



## Solution-processed hybrid p–n junction vertical diode

Jia Sun, Bhola Nath Pal, Byung Jun Jung, Howard E. Katz \*

Department of Materials Science and Engineering, Johns Hopkins University, 103 Maryland Hall, 3400 N Charles Street, Baltimore, MD 21218, United States

### ARTICLE INFO

#### Article history:

Received 27 February 2008

Received in revised form 27 August 2008

Accepted 27 August 2008

Available online 9 September 2008

#### PACS:

85.30 Kk

73.61 Ph

#### Keywords:

Diode

Rectification

Frequency

Zinc oxide

Polythiophene

### ABSTRACT

Solution-processed n-ZnO/p-poly(3,3'-didodecylquaterthiophene) (PQT-12) vertical p–n junction diodes were prepared on ITO-coated glass. A continuous film of ZnO nanoparticles was grown on the ITO glass by dip-coating and subsequent heat treatment of a zinc acetate film. PQT-12 was then spin-coated to form the ZnO/PQT-12 diode. Gold was chosen as the top electrode to complement ITO for this diode. The microstructures of ZnO films are studied by atomic force microscopy (AFM) and show a continuous, dense layer of ZnO nanoparticles. The current–voltage (*I*–*V*) measurement shows that the maximum current density for this p–n junction diode is 400 A/cm<sup>2</sup>, which is much higher than previously reported polymer diodes. Capacitance–voltage (*C*–*V*) data also provide evidence of formation of the p–n junction. The rectification was characterized by observation of full input-half output waves. Data indicate that these devices can operate up to frequencies of 14 MHz under ambient environment conditions. This rectification frequency is higher than other reported polymer Schottky diodes under these conditions. Turnon voltages of this diode are also much lower than for the reported polymer diodes.

© 2008 Elsevier B.V. All rights reserved.

### 1. Introduction

There is great interest in electronic devices based on solution-processed polymer [1–7], organic [8,9] and inorganic oxide [10,11] semiconductors in recent years because of the possibility of producing printable, low-cost, large-area, lightweight and flexible devices. Most of these reports concern field effect transistors and diodes for applications including light-emitting diodes [12,13], solar cells [14,15], non-volatile memory [16,17], and logic circuits [18,19]. Fast device response is very important for a broad spectrum of electronic applications including high frequency identification (RF-ID) tag circuits [21,22]. For diodes, one evaluates response speed by studying the rectification property of the device at different frequencies [20]. From the manufacturing point of view, it is desirable to use solution-processable semiconductors to enable printing and roll-to-roll processing, which facilitates low-cost fabrication using an all-in-line printing process [23].

An RF-ID circuit comprises a high-speed diode which can operate at frequencies of 13.54 MHz with a high rectification ratio [24,25]. A number of groups have tried to develop a solution-processed Schottky diode [1,2,4–7], however, the performance was inadequate for application due to very poor current density [1,2,4–7], high turnon voltage [1,2,4–7], and high reverse bias current [1,5,6]. On the other hand, in the case of inorganic oxide p–n junction diodes, performance is limited due to the non-availability of good quality p-type oxide semiconductors [10,26–29]. For these reasons, none of these diodes have been tested for high frequency rectification. In our present work we introduce one solution-processed inorganic semiconductor with a polymeric material to fabricate a p–n junction diode in which diode parameters are improved. We employ high-mobility, highly stable ZnO (inorganic) as the n-semiconductor and high-mobility poly(3,3'-didodecylquaterthiophene) (PQT-12) as the p-semiconductor. We also provide additional evidence for the correlation between morphology and current density from a study of poly(3-hexylthiophene)-aluminum (P3HT-Al) Schottky diodes. These are the solution-processable p–n junction

\* Corresponding author. Tel.: +1 410 516 6141; fax: +1 410 516 5293.  
E-mail address: [hekatz@jhu.edu](mailto:hekatz@jhu.edu) (H.E. Katz).

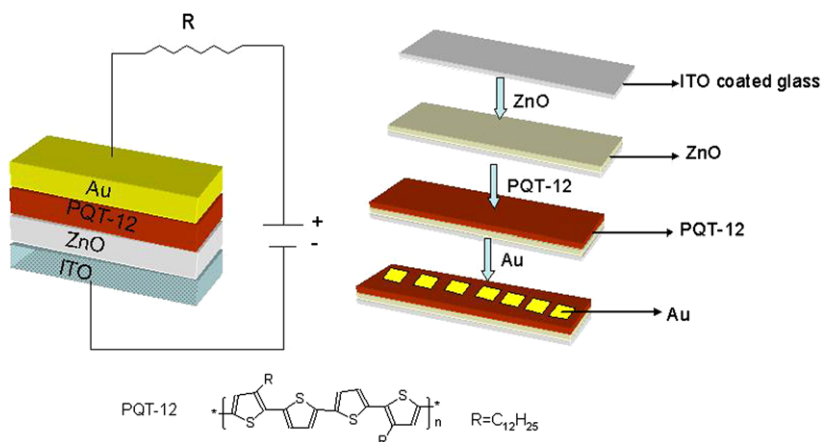


Fig. 1. Schematic of the device structure of ITO–ZnO(n)–PQT-12(p)–Au diode.

vertical diodes which can operate at MHz frequency, with much higher current density and low turn on voltage than related previously reported diodes [2,20,24,25].

In order to fabricate high current density and high-speed diodes, one needs materials that allow high forward current with considerably low operating voltage and very low reverse current with quite high reverse breakdown voltage. Normally this is achieved using electrodes that match in energy position, or make low potential barriers, to the energy levels of the semiconductors. In the case of a p–n junction diode, electrons and holes move towards the depletion region at forward bias and recombine. In case of thin film vertical diodes where electrons and holes cross one or two nanometer-scale grains from electrodes to the recombination zone, current density and speed can be expected to be higher compared to devices where numerous grain boundaries and defect sites must be crossed. Another important factor is relative band structure of two type semiconductors. The energy barrier at the depletion region depends on the differences between bulk Fermi energy levels of the two semiconductors [30]. For low turnon voltage and high current density this barrier is desirably be low [31]. The polymer/inorganic semiconductor p–n junction

discussed here meets these criteria. Although, we use two different classes of semiconductor, they are compatible for fabrication because they are deposited in separate steps (one dip-coating another spin-coating, from very different solvents) which are very well known and established techniques in solution-processed device fabrication.

## 2. Device and band structure of semiconductors

The device structure is shown in Fig. 1. In n–ZnO/p–PQT-12 vertical p–n junction diodes, indium tin oxide (ITO) and gold (Au) metals were chosen as bottom and top electrodes, respectively. Fig. 2a shows the schematic energy band diagram of an ITO/ZnO/PQT-12/Au device. Work functions of ITO and Au are 4.7 and 5.1 eV, respectively. The electron injection barrier at the ITO/ZnO interface and the hole injection barrier at the Au/PQT-12 interface are low, resulting in almost ohmic contacts at these interfaces. In Fig. 2b, we show the band diagram for the ZnO and PQT-12 after their heterojunction formation at thermal equilibrium. The band gaps of the two semiconductors are, respectively, 3.30 and 2.27 eV [18,32]. At thermal equilibrium the quasi-Fermi levels of both semiconductors are

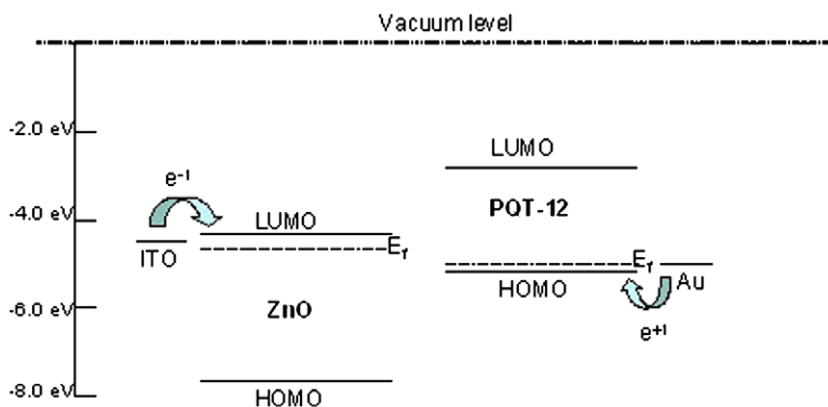
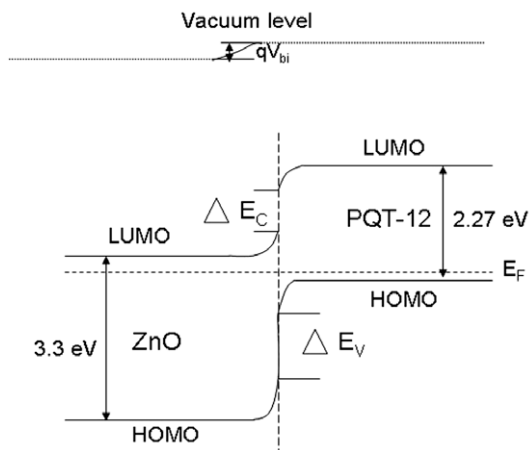


Fig. 2a. Schematic energy band diagram of ITO/ZnO/PQT-12/Au device.



**Fig. 2b.** Band diagram for ZnO and PQT-12 after heterojunction formation at thermal equilibrium.

equal to the equilibrium Fermi level  $E_F$ . On the same figure,  $\Delta E_C$  and  $\Delta E_V$  correspond to the band offset for conduction bands and valence bands, respectively. Since  $\Delta E_C$  is much lower than  $\Delta E_V$ , the energetic barrier for electrons is lower than for holes. Thus, electrons are the major carriers through these heterojunctions [31]. The  $qV_{bi}$  is the energy barrier of the junction which is equal to the difference between the bulk Fermi levels of the two semiconductors, where  $V_{bi}$  indicates the barrier potential of the junction. From this figure it is very clear that this barrier height is quite low, which enables high current density, high-speed rectification and low turnon voltage [31,33].

### 3. Experiment

Fig. 1 provides the schematic illustration of the polymer-inorganic hybrid p–n junction diode, which comprises an ITO–ZnO(n)–PQT-12(p)–Au structure. For this device, a clean ITO-coated glass was taken as substrate ( $<0.005 \Omega \text{ cm}$ ). For a solution-processed ZnO film, we used zinc acetate [ $\text{Zn}(\text{OAc})_2$ ] (40 mM) solution in ethanol solvent. The substrate was then dip-coated with this solution with a speed approximately 2 mm/s with an angle  $60^\circ$  with horizontal and immediately was placed on a  $70^\circ \text{C}$  heater. This process was carried out four times. The zinc acetate-coated substrate was annealed on a  $300^\circ \text{C}$  hot plate for 30 min to form a thin layer of continuous dense polycrystalline ZnO nanoparticle film. Around 30 nm of ZnO film thickness was measured by SEM. The detailed morphology of ZnO film was also studied by AFM. PQT-12 (warmed at  $60^\circ \text{C}$ ) of concentration 7 mg/ml was then spin-coated (at 800 rpm) from 1,2-dichlorobenzene to form a polymer film over the ZnO-coated ITO substrate. The thickness of PQT-12 (150 nm) was determined by scratching the PQT-12 film and measuring by AFM. Subsequently 50 nm-thick gold electrodes were deposited using a TEM grid (200 mesh) as shadow mask. After this the whole substrate was annealed at  $140^\circ \text{C}$  for 10 min then cooled down slowly at approximate  $2^\circ \text{C}/\text{min}$ . DC electrical characteristics of diodes were measured by using a semiconductor

parameter analyzer (Agilent 4155C). All electrical characterization results reported in this paper were obtained under ambient atmospheric conditions.

### 4. Results and discussion

Fig. 3a shows the current density–voltage ( $I$ – $V$ ) characteristics of our present device. The current density is  $400 \text{ A}/\text{cm}^2$ , which is few orders of magnitude higher than recent polymer vertical diodes [2–4]. The DC rectification ratio at  $\pm 2.5 \text{ V}$  is around  $4 \times 10^2$  (Fig. 3b). The turnon voltage is 1.2 V, which is considerably lower than the previously reported polymer diode [1–4]. The breakdown voltage of our diode is 15 V, 13 times higher than the threshold voltage. The forward bias was analyzed using the thermionic emission model and reverse bias using the reverse soft breakdown model [34,35]. The total current can be written as

$$I = I_s [\exp(qV/\eta kT) - 1] - I_{\text{tun}} [\exp(-qV/\eta_{\text{tun}} kT) - 1] \quad (1)$$

where  $I_s$  and  $I_{\text{tun}}$  are the reverse saturation current and tunneling saturation current, respectively, and  $\eta$  and  $\eta_{\text{tun}}$  are the ideality factor and tunneling ideality factor. The fitted values of  $I$ – $V$  parameters are listed below, and are com-

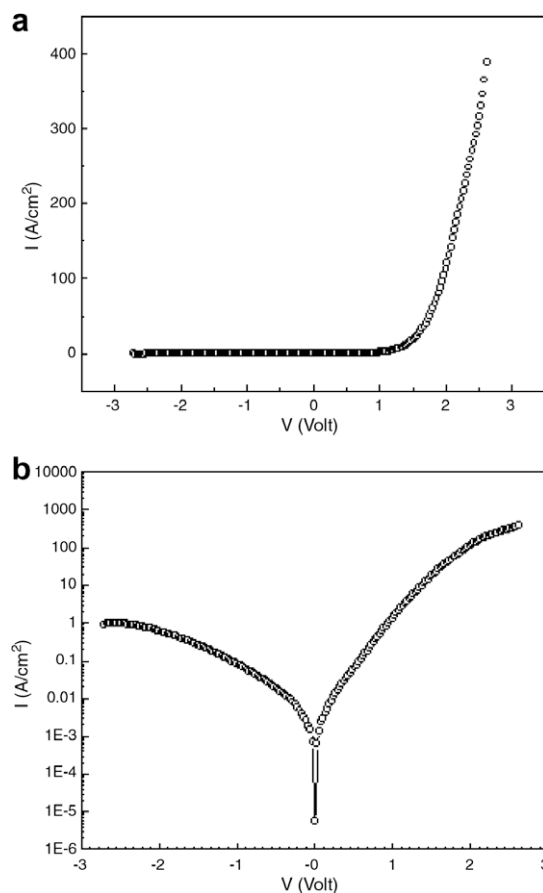


**Fig. 3.** Current–voltage characteristics of a typical ITO/ZnO/PQT-12/Au device (a) in normal scale and (b) in semi-log scale.

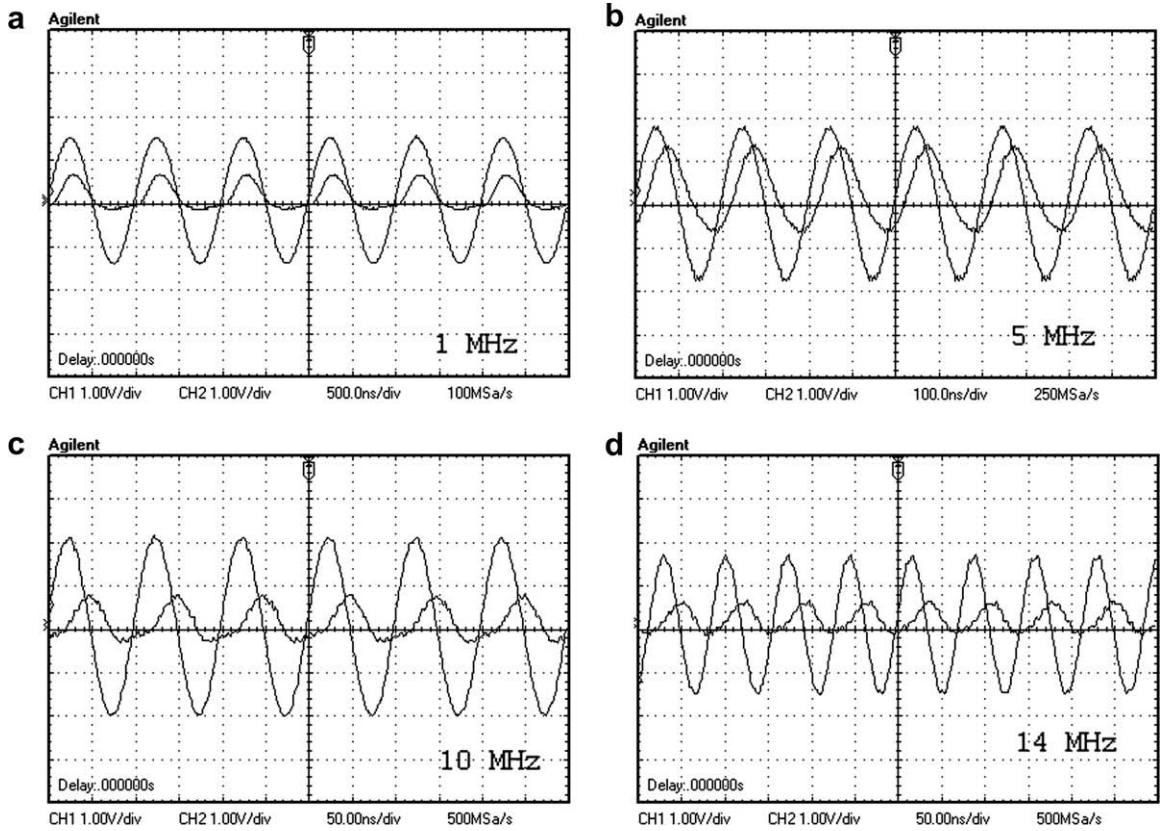


Fig. 4. Rectification behavior at (a) 1 MHz, (b) 5 MHz, (c) 10 MHz, (d) 14 MHz.

parable with other kinds of thin film p–n junction diodes [36].

$I_s$ (A)	$\eta$	$I_{tun}$ (A)	$\eta_{tun}$
$9.02 \times 10^{-5}$	17.8	$5.5 \times 10^{-5}$	43.5

Fig. 4 shows the half wave rectification behavior from the fabricated device. In Fig. 4(a–d), input signals were around

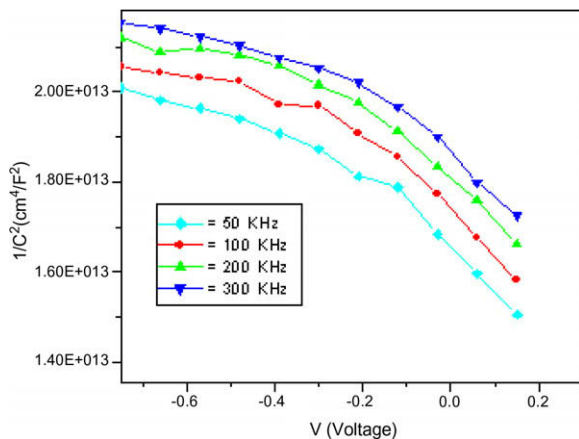


Fig. 5.  $1/C^2$  vs.  $V$  relationship of ITO/ZnO/PQT-12/Au device.

3 V peak to peak. We have taken this signal across  $100 \Omega$ . Channels 1 and 2 refer to the input and rectified signals, respectively. The left and right scales of the plots show

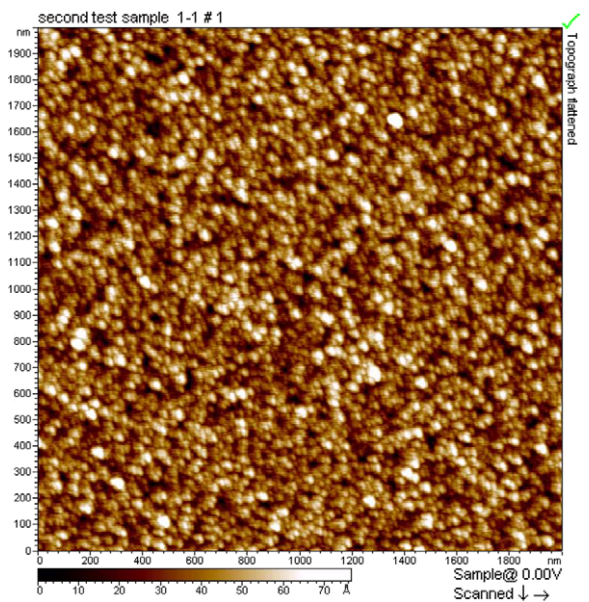


Fig. 6. Atomic force microscope image of polycrystalline ZnO film.

the input signal voltage and the rectified current density, respectively. There is a phase shift in the rectified signal which increases with frequency and is caused by the connecting wires, a limitation of our setup. The rectified signal for a particular device remained the same under six hours of steady observation. The long term storage stability of the device was also studied. The device was kept two months in dark and low vacuum, and retested. The results indicate that it essentially maintains its original characteristics. With respect to open atmosphere measurement, the response speed of this device is much higher than the previously reported polymer vertical Schottky diode with relatively less operating voltage.

The  $C$ - $V$  characteristic of the  $p$ - $n$  junction diode was measured in the frequency range 50–300 kHz using an LCR meter (Agilent 4284A). The capacitance per unit area of this kind of heterojunction can be described by Anderson's model, which can be expressed as [37,38]

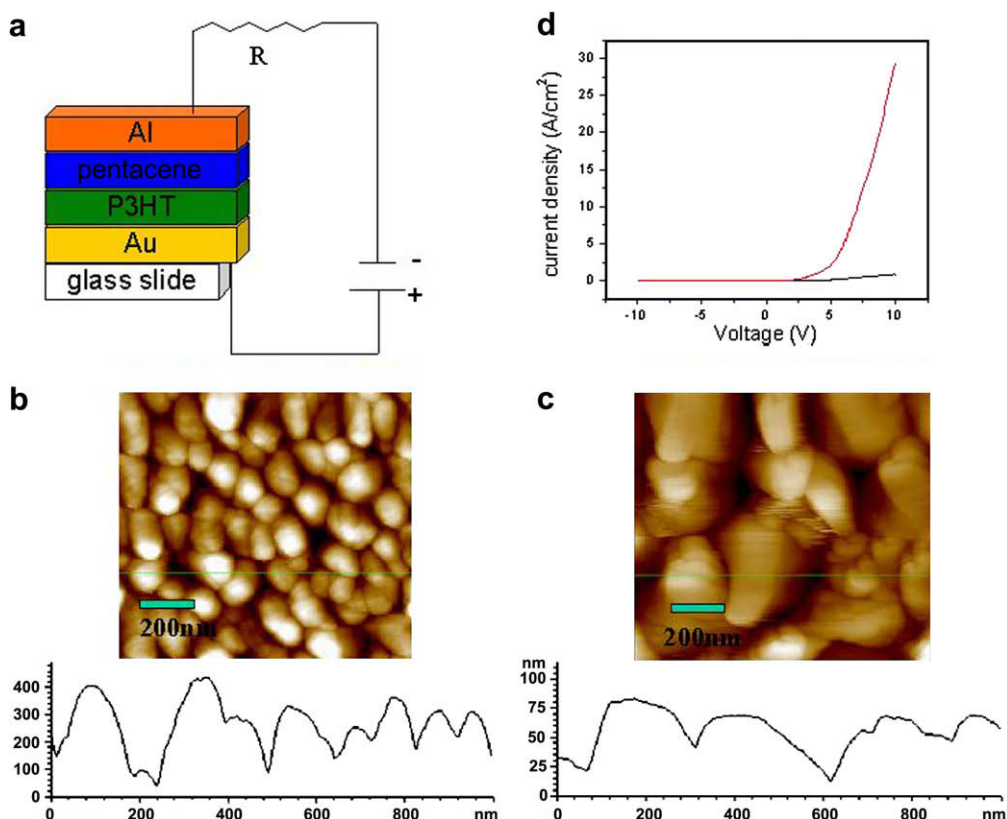
$$C^2 = \frac{qN_D N_A \epsilon_0 \epsilon_1 \epsilon_2}{2(N_A \epsilon_1 + N_D \epsilon_2)} \frac{1}{(V_D + V_b)} \quad (2)$$

where  $q$  is the electronic charge,  $\epsilon_0$  is the vacuum permittivity,  $\epsilon_1$  and  $\epsilon_2$  are the dielectric constants of  $n$ -ZnO and  $p$ -PQT-12, respectively,  $N_D$  and  $N_A$  are the doping density concentrations in the ZnO and PQT-12, respectively,  $V_D$  is the diffusion voltage and  $V$  is the applied voltage. Fig. 5

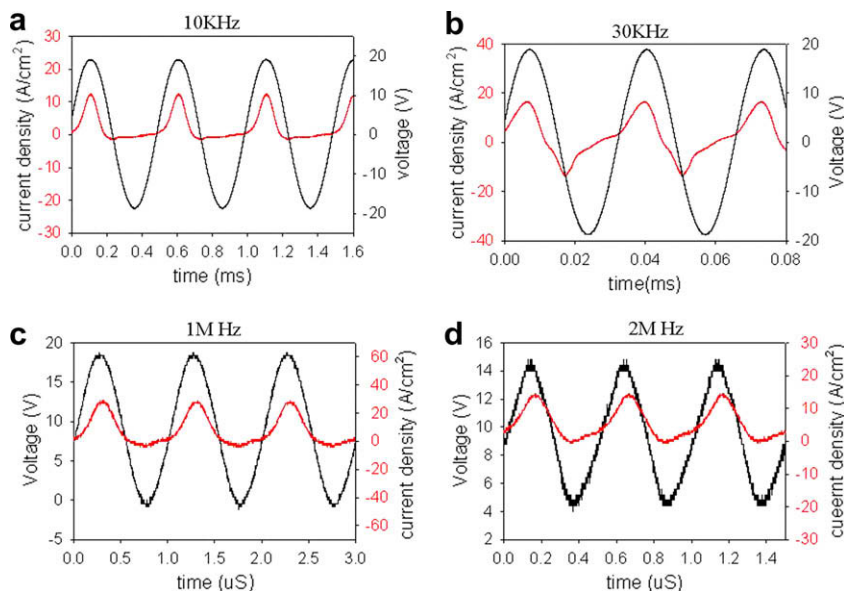
shows the  $1/C^2$  vs.  $V_D$  behavior of the measured devices, where almost linear behaviors in the 0.0 to  $-0.8$  V range are observed. This behavior is a clear indication that the fabricated diode is an abrupt junction.

Fig. 6 shows the AFM micrograph of the ZnO layer. The image shows a film of dense ZnO nanoparticles with average particle size around 40 nm. Detailed surface examination indicates that there is a lack of pinholes on the film, with low surface roughness (10 nm). This low roughness of the ZnO-coated film is favorable for the overlying polymer (PQT-12) film to avoid pinholes through the top surface. Thus, electrons cross one or two grains of ZnO particles from the ITO electrode whereas holes cross the nanometer-range film of PQT-12 from the top Au electrode to recombine at the interface. We believe this short range recombination mechanism is one of the key reasons for the high current density and high frequency rectification.

We also provide additional evidence for the correlation between morphology and current density from a parallel study of Au (50 nm)/P3HT (50 nm)/pentacene (225 nm)/Al (70 nm) Schottky diodes. Fig. 7a shows the schematic structure of this diode and Fig. 7b and c show AFM images of pentacene films on Au electrodes with and without P3HT. Larger grain sizes ( $\sim 250$  nm) were observed when pentacene was deposited on the P3HT-Au-electrode, preferable for charge transport.  $I$ - $V$  characteristics of the



**Fig. 7.** (a) Fabrication of the pentacene Schottky diodes with P3HT used as interface layer. (b) AFM image of pentacene film on bare Au electrode. (c) AFM image of pentacene film on P3HT/Au electrode. (d)  $I$ - $V$  measurement of pentacene Schottky diode with and without P3HT as interface layer, red curve represents pentacene Schottky diode with P3HT as interface layer. Black curve represents pentacene Schottky diode without P3HT as interface layer. (For interpretation of the references to colour in this figure legend, the reader is referred to the web version of this article.)



**Fig. 8.** (a and b) Current response (red) of pentacene-based Schottky diode without P3HT as interface layer under different frequencies of AC voltage input (black). (c and d) Current response of pentacene Schottky diode with P3HT as interface layer under different frequencies of AC voltage. (For interpretation of the references to colour in this figure legend, the reader is referred to the web version of this article.)

pentacene diode with and without P3HT as interface layer are shown in Fig. 7d. The maximum current density at 10 V was 30 A/cm<sup>2</sup> in the presence of the P3HT interface layer; however, without the interface layer, the current density was only 0.8 A/cm<sup>2</sup>. Thus, it can be concluded that carrier transport throughout the film was more facile when pentacene grain size increased from 150 to 250 nm (and the electrode junction became more graded) after adding P3HT as the interface layer. Fig. 8 showed the response speed of the pentacene-based Schottky diode with and without P3HT as interface layer. Response speed at frequencies of 2 MHz was achieved with the interface layer. Without the interface layer, the maximum rectification speed was only 30 kHz. Two megahertz is a lower response frequency relative to that of the ITO/ZnO/PQT-12/Au diode. From the AFM image, a large surface roughness of pentacene film compared to that of the ZnO film is apparent; such large surface roughness leads to the generation of pinholes, which increase contact resistance and affect diode characteristics. In addition, if the Au/P3HT/pentacene/Al diode device area is further decreased, and the pentacene film is further purified, much higher response frequency should be attained.

## 5. Conclusion

In summary, in this paper we report the fabrication and characterization of vertical p–n junction polymer-inorganic hybrid diodes. The maximum current density is 400 A/cm<sup>2</sup> and the AC rectification is fully maintained up to 14 MHz. The current density and rectification speed in the open atmosphere are much higher than previously reported all-polymer vertical diodes with relatively lower operating voltage, and the stability is encouraging. The

capacitance–voltage (C–V) study also implies that device structure can be portrayed as a p–n junction diode.

## Acknowledgments

We are grateful to the Air Force Office of Scientific Research (Contract FA9550-06-1-0076), the Department of Energy (Contract No. DE-FG02-07ER-46465 and also sub-contract with Los Alamos National Laboratory) for support of this work. We also thank Professor Peter Searson for the use of an Atomic Force Microscope.

## References

- [1] H. Tsutsumi, *Synth. Metals* 69 (1995) 143.
- [2] L.S. Roman, M. Berggren, O. Inganäs, *Appl. Phys. Lett.* 75 (1999) 3557.
- [3] G. Liang, T. Cui, K. Varshramyan, *Solid State Electron.* 47 (2003) 691.
- [4] R. Zhang, A. Barnes, Y. Wang, B. Chambers, P.V. Wright, *Adv. Funct. Mater.* 16 (2006) 1161.
- [5] F. Garnier, R. Hajlaoui, A. Yassar, P. Srivastava, *Science* 265 (1994) 1684.
- [6] J.H. Burroughes, C.A. Jones, R.H. Friend, *Nature* 335 (1988) 137.
- [7] F. Hide, Y. Greenwald, F. Wudl, A.J. Heeger, *Synth. Metals* 85 (1997) 1255.
- [8] M. Berggren, D. Nilsson, N.D. Robinson, *Nat. Mater.* 6 (2007) 3.
- [9] D.H. Kim, D.Y. Lee, H.S. Lee, W.H. Lee, Y.H. Kim, J.I. Han, K. Cho, *Adv. Mater.* 19 (2007) 678.
- [10] B. Pradhan, S.K. Batabyal, A.J. Pal, *Appl. Phys. Lett.* 89 (2006) 233109.
- [11] K. Mohanta, S.K. Batabyal, A.J. Pal, *Chem. Mater.* 19 (2007) 3662.
- [12] V.L. Colvin, M.C. Schlamp, A.P. Allivisatos, *Nature* 370 (1994) 354.
- [13] D.K. Hwang, S.H. Kang, J.H. Lim, E.J. Yang, J.Y. Oh, J.H. Yang, S.J. Park, *Appl. Phys. Lett.* 86 (2005) 222101.
- [14] W.J.E. Beek, M.M. Wienk, M. Kemerink, X. Yang, R.A.J. Janssen, *J. Phys. Chem. B* 109 (2005) 9505.
- [15] M. Law, L.E. Greene, J.C. Johnson, R. Saykally, P. Yang, *Nat. Mater.* 4 (2005) 455.
- [16] Q. Ling, Y. Song, S.J. Ding, C. Zhu, D.S. Chan, D.L. Kwong, E.T. Kang, K.G. Neoh, *Adv. Mater.* 17 (2005) 455.
- [17] B. Pradhan, S.K. Batabyal, A.J. Pal, *J. Phys. Chem. B* 110 (2006) 8274.
- [18] B.S. Ong, Y. Wu, P. Liu, S. Gardner, *Adv. Mater.* 17 (2005) 1141.
- [19] S.K. Park, T.N. Jackson, J.E. Anthony, D.A. Mourey, *Appl. Phys. Lett.* 91 (2007) 063514.

- [20] L. Ma, J. Ouyang, Y. Yang, *Appl. Phys. Lett.* 84 (2004) 4786.
- [21] M. Ghovanloo, K. Najafi, *IEEE J. Solid State Circ.* 39 (2004) 1976.
- [22] B. Jamali, P. Cole, D. Ransinghe, Z. Zhu, in: *Proceedings of SPIE*, vol. 5649, 2005, p. 323.
- [23] V. Subramanian, P.C. Chang, J.B. Lee, S.E. Molesa, S.K. Volkman, *IEEE Trans. Compon. Pack. Technol.* 28 (2005) 742.
- [24] S. Steudel, K. Myny, V. Arkhipov, C. Deibel, S. De Vusser, J. Genoe, P. Heremans, *Nat. Mater.* 4 (2005) 597.
- [25] S. Steudel, S. De Vusser, K. Myny, M. Lenes, J. Genoe, P. Heremans, *J. Appl. Phys.* 99 (2006) 114519.
- [26] Z.P. Wei, Y.M. Lu, D.Z. Shen, Z.Z. Zhang, B. Yao, B.H. Li, J.Y. Zhang, D.X. Zhao, X.W. Fan, Z.K. Tang, *Appl. Phys. Lett.* 90 (2007) 042113.
- [27] J.G. Lu, Z.Z. Ye, G.D. Yuan, Y.J. Zeng, F. Zhuge, L.P. Zhu, B.H. Zhao, S.B. Zhang, *Appl. Phys. Lett.* 89 (2006) 053501.
- [28] S.J. Jiao, Z.Z. Zhang, Y.M. Lu, D.Z. Shen, B. Yao, J.Y. Zhang, B.H. Li, D.X. Zhao, X.W. Fan, Z.K. Tang, *Appl. Phys. Lett.* 88 (2006) 031911.
- [29] J.M. Bian, X.M. Li, C.Y. Zhang, W.D. Yu, X.D. Gao, *Appl. Phys. Lett.* 85 (2004) 4070.
- [30] Hongxia Qi, Qingshan Li, Caifeng Wang, Lichun Zhang, Lei Lv, *Vacuum* 81 (2007) 943.
- [31] J.D. Ye, S.L. Gu, S.M. Zhu, W. Liu, S.M. Liu, R. Zhang, Y. Shi, Y.D. Zheng, *Appl. Phys. Lett.* 88 (2006) 182112.
- [32] Ü. Özgür, Y.I. Alivov, C. Liu, A. Teke, M.A. Reshchikov, S. Doğan, V. Avrutin, S.-J. Cho, H. Morkoç, *J. Appl. Phys.* 98 (2005) 041301.
- [33] K.M. Chen, Y.X. Zhang, G.G. Qin, S.X. Jin, K. Wu, C.Y. Li, Z.N. Gu, X.H. Zhou, *Appl. Phys. Lett.* 69 (1996) 3557.
- [34] S.M. Sze, *Physics of Semiconductor Devices*, Wiley, New York, 1981.
- [35] K.Y. Chiang, H.Y. Tseng, C.Y. Lin, C.P. Kung, W.H. Hou, *Mater. Res. Soc. Symp. Proc.* 965 (2007). 0965S0518.
- [36] P. Deb, H. Kim, Y. Qin, R. Lahiri, M. Oliver, R. Reifenberger, T. Sands, *Nano Lett.* 6 (2006) 2893.
- [37] D. Song, D.H. Neuhaus, J. Xia, A.G. Aberle, *Thin Solid Films* 422 (2002) 180.
- [38] R. Romero, M.C. López, D. Leinen, F. Martin, J.R. Ramos-Barrado, *Mater. Sci. Eng. B* 110 (2004) 87.



## Ferromagnetic cobalt and iron top contacts on an organic semiconductor: Evidence for a reacted interface

V.Yu. Aristov<sup>a,b</sup>, O.V. Molodtsova<sup>a</sup>, Yu.A. Ossipyan<sup>b</sup>, B.P. Doyle<sup>c</sup>, S. Nannarone<sup>c,d</sup>, M. Knupfer<sup>a,\*</sup>

<sup>a</sup> IFW Dresden, 'Electronic and Optical Properties', Postfach 270116, D-01171 Dresden, Germany

<sup>b</sup> Institute of Solid State Physics, Russian Academy of Sciences, Chernogolovka, Moscow District 142432, Russia

<sup>c</sup> TASC-INFM Laboratory, Area Science Park – Basovizza, I-34012 Trieste, Italy

<sup>d</sup> Dipartimento di Ingegneria dei Materiali e dell'Ambiente, Università di Modena e Reggio Emilia, Italy

### ARTICLE INFO

#### Article history:

Received 14 September 2007

Received in revised form 21 August 2008

Accepted 1 September 2008

Available online 12 September 2008

#### PACS:

72.80.Le

85.75.-d

79.60.Fr

#### Keywords:

Energy level alignment

Organic spintronic

Interfaces

Photoemission spectroscopy

### ABSTRACT

The interface formation between the organic semiconductor copper-phthalocyanine and the ferromagnets Co and Fe has been investigated for the case of metal deposition onto the organic film using photoemission as well as X-ray absorption spectroscopy. Such interfaces might allow the injection of spin polarized currents into organic semiconductors. Our data reveal the formation of interfaces which are characterized by chemical reactions in the interfacial region.

© 2008 Elsevier B.V. All rights reserved.

The active control and the manipulation of spin degrees of freedom in electronic devices – often called spintronics – is anticipated to enable the fabrication of future electronic systems [1]. Recently, it has been demonstrated that it is possible to inject spin polarized currents in organic semiconductors [2,3] or to built organic based spin valves [4–6] and tunnel magnetoresistance (TMR) units [7,8]. These observations can be regarded as the starting point of an organic spintronics, which combines the flexibility and variability of organic semiconducting materials with a further degree of freedom: to switch or control a device via external magnetic or electric fields.

The metallic electrode contacts in organic spintronic devices are required to have a substantial spin polarization of their conduction electrons, and consequently materials such as the metallic ferromagnets Fe, Ni, Co or corresponding alloys (e.g. permalloy) are obvious candidates for such contact electrodes and have already been used in a number of cases [4–9]. Moreover, recent studies of spin injection into organic semiconductors indicate that spin polarized electrons can be injected from a ferromagnet into an organic semiconductor with high efficiency [9–11].

Often, it is necessary to produce top contacts on an organic semiconducting layer via the deposition of the respective materials in vacuum chambers, but it is unclear to what extent this production procedure results in well defined contact interfaces, which is in contrast to the importance of the contacts for the device performance.

\* Corresponding author. Tel.: +49 351 4659 544; fax: +49 351 4659 440.

E-mail address: [m.knupfer@ifw-dresden.de](mailto:m.knupfer@ifw-dresden.de) (M. Knupfer).



In general, interfaces between metals and organic semiconductors have been extensively studied in the past [12–17], and most of these interfaces are characterized by the presence of a short range interface dipole, whereas the origin of this interface dipole is not yet fully understood [18]. Moreover, it has been demonstrated that the deposition of metals onto organic semiconductors in the majority of cases results in reactions at these interfaces, often accompanied by a diffusion of metal atoms deep into the organic layer [14,19–23]. The knowledge of the interface energy level alignment, interface reactions and charge carrier injection barriers is an indispensable prerequisite for the understanding and modelling of the device performance as well as for potential optimization of the devices.

In this contribution we present a detailed analysis of interfaces that are produced by thermal deposition of the ferromagnetic elements Fe and Co onto the model organic semiconductor copper-phthalocyanine (CuPc) using two complementary spectroscopic methods, photoemission spectroscopy and near edge X-ray absorption fine structure (NEXAFS) measurements. If such interfaces will turn out to be sharp, this would demonstrate again the potential for high efficiency of spin polarized electron injection from the deposited Co (and Fe) contact into a CuPc thin film substrate [9,11].

X-ray photoemission spectroscopy (XPS) measurements were carried out using a commercial PHI 5600 system, which was equipped with a monochromatized Al-K $\alpha$  X-ray source providing photons with 1486.6 eV. The total-energy resolution of the spectrometer was determined by analyzing the width of a Au Fermi edge to be 350 meV. The energy scale was aligned by measuring the Fermi edge (0 eV), as well as the 4f<sub>7/2</sub> emission (84.0 eV) of the gold substrate. The error produced by this alignment procedure is smaller than 0.1 eV. All measurements were carried out at room temperature.

The NEXAFS experiments were performed at the ELETTRA (Trieste, Italy) synchrotron radiation facility using

soft-X-ray light emitted by the BEAR high energy resolution dipole beam line [24]. The soft-X-ray absorption spectra were recorded in the total electron yield mode and normalized to the incident photon flux. The resolution for the NEXAFS measurements is determined exclusively by the performance of the beam line and was about 100 meV FWHM for the transition metal absorption edges shown below. The acquired spectra were energy calibrated using the C 1s  $\rightarrow \pi^*$  and N 1s  $\rightarrow \pi^*$  photoionization spectra of Ar and N<sub>2</sub> gases [25]. The pressure in the experimental system during data acquisition was always better than  $1.5 \times 10^{-10}$  Torr.

As substrate for CuPc film deposition, we used the (100) surface of a gold single crystal. The surface was prepared by repeated sputtering and annealing cycles after which a  $5 \times 20$  surface reconstruction was observed using low energy electron diffraction, while no remaining contamination was detected in the core level photoemission spectra. The CuPc film was deposited in sample preparation chambers directly linked to analyzer chambers. The deposition rate, monitored by a quartz microbalance, was 1–2 Å/min. The core level photoemission spectra indicated clean CuPc films without detectable traces of contamination including oxygen. The CuPc films used for our studies were about 70 Å thick, which is large enough to minimize contributions from the gold substrate in the photoemission spectra, and small enough to avoid charging effects.

Fe and Co were evaporated onto the CuPc films from molybdenum crucibles heated by electron bombardment. The deposition rates, measured by a quartz thickness monitor, were 0.5–1 Å/min. In addition, the total amount of metal coverage at each step of deposition was evaluated from a comparison of the relative intensities of the core levels of substrate atoms and deposited metals. The sensitivity factors of the core-levels for the corresponding photon energies were taken from tabulated cross-sections [26]. Other experimental details can be found elsewhere [23,27].

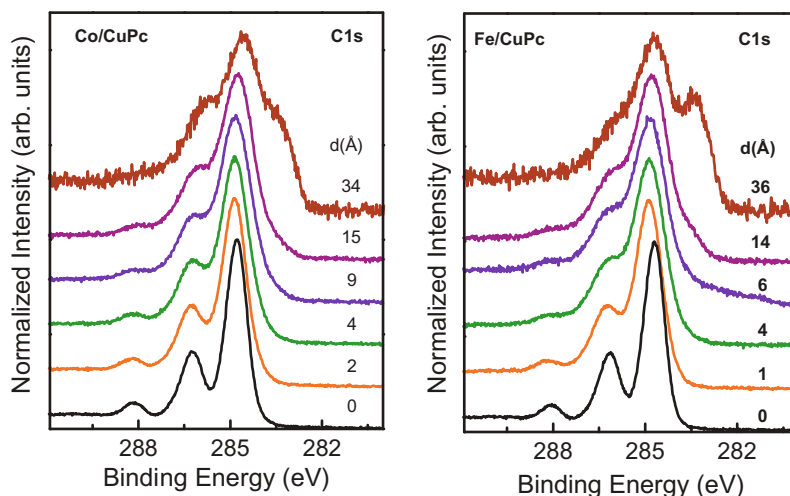


**Fig. 1.** Normalized C 1s core level photoemission data of CuPc thin films as a function of Co (left panel) and Fe deposition (right panel). The metal overlayer thickness is indicated. The data are normalized to equal intensity to ease comparison. The absolute intensity is strongly reduced upon metal addition (see text).

In Fig. 1 we show the evolution of the C 1s core level photoemission spectra as a function of Co and Fe deposition onto CuPc. Note that the data are normalized to equal intensities for comparison. The absolute C 1s photoemission intensity is strongly reduced upon metal addition. At a metal coverage of about 35 Å it is only about 2–3% of its starting value. This is well consistent with a homogeneous metal coverage on top of CuPc and the corresponding exponential thickness ( $d$ ) dependence of the photoemission intensity ( $\exp(-d/\lambda)$ ) taking into account an electron mean free path ( $\lambda$ ) of about 10 Å for electrons with a kinetic energy of about 1200 eV (i.e. C 1s core level emission).

The C 1s signal (resulting from C atoms of CuPc) is characterized by a distinct fine structure due to chemically inequivalent carbon sites in the CuPc molecule and the appearance of satellite features, as has been described in

detail previously [27,28]. Upon initial metal deposition there is a small upshift of the spectra, while the spectral shape remains unchanged. We attribute this initial energy shift to the formation of a short range interface dipole of about 0.1 eV and 0.2 eV for Co and Fe on CuPc, respectively. Further Co or Fe addition at first does not lead to further changes of the spectral shape, for thicker metal overlayers however, the C 1s spectra change substantially. We observe the occurrence of an additional C 1s feature at the low binding energy side. Since with growing overlayer thickness the C 1s signal increasingly arises from the CuPc molecules situated directly at the interface, the data in Fig. 1 are a clear indication that Co and Fe do not diffuse into the organic CuPc film but a sharp interface is formed. At this interface, though, there is chemical interaction resulting in the spectral changes seen in Fig. 1, i.e. carbon atoms with a different chemical environment.

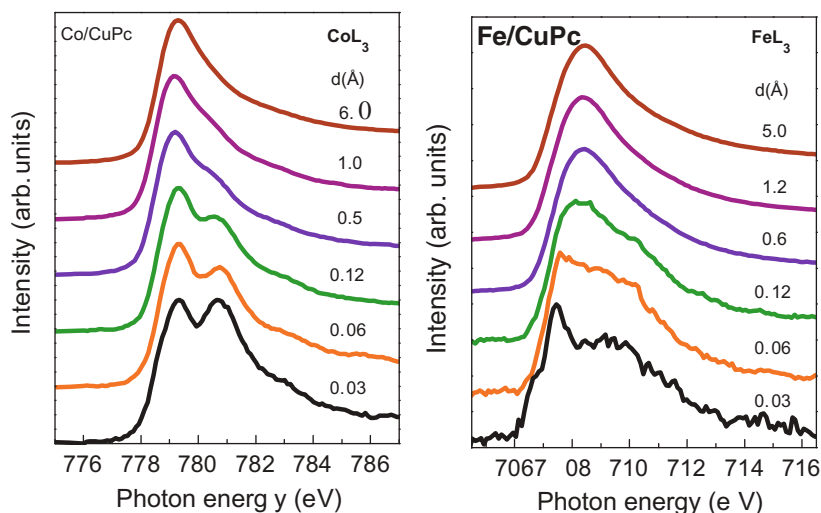


**Fig. 2.** Co  $L_3$  (left panel) and Fe  $L_3$  (right panel) absorption edges as a function of Co or Fe overlayer thickness on CuPc as indicated. The data are normalized to equal intensity, the absolute intensity scales with the metal overlayer thickness.

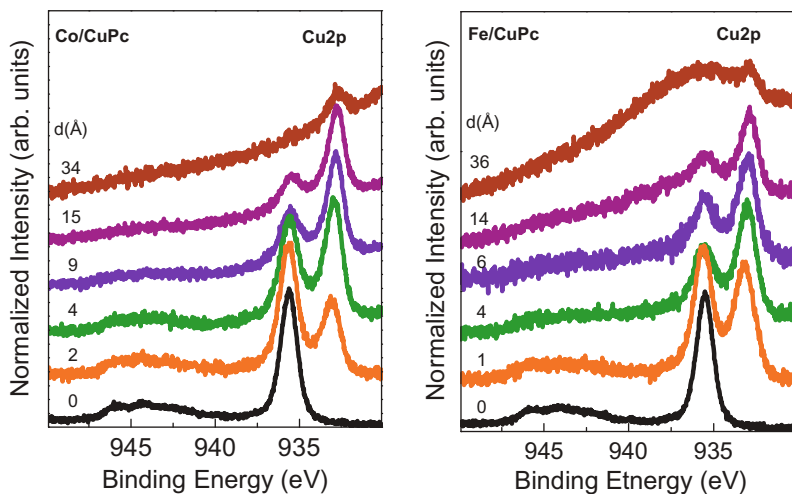


**Fig. 3.** Normalized Cu 2p core level photoemission data of CuPc thin films as a function of Co (left panel) and Fe deposition (right panel). The metal overlayer thickness is indicated.

This conclusion is corroborated in Fig. 2 where we show the Co and Fe  $L_3$  NEXAFS spectra, again as a function of metal overlayer thickness and normalized to equal intensity. For thin metal films on top, the data clearly consist of two components, which reveal Co or Fe atoms with different chemical environments. The feature at lower excitation energy grows upon increasing metal film thickness, while the second excitation feature disappears. These data can be rationalized by the presence of oxidized (i.e. cationic) Co or Fe atoms directly at the the Co/CuPc or Fe/CuPc interface, giving rise to the higher energy core level excitation. With increasing metal film thickness this excitation feature vanishes because its relative weight decreases, and only the typical NEXAFS spectral shape for the respective metal is observed.

The Cu 2p core level photoemission data shown in Fig. 3 complete our picture on the interface reaction at the (Co,Fe)/CuPc interfaces. Already the deposition of small amounts of metal results in the appearance of a spectral feature at the low binding energy side, which is reminiscent of the XPS data of Cu(I) compounds such as  $Cu_2O$  [29]. This low binding energy feature grows with increasing overlayer thickness, which again demonstrates that the corresponding reaction only occurs directly at the interface. Therefore we infer, that as a consequence of Co or Fe deposition onto CuPc, copper atoms at the interface are reduced from Cu(II) to Cu(I), while Co or Fe are oxidized as indicated in Fig. 2. The metal core level data in Figs. 2 and 3 would be consistent with a scenario where deposited Co or Fe atoms replace Cu in the center of the phthalocyanine, whereas the released Cu remains at the interface. This would parallel the effects of Li deposition onto CuPc, where it has been reported that Cu atoms are liberated from CuPc [30]. The C 1s data as shown in Fig. 1, however, evidence that this picture is too simple and that the phthalocyanine molecule as a whole is affected by the interface reactions. The situation at the Co/CuPc and Fe/CuPc interfaces studied here might be similar to what has been observed for the deposition of Al onto phthalocyanine molecules [20]. In this case, it has been proposed that Al–Pc complexes form, resulting in core level spectra similar to what is observed in Figs. 1 and 3. Moreover, a recent study on the deposition of Co on pentacene layers has revealed that Co only slightly penetrates into the pentacene films and that the interface is characterized by chemical reaction, equivalent to our results [31].

In summary, we have investigated the chemistry and the electronic structure of interfaces that are produced by deposition of the ferromagnets Co and Fe onto the organic semiconductor CuPc using two complementary spectroscopic methods, XPS and NEXAFS. In contrast to the deposition of other metals onto CuPc, our results demonstrate that for both metals there is no evidence of metal diffusion into the organic film, which is favorable for the application of such interfaces in organic spintronic devices. These interfaces however are characterized by chemical

interactions in the interfacial region, which might lead to the formation of interface electronic states that can act as charge carrier traps and thus have an unwanted impact on the injection of spin polarized currents.

## Acknowledgements

This work was supported by the DFG (KN393/5 and No. 436RUS17/52/06). We thank R. Hübel, R. Schönfelder and S. Leger for technical assistance. Two of the authors (Y.A.O. and V.Y.A.) thank the RFBR (Grant No. 08-02-01170).

## References

- [1] S.A. Wolf, D.D. Awschalom, R.A. Buhrman, J.M. Daughton, S. Von Molnar, M.L. Roukes, A.Y. Chtchelkanova, D.M. Treger, *Science* 294 (2001) 1488.
- [2] V. Dediu, M. Murgia, F.C. Matocotta, C. Taliani, S. Barbanera, *Solid State Commun.* 122 (2002) 181.
- [3] E. Shikoh, A. Fujiwara, Y. Ando, T. Miyazaki, *Jpn. J. Appl. Phys.* 45 (2006) 6897.
- [4] Z.H. Xiong, D. Wu, Z.V. Vardeny, J. Shi, *Nature* 427 (2004) 821.
- [5] S. Majumdar, H.S. Majumdar, R. Laiho, R. Osterbacka, *J. Alloy Compd.* 423 (2006) 169.
- [6] Z.-Y. Pang, Y.-X. Chen, T.-T. Liu, Y.-P. Zhang, S.-J. Xie, S.-S. Yan, S.-H. Han, *Chinese Phys. Lett.* 23 (2006) 1566.
- [7] T.S. Santos, J.S. Lee, P. Migdal, I.C. Lekshmi, B. Satpati, J.S. Moodera, *Phys. Rev. Lett.* 98 (2007) 016601.
- [8] W. Xu, G.J. Szulczewski, P. LeClair, I. Navarette, R. Schad, G. Miao, H. Guo, A. Gupta, *Appl. Phys. Lett.* 90 (2007) 072506.
- [9] J.H. Shim, K.V. Raman, Y.J. Park, T.S. Santos, G.X. Miao, B. Satpati, J.S. Moodera, *Phys. Rev. Lett.* 100 (2008) 226603.
- [10] T. Ikegami, I. Kawayama, M. Tonouchi, S. Nakao, Y. Xamashita, H. Tada, *Appl. Phys. Lett.* 92 (2008) 153304.
- [11] T. Shimada, H. Nogawa, T. Noguchi, Y. Furubayashi, Y. Yamamoto, Y. Hirose, T. Hitosugi, T. Hasegawa, *Jpn. J. Appl. Phys.* 47 (2008) 1184.
- [12] H. Ishii, K. Sugiyama, E. Ito, K. Seki, *Adv. Mater.* 11 (1999) 605.
- [13] W.R. Salaneck, K. Seki, A. Kahn, J.J. Pireaux, *Conjugated Polymer and Molecular Interfaces: Science and Technology for Photonic and Optoelectronic Applications*, Marcel Dekker, New York, 2002.
- [14] A. Kahn, N. Koch, W. Gao, *J. Polym. Sci. B* 41 (2003) 2529.
- [15] W.R. Salaneck, M. Fahlman, *J. Mater. Res.* 14 (2004) 1917.
- [16] M. Knupfer, H. Peisert, *Phys. Status Solidi A* 201 (2004) 1055.
- [17] D. Cahen, A. Kahn, E. Umbach, *Mater. Today* 8 (2005) 32.
- [18] M. Knupfer, G. Paasch, *J. Vac. Sci. Technol. A* 23 (2005) 1072.
- [19] C. Shen, A. Kahn, J. Schwartz, *J. Appl. Phys.* 89 (2001) 449.
- [20] C. Shen, A. Kahn, J. Schwartz, *J. Appl. Phys.* 90 (2001) 6236.
- [21] C. Shen, A. Kahn, *J. Appl. Phys.* 90 (2001) 4549.
- [22] L. Lozzi, S. Santucci, S. La Rosa, *J. Vac. Sci. Technol. A* 22 (2004) 1477.
- [23] V. Yu. Aristov, O.V. Molodtsova, V.M. Zhilin, D.V. Vyalikh, M. Knupfer, *Phys. Rev. B* 72 (2005) 165318.
- [24] S. Nannarone, F. Borgatti, A. DeLuisa, B.P. Doyle, G.C. Gazzadi, A. Giglia, P. Finetti, N. Mahne, L. Pasquali, M. Pedio, G. Selvaggi, G. Naletto, M.G. Pelizzo, G. Tondello, in: *AIP Conference Proceedings*, vol. 705, 2004, p. 450.
- [25] T.K. Sham, B.X. Yang, J. Kirz, J.S. Tse, *Phys. Rev. A* 40 (1989) 652.
- [26] X-ray Photoelectron Spectroscopy (XPS) Database, Version 3.4, <<http://srdata.nist.gov/xps/>>.
- [27] T. Schwiager, H. Peisert, M.S. Golden, M. Knupfer, J. Fink, *Phys. Rev. B* 66 (2002) 155207.
- [28] H. Peisert, M. Knupfer, J. Fink, *Surf. Sci.* 515 (2002) 491.
- [29] J. Ghijsen, L.H. Tjeng, J. van Elp, H. Eskes, J. Westerink, G.A. Sawatzky, M.T. Czyzyk, *Phys. Rev. B* 38 (1988) 11322.
- [30] S.H. Su, C.-H. Chou, M. Yokoyama, *Electrochem. Solid-State Lett.* 6 (2003) H17.
- [31] M. Popinciuc, H.T. Jonkman, B.J. van Wees, *J. Appl. Phys.* 100 (2006) 093714.



# Fully aromatic polyimide gate insulators with low temperature processability for pentacene organic thin-film transistors

Taek Ahn, Yoojeong Choi, Hyun Min Jung, Mihye Yi\*

Information and Electronics Polymer Research Center, Korea Research Institute of Chemical Technology, 19 Sinseongno, Yuseong-gu, Daejeon 305-600, Republic of Korea

## ARTICLE INFO

### Article history:

Received 20 March 2008

Received in revised form 6 September 2008

Accepted 6 September 2008

Available online 23 September 2008

### PACS:

72.80.Le

72.80.Sk

### Keywords:

Polyimide

Low temperature processability

Imidization ratio

Gate insulator

Organic thin-film transistor

## ABSTRACT

This paper demonstrates the effects of the imidization ratio of polyimide gate insulators on the performance of organic thin-film transistors (OTFTs). We report the synthetic results of polyimide films imidized at a temperature of 200 °C along with an easily removed organic base catalyst (1,8-diazabicyclo[5.4.0]undec-7-ene, DBU), and their application in gate insulators of organic thin-film transistors. The degree of imidization increased to almost 100% after a thermal treatment at 200 °C for 40 min in the presence of DBU. The performance of the pentacene OTFT dramatically improved by using low temperature cured polyimide film as the gate insulator.

© 2008 Elsevier B.V. All rights reserved.

## 1. Introduction

Research on organic thin-film transistors (OTFTs) has been rapidly growing in recent years. They are potential candidates for use in wide range of applications in low-cost and large area electronics. The performance of OTFTs including organic gate insulators has been significantly improved. Organic gate insulators are required to have a relatively high dielectric constant, heat and chemical resistance, pinhole-free thin-film formability, and comparability with organic semiconductors [1–7]. In addition, since OTFTs are targeting low-cost and large area flexible applications, their processing temperature should be low enough to be integrated on inexpensive plastic substrates, such as polyethyleneterephthalate (PET), polyethyl-

enenaphthalate (PEN), and polyethersulfone (PES). Several polymeric gate insulators, such as poly(vinylphenol) (PVP) [8–10], poly(methylmethacrylate) (PMMA) [11], polyvinylalcohol (PVA) [12], polyimide (PI) [13,14], and benzocyclobutene (BCB) [13] have been investigated. Among these materials, polyimides are currently considered promising gate insulators because of their excellent chemical resistance and mechanical properties. However, a major obstacle to the use of polyimides is their high processing temperature. Usually, fully aromatic polyimide has been extensively used in the microelectronics industry as interdielectric layers and passivation layers due to its excellent chemical, physical, and mechanical properties. We recently reported poly(amic-acid) based polyimide gate insulators for the application of OTFT [15,16]. However, those polyimides were not perfect candidates for OTFTs due to their high processing temperature, more than 250 °C, which is much higher than the glass transition temperature of

\* Corresponding author. Tel.: +82 42 860 7291; fax: +82 42 861 4151.  
E-mail address: [mhyi@kriict.re.kr](mailto:mhyi@kriict.re.kr) (M. Yi).

plastic substrates. We also published soluble polyimide gate insulators which can be processed into thin-film at low temperature. In that case, however, polyimides did not have fully aromatic structure, therefore, mechanical and leakage current properties of them were somewhat poor [17]. Basically if the imidization reaction of polyimide is conducted below 350–400 °C, the conversion of the poly(amic acids) to the PI is incomplete, which can result in high leakage current for the OTFT devices. In this paper, we describe new synthetic results of fully aromatic polyimide films imidized at the low temperature of 200 °C in the presence of an organic base catalyst, which can be easily removed after the imidization reaction, and investigate the performance of organic thin-film transistors fabricated with the polyimides as gate insulators.

## 2. Experimental

We have prepared new fully aromatic polyimide precursor, the poly(amic acid) from rigid aromatic dianhydride, 3,3',4,4'-biphenyl tetracarboxylic dianhydride (BPDA) and rigid aromatic diamines, *p*-phenylenediamine (*p*-PDA) in *N*-methyl-2-pyrrolidone (NMP). The molar ratio of the two monomers (BPDA: *p*-PDA) for the preparation of the poly(amic acid) was 1:1. The poly(amic acid) was converted into the corresponding polyimide, PI(NC)-200, without the catalyst through only a thermal imidization reaction, which was conducted at 200 °C for 40 min on a hot plate. PI(C)-200 was synthesized from the poly(amic acid) solution containing 5 wt% [weight percent to the poly(amic acid)] of DBU under the same thermal imidization conditions as that of PI(NC)-200.

To determine the capacitance and gate leakage of the polyimide gate insulators, MIM (metal–insulator–metal) capacitor structures were prepared on the patterned ITO coated glass substrates. The fully aromatic polyimide solutions were spin coated on top of the bottom ITO electrode

and then the film was annealed at 90 °C for 10 min and 200 °C for 40 min. MIM devices were then completed by a deposition of the top gold electrodes. The final thicknesses of all films were controlled to 300 nm. The active area of a MIM device was 50.24 mm<sup>2</sup>.

The OTFT device geometry for all electrical characterizations was a top-contact. Indium tin oxide (ITO) coated glass was used as the substrate and the ITO was patterned (2 mm wide stripes) to produce the gate electrode with a conventional photolithographic method: coating with a photoresist, ultraviolet light exposure, then developing and etching. The patterned ITO substrate was cleaned using a typical cleaning process for electronic applications: sonication in detergent, deionized water, acetone, and isopropyl alcohol in that order for 20 min at room temperature. The pentacene OTFT devices were fabricated using the polyimides as gate insulators. The final thickness of the polyimide gate insulators were adjusted to about 300 nm. A 60-nm-thick layer of pentacene was deposited on top of the gate insulator through a shadow mask by thermal evaporation at a pressure  $1 \times 10^{-6}$  Torr. The evaporation rate of the pentacene was 1 Å/s and the substrate temperature was 90 °C. The OTFTs were then completed by thermal evaporating 50-nm-thick gold source and drain electrodes on top of the pentacene layer through a shadow mask, creating transistors with channel lengths (*L*) and widths (*W*) of 50 and 1000 μm, respectively.

## 3. Results and discussion

### 3.1. Polyimide gate insulators and pentacene

The chemical structures of the polyimides are shown in Fig. 1. The structures of the poly(amic acid), PI(NC)-200, and PI(C)-200 were characterized by <sup>1</sup>H NMR and FT-IR spectroscopy. We determined the imidization degree of the polyimide films by comparing the characteristic

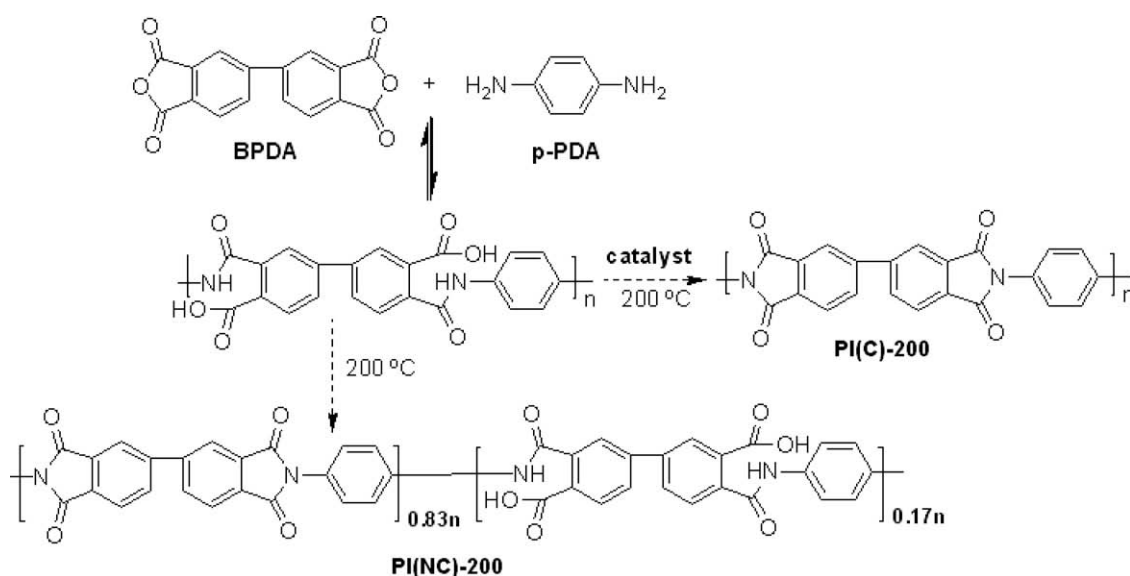


Fig. 1. Chemical structures of the PI(NC)-200 and PI(C)-200.

absorption bands at 1515 ( $\nu_{C=C}$ )  $\text{cm}^{-1}$  and 1357  $\text{cm}^{-1}$  ( $\nu_{C-N}$ ) using Eq. (1) where  $A_{1357}$  stands for the absorbance of characteristic imide II band ( $\nu_{C-N}$ ) and  $A_{1515}$  is the absorbance of aromatic ring stretching band ( $\nu_{C=C}$ ). The poly(amic acid) (PAA<sub>init</sub>) film dried at 100 °C for 1 h in a vacuum oven and the fully imidized polyimide (PI<sub>ref</sub>) film cured at 350 °C for 1 h were used as reference films.

$$DI (\%) = \frac{\left(\frac{A_{1357}}{A_{1515}}\right)_{\text{sample}} - \left(\frac{A_{1357}}{A_{1515}}\right)_{\text{PAA}_{\text{init}}}}{\left(\frac{A_{1357}}{A_{1515}}\right)_{\text{PI}_{\text{ref}}} - \left(\frac{A_{1357}}{A_{1515}}\right)_{\text{PAA}_{\text{init}}}} \times 100 \quad (1)$$

As shown in Fig. 2, the characteristic absorption bands due to the carbonyl group of the poly(amic acid), normally appearing at 1650 ( $\nu_{C=O}$ )  $\text{cm}^{-1}$ , had disappeared with an increasing imidization temperature. And, the characteristic absorption bands of the imide ring appeared at 1774 ( $\nu_{C=O}$ , asym), 1715 ( $\nu_{C=O}$ , sym.), 1357 ( $\nu_{C-N}$ ), and 725 (deformation)  $\text{cm}^{-1}$  in the IR spectra. Especially, the imidization degree of the PI(C)-200 film fabricated at 200 °C in the presence of the DBU was close to 100%, which was a remarkable increase compared to that of PI(NC)-200 cured at same temperature without the catalyst (83%). That is, the introduction of an organic base catalyst into the poly(amic acid) solution made it possible to prepare a fully imidized polyimide film at a temperature of 200 °C.

We also investigated the surface properties of the PI(NC)-200 and PI(C)-200 films. Fig. 3 shows the contact angles and surface energies of the PI(NC)-200 and PI(C)-200 were somewhat different. The surface energies of the PI(NC)-200 and PI(C)-200, calculated from the contact angle of water and diiodomethane, were 52.9 and 55.0 dyne/cm, respectively. The contact angle of a water drop on the PI(C)-200 and PI(NC)-200 films were similar, but the contact angle of a diiodomethane drop on the PI(C)-200 and PI(NC)-200 films were 29.4° and 18.1°, respectively, which was decreased by the introduction of

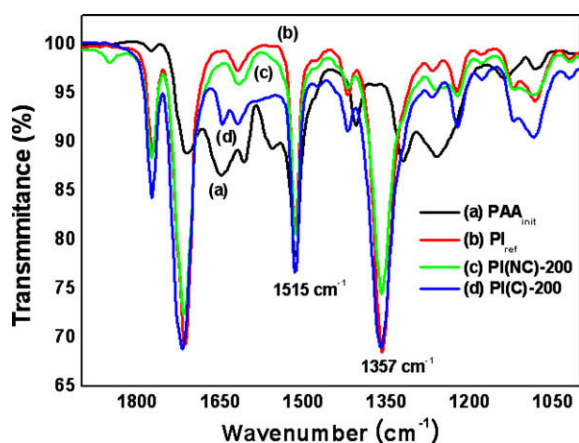


**Fig. 2.** FT-IR spectra of the polyimides. (a) PAA<sub>init</sub>: the poly(amic acid) baked at 90 °C for 10 min and dried at 100 °C for 1 h in a vacuum oven. (b) PI<sub>ref</sub>: the polyimide cured at 200 °C and 250 °C for 30 min, and 350 °C for 1 h in a convection oven. (c) PI(NC)-200 baked at 90 °C for 10 min and then cured at 200 °C for 40 min on a hot plate. (d) PI(C)-200 baked at 90 °C for 10 min and then cured at 200 °C for 40 min on a hotplate in the presence of 5 wt% of DBU as a catalyst.

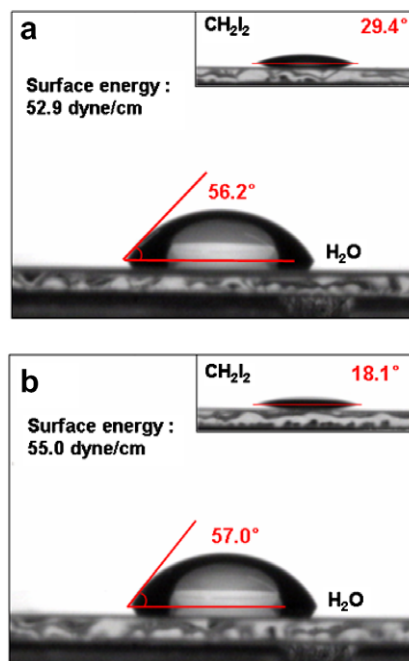


**Fig. 3.** Optical microscopy images of water and diiodomethane drops on the surface of (a) PI(NC)-200 and (b) PI(C)-200.

the imidization catalyst. This means that the surface of the PI(C)-200 becomes more hydrophobic with an increase in the degree of imidization.

Surface properties are known to influence the mechanism of the initial growth of pentacene and thus the performance of OTFTs. AFM experiments were performed in order to investigate the effect of the surface property on the morphology of the pentacene thin layers deposited on the gate insulator. AFM images of the 60 nm thick pentacene on the gate insulators are shown in Fig. 4. The morphology of the pentacene on both insulators showed similar dendritic structures. On the other hand, the grain size of the pentacene on the PI(C)-200, with its smaller diiodomethane contact angle, was larger than that of the pentacene on the PI(NC)-200. This would be due to the high inter-molecular interaction of the pentacene molecule with the PI(C)-200. That is, the surface of the PI(C)-200 becomes more hydrophobic with an increase in the degree of imidization, resulting in a higher diffusion rate of the pentacene molecules in the in-plane direction and considerable increase the nucleation density. The pentacene on PI(C)-200 film shows the corresponding XRD peaks is composed of a series of sharp (001) peaks indicating that the pentacene is highly ordered. The main XRD peak at 5.7° was observed from the thin-film phase. The measured Bragg reflection angles of 5.7° correspond to tilts of the c-axis of the pentacene molecules with respect to the surface normal of 15.0°.

The leakage current density of the device with the PI(NC)-200 insulator was less than  $9.2 \times 10^{-11}$  A/cm<sup>2</sup>, while biased from 0 to 50 V. The breakdown voltage and the capacitance were more than 1.5 MV/cm and 129.5 pF/mm<sup>2</sup>, respectively. On the other hand, the device with

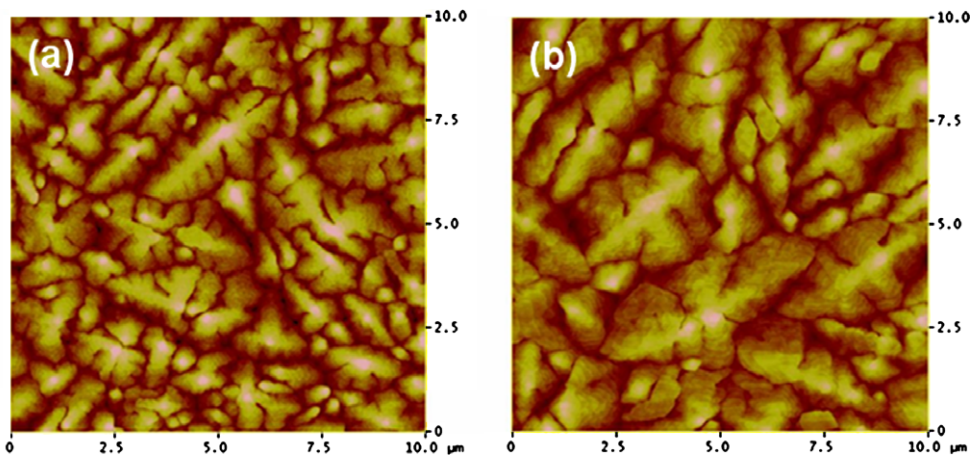


Fig. 4. AFM images ( $10\ \mu\text{m} \times 10\ \mu\text{m}$ ) of pentacene (60 nm) on (a) PI(NC)-200 and (b) PI(C)-200.

the fully imidized polyimide insulator, the PI(C)-200, showed a leakage current density of  $5.9 \times 10^{-11}\ \text{A}/\text{cm}^2$ , which was lower than the device with the PI(NC)-200 insulator. The breakdown voltage and capacitance were similar to the device with the PI(NC)-200 insulator, 1.5 MV/cm and  $140.0\ \text{pF}/\text{mm}^2$ , respectively. These results showed that the fully aromatic polyimide prepared from BPDA and *p*-PDA monomers in this study had a higher chain packing density owing to strong  $\pi$ - $\pi$  bond interaction between the phenyl rings, which resulted in remarkably improved insulating properties compared to those of the alicyclic polyimide insulators reported by our group ( $3.5 \times 10^{-8}$ – $1.5 \times 10^{-9}\ \text{A}/\text{cm}^2$ ) [16,17]. For comparison, the energy-minimized structures of the polyimides synthesized from different monomers were calculated by a HyperChem<sup>®</sup> v 7.5 program. As shown in Fig. 5, the alicyclic polyimide (a) connected with a flexible methylene linkage had a more bent structure than that of the polyimide [PI(C)-200] and (b) prepared from BPDA and *p*-PDA with rigid, flat monomer structures.

### 3.2. Device characteristics

The output ( $I_{\text{ds}}$  vs.  $V_{\text{ds}}$ ) characteristics of the OTFTs having the PI(NC)-200 and PI(C)-200 as insulators were investigated. The OTFTs exhibit typical *p*-type characteristics with a transition from linear to saturation behavior in both devices. At a given negative gate voltage ( $V_{\text{gs}}$ ),  $I_{\text{ds}}$  initially increases linearly with a small negative  $V_{\text{ds}}$  and then saturates due to a pinch off of the accumulation layer. Clear saturation behavior was observed for the OTFT device with the PI(C)-200 gate insulator with a high imidization ratio, which might be due to the complete removal of the carboxylic acids and amide groups of the original poly(amic acid). Fig. 6 exhibits transfer ( $I_{\text{ds}}$  vs.  $V_{\text{gs}}$ ) characteristic curves of the OTFTs fabricated with the PI(NC)-200 and PI(C)-200. The field-effect mobility ( $\mu$ ) was calculated from the plot of the square root of the drain current ( $I_{\text{ds}}^{1/2}$ ) and gate voltage ( $V_{\text{gs}}$ ) in the saturation regime. The threshold voltage ( $V_{\text{T}}$ ) of the device was determined from the plot of ( $I_{\text{ds}}^{1/2}$ ) and  $V_{\text{gs}}$  by extrapolating the measured data to

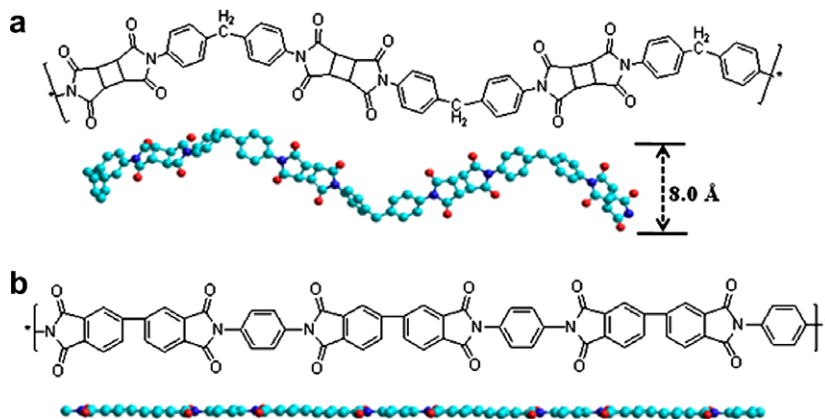
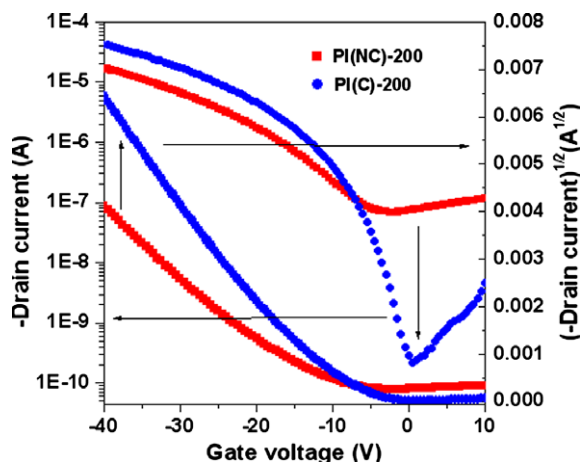


Fig. 5. Energy minimized structures of the polyimides (calculated by a HyperChem<sup>®</sup> v 7.5). (a) Polyimide based on CBDA and MDA16 and (b) polyimide based on BPDA and *p*-PDA [PI(C)-200].



**Fig. 6.** Transfer characteristics (for the square root of the drain current vs. gate voltage,  $I_{ds}^{1/2}$  vs.  $V_{gs}$  and drain current vs. gate voltage,  $I_{ds}$  vs.  $V_{gs}$ ) of OTFTs with PI(NC)-200 and PI(C)-200. The drain voltage ( $V_{ds}$ ) is set to  $-30$  V. Note that the Y-axis is in (a)  $\log(-I_{ds})$  and (b)  $(-I_{ds})^{1/2}$ .

$I_{ds} = 0$ . When  $V_{gs}$  was swept from  $+20$  to  $-40$  V and  $V_{ds}$  was set at  $-30$  V, the mobility, off-current, on/off ratio, and subthreshold swing (SS) of the pentacene OTFT with the PI(NC)-200 gate insulator were  $0.18 \text{ cm}^2/\text{Vs}$ ,  $6.9 \times 10^{-8}$  A,  $2.5 \times 10^2$ , and  $10.1 \text{ V/dec}$ , respectively. On the other hand, the mobility, off-current, on/off ratio, and subthreshold slope (SS) of the pentacene OTFT with the PI(C)-200 gate insulator were  $0.36 \text{ cm}^2/\text{Vs}$ ,  $2.1 \times 10^{-10}$  A,  $2.0 \times 10^5$ , and  $2.1 \text{ V/dec}$ , respectively. That is, when the PI(C)-200 was introduced as a gate insulator, the mobility increased by about two times ( $0.36 \text{ cm}^2/\text{Vs}$ ). In addition, it is clearly seen that the leakage current of OTFTs with PI(C)-200 was reduced dramatically by two orders of magnitude from  $6.9 \times 10^{-8}$  to  $2.1 \times 10^{-10}$  A, the value of SS also decreased significantly from  $10.1$  to  $2.1 \text{ V/s}$ . These results are much similar with the research reported by Yagi et al. They showed that traps at the pentacene/ $\text{SiO}_2$  interface were suppressed with 1,1,1,3,3,3-hexamethyldisilazane treatment, which improved off-current conduction. In their experiment, they showed that the hydrophobic surface treatment effectively improved of the off-current of the devices and the off-current suppression could be caused by the reduction of the interfacial charge trapping at the pentacene/ $\text{SiO}_2$  interface [18]. As mentioned in our text, the off-current of the pentacene OTFT device with a PI(C)-200 gate insulator is improved compared to that of the device with the PI(NC)-200, and it might be due to the complete removal of the hydrophilic carboxylic acids and amide groups of the original poly(amic acid). It has been well known that the carboxylic acids and amide groups of the poly(amic acid) easily absorb the water molecule from the atmosphere. As reported by Kumaki et al., it can be considered that the chemical reaction between the carboxylic acids on the gate-insulator surface and the absorbed water molecules is associated with the high off-current of the pentacene OTFT device even at zero and positive gate voltage [19]. We have also investigated the transfer characteristics of the devices with different direction of the gate voltage sweep to get more information about

the effects of the interface between the dielectric-semiconductor on the performance of organic transistors. The hysteresis was observed in the drain current ( $I_{ds}$ ) vs. gate voltage ( $V_{gs}$ ) characteristics (recorded under constant  $S/D$  bias  $V_{ds}$ ) when  $V_{gs}$  was swept from  $-10$  to  $+5$  V and back to  $-10$  V. That is, when sweeping  $V_{gs}$  back from  $+5$  to  $-10$  V, we observed a shift in the recorded  $I_{ds}$ - $V_{gs}$  toward the positive  $V_{gs}$  side. A significant dependence of the hysteresis on the type of gate insulators was also observed. The device fabricated with less-polar gate insulator, PI(C)-200 showed much smaller hysteresis compared to that of the devices with the polar interface. The width of the hysteresis in  $V_{gs}$  exhibited a significant dependence on the surface polarity of the gate insulator. As shown in Fig. 7, The difference in the threshold voltage values due to hysteresis increased from near zero for PI(C)-200 to  $2.5$  V for PI(NC)-200. The positive shift of the  $V_{th}$  reveals that the hole is accumulated at the channel region of pentacene layer even at zero and positive gate voltage, which can be attributed to the influence of the trap site, which is caused by the adsorption of the water molecules. These results suggest that the hysteresis is caused by the high polarity of the gate insulators.

Furthermore, it can be seen that the performance of OTFTs can be affected by the grain size, orientation, and crystallinity of an organic semiconductor. These properties are usually determined by the surface properties of gate insulators, which can affect the crystal structure of organic semiconductors. The surface of the PI(C)-200 becomes more hydrophobic with an increase in the imidization degree, which leads to the formation of a more stable interface and well-aligned crystalline structure, contributing

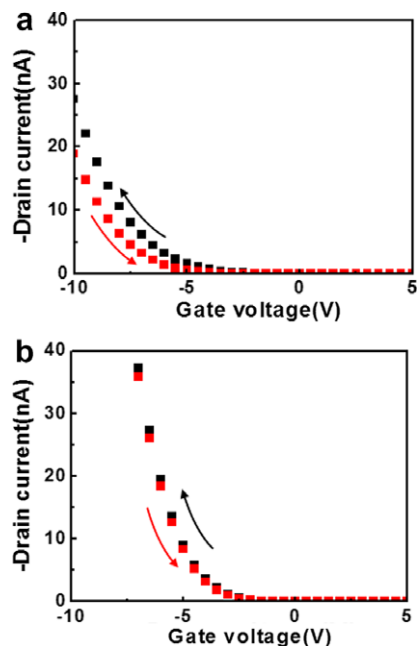


**Fig. 7.** (a)  $I_{ds}$ - $V_{gs}$  curves recorded for the OTFT device made of PI(NC)-200 as the gate insulator under the  $V_{gs}$  sweep rates of  $1.35 \text{ V/s}$ . Bias voltage,  $V_{ds} = 30$  V. (b)  $I_{ds}$ - $V_{gs}$  curves recorded for the OTFT device made of PI(C)-200 as the gate insulator under the same measuring condition of (a).



to an improvement of field-effect mobility of pentacene OTFT with PI(C)-200. As increasing the imidization degree of PI(C)-200 with the catalyst, the leakage current also was decreased effectively by the complete removal of the carboxylic acids and amide groups from polyimide insulator. This performance improvement in the pentacene OTFT with the PI(C)-200 gate insulator indicates that the high imidization degree obtained by the introduction of the base catalyst could be an effective approach to improving OTFT performance.

#### 4. Concluding remarks

In this study, we have reported a new synthetic route to convert the poly(amic acid) to the polyimide at a temperature of 200 °C by the introduction of an organic base catalyst. The effect of the imidization ratio on the performance of pentacene OTFT devices has been investigated. The device fabrication temperature of a pentacene OTFT with fully aromatic polyimide as a gate insulator was lowered to 200 °C, which was a remarkably lower temperature, compared to conventional thermal imidization processes without the catalyst. The leakage current of the pentacene OTFT device with a PI(C)-200 gate insulator was remarkably improved compared to that of the device with the PI(NC)-200, which might be due to the complete removal of the carboxylic acids and amide groups of the original poly(amic acid). In addition, the mobility of the OTFT with the PI(C)-200 was 0.36 cm<sup>2</sup>/Vs, which is two times larger than that of the OTFT device fabricated with the PI(NC)-200. Further, the SS of OTFTs with the PI(C)-200 decreased from 10.1 to 2.1 V/dec. The lowered SS indicates that the lower density of the trap exists at the interface between a gate insulator and semiconductor due to the more pentacene growth-friendly gate insulator. Consequently, by employing a base-catalyzed imidization method of fully aromatic polyimide, many aromatic polyimide with difference structures can be utilized not only for gate

insulator of OTFT and also for other organic electronic devices which require low processing temperature.

#### Acknowledgements

Research on the gate insulator at KRICT was financially supported by the Korean Ministry of Science and Technology through the 21 C Frontier Program, and the Top Brand Project.

#### References

- [1] A. Salleo, M.L. Chabinyk, M.S. Yang, R.A. Street, *Appl. Phys. Lett.* 81 (2002) 4383.
- [2] A.R. Völkel, R.A. Street, D. Knipp, *Phys. Rev. B* 66 (2002) 195336.
- [3] H. Sirringhaus, N. Tessler, R.H. Friend, *Synth. Met.* 102 (1999) 857.
- [4] T.C. Gorjanc, I. Levesque, M. Dlorio, *Appl. Phys. Lett.* 84 (2004) 930.
- [5] K. Shankar, T.N. Jackson, *J. Mater. Res.* 19 (2004) 2003.
- [6] M. Matters, D.M. de Leeuw, P.T. Herwig, A.R. Brown, *Synth. Met.* 102 (1999) 998.
- [7] D.J. Gundlach, C.-C.S. Kuo, C. Sheraw, J.A. Nicols, T.N. Jackson, *Proc. SPIE* 3366 (2001) 54.
- [8] M. Matters, D.M. de Leeuw, M.J.C.M. Vissenberg, C.M. Hart, P.T. Herwig, T. Geuns, C.M.J. Mutsaers, S.J. Drury, *Opt. Mater.* 12 (1999) 189.
- [9] S. Scheinert, G. Paasch, M. Schrodner, H.-K. Roth, S. Sensfub, *J. Appl. Phys.* 92 (2002) 330.
- [10] H. Klauk, M. Halik, U. Zschieschang, F. Eder, G. Schmid, C. Dehm, *Appl. Phys. Lett.* 82 (2003) 4175.
- [11] G. Horowitz, F. Deloffre, F. Garnier, R. Hajlaoui, M. Hmyene, A. Yassar, *Synth. Met.* 54 (1993) 435.
- [12] R. Schroeder, L.A. Majewski, M. Grell, *Appl. Phys. Lett.* 84 (2004) 1004; R. Schroeder, L.A. Majewski, M. Grell, *Appl. Phys. Lett.* 83 (2003) 3201.
- [13] C.D. Sheraw, D.J. Gundlach, T.N. Jackson, *Mater. Res. Soc. Symp. Proc.* 558 (2000) 403.
- [14] Y. Kato, S. Iba, R. Teramoto, T. Sekitani, T. Someya, *Appl. Phys. Lett.* 84 (2004) 3789.
- [15] S.M. Pyo, M.Y. Lee, J.H. Jeon, K.Y. Choi, M.H. Yi, J.S. Kim, *Adv. Funct. Mater.* 15 (2005) 619.
- [16] S.M. Pyo, J. Choi, Y. Oh, H.S. Son, M.H. Yi, *Appl. Phys. Lett.* 88 (2006) 173501.
- [17] S.M. Pyo, H.S. Son, K.Y. Choi, M.H. Yi, S.K. Hong, *Appl. Phys. Lett.* 86 (2005) 133508.
- [18] I. Yagi, K. Tsukagoshi, Y. Aoyagi, *Appl. Phys. Lett.* 86 (2005) 103502.
- [19] D. Kumaki, T. Umeda, S. Tokito, *Appl. Phys. Lett.* 92 (2008) 093309.



# Post-fabrication electric field and thermal treatment of polymer light emitting diodes and their photovoltaic properties

Ali Osman Sevim, Senol Mutlu \*

Department of Electrical and Electronics Engineering, Bogazici University, 34342 Istanbul, Turkey

## ARTICLE INFO

### Article history:

Received 20 April 2008

Received in revised form 8 September 2008

Accepted 18 September 2008

Available online 30 September 2008

### PACS:

73.50.Pz

73.61.Ph

81.05.Lg

85.60.Jb

85.60.Gz

### Keywords:

PEDOT:PSS

MEH-PPV

PLED

Post-fabrication treatment in reverse bias

Photovoltaic response

## ABSTRACT

This work presents post-fabrication electric field and heat treatment methods developed for polymer light emitting diodes (PLEDs), which have degraded due to exposure to oxygen and water vapors during low-cost fabrication performed in standard room conditions. Investigated PLEDs have structures composed of indium tin oxide (ITO), poly(3,4-ethylenedioxythiophene), poly(styrenesulfonate), (PEDOT:PSS), poly[2-methoxy-5-(2'-ethyl-hexyloxy)-1,4-phenylene vinylene] (MEH-PPV), and aluminum (Al). Heat treatment restores the light emitting function of dysfunctional PLEDs but also causes a high turn-on voltage of 10 V. Electric field treatment utilizing  $-1$  V reduces this high turn-on voltage to 3 V. This procedure also improves open circuit voltages from 5 mV to 55 mV, and short circuit currents from 0.5 nA to 5 nA when PLEDs are operated as photovoltaic cells under a light intensity of 500 mW/m<sup>2</sup>. Repeated  $I$ - $V$  sweep measurements additionally show improved stability and uniformity. The reasons for these improvements, the usage of an optimal treatment temperature of 130 °C, and the usage of treatment voltages of 0 and  $-1$  V are discussed.

© 2008 Elsevier B.V. All rights reserved.

## 1. Introduction

Conjugated polymers are semiconductors used in fabricating light emitting diodes [1], polymer transistors [2], electronic circuits [3] and photovoltaic cells [4]. Their varied capabilities make them attractive for monolithic integration of electronic, optoelectronic, microelectromechanical, and sensory devices [5,6] on a single substrate. In addition, polymer based systems are flexible, light, easy to fabricate, low in cost and are amenable to roll production [7]. However, when compared to their inorganic counterparts, current polymer semiconductor devices have lower performance, are less reliable, and have shorter lifetimes [8–10] due to ra-

pid degradation of performance on exposure to oxygen and water vapor under ambient atmosphere.

It has been shown by several groups that increased stability and performance characteristics of polymer light emitting diodes [11–15] and solar cells [16] can be attained by the use of treatment methodologies such as UV ozone, oxygen plasma or chemical treatments applied to ITO or conducting polymers [11–16]. High efficiencies can be achieved if the fabrication is performed under an inert atmosphere, such as nitrogen and argon, to prevent contamination of the semiconductor devices and degradation of the polymers [17–19]. Although fabrication under an inert atmosphere improves performance, it also increases the complexity and cost of fabrication.

This paper presents a two-step post-fabrication heat treatment and electric field treatment method, and its influences on the performance of PLEDs fabricated using ITO/PEDOT:PSS/MEH-PPV/Al layers. Differing from typical

\* Corresponding author. Tel.: +90 212 3597442; fax: +90 212 2872465.  
E-mail addresses: [ali.sevim@boun.edu.tr](mailto:ali.sevim@boun.edu.tr) (A.O. Sevim), [senol.mutlu@boun.edu.tr](mailto:senol.mutlu@boun.edu.tr) (S. Mutlu).

fabrication process in literature; fabrication is performed in standard room conditions without using glove-boxes. Therefore, during each fabrication step, the polymer materials are contaminated by humidity and oxygen in the environment and the resulting devices do not emit light when forward biased. However, the post-fabrication thermal treatment restores the electroluminescent function of PLEDs. The electric field treatment following the heat treatment improves this function by lowering their turn-on voltages. Furthermore, it improves their photovoltaic function by increasing their open circuit voltages and short circuit currents by an order of magnitude. This way fabrication is made easier and the cost is lowered since the equipment consisting of spin-coater, hotplate, stirrer, high vacuum thin film evaporator, wiring tools, and packaging tools used in the production of PLEDs does not have to be connected together inside a big glove-box to secure an inert atmosphere.

Previously, similar post-fabrication treatment have been shown to work on polymer solar cells [20,21], organic light emitting diodes (OLED) based on dendrimers [22], double layer OLEDs [23] and PLEDs [24]. In [20], the solar cell structure is ITO/PEDOT:PSS/poly(3-hexylthiophene) (P3HT) : [6,6]-phenylC<sub>61</sub>-butyric acid methyl ester (PCBM)/lithium fluoride (LiF)/Al. A thermal treatment at 75 °C and a forward biased voltage treatment at 2.7 V increase the short circuit current and the efficiency of the solar cells. In [21], the solar cell structure is ITO/PEDOT:PSS/MEH-PPV:Fullerene (C<sub>60</sub>)/Al. In this case, thermal anneal under reverse bias of -6 V increases the short circuit current and the efficiency of the solar cells. In [22], the OLED structure is ITO/PEDOT/Dendrimer:2-(4-biphenyl)-5-(4-tert-butylphenyl)-1,3,4-oxadiazole (PBD)/Calcium(Ca)/Al. Electrical annealing with a forward bias of 12.4 V without any thermal treatment reduces turn-on voltages of the devices and increases their brightness and efficiency. In [23], the OLED structure is ITO/N,N'-diphenyl-N,N'-(3-methylphenyl)-1,1'-biphenyl-4,4'-diamine (TPD)/tris(8-hydroxyquinonate)aluminum (Alq<sub>3</sub>)/magnesium (Mg):silver (Ag). Short-circuit electrical treatment at atmospheric pressure for 10 min or reverse bias treatment at -5 V for 10 min without a thermal treatment decreases the driving voltage and recovers the drop in luminance that occurs during the device operation. In [24], the PLED structure is ITO/MEH-PPV/Al. The devices are electrically treated at forward bias of 15 V after being thermally treated. As a result, turn-on voltages of the devices are reduced significantly to 3 V and their efficiency are enhanced dramatically.

The usage of forward bias or reverse bias electric field treatment on polymer solar cells, OLEDs and PLEDs for performance improvement changes from device to device in the literature. Improvement due to forward bias treatment is typically attributed to enhanced charge injection facilitated by an ionic dipole moment or space charge field near the electrodes formed by the ionic diffusion induced by the applied electric field [22,24]. Reverse bias treatment, on the other hand, is suggested to improve the performance by enhancing charge mobility through the modification and reorientation of the polymer chains along the direction of the applied electric field [21]. To date, thermal treatment with reverse bias electrical treatment has been shown to work only on solar cells [21]. Furthermore, none

of the related works have studied the effects of the electrical treatments on the electroluminescent and photovoltaic properties of PLEDs at the same time. This work shows, for the first time, that post-fabrication treatments to PLEDs based on MEH-PPV with the PEDOT:PSS layer must start with a thermal treatment and must be followed with an electrical treatment under reverse bias.

In this paper, the fabrication steps used to produce PLEDs are presented in detail. They are followed by an explanation of the details used in the post-fabrication thermal and electric field treatments. The effects of the heat treatment alone, and the effects of the electric field treatment following the heat treatment on the turn-on voltages and photovoltaic properties of PLEDs are presented, analyzed and discussed.

## 2. Experiment

### 2.1. Fabrication

All fabrication steps are performed in standard room conditions, with a relative humidity level of 40–50% and a temperature of 21–26 °C. The substrate material chosen for fabrication is ITO coated PET sheets with a sheet resistivity of 35 ohm/square, purchased from Aldrich. The sheets are cut into circular, wafer-shaped segments with diameters of 4" and attached to 1 mm thick glass wafers with silicone gel. They are cleaned in acetone, isopropyl alcohol, and deionized water consecutively for 3 min using an ultrasonic cleaner. To eliminate the hydrophobic nature of the PET surface against PEDOT:PSS, which is an aqueous solution, and to cleanse the surface of ITO from organic residuals, an oxygen plasma with a power of 1.3 W is used for 15 min in a 300 mTorr vacuum. In addition, oxygen plasma treatment of ITO improves the performance of the device as it decreases surface roughness [25] and increases the work function of ITO [26]. PEDOT:PSS is purchased from Sigma as an aqueous solution. After the filtration of PEDOT:PSS with a 0.25 µm syringe filter, a film approximately 80 nm in thickness is obtained on the wafer by spin-coating the solution at 1200 rpm for 30 s. To increase the conductivity of the PEDOT:PSS film, the sample is baked at 110 °C under nitrogen atmosphere for one hour and then baked in a vacuum of 150 Torr for 1 h. To minimize thermal stress, temperature is increased and decreased gradually. Next, a 4 mg/ml MEH-PPV/toluene solution is stirred at 50 °C on a hot plate for at least 4 h until the polymer is fully dissolved. After filtering the mixture with a 0.25 µm Teflon syringe filter, the MEH-PPV solution is spin coated onto the wafer at 1000 rpm. Then, the film is baked at 65 °C for 1 h. This obtains a film thickness of approximately 100 nm. For the deposition of the aluminum electrodes, a shadow mask is prepared from a 50 µm thick copper foil. A vacuum chamber with a base pressure of 10<sup>-6</sup> Torr is then used to evaporate a 120 nm aluminum layer. The shadow mask with 3 mm wide holes is aligned perpendicular to the patterned ITO and forms 3 × 3 mm<sup>2</sup> square test cells. Drawings of the cross-sectional and the top view of the test samples are shown in Fig. 1.

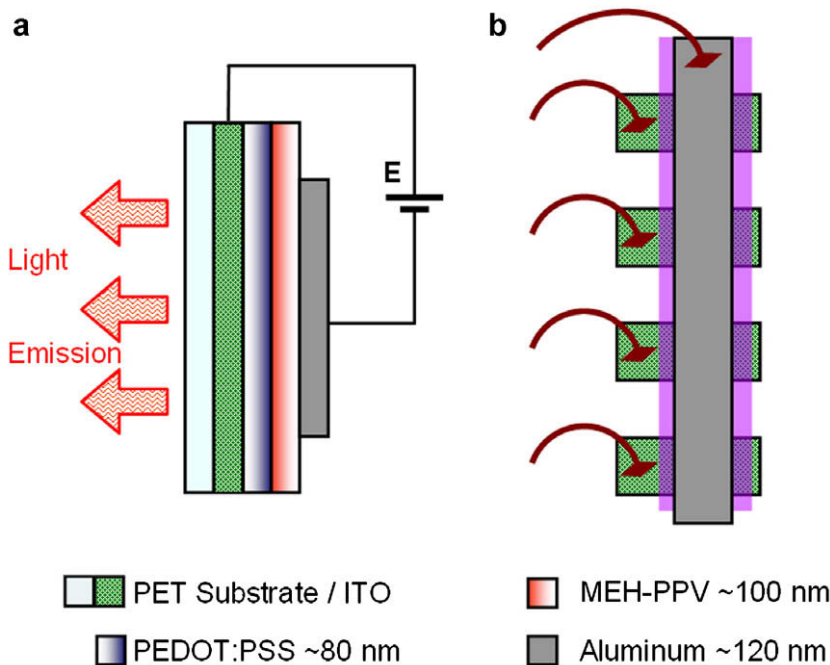


Fig. 1. (a) Cross sectional view of PLED and (b) top view of the wire bonded samples.

## 2.2. Post processing treatments

The post-fabrication treatments utilized in this work consist of two stages: heat treatment and electric field treatment immediately following it under the same environmental conditions. Heat treatment is performed on a hotplate inside a vacuum chamber with in-situ packaging capability. Open atmospheric fabrication of these devices inevitably lead to absorption of water vapor and oxygen in the thin film layers of these devices, which are detrimental to their performance. This treatment removes most of the oxygen and water vapors absorbed inside the devices.

In the heat treatment process, different temperatures are experimented with to determine an optimum value. Square PLED cells with an area of  $3 \times 3 \text{ mm}^2$  are chosen from the wafer with close proximity to one another. This reduces the effect of process variations between batches, allowing the treatment to be tested on similar samples. Temperature annealing is proposed to take place for one hour. At the end of the experimental trials, no significant further improvement was observed by heat treating the PLEDs for more than an hour as also reported in a similar work [27]. Temperature is changed gradually in stages to minimize the thermal stress between the layers. Treatment is performed in a vacuum of 150 Torr in a dark

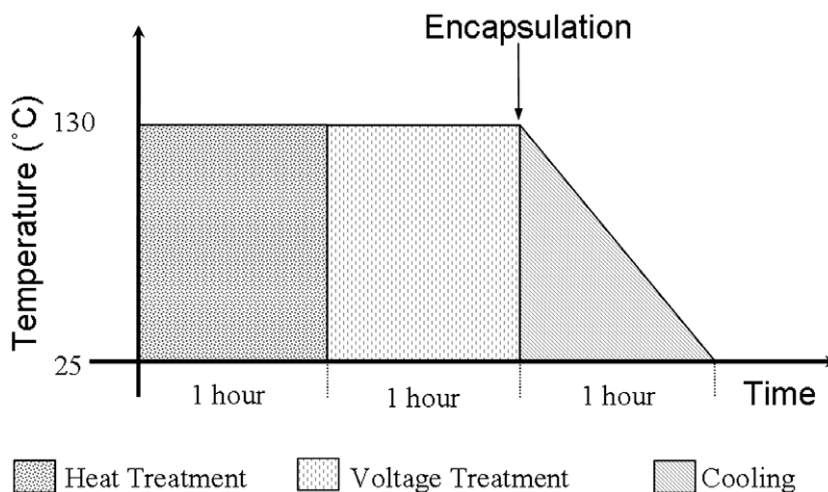


Fig. 2. Temperatures of the treatment stages.

environment. Following the heat treatment, the devices are electrically reversed-biased at voltages varying from 0 to  $-8$  V. Finally, encapsulation and cooling stages are ex-

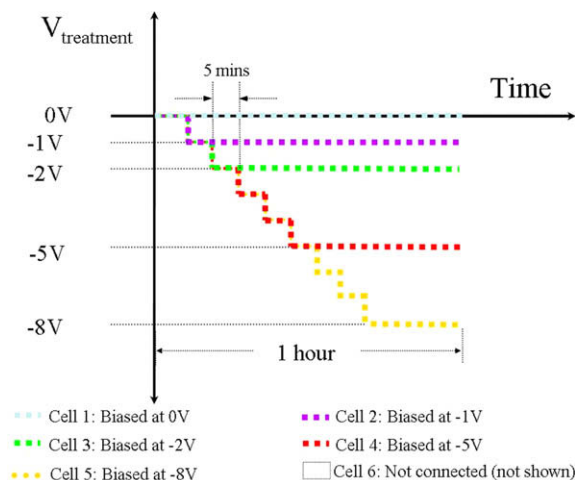


Fig. 3. Biasing steps involved in the electric field treatment.

cuted. The phases of treatments, their durations and temperatures are given in Fig. 2. In the electric field treatment phase, the magnitude of the negative bias voltage of each sample is increased in steps of 1 V/5 min, as shown in Fig. 3. In addition to a reference cell which is not connected to a certain bias supply, 0,  $-1$ ,  $-2$ ,  $-5$  and  $-8$  V potential levels are used in this phase. Different magnitudes are used to determine the effects of potential magnitude on device performance. The reference cell in this case is a device that receives only heat treatment.

At the end of treatment processes, samples are packaged immediately without breaking vacuum. The experimental setup used to apply heat, electrical field treatment, and the packaging under vacuum conditions is shown in Fig. 4. A layer of hot melted silicone approximately 2 mm thick purchased from Henkel is used to encapsulate the devices. The silicone is melted above  $90$  °C by turning on a separate custom-made heater, which holds solid silicone pieces. This heater is located on the surface of the primary hot plate. It is thermally isolated from the hot plate using glass supports. The whole setup is inside the vacuum chamber. The electrical controls for this custom-made heater and the primary heater are outside the chamber. The encapsulating silicone is intention-

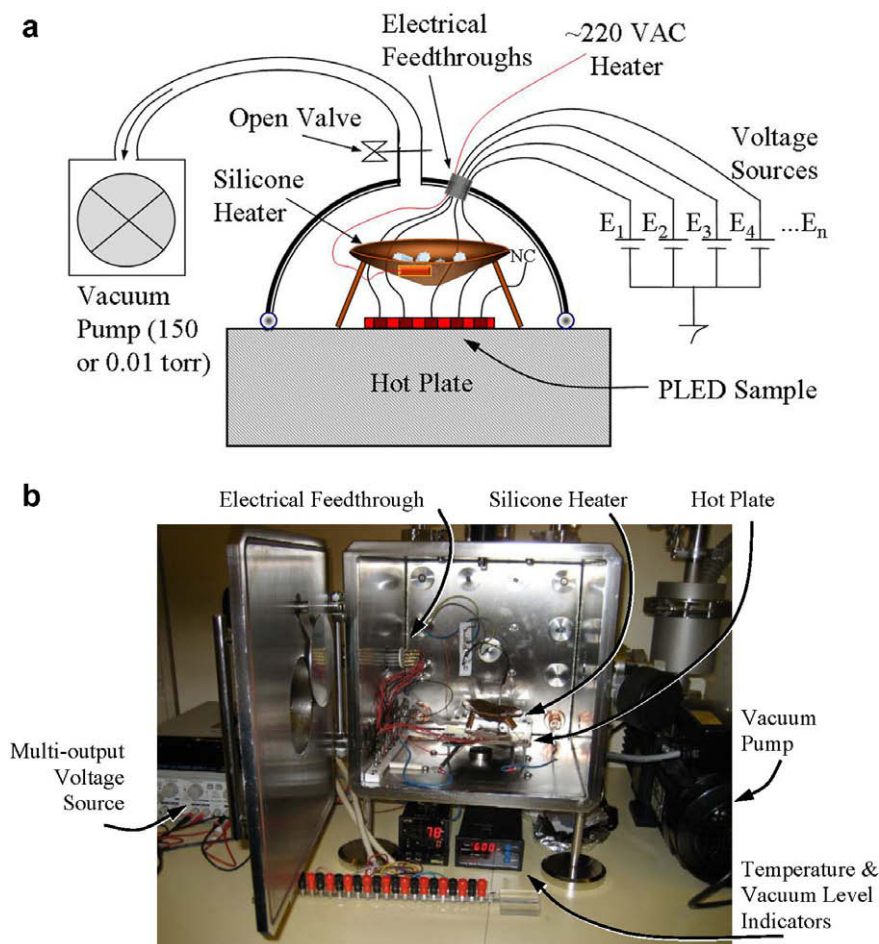


Fig. 4. (a) Depiction of the experiment setup for heat and electric field treatment (b) Photograph of the real setup.

ally deposited in a thick layer to eliminate water and oxygen diffusion to the semiconductor polymers. After encapsulation, the samples are cooled to room temperature without breaking vacuum so that the silicone layer solidifies and acts as a diffusion barrier. This encapsulation additionally makes the devices robust against mechanical disturbances.

The optical characteristics of PLEDs are determined with an optical setup composed of equipment purchased from Ocean Optics. For relative measurements, a bare fiber optic probe with a 200  $\mu\text{m}$  radius is used. The same fiber optic probe is also used to determine the light spectra of the PLEDs. The luminance observed by the fiber optic probe is measured with a fiber optic spectrometer (Ocean Optics USB 4000). For absolute measurements, a fiber optic integrating sphere (FOIS-1) is used to capture the total luminous emitted from the device. One side of the fiber optic probe is attached to integrating sphere (IS) and other side is connected to the fiber optic spectrometer. Calibrations are performed with a calibrated light source (LS-1-CAL-INT). Electrical measurements of the device parameters are performed using a Keithley 4200 Semiconductor Characterization System, an Agilent 34410A Digital Multimeter, and adjustable DC power supplies.

### 3. Results and discussion

It has been proven that heat treatment, also referred to as thermal annealing of polymer junctions, after fabrication is an effective tool for improving device performance. It decreases contact resistance, improves morphology, and enhances junction characteristics. The temperature of annealing must be higher than the glass transition temperature of the polymers [27].

Heat treatment under partial vacuum followed by packaging under the same conditions restores the light emitting characteristics of PLEDs. However, this result in devices with high turn-on voltages, around 10 V, compared to 2.1 V, which is the turn-on voltage of an ideal PLED based on MEH-PPV [28]. Furthermore, photovoltaic properties of the devices are hardly measurable.

Four different temperature levels, 90, 110, 130 and 150  $^{\circ}\text{C}$  are tested in the heat treatment stage.  $I$ - $V$  curves of the devices in Fig. 5 show that the most effective temperature for heat treatment is 150  $^{\circ}\text{C}$ . These results also indicate that temperatures higher than 150  $^{\circ}\text{C}$  may improve the  $I$ - $V$  curves even further, similar to the results of [27], which show further improvement in the device performance with a thermal treatment at 170  $^{\circ}\text{C}$ . However, due to increased thermal stress and operation difficulties encountered with PET substrates at temperatures greater than 130  $^{\circ}\text{C}$ , 130  $^{\circ}\text{C}$  is selected as optimal value and used in the remainder of the treatments.

The effect of electric field treatments is tested on both light emitting and photovoltaic properties of PLEDs. Fig. 6 shows the pictures of PLED samples, which are electrically treated with different voltages, taken at the given test voltages. For the devices that have been heat treated but not electric field treated, shown as unbiased cell on the column named NC (not connected), the turn-on voltage is relatively high and the uniformity is very poor. By treating de-

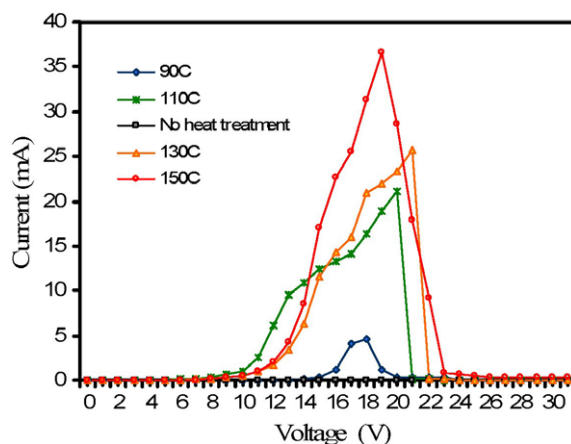


Fig. 5. Voltage–current characteristics of PLEDs heat treated at different temperatures.

VICES with negative electric fields after fabrication, the turn-on voltages of the PLEDs drop to lower voltages. Turn-on voltages increase slowly with the magnitude of the negative voltage treatment. For example, a device that experienced only heat treatment (NC column in Fig. 6) has a turn-on voltage of around 10 V. However, a device that experiences both heat treatment and an electric field treatment with  $-1$  V ( $-1$  column in Fig. 6), has a turn-on voltage of around 3 V. A device that is treated with  $-5$  V ( $-5$  column in Fig. 6), has a turn-on voltage of around 4 V. This is also true for the voltage levels at which PLEDs are most luminous. These results can be better understood in Fig. 7. This figure shows how the relative illuminance of PLEDs that are electrically treated with different negative voltages are altered upon applying test voltages. Electrical field treatments with 0 and  $-1$  V give the lowest turn-on voltages and produce wide operating regions with better uniformity.

Another important advantage of the electric field treatment is that the turn-on and maximum illumination voltage levels of the devices, which in electrically untreated cells are unstable and vary over the lifetime of operation, are stabilized to certain values that are determined by the magnitudes of the treatment voltages. This is clearly shown in Fig. 8b where thermal (130  $^{\circ}\text{C}$ ) and electrical ( $-1$  V) treatment in combination produces a stable, uniform and repeatable  $I$ - $V$  characteristics measured using a Keithley 4200 Semiconductor Characterization System with sweeping drive voltages in upward and downward directions. However, samples that are thermally treated (130  $^{\circ}\text{C}$ ) but not electrically treated have non-uniform and unstable response with large hysteresis in the  $I$ - $V$  sweeps. They typically fail after several sweeps, as shown in Fig. 8a. The electric field treatment additionally improves the uniformity of the light emitting surface.

Another point which should be addressed concerning the electric field treatment process is that if the voltage bias applied during the treatment stage is not removed before cooling, the performance of the polymer light emitting devices significantly degrades. Therefore, the wire connection between the voltage supply and the polymer junctions

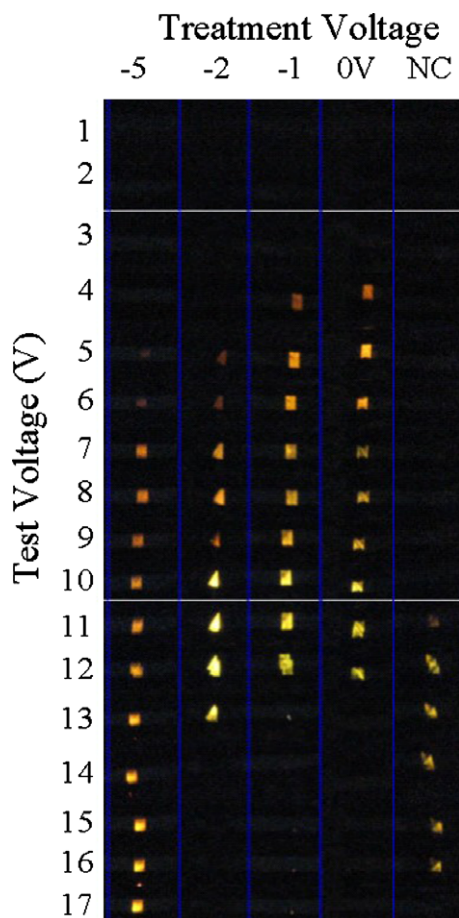


Fig. 6. Pictures of PLED samples, which are electrically treated with different voltages, taken at the given test voltages.

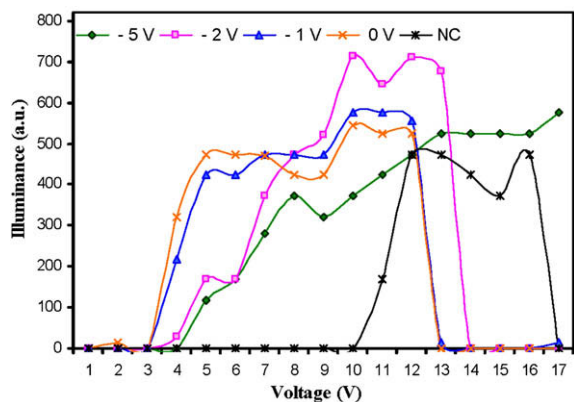


Fig. 7. Electroluminescence responses of the devices treated with various voltage levels.

must be opened before the cooling stage begins. Although the reason for this behavior is still under investigation, we believe that the molecular arrangement of the polymeric chains may be disturbed by the applied electric field when the temperature is under the  $T_g$  (65 °C) of MEH-PPV

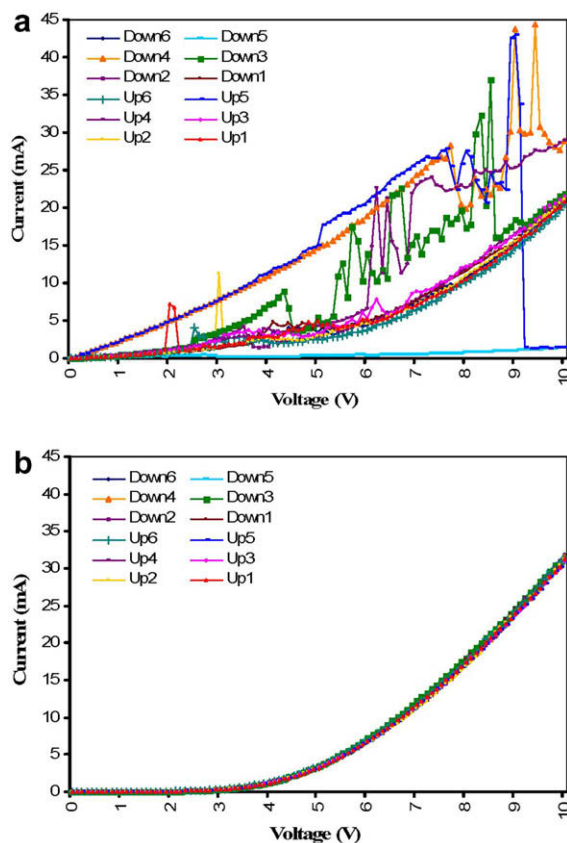
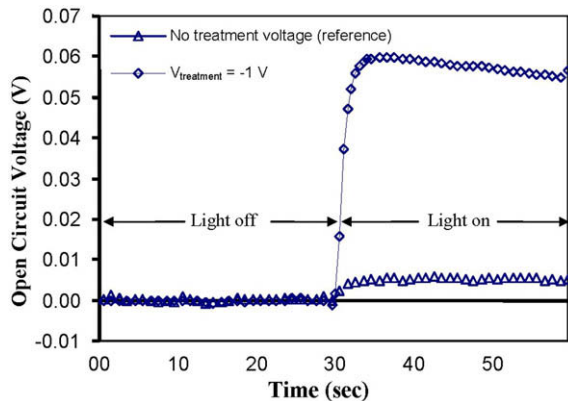


Fig. 8. (a)  $I$ - $V$  sweep measurement of a heat treated (130 °C) but not electrically treated sample and (b)  $I$ - $V$  sweep measurement of a heat treated (130 °C) and electrically treated (-1 V) sample.

( $M_n = 400,000$ ,  $M_w = 626,000$ ) [27] but is above the  $T_g$  (40 °C) of PEDOT:PSS [29].

The photovoltaic responses of PLEDs are tested by measuring open circuit voltages and short circuit currents in a dark environment, as well as under the light of a solar simulator with a light intensity of 500 W/m<sup>2</sup>. Figs. 9 and 10 show the transient responses of the devices in the dark environment when exposed to the light under the solar simulator. The measured open circuit voltage of the heat treated but not electrically treated PLED is noisy and its average value when the device is exposed to the light is indistinguishable. However, the output voltage of the polymer device that is treated with both the heat and electric field treatments is stabilized at a certain level and its average value (55 mV for -1 V treatment) is an order of magnitude higher than the electrically untreated (heat treated but not electric field treated) ones (5 mV) as shown in Fig. 9. Similar to the open circuit voltage characteristics, short circuit currents are enhanced significantly after the electric field treatment (Fig. 10). Without electric field treatment, the short circuit response of the devices when exposed to the light can not be distinguished from the dark response. Unstable output fluctuates between 1 and -1 nA with a rough average estimate of 0.5 nA. However, for the devices treated with an electric field, the intensity of the



**Fig. 9.** Transient photovoltaic responses of PLEDs in the dark when they are exposed to a light with an intensity of  $500 \text{ mW/m}^2$ , showing the effect of electric field treatment on the open circuit voltages.

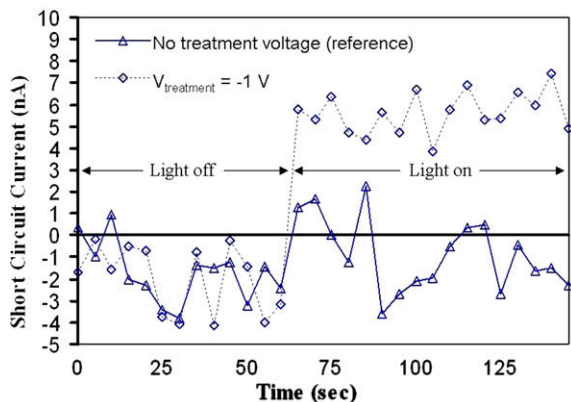


**Fig. 10.** Transient photovoltaic responses of PLEDs in the dark when they are exposed to a light with an intensity of  $500 \text{ mW/m}^2$ , showing the effect of electric field treatment on the short circuit currents.

light on the devices can be easily detected from their short circuit response (5 nA for  $-1 \text{ V}$  treatment).

The average open circuit voltages and average short circuit currents obtained from electric field treated samples are strongly dependent on the treatment voltages. Moreover, the heat treatment alone is not sufficient to allow PLEDs work as photovoltaic cells. Therefore, the average and standard deviation of the photovoltaic responses of the devices, which were treated at different voltage levels, are measured as shown in Fig. 11. The responses of the devices that were not treated with electric fields when exposed to light are not detectable. Furthermore, the results from devices in different batches vary significantly. On the other hand samples treated with  $-1 \text{ V}$  or  $-2 \text{ V}$  are very stable, and their electrical responses are easily measurable. It is worth mentioning that electric field treatment, which improves the light emitting operation of PLEDs as shown previously in Figs. 6 and 7, improves their photovoltaic operation as well. These results are significant as they show that when the correct electric field treatment is applied to PLEDs after fabrication, they can also be used as photovoltaic cells.

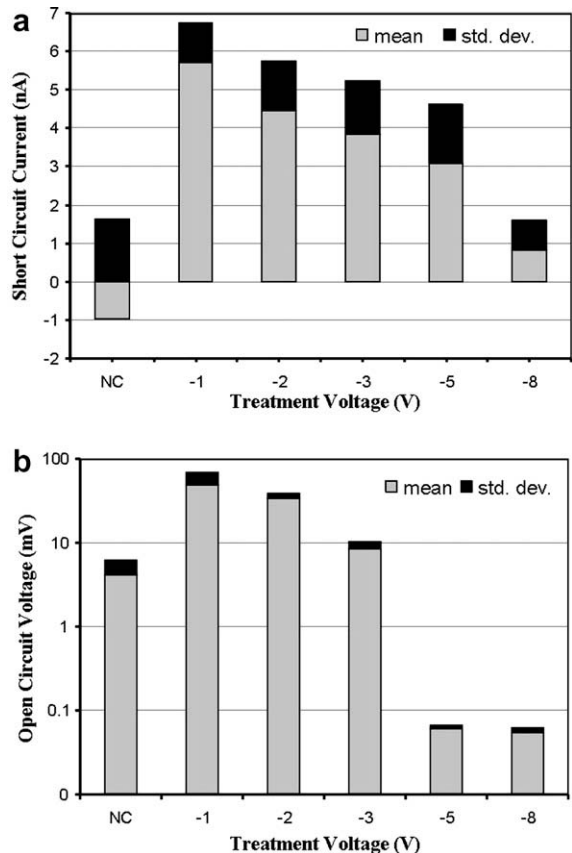


**Fig. 11.** Average values and standard deviations of (a) short circuit currents and (b) open circuit voltages of the photovoltaic responses of PLEDs under light intensity of  $500 \text{ mW/m}^2$  after different treatments.

The light emitting property of a PLED can be restored by the use of a heat treatment step alone because the heat treatment removes most of oxygen and water vapors absorbed by the PLED during fabrication. Further improvement of both the light emitting and photovoltaic functions of a PLED by the electric field treatment after heat treatment can be explained by the diode like molecular reorientation caused by the applied electric field as discussed in [30]. Electric field treatment above the glass transition temperatures of the polymers orients the polar molecules, improving molecular order. In this way, the barrier height between the polymers and electrodes is reduced for charge injection or extraction. This treatment also enhances charge mobility. Molecular order improvement, barrier height reduction, and charge mobility improvement after the application of an electric field treatment are shown to occur in [30]. In this case, the field is applied to a single polymer layer sandwiched between two aluminum layers at a temperature above the glass transition temperature. The improvement in the performance of polymer solar cells of ITO/PEDOT:PSS/MEH-PPV:C<sub>60</sub>/Al discussed in [21] due to the thermal treatment under reverse bias electric field treatment is also explained by the modified and ordered orientation of the active polymer chains due to the applied electric field. The work in [21] also claims that the treatment increases



the mobility of charge carriers. Similarly, above the glass transition temperatures, the polymer chains in the polymer layers of our devices become mobile. They are reoriented by the applied electric field resulting in more uniform structures. This new arrangement improves the chemical bonds between interfacial junctions and lowers the contact resistances and voltage barriers. Since the newly oriented polymer devices are cooled and packaged in these conditions, the molecules remain oriented. As evident from the sweep experiments shown in Fig. 8, this orientation remains stable during device operation.

Based on this explanation, it may be assumed that applying a zero bias voltage treatment does not form an electric field inside the polymer devices, and thus it should not improve the performance of the devices, contradicting our results. However, when a zero external bias voltage is applied to these devices, any diode, or any LED, a built-in electric field is formed across the junctions resulting in a built-in or junction potential. This built-in (intrinsic) electric field under zero bias orients polar molecules during electric field treatment, improving junction properties. This also explains why reverse bias treatments improve the device performance whereas the forward bias treatments do not. Applied reverse biases contribute to this built-in electric field, creating higher electric fields in the junction and orienting the molecules more effectively. However, forward biases reduce this built-in electric field. Thus, they do not improve the junction properties.

The results also show that reverse bias treatments up to certain voltages (0 and  $-1$  V) work more effectively than higher bias voltages. Above these voltages, even though the electric field treatment still improves the device performance, the rate of improvement decreases. This can be explained by the diffusion of anodic and cathodic materials into the polymers due to heat and the increase of their penetration thicknesses due to electric fields, which has been previously reported in [31]. Elevated electric fields increase the electrochemical reactions (oxidation–reduction) of the electrodes. Accelerated oxidation of electrodes, resulting from the high electric fields under reverse bias, and the diffusion of this oxide into the polymer layers can create barrier layers inside polymers. As a result, these barrier layers increase turn-on voltages and deteriorate the uniformity of the light emitting surfaces of the devices. Therefore, treatment voltages up to a threshold produce an obvious and long term improvement in both electroluminescent and photovoltaic response of PLEDs.

#### 4. Conclusions

In this work, the effect of post-fabrication heat treatment alone and heat treatment coupled with an electric field treatment on the performance of PLEDs has been investigated. PLEDs have been completely fabricated under ambient atmosphere without taking any preventive measures against exposure to oxygen and water vapors. This way, the fabrication is simplified and the cost is reduced. Heat treatment is performed at  $130$  °C, which is above the glass transition temperatures ( $T_g$ ) of MEH-PPV and PEDOT:PSS, for one hour and electric field treatment is per-

formed afterwards with voltage levels from 0 to  $-8$  V. Heat treatment after fabrication, followed by packaging under the same conditions, restores the light emitting properties of otherwise dysfunctional PLEDs. It removes the absorbed oxygen and water vapors inside the devices, restoring their functionality.

Reverse biased electric field treatment after heat treatment is applied to PLEDs based on MEH-PPV and PEDOT:PSS for the first time in this work. Electric field treatment performed after heat treatment lowers the turn-on voltage levels and the voltage levels at which PLEDs reach their maximum luminescence, when used as light emitting devices. The turn-on voltage of a PLED drops to 3 V when treated with a reverse bias voltage of  $-1$  V in comparison to 10 V when treated with heat and no bias voltage. Reverse biased electric field treatment increases the average short circuit current and open circuit voltage of the photovoltaic response of PLEDs by an order of magnitude compared to devices treated with heat only. Using a light intensity of  $500$  mW/m<sup>2</sup> in the photovoltaic measurements, a 5 mV open circuit voltage and a 0.5 nA short circuit current after heat treatment improve to 55 mV and 5 nA, respectively after an electric field treatment with  $-1$  V. Furthermore, the uniformity and stability of the light emitting surface increases significantly after electric field treatment, as evident from repeated  $I$ - $V$  sweep measurements.

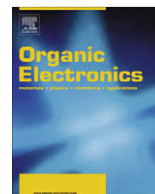
#### Acknowledgements

This work has been fully supported by Scientific and Technological Research Council of Turkey (TUBITAK) under the project INPOMIS-INtegrated Polymer Micro Systems, Project Number 106E013. It is also supported by Bogazici University Research Fund under Project Number 08A201.

#### References

- [1] J.H. Burroughes, D.D.C. Bradley, A.R. Brown, R.N. Marks, K. Mackay, R.H. Friend, P.L. Burns, A.B. Holmes, Light-emitting diodes based on conjugated polymers, *Nature* 347 (6293) (1990) 539–541.
- [2] J. Krumm, E. Eckert, W.H. Glauert, A. Ullmann, W. Fix, W. Clemens, A polymer transistor circuit using PDHTT, *IEEE Electron Device Letters* 25 (6) (2004) 346–361.
- [3] C.J. Drury, C.M.J. Mutsaers, C.M. Hart, M. Matters, D.M. de Leeuw, Low-cost all polymer integrated circuits, *Applied Physics Letters* 73 (1998) 108–110.
- [4] Y. Kim, K. Lee, N.E. Coates, D. Moses, T. Nguyen, M. Dante, A.J. Heeger, Efficient tandem polymer solar cells fabricated by all-solution processing, *Science* 317 (5835) (2000) 222–225.
- [5] R. Horning, B. Johnson, Polymer-based MEMS actuators for biomimetics, in: *Proceeding Neurotechnology Biomimetic Robots*, Nahant, MA, May 14–16, 2000.
- [6] C. Liu, Recent developments in polymer MEMS, *Advanced Materials* 19 (22) (2007) 3783–3790.
- [7] S. Forrest, P. Burrows, M. Thompson, The dawn of organic electronics, *IEEE Spectrum* 37 (8) (2000) 29–34.
- [8] J. Huang, X. Wang, A.J. deMello, J.C. deMello, D.D.C. Bradley, Efficient flexible polymer light emitting diodes with conducting polymer anodes, *Journal of Materials Chemistry* 17 (2007) 3551–3554.
- [9] Y. Shao, G.C. Bazan, A.J. Heeger, Long-lifetime polymer light-emitting electrochemical cells, *Advanced Materials* 19 (2007) 365–370.
- [10] D. Zou, M. Yahiro, T. Tsutsui, Spontaneous and reverse-bias induced recovery behavior in organic electroluminescent diodes, *Applied Physics Letters* 72 (1998) 2484–2486.
- [11] M. Atreya, S. Lia, E.T. Kanga, K.G. Neoha, Z.H. Mab, K.L. Tanb, W. Huangc, Stability studies of poly(2-methoxy-5-(2'-ethyl hexyloxy)-*p*-(phenylene vinylene) [MEH-PPV], *Polymer Degradation and Stability* 65 (2) (1999) 287–296.

- [12] A. Petr, F. Zhang, H. Peisert, M. Knupfer, L. Dunsch, Electrochemical adjustment of the work function of a conducting polymer, *Chemical Physics Letters* 385 (January) (2004) 140–143.
- [13] Z.Y. Zhong, Y.D. Jiang, Surface modification and characterization of indium tin oxide for organic light-emitting devices, *Journal of Colloid and Interface Science* 302 (August) (2006) 613–619.
- [14] C. Tengstedt, A. Kancierzewska, M.P. de Jong, S. Braun, W.R. Salaneck, M. Fahlman, Ultraviolet light-ozone treatment of poly(3,4-ethylenedioxy-thiophene)-based materials resulting in increased work functions, *Thin Solid Films* 515 (4) (2006) 2085–2090.
- [15] J. Morgado, R.H. Friend, F. Cacialli, Environmental aging of poly(*p*-phenylenevinylene) based light-emitting diodes, *Synthetic Metals* 114 (2) (2000) 189–196.
- [16] H. Jin, Y. Hou, X. Meng, Y. Li, Q. Shi, F. Teng, Enhanced photovoltaic properties of polymer-fullerene bulk heterojunction solar cells by thermal annealing, *Solid State Communications* 142 (2007) 181–184.
- [17] M. Suzuki, T. Hatakeyama, S. Tokito, F. Sato, High-efficiency white phosphorescent polymer light-emitting devices, *IEEE Journal of Selected Topics in Quantum Electronics* 10 (1) (2004) 115–120.
- [18] J. Huang, T. Watanabe, K. Ueno, Y. Yang, Highly efficient red emission polymer phosphorescent lighting emitting diodes based on two novel Ir(piq)<sub>3</sub> derivatives, *Advanced Materials* 19 (5) (2007) 739–743.
- [19] G. Xiong, J.C. Ostrowski, D. Moses, G.C. Bazan, A.J. Heeger, High-performance polymer-based electrophosphorescent light-emitting diodes, *Journal of Polymer Science, Part B (Polymer Physics)* 41 (21) (2003) 2691–2705.
- [20] F. Padinger, R.S. Rittberger, N.S. Sariciftci, Effects of postproduction treatment on plastic solar cells, *Advanced Functional Matter* 13 (1) (2003).
- [21] Y. Li, Y. Hou, Y. Wang, Z. Feng, B. Feng, L. Qin, F. Teng, Thermal treatment under reverse bias: Effective tool for polymer/fullerene bulk heterojunction solar cell, *Synthetic Metals* 158 (5) (2008) 190–193.
- [22] D. Ma, J.M. Lupton, R. Beavington, P.L. Burn, I.D.W. Samuel, Improvement of luminescence efficiency by electrical annealing in single-layer organic light-emitting diodes based on a conjugated dendrimer, *Journal of Physics D: Applied Physics* 35 (2002) 520–523.
- [23] M. Yahiro, D. Zou, T. Tsutsui, Recoverable degradation phenomena of quantum efficiency in organic EL devices, *Synthetic Metals* 111–112 (2000) 245–247.
- [24] T.-W. Lee, O.O. Park, Effect of electrical annealing on the luminous efficiency of thermally annealed polymer light-emitting diodes, *Applied Physics Letters* 77 (21) (2000) 3334–3336.
- [25] M. Jung, H. Choi, Surface treatment and characterization of ITO thin films using atmospheric pressure plasma for organic light emitting diodes, *Journal of Colloid and Interface Science* 310 (2007) 550–558.
- [26] Z. You, J. Dong, S. Fang, Surface modification of indium-tin-oxide anode by oxygen plasma for organic electroluminescent devices, *Physica Status Solidi A* 201 (14) (2004) 3221–3227.
- [27] T.-W. Lee, O. Park, The effect of different heat treatments on the luminescence efficiency of polymer light-emitting diodes, *Advanced Materials* 12 (11) (2000) 801–804.
- [28] I.D. Parker, Carrier tunneling and device characteristics in polymer light-emitting diode, *Journal of Applied Physics* 75 (3) (1994) 1656–1666.
- [29] Flexographic ink containing a polymer or copolymer of a 3,4-dialkoxythiophene, US Patènt 6890584, Agfa-Gevaert (Mortsel, BE), Appl. No. 175948, June 20, 2002.
- [30] C. Sentein, C. Fiorini, A. Lorin, J.M. Nunzi, Molecular rectification in oriented polymer structures, *Advanced Materials* 9 (10) (1997) 809–811.
- [31] D.E. Gallardo, C. Bertoni, S. Dunn, N. Gaponik, A. Eychmuller, Cathodic anodic material diffusion in polymer/semiconductor-nanocrystal composite devices, *Advanced Materials* 19 (20) (2007) 3364–3367.



## Annealing effect of polymer bulk heterojunction solar cells based on polyfluorene and fullerene blend

Jen-Hsien Huang<sup>a</sup>, Chuan-Yi Yang<sup>b</sup>, Zhong-Yo Ho<sup>c</sup>, Dhananjay Kekuda<sup>d</sup>, Meng-Chyi Wu<sup>b</sup>, Fan-Ching Chien<sup>d</sup>, Peilin Chen<sup>d</sup>, Chih-Wei Chu<sup>d,e,\*</sup>, Kuo-Chuan Ho<sup>a,c,\*</sup>

<sup>a</sup> Department of Chemical Engineering, National Taiwan University, Taipei, Taiwan

<sup>b</sup> Institute of Electronic Engineering, National Tsing Hua University, Hsinchu, Taiwan

<sup>c</sup> Institute of Polymer Science and Engineering, National Taiwan University, Taipei, Taiwan

<sup>d</sup> Research Center for Applied Sciences, Academia Sinica, Taipei, Taiwan

<sup>e</sup> Department of Photonics, National Chiao Tung University, Hsinchu, Taiwan

### ARTICLE INFO

#### Article history:

Received 18 July 2008

Received in revised form 19 September 2008

Accepted 20 September 2008

Available online 10 October 2008

#### PACS:

73.50.Pz

73.61.Ph

#### Keywords:

Photovoltaic device

Polymer

F8T2

Annealing effect

### ABSTRACT

Control of blend morphology at the nanoscale and high charge mobility is essential for polymer photovoltaic devices in terms of their power conversion efficiencies (PCE). In the case of bulk heterojunction solar cells, both blend morphology and charge mobility are influenced by thermal treatment. In this manuscript, we study the effects of annealing temperature on polymer PV devices with blends of poly[9,9'-dioctyl-fluorene-co-bithiophene] (F8T2) and [6,6]-phenyl-C<sub>61</sub>-butyric acid methyl ester (PCBM). The morphological changes of blended films were observed upon thermal annealing temperature near and above glass transition temperature (130 °C). Such microstructural transformations resulted in modified charge transport pathways and therefore greatly influenced the device performance. The highest PCE of 2.14% with an open-circuit voltage ( $V_{OC}$ ) of 0.99 V and a short-circuit current ( $J_{SC}$ ) of 4.24 mA/cm<sup>2</sup> was achieved by device annealing at 70 °C for 20 min.

© 2008 Elsevier B.V. All rights reserved.

### 1. Introduction

Polymer photovoltaic (PV) cells offer great technological potential as a renewable, alternative source of electrical energy including the possibility of low-cost fabrication, low specific weight, and mechanical flexibility. Since solution processed bulk heterojunction (BHJ) solar cells were first reported in mid-1990s, they have been the subject of

intense research interests due to their processing advantage as well as the superior mechanical properties of the polymers, such as flexibility. Although the BHJ provides quite a large interface for charge separation, the power conversion efficiency (PCE) is still limited by the space-charge effects inherent in the BHJ structure due to the imbalance between electron ( $\mu_e$ ) and hole mobility ( $\mu_h$ ) and the unfavorable morphology [1,2]. Regioregular poly(3-hexylthiophene) (P3HT) and [6,6]-phenyl C<sub>61</sub>-butyric acid methyl ester (PCBM) blend is one of the most promising candidates for realizing high power conversion efficiency (PCE) because P3HT possesses some unique properties over other polymers including its high self-organization capability [3,4], high hole mobility, and extended absorption in the red region of the electromagnetic

\* Corresponding authors. Address: Research Center for Applied Sciences, Academia Sinica, Taipei, Taiwan. Tel.: +886 2 27898000(x)70; fax: +886 2 27826680 (C.-W. Chu), tel.: +886 2 23660739; fax: +886 2 23623040 (K.-C. Ho).

E-mail addresses: [gchu@gate.sinica.edu.tw](mailto:gchu@gate.sinica.edu.tw) (C.-W. Chu), [kcho@ntu.edu.tw](mailto:kcho@ntu.edu.tw) (K.-C. Ho).

spectrum. Various independent approaches have been demonstrated to improve the PCE of blends consisted P3HT and PCBM. These approaches include thermal annealing [5], post-fabrication annealing at high temperature [6], and slow film growth by controlling the solvent evaporation rate of the active layer which resulted in the reduced series resistance and improved optical absorption of the devices. Subsequent annealing of the PV cells at a high temperature promotes the aggregation of PCBM which forms bi-continuous pathways in the entire active layer with the ordered P3HT phase and enhances efficient charge separation and transport. The slow solvent evaporation speed facilitates the growth of a highly crystalline film, interchain interactions become stronger and thus improve the electroconductivities, significantly [7]. These efficient enhancements are based on the unique chemical structure of P3HT. It crystallizes along its moderately long alkyl group at the 3-position and forms a more ordered structure leading to higher charge mobilities. Subsequently, an entirely positive effect in terms of solar cell efficiency has been reported due the smaller  $\mu_h$  compared with  $\mu_e$  in the blend in generally.

Recently, a group of polymers that works well in solar cells is an alternating copolymer based on fluorene. Polyfluorene copolymers are well known for their high charge

carrier mobility, good processability, and high absorption coefficients. The physical properties of polyfluorene derivatives can be easily tuned through the design of various alternating copolymers. Currently, PCE approaching 3.5–5.5% have been reported by several groups for organic PV devices based on blend films of polyfluorene copolymers and PCBM [8–10]. These results indicate that the PV cells based on polyfluorene copolymers are good candidates for conversion solar energy into electricity. However, the annealing and slow growth effects on the polymer based on fluorene copolymer is still not clear. The fluorene-bithiophene copolymer, poly[9,9'-dioctyl-fluorene-co-bithiophene] (F8T2) reveals good hole transporting properties [11] and excellent thermotropic liquid crystallinity [12–15]. It has also well been explored in the area of organic field-effect transistors, with good hole transporting properties [16]. On the basis of the result, it can be expected that the charge transport in F8T2:PCBM is strongly balanced. Therefore, it appears to be one of the most promising candidates among the conjugated polymers for high efficiency polymer solar cell. In this manuscript, we fabricate PV devices based on F8T2 and PCBM. We demonstrate the annealing effect on F8T2:PCBM devices through the nano-scale morphology aspect and clarify how it influences the associated PV performance.

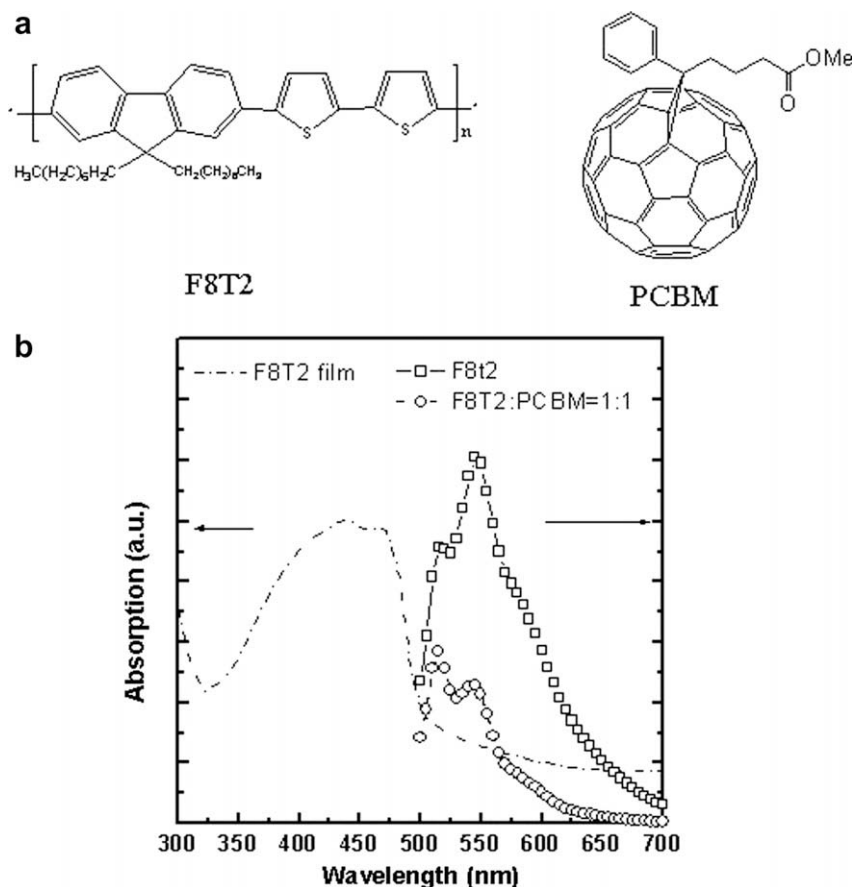


Fig. 1. (a) Chemical structure of F8T2, PCBM (b) absorption and photoluminescence spectra of pristine F8T2 and blend.

## 2. Experimental

The polymer PV cells in this study consists of a layer of F8T2:PCBM blend thin film sandwiched between transparent anode indium tin oxide (ITO) and metal cathode. Before device fabrication, the ITO glasses ( $1.5 \times 1.5 \text{ cm}^2$ ) were ultrasonically cleaned in detergent, de-ionized water, acetone and isopropyl alcohol before the deposition. After routine solvent cleaning, the substrates were treated with UV ozone for 15 min. Then a modified ITO surface was obtained by spin-coating a layer of poly(ethylene dioxythiophene): polystyrenesulfonate (PEDOT:PSS) ( $\sim 30 \text{ nm}$ ). Subsequently, the active layer of F8T2:PCBM (1:1 w/w) was spin coated from 1,2,4-trichlorobenzene (TCB) on the PEDOT:PSS modified ITO surface. Finally, 30 and 100 nm thick calcium and aluminium were thermally evaporated under vacuum at a pressure below  $6 \times 10^{-6}$  Torr through a shadow mask. The active area of the device was  $0.12 \text{ cm}^2$ .

Heavily doped p-type silicon ( $p^+$ -Si) wafer and a 300 nm thermally oxidized  $\text{SiO}_2$  film were used as the gate and dielectric for the F8T2-based field-effect transistors (FETs). The substrates were cut to  $1.5 \text{ cm} \times 1.5 \text{ cm}$  in size through mechanical scribing. Prior to the deposition, the substrates were cleaned by acetone and isopropanol in an ultrasonic bath followed by UV–ozone cleaning for 15 min. The semiconductor layer F8T2 was prepared by spin-coating a solution of F8T2 (2 wt%) in TCB at 2500 rpm and with a thickness of around 110–130 nm. The F8T2 film was baked at different annealing temperature 70–250 °C for 30 min to remove the residual solvent. Finally, the 50 nm thick gold film was thermally evaporated onto the F8T2 film through a shadow mask to form the source/drain electrodes.

The solar cell testing was done inside a glove box under simulated AM 1.5 G irradiation ( $100 \text{ W/cm}^2$ ) using a Xenon lamp based solar simulator (Thermal Oriel 1000 W). The electrical measurements of the F8T2 based FETs were also performed at room temperature in a nitrogen environment inside a glove box by using HP 4156C. The absorption and photoluminescence (PL) spectra were obtained from Jasco-V-670 UV–visible spectrophotometer and Hitachi F-4500, respectively. Surface morphology and cross sections of thin films images were obtained using atomic force microscopy (AFM, Digital instrument NS 3a controller with D3100 stage) and scanning electron microscopy (SEM, Hitachi S-4700), respectively. X-ray diffraction (XRD) studies were performed by Philips X'Pert/MPD. Fluorescence lifetime signal was measured by the confocal laser scanning microscope (FV300, Olympus Corporation Inc.) with a configuration of PCI-board for time-correlated single photon counting (TimeHarp 200, PicoQuant GmbH) combined a detector of single photon avalanche diode (PDM series, PicoQuant GmbH). Excitation light source was 470 nm of pulse diode laser (LDH-P-C-470, PicoQuant GmbH) and acquisition time for each lifetime signal was 5 s.

## 3. Results and discussion

Fig. 1a shows the chemical structure of F8T2 and PCBM. The UV–visible absorption and PL emission spectra of pristine F8T2 and their blend films with PCBM are shown in

Fig. 1b. The F8T2 film absorption peak is at 460 nm with a shoulder at 490 nm. The onset of the absorption occurred at 520 nm, from which the band gap was estimated to be approximately 2.4 eV. Based on cyclic voltamperometry measurements reported previously, the highest occupied molecular orbital (HOMO) level and lowest unoccupied molecular orbital (LUMO) of the polymer can be estimated at the onset point [17]. Therefore, the HOMO and LUMO levels are estimated to be 5.5 and 3.1 eV, respectively. It can be seen the band gap offset between the LUMOs of donor and acceptor is enough for electrons to be driven forward from the energy level diagram. The solid-state photoluminescence (PL) of the polymer lies near the green region with a maximum of emission at 545 nm with a vibrotic feature at 515 and 585 nm. The PL emission is significantly quenched by the addition of 50 wt% PCBM. This highly efficient photoluminescence quenching is the consequence of ultrafast photoinduced charge transfer from the polymer to PCBM.

Side view cross-sections of the films for annealing at 100 and 250 °C are shown in Fig. 2. The nanodomains are embedded within the F8T2:PCBM films. The nanodomains

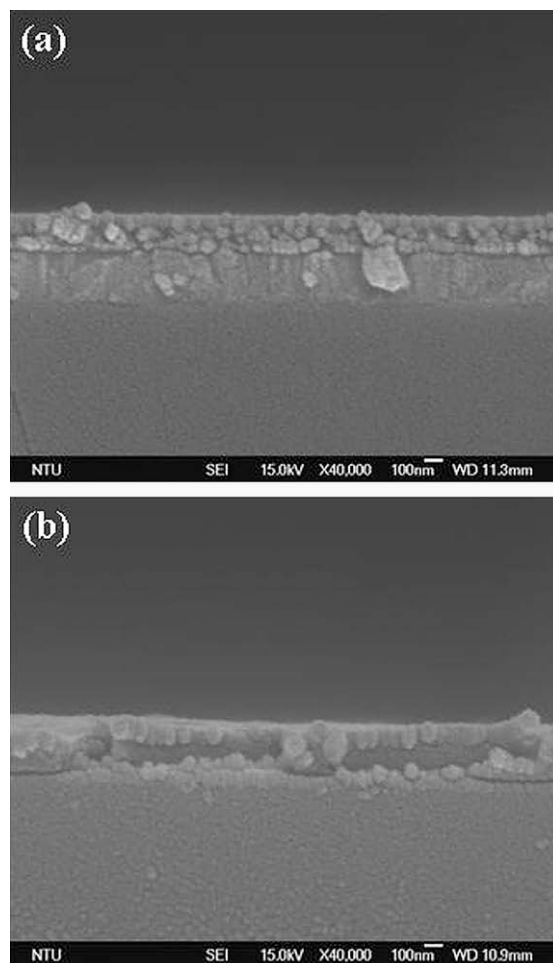


Fig. 2. SEM side views of F8T2:PCBM blend films cast from TCB annealed at (a) 100 °C (b) 250 °C.

under different annealing temperatures with diameters increased from 30–40 (100 °C) to 70–80 nm (250 °C) are assigned to the F8T2 with a coil structure formed by several polymer chains. This means the F8T2 polymer chains tend to crystallize after annealing at high temperature. The nanodomains are dispersed within the film annealed at 100 °C. Therefore, the F8T2 nanodomains and PCBM clusters are well-mixed which can achieve bi-continuous pathways in the entire layer for efficient charge separation and transport. However in the case of film annealed at 250 °C, much larger PCBM clusters can be seen. The PCBM clusters are surrounded by the polymer nanoparticles. It is expected that much of the photoexcitations will lead to recombine within the surrounding F8T2 layer. A similar result was also found for the blends based on poly[2-methoxy-5-(3,7-dimethyloxy)-1,4-phenylenevinylene (MDMO-PPV) and PCBM [18,19]. The reorganization of the F8T2 nanodomains under different annealing temperatures can be further confirmed by the observation of the surface morphology. Fig. 3 presents the AFM images for the as-cast film and the ones with thermal annealing. For the as-cast film, the surface is very smooth with a root mean square (RMS) roughness of 0.55 nm. However after undergoing thermal treatment at 130, 190 and 250 °C for 30 min, the RMS roughness increased to 0.91, 1.98 and 6.73 nm. The film without thermal annealing reveals an uniform and featureless morphology. With increasing the annealing temperature, the chain-like morphology running across the surfaces forms gradually. The features are the domains of pristine F8T2 crystallites originated from the highly

tight stack of several polymer chains. For the case of annealing at 250 °C, the formation of lamella-like crystallites can be observed. The crystallites are similar to those of P3HT with the *a*-axis orientation (backbone parallel and side-chains perpendicular to the substrate) [20].

Fig. 4 shows the UV-vis and PL emission spectra under various annealing temperatures. The films annealed at the temperatures higher than 130 °C show an increase and red-shift in the UV-vis absorption. Such shifts have been observed for conjugated polymers with a strong interchain interaction [7]. The thermal annealing process enables spatial rearrangement of the polymer chains leading to a tight stacking and a strong interchain interaction. Although a higher extraction of photocurrent can be expected in the case of strong absorption. PL emission spectra also show an increase after thermal annealing. That means the photo-induced charge tends to recombine before transporting to the electrodes. This can be well explained by the SEM cross sectional images as shown in Fig. 2. The F8T2 nanodomains are dispersed in the whole film annealed at 100 °C which forms percolated pathway for electrons and holes to transport. However in the case of blend annealed at higher temperatures, the PCBM clusters are surrounded by the F8T2 nanodomains offering an inappropriate morphology for charge transport. Therefore, most of the photogenerated holes simply recombine with electrons which transport through the polymer-rich matrix phase leading to a higher emission. XRD shows that structural changes occur due to high temperature annealing process. An increase in crystallinity of F8T2 can be seen clearly in

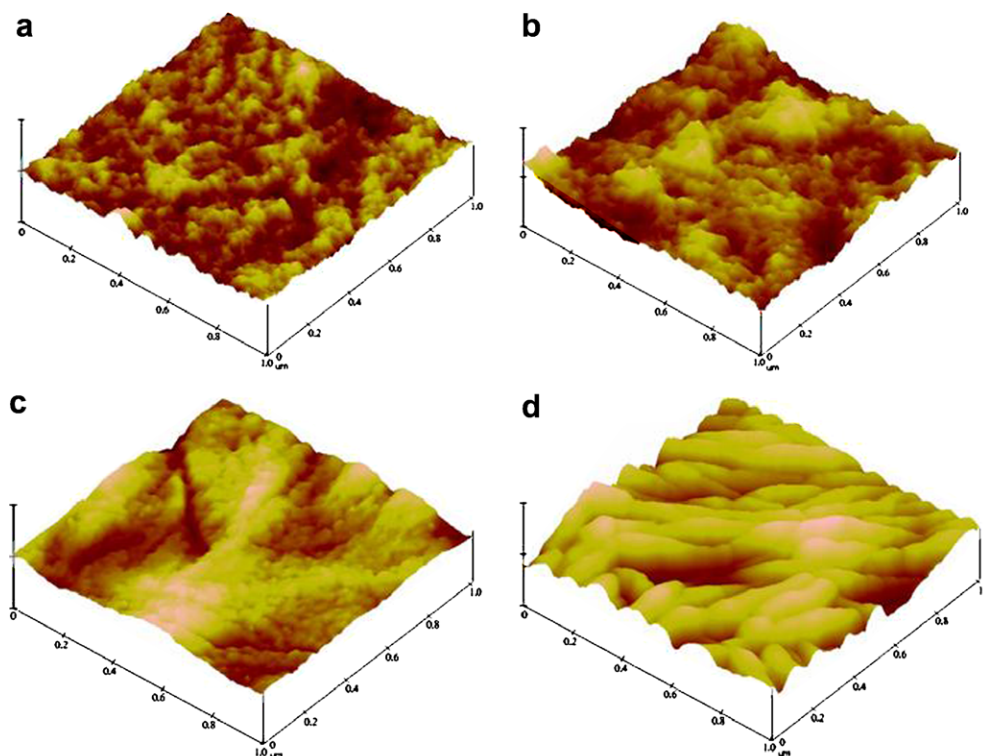


Fig. 3. AFM images of the blending films in various annealing temperature (a) as-cast film (b) 130 °C (c) 190 °C (d) 250 °C.

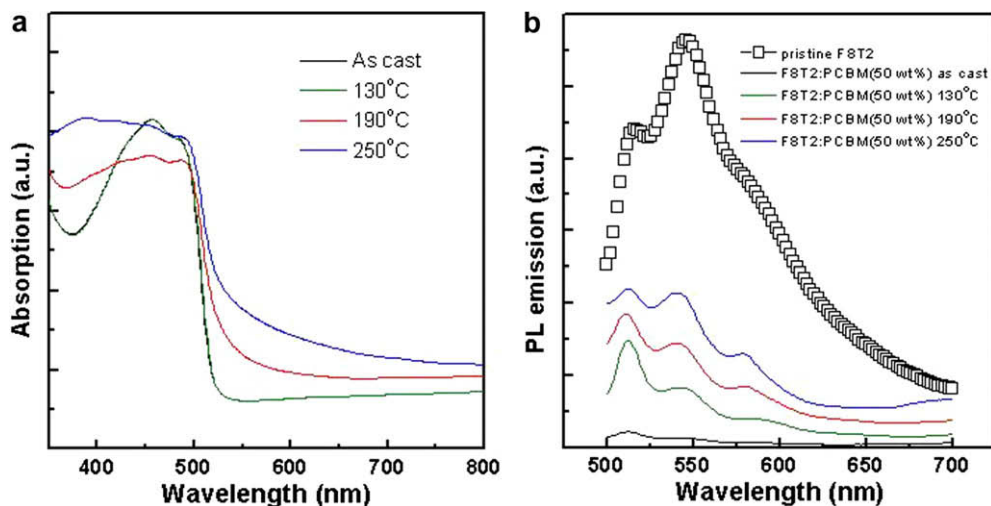


Fig. 4. (a) Absorption and (b) photoluminescence spectra of the blends annealed at different temperatures.

the results shown in Fig. 5. X-ray data show that prior to heating, the F8T2 is in a disordered state. Increased intensity is observed with increasing annealing temperature in the peak at  $2\theta \approx 5.7$  which corresponds to the layering distance,  $d_{100} = \text{\AA}$ , between the sheets of F8T2 chains associated with the plane perpendicular to their longitudinal axes. The features are in good agreement with the results of AFM images. This lamella structure appears due to the

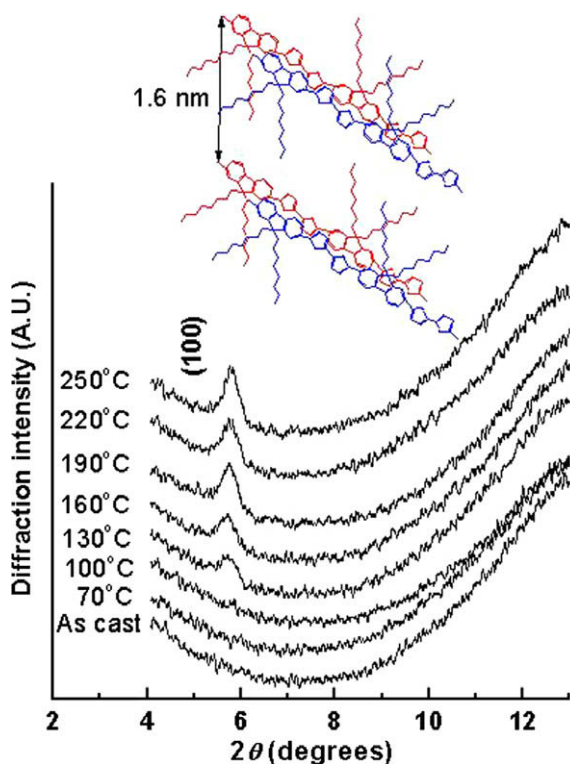


Fig. 5. XRD spectra of F8T2:PCBM films annealed at different temperatures.

segregation of main chain backbones to the aggregated alkyl side chains.

Additional evidence supporting the dependence of the crystallinity of F8T2 on the annealing temperature is provided by the observation of charge transport from field effect transistors (FETs) made with F8T2. Fig. 6 shows transfer characteristic of F8T2-based FETs at different annealing temperatures. The performance of F8T2 FETs is increased with rising up the annealing temperature. The improvement of device performance is attributed to the degree of F8T2 film crystallization which is coincident with above results. When annealing temperature is at 250 °C, the corresponding devices exhibit highest hole field effect mobility,  $2.7 \times 10^{-4} \text{ cm}^2/\text{Vsec}$ , depicting superior performance in p-channel conduction among the various annealing temperature conditions.

In order to get more careful investigation of the photo-physics in the F8T2:PCBM systems, we perform the time-resolved PL to see the exciton decay as a function of annealing temperature as shown in Fig. 7. It is found the PL life time (1.87 ns) for the blend without thermal treatment is shorter than that of the pristine F8T2 thin film (3.83 ns), indicating that the charge separation occurs at the interfaces between F8T2 and PCBM by providing a new non-radiative process for photogenerated excitons. However, the exciton life time increases with increasing the annealing temperature. This indicates the thermal process results in an unfavorable morphology. The unfavorable morphology reduces the interface between F8T2 and PCBM which is in good agreement with the SEM results as shown in Fig. 2 in the text. As the annealing temperatures increased from 70 to 250 °C, the poor morphology leads to a non-efficient charge separation and the exciton life time increases from 1.91 to 2.84 ns.

The current-voltage characteristics under illumination for PV devices that have undergone various thermal annealing are shown in Fig. 8 and the device parameters (PCE,  $V_{OC}$ ,  $J_{SC}$ , FF) are summarized in Table 1. Although the FET characteristics have shown the formation of more

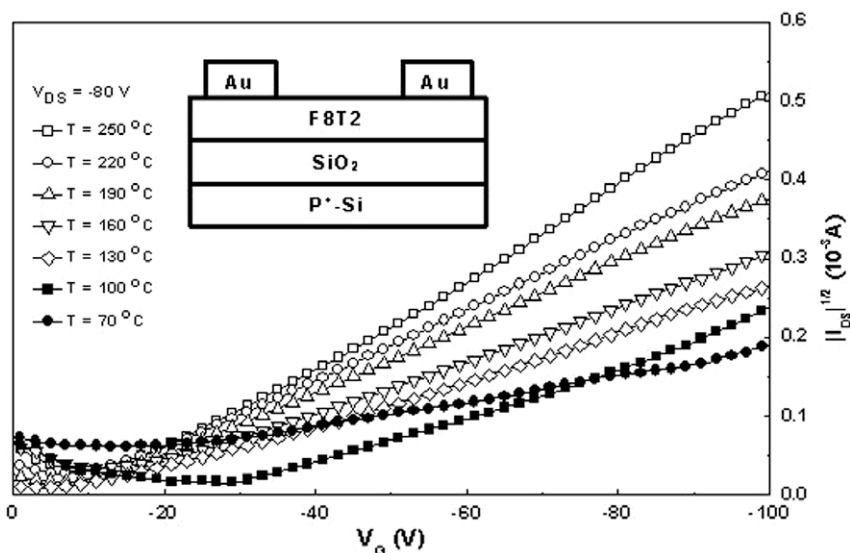


Fig. 6. Transfer characteristic of F8T2 based FETs at different annealing temperatures when drain to source voltage ( $V_{DS}$ ) is  $-80$  V. The inset is the schematic configuration of F8T2 FETs.

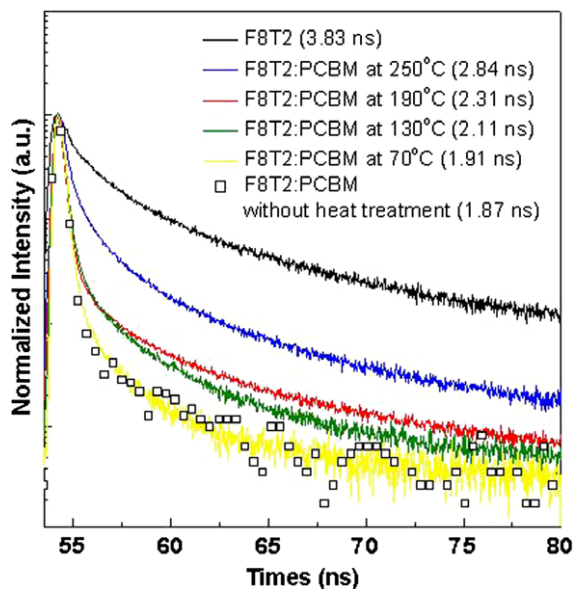


Fig. 7. Photoluminescence lifetime decay of the F8T2 and the blends annealed at various temperatures.

ordered structures in the blend by thermal treatment, thereby increasing the charge mobility, the unfavorable morphologies are also formed by the annealing process which leads to phase separation and charge recombination as shown in the SEM cross-sectional images. As a result of the influence by the two factors, it can be observed the photocurrent show an increase first and then a dramatic decrease while annealing temperature is higher than  $130$  °C. It is worthy to mention the temperature at which the values of  $J_{SC}$  and  $V_{OC}$  drop dramatically is the temperature that crystallization takes place. This means the performance of the PV devices is largely dominated by a

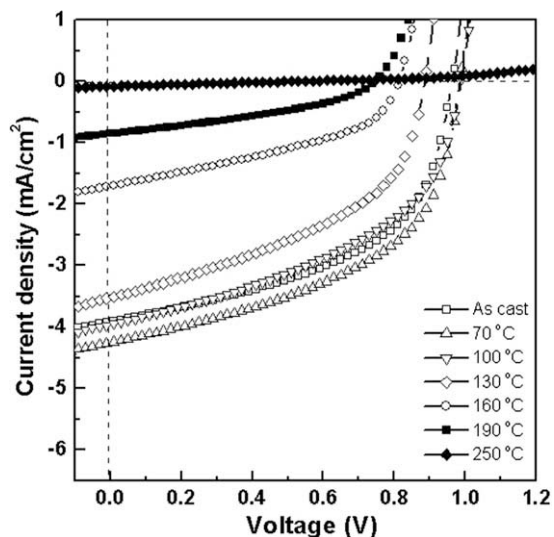


Fig. 8.  $J$ - $V$  characteristics under illumination for PV devices based on F8T2:PCBM (1:1) with different annealing temperatures.

Table 1

Short-circuit current ( $J_{SC}$ ), open circuit-voltage ( $V_{OC}$ ), fill factor (FF) and power conversion efficiency (PCE) as a function of annealing temperature for the PV devices based on F8T2:PCBM with PCBM concentration equal to 50 wt%.

Annealing temp (°C)	$J_{SC}$ (mA/cm <sup>2</sup> )	$V_{OC}$ (V)	FF (%)	PEC (%)
As-cast	3.91	0.97	51.4	1.95
70	4.24	0.99	50.8	2.13
100	3.94	0.99	46.7	1.82
130	3.51	0.89	45.4	1.42
160	1.71	0.82	40.5	0.57
190	0.85	0.75	37.0	0.23
250	0.08	0.48	22.0	0.01



favorable morphology and not a higher charge mobility in the F8T2:PCBM system. This results quite differ from the case in P3HT:PCBM. Several researches have been shown independently a positive effect on solar cell performance with the thermal treatment [21–23]. The best device performance was obtained at 70 °C, and the values were  $J_{SC} = 4.24 \text{ mA/cm}^2$ ,  $V_{OC} = 0.99$ ,  $FF = 0.51$ , and  $PCE = 2.14\%$  with 50 wt% PCBM cast from TCB.

#### 4. Conclusion

In conclusion, the F8T2:PCBM blends with thermal annealing at various temperatures leads to a tunable hole mobility. Our results demonstrate that the phase separation plays a more significant role than the one of charge mobility in terms of solar cell performance. Based on the results, too high annealing temperature is unfavorable to the performance of PV devices. Consequently, the optimal annealing temperature appears to be 70 °C and the PCE up to 2.14% can be obtained.

#### Acknowledgements

The authors are also grateful to the National Science Council (NSC), Taiwan, (NSC 97-2120-M-002-012 and NSC 96-2221-E-001-017-MY2) and Academia Sinica Research Program on Nanoscience and Nanotechnology for financial support.

#### References

- [1] C. Goh, R.J. Kline, M.D. McGehee, E.N. Kadnikova, J.M.J. Frechet, *Appl. Phys. Lett.* 86 (2005) 122110.

- [2] V.D. Mihailetchi, J.K.J. van Duren, P.W.M. Blom, J.C. Hummelen, R.A.J. Janssen, J.M. Kroon, M.T. Rispens, W.J.H. Verhees, M.M. Wienk, *Adv. Funct. Mater.* 13 (2003) 43.
- [3] M. Campoy-Quiles, T. Ferenczi, T. Agostinelli, P.G. Etchegoin, Y. Kim, T.D. Anthopoulos, P.N. Stavrinou, D.D.C. Bradley, J. Nelson, *Nat. Mater.* 7 (2008) 158.
- [4] V. Shrotriya, Y. Yao, G. Li, Y. Yang, *Appl. Phys. Lett.* 89 (2006) 063505.
- [5] F. Padinger, R.S. Rittberger, N.S. Sariciftci, *Adv. Funct. Mater.* 13 (2003) 85.
- [6] A.K. Pandey, J.M. Nunzi, H. Wang, C.C. Oey, A.B. Djurišić, M.H. Xie, Y.H. Leung, K.K.Y. Man, W.K. Chan, *Org. Electron.* 8 (2007) 396.
- [7] G. Li, V. Shrotriya, J. Huang, Y. Yao, T. Mariarty, K. Emery, Y. Yang, *Nat. Mater.* 4 (2005) 864.
- [8] K.G. Jespersen, F. Zhang, A. Gadisa, V. Sundström, A. Yartsev, O. Inganäs, *Org. Electron.* 7 (2006) 235.
- [9] A. Gadisa, W. Mammo, L.M. Andersson, S. Admassie, F. Zhang, M.R. Andersson, O. Inganäs, *Adv. Funct. Mater.* 17 (2007) 3836.
- [10] E.G. Wang, L. Wang, L.F. Lan, C. Luo, W.L. Zhuang, J.B. Peng, Y. Cao, *Appl. Phys. Lett.* 92 (2008) 033307.
- [11] J. Boucle, P. Ravirajan, J. Nelson, *J. Mater. Chem.* 17 (2007) 3141.
- [12] J. Jo, D. Vak, Y.Y. Noh, S.S. Kim, B. Lim, D.Y. Kim, *J. Mater. Chem.* 18 (2008) 654.
- [13] M.C. Gather, D.D.C. Bradley, *Adv. Funct. Mater.* 17 (2007) 479.
- [14] L.R. Pattison, A. Hexemer, E.J. Kramer, S. Krishnan, P.M. Petroff, D.A. Fischer, *Macromolecules* 39 (2006) 2225.
- [15] H. Sirringhaus, T. Kawase, R.H. Friend, T. Shimoda, M. Inbasekaran, W. Wu, E.P. Woo, *Science* 290 (2000) 2123.
- [16] E. Lim, B.J. Jung, M. Chikamatsu, R. Azumi, Y. Yoshida, K. Yase, L.M. Do, H.K. Shim, *J. Mater. Chem.* 17 (2007) 1416.
- [17] T. Ishwara, D.D.C. Bradley, J. Nelson, P. Ravirajan, I. Vanseveren, T. Cleij, D. Vanderzande, L. Lutsen, S. Tierney, M. Heeney, I. McCulloch, *Appl. Phys. Lett.* 92 (2008) 053308.
- [18] H. Hoppe, N.S. Sariciftci, *J. Mater. Chem.* 16 (2006) 45.
- [19] H. Hoppe, M. Niggemann, C. Winder, J. Kraut, R. Hiesgen, A. Hinsch, D. Meissner, N.S. Sariciftci, *Adv. Funct. Mater.* 14 (2004) 1005.
- [20] T.A. Chen, X. Wu, R.D. Rieke, *J. Am. Chem. Soc.* 117 (1995) 233.
- [21] Y. Kim, S.A. Choulis, J. Nelson, D.D.C. Bradley, *Appl. Phys. Lett.* 86 (2005) 063502.
- [22] A. Zen, J. Pflaum, S. Hirschmann, W. Zhuang, F. Jaiser, U. Asawapirom, J.P. Rabe, U. Scherf, D. Neher, *Adv. Funct. Mater.* 14 (2004) 757.
- [23] G. Li, V. Shrotriya, Y. Yao, J.S. Huang, Y. Yang, *J. Mater. Chem.* 17 (2007) 3126.



## A new p- and n-dopable selenophene derivative and its electrochromic properties

Gülben Ardahan Çetin<sup>a</sup>, Abidin Balan<sup>a</sup>, Asuman Durmuş<sup>a</sup>, Görkem Günbaş<sup>a,1</sup>, Levent Toppare<sup>a,\*</sup>

<sup>a</sup> Department of Chemistry, Middle East Technical University, Ankara 06531, Turkey

### ARTICLE INFO

#### Article history:

Received 5 June 2008

Received in revised form 1 September 2008

Accepted 20 September 2008

Available online 1 October 2008

#### PACS:

82.35.Cd

42.70.Qs

61.72.uf

61.72.uj

#### Keywords:

Conducting polymer

Low band-gap polymer

N and p dopable polymer

Selenophene

### ABSTRACT

A novel electrically conducting polymer, poly(2-dodecyl-4,7-di(selenophen-2-yl)benzotriazole) (PSBT), containing selenophene as the strong donor and benzotriazole as the strong acceptor groups was synthesized by electrochemical polymerization. Homopolymerization and copolymerization (in the presence of 3,4-ethylenedioxythiophene (EDOT)) were achieved in acetonitrile/dichloromethane(95/5 v/v) with 0.1 M tetrabutylammonium hexafluorophosphate (TBAPF<sub>6</sub>). The electrochemical and optical properties of homopolymer and copolymer were investigated by cyclic voltammetry, UV–Vis, near IR Spectroscopy. Cyclic voltammetry and spectroelectrochemistry studies demonstrated that homopolymer can be reversibly reduced and oxidized (both n- and p-doped) between –1.9 V and +1.4 V, at a scan rate of 100 mV/s. The homopolymer revealed a transmissive light blue color in the oxidized state, and a red-purple color in the neutral state. A transmissive light blue color was also observed in the reduced state. Homopolymer films could be fully switched between their reduced and oxidized forms in 2.4 s and 0.4 s with a percent transmittance of 32% and 56% at 511 and 1200 nm, respectively. Poly(SBT) exhibits a  $\lambda_{\text{max}}$  value of 511 nm and a band gap of 1.67 eV which is quite low among the selenophene-containing polymers reported so far except for poly(1,2-bis(2-seleninyl)ethane).

© 2008 Elsevier B.V. All rights reserved.

### 1. Introduction

In recent years, the design and synthesis of low band-gap polymers have been an area of intense interest since the band gap of polymer determines the intrinsic electrical and optical properties in doped state and their ability to be both p- and n-type doped [1–4]. Several ways have been developed to synthesize low band-gap polymers [5]. One of the most successful approaches is the application of an alternating sequence of donor–acceptor (D–A) units in the  $\pi$ -conjugated polymer chain. Alternating electron releasing and withdrawing units will consequently increase the HOMO level or lower the LUMO level which in return decrease the band gap of the molecule [6–8].

The search for organic conducting polymers started in the 1970s and up to date is largely focused on polyfuran [9], polythiophene [10], polypyrrole [11] and their derivatives. Relatively little work was conducted on higher selenium-containing analogues [12–14]. In comparison, the differences in the chemistry of selenium and sulfur include the metallic character and the electronegativity of the heteroatom [15]. Hence, selenophene has a lower oxidation potential and higher electron donating character than the sulfur analogue [16]. Lower oxidation potential engenders high quality polymer films during electropolymerization by minimizing harmful effects of high polymerization potentials which causes the degradation of the polymer films [17].

In our search for low band-gap conjugated polymers, we synthesized a polymer consisting of electron rich selenophene and electron deficient benzotriazole units. The molecule contains an electron withdrawing imine (C=N) group which exhibits  $\pi$ -deficient nature [18]. Here we

\* Corresponding author. Tel.: +90 3122103251; fax: +90 3122103200.

E-mail address: [toppare@metu.edu.tr](mailto:toppare@metu.edu.tr) (L. Toppare).

<sup>1</sup> Present address: Department of Chemistry, University of California, Davis.

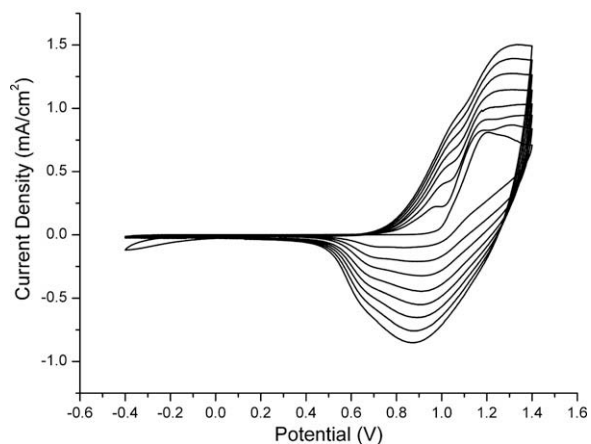


**Fig. 1.** Cyclic voltammogram of SBT in 0.1 M TBAPF<sub>6</sub>/ACN/DCM (95/5 v/v) at a scan rate of 100 mV/s. (ITO working electrode versus Ag wire pseudo reference electrode.)

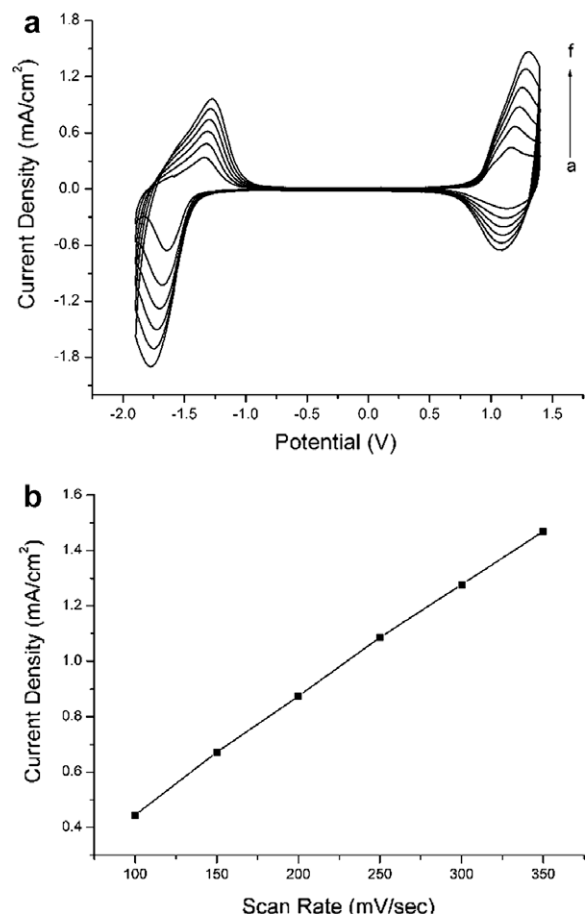


**Fig. 2.** (a) Scan rate dependence of poly(SBT) and (b) relation between current density and scan rate. (Pt working electrode versus Ag wire pseudo reference electrode.)

report the synthesis, characterization and electrochromic properties of a selenium-containing polymer, poly(SBT).

The electrochemical copolymerization of SBT with EDOT was also achieved to investigate the properties of the resultant copolymer. EDOT was the choice as a comonomer due to its excellent electrochromic properties and its oxidation potential which is close to SBT.

## 2. Results and discussion

### 2.1. Monomer synthesis

The donor–acceptor type monomer (SBT) was generated through Stille coupling reaction between 4,7-dibromo-2-dodecylbenzotriazole and tributyl(2-selenophenyl)stannane with a relatively good yield of 63%. Tributyl stannyl group is located on the electron rich selenophene unit whereas, the bromo substituent is on the electron deficient benzotriazole [8,19].

### 2.2. Cyclic voltammetry

In Fig. 1 the oxidative electrochemical polymerization of SBT is shown. An irreversible oxidation peak emerges

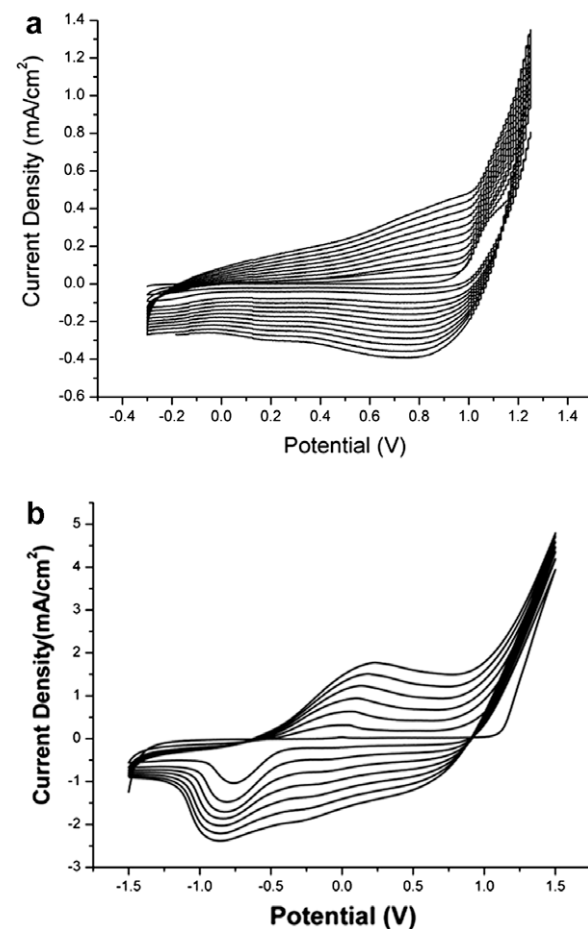


**Fig. 3.** (a) Electrochemical synthesis of poly(SBT-co-EDOT) in 0.1 M TBAPF<sub>6</sub>/ACN/DCM and (b) electrochemical synthesis of PEDOT in 0.1 M TBAPF<sub>6</sub>/ACN/DCM at a scan rate of 100 mV/s. (ITO working electrode versus Ag wire pseudo reference electrode.)

on the first cycle at a potential of +1.2 V versus Ag wire pseudo reference electrode (0.35 V versus SCE) indicating the formation of a reactive intermediate. The monomer oxidation potential is comparatively lower than selenophene (+1.48 V), an indication of more extensive conjugation for this monomer. As the polymerization proceeds, the peak current increases with successive scans, indicating the growth of polymer on ITO coated glass slides revealing an oxidation potential ( $E_{pa}$ ) at +1.0 V and a reduction potential ( $E_{pc}$ ) at +0.8 V versus the same reference electrode.

The n-doping property of the polymer was investigated using CV in a monomer free solution. The polymer deposited on Pt can reversibly be reduced and oxidized between  $-1.9$  V and  $+1.4$  V versus Ag wire pseudo reference electrode in TBAPF<sub>6</sub>/ACN. The cyclic voltammogram of Poly(SBT) is shown in Fig. 2. A redox couple with an oxidation potential of  $-1.3$  and a reduction potential of  $-1.7$  V was observed which is an important indication of an n-dopable character of the film. Further supporting data on n-doping properties of the polymer was provided with spectroelectrochemistry. The scan rate dependence of the polymer films were also investigated. The current was found to be proportional to the scan rate indicating the adherence of the polymers to the electrode surface. Hence, charge transfer process was not dominated by diffusion effects [20].

A 20  $\mu$ m polymer film was prepared on a platinum electrode. The polymer was peeled off and the standard four probe method was performed on the free standing polymer film where a current was supplied through the outer probes while measuring the voltage drop across the inner two. The conductivity was calculated to be  $1 \times 10^{-2}$  S/cm.

The electrochemical behavior of the Poly(SBT-co-EDOT) was investigated using CV in the presence of EDOT under same experimental conditions. The cyclic voltammogram

of copolymer is shown in Fig. 3. A redox couple with an oxidation potential of +0.85 V and a reduction potential of +0.8 V versus same reference electrode were observed (Fig. 3a). The oxidation and reduction potentials of the material were different than those of SBT and pristine EDOT (Fig. 3b), which in fact, could be interpreted as the formation of copolymer.

The conductivity of the copolymer prepared on platinum electrode was calculated to be  $2 \times 10^{-1}$  S/cm.

### 2.3. Spectroelectrochemistry

For optoelectrochemical studies, after homogeneous polymer films were electrochemically deposited on ITO coated glass in dichloromethane/acetonitrile (5/95, v/v) with 0.1 M TBAPF<sub>6</sub>, UV–Vis spectra were taken in a monomer free solution at various potentials to monitor the changes in absorbance as the polymer film is oxidized. Fig. 4 reveals spectroelectrochemistry and the corresponding colors of electrochemically prepared films at neutral and doped states. Stepwise oxidation of the polymer shows the fading of absorbance at 511 nm and typical evolution of peaks at 800 nm and 1200 nm corresponding to polaronic and bipolaronic bands, respectively. Dedoped polymer has two distinct absorption bands as expected from a donor–acceptor type polymer [21], centered at 483 nm and 511 nm. The band gap, onset of the  $\pi \rightarrow \pi^*$  transition for the neutral polymer is calculated as 1.67 eV using the absorption band centered at 511 nm. Compared to neutral dedoped polyselenophene ( $E_g$ : 2.0 eV) and some other selenophene containing polymers [22], poly(SBT) exhibits lower optical band gap.

Moreover, spectroelectrochemistry studies were performed in order to prove the n-type doping process of a conjugated polymer system since formation of a redox

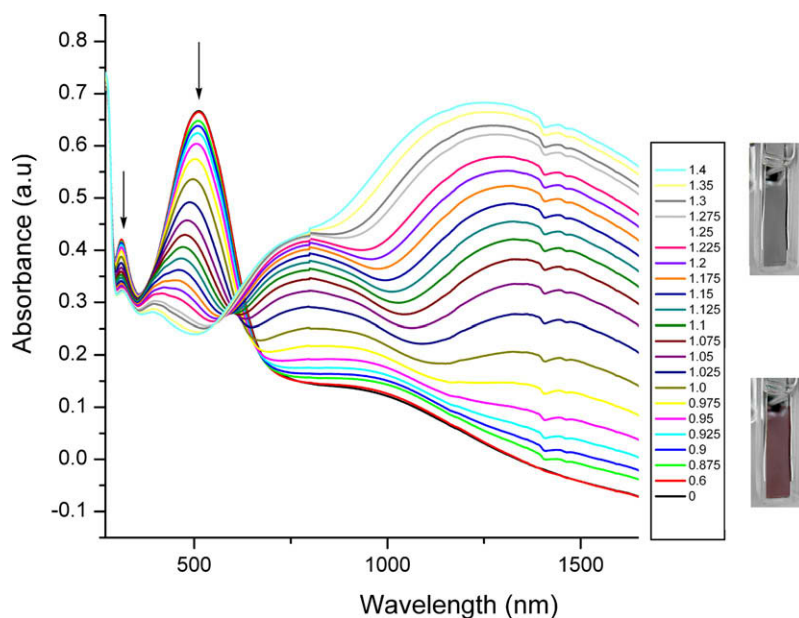


Fig. 4. Optoelectrochemical analysis of poly(SBT) in 0.1 M TBAPF<sub>6</sub>/ACN at applied potentials between 0 V and 1.4 V.

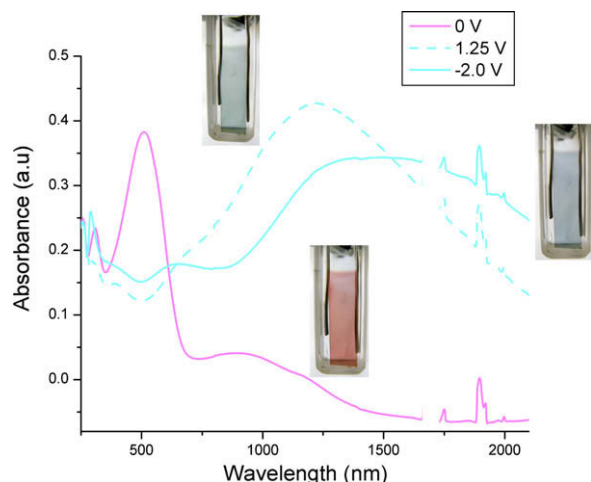


Fig. 5. Optoelectrochemical analysis of poly(SBT) in 0.1 M TBAPF<sub>6</sub>/ACN at applied potentials of (a) 1.25 V, (b) 0 V, and (c) -2.0 V.

couple at a negative potential in cyclic voltammetry is not adequate information. A drastic change in the NIR region was known to be one of the most important proofs of true n-type doping process [23]. As shown in Fig. 5, the optical spectrum of poly(SBT) reveals the changes in the color of the polymer film. Hence, it can be concluded that poly(SBT) is a true n-type dopable polymer [24].

Copolymer exhibits a  $\lambda_{\max}$  value of 560 nm and a band gap of 1.54 eV (Fig. 6). On the other hand, the band gap of Poly(EDOT) and the  $\lambda_{\max}$  of  $\pi \rightarrow \pi^*$  transition were reported as 1.6 eV and 620 nm, respectively. In conclusion, the band-gap energy and absorption maxima of the copolymer are different than the values for Poly(EDOT) and Poly(SBT) as expected. In addition, the  $\lambda_{\max}$  of the

copolymer is red shifted compared to that of the homopolymer with a lower optical band gap among such polymers.

#### 2.4. Switching

The optical switching studies were investigated using a square wave potential step method coupled with optical spectroscopy known as chronoabsorptometry in a monomer free solution. The percent transmittance versus time was monitored at  $\lambda_{\max}$  while the polymer on ITO coated glass slides was repeatedly switched between the reduced (0 V) and oxidized (+1.2 V) states for a residence time of 5 s. The optical contrast was measured as the difference in percent transmittance between neutral and oxidized forms and noted as  $\Delta T\%$ . Fig. 7 reveals the electrochromic switching properties of Poly(SBT). The optical contrast for Poly(SBT) is 32% at 511 nm and 56% at 1200 nm. The coloration efficiency which provides information about the contrast ratio acquired for a certain amount of charge introduced in the material is calculated as  $143 \text{ cm}^2/\text{C}$  (at 100% of full switch at 511 nm). It is the relation between the injected and ejected charge per unit area of the electrode and the change in optical density at a specific dominant wavelength.

Switching time is an important parameter for a polymer since it indicates the speed of ions move into the polymer chains during doping process [25]. The switching time was determined by monitoring the absorption intensity at 511 nm and 1200 nm while switching the applied voltage between 0 V and +1.2 V. It is calculated at 95% of contrast ratio. The homopolymer revealed a switching time of 2.4 s and 0.4 s at 511 nm and 1200 nm, respectively. Moreover, copolymerization studies show that copolymer has fast switching times (0.48 and 0.42 s) and high optical contrasts (42% and 68%) at 560 nm and 1400 nm, respectively (Fig. 8).

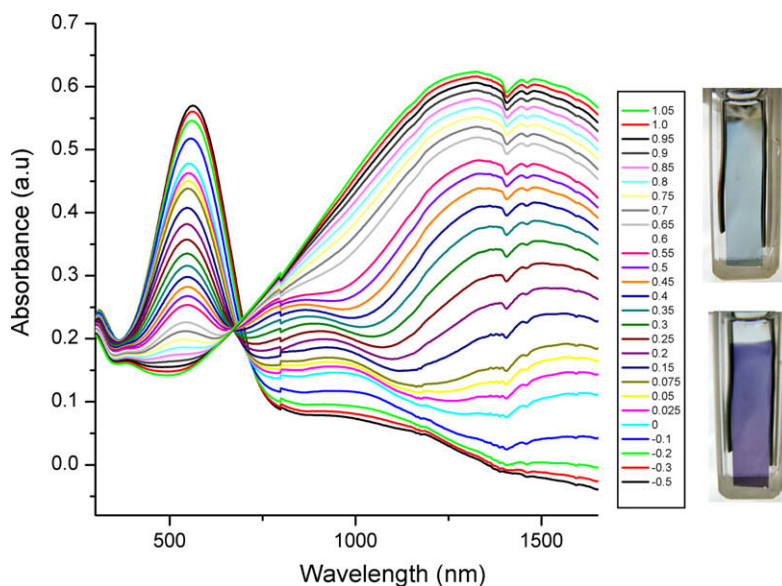


Fig. 6. Optoelectrochemical analysis of poly(SBT-co-EDOT) in 0.1 M TBAPF<sub>6</sub>/ACN with applied potentials between -0.5 V and 1.05 V versus Ag wire.

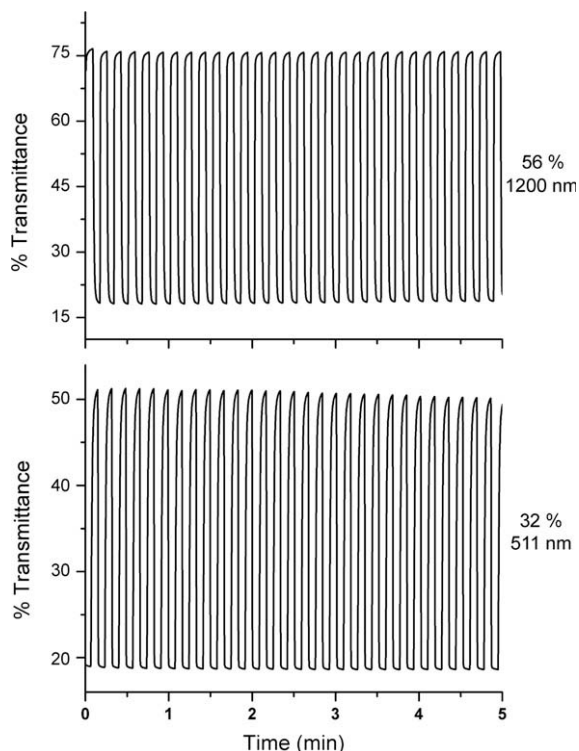


Fig. 7. Electrochromic switching, optical absorbance monitored for poly(SBT) in the presence of 0.1 M TBAPF<sub>6</sub>/ACN.

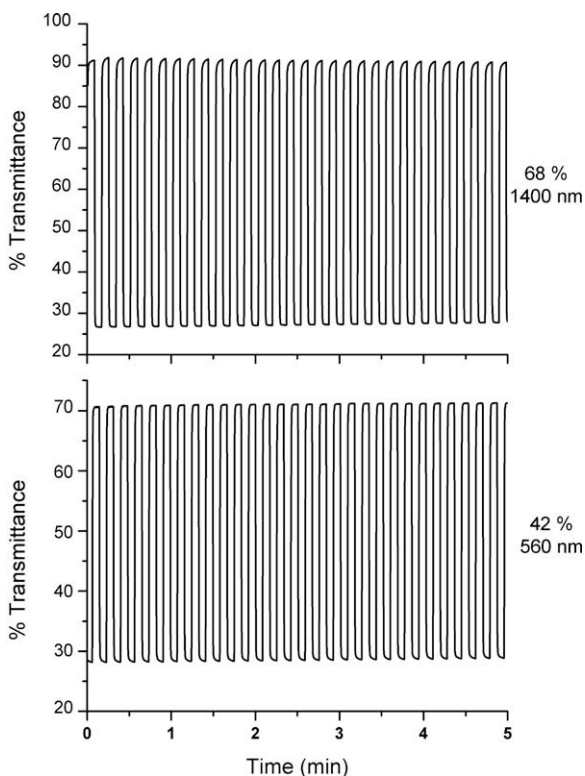


Fig. 8. Electrochromic switching, optical absorbance monitored for poly(SBT-co-EDOT) in the presence of 0.1 M TBAPF<sub>6</sub>/ACN.

Table 1

Electrochemical, electronic, and electrochromic properties

Material	E (V)	Color	<i>L</i>	<i>a</i>	<i>b</i>
PSBT	-2.0	Transmissive light blue	84.277	-8.847	-3.458
	0	Red-purple	79.897	8.298	7.365
	1.25	Transmissive light blue	86.947	-10.01	0.973
PSBT-co-EDOT	0.5	Purple	61.912	4.481	-10.93
	1.05	Transmissive light blue	79.328	-7.982	0.891

### 2.5. Colorimetry

Colorimetry is used to measure the color with an objective and quantitative practice, which allows matching of the colors in electrochromic devices. Color is made up of three attributes: hue, saturation, and luminance, and color systems, such as CIE, are used as a quantitative scale to define and compare colors. The three identifications of the colors (*L*, *a*, *b*) were measured and summarized in Table 1.

### 3. Conclusion

A novel donor–acceptor type polymer was synthesized and its electrochromic properties were investigated. Spectroelectrochemistry depicted that poly(SBT) reveals two absorption bands as expected for this type of donor–acceptor polymer, at 483 and 511 nm. The optical contrasts of the poly(SBT) film were calculated to be 32% and 56% at 511 nm and 1200 nm, respectively. Kinetic studies also revealed that the polymer films switch between their fully oxidized and fully reduced states in nearly two seconds in the visible and less than 0.5 s in the NIR regions. In addition to high optical contrasts and fast switching times, the polymer films did not reveal any degradation during kinetic studies. The colorimetry analysis showed that Poly(SBT) has a red-purple color in the neutral state and a transmissive-blue color in the oxidized state. The band gap of the Poly(SBT) is calculated as 1.67 eV which is quite low among the selenophene-containing polymers. Furthermore, the polymer has been shown to be n-dopable, as proven by reduction waves in CV and a significant change in the NIR region of spectrum upon reduction. These preliminary results are very promising for selenophene-containing donor–acceptor type polymers. Although our initial studies with 1,4-di(selenophen-2-yl)-benzene did not yield these superior characteristics, this polymer proves that use of an acceptor and a donor selenophene groups may be a key argument for the electrochromic properties of such compounds. Many other potential acceptor groups can be inserted in the structure to tune these properties to yield the best candidate selenophene-containing donor–acceptor polymer for ECD applications. Besides these promising results, it was also shown that this type of donor–acceptor monomers can be used as a comonomer for the synthesis of copolymers with superior properties. In this report EDOT was chosen as the comonomer due to its spectacular properties. The resulting copolymer

also revealed high quality characteristics as an electrochromic material.

## 4. Experimental section

### 4.1. Materials

All chemicals were purchased from Aldrich except for anhydrous tetrahydrofuran (THF) which was supplied from Acros. Tributyl(2-selenophenyl)stannane [26] was synthesized according to previously described method. All reactions were performed under argon atmosphere unless otherwise indicated (Scheme 1).

### 4.2. Synthesis of monomer

#### 4.2.1. Synthesis of 2-dodecylbenzotriazole

The synthesis of 2-dodecylbenzotriazole was performed according to methodology described in literature [27]. 1,2,3-Benzotriazole (5.0 g, 42 mmol) was dissolved in methanol (50 ml) together with potassium tert-butoxide (5.0 g, 44 mmol). Bromododecane (12.2 g, 49 mmol) was added dropwise to mixture. The mixture was refluxed for 12 h and the reaction was monitored by TLC. After removal of the solvent by evaporation, the residue was washed with H<sub>2</sub>O and extracted with CHCl<sub>3</sub>. The organic extract was dried over MgSO<sub>4</sub> and the solvent was evaporated under reduced pressure. The crude product was purified by column chromatography on a SiO<sub>2</sub> column to obtain 2-dodecylbenzotriazole; Yield: 3.73 g, 31%, colorless oil, Rf (3:2, hexane:CHCl<sub>3</sub>) 0.29. <sup>1</sup>H NMR spectrum of monomer: C<sub>18</sub>H<sub>29</sub>N<sub>3</sub>, δ (400 MHz; CDCl<sub>3</sub>; Me<sub>4</sub>Si): 7.76 (2H, m), 7.26

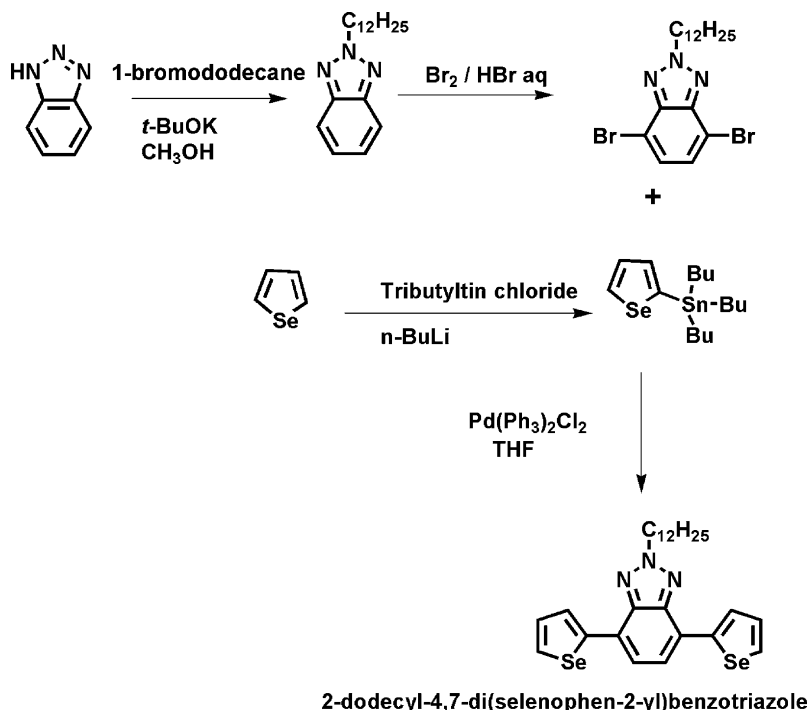
(2H, m), 4.62 (2H, t, *J* = 7.1 Hz), 2.22 (2H, m), 1.25–1.15 (18H, m), 0.78 (3H, t, *J* = 6.0 Hz). <sup>13</sup>C NMR spectrum of the monomer: <sup>13</sup>C NMR δ (100 MHz; CDCl<sub>3</sub>; Me<sub>4</sub>Si): 144.3, 126.1, 117.9, 56.6, 31.8, 30.0, 29.5, 29.5, 29.4, 29.3, 29.3, 29.0, 26.5, 22.6, 14.0.

#### 4.2.2. Synthesis of 4,7-dibromo-2-dodecylbenzotriazole

Synthesis of 4,7-dibromo-2-dodecylbenzotriazole was achieved as described in literature [27]. 2-Dodecylbenzotriazole (4.8 g, 16.8 mmol) and an aqueous HBr solution (5.8 M, 15 ml) were added to a flask, and the mixture was stirred for 1 h at 100 °C. Bromine (5.9 g, 36 mmol) was added, and the mixture was stirred for 12 h at 135 °C and the reaction was monitored by TLC. After cooling the mixture to room temperature, an aqueous solution of NaHCO<sub>3</sub> was added and the product was extracted with CHCl<sub>3</sub>. The organic extract was dried over MgSO<sub>4</sub> and the solvent was evaporated under reduced pressure. The crude product was purified by column chromatography on a SiO<sub>2</sub> column to obtain 4,7-dibromo-2-dodecylbenzotriazole; Yield: 4.0 g, 55%, oily at room temperature, Rf (1:1 hexane:CHCl<sub>3</sub>) 0.33. C<sub>18</sub>H<sub>27</sub>Br<sub>2</sub>N<sub>3</sub>, δ (400 MHz; CDCl<sub>3</sub>; Me<sub>4</sub>Si): 7.36 (2H, s), 4.70 (2H, t, *J* = 7.0 Hz), 2.00 (2H, m), 1.28–1.12 (18H, m), 0.80 (3H, t, *J* = 6.9 Hz). <sup>13</sup>C NMR: δ (100 MHz; CDCl<sub>3</sub>; Me<sub>4</sub>Si): 143.7, 129.4, 109.9, 57.4, 31.8, 31.5, 30.1, 29.5, 29.5, 29.4, 29.3, 28.9, 26.4, 22.6, 14.0.

#### 4.2.3. Synthesis of 2-dodecyl-4,7-di(selenophen-2-yl)benzotriazole (SBT)

4,7-Dibromo-2-dodecylbenzotriazole (100 mg, 0.224 mmol), and tributyl(2-selenophenyl)stannane (470 g, 1.12 mmol) were dissolved in anhydrous THF (100 ml), the



Scheme 1. Synthetic route of monomer.

solution was purged with argon for 30 min and dichlorobis(triphenyl phosphine)-palladium(II) (50 mg, 0.045 mmol) was added at room temperature. The mixture was refluxed for 18 h under argon atmosphere. Solvent was evaporated under vacuum and the crude product was purified by column chromatography on a SiO<sub>2</sub> column to obtain 2-dodecyl-4,7-di(selenophen-2-yl)benzotriazole; (scheme 1) Yield: 78 mg, 63%, yellow solid, R<sub>f</sub> (2:1 hexane:CHCl<sub>3</sub>) 0.45, <sup>1</sup>H NMR spectrum of monomer: C<sub>26</sub>H<sub>33</sub>N<sub>3</sub>Se<sub>2</sub>, δ (400 MHz; CDCl<sub>3</sub>; Me<sub>4</sub>Si): 8.12 (2H, d, *J* = 3.6 Hz), 8.01 (2H, d, *J* = 5.5 Hz), 7.52 (2H, s), 7.35 (2H, d-d, *J* = 3.8–1.5 Hz), 4.74 (2H, t, *J* = 7.1 Hz), 2.16–2.09 (2H, m), 1.37–1.18 (18H, m), 0.81 (3H, t, *J* = 6.9 Hz). <sup>13</sup>C NMR: δ (100 MHz; CDCl<sub>3</sub>; Me<sub>4</sub>Si): 144.1, 140.9, 130.3, 129.4, 127.2, 124.4, 122.0, 55.8, 30.8, 28.9, 28.6, 28.5, 28.4, 28.4, 28.3, 28.0, 25.5, 21.6, 13.0 (Figs. 9 and 10). *m/z*: 547.3 (100%), 545.1 (95%), 543.1 (55%). The details of MS spectrum are given in Fig. 11.

#### 4.2.4. Synthesis of homopolymer by electrochemical polymerization

Polymerization of SBT was performed in the presence of 0.01 M SBT, 0.1 M TBAPF<sub>6</sub> in acetonitrile/dichloromethane (95/5 v/v) in a three-electrode cell equipped with Pt counter electrode and a Ag wire pseudo reference electrode. Polymer films were grafted on Pt foil or an ITO glass working electrode by potentiodynamic scanning wherein the potential was cycled between –0.4 V and +1.4 V with 100 mV/s scan rate. The free standing film was washed with ACN to remove unreacted monomer and excess TBAPF<sub>6</sub> after the electrolysis.

#### 4.2.5. Synthesis of copolymer of SBT with 3,4-ethylenedioxythiophene (EDOT)

For the synthesis of conducting copolymer, poly(SBT-co-EDOT), EDOT was used as the comonomer. Copolymer was synthesized with a [EDOT]/[SBT] molar ratio of two. A similar oxidative electrochemical polymerization proce-

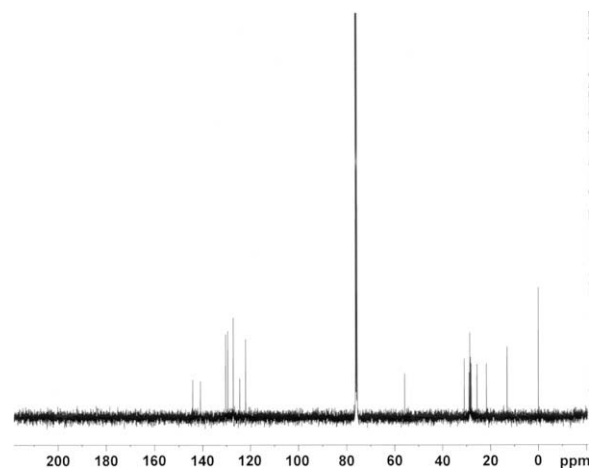


Fig. 10. <sup>13</sup>C NMR spectrum of SBT.

dure was carried out in acetonitrile/dichloromethane (95/5 v/v) via cyclic voltammetry (CV) at a scan rate of 100 mV/s. Resulting copolymer film was washed with ACN to remove unreacted monomer and excess TBAPF<sub>6</sub> after the electrolysis.

#### 4.2.6. Equipments

Polymer film was grafted on working electrode by potentiodynamic method, wherein the potential was cycled between oxidized and neutral states at 100 mV/s without significant decomposition of the material. Electrochemical polymerization was performed in a three-electrode cell consisting of Pt foil or Indium tin oxide coated glass slide (ITO) as the working electrode, platinum wire as the counter electrode and Ag wire as the pseudo reference electrode. Polymerizations were carried out under argon atmosphere using Voltalab PST 50 potentiostat.

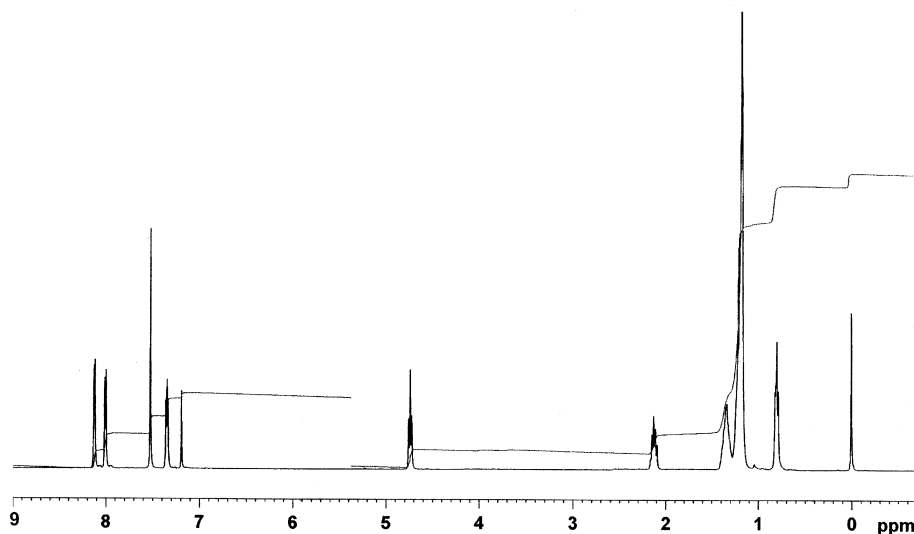


Fig. 9. <sup>1</sup>H NMR spectrum of SBT.



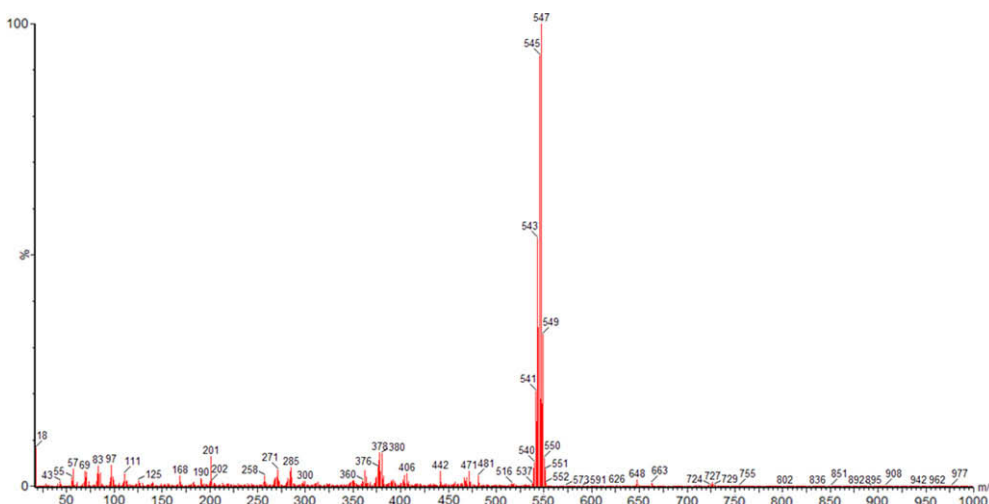


Fig. 11. MS spectrum of SBT.

Tetrabutylammonium hexafluorophosphate (TBAPF<sub>6</sub>) in acetonitrile/dichloromethane (95/5 v/v) was used as the electrolytic medium. <sup>1</sup>H NMR spectra of the monomer was recorded on a Bruker-Instrument-NMR Spectrometer (DPX-400) operating at 400 MHz. <sup>13</sup>C NMR spectra were recorded at 100 MHz with CDCl<sub>3</sub> as the solvent and chemical shifts ( $\delta$ ) were given relative to tetramethylsilane as the internal standard. Spectroelectrochemical studies were carried out on a Varian Cary 5000 UV–Vis–NIR spectrophotometer. Colorimetry measurements were obtained by a Konica Minolta CS-100A Chroma Meter with a 0/0 (normal/normal) viewing geometry as recommended by CIE. During measurement, samples were placed in a light booth system where it was illuminated from behind by a D65 light source. A direct pyrolysis mass spectrometry (DPMS) system consisting of a 5940 Quatro micromass quadrupole mass spectrometer a mass range of 10–1500 Da was coupled to direct inter probe ( $T_{\max}$  = 650 °C). In the experiment, the temperature was elevated up to 250 °C at a heating rate of 10 °C/min, and kept constant for an additional 1 min at 250 °C. Sample (0.010 mg) was pyrolyzed in the quartz glass sample vials. Pyrolysis mass spectrum was recorded using 20 eV.

## Acknowledgements

Authors gratefully thank METU and TUBA Grants for financial support.

## References

- [1] T.A. Skotheim, R.L. Elsenbaumer, J.R. Reynolds, *Handbook of Conducting Polymers*, second ed., Marcel Dekker Inc., New York, 1998, pp. 277–279.
- [2] M. Pfeiffer, K. Leoa, X. Zhoua, J.S. Huang, M. Hofmanna, A. Wernera, J. Blochwitz-Nimothb, *Org. Electron.* 4 (2003) 89.
- [3] Y.A. Udum, A. Durmuş, G.E. Gunbas, L. Toppare, *Org. Electron.* 9 (2008) 501.
- [4] F. Ozyurt, G. Gunbaş, A. Durmuş, L. Toppare, *Org. Electron.* 9 (2008) 296.
- [5] Y. Lee, S. Sadki, B. Tsuie, P. Schottland, J.R. Reynolds, *Synth. Met.* 119 (2001) 77.
- [6] M. Heeney, W. Zhang, D.J. Crouch, M.L. Chabinc, S. Gordeyev, R. Hamilton, S.J. Higgins, I. McCulloch, P.J. Skabara, D. Sparrowe, S. Tierney, *Chem. Commun.* 5061 (2007) 5061.
- [7] C.J. Du Boris Jr., F. Larmat, D.J. Irvin, J.R. Reynolds, *Synth. Met.* 199 (2001) 321–322.
- [8] H.A.M. Mullekom, J.A.J.M. Vekemans, E.E. Havinga, E.W. Meijer, *Chem. Eur. J.* 4 (1998) 1235.
- [9] S. Glenis, M. Benz, E. Legoff, J.L. Schindler, C.R. Kannewurf, M.G. Kanatzidis, *J. Am. Chem. Soc.* 115 (1993) 12519.
- [10] M. Kobayashi, J. Chen, T.-C. Chung, F. Moraes, A.J. Heeger, F. Wudl, *Synth. Met.* 9 (1984) 77.
- [11] A.R. Hillman, E.F. Mallen, *J. Electroanal. Chem.* 281 (1990) 109.
- [12] E. Aqad, M.V. Lakshmikantham, M.P. Cava, *Org. Lett.* 3 (26) (2001) 4283.
- [13] S. Glenis, D.S. Ginley, A.J. Frank, *J. Appl. Phys.* 62 (1987) 190.
- [14] A. Patra, Y.H. Wijsboom, S.S. Zade, M. Li, Y. Sheynin, G. Leitius, M. Bendikov, *J. Am. Soc. Chem.* 130 (2008) 6734.
- [15] S. Pu, J. Hou, J. Xu, G. Nie, S. Zhang, L. Shen, Q. Xiao, *Mater. Lett.* 59 (2005) 1061.
- [16] J. Xu, J. Hou, S. Zhang, G. Nie, S. Pu, L. Shen, Q. Xiao, *J. Electroanal. Chem.* 578 (2005) 345.
- [17] S. Jin, G. Xue, *Macromolecules* 30 (1997) 5753.
- [18] A. Tanimoto, T. Yamamoto, *Adv. Synth. Catal.* 346 (2004) 1818.
- [19] T.T. Ong, S.C. Ng, H.S.O. Chan, *Polymer* 44 (2003) 5597.
- [20] G. Sonmez, H. Meng, Q. Zhang, F. Wudl, *Adv. Funct. Mater.* 13 (2003) 726.
- [21] A. Berlin, G. Zotti, S. Zecchin, G. Schiavon, B. Vercelli, A. Zanelli, *Chem. Mater.* 16 (2004) 3667.
- [22] S.C. Ng, H.S.O. Chan, T.T. Ong, K. Kumura, Y. Mazaki, K. Kobayashi, *Macromolecules* 31 (1998) 1221.
- [23] B.C. Thompson, Y. Kim, T.D. McCarley, J.R. Reynolds, *J. Am. Chem. Soc.* 128 (2006) 12714.
- [24] D.J. Irvin, C.J. DuBois, J.R. Reynolds, *Chem. Commun.* 20 (1999) 2121.
- [25] D.M. Welsh, A. Kumar, M.C. Morvant, J.R. Reynolds, *Synth. Met.* 102 (1999) 967.
- [26] K. Aydemir, S. Tarkuc, A. Durmuş, G.E. Gunbas, L. Toppare, *Polymer* 49 (2008) 2029.
- [27] A. Tanimoto, T. Yamamoto, *Macromolecules* 39 (2006) 3546.



# Efficient red-light-emitting diodes based on novel amino-alkyl containing electrophosphorescent polyfluorenes with Al or Au as cathode

Lei Ying, Yunhua Xu, Wei Yang\*, Lei Wang, Hongbin Wu, Yong Cao

*Institute of Polymer Optoelectronic Materials and Devices, South China University of Technology, Key Lab of Specially Functional Materials, Ministry of Education, Guangzhou 510640, China*

## ARTICLE INFO

### Article history:

Received 3 June 2008

Received in revised form 25 September 2008

Accepted 2 October 2008

Available online 8 October 2008

### PACS:

72.80.Le

78.60.Fi

85.60.Jb

### Keywords:

Red-light-emitting diode

Al or Au cathode

Amino-alkyl containing polyfluorene

Ir complex

## ABSTRACT

Novel amino-alkyl containing polyfluorenes with Ir complex in pendant chain were synthesized by Suzuki polycondensation and efficient red-light-emitting devices based on the polymers that were fabricated using high work-function metal (Al or Au) as cathode. It was found that the prepared polyfluorenes exhibit good device performances, and the best device efficiency was achieved based on PFN-Irpiq1 that showed a maximal quantum efficiency ( $QE_{max}$ ) of 3.7% and 1.6% for Al and Au as cathode, respectively, which was comparable to that of 5.5% for low work-function metals Ba as cathode. The efficiencies of devices from the aforementioned polymers showed a reduced roll-off upon the increase of current density, which is beneficial for the highly efficient phosphorescent dye/host-doped systems. The obtained high efficiencies with air-stable metals as cathode reflect that the copolymers have dual functions of being efficient light-emitting and electron injection ability. The results indicated that the incorporation of Ir complex into amino-alkyl containing polyfluorenes side chain is a potential approach to achieve efficient light-emitting devices with air-stable high work-function metal as the cathode.

Crown Copyright © 2008 Published by Elsevier B.V. All rights reserved.

## 1. Introduction

Since remarkable progress has been made in polymer light-emitting diodes (PLEDs) during the last decade, light-emitting devices with high brightness and low drive voltage could be achieved for high-efficiency, full-color applications [1]. To obtain high-efficiency, low work-function metals (such as Ca or Ba) are generally employed as cathode to facilitate electron injection. However, these metals are very sensitive to moisture and oxygen, and detrimental quenching sites might be formed near the interface between the light-emitting layer (EML) and the cathode. To circumvent such problems, many efforts have been devoted to employing environmental stable high

work-function metals (such as Al, Ag or Au) as the cathode [2]. In this scenario, electron injection layers, (EIL or cathode buffer) such as metal fluoride (LiF, CsF, etc.), aluminum oxide layer, organic surfactants [3–6], or ammonium-functionalized polyfluorene derivatives [7–12] have been developed as EIL to facilitate electron injection. Recently, Huang et al. [7–11] reported a series of conjugated amino-alkyl containing polyfluorenes with various emissive wavelengths, which can significantly enhance the device performance using high work-function metal as cathode. However, the reported amino-alkyl substituted polyfluorenes [7–9] show a relative low emission efficiency, which limits their applications.

Electrophosphorescent polymers have attracted much attention since they can make use of both singlet and triplet exciton owing to a strong spin–orbit coupling, and theoretically 100% of internal quantum efficiency can be achieved. The phosphorescent conjugated polymers based

\* Corresponding author. Tel.: +86 20 87114346x17; fax: +86 20 87110606.

E-mail address: [pswyang@scut.edu.cn](mailto:pswyang@scut.edu.cn) (W. Yang).

on polyfluorene backbone with diketone pendant attached to 9-carbon position of fluorene were reported by Chen et al. [13]. The device from polymer which grafted with 1.3 mol% iridium(III)bis(2-(2'-benzothienyl)pyridinato-N,C<sup>3'</sup>) acetylacetonate complex [(btp)<sub>2</sub>Ir(acac)] in diketone pendant at 9-position of fluorene unit has shown a high external quantum efficiency of 1.59% ph/el and a power efficiency of 2.8 cd/A at 7.0 V with a luminance of 65 cd/m<sup>2</sup> and peak emission at 610 nm. Jiang et al. [14] reported a series of high-efficiency electrophosphorescent polymers by grafting Ir complexes into poly(fluorene-*alt*-carbazole) pendant chain, and QE<sub>ext</sub> of 4.9% and LE of 4.0 cd/A with 240 cd/m<sup>2</sup> at a bias voltage of 7.7 V and a peak emission of 610 nm were achieved. A very similar approach of incorporated Ir complexes conjugatively into polymer main chain was reported by Zhen et al. [15,16], and yellow and red electrophosphorescent copolymers with Ir complexes on the backbone of poly(fluorene-*alt*-carbazole) (PFCz) and polyfluorene (PFO) were synthesized to achieve maximal external quantum efficiencies of 4.6% and 7.0% ph/el, respectively. However, the efficient electrophosphorescent PLED was achieved based on low functional metals Ba as cathode [14–16]. In order to employ an air-stable metal such as Au or Al as cathode for the single active layer devices, Zhang et al. [17,18] reported a series of phosphorescent polyelectrolytes and their neutral precursor, in which Ir complex was conjugatively incorporated into a polymer main chain, but the device performance does not enhance evidently. In this paper, we introduce Ir complex into amino-alkyl containing polyfluorenes side chain by a long alkyl chain. Efficient red light-emitting devices are fabricated using high work-function metal (Al or Au) as cathode.

## 2. Experimental section

### 2.1. Materials and measurements

All solvents were purified and freshly distilled prior to use according to the literature procedures. All reagents were obtained from Acros, Aldrich or TCI chemical company and used as received. All manipulations involving air-sensitive reagents were performed under high purified argon or nitrogen atmosphere.

NMR spectra were recorded on a Bruker 300 in deuterated chloroform solution operating with tetramethylsilane as reference. Weight-average molecular weight ( $M_w$ ) and polydispersity index (PDI) were determined by a Water GPC 2410 spectrometer in tetrahydrofuran (THF) using a calibration curve with a standard polystyrene as a reference. Elemental analyses were performed on Vario EL Elemental analysis instrument (Elementar Company). UV-vis absorption spectra were recorded on a Hitachi UV-3010 spectrometer. The PL quantum yields were determined in an integrating sphere ISO80 (Labsphere) with 325 nm excitation of HeCd laser (Mells Griot). Cyclic voltammetry was carried out on a CHI660A electrochemical workstation with platinum at a scan rate of 50 mV s<sup>-1</sup> against a saturated calomel reference electrode with nitrogen-saturated solution of 0.1 M tetrabutylammonium hexafluorophosphate

(Bu<sub>4</sub>NPF<sub>6</sub>) in acetonitrile (CH<sub>3</sub>CN) for copolymers. Glass transition temperatures ( $T_g$ s) were measured on a TA 5200M DSC instrument at a heating rate of 10 °C min<sup>-1</sup> in nitrogen. Thermogravimetric analyses (TGA) were conducted on a NETZSCH TG 209 under a heating rate of 10 °C min<sup>-1</sup>.

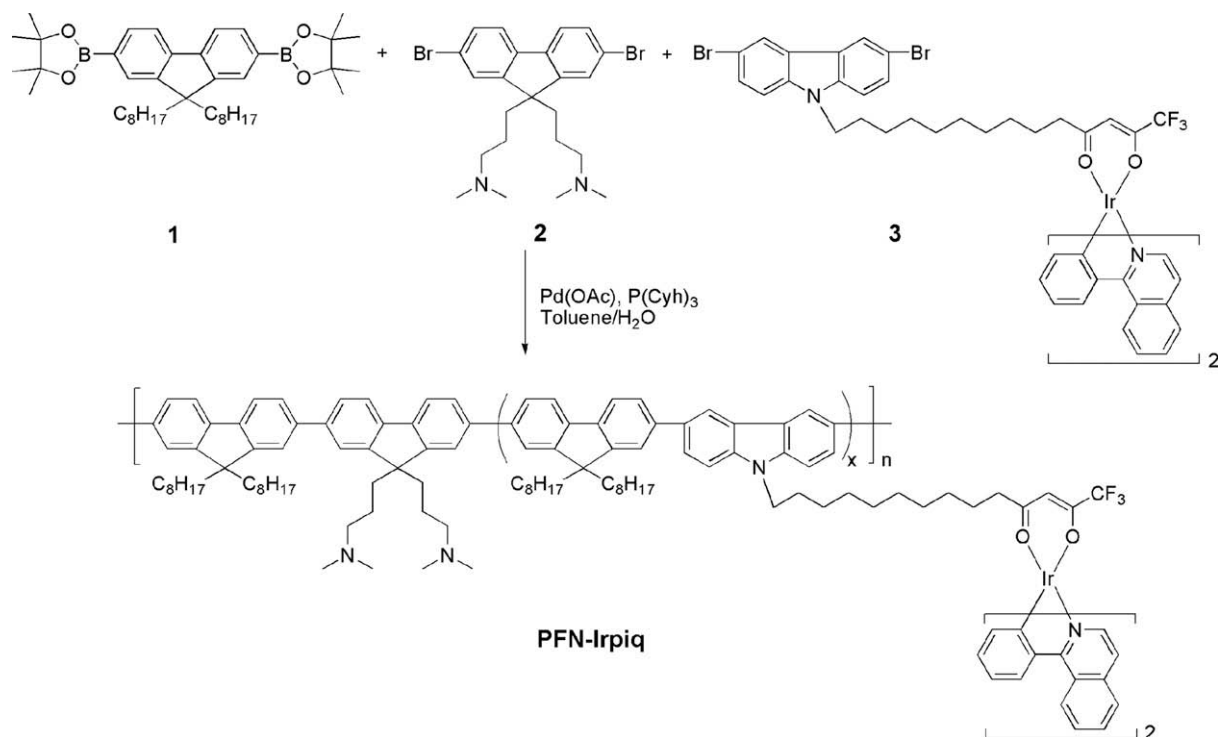
### 2.2. General procedure of Suzuki polycondensation taking PFN-Irpiq05 as an example

2,7-Bis(4,4,5,5-tetramethyl-1,3,2-dioxaborolan-2-yl)-9,9-dioctylfluorene [19] (**1**, 0.3213 g, 0.5 mmol), 2,7-dibromo-9,9-bis(3'-(*N,N*-dimethylamino)propyl)fluorene (**2**, 0.2447 g, 0.495 mmol), 3,6-dibromo-9-(iridium(III)bis(1-phenylisoquinoline-N,C<sup>2'</sup>))-14-trifluoro-11,13-tetradecylidiketone)carbazole [15] (**3**, 6.02 mg, 0.005 mmol), and palladium(II) acetate (1.5–2 mol%) and tricyclohexylphosphine (4–6 mol%) were dissolved in the mixture of toluene (8 ml) and THF (5 ml), stirred for 30 min in argon atmosphere, then Et<sub>4</sub>NOH (35 wt%) aqueous solution (2 ml) and deionized water (2 ml) were added. The mixture was heated to 90 °C and stirred for 48 h followed by stirring with 2-(4,4,5,5-tetramethyl-1,3,2-dioxaborolan-2-yl)-9,9-dioctylfluorene (50.00 mg) 12 h. Then bromobenzene (0.2 ml) was added and stirred for another 12 h. The whole mixture was poured into methanol with stirring. The precipitated polymer was collected by filtration and purified by Al<sub>2</sub>O<sub>3</sub> column chromatography with toluene as eluent to remove catalyst residue and small molecules (yield 70%). <sup>1</sup>H NMR (CDCl<sub>3</sub>) δ = 7.90–7.82 (m, 4H, fluorene ring), 7.71–7.57 (m, 8H, fluorene ring), 2.30–1.95 (m, 24H, -NCH<sub>2</sub>, -NCH<sub>3</sub>, H-alkyl), 1.22–1.04 (m, 28H, H-alkyl), 0.87–0.72 (m, 6H). Element Anal. Found C 85.78, H 8.85, N 3.40.

## 3. Results and discussion

### 3.1. Synthesis and characterization of polymers

Copolymers derived from monomers 2,7-bis(4,4,5,5-tetramethyl-1,3,2-dioxaborolan-2-yl)-9,9-dioctylfluorene (**1**), 2,7-dibromo-9,9-bis(3'-(*N,N*-dimethylamino)propyl)fluorene (**2**) and 3,6-dibromo-9-(iridium(III)bis(1-phenylisoquinoline-N,C<sup>2'</sup>))-14-trifluoro-11,13-tetradecylidiketone)carbazole (**3**) were prepared by Suzuki polycondensation (Scheme 1) with a feed ratio of 50:49.5:0.5, 50:49:1 and 50:48:2, and the resulted polymers are named PFN-Irpiq05, PFN-Irpiq1 and PFN-Irpiq2, respectively. The copolymers exhibit good solubility in common organic solvents such as THF, chloroform, toluene and xylene. The weight average molecular weight ( $M_w$ ) of the copolymers estimated by gel permeation chromatography (GPC) against the polystyrene standard with THF as eluent solvent ranges from 89,000 to 1,32,000 with a polydispersity index (PDI) ( $M_w/M_n$ ) from 1.65 to 1.90. The thermal stabilities of copolymers were studied by TGA and DSC measurements. As can be seen from Fig. 1, the Ir complex containing copolymer PFN-Irpiq1 exhibits a good thermal stability with an onset of degradation temperature at around 430 °C and with a glass transition temperature



**Scheme 1.** Synthetic procedure of copolymers.

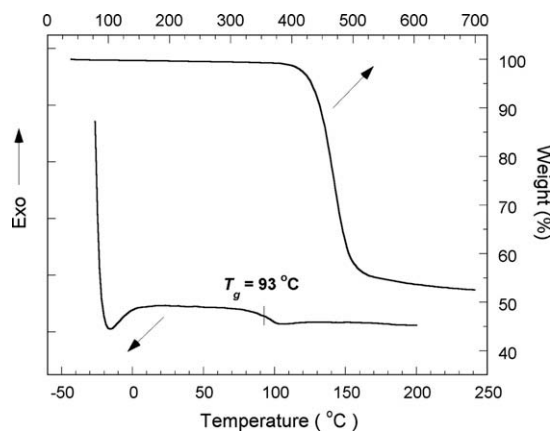


**Fig. 1.** Thermal properties of PFN-Irpiq1.

( $T_g$ ) of 93 °C. The distinct improved  $T_g$  of PFN-Irpiq1 compared to poly(9,9-dioctylfluorene) (PFO, with  $T_g$  of 72 °C) [20] might be ascribed to the intra-molecular interaction owing to the substituted amino-alkyl side chains. Likewise, other resulted copolymers also exhibit similar good thermal properties as PFN-Irpiq1.

### 3.2. Electrochemical properties

The electrochemical behavior of these polymers was investigated by cyclic voltammetry (CV) in the solution of 0.1 M tetrabutylammonium hexafluorophosphate ( $\text{Bu}_4\text{NPF}_6$ ) in acetonitrile ( $\text{CH}_3\text{CN}$ ). The copolymers show

a reversible oxidation wave with an onset at around 1.2 V of the oxidation potential of amino-alkyl containing copolymer main chain. The onset oxidation potentials are used to determine the highest occupied molecular orbital (HOMO) energy level, and the differences between the HOMO levels and the optical energy gap ( $E_g$ ) are used to estimate their lowest unoccupied molecular orbital (LUMO) energy levels, where  $E_g$  is inferred from the onset absorption. HOMO and LUMO levels of polymers are calculated according to empirical formulas  $E_{\text{HOMO}} = -e(E_{\text{ox}} + 4.40)$  eV [21]. The HOMO and LUMO levels of the copolymers show a little difference with a diverse Ir complex content. Table 1 summarizes the photophysical and electrochemical properties of Ir complexes and the redox potentials of the copolymers.

### 3.3. Photophysical properties

Fig. 2 shows the absorption spectrum of a model compound Ir complex bis-(1-phenylisoquinolyl)iridium(III)(1-

**Table 1**  
Photophysical and electrochemical properties of copolymers.

Polymers	$\lambda_{\text{abs}}$ / nm	$E_{\text{ox}}$ / V	HOMO/ eV	LUMO <sup>a</sup> / eV	$E_g^b$ / eV	$\lambda_{\text{PL}}$ /nm	QE <sub>PL</sub> / %
PFN	390	1.21	-5.61	-2.14	3.47	425, 449	37
PFN-Irpiq05	390	1.26	-5.66	-2.18	3.48	425, 618	28
PFN-Irpiq1	389	1.24	-5.64	-2.15	3.49	425, 619	34
PFN-Irpiq2	386	1.26	-5.66	-2.17	3.49	619	36

<sup>a</sup> Calculated from LUMO = HOMO +  $E_g^{\text{opt}}$ .

<sup>b</sup> Estimated from the onset absorption of copolymers.

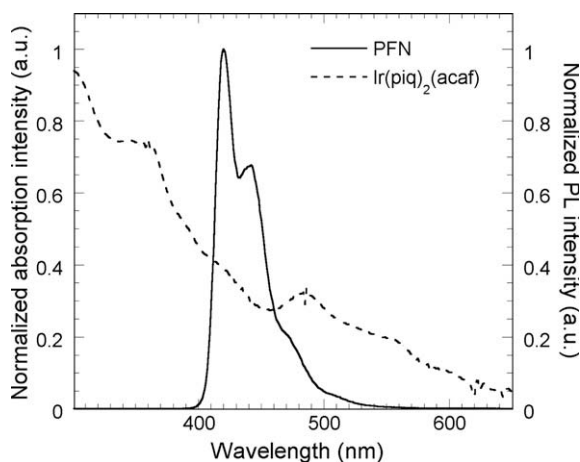


Fig. 2. Absorption of Ir(piq)<sub>2</sub>(acaf) and PL of PFN.

trifluoro)acetylacetonate [Ir(piq)<sub>2</sub>(acaf)] [22] and photoluminescence spectrum (PL) of poly[(9,9-bis(3'-(*N,N*-dimethyl)propyl)-2,7-fluorene)-2,7-(9,9-dioctyl-fluorene)] (PFN) [7]. The Ir complex shows broad absorption band from about 270 nm to more than 600 nm. The intense absorption peak below 350 nm is attributed to the spin-allowed singlet state  $\pi$ - $\pi^*$  transition of cyclometalated ligands, and the weak absorption peak at about 422 nm can be assigned to the spin-allowed singlet metal-to-ligand charge transfer (<sup>1</sup>MLCT) transition. The absorption peak of 486 nm is due to the triplet metal-to-ligand charge transfer (<sup>3</sup>MLCT) transition. The spin-forbidden <sup>3</sup>MLCT transition is gained by mixing it with the higher spin-allowed <sup>1</sup>MLCT transition through the strong spin-orbit coupling of iridium. As can be seen from Fig. 2, fairly good overlap is found in the PL of the host PFN and the absorption of the guest Ir(piq)<sub>2</sub>(acaf), thus the efficient Förster energy transfer from the PFN to the Ir complex can be expected [23].

The emission of the copolymers in Fig. 3 is dominated by the peak around 619 nm, which corresponds to the triplet emission of the Ir complex. Besides, the weak emission

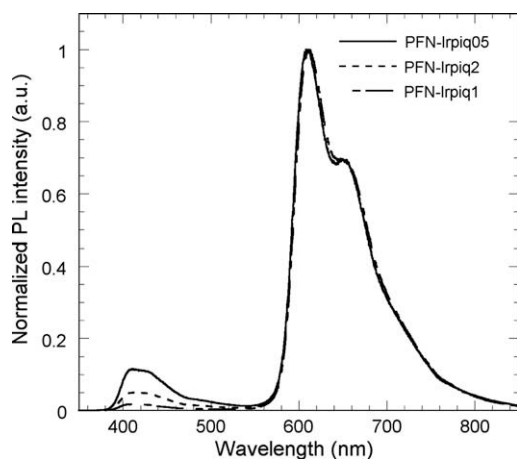


Fig. 3. PL spectra of PFN-Irpiq in solid films.

at 425 nm (emission from PFN) is also found in the copolymer with 0.5 mol% content of Ir complex (PFN-Irpiq 05), indicating that the energy transfer from the host PFN main chain to the low content Ir complex is incomplete. Indeed, with the increase of Ir complex content up to 2 mol%, the emission of PFN segment in copolymers is found to be quenched completely. Moreover, the emission at 425 nm is found to descend with the increase of Ir complex content in the copolymers. The PL efficiencies of the copolymers are in the range of 28.4–37.3% (Table 1), which are much higher than that of the previously reported electrophosphorescent polymers PFN-IrDPPy [13], in which neutral Ir complex is conjugatively incorporated into polyfluorenes main chain, suggesting that the incorporation of Ir complex into side chain is a better way to achieve more efficient emission.

### 3.4. Device performances

The light-emitting devices are fabricated in configuration: ITO/PEDOT/PVK/emissive layer/cathode. Here low work-function metal Ba (−2.8 eV) and high work-function Al (−4.3 eV) and Au (−5.2 eV) are used as cathode for comparison. As shown in Fig. 4, EL emission (Fig. 4) from the backbone of the copolymers is quenched completely although the Ir complex content is as low as 0.5 mol%. The substantial difference between the PL (Fig. 3) and EL (Fig. 4) of the copolymers implies that the excitation mechanism for the PL and EL process is different [23–25]. Under photoexcitation, singlet excited state is created on the polymer main chain and subsequently transferred to the iridium complex by Förster energy transfer [26, 27]. In contrast, since the HOMO and LUMO energy level of incorporated Ir(piq)<sub>2</sub>(acaf) (which is −5.0 and −2.7 eV, respectively) lies between that of host PFN (which is −5.6 and −2.1 eV, respectively), thus for electrical excitation process, electrons and hole are readily trapped on the Ir complex sites when charge carriers are injected from the electrodes, as can be referred from the energy level diagram. In other words, charge trapping mechanism is dominant in the electroluminescent process of our devices.

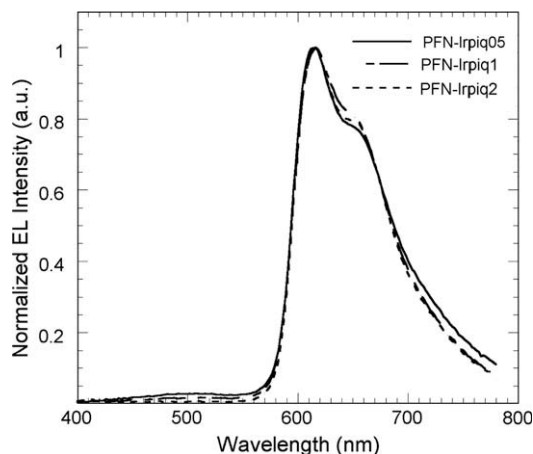


Fig. 4. EL spectra of PFN-Irpiq copolymers (ITO/PEDOT/PVK/PFN-Irpiq/Ba/Al).

**Table 2**  
EL performances of polymers.

Polymers	Cathode	$\lambda_{\text{ELmax}}/\text{nm}$	$V_{\text{th}}/\text{V}$	$\text{QE}_{\text{ext}}/\%$	$\text{LE}_{\text{max}}/\text{cd A}^{-1}$	$L_{\text{max}}/\text{cd m}^{-2}$
PFN-Irpiq05	Ba/Al	616	13.1	1.80	0.80	190
	Al	618	15.0	1.54	0.66	200
	Au	628	15.0	0.32	0.14	129
PFN-Irpiq1	Ba/Al	616	14.2	5.50	2.44	750
	Al	616	13.5	3.70	1.64	1032
	Au	629	15.0	1.60	0.71	361
PFN-Irpiq2	Ba/Al	615	14.0	1.34	0.59	170
	Al	616	13.2	1.10	0.48	160
	Au	629	14.0	0.16	0.07	58

Device structure: ITO/PEDOT/PVK/emissive layer/cathode.

It is interesting to note that, despite different metals with different work-functions being employed as cathodes, all copolymers exhibit a comparable device performance in terms of external quantum efficiency ( $\text{QE}_{\text{ext}}$ ). The best device performance is found in PFN-Irpiq1, in which Ir complex content of 1 mol% is used as EML. The  $\text{QE}_{\text{max}}$  of 5.50%, which corresponds to a luminous efficiency ( $\text{LE}_{\text{max}}$ ) of  $2.44 \text{ cd A}^{-1}$  and a maximal luminance of  $750 \text{ cd m}^{-2}$  is obtained with Ba/Al as cathode. When high work-function Al is employed, the  $\text{QE}_{\text{max}}$  and  $\text{LE}_{\text{max}}$  are 3.70% and  $1.64 \text{ cd A}^{-1}$ , respectively, with a maximal luminance of  $1032 \text{ cd m}^{-2}$ . Moreover, when noble metal Au is employed as cathode, the  $\text{QE}_{\text{max}}$  and  $\text{LE}_{\text{max}}$  could reach 1.60% and  $0.71 \text{ cd A}^{-1}$ , respectively, with a maximal luminance of  $361 \text{ cd m}^{-2}$ . It is important to note that the noble metal Au is commonly used as good hole-injection electrode and devices fabricated from traditional conjugated polymers with Au as cathode cannot emit light due to their extremely high work-function [10]. However, our devices based on PFN derivatives with Au as cathode show a remarkable efficiency, in consistence with what was reported previously [10]. The device performances in detail with different device configurations are summarized in Table 2.

Fig. 5 shows the  $\text{QE}_{\text{ext}}$  and luminance ( $L$ ) as a function of current density ( $J$ ) for the devices with different cathodes. It can be seen that Al and Au devices exhibit comparable

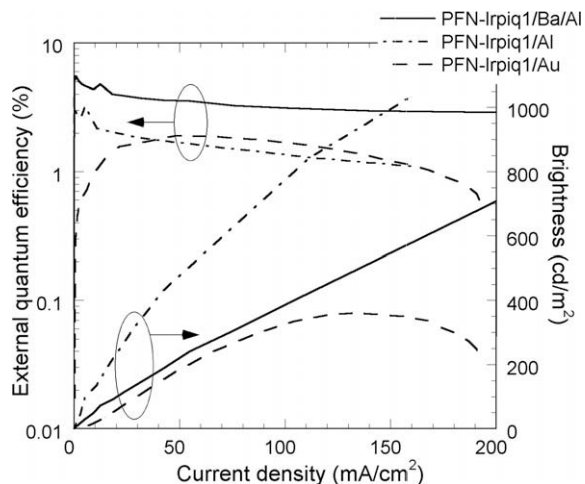


**Fig. 5.** Characteristics of  $\text{QE}$ - $J$ - $L$  with different cathodes.

overall efficiency than that with Ba device (Fig. 5). We speculate that a strong interaction between amino-alkyl moieties and high work-function metal can induce interfacial dipole [10,11], which can shift the vacuum level of the polymer upwards and is responsible for the enhanced electron injection from Al and Au. Despite that the mechanism being not fully understood, the obtained efficient devices with air-stable metals including Al or Au as cathode reveal that the copolymers have dual functions of being efficient light-emitting material and efficient electron injection ability. Furthermore, the  $\text{QE}_{\text{ext}}$  in Fig. 5 slightly decays with the increase of current density regardless of the employed cathodes, indicating that the incorporation of Ir complex into polymer side chain [15–18] is an effective way to inhibit the concentration quenching at the high current density due to the complex aggregation while depressing the triplet-triplet annihilation.

#### 4. Conclusion

A series of novel amino-alkyl containing polyfluorenes with Ir complex in pendant chain were synthesized by Suzuki polycondensation. The devices based on the resulted copolymers using air-stable high work-function metals including Al and Au as the cathode exhibited comparable device performance with that of low work-function metals Ba as cathode. The efficiencies of device from the prepared polymers show a reduced roll-off upon the increase of current density and Ir complex content, which is positive for the highly efficient phosphorescent dye/host doping systems.

#### Acknowledgments

We thank the Ministry of Science and Technology of China (Project No. 2002CB613403) and the National Natural Science Foundation of China (No. 20574021, U0634003 and 50433030) for the financial support.

#### References

- [1] B.W. D'Andrade, S.R. Forrest, *Adv. Mater.* 16 (2004) 1585.
- [2] D. Braun, A.J. Heeger, *Appl. Phys. Lett.* 58 (1991) 1982.
- [3] S.L. Hung, C.W. Tang, M.G. Mason, *Appl. Phys. Lett.* 70 (1997) 152.
- [4] X.H. Yang, Y.Q. Mo, W. Yang, G. Yu, Y. Cao, *Appl. Phys. Lett.* 79 (2001) 563.
- [5] F. Li, H. Tang, J. Andereg, J. Shinar, *Appl. Phys. Lett.* 70 (1997) 1233.
- [6] Y. Cao, G. Yu, A.J. Heeger, *Adv. Mater.* 10 (1998) 917.
- [7] F. Huang, H.B. Wu, D.L. Wang, W. Yang, Y. Cao, *Chem. Mater.* 16 (2004) 708.

- [8] F. Huang, L.T. Hou, H.B. Wu, X.H. Wang, H.L. Shen, W. Cao, W. Yang, Y. Cao, *J. Am. Chem. Soc.* 126 (2004) 9845.
- [9] F. Huang, Y.H. Niu, Y. Zhang, J.W. Ka, M.S. Liu, A.K.Y. Jen, *Adv. Mater.* 19 (2007) 2010.
- [10] H.B. Wu, F. Huang, Y.Q. Mo, W. Yang, D.L. Wang, J.B. Peng, Y. Cao, *Adv. Mater.* 16 (2004) 1826.
- [11] H.B. Wu, F. Huang, J.B. Peng, Y. Cao, *Org. Electron.* 6 (2005) 118.
- [12] W.J. Zeng, H.B. Wu, C. Zhang, F. Huang, J.B. Peng, W. Yang, Y. Cao, *Adv. Mater.* 19 (2007) 810.
- [13] X.W. Chen, J.L. Liao, Y.M. Liang, M.O. Ahmed, H.E. Tseng, S.A. Chen, *J. Am. Chem. Soc.* 125 (2003) 636.
- [14] J.X. Jiang, C.Y. Jiang, W. Yang, H.Y. Zhen, F. Huang, Y. Cao, *Macromolecules* 38 (2005) 4072.
- [15] H.Y. Zhen, C.Y. Jiang, W. Yang, J.X. Jiang, F. Huang, Y. Cao, *Chem. Eur. J.* 11 (2005) 5007.
- [16] H.Y. Zhen, C. Luo, W. Yang, W.Y. Song, B. Du, J.X. Jiang, C.Y. Jiang, Y. Zhang, Y. Cao, *Macromolecules* 39 (2006) 1693.
- [17] N.R. Evans, L.S. Devi, C.S.K. Mak, S.E. Watkins, S.I. Pascu, A. Kohler, R.H. Friend, C.K. Williams, A.B. Holmes, *J. Am. Chem. Soc.* 128 (2006) 6647.
- [18] Y. Zhang, Y.H. Xu, Q.L. Niu, J.B. Peng, W. Yang, X.H. Zhu, Y. Cao, *J. Mater. Chem.* 17 (2007) 992.
- [19] Y. Zhang, Y. Xiong, Y.H. Sun, X.H. Zhu, J.B. Peng, Y. Cao, *Polymer* 48 (2007) 3468.
- [20] W. Yang, Q. Hou, C.Z. Liu, Y.H. Niu, J. Huang, R.Q. Yang, Y. Cao, *J. Mater. Chem.* 13 (2003) 1351.
- [21] W. Yang, J. Huang, C.Z. Liu, Y.H. Niu, Q. Hou, R.Q. Yang, Y. Cao, *Polymer* 45 (2004) 865.
- [22] D.M. Leeuw, M.M.J. Simenon, A.R. Brown, R.E.F. Einerhand, *Synth. Met.* 87 (1997) 53.
- [23] Y.H. Xu, J.B. Peng, J.X. Jiang, W. Xu, W. Yang, Y. Cao, *Appl. Phys. Lett.* 87 (2005) 193502.
- [24] X. Gong, J.C. Ostrowski, D. Moses, G.C. Bazan, A.J. Heeger, *Adv. Funct. Mater.* 13 (2003) 439.
- [25] P.A. Lane, L.C. Palilis, D.F. O'Brien, C. Giebeler, A.J. Cadby, D.G. Lidzey, A.J. Campbell, W. Blau, D.D.C. Bradley, *Phys. Rev. B* 63 (2001) 235206.
- [26] X. Gong, M.R. Robinson, J.C. Ostrowski, D. Moses, G.C. Bazan, A.J. Heeger, *Adv. Mater.* 14 (2002) 581.
- [27] T. Förster, *Discuss. Faraday Soc.* 27 (1959) 7.



## Organic bistable memory device using MoO<sub>3</sub> nanocrystal as a charge trapping center

Kyoung Soo Yook<sup>a</sup>, Soon Ok Jeon<sup>a</sup>, Chul Woong Joo<sup>a</sup>, Jun Yeob Lee<sup>a,\*</sup>,  
Sung Hyun Kim<sup>b</sup>, Jyongsik Jang<sup>b</sup>

<sup>a</sup> Department of Polymer Science and Engineering, Dankook University, Jukjeon-dong, Suji-gu, Yongin-si, Gyeonggi-do, Seoul 448-701, Republic of Korea

<sup>b</sup> School of Chemical and Biological Engineering, Seoul National University, Shinlim-dong, Kwanak-gu, Seoul 151-742, Republic of Korea

### ARTICLE INFO

#### Article history:

Received 1 July 2008

Received in revised form 28 September 2008

2008

Accepted 2 October 2008

Available online 10 October 2008

#### PACS:

85.60.jb

#### Keywords:

Organic memory device

MoO<sub>3</sub> nanocrystal

Bistability

### ABSTRACT

Organic bistable memory devices (OBDs) with MoO<sub>3</sub> as a nanocrystal inside organic layer were developed and bistability of MoO<sub>3</sub> based OBDs was investigated. High on/off ratio over 200 was obtained at a low reading voltage of 1 V. MoO<sub>3</sub> OBDs could be electrically switched between high conductance state and low conductance state over more than 100 cycles and space charge limited conduction mechanism dominated switching behavior in MoO<sub>3</sub> OBDs.

© 2008 Elsevier B.V. All rights reserved.

## 1. Introduction

Organic bistable memory devices (OBDs) have attracted great attention due to many advantages such as high on/off ratio, high switching speed and simple fabrication process [1–14]. In addition, it can be made into flexible form on plastic substrate [1].

There have been many studies about OBDs with bistable memory characteristics and most OBDs had nanocrystals inside organic layer as a charge trapping center [2–9]. Al has been widely used as a nanocrystal for charge trapping and it showed stable memory characteristics with various organic materials [2–4]. Au was also effective as a nanocrystal and stable memory characteristics were realized in Au based OBDs [5–9]. Uniform dispersion of Au nanocrystal was achieved by self-assembly and high on/off ratio

over 1000 was obtained [8]. Alkanethiol capping of Au nanoparticle was found to be important for bistability in OBDs and dodecanethiol capping of Au improved switching performances of OBDs [6]. Other than Al and Au, CdSe capped with ZnS nanocrystal could play a role of nanoparticle for charge trapping inside C60 [10].

In this work, OBDs with MoO<sub>3</sub> as a nanoparticle for bistable memory characteristics were fabricated and memory behavior was investigated. MoO<sub>3</sub> was introduced as an interlayer inside tris(8-hydroxyquinoline) aluminium (Alq<sub>3</sub>). Detailed mechanism for bistability in MoO<sub>3</sub> OBDs was studied and it was correlated with energy level of Alq<sub>3</sub> and MoO<sub>3</sub>.

## 2. Experimental

Device structure for OBDs was indium tin oxide (ITO, 150 nm)/Alq<sub>3</sub>(50 nm)/MoO<sub>3</sub>(5 nm)/Alq<sub>3</sub>(50 nm)/Al(150 nm). Single layer OBDs with Alq<sub>3</sub> were also fabricated as a

\* Corresponding author. Tel./fax: +82 31 8005 3585.

E-mail address: [leej17@dankook.ac.kr](mailto:leej17@dankook.ac.kr) (J.Y. Lee).



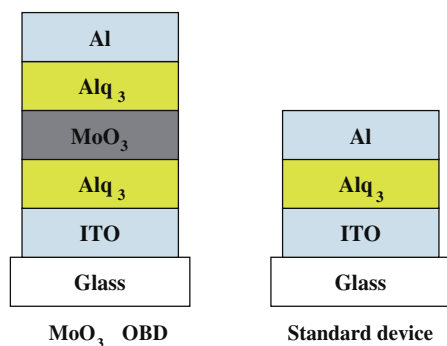


**Fig. 1.** Device structure of Alq<sub>3</sub> organic bistable memory devices with and without MoO<sub>3</sub> nanoparticles.

standard device. Device structure of OBDs is shown in Fig. 1. Pixel size of the device was 2 mm × 2 mm with an active area of 4 mm<sup>2</sup>. Deposition rate of Alq<sub>3</sub> was 0.1 nm/s, while MoO<sub>3</sub> was evaporated at a deposition rate of 0.02 nm/s. All materials were evaporated at a vacuum pressure under 1.0 × 10<sup>-6</sup> Torr. The device was encapsulated with CaO getter and a glass lid. Morphology of MoO<sub>3</sub> on Alq<sub>3</sub> was observed with transmission electron microscope (TEM, Jeol) at a magnification of 100,000. Current density–voltage relationship was measured with Keithley 2400 source measurement unit. All measurements were carried out after encapsulation in air. Pulse test of the OBD was performed with a semiconductor analyzer with a pulse width of 1 μs.

### 3. Results and discussion

MoO<sub>3</sub> has been known as a p-type dopant and charge transfer complex formation with aromatic amine materials was reported [15]. Valence band of MoO<sub>3</sub> has been known to be 5.3–5.5 eV. Therefore, charge trapping by MoO<sub>3</sub> can be induced when it is combined with Alq<sub>3</sub> with the highest occupied molecular orbital (HOMO) of 5.8 eV and the lowest unoccupied molecular orbital (LUMO) of 3.0 eV in our cyclovoltametry measurement. Hole trapping by MoO<sub>3</sub> in Alq<sub>3</sub> matrix can be expected at the interface between Alq<sub>3</sub> and MoO<sub>3</sub> and bistable memory performances can be induced by MoO<sub>3</sub>. The advantage of MoO<sub>3</sub> based memory device compared with Al embedded Alq<sub>3</sub> memory devices is that it is possible to get stable and reproducible memory performances. Al is sensitive to oxygen and it is difficult to guarantee reproducibility of device performances. MoO<sub>3</sub> is not sensitive to oxygen and memory device data are reproducible. In addition, it can be simply deposited by thermal evaporation in organic crucible at low temperature compared with other metals.

It is important to get uniform dispersion of nanoparticles to secure stable switching behavior in OBDs and morphology of MoO<sub>3</sub> on Alq<sub>3</sub> was analyzed. Fig. 2 shows TEM picture of MoO<sub>3</sub> deposited on Alq<sub>3</sub> at a thickness of 5 nm. Average size of MoO<sub>3</sub> nanoparticle on Alq<sub>3</sub> was around 30 nm and MoO<sub>3</sub> was uniformly dispersed on Alq<sub>3</sub> even though there was some scattering of particle size. Continuous film formation was not observed in TEM image of

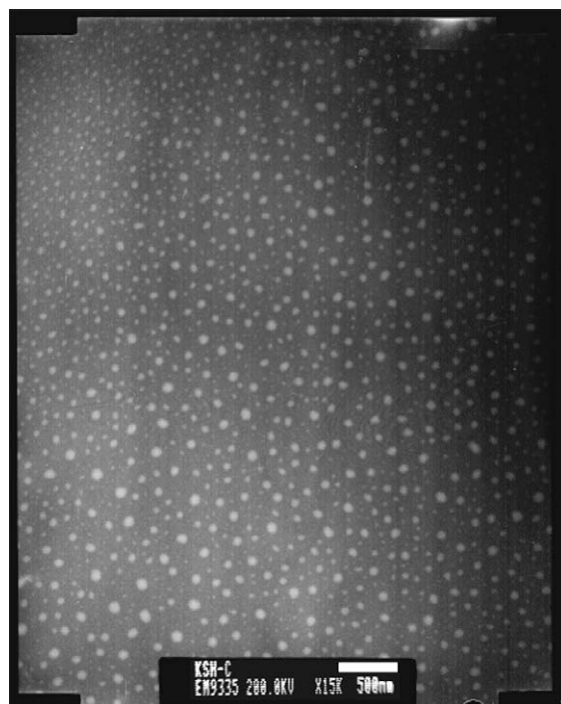


**Fig. 2.** Transmission electron microscopic picture of 5 nm thick MoO<sub>3</sub> deposited on Alq<sub>3</sub>.

MoO<sub>3</sub> on Alq<sub>3</sub> and island growth of MoO<sub>3</sub> dominated morphology of MoO<sub>3</sub>.

Memory characteristics of MoO<sub>3</sub> OBDs were measured by scanning voltage from 0 V to 7 V after applying writing and erasing voltage to the OBD. Current density–voltage plots of MoO<sub>3</sub> OBDs are shown in Fig. 3. MoO<sub>3</sub> OBDs showed bistable memory characteristics with high conductance state (ON state) and low conductance state (OFF state). Bistability was observed during forward scans depending on the writing voltage. Current density level was gradually increased according to voltage and sharp rise of current density was observed between 2.1 V and 2.4 V. The device was changed from low conductance state to high conductance state at 2.4 V. After sharp rise of current level, negative differential resistance behavior was observed. The high current state was observed after applying 2.5 V during scan from 0 V to 7 V. Large hysteresis required for bistable memory devices was clearly observed during voltage scan from 0 V to 7 V. To elucidate the switching mechanism of MoO<sub>3</sub> OBDs, single layer device of ITO/Alq<sub>3</sub>(100 nm)/Al was fabricated and its current density–voltage data were compared with those of MoO<sub>3</sub> OBDs. In contrast to MoO<sub>3</sub> OBDs, Alq<sub>3</sub> device did not show any hysteresis during voltage scans, indicating that MoO<sub>3</sub> nanoparticles are responsible for bistable current behavior in MoO<sub>3</sub> OBDs. The origin for bistable memory performances of MoO<sub>3</sub> OBDs can be found in the charge trapping by MoO<sub>3</sub>. Charges can be trapped by MoO<sub>3</sub> interlayer because there is 0.5 eV energy gap between valence band of MoO<sub>3</sub> and HOMO of Alq<sub>3</sub>. Therefore, the bistability mechanism can be explained by Simmons and Verderer mechanism

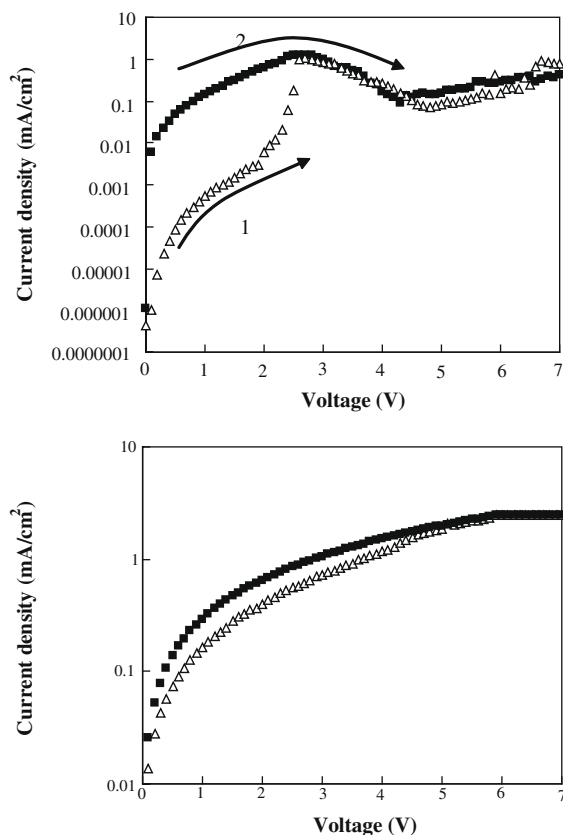


**Fig. 3.** Log (current density) -voltage curves of MoO<sub>3</sub> memory devices based on Alq<sub>3</sub>. Voltage was scanned from 0 V to 7 V after switching on the device at 2.5 V and switching off the device at 4.5 V. (a) Alq<sub>3</sub> based organic memory device with MoO<sub>3</sub>. (b) Alq<sub>3</sub> based organic memory device without MoO<sub>3</sub>.

which is based on charge trapping and detrapping [16,17]. Large amount of charges can be trapped by MoO<sub>3</sub> at high voltage and reading at low voltage (1 V) after charge trapping by MoO<sub>3</sub> gives high conductance state. Charge transport can be facilitated because charge traps are filled with holes. A sharp increase of current density is observed after the charge traps is occupied. However, the space charge formation limits the charge transport, leading to negative differential resistance region. Reading between 0 V and

2.5 V gives high conductance state after applying 2.5 V (curve 2) and low conductance state after applying 4.5 V (curve 1). Negative differential resistance behavior of MoO<sub>3</sub> OBDs supports this explanation. In off state, first scan from 0 V to 7 V (curve 1) shows low conductance state and the low conductance state is changed into high conductance state at 2.4 V. However, space charge formation at a voltage higher than 2.4 V leads to the decrease of current density level. Therefore, low conductance state can be induced by applying 4.5 V at which current density level is minimum and high conductance state can be recovered at 2.5 V at which current density level is maximum in negative differential resistance region. Current density–voltage curve after switching at 2.5 V followed the curve 2. Schematic diagram describing the on and off state is shown in Fig. 4. Even though negative bias region was not shown in Fig. 3, the device could be erased at negative bias due to charge detrapping.

To study detailed process for current flow in MoO<sub>3</sub> OBDs, charge transport mechanism of MoO<sub>3</sub> OBDs was investigated. Fig. 5 shows log–log plot of current density–voltage relationship at low conductance state. Linear relationship between log (current density) and log (voltage) was observed at low conductance state, indicating space charge limited charge transport behavior by MoO<sub>3</sub> [18,19]. This supports space charge limited switching behavior of MoO<sub>3</sub> OBDs at low conductance state.

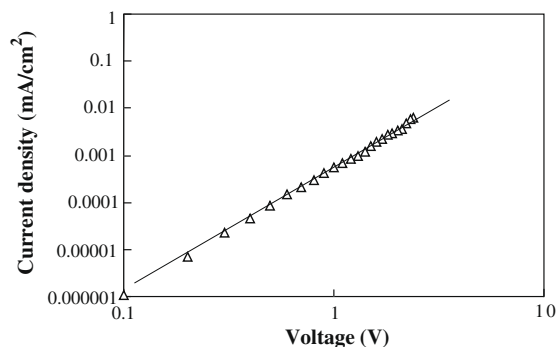


**Fig. 5.** Log (current density)–log (voltage) curves of Alq<sub>3</sub> based organic memory device with MoO<sub>3</sub> interlayer at low conductance state after applying erasing voltage of 4.5 V.

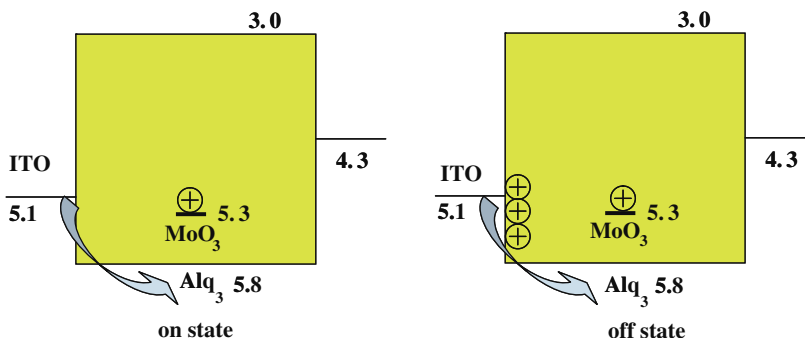


**Fig. 4.** Schematic diagram of the on and off state.

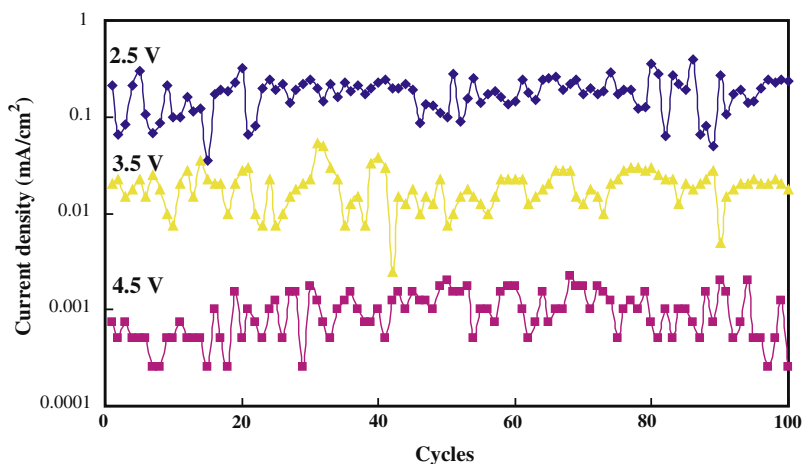


**Fig. 6.** Multilevel switching behavior of Alq<sub>3</sub> based organic memory device with 5 nm thick MoO<sub>3</sub> interlayer at a writing voltage of 2.5 V, 3.5 V and 4.5 V. Reading voltage was 1 V and the switching test was conducted 100 times.

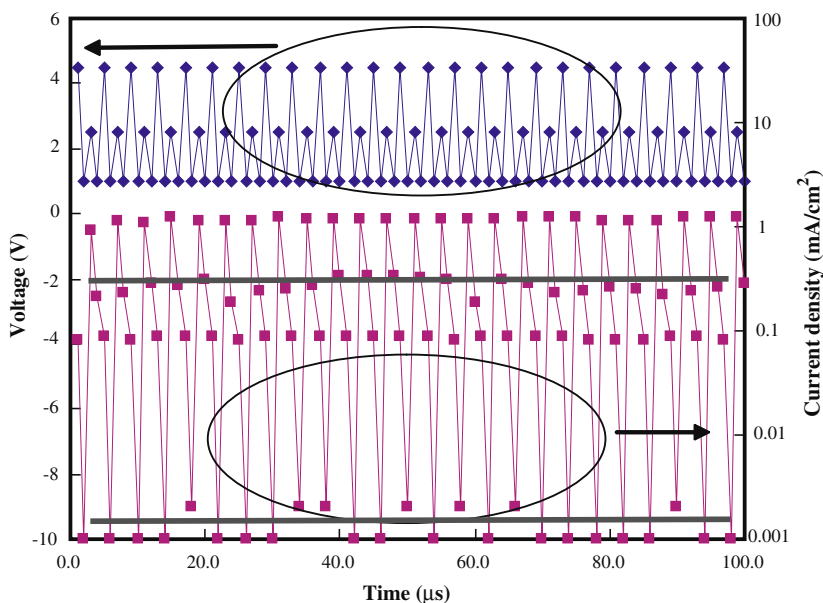


**Fig. 7.** Switching performance test results of Alq<sub>3</sub> based organic memory device with 5 nm thick MoO<sub>3</sub> interlayer. Pulse width was 1 µs and programming voltages were 2.5 V for writing and 4.5 V for erasing with a reading voltage of 1 V.

Multilevel switching can be realized by changing the writing voltage of MoO<sub>3</sub> nanoparticles based OBDs. Fig. 6 shows the multilevel switching test results of OBDs. Reading voltage was 1 V and writing voltage was 2.5 V, 3.5 V and 4.5 V. It can be clearly seen that different current density level was obtained depending on the writing voltage. Average current density level at 1 V after switching on MoO<sub>3</sub> OBDs at 2.5 V was 0.2 mA/cm<sup>2</sup>, while average current density level at 1 V after switching off MoO<sub>3</sub> OBDs at 4.5 V was 0.00075 mA/cm<sup>2</sup>. Current density level of OBDs after switching OBDs at 3.5 V was 0.02 mA/cm<sup>2</sup>. Three level switching could be effectively induced by changing the writing voltage in negative differential resistance region.

The switching test results also agree with the data proposed by Simmons and Verderber and support the charge trapping and detrapping mechanism [16]. High average on/off ratio over 200 could be obtained after programming MoO<sub>3</sub> OBDs at 2.5 V and 4.5 V with a reading voltage of 1 V. The on/off ratio was quite stable even though there was some scattering of current density level during multicycle test.

To get more detailed information about the switching behavior of the OBD, pulse voltage with a pulse width of 1 µs was applied to the OBD. Programming voltages were 4.5 V and 2.5 V, while the reading voltage was 1 V. Fig. 7 shows switching test results of the OBD with MoO<sub>3</sub> nano-

crystals. The OBD with MoO<sub>3</sub> nanocrystal inside Alq<sub>3</sub> showed good switching performances between on and off states. The on and off currents were maintained during measurements without any decrease.

#### 4. Conclusions

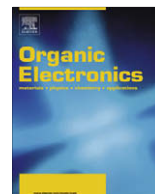
In summary, bistable memory devices could be fabricated by using MoO<sub>3</sub> as a nanoparticle to trap charges. Stable memory characteristics could be obtained by inserting MoO<sub>3</sub> between Alq<sub>3</sub> organic layers and high on/off ratio over 200 could be realized at a writing voltage of 2.5 V and erasing voltage of 4.5 V. The high on/off ratio could be maintained even after multicycle test over 100 times.

#### Acknowledgement

The present research was conducted in 2008 using research funds supplied by the Strategic Research Institute, Dankook University.

#### References

- [1] L. Li, Q. Ling, S. Lim, Y. Tan, C. Zhu, D.S.H. Chan, E. Kang, K. Neoh, *Org. Electron.* 8 (2007) 401.
- [2] J. Ouyang, C. Chu, C.R. Szmanda, L. Ma, Y. Yang, *Nat. Mater.* 3 (2004) 918.
- [3] L.D. Bozano, B.W. Kean, M. Beinhoff, K.R. Carter, P.M. Rice, J.C. Scott, *Adv. Funct. Mater.* 15 (2005) 1933.
- [4] Y. Yang, J. Ouyang, L. Ma, R.J. Tseng, C. Chu, *Adv. Funct. Mater.* 16 (2006) 1001.
- [5] R.J. Tseng, J. Huang, J. Quyang, R.B. Kaner, Y. Yang, *Nano Lett.* 5 (2005) 1077.
- [6] J. Quyang, C. Chu, D. Sieves, Y. Yang, *Appl. Phys. Lett.* 86 (2005) 123507.
- [7] A. Prakash, J. Ouyang, J. Lin, Y. Yang, *J. Appl. Phys.* 100 (2006) 054309.
- [8] H.P. Wang, S. Pigeon, R. Izquierdo, R. Martel, *Appl. Phys. Lett.* 89 (2006) 183502.
- [9] C. Tu, D. Kwong, Y. Lai, *Appl. Phys. Lett.* 89 (2006) 252107.
- [10] F. Li, D. Son, J. Ham, B. Kim, J.H. Jung, T.W. Kim, *Appl. Phys. Lett.* 91 (2005) 162109.
- [11] Y. Lai, C. Tu, D. Kwong, J.S. Chen, *Appl. Phys. Lett.* 87 (2005) 122101.
- [12] M. Lauters, B. McCarthy, D. Sarid, G.E. Jabbour, *Appl. Phys. Lett.* 87 (2005) 231105.
- [13] J. Chen, L. Xu, J. Lin, Y. Geng, L. Wang, D. Ma, *Appl. Phys. Lett.* 89 (2006) 083514.
- [14] A. Kanwal, M. Chhowalla, *Appl. Phys. Lett.* 89 (2006) 203103.
- [15] H. Ikeda, J. Sakata, M. Hayakawa, T. Aoyama, T. Kawakami, K. Kamata, Y. Iwaki, S. Seo, Y. Noda, R. Nomura, S. Yamazaki, *SID Digest* 37 (2006) 923.
- [16] J.G. Simmons, R.R. Verderber, *Proc. R. Soc. London, Ser. A* 301 (1967) 77.
- [17] L.D. Bozano, B.W. Kean, V.R. Deline, J.R. Salem, J.C. Scott, *Appl. Phys. Lett.* 84 (2004) 607.
- [18] M.A. Lampert, P. Mark, *Current Injection in Solids*, Academic, New York, 1970.
- [19] J.Y. Lee, *J. Ind. Eng.* (2008), doi:10.1016/j.jiec.2008.04.007.



## Second order nonlinear optical networks with excellent poling stability from a new trifunctional thiophene based chromophore

Fabio Borbone<sup>a</sup>, Ugo Caruso<sup>a</sup>, Rosita Diana<sup>a</sup>, Barbara Panunzi<sup>b,\*</sup>, Antonio Roviello<sup>a</sup>, Marco Tingoli<sup>b</sup>, Angela Tuzi<sup>a</sup>

<sup>a</sup> Dipartimento di Chimica "Paolo Corradini", Università degli Studi di Napoli "Federico II", Complesso Universitario di Monte S. Angelo, via Cintia, 80126 Napoli, Italy

<sup>b</sup> Dipartimento di Scienza degli Alimenti, Università degli Studi di Napoli "Federico II", via Università 100, 80155 Portici, Napoli, Italy

### ARTICLE INFO

#### Article history:

Received 17 June 2008

Received in revised form 30 September 2008

Accepted 5 October 2008

Available online 14 October 2008

#### PACS:

82.35.Ej

61.25.hp

81.05.Zx

#### Keywords:

Thiophene dye

NLO properties

Crosslinked material

### ABSTRACT

Two new trifunctional thiophene based dyes suited for crosslinking were synthesised from the same structural core, i.e. 4-[[5-[(4-nitrophenyl)azo]-2-thienyl]azo]benzenamine. Crystal structure and second order nonlinear optical properties were determined on a related difunctional dye that can be considered as a representative and simplified model of the trifunctional compounds, determining on it the  $\mu\beta$  value of  $4950 \times 10^{-48}$  esu ( $6111 \times 10^{-80} \text{C}^2 \text{m}^4 \text{V}^{-2}$ ).

The presence of three acrylic or hydroxyl functional groups in the dyes allowed to incorporate the chromophoric fragment into two different kinds of crosslinked materials possessing "frozen" long-lasting dipole order. The traditional guest-host approach used for one of them was exceeded by covalently anchoring the chromophore to a functionalised polymer in a three-dimensional unique network. In this way a promising NLO active material was obtained. The value of the  $d_{33}$  coefficient (determined by SHG measurement using the Maker fringe technique) was 11 pm/V for the poled/crosslinked film. Very good thermal and temporal stability of the chromophore poling-induced dipole alignment was attained.

© 2008 Elsevier B.V. All rights reserved.

### 1. Introduction

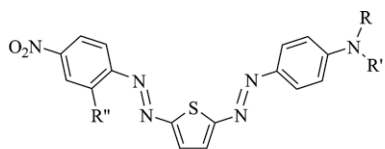
Compounds exhibiting disazo-thiophene groups have been extensively investigated, especially for their properties of colouring textiles and plastics or in general as dispersed pigments [1,2]. More recently, thiophene has been largely used as electron-rich molecule for a variety of optical and electrooptical applications [3–5]. Thiophene based dyes typically contain aromatic rings linked by unsaturated moieties. The influence on electron donor effects of the thiophene ring has been extensively examined [6] and the use of this heterocycle in compounds for nonlinear optics has

gained increasing consideration [7–9]. In particular, theoretical investigations indicated that the replacement of a phenyl ring with a thiophenic one significantly improves the values of molecular hyperpolarizability [10–12]. Thiophene not only behaves as one of the most effective heterocyclic rings in enhancing NLO properties of typical push-pull chromophores even in relatively short conjugated systems, but also prompts the desirable targets of high solubility of the dyes and easy processability of materials.

In this work, we report the synthesis of three functionalised derivatives having the same core, 4-[[5-[(4-nitrophenyl)azo]-2-thienyl]azo]benzenamine (C type compounds in Fig. 1) and their precursors (C' type compounds in Fig. 1).

In the new dyes the thiophene ring is interposed between two highly conjugated moieties bringing donor and acceptor substituents. The unsaturated moieties are

\* Corresponding author. Tel.: +39 081 674170; fax: +39 081 674090.  
E-mail address: [barbara.panunzi@unina.it](mailto:barbara.panunzi@unina.it) (B. Panunzi).



$R = \text{CH}_3$ ; $R' = \text{CH}_2\text{CH}_2\text{OCOCH}=\text{CH}_2$ ; $R'' = \text{OH}$	$\mathbf{C}'_{\text{Diacr}}$
$R = R' = \text{CH}_2\text{CH}_2\text{OCOCH}=\text{CH}_2$ ; $R'' = \text{OH}$	$\mathbf{C}'_{\text{Triacr}}$
$R = R' = \text{CH}_2\text{CH}_2\text{OH}$ ; $R'' = \text{OH}$	$\mathbf{C}'_{\text{Triox}}$
$R = \text{CH}_3$ ; $R' = \text{CH}_2\text{CH}_2\text{OCOCH}=\text{CH}_2$ ; $R'' = \text{OCOCH}=\text{CH}_2$	$\mathbf{C}_{\text{Diacr}}$
$R = R' = \text{CH}_2\text{CH}_2\text{OCOCH}=\text{CH}_2$ ; $R'' = \text{OCOCH}=\text{CH}_2$	$\mathbf{C}_{\text{Triacr}}$
$R = R' = \text{CH}_2\text{CH}_2\text{OH}$ ; $R'' = \text{OCH}_2\text{CH}_2\text{OH}$	$\mathbf{C}_{\text{Triox}}$

**Fig. 1.** Chemical diagrams of the chromophores (**C** type compounds) and their precursors (**C'** type compounds).

azo bridges, that are claimed to be the most efficient ones in push–pull systems [13].

In contrast with the extended use of thiophene in NLO active polymers and materials [14–16], only a few examples of disazo-thiophene dyes for the synthesis of NLO active materials are known [17,18]. To our knowledge no example of disazo-thiophene dye in crosslinked materials was reported.

The strategy generally used to produce NLO active materials with enduring polar order involves the synthesis of polymers crosslinkable under electric field [19,20]. Alternatively, polyfunctionalised monomers, eventually pre-polymerised, are poled and crosslinked under poling conditions to give the final network [21,22].

In our case, according to the last approach,  $\mathbf{C}_{\text{Triacr}}$  was simply reacted with non NLO active polyfunctional monomers under an electric field. For  $\mathbf{C}_{\text{Triox}}$  another recently proposed approach [23] was implemented. The dispersed chromophore, polyglycidyl methacrylate (PGMA) and a passive co-crosslinker were thermally seized by covalent bonding in a single network under poling conditions. The most promising crosslinked material presented in this paper was achieved in this case, getting materials with both high NLO activity and excellent temporal stability of the dipolar alignment.

The difunctional compound  $\mathbf{C}_{\text{Diacr}}$  was tailored as a model compound for EFISH and spectroscopic measurements. X-ray single crystal diffraction analysis was also effected, in order to relate crystal structure and optical properties and to achieve information on the factors affecting solubility.

## 2. Results and discussion

### 2.1. Synthesis and characterization of dyes

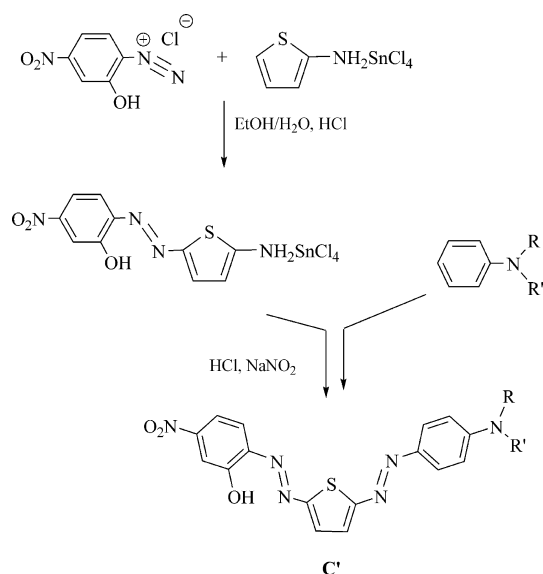
Three thiophene based functionalised push–pull chromophores ( $\mathbf{C}_{\text{Diacr}}$ ,  $\mathbf{C}_{\text{Triacr}}$  and  $\mathbf{C}_{\text{Triox}}$  in Fig. 1) were synthesised and characterized. The dye skeleton includes a nitro acceptor group and a substituted amino donor group on

phenyl rings linked by a conjugated system made up of two azo bridges and one thiophene unit. The syntheses of similar 2,5-disazo-thiophene compounds reported in literature [18,24] is often cumbersome. We have followed a synthetic pathway somehow different and simplified respect to the previously described ones [8,15,18]. According to a previous report [8], a nitro group in 2 position on a thiophene ring can be converted into an aminic one by reduction with tin. Isolation of a  $\text{SnCl}_4$ -aminothiophene hydrochloride complex avoided the use of the poorly stable free 2-aminothiophene. The complex was then converted into the acetamido derivative that was successively nitrated and then deprotected to nitroamine [8]. In our case, we have directly copulated 2-hydroxy-4-nitrobenzenediazonium chloride with  $\text{SnCl}_4$ -aminothiophene hydrochloride, the metal group acting as a protector group in the synthesis of the first azo bridge. We built the second azo bridge by amine diazotation on this metalated intermediate after easy de-protection in mildly acid solution. Thus, such use of the not isolated intermediate complex allowed easy and fast *one-pot* synthesis of the **C'** type chromophores (Scheme 1), that were used as precursors of **C** type ones.

Starting from **C'** chromophores, three different dyes (**C** type compounds, Fig. 1) were easily obtained as acrylic or hydroxylic derivatives. The trifunctional compounds,  $\mathbf{C}_{\text{Triacr}}$  and  $\mathbf{C}_{\text{Triox}}$ , were designed to be employed in the synthesis of two kinds of crosslinked materials.

The three chromophores are all crystalline greenish gray solids, affording blue solutions in chloroform. The  $^1\text{H}$  NMR spectra gave evidence of high purity for all products. In particular, the singlet pertaining to the thiophene proton, observed at 8.36 ppm, can be considered diagnostic. Thermodynamic data for **C** chromophores and their precursors **C'** are reported in Table 1.

According to thermogravimetric analyses, the 5% weight loss temperatures are higher than 200 °C for all



**Scheme 1.** Synthetic pathway for **C'** type compounds.

**Table 1**

Thermodynamic data for the chromophores (C type compounds) and their precursors (C' type compounds).

Sample	$T_m$ (°C)	$\Delta H$ (J/g)	$T_{dec}$ (°C) <sup>a</sup>
C <sup>Diacr</sup>	199.5	15.6	218
C <sup>Triacr</sup>	169.8	20.4	213
C <sup>Triox</sup>	160.4	11.7	222
C' <sup>Diacr</sup>	148.0	<sup>b</sup>	215
C' <sup>Triacr</sup>	123.0	65.6	210
C' <sup>Triox</sup>	157.0	11.4	220

<sup>a</sup> Decomposition temperature, calculated as the 5% weight loss temperature in N<sub>2</sub>.

<sup>b</sup> Not integrable.

compounds. DSC–TGA curves for the acrylic derivatives C<sup>Diacr</sup> and C<sup>Triacr</sup> are similar. Fig. 2 shows, as an example, DSC and TGA curves for C<sup>Triacr</sup>.

It can be observed that the DSC curve shows the endothermic peak related to melting immediately followed by a broad exothermic signal, probably as a consequence of thermo-induced breakage of the double bonds. A gradual partial degradation not involving significant weight loss occurs together with this transition, as confirmed by <sup>1</sup>H NMR, UV spectra, optical observation, DSC and TGA analysis effected on a thermally treated sample. This behaviour could be compared with the well known photochemical degradation reaction of phenylazo-thiophenes containing electron donors and attractors [25,26].

The OH-functionalised derivatives C'<sup>Triox</sup> and C<sup>Triox</sup> show a larger range of stability after melting and no degradation is detected till about 220 °C. This behaviour makes them better candidates for NLO applications.

The difunctional dye C<sup>Diacr</sup> was most easily obtained in pure form, and was considered as a “model” suitable for X-ray and EFISH measurements.

The X-ray single crystal molecular structure of C<sup>Diacr</sup> is shown in Fig. 3, selected bond lengths and angles are reported in Table 2.

Except for the two acrylic groups, the molecule is overall planar and a bent shape is observed. The two N=N moieties with E geometry are in mutual syn arrangement on

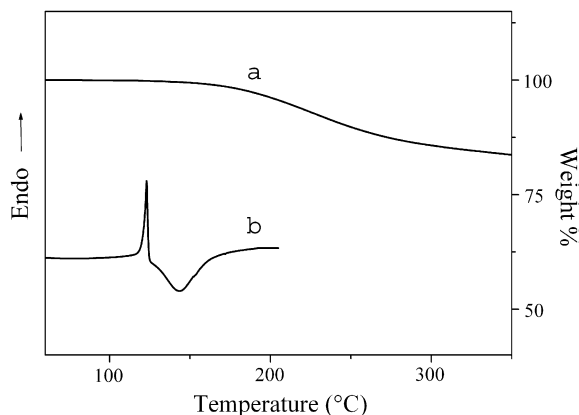


**Fig. 2.** Example of thermogravimetric and calorimetric curves for the acrylic C type compounds. TGA (a) and DSC (b) curves for C<sup>Triacr</sup>.

the thiophene ring. Both acrylic groups are planar and substantially perpendicular to the mean plane of the molecule (torsion angles around C4–O3 and N6–C20 bonds are 102.6(4)° and 95.4(4)°, respectively). The nitro group is almost co-planar with the attached phenyl ring, and a clear trigonal planar geometry is observed around N6. The flat shape of the molecule and the analysis of geometric parameters are in keep with extension of conjugation to the entire molecule.

The above results indicate that the core of the dyes satisfies basic conditions required to exhibit good NLO properties. In fact, it was demonstrated that a long conjugation path is expected to enhance second order non-linear hyperpolarizability and a bent molecular shape is claimed to favour efficient orientation of the chromophore in the material under poling conditions [27]. The bent shape, in addition to the presence of aliphatic chains, is also expected to favour solubility in common organic solvents. In fact, it is to remark that the dyes here described display good solubility in organic solvents at variance with most of the analogous rod-like all-benzenoid compounds [7], whose solubility is often to be enhanced by introduction of suited substituents [28].

EFISH measurements were effected on compound C<sup>Diacr</sup>. The  $\mu\beta$  value measured by EFISH technique in chloroform solutions at  $\lambda = 1.907 \mu\text{m}$ , is  $4950 \times 10^{-48}$  esu ( $6111 \times 10^{-80} \text{C}^2 \text{m}^4 \text{V}^{-2}$ ). To our knowledge this is by far the highest value found for similar thiophene based dyes and is about twice higher than the ones typically displayed by analogous all-benzenoid compounds [29,30].

UV–vis spectra were also recorded on the model chromophore C<sup>Diacr</sup> in solvents with different polarity (see Table 3) and show the existence of a relevant solvatochromic shift as well as low levels of optical absorption at some typical NLO operating wavelengths.

## 2.2. Polymeric networks

Covalently crosslinked polymeric networks (NET1 and NET2) were obtained, respectively, from C<sup>Triacr</sup> and C<sup>Triox</sup>.

Our attempts to react the acrylic groups of C<sup>Triacr</sup> by radical activation gave variable (by changing type of initiator and reaction temperature) amounts of decomposed material. In fact, as for the radical induced reactivity of acrylic monomers, it was demonstrated [25,26] that while azobenzenes containing a push–pull donor–acceptor conjugated system are moderately robust, the corresponding 2,5-substituted azothiophenes easily undergo photodegradation reactions.

Thus, in order to avoid damage to the system during crosslinking and to preserve reproducibility of the NLO signal, we reacted C<sup>Triacr</sup> by use of a procedure not involving radicals. It is well known [31] that primary or secondary amines easily add to vinyl bonds activated by electron attracting groups. The reaction is substantially a nucleophilic ionic addition. To obtain a network we used this reaction in bulk between C<sup>Triacr</sup> and a secondary diamine, 4,4'-trimethylene-dipiperidine. Eventually a passive co-crosslinker was added. The two polyfunctional monomers were layered by spinning as thin films and thermally cross-linked during poling.

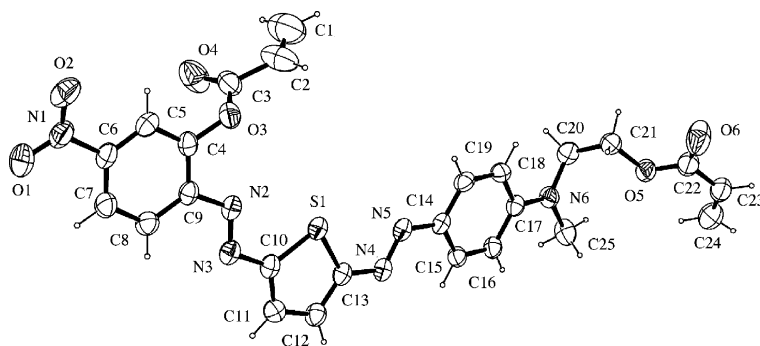


Fig. 3. Molecular structure of **C<sub>Diacr</sub>** obtained from single crystal X-ray analysis (thermal ellipsoids are drawn at 30% probability level).

Table 2

Selected bond lengths (Å) and angles (°) for **C<sub>Diacr</sub>** with esd's in parentheses.

Bond lengths (Å)		Torsion angles (°)	
S1–C10	1.731(4)	N2–N3–C10–S1	0.2(4)
S1–C13	1.744(3)	N5–N4–C13–S1	2.8(4)
N2–N3	1.278(4)	C17–N6–C20–C21	95.4(4)
N2–C9	1.424(4)	C9–C4–O3–C3	102.6(4)
N3–C10	1.395(4)		
N4–N5	1.275(4)		
N4–C13	1.388(4)		
N5–C14	1.406(4)		

Table 3

UV–vis data for the model chromophore **C<sub>Diacr</sub>**.

Solvent	$\mu$ (D) <sup>a</sup>	$\lambda_{\max}$ (nm) <sup>b</sup>	$\epsilon$ (L/cm mol) <sup>c</sup>
<b>C<sub>Diacr</sub></b>			
Ethyl acetate	1.78	599	45,500
Acetone	2.88	610	45,695
DMSO	3.96	639	45,270

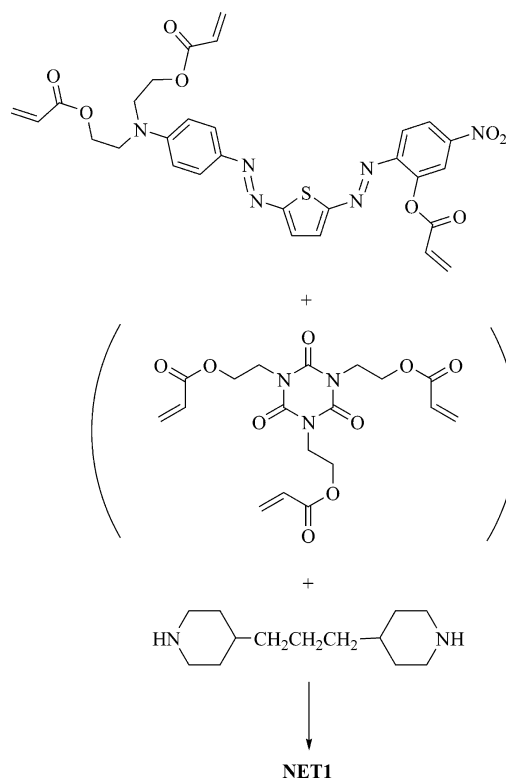
<sup>a</sup> Solvent dipole moment by Handbook of Chemistry and Physics, 59th ed., CRC Press, Inc.

<sup>b</sup> Wavelength of UV–vis absorbance maximum.

<sup>c</sup> Molar absorbance coefficient.

Constituents of the crosslinked film **NET1** are shown in Scheme 2.

By this synthetic route we easily obtained homogeneous crosslinked thin films either balancing stoichiometrically the aminic functions of 4,4'-trimethylene-dipiperidine only with the acrylic groups of **C<sub>Triacr</sub>**, or employing also tris[2-(acryloyloxy)ethyl]isocyanurate as a non NLO active crosslinker. This component was added in order to dilute the system and so contrast the depressing effect of dipole–dipole interactions on poling. In this case, the total amount of aminic functions was stoichiometrically balanced by the total acrylic functions, obtaining films at 5%, 10%, 20%, 30% by weight in chromophore. Although crosslinked insoluble films were obtained, no relevant SHG signal were recorded on them. Since crosslinking started on mixing of constituents, before thermal and electrical induction, it seems reasonable that the high rate of the reaction prevents efficient poling. Studies on the mechanism of Michael reaction of acrylates with primary and secondary amines gave evidence of possible sterical control of the



Scheme 2. Constituents of **NET1** film.

reaction rate [32]. However, attempts to lower the reaction rate by use of encumbered amines did not result in substantial improvements. The failure of the use of the passive crosslinker supports the hypothesis of a too fast crosslinking rate [33].

The presence of hydroxylic instead than acrylic functions in **C<sub>Triox</sub>**, should reasonably imply a more moderate reactivity of the dye, maintaining anyway good crosslinking aptitude. We recall that a recently employed approach [23] to stable NLO active materials is grounded on covalent crosslinking of a tailored polymer with the chromophore under poling conditions. We used **C<sub>Triox</sub>** substantially in similar way, but in our case a very simple monofunctional polymer was used and the covalent link was based on fac-



ile epoxy chemistry [34] in absence of initiator. We achieved (Scheme 3) the epoxy ring-opening of PGMA by reaction with the alcoholic functions of the chromophore and of the co-crosslinker to obtain the material **NET2**.

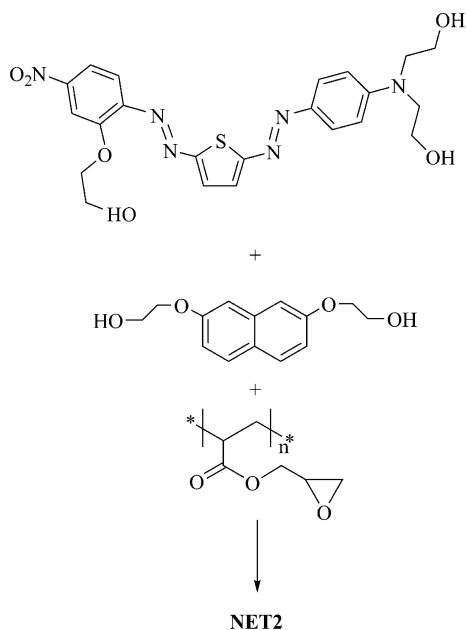
The total amount of epoxy functions was stoichiometrically balanced by the total alcoholic functions [35]. The glass transition temperature of pure PGMA (108 °C) is low enough to allow the entire system to be fluid and steerable at relatively low temperatures (about 10–20 °C below the glass transition). In these conditions the cross-linking reaction starts without catalyst while electric field is applied. Differently than for **NET1**, in the best poling conditions (140 °C for 4 h) the crosslinking rate results to be slow enough to allow satisfactory polar order before network “freezing”.

A set of crosslinked poled films was prepared according to Scheme 3 at 5%, 10%, 20%, 30%, 40%, and 54% by weight of chromophore, the latter corresponding to the stoichiometric amount in absence of co-crosslinker. Second order optical nonlinearity of **NET2** was evaluated by determining the  $d_{33}$  coefficient of the films by means of Maker fringe technique. In the above range of dye loading the value of  $d_{33}$  grows up to a maximum (at 30%), thereafter decreasing. This behaviour is in agreement with assessed theoretical expectation [36].

Fig. 4 shows the Maker fringe pattern for the 30% film, where the full-line corresponds to the best-fit curve.

In spite of the high chromophore NLO activity the SHG signal is in the average range for organic polymeric materials [37]. In fact, the  $d_{33}$  coefficient reaches a value of 11 pm/V for a 30% film poled in the best conditions. This finding could be related to the thermal epoxy ring-opening reaction that partially binds the dyes even at low temperature.

On the other hand, the nonlinear activity is well retained in time as demonstrated by thermal treatment of



**Scheme 3.** Constituents of **NET2** film.

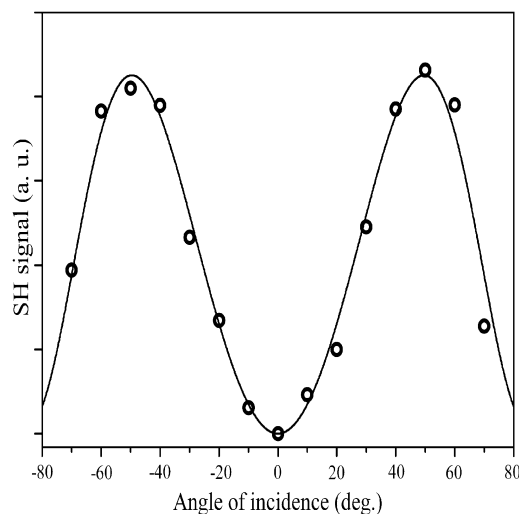


**Fig. 4.** The Maker fringes pattern of transmitted SH signal for **NET2** (30%) poled film. Open circle and full-line curve represent the experimental data and the best-fit curve, respectively.

films with various chromophore weight. In particular, Fig. 5 shows no detectable loss of activity within the experimental error for a 30% sample kept at 85 °C in air during several days.

This excellent stability of **NET2** is not typical of simple guest-host systems and is certainly due to strong degree of crosslinking. Additional stabilising effect could also be reasonably ascribed to the rigidity of naphthalene containing bridges from the passive co-crosslinker. It is to recall that also crosslinked polyglycidylmethacrylate based NLO polymers including chromophore pendants in the polymeric chains can attain high temporal stability of the nonlinear response. In fact, the SHG signal of poled samples was reported to retain from about 80% [38] to 100% [39] of its initial value. Our system attains in simple way a similar result.

The intermolecular crosslinks deriving by the thermal reaction of the hydroxyl groups of **C<sub>TrioX</sub>** and of 2,2'-(naph-

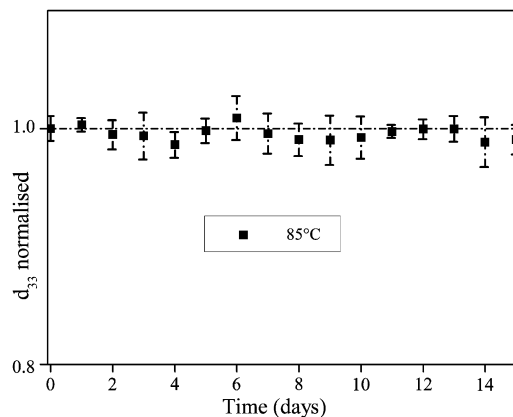


**Fig. 5.** SHG decay of **NET2** (30%) poled film at 85 °C, showing the temporal stability of the normalized NLO coefficient [ $d_{33}(t)/d_{33}(0)$ ].

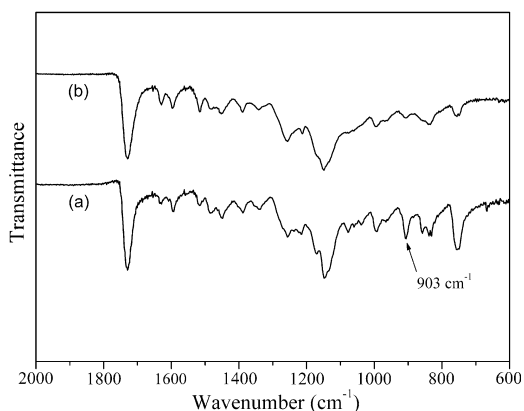


**Fig. 6.** IR spectra of NET2 (30%) film before (a) and after (b) crosslinking. The characteristic epoxy signal at  $903\text{ cm}^{-1}$  is marked.

thalene-2,7-diylbis(oxy)diethanol with the glycidyl groups of PGMA can be evidenced by FTIR spectroscopy [38]. The decrease of epoxy signal ( $903\text{ cm}^{-1}$ , see Fig. 6) is diagnostic, indicating that a consistent thermo-crosslinking has occurred in NET2 film.

### 3. Experimental part

#### 3.1. Materials and methods

Thiophene, 2-amino-5-nitrophenol, *N*-phenyldiethanolamine, *N*-methyl aniline, acryloyl chloride, 4,4'-trimethylene-dipiperidine, 2-bromoethanol, tris[2-(acryloyloxy)ethyl]isocyanurate, tin powder, are commercially available. All commercial products and solvents were used without further purification.

2,2'-(Naphthalene-2,7-diylbis(oxy)diethanol was synthesised according to the procedure reported for the 2,6-isomer [40]. The synthesis of 2-nitrothiophene [8], 2-hydroxy-4-nitrobenzenediazonium chloride [41], 2-(methyl(phenyl)amino)ethyl acrylate [42], 2,2'-(phenylazenedyl)bis(ethane-2,1-dyl)diacrylate [42],  $\text{SnCl}_4$ -2-aminothiophene hydrochloride [8] were performed according to literature. PGMA was obtained by a typical radicalic polyaddition in DMF at  $70\text{ }^\circ\text{C}$  with AIBN as initiator [42].

Optical observation was performed by using a Zeiss Axiocop polarizing microscope equipped with FP90 Mettler heating stage. Phase transition temperatures and enthalpies were measured using a DSC scanning calorimeter Perkin Elmer Pyris using a scanning rate of  $10\text{ }^\circ\text{C}/\text{min}$ , under nitrogen flow. UV-vis absorption spectra were recorded at room temperature by use of a Jasco V-560 Spectrophotometer. Thermogravimetric analysis was performed in air by a TA Instruments SDT 2960 Simultaneous DTA-TGA.  $^1\text{H}$  NMR spectra were recorded using Varian Spectrometers operating at 200 and 300 MHz. The mass spectra of the chromophores were recorded with a MALDI TOF DE-PRO apparatus on a matrix of 2,5-dihydroxybenzoic acid. IR spectra were recorded on a FT/IR-430 JASCO spectrophotometer.

Single crystals of  $\text{C}'_{\text{Diacr}}$  were obtained by slow evaporation of chloroform/hexane solution. One suitable crys-

tal was mounted at room temperature on a Bruker-Nonius Kappa-CCD diffractometer (Mo  $\text{K}\alpha$  radiation, graphite monochromator, CCD rotation images,  $\phi + \omega$  scans to fill asymmetric unit). The structure was solved by direct methods (SIR97 package [43]) and anisotropically refined by the full matrix least-squares method on  $F^2$  against all independent measured reflections (SHELXL program of SHELX97 package [44]). Hydrogen atoms were introduced in calculated positions and refined as riding on their carrier atoms. Crystal data for  $\text{C}'_{\text{Diacr}}$ :  $\text{C}_{25}\text{H}_{22}\text{N}_6\text{O}_6\text{S}$ ,  $M_r = 534.55$  triclinic, space group  $P-1$ ,  $D_{\text{calcd}} = 1.362\text{ g cm}^{-3}$ ,  $Z = 2$ ,  $a = 8.176(2)\text{ \AA}$ ,  $b = 11.859(3)\text{ \AA}$ ,  $c = 15.016(3)\text{ \AA}$ ,  $\alpha = 67.61(2)^\circ$ ,  $\beta = 75.52(2)^\circ$ ,  $\gamma = 85.57(3)^\circ$ ,  $V = 1303.2(5)\text{ \AA}^3$ . Approximate crystal dimensions  $0.57 \times 0.15 \times 0.08\text{ mm}$ . Numbers of measured and unique reflections were 15046 and 5362, respectively ( $R_{\text{int}} = 0.0647$ ). Final  $R_1 = 0.0629$ ,  $wR_2 = 0.1630$  for 344 parameters and 2575 reflections with  $I > 2\sigma(I)$  and  $2.80^\circ < \theta < 26.62^\circ$ . Largest difference peak and hole were  $0.566$  and  $-0.262\text{ e}\text{\AA}^{-3}$  [45].

#### 3.2. Synthesis of the chromophores

##### 3.2.1. $\text{C}'$ precursors

The synthesis of  $\text{C}'$  precursors was performed by the same general one-step procedure, and no two-rings intermediate was isolated. As an example the synthesis of  $\text{C}'_{\text{Diacr}}$  is described.

**3.2.1.1.  $\text{C}'_{\text{Diacr}}$ .** To a solution of 2-hydroxy-4-nitrobenzenediazonium chloride (0.75 g, 2.78 mmol) in ethanol (80 mL) cooled at  $10\text{ }^\circ\text{C}$ , a solution of  $\text{SnCl}_4$ -aminothiophene hydrochloride (1.00 g, 2.78 mmol) in water (20 mL) with HCl (1 mL, 37% solution) was added under stirring. The mixture turned to dark red and was kept under stirring for about 30 min. After this time HCl (3 mL, 37%) and then a solution of  $\text{NaNO}_2$  (1.28 g, 18.5 mmol) in water (10 mL) were slowly added, and the mixture was kept at room temperature for 15 min. A solution of 2-(methyl(phenyl)amino)ethyl acrylate (1.40 g, 6.82 mmol) in ethanol (20 mL) was added and the mixture was stirred at room temperature for 1 h. After this time, the mixture was poured on ice/water and pH was regulated at about five with sodium acetate, ensuing precipitation of a blue solid. The product was recovered by filtration, washed twice with water, and dried at  $70\text{ }^\circ\text{C}$ . The compound was dissolved in a minimum amount of acetone and the solution adsorbed on about 3 g of Florisil (100–200 mesh). The solvent was removed by mild warming in an oven, and the solid was layered on the top of a column containing about 200 g of Florisil. Elution with chloroform afforded first an orange fraction, and then the blue fractions containing the product. By concentrating the blue solution to a small volume (about 10 mL) and adding hexane the product was recovered. Two further crystallisations in  $\text{CHCl}_3$ /hexane (2:1) gave  $\text{C}'_{\text{Diacr}}$  as a crystalline dark green solid (dark-blue in solution). Yield: 45%.

$^1\text{H}$  NMR ( $\text{CDCl}_3$ ;  $\text{Me}_4\text{Si}$ ; 200 MHz)  $\delta$ : 3.20 (s, 3H), 3.79 (t, 2H,  $J = 5.8$ ), 4.40 (t, 2H,  $J = 5.6$ ), 5.86 (dd, 1H,  $J = 10.2$ ,  $J = 1.4$ ), 6.20 (dd, 1H,  $J = 17.2$ ,  $J = 10.5$ ), 6.38 (dd, 1H,

$J = 17.4$ ,  $J = 1.7$ ), 6.82 (d, 2H,  $J = 9.0$ ), 7.64 (d, 1H,  $J = 4.6$ ), 7.85 (6H, m), and 11.73 (1H, s).

MS ( $m/s$ ) 480.12 ( $M$  calc. 480.50).

**3.2.1.2.  $C'_{Triacr}$ .** It was obtained by employing 2,2'-(phenylazenedyl)bis(ethane-2,1-dyl)diacrylate and purified by the same pathway of  $C'_{Diacr}$ . Yield: 50%.

$^1H$  NMR ( $CDCl_3$ ;  $Me_4Si$ ; 200 MHz)  $\delta$ : 3.69 (t, 2H,  $J = 6.0$ ), 4.29 (t, 2H,  $J = 5.7$ ), 5.77 (dd, 2H,  $J = 10.5$ ,  $J = 1.4$ ), 6.01 (dd, 2H,  $J = 17.1$ ,  $J = 10.2$ ), 6.30 (dd, 2H,  $J = 17.4$ ,  $J = 1.6$ ), 6.76 (d, 2H,  $J = 8.7$ ), 7.55 (d, 1H,  $J = 4.5$ ), 7.66 (d, 1H,  $J = 4.5$ ), 7.73 (5H, m), and 11.00 (1H, s).

MS ( $m/s$ ) 564.14 ( $M$  calc. 564.18).

**3.2.1.3.  $C'_{Triox}$ .** It was obtained by employing *N*-phenyldiethanolamine and purified by the same pathway of  $C'_{Diacr}$ . Yield: 44%.

$^1H$  NMR (DMSO; 200 MHz)  $\delta$ : 3.21 (8H, m), 4.79 (2H, s), 6.79 (d, 2H,  $J = 9.3$ ), 7.60 (5H, m), 7.70 (1H, s), 7.94 (d, 1H,  $J = 4.5$ ), and 11.03 (1H, s).

MS ( $m/s$ ) 456.12 ( $M$  calc. 456.20).

### 3.2.2. C dyes

$C_{Diacr}$ ,  $C_{Triacr}$  and  $C_{Triox}$  were obtained by alkylation of the phenolic function of the correspondent  $C'$  precursors. This alkylation, affording the  $C$  derivatives, was made with minor modifications as reported elsewhere [42]. All compounds were purified on a Florisil column.

**3.2.2.1.  $C_{Diacr}$ .** Yield: 87%.  $^1H$  NMR ( $CDCl_3$ ;  $Me_4Si$ ; 200 MHz)  $\delta$ : 3.16 (3H, s), 3.80 (t, 2H,  $J = 6.0$ ), 4.40 (t, 2H,  $J = 5.9$ ), 5.87 (dd, 1H,  $J = 10.2$ ,  $J = 1.5$ ), 6.10 (2H, m), 6.40 (2H, m), 6.76 (dd, 1H,  $J = 17.1$ ,  $J = 1.0$ ), 6.84 (d, 2H,  $J = 9.3$ ), 7.62 (d, 1H,  $J = 4.4$ ), 7.80 (d, 2H,  $J = 9.3$ ), 7.92 (2H, m), and 8.35 (2H, m).

MS ( $m/s$ ) 534.39 ( $M$  calc. 534.13).

**3.2.2.2.  $C_{Triacr}$ .** Yield: 90%.  $^1H$  NMR ( $CDCl_3$ ;  $Me_4Si$ ; 200 MHz)  $\delta$ : 3.82 (t, 4H,  $J = 5.8$ ), 4.41 (t, 4H,  $J = 5.7$ ), 5.87 (dd, 2H,  $J = 10.4$ ,  $J = 1.0$ ), 6.15 (5H, m), 6.45 (4H, m), 6.74 (dd, 2H,  $J = 17.0$ ,  $J = 1.5$ ), 6.87 (d, 2H,  $J = 9.2$ ), 7.68 (dd, 1H,  $J = 4.4$ ,  $J = 1.2$ ), 7.87 (d, 2H,  $J = 9.0$ ), and 7.80 (4H, m).

MS ( $m/s$ ) 618.33 ( $M$  calc. 618.15).

**3.2.2.3.  $C_{Triox}$ .** Yield: 80%.  $^1H$  NMR (DMSO; 200 MHz)  $\delta$ : 3.24 (12H, m), 4.77 (2H, s), 4.90 (1H, s), 6.77 (d, 2H,  $J = 9.0$ ), 7.67 (5H, m), 7.93 (2H, m).

MS ( $m/s$ ) 500.42 ( $M$  calc. 500.15).

### 3.3. Poling and curing conditions of the crosslinked films

#### 3.3.1. Preparation and poling of **NET1** film (30% in chromophore)

A solution of  $C_{Triacr}$  (0.030 g, 0.048 mmol), tris[2-(acryloyloxy)ethyl]isocyanurate (0.031 g, 0.074 mmol) and of 4,4'-trimethylene-dipiperidine (0.039 g, 0.184 mmol) in chloroform (1 mL) was filtered on a 0.2  $\mu$  PTFE filter and spin-coated on glass substrate. The film was corona poled by applying a voltage of 7 kV while temperature was raised from 25 to 110 °C. After 2 h the sample was cooled to room temperature and the electric field removed. The same pro-

cedure was followed for the systems with 5%, 10%, 20% chromophore content.

#### 3.3.2. Preparation and poling of **NET2** film (30% in chromophore)

A solution of PGMA (0.050 g, 0.352 mmol glycidyl groups),  $C_{Triox}$  (0.030 g, 0.059 mmol) and 2,2'-(naphthalene-2,7-diylbis(oxy))diethanol (0.021 g, 0.086 mmol) in THF (2 mL) was filtered on a 0.2  $\mu$  PTFE filter and spin-coated on glass substrate. The film was corona poled by applying a voltage of 7 kV while temperature was raised from 25 to 140 °C. After 4 h the sample was cooled to room temperature and the electric field removed.

The same procedure was followed for the systems with 5%, 10%, 20%, 40% and 54% chromophore weight content.

### 3.4. EFISH measurements

Measurement of  $\mu\beta$  nonlinearity of the chromophore  $C_{Diacr}$  was obtained by the EFISH technique. The set-up allows the determination of the scalar  $\mu\beta$  product where  $\mu$  is the ground state dipole moment and  $\beta$  the vector part of the quadratic hyperpolarizability tensor. The light source was a Q-switched Nd:Yag laser whose emission at 1.06  $\mu$ m was shifted to 1.907  $\mu$ m by stimulated Raman scattering. Measurements were calibrated relative to a quartz wedge: the experimental value of  $d_{11} = 1.2 \times 10^{-9}$  esu at 1.06  $\mu$ m was extrapolated to  $1.1 \times 10^{-9}$  esu at 1.907  $\mu$ m. The projection  $\beta$  of the vector part of tensor  $\beta_{ijk}$  along the direction of the dipole moment was finally determined, neglecting the purely electronic contribution compared to the orientational part and allowing Kleinman symmetry. Measurements were made in molar chloroform solution at 5 kV. The  $\mu\beta$  value for  $C_{Diacr}$ , at  $\lambda = 1.907$   $\mu$ m, is  $4950 \times 10^{-48}$  esu ( $6111 \times 10^{-80}$  C<sup>2</sup> m<sup>4</sup> V<sup>-2</sup>).

### 3.5. SHG measurements

SHG experimental data relative to  $p \rightarrow p$  experiments (incident  $p$ -polarised wave  $\rightarrow$  detected  $p$ -polarised SH signal) were recorded as the incidence function at 1500 nm wavelength (SH = 750 nm) and fitted according to Hermann and Hayden SH power equation [46]. The calibration of the experimental setup was performed through SHG measurements on a sample with known second order NLO susceptibility. A 1 mm thick X-cut quartz plate was used ( $d_{11} = 0.30$  pm/V [47]). The conditions  $d_{15} = d_{31}$  (Kleinmann symmetry [48]) and  $d_{31} = 1/3d_{33}$  [49] were assumed for the polymeric poled film and hence used in the expression of  $d_{eff}$  [47].

Measurements of nonlinear coefficient  $d_{33}$  were performed by means of the Maker fringes technique. The laser beam at fundamental frequency was provided by an optical parametric oscillator (OPO) whose wavelength could be tuned in the near-infrared range (800–1600 nm). The OPO was pumped by a Q-switched Nd:YAG laser having 10 ns pulse duration and 10 Hz repetition rate. The laser beam impinged on a variable attenuator made by a half-wave retardation plate and a polarizing beam splitter cube, allowing continuous variation of optical power impinging on the sample. The fundamental beam reflected by the

polarizing beam splitter cube was directed on a potassium dideuterophosphate (KDP) crystal, whose second harmonic signal, detected by a photodiode, was employed as a reference signal in order to take into account of the power fluctuations of the fundamental laser beam. A double Fresnel rhomb selected the proper polarization direction of the fundamental beam impinging on the sample, which was placed on a goniometric stage to allow variation of the incidence angle. A coloured filter absorbed the unwanted fundamental wavelength signal transmitted through the sample, while the second harmonic signal was detected by a high sensitivity amplified photodiode. Both the electric signals coming from photodiodes were acquired by a computer interfaced Tektronix TDS540 500 MHz bandwidth digitizing oscilloscope.

#### 4. Conclusions

Our results show that the use of disazo-thiophene based chromophores can afford unprecedented NLO active cross-linked materials with excellent temporal stability of poling. The level of the NLO properties displayed by the “model” dye is higher than for analogous known benzenoid structures, while NLO properties of crosslinked films are in medium range displayed by similar polymeric systems. The approach used for the attainment of the material is grounded on covalent bonding of the chromophore with a simple reactive polymer. Crosslinking was attained with straightforward epoxy chemistry in absence of initiator by reaction of the dye with the monofunctional polymer. The synthesis of the trifunctional chromophores was simplified with respect to previous related protocols by direct use of tin intermediates in the coupling step.

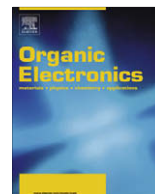
#### Acknowledgements

The authors thank the “Centro Interdipartimentale di Metodologie Chimico Fisiche” (CIMCF) of the University of Naples “Federico II” for NMR and X-ray facilities. Thanks are also due to Professor P. Maddalena, University of Naples “Federico II” for SHG facilities and to Professor Alain Fort, IPCMS-CNRS, Groupe d’Optique Nonlinéaire et d’Optoélectronique, 23 Rue de Loess, BP 43, 67034 Strasbourg Cedex 2, France, for the  $\mu\beta$  measurement.

#### References

- [1] Y. Yabuki, T. Chino, T. Fujiwara, EP Patent # 1437387, 2004.
- [2] A.T. Leaver, WO Patent # 9704030, 1997.
- [3] A. Seed, G.J. Cross, K.J. Toyne, J.W. Goodby, *Liq. Cryst.* 30(9)(2003) 1089.
- [4] L. Tong, J. Wang, X. Jian, Q. Zhang, *Gongneng Gaofenzi Xuebao* 17(3) (2004) 535.
- [5] A. Michaleviciute, G. Buika, J.V. Grazulevicius, F. Tran-Van, C. Chevrot, V. Jankuskas, *Mol. Cryst. Liq. Cryst.* 468 (2007) 459.
- [6] C.R. Moylan, B.J. McNelis, L.C. Nathan, M.A. Marques, E.L. Hermstad, B.A. Brichler, *J. Org. Chem.* 69 (24) (2004) 8239.
- [7] A.K.-Y. Jen, V. Pushkara Rao, K.Y. Wong, K.J. Drost, *J. Chem. Soc., Chem. Commun.* (1993) 90.
- [8] S. Yuquan, Z. Yuxia, L. Zao, W. Jianghong, Q. Ling, L. Shixiong, Z. Jianfeng, Z. Jiayun, *J. Chem. Soc., Perkin Trans. 1* (1999) 3691.
- [9] K. Guo, J. Hao, T. Zhang, F. Zu, J. Zhai, L. Qiu, Z. Zhen, X. Liu, Y. Shen, *Dyes Pigments* 77 (2008) 657.
- [10] P.R. Varanasi, A.K.-Y. Jen, J. Chandrasekhar, I.N.N. Namboothiri, A. Rathna, *J. Am. Chem. Soc.* 118 (1996) 12443.

- [11] I.D.L. Albert, J.O. Morley, D. Pugh, *J. Phys. Chem.* 99 (1995) 8024.
- [12] E.M. Breitung, C.-F. Shu, R.J. McMahon, *J. Am. Chem. Soc.* 122 (2000) 1154.
- [13] H. Xu, S. Yin, W. Zhu, Y. Song, B. Tang, *Polymer* 47 (2006) 6986.
- [14] C. Zhang, C. Wang, L.R. Dalton, H. Zhang, W.H. Steier, *Macromolecules* 34 (2001) 253.
- [15] Z. Yuxia, L. Zhao, Q. Ling, Z. Jianfen, Z. Jiayun, S. Yuquan, X. Gang, Y. Peixian, *European Polym. J.* 37 (2001) 445.
- [16] D.W. Kim, J.J. Choi, J.-S. Lim, C. Lee, *Mol. Cryst. Liq. Cryst.* 463 (2007) 325.
- [17] F.-H. Zu, L. Qiu, Y.-Q. Shen, X.-X. Deng, J.-H. Zhou, Q.-S. Shen, Z.-Q. Cao, *Gaodeng Xuexiao Huaxue Xuebao* 27 (3) (2006) 562.
- [18] Y. Shen, L. Qiu, F. Zu, T. Zhang, K. Guo, CN Patent # 1814595, 2006.
- [19] C. Monneréau, E. Blart, B. Illien, M. Paris, F. Odobel, *J. Phys. Org. Chem.* 18 (2005) 1050.
- [20] A. Apostoluk, J.-M. Nunzi, V. Boucher, A. Essahlaoui, R. Seveno, H.W. Gundel, C. Monneréau, E. Blart, F. Odobel, *Opt. Commun.* 260 (2006) 708.
- [21] J. Hao, M.-J. Han, K. Guo, J. Zhai, T. Zhang, X. Meng, J. Liang, L. Qiu, Y. Shen, *React. Funct. Polym.* 67 (8) (2007) 758.
- [22] N. Tsutsumi, S. Yoshizaki, W. Sakai, T. Kiyotsukuri, *Macromolecules* 28 (1995) 6437.
- [23] T.-D. Kim, J. Luo, J.-W. Ka, S. Hau, Y. Tian, Z. Shi, N.M. Tucker, S.-H. Jang, J.-W. Kang, A.K.-J. Jen, *Adv. Mater.* 18 (2006) 3038.
- [24] M. Onishi, H. Matsumoto, JP Patent # 01266167, 1989.
- [25] J.O. Morley, O.J. Guy, M.H. Charlton, *J. Phys. Chem. A* 108 (2004) 10542.
- [26] J.O. Morley, O.J. Guy, M.H. Charlton, *J. Photochem. Photobiol. A: Chem.* 173 (2005) 174.
- [27] L.R. Dalton, A.W. Harper, R. Ghosn, W.H. Steier, M. Ziari, H. Fetterman, Y. Shi, R.V. Mustacich, A.K.-Y. Jen, K.J. Shea, *Chem. Mater.* 7 (1995) 1060.
- [28] U. Caruso, M. Casalbani, A. Fort, M. Fusco, B. Panunzi, A. Quatela, A. Roviello, F. Sarcinelli, *Opt. Mater.* 27 (12) (2005) 1800.
- [29] I.D.L. Albert, T.J. Marks, M.A. Ratner, *J. Am. Chem. Soc.* 119 (1997) 6575.
- [30] J.O. Morley, D. Pugh, *J. Chem. Soc. Faraday Trans.* 87 (18) (1991) 3021.
- [31] A.S. Angeloni, M. Laus, C. Castellari, G. Galli, P. Ferruti, E. Chiellini, *Makromol. Chem.* 186 (1985) 977.
- [32] D. Wu, Y. Liu, C. He, T. Chung, S. Goh, *Macromolecules* 37 (2004) 6763.
- [33] A drawback of poling efficiency due to film conductivity should be excluded, taking in account that a relevant attainment of charged species during the crosslinking/poling process seems not in keep with the chemistry of the system, and that no film corrosion was observed in the experiment.
- [34] J. March, *Advanced Organic Chemistry: Reactions, Mechanisms, and Structure*, fourth ed., Wiley, New York, NY, 1992.
- [35] This approach could be compared with the well known use of the reaction of the epoxy groups with phenolic [38] or carboxylic [39] groups for the attainment of NLO active networks.
- [36] L.R. Dalton, A.W. Harper, B.H. Robinson, *Proc. Natl. Acad. Sci. USA* 94 (1997) 4842.
- [37] S. Fusco, R. Centore, P. Riccio, A. Quatela, G. Stracci, G. Archetti, H.-G. Kuball, *Polymer* 49 (2008) 186.
- [38] L.Z. Zhang, Y. Li, Z.X. Liang, Q.S. Yu, Z.G. Cai, *React. Funct. Polym.* 40 (1999) 255.
- [39] D. Bosc, F. Foll, B. Boutevin, A. Rousseau, *J. Appl. Polym. Sci.* 74 (4) (1999) 974.
- [40] H.H. Wang, U.E. Yuen, *J. Appl. Polym. Sci.* 102 (2006) 607.
- [41] B.D. Baignie, *Res. Disclos.* 175 (1978) 32.
- [42] U. Caruso, R. Diana, A. Fort, B. Panunzi, A. Roviello, *Macromol. Symp.* 234 (2006) 87.
- [43] A. Altomare, M.C. Burla, M. Camalli, G.L. Cascarano, C. Giacovazzo, A. Guagliardi, A.G.G. Moliterni, G. Polidori, R. Spagna, *J. Appl. Cryst.* 32 (1999) 115.
- [44] G.M. Sheldrick, SHELXL-97 Program, University of Göttingen, Germany, 1997.
- [45] All crystallographic data have been deposited at the Cambridge Crystallographic Data Centre (CCDC). Deposition number is CCDC 685786. These data can be obtained at <[www.ccdc.cam.ac.uk/conts/retrieving.html](http://www.ccdc.cam.ac.uk/conts/retrieving.html)> free of charge.
- [46] W.N. Herman, L.M. Hayden, *J. Opt. Soc. Am. B* 12 (3) (1995) 416.
- [47] I. Shoji, T. Kondo, R. Ito, *Opt. Quant. Electron.* 34 (2002) 797.
- [48] D.A. Kleinman, *Phys. Rev.* 126 (1962) 1977.
- [49] D.J. Williams, Nonlinear optical properties of guest-host polymer structures, in: D.S. Chemla, J. Zyss (Eds.), *Nonlinear Optical Properties of Organic Molecules and Crystals*, Academic, Orlando, FL, 1987.



## Thermal degradation mechanisms of PEDOT:PSS

E. Vitoratos<sup>a,\*</sup>, S. Sakkopoulos<sup>a</sup>, E. Dalas<sup>b</sup>, N. Paliatsas<sup>a</sup>, D. Karageorgopoulos<sup>a</sup>, F. Petraki<sup>c</sup>, S. Kennou<sup>c</sup>, S.A. Choulis<sup>d</sup>

<sup>a</sup> Department of Physics, University of Patras, 265 00 Patras, Greece

<sup>b</sup> Department of Chemistry, University of Patras, 265 00 Patras, Greece

<sup>c</sup> Department of Chemical Engineering, University of Patras, 265 00 Patras, Greece

<sup>d</sup> Department of Mechanical Engineering and Materials Science and Engineering, Cyprus University of Technology, 3603 Limassol, Cyprus

### ARTICLE INFO

#### Article history:

Received 4 July 2008

Received in revised form 5 October 2008

Accepted 7 October 2008

Available online 21 October 2008

#### PACS:

72.80.-r

73.61.Ph

82.35.Cd

#### Keywords:

Conducting polymers

Conductivity degradation mechanisms

Thermal stability

PEDOT/PSS

Organic light emitting diodes

Organic solar cells

### ABSTRACT

The thermal stability of thin (50 nm) PEDOT:PSS films, was investigated by dc conductivity measurements, X-ray and UV photoelectron spectroscopies as a function of heating temperature and heating time. The mechanism of electrical conductivity as a function of temperature is consistent with a hopping type carrier transport. The electrical conductivity decreased, as a function of time, in agreement with a granular metal type structure, in which aging is due to the shrinking of the PEDOT conductive grains. XPS and UPS spectra indicate that conformational changes of the PEDOT:PSS film are responsible for this behaviour and a model for these modifications is proposed.

© 2008 Elsevier B.V. All rights reserved.

## 1. Introduction

Organic semiconductors are of increasing interest as new materials for optoelectronic devices. This class of semiconductors is processed from solution, offering a huge potential for low fabrication costs and flexibility. Polymer emitting diodes (PLEDs), photodiodes and solar cells are the optoelectronic applications under intense study [1]. One of the fundamental requirements for reliable operation of all organic optoelectronic devices is a stable anode interface. Indium tin oxide (ITO) has been the preferred anode for all organic optoelectronic devices due to its optical

transparency and high conductivity [1–3]. However, the work function of ITO is quite low (even after special ITO treatment procedures such as plasma or oxygen treatment) [4]. The most common way to improve hole injection/collection is to incorporate a hole transporting layer (buffer layer) on top of the ITO surface [4,5]. The most common buffer layer is the poly(ethylenedioxythiophene):polystyrene sulphonate (PEDOT:PSS) [5].

Poly(3,4-ethylenedioxythiophene) (PEDOT), a  $\pi$ -conjugated polymer, combines high electrical conductivity with excellent optical transparency [6]. The problem with its low solubility is solved by the use of the water soluble polyelectrolyte poly(styrene sulfonic acid) PSS as a charge balancing dopant. PEDOT mixed with PSS forms an easily processible colloidal solution in water. For organic

\* Corresponding author. Tel.: +30 2610 997487; fax: +30 2610 997428.  
E-mail address: [vitorato@physics.upatras.gr](mailto:vitorato@physics.upatras.gr) (E. Vitoratos).

optoelectronic applications PEDOT:PSS is an essential part of the bottom electrode providing a high selective carrier contact. The stability of PEDOT:PSS layer is of high importance and determines the lifetime performance of organic optoelectronic devices. Despite the common use of PEDOT:PSS the correlation between the electrical conductivity and the morphology and especially the irreversible structural changes occurring during thermal degradation are not fully understood [7,8]. The purpose of this investigation is to study the thermal aging of the electrical conductivity of PEDOT:PSS thin films and correlate this with the morphological, composition and electronic structure changes occurring during the thermal degradation.

## 2. Methods

### 2.1. Materials

All measurements performed on 50 nm PEDOT:PSS films coated on pristine plastic substrates (PET). An aqueous dispersion of PEDOT:PSS (CLEVIOS PH 500, H.C. Starck) was used, where the ratio PEDOT-to-PSS was 1:2.5 by weight.

### 2.2. Conductivity measurements

Temperature dependence d.c. conductivity measurements  $\sigma = \sigma(T)$  performed using a four-probe method. For the temperature dependent studies a He filled cryostat was used [9]. Samples from the same PEDOT:PSS film were thermally treated at 120 °C in a thermostated oven under environmental conditions for different times. The 0 h time includes only the annealing step during the preparation process 20 min. The conductivity versus temperature was then measured after the heat treatment at every time. These successive measurements give a set of  $\sigma = \sigma(T)$  curves and the whole procedure is repeated until saturation in conductivity is observed.

### 2.3. X-ray photoelectron and ultra-violet photoelectron spectroscopies

X-ray photoelectron spectroscopy (XPS) was used to investigate the variation in the chemical structures of the sample surface of the PEDOT:PSS films before and after the thermal degradation, while the variation of the PEDOT:PSS valence band was investigated by ultra-violet photoelectron spectroscopy (UPS). The photoelectron spectroscopy measurements were carried out in a commercial ultra-high vacuum (UHV) system which consists of a fast entry specimen assembly, a preparation and an analysis chamber. The analysis chamber is equipped with a hemispherical electron analyzer (SPECS LH-10), a twin anode X-ray gun and a discharge lamp for X-ray and ultra-violet photoelectron spectroscopy (XPS and UPS) measurements. The base pressure was  $5 \times 10^{-10}$  mbar. The XPS measurements were carried out with a non-monochromatic Mg K $\alpha$  line at 1253.6 eV and a constant analyzer pass energy of 36 eV, while for UPS the He I (21.22 eV) radiation was used. The spectrometer was calibrated by the Au4f $_{7/2}$  core

level ( $84.00 \pm 0.05$  eV) for a clean Au foil. The XPS resolution, measured by the full width at half maximum (FWHM) of the Au4f $_{7/2}$ , was 1.10 eV for a constant pass energy of 36 eV. The analyzer resolution for the UPS measurements is determined from the width of the Au Fermi edge and is found 0.16 eV. A negative bias of 12.30 V was applied to the sample during UPS measurements in order to separate sample and analyzer high binding energy cut-offs and estimate the absolute work function from the UV photoemission spectra.

## 3. Results and discussion

In Fig. 1 the d.c. conductivity  $\sigma$  as a function of temperature  $T$  is shown for PEDOT:PSS exposed to thermal treatment times ranging from 0 to 55 h at 120 °C. The mechanism of carrier (hole polarons) transport in PEDOT:PSS is determined by its morphology. Conductive PEDOT oligomers consisted of 5–15 repeat units are electrostatically attached to twisted long insulating PSS chains, which form grains 20–70 nm in diameter, whose surfaces are rich in PSS [10,11]. So, in PEDOT:PSS, with its granular structure of conductive PEDOT-rich grains enclosed in insulating PSS-rich shells, the electrical conductivity is not determined only from the hole polarons transport into the PEDOT segments, but also by their hopping between segments and grains.

Despite different interpretations of the temperature dependence of the experimentally obtained conductivities, typically  $\sigma = \sigma(T)$  is given by

$$\sigma(T) = \sigma_0 \exp \left[ - \left( \frac{T_0}{T} \right)^\alpha \right] \quad (1)$$

which generally describes a hopping transport, where  $T_0$  is a measure of the potential barrier height, as carriers get thermally activated hopping among localized states at different energies [12–14]. On the other hand  $\sigma_0$  is related to the intrinsic conductivity of the grains, their size contribution, mean volume occupied by the conducting grains in the material, etc. [15].

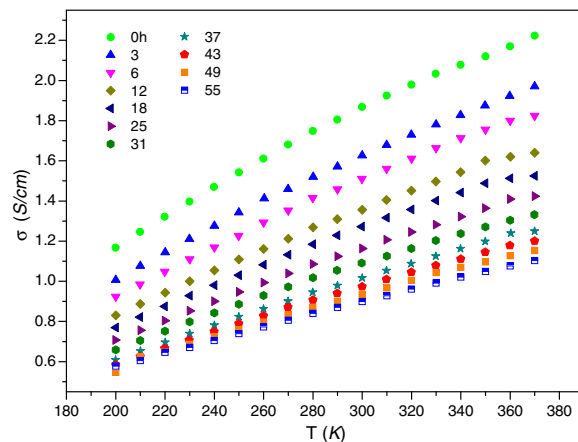


Fig. 1. Thermal degradation of the d.c. electrical conductivity of a 50 nm thick PEDOT:PSS film heated at 120 °C under environmental conditions for times between 0 and 55 h.

In a material consisting of conductive grains embedded into an insulating matrix, thermal degradation can be considered as a corrosion – a process which is reducing the size of the grains and consequently enhancing their distance, or equivalently increasing the potential barrier for polaron transport between them. In this case the conductivity can be described by the following equation

$$\ln \sigma = \sigma_1 \exp[-(t/\tau)^{1/2}] \quad (2)$$

in which  $t$  is the time of the thermal treatment and  $\tau$  is a parameter characteristic of the aging rate. The higher the  $\tau$  value, the slower the rate of degradation [16].

In the variable-range hopping (VRH) model of transport the exponent  $\alpha$  in Eq. (1) does not depend only on the number of the hopping process dimensions  $D$ , but also on the exponent  $\mu$  of the density of states  $g(E) \propto (E-E_F)^\mu$  near the Fermi energy level  $E_F$ , according to the formula  $\alpha = \mu + 1/(\mu + D + 1)$  [17].

In disordered systems, in which a self-assembled network of conductive polymer, PEDOT in our case, spreads in a matrix of insulating PSS, the carrier eigenstates display spatial fluctuations described by a multifractal analysis, in which the electrical conductivity follows Eq. (1) with the exponent  $\alpha$  decreasing systematically from 1 to 0.25 with increasing the volume fraction of the conductive component [18,19]. The exponent  $\alpha = 1$  indicates a nearest-neighbor hopping (nn-H) between PEDOT particles [12]. On the other hand, hopping conductivity in granular disordered systems follows Eq. (1) with the exponent  $\alpha$  ranging from 0.25 to 1 depending on the distribution of grain sizes. The decrease of the particle size results in the reduction of the exponent  $\alpha$  from values about unity to 0.5 or 0.25 [20]. An exponent  $\alpha = 0.25$  is consistent to a three-dimensional VRH, though an exponent  $\alpha = 1/2$  can be attributed to many cases. For example, the existence of an energy gap caused by Coulomb interactions between the carriers results in a  $\alpha = 1/2$ . However, the non-zero density of states at the Fermi level reveals that such an energy gap does not exist in PEDOT:PSS [12]. Another explanation for the  $\alpha = 1/2$  value is in the framework of the charging-energy limited tunnelling (CELT) model, where carriers tunnel between small conductive grains separated by insulating material [21,22]. From the above it is apparent that the exponent  $\alpha$  can reveal valuable information about the conduction mechanism in PEDOT:PSS.

In Fig. 2 the exponent  $\alpha$  of Eq. (1) is shown for increasing heat treatment time at 120 °C. For the fresh samples ( $t = 0$  h)  $\alpha \approx 1$  decreasing with thermal aging to the value  $\alpha \approx 0.5$  at the end of it, after 55 h of heat treatment. Taken into account the morphology of PEDOT:PSS, this means that for the first stages of the heat treatment, the nearest-neighbor hopping prevails, though later the charging-energy limited tunnelling between adjacent conductive grains determines the conduction. For  $\alpha \sim 1$ , Eq. (1) takes the well known Arrhenius formula, from which the mean of the potential barrier height can be estimated to  $E \sim 0.022 \pm 0.001$  eV for the fresh samples.

XPS and UPS were used to investigate the composition and electronic structure changes due to the thermal aging process. In Fig 3 the XPS spectra S 2p for PEDOT:PSS sam-

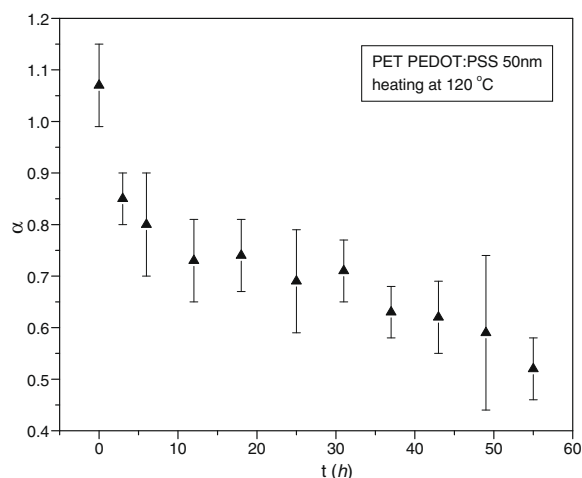


Fig. 2. The exponent  $\alpha$  of Eq. (1) vs. thermal treatment time for the same PEDOT:PSS sample, as in Fig. 1.

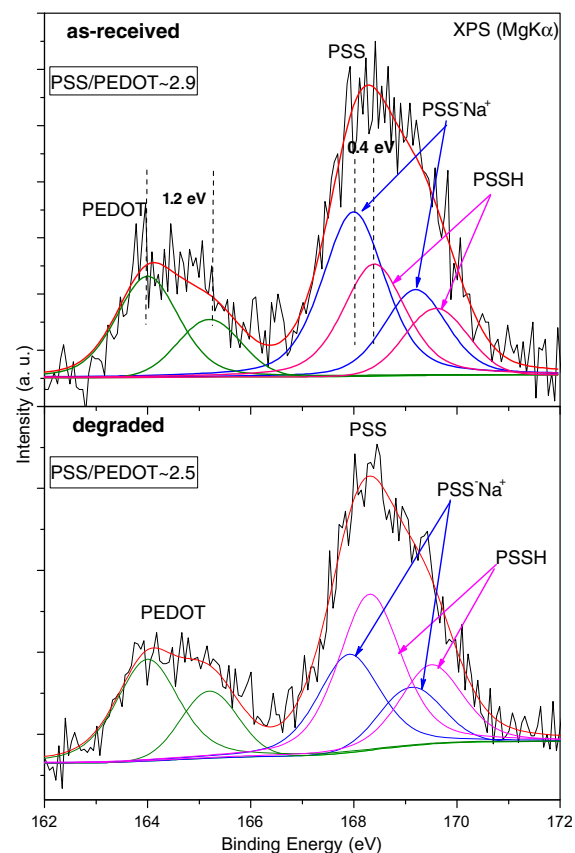


Fig. 3. S(2p) spectra from (a) a fresh PEDOT:PSS sample and (b) from the same sample after heat treatment at 120 °C under environmental conditions for 55 min.

ples (a) fresh and (b) after heat treatment at 120 °C for 55 h are shown. In both cases the S 2p spectrum appears in two components. The component at lower binding energies is attributed to the contribution of PEDOT and in particular,

to sulphur atoms linked to carbon in the chemical structure of PEDOT and the peak at higher binding energies corresponds to the sulphur atoms in the PSS polymer. The spectra were fitted with mixed Gaussian–Lorentzian peaks after Shirley background subtraction. The PEDOT component is fitted in all cases with a single spin-orbit doublet at  $164.0 \pm 0.1$  eV and  $165.2 \pm 0.1$  eV binding energy and a  $2p_{3/2}$  to  $2p_{1/2}$  ratio of 2:1, the splitting of 1.2 eV being that expected for S 2p. The contribution of PSS to the S 2p peak is due to the doping ions  $\text{PSS}^- \text{H}^+$  (spin-orbit doublet at 168.4 eV and 169.6 eV binding energy) and to the  $\text{PSS}^- \text{Na}^+$  salt [23,24] (spin-orbit doublet at 168.0 eV and 169.2 eV binding energy).  $\text{Na}^+$  residues originate from  $\text{Na}_2\text{S}_2\text{O}_8$  oxidizing agent used during the polymerization of PEDOT [25]. The original ratio of PSS-Na to the PSS-H in the PSS layer is found equal to 1.5 and it drops to 0.6 after the heat treatment. From them it can be seen that there is a decrease of the PSS-Na bond in the PSS chains due to thermal aging. The PEDOT-to-PSS ratio in the surface region can be calculated from the total area under the S2p core level spectra and it was found 1:2.9 for the PEDOT:PSS before thermal degradation. After thermal degradation up to 55 h at 120 °C this ratio becomes 1:2.4. As has also reported before for the fresh PEDOT:PSS the spectra indicate that there is phase segregation with an excess of PSS [25]. During this work we show that after 55 h at 120 °C the excess of PSS is slightly reduced.

In order to estimate the thickness  $d$  of the outermost PSS layer, we consider PSS and PEDOT as two separated polymers growing in the form of a “layer over layer” structure ending in a pure PSS layer and compare the intensities from the contribution to the S2p peak of each polymer. The thickness is given by the expression

$$d = \lambda \ln[(I_{\text{PSS}}/I_{\text{PSS}}^0)/(I_{\text{PEDOT}}/I_{\text{PEDOT}}^0) + 1] \quad (3)$$

where  $\lambda = 2.7 \pm 0.3$  nm, is the electron inelastic mean free path, and  $I_x, I_x^0$  are the measured and expected signal intensities from species X, respectively [23]. The above equation yields an outermost PSS layer thickness of 3.6 nm for the PEDOT:PSS before thermal degradation and 3.4 nm after thermal aging at 120 °C for 55 h, verifying that there is a thinning of the PSS layer on the surface.

From UPS spectra of the same PEDOT:PSS sample before and after the heat treatment at 120 °C, it can be seen that the density of the electronic states near the Fermi level slightly increases, although the work function of the surface decreases from 4.7 eV for the fresh sample to 3.7 eV at the end of the heat treatment. These can be attributed to the removal of the insulating PSS from the surface, which leaves an area enriched in PEDOT, from which is easier to remove carriers and as a p-doped conjugated polymer has occupied valence band states near the Fermi level [26].

From Fig. 3 it can also be seen that the peaks corresponding to the PSSH bond diminish with aging. This indicates that there is enough energy for the breaking of the electrostatic bonding between PSS and PEDOT, which gradually leads to the reeling off the PSS chains and on the other hand to the formation of PEDOT-rich clusters between the PSS chains [13,23].

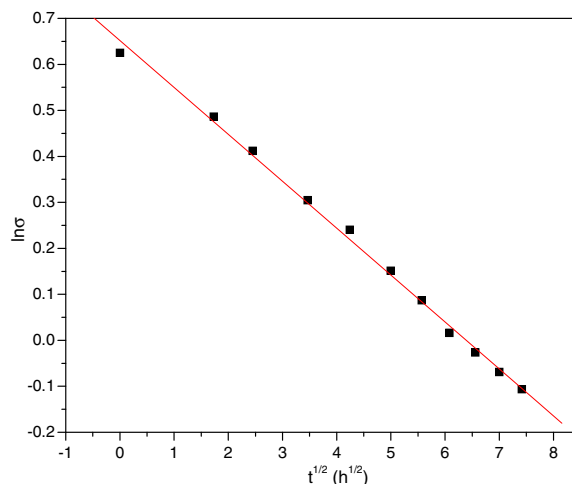


Fig. 4.  $\ln \sigma = f(t^{1/2})$  experimental data at 300 K for heating temperature 120 °C.

From Fig. 4 it is shown that for heating temperature 120 °C the experimental data follow very well Eq. (2). Moreover, from the fitting of the experimental data, the parameter  $\tau$  takes the value 96 h and from Eq. (2) it can be calculated that the time of heating, for the conductivity of the sample to become half of its original value, is 46.1 h, in excellent agreement with the experiment, from which this time is 46.3 h. This is consistent with a granular structure of PEDOT:PSS and an electrical conductivity degradation, in which the main contribution comes from the progressive increase of the potential barriers between the conductive grains with heat treatment.

The above experimental results can be explained by the following model of conformational changes during the thermal aging. At the first stage of heating, the PSS chains are perplexed, as it is shown in Fig. 5 and the agitation of the  $\text{Cl}^-$  ions (their existence is verified by EDX spectrograms) attached weakly to the hole polarons on the PEDOT

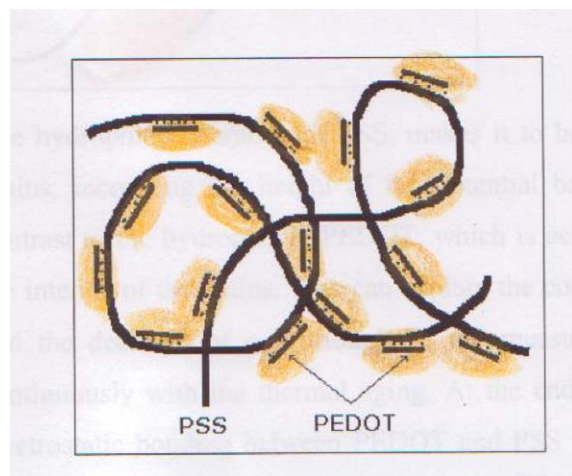


Fig. 5. Perplexed PSS chains at the first stage of heating.



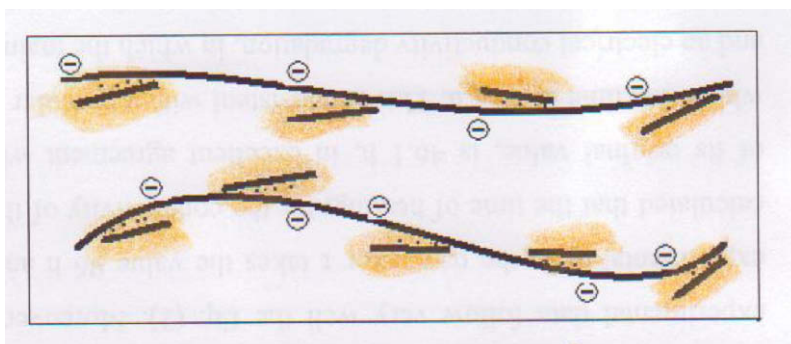


Fig. 6. The ionic bonds between PEDOT and the PSS chains start to break.

oligomers, makes them to wander further away from the polaron vicinity, increasing the mobility of the latter. This makes the grains more conductive as it is revealed from the decrease of the exponent  $\alpha$  and the increase of  $\sigma_0$ .

At a second stage of the heat treatment, shown in Fig. 6, the ionic bonds between the PEDOT oligomers and the PSS chains start to break.

The remaining negative charges on the PSS chains repulse each other resulting in an improvement of their alignment. In this stage the conductive PEDOT oligomers concentrate between the aligned PSS chains forming grains of enhanced conductivity, as it is shown in Fig. 7.

The hydrophilic character of PSS, makes it to be concentrated at the surface of the grains, increasing the height of the potential barriers, as this stage progresses, in contrast to the hydrophobic PEDOT, which is accumulated in increasing numbers in the interior of the grains. This can explain the continuous decrease of the exponent  $\alpha$  and the decrease of  $\sigma_0$ , although  $T_0$ , the measure of the barriers height increases continuously with the thermal aging. At the end of the heat treatment, most of the electrostatic bonding between PEDOT and PSS is removed, as it is revealed by the XPS spectrograms.

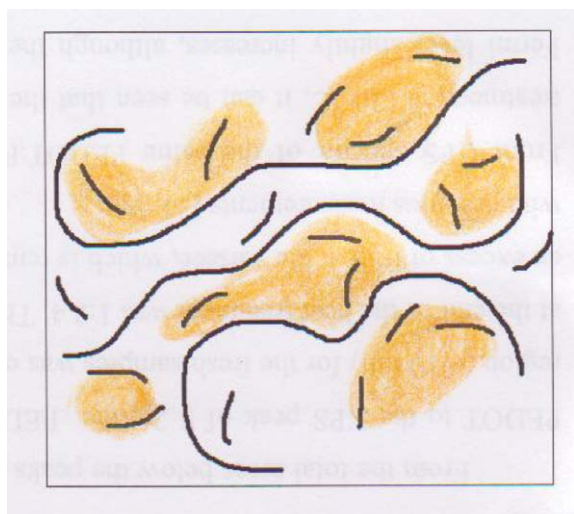


Fig. 7. PEDOT oligomers start to form conducting grains.

From Fig. 4 it is shown that for heating temperature 120 °C the experimental data follow very well Eq. (2). Moreover, from the fitting of the experimental data, the parameter  $\tau$  takes the value 96 h and from Eq. (2) it can be calculated that the time of heating, for the conductivity of the sample to become half of its original value, is 46.1 h, in excellent agreement with the experiment, from which this time is 46.3 h. This is consistent with a granular structure of PEDOT:PSS and an electrical conductivity degradation, in which the main contribution comes from the progressive increase of the potential barriers between the conductive grains with heat treatment.

From the total areas below the peaks representing the contribution of PSS and PEDOT to the XPS peak of S2p, the PEDOT-to-PSS molar ratio in the surface region ( $\sim 10$  nm) for the fresh samples was estimated to 1:2.9, though for the samples at the end of the heat treatment was 1:2.4. This indicates that in fresh samples there is an excess of PSS at the surface, which is removed by the heat treatment, in agreement with previous measurements [23–25].

From UPS spectra of the same PEDOT:PSS sample before and after the heat treatment at 120 °C, it can be seen that the density of the electronic states near the Fermi level slightly increases, although the work function of the surface decreases from 4.7 eV for the fresh sample to 3.7 eV at the end of the heat treatment. These can be most likely attributed to the removal of the insulating PSS from the surface, which leaves an area enriched in PEDOT, from which is easier to remove carriers and as a p-doped conjugated polymer has occupied valence band states near the Fermi level [26]. As has already been reported by differential scanning calorimetry (DSC) and other thermal degradation studies [27,28], decrease of the work function due to the decomposition of PEDOT:PSS, as Diels–Alder reaction ( $\text{SO}_2$ -extrusion), starts at higher temperatures (225–230 °C) from the ones used in this study (120 °C).

#### 4. Summary and conclusions

The aging of PEDOT:PSS films 50 nm thick was investigated by dc conductivity measurements, X-ray and UV photoelectron spectroscopies for thermal treatment at 120 °C under environmental conditions. The electrical conductivity versus T followed the formula

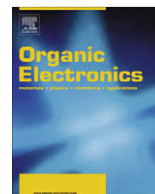
$\sigma = \sigma_0 \exp[-(T_0/T)^\alpha]$ , consistent with a carrier transport of the hopping type. The exponent  $\alpha$ , decreased with aging from a value of  $\sim 1$  for the fresh samples to a value  $\sim 0.5$  at the end of the thermal treatment. This indicates a change in the conduction mechanism from the nearest-neighbour hopping at the beginning of the heat treatment to the charging-energy limited tunnelling between the conductive grains as thermal aging progresses. On the other hand the electrical conductivity at room temperature vs.  $t$ , the time of the heat treatment, decreased following the formula  $\sigma = \sigma_1 \exp[-(t/\tau)^{1/2}]$ , in agreement with a granular metal type structure, in which aging is due to the shrinking of the conductive grains, with  $\tau = 96$  h. From the last formula the time  $t$  for which  $\sigma$  becomes half of its original value, is calculated to be 46.1 h in agreement with the value 46.3 h obtained from the  $\sigma = \sigma(T)$  curves for different  $t$ . Moreover, the XPS and the UPS spectra before and after thermal degradation revealed a slight decrease of the insulating PSS from the surface. According to the proposed model thermal aging starts with an increase of the mobility of the hole polarons in PEDOT oligomers attached to insulating PSS chains, improving conductivity into the grains, which reduces  $\alpha$  and increases  $\sigma_0$ . At a second stage, the ionic bonds between PEDOT and PSS start to break, the PSS chains bearing negative charge at intervals align better themselves and PEDOT oligomers concentrate between them, further enhancing the conductivity of the grains. At the final stage the bonds between PEDOT and PSS break down, as XPS spectrograms reveal. The conducting PEDOT being hydrophobic concentrates into the interior of the grains, although the insulating PSS being hydrophilic concentrates at the borders of the grains enhancing the potential barriers between the grains. These can explain the increase of  $\sigma_0$  and  $T_0$  with thermal treatment.

## Acknowledgments

This work was partially financed by the Research Committee of the University of Patras under the framework of the “K. Karatheodori” program for basic research strengthening.

## References

- [1] H. Burroughes, D.D.C. Bradley, A.R. Brown, R.N. Marks, K. Mackay, R.H. Friend, P.L. Burn, A.B. Holmes, Light-emitting diodes based on conjugated polymers, *Nature* 347 (6293) (1990) 539–541.
- [2] G. Yu, K. Pakbaz, A.J. Heeger, Semiconducting polymer diodes: large size, low cost photodetectors with excellent visible-ultraviolet sensitivity, *Applied Physics Letters* 64 (25) (1994) 3422–3424.
- [3] C.N. Hoth, S.A. Choulis, P. Schilinsky, C.J. Brabec, High photovoltaic performance of inkjet printed polymer:fullerene blends, *Advanced Materials* 19 (22) (2007) 3973–3978.
- [4] S.A. Choulis, A. Patwardhan, M.K. Mathai, V.-E. Choong, F. So, Interface modification to improve hole-injection properties in organic electronic devices, *Advanced Functional Materials* 16 (8) (2006) 1075–1080.
- [5] T.M. Brown, J.S. Kim, R.H. Friend, F. Cacialli, R. Daik, W.J. Feast, Built-in field electroabsorption spectroscopy of polymer light-emitting diodes incorporating a doped poly(3,4-ethylene dioxythiophene) hole injection layer, *Applied Physics Letters* 75 (12) (1999) 1679–1681.
- [6] J. Huang, P.F. Miller, J.S. Wilson, A.J. de Mello, J.C. de Mello, D.D.C. Bradley, Investigation of the effects of doping and post-deposition treatments on the conductivity, morphology and work function of poly(3,4-ethylenedioxythiophene)/poly(styrene sulfonate) films, *Advanced Functional Materials* 15 (2) (2005) 290–296.
- [7] I. Winter, C. Reese, J. Hormes, G. Heywang, F. Jonas, The thermal aging of poly(3,4-ethylenedioxythiophene). An investigation by X-ray absorption and X-ray photoelectron spectroscopy, *Chemical Physics* 194 (1) (1995) 207–213.
- [8] <<http://www.baytron.com/pages/985/scopeandlimitations.pdf>>.
- [9] H.H. Wieder, *Laboratory Notes of Electrical and Galvanomagnetic Measurements*, vol. 2, Elsevier, Amsterdam, 1979, ISBN 044441763X.
- [10] M.M. de Kok, M. Buechel, S.I.E. Vulto, P. van de Weijer, E.A. Meulenkaamp, S.H.P.M. de Winter, A.J.G. Mank, H.J.M. Vorstenbosch, C.H.L. Weijtens, V. van Elsbergen, Modification of PEDOT:PSS as hole injection layer in polymer LEDs, *Physica Status Solidi (a)* 201 (6) (2004) 1342–1359.
- [11] R.R. Smith, A.P. Smith, J.T. Stricker, B.E. Taylor, M.F. Durstock, Layer-by-layer assembly of poly(3,4-ethylenedioxythiophene):poly(styrenesulfonate), *Macromolecules* 39 (18) (2006) 6071–6074.
- [12] A.M. Nardes, M. Kemerink, R.A.J. Janssen, Anisotropic hopping conduction in spin-coated PEDOT:PSS thin films, *Physical Review B* 76 (8) (2007) 085208–085214.
- [13] A.M. Nardes, M. Kemerink, R.A.J. Janssen, J.A.M. Bastiaansen, N.M.M. Kiggen, B.M.W. Langeveld, A.J.J.M. van Breemen, M.M. de Kok, Microscopic understanding of the anisotropic conductivity of PEDOT:PSS thin films, *Advanced Materials* 19 (9) (2007) 1196–1200.
- [14] N. Mott, E.A. Davis, *Electronic Processes in Non-crystalline Materials*, Clarendon Press, Oxford, 1979, ISBN 0198512880.
- [15] E. Vitoratos, An analysis of DC conductivity in terms of degradation mechanisms induced by thermal aging in polypyrrole/polyaniline blends, *Current Applied Physics* 5 (6) (2005) 579–582.
- [16] E. Vitoratos, S. Sakkopoulos, E. Dalas, P. Malkaj, A. Anestis, D.C. conductivity and thermal aging of conducting zeolite/polyaniline and zeolite/polypyrrole blends, *Current Applied Physics* 7 (5) (2007) 578–581.
- [17] M.M. Fogler, S. Teber, B.I. Shklovskii, Variable-range hopping in quasi-one-dimensional electron crystals, *Physical Review B* 69 (3) (2004) 035413-1–035413-18.
- [18] M. Schreiber, H. Grussbach, Fluctuations in mesoscopic systems, *Philosophical Magazine B* 65 (4) (1992) 707–714.
- [19] M. Reghu, C.O. Yoon, C.Y. Yang, D. Moses, P. Smith, A.J. Heeger, Y. Cao, Transport in polyaniline networks near the percolation threshold, *Physical Review B* 50 (19) (1994) 13931–13941.
- [20] P. Sheng, J. Klafter, Hopping conductivity in granular disordered systems, *Physical Review B* 27 (4) (1983) 2583–2586.
- [21] L. Zuppiroli, M.N. Bussac, S. Paschen, Hopping in disordered conductivity polymers, *Physical Review B* 50 (8) (1994) 5196–5203.
- [22] A.N. Aleshin, S.R. Williams, A.J. Heeger, Transport properties of poly(3,4-ethylenedioxythiophene)/poly(styrenesulfonate), *Synthetic Metals* 94 (2) (1998) 173–177.
- [23] G. Greczynski, Th. Kugler, M. Keil, W. Osikowicz, M. Fahlman, W.R. Salanec, Photoelectron spectroscopy of thin films of PEDOT:PSS conjugated polymer blend: a mini-review and some new results, *Journal of Electron Spectroscopy and Related Phenomena* 121 (1–3) (2001) 1–17.
- [24] F. Petraki, S. Kennou, S. Nespurek, The electronic properties of the interface between nickel phthalocyanine and a PEDOT:PSS film, *Journal of Applied Physics* 103 (3) (2008) 033710-1–033710-15.
- [25] J. Hwang, F. Amy, A. Khan, Spectroscopic study on sputtered PEDOT. PSS: role of surface PSS layer, *Organic Electronics* 7 (5) (2006) 387–396.
- [26] K.Z. Xing, M. Fahlman, X.W. Chen, O. Inganas, W.R. Salanec, The electronic structure of poly(3,4-ethylene-dioxythiophene): studied by XPS and UPS, *Synthetic Metals* 89 (3) (1997) 161–165.
- [27] T.P. Nguyen, S.A. de Vos, An investigation into the effect of chemical and thermal treatments on the structural changes of poly(3,4-ethylenedioxythiophene)/polystyrenesulfonate and consequences on its use on indium tin oxide substrates, *Applied Surface Science* 221 (1–4) (2004) 330–339.
- [28] Y. Yosioka, G. Jabbar, Inkjet printing and patterning of PEDOT–PSS: application to optoelectronic devices, in: T.A. Skothein, J.R. Reynolds (Eds.), *Conjugated Polymers, Processing and Applications*, CRC Press, New York, 2007, pp. 3–1–3–21. ISBN 1420043609.



# An inkjet-printed passivation layer based on a photocrosslinkable polymer for long-term stable pentacene field-effect transistors

Sooji Nam, Hayoung Jeon, Se Hyun Kim, Jaeyoung Jang, Chanwoo Yang, Chan Eon Park \*

Polymer Research Institute, Department of Chemical Engineering, Pohang University of Science and Technology (POSTECH), Pohang 790-784, Republic of Korea

## ARTICLE INFO

### Article history:

Received 7 July 2008

Received in revised form 6 October 2008

Accepted 7 October 2008

Available online 22 October 2008

### PACS:

72.20.Jv

72.80.Le

### Keywords:

Inkjet-printing

Passivation

Pentacene FETs

Photocrosslinkable polymer

## ABSTRACT

Herein, we investigate the effects of the solvents used in the passivation process on the behavior of pentacene field-effect transistors (FETs) and report on the fabrication of a passivation layer for pentacene FETs via inkjet-printing using photocrosslinkable poly(vinyl alcohol), N-methyl-4(4'-formylstyryl) pyridinium methosulfate acetal (SbQ-PVA). The passivated pentacene FETs – composed of inkjet-printed SbQ-PVA containing polystyrene/SiO<sub>2</sub> and poly(4-vinyl phenol)/SiO<sub>2</sub> dual-layer gate dielectrics – retain their electrical properties for much longer periods than the unpassivated devices. Studies of the device performance show that inkjet-printed passivation is better than spin-coated passivation.

© 2008 Elsevier B.V. All rights reserved.

## 1. Introduction

In recent years, pentacene field-effect transistors (FETs) exhibiting high-performance have been reported by many research groups. The behaviors of some of these devices are comparable to those of amorphous silicon transistors [1,2]. However, although pentacene FETs show good performance in the short term, their electrical properties are significantly degraded over time by water and oxygen species present in ambient air [3–6]. Accordingly, the introduction of a passivation layer is necessary to protect the devices from the effects of water and oxygen. There are two representative ways to form a passivation layer, namely, vacuum deposition [7–9] and solution deposition [10,11]. To date, vacuum deposition processes, such as atomic layer deposition [7] and chemical vapor deposition [8,9], have been predominantly used to produce passivation layers. However, these processes have many draw-

backs, including long processing times and high costs. Solution-deposition processes, by contrast, have the advantages of allowing simple and low-cost processing in short times. Therefore, in this study, we fabricate two distinct kinds of solution-processed passivation layers by means of inkjet-printing and spin-coating. Our results show that the inkjet-printing technique has many advantages over spin-coating. In the former case, no photolithography process is required, because it is possible to pattern directly on the surface. Therefore, inkjet-printing can be conveniently applied to active-matrix displays and integrated circuits [12].

It is very important to choose appropriate solvents for the fabrication of solution-processed passivation layers, because the performance of the pentacene FETs is significantly affected by the solvent used. Gundlach et al. [13] showed that exposure of a pentacene film to solvents, such as acetone, isopropanol, and ethanol, induces a phase transition within the film from the thin-film to the bulk phase. Here, we investigate the solvent effects on the structure and morphology of pentacene films by using atomic force

\* Corresponding author. Tel.: +82 54 279 2269; fax: +82 54 279 8298.  
E-mail address: [cep@postech.ac.kr](mailto:cep@postech.ac.kr) (C.E. Park).

microscopy (AFM) and X-ray diffraction (XRD). We also fabricated passivation layers for pentacene FETs, using photocrosslinkable poly(vinyl alcohol), N-methyl-4(4'formylstyryl) pyridinium methosulfate acetal (SbQ-PVA) (Polysciences, Inc.), and characterized the time-dependent electrical performance of the devices.

## 2. Experiments

We fabricated high-performance pentacene FETs using a heavily doped Si wafer as gate substrate (see Fig. 1a). A dual-layer composed of thermally grown 300-nm-thick SiO<sub>2</sub> and spin-coated 40-nm-thick polymer films of polystyrene (PS) or poly(4-vinyl phenol) (PVP) was used as gate dielectric. PVP was thermally crosslinked (at 200 °C for 2 h) using poly melamine-co-formaldehyde as crosslinking agent. Subsequently, a 50-nm-thick pentacene film was deposited onto the dielectric layer by means of organic molecular beam deposition under high vacuum (i.e., 10<sup>-7</sup> Torr) and at a rate of 0.2 Å/s through shadow mask. For the top-contact geometry of the pentacene FETs, we deposited the source/drain electrodes by thermally evaporating gold through a shadow mask on the active layer. We used two kinds of shadow masks, with channel width (*W*)/length (*L*) ratios of 10 and 15.

To investigate the effects of the solvent on the crystallinity of the pentacene films, the organic-semiconductor layers were exposed to deionized (DI) water, ethanol, and toluene (by spin-coating), and the film morphologies and molecular orderings were investigated using an AFM (Digital Instruments Multimode SPM) and an XRD (Pohang Accelerator Laboratory 10C1 beam line), respectively. The polymer SbQ-PVA was dissolved in DI water and either inkjet-printed or spin-coated onto the pentacene FETs. The inkjet printer was equipped with a drop-on-demand piezoelectric print head with a nozzle size of 50 μm (manufactured by Microfab Technologies, Inc.). Uniform droplets of 1.3 wt% SbQ-PVA in DI water were gained at a frequency of 200 Hz and a substrate temperature of 50 °C. The dot-to-dot distance was 50.8 μm. An optical microscopy (OM) image of the inkjet-printed passivation layer is shown in Fig. 1b. A 200-nm-thick SbQ-PVA layer was deposited by spin-coating a 6.3 wt% solution in DI water at 1500 rpm. This film was then exposed to a fluorescent lamp for one hour and to UV light ( $\lambda = 365$  nm,

power = 7 W, ENF-240C, Spectroline<sup>®</sup>) for 20 min to conduct photocrosslinking. The thickness of the film was measured with a surface profiler (Alpha-step<sup>®</sup> 500, KLA Tencor). A UV-vis-NIR spectrophotometer (Cary 5000, Varian Co.) was used to study the UV absorbance and the degree of crosslinking. The electrical characteristics of the pentacene FETs were measured with Keithley 2400 and 236 source/measure units. The capacitances were characterized using a 4284A LCR meter (Agilent Tech.).

## 3. Results and discussion

Fig. 2 shows the effects of varying the solvent on the studied pentacene films. Specifically, Fig. 2a displays the height-mode AFM topography of a nonexposed pentacene surface, and Fig. 2b–d shows images of the pentacene film after exposure to DI water, ethanol, and toluene. Fig. 2e shows XRD analyses of pentacene films before and after exposure to different solvents. After exposure to DI water, the film exhibits the morphology similar to that of the pristine pentacene layer, with a root-mean-square (Rq) roughness of 7.4 nm (see Fig. 2a and 2b). In addition, the DI water-exposed film is characterized by a thin-film phase with an interlayer spacing  $d_{001}$  of  $15.5 \pm 0.1$  Å, which is similar to that of the pristine layer. The pentacene films exposed to other solvents exhibit high Rq roughnesses (between 15 and 30 nm). The XRD results indicate a phase transition from the thin-film to the bulk phase after ethanol and toluene exposure. Therefore, DI water is the most suitable solvent for the passivation of pentacene FETs, because the organic solvents damage the pentacene thin-film. These results coincide with those recently reported by Han et al. [11]. Thus, water-soluble SbQ-PVA can be used as a passivation layer. SbQ-PVA has powerful advantages over poly(vinyl alcohol) (PVA), which is commonly employed as a passivation layer, as the latter material is not completely adequate for this purpose due to its ultra-hydrophilic properties and high water-vapor transmission rate [14]. Therefore, an additional crosslinking agent and/or the introduction of another hydrophobic layer must be used in conjunction with PVA. SbQ-PVA can be photocrosslinked via a [2+2]-cycloaddition [15,16], which enhances its barrier properties (see Fig. 3a). Fig. 3b shows UV-vis absorption spectra of the SbQ-PVA film before and after UV exposure. The absorbance of the UV-exposed film is

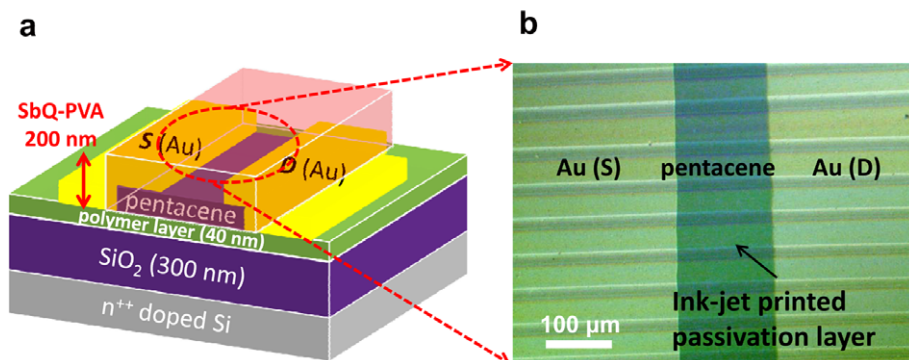
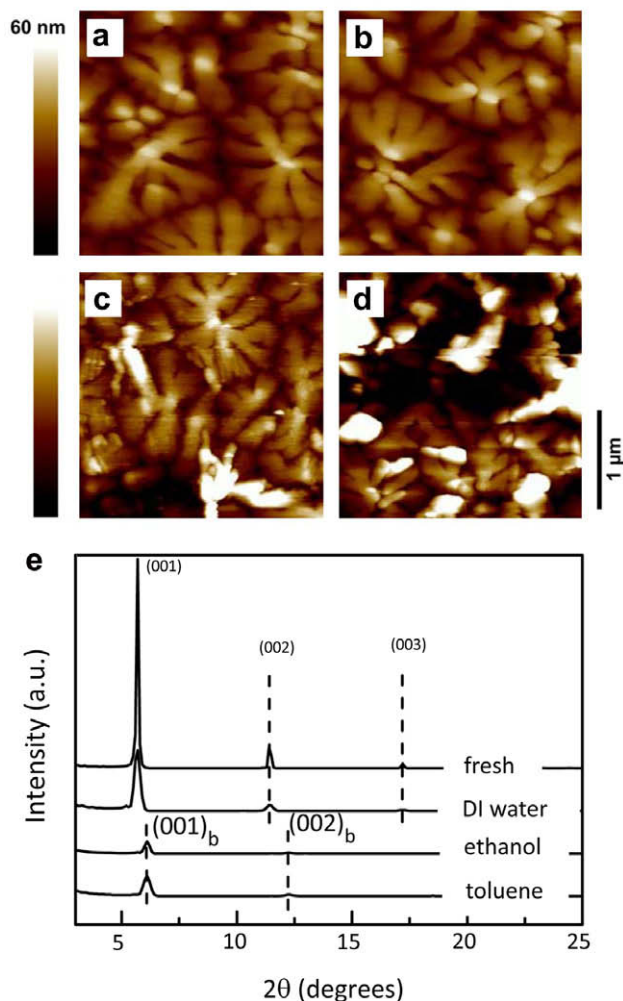


Fig. 1. (a) Schematic representation of a pentacene FET and (b) OM image of an inkjet-printed passivation layer on a pentacene FET ( $\times 200$ ).



**Fig. 2.** Height-mode AFM images of (a) a pristine pentacene film, (b) a DI water-exposed pentacene film, (c) an ethanol-exposed pentacene film, (d) a toluene-exposed pentacene film, and (e) XRD patterns of a pristine pentacene film and of various solvent-exposed pentacene films.

remarkably diminished relative to that of the pristine film, which verifies photocrosslinking due to quenching of the C=C double bond of the 4(4'-formylstyryl) pyridinium methosulfate salts to form the [2+2]-cycloaddition products. The crosslinked SbQ-PVA film was found to be robust, even after 20 min of ultrasonication in DI water, which indicated that it had been photocrosslinked by fluorescent light.

In previous studies, the degradation of pentacene FETs was mainly due to water present in ambient air rather than to oxygen [17,18]. Therefore, we focus here on the effect of water on the degradation of the devices. Fig. 4 shows the degradation of the electrical characteristics of pentacene FETs (PS/SiO<sub>2</sub> dual-layer gate dielectrics) without, with inkjet-printed, and with spin-coated passivation layers after 10 days. The field-effect mobility ( $\mu$ ) was obtained from the slope of a plot of the square root of the drain current ( $I_D$ ) versus the gate voltage ( $V_G$ ) in the saturation regime using the following equation:  $I_D = (WC_i/2L)\mu(V_G - V_{th})^2$ , where  $I_D$  is the drain current,  $C_i$  is the

capacitance per unit area of dielectrics (10 nF/cm<sup>2</sup> at 100 kHz), and  $V_{th}$  is the threshold voltage in ambient air (with a humidity of 60–80%) at room temperature. The pentacene FETs lacking a passivation layer showed a significant decrease in mobility, from the initial value ( $\mu_0$ ) of 0.71 cm<sup>2</sup>/Vs to 0.22 cm<sup>2</sup>/Vs (30% of  $\mu_0$ ), as shown in Fig. 4a. Water molecules in ambient air have been reported to diffuse into the grain boundaries of the polycrystalline semiconductor layer and/or the interface between the semiconductor and the gate dielectric, thereby generating both donor- and acceptor-like traps and leading to a significant degradation of the mobility [18].

The devices containing a passivation layer did not undergo a significant change in mobility when compared with the unpassivated devices (see Fig. 4b and 4c). The changes in  $V_{th}$ , the on/off ratio ( $I_{on/off}$ ), and the subthreshold swing (SS) were negligible. The device containing the inkjet-printed passivation layer showed a better electrical performance than that based on the spin-coated film. Since inkjet-printing allows the deposition of well-defined,

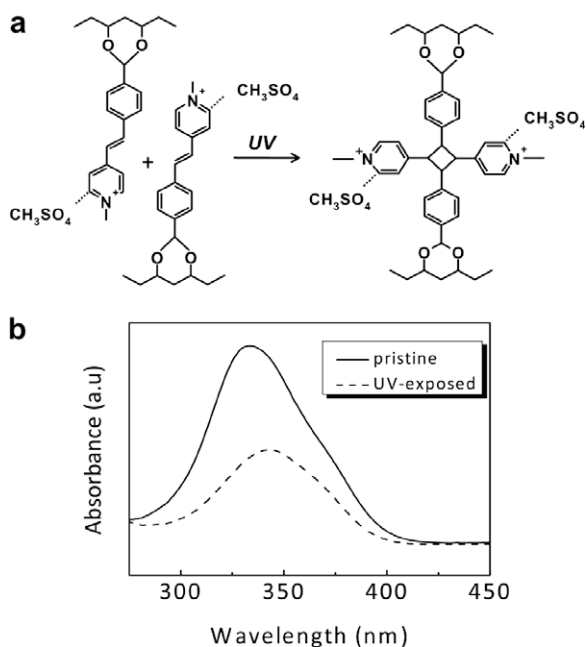


**Fig. 3.** (a) Chemical structures of SbQ-PVA (left) and photochemically crosslinked SbQ-PVA (right) and (b) Changes in the UV-vis absorption spectra of a SbQ-PVA film.

high-resolution lines (with dimensions of several tens of micrometers), while spin-coating takes place on the whole semiconductor area, less passivation solvent will come in contact with the semiconductor in the first case, which results in less degradation of the performance of the inkjet-printed devices.

Fig. 5 shows the transfer characteristics of pentacene FETs (PVP/SiO<sub>2</sub> dual-gate dielectrics) without a passivation layer, and with inkjet-printed and spin-coated layers. The characteristics are reported for a period of 100 days in ambient air (with a humidity of 60–80%) at room temperature. The  $I_D$ - $V_G$  transfer curves of the pentacene FETs were obtained in the linear regime ( $V_D = -6$  V). The  $\mu_0$  values for the devices without, with inkjet-printed, and with spin-coated passivation layers were 0.21, 0.22, and 0.24 cm<sup>2</sup>/Vs, respectively. These values were calculated by fitting the experimental data to the following equation:  $\mu = (L/WC_i V_D)(\partial I_D / \partial V_G)$ , where  $C_i$  was 9.4 nF/cm<sup>2</sup> at 100 kHz. After 100 days, the relative mobility ( $\mu/\mu_0$ ) of the pentacene FETs without a passivation layer dropped to 0.6, whereas those of the devices containing inkjet-printed and spin-coated passivation layers decreased to 0.7 and 0.65, respectively. In particular, the changes in the values of the turn-on voltage ( $V_{\text{turn-on}}$ ),  $V_{\text{th}}$ , and  $I_{\text{OFF}}$  are much larger in the devices without passivation than those with passivation (see Fig. 6).  $V_{\text{turn-on}}$  is the voltage where sub-threshold current starts increasing exponentially.

These results can be attributed to the presence of adsorbed water molecules on the pentacene layer close to the gate dielectrics, which act as acceptor-like traps that can be filled with injected electrons at positive  $V_G$  values, thus leading to the accumulation of negative charges. As a consequence, extra holes are required to balance the stored negative charges, and  $V_{\text{turn-on}}$  and  $V_{\text{th}}$  move to more positive values. Moreover, the value of  $I_{\text{OFF}}$  at positive  $V_G$  is higher than that of the devices without acceptor-like traps [19,20].

In addition to the variations in  $V_{\text{turn-on}}$ ,  $V_{\text{th}}$ , and  $I_{\text{OFF}}$ , the time dependence of  $SS$  also shows certain differences between the passivated and unpassivated devices. The

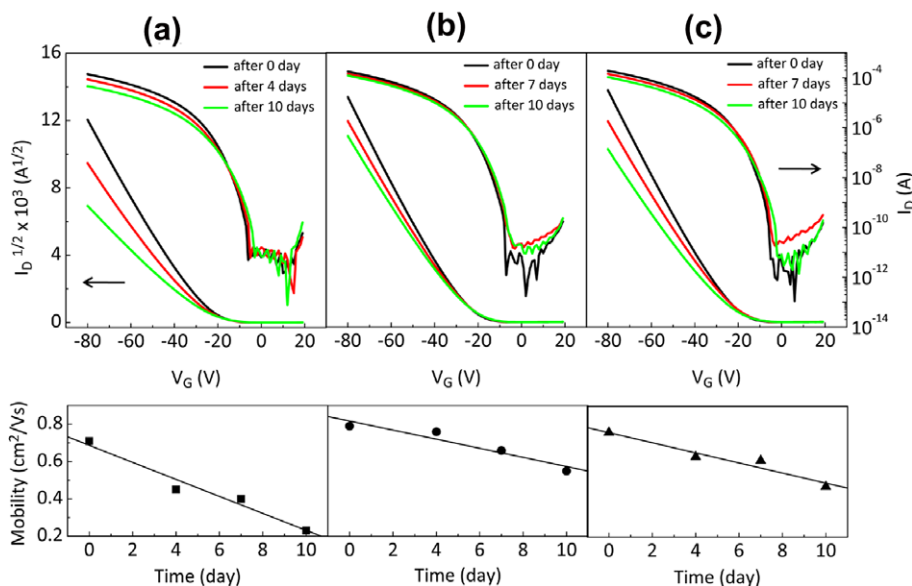


**Fig. 4.** Transfer characteristics and mobility drops of pentacene FETs (PS/SiO<sub>2</sub> dual-gate dielectrics) (a) without a passivation layer, (b) with an inkjet-printed passivation layer, and (c) with a spin-coated passivation layer. The characteristics were measured for 10 days. In the top graphics, the left curves represent the square root of  $I_D$  versus  $V_G$ , whereas the right ones are  $I_D$  versus  $V_G$ .

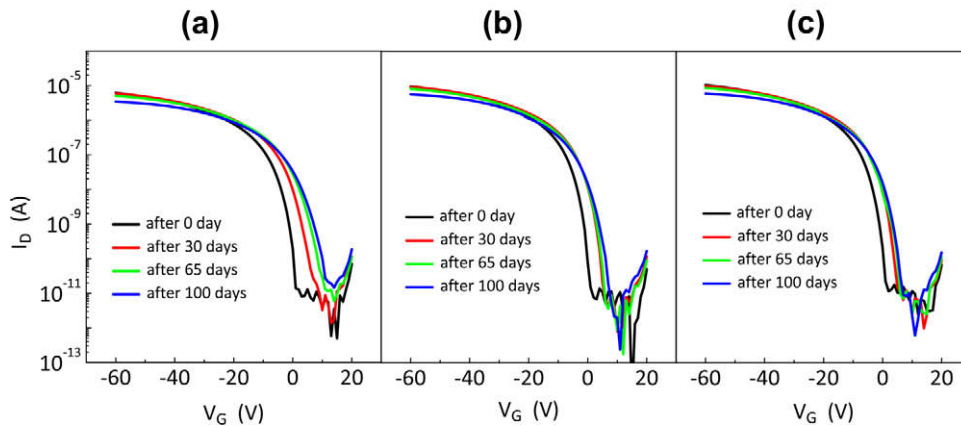


**Fig. 5.** Transfer characteristics of pentacene FETs (PVP/SiO<sub>2</sub> dual-gate dielectrics) (a) without passivation layer, (b) with an inkjet-printed passivation layer, and (c) with a spin-coated passivation layer. The characteristics were followed for 100 days. The  $I_D$ - $V_G$  transfer curves were measured in the linear regime ( $V_D = -6$  V).

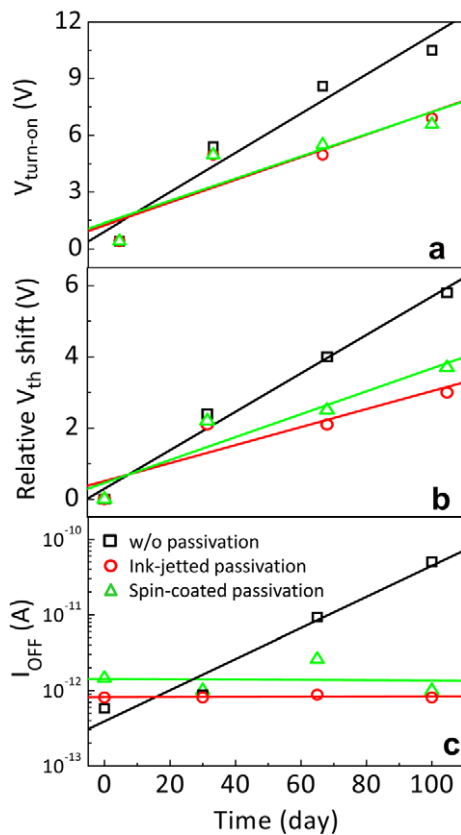


**Fig. 6.** Time-dependent changes of the (a)  $V_{\text{turn-on}}$ , (b) relative  $V_{\text{th}}$ , and (c)  $I_{\text{OFF}}$  values of pentacene FETs (PVP/SiO<sub>2</sub> dual-gate dielectrics) with and without passivation layer.

parameter SS is an important factor determining the voltage swing when a device is turned from the “off” to the “on” state and should be kept as low as possible. As mentioned above, the water molecules in the semiconductor act as trap sites, thus resulting in an increase of SS [20].

The SS value of the unpassivated device changed from 1.4 to 2.75 V/decade, whereas that of the device containing the inkjet-printed passivation layer only showed a small variation (from 1.3 to 1.7 V/decade).

We can conclude that the water-repellent properties of SbQ-PVA can protect the passivated devices from water molecules present in ambient air, so that the values of  $V_{\text{th}}$ ,  $I_{\text{OFF}}$ , and SS are less affected in this case relative to the unpassivated devices. Since the FETs based on inkjet-printed passivation layers show the most stable electrical properties, we can affirm that inkjet-printing is a promising solution-processing passivation technique with the advantage that it allows direct patterning with high-resolution.

#### 4. Summary

We investigated how the solvent used for passivation affects pentacene thin-films. The results showed that water is the most adequate solvent because it does not disrupt the pristine crystalline structure of the pentacene films. We introduced water-soluble and photocrosslinkable SbQ-PVA as a passivation material for pentacene FETs. Although this material normally dissolves well in water, it shows good water-resistant properties after photocross-linking. Pentacene FETs containing an inkjet-printed and photocrosslinked SbQ-PVA passivation layer showed good time-dependent electrical performance, even after 100 days of aging in ambient air with 60–80% humidity. In addition, we found that inkjet-printing is a better procedure than spin-coating, because it leads to better device performance and offers additional advantages during the manufacturing process, for example, direct patterning and high-resolution.

#### Acknowledgements

This work was supported by the Korea Research Foundation Grant No. KRF-2004-0005-D00004.

## References

- [1] C.D. Dimitrakopoulos, P.R.L. Malenfant, *Adv. Mater.* 14 (2002) 99.
- [2] S.R. Forrest, *Nature* 428 (2004) 911.
- [3] Y. Qiu, Y. Hu, G. Dong, L. Wang, J. Xie, Y. Ma, *Appl. Phys. Lett.* 83 (2003) 1644.
- [4] D. Li, E.-J. Borkent, R. Nortrup, H. Moon, H. Katz, Z. Bao, *Appl. Phys. Lett.* 86 (2005) 042105.
- [5] O.D. Jurchescu, J. Baas, T.T.M. Palstra, *Appl. Phys. Lett.* 87 (2005) 052102.
- [6] R. Ye, M. Baba, K. Suzuki, Y. Ohishi, K. Mori, *Thin Solid Films* 464–465 (2004) 437.
- [7] S. Ferrari, F. Perissinotti, E. Peron, L. Fumagalli, D. Natali, M. Sampietro, *Org. Electron.* 8 (2007) 407.
- [8] K. Tsukagoshi, I. Yagi, K. Shiget, K. Yanagisawa, J. Tanabe, Y. Aoyagi, *Appl. Phys. Lett.* 87 (2005) 183502.
- [9] T. Sekitani, T. Someya, *Jpn. J. Appl. Phys.* 46 (2007) 4300.
- [10] S.H. Han, J.H. Kim, J. Jang, S.M. Cho, M.H. Oh, S.H. Lee, D.J. Choo, *Appl. Phys. Lett.* 88 (2006) 073519.
- [11] S.H. Han, J.H. Kim, Y.R. Son, K.J. Lee, W.S. Kim, G.S. Cho, J. Jang, S.H. Lee, D.J. Choo, *Electrochem. Solid-State Lett.* 10 (2007) J68.
- [12] B.-J. de Gans, P.C. Duineveld, U.S. Schubert, *Adv. Mater.* 16 (2004) 203.
- [13] D.J. Gundlach, T.N. Jackson, D.G. Schlom, S.F. Nelson, *Appl. Phys. Lett.* 74 (1999) 3302.
- [14] M. Avella, M.E. Errico, R. Rimedio, *J. Mater. Sci.* 39 (2004) 6133.
- [15] E.S. Cockburn, R.S. Davidson, J.E. Pratt, *J. Photoch. Photobiochem. A: Chem.* 94 (1999) 83.
- [16] J. Jang, S.H. Kim, S. Nam, D.S. Chung, C. Yang, W.M. Yun, C.E. Park, J.B. Koo, *Appl. Phys. Lett.* 92 (2008) 143306.
- [17] S.H. Kim, H. Yang, S.Y. Yang, K. Hong, D. Choi, C. Yang, D.S. Chung, C.E. Park, *Org. Electron.* 9 (2008) 673.
- [18] D. Knipp, A. Benor, V. Wagner, T. Muck, *J. Appl. Phys.* 101 (2007) 044504.
- [19] G. Gu, M.G. Kane, J.E. Doty, A.H. Firester, *Appl. Phys. Lett.* 87 (2005) 243512.
- [20] S.H. Kim, J. Jang, H. Jeon, W.M. Yun, S. Nam, C.E. Park, *Appl. Phys. Lett.* 92 (2008) 183306.





# Thin-film transistors based on liquid-crystalline tetrafluorophenylter thiophene derivatives: thin-film structure and carrier transport

Fapei Zhang<sup>a</sup>, Masahiro Funahashi<sup>a,\*</sup>, Nobuyuki Tamaoki<sup>b,\*</sup>

<sup>a</sup> Department of Chemistry and Biotechnology, School of Engineering, University of Tokyo, 7-3-1 Hongo, Bunkyo-ku, Tokyo 113-8656, Japan

<sup>b</sup> Nanotechnology Research Institute, National Institute of Advanced Industrial Science and Technology, 1-1-1 Higashi, Tsukuba 305-8565, Ibaraki, Japan

## ARTICLE INFO

### Article history:

Received 25 July 2008

Received in revised form 6 October 2008

Accepted 7 October 2008

Available online 7 November 2008

### PACS:

71.20.Rv

71.23.-k

72.20.Ee

72.80.Le

73.40.Sx

73.61.Ph

### Keywords:

Liquid-crystalline semiconductors

Thin-film transistor

Carrier mobility

Smectic phase

Tetrafluorophenyl

## ABSTRACT

The authors fabricated thin films by solution processes using liquid-crystalline (LC) semiconductors, 5-alkyl-5''-(4-hexyltetrafluorophenyl)-2,2':5',2''-terthiophene (**2–5**). Films of 5-propyl-5''-(4-hexyltetrafluorophenyl)-2,2':5',2''-terthiophene (**2**) show similar molecular packing as their non-fluorinated counterparts. However, the degree of molecular packing ordering from X-ray diffraction measurement is higher, and the films exhibit a more crystal-like structure. Moreover, fluorination has a remarkable effect on their mesomorphic behaviors. Films of **2** consist of large size LC domains (in the range of 100  $\mu\text{m}$ ) at room temperature. Thin-film transistors (TFTs) of **2** show p-type operation with good hole mobility up to 0.027  $\text{cm}^2/\text{Vs}$  as well as improved operation stability under ambient conditions and high on/off ratio. Tetrafluorophenyl substitution leads to lowering of HOMO energy by 0.15 eV for **2** and 0.35 eV for **5**, resulting in operation stability. Variable-temperature current-voltage measurements indicate intrinsic carrier transport in films of **2**.

© 2008 Elsevier B.V. All rights reserved.

## 1. Introduction

In the quest for commercially successful organic field-effect transistors (OFETs), device fabrication by a solution process will be favorable due to its potential for large-area applicability and low cost production. However, the mobility of OFETs prepared by such a process is usually lower than that of devices fabricated by vacuum deposition. In addition, soluble conjugated polymers [1–3], solution-

processable pentacene [4], and soluble precursors that can be converted into polycrystalline thin films [5] have been utilized to fabricate OFETs; however, a number of defects that inhibit smooth carrier transport are formed when polycrystalline thin films are formed.

Recently, liquid-crystalline (LC) semiconductors have emerged as promising materials for organic electronics [6–8]. They are solution-processable because of the thermal movement of the long alkyl chains attached to the LC molecules, which can self-assemble into large-area domains with a crystal-like structure and low defect density. Thus, the influence of grain boundaries, which seriously hinder charge carrier transport in polycrystalline materials,

\* Corresponding authors. Tel.: +81 3 5841 7441; fax: +81 3 5841 8661.  
E-mail addresses: [funahashi@chembio.t.u-tokyo.ac.jp](mailto:funahashi@chembio.t.u-tokyo.ac.jp) (M. Funahashi),  
[n.tamaoki@aist.go.jp](mailto:n.tamaoki@aist.go.jp) (N. Tamaoki).

is significantly suppressed [9]. Such capability of LCs to self-organize into ordered thin films is also favorable to electronic applications requiring homogeneity over large-area.

Bulk carrier mobility in columnar [10–12], smectic [13–16], nematic, and cholesteric [17–20] phases has been determined by the time-of-flight (TOF) technique. High carrier mobility, in excess of  $0.1 \text{ cm}^2/\text{Vs}$ , has been observed in highly ordered columnar and smectic phases of LC molecules with a large  $\pi$ -conjugated system. It should be noted that a domain structure with size exceeding several  $\mu\text{m}$  is often formed in LC phases, and the domain boundary does not inhibit electronic carrier transport [9] when compared with molecular crystals. Recently, large-area LC thin-film transistors (TFTs) were fabricated [21–23] by utilizing the self-organization properties of LC semiconductors, although most LC semiconductors recrystallize at room temperature, leading to an increase in the density of defects and carrier traps.

Recently, our group developed the LC material: 5-propyl-5''-(4-pentylphenyl)-2,2':5',2''-terthiophene (**1**) [23]. It exhibits a highly ordered smectic phase at room temperature and fast ambipolar transport with the hole and electron mobility of  $0.07 \text{ cm}^2/\text{Vs}$  and  $0.2 \text{ cm}^2/\text{Vs}$  in the bulk state, respectively. LC thin films with a thickness of 50 nm were fabricated by the spin-coating method and they can be applied to TFTs. The hole mobility of  $0.04 \text{ cm}^2/\text{Vs}$  was achieved on TFTs using this solution-processable LC semiconductor [24]. This good performance of the devices could be attributed to the highly ordered structure of the LC thin films with low defect density and domain size as compared to the channel length.

The stabilization of the LC thin films against oxidation is indispensable for the realization of practical FET devices working under ambient air for long time periods. For this, an increase in the oxidation potential by the introduction of electron withdrawing moieties is effective. The tetrafluorophenyl group has moderate electronegativity and does not deteriorate molecular linearity because of the small van der Waals radius of the fluorine atoms and its symmetry. In addition, it is known that when the tetrafluorophenyl moiety is introduced in LC molecules, it lowers their phase transition temperatures and increases their mobility [25]. It is expected that this property would result in the formation of large domains during LC thin-film formation. The effect of the tetrafluorophenyl group on the liquid crystallinity of phenylbithiophene derivatives [25] and conju-

gated polymers [26] has been studied. However, no examples of LC semiconductors with low molecular weight for TFTs exist.

In this work, we developed LC terthiophene derivatives with the tetrafluorophenyl group, 5''-(4-hexyltetrafluorophenyl)-2,2':5',2''-terthiophene derivatives (**2–4**), as well as a more electronegative LC terthiophene compound with both tetrafluorophenylene and perfluoroalkyl groups 5-perfluoro-hexyl-5''-(4-hexyl-tetrafluorophenyl)-2,2':5',2''-terthiophene (**5**), both of which are analogues of compound **1**. We performed a detailed investigation of the fluorination effect on LC phase transition, molecular packing, and film structure as well as their relationship with carrier transport in the TFTs.

## 2. Results and discussion

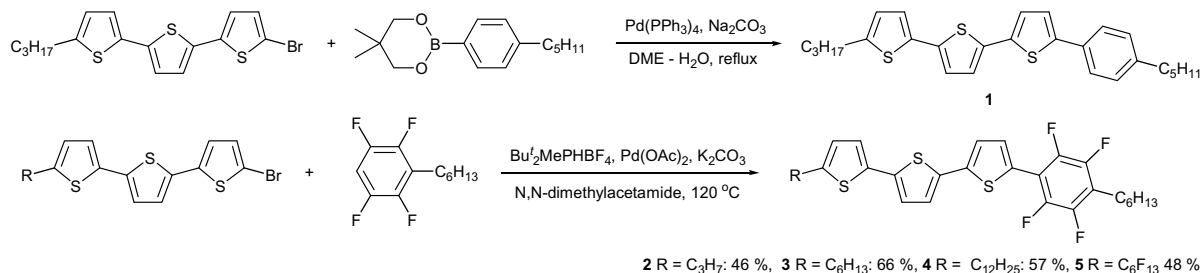
### 2.1. Material design and synthesis

As shown in Scheme 1, 5-(4-hexyl-2,3,5,6-tetrafluorophenyl)-5''-alkyl-2,2':5',2''-terthiophene (**2–4**) and 5-(4-hexyl-2,3,5,6-tetrafluorophenyl)-5''-perfluoro-hexyl-2,2':5',2''-terthiophene (**5**) were synthesized by a cross-coupling reaction between 5-bromo-5''-alkyl-2,2':5',2''-terthiophene and 1-hexyl-2,3,5,6-fluorobenzene catalyzed by palladium (II) acetate and di-*tert*-butylmethylphosphonium tetrafluoroborate in *N,N*-dimethylacetamide, a process reported by Fagnou et al. [27], because of the low reactivity of tetrafluorophenyl borate under a conventional Suzuki coupling reaction. In contrast, non-fluorinated compound **1** can be synthesized by the conventional Suzuki coupling reaction between alkylphenylboric acid and 5-bromo-5''-alkyl-2,2':5',2''-terthiophene [23]. Tetrafluorophenylterthiophene derivatives **2–5** were obtained in satisfactory yield and the crude products were purified by silica gel column chromatography and recrystallization from *n*-hexane.

### 2.2. Mesomorphic behaviors

The phase transition temperature was determined by differential scanning calorimetry (DSC) and the observation of optical textures under a polarized light microscope (POM). The LC phase structure was investigated by X-ray diffraction (XRD).

Compound **2** exhibits an enantiotropic nematic (N) phase and a highly ordered mesophase (M), as well as a



Scheme 1. Synthetic route of tetrafluorophenylterthiophene derivatives.

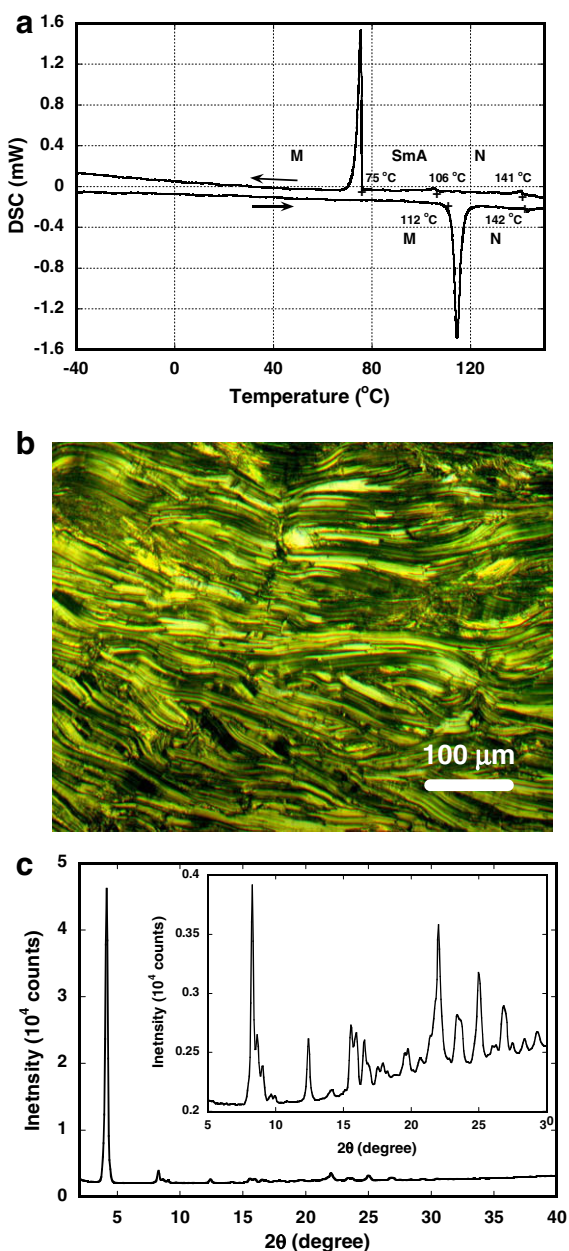


**Fig. 1.** (a) DSC profile of tetrafluorophenylterthiophene derivative **2**. (b) Micrographic textures in the mesophase of compound **2** at room temperature under a polarized light microscope. (c) X-ray diffraction in the mesophase of compound **2** at room temperature.

monotropic smectic A (SmA) phase. In the DSC curve of compound **2**, shown in Fig. 1(a), two peaks corresponding to an isotropic-N phase transition at 141 °C and a N-SmA at 106 °C with small transition enthalpies of 0.2 J/g as well as a peak corresponding to SmA-M transitions at 75 °C with a transition enthalpy of 8.4 J/g were observed in the cooling process. In the heating process, the curve exhibits one strong peak corresponding to the transition between the M phase and the N phases at 112 °C as well as a weak peak corresponding to the transition between the N and isotropic phases at 142 °C. When the M phase was cooled to  $-50$  °C, no glass transition was observed. From the schlieren and fan-like textures under the observation of a polarized light microscope, the two phases that appear in the high-temperature region were identified as N and SmA phases, respectively. The result of X-ray diffraction also supports that these two phases are nematic and smectic phases, respectively. In the M phase, mosaic texture with defect lines as shown in Fig. 1b was observed. In the X-ray diffraction of the M phase of compound **2** (Fig. 1c), which appears below 75 °C in the cooling process, the strong diffraction (100) at  $2\theta = 4.14^\circ$  indicates a layer structure whose spacing is 23.1 Å. This value is slightly smaller than the molecular length (29.8 Å) with all-trans conformation, determined by MM2 calculation. And a number of peaks were observed between  $2\theta = 10^\circ$  and  $30^\circ$ , indicating that this phase has crystal-like 3-D structures. However, this phase exhibits fluidity above 100 °C on heating, below phase transition to the N phase, indicating that this is a mesophase with a freedom of molecular thermal movement. The optical micrographic texture revealed domains with a relatively large size exceeding several ten  $\mu\text{m}$ . Such a mesophase of 3-D order was observed in dithenylbenzene derivatives reported by Shimizu et al. [28]. It should be noted that this mesophase is retained below room temperature and compound **2** possessed no phase transition when it was cooled to  $-50$  °C. The freedom of molecular thermal movement in the mesophase should cause the reorientation of molecules in the thin-film state in a thermal annealing process, resulting in large domain formation in the thin films.

Compound **3** also exhibits N, SmA, and highly ordered mesophase in both heating and cooling processes. Compound **4**, which has a long alkyl chain, exhibits a SmA and a highly ordered mesophase in a heating process. In a cooling process, an additional mesophase appears between the smectic A phase and the highly ordered mesophase. The phase transition temperatures are summarized in Table 1. The highly ordered mesophases of compounds **3** and **4** also exhibit fluidity to some extent below the phase transition

**Table 1**

Phase transition temperature of 5-(4-hexyltetrafluorophenyl)-5'-alkyl-2,2':5',2"-terthiophene derivatives.

	Heating	Cooling
<b>2</b> R = C <sub>3</sub> H <sub>7</sub>	M 112 °C N 142 °C Iso	Iso 141 °C N 106 °C SmA 75 °C M
<b>3</b> R = C <sub>6</sub> H <sub>13</sub>	M 114 °C SmA 130 °C N 139 °C Iso	Iso 138 °C N 130 °C SmA 90 °C M
<b>4</b> R = C <sub>12</sub> H <sub>25</sub>	M <sub>2</sub> 89 °C SmA 135 °C Iso	Iso 134 °C SmA 78 °C M <sub>1</sub> 67 °C M <sub>2</sub>
<b>5</b> R = C <sub>6</sub> F <sub>13</sub>	Cryst. 149 °C SmA 209 °C Iso	Iso 206 °C SmA 130 °C Cryst.

M, M<sub>1</sub>, and M<sub>2</sub> are unidentified mesophases.

temperature between the highly ordered mesophase and the SmA phase. Therefore, the mesophases should also be a kind of plastic crystal phase with some extent of molecular thermal movement.

The phase transition temperatures were lowered by ca. 50 °C as compared with the non-fluorinated counterpart 5-(4-alkylphenyl)-5''-alkyl-2,2':5',2''-terthiophene [23]. For example, compound **2** exhibited a nematic phase between 112 °C and 142 °C and a highly ordered smectic phase below 112 °C, in contrast to 5-(4-propylphenyl)-5''-hexyl-2,2':5',2''-terthiophene (**1**), which exhibits a nematic phase between 217 °C and 202 °C and a highly ordered smectic phase below 202 °C [23]. Such a lowering of the phase transition temperature was reported in tetrafluorophenyl-bithiophene derivatives [25].

Compound **5**, which has a perfluoroalkyl chain, does not exhibit mesophases at room temperature. The phase at room temperature has a 3-D crystal-like order and no fluidity even near the phase transition to the SmA phase.

### 2.3. Structural characterization of mesomorphic thin films

The tetrafluorophenyl substituted compounds **2–4** show high solubility in common organic solvents. In this work, the investigation of the fabrication of the films and TFTs was focused on compound **2** due to the high similarity of molecular structure to non-fluorinated compound **1**.

Homogeneous thin films of compounds **2** could be deposited on the surface of a SiO<sub>2</sub> layer treated with hexamethyldisilazane (HMDS) from their chlorobenzene solution by the spin-coating method. The polarized optical micrograph of as-prepared films of compound **2** in Fig. 2a shows the fine-threaded texture consisting of small domains with submicron size. Upon annealing at 85–90 °C for 10 min, a mosaic texture appears, corresponding to a highly ordered smectic phase (in Fig. 2b). This indicates that the thermal movement of the LC molecules caused the reorganization of macroscopic molecular alignment during the thermal annealing process below the phase transition temperature between the mesophase and the smectic A phase. This phenomenon should be associated with the freedom of molecular thermal movement in the mesophase. In particular, the films exhibited very large size of LC domains, exceeding several hundred μm, which was much larger than that in the film of non-fluorinated molecule **1** [23,24]. The tetrafluorophenyl group should increase molecular mobility in the mesophase because of weak intermolecular interaction.

The above facts were further confirmed by an atomic force microscope (AFM) observation. The film consists of large-area grains in the range of 20–50 μm (and even larger) with a lamellar structure. Fig. 2c and d show the AFM images within an individualized grain exhibiting a terrace structure on the surface. The height of the steps

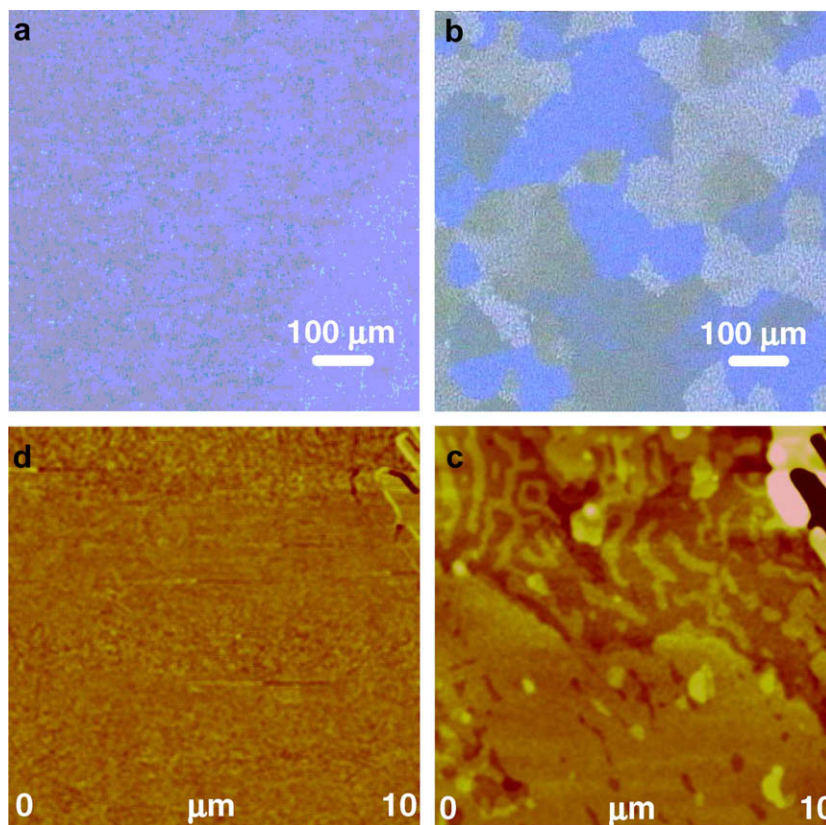


**Fig. 2.** Polarized-light microscopic textures at room temperature of thin film of compound **2** (a) as-cast and (b) annealed at 85 °C for 10 min. (c) AFM topographic and (d) phase images of thin film of compound **2**.

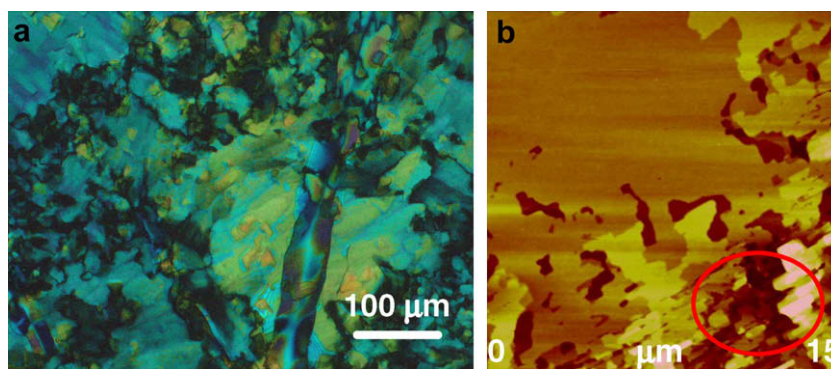


Fig. 3. (a) POM texture and (b) AFM topographic image of film of compound **5** from solution casting. The circled part is the less-ordered region.

separating the terraces is ca. 2.1 nm, corresponding to the thickness of one smectic layer of molecule **2** (vide infra). And the layers are thus parallel to the surface of the substrate. The large domain size is due to the higher mobility of the fluorinated molecules that originates from the weak interaction between tetrafluorophenyl groups. The high mobility of molecule **2** also causes partial dewetting of the film from the hydrophobic surface of the substrate during the annealing.

Homogenous thin films of compound **5** could not be fabricated by the spin-coating method at room temperature. Relatively homogenous films of the compound were prepared from the solution cast at 70 °C. They consist of domains with various sizes under POM observation, as shown in Fig. 3a. The AFM graph in Fig. 3b reveals the large

size domains with a layer structure. The height of the steps is 2.5 nm, corresponding to the molecular length, larger than that in the film of compound **2**. However, we found some less-ordered regions (the circled part in Fig. 3b) between the highly ordered grains. In the less-ordered regions, the layers should be perpendicular to the surface, in contrast to the ordered regions, in which the layers are parallel to the surface of the substrate. In the FET devices, carriers move within the layers, and carrier movement should be inhibited in the less-ordered regions. This may be attributed to the stiffness of the rod-like fluoroalkyl chains in molecule **5**, which hinders effective molecular assembly during film growth Table 2.

In the specular ( $\theta/2\theta$ ) X-ray diffraction patterns (in Fig. 4a and b), the as-deposited films of compound **2** show two distinct series of intense peaks, suggesting the presence of two different LC phases. The dominant phase (denoted as Phase I) has an interlayer spacing (d-spacing) of 2.8 nm, larger than the second phase (phase II). Such a d-spacing value is nearly the same as that in the bulk mesophase (2.83 nm), in agreement with the POM observation. After the thermal annealing, phase I disappears completely and the intensity of the reflection peak from phase II is considerably enhanced, corresponding to complete phase transition into the mesophase. The annealed film shows a

Table 2

Molecular length, d-spacing, and molecular tilt angle in thin films of compounds **2**, **5**, and **1**.

Compound	Molecular length	d-Spacing	Tilt angle
2	2.8 nm	2.104 nm	38°
5	3.2 nm	2.660 nm	43°
1	2.7 nm	2.315 nm	31°

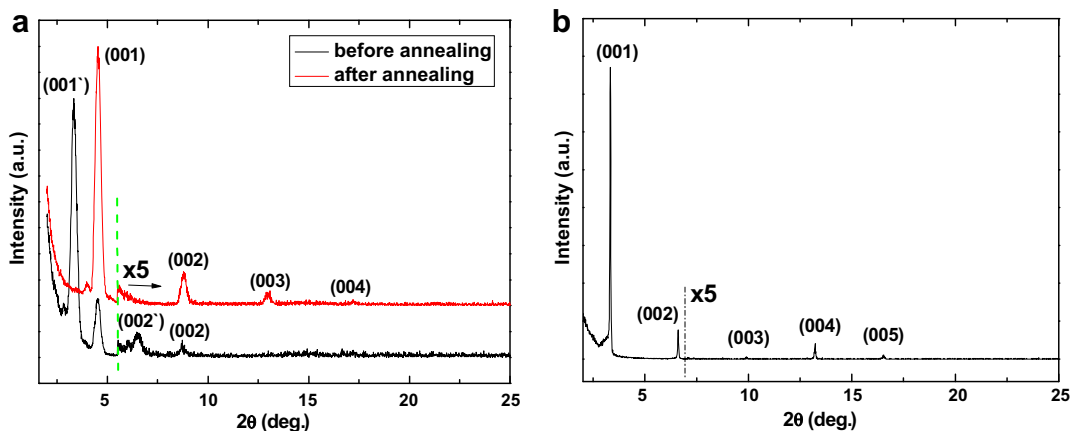


Fig. 4. X-ray diffraction of thin films of compounds **2** and **5**. (a) Out-of-plane pattern of film based on **2**, (b) out-of-plane pattern of film based on **5**.

strong reflection peak at an angle of  $2\theta = 3.8^\circ$  and three higher-order reflections attributed to (00n) reflections, indicating a clear layer structure. Using Bragg law, the interlayer spacing was calculated as 2.1 nm, in agreement with the step height of the molecular layers measured by AFM. This indicates that the molecular layer in the film is parallel to the substrate surface with the tilting of the molecular long axis with respect to the surface normal. In contrast, the XRD pattern exhibits only two (00n) reflection peaks for the film from fluorine-free molecule **1** [23,24]. These results indicate that the ordering of the stacking between the layers is enhanced by the fluorination of the phenyl group. The tilt angle of molecule **2** increases to  $43^\circ$  as compared to  $31^\circ$  in the case of molecule **1** (the molecular length of compound **1** is 2.7 nm), as shown in Table 1. The interdigitation of the alkyl chains of the LC molecules also lead to the shorter layer spacing. However, similar enhancement of the molecular tilt angle was found on films of fluoroarene-thiophenes [29].

For films of compound **5** with both tetrafluorophenyl and fluoroalkyl substitutions, the XRD pattern (in Fig. 4(b)) shows more higher-order (00n) reflection peaks up to  $n = 6$ , suggesting a highly orientated film structure. The d-spacing is 2.7 nm, as calculated from the first-order reflection at an angle of  $3.8^\circ$ . Compared with the films of compound **2** (with only fluorophenyl ring), the tilt angle of molecule **5** is reduced to  $38^\circ$  (Fig. 5).

The in-plane structure of the films was studied using grazing incidence XRD (in Fig. 4). The annealed films of compound **2** show a reflection peak at an angle of about  $16^\circ$  (corresponding to a d-spacing of 0.56 nm). A few reflections appear in the range of the higher angle for the film of compound **5**, suggesting a long-range ordering within the molecular layers of films of compounds **2** and **5**. However, weak intensity of the diffraction peaks (due to the limitation of intensity of X-ray source) prevents detailed structural analysis. In addition, a strong peak appears at the low angle corresponding to a d-spacing of 1.9 nm. This indicates the possible existence of a minor phase with the molecular layer perpendicular to the substrate surface. Such a phase may be located at less-ordered

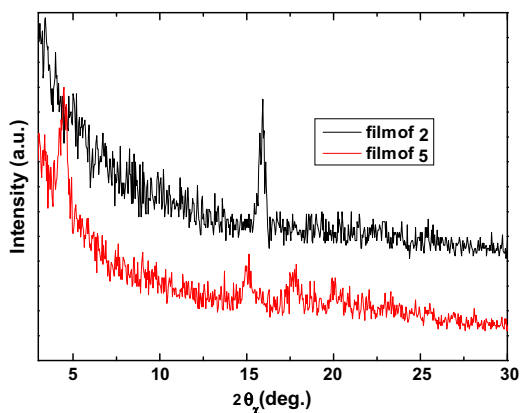


Fig. 5. In-plane X-ray diffraction patterns of films of compounds **2** and **5** (after annealing). The crystallographic assignments of the peaks are labeled.

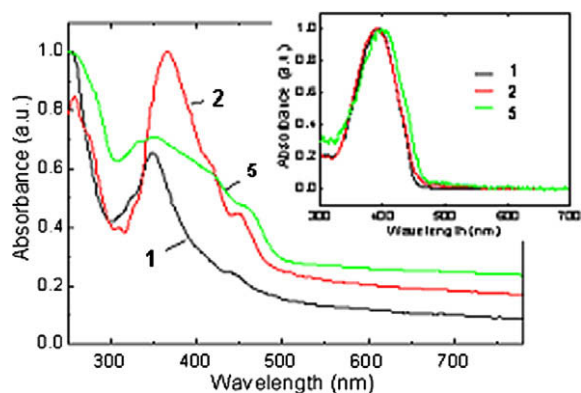


Fig. 6. Optical absorption spectra of compounds **1**, **2**, and **5** as films (inset shows optical absorption in chlorobenzene).

regions between the highly ordered grains or at the dielectric-organic interface. Further investigation is required to elucidate its origin.

#### 2.4. Absorption spectra of these compounds

Optical absorption spectra of compounds **1**, **2**, and **5** were measured both in solution and on thin films to study the effect of fluorophenyl and perfluoroalkyl-substitution on molecular packing and optical energy gap. The UV-VIS absorption spectra of the solutions (inset of Fig. 6) are free of fine structures. The absorption maximum ( $\lambda_{\text{abs}}$ ) corresponds to the  $\pi-\pi^*$  absorption band of the conjugated  $\pi$ -electron system of the core. The  $\lambda_{\text{abs}}$  of compound **2** in chlorobenzene is located at the same position as that of fluorine-free compound **1**.

UV-VIS data for the thin films of compounds **2** and **5** are shown in Fig. 6. The baselines of the spectra exhibit non-zero-values because of the light scattering. If the influence of the light scattering is excluded, the baselines should exhibit zero. All films show a similar absorption feature with a blue-shift of the maximum and a simultaneous red-shift of the onset compared to the solution spectra. The absorption maxima of films of compounds **2** and **5** are almost the

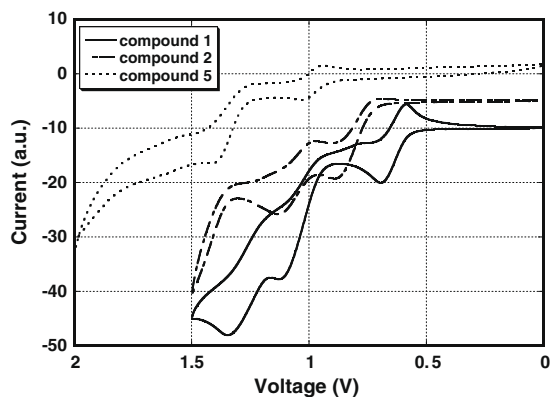


Fig. 7. Cyclic voltammogram of compounds **1**, **2**, and **5** in 0.05 M tetraethyl ammonium tetrafluoroborate/ $\text{CH}_2\text{Cl}_2$  solution with an Ag/AgCl standard electrode. The scan rate was 0.01 V/min.

same and the optical band gap is estimated to be 2.6 eV for compounds **2** and **5**. This suggests a similar patterning of molecular packing in films of fluorinated molecules **2** and **5** as well as non-fluorinated material **1**.

A similar feature was observed for different kinds of oligothiophene films and it was attributed to the formation of H aggregates [22,30].

### 2.5. Measurement of oxidation potential

Fig. 7 shows cyclic voltammetry (CV) plots of compounds **1**, **2**, and **5**. Non-fluorinated molecule **1** and fluorinated molecules **2** and **5** exhibit quasi-reversible one-electron oxidation at 0.65 V, 0.80 V, and 0.99 V, respectively (vs. Ag/AgCl in 0.05 M TEABF<sub>4</sub>/CH<sub>2</sub>Cl<sub>2</sub> solution). This indicates the lowering of the HOMO energy by 0.15 eV and 0.35 eV upon substitution with the tetrafluorophenyl group and both the tetrafluorophenyl and perfluoroalkyl groups, respectively. Considering the similar optical gap for compounds **2** and **5**, as observed from the UV–VIS spectra, the LUMO level is also lowered by 0.15 eV and 0.35 eV for compounds **2** and **5** with respect to liquid crystal **1**, respectively. Considering the similar optical gap for compounds **1**, **2**, and **5**, as observed from the UV–VIS spectra, the LUMO level is also lowered by 0.15 eV and 0.35 eV for **2** and **5** with respect to **1**, respectively. This is consistent with the results of oligothiophene systems with a strong electron withdrawing tetrafluorophenyl or perfluoroalkyl group [31,32]. Such modification of the HOMO and LUMO levels will have a significant effect on the carrier transport process of organic semiconductors. The lowering of the HOMO levels of compound **2** should contribute to the stabilization of LC semiconductors for oxidation under air.

### 2.6. Time-of-flight measurement

The bulk carrier mobility in the mesophase of tetrafluorophenylterthiophene derivative **2** was measured by the conventional time-of-flight technique [33].

Under the application of an electric field, the photogenerated carriers drift across the bulk of the sample, inducing

a transient photocurrent through the serial resistor. When the charge carriers reach the counter electrode, the induced photocurrent decays to zero. Therefore, a kink point in the transient photocurrent curve corresponds to the transit time  $t_T$ . Using Eq. (1), the carrier mobility ( $\mu$ ) can be calculated from the values of  $t_T$ , sample thickness  $d$ , and applied voltage  $V$ :

$$\mu = \frac{d^2}{Vt_T} \quad (1)$$

Illuminating the electrode under a positive or negative bias facilitates the determination of positive or negative carrier mobility, respectively.

When the absorption coefficient of a sample is sufficiently large, the excitation pulse is absorbed and a sheet of photo-carriers is generated at the interface between the illuminated electrode and the liquid crystal layer. In this study, a neat film of the compound exhibits a strong absorption band at around 370 and 250 nm in the smectic phase; the depth of penetration of the excitation light at 356 nm was estimated to be less than 0.5  $\mu\text{m}$ , i.e., it was much smaller than the sample thickness (25  $\mu\text{m}$ ).

The highly ordered smectic phase of the compound has a relatively rigid structure with high viscosity; further, no change in the micrographic texture is observed when an electric field of the order of  $10^5$  V/cm is applied to the sample. The liquid crystal molecules in the sample are aligned parallel to the electrode surface; therefore, carrier transport within a smectic layer perpendicular to the electrode surface should be observed in the TOF measurement.

Fig. 8a shows transient photocurrents for the hole in the mesophase of compound **2** at room temperature. The obtained photocurrents are dispersive; however, transit times are estimated in a double logarithmic plot. The hole mobility is 0.07  $\text{cm}^2/\text{Vs}$ , which is independent of the electric field and temperature between 100 and 50  $^\circ\text{C}$ . Below 50  $^\circ\text{C}$ , it decreases to 0.03  $\text{cm}^2/\text{Vs}$  at room temperature. This decrease in the hole mobility should be attributed to the formation of defects that are caused by shrinkage when the sample was cooled, but not the intrinsic property of the liquid crystal material. If the defects are not formed with volume shrinkage, the hole mobility would be maintained constant.

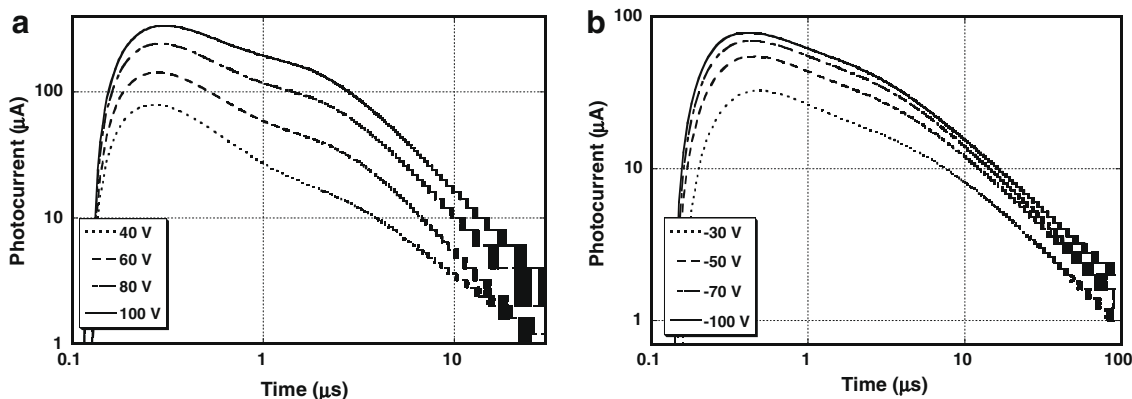


Fig. 8. Transient photocurrent curves in the mesophase of compound **2** at room temperature (a) for hole and (b) for electron. The sample thickness was 25  $\mu\text{m}$ .

Fig. 8b shows transient photocurrents for the electron in the highly ordered mesophase around room temperature. The electron mobility at room temperature is  $0.02 \text{ cm}^2/\text{Vs}$ , which is independent of the electric field but not the temperature. The electron mobility is lower than that of the hole, suggesting that the electron transport process should be influenced from the electron traps in the bulk state.

In the crystal phase of compound **5**, only photocurrent decay is observed. Because of the crystallinity of compound **5**, the sample contains a number of defects that form deep traps, in contrast to the low defect density of the mesophase of compounds **1** and **2**.

### 2.7. FET characterization

The TFTs from compounds **2** and **5** were fabricated in the top-contact configuration. As shown in the section of the structural characterization of mesomorphic thin films, molecules are perpendicular to the substrates in the mesomorphic thin films. Therefore the carriers should move within the layers consisting of the liquid crystal molecules in the channel area. Fig. 9a shows the  $I_D$ - $V_D$  characteristics for TFTs of compound **2** measured in ambient air. The devices exhibit a typical p-type operation. The hole mobility is calculated as  $1.6$ – $2.1 \times 10^{-2} \text{ cm}^2/\text{Vs}$  for most devices in a saturation region (see Fig. 9b). The current on/off ratio is more than  $10^6$ . The highest value of the mobility is up to  $2.7 \times 10^{-2} \text{ cm}^2/\text{Vs}$  in the best devices. Such a value is close to that obtained from the time-of-flight (TOF) measurement in the bulk state ( $0.07 \text{ cm}^2/\text{Vs}$  at  $50 \text{ }^\circ\text{C}$ ), which represents the upper limit of transport properties of the TFTs [24]. This should be attributed to the formation of highly ordered LC domains with size larger than the channel length ( $20$ – $30 \text{ }\mu\text{m}$ ) of the TFTs and thus, the effect of the grain boundary is significantly suppressed. The mobility is also comparable to that of the TFTs of non-fluorinated compound **1** [23,24]. Moreover, the TFTs of compound **2** exhibit enhanced stability of operation in ambient air. They can switch on continuously with less decay of drain current and mobility as compared to the TFTs of **1**. The devices

using compound **2** can maintain characteristics such as mobility, on/off ratio, and threshold voltage for 1 month. The on/off ratio is also higher than those of devices using compound **1** ( $10^5$ – $10^6$ ) fabricated under the same condition (on HMDS-treated  $\text{SiO}_2$ ). This may be due to the strong electron withdrawing characteristics of the tetrafluorophenyl group, which raises the oxidation potential of the aromatic core to make the material less susceptible to air oxidation.

The TFTs of compound **3** and **4** also exhibited p-type operation with the lower carrier mobilities. The mobilities were  $1 \times 10^{-2} \text{ cm}^2/\text{Vs}$  for compound **3** and  $8 \times 10^{-3} \text{ cm}^2/\text{Vs}$  for compound **4**, respectively.

On the other hand, TFTs of compound **5** show a much lower performance. The hole mobility is only about  $1 \times 10^{-5} \text{ cm}^2/\text{Vs}$  and on/off ratio is  $10^2$ . Presently, the exact origin of this low performance is not clear. One possible reason may be the existence of disordered regions and the smaller size of grains in the film, by which large amounts of electrical traps will be formed to hinder charge transport.

To evaluate the conduction mechanism and trap states in the films of compounds **2** and **5**, temperature-variable electrical characterization was performed for the TFTs from room temperature to  $120 \text{ }^\circ\text{C}$  in a hot stage (in Fig. 10). The hole mobility of the TFTs of **2** remains nearly constant from room temperature to  $70 \text{ }^\circ\text{C}$  and then decreases slightly (measurement was not performed at temperatures above  $80 \text{ }^\circ\text{C}$  because of the dewetting of the film from the substrate). The threshold voltage also remains unchanged. Such behavior is in contrast to the thermally activated behavior observed on normal OTFTs of polycrystalline films [34–37], but similar to the characteristic carrier transport of LC semiconductors in the bulk, where field- and temperature-independent mobility are often observed [10–15]. This indicates that the electrical trap may not be a dominant factor to control carrier transport in such LC films, although some amount of trap states still exists at the dielectric-LC interface [38]. This should be due to the formation of highly ordered domains with a large size that exceeds the electrode gap. Such a behavior is attrib-

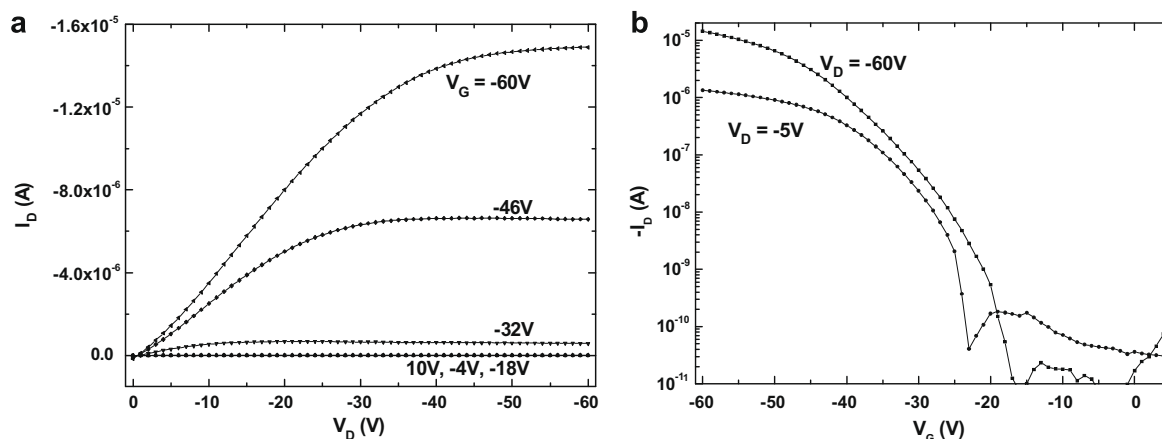


Fig. 9. (a) The output and (b) transfer characteristics of the TFT of compound **2** measured in ambient air. Channel length and width are  $30 \text{ }\mu\text{m}$  and  $5 \text{ }\mu\text{m}$ , respectively.



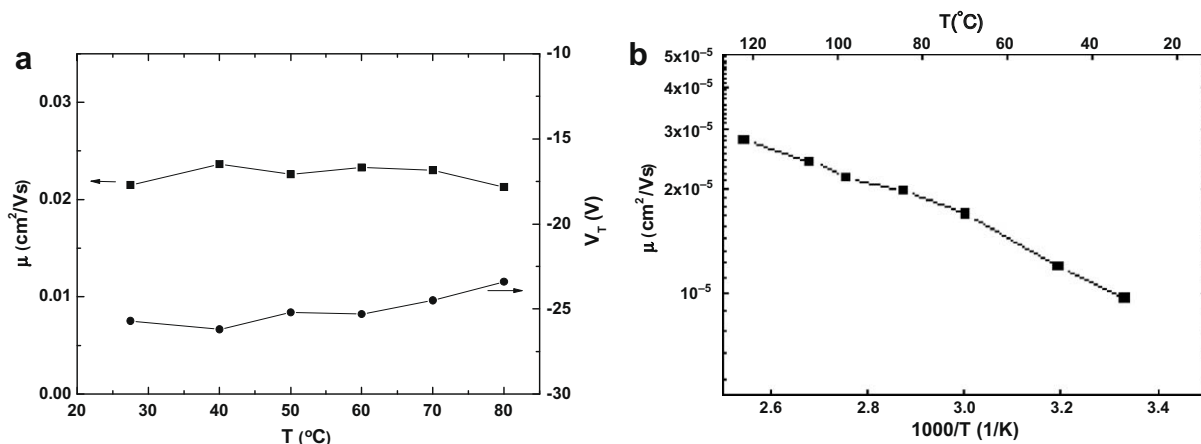


Fig. 10. Temperature dependence of saturation mobility and threshold voltage of TFTs based on (a) 2 and (b) 5.

uted to self-healing of the positional disorder by thermal movement of the LC molecules. It should be emphasized that this introduction of the tetrafluorophenyl moiety should increase the mobility of the liquid crystal molecules, resulting in the formation of large domains greater than the channel length and a reduction in the defect density.

However, the mobility of the TFTs of compound 5 shows thermally activated behavior. It increases nearly exponentially with temperature ( $\mu \propto \exp(E_A/kT)$ ) at an activation energy  $E_A$  of 50 meV. Therefore the carrier transport is trap-dominated, indicating the presence of large amounts of traps in the films. This is consistent with the microscopic observation shown above.

In this work, n-type operation was not observed in TFTs of compound 2 in ambient air and even in vacuum ( $10^{-3}$  Torr) although the gold, calcium, and samarium were used as the source and drain electrodes. This is different from the ambipolar behavior in their bulk state with an electron mobility of  $0.02 \text{ cm}^2/\text{Vs}$ , as obtained by the TOF technique. The result is also in contrast to cases of TFTs from dipentafluorophenyloligo thiophene or diperfluorohexyloligothiophene [29,39,40], in which a high electron mobility of  $0.4 \text{ cm}^2/\text{Vs}$  was obtained. It should be noted that our compound 2 showed a similar lowering of the LUMO energy relative to its non-fluorinated counterpart 1, as observed in the cases of perfluoroarene substitution.

The absence of n-type behavior in the TFTs may be partially attributed to the high barrier of electron injection due to the relatively high-lying LUMO level of our materials. However, the dominant factor must lie in the attack by environmental oxygen because the solution processing of our TFTs was done in ambient air. For molecule 2, an alkyl-tetrafluorophenyl group on one side of terthiophene is unable to provide sufficient screening of environmental  $\text{O}_2$  or residual oxygen to the dielectric, which inhibits electron transport near the organic-dielectric interface [41]. Similarly, the absence of electron transport was observed in TFTs of oligothiophenes bearing a central tetrafluorophenylene ring [29,32]. For compound 5 with both tetrafluorophenyl and perfluoroalkyl substitutions, the absence of

n-type behavior may be attributed to a large amount of structural defects during film growth; these defects act as electron traps. Improved processing conditions (e.g., inert atmosphere) and better control of growth parameters of thin films should be provided to reduce the defect density in the LC domains as well as oxygen attack, in order to achieve n-type operation in the TFTs.

### 3. Experimental section

#### 3.1. Synthesis

All solvents were used as obtained. 5-Propyl-5''-bromo-2,2':5',2''-terthiophene; 5-hexyl-5''-bromo-2,2':5',2''-terthiophene; and 5-dodecyl-5''-bromo-2,2':5',2''-terthiophene were synthesized by the procedure reported by Y. Geng et al. [42]. Other chemicals were used as obtained without further purification. <sup>1</sup>H NMR spectra were measured on a Varian NMR-300 spectrometer using chloroform-d as a solvent. IR spectra were measured using a Shimadzu IR-600 spectrometer. Mass spectra were recorded on a Voyager MALDI TOF Mass equipment.

#### 3.2. 5-Propyl-5''-(4-hexyl-2,3,5,6-tetrafluorophenyl)-2,2':5',2''-terthiophene (2)

A mixture of 5-bromo-5''-propyl-2,2':5',2''-terthiophene, 0.49 g (1.3 mmol); 1-hexyl-2,3,5,6-tetrafluorobenzene, 0.49 g (2.1 mmol); palladium acetate, 16.6 mg (0.074 mmol); di(*t*-butyl)methylphosphonium tetrafluoroborate, 40.3 mg (0.16 mmol); and potassium carbonate, 2.3 g (17 mmol), was dissolved in dimethyl acetamide, 10 ml, and stirred for 2 h at 130 °C. After cooling to room temperature, water was added to the reaction mixture. The precipitates were filtered off and the crude product was purified by column chromatography on silica gel with hot hexane. Recrystallization of the product from hexane afforded 0.25 g (0.59 mmol, 46%) of pure product as yellow crystals.

<sup>1</sup>H NMR (300 MHz,  $\text{CDCl}_3$ )  $\delta$  (ppm): 0.89 (3H, t,  $J = 6.8$  Hz), 1.00 (3H, t,  $J = 7.4$  Hz), 1.26–1.44 (6H, m),

1.56–1.66 (2H, m), 1.72 (2H, sext,  $J = 7.4$  Hz), 2.74 (2H, t,  $J = 7.8$  Hz), 2.78 (2H, t,  $J = 7.4$  Hz), 6.69 (1H, d,  $J = 3.6$  Hz), 7.00 (1H, d,  $J = 3.8$  Hz), 7.01 (1H, d,  $J = 4.0$  Hz), 7.12 (1H, d,  $J = 3.8$  Hz), 7.18 (1H, d,  $J = 4.0$  Hz), 7.50 (1H, d,  $J = 4.0$  Hz).  $^{13}\text{C}$  NMR (300 MHz),  $\text{CDCl}_3$   $\delta$  (ppm): 13.7, 14.1, 22.6, 22.9, 24.9, 29.0, 29.3, 31.5, 32.3, 119.1, 119.3, 123.4, 123.7, 123.8, 125.0, 125.1, 130.6, 130.7, 130.8, 134.4, 134.6, 137.8, 139.5, 139.6, 145.7. IR (KBr disc) 2957.3, 2927.4, 2869.6, 2858.9, 1652.7, 1477.2, 1442.5, 1394.3, 1378.9, 1251.6, 1224.6, 1196.6, 1155.2, 1123.3, 1055.8, 1024.0, 944.9, 856.2, 787.8, 735.7, 725.1, 479.2  $\text{cm}^{-1}$ . MS (MALDI):  $m/z$  (%): 522.6 (100%), 523.6 (29.5%), 524.6 (13.6%), 525.6 (4.9%) [ $\text{M}^+$ ] ( $\text{C}_{27}\text{H}_{26}\text{F}_4\text{S}_3$ ). Anal. Calcd. for 522.68: C 62.04, H 5.01, F 14.54, S 18.40; found: C 62.52, H 4.99.

### 3.3. 5-Hexyl-5''-(4-hexyl-2,3,5,6-tetrafluorophenyl)-2,2':5',2''-terthiophene (3)

A mixture of 5-bromo-5''-hexyl-2,2':5',2''-terthiophene, 0.51 g (1.2 mmol); 1-hexyl-2,3,5,6-tetrafluorobenzene, 0.51 g (2.15 mmol); palladium acetate, 18.1 mg (0.081 mmol); di(*t*-butyl)methylphosphonium tetrafluoroborate, 46.3 mg (0.18 mmol); and potassium carbonate, 0.55 g (4 mmol), was suspended in dimethyl acetamide, 5 ml, and stirred for 2 h at 130 °C. After cooling to room temperature, water was added to the reaction mixture. The precipitates were filtered off and the crude product was purified by column chromatography on silica gel with hot hexane. Recrystallization of the product from hexane afforded 0.45 g (0.80 mmol, 67%) of pure product as yellow crystals.

$^1\text{H}$  NMR (300 MHz,  $\text{CDCl}_3$ )  $\delta$  (ppm): 0.89 (3H, t,  $J = 6.8$  Hz), 1.00 (3H, t,  $J = 7.4$  Hz), 1.24–1.44 (12H, m), 1.56–1.66 (2H, m), 1.72 (2H, sext,  $J = 7.4$  Hz), 2.75 (2H, t,  $J = 7.8$  Hz), 2.80 (2H, t,  $J = 7.4$  Hz), 6.69 (1H, d,  $J = 3.6$  Hz), 7.00 (1H, d,  $J = 3.8$  Hz), 7.02 (1H, d,  $J = 4.0$  Hz), 7.13 (1H, d,  $J = 3.8$  Hz), 7.19 (1H, d,  $J = 4.0$  Hz), 7.50 (1H, d,  $J = 4.0$  Hz).  $^{13}\text{C}$  NMR (300 MHz),  $\text{CDCl}_3$   $\delta$  (ppm): 13.6, 13.7, 22.1, 22.2, 22.4, 28.3, 28.4, 28.5, 28.8, 29.8, 31.0, 31.1, 118.6, 118.8, 122.9, 123.2, 123.3, 124.5, 124.6, 130.1, 130.2, 130.3, 133.8, 134.1, 137.3, 139.1, 139.5, 145.5. IR (KBr disc) 2957.3, 2926.5, 2891.5, 2855.1, 1652.7, 1476.2, 1444.4, 1389.5, 1377.9, 1225.5, 946.9, 858.2, 787.8, 758.9, 505.3, 490.8, 476.3  $\text{cm}^{-1}$ . MS (MALDI):  $m/z$  (%): 564.6 (100%), 565.6 (29.5%), 566.6 (13.6%), 567.6 (4.9%) [ $\text{M}^+$ ] ( $\text{C}_{30}\text{H}_{32}\text{F}_4\text{S}_3$ ). Anal. Calcd. for 564.76: C 63.80, H 5.71, F 13.46, S 17.03; found: C 64.30, H 5.70.

### 3.4. 5-Dodecyl-5''-(4-hexyl-2,3,5,6-tetrafluorophenyl)-2,2':5',2''-terthiophene (4)

A mixture of 5-bromo-5''-dodecyl-2,2':5',2''-terthiophene, 0.52 g (1.05 mmol); 1-hexyl-2,3,5,6-tetrafluorobenzene, 0.46 g (1.9 mmol); palladium acetate, 18.1 mg (0.081 mmol); di(*t*-butyl)methylphosphonium tetrafluoroborate, 49.5 mg (0.20 mmol); and potassium carbonate, 0.4 g (4 mmol), was dissolved in dimethyl acetamide, 5 ml, and stirred for 2 h at 130 °C. After cooling to room temperature, water was added to the reaction mixture.

The precipitates were filtered off and the crude product was purified by column chromatography on silicagel with hot hexane. Recrystallization of the product from hexane afforded 0.45 g (0.69 mmol, 66%) of pure product as yellow crystals.

$^1\text{H}$  NMR (300 MHz,  $\text{CDCl}_3$ )  $\delta$  (ppm): 0.89 (3H, t,  $J = 6.8$  Hz), 1.00 (3H, t,  $J = 7.4$  Hz), 1.22–1.44 (24H, m), 1.56–1.66 (2H, m), 1.72 (2H, sext,  $J = 7.4$  Hz), 2.75 (2H, t,  $J = 7.8$  Hz), 2.79 (2H, t,  $J = 7.4$  Hz), 6.69 (1H, d,  $J = 3.6$  Hz), 7.00 (1H, d,  $J = 3.8$  Hz), 7.02 (1H, d,  $J = 4.0$  Hz), 7.13 (1H, d,  $J = 3.8$  Hz), 7.19 (1H, d,  $J = 4.0$  Hz), 7.50 (1H, d,  $J = 4.0$  Hz).  $^{13}\text{C}$  NMR (300 MHz),  $\text{CDCl}_3$   $\delta$  (ppm): 13.6, 13.7, 22.1, 22.3, 22.4, 28.5, 28.7, 28.8, 28.9, 29.1, 29.2, 29.3, 29.4, 29.8, 31.0, 31.2, 31.5, 118.5, 118.8, 122.9, 123.2, 123.3, 124.4, 124.5, 130.1, 130.2, 130.3, 133.8, 134.1, 137.3, 139.1, 145.5. IR (KBr disc) 2956.4, 29871.5, 2848.4, 1480.1, 1468.5, 1446.4, 1227.5, 1130.1, 993.2, 944.0, 856.2, 810.0, 801.3, 791.6, 727.6, 478.3  $\text{cm}^{-1}$ . MS (MALDI):  $m/z$  (%): 648.7 (100%), 649.7 (29.5%), 650.6 (13.6%), 651.7 (4.9%) [ $\text{M}^+$ ] ( $\text{C}_{36}\text{H}_{44}\text{F}_4\text{S}_3$ ). Anal. Calcd. for 648.92: C 66.63, H 6.83, F 11.71, S 14.82; found: C 67.04, H 6.94.

### 3.5. 5-Perfluorohexyl-5''-(4-hexyl-2,3,5,6-tetrafluorophenyl)-2,2':5',2''-terthiophene (4)

A mixture of 5-bromo-5''-perfluorohexyl-2,2':5',2''-terthiophene, 0.52 g (1.05 mmol); 1-hexyl-2,3,5,6-tetrafluorobenzene, 0.46 g (1.9 mmol); palladium acetate, 18.1 mg (0.081 mmol); di(*t*-butyl)methylphosphonium tetrafluoroborate, 49.5 mg (0.20 mmol); and potassium carbonate, 0.4 g (4 mmol), was dissolved in dimethyl acetamide, 5 ml, and stirred for 2 h at 130 °C. After cooling to room temperature, water was added to the reaction mixture. The precipitates were filtered off and the crude product was purified by column chromatography on silicagel with hot hexane. Recrystallization of the product from hexane afforded 0.45 g (0.69 mmol, 66%) of pure product as yellow crystals.

$^1\text{H}$  NMR (300 MHz,  $\text{CDCl}_3$ )  $\delta$  (ppm): 0.96 (3H, t,  $J = 6.9$  Hz), 1.24–1.45 (6H, m), 1.69 (2H, sext,  $J = 6.3$  Hz), 2.82 (2H, t,  $J = 7.5$  Hz), 7.25–7.33 (4H, d, m), 7.52 (1H, d,  $J = 4.0$  Hz), 7.69 (1H, d,  $J = 4.0$  Hz).  $^{13}\text{C}$  NMR (300 MHz),  $\text{CDCl}_3$   $\delta$  (ppm): 13.7, 14.1, 22.6, 22.9, 24.9, 29.0, 29.3, 31.5, 32.3, 119.1, 119.3, 123.4, 123.7, 123.8, 125.0, 125.1, 130.6, 130.7, 130.8, 134.4, 134.6, 137.8, 139.5, 139.6, 145.7. IR (KBr disc) 2960.2, 2939.9, 2930.3, 2910.1, 2856.1, 1476.3, 1456.0, 1361.5, 1234.2, 1210.1, 1179.3, 1138.8, 787.8  $\text{cm}^{-1}$ . MS (MALDI):  $m/z$  (%): 766.4 [ $\text{M-S}^-$ ] ( $\text{C}_{30}\text{H}_{19}\text{F}_{17}\text{S}_2$ ).

### 3.6. Characterization of mesomorphic behaviors

Phase transition behaviors of the liquid crystals were observed in micrographic optical textures under a polarized light microscope (Nikon OPTIPHOT2-POL) with a hot stage (Mettler F82HT hot stage) and thermograms were recorded by DSC (Seiko Instrument DSC-330). X-ray diffraction patterns were recorded on a Rigaku-denshi diffractometer RINT (Cu  $K\alpha$ : 1.541 Å) with an imaging plate.

### 3.7. Characterization of thin-film structure

Out-of-plane and in-plane X-ray diffraction (XRD) of thin films was acquired using a Rigaku RINT-Ultima X X-ray diffractometer with Cu K $\alpha$ 1 ( $\lambda = 1.5418 \text{ \AA}$ ). The surface morphology of thin films was measured in air using a Veeco Dimension 3100 atomic force microscope (AFM). UV-vis absorption spectra were obtained using JASCO V-570 UV-VIS-NIR spectro-photometer. The optical texture of thin films and bulk compounds was observed using an Olympus BX 60 polarized optical microscope.

### 3.8. Time-of-flight measurement

The time-of-flight setup comprised an Nd:YAG pulse laser equipped with a THG non-linear optical crystal (Continuum Minilite I FN, wavelength = 356 nm, pulse width = 2 ns), hand-made hot stage, source measurement unit (Advantest R-8252) as a DC voltage source, and digital oscilloscope (Tektronics TDS3044B). The liquid crystal compounds were capillary-filled into cells consisting of two ITO-coated glass plates on a hot stage heated above the mesophase–isotropic phase transition temperature. The liquid crystal cell was mounted on the hot stage. Under the application of the electric field by the DC voltage source, the pulse laser light was illuminated on the liquid crystal cell. The induced transient photocurrent was recorded in the digital oscilloscope through a serial resistor (100  $\Omega$ ).

### 3.9. Fabrication and characterization of field-effect transistors

Thin films of compound **2** were prepared by the spin-coating method. Then, 0.5–0.7% chlorobenzene solution was spun on doped Si wafers with a 300-nm SiO<sub>2</sub> layer. Thin films of compound **5** were grown by solution casting of 0.1–0.2% solution in chlorobenzene at 70 °C. The preparation by spin-coating was not successful because the films prepared were too thin (<10 nm) and uncontinuous even at a low rotation speed of the spin coater. Prior to film deposition, the wafer was cleaned in a UV ozone cleaner and subsequently treated with hexamethyldisilazane (HMDS). After film deposition, samples of **2** and **5** were annealed in a vacuum oven at 85–90 °C and 110 °C for 10 min, respectively. Gold source and drain electrodes with a thickness of 60 nm were deposited under high vacuum (10<sup>-4</sup> Pa) through a shadow mask to define the top-contact FET structure with a channel length of 20–30  $\mu\text{m}$  and channel width of 5 mm. Transistor characteristics were measured using a two-channel source meter (Kethley 2612) in a light-shield box under ambient conditions with low humidity or in a vacuum of 10<sup>-3</sup> Torr. The temperature-dependent electrical measurement of the TFTs was performed over a temperature range of 25 °C to 120 °C on a hot stage, where the temperature was controlled using a PID thermo-controller with an accuracy of 0.1 °C.

### Acknowledgments

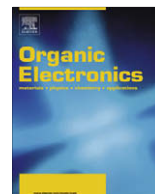
This work is financially supported by a NEDO Industrial Technology Research Grant, Grant in Aid for Scientific Re-

search (No. 19550183) from the Ministry of Education and Culture, and Research Grant from Asahi Glass Company. We thank the Nano-Processing Facility in National Institute of Advanced Industrial Science and Technology (AIST) for providing the XRD and AFM apparatus and Dr. Hiroyuki Minamikawa for assistance with X-ray diffraction measurement. We also thank Dr. R. Azumi and Dr. M. Chikamatsu of Photonics Research Institute of AIST for fruitful discussions on the characterization of the FET devices, and Prof. T. Kato for his valuable comment on the material design.

### References

- [1] Z. Bao, A. Dodabalapur, A.J. Lovinger, *Appl. Phys. Lett.* 69 (1996) 4108.
- [2] B.S. Ong, Y. Wu, P. Liu, S. Gardner, *J. Am. Chem. Soc.* 126 (2004) 3378.
- [3] R.J. Kline, M.D. McGehee, M.F. Toney, *Nature Mater.* 5 (2006) 222.
- [4] M.M. Payne, S.R. Parkin, J.E. Anthony, C.-C. Kuo, T.N. Jackson, *J. Am. Chem. Soc.* 127 (2005) 4986.
- [5] A.R. Murphy, P.C. Chang, P. VanDyke, J. Liu, J.M.J. Fréchet, V. Subramanian, D.M. DeLongchamp, S. Sambasivan, D.A. Fischer, E.K. Lin, *Chem. Mater.* 17 (2005) 6033.
- [6] M. Funahashi, *Transworld Res. Network, Recent Develop. Appl. Phys.* 6 (2003) 839.
- [7] Y. Shimizu, K. Oikawa, K. Nakayama, D. Guillon, *J. Mater. Chem.* 17 (2007) 4223.
- [8] S. Sergeev, W. Pisula, Y.H. Geerts, *Chem. Soc. Rev.* 36 (2007) 1902.
- [9] H. Maeda, M. Funahashi, J. Hanna, *Mol. Cryst. Liq. Cryst. Sci. Technol. Sect. A* 346 (2000) 183.
- [10] A. Pecchia, O.R. Lozman, B. Movaghar, N. Boden, R.J. Bushby, *Phys. Rev. B* 65 (2002) 104204.
- [11] D. Adam, F. Closs, T. Frey, D. Funhoff, D. Haarer, H. Ringsdorf, P. Schuhmacher, K. Siemensmeyer, *Phys. Rev. Lett.* 70 (1993) 457.
- [12] D. Adam, P. Schuhmacher, J. Simmerer, L. Häußling, K. Siemensmeyer, K.-H. Etzbach, H. Ringsdorf, D. Haarer, *Nature* 371 (1994) 141.
- [13] M. Funahashi, J. Hanna, *Phys. Rev. Lett.* 78 (1997) 2184.
- [14] M. Funahashi, J. Hanna, *Appl. Phys. Lett.* 71 (1997) 602.
- [15] M. Funahashi, J. Hanna, *Appl. Phys. Lett.* 76 (2000) 2574.
- [16] M. Funahashi, J. Hanna, *Adv. Mater.* 17 (2005) 594.
- [17] S.R. Farrar, A.E.A. Contoret, M. O'Neill, J.E. Nicholls, G.J. Richards, S.M. Kelly, *Phys. Rev. B* 66 (2002) 125107.
- [18] M. Funahashi, N. Tamaoki, *ChemPhysChem* 7 (2006) 1193.
- [19] K.L. Woon, M.P. Aldred, P. Vlachos, G.H. Mehl, T. Stirner, S.M. Kelly, M. O'Neill, *Chem. Mater.* 18 (2006) 2311.
- [20] M. Funahashi, N. Tamaoki, *Chem. Mater.* 19 (2007) 608.
- [21] A.J.J.M. van Breemen, P.T. Herwig, C.H.T. Chlon, J. Sweelssen, H.F.M. Schoo, S. Setayesh, W.M. Hardeman, C.A. Martin, D.M. de Leeuw, J.J.P. Valetton, C.W.M. Bastiaansen, D.J. Broer, A.R. Popa-Merticaru, S.C.J. Meskers, *J. Am. Chem. Soc.* 128 (2006) 2336.
- [22] K. Oikawa, H. Monobe, K. Nakayama, T. Kimoto, K. Tsuchiya, B. Heinrich, D. Guillon, Y. Shimizu, M. Yokoyama, *Adv. Mater.* 19 (2007) 1864.
- [23] M. Funahashi, F. Zhang, N. Tamaoki, *Adv. Mater.* 19 (2007) 353.
- [24] F. Zhang, M. Funahashi, N. Tamaoki, *Appl. Phys. Lett.* 91 (2007) 063515.
- [25] A.S. Matharu, S.J. Cowling, G. Wright, *Liq. Cryst.* 34 (2007) 489.
- [26] D. Sainova, S. Janietz, U. Asawapirom, L. Romaner, E. Zojer, N. Koch, A. Vollmer, *Chem. Mater.* 19 (2007) 1472.
- [27] M. Lafrance, C.N. Rowley, T.K. Woo, K. Fagnou, *J. Am. Chem. Soc.* 128 (2006) 8754.
- [28] K. Oikawa, H. Monobe, J. Takahashi, K. Tsuchiya, B. Heinrich, D. Guillon, Y. Shimizu, *Chem. Commun.* (2005) 5337.
- [29] M.-H. Yoon, A. Facchetti, C.E. Stern, T.J. Marks, *J. Am. Chem. Soc.* 128 (2006) 5792.
- [30] Y. Kanemitsu, N. Shimizu, K. Suzuki, Y. Shiraishi, M. Kuroda, *Phys. Rev. B* 54 (1996) 2198.
- [31] A. Facchetti, M.-H. Yoon, C.L. Stern, G.R. Hutchison, M.A. Ratner, T.J. Marks, *J. Am. Chem. Soc.* 126 (2004) 13480.
- [32] D.J. Crouch, P.J. Skabara, J.E. Lohr, J.J.W. McDouall, M. Heeney, I. McCulloch, D. Sparrowe, M. Shkunov, S.J. Coles, P.N. Horton, M.B. Hursthouse, *Chem. Mater.* 17 (2005) 6567.
- [33] R.G. Kepler, *Phys. Rev.* 119 (1960) 1226.

- [34] G. Horowitz, R. Hajlaoui, P. Delannoy, *J. Phys.* III 5 (1995) 355.
- [35] R.J. Chesterfield, J.C. McKeen, C.R. Newman, P.C. Ewbank, D.A. Da Silva Filho, J.-L. Bredas, L.L. Miller, K.R. Mann, C.D. Frisbie, *J. Phys. Chem. B* 108 (2004) 19281.
- [36] R.J. Chesterfield, C.R. Newman, T.M. Pappenfus, P.C. Ewbank, M.H. Haukaas, K.R. Mann, L.L. Miller, C.D. Frisbie, *Adv. Mater.* 15 (2003) 1278.
- [37] S. Mohapatra, B.T. Holmes, C.R. Newman, C.F. Frendergast, C.D. Frisbie, M.D. Ward, *Adv. Funct. Mater.* 14 (2004) 605.
- [38] V. Podzorov, E. Menard, A. Borissov, V. Kiryukhin, J.A. Rogers, M.E. Gershenson, *Phys. Rev. Lett.* 93 (2004) 086602.
- [39] A. Facchetti, M.-H. Yoon, C.L. Stern, H.E. Katz, T.J. Marks, *Angew. Chem. Int. Ed.* 42 (2003) 3900.
- [40] A. Facchetti, M. Musherush, M.-H. Yoon, G.R. Hutchison, M.A. Ratner, T.J. Marks, *J. Am. Chem. Soc.* 126 (2004) 13859.
- [41] L.-L. Chua, J. Zaumseil, J.-F. Chang, E.C.-W. Ou, P.K.-H. Ho, H. Sirringhaus, R.H. Friend, *Nature* 434 (2005) 194.
- [42] Y. Geng, A. Fechtenkötter, K. Müllen, *J. Mater. Chem.* 11 (2001) 1634.



## An amphiphilic C<sub>60</sub> penta-addition derivative as a new U-type molecular rectifier

Sandhyarani Acharya, Hyunwook Song, Jongman Lee, Pil Sook Kwon, Jung-pil Lee, Gottikunda Yogendranath, Young Ha Kim, Yun Hee Jang, Takhee Lee, Shashadhar Samal\*, Jae-Suk Lee\*

Department of Materials Science and Engineering, Gwangju Institute of Science and Technology (GIST), 261 Cheomdan-gwagiro (Oryong-dong), Buk-gu, Gwangju 500-712, Republic of Korea

### ARTICLE INFO

#### Article history:

Received 5 May 2008  
Received in revised form 8 August 2008  
Accepted 7 October 2008  
Available online 26 October 2008

#### PACS:

61.48.-c  
62.23.-c  
68.55.ap  
72.80.Rj  
81.05.Tp

#### Keywords:

Molecular electronics  
Fullerene pentapod  
Langmuir–Blodgett (LB) monolayer  
Conducting atomic force microscopy (CAFM)  
Rectification

### ABSTRACT

Unimolecular rectification behavior of a known amphiphilic fullerene derivative, 1,4,11,15,30-pentakis(4-hydroxyphenyl)-2H-1,2,4,11,15,30-hexahydro-[60]fullerene, (4-HOC<sub>6</sub>H<sub>4</sub>)<sub>5</sub>HC<sub>60</sub> (referred to here as the fullerene pentapod), is reported. The HOMO and LUMO energy levels of the pentapod were determined by density functional theory calculations (B3LYP/6-31G\*\*). It was found that the HOMO of the donor moiety and the LUMO of the acceptor are in the same fullerene cage, quite unlike the fullerene derivatives so far reported as molecular rectifiers. The molecule formed a stable Langmuir–Blodgett film at the air–water interface. Characterization of the film indicated that it constitutes mostly a monolayer of molecules with the hydrophobic C<sub>60</sub> moiety pointing upwards. The LB film was transferred over Au(111) substrate and electrical conductivity of the film was measured by conducting atomic force microscopy. An asymmetric electrical rectification behavior was observed in the voltage range of ±1.0 V to ±2.0 V. Beyond a bias voltage of ±2.0 V, rectification ratio decreased steadily, until at ±2.5 V the current–voltage curve became symmetric. The observed electrical rectification behavior was ascribed to resonant electron tunneling between the Fermi level of the electrode and the molecular orbital levels of the fullerene pentapod. Charge transport in the preferred direction under a suitable applied bias was facilitated due to efficient electronic interactions of the molecular orbitals through a combined effect of homo- and peri-conjugation. This constitutes a new class of donor–acceptor system and a step forward in the field of molecular electronics.

© 2008 Published by Elsevier B.V.

### 1. Introduction

Stable molecular diodes neatly arranged without defects are a viable answer to continued quest for ultimate device miniaturization in electronics [1,2]. The possibility that a single molecule could function as a rectifier was proposed by Aviram and Ratner with an exemplary theory of rectification [3]. This initial theory, modified subsequently

[4], led to a wide interest in the field of unimolecular rectification for over a decade [5]. ‘Unimolecular rectification’ is a conventional terminology, which in reality concerns the rectification behavior of an ordered assembly of molecules, since isolating and probing the electrical behavior of a single molecule is rather impractical. A number of systematic studies have been devoted to understand the rectification behavior of an organized array of molecules in Langmuir–Blodgett (LB) films, or self-assembled monolayers (SAM) of organic molecules. The molecules invariably contained an electron donor moiety (D) bound to an electron acceptor (A) through an insulating saturated σ-

\* Corresponding authors. Tel.: +82 62 970 2306; fax: +82 62 970 2304.  
E-mail addresses: [samal@gist.ac.kr](mailto:samal@gist.ac.kr) (S. Samal), [jslee@gist.ac.kr](mailto:jslee@gist.ac.kr) (J.-S. Lee).

conjugated  $\pi$ -bridge. Most devices involved monolayers of such archetypal organic molecules sandwiched between two metal-electrodes, one bottom electrode plate and the tip of the atomic force microscope as the top contact electrode, or an ordered assembly of molecules in a nanopore or a nanogap connected to two electrodes [6]. Unimolecular rectification across a LB monolayer was first demonstrated for hexadecylquinolinium tricyanoquinodimethanide [5,6d,7], a D- $\pi$ -A-type molecule.

Fullerenes are ideal materials for various nanoscale electronic devices. These molecules have a very strong affinity towards electrons.  $C_{60}$  is known as one of the strongest electron acceptors. When a suitable donor molecule is covalently or non-covalently bound to it, the donor-acceptor assembly shows many interesting properties with promising applications. For the rectification studies involving  $C_{60}$  derivatives, there should be an ordered assembly of preferably a monolayer of molecules over a suitable substrate. One of the deterrent factors, however, is that these molecules have a strong tendency to aggregate due to the hydrophobic fullerene–fullerene interactions [8]. This aggregation problem could easily be circumvented by attaching strong hydrophilic head groups to the fullerene [8f,9], blocking the contact of fullerene core by encapsulation [8g,10], and introducing structural constraints in the molecule [11]. Indeed, several amphiphilic fullerene derivatives are now known to form stable LB films at the air–water interface [12,13]. Similarly SAMs of fullerene derivatives, particularly those with appended thiol moiety, have produced highly ordered and densely packed structures on gold substrate [11]. The first  $C_{60}$ -based compound, dimethylaminophenylazafullerene [14], the LB film of which was sandwiched between two gold electrode layers, showed a tremendous apparent rectification ratio as high as 20,000, which was ascribed to the defects that grew at the domain boundaries. A Langmuir–Schaefer monolayer of another fullerene derivative [15] exhibited pronounced rectification with rectification ratio up to 16.5 when compared to the sample from the LB film. Interest in fullerene-based rectifier molecules with donor organic moiety

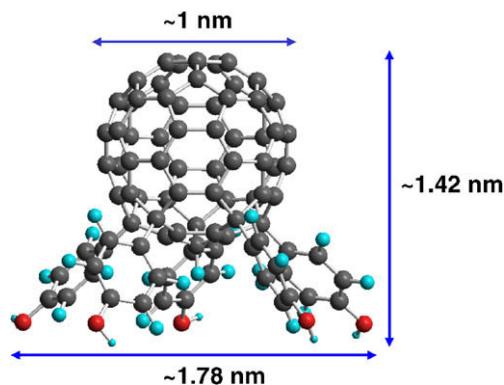


**Fig. 1.** Energy minimized structure of 1,4,11,15,30-pentakis(4-hydroxyphenyl)-2H-1,2,4,11,15,30-hexahydro-[60]fullerene,  $(4\text{-HOC}_6\text{H}_4)_5\text{HC}_{60}$ , the amphiphilic fullerene pentapod, with molecular dimensions. Color code: grey – carbon, green – hydrogen, and red – oxygen. (For interpretation of the references to color in this figure legend, the reader is referred to the web version of this article.)

attached to the acceptor  $C_{60}$  through a suitable spacer continues unabated [16].

Herein, we report our studies on the monolayer of LB film of the fullerene pentapod formed at the air–water interface. The energy minimized structure of the molecule is shown in Fig. 1. This amphiphilic fullerene derivative is expected to form stable LB film at the air–water interface and afford a very robust structure through the five –OH groups anchored to the substrate. The electrical behavior of the film on Au(111) substrate measured using conducting atomic force microscopy (CAFM) showed that the molecule behaves as a rectifier when an appropriate bias voltage was applied. A suitable mechanism of rectification is proposed.

## 2. Experimental

### 2.1. Materials

The fullerene pentapod,  $(4\text{-HOC}_6\text{H}_4)_5\text{HC}_{60}$ , synthesized following the procedure reported by Nakamura and coworkers [17–19] was isolated in gram quantities in highly pure form. The compound is readily soluble in polar solvents like tetrahydrofuran, *N*-methyl pyrrolidinone, pyridine, and *N,N*-dimethyl formamide. In nonpolar solvents like toluene solubility is low ( $\sim 0.001$  g/ml). The compound is very stable towards oxidation under ambient conditions as studied by  $^1\text{H}$  NMR monitoring the C–H peak intensity at 5.6 ppm. No change in spectral pattern was observed over a period of several weeks.

### 2.2. Computations

The geometry of free  $(4\text{-HOC}_6\text{H}_4)_5\text{HC}_{60}$  was optimized using the density functional theory (DFT) method with the B3LYP functional [20] and the 6-31G\*\* basis set. The HOMO and LUMO energy levels were determined on the final geometry by reading the DFT eigenvalues as well as by calculating the ionization potential ( $\text{IP} = E_{\text{CATION}} - E_{\text{NEUTRAL MOLECULE}} \approx -E_{\text{HOMO}}$ ) and electron affinity ( $\text{EA} = E_{\text{NEUTRAL MOLECULE}} - E_{\text{ANION}} \approx -E_{\text{LUMO}}$ ). In order to estimate roughly the error attributable to the functional-dependence of DFT, the energy levels were estimated using both B3LYP (hybrid) and PBE (GGA) functionals [21]. It should be noted that though the device in the present case is metal-organic-metal type, the shift and broadening of the energy levels due to the substrate (Au) were not taken into account in our calculations on this “free” isolated molecule. All the calculations were done with Jaguar v6.5 (Schrodinger Inc., Portland, OR).

### 2.3. Langmuir-Blodgett film

The LB film was cast using a PC controlled KSV MINIT-ROUGH instrument attached to a constant temperature bath. The quality of the LB monolayer at the air–water interface was monitored by KSV Win LB computational program. A 70  $\mu\text{l}$  dilute solution of the fullerene pentapod (0.0235 mg/ml in toluene) was spread on the air–water interface and the trough area decreased at a rate of 200  $\text{cm}^2/\text{min}$ . The film was transferred at a constant rate

of 5 mm/min and a surface pressure of 20 mN/M onto a freshly prepared hydrophilic Au(111) substrate, which was submerged in the subphase before spreading and compressing the LB film. All the experiments were performed at 21 °C using pure deionized water as the subphase.

#### 2.4. Atomic force microscopy

The LB film was examined by atomic force microscopy (AFM) to determine the height of the particles. The AFM images were acquired with a Nanoscope III dimension (Digital Instruments Inc. Santa Barbara, CA). Super sharp silicon tapping mode with a cantilever (Nanosensor, Wetzlar-Blankenfeld, Germany) having resonance frequency of ca. 330 kHz and scan rate of 0.5 Hz was used. The tip of the cantilever has a normal radius of ca. 2 nm. The samples for AFM measurement were prepared by LB deposition method at the air–water interface over Au(111) substrate.

#### 2.5. Ellipsometry

Variable angle spectroscopic ellipsometry measurement was done on a NFT I-ELLI 2000 ellipsometer equipped with a Nd:YAG LASER at 65°, 70° and 75° angles of incidence in the wavelength range of 300–1000 nm. The optical constants for bare gold were measured immediately before measuring the fullerene pentapod film-coated substrate. A refractive index of 1.533 was assumed for all measurements. The thickness of the film using three samples was calculated from variation of the ellipsometric parameters  $\Delta$  and  $\Psi$ . Repeated measurements were made at different positions all through the substrate for obtaining accurate results.

#### 2.6. Contact angle measurement

The wettability of the LB film was investigated by measuring the contact angle of water of a freshly prepared sample using CA-S150, KYOWA instrument. Ten microlitre of ultra pure water (Barnstead Easypure LF, 18.3 M $\Omega$  cm) was used throughout the experiment. The contact angle was read only on one side of the drop.

#### 2.7. Conducting atomic force microscopy

Samples for CAFM measurements are the fullerene pentapod LB films transferred over Au(111) substrate. These were dried in a vacuum desiccator for 48 h prior to the electrical measurements. Precautions were taken to prevent damage to the film in view of its fragile nature by thermal radiation. Current–voltage ( $I$ – $V$ ) measurement was performed using a commercially available AFM system (PSIA, XE-100 model) with conductive AFM tips that were made from Au (20 nm)/Cr (20 nm) coating around conventional AFM tips. Two terminal DC  $I$ – $V$  data were acquired using a semiconductor parameter analyzer (HP4145B). Voltage was applied to CAFM tip while the Au substrate was grounded. All the electrical measurements were carried out inside a covered AFM chamber through which nitrogen gas was passed to minimize the formation of contaminants on the surface of the film. From Johnson–Ken-

dall–Roberts (JKR) model [22] the radius of the contact area under the CAFM tip was estimated to be less than 10 nm [23].

### 3. Results and discussion

#### 3.1. Computations

The outer diameter of C<sub>60</sub> is ~1 nm estimated by taking into account the size of the  $\pi$ -electron cloud associated with the carbon atoms [24]. This value was taken as the diameter of the fullerene moiety in the pentapod (see Fig. 1). The five phenolic groups form a circular face, the diameter of which was ~1.78 nm. The difference between the diameters of the top fullerene moiety and bottom circular face is 0.78 nm. This is large enough to prevent fullerene–fullerene interaction among the neighboring molecules if uniformly oriented in a monolayer. Similar observations have been made for fullerene derivative C<sub>60</sub>-MPPA [11] where aggregation was prevented due to the difference in size between the fullerene head group attached to a relatively larger MPAA unit.

In the study of molecular electronics, computational calculations of the molecular energy levels relative to metal-electrode energies bear specific significance. Such calculations have been made for several fullerene derivatives [14,15,25]. Even though the device in the present case is metal-organic-metal type, the shift and broadening of these energy levels due to the substrate (Au) was not taken into account in our calculations on the “free” isolated molecule. Thus, the calculated HOMO and LUMO levels, shown in Fig. 2, should be taken as approximate.

The two functionals of DFT, B3LYP and PBE, result in essentially the same electronic structure. Both of them predict the same molecular energy diagram. The HOMO and HOMO – 1 are very close in energy and hence considered as degenerate MOs, and similarly the LUMO and LUMO + 1 constitute a pair of degenerate orbitals. The energy levels taken from the B3LYP eigenvalues are as follows (in eV): –5.45 ( $E_{\text{HOMO}}$ ), –5.47 ( $E_{\text{HOMO} - 1}$ ), –5.63 ( $E_{\text{HOMO} - 2}$ ), –5.84 ( $E_{\text{HOMO} - 3}$ ), –5.94 ( $E_{\text{HOMO} - 4}$ ), and –5.96 ( $E_{\text{HOMO} - 5}$ ) for the HOMO levels; –2.47 ( $E_{\text{LUMO}}$ ), –2.45 ( $E_{\text{LUMO} + 1}$ ), and –2.32 ( $E_{\text{LUMO} + 2}$ ) for the LUMO levels. Both functionals also predict that the frontier MOs of the molecule are essentially localized on the same C<sub>60</sub> moiety, which is in sharp contrast to other fullerene derivative-based donor–acceptor systems studied for molecular rectification where the donor HOMO is located on the exocyclic group and the acceptor LUMO is on C<sub>60</sub> [14–16,26].

The two functionals, however, show discrepancy in the precise locations of these energy levels (Table 1). The HOMO–LUMO gaps calculated with B3LYP are significantly larger than those calculated with PBE, as observed previously [27]. Interestingly this discrepancy becomes small when estimated from the IP and EA values. Since the PBE functional is known to underestimate the HOMO–LUMO gap, we focus on analyzing the experimental data only based on the two B3LYP values in the following discussion.

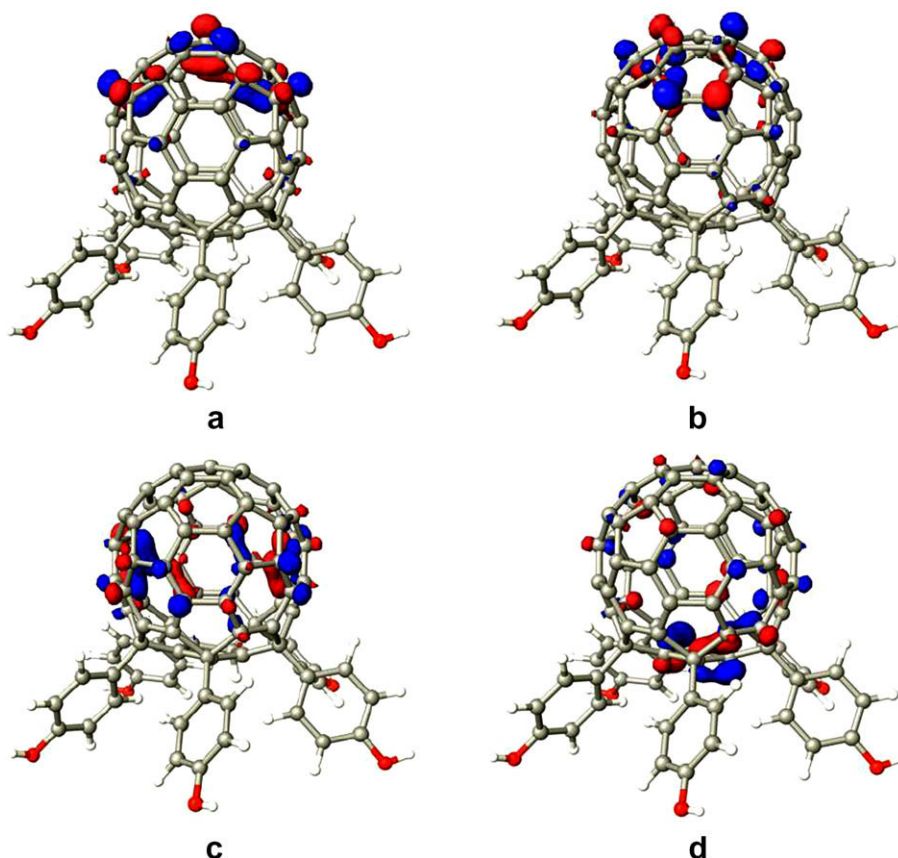


**Fig. 2.** Molecular orbitals of the fullerene pentapod generated by DFT calculations (B3LYP/6-31G<sup>\*\*</sup>). (a) LUMO (−2.47 eV) (b) LUMO + 1 (−2.45 eV), (c) HOMO (−5.45 eV), and (d) HOMO − 1 (−5.47 eV). Color code: grey – carbon, white – hydrogen, and red – oxygen. (For interpretation of the references to colour in this figure legend, the reader is referred to the web version of this article.)

**Table 1**  
HOMO–LUMO gap calculated by B3LYP and PBE functionals.

Method	$E_{\text{HOMO}}$ (eV)	$E_{\text{LUMO}}$ (eV)	HOMO–LUMO gap (eV)
B3LYP	−5.5	−2.5	3.0
B3LYP IP/EA	−6.3	−1.6	4.7
PBE	−4.8	−3.0	1.8
PBE IP/EA	−5.9	−1.7	4.2

### 3.2. LB film

The LB pressure–area isotherm of the fullerene pentapod is shown in Fig. 3. From the isotherm, the mean molecular area per molecule,  $A_0$ , obtained by extrapolating the pressure–area isotherm to zero pressure was  $0.98 \text{ nm}^2 \text{ molecule}^{-1}$ , which corresponds to a mean diameter of 1.117 nm per molecule. The LB films of unmodified dilute C<sub>60</sub> solution show a limiting area of  $0.98 \text{ nm}^2 \text{ molecule}^{-1}$  [8a,8c,8e], as against the theoretically predicted value of  $0.866 \text{ nm}^2 \text{ molecule}^{-1}$  for a monolayer of the molecule [9b,28]. This suggested that the pentapod formed a monolayer at the air–water interface rather than an irreversible aggregation of the fullerene clusters [12]. The mean molecular area at the inflection point ( $A_c$ ) calculated at the collapse pressure  $\Pi_c$  of 33 mN/M was  $0.83 \text{ nm}^2 \text{ molecule}^{-1}$ . Above the collapse pressure, the nature of the

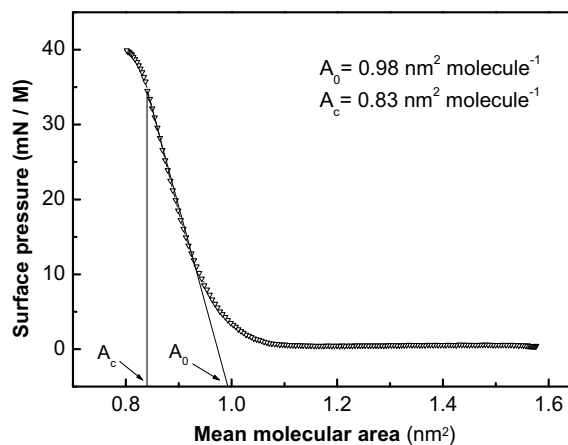


**Fig. 3.** Pressure–area isotherm ( $\Pi$ - $A$ ) of the LB film at the air–water interface obtained by spreading the fullerene pentapod solution in toluene.

curve changed indicating phase transition, possibly from one closely packed structure to another. The pentapod was transferred atop the Au(111) substrate at a transfer pressure,  $\Pi_{\text{tr}}$ , of 20 mN/M. The mean molecular area at the transfer pressure,  $A_{\text{tr}}$ , was  $0.90 \text{ nm}^2 \text{ molecule}^{-1}$ , from



which the mean diameter per molecule was calculated to be  $\sim 1.07$  nm.

The diameter of the bottom circular face of the molecule calculated from computational measurement is  $\sim 1.78$  nm. This should be the nearest neighbor distance between the molecules if they are in direct contact. However, an examination of the energy minimized structure of the molecule showed that there is enough space between the phenolic rings to allow the neighboring molecules to interdigitate as schematically shown in Fig. 4. This evidently means that the molecules could be packed more closely than 1.78 nm, i.e., even when the mean molecular diameter was 1.07 nm, the molecules could still form a monolayer without vertical stacking. It may be noted here that the molecules in the LB film though seem to interdigitate at the transfer pressure could get organized further while drying to optimize the intermolecular order. The mean molecular area of 1.07 nm is in close agreement with the nearest neighbor distance in a close-packed (111) plane of the  $C_{60}$  molecules [8e]. The LB film of  $C_{60}$ ,  $C_{60}O$  and  $C_{61}H_2$  showed (111) close-pack arrangement for the molecules with nearest neighbor distances of 1.002, 1.003 and 1.003 nm, respectively. Hexagonal (111) face-centered cubic lattice with

neighboring distance of 0.95 nm is reported for other fullerene derivatives [29].

The thickness of the LB film, determined from ellipsometry ( $1.5 \pm 0.01$  nm) and the height image of atomic force microscopy (AFM) studies (Fig. 5), was consistent with the height of the molecule from computational measurement. Thus, the LB film is mostly a monolayer of the molecules. Water contact angle of the film on Au(111) substrate was  $97^\circ$ . The high contact angles of  $H_2O$  on LB film suggested the hydrophobic nature of the film, which is expected of the film with the fullerene moieties exposed to air. Thus the molecule on the substrate surface formed a homogeneous monomolecular film with the five functional groups anchored to the substrate leading to a robust structure without aggregation. Recently Nakamura and coworkers [30] have reported the photophysical properties of the monolayer of the benzoic acid derivative of a series of fullerene penta-addition derivatives, which show the same anchoring behavior to the substrate.

Control experiments were performed using two other fullerene penta-addition derivatives,  $(C_6H_5)_5HC_{60}$  and  $(4-CH_3SC_6H_4)_5HC_{60}$ . From the pressure-area isotherms,  $A_0$  was  $1.98 \text{ nm}^2 \text{ molecule}^{-1}$  for  $(C_6H_5)_5HC_{60}$  and

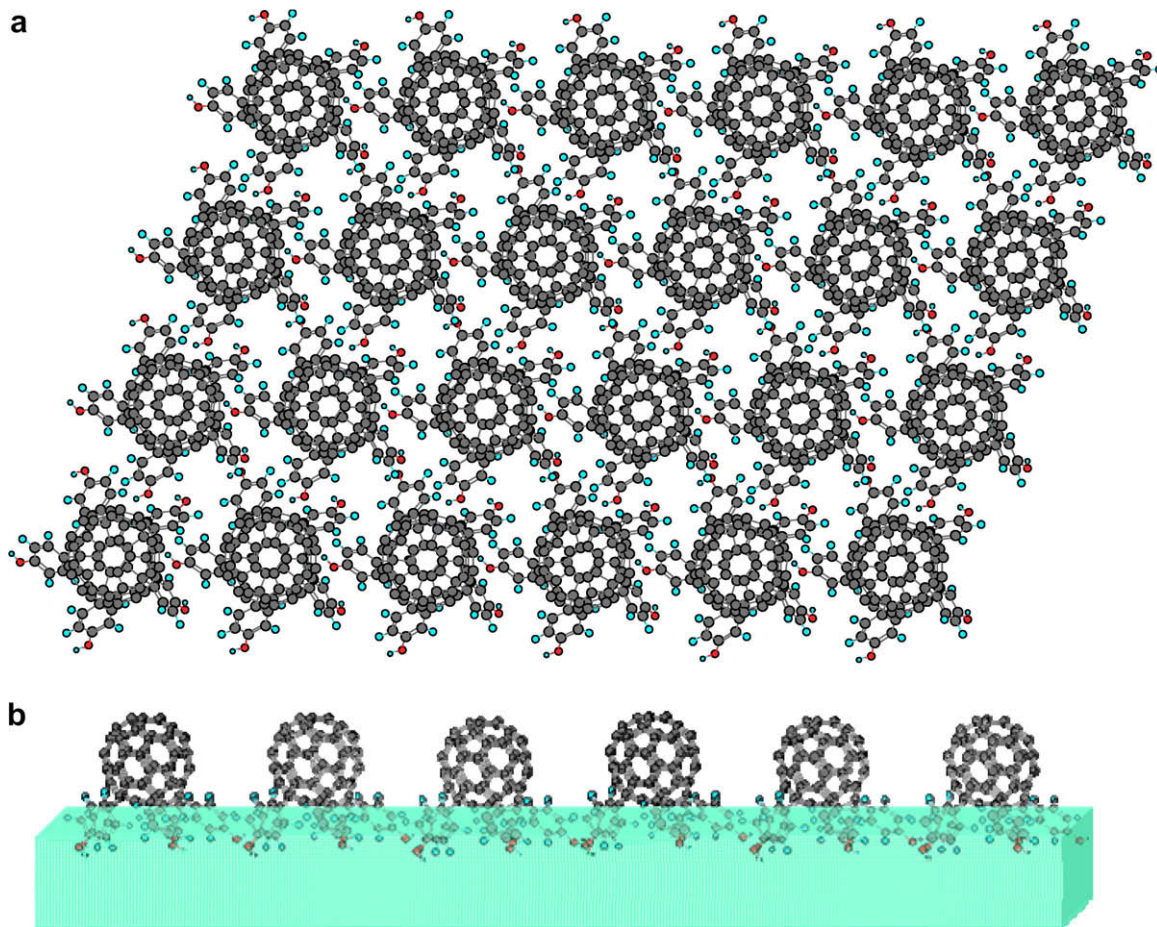


**Fig. 4.** Schematic arrangement of fullerene pentapods in the LB film. (a) Top view of the molecules showing the phenolic groups of neighboring molecules to interdigitate resulting in close-packing of the molecules. (b) Side view of the molecules showing arrangement at the air–water interface (shown for a single row of molecules).

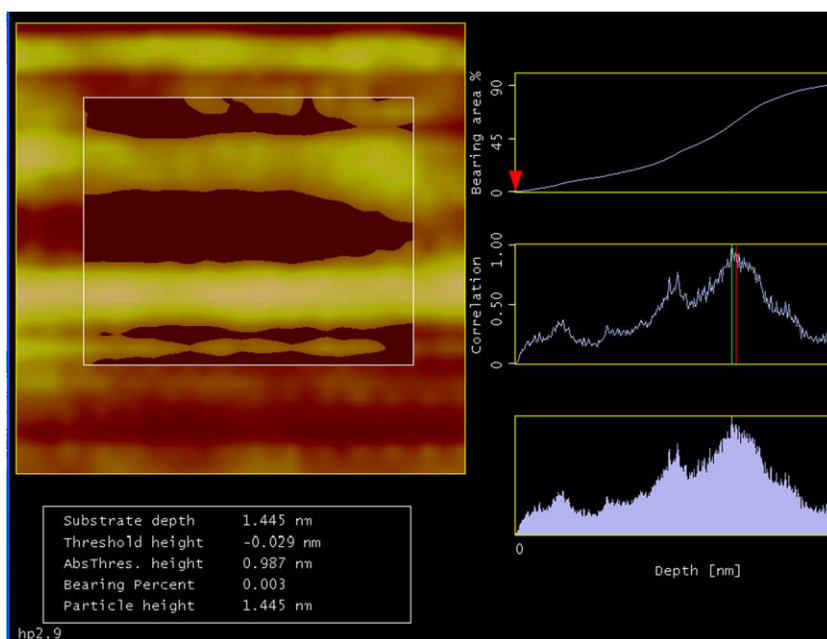


Fig. 5. Atomic force microscopy picture of the  $(4\text{-HOC}_6\text{H}_4)_5\text{HC}_{60}$  LB film on Au(111) substrate showing particle height of 1.445 nm.

$2.09 \text{ nm}^2 \text{ molecule}^{-1}$  for  $(4\text{-CH}_3\text{SC}_6\text{H}_4)_5\text{HC}_{60}$ , which correspond to mean diameters of 1.587 nm and 1.631 nm per molecule, respectively. In comparison, the mean diameter of  $(4\text{-HOC}_6\text{H}_4)_5\text{HC}_{60}$  was 1.117 nm per molecule. The large molecular diameters of  $(\text{C}_6\text{H}_5)_5\text{HC}_{60}$  and  $(4\text{-CH}_3\text{SC}_6\text{H}_4)_5\text{HC}_{60}$  imply that the derivatives are randomly oriented at the air–water interface due to their poor amphiphilic nature.

### 3.3. $I$ – $V$ measurement

The  $I$ – $V$  measurements for the LB films of the fullerene pentapods performed using CAFM method [31] with gold as the top and the bottom electrodes is schematically shown in Fig. 6. The LB monolayer exhibited electrical rectification when a positive bias was applied to the CAFM tip (Fig. 7). The  $I$ – $V$  characteristics showed current rectification at bias voltage of  $\pm 1.0$  V measured at different monolayer junctions, with high rectification ratios (RR) registered at each junction. The LB monolayer exhibited larger current flow when a positive bias was applied to the CAFM tip. In this condition, current flows from the CAFM tip top electrode to the bottom gold electrode. The direction of electron transport as shown in Fig. 6 is opposite to that seen in previous unimolecular rectifiers using either Al or Au electrodes [6b,6d,6g,7c,14]. Our observation on the direction of rectification is consistent with elastic transport model [32] and opposite to that predicted by Aviram–Ratner inelastic transport model [3].

Fig. 8 represents the  $I$ – $V$  curves of the pentapod LB film measured up to higher bias voltages of  $\pm 1.5$  V,  $\pm 2.0$  V,  $\pm 2.5$  V, and  $\pm 3.0$  V. In the bias voltages  $\pm 1.0$  V,  $\pm 1.5$  V, and  $\pm 2.0$  V high current asymmetries were observed with rectification ratios of 1.3–48.0, 2.0–32.6, and 2.0–19.5, respectively. However, further increase of voltage sweep up to

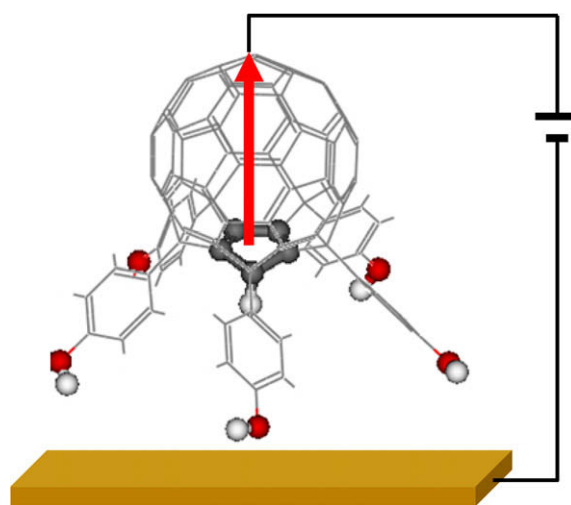
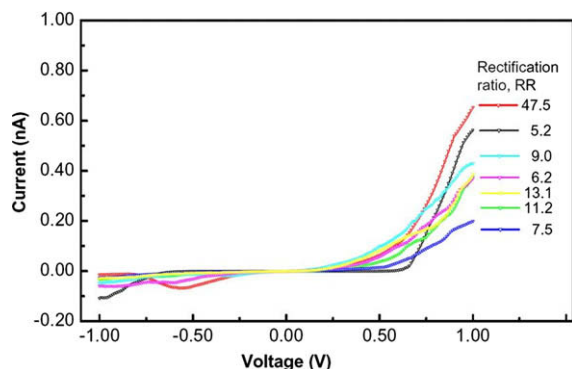


Fig. 6. Schematic representation of the  $I$ – $V$  measurement of the fullerene pentapod by CAFM. The arrow indicates the direction of electron transport when positive bias is applied to the CAFM tip (top electrode). The Au substrate (bottom electrode) is grounded.

$\pm 2.5$  V led to gradual increase in current in the negative bias direction with lowering of rectification ratios to 1.0 at  $\pm 2.5$  V and 0.9 at  $\pm 3.0$  V. Thus current asymmetry was substantially reduced for higher voltage sweeps. The best results were obtained at bias voltages of  $\pm 1.0$  V and  $\pm 1.5$  V, when there was negligible current flow in the negative bias direction. Current started flowing in the negative direction once the bias voltage exceeded  $\pm 1.5$  V. The asymmetric nature persisted with gradual lowering of RR and at  $\pm 2.5$  V the  $I$ – $V$  curve became symmetrical (RR  $\approx 1$ ). A plausible explanation for such behavior is presented (see below).



**Fig. 7.**  $I$ - $V$  characteristics of the LB film of the fullerene pentapod showing current rectification at bias voltage of  $\pm 1.0$  V measured at different junction positions, with high rectification ratios (RR) registered at each junction.

The  $I$ - $V$  measurements were taken repeatedly by changing the position of the CAFM tip and the rectification ratio for each position was recorded. It was observed that the molecule showed rectification behavior in almost 80% of the devices measured. From the statistical histograms (Fig. 9) the mean rectification ratios were 10.8 and 14.7, at bias voltages of  $\pm 1.0$  V and  $\pm 1.5$  V, respectively.

The  $I$ - $V$  characteristics of LB films from fullerene pentadervatives,  $(C_6H_5)_5HC_{60}$  and  $(4-CH_3SC_6H_4)_5HC_{60}$  were studied. For these molecules no rectification was observed in the same applied tip bias voltage ranges in which the fullerene pentapod  $(4-HOC_6H_4)_5HC_{60}$  showed rectification. Evidently, in the LB films,  $(C_6H_5)_5HC_{60}$  and  $(4-CH_3SC_6H_4)_5HC_{60}$  are not as uniformly oriented as the highly amphiphilic  $(4-HOC_6H_4)_5HC_{60}$ . Furthermore, the  $I$ - $V$  characteristics of the alkane thiol SAMs under a similar

experimental set up used for the present study were symmetric with a mean RR value of 1.17 [33a]. Thus, the observed current rectification behavior of  $(4-HOC_6H_4)_5HC_{60}$  is a characteristic attributable to the typical structural feature of the pentapod.

### 3.4. Mechanism of electron transport

The mechanism of the electron transport is explained by the interaction between the molecular energy levels obtained from the DFT calculation of the fullerene pentapod and the Fermi level of the electrode. Here the work function of Au was taken as  $-4.6$  eV though in the literature there is considerable variation of this value from  $-4.70$  eV to  $-5.40$  eV [34], depending upon the crystal face of Au and the method of measurement.

According to the B3LYP eigenvalues the HOMO and LUMO energies of the free molecule are separated by 2.98 eV, but this separation is expected to be smaller in the actual device as the interaction with the electrodes would broaden the molecular energy levels. At zero bias, the HOMO and HOMO  $- 1$  levels of the free molecule are located  $\sim 0.9$  eV below the Fermi level ( $E_F$ ) of Au, and the LUMO and LUMO  $+ 1$  levels are located  $\sim 2.1$  eV above the  $E_F$ .

When a bias of  $+1.0$  V is applied to the top electrode,  $E_F$  of Au goes down approximately by 1 eV relative to the cathode and becomes  $-5.6$  eV, approaching resonance with the HOMO and HOMO  $- 1$  levels of the molecule ( $E_{HOMO} = -5.45$  eV,  $E_{HOMO - 1} = -5.47$  eV) (Fig. 10). Hence current flow in the forward direction is favored. When a negative bias voltage ( $-1.0$  V) is applied to the top electrode, the  $E_F$  of Au goes up to  $-3.6$  eV, and neither the HOMOs nor the LUMOs are aligned with the electrode energy levels, thus impeding current flow in the reverse

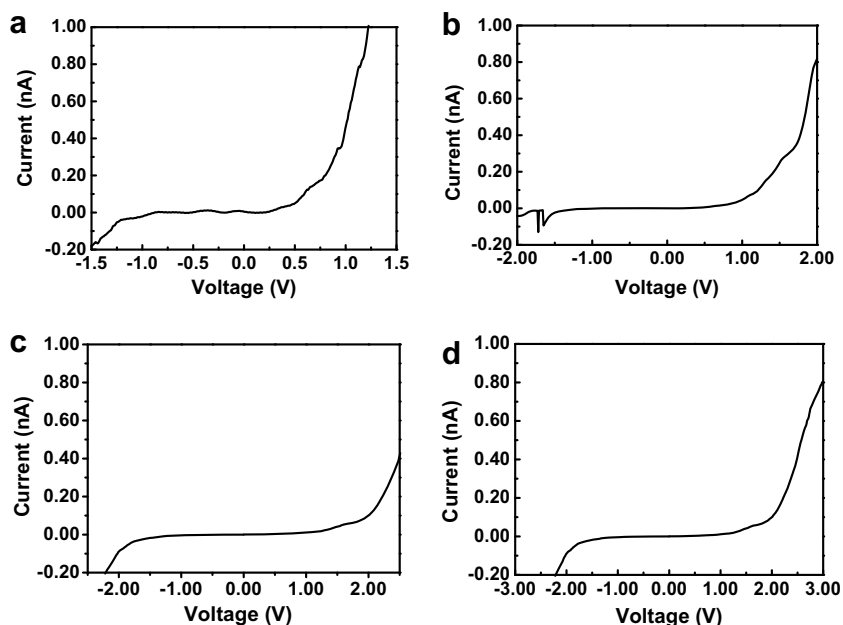


**Fig. 8.** Typical  $I$ - $V$  plots measured up to a higher bias than  $\pm 1.0$  V. (a) RR = 12.0 at  $\pm 1.5$  V, (b) RR = 19.5 at  $\pm 2.0$  V, (c) RR = 1.0 at  $\pm 2.5$  V, and (d) RR = 0.9 at  $\pm 3.0$  V.

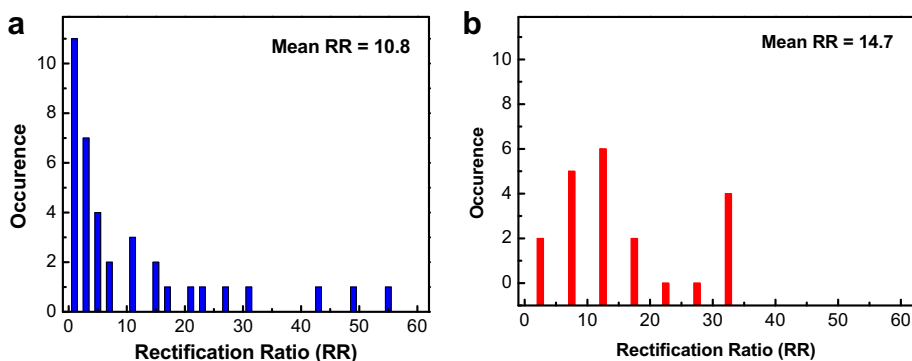


Fig. 9. Statistical histograms of rectification ratio data showing mean RR values of (a) 10.8 at  $\pm 1.0$  V and (b) 14.7 at  $\pm 1.5$  V.

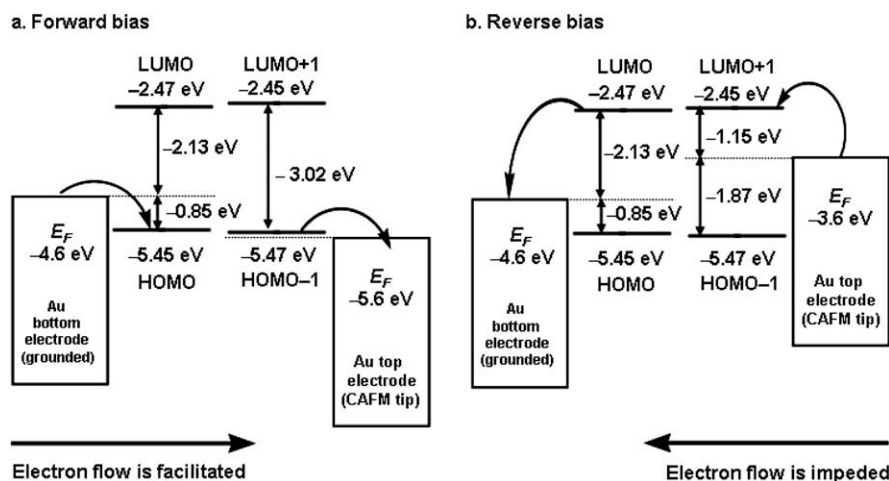


Fig. 10. Energy levels of the device under applied bias voltage. (a) A forward bias voltage of  $+1.0$  V facilitates the electron transport from the bottom Au electrode to the top CAFM tip electrode, and (b) a reverse bias voltage of  $-1.0$  V impedes it in the opposite direction. The HOMO and HOMO  $-1$  levels are of nearly similar energy and so are LUMO and LUMO  $+1$ . Hence these are shown to take part in the electron tunneling process as though they are degenerate orbitals.

direction. When a bias voltage of  $+2.0$  V is applied ( $E_F = -6.6$  V), lower HOMO levels, such as HOMO  $-10$  ( $E_{\text{HOMO}-10} = -6.22$  eV), become energetically favorable and participate in the current flow process. At  $-2.0$  V the LUMO levels ( $E_{\text{LUMO}} = -2.47$  eV,  $E_{\text{LUMO}+1} = -2.45$  eV) approach resonance with  $E_F$  of Au ( $-2.6$  V). Hence, some current starts flowing in the reverse direction as well. Apparently, for higher bias voltages, lower HOMO  $-X$  and upper LUMO  $+X$  levels had energies aligned to a similar extent with  $E_F$  of Au, facilitating current flow in both the directions with equal ease.

It may be pointed out here that the conventional use of the one-electron molecular orbitals from a DFT calculation may be an approximation to the many-electron states that will influence the real transport processes. Nevertheless, it is not actually the reaching of resonances that leads to the rectification but rather the approaching of resonances. Hence the explanation of charge transport in a preferred direction based on alignment of calculated orbital energies with those of the Fermi levels of the electrodes using the present method of computation, though qualitative, is a rational approach at the moment.

Besides, in the present case, there is homo-conjugation [35] between the cyclopentadiene moiety with the rest of the 50  $sp^2$  carbon atoms of the fullerene and peri-conjugation [36] between the  $p_z$ - $\pi$  orbitals of phenolic groups and orbitals of adjoining fullerene carbon atoms. Thus, the phenolic groups, the cyclopentadiene moiety, and the rest of the fullerene molecule in the pentapod electronically interact. From the B3LYP calculation it was found that the fullerene pentapod has a high ground state dipole moment of 3.23 debye (4.53 debye calculated from PBE), and hence the molecule is quite polar.  $C_{60}$  accepts six electrons electrochemically to form hexa-anion whereas oxidation is relatively difficult [37]. The electron affinity of  $C_{60}$  is  $2.65 \pm 0.05$  eV and the first ionization potential is 7.58 eV [38]. The values for the hydroxypentapod, calculated using B3LYP/6-31G<sup>\*\*</sup>, are 1.6 eV and 6.3 eV, respectively (1.7 eV and 5.9 eV from PBE/6-31G<sup>\*\*</sup>). Thus, the pentapod has retained to a significant extent the characteristic electron-withdrawing ability of  $C_{60}$ . Considering that the  $C_{50}$  moiety of the pentapod is still strongly electron-withdrawing, the direction of the dipole moment must be towards the fullerene moiety. Besides, the molecule could undergo further

polarization in this direction when a positive bias is applied to the CAFM tip electrode. Hence electron transport in the forward bias condition should be facilitated, as has been actually observed. Similar rectification behavior has been explained by polarization of the electron cloud of the molecule under an applied potential [39].

Three mechanisms, S-, A- or U-types, have been suggested to explain current rectification in metal-organic-metal devices [5,7a]. When the current passing through a molecule involves electron transfer between its own molecular orbitals, or asymmetry in the molecule itself causes asymmetry in current flow it is called the U-type of electrical rectification. Previously, the mechanism of electrical rectification in fullerene derivatives involve electron transfer in which C<sub>60</sub> acts as an acceptor and exohedral functional groups attached to it act as donors [14,16,26]. The donor is attached to the acceptor by a  $\sigma$ -bond and there is through-bond electron transfer from the HOMO of the donor to the LUMO of the acceptor. However, in the present case, both the HOMO and the LUMO are in the same fullerene cage interacting with each other through homo-conjugation. Under a suitable applied bias, electron from the HOMO level is transferred to the LUMO level through the fullerene cage itself. This is completely a new case observation in the field of molecular rectification of the fullerene derivatives and a novel example of a true U-type unimolecular rectifier.

#### 4. Conclusions

An amphiphilic fullerene pentapod, (4-HOC<sub>6</sub>H<sub>4</sub>)<sub>5</sub>HC<sub>60</sub>, formed well-defined LB film at the air–water interface and constitutes mostly a monomolecular arrangement with C<sub>60</sub> facing upwards. The LB film transferred over Au(111) substrate afforded a robust structure through anchoring of the five phenolic –OH groups. When the device was subjected to a forward bias using the CAFM tip as the top electrode in contact with the fullerene moiety, electrons moved from the bottom negative electrode to the top electrode through the fullerene molecule. When a negative bias was applied to the CAFM tip electron transport was significantly less in the opposite direction. The rectification was appreciable up to an applied bias of  $\pm 2.0$  V; decreasing thereafter until at  $\pm 2.5$  V there was no rectification. Two other fullerene derivatives, (C<sub>6</sub>H<sub>5</sub>)<sub>5</sub>HC<sub>60</sub> and (4-CH<sub>3</sub>SC<sub>6</sub>H<sub>4</sub>)<sub>5</sub>HC<sub>60</sub>, did not show any electrical rectification. These molecules are not as uniformly oriented on the substrate surface in contrast to (4-HOC<sub>6</sub>H<sub>4</sub>)<sub>5</sub>HC<sub>60</sub>. Thus, (4-HOC<sub>6</sub>H<sub>4</sub>)<sub>5</sub>HC<sub>60</sub> constitutes a new class of molecule, in which the donor HOMO and acceptor LUMO levels are on the same fullerene cage and hence represent true unimolecular U-type rectifier.

#### Acknowledgements

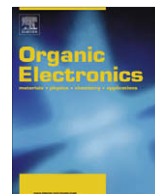
The authors T.L. and H.S. acknowledge the National Research Laboratory (NRL) Program of Korea. S.A. thanks the Brain Pool Program of the Korean Federation of Science and Technology (KOFST) for financial support. We thank Prof. Jae Geun Noh for helpful discussions. This work is sup-

ported by Program for Integrated Molecular System (PIMS), GIST, Korea.

#### References

- [1] C. Joachim, J.K. Gimzewski, A. Aviram, *Nature* 408 (2000) 541.
- [2] (a) F.L. Carter (Ed.), *Molecular Electronic Designs I*, Marcel Dekker, New York, 1987; (b) F.L. Carter (Ed.), *Molecular Electronic Designs II*, Marcel Dekker, New York, 1987.
- [3] A. Aviram, M. Ratner, *Chem. Phys. Lett.* 29 (1974) 277.
- [4] (a) G.J. Ashwell, J.R. Sambels, A.S. Martin, W.G. Parker, M. Szablewski, *J. Chem. Soc., Chem. Commun.* (1990) 1374; (b) A. Martin, J.R. Sambels, G.J. Ashwell, *Phys. Rev. Lett.* 70 (1993) 218; (c) G.J. Ashwell, R. Hamilton, L.R.H. High, *J. Mater. Chem.* 13 (2003) 1501. The current rectification ratio is 11 at 1 V (The limiting currents on the vertical axis of Figure 2 of the communication should read from +1.0 nA to –1.0 nA rather than from +10 nA to –10 nA); (d) G.J. Ashwell, W.D. Tyrell, A.J. Whittam, *J. Mater. Chem.* 13 (2003) 2855. SAMs of a D- $\sigma$ -A dye linked via S-C<sub>3</sub>H<sub>6</sub> to a gold coated substrate alters its *I*-*V* characteristics from asymmetric to symmetric when the intramolecular charge-transfer is disrupted by protonation.
- [5] (a) R.M. Metzger, *Acc. Chem. Res.* 32 (1999) 950; (b) R.M. Metzger, *Chem. Rev.* 103 (2003) 3803.
- [6] (a) A.C. Brady, B. Hodder, A.S. Martin, J.R. Sambels, C.P. Ewels, R. Jones, P.R. Briddon, A.M. Musa, C.A. Panetta, D.L. Mattern, *J. Mater. Chem.* 9 (1999) 2271; (b) J.W. Baldwin, R.R. Amaresh, I.R. Peterson, W.J. Shumate, M.P. Cava, M.A. Amiri, R. Hamilton, G.J. Ashwell, R.M. Metzger, *J. Phys. Chem. B* 106 (2002) 12158; (c) J. Ferraris, D.O. Cowan, V. Walatka Jr., J.H. Perlstein, *J. Am. Chem. Soc.* 95 (1973) 948; (d) R.M. Metzger, T. Xu, I.R. Peterson, *J. Phys. Chem. B* 105 (2001) 7280; (e) G.J. Ashwell, A. Chwialkowska, L.R.H. High, *J. Mater. Chem.* 14 (2004) 2389; (f) D. Vuillaume, B. Chen, R.M. Metzger, *Langmuir* 15 (1999) 4011; (g) T. Xu, I.R. Peterson, M.V. Laxmikantham, R.M. Metzger, *Angew. Chem. Int. Ed.* 40 (2001) 1749; (h) G.J. Ashwell, W.D. Tyrell, A.J. Whittam, *J. Am. Chem. Soc.* 126 (2004) 7102.
- [7] (a) R.M. Metzger, *Chem. Record* 4 (2004) 291; (b) B. Chen, R.M. Metzger, *J. Phys. Chem. B* 103 (1999) 4447; (c) R.M. Metzger, B. Chen, U. Hopfner, M.V. Lakshmiikantham, D. Vuillaume, T. Kawai, X. Wu, H. Tachibana, T.V. Hughes, H. Sakurai, J.W. Baldwin, C. Hosch, M.P. Cava, L. Brehmer, G.J. Ashwell, *J. Am. Chem. Soc.* 119 (1997) 10455.
- [8] (a) Y. Obeng, A. Bard, *J. Am. Chem. Soc.* 113 (1991) 6279; (b) T. Nakamura, H. Tachibana, M. Yumura, M. Matsumoto, R. Azumi, M. Tanaka, Y. Kawabata, *Langmuir* 8 (1992) 4; (c) C. Jehoulet, Y. Obeng, Y. Kim, F. Zhou, A. Bard, *J. Am. Chem. Soc.* 114 (1992) 4237; (d) L. Bulhoes, Y. Obeng, A. Bard, *Chem. Mater.* 5 (1993) 110; (e) N.C. Maliszewskij, P.A. Heiney, D.R. Jones, R.M. Strongin, M.A. Cichy, A.B. Smith III, *Langmuir* 9 (1993) 1439; (f) J. Gallani, D. Felder, D. Guillon, B. Heinrich, J. Nierengarten, *Langmuir* 18 (2002) 2908; (g) P. Wang, M. Shamsuzzoha, X. Wu, W. Lee, R.M. Metzger, *J. Phys. Chem.* 96 (1992) 9025.
- [9] (a) C. Hawker, P. Saville, J. White, *J. Org. Chem.* 59 (1994) 3503; (b) M. Maggini, A. Karlsson, L. Pasimeni, G. Scorrano, L. Valli, *Tetrahedron Lett.* 35 (1994) 2985; (c) M. Maggini, L. Pasimeni, M. Prato, G. Scorrano, L. Valli, *Langmuir* 10 (1994) 4164; (d) S. Ravaine, F. Lepecq, C. Mingotaud, P. Delhaes, J. Hummelen, F. Wudl, L. Patterson, *J. Phys. Chem.* 99 (1995) 9551; (e) M. Carrano, P. Ceroni, F. Paolucci, S. Roffia, T. Da Ros, M. Prato, M. Sluch, C. Pearson, M. Petty, M. Bryce, *J. Mater. Chem.* 10 (2000) 269; (f) D. Guldii, M. Maggini, S. Mondini, F. Guerin, J. Fendler, *Langmuir* 16 (2000) 1311; (g) J. Jin, L. Li, Y. Li, Y. Zhang, X. Chen, D. Wang, S. Jiang, T. Li, L. Gan, C. Huang, *Langmuir* 15 (1999) 4565.
- [10] (a) P. Wang, R.M. Metzger, B. Chen, *Thin Solid Films* 329 (1998) 96; (b) J. Nierengarten, C. Schall, J. Nicoud, B. Heinrich, D. Guillon, *Tetrahedron Lett.* 39 (1998) 5747; (c) G. Felder, J. Gallani, D. Guillon, B. Heinrich, J. Nicoud, J. Nierengarten, *Angew. Chem. Int. Ed.* 39 (2000) 201; (d) J. Nierengarten, *Chem. Eur. J.* 6 (2000) 3667;

- (e) D. Felder, M. Carreon, J. Gallani, D. Guillon, J. Nierengarten, C. Thierry, R. Deschenaux, *Helv. Chim. Acta* 84 (2001) 1119.
- [11] S.H. Kang, H. Ma, M.-S. Kang, K.S. Kim, A. K.-Y. Jen, M.H. Zareie, M. Sarikaya, *Angew. Chem. Int. Ed.* 43 (2004) 1512.
- [12] Y. Gao, Z. Tang, E. Watkin, J. Majweski, H.L. Wang, *Langmuir* 21 (2005) 1416.
- [13] T. Kawai, S. Scheib, P.M. Cava, R.M. Metzger, *Langmuir* 13 (1997) 5627.
- [14] R.M. Metzger, J.W. Baldwin, W.J. Shumate, I.R. Peterson, P. Mani, G.J. Mankey, T. Morris, G. Szulczewski, S. Bosi, M. Prato, A. Comito, Y. Rubin, *J. Phys. Chem. B* 107 (2003) 1021.
- [15] A. Honcius, A. Jaiswal, A. Gong, K. Ashworth, C.W. Spangler, I.R. Peterson, L.R. Dalton, R.M. Metzger, *J. Phys. Chem. B* 109 (2005) 857.
- [16] A. Honcius, R.M. Metzger, A. Gong, C.W. Spangler, *J. Am. Chem. Soc.* 129 (2007) 8310.
- [17] M. Sawamura, K. Kawai, Y. Matsuo, K. Kanie, T. Kato, E. Nakamura, *Nature* 419 (2002) 702.
- [18] (a) M. Sawamura, H. Likura, E. Nakamura, *J. Am. Chem. Soc.* 118 (1996) 12850;  
(b) M. Sawamura, H. Likura, H. Ohama, U.E. Hackler, E. Nakamura, *J. Organometal. Chem.* 599 (2000) 32;  
(c) M. Sawamura, M. Toganoh, Y. Kuninobu, S. Kato, E. Nakamura, *Chem. Lett.* (2000) 262;  
(d) M. Sawamura, N. Nagahama, M. Toganoh, E. Nakamura, *J. Organometal. Chem.* 652 (2002) 31.
- [19] E. Nakamura, M. Sawamura, *Pure Appl. Chem.* 73 (2) (2001) 355.
- [20] (a) J.C. Slater, *Quantum Theory of Molecules and Solids. The Self-Consistent Field for Molecules and Solids*, vol. 4, McGraw Hill, New York, 1974;  
(b) A.D. Beck, *Phys. Rev. A* 38 (1998) 3098;  
(c) S.H. Vosko, L. Will, M. Nusair, *Can. J. Phys. Chem.* 58 (1980) 1200;  
(d) C. Lee, W. Yang, R.G. Parr, *Phys. Rev. B* 37 (1998) 785;  
(e) B. Miehlich, A. Savin, H. Stoll, H. Preuss, *Chem. Phys. Lett.* 157 (1988) 200.
- [21] (a) J.P. Perdew, K. Burke, M. Ernzerhof, *Phys. Rev. Lett.* 77 (1996) 3865;  
(b) J.P. Perdew, K. Burke, M. Ernzerhof, *Phys. Rev. Lett.* 78 (1997) 1396.
- [22] K.L. Johnson, K. Kendall, A.D. Robert, *Proc. Roy. Soc. Lond. A* 324 (1971) 301.
- [23] T. Lee, W. Wang, J.F. Klemic, J.J. Zhang, J. Su, M.A. Reed, *J. Phys. Chem. B* 108 (2004) 8742.
- [24] (a) R. Tycko, R.C. Haddon, G. Dabbagh, S.H. Glarum, D.C. Douglass, A.M. Mjuscje, *J. Phys. Chem.* 95 (1991) 518;  
(b) R.D. Johnson, D.S. Bethume, C.S. Yannoni, *Acc. Chem. Res.* 25 (1992) 169.
- [25] A. Hirsh, I. Lamparth, T. Grösser, *J. Am. Chem. Soc.* 116 (1994) 9385.
- [26] S.S. Gayatri, A. Patnaik, *Chem. Commun.* (2006) 1977.
- [27] (a) Y.H. Jang, W.A. Goddard III, *J. Phys. Chem. C* 112 (2008) 8715;  
(b) Y.H. Jang, S. Hwang, Y.H. Kim, S.S. Jang, W.A. Goddard III, *J. Am. Chem. Soc.* 126 (2004) 12636.
- [28] P.A. Heiney, J.E. Fischer, A.R. McGhie, W.J. Romanow, A.M. Denenstien, J.P. McCauley Jr., A.B. Smith III, D.-E. Cox, *Phys. Rev. Lett.* 66 (1991) 2911.
- [29] M. Matsumoto, H. Tachibana, R. Azumi, M. Tanaka, J. Nakamura, *Langmuir* 11 (1995) 660.
- [30] Y. Matsuo, K. Kanaizuka, K. Matsuo, Y.-W. Zhong, T. Nakae, E. Nakamura, *J. Am. Chem. Soc.* 130 (2008) 5016.
- [31] (a) L. Andolfi, S. Cannistraro, *Surface Science* 598 (2005) 68;  
(b) D.J. Wold, C.D. Frisbie, *J. Am. Chem. Soc.* 123 (2001) 5549;  
(c) J. Zhao, K. Uosaki, *Nanoletter* 2 (2002) 137;  
(d) X.D. Cui, A. Primak, X. Zarate, J. Tomfohr, O.F. Sankey, A.L. Moore, T.L. Moore, D. Gust, G. Harris, S.M. Lindsay, *Science* 294 (2001) 571;  
(e) J.M. Beebe, V.B. Engelkes, L.L. Miller, C.D. Frisbe, *J. Am. Chem. Soc.* 124 (2002) 11268;  
(f) X.D. Cui, A. Primak, X. Zarate, J. Tomfohr, O.F. Sankey, A.L. Moore, T.A. Moore, D. Gust, G. Harris, S.M. Lindsay, *Nanotechnology* 13 (2002) 5.
- [32] J.W. Baldwin, B. Chen, S.C. Street, V.V. Konovaloy, H. Sakurai, T.V. Hughes, C.S. Simpson, M.V. Laxmikantham, M.P. Cava, L.D. Kispert, R.M. Metzger, *J. Phys. Chem. B* 103 (1999) 4269.
- [33] (a) H. Song, C. Lee, Y. Kang, T. Lee, *Colloids and Surfaces A: Physiochem. Eng. Aspects* 284–285 (2006) 583;  
(b) H. Song, H. Lee, T. Lee, *J. Am. Chem. Soc.* 129 (2007) 3806.
- [34] D.E. Gray, *American Institute of Physics Hand Book*, second ed., McGraw-Hill Book Co., New York, 1963.
- [35] H. Likura, S. Mori, M. Sawamura, E. Nakamura, *J. Org. Chem.* 62 (1997) 7912.
- [36] T. Ohno, N. Martin, B. Knight, F. Wudl, T. Suzuki, H. Yu, *J. Org. Chem.* 61 (1996) 1306.
- [37] (a) L.J. Wilson, S. Flanagan, L.P.F. Chibante, J.M. Alford, in: W.E. Billups, M.A. Ciufolini (Eds.), *Buckminsterfullerenes*, Macmillan, New York, 1993. Chapter 11;  
(b) F. Arias, L. Echegoyen, S.R. Wilson, Q. Lu, Q. Lu, *J. Am. Chem. Soc.* 117 (1995) 1442.
- [38] (a) S.H. Yang, C.L. Pettiette, J. Conceicao, O. Chesnovsky, R.E. Smalley, *Chem. Phys. Lett.* 139 (1987) 233;  
(b) M.S. Dresselhaus, G. Dresselhaus, P.C. Eklund, in: *Science of Fullerenes and Carbon Nanotubes*, Academic Press, 1996, p. 63. Chapter 3.
- [39] I.R. Peterson, D. Vuillaume, R.M. Metzger, *J. Phys. Chem. A* 105 (2001) 4702.



# Prediction of the current versus voltage behavior of devices based on organic semiconductor guest–host systems

Fredrik L.E. Jakobsson, Xavier Crispin \*, Magnus Berggren

Department of Science and Technology (ITN), Linköping University, S-60174 Norrköping, Sweden

## ARTICLE INFO

### Article history:

Received 6 August 2008

Accepted 5 October 2008

Available online 17 October 2008

### PACS:

73.50.Gr

73.61.Ph

85.30.De

### Keywords:

Host–guest system

Diode

Trapping

Modeling

Hopping

Gaussian density of states

## ABSTRACT

Organic semiconductor blends are commonly used in organic based (opto-) electronic devices. They are composed of two types of (macro-) molecules, referred to as the guest and host. To achieve optimum device operation, the chemical nature, electronic structure, molecular order and the relative concentration of the guests and host are crucial. Here, we present simulation results of the current density versus the voltage ( $J$ – $V$ ) behavior of a two terminal device based on a variable-range hopping model in which the electronic states of the guest and host are represented by two Gaussian distributions. The  $J$ – $V$  behavior is investigated for various energetic mismatches between guest and host states, widths of the distribution as well as the guest concentrations. Finally, a simple tool enabling easy prediction of the  $J$ – $V$  behavior of organic host–guest diodes is derived.

© 2008 Published by Elsevier B.V.

## 1. Introduction

The introduction of guest molecules into a host matrix has become a successful approach to improve efficiency and to define new functionalities of organic electronic devices. For instance, blending donor and acceptor materials improves exciton dissociation and enables high-efficiency of photovoltaics [1]. Blending phosphorescent dyes into an electroluminescent matrix provides harvesting of triplet states, thus improving the efficiency of light-emitting diodes [2,3]. Tuning the emission wavelength in light-emitting diodes and lasers have been achieved in tailor-made blends combining luminescent dyes, or inorganic nanoparticles, and organic semiconductors [4,5]. Switchable charge

traps have been demonstrated in diodes consisting of blends of a semiconductor host and photochromic guest molecules [6,7].

Organic electronic devices are commonly fabricated in less rigorously controlled environments than traditional inorganic electronic devices, increasing the risk of contamination of the materials. Moreover, organic materials are prone to degradation if not processed and operated in inert atmosphere and under proper light conditions. The resulting organic semiconductor can be regarded as an unintentional blend of a pristine intrinsic material, the host, and an ensemble of impurity molecules or degraded molecules considered as the guest.

Several factors govern charge transport in host–guest systems. First, if the highest occupied molecular orbital (HOMO) of the guest molecule (lowest unoccupied molecular orbital, (LUMO)) is above (below) the HOMO (LUMO) of the host molecule, the guest site is energetically more favorable for holes (electrons). Therefore, in a device at thermal

\* Corresponding author. Tel.: +46 11 363485; fax: +46 11 363270.  
E-mail address: [xavcr@itn.liu.se](mailto:xavcr@itn.liu.se) (X. Crispin).

equilibrium, the guest sites have a higher probability to be occupied than the host sites; the guest sites acts as a traps for the charge carriers (Fig. 1a) [8]. Second, a guest molecule with a large dipole moment reshapes the surrounding electrostatic landscape due to charge-dipole interactions. The energy of some host sites near the guest is lowered, and these sites might act as traps for carriers (Fig. 1b) [7,9]. Note however, dipole-charge interaction acts over a long range, which results in a smoother transition from the unperturbed host energy levels to the bottom of the trap. Therefore it is reasonable to assume that dipole traps might be less severe than energy level traps. Finally, in a situation where the host and guest have similar transport energy level, the difference in charge hopping rate between guest-host and host-host transitions can affect the charge transport behavior. This can originate from a different electronic coupling between guest-host and host-host, or reorganization energy between hosts and guests [10].

In order to optimize organic host-guest systems for (opto-) electronic devices, it is highly desirable to understand and to be able to predict the current-voltage behavior of devices. In this report, we focus on the case of guests acting as energy level traps and investigate how they affect the  $J$ - $V$  behavior diodes (Fig. 1a). We assume that the dipole moments of the guest and host molecules are similar, so that the electrostatic potential felt by the host molecules is not affected by the presence of guest molecules. Furthermore, the electronic coupling between the guest and host are considered to be the same as between hosts.

In general, the  $J$ - $V$  behavior of diodes in the presence of traps can be divided into three regimes (Fig. 1c). At low voltages (trap-limited regime (i)), the carrier concentration is significantly lower than the trap concentration. The traps

are to a large extent empty and therefore the transport is strongly limited by the traps. In this regime the current density is low and proportional to  $V^2$  and the mobility is approximately constant. For higher but intermediate voltages (trap-filling regime (ii)), the carrier concentration is high enough to increase significantly the occupancy of the traps. Equivalently, the Fermi level,  $E_F$ , is shifted towards higher energies and moves through the trap distribution. The sites that are below  $E_F$  are filled and do not contribute to the transport anymore. In other words, there are fewer active trap states to limit the mobility. Therefore the current density is increased rapidly in this region, with  $J \sim V^\beta$  and  $\beta \gg 2$ .  $\beta$  increases as the energy distribution of the trap levels is widened. As  $E_F$  is shifted above the energy levels of the traps practically all trap states are filled and the mobility is no longer suppressed by trapping (trap-free regime (iii)). In this regime, the current density follows the familiar  $J \sim V^2$  behavior in the case of an otherwise constant mobility. The voltage at which the  $J$ - $V$  behavior transits from the trap-filling to the trap-free behavior is traditionally called the trap-filled limit,  $V_{TFL}$ .

An analytical relation for the  $J$ - $V$  behavior in the trap-filling regime was first deduced by Mark et al. [11], assuming an exponential distribution of traps extending into the band gap from the conduction band edge and freely moving carriers in the conduction band. The resulting  $J$ - $V$  behavior follows a  $J \sim V^{r+1}/t^{2r+1}$  dependence, where  $r = T_t/T$  is a measure of the width of the trap distribution and  $t$  is the thickness of the active layer of the device, see Fig. 1d. This model was recently extended by Mandoc et al. [12] to the case of a Gaussian distribution of the host states and an exponential distribution of the guest states, energetically well below the distribution of host states. Several numerical models have been suggested to describe the  $J$ - $V$  behavior over the whole voltage range (i.e. for all charge transport regimes) [13–19]. The common denominator in those models is the concept of multiple-trapping [8]; i.e., the carriers move in extended states, with constant mobility, but are repeatedly trapped and released. At any given moment only carriers that are free, i.e. that does not reside at a trap site, contribute to the charge transport. Using this approach, the device behavior have been investigated for several archetypal trap distributions; e.g. discrete- [19], exponential- [17] and Gaussian- [13] trap distributions. A disadvantage with multiple-trapping models is the need to distinguish between trapped and free carriers. In disordered organic materials all states are localized and there are no free charge carriers. Therefore, the concept of trapped and free carriers is ambiguous for these materials.

In this report, we use a carrier concentration dependent mobility model derived by Martens et al. [20] and further elaborated on by Coehoorn et al. [21,22]. In this model all carriers reside in a density of states (DOS) composed of states from the guest and the host. In this way, the occupancy of the states is explicitly taken care of in the mobility model and the concept of trapped versus free carriers is circumvented. Both the host and the guest states are represented with a Gaussian DOS distribution, and the total DOS equals the sum of the two Gaussians, see Fig. 2a. We investigate the impact of (i) the width of the Gaussian guest- and host DOS (Fig. 2b), the position of the center of the guest DOS

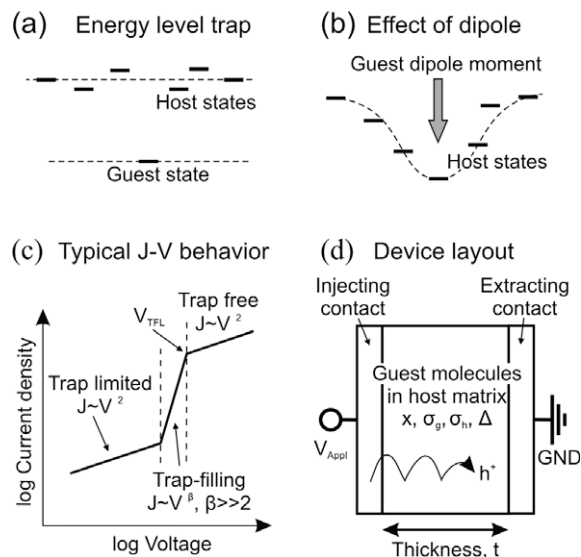


**Fig. 1.** Frontier energy levels of the organic semiconductor host-guest system where the guest molecule creates a charge trap: (a) either because its frontier level is more stable than the host; (b) or because its strong dipole moment perturbs the electrostatic landscape of the host. The general  $J$ - $V$  characteristic of a device with one type of charge traps is depicted in (c). In (d) the device layout is shown.



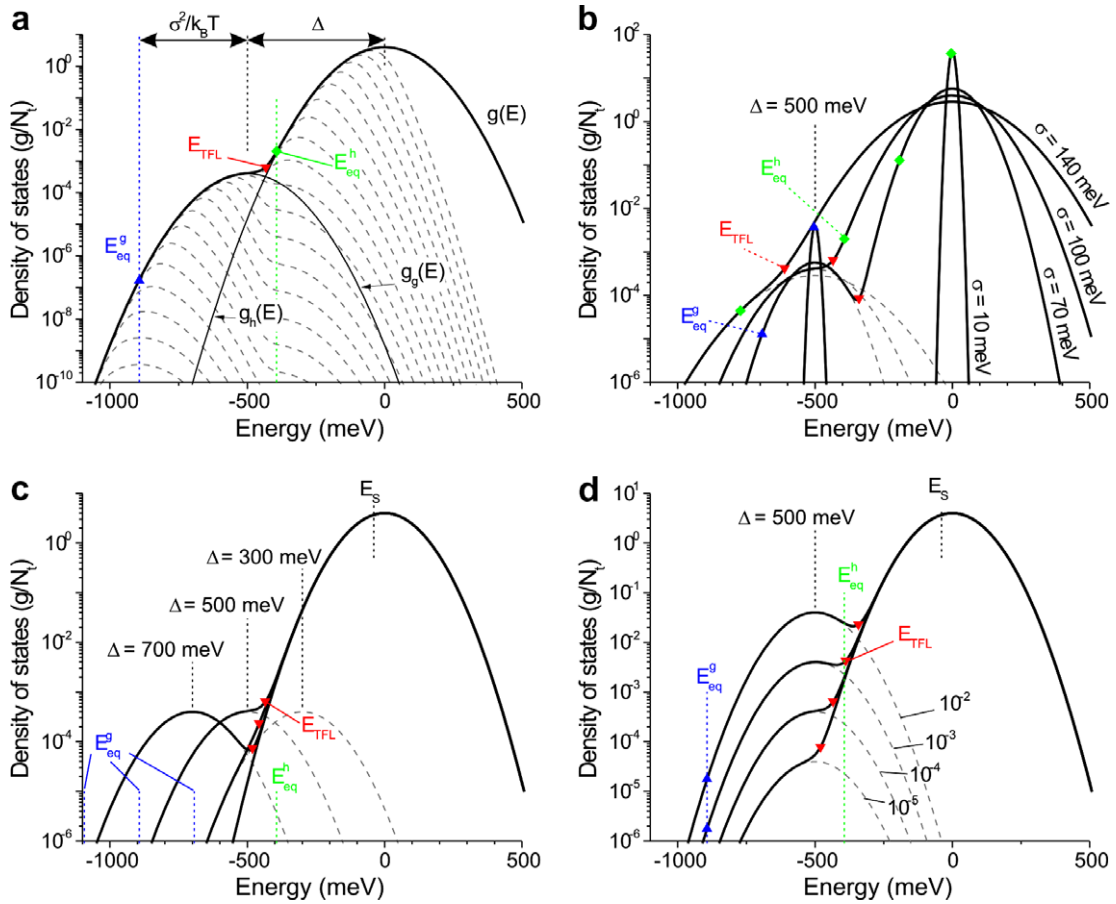


**Fig. 2.** (a) The total density of states,  $g(E)$ , consists of the sum of the host DOS,  $g_h(E)$ , and the guest DOS,  $g_g(E)$ . In this case  $\sigma_g = \sigma_h = 100$  meV,  $\Delta = 500$  meV and  $x = 10^{-4}$ . This gives  $E_{TFL} = -434$  meV,  $E_{eq}^h = -394$  meV and  $E_{eq}^g = -894$  meV. The ODOS is shown in dashed lines, starting with  $E_F = 0$  meV for the rightmost ODOS and with decreasing  $E_F$  by 50 meV for each successive ODOS. The effects of various parameters of the organic host-guest system on the device behavior are investigated; (b) the width  $\sigma$  of the DOS; (c) the energy difference  $\Delta$  (or trap depth) between the guest DOS and the host DOS; and, (d) the guest concentration  $x$ . In (b), (c) and (d) the total DOS is plotted in bold and the guest DOS is plotted in dashed lines.  $E_S$  is the position of the optimal transport energy,  $E_{TFL}$  marks the trap-filled limit (red down triangles).  $E_{eq}^g$  (blue up triangles) and  $E_{eq}^h$  (green rhombs) are the guest- and host equilibrium energy, respectively. (For interpretation of the references to colour in this figure legend, the reader is referred to the web version of this article).

with respect to the host DOS (Fig. 2c) and the concentration of guests (Fig. 2d).

## 2. Methodology

### 2.1. Mobility model

The Martens model [20] is an extension of the variable-range-hopping model introduced by Mott [23] but for arbitrary density of states. Despite its relative simplicity, the mobility is in good agreement with more sophisticated models [21,22]. The total DOS,  $g(E)$ , is the sum of the guest- and host-Gaussian DOS:

$$g(E) = g_h(E) + g_g(E) = \frac{(1-x)N_t}{\sqrt{2\pi}\sigma_h} \exp\left(-\frac{E^2}{2\sigma_h^2}\right) + \frac{xN_t}{\sqrt{2\pi}\sigma_g} \exp\left(-\frac{(E+\Delta)^2}{2\sigma_g^2}\right) \quad (1)$$

where  $g_h(E)$  and  $g_g(E)$  are the host and guest DOS, respectively;  $x$  is the concentration of guest sites, and  $N_t$  is the total density of sites.  $(1-x)N_t$  and  $xN_t$  are the density of host and guest sites;  $\sigma_h$  and  $\sigma_g$  are the width of the host and guest distributions.  $\Delta$  is the energy difference between the center of  $g_g(E)$  and  $g_h(E)$  (Fig. 2a). The energy disorder is assumed to be mainly due to electrostatic fluctuations arising from molecular electric dipoles or quadrupoles [24,25]. Furthermore, the guest molecules are considered to be well dispersed in the host matrix, i.e. no phase separation. Also, the guest and host molecules experience the same electrostatic environments and the width of both DOS distributions can be assumed to be the same ( $\sigma_g = \sigma_h = \sigma$ ).

The charge transport is governed by carriers hopping from an initial state near the Fermi level,  $E_F$ , to a final state lying at an optimal transport energy,  $E_S$ , over an optimal spatial hopping distance,  $R_S$ . The activation energy for the hopping process can be defined as  $E_A = E_S - E_F$ . Given the carrier concentration,  $p$ , the Fermi level is found by solving:

$$p = \int_{-\infty}^{\infty} g(E) f_{FD}(E, E_F) dE \quad (2)$$

where  $f_{FD}$  is the Fermi-Dirac distribution. The mobility is given by:

$$\mu = \frac{\sigma_0}{ep} \exp\left(-\alpha R_s - \frac{E_F - E_s}{k_B T}\right) \quad (3)$$

where  $e$  is the elementary charge,  $T$  is the temperature and  $\sigma_0$  is a constant prefactor.  $\alpha$  is the inverse localization length and describes the spatial extent of the localized state.  $\alpha^{-1}$  is proportional to the decay of the electronic density away from the molecules. In all simulations,  $\alpha = (0.1a)^{-1}$  and  $N_t = a^{-3}$ , where  $a$  is the average site-to-site distance and is assumed to be  $a = 1$  nm.

According to Mott's model, there is only one state to hop to within the optimal hopping distance  $R_s$  with energy lower than the optimal transport energy,  $E_s$ . In other words within the volume  $V_s = 4\pi R_s^3/3$ , there is only one available (i.e. one unoccupied) final state with energy less than  $E_s$ . This can also be expressed as  $V_s N(E_s) = 1$ , where  $N(E_s)$  is the number of available final states per unit volume with energy less than  $E_s$ . Coehoorn et al. [22] have suggested that this should be modified to  $V_s N(E_s) = B$  in order to take into account the percolative nature of charge transport in organic disordered materials.  $B$  is a parameter introduced to represent the average number of sites within the volume when percolation is achieved. In this study,  $B = 1.969$  is used as suggested by Coehoorn.

The mobility is found by optimizing the right-hand side of Eq. (3) with respect to  $R_s$  and  $E_s$ . In the case of a bi-modal Gaussian distribution, this translates into first solving the following Eq. (4) to get  $E_s$ :

$$\frac{\sqrt{\frac{2}{9\pi}} \left(\frac{3B\sigma_g^2}{2\pi N_t}\right)^{\frac{1}{3}} \left( (1-x) \exp\left(-\frac{E_s^2}{2\sigma_h^2}\right) + x \frac{\sigma_h}{\sigma_g} \exp\left(-\frac{(E_s+\Delta)^2}{2\sigma_g^2}\right) \right)}{\left( (1-x) \left( \operatorname{erf}\left(\frac{E_s}{\sqrt{2}\sigma_h}\right) - \operatorname{erf}\left(\frac{E_F}{\sqrt{2}\sigma_h}\right) \right) + x \left( \operatorname{erf}\left(\frac{E_s+\Delta}{\sqrt{2}\sigma_g}\right) - \operatorname{erf}\left(\frac{E_F+\Delta}{\sqrt{2}\sigma_g}\right) \right) \right)^{\frac{4}{3}}} - \frac{\sigma_h}{k_B T} = 0 \quad (4)$$

$R_s$  is then given by the relation  $V_s N(E_s) = B$ :

$$R_s = \left( \frac{3B_M}{2\pi N_t} \left/ \left( (1-x) \left( \operatorname{erf}\left(\frac{E_s}{\sqrt{2}\sigma_h}\right) - \operatorname{erf}\left(\frac{E_F}{\sqrt{2}\sigma_h}\right) \right) + x \left( \operatorname{erf}\left(\frac{E_s+\Delta}{\sqrt{2}\sigma_g}\right) - \operatorname{erf}\left(\frac{E_F+\Delta}{\sqrt{2}\sigma_g}\right) \right) \right) \right)^{\frac{1}{3}} \right) \quad (5)$$

Finally, the mobility is found by inserting  $E_s$  and  $R_s$  into Eq. (3).

For a given  $\sigma$ , a realistic carrier concentration for diodes ( $p < 10^{-3} N_t$ ) and at low- to moderate guest concentrations ( $x < 10^{-2}$ ), both  $R_s$  and  $E_s$  are to a very good approximation constant and are positioned slightly below the center of the host DOS. Physically, this means that the final state of the jumps is within the host distribution, and therefore the limiting processes for charge transport are guest-to-host or host-to-host jumps. As the guest concentration is increased above  $x \sim 10^{-1}$ ,  $E_s$  shifts towards the center of the guest DOS (towards  $-\Delta$ ), indicating that hopping directly between guest states becomes important. In this paper, we assume that the guest concentration is low enough

so that direct guest-to-guest hopping can be neglected, i.e.  $x < 10^{-2}$ . In this case, both  $R_s$  and  $E_s$  are nearly constant and therefore the carrier concentration dependence of the mobility originates from the dependence of  $E_F$  on  $p$ , and from the relative position of  $E_F$  to  $E_s$ .

In general, the charge carrier mobility in disordered organic semiconductors depends on both the charge carrier concentration and the electric field. In the above described model by Martens, the charge carrier concentration dependence of the mobility is well modeled, while the effect of the electric field is neglected. In our study, the charge carrier concentration is the most important parameter for the mobility in order to understand the effect of filling of deep guest (trap) states on the  $J$ - $V$  behavior. Furthermore, the carrier concentration dependence of the mobility is much stronger than the electric field dependence in disordered organic materials at low and intermediate fields [26]. Deviations from the calculated  $J$ - $V$  behavior can be expected at low temperatures due to the effect of the electric field on the activation barrier for charge hopping. To avoid that, all calculations are performed for a temperature set to 295 K.

## 2.2. Simulation of the $J$ - $V$ behavior

This study is restricted to the case of a single carrier device, consisting of a single organic host-guest layer with ideal ohmic contacts. The contacts can supply the bulk with unlimited amount of charges, i.e. the current is only limited by the charge transport phenomenon in the bulk of the organic material. The  $J$ - $V$  behavior is found by simultaneously solving the drift-diffusion equation:

$$J = ep(x)\mu(p(x))E(x) - eD(p(x))\frac{dp(x)}{dx} \quad (6)$$

and the Poisson's equation:

$$\frac{d^2\Psi(x)}{dx^2} = -\frac{e}{\varepsilon_0\varepsilon_r}p(x) \quad (7)$$

where  $\varepsilon_r$  and  $\varepsilon_0$  are the relative permittivity and the permittivity of vacuum, respectively; and,  $\Psi$  is the electric potential. The diffusion coefficient is estimated through the Einstein relation  $D = (k_B T/q)\mu$ .

Ohmic contacts are modeled by assuming that the carrier concentration at both contacts is fixed at a sufficiently high value. No difference to the solution of Eqs. (6) and (7) is found for carrier concentrations greater than  $p = 10^{25} \text{ m}^{-3}$ , and therefore this carrier concentration is used as the boundary conditions at the contacts. The voltage is applied to the injecting contact and the extracting contact is grounded. These four boundary conditions can be summarized as: (i)  $\Psi(0) = V_{\text{App}}$ ; (ii)  $\Psi(t) = 0$ ; (iii)  $p(0) = p_0$ ; and (iv)  $p(t) = p_0$ , where  $p_0 = 10^{25} \text{ m}^{-3}$  and  $t$  is the thickness of the organic layer. To eliminate the effect of filling of deep states due to diffusion from the electrodes into very thin films [15,27], all simulations have been performed for 300 nm-thick organic layers. In the following discussion, the carrier concentration in the middle of the device (i.e.  $p(x = t/2)$ ) is considered if not else explicitly stated.

### 3. Results and discussion

#### 3.1. General features of the modeled $J$ - $V$ behavior

##### 3.1.1. $J$ - $V$ behavior in the absence of guests

In order to identify the effect of guests, it is illustrative to first consider the simple case of a single-compound system. This corresponds to a pristine host system, without guests, described by a single Gaussian DOS (Fig. 3a). To visualize the occupation of the DOS, the occupied density of states (ODOS = product of the Fermi-Dirac distribution and the DOS) is also plotted. The evolution of the mobility versus charge carrier concentration is depicted in Fig. 3c (dashed line); while the expected  $J$ - $V$  behavior is shown in Fig. 3d (dashed line).

Let us first assume that the majority of the carriers, contributing to the charge transport, have their initial states close to the maximum of the ODOS and their final states for hopping at the transport level  $E_S$ . At high carrier concentrations, the maximum of the ODOS is to a good approximation near  $E_F$ . Hence, an increase of the carrier concentration is accompanied by a shift of  $E_F$  (and the maximum of the ODOS) towards higher energy, thus reducing the activation energy defined by  $E_F - E_S$ ; the mobility increases with  $p$ .

However, at low carrier concentration, the increase of the Gaussian DOS matches the fall-off of the Fermi-Dirac distribution, in such a way that the ODOS peak stays in the same position at the so-called equilibrium energy, given by  $E_{eq} = -\sigma^2/k_B T$  [28]. In this case, the activation energy for transport is instead given by  $E_{eq} - E_S$ . Since both  $E_{eq}$  and  $E_S$  are constant with  $p$ , the activation energy is constant; the mobility is independent of  $p$ . This regime of constant mobility occurs when  $E_F$  is several  $k_B T$  below  $E_{eq}$ . This can also be understood mathematically by replacing the Fermi-Dirac distribution in Eq. (2) with the Boltzman distribution, which is a reasonable approximation for low values of  $p$ . The resulting carrier concentration is proportional to  $p \sim \exp(E_F/k_B T)$ ; and consequently, the  $E_F$ -dependences in Eq. (3) cancel out and the mobility becomes constant. Note that this is a property of the Gaussian shape of the DOS [22], and it is in general not the case for an arbitrary shape of the DOS. For example, in the case of an exponential DOS, the maximum of the ODOS follows  $E_F$  also for small carrier concentrations and there is no well-defined  $E_{eq}$ .

$E_F$  is below  $E_{eq}$  for the entire voltage range in Fig. 3d (dashed line) and therefore the mobility is approximately constant. As a consequence, the  $J$ - $V$  behavior follows the  $J$ - $V^2$  behavior described by the Mott-Gurney law. Note that

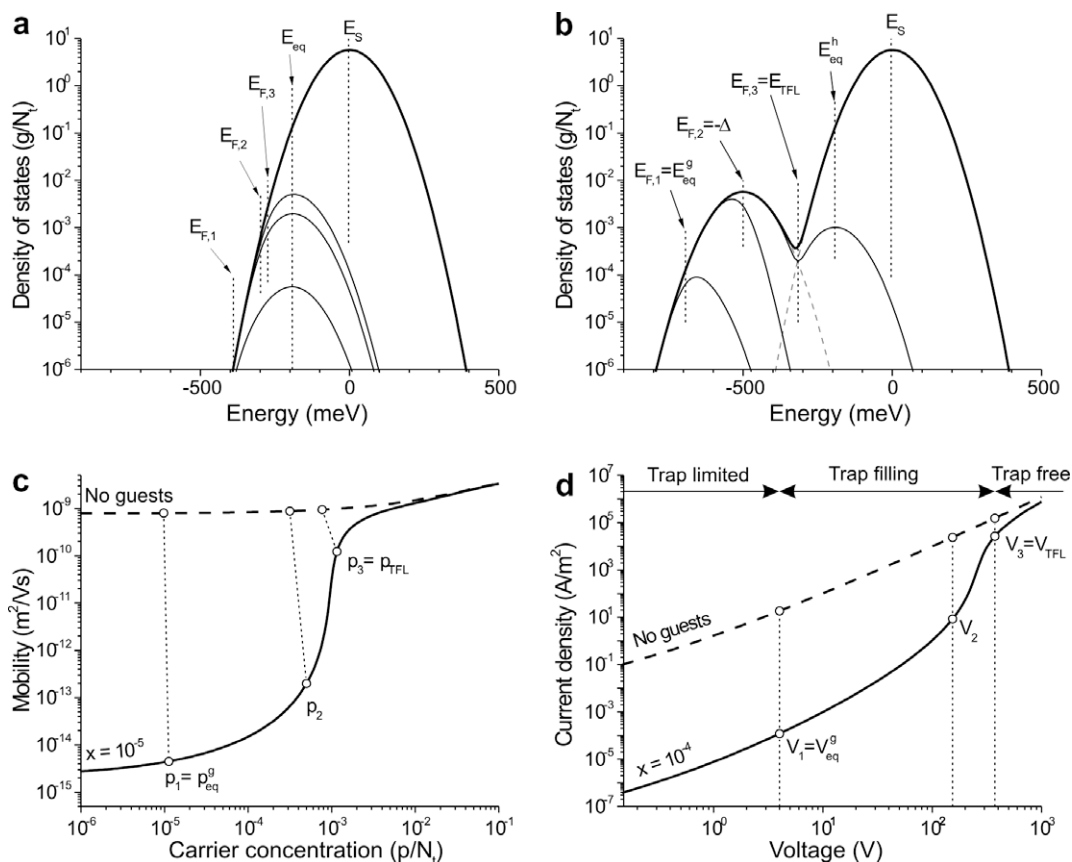


**Fig. 3.** (a) The DOS of an organic layer without guests, i.e. composed only of similar molecular levels with a certain disorder represented by the width  $\sigma = 70$  meV of the Gaussian. (b) The DOS of a host-guest system described by the sum of a Gaussian host DOS and a Gaussian guest DOS located 500 meV below the center of the host DOS. Mobility and  $J$ - $V$  behavior for the case with and without guest (c and d). Three marked Fermi-levels in (a) and (b) corresponds to the three carrier concentrations in (c) and the three voltages in (d). Note that the voltage range in (d) is much wider than what is accessible in an experiment.

in the case of Fig. 3d the width of the Gaussian DOS is only  $\sigma = 70$  meV, i.e. at the lower limit reported for organic disordered materials [29]. As disorder increases the mobility becomes dependent on the carrier concentration at lower voltage, resulting in a deviation from the Mott-Gurney behavior.

### 3.1.2. The $J$ - $V$ behavior in presence of guests

Fig. 3b shows the DOS of a host-guest system described by a bi-modal Gaussian distribution. The mobility versus carrier concentration and the  $J$ - $V$  behavior are displayed in Figs. 3c and d (solid line). The presence of guests does not modify the average density of charge carriers significantly but strongly changes the energy distribution of the carriers. The presence of guest states shifts the ODOS towards lower energy, which results in a lower  $E_F$  for the same carrier concentration as in the guest-free case. As a consequence, the activation energy for hopping increases and the mobility diminishes (Fig. 3c). The overall change in mobility due to the presence of guests depends on the degree of deformation of the total DOS caused by the guest states.

In order to explain qualitatively the mobility dependence on the carrier concentration in host-guest systems, we use a similar approach as adopted for the guest-free case. The carrier concentration sets the position of the Fermi level with respect to the defined equilibrium energy. The latter is an indicator to identify the region of constant mobility. For the host-guest system, two different equilibrium energies are worth defining (Fig. 3b):

$$E_{\text{eq}}^g = -\Delta - \sigma^2/k_B T \quad (8a)$$

$$E_{\text{eq}}^h = -\sigma^2/k_B T \quad (8b)$$

At sufficiently low carrier concentrations, the maximum of the ODOS is in the guest DOS at  $E_{\text{eq}}^g$ , and the mobility is constant as long as  $E_F < E_{\text{eq}}^g$ . Since  $E_{\text{eq}}^g$  is lower in energy than  $E_{\text{eq}}$  in absence of guests, the transition to a carrier dependent mobility occurs at lower  $E_F$  or equivalently at lower carrier concentrations as compared to the guest-free case. When  $E_F$  is shifted above  $-\Delta$  ( $E_{F2}$ ), the density of states starts to decrease again. As a consequence, a small change in carrier concentration results in a larger shift of  $E_F$  and thus a reduction of the activation barrier for the jumps ( $E_F - E_S$ ). Therefore, the mobility increases strongly with carrier concentration in this region of the DOS. As the guest states are filled up, the ODOS moves into the part of the total DOS that is dominated by host states ( $E_F = E_{F3}$ ). If the host and guest DOS are well separated and if the guest concentration is low, there is an intermediate carrier concentration regime where the mobility again becomes approximately independent on  $p$ . This occurs when  $E_F$  has passed into the host DOS but is still several  $k_B T$  below  $E_{\text{eq}}^h$ . If  $E_F$  is increased above  $E_{\text{eq}}^h$  the mobility again becomes dependent on the carrier concentration.

At low voltages ( $V < V_1$  in Fig. 3d), the carrier concentration is low and the carriers occupy states within the tail of the guest DOS, near  $E_{\text{eq}}^g$ . Hence,  $p$  is in the Boltzmann limit, the activation energy for hopping is high, and the mobility is effectively constant and low. This corresponds to the trap-limited regime. As the voltage is increased,  $E_F$  is shifted above  $E_{\text{eq}}^g$ , and the mobility becomes strongly carrier con-

centration dependent. This corresponds to the trap-filling regime. The increase in mobility results in a steeper slope of the  $J$ - $V$  behavior, peaking at  $V = V_2$  before it increases less steeply again. At even higher applied voltages ( $V > V_3$ ), the guest states start to be filled up significantly, such that  $E_F$  transits into the part of the DOS dominated by the host states. At this point the slope of the  $J$ - $V$  curve is reduced and the behavior approaches the trap-free case. This corresponds to the trap-free regime.

Since the DOS is not a discrete function, the filling of the guest states is a continuous process. Therefore the transition from the trap-filling regime to the trap-free regime is smooth and the definition of a trapped-filled limit,  $V_{\text{TFL}}$ , is ambiguous. We have chosen to define  $V_{\text{TFL}}$  as the voltage when  $E_F$  is equal to the crossing point,  $E_{\text{TFL}}$ , between the individual guest- and the host DOS. At  $E_{\text{TFL}}$ , the guest DOS and host DOS has the same magnitude; the initial states for hopping is equally probable to be a guest state as a host state. When  $E_F$  is further increased, the transport process becomes dominated by charge carriers hopping from states within the host DOS, i.e. by host-to-host hopping. Assuming that  $\sigma_g = \sigma_h = \sigma$ , it is straight-forward from  $g_g(E_{\text{TFL}}) = g_h(E_{\text{TFL}})$  to derive the following expression for  $E_{\text{TFL}}$ :

$$\text{TFL} = \frac{\sigma^2}{\Delta} \ln \left( \frac{x}{1-x} \right) - \frac{\Delta}{2} \quad (9)$$

Note that the definition of  $E_{\text{TFL}}$  and  $E_{\text{eq}}^g$  is only meaningful as long as  $E_{\text{TFL}} > E_{\text{eq}}^g$ , since otherwise the difference between the trap-limited and the trap-free regimes vanishes and the guests do no longer act as traps. Above the  $V_{\text{TFL}}$ , the  $J$ - $V$  behavior approaches the trap-free case.

The evolution of the  $J$ - $V$  behavior as states are filled in the DOS can be summarized by:

- (1) Trap-limited regime ( $E_F < E_{\text{eq}}^g$ ; i.e.,  $V < V_{\text{eq}}^g$ ): the ODOS is in the tail of the guest DOS and the mobility is approximately constant.
- (2) Trap-filling regime ( $E_{\text{eq}}^g < E_F < E_{\text{TFL}}$ ; i.e.,  $V_{\text{eq}}^g < V < V_{\text{TFL}}$ ): the mobility is strongly  $p$ -dependent and the slope of the  $\log J$ - $\log V$  is larger than
- (3) Trap-free regime ( $E_{\text{TFL}} < E_F$ ; i.e.,  $V_{\text{TFL}} < V$ ): Most guest states are filled and the  $J$ - $V$  behavior approaches the trap-free case.

There are two appealing reasons for this definition of the three different regimes. First, both  $E_{\text{eq}}^g$  and  $E_{\text{TFL}}$  are well-defined, which circumvents the problem with ambiguous definitions conceivable in the case of smooth transitions as with disordered materials [30]. Second, this definition is consistent with the traditional definition of the regimes, in that  $J$  follow a  $V^2$ -relationship (since the mobility is constant) in the trap-limited and trap-free regimes, and follows a considerably stronger  $V$ -dependence in the trap-filling regime.

### 3.2. $J$ - $V$ behavior and mobility for various shapes of the DOS

In the following sections the  $J$ - $V$  behavior for varying shape of the DOS is investigated. The width of the Gaussian DOS ( $\sigma$ ), the energy difference between the frontier levels

of the guest and host molecules in the blend ( $\Delta$ ) and the concentration of guest molecules in the host matrix ( $x$ ) is varied one at a time.

### 3.2.1. Influence of the Gaussian DOS width

Tuning the width of the Gaussian partial DOS for host and guest molecules (Fig. 4a) is a way to simulate the importance of energetic disorder in molecular host–guest systems. In the case of a very ordered and homogeneous system ( $\sigma = 10$  meV),  $E_F$  shifts negligibly until the guest DOS is almost filled. When the carrier concentration is further increased, the charge carriers start to occupy the host states, resulting in an abrupt shift of  $E_F$  into the host DOS. As a consequence, the activation barrier for jumps (i.e.  $E_S - E_F$ ) is dramatically reduced and the mobility becomes significantly enhanced (Fig. 4b). In the  $J$ – $V$  behavior, this appears as a narrow trap-filling regime and a steep transition from the trap-limited to the trap-free regime (Fig. 4c).

When disorder is increased to a realistic value for organic semiconductors (70–140 meV [26,29]), the trap-filling regime becomes stretched out, and the slope of the  $J$ – $V$  behavior in the trap-filling regime becomes less steep. Since the range of carrier concentration is still the same ( $10^{-6}N_t < p < 10^{-3}N_t$ ), the impact on the diode  $J$ – $V$  behavior becomes less dramatic. This implies that as  $\sigma$  becomes larger, the  $J$ – $V$  behavior becomes less sensitive to the presence of the guest DOS. As  $\sigma$  is increased,  $E_{eq}^g$  is shifted towards lower energy. Therefore, for  $\sigma > 100$  meV the trap-limited regime is most likely not accessible within the electric field span of real experiments.

### 3.2.2. Influence of the host–guest energy mismatch

The impact of  $\Delta$  on the  $J$ – $V$  behavior depends on the width of the distributions ( $\sigma$ ). If  $\Delta$  is small compared to  $\sigma$ , the guest DOS is almost entirely engulfed in the host DOS and the associated effect on the charge transport is small. In Fig. 5a, four different cases are shown: no guests,  $\Delta = 300$  meV, 500 meV and 700 meV for  $\sigma = 100$  meV and  $x = 10^{-4}$ . The host states are completely dominating the DOS when  $\Delta \leq 300$  meV (i.e.  $\sigma/\Delta \leq 3$ ). In this case, the shape of the ODOS and the position of  $E_F$  follow that of the guest-free case when  $V$  is varied. As a result, guests have very little impact on both the mobility (Fig. 5b) and the  $J$ – $V$  behavior (Fig. 5c). For  $\Delta$  values larger than 300 meV, the guest DOS is now clearly visible in the total DOS. The ODOS and  $E_F$  are at lower energy as compared to the guest-free case, resulting in an increased activation barrier for hopping and a reduced mobility. Increasing  $\Delta$  from 300 meV to 500 meV decreases the current density in the trap-limited regime with three orders of magnitude and increases the slope of the  $\log J$  vs.  $\log V$  curve from 4.5 to 16.5 in the trap-filling regime.

### 3.2.3. Influence of the guest concentration

As the guest concentration is increased, the shoulder in the total DOS grows (Fig. 6a). This is accompanied with a shift of the  $\mu$ – $p$  curve towards higher carrier concentration values (Fig. 6b) and a dramatic drop of the mobility for low charge carrier concentration. The shift of the  $p$ -dependent mobility implies that the trap-limited and trap-filling re-

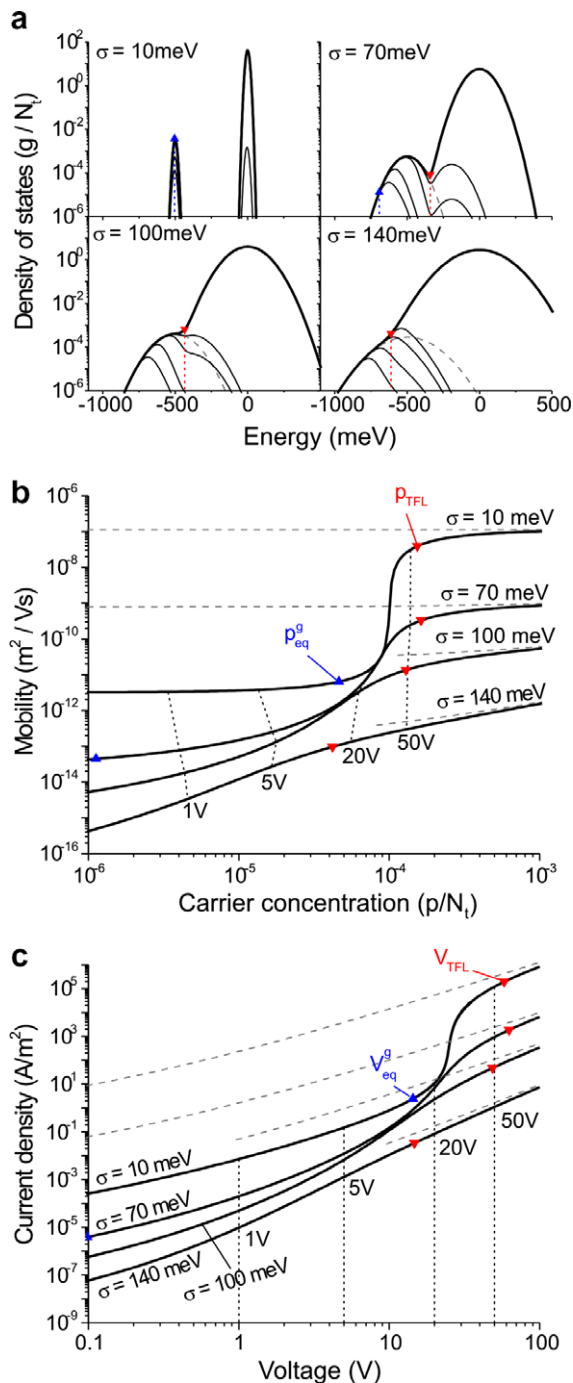


**Fig. 4.** The progression of the  $J$ – $V$  behavior for  $\sigma = 10$  meV, 70 meV, 100 meV and 140 meV. The DOS is shown in (a), and the mobility and  $J$ – $V$  behavior in (b) and (c). The guest equilibrium point  $E_{eq}^g$  and trap-fill limit  $E_{TFL}$  are marked with blue up triangles and red down triangles, respectively. The mobility and  $J$ – $V$  behavior in the absence of guests are shown in dashed. The ODOSs in (a) and the mobilities and concentrations in (b) corresponds to the voltages at the dotted lines in (c), i.e.  $V = 1$  V, 5 V, 20 V and 50 V.

gimes extend into higher carrier concentrations. When the carrier concentration reaches the same order of magnitude as the guest concentration, the mobility starts to increase

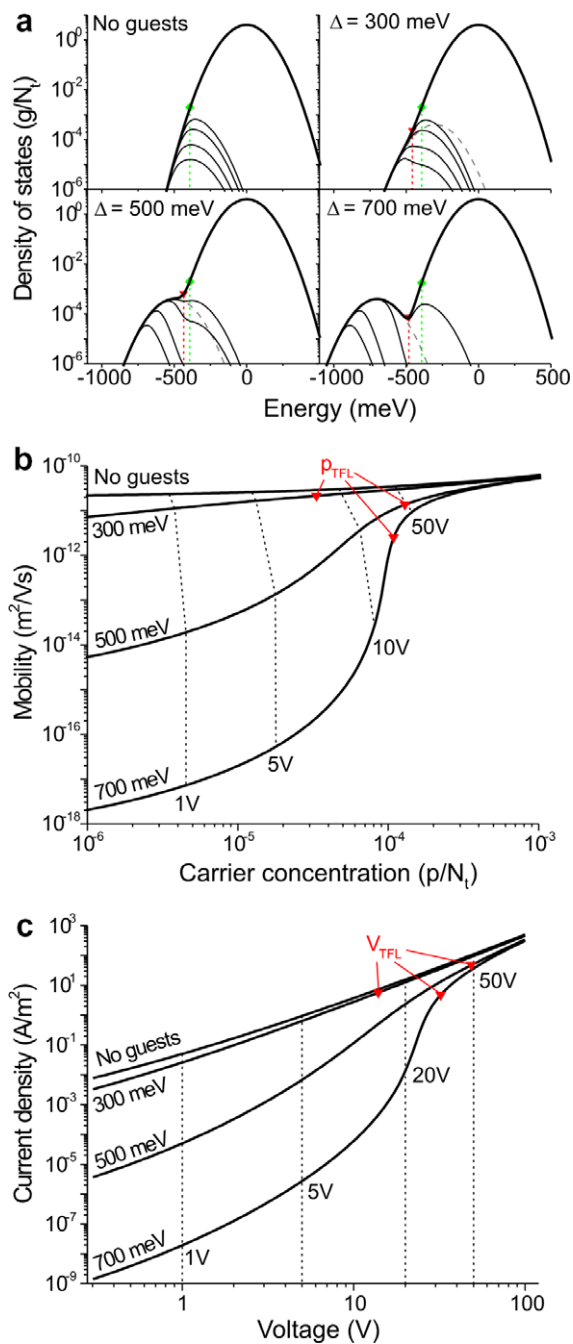


**Fig. 5.** The progression of the  $J$ - $V$  behavior for  $\Delta = 0$  meV, 300 meV, 500 meV and 700 meV, for  $\sigma = 100$  meV and  $x = 10^{-4}$ . The DOS is shown in (a) and the mobility and  $J$ - $V$  behavior in (b) and (c). The ODOs in (a) and the mobilities and concentrations at the dotted lines in (b) corresponds to the voltages at the dotted lines in (c), i.e.  $V = 1$  V, 5 V, 20 V and 50 V. The trap-fill limit and the host equilibrium point are marked with red down triangles and green diamonds, respectively. In this case the guest equilibrium point occurs for very low carrier concentrations and is therefore not visible in the figure.

towards the guest-free value and eventually reaches the value of the trap-free regime. The  $J$ - $V$  behavior in Fig. 6c follows the mobility behavior. At 5 V, the current density is

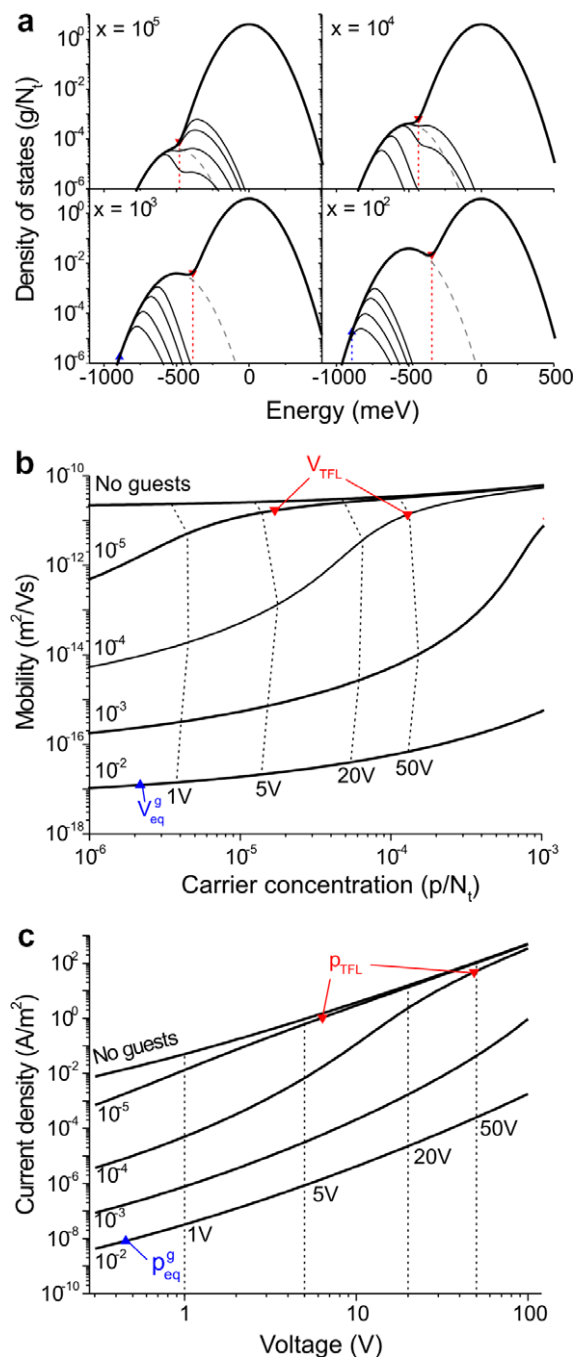


**Fig. 6.** The progression of the  $J$ - $V$  behavior for  $x = 10^{-5}$ ,  $10^{-4}$ ,  $10^{-3}$  and  $10^{-2}$ , for  $\sigma = 100$  meV and  $\Delta = 500$  meV. The DOS is shown in (a) and the mobility and  $J$ - $V$  behavior in (b) and (c). The ODOs in (a) and the mobilities and concentrations at the dotted lines in (b) corresponds to the voltages at the dotted lines in (c), i.e.  $V = 1$  V, 5 V, 20 V and 50 V. In all the graphs, the trap-fill limit is marked with a red down triangle and the guest equilibrium limit is marked with a blue up triangle. (For interpretation of the references to colour in this figure legend, the reader is referred to the web version of this article).

two orders of magnitude lower with a guest concentration of  $x = 10^{-4}$  than in the guest-free case.  $V_{\text{TFL}}$  is shifted from

6.4 V to 48.6 V when the guest concentration is changed from  $x = 10^{-5}$  to  $10^{-4}$ .

It is worth noting two limiting cases for the example considered. First, it is unlikely that the trap-filled limit can be reached for  $x > 10^{-2}$  in a diode configuration since the diode would likely break down before the transition is reached. Second, for very low guest concentrations ( $x < 10^{-4}$ ), the current transition is so smooth that it is hardly discernable. Note that if the guest concentration is increased above  $x > 10^{-2}$ , guest-to-guest hopping eventually starts to dominate the charge transport process. Assuming that the guest–guest electronic coupling is on the same order as (or even higher than) the host–host elec-

tronic coupling, the mobility will then increase with the guest concentration [21]. However, as noted above, this situation is outside the scope of this study.

### 3.3. Prediction of the dominant regime

#### 3.3.1. Estimation of $p_{eq}^g$ and $p_{TFL}$ for organic host–guest systems

Since the  $J$ – $V$  behavior is dramatically different in the trap-limited, trap-filling and trap-free regimes, it is desirable to be able to predict the dominant regime for a diode based on a certain organic host–guest system characterized by a set of  $\sigma$ ,  $\Delta$  and  $x$ . In order to do that, a correlation

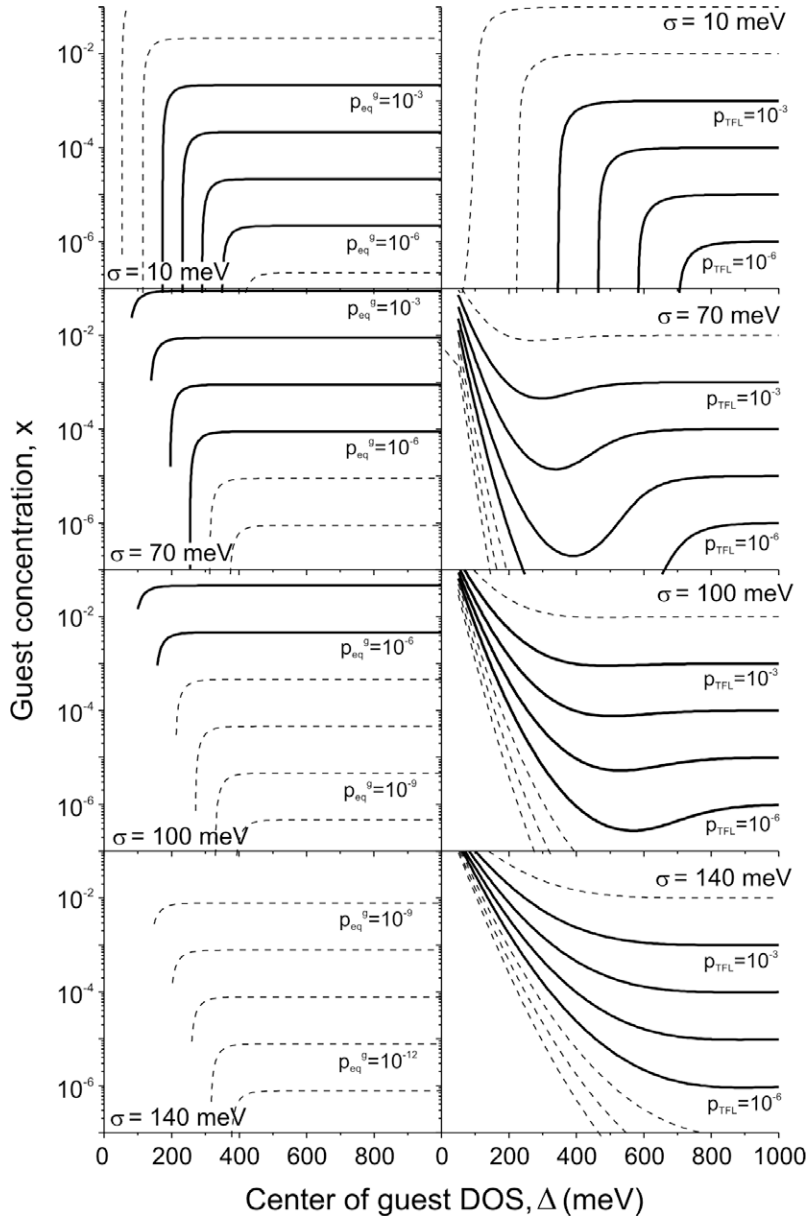


**Fig. 7.** Isodensity contours of  $p_{eq}^g$  (left column) and  $p_{TFL}$  (right column) for  $\sigma_h = \sigma_g = 10$  meV, 70 meV, 100 meV and 140 meV, as a function of  $x$  and  $\Delta$ . The bold lines correspond to  $p_{eq}^g$  or  $p_{TFL} = 10^{-3}N_t$ ,  $10^{-4}N_t$ ,  $10^{-5}N_t$  and  $10^{-6}N_t$ . The dashed lines correspond to one decade change of carrier concentration. Note that in the case of  $p_{eq}^g$  the contour lines are only plotted for  $E_{eq}^g < E_{TFL}$ , since otherwise the definition of  $E_{eq}^g$  is not relevant.

is needed between the range of the applied voltage and the range of accessible charge carrier densities in the device. With the definitions given above, the device is in the trap-filling regime when  $E_{\text{eq}}^g < E_F < E_{\text{TFL}}$ . Using Eq. (2), this condition translates into carrier concentrations as  $p_{\text{eq}}^g < p < p_{\text{TFL}}$ , where  $p_{\text{eq}}^g$  and  $p_{\text{TFL}}$  are the carrier concentrations when  $E_F = E_{\text{eq}}^g$  and  $E_F = E_{\text{TFL}}$ , respectively. At lower carrier concentrations ( $p < p_{\text{eq}}^g$ ), the device is in the trap-limited regime, while at higher carrier concentrations ( $p > p_{\text{TFL}}$ ), the system is in the trap-free regime. The isodensity contours of  $p_{\text{eq}}^g$  and  $p_{\text{TFL}}$  as a function of  $\Delta$  and  $x$  are extracted from Eq. (2) and given in Fig. 7. The difference between two neighboring lines in the figure corresponds to one decade difference in carrier concentration. In the case of  $p_{\text{eq}}^g$ , the contour lines are only plotted for  $E_{\text{eq}}^g < E_{\text{TFL}}$ , since otherwise the definition of  $E_{\text{eq}}^g$  is not relevant.

When the contacts are ohmic, the carrier concentration profile in the device at thermal equilibrium is determined by the build-up of charge near the injecting contact, irrespective of the transport mechanism in the bulk of the material. The amount of charge stored in the material is given by the product of the geometrical capacitance,  $C_g = \epsilon_r \epsilon_0 / t$  [F/m<sup>2</sup>], and the applied voltage,  $V_{\text{AppI}}$ . At intermediate to high carrier concentrations, an approximation of the average charge carrier concentration,  $p_{\text{av}}$ , is then given by  $p_{\text{av}} \approx C_g V_{\text{AppI}} / e = \epsilon_r \epsilon_0 V_{\text{AppI}} / et^2$  [8]. This simple estimate of the average charge concentration is independent on the DOS parameters ( $\sigma$ ,  $\Delta$  and  $x$ ), thus not rigorously accurate. However, it gives the same order of magnitude as the true value, with the shape of the DOS taken into consideration, of the carrier concentration in the center of the device. For a thickness of the organic layer of a few hundred nanometers and with an applied voltage close to the breakdown voltage of the organic layer, the realistic upper-limit for the carrier concentration in a diode is on the order of  $p_{\text{av}} \approx 10^{-3} N_t$ . With the same thickness, the lower limit of the carrier concentration in the device is  $p_{\text{av}} \approx 10^{-6} N_t$  due to diffusion of carriers from the ohmic contacts [27]. With this motivation, we conclude that the carrier concentration in diodes under realistic voltages is in the range of  $10^{-6} N_t < p < 10^{-3} N_t$ . In Fig. 7,  $p_{\text{eq}}^g$  and  $p_{\text{TFL}}$  belonging to this accessible range of carrier concentrations are plotted in bold lines, while those outside this range appears as dotted lines.

For large  $\Delta$  (e.g.  $\Delta = 700$  meV in Fig. 5a), the guest and the host DOSs are well separated and  $E_{\text{TFL}}$  is low. Few carriers occupy states in the host DOS and most states in the guest DOS are filled, according to the definition of  $E_{\text{TFL}}$ . Consequently,  $p_{\text{TFL}} \approx x N_t$  and is independent on  $\Delta$ . This appears in Fig. 7 as horizontal isodensity lines for large enough  $\Delta$ . When  $\Delta$  diminishes (e.g.  $\Delta = 500$  meV in Fig. 5a),  $E_{\text{TFL}}$  is sliding upwards along the crossing between the guest and the host DOS. As long as  $E_{\text{TFL}} < E_{\text{eq}}^h$ , an approximation for  $p_{\text{TFL}}$  in this intermediate range of  $\Delta$  can be found using Eq. (2), according to:

$$p_{\text{TFL}} = \int_{-\infty}^{\infty} g(E) f_{\text{FD}}(E, E_{\text{TFL}}) dE \approx x N_t + N_{\text{eff}} \exp((E_{\text{TFL}} - E_{\text{eq}}^h) / k_B T) \quad (10)$$

where  $N_{\text{eff}} \approx \int g_h(E) f_{\text{FD}}(E, E_{\text{eq}}^h) dE$  is the effective density of states of the host DOS at  $E_{\text{eq}}^h$  [31]. The two terms in Eq.

(10) corresponds to the charge carriers residing in the guest states (first term) and the host states (second term). As  $\Delta$  decreases further,  $E_{\text{TFL}} - E_{\text{eq}}^h$  becomes larger and the second term in Eq. (10) increases abruptly. In order to stay on the same isodensity contour,  $p_{\text{TFL}}$  must be kept constant by decreasing  $x$ . This appears as a downward bending of the  $p_{\text{TFL}}$  isodensity contours for intermediate  $\Delta$ .

For small  $\Delta$  (e.g.  $\Delta = 300$  meV in Fig. 5a), the guest DOS is almost entirely engulfed in the host DOS. The number of charge carriers residing in the guest states is therefore no longer accurately described by the first term in Eq. (10). In this case, a better estimate of  $p_{\text{TFL}}$  is given by the second term alone, i.e.  $p_{\text{TFL}} \approx N_{\text{eff}} \exp((E_{\text{TFL}} - E_{\text{eq}}^h) / k_B T)$ . The only way to maintain  $p_{\text{TFL}}$  constant while reducing  $\Delta$  is to keep  $E_{\text{TFL}}$  constant, since both  $N_{\text{eff}}$  and  $E_{\text{eq}}^h$  are constant. From Eq. (9), it follows that this can only be accomplished by increasing  $x$ . This trend is depicted as isodensity contours bending upwards towards larger  $x$  for small  $\Delta$ .

For large and intermediate  $\Delta$ ,  $E_{\text{eq}}^g < E_{\text{TFL}}$  and most of the carriers contributing to  $p_{\text{eq}}^g$  are located on guest molecules. Therefore, the  $p_{\text{eq}}^g$  isodensity contours are constant with  $x$

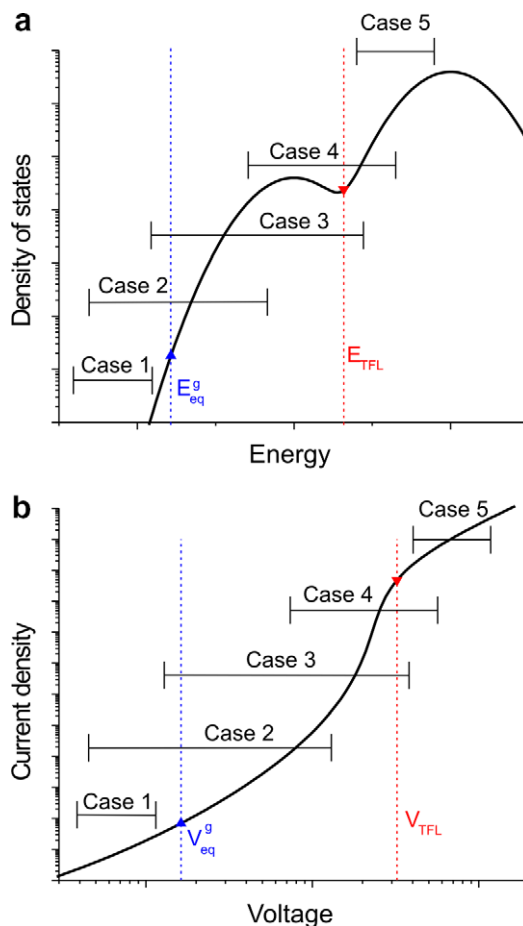


**Fig. 8.** Five possible cases for host-guest systems illustrated with sketches of the DOS (a) and the  $J$ - $V$  behavior (b) of the diode. The horizontal bars represent the energy- and voltage range corresponding to the carrier concentration range of  $10^{-6} N_t < p < 10^{-3} N_t$ . Note that this is only a sketch and the energy- and voltage ranges are mapped onto one DOS to fit all the cases into the same figure.



in this  $\Delta$  range. For small  $\Delta$ , such that  $E_{\text{eq}}^g > E_{\text{TFL}}$ , states from the host DOS contribute significantly to  $p_{\text{eq}}^g$ . In order to keep  $p_{\text{eq}}^g$  constant while decreasing  $\Delta$ , the guest concentration  $x$  is reduced and the isodensity contours diverge into vertical lines.

### 3.3.2. Organic host–guest systems classified in cases

On one hand, two key carrier concentrations  $p_{\text{eq}}^g$  and  $p_{\text{TFL}}$ , characterize a specific organic host–guest system, i.e. they are defined by a particular set of  $\sigma$ ,  $\Delta$  and  $x$  (see Fig. 7). On the other hand, the carrier concentration in a diode typically varies with the applied voltage from  $10^{-6}N_t$  to  $10^{-3}N_t$ . Depending on where  $p_{\text{eq}}^g$  and  $p_{\text{TFL}}$  are located within the range of the accessible  $p$ , six different cases of organic host–guest systems can be identified. While examples for each case can be found in the previous Section 3.2, we have here chosen a simplified representation in order to be able to represent all cases in one graph. Fig. 8 is not a rigorous scientific representation of the different cases, but a sketch that helps the reader to understand the physical origin of the mobility behavior of these different organic systems. The accessible carrier concentration span ( $10^{-6}N_t$ – $10^{-3}N_t$ ) in the device is translated into the accessible energy range for the Fermi level in the DOS of each specific system, which is represented by a horizontal bar in Fig. 8. The six cases are:

- (1)  $10^{-3}N_t < p_{\text{eq}}^g$ : Only the trap-limited regime is accessible. A requirement for a large  $p_{\text{eq}}^g$  is that  $E_{\text{eq}}^g$  is in a high-density part of the DOS, i.e. either close to the center of the guest DOS (if  $x$  is large) or well within the host DOS (a small  $\Delta$ ). Since  $E_{\text{eq}}^g$  is proportional to the square of  $\sigma$ , this is only satisfied if  $\sigma$  is small, i.e. for an ordered film. Interestingly, this situation is not observed in the simulations performed with realistic  $\sigma$  values for disordered organic semiconductor ( $\sigma > 70$  meV).
- (2)  $10^{-6}N_t < p_{\text{eq}}^g < 10^{-3}N_t < p_{\text{TFL}}$ : The  $J$ – $V$  behavior starts in the trap-limited regime, transits into the trap-filling regime, but never reaches the trap-free limit.
- (3)  $10^{-6}N_t < p_{\text{eq}}^g < p_{\text{TFL}} < 10^{-3}N_t$ : The  $J$ – $V$  behavior starts in the trap-filled regime, proceeds into the trap-filling regime and eventually reaches the trap-free regime.
- (4)  $p_{\text{eq}}^g < 10^{-6}N_t < p_{\text{TFL}} < 10^{-3}N_t$ : The trap-limited regime is not accessible; the  $J$ – $V$  behavior begins in the trap-filling regime, and transits into the trap-free regime.
- (5)  $p_{\text{eq}}^g < p_{\text{TFL}} < 10^{-6}N_t$ : Only the trap-free regime is accessible, i.e. the guest states have little impact on the  $J$ – $V$  behavior.
- (6)  $p_{\text{eq}}^g \geq p_{\text{TFL}}$ , or equivalently  $E_{\text{eq}}^g \geq E_{\text{TFL}}$ : The trap-filling regime vanishes and the guests no longer acts as traps.

## 4. Conclusions

Organic semiconductor blends, obtained by introducing guest molecules into a host matrix, have been demonstrated to improve efficiency and give new functionality

in two terminal devices, like diodes. Here, the evolution of the mobility vs. charge carrier concentration and the current density–voltage behavior of the device are explained and simulated by following how the charge carriers reside in a density of states of the organic host–guest system.

An organic semiconductor host–guest system is defined by three parameters: the width of the Gaussian guest– and host DOS, the position of frontier energy levels of the guest molecules compared to those of the host molecular matrix, as well as the concentration of guests. The impact of the guest states on the  $J$ – $V$  behavior is determined by the level of modification of the total DOS introduced by the guest DOS. Several major trends are observed: Firstly, when molecular disorder is increased, the transition from the trap-limited to the trap-free regime becomes smoother. In a strongly disordered system, the guest DOS needs to deviate strongly from the host DOS to have an impact on the  $J$ – $V$  behavior. Secondly, the transition from the trap-limited to the trap-free regimes occurs over approximately the same voltage range, but the transition is much steeper for larger energy mismatch between guest and host frontier  $\pi$ -levels. Thirdly, an increase of guest concentration in the organic system shifts the  $J$ – $V$  behavior towards higher voltages.

From the above analysis, we propose simple criteria to predict the  $J$ – $V$  behavior of a two terminal device composed of an organic semiconductor host–guest system defined with its three parameters ( $\sigma$ ,  $\Delta$ ,  $x$ ). An organic host–guest system is characterized by two key charge carrier concentrations,  $p_{\text{eq}}^g$  and  $p_{\text{TFL}}$ , easily accessible in this report. The position of  $p_{\text{eq}}^g$  and  $p_{\text{TFL}}$  within the range of charge carrier concentration accessible in device [ $10^{-6}N_t$ – $10^{-3}N_t$ ] allows to predict the regimes of charge transport (trap filling, trap-filled, trap free) accessible for that specific organic host–guest system. We believe these criteria will help device scientists to select the right molecular host–guest pair and host/guest ratio to access the desired  $J$ – $V$  behavior for a given (opto) electronic application.

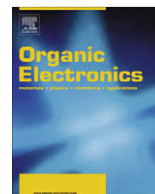
## Acknowledgement

The authors gratefully acknowledge The Swedish Foundation for Strategic Research (COE@COIN), VINNOVA, The Royal Swedish Academy of Sciences and The Swedish Research Council for financial support of this project. The authors acknowledge P.A. Bobbert and P. Andersson for invaluable discussions.

## References

- [1] G. Yu, A.J. Heeger, J. Appl. Phys. 78 (1995) 4519.
- [2] M.A. Baldo, D.F. O'Brien, Y. You, A. Shoustikov, S. Sibley, M.E. Thompson, S.R. Forrest, Nature 395 (1998) 151.
- [3] M.A. Baldo, M.E. Thompson, S.R. Forrest, Nature 403 (2000) 750.
- [4] Y. Kawamura, S. Yanagida, S.R. Forrest, J. Appl. Phys. 92 (2002) 87.
- [5] M. Berggren, A. Dodabalapur, R.E. Slusher, Z. Bao, Nature 389 (1997) 466.
- [6] P. Andersson, N.D. Robinson, M. Berggren, Adv. Mater. 17 (2005) 1798.
- [7] P. Toman, S. Nespurek, M. Weiter, M. Vala, J. Sworakowski, W. Bartkowiak, M. Mensik, Polym. Adv. Technol. 17 (2006) 673.
- [8] M. Pope, C.E. Swenberg, Electronic Processes in Organic Crystals and Polymers, Oxford University Press, Oxford, 1999.

- [9] S. Nespurek, J. Sworakowski, *Thin Solid Films* 393 (2001) 168.
- [10] J.-L. Brédas, D. Beljonne, V. Coropceanu, J. Cornil, *Chem. Rev.* 104 (2004) 4971.
- [11] P. Mark, W. Helfrich, *J. Appl. Phys.* 33 (1962) 205.
- [12] M.M. Mandoc, B. de Boer, G. Paasch, P.W.M. Blom, *Phys. Rev. B* 75 (2007) 193202.
- [13] V.I. Arkhipov, P. Heremans, E.V. Emelianova, G.J. Adriaenssens, *Appl. Phys. Lett.* 79 (2001) 4154.
- [14] B. Bohnenbuck, E. von Hauff, J. Parisi, C. Deibel, V. Dyakonov, *J. Appl. Phys.* 99 (2006) 024506.
- [15] M. Koehler, I. Biaggio, *Phys. Rev. B* 68 (2003) 075205.
- [16] V.R. Nikitenko, H. Heil, H. von Seggern, *J. Appl. Phys.* 94 (2003) 2480.
- [17] J. Shen, *J. Appl. Phys.* 83 (1998) 7706.
- [18] M.-J. Tsai, H.-F. Meng, *J. Appl. Phys.* 97 (2005) 114502.
- [19] J. Yang, J. Shen, *J. Appl. Phys.* 85 (1999) 2699.
- [20] H.C.F. Martens, I.N. Hulea, I. Romijn, H.B. Brom, W.F. Pasveer, M.A.J. Michels, *Phys. Rev. B* 67 (2003) 121203(R).
- [21] R. Coehoorn, *Phys. Rev. B* 75 (2007) 1.
- [22] R. Coehoorn, W.F. Pasveer, P.A. Bobbert, M.A.J. Michels, *Phys. Rev. B* 72 (2005) 155206.
- [23] N.F. Mott, *Phil. Mag.* 19 (1969) 835.
- [24] A. Dieckmann, H. Bässler, *J. Chem. Phys.* 99 (1993) 8136.
- [25] D.H. Dunlap, P.E. Parris, V.M. Kenkre, *Phys. Rev. Lett.* 77 (1996) 542.
- [26] W.F. Pasveer, J. Cottar, C. Tanase, R. Coehoorn, P.A. Bobbert, P.W.M. Blom, D.M. de Leeuw, M.A.J. Michels, *Phys. Rev. Lett.* 74 (2005) 206601.
- [27] N.I. Craciun, J.J. Brondijk, P.W.M. Blom, *Phys. Rev. B* 77 (2008) 035206.
- [28] H. Bässler, *Phys. Status Solidi (b)* 175 (1993) 15.
- [29] L.M. Andersson, O. Inganäs, *Organ. El.* 8 (2007) 423.
- [30] S.C. Jain, A.K. Kapoor, W. Geens, J. Poortmans, R. Mertens, M. Willander, *J. Appl. Phys.* 92 (2002) 3752.
- [31] C.M. Wolfe, N. Holonyak Jr., G.E. Stillman, *Physical Properties of Semiconductors*, Prentice-Hall Inc., Engelwood Cliffs, New Jersey, 1989.



## Pentacene thin film transistors fabricated by solution process with directional crystal growth

Yutaka Natsume\*, Takashi Minakata, Takeshi Aoyagi

Asahi Kasei Corporation, Analysis and Simulation Center, 2-1 Samejima, Fuji, Shizuoka 4168501, Japan

### ARTICLE INFO

#### Article history:

Received 28 August 2008  
Received in revised form 7 October 2008  
Accepted 8 October 2008  
Available online 14 October 2008

#### PACS:

68.55.Am  
81.10.Dn  
85.30.Tv

#### Keywords:

Pentacene  
Solution process  
Crystal growth  
Field effect transistor

### ABSTRACT

We have fabricated solution-processed pentacene thin film transistor arrays with mobilities as high as  $1.0 \text{ cm}^2/\text{V s}$ , evaluated at a low drain voltage of  $-10 \text{ V}$ . This is achieved by controlling the growth direction of the pentacene films from solution, and by optimizing conditions for drop casting. Crystal growth of the solution-processed pentacene films is found to proceed in one direction on a tilted substrate. Grazing incidence X-ray diffraction and electron diffraction reveal that the crystal growth azimuth corresponds to the direction along the minor axis of the  $a$ - $b$  plane in the unit cell of the pentacene crystal. This directional growth method is extended to solution processing on large glass substrates with an area of  $150 \times 150 \text{ mm}^2$ , thereby yielding transistor arrays with two-dimensional uniformity and high carrier mobility.

© 2008 Elsevier B.V. All rights reserved.

### 1. Introduction

In recent years, thin film transistors (TFTs) based on organic semiconductors have attracted significant attention because of the relatively high mobility up to  $10 \text{ cm}^2/\text{Vs}$  of single crystals and applicability to flexible substrates [1–5]. Solution processing can be applied using organic semiconductors with flexible substrates at much lower temperatures compared to conventional processes for inorganic semiconductors, thus allowing for studies using novel soluble materials [6–10]. One of the organic semiconductors under investigation, pentacene, has shown high carrier mobility comparable to amorphous silicon [11]. However, it has been typically used as the source for vacuum deposition due to its low solubility. To obtain higher solubility, it is necessary to modify the molecular

structure of pentacene by adding some functional groups to the parent structure. Diels–Alder-adducted pentacene derivatives [12,13] and 6,13-bis(triisopropyl-silylethynyl)pentacene [14], for example, were investigated and exhibited high field effect mobilities of  $0.1$ – $1 \text{ cm}^2/\text{Vs}$ .

We have investigated and reported direct solution processing of organic thin films, without the need for particular syntheses to obtain pentacene derivatives [15]. These organic thin film transistors (OTFTs) fabricated by direct solution processing also exhibited high carrier mobilities, up to  $0.5 \text{ cm}^2/\text{Vs}$ . Moreover, our solution-processed pentacene films had widespread crystalline domains up to several hundred micrometers and exhibited an interlayer spacing of  $d(001)$  similar to that of the bulk phase ( $d = 14.4 \text{ \AA}$ ). Although the maximum carrier mobility in our previous reports was sufficiently high to be applicable in electronic devices, such as the active-matrix of a liquid crystal display and electronic paper, little attention has been paid to controlling the quality of the films, thereby

\* Corresponding author. Tel.: +81 545 62 3191; fax: +81 545 62 3179.  
E-mail address: [natsume.yc@om.asahi-kasei.co.jp](mailto:natsume.yc@om.asahi-kasei.co.jp) (Y. Natsume).

obtaining reproducibly high carrier mobilities. To this end, it is important to clarify the crystal growth mechanism in the solution process and to extract key parameters for optimum growth conditions.

In this report, we focus on the crystal growth of pentacene from a solution, and discuss the application of directional growth of pentacene thin films. In the solution process, the surface-area-normalized amount of dropped solution and the concentration of the pentacene solution were optimized as primary parameters. The obtained TFT arrays showed uniformly high carrier mobilities, and accordingly this solution process was utilized for the preparation of transistor arrays for 5-inch-diagonal-sized liquid crystal displays (LCDs) [16].

## 2. Experimental procedure

Pentacene was purchased from Tokyo Chemical Industry Co. (refined product by sublimation) and used without further purification. Commercially available 1,2,4-trichlorobenzene (TCB) was used as the solvent after distillation. Pentacene was added to the TCB and heated at 200 °C to obtain 0.01–0.07 wt% solutions in a glove box under a nitrogen atmosphere. The solution was coated onto a substrate previously heated to 200 °C to form a pentacene thin film by evaporating the TCB. To enhance wetting of the solution on the substrate surface, we added polydimethylsiloxane (PDMS), obtained from Aldrich, to the pentacene solution to a concentration less than 50 ppm.

We used glass substrates with a 280 nm-thick silicon dioxide film as an insulator, which was prepared from polysilazane spin-coated over the 100 nm-thick Cr gate electrode and heated to 300 °C [16]. The source and drain electrodes were prepared using photolithography methods, electron beam deposition of 22/3 nm-thick Au/Ti, and cleaning by reactive-ion etching after a lift-off process. The bottom-contact configuration was adopted as the geometry of the electrode with a channel width ( $W$ ) of 500  $\mu\text{m}$  for all devices, and the channel length ( $L$ ) was varied from 5 to 50  $\mu\text{m}$ . The substrates were cleaned with oxygen plasma prior to the preparation of the pentacene thin films.

The electrical properties of the OTFTs were measured with a semiconductor parameter analyzer (Keithley 4200SC). The field effect mobility  $\mu$  was calculated in the saturation region from the slope of the linear part of the  $I_{\text{D,sat}}^{1/2}$  vs.  $V_{\text{G}}$  plot in the saturation region, using the following equation:

$$I_{\text{D,sat}} = \frac{WC_{\text{ox}}}{2L} \mu (V_{\text{G}} - V_{\text{th}})^2, \quad (1)$$

where  $C_{\text{ox}}$  is the capacitance of the insulator per unit area,  $V_{\text{G}}$  is the gate voltage and  $V_{\text{th}}$  is the threshold voltage, which can be estimated from the intercept of a line drawn through the linear part of the  $I_{\text{D,sat}}^{1/2}$  vs.  $V_{\text{G}}$  plot.

*In-situ* observations of crystal growth were carried out using an optical microscope with a heating and cooling stage (1002LS, Japan High Tech Co. Ltd.). The dispersed pentacene in TCB was enclosed in a cell of the stage unit under a nitrogen atmosphere, and the cell was mounted

on the microscope stage. The dispersion in the cell was heated initially to 200 °C to form a uniform ca. 0.07 wt% solution of pentacene. Thereafter, the solution was cooled to yield crystal growth at a cooling rate of 2 or 15 °C/min. The grown crystal domains were observed by polarized light.

Electron diffraction (ED) studies of the flat domain of the solution-processed pentacene thin films were carried out using a transmission electron microscope (TEM; HF-2000, Hitachi Ltd.). The pentacene films were covered with a water-soluble resin and were exfoliated together from the substrate. This was then floated on water to dissolve the resin, and the pentacene films left behind were picked up with a copper grid. The electron beam ( $\lambda = 0.0251 \text{ \AA}$ ) was irradiated onto the sample in a perpendicular direction to the pentacene films on the copper grid. The stripe patterns on the pentacene film, corresponding to the growth direction, were checked prior to the ED analysis to confirm the direction of crystal growth.

The in-plane structure of the solution-processed thin films was investigated by grazing incidence X-ray diffraction (GIXD) [17], to confirm the relationship between the direction of the thin film formation in the process and the crystallographic structure. The GIXD measurement was performed using an ATX-GSOR diffractometer with synchrotron radiation ( $\lambda = 1.00 \text{ \AA}$ ) at the BL46XU in the SPring-8. The incident X-ray beam is radiated onto the sample surface at a grazing angle (typically  $<0.5^\circ$ ). The X-ray detector is scanned in the in-plane direction to observe in-plane diffraction of the films. In this measurement, lattice planes perpendicular to the film surface can be detected. In addition, the in-plane two-dimensional azimuth of the pentacene crystalline film was subsequently analyzed by rotating the sample ( $\phi$  axis) with a fixed angle of the detector at  $2\theta_{\chi} = 18.0^\circ$ , wherein the strongest diffraction was obtained in the previous measurements of the  $\phi/2\theta_{\chi}$  scan. Here, the origin of the sample rotation was set as the direction of the stripe patterns on the thin film surface.

## 3. Results and discussion

### 3.1. Directional growth of the solution-processed film

*In-situ* observations of pentacene crystal growth in the TCB solvent were carried out using the optical microscope with the thermally controllable stage unit. Fig. 1 shows the crystal morphology for different cooling rates. The low cooling rate of 2 °C/min leads to plate-like crystal growth, while the high cooling rate of 15 °C/min results in dendritic pentacene crystals. The cooling rate is related to supersaturation of the solution, in other words, a fast cooling rate provides high supersaturation and vice versa. Furthermore, the plate-like crystal growth should evolve into flat domains of the solution-processed pentacene films, which always exhibit the stripe pattern. Here, we call these structures macro-stripe patterns. We have assumed that the macro-stripe patterns are related to the growth direction of the pentacene crystalline films.

The solution-processed films, in which the flat domains showed different directions of the macro-stripe patterns, were observed by a polarizing microscope. Some domains could be distinguished from the polarized image, with each domain having a different direction of the macro-stripe pattern. This implies that the macro-stripe patterns correspond to the crystal azimuth of the respective flat domains. We considered that the directionality of crystal growth is related to the evaporation direction. Drop casting was therefore carried out on a tilted substrate with a tilt angle of up to  $0.5^\circ$ . With a tilted substrate, the growth of the thin film proceeds approximately in one direction, since the thickness of the solution has a one-dimensional gradient. As shown in Fig. 2, the obtained films showed a directionality of the macro-stripe patterns, with the direction of the macro-stripes mostly oriented towards the direction of the thin film growth.

### 3.2. Growth azimuth of the pentacene crystalline film

To investigate the relationship between the growth direction and crystal azimuth in the pentacene solution-processed films, we employed TEM measurements, and the TEM images obtained are shown in Fig. 3. Another stripe pattern of ca.  $0.2 \mu\text{m}$  width was observed in the TEM images; we named this the micro-stripe pattern. Although the direction of the micro-stripe patterns did not necessarily correspond to that of the macro-stripe patterns, we focused on the regions where the direction of both stripe patterns corresponded to each other in the azimuth. The inset image in Fig. 3 represents the ED pattern observed simultaneously in the TEM measurement. In addition, the obtained ED pattern was compared with ED simulation [18] using the solution-grown crystal structure reported by Campbell et al. with the lattice parameters of  $a = 7.90 \text{ \AA}$ ,  $b = 6.06 \text{ \AA}$ ,  $c = 16.01 \text{ \AA}$ ,  $\alpha = 101.9^\circ$ ,  $\beta = 112.6^\circ$ ,

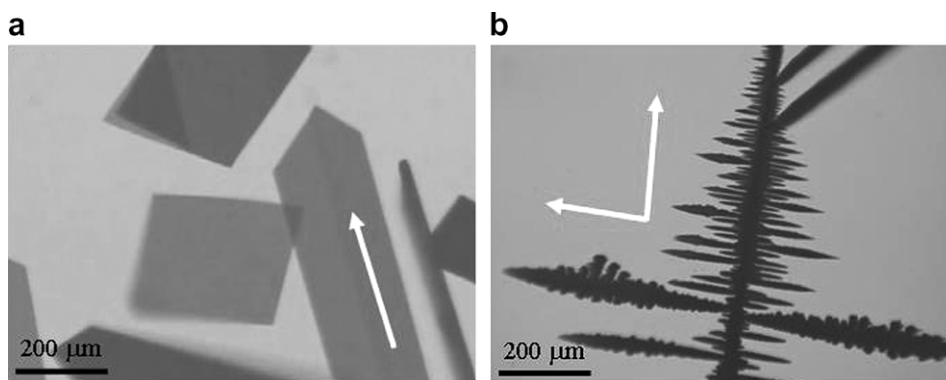


**Fig. 1.** Crystal morphologies of pentacene obtained by solution growth using a cooling rate of (a)  $2^\circ\text{C}/\text{min}$  and (b)  $15^\circ\text{C}/\text{min}$ . The arrows in the images represent the growth directions.

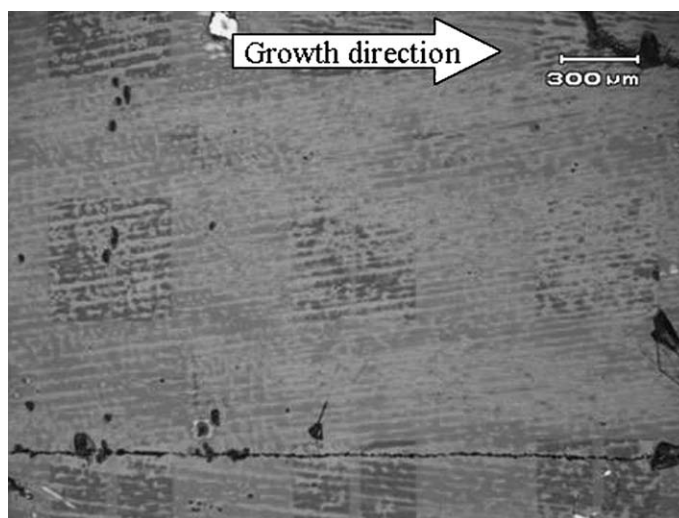


**Fig. 2.** Optical microscope image for the solution-processed pentacene film obtained with directional growth. The arrow represents the evaporation direction. The macro-stripe patterns were structured along the evaporation direction. The rectangles in the figure represent source and drain electrodes.

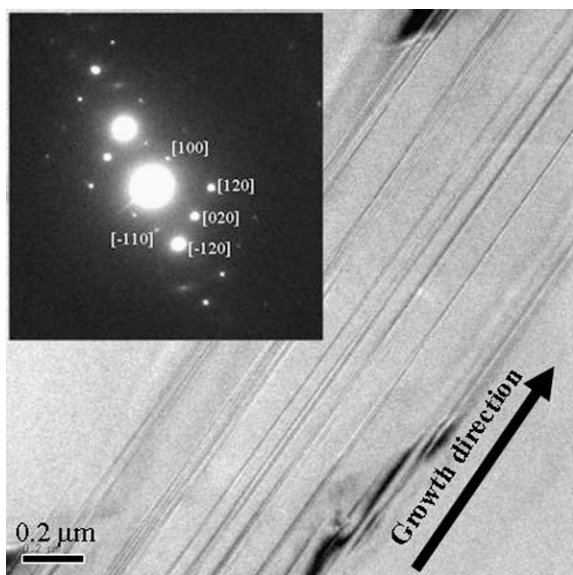


**Fig. 3.** TEM image of the solution-processed pentacene film. The inset image is the electron diffraction pattern observed simultaneously with TEM. The direction of the micro-stripe pattern is in agreement with the growth direction of the solution-processed pentacene film in this case (the arrow in the figure).

and  $\gamma = 85.8^\circ$  [19], in order to assign the respective diffractions. Recently, Siegrist et al. reported that the high-temperature pentacene polymorph is stable above  $190^\circ\text{C}$ ,

and that the unit cell parameters of this polymorph were similar to those reported by Campbell [20]. Furthermore, Della Valle et al. suggested that the structure reported by Campbell corresponds to the deepest minimum structure, using energy-minimization calculations with the quasi-Monte-Carlo sampling method [21]. These reports imply that pentacene crystal grown above  $190^\circ\text{C}$  tends to have the structure reported by Campbell. In fact, the solution-processed pentacene thin film in our earlier work was found to have a structure close to that determined by Campbell [22]. Therefore, in the following, the crystal structure of pentacene will be discussed on the basis of the Campbell's structure. In the ED simulation, Campbell's structure was redefined as  $a = 6.06 \text{ \AA}$ ,  $b = 7.90 \text{ \AA}$ ,  $c = 14.88 \text{ \AA}$ ,  $\alpha = 83.26^\circ$ ,  $\beta = 100.54^\circ$ , and  $\gamma = 85.80^\circ$ , since the original structure is not a reduced cell, namely, the  $c$  axis of the original cell is much inclined. The difference in the definition of a unit cell is displayed in Fig. 4. The ED measurement in Fig. 3 revealed that the direction of the stripe patterns on the film surface corresponded to (100) direction in the reduced Campbell's structure, that is, the (010) direction of the original one.

As further verification of the growth azimuth of the pentacene films, GIXD measurements were also carried out using synchrotron radiation at the SPring-8 ( $\lambda = 1.00 \text{ \AA}$ ). The GIXD pattern of the  $\phi/2\theta_\chi$  scan for the solution-processed pentacene film with directional growth is shown in Fig. 5a. A very strong peak is observed at  $2\theta_\chi = 18.0^\circ$ , which corresponds to the  $d$  spacing of  $0.32 \text{ nm}$ . This diffraction peak is assigned to the (1–2–1)

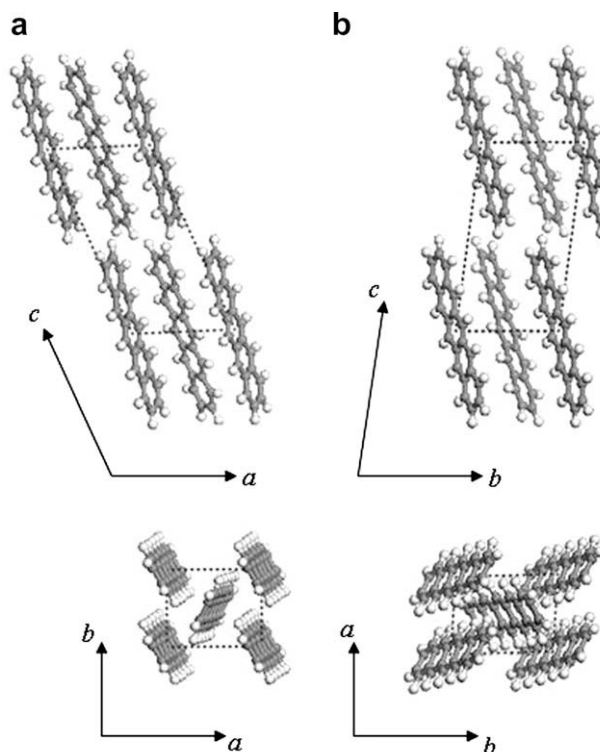


**Fig. 4.** Crystal structure of pentacene (a) determined by Campbell et al. and (b) redefined structure in this study.

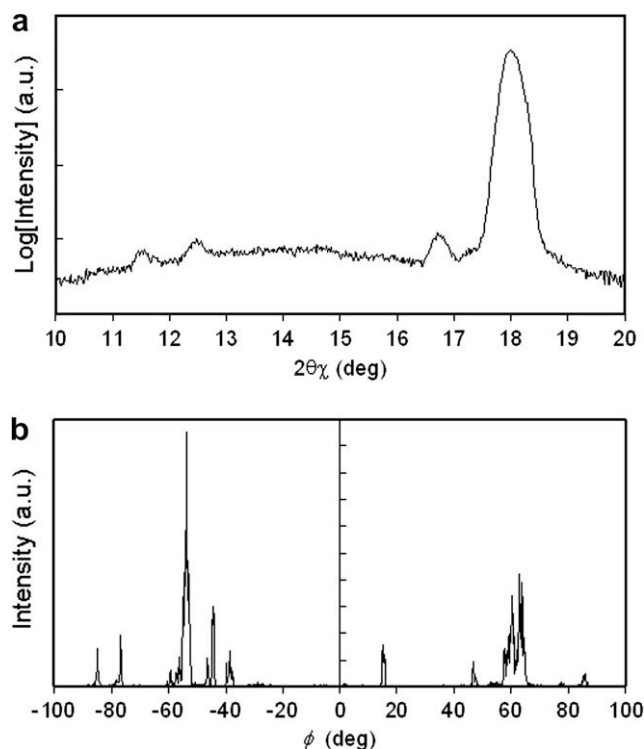


**Fig. 5.** (a) GIXD pattern ( $\lambda = 1.00 \text{ \AA}$ ) of the solution-processed pentacene thin film with directional growth. (b) In-plane distribution of diffraction at  $2\theta_\chi = 18.0^\circ$ , fixing the position of the detector during sample rotation of the  $\phi$  axis.

lattice plane of the reduced Campbell's structure (calculated to be  $2\theta_\chi = 18.0^\circ$ ). The  $(1-2-1)$  plane is confirmed to be almost perpendicular to the  $(001)$  plane, since the angle between these planes is calculated to be  $90.4^\circ$  from crystal structure data of the reduced Campbell's structure. In order to avoid confusion, the  $(120)$  and  $(1-20)$  planes, which were also confirmed in the ED measurement, should be mentioned here. The calculated angle between  $(120)$  and  $(001)$  is  $90.3^\circ$ , almost perpendicular; however, the corresponding  $d$  spacing is  $0.34 \text{ nm}$  which should be observed at  $2\theta_\chi = 16.8^\circ$ . The  $(120)$  diffraction was actually confirmed at  $2\theta_\chi = 16.82^\circ$  with a low intensity of  $10^3 \text{ cps}$  in this measurement. On the other hand, simulations indicated that the  $(1-20)$  plane was at  $2\theta_\chi = 18.42^\circ$  ( $d$  spacing =  $0.31 \text{ nm}$ ) with low intensity, and the dihedral angle toward the  $(001)$  plane was estimated to be  $78.0^\circ$ . The  $(1-20)$  plane cannot be detected in the GIXD measurement. Thus, it is reasonable to assign the peak at  $18.0^\circ$  to the  $(1-2-1)$  lattice plane. As shown in Fig. 5b, the in-plane distribution of the strong peak at  $2\theta_\chi = 18.0^\circ$  was subsequently investigated by rotating the sample ( $\phi$  axis) with the fixed angle of detector at  $2\theta_\chi = 18.0^\circ$ . In this measurement, we set the origin of the rotation angle approximately to the direction of the macro-stripe patterns, which was visible to the eye. It was revealed that the strongest peak was obtained in the narrow angle region from  $-56^\circ$  to  $-52^\circ$  with the peak top at  $-53.6^\circ$ , while several peaks were detected in the other azimuth. In addition, the angle between  $(100)$  and  $(1-2-1)$  was calculated to

be  $54.9^\circ$  from the crystal structure data. Since the difference in the azimuthal angle is only  $1.3^\circ$ , we conclude that the pentacene crystal growth from a solution proceeds along the minor axis (ca.  $6 \text{ \AA}$ ) in the  $a$ - $b$  plane of the crystal structure of pentacene.

Using density functional calculations, Northrup et al. predicted an equilibrium crystal shape in terms of the surface energy of the crystal structure [23]. They employed the original Campbell's structure without any structural redefinition, and calculated the surface energies for the  $(001)$ ,  $(100)$ ,  $(010)$ ,  $(110)$ , and  $(1-10)$  surfaces. In addition, the theoretical form of the crystal can be derived from the relative growth rates of various low-index faces, since the growth rate of the crystal face is assumed to be proportional to its surface-formation energy [24,25]. The corresponding formation energies were also calculated to be  $0.15$ ,  $0.45$ ,  $0.75$ ,  $0.71$ , and  $0.72 \text{ eV/cell}$  respectively in Ref. [23], that is, the  $(010)$  surface has the largest surface-formation energy. Therefore, pentacene molecules in a solution are likely to cohere to the  $(010)$  surface, and this facet will disappear from the equilibrium crystal shape [23]. It is worth noting again that the  $(010)$  surface mentioned here corresponds to the  $(100)$  surface of the reduced Campbell's structure in the present study. Hence, the crystal growth was theoretically predicted to proceed preferably along the minor axis in the  $a$ - $b$  plane of the pentacene crystal under equilibrium condition. This prediction implies that the flat domain growth in this process takes place under nearly equilibrium condition.

### 3.3. Fabrication of transistor array

The solution process with directional growth was applied to a glass substrate with an area of  $150 \times 150 \text{ mm}^2$ , wherein 10,000 transistors ( $W = 500 \mu\text{m}$ ) were prepared in the center region of  $100 \times 100 \text{ mm}^2$  area (cf. Fig. 7). The glass substrate was placed on a hot plate with a slight tilt and was sufficiently heated at  $200 \text{ }^\circ\text{C}$  before drop casting of the pentacene solution. The direction of thin film growth was parallel to that of the channel.

First, we emphasize that wetting of the solution on the substrate is important to stably provide two-dimensional growth of thin films. Since the drop casting itself is essentially a non-equilibrium process, it was difficult to control and restrain a phenomenon such as *stick and slip movement* at the edge of dropped solution without additives. It was found that the addition of PDMS of less than 50 ppm to the pentacene solution provides preferable wetting of the solution on the substrate, and that the solution on the tilted substrate can continuously evaporate from the upper side to the lower side of the dropped solution, even in the case of large-area substrates. Moreover, the evaporation rate becomes moderate after starting the two-dimensional growth. The enhancement of wetting can be attributed to appropriate lowering of the surface tension of the solution and the interfacial tension between the solution and the substrate due to the presence of an appropriate amount of PDMS. Although the exact mechanism for the enhancement in wetting has not been fully investigated at the present stage, this treatment was clearly found to make the drop casting controllable with simple experimental parameters as described below.

We focused on the surface-area-normalized amount of dropped solution and the concentration of the solution as process parameters to control the quality of the thin films. It is possible to apply the same condition to substrates with different sizes, by defining the surface-area-normalized amount of the dropped solution. These two parameters were optimized so that the best transistor characteristics were obtained. The optimum conditions for the amount

and concentration of the dropped solution were found to be  $0.058 \text{ ml/cm}^2$  and  $0.05 \text{ wt\%}$ , respectively. In Fig. 6a, distributions of the transistor characteristics, mobility and threshold voltage in the TFT arrays fabricated using the best condition (condition 2) are displayed, and compared with conditions of  $0.044 \text{ ml/cm}^2$  and  $0.07 \text{ wt\%}$  (condition 1). The characteristics of transistors with  $L = 10 \mu\text{m}$  were evaluated at a drain voltage of  $-10 \text{ V}$ , wherein 40 TFTs were randomly sampled from the TFT array of  $100 \times 100 \text{ mm}^2$  area. For condition 2, the characteristics converged well within a small distribution ranging from  $0.2$  to  $1.1 \text{ cm}^2/\text{Vs}$  for the carrier mobility ( $0.62 \text{ cm}^2/\text{Vs}$  on average with standard deviation of  $0.19 \text{ cm}^2/\text{Vs}$ ), and from  $-2.6$  to  $-0.9 \text{ V}$  for the threshold voltage ( $-1.8 \text{ V}$  on average with standard deviation of  $0.2 \text{ V}$ ), respectively. Moreover, the on/off ratio and the subthreshold slope showed good values of more than  $10^4$  and ranging from  $0.5$  to  $1.1 \text{ V/decade}$ , respectively. The transfer characteristics of OTFTs with the highest carrier mobility are shown in Fig. 6b. The maximum carrier mobility of  $1.1 \text{ cm}^2/\text{Vs}$  obtained may be one of the highest values ever reported measured at a low drain voltage in solution-processed OTFTs. In contrast, condition 1 resulted in low carrier mobility ranging from  $0.01$  to  $0.52 \text{ cm}^2/\text{Vs}$  with an average mobility of  $0.13 \text{ cm}^2/\text{Vs}$ .

The area with lower carrier mobility in the array is comprised of dendritic domains. The formation of dendritic domains occurs at the initial stage of film growth owing to high supersaturation accompanied by fast evaporation. In addition, the smaller amount of dropped solution results in widespread dendritic domains. Solution-processed films on  $150 \times 150 \text{ mm}^2$  glass substrates obtained using both conditions are shown in Fig. 7. In the pictures, a part of the thin film is clouded due to the presence of dendritic domains or large roughness of the thick domains. In the case of condition 2, most of the area in the TFT arrays was covered with flat domains, and at the same time, the area of the dendritic domain was restricted to the edge of the glass substrate (Fig. 7b), while the dendritic and thick domains covered a considerable area of the substrate when condition 1 was used (Fig. 7a). In the course of the evaporation,

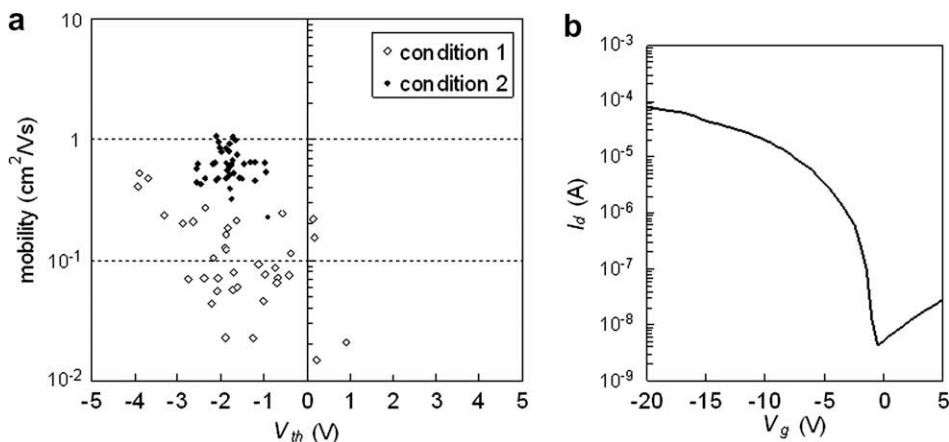


**Fig. 6.** (a) Distributions of carrier mobility as a function of threshold voltage for conditions 1 and 2. In both cases, 40 TFTs were randomly sampled from each part of the TFT array. (b) Transfer characteristic of OTFT with the best carrier mobility from the TFT array fabricated using condition 2. The geometry of TFTs was  $W/L = 500/10 \mu\text{m}$ , and the applied drain voltage was  $-10 \text{ V}$  for all measurements.



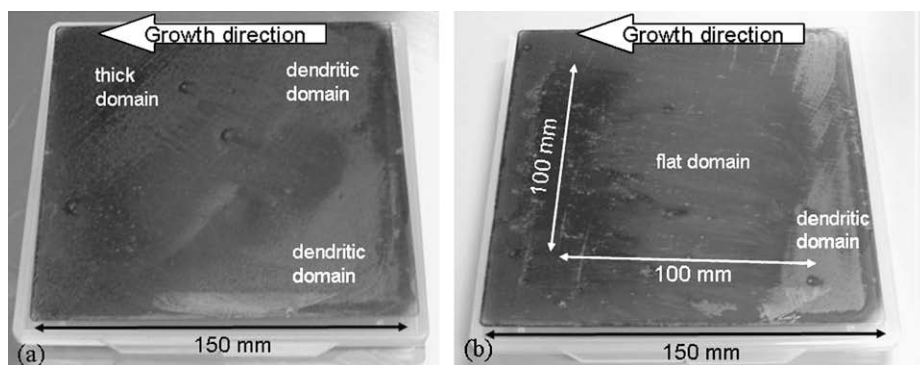


**Fig. 7.** Solution-processed pentacene thin film on a glass substrate of area  $150 \times 150 \text{ mm}^2$ , fabricated using (a) condition 1 and (b) condition 2. Both substrates were placed on a cover case for a 6-inch-square photomask. The outer area of the TFT array in the glass substrates was partially covered with gold in the electron beam deposition.

the increasing vapor pressure should reduce the evaporation rate to change the growth mode from dendritic growth to two-dimensional growth, owing to lowering of the supersaturation. A similar phenomenon was confirmed in the *in-situ* observations of pentacene crystal growth.

The directionally grown films have color gradation from blue to violet, as seen in Fig. 7. This color gradation is attributed to the gradient of the film thickness. The distribution of the film thickness obtained using condition 2 is displayed in Fig. 8b. The thickness was measured from cross-sectional profiling of the films, and 45 points (five points per division and nine divisions in an array) were evenly sampled from the respective area of the TFT array in the substrate. The TFT array was classified into nine divisions by separating three sections for each side, as *a–c* for the *x*-axis and 1–3 for the *y*-axis, respectively. The film growth proceeded in the direction from *a* to *c* along the *x*-axis. The thickness increased from 100 to 200 nm, accompanied by film growth, and the averaged thickness was approximately 150 nm. The distribution of the film thickness using condition 1 is also shown in Fig. 8a. The thickness gradually increased from 150 to 250 nm, accompanied by film formation, and the average thickness was ca. 200 nm. The concentration of the solution is roughly correlated with the thickness of the pentacene films. The dense solution yielded thick films particularly at the end of evaporation, resulting in large roughness of the films. The rough surface could be an impediment in the post-processing of pentacene film formation, for example the seal-

ing process for the liquid crystal layer. Thus, the intermediate concentration of 0.05 wt% was found to be desirable for application to TFT arrays [16].

The optimized process parameters thus successfully provided high quality solution-processed pentacene films, yielding high carrier mobilities. The directional growth also contributes to the high uniformity of TFT characteristics, even on large-area substrates, since the pentacene crystal has been reported to exhibit anisotropic carrier mobility both theoretically and experimentally [26,27]. This solution process was applied for the preparation of transistor arrays for 5-inch-diagonal-sized LCDs, which were also driven successfully [16].

#### 4. Conclusions

We have successfully fabricated directional-solution-grown pentacene TFT arrays with high carrier mobilities, up to  $1.1 \text{ cm}^2/\text{Vs}$ , at a low drain voltage of  $-10 \text{ V}$ . In addition, the distribution of TFT performance in an array showed high uniformity for both carrier mobility and threshold voltage, which were respectively  $0.62 \text{ cm}^2/\text{Vs}$  on average with standard deviation of  $0.19 \text{ cm}^2/\text{Vs}$  and  $-1.8 \text{ V}$  on average with standard deviation of  $0.2 \text{ V}$ .

We found that the crystal growth direction in the pentacene film was accompanied by the thin film growth direction, and that crystal growth proceeded preferably along the minor axis of the *a–b* plane in the crystal structure of pentacene. We applied this phenomenon to our solution

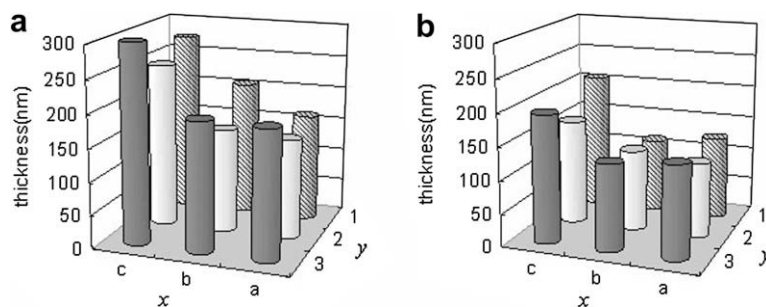


**Fig. 8.** Distribution of thickness for the solution-processed pentacene film prepared using (a) condition 1 and (b) condition 2.

process by dropping the solution onto tilted substrates, thereby obtaining high directionality of film growth.

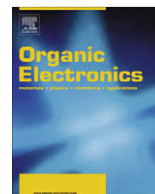
This solution process with directional growth was applied to a large glass substrate with an area of  $150 \times 150 \text{ mm}^2$ . To enhance the wetting of the pentacene solution on the substrate, we added a small amount of PDMS to the solution. With this treatment, good wetting on the substrate was realized, thereby making the drop casting process controllable. We optimized the amount of the dropped solution and the concentration of the solution as prime parameters in the process to obtain the preferred films. This method was applicable to TFT arrays for LCDs. In summary, we have demonstrated the possibility of application of the direct solution process to electronic devices. We believe that OTFT using small molecules is the most promising candidate for flexible displays manufactured by printing technologies.

### Acknowledgements

The authors would like to acknowledge Dr. Y. Yoshida (AIST) and Dr. S. Kuwajima (Kyoto University) for GIXD measurements, carried out with the approval of JASRI (Proposal No. 2007B1826). We also thank Mr. T. Nakao and Mr. T. Yamaguchi (Asahi Kasei) for TEM and ED measurements. This work was partially supported by the New Energy and Industrial Technology Development Organization (NEDO) as an Advanced Organic Device Project. We are grateful to Mr. M. Kawasaki (Hitachi Ltd.) for cooperation on fabrication and characterization of TFT arrays for LCDs in the project.

### References

- [1] B. Crone, A. Dodabalapur, Y.-Y. Lin, R.W. Filas, Z. Bao, A. LaDuca, R. Sarpeshkar, H.E. Katz, W. Lin, *Nature* 403 (2000) 521.
- [2] P.F. Baude, D.A. Ender, M.A. Haase, T.W. Kelly, D.V. Muyres, S.D. Theiss, *Appl. Phys. Lett.* 82 (2003) 3964.
- [3] B. Crone, A. Dodabalapur, A. Gelperin, L. Torsi, H.E. Katz, A.J. Lovinger, Z. Bao, *Appl. Phys. Lett.* 78 (2001) 2229.
- [4] C.D. Dimitrakopoulos, P.R.L. Malenfant, *Adv. Matter* 14 (2002) 99.
- [5] Y.-Y. Lin, D.J. Gundlach, S.F. Nelson, T.N. Jackson, *IEEE Electron Devic. Lett.* 18 (2002) 606.
- [6] M.M. Payne, S.A. Odom, S.R. Parkin, J.E. Anthony, *Org. Lett.* 6 (2004) 3325.
- [7] H. Meng, J. Zheng, A.J. Lovinger, B.-C. Wang, P. Gregory, V. Patten, Z. Bao, *Chem. Mater.* 5 (2003) 1778.
- [8] M. Mas-Torrent, P. Hadley, S. Bromley, X. Ribas, J. Tarres, M. Mas, E. Molins, J. Veciana, C. Rovira, *J. Am. Chem. Soc.* 126 (2004) 8546.
- [9] K. Takimiya, H. Ebata, K. Sakamoto, T. Izawa, T. Otsubo, Y. Kunugi, *J. Am. Chem. Soc.* 128 (2006) 12604.
- [10] F. Valiyev, W.-S. Hu, H.-Y. Chen, M.-Y. Kuo, I. Chao, Y.-T. Tao, *Chem. Mater.* 19 (2007) 3018.
- [11] H. Klauk, D.J. Gundlach, J.A. Nichols, C.D. Sheraw, M. Bonse, T.N. Jackson, *Solid State Technol.* 43 (2000) 63.
- [12] P.T. Herwig, K. Mullen, *Adv. Mater.* 11 (1999) 480.
- [13] A. Afzali, C.D. Dimitrakopoulos, T.L. Breen, *J. Am. Chem. Soc.* 124 (2004) 8812.
- [14] S.K. Park, T.N. Jackson, J.E. Anthony, D.A. Mourey, *Appl. Phys. Lett.* 91 (2007) 063514.
- [15] T. Minakata, Y. Natsume, *Synth. Met.* 153 (2005) 1.
- [16] M. Kawasaki, S. Imazeki, S. Hirota, T. Arai, T. Shiba, M. Ando, Y. Natsume, T. Minakata, S. Uemura, T. Kamata, *SID Int. Symp. Dig. Tech. Papers* 38 (2007) 1761.
- [17] S. Matsuno, M. Kuba, T. Nayuki, S. Soga, P.W.T. Yuen, *Rigaku J.* 17 (2000) 36.
- [18] DIFFRACTION code implemented in Cerius<sup>2</sup> ver. 3.8 (accelrys) was used for the simulation of electron diffraction patterns.
- [19] R.B. Campbell, J.M. Robertson, J. Trotter, *Acta Crystallogr.* 15 (1962) 289.
- [20] T. Siegrist, C. Besnard, S. Haas, M. Schiltz, P. Pattison, D. Chernyshov, B. Batlogg, C. Kloc, *Adv. Mater.* 19 (2007) 2079.
- [21] R.G. Della Valle, E. Venuti, A. Brillante, A. Girlando, *J. Chem. Phys.* 118 (2003) 807.
- [22] Y. Natsume, et al. *Synth. Met.* (2008), doi:10.1016/j.synthmet.2008.09.007.
- [23] J.E. Northrup, M.L. Tiago, S.G. Louie, *Phys. Rev. B* 66 (2002) 121404.
- [24] R. Docherty, G. Clydesdale, K.J. Roberts, P. Bennema, *J. Phys. D* 24 (1991) 89.
- [25] Z. Berkovitch-Yellin, *J. Am. Chem. Soc.* 107 (1985) 8239.
- [26] A. Troisi, G. Orlandi, *J. Phys. Chem. B* 109 (2005) 1849.
- [27] J.Y. Lee, S. Roth, Y.W. Park, *Appl. Phys. Lett.* 88 (2006) 252106.



## Negative capacitance and its photo-inhibition in organic bulk heterojunction devices

C. Lungenschmied<sup>a,1</sup>, E. Ehrenfreund<sup>a,b,\*</sup>, N.S. Sariciftci<sup>a</sup>

<sup>a</sup> Linz Institute for Organic Solar Cells (LIOS), Johannes Kepler University, 4040 Linz, Austria

<sup>b</sup> Physics Department, Technion, Israel Institute of Technology, Haifa 32000, Israel

### ARTICLE INFO

#### Article history:

Received 21 April 2008

Received in revised form 8 September 2008

Accepted 9 October 2008

Available online 1 November 2008

#### PACS:

73.50.Gr

73.50.Pz

73.61.Ph

73.61.Wp

#### Keywords:

Negative capacitance

P3HT:PCBM heterojunctions

Solar cells

Photo-capacitance

### ABSTRACT

We report the dynamic admittance, both in the dark and under illumination, of heterojunctions made of poly(3-hexyl thiophene)/1-(3-methoxycarbonyl)propyl-1-phenyl[6,6]C<sub>61</sub> (P3HT:PCBM) blends, which are used in efficient organic solar cells. In the dark there appears a huge low frequency negative capacitance which we associate with slow electron hole bimolecular recombination at the heterojunction interfaces. Surprisingly, under photoexcitation the negative capacitance gradually disappears with increasing light intensity. We attribute this positive photoinduced capacitance to the combined effect of (1) long lived photogenerated charges at the P3HT:PCBM interfaces that increase electron-hole bimolecular recombination rate, which in turn renders the capacitance less negative and (2) trapped photogenerated charges that increase the capacitance upon re-emission.

© 2008 Elsevier B.V. All rights reserved.

### 1. Introduction

We report a huge dark negative capacitance (NC) and its disappearance under illumination in organic bulk heterojunction devices made of poly(3-hexylthiophene)(P3HT) and 1-(3-methoxy carbonyl)propyl-1-phenyl[6,6]C<sub>61</sub> (PCBM). Photovoltaic cells based on P3HT:PCBM blends are among the most efficient in this class of devices [1–4]. The NC phenomenon in various devices, such as inorganic Schottky diodes, inorganic homojunction photo-detectors, organic light emitting devices and more, has been reported previously, while its origin is still under de-

bate [5–9]. In many cases, the frequency,  $\omega$ , dependence of the NC spectrum,  $C(\omega)$ , has been shown to be directly related to current relaxation [5,6] or electron–hole (e–h) recombination in bipolar organic devices [7,9]. The primary cause for the NC is probably different in different systems. In the present case of organic heterojunction devices, the NC is observed under bipolar charge injection conditions. At low enough frequencies the NC saturates reaching (in absolute value) up to  $\approx 500$  times the geometrical capacitance at low frequencies. The bias voltage and frequency dependencies of NC enable us to determine the e–h bimolecular recombination (BMR), which is responsible for the spectral behavior of the NC and the corresponding dynamic sample conductance.

Upon photoexcitation the NC diminishes in magnitude and the capacitance reaches even positive values under sufficiently intense illumination. We attribute this positive photoinduced capacitance to the combined effect of (1)

\* Corresponding author. Address: Physics Department, Technion, Israel Institute of Technology, Haifa 32000, Israel. Tel.: +972 4829 3610; fax: +972 4823 5107.

E-mail address: [eitane@tx.technion.ac.il](mailto:eitane@tx.technion.ac.il) (E. Ehrenfreund).

<sup>1</sup> Present address: Konarka Austria GmbH, Altenbergerstrasse 69, 4040 Linz, Austria.

long lived photogenerated charges at the P3HT:PCBM interfaces that increase e–h BMR rate, which in turn renders the capacitance less negative and (2) trapped photogenerated charges that increase the capacitance upon re-emission.

## 2. Experimental

Thoroughly cleaned indium tin oxide (ITO) covered glass slides are used as substrate. An  $L \approx 800$  nm thick photo-active layer made from a regio-regular (rr)-P3HT:PCBM solution (1:1, 2% in chloroform) was cast by the doctor blade technique on the substrate. The Al top contacts were applied by vacuum deposition, followed by an annealing step (5 min at 120 °C). The diodes (active area  $A \approx 12$  mm<sup>2</sup>) showed a rectification ratio of  $\approx 10^4$  at  $\pm 1$  V (Fig. 4, inset). Forward (positive) bias conditions are obtained when the ITO is wired (+) and Al wired (-). An HP 4284A LCR-meter operated in the frequency range  $f = \omega/2\pi = 20 - 10^6$  Hz (20 mV ac voltage) was used to measure the complex admittance  $Y(\omega)$ , from which the capacitance  $C(\omega) = \text{Im}Y(\omega)/\omega$  and the conductance  $G(\omega) = \text{Re}Y(\omega)$  were extracted. We carefully analyzed the low frequency regime in order to make sure that the extracted  $C(\omega)$  and  $G(\omega)$  are not influenced by any parasitic circuit reactance [10]. The 532 nm line of a Nd:YVO<sub>4</sub> laser was used as light source for the photoinduced admittance measurements. All measurements reported here were done at room temperature.

## 3. Results

In Fig. 1 we display the measured frequency dependent capacitance of the ITO-P3HT:PCBM-Al device in the dark at various applied forward bias voltages. For  $V_{\text{bias}} > 0.3$  V, we observe a negative contribution to the capacitance and relate it to current relaxation [5] due to e–h recombination in the bipolar injection regime [6,9]. This negative contribution becomes more dominant as the voltage increases above 0.35 V, where  $C(\omega)$  becomes more negative as the

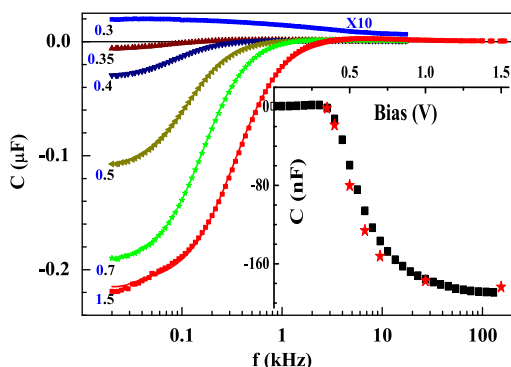


**Fig. 1.** Frequency dependent capacitance measured on an ITO-P3HT:PCBM-Al device shown for various forward bias from 0.3 to 1.5 V (as marked). Symbols: data points, solid lines: fits to the data. The 0.3 V data is multiplied by 10 for clarity. Inset:  $C(50$  Hz) vs bias voltage. Black squares – data points and red stars – fit (see text).

bias increases. The effect of increasing bias on NC is shown in the inset of Fig. 1 where the measured capacitance at 50 Hz,  $C(50$  Hz), is plotted as a function of  $V_{\text{bias}}$ . At 1.5 V,  $C(50$  Hz)  $\approx -200$  nF, which is (in absolute value)  $\approx 500$  times the geometrical capacitance,  $C_g = \epsilon A/L \approx 0.4$  nF ( $\epsilon \approx 3\epsilon_0$  is the sample static dielectric constant and  $\epsilon_0$  is the vacuum permittivity).

The decrease in capacitance as  $f$  decreases below  $\approx 5$ –10 kHz, is accompanied by a corresponding increase in the conductance, as shown in the inset to Fig. 2. The zero value  $G(f \approx 0)$  corresponds to the static conductance  $dI/dV$ . Denoting  $\Delta G(f) \equiv G(0) - G(f)$ , the quantity  $\Delta G(f)/f$  (up to  $f \approx 10$  kHz) is proportional [11] to the corresponding changes in  $\epsilon''(f)$ , the imaginary part of the dielectric function associated with the process. In Fig. 2,  $\Delta G(f)/f$  is displayed for various bias voltages, showing the bell shaped curves characteristic to  $\epsilon''$ . Note the shift of the curves' maximum towards higher frequencies for higher bias; this is consistent with the observed faster recombination process at higher voltages (see discussion below).

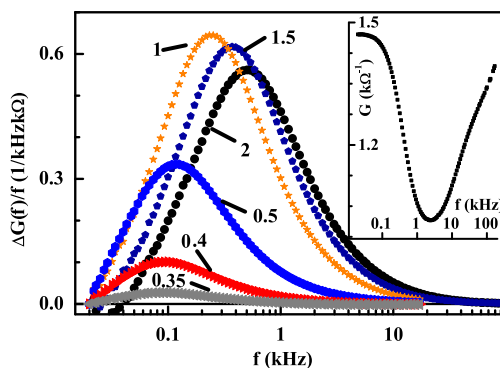


**Fig. 2.** The frequency dependence of  $\Delta G(f)/f \equiv [G(20$  Hz) –  $G(f)]/f$  for the same device as in Fig. 1, showing the typical bell shaped loss function behavior. Symbols: data points at various bias voltages (in V) as marked. Inset:  $G(f)$  vs  $f$  for  $V_{\text{bias}} = 1.5$  V.

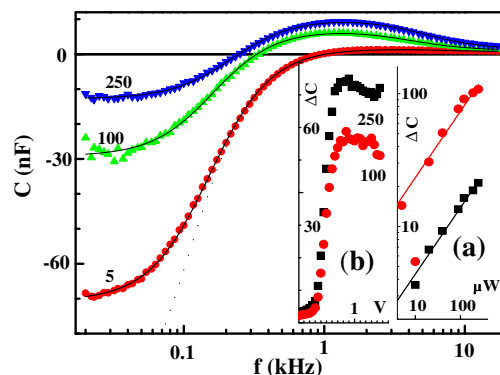


**Fig. 3.** The capacitance of the ITO-P3HT:PCBM-Al device vs frequency measured under laser illumination (532 nm) at  $I_L = 5, 100, 250$   $\mu$ W, as marked ( $V_{\text{bias}} \approx 0.6$  V). For clarity, only the frequency range 0.02–15 kHz is shown. Inset (a): the photoinduced changes  $\Delta C \equiv C_{\text{light}} - C_{\text{dark}}$  (in nF) at  $f = 50$  Hz vs  $I_L$  (on a log–log plot) for  $V_{\text{bias}} = 0.35$  (black square) and 0.5 V (red dots). The solid lines are fits to  $\Delta C \propto I_L^{1/2}$  law. Inset (b):  $\Delta C$  (in nF) at  $f = 50$  Hz vs  $V_{\text{bias}}$  for  $I_L = 100$   $\mu$ W (red dots) and 250  $\mu$ W (black square).

We now turn to the effect of photoexcitation on NC. In Fig. 3 the measured capacitances of a ITO-P3HT:PCBM-Al device under 532 nm continuous irradiation ( $C_{\text{light}}$ ) are shown in the bipolar charge injection regime for various light intensities,  $I_L$ . A significant increase in the capacitance due to illumination is observed at low frequencies. Above 15 kHz up to 1 MHz the photoinduced changes in the capacitance are very small (not shown in Fig. 3). The photoinduced changes in the capacitance,  $\Delta C \equiv C_{\text{light}} - C_{\text{dark}}$ , are sensitive to both the light intensity and applied bias. Inset (a) to Fig. 3 shows the dependence of  $\Delta C(50 \text{ Hz})$  on  $I_L$  at fixed  $V_{\text{bias}}$ . The observed  $\Delta C \propto I_L^{1/2}$  for both  $V_{\text{bias}} = 0.35$  and  $0.5 \text{ V}$  is indicative of a BMR mechanism for the photoinduced carriers. Inset (b) to Fig. 3 shows the dependence of  $\Delta C(50 \text{ Hz})$  on  $V_{\text{bias}}$  at fixed  $I_L$ . Below  $V_{\text{bias}} \approx 0.35 \text{ V}$   $\Delta C(50 \text{ Hz}) \leq 3\text{--}4 \text{ nF}$ , then a sharp rise at  $V_{\text{bias}} \approx 0.35 \text{ V}$  followed by a plateau (where  $\Delta C(50 \text{ Hz}) \geq 100 \text{ nF}$  for  $I_L \geq 100 \mu\text{W}/\text{cm}^2$ ) above  $\approx 0.6 \text{ V}$  are evident.

#### 4. Discussion

The negative contribution to the dark  $C(\omega)$  is observed here only at  $V_{\text{bias}} > 0.3 \text{ V}$ , under the conditions of bipolar injection. NC is more pronounced at higher forward bias voltages, where the conductance of the device is higher. The maximum frequency at which NC is observed is restricted approximately to  $f < 2 \text{ kHz}$  at  $V_{\text{bias}} = 1.5 \text{ V}$  where NC is most pronounced. Such low frequencies represent time scales which are much longer than the single carrier transit time in this device ( $\approx 5 \mu\text{s}$  at  $1 \text{ V}$ ). It is therefore plausible to analyze the NC as a separate process dominating the other transport processes in this frequency range. Previously, such an approach was used by Penin [5] in order to account for NC in semiconductor Schottky diodes via impact ionization of impurity atoms and in GaAs homojunctions via interface states mediated recombination [6]. In our previous publication [9] we have shown that the NC spectrum measured in organic semiconductor devices could be accurately described when treating NC as a separate mechanism in addition to the effect of space charge. In all these approaches the recombination plays an important role. Under bipolar injection conditions (with dc conductance  $G_0 = dl/dV$ ) and for a finite recombination time,  $\tau_r$ , a negative contribution (of the order of  $\tau_r G_0$ ) to the capacitance should be expected at frequencies  $\omega < \tau_r^{-1}$ ; this is similar to the negative contribution to the capacitance which occurs simultaneously with an increase in conductance at frequencies below the reciprocal transit time in a unipolar SCLC device. The effect of recombination on the capacitance and conductance can be summarized as follows [5,6,9]:

$$C_r(\omega) = -\frac{G_0 \tau_r}{1 + \omega^2 \tau_r^2}; \quad G_r(\omega) = G_0 - \frac{G_0 \omega^2 \tau_r^2}{1 + \omega^2 \tau_r^2}, \quad (1)$$

where  $G_0$  is the conductance associated with the process. As can be seen from Eq. (1), the maximum of the conductance (and most negative capacitance) occurs for  $\omega \ll \tau_r^{-1}$  near  $\omega \approx 0$ ; at higher frequencies the conductance decreases due to the diminishing carrier density ( $\propto (\omega \tau_r)^{-2}$  for  $\omega \gg \tau_r^{-1}$ ) and the capacitance becomes less negative.

It is important to note that the shorter is the recombination time, the wider is the frequency range in which NC can be observed experimentally. We can now use Eq. (1) in order to fit the data in the bipolar injection regime ( $V_{\text{bias}} \geq 0.35 \text{ V}$  in Fig. 1). In the relevant range where the NC is dominant (up to 5 kHz), the fits (solid lines, Fig. 1) account very well for  $C(\omega)$ . In particular, we notice the experimentally observed leveling off of  $C(f)$  below 30–40 Hz, that is very well accounted for by Eq. (1). Furthermore, the voltage dependence of  $C$  is also fully explained by our analysis, as can be seen in the inset to Fig. 1, where the stars denote the capacitance calculated using the parameters obtained from the frequency fits at each voltage.

The losses due to e–h recombination in the bipolar injection regime are clearly revealed in the  $\Delta G(f)/f$  plots shown in Fig. 2. The changes  $\Delta \mathcal{E}''(\omega) \equiv [G_r(0) - G_r(\omega)]/\omega = G_0 \omega \tau_r^2 / (1 + \omega^2 \tau_r^2)$  (Eq. (1)), can be ascribed to the losses due to recombination. As formally expected from the inter-relation between  $C(f)$  and  $G(f)$ , exactly the same parameters,  $\tau_r$  and  $G_0$ , obtained from the  $C(\omega)$  fits in Fig. 1, account accurately for the peak frequency and peak height of  $\Delta G(f)/f$  in Fig. 2.

Interestingly, the voltage dependence of the fitted conductance,  $G_0$ , follows exactly that of the static conductance,  $dl/dV$ , as seen in Fig. 4, where we find that  $G_0(V) \propto dl/dV$  for the entire bias range. The proportionality of the fitted  $G_0$  (from the complex admittance experiment, Figs. 1 and 2) and the measured  $dl/dV$  (from the dc I–V experiment, Fig. 4, inset) further supports the inter-consistency of the experimental results.

The recombination rate,  $\tau_r^{-1}$ , extracted from the fits shows a linear dependence on  $V_{\text{bias}}$ , as shown in Fig. 4. From the  $dl/dV$  curve we see that bipolar injection (as well as NC) starts at  $V_{\text{bias}} \approx 0.35 \text{ V}$ ; thus the actual injection voltage is  $V = V_{\text{bias}} - 0.35 \text{ V}$ . The straight dashed line in Fig. 4 is a linear fit to the data. The linear dependence on  $V$  implies a BMR mechanism under bipolar injection, where the average BMR rate,  $\tau_{\text{BM}}^{-1}$ , may then be written as [12]

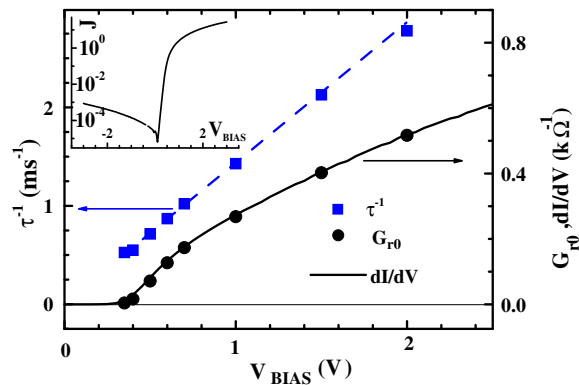


Fig. 4. The recombination parameters  $\tau_r^{-1}$  (left axis) and  $G_0$  (right axis), extracted from the fits to the NC data of Fig. 1, are shown vs  $V_{\text{bias}}$ . The straight dashed line is a linear fit,  $1/\tau_r (\text{ms}^{-1}) = 0.55 + 1.45(V_{\text{bias}} - 0.35 \text{ V})$ . The static admittance  $dl/dV$  (multiplied by 0.3) is overlaid (right axis) on the extracted  $G_0$  for comparison. Inset: current density  $J$  (in  $\text{mA}/\text{cm}^2$ ) vs  $V_{\text{bias}}$  (in V).

$$\tau_{\text{BM}}^{-1} = \gamma \bar{n} = \frac{4V}{L^2} \left[ \frac{\mu_n \mu_p \varepsilon \gamma}{2e(\mu_n + \mu_p)} \right]^{1/2}, \quad (2)$$

where  $\gamma = \bar{v} \sigma_R$  is the BMR coefficient,  $\bar{v}$  is the average e–h microscopic relative velocity,  $\sigma_R$  is their recombination cross section, and  $\bar{n}$  is the average carrier density. The measured mobility of the carriers in annealed rrP3HT:PCBM is of the order  $\mu \approx 10^{-3} \text{ cm}^2/\text{Vs}$  for both electrons and holes [13]. The linear fit of the data in Fig. 4 then yields  $\gamma \approx 10^{-12} \text{ cm}^3/\text{s}$ , similar to the value observed by other techniques [7,14,15]. This BMR coefficient,  $\gamma$ , is  $\approx 10^3$  times smaller than the Langevin BMR coefficient:  $\gamma_L = 2e(\mu_n + \mu_p)/\varepsilon$ . Obviously, a high recombination coefficient inhibits the efficiency of organic photovoltaic devices. The reduced BMR coefficient has been suggested to be the result of different pathways for electrons and holes in the heterojunction device [14,16]. Being confined to different phases or pathways, electrons and holes would recombine only at the interfaces between the phases. Thus the volume in which the recombination occurs is only a small fraction of the total volume in which the current flows.

Under bipolar injection, where the NC is dominant, it is surprising that by adding photoinduced carriers the NC decreases in magnitude, as shown in Fig. 3. Moreover, the reduction in NC,  $\Delta C$ , increases dramatically in forward bias as seen in Fig. 3 (inset (b)). Inset (a) of Fig. 3 shows that  $\Delta C \propto I_L^{1/2}$ . Assuming that  $\Delta C$  is proportional to the steady state density of the photogenerated carriers, the square root dependence on  $I_L$  implies that the photogenerated carriers undergo BMR process, in agreement with previous observations [14].

The photoinduced positive contribution  $\Delta C$  increases sharply at the onset of bipolar injection. It may therefore be related to the phenomenon of negative capacitance, which also appears only under bipolar injection. Such inhibition of the negative capacitance may be due to an increase in recombination rate by the photoinduced carriers decreasing thereby the magnitude of the NC, according to Eq. (1). Such photo-enhancement of the BMR may not be surprising since the photoinduced charges are predominantly created at the heterojunctions, where the local electric field breaks the photoexcited excitons. The increased carrier density at the heterojunction, where most of the bimolecular recombination takes place, shortens thus the recombination time. Alternatively, positive  $\Delta C$  may arise from trapped photoinduced carriers: upon re-emission from the traps the capacitance increases [17]. The effect of traps may be more evident from the maximum observed in the spectrum of  $C_{\text{light}}(f)$  at around  $f \approx 1 \text{ kHz}$  (Fig. 3 at  $I_L = 100$  and  $250 \mu\text{W}$ ). It is plausible that the 532 nm illumination excites deep compensated donors or acceptors, which may then become deep traps for the injected carriers. If the emission rate from these photogenerated traps (PGT) is  $e_{\text{PGT}}$ , then the increase of the capacitance due to the traps is  $\Delta C_{\text{PGT}}(\omega) \propto 1/(1 + \omega^2/e_{\text{PGT}}^2)$  [18]. Taking now into consideration both the effect of NC inhibition (i.e. reduced NC under light) and the PGT contribution ( $\Delta C_{\text{PGT}}$ ), the frequency dependent admittance data under illumination at  $I_L = 0.1$  and  $0.25 \mu\text{W}$  is very well accounted for with  $e_{\text{PGT}} \approx 3 \times 10^4 \text{ s}^{-1}$  (Fig. 3, solid lines). Emission

rates of the same order of magnitude were previously found for deep traps in organic diodes [19].

## 5. Summary

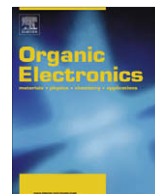
In summary, we have shown that in bulk heterojunction diodes made of annealed composites of rrP3HT and PCBM and under forward bias conditions a huge (up to  $\approx 500C_g$ ) negative capacitance is observed. We show that finite electron hole recombination times make it possible to observe the negative capacitance in the bipolar injection regime. We extract the bimolecular recombination coefficient and show that it is  $\approx 1000$  smaller than the Langevin value. Under illumination, the total capacitance becomes less negative reaching even positive values at sufficient intensities. This phenomenon may arise from an enhancement of the BMR rate at the heterojunction interfaces due to the extra carrier photoinduced density at exactly these donor-acceptor interfaces. Alternatively, it may arise from trapped photoinduced carriers.

## Acknowledgements

We thank Dr. G. Dennler for very valuable discussions. This work has been supported by the Austrian fund for the Advancement of Science (FWF, S9711-NO8). E.E. acknowledges the support of the Israel Science Foundation (ISF 745/08).

## References

- [1] P. Schilinsky, C. Waldauf, C.J. Brabec, Appl. Phys. Lett. 81 (2002) 3885.
- [2] F. Padinger, R. Rittberger, N.S. Sariciftci, Adv. Funct. Mater. 13 (2003) 85.
- [3] Y. Kim, S.A. Choulis, J. Nelson, D.D.C. Bradley, S. Cook, J.R. Durrant, Appl. Phys. Lett. 86 (2005) 063502.
- [4] W. Ma, C. Yang, X. Gong, K. Lee, A.J. Heeger, Adv. Funct. Mater. 15 (2005) 1617.
- [5] N.A. Penin, Semiconductors 30 (1996) 340.
- [6] A.G.U. Perera, W.Z. Shen, M. Ershov, H.C. Liu, M. Buchanan, W.J. Schaff, Appl. Phys. Lett. 74 (1999) 3167.
- [7] H.H.P. Gommans, M. Kemerink, R.A.J. Janssen, Phys. Rev. B 72 (2005) 235204.
- [8] N.D. Nguyen, M. Schmeits, H.P. Loeb, Phys. Rev. B 75 (2007) 075307.
- [9] E. Ehrenfreund, C. Lungenschmied, G. Dennler, H. Neugebauer, N.S. Sariciftci, Appl. Phys. Lett. 91 (2007) 012112.
- [10] K.S.A. Butcher, T.L. Tansley, D. Alexiev, Solid State Electron. 39 (1996) 333.
- [11] K.L. Ngai, R.W. Rendell, Dielectric and conductivity relaxation in conducting polymers, in: T.A. Skotheim (Ed.), Handbook of Conducting Polymers, vol. 2, 1986 (Chapter 28).
- [12] M.A. Lampert, P. Mark, Current Injection in Solids, Academic Press, New York, 1970.
- [13] A. Pivrikas, N.S. Sariciftci, G. Juška, R. Österbacka, Prog. Photovolt: Res. Appl. 15 (2007) 677.
- [14] A. Pivrikas, G. Juška, A.J. Mozer, M. Scharber, K. Arlauskas, N.S. Sariciftci, H. Stubb, R. Österbacka, Phys. Rev. Lett. 94 (2005) 176806.
- [15] G. Juška, G. Sliuzys, K. Genevičius, K. Arlauskas, A. Pivrikas, M. Scharber, G. Dennler, N.S. Sariciftci, R. Österbacka, Phys. Rev. B 74 (2006) 115314.
- [16] L.J.A. Koster, V.D. Mihailetschi, P.W.M. Blom, Appl. Phys. Lett. 88 (2006) 052104.
- [17] H.C.F. Martens, H.B. Brom, P.W.M. Blom, Phys. Rev. B 60 (1999) 8489.
- [18] G. Vincent, D. Bois, P. Pinard, J. Appl. Phys. 46 (1975) 5173.
- [19] O. Gaudin, R.B. Jackman, T.-P. Nguyen, P.L. Rendu, Mat. Res. Soc. Symp. Proc. 725 (2002) P11.7.



# Self-assembled monolayers for electrode fabrication and efficient threshold voltage control of organic transistors with amorphous semiconductor layer

Caroline Celle<sup>a</sup>, Clément Suspène<sup>a</sup>, Jean-Pierre Simonato<sup>a,\*</sup>, Stéphane Lenfant<sup>b</sup>, Marc Ternisien<sup>b</sup>, Dominique Vuillaume<sup>b</sup>

<sup>a</sup>CEA-Grenoble, LITEN/DTNM/LCH, 17, Rue des Martyrs, 38054 Grenoble Cedex 9, France

<sup>b</sup>Molecular Nanostructures and Devices Group, Institute for Electronics Microelectronics and Nanotechnology CNRS, Avenue Poincaré, F-59652 Cedex, Villeneuve d'Ascq, France

## ARTICLE INFO

### Article history:

Received 29 July 2008

Received in revised form 9 October 2008

Accepted 9 October 2008

Available online 18 October 2008

### PACS:

68.35.bm

68.35.bj

73.61.Ph

### Keywords:

Organic thin film transistor

Self-assembled monolayers

Threshold voltage

Electrodes

Amorphous organic semiconductor

## ABSTRACT

In this paper we show that thiolated self-assembled monolayers (SAMs) can be used to anchor source–drain gold electrodes on the substrate, leading to excellent electrical performances of the organic field-effect transistor (OFET) on a par with those using a standard electrode process. Using an amorphous semiconductor and a gate dielectric functionalized with SAMs bearing different dipole moments, we demonstrate that we can tune the threshold voltage alone, while keeping nearly unchanged the other electrical properties (hole carrier mobility,  $I_{on}/I_{off}$  ratio, subthreshold swing). This differs from previous studies for which SAMs functionalization induced significant changes in all the OFET electrical performances. This result opens doors to design organic circuits using reproducible amorphous semiconductor based OFETs for which only the threshold voltage can be tuned on demand.

© 2008 Elsevier B.V. All rights reserved.

## 1. Introduction

During the past decade, research on new materials for organic thin film transistors (OTFT) has received a fast growing interest, resulting in significant improvements of the electrical performances and leading to promising demonstrators [1]. Various organic materials have been developed due to their electronic tunability by molecular design. Good intrinsic properties are now accessible, but interestingly the interface properties of these new organic

species with other materials have been less studied whilst they can lead to dramatic changes in OTFT behaviour [2].

For instance, it is possible to modulate charge injection from the electrodes into the semiconductors by modifying the surfaces of electrodes with self-assembled monolayers (SAMs) [3–6]. Chemically modifying the interface properties between organic semiconductor (OSC) and insulator can also lead to phenomena of overwhelming importance. One of the most remarkable effects was reported in 2005: Chua et al. showed that trapping of electrons at the semiconductor–dielectric interface by hydroxyl groups prevented most conjugated polymers to yield n-channel field-effect transistor conduction [7]. Interface engineering by SAMs to achieve control of channel conductance and/or

\* Corresponding author. Tel.: +33 438781139; fax: +33 438785117.

E-mail address: [jean-pierre.simonato@cea.fr](mailto:jean-pierre.simonato@cea.fr) (J.-P. Simonato).

charge carrier density has been reported, but the role of the SAMs is still controversial since it can result in several effects such as (i) changes in the molecular orientation in the OSC, (ii) neutralization of surface defects, (iii) modification of surface roughness, interface dipole and surface energy. In most cases, a combination of these effects is likely, some of them being certainly dependent on both the dielectrics and the OSCs. As a consequence, several transistors parameters are modified simultaneously, and this feature prevents a clear understanding of the effect of the SAMs.

For further development of organic electronics, it is mandatory to find a way to precisely control the threshold voltage of OFET. This is a strong constraint to allow a reliable design of organic circuitries. It could be very interesting to fabricate and study organic transistors with similar electrical properties (i.e. charge carrier mobility,  $I_{\text{on}}/I_{\text{off}}$  ratio and subthreshold swing) except for the threshold voltage, this latter being precisely controlled and adjusted. Up to now, gate dielectric interface variations leading to modification of the threshold voltage came-along with charge carrier mobility changes that have mainly been attributed to modifications of the semiconductor morphology [8–10]. The chain alignment of polymeric OSCs at the interface is a well known process which can induce significant improvement of the mobility. For instance, poly-(3-hexylthiophene) (P3HT) enhancement in mobility by SAM-treated silicon oxide is linked to the highly oriented crystals at the interface between the polymer and the dielectric [11–16]. A similar effect was also observed for other molecules such as thermally evaporated pentacene [10,13,17,18], PQT-12 [18] and more recently on a fused-ring thieno-thiophene polymer [19]. For instance, surface modification of the gate dielectric by surface chemistry (using SAMs) can lead to a better  $\pi$ - $\pi$  stacking, resulting in an increase of the charge carrier mobility.

In the meantime, threshold voltage shifts were consistently observed, depending on the chemical nature of the SAMs. Thus, it was not possible to modify selectively the threshold voltage without modification of the overall electrical performances of the OFET, due to the interplay with changes in the structural organization of the OSCs.

In order to avoid any molecular ordering or crystallization effects, we decided to study the impact of organosilane self-assembled monolayers on OTFT fabricated with an amorphous OSC material. Despite the moderate hole mobility observed with PolyTriArylAmine (PTAA), this semiconductor material presents several advantages. It is easy to handle, to spin-coat from organic solutions, and thin films of PTAA exhibit excellent stability to air and light, thus, avoiding doping side-effect [20–25].

In addition to gate dielectric functionalization, SAMs have also been investigated to modify the surface properties of metal source–drain surfaces. This treatment improves the charge injection in the OSC, it can also help getting a better structural organization in the OSC film [26]. In this paper, we present an approach in which SAMs are used underneath the source–drain electrodes as an anchoring layer. Gold electrodes are made by metal evaporation directly on thiolated self-assembled monolayers. We demonstrate electrical performances identical to the

commonly used Ti/Au contacts made by lift-off. The benefit is a simplified one-step process, compatible with many substrates, including plastic ones.

Using these electrodes, we studied the effect of different SAMs at the dielectric/organic semiconductor interface on the electronic performances of the transistor, with the amorphous organic semiconductor PTAA. We demonstrate that threshold voltage can be significantly changed by choosing the orientation and magnitude of the molecule dipole, while other important parameters (charge carrier mobility, on/off ratio, subthreshold swing) are slightly affected, in contrast with previous results [8–17].

## 2. Thiol based SAM as anchoring layer for electrodes

Two types of devices with bottom gate/bottom contact geometry were fabricated on a heavily doped (100) silicon wafer ( $n^{++}$ , 2–5 m $\Omega$  cm) covered by a thermally grown silicon dioxide (200 nm). The source and drain electrodes of the first device were patterned by optical photolithography, followed by Ti (10 nm) and Au (90 nm) evaporation and lift-off. The second substrate was treated with piranha solution ( $\text{H}_2\text{SO}_4/\text{H}_2\text{O}_2$ , 1/1 (v:v)), followed by oxygen plasma treatment (20 mTorr, 10 sccm  $\text{O}_2$ , 10 W, 300 s) and immersion in a  $\text{HCl}/\text{H}_2\text{O}_2/\text{H}_2\text{O}$  (1:1:8) mixture. The sample was then exposed to vapour-phase of 3-mercaptopropyltrimethoxysilane (MPTS) for 6 h under vacuum ( $10^{-2}$  mBar). The water contact angle measured on the SAM was  $60^\circ \pm 2^\circ$  (Kruss DSA-10), which is in fair agreement with reported values [27,28]. The surface morphology of the organic layer was determined by imaging using a Veeco Dimension 3100 atomic force microscope (AFM) in tapping mode. We measured a root-mean square surface roughness of  $\sim 1 \text{ \AA}$  over a  $1 \mu\text{m}^2$  area ( $2.3 \text{ \AA}$  over a  $10 \mu\text{m}^2$  area), identical to the roughness of silicon oxide. Gold (90 nm) was then deposited by evaporation using photolithography techniques and etched by a solution of  $\text{KI}/\text{I}_2$ . The measured RMS roughness value of the gold electrode surface was  $\sim 7 \text{ \AA}$ , which is much better than the roughness ( $\sim 18 \text{ \AA}$ ) obtained by Au deposition on Ti. These results are consistent with those reported recently by Janes and Coll [29], and in addition to the stability tests mentioned in this paper we tried the commonly used “Scotch<sup>®</sup> tape peel test”. We observed no difference between the two types of electrodes, both of them remaining unaffected by this test. A schematic device structure is presented in Fig. 1.

A 1 wt% solution of PTAA in toluene was spin-coated on both substrates and devices were annealed at  $100^\circ\text{C}$  for 20 min. In both cases, uniform thin films of 50 nm, as measured by ellipsometry (Sopra ES4G spectroscopic ellipsometer) were obtained. No particular care was taken to prevent atmosphere contact since PTAA is an air-stable polymer. Electrical measurements were carried out on interdigitated source–drain transistors with channel length of  $10 \mu\text{m}$  and channel width of  $10,000 \mu\text{m}$  ( $W/L = 1000$ ) with an Agilent 4156b semiconductor parameter analyser.

Typical transfer curves of both devices are presented in Fig. 2 in the saturation regime ( $V_{\text{DS}} = -60 \text{ V}$ ). The performances measured on 10 devices indicated that both



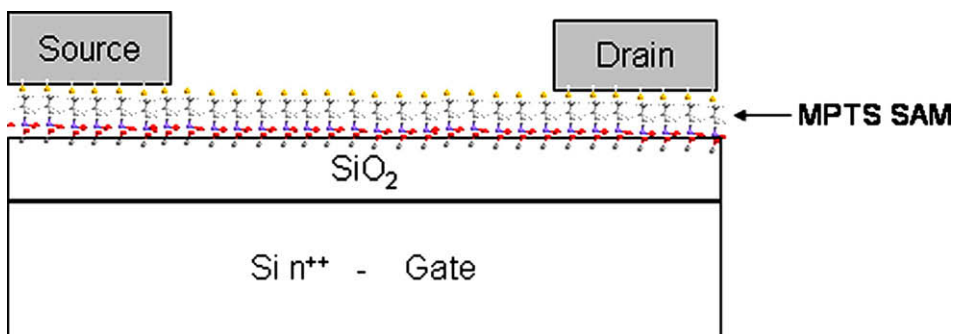


Fig. 1. Schematic structure of the devices with MPTS as anchoring layer for gold electrodes.

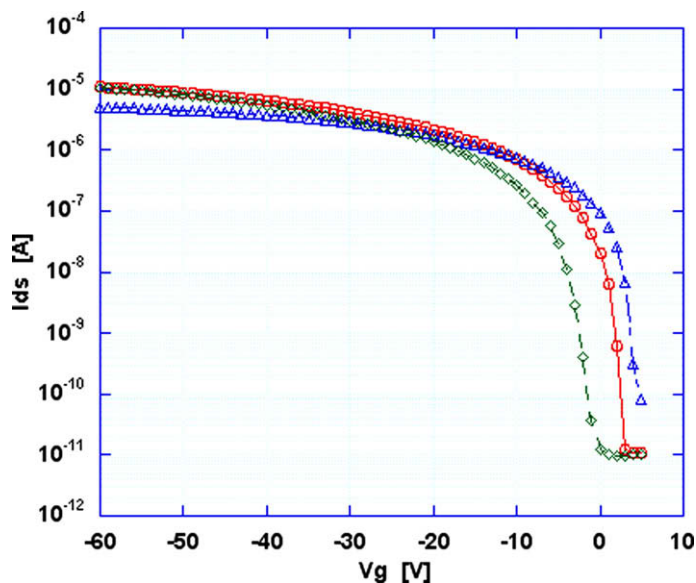


Fig. 2. Transfer curves of devices fabricated with PTAA as semiconductor, in the saturation regime ( $V_{DS} = -60$  V) (a) Diamonds: Ti (10 nm)/Au (90 nm) (b) Circles: MPTS/Au (100 nm) (c) Triangles: MPTS/Au (100 nm) after removal of organics in the channel by  $O_2$  plasma.

source–drain technologies led to very similar performances. The effective mobility of the devices is extracted from the slope of the current voltage characteristics according to the following equation

$$I_{ds,sat} = \frac{W}{2L} \mu_{sat} C_i (V_g - V_{th})^2 \quad (1)$$

where  $L$  is the channel length of the device,  $W$  is the channel width, and  $C_i$  is the gate dielectric capacitance. Capacitance of the SAM was neglected with regard to the 200 nm thickness of silicon dioxide, and according to recent results [9]. Charge carrier mobility values for both types of devices were similar ( $2\text{--}5 \times 10^{-4} \text{ cm}^2 \text{ V}^{-1} \text{ s}^{-1}$ ), as well as  $I_{on}/I_{off}$  ratios ( $>10^4$ ). A slight change of the threshold voltage was observed, this point will be discussed thereafter.

These results demonstrate that it is possible to fabricate substrates for OTFT using thiolated SAMs to anchor gold electrodes instead of chromium or titanium. Moreover, smooth surfaces for electrodes and channel are obtained

by this technique, which might be advantageous since surface roughness may be a critical parameter for organic transistor fabrication [30,31]. No significant differences were observed between the two systems, indicating that charge injection is not altered by this unconventional fabrication process.

### 3. Effect of different gate dielectric functionalization

As discussed in the introduction, self-assembled monolayers are known to strongly modify the OFET characteristics, leading generally to significant changes of electrical properties, notably for charge carrier mobility.

To study the effect of SAM molecules at the interface between dielectric and PTAA, we used devices made with the previously described MPTS/Au electrodes. The remaining SAMs in the channel were removed by  $O_2$  plasma and trialkoxy or trichlorosilane reagents were used to synthesize SAMs with different terminal groups.

Six chemically different surfaces were prepared between source and drain electrodes. The hydroxyl rich surface was obtained after oxygen plasma, and  $C_6F_5-(CH_2)_3-SiCl_3$  (3-perfluorophenyl-propyl-trichlorosilane, PFTS),  $HS-(CH_2)_3-Si(OMe)_3$  (MPTS),  $H_2N-(CH_2)_3-Si(OEt)_3$  (3-aminopropyl-triethoxysilane, APTS),  $4-(Ph_2N)-C_6H_4-NHC(O)NH-(CH_2)_3-Si(OEt)_3$  (1-(4-(diphenylamino)-phenyl)-3-(2-(triethoxysilyl)-propyl)-urea, a triarylamine triethoxysilane derivative, TAATS), and  $CH_3-(CH_2)_{17}-SiCl_3$  (octadecyltrichlorosilane, OTS) were used as starting molecules for the SAMs (Fig. 3) [32]. TAATS was synthesized in three steps [33].

APTS and MPTS were deposited under vacuum ( $10^{-2}$  mBar, respectively, 15 min and 6 h) whereas OTS, FTS and TAATS were grafted by immersion of the substrates in a  $10^{-3}$  M organic solution for 2 h. After synthesis, SAMs were characterized by advancing water contact angle measurements. Values reported in Table 1 were in good agreement with those reported in the literature [34,35].

A similar procedure as described previously (*vide supra*) was carried out for PTAA film formation. Homogeneous OSC thin films were achieved for all SAMs, except for the OTS one. In this case, we observed dewetting of the PTAA, which may probably be related to the highly hydrophobic nature of the long alkyl chains grafted on the silicon oxide surface ( $\theta = 110^\circ$ ).

Fig. 4a depicts the  $I-V$  characteristics of a typical OFET with PTAA, which conformed to the conventional transistor behaviours in both linear and saturated regimes.

In this figure, the MPTS self-assembled monolayer was used. Similar curve shapes were obtained for all devices. The output curves showed good saturation behaviours with no observable contact resistance (see inset of Fig. 4a), while the transfer curve in the saturated regime shown in Fig. 4b exhibited a near quadratic increase in current as a function of gate biases (see inset of Fig. 4b). The extracted mobility in the linear regime was slightly lower than that in the saturated regime, and this was quite similar to OFETs with most organic semiconductors. Table 2

summarizes the mean mobility values in the saturation regime, threshold voltages, subthreshold slopes and current  $I_{on}/I_{off}$  current ratios, with their standard deviation observed at least on five similar structures for each SAM. No significant deviation was observed for the hole carrier mobility values, which differs strongly from the poly-crystalline materials for which mobilities can vary by a factor of a few hundreds, depending both on the chemical formula of the SAMs and on the OSC material [8,18,19]. The  $I_{on}/I_{off}$  ratios ( $\sim 10^4$  to  $10^5$ ) as well as the subthreshold swing values were also in the same range, with low deviation. These results are in good agreement with the fact that the OSC remains mainly unaffected by the SAMs at the interface with the dielectric. As expected, the fact that PTAA is an amorphous material avoids any morphologic effect and, thus, any charge carrier mobility variation inherent to the crystal packing of the OSC.

In sharp contrast, the  $V_t$  values were strongly modified by the SAMs (Fig. 5).

A significant modulation was obtained, spanning over a 70 V range. PFTS SAM tends to shift positively the  $V_t$  values whereas amine derivatives (APTS and TAATS) lead to very negative values. Depending on their functional groups, SAMs are known to generate a built-in electric field [6,8], which modify the charge carrier density in the transistor channel. Fluorinated SAMs have tendency to generate local electric field that accumulates holes, and on the contrary, devices with APTS or TAATS accumulate electrons, leading to the need of a very large negative gate bias to turn on the PTAA into hole accumulation mode.

**Table 1**

Advancing water contact angle after different functionalizations of the channel.

Water contact angle ( $\theta$ )					
O <sub>2</sub> plasma	PFTS	MPTS	APTS	TAATS	OTS
ND	$91.7 \pm 1.2$	$60.1 \pm 1.8$	$72.3 \pm 0.7$	$89.0 \pm 1.4$	$110.0 \pm 1.2$

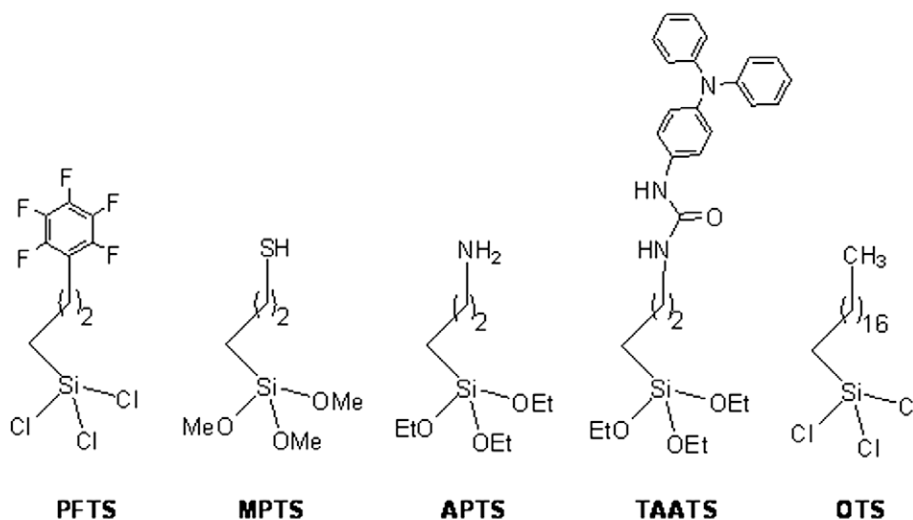


**Fig. 3.** Chemical structures of organosilane molecules used for the synthesis of SAMs.

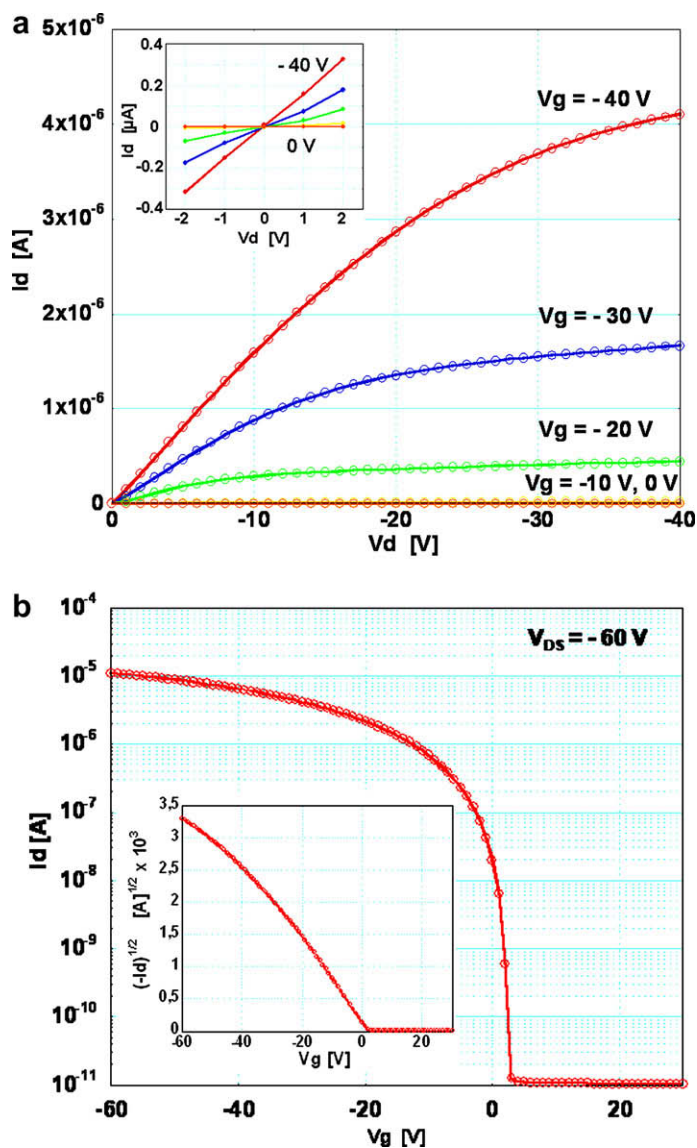


**Fig. 4.** Typical curves of devices fabricated with PTAA as semiconductor, with MPTS in the channel and as anchoring layer for gold electrodes (channel length = 10  $\mu\text{m}$ , channel width = 10,000  $\mu\text{m}$ ). (a) Output characteristics at different gate voltages and zoom in the  $V_{\text{DS}} = 0$  region (inset); (b) Transconductance characteristics in the saturated regime at constant source–drain voltage of  $-60$  V and square root of the absolute value of current as a function of gate voltage (inset).

This local electric field is related to the dipole moment of the molecules. We calculated the dipole moment using MOPAC [36] and the semi-empirical method PM3. The dipole values (see Table 3) were calculated for isolated molecules with a  $\text{SiH}_3$  group at the bottom. We considered that the leaving groups of the silane derivatives (OMe, OEt, Cl) are not present after the grafting reaction, and, therefore, no longer contribute to the molecular dipole. From these dipole moment values, we calculated the surface charge density according to the following equation

$$Q_s = \frac{N\mu_D \cos \theta}{d} \quad (2)$$

**Table 2**

Summarized electrical properties as a function of the channel modification.

SAM	$\mu$ ( $\text{cm}^2 \text{V}^{-1} \text{s}^{-1}$ )	$I_{\text{on}}/I_{\text{off}}$	$S$ (V/dec)	$V_t$ (V)
PFTS	$5.2 (\pm 1.3) \times 10^{-4}$	$1.0 (\pm 2.7) \times 10^4$	$5.0 (\pm 0.6)$	$18.6 (\pm 2.5)$
MPTS	$5.2 (\pm 1.5) \times 10^{-4}$	$3.0 (\pm 4.4) \times 10^5$	$2.7 (\pm 1.1)$	$5.5 (\pm 2.7)$
–	$1.9 (\pm 0.8) \times 10^{-4}$	$1.5 (\pm 2.3) \times 10^4$	$5.5 (\pm 2.4)$	$13.1 (\pm 5.2)$
APTS	$1.4 (\pm 0.7) \times 10^{-4}$	$7.0 (\pm 5.3) \times 10^4$	$5.4 (\pm 4.0)$	$-32.0 (\pm 5.6)$
TAATS	$2.0 (\pm 0.1) \times 10^{-4}$	$2.1 (\pm 0.7) \times 10^5$	$2.8 (\pm 1.6)$	$-41.5 (\pm 0.7)$

where  $N$  is the surface density of molecule,  $\mu_D$  the dipole moment,  $d$  the length of the molecule and  $\theta$  the (average) angle between the long axis of molecule and the normal

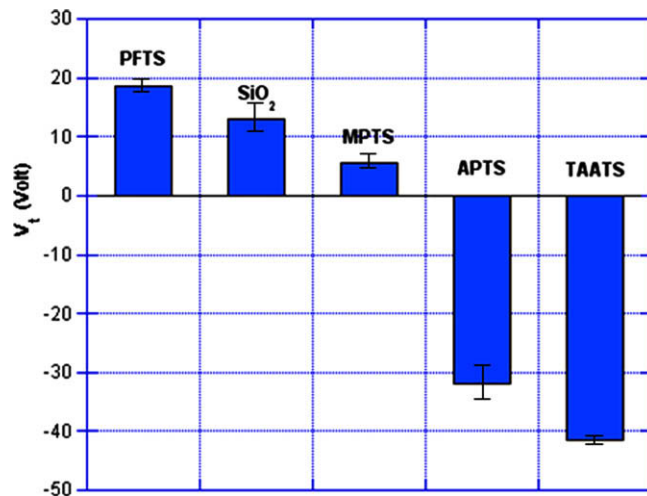


Fig. 5.  $V_t$  as a function of the channel modification.

Table 3

Calculated dipole moment along the long axis of the molecule, molecule length and steric hindrance, calculated with MOPAC (PM3). The positive (negative) dipole points upstairs (downstairs) leading to positive (negative) charges at the surface of the monolayer. The surface charge density is calculated according to Eq. (2). Dipole moment of the APTS is calculated for the ammonium derivative. Dipole moment of the TAATS is calculated for the cationic form of the triphenylamine group.

SAM	Dipole moment (D)	Length (Å)	Area (Å <sup>2</sup> )	$Q_s$ (cm <sup>-2</sup> )
PFTS	-1.66	9.9	37	$-1.2 \times 10^{13}$
MPTS	-1.6	7.2	23	$-2.7 \times 10^{13}$
APTS	7	7.3	21	$9.6 \times 10^{12}$
TAATS	7.7	18.3	61	$1.4 \times 10^{13}$

at the surface. The lengths  $d$  were calculated for the optimized conformations of the molecules (energy minimum optimization performed with MOPAC, see Table 3).

Without a precise knowledge of the molecular organization and packing inside the SAM, we assume here that  $\theta = 0$ , and we consider an average molecular density  $N = 2.5 \times 10^{14}$  molecules cm<sup>-2</sup> ( $\pm 1 \times 10^{14}$  cm<sup>-2</sup>). This value corresponds to an average surface per molecule of 40 Å<sup>2</sup> (steric hindrance calculated with MOPAC ranges from ~20–60 Å<sup>2</sup> (from APTS to TAATS, respectively). To explain the negative threshold voltage, we have to assume that APTS and TAATS molecules, or a fraction of them, are in a cationic form. In ambient and usual pH condition, only ca. 10% of the APTS molecules are in the ammonium form, and we used in Eq. (2) an effective dipole of 1/10 of the calculated one [37,38]. Similarly, we assume 50% for the TAATS which is more easily converted into its cationic form [39,40].

Fig. 6 shows the experimental threshold voltage versus the surface charge density deduced from the dipole calculation. A rough (according to the assumption done for the dipole calculation) linear relationship can be estimated (solid line). A slope of ca.  $-2.5 \times 10^{-12}$  V cm<sup>2</sup> is estimated, as well as, a zero-charge threshold voltage  $V_{T0}$  of -15 V. In an organic FET working in accumulation regime, the

threshold voltage corresponds to the so-called flat-band voltage of the metal–insulator–semiconductor structure. Thus, we can write

$$V_T = \Phi_{MS} - \frac{Q_B}{C_{ox}} - \frac{Q_S}{C_{ox}} = V_{T0} - \frac{Q_S}{C_{ox}} \quad (3)$$

where  $\Phi_{MS}$  is the work-function difference between the gate (here Si) and the semiconductor,  $Q_B$  the bulk density of charges in the gate dielectric,  $Q_S$  the surface charge density and  $C_{ox}$  the gate oxide capacitance.  $\Phi_{MS}$  cannot be easily calculated (it depends on the doping level in the semiconductor, which is not known here), but a negative  $V_T$  corresponds to  $Q_B > 0$  as expected for SiO<sub>2</sub> due to the well known presence of positively-charged traps and/or a possible positive ions contamination [41].

Notice that the measured  $V_T$  in the case of the pristine SiO<sub>2</sub> (Fig. 5) is positive. This is due to the negative charges at the surface ( $Q_S$ ) trapped by the hydroxyl surface groups. With a 200 nm thick oxide, the theoretical slope ( $-1/C_{ox}$ ) is  $9.4 \times 10^{-12}$  V cm<sup>2</sup>, i.e. a factor 3.7 larger than the experimental determination. In addition to the crude estimate of the dipole and charge (Section 2), another feature can explain this difference. The dipoles were calculated for isolated molecules, and it is well known that in a monolayer, the dipole is reduced due to the Coulomb interaction between the parallel dipoles. For instance, more detailed calculations have predicted a screening of the dipole by a factor of ca. 3 [42]. Such an effect reduces the surface charge density and, thus, increases the slope towards the expected value.

#### 4. Conclusion

In conclusion, we have shown how thiolated SAMs can be used for anchoring source and drain gold electrodes. We have demonstrated that this simple process leads to OFETs with similar performances as those using standard titanium anchoring layer. We have also fabricated OFETs with an amorphous semiconductor (PTAA) deposited on a gate

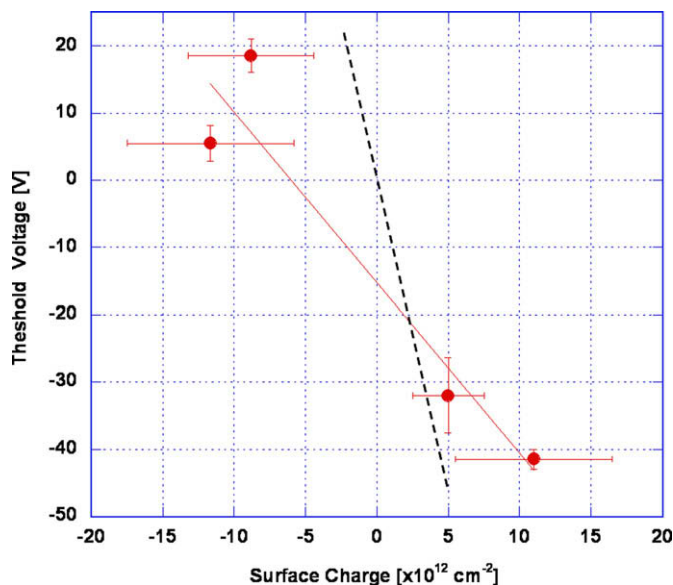


**Fig. 6.** Measured threshold voltage shift versus the calculated surface charge. The solid line is a linear fit,  $y = -15.2 - 2.54x$ . The dotted line is the expected slope given by  $(-1/C_{ox})$  where  $C_{ox}$  is the oxide capacitance.

dielectric functionalized by different SAMs. By virtue of the amorphous nature of the OSC, the molecular organization in the OSC is not strongly affected by the chemical nature of the SAM, and this feature allowed us to study the effect of the SAM on the threshold voltage, all the other parameters (hole carrier mobility,  $I_{on}/I_{off}$  ratio, subthreshold swing) remaining almost unchanged. By choosing molecules bearing different dipole moments, we observed an almost linear relationship between the surface charges at the monolayer/OSC interface and the threshold voltage, in agreement with the expected field-effect. This result opens the way for fabricating circuits with identical transistors, based on amorphous organic semiconductors, that can be adjusted to switch on at different selected voltages. The proposed method can also be extended to crystalline organic semiconductors by designing organosilanes that contain various dipoles embedded in the organic structure, but with an identical end group to ensure constant interface with the OSC.

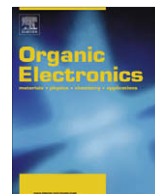
## Appendix A. Supplementary material

Supplementary data associated with this article can be found, in the online version, at [doi:10.1016/j.orgel.2008.10.007](https://doi.org/10.1016/j.orgel.2008.10.007).

## References

- [1] A. Dodabalapur, *Materials Today* 9 (2006) 24.
- [2] Y. Don Park, J.A. Lim, H.S. Lee, K. Cho, *Materials Today* 10 (2007) 46.
- [3] K. Asadi, F. Gholamrezaie, E.C.P. Smits, P.W.M. Blom, B. de Boer, *Journal of Materials Chemistry* 17 (2007) 1947.
- [4] P. Stoliar, R. Kshirsagar, M. Massi, P. Annibale, C. Albonetti, D.M. de Leeuw, F. Biscarini, *Journal of the American Chemical Society* 129 (2007) 6477.
- [5] I. Kymissis, C.D. Dimitrakopoulos, S. Purushothaman, *IEEE Transactions on Electron Devices* 48 (2001) 1060.
- [6] I.H. Campbell, S. Rubin, T.A. Zawodzinski, J.D. Kress, R.L. Martin, D.L. Smith, N.N. Barashkov, J.P. Ferraris, *Physical Review B* 54 (1996) R14321.
- [7] L.-L. Chua, J. Zaumseil, J.-F. Chang, E.C.W. Ou, P.K.H. Ho, H. Sirringhaus, R.H. Friend, *Nature* 434 (2005) 194.
- [8] S. Kobayashi, T. Nishikawa, T. Takenobu, S. Mori, T. Shimoda, T. Mitani, H. Shimotani, N. Yoshimoto, S. Ogawa, Y. Iwasa, *Nature Materials* 3 (2004) 317.
- [9] J. Yunseok, C. Jeong Ho, K. Do Hwan, P. Yeong Don, H. Minkyu, C. Kilwon, *Applied Physics Letters* 90 (2007) 132104.
- [10] K.P. Pernstich, S. Haas, D. Oberhoff, C. Goldmann, D.J. Gundlach, B. Batlogg, A.N. Rashid, G. Schitter, *Journal of Applied Physics* 96 (2004) 6431.
- [11] R. Joseph Kline, M.D. McGehee, M.F. Toney, *Nature Materials* 5 (2006) 222.
- [12] S. Grecu, M. Roggenbuck, A. Opitz, W. Brütting, *Organic Electronics* 7 (2006) 276.
- [13] L.A. Majewski, R. Schroeder, M. Grell, P.A. Glarvey, M.L. Turner, *Journal of Applied Physics* 96 (2004) 5781.
- [14] D.H. Kim, Y.D. Park, Y. Jang, H. Yang, Y.H. Kim, J.I. Han, D.G. Moon, S. Park, T. Chang, C. Chang, M. Joo, C.Y. Ryu, K. Cho, *Advanced Functional Materials* 15 (2005) 77.
- [15] H. Sirringhaus, P.J. Brown, R.H. Friend, M.M. Nielsen, K. Bechgaard, B.M.W. Langeveld-Voss, A.J.H. Spiering, R.A.J. Janssen, E.W. Meijer, P. Herwig, D.M. de Leeuw, *Nature* 401 (1999) 685.
- [16] Z. Bao, A. Dodabalapur, A.J. Lovinger, *Applied Physics Letters* 69 (1996) 4108.
- [17] G. Yoshikawa, J.T. Sadowski, A. Al-Mahboob, Y. Fujikawa, T. Sakurai, Y. Tsuruma, S. Ikeda, K. Saiki, *Applied Physics Letters* 90 (2007) 251906.
- [18] Y. Wu, P. Liu, B.S. Ong, T. Srikumar, N. Zhao, G. Botton, S. Zhu, *Applied Physics Letters* 86 (2005) 142102.
- [19] R. Rawcliffe, M. Shkunov, M. Heeney, S. Tierney, I. McCulloch, A. Campbell, *Chemical Communications* (2008) 871.
- [20] R. Schroeder, L. Majewski, A.M. Grell, J. Maunoury, J. Gautrot, P. Hodge, M. Turner, *Applied Physics Letters* 87 (2005) 113501.
- [21] Y. Shirota, *Journal of Materials Chemistry* 15 (2005) 75.
- [22] J. Veres, S. Ogier, G. Lloyd, D. de Leeuw, *Chemistry of Materials* 16 (2004) 4543.
- [23] L.A. Majewski, M. Grell, S.D. Ogier, J. Veres, *Organic Electronics* 4 (2003) 27.
- [24] J. Veres, S.D. Ogier, S. Leeming, B. Brown, D. Cupertino, *Materials Research Society Symposium Proceedings* 708 (2002) 243.
- [25] D. Zielke, C.A. Hubler, U. Hahn, N. Brandt, M. Bartzsch, U. Fugmann, T. Fischer, J. Veres, S. Ogier, *Applied Physics Letters* 87 (2005) 123508.

- [26] D.J. Gundlach, J.E. Royer, S.K. Park, S. Subramanian, O.D. Jurchescu, B.H. Hamadani, A.J. Moad, R.J. Kline, L.C. Teague, O. Kirillov, C.A. Richter, J.G. Kushmerick, L.J. Richter, S.R. Parkin, T.N. Jackson, J.E. Anthony, *Nature Materials* 7 (2008) 216.
- [27] E. Pavlovic, A.P. Quist, U. Gelius, S. Oscarsson, *Journal of Colloid and Interface Science* 254 (2002) 200.
- [28] D. Aswal, S. Lenfant, D. Guerin, J. Yakhmi, D. Vuillaume, *Small* 1 (2005) 725.
- [29] A.K. Mahapatro, A. Scott, A. Manning, D.B. Janes, *Applied Physics Letters* 88 (2006) 151917.
- [30] J.I. Jung, J.Y. Song, J.H. Kim, H.R. Kim, *Molecular Crystals and Liquid Crystals* 476 (2007) 403.
- [31] Y. Jung, J.R. Kline, D.A. Fischer, E.K. Lin, M. Heeney, I. McCulloch, D.M. DeLongchamp, *Advanced Functional Materials* 18 (2008) 742.
- [32] OTS, MPTS and APTS were purchased from Aldrich and PFTS from Gelest. Products were used as received.
- [33] The complete description of the organic synthesis and characterizations are available as supplementary materials.
- [34] D.K. Aswal, S. Lenfant, D. Guerin, J.V. Yakhmi, D. Vuillaume, *Analytica Chimica Acta* 568 (2006) 84.
- [35] N. Balachander, C.N. Sukenik, *Langmuir* 6 (1990) 1621.
- [36] Cambridge Soft Corporation, Cambridge, UK, 1996.
- [37] O. Bouloussa, F. Rondelez, Private Communication.
- [38] H. Zhang, H.-X. He, T. Mu, Z.-F. Liu, *Thin Solid Films* 327–329 (1998) 778.
- [39] E.T. Seo, R.F. Nelson, J.M. Fritsch, L.S. Marcoux, D.W. Leedy, R.N. Adams, *Journal of American Chemical Society* 88 (1966) 3498.
- [40] K. Yuan Chiu, T. Xiang Su, J. Hong Li, T.-H. Lin, G.-S. Liou, S.-H. Cheng, *Journal of Electroanalytical Chemistry* 575 (2005) 95.
- [41] E.H. Nicollian, J.R. Brews, *MOS (Metal-oxide-semiconductor) Physics and Technology*, Wiley, New York, 1982.
- [42] C. Krzeminski, C. Delerue, G. Allan, D. Vuillaume, R.M. Metzger, *Physical Review B* 64 (2001) 085405.



# Horizontal orientation of linear-shaped organic molecules having bulky substituents in neat and doped vacuum-deposited amorphous films

Daisuke Yokoyama<sup>a,b</sup>, Akio Sakaguchi<sup>c</sup>, Michio Suzuki<sup>c</sup>, Chihaya Adachi<sup>a,b,\*</sup>

<sup>a</sup> Center for Future Chemistry, Kyushu University, 744 Motoooka, Nishi, Fukuoka 819-0395, Japan

<sup>b</sup> CREST Program, Japan Science and Technology Agency (JST), 1-32-12 Higashi, Shibuya, Tokyo 150-0011, Japan

<sup>c</sup> J. A. Woollam Japan Corporation, 5-22-9 Ogikubo, Suginami, Tokyo 167-0051, Japan

## ARTICLE INFO

### Article history:

Received 19 August 2008

Received in revised form 7 October 2008

Accepted 13 October 2008

Available online 22 October 2008

### PACS:

78.20.Ci

78.20.Fm

78.66.Jg

78.66.Qn

### Keywords:

Horizontal orientation

Organic amorphous film

Cutoff emission

Variable angle spectroscopic ellipsometry

Styrylbenzene derivatives

## ABSTRACT

Organic amorphous films fabricated by vacuum deposition have been widely used in organic light-emitting devices, making use of their high-performance optical and electrical characteristics and taking advantage of the easy fabrication of pinhole-free thin smooth layers of a desired thickness. However, random orientation in amorphous films often makes it difficult to utilize their best optical and electrical potential. Here the authors demonstrate that the linear-shaped molecules of fluorescent styrylbenzene derivatives are horizontally oriented in organic amorphous films fabricated by conventional vacuum deposition even when the molecules are doped in an isotropic host matrix film. The longer the molecular length is, the larger the anisotropy of the molecular orientation becomes. The weak interaction between adjacent molecules and the linear-shaped molecular structure probably cause the horizontal orientation. The fact that the horizontal molecular orientation occurs on any underlying layers shows the high versatility of the horizontal orientation for various applications. Their findings will provide a new guideline for molecular designs that can be used to improve optical and electrical characteristics of organic optoelectronic devices, such as organic light-emitting diodes and organic laser devices.

© 2008 Elsevier B.V. All rights reserved.

## 1. Introduction

Organic amorphous films fabricated by vacuum deposition have played an important role in the development of organic light-emitting diodes (OLEDs) [1] and organic laser devices [2,3]. Amorphous films that have smooth interfaces are essential in the fabrication of fine structures in devices that control as planned light and charge carriers because randomly rough interfaces—for example, due to polycrystalline texture—cause undesirable light scattering or leak current. The vacuum-deposited amorphous films

also greatly contribute to the manufacture of practical pinhole-free multilayer films using simplified fabrication techniques that have in turn significantly increased the rate of development of organic thin film devices in the past 20 years.

However, it has been taken for granted that the full optical and electrical potential of organic molecules cannot be achieved because the molecules in organic vacuum-deposited amorphous films are randomly oriented and the films themselves are isotropic. In OLEDs fabricated by vacuum deposition, for example, light out-coupling efficiency is limited by the randomly oriented transition dipole moments of the emitting molecules [4–6]. If we can make the orientation of the transition dipole moments of the emitting molecules in OLEDs completely parallel to the substrate, the light out-coupling efficiency becomes

\* Corresponding author. Address: Center for Future Chemistry, Kyushu University, 744 Motoooka, Nishi, Fukuoka 819-0395, Japan. Tel./fax: +81 92 802 3294.

E-mail address: [adachi@cstf.kyushu-u.ac.jp](mailto:adachi@cstf.kyushu-u.ac.jp) (C. Adachi).

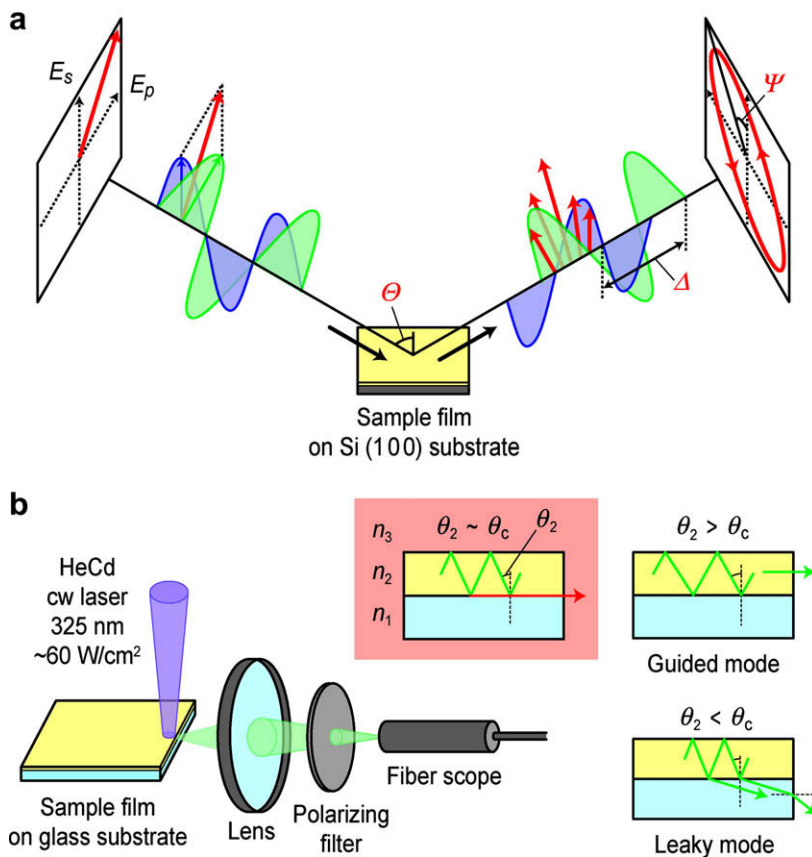


**Fig. 1.** (Color online) Schematic illustrations of experimental setup of two independent methods for detection of anisotropy in organic amorphous films. (a) Variable angle spectroscopic ellipsometry (VASE) [7]. Linearly polarized light is incident to an organic film deposited on a Si substrate with different incident angles of  $\theta$ . The ellipsometry parameters  $\Psi$  and  $\Delta$ , which represent the ratio of amplitudes of s- and p-polarized components of the incident light and the phase difference between them, respectively, are obtained for multiple incident angles and wavelengths. (b) Cutoff emission measurement (CEM). Organic films on glass substrates were optically pumped near the edges of the substrates by ultraviolet light from a cw He–Cd laser. Spectral shapes of edge emissions often significantly differ from the normal PL spectral shapes, and the peak wavelengths of the narrowed bands are in good agreement with the cutoff wavelengths of the slab waveguides composed of the glass substrate (with a refractive index of  $n_1$ ), organic film ( $n_2$ ) and air ( $n_3$ ). The cutoff emission occurs as a boundary phenomenon between the cases where light is guided and where light is leaky, which means that the incident angle in the organic film  $\theta_2$  corresponds to the critical angle of the waveguide  $\theta_c$ .

~50% higher than when the orientation of the transition dipole moments is random [6]. In organic semiconductor laser devices, the random orientation is also not favorable because the alignment of transition dipole moments of emitting molecules makes it easy for stimulated emissions to occur. Furthermore, the alignment of molecules can facilitate charge carrier transport because it makes the overlap of  $\pi$ -orbitals of adjacent molecules larger.

Although complete alignment of molecules is natural in organic single crystals, it is not easy to prepare single crystal thin films having a desired thickness and a smooth flat surface on a nm-scale by a simple fabrication technique. Therefore, instead of preparing ideal molecular single crystal films, realization of quasi-molecular orientation in smooth organic amorphous films is a right strategy to fabricate large-area organic high-performance devices with low cost. In this study, we pay attention on this viewpoint and investigate the molecular orientation in neat and doped organic amorphous films and its mechanism.

The molecular orientation in thin films can be detected by measuring the optical anisotropy in the films. One of the

best methods of investigating the optical properties of thin films is spectroscopic ellipsometry [7]. In particular, variable angle spectroscopic ellipsometry (VASE) is very sensitive to optical anisotropy in films and has been widely used to determine optical constants of anisotropic films. Variable angle spectroscopic ellipsometry has also been used to investigate many kinds of anisotropic films made from spin-coated polymers [8–11], and is reliable technique for determining optical properties not only of inorganic films but also of organic films. Because a smooth surface of a film makes it easier to analyze and determine optical constants, organic amorphous films are also good subjects for VASE measurement. Recently, Lin et al. [12] first reported the application of this technique to vacuum-deposited organic amorphous films and detected uniaxial anisotropies in ter(9,9-diarylfuorene)s thin films. They also demonstrated that the molecular orientation affect the amplified spontaneous emission thresholds of the films [13].

The other method used to detect anisotropy in films is measurement of emissions at cutoff wavelengths [14] from



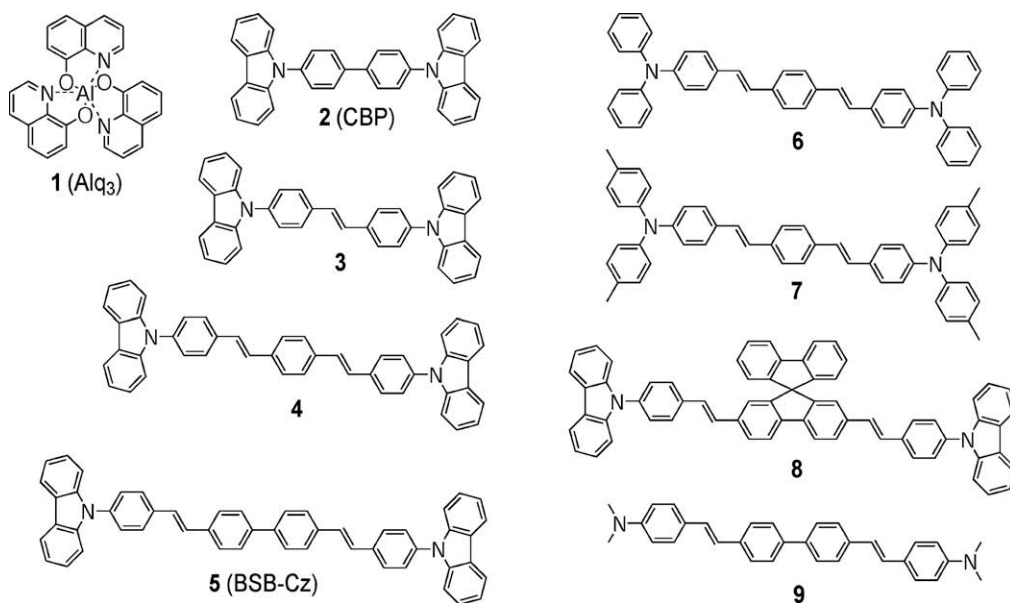


Fig. 2. Molecular structures of materials used in this study.

edges of substrates though it can only be applied to light-emitting films having a smooth surface [15–22]. With this method, a characteristic spectrum having a narrow band at the cutoff wavelength can be observed in the direction parallel to the substrate surface. Because the polarization characteristics of the emissions are related to the direction of the transition dipole moments of the emitting molecules, optical anisotropy in films can be detected. Using this cutoff emission measurement (CEM), anisotropy of spin-coated polymers has been investigated [15–20]. However, detailed analysis of the relation between peak wavelengths of the emissions and anisotropic refractive indices has not yet been completed.

Recently, we observed spectrally narrow emissions from organic vacuum-deposited amorphous films [21,22] and found that they originate in the cutoff phenomenon [22]. Here, we demonstrate that there are large anisotropies in vacuum-deposited amorphous films of fluorescent bis-styrylbenzene derivatives and that the ordinary refractive indices of the films of the bis-styrylbenzene derivatives are significantly higher than the extraordinary ones, showing the horizontal orientation of the molecules in the amorphous films fabricated by vacuum deposition. Using VASE, we proved the large anisotropy in the films of the bis-styrylbenzene derivatives. We also show the dependence of the anisotropy on molecular structures and underlying layers and discuss the mechanism causing the anisotropy in vacuum-deposited amorphous film. Furthermore, we demonstrate the optical anisotropy in the films of the bis-styrylbenzene derivatives by using CEM in addition to VASE. Detailed analysis of the relation between peak wavelengths of the cutoff emissions and anisotropic refractive indices is also performed. Although the two methods are completely independent of each other, as shown in Figs. 1a and b, there was excellent agreement between their results, showing the reliability of the results

obtained by the two methods. By using CEM on doped amorphous films, furthermore, we also found the horizontal orientation of doped molecules even in isotropic host matrix films.

## 2. Results and discussion

### 2.1. VASE analysis

Molecular structures of materials studied in this study are listed in Fig. 2. We selected styrylbenzene derivatives (materials 3–9) having carbazole or diphenylamine groups at both ends of the molecules. Although it seems from the formulas that these styrylbenzene derivatives have planar structures, they actually twist to avoid steric repulsion. We also previously demonstrated that bis-styrylbenzene derivatives are laser-active materials whose doped films have extremely low ASE thresholds [23,24]. The neat films fabricated by vacuum deposition are amorphous except material 9. Tris(8-hydroxyquinoline)aluminum ( $\text{Alq}_3$ , material 1) was used as a reference having an isotropic optical property. 4,4'-bis(*N*-carbazole)-biphenyl (CBP, material 2) was used as a material having a short molecular length. CBP was also used as a host material for the doped films.

Figures 3a–c show the experimental and simulated ellipsometric parameters  $\Psi$  and  $\Delta$  of the  $\text{Alq}_3$ , CBP and 4,4'-bis[(*N*-carbazole)styryl]biphenyl (BSB-Cz, material 5 in Fig. 2) films with the thickness of  $\sim 100$  nm on silicon substrates, respectively. Their surface appearances are very smooth and they are amorphous. The values of root mean square (RMS) of the surface roughness of the  $\text{Alq}_3$ , CBP and BSB-Cz films measured by atomic force microscope (AFM) were 0.5, 0.9 and 0.4 nm, respectively.

All the ellipsometric parameters of the  $\text{Alq}_3$  film obtained by VASE measurement were exactly simulated using an isotropic model. As shown in Fig. 3a, the experi-

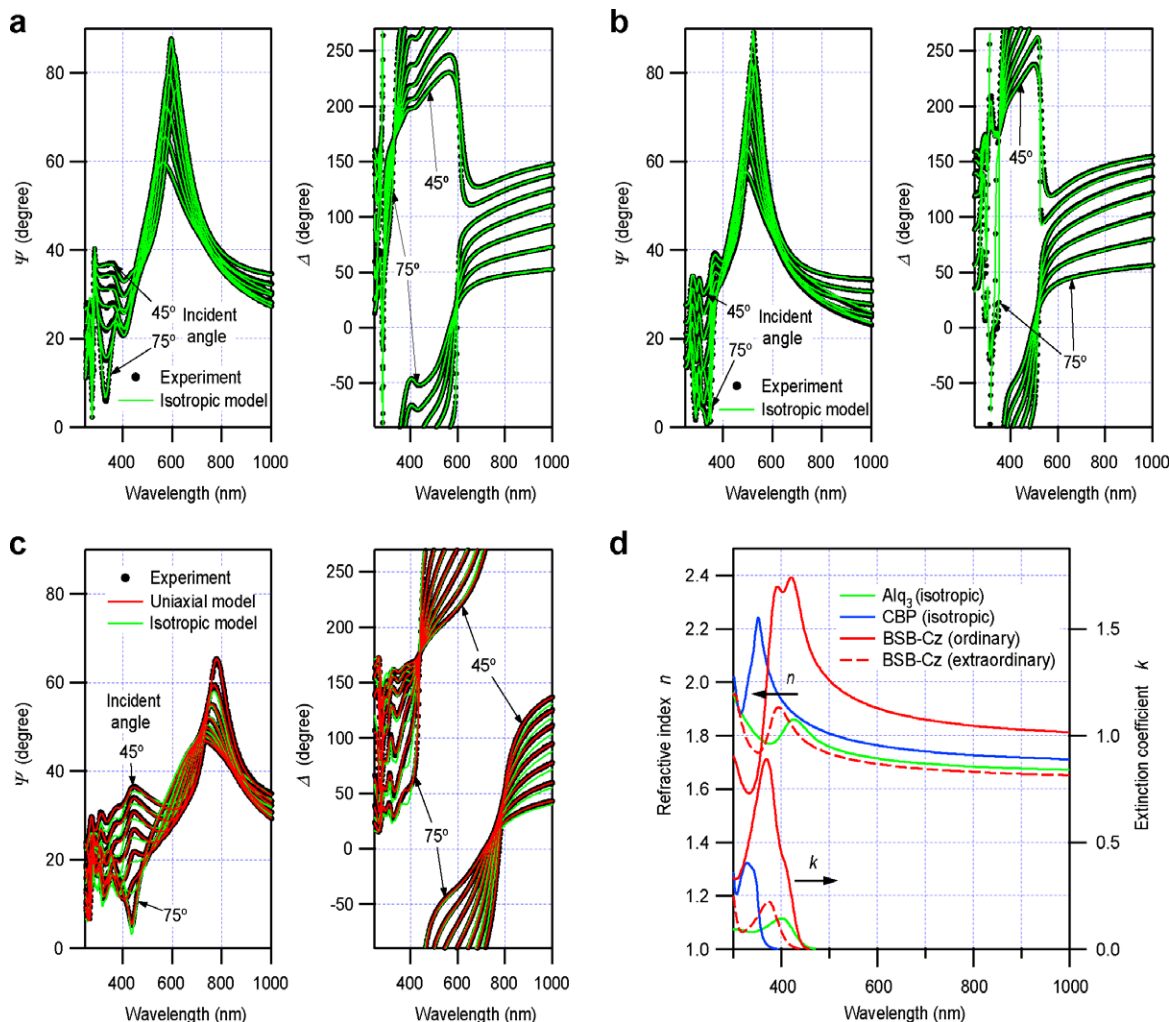


**Fig. 3.** (Color online) Experimental and simulated ellipsometric parameters  $\Psi$  and  $\Delta$ , and determined refractive indices of organic films. (a)–(c) Experimental (black dots) and simulated (green and red lines) ellipsometry parameters at incident angles from  $45^\circ$  to  $75^\circ$  in steps of  $5^\circ$  in the spectral region from 245 to 1000 nm for Alq<sub>3</sub> (a), CBP (b) and BSB-Cz (c). Because only the values simulated with an isotropic model (green lines) of the BSB-Cz film are not in good agreement with the experimental values, a uniaxial anisotropic model (red lines) is also used in the case of BSB-Cz. (d) Refractive indices and extinction coefficients of Alq<sub>3</sub> (green lines), CBP (blue lines) and BSB-Cz (red solid and broken lines) films. The ordinary refractive index of the BSB-Cz film is much higher than the extraordinary refractive index, meaning that there is horizontal orientation of BSB-Cz molecules in the BSB-Cz films.

mental and simulated curves exactly overlap. As well as the Alq<sub>3</sub> film, the ellipsometric parameters of the CBP film were also simulated using an isotropic model as shown in Fig. 3b.

In contrast to the Alq<sub>3</sub> and CBP films, the ellipsometric parameters of the BSB-Cz film could not be well simulated using an isotropic model even if many oscillators were included in the analysis. Other complicated models could also not compensate the deviation. For example, we tried to simulate the parameters on the assumption of a non-uniform refractive index in the film or existence of the interface layer between the substrate and the organic layer, but a good fitting could not be obtained. The ellipsometric parameters of the BSB-Cz film could be well simulated only using a uniaxial anisotropic model. This shows the uniqueness of analysis by VASE. As shown in Fig. 3c,

the ellipsometric parameters simulated using the uniaxial anisotropic model were in excellent agreement with the experimental parameters whereas the parameters simulated using the isotropic model do not correspond well. These results demonstrate the anisotropy in the BSB-Cz film. We also checked whether the in-plane anisotropy exists in the BSB-Cz film by rotating the sample, resulting in no in-plane difference.

The degree of fitting can be relatively quantified by a mean square error (MSE) [25]. The MSE values for the Alq<sub>3</sub>, CBP and BSB-Cz films obtained using the isotropic models were 5.8, 8.2 and 35, respectively. The much higher value for the BSB-Cz film means that the parameters could not be well simulated by the isotropic model. The MSE value for the BSB-Cz film obtained using the uniaxial anisotropic model was 4.2, which is comparable to that for the

Alq<sub>3</sub> film obtained using the isotropic model. The slightly higher MSE value for the CBP film than that for the Alq<sub>3</sub> film indicate the very slight anisotropy in the CBP film, as shown later. Actually, the MSE value for the CBP film became 2.8 when using a uniaxial anisotropic model.

The refractive indices and the extinction constants of the Alq<sub>3</sub>, CBP and BSB-Cz films are shown in Fig. 3d. The BSB-Cz film has uniaxial anisotropy, and the ordinary refractive index is much higher than the extraordinary one. The difference between them at 550 nm (near the center of visible wavelength),  $\Delta n$ , is 0.23, which means a very large birefringence of the film. The validity of the obtained refractive indices is demonstrated again by CEM, as shown later. The ordinary extinction constant is also much higher than the extraordinary one.

Because the transition dipole moment of the BSB-Cz molecule is almost along the molecular long axis, the ordinary extinction constant that is higher than the extraordinary one means that the BSB-Cz molecules in the film lie nearly parallel to the silicon substrate surface. The ordinary refractive index is also much higher than the extraordinary one because  $\pi$ -electrons in molecules can be moved by external electric fields more easily in the direction of the molecular long axis than in the direction perpendicular to it. Furthermore, no in-plane anisotropy means that the BSB-Cz molecules lie in random directions in the film. In our separate experiment, we could not observe apparent peaks in the X-ray diffraction (XRD) patterns of the BSB-Cz film as well as the Alq<sub>3</sub> films. From these results, we conclude that the BSB-Cz film is in a “horizontally oriented amorphous state”, where molecules are horizontally oriented on the substrate, but there is no crystallographic structure because the in-plane molecular orientation is random. The similar results of the horizontal molecular orientation in ter(9,9-diarylfuorene)s thin films using VASE were reported by Lin et al. [12].

We further investigated the dependence of the anisotropy on molecular structures of styrylbenzene derivatives to determine the mechanism causing anisotropy in vacuum-deposited amorphous film. The anisotropies in the amorphous films made from the materials in Fig. 2 are summarized in Table 1. Variable angle spectroscopic ellipsometry measurement and analysis of each film were carried out in the same way as for the BSB-Cz film to compare the results equally. We found that the films of all the styrylbenzene derivatives (materials 3–8) also have smooth surfaces and optical anisotropies except material 9 which forms a polycrystalline state with a rough surface by vacuum deposition. First, we focused attention on molecular length because the anisotropy in vacuum-deposited polycrystalline films of paraffin changes depending on the molecular length [26,27]. By comparison of the anisotropy in the film of materials 2–5, we found that a long molecular structure is essential for large anisotropy. Figures 4a–d show the optical constants of the film of materials 2–5 determined by VASE using uniaxial anisotropic models. The longer the molecular length is, the larger the birefringence  $\Delta n$  becomes.

The birefringence of the films, however, does not directly reflect the anisotropy of the molecular orientation

because each molecule itself has the anisotropy of molecular polarizability. To clarify the relation between the molecular orientation and the molecular structure, we introduced an orientation order parameter  $S$  as an index of molecular orientation [28]; that is

$$S = P_2(\cos \theta) = \frac{1}{2} (3 \cos^2 \theta - 1) = \frac{k_e - k_o}{k_e + 2k_o}, \quad (1)$$

where  $P_2(x)$  is the second Legendre polynomial,  $\langle \dots \rangle$  indicates ensemble average,  $\theta$  is the angle between the molecular long axis and the direction perpendicular to the substrate surface, and  $k_o$  and  $k_e$  are the ordinary and extraordinary extinction coefficients at the peak wavelength, respectively.  $S = -0.5$  if the molecules are completely parallel to the surfaces,  $S = 0$  if they are randomly oriented, and  $S = 1$  if they are completely perpendicular to the surface. The last term in Eq. (1) can be calculated using extinction coefficients determined by VASE using uniaxial anisotropic models, which is based on the assumption that the transition dipole moment of the molecule is parallel to the molecular axis. The values of  $S$  are also summarized in Table 1. The results of materials 2–5 clearly demonstrate the relation between the molecular orientation and the molecular length; that is, the longer the molecular length is, the larger the anisotropy of the molecular orientation becomes. From the results of materials 6 and 7, we found that bis-styrylbenzene derivatives having diphenylamine groups at both ends are also horizontally oriented in the films. Furthermore, the difference in  $S$  of materials 5 and 8 shows that the introduction of bulky central moieties makes anisotropy small.

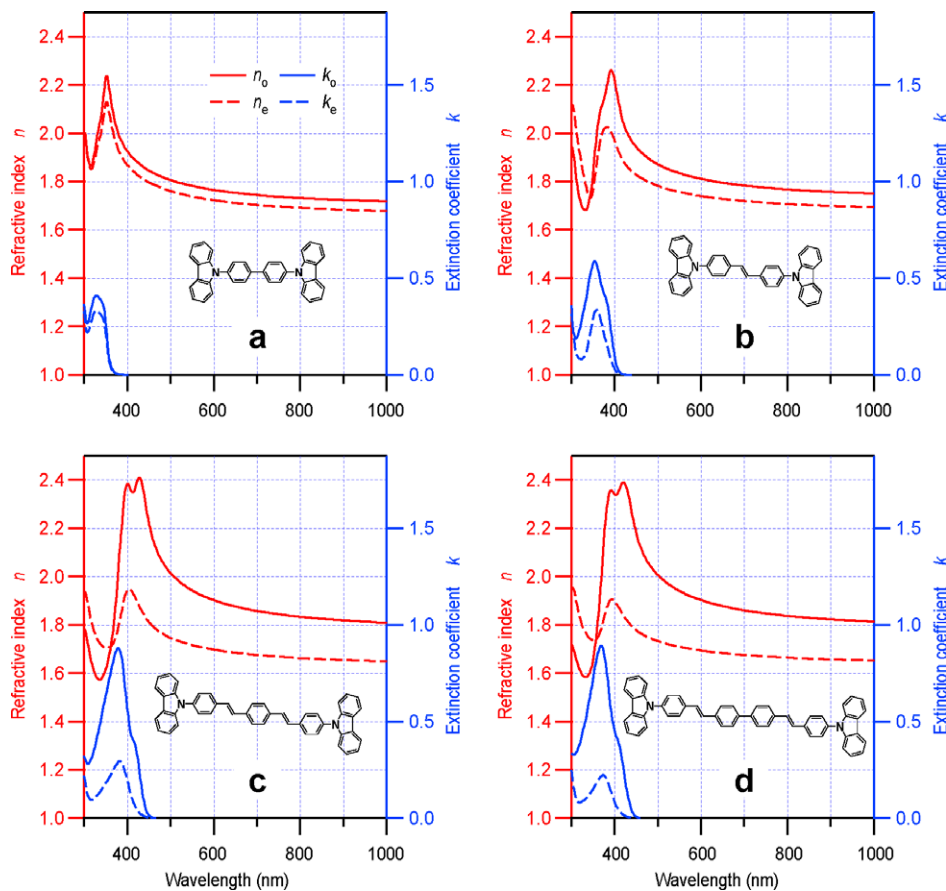
Interestingly, we found that the horizontal molecular orientation can occur on any underlying layers, as shown in Table 2. The large anisotropies in the BSB-Cz films on a silicon substrate, a glass substrate, a 50-nm-thick CBP layer, a 100-nm-thick Ag layer, and a 30-nm-thick smooth ITO layer with an RMS of 0.6 nm were obtained. These results are very important because they mean the high versatility of the horizontal orientation for various applications to organic devices, such as OLEDs, in which an emitting layer is usually sandwiched between electrodes and/or other organic layers.

From the above results, it is reasonable to assume that the molecular orientation in amorphous film is caused only by the weak interactions between the molecule and the underlying layer and the successive weak interaction between the adjacent molecules. As shown in Fig. 5a, in the case of a molecule which has a linear-shaped structure with no bulky substituent, such as material 9, there is a very strong interaction between the molecules. We think that although the molecules are horizontally oriented just after deposition due to the van der Waals interaction between the molecule and the underlying layer, successive aggregation and crystallization occur due to the strong interaction between the molecules. In contrast, in the case of a molecule which has a linear-shaped structure and bulky substituents, such as BSB-Cz, the bulky substituents avoid aggregation and crystallization, resulting in keeping the horizontal orientation, as shown in Fig. 5b. The van der Waals interaction between the molecules is not so

**Table 1**

Ordinary and extraordinary refractive indices of films on Si substrates at wavelength of 550 nm and orientation order parameters.

Material	Molecular length (Å)	Ordinary refractive index $n_o$	Extraordinary refractive index $n_e$	Birefringence $\Delta n = n_o - n_e$	Orientation order parameter $S$
<b>2</b> (CBP)	19	1.78	1.74	0.04	-0.07
<b>3</b>	21	1.83	1.76	0.08	-0.17
<b>4</b>	28	1.94	1.72	0.23	-0.29
<b>5</b> (BSB-Cz)	32	1.94	1.71	0.23	-0.33
<b>6</b>	27	1.98	1.73	0.24	-0.26
<b>7</b>	28	1.95	1.70	0.25	-0.26
<b>8</b>	31	1.86	1.76	0.10	-0.28

**Fig. 4.** (Color online) Dependence of ordinary and extraordinary refractive indices (red lines) and extinction coefficients (blue lines) on molecular length. (a) Material **2** (CBP), (b) material **3**, (c) material **4**, (d) material **5** (BSB-Cz). The longer the molecular length is, the larger the differences of ordinary and extraordinary optical constants become.**Table 2**

Dependence of ordinary and extraordinary refractive indices of BSB-Cz films at wavelength of 550 nm and orientation order parameters on underlying layer.

Underlying layer	Ordinary refractive index $n_o$	Extraordinary refractive index $n_e$	Birefringence $\Delta n = n_o - n_e$	Orientation order parameter $S$
Si substrate	1.94	1.71	0.23	-0.33
Glass substrate	1.97	1.74	0.23	-0.45
CBP layer (50 nm) on Si substrate	1.93	1.70	0.23	-0.39
Ag layer (100 nm) on glass substrate	1.90	1.71	0.19	-0.36
ITO layer (30 nm) on glass substrate	1.93	1.76	0.18	-0.31

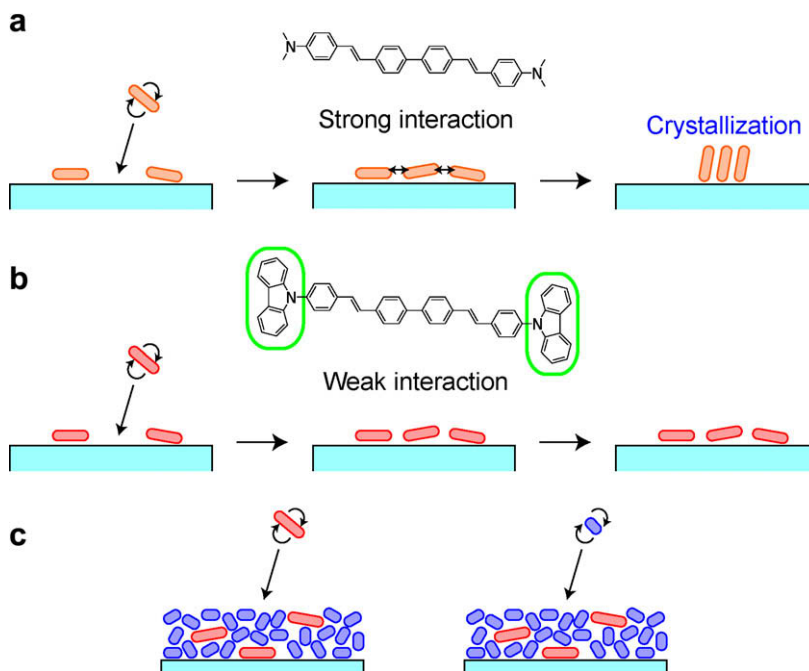


**Fig. 5.** (Color online) Schematic illustrations of horizontal molecular orientation. (a) Aggregation of molecules having linear-shaped structure without bulky substituents, (b) horizontal orientation of molecules having linear-shaped structure with bulky substituents, and (c) independent depositions of guest and host molecules on flat surface of doped film in which guest molecules having linear-shaped structure are horizontally oriented in a host matrix.

strong due to the presence of rather bulky substituents of carbazole or diphenylamine groups and the primary van der Waals interactions between the molecule and the underlying layer induce horizontal orientation to minimize the surface energy. After the formation of the horizontal orientation of the first molecular layer on the underlying layer, successive molecular orientations would occur due to the weak van der Waals interaction between the molecules without significant aggregation and crystallization.

## 2.2. CEM analysis

Next, we demonstrate that the molecular orientation based on the results of CEM. Figures 6a–d show cutoff emission spectra of the Alq<sub>3</sub>, CBP, BSB-Cz and 6 wt%-BSB-Cz-doped CBP films with 15 different thicknesses on glass substrates under optical excitation. We observed spectrally narrow bands that were strongly polarized in transverse electric (TE) mode or transverse magnetic (TM) mode. The electric field in TE mode is polarized parallel to the substrate surface, and that in TM mode is polarized in the plain perpendicular to it. All the TE and TM spectra in Figs. 6a–d are normalized such that the peak intensities of the TE spectra become unity while keeping the ratios of the intensities of the TE and TM spectra. The ratios of the intensities of the TE and TM emissions reflect both the direction of the transition dipole moment of the emitting molecules in the organic film and the intensity of the normal photoluminescent (PL) spectrum of the film at the peak wavelengths of the narrow TE and TM emissions. In the case of the isotropic Alq<sub>3</sub> and CBP films, the intensities of the TE and TM emissions were almost identical on the

whole, as shown in Figs. 6a and b. In contrast, Fig. 6c shows that the intensities of the TE emissions of the BSB-Cz films are much higher than those of the TM emissions. This result means that the transition dipole moments of the molecules in the film are nearly parallel to the polarization direction of the TE emissions. Thus, the horizontal orientation of the molecules on glass substrates is demonstrated by CEM independently of VASE.

Furthermore, because the weak interaction between molecules causes the horizontal orientation, guest molecules having a linear-shaped structure can be horizontally oriented in host films. Fig. 6d shows the cutoff emissions from the edges of 6 wt%-BSB-Cz-doped CBP films. It should be noted that the TM emissions from the BSB-Cz-doped CBP films were depressed compared to the TM emissions from the neat CBP films shown in Fig. 6b. (Although the high TM intensities are apparently seen at the thicknesses of ~100 and ~380 nm in Fig. 6d, it does not mean random orientation or normal orientation. Because the cutoff wavelengths of TE modes at these thicknesses are accidentally out of the PL spectral region, as shown later, the absolute intensities of the TE emissions became low. Furthermore, because the cutoff wavelengths of the TM emissions are inside the PL region, the intensities of the TM emissions became *relatively* high compared to those of the TE emissions at these thicknesses.) This result shows the horizontal orientation of the guest BSB-Cz molecules even in the isotropic host matrix of the CBP film. It can be well understood with assumptions that the surface of the films is always smooth on nm-scale during co-deposition and that the depositions of each BSB-Cz and CBP molecules are independent due to the weak interaction

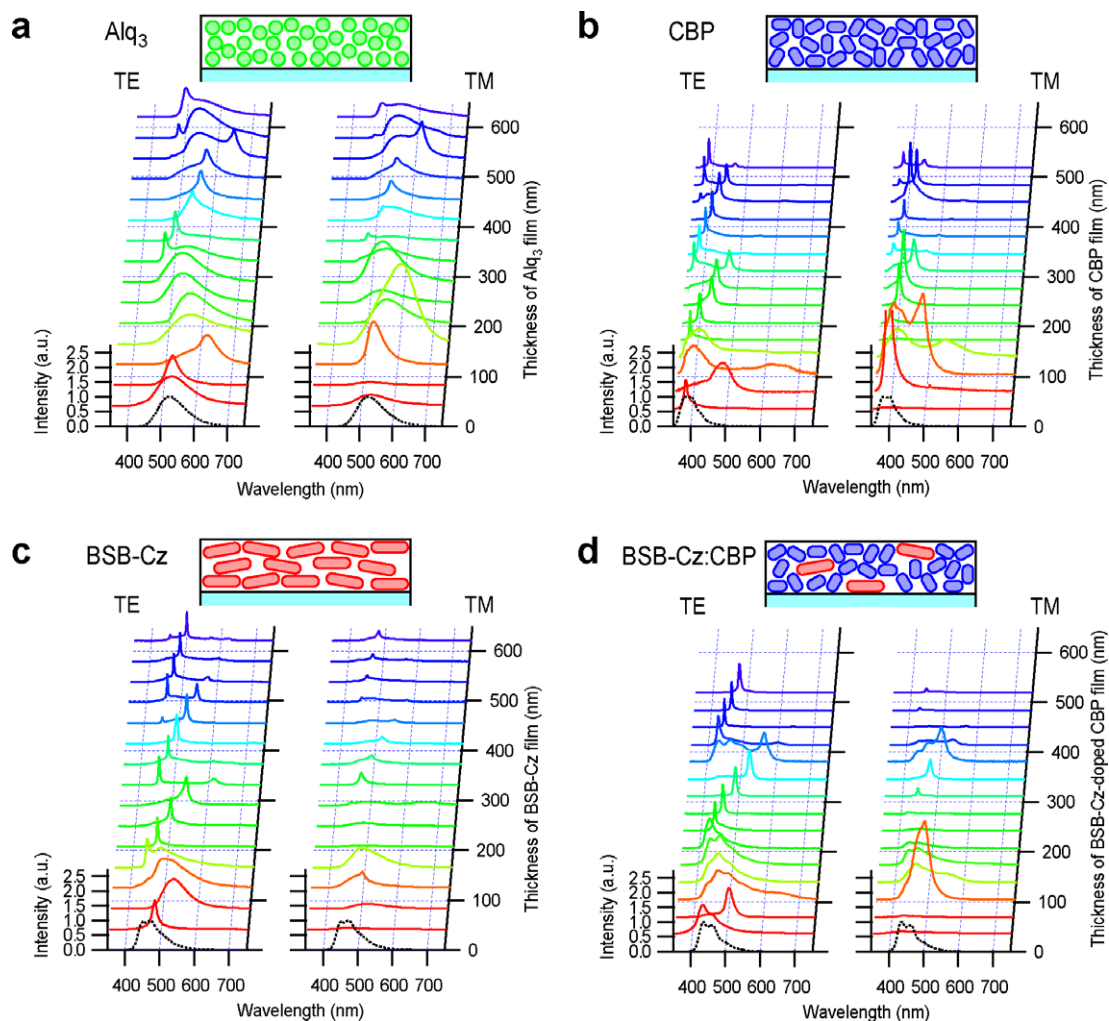


**Fig. 6.** (Color online) Dependence of cutoff emission spectrum on polarization direction and thickness of organic film. (a) Alq<sub>3</sub>, (b) CBP, (c) BSB-Cz, and (d) 6 wt%-BSB-Cz-doped CBP. Insets: Schematic illustrations of molecular orientations in films. All the TE and TM spectra are normalized such that the peak intensities of the TE spectra become unity while keeping the ratios of intensities of the TE and TM spectra. Normal PL spectra are shown by black broken lines. In the case of the isotropic films (Alq<sub>3</sub> and CBP), the intensities of the TE and TM spectra are not so different on the whole. In contrast, the intensities of the TE spectra are higher than those of the TM spectra on the whole in the case of BSB-Cz and 6 wt%-BSB-Cz-doped CBP, showing the orientation of BSB-Cz molecules.

between them, as shown in Fig. 5c. The BSB-Cz molecules are horizontally deposited on the surface of the doped film, as in the case where BSB-Cz molecules are deposited on a CBP underlying layer (see Table 2).

The validity of the results obtained by VASE and CEM is also shown in Fig. 7a–d, in which the peak wavelength of the cutoff emissions and the calculated cutoff wavelength of the films with different thicknesses are both shown. The former was obtained by CEM, and the latter was obtained by calculations according to the process written in Section 4 using refractive indices obtained by VASE (shown in Fig. 3d). They were obtained by the two independent methods using different substrates. The cutoff wavelengths of the slab waveguide composed of a glass substrate, an isotropic organic film (Alq<sub>3</sub> or CBP), and air were directly calculated using Eqs. (6) and (7) in Section 4. As shown in Figs. 7a and b, the peak

wavelength of the cutoff emissions and the calculated cutoff wavelength are in good agreement with each other. The peak wavelengths shift in the spectral region of the normal PL spectrum with an increase in the film thickness, and then the narrow emission having the next mode number appear from the short-wavelength side. The peak wavelengths of the TE and TM emissions are adjacent to each other and the wavelengths of the TE emissions are slightly longer than those of the TM emissions, which are the characteristics of a slab waveguide with an isotropic layer.

In contrast, the peak wavelengths of the emissions from the neat BSB-Cz films change in a different way, depending on the thickness, as shown in Fig. 5c. The peak wavelengths of the TE and TM emissions are not always adjacent. Here, we succeeded in simulating this behavior by a calculation in which we took into account the anisotropy in the BSB-

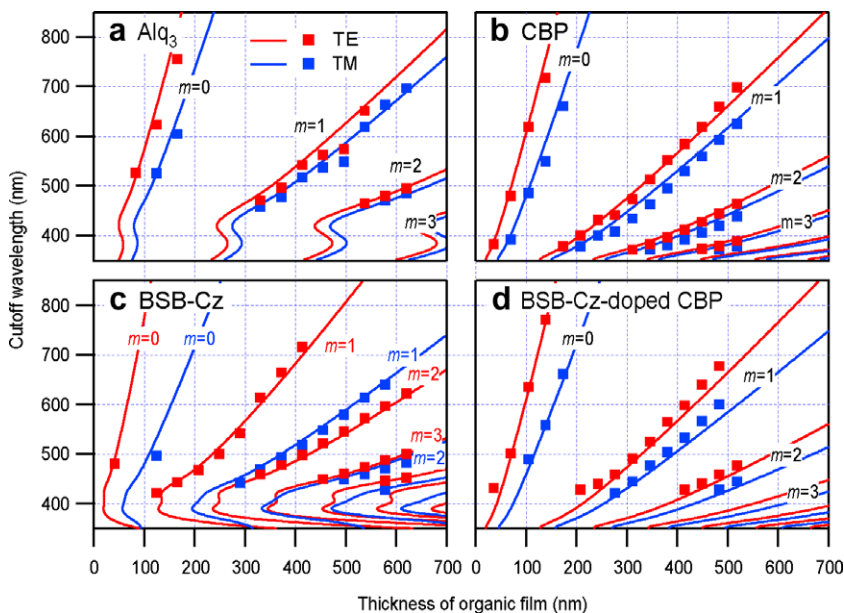


**Fig. 7.** (Color online) Agreement of experimental peak wavelengths of cutoff emissions and calculated cutoff wavelengths of slab waveguides. The peak wavelengths of the TE and TM emissions (red and blue squares, respectively) and the cutoff wavelengths calculated using the refractive indices (red and blue lines, respectively) are indicated. (a) Alq<sub>3</sub>, (b) CBP, (c) BSB-Cz, and (d) 6 wt%-BSB-Cz-doped CBP. The cutoff wavelengths in (d) are calculated using isotropic optical constants of a neat CBP film. Except for BSB-Cz, the peak wavelengths of the TE and TM emissions are always adjacent to each other. This is a characteristic of a slab waveguide with an isotropic core layer. Only the peak wavelengths of the emission from the neat BSB-Cz films change in a different way depending on the thickness and can be simulated using the equation of the index ellipsoid of the anisotropic film.

Cz film according to the process using the equation of the index ellipsoid, as shown in Section 4. The peak wavelengths and the calculated cutoff wavelength exactly corresponded, demonstrating the validity of the results obtained by both VASE and CEM.

The peak wavelengths of the cutoff emissions from the BSB-Cz-doped CBP films nearly corresponded to the calculated cutoff wavelengths of the waveguide with the isotropic CBP film though slight deviations were found, as shown in Fig. 5d. The deviation of the TE modes in the short-wavelength region is due to perturbation by the doped BSB-Cz molecules because the ordinary refractive index of the BSB-Cz film is much higher than that of the CBP film. This result demonstrates the horizontal orientation of doped emitting molecules in the host film having the low ordinary refractive index, which is necessary to improve out-coupling efficiency of OLEDs. The out-coupling efficiency is affected not only by the orientation of transition dipole moments but also by the refractive index of emitting layer  $n_{em}$  with the  $1/n_{em}^2$  relation [6]. Thus, a high ordinary refractive index is not favorable because it cancels out the effect of the horizontal orientation on the out-coupling efficiency. In addition, the horizontal orientation of emitting molecules in doped film is important because doping techniques are frequently used in the fabrication of OLEDs and organic laser devices to avoid concentration quenching.

### 3. Conclusions

In this study, we found that the linear-shaped molecules of fluorescent styrylbenzene derivatives are horizon-

tally oriented in organic amorphous films fabricated by conventional vacuum deposition even when the molecules are doped in an isotropic host matrix film. The weak interaction between adjacent molecules and the linear-shaped molecular structure probably cause the horizontal orientation. The fact that the horizontal molecular orientation occurs on any underlying layers shows the high versatility of the horizontal orientation for various applications. Our findings will lead to an improvement in optical and electrical characteristics of organic amorphous films and optoelectronic devices made from them. Moreover, there is a possibility that the horizontal molecular orientation inheres in many amorphous films having high-performance optical or electrical characteristics though it has not yet been noticed. Actually, we recently also detected the anisotropies in the films of many hole and electron transport materials having long or planar structures [29]. We think that it is meaningful to reevaluate the optical and electrical properties of organic materials in terms of their molecular orientation.

### 4. Experimental and calculations

All samples of organic films for ellipsometry measurement were prepared by vacuum deposition. Silicon (100) substrates were cleaned using detergent and organic solvents. Glass substrates with and without a 30-nm-thick ITO layer were cleaned using detergent and organic solvents and then subjected to UV-ozone treatment. A glass substrate with a 100-nm-thick Ag layer was also prepared by deposition of Ag on the cleaned glass substrate at an evaporation rate of  $\sim 0.1$  nm/s in a vacuum of

$<1 \times 10^{-3}$  Pa and kept without air exposure. All organic films were thermally evaporated on the substrates in a vacuum of  $<3 \times 10^{-3}$  Pa at an evaporation rate of  $\sim 0.2$  nm/s. A 6 wt%-BSB-Cz-doped CBP film was also fabricated by co-deposition. The thicknesses of all the samples were  $\sim 100$  nm.

Surface roughness of the films was measured using an AFM (D-3000, Veeco Instruments Inc.). Out-of-plane and in-plane XRD patterns of the Alq<sub>3</sub> and BSB-Cz films on silicon substrate were measured using a high-resolution XRD diffractometer (SmartLab, Rigaku Corporation).

Variable angle spectroscopic ellipsometry was performed using a fast spectroscopic ellipsometer (M-2000U, J. A. Woollam Co., Inc.). Measurements were taken at seven multiple angles of the incident light from 45° to 75° in steps of 5°. At each angle, experimental ellipsometric parameters  $\Psi$  and  $\Delta$  were simultaneously obtained in steps of 1.6 nm throughout the spectral region from 245 to 1000 nm. All measurements for one sample were done only at  $\sim 90$  s.

The analysis of the data was performed using the software “WVASE32” (J. A. Woollam Co., Inc.), which can perform a batch analysis of all the data at all the different incident angles and wavelengths. The model function system of dielectric constants  $\epsilon_1$  and  $\epsilon_2$  of the organic films, which satisfies the Kramers-Kronig consistency, was composed of Gaussian and Tauc-Lorentz oscillators [30] with a Sellmeier background. Physically reasonable values were adopted as the initial values of the structural and optical parameters of the model functions. Then, the parameters were optimized to fit the simulated values of  $\Psi$  and  $\Delta$  to the experimental values to minimize the value of the MSE [25]. The complex refractive indices of the films  $N = n + ik$  were also calculated using the values determined for  $\epsilon_1$  and  $\epsilon_2$ . Analysis using uniaxial anisotropic models [7] was also performed to determine the anisotropy in the films of the styrylbenzene derivatives. Only the amplitudes of the oscillators were independently changed in the model function systems of the ordinary and extraordinary dielectric constants. The other parameters were changed while keeping the common values in these systems. The dielectric constants of the ITO layer were estimated in advance using Drude and Tauc-Lorentz oscillators. Throughout all the above analysis, we assumed a uniform optical property of the films with a smooth surface, and complicated models, such as a surface roughness layer, a non-uniform layer, or an interface layer, were not used because they make the uniqueness of analysis low.

Molecular lengths of materials were roughly estimated from the optimized geometries obtained by density functional theory calculations using GAUSSIAN 03 program [31]. B3LYP calculations were performed using 6-31G(d) basis.

All samples of organic films for measurement of cutoff emissions were also prepared by vacuum deposition under the same conditions. The organic films, which had 15 different thicknesses, were deposited on the clean glass substrates having a refractive index of 1.524. The glass substrates with the organic film were cleaved, and the organic films were optically pumped near the edge of the cleavage face using a cw He–Cd laser (IK3102R-G, Kimmon

Electric Co.). An incident beam with a wavelength of 325 nm was focused on the surface of the organic films by a lens. The excitation energy of the beam was 60 W/cm<sup>2</sup>. The edge emissions were collected using a multichannel spectrometer (PMA-11, Hamamatsu Photonics Co.) that has an optical fiber with a receiving diameter of 1 mm. The polarization characteristics of the edge emissions were measured through a polarizing filter placed between the sample and the end of the fiber.

The cutoff wavelengths of waveguides with an isotropic and uniaxial anisotropic organic core layers were calculated as below. The wavelength of the light that propagates in a waveguide should satisfy the phase matching condition represented by

$$\frac{4\pi n_2 d \cos \theta_2}{\lambda} + \phi_{21} + \phi_{23} = 2m\pi, \quad (2)$$

where  $d$  is the thickness of the core layer,  $\lambda$  is the free space wavelength of light,  $\phi_{21}$  and  $\phi_{23}$  are the phase shifts at interfaces 21 and 23, respectively, and  $m$  is the mode number ( $m = 0, 1, 2, \dots$ ) (see also Fig. 1b). The phase shifts depend on the polarization direction and are represented for the TE and TM modes by

$$\phi_{2i}^{\text{TE}} = -2 \tan^{-1} \frac{(n_2^2 \sin^2 \theta_2 - n_i^2)^{1/2}}{n_2 \cos \theta_2} \quad (i = 1 \text{ or } 3) \quad (3)$$

and

$$\phi_{2i}^{\text{TM}} = -2 \tan^{-1} \frac{n_2(n_2^2 \sin^2 \theta_2 - n_i^2)^{1/2}}{n_i^2 \cos \theta_2} \quad (i = 1 \text{ or } 3) \quad (4)$$

respectively. If the wavelength of light is very close to the cutoff wavelength, incident angle  $\theta_2$  corresponds to the critical angle  $\theta_c$ , that is

$$\theta_2 = \theta_c = \sin^{-1}(n_1/n_2). \quad (5)$$

From Eqs. (2)–(5), we obtain the cutoff wavelength for the TE and TM modes,

$$\lambda_c^{\text{TE}} = \frac{2\pi d(n_2^2 - n_1^2)^{1/2}}{\tan^{-1} \left( \frac{n_1^2 - n_2^2}{n_2^2 - n_1^2} \right)^{1/2} + m\pi} \quad (6)$$

and

$$\lambda_c^{\text{TM}} = \frac{2\pi d(n_2^2 - n_1^2)^{1/2}}{\tan^{-1} \left[ \frac{n_2^2}{n_3^2} \left( \frac{n_1^2 - n_2^2}{n_2^2 - n_1^2} \right)^{1/2} \right] + m\pi}, \quad (7)$$

respectively. Here,  $d$  is the thickness of the organic film, and  $n_1$ ,  $n_2$ , and  $n_3$  are the refractive indices of the glass substrate ( $n_1 = 1.524$ ), the organic film, and air ( $n_3 = 1$ ), respectively. The refractive indices of the organic films  $n_2$  in all the above equations depend on the wavelength of light. Using Eqs. (6) and (7), we can directly calculate cutoff wavelengths of a waveguide with an isotropic core layer at a certain thickness. When a core layer has a uniaxial anisotropic property, the calculations become more complicated because the refractive indices for the light of the TE and TM modes are different. The refractive index for the light of the TE mode  $n_2^{\text{TE}}$  is simply equal to the ordinary refractive index, while that of the TM mode  $n_2^{\text{TM}}$  depends on



angle  $\theta_2$  according to the equation of an index ellipsoid. They are represented by

$$n_2^{\text{TE}} = n_o, \quad (8)$$

and

$$\frac{1}{n_2^{\text{TM}}(\theta_2)^2} = \frac{\cos^2 \theta_2}{n_o^2} + \frac{\sin^2 \theta_2}{n_e^2}, \quad (9)$$

respectively [32]. The cutoff wavelength for the TE mode is obtained by substituting Eq. (8) into Eq. (6). To calculate the cutoff wavelength for the TM mode, it is necessary to determine angle  $\theta_2$  at each wavelength because the refractive index depends on this angle. The equation for the cutoff condition, Eq. (5), is replaced with

$$\theta_2 = \sin^{-1}(n_1/n_2^{\text{TM}}(\theta_2)). \quad (10)$$

From (9) and (10) we obtain the equation for determining  $\theta_2$ ,

$$n_1 - n_o n_e (n_o^2 \sin^2 \theta_2 + n_e^2 \cos^2 \theta_2)^{-1/2} \sin \theta_2 = 0. \quad (11)$$

Eq. (11) can be solved for  $\theta_2$  numerically at each wavelength, and the  $n_2^{\text{TM}}$  determined by Eq. (9) is substituted into Eq. (7). In this way, we can calculate the cutoff wavelength in both cases: when the core layer is isotropic and when it is anisotropic.

## Acknowledgements

We gratefully acknowledge the help given to us by Rigaku Corporation in measuring XRD patterns of organic films. We thank the Research Center for Computational Science (RCCS), Okazaki National Research Institutes for the use of SGI Altix4700 computer. This work was supported by a Grant-in-Aid for the Global COE Program, "Science for Future Molecular Systems" from the Ministry of Education, Culture, Sports, Science and Technology of Japan.

## References

- [1] C.W. Tang, S.A. VanSlyke, *Appl. Phys. Lett.* 51 (1987) 913–915.
- [2] V.G. Kozlov, V. Bulovic, P.E. Burrows, M. Baldo, V.B. Khalfin, G. Parthasarathy, S.R. Forrest, Y. You, M.E. Thompson, *J. Appl. Phys.* 84 (1998) 4096–4108.
- [3] M.A. Baldo, R.J. Holmes, S.R. Forrest, *Phys. Rev. B* 66 (2002) 035321.
- [4] T. Tsutsui, E. Aminaka, C.P. Lin, D.-U. Kim, *Phil. Trans. R. Soc. Lond. A* 355 (1997) 801–804.
- [5] G. Gu, D.Z. Garbuzov, P.E. Burrows, S. Venkatesh, S.R. Forrest, M.E. Thompson, *Opt. Lett.* 22 (1997) 396–398.
- [6] J.-S. Kim, P.K.H. Ho, N.C. Greenham, R.H. Friend, *J. Appl. Phys.* 88 (2000) 1073–1081.
- [7] H. Fujiwara, *Spectroscopic Ellipsometry: Principles and Applications*, Wiley, New York, 2007.
- [8] E.K. Miller, M.D. McGehee, M. Diaz-Garcia, V. Srikant, A.J. Heeger, *Synth. Met.* 102 (1999) 1091–1092.
- [9] C.M. Ramsdale, N.C. Greenham, *Adv. Mater.* 14 (2002) 212–215.
- [10] M. Losurdo, M.M. Giangregorio, P. Capezzuto, G. Bruno, F. Babudri, D. Colangiuli, G.M. Farinola, F. Naso, *Synth. Met.* 138 (2003) 49–53.
- [11] J.M. Winfield, C.L. Donley, J.-S. Kim, *J. Appl. Phys.* 102 (2007) 063505.
- [12] H.-W. Lin, C.-L. Lin, H.-H. Chang, Y.-T. Lin, C.-C. Wu, Y.-M. Chen, R.-T. Chen, Y.-Y. Chien, K.-T. Wong, *J. Appl. Phys.* 95 (2004) 881–886.
- [13] H.-W. Lin, C.-L. Lin, C.-C. Wu, T.-C. Chao, K.-T. Wong, *Org. Electron.* 8 (2007) 189.
- [14] D. Marcuse, *Theory of Dielectric Optical Waveguides*, second ed., Academic Press, San Diego, 1991.
- [15] X. Peng, L. Liu, J. Wu, Y. Li, Z. Hou, L. Xu, W. Wang, F. Li, M. Ye, *Opt. Lett.* 25 (2000) 314–316.
- [16] A.K. Sheridan, G.A. Turnbull, A.N. Safonov, I.D.W. Samuel, *Phys. Rev. B* 62 (2000) R11929–R11932.
- [17] T. Kawase, D.J. Pinner, R.H. Friend, T. Shimoda, *Synth. Met.* 111–112 (2000) 583–586.
- [18] M. Pauchard, M. Vehse, J. Swensen, D. Moses, A.J. Heeger, E. Perzon, M.R. Andersson, *J. Appl. Phys.* 94 (2003) 3543–3548.
- [19] F. Li, O. Solomeshch, P.R. Mackie, D. Cupertino, N. Tessler, *J. Appl. Phys.* 99 (2006) 013101.
- [20] K.-H. Yim, R.H. Friend, J.-S. Kim, *J. Chem. Phys.* 124 (2006) 184706.
- [21] H. Nakanotani, C. Adachi, S. Watanabe, R. Kato, *Appl. Phys. Lett.* 90 (2007) 231109.
- [22] D. Yokoyama, M. Moriwake, C. Adachi, *J. Appl. Phys.* 103 (2008) 123104;
- [23] D. Yokoyama, M. Moriwake, C. Adachi, *J. Appl. Phys.* 104 (2008) 039909.
- [24] T. Aimonio, Y. Kawamura, K. Goushi, H. Yamamoto, H. Sasabe, C. Adachi, *Appl. Phys. Lett.* 86 (2005) 071110.
- [25] H. Nakanotani, S. Akiyama, D. Ohnishi, M. Moriwake, M. Yahiro, T. Yoshihara, S. Tobita, C. Adachi, *Adv. Funct. Mater.* 17 (2007) 2328–2335.
- [26] G.E. Jellison Jr., *Data analysis for spectroscopic ellipsometry*, *Thin Solid Films* 234 (1993) 416–422.
- [27] K. Tanaka, N. Okui, T. Sakai, *Thin Solid Films* 196 (1991) 137–145.
- [28] A. Kubono, N. Okui, *Prog. Polym. Sci.* 19 (1994) 389–438.
- [29] I.M. Ward, *Structure and Properties of Oriented Polymers*, Applied Science Publishers, London, 1975.
- [30] D. Yokoyama, A. Sakaguchi, M. Suzuki, C. Adachi, *Appl. Phys. Lett.* 93 (2008) 173302.
- [31] R.A. Synowicki, T.E. Tiwald, *Thin Solid Films* 455–456 (2004) 248–255.
- [32] M.J. Frisch, G.W. Trucks, H.B. Schlegel et al., *GAUSSIAN 03*, Revision E.01, Gaussian, Inc., Wallingford, CT, 2004.
- [33] B.E.A. Saleh, M.C. Teich, *Fundamentals of Photonics*, Wiley, New York, 1991.



# Carrier transport mechanism in aluminum nanoparticle embedded $AlQ_3$ structures for organic bistable memory devices

V.S. Reddy, S. Karak, S.K. Ray, A. Dhar \*

Department of Physics and Meteorology, IIT Kharagpur, Kharagpur 721 302, India

## ARTICLE INFO

### Article history:

Received 4 July 2008

Received in revised form 2 October 2008

Accepted 16 October 2008

Available online 31 October 2008

### PACS:

72.80.Le

73.61.Ph

85.30.De

85.65.+h

### Keywords:

Organic semiconductor

Memory device

Conduction mechanism

Nanoparticle

## ABSTRACT

Electrical bistability is demonstrated in organic memory devices based on *tris*-(8-hydroxyquinoline)aluminum ( $AlQ_3$ ) and aluminum nanoparticles. The role of the thickness of middle aluminum layer and the size of the nanoparticles in device performance is investigated. Above a threshold voltage, the device suddenly switches from a low conductivity OFF state to a high conductivity ON state with a conductivity difference of several orders of magnitude. The OFF state of the device could be recovered by applying a relatively high voltage pulse. The electronic transition is attributed to an electric field induced transfer of charge between aluminum nanoparticles and  $AlQ_3$ . The type of charge carriers responsible for conductance switching is investigated. The charge carrier conduction mechanism through the device in ON and OFF states is studied by temperature dependent current–voltage characteristics and analyzed in the framework of existing theoretical models. The conduction mechanism in the OFF state is dominated by field-enhanced thermal excitation of charge carriers from localized centers, whereas it changes to Fowler–Nordheim tunneling of charge carriers in the ON state. The device exhibited excellent stability in either conductivity states. The results indicate the strong potential of the device towards its application as a nonvolatile electronic memory.

© 2008 Elsevier B.V. All rights reserved.

## 1. Introduction

During the past fifteen years, tremendous work has been done in the field of organic semiconductor based electronic devices. Devices such as light emitting diodes [1–3], field effect transistors [4–6] and solar cells [7–9] have shown great potential towards future technologies. Organic semiconductor based devices exhibit unique advantages such as low fabrication cost, high mechanical flexibility and versatility of the material chemical structure compared with the inorganic semiconductor devices. However, to widen the application of organic semiconductors to varieties of electronics systems, organic based memory devices are essential [10–16]. The basic feature of a memory device is to exhibit bistable behavior having two different resistance states at the same applied voltage. Ma et al. have

demonstrated memory effects in a three layer organic/metal nanoparticle/organic structure embedded between two electrodes [17]. Bozano and coworkers have studied the important role of different metal nanoparticles in a three layer memory structure [18]. During the device operation, when applied voltage exceeds a certain value, the device suddenly switches from a low conductivity ‘OFF’ state to a high conductivity ‘ON’ state, with a conductivity difference of several orders of magnitude. This high conductivity state will be memorized until an ‘OFF’ voltage is applied to erase it. Despite the superior performance of organic memory devices, the charge carrier transport mechanism in the ‘ON’ and ‘OFF’ states and the type of carriers responsible for bistability are not understood clearly.

In this paper, we describe the fabrication and operation of the tri-layer organic/metal/organic and the single layer memory structures sandwiched between two electrodes. The effect of the thickness of intermediate metal layer and the size of the nanoparticles in device performance is

\* Corresponding author. Tel.: +91 3222 283830; fax: +91 3222 255303.  
E-mail address: [adhar@phy.iitkgp.ernet.in](mailto:adhar@phy.iitkgp.ernet.in) (A. Dhar).

investigated. The charge carrier conduction mechanism through the device in 'ON' and 'OFF' states is studied by temperature dependent current–voltage characteristics and analyzed in terms of existing theoretical models. The type of carriers responsible for conductance switching is also investigated.

## 2. Experimental

In present investigation, three different types of device structures were studied. The first type (type-I) is the tri-layer  $\text{AlQ}_3/\text{Al}$  nanoislands/ $\text{AlQ}_3$  structure sandwiched between two electrodes (hereafter called tri-layer device), the second one (type-II) is a single  $\text{AlQ}_3$  layer embedded between two electrodes (hereafter called single layer device), and the third type (type-III) is the ITO/Poly(3,4-ethylenedioxythiophene)-poly(styrenesulfonate) (PEDOT:PSS)/ $\text{AlQ}_3/\text{Al}$  nanoislands/ $\text{AlQ}_3/\text{Al}$  device. For all types of devices, patterned indium tin oxide (ITO) (SPI Inc.) with sheet resistance  $10 \Omega/\square$  was used as the bottom electrode. Prior to  $\text{AlQ}_3$  deposition, ITO substrates were cleaned thoroughly in acetone, isopropyl alcohol and de-ionized water in sequence by an ultrasonic cleaner followed by drying with nitrogen gas. For the fabrication of tri-layer structure, both the  $\text{AlQ}_3$  and Al middle layers were deposited by thermal evaporation at a base pressure of  $5 \times 10^{-6}$  mbar. The thickness of the each  $\text{AlQ}_3$  layer was about 50 nm and that of the middle Al layer was varied between 5 and 20 nm. The deposition rate of the middle Al layer was controlled by a quartz crystal thickness monitor. In order to obtain the nanoscale metal islands, a low evaporation rate of less than 0.1 nm/s was used. For the single layer device structure,  $\text{AlQ}_3$  (100 nm) was thermally evaporated on ITO electrodes. For the fabrication of ITO/PEDOT:PSS/ $\text{AlQ}_3/\text{Al}$  nanoislands/ $\text{AlQ}_3/\text{Al}$  device, a 40 nm thick PEDOT:PSS layer was spin coated on ITO substrates from a 2.8 wt.% water solution (Aldrich). Post baking was done for 1 h at around 110 °C to remove the solvent completely. Deposition of all other layers of this device was done in the same manner as the tri-layer device. Finally, aluminum top electrode strips were deposited by thermal evaporation through a shadow mask.

The thickness of different layers was monitored by quartz crystal monitor and was verified by stylus profilometer (Veeco Dektak3). Cross sectional scanning electron

microscopy (SEM) images of the device were taken using a ZEISS SUPRA 40 field emission (FE) microscope. Atomic force microscopy (AFM) (Veeco Nanoscope-IV) in tapping mode was used to evaluate the surface morphology of the middle Al layer. Fourier-transform infrared (FTIR) spectra of the middle Al layer in the wave number range  $400\text{--}4000 \text{ cm}^{-1}$  were obtained using a Nexus 870 Thermo Nicolet spectrometer. The optical transmission spectra were measured in the wavelength range 300–1100 nm using a UV–vis–NIR spectrophotometer (Perkin–Elmer Lambda 45). The dc current–voltage characteristics of the devices were obtained using a Keithley 485 Pico ammeter and an Advantest R6144 programmable dc voltage generator.

## 3. Results and discussion

Fig. 1 shows the cross sectional view of a typical tri-layer memory structure (type-I) sandwiched between ITO and Al electrodes. The FE–SEM micrograph clearly indicates ITO, two  $\text{AlQ}_3$  layers and Al layer with sharp interfaces. The thickness of bottom  $\text{AlQ}_3$ , top  $\text{AlQ}_3$ , ITO and Al layers are estimated to be 70 nm, 50 nm, 400 nm and 200 nm, respectively.

The performance of organic bistable device is sensitive to metal nanoparticles and the thickness of the middle metal layer. The ON/OFF current ratio, for example, depends strongly on the size and density of the nanoparticles. Morphology and the thickness of the middle Al layer depends on the evaporation rate and is controlled by quartz crystal monitor. Films deposited with a higher deposition rate led to continuous films and, hence, non-switching devices. A deposition rate less than 0.1 nm/s resulted in island like growth and bistable devices. Detailed information about the nanostructure of the middle Al layer has been obtained by AFM. Fig. 2a illustrates the surface morphology of the middle Al layer of thickness 5 nm. It clearly shows disconnected metal islands of various sizes. The size distribution of nanoislands is estimated from this AFM image and is shown in Fig. 2b. The island size varies from 5 nm to about 25 nm with peak of the distribution at 15 nm. When the thickness of the film is increased to 10 nm, the size of nanoislands increases slightly as shown in Fig. 2c. For this film the island size distribution ranges from 8 nm to about 35 nm and peaks at 20 nm, as shown in Fig. 2d. The gaps

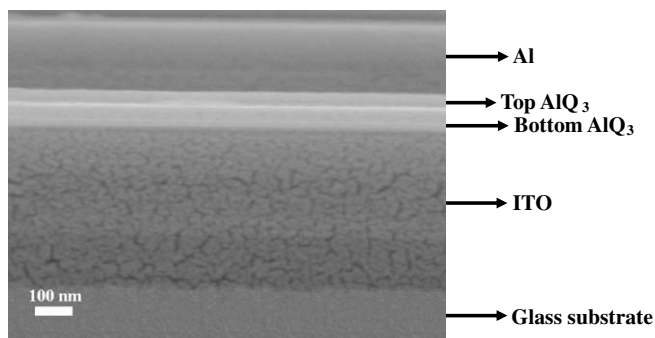


Fig. 1. Cross sectional SEM image of the tri-layer memory device, ITO/ $\text{AlQ}_3/\text{Al}/\text{AlQ}_3/\text{Al}$  (type-I).

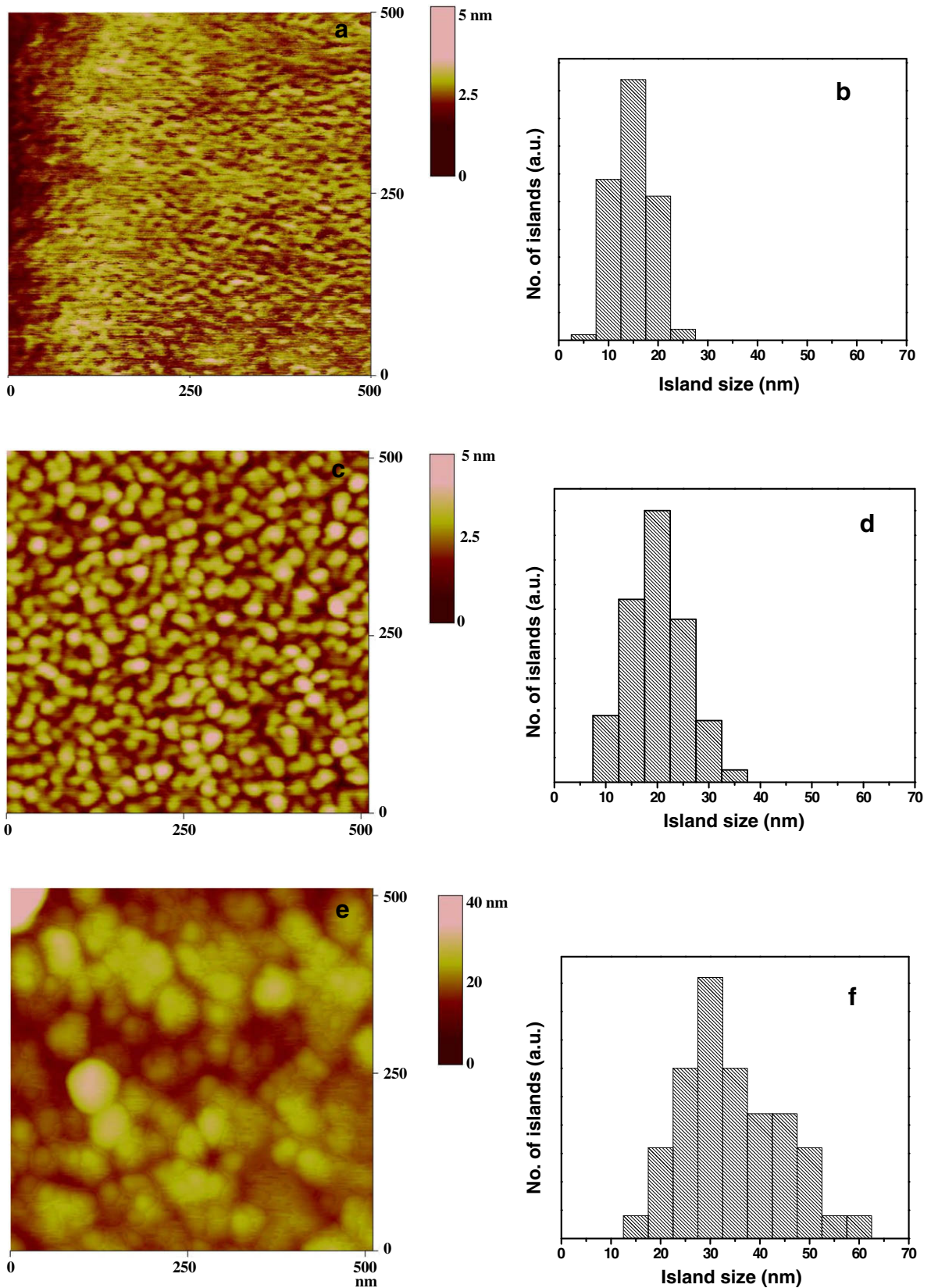


Fig. 2. Surface morphology and island size distribution of the middle aluminum layer of thickness (a, b) 5 nm; (c, d) 10 nm and (e, f) 15 nm.

between the islands are of the order of 3–7 nm. Coalescence of nanoislands is observed with further increase in film thickness as shown in Fig. 2e. Here the thickness of the middle Al layer is about 15 nm. A large variation in the size of the nanoislands (from 15 to 60 nm) is observed in Fig. 2f, with the peak of the distribution at 30 nm.

Though the deposition of Al nanoparticles is performed at  $5 \times 10^{-6}$  mbar, there is a time delay between the deposition of nanoparticles and top AlQ<sub>3</sub> layer. During this time a thin oxide shell is formed on the nanoparticles. Since the deposition is done under high vacuum, a large fraction of the aluminum remains as a metallic core surrounded by a thin oxide shell [18]. Formation of oxide shell was also mentioned by other authors. Ma et al. have performed *in situ* X-ray photoemission spectroscopy measurements and confirmed the formation of 16 Å oxide shell [11]. Fig. 3a shows the FTIR spectra of the middle Al layer of thickness 10 nm in the range 400–2000 cm<sup>-1</sup>. The strong band observed at 538 cm<sup>-1</sup> (labeled A) is assigned to octahedral Al–O stretching vibrations, whereas the broad band centered at 812 cm<sup>-1</sup> (labeled B) is assigned to tetrahedral Al–O stretching vibrations [19–21]. These results clearly indicate the presence of oxide shell on the metal islands.

In addition to AFM and FTIR, UV–vis transmission spectra have been used to study the middle Al layer deposited on AlQ<sub>3</sub>. Fig. 3b shows the transmission spectra of the middle Al layer of different thickness deposited on 50 nm thick AlQ<sub>3</sub> film. Transmission spectrum of pure AlQ<sub>3</sub> film is also shown as a reference. For the Al film that appears in normal metallic color, the transmission is relatively low in the UV–vis region. It indicates that most of the radiation from the light source is reflected away by the continuous metal film. The film containing Al nanoislands appears in deep blue color and shows relatively high transparency in the UV–vis region, as shown in Fig. 3b. The devices fabricated using this deep blue color Al films have shown bistable behavior.

Fig. 4 shows typical current–voltage (*I*–*V*) characteristics of the tri-layer nanoparticle memory device (type-I) on a semi logarithmic scale obtained by sweeping the volt-

age from –5 to +5 V and then back to –5 V. Here the thickness of the middle Al layer is about 15 nm. Almost symmetric *I*–*V* characteristics are observed for both the polarities of the voltage. This figure can be used to define the key parameters of the device. Initially, the device remains in the high resistance ‘OFF’ state at a smaller bias. When the applied voltage reaches a threshold value ( $V_{th}$ ), resistance of the device decreases abruptly and the device current increases by several orders of magnitude. The value of  $V_{th}$  is in the range 1.7–2.3 V. As shown in Fig. 4, the device current switches between the states of high and low resistance at the threshold, reaches the maximum ( $V_{ON}$ ), and then goes through a negative differential resistance (NDR) region to a minimum (till  $V_{OFF}$ ), after which it increases again almost exponentially. When the voltage is decreased towards zero, the current follows the upper curve and the device is set in its ‘ON’ state until the voltage near  $V_{OFF}$  is applied. An ‘N-shaped’ *I*–*V* curve is obtained in the ‘ON’ state of the device. The low voltage region below  $V_{th}$  is the region of bistability, in which the state of the device can be read ( $V_{read}$ ). The ‘ON’ state of the device is obtained by applying a voltage near  $V_{ON}$  and the ‘OFF’ state is recovered by applying a voltage beyond  $V_{OFF}$ .

Fig. 5 shows the current–voltage characteristics of the tri-layer devices ITO/AlQ<sub>3</sub>/Al/AlQ<sub>3</sub>/Al (type-I) with different thickness of middle Al layer. The characteristics of the device without middle Al layer, is also shown for comparison. Both the devices show bistable properties. The bistability is attributed to the presence of metal nanoparticles in the AlQ<sub>3</sub> matrix. For tri-layer devices, the middle thin Al layer contains the nanoparticles. In case of single layer devices, metal nanoparticles are incorporated in AlQ<sub>3</sub> layer by diffusion during the evaporation of top electrode [22]. The threshold voltage is in the range 1.7–2.3 V for the devices with different thickness of middle Al layer. The ON/OFF current ratio is very small (~10) for single layer device and increases with increasing thickness of the middle Al layer till 10 nm. The devices with 10 nm thick middle Al layer have shown better switching properties with large ON/OFF current ratio ( $>10^5$ ) at a read volt-

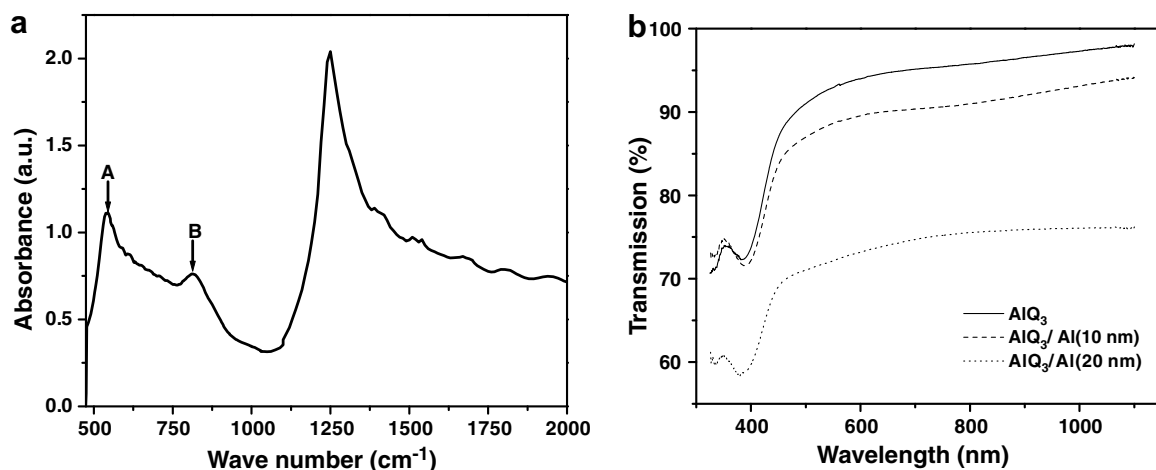


Fig. 3. (a) FTIR spectra of the middle Al layer of thickness 10 nm, and (b) transmission spectra of Al films of different thickness deposited on 50 nm thick AlQ<sub>3</sub> film.

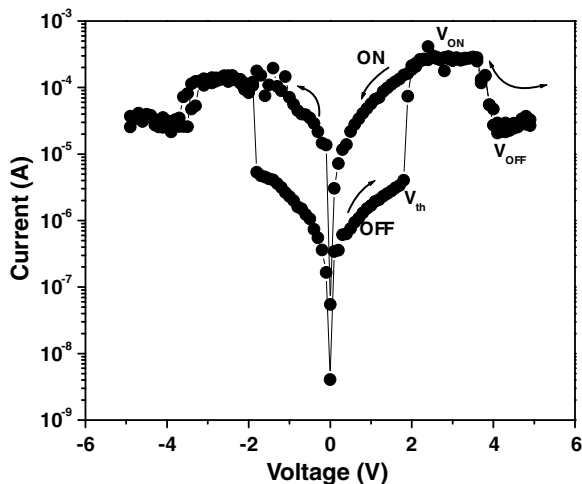


Fig. 4. Current–voltage characteristics of the tri-layer memory device, ITO/AlQ<sub>3</sub>/Al(15 nm)/AlQ<sub>3</sub>/Al (type-I) at room temperature.

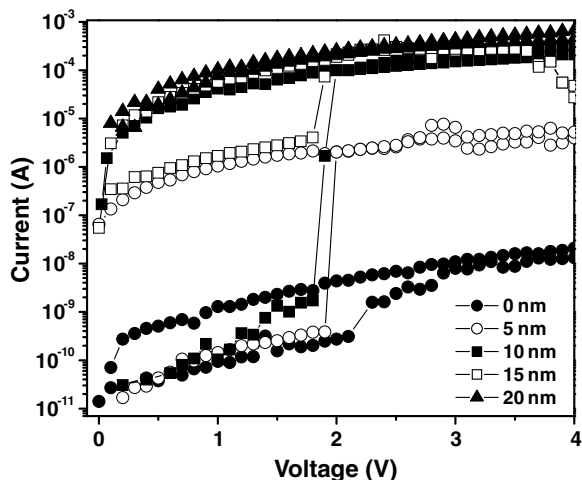


Fig. 5. Current–voltage characteristics of the single layer device and tri-layer device, ITO/AlQ<sub>3</sub>/Al/AlQ<sub>3</sub>/Al, with different thickness of middle Al layer (type-I and type-II).

age of 1 V. If the thickness of the middle Al layer is increased beyond 10 nm, the ON/OFF ratio decreases sharply and the switching properties almost vanish at a thickness of 20 nm as shown in Fig. 5. At higher thicknesses of middle Al layer, for example at 15 nm, Al nanoparticles grow in size and join with the neighboring particles as shown in AFM image (Fig. 2f). Then the number of isolated particles that can store charge becomes less and hence the ON/OFF ratio goes down. Single layer devices exhibit lower current because of the mismatch of electrode work functions to the HOMO and LUMO levels of AlQ<sub>3</sub>. The current in both ON and OFF states increases with increasing thickness of the middle Al layer. These results suggest that the nanoparticles not only induce bistability, but also contribute to the conduction process.

The retention of the ON and OFF states and device performance under electrical stress is important for practical

applications. Stress tests have been performed by subjecting the device to a low bias of 1 V over prolonged periods of time in both ON and OFF states and by recording the currents at different times. When subjected to stress test, the device in the OFF state retains its conductivity and do not undergo any transition to the ON state, as shown in Fig. 6. Similar tests have been performed on the device in the ON state. The current in both ON and OFF states remains constant even after a prolonged period of continuous stress test. It shows that there is no significant degradation of the device in both ON and OFF states, indicating the stability of both material and material/electrode interfaces.

To understand the conduction mechanism through the device in both ON and OFF states, the current–voltage characteristics at different temperatures have been measured and analyzed in the framework of existing theoretical models. Fig. 7 shows the current–voltage characteristics of the device, ITO/AlQ<sub>3</sub>/Al(10 nm)/AlQ<sub>3</sub>/Al (type-I), at different temperatures. The threshold voltage of the device decreases with increasing temperature. The device current in the OFF state has shown strong temperature dependence. This thermally activated charge transport may be either due to Poole–Frenkel (PF) emission of charge carriers or to the Schottky contact at the Al/AlQ<sub>3</sub> interface. The PF emission is due to the field-enhanced thermal excitation of charge carriers from localized centers or potential wells within the bulk of the semiconductor, whereas the Schottky effect results from the injection of charge carriers from the electrode into the semiconductor. In order to differentiate between these two conduction mechanisms, current–voltage characteristics are measured at both the polarities of voltage. In present study, an asymmetric electrode structure (ITO and Al electrodes) is used for the fabrication of all the devices. The difference between the work functions of ITO and Al is 0.6 eV (the work functions of ITO and Al are 4.9 and 4.3 eV, respectively). For the Schottky controlled conduction in an asymmetric electrode structure, the current–voltage characteristics should also be asymmetrical when the voltage is reversed. However, all

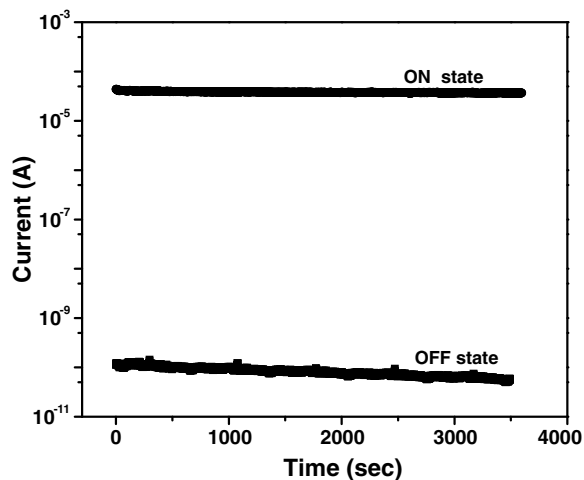


Fig. 6. Voltage stress test of the device in the ON and OFF states at a read voltage of 1 V.

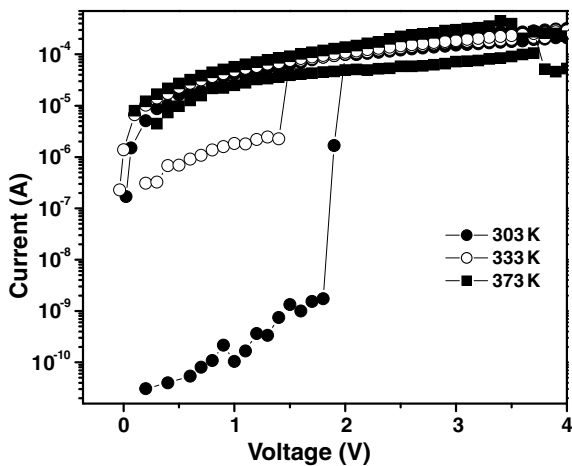


Fig. 7. Current–voltage characteristics of ITO/AlQ<sub>3</sub>/Al(10 nm)/AlQ<sub>3</sub>/Al device at different temperatures.

the devices have shown symmetric current–voltage characteristics in the OFF state as shown in Fig. 4. Therefore, the current conduction is dominated by PF emission in the OFF state of the device.

This PF mechanism is further confirmed by analyzing the current–voltage characteristics. The reported values of HOMO and LUMO levels of AlQ<sub>3</sub> are around 5.8 and 3.0 eV, respectively [18,23]. In case of PF emission, the theoretical energy barrier for the emission of electrons is 1.3 eV. The current through the device in case of PF emission is given by [24]

$$I = CV \exp \left[ -\frac{q}{kT} \left( \Phi - \left( \frac{qV}{\pi\epsilon l} \right)^{1/2} \right) \right] \quad (1)$$

where  $q$  is the electronic charge,  $\Phi$  is the ionization energy of the traps,  $\epsilon$  is the dynamic permittivity of AlQ<sub>3</sub>,  $k$  is the Boltzmann constant,  $T$  is the temperature, and  $C$  is a constant. A linear relation between  $\log(I/V)$  and  $V^{1/2}$  is ob-

served in the OFF state of the device as shown in Fig. 8a. The experimental activation energy obtained from the temperature dependant current characteristics is 1.6 eV, which is in close agreement with the theoretical ionization energy of PF emission. These results confirm the predominance of PF emission in the OFF state of the device.

The current–voltage and current–temperature relations have changed after electrical transition to the ON state. A linear relation is observed between  $\log(I/V^2)$  and  $1/V$  as shown in Fig. 8b. In addition, the current in the ON state is insensitive to temperature. These results suggest that the current conduction in the ON state is probably due to Fowler–Nordheim tunneling of charge carriers through a triangular barrier. The current in case of Fowler–Nordheim tunneling is given by [24]

$$I = C_1 V^2 \exp \left[ -\frac{4d(q\Phi)^{3/2} (2m^*)^{1/2}}{3qhV} \right] \quad (2)$$

where  $\Phi$  is the energy barrier height,  $d$  is the tunneling distance,  $m^*$  is the reduced mass of the charge carrier, and  $C_1$  is a constant. Thus, the current conduction mechanism changed from the Pool–Frenkel emission in the OFF state to Fowler–Nordheim tunneling in the ON state.

In order to investigate the type of carriers (either electrons or holes) responsible for conductance switching, a hole injecting material PEDOT:PSS is deposited between ITO electrode and bottom AlQ<sub>3</sub> layer. The current–voltage characteristics of ITO/PEDOT:PSS/AlQ<sub>3</sub>/Al(10 nm)/AlQ<sub>3</sub>/Al device exhibit slight hysteresis and no obvious switching behavior as shown in Fig. 9. Moreover, emission of light from the device is observed after the incorporation of PEDOT:PSS layer. In case of ITO/AlQ<sub>3</sub>/Al(10 nm)/AlQ<sub>3</sub>/Al device, electrons injected from the Al electrode are trapped inside Al nanoislands and produces bistability. Probability of electron–hole recombination is very small because of the less number of available holes. PEDOT:PSS enhances the injection of holes into the AlQ<sub>3</sub> layer and hence increases the probability of electron–hole recombination [25]. The process of recombination results in smearing

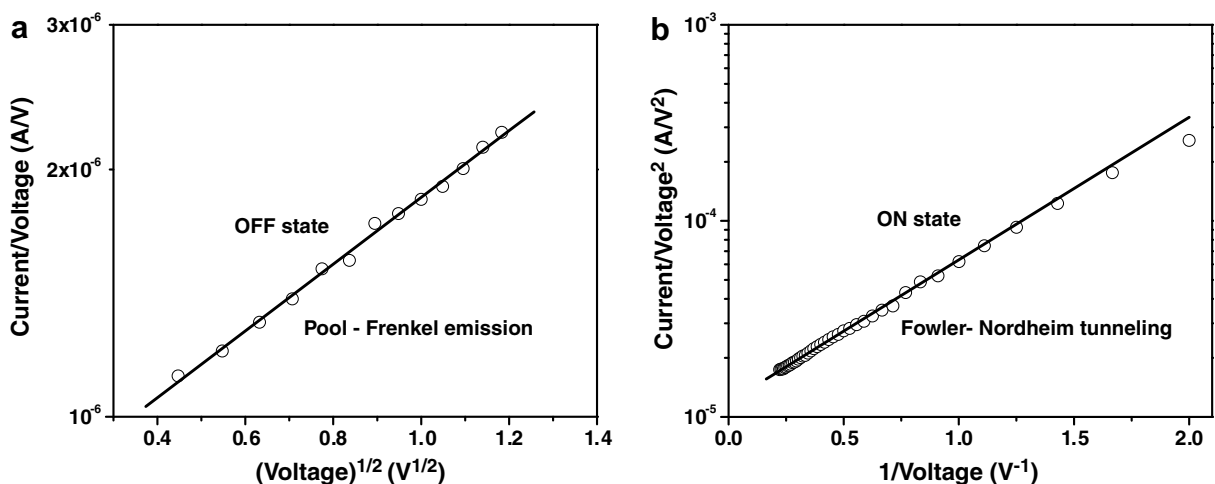


Fig. 8. (a) Variation of  $\log(I/V)$  with  $V^{1/2}$  in the OFF state of the device, and (b) variation of  $\log(I/V^2)$  with  $1/V$  in the ON state of the device. Symbols are the experimental data and the solid lines are the fitting data using theoretical models.

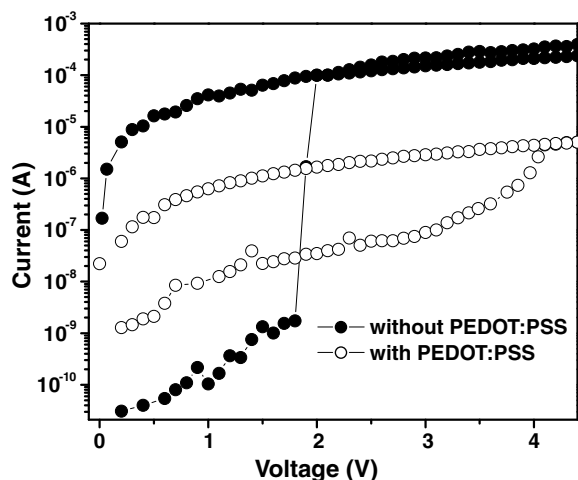


Fig. 9. Current–voltage characteristics of ITO/AlQ<sub>3</sub>/Al(10 nm)/AlQ<sub>3</sub>/Al device with and without PEDOT:PSS layer between ITO and bottom AlQ<sub>3</sub>.

out of bistability and emission of light. Thus the electrons are majority carriers and holes are minority carriers in case of our organic bistable devices.

In the light of above experimental results, we propose that the electronic transition is due to an electric field induced transfer of charge between aluminum nanoparticles and AlQ<sub>3</sub>. When the applied electric field is high enough, electrons in the AlQ<sub>3</sub> may gain enough energy and tunnel through aluminum oxide shell into the core of aluminum nanoparticles. The charge on the aluminum nanoparticles may be stable due to the presence of insulating aluminum oxide shell, which prevents the recombination of charge after the removal of external electric field. The OFF state of the device can be recovered by applying a voltage near  $V_{\text{OFF}}$ , which is due to the removal of charge from the core of the aluminum nanoparticles.

#### 4. Conclusions

In conclusion, electrically bistable devices using AlQ<sub>3</sub> and aluminum nanoparticles have been demonstrated. The effect of the thickness of middle aluminum layer and the size of the nanoparticles on device performance is investigated. It is observed that the bistability is very sensitive to nanostructure of the middle aluminum layer. For obtaining the devices with well controlled bistability, the middle aluminum layer should have island like structure, instead of continuous metal layer. These nanoislands act as the charge storage elements, which enable the nonvolatile electrical bistability when biased to a sufficiently high voltage. The charge carrier conduction mechanism through the device in ON and OFF states is studied by temperature dependent current–voltage characteristics and analyzed in

the framework of existing theoretical models. The charge conduction for the device in the OFF state is mainly due to the field-enhanced thermal excitation of charge carriers from localized centers, whereas it changes to Fowler–Nordheim tunneling of charge carriers in the ON state. Present study reveals that the electrons are majority carriers in these organic bistable devices. The devices exhibit a repeatable bistable behavior and stability in either state. These characteristics indicate that the tri-layer device has a strong potential towards its application as nonvolatile electronic memory.

#### Acknowledgements

The authors acknowledge CSIR, Government of India for partially supporting the present work under Grant No. 03/1016/05/EMR-II and for awarding VSR with SRF.

#### References

- [1] R.H. Friend, R.W. Gymer, A.B. Holmes, J.H. Burroughes, R.N. Marks, C. Taliani, D.D.C. Bradley, D.A. Dos Santos, J.L. Bredas, M. Logdlund, W.R. Salaneck, *Nature* 397 (1999) 121.
- [2] P.E. Burrows, Z. Shen, V. Bulovic, D.M. McCarty, S.R. Forrest, J.A. Cronin, M.E. Thompson, *J. Appl. Phys.* 79 (1996) 7991.
- [3] J. Meyer, S. Hamwi, T. Bulow, H.H. Johannes, T. Riedl, W. Kowalsky, *Appl. Phys. Lett.* 91 (2007) 113506.
- [4] J.B. Lee, P.C. Chang, J.A. Liddle, V. Subramanian, *IEEE Trans. Electron. Dev.* 52 (2005) 1874.
- [5] C.D. Dimitrakopoulos, P.R.L. Malenfant, *Adv. Mater.* 14 (2002) 99.
- [6] J.H. Kwon, J.H. Seo, S. Shin II, K.H. Kim, D.H. Choi, I.B. Kang, H. Kang, B.K. Ju, *IEEE Tran. Electron. Dev.* 55 (2008) 500.
- [7] C.J. Brabec, N.S. Sariciftci, J.C. Hummelen, *Adv. Funct. Mater.* 11 (2001) 15.
- [8] P. Peumans, S. Uchida, S.R. Forrest, *Nature* 425 (2003) 158.
- [9] S. Gunes, H. Neugebauer, N.S. Sariciftci, *Chem. Rev.* 107 (2007) 1324.
- [10] L.D. Bozano, B.W. Kean, V.R. Deline, J.R. Salem, J.C. Scott, *Appl. Phys. Lett.* 84 (2004) 607.
- [11] L. Ma, S. Pyo, J. Ouyang, Q. Xu, Y. Yang, *Appl. Phys. Lett.* 82 (2003) 1419.
- [12] Chia-Hsun Tu, Yi-Sheng Lai, Dim-Lee Kwong, *IEEE Electron. Dev. Lett.* 27 (2006) 354.
- [13] H.T. Lin, Z. Pei, Y.J. Chan, *IEEE Electron. Dev. Lett.* 28 (2007) 569.
- [14] D. Tondelier, K. Lmimouni, D. Vuillaume, C. Fery, G. Haas, *Appl. Phys. Lett.* 85 (2004) 5763.
- [15] L. Li, Q.D. Ling, S.L. Lim, Y.P. Tan, C. Zhu, D.S.H. Chan, E.T. Kang, K.G. Neoh, *Org. Electron.* 8 (2007) 401.
- [16] B. Mukherjee, A.J. Pal, *Org. Electron.* 7 (2006) 249.
- [17] L.P. Ma, J. Liu, Y. Yang, *Appl. Phys. Lett.* 80 (2002) 2997.
- [18] L.D. Bozano, B.W. Kean, M. Beinhoff, K.R. Carter, P.M. Rice, J.C. Scott, *Adv. Funct. Mater.* 15 (2005) 1933.
- [19] S. Kudela Jr., S. Oswald, S. Kudela, K. Wetzig, *Anal. Bioanal. Chem.* 390 (2008) 1477.
- [20] Y.C. Kim, H.H. Park, J.S. Chun, W.J. Lee, *Thin Solid Films* 237 (1994) 57.
- [21] Rajesh Katamreddy, R. Inman, G. Jursich, A. Soulet, A. Nicholls, C. Takoudis, *Thin Solid Films* 515 (2007) 6931.
- [22] W. Tang, H. Shi, G. Xu, B.S. Ong, Z.D. Popovic, J. Deng, J. Zhao, *Adv. Mater.* 17 (2005) 2307.
- [23] P.E. Burrows, S.R. Forrest, *Appl. Phys. Lett.* 64 (1994) 2285.
- [24] S.M. Sze, *Physics of Semiconductor Devices*, John Wiley and Sons, New York, 1981.
- [25] A.S. Wan, A.J. Makinen, P.A. Lane, G.P. Kushto, *Chem. Phys. Lett.* 446 (2007) 317.





# Low-voltage organic ferroelectric field effect transistors using Langmuir–Schaefer films of poly(vinylidene fluoride-trifluoroethylene)

Chien A. Nguyen\*, Junling Wang, Lang Chen, Subodh G. Mhaisalkar, Pooi See Lee

School of Materials Science and Engineering, Nanyang Technological University, Block N4.1, 50 Nanyang Avenue, Singapore 639798, Singapore

## ARTICLE INFO

### Article history:

Received 18 April 2008  
Received in revised form 18 October 2008  
Accepted 18 October 2008  
Available online 5 November 2008

### PACS:

81.07.–b  
81.16.Rf  
77.55.+f

### Keywords:

Langmuir–Schaefer film  
P(VDF-TrFE)  
Non-volatile memory

## ABSTRACT

Langmuir–Schaefer transfer was used to fabricate ultrathin films of ferroelectric copolymer, poly(vinylidene fluoride-trifluoroethylene) (70–30 mol%), for non-volatile memory application at low operating voltage. Increasing the number of transferred monolayers up to 10 led to improved film crystallinity in the “in-plane” direction, which reduced surface roughness of the semicrystalline film. Treatment of the substrate surface by plasma results in different film coverage which was subsequently found to be governed by interaction of the deposited film and surface condition. Localized ferroelectric switching was substantially attained using piezo-force tip at 10 V on 10-monolayer films. Integrating this film as a dielectric layer into organic capacitor and field effect transistor yields a reasonably good leakage current ( $<10^{-7}$  A/cm<sup>2</sup>) with hysteresis in capacitance and drain current with ON/OFF ratio of  $10^3$  for organic ferroelectric memory application at significantly reduced operating voltage of [15] V.

© 2008 Elsevier B.V. All rights reserved.

## 1. Introduction

Polyvinylidene fluoride (PVDF) and copolymer with trifluoroethylene P(VDF-TrFE) are well-known for their ferroelectric properties in crystalline forms [1,2]. The polymers have a vast application in sensors, actuators [3,4], and non-volatile memory [5–8]. These applications usually require a thin film fabricated by spin-coating or mechanical pressing. Crystallization of the polymer chains can be resulted from either post-process annealing or recrystallization from melting. Recently, a new method of forming P(VDF-TrFE) copolymer films has been reported using Langmuir–Schaefer transfer mechanism [9,10]. The method includes two main steps – first, compressing to form monolayer (ML) of compact polymer chains at the air-liquid interface and second, transferring the monolayer onto a substrate surface. Film thickness can be controlled by the

number of transfers at a certain compressing pressure [11]. Film crystallinity can be enhanced by annealing at temperatures below melting point similar to those of spin-coated films [12]. In addition, Langmuir–Schaefer (LS) method has a potential for realizing a polymer monolayer by aligning and packing its molecular chains without anneal crystallization.

Forming and transferring the LS-films of P(VDF-TrFE) copolymer have been intensively performed by Nalwa [9]. Different properties and characteristic of monolayer P(VDF-TrFE) can be observed including ferroelectricity, optical and energy band etc., as well as the proposed intrinsic switching polarization [9]. While Ducharme et al. have advocated for the intrinsic switching mechanism based on both experimental data and theoretical prediction [9], some other researchers have been expressing concerns regarding to the theoretical conditions of the data interpretation. Recent experimental works by Kliem et al. revealed that the switching process below a certain critical thickness could not be sufficiently explained by either intrinsic or extrinsic model alone [13]. Especially, Naber

\* Corresponding author.

E-mail addresses: [acnguyen@ntu.edu.sg](mailto:acnguyen@ntu.edu.sg) (C.A. Nguyen), [pslee@ntu.edu.sg](mailto:pslee@ntu.edu.sg) (P.S. Lee).

et al. have been able to obtain the experimental evidence of ferroelectric switching with bulk characteristics for ultrathin films with thickness ranging from 3 to 10 nm [14]. They have attributed this observation to the improved surface interfacing between the metal electrodes and the ultrathin ferroelectric polymer film. The intrinsic switching mechanism in the PVDF nanostructures and ultrathin films is beyond the scope of this report. However, it can be seen that various important properties of ferroelectric materials remain to be explored in spite of the tremendous efforts and achievements have been obtained in the field.

The application of LS-transfer P(VDF-TrFE) for non-volatile memory using hybrid device with Si-technology has been shown but limited to rather thick film of 100 ML [10]. A unique feature of the LS-transfer film is being strongly governed by the interfacial interaction with substrate that leads to formation of different nanostructures by simple annealing process [15]. It has been well postulated that the nucleation in ferroelectrics substantially occurs at defects or crystal boundaries. For the mesa nanostructures or ultrathin films, the domain-wall motion is in the film plane due to the highly anisotropic dimensions. It hence allows more precise control of nucleation locations and domain-wall motion direction in the switching process. With the lateral size in the range of less than 200 nm, a group of these separately and accurately positioned nanostructures can serve as an equivalent memory element (1 bit) that can improve the storage density as well as reduce cross-talk noise between bits. These understandings are potentially useful for memory application in terms of enhanced device density and performance [10]. To date, demonstration of non-volatile memory behavior of thin LS-transfer films (<100 ML) has been lacking and the memory functionality of the ultrathin P(VDF-TrFE) is not fully explored. Furthermore, realization of organic ferroelectric field effect transistors (FeFET) with LS-transfer film has not yet been reported.

In this paper, we investigate the crystallization of the polymers upon annealing in the paraelectric phase, as a function of the number of transferred layers. We attained localized area switching using piezo-force microscopy and demonstrate a low voltage ferroelectric memory (<15 V) using 10 ML of the LS-transfer P(VDF-TrFE) film as dielectric layer in capacitors and ferroelectric field effect transistors. The electrical behavior and memory functionality is correlated to polarization properties of the LS-transfer films.

## 2. Experimental

P(VDF-TrFE) (70–30 mol%) was purchased from Solvay and used without purification. Copolymer pellets were dissolved in methyl ethyl ketone (MEK) at concentration of 0.1 mg/cc. The solution was then filtered by using 0.2  $\mu\text{m}$  pore-size Teflon filter and promptly used for deposition to maintain a consistent concentration. N-type Silicon wafer was used as transfer substrates. The wafers were cleaned with Piranha solution (1H<sub>2</sub>O<sub>2</sub>:2H<sub>2</sub>SO<sub>4</sub>), SC2 solution (1NH<sub>4</sub>OH:1HCl:10H<sub>2</sub>O), followed by acetone, metha-

nol and DI water and blow-dried by N<sub>2</sub> gas. Plasma treatment was done on cleaned substrates with ambient medium for 2 min.

LS-transfer film fabrication was done using Langmuir KSV5000 trough. Ultra-purified water with resistivity of 18.2 M $\Omega$  cm was used as subphase medium. The copolymer solution was manually spread onto the subphase surface between the two automatically moving barriers with surface pressure measured by a platinum Wilhelmy plate. The monolayers were manually transferred onto substrates horizontally at 25 °C and surface pressure of 5 mN/m. All transferred samples were then annealed in the ambient at 120 °C for 1 h using a slow ramping oven (1 °C/min). Film crystallinity was determined by Rigaku X-ray diffractometer (XRD) (40 KV, 30 mA) with an incident angle of 0.5° and step of 0.02. The surface morphology of all layers was characterized by atomic force microscopy (AFM) (digital instruments) in tapping mode using nonconductive tip.

Polarization switching of the transferred films was observed by piezo-force microscopy (PFM) with conductive Si tip in contact mode. The closed circuit of sample and PFM equipment was made through the contact from the conductive tip to the LS-film surface and the back of the Si-wafer substrate using silver paste to reduce contact resistance. The surface morphology was first scanned with 10  $\times$  10  $\mu\text{m}^2$  dimensions. Next a voltage of +10 V was applied to an area of 6  $\times$  6  $\mu\text{m}^2$  and a reversed voltage of -10 V was lastly applied to area of 2  $\times$  2  $\mu\text{m}^2$  as shown in Fig. 2. The metal-ferroelectric-semiconductor (M-F-S) capacitor devices were fabricated by thermal evaporation of gold (99.9% purity) through a shadow mask (diameter of 300  $\mu\text{m}$ ) onto annealed film samples. The leakage current was measured by Keithley 4200 analyzer and capacitance data was obtained by using HP4284 LCR meter (AC signal of 50 mV and 1 kHz). Ferroelectric field effect transistor (FeFET) was fabricated using Si-wafer with 5 nm thick thermal oxide. The transistor was formed by evaporation of pentacene on top of the transferred P(VDF-TrFE) layers in vacuum (5  $\times$  10<sup>-7</sup> torr) at 1–2 Å/s rate. It was then followed by evaporation of gold electrodes for source and drain formation using shadow mask. The transistor operation was then characterized by the Keithley analyzer in dark vacuum ambient.

## 3. Results and discussion

To examine the formation of continuous thin film by LS-transfer method, multiple monolayers were transferred onto cleaned Si-wafer followed by annealing as described. Fig. 1 presents the surface morphology and crystalline structure of films with thickness from 2 to 10 ML. After annealing, it can be seen that nano-mesas and nanowells were formed for 2 and 6 ML thick film, respectively, as well as fully covered film for 10 ML thick sample. Final thickness of the nano-mesa and nanowell samples is below 20 nm while that of the 10 ML sample is in the range of 20  $\pm$  2 nm as determined by AFM line-profiling. Both the nanostructure formations and dimensions are in agreement with the previously reported data (1.8 nm per monolayer) especially in the case of fully covered film of 10 ML

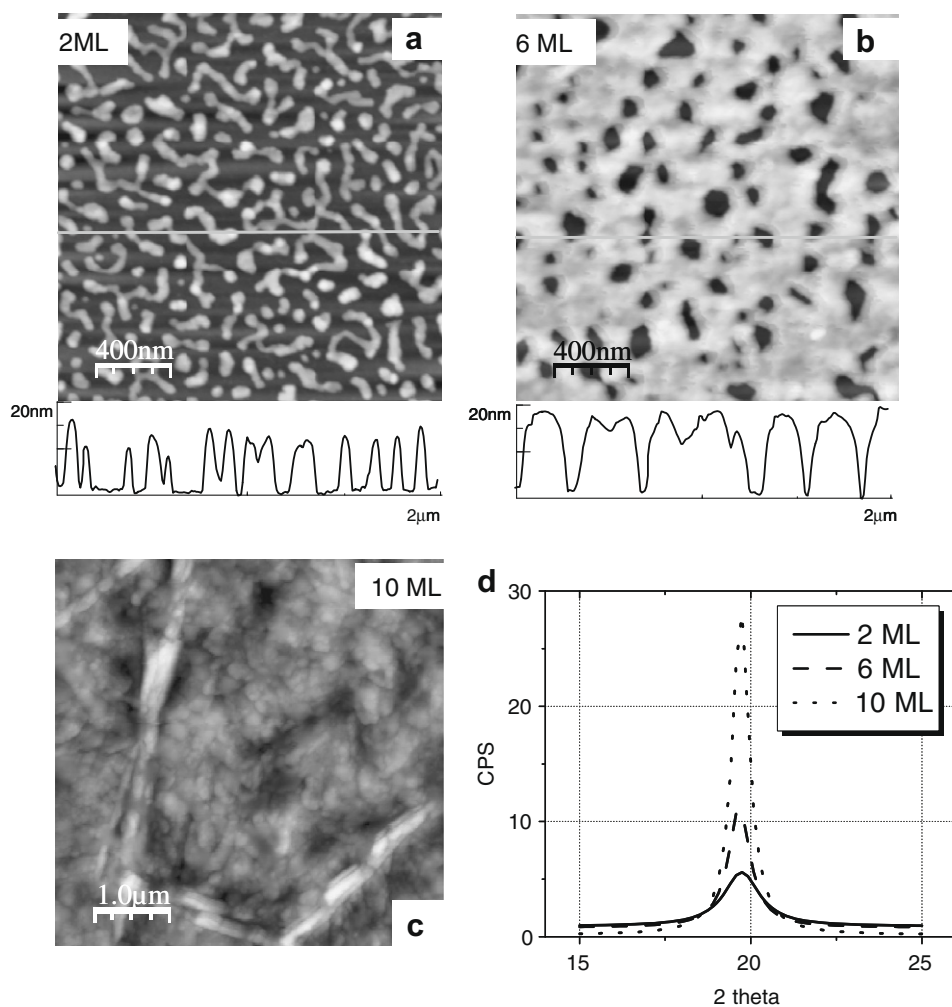


**Fig. 1.** Changes in surface morphology and crystallinity of the LS-transfer P(VDF-TrFE) films as thicknesses were increased (a), (b) and (c) 2, 6, and 10 ML, (d) XRD data of all the three films.

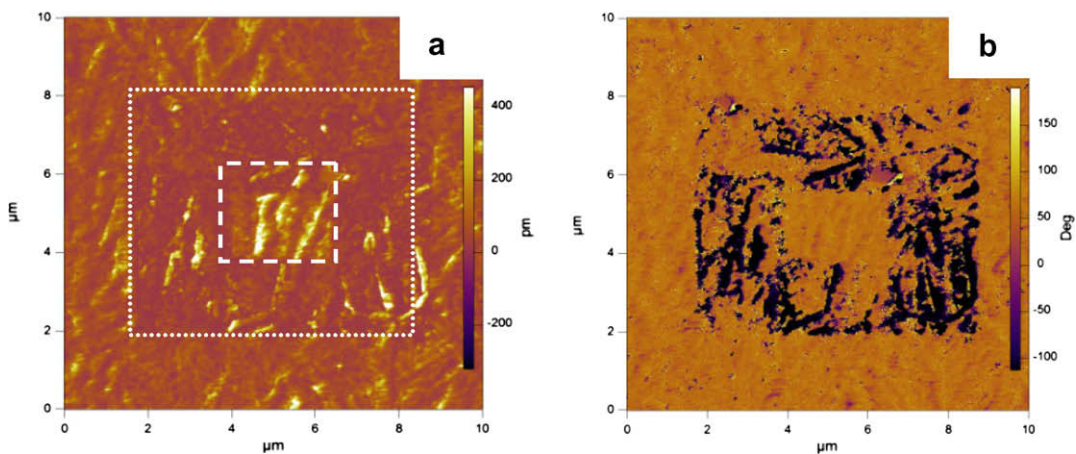


**Fig. 2.** PFM images of 10 ML LS-transfer sample (a)  $d_{33}$  coefficient image and (b) phase image. The dashed and dotted boxes in (a) indicate the scanning areas of different voltage application and the contrast difference in (a) and (b) represents the polarization switching.

layer [16]. The small variation in thickness suggests the crystallization of P(VDF-TrFE) copolymer occurred in a planar manner with crystallinity increasing with more transferred layers. While the 6 ML-film appears with vertical holes through the film thickness, no specific grain formation is observed on the covered regions by the copolymer. On the other hand, grain formation can be seen on the fully covered 10 ML film. The film surface mainly consists of small and round-shaped grains, which results in roughness value (RMS) less than 9 nm. Besides, occasional appearance of rod-like crystals is also observed as shown in Fig. 1c. At the locations of the rod-like grain, the vertical dimension can eventually reach up to 50 nm indicating the crystallization propagates along the normal direction to the film only after the substrate surface had been fully covered. The rod-like grains with polymer lamellas packing along the grain direction appears as vertical walls which intercept each others leading to rough topography and deep valleys usually found on thicker film fabricated by spin-coating [17]. Formation of the 10 ML thin film (10 ML) with limited rod-like grain and good crystallinity (Fig. 1) is anticipated to improve the quality of multilayer ferroelectric memory device.

The XRD data (Fig. 1d) of 2, 6 and 10 ML samples show that both ferroelectric and paraelectric phases coexist [1,2]. Previous report [18] suggested that formation of nanostructures had only taken place in the copolymer paraelectric phase. The observation of ferroelectric phase here is hence believed to be due to the slow cooling process after annealing that resulted in paraelectric–ferroelectric phase transition even in the nanostructures. Measurement to confirm polarization properties was hence done by PFM method on all the samples shown in Fig. 1. It was found that only fully covered sample with 10 ML transferred possessed switchable regions under the tip bias application while it was unable to capture any responsive signals from samples with nanostructures (2 and 6 ML). We attribute this to the limitation of applied voltage in the PFM system (maximum applied voltage of  $|10|$  V) as compared to the much higher value of intrinsic coercive field ( $\sim 0.5$  GV/m) which has been estimated for ultrathin ( $<15$  nm) Langmuir–Blodgett film [19]. Polarization switching examined in a 10-ML sample on Si-wafer substrate by the  $d_{33}$  coefficient and phase images are presented in Fig. 2. The experiment was performed in two steps – first,  $6 \times 6 \mu\text{m}^2$  (dotted box) scan with +10 V that

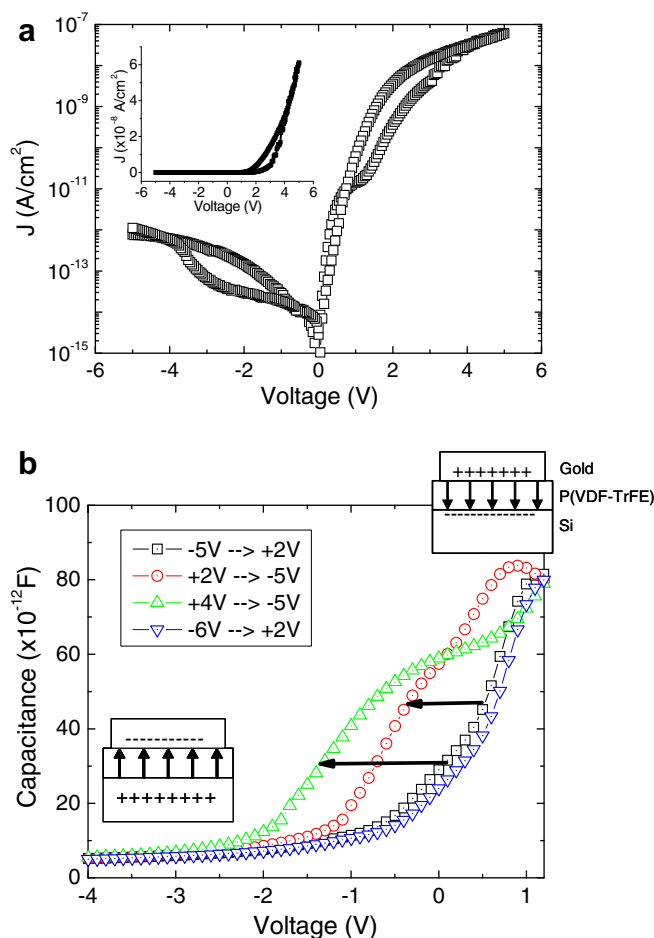


**Fig. 3.** Electrical characteristic of 10 ML M-F-S capacitor device (a) leakage current  $J$ - $V$  curve. The electrode area is  $7.07 \times 10^{-4} \text{ cm}^2$ . The inset shows the linear plot. (b) Capacitance hysteresis  $C$ - $V$  curves. Two insets present the device structure with hysteresis mechanism.

registered “down” dipoles (point towards substrate) appearing as dark contrast, and then  $2 \times 2 \mu\text{m}^2$  scan (dashed box) that reversed the polarization to “up” dipoles (pointing away from substrate) appears as different contrast in Fig. 2b. The bright contrast in the dashed box of Fig. 2a clearly indicates the strong dipolar response which could only be resulted from the orientation switching as compared to the outer areas where polarization was not disturbed. The stable existence of the switched region ( $2 \times 2 \mu\text{m}^2$  box) after continuous scanning enables the storing of information in an ultrathin film device without the adverse effects by depolarization.

Non-volatile memory behavior was studied using M-F-S device with 10 ML thick P(VDF-TrFE) film as a dielectric layer. Fig. 3a shows the leakage current profile which is reasonably low (less than  $10^{-7} \text{ A/cm}^2$ ) for device application with the inset showing a typical diode behavior. It can be seen the current is asymmetric across the vertical axis but has the minimum value at 0 V. The asymmetric shape of the current curve is believed to be caused by different barrier heights at P(VDF-TrFE)/Au and P(VDF-TrFE)/Si interfaces. With potential applied at the bottom electrode to the silicon substrate, higher current obtained by positive biases means the apparent barrier height of charge injection at the top electrode (Au) is lower than that at bottom one (Si). The minimum current at 0 V possibly indi-

cates the absence of detrapping current by charges existing near the interfacial regions. The memory function is hence mainly resulted from the switching polarization of the P(VDF-TrFE) dipoles as explained by the capacitance hysteresis below.

Fig. 3b presents the capacitance hysteresis data obtained by different sweeping voltages with the first curve ( $-5 \text{ V}$  to  $+2 \text{ V}$ ) as reference curve. As voltage was swept in the reversed direction ( $+2 \text{ V}$  to  $-5 \text{ V}$ , dash curve), a capacitance hysteresis was obtained with a shift in flat-band voltage of  $0.7 \text{ V}$  to the negative potential. This can be explained from the direction of dipole vectors. The positive bias ( $+2 \text{ V}$ ) at the top metal electrode caused the dipole pointing down towards the Si substrate and led to accumulation in Si. As the voltage was swept to negative bias ( $-5 \text{ V}$ ), the field across the device must overcome the dipolar coercive field to revert the dipole direction. As a result the charges were accumulated in the Si until coercive field was reached and led to depletion as displayed in the insets of Fig. 3b. The charge accumulation and depletion in the semiconductor can be treated as ON and OFF state, respectively, for the non-volatile memory. An estimation of the switching field for this device including voltage of  $|1| \text{ V}$  over thickness of  $18 \text{ nm}$  yields a value of  $|56| \text{ MV/m}$  similar to previous report [2] for spin-coated films. Furthermore, Fig. 3b also displays variability of

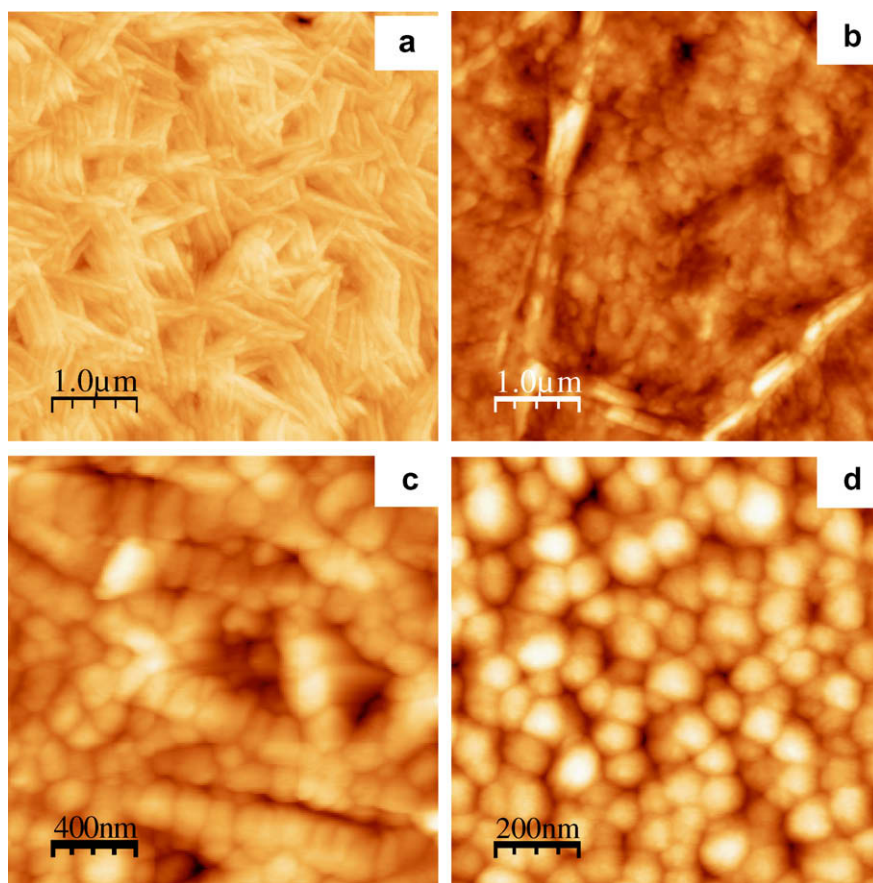


**Fig. 4.** Comparison of surface morphology of (a) spin-coated film (200 nm thick) and (b) 10 ML ( $\sim 20 \text{ nm}$  thick) LS-transfer film. Morphology of pentacene layers grown on both films are shown in (c) and (d), respectively.

flat-band voltage shift or memory window of the device with the application of different voltage amplitudes. When the “writing” voltage was increased to +4 V, the voltage shift could be extended up to 1.3 V (dot curve). To bring the device back to the original state, an “erasing” voltage was applied at –6 V (dash-dot curve). To read the data in the device, a small “reading” voltage should be used e.g. –0.5 V without destroying or reversing the polarization state, which will result in a capacitance difference of up to 40 pF for +4 V “writing” voltage. Hence this proves the versatility and applicability of thin ferroelectric polymer for low voltage non-volatile memory application.

It can be seen that the accumulation in the M-F-S device is unstable which coincides with the high leakage current in the device (Fig. 3). In order to improve the device stability during accumulation for field effect transistor, the semiconductor layer of Si is replaced with pentacene which is an organic p-type semiconductor with lower charge carrier concentration ( $\sim 3 \times 10^{17} \text{ cm}^{-3}$  [20]) while the n-type Si-wafer serves as an electrode. Surface morphology of the evaporated pentacene layer (50 nm thick) on spin-coated and LS-transfer (10 ML) films are shown for comparison in Fig. 4. The surface roughness of the spin-coated P(VDF-TrFE) film is about 17–20 nm as previously reported [6]. For the 10-ML LS-transfer film, pre-scans of surface morphology by AFM were performed to select regions with minimal appearance of the rod-crystallite. As a result, the effective surface roughness of the LS-film was maintained below 10 nm. The average size of pentacene grains is found from the AFM profile to be around 100 nm for both types of P(VDF-TrFE) films. However the pentacene grain-growth is seen to follow the morphology of the rod-like grains on the spin-coated film (Fig. 4c), which limits the intergrain connection in the thin ( $\sim 50$  nm) semiconductor layer. This resulted in weak semiconducting behavior of the pentacene film and negligible transistor device characteristics. In the contrary, pentacene grains on the LS-transfer film (Fig. 4d) are generally in circular shape and unaffected by the underneath surface morphology. The average small grain size is probably due to the low surface energy of the P(VDF-TrFE) copolymer [21,22].

The electrical characteristics ( $I_D$ - $V_D$ ,  $I_D$ - $V_G$ ) of the FeFET device fabricated on the LS-transfer film are shown in Fig. 5. Both of drain and gate voltages were applied in ascending order for  $I_D$ - $V_D$ . The mobility is calculated in the saturation regime from Fig. 5a yielding value of  $0.003 \text{ cm}^2/\text{Vs}$  for device with an effective capacitance of  $3.1 \times 10^{-7} \text{ F/cm}^2$  and channel length and width of 75 and 4000  $\mu\text{m}$ , respectively. The value of mobility is likely affected by the smaller grain size [23] and the lower dielectric constant of  $\text{SiO}_2$  ( $\kappa = 3.9$  as compared to  $\kappa = 13$  of P(VDF-TrFE)) in the composite insulating layer. The transfer characteristic shows hysteresis in drain current (ON/OFF ratio around  $2 \times 10^3$  at zero gate bias) which follows the polarization switching of the copolymer dipoles and is in agreement with previously reported devices fabricated by spin-coating P(VDF-TrFE) film [5,6]. As switching current peaks seen from the inset of Fig. 5b are around  $V_G = |5| \text{ V}$ , a sweeping gate voltage of  $|15| \text{ V}$  is hence sufficient to induce saturated polarization in the ferroelectric layer. One of the clear advantages is hence the saturating

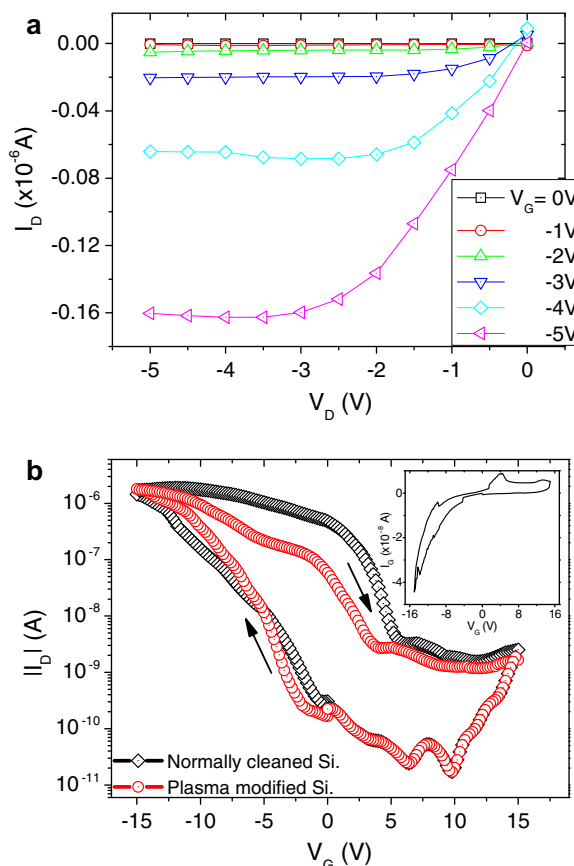


Fig. 5. Device characteristics of pentacene transistors with 10 ML transferred dielectric layer on normally cleaned and plasma-modified Si substrates (a)  $I_D$ - $V_D$  (device on normally cleaned Si substrate). (b)  $I_D$ - $V_G$  measured at  $V_D = -5 \text{ V}$ . The inset shows the gate current  $I_G$ - $V_G$  of device on normally cleaned Si substrate.

of polarization at low bias ( $\sim |15| \text{ V}$ ) which results in low voltage application device.

The formation of nanostructures from the first few monolayers is governed by both of the elastic and surface energy density [18]. We attempted to improve the contact formation between the LS-transferred film and the substrate surface by briefly subjecting the Si surface to ambient plasma for 2 min. The obtained result was a more hydrophilic surface (with smaller contact angle of  $7.72^\circ$  as compared to  $25.27^\circ$  of normally cleaned Si-wafer). The higher surface energy led to pattern coarsening to minimize the interface area during annealing in paraelectric phase [18]. Examination by AFM of annealed 1 ML sample on both types of treated surfaces shows different nanostructure formation. While separating nano-islands were seen on the normally cleaned sample, percolating nanomesa with larger coverage of substrate surface was obtained for the plasma-modified sample as previously described [15]. FeFET device with 10 ML film transferred onto the plasma-modified surface shows similar drain current hysteresis and carrier mobility in the semiconductor channel as the ones on normally cleaned substrate (Fig 5b). However the ON/OFF ratio is reduced to 350 due to lower current retention at zero gate bias. It is possibly

resulted from the defects generated during plasma-modification. The plasma ion bombardment partially removed the topmost oxygen-bonding layer and left unsaturated bonds on the Si surface that makes it more susceptible to trapping of mobile charges during the transfer of first few layers. The existence of trapped charges between the SiO<sub>2</sub> and the P(VDF-TrFE) layer subsequently caused the non-switching polarization which induced higher drain current during strong accumulation but did not retain the current as gate voltage drop to 0 V [6]. It is hence required further improvement in the engineering of interface between substrate and the transferred films to obtain denser dielectric layer of ultrathin thickness.

#### 4. Conclusion

We have demonstrated the fabrication of good quality ultrathin Langmuir–Schaefer films for the application in non-volatile memory device. Study of crystallinity evolution and surface morphology in the process of film formation indicates planar crystallization occurring in the LS-film with transferring of up to 10 ML. The good coverage of this film with high crystallinity of small flat grains allows the demonstration of non-volatile memory devices. The memory behavior was presented in MFS capacitor as well as FET with the retention by the dipolar polarization. Different states of data storing and erasing was demonstrated with operation voltages less than 15 V. One of the detrimental defects has been identified as mobile charge trapping at the interface that worsens the current retention when the substrate is plasma treated to improve the LS-film coverage. This hence prompt for more attention in optimizing the crystallization of the LS-film and the engineering of the surface morphology. In spite of those shortcomings, the LS-transfer method offers the advantages of simple processing conditions and small volume of consumed material. The ferroelectric LS-film is proven to be versatile and applicable for device application that requires low operation voltages.

#### Acknowledgements

One of the authors, C.A. Nguyen, would like to acknowledge the research scholarship awarded by Nanyang Technological University, Singapore. This work is supported by A Star Grant No. 0521170032 and NTU Acfr Grant No. RG26/05.

#### References

- [1] A.J. Lovinger, *Science* 220 (1983) 1115.
- [2] T. Furukawa, *Adv. Coll. Int. Sci.* 71–72 (1997) 183.
- [3] Q.M. Zhang, V. Bharti, X. Zhao, *Science* 280 (1998) 2101.
- [4] S.B. Lang, S. Muensit, *Appl. Phys. A* 85 (1998) 125.
- [5] R.C.G. Naber, C. Tanase, P.W.M. Blom, G.H. Gelinck, A.W. Marsman, F.J. Touwslager, S. Setayesh, D.M. De Leeuw, *Nature Mater.* 4 (2005) 243.
- [6] C.A. Nguyen, P.S. Lee, S.G. Mhaisalkar, *Org. Electron.* 8 (2007) 415.
- [7] K.N. Narayanan Unni, R. de Bettignies, S. Dabos-Seignon, J.M. Nunzi, *Appl. Phys. Lett.* 85 (2004) 1823.
- [8] B. Stadlober, M. Zirkel, M. Beult, G. Leising, *Appl. Phys. Lett.* 86 (2005) 242902.
- [9] H.S. Nalwa (Ed.), *Handbook of thin film materials, Ferroelectric Polymer Langmuir–Blodgett Films*, vol. 3, Academic Press, San Diego, 2002. Chapter 11.
- [10] S. Durchame, T.J. Reese, C.M. Othon, R.K. Rannow, *IEEE Trans. Device Mater. Reliab.* 5 (2005) 720.
- [11] M. Bai, A.V. Sorokin, D. Thompson, M. Poulsen, S. Durchame, C.M. Herzinger, S.P. Palto, V.M. Fridkin, S.G. Yudin, V.E. Sachenko, L.K. Gribova, *J. Appl. Phys.* 95 (2004) 3372.
- [12] T. Furukawa, H. Matsuzaki, M. Shiina, Y. Tajitsu, *Jpn. J. Appl. Phys.* 24 (1985) L661.
- [13] H. Kliem, R. Tadros-Morgane, *J. Phys. D Appl. Phys.* 38 (2005) 1860.
- [14] R.C.G. Naber, P.W.M. Blom, D.M. de Leeuw, *J. Phys. D Appl. Phys.* 39 (2006) 1984.
- [15] M. Bai, S. Ducharme, *Appl. Phys. Lett.* 85 (2004) 3528.
- [16] M. Bai, M. Poulsen, S. Ducharme, *J. Phys. Condens. Mat.* 18 (2006) 7383.
- [17] K. Matsushige, H. Yamada, *Ann. NY. Acad. Sci.* 960 (2002) 1.
- [18] J. Li, Y. Luo, M. Bai, S. Ducharme, *Appl. Phys. Lett.* 87 (2005) 213116.
- [19] S. Ducharme, V.M. Fridkin, A.V. Bune, S.P. Palto, L.M. Blinov, N.N. Petukhova, S.G. Yudin, *Phys. Rev. Lett.* 84 (2000) 175.
- [20] Y.S. Lee, J.H. Park, J.S. Choi, *Opt. Mater.* 21 (2002) 433.
- [21] S.Y. Yang, K. Shin, C.E. Park, *Adv. Func. Mater.* 15 (2005) 186.
- [22] G. Teyssedre, A. Bernes, C. Lacabanne, *J. Polym. Sci. B Polym. Phys.* 33 (1995) 879.
- [23] A. Facchetti, C. Kim, T.J. Marks, *Mater. Res. Soc. Symp. Proc.* 1003 (2007) 1003-001-08.



# Efficient solution-processed electrophosphorescent devices using ionic iridium complexes as the dopants

Lei He, Lian Duan, Juan Qiao, Deqiang Zhang, Guifang Dong, Liduo Wang, Yong Qiu \*

Key Lab of Organic Optoelectronics and Molecular Engineering of Ministry of Education, Department of Chemistry, Tsinghua University, Beijing 100084, PR China

## ARTICLE INFO

### Article history:

Received 20 July 2008

Received in revised form 19 October 2008

Accepted 20 October 2008

Available online 26 October 2008

### PACS:

72.80.Ga

72.80.Le

78.60.Fi

85.60.Jb

### Keywords:

Ionic iridium complexes

Dopants

Blue

Electrophosphorescent devices

## ABSTRACT

Efficient solution-processed electrophosphorescent devices using two blue-emitting ionic iridium complexes (complex 1 and complex 2) were fabricated, with poly(*N*-vinylcarbazole) (PVK):1,3-bis(5-(4-*tert*-butylphenyl)-1,3,4-oxadiazol-2-yl)benzene (OXD-7) as the host and Cs<sub>2</sub>CO<sub>3</sub>/Al as the cathode. Using complex 1 as the dopant, we obtained efficient blue-green electrophosphorescence from single-layer devices with a maximum efficiency of 12.2 cd A<sup>-1</sup>, a maximum brightness of 12,600 cd m<sup>-2</sup> and CIE (Commission Internationale de l'Éclairage) coordinates of (0.19, 0.45). And the maximum efficiency of the device based on complex 1 can be further improved to 20.2 cd A<sup>-1</sup>, when a thin 1,3,5-tris(1-phenyl-1H-benzo[d]imidazol-2-yl)benzene (TPBI) layer was inserted between the light-emitting layer and the cathode. Using complex 2 as the dopant, we obtained deep-blue electrophosphorescence with the emission peak at 458 nm and CIE coordinates of (0.16, 0.22). Our work suggests that ionic iridium complexes are promising phosphors for obtaining efficient electrophosphorescence in the blue region.

© 2008 Elsevier B.V. All rights reserved.

## 1. Introduction

The past two decades have witnessed the great development of organic light-emitting diodes (OLEDs), which are promising candidates for display and solid-state lighting applications [1]. Through the recombination of holes and electrons, singlet and triplet excitons are generated in OLEDs. For OLEDs containing fluorescent dopants, only singlet excitons can generate light; while for OLEDs containing phosphorescent dopants, both singlet and triplet excitons can generate light [2]. In theory, the efficiency of electrophosphorescent devices is nearly three times higher than that of electrofluorescent devices, given that the ratio between singlet and triplet excitons generated in OLEDs is about 1:3 [2,3]. To achieve high efficiency, electrophospho-

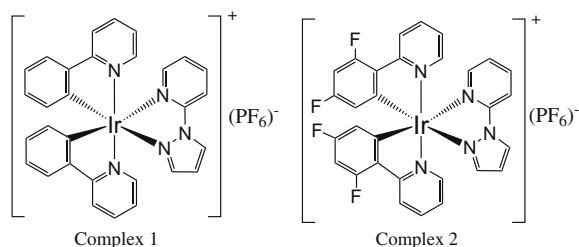
rescent devices containing phosphorescent dopants are more favorable choices.

Phosphorescent dopants commonly used in OLEDs are transition metal complexes [2,4]. The involvement of transition metal ions is essential because they can provide strong spin-orbit coupling which allows the spin-forbidden triplet excitons to decay radiatively. Many kinds of transition metal complexes, i.e., rhenium, osmium, ruthenium, platinum and iridium complexes, have been developed and utilized as efficient phosphorescent dopants in OLEDs [4]. These transition metal complexes are mostly neutral and, thus, evaporable to fabricate vacuum-deposited devices. In recent years, ionic transition metal complexes (iTMCs), including ionic copper, ruthenium, osmium and iridium complexes, have drawn more and more attention [5,6]. The application of iTMCs in organic electroluminescence have resulted in another kind of device, named light-emitting electrochemical cells (LECs), which have

\* Corresponding author. Tel.: +86 10 62779988; fax: +86 10 62795137.  
E-mail address: [qiyu@mail.tsinghua.edu.cn](mailto:qiyu@mail.tsinghua.edu.cn) (Y. Qiu).



many advantages (i.e., single-layer, solution-process and air-stable cathodes) over conventional multilayer OLEDs, though they suffer from long response time and limited device stability [5,6]. To obtain highly efficient LECs, various iTMCs with controllable emission colors and high photoluminescent quantum yields (PLQY) have been developed [5,6,8]. Surprisingly, these iTMCs, despite their impressive photophysical and electrochemical characteristics, have seldom been used as phosphorescent dopants in OLEDs. For LEC devices, the light-emitting layer is composed of neat iTMCs, which results in severe excited-state quenching and, thus, depressed device performance [7,8]. It is expected that the severe excited-state quenching in LEC devices will be significantly relieved as the iTMCs are used as dopants in OLEDs. Carlson et al. reported single-layer polymer OLEDs with ionic osmium complexes as dopants, which gave red light emission with a maximum external quantum efficiency of 2.2% [9]. Zhang et al. used ionic copper complexes as dopants in multilayer polymer OLEDs, which emitted green light with a maximum efficiency of 10.5 cd A<sup>-1</sup> [10]. Plummer et al. reported yellow-emitting polymer OLEDs using an ionic iridium complex as the dopant, which gave a maximum efficiency of 22.5 cd A<sup>-1</sup> [11]. However, as far as we know, there is no report on blue-emitting OLEDs with iTMCs dopants till now, as iTMCs emitting light in the blue region are rare [6,8]. In this paper, we report efficient electrophosphorescent devices using two blue-emitting ionic iridium complexes as the dopants (Scheme 1). Previously, we used these two ionic iridium complexes to fabricate blue LECs and found severe excited-state-quenching in LEC devices, though blue light emission was achieved [8]. In single-layer devices with the host of poly(*N*-vinylcarbazole) (PVK):1,3-bis(5-(4-tert-butylphenyl)-1,3,4-oxadiazol-2-yl)benzene (OXD-7) and the cathode of Cs<sub>2</sub>CO<sub>3</sub>/Al, we obtained efficient blue-green electrophosphorescence with a maximum efficiency of 12.2 cd A<sup>-1</sup>, a maximum brightness of 12,600 cd m<sup>-2</sup> and CIE (Commission Internationale de l'Éclairage) coordinates of (0.19, 0.45) when complex 1 was used as the dopant. After a thin 1,3,5-tris(1-phenyl-1H-benzodimidazol-2-yl)benzene (TPBI) layer was inserted between the light-emitting layer and the cathode, the maximum efficiency of the blue-green device was further improved to 20.2 cd A<sup>-1</sup>. We also obtained deep-blue electrophosphorescence with the emission peak at 458 nm and CIE coordinates of (0.16, 0.22) when complex 2 was used as the dopant.



**Scheme 1.** Chemical structures of the ionic iridium complexes.

## 2. Experimental

### 2.1. Photophysical characterization

Complex 1 and complex 2 were synthesized according to our previous publication and were further purified by recrystallization from acetonitrile and ether before use [8]. Thin films with the thickness of approximate 100 nm for photophysical characterization were deposited onto quartz substrates by spin-coating from 1,2-dichloroethane solutions. Absorption spectra were recorded with a UV-vis spectrophotometer (Agilent 8453) and PL spectra were recorded with a fluorospectrophotometer (Jobin Yvon, FluoroMax-3).

### 2.2. Fabrication and characterization of electrophosphorescent devices

Film thickness and surface morphology of thin films were determined with the atomic force microscopy (AFM, SPA-400). The ITO substrates with sheet resistance of 15 Ω/□ were sufficiently cleaned by ultrasonication in detergent and then in deionized water and treated with oxygen plasma before use. The PEDOT:PSS layer was spin-coated in ambient atmosphere and then baked at 200 °C for 10 min, yielding a smooth film with a thickness of approximate 60 nm and a root mean square (RMS) value of 1.25 nm (for an area of 5 × 5 μm<sup>2</sup>). The light-emitting layer was then spin-coated onto the PEDOT:PSS-coated substrate from a mixed solution of PVK:OXD-7:complex 1 (or complex 2) in 1,2-dichloroethane in a nitrogen atmosphere glove box. The film was then baked at 80 °C for 30 min, yielding a smooth film with a thickness of approximate 85 nm and a RMS value of 0.93 nm (for an area of 5 × 5 μm<sup>2</sup>). The substrate was then transferred into an evaporation chamber, where the TPBI (if needed) was evaporated at an evaporation rate of 1–2 Å/s under a pressure of 4 × 10<sup>-4</sup> Pa and the Cs<sub>2</sub>CO<sub>3</sub>/Al bilayer cathode was evaporated at evaporation rates of 0.2 and 10 Å/s for Cs<sub>2</sub>CO<sub>3</sub> and Al, respectively, under a pressure of 1 × 10<sup>-3</sup> Pa. The current-voltage-brightness characteristics of the devices were characterized with Keithley 4200 semiconductor characterization system. The electroluminescent spectra were collected with a Photo Research PR705 Spectrophotometer. All measurements of the devices were carried out in ambient atmosphere without further encapsulations.

## 3. Results and discussion

### 3.1. Photophysical characterization

Fig. 1 depicts the absorption and photoluminescent (PL) spectra of complex 1, complex 2 and PVK:OXD-7 in thin films. The intense absorptions at the ultra-violet region from 200 to 350 nm are ascribed to <sup>1</sup>π-π\* transitions from the ligands while the relatively weak absorptions from 350 nm to the visible region are ascribed to metal-to-ligand charge-transfer transitions (MLCT) of the complexes. As Fig. 1 shows, the overlap between the emission

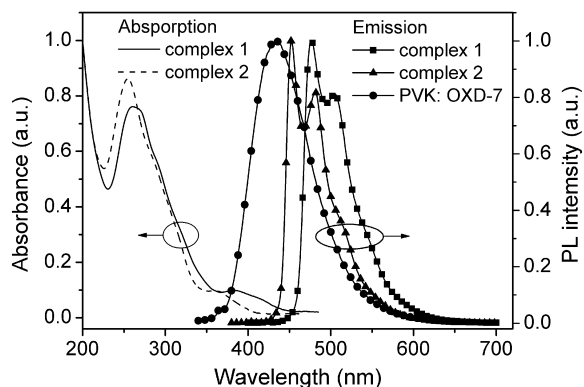


**Fig. 1.** Absorption and emission spectra of complex 1 (5% doped in PMMA), complex 2 (5% doped in PMMA) and PVK:OXD-7 (2:1, weight ratio) in thin films.

spectra of PVK:OXD-7 and the MLCT absorption bands of complex 1 is quite large, indicating that the Förster energy transfer from PVK:OXD-7 to complex 1 would be efficient. As for complex 2, the overlap is relatively weak. When lightly doped at 5 wt.% into poly(methyl methacrylate) (PMMA), complex 1 and complex 2 both give blue light emission with the emission peak at 476 and 452 nm, respectively. More photophysical characterizations of complex 1 and complex 2 can be found in our previous publication [8].

### 3.2. Electrophosphorescent devices based on complex 1

PVK:OXD-7 (2:1, weight ratio) was selected as the host for the ionic iridium complexes. The electron-transporting material OXD-7 was mixed into PVK to facilitate the electron transport in the light-emitting layer [12–14]. The device structure is ITO/PEDOT:PSS (60 nm)/PVK:OXD-7:*x*% complex 1 (85 nm)/Cs<sub>2</sub>CO<sub>3</sub> (*y* nm)/Al (200 nm), where the doping concentration of complex 1 and the thickness of Cs<sub>2</sub>CO<sub>3</sub> layer were varied to optimize the device performance.

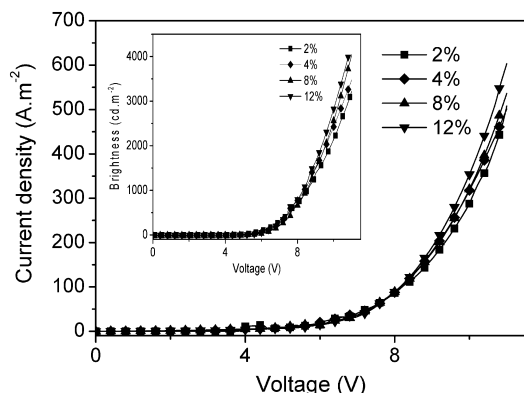


**Fig. 2.** Current density–voltage characteristics of ITO/PEDOT:PSS (60 nm)/PVK:OXD-7:*x*% complex 1 (85 nm)/Cs<sub>2</sub>CO<sub>3</sub> (2 nm)/Al (200 nm) with different doping concentrations (*x*%) of complex 1. The inset shows the corresponding brightness–voltage curves of the devices.

**Fig. 2** shows the current density–voltage characteristics of devices with different doping concentrations of complex 1. The inset in **Fig. 2** depicts the corresponding brightness–voltage curves of the devices. Detailed electrical characteristics of the devices are summarized in **Table 1**. For all devices, the thickness of the Cs<sub>2</sub>CO<sub>3</sub> layer was fixed at 2 nm. As **Fig. 2** shows, the current density–voltage curves shift towards the low voltages as the doping concentration of complex 1 increases. This can be explained by the energy level diagram of the device (**Scheme 2**). The lowest unoccupied molecular orbital (LUMO) energy level of complex 1 (−3.2 eV) is much lower than that of PVK (−2.2 eV) and comparable to that of OXD-7 (−3.0 eV). Thus, as the doping concentration of complex 1 increases, electrons are expected to be able to move along the LUMO orbitals of complex 1. Consequently, the electron transport in the device is facilitated, which explains the increased current density at a fixed voltage as the doping concentration of complex 1 increases. Noticeably, as the doping concentration of complex 1 increases, the brightness of the device at a fixed voltage also increases (see the inset of **Fig. 2**). The net result is that the efficiency of the devices does not vary very much as the doping concentration of complex 1 varies from 2% to 12% (**Table 1**). At a doping concentration of 8%, the device reaches a maximum efficiency of 10.5 cd A<sup>−1</sup> and a maximum brightness of 10,080 cd m<sup>−2</sup>. Besides, all devices show low turn-on voltages at around 4.0 V, indicating that both the hole injection from the ITO/PEDOT:PSS anode and the electron injection from the Cs<sub>2</sub>CO<sub>3</sub>/Al cathode into the light-emitting layer are efficient.

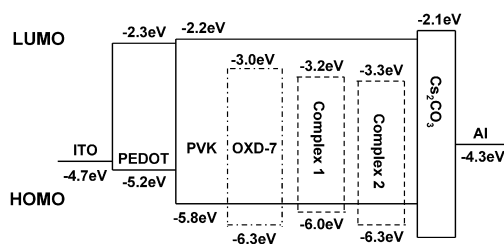
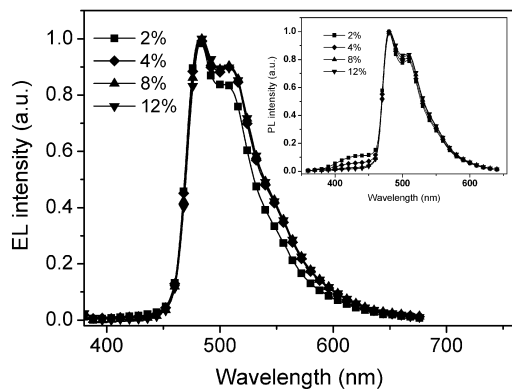
All devices show bright blue–green light emission with the emission peak at around 482 nm and CIE coordinates varying a little from (0.19, 0.45) to (0.20, 0.48) as the doping concentration of complex 1 varies from 2% to 12% (**Table 1**). **Fig. 3** shows the electroluminescent (EL) spectra of the devices and the inset shows the corresponding PL spectra of the light-emitting layers. In the PL spectra of thin films of PVK:OXD-7:2% or 4% complex 1, the emission from PVK:OXD-7 (around 410 nm) was observed, indicating incomplete energy transfer from PVK:OXD-7 to complex 1 at a low doping concentration of the dopant. However, in the EL spectra, the emission from PVK:OXD-7 disappears completely, indicating that the charge-trapping plays an important role in the operation of the devices [15]. The charge-trapping mechanism mainly corresponds to the trap of electrons considering the low-lying LUMO energy level of complex 1 (**Scheme 2**).

To further improve the device performance, the thickness of the Cs<sub>2</sub>CO<sub>3</sub> electron-injection layer was also optimized [16,17]. **Fig. 4** depicts the current density–voltage characteristics of devices with Cs<sub>2</sub>CO<sub>3</sub> layers of different thicknesses. The inset in **Fig. 4** depicts the corresponding brightness–voltage curves of the devices. Detailed electrical characteristics are also summarized in **Table 1**. For all devices, the doping concentration of complex 1 was fixed at 8%. As the thickness of Cs<sub>2</sub>CO<sub>3</sub> layer increases, the current density–voltage curves shift towards the high voltages. And, at the same time, the brightness–voltage curves shift slightly towards the low voltages. As a result, the efficiency of the device increases as the thickness of Cs<sub>2</sub>CO<sub>3</sub> layer increases (**Table 1**). With a 4 nm thick Cs<sub>2</sub>CO<sub>3</sub>

**Table 1**

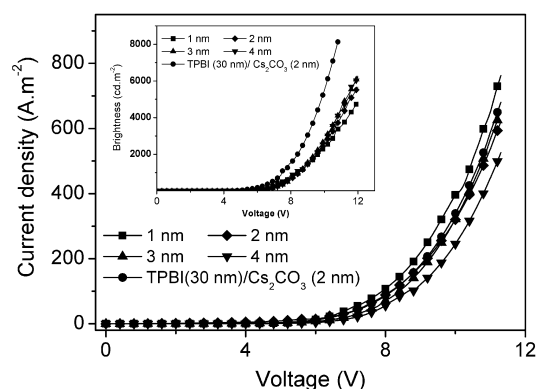
Electrical characteristics of devices based on complex 1.

Device <sup>a</sup>		$V_{on}$ (V) <sup>b</sup>	$J$ at 9 V, 11 V ( $A\ m^{-2}$ ) <sup>c</sup>	$\eta_{c,max}$ ( $cd\ A^{-1}$ ) <sup>d</sup>	$B_{max}$ ( $cd\ m^{-2}$ ) <sup>e</sup>	CIE ( $x, y$ )
$x$ (%)	$y$ (nm)					
2	2	4.0	162.6, 508.1	10.5	8400	(0.19, 0.45)
4	2	3.9	179.9, 501.2	9.4	8300	(0.20, 0.47)
8	2	4.2	177.6, 536.6	10.5	10,080	(0.20, 0.48)
12	2	4.0	189.7, 603.5	10.1	9600	(0.20, 0.48)
8	1	4.1	219.4, 649.0	7.6	7200	(0.20, 0.48)
8	3	4.0	163.5, 568.4	11.2	10,400	(0.20, 0.48)
8	4	4.1	121.0, 448.2	12.2	12,600	(0.20, 0.48)
8	2 <sup>f</sup>	3.8	180.8, 590.1	20.2	>26,000	(0.18, 0.47)

<sup>a</sup> The device structure is ITO/PEDOT:PSS (60 nm)/PVK:OXD-7: $x\%$  complex 1 (85 nm)/Cs<sub>2</sub>CO<sub>3</sub> ( $y$  nm)/Al (200 nm).<sup>b</sup>  $V_{on}$  denotes the turn-on voltage.<sup>c</sup>  $J$  denotes the current density.<sup>d</sup>  $\eta_{c,max}$  denotes the maximum current efficiency.<sup>e</sup>  $B_{max}$  denotes the maximum brightness.<sup>f</sup> For this device, a 30 nm thick TPBI layer was inserted between the light-emitting layer and the Cs<sub>2</sub>CO<sub>3</sub> (2 nm) layer.**Scheme 2.** Energy level diagram of ITO/PEDOT:PSS/PVK:OXD-7:complex 1(or complex 2)/Cs<sub>2</sub>CO<sub>3</sub>/Al, where the highest occupied molecular orbitals (HOMO) and LUMO values of complex 1 (or complex 2) were calculated from their oxidation potentials in CH<sub>3</sub>CN solutions together with their optical band gaps obtained from the absorption spectra [8].**Fig. 3.** EL spectra of ITO/PEDOT:PSS (60 nm)/PVK:OXD-7: $x\%$  complex 1 (85 nm)/Cs<sub>2</sub>CO<sub>3</sub> (2 nm)/Al (200 nm) with different doping concentrations ( $x\%$ ) of complex 1. The inset shows the corresponding PL spectra of the light-emitting layers.

layer, the device reaches a maximum efficiency of 12.2  $cd\ A^{-1}$  and a maximum brightness of 12,600  $cd\ m^{-2}$ .

Generally, for single-layer devices, severe exciton-quenching exists at the cathode interface, resulting in degraded device performance. To improve the performance of the device based on complex 1 further, a thin (30 nm) TPBI electron-transporting/exciton-confining layer was inserted

**Fig. 4.** Current density–voltage characteristics of ITO/PEDOT:PSS (60 nm)/PVK:OXD-7:8% complex 1 (85 nm)/Cs<sub>2</sub>CO<sub>3</sub> ( $y$  nm)/Al (200 nm) with different thicknesses ( $y$  nm) of Cs<sub>2</sub>CO<sub>3</sub> layer. The inset shows the corresponding brightness–voltage curves of the devices.

between the light-emitting layer and the cathode [11,18]. As shown in Fig. 4, the brightness of the device with a TPBI layer was significantly increased compared with those of single-layer devices. After the insertion of the TPBI layer, the maximum efficiency of the blue-green device was largely improved to 20.2  $cd\ A^{-1}$  (Table 1), demonstrating that complex 1 is a promising phosphor for achieving highly efficient blue-green electrophosphorescence.

### 3.3. Electrophosphorescent devices based on complex 2

Complex 2 with fluorine-substituted cyclometalated ligands shows further blue-shifted emission spectra (Fig. 1). As blue phosphorescent dopants with saturated color purity are rare, we used complex 2 to fabricate deep-blue electrophosphorescent devices. The device structure is ITO/PEDOT:PSS (60 nm)/PVK:OXD-7: $x\%$  complex 2 (85 nm)/Cs<sub>2</sub>CO<sub>3</sub> (2 nm)/Al (120 nm), where the doping concentration of complex 2 was varied to optimize the device performance.

Fig. 5 depicts the EL spectra of the devices and the inset depicts the corresponding PL spectra of the light-emitting layers. All devices show deep-blue light emission with

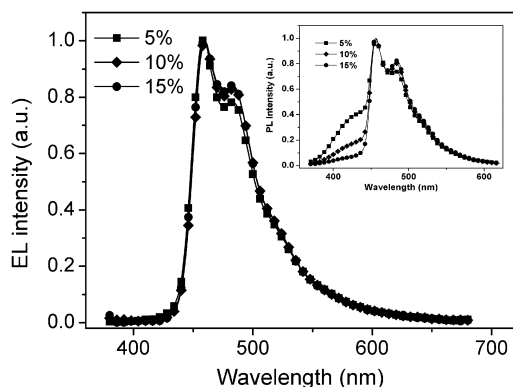


**Fig. 5.** EL spectra of ITO/PEDOT:PSS (60 nm)/PVK:OXD-7:*x*% complex 2 (85 nm)/Cs<sub>2</sub>CO<sub>3</sub> (2 nm)/Al (200 nm) with different doping concentrations (*x*%) of complex 2. The inset shows the corresponding PL spectra of the light-emitting layers.

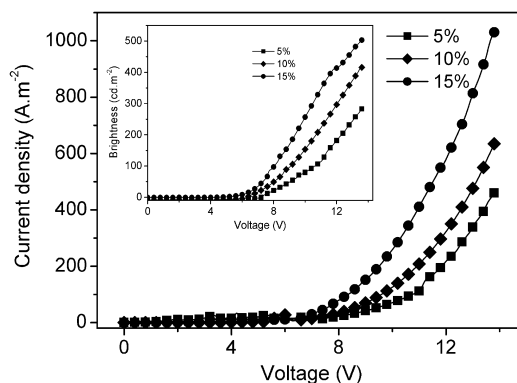


**Fig. 6.** Current density–voltage characteristics of ITO/PEDOT:PSS (60 nm)/PVK:OXD-7:*x*% complex 2 (85 nm)/Cs<sub>2</sub>CO<sub>3</sub> (2 nm)/Al (200 nm) with different doping concentrations (*x*%) of complex 2. The inset shows the corresponding brightness–voltage curves of the devices.

the emission peak at 458 nm and CIE coordinates of (0.16, 0.22), which is, to the best of our knowledge, the bluest electrophosphorescence from ionic iridium complexes. This light emission is also much bluer compared to the electrophosphorescence from the widely used blue phosphorescent dopant of bis[(4,6-difluorophenyl)-pyridinato-N,C<sup>2</sup>] iridium(III) (picolinate) (Flrpic), which shows sky-blue electrophosphorescence with the emission peak at around 474 nm [19]. Interestingly, the PL spectra of the light-emitting layers show considerable emission intensity from PVK:OXD-7 (around 410 nm) even at a doping concentration up to 10%, indicating that the energy transfer from PVK:OXD-7 to complex 2 is not complete. This is consistent with the weak overlap between the emission spectrum of PVK:OXD-7 and the absorption spectrum of complex 2 in thin films (Fig. 1). However, in EL spectra, only light emission from complex 2 was observed, indicating that charge-trapping plays an important role in the operation of the devices based on complex 2 [15]. The charge-trapping mechanism mainly corresponds to the trap of electrons considering that the LUMO energy level of complex 2 (−3.3 eV) is much lower than that of PVK (−2.2 eV) (Scheme 2).

Fig. 6 shows the current density–voltage characteristics of the devices with different doping concentrations of com-

plex 2 and detailed electrical characteristics are summarized in Table 2. As the doping concentration of complex 2 increases, the current density–voltage curves shift towards the low voltages. Though complex 2 has a LUMO energy level (−3.3 eV) much lower than that of PVK (−2.2 eV) (Scheme 2) and, thus, would behave as strong electron traps, the doping of complex 2 would also facilitate the electron transport when the doping concentration of complex 2 is beyond the percolation where electrons are expected to be transported by directly hopping between molecules of complex 2. Noticeably, the current density of the devices based on complex 2 is much lower than that of the devices based on complex 1, suggesting that complex 2 might behave as much stronger electron traps than complex 1 does. The efficiency of the devices based on complex 2 does not vary very much either as the doping concentration of complex 2 varies from 5% to 15% (Table 2). At a doping concentration of 10%, the device reaches a maximum efficiency of 1.5 cd A<sup>−1</sup> and a maximum brightness of 595 cd m<sup>−2</sup>. When the film thickness of the light-emitting layer was increased to 140 nm, the efficiency of the device was improved to 2.4 cd A<sup>−1</sup> at the expense of a higher driving voltage and degraded color purity (due to the microcavity effect [14,20]) (Table 2). When a thin (30 nm) TPBI layer was inserted between the light-

**Table 2**

Electrical characteristics of devices based on complex 2.

Device <sup>a</sup>	<i>V</i> <sub>on</sub> (V) <sup>b</sup>	<i>J</i> at 9 V, 11 V (A m <sup>−2</sup> ) <sup>c</sup>	<i>η</i> <sub>c,max</sub> (cd A <sup>−1</sup> ) <sup>d</sup>	<i>B</i> <sub>max</sub> (cd m <sup>−2</sup> ) <sup>e</sup>	CIE ( <i>x</i> , <i>y</i> )	
<i>x</i> (%)	<i>d</i> (nm)					
5	85	5.3	41.5, 112.0	1.1	568	(0.16, 0.22)
10	85	5.1	69.6, 208.0	1.5	595	(0.16, 0.22)
15	85	4.6	151.3, 411.0	1.3	572	(0.16, 0.23)
10	140	8.5	0.36, 2.0	2.4	995	(0.16, 0.28)
10	85 <sup>f</sup>	4.1	155.1, 515.7	2.5	1950	(0.16, 0.27)

<sup>a</sup> The device structure is ITO/PEDOT:PSS (60 nm)/PVK:OXD-7:*x*% complex 2 (*d* nm)/Cs<sub>2</sub>CO<sub>3</sub> (2 nm)/Al (200 nm).

<sup>b</sup> *V*<sub>on</sub> denotes the turn-on voltage.

<sup>c</sup> *J* denotes the current density.

<sup>d</sup> *η*<sub>c,max</sub> denotes the maximum current efficiency.

<sup>e</sup> *B*<sub>max</sub> denotes the maximum brightness.

<sup>f</sup> For this device, a 30 nm thick TPBI layer was inserted between the light-emitting layer (85 nm) and the Cs<sub>2</sub>CO<sub>3</sub> (2 nm) layer.

emitting layer and the Cs<sub>2</sub>CO<sub>3</sub> layer, the device efficiency was improved to 2.5 cd A<sup>-1</sup> at the expense of degraded color purity (also due to the microcavity effect [14,20]) (Table 2). The relatively low efficiency and brightness of the devices based on complex 2 are presumably due to the relatively low triplet-energy of the PVK host [21,22] or the inefficient energy transfer from PVK:OXD-7 host to complex 2 (vide supra). Further work is to dope complex 2 into a host with higher triplet-energy to improve the efficiency of the deep-blue device.

#### 4. Conclusion

Efficient electrophosphorescent devices were fabricated using two blue-emitting ionic iridium complexes as the dopants and PVK:OXD-7 as the host. For single-layer devices, we obtained efficient blue-green electrophosphorescence with a maximum efficiency of 12.2 cd A<sup>-1</sup>, a maximum brightness of 12,600 cd m<sup>-2</sup> and CIE coordinates of (0.19, 0.45). After a thin TPBI layer was inserted between the light-emitting layer and the cathode, the maximum efficiency of the blue-green device was further improved to 20.2 cd A<sup>-1</sup>. We obtained deep-blue electrophosphorescence with the emission peak at 458 nm and CIE coordinates of (0.16, 0.22). Our work suggests that ionic iridium complexes are promising phosphors for obtaining efficient electrophosphorescence in the blue region.

#### Acknowledgements

This work was supported by the National Natural Science Foundation of China (Grant No. 50573039) and the

National Basic Research Program of China (Grant No. 2006CB806200).

#### References

- [1] C.W. Tang, S.A. Vanslyke, *Appl. Phys. Lett.* 51 (1987) 913.
- [2] M.A. Baldo, D.F. O'Brien, Y. You, A. Shoustikov, S. Sibley, M.E. Thompson, S.R. Forrest, *Nature* 395 (1998) 151.
- [3] M.A. Baldo, D.F. O'Brien, *Phys. Rev. B* 60 (1999) 14422.
- [4] E. Holder, Bea M.W. Langeveld, U.S. Schubert, *Adv. Mater.* 17 (2005) 1109.
- [5] J. Slinker, D. Bernards, P.L. Houston, H.D. Abbruña, S. Bernhard, G.G. Malliaras, *Chem. Commun.* (2003) 2392.
- [6] J.D. Slinker, J. Rivnay, J.S. Moskowitz, J.B. Parker, S. Bernhard, H.D. Abbruña, G.G. Malliaras, *J. Mater. Chem.* 17 (2007) 2976.
- [7] H.J. Bolink, L. Cappelli, S. Cheylan, E. Coronado, R.D. Costa, N. Lardiés, M.K. Nazeeruddin, E. Ortí, *J. Mater. Chem.* 17 (2007) 5032.
- [8] Lei He, Lian Duan, Juan Qiao, Ruji Wang, Peng Wei, Liduo Wang, Yong Qiu, *Adv. Funct. Mater.* 18 (2008) 2123.
- [9] B. Carlson, G.D. Phelan, W. Kaminsky, L. Dalton, X.Z. Jiang, S. Liu, A.K.-Y. Jen, *J. Am. Chem. Soc.* 124 (2002) 14162.
- [10] Q.S. Zhang, Q.G. Zhou, Y.X. Cheng, L.X. Wang, D.G. Ma, X.B. Jing, F.S. Wang, *Adv. Mater.* 16 (2004) 432.
- [11] E.A. Plummer, V.A. Dijken, H.W. Hofstraat, L.D. Cola, K. Brunner, *Adv. Funct. Mater.* 15 (2005) 281.
- [12] A. Nakamura, T. Tada, M. Mizukami, S. Yagyua, *Appl. Phys. Lett.* 84 (2004) 130.
- [13] X.H. Yang, F. Jaiser, S. Klinger, D. Nehera, *Appl. Phys. Lett.* 88 (2006) 021107.
- [14] M.K. Mathai, V.E. Choong, S.A. Choulis, B. Krummacher, Franky So, *Appl. Phys. Lett.* 88 (2006) 243512.
- [15] X. Gong, J.C. Ostrowski, D. Moses, G.C. Bazan, A.J. Heeger, *Adv. Funct. Mater.* 13 (2003) 439.
- [16] J.S. Huang, Z. Xu, Y. Yang, *Adv. Funct. Mater.* 17 (2007) 1966.
- [17] J.S. Huang, T. Watanabe, K. Ueno, Y. Yang, *Adv. Mater.* 19 (2007) 739.
- [18] K.M. Vaeth, C.W. Tang, *J. Appl. Phys.* 92 (2002) 3447.
- [19] C. Adachi, R.C. Kwong, P. Djurovich, V. Adamovich, M.A. Baldo, M.E. Thompson, S.R. Forrest, *Appl. Phys. Lett.* 79 (2001) 2082.
- [20] Z.X. Wu, L.D. Wang, G.T. Lei, Y. Qiu, *J. Appl. Phys.* 97 (2005) 103105.
- [21] G. Rippen, G. Kaufmann, W. Klöpffer, *Chem. Phys.* 52 (1980) 165.
- [22] G. Rippen, G. Kaufmann, W. Klöpffer, *J. Chem. Phys.* 65 (1976) 272.



## A new ambipolar blue emitter for NTSC standard blue organic light-emitting device

Tsung-Cheng Tsai<sup>a</sup>, Wen-Yi Hung<sup>a,\*</sup>, Liang-Chen Chi<sup>b</sup>, Ken-Tsung Wong<sup>b,\*</sup>,  
Cheng-Chih Hsieh<sup>b</sup>, Pi-Tai Chou<sup>b,\*</sup>

<sup>a</sup> Institute of Optoelectronic Sciences, National Taiwan Ocean University, Keelung 202, Taiwan

<sup>b</sup> Department of Chemistry, National Taiwan University, Taipei 106, Taiwan

### ARTICLE INFO

#### Article history:

Received 22 August 2008

Received in revised form 21 October 2008

Accepted 21 October 2008

Available online 5 November 2008

#### PACS:

73.50.-h

73.61.Ph

78.55.Qr

78.60.Fi

78.66.Qn

#### Keywords:

Organic light-emitting diodes

Deep blue emitter

Ambipolar transport

Coplanar molecule

### ABSTRACT

A novel blue emitter, **In2Bt**, featured with a rigid and coplanar distyryl-*p*-phenylene backbone flattened by two different bridging atoms (i.e. carbon and sulfur) exhibits high thermal and morphological stability ( $T_g \sim 192$  °C) and ambipolar charge carrier mobilities in the range of  $10^{-4} \sim 10^{-5} \text{ cm}^2 \text{ V}^{-1} \text{ s}^{-1}$ . OLED device: ITO/PEDOT:PSS (300 Å)/ $\alpha$ -NPD (200 Å)/TCTA (100 Å)/**In2Bt** (200 Å)/TPBI (500 Å)/LiF (5 Å)/Al (1500 Å) utilized **In2Bt** as an emitter gave a maximum brightness as high as  $8000 \text{ cd m}^{-2}$  (12 V) and saturated-blue emission with CIE chromaticity coordinates of (0.16, 0.08), which is very close to the National Television Standards Committee (NTSC) standard blue gives an enlarged palette of colors for color displays.

© 2008 Elsevier B.V. All rights reserved.

### 1. Introduction

In recent years, the development of deep blue emitters for OLED, which can match the National Television System Committee (NTSC) standard blue CIE ( $x, y$ ) coordinates of (0.14, 0.08) has drawn considerable attentions [1–5]. Such a device not only can effectively reduce the power consumption of a full-color OLED but also can be utilized to generate emission of other colors through energy transfer. However, the molecular design for a deep blue emitter is

quite challenging in terms of molecular structures. Molecules that can emit deep blue light normally have a restricted  $\pi$ -conjugated length, which consequently limits the spaces for tailoring the desired chromophore with sufficient thermal and thin film morphological stability. Thus, only few materials can meet these requirements so far [1–5]. Recently, the ladder-type oligomers and polymers [6–14], due to their rigid and coplanar structures which can enhance the  $\pi$ -conjugation, charge mobility, and luminescence intensity have emerged as potential materials for optoelectronic applications. In this regard, the physical properties and possible applications of ladder-type oligo- or poly(*p*-phenylene)s with various heteroatom bridges have been extensively studied [15–18]. More importantly, the physical properties of ladder-type materials can be

\* Corresponding authors. Tel.: +886 2 33661665; fax: +886 2 33661667 (K.-T. Wong).

E-mail addresses: [wenhung@mail.ntou.edu.tw](mailto:wenhung@mail.ntou.edu.tw) (W.-Y. Hung), [kenwong@ntu.edu.tw](mailto:kenwong@ntu.edu.tw) (K.-T. Wong).

tailored by modulating the degree of conformational flexibility between consecutive backbone units or, more effectively, manipulating the electronic properties by flattening the  $\pi$ -conjugated molecular framework with heteroatoms. In this paper, we report a new blue light-emitting material based on a coplanar molecular structure, in which benzothiophene was fused to neighboring phenylene ring through intramolecular annulation via  $sp^3$ -hybridized carbon atoms bearing two *p*-tolyl groups as peripheral substituents [19]. The non-doped OLED device shows an external quantum efficiency of 1.3% and saturated-blue emission with CIE chromaticity coordinates (0.16, 0.08), which is almost the National Television Standards Committee (NTSC) standard blue.

## 2. Results and discussion

Fig. 1 depicts the molecular structure of blue emitter: 7,14-dihydro-7,7,14,14-tetrakis(4-methylphenyl)-s-indaceno[1,2-b:5,6-b']bis[1]benzothiophene (**In2Bt**) featured with a rigid and coplanar distyryl-*p*-phenylene backbone flattened by two different bridging atoms (i.e. carbon and sulfur). The synthesis and X-ray structural analysis of **In2Bt** have been reported by our group previously [19]. The peripheral *p*-tolyl substituents occupy the top and bottom faces of the main conjugated backbone prevent undesirable aggregation and improve thermal and morphological stability efficiently. We characterized the morphological and thermal properties of **In2Bt** using differential scanning calorimetry (DSC) and thermogravimetric analyses (TGA), respectively. **In2Bt** exhibits a distinct glass transition temperature ( $T_g \sim 192$  °C), which allows to form homogeneous and stable amorphous films upon thermal evaporation, a critical issue for OLED application. We ascribed the amorphous behavior and high values of  $T_g$  to the rigidity of the conjugated backbone and the presence of the *p*-tolyl substituents, which can effectively suppress intermolecular interactions and crystallization. The aryl substituents impart the oligomers with a high tolerance to heat, as indicated by their high decomposition temperatures ( $T_d \sim 408$  °C, corresponding to a 5% weight loss).

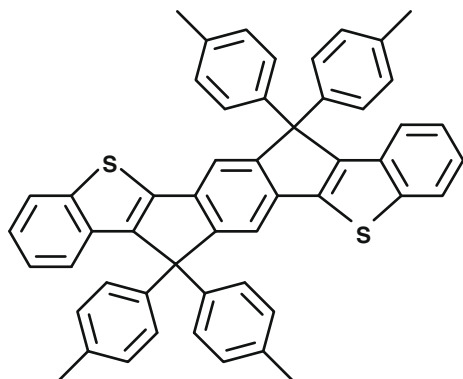


Fig. 1. Chemical structure of **In2Bt**.

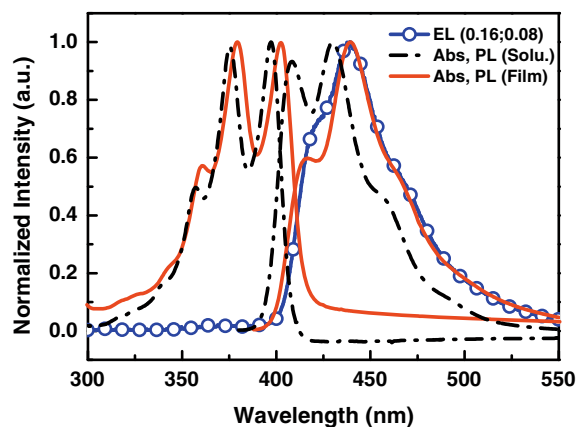


Fig. 2. The optical absorption, photoluminescence (PL) spectra of **In2Bt** in solution and thin film, and the electroluminescence (EL) spectra of device using **In2Bt** as an emitter.

Fig. 2 summarizes the electronic absorption (Abs) and photoluminescence (PL) spectra of **In2Bt** in chloroform solution and as solid films. Due to the coplanar conformation of the main chromophore, the absorption spectra of **In2Bt** in dilute solution and in thin film are almost superimposable with slightly red-shifted maxima in solid state (Abs  $\lambda_{\max}$  in solution, 375, 397 nm, and in film, 385, 402 nm). The thin film emission spectra of **In2Bt** exhibit slightly red-shifted maxima (PL  $\lambda_{\max}$  in solution 408, 430 nm, and in film 416, 439 nm). In addition, the small Stokes shifts ( $\Delta\lambda \sim 11$  nm in solution) and the mirror images of the absorption and emission spectra are consistent with the molecular rigidity observed in the solid state structures [19,20]. We estimated the  $\pi-\pi^*$  band gap ( $\Delta E_g \sim 3$  V) from the lowest energy absorption edges (ca. 413 nm) in the UV-Vis absorption spectra. The thin film photoluminescence quantum yield (PLQY) of **In2Bt** measured by a calibrated integral sphere (HAMAMATSU C9920) is ca. 14%. In order to gain more insight into the low PLQY of **In2Bt** in thin film, we have employed time-correlated single photon counting measurement with a time resolution of  $\sim 30$  ps. Upon excitation at 390 nm and monitoring the emission at e.g. 450 nm, the observed lifetime ( $\tau_{\text{obs}}$ ) for **In2Bt** in thin film was determined to be 268 ps. From the PLQY and observed lifetime, the radiative ( $k_r$ ) and non-radiative ( $k_{\text{nr}}$ ) decay rate constants, deduced by Eq. (1), were  $5.2 \times 10^8 \text{ s}^{-1}$  and  $3.2 \times 10^9 \text{ s}^{-1}$ , respectively,

$$\text{PLQY}(\Phi) = \frac{\tau_{\text{obs}}}{\tau_r} = \frac{k_r}{k_{\text{obs}}} = \frac{k_r}{k_r + k_{\text{nr}}} \quad (1)$$

Normally, a skeleton possessing a rigid distyryl-*p*-phenylene backbone is expected to provide a reasonably high PLQY. The large  $k_{\text{nr}}$  (c.f.  $k_r$ ) value and hence low PLQY for **In2Bt** in thin film is of fundamental interest and, to our viewpoint, can be tentatively attributed to two factors associated with the sulfur atom and/or the molecular framework. On one hand, sulfur atoms embedded inside the chromophore backbone may facilitate the non-radiative processes due to the heavy atom effect, a common phenomenon occasionally reported in sulfur-containing oligoaryls [21]. On the other hand, the soft sulfur atom pos-

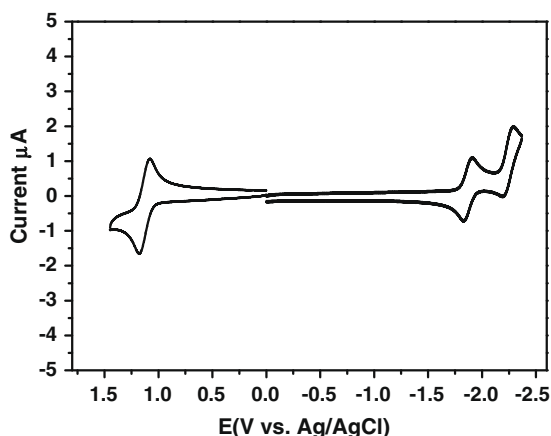


Fig. 3. The cyclic voltammogram of **In2Bt**.

sesses a lower lying non-bonding orbital that may facilitate the non-radiative process via certain vibronic coupling modes. Such modes may be associated with the slightly twisted molecular plane of **In2Bt** in thin film [12]. At room temperature or upon cooling to 77 K, phosphorescence of the **In2Bt** thin film was obscure. Therefore, the former case of heavy atom enhanced spin-orbit coupling and hence the intersystem crossing is less likely. Nevertheless, at this stage, the actual deactivation mechanism is still pending for resolution. Note we also cannot eliminate the possibility that relatively low PLQY, in part, is attributed to the re-absorption problem occurring in solid states.

Fig. 3 depicts the electrochemical properties of **In2Bt** studied by cyclic voltammetry (CV). We detected one reversible oxidation potential occurred at 1.13 V (V vs. Ag/AgCl, in  $\text{CH}_2\text{Cl}_2$  using a glassy carbon electrode with 0.1 M of  $n\text{Bu}_4\text{NPF}_6$  as electrolyte) and one reversible reduction potential at  $-1.87$  V together with one quasi-reversible reduction at  $-2.25$  V (V vs. Ag/AgCl in dimethylformamide using a glassy carbon electrode with 0.1 M of  $n\text{Bu}_4\text{ClO}_4$  as electrolyte). Thus, **In2Bt** exhibits bipolar character with excellent electrochemical stability. The HOMO energy level of **In2Bt** (ca.  $-5.7$  eV) was calculated using a linear correlation with  $\alpha$ -NPB (HOMO = ca.  $-5.3$  eV), which exhibits an  $E_{1/2}^{\text{OX}}$  at 0.74 V measured under the same conditions [22]. And the corresponding LUMO (ca.  $-2.7$  eV) of **In2Bt** was then derived by subtracting the corresponding optical band gap from the HOMO energy.

We used time-of-flight (TOF) techniques with a device structure of glass/Ag (30 nm)/**In2Bt** (2.1  $\mu\text{m}$ )/Ag (200 nm) to measure the charge carrier mobilities of **In2Bt** [23]. Fig. 4a and b shows representative TOF transients for electrons and holes of under an applied field, respectively. The TOF transients reveal that **In2Bt** exhibits slightly dispersive carrier-transport characteristics. In the double-logarithmic representation (inset of Fig. 4a and b), the carrier-transit time,  $t_T$ , needed for determining carrier mobilities can be clearly extracted from the intersection point of two asymptotes. The field dependence of hole mobility  $\mu$  thus determined (Fig. 4c) from the transit time  $t_T$  according to the relation  $\mu = d^2/Vt_T$ , where  $d$  is the sample thickness and  $V$  is the applied voltage. Apparently,

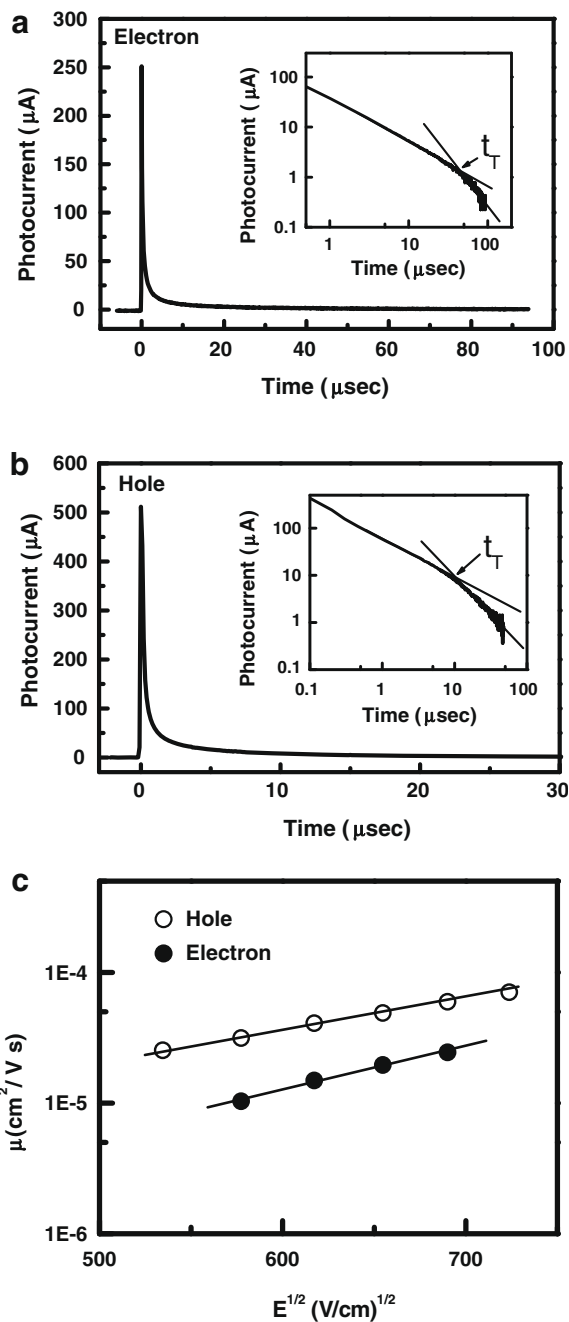


Fig. 4. TOF transients for **In2Bt** (2.1  $\mu\text{m}$  thick): (a) electron,  $E = 4.8 \times 10^5 \text{ V cm}^{-1}$ ; (b) hole,  $E = 4.3 \times 10^5 \text{ V cm}^{-1}$ . Insets are the double-logarithmic plots of (a) and (b). (c) Electron and hole mobilities vs.  $E^{1/2}$ .

**In2Bt** exhibits bipolar charge-transport properties, which has similar electron and hole mobilities in the range of  $10^{-4} \sim 10^{-5} \text{ cm}^2 \text{ V}^{-1} \text{ s}^{-1}$  ( $E = 3 \times 10^5 \sim 5 \times 10^5 \text{ V cm}^{-1}$ ) at room temperature.

To assess the feasibility of using **In2Bt** as an emitting material, multilayer device with the configuration of ITO/PEDOT:PSS (300 Å)/ $\alpha$ -NPB (200 Å)/TCTA (100 Å)/**In2Bt** (200 Å)/TPBI (500 Å)/LiF (5 Å)/Al (1500 Å) was fabricated.



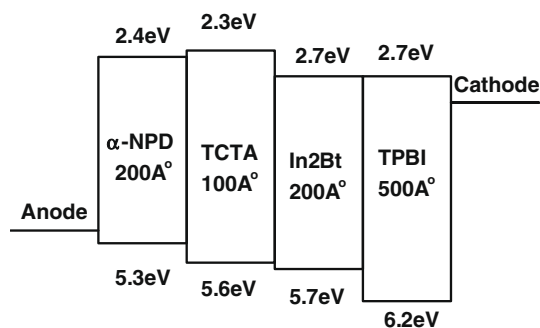


Fig. 5. HOMO and LUMO energy level diagram of the organic materials in the device.

Here, the conducting polymer, poly(ethylene dioxythiophene)/poly(styrene sulfonate) (PEDOT:PSS) is used as the hole-injection layer [24], 4,4'-bis(*N*-(1-naphthyl)-*N*-phenyl)biphenyldiamine ( $\alpha$ -NPD) [25] and 4,4'-tri(*N*-carbazolyl)triphenylamine (TCTA) as hole-transport layers [26], **In2Bt** as an emitting layer, 1,3,5-tris(*N*-phenylbenzimidazol-2-yl)benzene (TPBI) [27] as an electron-transport and hole-blocking layer, LiF as an electron-injection layer and Al as a cathode, respectively. The energy levels alignment diagram of this blue OLED is shown in Fig. 5. The holes transport through the HTLs of  $\alpha$ -NPD and TCTA with a stepwise increase in HOMOs into the emitting layer, and

subsequently are blocked by the higher energy barrier at the interface of **In2Bt** and TPBI. In the meantime, the electrons are injected into **In2Bt** layer from TPBI and blocked by the higher energy barrier at the interface of TCTA and **In2Bt**. Therefore, it is reasonable to anticipate that the recombination region is restricted only within the **In2Bt** layer. Consequently, a pure deep blue EL spectrum from **In2Bt** was obtained, which is corresponding well to the thin film PL spectrum (Fig. 2).

Fig. 6a shows the current density and the luminance vs. voltage for the device. The device exhibits a rather low turn-on voltage of 3 V and low operation voltage ( $100 \text{ cd m}^{-2}$  at 6 V,  $1000 \text{ cd m}^{-2}$  at 8.5 V). The device exhibits unusual high currents  $\sim 3860 \text{ mA cm}^{-2}$  for 12 V, giving a maximal brightness of  $8000 \text{ cd m}^{-2}$ . Such high current density is ascribed to the well-matched energy levels of various functional layers used, rendering the device with a balanced holes and electrons recombination ratio. However, this device inevitably suffers from the re-absorption phenomena occurred in the solid states. The EL external quantum efficiency (EQE) shows a maximum at 1.3% ( $0.86 \text{ cd A}^{-1}$ ) and a maximal power efficiency of  $\sim 0.76 \text{ lm W}^{-1}$  (Fig. 6b). It is worthy to note that the non-doped device shows a pure deep blue emission (Fig. 2) with CIE coordinates of (0.16, 0.08), which is almost perfectly match to the National Television Standards Committee (NTSC) standard blue value. The observed external quantum yield and luminance efficiencies is comparable to commonly non-doped deep blue devices, which warrants further investigations of analogous derivatives to afford materials with improved EL properties.

### 3. Experimental

#### 3.1. Device fabrication and measurement

All chemicals were purified through vacuum sublimation prior to use. The OLEDs were fabricated by vacuum deposition of the materials at  $10^{-6}$  torr. onto ITO-coated glass substrates having a sheet resistance of  $15 \Omega/\text{square}$ . The ITO surface was cleaned through ultrasonication sequentially with acetone, methanol, and deionized water and then it was treated with UV-ozone. The deposition rate of each organic material was ca.  $1\text{--}2 \text{ \AA s}^{-1}$ . Subsequently, LiF was deposited at  $0.1 \text{ \AA s}^{-1}$  and then capped with Al (ca.  $5 \text{ \AA s}^{-1}$ ) by shadow masking without breaking the vacuum.

The current–voltage–brightness ( $I$ – $V$ – $L$ ) characteristics of the devices were measured simultaneously using a Keithley 6430 source meter and a Keithley 6487 picoammeter equipped with a calibration Si-photodiode. EL spectra were measured using an ocean optics spectrometer.

#### 3.2. Time-of-flight mobility measurements

The samples for the TOF measurement were prepared by vacuum deposition using the structure: glass/Ag (30 nm)/organic ( $2\text{--}3 \mu\text{m}$ )/Al (150 nm), and then placed inside a cryostat and kept under vacuum. The thickness of organic films were monitored in situ with a quartz crys-

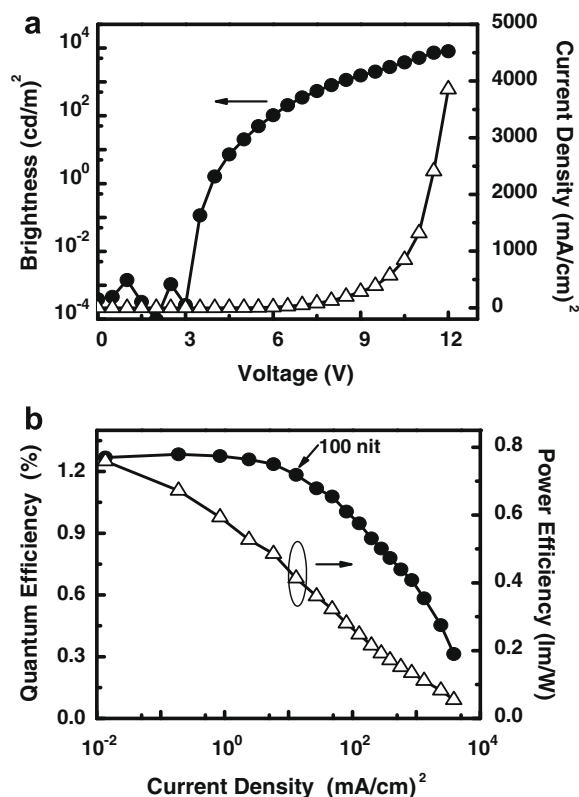


Fig. 6. (a) Brightness and current density vs. voltage. (b) External quantum efficiency and power efficiency vs. current density.

tal sensor and calibrated by a profilometer (Tencor Alpha-step 500). A pulsed nitrogen tunable dye laser was used as the excitation light source (to match the absorption of organic films) through the semitransparent electrode (Ag) induced photogeneration of a thin sheet of excess carriers. Under an applied dc bias, the transient photocurrent was swept across the bulk of the organic film toward the collection electrode (Al), and then recorded with a digital storage oscilloscope. Depending on the polarity of the applied bias, selected carriers (holes or electrons) are swept across the sample with a transit time of  $t_T$ . With the applied bias  $V$  and the sample thickness  $D$ , the applied electric field  $E$  is  $V/D$ , and the carrier mobility is then given by  $\mu = D/(t_T E) = D^2/(V t_T)$ , in which the carrier-transit time,  $t_T$ , can be extracted from the intersection point of two asymptotes to the plateau and the tail sections in double-logarithmic plots.

#### 4. Conclusions

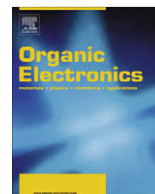
In summary, we reported a new deep blue emitter, **In2Bt**, which is based on a coplanar distyryl-*p*-phenylene core flattened through the incorporation of two different bridging atoms (i.e. carbon and sulfur). The promising physical properties of **In2Bt** including deep blue emission, high morphological stability, and bipolar charge-transport properties allow us to use it to achieve a non-doped deep blue device. The device fabricated use **In2Bt** as deep blue emitter leads to a NTSC pure blue electroluminescence (CIE coordinates = 0.16, 0.08) with respectable device performances.

#### Acknowledgement

This study was supported financially by the National Science Council of Taiwan.

#### References

- [1] Y.-H. Kim, D.-C. Shin, S.-H. Kim, C.-H. Ko, H.-S. Yu, Y.-S. Chae, S.-K. Kwon, *Adv. Mater.* 16 (2001) 1690.
- [2] Y.-H. Kim, H.-C. Jeong, S.-H. Kim, K. Yang, S.-K. Kwon, *Adv. Funct. Mater.* 15 (2005) 1799.
- [3] Y.-H. Niu, B. Chen, T.-D. Kim, M.S. Liu, A.K.-Y. Jen, *Appl. Phys. Lett.* 85 (2004) 5433.
- [4] Z.Q. Gao, Z.H. Li, P.F. Xia, M.S. Wong, K.W. Cheah, C.H. Chen, *Adv. Funct. Mater.* 17 (2007) 3194.
- [5] S. Tang, M.R. Liu, P. Lu, H. Xia, M. Li, Z.Q. Xie, F.Z. Shen, C. Gu, H.P. Wang, B. Yang, Y. Ma, *Adv. Funct. Mater.* 17 (2007) 2869.
- [6] S. Merlet, M. Birau, Z.Y. Wang, *Org. Lett.* 4 (2002) 2157.
- [7] C. Xu, A. Wakamiya, S. Yamaguchi, *J. Am. Chem. Soc.* 127 (2005) 1638.
- [8] J. Jacob, S. Sax, M. Gaal, E.J.W. List, A.C. Grimsdale, K. Müllen, *Macromolecules* 38 (2005) 9933.
- [9] D. Vak, B. Lim, S.-H. Lee, D.-Y. Kim, *Org. Lett.* 7 (2005) 4229.
- [10] A.C. Grimsdale, K. Müllen, *Adv. Polym. Sci.* 199 (2006) 1.
- [11] D. Horhant, J.-J. Liang, M. Virboul, C. Poriel, G. Alcaraz, J. Rault-Berthelot, *Org. Lett.* 8 (2006) 257.
- [12] K.-T. Wong, L.-C. Chi, S.-C. Huang, Y.-L. Liao, Y.-H. Liu, Y. Wang, *Org. Lett.* 8 (2006) 5029.
- [13] F. Laquai, A.K. Mishra, M.R. Ribas, A. Petrozza, J. Jacob, L. Akcelrud, K. Müllen, R.H. Friend, G. Wegner, *Adv. Funct. Mater.* 17 (2007) 3231.
- [14] Y. Wu, J. Zhang, Z. Bo, *Org. Lett.* 9 (2007) 4435.
- [15] S.A. Patil, U. Scherf, A. Kadashchuk, *Adv. Funct. Mater.* 13 (2003) 609.
- [16] S. Wakim, J. Bouchard, N. Blouin, A. Michaud, M. Leclerc, *Org. Lett.* 6 (2004) 3413.
- [17] H. Ebata, E. Miyazaki, T. Yamamoto, K. Takimiya, *Org. Lett.* 9 (2007) 4499.
- [18] L. Li, J. Xiang, C. Xu, *Org. Lett.* 9 (2007) 4877.
- [19] K.-T. Wong, T.-C. Chao, L.-C. Chi, Y.-Y. Chu, A. Balaiah, S.-F. Chiu, Y.-H. Liu, Y. Wang, *Org. Lett.* 8 (2006) 5033.
- [20] C. Poriel, J. Rault-Berthelot, F. Barriere, A.M.Z. Slawin, *Org. Lett.* 10 (2008) 373.
- [21] K.R. Radke, K. Ogawa, S.C. Rasmussen, *Org. Lett.* 7 (2005) 5253.
- [22] B.W. D'Andrade, S. Datta, S.R. Forrest, P. Djurovich, E. Polikarpov, M.E. Thompson, *Org. Electron.* 6 (2005) 11.
- [23] P.M. Borsenberger, D.S. Weiss, *Organic Photoreceptors for Imaging Systems*, Marcel Dekker, New York, 1993.
- [24] P. Strohriegel, J.V. Grazulevicius, *Adv. Mater.* 14 (2002) 1439.
- [25] A. Berntsen, Y. Croonen, C. Liednbaum, H. Schoo, R.J. Visser, J. Vlegaar, P. van de Weijer, *Opt. Mater.* 9 (1998) 125.
- [26] Y. Kuwabara, H. Ogawa, H. Inada, N. Noma, Y. Shirota, *Adv. Mater.* 6 (1994) 677.
- [27] J. Shi, C.W. Tang, C.H. Chen, U.S. Patent No. 5,646,948, 1997.



# Efficient blue organic light-emitting diodes using newly-developed pyrene-based electron transport materials

Hyoungh-Yun Oh<sup>a</sup>, Changhee Lee<sup>b</sup>, Seonghoon Lee<sup>a,\*</sup>

<sup>a</sup> Molecular Electronics and NanoStructures Lab, School of Chemistry, Seoul National University, Shilim-dong, San 56-1, Seoul 151-747, Republic of Korea

<sup>b</sup> School of Electrical Engineering and Computer Science, Seoul National University, Gwanak, P.O. Box 34, Seoul 151-600, Republic of Korea

## ARTICLE INFO

### Article history:

Received 6 September 2008

Received in revised form 24 October 2008

Accepted 25 October 2008

Available online 5 November 2008

### PACS:

42.70.-a

85.60.Jb

42.70.Jk

81.05.Lg

### Keywords:

Blue OLED

Degradation

Pyrene-based electron transport material

## ABSTRACT

We synthesized new kinds of pyrene-based electron transport materials: 1,6-di(pyridin-3-yl)-3,8-di(naphthalen-1-yl)pyrene (N1PP) and 1,6-di(pyridin-3-yl)-3,8-di(naphthalen-2-yl)pyrene (N2PP). The external quantum efficiencies of the device with these electron transport materials increase by more than 50% at  $1 \text{ mA cm}^{-2}$  compared with those of the device with representative  $\text{Alq}_3$  as an electron transport material. The enhanced quantum efficiency is due to a balanced charge recombination in an emissive layer. Electron mobilities in N1PP and N2PP films are three times higher than that in  $\text{Alq}_3$ . Highly enhanced power efficiency is achieved due to a low electron injection barrier and a high electron mobility. We find that the luminance degradation in the blue OLEDs is correlated with the HOMO energy levels of electron transport materials.

© 2008 Elsevier B.V. All rights reserved.

## 1. Introduction

Since the first report on light emission from double-layered OLEDs by Tang and Van Slyke [1], advances in luminescent RGB materials, device structures, and manufacturing processes have led to the demonstration of full-color OLED displays that are capable of showing video rate images. There are still obstacles for the commercialization of full-color OLED displays. Among them, development of highly efficient blue emitters with sufficient operational stability should be made. Substantial performance enhancement can be achieved through synthesizing new blue luminescent organic materials by way of rational design of the photoactive chemical structure. A phosphorescent (triplet emission) blue electroluminescence (EL) with a high external quantum efficiency and a saturated blue color has been thought

to be an alternative but its instability problems remain unresolved [2–4]. Another approach to achieve maximum device efficiency is to balance charge carrier recombination, because the hole mobility in the OLED is usually much higher than the electron mobility under the same electric field [5,6]. And thus, emitting and charge-transporting materials with a high ionization potential value such as oxadiazole [7], benzimidazole [8], diarylsilole group materials [9] and electron transport materials [10,11] were synthesized and applied to OLEDs. The lifetimes of the devices made with these electron transport materials (ETMs) are short compared with those of the devices using a small molecule  $\text{Alq}_3$ . There are needs to develop emitting and charge-transporting materials with a longer lifetime and to understand the degradation mechanism. The increased luminance efficiency and the understanding of luminance degradation in OLEDs will be keys to the use of OLED technology in the next generation flat displays and light sources. Here, we report the development of the new kinds of ETMs based on

\* Corresponding author. Tel.: +82 2 880 1456; fax: +82 2 889 1568.  
E-mail address: [shnlee@snu.ac.kr](mailto:shnlee@snu.ac.kr) (S. Lee).

pyrene molecules and the measurement of the lifetime of ETMS and find the luminance degradation process of the blue OLEDs.

## 2. Experimental

### 2.1. Materials

Dibromo pyrene and 3-pyridinyl boronic acid were purchased from SFC Co. Ltd. All other reagents and solvents were purchased from Aldrich Chemical Co. and Fluka. Those were used as received. For absorption and emission experiments, spectroscopic grade  $\text{CH}_2\text{Cl}_2$  (Aldrich) was used.

#### 2.1.1. 1,6-Di(pyridin-3-yl)-pyrene

To a solid mixture of 1,6 dibromo-pyrene (7.2 g, 20 mmol) and 3-pyridinyl boronic acid (7.4 g, 60 mmol) were added a solution of 70 ml tetrahydrofuran (THF) and 10 ml toluene. After 60 ml of 2 M aqueous potassium carbonate was added to the mixture, it was degassed by bubbling nitrogen for 30 min. Finally, 0.6 mmol of tetrakis(tri-phenylphosphine)palladium ( $\text{Pd}(\text{Ph}_3)_4$ ) was added to the mixture. The mixture was vigorously refluxed under nitrogen for 24 h. When the reaction mixture was cooled down to room temperature, it was poured into 200 ml methanol. After filtering it off, the crude solid was re-precipitated from chloroform and methanol. Light-yellow powder (5.3 g, 74%) was more purified by flash chromatography with chloroform. mp 249 °C.  $\delta_{\text{H}}$  (500 MHz;  $\text{CDCl}_3$ ;  $\text{Me}_4\text{Si}$ ) 8.88 (2H, s), 8.73 (2H, d, *J* 3.5), 8.27 (2H, d, *J* 7.7), 8.15 (4H, m), 7.97 (4H, m), 7.52 (2H, m). Elemental analysis: Found: C, 87.27%; H, 4.35%; N, 7.97%; Calc. for  $\text{C}_{26}\text{H}_{16}\text{N}_2$ : C, 87.62%; H, 4.52%; N, 7.86%;  $M^+$ , 357.

#### 2.1.2. 1,6-Di(pyridin-3-yl)-3,8-dibromo-pyrene

Pyridinium hydrobromide perbromide (7.97 g, 25 mmol) was added to a solution of 1,6-di(pyridin-3-yl)-pyrene (3.56 g, 10 mmol) in 1,2 dichlorobenzene (200 ml). The mixture was refluxed for 12 h. After cooling, 100 ml of methanol was slowly added and the precipitate was filtered. Pure product (3.6 g, 70%) was obtained from re-precipitation with pyridine and methanol. mp: 378 °C.  $\delta_{\text{H}}$  (500 MHz;  $\text{CDCl}_3$ ;  $\text{Me}_4\text{Si}$ ) 8.89 (2H, s), 8.79 (2H, d, *J* 5.0), 8.50 (2H, d, *J* 9.5), 8.3 (2H, s), 8.16 (2H, d, *J* 10.0), 7.95 (2H, d, *J* 10.0), 7.54 (2H, m). Elemental analysis: Found: C, 60.93%; H, 2.90%; N, 5.67%; Calc. for  $\text{C}_{26}\text{H}_{14}\text{Br}_2\text{N}_2$ : C, 60.73%; H, 2.74%; N, 5.45%;  $M^+$ , 515.

#### 2.1.3. 1,6-Di(pyridin-3-yl)-3,8-di(naphthalen-1-yl)pyrene (N1PP)

To a solid mixture of 1,6-di(pyridin-3-yl)-3,8-dibromopyrene (5.1 g, 10 mmol) and 1-naphthyl boronic acid (4.3 g, 25 mmol) were added a solution of 70 ml tetrahydrofuran (THF) and 10 ml toluene. After 60 ml of 2 M aqueous potassium carbonate was added to the mixture, it was degassed by bubbling nitrogen for 30 min. Finally, 0.05 mmol of tetrakis(tri-phenylphosphine)palladium ( $\text{Pd}(\text{Ph}_3)_4$ ) was added to the mixture. The mixture was vig-

orously refluxed under nitrogen for 24 h. When the reaction mixture was cooled down to room temperature, it was poured into 200 ml methanol. After filtering it off, the crude solid was re-precipitated from chloroform and methanol. Light-yellow powder (4.9 g, 80%) was more purified by flash chromatography with chloroform. mp 377 °C.  $\delta_{\text{H}}$  (500 MHz;  $\text{CDCl}_3$ ;  $\text{Me}_4\text{Si}$ ) 8.91 (2H, s), 8.66 (2H, d, *J* 4.0), 8.05 (2H, s), 8.03 (2H, d, *J* 7.9), 7.99 (2H, t, *J* 3.9), 7.96 (4H, m), 7.75 (2H, d, *J* 7.9), 7.65 (4H, m), 7.50 (2H, t), 7.46 (2H, d, *J* 7.0), 7.40 (2H, m), 7.32 (2H, t). Elemental analysis: Found C, 90.74%; H, 4.66%; N, 4.53%; Calc. for  $\text{C}_{46}\text{H}_{28}\text{N}_2$ : C, 90.76%; H, 4.64%; N, 4.60%;  $M^+$ , 609.

#### 2.1.4. 1,6-Di(pyridin-3-yl)-3,8-di(naphthalen-2-yl)pyrene (N2PP)

Synthetic procedure is the same as in N1PP, except using 2-naphthyl boronic acid instead of 1-naphthyl boronic acid. Yellow powder (4.8 g, 80%), mp 340 °C.  $\delta_{\text{H}}$  (500 MHz;  $\text{CDCl}_3$ ;  $\text{Me}_4\text{Si}$ ) 8.96 (2H, s), 8.72 (2H, d, *J* 4), 8.28 (2H, d, *J* 8.0), 8.14 (6H, m), 8.05 (4H, m), 7.94 (4H, m), 7.80 (2H, d, *J* 7.0), 7.59 (4H, m), 7.51 (2H, m). Elemental analysis: Found: C, 90.74%; H, 4.61%; N, 4.45%; Calc. for  $\text{C}_{46}\text{H}_{28}\text{N}_2$ : C, 90.76%; H, 4.64%; N, 4.60%.  $M^+$ , 609.

### 2.2. Instrument

#### 2.2.1. Solution electrochemistry and UV-vis spectroscopy

Cyclic voltammetry was performed in 0.5 mM solution of the compounds with a Potentiostat & Galvanostat (EG&G Princeton Applied Research, Model 273A). All oxidation measurements were carried out in nitrogen-purged anhydrous  $\text{CH}_2\text{Cl}_2$  containing 0.1 M tetraethyl ammonium tetrafluoroborate ( $\text{Et}_4\text{NBF}_4$ , Aldrich) as a supporting electrolyte. Platinum disk (2 mm in diameter), platinum wire, and Ag/AgCl (saturated) were used as the working, counter, and reference electrodes, respectively. The voltage between the working and counter electrodes was swept at a scan rate of  $50 \text{ mV s}^{-1}$ . The potentials for all the materials were traced to the first anodic peak by using a differential pulse mode. Absorption spectra of  $10^{-5} \text{ M}$  solution of the samples were collected using a spectrophotometer (SCINCO UVS2100). The optical bandgap was determined from the absorption onset of that spectrum.

#### 2.2.2. OLED fabrication

Patterned indium tin oxide (ITO)-coated glass substrates (NHT,  $2 \text{ mm} \times 2 \text{ mm}$ ,  $20 \Omega \text{ cm}^{-2}$ ) were thoroughly cleaned, treated with oxygen plasma (150 W, 5 min,  $4 \times 10^{-2} \text{ torr}$ ). Organic materials were purified by train-sublimation method prior to device experiments. OLEDs were prepared in multiple-source thermal evaporation system at a base pressure of  $3 \times 10^{-6} \text{ torr}$  or lower. The deposition rate, which is controlled using a deposition controller (Inficon IC/5), was  $2 \text{ \AA s}^{-1}$  for organic materials, except for dopants which were co-evaporated at an appropriate rate to obtain the desired doping level. All the OLEDs were characterized by using a source-unit (Keithley 2400) and a spectroradiometer (Photo Research PR650). To determine the OLED lifetimes, the devices were driven at a constant DC current, while the emission

intensity was monitored using a silicon photodiode at room temperature.

### 2.2.3. Transient EL and PL

The ITO treatments and organic evaporating conditions are all the same as described in the OLED fabrication. The NPB (60 nm) as a HTL was coated on the ITO, and then electron transport materials (they also behave as emitting materials in this case, 85 nm) were coated on that. Al (100 nm) was used as a cathode. During measurement, a rectangular voltage pulse (amplitude 6–8 V, pulse duration time 3  $\mu$ s) was applied to an OLED using a pulse generator (HP model 241B). The time-resolved EL from the OLED was measured by placing a miniature photomultiplier tube (PMT, Acton spectra pro 300i Hamamatsu Model 5783-02) directly on the top of the OLED. The output photocurrent from the PMT was sourced into a sensing resistor from which the transient EL signal can be displayed on a storage oscilloscope (Tektronix TDS 754B). The electron mobility was then calculated using  $\mu = d/(\tau_d E)$ , with  $d$  denoting the film thickness and  $E$  the applied field, assuming the field drops across the sample compound and neglecting the built-in potential. For the PL measurement, sample thin films (45 nm) were prepared on the ITO glass and Al (100 nm) was coated to protect the films from air. Fluorescence spectra upon excitation with 355 nm were collected by a PMT.

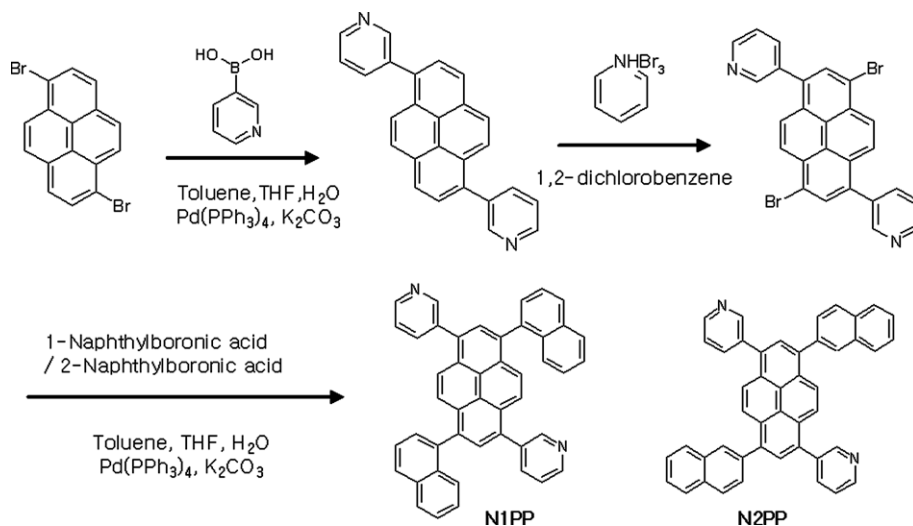
## 3. Results and discussion

The polycyclic aromatic hydrocarbons such as naphthalenes, anthracenes, and pyrenes, compared with other hetero-aromatic compounds, are known to be not suitable for ETMs because of their high reduction potentials, but they have good thermal stability and no absorption at longer wavelengths than 430 nm [12]. Among them, the pyrene has relatively high electron affinity values and better thermal stability [13]. Moreover, it has four possible positions for substitution reaction (1, 3, 6, and 8 positions), so we

can introduce various kinds of functional groups to it to tailor the desired electrical and optical properties. To increase the electron affinity of pyrene-based aromatic hydrocarbons, we attached two 3-pyridyl moieties at the 1 and 6 positions. Additionally, in order to ensure morphologically stable amorphous film, we introduced two naphthyl moieties into 3 and 8 positions. Expecting the positional dependence of physical properties, we used 1-naphthyl boronic acid and 2-naphthyl boronic acid to synthesize 1,6-di(pyridin-3-yl)-3,8-di(naphthalen-1-yl)pyrene (hereafter, N1PP) and 1,6-di(pyridin-3-yl)-3,8-di(naphthalen-2-yl)pyrene (hereafter, N2PP), respectively. Synthetic routes to the new ETMs (N1PP and N2PP) are shown in Scheme 1. (The detailed description is given in Section 2.)

The molecular structures of N1PP and N2PP were confirmed by  $^1\text{H}$  NMR, mass spectrometry, and elemental analysis. Thermal properties of N1PP and N2PP were investigated by means of differential scanning calorimetry (DSC). A glass transition temperature ( $T_g$ ) was obtained from the second heating scan of the glassy samples cooled after the first heating up to melting temperature ( $T_m$ ). The heating rate was 10  $^\circ\text{C min}^{-1}$ . The  $T_m$ 's of N1PP and N2PP appear at 377 and 337  $^\circ\text{C}$ , respectively, and N1PP shows 20  $^\circ\text{C}$  higher  $T_g$  than N2PP (shown in Table 1). Because the 1-naphthyl group is expected to be more properly oriented towards the pyrene backbone than the 2-naphthyl group is, N1PP molecule may form a more rigid structure where the intermolecular dipole interactions are favored [14,15]. The crystallization temperature ( $T_c$ ) of N1PP was observed at 250  $^\circ\text{C}$  by the second heating, but no  $T_c$  of N2PP was found (Supplementary information), which indicates that N2PP has more glass-like property. However,  $T_g$ 's of N1PP and N2PP are high enough to keep the amorphous films from being crystallized during the device operation.

The oxidation potentials for the compounds were measured by a differential pulse voltammetry and were used for the estimation of the highest occupied molecular orbital (HOMO) levels, based upon the known linear correla-



Scheme 1. Synthetic routes of N1PP and N2PP.

tion between the two parameters [16]. Because Alq<sub>3</sub>, N1PP, and N2PP did not undergo reversible oxidation, the potentials given for these molecules are the first irreversible anodic peak potentials, which are considered as the half-wave oxidation potentials ( $E_{1/2}^{OX}$ ). The anodic peak potential of ferrocene measured by a differential pulse voltammetry corresponded within 30 mV to its half-wave oxidation potential obtained from the anodic peak ( $E_p^a$ ) and the cathodic peak potential ( $E_p^c$ ). The bandgap energies were estimated from the onset of UV–vis absorption spectra in dilute solution (Supplementary information).

N2PP ( $E_g = 2.9$  eV) has a smaller bandgap than N1PP ( $E_g = 3.0$  eV). HOMO's and LUMO's of N1PP and N2PP are shown in Fig. 1. Furthermore, in order to get more detailed substituent positional effect, we calculated electronic energy of N1PP and N2PP, using the density functional theory (DFT) B3LYP/6-31G\* level Spartan'06 program. Dihedral angles between a naphthyl unit and a pyrene backbone in N1PP and N2PP are and 73.6° and 54.5°, respectively. The conjugation between naphthalene moiety and pyrene moiety is more favourable in N2PP than in N1PP. N2PP shows more bathochromic shift of  $\pi$ - $\pi^*$  transition as shown in Table 1. The two materials, however, show rela-

tively higher oxidation potentials and larger bandgap energy than Alq<sub>3</sub>, as shown in Table 1.

The blue OLEDs were fabricated by high-vacuum thermal evaporation of OLED materials onto ITO-coated glass that was used as the anode. All the devices, we fabricated have the same architectures as one shown in the left-half of Fig. 1, differing in the component of electron transport layer. We tested Alq<sub>3</sub>, newly-synthesized N1PP and N2PP as electron transport layer (ETL) or electron transport material (ETM).

Firstly, a 60-nm-thick hole injection layer (HIL) consisting of 4,4'-bis[N-(4-{N,N-bis(3-methylphenyl)amino}phenyl)-N-phenylamino]biphenyl (DNTPD) was deposited, and followed by a 30-nm-thick 4,4'-bis [N-(1-naphthyl)-N-phenylamino]biphenyl (NPB) as a hole transport layer (HTL). Secondly, a 25-nm-thick emissive material layer (EML) was formed by co-depositing 3 wt% of 2,5,8,11-tetra(tert-butyl)perylene (TBP) as a dopant and 9,10-di-(2-naphthyl)anthracene (ADN) as a host [17]. Finally, a 25-nm-thick electron transport layer (ETL) consisting of Alq<sub>3</sub> for device 1 (N1PP for device 2, N2PP for device 3) was deposited. LiF (0.5 nm) and Al (100 nm) worked as an electron injection facilitating a layer and a cathode

**Table 1**

Physical properties of electron transport materials (N1PP and N2PP) used in this work.

Compound	$T_g$ [°C]	$\lambda_{max}^{abs}$ [nm] <sup>b</sup>	$\lambda_{max}^{PL}$ [nm] <sup>c</sup>	$E_{1/2}^{OX}$ [mV] <sup>d</sup>	HOMO [eV] <sup>e</sup>	Bandgap [eV] <sup>f</sup>
Alq <sub>3</sub>	175 <sup>a</sup>	386	512	1140	5.51	2.80
N1PP	172	380	421	1570	6.14	3.03
N2PP	152	386	434	1320	5.79	2.94

<sup>a</sup> Literature value [15].

<sup>b</sup> 0.01 mM solutions in CH<sub>2</sub>Cl<sub>2</sub>.

<sup>c</sup> 0.01 mM solutions in CH<sub>2</sub>Cl<sub>2</sub> upon excitation at 355 nm.

<sup>d</sup> The first irreversible anodic peak potential measured by a differential pulse voltammetry was considered as the half-wave oxidation potential ( $E_{1/2}^{OX}$ ) (see Supplementary information).

<sup>e</sup> Estimated using a linear correlation by the measured anodic peak potential [16].

<sup>f</sup> Estimated from the absorption onset.

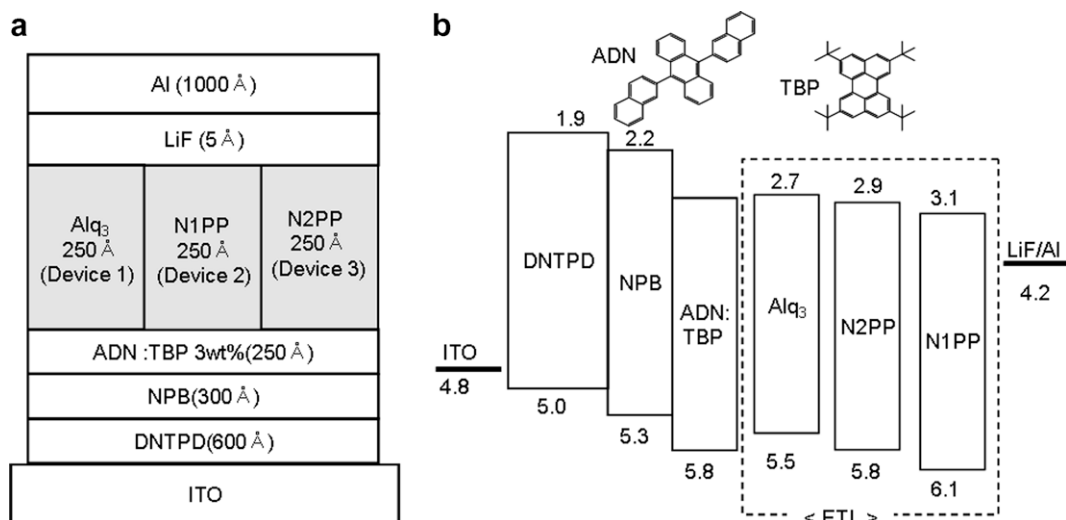


**Fig. 1.** (a) Device architecture for OLED, where ETM is Alq<sub>3</sub> for device 1, N1PP for device 2, and N2PP for device 3. (b) Energy diagram of multi layer devices; HOMO and LUMO levels of DNTPD, Alq<sub>3</sub>, N1PP, and N2PP are estimated from the first oxidation potential and the absorption onset (Section 2). Those of NPB and ADN are previously reported values [22].

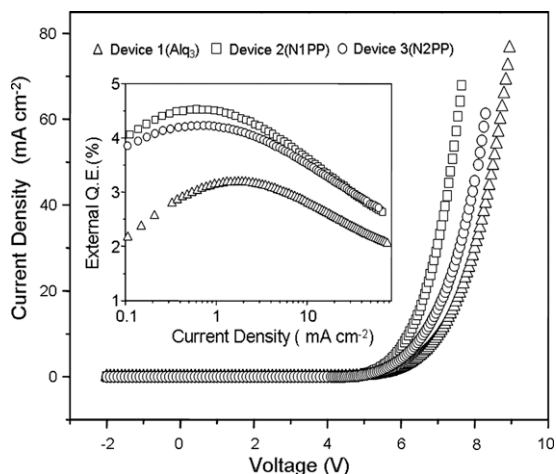


**Fig. 2.** The  $J$ - $V$  (current-density-voltage) curves of blue devices based on different ETMs. The inset shows the external quantum efficiency as a function of current density.

layer, respectively. Inside a glove box, all the devices were encapsulated by a 1-mm-thick glass cover containing a humidity absorber (Dyvic). Devices 1, and 2, and 3 have Alq<sub>3</sub>, N1PP, and N2PP as an electron transport layer (ETL), respectively.

The current density ( $J$ )-voltage ( $V$ )-luminescence ( $L$ ) characteristics of the blue OLEDs with different ETMs were measured by source-measure-units (Keithley 2400) and a spectrometer (Photo research PR650). The  $J$ - $V$  characteristics are shown in Fig. 2 and the external quantum efficiencies as a function of  $J$  are also shown in the inset of Fig. 2. Applying approximately  $10 \text{ mA cm}^{-2}$  to the devices, the driving voltages of the devices 1, 2, and 3 are 7.05 V ( $10.1 \text{ mA cm}^{-2}$ ), 6.25 V ( $10.4 \text{ mA cm}^{-2}$ ), and 6.65 V ( $10.4 \text{ mA cm}^{-2}$ ), respectively. The external quantum efficiencies of the devices are 2.8%, 3.6%, and 3.5%, respectively. The required operating voltage for  $10 \text{ mA cm}^{-2}$  is in the order of device 1 > device 3 > device 2, which corresponds to the height of the electron injection barrier estimated by the electrochemical data (Alq<sub>3</sub> > N2PP > N1PP shown in the right-half of Fig. 1, i.e. N1PP has the lowest injection barrier among them.).

Additionally, the external quantum efficiencies of the device with the newly-developed pyrene-based molecules as electron transport materials increase by more than 50% at  $1 \text{ mA cm}^{-2}$  compared with those of the device with Alq<sub>3</sub> as an electron transport material. This enhancement is due to the newly-developed pyrene-based molecules as electron transport materials through an improved electron mobility and a lower injection barrier. In order to confirm this fact, we fabricated three kinds of devices to measure the electron mobility by the transient electroluminescence (EL) with ITO/NPB (60 nm)/ETM (85 nm)/Al device structure, where ETM is Alq<sub>3</sub>, N1PP, or N2PP (described in Section 2) [18]. The typical transient EL signals for the three devices are shown in the inset of Fig. 3, where the time delay ( $\tau_d$ ) of Alq<sub>3</sub> film is  $1.1 \mu\text{s}$  and both N1PP and N2PP films have about  $0.3 \mu\text{s}$  of  $\tau_d$  around 5.5 V. We collect  $\tau_d$  by varying the electric field. The electron mobility is

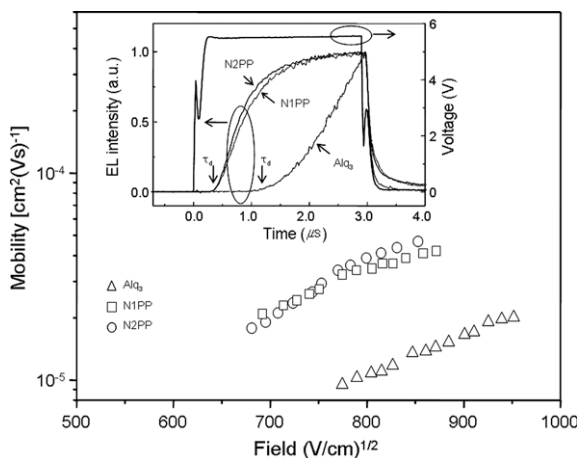


**Fig. 3.** The electron mobilities in Alq<sub>3</sub>, N1PP, and N2PP are plotted as a function of the square-root of the electric field. Their transient electroluminescent signals around 5.5 V are also shown in the inset (more specifically, applied voltages for Alq<sub>3</sub>, N1PP, and N2PP devices are 5.67 V, 5.52 V, and 5.45 V, respectively).

plotted as a function of the square-root of the electric field and is given in Fig. 3. For the electric field at  $0.7 \text{ MV cm}^{-1}$ , the estimated electron mobility in Alq<sub>3</sub> film is  $1.4 \times 10^{-5} \text{ cm}^2 (\text{V s})^{-1}$  that is in a good agreement with the reported value,  $10^{-6} \sim 10^{-5} \text{ cm}^2 (\text{V s})^{-1}$  [5,19]. Those in N1PP and

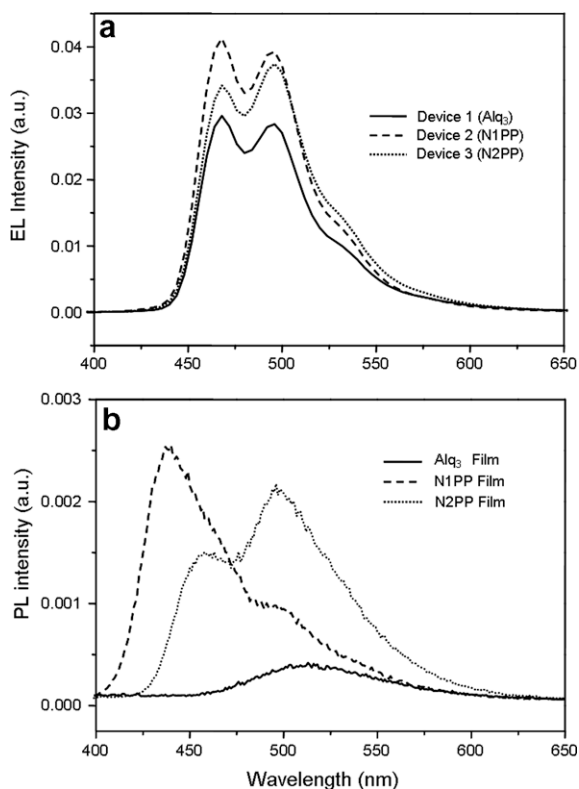


**Fig. 4.** (a) EL spectra of devices 1, 2, and 3 at  $J = 10 \text{ mA cm}^{-2}$ . (b) Photoluminescence spectra of the vacuum-deposited amorphous thin films of Alq<sub>3</sub>, N1PP and N2PP upon UV excitation at 355 nm.

N2PP films are  $3.7 \times 10^{-5} \text{ cm}^2 (\text{V s})^{-1}$  and  $4.3 \times 10^{-5} \text{ cm}^2 (\text{V s})^{-1}$ , respectively. As expected, the electron mobilities in the newly-developed pyrene-based electron transport materials (N1PP and N2PP) turned out to be higher than that in better-known  $\text{Alq}_3$ , and thus enhanced the external quantum efficiency of devices 2 and 3 using N1PP and N2PP as ETLs which can be explained in terms of an efficient balanced carrier recombination in the emissive material layer (EML).

The EL spectra of the three devices at  $10 \text{ mA cm}^{-2}$  are also shown in Fig. 4a together with their PL spectra in Fig. 4b. The luminescences with 1931 Commission Internationale del' Eclairage (CIE) coordinates ( $x, y$ ) of devices 1, 2, and 3 are  $495 \text{ cd m}^{-2}$  with (0.148, 0.294),  $627 \text{ cd m}^{-2}$  with (0.138, 0.276), and  $672 \text{ cd m}^{-2}$  with (0.148, 0.318), respectively. Device 2 (with N1PP as an ETL) emits the most saturated blue color and the intense peak at 468 nm. Device 3 (with N2PP as an ETL) shows a little bit broader spectrum and the intense peak centered at 496 nm. The difference in spectral feature among these results from the enhanced blue emission. Gathering from the PL data shown in Fig. 4b, the totally enhanced portion of blue emission in device 2 with N1PP as an ETL, compared with device 1 with  $\text{Alq}_3$  as an ETL, comes from an improved carrier recombination in an EML due to the HOMO energy level of N1PP as a hole barrier and three times higher electron mobility of N1PP than that of  $\text{Alq}_3$ . If some of the enhanced portion of the blue emission in device 2 with N1PP as an ETL come from the blue emission of N1PP itself, then the blue emission around 430 nm should be shown in the EL spectrum of device 2. In fact, it is not shown in the EL spectrum of device 2 as given in Fig. 4a. On the other hand, the excimer peaks of pyrene [20] around 500 nm are generated from both N1PP and N2PP, but N2PP having more planar structure for easier formation of excimers shows much stronger excimer peak, for device 3 with N2PP as an ETL, considering that 9,10-di(2-naphthyl)anthracene (ADN) is so ambipolar [21] that the holes passing over it can reach the ETL of N2PP, some of the enhanced portion of blue emission can be originated from N2PP and its excimer themselves.

With the newly-developed pyrene-based molecules (N1PP and N2PP) as an ETL, we get the enhanced blue emission due to 3 times higher electron mobility in those and the HOMO levels of those, compared with  $\text{Alq}_3$  as an ETL. More specifically, the totally enhanced portion of the blue emission with N1PP as an ETL originates from the HOMO energy level of N1PP as a hole barrier and three times higher electron mobility, while some of the enhanced portion of the blue emission with N2PP as an ETL results from an improved carrier recombination at EML due to three times higher electron mobility and the others come from the blue emission of N2PP and its excimer themselves. We have performed an accelerated lifetime test at  $2000 \text{ cd m}^{-2}$  initial brightness for the three devices. Applied current and voltage are  $52.8 \text{ mA cm}^{-2}$  and  $8.55 \text{ V}$  for the device 1,  $42.2 \text{ mA cm}^{-2}$  and  $7.25 \text{ V}$  for device 2, and  $37.3 \text{ mA cm}^{-2}$  and  $7.80 \text{ V}$  for the device 3. The accelerated test data are given in Fig. 5. The operation times of 40% light emission reduction occurring for devices 1, 2, and 3 are 620 h, 87 h, and 517 h, respectively.

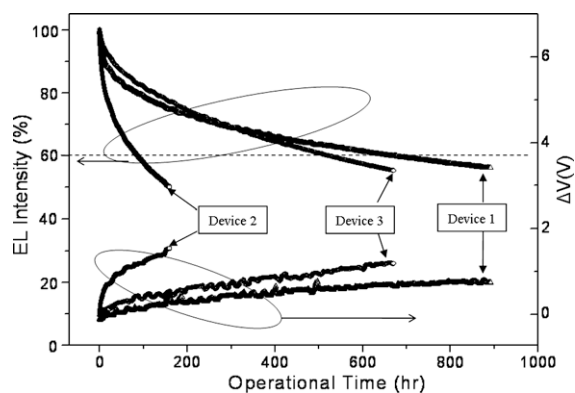


Fig. 5. Luminance deteriorations and drive voltage variation curves ( $\Delta V$ ) of the devices as a function of time at  $2000 \text{ cd m}^{-2}$ .

Interestingly, the lifetime of the device 2 with N1PP is shortened by a factor of 5, compared with device 3 with N2PP, even though the only difference in the two structures is the substituent (1-naphthyl or 2-naphthyl). This observation gives some light on the device degradation. According to the energy levels of each material shown in Fig. 1b, device 2 with N1PP as an electron transport layer has a hole injection barrier between an emissive material layer (EML) and an electron transport layer (ETL), but device 3 with N2PP as an ETL does not have a hole injection barrier. The holes in device 3 (with no hole injection barrier) can penetrate the ETL layer deeply and spread over larger area and disappear away with electrons than those in device 2 with N1PP as an ETL. The hole accumulation caused by a hole injection barrier accelerate the material decomposition through a higher concentration of ionized carbocation species in the emissive materials layer [22–24]. Compared to  $\text{Alq}_3$  and N2PP, N1PP has the highest hole injection barrier. And thus the device 2 with N1PP as an ETM degrades faster than the others. Usually, the deterioration of the light emission is observed in company with an increase in the drive voltage. The drive voltage variations,  $\Delta V$ 's of devices 1, 2, and 3 at 40% light emission reduction, are 0.68 V, 1.2 V, and 1.0 V, respectively. The highest drive voltage increase ( $\Delta V = 1.2 \text{ V}$ ) is also observed in the device 2 with N1PP as an ETL, with which we can suppose that the voltage increase during the lighting process has a strong correlation with some degradation at the interface between EML and ETL as well. The luminance degradation in the blue OLEDs was correlated with the HOMO energy levels of electron transport materials. Based upon the fact that N1PP and N2PP have 3 times higher mobility than  $\text{Alq}_3$  and the understanding on the device degradation with N1PP and N2PP, further works on the better devices with a longer lifetime are in progress.

#### 4. Conclusions

In conclusion, we synthesized new kinds of pyrene-based electron transport materials: 1,6-di(pyridin-3-yl)-3,8-di(naphthalen-1-yl)pyrene (N1PP) and 1,6-di(pyridin-3-yl)-3,8-di(naphthalen-2-yl)pyrene (N2PP). The external



quantum efficiencies of the device with the newly-developed pyrene-based molecules as electron transport materials increase by more than 50% at  $1 \text{ mA cm}^{-2}$  compared with those of the device with representative  $\text{Alq}_3$  as an electron transport material. The enhanced quantum efficiency is due to the balanced charge recombination in an emissive layer. Electron mobilities in N1PP and N2PP films are  $3.7 \times 10^{-5} \text{ cm}^2 (\text{V s})^{-1}$  and  $4.3 \times 10^{-5} \text{ cm}^2 (\text{V s})^{-1}$ , respectively. These values are three times higher than that of  $\text{Alq}_3$ . Highly enhanced power efficiency (e.g.,  $1.4 \text{ lm W}^{-1}$  for device 1 with  $\text{Alq}_3$ ,  $2.0 \text{ lm W}^{-1}$  for device 2 with N1PP, and  $2.1 \text{ lm W}^{-1}$  for device 3 with N2PP at  $2000 \text{ cd m}^{-2}$ ) is achieved due to a low electron injection barrier and a high electron mobility. We find that the luminance degradation in the blue OLEDs is correlated with the HOMO energy levels of electron transport materials.

### Acknowledgements

This work was supported in part by MOE through BK21 program and Seoul R&BD program. We thank KOSEF and CNNC for supporting this research. We also acknowledge the student support from the Korea Science and Engineering Foundation through NanoSystems Institute – National Core Research Center.

### Appendix A. Supplementary data

Supplementary data associated with this article can be found, in the online version, at [doi:10.1016/j.orgel.2008.10.015](https://doi.org/10.1016/j.orgel.2008.10.015).

### References

- [1] C.W. Tang, S.A. Van Slyke, *Appl. Phys. Lett.* 51 (1987) 913.
- [2] R.J. Holmes, B.W. D'Andrade, S.R. Forrest, X. Ren, J. Li, M.E. Thompson, *Appl. Phys. Lett.* 83 (2003) 3818.
- [3] S.-J. Yeh, M.-F. Wu, C.-T. Chen, Y.-H. Song, Y. Chi, M.-H. Ho, S.-F. Hsu, C.H. Chen, *Adv. Mater.* 17 (2005) 285.
- [4] X. Ren, J. Li, R.J. Holmes, P.I. Djurovich, S.R. Forrest, M.E. Thompson, *Chem. Mater.* 16 (2004) 4743.
- [5] B.J. Chen, W.Y. Lai, Z.Q. Gao, C.S. Lee, S.T. Lee, W.A. Gambling, *Appl. Phys. Lett.* 75 (1999) 4010.
- [6] T.-Y. Chu, O.-K. Song, *Appl. Phys. Lett.* 90 (2007) 203512.
- [7] S. Tokito, H. Tanaka, N. Koda, A. Okada, Y. Tago, *Macromol. Symp.* 125 (1997) 181.
- [8] J. Shi, C.W. Tang, C.H. Chen, US Patent 5646948, 1997.
- [9] M. Uchida, T. Izumizawa, T. Nakano, S. Yamaguchi, K. Tamao, K. Furukawa, *Chem. Mater.* 13 (2001) 2680.
- [10] A.P. Kulkarni, C.J. Tonzola, A. Babel, S.A. Jenekhe, *Chem. Mater.* 16 (2004) 4556.
- [11] P. Stroehriegel, J.V. Grazulevicius, *Adv. Mater.* 14 (2002) 1439.
- [12] C.J. Tonzola, M.M. Alam, W. Kaminsky, S.A. Jenekhe, *J. Am. Chem. Soc.* 125 (2003) 13548.
- [13] R.S. Becker, W.E. Wentworth, *J. Am. Chem. Soc.* 85 (1963) 2210.
- [14] D.E. Loy, B.E. Koene, M.E. Thompson, *Adv. Funct. Mater.* 12 (2002) 245.
- [15] K. Naito, A. Miura, *J. Phys. Chem.* 97 (1993) 6240.
- [16] B.W. D'Andrade, S. Datta, S.R. Forrest, P. Djurovich, E. Polikarpov, M.E. Thompson, *Org. Electron.* 6 (2005) 11.
- [17] J. Shi, C.W. Tang, *Appl. Phys. Lett.* 80 (2002) 3201.
- [18] C. Hosokawa, H. Tokailin, H. Higashi, T. Kusumoto, *Appl. Phys. Lett.* 60 (1992) 1221.
- [19] S.C. Tse, H.H. Fong, S.K. So, *J. Appl. Phys.* 94 (2003) 2033.
- [20] (a) T. Forster, K. Kasper, *Z. Physik Chem. N.F.* 1 (1954) 275; (b) N.J. Turro, in: *Modern Molecular Photochemistry*, Univ. Science Books, Mill Valley, California, 1991 (Ch. 5).
- [21] S.C. Tse, S.K. So, M.Y. Yeung, C.F. Lo, S.W. Wen, C.H. Chen, *Chem. Phys. Lett.* 353 (2002) 407.
- [22] S.W. Culligan, A.C.-A. Chen, J.U. Wallance, K.P. Klubek, C.W. Tang, S.H. Chen, *Adv. Funct. Mater.* 16 (2006) 1481.
- [23] H. Aziz, Z.D. Popovic, N.X. Hu, A. Hor, G. Xu, *Science* 283 (1999) 1900.
- [24] Y.C. Luo, H. Aziz, G. Xu, Z.D. Popovic, *Chem. Mater.* 19 (2007) 2079.



# High efficiency deep blue phosphorescent organic light-emitting diodes

Kyoung Soo Yook, Soon Ok Jeon, Chul Woong Joo, Jun Yeob Lee \*

Department of Polymer Science and Engineering, Dankook University, Jukjeon-dong, Suji-gu, Yongin-si, Gyeonggi-do, 448-701, Republic of Korea

## ARTICLE INFO

### Article history:

Received 23 July 2008

Accepted 29 October 2008

Available online 6 November 2008

### PACS:

85.60.jb

### Keywords:

Deep blue phosphorescent devices

Quantum efficiency

Pure blue color

## ABSTRACT

Deep blue phosphorescent organic light-emitting diodes have been developed by using tris((3,5-difluoro-4-cyanophenyl)pyridine) iridium (FCNir) as a blue phosphorescent dopant. The FCNir showed a wide triplet bandgap of 2.8 eV for deep blue emission due to a strong electron withdrawing CN substituent in addition to F unit. Doping of the FCNir in N,N'-dicarbazolyl-3,5-benzene gave a high quantum efficiency of 9.2% with a CIE color coordinate of (0.15, 0.16).

© 2008 Elsevier B.V. All rights reserved.

## 1. Introduction

Deep blue phosphorescent organic light-emitting diodes (PHOLEDs) are critical to get a low power consumption in organic light-emitting diodes because the efficiency of blue fluorescent device is low compared with that of red and green devices [1].

There have been many studies to develop blue PHOLEDs. Iridium(III) bis(4,6-(di-fluorophenyl)-pyridinato-N,C2') picolinate (Flrpic) is the most well-known blue phosphorescent dopant, but its color performances were poor with a color coordinate of (0.15,0.32) [2]. Bis[2-(4',6'-difluorophenyl)pyridinato-N,C2']tetrakis(1-pyrazolyl)borate was also developed as a blue phosphorescent dopant, but its electroluminescence performances were not good enough as a deep blue dopant [3]. Color coordinate of (0.16, 0.26) was obtained with a quantum efficiency of about 10%. Fluorine substituted phenylpyridine derivatives were synthesized as blue dopants, but it gave a light blue emission in spite of high efficiency in soluble devices [4]. Other than these studies, a triazole based ancillary ligand structure was combined with fluorine substituted phenylpyridine

ligand structure and color coordinate of (0.16,0.24) was obtained [5].

In this work, a deep blue PHOLED with a color coordinate of (0.15,0.16) was developed by using an iridium based phenylpyridine derivative with strong electron withdrawing substituents. N,N'-Dicarbazolyl-3,5-benzene(mCP) was used as a host to get a high quantum efficiency in deep blue PHOLEDs.

## 2. Experimental

A device architecture of indium tin oxide(ITO, 150 nm)/N,N'-diphenyl-N,N'-bis-[4-(phenyl-m-tolyl-amino)-phenyl]-biphenyl-4,4'-diamine (60 nm)/N, N'-di(1-naphthyl)-N,N'-diphenylbenzidine(20 nm)/mCP(10 nm)/mCP: tris((3,5-difluoro-4-cyanophenyl)pyridine) iridium(FCNir, 30 nm)/2,9-dimethyl-4,7-diphenyl-1,10-phenanthroline(BCP, 5 nm)/tris(8-hydroxyquinoline) aluminium(Alq<sub>3</sub>, 20 nm)/LiF (1 nm)/Al(200 nm) was used to fabricate deep blue devices. Blue PHOLEDs with 4,7-diphenyl-1,10-phenanthroline (BPhen) as an electron transport layer were also fabricated to study the effect of the electron transport layer on device performances of deep blue PHOLEDs. The doping concentration of FCNir in mCP was controlled as 5%, 10% and 15%. Chemical structures and the device structure

\* Corresponding author. Tel./fax: +82 31 8005 3585.

E-mail address: [leej17@dankook.ac.kr](mailto:leej17@dankook.ac.kr) (J.Y. Lee).

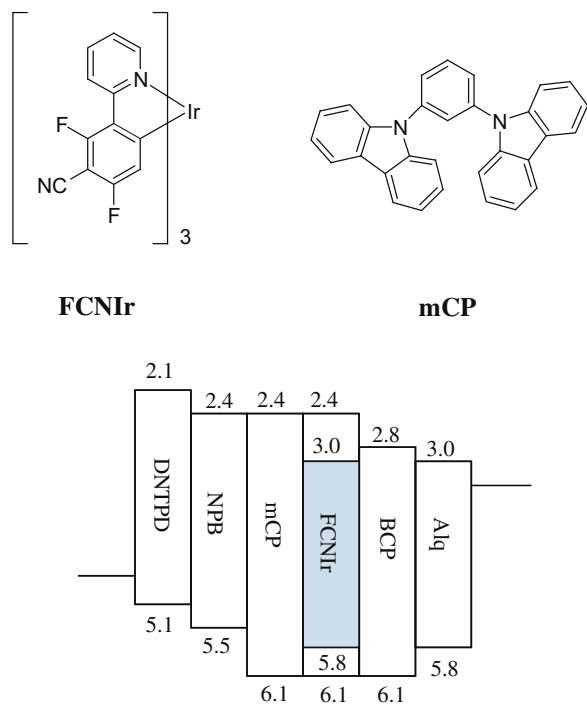


Fig. 1. A chemical structure of FCNIr and device structures of deep blue PHOLEDs.

are shown in Fig. 1. Synthesis of FCNIr will be reported in other work. Ultraviolet–visible (UV–visible) and photoluminescence (PL) spectra of host and dopant materials were measured with JASCO FP-750 fluorescence spectrometer. Current density–voltage–luminance characteristics of the devices were measured with Keithley 2400 source measurement unit and CS-1000 spectrophotometer.

### 3. Results and discussion

FCNIr was designed as a deep blue phosphorescent dopant because a strong electron withdrawing group in phenyl unit of main ligand can induce a blue shift of emission spectrum [6]. Fig. 2 shows PL spectra of FCNIr and Flrpic

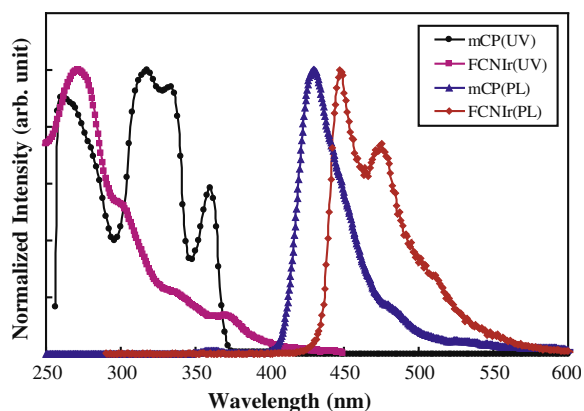


Fig. 2. Ultraviolet–visible absorption and photoluminescence spectra of mCP and FCNIr materials.

dopant materials. The PL emission peak of FCNIr was observed at 448 nm with a vibrational peak at 476 nm. The FCNIr showed a deep blue emission peak due to the strong electron withdrawing CN group in the phenyl unit of main ligand. An electron withdrawing group in phenyl unit shifts the highest occupied molecular orbital (HOMO) and a deep HOMO level of 5.8 eV was observed in FCNIr from photoelectron spectroscopy. UV–visible absorption and PL emission spectra of mCP are also shown in Fig. 2 and it can be clearly seen that PL emission spectra of mCP are overlapped with metal to ligand charge transfer absorption of FCNIr with a peak position between 400 nm and 450 nm. Therefore, an efficient energy transfer from host materials to FCNIr is expected. In addition, the triplet bandgap of mCP is 2.9 eV compared with 2.8 eV of FCNIr and a triplet dexter energy transfer can be induced.

Fig. 3 shows current density–voltage–efficiency curves of FCNIr doped blue PHOLEDs with BCP/Alq<sub>3</sub> and BPhen electron transport layer. The doping concentration of FCNIr was 10%. The blue PHOLED with BPhen showed a higher current density than the blue PHOLED with BCP/Alq<sub>3</sub>. Bphen is known to have a high electron mobility [7], leading to high current density at the same voltage. High electron mobility of BPhen can be beneficial to the quantum efficiency in hole transport type mCP based devices. Therefore, Bphen was chosen as an electron transport layer of deep blue PHOLEDs and device performances were studied according to doping concentration.

Current density–voltage–luminance curves of deep blue PHOLEDs with Bphen electron transport layer are shown in Fig. 4a. Current density was increased as the doping concentration was increased. A maximum current density was obtained in the device with 15% doping concentration. The high current density in the highly doped device can be explained by charge trapping effect in the light-emitting layer [8]. The FCNIr has a HOMO of 5.8 eV and the lowest unoccupied molecular orbital (LUMO) of 3.0 eV. As can be seen in Fig. 1, electron is strongly trapped by FCNIr due to a LUMO gap of 0.6 eV between mCP and FCNIr. A HOMO gap between mCP and FCNIr is 0.3 eV, which is much lower than the LUMO gap between mCP and FCNIr. Therefore, electrons are strongly trapped by FCNIr and the electron transport in FCNIr doped mCP is retarded by the electron trapping effect. The electron transport is facilitated at high doping concentration because of a reduced hopping distance between dopant materials, resulting in the high current density at high doping concentration. A similar result was observed in the luminance data of blue PHOLEDs and a high luminance was obtained in the highly doped blue PHOLED due to high charge density at high doping concentration [9].

The quantum efficiency of the deep blue PHOLEDs was plotted against the luminance and it is shown in Fig. 4b. The quantum efficiency was enhanced at high doping concentration and a high quantum efficiency of 9.1% was obtained at 500 cd/m<sup>2</sup>. The high quantum efficiency of deep blue PHOLEDs doped with 15% FCNIr can be explained by a charge balance in the light-emitting layer. The mCP host material is a hole transport type host material and a hole injection is better than an electron injection. Therefore, a hole density is higher than the electron density in the

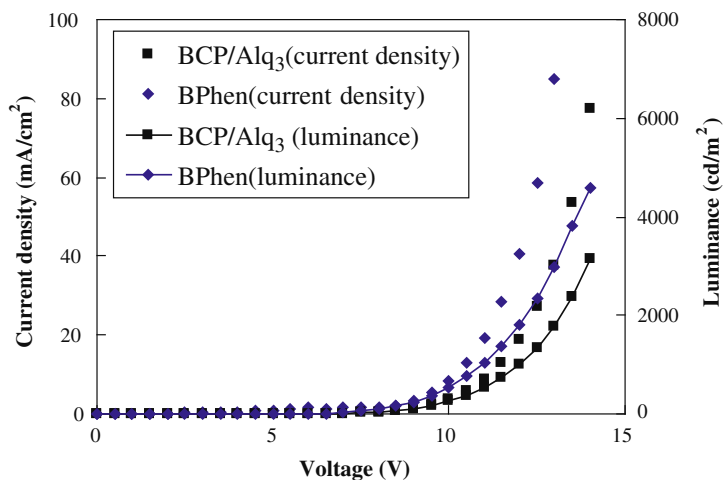


Fig. 3. Current density–voltage–luminance characteristics of blue PHOLEDs with BCP/Alq<sub>3</sub> and BPhen electron transport layers.

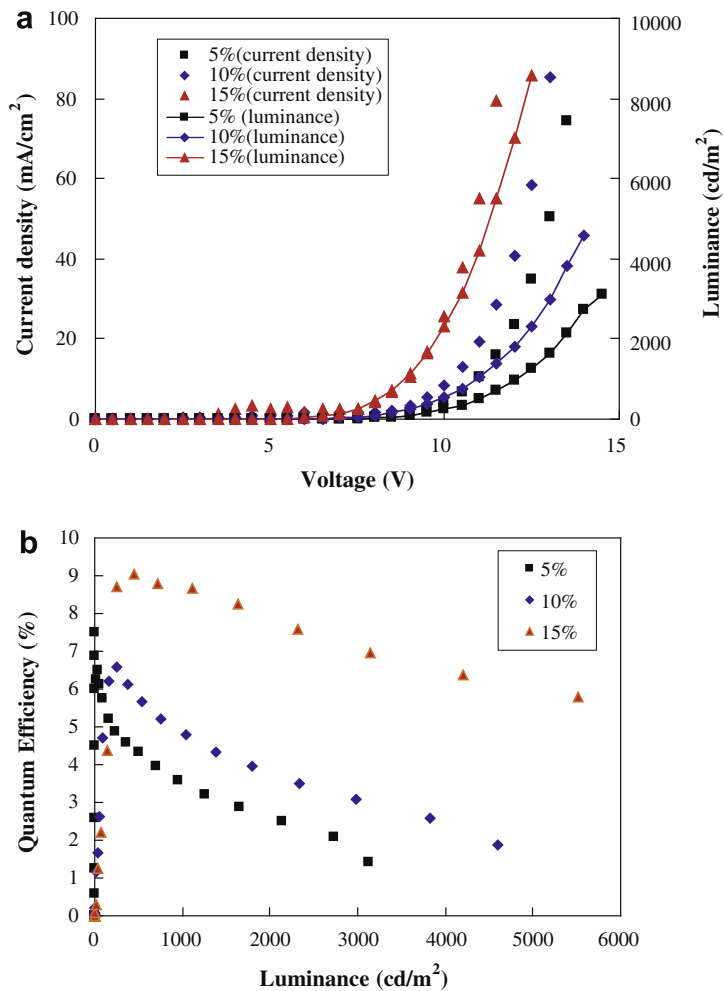
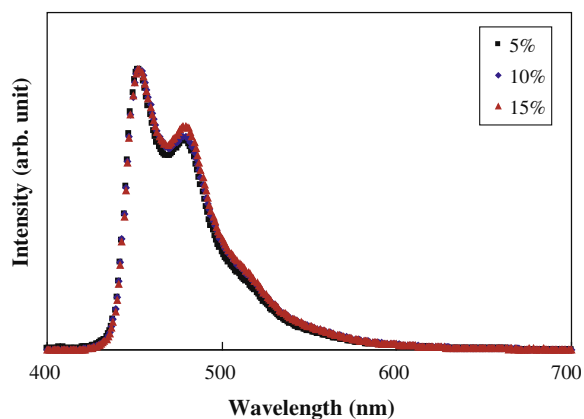


Fig. 4. Current density–voltage–luminance curves (a) and quantum efficiency–luminance curves (b) of blue PHOLEDs with Bphen according to FCNIR doping concentration.



**Fig. 5.** Electroluminescence spectra of blue PHOLEDs with different FCNir doping concentrations.

mCP based emitting layer and more electron injection enhances the charge balance. The electron transport is improved at high doping concentration due to a reduced hopping distance and the electron density is increased at high doping concentration, resulting in better holes and electrons balance in the light-emitting layer. A high current efficiency of 11 cd/A was observed in 15% FCNir doped devices.

Electroluminescence spectra of deep blue PHOLEDs are shown in Fig. 5. The peak maximum of blue PHOLEDs was 454 nm and a shoulder peak at 482 nm was observed. The color coordinate of 5% FCNir doped PHOLED was (0.14, 0.15) compared with (0.17, 0.33) of common phos-

phorescent blue dopant materials in our measurement. The color coordinate is better than any other data reported in the literature [2–5]. The blue PHOLED with 15% doping concentration was (0.15, 0.16) with a current efficiency of 11 cd/A. Therefore, a true deep blue PHOLED with a high efficiency over 10 cd/A could be obtained by controlling the doping concentration and the electron transport layer of the blue PHOLEDs.

#### 4. Conclusions

In summary, a true deep blue PHOLED could be fabricated by doping FCNir in the mCP host material. A high quantum efficiency of 9.2% and a current efficiency of 11 cd/A were obtained in the deep blue PHOLED with a color coordinate of (0.15, 0.16) at 500 cd/m<sup>2</sup>.

#### References

- [1] J.Y. Lee, J.H. Kwon, H.K. Chung, *Org. Electron.* 4 (2003) 143.
- [2] C. Adachi, R.C. Kwong, P. Djurovich, V. Adamovich, M.A. Baldo, M.E. Thompson, S.R. Forrest, *Appl. Phys. Lett.* 79 (2001) 2082.
- [3] R.J. Holmes, B.W.D. Andrade, S.R. Forrest, X. Ren, J. Lee, M.E. Thompson, *Appl. Phys. Lett.* 83 (2003) 3818.
- [4] H. Liu, P. Wang, J. He, C. Zheng, X. Zhang, S. Chew, C. Lee, J. Chang, S.T. Lee, *Appl. Phys. Lett.* 92 (2008) 023301.
- [5] S. Yeh, M. Wu, C. Chen, Y. Song, Y. Chi, M. Ho, *Adv. Mater.* 17 (2005) 285.
- [6] S. Lamansky, P. Djurovich, D. Murphy, F. Abdel-Razzaq, H. Lee, C. Adachi, P.E. Burrows, S.R. Forrest, M.E. Thompson, *J. Am. Chem. Soc.* 123 (2001) 4304.
- [7] S. Naka, H. Okada, H. Onnagawa, T. Tsutsui, *Appl. Phys. Lett.* 76 (2000) 197.
- [8] S.H. Kim, J. Jang, J.Y. Lee, *Appl. Phys. Lett.* 89 (2006) 153503.
- [9] J.Y. Lee, *J. Ind. Eng. Chem.* (2008), doi:10.1016/j.jiec.2008.04.007.



# Ultra-thin polymer gate dielectrics for top-gate polymer field-effect transistors

Yong-Young Noh<sup>a,b,\*</sup>, Henning Sirringhaus

<sup>a</sup> Cavendish Laboratory, University of Cambridge, JJ Thomson Avenue, Cambridge CB3 0HE, United Kingdom

<sup>b</sup> Convergence Components and Materials Laboratory, Electronics and Telecommunications Research Institute (ETRI), 161 Gajeong-dong, Yuseong-gu, Daejeon 305-350, Republic of Korea

## ARTICLE INFO

### Article history:

Received 23 July 2008

Received in revised form 29 October 2008

Accepted 29 October 2008

Available online 12 November 2008

### PACS:

85.30.Tv

81.05.Lg

77.84.-s

### Keywords:

Organic field-effect transistor

Polymer gate dielectrics

## ABSTRACT

We have demonstrated top-gate polymer field-effect transistors (FETs) with ultra-thin (30–50 nm), room-temperature crosslinkable polymer gate dielectrics based on blending an insulating base polymer such as poly(methyl methacrylate) with an organosilane cross-linking agent, 1,6-bis(trichlorosilyl)hexane. The top-gate polymer transistors with thin gate dielectrics were operated at gate voltages less than  $-8$  V with a relatively high dielectric breakdown strength ( $>3$  MV/cm) and a low leakage current ( $10$ – $100$  nA/mm<sup>2</sup> at 2 MV/cm). The yield of thin gate dielectrics in top-gate polymer FETs is correlated with the roughness of underlying semiconducting polymer film. High mobilities of  $0.1$ – $0.2$  cm<sup>2</sup>/V s and on and off state current ratios of  $10^4$  were achieved with the high performance semiconducting polymer, poly(2,5-bis(3-alkylthiophen-2-yl)thieno[3,2-b]thiophene).

© 2008 Elsevier B.V. All rights reserved.

## 1. Introduction

Research into solution-processible organic field-effect transistors (OFETs) has been dramatically increasing in the past decade motivated by applications in low-cost, large-area electronics on flexible substrates. Many studies have focused on the development of high performance polymer semiconductor materials and methods for improving their ordering to achieve high charge carrier mobility via inter-molecular hopping [1–5]. Research on gate dielectrics and their properties has attracted less attention even though the device operates through the modulation of charge carrier flow at the semiconductor–dielectric interface. Earlier works on development of solution-processible

gate dielectrics focused mainly on high permittivity [6–9] and silicon-based materials motivated by the superb properties of silicon dioxide (SiO<sub>2</sub>) as a gate dielectric for silicon FETs [10]. However, reports of a dependence of field-effect mobility on the dielectric constant of the gate dielectric [11] and of the general observation of n-type behavior in organic semiconductors via controlling the semiconductor–dielectric interface [12] illustrate clearly the importance of selecting the right gate dielectric material. New polymer dielectrics are now considered as a key area of development for improving the performance and reliability of OFETs and to accelerate commercialization.

A key requirement for a polymer gate dielectric is the ability to form a thin film with good dielectric properties [13,14]. The thickness of the gate dielectric determines directly the operating voltage of the FET, and for devices with short channel length  $L$  the gate dielectric thickness needs to be sufficiently thin to fulfill basic transistor scaling relationships (typically  $d/L < 1/4$ ) [15,16]. With conventional polymer insulators such as poly(methyl

\* Corresponding author. Address: Convergence Components and Materials Laboratory, Electronics and Telecommunications Research Institute (ETRI), 161 Gajeong-dong, Yuseong-gu, Daejeon 305-350, Republic of Korea.

E-mail addresses: [yynoh@etri.re.kr](mailto:yynoh@etri.re.kr) (Y.-Y. Noh), [hs220@cam.ac.uk](mailto:hs220@cam.ac.uk) (H. Sirringhaus).

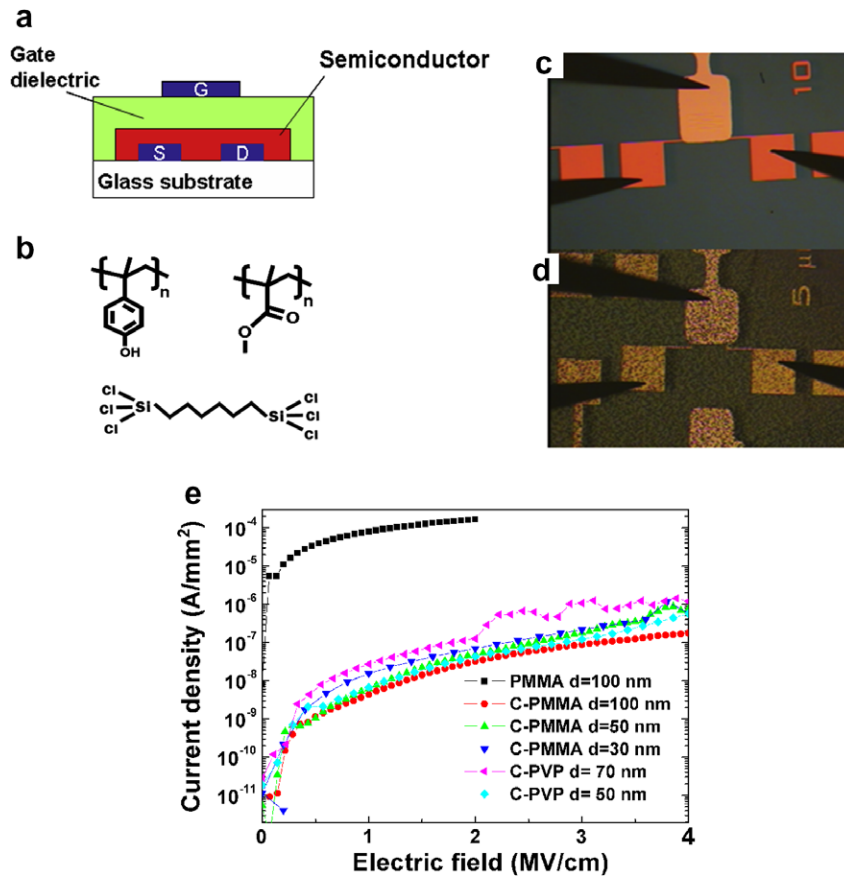


**Fig. 1.** (a) Chemical structure of poly(methyl methacrylate) (PMMA), poly-4-vinylphenol (PVP) and 1,6-bis(trichlorosilyl)hexane ( $C_6$ -Si) used as a base polymer and crosslinking agent for thin gate dielectrics in this study. (b) Schematic diagram of top-gated polymer transistor. Optical micrograph view of the top of poly(9,9-dioctylfluorene-co-bithiophene) (F8T2) transistors with (c) crosslinked PMMA (C-PMMA), and (d) crosslinked polystyrene as a gate dielectric (the size of for the square source and drain contact pads is  $500 \times 500 \mu\text{m}$ ). (e) Leakage current density versus applied voltage for C-PMMA (100, 50 and 30 nm), C-PVP (70 nm and 50 nm), or PMMA (100 nm)/30 nm F8T2 films sandwiched between gold electrodes.

methacrylate) (PMMA) or polystyrene (PS) it is very difficult to achieve thin dielectrics less than 100 nm without pinholes due to their large free volume and low breakdown voltage (see Fig. 1e). Some research groups have introduced crosslinkable polymer systems with high breakdown voltage and low free volume as a thin gate insulator ( $d < 50 \text{ nm}$ ), but these are all applied in a bottom-gate architecture in which the gate insulator is formed on an underlying smooth highly doped silicon substrate as a gate electrode prior to deposition of the organic semiconductor [14,17,18].

For some technological applications top-gate device architectures are advantageous:

- (i) The gate-line can be deposited at the top of device and can therefore be formed by a cheap printing process and the conductivity of gate-line can be controlled via selection of conductive inks such as a metal nanoparticle to reduce RC-delay in large-area active matrix liquid crystal displays [19].
- (ii) Source-drain electrode can be formed on the substrate by high-resolution patterning processes such as photolithography, printing or imprinting without

degrading the surface properties of an underlying gate dielectric/semiconducting layer.

- (iii) The presence of a gate dielectric and gate electrode on top of the organic semiconductor can provide an encapsulation effect against environmental exposure.
- (iv) The top-gate architecture enables use of a staggered device configuration with lower contact resistance than what can be achieved in bottom-gate, bottom-contact devices [20].

However, there are difficulties to apply crosslinkable polymer thin gate dielectrics in top-gate architectures including (i) a high curing temperature for crosslinking causing damage to the underlying semiconductor film; (ii) the difficulty to find an orthogonal, stable solvent to avoid dissolution of the underlying semiconducting layer and (iii) increased leakage current related to the roughness of the semiconducting film, which is often higher than that of a smooth substrate such as a silicon wafer. Most systems require high curing temperatures over  $150 \text{ }^\circ\text{C}$  for more than 30 min [13,17,18]. We show here that the crosslinkable polymer blend (CPB) system recently introduced by Yoon

et al. [14] for bottom-gate architectures is able to meet the requirements for integration into a top-gate architecture.

We have realized ultra thin polymer gate dielectrics (~30 nm) for top-gate polymer FETs via blending a conventional insulating polymer with the crosslinking agent, 1,6-bis(trichlorosilyl)hexane (C<sub>6</sub>-Si). The main advantage of this system is that the crosslinking takes place at room-temperature spontaneously in the presence of moisture and therefore the system can be applied in top-gate configuration while avoiding damage to the underlying conjugated polymer. Using this approach we have fabricated polymer FETs operating at voltages less than -8 V with a relatively high dielectric breakdown strength and a low leakage current (10–100 nA/mm<sup>2</sup> at 2 MV/cm). The polymer transistors with thin gate dielectrics exhibit high yield, which is correlated with the roughness of semiconducting polymer film. High mobilities of 0.1–0.2 cm<sup>2</sup>/V s and on-off current ratios of 10<sup>4</sup> were achieved with the high performance semiconducting polymer, poly(2,5-bis(3-alkylthiophen-2-yl)thieno[3,2-b]thiophene (pBTTT).

## 2. Experiment

Corning 7059 glass slides were used as substrates after cleaning sequentially in an ultrasonic bath with deionised water, acetone and isopropanol for 10 min each. The gold patterns for source and drain electrode were fabricated using conventional lift-off photolithography. The semiconducting polymer, poly(9,9-dioctylfluorene-co-bithiophene) (F8T2) (Dow Chemical Company), poly(3-hexylthiophene) (P3HT) (Rieke Metal Inc.), and pBTTT (Merck Chemicals) was dissolved in anhydrous xylene (0.7 wt.%; F8T2) or trichlorobenzene (1 wt.%; P3HT and 0.5 wt.%; pBTTT), respectively. For the case of F8T2 or P3HT films, films were annealed at 100 °C for 30 min to remove the solvent after spinning (2000 rpm, 1 min (F8T2) or 3 min (P3HT)) in a glove box with low oxygen and moisture level (<5 ppm). pBTTT films were annealed at 100 °C for 30 min in the same glove box to remove the solvent and 170 °C for 10 min to achieve high molecular ordering. For thin polymer dielectrics, PMMA (Aldrich, MW = 120,000) or poly-4-vinylphenol (PVP) (Aldrich, MW = 20,000) was used without further purification. The crosslinking agent, 1,6-bis(trichlorosilyl)hexane (Acro Organics, UK), was purified by distillation under inert atmosphere. For a 30–50 nm thickness film, PMMA or PVP (15–20 mg/ml in anhydrous n-butyl acetate) was blended with 1,6-bis(trichlorosilyl)hexane (5–7 μl) and then the mixture was filtered via 0.1 μm syringe filter and spin-coated at 4000–6000 rpm onto the semiconductor. All steps except spin-coating of the gate dielectric were performed in the glove box. The film was annealed on hot plate at 100 °C for 10 min to remove solvent in air. Top-gate transistors were completed by formation of a gate electrode via inkjet printing of the conducting polymer poly(3,4-ethylenedioxythiophene) doped with poly(styrene sulfonate) (PEDOT:PSS) or evaporation of thin Au or Al films through a shadow mask. Some FETs with P3HT and pBTTT were annealed after making full devices at hotplate (80 °C, 30 min) in nitrogen filled glove box to improve on-off current ratio. The electrical characteristics were measured with HP 4155B semiconductor

parameter analyzer and HP 4192A impedance analyzer in nitrogen atmosphere. The transistors parameters such as charge carrier mobility were calculated in the saturation or linear regime using the standard formalism for field-effect transistors [6]. The surface morphology of films was investigated by atomic force microscopy (Dimension 3100, Veeco Instrument Inc.) in tapping-mode.

## 3. Result and discussion

Fig. 1a and b displays the device configuration of our top-gated FETs and the molecular structure of PMMA and PVP used as a base polymer and C<sub>6</sub>-Si as crosslinking agent, named as C-PMMA and C-PVP, respectively. To spin-coat a thin dielectric film on top of the semiconducting polymer layer, the base polymer was dissolved in an orthogonal solvent, anhydrous n-butyl acetate, and blended with the crosslinking agent in a glove box (oxygen and moisture concentration < 5 ppm). The orthogonal solvent was selected to provide (i) a good solubility for the insulating polymer; (ii) a poor solubility for the underlying semiconductor film to avoid dissolution and swelling; (iii) a low vapor pressure (15 mm Hg at 25 °C for n-butyl acetate) to give sufficient time for full crosslinking before evaporation of solvent and (iv) absence of hydroxyl group to avoid crosslinking with the solvent. We have tried a range of base polymers and PMMA and PVP exhibited clear and smooth films (Figs. 1c and 2a) and the best performance and yield in our top-gated polymer transistors. The proper combination of a base polymer and an orthogonal solvent was important to obtain a pinhole free, smooth film. For example, PS films deposited from n-butyl acetate with C<sub>6</sub>-Si showed much higher surface roughness and large leakage current (Fig. 1d) in contrast to smooth PS films deposited from the same solvent but without the C<sub>6</sub>-Si crosslinker or crosslinked PS film deposited from xylene. Details about this are well-described in another paper published recently [21]. The dissolution and swelling of a F8T2 layer in the orthogonal solvent, n-butyl acetate, was checked by measuring atomic force microscopy topographs before and after spin-coating of the pure solvent. There was no dissolution of the F8T2 film by the solvent and the roughness of film was only slightly increased from a root mean square (rms) value of 0.52 nm before to 1.1 nm after the spinning.

To investigate the minimum possible thickness that can be achieved in this way in comparison with conventional, non-crosslinked insulating polymer films, we measured the current density versus applied field characteristics of a series of 1 mm<sup>2</sup> Au/C-PMMA (*d* = 100, 50 and 30 nm)/F8T2 (30 nm)/Au metal-insulator-semiconductor (MIS) diodes and compared these with reference structures using a 100 nm uncrosslinked PMMA dielectric layer (Fig. 1e). The ultra-thin, 30 nm C-PMMA films on F8T2 exhibited gate dielectric breakdown strength exceeding 3 MV/cm with low leakage current of <100 nA/mm<sup>2</sup>. This is much better performance than what could be achieved with 100 nm, uncrosslinked PMMA films. The performance of the C-PMMA films is comparable to that of thermal SiO<sub>2</sub> on Si [22]. The measured capacitance values (10 kHz) are 103.3 nF cm<sup>-2</sup> for 30 nm C-PMMA and 180.3 nF cm<sup>-2</sup> for



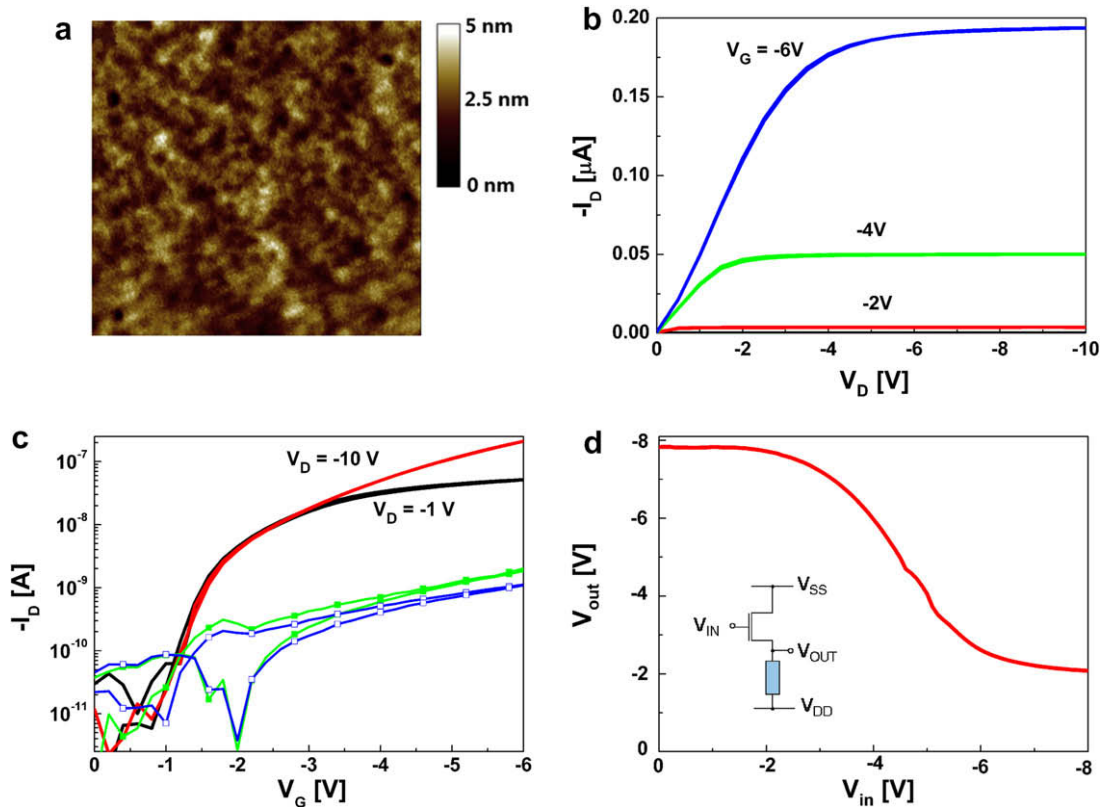


**Fig. 2.** (a) Atomic force microscopy image of C-PMMA film on F8T2 film ( $5 \mu\text{m} \times 5 \mu\text{m}$ ). (b) Output and (c) transfer characteristics of top-gated F8T2 FET ( $W/L = 1 \text{ mm}/20 \mu\text{m}$ ) with C-PMMA ( $t \sim 30 \text{ nm}$ ). The gate leakage currents were measured at  $V_D = -1 \text{ V}$  (opened square) and  $-10 \text{ V}$  (closed square) at the same time. (d) Static characteristics of a resistor load inverter ( $W/L = 1 \text{ mm}/20 \mu\text{m}$ ) with a printed PEDOT:PSS resistor load ( $R_L = 30 \text{ M}\Omega$ ) and the corresponding circuit diagram (inset).

30 nm C-PVP which is in good agreement with the theoretically expected values using dielectric constants of 3.5 and 6.4 for C-PMMA and C-PVP, respectively [14]. The possible minimum thickness was dependent of the roughness of the underlying semiconductor film and 30 nm thickness was successfully achieved for F8T2 with more than 90% yield. Yield details will be discussed below. C-PVP film on F8T2 exhibited similar properties in terms of dielectric break down strength and leakage current as C-PMMA at the same thickness (Fig. 1e).

To fabricate top-gate polymer FETs F8T2 was coated on a glass substrate in the glove box with Au source and drain electrodes pre-patterned by photolithography and then C-PMMA solution was spin-coated onto the semiconducting layer in air atmosphere. The crosslinking took place spontaneously during the spinning process with the help of moisture in air and no annealing process was necessary. (Note: The blending of the crosslinking agent,  $C_6\text{-Si}$  into the PMMA solution must be done in the glove box to avoid the crosslinking in the formulation before coating of C-PMMA.) The C-PMMA film (30 nm) on F8T2 exhibited a very smooth surface with less than 0.8 nm rms roughness which is similar to the surface roughness of the underlying F8T2 film (Fig. 2a). The top-gated FETs were completed by the evaporation of a metal (Au or Al) or printing of PEDOT:PSS as a gate electrode. Typical output and transfer curves are shown in Fig. 2b and c. All devices operated be-

low  $-8 \text{ V}$  with a saturation mobility ( $\mu_{\text{sat}}$ ) of  $0.005 \text{ cm}^2/\text{V s}$  typical of F8T2 [4,23] and a low threshold voltage ( $V_{\text{TH}}$ ) of  $-1.5 \text{ V}$ . Very low gate leakage current was observed ( $<1 \text{ nA}$ ) at  $V_G = -6 \text{ V}$  and there is no significant increase of gate leakage ( $<10 \text{ nA}$ ) even at  $V_G = -20 \text{ V}$  when the gate field corresponds to  $\sim 6 \text{ MV/cm}$  (Fig. 4b). Inverters were realized in a simple resistor load configuration using an inkjet printed PEDOT:PSS load resistor ( $30 \text{ M}\Omega$ ) and exhibited a good voltage gain of 2 at  $V_{\text{DD}} = -8 \text{ V}$  (Fig. 2d). Top-gated F8T2 FETs with 50 nm C-PVP showed similar performance to that of C-PMMA devices (Fig. 3a and b).

Thin polymer gate dielectrics were successfully applied also on semicrystalline polymer semiconductors, such as P3HT and pBTTT in top-gate architecture. Regioregular P3HT (molecular weight = 45,000, regio-regularity  $\sim 98\%$ ) film showed a typical nanoribbon morphology when deposited from the high boiling point trichlorobenzene solution (Fig. 4c). The rms roughness of the film was 3.5 nm, which is much increased from that of amorphous, as-deposited films of F8T2. Top-gated P3HT FETs were demonstrated successfully with 30 nm thin C-PMMA as gate dielectric. The calculated  $\mu_{\text{sat}}$  was  $0.007\text{--}0.01 \text{ cm}^2/\text{V s}$  which was similar to that of reference top-gate P3HT FETs with uncrosslinked PMMA [24]. The as-deposited P3HT transistors exhibit low on-off current ratio on the order of 100 presumably due to doping of P3HT during spin-coating of the gate dielectric in air (Fig. 4a). The poor on-off

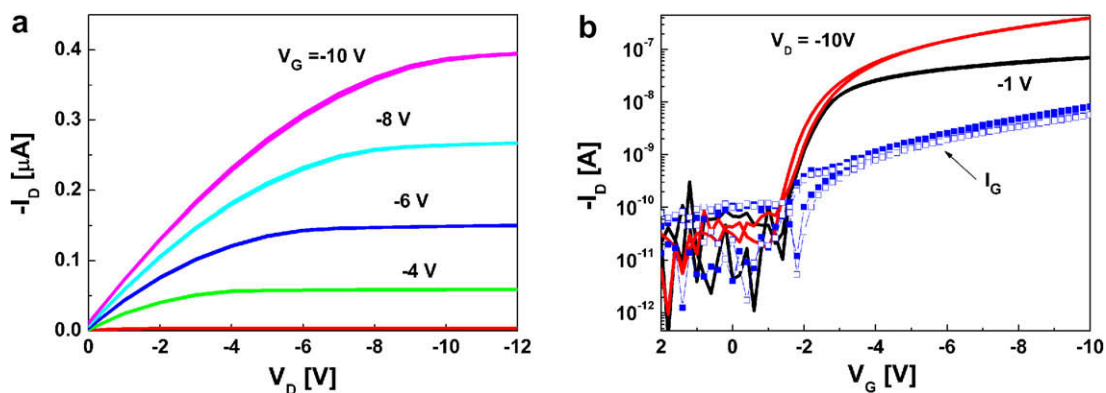


**Fig. 3.** (a) Output and (b) transfer characteristics of top-gated F8T2 FET ( $W/L = 1 \text{ mm}/10 \mu\text{m}$ ) with C-PVP ( $t \sim 50 \text{ nm}$ ). Gate current leakages were measured at  $V_D = -10 \text{ V}$  (closed square) and  $-1 \text{ V}$  (opened square) at the same time.

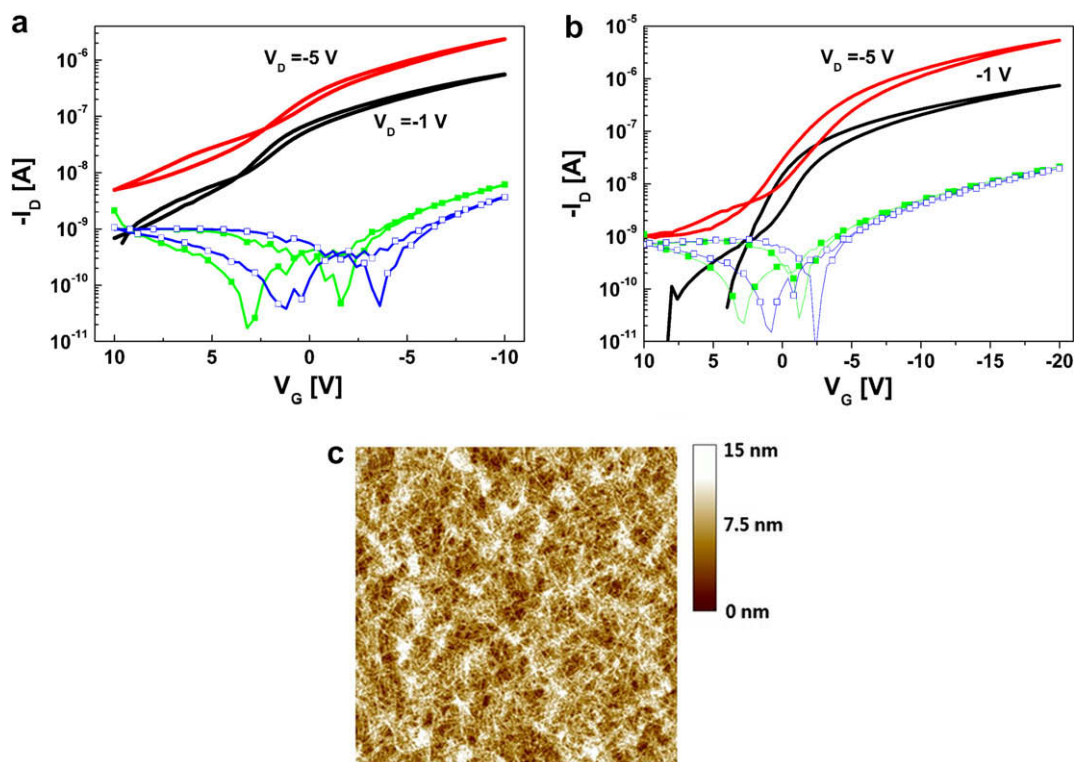


**Fig. 4.** Transfer characteristics of top-gated poly(3-hexylthiophene) (P3HT)/C-PMMA ( $t \sim 30 \text{ nm}$ ) FET ( $W/L = 1 \text{ mm}/20 \mu\text{m}$ ) measured (a) before and (b) after post-annealing ( $80 \text{ }^\circ\text{C}$ , 30 min) in a glove box. The gate leakage currents were measured at  $V_D = -1 \text{ V}$  (opened square) and  $-5 \text{ V}$  (closed square) at the same time. (c) Atomic force microscopy image of the P3HT surface morphology on glass ( $5 \mu\text{m} \times 5 \mu\text{m}$ ).

current ratio could be significantly improved to values of 1000 by de-doping the films via post-fabrication annealing ( $80 \text{ }^\circ\text{C}$ , 30 min) in nitrogen (Fig. 4b).

Finally, high performance top-gated polymer transistors were demonstrated with pBTTT. pBTTT FETs had been shown to exhibit a remarkably high-mobility of up to  $0.6 \text{ cm}^2/\text{V s}$  on octyltrichlorosilane (OTS) treated  $\text{SiO}_2$  in the bottom-gate configuration and the mobility was further improved to  $1 \text{ cm}^2/\text{V s}$  with the low contact resistance Pt source/drain electrode [3,25]. The high performance was

attributed to their exceptional molecular ordering obtained via cooling from the liquid crystalline (LC) mesophase. The performance was shown to be highly sensitive to the surface chemistry of the substrate resulting in large difference of grain size on different surfaces [26]. Samples fabricated on a bare  $\text{SiO}_2$  surface showed much poorer mobility ( $<0.005 \text{ cm}^2/\text{V s}$ ) and smaller granular grain size ( $\sim 50\text{--}100 \text{ nm}$ ) than samples on OTS/ $\text{SiO}_2$  with large, terraced grains ( $\sim 200 \text{ nm}$ ). Our top-gate pBTTT transistors with 30–50 nm C-PMMA exhibit high  $\mu_{\text{sat}}$  values of  $\sim 0.1\text{--}$

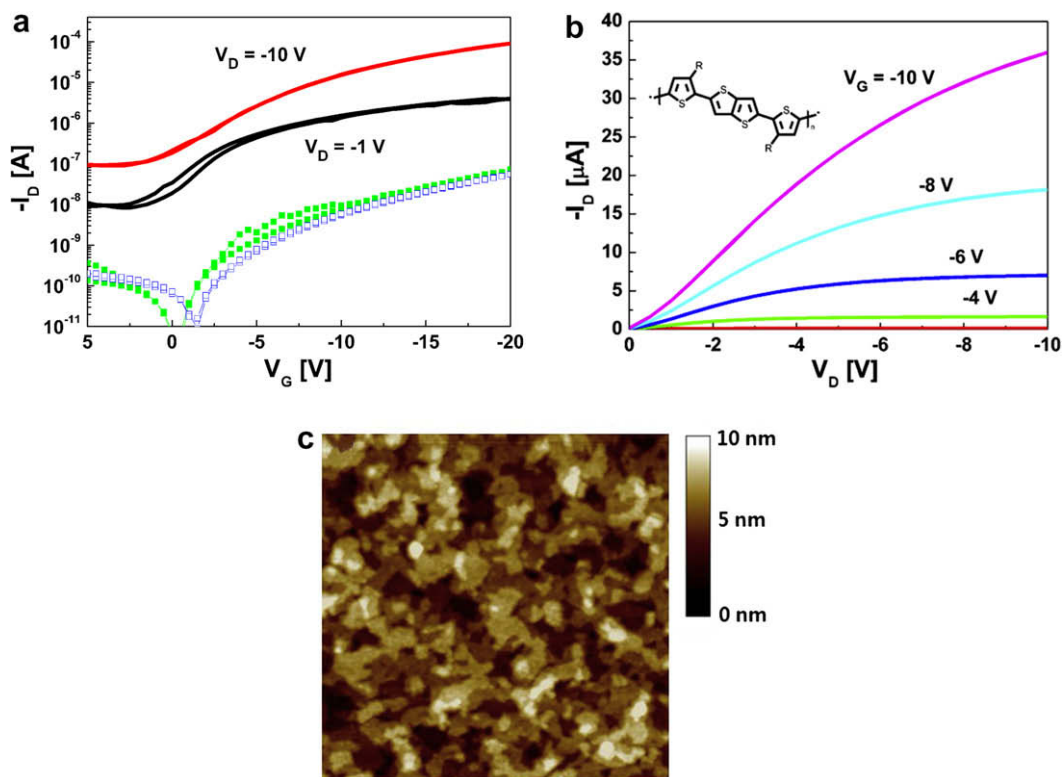


**Fig. 5.** (a) Transfer and (b) output characteristics of top-gated poly(2,5-bis(3-alkylthiophen-2-yl)thieno[3,2-b]thiophene (pBTTT)/C-PMMA ( $t \sim 30$  nm) FET ( $W/L = 1$  mm/20  $\mu$ m) measured after post-annealing (80  $^{\circ}$ C, 30 min) in glove box. The gate leakage currents were measured at  $V_D = -1$  V (opened square) and  $-10$  V (closed square) at the same time. Inset shows the chemical structure of pBTTT. (c) Atomic force microscopy image of the pBTTT surface morphology on glass (2  $\mu$ m  $\times$  2  $\mu$ m).

0.2  $\text{cm}^2/\text{Vs}$ . To the best of our knowledge this mobility is the highest value reported for a top-gate polymer FET. Fig. 5a and b shows typical transfer and output characteristics of a pBTTT top-gate FET after 30 min post-fabrication annealing. The as-deposited pBTTT devices showed poor on-off current ratio on the order of 100 similar to the behavior observed for P3HT. Overnight annealing of the devices in nitrogen leads to a slight decrease of on current but to a significant increase of the on-off current ratio to values of  $>10^4$ . The relatively large grain size of pBTTT films ( $>200$  nm, Fig. 5c) on glass substrates explains the high-mobility values obtained in our top-gate pBTTT FETs. It is interestingly noted that we can get the large grains on glass substrate without OTS treatment and different from other group's reports that the large grains only can ob-

tained on OTS treated  $\text{SiO}_2$  surface in bottom-gated FETs [3,26,27]. Even though top-gated pBTTT transistors show the relatively high performance with thin polymer gate dielectrics, the output characteristics seemed somewhat a nonlinear drain current increase near the origin (Fig. 5b). The reason of poor output characteristics does not clarified yet but it may be due to pBTTT itself because other publications also showed the similar poor output curve with thick  $\text{SiO}_2$  (200 nm) [25].

Finally, we comment on the device yield due to dielectric breakdown and gate leakage of top-gated FETs with thin C-PMMA or C-PVP films. For the thinnest gate dielectrics (30–50 nm) this was strongly correlated with the roughness of the semiconductor surface and the size of the active area (see Table 1). FETs with an amorphous

**Table 1**

Device performance and yield due to dielectric breakdown/gate leakage of top-gated polymer transistors with 30 nm C-PMMA or C-PVP.

Gate dielectric	Channel length/width	Semiconducting polymer	$\mu_{\text{sat}}$ ( $\text{cm}^2/\text{Vs}$ )	$V_{\text{TH}}$ (V)	Yield (%) <sup>a</sup>
C-PMMA	20 $\mu\text{m}/1$ mm	F8T2	0.005–0.001	0 to –2	100
	10 $\mu\text{m}/1$ mm	P3HT	0.008–0.015	1 to –2	45
	5 $\mu\text{m}/1$ mm	P3HT	0.007–0.01	0 to –3	60
	5 $\mu\text{m}/1$ mm	pBTTT	0.1–0.2	–1 to –4	80
C-PVP	20 $\mu\text{m}/1$ mm	F8T2	0.005–0.001	–1 to –2	90
	5 $\mu\text{m}/1$ mm	F8T2			95

<sup>a</sup> The yield was determined from measurements of more than 20 transistors from four different batches. A transistor was considered to have failed if the gate leakage current was the same as the drain current of transistor.

semiconducting polymer such as F8T2 always exhibited near perfect yield due to their smooth surface morphology. However, we observed that the yield of transistors decreased for semicrystalline semiconductors, such as P3HT or pBTTT due to their significantly rougher surface morphology.

#### 4. Conclusion

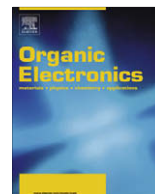
In conclusion, we have demonstrated high performance top-gate polymer FETs with ultra-thin (30–50 nm), room-temperature crosslinkable polymer gate dielectrics based on blending an insulating base polymer with an organosilane crosslinking agent. The crosslinking system can be extended to other systems with different dielectric permittivities by careful selection of the base polymer. The approach enables low-voltage operation below 10 V and high yield and is compatible with a range of state-of-the-art high-mobility polymer semiconductors.

#### Acknowledgements

The research was supported by the Engineering and Physical Sciences Research Council (EPSRC). The authors thank Merck Chemicals for providing pBTTT, the Dow Chemical Company for providing F8T2, Dr. Antonio Facchetti (Northwestern University), Mr. Xiaoyang Cheng, Ms. Ni Zhao, and Dr. R.L. Peterson, (Cavendish Laboratory) for helpful discussion and support.

#### References

- [1] B.S. Ong, Y.L. Wu, P. Liu, S. Gardner, *J. Am. Chem. Soc.* 126 (2004) 3378.
- [2] M. Heeney, C. Bailey, K. Genevicius, M. Shkunov, D. Sparrowe, S. Tierney, I. McCulloch, *J. Am. Chem. Soc.* 127 (2005) 1078.
- [3] I. McCulloch, M. Heeney, C. Bailey, K. Genevicius, I. Macdonald, M. Shkunov, D. Sparrowe, S. Tierney, R. Wagner, W.M. Zhang, M.L. Chabinyc, R.J. Kline, M.D. McGehee, M.F. Toney, *Nat. Mater.* 5 (2006) 328.
- [4] H. Sirringhaus, R.J. Wilson, R.H. Friend, M. Inbasekaran, W. Wu, E.P. Woo, M. Grell, D.D.C. Bradley, *Appl. Phys. Lett.* 77 (2000) 406.
- [5] H. Sirringhaus, P.J. Brown, R.H. Friend, M.M. Nielsen, K. Bechgaard, B.M.W. Langeveld-Voss, A.J.H. Spiering, R.A.J. Janssen, E.W. Meijer, P. Herwig, D.M. de Leeuw, *Nature* 401 (1999) 685.
- [6] C.D. Dimitrakopoulos, I. Kymissis, S. Purushothaman, D.A. Neumayer, P.R. Duncombe, R.B. Laibowitz, *Adv. Mater.* 11 (1999) 1372.
- [7] H. Klauk, M. Halik, U. Zschieschang, G. Schmid, W. Radlik, W. Weber, *J. Appl. Phys.* 92 (2002) 5259.
- [8] H.G.O. Sandberg, T.G. Backlund, R. Osterbacka, H. Stubb, *Adv. Mater.* 16 (2004) 1112.
- [9] R. Parashkov, E. Becker, G. Ginev, T. Riedl, H.H. Johannes, W. Kowalsky, *J. Appl. Phys.* 95 (2004) 1594.
- [10] Z. Bao, V. Kuck, J.A. Rogers, M.A. Paczkowski, *Adv. Funct. Mater.* 12 (2002) 526.
- [11] J. Veres, S.D. Ogier, S.W. Leeming, D.C. Cupertino, S.M. Khaffaf, *Adv. Funct. Mater.* 13 (2003) 199.
- [12] L.L. Chua, J. Zaumseil, J.F. Chang, E.C.W. Ou, P.K.H. Ho, H. Sirringhaus, R.H. Friend, *Nature* 434 (2005) 194.
- [13] L.L. Chua, P.K.H. Ho, H. Sirringhaus, R.H. Friend, *Appl. Phys. Lett.* 84 (2004) 3400.
- [14] M.H. Yoon, H. Yan, A. Facchetti, T.J. Marks, *J. Am. Chem. Soc.* 127 (2005) 10388.
- [15] G.S. Tulevski, C. Nuckolls, A. Afzali, T.O. Graham, C.R. Kagan, *Appl. Phys. Lett.* 89 (2006) 183101.
- [16] Y.-Y. Noh, N. Zhao, M. Caironi, H. Sirringhaus, *Nat. Nanotechnol.* 2 (2007) 784.
- [17] S.Y. Yang, S.H. Kim, K. Shin, H. Jeon, C.E. Park, *Appl. Phys. Lett.* 88 (2006) 173507.
- [18] Y. Jang, D.H. Kim, Y.D. Park, J.H. Cho, M. Hwang, K.W. Cho, *Appl. Phys. Lett.* 88 (2006) 072101.
- [19] C.S. Chiang, S. Martin, J. Kanicki, Y. Ugai, T. Yukawa, S. Takeuchi, *Jpn. J. Appl. Phys. Part 1* 37 (1998) 5914.
- [20] T.J. Richards, H. Sirringhaus, *J. Appl. Phys.* 102 (2007) 094510.
- [21] C. Kim, Z. Wang, H.-J. Choi, Y.-G. Ha, A. Facchetti, T.J. Marks, *J. Am. Chem. Soc.* 130 (2008) 6867.
- [22] D.J. Frank, R.H. Dennard, E. Nowak, P.M. Solomon, Y. Taur, H.S.P. Wong, *Proc. IEEE* 89 (2001) 259.
- [23] H. Sirringhaus, T. Kawase, R.H. Friend, T. Shimoda, M. Inbasekaran, W. Wu, E.P. Woo, *Science* 290 (2000) 2123.
- [24] J. Veres, S. Ogier, G. Lloyd, D. de Leeuw, *Chem. Mater.* 16 (2004) 4543.
- [25] B.H. Hamadani, D.J. Gundlach, I. McCulloch, M. Heeney, *Appl. Phys. Lett.* 91 (2007) 243512.
- [26] M.L. Chabinyc, M.F. Toney, R.J. Kline, I. McCulloch, M. Heeney, *J. Am. Chem. Soc.* 129 (2007) 3226.
- [27] T. Umeda, S. Tokito, D. Kumaki, *J. Appl. Phys.* 101 (2007) 054517.



# Hole mobilities of thermally polymerized triaryldiamine derivatives and their application as hole-transport materials in organic light-emitting diodes (OLEDs)

Chi-Yen Lin<sup>a</sup>, You-Ming Chen<sup>a</sup>, Hsiao-Fan Chen<sup>a</sup>, Fu-Chuan Fang<sup>a</sup>, Yu-Cheng Lin<sup>b</sup>, Wen-Yi Hung<sup>b,\*</sup>, Ken-Tsung Wong<sup>a,\*</sup>, Raymond C. Kwong<sup>c</sup>, Sean C. Xia<sup>c</sup>

<sup>a</sup> Department of Chemistry, National Taiwan University, Taipei 106, Taiwan, ROC

<sup>b</sup> Institute of Optoelectronic Sciences, National Taiwan Ocean University, Keelung 202, Taiwan, ROC

<sup>c</sup> Universal Display Corporation, 375 Phillips Blvd, Ewing, NJ 08618, USA

## ARTICLE INFO

### Article history:

Received 21 August 2008

Received in revised form 5 November 2008

Accepted 7 November 2008

Available online 18 November 2008

### PACS:

73.50.-h

73.61.Ph

78.30.Jw

78.55.Kz

78.60.Fi

78.66.Qn

### Keywords:

Solution process

Thermal polymerization

Time-of-flight (TOF)

Hole mobility

## ABSTRACT

This paper describes the synthesis of three triaryldiamine derivatives presenting two thermally polymerizable trifluorovinyl ether groups that can be polymerized through thermal curing to form perfluorocyclobutyl (PFCB) polymers. These PFCB polymers, studied using time-of-flight techniques for the first time, exhibited remarkable non-dispersive hole-transport properties, with values of  $\mu_h$  of ca.  $10^{-4} \text{ cm}^2 \text{ V}^{-1} \text{ s}^{-1}$ . When we employed these thermally polymerized polymers as hole-transport layers (HTLs) in electroluminescence devices containing tris(8-hydroxyquinolate) aluminum ( $\text{Alq}_3$ ) as the emission layer, we obtained high current densities (ca.  $3400 \text{ mA cm}^{-2}$ ), impressive brightnesses ( $5 \times 10^4 \text{ cd m}^{-2}$ ), and high external quantum efficiencies (EQEs = 1.43%). These devices exhibited the same turn-on voltage, but higher EQEs, relative to those incorporating the vacuum-processed model compound  $N,N'$ -di(1-naphthyl)- $N,N'$ -diphenylbenzidine ( $\alpha$ -NPD) (EQE = 1.37%) as the HTL under the same device structure.

© 2008 Elsevier B.V. All rights reserved.

## 1. Introduction

Organic and polymer light-emitting diodes are promising devices for use in future lighting and display applications because of their low power consumption, light weight, fast response, and wide viewing angle [1,2]. To increase their efficiency, most organic light-emitting diodes (OLEDs) are configured with a variety of functional materials into a multilayer structure—fabricated through succes-

sive vacuum deposition of small molecules—and then covered by a metal cathode. It is generally inherently difficult to form polymer-based OLEDs in multilayer structures through solution-processing techniques, such as spin-coating, because of solvent erosion of the previously deposited layers during spin-coating [3]. One of the most promising approaches toward achieving purely solution-processed multiple-layer polymer-based OLEDs is utilizing soluble precursor materials to produce insoluble polymer networks through polymerization and/or cross-linking reactions. This strategy allows the sequential deposition of various functional layers [4,5]. The flexibility of using the chemical modifications of a wide variety of materials

\* Corresponding authors. Tel.: +886 2 33661665; fax: +886 2 33661667.  
E-mail addresses: [wenhung@mail.ntou.edu.tw](mailto:wenhung@mail.ntou.edu.tw) (W.-Y. Hung), [kenwong@ntu.edu.tw](mailto:kenwong@ntu.edu.tw) (K.-T. Wong).

possessing various functional moieties—such as siloxan [6–9], norbornene [10,11], oxetane [4,5], vinyl [12,13], and trifluorovinyl ether [14–18] units—as polymerizable groups under UV irradiation or thermal curing allows the construction of copolymers in nearly any designated composition. For example, trifluorovinyl ether (TFVE)-containing compounds are useful as reactive monomers that undergo thermal cyclopolymerization to afford a new class of thermally stable perfluorocyclobutane (PFCB) polymers [19–21]. Taking advantage of this strategy, PFCB-based hole-transport materials have been developed to increase the efficiency of OLED devices [22–28]. This superior performance is ascribed mainly to the homogeneous surface morphology of the thermally treated thin films, as probed using atomic force microscopy (AFM). Nevertheless, to the best of our knowledge, the intrinsic charge transporting characteristic, one of the most critical factors in optoelectronic devices, of PFCB-based hole-transport materials has not been reported previously. In this paper, we report the synthesis, characterization, and application of three triaryldiamine derivatives attached to two thermally polymerizable trifluorovinyl ether (TFVE) groups that can be polymerized through thermal curing to form PFCB polymers. More importantly, we have used time-of-flight (TOF) techniques to study the hole-transport properties of these polymers. We have found that PFCB-based polymers possess remarkable hole-transport properties, with values of  $\mu_h$  of ca.  $10^{-4} \text{ cm}^2 \text{ V}^{-1} \text{ s}^{-1}$ . These thermally polymerized polymers are useful as hole-transport layers (HTLs) in electroluminescence (EL) applications, as evidenced by the high external quantum efficiency of 1.43% achieved when employing one such system with tris(8-hydroxyquinolate) aluminum (Alq<sub>3</sub>) as the emission layer.

## 2. Experimental

### 2.1. Synthesis

**Compound 5:** Compound **4** (5.08 g, 10 mmol), *N*-phenyl-1-naphthylamine (4.39 g, 20 mmol), Pd(OAc)<sub>2</sub> (67 mg, 0.3 mmol), and sodium *tert*-butoxide (7.68 g, 80 mmol) were dissolved in toluene (100 mL) and then tri-*tert*-butylphosphine (6 mL, 0.05 M in toluene, 0.3 mmol) was added. The mixture was heated under reflux under argon for 72 h and then quenched with water. The solution was partitioned between ethyl acetate and brine. The combined organic extracts were dried (MgSO<sub>4</sub>) and concentrated. The resulting solid was washed with hexane to afford a yellow product (6.41 g, 82%). M.p. 254–255 °C. IR (KBr)  $\nu$  3544 (w), 3055 (w), 1609 (m), 1592 (s), 1573 (m), 1507 (s), 1489 (s), 1464 (s), 1434 (m), 1392 (m), 1302 (m), 1269 (s), 1172 (m), 1015 (m) cm<sup>-1</sup>. <sup>1</sup>H NMR (DMSO-*d*<sub>6</sub>, 400 MHz):  $\delta$  9.29 (s, 2H), 7.97 (d, *J* = 8.0 Hz, 2H), 7.84 (d, *J* = 8.4 Hz, 2H), 7.76 (d, *J* = 8.4 Hz, 2H), 7.56–7.48 (m, 6H), 7.37 (t, *J* = 7.4 Hz, 2H), 7.28 (d, *J* = 7.2 Hz, 2H), 7.16 (t, *J* = 7.6 Hz, 4H), 6.92–6.84 (m, 8H), 6.78 (s, 2H), 6.51 (d, *J* = 8.8 Hz, 4H), 6.41 (d, *J* = 8.4 Hz, 4H). <sup>13</sup>C NMR (DMSO-*d*<sub>6</sub>, 100 MHz):  $\delta$  155.5, 152.2, 147.5, 146.5, 142.6, 135.3, 134.7, 132.9, 130.1, 129.1, 128.4, 128.2, 126.6, 126.4, 126.3, 126.1, 123.4, 121.6, 121.1, 120.4, 120.2, 118.8,

114.6, 63.0. MS (FAB<sup>+</sup>, *m/z*) 785 (100), 784 (65), 154 (70), 136 (65), 57 (65). HRMS (FAB<sup>+</sup>, [M+H]<sup>+</sup>) Calcd. C<sub>57</sub>H<sub>41</sub>N<sub>2</sub>O<sub>2</sub> 785.3170, found 785.3165.

**Compound 6:** A mixture of **5** (2.93 g, 3.73 mmol) and triethylamine (3 mL, 21.6 mmol) in dry dichloromethane (260 mL) was cooled to –10 °C. Trifluoromethanesulfonic anhydride (1.9 mL, 11.2 mmol) in dry dichloromethane (90 mL) was added dropwise and then the reaction mixture was warmed to room temperature and stirred for 16 h. The reaction was quenched by pouring the mixture into ice water. The organic layer was separated and the aqueous phase was extracted twice with dichloromethane. The combined organic extracts were washed with saturated NaHCO<sub>3</sub> solution and brine and then dried (MgSO<sub>4</sub>). The solvents were evaporated and the resulting residue was purified through re-precipitation from dichloromethane and methanol to afford a yellow product (3.18 g, 81%). M.p. 136–138 °C. IR (KBr)  $\nu$  3059 (w), 1609 (m), 1592 (m), 1573 (m), 1494 (s), 1468 (s), 1455 (m), 1426 (s), 1392 (m), 1271 (m), 1249 (m), 1212 (s), 1140 (s), 884 (m), 774 (m) cm<sup>-1</sup>. <sup>1</sup>H NMR (DMSO-*d*<sub>6</sub>, 400 MHz):  $\delta$  7.96 (d, *J* = 8.4 Hz, 2H), 7.85 (d, *J* = 8.0 Hz, 2H), 7.72 (d, *J* = 8.0 Hz, 2H), 7.62 (d, *J* = 8.4 Hz, 2H), 7.53–7.46 (m, 4H), 7.37–7.27 (m, 8H), 7.15 (t, *J* = 7.6 Hz, 4H), 7.00 (d, *J* = 8.4 Hz, 4H), 6.92–6.89 (m, 4H), 6.84 (d, *J* = 8.4 Hz, 6H). <sup>13</sup>C NMR (DMSO-*d*<sub>6</sub>, 100 MHz):  $\delta$  149.9, 147.7, 147.2, 146.9, 145.0, 142.3, 134.7, 132.8, 129.9, 129.3, 129.0, 128.4, 126.7, 126.5, 126.4, 126.3, 126.0, 123.2, 121.8, 121.3, 121.1, 120.8, 119.6, 118.3, 116.4, 63.6. MS (FAB<sup>+</sup>, *m/z*) 1048 (100), 916 (15), 690 (20), 218 (40), 217 (35). HRMS (FAB<sup>+</sup>, M<sup>+</sup>) Calcd. C<sub>59</sub>H<sub>38</sub>F<sub>6</sub>N<sub>2</sub>O<sub>6</sub>S<sub>2</sub> 1048.2075, found 1048.2076.

**TFVE1: 1** (380 mg, 0.87 mmol), **2** (515 mg, 2.18 mmol), Pd(OAc)<sub>2</sub> (10 mg, 0.04 mmol), and sodium *tert*-butoxide (210 mg, 2.18 mmol) were dissolved in toluene (10 mL) and then tri-*tert*-butyl phosphine (1.6 mL, 0.05 M in toluene, 0.08 mmol) was added. The mixture was heated under reflux under argon for 24 h and then quenched with water. The solvent was evaporated and then the reaction mixture was extracted with dichloromethane and dried (MgSO<sub>4</sub>). The crude product was purified through column chromatography (SiO<sub>2</sub>; EtOAc/hexane, 1:15) to afford **TFVE1** (485 mg, 72%) as a white solid. IR (KBr)  $\nu$  3046 (w), 1600 (w), 1497 (s), 1460 (w), 1397 (m), 1311 (m), 1274 (s), 1192 (m), 1159 (m), 1136 (m) cm<sup>-1</sup>. <sup>1</sup>H NMR (acetone-*d*<sub>6</sub>, 400 MHz):  $\delta$  7.98 (d, *J* = 8.0 Hz, 2H), 7.94 (d, *J* = 8.0 Hz, 2H), 7.89 (d, *J* = 8.0 Hz, 2H), 7.55 (t, *J* = 8.0 Hz, 2H), 7.52–7.45 (m, 6H), 7.43–7.36 (m, 4H), 7.14–7.07 (m, 8H), 7.00 (d, *J* = 8.0 Hz, 4H). <sup>13</sup>C NMR (acetone-*d*<sub>6</sub>, 100 MHz):  $\delta$  148.0, 146.3, 143.8, 136.2, 134.5, 131.8, 129.3, 127.9, 127.8, 127.6, 127.3, 127.2, 127.0, 124.5, 124.2, 122.3, 117.6. <sup>19</sup>F NMR (acetone-*d*<sub>6</sub>, 376 MHz):  $\delta$  –117.1 (dd, *J* = 99.6, 55.6 Hz, 2F), –124.3 (dd, *J* = 108.3, 99.3 Hz, 2F), 130.6 (dd, *J* = 108.3, 56.4 Hz, 2F). MS (FAB<sup>+</sup>, *m/z*) 780 (100), 467 (25), 217 (35). HRMS (FAB<sup>+</sup>, M<sup>+</sup>) Calcd. C<sub>47</sub>H<sub>28</sub>N<sub>4</sub> 780.2211, found 780.2208.

**TFVE2:** A flask containing **3** (2.46 g, 4.88 mmol), 1-aminonaphthalene (2.09 g, 14.6 mmol), Pd<sub>2</sub>(dba)<sub>3</sub> (224 mg, 0.25 mmol), and sodium *tert*-butoxide (1.41 g, 14.7 mmol) was evacuated and recharged with argon, then dry toluene (30 mL) and tri-*tert*-butylphosphine (9.8 mL,

0.05 M in toluene, 0.49 mmol) were added. The mixture was heated under reflux for 48 h and then cooled to room temperature. The mixture was filtered through a short path of Celite and then washed with dichloromethane, and the filtrate was extracted with dichloromethane and dried (MgSO<sub>4</sub>). The solvent was partially removed using a rotary evaporator and then hexane (30 mL) was added to give a yellow solid that was collected through filtration and washed with hexane. The crude solid (1.9 g, 3.02 mmol) was combined with Pd(OAc)<sub>2</sub> (34 mg, 0.15 mmol), **2** (1.91 g, 7.5 mmol), and sodium *tert*-butoxide (1.44 g, 15 mmol) and then dry toluene (40 mL) and tri-*tert*-butylphosphine (6 mL, 0.05 M in toluene, 0.3 mmol) were added. The mixture was filtered through a short path of Celite and washed with ethyl acetate, and the filtrate was extracted with ethyl acetate and dried (MgSO<sub>4</sub>). The solvent was removed using a rotary evaporator to give a crude product, which was purified through column chromatography (SiO<sub>2</sub>; EtOAc:hexane, 1:20) to afford **TFVE2** (2.3 g, 49% over two steps) as a yellow solid. IR (KBr)  $\nu$  3048 (m), 2917 (w), 2869 (w), 1831 (w), 1604 (m), 1573 (w), 1499 (s), 1465 (s), 1440 (m), 1392 (m), 1311 (s), 1274 (s), 1192 (s), 1164 (m), 1137 (s), 1019 (w), 816 (m), 798 (m), 772 (m) cm<sup>-1</sup>. <sup>1</sup>H NMR (CDCl<sub>3</sub>, 400 MHz):  $\delta$  7.94 (d, *J* = 4.2 Hz, 2H), 7.83 (t, *J* = 8.8 Hz, 4H), 7.56 (d, *J* = 4.6 Hz, 2H), 7.49 (t, *J* = 8 Hz, 4H), 7.35 (t, *J* = 6.8 Hz, 2H), 7.28 (d, *J* = 3.4 Hz, 2H), 7.06 (d, *J* = 4.6 Hz, 4H), 6.96 (m, 8H), 6.85 (d, *J* = 4 Hz, 4H), 6.74 (d, *J* = 4.2 Hz, 4H), 2.21 (s, 6H). <sup>13</sup>C NMR (CDCl<sub>3</sub>, 100 MHz):  $\delta$  152.5, 149.6, 147.4, 145.7, 143.3, 142.6, 135.8, 135.5, 134, 130.6, 128.6, 128.5, 127.7, 126.7, 126.6, 126.4, 126.2, 123.9, 123.4, 121, 120.4, 119.5, 116.8, 64.6, 20.2. <sup>19</sup>F NMR (CDCl<sub>3</sub>, 376 MHz):  $\delta$  -115.8 (dd, *J* = 98.9, 56.4 Hz, 2F), -123.0 (dd, *J* = 108.3, 99.3 Hz, 2F), -129.2 (dd, *J* = 107.5, 55.6 Hz, 2F). MS (FAB<sup>+</sup>, *m/z*) 973 (100), 972 (35), 881 (15), 659 (30), 217 (20). HRMS (FAB<sup>+</sup>, [M+H]<sup>+</sup>) Calcd. C<sub>63</sub>H<sub>43</sub>O<sub>2</sub>N<sub>2</sub>F<sub>6</sub>: 973.3230, found: 973.3238.

**TFVE3: 6** (2.1 g, 2 mmol), **7** (1.44 g, 4.8 mmol), and Pd(PPh<sub>3</sub>)<sub>4</sub> (0.1 g, 0.086 mmol) were dissolved in 1,4-dioxane (25 mL) and then sodium carbonate (10 mL, 2 M in H<sub>2</sub>O) was added. The mixture was heated under reflux under Ar for 72 h and then quenched with water, extracted with dichloromethane, and dried (MgSO<sub>4</sub>). The crude product was purified through column chromatography (SiO<sub>2</sub>; toluene/hexane, 1:3) to afford **TFVE3** (1.2 g, 55%) as a yellow solid. IR (KBr)  $\nu$  3056 (w), 2942 (w), 1592 (m), 1574 (m), 1492 (s), 1465 (m), 1429 (m), 1387 (w), 1310 (m), 1273 (s), 1197 (m), 1175 (m), 1138 (m) cm<sup>-1</sup>. <sup>1</sup>H NMR (DMSO-*d*<sub>6</sub>, 400 MHz):  $\delta$  7.96 (d, *J* = 7.6 Hz, 2H), 7.84 (d, *J* = 8.0 Hz, 2H), 7.76 (d, *J* = 8.4 Hz, 2H), 7.64 (t, *J* = 8.0 Hz, 6H), 7.53–7.46 (m, 4H), 7.40–7.36 (m, 10H), 7.30 (d, *J* = 6.8 Hz, 2H), 7.18 (t, *J* = 8.0 Hz, 4H), 6.93–6.84 (m, 14H). <sup>13</sup>C NMR (DMSO-*d*<sub>6</sub>, 100 MHz):  $\delta$  153.4, 150.8, 147.3, 146.7, 143.9, 142.4, 137.0, 136.4, 134.7, 133.0, 129.9, 129.0, 128.7, 128.4, 128.2, 127.7, 126.5, 126.4, 126.2, 126.0, 123.3, 121.8, 121.4, 120.6, 120.5, 118.4, 115.9, 63.8. <sup>19</sup>F NMR (DMSO-*d*<sub>6</sub>, 376 MHz):  $\delta$  -117.8 (dd, *J* = 96.3, 54.9 Hz, 2F), -125.6 (dd, *J* = 107.5, 96.6 Hz, 2F), -133.6 (dd, *J* = 107.5, 55.6 Hz, 2F). MS (FAB<sup>+</sup>, *m/z*) 1097 (100), 880 (15), 217 (35). HRMS ([M+H]<sup>+</sup>, FAB<sup>+</sup>) Calcd. C<sub>73</sub>H<sub>47</sub>F<sub>6</sub>N<sub>2</sub>O<sub>2</sub> 1097.3543, found 1097.3534.

## 2.2. Time-of-flight (TOF) mobility measurements

In the TOF method, a sheet of carriers is created near one of the contacts using a short laser pulse (nitrogen pulse laser). The sample is illuminated from the indium tin oxide (ITO) side to generate a sheet of charge carriers in the organic layer. Under the influence of an applied electric field, these carriers drift toward the counter electrode (Ag), resulting in a transient current through the sample. When the carriers reach the counter electrode, the current drops to zero; the point at which this happens corresponds to the transit time of the carriers (*t<sub>T</sub>*). Depending on the polarity of the applied bias, selected photogenerated carriers (holes or electrons) are swept across the sample thickness *D*; the applied electric field *E* is then equal to *V/D*, and the carrier mobility ( $\mu$ ) is given by  $D/(t_T E)$ .

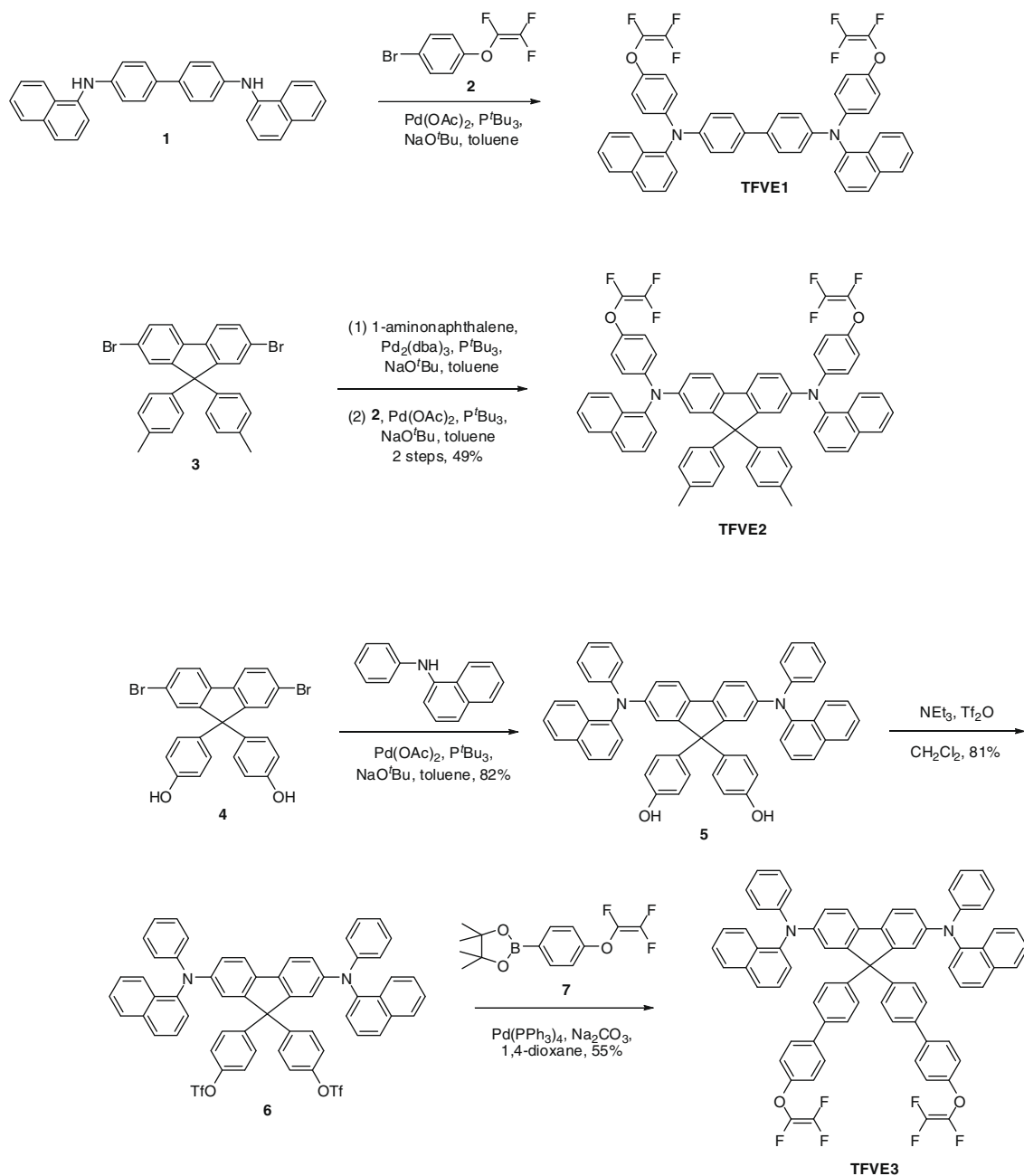
## 2.3. OLED device

The OLEDs were fabricated on ITO sheets having a resistance of 15  $\Omega/\square$ . The substrates were washed sequentially with isopropyl alcohol, acetone, and methanol in an ultrasonic bath, followed by UV-ozone treatment prior to use. A hole injecting poly(ethylene dioxythiophene): polystyrene sulfonate (PEDOT:PSS) layer was spin-coated onto the substrates and dried at 130 °C for 30 min to remove residual water. The substrates were transferred to a N<sub>2</sub>-filled glove box. The crosslinkable **TFVE1–3** monomers (1.2 wt%) were dissolved in THF, dip-coated atop the PEDOT:PSS layer to yield ca. 50-nm-thick films, and then cured at 230 °C for 30 min to promote crosslinking. To prepare the emissive and electron transport layer, a 60-nm layer of Alq<sub>3</sub> was vacuum-deposited on top of the spin-coated HTL. The devices were then completed through thermal evaporation of the back electrode [LiF (0.5 nm)/Ag (100 nm)] through a shadow mask. All evaporations were performed under a vacuum of less than 10<sup>-6</sup> torr. Each device pixel had an active area of 0.25 $\pi$  mm<sup>2</sup>. The current–voltage–brightness (*I–V–L*) characteristics of the devices were measured simultaneously using a Keithley 6430 source meter and a Keithley 6487 picoammeter equipped with a calibration Si-photodiode. EL spectra were measured using an ocean optics spectrometer.

## 3. Results and discussion

### 3.1. Materials

**Scheme 1** depicts the syntheses of monomers **TFVE1–3**, which were derivatives of the well-established hole-transporting material *N,N'*-di(1-naphthyl)-*N,N'*-diphenylbenzidine ( $\alpha$ -NPD). **TFVE1**, possessing two trifluorovinyl ether (TFVE) groups linked to the terminal phenylene rings of  $\alpha$ -NPD, was synthesized in an isolated yield of 72% through Pd-catalyzed amination of diamine **1** and compound **2** [20]. **TFVE2**, which had similar structural features to the terminal groups of **TFVE1**, but with the diarylamino groups attached to a coplanar rigid core (fluorene) to modulate the electronic properties, was synthesized through the reaction of 2,7-dibromo-9,9-ditolylfluorene (**3**) [29] with



**Scheme 1.** Synthesis of trifluorovinyl ether-functionalized monomers **TFVE1–3**.

1-aminonaphthalene in the presence of a catalytic amount of  $\text{Pd}_2(\text{dba})_3$  to furnish an aminated crude product that was subsequently subjected to Pd-catalyzed amination with compound **2** (49% yield over two steps). Without structural perturbation of the active chromophore, the two TFVE groups of **TFVE3** were introduced onto the peripheral biphenyl substituents of the central fluorene unit. The amination of compound **4** [30] with *N*-phenyl-1-naphthylamine in the presence of a catalytic amount of  $\text{Pd(OAc)}_2$  and tri-*tert*-butyl phosphine gave compound **5** in 82% yield. The treatment of the phenol groups in **5** with trifluoromethane-

sulfonic anhydride afforded the disulfonate **6** in 81% yield. **TFVE3** was then obtained in 55% yield after Suzuki coupling of the boronic ester **7** [15] and compound **6**.

### 3.2. Physical properties

The morphological properties of the monomers **TFVE1–3** were investigated using differential scanning calorimetry (DSC). The introduction of two TFVE groups had a pronounced effect on the morphology. As indicated in Fig. 1, no evident glass transition could be detected for **TFVE1**; in-



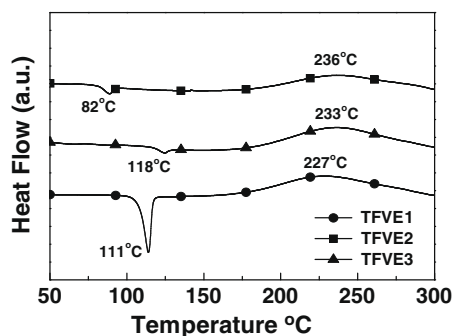


Fig. 1. DSC analyses of the thermally polymerizable monomers TFVE1–3.

stead, we observed an endothermic peak centered at 111 °C, which corresponded to the melting point of TFVE1. The increased molecular rigidity of TFVE2 led to a distinct glass transition temperature ( $T_g$ ) detected at 82 °C, which remained significantly lower than that of its parent compound (127 °C) [29]. TFVE3, with its two TFVE groups attached to the peripheral biphenyl substituents of the central fluorene unit, possesses a value of  $T_g$  of 118 °C. The exothermic peaks of TFVE1–3 at ca. 230 °C in the DSC traces correspond to their thermal polymerizations, consistent with the previously reported polymerization temperatures of TFVE groups [14–28]. The three TFVE monomers were soluble in common organic solvents, such as chloroform, tetrahydrofuran (THF), and toluene. After dip-coating solutions of the TFVEs in THF onto ITO substrates, the films were baked at 100 °C for 30 min to remove any residual solvent. Atomic force microscopy (AFM) reveals that the films prepared through this dip-coating process had smooth surfaces with no obvious crystallization, pinholes, or cracks (Fig. 2). After curing at 230 °C for 60 min, the films of the PFCB polymers became

insoluble in most organic solvents. The AFM images of these PFCB polymer films reveal some clusters formed after thermal polymerization at high temperature.

Fig. 3a displays UV–vis absorption and photoluminescence spectra of the thin films of vacuum-deposited  $\alpha$ -NPD and TFVE1–3 after thermal polymerization. The absorption spectrum ( $\lambda_{\text{max}} = 344$  nm) of TFVE1 polymer matches well with that of  $\alpha$ -NPD, whereas polymers of TFVE2 and TFVE3 exhibit red-shifted absorption maxima (by ca. 40 nm), due to the coplanar structure of their cores. There were no significant changes in the absorption spectra of TFVE1–3 after the treatment at high temperature (Fig. 3b and c). In contrast to their electronic transitions, the emission spectra of the thermally polymerized thin films of TFVE1–3 exhibit slightly red-shifted maxima with broader half-widths of the emission peaks, relative to that of the  $\alpha$ -NPD thin film and the thin films of TFVE1–3 prior to thermal polymerization. These results contrast those from a previous report by Jen et al., where a thin film of a  $N,N'$ -di(3-methylphenyl)- $N,N'$ -diphenylbenzidine (TPD)-based PFCB polymer exhibited an obviously red-shifted emission maximum relative to that of its monomer film as a result of strong aggregation and excimer emission [22–28]. The observed limited red shifts in the emission of TFVE1–3 polymers and their long-wavelength tails could be attributable to the changes in the dielectric environments upon thermal treatment. The chromophores surrounded by TFVE moieties in the monomeric states should behave differently from those in the polymeric forms, in which the TFVE groups have been converted into PFCB moieties. Nevertheless, we cannot exclude the possibility of weak interchromophore interactions leading to long-wavelength emission regions in the polymer films after high-temperature thermal polymerization.

To characterize the hole transport in these thermally polymerized TFVE1–3 polymers and to quantify their mobilities, we used time-of-flight (TOF) techniques [31]

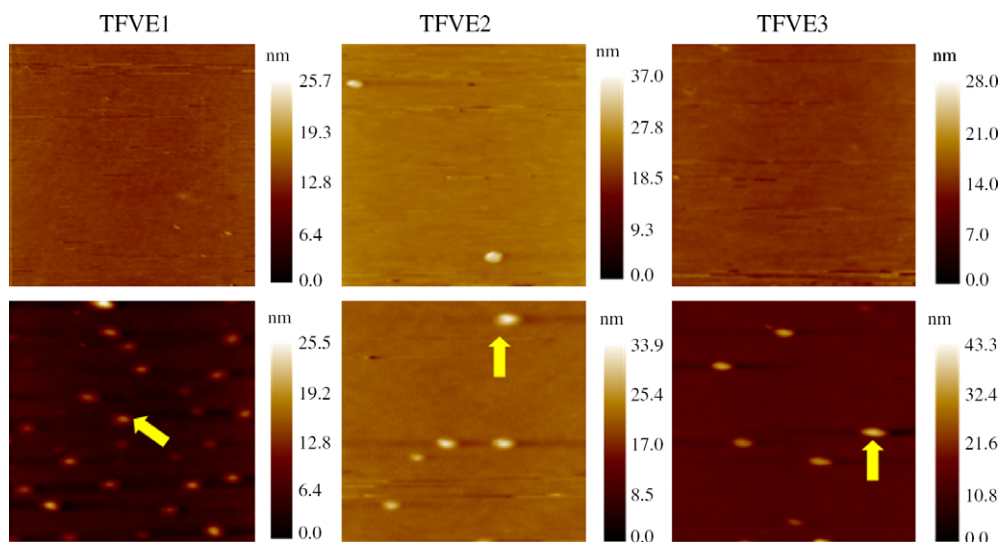
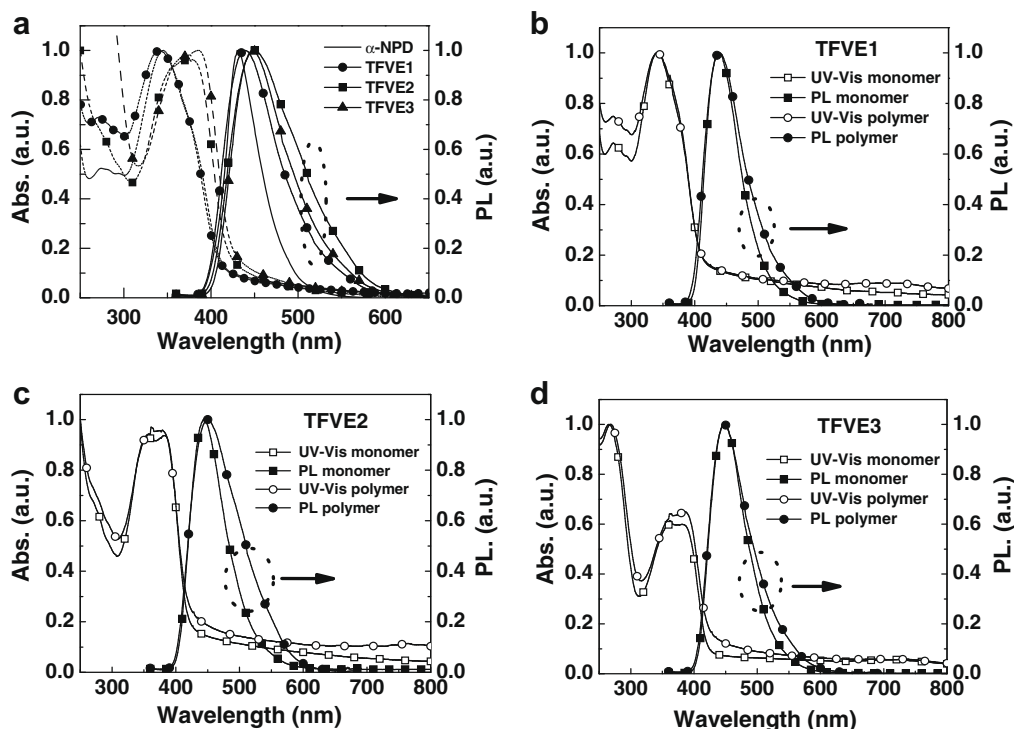


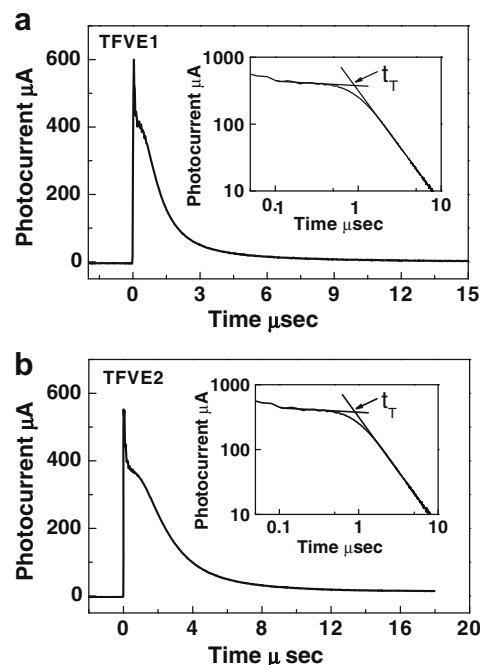
Fig. 2. AFM images ( $5 \times 5 \mu\text{m}$ ) of TFVE1–3 thin films before (top) and after (bottom) thermal polymerization. The indicated clusters with heights of TFVE1 (11 nm), TFVE2 (13 nm), and TFVE3 (16 nm), respectively.



**Fig. 3.** (a) UV-vis absorption and photoluminescence spectra of thin films of thermally polymerized TFVE1–3 and vacuum-deposited  $\alpha$ -NPD and (b–d) comparisons of photophysical properties of TFVE1–3 thin films before (monomers) and after thermal polymerization (polymers).

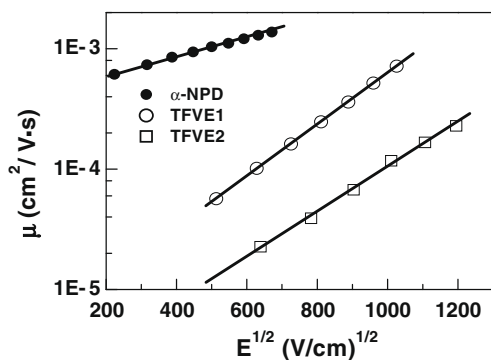
to measure the charge carrier mobility. This technique has been successfully applied to investigate the charge transport behavior of a wide range of polymers and small molecules, but it has not been applied previously to measure the charge mobility of any thermal polymerized and/or cross-linked polymers. TOF samples were prepared by dissolving appropriate weight ratios (up to 25 wt%) of the monomers TFVE1 and TFVE2 in THF and then dip-coating the solutions onto an ITO substrate within a glove box. For TFVE3, however, poor solubility in THF meant that we could not obtain a solution of sufficiently high concentration to yield a sample that was thick enough for TOF measurement. We were able to control the film thicknesses by varying the solution concentrations and the dip-coating conditions; the films were subsequently dried through baking at 100 °C for 30 min to remove the residual solvent and then curing at 230 °C for 60 min to form the polymers. We used a Dektak surface profilometer to measure the thicknesses of the TFVE1 (ca. 760 nm) and TFVE2 (ca. 500 nm) polymer films. The samples were then completed through thermal deposition of the back electrode [Ag (100 nm)] through a shadow mask.

Fig. 4 displays the TOF transients of the TFVE1 and TFVE2 polymer films. Distinctive plateaus are visible in the typical TOF transient photocurrents, indicating the non-dispersive transport behavior of the TFVE1 and TFVE2 polymers toward holes. We estimated the carrier transit times  $t_T$  from the asymptotes of the log–log plots (insets to Fig. 4); from these values, we deduced the hole mobilities ( $\mu$ ) using the relation  $\mu = d/(Et_T)$ , where  $E$  and  $d$  are the applied electric field and the thickness of the organic film,



**Fig. 4.** Representative TOF transients for polymer films derived from (a) TFVE1 (at  $E = 5.3 \times 10^5$  cm V<sup>-1</sup>) and (b) TFVE2 (at  $E = 6.1 \times 10^5$  cm V<sup>-1</sup>) at room temperature. The insets present double-logarithmic plots of the data.

respectively. Fig. 5 presents the room-temperature hole mobilities of the model compound  $\alpha$ -NPD and of the



**Fig. 5.** Plots of hole mobilities vs.  $E^{1/2}$  for the thermally polymerized films of **TFVE1** and **TFVE2** and of a film of the model compound  $\alpha$ -NPD obtained through thermal evaporation.

PFCB-based polymer films derived from **TFVE1** and **TFVE2** plotted against the square root of the applied electric field. The linear correlation follows the universal Poole–Frenkel relationship,  $\mu = \mu_0 \exp(\beta E^{1/2})$ , where  $\mu_0$  is the zero-field mobility,  $\beta$  is the Poole–Frenkel factor and  $E$  is the electric field [32]. The hole mobilities ranged from  $2 \times 10^{-5}$  to  $10^{-3}$   $\text{cm}^2 \text{V}^{-1} \text{s}^{-1}$  for fields varying from  $4 \times 10^4$  to  $1.4 \times 10^6$   $\text{V cm}^{-1}$  and the values ( $\mu_0$  and  $\beta$ ) of fitting data are summarized in Table 1.

The observed hole mobility ( $\mu_{\text{th}} = \text{ca. } 10^{-4}$   $\text{cm}^2 \text{V}^{-1} \text{s}^{-1}$ ) of the **TFVE1**-derived polymer film was about one order of magnitude lower than that of the model compound  $\alpha$ -NPD ( $\mu_{\text{th}} = 1.2 \times 10^{-3}$   $\text{cm}^2 \text{V}^{-1} \text{s}^{-1}$ ) under the same electric field ( $E = 3.6 \times 10^5$   $\text{V cm}^{-1}$ ). In addition, as indicated by its larger value of  $\beta$ , the **TFVE1**-derived polymer film exhibited a stronger electric-field-dependent hole mobility. We ascribe these phenomena to the presence of the PFCB units of the **TFVE1**-derived polymer; i.e., the more rigid structure and the larger distance and steric hindrance between neighboring chromophores increased the carrier hopping distance, thus retarding hole migration. The aggregates observed in the AFM images of the thermally treated thin films might also have been another attribute responsible for the lower hole mobility. The steric effect on hole transportation was also evident from the lower hole mobility of

**Table 1**

The values of zero-field hole mobility ( $\mu_0$ ) and Poole–Frenkel factor ( $\beta$ ) obtained by fitting the data in Fig. 5 with the Poole–Frenkel equation.

HTL	$[\text{cm}^2 \text{V}^{-1} \text{s}^{-1}]$	$\beta$
$\alpha$ -NPD	$4.18 \times 10^{-4}$	$1.79 \times 10^{-3}$
<b>TFVE1</b>	$4.53 \times 10^{-6}$	$4.93 \times 10^{-3}$
<b>TFVE2</b>	$1.46 \times 10^{-6}$	$4.27 \times 10^{-3}$

**Table 2**

Device characteristics of OLEDs incorporating cross-linked **TFVE1–3** and vacuum-deposited  $\alpha$ -NPD as HTLs.

HTL	$V_{\text{on}}$ [V]	$L_{\text{max}}$ [ $\text{cd m}^{-2}$ ]	$I_{\text{max}}$ [ $\text{mA cm}^{-2}$ ]	$\eta_{\text{ext}}$ (max) [% $\text{cd A}^{-1}$ ]	$\eta_{\text{p}}$ (max) [ $\text{lm W}^{-1}$ ]
$\alpha$ -NPD	2	86,000 (11.5 V)	3500	1.36, 4.4	4
<b>TFVE1</b>	2	50,000 (14.0 V)	3400	1.43, 4.6	3.6
<b>TFVE2</b>	2	43,000 (13.5 V)	4600	1.32, 4.2	3.6
<b>TFVE3</b>	2	26,600 (14.0 V)	3900	1.32, 4.2	2.4

the **TFVE2**-derived polymer (a 9,9-ditylfluorene-based diamine) relative to that of the **TFVE1**-derived polymer (a biphenylene-based diamine) [33].

### 3.3. Device

To evaluate the performances of devices incorporating the thermally polymerized **TFVE1–3** films as HTLs, we fabricated two-layer devices having the configuration ITO/PEDOT:PSS (30 nm)/polymeric **TFVE1–3** (ca. 50 nm)/ $\text{Alq}_3$  (60 nm)/LiF (0.5 nm)/Al (100 nm). Uniform films were formed through first dip-coating the solution of **TFVE1–3** (1.2 wt% in THF) onto the pre-dried (130 °C for 30 min) PEDOT:PSS layer on an ITO substrate [34,35] and then polymerizing under thermal treatment at 230 °C for 30 min. Integrating the conductive HIL and the thermally polymerized HTL together resulted in a low driving

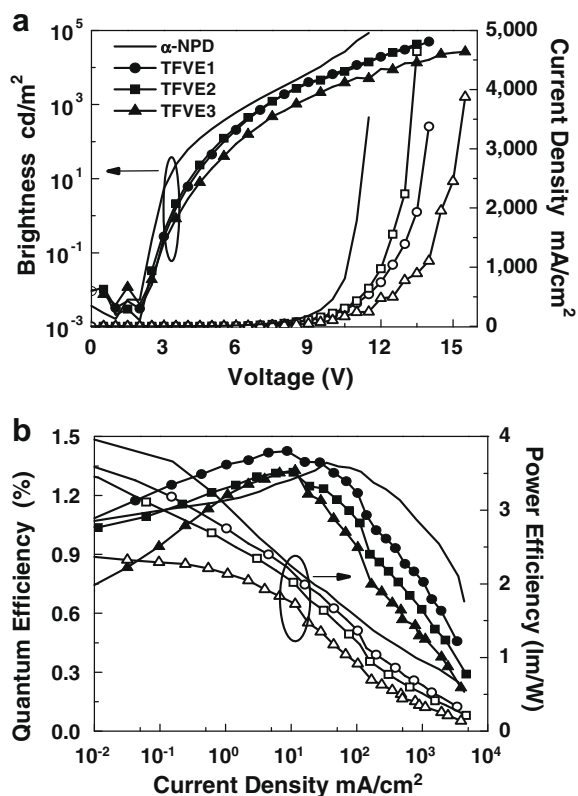


**Fig. 6.** Performances of typical two-layer devices incorporating thermally polymerized HTLs and  $\alpha$ -NPD. Plots of (a) brightness (solid symbols) and current (open symbols) vs. voltage and (b) quantum efficiency (solid symbols) and power efficiency (open symbols) vs. current.

voltage, cascade hole injection, and effective electron blocking/exciton confinement in the Alq<sub>3</sub> layer. All devices exhibited the same emission, which originated exclusively from the Alq<sub>3</sub> layer.

Table 2 and Fig. 6 summarize the EL characteristics of the OLEDs incorporating the thermally polymerized **TFVE1–3** monomers and vacuum-deposited  $\alpha$ -NPD as HTLs. These hybrid OLEDs exhibit noteworthy properties relative to those of conventional vacuum-deposited OLEDs. For example, the thermally polymerized HTLs functioned well without decreasing the device performance [10]. As indicated in Fig. 5a, the devices turned on sharply at low voltages (ca. 2 V), probably because the HOMO and LUMO energy levels of the active triaryldiamine chromophores, which remained intact before and after thermal polymerization, were matched well with those of ITO and Alq<sub>3</sub>. Among our three new thermally polymerizable HTL materials, the **TFVE1**-derived polymer exhibited the best performance. Fig. 5b indicates that the highest efficiency was achieved when using the **TFVE1**-derived polymer as the HTL: the maximum EQE was 1.43% (4.6 cd A<sup>-1</sup>) and the maximum power efficiency was 3.6 lm W<sup>-1</sup>. It is generally accepted that polymers exhibiting high morphological stability in their thin film form result in devices that can endure relatively high current densities (ca. 3400 mA cm<sup>-2</sup>) and, consequently, emit an impressive maximum brightness of nearly 5 × 10<sup>4</sup> cd m<sup>-2</sup> at ca. 14 V from the non-doped Alq<sub>3</sub>. Despite the lower hole mobility of the **TFVE1**-derived polymer films, compared with that of the vacuum-deposited model compound  $\alpha$ -NPD, the device incorporating the former as the HTL exhibited the same turn-on voltage and slightly higher EQE (1.43%) relative to that of the latter (EQE = 1.37%) under the same device structure. We attributed the higher EQE achieved in the hybrid OLED to a more balanced recombination of holes and electrons.

#### 4. Conclusions

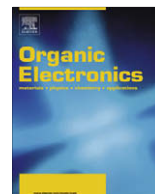
In summary, we have synthesized and characterized three thermally polymerizable hole-transporting materials, **TFVE1–3**, derived from the parent  $\alpha$ -NPD core through the attachment of TFVE groups. The thermally polymerized monomers exhibited good thermal properties, solvent resistance, and relatively high surface smoothness. More importantly, for the first time we used TOF techniques to measure the hole-transporting characteristics of  $\alpha$ -NPD-based PFCB polymers. We observed a hole mobility of ca. 10<sup>-4</sup> cm<sup>2</sup> V<sup>-1</sup> s<sup>-1</sup> for **TFVE1**-derived polymer films, ca. one order of magnitude lower than that of the model compound  $\alpha$ -NPD (i.e., in the absence of TFVE groups) under the same electric field. We ascribe the lower mobilities of the PFCB-based polymers to their larger degrees of spatial and steric hindrance leading to blocking of carrier hopping. We fabricated hybrid OLEDs incorporating the **TFVE1**-derived polymer film as the HTL. These devices exhibited high current densities (ca. 3400 mA cm<sup>-2</sup>), impressive brightness (5 × 10<sup>4</sup> cd m<sup>-2</sup>), and high external quantum efficiency (1.43%).

#### Acknowledgement

This study was supported financially by the National Science Council of Taiwan.

#### References

- [1] C.W. Tang, S.A. VanSlyke, *Appl. Phys. Lett.* 51 (1987) 913.
- [2] A.R. Brown, R.N. Marks, K. Mackay, R.H. Friend, P.L. Burns, A.B. Holmes, *Nature (London)* 3471 (1990) 539.
- [3] B. Yan, B.J. Scott, Q. Huang, Q. Marks, *Adv. Mater.* 16 (2004) 1948.
- [4] C.D. Müller, A. Falcou, N. Reckefuss, M. Rojahn, V. Wiederhirn, P. Rudati, H. Frohne, O. Nuyken, H. Becker, K. Meerholz, *Nature (London)* 421 (2003) 829.
- [5] M.C. Gather, A. Köhnen, A. Falcou, H. Becker, K. Meerholz, *Adv. Funct. Mater.* 17 (2007) 191.
- [6] R.J.P. Corriu, D. Leclercq, *Angew. Chem., Int. Ed. Eng.* 35 (1996) 1420.
- [7] U. Schubert, N. Hüsing, A. Lorenz, *Chem. Mater.* 7 (1995) 2010.
- [8] W. Li, Q. Wang, J. Cui, H. Chou, S.E. Shaheen, G.E. Jabbour, J. Anderson, P. Lee, B. Kippelen, N. Peyghambarian, N.R. Armstrong, T.J. Marks, *Adv. Mater.* 11 (1999) 730.
- [9] J.G.C. Veinot, T.J. Marks, *Accounts Chem. Res.* 38 (2005) 632.
- [10] E. Bellmann, S.E. Shaheen, S. Thayumanavan, S. Barlow, R.H. Grubbs, S.R. Marder, B. Kippelen, N. Peyghambarian, *Chem. Mater.* 10 (1998) 1668.
- [11] A. Kimyonok, B. Domercq, A. Haldi, J.-Y. Cho, J.R. Carlise, X.-Y. Wang, L.E. Hayden, S.C. Jones, S. Barlow, S.R. Marder, B. Kippelen, M. Weck, *Chem. Mater.* 19 (2007) 5602.
- [12] A. Bacher, C.H. Erdelen, W. Paulus, H. Ringsdorf, H.-W. Schmidt, P. Schuhmacher, *Macromolecules* 32 (1999) 4551.
- [13] Y.-H. Niu, M.S. Liu, J.-W. Ka, J. Bardeker, M.T. Zin, R. Schofield, Y. Chi, A.K.-Y. Jen, *Adv. Mater.* 19 (2007) 300.
- [14] B.K. Spraul, S. Suresh, U.Y. Jin, D.W. Smith Jr., *J. Am. Chem. Soc.* 128 (2006) 7055.
- [15] B. Lim, J.-T. Hwang, J.Y. Kim, J. Ghim, D. Vak, Y.-Y. Noh, S.-H. Lee, K. Lee, A.J. Heeger, D.-Y. Kim, *Org. Lett.* 8 (2006) 4703.
- [16] B.K. Spraul, S. Suresh, S. Glaser, D. Perahia, J. Ballato, D.W. Smith Jr., *J. Am. Chem. Soc.* 126 (2004) 12772.
- [17] A.R. Neilson, S.M. Budy, J.M. Ballato, D.W. Smith Jr., *Macromolecules* 40 (2007) 9378.
- [18] J. Ghim, H.-S. Shim, B.G. Shin, J.-H. Park, J.-T. Hwang, C. Chun, S.-H. Oh, J.-J. Kim, D.-Y. Kim, *Macromolecules* 38 (2005) 8278.
- [19] J. Ji, S. Narayan-Sarathy, R.H. Neilson, J.D. Oxley, D.A. Babb, N.G. Rondan, D.W. Smith, *Macromolecules* 17 (1998) 783.
- [20] D.W. Smith, D.A. Babb, *Macromolecules* 29 (1996) 852.
- [21] D.A. Babb, B.R. Ezzell, K.S. Clement, W.F. Richey, A.P. Kennedy, *J. Polym. Sci. Part A: Polym. Chem.* 31 (1993) 3465.
- [22] Y.-H. Niu, Y.-L. Tung, Y. Chi, C.-F. Shu, J.H. Kim, B. Chen, J. Luo, A.J. Carty, A.K.-Y. Jen, *Chem. Mater.* 17 (2005) 3532.
- [23] X. Gong, D. Moses, A.J. Heeger, S. Liu, A.K.-Y. Jen, *Appl. Phys. Lett.* 83 (2003) 183.
- [24] X. Jiang, S. Liu, M.S. Liu, P. Herguth, A.K.-Y. Jen, H. Fong, M. Sarikaya, *Adv. Funct. Mater.* 12 (2002) 745.
- [25] S. Liu, X. Jiang, H. Ma, M.S. Liu, A.K.-Y. Jen, *Macromolecules* 33 (2000) 3514.
- [26] X. Jiang, M.S. Liu, A.K.-Y. Jen, *J. Appl. Phys.* 91 (2002) 10147.
- [27] Y.H. Niu, B. Chen, S. Liu, H. Yip, J. Bardecker, A.K.-Y. Jen, J. Kavitha, C.-F. Shu, Y. Chi, Y.-H. Tseng, C.-H. Chien, *Appl. Phys. Lett.* 85 (2004) 1619.
- [28] J. Zhao, J. Bardecker, A.M. Munro, M.S. Liu, Y. Niu, I.-K. Ding, J. Luo, B. Chen, A.K.-Y. Jen, D.S. Ginger, *Nano Lett.* 6 (2006) 463.
- [29] K.-T. Wong, Z.-J. Wang, Y.-Y. Chien, C.-L. Wang, *Org. Lett.* 3 (2001) 2285.
- [30] C.-H. Chou, C.-F. Shu, *Macromolecules* 35 (2002) 9673.
- [31] P.M. Borsenberger, D.S. Weiss, *Organic Photoreceptors for Imaging Systems*, Marcel Dekker, New York, 1993.
- [32] P.M. Borsenberger, L. Pautmeier, H. Bässler, *J. Chem. Phys.* 94 (1991) 5447.
- [33] Y.-L. Liao, W.-Y. Hung, T.-H. Hou, C.-Y. Lin, K.-T. Wong, *Chem. Mater.* 19 (2007) 6350.
- [34] Y. Cao, G. Yu, C. Zhang, R. Menon, A.J. Heeger, *Synth. Metal.* 87 (1997) 171.
- [35] A. Berntsen, Y. Croonen, C. Liednbaum, H. Schoo, R.-J. Visser, J. Vleggaar, P. van de Weijer, *Opt. Mater.* 9 (1998) 125.



## Letter

## Small molecule interlayer for solution processed phosphorescent organic light emitting device

Jung Joo Park<sup>a</sup>, Tae Jin Park<sup>a</sup>, Woo Sik Jeon<sup>a</sup>, Ramchandra Poda<sup>b</sup>, Jin Jang<sup>a</sup>, Jang Hyuk Kwon<sup>a,\*</sup>, Eun-Sun Yu<sup>c</sup>, Mi-Young Chae<sup>c</sup>

<sup>a</sup> Department of Information Display, Kyung Hee University, Dongdaemun-gu, Seoul 130-701, Republic of Korea

<sup>b</sup> Department of Physics, Kyung Hee University, Dongdaemun-gu, Seoul 130-701, Republic of Korea

<sup>c</sup> Cheil Industries Inc., Gocheon-dong, Uiwang-si, Gyeonggi-do 332-2, Republic of Korea

## ARTICLE INFO

## Article history:

Received 14 April 2008

Received in revised form 11 July 2008

Accepted 25 August 2008

Available online 6 September 2008

## PACS:

72.80.Le

73.50.Ph

78.61.r

## Keywords:

Interlayer

Phosphorescent

Solution

OLED

## ABSTRACT

Using a 4,4',4''-tris(*N*-carbazolyl)-triphenylamine (TCTA) small molecule interlayer, we have fabricated efficient green phosphorescent organic light emitting devices by solution process. Significantly a low driving voltage of 3.0 V to reach a luminance of 1000 cd/m<sup>2</sup> is reported in this device. The maximum current and power efficiency values of 27.2 cd/A and 17.8 lm/W with TCTA interlayer (thickness 30 nm) and 33.7 cd/A and 19.6 lm/W with 40 nm thick interlayer are demonstrated, respectively. Results reveal a way to fabricate the phosphorescent organic light emitting device using TCTA small molecule interlayer by solution process, promising for efficient and simple manufacturing.

Crown Copyright © 2008 Published by Elsevier B.V. All rights reserved.

Solution processible organic light emitting diodes (OLEDs) are attracting much attention as potential candidates for flat-panel displays and solid state lighting, owing to their easy processing and low manufacturing cost [1,2]. Requirement for use in these applications, the high luminance at lower current density and efficient operation, are realized by the balance charge carriers injection from the electrodes into the emitting layer. Poly(3,4-ethylenedioxythiophene)-poly(4-stylenesulfonate) (PEDOT:PSS) hole injection layer on the top of indium-tin-oxide (ITO) surface is most widely used to improve the hole injection [3–5]. Further, the insertion of a thin interlayer (thickness 10–30 nm) between the PEDOT:PSS and the light emitting

layer (EML) significantly improves the device efficiency and lifetime. Conjugated polymer materials such as poly(*p*-phenylene vinylene), poly(9,9'-dioctylfluorene) (PFO) and poly(9,9'-dioctylfluorene-*alt*-benzothiadiazole) [6], poly(2,7-(9,9-di-*n*-octylfluorene)-*alt*-(1,4-phenylene-((4-*sec*-butylphenyl)imino)-1,4-phenylene)) (TFB) [7,8], and poly(9,9'-dioctylfluorene-co-bis-*N,N'*-(4-butylphenyl)-bis-*N,N'*-phenyl-1,4-phenylenediamine) (PFB) [9] were used for this purpose. To date, non-conjugated materials, poly(*N*-vinylcarbazole) (PVK) [9] and crosslinked non-conjugated materials [10–12] having hole transporting chemical units were mostly reported for this purpose. However, such interlayer polymers have several issues for use in practical devices such as considerably high exchange energy, 1.0–1.5 eV values, between the singlet and triplet states [13]. As a consequence, conjugated polymers

\* Corresponding author. Tel.: +82 2 961 0948; fax: +82 2 961 9154.

E-mail address: [jhkwon@khu.ac.kr](mailto:jhkwon@khu.ac.kr) (J.H. Kwon).

generally are not suitable as phosphorescent host materials [14]. Further, these polymers in phosphorescent OLEDs may act as a potential quencher at the interface of EML. Owing to low solubility in several organic solvents, conjugated polymers also offer a serious difficulty for the printing process and in removing the undesired material from the substrate. Although TFB is widely used as an interlayer, its low triplet emission energy (2.2–2.3 eV) causes some quenching of the phosphorescence emission in green phosphorescent devices. While 4,4',4''-tris(*N*-carbazolyl)-triphenylamine (TCTA) small molecule has a good film forming properties, solubility, and high triplet emission energy (2.7 eV). We, therefore, propose that the use of small molecule material interlayer may be a good approach in solution processed phosphorescent OLEDs. In the present work, phosphorescent green light emitting devices using a solution process with a small molecule TCTA interlayer have been fabricated and studied.

The TCTA hole transport material (HTL), known to confine excitons and electrons in emitting layer and reported as a suitable host material in green phosphorescent OLEDs [15,16], usually has been deposited using the vacuum evaporation process in OLEDs fabrication. In order to acquire more knowledge about amorphous nature of spin-coated TCTA film, the vacuum thermal evaporated TCTA and the spin-coated TCTA and well known TFB interlayer films (30 nm thick) were fabricated on glass substrates. The average surface roughness ( $R_{\text{ave}}$ ) values of spin-coated and sublimated TCTA surface, measured by using Atomic Force Microscopy (AFM), are about 4.17 Å and 3.38 Å, while the surface roughness value of 5.49 Å in the spin-coated TFB interlayer is observed as shown in Fig. 1. This unlike value of surface roughness in a spin-coated TCTA film than the vacuum thermal evaporated may be attributed to the solvent evaporation during the process of spin coating. A good amorphous film formation characteristic of the TCTA has been ascribed to three dimensional molecular structure of TCTA. A Half circle shape structure of the TCTA molecule with coplanar two carbazole units and remaining one carbazole unit vertically orthogonal to the plane containing two carbazole units contributes to the amorphous molecular packing, indicating that the crystallization of the TCTA film during spin-coating and baking process is practically missing. The good surface characteristic of spin-coated TCTA film is well suited for use as an interlayer material. Furthermore, to check the possibility of use of well known TPD and NPB hole transport materials

as an interlayer in wet processed OLEDs, spin-coated TPD and NPB films (40 nm) on the glass substrate were fabricated and investigated, respectively. Evidences of non-uniform surface with high roughness due to crystallization of TPD and NPB molecules upon thermal treatment in solution processed films make them unsuitable for wet processed OLEDs.

To fabricate OLED devices, clean glass substrates of size 2 cm × 2 cm precoated with a 150 nm thick indium-tin-oxide (ITO) layer with a sheet resistance of 12 Ω/square were used. The ITO glass was cleaned by sonification in an isopropylalcohol (IPA) and acetone, rinsed in deionized water, and finally irradiation in a UV-ozone chamber. The line pattern of ITO was formed by photolithography process. The PEDOT:PSS was spin-coated on the ITO substrates pretreated with UV ozone to a thickness of 40 nm and dried at 120 °C for 20 min on a hot plate to remove the solvent. Subsequently, the interlayer solution either TCTA or TFB 0.5 wt% in toluene (thickness of about 30 nm) was spin coated and later dried at 180 °C for 30 min on a hot plate. PVK described as an unipolar hole transporter and 4,4'-*N,N'*-dicarbazolebiphenyl (CBP) recognized to have bipolar transport character were used as mixed host materials in the present work. The 40 nm-thick EML of PVK:CBP system mixed in the proportion of 1:1 and doped with 13 wt% of tris(2-(4-tolyl)phenylpyridine) iridium ( $\text{Ir}(\text{mpy})_3$ ) in chlorobenzene was spin-coated on the top of interlayer film. The spin-coated EML was then baked on a hot plate at 120 °C for 60 min to remove the solvent present, if any. The spin coating and baking processes were carried out in a nitrogen atmosphere glove box. Subsequently, The TPBi (2,2',2''-(1,3,5-phenylene)tris(1-phenyl-1*H*-benzimidazole)) (30 nm) was deposited in organic chamber using vacuum thermal evaporation in a base pressure of  $10^{-7}$  Torr, while LiF (1 nm) and Al (100 nm) were deposited in a metal chamber without breaking the vacuum of the system. The following devices were fabricated:

- Device 1: ITO/PEDOT:PSS (40 nm)/TFB (30 nm)/EML (40 nm)/TPBi (30 nm)/LiF (1 nm)/Al (100 nm), and
- Device 2: ITO/PEDOT:PSS (40 nm)/TCTA (30 nm)/EML (40 nm)/TPBi (30 nm)/LiF (1 nm)/Al (100 nm).

The emission area of devices was 2 mm × 2 mm. The current density–voltage ( $I$ – $V$ ) and luminance–voltage ( $L$ – $V$ ) characteristics of fabricated OLEDs were measured by using a Keithley SMU 238 and Minolta CS-100A.

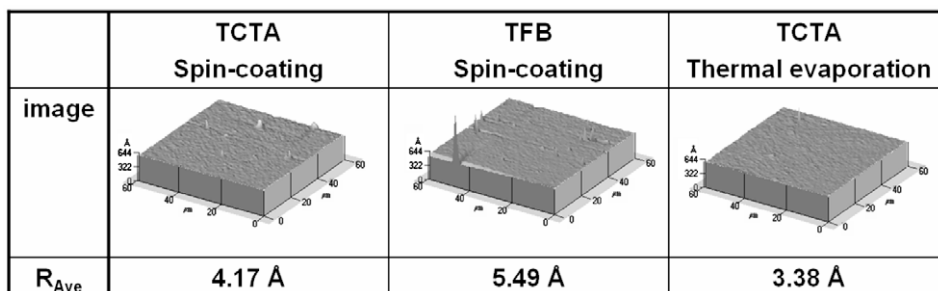


Fig. 1. Surface morphology of sublimated TCTA, spin-coated TCTA, and TFB.

Electroluminescence (EL) spectra and CIE color coordinate were obtained by using a photo-research PR-650 spectroradiometer.

Fig. 2a shows the luminance and current density as a function of applied voltage. The turn voltage value of 4.0 V to attain a luminance of 1000 cd/m<sup>2</sup> in device 1 with TFB interlayer is reported, while this value is 3.0 V in device 2 with TCTA interlayer. Device 2 with TCTA interlayer seems to offer a low barrier for hole injection into emitting layer. To substantiate our argument, hole only devices, having configuration of ITO/PEDOT:PSS (40 nm)/TCTA or TFB (70 nm)/LiF (1 nm)/Al (100 nm), were fabricated. As

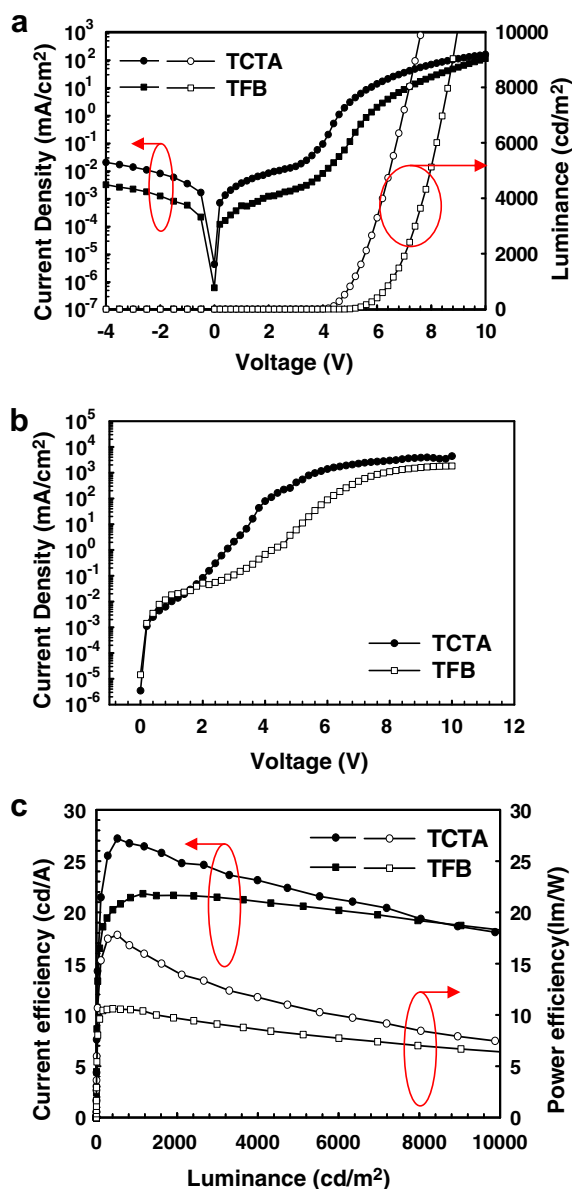


Fig. 2. I-V-L and efficiency characteristics of fabricated PHOLED devices. (a) luminance and current density versus voltage devices 1 & 2, (b) current versus voltage characteristics of fabricated hole only devices, (c) current and efficiency versus luminance in devices 1 & 2.

evident from the results shown in Fig. 2b, low resistance to hole transport and conduction in hole only device with TCTA interlayer is noticed. Clearly, these results corroborate the superior electrical performance of device 2 with the TCTA interlayer. Further, to perceive whether the large difference in space charge current is still true, hole only devices were fabricated using Al cathode (work function = 4.28 eV, electron injection barrier to TFB = 2.18 eV and TCTA = 1.98 eV) which does not inject electrons either into TFB or TCTA. We have obtained results similar to LiF/Al cathode, thus substantiating the hypothesis of better transport properties of TCTA interlayer.

Fig. 2c shows the current and power efficiencies as a function luminance. Current and power efficiency values of 21.5 cd/A and 10.5 lm/W in device 1 with TFB interlayer at a luminance of 1000 cd/m<sup>2</sup> are observed, whereas these values in device 2 with TCTA interlayer are 26.5 cd/A and 16.0 lm/W. The maximum current and power efficiency values with TCTA interlayer are 27.2 cd/A and 17.8 lm/W and 21.7 cd/A and 10.6 lm/W with TFB interlayer, respectively. Better performance of the device 2 with TCTA interlayer, therefore, is of interest to manufacturers.

Furthermore, improvement of the device performance due to increase of the thickness of TCTA interlayer from 30 to 40 nm is observed. The values of current and power efficiencies of 32.0 cd/A and 15.9 lm/W at the luminance of 1000 cd/m<sup>2</sup> were measured, respectively. The maximum current and power efficiencies were 33.7 cd/A and 19.6 lm/W in this device, respectively. Further enhancement of TCTA interlayer thickness deteriorates the device performance as listed in Table 1.

To investigate the dissolution issue of interlayer, if any, in the solvent of emitting layer, thick interlayers (70 nm) of TFB and TCTA in toluene were spin coated on glass substrates and dried at 180 °C for 30 min on a hot plate. Subsequently, EML solvent chlorobenzene was spin-coated on the top of TFB and TCTA interlayers, baked on a hot plate at 120 °C for 60 min, and thicknesses of the final layers were then measured. The thickness of TFB was reduced about 8–10 nm while that of TCTA by 20–22 nm. These dissolution values of TFB and TCTA in the EML solvent are not a serious issue for making spin-coated phosphorescent OLEDs.

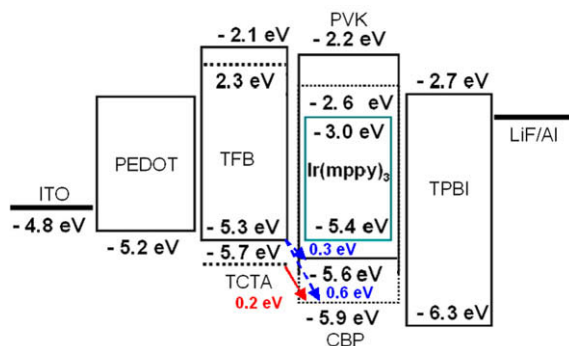


Fig. 3. Device structure and energy band diagram of the devices using hole transporting interlayer.

**Table 1**

Performance of ITO/PEDOT/TCTA/PVK + CBP:Ir(mppy)<sub>3</sub> (1:1, 13 %)/TPBI/LiF/Al PHOLEDs with different interlayer thicknesses

TCTA thickness (Å)	300	400	500–600
Turn-on voltage (V)	3	3.8	4.6
At 1000 cd/m <sup>2</sup>			
Voltage	5.2	6.4	8.0
current efficiency (cd/A)	26.5	32	18.1
Power efficiency (lm/W)	16.0	15.9	7.1
Max.			
Current efficiency (cd/A)	27.2	33.7	18.6
Power efficiency (lm/W)	17.8	19.6	8.6

**Table 2**

HOMO and LUMO energy levels of interlayers, host materials and excitation blocking layers

Materials	HOMO(eV)	LUMO(eV)	Triplet energy T <sub>1</sub> (eV)	Reference
TFB	5.3	2.1	2.2–2.3	17
TCTA	5.7	2.3	2.7	18, 19
	5.7	2.4		20
PVK	5.4	1.9		21
	5.6	2.2	2.5	22
CBP	6.1	3.0	2.6	23, 19
	5.9	2.6		20
TPBI	6.3	2.8		24
Ir(mppy) <sub>3</sub>	5.4	2.4, 3.0(T <sub>1</sub> )	2.4	25, 26

Indeed, interesting and intriguing results on the device performance with the TCTA small molecule interlayer deposited using spin coating are obtained. These results may be explained as electrons/holes charge carriers injection and transport and confinement of triplet excitons in emissive layers on the basis of the existing knowledge of energy levels of materials used in device fabrication. Highest occupied molecular orbital (HOMO) and lowest unoccupied molecular orbital (LUMO) energy levels of interlayers, host materials, phosphorescent dopant, and excitation blocking layers are summarized in Table 2 [17–26]. As the HOMO level of TCTA (–5.9 eV or –5.7 eV) is close the HOMO energy of host layer (–5.8 eV or 5.6 eV in PVK and –5.91 eV or 5.9 eV in CBP), a low hole injection barrier (~0.2 eV) into PVK + CBP:Ir(mppy)<sub>3</sub> emissive layer significantly facilitates carrier injection (Fig. 3). While holes injected from TFB into PVK + CBP:Ir(mppy)<sub>3</sub> emissive layer have to overcome a barrier of ~0.3–0.6 eV, high com-

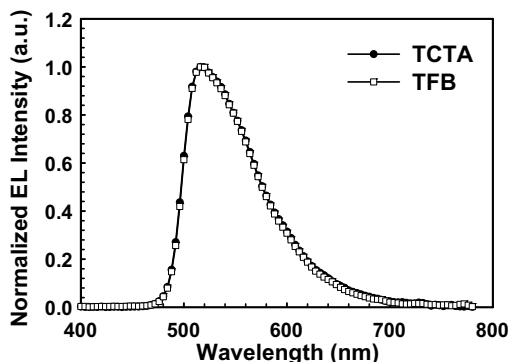


Fig. 4. Electroluminescence spectra of fabricated devices.

pared to TCTA. Finally, injected holes are trapped at the HOMO of Ir(mppy)<sub>3</sub> (5.4 eV) (Fig. 3). Thus, the hole injection efficiency in TCTA interlayer based device is significantly improved. The electrons injected from the cathode transport freely with a negligible barrier, recombine with the trapped holes on the Ir(mppy)<sub>3</sub> dopant molecules in the emissive layer, and finally result in an improved green phosphorescence emission. Whereas in case of TFB interlayer, the triplet energy levels of TFB are in the range of 2.2–2.3 eV, lower than the triplet emission energy of Ir(mppy)<sub>3</sub> (2.4 eV). Thus, low triplet energy of TFB provides a nonradiative path for exciton quenching and reduced the phosphorescence light emission of the PHOLEDs. No such phenomenon is observed in PHOLEDs with a TCTA interlayer as triplet emission energy of TCTA (2.7 eV). Moreover, TCTA interlayer confines excitons and electrons in the emitting layer, contributing to enhanced device performance. Furthermore, the clean emission peak in green region at 520 nm (CIE coordinates (0.33, 0.61) at 1000 cd/m<sup>2</sup>) in the fabricated TCTA interlayer device also reveals no leakage of electrons into HTL layer (Fig. 4), thereby confining electrons in the EML.

In summary, we have fabricated TCTA small molecular interlayer based green phosphorescent devices using a spin-coating process. The TCTA has a good solubility in toluene and thin film forming properties by spin coating process. Low turn-on voltage value of 3.0 V to obtain luminance of 1000 cd/m<sup>2</sup> and maximum current and power efficiencies values of 27.3 cd/A and 18.0 lm/W are reported in this device, respectively. The maximum current and power efficiencies of 33.7 cd/A and 19.6 lm/W with TCTA thickness of 40 nm were reported. In conclusion, demonstration of solution processible efficient green phosphorescent OLEDs with TCTA small molecule interlayer could be a promising way for simple manufacturing process.

## References

- [1] A.R. Duggal, C.M. Heller, J.J. Shiang, J. Liu, L.N. Lewis, *J. Display Technol.* 3 (2007) 184.
- [2] S.A. Choulis, Vi-En Choong, M.K. Mathai, F. So, *Appl. Phys. Lett.* 87 (2005) 113503.
- [3] T.M. Brown, J.S. Kim, R.H. Friend, F. Cacialli, R. Dai, W.J. Feast, *Appl. Phys. Lett.* 75 (1999) 1679.
- [4] P.K.H. Ho, J.S. Kim, J.H. Burroughes, H. Becker, S.F.Y. Li, T.M. Brown, F. Cacialli, R.H. Friend, *Nature* 404 (2000) 481.
- [5] Y. Yang, A.J. Heeger, *Appl. Phys. Lett.* 64 (1994) 1245.
- [6] J. Morgado, R.H. Friend, F. Cacialli, *Appl. Phys. Lett.* 80 (2002) 2436.
- [7] J. Kim, R.H. Friend, I. Grizzi, J.H. Burroughes, *Appl. Phys. Lett.* 87 (2005) 023506.
- [8] S.A. Choulis, Vi-En Choong, A. Patwardhan, M.K. Mathai, F. So, *Adv. Funct. Mater.* 16 (2006) 1075.
- [9] T.-W. Lee, M.G. Kim, S.Y. Kim, S.H. Park, O. Kwon, T. Noh, T.-S. Oh, *Appl. Phys. Lett.* 89 (2006) 123505.
- [10] H. Yan, P. Lee, N.R. Armstrong, A. Graham, G.A. Evononenkes, P. Dutta, T.J. Marks, *J. Am. Chem. Soc.* 127 (2005) 3172.
- [11] M.C. Gather, A. Kohnen, A. Falcou, H. Becker, K. Meerholz, *Adv. Funct. Mater.* 17 (2007) 191.
- [12] Y.-H. Niu, M.S. Liu, J.-W. Ka, J. Bardeker, M.T. Zin, R. Schofield, Y. Chi, A.K.-Y. Jen, *Adv. Mater.* 19 (2007) 300.
- [13] A.P. Monkman, H.D. Burrows, L.J. Hartwell, L.E. Horsburgh, I. Hamblett, S. Navaratnam, *Phys. Rev. Lett.* 86 (2001) 1358.
- [14] M. Sudhakar, P.I. Djurovich, T.E. Hogen-Esch, M.E. Thompson, *J. Am. Chem. Soc.* 125 (2003) 7796.
- [15] S. Reineke, G. Schwartz, K. Walzer, K. Leo, *Appl. Phys. Lett.* 91 (2007) 123508.



- [16] J. Meyer, S. Hamwi, T. Bülow, H.-H. Johannes, T. Riedl, W. Kowalsky, *Appl. Phys. Lett.* 91 (2007) 113506.
- [17] M. Redecker, D.D.C. Bradley, M. Inbasekaran, W.W. Wu, E.P. Woo, *Adv. Mater.* 11 (1999) 241.
- [18] Y.-H. Niu, M.S. Liu, J.-W. Ka, A.K.-Y. Jen, *Appl. Phys. Lett.* 88 (2006) 093505.
- [19] A. van Dijken, K. Brunner, H. Borner, B.M.W. Langeveld, in: H. Yersin (Ed.), *Highly Efficient OLEDs with Phosphorescent Materials*, Wiley-VCH Verlag GmbH & Co. KGaA, Weinheim, Germany, 2008, p. 317.
- [20] S.-H. Kim, J.-S. Jang, K.-S. Yook, J.-Y. Lee, M.-S. Gong, S. Ryu, G.-K. Chang, H.J. Chang, *Appl. Phys. Lett.* 103 (2008) 054502.
- [21] R.A. Negres, X. Gong, J.C. Ostrowski, G.C. Bazan, D. Moses, A.J. Heeger, *Phys. Rev. B* 68 (2003) 115209.
- [22] X.-H. Yang, F. Jaiser, D. Neher, in: H. Yersin (Ed.), *Highly Efficient OLEDs with Phosphorescent Materials*, Wiley-VCH Verlag GmbH & Co. KGaA, Weinheim, Germany, 2008, p. 223.
- [23] T. Tsuzuki, S. Tokito, *Adv. Mater.* 19 (2007) 276.
- [24] Brian W.D. Andrade, R.J. Holmes, S.R. Forrest, *Adv. Mater.* 16 (2004) 624.
- [25] G. He, M. Pfeiffer, K. Leo, M. Hofmann, J. Birnstok, R. Pudzich, J. Salbeck, *Appl. Phys. Lett.* 85 (2004) 3911.
- [26] M. Ikai, S. Tokito, Y. Sakamoto, T. Suzuki, Y. Taga, *Appl. Phys. Lett.* 79 (2001) 156.



## Letter

# Flexible high mobility pentacene transistor with high-*k*/low-*k* double polymer dielectric layer operating at $-5$ V

Kwang H. Lee<sup>a</sup>, Kimoon Lee<sup>a</sup>, Min Suk Oh<sup>a</sup>, Jeong-M. Choi<sup>a</sup>, Seongil Im<sup>a,\*</sup>, Sungjin Jang<sup>b</sup>, Eugene Kim<sup>b</sup>

<sup>a</sup> Institute of Physics and Applied Physics, Yonsei University, Seoul 120-749, Republic of Korea

<sup>b</sup> Department of Information and Display, Hongik University, Seoul 121-791, Republic of Korea

## ARTICLE INFO

## Article history:

Received 30 June 2008

Received in revised form 20 August 2008

Accepted 24 September 2008

Available online 2 October 2008

## PACS:

72.80.Le

77.84.Jd

85.30.Tv

## Keywords:

Organic thin-film transistor

Pentacene

Low voltage

Polymer dielectric

High mobility

Flexible

## ABSTRACT

We report on the fabrication of pentacene-based thin-film transistors (TFTs) with a 230 nm-thick double polymer dielectric composed of 30 nm-thin low-*k* poly-4-vinylphenol (PVP) and 200 nm-thick high-*k* poly(vinylidene fluoride/trifluoroethylene) [P(VDF-TrFE)] dielectric on polyethersulfone (PES) films. Our 230 nm-thick double (high-*k*/low-*k*) polymer showed a good dielectric strength of  $\sim 2$  MV/cm, a high capacitance of 26 nF/cm<sup>2</sup> with  $k = \sim 7$ . Based on this double polymer dielectric, our flexible pentacene TFT displayed a high saturation mobility of 1.22 cm<sup>2</sup>/V s, a threshold voltage of  $-2.5$  V, and on/off ratio of 10<sup>3</sup>, stably operating under  $-5$  V.

© 2008 Elsevier B.V. All rights reserved.

## 1. Introduction

Pentacene organic thin-film transistors (OTFTs) have attracted much attention, looking for practical applications such as flat-panel displays, logic devices, and radio frequency identification tag, and other portable devices in general [1–5]. Very recently, electrophoretic display or E-book emerges to be one of the most appropriate applications in such OTFT device field [6–8]. The E-book driving TFTs preferably require flexible substrate and low voltage operation, as well as device stability. In order to realize these low voltage driven OTFTs, many research groups have focused on the study about the gate dielectric layers

(for example, thin-polymers, self-assembled monolayer (SAM), high-*k* metal oxide, and thin polymer/thick high-*k* oxide hybrid layer) [9–12]. However, low voltage OTFT adopting flexible plastic substrate is still in lack of report. Moreover high mobility operations on flexible substrates are even more difficult to find from literature. It is because such device needs high-*k* polymer dielectric to support the low voltage operation while usual polymer has low-*k* dielectric properties unlike inorganic dielectrics. (But inorganic high-*k* dielectric has a limited process-compatibility with flexible plastic substrate and a limited flexibility by itself.) High-*k* polymer with smooth surface and good electric strength is quite difficult to find and further difficult to fabricate without high current leakage paths while thin low-*k* polymer is easy to be broken down under gate voltage stress [9]. One way to satisfactorily meet the condition

\* Corresponding author. Tel.: +82 2 2123 2842; fax: +82 2 392 1592.  
E-mail address: [semicon@yonsei.ac.kr](mailto:semicon@yonsei.ac.kr) (S. Im).

of low voltage operation on flexible substrate may be to adopt both low- $k$  and high- $k$  polymer dielectric layer in stack since the low- $k$  polymer provides good electric strength and surface smoothness while the high- $k$  one may make the low voltage TFT operation possible. In the present study of low voltage flexible pentacene OTFT fabrication, we thus adopt a leakage-resistant 200 nm-thick poly(vinylidene fluoride/trifluoroethylene) [P(VDF-TrFE)] as a high- $k$  polymer ( $k = 6-9$ ) beneath a 30 nm-thin low- $k$  poly-4-vinylphenol (PVP) dielectric, that interfaces pentacene channel. Our pentacene OTFT demonstrates a high mobility of  $1.22 \text{ cm}^2/\text{V s}$  operating at  $-5 \text{ V}$  on flexible plastic substrate.

## 2. Experimental section

Al gate electrodes (width  $320 \mu\text{m}$ ) were patterned by thermal evaporation on polyethersulfone (PES) films in a vacuum chamber. The 200 nm-thick film of P(VDF-TrFE) 75/25 mol% copolymer was coated by spin casting 6 wt% cyclohexanone solutions on Al gate pattern and the high- $k$  polymer was quenched by blowing  $\text{N}_2$  gas (99.9% purity) at room temperature (RT) after being cured at  $160^\circ\text{C}$  for 2 h in a vacuum oven, so that the P(VDF-TrFE) has little crystalline ordering inside the film. Sequentially, the 30 nm-thick PVP layer was coated by spin casting 1 wt% solutions and was exposed under UV lamp (254 nm wavelength) for 10 min in air at RT as a curing process [13]. The 240 nm-thick PVP single layer was coated by spin casting 8 wt% solutions and was cured at  $175^\circ\text{C}$  for 1 h in a vacuum oven [14]. Pentacene (Aldrich Chem. Co., 99% purity, with no other purification) active channel layer was patterned on the double polymer dielectric through a shadow

mask at room temperature (RT) by thermal evaporation. Deposition rate was fixed to  $1 \text{ \AA/s}$  using an effusion cell (ALPHAPLUS Co., LTE-500S) in a vacuum chamber (base pressure  $\sim 1 \times 10^{-7}$  Torr). The thickness of pentacene films was 50 nm as monitored by a quartz crystal oscillator and confirmed by ellipsometry. Au pads were finally deposited as source and drain electrodes by thermal evaporation in a vacuum chamber (base pressure  $\sim 2 \times 10^{-6}$  Torr). The nominal channel length ( $L$ ) and width ( $W$ ) of our pentacene TFTs were 90 and  $500 \mu\text{m}$ , respectively. Fig. 1a shows the schematic cross-sectional views of our low voltage pentacene TFT with double polymer dielectric and high voltage reference TFT with single PVP. Fig. 1b is a picture displaying our flexible pentacene TFTs.

The electrical properties of the double polymer and PVP single dielectric layers were measured with  $250 \mu\text{m}$ -dia Al dot/dielectric/indium-tin-oxide (ITO) glass structures by capacitance-voltage ( $C-V$ ) and current density-electric field ( $J-E$ ) tests. All current-voltage ( $I-V$ ) properties of our TFTs and test structures were measured with a semiconductor parameter analyzer (HP 4155C, Agilent Technologies), and  $C-V$  measurements were made with a capacitance meter (HP 4284 LCR meter, Agilent Technologies, 1 MHz) in the dark and in an air ambient (relative humidity  $\sim 40\%$ ) at RT. The dielectric surface morphologies were observed by atomic force microscopy (AFM) (XE-100, PSIA).

## 3. Results and discussion

Fig. 1c and d shows  $C-V$  and  $J-E$  characteristics of the 230 nm-thick PVP/P(VDF-TrFE) double and 240 nm-thick PVP single dielectric layers on ITO glass, respectively. The

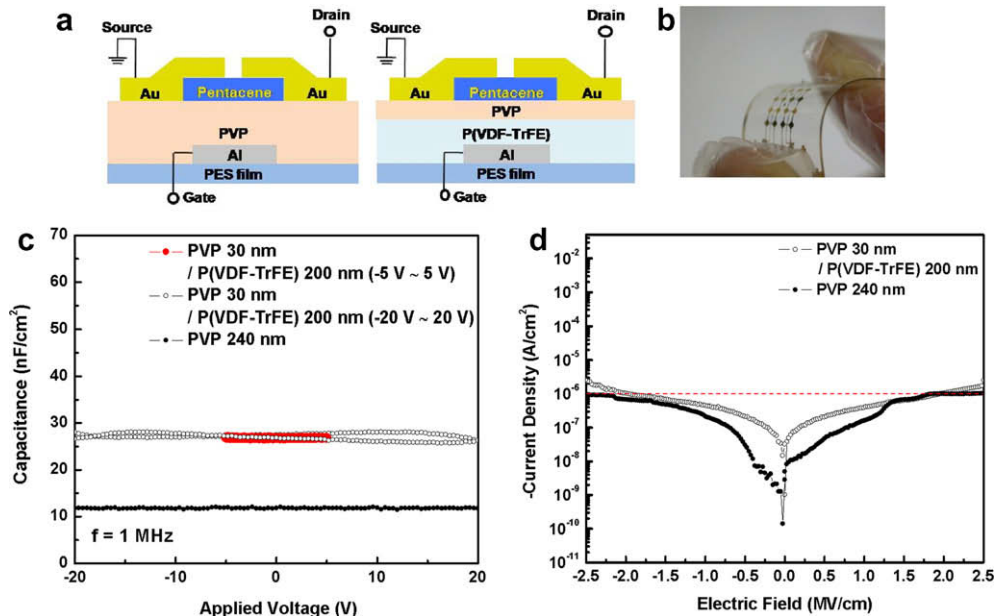


**Fig. 1.** (a) Schematic cross-section of our pentacene TFT with 240 nm-thick PVP single and 230 nm-thick double polymer insulator. (b) The photograph of flexible pentacene TFTs on PES films. (c) Capacitance-voltage ( $C-V$ ) curves of 240 nm-thick PVP single and 230 nm-thick double polymer dielectric insulators on ITO glass as measured from  $250 \mu\text{m}$ -dia Au dot/dielectric/electrode structures at 1 MHz (d) Current density-electric field ( $J-E$ ) characteristics of both insulators.

capacitance of the double polymer and PVP single dielectric layers were  $26\sim 28\text{ nF/cm}^2$  and  $12\text{ nF/cm}^2$ , respectively. Also, the dielectric constant ( $k$ ) of the double

polymer and PVP single dielectric layers were  $\sim 7.1$  and  $\sim 3.2$ , respectively, estimated from the measured capacitance values. The high capacitance of double polymer layer

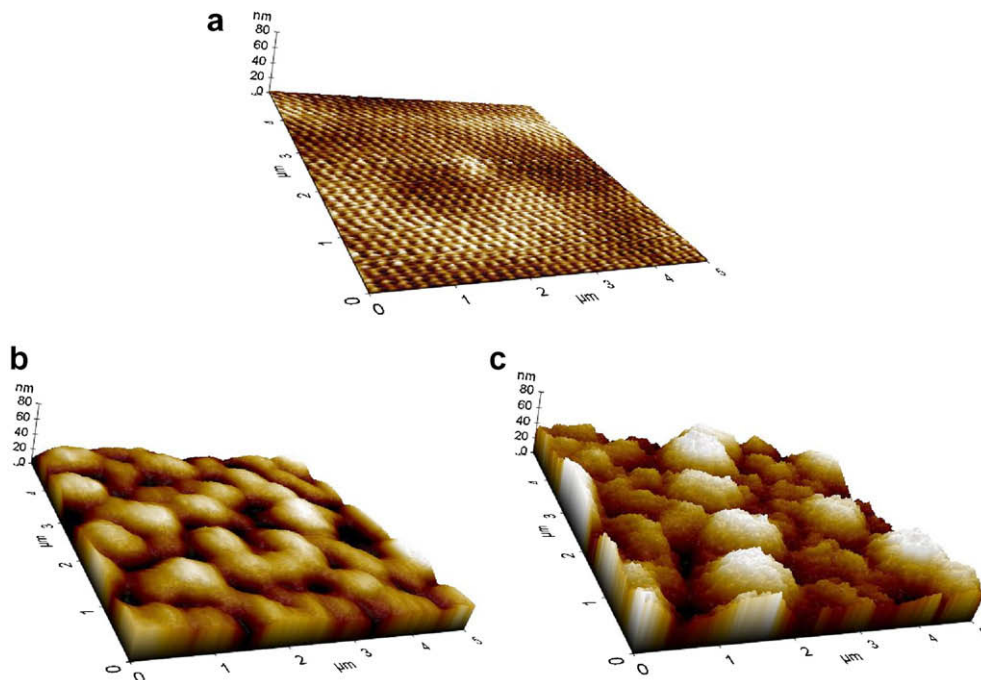


**Fig. 2.** (a) AFM images of 240 nm-thick PVP single insulator, (b) 30 nm-thin PVP layer on 200 nm-thick P(VDF-TrFE) layer, and (c) 200 nm P(VDF-TrFE) layer deposited on ITO glass ( $5\ \mu\text{m} \times 5\ \mu\text{m}$ ).

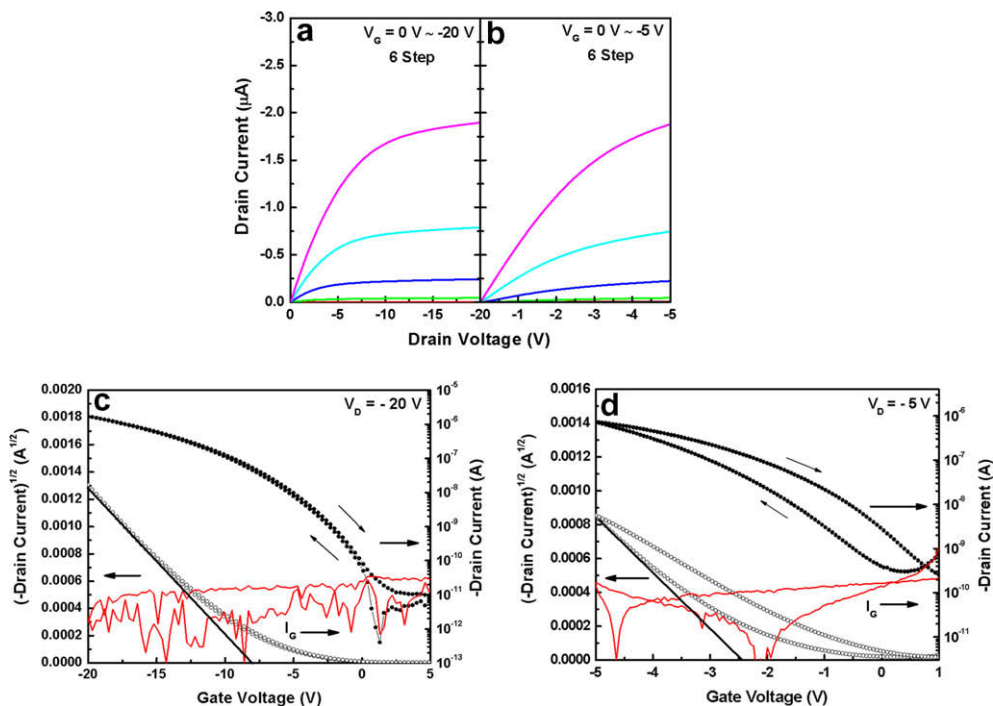


**Fig. 3.** Drain current–drain voltage ( $I_D$ – $V_D$ ) output curves obtained from our pentacene TFTs with (a) 240 nm-thick PVP single layer and (b) 230 nm-thick double polymer dielectric layers. Transfer curves ( $\sqrt{-I_D}$ – $V_G$  and  $\log_{10}(-I_D)$ – $V_G$ ) of the pentacene TFTs with (c) PVP single and (d) double polymer dielectric layers (obtained at  $V_D = -20\text{ V}$  and  $V_D = -5\text{ V}$ , respectively).

would assist the flexible organic TFT to operate in low voltage range. Similar dielectric strength of  $\sim 2$  MV/cm was shown in the both double polymer and PVP single dielectric layers. In spite of generic high leakage profile of crystalline-ordered high- $k$  polymer (data not shown here) [15], the double polymer dielectric layer composed of 30 nm-thin PVP and 200 nm-thick P(VDF-TrFE) showed quite good leakage property. It is mainly because the thin PVP layer inhibits the current leakage covering the rough surface of P(VDF-TrFE) layer, and also because our P(VDF-TrFE) layer obtained by  $N_2$  gas-quenching after the 160 °C curing has fewer leakage paths than normal crystalline-ordered polymer, which is conventionally obtained by 135 °C curing and subsequent long term cooling for good crystalline ordering. We expect that our P(VDF-TrFE) layer is amorphous-like with little crystalline ordering. Also interesting to note is that the  $C-V$  curve of our double polymer shows broad and weak butterfly peaks in the voltage range between  $-20$  and  $+20$  V although the butterfly effect vanishes in low voltage range ( $-5$  to  $+5$  V). It is because our amorphous-like polymer still pos-

sess a little of ferroelectric property. However, those ferroelectric properties are dejected by PVP-induced depolarization during TFT gating and also subside by operating the TFT under a low voltage which is much lower than coercive voltage ( $\sim \pm 12$  V according to the present  $C-V$  data). This means that our double polymer layer can be used as a dielectric for low voltage TFT without any problem.

Fig. 2a–c shows the AFM surface images of the 240 nm-thick PVP single layer, 230 nm-thick PVP/P(VDF-TrFE) double polymer layer, and 200 nm-thick P(VDF-TrFE) single layer on ITO glass. According to the Figs. 2a, b and c, the surface roughness of PVP single, PVP/P(VDF-TrFE) double, and P(VDF-TrFE) single layers on ITO glass was 0.4, 5 and 10 nm, respectively. Although initial surface of P(VDF-TrFE) single layer was very rough, the final surface of PVP/P(VDF-TrFE) double layer became much smoother due to the thin PVP over layer.

Fig. 3a and b displays the drain current–drain voltage ( $I_D-V_D$ ) output curves obtained from our pentacene-based TFTs with the 240 nm-thick PVP single and 230 nm-thick

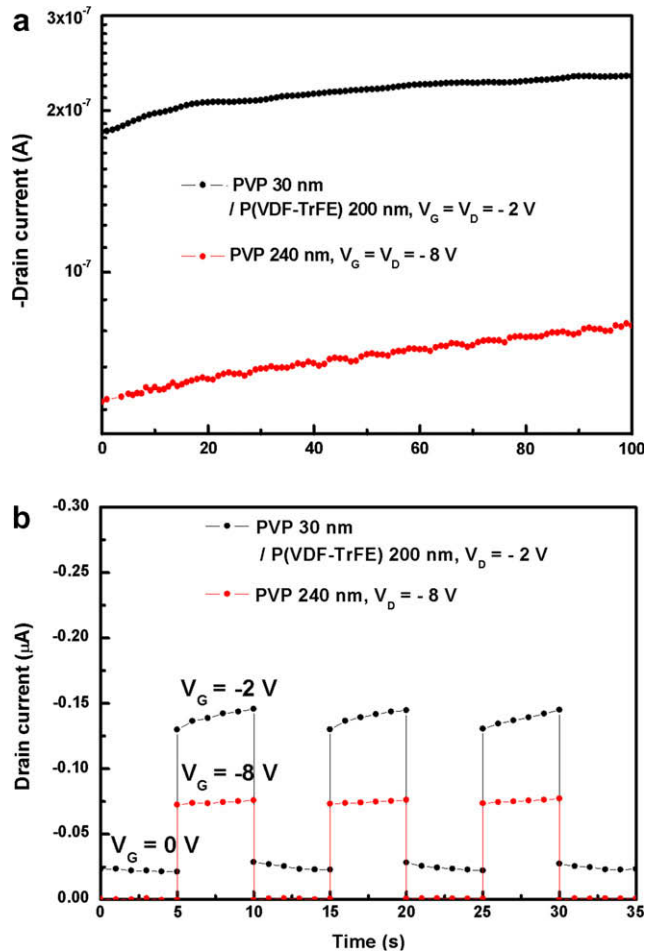


**Fig. 4.** Drain current behavior of the both devices observed under (a) constant gate bias stress (vertical scale range:  $5 \times 10^{-8}$ – $3 \times 10^{-7}$  A) and (b) dynamic bias stress conditions (5 s on/off periods). On-state condition was  $V_G = V_D = -2$  V for device with double polymer layer and was  $V_G = V_D = -8$  V for the other device with single PVP dielectric, while off-state condition was  $V_G = 0$  V at  $V_D = -2$  and at  $-8$  V for the devices with double polymer and single PVP, respectively.

double polymer dielectric layers on PES films. Similar maximum saturation current ( $\sim 2 \mu\text{A}$ ) was achieved from the TFTs with single PVP dielectric and double dielectric layers but under different gate biases of  $-20 \text{ V}$  and only  $-5 \text{ V}$ , respectively. According to the drain current–gate voltage ( $\sqrt{I_D - V_G}$ ) transfer curves of Fig. 3c and d, the pentacene TFT with the double polymer dielectric showed a high field mobility (saturation mobility) of  $1.22 \text{ cm}^2/\text{V s}$  at  $-5 \text{ V}$  while that with PVP single dielectric layer displayed a field mobility of  $0.38 \text{ cm}^2/\text{V s}$  at  $-20 \text{ V}$ . The threshold voltages ( $V_T$ ) of pentacene TFTs with double polymer (Fig. 3d) and PVP single layers (Fig. 3c) were about  $-2.5 \text{ V}$  and  $-7.5 \text{ V}$ , respectively, but the pentacene TFT with double polymer dielectric showed a relatively large gate-bias hysteresis while the other TFT with PVP single layer did not display such hysteresis. It is very likely that the present double polymer dielectric is somewhat unstable under gate biases, because the P(VDF–TrFE) in our double polymer layer is as weak as to allow the charge injection from the gate electrode [16] or to allow the residual poling (slow polarization) effect under negative gate bias sweep [16]. In contrast the  $240 \text{ nm}$ -thick PVP single layer is known to be very stable under the gate bias stress if gone through the right curing process [14]. Since the leakage property of our double polymer containing the high- $k$  layer is a little inferior to that of the single PVP (see  $J$ – $E$  curves of Fig. 1), gate electron injection to the bottom P(VDF–TrFE) is quite a reasonable conjecture to explain this gate instability. The  $\log_{10}(-I_D) - V_G$  curves of Fig. 3c and d showed the on/off current ratios of  $3 \times 10^3$  for the double polymer dielectric device and  $\sim 10^6$  for the PVP single layer device. The maximum gate leakage current ( $I_G$ ) level is kept under less than  $1 \text{ nA}$  for the both cases.

Since the TFT with double polymer layer showed such gate-hysteresis, we measured the gate stability of the two TFTs under continuous and dynamic gate-bias stress as shown in Fig. 4a and b, respectively [17]. As expected, the drain current of pentacene TFT with the double polymer dielectric layers continuously and more rapidly increased (after on:  $V_G = -2 \text{ V}$ ) or decreased (after off:  $V_G = 0 \text{ V}$ ) than that of the other TFT with thick single PVP (on:  $V_G = -8 \text{ V}$ ) as measured in repetitive  $5 \text{ s}$  periods (Fig. 4b), but according to Fig. 4a the  $I_D$  increase of the TFT with double-polymer dielectric becomes quite saturated as the stress time elapses, although its initial increase was rapid. We do not exactly know why this saturation takes place but it seems that injected electrons stay somewhere in the bottom P(VDF–TrFE) making some negative charge states, finally to play as coulomb blockade against the next coming gate electrons. Time dependent dielectric breakdown experiments on our double polymer layer are necessary as a future study but it is now regarded that our pentacene TFT with the double polymer dielectric is not so much unstable and is possibly promising as a driving component in E-book application.

#### 4. Conclusion

In summary, we have fabricated flexible low-voltage pentacene TFTs with  $30 \text{ nm}$ -thin PVP/ $200 \text{ nm}$ -thick P(VDF–TrFE) double polymer dielectric. The  $230 \text{ nm}$ -thick double polymer dielectric layer showed a good dielectric strength ( $\sim 2 \text{ MV/cm}$ ) and a high capacitance (over  $\sim 26 \text{ nF/cm}^2$ ), allowing our pentacene TFT to operate under a low voltage of  $-5 \text{ V}$  along with a maximum channel mobility of  $1.22 \text{ cm}^2/\text{V s}$  and an on/off current ratio of  $\sim 3 \times 10^3$ . Although our TFT displayed some degree of  $I_D$ – $V_G$  hysteresis due to the gate electron injection and remnant polarization in P(VDF–TrFE) layer, we conclude that our thick double polymer layer is quite a promising candidate as a gate dielectric for flexible low-voltage driven pentacene TFTs.

#### Acknowledgements

The authors acknowledge the financial support from LG Display (project year 2005), Brain Korea 21 Project and a grant of Information Display R&D center, one of the 21st Century Frontier R&D Program funded by the Ministry of Knowledge Economy of Korean government. One of authors (Kwang H. Lee) acknowledges the support from the KOSFFL fellowship.

#### References

- [1] C.D. Sheraw, L. Zhou, J.R. Huang, D.J. Gundlach, T.N. Jackson, M.G. Kane, I.G. Hill, M.S. Hammond, J. Campi, B.K. Greening, J. Francl, J. West, *Appl. Phys. Lett.* 80 (2002) 1088.
- [2] H. Klauk, M. Halik, U. Zschieschang, F. Eder, G. Schmid, C. Dehm, *Appl. Phys. Lett.* 82 (2003) 4175.
- [3] H. Klauk, M. Halik, U. Zschieschang, F. Eder, D. Rohde, G. Schmid, C. Dehm, *IEEE T. Electron. Dev.* 52 (2005) 618.
- [4] M.S. Oh, D.K. Hwang, K. Lee, S. Yi, S. Im, *Appl. Phys. Lett.* 90 (2007) 173511.
- [5] P.F. Baude, D.A. Ender, M.A. Haase, T.W. Kelley, D.V. Muires, S.D. Theiss, *Appl. Phys. Lett.* 82 (2003) 3964.
- [6] L. Zhou, A. Wang, S.C. Wu, J. Sun, S. Park, T.N. Jackson, *Appl. Phys. Lett.* 88 (2006) 083502.
- [7] B. Comiskey, J.D. Albert, H. Yoshizawa, J. Jacobson, *Nature* 394 (1998) 253.
- [8] J. Jang, *Mater. Today* 9 (2006) 46.
- [9] M.H. Yoon, H. Yan, A. Facchetti, T.J. Marks, *J. Am. Chem. Soc.* 127 (2005) 10388.
- [10] M. Halik, H. Klauk, U. Zschieschang, G. Schmid, C. Dehm, M. Schutz, S. Malsch, F. Effenberger, M. Brunnbauer, F. Stellacci, *Nature* 431 (2004) 963.
- [11] C.D. Dimitrakopoulos, S. Purushothaman, J. Kymissis, A. Callegari, J.M. Shaw, *Science* 283 (1999) 822.
- [12] D.K. Hwang, C.S. Kim, J.M. Choi, K. Lee, J.H. Park, E. Kim, H.K. Baik, J.H. Kim, *S. Im, Adv. Mater.* 18 (2006) 2299.
- [13] J.M. Choi, J.H. Kim, S. Im, *Appl. Phys. Lett.* 91 (2007) 083504.
- [14] D.K. Hwang, J.H. Park, J. Lee, J.M. Choi, J.H. Kim, E. Kim, S. Im, *J. Electrochem. Soc.* 153 (2005) G23.
- [15] W.J. Choi, S.H. Noh, D.K. Hwang, J.M. Choi, S. Jang, E. Kim, S. Im, *Electrochem. Solid St.* 11 (2007) H47.
- [16] D.K. Hwang, M.S. Oh, J.M. Hwang, J.H. Kim, S. Im, *Appl. Phys. Lett.* 92 (2008) 013304.
- [17] D.K. Hwang, K. Lee, J.H. Kim, S. Im, J.H. Park, E. Kim, *Appl. Phys. Lett.* 89 (2006) 093507.



## Letter

## Rubrene thin-film transistors with crystalline channels achieved on optimally modified dielectric surface

Jeong-M. Choi<sup>a</sup>, Seong Hun Jeong<sup>a</sup>, Do Kyung Hwang<sup>a</sup>, Seongil Im<sup>a,\*</sup>, Byoung H. Lee<sup>b</sup>, Myoung M. Sung<sup>b</sup>

<sup>a</sup> Institute of Physics and Applied Physics, Yonsei University, Seoul 120-749, Republic of Korea

<sup>b</sup> Department of Chemistry, Hanyang University, Seoul 133-791, Republic of Korea

## ARTICLE INFO

## Article history:

Received 25 February 2008

Received in revised form 9 July 2008

Accepted 26 September 2008

Available online 2 October 2008

## PACS:

85.30.Tv

81.40.-z

## Keywords:

Organic thin-film transistor

Rubrene

Self-assembled-monolayer

Surface treatment on dielectrics

## ABSTRACT

We report on the fabrication of rubrene thin-film transistors (TFTs) with surface-modified dielectrics adopting several kinds of self-assembled-monolayer (SAM) on SiO<sub>2</sub>/p<sup>+</sup>-Si substrate. With the dielectric of lower surface energy, the crystalline rubrene growth or amorphous-to-crystalline transformation kinetics is faster during in-situ vacuum post-annealing, which was performed after rubrene vacuum deposition. In the present study, hexamethyldisilazane (HMDS) was finally determined to be the most effective SAM interlayer for polycrystalline rubrene channel formation. Our rubrene TFT with HMDS-coated SiO<sub>2</sub> dielectric showed quite a high field mobility of  $\sim 10^{-2}$  cm<sup>2</sup>/V s and a high on/off current ratio of  $\sim 10^5$  under 40 V.

© 2008 Elsevier B.V. All rights reserved.

### 1. Introduction

Rubrene transistors with crystalline channels, as fabricated by solution- or vapor-induced processes, recently attracted much attention, displaying high mobilities exceeding those of pentacene thin-film transistors (TFTs) that usually have vacuum-deposited patterned channels [1–6]. This means that rubrene TFTs may have higher potentials than those of pentacene TFTs even in patterned device form. However, until recent years rubrene TFTs could hardly draw such a desirable device performance from vacuum-deposited patterned channels [7]. It is mainly due to process-dependent difficulties of vacuum-deposition (thermal evaporation) method in obtaining crystalline channels on a dielectric substrate; this vacuum

process could hardly obtain good crystalline rubrene film because the evaporated rubrene molecules could not easily overcome the energy barrier to the planar conformation [8]. In addition, considering the fact that the surface chemical state of the dielectric is important for the formation of crystalline organic semiconductor layers although those studies appeared in lack of systematic understanding or uncertain in terms of device performance [6,9]. Therefore, in order to achieve a high performance rubrene TFT with vacuum-deposited channel pattern, it is very desirable to exploit the previously-found deposition conditions [10] on an optimally-modified dielectric surface. We thus, as the first step, implemented a systematic study for the crystalline growth of vacuum-deposited rubrene film on several dielectric surfaces modified with such a variety of self-assembled-monolayers (SAMs) as Hexamethyldisilazane (HMDS), 7-octenyltrichlorosilane (7-OTS), and Trichloro(1H,1H,2H,2H-perfluorooctyl)Silane (FTS) in the

\* Corresponding author. Tel.: +82 2 2123 2842; fax: +82 2 392 1592.  
E-mail address: [semicon@yonsei.ac.kr](mailto:semicon@yonsei.ac.kr) (S. Im).

order of hydrophobic tendency. Then as the next step of research, we have fabricated channel patterned rubrene TFTs with those surface-modified dielectrics to determine an optimal SAM layer leading to the best performance rubrene TFTs with enhanced mobilities.

## 2. Experimental section

A 200 nm-thick conventional thermal silicon oxide ( $\text{SiO}_2$ ) on  $p^+-\text{Si}$  was used as substrates (or gate dielectrics). In order to modify the surface states of our dielectrics, HMDS, 7-OTS, and FTS were applied onto the substrates using the following universal methods [11–15]; prior to the surface modification of  $\text{SiO}_2$  substrates, the substrates were cleaned with acetone, methanol, and de-ionized water in that order, and then the substrates reacted with 7-OTS and FTS solution (0.1 wt.%) using hexane as the solvent by immersion for 1 h at room temperature (RT). In HMDS coated sample case, it was coated on the  $\text{SiO}_2$  substrates by spin casting at RT. After that, the SAM-modified samples were dried in the vacuum oven at 100 °C for 1 h.

The rubrene channel layers (Aldrich, ~99.19% purity) were initially deposited on the substrates at 40 °C by thermal evaporation. After deposition, we immediately carried out in-situ post-annealing at 80 °C for 17 h. For source/drain (S/D) of the rubrene TFTs, 100 nm-thick Au was then evaporated onto the rubrene channels at RT. Nominal channel length and width of our rubrene TFTs were 90 and 500  $\mu\text{m}$ , respectively. All electrical characterizations were carried out with a semiconductor parameter analyzer (Model HP 4155C, Agilent Technologies) in the dark. Atomic force microscopy (AFM: model XE-100, PSIA) was carried out on the surfaces of our rubrene channels and SAM-treated dielectrics. Absorption measurements were also performed for HMDS-, 7-OTS-, FTS-functionalized, and unfunctionalized 80 nm-thick rubrene films on Corning glass with a Varian Cary 5G Spectrophotometer.

## 3. Results and discussion

Table 1 shows the information on the de-ionized water contact angles (c.a.) of pristine, HMDS-treated, 7-OTS-treated, and FTS-treated  $\text{SiO}_2$ , listed in the order of dielectric surface energy. In view of AFM image those pristine or modified dielectric surfaces appeared nearly identical (root-mean-square roughness,  $R_{\text{rms}}$ ; 0.2–0.3 nm for all). The information on the c.a. is very important here because only the surface energy may influence on the rubrene channel formation and the effects from surface roughness can be ignored in our experiments.

Fig. 1a–d are the optical micrographs of rubrene surfaces obtained by thermal evaporation of rubrene molecules at a substrate temperature of 40 °C and subsequent

in-situ vacuum annealing at 80 °C for 17 h. [10] on  $\text{SiO}_2$  substrate surfaces modified with various SAMs: (a) pristine, (b) HMDS, (c) 7-OTS, and (d) FTS. In the figures, the photos I, II, and III are  $\times 90$ ,  $\times 140$ , and  $\times 3.5$  times magnified images of rubrene film surfaces, respectively. According to the photo I in Fig. 1a–d, the final radii of crystalline rubrene discs grown in the same post-anneal period were observed to be 300  $\mu\text{m}$ , 400  $\mu\text{m}$ , 500  $\mu\text{m}$ , and more than 500  $\mu\text{m}$  on pristine, HMDS-, 7-OTS-, and FTS-treated  $\text{SiO}_2$ , respectively, along in the inverse order of the hydrophobic tendency of dielectric surfaces. This means that the growth rate of the nuclei becomes faster with the lower dielectric surface energy. These phenomena may be understandable based on a classical nucleation and growth theory as we deploy it in a simplified manner as follows;

$$\Delta G = \pi R^2 d \Delta G_c + \pi R^2 (\gamma_3 - \gamma_1) + 2\pi R d \gamma_2 \quad (1)$$

where  $\Delta G$  is the total free energy necessary for the amorphous-to-crystalline phase transition of rubrene disc,  $R$  and  $d$  are the radius and thickness of the crystalline rubrene disc,  $\Delta G_c$  is bulk free energy for the phase transition,  $\gamma_1$  and  $\gamma_3$  are the interface energies of dielectric/amorphous and dielectric/crystalline rubrene, respectively.  $\gamma_2$  is the interface energy between amorphous and crystalline rubrene. Since we want to derive a critical radius ( $R_c$ ) of crystal rubrene disc, it can be determined from the following Eq. (2) if the equation satisfies the next conditional formula (3).

$$\left(\frac{\partial \Delta G}{\partial R}\right) = 2\pi(d\Delta G_c + \gamma_3 - \gamma_1)R + 2\pi d\gamma_2 = 0 \quad (2)$$

$$\left(\frac{\partial^2 \Delta G}{\partial R^2}\right) = 2\pi(d\Delta G_c + \gamma_3 - \gamma_1) < 0$$

Here,  $\Delta G_c$  and  $\gamma_3 - \gamma_1$  are always negative values because crystalline phase must be more stable than amorphous phase ( $\Delta G_c < 0$ ) and  $\gamma_3$  is usually smaller than  $\gamma_1$  ( $\gamma_3 - \gamma_1 < 0$ ).

Therefore formula (3) is satisfied. We thus could derive  $R_c$  from Eq. (2).

$$R_c = -\frac{d\gamma_2}{(d\Delta G_c + \gamma_3 - \gamma_1)} \quad (3)$$

Here  $\gamma_1$  is probably almost the same for all the SAM-modified  $\text{SiO}_2$  while  $\gamma_3$  should vary with the chemical state of dielectric substrate. According to our experimental results on the growth rate, it is deduced that the  $\gamma_3$  decreases with the hydrophobic tendency of dielectrics and also that with the stronger hydrophobic dielectric surface the magnitude of  $R_c$  becomes smaller. This means that the crystalline rubrene nuclei on the FTS-modified  $\text{SiO}_2$  are relatively easy to go to the stable growth stage due to their small  $R_c$  or small energy barrier conditions compared to those of pristine  $\text{SiO}_2$ . Since the growth of the crystalline disc becomes fast once they overcome the  $R_c$  condition, it is now understandable that why the dielectrics of the low surface energy display large-sized rubrene discs here. Photo II shows a merged form of crystalline nuclei and their grain boundaries.

**Table 1**

Contact angle measured from (a) Pristine, (b) HMDS treated, (c) 7-OTS treated, and (d) FTS treated  $\text{SiO}_2$ .

	Pristine	HMDS	7-OTS	FTS
Contact angle	~40°	~60°	~85°	~117°



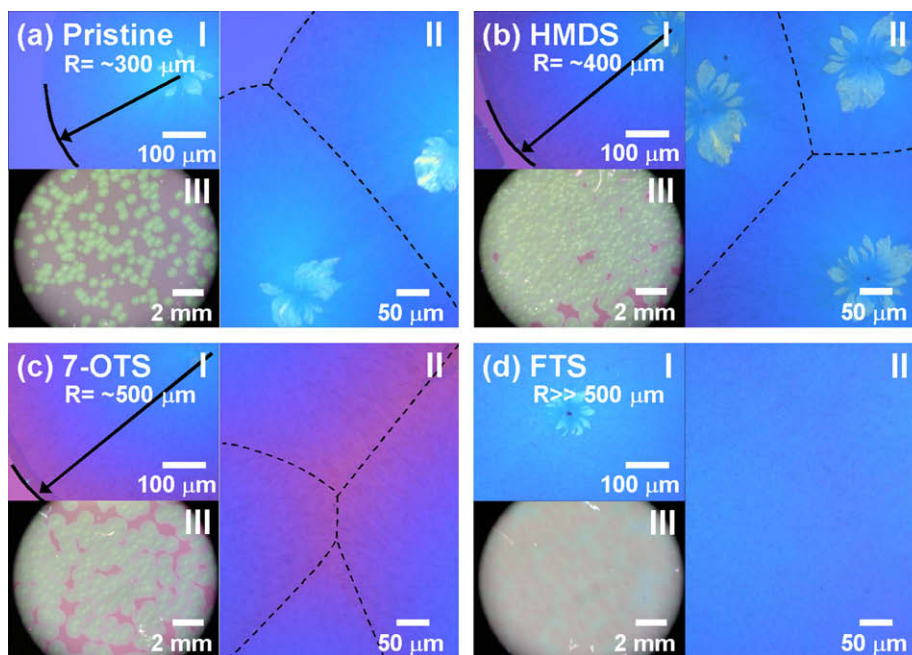


**Fig. 1.** Optical microscope images of rubrene thin-film surfaces prepared by in-situ vacuum annealing (at 80 °C for 17 h), which follows the rubrene film deposition at 40 °C on various SiO<sub>2</sub> substrates with (a) Pristine, (b) HMDS-treated, (c) 7-OTS-treated, and (d) FTS-treated surfaces. Photo I, II, and III are  $\times 90$ ,  $\times 140$ , and  $\times 3.5$  magnified surface images of rubrene film.

On the one hand, it is also worthy of note from the photo III of Fig. 1a–d that the number of rubrene crystal discs dwindles with the lowered surface energy. Although why the number of crystals decreases with the surface energy decrease of dielectric is not quite clear, we can suggest an assumption that the number of nucleation sites are somewhat related to that of OH groups on the dielectric surface or that the surface OH groups play as main seeds of nucleation sites for the crystalline discs. As an extreme case, FTS-treated SiO<sub>2</sub> surface rarely allows to show any disc shape crystals but seems to show only one grain of crystalline rubrene because it has very small surface energy and thus contains only a small number of nuclei while the growth rate of the nuclei is much fast enough to cover the whole surface area during the process time after all. The next best coverage (>90%) with the crystalline phase resulted from the HMDS-modified SiO<sub>2</sub> surface. This good result might come from an optimum phase transition condition which is achievable with large numbers of nucleation site and proper growth rate as well. Since the surface coverage with the crystalline phase is important to obtain a high mobility TFT device, this nucleation and growth issue must be taken into good consideration. In the case of bare hydrophilic SiO<sub>2</sub> dielectric, the nucleation site is many but the growth speed is too slow to cover the whole area of the dielectric surface with the crystalline phase (resulting in only ~40% coverage). In contrast, the 7-OTS-modified SiO<sub>2</sub> contains only a small number of nucleation sites while it allows the nuclei to grow so fast (~70% coverage).

Fig. 2a–d shows AFM images of 80 nm-thick rubrene films grown on (a) pristine SiO<sub>2</sub>, (b) HMDS-treated SiO<sub>2</sub>,

(c) 7-OTS-treated SiO<sub>2</sub>, and (d) FTS-treated SiO<sub>2</sub>. The AFM surface image (5 μm  $\times$  5 μm) of rubrene in a few hundred μm-dia. crystalline disc on pristine SiO<sub>2</sub> shows lamellar-like orientation and is generally similar to those of crystalline films grown on HMDS- and 7-OTS-treated SiO<sub>2</sub>. (They showed (200) orientation in previous X-ray diffraction analysis [10]). It is very interesting, however, that the rubrene films on FTS-treated SiO<sub>2</sub> substrates show somewhat different AFM surface image distinguishable from those of other samples. Crystalline rubrene film grown on FTS-treated SiO<sub>2</sub> displayed rather directionless micro-grains unlike the other cases. The growth speed of rubrene crystals on FTS-modified SiO<sub>2</sub> is probably too high to keep the directional morphologies and thus the speed results in somewhat directionless or dendritic outcome as micro-grains, whose appears random and their sizes are so small (~1 μm dia.). In addition to optical microscopy and AFM analysis, we implemented absorption measurement to again confirm the crystalline quality of the four types of 80 nm-thick rubrene films on clear glass substrate, which has correspondingly SAM-modified surfaces. As shown in this optical measurement of Fig. 2e, we clearly observed the rubrene crystalline quality with respect to the substrate hydrophobicity. As expected, HMDS- and FTS-functionalized rubrene films displayed the similarly intense peak signatures representing the best crystalline quality among the four samples while the rubrene film on bare SiO<sub>2</sub> showed weak crystalline signature. These results are quite consistent with those from optical microscopy of Fig. 1a–d, where our HMDS- and FTS-functionalized rubrene films displayed similar crystalline coverage of 90% and 100%.

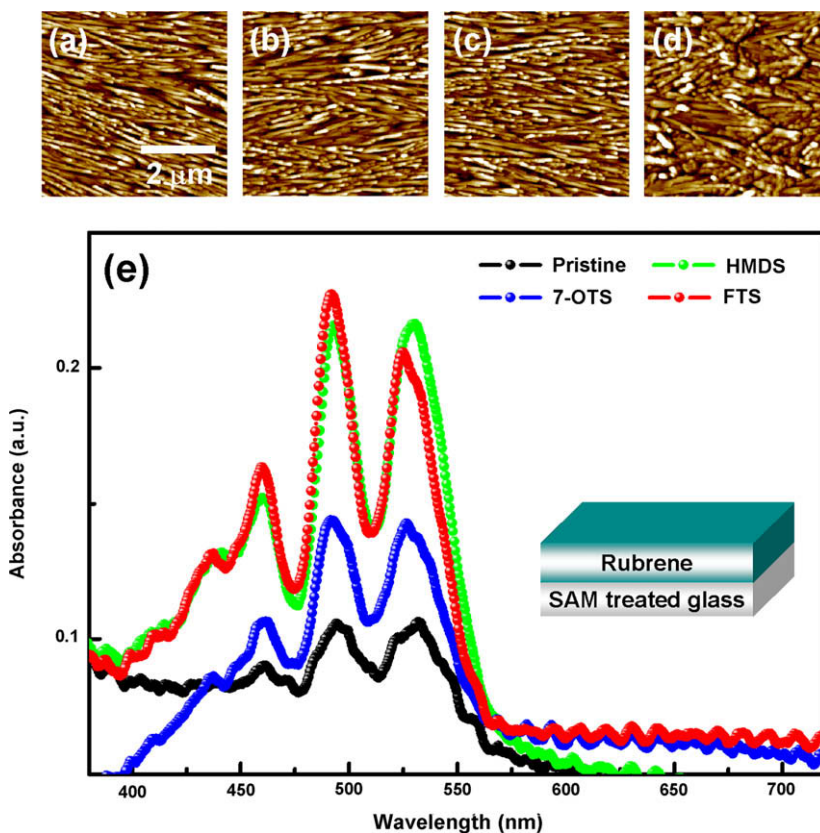


**Fig. 2.** AFM images of rubrene thin-film deposited on (a) Pristine, (b) HMDS-treated, (c) 7-OTS-treated, (d) FTS-treated  $\text{SiO}_2$ , and (e) absorption spectra of those 80 nm-thick rubrene thin-films deposited on correspondingly SAM-treated glass.

In order to determine the optimum rubrene TFT with the highest performance potentials, we have fabricated four types of TFT devices adopting aforementioned SAM-modified  $\text{SiO}_2$  and pristine  $\text{SiO}_2$  as gate dielectrics. The inset of Fig. 3 shows 3-dimensional (3-D) schematic drawing of our rubrene TFTs and the Fig. 3 shows the drain current–drain voltage ( $I_D$ – $V_D$ ) output curves obtained from the four rubrene TFTs: TFTs on pristine, HMDS-treated,

7-OTS-treated, and FTS-treated 200 nm-thick  $\text{SiO}_2$  dielectrics. According to the output curves, rubrene TFTs with pristine and 7-OTS-treated  $\text{SiO}_2$  exhibited almost the same saturation level of drain current ( $I_{D,\text{sat}} \sim 60$  nA) at the gate bias ( $V_G$ ) of  $-40$  V but the  $I_{D,\text{sat}}$  level of devices obtained from HMDS-treated and FTS-treated  $\text{SiO}_2$  were 220 and 245 nA, respectively which are much higher than 60 nA at the same  $V_G$ . These results were reflected by the

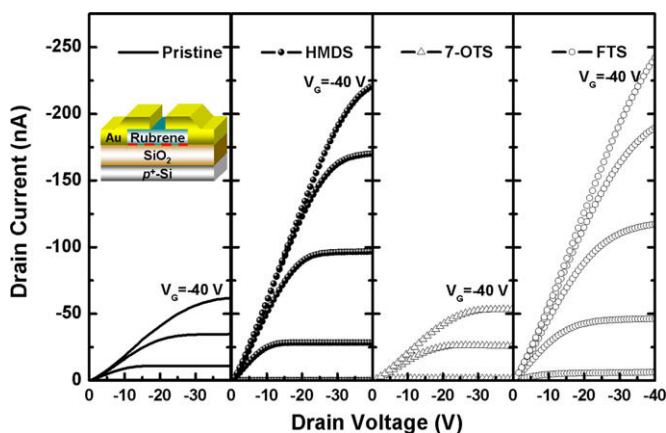


**Fig. 3.** Output characteristics ( $I_D$  vs.  $V_D$ ) of the rubrene TFTs with pristine, HMDS-, 7-OTS-, and FTS-treated  $\text{SiO}_2$  dielectrics.

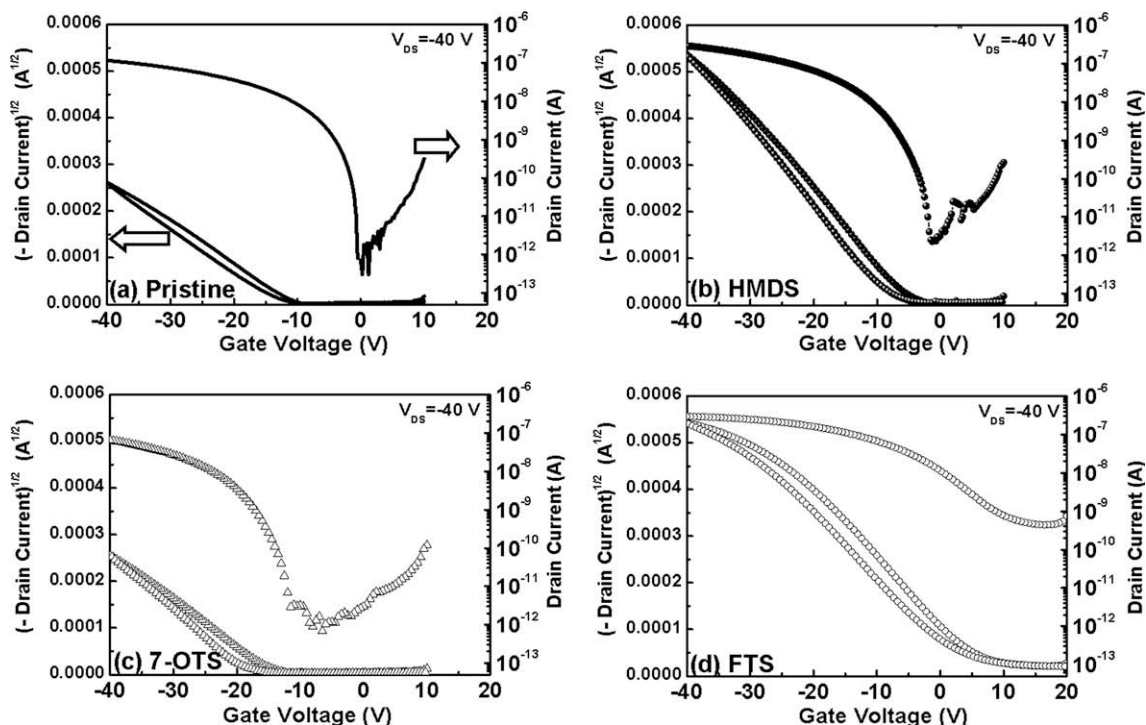


Fig. 4.  $\sqrt{-I_D}$  vs.  $V_G$  and  $\text{Log}(-I_D)$  vs.  $V_G$  transfer curves of the rubrene TFTs with (a) pristine, (b) HMDS-, (c) 7-OTS-, and (d) FTS-treated  $\text{SiO}_2$  dielectrics.

corresponding drain current-gate bias ( $I_D$ - $V_G$ ) transfer curves of Fig. 4a–d. Under a drain-source bias ( $V_{DS}$ ) of  $-40$  V our organic TFTs with (a) pristine, (b) HMDS treated, (c) 7-OTS treated, and (d) FTS-treated  $\text{SiO}_2$  dielectrics exhibited the saturation field effect mobilities of 0.0020, 0.0080, 0.0024, and 0.0050  $\text{cm}^2/\text{V s}$ , respectively (and by extending the annealing time (24 h) for the rubrene film on HMDS-treated surface, we could achieve a little higher mobility of  $\sim 0.01$   $\text{cm}^2/\text{V s}$ ). All the rubrene TFTs displayed on/off current ratio of  $\sim 10^5$  except the one with FTS-treated  $\text{SiO}_2$ , which showed only  $\sim 10^3$ . In terms of on-state current and mobility, we could regard that the organic TFTs with HMDS- and FTS-treated dielectrics displayed good potentials toward device performance. Their high mobilities are certainly because their rubrene channels have been mostly covered by crystalline phase, which must be true in that the crystalline coverage of the HMDS- and FTS-treated cases was 90% and 100%, respectively (see Fig. 1a–d). However, in terms of the off-state current and sub-threshold swing the OTFT with FTS-treated  $\text{SiO}_2$  appears less desirable than the other one with HMDS-treated  $\text{SiO}_2$  dielectric, displaying two orders of magnitude higher off-current. As the AFM image of crystalline rubrene film grown on FTS-treated dielectric shown in Fig. 2d, the film contains many micro-grains as a result of the fast crystalline growth. Consequently the total grain boundary area becomes large and as a matter of fact the boundary area may play as carrier trap center. Many of trapped whole charges are de-trapped at a depletion state under a gate bias for off-state, resulting in an elevated level of off-state current.

#### 4. Conclusion

In summary, we have implemented a systematic study for the crystalline growth of vacuum-deposited rubrene film on several dielectric surfaces modified with HMDS, 7-OTS, and FTS in the order of hydrophobic tendency, in order to achieve or determine an optimal SAM layer leading to optimum OTFT performance in both terms of mobility and on/off ratio. Our rubrene TFT with HMDS-coated  $\text{SiO}_2$  dielectric showed quite high field mobility of 0.008–0.01  $\text{cm}^2/\text{V s}$  and on/off current ratio of  $\sim 10^5$  under 40 V. We conclude that HMDS is presently the most effective and promising SAM interlayer for polycrystalline rubrene channel formation, which involves an amorphous-to-crystalline phase transition during post-annealing.

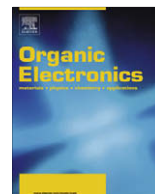
#### Acknowledgement

This research was performed with the financial support from LG. Philips LCD (project year 2005). The authors also acknowledge the support from Brain Korea 21 Project. Among these authors, J.-M. Choi acknowledges Seoul Science Fellowship.

#### References

- [1] X.-H. Zhang, B. Domercq, X. Wang, S. Yoo, T. Kondo, Z.L. Wang, B. Kippel, *Org. Electron.* 8 (2007) 718.
- [2] T. Cahyadi, H.S. Tan, E.B. Namdas, S.G. Mhaisalkar, P.S. Lee, Z.-K. Chen, C.M. Ng, F.Y.C. Boey, *Org. Electron.* 8 (2007) 455.
- [3] N. Stingelin-Stutzmann, E. Smits, H. Wonderegern, C. Tanase, P. Blom, P. Smith, D.D. Leeuw, *Nature Mater.* 4 (2005) 601.

- [4] V.C. Sundar, J. Zaumseil, V. Podzorov, E. Menard, R.L. Willett, T. Someya, M.E. Gershenson, J.A. Rogers, *Science* 303 (2004) 1644.
- [5] V. Podzorov, V.M. Pudalov, M.E. Gershenson, *Appl. Phys. Lett.* 82 (2003) 1739.
- [6] A.L. Briseno, S.C.B. Mannsfeld, M.M. Ling, S. Liu, R.J. Tseng, C. Reese, M.E. Roberts, Y. Yang, F. Wudl, Z. Bao, *Nature* 444 (2006) 913.
- [7] S. Seo, B.-N. Park, P.G. Evans, *Appl. Phys. Lett.* 88 (2006) 232114.
- [8] D. Käfer, G. Witte, *Phys. Chem. Chem. Phys.* 7 (2005) 2850.
- [9] C.H. Hsu, J. Deng, C.R. Staddon, P.H. Beton, *Appl. Phys. Lett.* 91 (2007) 193505.
- [10] S.-W. Park, S.H. Jeong, J.-M. Choi, J.M. Hwang, J.H. Kim, S. Im, *Appl. Phys. Lett.* 91 (2007) 033506.
- [11] A. Ulman, *Chem. Rev.* 96 (1996) 1533.
- [12] J.H. Cho, Y.D. Park, D.H. Kim, W.-K. Kim, H.W. Jang, J.-L. Lee, K. Cho, *Appl. Phys. Lett.* 88 (2006) 102104.
- [13] P. Marmont, N. Battaglini, P. Lang, G. Horowitz, J. Hwang, A. Kahn, C. Amato, P. Calas, *Org. Electron.* 9 (2008) 419.
- [14] H. Yang, T.J. Shin, M.-M. Ling, K. Cho, C.Y. Ryu, Z. Bao, *J. Am. Chem. Soc.* 127 (2005) 11542.
- [15] I. Yagi, K. Tsukagoshi, Y. Aoyagi, *Appl. Phys. Lett.* 86 (2005) 103502.



## Letter

## Effects of thickness and thermal annealing of the PEDOT:PSS layer on the performance of polymer solar cells

Youngkyoo Kim<sup>a,b,\*</sup>, Amy M. Ballantyne<sup>b</sup>, Jenny Nelson<sup>b</sup>, Donal D.C. Bradley<sup>b</sup><sup>a</sup> Organic Nanoelectronics Laboratory, Department of Chemical Engineering, Kyungpook National University, Daegu 702-701, Republic of Korea<sup>b</sup> Blackett Laboratory, Department of Physics, Imperial College London, Prince Consort Road, London SW7 2AZ, United Kingdom

## ARTICLE INFO

## Article history:

Received 10 July 2008

Received in revised form 10 September 2008

Accepted 5 October 2008

Available online 14 October 2008

## PACS:

72.80.Le

73.40.-C

82.35.Cd

## Keywords:

Polymer solar cells

PEDOT:PSS

Thermal annealing

P3HT

PCBM

## ABSTRACT

We report the influence of thickness and thermal annealing of the poly(3,4-ethylenedioxythiophene):poly(styrenesulfonate) (PEDOT:PSS) layer on the performance of bulk heterojunction solar cells made from blends of regioregular poly(3-hexylthiophene) and 1-(3-methoxycarbonyl)-propyl-1-phenyl-(6,6)C<sub>61</sub>. Results show that the power conversion efficiency was significantly improved by inserting the PEDOT:PSS layer but was not strongly sensitive to either the layer thickness or the annealing temperature. Although the short circuit current density was enhanced slightly by annealing the PEDOT:PSS layer at high temperatures, the fill factor was slightly decreased. The trend in device performance could not be explained by the observed changes in the work function of the PEDOT:PSS layer.

© 2008 Elsevier B.V. All rights reserved.

Since the first reports of organic solar cells based on blends of conjugated polymers and fullerene derivatives [1,2], device performance has been greatly improved by selection of materials with suitable energy levels, control of nanomorphology [3] either during film deposition [4] or using post-fabrication procedures such as thermal annealing [5–9], and by optimisation of electrode materials [10]. Devices made from the well studied combination of poly(3-hexylthiophene) (P3HT) and 1-(3-methoxycarbonyl)-propyl-1-phenyl-(6,6)C<sub>61</sub> (PCBM) have been reported to produce power conversion efficiency (PCE) of

4–5% [4,7,8,10], while devices made from poly[2,6-(4,4-bis-(2-ethylhexyl)-4H-cyclopenta[2,1-b;3,4-b']-dithiophene)-alt-4,7-(2,1,3-benzothiadiazole)] (PCPDTBT):PCBM blend have been reported to produce PCE of up to 5.5% [11].

Most of these high efficiency polymer:fullerene solar cells are made with a poly(3,4-ethylenedioxythiophene):poly(styrenesulfonate) (PEDOT:PSS) layer, which is inserted between the transparent electrode, typically indium-tin oxide (ITO) and the light-absorbing organic layer. The positive effect of this PEDOT:PSS layer on device performance has been attributed to improved selectivity of the anode, on account of the higher work function relative to ITO [12], improved smoothness of the electrode/active layer contact [13], and increased photovoltage through the surface enrichment of PSS components [14]. Despite

\* Corresponding author. Address: Organic Nanoelectronics Laboratory, Department of Chemical Engineering, Kyungpook National University, Daegu 702-701, Republic of Korea.

E-mail address: [ykimm@knu.ac.kr](mailto:ykimm@knu.ac.kr) (Y. Kim).

the apparent importance of the PEDOT:PSS layer for high efficiency [4,7,8,11], the device performance has not yet been correlated to the specific properties of the PEDOT:PSS layer such as thickness, conductivity and morphology. Moreover, the literature contains quite a range of PEDOT:PSS layer thicknesses and annealing treatments, even for otherwise similar devices [6,15–18].

Here we report studies of the effect of thickness and annealing temperature of the PEDOT:PSS layer on the performance of bulk heterojunction solar cells made with blends of regioregular P3HT and PCBM. The results are considered in terms of variations in work function, conductivity and surface morphology of the PEDOT:PSS layers.

The P3HT:PCBM (50 wt.% PCBM) solution was prepared in chlorobenzene as reported previously [6]. PEDOT:PSS (Baytron P standard grade, HC Starck) layers were prepared by spin-coating onto pre-cleaned ITO-coated glass substrates [6]. For the study of thickness dependence, layer thickness was varied from 60 to 165 nm by varying spin rate, and films were then soft-baked at 50 °C for 15 min. A 70 nm thick P3HT:PCBM active layer was then deposited by spin-coating at 2500 rpm. To study annealing temperature, the thickness of PEDOT:PSS layer was fixed at 70 nm and the PEDOT:PSS coated substrates were annealed for 15 min at temperatures from 75 °C to 230 °C using a precision hot plate which has a glass cover to protect samples from moisture attack from outside. A 90 nm thick P3HT:PCBM layer was then deposited on top by spin-coating at 1500 rpm. Devices of 4.5 mm<sup>2</sup> were defined by thermal evaporation of aluminium top contacts through a shadow mask. In each case about 18 devices were fabricated to check the reproducibility of resulting data. In order to minimize the sample-to-sample variation of device performance we measured pixels in similar positions on each substrate. Since annealing of the active layer (after complete device fabrication) significantly affects device performance and may also affect the PEDOT:PSS layer, each device set was replicated. One set of devices was not further annealed (non-annealed or 'NAN' devices) and the other set was further annealed at 140 °C for 15 min (annealed or 'AN' devices).

The photovoltaic characteristics of devices were measured as described in Ref. 6, but with an incident light intensity of simulated solar light of 85 mW/cm<sup>2</sup>. The work functions of the PEDOT:PSS layers were calculated from the chemical potential that was measured by using a Kelvin probe (Kelvin Control 07, Besocke Delta Phi GmbH) by comparison to a gold reference. The surface morphology of the PEDOT:PSS layers and ITO was measured by using an atomic force microscope (AFM, Burleigh). The sheet conductivity was measured using a four point probe (Newport).

Fig. 1a shows the current density – voltage (*J*–*V*) characteristics of as-fabricated P3HT:PCBM devices with different PEDOT:PSS layer thicknesses. The data show that device performance is improved by inserting the PEDOT:PSS layer, irrespective of its thickness. This result is in good agreement with the previous result for vacuum deposited small molecule (C<sub>60</sub>: copper phthalocyanine) solar cells [19]. Here the sigmoidal *J*–*V* shape for the device without the PEDOT:PSS layer can be attributed to an interfacial barrier

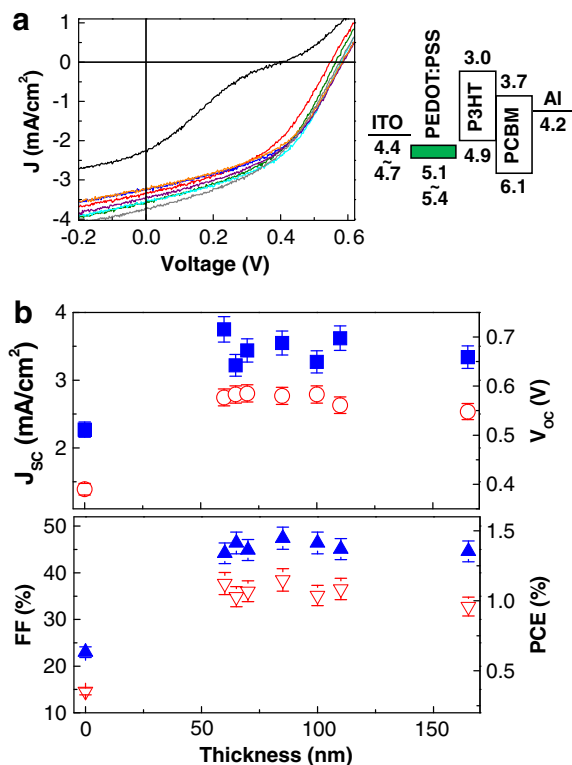


**Fig. 1.** (a) (Left) *J*–*V* characteristics (AM 1.5, 85 mW/cm<sup>2</sup>) of devices with non-annealed P3HT:PCBM layer (70 nm) and non-annealed PEDOT:PSS layer of which thickness is 0 (ITO only; black line), 60 (gray line), 65 (orange line), 70 (purple line), 85 (sky blue line), 100 (blue line), 110 (green line), and 165 nm (red line). (Right) Ideal flat energy band diagram for the device with the PEDOT:PSS layer; (b) *J*<sub>sc</sub> (filled squares), *V*<sub>oc</sub> (open circles), FF (filled upward triangles), and PCE (open downward triangles) as a function of PEDOT:PSS layer thickness. (For interpretation of the references to color in this figure legend, the reader is referred to the web version of this article).

between ITO and the active layer which can cause slow charge transfer [20]. The increased short circuit current density (*J*<sub>sc</sub>) and fill factor (FF) on inclusion of the PEDOT:PSS layer are attributed to the improved efficiency of hole transfer between P3HT and PEDOT:PSS compared to hole transfer between P3HT and ITO. Because the work function of ITO is approximately 0.3–0.5 eV lower than the ionisation potential of P3HT, a barrier exists for hole injection at the ITO–P3HT interface. In contrast, the higher work function of PEDOT:PSS (measured by Kelvin probe and shown in Fig. 3) means that the contact will be ohmic for holes (see the flat energy band diagram in Fig. 1a).

The open circuit voltage (*V*<sub>oc</sub>) was also observed to increase on insertion of the PEDOT:PSS layer. Since the same P3HT:PCBM layer is used for each device, this change in *V*<sub>oc</sub> can be attributed primarily to the effect of the significantly (>0.4 eV) increased work function relative to ITO: Better matching of the electrode work functions with the transport levels of the active materials allows the open circuit voltage to approach closer to the theoretical limit for any combination of donor and acceptor. As a result, the insertion of PEDOT:PSS layer improved PCE by a factor of 1.8.

Device performance was not strongly sensitive to PEDOT:PSS film thickness over the range measured (60–165 nm). The trend in  $J_{SC}$  is in moderately good agreement with theoretical calculations which predict a gradual decrease in  $J_{SC}$  of some 10% of its value as the PEDOT:PSS layer thickness is increased from 50 nm to 160 nm, with a local maximum in the region 100–140 nm, for the active layer thickness used here [17]. Only approximate agreement can be expected with such calculations for perfectly planar structures, on account of the roughness of the ITO and PEDOT:PSS layers (see below) that are used in practice. Finally, we note that the shape of  $J$ - $V$  curves was not influenced by the PEDOT:PSS layer thickness. This indicates that the overall charge collection efficiency is not strongly affected by any variation in PEDOT:PSS film morphology due to different spin-coating speed. The linear shape of the  $J$ - $V$  curves near  $V_{OC}$  is most likely the result of serial resistance due to relatively low conductivity of the soft-baked PEDOT:PSS films, as discussed in detail below.

Next, the effect of thermal annealing of the PEDOT:PSS layer (thickness = 70 nm) was studied for both NAN devices and AN devices. As shown in Fig. 2a and b, the  $J$ - $V$  characteristics of neither set of devices was significantly affected by the annealing temperature of the PEDOT:PSS

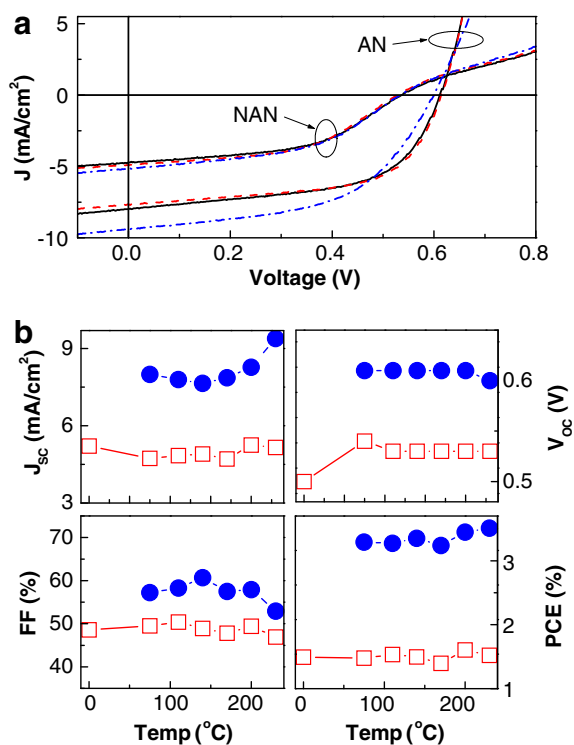


**Fig. 2.** (a)  $J$ - $V$  characteristics (AM 1.5, 85 mW/cm<sup>2</sup>) of devices: 'NAN' denotes the devices with non-annealed P3HT:PCBM layer (90 nm) and PEDOT:PSS layer (70 nm) annealed at 75 (black solid line), 140 (red dashed line), 230 °C (blue dash-dot line), while 'AN' represents the annealed devices of the 'NAN' devices at 140 °C for 15 min. (b)  $J_{sc}$ ,  $V_{oc}$ , FF, and PCE as a function of PEDOT:PSS annealing temperature: Red open squares and blue filled circles denote 'NAN' and 'AN' devices, respectively. (For interpretation of the references to color in this figure legend, the reader is referred to the web version of this article).

layer, although all AN devices show a much higher  $J_{SC}$  than NAN devices, as previously reported [4–6]. Both NAN and AN devices show a slight increase in  $J_{SC}$  upon annealing the PEDOT:PSS layer at high temperatures (Fig. 2b) while the FF reduces slightly. As the annealing temperature of the PEDOT:PSS film affects the intensity but not the shape of external quantum efficiency spectra (data not shown), these  $J_{SC}$  trends are unlikely to be caused by a change in morphology of the photoactive layer but may relate to the morphology or conductivity of the PEDOT:PSS layer. Therefore the effect of thermal annealing of the PEDOT:PSS layer on these properties was studied.

The work function (Fig. 3 top panel) is observed to decrease monotonically with the annealing temperature, in accordance with a previous report by Huang et al. [21]. This suggests that the surface concentration of PSS components is reduced with an increase in annealing temperature. The drop in work function cannot explain the increase in  $J_{SC}$  but is small enough (<0.15 eV) for the PEDOT:PSS – P3HT contact to remain approximately ohmic over the range of annealing temperatures explored, and therefore it is unlikely to be expected to degrade performance. In contrast, as shown in Fig. 3 (bottom panel), the conductivity is observed to increase as annealing temperature is increased above 100 °C, and then decrease as the annealing temperature is increased above 200 °C. This change in conductivity is likely due to a change in oxidation state of the polymer, where heating at temperatures between 100 and 200 °C cause an increase in oxidation state, but heating above 200 °C causes over-oxidation and degradation of the film [21–24]. Although the change in sheet conductivity at high annealing temperatures correlates with FF, possibly due to an increase in series resistance, it does not correlate to the change in  $J_{SC}$ , and so cannot explain the increase in  $J_{SC}$  at annealing temperatures in the range 160–200 °C. However, the four point probe technique is not sensitive to changes in conductivity in the direction perpendicular to the substrate, which could result in this case from changes in the vertical distribution of PSS within the layer and could also

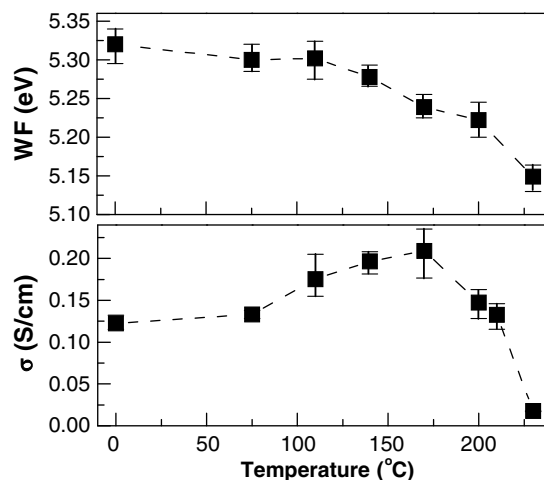


**Fig. 3.** Work function (WF, top panel) and conductivity ( $\sigma$ , bottom panel) of PEDOT:PSS layers (70 nm thick) as a function of annealing temperature.

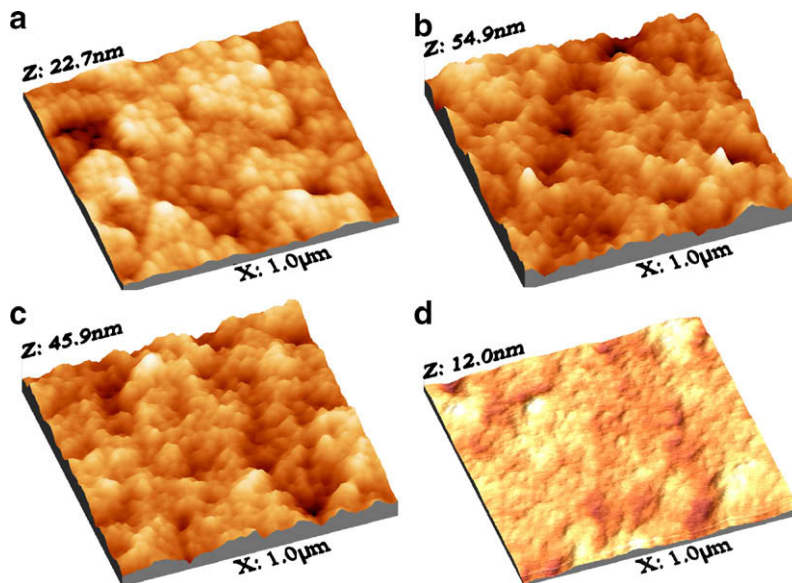


**Fig. 4.** AFM images ( $1 \times 1 \mu\text{m}$ ) of ITO surface (a;  $R_g = 3.3 \text{ nm}$ ) and PEDOT:PSS layer (70 nm thick) annealed at  $75 \text{ }^\circ\text{C}$  (b;  $R_g = 6.9 \text{ nm}$ ),  $140 \text{ }^\circ\text{C}$  (c;  $R_g = 5.8 \text{ nm}$ ), and  $230 \text{ }^\circ\text{C}$  (d;  $R_g = 1.4 \text{ nm}$ ).

influence  $J_{SC}$ . Measurements of the change in surface roughness of the PEDOT:PSS layer upon thermal annealing suggest an alternative explanation for the increase in  $J_{SC}$ . AFM images (Fig. 4) show that while annealing of the PEDOT:PSS layer at  $140 \text{ }^\circ\text{C}$  leads to fluctuations in thickness of tens of nm, a much smoother film results from annealing above  $200 \text{ }^\circ\text{C}$ . The smoother surface should enable a more uniform interfacial contact between the PEDOT:PSS and P3HT:PCBM layers, after thermal annealing of the active layer, and so avoid local fluctuations in collection efficiency that could limit  $J_{SC}$ .

With regards to  $V_{OC}$ , thermal annealing of the PEDOT:PSS layer improved  $V_{OC}$  for NAN devices irrespective of annealing temperature. As for  $J_{SC}$ , this cannot be attributed to the enrichment of PSS components on the surface of PEDOT:PSS layer as previously reported [14]. The higher  $V_{OC}$  in AN devices than NAN devices (regardless of PEDOT:PSS annealing temperature) can be explained by the previously reported effects of thermal annealing on charge recombination kinetics [7] and on vertical distribution of components [25]. The combined trends lead to the highest PCE (3.5%) for annealed devices at a PEDOT:PSS annealing temperature of  $230 \text{ }^\circ\text{C}$  but no clear optimum for non-annealed devices.

In summary, the performance of P3HT:PCBM blend solar cells was significantly improved by addition of a PEDOT:PSS layer, as previously reported. The short circuit current density decreases slightly with increasing thickness of this layer (over a range 60–165 nm) in agreement with theoretical calculations. Thermal annealing of the PEDOT:PSS layer at high temperatures ( $200\text{--}230 \text{ }^\circ\text{C}$ ) increased  $J_{SC}$  slightly but decreased FF. It is proposed that these influences are caused by variations in conductivity and surface roughness of the PEDOT:PSS layers with thermal annealing temperature. The work function was also

observed to decrease with an increase in annealing temperature whilst remaining high enough to provide an ohmic contact with P3HT and is consistent with the small observed trend in  $V_{OC}$ . The small variation in PCE with annealing temperature is consistent with the large variation in annealing temperature ( $10\text{--}230 \text{ }^\circ\text{C}$ ) of PEDOT:PSS layers commonly used in devices reported in the literature.

### Acknowledgements

The authors thank Merck Chemicals Ltd for supplying the P3HT polymer and BP Solar (OSCEP project), the Department of Trade and Industry (project no. TP/2/RT/6/I/10384) and the Korea Science and Engineering Foundation (KOSEF) grant funded by the Korea government (MOST) (No. R01-2007-000-10836-0) for financial support. The authors thank James Durrant, Dmitry Poplavskyy, Jingsong Huang, and Xuhua Wang for useful discussions and help with Kelvin and 4-point probe measurements.

### References

- [1] G. Yu, J. Gao, J.C. Hummelen, F. Wudl, A.J. Heeger, *Science* 270 (1995) 1789.
- [2] C.W. Tang, *Appl. Phys. Lett.* 48 (1986) 183.
- [3] S.E. Shaheen, C.J. Brabec, N.S. Sariciftci, F. Padinger, T. Fromherz, J.C. Hummelen, *Appl. Phys. Lett.* 78 (2001) 841.
- [4] G. Li, V. Shrotriya, J. Huang, Y. Yao, T. Moriarty, K. Emery, Y. Yang, *Nat. Mater.* 4 (2005) 864.
- [5] F. Padinger, R.S. Ritterberger, N.S. Sariciftci, *Adv. Funct. Mater.* 13 (2003) 85.
- [6] Y. Kim, S.A. Choulis, J. Nelson, D.D.C. Bradley, S. Cook, J.R. Durrant, *Appl. Phys. Lett.* 86 (2005) 063502.
- [7] Y. Kim, S. Cook, S.M. Tuladhar, J. Nelson, J.R. Durrant, D.D.C. Bradley, M. Giles, I. McCulloch, M. Ree, C.S. Ha, *Nat. Mater.* 5 (2006) 197.
- [8] M. Reyes-Reyes, K. Kim, J. Dewald, R. López-Sandoval, A. Avadhanula, S. Curran, D.L. Carroll, *Org. Lett.* 7 (2005) 5749.
- [9] P. Peumans, S. Uchida, S.R. Forrest, *Nature* 425 (2003) 158.



- [10] M.D. Irwin, D.B. Buchholz, A.W. Hains, R.P.H. Chang, T.J. Marks, *Proc. Nat. Acad. Sci.* 105 (2008) 2783.
- [11] J. Peet, J.Y. Kim, N.E. Coates, W.L. Ma, D. Moses, A.J. Heeger, *Nat. Mater.* 6 (2007) 497.
- [12] S. Khodabakhsh, B.M. Sanderson, J. Nelson, T.S. Jones, *Adv. Funct. Mater.* 16 (2006) 95.
- [13] A.C. Arias, M. Granström, D.S. Thomas, K. Petritsch, R.H. Friend, *Phys. Rev. B* 60 (1999) 1854.
- [14] F.L. Zhang, A. Gadisa, O. Inganäs, M. Svensson, M.R. Andersson, *Appl. Phys. Lett.* 84 (2004) 3906.
- [15] G. Li, V. Shrotriya, Y. Yao, Y. Yang, *J. Appl. Phys.* 98 (2005) 043704.
- [16] R.C. Hiorns, R. de Bettignies, J. Leroy, S. Baily, M. Firon, C. Sentein, A. Khoukh, H. Preud'homme, C. Dagron-Lartigau, *Adv. Funct. Mater.* 16 (2006) 2263.
- [17] A.J. Moule, K. Meerholz, *Appl. Phys. B* 86 (2007) 721.
- [18] A.M. Ballantyne, L. Chen, J. Nelson, D.D.C. Bradley, Y. Astuti, A. Maurano, C.G. Shuttle, J.R. Durrant, M. Heeney, W. Duffy, I. McCulloch, *Adv. Mater.* 19 (2007) 4544.
- [19] P. Peumans, S.R. Forrest, *Appl. Phys. Lett.* 79 (2001) 126.
- [20] J. Nelson, J. Kirkpatrick, P. Ravirajan, *Phys. Rev. B* 69 (2004) 035337.
- [21] J. Huang, P.F. Miller, J.S. Wilson, A.J. de Mello, J.C. de Mello, D.D.C. Bradley, *Adv. Funct. Mater.* 15 (2005) 290.
- [22] F. Mohammad, P.D. Calvert, N.C. Billingham, *Synth. Met.* 66 (1994) 33.
- [23] P. Rannou, M. Nechtschein, *Synth. Met.* 101 (1999) 474.
- [24] I. Winter, C. Reese, J. Hormes, G. Heywang, F. Jonas, *Chem. Phys.* 194 (1995) 207.
- [25] M. Campoy-Quiles, T. Ferenczi, T. Agostinelli, P.G. Etchegoin, Y. Kim, T. Anthopoulos, P.N. Stavrinou, D.D.C. Bradley, J. Nelson, *Nat. Mater.* 7 (2008) 158.



## Letter

Ambipolar permeable metal-base transistor based on NPB/C<sub>60</sub> heterojunctionJinying Huang<sup>a</sup>, Mingdong Yi<sup>a</sup>, Ivo A. Hümmelgen<sup>b,\*</sup>, Dongge Ma<sup>a,\*</sup><sup>a</sup>State Key Laboratory of Polymer Physics and Chemistry, Changchun Institute of Applied Chemistry, Graduate School of the Chinese Academy of Sciences, Chinese Academy of Sciences, Changchun 130022, People's Republic of China<sup>b</sup>Group of Organic Optoelectronic Devices, Departamento de Física, Universidade Federal do Paraná, Caixa Postal 19044, 81531-990 Curitiba PR, Brazil

## ARTICLE INFO

## Article history:

Received 23 July 2008

Received in revised form 17 October 2008

Accepted 29 October 2008

Available online 6 November 2008

## PACS:

81.07.Pr

73.40.Vz

85.30.De

## Keywords:

Ambipolar

Organic

Permeable metal-base transistor

Heterojunction

Air stable

## ABSTRACT

In this paper, we report the fabrication of permeable metal-base organic transistors based on *N,N'*-diphenyl-*N,N'*-bis(1-naphthylphenyl)-1,1'-biphenyl-4,4'-diamine (NPB)/C<sub>60</sub> heterojunction as both emitter and collector. By applying different polarities of voltage bias to the collector and the base, and input current to the emitter, the ambipolar behavior can be observed. The device demonstrates excellent common-base characteristics both in *P*-type and *N*-type modes with common-base current gains of 0.998 and 0.999, respectively.

© 2008 Elsevier B.V. All rights reserved.

In recent years, organic transistors are technologically interesting because they could serve as the main component in cheap and flexible electronic circuits, such as flexible displays [1,2] and integrated circuits [3,4]. For the development of electronic circuits based on organic semiconductors, the transistors need to go beyond unipolarity. The simultaneous transport of both types of carriers could lead to a simplification in the design of the complementary logic circuits, allowing at the same time to reduce power dissipation and increase noise margins. As a consequence, a lot of efforts have been made towards the fabrication and optimization of ambipolar transistors [5–11].

Ambipolar organic transistors have been fabricated by applying blends [5–7], bilayers of holes and electrons transporting materials [8], interface dopant [9] and electron injection electrodes [10]. Recently, transistor with vertical structure achieving ambipolar characteristics by inserting a transition-metal-oxide layer at the source/organic interface to form a unique nanoscale structure was reported [11]. In this letter, we fabricated another type of vertical structure organic transistors, namely permeable metal-base organic transistors, based on *N,N'*-diphenyl-*N,N'*-bis(1-naphthylphenyl)-1,1'-biphenyl-4,4'-diamine (NPB)/C<sub>60</sub> heterojunction as the emitter and the collector, and Al/Al:Ca/Al base electrode. It is found that the devices showed ambipolar behavior with common-base current gains of 0.99 for both, *P*-type and *N*-type modes, respectively.

Fig. 1a shows the schematic diagram of the studied device structure. The patterned ITO glass substrate was first cleaned and dried, and then put in a vacuum chamber.

\* Corresponding authors. Tel.: +86 431 85262357; fax: +86 431 85262873 (D. Ma).

E-mail addresses: [iah@fisica.ufpr.br](mailto:iah@fisica.ufpr.br) (I.A. Hümmelgen), [mdg1014@ciac.jl.cn](mailto:mdg1014@ciac.jl.cn) (D. Ma).

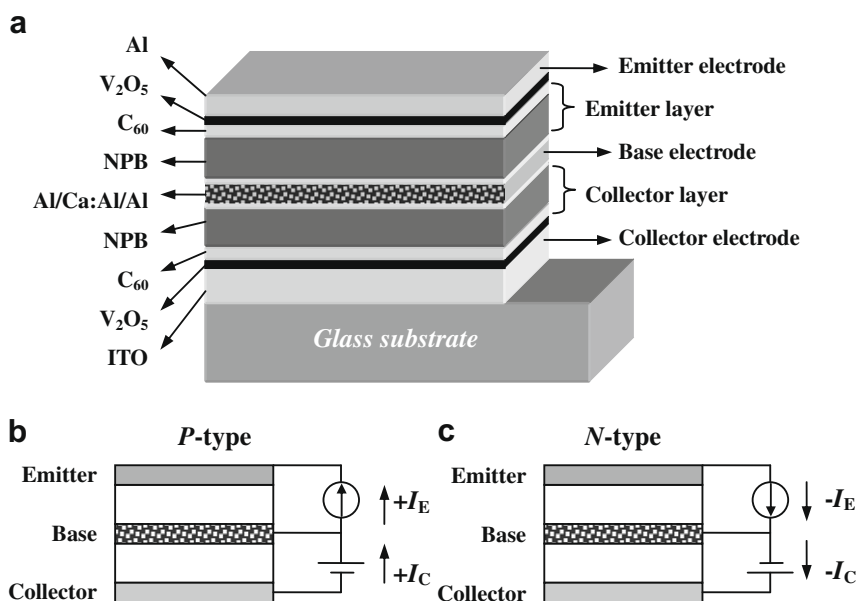


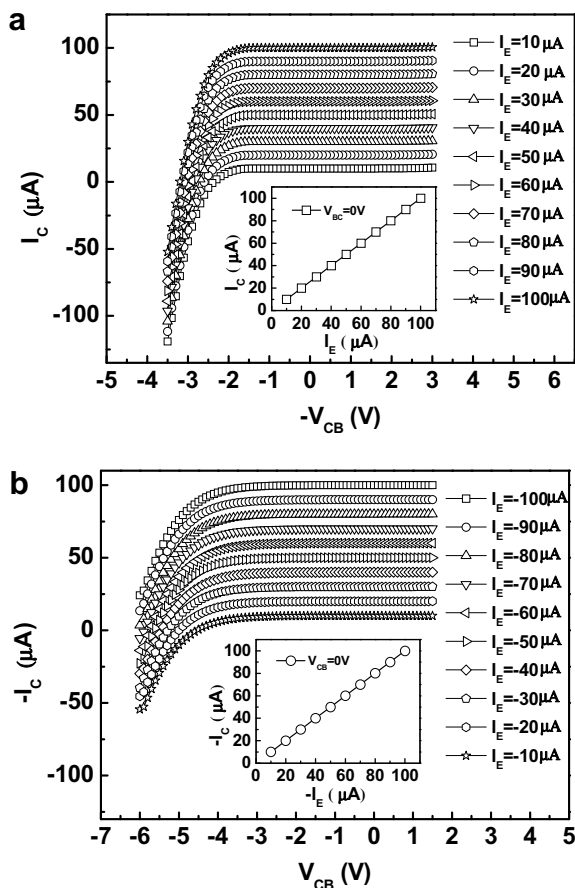
**Fig. 1.** (a) The schematic diagram of the proposed ambipolar PBT structure. (b) Ambipolar device operating modes for *P*-type. (c) Ambipolar device operating modes for *N*-type.

At a pressure of  $\sim 5 \times 10^{-4}$  Pa, a 5 nm thick vanadium oxide ( $V_2O_5$ ) film, a 10 nm  $C_{60}$  film, a 50 nm NPB film, a 5 nm Al film and a 15 nm Ca:Al alloy film were evaporated in sequence on ITO. Amongst, the heterojunction consisting of  $C_{60}$ /NPB was used as the collector, and the  $V_2O_5$  was used as the buffer layer to enhance the injection of charge carriers. Ca and Al were co-evaporated to form the Ca:Al alloy layer. The evaporation rates of aluminum and calcium were 0.2 nm/s and 0.1 nm/s, respectively. At this time, taking out the samples and annealing them at 120 °C for five minutes in air. After annealing, the samples were putted in the vacuum again. When the vacuum achieved  $\sim 5 \times 10^{-4}$  Pa, then a 5 nm Al, 50 nm NPB, 10 nm  $C_{60}$ , 5 nm  $V_2O_5$  and 120 nm Al films were in turn deposited to finish the fabrication of the devices. Thus the NPB/ $C_{60}$  heterojunction forms the emitter and the Al/Ca:Al/Al forms the base. All the organic layers and  $V_2O_5$  were deposited at a rate of 0.2 nm/s with the substrate temperature maintained at room temperature. The device area defined as the overlap of three electrodes was 6 mm<sup>2</sup>. The electric characteristics measurements were performed in the dark using two Keithley 2400 Sourcemeters. For the measured results throughout this work, we use the following definition,  $V_{BE} \equiv V_B - V_E$ ;  $V_{CB} \equiv V_C - V_B$ , and when the device is in *P*-type mode,  $I_E$  and  $I_C$  are positive, whereas the input/output currents are negative, this device operates in *N*-type mode. The subscripts E, B and C denote emitter, base and collector, respectively. Fig. 1b and c show the operating modes for *P*-type and *N*-type cases, respectively.

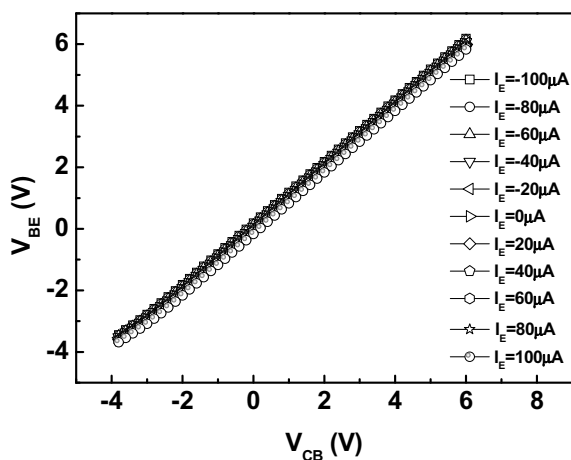
By applying different polarities of voltage biases between the collector and the base, and the input current to the emitter, the ambipolar behavior can be observed. In Fig. 2a and b, the common-base characteristics are plotted for *P*- and *N*-type devices. When operated as a *P*-type device with the measurement shown in Fig. 1b, the device demonstrates excellent common-base characteristics, as shown in

Fig. 2a. For increasingly negative  $-V_{CB}$ , there is a sharp increase in negative  $I_C$  for holes injection from the collector through the  $C_{60}$ /NPB heterojunction to the base. When  $-V_{CB}$  increases to positive values, the  $I_C$  meets a plateau soon and keeps the value  $I_C \cong I_E$  afterward. The device also gives out fine *N*-type common-base characteristics, as presented in Fig. 2b, when working in *N*-type mode in Fig. 1c. It can be observed that  $-I_C$  is negative and large at  $V_{CB} = -6$  V, accounting for the presence of electrons injection between the collector and the base, and increases with the increasing of  $V_{CB}$  up to a saturation value close to the selected  $-I_E$ . The insets depict output current  $I_C$  dependence on input current  $I_E$  at  $V_{CB} = 0$  V, which offer the calculation of the common-base gain  $\alpha \equiv \frac{\partial I_C}{\partial I_E}$ , to be about 0.998 and 0.999 for *P*- and *N*-type modes, respectively. These high common-base gains indicate that whether charge carriers are injected by the emitter are able to be transferred through the  $C_{60}$ /NPB heterojunction and cross the base, being collected by the collector.

Fig. 3 shows the variation of  $V_E$  necessary to maintain  $I_E$  constant during the  $V_{CB}$  scan. As can be seen,  $|dV_{EB}/dV_{CB}| \cong 1$  at different values of  $I_E$ , ranging from 100  $\mu$ A (bottom) to  $-100$   $\mu$ A (top) at steps of  $-10$   $\mu$ A, indicating that the device operates as PBT both in *P*-type and *N*-type modes [12]. As known, the process that charge transfer between the emitter and collector occurs mainly through small openings in the base layer, rather than by ballistic transport across it, is the principle behind PBTs [12]. In our devices, openings formed by annealing. Annealing caused the base layer Al:Ca to be oxidized partially and result in a ultra thin oxidized surface and pin-like-oxide penetrated into the base layer due to the easier oxidation of the calcium in air with respect to aluminum. Obviously, the pin-like-oxide can act as the efficient openings, thus the carriers transport from the emitter to the collector, rather than shield by the thick base electrode [13].



**Fig. 2.** (a) Common-base characteristics of the ITO/ $V_2O_5$ / $C_{60}$ /NPB/Al/AI:Ca/Al/NPB/ $C_{60}$ / $V_2O_5$ /Al device operating at P-type mode. (b) Common-base characteristics of the device operating at N-type mode. The insets show  $I_C$  as a function of  $I_E$  at  $V_{CB} = 0$  V.



**Fig. 3.**  $-V_{BE}$  ( $-V_{CB}$ ) characteristics of the ITO/ $V_2O_5$ / $C_{60}$ /NPB/Al/AI:Ca/Al/NPB/ $C_{60}$ / $V_2O_5$ /Al device at different  $I_E$  values.

Moreover, the ambipolar PBTs exhibit good air stability. After 33 days exposed to environmental atmosphere, the devices were measured again and there was no observable

changes in common-base characteristics. P-type PBTs based on NPB as emitter and collector showed different behavior, i.e., did not demonstrate any performance expected for PBTs after only 5 days stored in air. We consider that the air stability of the ambipolar PBTs can be attributed to the utilization of  $C_{60}$ /NPB heterojunction with the air-stable  $C_{60}$ .

It can be seen that the ambipolar characteristics can not be achieved when the  $C_{60}$ /NPB heterojunction is not used in such devices. It is well known that heterojunctions can well be used to improve the performance of organic optoelectronic devices due to the possibility of control of the charge injection, transport and confinement by the change of energy barriers [14,15]. Obviously, the  $C_{60}$ /NPB heterojunction plays an important role in the achievement of the ambipolar characteristics in our PBTs, also contribution to the long term stability of the devices, which constitute a key point when practical applications are considered.

For further understanding of the origin of ambipolar properties, we fabricated diodes based on  $C_{60}$ /NPB heterojunction with structures of Al(1)/NPB/ $C_{60}$ / $V_2O_5$ /Al(2) and Al(1)/NPB/ $C_{60}$ /Al(2). Here the devices are defined as positive bias when Al (1) is set as anode and Al (2) as cathode, whereas the devices are negative biased.  $I$ - $V$  characteristics of the two diodes are shown in Fig. 4. It can be seen that the device with  $V_2O_5$  shows higher current than that of the device without  $V_2O_5$  under positive and negative bias. This indicates that there are more electrons or holes to be injected into the device in Al(1)/NPB/ $C_{60}$ / $V_2O_5$ /Al(2). In the case of positive bias, hole injection of the two devices are identical, obviously the more currents in Al(1)/NPB/ $C_{60}$ / $V_2O_5$ /Al(2) owe to the more electrons injection from Al(2) electrode. While negative biased, electron injection of the two devices are same, the more currents in Al(1)/NPB/ $C_{60}$ / $V_2O_5$ /Al(2) evidently attribute to holes injection from Al(2) to  $C_{60}$ /NPB. That is to say, the utilization of  $V_2O_5$  greatly enhances electron injection and favors hole injection, which had been proven in our previous works [16,17]. All above should be account for ambipolar properties of the devices based on NPB/ $C_{60}$  heterojunction. The deep understanding of the organic heterojunction will be helpful for further developing environmentally stable, or even long operational lifetime encapsulated high performance PBTs.

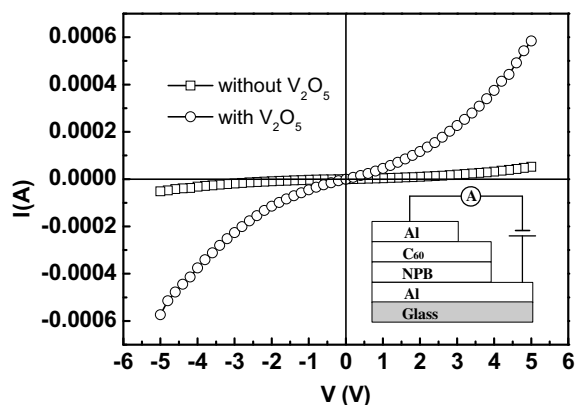


**Fig. 4.**  $I$ - $V$  characteristics of the diodes based on  $C_{60}$ /NPB heterojunction. The inset shows the structure of the devices.

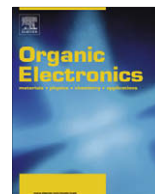
In summary, vertical architecture ambipolar permeable metal-base organic transistors were realized by using C<sub>60</sub>/NPB heterojunction as the emitter and collector. The device demonstrates excellent common-base characteristics both in *P*-type and *N*-type modes with common-base gains of 0.998 and 0.999, respectively. This opens an effective method to fabricate ambipolar organic PBTs.

### Acknowledgements

The authors would like to thank the Hundreds Talents program of Chinese Academy of Sciences, National Science Fund for Distinguished Young Scholars of China (50325312), Science Fund for Creative Research Groups of NSFC (20621401), and the Brazilian institutions CNPq, Renami/CNPq and Instituto do Milênio/CNPq for research grants.

### References

- [1] L.S. Zhou, A. Wanga, S.C. Wu, J. Sun, S. Park, T.N. Jackson, *Appl. Phys. Lett.* 88 (2006) 083502.
- [2] S. Lee, B. Koo, J.G. Park, H. Moon, J. Hahn, J.M. Kim, *MRS Bull.* 31 (2006) 455.
- [3] H. Klauk, M. Halik, U. Zschieschang, F. Eder, G. Schmid, C. Dehm, *Appl. Phys. Lett.* 82 (2003) 4175.
- [4] Y. Watanabe, H. Iechi, K. Kudo, *Thin Solid Films* 516 (2008) 2731.
- [5] E.J. Meijer, D.M. de Leeuw, S. Setayesh, E. van Veenendaal, B.H. Huisman, P.W.M. Blom, J.C. Hummelen, U. Scherf, T.M. Klapwijk, *Nat. Mater.* 2 (2003) 678.
- [6] A. Babel, J.D. Wind, S.A. Jenekhe, *Adv. Funct. Mater.* 14 (2004) 891.
- [7] Y. Hayashi, H. Kanamori, I. Yamada, A. Takasu, S. Takagi, K. Kaneko, *Appl. Phys. Lett.* 86 (2005) 052104.
- [8] H.B. Wang, J. Wang, X.J. Yan, J.W. Shi, H.K. Tian, Y.H. Geng, D.H. Yan, *Appl. Phys. Lett.* 88 (2006) 133508.
- [9] M. Ahles, R. Schmechel, H.V. Seggern, *Appl. Phys. Lett.* 85 (2004) 4499.
- [10] T. Yasuda, T. Goto, K. Fujita, T. Tsutsui, *Appl. Phys. Lett.* 85 (2004) 2098.
- [11] S.H. Li, Z. Xu, L.P. Ma, C.W. Chu, Y. Yang, *Appl. Phys. Lett.* 91 (2007) 083507.
- [12] M.S. Meruvia, I.A. Hümmelgen, *Adv. Funct. Mater.* 16 (2006) 459.
- [13] J. Huang, M. Yi, D. Ma, I.A. Hümmelgen, *Appl. Phys. Lett.* 92 (2008) 232111.
- [14] C.W. Tang, S.A. VanSlyke, *Appl. Phys. Lett.* 51 (1987) 913.
- [15] A. Dodabalapor, H.E. Katz, L. Torsi, R.C. Haddon, *Science* 269 (1995) 1560.
- [16] M. Yi, S. Yu, D. Ma, C. Feng, T. Zhang, M.S. Meruvia, I.A. Hümmelgen, *Org. Electron.* 8 (2007) 311.
- [17] C. Feng, M. Yi, S. Yu, I.A. Hümmelgen, T. Zhang, D. Ma, *J. Nanosci. Nanotechnol.* 8 (2007) 2037.



## The effects of metal impurities in poly[(2,5-bis(3-decylthiophen-2-yl)-thieno[2,3-b]thiophene)] on field-effect transistor properties

Niklas Björklund<sup>a,\*</sup>, Jan-Olof Lill<sup>a,b</sup>, Johan Rajander<sup>c</sup>, Ronald Österbacka<sup>a</sup>, Steven Tierney<sup>d</sup>, Martin Heeney<sup>d,1</sup>, Iain McCulloch<sup>d,2</sup>, Michael Cölle<sup>d</sup>

<sup>a</sup> Centre of Excellence for Functional Materials and Department of Physics, Åbo Akademi University, Porthansgatan 3, 20500 Åbo, Finland

<sup>b</sup> Accelerator Laboratory, Åbo Akademi University, Porthansgatan 3, 20500 Åbo, Finland

<sup>c</sup> Laboratory of Analytical Chemistry, Åbo Akademi University, Porthansgatan 3, 20500 Åbo, Finland

<sup>d</sup> Merck Chemicals Ltd., University Parkway, Southampton SO16 7QD, United Kingdom

### ARTICLE INFO

#### Article history:

Received 11 August 2008

Received in revised form 28 October 2008

Accepted 3 November 2008

Available online 20 November 2008

#### PACS:

71.55.-i

72.80.Le

82.35.Lr

82.80.Ej

85.30.Tv

#### Keywords:

Field-effect transistor

PIXE

Nuclear analysis

Purity

OFET

### ABSTRACT

We have used particle induced X-ray emission analysis and particle induced gamma-ray emission analysis to determine the elemental impurity concentrations in poly[(2,5-bis(3-decylthiophen-2-yl)thieno[2,3-b]thiophene)] samples that have undergone different washing and extraction procedures to remove impurities. Field-effect transistors (FETs) were fabricated from the materials and their electrical characteristics show no significant differences between the devices made from different material samples. Reducing the metal residue levels below the ones measured in the starting material (300 mg/kg Fe, 7 mg/kg Zn, 3000 mg/kg Pd and 12000 mg/kg Sn) does not improve the FET performance. This suggests that it is not necessary to completely remove metal residues in the polymer for FET applications.

© 2008 Elsevier B.V. All rights reserved.

## 1. Introduction

During the last few years semi-conducting polymers have attracted a considerable amount of attention due to their potential electronic applications in field-effect transistors, solar cells, light emitting diodes, electronic memories and other devices [1–4]. The advantages of polymers

over conventional inorganic semi-conductors, such as silicon and germanium, include solution-processability, large area fabrication, low costs and flexibility. One of the requirements on organic semi-conductors for use in organic field-effect transistors (OFETs) is a high chemical purity level, since impurities can act as charge-trapping sites [2]. However, the effects of impurities in semi-conducting polymers on OFET performance are not well understood.

In organic semi-conductors the charge carriers are more localized than in their inorganic counterparts; resulting in a smaller radius of influence for impurities [5]. Depending on the nature of the impurity it can influence device performance in different ways. Charged impurities could act as dopants that interact coulombically with localized

\* Corresponding author. Tel.: +358 2 215 4914; fax: +358 2 215 4776.

E-mail address: [niklas.bjorklund@abo.fi](mailto:niklas.bjorklund@abo.fi) (N. Björklund).

<sup>1</sup> Present address: Queen Mary, University of London, Department of Materials, Mile End Road, London E1 4NS, United Kingdom.

<sup>2</sup> Present address: Imperial College London, Department of Chemistry, London SW7 2AZ, United Kingdom.

carriers, resulting in a broadened density-of-states which could reduce the charge carrier mobility [6]. Charge neutrality must be maintained when ionized moieties are introduced into the system. One way to accomplish this is by electrochemical doping, where the dopants injects mobile majority carriers, giving rise to an increased energetic disorder [6]. Another possibility is to introduce a neutral entity whose electron affinity allows for charge transfer from the semiconductor to the dopant [7]. Metallic residues in the material acting as charge-trapping sites could also produce hysteresis in a device [8], while any impurities acting as bulk traps will increase the off-currents [9]. The drain voltage dependence of the subthreshold current is also affected by interface-traps. Scheniert et al. have suggested that this effect is caused by recharging of incompletely ionized acceptors or traps in the interface and in the bulk [10]. It is also possible that the impurities are charge neutral and chemically inert, having no effect on the device performance.

To the best of our knowledge, only a few studies of the effects of impurities in semi-conducting polymers on electronic device performance have been published [5,8,11]. Urien et al. performed Particle Induced X-ray Emission (PIXE) analysis on poly(3-hexylthiophene) (P3HT), revealing several impurity atom species and an increase in organic field-effect transistor (OFET) performance upon removal of these impurities [5]. They did not, however, quantify the levels of impurities. Kawamura et al. reported a decrease in OFET off-currents upon the removal of Zn and Ni impurities from P3HT, suggesting the metal residues acted as bulk traps [11]. Sonar et al. presented a study of poly(9,9-dioctylfluorene) fabricated by two different methods and purified a number of times, resulting in different Pd and Ni levels [8]. They concluded that it is not necessary to remove all traces of palladium to obtain satisfactory device performance, suggesting that complete removal of metal residues from semiconductors may not be necessary for OFET applications.

In this article, we aim to investigate the effects of impurities in poly[(2,5-bis(3-decylthiophen-2-yl)thieno[2,3-b]thiophene)] on the electronic properties of OFETs. Eight batches of the polymer were obtained after different purification and extraction steps, resulting in samples containing different impurity levels. PIXE and PIGE were chosen for the elemental analyzes due to their ability, when combined, to give the concentrations of most elements present in a solid target [12].

In recent years an external ion beam set-up has been developed at the Åbo Akademi University [13]. Equipped with a high precision beam current monitor [14] and a computer controlled XY-stage the set-up offers accurate determinations of elemental concentrations and distributions in solid materials. Hence, the PIXE and PIGE analysis can be performed on a small amount of dry polymer mate-

rial, thus avoiding contaminations from solvents and interference from the substrate. The small amount of material required also makes these methods suitable for testing materials produced on laboratory scale. The methods are also fast, and cover a wide range of concentrations.

## 2. Materials

The polymer, poly[2,5-bis(3-decylthiophen-2-yl)thieno[2,3-b]thiophene], was prepared by a microwave-assisted Stille coupling as illustrated in Fig. 1 [15]. Sample 1 was obtained by direct precipitation of the reaction mixture, and materials 2 to 4 by sequential washing in acetone, petrol and methanol *via* Soxhlet extraction. Material sample 4 was then split into four batches that all underwent different purification procedures to yield samples 5 through 8. The extraction methods are summarized in Table 1. A more detailed description of the synthetic method and the subsequent extraction methods can be found in the experimental section below.

The purpose of the different purification and extraction methods was to test the relative effectiveness of each of these steps and identify which steps were critical for the reduction of metal impurity content. Furthermore, by gaining a deeper understanding of which steps were critical for the removal of metal impurities, a more efficient standard purification protocol could be constructed for polymers prepared by this synthetic method.

Poly[(2,5-bis(3-alkylthiophen-2-yl)thieno[2,3-b]thiophene)] materials demonstrate excellent air stability in FET devices [16]. This is due to the deeper and more stable HOMO energy level of the polymer class that results in a material that is much less susceptible to oxidative doping compared to P3HT. For poly[(2,5-bis(3-decylthiophen-2-yl)thieno[2,3-b]thiophene)], the HOMO level energy was determined by photoelectron spectroscopy AC-2 measurements and measured as HOMO = -5.3 eV [21].

## 3. Elemental analysis

About 15 mg of the polymer sample material was pressed to a pellet (diameter 13 mm). Pure graphite was used as backing material to minimize the amount of sample material [17]. The samples were irradiated with a 3 MeV proton beam from the Åbo Akademi MGC-20 cyclotron. The acquisition time was about 500 s with a beam current of 10 nA. All irradiations were performed in air to avoid heating and charge build-up. A strong ion luminescence from the irradiated spot on the polymer samples was observed in the beginning of the proton irradiation but faded away within a few seconds. This phenomenon indicates some changes in the molecular structure but does not affect the elemental concentration measure-

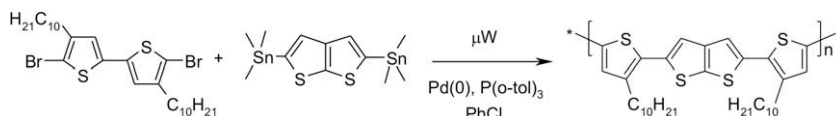


Fig. 1. Illustration of the preparation of poly[(2,5-bis(3-decylthiophen-2-yl)thieno[2,3-b]thiophene)] by a microwave-assisted Stille coupling.

**Table 1**

Summary of the purification and extraction procedures used for the material samples, and the number ( $M_n$ ) and weight ( $M_w$ ) average molecular weights for the samples.

Sample	Starting sample	Procedure	$M_n$	$M_w$
1		Re-precipitation	36200	73200
2	1	Acetone Soxhlet extraction	38000	76700
3	2	Petrol Soxhlet extraction	33800	74400
4	3	Methanol Soxhlet extraction	35900	73900
5	4	Re-precipitation	35000	77200
6	4	Silica treatment	31200	62000
7	4	Thiol-silica treatment	33800	64000
8	4	Thiourea-silica treatment	38000	65100

ments. The radiation emitted from the sample during the irradiation was measured with an IGP X-ray detector for PIXE analysis and with an HPGe gamma detector for PIGE analysis. The integrated charge on the target needed for quantification was determined from measurements of light induced in air by the proton beam [14]. The obtained PIXE spectra were analyzed using the GUPIX software package [18]. The calibration was checked using the USGS granite CRM G-2. The sodium and magnesium concentrations were obtained from peak height analyzes of the gamma spectra using the SAMPO 90 program [19]. The calibration method and the calculation of the limits of detection have been described earlier [20].

## 4. Results and discussion

### 4.1. Elemental analysis

Fig. 2 shows a typical PIXE spectrum, it has clear peaks from S, Fe, Br, Pd and Sn. Detailed results of the PIXE analysis are shown in Table 2. Sulfur can be found in the polymer backbone and bromine in the ends of the polymer chain, the other elements are considered to be impurities. Sample number 1 is the crude polymer, containing the highest level of impurities. The high ratio between bromine and sulfur in the starting material, compared to the

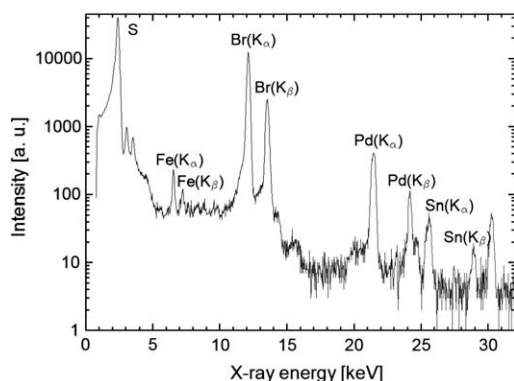


**Fig. 2.** Energy spectrum of sample 3 as an example of a typical spectrum for the polymer. The  $K_\alpha$  peaks correspond to transitions from the L- to the K-shell, transitions from higher shells gives the  $K_\beta$  peaks.

other samples, suggests that it either contains free bromine impurities (either ionic or organic) or low weight polymers (with a high ratio of bromine end groups) that were removed in the subsequent cleaning steps. The acetone Soxhlet extraction removed almost 90% of the impurities, the result of which can be seen in column 2 of Table 2. The following petrol Soxhlet extraction reduced the zinc and palladium contents but increased the tin and iron levels. The methanol Soxhlet extraction reduced the iron and tin content (column 4 of Table 2), but increased the palladium level slightly. Sample 6 contained about the same iron than the precursor material 4, the other extraction procedures resulted in slightly higher iron concentrations in the samples (5, 7 and 8). Sample 7 displayed a higher zinc concentration than material 4; in the others (5, 6, and 8) it was unaffected. All extraction procedures reduced the palladium content, the thiourea-silica treatment the most. The tin concentration in sample 8 was reduced from the starting sample 4, in the other three it increased. The increase in impurity concentrations might be due to impurities transferred from the solvents used in the purification, or more plausibly from the removal of polymer material in the purification that was less rich in these impurities. The silica and the thiourea-silica treatments gave the best results. The silica treatment gave the lowest levels of iron and zinc, and low levels of palladium; the lowest total impurity level was obtained with the thiourea-silica treatment, which also gave the lowest level of tin.

The additional information from the PIGE analysis was that sample 5 contained 17 mg/kg and sample 7 contained 30 mg/kg of sodium. The sodium contents in the rest of the samples were below the limit of detection (7 mg/kg). The concentrations of manganese were below the limit of detection (330 mg/kg) for all samples.

### 4.2. Homogeneity analysis

The homogeneity of the elemental composition was determined by performing additional PIXE analysis on two different material samples. Nine points on each sample were analyzed and the elemental concentrations at each point calculated. Average concentrations and standard deviations for the samples are shown in Table 3. If the relative standard deviation (RSD), the ratio between the standard deviation between the points and the average concentration, is less than or roughly of the same size as the statistical error of the PIXE measurement the impurity concentration is considered homogeneous. In sample 3 the zinc impurities were homogeneously distributed, since the RSD was only 5,5% compared to the statistical error of 16,5%. For the other impurities in material 3, the RSD for Fe (15,4%), Pd (30,3%) and Sn (26,8%), exceeded the statistical errors (6,1%, 2,3% and 7,7%), thus the distribution of these impurities were considered inhomogeneous. For sample 7 the RSD for both Pd (5,5%) and Sn (8,2%) were of the same order as the statistical errors (3,3% and 4,9%), and therefore considered homogeneously distributed. The RSD for both Fe (30,8%) and Zn (59,4%) were larger than the statistical errors (14,9% and 6,2%), suggesting an inhomogeneous distribution of these impurities. The Zn and Fe levels are close to the limit of quantification ( $\sim 3$  \* limit of



**Table 2**

Elemental concentrations in the material samples (1–8) given in mg/kg of dry weight. Typical statistical errors in% and limit of detection (LOD) in mg/kg are in the columns to the right. The bottom row contains the sum of the impurity concentrations (Fe, Zn, Pd and Sn).

	Sample								Error [%]	LOD
	1	2	3	4	5	6	7	8		
S	148046	211003	213186	211869	223685	225432	215227	232811	0.2	172.8
Br	15268	6397	5875	6167	5487	5350	5327	5236	0.4	4.0
Fe	305.9	19.1	134.0	7.7	23.9	8.3	33.5	80.5	6.9	8.9
Zn	7.4	7.1	5.2	6.4	6.7	6.1	32.6	11.0	13.8	2.7
Pd	3124	1470	1390	1511	829	517	508	604	2.8	11.0
Sn	12257	295	367	312	376	571	730	277	8.1	35.5
Sum	15694	1791	1896	1837	1235	1103	1304	973		

detection), which partially explain the high RSD. Sample 7 is more homogeneous than sample 3, suggesting that the additional cleaning and extraction steps improve the homogeneity of the material.

### 4.3. OFET characteristics

Typical transfer curves ( $I_d$ - $V_g$  traces) for the devices are shown in Fig. 3a and 3b. All devices displayed the same  $I$ - $V$

**Table 3**

Average concentrations ( $C_{ave}$ ) in mg/kg and standard deviations ( $\sigma$ ) in impurity concentrations for materials 3 and 7. The RSD-column contains the ratio between the standard deviation and average concentration in per cent. The error column contains the statistical error from the PIXE analysis for the first measurement point.

$C_{ave}$ [mg/kg]	$\sigma$ [mg/kg]	RSD [%]	Error [%]	LOD	
			For point #1		
<b>Material 3</b>					
Fe	123.7	19.0	15.4	6.1	11.1
Zn	606.9	33.5	5.5	16.5	3.1
Pd	1948.8	589.7	30.3	2.3	26.7
Sn	373.0	100.0	26.8	7.7	35.5
<b>Material 7</b>					
Fe	45.4	14.0	30.8	14.9	9.4
Zn	50.2	29.9	59.4	6.2	2.8
Pd	606.9	33.5	5.5	3.3	22.3
Sn	721.2	58.9	8.2	4.9	18.1

characteristics, except for a small variation in the turn-on-voltage. On/Off ratios of  $10^4$ – $10^5$  were routinely achieved for the devices. The on-currents in the saturated regime (Fig. 3a) were typically on the order of  $10^{-6}$  A, and slightly lower in the linear regime (Fig. 3b). In the off-state, the currents regularly reached levels of  $10^{-9}$ – $10^{-10}$  A. The variations in on-currents seen in Fig. 3a and b are due to the turn-on-voltage shift between the devices. The conductivity in the off-state can be increased by impurities in the semiconductor, resulting in leak currents to the gate and low on/off-ratios [21]. Off-currents in devices made from the same sample material display fluctuations on the same order of magnitude as devices made from different samples. We therefore conclude that the differences in off-currents in Fig. 3a are statistical. We also found that manual patterning of the devices, i.e. reducing the area of the semi-conductor, reduced the off-current with up to one order of magnitude.

Sonar et al. reported that metal residues, especially palladium, causes hysteresis in poly(9,9-dioctylfluorene) OFET devices [8]. Their devices displayed less hysteresis when fabricated from polymers containing 2000 mg/kg palladium than from polymers with higher palladium levels (3300 mg/kg or 4000 mg/kg). We did not observe this kind of behavior in our transistors. Little or no hysteresis could be observed while operating the devices in the on-state, and there were no systematic difference between the devices.

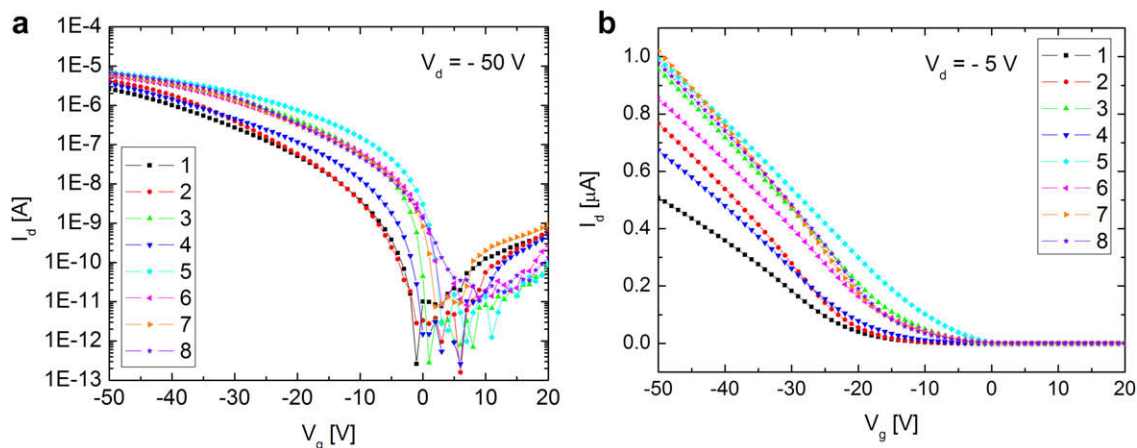


**Fig. 3.** Typical transfer curves for the material samples, measured at a constant drain bias of (a)  $-50$  V and (b)  $-5$  V. The channel length,  $L$ , was  $35 \mu\text{m}$  and the width,  $W$ ,  $1.5 \text{ mm}$ .

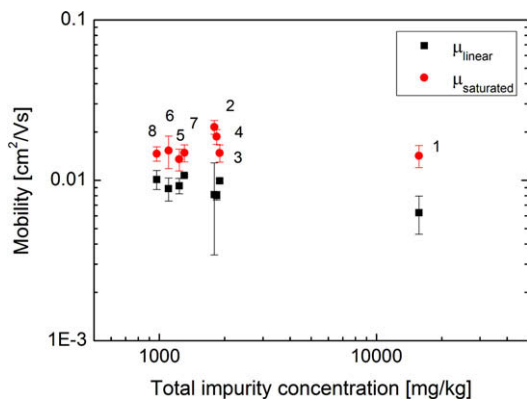


**Fig. 4.** Typical field-effect mobilities. The linear mobilities were measured at a constant drain voltage of  $V_d = -5$  V and the saturated at  $V_d = -50$  V. The error bars show the maximum deviation between the measured mobility values and average mobilities.

The field-effect mobilities measured in both the linear and saturated regimes are plotted as a function of the total impurity concentrations in Fig. 4. The linear mobilities typically ranged from  $\sim 0.008$  to  $0.01$   $\text{cm}^2\text{V}^{-1}\text{s}^{-1}$  and the saturated from  $\sim 0.01$  to  $0.03$   $\text{cm}^2\text{V}^{-1}\text{s}^{-1}$ , the latter agrees with earlier reported mobilities [16]. The linear mobilities are lower than the saturated, but no systematic difference in the mobilities with respect to the measured impurity concentrations could be observed.

The  $\text{SiO}_2$ -semiconductor interface is very sensitive to the device fabrication methods [21,22] and small variations in fabrication parameters might lead to different results. It has been shown that plasma treating the  $\text{SiO}_2$ -surface for different times introduces different amounts of charges to the surface [21], such charges will shift the turn-on voltage [23]. Turn-on voltage as a function of impurity concentration for some typical devices is shown in Fig. 5.  $V_0$  is very sensitive to device fabrication, which explains the offset between the turn-on voltages for the two series. All devices in the same series were fabricated at the same time under the same conditions, making the turn-on voltages comparable within the same series. No clear trends can be observed in the turn-on voltage with regards to the impurity concentrations.

## 5. Conclusions

We have used PIXE and PIGE to determine the elemental concentrations in poly[(2,5-bis(3-alkylthiophen-2-yl)thieno[2,3-b]thiophene)] samples that have undergone successive washing and extraction procedures to remove impurities. The levels of impurities in each sample were measured and FETs were made from the materials. Analysis of the homogeneity of impurity levels showed that the successive cleaning and extraction procedures improved the homogeneity of the Sn and Pd impurities. Characterisation of the FETs shows that there were no significant

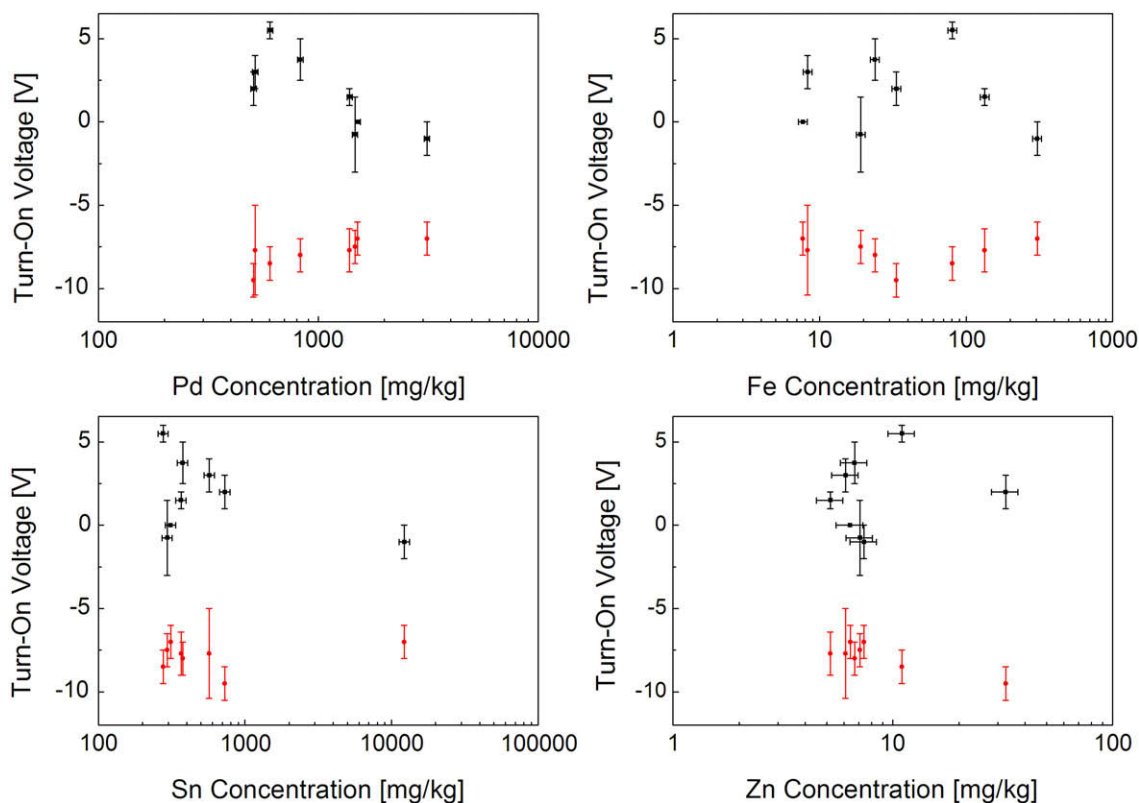


**Fig. 5.** Turn-on voltages as function of impurity concentrations for two series of devices. The error bars show the maximum deviation between the measured turn-on-voltages and average turn-on-voltages.

differences between the devices made from different material samples. We have shown that reducing the metal residue levels below the one measured in sample 1 (300 mg/kg Fe, 7 mg/kg Zn, 3000 mg/kg Pd and 12000 mg/kg Sn) does not improve the FET performance. The methods presented in this article could be used to study most semi-crystalline polymer semi-conductors, to determine if present day large-scale synthesis provides sufficiently pure materials for organic transistor applications.

## 6. Experimental

### 6.1. Polymer synthesis

A 20 ml glass vial was charged with a stirrer bar, 5,5'-dibromo-4,4'-didecylbithiophene (0.967 g, 1.6 mmol), 2,5-bis(trimethylstannyl)thieno[2,3-b]thiophene (0.745 g, 1.6 mmol), tris(dibenzylideneacetone)dipalladium (0) (29 mg, 2 mol.%), tri(o-tolyl)phosphine (39 mg, 8 mol.%) and chlorobenzene (16 mL). The glass vial was purged with nitrogen and securely sealed. The glass vial was placed into a microwave reactor (Emrys Creator, Personal Chemistry Ltd) and heated to 180 °C. A temperature ramp was used such that the vial was heated with stirring at 140 °C for 120 s, then at 160 °C for 120 s and finally at 180 °C for 15 min. Elapsed time was only calculated once the temperature had been reached. Bromobenzene (33  $\mu$ L, 20 mol.%) was added *via* syringe and the reaction mixture heated at 160 °C for 60 s in the microwave reactor. Tributylphenyltin (107  $\mu$ L, 20 mol.%) was added *via* syringe and the reaction mixture heated at 160 °C for 60 s in the microwave reactor.

### 6.2. Purification and extraction methods

The reaction mixture was precipitated into a mixture of 37% hydrochloric acid (50 mL) and methanol (500 mL) and stirred for 1 h. The polymer was collected by filtration, washed with water followed by methanol, and dried under vacuum to yield sample 1. Sample 1 was washed (*via* Soxhlet extraction) with acetone for 24 h and dried under vacuum to yield sample 2. Sample 2 was further washed (*via* Soxhlet extraction) with petrol 40–60 for 24 h and dried under vacuum to yield sample 3. Sample 3 was further washed (*via* Soxhlet extraction) with methanol for 24 h and dried under vacuum to yield sample 4. A bulk solution of sample 4 was formulated in hot chloroform (100 mL). A portion of the sample 4 bulk solution (25 mL) was precipitated from methanol (200 mL), and the polymer was collected by filtration, washed with methanol, and dried under vacuum to yield sample 5. Another portion of the sample 4 bulk solution (25 mL) was stirred at 50 °C over silica (1 g) for 1 h under N<sub>2</sub>. The solution was filtered through a plug of cotton wool, which was washed with hot chloroform. The filtrate was precipitated from methanol (200 mL). The polymer was collected by filtration, washed with methanol, and dried under vacuum to yield sample 6. A portion of the sample 4 bulk solution (25 mL) was also stirred at 50 °C over thiol-functionalized silica (1 g) for 1 h under N<sub>2</sub>. The solution was filtered through a plug of cotton wool, which was washed with hot chloroform. The filtrate

was precipitated from methanol (200 mL). The polymer was collected by filtration, washed with methanol, and dried under vacuum to yield sample 7. Another portion of the sample 4 bulk solution (25 mL) was stirred at 50 °C over thiourea-functionalized silica (1 g) for 1 h under N<sub>2</sub>. The solution was filtered through a plug of cotton wool, which was washed with hot chloroform. The filtrate was precipitated from methanol (200 mL). The polymer was collected by filtration, washed with methanol, and dried under vacuum to yield sample 8.

### 6.3. OFET fabrication

The poly[(2,5-bis(3-decylthiophen-2-yl)thieno[2,3-b]thiophene)] samples were received from Merck Chemicals Ltd. Molecular weight determinations were carried out in chlorobenzene solution on an Agilent 1100 series HPLC using two PL Mixed B columns in series and the system was calibrated against narrow weight PL polystyrene calibration standards. 10 mg/ml solutions were made in 1,2-dichlorobenzene from each polymer sample under dry nitrogen atmosphere in a glove box. The solutions were heated on a hot plate at 80 °C for 2 h.

Thin-film organic field-effect transistors were fabricated on doped silicon substrates with 300 nm thermally grown silicon oxide (SiO<sub>2</sub>), where the substrate served as a common gate electrode. The capacitance of the insulating SiO<sub>2</sub> layer, C<sub>i</sub>, was calculated to be 11.5 nF(cm)<sup>-2</sup>, assuming the permittivity of SiO<sub>2</sub> to be 3.9 nF. Prior to organic film deposition the substrates were ultrasonicated at 60 °C in H<sub>2</sub>O, acetone and IPA successively for 10 min. The substrates were etched for 30 s in an O<sub>2</sub>-plasma and treated with a silylating agent octadecyltrichlorosilane at 10 mM concentration in toluene for 15 min at 60 °C, before the film deposition. Semi-conductor films were deposited on the substrates in dry nitrogen atmosphere in a glove box by spin coating at 2000 rpm for 78 s and annealed at 100 °C for 60 min on a hot plate inside the box. About 30 nm thick Au electrodes were vacuum evaporated on top of the semiconductor film using a custom built evaporator inside the glove box. All transistors were fabricated with top-electrode bottom-gate configuration with a channel length, L, of 35  $\mu$ m and channel width, W, of 1.5 mm. Several series of devices were fabricated to verify the reproducibility of the results. All samples in one series were manufactured at the same time, making the elemental concentrations in the material the only difference between the samples.

### 6.4. Electrical characterization

Electrical characterization of the devices was performed in a custom built probe station inside the glove box. An Agilent 4142B parameter analyzer controlled via Labview on a PC was used to conduct the measurements. Characterization of the transistors was conducted at constant drain bias, V<sub>d</sub>, -5 V for the linear regime and -50 V for the saturated. The gate voltage, V<sub>g</sub>, was swept from +20 V to -50 V in steps of 1 V and the drain current, I<sub>d</sub>, was measured. Standard methods were used to calculate the field-effect mobilities and threshold voltages [22]. V<sub>0</sub> is graphically

calculated as the gate voltage where  $I_d$  starts growing exponentially.

### Acknowledgements

The authors would like to thank Tomas Bäcklund for fruitful discussions and Kristijonas Genevicius for his assistance with the device fabrication techniques. We also thank the Academy of Finland for their financial support through project numbers: 107684 and 116995 and the M. Ehrnrooth foundation.

### References

- [1] S.R. Forrest, *Nature* 428 (2004) 911.
- [2] A. Facchetti, *Mater. Today* 10 (2007) 28.
- [3] R.H. Friend, R.W. Gymer, A.B. Holmes, J.H. Burroughes, R.N. Marks, C. Taliani, D.D.C. Bradley, D.A. Dos Santos, J.L. Brédas, M. Lögdlund, W.R. Salaneck, *Nature* 397 (1999) 121.
- [4] J.-M. Nunzi, *Physique* 3 (2002) 523–542.
- [5] M. Urien, G. Wantz, E. Cloutet, L. Hirsch, P. Tardy, L. Vignau, H. Cramail, J.-P. Parneix, *Org. Elect.* 6 (2007) 727–734.
- [6] V.I. Arkhipov, P. Heremans, E.V. Emilianova, H. Bässler, *Phys. Rev. B* 71 (2005) 045214.
- [7] B. Maennig, M. Pfeiffer, A. Nollau, X. Zhou, K. Leo, P. Simon, *Phys. Rev. B* 64 (2001) 195208.
- [8] P. Sonar, A.C. Grimdale, M. Heeney, M. Shkunov, I. McCullouch, K. Müllen, *Synth. Met.* 157 (2007) 872–875.
- [9] S. Scheinert, G. Paasch, T. Doll, *Synth. Met.* 139 (2003) 233–237.
- [10] S. Scheinert, G. Paasch, M. Schrödner, H.-K. Roth, S. Sensfuß, *J. Appl. Phys.* 92 (2002) 330.
- [11] S. Kawamura, M. Yoshida, S. Hoshino, T. Kamata, *Mater. Res. Soc. Symp. Proc.* 871E (2005).
- [12] S.A.E. Johansson, J.L. Campbell, K.G. Malmqvist, *Chemical Analysis* 135, Wiley, New York, 1995.
- [13] J.-O. Lill, Ion Beam Analysis at Åbo Akademi University, Available at: <<http://web.abo.fi/~jlill/IonBeams.html>> (Accessed 15.05.2008).
- [14] J.-O. Lill, *Nucl. Instr. Meth. B* 150 (1999) 114–117.
- [15] S. Tierney, M. Heeney, I. McCulloch, *Synth. Met.* 148 (2005) 195.
- [16] M. Heeney, C. Bailey, K. Genevicius, M. Shkunov, D. Sparrowe, S. Tierney, I. McCulloch, *J. Am. Chem. Soc.* 127 (2005) 1078–1079.
- [17] K.-E. Saarela, J.-O. Lill, F.J. Hernberg, L. Harju, A. Lindroos, S.-J. Heselius, *Nucl. Instr. Meth. B* 1003 (1995) 466–472.
- [18] J.A. Maxwell, J.L. Campbell, W. Teesdale, *Nucl. Instr. Meth. B* 43 (1989) 218–230.
- [19] J.T. Routti, M.T. Nikkinen, P.A. Aarnio, *Meth. Appl. Radioanal. Chem., Kona, Hawaii*, April 21–27, 1991.
- [20] J.-O. Lill, L. Harju, K.-E. Saarela, A. Lindroos, S.-J. Heselius, *Anal. Chim. Acta* 378 (1999) 273–278.
- [21] C.R. Newman, C.D. Frisbie, D.A. Da Silva Filho, J.-L. Brédas, P.C. Ewbank, K.R. Mann, *Chem. Mater.* 16 (2004) 4436–4451.
- [22] J. Veres, S. Ogier, G. Loud, *Chem. Mater.* 16 (2004) 4543–4555.
- [23] E.J. Meijer, C. Tanase, P.W.M. Blom, E. Van Veenendaal, B.-H. Huisman, D.M. De Leeuw, T.M. Klapwijk, *Appl. Phys. Lett.* 80 (2002) 3838–3840.



## Characteristics of tetracene-based field-effect transistors on pretreated surfaces

Young-Se Jang, Hoon-Seok Seo, Ying Zhang, Jong-Ho Choi \*

Department of Chemistry and Center for Electro- and Photo-Responsive Molecules, Korea University, Anam-Dong, Seoul 136-701, Republic of Korea

### ARTICLE INFO

#### Article history:

Received 26 August 2008

Received in revised form 3 November 2008

Accepted 8 November 2008

Available online 17 November 2008

#### PACS:

73.40.-c

73.61.Ph

#### Keywords:

Tetracene

Organic thin-film transistor (OTFT)

Neutral cluster beam deposition (NCBD)

Octadecyltrichlorosilane (OTS)

Temperature-dependence of field-effect mobility ( $\mu_{eff}$ )

### ABSTRACT

Tetracene-based organic thin-film transistors (OTFTs) were prepared using a neutral cluster beam deposition (NCBD) method. The effect of surface modification with an amphiphilic surfactant, octadecyltrichlorosilane (OTS), on the formation of thin films and the geometric influence of channel length and width on the transistor characteristics were systematically examined. The estimated trap density and temperature-dependence of the field-effect mobility in the range of 10–300 K demonstrated that surfactant pretreatment decreased the total trap density and activation energy for hole-transport by reducing structural disorder in the active layer. In particular, the room-temperature hole mobilities of 0.162 and 0.252  $\text{cm}^2/\text{Vs}$  for untreated and OTS-pretreated devices were among the best to date for polycrystalline tetracene-based transistors using  $\text{SiO}_2$  gate dielectric layers without any thermal post-treatment.

© 2008 Elsevier B.V. All rights reserved.

### 1. Introduction

Compared to conventional electronic devices made of inorganic materials, organic-based semiconductor electronics have many advantages, such as their large-area coverage, structural flexibility, and low-cost fabrication. The performance of some organic thin-film devices is comparable to that of hydrogenated, amorphous Si-based devices [1–7]. Organic thin-film devices utilizing fused-ring polycyclic aromatic hydrocarbon compounds have been extensively investigated. This is well-demonstrated by the polyacene-based devices including tetracene, a  $\Pi$ -conjugated molecule consisting of four aligned condensed benzene rings (Fig. 1) in organic thin-film transistors (OTFTs), light-emitting transistors and solar cells [8–14]. De Boer et al. fabricated the transistors based upon the

free-standing tetracene single crystals by applying the physical vapor deposition method under temperature-gradient conditions to obtain a high room-temperature mobility of 0.4  $\text{cm}^2/\text{Vs}$  [8]. Gundlach and co-workers studied the polycrystalline tetracene-based transistors using the amphiphilic surfactant, octadecyltrichlorosilane (OTS), and obtained a mobility as high as 0.1  $\text{cm}^2/\text{Vs}$  [9].

In fabricating high-performance OTFTs, both preparation of highly crystalline active layers and systematic optimization of device structures are important prerequisites. Various techniques such as traditional vapor deposition and solution processing methods have been proposed to produce high-quality thin films. Conversely, the neutral cluster beam deposition (NCBD) method is less popular but highly promising [15–21]. The NCBD scheme utilizes weakly bound clusters produced when the organic vapor-phase molecules sublimated by resistive heating undergo adiabatic expansion into a high vacuum. Due to the large translational energy of cluster beams with high

\* Corresponding author. Tel.: +82 2 3290 3135; fax: +82 2 3290 3121.  
E-mail address: [jhc@korea.ac.kr](mailto:jhc@korea.ac.kr) (J.-H. Choi).

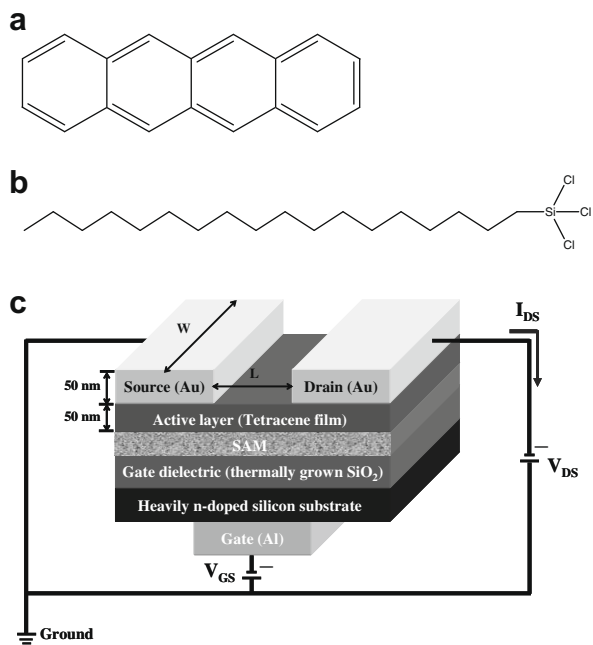


**Fig. 1.** Molecular structures of (a) tetracene and (b) OTS (octadecyltrichlorosilane). (c) A schematic view of the tetracene-based transistor with its bias condition.

directionality, the collision of clusters with the substrate results in efficient decomposition into individual molecules, and the subsequent migration leads to very smooth, uniform thin films. The NCBD scheme has demonstrated significant enhancement in the surface morphology, crystalline quality, and film packing density. In particular, the distinctive advantage of low substrate-temperature deposition cannot be accomplished simply by employing conventional deposition techniques.

In this paper, we describe our systematic investigation of the performance of tetracene-based OTFTs prepared by the NCBD method. No comparative study examining the effects of surface pretreatment and geometry on device performance and transport characteristics has been reported to the best of our knowledge. We first focused on the effects of surface modification with an amphiphilic OTS surfactant on the morphology, crystallinity, and packing density of tetracene thin films. Secondly, we investigated the influence of the geometric dimensions upon device characteristics to optimize the transistor structure for higher performance. Finally, the transport mechanisms were examined in the temperature range of 10–300 K. The strong correlation of device performance with structural and morphological properties of the active layers is discussed.

## 2. Experiment

Fig. 1 displays molecular structures of the tetracene and OTS, and a schematic diagram of a top-contact transistor along with the bias condition. The substrates used in this study consisted of a highly doped, n-type Si wafer coated

with an aluminum layer as the gate electrode and thermally grown 1000 Å-thick SiO<sub>2</sub> layers as the gate dielectric. The substrates were first cleaned by a series of sequential ultrasonic treatments in acetone, hot trichloroethylene, acetone, HNO<sub>3</sub>, methanol, and deionized water, and finally blown dry with dry N<sub>2</sub> [22]. The substrates were finally exposed to UV (254 nm) for 15 min [23]. Such a rigorous cleaning procedure significantly increased device performance. For surface modification, the cleaned substrates were immersed in a 1 × 10<sup>−3</sup> M solution of OTS in *n*-hexane (Aldrich Co.) for 24 h at room temperature.

The active layers of the tetracene thin films were prepared by a homemade NCBD apparatus previously described in detail [15], and therefore, only a relevant account is presented here. The as-received tetracene sample (Sigma-Aldrich Co.) was placed inside the enclosed, cylindrical, crucible cell with a diameter of 1.0 and 1.0 mm-long nozzle. The sample was sublimated by resistive heating between 520 and 550 K, and then the tetracene vapor underwent adiabatic, supersonic expansion into the high-vacuum drift region at a working pressure of 3 × 10<sup>−6</sup> Torr. The resultant, highly-directional, weakly bound neutral cluster beams were produced at the nozzle throat and deposited directly onto the substrates with an average thickness of ca. 500 Å, and a deposition rate of 5 Å/s. Electron-beam evaporation using a rectangular-shaped shadow mask was utilized to produce 500 Å-thick Au source and drain electrodes. To determine the influence of the geometric dimensions on device performance, the devices were prepared with several channel lengths (*L*) of 200, 660, 800, and 1400 μm, at a fixed channel width (*W*) of 500 μm. Depending on the channel length, the four different kinds of devices were grouped into class I, II, III and IV, respectively.

The thickness, contact angle, surface morphology, and structural properties were characterized using an alpha-step surface profile monitor, a contact angle goniometer, atomic force microscopy (AFM), and X-ray diffractometry (XRD). The current–voltage (*I*–*V*) characteristics of the OTFTs and their temperature-dependence were measured by an optical probe station connected to a HP4140B pA meter-dc voltage source unit and a 10 K-closed cycle refrigerator at a base pressure of 1 × 10<sup>−2</sup> Torr over the temperature range of 10–300 K. Various parameters were derived from the fits of the *I*–*V* characteristics.

## 3. Results and discussion

### 3.1. Comparison of surface morphological and structural properties

Surface analysis using an AFM apparatus in the non-contact mode was employed to characterize the morphology of the tetracene active layers. Fig. 2a shows the 2-dimensional AFM images taken over an area of 5 × 5 μm<sup>2</sup> for the untreated and OTS-pretreated tetracene films at a nominal thickness of 500 Å. Both films were completely covered with highly packed grain crystallites. Compared to the data obtained at the same deposition rate using the conventional vacuum sublimation method [12], our grain size appeared larger in both untreated and

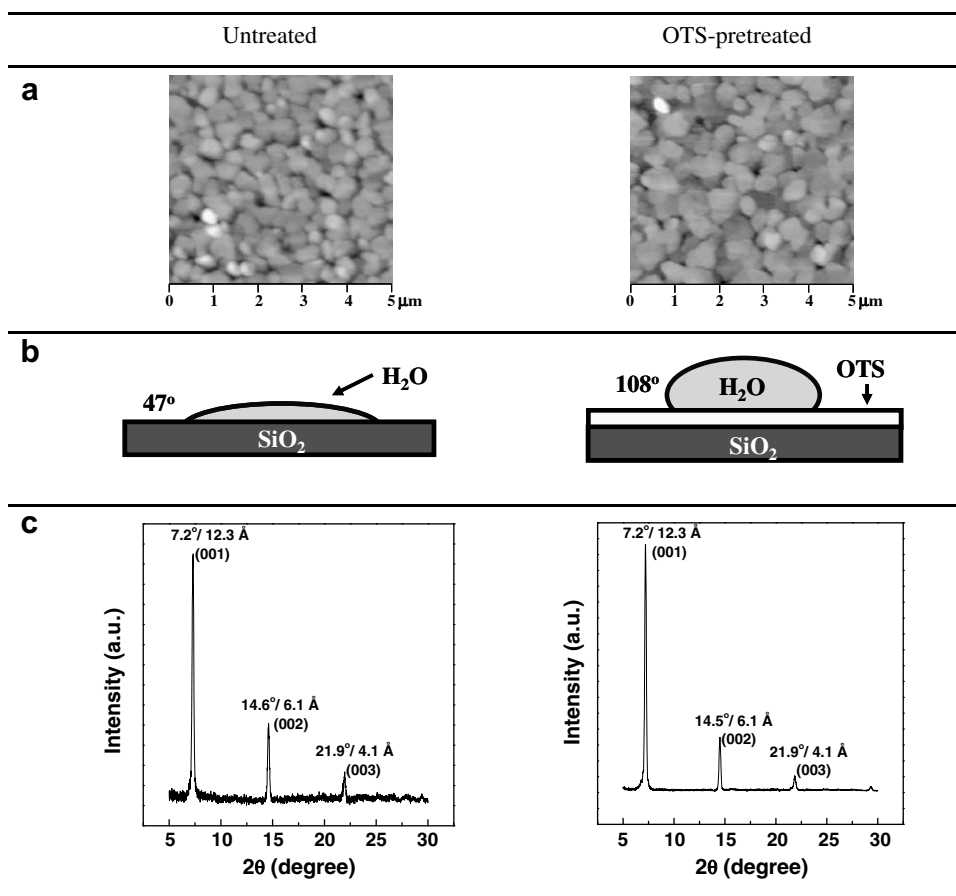


**Fig. 2.** Comparison of (a) 2-dimensional AFM micrographs ( $5 \times 5 \mu\text{m}^2$ ), (b) contact angles with water, and (c) XRD spectra for the 500 Å-thick tetracene thin films prepared on untreated and OTS-pretreated SiO<sub>2</sub> substrates at room temperature using the NCBD method.

OTS-pretreated films. The increase can be ascribed to the characteristics of the neutral cluster beam method, in which the larger energetic cluster seeds enhance the formation of grain crystallites on the early stages of growth. The quantitative values of the root-mean-square roughness of the films were obtained by conducting section analyses over at least four areas in the  $5 \times 5 \mu\text{m}^2$  films using the built-in software of the AFM apparatus. The roughness values for the untreated and OTS-pretreated tetracene films were measured to be 40 and 30 Å on the average, respectively.

The pretreated tetracene films showed a lower roughness and a higher packing density, suggesting that the amphiphilic OTS molecules capable of forming bonds with hydrophobic tetracene and hydrophilic SiO<sub>2</sub> provided favorable deposition conditions. This result is also consistent with the contact angle measurement in Fig. 2b. The surface pretreatment increased the contact angle with water from 47° to 108°, indicating that the OTS-covered substrate surface becomes highly non-polar and leads to a significant reduction in the structural mismatch at the interface during the initial accumulation of tetracene molecules.

The effect of the surface pretreatment was also clearly demonstrated in the X-ray diffraction measurements ob-

tained using Cu K $\alpha$  radiation in a symmetric reflection, coupled  $\theta$ - $2\theta$  scanning mode. Fig. 2c shows the comparative XRD results for the 500 Å-thick tetracene thin films deposited on the untreated and OTS-pretreated SiO<sub>2</sub> substrates at room temperature. Tetracene single crystals are known to have a triclinic structure with two molecules in the unit cell [24–27]. The strong and sharp first-order peak, as well as distinctive higher-order multiple peaks, can be fitted to a series of (001) reflection lines with multiple  $d$  spacing. The interplanar spacing  $d_{001}$  from the peak positions is determined to be 12.3 Å for both films, which is in good agreement with the previous XRD reports of  $d_{001} = 12.1$  and 12.4 Å for as-deposited tetracene films [17,24,25]. The higher signal-to-noise in the XRD patterns of OTS-pretreated films suggests that the amphiphilic surfactant appears to substantially affect the growth of tetracene films and the packing between tetracene crystallites as a well-ordered monolayer template, which is consistent with the results shown in the AFM micrographs. The observed, unique advantage of the facile growth of smooth crystalline films through the low substrate-temperature mechanism is characteristic of the NCBD method. In addition, the formation of well-packed tetracene films is very likely to improve performance of the OTFT devices due to

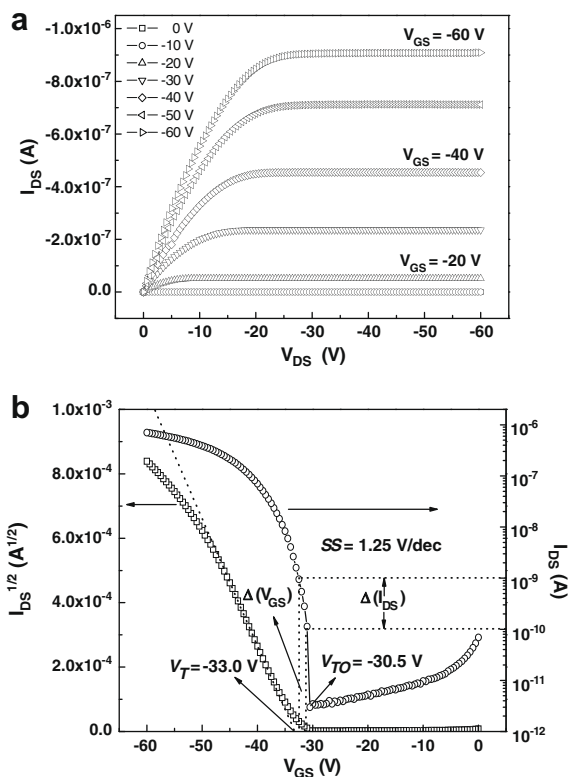


**Fig. 3.** (a) Current–voltage characteristics at various gate voltages for the OTS-pretreated tetracene-based transistors in class IV. (b) Variation of  $I_{DS}^{1/2}$  (left axis) and  $\log(I_{DS})$  (right axis) vs.  $V_{GS}$  at a constant  $V_{DS} = -60$  V.

more favorable hopping of the polaron charge carriers between the grain crystallites.

### 3.2. Comparison of mobilities, geometry effects and trap densities

A comparative characterization analysis of top-contact, tetracene-based transistors grouped into the 4 classes, I, II, III, and IV, depending on  $W/L$ , was performed. The  $I$ – $V$  characteristics of untreated and OTS-pretreated transistors were similar to those for typical p-type semiconductors and complied well with the standard field-effect transistor equations working in the accumulation mode. Fig. 3 demonstrates the typical plots of drain-source current ( $I_{DS}$ ) as a

function of the drain-source voltage ( $V_{DS}$ ) for various gate-source voltages ( $V_{GS}$ ). At a fixed  $V_{GS}$ ,  $I_{DS}$  increases linearly with  $V_{DS}$  in the low  $V_{DS}$  regime, and then the  $I_{DS}$  tends to saturate in the large  $V_{DS}$  regime due to the pinch off in the accumulation layer. In the saturation regime,  $I_{DS}$  increases with  $V_{GS}$  and satisfies the following relationship

$$I_{DS} = \frac{WC_i\mu}{2L}(V_{GS} - V_T)^2$$

where  $C_i$  is the capacitance per unit area of the  $\text{SiO}_2$  gate dielectric,  $\mu$  the field-effect mobility, and the channel lengths ( $L$ ) of 200, 660, 800, and 1400  $\mu\text{m}$  are at a fixed channel width ( $W$ ) of 500  $\mu\text{m}$ . For thermally grown, 1000  $\text{\AA}$ -thick  $\text{SiO}_2$ , the value for  $C_i$  is known to be 34.5  $\text{nF}/\text{cm}^2$ . From the analysis of the observed  $I$ – $V$  characteristics, several device parameters such as  $\mu$ , current on/off ratio ( $I_{on}/I_{off}$ ), threshold voltage ( $V_T$ ), subthreshold slope ( $SS$ ), and trap density ( $N_{trap}$ ) could be deduced.

Various derived device parameters are listed in Table 1 and were obtained for more than 160 untreated and OTS-pretreated transistors: on the average, 20 devices for each of eight different groups belonging to classes I–IV. In the case of the mobility data, the maximum mobilities ( $\mu_{eff}$ ) are listed with the average mobilities ( $\mu_{eff}^{avg}$ ) with the standard deviation. Three characteristic features with respect to the device performance can be found in Table 1.

Firstly, the whole groups of the NCBD-based transistors in this study showed room-temperature mobilities greater than  $4.5 \times 10^{-2} \text{ cm}^2/\text{Vs}$ , and the surface modification with OTS always enhanced the mobilities. Although the devices in class I showed lower mobilities compared to other class devices, still, these mobilities were comparable to or higher than those from typical tetracene-based transistors, which ranged between ca.  $1 \times 10^{-4}$  and  $0.12 \text{ cm}^2/\text{Vs}$  [9,28]. The observed high mobilities can be rationalized that after the surface pretreatment, the formation of the smooth tetracene active layer, with higher structural organization, induces more efficient charge-carrier transport via face-to-face intermolecular interactions between the  $\Pi$ – $\Pi$  stacks. The outcome of the pretreatment also suggests that the grain boundary-scattering of hole carriers in the tetracene active layers was the key obstacle to favorable charge conduction, as in poly-silicon- and pentacene-based transistors [22]. Furthermore, one of the critical factors determining device performance was the production of highly ordered thin films with good film connectivity, which was consistent with the AFM images and XRD diffractograms described in the previous section.

**Table 1**

Device parameters deduced from current–voltage characteristics.

	$W/L$	Surface pretreatment	$\mu_{eff}$ ( $\text{cm}^2/\text{Vs}$ ) <sup>a</sup>	$\mu_{eff}^{avg} \pm \sigma$ ( $\text{cm}^2/\text{Vs}$ ) <sup>a</sup>	$I_{on}/I_{off}$	$V_T$ (V)	$SS$ (V/dec)	$N_{trap}$ ( $10^{12}/\text{cm}^2$ )
Class I	500 $\mu\text{m}/200 \mu\text{m}$	untreated	$5.7 \times 10^{-2}$	$0.045 \pm 0.011$	$10^5$	–37	1.21	1.25
		OTS	0.126	$0.098 \pm 0.014$	$10^6$	–40	0.78	0.96
Class II	500 $\mu\text{m}/660 \mu\text{m}$	untreated	$9.1 \times 10^{-2}$	$0.064 \pm 0.018$	$10^5$	–34	1.32	0.93
		OTS	0.148	$0.11 \pm 0.02$	$10^6$	–33	0.84	0.85
Class III	500 $\mu\text{m}/800 \mu\text{m}$	untreated	0.124	$0.10 \pm 0.02$	$10^5$	–38	1.58	0.81
		OTS	0.208	$0.15 \pm 0.02$	$10^6$	–26	0.85	0.74
Class IV	500 $\mu\text{m}/1400 \mu\text{m}$	untreated	0.162	$0.12 \pm 0.03$	$10^5$	–37	1.59	0.62
		OTS	0.252	$0.19 \pm 0.03$	$10^5$	–33	1.25	0.48

<sup>a</sup> The hole mobility data in the text represents the maximum values ( $\mu_{eff}$ ). Considering the distributions of the OTFT characteristics derived, most of the  $\mu_{eff}$  values lie within  $\mu_{eff}^{avg} \pm 2\sigma$  (standard deviation).



Secondly, the geometric configuration effect on the mobilities was examined for the four different  $W/L$  ratios of the untreated and OTS-pretreated devices in classes I–IV. Fig. 4 represents the summarized results of the dimension effect on the mobilities whereby the obtained data showed that, at a constant channel width, the field-effect mobility increased as the channel length became longer (with decreasing  $W/L$  ratio), irrespective of surface modification. The maximum hole mobilities of 0.162 and 0.252  $\text{cm}^2/\text{Vs}$  for untreated and OTS-pretreated devices in class IV were among the best for the polycrystalline tetracene-based OTFTs reported to date for a  $\text{SiO}_2$  gate dielectric layer. We note that the  $W/L$  ratio of our devices is less than  $W/L = 10$  which is recommended to ignore a contribution of stray currents in these devices. As a result the mobilities might be slightly overestimated. However, when extrapolating the mobilities in Fig. 4 to smaller channel lengths of  $W/L > 10$  where the stray current contribution is negligible, the observed mobilities of 0.1  $\text{cm}^2/\text{Vs}$  are still equal or slightly higher than those reported previously.

Thirdly, the total trap density was also consistent with the device performance and surfactant pretreatment effect. The traps can be identified as structural disorders and/or defects. The  $N_{\text{trap}}$  value was estimated by the following relationship:

$$N_{\text{trap}} = \frac{C_i |V_T - V_{TO}|}{e}$$

where  $e$  the elementary charge and  $V_{TO}$  is the turn-on voltage, at which the drain current starts to increase exponentially as indicated in Fig. 3 [29]. There have been no other tetracene-based devices to which our current  $N_{\text{trap}}$  results can be directly compared. In Table 1, the surface modification with OTS clearly reduced the trap densities in all active layers. It should be noted that the tetracene thin films were deposited on  $\text{SiO}_2$  substrates at room temperature without any thermal post-treatment. In comparison to the previous reports involving thermal post-treatment, the observed low trap densities of the OTS-pretreated thin films can be attributed to the characteristic growth of well-connected, polycrystalline thin films produced by the weakly bound neutral cluster beams.

### 3.3. Comparison of transport characteristics

The temperature-dependence of the field-effect mobility was examined over a wide temperature range from 300 to 10 K. Fig. 5 represents the typical behavior of the mobilities as a function of temperature in class IV. Two domains in both logarithmic plots were observed: temperature-dependent region II (50 K  $< T < 300$  K) and temperature-independent region I (10 K  $< T < 50$  K). In low-temperature region I, the conduction of the majority hole carriers can be described by a so-called tunneling process occurring at the Au–(OTS-)tetracene interfaces. On the other hand, region II is attributed to a thermally activated transport mechanism, where the hole conduction is governed by thermal overcoming of the shallow traps present in the tetracene active layers. The behavior in region II was well fitted to the Arrhenius relation:

$$\mu_{\text{eff}} \propto \exp(-E_a/kT)$$

where  $E_a$  and  $k$  are the activation energy and Boltzmann constant, respectively. From the analysis of the slope of the logarithmic plot, the activation energies were estimated to be 42.2 and 28.4 meV for the untreated and OTS-pretreated devices.

The low activation energies derived from the temperature-dependence are consistent with the aforementioned device characteristics. Since the origin of the thermal activation process lies mainly in overcoming the traps produced by the structural imperfections in the active layers, the low activation energies derived in Fig. 5 correlated strongly with the good crystallinity of the tetracene thin films and the low trap densities in Table 1. The high quality of the NCBD-based thin films is also evidently manifested in the comparison to those reported elsewhere. For instance, Newman et al. examined device performance of bottom-contact, single crystal, tetracene-based transistors and reported that the mobility over the range of 220 K  $< T < 270$  K was thermally activated with an  $E_a$  of 49–51 meV [30]. In the case of OTS-pretreated, pentacene-based transistors prepared by thermal evaporation, Minari et al. reported an  $E_a$  of 54.8 meV [31]. The lower activation energy and trap density observed in this study strongly imply that the higher quality of the surface-modified NCBD

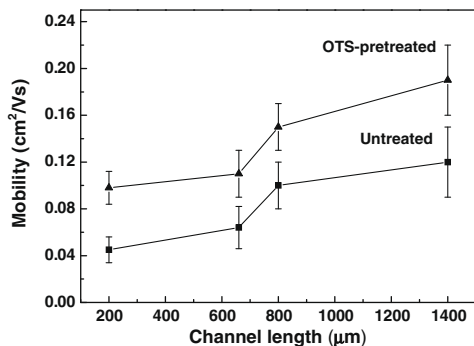


Fig. 4. Variation of field-effect mobilities as a function of channel length for untreated and OTS-pretreated tetracene-based transistors.

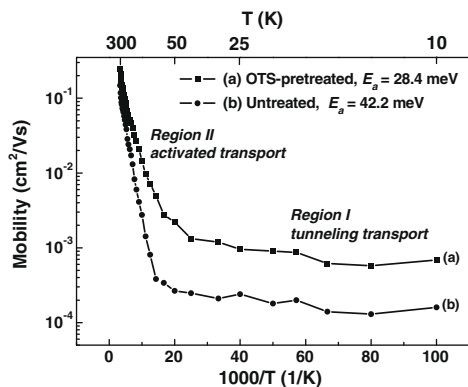


Fig. 5. Temperature-dependence of the field-effect mobilities for (a) OTS-pretreated, and (b) untreated tetracene-based transistors in class IV.

films eventually results in highly effective hole conduction between the well-connected polycrystalline grains, as well as the excellent mobilities in the tetracene-based transistors.

#### 4. Summary

Tetracene-based, top-contact OTFTs fabricated using a neutral cluster beam deposition method were characterized. In comparison to untreated thin films, surface modification with an amphiphilic OTS surfactant improved growth of tetracene active layers, as manifested in the contact angles, AFM, and XRD measurements. The trap density and temperature-dependence of the field-effect mobility in the range of 10–300 K demonstrated that the OTS pretreatment decreased the total trap density and activation energy for hole conduction by reducing structural disorder in the active layer. The influence of device configuration on the transistor characteristics was systematically examined: the field-effect mobility increased as the channel length became longer at a constant channel width. In particular, room-temperature hole mobilities as high as 0.162 and 0.252 cm<sup>2</sup>/Vs for untreated and OTS-pretreated devices were among the best to date for polycrystalline tetracene-based transistors using SiO<sub>2</sub> gate dielectric layers without any thermal post-treatment.

#### Acknowledgments

H.-S. Seo is grateful for the Seoul Science Fellowship. This work was supported by a Korea University grant and the Korea Science and Engineering Foundation (KOSEF) grant funded by the Korea government (MEST) (No. M10500000023-06J0000-02310).

#### References

- [1] G. Horowitz, *Adv. Mater.* 10 (1998) 365.  
 [2] M.M. Ling, Z. Bao, *Chem. Mater.* 16 (2004) 4824.

- [3] C.D. Dimitrakopoulos, P.R.L. Malenfant, *Adv. Mater.* 14 (2002) 99.  
 [4] L.A. Majewski, M. Grell, *Synth. Met.* 151 (2004) 175.  
 [5] H.Y. Choi, S.H. Kim, J. Jang, *Adv. Mater.* 16 (2004) 732.  
 [6] T.W. Kelley, L.D. Boardman, T.D. Dunbar, D.V. Muyres, M.J. Pellerite, T.P. Smith, *J. Phys. Chem. B* 107 (2003) 5877.  
 [7] H. Klauk, M. Halik, U. Zschieschang, G. Schmid, W. Radlik, W. Weber, *J. Appl. Phys.* 92 (2002) 5259.  
 [8] R.W.I. De Boer, T.M. Klapwijk, A.F. Morpurgo, *Appl. Phys. Lett.* 83 (2003) 4345.  
 [9] D.J. Gundlach, J.A. Nichols, L. Zhou, T.N. Jackson, *Appl. Phys. Lett.* 80 (2002) 2925.  
 [10] F. Cicoira, C. Santato, *Adv. Func. Mater.* 17 (2007) 3421.  
 [11] C. Santato, F. Cicoira, P. Cosseddu, A. Bonfiglio, P. Bellutti, M. Muccini, R. Zamboni, F. Rosei, A. Mantoux, P. Doppelt, *Appl. Phys. Lett.* 88 (2006) 163511.  
 [12] F. Cicoira, C. Santato, F. Dinelli, M. Murgia, M.A. Loi, F. Biscarini, R. Zamboni, P. Heremans, M. Muccini, *Adv. Func. Mater.* 15 (2005) 375.  
 [13] C.-W. Chu, Y. Shao, V. Shrotriya, Y. Yang, *Appl. Phys. Lett.* 86 (2005) 243506.  
 [14] J.-M. Choi, K. Lee, D.K. Hwang, J.H. Park, E. Kim, S. Im, *Electrochem. Solid-State Lett.* 9 (2006) G289.  
 [15] J.-Y. Kim, E.-S. Kim, J.-H. Choi, *J. Appl. Phys.* 91 (2002) 1944.  
 [16] H. Lim, J.-H. Choi, *J. Chem. Phys.* 124 (2006) 014710.  
 [17] P.S. Abthagir, Y.-G. Ha, E.-A. You, S.-H. Jeong, H.-S. Seo, J.-H. Choi, *J. Phys. Chem. B* 109 (2005) 23918.  
 [18] Y.-G. Ha, E.-A. You, B.-J. Kim, J.-H. Choi, *Synth. Met.* 153 (2005) 205.  
 [19] E.-A. You, Y.-G. Ha, Y.-S. Choi, J.-H. Choi, *Synth. Met.* 153 (2005) 209.  
 [20] M. Kim, B.-H. Jeon, J.-Y. Kim, J.-H. Choi, *Synth. Met.* 135–136C (2003) 743.  
 [21] H. Lim, B.-J. Kim, J.-H. Choi, *Synth. Met.* 135–136C (2003) 81.  
 [22] S.J. Kang, M. Noh, D.S. Park, H.J. Kim, C.N. Whang, C.H. Chang, *J. Appl. Phys.* 95 (2004) 2293.  
 [23] D. Guo, S. Entani, S. Ikeda, K. Saiki, *Chem. Phys. Lett.* 429 (2006) 124.  
 [24] H. Akimichi, T. Inoshita, S. Hotta, H. Noge, H. Sakaki, *Appl. Phys. Lett.* 63 (1993) 3158.  
 [25] S. Milita, M. Servidori, F. Cicoira, C. Santato, A. Pifferi, *Nucl. Instr. Meth. Phys. Res. B* 246 (2006) 101.  
 [26] D. Holmes, S. Kumaraswamy, A.J. Matzger, K.P.C. Vollhardt, *Chem. Eur. J.* 5 (1999) 3399.  
 [27] R.B. Campbell, J.M. Robertson, *Acta Cryst.* 15 (1962) 289.  
 [28] C. Santato, R. Capelli, M.A. Loi, M. Murgia, F. Cicoira, V.A.L. Roy, P. Stallinga, R. Zamboni, C. Rost, S.F. Karg, M. Muccini, *Synth. Met.* 146 (2004) 329.  
 [29] K.P. Pernstich, S. Haas, D. Oberhoff, C. Goldmann, D.J. Gundlach, B. Batlogg, A.N. Rashid, G. Schitter, *J. Appl. Phys.* 96 (2004) 6431.  
 [30] R. Newman Christopher, J. Chesterfield Reid, A. Merlo Jeffrey, C. Daniel Frisbie, *Appl. Phys. Lett.* 85 (2004) 422.  
 [31] T. Minari, T. Nemoto, S. Isoda, *J. Appl. Phys.* 99 (2006) 034506.



## Lithium phenolate complexes for an electron injection layer in organic light-emitting diodes

Yong-Jin Pu<sup>\*</sup>, Masashi Miyamoto, Ken-ichi Nakayama, Toshiro Oyama, Yokoyama Masaaki, Junji Kido<sup>\*</sup>

Department of Organic Device Engineering, Yamagata University, Yonezawa, Yamagata 992-8510, Japan

### ARTICLE INFO

#### Article history:

Received 29 July 2008  
Received in revised form 7 November 2008  
Accepted 7 November 2008  
Available online 17 November 2008

#### PACS:

61.66.Hq  
78.55.Fv  
78.55.Kz  
78.60.Fi

#### Keywords:

Lithium complexes  
Electron injection  
Organic light-emitting diode

### ABSTRACT

We synthesized  $\pi$ -conjugated lithium phenolate complexes, lithium 2-(2-pyridyl)phenolate (LiPP), lithium 2-(2', 2''-bipyridine-6'-yl)phenolate (LiBPP), and lithium 2-(isoquinoline-1'-yl)phenolate (LiQP). These complexes showed lower sublimation temperatures of 305–332 °C compared to 717 °C of LiF. The organic light-emitting devices (OLEDs) using these complexes as an electron injection layer exhibited high efficiencies which are comparable to that of the device using LiF. Especially, a 40-nm thick film of LiBPP or LiPP was effective as an electron injection material, providing low driving voltages, while such a thick film of LiF serves as a complete insulator, resulting in high driving voltages.

© 2008 Elsevier B.V. All rights reserved.

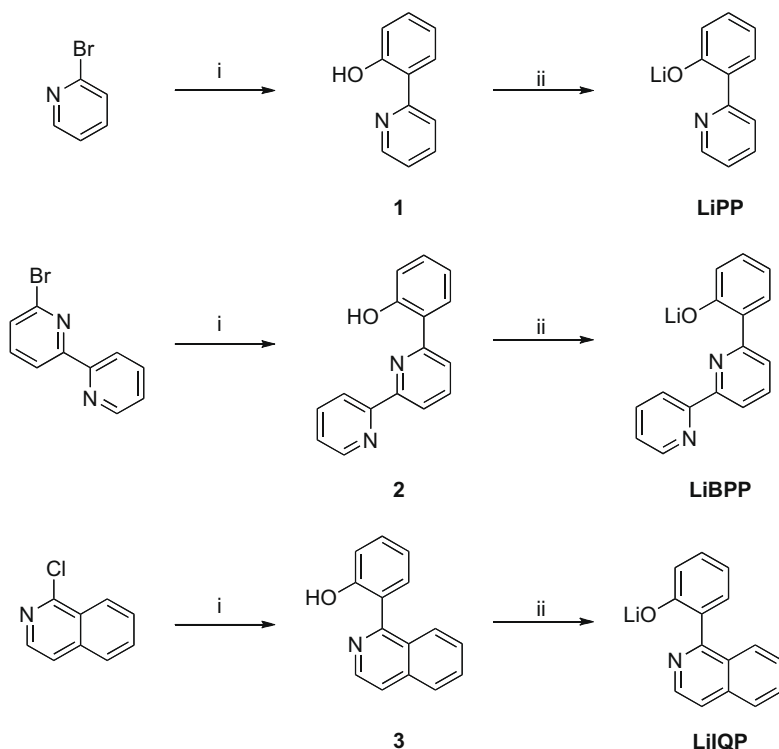
### 1. Introduction

In organic light-emitting devices (OLEDs), aluminum metal has been widely used for cathode because of its high stability in air and easy processability. However, work function of Al (4.2 eV) as an anode is not low enough to inject electrons into organic layer at low driving voltages. In the first report on an efficient OLED by Tang and Van Slyke, Mg:Ag alloy was used to improve electron injection from cathode [1]. Later, Li:Al alloy and double layer cathode of Li/Al were found to reduce driving voltage drastically [2]. These effects are due to lower work function of Li than that of Mg. Insertion of thin inorganic Li salt layer, such as Li<sub>2</sub>O [3] or LiF [4], between organic layer and cathode Al was found to be also very effective

to reduce electron injection barrier to the organic layer, and now it is widely used. LiF is expected to be reduced to Li by thermally activated hot Al in successive deposition, and interacts with an electron-transporting material like an electron donor [5]. That is why the thickness of LiF has to be very thin, no thicker than 1 nm, to be fully reacted by Al and not to leave unreduced insulating part of LiF. High temperature is also required to evaporate LiF under vacuum. Such thin thickness and low processability are disadvantages, especially in industrial process and large area deposition. On the other hand, organic  $\pi$ -conjugated ligands can be helpful to reduce evaporation temperature in a deposition process, and give charge-transporting ability to the complex. We previously reported that lithium quinolinolate complex (Liq) serves as an excellent electron injection material (EIM), and its thickness is much less sensitive to a performance of the device than that of LiF, because of an electron-transporting ability of Liq [6].

<sup>\*</sup> Corresponding authors.

E-mail addresses: [pu@yz.yamagata-u.ac.jp](mailto:pu@yz.yamagata-u.ac.jp) (Y.-J. Pu), [kid@yz.yamagata-u.ac.jp](mailto:kid@yz.yamagata-u.ac.jp) (J. Kido).



**Scheme 1.** Synthetic route of the lithium complexes. Reagents and conditions: (i) 2-hydroxyphenylboronic acid, Pd(PPh<sub>3</sub>)<sub>4</sub>, K<sub>2</sub>CO<sub>3</sub> aqueous, toluene, ethanol, reflux, 8 h and (ii) LiOH·H<sub>2</sub>O, methanol, r.t., 1 h.

In this paper, we report new series of Li complexes, such as lithium 2-(2-pyridyl)phenolate (LiPP), lithium 2-(2', 2''-bipyridine-6'-yl)phenolate (LiBPP), and lithium 2-(isoquinoline-1'-yl)phenolate (LiIQP), and their improved electron-transporting ability in OLED due to their more extended  $\pi$ -conjugated ligand than that of Liq.

## 2. Results and discussion

### 2.1. Synthesis, thermal and optoelectrochemical properties

Phenol ligands **1–3**, substituted 2-pyridyl or 2-quinolyl group on ortho position, were synthesized by Suzuki coupling of 2-hydroxyphenylboronic acid and the corresponding bromopyridine or chloroquinoline. Complexation reactions of the phenols and lithium hydroxide in methanol were straightforward, and the yields were quantitative (Scheme 1). All these complexes were further purified by train sublimation, and characterized with <sup>1</sup>H NMR and elemental analysis. Melting points of the complexes were relatively high (>300 °C) although their molecular weight is only around 200, probably because of their strong molecular interaction derived from their ionic property (Table 1). The complexes were sublimable, and the sublimation temperatures  $T_s$ s of the complexes were estimated from 10 wt% loss temperature in thermal gravimetric analysis under vacuum (Fig. 1). The lithium phenolate complexes showed much lower  $T_s$ s around 300 °C, while LiF showed a high  $T_s$  of 717 °C. These  $T_s$ s are nearly 100 °C lower than their decomposition temperatures, suggesting that the

complexes are not decomposed and do not release lithium ion or neutral atom during the thermal evaporation process.

UV–vis and photoluminescence (PL) spectra of the film on quartz substrates are shown in Fig. 2. LiPP showed a widest  $\pi$ – $\pi^*$  energy gap derived from the ligand **1**, which is estimated from the absorption edge, and LiBPP showed the narrowest gap, derived from the ligand **2**. The photoluminescence of the complexes was blue to green, and the order of  $\lambda_{\text{max}}$  is consistent with the order of energy gap from UV spectra. The highest occupied molecular orbital (HOMO) levels of the complexes, or the ionization potentials ( $I_p$ s), determined from photoelectron spectrometer surface analysis, were 5.56–5.70 eV, and the lowest unoccupied molecular orbital (LUMO) levels, estimated by the difference of  $I_p$  and optically obtained energy gap, were 2.49–2.68 eV.

**Table 1**  
Thermal and optoelectrochemical properties of the lithium phenolate complexes.

	$T_m^a$ (°C)	$T_d^b$ (°C)	$T_s^c$ (°C)	$E_g$ (eV)	PL (nm)	$I_p$ (eV)	$E_a$ (eV)
LiF	845	–	717	–	–	–	–
LiPP	331	411	317	3.18	430	5.67	2.49
LiBPP	361	431	305	2.95	546	5.56	2.61
LiIQP	351	455	332	3.02	508	5.70	2.68

<sup>a</sup> Melting point.

<sup>b</sup> Decomposition temperature: 5 wt% loss at atmosphere.

<sup>c</sup> Sublimation temperature: 10 wt% loss at  $2.0 \times 10^{-5}$  Torr.

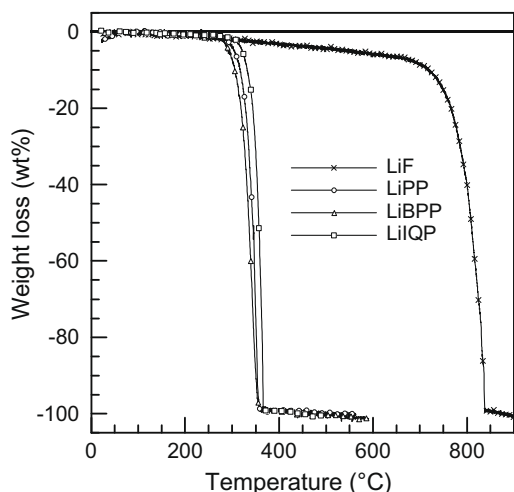


Fig. 1. Thermal gravimetric analysis of the complexes under vacuum.

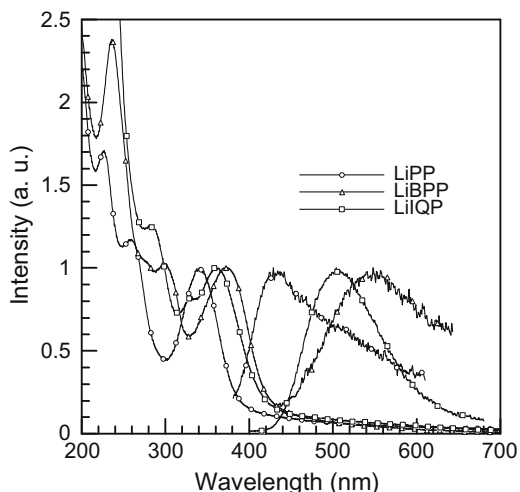


Fig. 2. UV-vis and PL spectra of the complexes in the film.

## 2.2. OLED performance

The OLEDs with the configuration of an ITO/*N,N'*-bis(naphthalen-1-yl)-*N,N'*-bis(phenyl)benzidine ( $\alpha$ -NPD) (50 nm)/tris(8-quinolinolato) aluminum ( $\text{Alq}_3$ ) (70 nm)/EIM (0.5–7.0 nm)/Al (100 nm) were fabricated. The device performance is summarized in Table 2. The devices without EIMs: ITO/ $\alpha$ -NPD (50 nm)/ $\text{Alq}_3$  (70 nm)/Al (100 nm) showed much higher driving voltage and much lower efficiencies compared with those with EIMs. These results demonstrated that the electron injection from Al cathode (4.2 eV) was not blocked by the higher LUMO levels of the lithium complexes, but was rather facilitated, although the LUMO levels of the EIMs (2.5–2.7 eV) are higher than that of  $\text{Alq}_3$  (3.2 eV). This improvement of the electron injection is probably because of the low barrier height for the electron injection from the Al cathode, which are the results from the lithium metal doping of the EIL materials

at the cathode interface. As reported [6], the lithium ion in the organic lithium complexes can be reduced by thermally activated Al to release lithium metal, which dopes the EIL materials at the interface to form the gap states. When a thin layer, <3.0 nm, of the lithium complexes was used as an EIM, the turn-on voltages at 1  $\text{cd/m}^2$  in the all devices were around 3–4 V, and the driving voltages at 100  $\text{cd/m}^2$  were 6–8 V. The efficiencies are comparable to those of the device using LiF as an EIM. On the other hand, the life time of the devices using these lithium phenolate complexes was the same as that of the device using LiF, and so there was no negative effect of the phenolate ligand for the device stability. These results reveal that the three lithium complexes can be alternative to LiF as an EIM.

In contrast to LiF, these complexes have a  $\pi$ -conjugated ligand, which may act as a charge-transporting moiety. To investigate the electron-transporting ability of the complexes, the devices with a thick EIM layer, having a structure of an ITO/NPD (50 nm)/ $\text{Alq}_3$  (70– $x$  nm)/EIM ( $x = 20$  or 40 nm)/Al (100 nm), were fabricated. Fig. 3 shows the dependency of driving voltage on the thickness of EIM. As the thickness of LiPP increased from 3.0 to 40 nm, the turn-on voltage at 1  $\text{cd/m}^2$  increased by 8.8–13.2 V. On the other hand, the turn-on voltage with LiBPP and LiIQP increased only by 2.1 and 2.6 V, respectively, with increase of the thickness from 3.0 to 40 nm. At 100  $\text{cd/m}^2$ , LiBPP and LiIQP also showed less increase in the driving voltage compared with that of LiPP. These results show that LiBPP and LiIQP may have higher electron-transporting mobility than LiPP, resulting from their wider  $\pi$ -conjugation.

The EL emissions of the devices were green and ascribed to the emission of  $\text{Alq}_3$ . However, the EL spectra with a thick LiPP layer exhibited a shoulder peak around 430 nm derived from LiPP emission (Fig. 4). The shoulder peak was increased as the thickness of LiPP increased from 20 to 40 nm. These shoulder peaks indicate that all injected holes were not consumed through recombination in  $\text{Alq}_3$  because of a poorer electron-transporting ability of LiPP, and some of the holes reached into LiPP layer to give a blue emission of LiPP (Scheme 1).

When BCP (bathocuproine), which has a more crystalline feature than  $\text{Alq}_3$ , was used as 0.5 nm of thin ETL between  $\text{Alq}_3$  and EIL (device: ITO/NPD (50 nm)/ $\text{Alq}_3$  (60 nm)/BCP (10 nm)/EIM (LiF or LiPP) (0.5 nm)/Al (100 nm)), LiPP showed a slightly poorer electron injection compared with LiF. This result is probably because LiF having smaller molecular size than LiPP could make a better contact with rough BCP surface, while there were no differences between LiF and LiPP for the electron injection to amorphous  $\text{Alq}_3$  layer. Further investigation on the effect of roughness of ETL and on the size of the lithium complexes is ongoing.

## 3. Conclusion

$\pi$ -Conjugated lithium phenolate complexes, lithium 2-(2-pyridyl)phenolate (LiPP), lithium 2-(2', 2''-bipyridine-6'-yl)phenolate (LiBPP), and lithium 2-(isoquinoline-1'-yl)phenolate (LiIQP), were synthesized. The complexes

**Table 2**

OLED performances with the various thicknesses of the EIM.

EIM <sup>a</sup> (nm)		1 cd/m <sup>2</sup>				100 cd/m <sup>2</sup>				1000 cd/m <sup>2</sup>				
		(V)	(V)	(lm/W)	(cd/A)	(%)	(V)	(lm/W)	(cd/A)	(%)	(V)	(lm/W)	(cd/A)	(%)
No EIM <sup>b</sup>		9.1	14.8	0.4	0.8	0.6	18.2	0.4	2.1	0.6				
LiPP	0.5	3.9	7.6	1.5	3.6	1.1	10.4	1.3	4.4	1.4				
	1.0	3.1	5.9	1.6	3.1	1.0	8.6	1.4	3.7	1.2				
	2.0	3.4	6.8	1.7	3.8	1.2	9.8	1.4	4.5	1.5				
	3.0	4.4	8.9	1.0	3.0	0.9	12.3	0.9	3.5	1.1				
	5.0	7.5	14.2	0.1	0.3	0.1	–	–	–	–				
	20	9.1	14.8	0.1	0.3	0.1	–	–	–	–				
	40	13.2	19.1	0.2	0.9	0.3	–	–	–	–				
LiBPP	0.5	4.0	7.7	1.5	3.6	1.2	10.6	1.2	4.2	1.3				
	2.0	4.0	7.3	1.4	3.3	1.0	10.1	1.2	3.9	1.3				
	3.0	2.9	5.6	1.7	3.0	1.0	8.2	1.4	3.6	1.1				
	5.0	3.4	7.3	0.6	1.4	0.4	10.8	0.5	1.7	0.5				
	7.0	4.5	9.2	0.9	2.5	0.8	12.6	0.8	3.0	0.9				
	20	4.7	9.7	1.0	3.1	1.0	13.1	0.8	3.4	1.1				
	40	5.0	10.6	0.7	2.5	0.8	14.1	0.6	2.6	0.8				
LiIQP	0.5	3.0	6.3	1.8	3.6	1.2	9.1	1.5	4.3	1.4				
	2.0	3.1	6.6	1.2	2.6	0.8	9.5	1.0	3.2	1.0				
	3.0	3.0	6.1	1.5	2.9	0.9	8.8	1.2	3.4	1.1				
	5.0	3.6	7.6	1.1	2.6	0.8	10.8	0.9	3.0	0.9				
	20	6.0	11.0	0.8	2.8	0.8	14.2	0.7	3.2	1.0				
	40	5.6	11.0	0.7	2.6	0.8	14.6	0.6	3.0	0.9				

<sup>a</sup> EIM, 0.5–7.0 nm: ITO/NPD (50 nm)/Alq<sub>3</sub> (70 nm)/EIM (0.5–7.0 nm)/Al (100 nm) and EIM, 20 or 40 nm: ITO/NPD (50 nm)/Alq<sub>3</sub> (70 – x nm)/EIM (x nm)/Al (100 nm).

<sup>b</sup> ITO/NPD (50 nm)/Alq<sub>3</sub> (70 nm)/Al (100 nm).

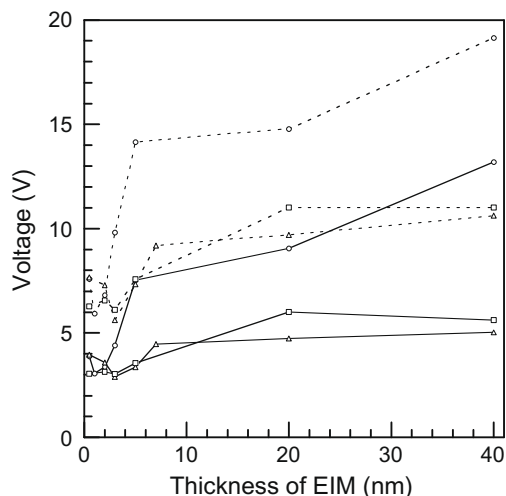


**Fig. 3.** Driving voltage at 1 cd/m<sup>2</sup> (solid line) and 100 cd/m<sup>2</sup> (dotted line) of LiPP (circle), LiBPP (triangle) and LiIQP (square). Device structures: ITO/NPD (50 nm)/Alq<sub>3</sub> (70 nm)/EIM (0.5–7.0 nm)/Al (100 nm); ITO/NPD (50 nm)/Alq<sub>3</sub> (50 nm)/EIM (20 nm)/Al (100 nm) and ITO/NPD (50 nm)/Alq<sub>3</sub> (30 nm)/EIM (40 nm)/Al (100 nm).

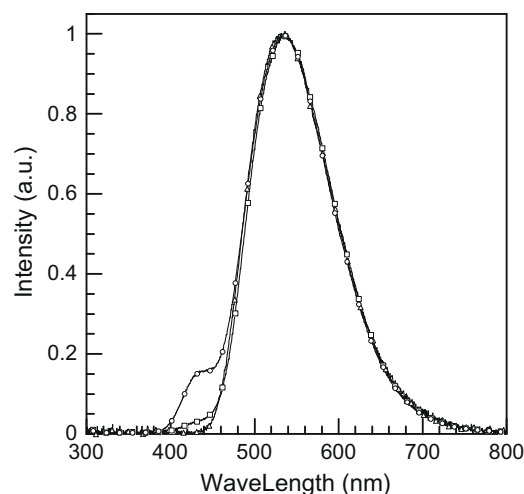


**Fig. 4.** EL spectra of the OLED devices with LiPP at 20 mA/cm<sup>2</sup>. Circle: ITO/NPD (50 nm)/Alq<sub>3</sub> (30 nm)/LiPP (40 nm)/Al (100 nm); square: ITO/NPD (50 nm)/Alq<sub>3</sub> (50 nm)/LiPP (20 nm)/Al (100 nm) and triangle: ITO/NPD (50 nm)/Alq<sub>3</sub> (70 nm)/LiF (0.5 nm)/Al (100 nm).

were readily sublimated under vacuum, compared with LiF. The organic light-emitting diodes (OLEDs) using these complexes as an electron injection layer exhibited a facilitated electron injection from Al cathode to Alq<sub>3</sub> emitting layer, as well as the device using LiF, and even in 40 nm of thick film, LiBPP and LiPP were still effective because of their electron-transporting  $\pi$ -conjugated ligand.

## 4. Experimental

### 4.1. Materials

6-Bromo-2, 2'-dipyridyl was synthesized according to the literature. 2-Hydroxyphenylboronic acid was purchased from Wako Chemical.

## 4.2. Measurements

The  $^1\text{H}$  NMR spectra were measured in deuterated solvents with JEOL ECX 400 MHz spectrometers. Elemental analyses were carried out in the Elemental Analysis Service, Yamagata University, Japan. Mass spectra were obtained by a JEOL JMS-K9 mass spectrometer. Thermal gravimetric analysis was performed on SII EXSTAR 6000 and TGA/DTA 62000. Ionization potentials were measured with Photoelectron Spectrometer Surface Analyzer (RIKEN KEIKI AC-3). UV–visible absorption spectra were recorded with a Shimadzu UV-3150 spectrometer. PL spectra were recorded using a Jobin Yvon Fluoromax-2 fluorometer. The EL devices were fabricated on indium tin oxide (ITO) coated glass substrates, ultrasonicated sequentially in detergent, methanol, 2-propanol, and acetone and exposed under UV–ozone ambient for 20 min. NPD and  $\text{Alq}_3$  materials were deposited by thermal evaporation under  $2 \times 10^{-4}$  Pa. EIM and aluminum were finally deposited under  $1 \times 10^{-3}$  Pa as a cathode through a shadow mask, and its active area is  $5 \times 5 \text{ mm}^2$ . Layer thickness calibration was performed using Dektak 3 surface profilometer. The EL spectra were measured on a Hamamatsu photonic multichannel analyzer PMA-11. The current–voltage (I–V) characteristics and luminance were measured using Keithley 2400 Source Meter and Konika Minolta CS-200, respectively. External quantum efficiencies were calculated assuming Lambertian emission pattern and considering all spectral features in the visible.

**Ligand 1:** A mixture of 2-bromopyridine (5.21 g, 33.0 mmol), 2-hydroxyphenylboronic acid (4.14 g, 30.0 mmol), toluene (120 ml), ethanol (60 ml), aqueous potassium carbonate (2.0 mol/l, 30 ml) and tetrakis(triphenylphosphine)palladium (0) was heated at 80 °C for 8 h under nitrogen. The mixture was allowed to cool to room temperature, and then toluene was added. The organic layer was washed with water, dried over magnesium sulfate and filtered. The solvent was removed in vacuo, and the residue was purified by column chromatography over silica using a chloroform–hexane mixture (1:1) as eluent to give **1** (3.4 g, 66%).  $^1\text{H}$  NMR (400 MHz,  $d_6\text{DMSO}$ , ppm) 8.62 (1H, d,  $J = 4.1$  Hz), 8.21 (1H, d,  $J = 8.6$  Hz), 8.03–8.00 (2H, m), 7.43 (1H, t,  $J = 6.1$  Hz), 7.30 (1H, t,  $J = 7.5$  Hz), 6.91 (2H, t,  $J = 4.1$  Hz). EI–MS ( $m/z$ ) calcd. 171.2. found 171. Elemental analysis calcd. for  $\text{C}_{11}\text{H}_9\text{NO}$ : C, 77.17; H, 5.30; N, 8.18. found: C, 77.08; H, 5.39; N, 8.17.

**Ligand 2:** A mixture of 6-bromo-2,2'-dipyridyl (5.05 g, 21.5 mmol), 2-hydroxyphenylboronic acid (3.27 g, 23.7 mmol), toluene (100 ml), ethanol (50 ml), aqueous potassium carbonate (2.0 mol/l, 24 ml), and tetrakis(triphenylphosphine)palladium (0) was heated at 70 °C for 8 h under nitrogen. The mixture was allowed to cool to room temperature, and then toluene was added. The organic layer was washed with water, dried over magnesium sulfate, and filtered. The solvent was removed in vacuo, and the residue was purified by column chromatography over silica using a chloroform–ethyl acetate mixture (9:1) as eluent to give **2** (4.8 g, 90%).  $^1\text{H}$  NMR (400 MHz,  $d_6\text{DMSO}$ , ppm) 8.77 (1H, d,  $J = 4.5$  Hz), 8.32–8.26 (2H, m), 8.19–8.13 (2H, m), 8.09–8.03 (2H, m), 7.53 (1H, dd,  $J = 7.7, 5.0$  Hz), 7.34 (1H, t,  $J = 7.7$  Hz), 6.98–6.94 (2H, m). EI–MS ( $m/z$ ) calcd. 248.3. found 248. Elemental analysis

calcd. for  $\text{C}_{16}\text{H}_{12}\text{N}_2\text{O}$ : C, 77.40; H, 4.87; N, 11.28. found: C, 77.34; H, 4.93; N, 11.32.

**Ligand 3:** A mixture of 1-chloroisoquinoline (5.20 g, 31.8 mmol), 2-hydroxyphenylboronic acid (5.21 g, 37.8 mmol), toluene (100 ml), ethanol (60 ml), aqueous potassium carbonate (2.0 mol/l, 38 ml) and tetrakis(triphenylphosphine)palladium (0) was heated at 70 °C for 8 h under nitrogen. The mixture was allowed to cool to room temperature, and then toluene was added. The organic layer was washed with water, dried over magnesium sulfate, and filtered. The solvent was removed in vacuo, and the residue was purified by column chromatography over silica using a toluene–ethyl acetate mixture (9:1) as eluent to give **3** (5.5 g, 78%).  $^1\text{H}$  NMR (400 MHz,  $d_6\text{DMSO}$ , ppm) 9.67 (1H, s), 8.53 (1H, d,  $J = 6.0$  Hz), 7.99 (1H, d,  $J = 8.2$  Hz), 7.81 (1H, d,  $J = 6.0$  Hz), 7.76–7.71 (2H, m), 7.57 (1H, t,  $J = 7.6$  Hz), 7.35–7.27 (2H, m), 7.01–6.94 (2H, m). EI–MS ( $m/z$ ) calcd. 221.3. found 221. Elemental analysis calcd. for  $\text{C}_{15}\text{H}_{11}\text{NO}$ : C, 81.43; H, 5.01; N, 6.33. found: C, 81.46; H, 5.07; N, 6.33.

## 4.3. General procedure of the complexation

A methanol solution (2.5 ml) of a ligand (1.0 mmol) was slowly added to a methanol solution (2.5 ml) of lithium hydroxide monohydrate (1.0 mmol), and the mixture was stirred at room temperature. After 30 min, the solvent was evaporated in vacuum to give a yellow solid. The obtained compounds were purified with train sublimation.

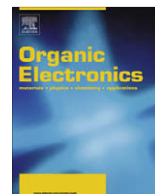
**LiPP:**  $^1\text{H}$  NMR (400 MHz,  $d_6\text{DMSO}$ , ppm) 8.45 (1H, d,  $J = 7.7$  Hz), 8.40 (1H, d,  $J = 4.5$  Hz), 7.68–7.64 (2H, m), 7.06 (1H, t,  $J = 5.9$  Hz), 6.86 (1H, t,  $J = 7.5$  Hz), 6.39 (1H, d,  $J = 7.7$  Hz), 6.15 (1H, s). Elemental analysis calcd. for  $\text{C}_{11}\text{H}_8\text{NO}$ : C, 74.59; H, 4.55; N, 7.91. found: C, 74.64; H, 4.44; N, 7.85.

**LiBPP:**  $^1\text{H}$  NMR (400 MHz,  $d_6\text{DMSO}$ , ppm) 8.88 (1H, d,  $J = 7.7$  Hz), 8.64 (1H, d,  $J = 3.6$  Hz), 8.43 (1H, d,  $J = 7.7$  Hz), 8.00 (1H, d,  $J = 7.7$  Hz), 7.96–7.92 (2H, m), 7.73 (1H, t,  $J = 7.9$  Hz), 7.40 (1H, t,  $J = 5.8$  Hz), 6.87 (1H, t,  $J = 7.5$  Hz), 6.46 (1H, d,  $J = 8.2$  Hz), 6.18 (1H, t,  $J = 7.0$  Hz). Elemental analysis calcd. for  $\text{C}_{16}\text{H}_{11}\text{N}_2\text{O}$ : C, 75.59; H, 4.36; N, 11.02. found: C, 75.58; H, 4.23; N, 11.01.

**LiIQP:**  $^1\text{H}$  NMR (400 MHz,  $d_6\text{DMSO}$ , ppm) 8.34 (1H, d,  $J = 5.9$  Hz), 8.10 (1H, d,  $J = 8.2$  Hz), 7.85 (1H, d,  $J = 8.2$  Hz), 7.64 (1H, t,  $J = 7.5$  Hz), 7.57 (1H, d,  $J = 5.9$  Hz), 7.46 (1H, t,  $J = 7.7$  Hz), 6.96–6.88 (2H, m), 6.37 (1H, d,  $J = 8.2$  Hz), 6.08 (1H, t,  $J = 7.3$  Hz). Elemental analysis calcd. for  $\text{C}_{15}\text{H}_{10}\text{NOLi}$ : C, 79.30; H, 4.44; N, 6.17. Found: C, 79.13; H, 4.31; N, 6.15.

## References

- [1] C.W. Tang, S.A. VanSlyke, Appl. Phys. Lett. 51 (1987) 913.
- [2] J. Kido, K. Nagai, Y. Okamoto, IEEE Trans. Electron Devices 40 (1993) 1342.
- [3] T. Wakimoto, Y. Fukuda, K. Nagayama, A. Yokoi, H. Nakada, M. Tsuchida, IEEE Trans. Electron Devices 44 (1997) 1245.
- [4] L.S. Hung, C.W. Tang, M.G. Mason, Appl. Phys. Lett. 70 (1997) 152.
- [5] (a) Q.T. Le, L. Yan, Y. Gao, M.G. Mason, D.J. Giesen, C.W. Tang, J. Appl. Phys. 87 (2000) 375; (b) M.G. Mason, C.W. Tang, L.-S. Hung, P. Raychaudhuri, J. Madathil, D.J. Giesen, L. Yan, Q.T. Le, Y. Gao, S.-T. Lee, L.S. Liao, L.F. Cheng, W.R. Salaneck, D.A.D. Santos, J.L. Brédas, J. Appl. Phys. 89 (2001) 2756; (c) L.S. Hung, R.Q. Zhang, P. He, G. Mason, J. Phys. D: Appl. Phys. 35 (2002) 103; (d) C.-I. Wu, G.-R. Lee, T.-W. Pi, Appl. Phys. Lett. 87 (2005) 212108.
- [6] J. Endo, T. Matsumoto, J. Kido, Jpn. J. Appl. Phys. 41 (2002) 800.



## Contact effects in organic thin-film transistor sensors

Luisa Torsi \*, Francesco Marinelli, M. Daniela Angione, Antonio Dell'Aquila, Nicola Cioffi, Elvira De Giglio, Luigia Sabbatini

Dipartimento di Chimica, Università degli Studi di Bari, via Orabona 4, 70126 Bari, Italy

### ARTICLE INFO

#### Article history:

Received 20 October 2008

Received in revised form 12 November 2008

Accepted 13 November 2008

Available online 30 November 2008

#### PACS:

72.80.Le

73.40.Cg

85.30.Tv

87.85.fk

#### Keywords:

Thin films

Transistors

Chemo-bio sensors

Conducting polymers

Molecular electronics

### ABSTRACT

Contact effects in organic thin-film transistors (OTFTs) sensors are here investigated specifically respect to the gate field-induced sensitivity enhancement of more than three orders of magnitude seen in a DH $\alpha$ 6T OTFT sensor exposed to 1-butanol vapors. This study shows that such a sensitivity enhancement effect is largely ascribable to changes occurring to the transistor channel resistance. Effects, such as the changes in contact resistance, are seen to influence the low gate voltage regime where the sensitivity is much lower.

© 2008 Elsevier B.V. All rights reserved.

## 1. Introduction

The scientific and technological driving force towards the development of performing conducting polymer (CP) based solid state sensors is still very strong despite this field has been initiated more than 30 years ago [1]. Recently, organic thin-film transistor (OTFT) sensors have risen the interest of the scientific community for their enhanced level of performance [2–6]. In this configuration, highly repeatable responses were measured by properly gate biasing the device [2,3] whereas broad chemical selectivity was conferred either by covalently bound side groups [7] or by means of CP blends [8]. Besides, an important assessment of their selectivity capabilities was achieved with a chiral OTFT, that exhibited field-effect

amplified sensitivity allowing detection of optical isomers in the tens part-per-million (ppm) concentration range [9], *i.e.* with a three order of magnitude sensitivity improvement [10,11].

This report aims to demonstrate that the sensing process, in particular the field-induced sensitivity enhancement, can be largely ascribed to changes of the channel resistance  $R_{ch}$ , eventually ruling out dominating contributions from of the contact resistance ( $R_c$ ) or leakage current variations. The results reported can also shed light on the origin of the contact resistance in OTFTs.

## 2. Experimental methods

### 2.1. Organic thin-film transistors fabrication

The transistors used for this study have a bottom-gate structure and consist of a highly *n*-doped silicon wafer

\* Corresponding author.

E-mail address: [torsi@chimica.uniba.it](mailto:torsi@chimica.uniba.it) (L. Torsi).



(resistivity: 0.02–1  $\Omega/\text{cm}$ ) coated by a 300 nm thick  $\text{SiO}_2$  thermal oxide (dielectric capacitance per unit area:  $C_i = 10 \text{ nF cm}^{-2}$ ). Each sample was fabricated on a cleaved wafer piece of ca. 2  $\text{cm}^2$ . The silicon substrate with a gold pad acts as the gate contact (G) while the silicon dioxide is the gate dielectric. The  $\text{SiO}_2$  surface was alkyl functionalized by treatment in 1,1,1,3,3,3-hexamethyldisilazane saturated vapors for 24 h. The dielectric surface was covered by a  $\alpha,\omega$ -dihexyl-hexathiophene (DH $\alpha$ 6T) thin-film deposited by thermal evaporation at a base pressure of  $8 \times 10^{-7}$  with the substrate kept at room temperature. A series of 30 gold source (S) and drain (D) contacts were defined, by thermal evaporation through a shadow mask, directly on the organic films. Before the measurements, the OTFTs were annealed under a vacuum of  $10^{-5}$  Torr at 100  $^\circ\text{C}$  for 30 min. Transistors were produced with different channel lengths (distance between the two probed pads), namely:  $L = 0.2 \text{ mm}$ , 0.6 mm and 1 mm, while the channel width (the pads' longer dimension,  $W$ ), was kept constant at 4 mm. The sensors were fabricated and measured in a standard laboratory environment and operated at room temperature. The synthetic approach for preparing the  $\alpha,\omega$ -dihexylhexathiophene comprised a Stille coupling between the 5,5'-bis-trimethylstannyl-2,2'-bithiophene and the 5-bromo-5'-hexyl-2,2'-bithiophene. The product precipitated from the reaction medium as a red powder and was purified from soluble byproducts by subsequent Soxhlet washing with methanol, chloroform, acetone and *n*-hexane.

## 2.2. Sensing measurements

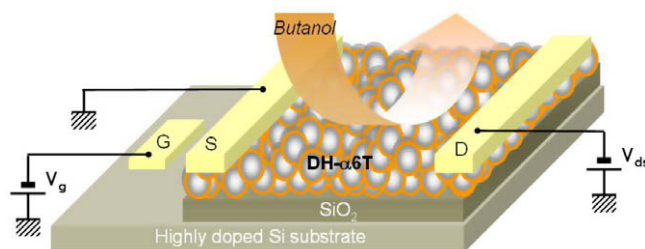
The analyte, in a nitrogen stream and at a controlled concentration, was delivered through a nozzle (positioned at a fixed distance of few mm from the device channel surface) directly onto the active layer surface, as depicted in Scheme 1. The  $I_{\text{ds}}-V_{\text{g}}$  transfer characteristics were measured by biasing the device in a common source configuration by sweeping  $V_{\text{g}}$  (from positive to negative potentials) at a fixed  $V_{\text{ds}}$ , namely  $-50 \text{ V}$ . The current,  $I_{\text{ds}}$ , flowing in the channel region was measured in nitrogen and in a flux of controlled butanol concentration in  $\text{N}_2$ , obtained through a system of computer controlled flow meters. The response measurements were performed at relatively high analyte concentrations (3750–11,250 ppm) as this condition allowed to better discriminate the effects of the contact resistance variation. Both the transfer characteristics (measured in  $\text{N}_2$  and in the analyte atmosphere), lasted for 45 s with a total flux of 200 ml/min. Before starting

each run the unbiased device was conditioned by exposure to the analyte atmosphere for 45 s.

## 3. Results and discussion

The system investigated is a  $\alpha,\omega$ -dihexylhexathiophene (DH $\alpha$ 6T) OTFT with a bottom-gate top contact configuration (Scheme 1). Such a device has been widely investigated for 15 years now [12–17] and can, in many respects, be taken as a model system. The DH $\alpha$ 6T thin-film, exhibiting a morphology formed of a three dimensional percolation-type network, with nano-sized crystalline domains separated by voids of comparable size [18], acts both as transistor channel material and as sensing layer. In agreement to what already reported for OTFTs exposed to volatile organic compounds, changes in the drifting source-drain current were seen upon exposure of the DH $\alpha$ 6T OTFT to 1-butanol and the response and recovery times were generally quite short, falling in the 10–100 s of seconds range at most [2,3]. Weak chemical interactions are likely to occur between the DH $\alpha$ 6T thin-film and the alcohol molecules, the latter being eventually partitioned between the solid (the DH $\alpha$ 6T thin-film) and the gaseous phase. Since diffusion of the molecules into the crystalline grains is unlikely, such molecules largely percolate through the voids around the grains till the interface with the dielectric is reached. The analyte molecules are physisorbed at the grains surface and this can enhance the potential barriers at the boundaries [19], generating also charge trapping effects. The degree of physisorption is a function of the chemical affinity between the active layer and the analyte [7], and it occurs in the DH $\alpha$ 6T bulk, as well as at the interface with the dielectric, where the two-dimensional transport takes place.

Typical DH $\alpha$ 6T OTFT current–voltage characteristics in the inert  $\text{N}_2$  atmosphere are reported in Fig. 1a. Here, the source-drain current ( $I_{\text{ds}}$ ) is reported as a function of the source-drain bias ( $V_{\text{ds}}$ ) for different gate biases ( $V_{\text{g}}$ ). As DH $\alpha$ 6T is a p-type semiconductor, negative values of  $V_{\text{ds}}$  and  $V_{\text{g}}$  ( $|V_{\text{g}}| > |V_{\text{t}}|$ ) drive the device in the *on-state* (accumulation mode), while  $V_{\text{g}}$  values below the threshold voltage,  $V_{\text{t}}$ , generate a regime of charge depletion (*off-state* or depletion mode) [2]. The field-effect mobility ( $\mu$ ) and the threshold voltage,  $V_{\text{t}}$ , are graphically extracted from the relevant square root of  $I_{\text{ds}}$  vs.  $V_{\text{g}}$  plot (Fig. 1b) resulting in  $\mu = 0.1 \text{ cm}^2/\text{Vs}$ ,  $V_{\text{t}}$  below  $-2 \text{ V}$  while a current amplification of  $10^4$  can be achieved. These figures of merit are state of the art values for DH $\alpha$ 6T [12–15], although best mobility



**Scheme 1.** DH $\alpha$ 6T thin-film transistor sensor structure upon exposure to 1-butanol vapors along with biasing details.

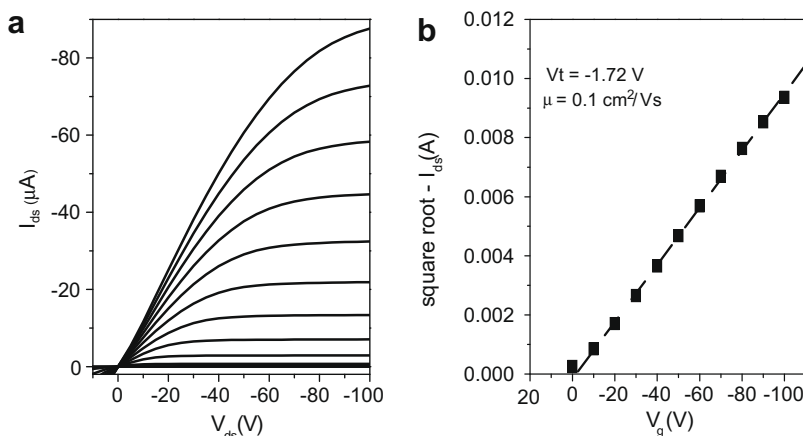


**Fig. 1.** (a) DH $\alpha$ 6T current–voltage characteristics in a nitrogen flux. Gate voltages go from 20 V to  $-100$  V in steps of  $-10$  V. (b) The relevant square root of source–drain current as a function of the gate bias is reported ( $L = 0.2$  mm).

values can reach  $0.5\text{--}1\text{ cm}^2/\text{Vs}$  [16,17]. Data reported in the supporting information show  $I_{ds}$  values at zero  $V_{ds}$  biases at different  $V_g$ . It is apparent that the highest leakage current ( $I_{ds}$  values at zero  $V_{ds}$ ) is at most of ca. 60 nA. Since the  $I_{ds}$  currents measured reach  $100\text{ }\mu\text{A}$ , the sum of the leakage currents is below 0.1% of  $I_{ds}$ , this being a figure generally considered as adequate.

The field-effect mobility in a OTFT is generally gate bias dependent and can be better estimated by considering the channel conductance

$$g_{ds} = \frac{\partial I_{ds}}{\partial V_g} \quad (1)$$

measured at low drain voltages ( $V_{ds} < -5$  V) [20]. In this case being  $V_{ds} \ll V_g$ ,  $g_{ds}$  can be expressed as follows:

$$g_{ds} = \frac{\partial I_{ds}}{\partial V_{ds}} \approx \frac{W}{L} \mu C_i (V_g - V_t) \quad (2)$$

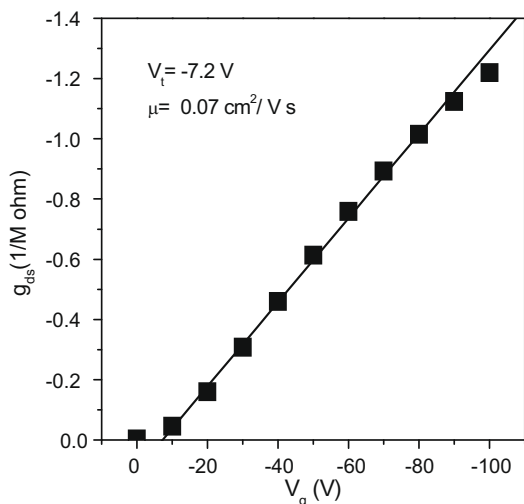


**Fig. 2.** DH $\alpha$ 6T OTFT channel conductance,  $g_{ds}$ , plotted as a function of the gate bias.

This equation is, at first approximation, valid also for non-constant mobility. In Fig. 2 the data for the channel conductance,  $g_{ds}$ , extracted from the  $I$ – $V$  characteristics of Fig. 1 at low source–drain voltage ( $0 < V_{ds} < |-5$  V]), are reported as a function of  $V_g$ . The extracted mobility is of  $0.07\text{ cm}^2/\text{Vs}$  in this case. The data modeling within this framework allows also to give a first estimate of the contact resistance effects. In the case of zero contact resistance Eq. (2) holds, at low  $V_{ds}$  (linear region). Introducing a series resistance as contact resistance,  $R_c$ , results in changing  $V_{ds}$  by a  $V_{ds} - I_{ds}R_c$  and Eq. (2) becomes

$$g_{ds} \approx \frac{W/L \cdot C_i \mu (V_g - V_t)}{1 + W/LC_i \mu R_c (V_g - V_t)} \quad (3)$$

The transport in the channel region appears as not limited by the contact resistance, since  $g_{ds}$  shows a quite good linear dependence from  $V_g$  (correlation factor of 0.9997). A slight deviation from linearity at higher  $V_g$  biases is indeed observed and this calls for further investigations. To quantitatively extract the contribution of the contact resistance the transfer line method, TLM [21,22] was used. Accordingly, the  $I$ – $V$  characteristics of a set of three DH $\alpha$ 6T OTFTs, with channel lengths of  $L = 0.2, 0.6$  and  $1$  mm were measured in  $N_2$ . The total device resistance,  $R$ , was extracted from the linear region ( $0 < V_{ds} < |-10$  V]) for each of the three OTFTs. In Fig. 3 the data are reported as  $(R * W)$  vs.  $L$  at different  $V_g$  voltages. According to the transfer line method, the total resistance,  $R$ , is the sum of the channel resistance,  $R_{ch}$ , and the contact resistance  $R_c$ , the latter being graphically extrapolated at  $L = 0$ .

In Fig. 4 the contact ( $R_c$ ) and channel ( $R_{ch}$ ) resistances of DH $\alpha$ 6T OTFTs with different channel lengths are plotted vs.  $V_g$ . As expected, in longer channel devices the contact resistance weights much less, while in the shorter channel devices they are of comparable size, at least at higher gate biases. This provides preliminary evidences that contact related effects are not dominating the *on-state* OTFT transport properties. Besides, the curves in Fig. 4 exhibit contact resistance at high  $V_g$  biases falling in the  $10^5\text{ }\Omega\text{ cm}$  range. Although lower  $R_c$  have been reported in some cases for

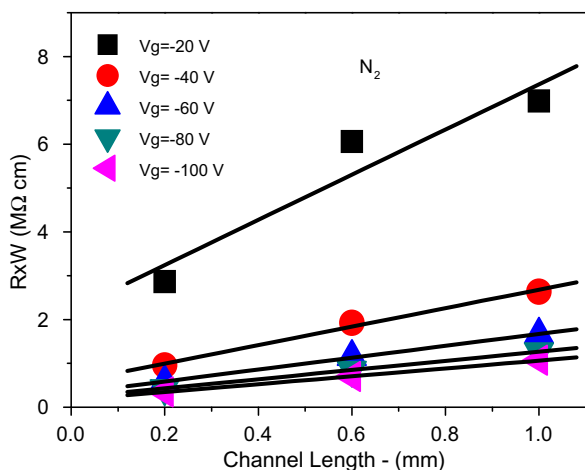


**Fig. 3.** The total device resistances ( $R$ ) extracted from the  $I_{ds}$ - $V_{ds}$  curves ( $0 < V_{ds} < |-10 \text{ V}|$  and  $V_g = -20 \text{ V}, -40 \text{ V}, -60 \text{ V}, -80 \text{ V},$  and  $-100 \text{ V}$ ) of DH $\alpha$ 6T OTFTs of different channel lengths exposed to nitrogen.  $W$  is the transistor channel width.

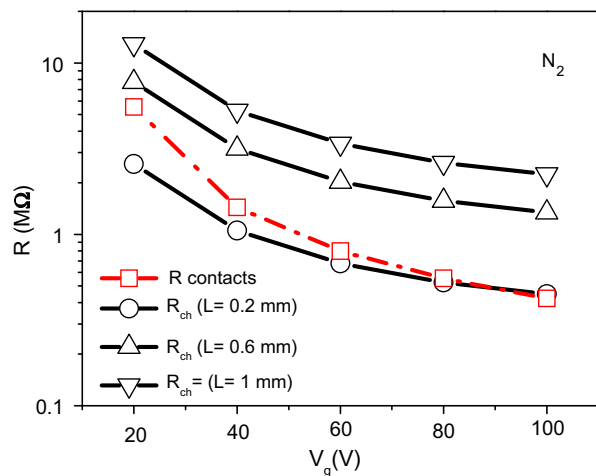


**Fig. 4.** DH $\alpha$ 6T OTFT contact and channel resistances as extracted from the plots in Fig. 3.

pentacene organic semiconductors [22,23], values in the  $10^5 \Omega \text{ cm}$  are typical for thiophene based materials contacted with gold electrodes [24,25].

The same DH $\alpha$ 6T OTFT devices were then exposed to saturated vapors of 1-butanol. A comparison of the device  $I$ - $V$  and transfer characteristics in nitrogen and butanol are reported in Fig. 5. The DH $\alpha$ 6T OTFT  $I_{ds}$ - $V_g$  transfer characteristics, are reported in Fig. 5a, along with the relevant log-plot (Fig. 5b), while typical device  $I_{ds}$ - $V_{ds}$  characteristics are reported in panel (c) and (d). The black solid curves in Fig. 5a and b show the current drifting in the channel region between the source and the drain contacts at a fixed drain-source bias ( $V_{ds} = -50 \text{ V}$ ) while sweeping  $V_g$  between 20 V and  $-100 \text{ V}$ . Generally, as it is apparent in Fig. 5 and as already widely reported, a *on-state*  $I_{ds}$  decrease occurs upon exposure of a thiophene based OTFT to alcohol vapors [3,25]. This can be explained by the elicited poten-

tial barrier increase at grain boundaries upon exposure to the analyte or, equivalently, by a charge trapping effect. However, a closer inspection of Fig. 5b, reveals that for gate biases falling below a cross-over point, a  $I_{ds}$  current increase occurs upon exposure to the analyte. This effect has been seen consistently in most sensing OTFT, using differently substituted thiophene as well as phenylene-thiophene based organic semiconductor, when exposed to organic vapors as well as to inorganic species [9]. It can be also seen on a recently published report, by a different laboratory [6]. In this case a doping effect can be postulated as an increase of the *off-current* is seen. Sample dependent features were for instance the gate bias at which the cross-over took place and in the intensity of the current differential change.

The response of the OTFT sensor  $\Delta I$  was defined as follows:

$$\Delta I = I_{ds}(N_2) - I_{ds}(1 - \text{butanol}) \quad (4)$$

In Fig. 5b it can be seen that different  $\Delta I$  values can be measured at different  $V_g$  biases and as  $I_{ds}$  are negative values,  $\Delta I$  is negative above the cross-over while is positive below. The DH $\alpha$ 6T  $I$ - $V$  characteristics, exposed to butanol at different concentrations, were measured for devices with different channel lengths and plots, similar to those reported in Fig. 3, were constructed. The relevant data are reported in Fig. 6a. Also in this case the  $R_{ch}$  and  $R_c$  data are extracted by the TLM and a comparison of the contact and channel resistances in  $N_2$  (data as in Fig. 4) and in butanol are given in Fig. 6b and c, respectively. In Fig. 7 the relevant  $R_{ch}$  and  $R_c$  variation are reported and the following features can be outlined. The  $\Delta R_c$  values can be several times lower than  $\Delta R_{ch}$ , especially for longer channel devices. This holds true also for the relative percentage variations as  $\Delta R_c/R$  is ca. 8% while  $\Delta R_{ch}/R$  can be as high as 20%. Moreover, the variations of the contact and channel resistances, upon exposure to 1-butanol vapors, go in opposite directions as  $\Delta R_{ch}$  are negative values while  $\Delta R_c$  are positive ones.

Such a result allows establishing some correlations. As already mentioned, a cross-over point, discriminating negative and positive  $\Delta I$  current changes, was identified in the transfer characteristics (curves in Fig. 5b being a typical example). It is straightforward to associate negative resistance changes to negative current variations and *vice versa*. This means that, when a negative  $\Delta I$  is seen, it is the channel resistance that is changing, while when  $\Delta I$  is positive, contact resistance variations are dominating. Therefore, the plot of the OTFT sensor transfer characteristics, measured in an inert and in the analyte atmosphere, gives an indication of the voltage range in which the contribution of contact effects dominates. To better understand the interplay occurring between the channel and the contact resistance changes in OTFT sensors a modeling of the data is in progress.

As a further step, the DH $\alpha$ 6T OTFT transfer characteristics have been measured also in atmospheres of butanol vapors at different concentrations. The  $\Delta I$  values were evaluated at different gate biases and at constant concentration as shown in Fig. 5b. The  $\Delta I$  values at a fixed  $V_g$  bias

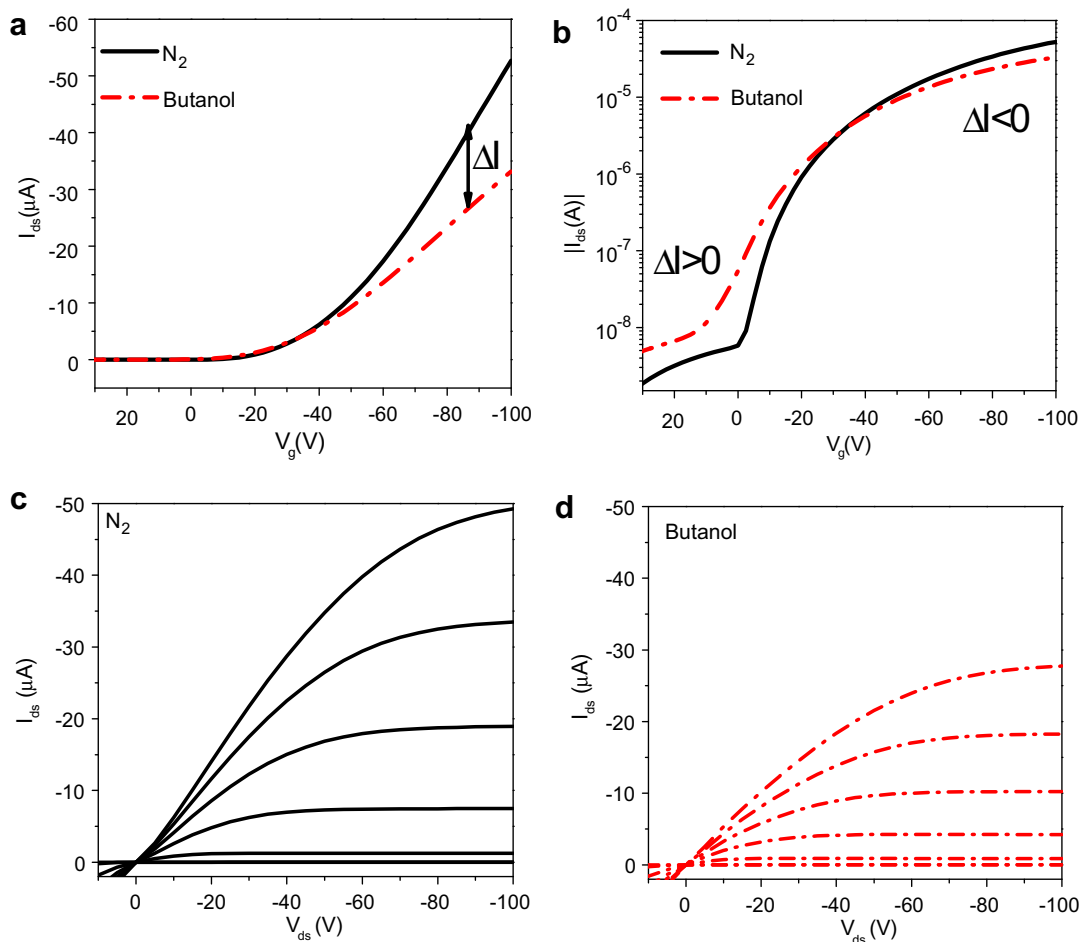


**Fig. 5.** DH $\alpha$ 6T OTFT transfer characteristics in N<sub>2</sub> and 1-butanol are reported in panel (a). Panel (b) shows the relevant log-plot.  $I$ - $V$  characteristics curves in N<sub>2</sub> and 1-butanol are reported in panels (c) and (d), respectively. The OTFT channel length is  $L = 0.2$  mm and the analyte concentration is 11,250 ppm.

and at different concentration constitute the data points for one calibration curve, the slope ( $m$ ) of each curve being the device sensitivity. The relevant  $m$  data are given in Fig. 8 for  $L = 0.2$  mm and  $L = 1.0$  mm DH $\alpha$ 6T OTFTs. The occurrence of a gate field dependent sensitivity is apparent and a sensitivity enhancement of more than three orders of magnitude is seen when the device is driven from the *off* to the *on*-state. Similar data were gathered for a phenylene-thiophene [9], as well as for differently substituted thiophene oligomers exposed to organic and inorganic species, showing that this can be a general property of OTFT sensors. Fig. 8 further shows that the slope values too can be positive (hollow red points) and negative (solid black points). Also in this case it is possible to associate the negative slopes to the channel resistance variation, while the positive ones to the contact resistance changes. This means that contact resistance dominates in the low gate voltage regime while channel resistance variations are responsible for the much higher sensitivity at gate biases that drive the transistor in the *on*-state. Since red points values are consistently orders of magnitude lower than negative ones, the contact resistance variations affect the field-enhanced sensitivity only negligibly. Besides, it is also

important to outline that the associated standard error on the response repeatability is much lower in the *on regime* than in the *off-one*. All the evidences provided so far show that the enhanced sensitivity observed is in fact not dominated by contact related effects. Such effects are present, but influence the TFT sensor low gate voltage regime. Interestingly, in this operating regime an OTFT is much more likely to behave as a chemiresistor. As to the leakage is concerned, it has been shown in the Supplementary information file that the leakage is limited to 0.1% of the maximum  $I_{ds}$  current, while the total relative current variation can be as high as 20%. Therefore, leakage current contribution to the total current variation is negligible too.

A final remark is due on the sensing mechanism. Upon exposure of the OTFT active layer to a volatile organic vapor a partition of the analyte molecules between the solid and the gaseous phase occurs. The chemical affinity between the analyte and the active layer modulates the degree of physisorption of the analyte molecules at the grains' surface. This in turn can enhance the potential barriers at the grain boundaries, eventually lowering the intensity of the drifting source-drain current, as seen in preliminary evidences [19,26]. This effect involves the

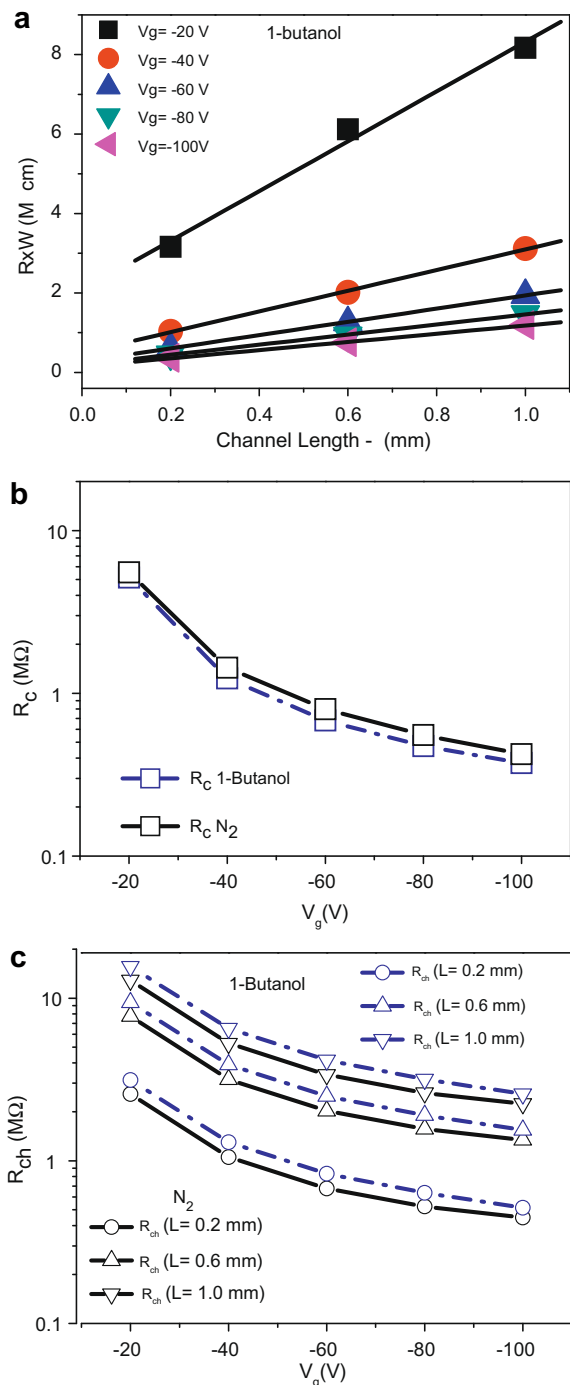


**Fig. 6.** (a) The total device resistances ( $R$ ) extracted from the  $I_{ds}$ - $V_{ds}$  curves ( $0 < V_{ds} < | -10$  V] and  $V_g = -20$  V,  $-40$  V,  $-60$  V,  $-80$  V,  $-100$  V) of DH $\alpha$ 6T OTFTs of different channel lengths exposed to 1-butanol,  $W$  is the transistor channel width. (b) Comparison of the contact resistances in 1-butanol and in N<sub>2</sub>. (c) Comparison of the channel resistances in 1-butanol and in N<sub>2</sub> for devices of different channel lengths.

whole bulk of the DH $\alpha$ 6T film down to the interface with the gate dielectric where the two-dimensional transport occurs [27]. The two-dimensional nature of the sensing

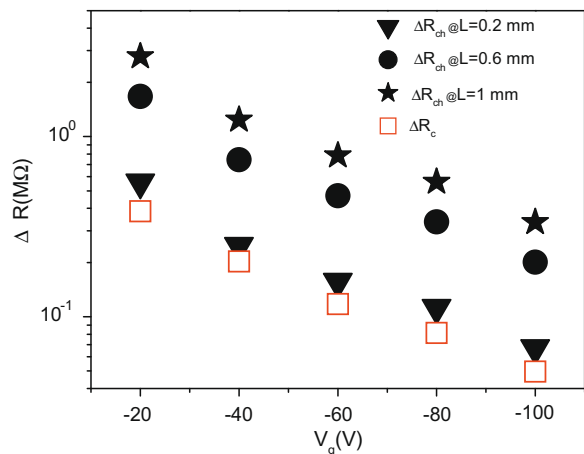


**Fig. 7.** Differential changes of  $R_c$  (hollow red squares) and  $R_{ch}$  (black solid symbols) parameters upon exposure to 1-butanol at different gate voltages and for different channel lengths (triangles:  $L = 0.2$  mm, circles:  $L = 0.4$  mm, stars:  $L = 1$  mm). Hollow red squares are positive values while solid black symbols are negative ones. (For interpretation of the references to colour in this figure legend, the reader is referred to the web version of this article.)

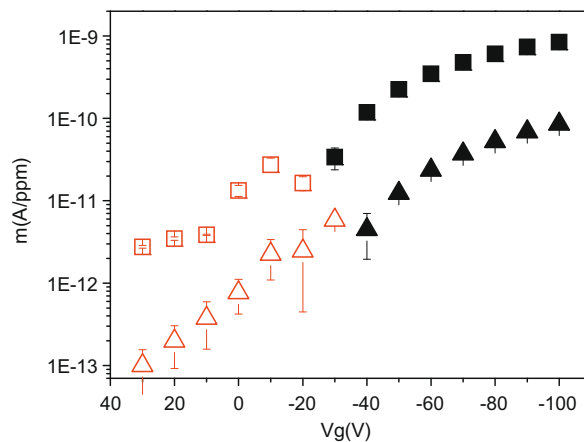


**Fig. 8.** Slopes ( $m$ ) of the calibration lines ( $\Delta I$  vs. [c]) measured at different  $V_g$  biases. Hollow red points stand for positive values, while solid black are negative ones. (For interpretation of the references to colour in this figure legend, the reader is referred to the web version of this article.)

mechanism was demonstrated too, as  $\Delta I$  responses were seen to be active layer thickness independent [9]. The field-induced sensitivity enhancement, can be seen as correlated to the comparably larger number of charges drifting in the device's channel in the *on-state* accumulation regime with the respect to the charges, drifting in the bulk, in the device *off state*. The data reported can also contribute to shed light on the origin of contact effects in OTFTs. A simple thermionic emission is generally postulated although this hypothesis is not supported by evidences such as the contact activation energy being much smaller than the estimated potential barriers determined by pho-

toemission spectroscopy. Also the channel potential measurements by Kelvin probe force microscopy and the four-probe methods, indicate that the contact resistances and temperature dependences associated with the individual source and drain electrodes are nearly identical [21]. Alternatively, the transport through the contacts can be limited by a disordered depletion region near the contacts, this being even more plausible in top contact devices. It is received that the charged carrier transport in OTFTs proceeds through thermionic emission through grains [28]. The data in Fig. 8 shows that, upon exposure to an alcohol, the contact resistance and the channel one change in opposite fashion, implying that they can be generated by two different mechanisms. This can be of further support to the hypothesis that the carrier diffusion through a disordered depletion region is the dominant contributing mechanism to OTFT contact resistance. A doping near the contacts could also be favored by the amorphous nature of the organic semiconductor in this region.

#### 4. Conclusions

A systematic study is reported on the role of contact resistance effects on OTFT sensors, in particular as it concerns the gate field-induced sensitivity enhancement. The *on-state* sensitivity enhancement is largely ascribable to changes occurring in the transistor channel transport and effects, such as contacts resistance or leakage current variations do not dominate the *on-state* sensor behavior. Their effect is seen in the low gate voltage regime where sensitivities are much lower. Besides, the evidences reported bring further support to the hypothesis of the OTFT contact resistances being mainly due to carrier diffusion through a disordered depletion region.

#### Acknowledgments

Prof. P. Mastrorilli, Prof. G.P. Suranna and Dr. G. Romanazzi are acknowledged for the synthesis of the high quality DH $\alpha$ 6T oligomers and Prof. F. Palmisano is acknowledged for useful discussions. This work was partially supported by the “PRIN-06 Project – 2006037708 – Plastic bio-FET sensors”.

#### Appendix A. Supplementary data

Supplementary data associated with this article can be found, in the online version, at doi:10.1016/j.orgel.2008.11.009.

#### References

- [1] K.C. Persaud, *Mater. Today* 8 (2005) 38.
- [2] L. Torsi, A. Dodabalapur, *Anal. Chem.* 77 (2005) 380A.
- [3] B. Crone, A. Dodabalapur, A. Gelperin, L. Torsi, H.E. Katz, A.J. Lovinger, Z. Bao, *Appl. Phys. Lett.* 78 (2001) 2229.
- [4] D.A. Bernards, D.J. Macaya, M. Nikolou, J.A. DeFranco, S. Takamatsu, G.G. Malliaras, *J. Mater. Chem.* 18 (2008) 116.
- [5] L. Torsi, *Anal. Bioanal. Chem.* 384 (2006) 309 (and papers therein).
- [6] K.C. See, A. Becknell, J. Miragliotta, H.E. Katz, *Adv. Mater.* 19 (2008) 3322.
- [7] L. Torsi, M.C. Tanese, N. Cioffi, M.C. Gallazzi, L. Sabbatini, P.G. Zambonin, G. Raos, S.V. Meille, M.M. Giangregorio, *J. Phys. Chem. B* 107 (2003) 7589.
- [8] J. Huang, J. Miragliotta, A. Becknell, H.E. Katz, *J. Am. Chem. Soc.* 129 (2007) 9366.
- [9] L. Torsi, G.M. Farinola, F. Marinelli, M.C. Tanese, O. Hassan Omar, L. Valli, F. Babudri, F. Palmisano, P.G. Zambonin, F. Naso, *Nature Mater.* 7 (2008) 412.
- [10] E.J. Severin, R.D. Scanner, B.J. Doleman, N.S. Lewis, *Anal. Chem.* 70 (1998) 1440.
- [11] B.P.J. de Lacy Costello, N.M. Ratcliffe, P.S. Sivanand, *Synth. Met.* 139 (2003) 43.
- [12] F. Garnier, A. Yassar, R. Hajlaoui, G. Horowitz, F. Deloffre, B. Servet, S. Ries, P.J. Alnott, *Am. Chem. Soc.* 115 (1993) 8716.
- [13] H.E. Katz, L. Torsi, A. Dodabalapur, *Chem. Mater.* 7 (1995) 2235.
- [14] H.E. Katz, A. Dodabalapur, L. Torsi, D. Elder, *Chem. Mater.* 7 (1995) 2238.
- [15] H.E. Katz, J.G. Laquindanum, A. Lovinger, *J. Chem. Mater.* 10 (1998) 633.
- [16] C.D. Dimitrakopoulos, B.K. Furman, T. Graham, S. Hegde, S. Purushothaman, *Synth. Met.* 92 (1998) 47.
- [17] M. Halik, H. Klauk, U. Zschieschang, G. Schmid, S. Ponomarenko, S. Kirchmeyer, W. Weber, *Adv. Mater.* 15 (2003) 917.
- [18] A.J. Lovinger, H.E. Katz, A. Dodabalapur, *Chem. Mater.* 10 (1998) 3275.
- [19] A. Dodabalapur, *SPIE Optics and Photonics 2007 – 26–30 August*, San Diego, CA.
- [20] G. Horowitz, M.E. Hajlaoui, R. Hajlaoui, *J. Appl. Phys.* 87 (2000) 4456.
- [21] M.J. Panzer, C.D. Frisbie, in: Z. Bao, J. Locklin (Eds.), *Organic Field-Effect Transistors*, CRC Press Taylor and Francis Group 2007 (Chapter. 2.4).
- [22] J. Zaumseil, K.W. Baldwin, J.A. Rogers, *J. Appl. Phys.* 93 (2003) 6117.
- [23] P.V. Pesavento, K.P. Puntambekar, C.D. Frisbie, J.C. McKeen, P.P. Ruden, *J. Appl. Phys.* 99 (2006) 094504.
- [24] E.J. Meijer, G.H. Gelinck, E. van Veenendaal, B.-H. Huisman, D.M. de Leeuw, T.M. Klapwijk, *Appl. Phys. Lett.* 82 (2003) 4576.
- [25] B.H. Hamadami, D. Natelson, *J. Appl. Phys.* 97 (2005) 064508.
- [26] T. Someya, H.E. Katz, A. Gelperin, A.J. Lovinger, A. Dodabalapur, *Appl. Phys. Lett.* 81 (2002) 3079.
- [27] A. Dodabalapur, L. Torsi, H.E. Katz, *Science* 268 (1995) 270.
- [28] G. Horowitz, M.E. Haifaoui, *Adv. Mater.* 12 (2000) 1046.



## Ideal host and guest system in phosphorescent OLEDs

Woo Sik Jeon<sup>a</sup>, Tae Jin Park<sup>a</sup>, Sun Young Kim<sup>a</sup>, Ramchandra Pode<sup>b,\*</sup>, Jin Jang<sup>a</sup>, Jang Hyuk Kwon<sup>a,\*</sup>

<sup>a</sup> Department of Information Display, Kyung Hee University, Dongdaemoon-ku, Seoul 130-701, Republic of Korea

<sup>b</sup> Department of Physics, Kyung Hee University, Dongdaemoon-ku, Seoul 130-701, Republic of Korea

### ARTICLE INFO

#### Article history:

Received 5 November 2008

Accepted 16 November 2008

Available online 6 December 2008

#### Keywords:

Host

Dopant

Phosphorescent

OLED

Energy transfer

Guest

### ABSTRACT

Ideal host-guest system for emission in phosphorescent OLEDs with only 1% guest doping condition for efficient energy transfer have been demonstrated in the present investigation. Using a narrow band-gap fluorescent host material, bis(10-hydroxybenzo[h]quinolino)beryllium complex (Bebq<sub>2</sub>), and red dopant bis(2-phenylquinoline)(acetylacetonate)iridium (Ir(phq)<sub>2</sub>acac), highly efficient red phosphorescent OLEDs (PHOLEDs) exhibiting excellent energy transfer characteristics with a doping concentration of 1% were developed. Fabricated PHOLEDs show a driving voltage of 3.7 V, maximum current and power efficiencies of 26.53 cd/A and 29.58 lm/W, and a maximum external quantum efficiency of 21%. Minimized electron or hole trapping at the phosphorescent guest molecules and efficient Förster and Dexter energy transfers from the Bebq<sub>2</sub> host singlet and triplet states to the emitting triplet of Ir(phq)<sub>2</sub>acac guest appear to be the key mechanism for ideal phosphorescence emission.

Crown Copyright © 2008 Published by Elsevier B.V. All rights reserved.

### 1. Introduction

Since the initial report by Baldo et al. [1], phosphorescent organic light-emitting devices (PHOLEDs) have been attracting much attention owing to their potential use in general illumination and flat panel displays. Phosphorescent based devices fabricated by doping host materials, having high-energy triplet states, with phosphorescent guest materials can theoretically produce 100% internal quantum efficiency (IQE). This is achieved by harvesting both singlet and triplet excitons generated by electrical injection which is four times that of fluorescent organic light-emitting devices (OLEDs) [2–4]. Förster and/or Dexter energy transfer processes [5] between host and guest molecules play an important role in confining the triplet energy excitons in the phosphorescent guest. This determines the triplet state emission efficiency in PHOLEDs. Förster energy transfer [6] is a long range process

(up to ~10 nm) due to dipole–dipole coupling of donor host and acceptor guest molecules, while Dexter energy transfer [7] is a short range process (typically ~1–3 nm) which requires overlapping of the molecular orbital of adjacent molecules (intermolecular electron exchange).

The phosphorescence emission in the conventional host-guest phosphorescent system occurs either with Förster transfer from the excited singlet S<sub>1</sub> state of the host to the excited singlet S<sub>1</sub> state of the guest and Dexter transfer from the excited triplet T<sub>1</sub> state of the host to the excited triplet T<sub>1</sub> state of the guest or direct exciton formation on the phosphorescent guest molecules, resulting in a reasonable good efficiency. However, emission mechanism in phosphorescent OLEDs whether due to charge trapping by guest molecules and/or energy transfer from the host to the guest, is not clearly understood. Till date, several researchers have reported that the charge trapping at guest molecules is the main cause for the emission of PHOLEDs.

Amongst well-known iridium (III) and platinum (II) phosphorescent emitters, iridium (III) complexes have been shown to be the most efficient triplet dopants employed in highly efficient PHOLEDs [8,9]. Usually, wide

\* Corresponding authors. Tel.: +82 2 961 0948; fax: +82 2 961 9154.

E-mail addresses: [rbpode@khu.ac.kr](mailto:rbpode@khu.ac.kr) (R. Pode), [jhkwon@khu.ac.kr](mailto:jhkwon@khu.ac.kr) (J.H. Kwon).

energy gap 4,4'-bis(*N*-carbazolyl)-1,1'-biphenyl (CBP) is used as a host material for red ( $\sim 2.0$  eV) or green ( $\sim 2.3$ – $2.4$  eV) phosphorescent guests [10,11]. Such a wide energy gap host has the advantage of a high  $T_1$  energy of 2.6 eV [12] or 2.55 eV [13] and long triplet lifetime  $>1$  s, [12] while the optical band-gap value ( $E_g$ ) is 3.1 eV [8].

Fig. 1a shows both the energy level diagram of *fac*-tris(2-phenyl-pyridinato)iridium(III) ( $\text{Ir}(\text{ppy})_3$ ) green and the tris(1-phenylisoquinoline)iridium ( $\text{Ir}(\text{piq})_3$ ) red phosphorescent complexes used in doping the CPB host. However, the wide band-gap host and narrow  $E_g$  guest system often cause an increase in driving voltage due to the difference in HOMO and/or LUMO levels between the guest and host materials [11]. Thus, the guest molecules are thought to act as deep trapping centers for electrons and holes in the emitting layer, causing an increase in the drive voltage of the PHOLED [14]. The dopant concentration in such a host-guest system is usually as high as about 6–10% by weight (wt%) because injected charges should move through guest molecules in the emitting layer. Therefore, self-quenching or triplet–triplet annihilation by guest molecules is an inevitable problem in host-guest systems with high doping concentrations. Earlier, Kawamura et al. had reported that the phosphorescence photoluminescence quantum efficiency of  $\text{Ir}(\text{ppy})_3$  could be decreased by  $\sim 5\%$  with an increasing in doping concentration from 2% to 6% [15]. Consequently, the selection of suitable host candidates is a critical issue in fabricating high efficiency PHOLEDs.

In this study, the minimized charge trapped host-guest system is investigated by using a narrow band-gap fluorescent host material in order to address device performance and manufacturing constraints. Here, we report an ideal host-guest system that requires only 1% guest doping condition for good energy transfer and provides ideal quantum efficiency in PHOLEDs. We also report that strong fluorescent host materials function very well in phosphorescent

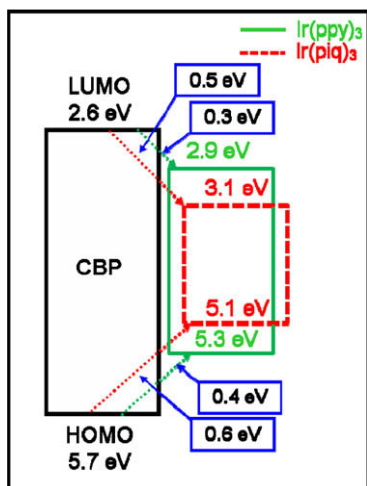


**Fig. 1a.** An Energy level diagram of the  $\text{Ir}(\text{ppy})_3$  green and  $\text{Ir}(\text{piq})_3$  red phosphorescent complex doped by the CPB host. (For interpretation of the references to colour in this figure legend, the reader is referred to the web version of this article.)

OLEDs due to efficient Förster energy transfers from the host singlet state to the guest singlet and triplet mixing state which appears to be the key mechanism for phosphorescence emission.

## 2. Experimental

*N,N'*-Di(4-(*N,N'*-diphenyl-amino)phenyl)-*N,N'*-diphenylbenzidine (DNTPD) as a hole transporting layer, CBP and bis(10-hydroxybenzo [h] quinolinato)beryllium complex ( $\text{Bebq}_2$ ) as host materials, bis(2-phenylquinoline)(acetylacetonate)iridium ( $\text{Ir}(\text{phq})_2\text{acac}$ ), tris(1-phenylisoquinoline)iridium ( $\text{Ir}(\text{piq})_3$ ) as red dopants, aluminum (III) bis(2-methyl-8-quinolinato)-4-phenylphenolate ( $\text{BALq}$ ) as a hole blocking layer and tris-(8-hydroxyquinoline)aluminum ( $\text{Alq}_3$ ) as an electron transporting layer were purchased from Gracel and Chemipro Corporation and were used. To fabricate OLED devices, clean glass substrates pre-coated with a 150-nm-thick indium tin oxide (ITO) layer with a sheet resistance of  $\sim 12 \Omega/\square$  were used. Line patterns of ITO were formed on glass by photolithography process. The ITO glass was cleaned by sonification in an isopropylalcohol and acetone, rinsed in deionized water, and finally irradiation in a UV–ozone chamber. All organic materials were deposited by the vacuum evaporation technique under a pressure of  $\sim 1 \times 10^{-7}$  Torr. The deposition rate of organic layers was about  $1 \text{ \AA}/\text{s}$ . Then, LiF and Al were deposited in another vacuum deposition system without breaking vacuum. Deposition rates of LiF and Al were  $0.1 \text{ \AA}/\text{s}$  and  $5$ – $10 \text{ \AA}/\text{s}$ , respectively. The current density–voltage ( $J$ – $V$ ) and luminance–voltage ( $L$ – $V$ ) data of PHOLEDs were measured by Keithley SMU 238 and Minolta CS-100A, respectively. The OLED area was  $2 \text{ mm}^2$  for all the samples studied in this work. Electroluminescence (EL) spectra and CIE coordinate were obtained using a Photoresearch PR-650 spectroradiometer.

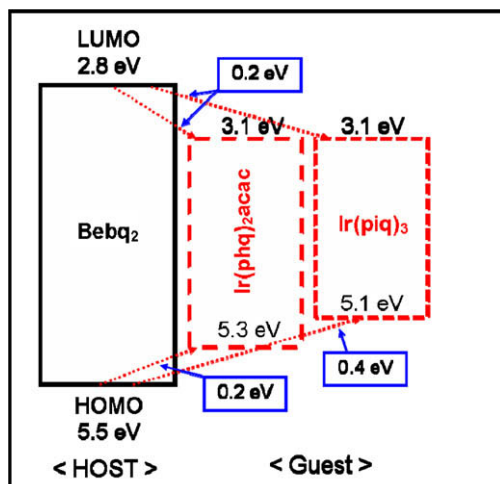
## 3. Result and discussion

Fig. 1b shows an energy band diagram of the fluorescent host and orange–red phosphorescent dopant materials used in the device fabrication. The simple bilayer PHOLED comprises a DNTPD hole transport layer (HTL), a  $\text{Bebq}_2$  narrow band-gap fluorescent host and an electron transport layer (ETL) plus  $\text{Ir}(\text{phq})_2\text{acac}$  dopant.  $\text{Bebq}_2$  and other beryllium complexes are known to have excellent electron transport characteristics with a high electron mobility of  $\sim 10^{-4} \text{ cm}^2/\text{Vs}$  [16,17] and a narrow band-gap. Earlier, Hamada et al. [18] used  $\text{Bebq}_2$  as an emitter to produce high luminance in OLEDs. More recently, we have demonstrated green [19] and red [20] emitting phosphorescent devices utilizing beryllium complexes as host and ETL. In the present investigation, the fabricated PHOLED was:

ITO/DNTPD(40 nm)/ $\text{Bebq}_2$  :  $\text{Ir}(\text{phq})_2\text{acac}$ (50 nm, 1%)  
/LiF(0.5 nm)/Al(100 nm)

Fig. 2a and b and Table 1 (device B) illustrate the electrical performance of the fabricated phosphorescent device. A luminance of  $1000 \text{ cd}/\text{m}^2$  was obtained with a driving voltage of 3.7 V, and a current and power efficiency





**Fig. 1b.** An Energy level diagram of the  $\text{Bebq}_2$  fluorescent host and  $\text{Ir}(\text{phq})_2\text{acac}$  and  $\text{Ir}(\text{piq})_3$  red phosphorescent dopant materials. (For interpretation of the references to colour in this figure legend, the reader is referred to the web version of this article.)

of 20.53 cd/A and 23.14 lm/W, respectively. Furthermore, the maximum current and power efficiency were 26.53 cd/A and 29.58 lm/W, respectively. The external quantum efficiency (EQE) value of 21% in the fabricated PHOLED slightly exceeded the theoretical limit of about 20% derived from simple classical optics. Moreover, this can be further improved by optimizing the output coupling. These remarkable results brought some pleasant surprises.

Indeed, because of the extraordinarily low doping concentration ( $\sim 1\%$ ) by contrast with most phosphorescent devices (6–10 wt%) we never expected the enhanced performance of the  $\text{Bebq}_2\text{:Ir}(\text{phq})_2\text{acac}$  PHOLEDs. In order to investigate the origin for the enhanced performance, we fabricated several PHOLEDs by varying the doping concentration from 0.5% to 2% in the host-guest system. Current and luminance as a function of voltage are presented in Fig. 2a, while current and power efficiencies as a function of luminance are presented in Fig. 2b. This data provides evidence for: (1) complete energy transfer from the fluorescent host to phosphorescent guest, except at extremely low doping concentrations ( $\sim 0.5\%$ ); (2) no significant difference between measured  $I$ - $V$  characteristics for identical

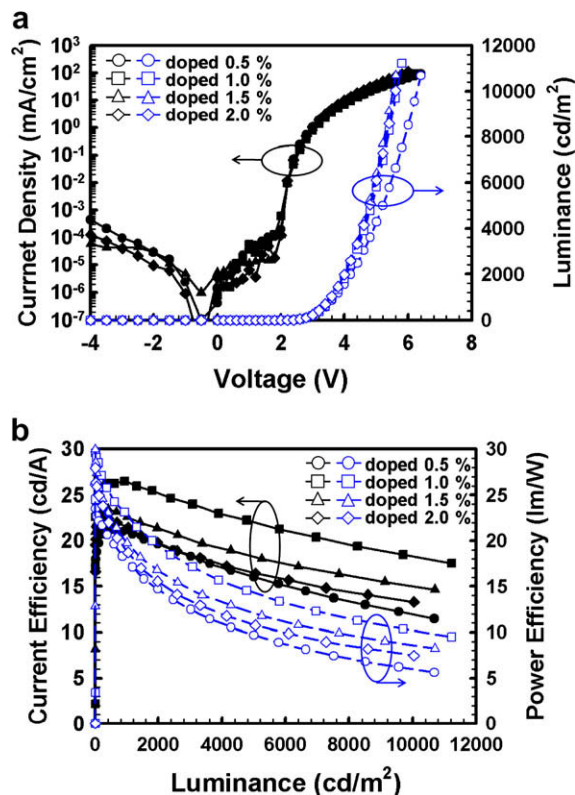


**Fig. 2.** (a) A  $J$ - $V$ - $L$  plot and (b) current and power efficiencies as a function of luminance from red PHOLEDs doped with different concentrations (0.5–2%) of  $\text{Ir}(\text{phq})_2\text{acac}$ . (For interpretation of the references to colour in this figure legend, the reader is referred to the web version of this article.)

devices but with different dopant concentrations lying between 0.5 and 2 wt%; and, (3) the quenching of both luminance, and current and power efficiencies with higher doping concentrations ( $\sim 2$  wt%). A summary of the key electrical and optical parameters (Table 1) reveals excellent device performance for doping concentration as low as 0.5–2%, in contrast with conventional PHOLEDs which require a guest concentration typically in the range of 6–10 wt%. Therefore, a highly efficient simple bilayer PHOLED structure with a  $\text{Ir}(\text{phq})_2\text{acac}$  guest doping concentration as low as 1% in the narrow band-gap  $\text{Bebq}_2$  fluorescent host is demonstrated here for the first time. Previously,

**Table 1**

Key parameters from  $\text{Bebq}_2\text{:Ir}(\text{phq})_2\text{acac}$  (0.5–2 wt%) orange-red emitting ITO/DNTPD (40 nm)/ $\text{Bebq}_2\text{:Ir}(\text{phq})_2\text{acac}$  (50 nm, 0.5–2%)/LiF(0.5 nm)/Al(100 nm) PHOLED devices.

$\text{Ir}(\text{phq})_2\text{acac}$ concentration (wt%)	Device A (0.5)	Device B (1.0)	Device C (1.5)	Device D (2.0)
Turn-on voltage (V) (at 1 $\text{cd/m}^2$ )	2.1	2.1	2.1	2.1
Operating voltage (V) (1000 $\text{cd/m}^2$ )	3.7	3.7	3.6	3.6
Efficiency (at 1000 $\text{cd/m}^2$ )				
Current (cd/A)	20.96	20.53	22.61	21.45
Power (lm/W)	18.29	23.14	19.73	18.72
Maximum efficiency				
Current (cd/A)	21.25	26.53	23.46	22.73
Power (lm/W)	24.62	29.58	29.94	27.94
CIE (x,y) (1000 $\text{cd/m}^2$ )	(0.61,0.38)	(0.62,0.37)	(0.62,0.37)	(0.62,0.37)
EQE (%) (maximum)	16.6	21.0	18.9	18.6

(ppy)<sub>2</sub>Ir(acac):Ir(piq)<sub>3</sub> (0.3–1 wt%) red [11] and CBP:Ir(phq)<sub>2</sub>acac (6 wt%) orange-red PHOLEDs [21] demonstrated an EQE of 9.2% with a power efficiency of 11.0 lm/W and a power efficiency of 17.6 cd/A with an EQE of 10.3% at 600 nit, respectively.

Fig. 3 provides evidence of energy transfer from the Bebq<sub>2</sub> fluorescent host to the Ir(phq)<sub>2</sub>acac phosphorescent guest by comparing the electroluminescence (EL) spectra of PHOLEDs as a function of Ir(phq)<sub>2</sub>acac doping concentration from 0.5% to 2%. The strong red light emission peak at 605 nm for all EL curves at 1000 nit is attributed to the phosphorescence of Ir(phq)<sub>2</sub>acac. The Commission Internationale de l'Éclairage (CIE) colour emission coordinates are (0.61, 0.38), (0.62, 0.37), (0.62, 0.37), (0.62, 0.37) for doping concentrations of 0.5, 1.0, 1.5, and 2.0 wt% of Ir(phq)<sub>2</sub>acac, respectively. A slight emission at 500 nm due to the Bebq<sub>2</sub> host plus a dominant doping peak at 605 nm when the doping concentration is extremely low (~0.5%), suggests an incomplete energy transfer from the Bebq<sub>2</sub> host to the Ir(phq)<sub>2</sub>acac guest. Furthermore, it indicates that the recombination of injected holes and electrons occurs at host molecule sites and then the excited energy is rapidly transferred from the host to the guest. The presence of a clean EL peak (no emissions at 500 nm) in other devices with doping concentrations of Ir(phq)<sub>2</sub>acac > 0.5% indicates a complete energy transfer from the host to the guest.

To understand the phosphorescence emission mechanism more precisely in the Bebq<sub>2</sub>:Ir(phq)<sub>2</sub>acac host-guest system, we fabricated and studied a series of PHOLEDs. Firstly, we used the well-known wide band-gap CBP host material instead of Bebq<sub>2</sub> and fabricated the device with a structure: NPB (40 nm)/CBP:Ir(phq)<sub>2</sub>acac (30 nm, 10%)/BAIq (5 nm)/Alq<sub>3</sub> (20 nm)/LiF (0.5 nm)/Al (100 nm). At a luminance of 1000 cd/m<sup>2</sup> the resultant operating voltage was 7.1 V with current and power efficiencies of 14.41 cd/A and 6.28 lm/W, respectively, and an EQE of 11.5%. Furthermore, the maximum current and power efficiency values were 14.43 cd/A and 8.99 lm/W, respectively. Obviously, the two fold increase in driving voltage is a consequence of the trapping of injected holes and electrons at deep Ir(phq)<sub>2</sub>acac molecules in the CBP:Ir(phq)<sub>2</sub>acac system. Direct charge trapping on the Ir(phq)<sub>2</sub>acac guest

molecules seems to be the key mechanism for phosphorescence emission in this host-guest system.

Later, a PHOLED device was fabricated using Ir(piq)<sub>3</sub> red emitting phosphorescent doping instead of Ir(phq)<sub>2</sub>acac and a Bebq<sub>2</sub> host. The fabricated device was: DNTPD (40 nm)/Bebq<sub>2</sub>:Ir(piq)<sub>3</sub> (50 nm, 4 wt%)/LiF (0.5 nm)/Al (100 nm). A weak emission peak at 500 nm in the EL spectra due to the Bebq<sub>2</sub> host arises at a doping concentration of 4 wt% (significantly high by comparison with an Ir(phq)<sub>2</sub>acac doping concentration ~0.5 wt%), accompanied by a strong peak at 620 nm (CIE coordinates  $x = 0.67$  and  $y = 0.32$ ) due to an Ir(piq)<sub>3</sub> doping molecule (Fig. 4). At luminance of 1000 cd/m<sup>2</sup>, the corresponding operating voltage, current and power efficiencies were 3.5 V, 8.41 cd/A and 7.34 lm/W, respectively. Furthermore, the maximum current and power efficiency values were 9.38 cd/A and 11.72 lm/W, respectively. Increasing the Ir(piq)<sub>3</sub> concentration to 6 wt% suppresses the Bebq<sub>2</sub> host emission and results in a clean EL red emitting peak at 620 nm due to the Ir(piq)<sub>3</sub> doping molecules. However, the device performance deteriorates with increasing doping concentration due to the self-quenching process.

The primary mechanism for phosphorescence emission in the Bebq<sub>2</sub>:Ir(piq)<sub>3</sub> host-guest system (Fig. 1 b) appears to be due to energetically favorable electron transport and hole trapping at deep trapping centers in Ir(piq)<sub>3</sub> molecules. Thus, an appropriate selection of host and phosphorescent dopant materials plays a significant role in determining the emission mechanism in phosphorescent devices. These results on phosphorescent emission in Bebq<sub>2</sub>:Ir(phq)<sub>2</sub>acac host-guest systems are very interesting and intriguing. The mechanism of phosphorescence emission is not believed to be due to direct charge trapping in Ir(phq)<sub>2</sub>acac phosphorescent guest molecules. Now an attempt is made here to explain these results on the basis of the existing knowledge of Förster and Dexter energy transfer processes in host-guest systems.

The Bebq<sub>2</sub> host material produces a strong fluorescence emission but no phosphorescence emission signature even at 77 K. The efficient use of Bebq<sub>2</sub> host in the described phosphorescent devices is an extraordinary phenomenon since strong fluorescent host materials are believed to provide poor phosphorescent performance. Therefore, we suspect efficient Förster energy transfer between the host

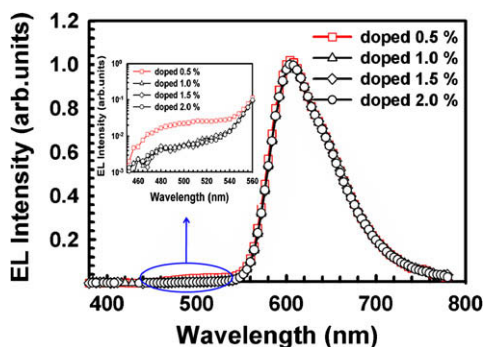


Fig. 3. EL spectra as a function of dopant concentration: Ir(phq)<sub>2</sub>acac of an ITO/DNTPD (40 nm)/Bebq<sub>2</sub>:Ir(phq)<sub>2</sub>acac (50 nm, 0.5–2%)/LiF(0.5 nm)/Al(100 nm) PHOLEDs at 1000 cd/m<sup>2</sup>.

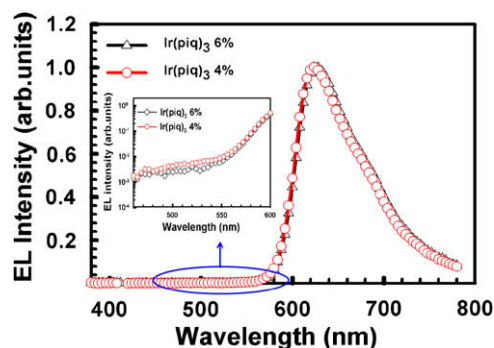


Fig. 4. EL spectra of DNTPD (40 nm)/Bebq<sub>2</sub>:Ir(piq)<sub>3</sub> (50 nm, 4 and 6 wt%)/LiF (0.5 nm)/Al (100 nm) PHOLEDs at 8000 cd/m<sup>2</sup>.

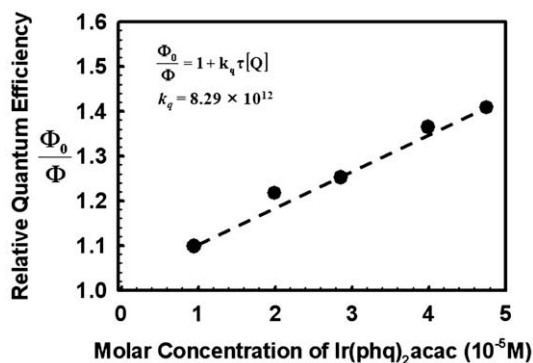


Fig. 5. Stern–Volmer plot showing the effect of Beq<sub>2</sub> fluorescence quenching by Ir(phq)<sub>2</sub>acac dopant.

singlet and the metal-to-ligand charge-transfer (MLCT) state of the iridium (III) metal complex. Earlier, Förster energy transfer in phosphorescent OLEDs was postulated by Gong et al. and Ramos-Ortiz et al. in solid photoluminescence studies [14,22]. To investigate Förster energy transfer from the Beq<sub>2</sub> host to the Ir(phq)<sub>2</sub>acac, time resolved spectroscopy and a Stern–Volmer plot in THF solution measurements techniques were employed. The singlet fluorescent lifetime of Beq<sub>2</sub> is 5.0 ns. From the slope of the linear Stern–Volmer plot (Fig. 5), the calculated energy transfer rate is  $k_q = 8 \times 10^{12} \text{ s}^{-1} \text{ M}^{-1}$ , indicating that the energy transfer from the excited singlet state of the host to the dopant triplet occurs quantitatively and ideally. Furthermore, the strong spin orbital coupling induced by the transition metal ion indicates that a narrow energy gap exists between the <sup>1</sup>MLCT and <sup>3</sup>MLCT states (~0.3 eV) and opens a pathway for efficient energy transfer from the singlet to the emitting triplet states. Therefore, two channels for Förster energy transfer from the host singlet to the <sup>1</sup>MLCT and <sup>3</sup>MLCT states of the iridium complex are available as shown in Fig. 6. Overlapping of the host emission and dopant absorption spectra substantiates the hypothesis of efficient Förster energy transfer from the host singlet to the guest emitting triplet states via two channels (Fig. 7). Furthermore, the strong fluorescent quantum efficiency of 0.39 in the host (Beq<sub>2</sub>) in solution, obtained using a relative quantum yield measurement, favors Förster energy transfer.

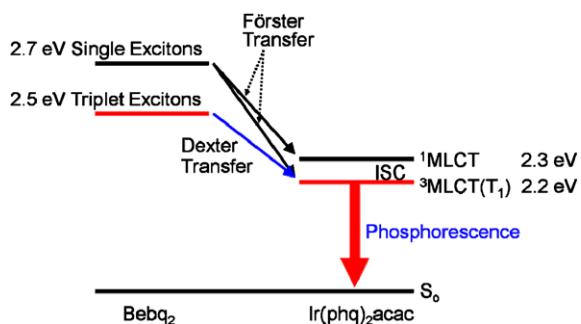


Fig. 6. Förster and Dexter energy transfer mechanism in the Beq<sub>2</sub>:Ir(phq)<sub>2</sub>acac system.

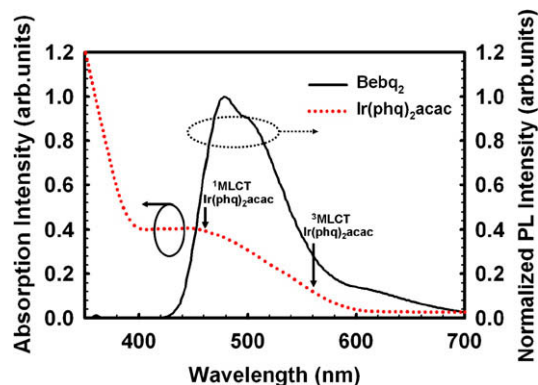


Fig. 7. Spectral overlapping of the photoluminescence spectrum from Beq<sub>2</sub> and the absorption spectrum from Ir(phq)<sub>2</sub>acac.

The Förster radius ( $R_0$ ), critical distance for the concentration quenching, was estimated as 1.3 nm (similar to a previously reported value [23]) using the following equation:

$$R_0^6 = \frac{9000(\ln 10)k^2\Phi_{PL}}{128\pi^5 N_A n^4} \int_0^\infty F_D(\lambda) \epsilon_A(\lambda) \lambda^4 d\lambda$$

where  $k^2$  = orientation factor,  $\Phi_{PL}$  = photoluminescence quantum efficiency,  $N_A$  = Avogadro's number,  $n$  = refractive index,  $\int_0^\infty F_D(\lambda) \epsilon_A(\lambda) \lambda^4 d\lambda$  = spectral overlap integral between donor photoluminescence ( $F_D(\lambda)$ ), and  $\epsilon_A \lambda$  = acceptor absorption, and  $\lambda$  = wavelength.

The triplet exciton energy transfer from the Beq<sub>2</sub> host to <sup>3</sup>MLCT is governed by Dexter energy transfer. The rate constant of Dexter energy transfer [23] is:

$$K_{ET} = KJ \exp(-2R_{DA}/L)$$

where  $K$  is related to the specific orbital interaction,  $J$  is a spectral overlap integral, and  $R_{DA}$  is donor–acceptor separation relative to their van der Waals radii,  $L$ . The ideal Dexter radius is the distance between the host and dopant molecule diameter considering overlapping molecular orbitals in adjacent molecules [24].

Using the equation:  $R = [(\text{molecular density in film}) \times \text{mol\% of the dopant in a film}]^{-1/3}$  as reported by Kawamura et al. [23] yields an average distance of about 58.5 Å and 44.9 Å between Ir(phq)<sub>2</sub>acac molecules for doping concentrations of 0.5% and 1.0%, respectively (Fig. 8). By considering the host (13.6 Å) and dopant (13.7 Å) diameters calculated using a molecular modeling program (DMOL3) [25] and van der Waals interaction distance (usually very small within ~2 Å) for the ideal Dexter energy transfer condition, the estimated distance between the host and guest molecules is about 15.6 Å (i.e. the half diameters of the host and dopant molecules are,  $13.7/2$  Å plus  $13.6/2$  Å, including a 2 Å van der Waals interaction distance). In solid state films, the minimum doping concentration is desirable to prevent triplet quenching processes.

Considering that two host molecules are located between two dopant molecules, an ideal Dexter condition (Fig. 8b), all host molecules are adjacent to a dopant molecule and dopant molecules are well separated in the host

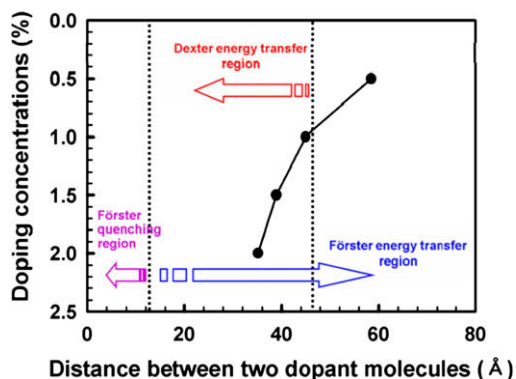


Fig. 8a. Förster and Dexter energy transfer conditions as a function of doping concentration and distance between two dopants.

matrix. In such a host and guest molecule arrangement, the separation between two dopant molecules appears to be about 46.9 Å. However, when the doping concentration is 0.5%, the estimated separation between Ir(phq)<sub>2</sub>acac molecules is 58.5 Å, suggesting that more than two host molecules are located between two dopant molecules (Fig. 8b). If the doping concentration is increased to 1%, the separation between dopant molecules is less than 46.9 Å, which results in an efficient energy transfer from the Bebq<sub>2</sub> host to the emitting triplet state of Ir(phq)<sub>2</sub>acac via Dexter processes. The triplets generated due to the Bebq<sub>2</sub> host molecules diffuse an average of only 15.6 Å, with a doping concentration of 1 wt%, until they are harvested by Ir(phq)<sub>2</sub>acac (Fig. 8b). If the doping concentration is increased to greater than 1%, the device performance deteriorates due to quenching processes of

triplet excitons caused by two closely separated dopant molecules.

The influence of the Förster quenching process in the described system is not serious at all doping concentrations (Fig. 8a). The singlet exciton energies generated by charge injection in host molecules can be transferred to triplet states of dopant molecules by the efficient Förster energy transfer. In our system, the rate constant of Förster energy transfer is much faster than that of the intersystem crossing of host singlet states. Typical intersystem crossing rate constants fall within the range  $\sim 10^6$ – $10^8$  s<sup>-1</sup> [26]. Thus, strong fluorescent materials, such as Bebq<sub>2</sub>, are excellent as host materials in PHOLEDs.

#### 4. Conclusions

In conclusion, we have demonstrated here an ideal host-guest energy transfer and quantum efficiency conditions with a dopant concentration of approximately 1% in phosphorescent OLEDs. We also report that strong fluorescent host materials function very well in phosphorescent OLEDs. The operating mechanism for the phosphorescence emission is twofold: Firstly, an efficient Förster energy transfer process from the host singlet exciton to the <sup>1</sup>MLCT and <sup>3</sup>MLCT states of the guest. And, secondly, Dexter energy transfer process from the host triplet exciton to the <sup>3</sup>MLCT state of the guest. The extremely low doping concept for highly efficient PHOLEDs has potential uses in future display and lighting applications.

#### Acknowledgements

The authors are thankful to Professor Ching Tang at the University of Rochester for helpful discussion and sugges-

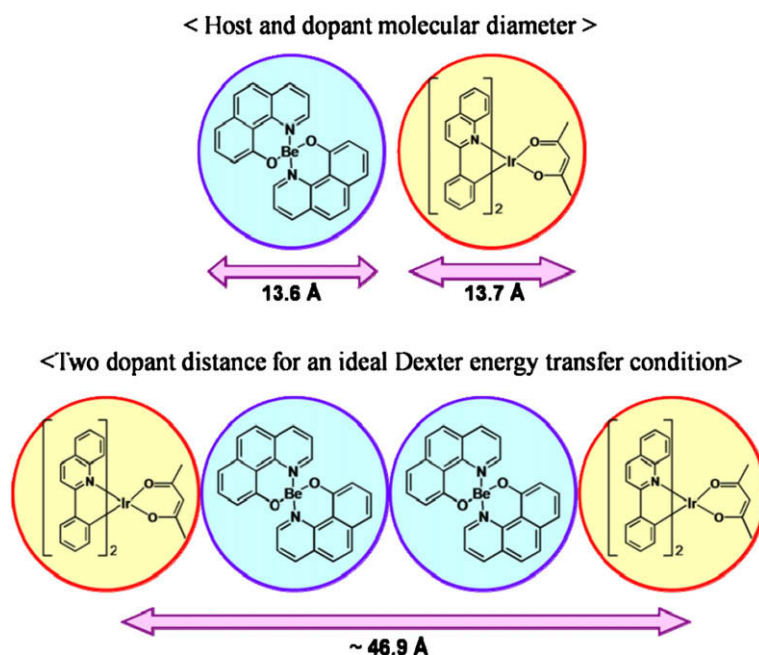
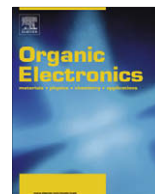


Fig. 8b. The molecular diameters of the host and dopant and the dopant–dopant distance for an ideal Dexter energy transfer.

tions. Also, the authors would like to thank Professor Kennedy for his suggestions during the preparation of this manuscript for publishing. This work has been supported by Ministry of Knowledge Economy of Korea.

## References

- [1] M.A. Baldo, D.F. O'Brien, Y. You, A. Shoustikov, S. Sibley, M.E. Thompson, S.R. Forrest, Highly efficient phosphorescent emission from organic electroluminescent devices, *Nature* 395 (1998) 151–154.
- [2] X. Gong, J.C. Ostrowski, D. Moses, G.C. Bazan, A.J. Heeger, Red electrophosphorescence from polymer doped with iridium complex, *App. Phys. Lett.* 81 (2002) 3711–3713.
- [3] T. Tsuzuki, N. Shirasawa, T. Suzuki, S. Tokito, Color tunable organic light emitting diodes using pentafluorophenyl-substituted iridium complexes, *Adv. Mater.* 15 (2003) 1455–1458.
- [4] C. Adachi, M.A. Baldo, S.R. Forrest, M.E. Thompson, High-efficiency organic electrophosphorescent devices with tris(2-phenylpyridine)iridium doped into electron-transporting materials, *App. Phys. Lett.* 77 (2000) 904–906.
- [5] I. Tanaka, S. Tokito, Energy-transfer processes between phosphorescent guest and fluorescent host molecules in phosphorescent OLEDs, in: H. Yersin (Ed.), *Highly Efficient OLEDs with Phosphorescent Materials*, Wiley-VCH Verlag GmbH and Co. KGaA, Weinheim, 2008.
- [6] T. Forster, Transfer mechanisms of electronic excitation, *Discuss. Faraday Soc.* 27 (1959) 7–17.
- [7] D.L. Dexter, A theory of sensitized luminescence in solids, *J. Chem. Phys.* 21 (1953) 836–850.
- [8] M.A. Baldo, S. Lamansky, P.E. Burrows, M.E. Thompson, S.R. Forrest, Very high-efficiency green organic light emitting devices based on electrophosphorescence, *App. Phys. Lett.* 75 (1999) 4–6.
- [9] C. Adachi, M.A. Baldo, M.E. Thompson, S.R. Forrest, Nearly 100% internal phosphorescence efficiency in an organic light emitting device, *J. Appl. Phys.* 90 (2001) 5048–5051.
- [10] B.D. Chin, M.C. Suh, M.H. Kim, S.T. Lee, H.D. Kim, H.K. Chung, Carrier trapping and efficient recombination of electrophosphorescent device with stepwise doping profile, *App. Phys. Lett.* 86 (2005) 133505–133507.
- [11] T. Tsuzuki, S. Tokito, Highly efficient, low-voltage phosphorescent organic light emitting diodes using an iridium complex as the host material, *Adv. Mater.* 19 (2007) 276–280.
- [12] M.A. Baldo, S.R. Forrest, Transient analysis of organic electrophosphorescence: I transient analysis of triplet energy transfer, *Phys. Rev. B* 62 (2000) 10958–10966.
- [13] I. Tanaka, Y. Tabata, S. Tokito, Energy-transfer and light-emission mechanism of blue phosphorescent molecules in guest-host systems, *Chem. Phys. Lett.* 400 (2004) 86–89.
- [14] X. Gong, J.C. Ostrowski, D. Moses, G.C. Bazan, A.J. Heeger, Electrophosphorescence from a polymer guest-host system with an iridium complex as guest: Forster energy transfer and charge trapping, *Adv. Funct. Mater.* 13 (2003) 439–444.
- [15] Y. Kawamura, K. Goushi, J. Brooks, J. Brown, H. Sasabe, C. Adachi, 100% phosphorescent quantum efficiency of Ir(III) complexes in organic semiconductor film, *App. Phys. Lett.* 86 (2005) 071104.
- [16] Y. Liu, J. Guo, J. Feng, H. Zhang, Y. Li, Y. Wang, High-performance blue electroluminescent devices based on hydroxyphenyl-pyridine beryllium complex, *App. Phys. Lett.* 78 (2001) 2300–2302.
- [17] S.A. Vanslyke, C.W. Tang, M.E. O'Brien, C.H. Chen, Electroluminescent device with organic electroluminescent medium, *US Pat.* 5061569, 1991.
- [18] Y. Hamada, T. Sano, M. Fujita, T. Fujii, Y. Nishio, K. Shibata, High luminance in organic electroluminescent devices with Bis(10-hydroxybenzo[h]quinolinato)beryllium as an emitter, *Chem. Lett.* 22 (1993) 905–906.
- [19] W.-S. Jeon, T.-J. Park, J.-J. Park, S.-Y. Kim, Y.-K. Lee, J. Jang, J.-H. Kwon, R. Pode, Highly efficient bilayer green phosphorescent organic light emitting devices, *App. Phys. Lett.* 92 (2008) 113311–113313.
- [20] Tae Jin Park, Woo Sik Jeon, Jung Joo Park, Sun Young Kim, Yong Kyun Lee, Jin Jang, Jang Hyuk Kwon, R. Pode, Efficient simple structure red phosphorescent organic light emitting devices with narrow band-gap fluorescent host, *App. Phys. Lett.* 92 (2008) 113308–113310.
- [21] R.C. Kwong, M.R. Nugent, L. Michalski, T. Ngo, K. Rajan, Y.-J. Tung, M.S. Weaver, T.X. Zhou, M. Hack, M.E. Thompson, S.R. Forrest, J.J. Brown, High operational stability of electrophosphorescent devices, *App. Phys. Lett.* 81 (2002) 162–164.
- [22] G. Ramos-Ortiz, Y. Oki, B. Domercq, B. Kippelen, Forster energy transfer from a fluorescent dye to a phosphorescent dopant: a concentration and intensity study, *Phys. Chem. Chem. Phys.* 4 (2002) 4109–4114.
- [23] Y. Kawamura, J. Brooks, J. Brown, H. Sasabe, C. Adachi, Intermolecular interaction and a concentration-quenching mechanism of phosphorescent Ir(III) complexes in a solid film, *Phys. Rev. Lett.* 96 (2006) 017404–017407.
- [24] N.J. Turro, *Modern Molecular Photochemistry*, vol. 305, University Science Books, USA, 1991.
- [25] B. Delley, From molecules to solids with the DMol3 approach, *J. Chem. Phys.* 113 (2000) 7756–7764.
- [26] N.J. Turro, *Modern Molecular Photochemistry*, vol. 186, University Science Books, USA, 1991.



# Highly efficient, orange–red organic light-emitting diodes using a series of green-emission iridium complexes as hosts

Zhiwei Liu, Zuqiang Bian\*, Feng Hao, Daobo Nie, Fei Ding, Zhuqi Chen, Chunhui Huang\*

Beijing National Laboratory for Molecular Sciences (BNLMS), State Key Laboratory of Rare Earth Materials Chemistry and Applications, College of Chemistry and Molecular Engineering, Peking University, Beijing 100871, PR China

## ARTICLE INFO

### Article history:

Received 29 July 2008

Received in revised form 27 October 2008

Accepted 16 November 2008

Available online 6 December 2008

### PACS:

72.80.Ga

78.60.Fi

85.60.Jb

### Keywords:

Iridium complex

Electroluminescence

Guest

Host

Energy transfer

## ABSTRACT

We investigated highly efficient phosphorescent organic light-emitting diodes (OLEDs) based on an orange–red emission iridium complex as the guest and five green emission iridium complexes as the host material, respectively. For comparison, a device using a common fluorescent host CBP (4,4'-bis(*N*-carbazolyl)-1,1'-biphenyl) has also been fabricated. Results show that the steric hindrance and exciton transporting property of the iridium complex host are found to be critical to this kind of doping system, a proper steric hindrance and improved exciton transporting ability result in reducing of triplet–triplet annihilation, thus improving of the device performance. In addition, all devices using iridium complexes as host have better performance than that of CBP, which arises from the fact that those green emission iridium complexes have a lower triplet excited energy befitting for energy confinement and a higher highest occupied molecular orbital (HOMO) level for hole injection.

© 2008 Elsevier B.V. All rights reserved.

## 1. Introduction

Recently, electrophosphorescent materials such as iridium, platinum, ruthenium, and osmium complexes, which use both singlet and triplet excitons, have received a great deal of attention due to their potential application in flat-panel displays [1–13]. The heavy metals such as iridium in the complex forms are known to induce intersystem crossing by strong spin-orbit coupling, leading to mixing of the singlet and triplet excited states. Thus, iridium complexes were known to have high photoluminescence efficiency with a relatively short excited state lifetime, which minimizes annihilation of triplet emissive states. Up to now, high brightness and efficiency of iridium complexes based OLEDs were achieved by using a host:guest

system to improve energy transfer and avoid triplet–triplet annihilation. Thus many host materials have been investigated, such as 4,4'-bis(*N*-carbazolyl)-1,1'-biphenyl (CBP) [6,14,15], 4,4',4''-tris(*N*-carbazolyl)-triphenylamine (TCTA) [16], 3-phenyl-4-(1'-naphthyl)-5-phenyl-1,2,4-triazole (TAZ) [17], and 9-[4-[5-(4-tert-butylphenyl)-[1,3,4]oxadiazol-2-yl]-benzyl]-9H-carbazole (t-CmOxa) [18]. However, most employed hosts were fluorescent materials, while the host:guest based OLEDs using phosphorescent materials as hosts are rare but their performances seem to be amazing [19,20].

In this study, we report a series of green-emission iridium complexes used as the host for an orange–red iridium complex guest for highly efficient OLEDs. In particular, we describe the electroluminescent (EL) properties of OLEDs based on five iridium complexes Ir(ppy)<sub>2</sub>(acac) [bis(2-phenylpyridinato-*N,C*<sup>2</sup>) iridium (acetylacetonate)] [21], Ir(ppy)<sub>2</sub>(dmd) [bis(2-phenylpyridinato-*N,C*<sup>2</sup>) iridium

\* Corresponding authors. Tel./fax: +86 10 62757156.

E-mail address: [chhuang@pku.edu.cn](mailto:chhuang@pku.edu.cn) (C. Huang).

(5,5-dimethylhexane-2,4-diketonate)], Ir(ppy)<sub>2</sub>(tmd) [bis(2-phenylpyridinato-*N,C*<sup>2</sup>) iridium (2,2,6,6-tetramethylheptane-3,5-diketonate)] [6], Ir(ppy)<sub>2</sub>(CBDK) [bis(2-phenylpyridinato-*N,C*<sup>2</sup>) iridium (1-(9H-carbazol-9-yl)-5,5-dimethylhexane-2,4-diketonate)] [22], and Ir(ppy)<sub>2</sub>(FBDK) [bis(2-phenylpyridinato-*N,C*<sup>2</sup>) iridium (1-(9-methylfluoren-9-yl)-6,6-dimethylheptane-3,5-diketonate)] used as hosts for the guest Ir(DBQ)<sub>2</sub>(acac) [bis(dibenzo[f,h]quinoxalinato-*N,C*<sup>2</sup>) iridium (acetylacetonate)] [2], and compare these results with the device using CBP as the host. The choice of these OLEDs provided us an opportunity for tracing the effect of the host: considering Ir(ppy)<sub>2</sub>(acac) as a reference, we investigated the effect of structural change of the iridium complex on the performance of this class of host:dopant system, such as exciton transporting ability and molecular steric hindrance; while considering CBP as a reference, we traced the differences between fluorescent and phosphorescent hosts.

## 2. Experimental

### 2.1. General information

<sup>1</sup>H NMR spectra were recorded on an ARX-400 NMR spectrometer, chemical shift data for each signal were reported in ppm units with tetramethylsilane (TMS) as internal reference, where  $\delta$  (TMS) = 0. Elemental analyses were performed on a VARIO EL instrument. The UV-vis absorption spectra were measured with Shimadzu UV-3100 spectrometer. The photoluminescence (PL) spectra were recorded on an Edinburgh Analytical Instruments FLS920 spectrometer after removing the oxygen by bubbling of nitrogen through the solution. Electrochemical measurements were recorded by a similar method reported before [23].

### 2.2. Materials

Ir(ppy)<sub>2</sub>(acac) [21], Ir(ppy)<sub>2</sub>(tmd) [6], Ir(DBQ)<sub>2</sub>(acac) [2], Ir(ppy)<sub>2</sub>(CBDK) [22], Hdmmd [24], HFBDK [23], and tris(8-hydroxyquinolinolato)aluminium (AlQ) [25] were synthesized according to the literature. Both *N,N'*-diphenyl-*N,N'*-bis(1-naphthyl)-1, 1'-diphenyl-4, 4'-diamine (NPB) and 2, 9-dimethyl-4, 7-diphenyl-1, 10-phenanthroline (BCP) were purchased from Aldrich. NPB, BCP and AlQ were all subjected to gradient sublimation prior to use.

### 2.3. Synthesis of Ir(ppy)<sub>2</sub>(FBDK)

[(ppy)<sub>2</sub>Ir( $\mu$ -Cl)]<sub>2</sub> [26] (0.536 g, 0.5 mmol), sodium carbonate (0.53 g, 5.0 mmol) and HFBDK (0.367 g, 1.1 mmol) were dissolved in 2-ethoxyethanol (30 mL). The reaction mixture was refluxed under a nitrogen atmosphere for 12 h and an excess of water was added after cooling the solution to room temperature. The resulting precipitate was collected by filtration and pumped dry. The solid was chromatographed using dichloromethane as eluent. <sup>1</sup>H NMR (400 MHz, CDCl<sub>3</sub>),  $\delta$ : 8.34 (d, 1H, *J* 7.3 Hz), 8.29 (d, 1H, *J* 6.6 Hz), 7.84 (d, 1H, *J* 8.0 Hz), 7.78 (d, 1H, *J* 8.0 Hz), 7.65–7.71 (m, 4H), 7.58 (d, 1H, *J* 8.9 Hz), 7.51 (d,

1H, *J* 8.9 Hz), 7.22–7.31 (m, 6H), 7.04 (t, 1H, *J* 13.0 Hz), 7.00 (t, 1H, *J* 14.5 Hz), 6.83 (t, 1H, *J* 14.9 Hz), 6.78 (t, 1H, *J* 14.9 Hz), 6.69 (t, 1H, *J* 16.2 Hz), 6.65 (t, 1H, *J* 14.8 Hz), 6.37 (d, 1H, *J* 8.6 Hz), 6.26 (d, 1H, *J* 8.6 Hz), 4.99 (s, 1H, CH), 1.96 (t, 2H, *J* 18.4 Hz, CH<sub>2</sub>), 1.39 (t, 2H, *J* 16.3 Hz, CH<sub>2</sub>), 1.32 (s, 3H, CH<sub>3</sub>), 0.79 (s, 9H, *t*-Bu); MS (TOF) *m/z* calcd. for C<sub>45</sub>H<sub>41</sub>IrN<sub>2</sub>O<sub>2</sub>, 834, found, 834. Anal. calcd. for C<sub>45</sub>H<sub>41</sub>IrN<sub>2</sub>O<sub>2</sub>, C 64.80, H 4.95, N 3.36. found: C 64.75, H 4.96, N 3.42.

### 2.4. Synthesis of Ir(ppy)<sub>2</sub>(dmd)

The synthesis of Ir(ppy)<sub>2</sub>(dmd) is similar to Ir(ppy)<sub>2</sub>(FBDK) except the Hdmmd (0.156 g, 1.1 mmol) was instead of HFBDK (0.367 g, 1.1 mmol). <sup>1</sup>H NMR (400 MHz, CDCl<sub>3</sub>),  $\delta$ : 8.49 (d, 1H, *J* 4.9 Hz), 8.43 (d, 1H, *J* 5.1 Hz), 7.85 (d, 1H, *J* 8.1 Hz), 7.80 (d, 1H, *J* 8.0 Hz), 7.67–7.73 (m, 2H), 7.56 (d, 1H, *J* 7.7 Hz), 7.51 (d, 1H, *J* 7.7 Hz), 7.09 (t, 2H, *J* 13.1 Hz), 6.78 (t, 2H, *J* 10.7 Hz), 6.66–6.71 (m, 2H), 6.40 (d, 1H, *J* 8.5 Hz), 6.23 (d, 1H, *J* 8.4 Hz), 5.32 (s, 1H, CH), 1.81 (s, 3H, CH<sub>3</sub>), 0.87 (s, 9H, *t*-Bu); MS (TOF) *m/z* calcd for C<sub>30</sub>H<sub>29</sub>IrN<sub>2</sub>O<sub>2</sub>, 642, found, 642. Anal. Calcd for C<sub>30</sub>H<sub>29</sub>IrN<sub>2</sub>O<sub>2</sub>, C 56.14, H 4.55, N 4.36. Found: C 55.20, H 4.46, N 4.42.

### 2.5. Computational details

All calculations have been carried out using Gaussian 03 package [27]. Ground state geometries of all the complexes were fully optimized with no symmetry or internal coordinate constrains. The hybrid density functional B3P86 [28,29] was used for all the calculations. For geometry optimization, the standard basis set 6-31g\* [30,31] was used and for single point energy calculations, a larger “triple- $\zeta$ ” basis 6-311g\* was employed.

### 2.6. Device fabrication and testing

Patterned anode used in our laboratory was commercially available with a sheet resistance of 7  $\Omega$ /sq. Before loading into a deposition chamber, the ITO coated glass were cleaned with organic solvents, deionized water and finally treated with ultraviolet (UV) ozone. The organic and metal layers were deposited in different vacuum chamber with a base pressure better than  $8 \times 10^{-5}$  Pa. The emissive area of the devices as defined by the overlapping area of the cathode and the anode was 9 mm<sup>2</sup>. All electric testing and optical measurements were performed under ambient conditions. The EL spectra were measured with a Spectra Scan PR650. The current–voltage (*I*–*V*) and luminance–voltage (*L*–*V*) characteristics were measured with a computer controlled Keithley 2400 Sourcemeter unit with a calibrated silicon diode.

## 3. Results and discussion

### 3.1. X-ray crystal structure

Single crystals of Ir(ppy)<sub>2</sub>(dmd), Ir(ppy)<sub>2</sub>(tmd), and Ir(ppy)<sub>2</sub>(FBDK) were all grown from an ethanol/chloroform

**Table 1**Crystallographic data for Ir(ppy)<sub>2</sub>(dmd), Ir(ppy)<sub>2</sub>(tmd), and Ir(ppy)<sub>2</sub>(FBDK).

Compound	Ir(ppy) <sub>2</sub> (dmd)	Ir(ppy) <sub>2</sub> (tmd)	Ir(ppy) <sub>2</sub> (FBDK)
Empirical formula	C <sub>30</sub> H <sub>29</sub> IrN <sub>2</sub> O <sub>2</sub>	C <sub>33</sub> H <sub>35.04</sub> IrN <sub>2</sub> O <sub>2.08</sub>	C <sub>45</sub> H <sub>41</sub> IrN <sub>2</sub> O <sub>2</sub>
Formula mass	641.75	685.21	834.00
Temperature (K)	113(2)	293(2)	113(2)
Crystal system	Triclinic	Rhombohedral	Orthorhombic
Space group	P1	R-3	P2(1)2(1)2(1)
a (Å)	9.4089(19)	32.504(5)	11.941(2)
b (Å)	10.646(2)	32.504(5)	16.817(3)
c (Å)	13.535(3)	14.581(3)	17.816(4)
α (°)	95.02(3)	90	90
β (°)	100.28(3)	90	90
γ (°)	106.35(3)	120	90
Volume (Å <sup>3</sup> )	1266.4(4)	13341(4)	3577.6(13)
Z	2	18	4
D <sub>calcd.</sub> (g cm <sup>-3</sup> )	1.683	1.535	1.548
F(000)	632	6133	1672
θ range (°)	2.31–25.02	1.25–25.01	1.67–25.02
Index ranges	−11 ≤ h ≤ 8 −12 ≤ k ≤ 12 −16 ≤ l ≤ 16	−37 ≤ h ≤ 38 −38 ≤ k ≤ 38 −13 ≤ l ≤ 17	−14 ≤ h ≤ 14 −20 ≤ k ≤ 20 −20 ≤ l ≤ 21
GOF on F <sup>2</sup>	1.024	1.146	1.117
R1, wR2 [I > 2σ(I)]	0.0490, 0.0917	0.0436, 0.1149	0.0470, 0.0823
R1, wR2 (all data)	0.0559, 0.0939	0.0493, 0.1238	0.0509, 0.0838

solution by slow evaporation at room temperature and characterized by X-ray diffraction analysis to establish their exact configuration [32]. Details of crystallographic data are given in Table 1.

The ORTEP diagram only for Ir(ppy)<sub>2</sub>(FBDK) is shown in Fig. 1 as an example. The Ir(ppy)<sub>2</sub>(LX) (LX = dmd, tmd, or FBDK) molecule consists of two phenylpyridine fragments as cyclometalated ligands and one β-diketonate as an ancillary ligand ranging in a distorted octahedral geometry around the iridium atom. The coordination geometries of these three complexes are the same as that reported for the chloride-bridged dimer complex [(ppy)<sub>2</sub>Ir(μ-Cl)]<sub>2</sub> [33] and Ir(ppy)<sub>2</sub>(acac) [6,21]. However, the average single molecular volume varied from 552 [21,34] to 894 [34] Å<sup>3</sup>

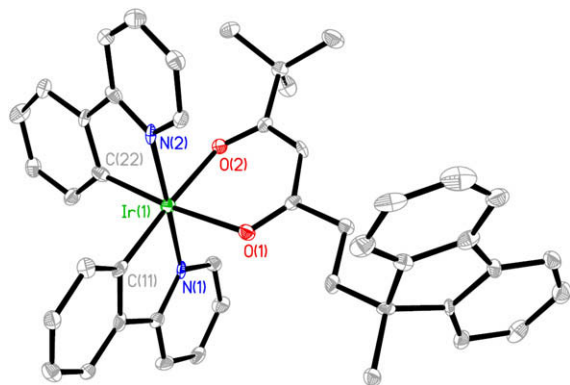


**Fig. 1.** ORTEP diagram of Ir(ppy)<sub>2</sub>(FBDK). The measurement temperature was 113(2) K and the thermal ellipsoids for the image represent 30% probability. The hydrogen atoms are omitted for clarity.

as the steric hindrance of β-diketonate increased from the small acac to the bulky FBDK.

### 3.2. Photophysical characterization

The UV–vis absorption and photoluminescence spectra of Ir(ppy)<sub>2</sub>(acac), Ir(ppy)<sub>2</sub>(dmd), Ir(ppy)<sub>2</sub>(tmd), Ir(ppy)<sub>2</sub>(CBDK), and Ir(ppy)<sub>2</sub>(FBDK) in CH<sub>2</sub>Cl<sub>2</sub> solution are shown in Fig. 2. For these Ir(ppy)<sub>2</sub>(LX) complexes, the difference in UV–vis absorption is only the transitions attributed to the different β-diketonates, while the singlet (~410 nm) and triplet (~460 nm) metal-to-ligand charge transfer (MLCT) transitions [6] are the same as those showing in 400–500 nm region. The maximum emission bands for Ir(ppy)<sub>2</sub>(acac), Ir(ppy)<sub>2</sub>(dmd), Ir(ppy)<sub>2</sub>(tmd), Ir(ppy)<sub>2</sub>(CBDK), and Ir(ppy)<sub>2</sub>(FBDK) in CH<sub>2</sub>Cl<sub>2</sub> solution examined at room temperature are at 518, 522, 523, 518, and 520 nm, respectively. These similar emissions are all likely to be <sup>3</sup>MLCT based transitions [21]. The phosphorescence quantum yields for Ir(ppy)<sub>2</sub>(dmd), Ir(ppy)<sub>2</sub>(tmd), and Ir(ppy)<sub>2</sub>(FBDK) were deduced to be 0.31, 0.28, and 0.24, respectively, which are a little lower than that of Ir(ppy)<sub>2</sub>(acac) (0.34 [6]), and a little higher than that of Ir(ppy)<sub>2</sub>(CBDK) (0.19 [22]).

The UV–vis absorption spectrum of Ir(DBQ)<sub>2</sub>(acac) in CH<sub>2</sub>Cl<sub>2</sub> solution, photoluminescence spectra of neat Ir(ppy)<sub>2</sub>(LX) films, and Ir(DBQ)<sub>2</sub>(acac)/Ir(ppy)<sub>2</sub>(LX) blend films doped with ~7 mol% Ir(DBQ)<sub>2</sub>(acac) are shown in Fig. 3. The absorptions at 440 and 530 nm can be assigned to <sup>1</sup>MLCT and <sup>3</sup>MLCT based transitions [2]. The maximum emission bands for neat Ir(ppy)<sub>2</sub>(acac), Ir(ppy)<sub>2</sub>(dmd), Ir(ppy)<sub>2</sub>(tmd), Ir(ppy)<sub>2</sub>(CBDK), and Ir(ppy)<sub>2</sub>(FBDK) films are 532, 532, 531, 529, and 531 nm, respectively. Since all five Ir(ppy)<sub>2</sub>(LX) have a maximum emission band around 530 nm, the triplet excited state (T<sub>1</sub>) energies were estimated to be ~2.3 eV, which is higher than that of Ir(DBQ)<sub>2</sub>(acac), ~2.0 eV. Furthermore, these observed emission bands fairly overlap with the <sup>3</sup>MLCT absorption of Ir(DBQ)<sub>2</sub>(acac), which indicates that there may be good energy transfer between Ir(ppy)<sub>2</sub>(LX) and Ir(DBQ)<sub>2</sub>(acac). By gradually increasing the concentration of Ir(DBQ)<sub>2</sub>(acac) in Ir(ppy)<sub>2</sub>(LX) host at 0, 1, 3, 5, 7, 9, and 11 mol%, respectively, pure emission was observed only when the concentration of the guest was up to ~7 mol%. The blend films doped with ~7 mol% Ir(DBQ)<sub>2</sub>(acac) emitted red light with maximum intensity at wavelengths 621, 619, 615, 615, and 615 nm for Ir(ppy)<sub>2</sub>(acac), Ir(ppy)<sub>2</sub>(dmd), Ir(ppy)<sub>2</sub>(tmd), Ir(ppy)<sub>2</sub>(CBDK), and Ir(ppy)<sub>2</sub>(FBDK), respectively. The phosphorescence of Ir(ppy)<sub>2</sub>(LX) was quenched, indicating that the triplet energy of Ir(ppy)<sub>2</sub>(LX) were efficiently transferred to Ir(DBQ)<sub>2</sub>(acac).

### 3.3. HOMO and LUMO Investigation

Because the highest occupied molecular orbital (HOMO) and the lowest unoccupied molecular orbital (LUMO) energy levels of the host are one of the most important factors for OLEDs, herein we investigated the HOMO and LUMO properties of these five iridium complexes both by cyclic voltammetry and density functional theory (DFT) calculations.



The oxidation potential for an iridium complex in HPLC grade  $\text{CH}_2\text{Cl}_2$  solution can be obtained via cyclic voltammetry [23], then the HOMO was deduced by assuming the energy level of ferrocene/ferrocenium to be  $-4.8$  eV [35]. Estimated from the UV–vis absorption spectrum, the energy bandgap of the iridium complex was obtained, thus the LUMO was calculated to be the sum of the energy bandgap and HOMO. Using the strategy mentioned above, the oxidation potentials for  $\text{Ir}(\text{ppy})_2(\text{acac})$ ,  $\text{Ir}(\text{ppy})_2(\text{dmd})$ ,  $\text{Ir}(\text{ppy})_2(\text{tmd})$ ,  $\text{Ir}(\text{ppy})_2(\text{CBDK})$ , and  $\text{Ir}(\text{ppy})_2(\text{FBDK})$  are estimated to be 0.35, 0.30, 0.25, 0.32, and 0.26 V higher than that of the ferrocene/ferrocenium couple, respectively. Thus the HOMO energy levels were deduced to be 5.15, 5.10, 5.05, 5.12, and 5.06 eV, respectively. The five iridium

complexes possess similar  $^3\text{MLCT}$  absorption bands whose edges reach the green-wavelength region with an absorption band limit of approximately 520 nm, and have the same bandgap of 2.36 eV; thus the LUMO energy levels are 2.79, 2.74, 2.69, 2.76, and 2.70 eV for  $\text{Ir}(\text{ppy})_2(\text{acac})$ ,  $\text{Ir}(\text{ppy})_2(\text{dmd})$ ,  $\text{Ir}(\text{ppy})_2(\text{tmd})$ ,  $\text{Ir}(\text{ppy})_2(\text{CBDK})$ , and  $\text{Ir}(\text{ppy})_2(\text{FBDK})$ , respectively. The cyclic voltammograms are compared in Fig. 4. The electrochemical data and energy levels of the complexes are summarized in Table 2, from which we can see that the HOMO and LUMO energy levels of the iridium complexes are similar.

Computational investigations have been proved to be very helpful in understanding the HOMO and LUMO properties of iridium complexes [20,21]. Herein, DFT calcula-

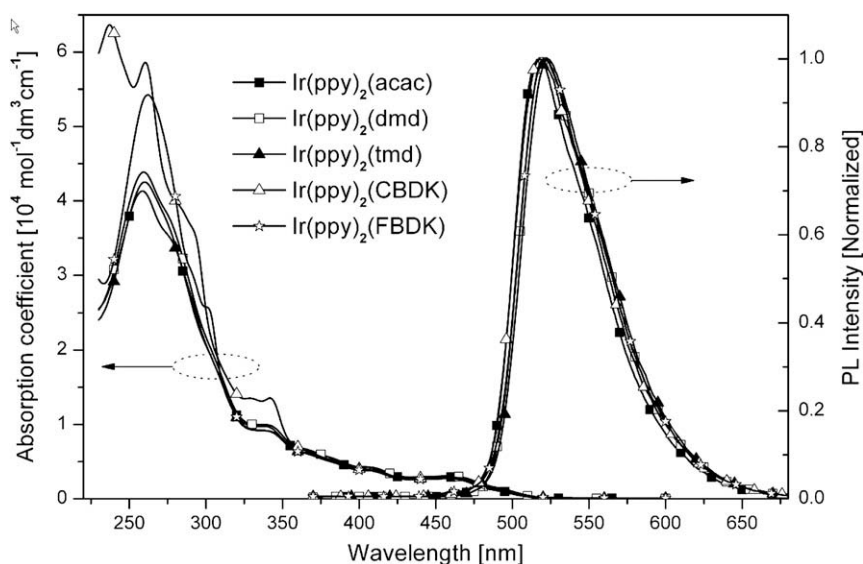


Fig. 2. UV–vis absorption and photoluminescence spectra of  $\text{Ir}(\text{ppy})_2(\text{LX})$  ( $\text{LX} = \text{acac}, \text{dmd}, \text{tmd}, \text{CBDK}, \text{or FBDK}$ ) in  $\text{CH}_2\text{Cl}_2$  solution.

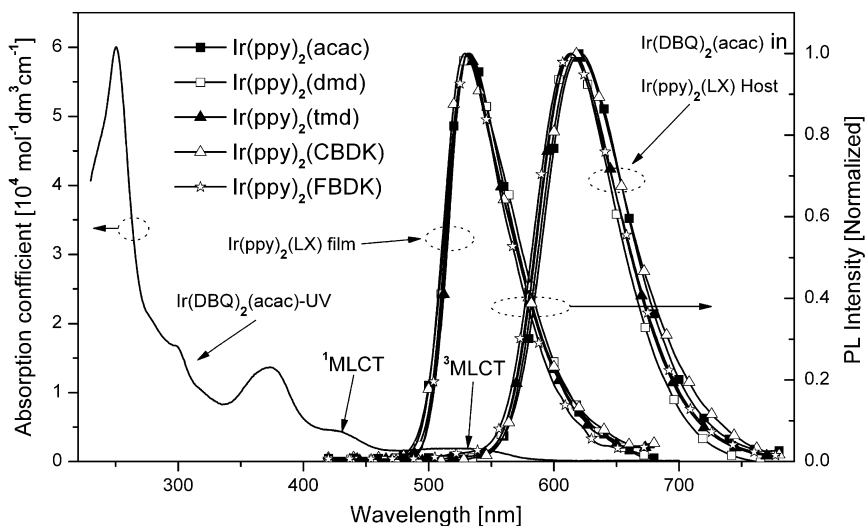


Fig. 3. UV–vis absorption spectrum of  $\text{Ir}(\text{DBQ})_2(\text{acac})$  in  $\text{CH}_2\text{Cl}_2$ , photoluminescence spectra of neat  $\text{Ir}(\text{ppy})_2(\text{LX})$  films, and  $\text{Ir}(\text{DBQ})_2(\text{acac})/\text{Ir}(\text{ppy})_2(\text{LX})$  ( $\text{LX} = \text{acac}, \text{dmd}, \text{tmd}, \text{CBDK}, \text{or FBDK}$ ) blend films doped with  $\sim 7$  mol%  $\text{Ir}(\text{DBQ})_2(\text{acac})$ .

tions were carried out on these five iridium complexes. The HOMO and LUMO of Ir(ppy)<sub>2</sub>(CBDK) are plotted in Fig. 5 as an example. Results show that in all five iridium complexes, the HOMO consists of a mixture of phenyl- $\pi$  and Ir-d orbitals, while the LUMO orbital is localized primarily on the pyridine- $\pi$  orbitals. That the HOMO and LUMO do not involve the  $\beta$ -diketonate fragments may be the best explanation for the observed phenomenon that they have similar HOMO and LUMO energy levels.

### 3.4. Electroluminescent properties

To understand the EL properties of Ir(DBQ)<sub>2</sub>(acac) doped in the phosphorescent hosts and compare these results with a common host CBP, six devices (I–VI) using Ir(ppy)<sub>2</sub>(acac), Ir(ppy)<sub>2</sub>(dmd), Ir(ppy)<sub>2</sub>(tmd), Ir(ppy)<sub>2</sub>(CBDK), Ir(ppy)<sub>2</sub>(FBDK), and CBP as a host material, respectively, were fabricated with the same configuration of ITO/NPB (50 nm)/Ir(DBQ)<sub>2</sub>(acac): Host (~7 mol%, 30 nm)/BCP (10 nm)/AlQ (30 nm)/Mg<sub>0.9</sub>Ag<sub>0.1</sub> (200 nm)/Ag (80 nm), in which NPB is used as the hole-transporting layer, and BCP and AlQ are used as the hole-blocking layer and electron-transporting layer, respectively. The Mg:Ag layer is used as the cathode with a Mg:Ag mass ratio of 9:1, and with an 80-nm thick Ag cap. The chemical structures of the materials and the structure of the EL devices are shown in Fig. 6. The EL performances of those devices are summarized in Table 3.

The EL spectra of device I are shown in Fig. 7 as an example. The observed emission is attributed to the guest Ir(DBQ)<sub>2</sub>(acac) at low voltages while a combined orange-red light from the host Ir(ppy)<sub>2</sub>(acac) and guest was observed at higher applied voltages. The emission color changes from red to orange-red due to the increasing Ir(ppy)<sub>2</sub>(acac) emission at higher current density, accompanied with the CIE chromaticity coordinates ( $x$ ,  $y$ )

**Table 2**

Electrochemical potentials and energy levels of the iridium complexes.

Iridium complex	$E^{\text{ox}}$ (V) <sup>a</sup>	$E_g$ (eV) <sup>b</sup>	HOMO (eV) <sup>c</sup>	LUMO (eV) <sup>d</sup>
Ir(ppy) <sub>2</sub> (acac)	0.35	2.36	5.15	2.79
Ir(ppy) <sub>2</sub> (dmd)	0.30	2.36	5.10	2.74
Ir(ppy) <sub>2</sub> (tmd)	0.25	2.36	5.05	2.69
Ir(ppy) <sub>2</sub> (CBDK)	0.32	2.36	5.12	2.76
Ir(ppy) <sub>2</sub> (FBDK)	0.26	2.36	5.06	2.70

<sup>a</sup> Oxidation potentials measured by cyclic voltammetry with ferrocene as the standard (the oxidation potential of ferrocene set as zero).

<sup>b</sup> Band gap estimated from the UV–vis absorption spectrum.

<sup>c</sup> Calculated from the oxidation potentials.

<sup>d</sup> Deduced from the HOMO and  $E_g$ .

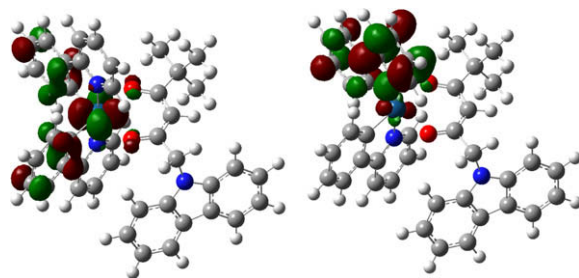


**Fig. 5.** Contour plot of HOMO (left) and LUMO (right) of Ir(ppy)<sub>2</sub>(CBDK).

changing from (0.60, 0.40) at 8 V to (0.57, 0.42) at 19 V. Similarly, the devices using the other four iridium complexes as the hosts have also combined orange-red light from the host Ir(ppy)<sub>2</sub>(LX) and guest Ir(DBQ)<sub>2</sub>(acac) at higher applied voltages, and the CIE chromaticity coordinates changes from (0.60, 0.40) at 8 V for all Ir(ppy)<sub>2</sub>(LX)-based devices to (0.57, 0.42) at 20 V for device II, (0.57, 0.43) at 16 V for device III, (0.58, 0.42) at 15 V for device

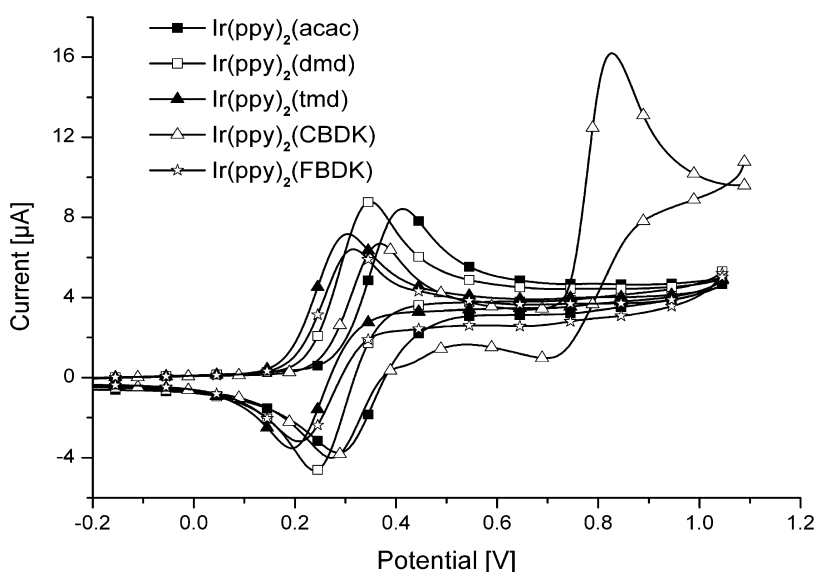


**Fig. 4.** Cyclic voltammograms of Ir(ppy)<sub>2</sub>(LX) (LX = acac, dmd, tmd, CBDK, or FBDK) in 0.1 M tetrabutylammonium hexafluorophosphate (TBAP) of CH<sub>2</sub>Cl<sub>2</sub> solution at a scan rate of 50 mV/s, and with ferrocene/ferrocenium couple as standard.

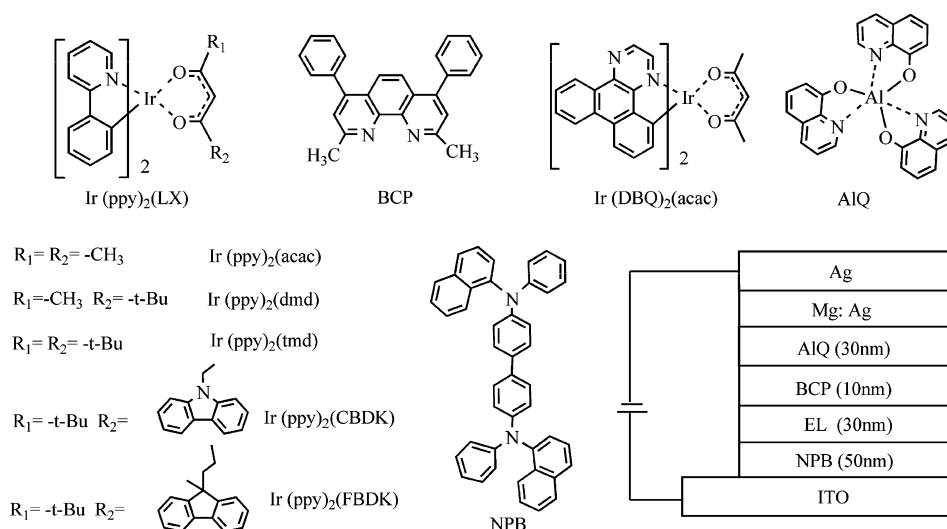


Fig. 6. Chemical structures of the materials used and the structure of the EL devices.

Table 3  
Performances of devices I–VI.

Device	$V^a$	$\eta_{ext}^b$	$L^c$	$\eta_c^d$	$\eta_p^e$
I	3.8	8.9, 3.8	4072	19.1, 6.0	14.2, 3.8
II	4.3	12.5, 4.9	2624	25.4, 4.9	15.5, 4.9
III	3.2	12.6, 3.4	13440	24.5, 3.4	22.6, 3.4
IV	3.0	12.7, 3.5	17660	24.5, 3.5	22.0, 3.5
V	5.0	9.1, 5.0	532.1	20.2, 5.0	12.7, 5.0
VI	6.5	8.7, 6.5	1462	16.9, 6.5	8.2, 6.5

<sup>a</sup> Turn-on voltage ( $V_{on}$ ).

<sup>b</sup> The maximum external quantum efficiency and applied voltage.

<sup>c</sup> The brightness at 15 V.

<sup>d</sup> The maximum current efficiency and applied voltage.

<sup>e</sup> The maximum power efficiency and applied voltage.

IV, and (0.59, 0.41) at 23 V for device V. The device VI in which CBP was used as the host has a pure EL spectrum that originates from Ir(DBQ)<sub>2</sub>(acac), and the CIE chromaticity coordinates does not change significantly from a value around (0.61, 0.39). The pure EL spectra of device VI may be attributed to a wide  $E_g$  between the host and guest leading to a completely energy transfer even at higher current density. Based on the reason mentioned above, pure EL spectra can be forecasted for all devices if a red-shifted guest, such as tris(1-phenylisoquinolinolato- $C^2, N$ )iridium(III) [Ir(piq)<sub>3</sub>], was used here [20,36].

Figs. 8 and 9 show the luminance–voltage and current–voltage curves for devices I–VI, respectively. The turn-on voltage is 3.8 V (1.86 cd m<sup>-2</sup>), 4.3 V (1.08 cd m<sup>-2</sup>), 3.2 V

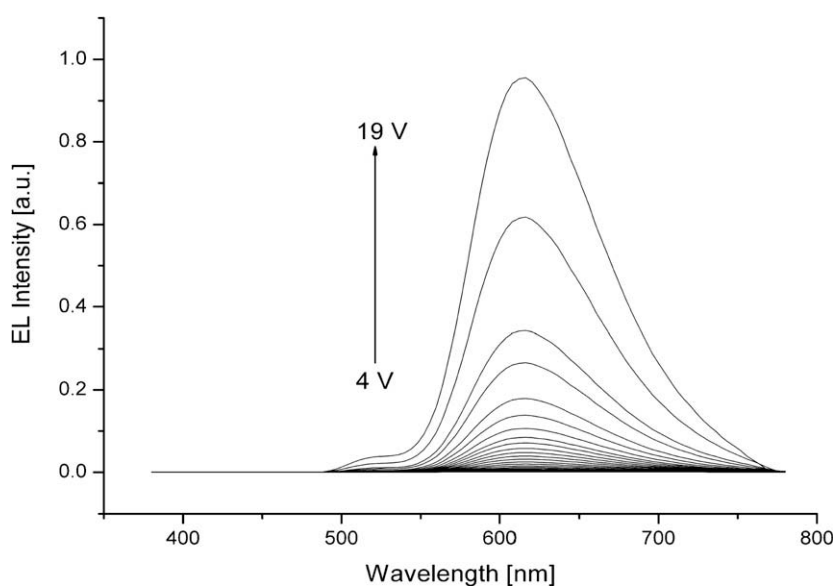


Fig. 7. Electroluminescent spectra of device I at different applied voltages.

( $1.34 \text{ cd m}^{-2}$ ), 3.0 V ( $1.85 \text{ cd m}^{-2}$ ), 5.0 V ( $2.20 \text{ cd m}^{-2}$ ), and 6.5 V ( $1.83 \text{ cd m}^{-2}$ ) for devices **I**, **II**, **III**, **IV**, **V**, and **VI**, respectively. Devices **I–V** using  $\text{Ir}(\text{ppy})_2(\text{LX})$  as host have lower turn-on voltages compared to device **VI**, in which CBP was used as the host. While among these devices based on  $\text{Ir}(\text{ppy})_2(\text{LX})$  host, devices **III** and **IV** have lower turn-on voltages. This phenomenon can also be observed when comparing luminance and current density under the same applied voltage. For example, for an applied voltage of 8 V, the luminance (current density) is  $102.3 \text{ cd m}^{-2}$  ( $0.756 \text{ mA cm}^{-2}$ ),  $58.0 \text{ cd m}^{-2}$  ( $0.534 \text{ mA cm}^{-2}$ ),  $531.1 \text{ cd m}^{-2}$  ( $2.84 \text{ mA cm}^{-2}$ ),  $618.2 \text{ cd m}^{-2}$  ( $6.50 \text{ mA cm}^{-2}$ ), and

$14.8 \text{ cd m}^{-2}$  ( $0.092 \text{ mA cm}^{-2}$ ) for devices **I**, **II**, **III**, **IV**, and **V**, respectively, which are higher than that of device **VI**,  $7.5 \text{ cd m}^{-2}$  ( $0.056 \text{ mA cm}^{-2}$ ). Moreover, devices **III** and **IV** have higher luminance and current density among devices **I–V**.

Fig. 10 shows the lumen efficiency as a function of current density for devices **I–VI**. All the devices **I–V** using iridium complexes as host have higher lumen efficiency than device **VI** based on CBP host. Among these devices **I–V**, devices **III** and **IV** exhibit the highest lumen efficiency. Device **III** displays a maximum brightness of  $22360 \text{ cd m}^{-2}$  at 16 V, a maximum external quantum efficiency of 12.6%, the highest power efficiency of  $22.6 \text{ lm W}^{-1}$  (3.4 V, 2.70 cd

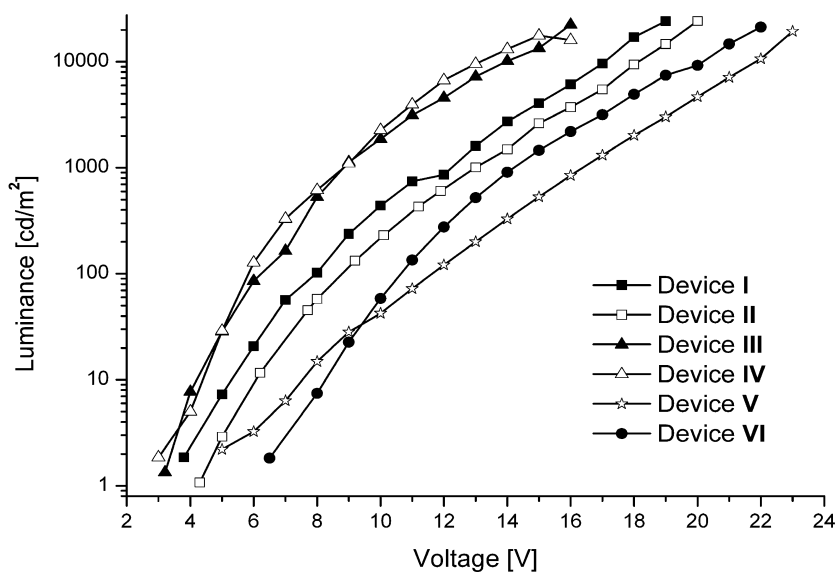


Fig. 8. Luminance–voltage curves for devices **I–VI**.

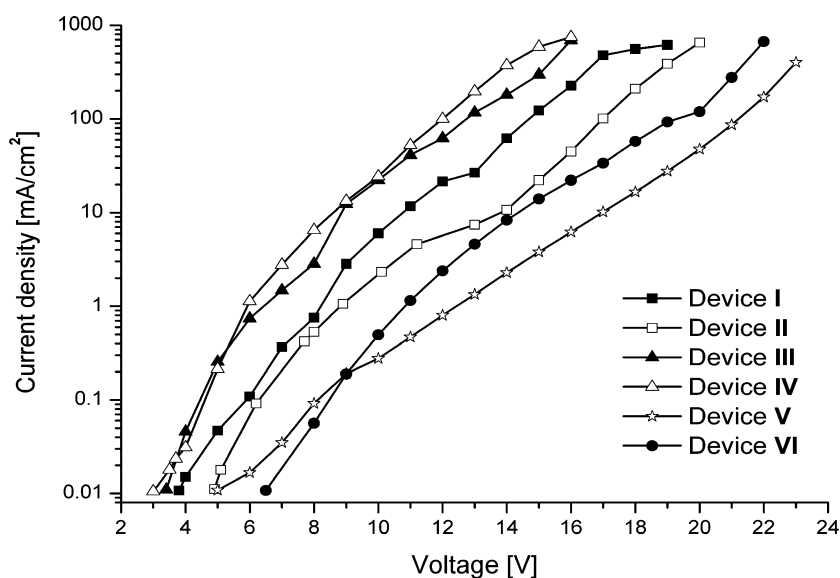


Fig. 9. Current–voltage curves for devices **I–VI**.

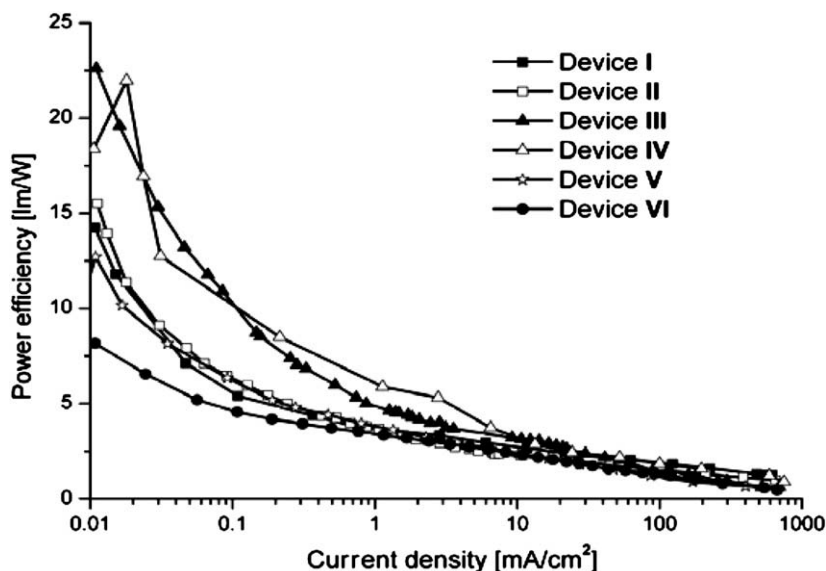


Fig. 10. Lumen efficiencies as function of current density for devices I–VI.

$\text{m}^{-2}$ ,  $0.011 \text{ mA cm}^{-2}$ ), and the highest current efficiency of  $24.5 \text{ cd A}^{-1}$ . In addition, when the brightness of device **III** was increased to  $531.1 \text{ cd m}^{-2}$  ( $2.84 \text{ mA cm}^{-2}$ ) it still had a power efficiency of  $4.0 \text{ lm W}^{-1}$  and current efficiency of  $18.7 \text{ cd A}^{-1}$  (external quantum efficiency 5.3%). Even at  $10180 \text{ cd m}^{-2}$  ( $181.2 \text{ mA cm}^{-2}$ ) the external quantum efficiency of 2.9% was kept. Device **IV** displays a maximum brightness of  $17660 \text{ cd m}^{-2}$  at 15 V, a maximum external quantum efficiency of 12.7%, the highest power efficiency of  $22.0 \text{ lm W}^{-1}$  ( $3.5 \text{ V}$ ,  $4.41 \text{ cd m}^{-2}$ ,  $0.018 \text{ mA cm}^{-2}$ ), and the highest current efficiency of  $24.5 \text{ cd A}^{-1}$ . The device **IV** also has excellent performances at higher current density or luminance. For example, when the brightness of device **IV** was increased to  $127.8 \text{ cd m}^{-2}$  ( $1.13 \text{ mA cm}^{-2}$ ) it still had a power efficiency of  $5.9 \text{ lm W}^{-1}$  and a current efficiency of  $11.8 \text{ cd A}^{-1}$  (external quantum efficiency 5.8%). Even at  $375.5 \text{ mA cm}^{-2}$  ( $>13,000 \text{ cd m}^{-2}$ ) the external quantum efficiency of 3.2% was maintained.

By comparing the electroluminescent properties of these devices, key factors that may influence the performances of this doped system could be emphasized. One is the steric hindrance of the host material. Comparing devices **I**, **II**, and **III** it can be seen that device **III** shows the best performance. This may arise from a larger distance between the central ions, which correspondingly reduce the triplet–triplet annihilation of the host [23]. However, the rule for steric hindrance is not the larger the better. The performance of device **V** can compare with device **III** only at higher current densities. It is likely that too large steric hindrance of the host material is not beneficial for exciton transportation. Another factor is the carrier-transporting property. When devices **IV** and **V** are compared, one can find that the performance of the former is much better than the later. This can be attributed to a carbazole group introduced to the  $\beta$ -diketone, which not only enhances its hole-transporting ability but also reduces the triplet–triplet annihilation [22,23]. In addition, it is

interesting to observe that the performances of those devices using iridium complexes as hosts are much better than that of CBP, performing lower driving voltages and higher efficiencies. The lower driving voltages were resulted from the easier hole injection from NPB to iridium complex based host because  $\text{Ir}(\text{ppy})_2(\text{LX})$  series have a higher HOMO level compare to that of CBP [37]. And the higher efficiency was arisen from the efficient energy transfer from  $\text{Ir}(\text{ppy})_2(\text{LX})$  to guest because they have a lower triplet excited level compare to that of CBP, which confined energy better on the guest molecules [38].

#### 4. Conclusion

In summary, phosphorescent OLEDs using an orange-red emitting iridium complex  $\text{Ir}(\text{DBQ})_2(\text{acac})$  as the guest and five green-emitting iridium complexes  $\text{Ir}(\text{ppy})_2(\text{acac})$ ,  $\text{Ir}(\text{ppy})_2(\text{dmd})$ ,  $\text{Ir}(\text{ppy})_2(\text{tmd})$ ,  $\text{Ir}(\text{ppy})_2(\text{CBDK})$ , or  $\text{Ir}(\text{ppy})_2(\text{FBDK})$  as the host, respectively, were demonstrated. Results show that these devices have better performance than that of the device based on CBP hosts. Moreover, the steric hindrance and exciton transporting property of the host are found to be the most important factors to this kind of doped system.

#### Acknowledgements

We thank the National Basic Research Program (2006CB601103), and the National Natural Science Foundation of China (20021101, 20423005, 50772003, 20671006) for financial support.

#### References

- [1] M.A. Baldo, D.F. O'Brien, Y. You, A. Shoustikov, S. Sibley, M.E. Thompson, S.R. Forrest, *Nature* 395 (1998) 151.
- [2] J.P. Duan, P.P. Sun, C.H. Cheng, *Adv. Mater.* 15 (2003) 224.

- [3] C.H. Yang, C.C. Tai, I.W. Sun, *J. Mater. Chem.* 14 (2004) 947.
- [4] X.W. Chen, J.L. Liao, Y.M. Liang, M.O. Ahmed, H.E. Seng, S.A. Chen, *J. Am. Chem. Soc.* 125 (2003) 636.
- [5] W.S. Huang, J.T. Lin, C.H. Chien, Y.T. Tao, S.S. Sun, Y.S. Wen, *Chem. Mater.* 16 (2004) 2480.
- [6] S. Lamansky, P. Djurovich, D. Murphy, F. Adbel-Razzaq, H.-E. Lee, C. Adachi, P.E. Burrows, S.R. Forrest, M.E. Thompson, *J. Am. Chem. Soc.* 123 (2001) 4304.
- [7] W. Lu, B.X. Mi, M.C.W. Chan, Z. Hui, N.Y. Zhu, S.T. Lee, C.M. Che, *Chem. Commun.* (2002) 206.
- [8] B.W. D'Andrade, J. Brooks, V. Adamovich, M.E. Thompson, S.R. Forrest, *Adv. Mater.* 14 (2002) 1032.
- [9] M. Buda, G. Kalyuzhny, A.J. Bard, *J. Am. Chem. Soc.* 124 (2002) 6090.
- [10] E.S. Handy, A.J. Pal, M.F. Rubbner, *J. Am. Chem. Soc.* 121 (1999) 3525.
- [11] C.M. Elliott, F. Pichot, C.J. Bloom, L.S. Rider, *J. Am. Chem. Soc.* 120 (1998) 6781.
- [12] X.Z. Jiang, A.K.-Y. Jen, B. Carlson, L.R. Dalton, *Appl. Phys. Lett.* 80 (2002) 713.
- [13] X.Z. Jiang, A.K.-Y. Jen, B. Carlson, L.R. Dalton, *Appl. Phys. Lett.* 81 (2002) 3125.
- [14] D.F. O'Brien, M.A. Baldo, M.E. Thompson, S.R. Forrest, *Appl. Phys. Lett.* 74 (1999) 442.
- [15] M.A. Baldo, S. Lamansky, P.E. Burrows, S.R.M.E. Thompson, S.R. Forrest, *Appl. Phys. Lett.* 75 (1999) 4.
- [16] M. Ikai, S. Tokito, Y. Sakamoto, T. Suzuki, Y. Taga, *Appl. Phys. Lett.* 79 (2001) 156.
- [17] C. Adachi, M.A. Baldo, M.E. Thompson, S.R. Forrest, *J. Appl. Phys.* 90 (2001) 5048.
- [18] M. Guan, Z. Chen, Z. Bian, Z. Liu, Z. Gong, W. Baik, H. Lee, C. Huang, *Org. Electron.* 7 (2006) 330.
- [19] R.C. Kwong, S. Lamansky, M.E. Thompson, *Adv. Mater.* 15 (2000) 1134.
- [20] T. Tsuzuki, S. Tokito, *Adv. Mater.* 19 (2007) 276.
- [21] S. Lamansky, P. Djurovich, D. Murphy, F. Abdel-Razzaq, R. Kwong, I. Tsyba, M. Bortz, B. Mui, R. Bau, M.E. Thompson, *Inorg. Chem.* 40 (2001) 1704.
- [22] Z.W. Liu, Z.Q. Bian, L. Ming, F. Ding, H.Y. Shen, D.B. Nie, C.H. Huang, *Org. Electron.* 9 (2008) 171.
- [23] Z.W. Liu, M. Guan, Z.Q. Bian, D.B. Nie, Z.L. Gong, Z.B. Li, C.H. Huang, *Adv. Funct. Mater.* 16 (2006) 1441.
- [24] F.W. Swamer, C.R. Hauser, U. Duke, N.C. Durham, *J. Am. Chem. Soc.* 72 (1950) 1352.
- [25] T.A. Hopkins, K. Meerholz, S. Shaheen, M.L. Anderson, A. Schmidt, B. Kippelen, A.B. Padias, H.K. Hall Jr., N. Peyghambarian, N.R. Armstrong, *Chem. Mater.* 8 (1996) 344.
- [26] M. Nonoyama, *Bull. Chem. Soc. Jpn.* 47 (1974) 767.
- [27] M.J. Frisch, G.W. Trucks, H.B. Schlegel, G.E. Scuseria, M.A. Robb, J.R. Cheeseman, J.A. Montgomery, T. Vreven Jr., K.N. Kudin, J.C. Burant, J.M. Millam, S.S. Iyengar, J. Tomasi, V. Barone, B. Mennucci, M. Cossi, G. Scalmani, N. Rega, G.A. Petersson, H. Nakatsuji, M. Hada, M. Ehara, K. Toyota, R. Fukuda, J. Hasegawa, M. Ishida, T. Nakajima, Y. Honda, O. Kitao, H. Nakai, M. Klene, X. Li, J.E. Knox, H.P. Hratchian, J.B. Cross, C. Adamo, J. Jaramillo, R. Gomperts, R.E. Stratmann, O. Yazyev, A.J. Austin, R. Cammi, C. Pomelli, J.W. Ochterski, P.Y. Ayala, K. Morokuma, G.A. Voth, P. Salvador, J.J. Dannenberg, V.G. Zakrzewski, S. Dapprich, A.D. Daniels, M.C. Strain, O. Farkas, D.K. Malick, A.D. Rabuck, K. Raghavachari, J.B. Foresman, J.V. Ortiz, Q. Cui, A.G. Baboul, S. Clifford, J. Cioslowski, B.B. Stefanov, G. Liu, A. Liashenko, P. Piskorz, I. Komaromi, R.L. Martin, D.J. Fox, T. Keith, M.A. Al-Laham, C.Y. Peng, A. Nanayakkara, M. Challacombe, P.M.W. Gill, B. Johnson, W. Chen, M.W. Wong, C. Gonzalez, J.A. Pople, B.05 ed., Gaussian Inc., Pittsburgh PA, 2003.
- [28] A.D. Becke, *J. Chem. Phys.* 98 (1993) 5648.
- [29] J.P. Perdew, *Phys. Rev. B* 33 (1986) 8822.
- [30] W.J. Hehre, R. Ditchfield, J.A. Pople, *J. Chem. Phys.* 56 (1972) 2257.
- [31] V.A. Rassolov, J.A. Pople, M.A. Ratner, T.L. Windus, *J. Chem. Phys.* 109 (1998) 1223.
- [32] CCDC 673949-673951 contains the supplementary crystallographic data for this paper. These data can be obtained free of charge via [www.ccdc.cam.ac.uk/data\\_request/cif](http://www.ccdc.cam.ac.uk/data_request/cif), by emailing [data\\_request@ccdc.cam.ac.uk](mailto:data_request@ccdc.cam.ac.uk) or by contacting. The Cambridge Crystallographic Data Centre, 12, Union Road, Cambridge CB2 1EZ, UK; fax: +44 1223 336033.
- [33] F.O. Graces, K.A. King, R.J. Watts, *Inorg. Chem.* 27 (1988) 3464.
- [34] The value was deduced by the cell volume and Z value.
- [35] J. Pommerehne, H. Vestweber, W. Guss, R.F. Mahrt, H. Bässler, M. Porsch, J. Daub, *Adv. Mater.* 7 (1995) 551.
- [36] A. Tsuboyama, H. Iwasaki, M. Furugori, T. Mukaide, J. Kamatani, S. Igawa, T. Moriyama, S. Miura, T. Takiguchi, S. Okada, M. Hoshino, K. Ueno, *J. Am. Chem. Soc.* 125 (2004) 12971.
- [37] T. Tsuzuki, Y. Nakayama, J. Nakamura, T. Iwata, S. Tokito, *Appl. Phys. Lett.* 88 (2006) 243511.
- [38] T. Tsuzuki, S. Tokito, *Appl. Phys. Express* 1 (2008) 021805.



## Pyrene functioned diarylfluorenes as efficient solution processable light emitting molecular glass

Feng Liu<sup>a</sup>, Chao Tang<sup>b</sup>, Qing-Quan Chen<sup>a</sup>, Shuang-Zhu Li<sup>a</sup>, Hong-Bin Wu<sup>c</sup>, Ling-Hai Xie<sup>b</sup>, Bo Peng<sup>a</sup>, Wei Wei<sup>a,\*</sup>, Yong Cao<sup>c</sup>, Wei Huang<sup>b</sup>

<sup>a</sup> State Key Laboratory for Advanced Photonic Materials and Devices, Fudan University, Shanghai 200433, PR China

<sup>b</sup> Jiangsu Key Lab of Organic Electronics and Information Displays and Institute of Advanced Materials (IAM), Nanjing University of Posts and Telecommunications (NUPT), Nanjing 210003, China

<sup>c</sup> Institute of Polymer Optoelectronic Materials and Devices, South China University of Technology, Guangzhou 510640, China

### ARTICLE INFO

#### Article history:

Received 4 October 2008

Received in revised form 18 November 2008

Accepted 22 November 2008

Available online 10 December 2008

#### PACS:

72.80.Le

73.61.Jc

78.60.Li

85.60.Jb

#### Keywords:

Fluorescence pyrene light emitting diodes  
molecular electronics

### ABSTRACT

In this paper, we described a new category of solution processable small molecule organic light emitting materials, the pyrene functioned diarylfluorenes: 2PE-PPF and DPE-PPF. They emit blue light in solution and green light in film, and show high thermal stability with the 5% weight loss temperature ( $T_d$ ) over 400 °C. The glass transition temperature ( $T_g$ ) for 2PE-PPF and DPE-PPF is 102 °C and 147 °C, respectively. These molecules are interesting molecular glass and they have good film forming abilities. Smooth and uniform film could be obtained by spin-coating. This character enables them able to be used in solution processed OLEDs by spin-coating or jet-printing. Single layered device using 2PE-PPF as the active material shows a turn-on voltage of 3.2 V, brightness over 8000 cd/m<sup>2</sup> and current efficiency up to 2.55 cd/A. Double layered device by inserting TPBI as the hole-blocking electron-transporting layer increases the maximum efficiency to 5.83 cd/A.

© 2008 Elsevier B.V. All rights reserved.

## 1. Introduction

Since the pioneering work by Tang and Friend in 1987 and 1990 [1], organic/polymeric light emitting diodes (OLEDs) have come to the commercial stage. Despite this progress, there are still many opportunities to improve the technology for both materials and devices. In OLEDs applications, amorphous materials are required for charge transporting and light emitting purpose. The amorphous materials with high thermal and morphological stability enable the fabrication of thermally stable OLEDs to increase device service time [2]. The materials with a low glass transition temperature and strong tendency to crys-

tallize are not proper for OLEDs because they will form grain boundaries which limit the charge transport and shorten the device lifetime [3].

Many stable amorphous molecules have been reported as functional materials in OLEDs for charge transporting/blocking and light emitting purpose, such as 4,4',4"-Tris-(carbazol-9-yl)-triphenylamine (TCTA) [4], 2,2',7'-tetrakis-(N,N-diphenylamino)-9,9'-spirobifluorene (spiro-TAD) [5], 1,3-bis[5-(*p*-tert-butylphenyl)-1,3,4-oxadiazol-2-yl]-benzene (OXD-7) [6], 2,2',2"--(1,3,5-benzenetriyl) tris[1-phenyl-1H-benzimidazole] (TPBI) [7] and many chromophores. [8] They have good thermal and morphological stability, as well as good film forming ability by vacuum deposition. For solution processed devices, the active materials are usually polymers, which could form smooth and uniform films without pinholes. The most famous examples are polyfluorenes blue emitters [9] and

\* Corresponding author.

E-mail addresses: [iamww@fudan.edu.cn](mailto:iamww@fudan.edu.cn) (W. Wei), [wei-huang@njupt.edu.cn](mailto:wei-huang@njupt.edu.cn) (W. Huang).

Poly(phenylenevinylene) (PPV) series green and red light emitting polymers [10]. Yet, light emitting polymers could not be purified by common purification methods such as column chromatography, recrystallization and vacuum sublimation. This drawback limits their purity, especially those defects and catalyst residues, which strongly quench light emission and trap injected carriers [11].

Recently, a new category of monodisperse materials: dendrimers [12], starbursts [13] and nanocomposites [14], have emerged as promising light emitting materials. They have well defined chemical structure, high purity, and could be deposited by cheap and efficient solution process. However, their synthesis and purification are quite laborious. An alternate solution to combine the advantage of small molecule and polymer is to develop efficient solution processable small molecules, which could be easily synthesized and purified, and have good film forming ability by spin-coating. Oligofluorenes are interesting solution processable molecules [15], yet their  $T_g$  is low. Structure modification is needed to increase their  $T_g$  to enhance thermal and morphological stability [16]. For the unique advantages of solution processable small molecular light emitting materials, there is a current need to gain more understanding of the correlation between molecular structure and device function. It is important to design and synthesize new molecules to accelerate their practical application.

In this article, we report a new methodology to design solution processable amorphous light emitting molecular glass. Pyrene is used as the building block for its high photoluminescence efficiency, high carrier mobility and enhanced hole-injection ability compared to fluorene based materials [17,18]. To endow the molecules high  $T_g$ , the diarylfluorene building block was employed [19]. We have recently reported several pyrene functioned fluorene molecules for vacuum deposited blue OLEDs, in which the C9 position of fluorene unit was modified by attaching a pyrene group [18]. This approach was also employed here for it could improve the thermal stability and increase the  $T_g$ . Diarylfluorene moiety is very rigid and its derivatives usually show low solubility and high tendency to crystallize. To overcome these problems, one 2-ethylhexyloxy solubilizing chain was introduced to the para- position of C9 substituted benzene group. Pyrenyl-ethynylene groups were kinked to the C2 and C7 position of diarylfluorene unit to extend the conjugation length and give rise to the emission color [20]. The resulted molecules show blue emission in dilute solution and green emission in film. They have good solubility and could form smooth and uniform films by spin-coating. Although a 2-ethylhexyloxy chain is presented in the molecules, their  $T_g$  is still above 100 °C, which is comparable to polyfluorenes (The  $T_g$  of fluorene copolymers lies between 80 and 100 °C [21]. For poly(9,9-dihexylfluorene), the  $T_g$  is 103 °C [22]). The synthetic procedure is quite easy and the target molecules could be purified by silica gel column. This design combines the synthetic simplicity and solution processability. In the device work, the molecules show green emission with high brightness and efficiency. These advantages make them interesting amorphous molecular glass for optoelectronic applications.

## 2. Experimental section

### 2.1. General experimental information

All reactions were monitored by TLC using pre-coated glass sheets purchased by Yantai Huiyou Silica Gel Developing Co. Ltd. (0.20 mm with fluorescent indicator UV254). Column chromatography was carried out using flash silica gel from Qingdao Haiyang Chemical Co. Ltd. (200 ~ 300 mesh).  $^1\text{H}$  NMR was recorded using a Varian spectrometer at 400 MHz. Molecular masses were determined by a SHIMADZU matrix-assisted laser desorption/ionization time-of-flight mass spectrometer (MALDI-TOF-MASS). Elemental analyses were performed on a Vario ELIII elemental analyzer. Thermogravimetric analysis (TGA) and differential scanning calorimetry (DSC) were performed using a purged nitrogen atmosphere at a heating rate of 20 °C/min. Absorption and photoluminescence (PL) emission spectra of the materials were measured in dichloromethane using a SHIMADZU UV-3150 spectrophotometer and a SHIMADZU RF-5301PC spectrophotometer, respectively. Cyclic voltammetry (CV) was performed on an Eco Chemie's Autolab. The quantum chemical calculations were performed using Gaussian 03, B.04 program. Fluorescent life time was measured with an Edinburgh FL-920 spectrometer. The AFM analysis was performed on DI MultiMode NanoScope IIIa Vecco. WAXRD was performed on Bruker Advance 8 powder XRD spectrometer.

*Synthesis of trimethyl(pyren-1-ylethynyl)silane (2):* To a 100 ml flask, 1.0 g (5.0 mmol) 1-bromopyrene, 0.24 g (0.25 mmol, 5%) Pd(PPh<sub>3</sub>)<sub>4</sub>, 47.5 mg (0.25 mmol, 5%) CuI was added. The flask was protected by N<sub>2</sub>. Then 30 ml degassed Et<sub>3</sub>N and 30 ml toluene was added. After stirred for several minutes, 10 ml (15 mmol) ethynyltrimethylsilane was added. The reaction was kept under 70 °C for 12 h. Silica-gel chromatograph yields yellow solid product 1.2 g (yield 80%).  $^1\text{H}$  NMR (400 MHz, CDCl<sub>3</sub>)  $\delta$  (ppm): 8.59 (d, 1H), 8.09 (m, 8H), 0.56 (s, 9H).

*Synthesis of 1-ethynylpyrene (3):* To a 100 ml flask, 1.2 g trimethyl(pyren-1-ylethynyl)silane (2) (4 mmol) was added. Then 30 ml THF and 30 ml MeOH were added. When compound 2 was dissolved, 5 g K<sub>2</sub>CO<sub>3</sub> was added. The reaction was stirred under room temperature overnight. Silica-gel chromatograph yield brown product 0.77 g (yield 86%).  $^1\text{H}$  NMR (400 MHz, CDCl<sub>3</sub>)  $\delta$  (ppm): 8.57 (d, 1H), 8.04 (m, 8H), 3.69 (s, 1H).

*Synthesis of 2-Bromo-9-(4'-(2"-ethylhexyloxyphenyl))-9-pyrenylfluorene (4a) and 2,7-Dibromo-9-(4'-(2"-ethylhexyloxyphenyl))-9-pyrenylfluorene (4b)* follows our previous procedure. For 4a:  $^1\text{H}$  NMR (400 MHz, CDCl<sub>3</sub>)  $\delta$  (ppm): 8.16 (d,  $J = 7.6$  Hz, 1H); 8.10 (d,  $J = 7.6$  Hz, 1H); 7.92–8.06 (m, 5H); 7.81 (d,  $J = 7.6$  Hz, 2H); 7.70 (d,  $J = 8.0$  Hz, 3H); 7.54–7.64 (broad, 1H); 7.38 (td,  $J = 7.6$  Hz, 0.8 Hz, 1H); 7.23 (td,  $J = 7.6$  Hz, 0.8 Hz, 1H); 3.80 (d, 5.6 Hz, 2H); 1.64–1.74 (m, 1H); 1.25–1.53 (m, 8H); 0.91 (s, 6H). For 4b:  $^1\text{H}$  NMR (400 MHz, CDCl<sub>3</sub>)  $\delta$ (ppm): 8.17 (d,  $J = 7.6$  Hz, 1H); 8.12 (d,  $J = 7.6$  Hz, 1H); 7.94–8.08 (m, 5H); 7.78–7.92 (broad, 2H); 7.67 (d,  $J = 8.0$  Hz, 4H); 7.51 (d,  $J = 8.0$  Hz, 2.0 Hz, 2H); 3.80 (d,  $J = 6.0$  Hz, 2H); 1.62–1.78 (m, 1H); 1.24–1.52 (m, 8H); 0.91 (s, 6H).



**Synthesis of 2PE-PPF:** To a 50 ml flask, compound 4a (0.65 g, 1 mmol), compound 3 (0.27 g, 1.2 mmol), tetrakis(triphenylphosphine) palladium (30.0 mg), and cuprous iodide (10.0 mg) was added. The flask was degassed and protected under N<sub>2</sub>, and then degassed toluene (15 ml) and diisopropylamine (15 ml) was injected. The reaction mixture was stirred at 70 °C for 48 h, and then cooled to room temperature. The solvent was stripped off under reduced pressure. The residue was purified by column chromatography on a silica-gel column, yield solid yellow product 0.64 g (yield 80%). <sup>1</sup>H NMR (400 MHz, CDCl<sub>3</sub>) δ (ppm): 8.56 (d, *J* = 9.2 Hz, 1H); 8.10–8.16 (m, 6H); 7.96–8.35 (m, 12H); 7.93–7.89 (m, 3H); 7.81 (d, *J* = 7.6 Hz, 1H); 7.68 (s, 1H); 7.44 (t, *J* = 7.2 Hz, 1H); 7.31–7.26 (m, 2H); 6.84 (broad, 2H); 3.82 (d, *J* = 4.8 Hz, 2H); 1.65–1.78 (m, 1H); 1.31–1.54 (m, 8H); 0.92 (m, 6H). <sup>13</sup>C NMR (100 MHz, CDCl<sub>3</sub>) δ (ppm): 158.53, 153.35, 140.46, 139.43, 132.06, 131.70, 131.45, 131.39, 131.29, 130.64, 129.92, 129.76, 128.61, 128.46, 128.30, 128.00, 127.70, 127.64, 127.44, 126.61, 126.52, 126.39, 126.21, 125.78, 125.43, 125.19, 124.95, 124.70, 124.52, 122.92, 121.04, 120.79, 118.00, 115.07, 96.24, 89.38, 70.69, 66.46, 53.70, 39.69, 30.80, 29.38, 24.13, 23.32, 14.38, 11.43. MALDI-TOF-MS (*m/z*): Anal. calcd. for C<sub>61</sub>H<sub>46</sub>O 795.0; found 795.4. Anal. calcd. C, 92.16; H, 5.83; found C, 92.11; H, 5.92.

**Synthesis of DPE-PPF:** To a 100 ml flask, compound 4b (0.73 g, 1 mmol), compound 3 (0.54 g, 2.4 mmol), tetrakis(triphenylphosphine) palladium (60.0 mg), and cuprous iodide (20.0 mg) was added. The flask was degassed and protected under N<sub>2</sub>, and then degassed toluene (30 ml) and diisopropylamine (30 ml) was injected. The reaction mixture was stirred at 70 °C for 48 h, and then cooled to room temperature. The solvent was stripped off under reduced pressure. The residue was purified by column chromatography on a silica-gel column, yield solid yellow product 0.78 g (yield 77%). <sup>1</sup>H NMR (400 MHz, CDCl<sub>3</sub>) δ (ppm): 8.54 (d, *J* = 9.2 Hz, 2H); 8.09–8.19 (m, 9H); 7.92–8.05 (m, 20H); 7.79 (d, *J* = 8.0 Hz, 2H); 7.34 (broad, 2H); 6.88 (d, *J* = 8.8 Hz, 2H); 3.82 (d, *J* = 6.0 Hz, 2H); 1.65–1.78 (m, 1H); 1.31–1.54 (m, 8H); 0.92 (m, 6H). <sup>13</sup>C NMR (400 MHz, CDCl<sub>3</sub>) δ (ppm): 158.66, 153.62, 139.66, 132.06, 131.82, 131.72, 131.44, 131.26, 130.67, 129.76, 129.70, 128.48, 128.33, 127.76, 127.70, 127.42, 126.76, 126.39, 126.25, 125.80, 125.74, 125.52, 125.29, 125.00, 124.69, 124.64, 124.49, 123.40, 121.12, 117.87, 115.15, 96.14, 89.82, 70.70, 66.47, 39.67, 30.78, 29.35, 24.11, 23.29, 14.34, 11.40. MALDI-TOF-MS (*m/z*): Anal. calcd. for C<sub>79</sub>H<sub>54</sub>O 1019.3; found 1019.5. Anal. calcd. C, 93.09; H, 5.34; found C, 93.01; H, 5.42.

**Device fabrication and testing:** LED was fabricated on pre-patterned indium–tin oxide (ITO) with sheet resistance 10–20 Ω/□. The substrate was ultrasonic cleaned with acetone, detergent, deionized water, and 2-propanol. Oxygen plasma treatment was made for 5 min as the final step just before film coating. Onto the ITO glass was spin-coated a layer of polyethylenedioxythiophene-polystyrene sulfonic acid (PEDOT: PSS) film with thickness of 40 nm from its aqueous dispersion. PEDOT: PSS film was dried at 80 °C for 12 h in the vacuum oven. The solution of the polymer was prepared under nitrogen atmosphere and spin-coated on to PEDOT: PSS layer. Typical thickness of

the emitting layer was 80 nm and heated at 60 °C for 30 min. Then a thin layer of 4 nm barium or 2 nm CsF as the electron injection cathode and the subsequent 120 nm thick aluminum protection layers were thermally deposited by vacuum evaporation through a mask at a base pressure below 4 × 10<sup>-4</sup> Pa. The cathode area defines the active area of the device. The typical active area of the devices in this study is 0.17 cm<sup>2</sup>. The EL layer spin-coating process and the device performance tests were carried out within a glove box under nitrogen atmosphere. Current–voltage (*I*–*V*) characteristics were recorded with a Keithley 236 source meter. EL spectra were measured by a PR 705 photometer (Photo Research). The external quantum efficiencies were determined by a Si photodiode with calibration in an integrating sphere (IS080, Labsphere).

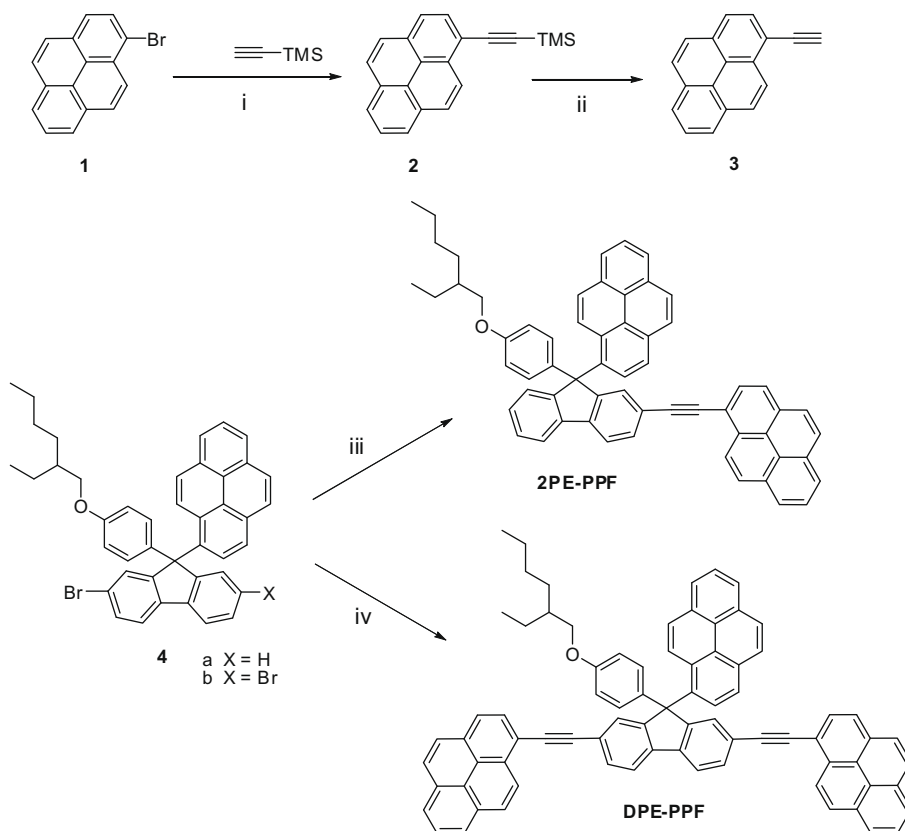
### 3. Results and discussion

#### 3.1. Synthesis and characterization

The pyrene functional diarylfluorenes, 2PE-PPF and DPE-PPF, were synthesized according to the procedure sketched in Scheme 1. Compound 2 was synthesized by Sonogashira reaction (82% yields) from 1-bromopyrene [23], then the TMS protecting group was eliminated by using KOH in THF/CH<sub>3</sub>OH solution. The intermediate 4 was prepared according to the procedure in our previous publication with excellent yield [18b]. The Sonogashira coupling reaction was employed between the pyrene ethylene and monobromide 4a or dibromide 4b to achieve the target compound 2PE-PPF and DPE-PPF with 80% and 77% yields, respectively. They showed good solubility in common solvents such as dichloromethane, THF and toluene. Both the two compounds in this report were purified by silica column chromatography. They were fully characterized by <sup>1</sup>H and <sup>13</sup>C NMR, MALDI-TOF-MASS and elemental analysis. The results were consistent with the proposed structures.

#### 3.2. Photophysical properties and electrochemistry

The UV–Vis absorption and photoluminescence spectra of the two materials were measured both in CH<sub>2</sub>Cl<sub>2</sub> and in film, the corresponding data were summarized in Table 1. In solution absorption spectra, the onset absorption edge showed a red shift about 28 nm from 2PE-PPF to DPE-PPF. This was due to the increasing of conjugation length, resulting from a more conjugated pyrenyl-ethynylene group at the C7 position of fluorene moiety in DPE-PPF (Fig. 1). The absorption spectra of the two molecules both in solution and in film were dominated by a series of peaks, which result from the combination of fluorene, pyrene and pyrenyl-ethynylene groups. The peak at about 350 nm came from the pyrene unit at the C9 position of fluorene unit [18b]. Peaks at longer wavelength were due to the absorption from pyrenyl-ethynylene functional fluorene backbone. In the solid state absorption spectra, the absorption edges red shifted about 20 nm compared to solution absorption for each molecule. The phenomena indicated strong intermolecular aggregation existed in film. The



**Scheme 1.** Reagents and conditions: (i)  $\text{PdCl}_2(\text{PPh}_3)_2$ , CuI, toluene/triethylamine, 70 °C, 24 h; (ii) KOH, THF/ $\text{CH}_3\text{OH}$ , RT, 24 h; (iii) 3/4a (1.2:1),  $\text{Pd}(\text{PPh}_3)_4$ , CuI, toluene/triethylamine, 70 °C, 48 h; (iv) 3/4b (2.4:1),  $\text{Pd}(\text{PPh}_3)_4$ , CuI, toluene/triethylamine, 70 °C, 48 h.

**Table 1**  
Photophysical properties of 2PE-PPF and DPE-PPF.

Molecules	$\Phi_{\text{PL}}^{\text{a}}$ (%)	$\lambda_{\text{abs,max}}$ (nm)	$\lambda_{\text{em,max}}$ (nm)		$\Delta E$ (eV) (abs. edge (nm))	HOMO (eV)	LUMO <sup>b</sup> (eV)
			Solution	Film			
2PE-PPF	47	240	412	514	2.95 (420)	-5.39	-2.44
DPE-PPF	51	240	439	495	2.77 (448)	-5.32	-2.55

<sup>a</sup> Absolute quantum yield of spin-coated film measured in the integrating sphere.

<sup>b</sup> LUMO = HOMO -  $\Delta E$  (solution state band gap).

absorption peak of C9-pyrene red shifted about 5 nm compared to solution absorption. This red shift was less pronounced compared to the red shift of absorption edges, indicating the intermolecular aggregation comes from the conjugated backbone. The intermolecular interaction of C9-pyrenes was very weak. The diarylfluorene was highly twisted in structure, and it could hamper the molecular aggregation to some extent. Thus we believe the strong red shift of the absorption edges comes from the  $\pi$ - $\pi$  stacking of C2 and C7 functionalized pyrenyl-ethynylene group.

The solution emission spectra of 2PE-PPF and DPE-PPF displayed well structured emission band with the maximum at 412 and 439 nm, respectively (Fig. 2). In the solid state emission, both the two materials red shifted to the

green emission region and the peaks are broad and structureless, which was typical excimer emission. 2PE-PPF showed a peak at 514 nm, and DPE-PPF showed a peak at 495 nm. Although DPE-PPF had a longer main chain conjugation, its film state emission located at the short wavelength region [24]. This was on the contrary to the absorption spectra. Pyrene had a strong tendency to form aggregation. This explained the remarkable red shift in emission from solution to film. The lower energy emission for 2PE-PPF was attributed to the aggregation nature of pyrene-ethynylene group at C2 position of fluorene unit. DPE-PPF was larger and more rigid in molecular structure. In the film forming process, it was less prone to form well packed aggregates than 2PE-PPF. The stronger aggregation

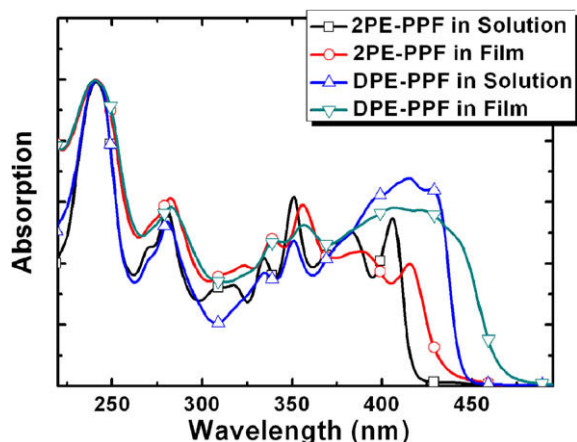


Fig. 1. UV-vis absorption spectra in  $\text{CH}_2\text{Cl}_2$  solution ( $10^{-6}$  M) and film.

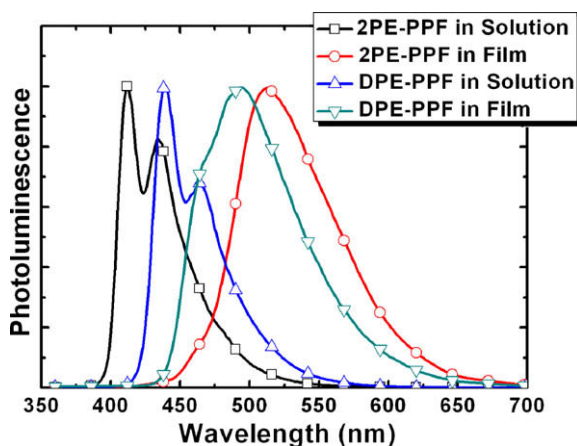


Fig. 2. Photoluminescence spectra in  $\text{CH}_2\text{Cl}_2$  solution ( $10^{-6}$  M) and film.

in 2PE-PPF caused its emission shifted to lower energy band. This explanation was supported by the observation of emission shoulders and tails. For 2PE-PPF, its emission shoulder and tail was stronger at lower energy region compared to DPE-PPF, indicating lower energy emission species existed in 2PE-PPF.

Fluorescent lifetime of 2PE-PPF and DPE-PPF films was measured with an Edinburgh FL-920 spectrometer [25]. The excitation source was a nanosecond flash lamp operating in the atmosphere of  $\text{H}_2$  gas (0.40–0.50 bar, 1.2 ns FWHM, 40 kHz repetition rate), whose output was filtered through a monochromator prior to the sample excitation. All fluorescent lifetimes were determined from the data using the Edinburgh Instruments software package. The film was pumped under 240 nm excitation and probed at their maximum emission wavelength. The fluorescence decay was plotted in Fig. 3. The fluorescent lifetime was deduced by bi-exponential fitting. For 2PE-PPF,  $\tau_1 = 2.23$  ns,  $\tau_2 = 7.62$  ns; for DPE-PPF,  $\tau_1 = 1.04$  ns,  $\tau_2 = 5.13$  ns. The lifetime decreased from 2PE-PPF to DPE-PPF [26].

The electrochemical behavior of the materials was investigated by cyclic voltammetry (CV) with a standard

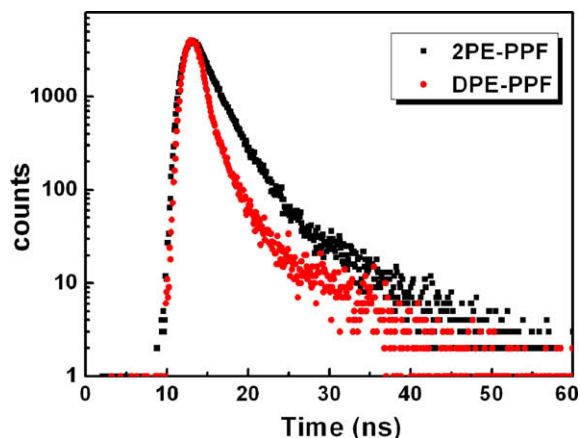


Fig. 3. Fluorescent life time measurement of 2PE-PPF and DPE-PPF films.

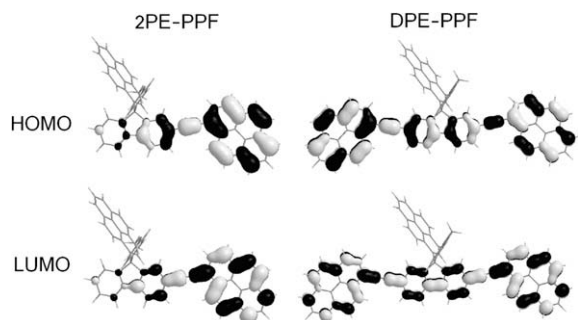
three electrodes electrochemical cell in a 0.1 M tetra-n-butylammonium hexafluorophosphate ( $\text{Bu}_4\text{NPF}_6$ ) in acetonitrile at room temperature under nitrogen with a scanning rate of 80 mV/s. A glassy carbon working electrode, a platinum counter electrode and an  $\text{Ag}/\text{AgNO}_3$  (0.1 M) reference electrode were used. The oxidation onset potentials were measured to be 0.66 V and 0.60 V for 2PE-PPF and DPE-PPF, respectively. The corresponding HOMO energy levels were thus estimated to be  $-5.37$  eV and  $-5.31$  eV for 2PE-PPF and DPE-PPF by the method  $-(E_{ox} + 4.71)$  reported by Li et al. [27]. This indicates that the pyrene center could improve the HOMO level, and thereby heighten the hole-affinity and hole-injection ability than conjugated fluorene derivatives (for polyfluorene, the HOMO level is  $-5.80$  eV [28]). The LUMOs can be estimated by  $\text{LUMO} = \text{HOMO} + \Delta E$  (band gap) method. The band gap was calculated from the solution absorption edges. The corresponding data were also summarized in Table 1.

### 3.3. Electronic structure

To gain deep insight into the materials, quantum chemistry was employed to investigate the electronic structure of the molecules. To minimize calculation cost, the 2-ethylhexyloxy group was substituted by methoxy group in the calculation. The ground state geometry of the molecules was fully optimized by AM1 and B3LYP/6-31G methods [29]. The energy of highest occupied molecular orbital (HOMO)/lowest unoccupied molecular orbital (LUMO) and energy gap was listed in Table 2. In the B3LYP calculation, the resulting data were much more close to experimental observation, because the DFT calculation took good account on the correlation effect [30]. In the molecular perspective, the energy level of HOMO for both molecules was around  $-5.0$  eV, indicating they had good hole-injection ability. And the energy gap decreased with the adding of the pyrenyl-ethynylene group, this was easy to understand because the conjugation was increased. It was interesting to note that from 2PE-PPF to DPE-PPF, with the adding of a pyrenyl-ethynylene group, the energy level of HOMO increased and the LUMO decreased, indicating

**Table 2**The calculated HOMO, LUMO, and the energy gap ( $\Delta E$ /eV) by AM1 and DFT-B3LYP/6-31G methods.

Methods	2PE-PPF			DPE-PPF		
	HOMO	LUMO	$\Delta E$	HOMO	LUMO	$\Delta E$
AM1	-7.967	-1.196	6.771	-7.931	-1.294	6.637
B3LYP/6-31G	-5.077	-1.887	3.190	-4.990	-2.063	2.928

**Fig. 4.** HOMO-LUMO orbitals of 2PE-PPF and DPE-PPF.

adding such a group enhanced both the hole-injection and electron injection. The HOMO and LUMO orbitals were shown in Fig. 4. They all localized on the main chain backbone, the C9-pyrene group had no contribution. This was because it was linked to the fluorene unit via a conjugation breaking manner.

### 3.4. Thermal and morphological properties

The thermal stability of the two materials was evaluated by thermogravimetric analysis (TGA) in nitrogen atmosphere. Thermal decomposition temperatures (5% weight loss temperature,  $T_d$ ) for 2PE-PPF and DPE-PPF were 409 °C and 436 °C, respectively. The TGA results indicated that the materials were stable enough to be used as EL materials. The phase-transition properties of the two materials were determined by DSC in nitrogen atmosphere at a heating rate of 20 °C/min, the result was shown in Table 3. The  $T_g$  of 2PE-PPE was 102 °C, and the  $T_g$  of DPE-PPF was 147 °C. No melting temperature ( $T_m$ ) was found for the two materials upon heating to 300 °C, revealing that 2PE-PPF and DPE-PPF were amorphous materials. Stable amorphous molecular materials were highly needed for long lifetime OLEDs. For solution processed OLEDs, this need was much more urgent. Solution processable light emitting molecules usually had a low  $T_g$ . This was because they were often substituted by long alkyl or alkoxy chains to enhance the solution processability (For the *n*-pentyl-substituted fluorene pentamer, the  $T_g$  is 72 °C [15]; for

**Table 3**

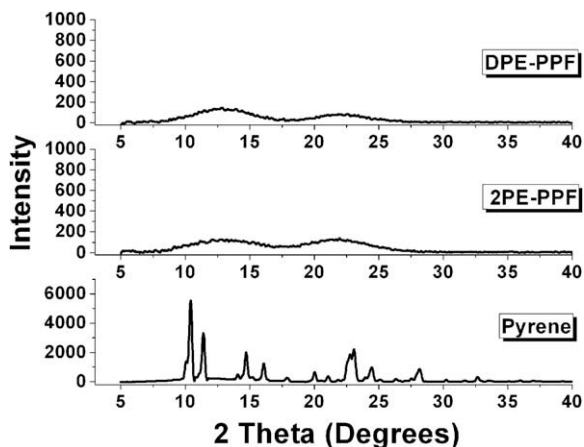
Thermal properties of 2PE-PPF and DPE-PPF.

Molecules	Molecular weight	$T_g$ /°C	$T_d$ /°C
2PE-PPF	795.02	102	409
DPE-PPF	1019.27	147	436

the low generation triazatruxene-centered starburst oligo-fluorenes, the  $T_g$  is 51 °C [13a]). For a small molecule bearing 2-ethylhexyloxy solubilizing chain with the molecular weight of 795, while still keeping a  $T_g$  higher than 100 °C, this was very rare. The thermal stable amorphous molecular glass could make the spin-coated film bearing a much stable morphology under annealing or device operation.

The amorphous characteristics of 2PE-PPF and DPE-PPF were further studied by powder wide-angle X-ray diffraction (WAXRD), and pyrene was also examined for comparison. The WAXRD pattern was shown in Fig. 5. For pyrene, a series of sharp peaks were recorded with high intensity. For 2PE-PPF and DPE-PPF, similar weak and broad amorphous peaks at  $2\theta = 14, 21$  (corresponding *d* values were 6.5 and 4.2 Å) were found, which were attributed to the  $\pi$ - $\pi$  stacking of pyrene segments. The WAXRD experiment indicated by kinking pyrenyl-ethynylene group with fluorene could effectively reduce the crystalline nature of pyrene to get amorphous materials.

2PE-PPF and DPE-PPF had good solubility in common solvent such as THF, toluene, chlorobenzene and  $\text{CHCl}_3$ . We dissolved the materials in chlorobenzene with the concentration of 40 mg/ml, and spin-coated on the glass substrates with the speed of 3200 rpm/min. The thickness of obtained film was about 80 nm. The film was heated at 80 °C in nitrogen for 30 min. The morphology of the film was examined by AFM using typical tapping mode, as shown in Fig. 6. For 2PE-PPF, very smooth and uniform film without pinholes was obtained. For DPE-PPF, the film was not as smooth as 2PE-PPF, and some pinholes were found, which was not ideal for device because the pinholes would cause large leakage current [31].

**Fig. 5.** WAXRD measurement of 2PE-PPF, DPE-PPF and pyrene.

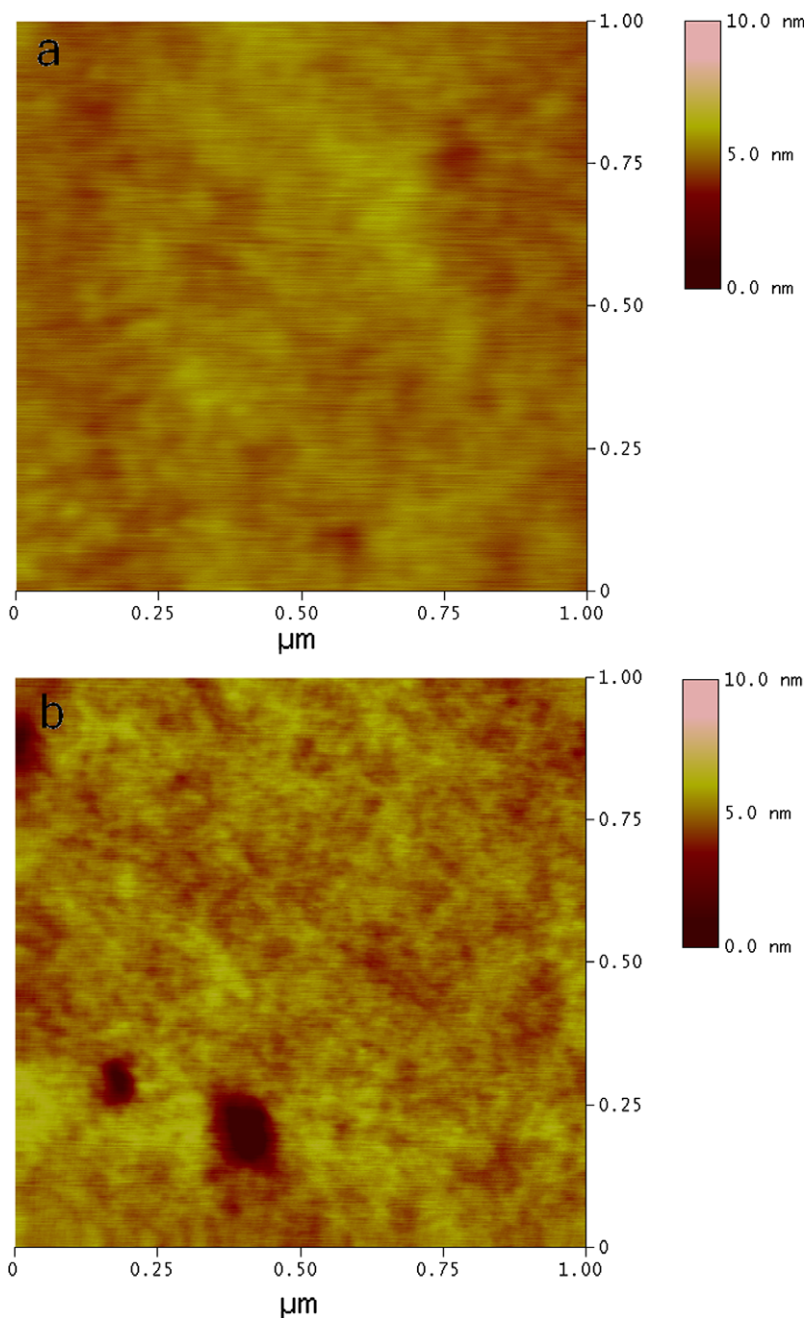


Fig. 6. AFM morphology of spin-coated film on glass substrate: (a) 2PE-PPF; (b) DPE-PPF.

### 3.5. Electroluminescence

Because of the good thermal stability and excellent film forming ability, 2PE-PPF was chosen as the active material in solution processed devices. Single layered device with the configuration of [ITO/PEDOT: PSS (40 nm)/2PE-PPF (80 nm)/Ba (4 nm) /Al (120 nm)] was fabricated (Device 1). It showed bright green emission with the peak at 522 nm. The turn-on voltage was 4.2 V, the maximal brightness was 3544 cd/m<sup>2</sup> and the maximal current efficiency reached 0.9 cd/A. The device performance was sum-

marized in Table 4. The electroluminescence spectra were presented in Figs. 7 and 8 and the  $I$ - $V$ - $L$  characteristic was shown in Figs. 9 and 10.

Single layered device was optimized by using CsF/Al as cathode with the device configuration of [ITO/PEDOT: PSS (40 nm)/2PE-PPF (80 nm)/CsF (2 nm)/Al (120 nm)] (Device 2). The device showed bright green emission with the peak located at 528 nm, little red shifted compare to Device 1. The emission color remains quite stable with increasing the current. While increasing the current from 1 mA to 20 mA, the emission remained identical (Fig. 8). Compared

**Table 4**

Electroluminescence properties of 2PE-PPF based devices.

Device	Structure	Turn-on (V)	Brightness (cd/m <sup>2</sup> )	LE (cd/A)	EQE (%)	CIE 1931
1	PEDOT/2PE-PPF/Ba	4.2	3544	0.90	0.36	(0.36, 0.54)
2	PEDOT/2PE-PPF/CsF	3.2	8325	2.55	1.12	(0.39, 0.54)
3	PEDOT/2PE-PPF/TPBI/Ba	6.2	2579	5.83	2.32	(0.28, 0.54)
4	PEDOT/PVK: 2PE-PPF/CsF	2.4	4262	2.06	1.13	(0.19, 0.30)

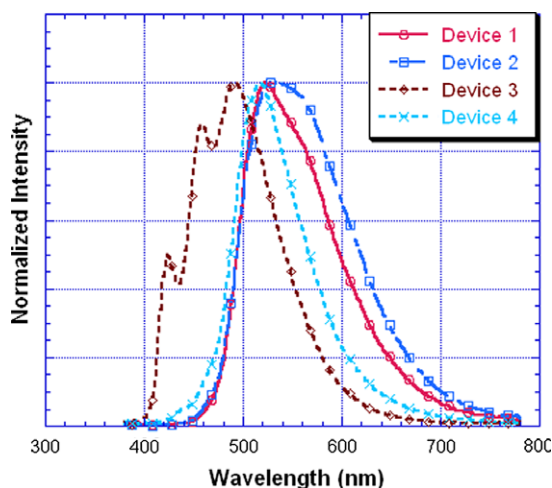


Fig. 7. Electroluminescence of devices with different structure.

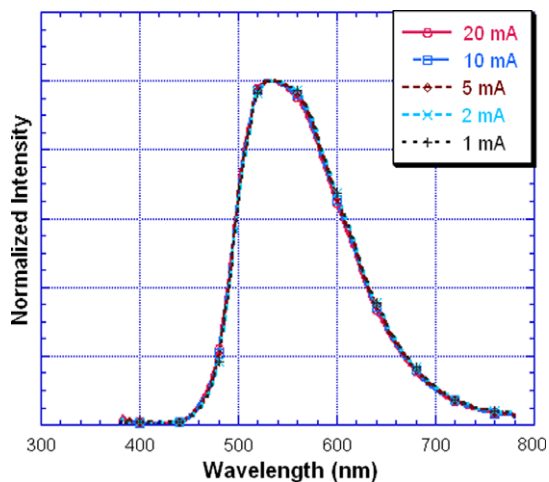


Fig. 8. Electroluminescence stability of Device 2.

to Device 1 using Ba electrode, Device 2 showed better performance. The turn-on voltage was reduced to 3.2 V, indicating that the CsF/Al cathode have better electron injection than Ba cathode [32], this could be seen from direct comparison of *I*–*V* characteristics of the two devices (Fig. 9). The brightness and current efficiency both increased to a great extent. For Device 2, the maximal current efficiency reached 2.55 cd/A (Fig. 10), and it remained quite stable with increasing the current density. The interesting efficiency-current density relationship was

similar to our previous pyrene functional material based OLEDs by vacuum deposition, [18] indicating 2PE-PPF was a promising light emitting material. The maximal brightness for Device 2 was over 8000 cd/m<sup>2</sup>, it was strong enough for lightening application. Based on this investigation and our previous work [13a], we found that for pyrene based materials, CsF was a more efficient cathode than barium in electron injection. This was because the Ba was still an injection limited cathode for 2PE-PPF. While using a thin layer of CsF, with the presence of Al capping cathode, free low work function alkali metal would be generated at the 2PE-PPF/CsF interface and the CsF layer produced an interfacial dipole. The combination of these two reasons lowered the Schottky barrier at the interface and enhanced the electron injection [33].

The device performance was further optimized by employing [1,3,5-tris (N-phenylbenzimidazol-2-yl)benzene] (TPBI) as the electron-transporting/hole-blocking layer. Double layered device using 2PE-PPF as the emitting material was fabricated with the structure of [ITO/PEDOT: PSS (40 nm)/2PE-PPF (80 nm)/TPBI (20 nm)/Ba (4 nm)/Al (120 nm)] (Device 3). Compared to Device 1 and 2, the emission blue shifted a little and its emission band was narrowed in FWHM (full-width at half-maximum). This was due to the adding of TPBI exciton blocking layer [34]. The turn-on voltage for Device 3 was increased to 6.2 V, this was due to the adding of 20 nm TPBI layer. The maximal brightness was over 2500 cd/m<sup>2</sup>, and the light efficiency was improved to 5.83 cd/A, which was quite high for solution processed small molecule OLEDs. We believe further optimization could improve the device performance and fully explore the potential of the material.

The fluorescence molecules could be used as the bulk emitter in a neat film. It could also be used as the dopant in the electroluminescent devices. Because 2PE-PPF had strong aggregation in neat film, it would be interesting to study the optoelectronic properties of the isolated molecules. We blended 2PE-PPF into PVK to study its optoelectronic response in blends. 2PE-PPF was 20 wt% compared to PVK in the blend. To increase the electron-transporting properties, [2-(4-bi-phenyl)-5-(4-tert-butylphenyl)-1,3,4-oxadiazole] (PBD) was added (30 wt% compared to PVK) [35]. The configuration of the device was [ITO/PEDOT: PSS (40 nm)/PVK: 2PE-PPF (80 nm)/CsF (2 nm)/Al (120 nm)] (Device 4). The turn-on voltage was 2.4 V, the maximal brightness was over 4200 cd/m<sup>2</sup> and the peak efficiency reached 2.06 cd/A, as shown in figures 8, 10 and 11. 2PE-PPF worked as an efficient dopant in PVK and the intermolecular aggregation was strongly reduced. The emission shifted to the sky blue region with the CIE 1931 coordinates of (0.19, 0.30) (For Device 2, the CIE 1931 coordinates of (0.39, 0.54)).

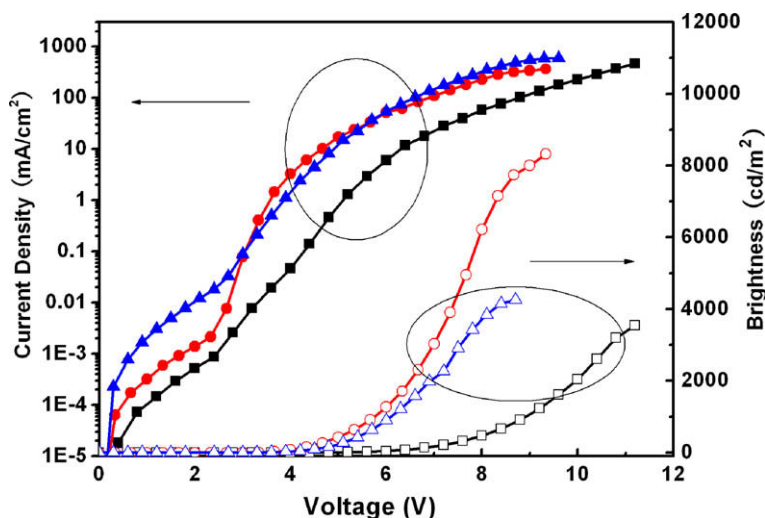


Fig. 9.  $I$ - $V$ - $L$  curve of devices 1 (black line), 2 (red line), 4 (blue line). (For interpretation of the references to colour in this figure legend, the reader is referred to the web version of this article.)

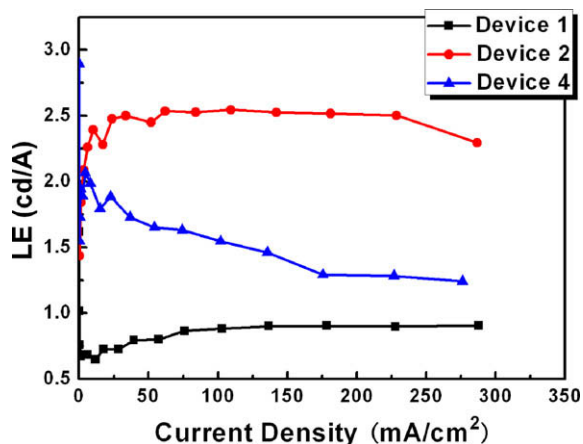


Fig. 10. Current efficiency of devices 1 (black line), 2 (red line), 3 (blue line). (For interpretation of the references to colour in this figure legend, the reader is referred to the web version of this article.)

ordinates were (0.39, 0.54)). The electroluminescence spectra were not the same as that of solution state photoluminescence, it was because in the solid state solution, the concentration for 2PE-PPF was still very high, and the electrical excitation was different from optical excitation in nature. These two reasons made the electroluminescence not the same as the solution state photoluminescence.

#### 4. Conclusion

In this paper, we demonstrated a promising molecular glass with high thermal and morphological stabilities for optoelectronic applications. The pyrene functioned diarylfluorenes, especially 2PE-PPF, is easy to be obtained by simple synthetic procedures and could be purified by column chromatography. The solid state emission comes from the pyrene excimer, which is broad and structureless and

red shifted a lot from the solution state photoluminescence. Although the molecule is very small, and contains only one alkoxy solubilizing group, it has good film forming ability, smooth and uniform film could be obtained by spin-coating. They have quite high  $T_d$  and  $T_g$ , which grant their service longevity in device operation. This material extends the device fabricating method of molecular glass. Single and double layered devices show efficient green emission, and the emission color remains quite stable with increasing the current. CsF is observed to be the optimal cathode for the material. Single layered device using CsF as the cathode shows a maximal current efficiency up to 2.55 cd/A and the maximal brightness over 8000 cd/m<sup>2</sup>, which is quite high for a solution processed small molecule OLEDs. The efficiency of single layered device remained quite stable when current density increased. This feature is very interesting in OLEDs application.

#### Acknowledgements

The authors are grateful to the Natural Science Foundation of China under Grants 60578039, 90406021, and 50428303 for financial support.

#### References

- [1] (a) C.W. Tang, S.A. Van Slyke, *Appl. Phys. Lett.* 51 (1987) 913; (b) J.H. Burroughes, D.D.C. Bradley, A.R. Brown, R.N. Marks, K. Mackay, R.H. Friend, P.L. Burn, A.B. Holmes, *Nature* 347 (1990) 539.
- [2] K. Müllen, U. Scherf, *Organic Light Emitting Devices Synthesis Properties and Applications*, WILEY-VCH Verlag GmbH and Co. KGaA, 2006. Chapter 7.
- [3] Y. Shirota, *J. Mater. Chem.* 15 (2005) 75.
- [4] Y. Kuwabara, H. Ogawa, H. Inada, N. Noma, Y. Shirota, *Adv. Mater.* 6 (1994) 677.
- [5] T.P.I. Saragi, T. Fuhrmann-Lieker, J. Salbeck, *Adv. Funct. Mater.* 16 (2006) 966.
- [6] D. O'Brien, A. Bleyer, D.G. Lidzey, D.D.C. Bradley, *J. Appl. Phys.* 82 (1997) 2662.
- [7] Z. Gao, C.S. Lee, I. Bello, S.T. Lee, R.-M. Chen, T.-Y. Luh, J. Shi, C.W. Tang, *Appl. Phys. Lett.* 74 (1999) 865.

- [8] (a) J.Y. Shen, C.Y. Lee, T.-H. Huang, J.T. Lin, Y.-T. Tao, C.-H. Chien, C. Tsai, *J. Mater. Chem.* 15 (2005) 2455;  
(b) P.-I. Shih, C.-Y. Chuang, C.-H. Chien, E.W.-G. Diau, C.-F. Shu, *Adv. Funct. Mater.* 17 (2007) 3141.
- [9] D. Neher, *Macromol. Rapid Commun.* 22 (2001) 1365.
- [10] L. Akcerud, *Prog. Polym. Sci.* 28 (2003) 875.
- [11] K. Pichler, *Phil. Trans. R. Soc. Lond. A* 355 (1997) 829.
- [12] (a) L. Zhao, C. Li, Y. Zhang, X.H. Zhu, J. Peng, Y. Cao, *Macromol. Rapid Commun.* 27 (2006) 914;  
(b) J. Ding, J. Gao, Y. Cheng, Z. Xie, L. Wang, D. Ma, X. Jing, F. Wang, *Adv. Funct. Mater.* 16 (2006) 575;  
(c) T.D. Anthopoulos, M.J. Frampton, E.B. Namdas, P.L. Burn, I.D.W. Samuel, *Adv. Mater.* 16 (2004) 557;  
(d) T.W. Kwon, M.M. Alam, S.A. Jenekhe, *Chem. Mater.* 16 (2004) 4657;  
(e) X.Y. Cao, W.B. Zhang, J.L. Wang, X.H. Zhou, H. Lu, J. Pei, *J. Am. Chem. Soc.* 125 (2003) 12430.
- [13] (a) F. Liu, W.-Y. Lai, C. Tang, H.-B. Wu, Q.-Q. Chen, B.P.W. Wei, W. Huang, Y. Cao, *Macromol. Rapid Commun.* 29 (2008) 659;  
(b) W.-Y. Lai, Q.-Y. Hei, R. Zhu, Q.-Q. Chen, W. Huang, *Adv. Funct. Mater.* 18 (2008) 265;  
(c) W.Y. Lai, R. Zhu, Q.L. Fan, L.T. Hou, Y. Cao, W. Huang, *Macromolecules* 39 (2006) 3707;  
(d) Q.D. Liu, J. Lu, J. Ding, M. Day, Y. Tao, P. Barrios, J. Stupak, K. Chan, J. Li, Y. Chi, *Adv. Funct. Mater.* 17 (2007) 1028;  
(e) A.L. Kanibolotsky, R. Berridge, P.J. Skabara, I.F. Perepichka, D.D.C. Bradley, M. Koeberg, *J. Am. Chem. Soc.* 126 (2004) 13695;  
(f) X.H. Zhou, J.C. Yan, J. Pei, *Org. Lett.* 5 (2003) 3543;  
(g) J. Pei, J.L. Wang, X.Y. Cao, X.H. Zhou, W.B. Zhang, *J. Am. Chem. Soc.* 125 (2003) 9944;  
(h) B. Li, J. Li, Y. Fu, Z. Bo, *J. Am. Chem. Soc.* 126 (2004) 3430;  
(i) D. Katsis, Y.H. Geng, J.J. Ou, S.W. Culligan, A. Trajkovska, S.H. Chen, L.J. Rothberg, *Chem. Mater.* 14 (2002) 1332.
- [14] (a) M.Y. Lo, C. Zhen, M. Lauters, G.E. Jabbour, A. Sellinger, *J. Am. Chem. Soc.* 129 (2007) 5808;  
(b) S. Sudhakar, Al. Sellinger, *Macromol. Rapid Commun.* 27 (2006) 247;  
(c) A. Sellinger, R. Tamaki, R.M. Laine, K. Ueno, H. Tanabe, E. Williams, G.E. Jabbour, *Chem. Commun.* 17 (2005) 3700.
- [15] Y. Geng, S.W. Culligan, Y. Trajkowska, J.U. Wallace, S.H. Chen, *Chem. Mater.* 15 (2003) 542.
- [16] S. Tang, M. Liu, P. Liu, H. Xia, M. Li, Z. Xie, F. Shen, C. Gu, H. Wang, B. Yang, Y. Ma, *Adv. Funct. Mater.* 17 (2007) 2869.
- [17] W.L. Jia, T.M. Cormick, Q.D. Liu, H. Fukutani, M. Motala, R.Y. Wang, Y. Tao, S.J. Wang, *J. Mater. Chem.* 14 (2004) 3344.
- [18] (a) C. Tang, F. Liu, Y.J. Xia, J. Lin, L.H. Xie, G.Y. Zhong, Q.L. Fan, W. Huang, *Org. Electron.* 7 (2006) 155;  
(b) C. Tang, F. Liu, Y.J. Xia, L.H. Xie, A. Wei, S.B. Li, Q.L. Fan, W. Huang, *J. Mater. Chem.* 16 (2006) 4074.
- [19] K.-T. Wong, Y.-Y. Chien, R.-T. Chen, C.-F. Wang, Y.-T. Lin, H.-H. Chiang, P.-Y. Hsieh, C.-C. Wu, C.H. Chou, Y.O. Su, G.-H. Lee, S.-M. Peng, *J. Am. Chem. Soc.* 124 (2002) 11576.
- [20] (a) Z. Zhao, J.-H. Li, X. Chen, P. Lu, Y. Yang, *Org. Lett.* 10 (2008) 3041;  
(b) Z. Zhao, J.-H. Li, X. Chen, P. Lu, Y. Yang, *Adv. Funct. Mater.* 17 (2007) 2203;  
(c) Z. Zhao, X. Xu, L. Xu, G. Yu, P. Lu, Y. Liu, *Synth. Metals* 157 (2007) 414;  
(d) Z. Zhao, X. Xu, F. Wang, G. Yu, P. Lu, Y. Liu, D. Zhub, *Synth. Metals* 156 (2006) 209.
- [21] G. Zeng, W.-L. Yu, S.-J. Chua, W. Huang, *Macromolecules* 35 (2002) 6907.
- [22] B. Liu, W.L. Yu, Y.H. Lai, W. Huang, *Chem. Mater.* 13 (2001) 1984.
- [23] Y. Liang, Y.X. Xie, J.H. Li, *J. Org. Chem.* 71 (2006) 379.
- [24] Z. Zhao, X. Xu, Z. Jiang, P. Lu, G. Yu, Y. Liu, *J. Org. Chem.* 72 (2007) 8345.
- [25] S. Fan, M. Sun, Z. Chen, J. Luo, Q. Hou, J. Peng, H. Yang, D. Zhang, F. Li, Y. Cao, *J. Phys. Chem. B* 111 (2007) 6113.
- [26] (a) L.-O. Pålsson, R. Beavington, M.J. Frampton, J.M. Lupton, S.W. Magennis, J.P.J. Markham, J.N.G. Pillow, P.L. Burn, I.D.W. Samuel, *Macromolecules* 35 (2002) 7891;  
(b) M. Endo, H. Wang, M. Fujitsuka, T. Majima, *Chem. Eur. J.* 12 (2006) 3735.
- [27] Q. Sun, H. Wang, C. Yang, Y.F. Li, *J. Mater. Chem.* 13 (2003) 800.
- [28] S. Janietz, D.D.C. Bradley, M. Grell, C. Giebeler, M. Inbasekaran, E.P. Woo, *Appl. Phys. Lett.* 73 (1998) 2453.
- [29] The quantum chemistry calculation was done using Gaussian W03.B4 software.
- [30] (a) T. Kugler, M. Logdlund, W.R. Salaneck, *Acc. Chem. Res.* 32 (1999) 225;  
(b) A.D. Becke, *Phys. Rev. A* 38 (1988) 3098;  
(c) C. Lee, W. Yang, R.G. Parr, *Phys. Rev. B* 37 (1988) 785.
- [31] (a) Y. Kim, D. Choi, H. Lim, C.-S. Ha, *Appl. Phys. Lett.* 82 (14) (2003) 2200;  
(b) Patent PCT/KR2006/003914.
- [32] (a) P. Piromreun, H. Oh, Y. Shen, G.G. Malliaras, J.C. Scott, P.J. Brock, *Appl. Phys. Lett.* 77 (15) (2000) 2403;  
(b) T.M. Brown, R.H. Friend, I.S. Millard, D.J. Lacey, J.H. Burroughes, F. Cacialli, *Appl. Phys. Lett.* 79 (2) (2001) 174;  
(c) G. Greczynski, M. Fahlman, W.R. Salaneck, *J. Chem. Phys.* 114 (2001) 8628.
- [33] N.K. Patel, S. Cinà, J.H. Burroughes, *IEEE J. Select. Topics Quantum Electron.* 8 (2002) 346.
- [34] (a) K.R.J. Thomas, J.T. Lin, Y.-T. Tao, C.-H. Chuen, *Chem. Mater.* 14 (2002) 3852;  
(b) H.B. Wu, F. Huang, J. Peng, Y. Cao, *Org. Electron.* 6 (2005) 118.
- [35] C. Jiang, W. Yang, J. Peng, S. Xiao, Y. Cao, *Adv. Mater.* 16 (2004) 537.





# Origin of improvement in device performance via the modification role of cesium hydroxide doped tris(8-hydroxyquinoline) aluminum interfacial layer on ITO cathode in inverted bottom-emission organic light-emitting diodes

Fengxia Wang, Tao Xiong, Xianfeng Qiao, Dongge Ma \*

State Key Laboratory of Polymer Physics and Chemistry, Changchun Institute of Applied Chemistry, Chinese Academy of Sciences, Graduate School of Chinese Academy of Sciences, Changchun 130022, People's Republic of China

## ARTICLE INFO

### Article history:

Received 7 August 2008

Received in revised form 4 November 2008

Accepted 24 November 2008

Available online 13 December 2008

### PACS:

85.60.Jb

81.20.Vj

### Keywords:

CsOH doped Alq<sub>3</sub>

Interfacial modification

IBOLED

## ABSTRACT

It has been found that cesium hydroxide (CsOH) doped tris(8-hydroxyquinoline) aluminum (Alq<sub>3</sub>) as an interfacial modification layer on indium-tin-oxide (ITO) is an effective cathode structure in inverted bottom-emission organic light-emitting diodes (IBOLEDs). The efficiency and high temperature stability of IBOLEDs with CsOH:Alq<sub>3</sub> interfacial layer are greatly improved with respect to the IBOLEDs with the case of Cs<sub>2</sub>CO<sub>3</sub>:Alq<sub>3</sub>. Herein, we have studied the origin of the improvement in efficiency and high temperature stability via the modification role of CsOH:Alq<sub>3</sub> interfacial layer on ITO cathode in IBOLEDs by various characterization methods, including atomic force microscopy (AFM), ultraviolet photoemission spectroscopy (UPS), X-ray photoemission spectroscopy (XPS) and capacitance versus voltage (C–V). The results clearly demonstrate that the CsOH:Alq<sub>3</sub> interfacial modification layer on ITO cathode not only enhances the stability of the cathode interface and electron-transporting layer above it, which are in favor of the improvement in device stability, but also reduces the electron injection barrier and increases the carrier density for current conduction, leading to higher efficiency.

© 2008 Elsevier B.V. All rights reserved.

## 1. Introduction

Interfacial phenomena represent a challenge and important area in organic light-emitting diode science and technology, and they have been the subjects of recent theoretical and experimental studies [1–10]. At present, a variety of interfacial treatments have been applied to both the cathode/organic and anode/organic interfaces, influencing interfacial stability and charge injection, and leading to varying degrees of the improvement in device performances in terms of luminance, efficiency and lifetime [11–14]. For representative vapor-deposited multi-

layer structure OLEDs, a significant increase in luminance and efficiency occurs upon the insertion of an interfacial layer (i.e. LiF [15], NaF [16], CsF [17], NaCl [18], alkali metal acetates [19], MgO [20], Liq [21], Cs<sub>2</sub>CO<sub>3</sub> [22], C<sub>60</sub> [23], and Cs:POPy<sub>2</sub> [24]) between the cathode and electron-transporting layer. Numerous mechanisms, including band bending, tunneling injection, LiF and CsF dissociation upon Al deposition, decrease of the Al surface potential, lowering the effective Al work function, as well as ETL protection during cathode deposition, have been suggested to explain the improvement in device performance.

As known, inverted bottom-emission organic light-emitting devices (IBOLEDs) are of considerable interest for display applications due to their easily integrating with either Si or organic thin film transistors for active-matrix displays [25]. However, generally, the structure of IBOLED

\* Corresponding author. Tel.: +86 431 85262357; fax: +86 431 85262873.

E-mail address: [mdg1014@ciac.jl.cn](mailto:mdg1014@ciac.jl.cn) (D. Ma).

has an indium-tin-oxide (ITO) as the bottom cathode. A dogged issue of using ITO as the cathode is the high electron injection barrier due to the high work function of ITO, even though inserting interfacial layers. Although the problem can recently be overcome by evaporating an ultrathin layer of magnesium (Mg) or introducing a lithium (Li) or cesium (Cs) doped 4,7-diphenyl-1,10-phenanthroline (BPhen) layer onto ITO [26–28]. There yet exist problems, for example, the ultrathin Mg and active Li and Cs are rather difficult to handle and deposit, and the introduction of the Mg layer affects the transparency of ITO. Therefore, there is a continuing need to develop more effective electron interfacial layer materials, especially using ITO as the cathode.

Chen et al. [29] ever reported that introducing a Cs<sub>2</sub>O:Bphen interfacial layer on ITO significantly enhanced the efficiency and lifetime of IBOLEDs, comparable with the conventional bottom-emission OLEDs. The improvement in device performance was attributed to the reduction in electron injection barrier from ITO, leading to the effective injection of electrons. Recently, we found [30] that cesium hydroxide (CsOH) doped Alq<sub>3</sub> as interfacial layer on ITO cathode could also significantly enhance the efficiency of IBOLEDs. More importantly, it was found that the device using CsOH:Alq<sub>3</sub> as the electron injection layer achieved 30–40% higher efficiency than that with Cs<sub>2</sub>CO<sub>3</sub>:Alq<sub>3</sub> interfacial layer. However, the origin of the improvement in efficiency via the modification role of CsOH:Alq<sub>3</sub> interfacial layer on ITO cathode in IBOLEDs is not yet understood well, and the complete studies on the effects of the CsOH:Alq<sub>3</sub> interfacial layer on the device stability of IBOLEDs are not still given.

In this paper, we carried out systematic studies on the role of CsOH:Alq<sub>3</sub> as interface modification layer on ITO cathode in the improvement of the efficiency and high temperature stability in IBOLEDs by atomic force microscopy (AFM), ultraviolet photoemission spectroscopy (UPS) and X-ray photoemission spectroscopy (XPS) and capacitance versus voltage (C–V). It is clearly seen that the CsOH:Alq<sub>3</sub> interfacial modification layer not only improves the stability of the interface at cathode and electron-transporting layer above it, leading to the stability at high temperature, but also reduces the electron injection barrier height, resulting in higher electron injection efficiency. More importantly, the free carrier density in CsOH:Alq<sub>3</sub> film is greatly enhanced with respect to Cs<sub>2</sub>CO<sub>3</sub>:BCP, Cs<sub>2</sub>CO<sub>3</sub>:Alq<sub>3</sub> films. As a result, the more electrons are injected, which is attributed to the higher efficiency compared to the case of Cs<sub>2</sub>CO<sub>3</sub> doping.

## 2. Experimental

The used device structure in this study was ITO/CsOH:Alq<sub>3</sub> (20 wt%, 10 nm)/Alq<sub>3</sub> (20 nm)/10-(2-benzothiazolyl)-2,3,6,7-tetrahydro-1,1,7,7-tetramethyl-1H,5H,11H-benzo[*l*]-pyrano-[6,7,8-*i*,*j*]quinolizin-11-one (C545T):Alq<sub>3</sub>(0.6%, 20 nm)/N,N'-di(naphthalene-1-yl)-N,N'-diphenyl-benzidine (NPB)(40 nm)/MoO<sub>3</sub> (6 nm)/Al (120 nm). For comparison, ITO/Cs<sub>2</sub>CO<sub>3</sub> (3 nm) or Cs<sub>2</sub>CO<sub>3</sub>:BCP (30 wt%, 10 nm), Cs<sub>2</sub>CO<sub>3</sub>:Alq<sub>3</sub> (5 wt%, 10 nm)/Alq<sub>3</sub>(20 nm)/(C545T):Alq<sub>3</sub>

(0.6%, 20 nm)/NPB(40 nm)/MoO<sub>3</sub> (6 nm)/Al (120 nm) devices were also investigated. The aforementioned structures of devices have been optimized. The inverted bottom-emission organic light-emitting diodes (IBOLEDs) and thin films for the thermal treatment studies were prepared by thermal evaporation in a high-vacuum system with pressure of less than  $5 \times 10^{-4}$  Pa. In order to study the influence of the cathode interfacial layer on the stability of the cathode interface and electron-transporting layer, the substrate temperature referred to the temperature of evaporating the electron interfacial layer and transport layer. For an example of the devices fabricated at high substrate temperature, the electron interfacial layer and transport layer were prepared when the substrate temperature reached 170 °C or 190 °C, and then the light-emitting layer and other layers were evaporated after the substrate temperature was reduced to about 85 °C. For the thin films fabricated at high substrate temperature, thermal treatment was the same as the fabrication processes of devices. In our experiments, the commercial ITO-coated glass with a sheet resistance of around 10 Ω/□ was used as the cathode. The evaporation rates for organic layer and Al were 0.2 nm/s and 1 nm/s, respectively, which were monitored by frequency counter and calibrated by Dektak 6M Profiler (Veeco). The overlap between ITO and Al electrodes was 16 mm<sup>2</sup> as the emissive size of devices. For the measurements energy levels and morphologies of Alq<sub>3</sub>, Cs<sub>2</sub>CO<sub>3</sub>/Alq<sub>3</sub>, Cs<sub>2</sub>CO<sub>3</sub>:BCP/Alq<sub>3</sub>, Cs<sub>2</sub>CO<sub>3</sub>:Alq<sub>3</sub>/Alq<sub>3</sub> and CsOH:Alq<sub>3</sub>/Alq<sub>3</sub> thin films at different substrate temperatures, they were deposited on ITO-coated glass substrates. The current–voltage–luminance characteristics were measured by a Keithley source measurement unit (Keithley 2400 and Keithley 2000) with a calibrated silicon photodiode. All the devices were measured without encapsulation at room temperature.

The morphology was measured by atomic force microscopy (AFM) (SIINT, SPA400). The electron concentration was measured by C–V (Agilent E 4980A). The interface electronic structure and variation in the work function were performed by XPS with Al *K*α X-ray source (1486.6 eV) and UPS with He discharge lamp (UV light of 21.22 eV) (Thermo ELECTRON CORPORATION, ESCALAB 250). The resolution of the spectra was 0.3 eV for XPS, 0.1 eV for UPS. The UPS measurements were performed with a –4 V bias voltage applied to the sample in order to enable the measurement of the secondary electrons cutoff.

## 3. Results and discussion

### 3.1. Electroluminescence properties of IBOLEDs

The electroluminescence (EL) performances of IBOLEDs with different interfacial modification layers on ITO cathode at different substrate temperatures were firstly investigated in detail. Fig. 1a and b show the current density–luminance–voltage, current efficiency–current density–power efficiency characteristics of devices with Cs<sub>2</sub>CO<sub>3</sub>, Cs<sub>2</sub>CO<sub>3</sub>:BCP, Cs<sub>2</sub>CO<sub>3</sub>:Alq<sub>3</sub> and CsOH:Alq<sub>3</sub> modification layers at room substrate temperature, respectively.

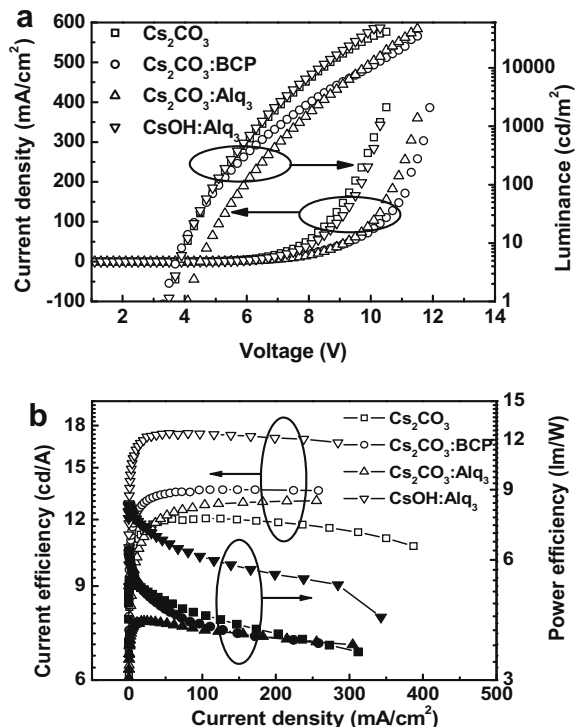


**Fig. 1.** Luminance–voltage–current density (a), current efficiency–current density–power efficiency (b) of ITO/cathode buffer layer/Alq<sub>3</sub>/Alq<sub>3</sub>:C545T/NPB/MoO<sub>3</sub>/Al at room substrate temperature.

The EL properties of ITO/Alq<sub>3</sub>/Alq<sub>3</sub>:C545T/NPB/MoO<sub>3</sub>/Al device without the modification layer structure are not shown in Fig. 1 because the luminance and current efficiency are lower than 100 cd/m<sup>2</sup>, 1 cd/A, respectively, due to high electron injection barrier between ITO cathode and Alq<sub>3</sub>. It is clearly seen that the device with CsOH:Alq<sub>3</sub> interfacial layer shows more efficient EL performances than the case of Cs<sub>2</sub>CO<sub>3</sub>, Cs<sub>2</sub>CO<sub>3</sub>:BCP and Cs<sub>2</sub>CO<sub>3</sub>:Alq<sub>3</sub> as the interfacial layers. The device with CsOH:Alq<sub>3</sub> interfacial layer shows higher luminance and current density than devices with the case of Cs<sub>2</sub>CO<sub>3</sub>:BCP and Cs<sub>2</sub>CO<sub>3</sub>:Alq<sub>3</sub> as the interfacial layer at the same voltage. As shown in Fig. 1b, the higher current efficiency and power efficiency are obtained in device with CsOH:Alq<sub>3</sub> interfacial layer than in devices with Cs<sub>2</sub>CO<sub>3</sub>, Cs<sub>2</sub>CO<sub>3</sub>:BCP and Cs<sub>2</sub>CO<sub>3</sub>:Alq<sub>3</sub> as the interfacial layers. The maximum current efficiency and power efficiency, respectively, reach 17.4 cd/A and 8.3 lm/W in device with CsOH:Alq<sub>3</sub> interfacial layer. They are significantly higher than 12.1 cd/A and 5.3 lm/W of device with Cs<sub>2</sub>CO<sub>3</sub> as the interfacial layer, 13.6 cd/A and 6.4 lm/W of device with Cs<sub>2</sub>CO<sub>3</sub>:BCP as the interfacial layer, and 13.0 cd/A and 4.2 lm/W of device with Cs<sub>2</sub>CO<sub>3</sub>:Alq<sub>3</sub> as the interfacial layer. These indicate that CsOH:Alq<sub>3</sub> should be an excellent electron injection interfacial material.

To further demonstrate the validity of CsOH:Alq<sub>3</sub> as interfacial layer, the EL performances of devices with different interfacial modification layers fabricated at different substrate temperatures are compared. Fig. 2 shows the EL performance characteristics of the devices with Cs<sub>2</sub>CO<sub>3</sub>,

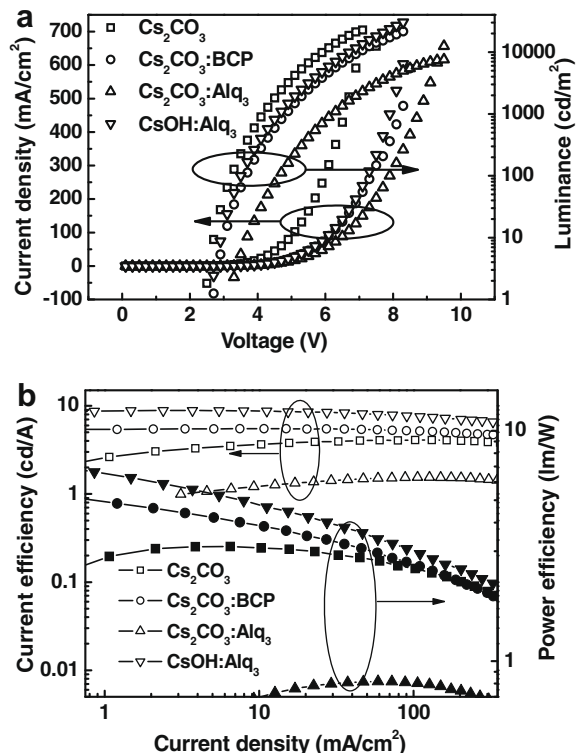


**Fig. 2.** Luminance–voltage–current density (a), current efficiency–current density–power efficiency (b) of ITO/cathode buffer layer/Alq<sub>3</sub>/Alq<sub>3</sub>:C545T/NPB/MoO<sub>3</sub>/Al at substrate temperature of 170 °C.

Cs<sub>2</sub>CO<sub>3</sub>:BCP, Cs<sub>2</sub>CO<sub>3</sub>:Alq<sub>3</sub> and CsOH:Alq<sub>3</sub> modification layers at substrate temperature of 170 °C. It can be seen that the device with CsOH:Alq<sub>3</sub> interfacial layer yet shows higher luminance and power efficiency, reaching 32,300 cd/m<sup>2</sup> and 7.24 lm/W, approximately equal to the luminance and power efficiency of device fabricated at room substrate temperature. However, the EL efficiencies of the devices with Cs<sub>2</sub>CO<sub>3</sub>, Cs<sub>2</sub>CO<sub>3</sub>:BCP and Cs<sub>2</sub>CO<sub>3</sub>:Alq<sub>3</sub> as the interfacial layer are greatly reduced. Especially, the EL efficiencies of the devices with Cs<sub>2</sub>CO<sub>3</sub> or Cs<sub>2</sub>CO<sub>3</sub>:Alq<sub>3</sub> as the interfacial layer are reduced to 4.09 cd/A (3.14 lm/W) and 1.54 cd/A (0.816 lm/W), obviously lower than the cases of room substrate temperature.

The reduction difference in luminance and EL efficiency is further obvious at higher substrate temperature. As the case of the devices fabricated at substrate temperature of 190 °C, which is above the glass transition temperature of Alq<sub>3</sub>, the EL performances are shown in Fig. 3. It can be seen that the device based on Cs<sub>2</sub>CO<sub>3</sub> or Cs<sub>2</sub>CO<sub>3</sub>:Alq<sub>3</sub> as the interfacial layer hardly emits light, whereas the EL efficiencies of device with Cs<sub>2</sub>CO<sub>3</sub>:BCP interfacial layer are reduced to 2.98 cd/A and 0.98 lm/W. However, as shown in Fig. 3, the device with CsOH:Alq<sub>3</sub> interfacial layer may still operate well with efficiencies of 6.27 cd/A and 2.06 lm/W. All of these results demonstrate that the CsOH:Alq<sub>3</sub> is an ideal cathode interfacial layer material in enhancing EL efficiency and high temperature stability of IBOLEDs.

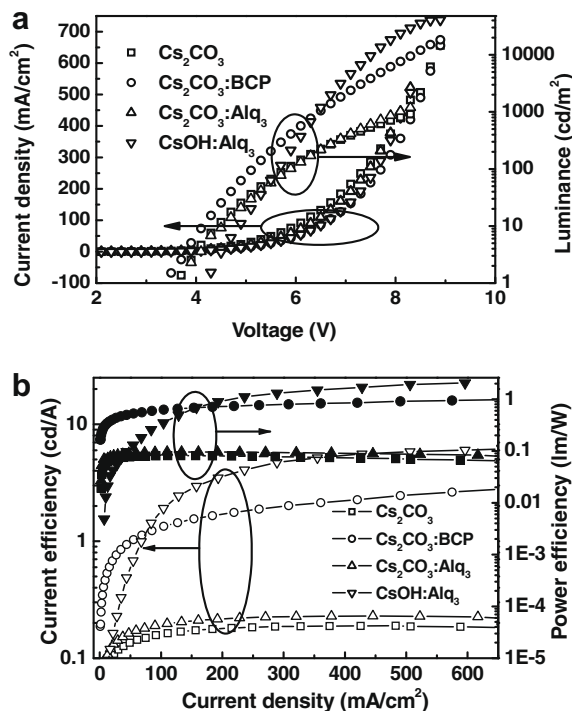


**Fig. 3.** Luminance–voltage–current density (a), current efficiency–current density–power efficiency (b) of ITO/cathode buffer layer/Alq<sub>3</sub>/Alq<sub>3</sub>:Cs<sub>2</sub>CO<sub>3</sub>/NPB/MoO<sub>3</sub>/Al at substrate temperature of 190 °C.

### 3.2. Morphology of electron-transporting layer

For insight into the origin of the observed great improvement in device performance due to the utilization of the CsOH:Alq<sub>3</sub> interfacial layer, the effects of different interfacial layers on the morphology of electron-transporting layer Alq<sub>3</sub> at different substrate temperatures were studied in detail by atomic force microscope (AFM). The atomic force microscopy images of Alq<sub>3</sub> (20 nm), Cs<sub>2</sub>CO<sub>3</sub> (3 nm)/Alq<sub>3</sub> (20 nm) (I), Cs<sub>2</sub>CO<sub>3</sub>:BCP (30 wt%, 10 nm)/Alq<sub>3</sub> (20 nm) (II), Cs<sub>2</sub>CO<sub>3</sub>:Alq<sub>3</sub> (5 wt%, 10 nm)/Alq<sub>3</sub> (20 nm) (IV) and CsOH:Alq<sub>3</sub> (20 wt%, 10 nm)/Alq<sub>3</sub> (20 nm) (V) films on ITO are shown in Fig. 4. It is clearly seen that the spots grow larger in some areas and spread to almost all regions of the samples for the case of ITO/Alq<sub>3</sub> and ITO/Cs<sub>2</sub>CO<sub>3</sub>:Alq<sub>3</sub>/Alq<sub>3</sub> fabricated at substrate temperature of 170 °C, and the spots become severe as the substrate temperature increases to 190 °C. Although the Alq<sub>3</sub> film above Cs<sub>2</sub>CO<sub>3</sub> and Cs<sub>2</sub>CO<sub>3</sub>:BCP interfacial layer keeps a basically featureless morphology with a small root mean square (RMS) roughness of 1.1 nm, 1.2 nm, respectively, in case of 170 °C substrate temperature, which are smaller than the RMS of 1.5 nm of Alq<sub>3</sub> without cathode buffer layer. However, the RMS roughness of Alq<sub>3</sub> film above Cs<sub>2</sub>CO<sub>3</sub> and Cs<sub>2</sub>CO<sub>3</sub>:BCP interfacial layer reaches 5.5 nm, 9.9 nm as the substrate temperature is up to 190 °C. This indicates that the Alq<sub>3</sub> films above these interfacial layers are crystallized, which will degrade the performances of IBOLEDs. Differently, the CsOH:Alq<sub>3</sub> interfacial layer keeps the stable morphology of Alq<sub>3</sub> film above it, even at substrate tem-

perature of 190 °C. A relatively flat surface with RMS roughness of 0.7 nm and 3.4 nm at 170 °C and 190 °C is obtained. These studies show that CsOH:Alq<sub>3</sub> as the interfacial layer greatly improves the stability of the morphology of Alq<sub>3</sub> film above it, which should favor the high temperature stability of IBOLEDs.

### 3.3. Electron injection barrier at interfaces

It is known that the improvement mechanism of Cs<sub>2</sub>CO<sub>3</sub> or Cs<sub>2</sub>CO<sub>3</sub> doping as an interfacial layer is attributed to the enhancement of electron injection due to the reduction of electron injection barrier [31–34]. One reason is that the Cs<sub>2</sub>CO<sub>3</sub> tends to decompose into Cs<sub>2</sub>O and CO<sub>2</sub> to form X–O–Cs complex during evaporation, thus enhancing the electron injection [32]. Another is that the metallic Cs is diffused into the Alq<sub>3</sub> surface to form an efficient electron injection contact during the thermal evaporation of Cs<sub>2</sub>CO<sub>3</sub> [33]. Furthermore, the increase of free electron density is also considered as to be one of the main reasons in the enhancement of electron injection in the case of Cs<sub>2</sub>CO<sub>3</sub> doping [34]. Similar processes may occur in the case of CsOH doping. However, as we can see, the CsOH doped Alq<sub>3</sub> as the interfacial layer significantly enhances the device efficiency with respect to Cs<sub>2</sub>CO<sub>3</sub> and Cs<sub>2</sub>CO<sub>3</sub> doped Alq<sub>3</sub>. In order to clearly elucidate the advantage of the CsOH doped Alq<sub>3</sub> as the interfacial layer, the effect of CsOH:Alq<sub>3</sub> on interfacial barrier is investigated by UPS. Fig. 5a and b show the UPS spectra of Cs<sub>2</sub>CO<sub>3</sub> (2 nm), Cs<sub>2</sub>CO<sub>3</sub>:BCP (2 nm), Cs<sub>2</sub>CO<sub>3</sub>:Alq<sub>3</sub> (2 nm) and CsOH:Alq<sub>3</sub> (2 nm) on ITO interface as well as ITO. As shown in UPS spectra, the work function ( $\phi_{\text{buffer}}$ ) of ITO is calculated to be 4.70 eV, and the work function of ITO with Cs<sub>2</sub>CO<sub>3</sub>, Cs<sub>2</sub>CO<sub>3</sub>:BCP, Cs<sub>2</sub>CO<sub>3</sub>:Alq<sub>3</sub> and CsOH:Alq<sub>3</sub> modification layer is reduced to 4.00 eV, 4.38 eV, 4.40 eV, and 4.50 eV, respectively. This lower work function due to the modification of interfacial layer has been ascribed to the formation of interfacial dipoles ( $ID_1 = \text{vacuum}_{\text{cathode buffer layer}} - \text{vacuum}_{\text{ITO}}$ ), which reduces the vacuum level, leading to lower electron injection barrier, thus facilitating electron injection.

Furthermore, the UPS spectra of ITO/Alq<sub>3</sub> (2 nm), and ITO/Cs<sub>2</sub>CO<sub>3</sub> (3 nm), Cs<sub>2</sub>CO<sub>3</sub>:BCP (10 nm), Cs<sub>2</sub>CO<sub>3</sub>:Alq<sub>3</sub> (10 nm), or Alq<sub>3</sub>:CsOH (10 nm)/Alq<sub>3</sub> (2 nm) films are performed, as shown in Fig. 5c and d. It can be calculated that the interfacial dipole ( $ID_2 = \text{vacuum}_{\text{Alq}_3} - \text{vacuum}_{\text{cathode buffer layer}}$ ) of 0.20 eV is generated at ITO/Alq<sub>3</sub>, the interfacial dipoles of –0.10 eV, –0.96 eV, –0.96 eV, –0.64 eV are formed for Cs<sub>2</sub>CO<sub>3</sub>/Alq<sub>3</sub>, Cs<sub>2</sub>CO<sub>3</sub>:BCP/Alq<sub>3</sub>, Cs<sub>2</sub>CO<sub>3</sub>:Alq<sub>3</sub>/Alq<sub>3</sub> and Alq<sub>3</sub>:CsOH/Alq<sub>3</sub>, respectively. Therefore, the utilization of the interfacial modification layer induces lower vacuum level of Alq<sub>3</sub> to reduce further electron-injection barrier height compared to that without interfacial modification layer.

The detailed values extracted from the Fig. 5 are shown in Fig. 6. In energy diagrams, the band bending effects are negligible because the change of HOMO is almost the same as the change of the vacuum level. From the optical band gap (2.7 eV for Alq<sub>3</sub>) and HOMO energy level, the evolution of the lowest unoccupied molecular orbital (LUMO) of Alq<sub>3</sub> can be determined. As the energy diagram shown in Fig. 6, the electron injection barrier from ITO to Alq<sub>3</sub> is 1.73 eV for

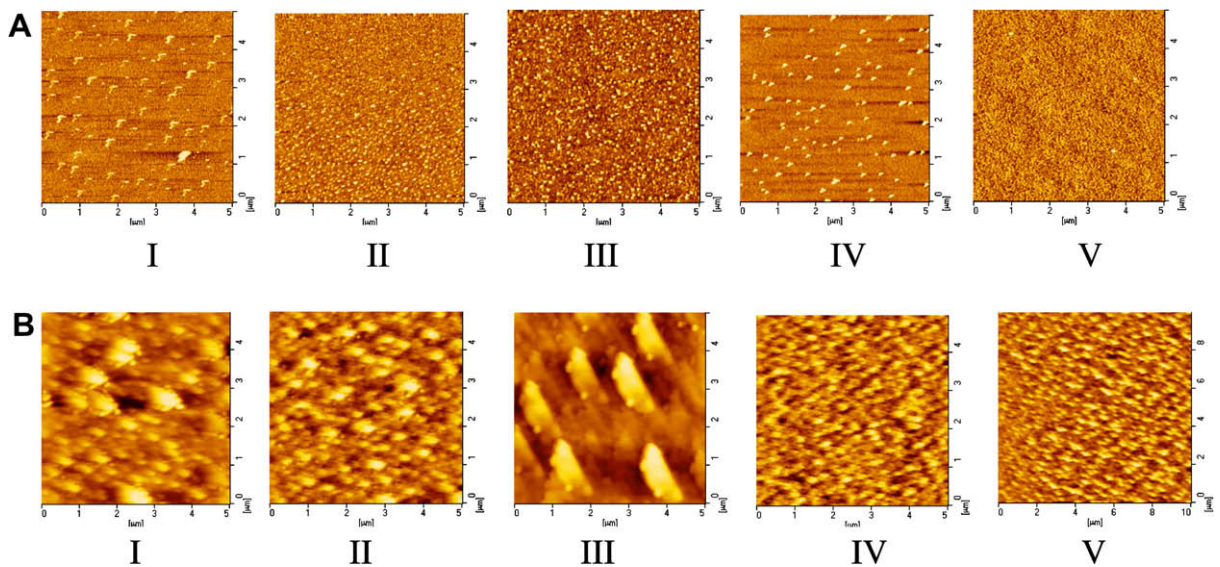


**Fig. 4.** Atomic force microscopy images of Alq<sub>3</sub> (I), Cs<sub>2</sub>CO<sub>3</sub>/Alq<sub>3</sub> (II), Cs<sub>2</sub>CO<sub>3</sub>:BCP/Alq<sub>3</sub> (III) and Cs<sub>2</sub>CO<sub>3</sub>:Alq<sub>3</sub>/Alq<sub>3</sub> (IV) CsOH:Alq<sub>3</sub>/Alq<sub>3</sub> (V) films fabricated at substrate temperature of 170 °C (A), and 190 °C (B).

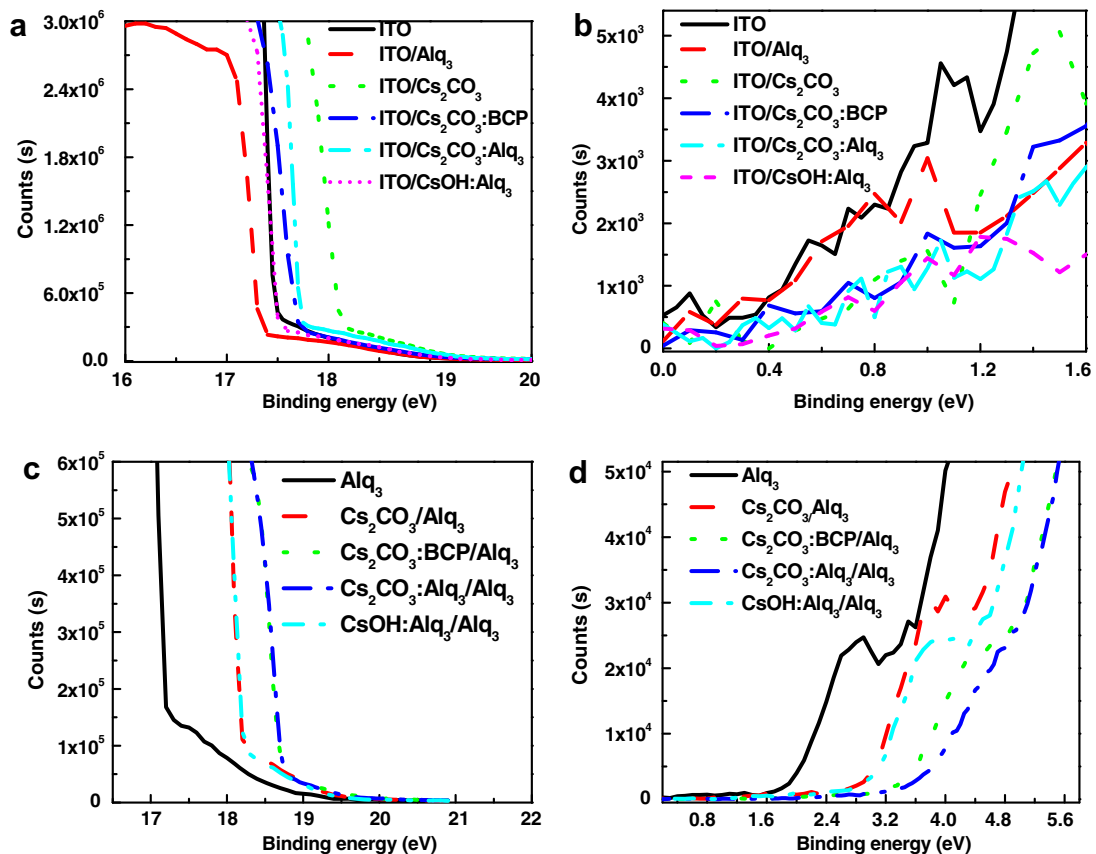


**Fig. 5.** UPS spectra ITO, ITO/Alq<sub>3</sub>, ITO/Cs<sub>2</sub>CO<sub>3</sub>, ITO/Cs<sub>2</sub>CO<sub>3</sub>:BCP, ITO/Cs<sub>2</sub>CO<sub>3</sub>:Alq<sub>3</sub>, and ITO/Alq<sub>3</sub>:CsOH shown in (a) and (b), ITO/Alq<sub>3</sub>, ITO/Cs<sub>2</sub>CO<sub>3</sub>/Alq<sub>3</sub>, ITO/Cs<sub>2</sub>CO<sub>3</sub>:BCP/Alq<sub>3</sub>, ITO/Cs<sub>2</sub>CO<sub>3</sub>:Alq<sub>3</sub>/Alq<sub>3</sub>, and ITO/Alq<sub>3</sub>:CsOH/Alq<sub>3</sub> shown in (c) and (d).

the case of ITO/Alq<sub>3</sub>, whereas the electron injection barriers are reduced to 0.74 eV, 0.26 eV, 0.19 eV and 0.68 eV,

respectively, as inserting Cs<sub>2</sub>CO<sub>3</sub>, Cs<sub>2</sub>CO<sub>3</sub>:BCP, Cs<sub>2</sub>CO<sub>3</sub>:Alq<sub>3</sub> and CsOH:Alq<sub>3</sub> interfacial layers between ITO and Alq<sub>3</sub>.

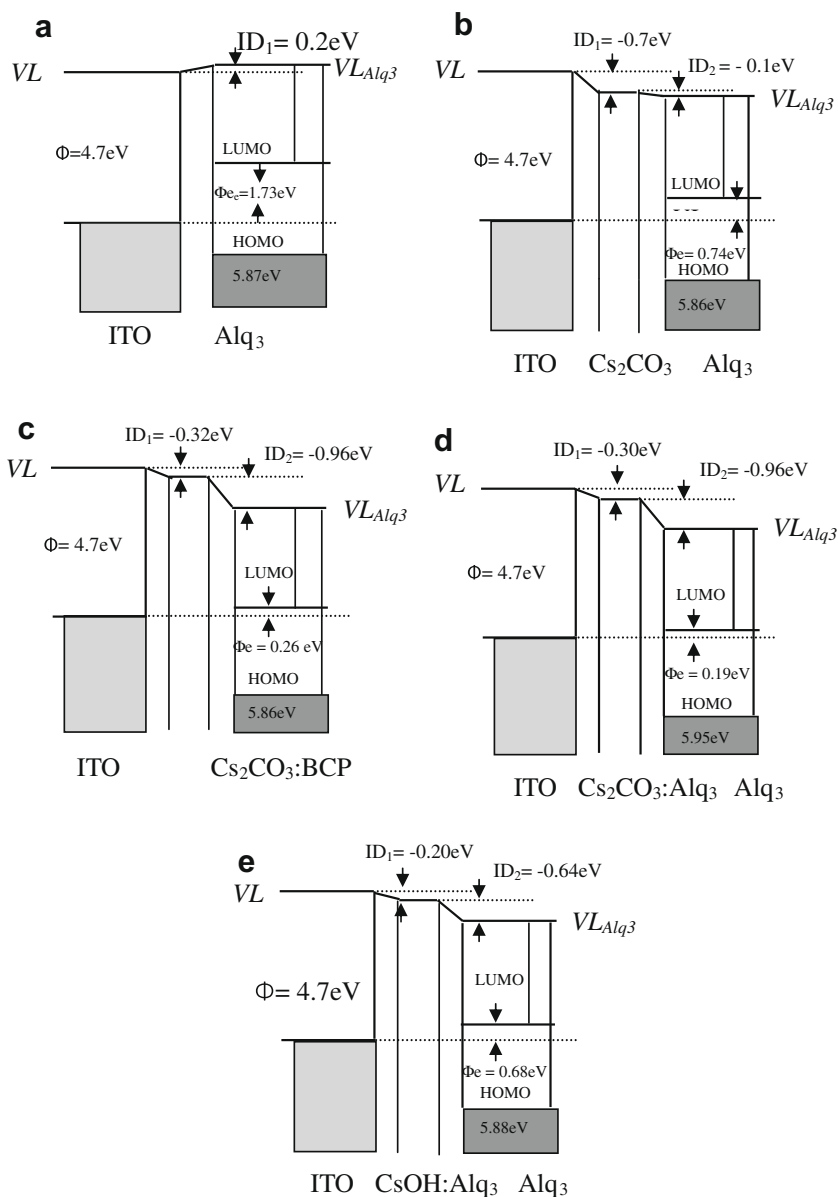


**Fig. 6.** Schematic energy diagrams of ITO/Alq<sub>3</sub> (a), ITO/Cs<sub>2</sub>CO<sub>3</sub>/Alq<sub>3</sub> (b), ITO/Cs<sub>2</sub>CO<sub>3</sub>:BCP /Alq<sub>3</sub> (c), ITO/Cs<sub>2</sub>CO<sub>3</sub>:Alq<sub>3</sub>/Alq<sub>3</sub> (d), ITO/Alq<sub>3</sub>:CsOH/Alq<sub>3</sub> (e) extracted from the UPS.

Obviously, these cathode interfacial modification layers greatly reduce the electron injection barrier, which should be benefit for the improvement of EL efficiency.

The XPS spectra of ITO, ITO/Cs<sub>2</sub>CO<sub>3</sub>:Alq<sub>3</sub> (2 nm), ITO/Cs<sub>2</sub>CO<sub>3</sub>:Alq<sub>3</sub> (30 nm), ITO/CsOH:Alq<sub>3</sub> (2 nm), and ITO/CsOH:Alq<sub>3</sub> (30 nm) films are shown in Fig. 7. It can be seen that the In and Sn binding energies shift to lower level after deposition of 2 nm Cs<sub>2</sub>CO<sub>3</sub>:Alq<sub>3</sub> or CsOH:Alq<sub>3</sub> film on ITO compared to that of bare ITO. Meanwhile, the Cs peak in the case of deposition of 2 nm Cs<sub>2</sub>CO<sub>3</sub>:Alq<sub>3</sub> or CsOH:Alq<sub>3</sub> film keeps higher binding energy than that in the case of 30 nm Cs<sub>2</sub>CO<sub>3</sub>:Alq<sub>3</sub> or CsOH:Alq<sub>3</sub> film. This indicates that there occurs electron transfer from CsOH (Cs<sub>2</sub>CO<sub>3</sub>) to ITO,

resulting in the vacuum level shift down. Furthermore, the reaction between ITO and CsOH (Cs<sub>2</sub>CO<sub>3</sub>) may also form the Sn or In–O–Cs complex [32], which further lowers the work function of ITO. As the experiment shown, the utilization of CsOH:Alq<sub>3</sub> interfacial layer greatly reduces the electron injection barrier from ITO, which is similar to that of Cs<sub>2</sub>CO<sub>3</sub> modification with respect to the case of bare ITO. However, the electron injection barrier is not further reduced due to the modification of CsOH:Alq<sub>3</sub> compared to the modification of Cs<sub>2</sub>CO<sub>3</sub>:Alq<sub>3</sub> and Cs<sub>2</sub>CO<sub>3</sub>:BCP. This indicates that the large enhancement in EL efficiency is not mainly originated from the reduction of the electron injection barrier as using CsOH:Alq<sub>3</sub> to modify ITO.

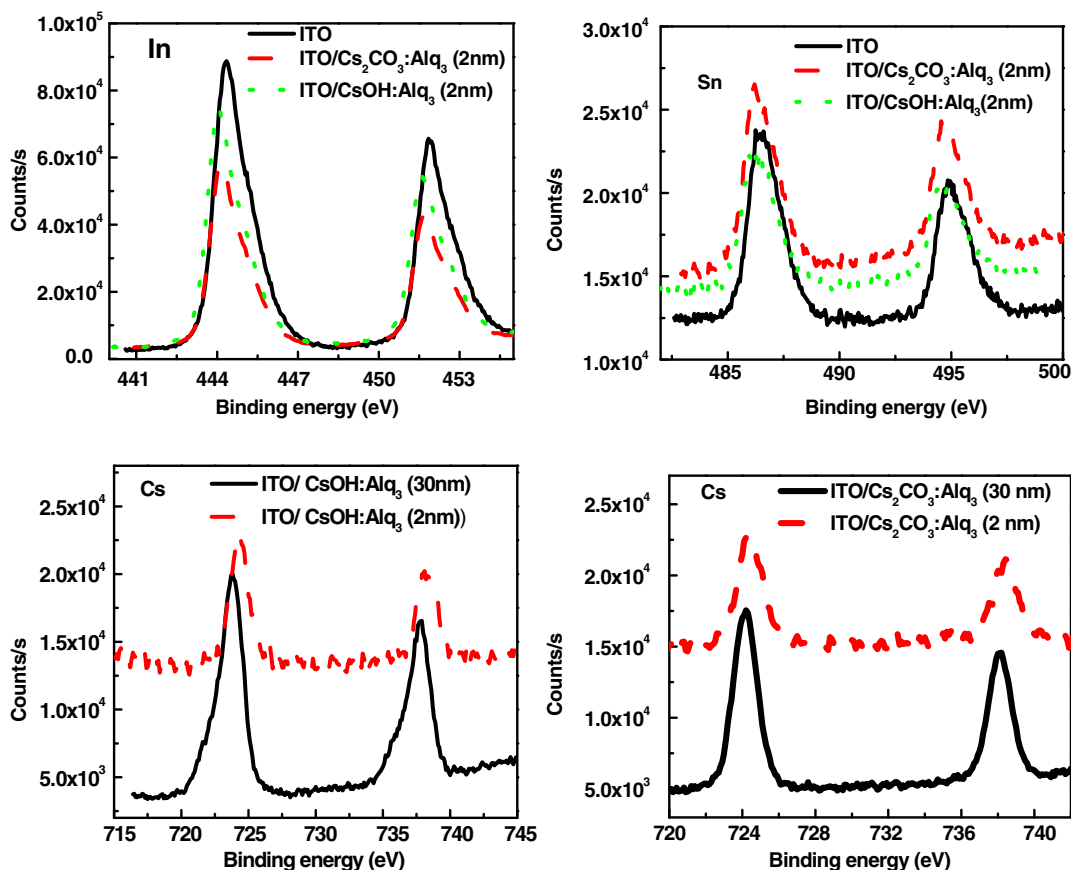


Fig. 7. XPS spectra of ITO, ITO/Cs<sub>2</sub>CO<sub>3</sub>:Alq<sub>3</sub> (2 nm), ITO/Cs<sub>2</sub>CO<sub>3</sub>:Alq<sub>3</sub> (30 nm), ITO/CsOH:Alq<sub>3</sub> (2 nm) and ITO/CsOH:Alq<sub>3</sub> (30 nm).

### 3.4. Free electron density

To elucidate the main origin of the improvement in EL efficiency due to the utilization of CsOH:Alq<sub>3</sub> interfacial modification layer, the capacitance–voltage characteristics of ITO/Alq<sub>3</sub>:Cs<sub>2</sub>CO<sub>3</sub> (100 nm), BCP: Cs<sub>2</sub>CO<sub>3</sub> (100 nm), Alq<sub>3</sub>:CsOH (100 nm)/Al were performed. As we know, capacitance–voltage characteristics have been widely used to investigate the electrical and charge transport properties in organic diodes. For one-sided injection organic diodes, i.e. one side contact is ohmic, the other side is injection limited, which controls the charge injection and forms the depletion layer, then the free charge carriers can be determined well by the capacitance–voltage characteristics [35–39]. In this case, the capacitance can generally be described as [40]:

$$\frac{1}{C^2} = \frac{2(V_{bi} - V)}{A^2 q \epsilon \epsilon_0 N_A} \quad (1)$$

where  $q$  is elementary charge,  $V_{bi}$  is the built-in potential,  $\epsilon$  is the relative dielectric constant,  $\epsilon_0$  is the vacuum permittivity,  $A$  is effective area of device, and  $N_A$  is the active concentration of free charge carriers.  $1/C^2 - V$  plots with different doped layer are shown in Fig. 8. It is found that the fitted lines are in good agreement with  $1/C^2$  versus the bias voltage curves, where all the relative coefficients

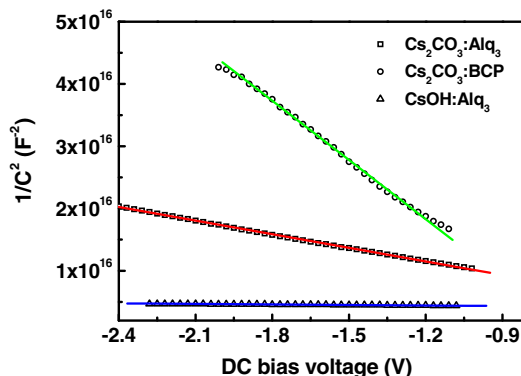


Fig. 8.  $1/C^2$  vs.  $V_{bias}$  plots of different doped layers.

( $R$ ) are above 0.98. The free carrier density can be easily extracted from the slope. The calculated carrier density values are summarized in Table 1. It is surprisingly found that the free carrier density is strongly dependent on the dopants in doped layers as determined by capacitance–voltage measurements. For example, the CsOH:Alq<sub>3</sub> film shows the highest value, which is much 10 times higher than Cs<sub>2</sub>CO<sub>3</sub>:Alq<sub>3</sub> and 20 times higher than Cs<sub>2</sub>CO<sub>3</sub>:BCP. The large increase of the free carrier density in the CsOH-

**Table 1**The parameters calculated by the C–V<sup>a</sup>.

	$k_A$	$R$	$N_A$ ( $10^{16}$ cm <sup>-3</sup> )
Cs <sub>2</sub> CO <sub>3</sub> :BCP	1.179E16	0.984	16.25
Cs <sub>2</sub> CO <sub>3</sub> :Alq <sub>3</sub>	6.768E15	0.999	27.17
CsOH:Alq <sub>3</sub>	4.669E14	0.993	393.81

<sup>a</sup> The relative dielectric constant  $\epsilon$  is assumed to be 3, and the active area of device is 16 mm<sup>2</sup>. For C–V measurements, 0.03 V signal oscillating at 1 kHz was added to dc bias.

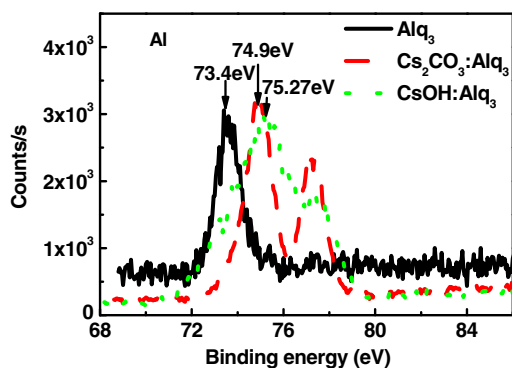


**Fig. 9.** XPS spectra of Alq<sub>3</sub> (30 nm), Cs<sub>2</sub>CO<sub>3</sub>:Alq<sub>3</sub> (30 nm) and CsOH:Alq<sub>3</sub> (30 nm) films.

H:Alq<sub>3</sub> film should be attributed to the most effective electron injection.

The larger increase of the free electron density in CsOH:Alq<sub>3</sub> film could be well elucidated by XPS spectral measurements. Fig. 9 shows the XPS spectra of the Alq<sub>3</sub> (30 nm), Cs<sub>2</sub>CO<sub>3</sub>:Alq<sub>3</sub> (30 nm) and CsOH:Alq<sub>3</sub> (30 nm) films. It can be seen that a new peak appears and Al peak shifts to higher binding energy value in the Cs<sub>2</sub>CO<sub>3</sub>:Alq<sub>3</sub> and CsOH:Alq<sub>3</sub> films. This indicates that there occurs charge transfer between the Cs<sub>2</sub>CO<sub>3</sub> and Alq<sub>3</sub> or CsOH and Alq<sub>3</sub>. Furthermore, the Al peak of CsOH:Alq<sub>3</sub> film shifts to higher binding energy than that of Cs<sub>2</sub>CO<sub>3</sub>:Alq<sub>3</sub> film, indicating that the more charge transfer states are formed between CsOH and Alq<sub>3</sub>. As known, the formed charge transfer state generally exhibits a high conductivity [41]. This should be used to explain the reason that the higher free carrier density occurs in CsOH:Alq<sub>3</sub> film. It can be seen that the electron injection properties strongly depend on the dopant structures and electron transport materials. The detailed mechanism investigation should be benefit for the understanding of the electron transport properties in doping organic films, thus further optimizing device performances.

#### 4. Conclusions

We have studied the origin of the improvement in EL efficiency and high temperature stability via the modification role of CsOH:Alq<sub>3</sub> interfacial layer on ITO cathode in inverted bottom-emission organic light-emitting diodes (IBOLEDs) in detail. The studies clearly demonstrated that the CsOH:Alq<sub>3</sub> interfacial modification layer on ITO cath-

ode significantly enhanced the stability of the cathode interface and reduced the electron injection barrier from ITO cathode. More importantly, inserting the CsOH:Alq<sub>3</sub> between ITO and electron-transporting layer greatly increased the free carrier density leading to the more effective electron injection.

#### Acknowledgement

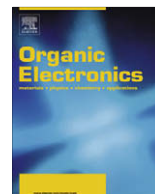
We would like to thank the Foundation of Jilin Research Council (20050517), Foundation of Changchun Research Council (2007GH06), Science Fund for Creative Research Groups of NSFC (20621401) and Ministry of Science and Technology of China (863 program No. 2006AA03A161, 973 program No. 2009CB930603, 2009CB623604) for financial support.

#### References

- [1] K. Demirkan, A. Mathew, C. Weiland, M. Reid, R.L. Opila, *J. Appl. Phys.* 103 (2008) 034505.
- [2] S.W. Tsang, Z.H. Lu, Y. Tao, *Appl. Phys. Lett.* 90 (2007) 132115.
- [3] S.V. Novikov, G.G. Malliaras, *Phys. Rev. B* 73 (2006) 033308.
- [4] A. Kraft, A.C. Grimsdale, A.B. Holmes, *Angew. Chem. Int. Ed.* 37 (1998) 402.
- [5] U. Mitschke, P. Baeuerle, *J. Mater. Chem.* 10 (2000) 1471.
- [6] B.N. Limketkai, M.A. Baldo, *Phys. Rev. B* 71 (2005) 085207.
- [7] C.H. Chen, J. Shi, C.W. Tang, *Macromol. Symp.* 125 (1997) 1.
- [8] R.H. Friend, R.W. Gymer, A.B. Holmes, J.H. Burroughes, R.N. Marks, C. Taliani, D.C.C. Bradley, D.A.D. Santos, J.L. Brédas, M. Lögdlund, W.R. Salaneck, *Nature* 397 (1999) 121.
- [9] M.A. Baldo, M.E. Thompson, S.R. Forrest, *Nature* 403 (2003) 750.
- [10] Q. Huang, J. Li, G.A. Evmenenko, P. Dutta, T.J. Marks, *Chem. Mater.* 18 (2006) 2431.
- [11] J. Huang, T. Watanabe, K. Ueno, Y. Yang, *Adv. Mater.* 19 (2007) 739.
- [12] H. You, Y. Dai, Z. Zhang, D. Ma, *J. Appl. Phys.* 101 (2007) 026105.
- [13] S.A. Van Slyke, C.H. Chen, C.W. Tang, *Appl. Phys. Lett.* 69 (1996) 2160.
- [14] Y. Lee, J. Kim, S. Kwon, C.K. Min, Y. Yi, J.W. Kim, B. Koo, M.P. Hong, *Organic Electron.* 9 (2008) 407.
- [15] L.S. Hung, C.W. Tang, M.G. Mason, *Appl. Phys. Lett.* 70 (1997) 152.
- [16] J. Lee, Y. Park, D.Y. Kim, H.Y. Chu, H. Lee, L.M. Do, *Appl. Phys. Lett.* 82 (2003) 173.
- [17] P. Piromreun, H.S. Oh, Y. Shen, G.G. Malliaras, J.C. Scott, P.J. Brock, *Appl. Phys. Lett.* 77 (2000) 2403.
- [18] S.J. Kang, D.S. Park, S.Y. Kim, C.N. Whang, K. Jeong, S. Im, *Appl. Phys. Lett.* 81 (2002) 2581.
- [19] C. Ganzorig, K. Suga, M. Fujihira, *Mater. Sci. Eng. B85* (2001) 140.
- [20] T. Wakimoto, Y. Fukuda, K. Nagayama, A. Yokoi, H. Nakada, M. Tsuchida, *IEEE Trans. Electron. Dev.* 44 (1997) 1245.
- [21] S.H. Kim, J. Jang, J.Y. Lee, *Appl. Phys. Lett.* 91 (2007) 103501.
- [22] J. Huang, G. Li, E. Wu, Q. Xu, Y. Yang, *Adv. Mater.* 18 (2006) 114.
- [23] X.D. Feng, C.J. Huang, V. Lui, R.S. Khangura, Z.H. Lu, *Appl. Phys. Lett.* 86 (2005) 143511.
- [24] T. Matsushima, C. Adachi, *Appl. Phys. Lett.* 89 (2006) 253506.
- [25] T.Y. Chu, J.F. Chen, S.Y. Chen, C.H. Chen, *Appl. Phys. Lett.* 89 (2006) 113502.
- [26] T.Y. Chu, J.F. Chen, S.Y. Chen, C.J. Chen, C.H. Chen, *Appl. Phys. Lett.* 89 (2006) 053503.
- [27] T.Y. Chu, S.Y. Chen, J.F. Chen, C.H. Chen, *J. Appl. Phys.* 45 (2006) 4948.
- [28] X. Zhou, M. Pfeiffer, J.S. Huang, J. Blochwitz-Nimoth, D.S. Qin, A. Werner, J. Drechsel, B. Maennig, K. Leo, *Appl. Phys. Lett.* 81 (2002) 922.
- [29] S.Y. Chen, T.Y. Chu, J.F. Chen, C.Y. Su, C.H. Chen, *Appl. Phys. Lett.* 89 (2006) 053518.
- [30] T. Xiong, F. Wang, X. Qiao, D. Ma, *Appl. Phys. Lett.* 92 (2008) 263305.
- [31] T.R. Briere, A.H. Sommer, *J. Appl. Phys.* 48 (1977) 3547.
- [32] J. Huang, Z. Xu, Y. Yang, *Adv. Funct. Mater.* 17 (2007) 1966.
- [33] C.I. Wu, C.T. Lin, Y.H. Chen, M.H. Chen, Y.J. Lu, C.C. Wu, *Appl. Phys. Lett.* 88 (2006) 152104.
- [34] Y. Li, D.Q. Zhang, L. Duan, R. Zhang, L.D. Wang, Y. Qiu, *Appl. Phys. Lett.* 90 (2007) 012119.



- [35] A. Rihani, N. Boutabba, L. Hassine, S. Romdhane, H. Bouchriha, *Synth. Metals* 145 (2004) 129.
- [36] M.E. Aydin, F. Yakuphanoglu, T. Kılıçoğlu, *Synth. Metals* 157 (2007) 1080.
- [37] M.E. Aydin, F. Yakuphanoglu, J.-H. Eom, D.-H. Hwang, *Physica B* 387 (2007) 239.
- [38] S. Karg, W. Riess, V. Dyakonov, M. Schwoerer, *Synth. Metals* 54 (1993) 427.
- [39] W.-J. Shin, J.-Y. Lee, J.C. Kim, T.-H. Yoon, T.-S. Kim, O.-K. Song, *Organic Electron.* 9 (2008) 333.
- [40] S.M. Sze, *Physics of Semiconductor Devices*, second ed., Wiley-Interscience, New York, 1981.
- [41] K. Walzer, B. Maennig, M. Pfeiffer, K. Leo, *Chem. Rev.* 107 (2007) 1233.



## Realization of negative differential resistance and switching devices based on copper phthalocyanine by the control of evaporation rate

Jian Lin, Dongge Ma\*

State Key Laboratory of Polymer Physics and Chemistry, Changchun Institute of Applied Chemistry, Chinese Academy of Sciences, Graduate School of the Chinese Academy of Sciences, Changchun 130022, PR China

### ARTICLE INFO

#### Article history:

Received 20 October 2008

Received in revised form 18 November 2008

Accepted 22 November 2008

Available online 10 December 2008

#### PACS:

85.30.De

73.40.Sx

#### Keywords:

CuPc

Evaporation rates

NDR

Traps

WORM

### ABSTRACT

We have observed, respectively, a negative differential resistance (NDR) and switching conduction in current–voltage ( $I$ – $V$ ) characteristics of organic diodes based on copper phthalocyanine (CuPc) film sandwiched between indium-tin-oxide (ITO) and aluminum (Al) by controlling the evaporation rate. The NDR effect is repeatable, which can be well controlled by sweep rate and start voltage, and the switching exhibits write-once-read-many-times (WORM) memory characteristic. The traps in the organic layer and interfacial dipole have been used to explain the NDR effect and switching conduction. This opens up potential applications for CuPc organic semiconductor in low power memory and logic circuits.

© 2008 Elsevier B.V. All rights reserved.

### 1. Introduction

Organic molecular semiconductors have been intensively studied for more than twenty years due to their envisioned applications in flexible, low-cost and light-weight organic optoelectronics [1–4]. The physical processes of electrical transport in organic semiconductors (charge injection, transport, and space charge effects) have also been widely explored [5], which are quite different from the crystalline inorganic semiconductors. Considering the injection process can be viewed as a supply vs. demand problem, the current–voltage ( $I$ – $V$ ) characteristics in organic devices are generally dominated by the charge injection or transport processes in organic semiconductor. On the other hand, it was found experimentally that some or-

ganic devices showed negative differential resistance (NDR) characteristics [6–11] that have tremendous potential in the applications of low power memory and logic circuits, or irreversible switching currents which possibility of obtaining write-once-read-many-times (WORM) memories for archiving non-editable databases [12–14]. These devices based on organic semiconductors could satisfy the requirement in the low end of the market and some of them have been reported in recent years.

In this paper, we realized a single-layer diodes with repeatable NDR and switching exhibiting WORM memory in  $I$ – $V$  characteristics based on copper phthalocyanine (CuPc), a macrocyclic metal complex, which has been one of the most popular organic semiconductors with high thermal and chemical stability suitable for thin film preparations [15], and widely reported in electrical transport and switching in organic devices [4,16–18]. It was found experimentally that the CuPc exhibits distinctly different  $I$ – $V$  characteristics by merely changing the evaporation

\* Corresponding author. Tel.: +86 431 85262357; fax: +86 431 85262873.

E-mail address: [mdg1014@ciac.jl.cn](mailto:mdg1014@ciac.jl.cn) (D. Ma).

rates of the CuPc. Our results demonstrate that CuPc is a hopeful organic semiconductor as memory medium in organic diodes for the applications in low power information storage and logic circuits.

## 2. Experimental details

The fabricated device in this study was a single-layer sandwich structure. Indium-tin-oxide (ITO) coated on glass substrate was used as one of the electrodes. CuPc was firstly thermally evaporated on ITO coated glass substrate at a controlled evaporation rate. The high, normal, and low deposition rate (H, N and L for short) of CuPc was, respectively, 0.50, 0.10, and 0.05 nm/s. Then 150 nm aluminum (Al) was thermally deposited on the CuPc film as another electrode. If using calcium (Ca)/Al electrode, 10 nm Ca was first deposited and then 150 nm Al was capped on Ca. For the case of molybdenum oxide ( $\text{MoO}_3$ )/Al electrode, 3 nm  $\text{MoO}_3$  layer was firstly deposited. The thickness of CuPc film was about 400 nm. All of the deposition processes were carried out in a vacuum of  $10^{-4}$  Pa. The  $I$ - $V$  characteristics were performed by Keithley 2400 sourcemeter controlled by a computer, and the positive electric voltage was defined the Al electrode as positive bias. The atomic force microscope (AFM) measurements were carried out on a scanning probe microscope (SPA-300HV, Seiko Instruments, Inc.). All the electrical measurements were done in ambient condition without any device encapsulation.

## 3. Results and discussion

It was experimentally found that a large NDR is observed in  $I$ - $V$  characteristics only when the organic layer was deposited by high rates and the applied voltage starts from certain negative voltage. Fig. 1 shows the typical  $I$ - $V$  characteristics of the ITO/CuPc (H)/Al device between voltages of  $-16$  to  $16$  V. As sweeping the voltage from  $-16$  to

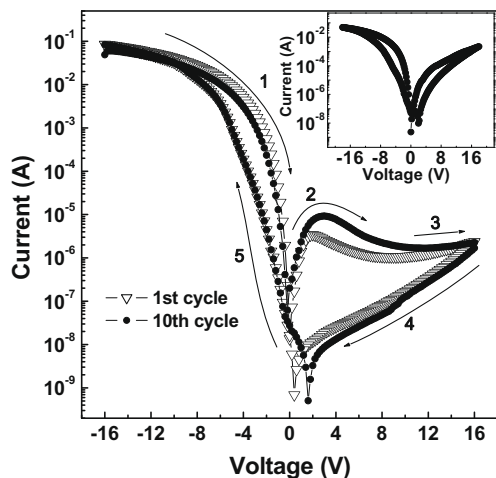


**Fig. 1.** Typical  $I$ - $V$  characteristics (the first cycle and tenth cycle) of the ITO/CuPc (H)/Al device. The arrows indicate the direction of voltage sweep. The insert shows the  $I$ - $V$  characteristics of ITO/CuPc (N)/Al.

positive bias, the current is initially high, and increases with bias voltage. When the bias voltage reaches a certain value, the current starts decrease with the bias, forming a NDR region. Finally, the current remained at a low current state from  $16$  V back to  $0$ . It can be seen that a high current state (ON state) and a low current state (OFF state) exist simultaneously at the same voltage in the positive region. It should be noted that the ON state and NDR characteristic can be recovered from the low current state by simply applying a negative bias voltage. However, the devices ITO/CuPc (N)/Al, whose organic layer deposited with normal rate, have no similar NDR  $I$ - $V$  characteristics, as shown in the insert of Fig. 1.

Furthermore, it can be seen that the occurrence of the hysteretic NDR and the ON/OFF current ratio depend strongly on the magnitude of the applied reverse start voltage in ITO/CuPc (H)/Al. As shown in Fig. 2, a higher negative start voltage leads to the occurrence of the larger hysteresis and higher ON/OFF current ratio, whereas the hysteresis and NDR vanish if the sweep voltage from negative is less than a critical value. The insert of Fig. 2 shows the currents of ON and OFF states at  $3$  V and the ON/OFF current ratio as a function of the negative sweep voltages. The maximum ON/OFF current ratio is over  $4600$ . It is noteworthy that the ON state current and ON/OFF current ratio are also greatly dependent on the sweep rate. Fig. 3 shows the  $I$ - $V$  characteristics of the ITO/CuPc (H)/Al device at different sweep rates after applying  $-16$  V reverse bias voltage for  $3$  s. It can be seen that a faster sweep rate results in larger ON current and larger ON/OFF current ratio.

The similar hysteresis and NDR phenomenon in  $I$ - $V$  characteristics are also observed in ITO/CuPc (H)/Ca/Al devices. However, as inserting an electron-blocking layer of  $\text{MoO}_3$  between CuPc and Al to fabricate devices of ITO/CuPc (H)/ $\text{MoO}_3$ /Al, the NDR is disappeared and the hysteresis is greatly reduced. Fig. 4 gives the comparison in  $I$ - $V$  characteristics of three different devices of ITO/CuPc (H)/Al, ITO/

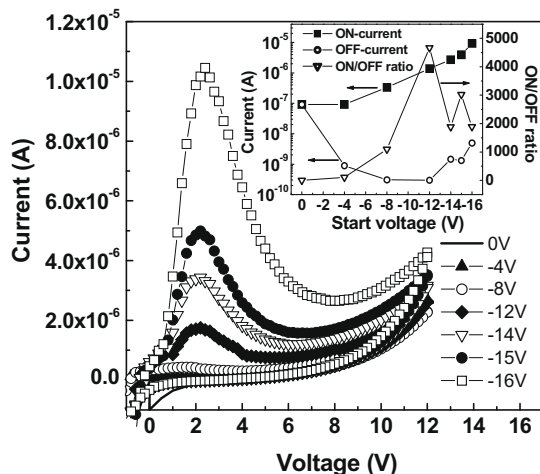


**Fig. 2.** Forward  $I$ - $V$  characteristics of the ITO/CuPc (H)/Al device at different negative sweep voltages. The ON state and OFF state currents at  $3$  V and the ON/OFF current ratio as a function of the negative sweep voltages are shown in the insert.

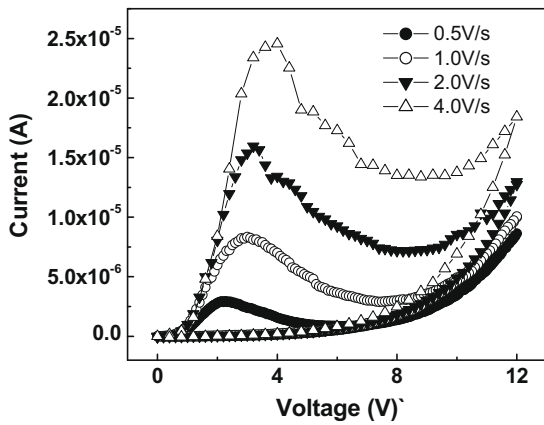


Fig. 3.  $I$ - $V$  characteristics of the ITO/CuPc/Al device at different sweep rates.

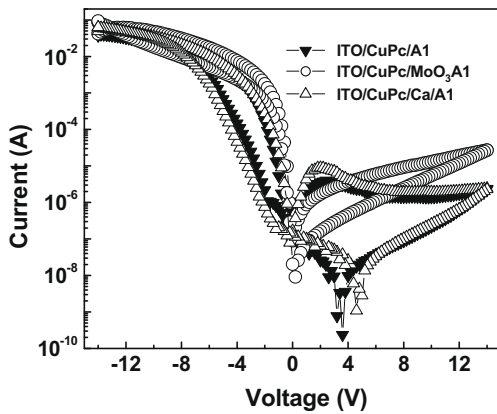


Fig. 4. Comparison of  $I$ - $V$  characteristics of the ITO/CuPc/Ca/Al, ITO/CuPc/MoO<sub>3</sub>/Al and ITO/CuPc/Al devices.

CuPc (H)/Ca/Al and ITO/CuPc (H)/MoO<sub>3</sub>/Al. This indicates that the electron injected in the device during the application of negative voltage plays an important role in the NDR properties.

However, it was found that the device ITO/CuPc (H/L)/Al with a 20 nm low-deposited CuPc layer between 270 nm high-deposited CuPc and Al electrode exhibit switching conduction in  $I$ - $V$  characteristics [19]. Fig. 5 shows the typical  $I$ - $V$  characteristics of the device ITO/CuPc (H/L)/Al, which were measured by scanning the voltage from 0 to  $V_{\max}$  (10 V) and then to 0. The current in ON state is increased linearly with the voltage and decreased abruptly as switching transition at a critical bias (about 4.8 V). Then the device remains the OFF state as the voltage sweeping to high value and back to 0. This OFF state will be retained permanently in the subsequent voltage sweeps. The typical ON/OFF current ratio observed in the sweep  $I$ - $V$  characteristics at 1.0 V, as shown in Fig. 5, is over  $5.6 \times 10^5$ . It was interestingly noted that the a repeatable NDR effect can be observed in the  $I$ - $V$  characteristics in the case of OFF state, as shown in the insert of Fig. 5. Fig. 6 shows the retention ability of the memory device, in which the cur-

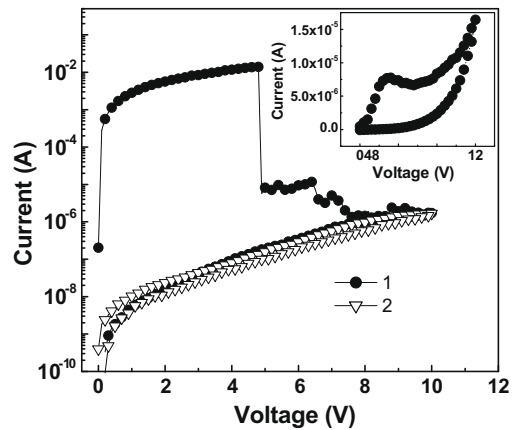


Fig. 5. Typical  $I$ - $V$  characteristics of the ITO/CuPc (H/L)/Al device, in which curve 1 is the switching  $I$ - $V$  characteristics from ON to OFF state, and curve 2 is the  $I$ - $V$  characteristics of OFF state. Insert shows the NDR effect in the OFF state, which is similar to the ITO/CuPc (H)/Al.

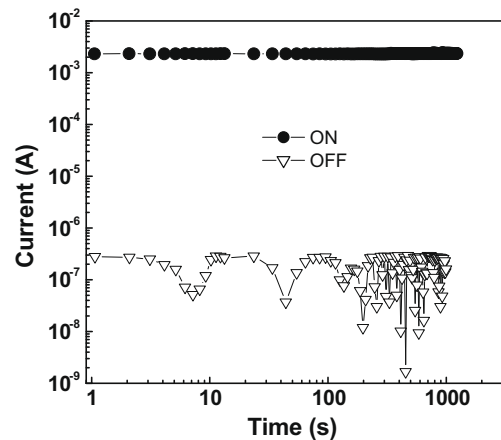


Fig. 6. The retention ability of the memory device ITO/CuPc (H/L)/Al. The currents of the ON and OFF states were measured continuously under a constant bias of 1.0 V.

rents of the ON and OFF states were measured continuously under a constant bias of 1.0 V. It can be seen that the device remains good stability without any degradation.

We further studied the  $I$ - $V$  characteristics of the ITO/CuPc (H/L)/Al device, and found that the currents of OFF states were injection limited, as previous reported [20,21], whereas the ON state currents are ohmic conduction. This means that a perfect ohmic contact at the interface of CuPc (L)/Al is formed as the currents transit to ON state from OFF state, i.e. the change of the injection barrier height leads to the ON-OFF state transition.

It is worthy noting that the voltage value shifts away zero as the current reaches the maximum value in the case of ITO/CuPc (H)/Al. This should indicate the existence of space charges in devices. Furthermore, as shown above, only by applying certain negative voltage bias can lead to the NDR. The bias polarity dependence demonstrates that the NDR characteristics in our devices should be due to the interface

effects [22], directly related to the interfacial traps [23], leading to the formation of space charge due to trapping.

To clearly demonstrate the mechanism of the NDR and switching conduction, the energy band diagrams of the devices at forward bias are depicted in Fig. 7. For the case of ITO/CuPc (H)/Al devices, some electrons are injected and trapped in CuPc near the side of Al at sufficient negative bias (ITO as anode and Al as cathode). In this state, when the voltage is swept to the positive value, the electric field at the Al/CuPc interface increases due to the existence of the trapped electrons, resulting in the band bending, thus greatly decreasing the injection barrier of holes, leading to high hole current, as shown in Fig. 7a. However, with the increase of forward voltage, the trapped electrons are released and neutralized by injected holes. In this case, the band bending will be gradually flattened, and the current will decrease due to the increase of hole injection barrier, forming the NDR region, which can be seen in Fig. 7b. When the voltage is swept faster, the current is larger because the processes of trapping electron releasing and injection barrier rising are slow. As the voltage keeps on increasing and sweeping back to zero, the current will remain at the low current state. Obviously, the processes are reproducible by simply applying a negative voltage.

The same operational mechanism can be observed in ITO/CuPc (H)/Ca/Al device. In this device, the low electron

injection barrier of the Ca electrode with respect to the case of Al electrode leads to more electrons to be trapped in CuPc near Ca electrode, resulting in larger NDR. However, for the case of ITO/CuPc (H)/MoO<sub>3</sub>/Al devices, the MoO<sub>3</sub> interfacial layer possesses a blocking role of electrons [24]. In this case, no more trapped electrons by applying negative bias voltage can make the processes of the band bending and band flattening with bias. Therefore, the NDR effect is disappeared. Accordingly, we can conclude that the interfacial traps and electron trapping are the main reasons of the NDR formation in our devices.

In the device ITO/CuPc (N)/Al, the hole injection barrier under positive voltage can also greatly decrease due to the existence of the trapped electrons, resulting in the band bending, leading to high hole current. However, there are much more traps because the trap concentration in the CuPc film will increase when the deposition rate decreasing [25]. It is much more difficult to release sufficient trapped electrons for flattening energy band and increasing the injection barrier. That is why the forward currents of the device with normal rate evaporated CuPc are larger and have no NDR effects, as shown in Fig. 7c.

As known, a very low deposition rate of organic molecules generally results in the much larger grain size [19]. It is well established that metal atoms can migrate inside the organic layer during the evaporation of a top electrode

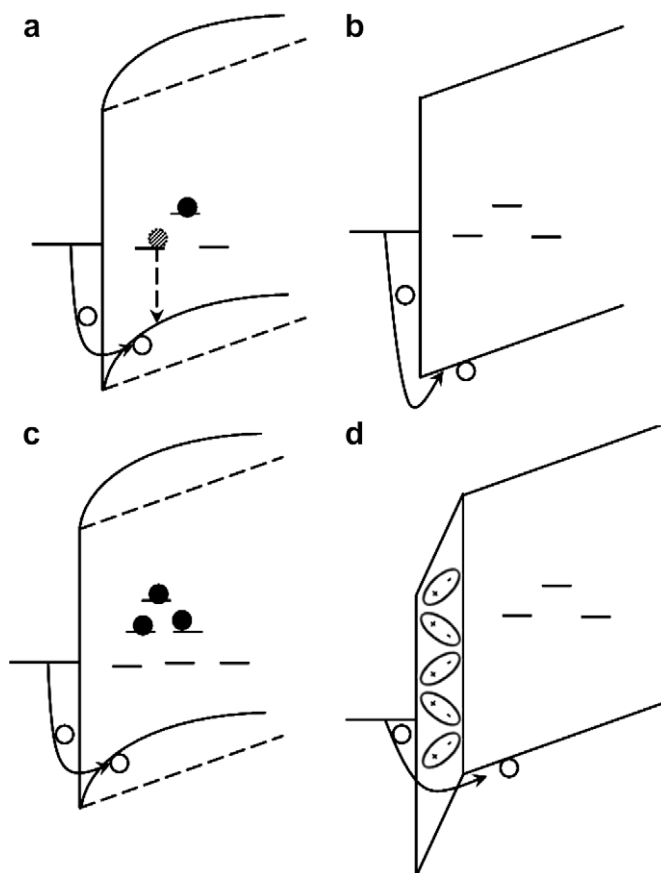


**Fig. 7.** Energy band diagrams (the side of anode) of the devices in the paper: (a) ON state of ITO/CuPc (H)/Al, (b) OFF state of ITO/CuPc (H)/Al or ITO/CuPc (H)/L)/Al, (c) ITO/CuPc (N)/Al, and (d) OFF state of ITO/CuPc (H/L)/Al.

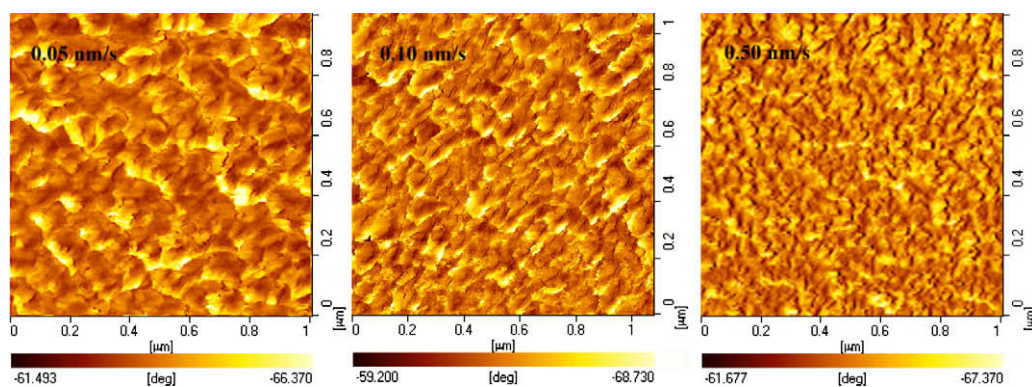


Fig. 8. AFM morphology images of the CuPc films with L, N, and H deposition rate on ITO, respectively.

and such an interdiffusion increases if the surface of organic film shows a larger grain size. As a result, a huge interface dipole is easily formed [26,27]. Fig. 8 show the AFM images of the morphology of CuPc films with L, N and H deposition rate, respectively. As seen, the film fabricated by low deposition rate indeed shows larger grain size. Therefore, in the case of ITO/CuPc (H/L)/Al device, since the interface dipole oriented in a suitable direction greatly pushes up the energy band of CuPc with respect to the vacuum level of metal, the barrier for hole injection is significantly reduced from a rectifying Schottky contact to an Ohmic contact. Then the hole injection from Al into organic layer is easier, forming the high ON state, as shown in Fig. 7d. This interface dipole can be destroyed due to a high space field caused by access hole injection, resulting in great increase of the barrier height for the hole injection, as shown in Fig. 7b. At this time, the hole injection is rather difficult due to higher barrier, leading to a abruptly decrease in current, and the destruction of the interface dipole under a critical bias voltage is irreversible. However, the injection barrier in the OFF state device may be temporarily decreased a little by the trapped electrons after negative biased, which is similar as the ITO/CuPc (H)/Al device.

#### 4. Conclusions

We have observed, respectively, a repeatable NDR effect and switching conduction in the  $I$ - $V$  characteristics of organic diodes based on CuPc film sandwiched between ITO and Al by the control of the CuPc deposition rate. It is found that a high deposition rate of CuPc results in a repeatable negative differential resistance (NDR), where a low deposition rate of CuPc near the metal electrode then leads to unrenovable switching property. The traps in the organic layer and interfacial dipole could well be used to explain the NDR effect and switching conduction. It is believed that these interesting characteristics could lead to more deep understanding of devices based on CuPc.

#### Acknowledgments

We thank the Hundreds Talents Program of Chinese Academy of Sciences, the National Science Fund for Distin-

guished Young Scholars of China (50325312), National Natural Foundation of China (50573075), Science Fund for Creative Research Groups of NSFC (20621401), Foundation of Jilin Research (20050517) and Ministry of Science and Technology of China (973 program No. 2002CB613400) for the support of this research.

#### References

- [1] L.S. Hung, C.H. Chen, *Mat. Sci. Eng. R.* 39 (2002) 143.
- [2] C.D. Dimitrakopoulos, P.R.L. Malenfant, *Adv. Mater.* 14 (2002) 99.
- [3] P. Peumans, S. Uchida, S.R. Forrest, *Nature (London)* 425 (2003) 158.
- [4] B. Mukherjee, A.J. Pal, *Org. Electron.* 8 (2007) 584.
- [5] A.B. Walker, A. Kambili, S.J. Martin, *J. Phys.: Condens. Matter.* 14 (2002) 9825.
- [6] L.D. Bozano, B.W. Kean, V.R. Deline, J.R. Salem, J.C. Scott, *Appl. Phys. Lett.* 84 (2004) 607.
- [7] S.Y. Quek, J.B. Neaton, M.S. Hybertsen, E. Kaxiras, S.G. Louie, *Phys. Rev. Lett.* 98 (2007) 066807.
- [8] R.A. Kiehl, J.D. Le, P. Candra, R.C. Hoye, T.R. Hoye, *Appl. Phys. Lett.* 88 (2006) 172102.
- [9] F. Verbakel, S.C.J. Meskers, R.A.J. Janssen, *J. Appl. Phys.* 102 (2007) 083701.
- [10] H.S. Majumdar, J.K. Baral, R. Österbacka, O. Ikkala, H. Stubb, *Org. Electron.* 6 (2005) 188.
- [11] C. Tu, D. Kwong, Y. Lai, *Appl. Phys. Lett.* 89 (2006) 252107.
- [12] S. Møller, C. Perlov, W. Jackson, C. Taussig, S.R. Forrest, *Nature* 426 (2003) 166.
- [13] E.Y.H. Teo, Q.D. Ling, Y. Song, Y.P. Tan, W. Wang, E.T. Kang, D.S.H. Chan, C. Zhu, *Org. Electron.* 7 (2006) 173.
- [14] Z. Liu, F. Xue, Y. Su, K. Varahramyan, *IEEE Electron. Dev. Lett.* 27 (2006) 151.
- [15] C.C. Leznoff, A.B.P. Lever, *Phthalocyanines, Properties and Applications*, vol. 1, VCH Publishers, New York, 1989.
- [16] H. Yamamoto, H. Kasajima, W. Yokoyama, H. Sasabe, C. Adachi, *Appl. Phys. Lett.* 86 (2005) 083502.
- [17] C.H. Tu, Y.S. Lai, D.L. Kwong, *Appl. Phys. Lett.* 89 (2006) 062105.
- [18] X.W. Tu, G. Mikaelian, W. Ho, *Phys. Rev. Lett.* 100 (2008) 126807.
- [19] J. Lin, D. Ma, *J. Appl. Phys.* 103 (2008) 024507.
- [20] B.N. Limketkai, M.A. Baldo, *Phys. Rev. B* 71 (2005) 085207.
- [21] A.K. Mahapatro, S. Ghosh, *J. Appl. Phys.* 101 (2007) 034318.
- [22] A. Sawa, T. Fujii, M. Kawasaki, Y. Tokura, *Appl. Phys. Lett.* 85 (2004) 4073.
- [23] P.H. Nguyen, S. Scheinert, S. Berleb, W. Brütting, G. Paasch, *Org. Electron.* 2 (2001) 105.
- [24] K.J. Reynolds, J.A. Barker, N.C. Greenham, R.H. Friend, G.L. Frey, *J. Appl. Phys.* 92 (2002) 7556.
- [25] R.D. Gould, *J. Phys. D: Appl. Phys.* 19 (1986) 1785.
- [26] A.C. Dürr, F. Schreiber, M. Kelsch, H.D. Carstanjen, H. Dosch, O.H. Seeck, *J. Appl. Phys.* 93 (2003) 5201.
- [27] M.A. Baldo, S.R. Forrest, *Phys. Rev. B* 64 (2001) 085201.



## Performance and stability of *poly*(phenylene vinylene) based polymer light emitting diodes with caesium carbonate cathode

Riikka Suhonen<sup>a,c,\*</sup>, Ralf Krause<sup>a</sup>, Fryderyk Kozłowski<sup>a</sup>, Wiebke Sarfert<sup>a</sup>, Ralph Pätzold<sup>b</sup>, Albrecht Winnacker<sup>c</sup>

<sup>a</sup>Siemens AG, CT MM 1, Günther-Scharowsky-Straße 1, 91058 Erlangen, Germany

<sup>b</sup>OSRAM Opto Semiconductors GmbH, Leibnizstraße 4, 93055 Regensburg, Germany

<sup>c</sup>Department of Material Science VI, University Erlangen-Nuremberg, Martensstraße 7, 91058 Erlangen, Germany

### ARTICLE INFO

#### Article history:

Received 9 June 2008

Received in revised form 17 November 2008

Accepted 26 November 2008

Available online 6 December 2008

#### PACS:

73.00.00

#### Keywords:

PLED

*Poly*(phenylene vinylene)

Lifetime

Caesium carbonate

### ABSTRACT

We have studied the phenomena resulting from the combination of a hole-conducting *poly*(phenylene vinylene) (PPV) based light emitting polymer with a highly efficient electron injection layer of caesium carbonate ( $\text{Cs}_2\text{CO}_3$ ) in light emitting diodes. A strong dependence between the thickness of the applied  $\text{Cs}_2\text{CO}_3$  and the electro-optical performance of the diodes is detected and already with ultrathin  $\text{Cs}_2\text{CO}_3$  layers high efficiency diodes are achieved. The  $\text{Cs}_2\text{CO}_3$  is shown to diffuse into the polymer layer leading to an increased electron density but also quenching of both electro and photoluminescence when the amount of applied  $\text{Cs}_2\text{CO}_3$  is increased. During electrical stressing the electron density decreases assumably through degradation of the *n*-doping and quenching  $\text{Cs}_2\text{CO}_3$  species inducing an unusual increasing luminescence behavior.

© 2008 Elsevier B.V. All rights reserved.

## 1. Introduction

Ever since their discovery polymer light emitting diodes (PLEDs) have raised great attention due to their potential in fabrication of low-cost light emitting devices [1,2]. Due to their solution processability and mechanical flexibility, PLEDs offer a possibility to be applied on flexible substrates with traditional roll-to-roll printing methods [3]. The potential applications for these devices include ultra-thin, ultra-light, low power consumption displays and lighting elements. Although some products containing PLED displays are already commercially available, a lot of research and development is still ongoing in order to enhance the

efficiency and especially the long-term stability of the materials involved in these polymer based devices.

The standard structure of a PLED consists of a transparent substrate and anode on which a hole-injection layer (HIL) is applied from solution. The HIL is then covered with a light emitting polymer (LEP) film followed by a vacuum deposited low work function metal electron injection layer (EIL) and a protective higher work function metal cathode. This asymmetric electrode structure is designed to supply the injection of both electrons and holes in the LEP-layer in order to achieve as efficient exciton formation as possible. Besides the injection of the charge carriers, also their transport in the LEP must be sufficient enough to ensure fast response times and low power consumption of the devices.

“Superyellow-PPV” (PDA-132 from Merck KGaA) is known as an efficient alkoxy-phenyl-substituted *poly*(phenylene vinylene) (PPV) based light emitting polymer [4].

\* Corresponding author. Address: Siemens AG, CT MM 1, Günther-Scharowsky-Straße 1, 91058 Erlangen, Germany. Tel.: +49 9131 731300; fax: +49 9131 732209.

E-mail address: [riikka.suhonen.ext@siemens.com](mailto:riikka.suhonen.ext@siemens.com) (R. Suhonen).

Like PPV-polymers in general, also SY is a hole-dominant polymer meaning that the hole mobility is higher than the mobility of electrons along the polymer chains [5–7]. Applying a low work function metal, like barium in this study, on top of the SY improves the electron injection from the aluminum cathode and thus also the diode performance significantly. Even though the electron injection is improved, due to the low electron mobility and the presence of electron traps in the PPV-polymer, the emission zone is still located in the vicinity of the cathode leading in to a partial loss of excitons via non-radiative energy transfer to the metal cathode [5,8]. Therefore, more efficient electron injection would be required to push the emission zone further away from the cathode thus minimizing the quenching and resulting in diodes with even higher efficiency due to the better balance between the charge carriers. Caesium carbonate ( $\text{Cs}_2\text{CO}_3$ ) has been reported to result in very low work function surfaces when fabricated via thermal evaporation [9]. Recently,  $\text{Cs}_2\text{CO}_3$  has also been shown to efficiently function as a solution processed electron injection layer in PLEDs as well as an *n*-dopant in the electron transport layer in vacuum deposited small molecule based OLEDs [10–14].

In this work, a thin layer of  $\text{Cs}_2\text{CO}_3$  was applied between the SY and aluminum by thermal evaporation to explore the effects initiated by a highly efficient electron injection layer being deposited on top of a highly efficient, hole-dominated LEP. As expected, diodes with higher efficiency were achieved with a SY– $\text{Cs}_2\text{CO}_3$  structure in comparison to the traditional SY–Ba structure. The strong increase in the electron injection of the  $\text{Cs}_2\text{CO}_3$  diodes is apparently caused by a highly conductive, *n*-doped layer resulting from the charge transfer reaction between  $\text{Cs}_2\text{CO}_3$  and SY, where by the magnitude of the reaction and resulting effects depend strongly on the amount of the applied  $\text{Cs}_2\text{CO}_3$ . This conclusion can be drawn from the LIV, impedance and photoluminescence measurements of the diodes with Ba and  $\text{Cs}_2\text{CO}_3$  cathodes. Impedance spectrometry (AC-field with varying frequency) is a powerful tool for investigation of the interfaces between organic layers and the effects of an *n*-doped layer on conductance and capacitance behavior have been shown in literature [15]. The tendencies in the impedance spectra measured for our  $\text{Cs}_2\text{CO}_3$  diodes align perfectly with the published study [15] implying that *n*-doping of the SY and the following increase in the number of intrinsic electrons indeed is the source of the more efficient electron injection. Further indications on the formation of an *n*-doped region are the quenching of the intensity and the shift of the maximum both in electro- and photoluminescence spectra. With the help of the simulated EL-spectra the shift in the maximum is concluded to result from the alteration in the location of the emission zone. A quenching, *n*-doped region would also consequentially explain the quenching of the intensity in the EL and PL spectra.

For industrial applications the long-term stability of the light emitting devices is of outmost importance and therefore the behavior of the  $\text{Cs}_2\text{CO}_3$  diodes during electrical stressing was investigated both electrically and optically. It is shown that the behavior of the highest efficiency  $\text{Cs}_2\text{CO}_3$ -diodes during electrical stressing is comparable to the behavior of the Ba-cathode. Interestingly, with thicker

$\text{Cs}_2\text{CO}_3$  layers, after an initial decay the light-output of the diodes increases strongly reaching a maximum near the initial luminescence. We attribute this behavior to result from a better charge carrier balance and the simultaneous decrease in the number of the quenching  $\text{Cs}_2\text{CO}_3$  species in the SY-layer. These conclusions are drawn based on the results from LIV, impedance and photoluminescence measurements before, during and after the electrical stressing.

## 2. Experimental

The poly(3,4-polyethylenedioxythiophene) poly(styrene sulfonate) (PEDOT:PSS) used in this study was Baytron® PVP CH 8000 purchased from H.C. Starck. Superyellow (SY) (PDA-132) (5 mg/ml in toluene) was acquired from Merck KGaA as a ready-to-use solution and was used as received. The caesium carbonate  $\text{Cs}_2\text{CO}_3$  was purchased from Sigma–Aldrich and stored in an inert atmosphere due to its highly hygroscopic nature.

The light emitting devices studied in this work consisted of glass-substrate/ITO/PEDOT:PSS (120 nm)/SY (100 nm)/Ba or  $\text{Cs}_2\text{CO}_3$ /Al and were processed as follows. The indium tin oxide (ITO) covered glass-substrates were cleaned in ultrasonic bath followed by drying and reactive ion etching (RIE) treatment. PEDOT:PSS was spin-coated on ITO and baked in order to avoid water contamination of the following layers. The SY-polymer was spin-coated on PEDOT:PSS from toluene in an inert  $\text{N}_2$ -atmosphere followed by a heat treatment.  $\text{Cs}_2\text{CO}_3$  and the protecting aluminum electrode were thermally evaporated on the substrates. The applied thicknesses of  $\text{Cs}_2\text{CO}_3$  were 0.05, 0.10, 0.15, 0.25, 0.50, 0.75, 1.0 and 1.50 nm measured with a calibrated oscillating quartz crystal. Theoretically, one monolayer of  $\text{Cs}_2\text{CO}_3$  molecules is formed with about 0.50 nm layer thickness. The thickness of the reference barium layer used in this study was 3 nm. After the cathode deposition, the diodes were encapsulated in an inert argon atmosphere followed by measurements in atmospheric conditions. The active area of the devices was 4 mm<sup>2</sup>.

The current–voltage characteristics of the diodes were measured with a computer controlled Keithley 238 high current source measure unit and the luminescence and spectra with a calibrated spectral camera Photo Research PR650. The influence of the varying location of the emission zone on the EL spectrum was simulated with commercially available optical simulation software *etfos* (FLUXiM) [16]. In order to study the interfacial properties of the SY-dielectric, impedance spectroscopy in a frequency range of 5 Hz–10 MHz was performed with a Hewlett Packard 4192A LF Impedance Analyzer.

## 3. Results and discussion

### 3.1. Diode performance dependency on the amount of applied $\text{Cs}_2\text{CO}_3$

#### 3.1.1. LIV characteristics

When  $\text{Cs}_2\text{CO}_3$  is used as an electron injection layer on the hole-dominant superyellow polymer, already with ul-



tra-thin layers a significant change in the LIV-characteristics of the diodes is detected. At a constant bias of 4.0 V, the current density of the diodes with only aluminum and 0.05 nm  $\text{Cs}_2\text{CO}_3$  is almost equal (Fig. 1a). However, the light-output at a constant 25 mA/cm<sup>2</sup> current density of the device with only Al as cathode material is roughly two orders of magnitude lower in comparison to the  $\text{Cs}_2\text{CO}_3$  diode (Fig. 2b). The unsubstantial difference in the current density but the significant difference in the luminescence indicates that the current is still hole-dominated in both devices (0 nm  $\text{Cs}_2\text{CO}_3$  device behaves like a single carrier device) but already an infinitesimal amount of  $\text{Cs}_2\text{CO}_3$  improves the electron injection into the SY-polymer in such a way that a substantial improvement in the light-output is detected. This behavior is in-line with the previously reported comparison between the Al and Ca cathodes [8]. As can be seen in Fig. 1a, when the thickness of the  $\text{Cs}_2\text{CO}_3$  layer is further increased, the current density at 4.0 V bias is also increased reaching its maximum at 0.50 nm after which the current density decreases going above the values of the reference Ba as the layer thickness of  $\text{Cs}_2\text{CO}_3$  reaches 1.50 nm.

Similarly with the current density plot in Fig. 1a, a curve with a maximum can also be seen in the efficiency versus  $\text{Cs}_2\text{CO}_3$  thickness plot at 4.0 V bias (Fig. 1b). The optimum ratio between the required voltage and the achieved light-output and therefore also the maximum efficiency (over a

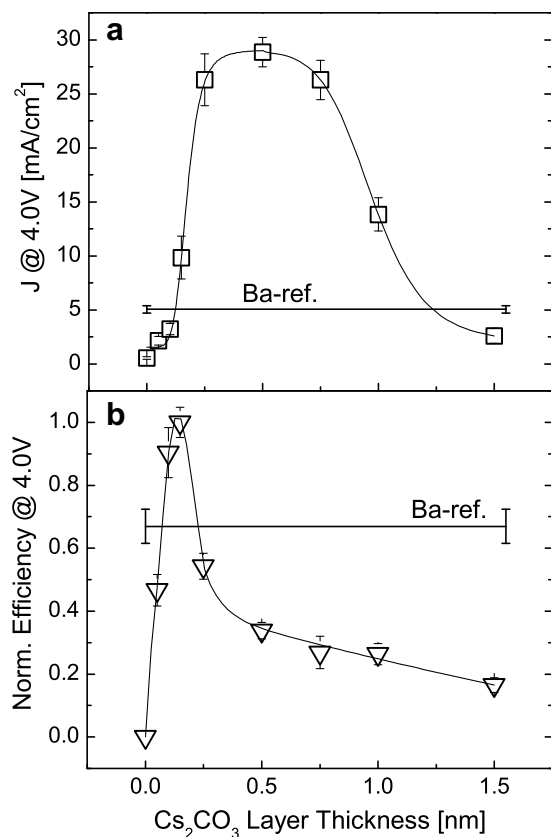


Fig. 1. (a) The current density and (b) the normalized power efficiency measured at 4.0 V for devices with varying  $\text{Cs}_2\text{CO}_3$  thickness and Ba.

third higher power efficiency [lm/W] at 4.0 V than reference Ba, Fig. 1b) is achieved with a layer thickness of 0.15 nm which corresponds not even to one monolayer of  $\text{Cs}_2\text{CO}_3$ .

The efficiency optimum can also be seen in the electroluminescence (EL) spectra of the devices detected at a constant current density of 25 mA/cm<sup>2</sup> (Fig. 2) as a significant increase in the EL-intensity when the  $\text{Cs}_2\text{CO}_3$  thickness is increased from 0 nm to 0.15 nm. As the  $\text{Cs}_2\text{CO}_3$  layer thickness increases above 0.15 nm, besides a decrease in the EL-intensity also a shift in the emission maximum towards higher wavelengths is detected (Fig. 2b). The  $\lambda_{\text{max}}$  for Ba and 0–0.15 nm  $\text{Cs}_2\text{CO}_3$  layers is located at 552 nm whereas the  $\lambda_{\text{max}}$  for thicker  $\text{Cs}_2\text{CO}_3$  layers is located at 596 nm. The onset of this red-shift can already be detected in the EL-spectrum of the 0.15 nm  $\text{Cs}_2\text{CO}_3$  as an increase of another peak next to the maximum.

### 3.1.2. Impedance and photoluminescence behavior

In order to investigate the change in the electrical properties of the  $\text{Cs}_2\text{CO}_3$  diodes further, impedance spectroscopy measurements were performed [15]. During these measurements a small harmonic AC-voltage is applied and both the amplitude and the phase difference of the AC-current are detected as a function of frequency ( $f$ ). The complex admittance ( $Y$  which is the inverse of the impedance) can then be written as a function of conductance ( $G$ ) and capacitance ( $C$ ) using the equation  $Y = G(\omega) + i\omega C(\omega)$ , where  $\omega = 2\pi f$ . While the DC-driven measurements (Figs. 1 and 2) provide information about the charge injection and transport properties in the devices, the information gained from the AC-measurements at zero applied bias is more related to the number of the intrinsic charge carriers in the device. As already mentioned,  $\text{Cs}_2\text{CO}_3$  has been shown to function as a very efficient  $n$ -dopant in small molecule based OLEDs [11,13,14]. An  $n$ -doping reaction would result in a formation of a charge-transfer complex and a following movement of the Fermi-level of the bulk material towards the donor-states introduced by the  $n$ -dopant [17]. Knowing that these doping states are immediately charged with electrons during deposition, the assumed  $n$ -doping reaction between SY and  $\text{Cs}_2\text{CO}_3$  should be detected as an increase in the number of intrinsic electrons in the layer.

In our measurements, a small 100 mV AC-pulse in the 5 Hz–10 MHz frequency range was applied between the electrodes and the detected capacitance and conductance as a function of frequency for different  $\text{Cs}_2\text{CO}_3$  thicknesses are shown in Fig. 3. From the curves it is clear that after the  $\text{Cs}_2\text{CO}_3$  thickness exceeds 0.15 nm, both the capacitance and the conductance of the SY-layer increase significantly at low frequencies. The strong increase in capacitance and conductance at low frequencies indicates that the applied  $\text{Cs}_2\text{CO}_3$  indeed forms a charge-transfer complex with SY thereby introducing doping states on which the electrons are then able to diffuse or tunnel with the oscillating field [15]. This  $n$ -doping is further enhanced by increasing the amount of applied  $\text{Cs}_2\text{CO}_3$  and thus also the intrinsic electron density in the SY layer. As the frequency of the AC-pulse increases above  $2 \times 10^5$  Hz (above  $2 \times 10^6$  Hz for 1.50 nm  $\text{Cs}_2\text{CO}_3$ ), the mobile intrinsic electrons are no

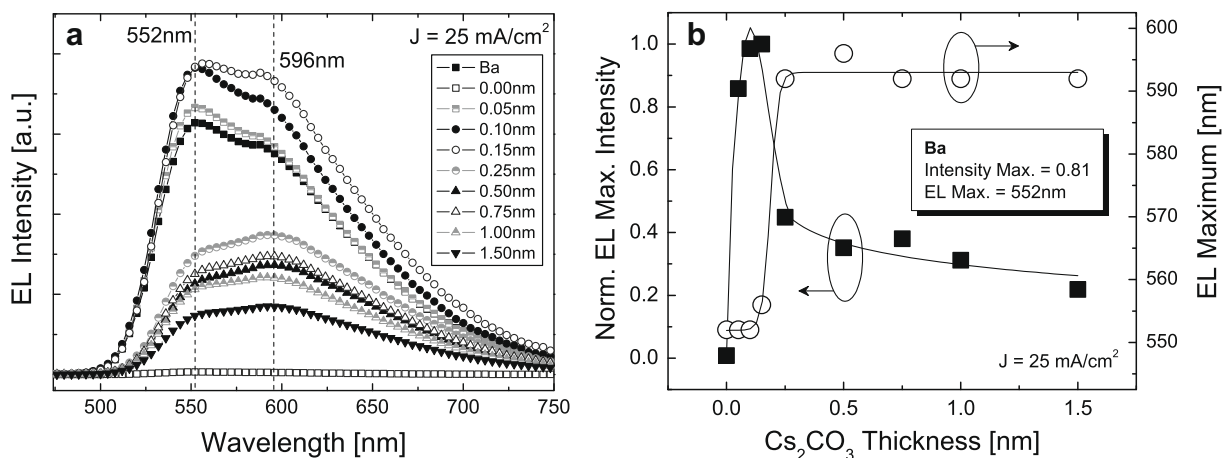


**Fig. 2.** The measured (a) EL-spectra for diodes with 0–1.50 nm  $\text{Cs}_2\text{CO}_3$  and reference Ba and (b) the normalized electroluminescence maximal intensity and the location of the electroluminescence maximum at a constant current density of  $25 \text{ mA/cm}^2$  for devices with varying  $\text{Cs}_2\text{CO}_3$  thickness.

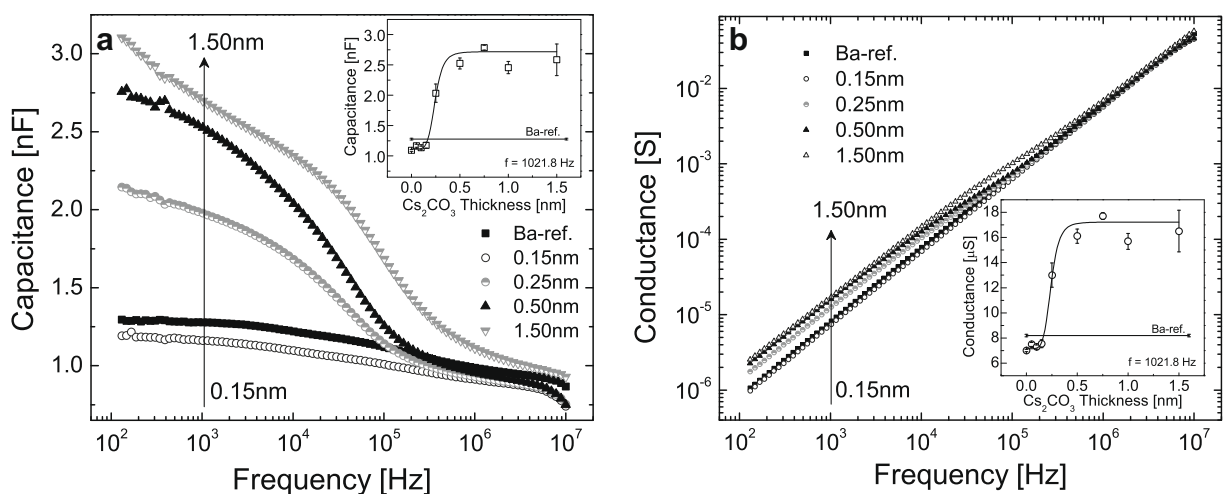


**Fig. 3.** Frequency dependency at zero bias of the (a) capacitance and (b) conductance of diodes with different  $\text{Cs}_2\text{CO}_3$  layer thickness. The inset in (a) shows the  $\text{Cs}_2\text{CO}_3$  layer thickness vs. capacitance at 1021.8 Hz and the inset in (b) the  $\text{Cs}_2\text{CO}_3$  layer thickness vs. conductance at 1021.8 Hz.

longer fast enough to follow the oscillation of the field and the dielectric (SY-polymer) response takes over both the capacitance and the conductance. This can be seen as an alignment of the capacitance and conductance curves at higher frequencies.

Gommans et al. [15] have reported similar results with another PPV-derivative as light emitting polymer and pure caesium metal as the cathode material. They concluded that the enhancement in capacitance and conductance is caused by the diffusion of the Cs atoms and following *n*-doping of the PPV-layer. This reaction was reported to lead into an increased hole transit time (resulting from a change in the field distribution inside the device due to band bending and potential drop at the cathode interface) and improved electron injection and/or higher electron mobility. In our study, diffusion profiles are not measured but from a simple calculation of the dielectric thickness derived from the geometrical capacitance ( $C = \epsilon_0 \epsilon A/d$ ), the calcu-

lated SY thickness at 1 kHz frequency for the thicker  $\text{Cs}_2\text{CO}_3$  layers is only half of the SY thickness calculated to the Ba-diode. This significant decrease in the electrically visible layer thickness of the dielectric indicates a strong diffusion of the  $\text{Cs}_2\text{CO}_3$  into the polymer layer.

Another indication of the diffusion of  $\text{Cs}_2\text{CO}_3$  in the SY-layer is the quenching of the photoluminescence (PL) intensity (Fig. 4a and b). In previous studies it has been shown that both *p*- and *n*-type dopants quench the EL and PL intensities as they are diffused into the emissive layer via exciton-dopant (in EL and PL) and exciton-polaron (in EL) type quenching [18]. Unlike in the case of electroluminescence, where charge injection and charge transport contribute to the exciton distribution (emission zone) and thus to the emission spectrum, in the PL the response consists of the emission from homogeneously distributed excitons in the layer. As shown in Fig. 4b, the PL intensity maximum of these homogeneously distributed excitons decays expo-

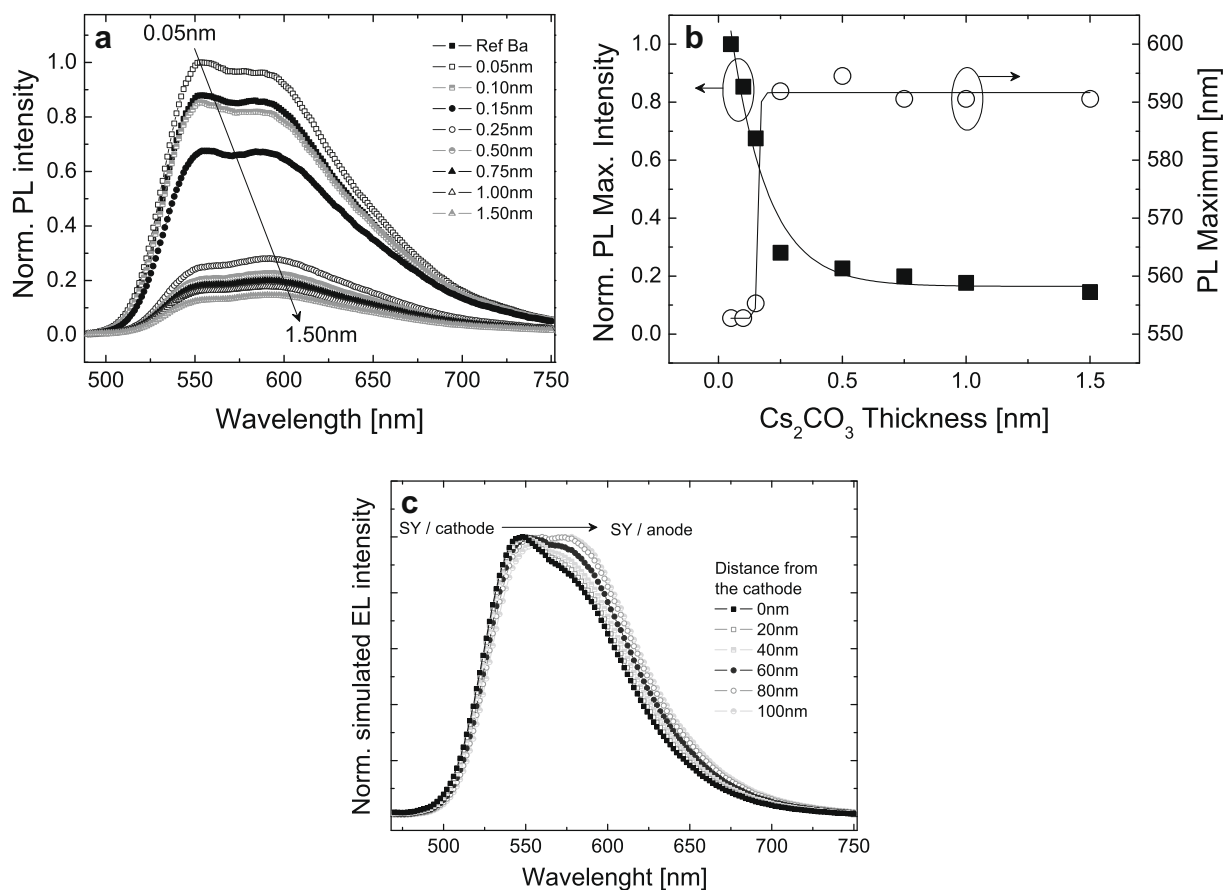


**Fig. 4.** The measured (a) PL-spectra for diodes with 0.05–1.50 nm Cs<sub>2</sub>CO<sub>3</sub> and reference Ba and (b) the PL-intensity and the location of the PL-maximum as a function of Cs<sub>2</sub>CO<sub>3</sub> thickness. (c) The EL-spectra simulated from the PL-spectrum of a pure superyellow-layer.

nentially as a function of increasing Cs<sub>2</sub>CO<sub>3</sub> thickness indicating clearly that the more Cs<sub>2</sub>CO<sub>3</sub> is applied the more the PL-emission is quenched. The mechanism for this non-radiative decay of the photoexcited excitons is assumed to be the exciton-dopant quenching [18].

In order to simulate the red-shift detected both in EL and PL spectra, a Gaussian-shaped 10 nm half-width emission zone was moved from the interface of the cathode towards the interface of the anode and was used as an input parameter for the optical simulation software (*etfos*) [16]. The shape, width and the position of the emission zone was chosen based on the hypothesis that Cs<sub>2</sub>CO<sub>3</sub> diffuses into the SY layer and quenches the emission starting from the cathode as a function of the amount of applied Cs<sub>2</sub>CO<sub>3</sub>. A red-shift similar to the measured PL- and EL-spectra (in Figs. 4a and 2a, respectively) can be detected if the emission zone is shifted in the optical simulation. As the emission zone is located at the SY-cathode interface, the simulated EL-spectrum has a similar shape than the spectra measured for Ba and 0.05–0.10 nm Cs<sub>2</sub>CO<sub>3</sub>. Whereas if the emission zone is located at the anode interface, the  $\lambda_{\text{max}}$  shifts towards higher wavelengths resembling the tendency of the PL- and EL-spectra measured for thicker Cs<sub>2</sub>CO<sub>3</sub> layers.

The red-shift detected in the PL-emission (Fig. 4a and b) is indeed a strong indication that by quenching the PL-

emission starting from the cathode interface, the diffused Cs<sub>2</sub>CO<sub>3</sub> leads into a formation of a gradually narrowing photo-emissive layer. If this quenching region would not exist, the excitons would emit homogeneously from the whole SY-layer and the shape and intensity of the PL-spectrum would remain the same for all cathodes and cathode thicknesses.

Based on the results from DC-, AC- and photo-excitation measurements a theory that Cs<sub>2</sub>CO<sub>3</sub> diffuses into the SY-layer forming a charge-transfer complex via an *n*-doping reaction is applicable. The magnitude of this *n*-doping is dependent on the amount applied Cs<sub>2</sub>CO<sub>3</sub> increasing the intrinsic electron density and decreasing the PL-intensity with increasing quantity of Cs<sub>2</sub>CO<sub>3</sub>. The long-term effects resulting from the diffused Cs<sub>2</sub>CO<sub>3</sub> are discussed in detail in the following chapter.

### 3.2. Long-term stability of the diodes with Cs<sub>2</sub>CO<sub>3</sub> and Ba cathodes

#### 3.2.1. LIV characteristics

The long-term stability of the SY-diodes with different Cs<sub>2</sub>CO<sub>3</sub> thicknesses was investigated in a lifetime measurement setup where the diodes were driven at a constant DC-

current corresponding to a certain initial luminescence. For diodes with a  $\text{Cs}_2\text{CO}_3$  thickness exceeding 0.25 nm, unusual increasing luminescence-curves were measured. Whereas in the case of  $\text{Cs}_2\text{CO}_3$  layer thickness below 0.25 nm the lifetime behavior was normally decreasing and aligned with the behavior of the Ba-diodes. In order to further investigate the unusual behavior of the thicker  $\text{Cs}_2\text{CO}_3$  diodes in comparison to the thinner  $\text{Cs}_2\text{CO}_3$ - and Ba-diodes during stressing, the device with 0.50 nm  $\text{Cs}_2\text{CO}_3$  is discussed here more in detail.

The behavior of the luminescence and driving voltage of the diodes with 0.15 nm  $\text{Cs}_2\text{CO}_3$ , 0.50 nm  $\text{Cs}_2\text{CO}_3$  and reference Ba are displayed in Fig. 5. The decay of the luminescence and the increase of the driving voltage of the Ba- and 0.15 nm  $\text{Cs}_2\text{CO}_3$  devices are standard behavior for SY-diodes and similar curves have also been reported elsewhere [19]. The luminescence of the Ba-diodes (and 0.15 nm  $\text{Cs}_2\text{CO}_3$ ) decays rapidly during the first hours of the measurement losing about 30% of its initial brightness. This has been reported to be due to the morphological changes of the PPV-film [20]. After this rapid decrease, the luminescence continues to decrease very slowly until

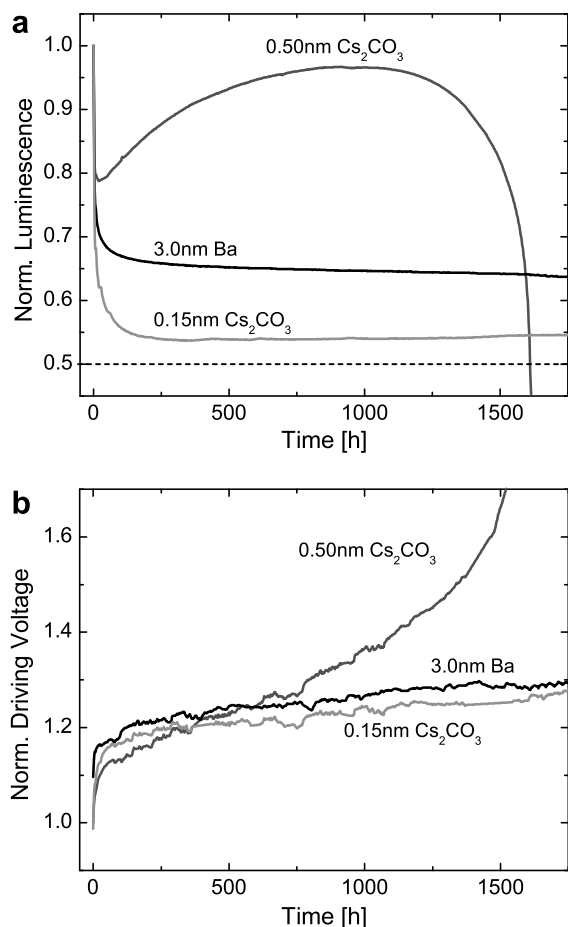
reaching its half-lifetime (50% of the initial brightness) after several thousands of hours. The luminescence over time for the 0.50 nm  $\text{Cs}_2\text{CO}_3$ -device shows similar rapid decrease in the beginning of the stressing but starts to increase again already after 30 h of stressing. The luminescence continues to increase until after reaching its maximum value at 1000 h, a decrease begins leading into a device failure after 1600 h of stressing.

After the initial rapid increase, the driving voltage of the Ba-diode (and 0.15 nm  $\text{Cs}_2\text{CO}_3$ ) continues to increase slowly during stressing (Fig. 5b). The gradually increasing driving voltage of the 0.50 nm  $\text{Cs}_2\text{CO}_3$ -diode is faster than that of the Ba-diode (and 0.15 nm  $\text{Cs}_2\text{CO}_3$ ) and after 550 h lifetime, the  $\text{Cs}_2\text{CO}_3$ -diode already consumes more voltage for its constant current than the Ba-diode.

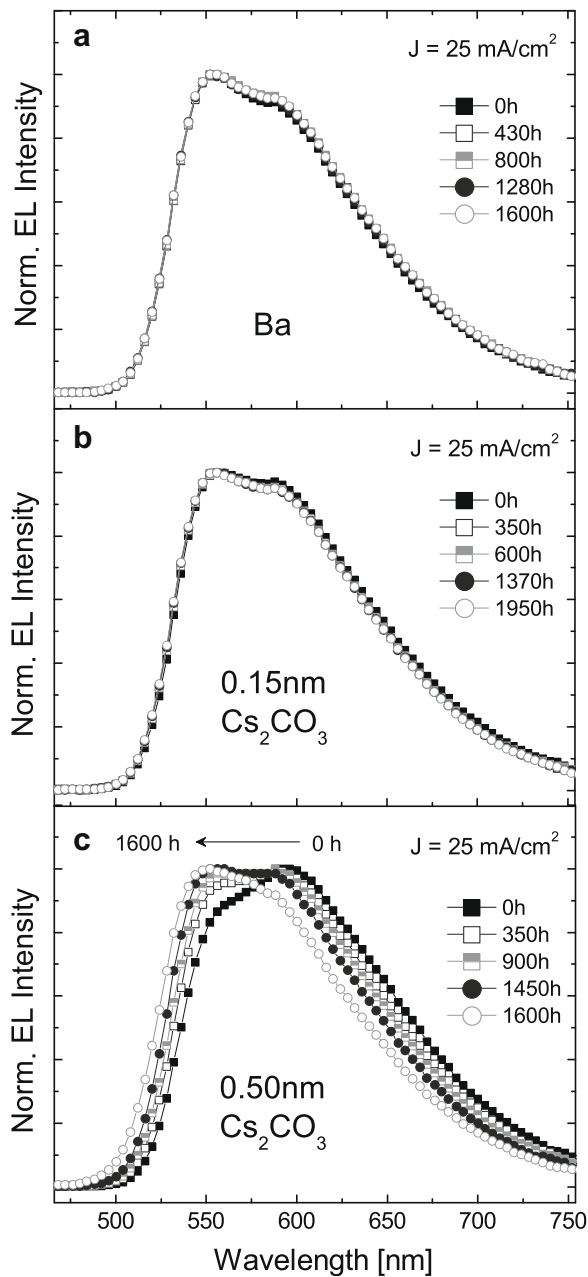
The increasing luminescence behavior seen in Fig. 5a resembles the published luminescence curves of the polymer light emitting electrochemical cells (PLEC). In PLEC-devices, under the influence of an applied electric field, the ionic species mixed into the polymer move to the electrode interfaces thereby enhancing the charge injection and leading to a relatively slow formation of a light emitting junction. The formation of this light emitting junction is detected as an increasing luminescence under electrical stressing. If such an ion drift were to happen also in the studied devices during stressing, a decrease in the driving voltage would be expected due to the enhanced charge injection [19]. This is however not the case but the driving voltage of the 0.50 nm  $\text{Cs}_2\text{CO}_3$  device (that shows the increasing luminescence) increases with increasing stressing time indicating that the injection and/or transport in the devices rather degrades than improves during electrical stressing. This could mean that the charge-transfer complexes providing the electrons to the LUMO of the SY, degrade during stressing weakening the electron injection and/or transport and thus increasing the resistance and driving voltage in the layer.

Fig. 6 shows the electroluminescence spectra of the SY-devices with Ba, 0.15 nm  $\text{Cs}_2\text{CO}_3$  and 0.50 nm  $\text{Cs}_2\text{CO}_3$  cathodes measured during stressing. For Ba and 0.15 nm  $\text{Cs}_2\text{CO}_3$  the spectra remain unchanged whereas a significant blue shift is detected in the emission maximum of the 0.50 nm  $\text{Cs}_2\text{CO}_3$ -diode with increasing stressing time (Fig. 6c). According to the optical simulations shown in Fig. 4c, this shift could result from a movement of the emission zone from the interface of the anode towards the interface of the cathode. Previously, an identical blue shift was detected as the  $\text{Cs}_2\text{CO}_3$  layer thickness decreased from 1.50 nm to 0.05 nm (Fig. 2a). The shift in the emission zone and the increasing driving voltage could result from the decreasing electron contribution in the SY-layer during electrical stressing. As Gommans et al. [15] reported the doping reaction changes the field distribution in the device leading to an increased hole transit time. If the doping reaction between SY and  $\text{Cs}_2\text{CO}_3$  degrades during stressing, that would also result in a gradually decreasing hole transit time. The decreasing hole transit time could then at least partly induce the shift in the location of the emission zone and thus also a shift in the EL-maximum.

The shift in the EL-spectrum is neither visible in the diode with Ba-cathode (Fig. 6a) nor with the thinner



**Fig. 5.** (a) Luminescence and (b) driving voltage behavior during lifetime for Ba, 0.15 nm  $\text{Cs}_2\text{CO}_3$  and 0.50 nm  $\text{Cs}_2\text{CO}_3$  cathodes measured at a constant 22 °C temperature. The diodes were driven at a constant DC-current calibrated to correspond 1000  $\text{cd/m}^2$  initial luminescence.



**Fig. 6.** Normalized electroluminescence spectra measured during stressing for (a) Ba, (b) 0.15 nm  $\text{Cs}_2\text{CO}_3$  and (c) 0.50 nm  $\text{Cs}_2\text{CO}_3$  cathodes.

0.15 nm  $\text{Cs}_2\text{CO}_3$  (Fig. 6b). This suggests that the emission zone in the Ba- and 0.15 nm  $\text{Cs}_2\text{CO}_3$  devices remain unchanged during stressing.

### 3.2.2. Impedance and photoluminescence behavior

While the conductance (and the capacitance, not shown here) of the 0.50 nm  $\text{Cs}_2\text{CO}_3$  diode in the low frequency range is strongly decreased during stressing (Fig. 7c), the conductance of the Ba-reference and 0.15 nm  $\text{Cs}_2\text{CO}_3$  diodes remain relatively constant during the measured time (Fig. 7a and b).

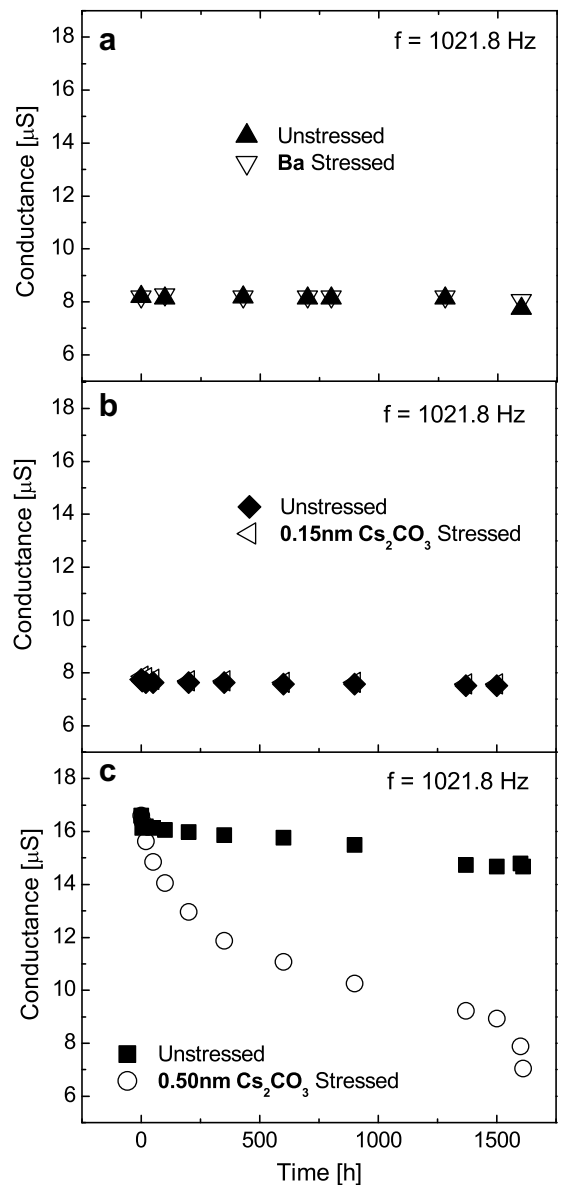


**Fig. 7.** The change in the conductance of (a) Ba, (b) 0.15 nm  $\text{Cs}_2\text{CO}_3$  and (c) 0.50 nm  $\text{Cs}_2\text{CO}_3$  diodes at 1021.8 Hz frequency during electrical stressing. "Unstressed" indicates to the pixel which has not been under an influence of a DC electric field and "Stressed" to a pixel that has been electrically stressed.

The decreasing conductance, the increasing driving voltage and the shift in the emission zone are all indications of the decrease in the electron contribution during electrical stressing in the 0.50 nm  $\text{Cs}_2\text{CO}_3$  diode. Knowing that before stressing, the SY-diode with 0.50 nm  $\text{Cs}_2\text{CO}_3$  has a very high density of electrons on the cathode side of the polymer which then gradually decreases during stressing and assuming that the hole transit time in the SY decreases as the doping degrades, it can be assumed that the ratio between the charge carriers changes from electron domination via optimal balance to a hole domination. This variation in the charge carrier balance could at

least partly explain the increasing luminescence of the  $\text{Cs}_2\text{CO}_3$  diode during stressing, the maximum luminescence representing the optimal charge carrier balance.

The slight decrease in the conductance of the unstressed  $\text{Cs}_2\text{CO}_3$  diode visible in Fig. 7c could be either due to the repeated DC-measurements and following degradation of the *n*-doping, or due to storage instability. The storage stability of the SY- $\text{Cs}_2\text{CO}_3$  diodes is currently under further investigation.

Interestingly, the PL-spectrum of the 0.50 nm  $\text{Cs}_2\text{CO}_3$  diode measured after the operational lifetime shows a strong increase in the PL intensity and also a blue shift in the spectral maximum (Fig. 8c) in comparison to a diode that has not been electrically stressed. This implies that

the  $\text{Cs}_2\text{CO}_3$  species which resulted into a quenched PL-spectrum (Fig. 4a and b) before electrical stressing are indeed no longer active in the SY-layer after stressing. Because no EL is detected at this point anymore we assume that the SY parts reacted with  $\text{Cs}_2\text{CO}_3$  have lost their conjugation leading into an electrical isolation of the still conjugated and emissive SY-chains. Also the electron injection is presumably decreased because of the decreasing number of the active  $\text{Cs}_2\text{CO}_3$ . Thus after the complete degradation of the diffused  $\text{Cs}_2\text{CO}_3$  species, the electron injection into the still conjugated parts of SY is no longer possible which leads into a complete disappearance of the electroluminescence. This decrease in the number of quenching units during stressing could also, together with the optimized charge balance, logically explain the increasing luminescence behavior (Fig. 5) of the thicker  $\text{Cs}_2\text{CO}_3$  devices.

In comparison to the PL-intensity before and after stressing, both the stressed Ba-diode and the stressed 0.15 nm  $\text{Cs}_2\text{CO}_3$  diode reach 70% from the intensity of the corresponding unstressed device. Also the stressed 0.50 nm  $\text{Cs}_2\text{CO}_3$  diode reaches about 75% from the intensity of the unstressed Ba-device. This is in good agreement with the EL-behavior where the electroluminescence is decreased to about 70% of the initial light-output (Fig. 5). The result also implies that after the initial morphological changes the SY-polymer is very stable against electrical stressing and goes through identical changes independently of the applied cathode material.

#### 4. Conclusions

We have investigated the effect of introducing a  $\text{Cs}_2\text{CO}_3$  interlayer as a cathode in PLED devices with a well known highly efficient PPV-derivative as a light emitting polymer. The  $\text{Cs}_2\text{CO}_3$  cathode strongly influences both the electrical and optical properties of the devices leading to a higher density of electrons and to a shift in the electroluminescence and photoluminescence emission maxima. These phenomena are dependent on the applied  $\text{Cs}_2\text{CO}_3$  layer thickness leading to more pronounced effects with increasing thickness. When the amount of the applied  $\text{Cs}_2\text{CO}_3$  is optimized, diodes with higher efficiency than the reference Ba but similar long-term behavior are obtained. After electrical and optical analysis of the  $\text{Cs}_2\text{CO}_3$  diodes before, during and after electrical stressing we conclude that as the amount of  $\text{Cs}_2\text{CO}_3$  is increased above the optimum,  $\text{Cs}_2\text{CO}_3$  diffuses in the SY-layer reacting with the conjugated double bonds forming an *n*-doped region on the cathode side of the polymer. This *n*-doping degrades during electrical stressing leading to a decrease in the intrinsic electron density and in the number of quenching units. These two phenomena result in a better charge carrier balance and weaker quenching of the emission in the device and thus into a shift in the emission zone. Consequently, an increasing luminescence curve and increased photoluminescence intensity during stressing are measured for the diodes with thicker  $\text{Cs}_2\text{CO}_3$  layer.

The results disclosed in this study are used to explain the functional principle of the  $\text{Cs}_2\text{CO}_3$ -cathode with a PPV-derivative as an emitting polymer. The outcome and

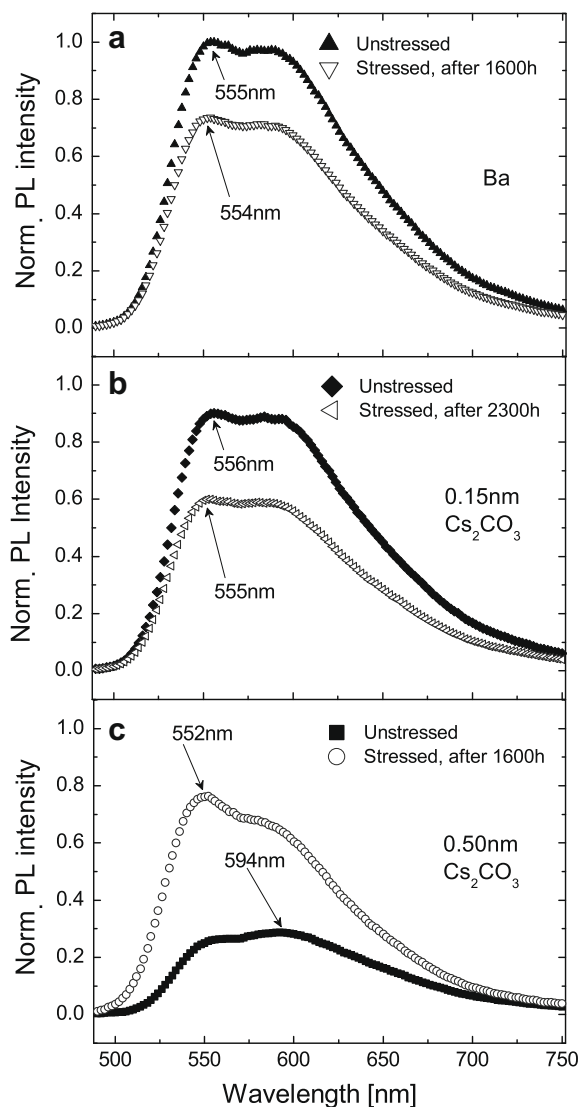


**Fig. 8.** PL intensity before and after a stressing period for (a) Ba, (b) 0.15 nm  $\text{Cs}_2\text{CO}_3$  and (c) 0.50 nm  $\text{Cs}_2\text{CO}_3$  diodes. The intensities are normalized to the PL-maximum of the unstressed Ba-diode in (a). "Unstressed" indicates to the pixel which has not been under an influence of a DC electric field and "Stressed" to a pixel that has been electrically stressed.

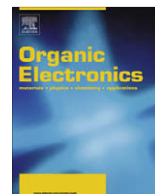
the experimental route will serve as a useful guideline for the future studies on other light emitting polymers and the  $\text{Cs}_2\text{CO}_3$ -cathode initiated effects on them.

### Acknowledgements

The authors would like to thank Dr. H. Becker from Merck KGaA, Dr. A. Kanitz, Dr. G. Schmid and U. Niedermeier from Siemens AG, and M. Kuik and H. Nicolai from the University of Groningen for the valuable discussions and Sabine Herder, Silke Scharner and Frank Ulsenheimer for their help in the device processing and measurements.

### References

- [1] J.H. Burroughes, D.D.C. Bradley, A.R. Brown, R.N. Marks, K. Mackay, R.H. Friend, P.L. Burns, A.B. Holmes, *Nature* 347 (1990) 539.
- [2] D. Braun, A.J. Heeger, *Appl. Phys. Lett.* 58 (1991) 1982.
- [3] M. Tuomikoski, R. Suhonen, M. Välimäki, T. Maaninen, A. Maaninen, M. Sauer, P. Rogin, M. Mennig, S. Heusing, J. Puetz, M.A. Aegerter, *Proc. SPIE* 6192 (2006) 619204.
- [4] H. Becker, H. Spreitzer, W. Kreuder, E. Kluge, H. Schenk, I. Parker, Y. Cao, *Adv. Mater.* 12 (2000) 42.
- [5] D.E. Markov, P.W.M. Blom, *Appl. Phys. Lett.* 87 (2005) 233511.
- [6] M.M. Mandoc, B. de Boer, G. Paasch, P.W.M. Blom, *Phys. Rev. B* 75 (2007) 193202.
- [7] F. Cicoira, C. Santato, *Adv. Funct. Mater.* 17 (2007) 3421.
- [8] P.W.M. Blom, M.C.J.M. Vissenberg, *Mater. Sci. Eng. R* 27 (2000) 53.
- [9] T.R. Briere, A.H. Sommer, *J. Appl. Phys.* 48 (1977) 3547.
- [10] J. Huang, G. Li, E. Wu, Q. Xu, Y. Yang, *Adv. Mater.* 18 (2006) 114.
- [11] C.-I. Wu, C.-T. Lin, M.-H. Chen, Y.-J. Lu, C.-C. Wu, *Appl. Phys. Lett.* 88 (2006) 152104.
- [12] J.-W. Ma, S.-W. Hwang, C.-C. Chang, S.F. Hsu, C.H. Chen, *SID 06 DIGEST P-196* (2006) 964.
- [13] M.-H. Ho, T.-M. Chen, P.-C. Yeh, S.-W. Hwang, C.H. Chen, *Appl. Phys. Lett.* 91 (2007) 233507.
- [14] G. Schmid, R. Krause, A. Hunze, G. Gieres, T. Dobbertin, B. Götz, *Presentation P010301* (2007) OEC-2007.
- [15] H.H.P. Gommans, M. Kemerink, G.G. Andersson, R.M.T. Pijper, *Phys. Rev. B* 69 (2004) 155216.
- [16] <http://www.fluxim.com>.
- [17] W. Gao, A. Kahn, *Org. Electron.* 3 (2002) 53.
- [18] C. Williams, S. Lee, J. Ferraris, A.A. Zakhidov, *J. Lumin.* 110 (2004) 396.
- [19] Y. Shao, G.C. Bazan, A.J. Heeger, *Adv. Mater.* 20 (2008) 1191.
- [20] I.D. Parker, Y. Cao, C.Y. Yang, *J. Appl. Phys.* 85 (1999) 2441.



# Raman spectroscopy applied to reveal polycrystalline grain structures and carrier transport properties of organic semiconductor films: Application to pentacene-based organic transistors

Horng-Long Cheng<sup>a,\*</sup>, Xin-Wei Liang<sup>a</sup>, Wei-Yang Chou<sup>a</sup>, Yu-Shen Mai<sup>a</sup>, Chou-Yu Yang<sup>a</sup>, Li-Ren Chang<sup>a</sup>, Fu-Ching Tang<sup>b</sup>

<sup>a</sup>Institute of Electro-Optical Science and Engineering, Center for Micro/Nano Science and Technology, and Advanced Optoelectronic Technology Center, National Cheng Kung University, Tainan 701, Taiwan, ROC

<sup>b</sup>Department of Physics, National Cheng Kung University, Tainan 701, Taiwan, ROC

## ARTICLE INFO

### Article history:

Received 27 August 2008

Received in revised form 28 November 2008

Accepted 1 December 2008

Available online 13 December 2008

### PACS:

72.80.Le

72.00.00

33.20.Fb

85.30.Tv

61.66.Hq

### Keywords:

Organic semiconductors

Charge transport properties

Organic thin-film transistors

Polycrystalline organic films

Raman spectroscopy

## ABSTRACT

We have fabricated high performance polycrystalline pentacene-based thin-film transistors using several dielectrics with different surface properties, including inorganic oxide and polymeric materials. These materials provide excellent samples for the analysis of charge transport properties, particularly the impact of the grain boundary and the molecular structural quality within the grain on the efficient charge transport. The carrier transport in polycrystalline organic films with grain structures is often interpreted using the grain boundary model. Assuming a large amount of charges are trapped at the boundaries, the model neglects the microstructural quality inside a grain. According to joint experimental and theoretical Raman spectra and normal modes analysis on these pentacene films, we present a new observation that the microscopic hopping transport parameters, i.e., intermolecular interactions and reorganization energy, in polycrystalline films govern the carrier transport. An obvious, positive correlation is found between the mobility and the molecular vibrational characteristics, especially the intermolecular vibrational coupling energy, under all varieties of grain size morphology. MicroRaman mapping methodology reveals that the grain size of pentacene films should not be taken for granted in structural quality and efficient charge transport. The microstructural qualities inside the grain play an important role in efficient charge transport.

© 2008 Elsevier B.V. All rights reserved.

## 1. Introduction

The use of organic semiconductors as active elements in optoelectronic devices has become prevalent, such as in thin-film transistors (TFTs), light-emitting diodes, solar cells, sensors, switches and others devices [1–3]. The charge transport properties of organic semiconductors [2–4] will have a critical role in integrating organic materials into useful devices and further optimizing device per-

formance. In particular, the organic TFT (OTFT) is one of the current hot topics in the research field of organic electronics applications, and the behavior of the charge transport can be investigated in these devices. Recently, the performance of OTFTs based on small molecule organic semiconducting materials, such as oligoacenes, oligothiophenes, and their derivatives, have demonstrated high carrier mobilities ( $\mu$ ) of above 1.0 and have surpassed that of amorphous silicon [2,5]. For most OTFT device applications, these small molecules are generally and easily deposited upon gate dielectrics using thermal evaporation to form thin-films. However, these organic thin-films are particularly challenging because of their polycrystalline

\* Corresponding author. Tel.: +886 6 2757575x65286; fax: +886 6 2095040.

E-mail address: [shlcheng@mail.ncku.edu.tw](mailto:shlcheng@mail.ncku.edu.tw) (H.-L. Cheng).



nature with a grainy texture morphology [1,2,5]: they do not form a single-crystal but instead are rife with multiple polymorphisms [6], grain boundary (GB) effects [7,8], orientation defects [9], static disorder [4c], and defects/impurities [10]. Despite existence of extensively studies devoted to the analysis of structure–carrier transport relationships of organic semiconducting films, carrier transport properties in polycrystalline films remain unclear, in particular, the role of GB and molecular microstructural quality within the grain.

Concerning the polycrystalline media, including inorganic materials (e.g., silicon, CdSe, etc.) and organic materials (e.g., oligoacenes, oligothiophenes, etc.), a grain boundary model has been proposed to research the charge transport mechanisms [7,11,12]. The  $\mu$  in a polycrystalline material could be described as

$$\frac{L_G + L_{GB}}{\mu} = \frac{L_G}{\mu_G} + \frac{L_{GB}}{\mu_{GB}} \quad (1)$$

where  $L_G$  and  $L_{GB}$  are the average lengths of the grain and GB, respectively;  $\mu_G$  and  $\mu_{GB}$  are the intragrain and the GB mobilities, respectively. The  $\mu$  qualities appear to be dominated by GB effects, assuming a large amount of charges are trapped at the boundary. For a small grain size, where  $L_{GB} \gg L_G$  and  $\mu_{GB} < \mu_G$ ,  $\mu$  is approaching the value of  $\mu_{GB}$ . Under this assumption, the microstructural quality within the intragrain can be neglected. Grain size dependent  $\mu$  values in oligothiophene [7] and pentacene [8] films have been reported. It has become demanding work to develop growth methods for realizing the super large grain (e.g., 100  $\mu\text{m}$  for pentacene [13]), producing single-crystalline films [14], or fabricating nanoscale OTFTs that enable charge transport in a single grain and eliminate GBs [15]. However, in some cases there was no direct relationship between  $\mu$  and grain size in organic films [5b,16]. Recently, we observed a tiny grain ( $\sim 0.1 \mu\text{m}$ ) pentacene OTFT with excellent electrical characteristics, including a  $\mu$  above  $1.0 \text{ cm}^2 \text{ V}^{-1} \text{ s}^{-1}$ , an on/off current ratio larger than  $10^6$ , and a subthreshold slope as low as 0.8 V/dec [17]. These results suggest that GBs may not act as a dominating mobility- and device performance-limiting mechanism. There are several interesting questions raised by the above discussion. For one, the traps are quite likely to reside in GBs rather than being uniformly distributed over the film according to the GB model, but what is the microstructural quality inside the grain? Is it acceptable to presume that there are single-crystal-like and/or trap-free microstructures inside the grain and that these should, therefore, be disregarded entirely?

In this study, to clarify the above questions, we applied microRaman spectroscopy to investigate the correlations between microscopic structural characteristics and charge transport properties in pentacene thin-films deposited on several dielectrics with different surface properties, including inorganic silicon dioxide ( $\text{SiO}_2$ ) and polymeric insulators. We discuss the structural characteristics of polycrystalline pentacene films in view of a molecular picture of charge transfer processes in  $\pi$ -conjugated organic semiconductors. Such transport processes can be described using two key microscopic parameters [4]: intermolecular electronic coupling (transfer integrals,  $J_{ab}$ ) and reorganiza-

tion energy ( $\lambda_{\text{reorg}}$ ). The  $J_{ab}$  is proportional to the intermolecular interactions and thus inversely proportional to the effective separation,  $R$ , between adjacent molecules. The  $\lambda_{\text{reorg}}$  is a measure of the strength of the interaction between the electronic structure and the vibrational states of the molecule and of the material. In order to ensure an efficient carrier transport process, the  $J_{ab}$  must be maximized, while the  $\lambda_{\text{reorg}}$  needs to be minimized [4]. In this paper, we show that microRaman spectroscopy provides a powerful and convenient tool for analyzing the actual microstructure and the microscopic transport parameters of organic films within the active channel of OTFTs. At the same time, the relevant information of  $J_{ab}$  and  $\lambda_{\text{reorg}}$  can be derived and related to the measured  $\mu$  in the OTFTs. Furthermore, microRaman mapping offers the ability to identify the quality of both the intragrain and GB microstructures of these films. Finally, the implications of crystal and grain size data obtained from X-ray diffraction (XRD) and atomic force microscopy (AFM) scans, respectively, are also discussed.

## 2. Experimental section

*Preparation of gate dielectrics:* Four type gate dielectrics were used as follows: (i) thermally grown  $\text{SiO}_2$  (denoted  $\text{TSiO}_2$ ): a heavily doped Si wafer was used as the gate electrode substrate. A 300 nm  $\text{SiO}_2$  layer was thermally grown on the substrate acted as the gate dielectrics; (ii) plasma-enhanced chemical vapor deposition (PECVD) grown  $\text{SiO}_2$  (denoted  $\text{PSiO}_2$ ): heavily doped Si wafer or glass substrates (with the indium–tin–oxide gate electrode upon the substrate) were used as the gate electrode substrate. Then, a 300 nm  $\text{SiO}_2$  gate dielectric layer was prepared by PECVD at 800 mtorr and 380 °C. The gases used were He,  $\text{O}_2$ , and tetraethylorthosilicate with corresponding gas quantities of 100, 3500, and 175 sccm, respectively; (iii) poly(methyl methacrylate) (PMMA): an approximately 60 nm PMMA (molecular weight ( $M_w$ ) =  $5.4 \times 10^5 \text{ g mol}^{-1}$ , Scientific Polymer Products, Inc.) layer was deposited by spin coating directly onto a  $\text{SiO}_2$  layer using a 1 wt% PMMA solution from *p*-xylene, and then was baked for 2 h at 120 °C; (iv) polyimide (PI, Nissan Chemical Co.): an approximately 80 nm PI layer was deposited by spin coating directly onto a  $\text{SiO}_2$  layer, and then was baked for 60 min at 220 °C. In this study, the root-mean-square surface roughness of  $\text{TSiO}_2$ ,  $\text{PSiO}_2$ , PMMA, and PI were 1.6, 2.8, 0.5, and 0.8 nm, respectively, and the surface free energies were 59, 62, 49, and 39  $\text{mJ m}^{-2}$ , respectively.

*Preparation of pentacene films:* Pentacene was purchased from Aldrich Chemical Company and was used as received without further purification. All of the pentacene was thermally evaporated upon dielectrics with a thickness of ca. 65 nm at a deposition rate of approximately  $0.5\text{--}1 \text{ \AA s}^{-1}$  and a pressure of  $2 \times 10^{-5}$  torr. The pentacene active layer was patterned using a shadow mask around the measured OTFTs to minimize the leakage. The thickness of pentacene films were calibrated using an AFM and monitored via the frequency shift of a quartz oscillator.

*OTFT fabrication and electrical characteristics measurements:* A bottom gate staggered transistor structure with rectangular gold top-contacts was used (also see Fig. 1).

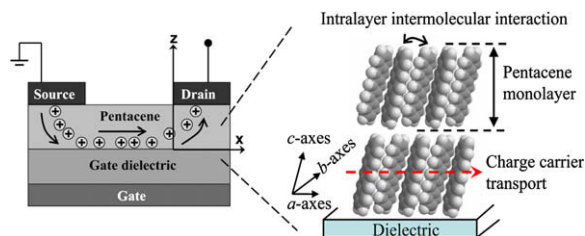


**Fig. 1.** Schematic cross-section of the thin-film transistor test structure and herringbone packing of the pentacene molecules grown upon the gate dielectric surface.

In the final step, the gold source–drain electrodes were deposited to form an electrode upon the surface of the pentacene film through a shadow mask in order to complete the top-contact OTFT device. The devices were then transferred to a dry nitrogen-atmosphere glove box to minimize the influence of H<sub>2</sub>O from the ambient air upon the electrical properties of devices [12c]. The electrical characteristics of OTFTs were measured by a Keithley 4200-SCS semiconductor parameter analyzer in the glove box under dark conditions. In the saturation regime, the saturated field-effect mobility ( $\mu_{\text{sat}}$ ) was calculated by fitting the metal-oxide-semiconductor field-effect transistor charge-sheet model equation described below [2,18]:

$$I_{\text{DS}} = \frac{W\mu_{\text{sat}}C_i}{2L}(V_G - V_{\text{th}})^2, \quad \text{if } (V_G - V_{\text{th}}) \leq V_D \quad (2)$$

where  $I_{\text{DS}}$  is the drain-to-source current,  $C_i$  is the gate capacitance,  $V_D$  is the drain bias,  $V_G$  is the gate bias,  $V_{\text{th}}$  is the threshold voltage, respectively, and  $W/L$  is the channel width-to-length ratio.

**Analytical methods:** The surface morphology and root-mean-square surface roughness were measured using AFM (Digital Instrument Multimode SPM AS-12VMF). The surface free energy was analyzed using the OCA15 contact angles goniometer (Dataphysics Co.). Raman spectra of pentacene films, produced by lattice phonons, were obtained using a Jobin Yvon LabRam HR spectrometer. A 532 nm solid state laser and a 633 nm He–Ne laser served as the excitation light source and were kept below 0.5 mW to prevent thermal damage to the pentacene thin-film. The spatial resolution of the beam spot was around 1  $\mu\text{m}$ , attained using a 100 $\times$  objective microscope lens. The spectrometer resolutions are 0.4 and 0.2  $\text{cm}^{-1}$  for using 532 and 633 nm excitation lines, respectively. Every Raman spectrum was taken an average of five spectrums and at least three spectra were measured for each sample. MicroRaman mapping measurements were generated by measuring Raman spectra for each with lines of over 5  $\mu\text{m}$  in step sizes of 0.1  $\mu\text{m}$ . The pentacene films on various substrates were studied by XRD (Rigaku D/Max-2500 diffractometer) in the symmetric reflection coupled  $\theta$ – $2\theta$  arrangement. XRD patterns were obtained using a 18 kW rotating-anode X-ray generator (Cu K $\alpha$  radiation,  $\lambda_{\text{K}\alpha 1} = 1.5406 \text{ \AA}$ ) and a wide-angle graphite monochromator. The data were collected with a step size of 0.01 $^\circ$  with a scanning rate of 1 $^\circ/\text{min}$ . A Si single-crystal (111) wafer was used to estimate the effect of the instrumental broadening in XRD experiments. The observed FWHM of the (111)

peak at ca. 28 $^\circ$   $2\theta$  is 0.061 $^\circ$  under the same instrumental conditions.

**Quantum mechanical calculations:** The GAUSSIAN 03 program [19] was used to perform the density functional theory (DFT) calculations. The BLYP method (Becke's 1988 exchange functional combined with the LYP correlation functional of Lee, Yang and Parr) [20] was used for geometry optimization, Raman spectrum, and normal modes calculations. In all cases, the 6-31G(d) basis set was used. The observed Raman modes were assigned based on the calculation. However, it should be noted that the theoretical calculated frequencies were scaled with a factor of 0.9613 to fit the experimental obtained frequencies, as recommended by Scott and Radom [21]. Comparison of theoretical and experimental Raman spectra, the agreement between theory and experimentation is generally very good [22]. Therefore, the contributions of each vibrational mode to the reorganization energy were calculated from the normal mode analysis using the same 6-31G(d) basis set. The  $\lambda_{\text{reorg}}$  is proportional to the extent of the molecular geometry change between the neutral-state and charge-state, including the inner- ( $\lambda_i$ ) and outer- ( $\lambda_o$ ) sphere contributions. The  $\lambda_i$  (intramolecular) arises from the molecular geometry modifications that occur when an electron is added to or removed from a molecule. The vibrational term  $\lambda_i$  is a sum of contributions from the Raman active normal modes [4,23],

$$\lambda_i = \sum \lambda_v = \frac{1}{2} \sum A_k^2 v_k = \sum S_k h v_k \quad (3)$$

In the harmonic approximation, the vibrational reorganization energy,  $\lambda_v$ , depends on the dimensionless displacement,  $\Delta_k$ , and  $v_k$  is the vibrational frequency of mode  $k$ . The displacement  $\Delta_k$  along normal mode  $k$  is between the equilibrium positions of the two electronic states, i.e., the ground and cation states. The Huang–Rhys factor  $S_k$  is the distortion parameter and  $h$  is Planck's constant. Calculated optimized geometries of neutral and cation states and the normal mode coordinates were used to derive the vibrational term  $\lambda_i$  [23]. The numerical procedure consists of the following steps: (i) the optimized neutral ( $q_k^0$ ) and cation ( $q_k^+$ ) geometries at charge 0 and charge +1, respectively, are determined. The vector  $\Delta q = (q_k^+ - q_k^0)$  describes the geometry change upon electronic excitation in the mass weighted Cartesian coordinates; (ii) the normal mode coordinates and the force constants are determined; (iii) the normal mode displacements,  $\Delta_k$ , are obtained by projecting the displacements  $\Delta q$  onto the normal mode vectors. By substituting the calculated quantities into Eq. (3), the  $S_k$ ,  $\lambda_v$ , and  $\lambda_i$  are obtained. The partition of the reorganization energy into the contributions of each vibrational mode is listed in Table 1.

### 3. Results and discussion

**Carrier mobilities in pentacene-based OTFTs:** We used a typical bottom gate configuration with a gold top-contact OTFT [2] (see Fig. 1a) to study the charge transport properties for the pentacene films grown on several dielectric surfaces with different surface properties. The measured

**Table 1**

DFT/B3LYP/6-31G(d) estimates of frequencies, Huang–Rhys factors,  $S$ , and vibrational reorganization energies,  $\lambda_v$ , and the experimental observation frequencies,  $\nu_{exp}$ , for pentacene in its neutral-state.

Frequency (cm <sup>-1</sup> )	$S$	$\lambda_v$		$\nu_{exp}$ (cm <sup>-1</sup> )
		(meV)	(%)	
264	0.0260	0.9	1.8	264
617	0.0001	0.0	0.0	600
647	0.0000	0.0	0.0	–
765	0.0009	0.1	0.2	753
800	0.0020	0.2	0.4	785
1029	0.0037	0.5	1.0	995
1194	0.0110	1.6	3.5	1158
1223	0.0525	8.0	17.0	1178
1348	0.0004	0.1	0.1	1350
1426	0.0740	13.1	27.9	1371
1451	0.0115	2.1	4.4	1409
1512	0.0021	0.4	0.9	1457
1572	0.0908	17.7	37.7	1498
1594	0.0115	2.3	4.8	1533
3175	0.0000	0.0	0.0	–
3180	0.0001	0.0	0.0	–
3184	0.0003	0.1	0.3	–
3210	0.0001	0.0	0.1	–
Total		47.0	100	

output and saturation transfer characteristics are shown in Fig. 2. When the pentacene was grown on a SiO<sub>2</sub> surface, it showed a very low output on-current. The output on-current was improved by nearly two orders of magnitude when pentacene was grown on the PI surfaces. The  $\mu_{sat}$  was extracted from the slope (see Fig. 2b) using Eq. (2). When the pentacene was deposited on a SiO<sub>2</sub> surface, the device generally displayed a poor  $\mu_{sat}$  of around 0.01–0.4 cm<sup>2</sup> V<sup>-1</sup> s<sup>-1</sup>. The obtained  $\mu_{sat}$  values of pentacene films in this work that grown on a native SiO<sub>2</sub> surface are consistent with previous studies done by other researchers [2,5,16]. However, when pentacene films were grown upon polymeric surfaces, the corresponding devices displayed excellent performance with  $\mu_{sat}$  values that were generally above 1.0 cm<sup>2</sup> V<sup>-1</sup> s<sup>-1</sup>. In particular, the mobility of penta-

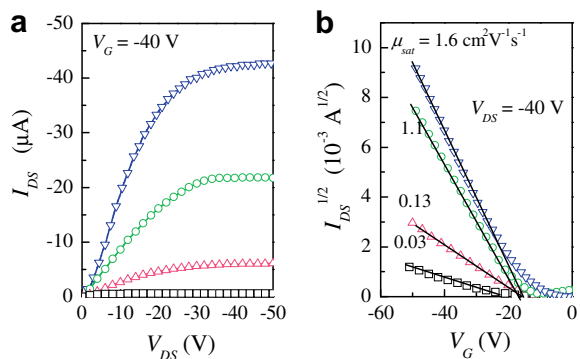


**Fig. 2.** Comparison of electrical characteristics of OTFTs using pentacene films grown on various dielectric surfaces: (□) TSiO<sub>2</sub>; (Δ) PSiO<sub>2</sub>; (○) PMMA; and (▽) PI. (a) Typical output characteristics: drain current ( $I_{DS}$ ) versus source–drain voltage ( $V_{DS}$ ) curves. (b) Saturated electrical-transfer characteristics:  $I_{DS}^{1/2}$  versus gate voltage ( $V_G$ ) curves. The solid lines indicate the linear fitting results. Calculated saturated field-effect mobilities ( $\mu_{sat}$ ) were also shown.

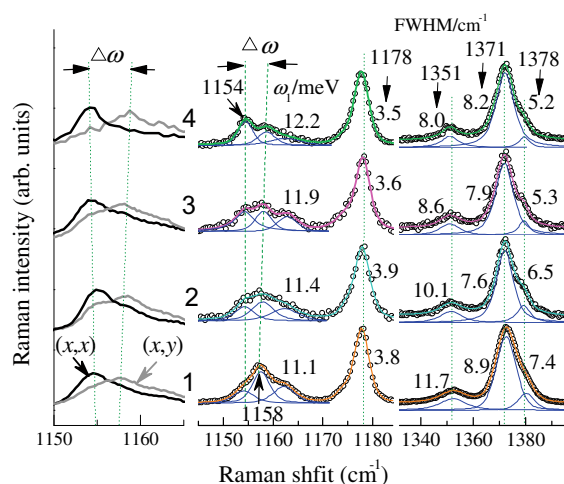


**Fig. 3.** Non-polarized ( $\lambda_{exc} = 532$  nm, right-panel) and polarized ( $\lambda_{exc} = 633$  nm, left-panel) Raman spectra of pentacene films grown on (1) TSiO<sub>2</sub>, (2) PSiO<sub>2</sub>, (3) PMMA, and (4) PI surfaces. The polarizations of the incident and detected light are parallel ( $x, x$ ) and perpendicular ( $x, y$ ) to each other. The Gaussian/Lorentzian functions used for the deconvolution are presented by a thin solid line. The thick solid lines represent the overall fit, while the open circles to the experimental data. The dashed lines serve as guidelines. The intermolecular vibrational coupling energy ( $\omega_1$ ) and the full width at half-maximum (FWHM) of selected bands were also shown.

cene on PI was above 1.6 cm<sup>2</sup> V<sup>-1</sup> s<sup>-1</sup>, which is close to two orders of magnitude improvement when compared to pentacene grown on a TSiO<sub>2</sub> dielectric.

**Raman scattering analysis:** The Raman spectra of the corresponding pentacene films are shown in Fig. 3. The bands at 1158 ( $A_g$ ) and 1178 ( $A_g$ ) cm<sup>-1</sup> are related to C–H in-plane bending modes, and the 1351 ( $A_g$ ), 1371 ( $A_g$ ), and 1379 ( $B_{3g}$ ) cm<sup>-1</sup> bands belong to the aromatic C–C stretching modes. These modes are shown in Fig. 4. A molecule under solid phase, Raman selection rules can be changed due to the static field-effect arising from the crystalline environment, and also due to the dynamic effect (called correlation field or Davydov splitting [24]) arising from the nonidentical spatial orientation of anisotropic molecules in the crystal and from the intermolecular forces between molecules. First, we have focused on a significant splitting  $\Delta\omega$  that occurred between ca. 1158 ( $\nu_0$  band) and ca. 1155 cm<sup>-1</sup> ( $\nu_1$  band) and was explained by Davydov splitting [25]. Evidently, the relative intensity ratio of  $\nu_1$  and  $\nu_0$  bands ( $I_{\nu_1}/I_{\nu_0}$ ) has explicitly changed by altering polarizations of incident and scattered light either parallel ( $x, x$ ) or perpendicular ( $x, y$ ) to each other (see Fig. 3, left-panel). We have observed that the  $\nu_1$  and  $\nu_0$  bands have the following features [22,26]: (i) compared with other Raman modes, the relative intensity of the  $\nu_1$  band was much more sensitive in response to the 633 nm excitation line that corresponds to the Davydov component in the absorption spectrum; (ii) the  $\Delta\omega$  was sensitive to the unit cell volume (i.e., the  $R$ ) due to that  $\Delta\omega$  could be enlarged at low temperatures; (iii) the  $\Delta\omega$  was related to the intermolecular coupling parallel to the  $a$ – $b$  lattice plane direction (also see Fig. 1), which is said to be parallel to active channel direction in OTFT geometry.

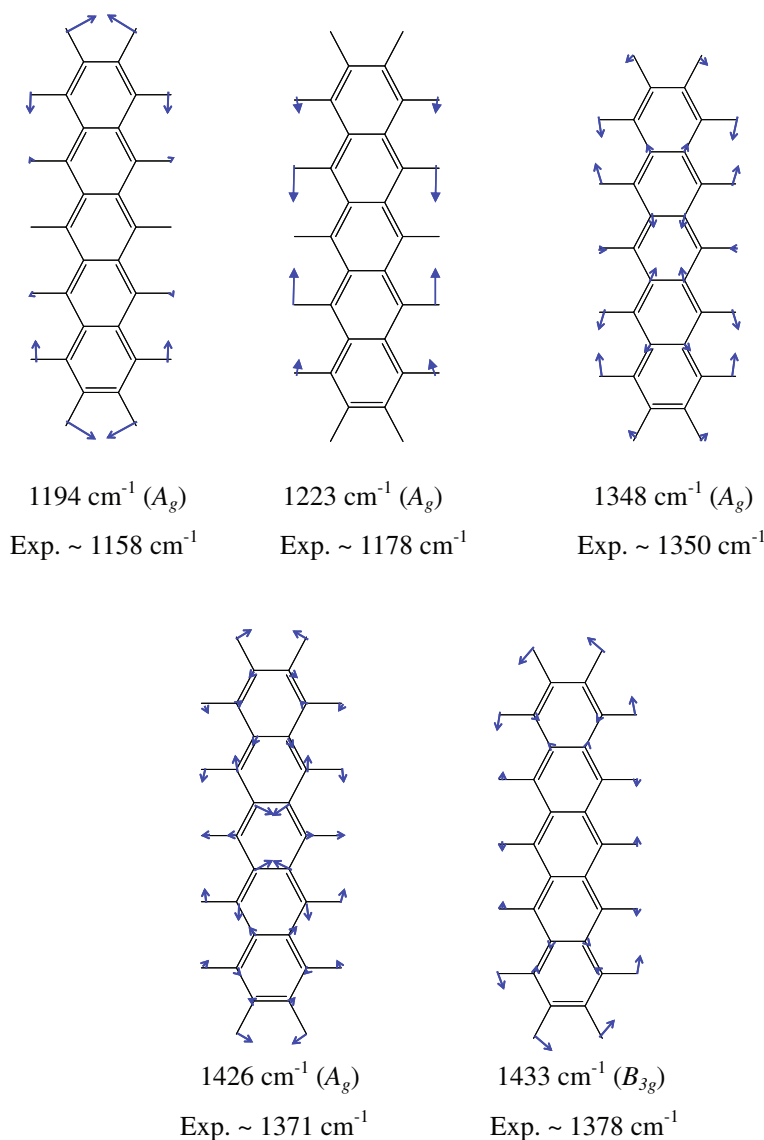


**Fig. 4.** Shows a representation of the selected  $A_g$  and  $B_{3g}$  vibrational modes of pentacene as determined by a DFT/B3LYP at 6-31G(d) calculation of an isolated pentacene. The vectors representing the atom displacements in the Cartesian coordinates are multiplied by a factor of three.

Recently, we have shown that the Davydov splitting of the Raman mode could be used to study the intermolecular interactions between molecules in films [22,26]. The intermolecular vibrational coupling energy,  $\omega_1$ , could be estimated by a simple coupled-oscillator model due to that the transfer of energy from internal vibrations to external vibrations (phonons) is equivalent to the damping of internal vibrations. In the weak-coupling regime, the splitting of the characteristic frequencies is given by  $\Delta\omega = \nu_0 - \nu_1 = \omega_1^2/2\omega_0$ , where  $\omega_0$  is the frequency of the internal molecular band. The peak centre of  $\nu_0$  and  $\nu_1$  bands could be obtained according to a curve-fitting procedure reported previously [27], thus obtaining the  $\Delta\omega$ . Alternatively, the obtained  $\Delta\omega$  could be further checked by using polarized Raman measurements (see Fig. 3, left-panel). Herein, both methods were used to determine the average

value of  $\omega_1$  based on at least six values from different locations. The results of  $\omega_1$  calculation are also shown in Fig. 3, indicating that pentacene films on polymeric surfaces have a higher value, e.g.,  $\omega_1 \sim 12$  meV. Such polycrystalline organic films do not have clear phonon modes in the low-frequency spectral region ( $<200$   $\text{cm}^{-1}$ ) due to the lack of long-range order [22]. Hence, the observed differences in  $\omega_1$  among these films bear useful information in identifying microstructural differences. Most importantly, in Fig. 5a, we can observe a linear relationship between  $\mu_{sat}$  and  $\omega_1$  on a semi-logarithmic scale. A clear relationship between the  $\mu_{sat}$  and  $I_{\nu_1}/I_{\nu_0}$  has also been discovered. The magnitude of Davydov splitting is directly dependent upon the  $R$  [22,24]. Consequently, there are good reasons to believe that the charge carrier mobility can be scaled to  $\omega_1$ .

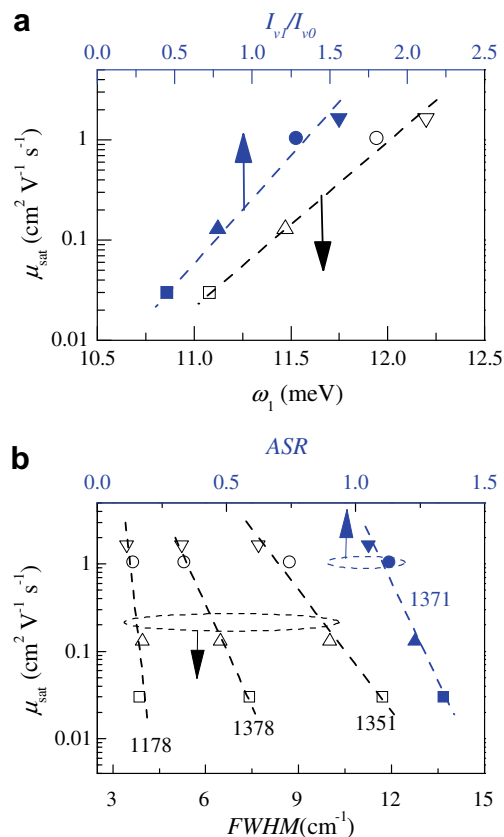


**Fig. 5.** Relationships between saturated field-effect mobility ( $\mu_{sat}$ ) and vibrational characteristics of pentacene films grown on different dielectric surfaces: ( $\square$ ) TSiO<sub>2</sub>; ( $\triangle$ ) PSiO<sub>2</sub>; ( $\circ$ ) PMMA; and ( $\nabla$ ) PI. (a) The  $\mu_{sat}$  versus the intermolecular vibrational coupling energy ( $\omega_1$ ) and the relative intensity ratio of  $v_1$  to  $v_0$  bands ( $I_{v1}/I_{v0}$ ). The standard deviations of the  $\omega_1$  and the  $I_{v1}/I_{v0}$  are within 0.15 meV and 6%, respectively. (b) The  $\mu_{sat}$  versus the FWHM of 1178, 1351, and 1379  $\text{cm}^{-1}$  bands and asymmetric ratio (ASR) of 1371  $\text{cm}^{-1}$  band. The standard deviations of the FWHM of 1178, 1351, and 1379  $\text{cm}^{-1}$  bands are within 0.1, 0.5, and 0.2  $\text{cm}^{-1}$ , respectively. At least three spectra were measured for each sample from different locations. Solid lines indicate the linear fitting results.

Raman spectroscopy provides a powerful tool not only for analyzing the molecular packing and orientation of organic molecules in thin layers and the thin-film uniformity (homogeneity) in a specific direction, but also for obtaining information on  $\lambda_{reorg}$  [4b,28]. When pentacene was grown on polymeric surfaces, the films had a narrow full width at half-maximum (FWHM) of 1178, 1351, and 1378  $\text{cm}^{-1}$  bands (see Fig. 3, right-panel). According to DFT calculations (also see Fig. 4), the 1178  $\text{cm}^{-1}$  band is the strongest C–H in-plane vibrational mode and is related to the motion of H-atoms located on both sides of the pentacene molecule. The 1351  $\text{cm}^{-1}$  band is the aromatic C–C stretching vibration and is strongly related to the completeness of the film parallel to the dielectric surface [22]. The 1379  $\text{cm}^{-1}$  band is due to the asymmetric C–C stretching vibration along the short molecular axis also in the molecular plane. The smaller FWHM of these bands indicated that the films have a higher environmental unity for molecular vibrations occurring parallel to a dielectric sur-

face (or called the horizontal direction, i.e., along the direction of the active channel of OTFT, also see Fig. 1) due to better molecular packing.

During the carrier transfer process, the total free energy of reaction could contribute to the FWHM of the vibronic bands that involve the excitation process and lead to an unsymmetrical shape; thus,  $\lambda_{reorg} \sim (\text{FWHM of the vibronic bands})^2$  [4b,28]. We found that the larger the  $\omega_1$  was in the experimental pentacene films, the smaller the FWHM of the vibration modes became. However, the FWHM of the strongest C–C band at 1371  $\text{cm}^{-1}$  does not show the same trend (see Fig. 3, right-panel). In fact, we have observed that the FWHM of this band decreased with the increase of pentacene film thickness [22]. DFT normal-coordinate displacement analysis suggested that the 1371  $\text{cm}^{-1}$  band (see Fig. 4) are more sensitive to the film quality in the vertical direction than that in the horizontal direction. Examining many pentacene films grown on various surfaces with the same thicknesses, we found that the FWHM of the 1371  $\text{cm}^{-1}$  band is highly related to the FWHM of the (001) diffraction peak from XRD scans (see Fig. 6). We could further quantify the degree of asymmetry of the 1371  $\text{cm}^{-1}$  band using an asymmetry ratio (ASR) [29] that is described as the ratio of the blue half to the red half of the FWHM. In general, the vibration modes have a higher ASR in an amorphous (disordered) region than in a crystalline (ordered) region, since the crystalline environment causes a shift of vibrational frequencies and possible splittings. Pentacene films grown on PI and PMMA have smaller ASRs of 1.05 and 1.13, respectively, than the obtained values of 1.34 and 1.23 on TSiO<sub>2</sub> and PSiO<sub>2</sub>, respectively. After an annealing process, which aims to improve the crystal quality, the band becomes more symmetrical.

In Fig. 5b, one can see that the  $\mu_{sat}$  is inversely proportional to the FWHM of these vibrational modes at 1178, 1351, and 1378  $\text{cm}^{-1}$  and the ASR of 1371  $\text{cm}^{-1}$ . According to the DFT computational results, the main contributions to the  $\lambda_i$  of a single molecule in the dimensionless situation come from a few normal modes, especially in the 1178 (17%), 1371 (28%), and 1498 (38%) [30]  $\text{cm}^{-1}$  bands (see Table 1). In single-crystals and thin-films, we have to consider the  $\lambda_o$  due to external environmental influences. A simulation approach suggests that  $\lambda_i$  has a strong dependence on the local intermolecular coupling; thus, the

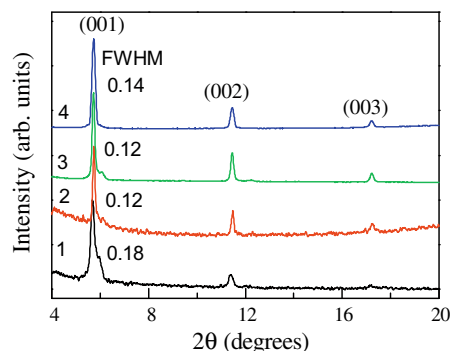


**Fig. 6.** XRD spectra of the corresponding pentacene films on different dielectric surfaces: (1) TSiO<sub>2</sub>, (2) PSiO<sub>2</sub>, (3) PMMA, and (4) PI. The FWHM of the (001) peak were also shown.

embedded pentacene molecule in a single-crystal has a lower  $\lambda_i$  value than that of a free molecule [31]. For conjugated oligomers and polymers, it has been reported [32] that the  $\lambda_{reorg}$  decreases with increasing degrees of inter-chain and intrachain orders. However, in an OTFT, we need to consider the influence of molecular packing and orientation on the vibrations as well as the direction of charge transport in the active channel. Consequently, the analysis results from these normal modes suggests that pentacene grown on PI and PMMA surfaces have a superior microstructure with closed molecular packing, thus lowering the  $\lambda_{reorg}$ , especially in the direction along the current flow.

**X-ray diffraction analysis:** As shown in Fig. 6, we have also studied the crystal structure of the corresponding pentacene films. All the films consist of only the (00*l*) lattice plane and show a dominant “thin-film” phase [33] with almost identical  $d_{001}$  spacing ( $\sim 15.4$  Å). The results indicated that the pentacene molecules are slightly tilted to the plane of dielectric surface and form a herringbone pattern within the layers [6]. The structural parameters, including the paracrystal size ( $L_{00i}$ , i.e., the mean dimension of the crystallites perpendicular to the (00*l*) plane) and the fluctuation factor ( $g_{ll}$ , i.e., the distance fluctuation between successive planes of the family (00*l*) or the degree of distortions of crystal structure), were calculated according to the paracrystal theory, repeating the methodology used before [33,34]. The estimated parameters are listed in Table 2. Contribution to the FWHM from instrumental broadening is negligible compared to the magnitude of the observed FWHM values. Therefore, the calculated crystallite size  $L_{001}$  is a minimum. As displayed in the table, the pentacene films on PSiO<sub>2</sub>, PMMA, and PI all have similar values for the FWHM of the (001) diffraction peak,  $L_{00i}$ , and  $g_{ll}$ . The obtained  $L_{00i}$  and  $g_{ll}$  values were similar to those reported in other publications [33]. In contrast, the pentacene film on TSiO<sub>2</sub> has significantly inferior crystal quality. From the present case, it is difficult to draw clear correlations between out-of-plane XRD data and  $\mu_{sat}$ . For OTFTs with top-contact configurations, the charge transport runs through the path that includes the channel near the dielectric surface at horizontal direction and the way from source and drain electrodes to the channel at the vertical direction (also see Fig. 1). Since there is only the (00*l*) lattice plane in the XRD pattern, we should mention the importance of crystal quality in the vertical direction of the substrate. It is established that the quality of vertical growth does not always determine the quality of horizontal growth for pentacene films. Sometimes we

could observe a good correlation between mobility and  $L_{001}$  [16d]. Large  $L_{001}$  and low  $g_{ll}$  would help the charges pass through the pentacene film easily, thus leading to lower bulk film resistance and higher output on-current.

Upon further analysis of these pentacene films at low thicknesses (ca. 1–2 monolayers), it was found that the films on polymeric surfaces still have higher coverage associated with a larger  $\omega_1$  (e.g., 10.5 and 10.3 meV for 50 Å pentacene films on PI and PMMA surfaces, respectively) and narrower FWHM of the Raman modes than those on the SiO<sub>2</sub> surface (e.g.,  $\omega_1$  of 9.1 meV for 50 Å pentacene films on SiO<sub>2</sub> surfaces, respectively) [22]. It should be noted that the results do not fully reflect the real situations of the films for charge transport, since several monolayers could possibly be incomplete layers, which is common for organic films. However, the subsequent growth of pentacene films at a higher thickness was strongly influenced by the bottom-most layer, i.e., the formation of a more completed bottom-most layer will benefit pentacene growth, thus higher mobility for real device applications (in general, a-few-10-nm thick organic films).

**MicroRaman mapping analysis of grain structures:** The microstructural quality inside the grain and near the GBs is another concern. The  $\nu_0$  and  $\nu_1$  bands featured within the grain and near GBs were investigated using microRaman mapping scans. In Fig. 7 (upper-panels), we could see that the pentacene films grown on PSiO<sub>2</sub> display larger grain sizes than those on PMMA surfaces. First, Raman line-mapping analyzes (spot size  $\sim 1$   $\mu\text{m}$  with step 0.1  $\mu\text{m}$ ) were performed for a pentacene film on PSiO<sub>2</sub> as shown in Fig. 7a (lower-panel). The intensities of  $\nu_1$  and  $\nu_0$  bands were normalized to the intensity of the strongest C–C bands at 1371  $\text{cm}^{-1}$  (as an internal standard) to eliminate the thickness variation effects due to granular morphology. We observed that both the relative intensities of  $\nu_1$  and  $\nu_0$  bands exhibit a wavy shape with scan position. The pinnacle and valley positions of the  $\nu_1$  band intensity were used to calculate the highest ( $\omega_1^H$ ) and the lowest ( $\omega_1^L$ ) intermolecular vibrational coupling energy, respectively. The positions with stronger  $\nu_1$  and  $\nu_0$  intensities are always associated with larger  $\omega_1$ , indicating a large contribution from the molecules within the grain. Because there are large quantities of pentacene molecules within the grain they form a more orderly crystal structure compared to that in GB. For a classical treatment, Raman scattering intensity is proportional to the density of scatters or molecules per cubic centimeter [35]. Moreover, only the pentacene in a crystal lattice can contribute to the  $\omega_1$  [24]. Hence, the lowest  $\nu_1$  and  $\nu_0$  intensities along with lower  $\omega_1$  occur at the positions near GBs. Based on the Raman mapping, the estimated grain size distributions at ca. 0.5–1  $\mu\text{m}$  are consistent with those obtained by AFM observations. Furthermore, the larger sizes of grains demonstrate the higher Raman intensities.

Fig. 7b (lower-panel) displays the Raman mapping of the pentacene film on PMMA featuring a very small grain size of ca. 0.1  $\mu\text{m}$ , which is far smaller than the spatial resolution of the Raman beam spot (ca. 1  $\mu\text{m}$ ). Thus the grain and GB locations could not be recognized clearly although the mapping measurements had a step of only 0.1  $\mu\text{m}$ . Whether due to grains or GBs, the film on PMMA had a

**Table 2**

Thin-film phase structural parameters of the pentacene films grown on various dielectric surfaces.

Dielectric surfaces	$d_{001}$ -spacing (Å)	FWHM of (001) peak (degree)	$L_{00i}^a$ (Å)	$g_{ll}^a$ (%)
TSiO <sub>2</sub>	15.5	0.18	263	2.84
PSiO <sub>2</sub>	15.4	0.12	363	1.60
PMMA	15.4	0.12	354	1.53
PI	15.4	0.14	350	1.75

<sup>a</sup>  $L_{00i}$  and  $g_{ll}$  are the mean dimension of the crystallites perpendicular to the (00*l*) plane and the distance fluctuation between successive planes of the family (00*l*), respectively.

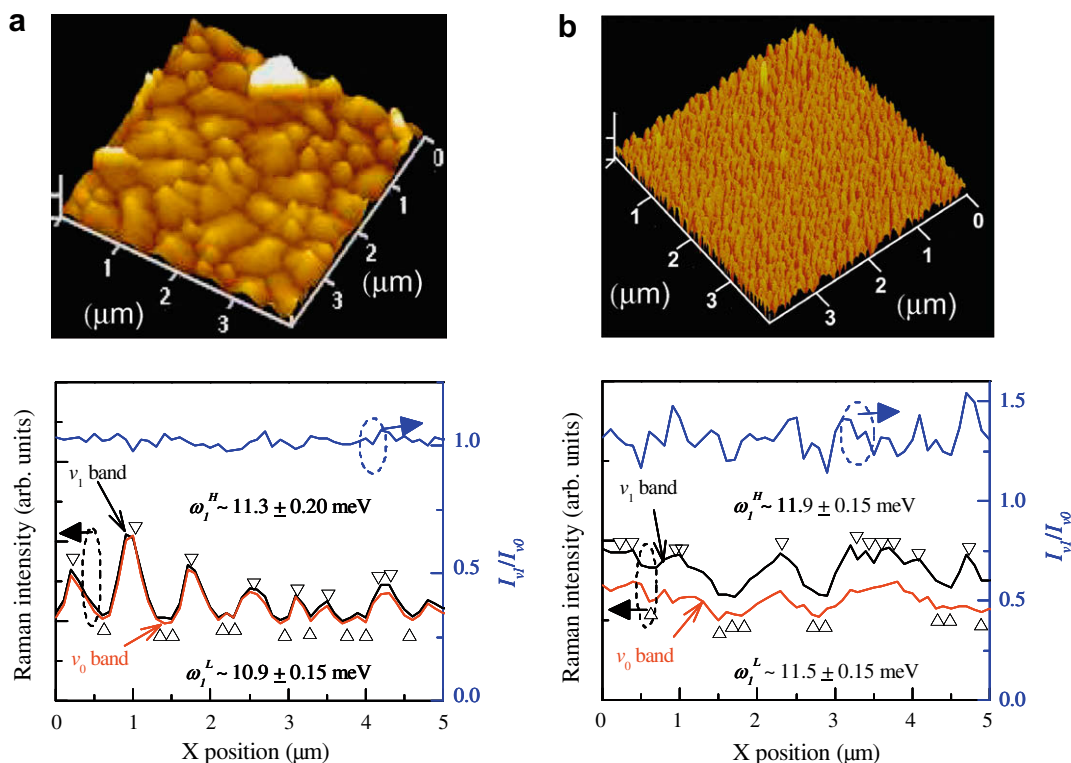


**Fig. 7.** AFM images (upper-panels,  $4 \mu\text{m} \times 4 \mu\text{m}$ ) and Raman mapping spectra ( $\lambda_{\text{exc}} = 633 \text{ nm}$ ) (lower-panels) of pentacene films grown on (a) PSiO<sub>2</sub> and (b) PMMA. Lower-panels: relative Raman intensities of  $\nu_1$  and  $\nu_0$  bands, respectively, normalized to the intensity of the strongest C–C band at  $1371 \text{ cm}^{-1}$  (left-axes) and relative intensity ratio of  $\nu_1$  to  $\nu_0$  bands ( $I_{\nu_1}/I_{\nu_0}$ ) (right-axes) as a function of scan length. Downtriangles and uptriangles indicate the positions used for calculating the highest ( $\omega_1^H$ ) and the lowest ( $\omega_1^L$ ) intermolecular vibrational coupling energy, respectively.

higher  $I_{\nu_1}/I_{\nu_0}$  and larger  $\omega_1$  than that on PSiO<sub>2</sub> featuring large grains. The results imply that the microstructure qualities inside the grain (i.e., the higher density crystals with close packing and thus highly ordered microstructures) of pentacene film on PMMA are far superior to that on PSiO<sub>2</sub>. At the early stage growth, other researchers [36] have observed that the pentacene on PMMA had higher first monolayer coverage than on the SiO<sub>2</sub> surfaces. Although the formed grain is bigger on the PSiO<sub>2</sub>, we suggest that with looser crystal packing comes worse microstructures. Evidently, the intragrain mobility is lower than that expected in single-crystals [37], thus Matsubara et al. [8b] suggested that there exist some limiting factors of charge transport other than the GBs. It should be noted that in Refs. [7,8], these researchers only used SiO<sub>2</sub> as the dielectric surface and their OTFTs have an inferior  $\mu$  below  $0.5 \text{ cm}^2 \text{ V}^{-1} \text{ s}^{-1}$ . This is valid if the density of formed crystals inside the grain was at a similar level. Indeed, we also observed an apparent grain size dependent  $\mu$  in pentacene OTFTs when one kind of surface, e.g., SiO<sub>2</sub>, was used. We argue that the GB model does not apply to the case where the density of crystals inside the grain has large disparities among the specimens. This viewpoint could be supported by using a higher  $M_w$  of PMMA, intended to increase the density of polymer chains on the surface, thus leading to the formed pentacene film becoming more dense and forming high a density crystal (since the polar functional groups on the PMMA surface could produce an extra

attraction force for the pentacene molecules). For instance, when using PMMA with a higher  $M_w$ , we observed a higher value of  $\mu_{\text{sat}}$ . Investigations into the effects of the  $M_w$  of polymer insulators (e.g., PMMA) on the electrical characteristics of pentacene OTFTs will be reported elsewhere. On the other hand, the pentacene film grown on PMMA has tiny grain morphology, thus someone may suggest that grain boundaries act as charge traps and consequently degrade OTFT characteristics, as well as the OTFTs may exhibit a larger hysteresis effects in the current–voltage characteristics. Interesting, we have not observed relationship between grain size and hysteresis effect in pentacene films. To the contrary, adding an extra PMMA layer upon SiO<sub>2</sub>, the hysteresis effects of pentacene-based OTFTs were reduced as compared to that only using SiO<sub>2</sub> [38]. Moreover, Uemura et al. have not observed hysteresis effects in the pentacene-based OTFTs by only using PMMA as gate dielectric [39]. The results suggest that the GBs should not be treated as an only dominant carrier transport/performance constraint factor in polycrystalline pentacene-based OTFTs.

For organic polycrystalline films with grain morphology, there are many influencing factors on charge carrier transportation. In the past, the GB effect is thought to be a significant limiting factor on charge transport taking dominance over others. As can be observed in the study, the microstructural quality within the grain, i.e., molecular packing, has a remarkable influence on  $\mu$  in pentacene

polycrystalline films. Recently, Matsubara et al. [8b] treated the carrier transport behavior in pentacene polycrystalline films on SiO<sub>2</sub> by a polycrystalline model with the diffusion theory that a mean free path of a charge carrier is smaller than the barrier width at GB. According to their GB model, the apparent  $\mu$  can be influenced both by the barrier height at the GB (grain size-dependent part) and the mobility in grain (in-grain-relevant part). Previous research papers are mainly concerned with the discussion of the grain size-dependent part on the charge transport, in which GB elimination is the main focus. Besides, we suggest the improvement of the in-grain-relevant part, e.g., the microstructural quality within the grain, is also very important in order to achieve ultrahigh  $\mu$  of organic polycrystalline films. Our observations do not contradict to previous reports from the point that the  $\mu$  is still limited by the GB region.

#### 4. Conclusions

To summarize, despite the use of different dielectrics with various surface properties, we report a clear relationship between the mobility and the  $\omega_1$  in the pentacene films regardless of grainy morphology. The microstructural qualities inside the grains must be considered case by case. In other words, the inferior microstructures may have a large grain appearance. Here, we have shown that microRaman mapping based on Davydov splitting, probing the intermolecular vibrational coupling on a micrometer scale, clearly shows that the grain morphology should not be taken for granted, for both structural quality and efficient charge transport. The GB effects (assuming large amounts of charge traps at the GBs) are found not to be a dominant performance factor, thus suggesting that the traps may be randomly distributed over the films. Our observations give a possible reason why some experimental efforts could not make carrier transport more efficient in samples featuring large grains, in a single grain, or within the grain. After all, eliminating GBs is still important since the microstructures are still inferior to inside the grain. However, the most important thing is to improve the microstructural qualities inside the grain, which was not addressed in previous studies. Furthermore, the microRaman mapping methodology we proposed here can also be used to check most organic semiconductors, both in films and in single-crystals, since there exist two types of molecular orientations in a unit cell. For example, the Davydov splitting in Raman spectroscopy has been observed in a n-type perylene tetracarboxylic dianhydride [40]. Consequently, we believe that the basic understanding of carrier transport properties of an organic film at the microscopic level will significantly contribute to the development of organic thin-film devices and the advancement of relevant technologies.

#### Acknowledgments

This work was supported by the National Science Council, Taiwan, through Grant NSC 97-2221-E-006-245 and NSC 96-2112-M-006-015-MY3. We are grateful to the National

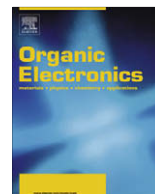
Center for High-performance Computing of Taiwan for computer time and facilities. The authors acknowledge J.M. Chen for the technical support and helpful discussion during the XRD measurements.

#### References

- [1] (a) For example, see: W. Brütting (Ed.), *Physics of Organic Semiconductors*, Wiley-VCH, Weinheim, Germany, 2005; (b) H. Klauk (Ed.), *Organic Electronics: Materials, Manufacturing and Applications*, Wiley-VCH, Weinheim, Germany, 2006.
- [2] (a) G. Horowitz, *Adv. Mater.* 10 (1998) 365; (b) C.D. Dimitrakopoulos, P.R.L. Malenfant, *Adv. Mater.* 14 (2002) 99.
- [3] M. Pope, C.E. Swenberg, *Electronic Processes in Organic Crystals and Polymers*, Oxford, New York, 1999.
- [4] (a) R.A. Marcus, *Rev. Mod. Phys.* 65 (1993) 599; (b) P.F. Barbara, T.J. Meyer, M.A. Ratner, *J. Phys. Chem.* 100 (1996) 13148; (c) V. Coropceanu, J. Cornil, D.A. da Silva Filho, Y. Olivier, R. Silbey, J.-L. Brédas, *Chem. Rev.* 107 (2007) 926.
- [5] (a) For example, see: Y.-Y. Lin, D.J. Gundlach, S.F. Nelson, T.N. Jackson, *IEEE Electron. Dev. Lett.* 8 (1997) 606; (b) T.W. Kelley, D.V. Muires, P.F. Baude, T.P. Smith, T.D. Jones, *Mater. Res. Soc. Symp. Proc.* 771 (2003) 169; (c) S. Lee, B. Koo, J. Shin, E. Lee, H. Park, H. Kima, *Appl. Phys. Lett.* 88 (2006) 162109.
- [6] (a) R.G.D. Valle, A. Brillante, E. Venuti, L. Farina, A. Girlando, M. Masino, *Org. Electron.* 5 (2004) 1; (b) C.C. Mattheus, G.A. de Wijs, R.A. de Groot, T.T.M. Palstra, *J. Am. Chem. Soc.* 125 (2003) 6323.
- [7] G. Horowitz, M.E. Hajlaoui, *Adv. Mater.* 12 (2000) 1046.
- [8] (a) A. Di Carlo, F. Piacenza, A. Bolognesi, B. Stadlober, H. Maresch, *Appl. Phys. Lett.* 86 (2005) 263501; (b) R. Matsubara, N. Ohashi, M. Sakai, K. Kudo, M. Nakamura, *Appl. Phys. Lett.* 92 (2008) 242108.
- [9] J.H. Kang, D. da Silva Filho, J.-L. Brédas, X.-Y. Zhu, *Appl. Phys. Lett.* 86 (2005) 152115.
- [10] V. Nádazdy, R. Durný, J. Puiggollers, C. Voz, S. Cheylan, K. Gmucová, *Appl. Phys. Lett.* 90 (2007) 092112.
- [11] Inorganic systems, for example, see: (a) J. Levinson, F.R. Shepherd, P.J. Scanlon, W.D. Westwood, G. Este, M. Rider, *J. Appl. Phys.* 53 (1982) 1193; (b) F.V. Farmakis, J. Brini, G. Kamarinos, C.T. Angelis, C.A. Dimitriadis, M. Miyasaka, *IEEE Trans. Electron. Dev.* 48 (2001) 701.
- [12] Organic systems, for example, see: (a) R.A. Street, D. Knipp, A.R. Völkel, *Appl. Phys. Lett.* 80 (2002) 1658; (b) G. Horowitz, *Adv. Funct. Mater.* 13 (2003) 53; (c) Y.W. Wang, H.L. Cheng, Y.K. Wang, T.H. Hu, J.C. Ho, C.C. Lee, T.F. Lei, C.F. Yeh, *Thin Solid Films* 467 (2004) 215.
- [13] F.-J. Meyer zu Heringdorf, M.C. Reuter, R.M. Tromp, *Nature* 412 (2001) 517.
- [14] Y. Wu, T. Toccoli, N. Koch, E. Jacob, A. Pallaoro, P. Rudolf, S. Iannotta, *Phys. Rev. Lett.* 98 (2007) 076601.
- [15] G.S. Tulevski, Q. Miao, A. Afzali, T.O. Graham, C.R. Kagan, C. Nuckolls, *J. Am. Chem. Soc.* 128 (2006) 1788.
- [16] For example, see: (a) M. Shtein, J. Mapel, J.B. Benziger, S.R. Forrest, *Appl. Phys. Lett.* 81 (2002) 268; (b) M.H. Choo, J.H. Kim, S. Im, *Appl. Phys. Lett.* 81 (2002) 4640; (c) D. Knipp, R.A. Street, A. Völkel, J. Ho, *J. Appl. Phys.* 93 (2003) 347; (d) W.Y. Chou, Y.S. Mai, H.L. Cheng, C.Y. Yeh, C.W. Kuo, F.C. Tang, D.Y. Shu, T.R. Yew, T.C. Wen, *Org. Electron.* 7 (2006) 445.
- [17] H.L. Cheng, Y.S. Mai, W.Y. Chou, L.R. Chang, *Appl. Phys. Lett.* 90 (2007) 171926.
- [18] S.M. Sze, *Physics of Semiconductor Devices*, Wiley-Interscience, New York, 1981.
- [19] M.J. Frisch, G.W. Trucks, H.B. Schlegel, G.E. Scuseria, M.A. Robb, J.R. Cheeseman, J.A. Montgomery Jr., T. Vreven, K.N. Kudin, J.C. Burant, J.M. Millam, S.S. Iyengar, J. Tomasi, V. Barone, B. Mennucci, M. Cossi, G. Scalmani, N. Rega, G.A. Petersson, H. Nakatsuji, M. Hada, M. Ehara, K. Toyota, R. Fukuda, J. Hasegawa, M. Ishida, T. Nakajima, Y. Honda, O. Kitao, H. Nakai, M. Klene, X. Li, J.E. Knox, H.P. Hratchian, J.B. Cross, V. Bakken, C. Adamo, J. Jaramillo, R. Gomperts, R.E. Stratmann, O. Yazyev, A.J. Austin, R. Cammi, C. Pomelli, J.W. Ochterski, P.Y. Ayala, K. Morokuma, G.A. Voth, P. Salvador, J.J. Dannenberg, V.G. Zakrzewski, S. Dapprich, A.D. Daniels, M.C. Strain, O. Farkas, D.K. Malick, A.D. Rabuck, K. Raghavachari, J.B. Foresman, J.V. Ortiz, Q. Cui, A.G. Baboul, S. Clifford, J. Cioslowski, B.B. Stefanov, G. Liu, A. Liashenko, P. Piskorz,



- I. Komaromi, R.L. Martin, D.J. Fox, T. Keith, M.A. Al-Laham, C.Y. Peng, A. Nanayakkara, M. Challacombe, P.M.W. Gill, B. Johnson, W. Chen, M.W. Wong, C. Gonzalez, J.A. Pople, Gaussian 03, Revision E.01, Gaussian, Inc., Wallingford, CT, 2004.
- [20] (a) A.D. Becke, *Phys. Rev. A* 38 (1988) 3098;  
(b) C.T. Lee, W.T. Yang, R.G. Parr, *Phys. Rev. B* 37 (1988) 785.
- [21] A.P. Scott, L. Radom, *J. Phys. Chem.* 100 (1996) 16502.
- [22] H.L. Cheng, Y.S. Mai, W.Y. Chou, L.R. Chang, X.W. Liang, *Adv. Funct. Mater.* 17 (2007) 3639.
- [23] V. Coropceanu, J.M. André, M. Malagoli, J.-L. Brédas, *Theor. Chem. Acc.* 110 (2003) 59.
- [24] A.S. Davydov, *Theory of Molecular Excitons*, McGraw-Hill, New York, 1971.
- [25] (a) T. Jentsch, H.T. Juepner, K.-W. Brzezinka, A. Lau, *Thin Solid Films* 315 (1998) 273;  
(b) R. He, I. Dujovne, L. Chen, Q. Miao, C.F. Hirjibehedin, A. Pinczuk, C. Nuckolls, C. Kloc, A. Ron, *Appl. Phys. Lett.* 84 (2004) 987.
- [26] H.L. Cheng, W.Y. Chou, C.W. Kuo, Y.W. Wang, Y.S. Mai, F.C. Tang, S.W. Chu, *Adv. Funct. Mater.* 18 (2008) 285.
- [27] H.L. Cheng, W.Y. Chou, C.W. Kuo, F.C. Tang, Y.W. Wang, *Appl. Phys. Lett.* 88 (2006) 161918.
- [28] (a) J.T. Hupp, R.D. Williams, *Acc. Chem. Res.* 34 (2001) 808;  
(b) D.G. Thompson, J.R. Schoonover, C.J. Timpson, T.J. Meyer, *J. Phys. Chem. A* 107 (2003) 10250.
- [29] B.R. Suffolk, R.K. Gilpin, *Anal. Chem.* 57 (1985) 596.
- [30] Although there is a large contribution to the  $\lambda_i$  from the 1498  $\text{cm}^{-1}$  mode, we could not obtain useful information on this in polycrystalline pentacene films due to the very weak signals.
- [31] S.T. Bromley, M. Mas-Torrent, P. Hadley, C. Rovira, *J. Am. Chem. Soc.* 126 (2004) 6544.
- [32] (a) J. Cornil, D.A. Dossantos, X. Crispin, R. Silbey, J.-L. Brédas, *J. Am. Chem. Soc.* 120 (1998) 1289;  
(b) J. Cornil, D. Beljonne, J.P. Calbert, J.L. Brédas, *Adv. Mater.* 13 (2001) 1053;  
(c) P.J. Brown, D.S. Thomas, A. Köhler, J.S. Wilson, J.S. Kim, C.M. Ramsdale, H. Sirringhaus, R.H. Friend, *Phys. Rev. B* 67 (2003) 064203.
- [33] (a) T. Minakata, H. Imai, M. Ozaki, K. Saco, *J. Appl. Phys.* 72 (1992) 5220;  
(b) D. Dimitrakopoulos, A.R. Brown, A. Pomp, *J. Appl. Phys.* 80 (1996) 2501.
- [34] W.Y. Chou, H.L. Cheng, *Adv. Funct. Mater.* 14 (2004) 811.
- [35] R.L. McCreery, *Raman spectroscopy for chemical analysis*, in: J.D. Winefordner (Ed.), *Wiley Chemical Analysis Series*, vol. 157, Wiley-Interscience, New York, 2000 (Chapter 2).
- [36] (a) S. Pratontep, F. Nüesch, L. Zuppiroli, M. Brinkmann, *Phys. Rev. B* 72 (2005) 085211;  
(b) B. Stadlober, U. Haas, H. Maresch, A. Haase, *Phys. Rev. B* 74 (2006) 165304.
- [37] D. Jurchescu, M. Popinciuc, B.J. van Weeks, T.T.M. Palstra, *Adv. Mater.* 19 (2007) 688.
- [38] C.Y. Yang, L.R. Chang, Y.S. Mai, H.Y. Wang, W.Y. Chou, Y.W. Wang, H.L. Cheng, in: *The 13th International Symposium on Electrets*, Tokyo, Japan, 2008.
- [39] S. Uemura, A. Komukai, R. Sakaida, T. Kawai, M. Yoshida, S. Hoshino, T. Kodzasa, T. Kamata, *Syn. Met.* 153 (2005) 405.
- [40] D.A. Tenne, S. Park, T.U. Kampen, A. Das, R. Scholz, D.R.T. Zahn, *Phys. Rev. B* 61 (2000) 14564.



# White emission polymer light-emitting devices with efficient electron injection from alcohol/water-soluble polymer/Al bilayer cathode

Ding An, Jianhua Zou, Hongbin Wu\*, Junbiao Peng, Wei Yang, Yong Cao\*

*Institute of Polymer Optoelectronic Materials and Devices, Key Laboratory of Specially Functional Materials of the Ministry of Education, South China University of Technology, 381 Wushan Road, Guangzhou 510640, PR China*

## ARTICLE INFO

### Article history:

Received 25 September 2008

Received in revised form 28 November 2008

Accepted 28 November 2008

Available online 10 December 2008

### Keywords:

White emission polymer light-emitting devices

Electron-injection layer

Alcohol/water-soluble polymer

## ABSTRACT

We demonstrate highly efficient white emission polymer light-emitting diodes (WPLEDs) from multilayer structure formed by solution processed technique, in which alcohol/water-soluble polymer, poly [(9,9-bis(3'-(*N,N*-dimethylamino)propyl)-2,7-fluorene)-alt-2,7-(9,9-dioctylfluorene)] (PFN) was incorporated as electron-injection layer and Al as cathode. It was found that the device performance was very sensitive to the solvents from solution of which the PFN electron-injection layer was cast. Devices with electron-injection layer cast from methanol solution show degraded performance while the best device performance was obtained when mixed solvent of water and methanol with ratio of 1:3 was used. We attribute the variation in device performance to washing out the electron transport material in the emissive layer due to rinse effect. As a result of alleviative loss of electron transport material in the emissive layer, the optimized device with a peak luminous efficiency of 18.5 cd A<sup>-1</sup> for forward-viewing was achieved, which is comparable to that of the device with same emissive layer but with low work-function metal Ba cathode (16.6 cd A<sup>-1</sup>). White emission color with Commission International de l'Eclairage coordinates of (0.321, 0.345) at current 10 mA cm<sup>-2</sup> was observed.

© 2008 Elsevier B.V. All rights reserved.

## 1. Introduction

White organic light-emitting devices (WOLEDs) are of intense interest because of their potential applications in full-color flat-panel displays, solid-state lighting source and backlights for liquid-crystal displays [1–3]. Various approaches towards realizing WOLEDs have been reported, which include doping of RGB fluorophors or phosphors in a small molecule or polymer host [4–8], synthesis of a single polymer incorporating RGB emitting moieties in the polymer backbone or side chain [9,10], use of excimer or exciplex formed by one or two dopants [11–13], multilayer device with consecutive evaporations of RGB-emitting compounds [14,15]. So far, efficiency of WOLEDs based

on vacuum deposited technology have exceeded that of the incandescent light bulb (12–17 lm W<sup>-1</sup>) [1]. In contrast, only a few demonstrations with high efficiency exceeding this benchmark were reported for WPLEDs [16,17], and for most of white emission PLEDs, their power efficiencies are still much lower than 10 lm W<sup>-1</sup> mainly due to unbalanced charge injection, unsatisfactory charge transport and weak confinement of electron and hole [15]. Therefore, one of the most critical factors in achieving high efficiency for a given polymer is to obtain balanced electron and hole injection and effective confinement over the charge carrier. To minimize the injection barrier height for electron, low work-function metals are usually employed as cathode [18,19]. However, since the low-work function metals are susceptible to degradation upon water vapor and oxygen, high work-function metal, thereby more stable electron injection cathodes are desirable, if they can provide comparable device efficiency. Over the past years, significant efforts have been made to develop

\* Corresponding authors. Tel.: +86 20 35902080/87114609; fax: +86 20 87110606.

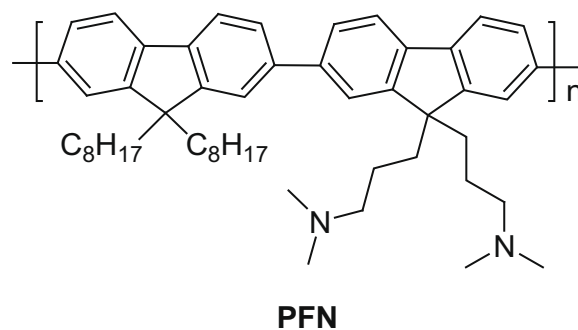
E-mail addresses: [hbwu@scut.edu.cn](mailto:hbwu@scut.edu.cn) (H. Wu), [poycao@scut.edu.cn](mailto:poycao@scut.edu.cn) (Y. Cao).

a new electron injection cathode from high work-function metals in order to reach a high environmental stability, easy fabrication in combination with high device efficiency and a low operating voltage. For example, Park et al. reported the use of the ionomer-type and salt-type electron-injection layer with air-stable metal Al as cathode [20,21]. Recently, several groups reported that thin film of alcohol- or water-soluble conjugated polymer in combination with air-stable metals (such as Al, Ag, and Au) can be used as efficient electron injection cathode for PLEDs with high efficiency of green or red-emitting devices [22–29]. And more recently, Zhang et al. have developed a novel method in which a thin layer of poly[9,9-bis(6'-(diethanolamino)hexyl)-fluorene] (PFN-OH) spin-coated from water/ethanol mixed solvent was used as electron-injection layer for WPLEDs consisting of two phosphores (blue Ir complex and orange Os complex) doped into poly(*N*-vinylcarbazole) (PVK), the device efficiency is much higher than that with PFN-OH cast from neat ethanol, to improve the performance of white phosphorescent PLEDs by manipulating the morphology of the electron-injection layer through solvent processing [17].

In this letter, we demonstrate that analogous concepts can be applied to fabricate highly efficient multilayer WPLEDs based on blue and red Ir complexes, Flrpic and Ir(piq), respectively, in which a water/alcohol-soluble polymer, poly[(9,9-bis(3'-(*N,N*-dimethylamino)propyl)-2,7-fluorene)-alt-2,7-(9,9-dioctylfluorene)] (PFN) [24] was used as electron-injection layer, and air-stable, high work-function metal Al was used as cathode. We also found out that the device performance was very sensitive to the solvent composition from which PFN layer was cast, which is consistent with previous report [17]. We proposed that washing out of electron transport materials, 1,3-bis[4-tert-butylphenyl]-1,3,4-oxadiazolyl phenylene (OXD-7) component in the EML layer upon spin-coating of PFN layer from methanol solution is an important reason responsible for degradation of such device performance. Addition of water into PFN methanol solution prevents erosion of Ir complexes/PVK layer underneath and makes efficient electron injection from bilayer cathode possible. This implies that multilayer configuration is an effective approach for producing low-cost, and large-area size white PLEDs by spin-coating.

## 2. Experimental details

Devices configurations used in this study is ITO/poly(ethylenedioxythiophene):poly(styrene sulfonic acid) (PEDOT:PSS) (40 nm)/PVK:OXD-7:Flrpic (5%):Ir(piq) (0.25%) (70–80 nm)/cathode, in which PVK (70 wt%)/OXD-7 (30 wt%) form the host matrix, iridium bis(2-(4,6-difluorophenyl)pyridinato-*N,C*<sup>2'</sup>) picolinate (Flrpic, blue emission) and iridium bis(1-phenylisoquinoline) (acetylacetonate) (Ir(piq), red emission) are efficient triplet emitters. PVK was purchased from Aldrich, Ir(piq) were obtained from America Dyes Sources, respectively, and used as received. Flrpic, OXD-7 and PFN were synthesized in our laboratory. The chemical structure of PFN is shown in Scheme 1. PEDOT:PSS (Baytron P 4083, Bayer AG) was purchased from H. C. Starck, Inc.



**Scheme 1.** Chemical structure of the water soluble polymer (PFN).

The fabrication of devices followed well-established processes [25]. Patterned indium tin oxide (ITO) coated glass with a sheet resistance of 15–20  $\Omega$ /square were cleaned by a surfactant scrub, then underwent a wet-cleaning process inside an ultrasonic bath, beginning with deionized water, followed by acetone and isopropanol. After oxygen plasma cleaning for 4 min, a 40 nm-thick PEDOT:PSS anode buffer layer of was spin-cast on the ITO substrate and then dried in vacuum oven at 80 °C overnight. The emitting layer, with thickness in the 70–80 nm range, was then deposited on top of PEDOT layer, by casting from a chlorobenzene solution containing PVK (60 wt%):OXD-7 (30 wt%):Flrpic (10 wt%):Ir(piq) (0.5 wt%), followed by thermal annealing at 120 °C for 30 min. A Tencor, Alfa-Step 500 surface profiler was used to determine thickness of the PEDOT and EL polymer films. Deposition of PFN layers and determination of their thickness follows a previously published paper [24,25] and thickness control is adjusted by spin speed between 600 rpm to 2500 rpm. In a word, the thickness of PFN was determined by a surface profiler (Alfa Step-500, Tencor) in combination with extrapolation from an absorbance–thickness curve assuming a linear dependence of absorbance at 380 nm of PFN peak on the film thickness. Prior to making the co-solvent solution, the solubility of PFN in methanol and water was checked, respectively. It was found when dissolved into methanol, with a few drops of acetic acid added and heating up to 60 °C, a concentration of 10–15 mg/ml was reached, yielding a clear solution with no sign of saturation. Nevertheless, the solubility decreases rapidly in water, for instance, even dissolving 2 mg of PFN in 1 mL of water requires heating, apparently due to the reduced solvent polarity. Given these conditions, when we handled with water/methanol (6v/1v) co-solvent solution, or any other co-solvent solution, we made PFN methanol solution first, for example, in a concentration of 2–5 mg/ml. Depending on the water/methanol blending ratio, corresponding amount of water is added to form the targeted diluted solution. When water was added in the prepared PFN methanol solution, the resulted mixed solution became slightly ropy whereas remained clear. Finally, 4 nm barium and 100 nm aluminum layer were evaporated with a shadow mask at a base pressure of  $3 \times 10^{-4}$  Pa. The thickness of the evaporated cathodes was monitored by a quartz crystal thickness/ratio monitor

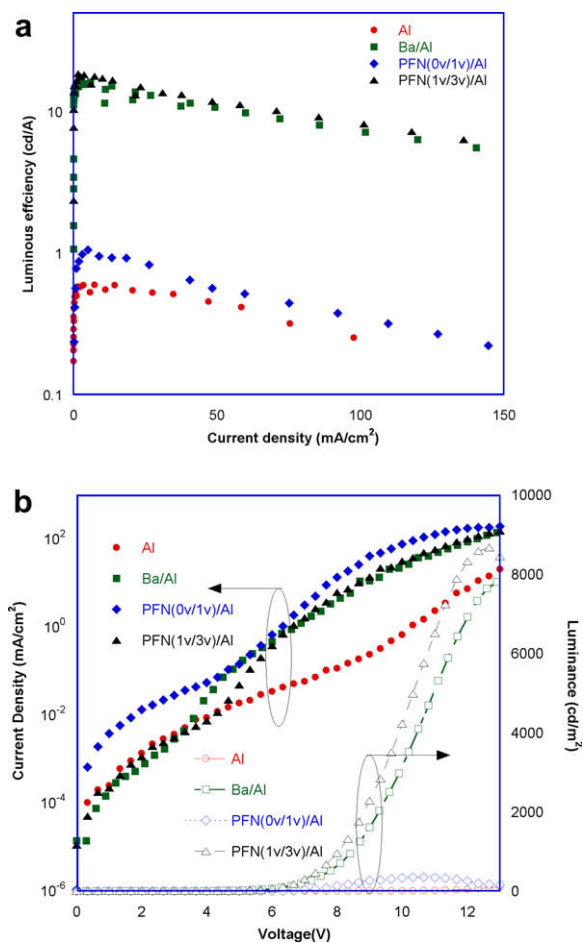
(Model: STM-100/MF, Sycon). The structure of electron-only devices we studied in this letter is ITO/Ba(20 nm)/EML(70–80 nm)/PFN(20 nm)/Al(120 nm). 20 nm barium layer were evaporated on the ITO substrate with a shadow mask at a base pressure of  $3 \times 10^{-4}$  Pa. The overlapping area between the cathode and anode defined a pixel size of  $17 \text{ mm}^2$ . Except for the deposition of the PEDOT layers, all the fabrication processes were carried out inside a controlled atmosphere of nitrogen dry-box (Vacuum Atmosphere Co.) containing less than 10 ppm oxygen and moisture. The current–luminance–voltage ( $I$ – $L$ – $V$ ) characteristic was measured using a Keithley 236 source–measurement unit and a calibrated silicon photodiode. The forward-viewing luminance was calibrated by a spectrophotometer (SpectraScan PR-705, Photo Research) and the forward-viewing LE was calculated accordingly. Throughout the whole manuscript, reported value of luminance and LE are for forward-viewing direction only. The external quantum efficiency of EL was collected by measuring the total light output in all directions in an integrating sphere (IS-O80, Labsphere). The photoluminescent spectra was recorded by a single-grating monochromator (Instaspec IV, Oriel Co.) equipped with a CCD detector,

and electroluminescent spectra was collected by a PR-705 photometer. The photovoltaic measurement was carried out under white-light illumination using a xenon lamp (150 W, Oriel) as a light source.

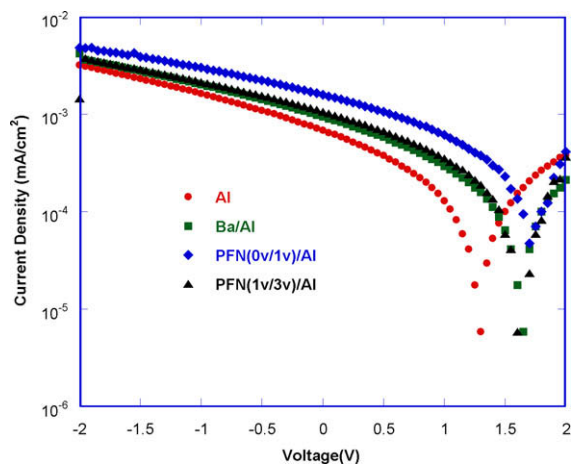
### 3. Results and discussion

Fig. 1a display the forward-viewing luminous efficiency–current density ( $LE$ – $J$ ) characteristics of the devices with different cathodes (Al, Ba/Al, PFN (methanol)/Al, PFN (water/methanol, 1v/3v)/Al, respectively). All the thickness of PFN was fixed at its optimized value of 20 nm. It was found that that the maximal  $LE$  of the device with neat Al as cathode is only  $0.59 \text{ cd A}^{-1}$ , which is consistent with the fact that Al has a work-function of 4.3 eV and a big electron injection barrier exists at the PVK/Al interface. On the other hand, it is interesting to note that changing the solution composition for PFN coating can make a substantial impact on the device performance. The maximal  $LE$  of the device with PFN (water/methanol, 1v/3v)/Al as cathode can be as high as  $18.5 \text{ cd A}^{-1}$ , while a maximal luminance of  $8672 \text{ cd m}^{-2}$  was obtained at 12.6 V (Fig. 1b). This is comparable to that of device with low work-function metal Ba as cathode (a peak forward-viewing  $LE$  of  $16.6 \text{ cd A}^{-1}$  and a maximal luminance of  $7823 \text{ cd m}^{-2}$  at 13.2 V, respectively). We also note that insertion of additional Ba between PFN (water/methanol, 1v/3v) layer and Al have minor effect on the device performance further indicating that the enhancement is originated from the incorporation of PFN layer itself. On the other hand, the maximal  $LE$  of device with the PFN (methanol)/Al device is only  $1.0 \text{ cd A}^{-1}$  with a maximal luminance of  $351 \text{ cd m}^{-2}$  at 10.6 V. We also note that the turn-on voltage (defined as voltage at which luminance of  $1 \text{ cd m}^{-2}$  was detected) of the device with the PFN (methanol)/Al is quite high (6.3 V), while for the device with PFN (water/methanol, 1v/3v)/Al, lower turn-on voltage of 4.8 V was observed, close to that of Ba/Al device (3.9 V).

$J$ – $L$ – $V$  characteristics of the devices with the four types of cathodes are presented in Fig. 1b. It is obvious that the



**Fig. 1.**  $LE$ – $J$  (a) and  $J$ – $L$ – $V$  (b) characteristic of the devices with different cathode (Al, Ba/Al, PFN (methanol)/Al, PFN (water/methanol, 1v/3v)/Al cathodes, respectively).



**Fig. 2.** Photovoltaic characteristics of the white emission PLEDs with different cathode.

PFN (water/methanol, 1v/3v)/Al bilayer cathode provides an efficient electron injection due to reduced electron injection barrier height [25,26] and the device performance with such bilayer cathode was dramatically enhanced over plain Al cathode devices. On the other hand, despite its poor device performance, the PFN(methanol)/Al device exhibit the maximal current density over any other devices at any voltage studied, suggesting that its device performance is limited by imbalanced charge carriers transport rather than by injection of electron itself. This is supported by built-in potential measurement [23,25] shown in Fig. 2. As deduced from the  $J$ - $V$  cure under illumination from solar simulator, the built-in across the device shift from 1.30 V for a plain Al device to about 1.60–1.70 V for the PFN(W/M)/Al, PFN(M)/Al and Ba/Al cathode device. This reveals that the built-in potentials of all of the three types of devices are very close (with difference of only 0.05 V), indicating electron injection barrier height of these devices are similar. In order to further clarify the influence of solvent composition on the charge transport properties of the device, it is necessary to compare the sole current of electron. Therefore, hole carrier flux must be suppressed by a large barrier to form an electron-only device. Since highest occupied molecular orbital (HOMO) of PVK is  $-5.8$  eV, an hole injection barrier of 3.0 eV is expected when using low work-function metal such as Ba (2.8 eV) as anode. Two sets of electron-only devices in configuration like ITO/Ba(20 nm)/EML(70–80 nm)/PFN(20 nm)/Al(120 nm) were fabricated with PFN layers processed from two types of solvents, respectively, and their  $J$ - $V$  characteristics is shown in Fig. 3. In order to obtain reliable anode/polymer contact with extra high injection barrier height, prior to spin-coating of EML, 20 nm of barium film was evaporated on precleaned ITO substrate with a shadow mask at a base pressure of  $3 \times 10^{-4}$  Pa. More importantly, anhydrous grade chlorobenzene (Aldrich) containing negligible water (less than 0.005 wt%) was used as solvent for the EML solution to alleviate ero-

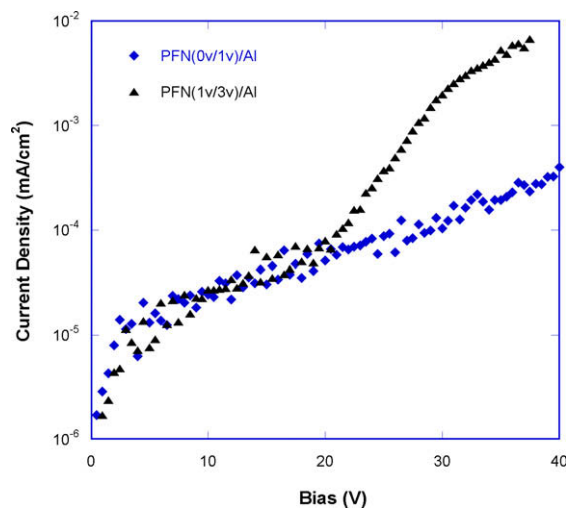


Fig. 3.  $J$ - $V$  characteristics of electron-only device with PFN (methanol)/Al and PFN (water/methanol, 1v/3v)/Al as cathode, respectively.

sion. Negligible emission from the resulted devices further confirmed that electron is the dominant charge carrier in the devices. In addition, diodes characteristics shown in Fig. 3 also confirmed that it is not likely the 20 nm of barium be oxidated by the residue water completely. It is found that electron current density through PFN (water/methanol, 1v/3v)/Al device is significantly higher than that of PFN(methanol)/Al device, which must be results of the better electron transport properties in the former device keeping in mind that the electron injection barriers are the same for these two type of devices. In addition, the fact that insufficient electron transport in the PFN(methanol)/Al device results in higher total current density through the device can be understood if one take into account the fact that electron accumulation at the internal interface can give rise to a significant redistribution of the electric field inside the device [30]. Furthermore, imbalanced charge transport in the bulk of PFN (methanol)/Al was also supported by the EL spectra of the PFN (methanol)/Al device (Fig. 4), which will be discussed later.

It is also worthy to point out that changing the ratio between water and methanol can significantly affect on the device performance of the WPLEDs. Table 1 presents the influence of various solvent ratios (from 6:1 to 1:10 by volume, water to methanol) on peak LE, peak luminance and CIE coordinates (at  $10 \text{ mA cm}^{-2}$ ) the devices. It can be seen that the best device performance (highest LE) is obtained when water/methanol ratio is 1v/3v.

Fig. 4 displayed the EL spectra of the white PLEDs with different cathodes (Al, Ba/Al, PFN(methanol)/Al, PFN(water/methanol, 1v/3v)/Al) at a current density of  $10 \text{ mA cm}^{-2}$ , which corresponded to CIE coordinates of (0.366,0.362), (0.320,0.369), (0.205,0.328), and (0.321, 0.345), respectively, very close to ideal white emission point (0.33, 0.33). For all of the EL spectra, two intense peaks around 470 nm and 620 nm and a small shoulder peak at 500 nm were clearly observed, which can be

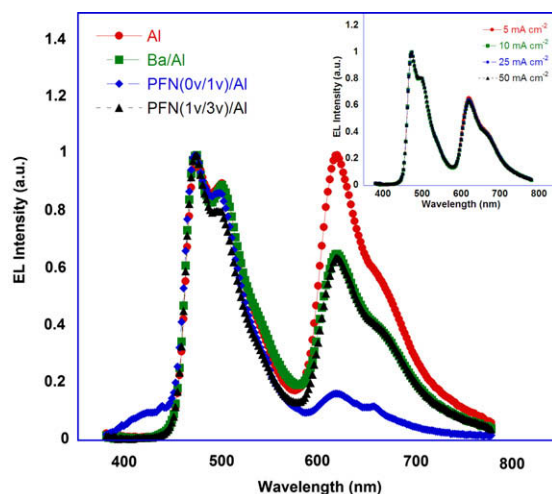
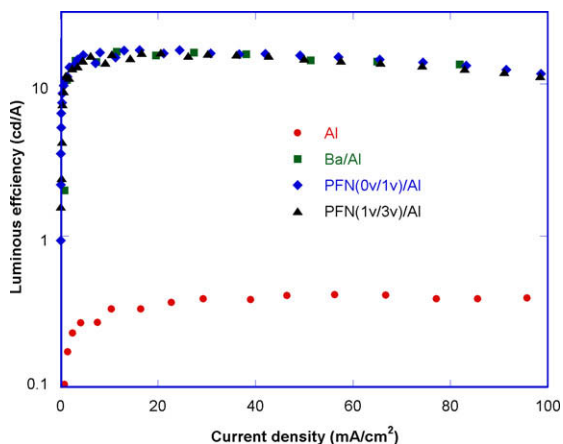


Fig. 4. EL spectra for the different cathode structure, of which with Al, Ba/Al, PFN (methanol)/Al, PFN (water/methanol, 1v/3v)/Al cathode, respectively. Inset: EL spectra for device with PFN (water/methanol, 1v/3v)/Al with different current density.

**Table 1**

Performances of the devices with PFN as EIL layer from various water/methanol concentrations. [Devices configurations: ITO/PEDOT:PSS(40 nm)/PVK:OXD-7:Irpic(5%):Irpic(0.25%) (70–80 nm)/PFN (20 nm)/Al (120 nm)].

Cathode (PFN/Al) (water/methanol)	Peak luminance (cd m <sup>-2</sup> )	Peak LE (cd A <sup>-1</sup> )	CIE (x,y)
6v/1v	1416	4.9	(0.364,0.362)
3v/1v	1547	8.5	(0.361,0.363)
1v/1v	9651	16.1	(0.348,0.361)
1v/3v	8672	18.5	(0.321,0.345)
1v/6v	1875	4.2	(0.331,0.359)
1v/10v	640	2.4	(0.235,0.354)
0v/1v	351	1.0	(0.205,0.328)



**Fig. 5.** LE–*J* characteristics of PLEDs based on green emitting poly [2-(4-(3',7'-dimethyloctyloxy)-phenyl)-*p*-phenylenevinylene] as active layer and Al, PFN (methanol)/Al and PFN (water/methanol, 1v/3v)/Al as cathode, respectively.

assigned to the emission from Irpic and Ir(piq). However, the device with PFN (methanol)/Al as cathode shows additional emission peak at 420 nm, which can be attributed to the EL emission of PFN layer itself, indicating that the excitation recombination zone shift towards cathode side as a result of imbalanced charge carrier transport in such device and accumulated electron at PFN/emissive layer interface. In contrast, PLEDs with single emissive component (i.e. phenylenevinylene or polyfluorene derivative) does not show such dependence on the solvent from which PFN layer was spin-cast. As clearly seen from Fig. 5, with green emitting poly[2-(4-(3',7'-dimethyloctyloxy)-phenyl)-*p*-phenylenevinylene] (P-PPV) as emissive layer, both PFN(M)/Al and PFN(W/M)/Al cathode device show significant enhancement with a peak luminous efficiency around 16 cd A<sup>-1</sup> when compared with the plain Al device (~0.40 cd A<sup>-1</sup>). We speculate that in the white emission device with PFN (methanol)/Al device, methanol dramatically affect on electron transport in the device by washing away OXD-7, resulting in imbalanced electron transport, therefore leading to degraded device performance. Since Irpic had been shown to exhibit bipolar transport properties [31], the reduced electron transport properties in the device had even greater impact on the excitation of Ir(piq),

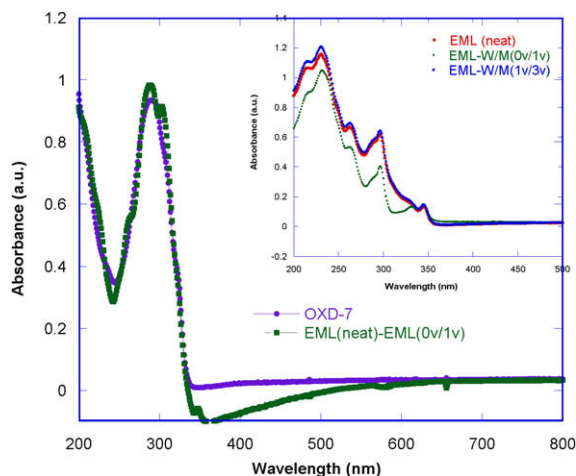


**Fig. 6.** The normalized spectral difference between the neat film and those treated by methanol and UV-Vis absorption spectra of OXD-7. Inset: the UV-Vis spectra of the EML, equivalent film treated by methanol and co-solvent (water/methanol, 1v/3v), respectively.

leading to a significantly reduced red emission from Ir(-piq). Furthermore, since charge trapping is the dominant process in the electrical excitation of these devices [8], and Ir(piq) serve as hole traps due to its high HOMO level, it is expected that a reduced electron transport will significantly influence the excitation of the Ir(piq), fully consistent with the observation shown in Fig. 4.

The emission color of the device with PFN (water/ethanol, 1v/3v)/Al as cathode showed minor color shift upon change of applied current density, for example, as the current density increase from 5 mA cm<sup>-2</sup> to 10, 20, and 50 mA cm<sup>-2</sup>, CIE coordinates shifted from (0.325,0.345) to (0.321,0.347). EL spectra for device with PFN (water/methanol, 1v/3v)/Al at different current density are also shown in the inset of Fig. 4.

In order to get insight into the strong dependence of device performance on the solvent composition, UV-Vis spectra of neat EML and equivalent film treated by methanol and mixed solvent (water/methanol, 1v/3v) were compared (inset in Fig. 6). As shown in Fig. 6, it was found that the spectral difference between the neat film and those treated by methanol is consistent with the UV-Vis spectra of OXD-7, while in contrast, UV-Vis spectra of the neat film and the film treated with mixed solvent (water/methanol, 1v/3v) was nearly identical, thus confirm removal of the small molecule in the EML in somehow upon drop casting of PFN from methanol solution atop. The mechanisms of alleviative erosion of PVK:OXD-7:Ir complexes upon incorporation of water into PFN methanol solution is not clear so far and will be investigated in the follow-up study.

#### 4. Conclusions

In summary, highly efficient white emission polymer light-emitting diodes was fabricated from multilayer structure formed by solution processed technique using a water/alcohol-soluble polymer as electron-injection layer, and air-stable, high work-function metal Al was used as

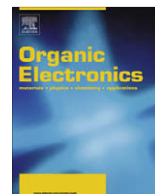
cathode. To obtain optimized device performance, 25% amount of water was added into PFN methanol solution to prevent erosion of Ir complexes/PVK layer underneath and makes efficient electron injection from bilayer cathode and transport possible. The maximal luminance efficiency of the resulting device increase immensely from  $0.59 \text{ cd A}^{-1}$  for device with neat Al cathode,  $1.0 \text{ cd A}^{-1}$  for device with PFN spin-coated from methanol to  $18.5 \text{ cd A}^{-1}$  for devices with optimized PFN/Al cathode, which is comparable to those obtained using Ba cathode. We found that washing out of electron transport materials, OXD-7 component in the EML layer upon spin-coating of PFN layer from methanol solution is an important reason responsible for degradation of such device performance. Addition of water into PFN methanol solution prevents erosion of Ir complexes/PVK layer underneath although the mechanism is not clear so far. Using air-stable metals as cathode makes these white emitting PLEDs promising candidates for lighting applications. Our study implies that multilayer configuration is an effective approach for producing low-cost, and large-area size white PLEDs by spin-coating.

### Acknowledgements

The authors are grateful to the Natural Science Foundation of China (Project Nos. 50433030 and U0634003) and the Ministry of Science and Technology Project (No. 2002CB613400) for the financial support.

### References

- [1] B.W. D'Andrade, S.R. Forrest, *Adv. Mater.* 16 (2004) 1585.
- [2] A. Misra, P. Kumar, M.N. Kamalasanan, S. Chandra, *Semicond. Sci. Technol.* 21 (2006) R35.
- [3] R. Duggal, J.J. Shiang, C.M. Heller, D.F. Foust, *Appl. Phys. Lett.* 80 (2002) 3470.
- [4] P.I. Shih, Y.H. Tseng, F.I. Wu, A.K. Dixit, C.F. Shu, *Adv. Funct. Mater.* 16 (2006) 1582.
- [5] S. Kim, J. Seo, H.K. Jung, J.-J. Kim, S.Y. Park, *Adv. Mater.* 17 (2005) 2077.
- [6] X. Gong, W.L. Ma, J.C. Ostrowski, G.C. Bazan, D. Moses, A.J. Heeger, *Adv. Mater.* 16 (2004) 615.
- [7] Y. Shao, Y. Yang, *Appl. Phys. Lett.* 86 (2005) 073510.
- [8] H.B. Wu, J.H. Zou, F. Liu, L. Wang, A. Mikhailovskiy, G.C. Bazan, W. Yang, Y. Cao, *Adv. Mater.* 20 (2008) 696.
- [9] G.L. Tu, C.Y. Mei, Q.G. Zhou, Y.X. Cheng, Y.H. Geng, L.X. Wang, D.G. Ma, X.B. Jing, F.S. Wang, *Adv. Funct. Mater.* 16 (2006) 101.
- [10] J. Jiang, Y. Xu, W. Yang, R. Guan, Z. Liu, H. Zhen, Y. Cao, *Adv. Mater.* 18 (2006) 1769.
- [11] E.L. Williams, K. Haavisto, J. Li, G.E. Jabbour, *Adv. Mater.* 19 (2007) 197.
- [12] V. Adamovich, J. Brooks, A. Tamayo, A.M. Alexander, P.I. Djurovich, B.W. D'Andrade, C. Adachi, S.R. Forrest, M.E. Thompson, *New J. Chem.* 26 (2002) 1171.
- [13] M. Mazzeo, D. Pisignano, F. Della Sala, J. Thompson, R.I.R. Blyth, G. Gigli, R. Cingolani, G. Sotgiu, G. Barbarella, *Appl. Phys. Lett.* 82 (2003) 334.
- [14] B.W. D'Andrade, J. Brooks, V. Adamovich, M.E. Thompson, S.R. Forrest, *Adv. Mater.* 14 (2002) 1032.
- [15] Y. Sun, N.C. Giebink, H. Kanno, B. Ma, M.E. Thompson, S.R. Forrest, *Nature* 440 (2006) 908.
- [16] J. Huang, G. Li, E. Wu, Q. Xu, Y. Yang, *Adv. Mater.* 18 (2006) 114.
- [17] Y. Zhang, F. Huang, Y. Chi, A.K.-Y. Jen, *Adv. Mater.* 20 (2008) 1565.
- [18] I.D. Parker, *J. Appl. Phys.* 75 (1994) 1656.
- [19] T.H. Kim, H.K. Lee, O.O. Park, B.D. Chin, S.H. Lee, J.K. Kim, *Adv. Funct. Mater.* 16 (2006) 611.
- [20] T.-W. Lee, O.O. Park, L.-M. Do, T. Zyung, T. Ahn, H.-K. Shim, *J. Appl. Phys.* 90 (2001) 2128.
- [21] T.-W. Lee, H.-C. Lee, O.O. Park, *Appl. Phys. Lett.* 81 (2006) 214.
- [22] F. Huang, Y.H. Niu, Y. Zhang, J.W. Ka, M.S. Liu, A.K.-Y. Jen, *Adv. Mater.* 19 (2007) 2010.
- [23] Y. Cao, G. Yu, A.J. Heeger, *Adv. Mater.* 10 (1998) 917.
- [24] F. Huang, H.B. Wu, D.L. Wang, W. Yang, Y. Cao, *Chem. Mater.* 16 (2004) 708.
- [25] H.B. Wu, F. Huang, Y.Q. Mo, W. Yang, D.L. Wang, J.B. Peng, Y. Cao, *Adv. Mater.* 16 (2004) 1826.
- [26] H.B. Wu, F. Huang, J.B. Peng, Y. Cao, *Org. Electron.* 6 (2005) 118.
- [27] L. Wang, B. Liang, F. Huang, J.B. Peng, Y. Cao, *Appl. Phys. Lett.* 89 (2005) 151115.
- [28] R.Q. Yang, H.B. Wu, Y. Cao, Y.G.C. Bazan, *J. Am. Chem. Soc.* 128 (2006) 14422.
- [29] S.H. Oh, D. Vak, S.I. Na, T.W. Lee, D.Y. Kim, *Adv. Mater.* 20 (2008) 1624.
- [30] H. Bassler, *Polym. Adv. Technol.* 9 (1998) 402–418.
- [31] N. Matsusue, Y. Suzuki, H. Naito, *Jpn. J. Appl. Phys.* 44 (2005) 3691.



## Trap-limited mobility in space-charge limited current in organic layers

José M. Montero<sup>a</sup>, Juan Bisquert<sup>a,\*</sup>, Germà Garcia-Belmonte<sup>a</sup>, Eva M. Barea<sup>a</sup>, Henk J. Bolink<sup>b</sup>

<sup>a</sup> Photovoltaic and Optoelectronic Devices Group, Departament de Física, Universitat Jaume I, 12071 Castelló, Spain

<sup>b</sup> Institut de Ciència Molecular, Universitat de València, Polígon La Coma s/n, 46980 Paterna, València, Spain

### ARTICLE INFO

#### Article history:

Received 28 July 2008

Received in revised form 11 November 2008

Accepted 29 November 2008

Available online 10 December 2008

#### Keywords:

OLED

Transport in organic materials

Trap

Mobility

Impedance

Capacitance

### ABSTRACT

Space-charge limited current transport in organic devices, relevant to the operation of a range of organic optoelectronic devices, is analyzed in the frequency domain. The classical multiple trapping picture with one transport state and one trap level is used as the basis for the descriptions. By varying the energetic and kinetic properties of the traps, we show that the admittance and the capacitance spectra are considerably modified depending on the interplay between the trap-limited mobility and the trap kinetics. We point out that capacitance steps at low-frequency, usually found in experiments, are observed only for slow traps.

© 2008 Elsevier B.V. All rights reserved.

## 1. Introduction

The discovery of electroluminescence in organic materials [1] launched a vast research effort for improving the performance and stability of organic semiconductors applied in optoelectronic devices such as organic light-emitting diodes (OLEDs) [2]. Polymer-based OLEDs are quite appealing for their easy processability by spin coating and ink-jet printing techniques [3]. However, further understanding of the physical behavior of such materials is needed. For instance, the description of the charge transport in organic layers by space-charge limited current (SCLC) model requires to include field [4–6] or density-dependent [7] mobility according to the percolation models [8]. Experimentally, the determination of transit times in single-carrier devices has been widely used to measure the mobility by time-of-flight (TOF) [9] and impedance spectroscopy techniques [10,11], among others [12]. It has also been recognized that the role of energetic disorder is crucial for an adequate knowledge and control of the

properties of organic transport layers. Transport in a single-carrier device has been often rationalized in terms of an extended state and a distribution of traps in the band-gap [13–15]. In this approach, the traps produce a decrease of the transport rate in the extended states [16]. However, in general the dynamics of traps is far more complex, since the traps relaxation intersects with the transport features throughout the layer [17]. While the trapping-diffusion dynamics can be solved completely in homogeneous situations [18], the typical carrier distribution at high injection currents in an organic layer in the SCLC regime is highly inhomogeneous [19].

The aim of this paper is to go beyond a quasistatic approximation to the trap-limited mobility (in which free and trapped charge remain in local equilibrium [13,20]) and to treat rather generally an apparently simple problem, a two level system composed of a transport state and a single trap level. The advantage of this model is that we can fully classify the different dynamic regimes of the system by the interplay of the relevant kinetic constants. This gives us physical insight in the interpretation of more general systems with a distribution of localized levels (e.g., exponential or Gaussian) which can be calculated

\* Corresponding author.

E-mail address: [bisquert@fca.uji.es](mailto:bisquert@fca.uji.es) (J. Bisquert).



numerically, a method also applied to dual-carrier devices [10,21,22]. However, the latter systems are beyond the scope of this paper.

The problem treated in this paper has been already considered some decades ago by Dascalu [23,24] and Kassing [25,26], for the particular case of a slow-shallow trap (i.e., when the transit time is shorter than trapping time) and this case is also solved numerically in the present paper. In addition, we consider the dynamic results in the frequency domain for fast traps, and also for deep traps. By formulating a general analytical model valid for a fast-shallow trap, we find a delay in the transit time (and thus, a mobility decrease) due to multiple trapping, as measured by means of impedance techniques [27].

The paper has the following structure. Firstly, a mathematical description is presented of the single-trap model, secondly, physical implications according to the applications of the model are discussed, and finally, we provide the main conclusions.

## 2. Single-trap model

The SCLC for single-carrier transport (neglecting diffusion) of electrons in a transport level with density  $n_c$  that drift in the electric field  $F$ , a trap level of occupancy  $f_t$  and total density  $N_t$ , is described by: the continuity equation, the drift-current equation, Poisson equation and the trap dynamics equation, respectively [9,18]

$$\frac{dJ}{dx} = 0 \quad (1)$$

$$J = q\mu_0 n_c F + \varepsilon_r \varepsilon_0 \frac{\partial F}{\partial t} \quad (2)$$

$$\frac{dF}{dx} = \frac{q}{\varepsilon_r \varepsilon_0} (n_c + N_t f_t) \quad (3)$$

$$\frac{\partial f_t}{\partial t} = cn_c [1 - f_t] - ef_t \quad (4)$$

Here  $q$  is the elementary charge,  $\mu_0$  is the mobility,  $\varepsilon_r \varepsilon_0$  the dielectric constant, and  $c$  and  $e$  are the coefficients for electron capture and release, respectively. The potential can be calculated by integrating the electrical field along the thickness  $L$

$$V = \int_0^L F dx \quad (5)$$

The population of the extended states at the energy level  $E_c$ , for a non-degenerate semiconductor, relates to the Fermi level  $E_F$  as

$$n_c = N_c e^{(E_F - E_c)/k_B T} \quad (6)$$

where  $N_c$  is an effective density of states in the transport level (conduction band). Assuming that the trap level at energy  $E_t$  reaches equilibrium with the extended states (with the same Fermi level), the trap occupancy is given by

$$f_t = \frac{1}{1 + e^{(E_t - E_F)/k_B T}} \quad (7)$$

In steady state, Eq. (4) gives

$$\hat{f}_t = \frac{1}{1 + e/(cn_c)} \quad (8)$$

Therefore, the detailed balance condition provides the following relationship for the trap emission and capture coefficients:

$$e = cN_c e^{(E_t - E_c)/k_B T} \quad (9)$$

Let us denote steady-state by  $\bar{x}$  and small perturbation by  $\hat{x}$  applied at a certain angular frequency  $\omega$ . Therefore every electrical variable can be expressed as  $x = \bar{x} + \hat{x}$  to linearize the whole system of equations up to the first order [28,29]. As shown in Ref. [17], by solving Eq. (4) for a small perturbation, we obtain

$$\hat{f}_t = \frac{1}{\hat{n}_c} \frac{\bar{f}_t(1 - \bar{f}_t)}{1 + i\omega/\omega_t} \hat{n}_c \quad (10)$$

This term gives the contribution to the spectra of the capacitance and conductance of the trap. The trap frequency is defined as

$$\omega_t = \frac{e}{1 - \bar{f}_t} \quad (11)$$

This is the maximum frequency that the trap is acting as such, since at higher frequencies the trap cannot follow the ac perturbation, as will be described in Section 3. Inserting Eq. (9) in Eq. (11), we find the dependence of  $\omega_t$  on the trap energy and the occupation, as

$$\omega_t = \frac{cN_c e^{(E_t - E_c)/k_B T}}{1 - \bar{f}_t} \quad (12)$$

It should be remarked that in the SCLC regime,  $\bar{f}_t$  is position-dependent along the organic layer. The impedance is defined as the quotient of potential to current density,

$$Z(\omega) = \frac{\hat{V}(\omega)}{\hat{J}(\omega)} \quad (13)$$

$\hat{V}(\omega)$  is determined by spatial integration of  $\hat{F}(\omega)$  from the solution of the above described model. The boundary conditions at the injecting contact used to solve the electrical variables along the thickness in  $dc$  and  $ac$  conditions are [30,31]

$$\hat{n}_c(x=0) = N_c \text{ and } \hat{F}(x=0) = 0 \quad (14)$$

Capacitance and conductance are defined as follows:

$$C'(\omega) = \text{Re} \left[ \frac{1}{i\omega Z(\omega)} \right] \quad (15)$$

$$g(\omega) = \text{Re} \left[ \frac{1}{Z(\omega)} \right] \quad (16)$$

## 3. Results and discussion

In this section we show the results of the calculations of the capacitance and the conductance spectra for different trap properties and voltages, compared to the trap-free case. We first describe the latter case as a reference, and then discuss variations of energetics ( $E_t$ ), by considering a shallow and a deep trap level, and the trap kinetics ( $c$ ),

for a fast and a slow trap. The different configurations are given in Table 1.

### 3.1. Trap-free

The well-known trap free SCLC model with constant mobility is given by the analytical expression for stationary and impedance responses as [32]

$$J = \frac{9}{8} \varepsilon \mu_0 \frac{V^2}{L^3} \quad (17)$$

$$Z(\omega) = \frac{6}{g_0(i\omega\tau_0)^3} \left[ 1 - i\omega\tau_0 + \frac{1}{2}(i\omega\tau_0)^2 - \exp(-i\omega\tau_0) \right] \quad (18)$$

where the transit time, the geometrical capacitance and the conductance are, respectively,

$$\tau_0 = \frac{4}{3} \frac{L^2}{\mu_0 V} \quad (19)$$

$$C_g = \frac{\varepsilon}{L} \quad (20)$$

$$g_0 = \frac{dJ}{dV} = \frac{3}{\tau_0} C_g \quad (21)$$

For low-frequency, the admittance is

$$Y(\omega) = g_0 + i\omega \frac{3}{4} C_g \quad (22)$$

and for high-frequency it is

$$Y(\omega) = \frac{2}{3} g_0 + i\omega C_g \quad (23)$$

It is well-known that the capacitance spectrum makes a step from  $\frac{3}{4} C_g$  to  $C_g$  at around the transit time frequency, i.e., when the small perturbation of charge carriers injected by the frequency perturbation voltage is able to arrive at the collecting contact. However, in experimental data, this ideal behavior is usually distorted, mainly at low-frequencies, by the trap contribution to capacitance.

### 3.2. Steady-state characteristics of organic layers with shallow and deep traps

Experimental measurements of  $J$ - $V$  curves have been used to determine the transport properties in organic layers [33,34]. Simulations of current density-voltage curves and the Fermi level distributions are displayed in Fig. 1 for two different trap energy levels configurations. These results are well understood and described in the literature [35]. For a shallow trap, the trap population is much less than the population of the transport level, hence the electric field distribution is not significantly altered, causing only a slight variation in the Mott-Gurney square law

$$J \approx \frac{9}{8} \varepsilon \theta \mu_0 \frac{V^2}{L^3} \quad (24)$$

where  $\theta$  is a carrier-density dependent factor of trapped and free charge defined as [27]

$$\theta^{-1} = \left( 1 + \frac{\langle \bar{n}_t \rangle}{\langle \bar{n}_c \rangle} \right) \quad (25)$$

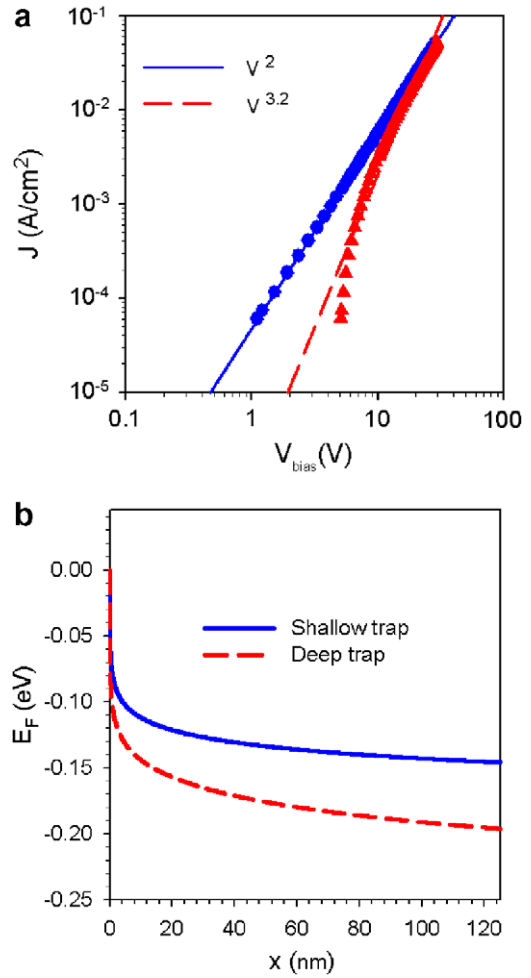


**Fig. 1.** Model simulations of shallow ( $E_c - E_t = 0.1$  eV) and deep ( $E_c - E_t = 0.5$  eV) trap configurations represented by blue solid lines and red dashed lines. (a) Current density voltage-characteristics for a shallow trap and a deep trap are plotted by blue dots and red triangles. Fittings provide the exponent of the voltage. (b) Fermi level representations at 6 V along the thickness, for a shallow trap (blue solid line) and a deep level (red dashed line). (For interpretation of the references to colour in this figure legend, the reader is referred to the web version of this article.)

with the brackets denoting an average over the thickness of the film. For a deep trap, the occupancy of the trap level increases and the trapped charges play a crucial role in the current density-voltage curves. At low bias, most carriers are trapped, thus significantly altering the carrier and electric field distributions with respect to trap-free case, leading to an abrupt increase of the current slope,  $J \propto V^m$  with  $m \geq 2$ . At high bias, the trapping sites are already filled and all the additional injected carriers are located in the transport level. This situation bends the curve from a higher voltage exponent than 2, towards a square law dependence.

### 3.3. Dynamic characterization of shallow traps

Let us now focus our attention on the dynamic properties of the electrical variables (capacitance and

conductance) in the case of the shallow trap. A general outline of the simulation results is displayed in Fig. 2. To accurately determine the *ac* transit times  $\tau_{ac}$ , it is worth to apply the representation of negative differential suscep-

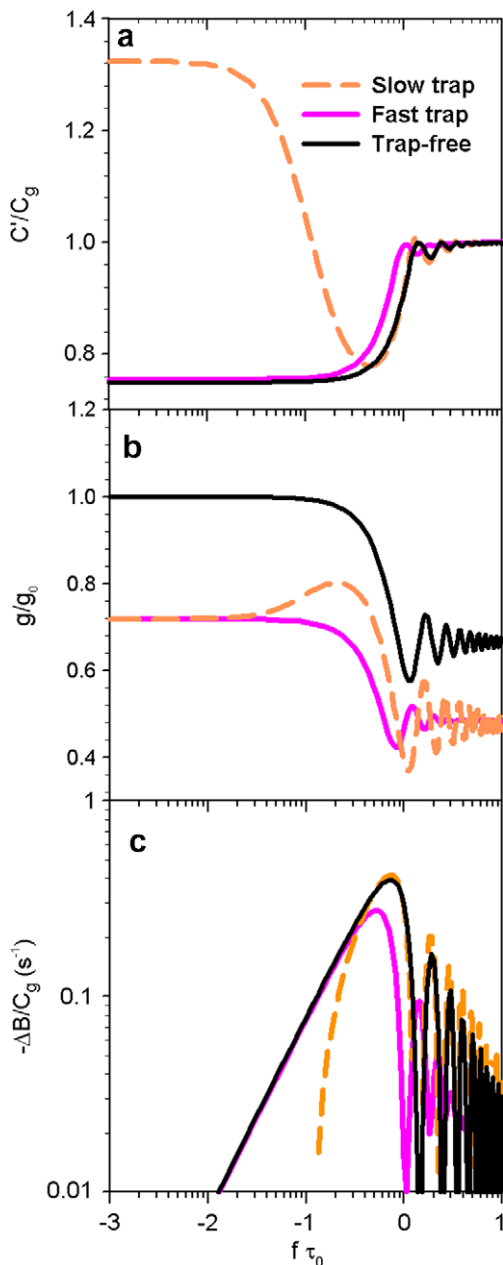


**Fig. 2.** Simulation spectra for shallow traps at 2 V. Fast traps are plotted by pink lines, slow traps by orange dashed lines and trap-free spectrum by black. (a) Capacitance spectra normalized to  $C_g$  for fast and slow traps. Low-frequency increase is displayed for slow traps whereas not for the fast ones. (b) Conductance spectra normalized to  $g_0$  for fast and slow traps. (c) Negative differential susceptance  $-\Delta B(\omega)$  normalized to  $C_g$  to extract transit times. In the case of fast trapping, *ac* transit time is  $\tau_{ac} = 1.36\tau_0$  ( $\tau_0 = 221.6 \mu\text{s}$ ) with  $\theta^{-1} \approx 1.40$ , whereas for slow trapping no deviation from the trap free is observed. (For interpretation of the references to colour in this figure legend, the reader is referred to the web version of this article.)

tance ( $-\Delta B(\omega) = \text{Im}(Y(\omega)) = -\omega(C'(\omega) - C_g)$ ), that provides peaks at certain frequencies  $f_{\text{max}}$  such that [36]

$$\tau_{ac} \approx 0.72 \cdot f_{\text{max}}^{-1} \quad (26)$$

Fig. 2a shows the capacitance spectra (normalized to  $C_g$ ) for the trap-free case, as a reference, and a shallow trap with two different trap kinetics, fast and slow (as specified below). At low-frequencies, the presence of a shallow trap in the organic layer implies (1) a deviation of the capacitance spectra for the slow case, and (2) of transit time for the fast one. At high frequencies, all the spectra converge to  $C_g$  with smooth and decaying oscillations as theoretically expected. In experiments, a slight decrease of the capacitance occurs due to the dielectric relaxation of the material [37].

As for conductance, Fig. 2b, the normalized low-frequency value decreases by a factor  $\theta$  and the calculated *ac* transit time (normalized to  $\tau_0$ ) is increased by  $\theta$ , although only for fast traps, thus in Fig. 2b we obtain for low-frequencies  $g = 0.71g_0$  and for high frequencies,  $g = 2\theta g_0/3$ . All these behaviors will be modeled and explained in terms of a quasi-equilibrium between the two states (trapping and transport levels) in the forthcoming subsections.

### 3.4. Fast-shallow traps

When the trap kinetics is fast, quasi-equilibrium prevails between carriers in the trap and transport levels. In this case we expect the standard formula of Rose [27] for trap limited transport to be valid

$$\mu = \theta\mu_0 \quad (27)$$

and therefore, the trap-limited transit time is

$$\tau = \theta^{-1}\tau_0 \quad (28)$$

In order to check Eq. (27), in Fig. 3 changes in the population of the traps were imposed by modifying  $N_t$ . The resulting capacitance spectra are well described by the trap-free case formulas by using the trap-limited values  $\tau$  and  $g$  instead of  $\tau_0$  and  $g_0$ . In particular we obtain

$$g = \frac{dJ}{dV} = \frac{3}{\tau}C_g = \theta g_0 \quad (29)$$

The inset of Fig. 3 shows that Eq. (28) is indeed satisfied.

The physical interpretation of this situation is given in terms of the interplay between trapping and detrapping and the carrier transit time. If fast-shallow traps are present in an organic layer, a delay in the transit time is expected and thereby, a mobility decrease. An experimental method to corroborate whether this kind of energetic disorder exists, consists on the evaluation of the *ac* transit time from admittance spectroscopy, Eq. (26), and the *dc* transit time, Eq. (19). The possible deviation should be attributed to the presence of fast-shallow traps.

### 3.5. Slow-shallow traps

If the trapped charge is not able to achieve the quasi-equilibrium with the carrier concentration in the transport

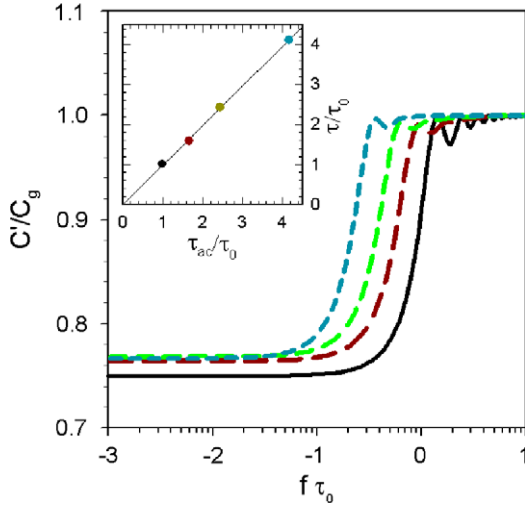


**Fig. 3.** Simulated capacitance spectra steps for fast-shallow traps at 6 V ( $\tau_0 = 73.8 \mu\text{s}$ ) with varying trap densities, from left to right:  $N_t = 8 \times 10^{17}$ ,  $4 \times 10^{17}$ ,  $2 \times 10^{17}$ ,  $0 \text{ cm}^{-3}$ . Inset shows an identification of the transit times between the models discussed in the text, and the *ac* conductance calculation.

levels, the spectra present a large low-frequency capacitance that increases above the  $3C_g/4$  value, Fig. 4. When exceeding the trap frequency  $\omega_t$  of Eq. (11), capacitance rapidly decreases as trapping action ceases for the rest of the frequency range. In contrast to the previous case, here carriers are able to cross the organic layer and reach the collecting contact before being trapped, avoiding any delay and following the trap-free transit time  $\tau_0$ . Dascalu and Kassing have given the analytical expression for the impedance in this situation [23–26]

$$Z(\omega) = \frac{6\alpha}{g_0} \sum_{k=0}^{\infty} \frac{\Gamma(\theta\alpha + 1)}{\Gamma(\theta\alpha + k + 2)} \frac{(-i\omega\tau_0)^k}{k + 3} \quad (30)$$

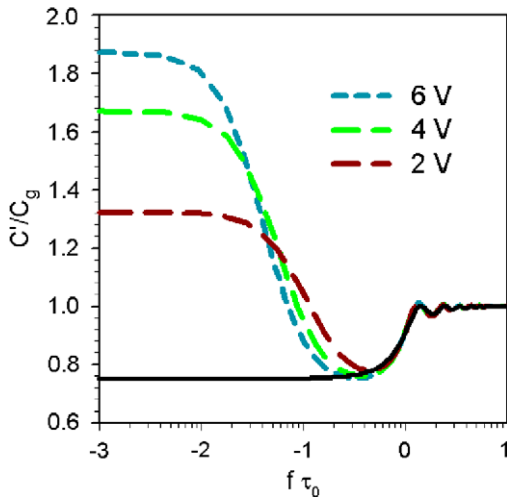


**Fig. 4.** Model representations of the capacitance spectra for slow-shallow traps at voltages 6, 4 and 2 V, from top to bottom. The trap-free spectrum is pictured in black.

with  $\alpha$  being

$$\alpha(\omega) = 1 + \frac{\omega_c}{\omega_e} \frac{1}{1 + i\omega/\omega_e} \quad (31)$$

Here  $\omega_c = c(N_t - \langle \bar{n}_t \rangle)$  and  $\omega_e = \beta(\langle \bar{n}_c \rangle + N_c e^{(E_t - E_c)/k_B T})$  are the reciprocal lifetimes for electrons in the conduction band and in the trap level, respectively. For low-frequency with  $N_t \gg \langle \bar{n}_t \rangle$ , we have the approximation [26]

$$Y(\omega) = g + i\omega \frac{C_g}{\omega_e \tau_0} \quad (32)$$

being  $g = \theta g_0$  and for high-frequency

$$Y(\omega) = \frac{2}{3}g + i\omega C_g \quad (33)$$

The low-frequency capacitance increase is usually found in experiments for single-carrier devices [11,38,10] and, according to our model, due to the slow-shallow trap contribution. The model also predicts a coincidence in transit times by *ac* and *dc* techniques unlike the previous case.

In Fig. 5, it is shown that the low-frequency capacitance dependence with the voltage exhibits a peak when quasi-Fermi level crosses the trap energy level ( $E_t$ ) corresponding to a maximum in the trap contribution to the capacitance, Eq. (10). The low-frequency conductance is similar to the trap-free value at high voltages since free charges dominate the injected carrier concentration.

### 3.6. Limit between fast- and slow-shallow traps

In the previous subsection, we have shown two extreme behaviors dominated either by transit or trapping time. It is interesting to establish the conditions that determine which regime prevails. Let us define the trap and transit time frequencies as

$$\langle \omega_{tr} \rangle \approx \frac{cN_c e^{(E_t - E_c)/k_B T}}{1 - \langle \bar{f}_t \rangle} \quad (34)$$

$$\omega_{tt} = 2\pi/\tau_0 \quad (35)$$

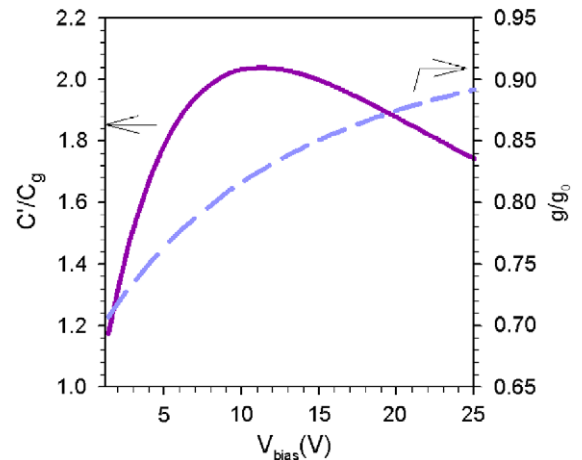


**Fig. 5.** Calculations of the low-frequency capacitance (violet solid line) and conductance (cyan dashed line) versus voltage at 1 Hz. (For interpretation of the references to colour in this figure legend, the reader is referred to the web version of this article.)

If the trap frequency is larger than the reciprocal transit time, the fast trap regime with the multiple trapping transit time  $\tau = \theta^{-1}\tau_0$  is present. In the opposite situation, the slow trap regime occurs with the trap-free transit time  $\tau_0$  value.

Inserting Eqs. (34) and (35) in  $\langle\omega_{tr}\rangle \approx \omega_{tt}$ , it is possible to quantify a critical capture coefficient  $c_c$  as

$$c_c \approx \frac{2\pi}{\tau_0} \frac{1 - \langle\bar{f}_t\rangle}{N_c e^{(E_t - E_c)/k_B T}} \quad (36)$$

According to the parameters of Table 1, this quantity is estimated as  $c_c \approx 10^{-13} \text{ cm}^3/\text{s}$ . If a trap capture coefficient is lower than this critical value the trap is slow, whereas if it is higher, the trap is fast. In Fig. 6, normalized transit times are plotted versus normalized trap frequency and both transit time regimes are depicted showing a narrow transition from the trap-free formula to the multiple trapping one.

As pointed out at the end of Section 3.4, to experimentally determine if shallow traps of an organic layer are slow or fast, the technique consists in comparing the transit times from *ac* (Eq. (26)) and *dc* (Eq. (19)). A coincidence would give us the slow result whereas a deviation indicates the presence of fast traps.

**Table 1**

Material parameters used in the simulation of transport in an organic layer.

$L$ (nm)	$N_c$ ( $\text{cm}^{-3}$ )	$\mu_0$ ( $\text{cm}^2/(\text{Vs})$ )	$E_t$ (eV)	$N_t$ ( $\text{cm}^{-3}$ )	$c$ ( $\text{cm}^3/\text{s}$ )
125	$10^{19}$	$4.7 \times 10^{-7}$		$10^{17}$	
Trap properties	Shallow		-0.1	Fast	$10^{-12}$
	Deep		-0.5	Slow	$10^{-14}$

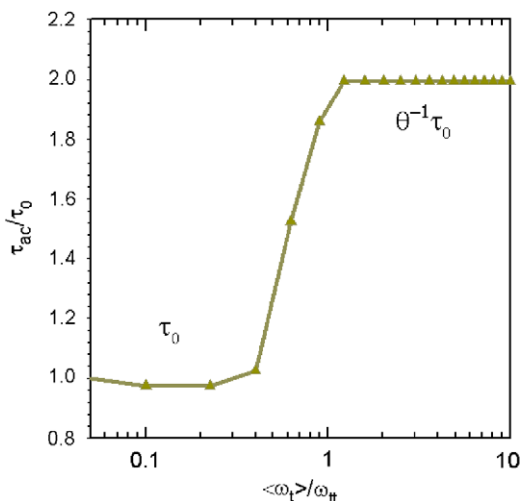


**Fig. 6.** Simulations of normalized transit times calculated from the *ac* conductance method versus normalized trap frequency at 6 V and  $N_t = 3 \times 10^{17} \text{ cm}^{-3}$ , describing a step up from the classical transit time  $\tau_0 = 73.8 \mu\text{s}$  to the multiple trapping one,  $\tau_{ac} = \theta^{-1}\tau_0$  with  $\theta^{-1} \approx 2$ . Classical transit time occurs for normalized trap frequency  $\langle\omega_t\rangle/\omega_{tt} = 85 \text{ kHz}$  ( $\langle\omega_t\rangle/\omega_{tt} < \theta$ ) and multiple trapping for  $\langle\omega_t\rangle/\omega_{tt} > 1$  according to dotted vertical marks.

### 3.7. Comparison between dynamic and static capacitance

Dynamic capacitance, obtained from admittance spectroscopy at low-frequencies, is frequently compared to the well-known static one [13]. In SCLC, the low-frequency capacitance has a value of  $3C_g/4$  [32,39], whereas the static capacitance is set at  $3C_g/2$  [13]. This reduced factor of 1/2 in the dynamic capacitance is attributed to the three contributions to the *ac* current (velocity modulation, density modulation and displacement term) [26]. In a two level system with a shallow trap, the static capacitance is calculated by integrating the charge stored in the device per voltage unit as [13]

$$C_{st} = \frac{q}{V} \left( \int_0^L \bar{n}_c(x) dx + \int_0^L \bar{n}_t(x) dx \right) \quad (37)$$

where  $V$  is the bias applied along the organic layer. In Fig. 7, the static capacitance is plotted versus bias-voltage. It is observed that the value remains at  $3C_g/2$  as in the trap-free case. At low voltages, the capacitance contribution essentially comes from the majority of the charge stored in the shallow trapping sites whereas at high voltages the capacitance is mainly due to free charge.

### 3.8. Dynamic characterization of deep traps

In contrast to the shallow trap energy level, where occupation is quite low, in the case of a deep trap, the opposite situation occurs as occupation is approaching the unity. This deviation strongly determines the contribution to the impedance from the trap dynamics Eq. (4). The trap levels are so heavily occupied that the temporal variation of  $\bar{f}_t$  is governed by the emitting rather than the trapping term. The numerical solution for the capacitance and the conductance is shown in Fig. 8a and b displaying distinct features with respect to the trap-free spectrum: a

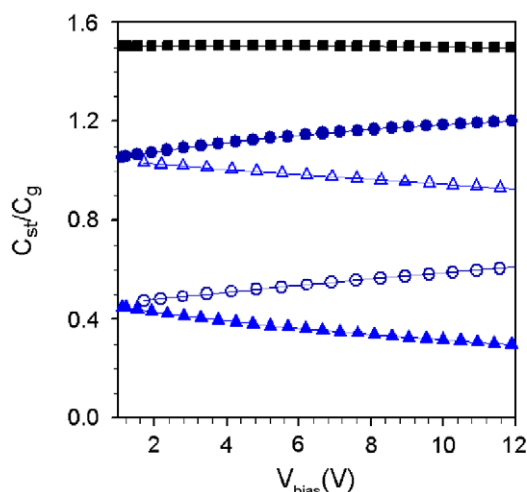


**Fig. 7.** Model calculations of the static capacitance versus voltage for a shallow trap (black squares). Free carrier contribution (solid and empty triangles) and trap carrier contribution (solid and empty circles) to static capacitance. Solid and empty symbols are for  $N_t = 1 \times 10^{17}, 5 \times 10^{17} \text{ cm}^{-3}$ , respectively.

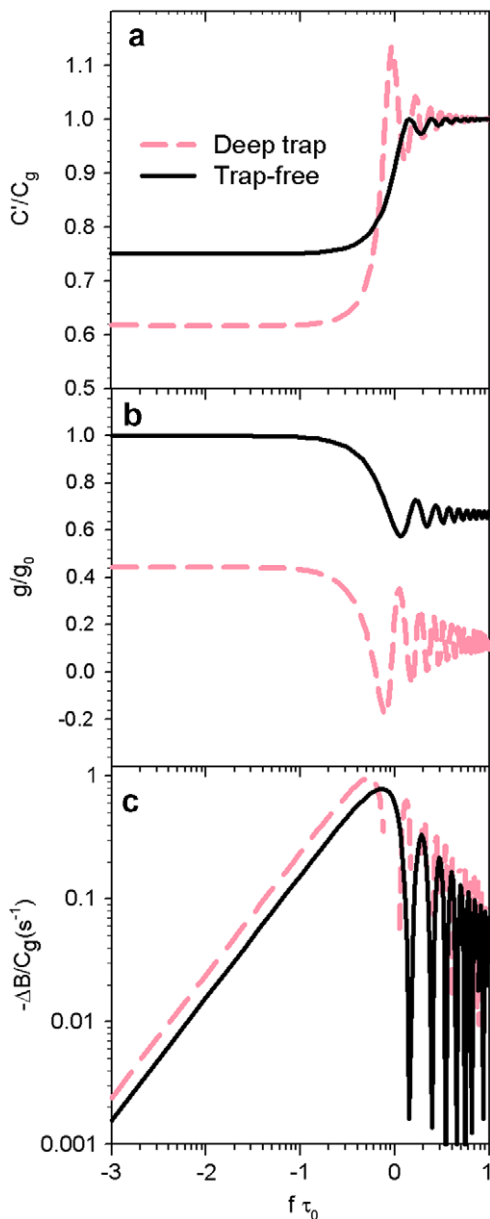


**Fig. 8.** Model solution of impedance spectra for deep trap at 6 V. Traps are plotted by maroon dashed lines and trap-free spectrum in black as a reference. (a) Capacitance spectra normalized to  $C_g$ . (b) Conductance spectra normalized to  $g_0$ . (c) Negative differential susceptance  $-\Delta B(\omega)$  normalized to  $C_g$ .

low-frequency capacitance below  $3C_g/4$ , a conductance spectrum significantly lower, and increased oscillation in the transition from low to high frequencies. These results are independent of the traps kinetics, which is another particularity in comparison to the shallow-trap results.

#### 4. Conclusions

The single-trap model has been described and numerically solved for SCLC for impedance studies in order to

determine the dynamical properties of carrier transport and storage depending on energy (shallow and deep) and kinetics (fast and slow) of the trap. For a fast-shallow trap, an analytical model is provided and validated by means of the multiple trapping formula for mobility  $\mu = \theta\mu_0$ , where  $\theta$  depends on the steady-state solution (trapped and free charge). For a slow-shallow trap, the available analytical model has been revised. Both regimes, fast and slow, have been characterized depending on the dominance of either trapping or transit processes and an experimental method has been also provided by comparing *dc* and *ac* transit times. A deep trap results in a decrease in the low-frequency capacitance (with respect to the trap-free case) and also in a delay in the transit times.

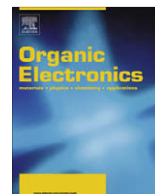
#### Acknowledgements

We thank financial support from MEC of Spain under programs: Consolider-Ingenio 2010 (Project HOPE CSD2007-00007), "Ramón y Cajal", FPI (Project MAT2004-05168) and ESF-EUROCORES project 05-SONS-FP-021 (MAT2006-28187-E). We are also grateful to the support from Bancaixa (Project P1 1B2005-12). We appreciate discussions with Dan Dascalu.

#### References

- [1] J.H. Burroughes, D.D.C. Bradley, A.R. Brown, R.N. Marks, K. MacKay, R.H. Friend, P.L. Burn, A.B. Holmes, *Nature* 347 (1990) 539.
- [2] S. Forrest, *Nature* 428 (2004) 911.
- [3] Y. Shen, A.R. Hosseini, M.W. Wong, G.G. Malliaras, *Chem. Phys. Chem.* 5 (2004) 16.
- [4] H. Bässler, *Phys. Status Solidi (b)* 175 (1993) 15.
- [5] P.N. Murgatroyd, *J. Appl. Phys.* D 3 (1970) 151.
- [6] P.S. Davids, I.H. Campbell, D.L. Smith, *J. Appl. Phys.* 82 (1997) 6319.
- [7] C. Tanase, P.W.M. Blom, D.M. Leeuw, *Phys. Rev. B* 70 (2004) 193202.
- [8] M.C.J.M. Vissenberg, M. Matters, *Phys. Rev. B* 57 (1998) 12964.
- [9] P.W.M. Blom, M.C.J.M. Vissenberg, *Mater. Sci. Eng.* R27 (2000) 53.
- [10] D. Poplavskyy, F. So, *J. Appl. Phys.* 99 (2006) 033707.
- [11] H.H.P. Gommans, M. Kemerink, G.G. Andersson, R.M.T. Pijper, *Phys. Rev. B* 69 (2004) 155216.
- [12] S. Shirota, H. Kageyama, *Chem. Rev.* 107 (2007) 953.
- [13] B. Ramachandran, H.G.A. Huizing, R. Coehoorn, *Phys. Rev. B* 73 (2006) 233306.
- [14] M.M. Mandoc, B. de Boer, P.W.M. Blom, *Phys. Rev. B* 73 (2006) 155205.
- [15] V.I. Arkhipov, E.V. Emelianova, G.J. Adriaenssens, *Phys. Rev. B* 64 (2001) 125125.
- [16] A.L. Alvarez, B. Arredondo, B. Romero, X. Quintana, A. Gutiérrez-Llorente, R. Mallavia, J.M. Otón, *IEEE Trans. Electron. Dev.* 55 (2008) 674.
- [17] J. Bisquert, *Phys. Rev. B* 77 (2008) 235203.
- [18] J. Bisquert, V.S. Vikhrenko, *Electrochim. Acta* 47 (2002) 3977.
- [19] G.T. Wright, *Solid-State Electron.* 2 (1960) 165.
- [20] J. Bisquert, *Phys. Chem. Chem. Phys.* 10 (2008) 3175.
- [21] N.D. Nguyen, M. Schmeits, *Phys. Rev. B* 75 (2007) 075307.
- [22] M. Schmeits, *J. Appl. Phys.* 101 (2007) 084508.
- [23] D. Dascalu, *Int. J. Electron.* 21 (1966) 183.
- [24] D. Dascalu, *Solid-State Electron.* 11 (1968) 491.
- [25] R. Kassing, E. Kähler, *Solid State Commun.* 15 (1974) 673.
- [26] R. Kassing, *Phys. Status Solidi (a)* 28 (1975) 107.
- [27] A. Rose, *Concepts in Photoconductivity and Allied Problems*, John Wiley and Sons, 1963.
- [28] A. van der Ziel, *Solid State Physical Electronics*, Prentice-Hall, Englewood Cliffs, 1976.
- [29] W. Brütting, S. Berleb, *Phys. Rev. Lett.* 89 (2002) 286601.
- [30] P.W.M. Blom, M.J.M. de Jong, M.G. van Munster, *Phys. Rev. B* 55 (1997).
- [31] N.F. Mott, R.W. Gurney, *Electronic Processes in Ionic Crystals*, Oxford University Press, London, 1940.

- [32] J. Shao, G.T. Wright, *Solid-State Electron.* 3 (1961) 291.
- [33] A.J. Campbell, M.S. Weaver, D.G. Lidzey, D.D.C. Bradley, *J. Appl. Phys.* 84 (1998) 6737.
- [34] F. So, B. Krummacher, M.K. Mathai, D. Poplavskyy, S.A. Choulis, *J. Appl. Phys.* 102 (2007) 091101.
- [35] M.A. Lampert, *Current Injection in Solids*, Academic Press, New York, 1970.
- [36] H.C.F. Martens, J.N. Huiberts, P.W.M. Blom, *Appl. Phys. Lett.* 77 (2000) 1852.
- [37] H.C.F. Martens, H.B. Brom, P.W.M. Blom, *Phys. Rev. B* 60 (1999) R8489.
- [38] J.M. Montero, J. Bisquert, G. Garcia-Belmonte, H. Bolink, E.M. Barea, *Phys. Status Solidi (a)* 204 (2007) 2402.
- [39] D. Dascalu, *Solid-State Electron.* 12 (1969) 444.



# Formation of low surface energy separators with undercut structures via a full-solution process and its application in inkjet printed matrix of polymer light-emitting diodes

Rubo Xing, Tengling Ye, Yan Ding, Dongge Ma, Yanchun Han\*

State Key Laboratory of Polymer Physics and Chemistry, Changchun Institute of Applied Chemistry, Chinese Academy of Sciences and Graduate University of the Chinese Academy of Sciences, 5625 Renmin Street, Changchun 130022, People's Republic of China

## ARTICLE INFO

### Article history:

Received 31 July 2008

Received in revised form 25 November 2008

Accepted 10 December 2008

Available online 25 December 2008

### PACS:

85.40.Hp

### Keywords:

Inkjet printing

Patterning

Polymer light-emitting diodes

## ABSTRACT

In this paper, low surface energy separators with undercut structures were fabricated through a full-solution process. These low surface energy separators are more suitable for application in inkjet printed passive-matrix displays of polymer light-emitting diodes. A patterned PS film was formed on the P4VP/photoresist film by microtransfer printing firstly. Patterned Au-coated Ni film was formed on the uncovered P4VP/photoresist film by electroless deposition. This metal film was used as mask to pattern the photoresist layer and form undercut structures with the patterned photoresist layer. The surface energy of the metal film also decreased dramatically from 84.6 mJ/m<sup>2</sup> to 21.1 mJ/m<sup>2</sup> by modification of fluorinated mercaptan self-assemble monolayer on Au surface. The low surface energy separators were used to confine the flow of inkjet printed PFO solution and improve the patterning resolution of inkjet printing successfully. Separated PFO stripes, complement with the pattern of the separators, formed through inkjet printing. The separators also realized the patterning of cathodes. A passive-matrix display device was obtained through the assistant patterning of low surface energy separators.

Crown Copyright © 2008 Published by Elsevier B.V. All rights reserved.

## 1. Introduction

Organic light-emitting diodes (OLEDs) have exhibit tremendous potential in flat panel displays (FPDs) since their high brightness, low power consumption, wide viewing angle and good contrast [1–5]. FPDs of polymer light-emitting diodes (PLEDs) attracted more attention in this field because of the color tunability of polymer materials within the entire visible spectrum, simpler manufacture processing, suitable for large area and soft substrate and so on. The light-emitting polymer with different color need to be patterned in a full color display of PLEDs. Many methods have been used to pattern the light-emitting polymers,

such as screen printing [6,7], transfer printing [8], inkjet printing [9–11] and photo-induced polymerization patterning [12].

Thereinto, inkjet printing is a most potential technique for application because of its simple and high efficient patterning process, suitable for solution process, easy to integration and automatization. To improve the patterning resolution of inkjet printing to up to par of patterning of FPD of PLEDs, high-resolution pattern with low surface energy was used to confine the wettability and flow of inkjet printed liquid and improve the patterning resolution of inkjet printing [13–17]. The high-resolution pattern normally formed by photolithography. Then, the pattern can be modified by fluorinated self-assembled monolayer (SAM) [14,15] or CF<sub>4</sub> plasma treating [16,17] to decrease its surface energy. Thereinto, modification by fluorinated SAM can be a simple and high selective approach.

\* Corresponding author. Tel.: +86 431 85262175; fax: +86 431 85262126.

E-mail addresses: [mdg1014@ciac.jl.cn](mailto:mdg1014@ciac.jl.cn) (D. Ma), [yhan@ciac.jl.cn](mailto:yhan@ciac.jl.cn) (Y. Han).



Another element need to be patterned is cathode for the FPD of PLEDs. Separators with undercut structure are the effective method to pattern the cathode in passive-matrix display of FPD [18,19]. The separators with undercut structures have been fabricated by photolithography [20–24] or soft lithography [25–27]. Photolithography has good stability and repeatability. But multilayer resist configuration or special photolithography process is needed which complicate the patterning process. Soft lithography is simple, high efficient and low cost compared with photolithography because of its characteristic, such as suitability with roll-to-roll printing and solution process, simpler patterning equipment and so on.

In this paper, based on transfer printing of soft lithography, a full-solution process was used to fabricate undercut structures with low surface energy. At first patterned PS film was formed on P4VP/photoresist films by microtransfer printing. Metal film was formed on the uncovered P4VP film by electroless deposition, which was simple and high efficient compared with traditional deposition and patterning process of metal films. This metal film pattern can be used as mask to pattern the photoresist and fabricate undercut structures, which can be used as separators to pattern metal cathode in the passive-matrix display. It also can be modified by fluorinated SAM to form separators with low surface energy, which can be used to assist the patterning of inkjet printing. Special separators, which were suit to assist the patterning of passive-matrix displays of inkjet printed PLEDs, were obtained.

## 2. Experimental

### 2.1. Materials

The positive photoresist was purchased from Suzhou Ruihong Electronic Chemical Co., Ltd., China. Polystyrene (PS, Mw:  $\sim 31600$ ,  $T_g = 103^\circ\text{C}$ ) and poly(4-vinylpyridine) (P4VP, Mw:  $\sim 60,000$ ,  $T_g = 137^\circ\text{C}$ ) were purchased from Aldrich. Polydimethylsiloxane (PDMS, Sylgard<sup>TM</sup> 184) was purchased from Dow Corning. ITO glass (glass slide with indium-tin-oxide films) was purchased from Chinese South Glass Holding (CSC) Co., Ltd. The hole-injection materials of poly(styrene sulfonic acid)-doped poly(3,4-ethylenedioxythiophene) (PEDOT, Baytron P VP.A14083) was purchased from H. C. Starck GmbH. Poly(9,9-di-n-octylfluorene) (PFO) was synthesized as shown in Ref. [28]. PS was dissolved in toluene with a concentration of 1.5 wt%. P4VP was dissolved in chloroform with a concentration of 0.8 wt%. PFO was dissolved in the mixture of iso-propylbenzene and cyclohexylbenzene (iso-propylbenzene/cyclohexylbenzene = 8/2 (w/w)) with a concentration of 0.8 wt%.

### 2.2. Patterning of metal film

The PDMS mold with a stripes pattern was obtained as our previous work reported [27]. Then PS film was spin coated on the PDMS mold at 2000 rms. Photoresist film was spin coated at 2000 rms on the ITO glass substrate and then baked at  $110^\circ\text{C}$  for 3 min. P4VP film was spin coated on the photoresist-coated ITO glass substrate at

2000 rms subsequently. The PDMS mold and the P4VP/photoresist-coated ITO glass substrate were baked at  $110^\circ\text{C}$  for 2 min. Then the PDMS mold was placed on the P4VP/photoresist-coated ITO glass substrate and baked at  $110^\circ\text{C}$  for 3 min sequentially. The PDMS mold was removed from the P4VP/photoresist-coated ITO glass substrate when their temperature dropped to  $\sim 80^\circ\text{C}$ . The PS film would remain on the P4VP film at the contact region. A patterned PS film formed on the P4VP film.

The glass substrate with the patterned PS film was dipped into  $\text{Na}_2\text{PdCl}_4$ /water solution (0.2 mg/ml) for 1 min. The  $\text{Pd}^{2+}$  was absorbed at the uncovered P4VP film. Subsequently, the glass substrate was dipped into  $\text{NaBH}_4$ /water solution (0.5 mg/ml) to reduce the  $\text{Pd}^{2+}$ . Then the glass substrate was dipped into electroless deposition solutions of nickel (Ni) for 2 min and gold (Au) for 30 s, respectively. The Au-coated Ni film deposited at the uncovered P4VP film. The components of the electroless deposition solutions were shown in Table 1.

### 2.3. Undercut structures fabrication and surface modification

The glass substrate with the patterned metal film was etched by oxygen reactive ion etch ( $\text{O}_2$ -RIE) at a power of 120 w and an oxygen flux of 100 sccm for 5 min to remove the PS and P4VP layer at the regions uncovered by metal film. Then the substrate was exposed to UV light and realized the UV-exposure of photoresist at the regions uncovered by metal film. The undercut structures consist of the metal film and the patterned photoresist, formed after developing process.

The glass substrate with the undercut structures was placed in the vapor atmosphere of fluorinated mercaptan (Heptadecafluoro-1-decanethiol, Aldrich) for 30 min at room temperature. The fluorinated mercaptan formed SAM on the gold surface and decreased its surface energy. Then the undercut structures were used as separators to assist the deposition of inkjet printed solution and to pattern the cathode of passive-matrix display.

### 2.4. Inkjet printing of PFO films and fabrication of PLEDs

The overall inkjet printing system consists of inkjet print head and its controller, a translation stage equipped with a hot plate for heating the substrate, and software to control the translation stage. The inkjet print head was manufactured by Microdrop Technique GmbH (Germany), with nozzle diameter of  $70\ \mu\text{m}$ . The PEDOT was spin coated on the substrate with the low surface energy separators at 3000 rms for 60 s and then baked at  $100^\circ\text{C}$  for 15 min to give a thickness of  $\sim 40\ \text{nm}$ . The PFO solution was inkjet printed into the grooves between the separators and formed PFO film. Then Ca/Al cathode was deposited on the PFO film by physical vapor deposition to complete the fabrication of PLEDs.

### 2.5. Characterization

The absorption and reduction of  $\text{Pd}^{2+}$  was proved by X-ray photoelectron spectra (XPS). The patterned PS film, metal film, undercut structures and inkjet printed polyflu-

**Table 1**  
The component of the electroless deposition solutions of nickel and gold<sup>a,b</sup>.

Electroless deposition solutions of nickel		Electroless deposition solutions of gold	
Materials	Concentration (g/L)	Materials	Concentration (g/L)
Nickel sulfate	2.00	Sodium tetrachloroaurate	3.62
Sodium hypophosphite	30.00	Hydroxylamine hydrochloride	6.95
Sodium citrate	10.00	Sodium hydrogen phosphate	11.36
Ammonium chloride	30.00	Sodium thiosulfate	12.64
		Sodium sulfite	40.32
pH	8.5	pH	8.0

<sup>a</sup> Sodium hydroxide was used to adjust the potential of hydrogen.

<sup>b</sup> The deposition temperatures are 40 °C for the electroless deposition of nickel and 56 °C for the electroless deposition of gold, respectively.

orene film were all observed by optical microscope. The undercut structures were also observed by ESEM/FEG scanning electron microscopy (XL30 ESEM, FEI Company). The surface energy of the metal film was measured by contact angle measuring system (Krüss DSA10-MK2, Germany). The brightness-voltage characteristics of the PLEDs were recorded using a computer-controlled sourcemeter (Keithley 2400) at room temperature under ambient conditions.

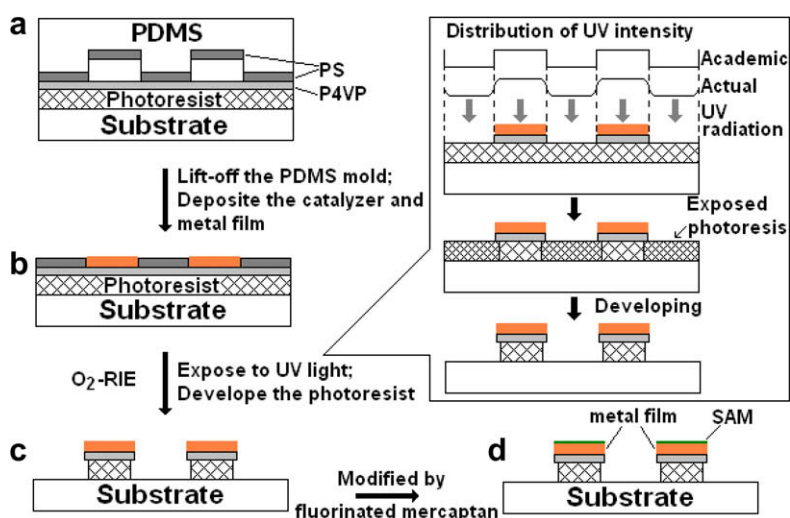
### 3. Result and discussion

Fig. 1 shows the over all patterning process of undercut structures with low surface energy. The first key step of the fabrication process is the patterning of PS film on the P4VP film. Microtransfer printing was used to pattern the PS film. In this patterning step, the PS-coated PDMS mold was placed on the P4VP/photoresist-coated glass substrate. The PS film contacted with the P4VP film at the protruded regions of the PDMS mold, as shown in Fig. 1(a). When the PDMS mold and the glass substrate were heated to 110 °C, which temperature was higher than the glass transition temperature ( $T_g$ ) of the PS ( $T_g = 103$  °C) slightly, the PS film and the P4VP film formed a stick because of

the movement of PS molecule. The movement of PS molecule frozen when the temperature was dropped to  $\sim 80$  °C. And the stick between the PS film and the P4VP film became stronger. The PS film remained on the P4VP film in the stick regions after the PDMS mold was removed from the glass substrate because of the low surface energy of the PDMS mold. A patterned PS film was obtained on the P4VP/photoresist-coated glass substrate. Fig. 2(a) shows the optical image of the patterned PS film.

The second step is the absorption of  $\text{Pd}^{2+}$  and electroless deposition of metal film. The patterned PS film was used as a mask to define the region of absorption of  $\text{Pd}^{2+}$ . Previous work has proved that P4VP and  $\text{Pd}^{2+}$  can form complex [29]. Fig. 3 shows the XPS analysis of the P4VP surface with patterned PS film after different treatment. It is obviously that absorption of  $\text{Pd}^{2+}$  has occurred on the P4VP surface. And a part of  $\text{Pd}^{2+}$  was reduced to Pd after the reduction step. This was proved by the decreased intensity at  $\sim 338.5$  eV and the slight increased intensity at  $\sim 335.7$  eV. The reduced Pd can be used as catalyzer to catalyze the electroless deposition of metal film.

Fig. 2(b) shows the optical image of the Au-coated Ni film through electroless deposition. The electroless deposition of metal film has happened at the uncovered P4VP



**Fig. 1.** The patterning process of undercut structures: (a) form patterned PS film on the P4VP/photoresist-coated substrate; (b) deposit metal film on the uncovered P4VP surface by electroless deposition; (c) expose the substrate to UV light and then develop to obtain the undercut structures; (d) modify the surface of the undercut structures by SAM of fluorinated mercaptan. Insert: detailed description of the UV exposing and developing process.

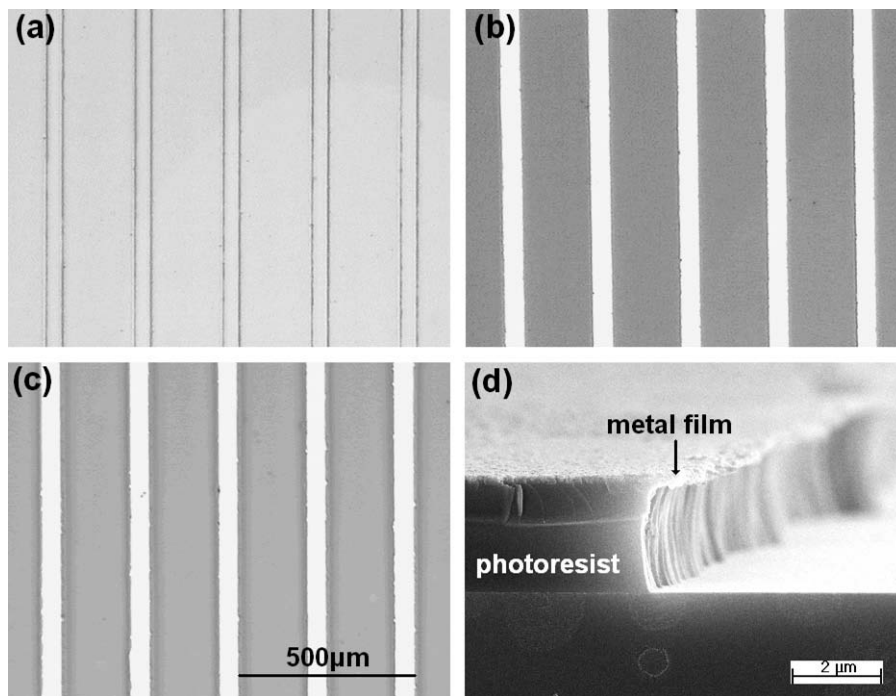


**Fig. 2.** Optical images of P4VP/photoresist-coated substrate with (a) patterned PS film and (b) electroless deposited metal film. (c) Optical image of patterned stripes with undercut structures and (d) its SEM image of the cross-section.

surface selectively. This also proved that the absorption of  $\text{Pd}^{2+}$  occurred at the uncovered P4VP surface. And the reduced Pd catalyzed the electroless deposition effectively. So patterned metal film, complement with the pattern of PS film, was obtained. The patterned PS film can also be used as hydrophobic layer to avoid the edge diffusion of metal film in the electroless deposition process. This ensured that the electroless deposited metal film pattern was confirmed with the uncovered P4VP regions.

The patterned metal film was used as mask to realize the selective UV-exposure of the photoresist layer at the regions uncovered by metal film. The UV-exposed photoresist layer can be dissolved and removed at the following

developing process. The remained photoresist pattern was same with the pattern of the metal film. In the developing process, a lateral dissolving of photoresist would occur at the edge of the unexposed regions because of the lateral nonideal exposure caused by the UV diffraction at corresponding region [30], as shown in the insert of Fig. 1. So the undercut structures, consist of the up-layer of the patterned metal film and the bottom-layer of the patterned photoresist, formed after the developing process. Fig. 2(c) and (d) show the optical and SEM images of the patterned undercut structures. It is obviously that a lateral dissolving has happened at the unexposed region. The undercut structures formed because of this lateral dissolving. These undercut structures can be used as separators to pattern the cathodes in the passive-matrix display.

The metal film can be modified by SAM of fluorinated mercaptan to decrease its surface energy. The metal film was placed in the vapor atmosphere of fluorinated mercaptan for 30 min at room temperature. A SAM of fluorinated mercaptan formed on the surface of metal film because of the chemical action between mercaptan and Au atom. The surface energy of the metal film decreased from  $84.6 \text{ mJ/m}^2$  to  $21.1 \text{ mJ/m}^2$  after the modification of SAM of fluorinated mercaptan. Fig. 4 also shows the contact angle between water and the metal film with or without the SAM of fluorinated mercaptan. The contact angle between water and the metal film has increased from  $20.3^\circ$  to  $100.6^\circ$ . The surface energy of the metal film has decreased dramatically through the SAM modification. This low surface energy separators can be used to confine the flow of the inkjet printed solution and improve the patterning resolution of inkjet printing.

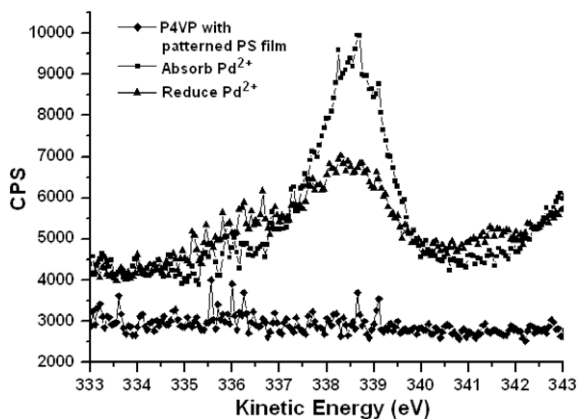


**Fig. 3.** Surface analysis of P4VP/photoresist-coated substrate by X-ray photoelectron spectra.

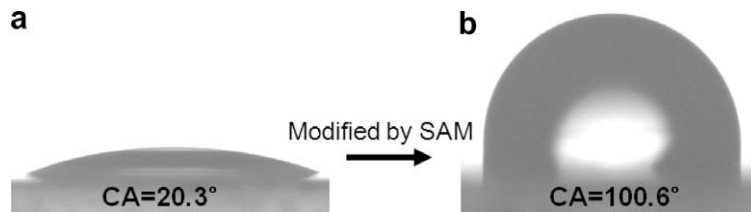


Fig. 4. Contact angle of water on the Au/Ni-coated substrate (a) with and (b) without the SAM of fluorinated mercaptan.

To demonstrate their application, the undercut structures with low surface energy were used as separators to assist the inkjet printing of PFO solution and pattern the

cathodes of passive-matrix display of PLEDs. Photolithography and wet-etching were used to realize the patterning of ITO anode firstly. The patterned ITO stripes have a width

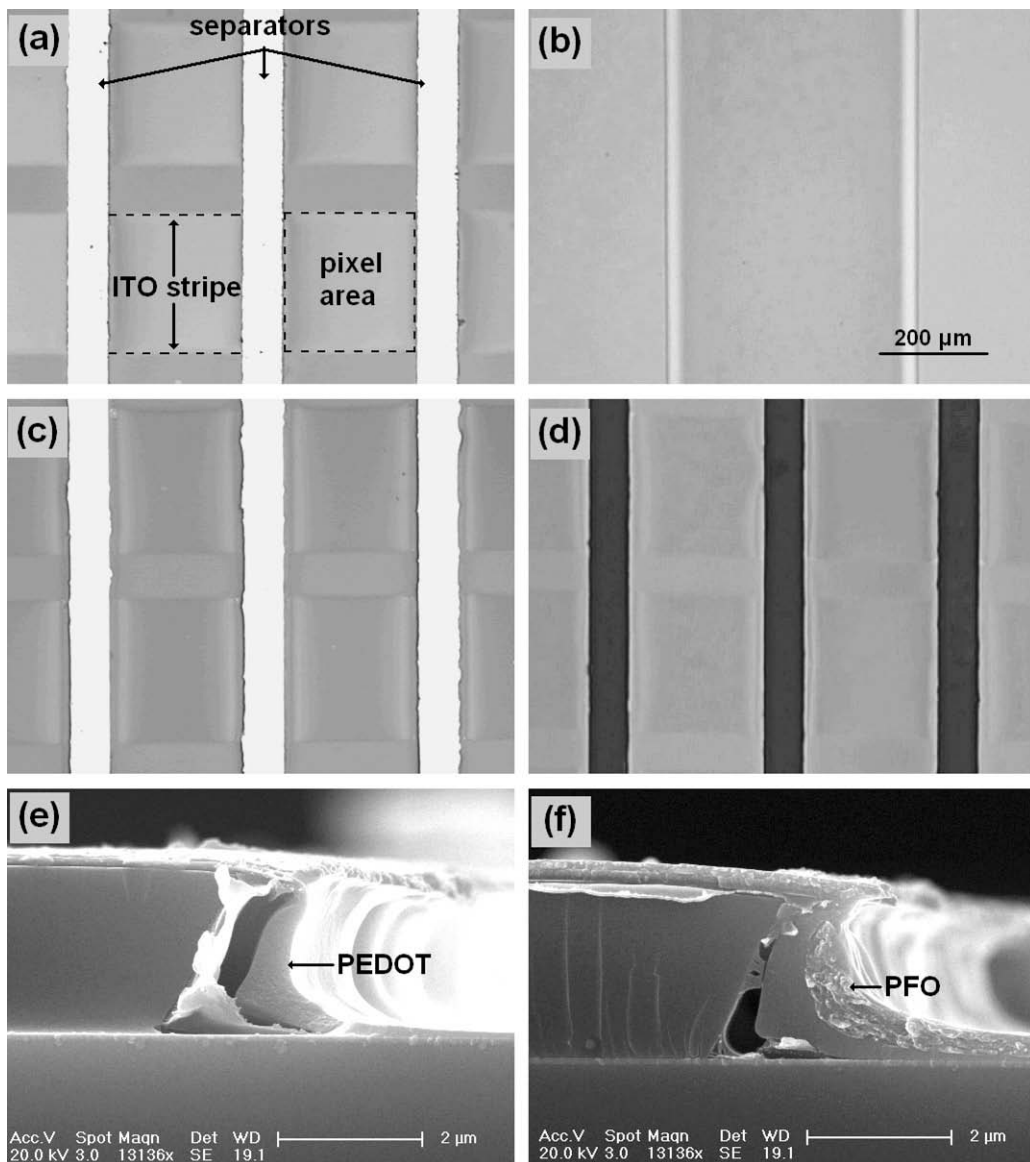


Fig. 5. Optical images of (a) spin-coated PEDOT film on substrate with low surface energy separators and inkjet printed PFO film on PEDOT-coated substrate (b) without and (c) with low surface energy separators. (d) Fluorescent image of inkjet printed PFO film on the substrate with low surface energy separators. SEM images of the cross-section of the separators with (e) PEDOT film and (f) PEDOT/PFO film.

of 200  $\mu\text{m}$  with a space of 50  $\mu\text{m}$ . Then a group of parallel stripes with undercut structures and low surface energy were fabricated using the method described above. The stripes, which were vertical with the ITO anode, were used as confined pattern to assist the inkjet printing and separators to pattern the cathodes. The stripes have a width of 50  $\mu\text{m}$  with a space of 200  $\mu\text{m}$ . So the dimension of the light-emitting region in every pixel of the passive matrix was 200  $\mu\text{m} \times 200 \mu\text{m}$ .

The PEDOT film was spin coated on the substrate with the low surface energy separators firstly. Fig. 5(a) and (e) show the optical and SEM images of the substrate with spin-coated PEDOT film. When the PEDOT film was spin coated on the substrate, the PEDOT/water solution dewetted from the separators surface because of its low surface energy. So the PEDOT film just deposited in the grooves between the separators and formed separated PEDOT stripes after the spin-coating process. The PEDOT film has obvious edge deposition at the edge of the grooves which caused by the morphology of the separators. The PFO solution was then inkjet printed into the grooves at ambient atmosphere and formed PFO film. Fig. 5(b) and (c) show the optical images of inkjet printed PFO film on PEDOT-coated substrate without and with low surface energy separators. Compared Fig. 5(b) with (c), low surface energy separators confined the wetting and spreading of inkjet printed solution effectively and improved patterning resolution. Fig. 5(d) and (f) also show the fluorescent image of the inkjet printed PFO film and the SEM image of the cross-section of low surface energy separators. The fluorescence of PFO film emitted from the regions of grooves only. There was no emitting of fluorescence at the regions of separators. The PFO film just formed in the grooves because of the confined flow of inkjet printed solution by separators with low surface energy. Separated PFO stripes were obtained by inkjet printing. There are also edge deposition of inkjet printed PFO film at the edge of the grooves which caused by the coffee-ring effect in the evaporating and drying process of PFO solution [31,32].

A thin layer of calcium (10 nm) followed by a layer of aluminum (100 nm) is deposited on the PFO/PEDOT/ITO coated glass substrate through a physics vapor deposition. The Ca/Al cathodes separated by the separators and formed stripes pattern which were vertical with the ITO stripes. A passive-matrix display device was obtained. Fig. 6 shows the optical image of light-emitting matrix and its bright-

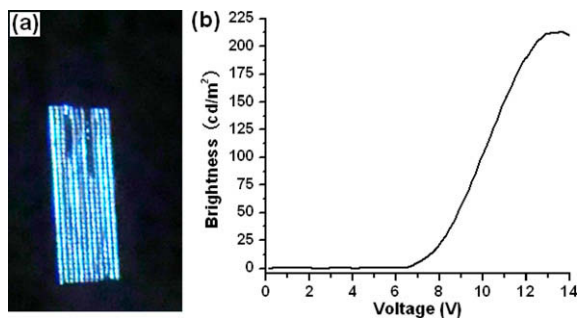


Fig. 6. (a) Optical image of the patterned PLEDs matrix; (b) the brightness-voltage characteristic of the devices.

ness-voltage curve. It is obvious that the patterned matrix of polymer light-emitting diodes have formed through inkjet printing. Certainly, there are some dead pixels in the light-emitting matrix which may be caused by the defects of the inkjet printed PFO film.

#### 4. Conclusion

A full-solution process was explored to fabricate separators with undercut structures and low surface energy. By microtransfer printed PS film as mask, patterned metal film was formed on the P4VP/photoresist film by electroless deposition. This metal pattern was used as mask to pattern the photoresist layer and form undercut structures with the patterned photoresist layer. The metal film can also be modified by SAM of fluorinated mercaptan to form low surface energy separators. The low surface energy separators were used to assist the deposition of inkjet printed PFO solution successfully. Separated PFO stripes formed through inkjet printing. The separators also realized the patterning of cathodes. A passive-matrix display device was obtained which proved the suitability of the low surface energy separators in the application of inkjet printed passive-matrix display of PLEDs.

#### Acknowledgement

This work was subsidized by the National Natural Science Foundation of China (20621401, 50573077) and the Ministry of Science and Technology of China (2009CB930603, 2009CB623600).

#### References

- [1] C.W. Tang, S.A. Vanslyke, *Appl. Phys. Lett.* 51 (1987) 913.
- [2] S.A. Vanslyke, C.H. Chen, C.W. Tang, *Appl. Phys. Lett.* 69 (1996) 2160.
- [3] J.H. Burroughes, D.D.C. Bradley, A.R. Brown, Q.N. Marks, K. Mackay, R.H. Friend, P.L. Burns, A.B. Holmes, *Nature* 347 (1990) 539.
- [4] D. Braun, A.J. Heeger, *Appl. Phys. Lett.* 58 (1991) 1982.
- [5] A. Sugimoto, H. Ochi, S. Fujimura, A. Yoshida, T. Miyadera, M. Tsuchida, *IEEE J. Select. Top. Quantum Electron.* 10 (2004) 107.
- [6] D.A. Pardo, G.E. Jabbour, N. Peyghambarian, *Adv. Mater.* 12 (2000) 1249.
- [7] J. Birnstock, J. Blassing, A. Hunze, M. Scheffel, M. Stossel, K. Heuser, G. Wittmann, J. Worle, A. Winnacker, *Appl. Phys. Lett.* 78 (2001) 3905.
- [8] T. Granlund, T. Nyberg, L.S. Roman, M. Svensson, O. Inganäs, *Adv. Mater.* 12 (2000) 269.
- [9] (a) J. Bharathan, Y. Yang, *Appl. Phys. Lett.* 72 (1998) 2660;  
(b) S.C. Chang, J. Bharathan, Y. Yang, R. Helgeson, F. Wudl, *Appl. Phys. Lett.* 73 (1998) 2561;  
(c) S.C. Chang, J. Liu, J. Bharathan, Y. Yang, J. Onohara, J. Kido, *Adv. Mater.* 11 (1999) 734.
- [10] T. Shimoda, K. Morii, S. Seki, H. Kiguchi, *MRS Bull.* 28 (2003) 821.
- [11] Q.L. Niu, Y.X. Shao, W. Xu, L. Wang, S.H. Han, N.H. Liu, J.B. Peng, Y. Cao, J. Wang, *Organic Electron.* 9 (2008) 95.
- [12] C.D. Müller, A. Falcou, N. Reckefuss, M. Rojahn, V. Wiederhirn, P. Rudati, H. Frohne, O. Nuyken, H. Becker, K. Meerholz, *Nature* 421 (2003) 829.
- [13] H. Sirringhaus, T. Kawase, R.H. Friend, T. Shimoda, M. Inbasekaran, W. Wu, E.P. Woo, *Science* 290 (2000) 2123.
- [14] J.Z. Wang, Z.H. Zheng, H.W. Li, W.T.S. Huck, H. Sirringhaus, *Nature Mater.* 3 (2004) 171.
- [15] N. Zhao, M. Chiesa, H. Sirringhaus, Y.N. Li, Y.L. Wu, B. Ong, *J. Appl. Phys.* 101 (2007) 064513.
- [16] C.W. Sele, T. von Werne, R.H. Friend, H. Sirringhaus, *Adv. Mater.* 17 (2005) 997.
- [17] T. Takashima, S. Takei, K. Morii, H. Hokari, R. Makiura, S. Seki, US Patent No.: US 7252570.

- [18] Y. Kihima, N. Asai, N. Kishii, S. Tamura, IEEE Transact. Electron. Devices 44 (1997) 1222.
- [19] S.W. Kim, B.H. Hwang, J.H. Lee, J.I. Kang, K.W. Min, W.Y. Kim, Curr. Appl. Phys. 2 (2002) 335.
- [20] H.S. Lee, J.B. Yoon, J. Micromech. Microeng. 15 (2005) 2136.
- [21] <[www.microchem.com](http://www.microchem.com)>.
- [22] Z.H. Huang, G.J. Qi, X.T. Zeng, W.M. Su, Thin Sol. Films 503 (2006) 246.
- [23] C. Py, M. D'Iorio, Y. Tao, J. Stapledon, P. Marshall, Synthetic Metals 113 (2000) 155.
- [24] <[www.microresist.com](http://www.microresist.com)>.
- [25] J. Rhee, J. Park, S. Kwon, H. Yoon, H.H. Lee, Adv. Mater. 15 (2003) 1075.
- [26] S.M. Seo, J.H. Kim, T.I. Kim, H.H. Lee, Appl. Phys. Lett. 88 (2006) 023118.1.
- [27] R.B. Xing, Y. Xuan, D.G. Ma, Y.C. Han, J. Vac. Sci. and Tech. B 26 (2008) 1.
- [28] J. Liu, G.L. Tu, Q.G. Zhou, Y.X. Cheng, Y.H. Geng, L.X. Wang, D.G. Ma, X.B. Jing, F.S. Wang, J. Mater. Chem. 16 (2006) 1431.
- [29] D.X. Wang, Y.J. Li, Y.Y. Jiang, Chinese J. Catal. 3 (1982) 78.
- [30] S.M. Sze, second ed., Semiconductor Devices: Physics and Technology, Wiley, New York, 2001. p. 400.
- [31] R.D. Deegan, O. Bakajin, T.F. Dupont, G. Huber, S.R. Nagel, T.A. Witten, Nature 389 (1997) 827.
- [32] R.D. Deegan, O. Bakajin, T.F. Dupont, G. Huber, S.R. Nagel, T.A. Witten, Phys. Rev. E 62 (2000) 756.



# An efficient bis(2-phenylquinoline) (acetylacetonate) iridium(III)-based red organic light-emitting diode with alternating guest:host emitting layers

Y. Divayana, X.W. Sun \*

School of Electrical and Electronic Engineering, Nanyang Technological University, Nanyang Avenue, Singapore 639798, Singapore

## ARTICLE INFO

### Article history:

Received 10 October 2008

Received in revised form 11 December 2008

Accepted 12 December 2008

Available online 24 December 2008

### PACS:

32.50.+d

33.50.Hv

78.40.Me

### Keywords:

Organic light-emitting diode

Efficiency roll-off

Forster process

Concentration quenching

## ABSTRACT

We report a highly efficient electrophosphorescent bis(2-phenylquinoline) (acetylacetonate) iridium(III) [Ir(2-phq)<sub>2</sub>(acac)]-based red organic light-emitting diode. The emission layer consists of a periodic thin layer of guest material of Ir(2-phq)<sub>2</sub>(acac) separated by host material of 4,4'-Bis(carbazol-9-yl)biphenyl. The guest and host thicknesses were optimized independently to obtain the best performance. The current efficiency reaches to a maximum of 16.2 cd/A then drops to 15 and 11 cd/A at brightness of 10 and 100 cd/m<sup>2</sup>, respectively. By reducing the thickness of the host layer, the power efficiency was further improved. Device with a maximum power efficiency of 8.3 lm/W was obtained. We also found that the concentration quenching in Ir(2-phq)<sub>2</sub>(acac) is dominated by molecular aggregation. Excitonic quenching by radiationless Förster process is miniscule.

© 2008 Elsevier B.V. All rights reserved.

## 1. Introduction

Organic light-emitting diode (OLED) has emerged as one of the most important display technologies for the future. Various techniques have been reported in literature to optimize the electroluminescence processes in OLED, including: balancing the carrier transport and injection [1,2], confining the excitons [3], doping the transport [4] and emission layers [5], and the most recent electrophosphorescence [6].

By harvesting the triplet excitons, electrophosphorescence enables improvement of the efficiency by four times. With further improvements in carrier balance and exciton confinement, both green [7] and yellow [8] emitting devices have reached the efficiency close to their maximum

theoretical limit. Red phosphorescent OLED, however, still has room for improvement. Li et al. reported a red phosphorescent OLED with a current efficiency of 13 cd/A at a current density of 20 mA/cm<sup>2</sup> [9]. Ho et al. reported a maximum external quantum efficiency of 12% photon/electron at low current density but drops to 3% photon/electron at 200 mA/cm<sup>2</sup> for their saturated red OLED [10].

In phosphorescent OLED, the emission layer (EML) is normally made of a host-guest system formed by co-evaporating a small amount of guest molecule in the matrix of host material [5,6]. Most excitons are formed in the matrix host which then transfer the energy to the guest molecules where final emission takes place. Host-guest system minimizes concentration quenching of guest molecules to enable high quantum yield.

Red emitting organic molecules suffer from a tremendous concentration quenching [11]. As the concentration of the emitting guest molecules increases, the quantum

\* Corresponding author.

E-mail address: [exwsun@ntu.edu.sg](mailto:exwsun@ntu.edu.sg) (X.W. Sun).

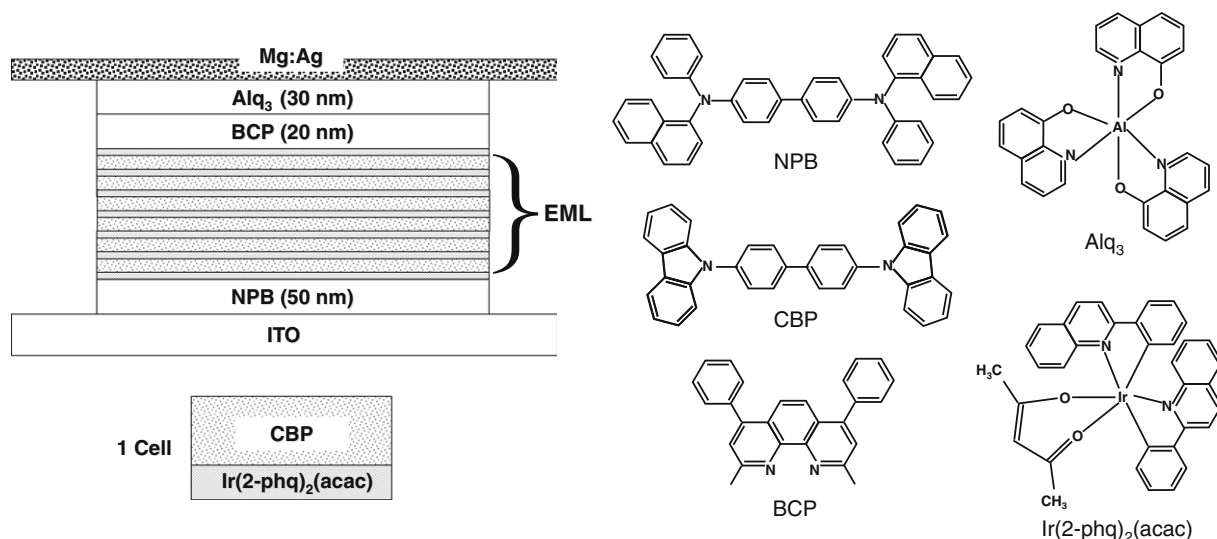


**Fig. 1.** Schematic diagram of fluorescent OLED fabricated with sequential doping with  $N$  cells and the molecular structures of the materials used in this work.

efficiency of the device drops significantly. Concentration quenching is originated from molecules aggregation [12] and long range dipole–dipole interaction between the guest molecules [13–15]. Molecular aggregation results in a much red-shifted emission spectrum followed by a significant drop in the efficiency [12]. On the other hand, excitonic quenching by long range dipole–dipole interaction only results in efficiency reduction without emission shift [13–15]. Depending on the molecule, the dominant factor is either molecular aggregation or dipole–dipole interaction. Since conventional doping only allows one parameter to be varied, the guest–host ratio, the effect of molecular aggregation or dipole–dipole interaction can not be controlled separately.

Recently we have introduced a technique termed sequential doping that allows two independent parameters to be varied for a better control of device performances [14]. In sequential doping, the EML consists of periodic thin layers of guest separated by the host. In this architecture, device performance can be tuned by adjusting the thicknesses of the guest and host layers independently. For molecules with a severe excitonic quenching due to molecular aggregation, the thickness of the guest layers can be minimized. On the other hand for molecules that suffer a large dipole–dipole quenching interaction, one may increase the thickness of the host layers for better device performance.

Reineke et al. showed a similar EML structure to the sequential doping, but compared to a neat film of guest molecules, they prepare the guest containing layers by co-evaporation of host and guest [16]. This method has been able to improve the efficiency roll-off with the critical current density increases from 140 to 270 mA/cm<sup>2</sup> by confining the exciton within the guest molecule. In spite of the better roll-off performance, the device reported by Reineke et al. shows a lower EQE value. The lack of guest molecules available for emission results in appearance of host emis-

sion and reduction in EQE due to incomplete energy transfer. Also the interlayer host thickness used is fixed at 2 nm. At such distance, the excitonic quenching by long range dipole–dipole process becomes significant.

In this letter, we utilized the sequential doping method to produce a highly efficient red OLED and to investigate the quenching mechanism in bis(2-phenylquinoline) (acetylacetonate) iridium(III) [Ir(2-phq)<sub>2</sub>(acac)]. Device with a maximum current efficiency of 16.2 cd/A (8.4% photon/electron) is reported. Interestingly the power efficiency can be improved by minimizing the thickness of the host layer. Using 3 nm of host layers, device with a maximum power efficiency of 8.3 lm/W is achieved. We also found that molecular aggregate dominates the exciton quenching in Ir(2-phq)<sub>2</sub>(acac).

## 2. Experimental

Here, we employed *N,N'*-di(naphth-2-yl)-*N,N'*-diphenylbenzidine [NPB] as the hole transporting layer, 4,4'-Bis(carbazol-9-yl)biphenyl [CBP] as the host, Ir(2-phq)<sub>2</sub>(acac) as the guest, and 2,9-dimethyl-4, 7-diphenylphenanthroline (BCP) as the hole blocking layer and tris-(8-hydroxyquinoline) aluminum [Alq<sub>3</sub>] as the electron transporting layer. Fig. 1 shows the schematic of the sequential doped device and the molecular structures of the materials used in this work.

The routine cleaning procedures, including ultra-sonication in acetone, ethanol, and rinsing in de-ionized water, were firstly carried out to clean ITO glass (50 Ω/square). Before deposition, the ITO was treated by oxygen plasma at 10 Pa for 2.5 min. The ITO substrates were then transferred to the main chamber under high vacuum for device fabrication. The deposition rate (thickness) is measured by a crystal sensor quartz oscillator combined with a frequency meter. Evaporation of organic materials and metals



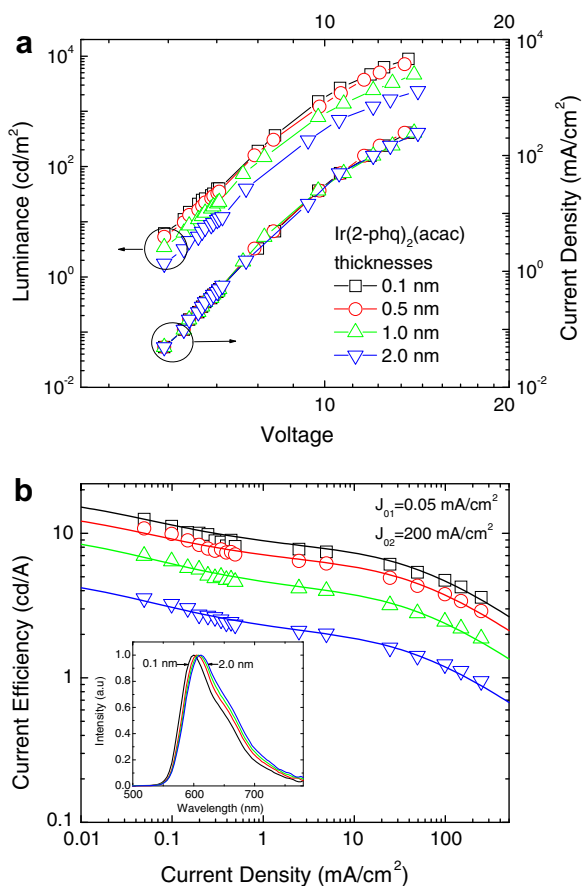


**Fig. 2.** (a)  $J$ - $V$  and  $L$ - $V$  curves for devices with various Ir(2-phq)<sub>2</sub>(acac) thicknesses (six cells). (b) Current efficiency versus current density for devices in (a). The efficiency roll-off can be fitted with a double TT annihilation model (with  $J_{01}$  and  $J_{02}$  of 0.05 and 200 mA/cm<sup>2</sup>, respectively). Inset in (b) shows the normalized emission spectra for devices in (a). Symbols in (a) also apply in (b).

was carried out in a high vacuum condition of about  $2 \times 10^{-4}$  Pa at a deposition rate of 0.5–4 Å/s.

Electroluminescence (EL) spectra of the fabricated devices were measured with a PR650 Spectra Scan spectrometer. Luminance–current density–voltage ( $L$ - $J$ - $V$ ) characteristics were recorded simultaneously with the measurements of the EL spectra by attaching the spectrometer to a programmable Keithley 236 source measurement unit. Assuming a Lambertian emission pattern, we calculated the EQE from the luminance, current density and EL spectrum. All measurements were carried out at room temperature under ambient atmosphere without any encapsulation.

### 3. Results and discussion

#### 3.1. Variation of guest's thicknesses

We fabricated devices with a structure of NPB/[Ir(2-phq)<sub>2</sub>(acac) ( $x$  nm)/CBP (5 nm)] (6 cells)/ Ir(2-phq)<sub>2</sub>(acac) ( $x$  nm)/ BCP/ Alq<sub>3</sub>, where  $x$  varies from 0.1, 0.5, 1, to 2.0 nm. Six cells were used to make sure the EML thick-

ness is larger than 20 nm to obtain a good carriers confinement [3]. Fig. 2a shows the current density and luminance versus voltage curves for devices with various guest thicknesses ( $x$ ). It can be seen that the current density does not vary much, while the luminance drops significantly as the guest thickness increases. This means the Ir(2-phq)<sub>2</sub>(acac) molecules do not trap or block charges significantly enough to influence the current flow. On the other hand, the large drop in the luminance for thicker guest layer can be attributed to molecular aggregation. Fig. 2b shows the current efficiency versus current density for various guest thicknesses. As the thickness of the guest layers increases, the degree of aggregation increases accordingly, resulting in a decrease in efficiency.

It can also be seen from Fig. 2b that the efficiency drops as the current increases. The efficiency roll-off is caused by biexcitonic interaction of triplet–triplet (TT) annihilation [17]. In the presence of triplet–triplet annihilation, the efficiency ( $\eta$ ) becomes

$$\eta = \eta_0 \frac{J_0}{4J} \left( \sqrt{1 + \frac{8J}{J_0}} - 1 \right) \quad (1)$$

where  $\eta_0$  is the maximum efficiency,  $J$  is the current density and  $J_0$  is the critical current density. The efficiency in Fig. 2b, however, cannot be fitted with a single TT annihilation model. Instead it can be fitted with a double TT annihilation process of

$$\frac{\eta}{\eta_0} = k_1 \frac{J_{01}}{4J} \left( \sqrt{1 + \frac{8J}{J_{01}}} - 1 \right) + k_2 \frac{J_{02}}{4J} \left( \sqrt{1 + \frac{8J}{J_{02}}} - 1 \right) \quad (2)$$

where  $k_1$  and  $k_2$  are constants,  $J_{01}$  and  $J_{02}$  represent the first and second critical current densities, respectively. Similar feature of double TT annihilation has been observed previously in various different OLEDs utilizing CBP as the host material [17]. The reason behind this phenomenon is not clear; however it may be related to exciton formation processes. At a low current injection, the excitons are only formed at the heterojunction interfaces. Therefore the TT annihilation is severe due to the thin recombination region. As the current increases, the exciton starts to be formed throughout the EML, increasing the effective recombination region, hence reducing the TT annihilation.

It can be seen from Fig. 2b that the data can be fitted nicely with double TT annihilations model.  $J_{01}$  and  $J_{02}$  values are independent of the guest thickness. This suggests that the TT annihilation is dominated by interaction between the planar guest layers since the host thickness is fixed. Later we shall see that variation of the host thickness changes the value of the critical current density.

Inset of Fig. 2b shows the emission spectrum of the device in Fig. 2a. It can be seen that the emission red-shifts with the increase in guest thickness. The emission peak shifts from 600 nm to 612 nm for Ir(2-phq)<sub>2</sub>(acac) thickness of 0.1 nm to 2.0 nm, respectively. This also supports the argument on molecule-aggregation. When two similar molecules are positioned close one another such that their electronic wavefunctions start to overlap, a new state is formed with different spectral properties compared to the molecular spectrum. In most cases the emission spec-

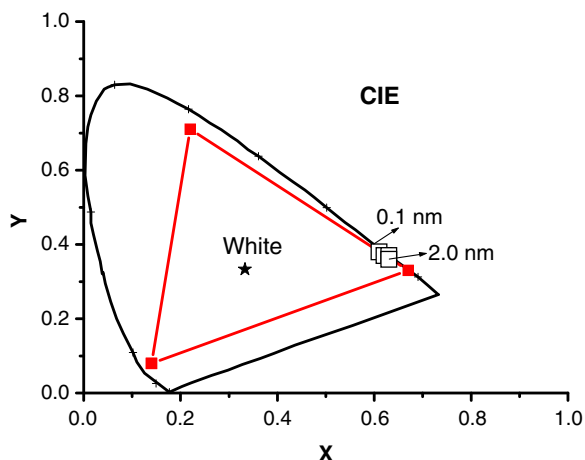


Fig. 3. CIE color coordinates of devices in Fig. 2.

trum is broaden and red-shifted with a much lower quantum efficiency than that of the molecule itself [12]. The large drop in the efficiency and shift of the emission spectrum show that Ir(2-phq)<sub>2</sub>(acac) molecules tend to form inefficient aggregates.

Fig. 3 shows the Commission Internationale de l'Eclairage (CIE) coordinate for devices in Fig. 2. It can be seen that there is a slight shift in CIE coordinate from ( $x = 0.61$ ,  $y = 0.38$ ) to ( $x = 0.63$ ,  $y = 0.36$ ) for devices with Ir(2-phq)<sub>2</sub>(acac) thickness from 0.1 nm to 2.0 nm. The CIE coordinate is very close to that of the National Television System Committee (NTSC) standard red color ( $x = 0.674$ ,  $y = 0.326$ ) [9].

### 3.2. Variation of host's thicknesses

We then varied the host thickness using a structure of NPB/[Ir(2-phq)<sub>2</sub>(acac) (0.1 nm)/CBP ( $y$  nm)] (6 cells)/Ir(2-phq)<sub>2</sub>(acac) (0.1 nm)/BCP/Alq<sub>3</sub>, where  $y$  varies from 3, 7, 10, to 15 nm. Fig. 4a shows the current density and luminance versus voltage curves for devices with various thicknesses of host layers. It can be seen that the current density and the luminance shift toward higher voltage as the thickness of the host increases. This is understandable due to a thicker device structure. The maximum luminance increases slightly with the host thickness. Fig. 4b shows the current efficiency for devices in Fig. 4a. It can be seen that the current efficiency increases slightly with the host thickness.

Similar to previous observation, the efficiency drops with the increase of current density. The efficiency roll-off in Fig. 4b can only be fitted with double TT annihilation model as shown by the solid line. The value of  $J_{01}$  is fixed at 0.05 mA/cm<sup>2</sup>. On the other hand  $J_{02}$  drops from 800 to 180 mA/cm<sup>2</sup> when CBP thickness reduces from 15 to 3 nm. The maximum value of  $J_{02}$  even exceeds that of the optimized device reported by Reineke et al. of 400 mA/cm<sup>2</sup>, which indicates the advantage of using our sequential doping method for this study [18]. The variation of  $J_{02}$  with CBP thickness shows that the TT annihilation processes oc-

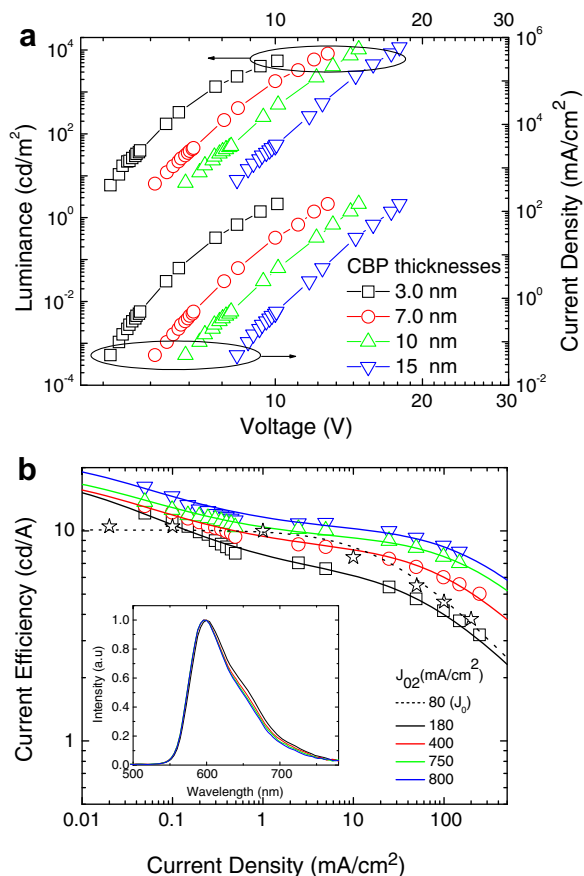


Fig. 4. (a)  $J$ - $V$  and  $L$ - $V$  curves for devices with various CBP thicknesses (six cells). (b) Current efficiency versus current density for devices in (a). Also shown here is the current efficiency of device from Ref. [10] (stars). Inset in (b) shows the normalized emission spectra for devices in (a). Symbols in (a) also apply in (b).

cur between the guest layers as mentioned before. When the guest layers are separated adequately, the TT annihilation is minimized as evidenced by the increase in the critical current density.

The TT annihilation between the Ir(2-phq)<sub>2</sub>(acac) within the planar guest layer is also minimized due to the large intermolecular spacing between the molecules. To estimate the intermolecular spacing of the Ir(2-phq)<sub>2</sub>(acac) layer, we assume that 0.1 nm of Ir(2-phq)<sub>2</sub>(acac) layer corresponds to 0.1 monolayer of Ir(2-phq)<sub>2</sub>(acac) film. Assuming that a monolayer square lattice of Ir(2-phq)<sub>2</sub>(acac) has intermolecular spacing of 1 nm [15,19], the intermolecular spacing of a 0.1 monolayer can be estimated as  $a = 1 \text{ nm} \times \frac{1}{\sqrt{0.1}}$ . We further assume that, two molecules may be closely spaced forming aggregate (dimer), the intermolecular spacing ranges between 3 and 6 nm. At this distance, the Ir(2-phq)<sub>2</sub>(acac) molecules are isolated, therefore minimizes the TT annihilation.

To our best knowledge this is the first time that Ir(2-phq)<sub>2</sub>(acac) molecule was incorporated as a red OLED. In the literature, a similar molecule of bis(1-phenylisoquinoline) (acetylacetonate)iridium(III) [Ir(piq)<sub>2</sub>(acac)] has

**Table 1**

Summary of performances of devices in this work.

Thickness of CBP (nm)	Thickness of Ir(2-phq) <sub>2</sub> (acac) (nm)	EQE (%) [Max, @ 10, 100 cd/m <sup>2</sup> ]	Current Efficiency (cd/A) [Max, @ 10, 100 cd/m <sup>2</sup> ]	Power Efficiency (lm/W) [Max, @ 10, 100 cd/m <sup>2</sup> ]	CIE (x,y)	Peak of Emission Spectrum (nm)
5	0.1	7.2, 6.6, 4.6	12.5, 11.2, 7.8	7.2, 6.0, 3.5	0.61, 0.38	600
5	0.5	6.9, 6.3, 4.4	10.8, 9.9, 6.8	6.3, 5.3, 3.0	0.62, 0.37	604
5	1	4.9, 3.9, 2.9	7.0, 5.6, 4.2	4.4, 2.8, 1.8	0.63, 0.37	608
5	2	2.5, 1.7, 1.4	3.5, 2.4, 2.0	2.5, 1.1, 0.8	0.63, 0.36	612
3	0.1	7.1, 6.4, 4.5	12.1, 11.2, 7.7	8.3, 7.5, 4.4	0.61, 0.38	600
7	0.1	7.2, 6.9, 5.0	13.1, 12.5, 8.9	7.2, 6.6, 3.9	0.61, 0.38	600
10	0.1	7.3, 6.9, 5.6	13.7, 12.6, 10.3	6.6, 5.8, 3.7	0.61, 0.38	600
15	0.1	8.4, 8.0, 6.0	16.2, 15.0, 11.0	6.1, 5.5, 3.3	0.61, 0.38	600

also been used for red OLED [10]. The current efficiency of a Ir(piq)<sub>2</sub>(acac) device fabricated using the conventional co-evaporation method was included in Fig. 4b represented as stars. The emission layer consists of 4 wt.% Ir(piq)<sub>2</sub>(acac) doped into CBP host. It is clear that the performance of the device fabricated using the conventional method is worse. The maximum current efficiency reaches up to 10.1 cd/A and drops to 4.5 cd/A at a current density of 100 mA/cm<sup>2</sup>. The  $J_0$  value is much lower of 80 mA/cm<sup>2</sup> [20].

Inset of Fig. 4b shows the emission spectrum of the device in Fig. 4a. No significant change was observed in the emission spectrum for devices with various thicknesses of CBP, which indicates the absence of molecular aggregate. The slight drops of the current efficiency for device with thinner layer of host material may arise from an increase in interaction between the guest molecules.

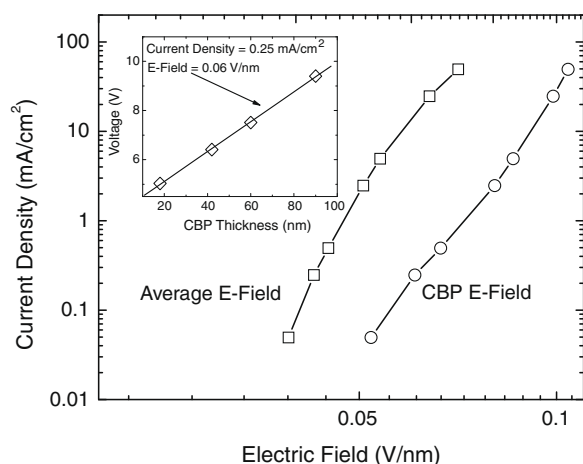
Previous studies have shown that Förster type interactions between the guest molecules result in excitonic quenching in host–guest system [13–15]. The long range interaction between the electronic and vibrational modes between two molecules is enabled by dipole–dipole interaction which applies up to a range of 20 nm [21]. In our case, it is clear that the long range excitonic quenching is much less significant than the aggregation effects. It can be seen that only a slight drops in current efficiency is observed for device with different CBP thicknesses (drops from 16.2 to 12.1 cd/A for CBP thicknesses of 15 to 3 nm, respectively). This means that the radiationless Förster radius between the Ir(2-phq)<sub>2</sub>(acac) molecule is small.

Table 1 summarized the performances for devices reported in this work. It worth mentioning that the current efficiency obtained in this work (16.2 cd/A) is one of the best for red OLED based on small molecule with CBP host. Furthermore, the current efficiency shows only a small roll-off with current density. At high current density of 100 mA/cm<sup>2</sup> the current efficiency still reaches 8.7 cd/A. At brightness values of 10 and 100 cd/m<sup>2</sup>, the current efficiency reaches 15 and 11 cd/A, respectively.

From Table 1 it can be seen that the best power efficiency (8.3 lm/W) is obtained for device with a thinner layer of CBP layer (3 nm) which corresponds to EML thickness of 18 nm. In OLED it is known that reducing the thickness of EML significantly reduces the efficiency due to

inadequate number of emitter molecules, which results in emission saturation [3]. Therefore sufficient EML thickness is required to achieve high power efficiency. In our case, the numbers of guest emitter molecules are fixed with variation of host thickness. Therefore the decrease of the efficiency is not due to emission saturation but increase intermolecular interaction between the guest molecules. The slight drop in current efficiency is followed by a significant reduction in operating voltage, which in overall increases the power efficiency as the thickness of the host reduces.

Inset of Fig. 5 shows the operating voltage for devices with various CBP thicknesses at a current density of 25 mA/cm<sup>2</sup>. It can be seen that the voltage increases linearly with CBP thickness, indicating that the electric field is constant throughout the CBP layer. The electric field within the CBP can be obtained from the slope of the fitting straight-line. Fig. 5 plots the average electric field and the CBP electric field at various current densities. The average electric field is determined by dividing the operating voltage with the total thickness of the device with EML thickness of 18 nm. It is clear that for a fixed current density the electric field in the CBP is almost two times higher than the average electric field. There-



**Fig. 5.** Current density versus the average and CBP electric-field. Inset shows the operating voltage for devices with various CBP thicknesses at a current density of 25 mA/cm<sup>2</sup>.

fore minimization of the CBP thickness effectively reduces the operating voltage and increases the power efficiency since the number of emitting guest molecules is unaltered.

It is worth mentioning that the device structure has the potential for further optimization, such as the usage of Alq<sub>3</sub> as the host, LiF [2] or CsF [22] cathodes, electron-blocking layer [4], corrugated substrate [23], or microcavity [24] and optimization of number of cells in order to further reduce the operating voltage and increases the current efficiency of the device.

#### 4. Conclusion

In conclusion, we have introduced sequential doping method for efficient phosphorescent red OLED. The method presented here has an advantage since it allows two independent parameters to be varied for optimization. Device with current efficiency of 16.2 cd/A has been produced. Interestingly, the power efficiency increases with reduction of the host thickness. Device with a power efficiency of 8.3 lm/W is achieved. The excitonic quenching in thin layer of Ir(2-phq)<sub>2</sub>(acac) was mainly due to appearance of aggregation state. We also observed a small amount of excitonic quenching due to inter-molecular energy transfer among Ir(2-phq)<sub>2</sub>(acac) molecules, i.e. by long range Förster process between the Ir(2-phq)<sub>2</sub>(acac) molecules in different layers.

#### Acknowledgement

Y.D. would like to thank the Singapore Millennium Foundation (SMF) for the financial support.

#### References

- [1] S.A. VanSlyke, C.H. Chen, C.W. Tang, *Appl. Phys. Lett.* 69 (1996) 2160.
- [2] L.S. Hung, C.W. Tang, M.G. Mason, *Appl. Phys. Lett.* 70 (1997) 152.
- [3] B.W. D'Andrade, S.R. Forrest, *J. Appl. Phys.* 94 (2003) 3101.
- [4] M. Pfeiffer, S.R. Forrest, K. Leo, M.E. Thompson, *Adv. Mater.* 14 (2002) 1633.
- [5] C.W. Tang, S.A. VanSlyke, C.H. Chen, *J. Appl. Phys.* 65 (1989) 3610.
- [6] M.A. Baldo, D.F. O'Brien, Y. You, A. Shoustikov, S. Sibley, M.E. Thompson, S.R. Forrest, *Nature* 395 (1998) 151.
- [7] C. Adachi, M.A. Baldo, S.R. Forrest, M.E. Thompson, *Appl. Phys. Lett.* 77 (2000) 904.
- [8] C. Adachi, M.A. Baldo, M.E. Thompson, S.R. Forrest, *J. Appl. Phys.* 90 (2001) 5048.
- [9] C.L. Li, Y.J. Su, Y.T. Tao, P.T. Chou, C.H. Chien, C.C. Cheng, R.S. Liu, *Adv. Funct. Mater.* 15 (2005) 387.
- [10] C.-L. Ho, W.-Y. Wong, Z.-Q. Gao, C.-H. Chen, K.-W. Cheah, B. Yao, Z.-Y. Xie, Q. Wang, D.-G. Ma, L.-X. Wang, X.-M. Yu, H.-S. Kwok, Z.-Y. Lin, *Adv. Funct. Mater.* 18 (2008) 319.
- [11] C.T. Chen, *Chem. Mater.* 16 (2004) 4389.
- [12] M. Pope, C.E. Swenberg, *Electronic Processes in Organic Crystals and Polymers*, second ed., Oxford University Press, Oxford, 1999.
- [13] Y. Kawamura, J. Brooks, J.J. Brown, H. Sasabe, C. Adachi, *Phys. Rev. Lett.* 96 (2006) 017404.
- [14] Y. Divayana, X.W. Sun, *Phys. Rev. Lett.* 99 (2007) 143003.
- [15] J.C. Ribierre, A. Ruseckas, K. Knights, S.V. Staton, N. Cumpstey, P.L. Burn, I.D.W. Samuel, *Phys. Rev. Lett.* 100 (2008) 017402.
- [16] S. Reineke, G. Schwartz, K. Walzer, K. Leo, *Appl. Phys. Lett.* 91 (2007) 123508.
- [17] M.A. Baldo, S.R. Forrest, *Phys. Rev. B* 62 (2000) 10958.
- [18] S. Reineke, K. Walzer, K. Leo, *Phys. Rev. B* 75 (2007) 125328.
- [19] S. Lamansky, P. Djurovich, D. Murphy, F. Abdel-Razzaq, R. Kwong, I. Tsyba, M. Bortz, B. Mui, R. Bau, M.E. Thompson, *Inorg. Chem.* 40 (2001) 1704.
- [20] The data from Ref. [10] can be fitted with single TT annihilation model.
- [21] T. Förster, *Discuss. Faraday Soc.* 27 (1959) 7.
- [22] M.Y. Chan, S.L. Lai, M.K. Fung, C.S. Lee, S.T. Lee, *Chem. Phys. Lett.* 374 (2003) 215.
- [23] Y.J. Lee, S.H. Kim, J. Huh, G.H. Kim, Y.H. Lee, S.H. Cho, Y.C. Kim, Y.R. Do, *Appl. Phys. Lett.* 82 (2003) 3779.
- [24] H. Peng, J. Sun, X. Zhu, X. Yu, M. Wong, H.S. Kwok, *Appl. Phys. Lett.* 88 (2006) 073517.



## Modification of para-sexiphenyl layer growth by UV induced polarity changes of polymeric substrates

G. Hernandez-Sosa<sup>a,\*</sup>, C. Simbrunner<sup>a</sup>, T. Höfler<sup>b</sup>, A. Moser<sup>c</sup>, O. Werzer<sup>c</sup>, B. Kunert<sup>c</sup>, G. Trimmel<sup>b</sup>, W. Kern<sup>d</sup>, R. Resel<sup>c</sup>, H. Sitter<sup>a</sup>

<sup>a</sup> Institute of Semiconductors and Solid State Physics, Johannes Kepler University Linz, Altenbergerstrasse 69, 4040 Linz, Austria

<sup>b</sup> Institute for Chemistry and Technology of Materials, Graz University of Technology, Stremayrgasse 16, 8010 Graz, Austria

<sup>c</sup> Institute of Solid State Physics, Graz University of Technology, Petersgasse 16, 8010 Graz, Austria

<sup>d</sup> Institute of Chemistry of Polymeric Materials, Montanuniversität Leoben, Franz-Josef-Strasse 18, 8700 Leoben, Austria

### ARTICLE INFO

#### Article history:

Received 25 September 2008

Received in revised form 10 December 2008

Accepted 13 December 2008

Available online 25 December 2008

#### PACS:

61.05.cp

68.37.Ps

68.55.am

82.50.m

#### Keywords:

Para-sexiphenyl

Hot wall epitaxy

Surface polarity

Photo-Fries rearrangement

Photochemistry

### ABSTRACT

We report on the deposition of para-sexiphenyl (PSP) on poly(diphenyl bicyclo[2.2.1]hept-5-ene-2,3-dicarboxylate) (PPNB) by hot wall epitaxy (HWE). The surface polarity of the substrate, PPNB, can be increased by UV-illumination via a photo-Fries rearrangement. The influence of the changed surface polarity on the surface morphology and the structure of the PSP layers were studied by atomic force microscopy (AFM), X-ray diffraction (XRD) and grazing incidence X-ray diffraction (GIXD). The observation of growth spirals and islands, providing mono-layer step heights of standing PSP molecules, underline a high crystallographic order of the films which is confirmed by XRD analysis. GIXD experiments show a strong preferential (001) orientation of the PSP layers with better alignment on substrates with smaller surface polarity. The  $\gamma$ - and Baker-crystal structures are present in the films grown at low substrate temperatures, but only Baker structure was found in the films deposited at high substrate temperatures. However the main influence on the growth of PSP, is caused by the polarity change induced by pre-treating the PPNB substrate by UV-illumination.

© 2008 Elsevier B.V. All rights reserved.

### 1. Introduction

Surface morphology and crystalline order are determining the electrical and optical properties such as mobility or electroluminescence of organic semiconducting films. Therefore it is of great importance to understand the growth kinetics of organic materials on surfaces with well controlled properties that could be potentially used for the fabrication of optoelectronic devices. Para-sexiphenyl (PSP) (C<sub>36</sub>H<sub>26</sub>), a six units oligomer of para-phenylene, is

a promising candidate as an electro active layer in organic LED displays due to its blue luminescence with high quantum yield [1,2]. Moreover, it is classified as a wide band gap organic semiconductor (3.1 eV) with photoluminescence in the blue visible range and polarisation dependent absorption and emission if the PSP films are highly ordered [3].

The hot wall epitaxy (HWE) technique was adapted for the deposition of organic materials. Highly ordered organic thin films can be obtained with this technique because it allows organic molecules to find the most suitable arrangement before settling into the crystal lattice [3,4]. Organic thin films grown by HWE have shown outstanding electrical and optical properties [5,6]. HWE grown PSP films have been already deposited on different substrates such as KCl

\* Corresponding author. Tel.: +43732 24689659; fax: +43732 24689696.

E-mail address: [Gerardo.HernandezSosa@jku.at](mailto:Gerardo.HernandezSosa@jku.at) (G. Hernandez-Sosa).

and muscovite mica and extensive morphological and structural characterization has been performed [7,8]. It is generally shown that the nature of the substrate and the growth conditions such as substrate temperature and deposition rate are determinant parameters for the molecular packing of the films.

In this contribution, an amorphous polymer poly(diphenyl bicyclo[2.2.1]hept-5-ene-2,3-dicarboxylate) (PPNB) containing photoreactive aryl-ester groups was used as substrate. Upon illumination with UV-light of  $\lambda < 280$  nm these ester groups isomerise to the corresponding hydroxyketones in the so-called photo-Fries reaction [9,10]. Fig. 1 shows the generally accepted mechanism [11–13]. As a first step photolysis proceeding from an excited singlet (S1) state leads to the cleavage of the C–O bond. The photogenerated radicals can recombine and yield a derivative of cyclohexadienone as the “cage product” (ortho and para product). Tautomerism then gives the hydroxyketone, which is the rearranged acyl migration product. Besides the release of free phenols as “escape” product, decarboxylation occurs as competing reaction [14,15].

The photo-Fries rearrangement is also observed in polymeric materials [16–18]. Recently, we have shown that the photoreaction in PPNB (Fig. 2) yields up to 21% hydroxyketones as photoproducts [19]. The UV induced reaction leads to a large increase of the refractive index as well as a change in surface polarity. This enhanced polarity and the generated new functional groups can be used for selective post-modification reactions [20]. As a consequence we expected a clear influence of the enhanced surface polarity on the growth mechanism of PSP layers.

## 2. Experimental

PPNB was synthesized as described previously [19]. A 10 mg/ml solution of PPNB in  $\text{CHCl}_3$  was prepared and stirred for 12 h. Subsequently, the solution was spin cast onto Si-substrates with a native 1.7 nm ( $\pm 0.4$  nm) thick oxide layer, resulting in 80 nm ( $\pm 10$  nm) film thickness of PPNB which was verified by ellipsometric measurements. Finally, the film was dried at 40 °C in vacuum.

In order to provide equivalent growth conditions while depositing PSP on UV-exposed and non-irradiated surfaces each substrate was divided in two regions. One half of the substrate was exposed for 20 min to UV-light (254 nm) while the other half was covered with a chromium mask.

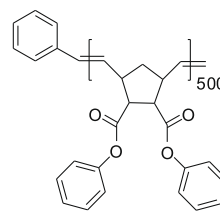


Fig. 2. Structure of PPNB.

The unfiltered light of an ozone-free mercury low pressure UV lamp (Heraeus Noblelight; 254 nm) was used. For these experiments, the light intensity (power density) at the sample surface was measured with a spectroradiometer (Solatell, Sola Scope 2000TM, measuring range from 230 to 470 nm). The integrated power density for the spectral range 240–270 nm was 1.41  $\text{mWcm}^{-2}$ . The illumination process was performed under inert gas atmosphere (nitrogen with a purity >99.95%) in order to avoid unwanted oxidation reactions. The surface tension  $\gamma$  of the illuminated and non-illuminated part was determined by measuring the contact angle with a Drop Shape Analysis System DSA100 (Krüss GmbH, Hamburg, Germany) using water and diiodomethane as test liquids (drop volume  $\sim 20$   $\mu\text{l}$ ). The contact angles were obtained by means of the sessile drop method and they were measured within 2 s. Based on the Owens–Wendt method, the surface tension  $\gamma$  as well as the dispersive and polar components ( $\gamma^D$  and  $\gamma^P$ ) were calculated [21]. The surface polarity is expressed as the ratio  $\gamma^P/\gamma$  and is given in percent (%). AFM investigation of the surface roughness (before and after 1 h annealing at 160 °C) resulted in RMS values between 0.2 and 0.6 nm no difference could be observed for the as prepared and illuminated parts of the substrate.

After the illumination process the substrates were transferred via a load lock to a HWE evaporation chamber working at a dynamic vacuum of  $9 \times 10^{-6}$  mbar. The working principles of a HWE system can be found elsewhere [22]. In order to reduce surface contaminations a 15 min in situ preheating procedure was applied. The substrate temperature during preheating is chosen the same as the growth temperature in order to permit constant thermal conditions during the whole deposition process. The preheating process also allows to remove any adsorbed species ( $\text{H}_2\text{O}$ ,  $\text{O}_2$  etc.) from the surface of the substrate. A complete series of samples was prepared varying growth

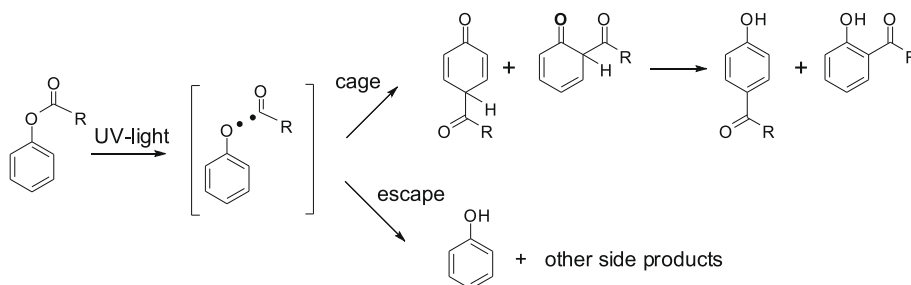


Fig. 1. Mechanism of photo-Fries rearrangement.

time (5–60 min) and substrate temperature (85–160 °C) whereas the source- (240 °C) and wall-temperature (260 °C) were kept constant resulting in a deposition rate of  $\sim 0.55$  nm/min. All steps of the sample preparation procedure are shown schematically in Fig. 3.

For the structural characterization, specular scans were performed on a SIEMENS D501 diffractometer using Cu  $K_{\alpha}$  radiation in Bragg–Brentano geometry equipped with a secondary graphite monochromator. Complementary to studies in our laboratory, grazing incidence X-ray diffraction (GIXD) was performed at the G2 line, Cornell high energy synchrotron source. The angle of incidence was optimised for maximum scattering intensity, values between 0.19° and 0.23° were used.

At the beam line a diffractometer in  $\kappa$ -geometry was operated with radiation of a wavelength of 0.12681 nm. Reciprocal space maps were taken with a one-dimensional detector collecting the scattered intensity in  $q_z$ -direction. Simultaneously an angular range of 6° was picked up with a resolution of 0.1°. The surface parallel component of the scattering vector ( $q_{xy}$ ) was varied by the goniometer in steps of 0.1°. Since the PSP crystallites do not have any specific in-plane orientation the GIXD measurements could be performed without sample rotation.

The vertical crystal size (in perpendicular direction to the substrate surface) was determined from the specular scans taking the integral width of the diffraction peaks. No corrections for the instrumental line broadening were used, since only relative changes in the peak width are of interest. The lateral crystal size (in parallel direction to the substrate surface) was determined from the GIXD pattern by using the Scherrer formula. The crystal sizes obtained from Williams–Hall plots reveal that the line broadening arises dominantly by size effects, this reveals that Scherrer formula can be applied [23,24].

Atomic force microscopy (AFM) studies of the deposited films were performed using a Digital Instruments Dimension 3100 in the tapping mode. The AFM characterization was performed on an area of 100  $\mu\text{m}^2$  with a SiC tip.

### 3. Results and discussion

In Table 1 the contact angle data of the non-illuminated and of the illuminated parts of the substrate are summa-

rized. Due to the illumination of the substrate the contact angle of water decreases from  $88 \pm 1^\circ$  to  $83 \pm 3^\circ$  while the contact angle of diiodomethane increases from  $34 \pm 1^\circ$  to  $43 \pm 2^\circ$  demonstrating that the surface becomes more hydrophilic. The overall surface tension decreases slightly upon illumination, due to a large decrease of the dispersive component. However, the polar component becomes higher, leading to an increase of the surface polarity from 2.3% to 6.5%.

Using AFM in tapping mode, a detailed surface morphology analysis of the sample series was performed. The influence of the polymer substrate on the surface properties of the grown PSP is analysed depending on substrate temperature, deposition time and UV-illumination of the substrate before deposition of PSP.

Fig. 4 depicts a chart with the AFM images (100  $\mu\text{m}^2$ ) of films grown at 85 °C, 100 °C, 130 °C and 160 °C varying the deposition time from 5 to 20 and 60 min. The height scale ( $z_0$ ) is presented at the bottom of each image. The morphology of the PSP film grown on the UV-illuminated side and on the as prepared surface are shown on the right and left side of each image, respectively. A clear morphological difference between non-illuminated and UV-illuminated regions can be observed. While on the non-illuminated side a more homogeneous PSP film is formed, UV-irradiation of the substrate prior to HWE leads to island formation. This can be clearly deduced in the height distribution from the AFM scans. The UV-treated side always shows two peaks in the height histogram, while the as prepared parts give only one. That means that the AFM tip reached the substrate in the first case between the islands, which does not occur for as prepared samples. This effect in the surface morphology can be attributed to the increase in surface polarity of the substrate, resulting from the photochemical reaction of PPNB, due to the fact that the preparation conditions of the sample were identical and the only change was the UV treatment.

Increasing the deposition time of PSP from 5 to 60 min is leading to a lateral expansion of the single islands. In the same way, an increase in size of the observed structures results from an increase of the substrate temperature. In Fig. 5 more detailed AFM images of the two regions of the sample grown at 160 °C for 20 min (Fig. 4-IVb) are pre-

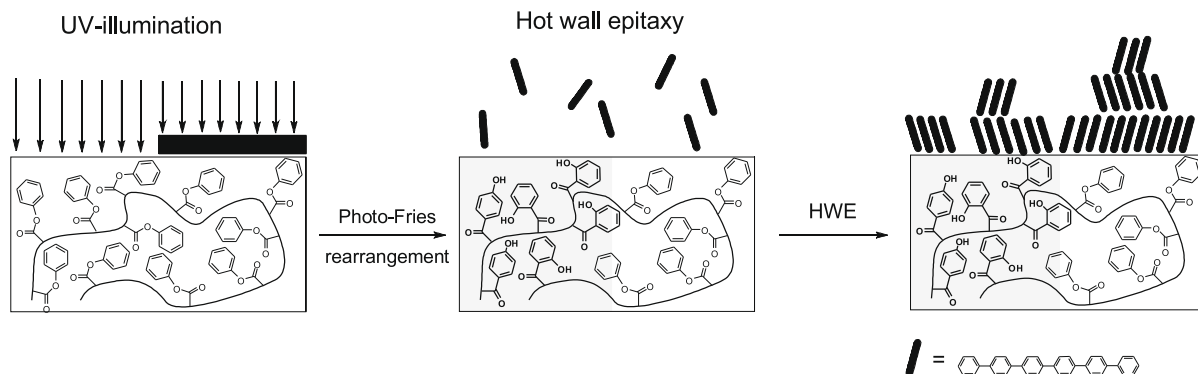


Fig. 3. Description of the sample preparation.

**Table 1**

Contact angle (sessile drop) of PPNB before and after UV-illumination, calculated values of the surface tension  $\gamma$  using the Owens–Wendt method as well as the dispersive and polar components ( $\gamma^D$  and  $\gamma^P$ ) and the surface polarity [21]. The surface polarity is expressed as ratio  $\gamma^P/\gamma \times 100$ .

PPNB	$\theta$ H <sub>2</sub> O (°)	$\theta$ CH <sub>2</sub> Cl <sub>2</sub> (°)	$\gamma$ (mJ <sup>-2</sup> )	$\gamma^D$ (mJ <sup>-2</sup> )	$\gamma^P$ (mJ <sup>-2</sup> )	Surface polarity (%)
Pristine	88 ± 1	34 ± 1	43.4	42.4	1.0	2.3(0.2)
UV-illumination <sup>a</sup>	83 ± 3	43 ± 2	40.6	38.0	2.7	6.5(0.3)

<sup>a</sup>  $\lambda = 254$  nm, illumination time 20 min, power density 1.4 mW cm<sup>-2</sup>.

sented. On the one hand, on the non-illuminated part (Fig. 5a, Fig. 4-IVb left) we can observe a closed film with growth spirals, which are characteristic for screw dislocations [25,26]. On the other hand, in the UV-illuminated side (Fig. 5c, Fig. 4-IVb right), crystallites with terraces of up to hundreds of nanometres in length can be observed. A substrate temperature of 160 °C seems to be the optimal growth parameter to observe such differences in morphological features. Fig. 5b and d shows the scan profiles indicated in Fig. 5a and c as black solid lines. The step heights of the observed features are in good agreement with the expected thickness of one mono-layer of standing PSP molecules corresponding to 2.6 nm. Similar results are found for other small organic molecules grown on different sub-

strates [27]. The resulting surface morphology and the observation of step heights corresponding to standing PSP molecules gives a clear hint that the PSP layers have a high degree of crystallographic order. Moreover, it is demonstrated that it is possible to influence the crystal morphology of PSP via a pre-treatment of the substrate by illumination.

In order to deduce additional information concerning the crystal structure of the samples detailed X-ray studies were performed, taking as a motivation the results obtained from the morphology studies. The thicker samples, grown at substrate temperatures between 85 °C and 160 °C (60 min of deposition time) were selected for diffraction experiments to ensure a higher intensity.

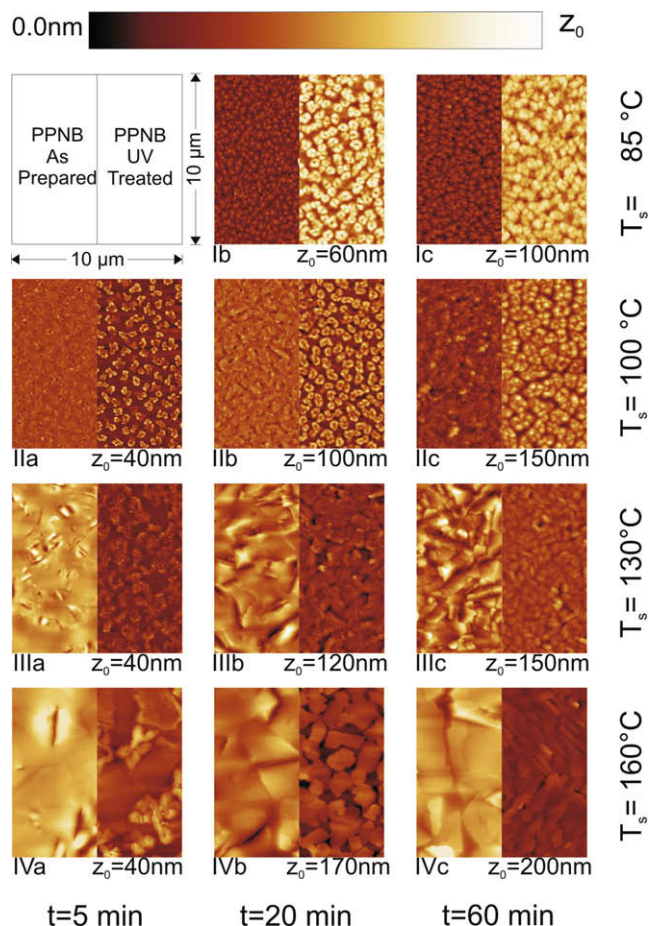


**Fig. 4.** Atomic force microscopy images of para-sexiphenyl on PPNB pre-treated with UV-light (right side of each image) and as prepared (left side) for different substrate temperatures and different deposition times.



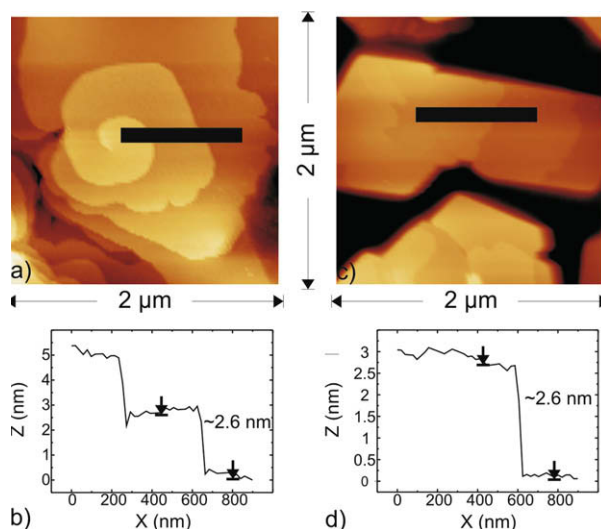


**Fig. 5.** AFM images and scan profiles along the indicated dark lines of the PSP crystallites deposited on the as prepared (a and b) and UV-illuminated (c and d) PPNB surface.

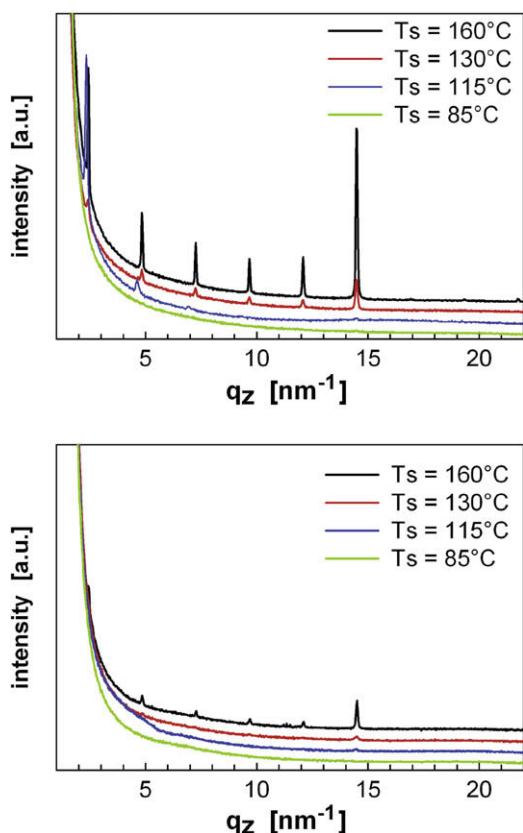


**Fig. 6.** Specular X-ray diffraction of PSP films grown on the as prepared surface (a) and on the UV-illuminated surface (b). The substrate temperature during the thin film growth was varied between 85 °C and 160 °C. The curves are vertically shifted for clarity.

The specular scans of the PSP films, deposited on the as prepared surface and on the UV-illuminated surface, are depicted in Fig. 6a and b, respectively. The film grown at a substrate temperature of 160 °C (Fig. 6a) shows a diffraction peak series, arising from an interplanar distance of 2.6 nm. Please note that the 6th order reflection observed at  $q_z = 14.51 \text{ nm}^{-1}$  shows enhanced intensity. The peak positions in the specular scan together with the indexed diffraction pattern of the reciprocal space map obtained by GIXD (not shown), reveal that the present crystal structure can be identified as the well-known “Baker” structure [28]. This crystal structure is a layered herringbone structure with lattice constants of  $a = 0.8091 \text{ nm}$ ,  $b = 0.5565 \text{ nm}$ ,  $c = 2.6241 \text{ nm}$  and  $\beta = 98.17^\circ$ . The reflections of the specular scan can be indexed as 00L arising from the crystallographic 001 plane parallel to the PPNB substrate. This plane with the herringbone structure has the lowest surface energy of the Baker structure [29]. In a real space picture the orientation of the molecules within the PSP crystals appears with up-right standing molecules with the long molecular axes tilted  $17^\circ$  to the surface normal.

At a substrate temperature of 115 °C, a considerable shift of the 00L reflections appears (Fig. 6a), which is most clearly visible at the 002 reflection at  $q_z = 4.61 \text{ nm}^{-1}$ . A change in the crystal structure can be concluded. The new crystal structure can be assigned to the  $\gamma$ -phase of PSP. This polymorph phase is also a layered herringbone structure [30]. In difference to the “Baker” structure, the long molecular axes of the PSP molecules are oriented perpendicular to the surface normal. The GIXD pattern allow an indexation of the  $\gamma$ -phase with lattice constants of  $a = 0.776 \text{ nm}$ ,  $b = 0.558 \text{ nm}$ ,  $c = 2.85 \text{ nm}$  and  $\beta = 106.3^\circ$ . The GIXD investigations of these samples confirm the simultaneous appearance of Baker and  $\gamma$ -phase for PSP crystals grown on the as prepared surface, however only the  $\gamma$ -phase was found at the UV-illuminated substrate.

The overall intensity of the 00L diffraction peaks decreases with decreasing substrate temperature. In case of the films prepared on the as prepared surface (Fig. 6a) strong diffraction peaks are observed for layers grown at a substrate temperature of 160 °C, but no clear peaks are present for layers grown at 85 °C. This decrease of intensity is even more pronounced for films grown on the UV-treated surface (Fig. 6b). This fact is clearly related to the mosaicity of the PSP layers: at lower substrate temperatures the 001 planes of PSP crystallites are much weaker oriented, than at high substrate temperatures. This fact is experimentally observed in the GIXD pattern where the thin films grown at 160 °C show comparable sharp diffraction spots as it is expected for a two-dimensional powder. The films grown at 115 °C show segments of circles (onset of Debye–Scherrer rings), which reveal a much higher mosaicity of the PSP crystals. The different mosaicity is also reflected in the different intensity of the 00L diffraction peaks between films grown on the as prepared and the UV-illuminated surface (compare Fig. 6a and 6b).

The vertical crystal size was determined from specular scans. Reliable values could be obtained only for the thin films grown at a substrate temperature of 160 °C. The small intensities of the 00L peaks for layers grown at lower

substrate temperatures, did not allow a crystal size determination. The PSP crystallites grown on the as prepared and on the UV-illuminated surface show a vertical crystal size of 70 nm and 60 nm, respectively.

Specific results of GIXD measurements are shown in Fig. 7. The figure shows the scattered intensity as a function of  $q_{xy}$  obtained from cuts through the reciprocal space maps at  $q_z = 1.5 \text{ nm}^{-1}$ . The strongest diffraction peaks of both PSP crystal structures (Baker as well as  $\gamma$  - structure) are visible. The lateral crystal size was determined from the peak widths. At a substrate temperature of 160 °C (Fig. 7a) the lateral crystal size was estimated with 40 nm which is comparable for films on both types of substrates. At a substrate temperature of 115 °C, a lateral crystal sizes of 40 nm and 20 nm is obtained for films grown on as prepared and UV-treated substrates, respectively. The lateral crystal size is not in the same range as the island size observed in AFM images, which means that the islands can contain grain boundaries, not observable by AFM.

The strongly preferred orientation of PSP crystallites with the 001 plane parallel to the substrate surface is known for isotropic surfaces such as glass or native oxide single crystal surfaces [31,32]. It is reported that the crystal orientation becomes more pronounced with increasing substrate temperature [33]. This tendency is also clearly seen on the PPNB substrate. This results from the fact that the PSP molecules become more mobile on the surface and are thereby able to arrange in larger crystallites. An additional contribution to this effect may stem from the fact that PPNB has a glass transition temperature ( $T_g$ ) of 96 °C. While below  $T_g$  the PPNB polymer is in a glassy state, at temperatures above  $T_g$  molecular motion on the scale of its repeating unit takes place. Therefore, the substrate can adapt its surface with the 001 facet of PSP crystals which have a lateral extension of 40 nm. With increasing sub-

strate temperature the softness of the substrate increases which causes that the PPNB thin film becomes more homogenous while the impinging PSP molecules become more mobile on the surface resulting in a better alignment of the 001 planes of PSP crystallites relative to the substrate.

Recently, Kim et al. reported that depositing pentacene on polymeric substrates below  $T_g$  results in better quality thin films than when the deposition temperature is above the glass transition temperature of the substrate [34]. At first glance these findings seem to follow the opposite trend of our observations. However, the temperature range investigated in Ref. [34] ended shortly above the glass transition and no data on higher temperatures are given. In our study, the samples around the glass transition temperature also exhibit a low order (samples prepared at 85 °C and 115 °C) compared to the samples prepared at higher substrate temperature (samples prepared at 130 °C and 160 °C). In these samples, the effect that at higher substrate temperatures higher quality films are obtained [33], seems to be predominant.

As already discussed the size of the PSP crystals is slightly smaller in the films grown on the UV-treated substrates than on the as prepared ones, 20 and 40 nm for the lateral crystal size (detected at  $T_s = 115$  °C) and 60 and 70 nm for the vertical crystal size (detected at  $T_s = 160$  °C). This fact correlates with AFM results which detects smaller lateral as well as vertical dimensions of the islands on the UV-treated surface. Moreover, the PSP thin film morphology shows a clear difference between the as prepared and the UV-treated surface. Elongated islands are observed at the UV-treated surface, especially at high substrate temperatures, while the typical island morphology of sexiphenyl is observed on the as prepared surface [32,35]. Different mechanisms of crystal formation, like spiral growth caused by screw dislocations at the as prepared surface, can be suggested. This can be correlated to the different surface polarity of the illuminated side of the substrate compared to the non-illuminated side. It is obvious that on the pristine surface (which contains ester groups and is non-polar) the interaction between the PSP and the polymer is enhanced. However, on the illuminated side, these ester groups are photochemically converted into hydroxyketones which results in a more polar surface. Higher polarity disturbs the favourable interaction between PSP and the substrate, and consequently more island formation during the growth process is observed.

No clear conclusion can be made for the observed polymorphism. The  $\gamma$ -phase can be classified as a surface mediated polymorph of sexiphenyl [30,36], as it is also known for other rod-like conjugated molecules like pentacene or sexithiophene. These phases are observed on silicon oxide surfaces at elevated substrate temperatures [33,37,38]. The appearance of the  $\gamma$ -phase of sexiphenyl on the polymeric substrate in a temperature range close to the glass transition temperature of the substrate layer can be induced by the smooth but not too flexible surface of the polymer, favouring the formation of a surface mediated polymorph structure at lower substrate temperatures.

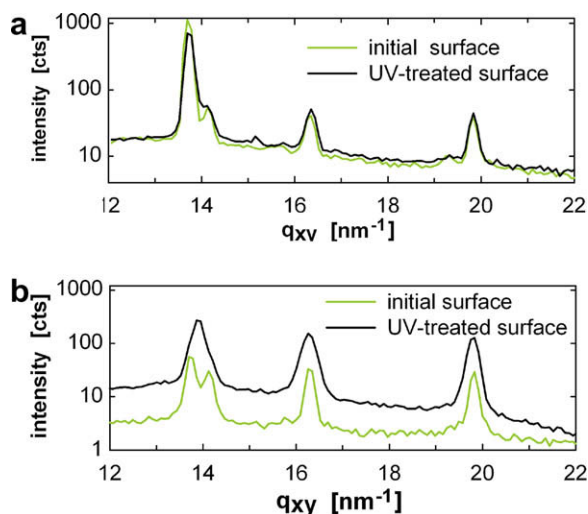


**Fig. 7.** Line scans of the grazing incidence X-ray diffraction pattern taken at  $q_z = 1.5 \text{ nm}^{-1}$ . The results of the thin films grown at a substrate temperature of 160 °C (a) and of the 115 °C (b) are depicted for the non-illuminated and the UV-treated polymer surface.

#### 4. Conclusions

Para-sexiphenyl films were successfully deposited on PPNB at different temperatures and deposition times. Careful AFM investigations demonstrate that PSP shows different growth morphology when deposited on UV-illuminated and as prepared PPNB substrates. Features such as terraces or screw dislocations with step heights corresponding to standing PSP molecules highlight the high order of the layers.

The lateral and vertical sizes of the PSP crystallites were estimated from the specular scans and line scans of the GIXD measurements. For the samples grown at  $T_s = 160^\circ\text{C}$  lateral and vertical crystal sizes of up to 40 and 70 nm were obtained, respectively. While for the samples grown at  $115^\circ\text{C}$  values of 20 nm and 40 nm for the lateral size of the as prepared and UV-treated substrates were respectively evaluated. The grown films show a strong 001 orientation with a better alignment on the as prepared than on the UV-treated substrate. It is also shown that at lower  $T_s$  the 001 planes of PSP crystallites are much weaker oriented relative to the surface than at high  $T_s$ . It is suggested that the strong preferred orientation of PSP crystallites with the 001 plane parallel to the substrate surface is related to the fact that the impinging PSP molecules become more mobile on the surface and is due to the effects caused by depositing at temperatures above the glass transition temperature of PPNB ( $T_g = 96^\circ\text{C}$ ). The specular scans together with the indexed diffraction pattern of the reciprocal space maps obtained by GIXD reveal the presence of two different crystal structures of PSP. The formation of Baker structure only was observed if elevated substrate temperatures were used ( $T_s \geq 130^\circ\text{C}$ ) and the simultaneous appearance of Baker and  $\gamma$ -phase was obtained when using low substrate temperatures.

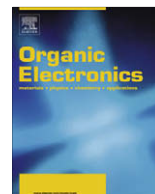
We have shown that a change in polarity of amorphous polymer films of PPNB does significantly influence the growth of PSP films prepared by HWE. The polarity change of the polymer film was generated by a photochemical reaction, the photo-Fries rearrangement of the aryl-ester units. In this reaction, the phenyl ester groups of PPNB undergo upon irradiation with UV-light a rearrangement reaction to the corresponding hydroxyketones which leads to an increase in surface polarity. Consequently, it is clearly demonstrated, that the growth on PSP can be modified by a simple and easily reproducible pre-treatment of the substrate surface and by the deposition conditions. This procedure can potentially control the optical and electrical properties of the films deposited on the different parts of the substrate thus opening new perspectives for the fabrication of devices by using the UV treatment of the substrates as pre-structuring process.

#### Acknowledgment

This work was supported by the Austrian Science Foundation Projects NFN-S9702, NFN-S9706 and NFN-S9708. G. Hernandez-Sosa wants to thank Consejo Nacional de Ciencia Tecnología (CONACYT), in México for scholarship.

#### References

- [1] S. Tasch, C. Brandstatter, F. Meghdadi, G. Leising, G. Froyer, L. Athouel, *Adv. Mater.* 9 (1997) 33.
- [2] G. Leising, S. Tasch, W. Graupner, *Fundamentals of electroluminescence in paraphenylene-type conjugated polymers and oligomers*, in: *Handbook of Conducting Polymers*, second ed., Dekker, New York, 1997.
- [3] A.Y. Andreev, G. Matt, C.J. Brabec, H. Sitter, D. Badt, H. Seyringer, N.S. Sariciftci, *Adv. Mater.* 12 (2000) 629.
- [4] D. Stifter, H. Sitter, *Appl. Phys. Lett.* 66 (1995) 679.
- [5] Th.B. Singh, N. Marjanovic, G.J. Matt, S. Gunes, N.S. Sariciftci, A.M. Ramiel, A. Andreev, H. Sitter, R. Schwodiauer, S. Bauer, *Org. Electron.* 6 (2000) 105.
- [6] F. Quochi, F. Cordella, R. Orrù, J.E. Communal, P. Verzeroli, A. Mura, G. Bongiovanni, A. Andreev, H. Sitter, N.S. Sariciftci, *Appl. Phys. Lett.* 84 (2004) 4454.
- [7] H. Plank, R. Resel, S. Pruger, J. Keckes, A. Thierry, B. Lotz, A. Andreev, N.S. Sariciftci, H. Sitter, *Phys. Rev. B* 64 (2001) 235423.
- [8] T. Haber, A. Andreev, A. Thierry, H. Sitter, M. Oehzelt, R. Resel, *J. Cryst. Growth* 284 (2005) 209.
- [9] J.C. Anderson, C.B. Reese, *Proc. Chem. Soc.* (1960) 217.
- [10] D. Bellus, *Adv. Photochem.* 8 (1981) 109.
- [11] C.E. Kalmus, D.M. Hercules, *J. Am. Chem. Soc.* 96 (1974) 449.
- [12] M.A. Miranda, F. Galindo, *Photo-fries reaction and related processes*, in: W. M. Horspool (Ed.), *CRC Handbook of Organic Photochemistry and Photobiology*, second ed., CRC Press, Boca Raton, FL, 2004.
- [13] S. Lochbrunner, M. Zissler, J. Piel, E. Riedle, A. Spiegel, T. Bach, *J. Chem. Phys.* 120 (2004) 11634.
- [14] G. Weiqiang, D.J. Abdallah, R.G. Weiss, *J. Photochem. Photobiol. A: Chem* 139 (2001) 79.
- [15] R.A. Finnegan, D. Knutson, *Tetrahedron Lett.* 9 (1968) 3429.
- [16] S.K.L. Li, J.E. Guillet, *Macromolecules* 10 (1977) 840.
- [17] L. Merle-Aubry, Y.M. Holden, J.E. Guillet, *Macromolecules* 13 (1980) 1138.
- [18] J.M.J. Frechet, T.G. Tessier, C.G. Wilson, H. Ito, *Macromolecules* 18 (1985) 317.
- [19] T. Höfler, T. Griesser, X. Gstrein, G. Trimmel, G. Jakopic, W. Kern, *Polymer* 48 (2007) 1930.
- [20] T. Griesser, T. Höfler, S. Temmel, W. Kern, G. Trimmel, *Chem. Mater.* 19 (2007) 3011.
- [21] D.K. Owens, R.C. Wendt, *J. Appl. Polym. Sci.* 13 (1969) 1741.
- [22] A. Lopez-Otero, *Thin Solid Films* 3 (1978) 4.
- [23] H.-J. Brandt, R. Resel, J. Keckes, B. Koppelhuber-Bitschnau, N. Koch, G. Leising, *Mater. Res. Soc. Symp. Proc.* 561 (1999) 61.
- [24] M. Birkholz, *Thin Film Analysis by X-ray Scattering*, Wiley-VCH, Weinheim, 2005.
- [25] J. Ackermann, C. Vidalot, P. Raynal, A. El Kassmi, P. Dumas, *Appl. Surf. Sci.* 212 (2003) 26.
- [26] R. Ruiz, D. Choudhary, B. Nickel, T. Toccoli, K.-C. Chang, A.C. Mayer, P. Clancy, J.M. Blakely, R.L. Headrick, S. Iannotta, G.G. Malliaras, *Chem. Mater.* 23 (2004) 4497.
- [27] Th.B. Singh, N.S. Sariciftci, H. Yang, L. Yang, B. Plochberger, H. Sitter, *Appl. Phys. Lett.* 90 (2007) 213512.
- [28] K.N. Baker, A.V. Fratini, T. Resch, H.C. Knachel, W.W. Adams, E.P. Socci, B.L. Farmer, *Polymer* 34 (1993) 1571.
- [29] D. Nabok, P. Puschnig, C. Ambrosch-Draxl, *Phys. Rev. B* 77 (2008) 245316.
- [30] R. Resel, N. Koch, F. Meghdadi, G. Leising, L. Athouel, G. Froyer, F. Hofer, *Cryst. Res. Technol.* 36 (2001) 47.
- [31] R. Resel, G. Leising, *Surf. Sci.* 409 (1998) 302.
- [32] E. Zojer, N. Koch, P. Puschnig, F. Meghdadi, A. Niko, R. Resel, C. Ambrosch-Draxl, M. Knapfer, J. Fink, L. Bredas, G. Leising, *Phys. Rev. B* 61 (2000) 16538.
- [33] R. Resel, N. Koch, F. Meghdadi, G. Leising, W. Unzog, K. Reichmann, *Thin Solid Films* 305 (1997) 232.
- [34] C. Kim, A. Facchetti, T.J. Marks, *Science* 318 (2007) 76.
- [35] S. Blumstengel, F. Meinardi, R. Tubino, A. Borghesi, *Synth. Met.* 137 (2003) 961.
- [36] L. Athouel, G. Froyer, M.T. Riou, *Synth. Met.* 55 (1993) 4734.
- [37] B. Servet, S. Ries, M. Trotel, P. Alnot, G. Horowitz, F. Garnier, *Adv. Mater.* 5 (1993) 461.
- [38] D.J. Gundlach, T.N. Jackson, D.G. Schlom, S.F. Nelson, *Appl. Phys. Lett.* 74 (1999) 3302.



## Modification of the electronic properties of rubrene crystals by water and oxygen-related species

L. Tsetseris<sup>a,b,\*</sup>, S.T. Pantelides<sup>b,c</sup>

<sup>a</sup> Department of Physics, Aristotle University of Thessaloniki, GR-54124 Thessaloniki, Greece

<sup>b</sup> Department of Physics and Astronomy, Vanderbilt University, Nashville, TN 37235, USA

<sup>c</sup> Oak Ridge National Laboratory, Oak Ridge, TN 37831, USA

### ARTICLE INFO

#### Article history:

Received 2 October 2008

Received in revised form 8 December 2008

Accepted 17 December 2008

Available online 27 December 2008

#### PACS:

72.80.Le

71.20.Rv

71.55.Ht

#### Keywords:

Rubrene

Impurities

First-principles

Acenes

Carrier traps

Water

### ABSTRACT

The presence of impurities in organic semiconductors is an important limitation for the performance of related devices. Here, we investigate with density-functional theory calculations the effect of water and oxygen-related species on the properties of the prototype system of rubrene, the current record-holder organic semiconductor in terms of carrier mobilities. We identify the most stable impurity structures, with species in either substitutional or interstitial configurations, and we analyze their complex role in changing the shape and profile of rubrene energy bands. In certain cases the impurities either give rise or help annihilate carrier traps, and we discuss the relevance of our findings for the optimization of rubrene-based electronic systems.

© 2008 Elsevier B.V. All rights reserved.

The absence of inter-molecular covalent bonding in organic semiconductors carries significant advantages such as flexibility and versatility of film growth, but it also relates to increased likelihood for impurity insertion. An understanding of the atomic-scale mechanisms that control the presence of extrinsic species and their effect on the properties of organic electronic materials is, therefore, essential for the optimization of related devices. The issue is even more pressing for materials like rubrene which has attracted a lot of interest recently [1–11] because its films show carrier mobilities that surpass those of any other organic semiconductor.

Rubrene is an oligoacene derivative which is formed by four phenyl rings linked (Fig. 1) on the side of a tetracene back-bone (TBB). In the crystalline orthorhombic form [12,13], large portions of the TBBs of neighboring molecules face off in parallel, while other parts of the crystal contain more open space. Impurities may be incorporated in either region and, indeed, experimental studies [14–18] have already reported oxygen-related effects on the electronic properties of rubrene samples. In addition to oxygen, water and hydrogen are known as key impurities in conventional Si-based devices [19–22], but also in organic electronic materials, for example in pentacene [23–27]. It can thus be expected that these species play an important role also in rubrene-based systems.

In this article, we use quantum-mechanical first-principles calculations to elucidate several prominent impurity effects in rubrene crystals. In particular, we examine

\* Corresponding author. Address: Department of Physics, Aristotle University of Thessaloniki, GR-54124 Thessaloniki, Greece. Tel.: +30 2310 998039.

E-mail address: [leonidas.tsetseris@vanderbilt.edu](mailto:leonidas.tsetseris@vanderbilt.edu) (L. Tsetseris).

oxygen impurities in ketone configurations, with or without hydrogen atoms attached, and we find that they can lead to distinct peaks formed out of the valence band of rubrene. We also find that it is energetically favorable for water molecules to enter rubrene crystals and that they can either appear in physisorbed configurations between phenyl groups, or they can dissociate to H atoms and hydroxyl groups attached on the TBB. An isolated hydroxyl group is shown to give rise to energy levels deep in the band gap of rubrene, an effect that is ameliorated upon the arrival of a H impurity.

The results were obtained using density-functional theory (DFT) calculations, with a local-density approximation (LDA) exchange-correlation (xc) functional [28],

plane waves as a basis set (the energy cutoff was set at 400 eV) and ultrasoft pseudopotentials to represent the ionic cores [29], as implemented in the code VASP [30]. As in a previous study that discussed the effect of hydrogen and interstitial oxygen atoms in rubrene [31], the energetics of impurity incorporation were studied with supercells that contain four molecules and which were constructed based on the experimental data for the unit cell [13] of rubrene.  $2 \times 2 \times 2$   $k$ -grids and the Monkhorst-Pack method for Brillouin zone sampling [32] were employed for total energy calculations, whereas to obtain the electronic density of states (DOS) we used larger  $6 \times 6 \times 6$   $k$ -meshes and the tetrahedron sampling method [33].

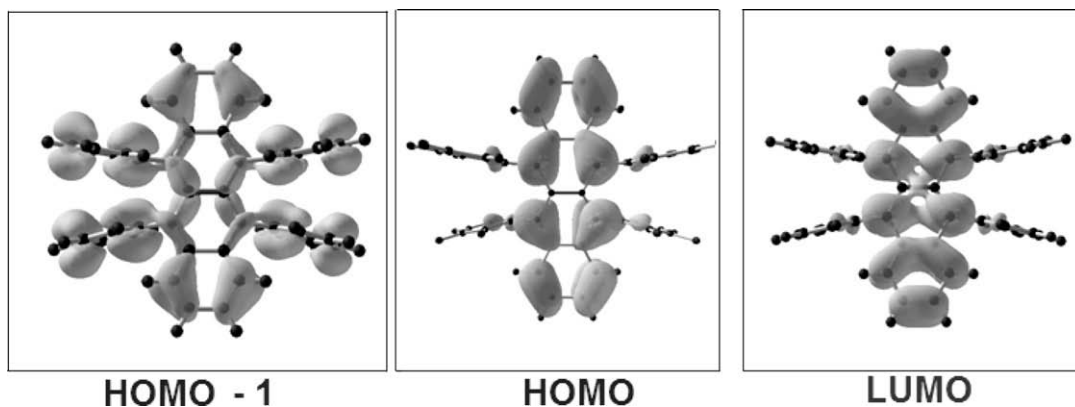


Fig. 1. Amplitude of the highest occupied (HOMO), lowest unoccupied (LUMO), and HOMO-1 orbitals of rubrene.

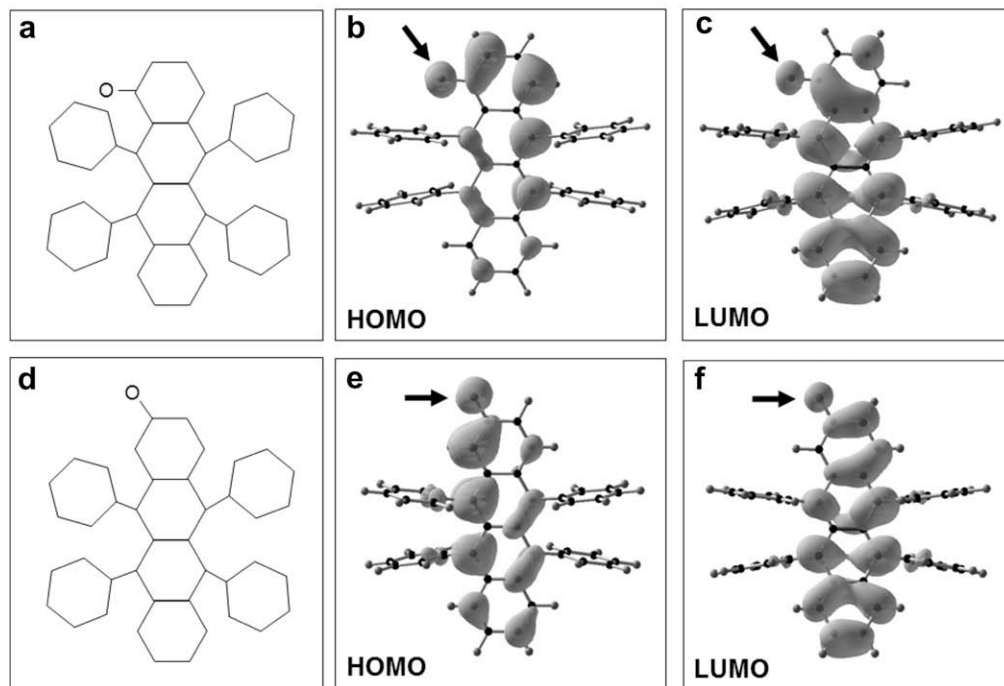


Fig. 2. Chemical structure and amplitude of the HOMO and LUMO for ketone impurities in a rubrene molecule. The arrows show the positions of the O atom that replaces a H atom in the defective molecule.

We start with results on substitutional oxygen impurities in rubrene crystals. We first consider an O impurity that replaces a H atom in a rubrene molecule and forms a ketone group with a double bond to the corresponding C atom. The most stable ketone configurations are shown in Fig. 2. Other defects with the C=O bond at different C sites have energies higher by 0.2–0.3 eV. If we assume that H and O atoms are exchanged with H<sub>2</sub> and O<sub>2</sub> molecules, respectively, then the formation of the ketone defect of Fig. 2b is an exothermic reaction with an energy gain of 0.73 eV.

In Fig. 2, we show the amplitudes of the highest occupied molecular orbitals (HOMO) and the lowest unoccupied molecular orbitals (LUMO) of rubrene molecules with ketone substitutional groups on their TBB's. For comparison, the HOMO, the HOMO-1, and the LUMO of a defect-free molecule are included in Fig. 1. The figures clearly show that the defects change the frontier orbitals considerably. This effect is more pronounced for the HOMO of Fig. 2b, where a substantial decrease in the weight of the wavefunction is noticed for the parts of the molecule away from the impurity.

The plots of frontier orbitals that are included in Fig. 1 and DFT results [34] on the projected density of states of rubrene demonstrate that the tetracene units have a dominant role in the formation of the valence and conduction bands of this organic semiconductor. As a result, any orbital changes similar to the ones depicted in Fig. 2 that disrupt the TBB stacking and the respective intermolecular electronic coupling are bound to have a considerable effect on the electronic properties of the crystal. Indeed, in com-

parison to the electronic density of states of defect-free rubrene, the DOS plots of Fig. 3 for 4-molecule supercells with isolated ketone groups show that the valence and conduction bands of the defective crystal split up and change their relative positions.

An especially important effect is noted for the ketone configuration of Fig. 2a: a distinct peak appears in the DOS and its distance of about 0.22 eV to the bands below is very close to the experimental value [15,16] of 0.25 eV for O-related carrier traps in rubrene. We should note that, the well known DFT band gap problem results in the theoretical underestimation of the energy separation between the HOMO and LUMO states, and introduces an uncertainty about the absolute position of defect levels. An approach like GW (wherein the electronic self-energy is given by the Green's function  $G$  and the screened interaction  $W$ ) can enhance the accuracy of the calculated values, but its use for large supercells requires excessive computational power. In fact, though DFT results on impurity energy levels lack in absolute accuracy, they are normally reliable in predicting the nature of impurity effects and, in particular, whether defects introduce deep or shallow levels in a semiconductor band gap.

As noted above, hydrogen is a typical impurity in many types of systems [22,20]. In its most stable configuration in rubrene [31] hydrogen is attached to the C atom that links the TBB to a phenyl group. The interaction of this H-structure with a ketone-containing molecule can lead to the formation of the hydroxyl group depicted in Fig. 4, an exothermic process that releases 1.6 eV of energy. The differences between the HOMO's and LUMO's of rubrene

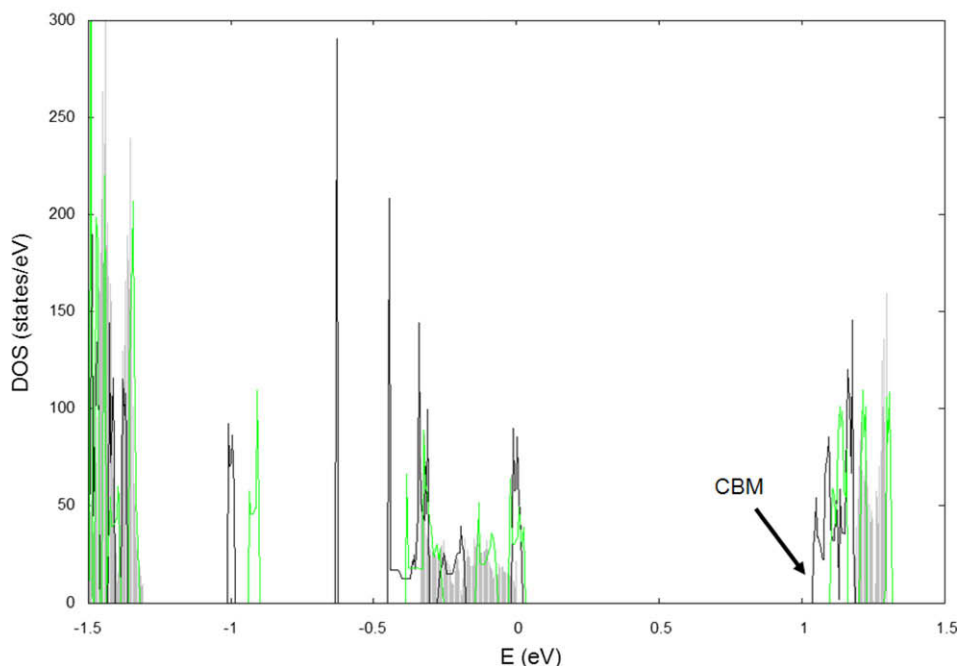


**Fig. 3.** Effect of ketone impurities on the electronic density of states (DOS) of a rubrene crystal. Dark (black) and light (green) lines for one defective rubrene molecule of the type of Fig. 2a and c, respectively, per 4 rubrene molecules in the crystal. The DOS for defect-free rubrene is shown with light impulses. The arrow shows the conduction band minimum (CBM). (For interpretation of the references to color in this figure legend, the reader is referred to the web version of this article.)

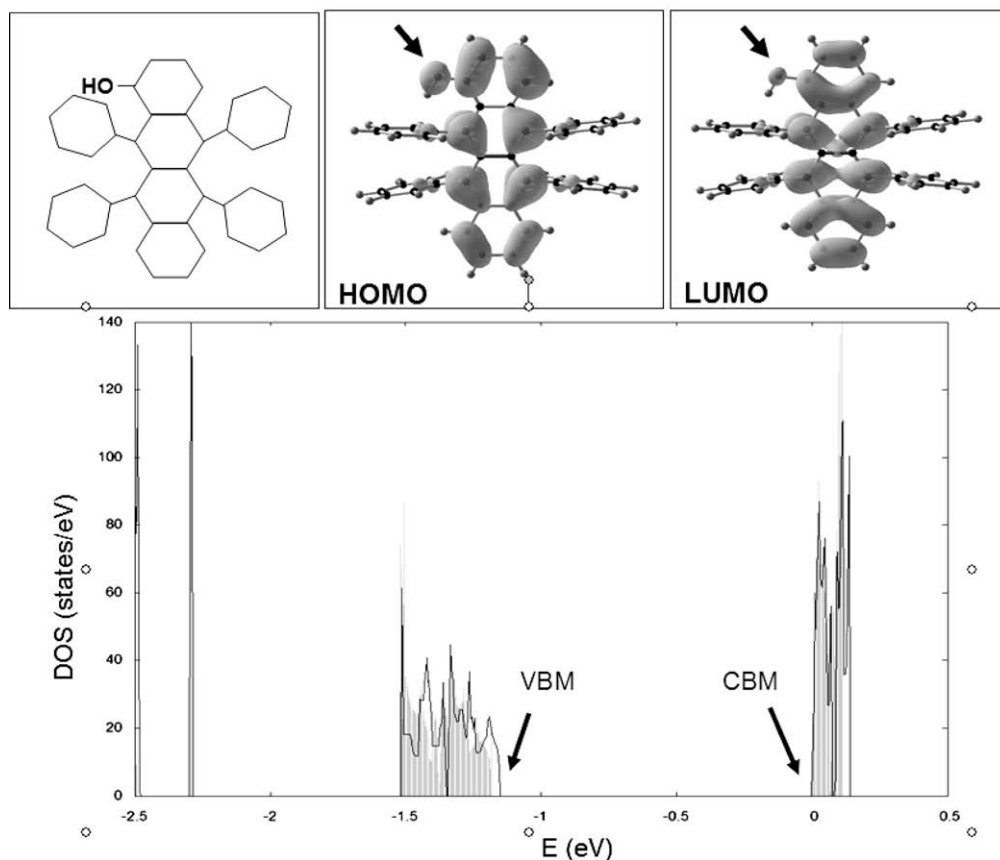


**Fig. 4.** Chemical structure and amplitude of the HOMO and LUMO for passivated ketone impurities (shown with arrows) in a rubrene molecule (upper part) and effect on the electronic DOS (lower part). The arrows show the valence band maximum (VBM) and conduction band minimum (CBM) in the lower part. The DOS for defect-free rubrene is shown with light impulses.

molecules with substitutional hydroxyl and those of defect-free rubrene molecules are much less pronounced compared to the case of ketone impurities. As a result, the effect of OH species on the electronic DOS of a rubrene crystal is also less pronounced. For example, the passivation of the ketone of Fig. 2a with a H atom results in a more compact form for the electronic DOS (Fig. 4) in the range of the valence band and the 0.2 eV peak of Fig. 3 disappears.

In addition to substitutional configurations, oxygen species may enter rubrene in interstitial structures, either as isolated atoms, or in pairs. The most stable configurations of extra O atoms are epoxy groups, wherein O atoms form triangles of bonds with two C atoms of the TBB of rubrene. The structural details of epoxy groups and their effect on the electronic properties of rubrene have been reported in Ref. [31]. In Fig. 5, we show a number of other configurations of a pair of O atoms in rubrene. They include variants of peroxy bridges, which have been suggested as likely oxidized rubrene configurations in previous studies [2,14], and non-dissociated O<sub>2</sub> molecules. All these structures are considerably less stable than the epoxy pairs since their energies are higher by at least 1.2 eV. We note that following the removal of one of the two O atoms in the configurations of Fig. 5a–c, the remaining O impurity relaxes to form bonds with two C atoms of rubrene, creating thus an isolated epoxy group.

We now turn our attention to the effect of water-related impurities in rubrene crystals. In Fig. 6a, we show the most stable configuration for a non-dissociated water molecule inside rubrene. The molecule physisorbs with a significant energy gain of 0.38 eV compared to an H<sub>2</sub>O species in vacuum. It gets trapped in the space between two side phenyl groups of a rubrene molecule, with the two O–H bonds pointing to two different C atoms. The distances between the H atoms of water and the two C atoms of the phenyl moieties are approximately equal to 2 Å. In another physisorbed configuration, which is similar to Fig. 6a and has an energy gain of 0.30 eV compared to vacuum, only one of the water O–H bonds points to a phenyl group, while the other O–H bond is directed to the space between neighboring molecules. When one of the O–H bonds points to the end of a TBB and the other to a neighboring molecule the energy gain for H<sub>2</sub>O insertion drops to 0.23 eV.

In addition to physisorbed configurations of non-dissociated H<sub>2</sub>O molecules in a rubrene crystal, we found stable impurity structures that can be viewed as the result of the breakup of water species. One such configuration is shown in Fig. 6b; it comprises a hydroxyl group and a hydrogen impurity that are both attached on the same rubrene molecule and the C sites that link the TBB to phenyl groups. This chemisorbed structure is, in fact, more stable than

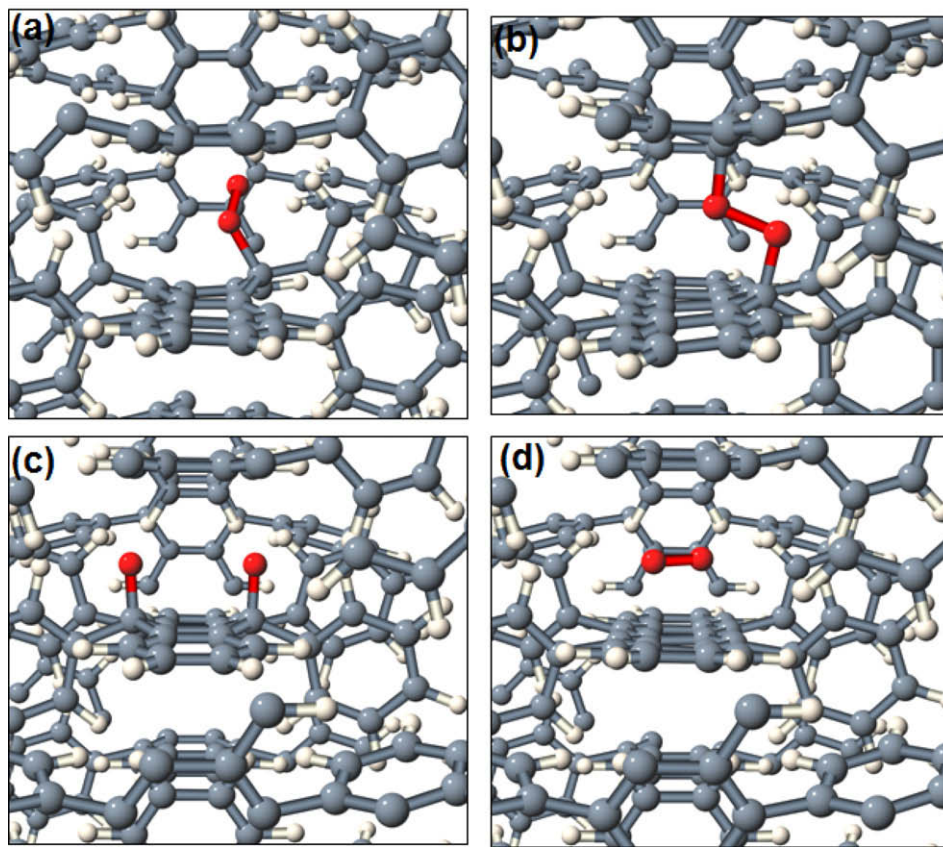


**Fig. 5.** Metastable configurations with oxygen impurities in endoperoxide or molecular configurations in rubrene. The energies of these configurations are at least 1.2 eV higher in energy than the epoxy pairs discussed in Ref. [31] [C: gray, O: dark gray (red), H: white spheres]. (For interpretation of the references to color in this figure legend, the reader is referred to the web version of this article.)

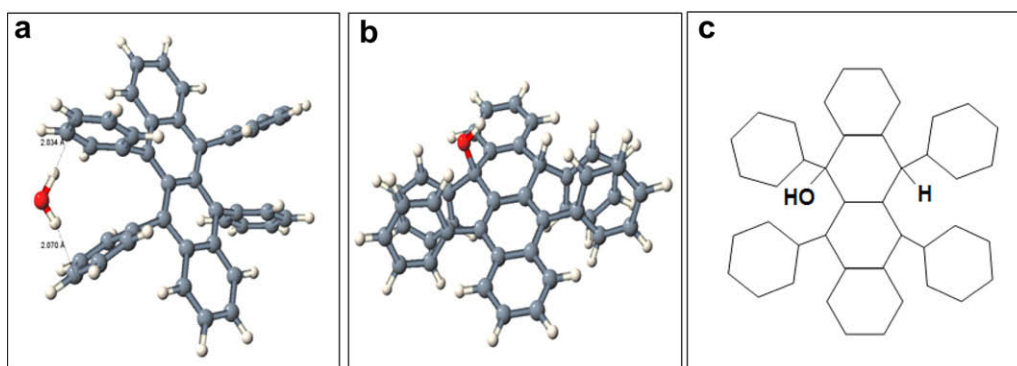


**Fig. 6.** Water-related impurities in a rubrene crystal: (a) a physisorbed water molecule, (b) vicinal OH and H impurities after dissociation of  $\text{H}_2\text{O}$ , and (c) chemical structure of (b). Only the defective molecule is shown for clarity. The energy of (b) is lower than that of (a) by 0.2 eV [C: gray, O: dark gray (red), H: white spheres]. (For interpretation of the references to color in this figure legend, the reader is referred to the web version of this article.)

the physisorbed configurations of the type of Fig. 6a by at least 0.2 eV of energy.

As might be expected, the physisorption of an  $\text{H}_2\text{O}$  molecule in the configuration of Fig. 6a has a minimal effect on the electronic DOS of rubrene. The corresponding DOS

curve is depicted in Fig. 7. The dissociation of an  $\text{H}_2\text{O}$  species, on the other hand, in the structure of Fig. 6b has a more discernible effect; it splits the valence band in two parts, and it introduces an isolated peak between this band and the one below it. Overall, the effect of attaching the OH



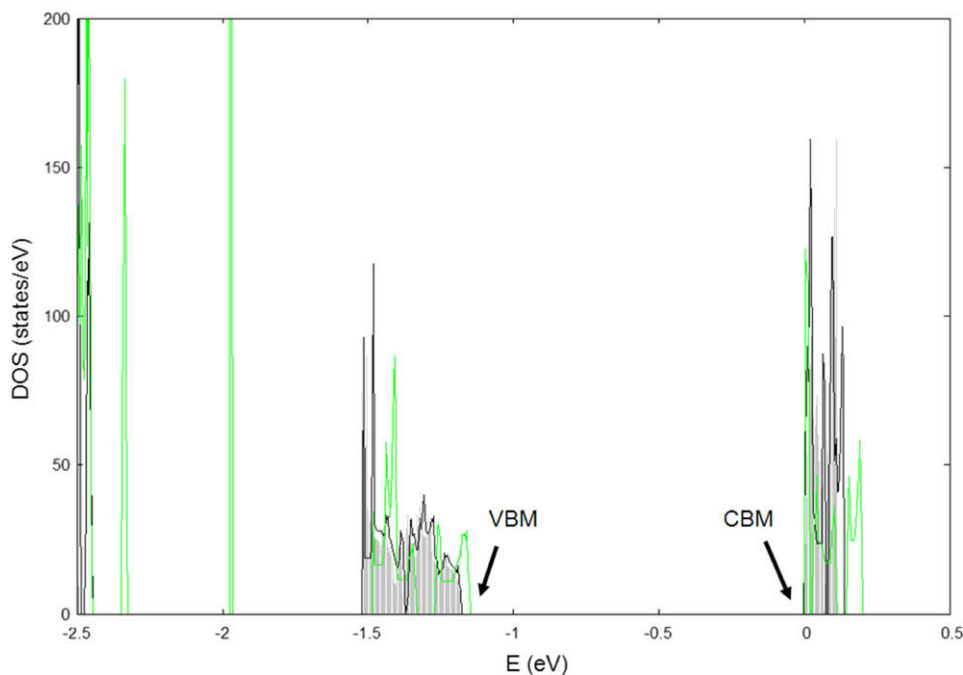


**Fig. 7.** Effect of water-related impurities on the electronic DOS of a rubrene crystal. Dark (black) and light (green) lines for one defective rubrene molecule of the type of Fig. 6a and b, respectively, per 4 rubrene molecules in the crystal. The arrows show the valence band maximum (VBM) and the conduction band minimum (CBM). The DOS for defect-free rubrene is shown with light impulses. (For interpretation of the references to color in this figure legend, the reader is referred to the web version of this article.)

and H species at C sites between a rubrene TBB and the side phenyl groups is similar to the corresponding change [31] in the DOS in the case of a configuration with two H atoms at the same positions.

A water-related impurity that introduces a more pronounced change in the DOS is an isolated hydroxyl group attached at the OH position of Fig. 6b. As shown in Fig. 8, the introduction of an OH species on a rubrene molecule breaks the symmetry of the impurity-free HOMO and LUMO. For this reason, it can be expected that this defect gives rise to changes in the DOS away from the bands of pristine rubrene. This qualitative argument is validated by the results of Fig. 8 for the DOS of the cell with an OH impurity, which show that the isolated hydroxyl species introduces a level that lies deep in energy band gap of rubrene, almost at the midgap position.

The attachment of a H atom on the molecule of Fig. 8 leads to the formation of the structure of Fig. 6b and an energy gain of 1.6 eV. In other words, the dissociation of the latter H–OH complex to H and OH species in rubrene carries an energy penalty of 1.6 eV. The role of H in the formation of the H–OH group is similar to its role in the creation of stable H–H complexes [31] in rubrene. In fact, the similarity extends as well to the effect of H on the electronic properties of rubrene: whereas isolated H and OH species introduce states deep in the energy band gap, H–OH complexes and H–H pairs lack such deep levels. Hydrogen has, therefore, a dual role in creating and annihilating carrier traps in rubrene.

The incorporation of impurities and, especially, the formation of levels in their energy band gap is fundamentally important in semiconductor physics. For example, oxygen species have been identified as acceptor states in rubrene [15] and impurities control the behavior of pentacene-based transistors under bias stress [35] and photo-oxidation [36]. Impurities like ketone groups may be incorporated in a rubrene molecule during synthesis, while other defects like water species may enter a rubrene crystal during growth or operation of rubrene-based devices. In addition, the pronounced effects of impurities on the shape and position of the valence and conduction bands of rubrene may provide mechanisms [31] for effective defect engineering in this prototype organic semiconductor. Finally, another possible role for impurities in rubrene that can be explored in the future relates to mechanisms of selective adsorption and of nucleation similar to the ones that have been suggested [37,38] or observed [39] for pentacene growth on substrates.

In summary, we examined the stability of water and oxygen-related impurities in rubrene and we showed that they have pronounced effects on the electronic properties of the host crystal, including the possibility of formation or annihilation of carrier traps. It is energetically favorable for water molecules to enter this system in either physisorbed or chemisorbed configurations, and ketone or hydroxyl groups create shallow and deep levels in the energy band gap of rubrene.

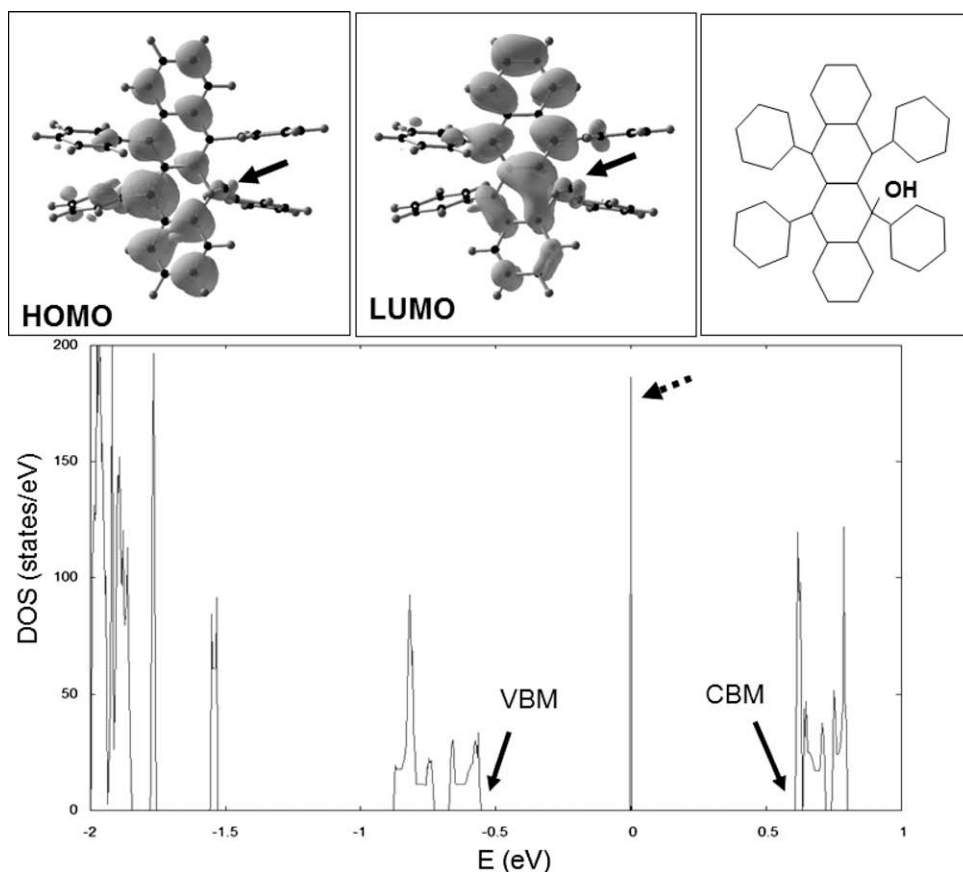


**Fig. 8.** Top: chemical structure and amplitude of the HOMO and LUMO for a hydroxyl impurity on a rubrene molecule. The arrows show the positions of the hydroxyl group. Bottom: effect of the OH impurity on the electronic DOS for one defective molecule per 4 rubrene species in a crystal. The dotted arrow shows the position of an impurity level in the energy band gap of rubrene. The solid arrows show the valence band maximum (VBM) and the conduction band minimum (CBM).

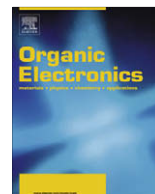
## Acknowledgements

We acknowledge support by the William A. and Nancy F. McMinn Endowment at Vanderbilt University, and by DOE Grant No. DEFG0203ER46096. The calculations were performed at ORNL's Center for Computational Sciences.

## References

- [1] V. Podzorov, V.M. Pudalov, M.E. Gershenson, *Appl. Phys. Lett.* 82 (2003) 1739.
- [2] V. Podzorov, V.M. Pudalov, M.E. Gershenson, *Appl. Phys. Lett.* 85 (2004) 6039.
- [3] V. Podzorov, E. Menard, A. Borissov, V. Kiryukhin, J.A. Rogers, M.E. Gershenson, *Phys. Rev. Lett.* 93 (2004) 086602.
- [4] C. Goldmann, S. Haas, C. Krellner, K.P. Pernstich, D.J. Gundlach, B. Batlogg, *J. Appl. Phys.* 96 (2004) 2080.
- [5] V.C. Sundar, J. Zaumseil, V. Podzorov, E. Menard, R.L. Willett, T. Someya, M.E. Gerzhenson, J.A. Rogers, *Science* 303 (2004) 1644.
- [6] D.A. da Silva Filho, E.G. Kim, J.L. Brédas, *Adv. Mater.* 17 (2005) 1072.
- [7] I.N. Hulea, S. Fratini, H. Xie, C.L. Mulder, N.N. Iossad, G. Rastelli, S. Ciuchi, A.F. Morpurgo, *Nature Mater.* 5 (2006) 982.
- [8] J. Takeya, M. Yamagishi, Y. Tominari, R. Hirahara, Y. Nakazawa, T. Nishikawa, T. Kawase, T. Shimoda, S. Ogawa, *Appl. Phys. Lett.* 90 (2007) 102120.
- [9] M. Yamagishi, J. Takeya, Y. Tominari, Y. Nakazawa, T. Kuroda, S. Ikehata, M. Uno, T. Nishikawa, T. Kawase, *Appl. Phys. Lett.* 90 (2007) 182117.
- [10] M.F. Calhoun, J. Sanchez, D. Olaya, M.E. Gershenson, V. Podzorov, *Nature Mater.* 7 (2008) 84.
- [11] K.P. Pernstich, B. Rössner, B. Batlogg, *Nature Mater.* 7 (2008) 321.
- [12] B.D. Chapman, A. Checco, R. Pindak, T. Siegrist, C. Kloc, *J. Cryst. Growth* 290 (2006) 479.
- [13] O.D. Jurchescu, A. Meetsma, T.T. Palstra, *Acta Cryst. B* 62 (2006) 330.
- [14] D. Käfer, G. Witte, *Phys. Chem. Chem. Phys.* 7 (2005) 2850.
- [15] O. Mitrofanov, D.V. Lang, C. Kloc, J.M. Wikberg, T. Siegrist, W.Y. So, M.A. Sergent, A.P. Ramirez, *Phys. Rev. Lett.* 97 (2006) 166601.
- [16] C. Krellner, S. Haas, C. Goldmann, K.P. Pernstich, D.J. Gundlach, B. Batlogg, *Phys. Rev. B* 75 (2007) 245115.
- [17] M. Kytka, A. Gerlach, F. Schreiber, J. Kovac, *Appl. Phys. Lett.* 90 (2007) 131911.
- [18] W. So, J.M. Wikberg, D.V. Lang, O. Mitrofanov, C.L. Kloc, T. Siegrist, A.M. Sergent, A.P. Ramirez, *Solid State Commun.* 142 (2007) 483.
- [19] M. Needels, J.D. Joannopoulos, Y. Baryam, S.T. Pantelides, *Phys. Rev. B* 43 (1991) 4208.
- [20] L. Tsetseris, S.W. Wang, S.T. Pantelides, *Appl. Phys. Lett.* 88 (2006) 051916.
- [21] I.G. Batyrev, B.R. Tuttle, D.M. Fleetwood, R.D. Schrimpf, L. Tsetseris, S.T. Pantelides, *Phys. Rev. Lett.* 100 (2008) 105503.
- [22] L. Tsetseris, D.M. Fleetwood, R.D. Schrimpf, X.J. Zhou, I.G. Batyrev, S.T. Pantelides, *Microelectr. Eng.* 84 (2007) 2344.
- [23] Z.T. Zhu, J.T. Mason, R. Dieckmann, G.G. Malliaras, *Appl. Phys. Lett.* 81 (2002) 4643.
- [24] J.E. Northrup, M.L. Chabiny, *Phys. Rev. B* 68 (2003) 041202.
- [25] C. Goldmann, D.J. Gundlach, B. Batlogg, *Appl. Phys. Lett.* 88 (2006) 063501.
- [26] L. Tsetseris, S.T. Pantelides, *Phys. Rev. B* 75 (2007) 153202.
- [27] K. Diallo, M. Erouel, J. Tardy, E. André, J.L. Garden, *Appl. Phys. Lett.* 91 (2007) 183508.

- [28] J.P. Perdew, A. Zunger, *Phys. Rev. B* 23 (1981) 5048.
- [29] D. Vanderbilt, *Phys. Rev. B* 41 (1990) 7892.
- [30] G. Kresse, J. Furthmüller, *Phys. Rev. B* 54 (1996) 11169.
- [31] L. Tsetseris, S.T. Pantelides, *Phys. Rev. B* 78 (2008) 115205.
- [32] D.J. Chadi, M.L. Cohen, *Phys. Rev. B* 8 (1973) 5747.
- [33] O. Jepsen, O.K. Andersen, *Solid State Commun.* 9 (1971) 1763.
- [34] L. Tsetseris, S.T. Pantelides, unpublished.
- [35] D.V. Lang, X. Chi, T. Siegrist, A.M. Sergent, A.P. Ramirez, *Phys. Rev. Lett.* 93 (2004) 086802.
- [36] W.L. Kalb, K. Mattenberger, B. Batlogg, *Phys. Rev. B* 78 (2008) 035334.
- [37] L. Tsetseris, S.T. Pantelides, *Appl. Phys. Lett.* 87 (2005) 233109.
- [38] L. Tsetseris, S.T. Pantelides, *Mater. Sci. Eng. B* 152 (2008) 109.
- [39] B.R. Conrad, E. Gormar-Nadal, W.G. Cullen, A. Pimpinelli, T.L. Einstein, E.D. Williams, *Phys. Rev. B* 77 (2008) 205328.



# Enhancement of top emission for organic light-emitting diode via scattering surface plasmons by nano-aggregated outcoupling layer

Ziyao Wang, Zhijian Chen \*, Lixin Xiao, Qihuang Gong \*

State Key Laboratory for Mesoscopic Physics and Department of Physics, Peking University, 100871, People's Republic of China

## ARTICLE INFO

### Article history:

Received 13 August 2008

Received in revised form 11 December 2008

Accepted 17 December 2008

Available online 25 December 2008

### PACS:

73.20.Mf

85.60.Jb

78.55.Kz

### Keywords:

Enhanced top emission

Surface plasmon

Organic light emitting diode

## ABSTRACT

A stable self nano-aggregated bathocuproine film was fabricated and introduced atop of a conventional organic light emitting diode for enhancing top emission. It leads to a 2.7–2.1-fold enhancement on top emission at applied voltage from 4 to 9 V which is much larger than the 1.5–1.3-fold enhancement for a device overlaid with an amorphous bathocuproine film. The more effective outcoupling of this method probably arises from surface plasmon modes being scattered by only the nanostructured surface, and thus without phase cancellation, at the bathocuproine/air boundary. Moreover, this method nearly preserves the original electroluminescent spectra and has no damage on electrical properties.

© 2009 Elsevier B.V. All rights reserved.

## 1. Introduction

Organic light-emitting diodes (OLEDs), typical structures of which consists of an anode, organic materials and a metallic cathode, have been attracting considerable attention because of their application to flat-panel displays. One problem that occurs though is that a large fraction of the power generated by excitons within the organic emissive layer is lost to surface plasmon (SP) modes, which are surface free electron density oscillations confined to the metallic electrode/organic layer interface and can not radiate out due to its larger wave vector than that of a freely propagating photon. Calculations have shown that as much as 40% of the light produced in a typical OLED based on small molecules may be lost via this decay route [1], and an even more significant SP loss for top electrolu-

minescence (EL) devices [2], that are practical and suitable for high-resolution active matrix displays; while the emitted light extraction efficiency is limited to be as low as ~20% [3–5]. Therefore, many fabrication methods, such as the incorporation of appropriate sub-wavelength scale periodic corrugations fabricated by holographic techniques [6], solvent assisted micromolding [7] and nanoimprint lithography [8,9], have been employed to outcouple SP modes to improve light extraction. For top EL devices in particular, the recovery of significant SP loss has been anticipated to be a desirable and powerful way to enhance light output [10]. In this work, a nano-aggregated bathocuproine (BCP) film has been layered in a simple manner on top of an Ag cathode of a conventional OLED based on tris-8-hydroxyquinoline aluminum (Alq<sub>3</sub>) to enhance top emission. This method avoids currently costly and complex fabrication processes and more importantly does not damage the electrical properties of the device. Its top emission intensity increases by a factor of 2.7–2.1 compared with that of the equivalent device without such a nanostruc-

\* Corresponding authors. Tel.: +86 10 62754990; fax: +86 10 62756567.  
E-mail addresses: [zjchen@pku.edu.cn](mailto:zjchen@pku.edu.cn) (Z. Chen), [qhong@pku.edu.cn](mailto:qhong@pku.edu.cn) (Q. Gong).

tured layer, while a similar device capped with an amorphous BCP layer exhibits 1.5–1.3 times enhancement. The experimental data emphasize the excellent outcoupling capability of a nano-aggregated BCP film on a single side of an Ag cathode, an arrangement ensuring no phase cancellation when scattering SP modes. Furthermore, this method does not modify the original EL spectra because of nonperiodic BCP nanostructures. All these properties are desirable for application in OLED displays.

## 2. Experimental

### 2.1. Nano-aggregated BCP layer formation

A 50 nm thick Ag film was deposited on a quartz substrate by vacuum evaporation, and then an 80 nm layer of BCP was deposited on Ag/quartz; meanwhile a sample of BCP (80 nm)/quartz was fabricated for comparison. The two samples were kept in vacuum at room temperature for 24 h, and then a stable self nano-aggregated BCP films were obtained. The top surface morphology of all the samples were measured by atomic force microscopy (AFM), as shown in Fig. 1.

### 2.2. Photoluminescence (PL) and lifetime measurements

To properly apply a nano-aggregated BCP film to an EL device, we first need to investigate the formation mechanism of such nanostructures and the SP resonance supported by these nanostructures. The relevant experiments are outlined as follows. The PL spectra of amorphous BCP film on quartz and nano-aggregated BCP films on both quartz and Ag film were recorded by a Hitachi F2500 fluorescence spectrophotometer in air at room temperature with ~15% relative humidity (RH). The fluorescence decay dynamics for nano-aggregated BCP films on quartz and on Ag film were studied at 383 nm (monomer emission) and 492 nm (excimer emission). The samples were excited by a femtosecond laser and then the fluorescence was recorded by a Hamamatsu streak camera system synchronized with laser repetition rate. For the above samples, intensity decays at 524 nm, viz. the wavelength of PL enhancement maximum, were investigated by an FL920 fluorometer. All the lifetime data were attained by using deconvolution methods with exponential functions.

### 2.3. EL device fabrication and characterization

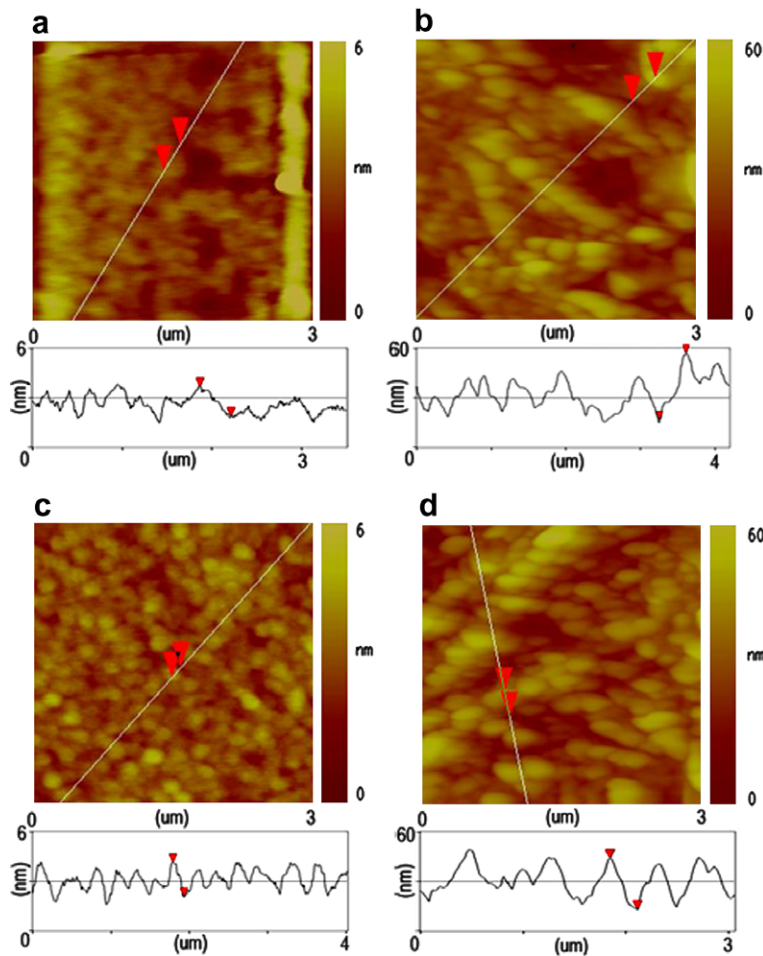
Such a nano-aggregated BCP film was introduced onto an EL device with the aim to improve top emission. The device, composed of glass/180 nm indium tin oxide (ITO) anode/40 nm 4,4-bis[N-(1-naphthyl)-N-phenylamino] biphenyl (NPB) hole transport layer/40 nm tris-8-hydroxyquinoline aluminum (Alq<sub>3</sub>) emitting layer/2 nm Ca for enhancing electron injection/28 nm Ag metallic cathode, was fabricated by vacuum deposition without thickness optimization. The active device region was confined to a 12.56 mm<sup>2</sup> area by a shadow mask during cathode evaporation. For comparison, half the area of the Ag cathode was covered by a 30 nm layer of BCP. The top EL properties of

the device were measured immediately after vacuum evaporation, during which time the fresh BCP film was still amorphous. And the top EL properties were measured again after the nano-aggregated structures were formed in BCP film by preserving in vacuum at room temperature. The current density–voltage–luminance and spectral characteristics were simultaneously recorded using a programmable array 3645A power supply and Photo research PR650 spectrophotometer. All measurements were carried out on an unencapsulated device in air with ~15% RH at room temperature.

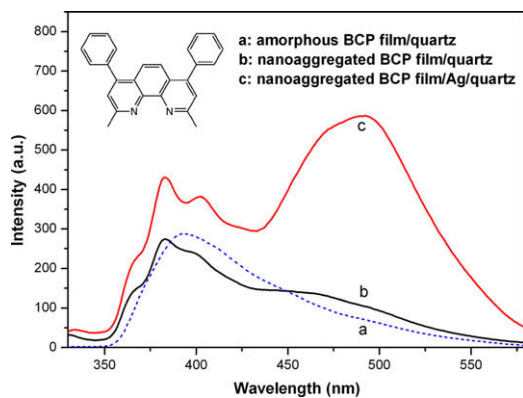
## 3. Results and discussion

Fig. 1a shows the amorphous BCP film on a quartz substrate examined immediately after vacuum evaporation revealing a surface roughness of 1.2 nm. Surface roughness of 9.9, 9.6 and 0.6 nm are found, respectively, for nano-aggregated BCP film on quartz (Fig. 1b), for nano-aggregated BCP film on Ag film (Fig. 1d), and for Ag film on quartz (Fig. 1c). Nano-aggregated BCP films on quartz and on Ag film exhibit similar topography. As shown in Fig. 2, compared with the emission spectrum of an amorphous BCP film on quartz, which displays only the monomer band (~383 nm), the spectral profile of a nano-aggregated BCP film on quartz, exhibits a slight decrease in monomer emission with a concomitant emergence of an emission band (~492 nm). This emission (~492 nm) substantially increases in the PL spectrum of a nano-aggregated BCP film on Ag film. In general, many aromatic hydrocarbons are subject to excimer formation, a diffusion-controlled process; the corresponding fluorescence band has red shift relative to that of the monomer and does not show vibronic bands [11]. These features can be observed in the PL spectra of nano-aggregated BCP films, indicating that BCP molecules, which themselves contain aromatic groups, have probably formed excimers. To further verify the existence of these excimers, the fluorescence decay dynamics for nano-aggregated BCP films on quartz and on Ag film were analyzed. As shown in Fig. 3, the intensity decay at 492 nm exhibits rise-times of 186 and 167 ps for nano-aggregated BCP films on quartz and on Ag film, respectively, with negative exponential prefactors. These values are close to the lifetimes of 251 and 236 ps for nano-aggregated BCP films on quartz and on Ag film, respectively, associated with the fast monomer decay at 383 nm. Because fast monomer decay lifetimes correspond to rise-times indicative of excimer formation [12], the emission band (~492 nm) occurring in the PL spectra of nano-aggregated BCP films on both quartz and Ag film should originate from excimers. Based on the AFM results and excimer presence reflecting molecular diffusion, we can deduce the formation mechanism of this nano-aggregated BCP film as follows [13]. The vacuum evaporation produces a film in non-equilibrium, and thus molecules diffuse and agglomerate to minimize the total surface energy. Finally, the original film arrives at an equilibrium state, i.e., forming a stable nanostructured film.

To ascertain the range of wavelengths of the SP resonance supported by the nano-aggregated BCP film, the



**Fig. 1.** AFM morphological images ( $3 \mu\text{m} \times 3 \mu\text{m}$ ) and depth profiles (along solid line) for (a) amorphous BCP film on quartz; (b) nano-aggregated BCP film on quartz; (c) Ag film on quartz; (d) nano-aggregated BCP film on Ag film. The pair of arrows in (a), (b), (c) and (d) indicate vertical distances are 1.8, 39.4, 2.1 and 31.2 nm, respectively.



**Fig. 2.** PL spectra of a: amorphous BCP film on quartz, b: nano-aggregated BCP film on quartz and c: nano-aggregated BCP film on Ag film. The chemical structure of BCP is shown in the inset.

experimental PL enhancement ratio of nano-aggregated BCP film on Ag film to that on quartz as a function of wavelength was obtained, as shown in the inset of Fig. 4 (curve

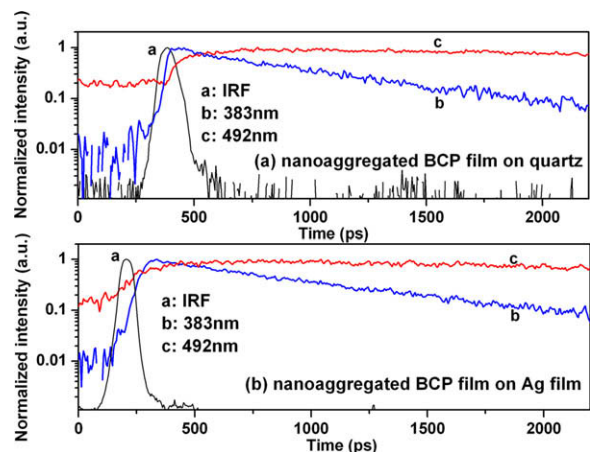


**Fig. 3.** PL decay dynamics of the nano-aggregated BCP film on quartz (a) and on Ag film (b). The emission was recorded at 383 and 492 nm and the excitation wavelength was 300 nm. IRF is the instrumental response function.

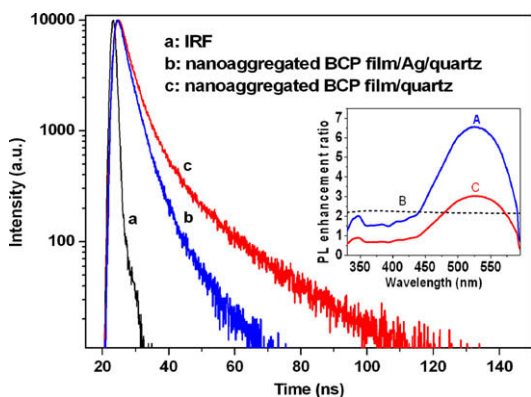


**Fig. 4.** PL decay dynamics of nano-aggregated BCP films on quartz and on Ag film. The excitation wavelength was 300 nm, and the emission was recorded at 524 nm. IRF is the instrumental response function. Curves in the inset show (A) the experimental PL enhancement ratio of nano-aggregated BCP film on Ag film to that on quartz; (B) the calculated PL enhancement ratio caused by reflection and interference; (C) the PL enhancement ratio of the data in (A) to that in (B) as a function of wavelength.

A). The PL intensity increases over a broad range of green emission wavelengths and the PL enhancement ratio reaches a maximum ( $\sim 6.5$  times) at 524 nm. We also calculated the PL enhancement ratio resulting from the reflection and interference of exciting light, as well as that of fluorescence, arising from the presence of Ag film, as shown in the inset of Fig. 4 (curve B). Those small values ( $\sim 2$  times) can not explain the larger experimental enhancement, which indicates the existence of another PL enhancement mechanism. Meanwhile, the intensity decays at 524 nm in Fig. 4 show both a reduced mean time ( $\tau_{\text{mean}} = 5.3$  ns) and an amplitude-weighted lifetime ( $\langle \tau \rangle = 3.8$  ns) for a nano-aggregated BCP film on Ag film as compared with a quartz control sample ( $\tau_{\text{mean}} = 14.6$  ns,  $\langle \tau \rangle = 7.0$  ns). The increased fluorescence, accompanied by the decreased lifetime in the presence of flat Ag film overlaid with a nanostructured layer, can be attributed to the resonant coupling of spontaneous emission into SPs, which can compete with nonradiative decays and can be scattered out to the far field by nanostructures, thus enhancing the output of light [14–18].

Accordingly, we introduced such a nano-aggregated BCP film onto a typical OLED based on the green emitter, Alq<sub>3</sub>, to improve top emission. As shown in Fig. 5, the curves of current density–voltage and top emission luminance–voltage from the bare Ag cathode for the device, both before and after BCP aggregation, are nearly identical for both measurements, indicating almost no degradation of electrical properties occurring. The inset of Fig. 5 depicts the EL spectrum at 8.4 V for both measurements. The top emission spectral shape from the nano-aggregated BCP film, the amorphous BCP film and the bare Ag cathode are almost the same. This result can be expected from non-periodic nanostructures and is favorable for OLEDs applications.

A previous report has demonstrated that a capping layer can enhance the light output in top-emitting OLEDs

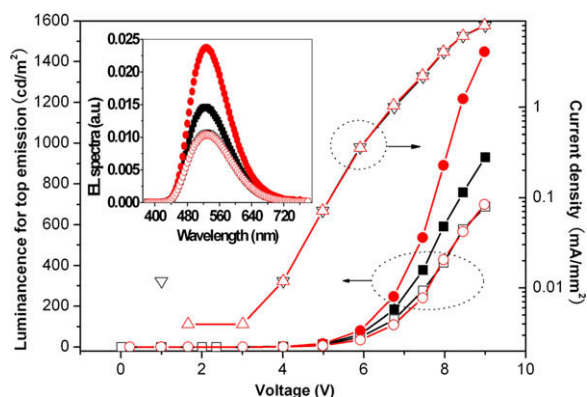


**Fig. 5.** Current density–voltage characteristics of the device for the first measurement, viz. before BCP aggregation (open triangle  $\Delta$ ), and for the second measurement, viz. after BCP aggregation (inverse open triangle  $\nabla$ ). Top emission luminescence–voltage characteristics for both measurements, and the corresponding EL spectra at 8.4 V (shown in the inset). For the first measurement: top emission from amorphous BCP film (solid square  $\blacksquare$ ) and from Ag cathode (open square  $\square$ ); for the second measurement: top emission from nano-aggregated BCP film (solid circle  $\bullet$ ) and from Ag cathode (open circle  $\circ$ ).

due to the reduction of an Ag cathode reflection [19]. As shown in Fig. 6, a similar phenomenon is observed in that the top EL intensity from the amorphous BCP film increases by a factor of 1.5–1.3 compared with that from the bare Ag cathode, while the top EL intensity from the nano-aggregated BCP film exhibits a 2.7–2.1-fold enhancement over applied voltage range of 4–9 V. To compare outcoupling capabilities, the outcoupling enhancement factor  $g$  is defined as:  $g = \frac{(E_{\text{nanostructured}} - E_{\text{amorphous}})}{E_{\text{amorphous}}} \times 100\%$ , where  $E_{\text{nanostructured}}$  and  $E_{\text{amorphous}}$  are top EL enhancements from nano-aggregated and amorphous BCP films, respectively. The calculated outcoupling enhancement factors demonstrate that the outcoupling capability of the nano-aggregated BCP film is  $\sim 60\%$  higher than that of the amorphous film. Because the absorption band of the nano-aggregated BCP

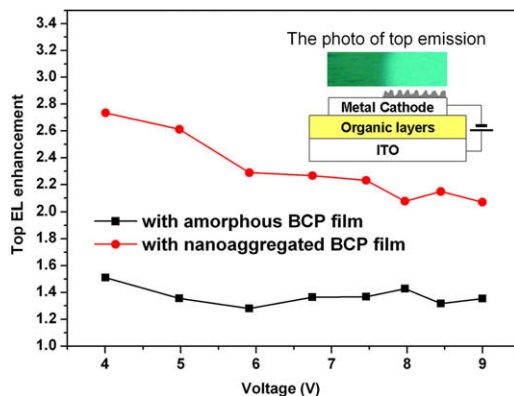


**Fig. 6.** Top EL enhancement for ITO/NPB/Alq<sub>3</sub>/Ca/Ag with amorphous (square) and nano-aggregated (circle) BCP film compared with ITO/NPB/Alq<sub>3</sub>/Ca/Ag as a function of voltage. The inset shows a schematic drawing of the EL device as well as a photo of top emission from bare Ag cathode and from nano-aggregated BCP film for the second measurement.

film does not overlap the EL emission band of Alq<sub>3</sub>, there is no PL from the overlaid nanostructured BCP layer to contribute to an enhanced light output. The improvement of the top emission from the nano-aggregated BCP film may be attributed to two factors [10,20,21]. First, the Ag cathode is thin enough to allow the fields of the SP modes associated with each metal interface to overlap. Organic materials with similar refractive indices on both sides of the Ag cathode enable those SP modes to interact due to wave vector matching of each SP mode, thus allowing the energy to transfer across the metal. Second, a pathway opens to recover energy in the SP modes as free light. In symmetric nanostructures used in previous studies, SP modes may be scattered by either metal surfaces of the cathode and light mediated via these two routes are out of phase [22], decreasing the strength of emission. In this work, the single nanostructured surface on one side of the Ag cathode ensures the absence of phase cancellation, thus supporting the more effective scattering of SP modes into free radiation. In general, the recovery of the trapped energy from the SPs relies on suitable surface corrugation. It has been reported that a surface depth modulation of approximately 30–40 nm can efficiently scatter SPs as light [23], and even the surface roughness on the order of 7–10 nm can scatter SPs [24]. Therefore, we believe that the nano-aggregated BCP film with a depth modulation of about 30–40 nm can offer similar recovery.

#### 4. Conclusion

Nano-aggregated BCP film, which is easily obtained, has been incorporated into a typical OLED based on Alq<sub>3</sub> and has been found to increase top emission by a factor of 2.7–2.1, compared with a typical OLED overlaid with amorphous BCP film, which exhibited only an enhancement of 1.5–1.3 times in top emission. Thus the outcoupling capability of the nano-aggregated BCP film is ~60% higher than that of the amorphous film. Moreover, this non-periodic nanostructured layer has proved beneficial in preserving the EL spectrum of the light emitting device, and its introduction won't have damage on current injection. All these properties are favorable in OLED applications.

#### Acknowledgments

This work was supported by the National Natural Science Foundation of China under Grant Nos. 10674011, 60677002, 60407004 and 10521002, and the National Basic Research Program under Grant No. 2007CB307000. The authors would like to thank Prof. G.Z. Ran and Prof. S.F. Wang of the Department of Physics for their kind assistance in the measurements of the decay dynamics of the fluorescence.

#### References

- [1] P.A. Hobson, S. Wedge, J.A.E. Wasey, I. Sage, W.L. Barnes, *Adv. Mater.* 14 (2002) 1393.
- [2] L.H. Smith, J.A.E. Wasey, W.L. Barnes, *Appl. Phys. Lett.* 84 (2004) 2986.
- [3] A. Chutinan, K. Ishihara, T. Asano, M. Fujita, S. Noda, *Org. Electron.* 6 (2005) 3.
- [4] G. Gu, D.Z. Garbuzov, P.E. Burrows, S. Venkatesh, S.R. Forrest, M.E. Thompson, *Opt. Lett.* 22 (1997) 396.
- [5] S.R. Forrest, *Org. Electron.* 4 (2003) 45.
- [6] J. Feng, T. Okamoto, *Opt. Lett.* 30 (2005) 2302.
- [7] C.J. Yates, I.D.W. Samuel, P.L. Burn, S. Wedge, W.L. Barnes, *Appl. Phys. Lett.* 88 (2006) 161105.
- [8] C. Liu, V. Kamaev, Z.V. Vardeny, *Appl. Phys. Lett.* 86 (2005) 143501.
- [9] K. Ishihara, M. Fujita, I. Matsubara, T. Asano, S. Noda, H. Ohata, A. Hirasawa, H. Nakada, N. Shimoji, *Appl. Phys. Lett.* 90 (2007) 111114.
- [10] S. Wedge, A. Giannattasio, W.L. Barnes, *Org. Electron.* 8 (2007) 136.
- [11] Bernard Valeur, *Molecular Fluorescence: Principles and Applications*, Wiley VCH, 2001, p. 94.
- [12] L. Mohanambe, S. Vasudevan, *J. Phys. Chem. B* 110 (2006) 14345.
- [13] S. Goncalves-Conto, M. Carrard, L. Si-Ahmed, L. Zuppiroli, *Adv. Mater.* 11 (1999) 112.
- [14] J.R. Lakowicz, Y.B. Shen, S. D'Auria, J. Malicka, J.Y. Fang, Z. Gryczynski, I. Gryczynski, *Anal. Biochem.* 301 (2002) 261.
- [15] Y.X. Zhang, K. Aslan, M.J.R. Previte, C.D. Geddes, *Appl. Phys. Lett.* 90 (2007) 173116.
- [16] Y.X. Zhang, K. Aslan, M.J.R. Previte, C.D. Geddes, *Appl. Phys. Lett.* 90 (2007) 053107.
- [17] S.L. Pan, L.J. Rothberg, *J. Am. Chem. Soc.* 127 (2005) 6087.
- [18] Z.Y. Wang, Z.J. Chen, Z.H. Lan, X.F. Zhai, W.M. Du, Q.H. Gong, *Appl. Phys. Lett.* 90 (2007) 151119.
- [19] S.F. Chen, Y. Zhao, G. Cheng, J. Li, C.L. Liu, Z.Y. Zhao, Z.H. Jie, S.Y. Liu, *Appl. Phys. Lett.* 88 (2006) 153517.
- [20] P. Andrew, W.L. Barnes, *Science* 306 (2004) 1002.
- [21] S. Wedge, J.A.E. Wasey, W.L. Barnes, I. Sage, *Appl. Phys. Lett.* 85 (2004) 182.
- [22] I.R. Hooper, J.R. Sambles, *Phys. Rev. B* 67 (2003) 235404.
- [23] K. Okamoto, I. Niki, A. Shvartsner, Y. Narukawa, T. Mukai, A. Scherer, *Nat. Mater.* 3 (2004) 601.
- [24] C.W. Lai, J. An, H.C. Ong, *Appl. Phys. Lett.* 86 (2005) 251105.





# Low-voltage, high-performance *n*-channel organic thin-film transistors based on tantalum pentoxide insulator modified by polar polymers

Linfeng Lan, Junbiao Peng\*, Mingliang Sun, Jianlin Zhou, Jianhua Zou, Jian Wang, Yong Cao

*Institute of Polymer Optoelectronic Materials and Devices, Key Laboratory of Special Functional Materials, South China University of Technology, Guangzhou 510640, China*

## ARTICLE INFO

### Article history:

Received 26 October 2008

Received in revised form 5 December 2008

Accepted 17 December 2008

Available online 25 December 2008

### PACS:

85.65.+h

71.23.-k

71.38.Fp

### Keywords:

Organic transistor

*n*-Channel

Polar polymer modification

## ABSTRACT

Polar polymers (polyfluorene copolymers, PFN–PBT) with different polarities are utilized to modify the surface of tantalum pentoxide ( $\text{Ta}_2\text{O}_5$ ) insulator in *n*-channel organic thin-film transistors (OTFTs). A high mobility of  $0.55 \text{ cm}^2/\text{Vs}$ , high on/off current ratio of  $1.7 \times 10^5$ , and low threshold voltage of 2.8 V are attained for the OTFT with the modification polymers, the performances of which are much better than those of OTFT with only  $\text{Ta}_2\text{O}_5$  insulator. The performances of the OTFT with only  $\text{Ta}_2\text{O}_5$  insulator are only  $0.006 \text{ cm}^2/\text{Vs}$  in mobility,  $5 \times 10^3$  in on/off ratio, and 12.5 V in threshold voltage. Furthermore, it is found that the threshold voltage of the OTFTs with PFN–PBT modification layer is easily tuned by polarities of the polymers. Further studies show that self-assembly dipole moments in the polymers play an important role in the improvement of the OTFT performances.

© 2008 Elsevier B.V. All rights reserved.

## 1. Introduction

In recent years, organic thin-film transistors (OTFTs) have received more and more attention due to their potential applications in low-cost and flexible electronics such as organic light-emitting diodes (OLEDs) and organic complementary circuits [1,2]. The performances of *p*-channel (hole transporting) OTFTs based on pentacene can be comparable to those of amorphous silicon transistors [3]. However, the performances of *n*-channel (electron transporting) OTFTs are not as good as those of *p*-channel OTFTs. So to improve *n*-channel OTFTs performances is urgent for many applications, such as in complementary circuit.

To date, most of *n*-channel OTFTs are based on low dielectric-constant materials (e.g.,  $\text{SiO}_2$  [4,5] or insulating polymers [6,7]) as the gate insulators, which may lead to high operating voltage or high threshold voltage. There-

fore, to reduce the operating voltage or threshold voltage is an important issue in investigation of OTFTs. Tantalum pentoxide ( $\text{Ta}_2\text{O}_5$ ) is one of the most promising materials for gate insulators due to its high dielectric-constant ( $\epsilon_r = 20\text{--}35$ ) [8–12] which would result in low operating voltage or low threshold voltage in OTFTs. However, the  $\text{Ta}_2\text{O}_5$  insulator has the problem of seriously trapping electrons at the interface between  $\text{Ta}_2\text{O}_5$  and *n*-type active semiconductors [13], which may cause low electron mobility and poor electrical stabilities in *n*-channel OTFTs.

In this work, we use polar polymers to modify the surface of  $\text{Ta}_2\text{O}_5$  insulators, and achieve great improved performances in *n*-channel OTFTs.

## 2. Experimental

The polar polymers used as the modification layers are based on Poly[(9,9-bis(3'-((*N,N*-dimethyl)-*N*-ethylammonium)propyl)-2,7-fluorene)-alt-2,7-(9,9-dioctylfluorene)]

\* Corresponding author. Fax: +86 20 87110606.

E-mail address: [psjbpeng@scut.edu.cn](mailto:psjbpeng@scut.edu.cn) (J. Peng).

(PFN, Fig. 1a), which is widely utilized in polymer light-emitting diodes to improve electron injection from the cathode into emission polymers due to its strong molecule polarity [14,15]. Here, polar PFN and its copolymers (Fig. 1b) are firstly used to fabricate OTFTs.

The copolymers (PFN-PBT) (Fig. 1b) were synthesized in our lab from monomers of 2,7-bis(4,4,5,5-tetramethyl-1,3,2-dioxaborolan-2-yl)-9,9-dioctylfluorene (1), 2,7-dibromo-9,9-bis(3'-(*N,N*-dimethylamino)propyl)fluorene (2), and 4,7-bis(5-bromo-*N*-methylpyrrol-2-yl)-2,1,3-benzothiadiazole (3), processed by using Pd-catalyzed Suzuki coupling methods. The co-monomer feed ratios of 3 to 1 + 2 are 1:99 and 5:95 and the corresponding polymers are named PFN-PBT1 and PFN-PBT5, respectively. Higher feed ratio copolymers are poor soluble in methyl alcohol solvent. The active material is *N,N*-didodecyl-3,4,9,10-perylene tetracarboxylic diimides (PTCDI, Fig. 1c), a typical *n*-type semiconductor [16].

The schematic structure of the OTFTs with top contact configuration is shown in Fig. 1d. A 600 nm thick tantalum (Ta) film was deposited on a cleaned glass substrate by a DC magnetron sputtering. The Ta<sub>2</sub>O<sub>5</sub> insulator was prepared by anodizing Ta. The anodizing process was performed as follows: the glass substrate with a Ta layer was immersed in a 0.01 wt.% citric acid solution. Ta acts as the anode of the circuit and platinum electrode is the cathode. A constant current density of 0.2 mA/cm<sup>2</sup> was established at the beginning with increasing the voltage up to about 100 V. The current would experience an exponential decay process when the voltage keeps constant (100 V) during anodizing [8], and then Ta<sub>2</sub>O<sub>5</sub> film with 200 nm thick was formed. The polymers of PFN, PFN-PBT1, and PFN-PBT5 were dissolved in methyl alcohol at the concentration of 5 mg/ml (a small amount of acetic acid was added in the methyl alcohol to improve the solubility). Then the solution was deposited, respectively, onto the Ta<sub>2</sub>O<sub>5</sub> film by spin-coating to form a 40 nm-thick polymer film. The polymer films were naturally dried in N<sub>2</sub> atmosphere overnight at room temperature. PTCDI was thermally evaporated onto the polymer films with a thickness of 50 nm. The initial deposition rate was controlled between 0.01 and 0.05 nm/s to form a 10 nm thick film. Then the rate was increased to about 0.2 nm/s for another 40 nm, because the first 10 nm-thick PTCDI is a key issue in optimizing performances of OTFTs. Finally the Al source and drain electrodes with 80 nm thick were thermally deposited through a shadow mask onto the PTCDI film. The transistor channel length and width were 0.1 and 10 mm, respectively. The OTFT characterization was performed in N<sub>2</sub> atmosphere by using a probe station and a semiconductor parameter analyzer (Agilent 4155C). The capacitance–voltage (*C*–*V*) measurements were carried out by using a HP4192A impedance analyzer.

### 3. Results and discussion

#### 3.1. Device characteristics for PTCDI OTFTs

Leakage current density vs. gate voltage (*V<sub>G</sub>*) is shown in Fig. 2. Clearly, the current density is remarkably reduced to

10<sup>−10</sup> A/cm<sup>2</sup> order in minimum for the device structure with PFN or its copolymers. It is noted that the *V<sub>G</sub>* values corresponding to the lowest leakage current density are not at zero but at a positive values in *V<sub>G</sub>* range (*V<sub>G</sub>* > 0) for the structure with PFN and its copolymers, which suggests the existence of an internal electric field induced by PFN or its copolymers, which will be discussed below.

Fig. 3a–d show the output characteristics (*I<sub>D</sub>* vs. *V<sub>D</sub>*) obtained from OTFTs based on Ta<sub>2</sub>O<sub>5</sub>, Ta<sub>2</sub>O<sub>5</sub>/PFN, Ta<sub>2</sub>O<sub>5</sub>/PFN-PBT1, and Ta<sub>2</sub>O<sub>5</sub>/PFN-PBT5 insulators, respectively. All types of the transistors show *n*-channel behavior with operating voltages lower than 16 V. In the transistor fabricated by using Ta<sub>2</sub>O<sub>5</sub> only, the drain current (*I<sub>D</sub>*) remarkably decreases in higher drain voltages (*V<sub>D</sub>*), indicating that the electron carriers are trapped seriously at the PTCDI/Ta<sub>2</sub>O<sub>5</sub> interface or in bulk of Ta<sub>2</sub>O<sub>5</sub> layer. Fortunately, in the transistors fabricated by using Ta<sub>2</sub>O<sub>5</sub>/PFN, Ta<sub>2</sub>O<sub>5</sub>/PFN-PBT1, and Ta<sub>2</sub>O<sub>5</sub>/PFN-PBT5, the output characteristics demonstrate typically saturated behavior, and the saturated *I<sub>D</sub>* reaches as high as 114 μA when the gate voltage (*V<sub>G</sub>*) is biased at 16 V for the OTFT based on Ta<sub>2</sub>O<sub>5</sub>/PFN insulator. Similarly, saturated current *I<sub>D</sub>* is about 45 and 39 μA at *V<sub>G</sub>* = 16 V for OTFTs based on Ta<sub>2</sub>O<sub>5</sub>/PFN-PBT1 and Ta<sub>2</sub>O<sub>5</sub>/PFN-PBT5 insulators, respectively. This implies that the electron transport properties are greatly improved when using a PFN, or PFN-PBT1, or PFN-PBT5 modification layer.

Fig. 4 shows *I<sub>D</sub>* vs. *V<sub>G</sub>*, and corresponding  $|I_D|^{1/2}$  vs. *V<sub>G</sub>* for the OTFTs with Ta<sub>2</sub>O<sub>5</sub>, Ta<sub>2</sub>O<sub>5</sub>/PFN, Ta<sub>2</sub>O<sub>5</sub>/PFN-PBT1, and Ta<sub>2</sub>O<sub>5</sub>/PFN-PBT5 insulators, respectively. Clearly, the on/off ratio reaches as high as 1.7 × 10<sup>5</sup> for the device with Ta<sub>2</sub>O<sub>5</sub>/PFN insulator while it is only 5 × 10<sup>3</sup> for the one based on Ta<sub>2</sub>O<sub>5</sub> only. It should be noted, the subthreshold swing (SS) tends to increase in the transistors with the modification layer from PFN to PFN-PBT1 to PFN-PBT5, which is different from the case of the transistors with modified surface of SiO<sub>2</sub> insulators [17]. It indicates fewer traps at the interface of PFN/PTCDI, or PFN-PBT1/PTCDI, or PFN-PBT5/PTCDI than those at the interface of Ta<sub>2</sub>O<sub>5</sub>/PTCDI. The detailed information for SS and on/off ratios is listed in Table 1.

The threshold voltages (*V<sub>T</sub>*) as illustrated in Fig. 4b for the transistors with Ta<sub>2</sub>O<sub>5</sub>, Ta<sub>2</sub>O<sub>5</sub>/PFN, Ta<sub>2</sub>O<sub>5</sub>/PFN-PBT1, and Ta<sub>2</sub>O<sub>5</sub>/PFN-PBT5 insulators are 12.5, 2.8, 4.8, and 6 V, respectively. Clearly, the *V<sub>T</sub>* decreases when Ta<sub>2</sub>O<sub>5</sub> insulator is modified by PFN or its copolymers, and tuned by PBT contents in PFN-PBT copolymers. We ascribe the *V<sub>T</sub>* changes to dipole moments formed at the interface of PFN/PTCDI or PFN-PBT/PTCDI, as discussed below.

The electron mobility (*μ*) in the saturated current regime is calculated as follows:

$$I_D = \frac{W\mu C_i}{2L}(V_G - V_T)^2 \quad (1)$$

where *L* is the channel length, *W* the channel width, and *C<sub>i</sub>* the capacitance per unit area of the dielectrics. The capacitances are 51.3 nF/cm<sup>2</sup> for Ta<sub>2</sub>O<sub>5</sub>, 43.1 nF/cm<sup>2</sup> for Ta<sub>2</sub>O<sub>5</sub>/PFN, 44.3 nF/cm<sup>2</sup> for Ta<sub>2</sub>O<sub>5</sub>/PFN-PBT1, 43.8 nF/cm<sup>2</sup> for Ta<sub>2</sub>O<sub>5</sub>/PFN-PBT5 dielectric layers, respectively, measured by an impedance instrument. The electron mobility of the OTFTs fabricated on Ta<sub>2</sub>O<sub>5</sub>/PFN reaches as high as 0.55 cm<sup>2</sup>/Vs which is almost 100 times large compared to

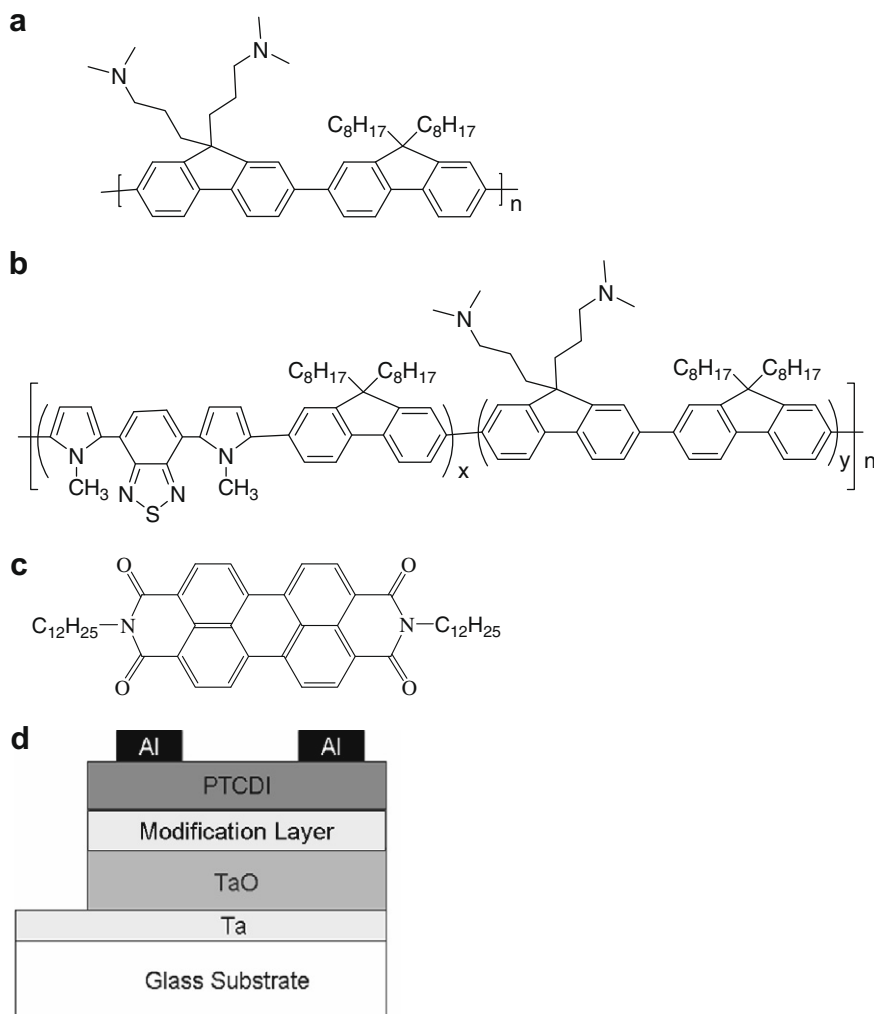


**Fig. 1.** Chemical structure of (a) PFN, (b) PFN-PBT, (c) PTCDI, and (d) schematic cross-section of the OTFTs.

that of the transistor with  $\text{Ta}_2\text{O}_5$  insulator ( $0.006 \text{ cm}^2/\text{Vs}$ ). This value is higher than that reported before [16], and can be comparable to those of many *p*-channel OTFTs [17]. Table 1 summarizes the data of  $\mu$  and  $V_T$ , suggesting that the PFN or PFN-PBT modification layer can greatly improve the performances of the *n*-channel OTFTs. Meanwhile, during comparing the mobilities of the OTFTs with PFN, PFN-PBT1, and PFN-PBT5 modification layers, we find that the PBT monomer seems disadvantageous for the *n*-channel OTFT performances (Table 1), probably it is due to the non-polarity of PBT monomers.

### 3.2. Interface structure between insulator and PTCDI

We now discuss the reasons for  $V_T$  changes with different polymer modification layers. We believe that the changes attribute to the different polarities of PFN, PFN-PBT1, and PFN-PBT5. In order to conform the speculation, we measure the water-contact angle of  $\text{Ta}_2\text{O}_5$ , PFN, PFN-PBT1, and PFN-PBT5 surfaces, respectively, as shown in Ta-

ble 1. We can see that PFN has the smallest water-contact angle and the angles increase with increasing PBT contents, suggesting that PFN has the strongest polarity and the polarity is reduced as the PBT content increases. Further-

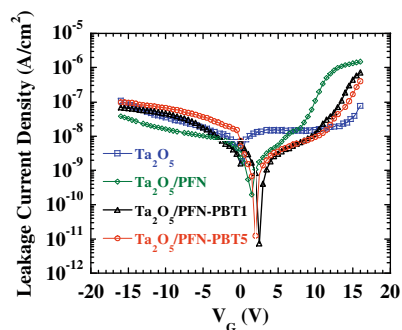


**Fig. 2.** Leakage current density vs. gate voltage ( $V_G$ ) for the capacitors with the structures of  $\text{Ta}/\text{Ta}_2\text{O}_5/\text{Al}$ ,  $\text{Ta}/\text{Ta}_2\text{O}_5/\text{PFN}/\text{Al}$ ,  $\text{Ta}/\text{Ta}_2\text{O}_5/\text{PFN-PBT1}/\text{Al}$ , and  $\text{Ta}/\text{Ta}_2\text{O}_5/\text{PFN-PBT5}/\text{Al}$ .

more, we speculate that the polar PFN or PFN–PBT may form self-assembly electric dipolar layer between PFN or PFN–PBT and PTCDI because of PFN and its copolymers containing the amino polar groups, similar case has been discussed by Wu in light-emitting diodes [14]. The speculation can be confirmed via measuring small angle X-ray diffraction (XRD). Fig. 5 displays the results of the samples of PTCDI deposited on Ta<sub>2</sub>O<sub>5</sub>, PFN, PFN–PBT1, and PFN–PBT5, respectively. No diffraction peaks are observed in Ta<sub>2</sub>O<sub>5</sub>/PTCDI structure. As for PFN/PTCDI structure, a peak located at  $2\theta = 2.58^\circ$  is observed, indicating the existence of an ordered structure with a spacing of  $\sim 34.2 \text{ \AA}$ , which is consistent with that reported in Ref. [13]. Similarly, a peak located at  $2\theta = 3.48^\circ$  (corresponding to a spacing of  $\sim 25.4 \text{ \AA}$ ) for the PFN–PBT1/PTCDI structure, and a peak at  $2\theta = 3.80^\circ$  (corresponding to a spacing of  $\sim 23.2 \text{ \AA}$ ) for the PFN–PBT5/PTCDI structure appear, showing decreased

both the spacing in the ordered layer and the diffraction intensities with increasing the PBT contents. It means that the dipoles are less ordered when the PBT contents increase, which would weaken the self-assemble electric dipole field. The changes of the intensity of the self-assemble electric dipole field will cause the  $V_T$  changes. The situation is quite similar to the statement of Campbell et al. [18]. They found that the dipole moment strength depends on the functional group of the investigated molecule. When such molecules form a self-assemble layer, the molecular dipoles will give rise to a net polarization to influence on the surface potential [19]. So, when PFN or PFN–PBT copolymers to modify non-polar Ta<sub>2</sub>O<sub>5</sub> insulator, the dipole field in the PFN or PFN–PBT copolymers would provide a surface potential which produces a similar effect as applying a (positive) gate voltage (Fig. 6). It means that a lower gate bias is high enough to turn on the OTFTs, i.e.,

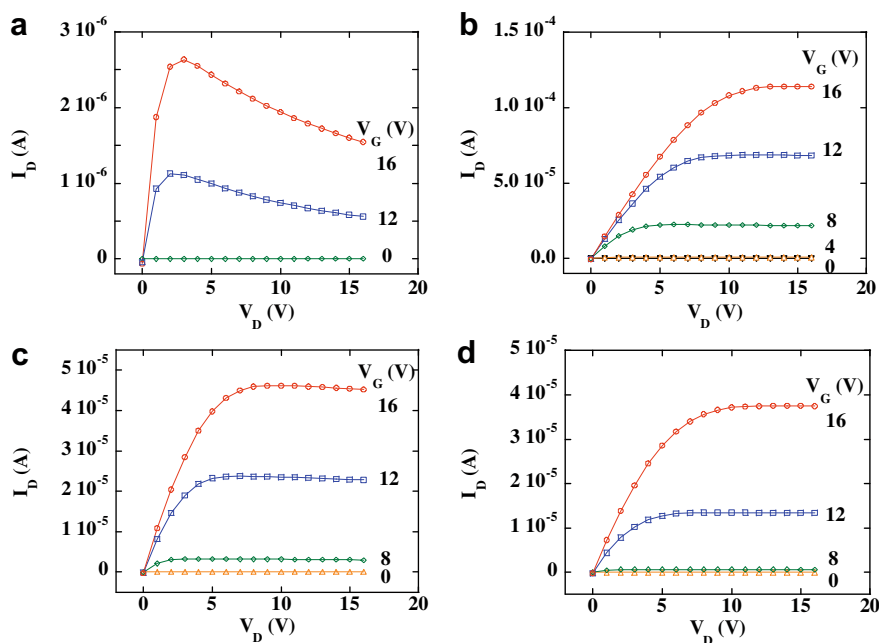


Fig. 3. Output characteristics for PTCDI OTFTs with insulators of (a) Ta<sub>2</sub>O<sub>5</sub>, (b) Ta<sub>2</sub>O<sub>5</sub>/PFN, (c) Ta<sub>2</sub>O<sub>5</sub>/PFN–PBT1, and (d) Ta<sub>2</sub>O<sub>5</sub>/PFN–PBT5.

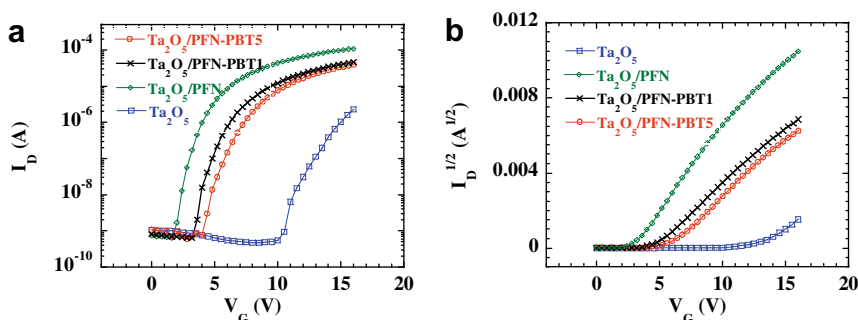


Fig. 4. Plots of (a)  $I_D$  vs.  $V_G$ , and (b) corresponding  $|I_D|^{1/2}$  vs.  $V_G$  for PTCDI OTFTs with insulators of Ta<sub>2</sub>O<sub>5</sub>, Ta<sub>2</sub>O<sub>5</sub>/PFN, Ta<sub>2</sub>O<sub>5</sub>/PFN–PBT1, and Ta<sub>2</sub>O<sub>5</sub>/PFN–PBT5 biased at  $V_D = 16 \text{ V}$ .

**Table 1**

Summarized properties of the transistors with various surface modification polymers.

Insulators	$V_T$ (V)	SS (V/dec)	$\mu$ ( $\text{cm}^2/\text{Vs}$ )	On/off ratio	$\Theta^a$ (deg)
Ta <sub>2</sub> O <sub>5</sub>	12.5	1.2	0.006	$5 \times 10^3$	90.6
Ta <sub>2</sub> O <sub>5</sub> /PFN	2.8	0.6	0.55	$1.7 \times 10^5$	29.0
Ta <sub>2</sub> O <sub>5</sub> /PFN-PBT1	4.8	0.7	0.30	$7.5 \times 10^4$	38.4
Ta <sub>2</sub> O <sub>5</sub> /PFN-PBT5	6.0	0.9	0.26	$6 \times 10^4$	52.0

<sup>a</sup>  $\Theta$  is the contact angle of water on different substrates.

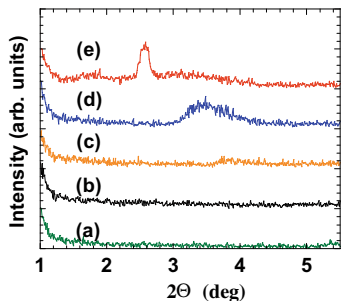


**Fig. 5.** X-ray diffraction patterns of (a) PTCDI (50 nm in thickness), (b) PTCDI (50 nm)/Ta<sub>2</sub>O<sub>5</sub> (200 nm) (c) PTCDI (50 nm)/PFN-PBT5 (40 nm), (d) PTCDI (50 nm)/PFN-PBT1 (40 nm), and (e) PTCDI (50 nm)/PFN (40 nm).

the  $V_T$  is lowered. The discussion coincides with the tendency of  $V_T$  changes (Table 1).

### 3.3. Traps at the interface

The traps at the insulator/semiconductor interface could strongly affect the performances of the OTFTs. As known, Ta<sub>2</sub>O<sub>5</sub> insulator can seriously trap electrons [13]. Therefore, to reduce the interface-traps is an important issue in fabricating *n*-channel OTFTs based on Ta<sub>2</sub>O<sub>5</sub> insulators. Fortunately, the interface-trap densities could be reduced greatly by modifying Ta<sub>2</sub>O<sub>5</sub> surface with PFN or PFN-PBT copolymer layer, and the electron mobility would be enhanced.

In order to investigate the trap densities at the interfaces of Ta<sub>2</sub>O<sub>5</sub>/PTCDI and polymer/PTCDI, capacitance–voltage (*C*–*V*) measurement on Ta/Ta<sub>2</sub>O<sub>5</sub>/PTCDI/Al and Ta/Ta<sub>2</sub>O<sub>5</sub>/polymer/PTCDI/Al structures has been carried out. The frequency and the amplitude for the AC component of the bias to the Ta electrode were 100 kHz and 50 mV, respectively. The DC component was swept between –16 and +16 V. The hysteresis swept forward and reverse reflects the trap density at the insulator/PTCDI interface or in the bulk of insulators.

Fig. 7 shows the *C*–*V* characteristics. The shifts of the flat-band voltages ( $\Delta V$ ) are 8.2, 1.4, 1.9, and 3.3 V for Ta<sub>2</sub>O<sub>5</sub>/PTCDI, PFN/PTCDI, PFN-PBT1/PTCDI, and PFN-PBT5/PTCDI interface, respectively. Assuming that  $\Delta V$  originated from trapped electrons at the insulator/PTCDI interface, the density of interface-traps (*N*) can be estimated by the following equation [17,20]:

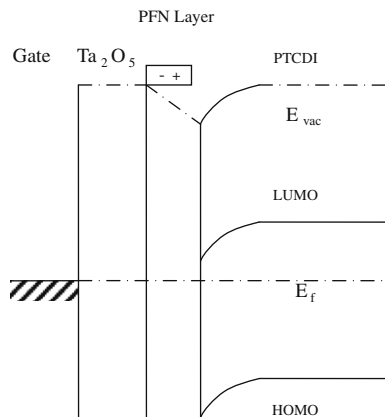


**Fig. 6.** Schematic energy level diagram of OTFTs with PFN modification layer (LUMO: the highest occupied molecular orbital energy level, HOMO: the lowest unoccupied molecular orbital energy level, Evac: vacuum energy level, Ef: Fermi level).

$$N \approx C_i \Delta V / q \quad (2)$$

where  $C_i$  is the capacitance per area of the insulator and  $q$  is the elementary charge. Using this formula, we are able to estimate the trap density to be  $3 \times 10^{12} \text{ cm}^{-2}$  for Ta<sub>2</sub>O<sub>5</sub>/PTCDI,  $5 \times 10^{11} \text{ cm}^{-2}$  for PFN/PTCDI,  $7 \times 10^{11} \text{ cm}^{-2}$  for PFN-PBT1/PTCDI, and  $1 \times 10^{12} \text{ cm}^{-2}$  for PFN-PBT5/PTCDI interfaces. As seen, the trap density is the smallest for the PFN/PTCDI interface. According to the data, we may conclude that the stronger polarity of the polymer modification layers will lead to fewer traps at the interface and higher electron mobility for the *n*-channel PTCDI OTFTs.

### 3.4. Gate bias stress effects

One of the obstacles for a commercialization of OTFTs is gate bias stress effects. The effects are often investigated by applying a fixed gate voltage for an extended time, followed by a measurement of the shift of the transfer characteristic [21].

Fig. 8 shows the  $V_T$  shift due to the gate bias stress. During the measurement, the gate bias was stressed at 16 V at the interval between every two sweeps, and the transfer curves were recorded at a drain bias of 16 V with the gate bias sweeping from –8 to 16 V. Five transfer curves were

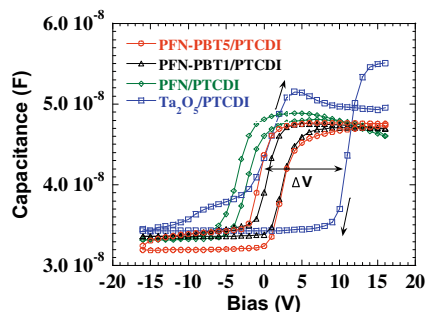


**Fig. 7.** *C*–*V* characteristics for Ta/Ta<sub>2</sub>O<sub>5</sub>/PTCDI/Al, Ta/Ta<sub>2</sub>O<sub>5</sub>/PFN/PTCDI/Al, Ta/Ta<sub>2</sub>O<sub>5</sub>/PFN-PBT1/PTCDI/Al, Ta/Ta<sub>2</sub>O<sub>5</sub>/PFN-PBT5/PTCDI/Al structures.

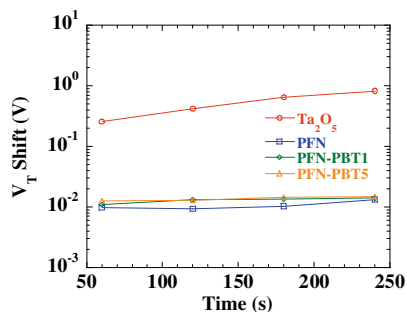


**Fig. 8.**  $V_T$  shifts under gate bias stress for PTCDI OTFTs with Ta<sub>2</sub>O<sub>5</sub>, PFN/Ta<sub>2</sub>O<sub>5</sub>, PFN-PBT1/Ta<sub>2</sub>O<sub>5</sub>, and PFN-PBT5/Ta<sub>2</sub>O<sub>5</sub> insulators.

recorded with interval time of 60 s. Clearly, very little  $V_T$  shift occurs in the OTFTs with PFN or PFN-PBT modification layer during the gate bias stress, while the OTFT without PFN or PFN-PBT layer displays large shift. The result is consistent with the hysteresis ( $\Delta V$ ) in  $C-V$  measurements. It should be noted that the effects of H<sub>2</sub>O and O<sub>2</sub> on the electrical instability can be neglected, because all of the measurements were carried out in a dry nitrogen atmosphere. Thus, the improvement in the electrical stability is most probably due to the reduction of the interface-trap density.

#### 4. Conclusion

We fabricated *n*-channel PTCDI OTFTs using Ta<sub>2</sub>O<sub>5</sub> as the insulator. The performances of OTFTs are significantly improved by using polar PFN and PFN-PBT polymers to modify the surface of Ta<sub>2</sub>O<sub>5</sub>. The electron mobilities of the OTFTs with PFN modification layer are increased by almost two orders (0.55 cm<sup>2</sup>/Vs) compared to that of the transistor with only Ta<sub>2</sub>O<sub>5</sub> insulator (0.006 cm<sup>2</sup>/Vs). The drain current is as high as 114  $\mu$ A. The reason for the improvement was discussed to be ascribed to the formation of self-assembly dipole moments in the polymers. The polarity of PFN-PBT can strongly influence on the performances of OTFTs. Strong polarity of the polymers can decrease both electron-trap density at the interface of insulator/PTCDI and the gate bias stress effect, and finally increase electron mobilities of OTFTs. The threshold voltages of the OTFTs decrease with increasing the polarity of

PFN-PBT, the stronger the polarity of the polymer is, the lower the threshold voltages of the OTFT are. We believe that it is an available way to improve the *n*-channel OTFT performances by using polar polymers to modify Ta<sub>2</sub>O<sub>5</sub> insulator surface.

#### Acknowledgement

The authors appreciate the financial supports have been given by National "973" Project of China (Grant No. 2009CB623604), the National Natural Science Foundation of China (under the Grant No. 50573024 and 50433030), the Key Project of Chinese Ministry of Education (Grant No. 104208).

#### References

- [1] F.J. Touwslager, N.P. Willard, D.M. de Leeuw, Appl. Phys. Lett. 81 (2002) 4556.
- [2] M. Halik, H. Klauk, U. Zschieschang, G. Schmid, W. Radlik, W. Weber, Adv. Mater. (Weinheim, Ger.) 14 (2002) 1717.
- [3] A.S. Dhoot, J.D. Yuen, M. Heeney, I. McCulloch, D. Moses, A.J. Heeger, PNAS 103 (2006) 11834.
- [4] Y.Y. Lin, D.J. Gundlach, S.F. Nelson, T.N. Jackson, IEEE Electron Device Lett. 18 (1997) 606.
- [5] C.R. Newman, R.J. Chesterfield, J.A. Merlo, C.D. Frisbie, Appl. Phys. Lett. 85 (2004) 422.
- [6] H. Klauk, M. Halik, U. Zschieschang, G. Schmid, W. Radlik, W. Weber, J. Appl. Phys. 92 (2002) 5259.
- [7] G.H. Gelinck, T.C.T. Geuns, D.M.d. Leeuw, Appl. Phys. Lett. 77 (2000) 1487.
- [8] J. Tate, J.A. Rogers, C.D.W. Jones, et al, Langmuir 16 (2000) 6054.
- [9] C. Bartic, H. Jansen, A. Campitelli, S. Borghs, Org. Electron. 3 (2002) 65.
- [10] H. Sakai, Y. Furukawa, E. Fujiwara, H. Tada, Chem. Lett. 33 (2004) 1172.
- [11] K. Ueno, S. Abe, R. Onoki, K. Saiki, J. Appl. Phys. 98 (2005) 114503.
- [12] Y. Iino et al, Jpn. J. Appl. Phys. 42 (2003) 299.
- [13] Y. Zhao, G. Dong, L. Wang, Y. Qiu, Appl. Phys. Lett. 90 (2007) 252110.
- [14] H. Wu, F. Huang, J. Peng, Y. Cao, Org. Electron. 6 (2005) 118.
- [15] F. Huang, L.T. Hou, H.B. Wu, X.H. Wang, H.L. Shen, W. Cao, W. Yang, Y. Cao, J. Am. Chem. Soc. 126 (2004) 9845.
- [16] R.J. Chesterfield, J.C. McKeen, C.R. Newman, P.C. Ewbank, D.A. da Silva Filho, J. Brédas, L.L. Miller, K.R. Mann, C.D. Frisbie, J. Phys. Chem. B 108 (2004) 19281.
- [17] K.P. Pernstich, S. Haas, D. Oberhoff, C. Goldmann, D.J. Gundlach, B. Batlogg, A.N. Rashid, G. Schitterb, J. Appl. Phys. 96 (2004) 6431.
- [18] I.H. Campbell et al, Phys. Rev. B 54 (1996) 14321.
- [19] H. Ishii, K. Sugiyama, E. Ito, K. Seki, Adv. Mater. (Weinheim, Ger.) 11 (1999) 605.
- [20] Dhananjay, S.B. Krupanidhi, J. Appl. Phys. 101 (2007) 123717.
- [21] D. Kumaki, T. Umeda, S. Tokito, Appl. Phys. Lett. 92 (2008) 093309.



## Letter

# Highly efficient photovoltaic diode based organic ultraviolet photodetector and the strong electroluminescence resulting from pure exciplex emission

Guang Zhang<sup>a</sup>, Wenlian Li<sup>a,\*</sup>, Bei Chu<sup>a,\*</sup>, Zisheng Su<sup>a</sup>, Dongfang Yang<sup>a</sup>, Fei Yan<sup>a</sup>, Yiren Chen<sup>a</sup>, Dongyu Zhang<sup>a</sup>, Liangliang Han<sup>a</sup>, Junbo Wang<sup>a</sup>, Huihui Liu<sup>a</sup>, Guangbo Che<sup>a</sup>, Zhiqiang Zhang<sup>b</sup>, Zhizhi Hu<sup>b</sup>

<sup>a</sup> Key Laboratory of Excited State Processes, Changchun Institute of Optics, Fine Mechanics and Physics, Chinese Academy of Sciences, 16-Dong NanHu Road, Changchun, Jilin 130033, PR China

<sup>b</sup> Organic Photoelectronic Materials and Technology Development Center, Liaoning University of Science and Technology, Anshan 114000, PR China

## ARTICLE INFO

## Article history:

Received 9 July 2008

Received in revised form 28 October 2008

Accepted 3 November 2008

Available online 20 November 2008

## PACS:

72.40.+w

## Keywords:

Ultraviolet photodetector

Exciplex

Photovoltaic

## ABSTRACT

We demonstrate organic photovoltaic (PV) and ultraviolet (UV) photodetector devices using 1,3,5-tris(3-methylphenyl-phenylamino)-triphenylamine and 1,3,5-tris(N-phenylbenzimidazol-2-yl)-benzene to function as the donor (D) and the acceptor (A), respectively. Two types of structural devices, a planar heterojunction of layer-by-layer and a bulk heterojunction with a D/A blend layer are fabricated, respectively. Under UV-365 irradiation, the PHJ device offers a power conversion efficiency of ~10%, while the BHJ device behaves with a responsivity of 135 mA/W at -4 V bias. The BHJ device can also obtain a high exciplex electroluminescence (EL). The dependencies of PV and EL performances on exciplex formation were also discussed.

© 2008 Elsevier B.V. All rights reserved.

Ultraviolet (UV) sensitive photovoltaic (PV) diodes can be used for environment monitoring, combustion flames, UV curing monitors, developing areas, and so on [1–7]. Moreover, the devices, especially the visible-blind (VB) device, also has potential applications in solar astronomy, missile plume detection, space-to-space transmission, and sterilization monitors. The wide-band-gap inorganic photodetectors based III-nitrides [2], SiC [3] and II–VI materials [4] are constructed on expensive substrates such as sapphire [5] or SiC [3], and the associated fabrication techniques are troublesome and costly. Differing from inorganic systems, organic UV photodetectors have undergone rapid development in recent years, which can be as-

cribed to simpler fabrication processes, lighter weight and lower costs [6,7]. However, organic UV photodetectors still exhibit lower responsivity, such as a peak responsivity of 30 mA/W [6]. Organic PV performances rely intensively on electrical properties including energy levels and the carrier mobility of the donor (D) and acceptor (A) materials and the diode structure. For this reason, we will select a new material system in which the D material has a low ionization potential (IP) and the A material presents a higher electron affinity (EA) and electron-mobility. 1,3,5-tris(3-methylphenyl-phenylamino)-triphenylamine (m-MTDATA) is a well-known effective D material due to its lower IP (5.1 eV) and high hole mobility of  $3 \times 10^{-5} \text{ cm}^2/\text{Vs}$  [8]. It has also been studied on various exciplex-type devices [9–11]. However, the efficiency of m-MTDATA based PV devices shows lower performance which may be due to the unmatched energy alignment between m-MTDATA and

\* Corresponding authors.

E-mail addresses: [wllioel@yahoo.com.cn](mailto:wllioel@yahoo.com.cn) (W. Li), [beichu@163.com](mailto:beichu@163.com) (B. Chu).

bathocuproine (BCP) [11]. Compared with BCP as an acceptor, 1,3,5-*tris*(*N*-phenyl-benzimidazol-2-yl) benzene (TPBi) presents a higher electron mobility (EM) over BCP and *tris*-(8-hydroxy-quinoline) aluminum (Alq<sub>3</sub>) [12]. Its electron mobility increases three times than that of BCP when the applied electrical field increased only two times, which lead to a decisive PV performance. TPBi is generally used as the exciton blocking and electronic transporting material to substitute BCP/Alq<sub>3</sub> layers in the field of OLED fabrications. In this Letter, a new PV diode was constructed where *m*-MTDATA and TPBi serve as D and A, respectively, and BCP was also employed as the exciton blocking layer (EBL).

All devices were fabricated on cleaned glass substrates pre-coated with conducting indium–tin–oxide (ITO) anode with a sheet resistance of 25 Ω/sq, and the substrates were treated by UV ozone in a chamber for 15 min after solvent cleaning. The organic films were thermally evaporated in high vacuum (<10<sup>-6</sup> Torr) using previously calibrated quartz crystal monitors to determine the deposition rate and the film thickness. The organic layers were deposited at a rate of 2 Å/s. The evaporating rate of LiF and Al cathode were controlled to be 0.5 Å/s and 10 Å/s with the thickness of 10 Å and 2000 Å, respectively. A 365 nm UV light with a

power of 0.426 mW/cm<sup>2</sup> was employed to illuminate both types of diodes at zero bias and various reverse biases.

Fig. 1 shows the chemical structures of the used materials and the schematic energy level diagram of the PHJ device. The function of three layers has been expatiated in the preamble. About 10 Å LiF was used as the complex cathode with Al to further increase the performance [13,14]. To compare the performance of the diodes, two types of devices were constructed. One is device-A with a structure of ITO/*m*-MTDATA(350 Å)/TPBi(500 Å)/BCP(120 Å)/LiF(10 Å)/Al. The other is device-B with a structure of ITO/*m*-MTDATA(300 Å)/*m*-MTDATA:TPBi (1:1, 100 Å)/TPBi(450 Å)/BCP(120 Å)/LiF(10 Å)/Al, which were called the planar heterojunction (PHJ) and bulk-heterojunction (BHJ) devices hereafter, respectively.

Fig. 2a shows *I*–*V* characteristics of the PHJ and BHJ devices. According to the figure, the open-circuit voltage (*V*<sub>OC</sub>), short-circuit current density (*J*<sub>SC</sub>), and fill factor (*FF*) for PHJ and BHJ devices were 2.26 and 2.22 V, 46.1 and 46.7 μA/cm<sup>2</sup>, 37.5% and 31.3%, yielding a power conversion efficiency (*η*<sub>p</sub>) of 9.15% and 7.63%, respectively. Compared with previous reports [15], the *η*<sub>p</sub> of 9.15% is highest found until now. The above data depicts that *η*<sub>p</sub> is higher for PHJ than for BHJ structure devices. It is

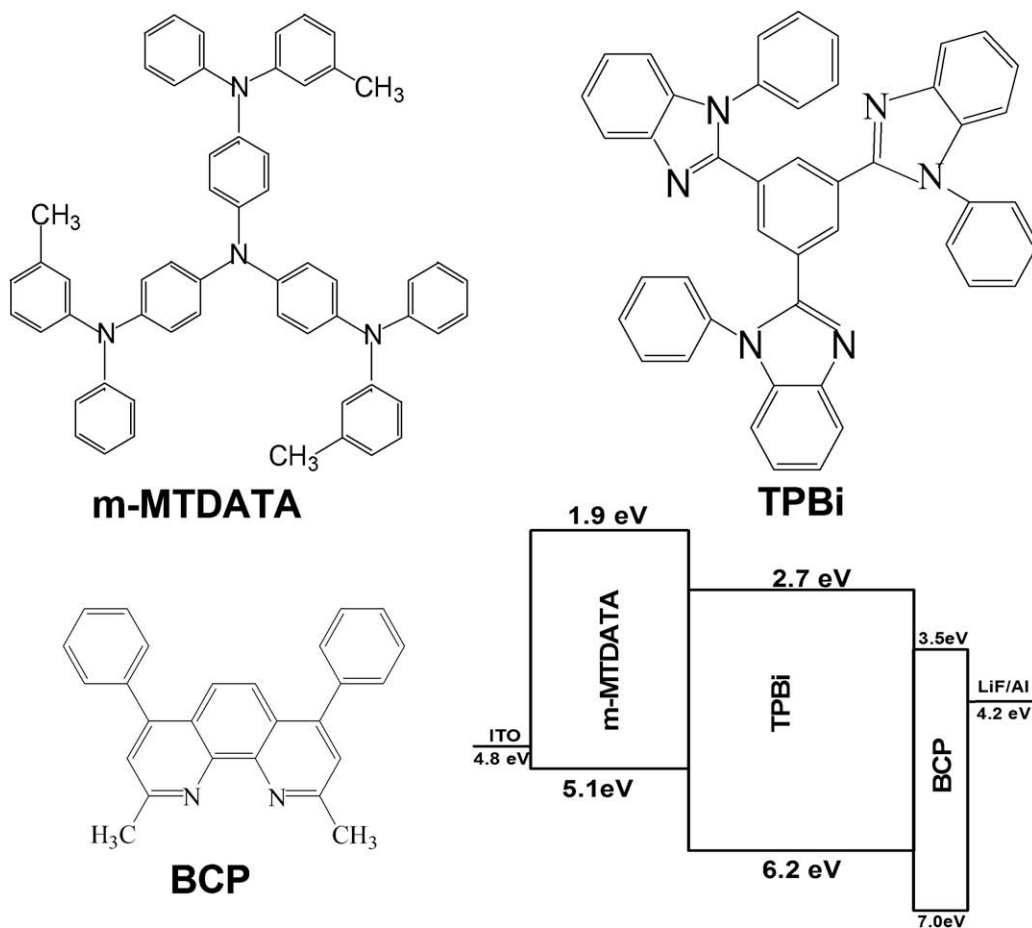
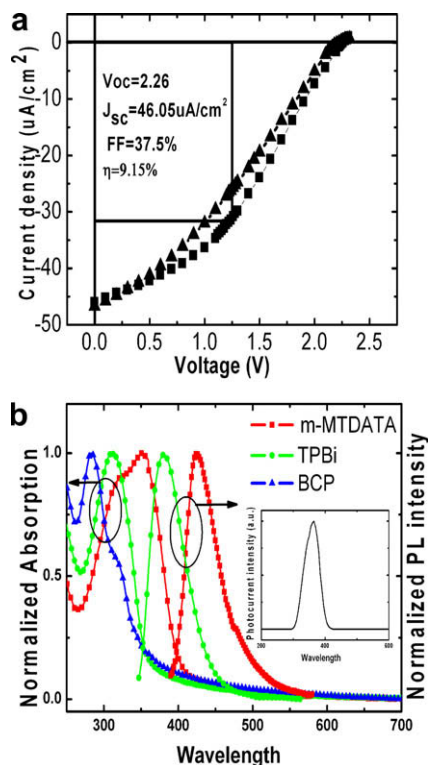


Fig. 1. Materials and schematic energy-level diagram of the PHJ device used in this work with the highest occupied molecular orbital (HOMO) level and the lowest unoccupied molecular orbital (LUMO) level which were cited from literatures (see Ref. [20,21]).





**Fig. 2.** (a)  $I$ - $V$  characteristics of the PHJ device (filled block) and BHJ device (filled triangle) under irradiation at 365 nm at an incident light density of  $0.426 \text{ mW/cm}^2$ . (b) Normalized absorption and PL spectra of neat m-MTDATA, TPBi and BCP neat films on quartz substrates. The insert shows the same photocurrent spectral response of PHJ and BHJ-devices.

interesting that this result is very different from the previous relationship in which the blend-device (BHJ) generally provides a higher PV property than that of a bilayer (PHJ) device reported in Yang's work [16]. The discrepancy in the phenomena of PV efficiency can be understood as follows. First of all, BHJ devices can provide a large interface area where photoinduced charge transfer by excitons into separated electrons and holes can efficiently occur. In this case, excitons are always generated within a diffusion length ( $\sim 3$ – $10 \text{ nm}$ ) of a donor-acceptor interface, potentially leading to higher cell efficiency than a planar heterojunction. Secondly, m-MTDATA is an amorphous film. It possesses a denser film structure and finer surface morphology than CuPc microcrystalline [17]. Because the charge mobility is higher in crystalline than in amorphous materials, the existence of crystalline structures is important for ensuring a low cell series resistance [16]. Thirdly, the mean distance between neighboring molecules of the same species in the mixed layer is larger than that in their respective homogeneous layers. The hopping mobilities are expected to decrease upon intermixing on the molecular scale. Both the second and third reasons lead to a larger internal series resistance in our BHJ device, which result in a lower  $FF$ , i.e., the  $FF$  is lower for the BHJ-device (0.313) than for the PHJ-device (0.375), consequently a lower  $\eta_p$  for the BHJ-device. In other words, the introduction of the blend layer produces a pair of contradictory processes

and results in a trade-off in which the highest  $\eta_p$  can be obtained. However, when the thickness of blend layer decreases from 20 to 2 nm, the  $\eta_p$  increases linearly and the maximum photocurrent is highest only at 10 nm. This suggested that the method of mixing D:A could be unfit for our system, and the causes will be illuminated at the latter of part of this paper.

Fig. 2b shows the normalized absorption and photoluminescence (PL) spectra of neat m-MTDATA, TPBi and BCP neat films on quartz substrates as well as the photocurrent spectral response of the PHJ-device. In the insert of Fig. 2b, it shows that both types of devices offer the same photocurrent spectral responses which mainly correspond with the absorption of m-MTDATA film. It proved that most of the excitons were generated in the m-MTDATA layer. An absorption peak of TPBi is located at 315 nm, at which the photons can be completely absorbed by ITO glass, leading to a smaller contribution of spectral response in TPBi layer. The spectral response is located at the band from 300 to 400 nm, which is just at the VB UV spectral position. We also found that these two types of diodes have a higher photoelectric detector effect under the irradiation of 365 nm UV light.

Fig. 3a depicts the dark-corrected photocurrent response as a function of the different reverse bias for the two types of devices. It is clearly shown that generation rate of the free carrier is prominently enhanced with the increase of the reverse bias voltage and gradually reach a

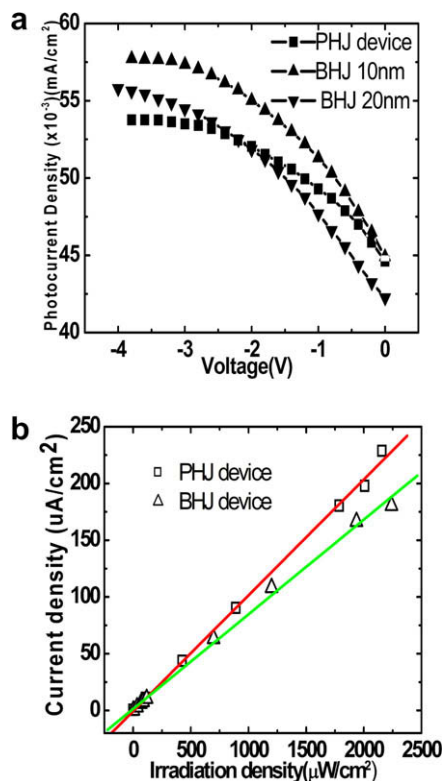


**Fig. 3.** (a) Dark-corrected photocurrent response as a function of different reverse biases for the different structure detector devices. (b) Dependence of photocurrent response on the 365 UV irradiation intensity at zero bias.

saturation value. The BHJ device has a higher photocurrent and saturation photocurrent density than the PHJ one, which is due to a higher amount of intermolecular contact between the D/A, which proves that the generation and disassociation ratio of the excitation in the BHJ device is easier than that of the PHJ. The difference between the photocurrents gradually increases with the increase of the reverse bias which indicates that the external electric field gradually plays a leading role over the built-in electric field. But the case is different when the thickness of the mixed layer is increased to 20 nm. That is, at lower reverse bias, the responsivity is higher for the PHJ device than for the BHJ one because the built-in field plays a dominating role in exciton dissociation. But as the reverse bias increases, the external electrical field plays a dominant role in exciton dissociation for the BHJ device, because the external electrical field could overcome the disadvantageous influence of the higher resistance at the blend layer while taking advantage of the much higher photogenerated exciton ratio, thus the photocurrent will be higher than that of the PHJ one but lower than the optimized BHJ device with a 10 nm blend layer (see Fig. 3a).

The dependence of the photocurrent response on the incident UV light intensity under zero bias was shown in Fig. 3b. From the slope of the fitted line, the responsivities of 100 and 85 mA/W for the PHJ and BHJ detectors were attained, respectively, which is three times higher than that reported by Ray's [6] and can be compared with that of

GaN (~100 mA/W) and of SiC (130 mA/W) based on inorganic UV detectors [2,3]. When the reverse bias rises to 4 V, the responsivity of the BHJ structure based detector can up to 135 mA/W, and the photodetector presents a constant at broad irradiation density range with only a sharp spectral response as shown in the insert of Fig. 2b.

Fig. 4a provides the current efficiency and luminance as a function of current density for the two devices. Fig. 4b indicates the EL and PL spectra of the PHJ and BHJ structure devices. Both the PHJ and BHJ devices show a bright green emission peak at 520 nm, which are completely different from the emission spectrum of m-MTDATA and TPBi monomers, proving it is caused by exciplex [10]. Exciplex is formed at the intermolecular interface between the excited state of m-MTDATA and the ground state of TPBi molecules [18]. We note that the emission of the BHJ and PHJ devices exhibit the maximum current efficiencies of 7.14 and 2.05 cd/A, and the peak luminance of 4182 and 1319 cd/m<sup>2</sup>, at 8.2 V and 7.5 V biases, respectively. That means these two types of devices have an EL effect and a PV effect, which were connected by exciplex and will be explained as below. There is a weak emission at blue waveband even extending to UV area in PHJ EL device and it increases with applied voltage. It is because the exciplex formation takes place only at the interface between m-MTDATA and TPBi. The increasing in the applied voltage leads to an increase in the number of injected holes and electrons, which recombine not only at the interface but also in the bulk of the TPBi layer, which can be proved from the PL spectrum of TPBi.

It is well known that the energy level offset of D and A at heterojunctions interface plays a very important role in the operation of the PV diode because exciton dissociation occurs at the D/A interface, while exciplex can be formed in the same place in some system. Based on our previous experiments [9,10,19], the formation of exciplex would be easier in the BHJ than for the PHJ structure device as there is a higher number of D/A molecular interactions. That is, the intensity of exciplex EL is higher for the BHJ device. Compared with the EL result, there is a contrary dependence on the PV performance in our system. That is, the PHJ device offers higher PV properties and better EL performance but its PL of exciplex is almost undetectable (data not shown), which is due to less contact and interaction among D/A molecules, while the BHJ device offers lower PV properties and better EL performance and its intensive PL of exciplex which is due to much more contact and interaction between D/A molecules (see Fig. 4b).

We deduced that there would be a competitive process between exciplex formation and photo-generated free charge carriers. Thus we supposed that they have a common precursor, which is most likely a similar non-emissive geminate pair. The PL of exciplex competes with the PV effect, which leads to a lower PV effect. The dynamic physical process may be like this: When the PV device was irradiated by a photon of a suitable energy, photo-generated excitons diffuse to the interface of the heterojunction and converse into non-emissive geminate pairs, and they are the generated common precursor. They will transform either into exciplex and emit photons or free charge carriers that drive the external circuit load. However, the

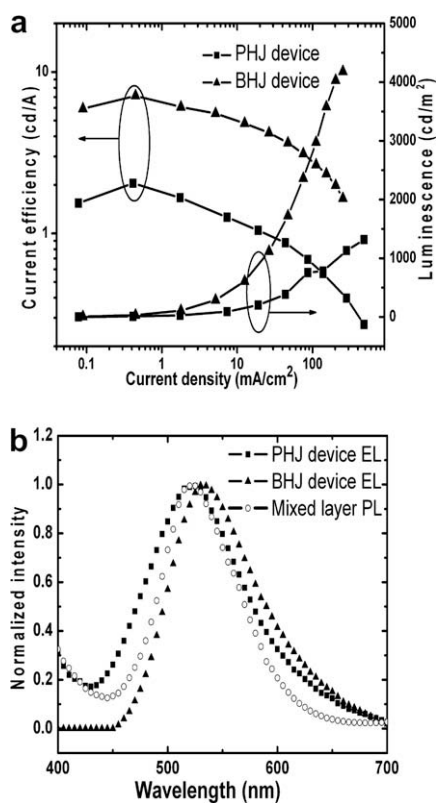


Fig. 4. (a) Plot of current efficiency and luminance as a function of current density for PHJ device and BHJ device. (b) The EL spectra of PHJ and BHJ devices and the PL spectrum of BHJ device.

dynamic factors that decide what the common precursor will change into are still confusing.

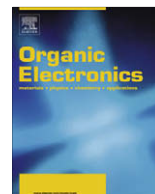
In conclusion, we have fabricated a high efficiency PHJ-PV device with the  $\eta_p$  of 9–10%. This diode could be used as a photodetector for its sharp response in VB-UV and a responsivity of 100 mA/W at zero bias. A maximum responsivity of 135 mA/W was achieved in the BHJ device with a 10 nm blend layer with 1:1 D:A at a  $-4$  bias, while this device has peak current efficiency and maximum luminance of 7.14 cd/A and 4182 cd/m<sup>2</sup> under electrical excitation. A new dependence of the PV and EL performances on the exciplex formation was discovered in our small molecular system, which will inspire us to design more efficient organic electronic diode devices.

### Acknowledgement

This work was supported by the National Natural Science Foundation of China under Grant No. 60877027.

### References

- [1] M. Razeghi, A. Rogalski, *J. Appl. Phys.* 79 (1996) 7433.
- [2] B. Butun, T. Tut, E. Ulker, T. Yelboga, E. Ozbay, *Appl. Phys. Lett.* 92 (2008) 033507.
- [3] X. Chen, H. Zhu, J. Cai, Z. Wu, *J. Appl. Phys.* 102 (2007) 024505.
- [4] A. Ohtomo, M. Kawasaki, Y. Sakurai, Y. Yoshida, H. Koinuma, P. Yu, Z.K. Tang, G.K.L. Wong, Y. Segawa, *Mater. Sci. Eng. B* 54 (1998) 24.
- [5] Y.D. Jhou, S.J. Chang, Y.K. Su, Y.Y. Lee, C.H. Liu, H.C. Lee, *Appl. Phys. Lett.* 91 (2007) 103506.
- [6] D. Ray, K.L. Narasimhan, *Appl. Phys. Lett.* 91 (2007) 093516.
- [7] T.P.I. Saragi, M. Fetten, J. Salbeck, *Appl. Phys. Lett.* 90 (2007) 253506.
- [8] C. Giebeler, H. Antoniadis, D.D.C. Bradley, Y. Shirota, *Appl. Phys. Lett.* 72 (1998) 2448.
- [9] W.M. Su, W.L. Li, Q. Xin, Z.S. Su, B. Chu, D.F. Bi, H. He, J.H. Niu, *Appl. Phys. Lett.* 91 (2007) 043508.
- [10] M. Li, W. Li, L. Chen, Z. Kong, B. Chu, B. Li, Z. Hu, Z. Zhang, *Appl. Phys. Lett.* 88 (2006) 091108.
- [11] L.L. Chen, W.L. Li, M.T. Li, B. Chu, *J. Lumin.* 122–123 (2007) 667.
- [12] Y.Q. Li, M.K. Fung, Z.Y. Xie, S.T. Lee, L.S. Hung, J. Shi, *Adv. Mater.* 14 (2002) 1317.
- [13] C.J. Brabec, S.E. Shaheen, C. Winder, N.S. Sariciftci, P. Denk, *Appl. Phys. Lett.* 80 (2002) 1288.
- [14] A.K. Pandey, K.N.N. Unni, J.-M. Nunzi, *Thin Solid Films* 511–512 (2006) 529.
- [15] J.Y. Kim, K. Lee, N.E. Coates, D. Moses, T.-Q. Nguyen, M. Dante, A.J. Heeger, *Science* 317 (2007) 222.
- [16] F. Yang, M. Shtein, S.R. Forrest, *Nat. Mater.* 4 (2005) 37.
- [17] S.-F. Chen, C.-W. Wang, *Appl. Phys. Lett.* 85 (2004) 765.
- [18] H.O.Y.S. Tetsuya Noda, *Adv. Mater.* 11 (1999) 283.
- [19] D. Wang, W. Li, B. Chu, Z. Su, D. Bi, D. Zhang, J. Zhu, F. Yan, Y. Chen, T. Tsuboi, *Appl. Phys. Lett.* 92 (2008) 053304.
- [20] M.Y. Chan, C.S. Lee, S.L. Lai, M.K. Fung, F.L. Wong, H.Y. Sun, K.M. Lau, S.T. Lee, *J. Appl. Phys.* 100 (2006) 094506.
- [21] P. Peumans, S.R. Forrest, *Appl. Phys. Lett.* 79 (2001) 126.



## Letter

## Vertical structure permeable-base hybrid transistors based on multilayered metal base for stable electrical characteristics

J.P.M. Serbena<sup>a,b</sup>, J.Y. Huang<sup>b</sup>, D. Ma<sup>b</sup>, Z.Y. Wang<sup>c</sup>, I.A. Hümmelgen<sup>a,\*</sup><sup>a</sup> Group of Organic Optoelectronic Devices, Departamento de Física, Universidade Federal do Paraná, Caixa Postal 19044, PR 81531-990 Curitiba, Brazil<sup>b</sup> State Key Laboratory of Polymer Physics and Chemistry, Changchun Institute of Applied Chemistry, Graduate School of the Chinese Academy of Sciences, Chinese Academy of Sciences, Changchun 130022, PR China<sup>c</sup> Department of Chemistry, Carleton University, 1125 Colonel By Drive, Ottawa, Ontario, Canada K1S 5B6

## ARTICLE INFO

## Article history:

Received 21 August 2008

Received in revised form 5 November 2008

Accepted 8 November 2008

Available online 17 November 2008

## PACS:

81.07.Pr

85.30.De

85.30.Tv

## Keywords:

Characterization

Permeable-base hybrid transistor

Organic semiconductor

Vertical-architecture transistor

## ABSTRACT

In this work we present a permeable-base transistor consisting of a 60 nm thick *N,N'*-diphenyl-*N,N'*-bis(1-naphthylphenyl)-1,1'-biphenyl-4,4'-diamine layer or a 40 nm thick 2,6-diphenyl-indenofluorene layer as the emitter, a Ca/Al/Ca multilayer as the metal base, and p-Si as collector. In the base, the Ca layers are 5 nm thick and the Al layer was varied between 10 and 40 nm, the best results obtained with a 20 nm thick layer. The devices present common-base current gain with both organic layer and silicon acting as emitter, but there is only observable common-emitter current gain when the organic semiconductor acts as emitter. The obtained common-emitter current gain,  $\sim 2$ , is independent on collector-emitter voltage, base current and organic emitter in a reasonable wide interval. Air exposure or annealing of the base is necessary to achieve these characteristics, indicating that an oxide layer is beneficial to proper device operation.

© 2008 Elsevier B.V. All rights reserved.

## 1. Introduction

The concept of the modern metal-base transistor (MBT) is almost 50 years old [1,2], but it was not widely explored because such devices constructed in the inorganic semiconductor/metal/inorganic semiconductor vertical structure suffered from severe limitations. These devices present complex production procedures showing poor electrical characteristics, despite the promise of operation at higher frequencies than bipolar transistors [3,4]. The interest on MBTs received a new impulse after many research groups used the approach of the substitution of the inorganic semiconductors by organic ones. By doing this, not only the fabrication process became easier, but

new possibilities of flexible [5,6] and hybrid organic/inorganic integrated devices were opened [7–10].

The MBT structure, which is a vertical stack of ultra-thin layers, is specially suitable for organic semiconductor applications. In this architecture high currents can be attained at low voltages due to the short paths for charge carriers, of the order of tens of nanometers, reducing the limitations imposed by the low charge carrier mobilities usually observed in organic semiconductors.

The MBT is constructed in the semiconductor/metal/semiconductor vertical structure, constituting a three-terminal device, named emitter, base and collector. In the case of inorganic semiconductors, the transistor is formed by two Schottky junctions, one is forward-biased (emitter/base junction) and the other is reverse-biased (base/collector junction), the emitter and collector semiconductors traditionally being crystalline ones. However, when organic semiconductors are used, the junction can be more

\* Corresponding author. Tel./fax: +55 41 33613645.  
E-mail address: [iah@fisica.ufpr.br](mailto:iah@fisica.ufpr.br) (I.A. Hümmelgen).

complex due to its amorphous and disordered character, interface polarization, etc. [11,12]. In general, these junctions are asymmetrical in order to increase the base transport factor, to improve current gains and to prevent a high leakage current or minority charge carrier injection. Additionally, as the charge carriers must be transported from the emitter through the base to reach the collector, a thin metal layer is required as the base and a low electron scattering is desired to improve device performance. In such ultra-thin base layers, typically of a few tens of nanometers, the existence of pinholes directly connecting emitter and collector is quite common. When this happens, the device is called permeable-base transistor (PBT) as characterized by the interdependence between emitter-base and collector-base voltages due to its inability of electric field shielding, analogous to the solid-state triode [13]. Using newly developed techniques, PBTs with controlled pinhole size and distribution and showing high current gains and on/off ratios have been demonstrated [14–17].

Recently, several PBTs containing organic materials were designed using different approaches, including electrochemically deposited metal base layer [18], bi-metal base layer [19], conducting polymer base layer [20] and organic collector and emitter layers [21,22], and all aimed at achieving improved electrical characteristics. Despite the high common-emitter current gains and low operational voltages already achieved, these devices suffer from high leakage currents and current gains dependent on emitter-collector voltage and base current, which leads to low on/off ratios and severely restricts practical applications related to signal amplification and modulation.

In this work we report the construction of hybrid PBTs with constant common-emitter current gain, i.e., independent of collector voltage and base current. The devices are constructed using a Ca/Al/Ca layered base. In addition, we compare two organic semiconductors with different band gaps as an emitter, observing only a slight dependence of device characteristics on the emitter materials and thus confirming the importance of the base structure for achieving high performance devices.

## 2. Experimental

The hybrid transistors were prepared onto p-type Si (100) substrate (resistivity 1–10  $\Omega$  cm). The silicon substrates were immersed in a 35% hydrofluoric acid (HF) aqueous solution to remove surface oxide. In the sequence, an insulating poly(methyl methacrylate) (PMMA) thick layer was deposited by spin-coating on part of the p-Si, in order to further prevent the direct contact between the emitter and collector electrodes, in the same geometry as reported elsewhere [24].

The deposition of the Ca/Al/Ca three-layer metal base was sequentially made without vacuum break on the p-Si polished side. The Ca layer thickness was maintained constant at 5 nm for all devices, while devices having different thickness  $\delta_{Al}$  of the Al layer ( $\delta_{Al} = 10, 15, 20$  or 40 nm) were prepared. After the Ca/Al/Ca base deposition the vacuum is broken, exposing the three-metal layer to air and allowing oxidation of the highly reactive Ca layer. These samples are not submitted to any thermal treatment. However, addi-

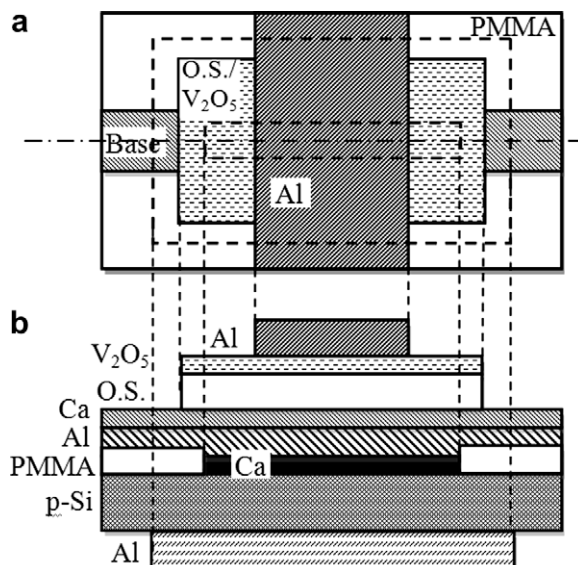


**Fig. 1.** Scheme of the structure in which the devices are constructed. O.S. means organic semiconductor, DPIF or NPB. (a) top view, the PMMA covers the entire silicon wafer, except inside the broken line rectangle, which lies under the base and emitter layers; (b) side view, layer-by-layer structure of the devices. The p-Si/Al corresponds to the collector, the Ca/Al/Ca to the base and the O.S./V<sub>2</sub>O<sub>5</sub>/Al to the emitter.

tional devices were made in which an  $\delta_{Al} = 20$  nm three-metal base was annealed in air at 120 °C for 5 min just after its deposition, being the sequence of device construction the same.

The organic emitter, a 60 nm thick layer of *N,N'*-diphenyl-*N,N'*-bis(1-naphthylphenyl)-1,1'-biphenyl-4,4'-diamine (NPB), or a 40 nm thick layer of 2,6-diphenylindeno[1,2-b]fluorene (DPIF), was further deposited by thermal sublimation in vacuum. To improve the hole injection into the organic semiconductor emitter layer, a 5 nm layer of nominally V<sub>2</sub>O<sub>5</sub> was deposited on top of the NPB layer [23,24] prior to the top contact metal electrode deposition, which consisted of a 120 nm thick Al layer. The resulting devices have an effective area of  $\sim 9$  mm<sup>2</sup>. Another 120 nm thick Al layer was deposited on the silicon unpolished backside to act as the back contact for the collector terminal. The layers thickness were controlled during device preparation using a quartz oscillator and all base and emitter related depositions were made at a base pressure lower than  $6 \times 10^{-6}$  torr. Fig. 1 presents the geometry in which the devices are constructed (Fig. 1a) together with the final structure of the transistors (Fig. 1b).

Two- and three-terminal electrical measurements carried out in the dark using two Keithley 2400 Sourcemeters were made in both, common-emitter and common-base mode. Furthermore, the devices were measured again after a period under air exposure to investigate degradation.

## 3. Results and discussion

As reported elsewhere [24], the energy levels of the involved materials favors holes as majority charge carriers. The metal work functions [25], the valence and conduction

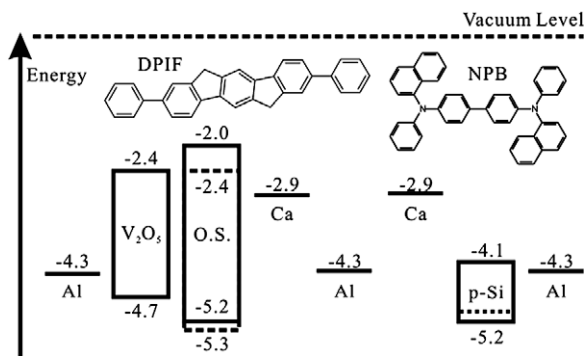


**Fig. 2.** Energy levels of materials used in this work and chemical structure of DPIF and NPB. O.S. means organic semiconductor, DPIF (full line) or NPB (broken line).

band energies of Si [26], and HOMO and LUMO levels of NPB [27] and DPIF [32] are summarized in Fig. 2. Both, NPB and DPIF are used in p-type conduction hybrid devices and their HOMO levels differ by approximately 0.1 eV. However, it must be pointed out that the Ca/Al/Ca layer was exposed to air after evaporation in all cases, so that the actual Ca work function during device operation can significantly differ from that presented in the figure, since the work function of CaO is around 1.7 eV [28].

Although the detailed energy level structure of this Ca/Al/CaO layer is difficult to predict, it plays an important role in device operation, as freshly-prepared devices do not work properly, their characteristics being not reproducible. However, after some days under air exposure, the device characteristics become more stable and the results highly reproducible. The following results for the NPB-based devices were acquired after four days device exposure to air, and for the DPIF-based devices the results were acquired one day after air exposure. However, the base of the DPIF-based device was submitted to the mentioned thermal treatment.

In the presentation of the electrical characteristics of the devices we will use the subscripts *E*, *B* and *C* to denote emitter, base and collector currents *I* and voltages *V*, respectively. Additionally, we define  $V_{ij} = V_i - V_j$  (*i,j* = *E*, *B* or *C*).

We made two-terminal current versus voltage measurements between each of the three terminals, i.e., collector/base, emitter/base and emitter/collector, maintaining the unmeasured electrode unconnected to the measurement setup. Fig. 3 presents these measurements for a  $\delta_{Al} = 20$  nm device, using NPB (Fig. 3a) or DPIF (Fig. 3b) as organic emitter. Considering the first device, it can easily be seen that the collector-base characteristic curve presents rectification. However, it seems not to follow a Schottky junction behavior. Instead, a series resistance appears to limit the injected current, possibly due to the oxidized Ca layer. The emitter-base characteristic curve also presents rectification. As expected from Fig. 2, the injection is favored when the emitter is positively biased, due to the different energy barriers for hole injection from  $V_2O_5$ /Al and Ca/CaO. Furthermore, the injected current is higher than the collector-base current for voltages  $V > 2$  V, favoring its use as the emitter electrode. The emitter-collector charac-

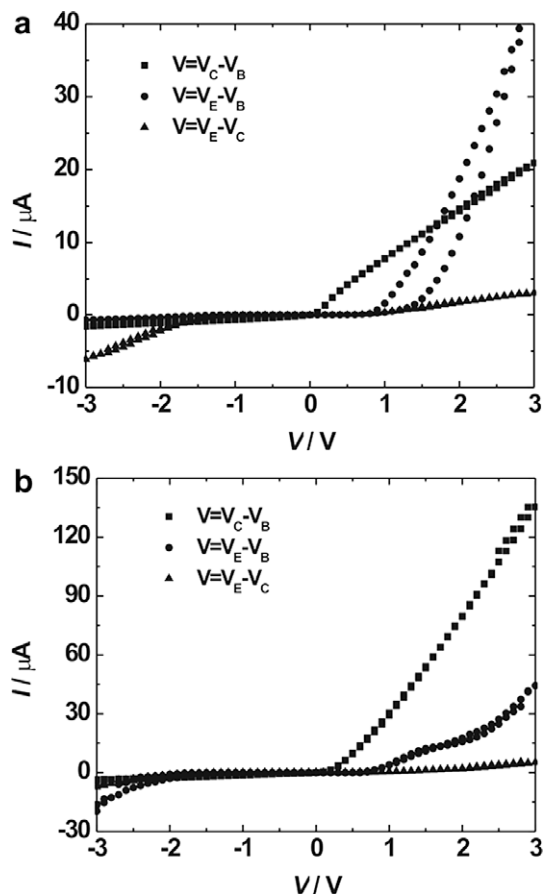


**Fig. 3.** Two terminal current versus voltage characteristics of  $\delta_{Al} = 20$  nm devices using as organic emitter (a) NPB and (b) DPIF.

teristic curve shows almost no rectification. Moreover, this current is lower than the previous ones, possibly due to the necessity of the charge carriers to transverse the base layer through pinholes. These results are similar to those obtained in  $\delta_{Al} = 40$  nm devices, while for all other devices ( $\delta_{Al} < 20$  nm) the base was not able to transport charge. Therefore, 20 nm is a critical thickness in this structure. The same behavior is observed for a device using DPIF as organic emitter (Fig. 3b), although different current values are achieved.

Fig. 3 presents the NPB-based device characteristics while operating in common-base mode. Interestingly, these devices can operate using the NPB or the p-Si as emitter electrode, as presented in Fig. 3a and b, respectively. The inset presents the measured  $I_C$  versus  $V_{CB}$ , for different  $I_E$  values, for devices with  $\delta_{Al} = 20$  nm. As can easily be seen, in this operation mode there is no leakage current, i.e.,  $I_C(I_E = 0) = 0$  in both cases. With NPB as the emitter (Fig. 4a), the  $I_C$  saturation value is not close to  $I_E$ , indicating a common-base current gain  $\alpha$  lower than the ideal value, which equals 1. The plot of the  $I_C$  versus  $I_E$  at  $V_{CB} = 0$  V allows the calculation of  $\alpha = \left. \frac{\partial I_C}{\partial I_E} \right|_{V_{CB}=\text{const.}}$  [29]. The slope of this straight line gives  $\alpha = 0.67$ , being lower than the previously reported values on p-type hybrid tran-

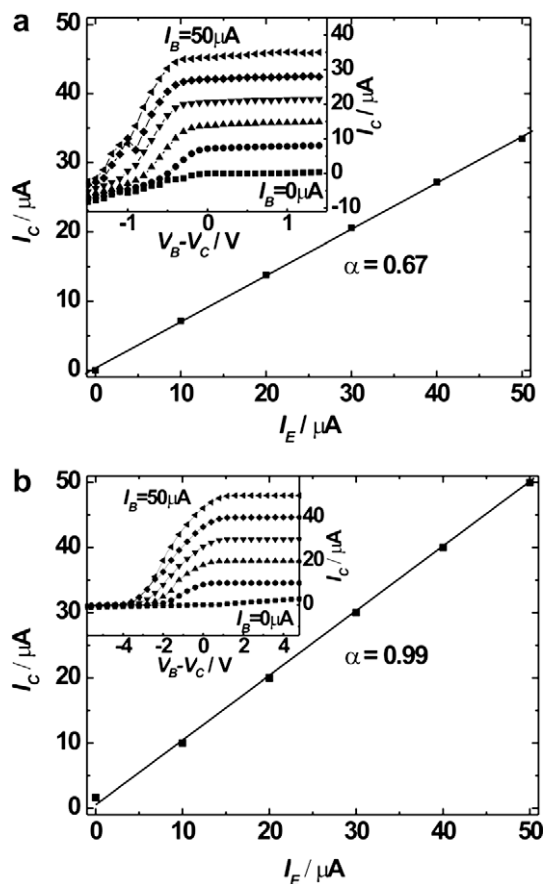


**Fig. 4.** Common-base characteristic curves of a  $\delta_{Al} = 20$  nm NPB-based device in case of (a) NPB operating as emitter and; (b) p-Si operating as emitter. Inset: Emitter currents ranging from 0 to 50  $\mu\text{A}$  in steps of 10  $\mu\text{A}$ .

sisters [24,30], but is highly reproducible. Furthermore, the devices suffer from a very slow degradation process, because after eleven days air exposure,  $\alpha$  dropped to 0.60, a fall of only  $\sim 10\%$ . The  $\delta_{Al} = 40$  nm device presented  $\alpha = 0.62$ . In contrast, when the p-Si is the emitter (Fig. 4b), the saturation  $I_C$  is close to  $I_E$ , indicating a nearly ideal  $\alpha = 0.99$  at  $V_{BC} = 3$  V. These devices support a maximum  $I_E$  of the order of 50  $\mu\text{A}$ , higher currents leading to saturation of  $I_C$  at  $\sim 50$   $\mu\text{A}$ .

The common-base characteristic curves of DPIF-based devices are presented in Fig. 5, for the organic material acting as emitter (Fig. 5a) and collector (Fig. 5b). These characteristics are very similar to those observed in the NPB-based devices for both emitters, DPIF and p-Si: low leakage currents and similar saturation currents, which lead to  $\alpha$  similar to that observed in NPB-based devices. This is a very interesting result because changing the organic emitter does not influence the device characteristics, despite energy level differences, and thus strongly indicates that in this system the base layer is the key terminal and determining factor to high device performance. It is reasonable to attribute this characteristic to the small difference in HOMO energies, 0.1 eV between NPB and DPIF, when compared to the energy difference between

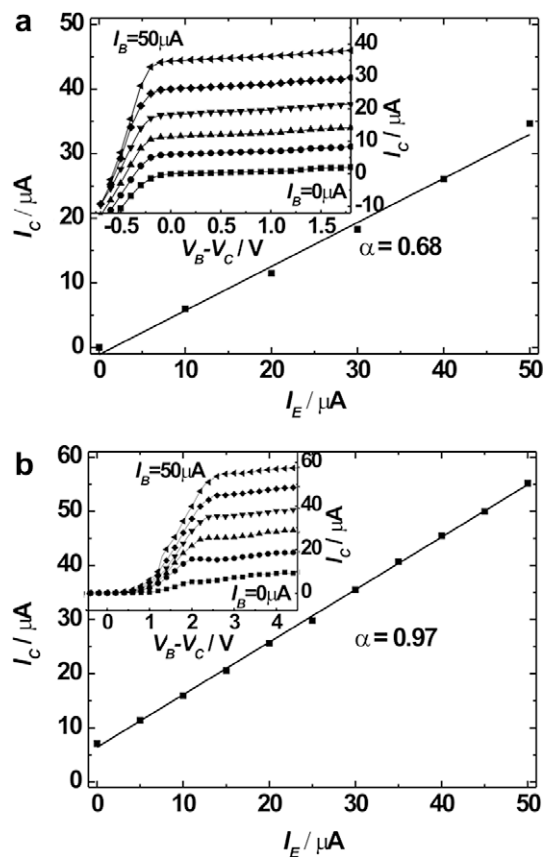


**Fig. 5.** Common-base characteristic curves of a  $\delta_{Al} = 20$  nm DPIF-based device in case of (a) DBIF operating as emitter and; (b) p-Si operating as emitter. Inset: emitter current ranging from 0 to 50  $\mu\text{A}$  in steps of 10  $\mu\text{A}$ .

CaO work function and NPB- or DPIF-HOMO, of the order of 3.5–3.6 eV. In all cases permeable-base characteristic was observed through the typical dependence of  $\partial V_{BE}/\partial V_{CB} = 1$  at a constant  $I_E$  [29]. Despite the fact that the total thickness of the metallic base is much thicker than the Fermi-Thomas length, across which an electric field is screened, we attribute the permeable-base characteristic of these devices to the roughness of the base layer, which can be of the same order as the layer thickness, creating natural pinholes that allow the direct connection of emitter and collector [24,30].

The common-emitter characteristics for  $\delta_{Al} = 20$  nm NPB- and DPIF-based devices are presented in Figs. 5a and b, respectively. These measurements show that, independent on the organic material used as emitter, the leakage current  $I_L = I_C$  ( $I_B = 0$ ) is low compared to previously reported hybrid p-type transistors [24,31,32], leading to higher on/off ratios. Additionally, it is easy to see that in both cases the difference between two  $I_C$  curves remains constant as  $V_{CE}$  changes, which leads to a constant common-emitter current gain  $\beta = \left. \frac{\partial I_C}{\partial I_B} \right|_{V_{CE}=\text{const.}}$ . Due to the step-wise character of our measurements, we considered the related quantity  $\beta^*$  defined as  $\beta^* = \frac{I_C - I_L}{I_B}$ . The obtained results are constant,  $\beta^* \cong 2$ , independent on  $I_B$  and on the

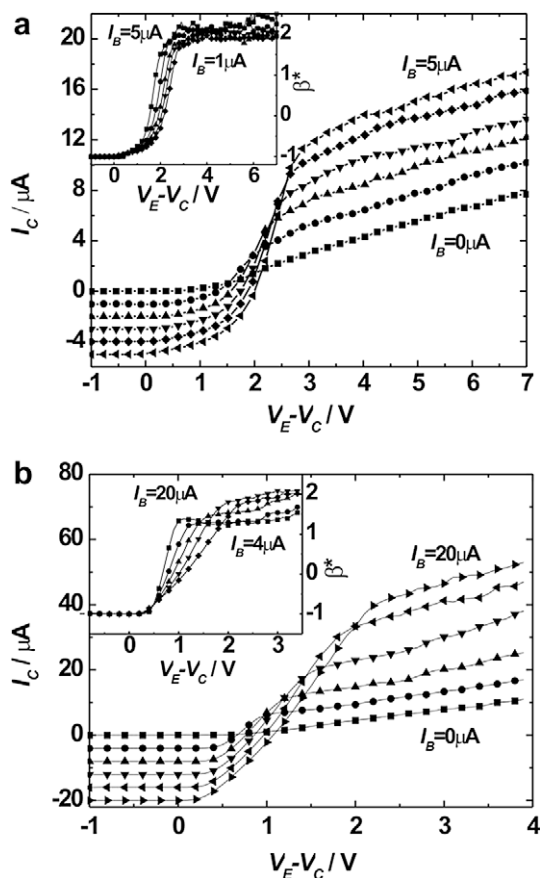


**Fig. 6.** Common-emitter characteristic curves of a  $\delta_{Al} = 20$  nm (a) NPB-based device and; (b) DPIF-based device. Base currents ranging from (a) 0 to 5  $\mu\text{A}$  in steps of 1  $\mu\text{A}$  and; (b) 0 to 20  $\mu\text{A}$  in steps of 4  $\mu\text{A}$ . Inset:  $\beta^*$  for different  $I_B$  values ranging from (a) 1 to 5  $\mu\text{A}$  in steps of 1  $\mu\text{A}$  and; (b) 4 to 20  $\mu\text{A}$  in steps of 4  $\mu\text{A}$ .

organic emitter material, as can be seen in the insets of Fig. 6. However, a small dependence of  $\beta^*$  on  $I_B$  in the DPIF-based device can be observed:  $\beta^*$  increases as  $I_B$  increases, reaching a saturation value of about 2 at  $I_B \cong 12 \mu\text{A}$ . Despite the low value, it represents an important achievement because previously reported permeable-base hybrid transistor devices show common-emitter current gain dependent on base current and collector voltage, restricting practical applications. Most of those reported devices show very high gains at very low base currents, but the gain strongly diminishes as the base current increases. Moreover, the operation voltage of our devices is low, near 3 V, with a low “turn-on” voltage of about 2 V. The same operation and “turn-on” voltages are achieved in the  $\delta_{Al} = 40$  nm NPB-based device, but in this case  $\beta^*$  drops to 1.6. In both devices, the maximum supported  $I_B$  is  $\sim 20 \mu\text{A}$ . Higher currents lead to saturation of  $I_C$  and, consequently, to lower  $\beta^*$ , possibly due to the low conductivity of the organic emitter, which cannot provide enough current to the collector, as demanded by the base. It is important to notice that these values of  $\alpha$  and  $\beta$  follow in all cases exactly the expected relation  $\beta = \frac{\alpha}{1-\alpha}$ , also valid for bipolar transistors [33].

At last, it was not possible to observe a common-emitter current gain when operating the devices using the organic materials as collector. Probably, this is because in order to operate in the active-forward mode while in the common-emitter configuration, the voltages required to drive the charge carriers through the collector are much higher than those used in the measurements. As a consequence, devices degrade before achieving the required operational condition.

As mentioned earlier, the reported characteristics are observed only after the devices are exposed to air. The most plausible hypothesis is that the Ca layer oxidizes completely, considering its thickness and period of air exposure. This could explain the dramatic change in the electrical properties in a fresh-prepared device and its late stability. In order to help supporting this hypothesis, we made a  $\delta_{Al} = 20$  nm NPB-based device and submitted it to a thermal treatment in air at 120  $^\circ\text{C}$  during 5 min. The obtained results were exactly the same as those presented above for long time air exposure devices. This result strengthens the hypothesis that an isolating layer between emitter and base is a key factor to improve device characteristics, as already reported elsewhere [7,21,22,34] for all-organic transistors, since higher temperature is expected to lead to faster oxidation.

Finally, despite the similarity in the structure of these devices and the one presented in previous work [24], the device characteristics are very different. The difference can be partially attributed to the substitution of the Ag by the Al in the base layer. However, the oxidation of the Ca layer cannot be neglected, as it may play an important role in defining device characteristics. The strong mismatch between CaO work function and NPB- and DPIF-HOMO probably imposes severe constraints for charge transport from NPB or DPIF through the Ca/CaO to the Al, effectively acting as an energy barrier and leading the device base to operate as a high impedance terminal. However, due to the high conductivity of the Al layer in the base, this high impedance base is able to act as an equipotential surface, producing a homogeneous potential drop in the NPB or DPIF layer between Al top metal electrode and Al in the base.

#### 4. Summary

In conclusion, we have demonstrated hybrid organic/inorganic metal base transistors with low leakage current in common-emitter mode and with a highly reproducible common-emitter current gain independent on both base current and collector voltage. These devices are stable when operated in air. Furthermore, a critical thickness of 20 nm is necessary for the proper base operation. A key factor to the stable device operation is related to the oxidation of the Ca base layer, since a device submitted to a short thermal treatment presents the same characteristics as those exposed to air for longer periods. Additionally, the observed nearly identical characteristics of the devices differing only by the organic emitter lead to a conclusion that in this system the base plays a key role in device characteristics.

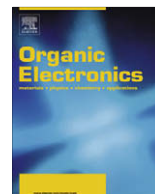


## Acknowledgements

The authors would like to acknowledge CAPES–PDEE, CNPq, Renami/CNPq, Instituto do Milenio/CNPq, The Natural Sciences and Engineering Research Council of Canada, the Hundreds Talents program of Chinese Academy of Sciences, National Science Fund for Distinguished Young Scholars of China (50325312) and Science Fund for Creative Research Groups of NSFC (20621401) for research grants.

## References

- [1] M. Atalla, D. Khang, *IEEE Trans. Electron. Dev.* 9 (1962) 507.
- [2] D.V. Geppert, in: *Proc. IRE*, vol. 50, 1962, p. 1527.
- [3] J.L. Moll, *IEEE Trans. Electron. Dev.* 10 (1963) 299.
- [4] M.M. Atalla, R.W. Soshea, *Solid-State Electron.* 6 (1963) 245.
- [5] Y. Watanabe, K. Kudo, *Appl. Phys. Lett.* 87 (2005) 223505.
- [6] Y. Watanabe, H. Iechi, K. Kudo, *Appl. Phys. Lett.* 89 (2006) 233509.
- [7] Y.C. Chao, M.H. Xie, M.Z. Dai, H.F. Meng, S.F. Horng, C.S. Hsu, *Appl. Phys. Lett.* 92 (2008) 093310.
- [8] K. Kudo, S. Tanaka, M. Iizuka, M. Nakamura, *Thin Solid Films* 438 (2003) 330.
- [9] Z. Xu, S.H. Li, L. Ma, G. Li, Y. Yang, *Appl. Phys. Lett.* 91 (2007) 092911.
- [10] W.J. da Silva, I.A. Hümmelgen, R.M.Q. Mello, D. Ma, *Appl. Phys. Lett.* 93 (2008) 053301.
- [11] M.A. Baldo, S.R. Forrest, *Phys. Rev. B: Condens. Matter Mater. Phys.* 64 (2001) 085201.
- [12] H. Ishii, K. Sugiyama, E. Ito, K. Seki, *Adv. Mater.* 11 (1999) 605.
- [13] J. McElvain, M. Keshavarz, H. Wang, F. Wudl, A.J. Heeger, *J. Appl. Phys.* 81 (1997) 6468.
- [14] K. Fujimoto, T. Hiroi, K. Kudo, M. Nakamura, *Adv. Mater.* 19 (2007) 525.
- [15] Y.C. Chao, H.F. Meng, S.F. Horng, C.S. Hsu, *Org. Electron.* 9 (2008) 310.
- [16] Y.C. Chao, H.F. Meng, S.F. Horng, *Appl. Phys. Lett.* 86 (2006) 223510.
- [17] K. Nakayama, S. Fujimoto, M. Yokoyama, *Appl. Phys. Lett.* 88 (2006) 153512.
- [18] R.G. Delatorre, M.L. Munford, Q. Zhou, A.A. Pasa, W. Schwarzacher, *Phys. Status Solidi A* 204 (2007) 940.
- [19] M. Yi, J. Huang, D. Ma, I.A. Hümmelgen, *Org. Electron.* 9 (2008) 539.
- [20] L. Rossi, M.S. Meruvia, I.A. Hümmelgen, W. Schwarzacher, A.A. Pasa, *J. Appl. Phys.* 100 (2006) 024504.
- [21] S. Zorba, Y. Gao, *Appl. Phys. Lett.* 86 (2005) 193508.
- [22] C.Y. Yang, T.M. Ou, S.S. Cheng, M.C. Wu, S.Y. Lin, I.M. Chan, Y.J. Chan, *Appl. Phys. Lett.* 89 (2006) 183511.
- [23] C.W. Chu, S.H. Li, C.W. Chen, S. Shrotriya, Y. Yang, *Appl. Phys. Lett.* 87 (2005) 193508.
- [24] C. Feng, M. Yi, S. Yu, I.A. Hümmelgen, T. Zhang, D. Ma, *J. Nanosci. Nanotechnol.* 8 (2008) 2037.
- [25] D.R. Lide, *CRC Handbook of Chemistry and Physics*, CRC Press, Boca Raton, USA, 1995.
- [26] F. Shimura, *Semiconductor Silicon Crystal Technology*, Academic Press, San Diego, USA, 1989.
- [27] S.J. Martin, G.L.B. Verschoor, M.A. Webster, A.B. Walker, *Org. Electron.* 3 (2002) 129.
- [28] S. Halas, S. Durakiewicz, *Appl. Surf. Sci.* 252 (2006) 6119.
- [29] M.S. Meruvia, I.A. Hümmelgen, *Adv. Funct. Mater.* 16 (2006) 459.
- [30] J.P.M. Serbena, I.A. Hümmelgen, T. Hadizad, Z.Y. Wang, *Small* 2 (2006) 372.
- [31] C. Feng, M. Yi, S. Yu, D. Ma, T. Zhang, M.S. Meruvia, I.A. Hümmelgen, *Appl. Phys. Lett.* 88 (2006) 203501.
- [32] T. Hadizad, J. Zhang, D. Yan, Z.Y. Wang, J.P.M. Serbena, M.S. Meruvia, I.A. Hümmelgen, *J. Mater. Sci.: Mater. Electron.* 18 (2007) 903.
- [33] S.M. Sze, *Physics of Semiconductor Devices*, John Wiley & Sons Inc., New Jersey, 1981.
- [34] K. Yutani, S. Fujimoto, K. Nakayama, M. Yokoyama, *Mol. Cryst. Liq. Cryst.* 462 (2007) 51.



## Letter

## Solution-processed organic field-effect transistors composed of poly(4-styrene sulfonate) wrapped multiwalled carbon nanotube source/drain electrodes

Kipyo Hong, Sooji Nam, Chanwoo Yang, Se Hyun Kim, Dae Sung Chung, Won Min Yun, Chan Eon Park \*

Polymer Research Institute, Department of Chemical Engineering, Pohang University of Science and Technology (POSTECH), Pohang 790-784, Republic of Korea

## ARTICLE INFO

## Article history:

Received 19 October 2008

Received in revised form 17 November 2008

Accepted 17 November 2008

Available online 28 November 2008

## PACS:

73.40.Cg

79.60.-i

61.10.-i

72.80.Le

## Keywords:

Organic transistor

Carbon nanotube

Multiwalled carbon nanotube

MWNT

OFET

Solution-processed

## ABSTRACT

Multiwalled carbon nanotubes (MWNTs) were solubilized in water by wrapping them non-covalently with poly(4-styrene sulfonate) (PSS). The PSS-wrapped MWNTs exhibited a high conductivity ( $2.0 \times 10^2$  S/cm) when compared to other solution-processed electrodes. Ultraviolet photoelectron spectroscopy results show the PSS-wrapped nanotubes have a work function of 4.83 eV, which is 0.36 eV higher than that of untreated MWNTs. We fabricated triisopropylsilylethynyl pentacene field-effect transistors (FETs) using the PSS-wrapped MWNTs as source/drain electrodes and found that the field-effect mobility of the thus obtained devices was  $0.043 \text{ cm}^2 \text{ V}^{-1} \text{ s}^{-2}$ . This mobility is four times higher than that of similar FETs containing gold electrodes ( $0.011 \text{ cm}^2 \text{ V}^{-1} \text{ s}^{-2}$ ).

© 2008 Elsevier B.V. All rights reserved.

In the past decade, there has been a growing interest in organic field-effect transistors (OFETs) because of their potential commercial applications as driving units in low-cost, large-area, and bendable electronics, for example, for the development of flexible displays, radio-frequency identification tags, smart cards, and so forth [1,2]. Intensive studies performed on OFETs using solution-processed small molecules and polymers, such as triisopropylsilylethynyl pentacene (TIPS-PEN), poly(3-hexylthiophene), and poly(2,5-bis(3-alkylthiophen-2-yl)thieno[3,2-b]thio-

phene), as the active layer have made it possible to achieve device performances comparable to those of amorphous-silicon transistors [3–5]. The electrode materials used in such OFETs must be highly conductive and flexible and exhibit a high work function (for p-type transistors) to ensure a good performance of the devices. Furthermore, the electrode materials should be solution-processable and printable to allow the fabrication of low-cost logic devices. To date, several materials, including poly(3,4-ethylenedioxythiophene):poly(styrene sulfonate), polyaniline, silver paste, and conductive polymer–carbon nanotube composites, have been tested as possible electrodes for OFETs [6–9]. However, these materials have not been shown to be good enough to replace the gold electrodes due to the

\* Corresponding author. Tel.: +82 54 279 2269; fax: +82 54 279 8298.  
E-mail address: [cep@postech.ac.kr](mailto:cep@postech.ac.kr) (C.E. Park).

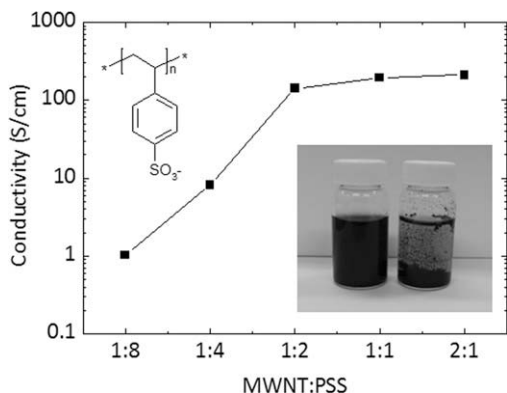


**Fig. 1.** Electrical conductivities of MWNT/PSS films as a function of the MWNT:PSS ratio. The inset at the bottom shows 20-ml vials containing PSS-wrapped MWNTs (left) and untreated MWNTs (right) in water.

low conductivity of the conductive polymers and the low work function of the silver paste.

Multiwalled carbon nanotubes (MWNTs), composed of co-axially arranged single-walled carbon nanotubes of different radii, are good candidates to be used as electrodes in OFETs. This is because of their high conductivity and mechanical strength [10,11]. However, their poor solubility and low work function have complicated their use. In this

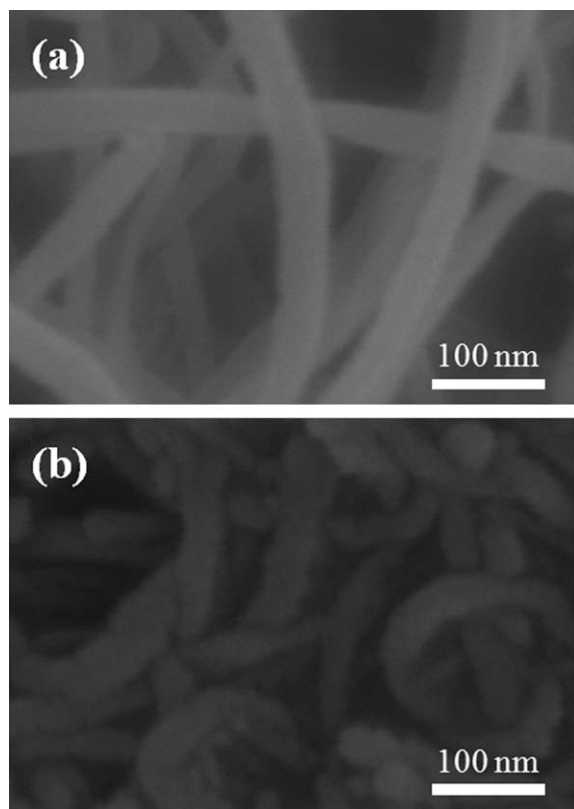


**Fig. 2.** SEM images of (a) as-received MWNT powder and (b) PSS-wrapped MWNTs.

work, we solubilized MWNTs in water by simply wrapping them with poly(4-styrene sulfonate) (PSS) [12]. The wrapping of the MWNTs with the water-soluble polymers was thermodynamically driven to eliminate the hydrophobic interface between the tubes and their aqueous medium [12–14]. In addition to the good solubility of the PSS-wrapped MWNTs in water, we also found—via ultraviolet photoemission spectroscopy (UPS) measurements—that their work function was high enough to allow their use as electrodes in OFETs. Using the PSS-wrapped nanotubes as source/drain electrodes, we fabricated solution-processed TIPS-PEN OFETs and examined their device performances.

The MWNTs were obtained from Carbon Nano-material Technology Co. Ltd. and used as received. PSS was purchased from Aldrich ( $M_w \approx 75,000$ ). The nanotubes were dispersed in a 2 wt.% solution of PSS in water (at a concentration of 20 mg/ml) by ultrasonication for 30 min. The homogeneous dispersion of the as-prepared PSS-wrapped MWNTs was stable and no phase separation with aggregation of nanotubes was observed—not even after two weeks. The conductivity of a PSS-covered MWNT film formed by drop-casting on a glass was calculated from the sheet resistance measured using the four-point probe method (KEITHLEY 2400 source meter). The film thickness was measured with a surface profiler (alpha step 500, TENCOR) at different MWNT:PSS ratios. Scanning electron microscopy images of both the PSS-wrapped MWNTs and the nanotube powder were obtained using a field-emission scanning electron microscope (FESEM, Hitachi S-4800) operating at 3 kV. All the materials, namely, the untreated MWNTs, the polymer (PSS), and the PSS-wrapped MWNTs spin-coated on the gold substrate, were characterized by UPS (Escalab 220IXL) with an He(I) emission of 21.2 eV to measure their work function. During the UPS measurements, a  $-5.0$  eV bias was applied to improve the transmission of low-kinetic-energy electrons and ensure the determination of the energy of the low-kinetic-energy edge.

OFETs with bottom-contact configurations, where the source/drain electrodes are built before depositing the

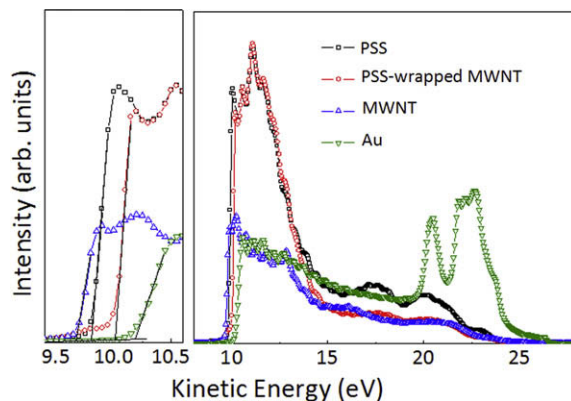


**Fig. 3.** Right: full UP spectra of a PSS film, PSS-wrapped MWNTs, and gold. Left: magnified view of the secondary electron region to determine the work function.

**Table 1**

Work functions of MWNTs, PSS, PSS-wrapped MWNTs, and Au calculated from UPS measurements.

	MWNTs	PSS	PSS-wrapped MWNTs	Au
Work function	4.47 eV	4.58 eV	4.83 eV	5.01 eV

semiconductor layer, were fabricated on heavily doped silicon wafers covered by thermally grown 300-nm-thick silicon-dioxide layers. The substrates were modified with hexamethyldisilazane (HMDS) after rinsing with acetone and cleaning with a UV–ozone cleaner, GCS-1700 (AHTECH LTS, Korea), for 20 min. In order to pattern the source/drain electrodes, the substrates were irradiated with an O<sub>2</sub> plasma (at 70 W for 6 s) through a shadow mask. Then, the PSS-wrapped MWNTs were spin-coated on these substrates. In this way, source/drain electrode patterns composed of PSS-wrapped MWNTs were formed on the irradiated areas. This patterning method has been described in previous reports [7,15,16]. Before spin-coating the PSS-wrapped MWNTs, we added glycerol to the modified nanotube solution (at a concentration of 0.8 g/ml) to obtain a clear pattern (it should be noted that glycerol does not affect the conductivity of the PSS-wrapped MWNTs). The electrode-patterned substrates were dried in a vacuum oven for one hour at 60 °C. A solution of TIPS-PEN in tolu-

ene (1 wt.%) was then dropped onto the patterned substrates and dried under ambient conditions. The electrical characteristics of the OFETs were measured in air using Keithley 2400 and 236 source/measure units.

The conductivities of MWNT/PSS films at different ratios of MWNTs and PSS—measured using the four-point probe method—are shown in Fig. 1. Upon varying the ratio of PSS and MWNTs from 2:1 to 4:1, and then to 8:1, we observe a decrease in the conductivity, which is caused by the excess of PSS. At an MWNT:PSS ratio of 1:1, the conductivity becomes saturated (at  $2.0 \times 10^2$  S/cm). However, at a ratio of 1:2, aggregates of MWNTs are observed due to a lack of PSS wrapping the tubes. Therefore, we can roughly say that a MWNT:PSS ratio of 1:1 is optimal in this case. The PSS-wrapped MWNTs (with a MWNT:PSS ratio of 1:1) are homogeneously dispersed in water, even after 2 weeks. However, if the MWNT content exceeds the PSS content, nanotube aggregates start to precipitate at the bottom of vial, as shown in the inset of Fig. 1. The surface

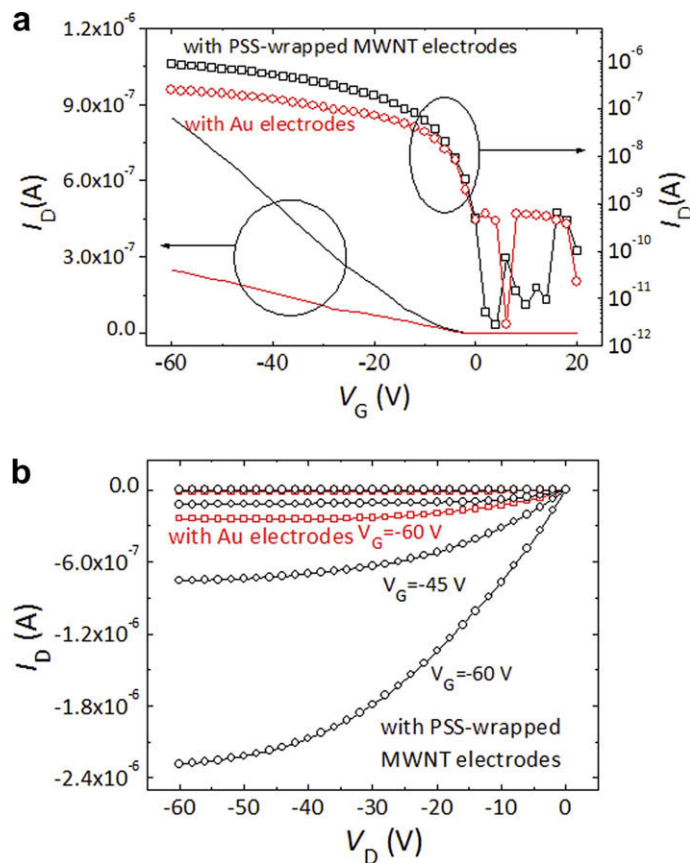


**Fig. 4.** (a)  $I_D$ – $V_G$  transfer characteristics in the linear regime (drain voltage,  $V_D = -6$  V) for TIPS-PEN OFETs containing source/drain electrodes composed of PSS-wrapped MWNTs and gold. (b)  $I_D$ – $V_D$  output characteristics of both devices. The values of  $W$  and  $L$  are 1000 and 100  $\mu\text{m}$ , respectively.

of the pristine MWNTs is smooth (see Fig. 2a), whereas that of the PSS-wrapped nanotubes is rough, with the polymers helically wrapping the surface of the MWNTs. Fig. 2b shows the successful fabrication of PSS-wrapped MWNTs with a MWNT:PSS ratio of 1:1.

The work functions of pristine MWNTs, the polymer (PSS), and PSS-wrapped nanotubes were determined from the UPS experiments shown in Fig. 3 and summarized in Table 1. The work function of the pristine nanotubes was found to be 4.47 eV, a value that is quite consistent with that reported previously [17]. The work function of the PSS-wrapped MWNTs was 0.36 eV above that of the pristine nanotubes. Since the work function of the surface of a PSS bulk film spin-coated on a gold substrate is 4.58 eV, we can conclude that the increased work function does not come from the PSS bulk. Ago et al. showed that carboxylic-acid groups introduced at the surfaces of MWNTs by acid oxidation increase the work function of the nanotubes from 4.4 to 5.1 eV due to the presence of oxygen-induced surface dipole moments [17]. Similarly, the increased work function observed here may originate from a negative dipole moment at the pendent group (benzene sulfonate) of the wrapping polymer, which is oriented away from the nanotube [18]. The increased work function of the PSS-wrapped MWNTs (i.e., 4.83 eV) is comparable to that of gold, the material generally used for source/drain electrodes in OFETs due to its high work function, which is comparable to the highest occupied molecular orbital (HOMO) of an organic semiconductor. Consequently, since the PSS-wrapped MWNTs exhibit good conductivity and a high work function, as well as good solubility, they represent good candidates to be used as electrodes in OFETs.

Fig. 4a shows typical drain current–gate voltage ( $I_D$ – $V_G$ ) transfer curves for TIPS-PEN OFETs fabricated using source/drain electrodes composed of PSS-wrapped MWNTs and gold. The carrier mobility was calculated in the linear regime from the slope of a plot of the drain current versus the gate voltage. This was done by fitting the data to the following equation:  $I_D = (WC_i/L)\mu(V_G - V_{th})V_D$ , where  $I_D$  is the drain current,  $\mu$  is the carrier mobility,  $V_{th}$  is the threshold voltage, and  $V_D$  is the drain voltage (namely, –6 V). The measured capacitance,  $C_i$ , was 10 nF/cm<sup>2</sup>. The carrier mobility of the pentacene OFETs containing the PSS-wrapped MWNTs was  $0.043 \pm 0.006$  cm<sup>2</sup>/V s whereas that of the devices based on gold substrates was  $0.011 \pm 0.004$  cm<sup>2</sup>/V s. Ohmic contact behavior was observed for the devices based on the modified nanotubes (see Fig. 4b), which implies that the contact resistance between the PSS-wrapped MWNTs and TIPS-PEN is negligible.

The mobility of OFETs containing PSS-wrapped MWNT electrodes is about four times higher than that of gold-based devices, even though the work function of gold is slightly higher than that of the modified nanotubes. In previous reports, a large downward vacuum level shift was observed between pentacene and gold [19,20] due to the high induced density of interface states (IDIS) originated from the strong local orbital exchange and the potential correlation between the metal and the semiconductor

[19–21]. This large vacuum level shift also leads to a large hole-injection barrier between pentacene and gold, despite the high work function of gold. In contrast, the electrodes having an organic surface show a smaller vacuum level shift—or no shift at all—between the electrode and pentacene. This is because no strong local orbital exchange or potential correlation are expected on the organic surface [20,22,23]. From this viewpoint, a large downward vacuum level shift at the interface between TIPS-PEN and the metallic surface of gold leads to a large hole-injection barrier. In contrast, the organic surface of PSS causes a small vacuum level shift between the PSS-wrapped MWNT electrode and TIPS-PEN, thus leading to a smaller hole-injection barrier. Since a smaller hole-injection barrier implies a smaller contact resistance in the OFETs [23,24], we can assume that the higher mobility of the devices containing the PSS-wrapped MWNT electrodes comes from their lower contact resistance relative to that of the transistors containing gold electrodes.

In conclusion, we have fabricated PSS-wrapped MWNT electrodes exhibiting a high work function (of 4.83 eV), high conductivity (of  $2.0 \times 10^2$  S/cm), and good solubility in water. The good performance of TIPS-PEN OFETs fabricated using these electrodes as source/drain electrodes demonstrates that PSS-wrapped MWNTs are a competitive material for the fabrication of OFET electrodes.

## Acknowledgment

This research was supported by a grant (F0004010-2008-31) from Information Display R&D Center, one of the 21st Century Frontier R&D Program funded by the Ministry of Knowledge Economy of Korean government.

## References

- [1] R.A. Street, W.S. Wong, S.E. Ready, M.L. Chabinyc, A.C. Arias, S. Limb, A. Salleo, R. Lujan, *Mater. Today* 9 (2006) 32.
- [2] T. Sekitani, M. Takamiya, Y. Noguchi, S. Nakano, Y. Kato, T. Sakurai, T. Someya, *Nature Mater.* 6 (2007) 413.
- [3] J.E. Anthony, J.S. Brooks, D.L. Eaton, S.R. Parkin, *J. Am. Chem. Soc.* 123 (2001) 9482.
- [4] R.J. Kline, M.D. McGehee, E.N. Kadnikova, J. Liu, J.M.J. Frechet, *Adv. Mater.* 15 (2003) 1519.
- [5] I. McCulloch, M. Heeney, C. Bailey, K. Genevicius, I. Macdonald, M. Shkunov, D. Sparrowe, S. Tierney, R. Wagner, W. Zhang, M.L. Chabinyc, R.J. Kline, M.D. McGehee, M.F. Toney, *Nature Mater.* 5 (2006) 328.
- [6] J.A. Lim, J.H. Cho, Y.D. Park, D.H. Kim, M. Hwang, K. Cho, *Appl. Phys. Lett.* 88 (2006) 082102.
- [7] K.S. Lee, G.B. Banchet, F. Gao, Y.-L. Loo, *Appl. Phys. Lett.* 86 (2005) 074102.
- [8] T. Takahashi, T. Takenobu, J. Takeya, Y. Iwasa, *Appl. Phys. Lett.* 88 (2006) 033505.
- [9] W.R. Small, F. Masdarolomoor, G.G. Wallace, M. Panhuis, *J. Mater. Chem.* 17 (2007) 4359.
- [10] R.A. Hatton, A.J. Miller, S.R.P. Silva, *J. Mater. Chem.* 18 (2008) 1183.
- [11] P.M. Ajayan, T.W. Ebbesen, *Rep. Prog. Phys.* 60 (1997) 1025.
- [12] M.J. O'Connell, P. Boul, L.M. Ericson, C. Huffman, Y. Wang, E. Haroz, C. Kuper, J. Tour, K.D. Ausman, R.E. Smalley, *Chem. Phys. Lett.* 342 (2001) 265.
- [13] A. Liu, I. Honma, M. Ichihara, H. Zhou, *Nanotechnology* 17 (2006) 2845.
- [14] J.N. Barisci, M. Tahan, G.G. Wallace, S. Badaire, T. Vaugien, M. Mauger, P. Poulin, *Adv. Funct. Mater.* 14 (2004) 133.
- [15] K.S. Lee, T.J. Smith, K.C. Dickey, J.E. Yoo, K.J. Stevenson, Y.-L. Loo, *Adv. Funct. Mater.* 16 (2006) 2409.

- [16] S. Kim, D. Choi, D. Chung, C. Yang, J. Jang, S.-H. Park, C.E. Park, *Appl. Phys. Lett.* 93 (2008) 113306.
- [17] H. Ago, T. Kugler, F. Cacialli, W.R. Salaneck, M.S.P. Shaffer, A.H. Windle, R.H. Friend, *J. Phys. Chem. B* 103 (1999) 8116.
- [18] D.M. Alloway, M. Hogmann, D.L. Smith, N.E. Gruhn, A.L. Graham, R. Colorado Jr., V.H. Wysocki, T.R. Lee, P.A. Lee, N.R. Armstrong, *J. Phys. Chem. B* 107 (2003) 11690.
- [19] P.G. Schroeder, C.B. France, J.B. Park, B.A. Parkinson, *J. Appl. Phys.* 91 (2002) 3010.
- [20] K. Hong, J.W. Lee, S.Y. Yang, K. Shin, H. Jeon, S.H. Kim, C. Yang, C.E. Park, *Org. Electron.* 9 (2008) 21.
- [21] H. Vazquez, R. Oszwaldowski, P. Pou, J. Ortega, R. Perez, F. Flores, A. Kahn, *Europhys. Lett.* 65 (2004) 802.
- [22] A. Wan, J. Hwang, F. Amy, A. Kahn, *Org. Electron.* 6 (2005) 47.
- [23] K. Hong, S.Y. Yang, C. Yang, S.H. Kim, D. Choi, C.E. Park, *Org. Electron.* 9 (2008) 864.
- [24] P. Marmont, N. Battaglini, P. Lang, G. Horowitz, J. Hwang, A. Kahn, C. Amato, P. Calas, *Org. Electron.* 9 (2008) 419.



## Letter

# Novel organic materials that permanently increase conductivity upon thermal or photo treatment

Ruhai Tian, Zheng Shi, Yi Liao \*

Department of Chemistry, University of Central Florida, Orlando, FL 32816, USA

## ARTICLE INFO

## Article history:

Received 21 October 2008

Received in revised form 8 December 2008

Accepted 9 December 2008

Available online 24 December 2008

## PACS:

72.80.Le

## Keywords:

Organic conducting material

Thermo-responsive

Photo-responsive

Permanent conductivity increase

## ABSTRACT

In this work, we tested an approach towards novel organic materials that can permanently increase conductivity upon thermal or photo treatment, and potentially, change from insulator to conductor or semiconductor. Using dichlorodicyanoquinone (DDQ) doped thermo and photo responsive pentacene precursors as model systems, we found that conductivity of the thermal responsive material increased over 2 orders of magnitude to  $10^{-3}$ – $10^{-2}$  S/cm after thermal treatment, while that of a photo responsive material did not significantly increase after photo irradiation even though the composites are same. Based on the results of conductivity measurement, SEM, XRD, UV–Vis, and FT–IR, the phenomena are attributed to that the crystalline morphology of thermally generated pentacene/DDQ thin films favored charge transfer while the amorphous morphology of the photo generated material favored solid-state Diels–Alder reaction. The result implies that the mechanism of solid-state reaction can be altered by controlling morphology.

© 2008 Elsevier B.V. All rights reserved.

Current research on organic electronic materials focuses on organic semiconductors and conductors. Our group is working on a novel type of organic electronic material that can permanently increase conductivity upon photo or thermal treatment, and potentially, change from insulator to conductor or semiconductor. Such materials may be applied to improve the interface between insulator, semiconductor and conductor. More interestingly, they have potential to largely simplify the process of multilayer interconnection; and allow ink-free printing of microcircuit with high resolution.

Substantial conductivity increase after intense UV irradiation and multistep processing has been reported in early works aimed at photo patterning of conducting polymer [1–4]. We are developing a systematic approach that can control electric property in a wide range with mild photo and/or thermal process. The approach is based on

the fact that nonconjugated organic materials are insulating; conjugated polymers or oligomers are semiconducting; and effectively doped conjugated polymers or oligomers can be highly conducting in the presence of a suitable morphology. Thus, converting nonconjugated structure to conjugated, or activating an ineffective dopant, i.e. converting a precursor dopant that is not oxidizing or reducing enough for charge transfer to a dopant that can induce charge transfer efficiently, can largely increase conductivity.

Inspired by the previous works that utilized precursor chemistry to solve solubility problems associated with aromatic polymers and oligomers [5–12], we utilized retro-Diels–Alder chemistry for converting nonconjugated structure to conjugated in the presence of an effective dopant. This process can potentially convert an insulating material to a conducting material, and thus largely increase conductivity. While the idea is straightforward, the process is complicated since it involves solid-state reaction, morphology change, and consequent change of

\* Corresponding author.

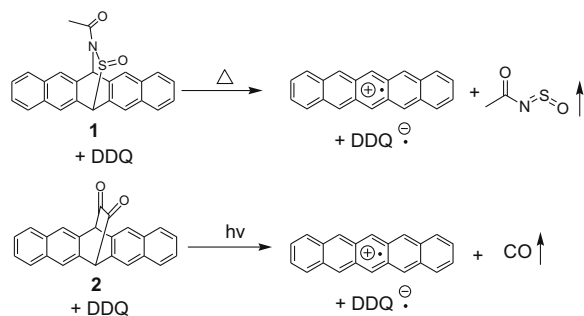
E-mail address: [yliao@mail.ucf.edu](mailto:yliao@mail.ucf.edu) (Y. Liao).

charge transfer and transport. Successful development of such materials requires understanding how factors including structures of polymers or oligomers, dopants, morphology and processing procedures affect solid-state reactions and charge transport. In this communication, we demonstrate a large conductivity increase using dichlorodicyanoquinone (DDQ) doped pentacene precursors as a model system. The factors that affect the conductivity change are carefully analyzed. In addition, we observed intriguing competition between charge transfer and solid-state reaction of pentacene and DDQ.

To demonstrate conductivity increase upon thermal and photo treatment, thermal responsive pentacene precursor **1** [9] and photo responsive pentacene precursor **2** [10] were doped by DDQ and spin cast into thin films. The idea is that **1** and **2** will be converted from nonconjugated structures to pentacene by thermal and photo treatment, respectively, followed by charge transfer between pentacene and DDQ, which will largely increase the conductivity. (Scheme 1)

Precursor **1** was developed by Afzali et al for solving the low solubility problem in preparing thin films of pentacene by solution process [9]. Thin films with charge mobility as high as  $0.1 \text{ cm}^2 \text{ V}^{-1} \text{ S}^{-1}$  were achieved after pentacene was generated from **1** via a retro-DA reaction at  $\sim 150^\circ\text{C}$ . It must be pointed out that, as described below, the conductivity of **1** is at least 2 orders of magnitude higher than the pentacene generated from it. Simply converting **1** to pentacene decreases conductivity though increases the charge mobility, which may be due to that ionic conductivity is predominant in low conductivity range. Precursor **2** can be converted to pentacene in solution or solid-state under UV-vis irradiation (Scheme 1) [10,13].

A solution of **1** and DDQ in  $\text{CH}_2\text{Cl}_2$  was spin cast to thin films (concentration:  $\sim 2\%$  total solid weight; spin rate: 1000 rpm; substrate: ITO or glass.) The molar ratio of DDQ/precursor was varied between 1:5 and 1:1. The conductivity was measured by a Keithley 2400 source meter using four-point technique and I–V scan. Thin films of **1** and DDQ showed a conductivity of  $10^{-6}$ – $10^{-5} \text{ S/cm}$  which was close to or slightly higher than that of the undoped **1** ( $2 \times 10^{-6} \text{ S/cm}$ ). Baking the film at  $150^\circ\text{C}$  under  $\text{N}_2$  induced the retro-DA reaction and changed the color of the film from light yellow to blue or greenish blue. The in-film retro-DA reaction was monitored by attenuated total



**Scheme 1.** Thermal and photo responsive composites based on DDQ doped pentacene.

reflection infrared (ATR-IR) and UV-vis spectroscopy. The aliphatic C–H stretch disappeared in IR after thermal treatment, which indicated that the retro-DA reaction is close to completion [9]. The change of UV-vis spectra between 350 nm and 900 nm is similar to that of the undoped **1** (Fig. 1a). No charge transfer band can be undoubtedly assigned in this range. However, the conductivity increased more than two orders of magnitude after heated for 15 min. The conductivity stayed in the same order of magnitude after a couple of days. The highest conductivity increase was  $\sim 570$  fold ( $3.6 \times 10^{-5} \text{ S/cm}$  to  $2.0 \times 10^{-2} \text{ S/cm}$ ) obtained from 1:3 DDQ/pentacene. The magnitude of conductivity change was reproducible with commercial DDQ and **1**. Additionally, a film of **1** without DDQ showed that a low conductivity of  $\sim 10^{-8}$ – $10^{-7} \text{ S/cm}$  after heated under the same condition, which is consistent with the fact that undoped pentacene has very low conductivity [14]; heating a mixture of **1** and  $\text{FeCl}_3$  and  $\text{NOSbF}_4$  [15] also substantially decreased conductivity, which confirmed that the conductivity increase was indeed caused by interaction between pentacene and DDQ.

Photoresponsive pentacene precursor **2** was synthesized according to a literature procedure [10]. Compound **2** was thermally stable. No decomposition was observed upon stationary heating at  $150^\circ\text{C}$ . Thin films of undoped **2** and DDQ doped **2** showed conductivity of  $10^{-6} \text{ S/cm}$ . UV-vis spectrum of **2** showed an absorption peak at 470 nm, while neither pentacene nor DDQ strongly absorbs at this wavelength. The 470 nm absorption is due to the diketone structure of the DA adduct **2**. Therefore we irradiated a thin film of DDQ doped **2** under nitrogen with a 472 nm LED bundle [16]. The 470 nm absorption peak disappeared after irradiation which indicated that conversion from **2** to pentacene was close to completion

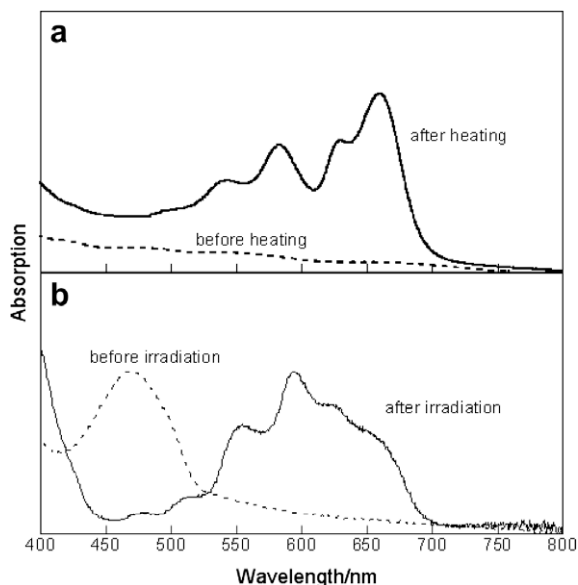


**Fig. 1.** (a) UV-vis spectra of DDQ doped **1** before and after thermal treatment. (b) UV-vis spectra of DDQ doped **2** before and after irradiated at 472 nm. Disappearance of the absorption at 470 nm after irradiation indicated that the precursor **2** had completely changed into pentacene.



[11] (Fig. 1b). While conductivity increase was observed as expected, the magnitude is much less than that of the thermal system. The conductivity only increased  $\sim 5$  fold in the best case.

The low conductivity increase of the photo generated pentacene/DDQ films may be attributed to three possible reasons: incomplete conversion from **1** to pentacene, inefficient charge transport due to undesirable morphology, and inefficient charge transfer between pentacene and DDQ due to undesirable molecular orientation. Prolonged irradiation did not increase (or decrease) conductivity which implies that the low conductivity increase was unlikely due to incomplete conversion. Scanning electron microscope (SEM) was applied to study the morphology of the thin films. After photo irradiation, bumps with diameter of  $\sim 300$  nm and average height of  $\sim 25$  nm appeared on the surface (Fig. 2). The height of the bump was measured by AFM. Elemental analysis of the bumping areas

and the adjacent areas by SEM did not show apparent difference, which indicated that the bumps are not aggregates of pure DDQ or pentacene. Since irradiation was at room temperature in nitrogen filled glove box, thermal mechanisms and air oxidation are also ruled out. Therefore, bumping must be due to release of CO during the retro-DA reaction (Scheme 1). Small CO molecules aggregated in the film before evaporated out, which caused the bumps. SEM of the thermal responsive films also showed morphology change after the retro-DA reaction. However, instead of bumps, crystalline domains appeared on the surface. (Fig. 2) This may be due to that the size of the N-sulfinyl dienophile released during the thermal reaction is much larger than CO, which makes them difficult to move and aggregate in the film. In addition, the thermal process provided energy for generated pentacenes to align themselves and fill the space left by the released dienophiles for reaching a low energy state stabilized by intermolecu-

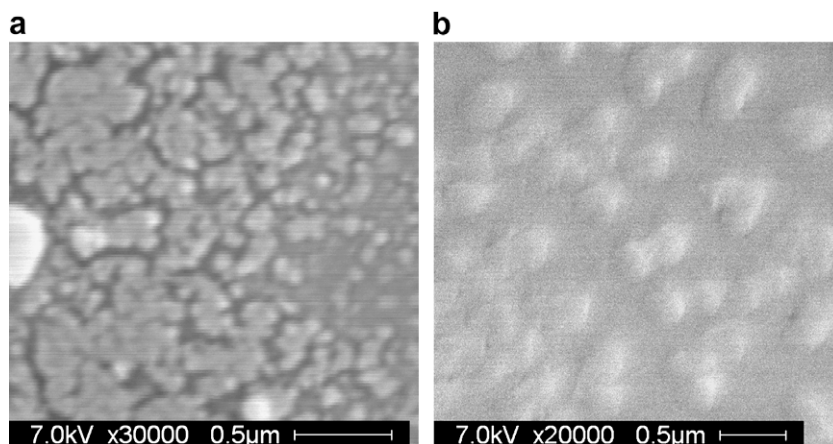


**Fig. 2.** SEM of thermal generated (a) and photo generated (b) pentacene/DDQ films. The films before thermal or photo treatment looked smooth and did not show any special feature (Supporting information Figures 3 and 4).

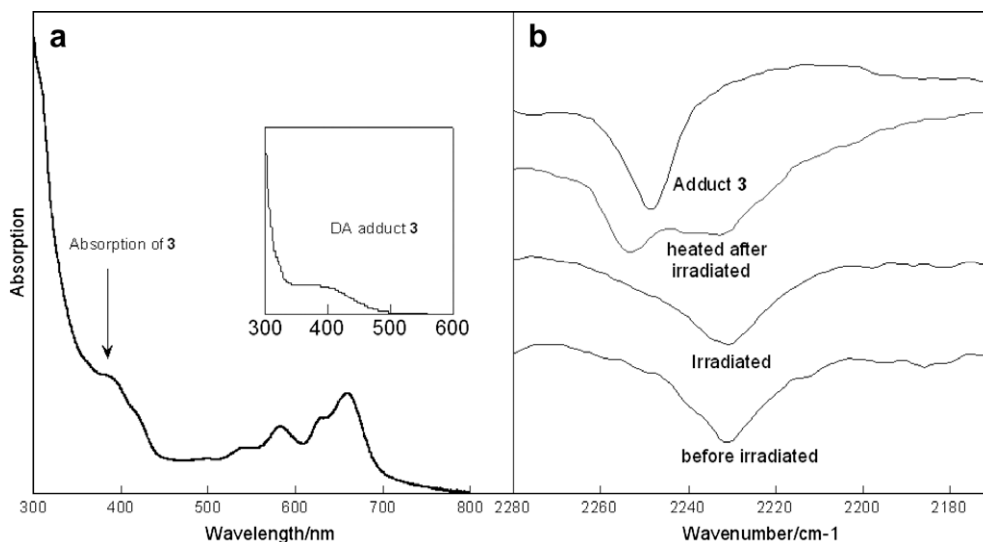
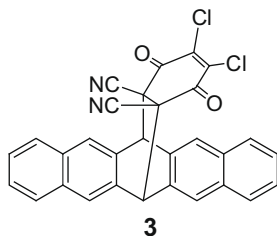


**Fig. 3.** UV-vis (a) and FTIR (b) of the photo generated pentacene/DDQ films after heated at 150 °C for 10 min. The spectra of the pure DA adduct **3** are also showed.

lar  $\pi$ – $\pi$  interactions. The difference in crystallinity was further proved by both X-ray diffraction (XRD) and UV–vis spectroscopy. Only the thermally treated thin films of **1** and DDQ showed the 001 peak of pentacene in XRD (Supporting information). Moreover, UV–vis indicated that pentacene generated from **2** by photo irradiation is disordered and amorphous. The coulomb interaction between a pentacene molecule and its surrounding is weak, which lead to low intensity of the Davydov doublet [17] (Fig. 1).



To improve the crystallinity of the photo generated films, a film of **2** and DDQ was heated at 150 °C for 10 min after photo irradiation. While the pentacene absorption in UV–vis became similar to that of the thermally generated films (Fig. 3) and SEM showed that the bumps became flat, no conductivity increase was observed. IR and UV–vis spectra showed that substantial amount of DDQ/pentacene DA adduct **3** was generated by the annealing process. (Fig. 3) This is an unexpected observation since the films of **1** and DDQ did not show notable absorption of **3** in UV–vis or IR after being heated at the same condition. Upon prolonged heating for over 1 h, only a small shoulder on the CN stretch peak of DDQ appeared in the IR, which may be due to the formation of **3** (Supporting information).

All the results can be attributed to that the morphology of DDQ and pentacene in the thermally generated films favored charge transfer interaction while that of the photo generated films favored solid-state Diels Alder reaction. Morphology includes both long-range alignment (crystallinity) and short-range relative molecular orientation between pentacene and DDQ. The precursor **1** and **2** interact differently with DDQ which may lead to different relative orientation between pentacene and DDQ after retro-DA reaction. While it is well known that molecular orientation is important for both bimolecular reaction and charge transfer, [18] the long-range alignment may also play an important role since it affects the energy levels of the donor and acceptor, and the subsequent charge separation [19]. Charge transfer will result in positively charged pentacene and negatively charged DDQ, which suppresses DA reaction since DA reaction normally requires electron-rich diene and electron-deficient dienophile. It is possible that the amorphous morphology of the photo-generated films cannot stabilize the charge transfer state as the crystalline morphology of the thermally generated ones and consequently favors the DA reaction.

In conclusion, we have demonstrated an approach towards organic materials that can permanently increase conductivity upon thermal or photo treatment. Over two

orders of magnitude conductivity increase to  $10^{-2}$  S/cm was achieved by thermally converting a DA adduct to pentacene in the presence of DDQ. The photo generated materials did not show large conductivity increase though the composition was the same as the thermally generated ones. This is attributed to undesirable morphology including long-range alignment and short-range molecular orientation. The observation that different morphologies can favor either charge transfer or solid-state reaction is both intriguing and important since it implies that the mechanism of a solid-state reaction can be altered by controlling the morphology. It is worth pointing out that two orders of magnitude conductivity increase is much less than the potential of the general approach described here. Future work will focus on further understanding the fundamentals by modeling the interactions between the precursors and dopants, measuring charge density and charge mobility, designing new oligomers and polymers as well as dopants, and testing processing conditions for desirable morphology.

## Appendix A. Supplementary data

SEM of the thin films before thermal and photo treatment; XRD of a pentacene/DDQ film generated from thermal treatment; FTIR of thermally generated pentacene/DDQ. Supplementary data associated with this article can be found, in the online version, at doi:10.1016/j.orgel.2008.12.003.

## References

- [1] S. Holdcroft, *Adv. Mater.* 13 (2001) 1753.
- [2] L. Dai, H.J. Griesser, X. Hong, A.W.H. Mau, T.H. Spurling, Y. Yang, J.W. White, *Macromolecules* 29 (1996) 282.
- [3] R. Baumann, J. Bargon, *Appl. Surf. Sci.* 106 (1996) 287.
- [4] B.M. Novak, E. Hagen, A. Viswanathan, L. Magde, *Polym. Prepr.* 31 (1990) 482.
- [5] J.H. Edwards, W.J. Feast, D.C. Bott, *Polymer* 25 (1984) 395.
- [6] C.B. Gorman, E.J. Ginsburg, R.H. Grubbs, *J. Am. Chem. Soc.* 115 (1993) 1397.
- [7] R.A. Wessling, *J. Polym. Sci., Polym. Symp.* 72 (1985) 55; R.A. Wessling, R.G. Zimmerman, US3532643 (1970).
- [8] L. Yu, L.R. Dalton, *Macromolecules* 23 (1990) 3439.
- [9] A. Afzali, C.D. Dimitrakopoulos, T.L. Breen, *J. Am. Chem. Soc.* 124 (2002) 8812; A. Afzali, C.D. Dimitrakopoulos, T.O. Graham, *Adv. Mater.* 15 (2003) 2066; A. Afzali, T.L. Breen, C.D. Dimitrakopoulos, US6963080 (2005).
- [10] H. Yamada, Y. Yamashita, M. Kikuchi, H. Watanabe, T. Okujima, H. Uno, T. Ogawa, K. Ohara, N. Ono, *Chem. Eur. J.* 11 (2005) 6212.
- [11] P. Hodge, G.A. Power, M.A. Rabjohns, *Chem. Commun.* 1 (1997) 73.
- [12] P.T. Herwig, K. Mullen, *Adv. Mater.* 11 (1999) 480.
- [13] R. Mondal, A.N. Okhrimenko, B.K. Shah, D.C. Neckers, *J. Phys. Chem. B* 112 (2008) 11.
- [14] P. Parisse, M. Passacantando, S. Picozzi, L. Ottaviano, *Organic Electron.* 7 (2006) 403–409.
- [15] K.-Y. Jen, G.G. Miller, R.L. Elsenbaumer, *J. Chem. Soc., Chem. Commun.* 17 (1986) 1346–1347.
- [16] The LED bundle was fabricated by parallel connecting 10 blue LED bulbs [472 nm, 4600 mcd] bought from Super Bright LEDs Inc. The diameter of the bundle was ~2 cm.
- [17] O. Ostroverkhova, S. Shcherbina, D.G. Cooke, R.F. Egerton, F.A. Hegmann, *J. Appl. Phys.* 98 (2005) 033701; K.O. Lee, T.T. Gan, *Chem. Phys. Lett.* 51 (1977) 120.
- [18] R.A. Marcus, *J. Chem. Phys.* 24 (1956) 966.
- [19] M.A. Fox, *Top. Curr. Chem.* 159 (1991) 67.



## Letter

## Improved device performances in polymer light-emitting diodes using a stamp transfer printing process

Chul Woong Joo, Soon Ok Jeon, Kyoung Soo Yook, Jun Yeob Lee \*

Department of Polymer Science and Engineering, Dankook University, Jukjeon-dong, Suji-gu, Yongin, Gyeonggi 448-701, Republic of Korea

## ARTICLE INFO

## Article history:

Received 18 October 2008

Received in revised form 25 November 2008

Accepted 17 December 2008

Available online 27 December 2008

## PACS:

85.60.jb

## Keywords:

Stamp transfer printing

Lifetime

Polymer light-emitting diodes

## ABSTRACT

The device performances of spin-coated and stamp transfer printed devices were compared. There was little difference of morphology between the spin-coated and stamp transfer printed devices. However, the stamp transfer printing process was better than the spin-coating process in terms of current density, light-emitting efficiency and lifetime. In particular, the lifetime of the stamp transfer printed device was doubled compared with that of the spin-coated device.

© 2008 Elsevier B.V. All rights reserved.

Polymer light-emitting diodes (PLEDs) have advantages over small molecule based organic light-emitting diodes (OLEDs) such as an easy fabrication process, less material consumption and scalability to large size. In particular, the PLEDs is superior to small molecule OLEDs for large size applications because large size PLEDs can be easily fabricated by a solution coating process.

Spin-coating and ink-jet printing has been typically used as film-forming methods in PLEDs [1]. The spin-coating is a simple method to form a thin polymer film and the ink-jet printing has been used as a color patterning method of PLEDs [1–3]. Other than the two methods, the laser induced thermal imaging has also been used in PLEDs [4,5]. A light-emitting polymer film spin-coated on a donor film was transferred from the donor film to the substrate with a hole transport layer by an excimer laser irradiation. The pattern transfer process depended on the interfacial adhesion between the light-emitting polymer and the hole transport layer. Even though the efficiency was not de-

graded by the laser transfer process, it is not good for the lifetime of the device. A stamp transfer printing method has also been developed as a film-forming method of polymers [6–8]. A polymer pattern could be effectively transferred by the stamp transfer printing method even though detailed device performances of the stamp transfer printed device were not reported.

In this work, the device performances of the stamp transfer printed PLEDs were compared with those of the spin-coated PLEDs. The extension of lifetime by the stamp transfer printing process was demonstrated in this work.

A device structure of indium tin oxide (ITO, 150 nm)/polyethylene-3,4-dioxythiophene:polystyrenesulfonate (PEDOT:PSS, 100 nm)/yellow emitting layer (30 nm)/LiF/Al was used to study the effect of coating process on device performances of PLEDs. Polyphenylenevinylene based super yellow polymer from Merck was a yellow emitting material. The spin-coating of the yellow polymer was carried out from 0.3 wt% toluene solution, while the stamp transfer printing of yellow polymers was carried out by spin-coating of the 0.3 wt% yellow polymer solution on Si substrate and a subsequent transfer printing of yellow

\* Corresponding author. Tel./fax: +82 31 8005 3585.

E-mail address: [leej17@dankook.ac.kr](mailto:leej17@dankook.ac.kr) (J.Y. Lee).

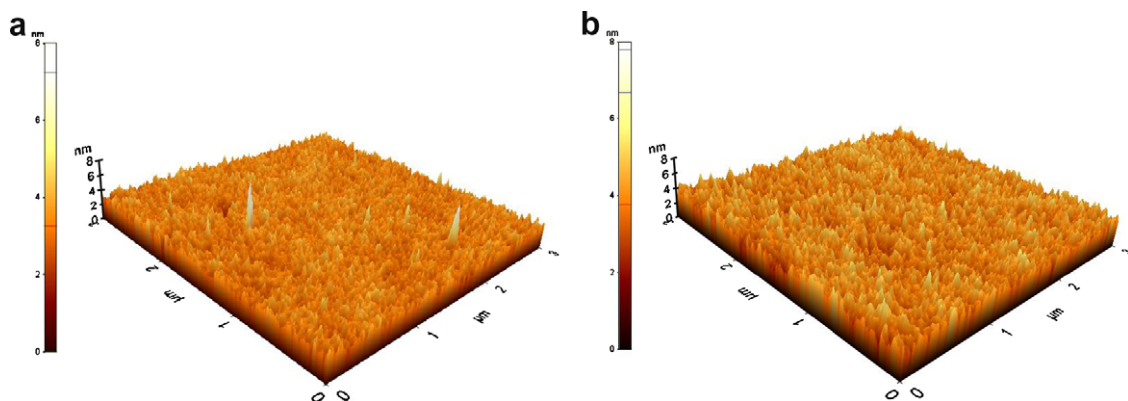


Fig. 1. Atomic force microscopic images of spin-coated and stamp transferred yellow polymer films. (a) Spin-coated film, (b) stamp transferred film.

polymer from the Si substrate to an ITO substrate using polydimethylsiloxane (PDMS) stamp. The PDMS stamp was fabricated by curing Sylgard<sup>®</sup> 184 from Dow Corning Co. at 95 °C for 2 h. The yellow polymer film was separated from the Si substrate by contacting the cured PDMS stamp with the yellow polymer coated Si substrate at room temperature. Then, the yellow polymer was transferred from the PDMS stamp to the PEDOT:PSS coated substrate by pressing the PDMS stamp on the substrate at 120 °C for 10 s. Hole only devices of spin-coated and stamp transfer printed yellow devices were fabricated to study the effect of film-forming process on the hole injection of yellow devices.

Morphology of spin-coated and stamp transfer printed yellow polymer films was analyzed with atomic force microscope and a non-contact method was used to get images from the films. Current density-voltage-luminance characteristics of the devices were obtained by Keithley 2400 source measurement unit and a CS 1000 spectrophotometer.

The transfer of the polymer film was carried out from Si substrate using a PDMS stamp. The use of Si substrate for the film transfer is advantageous because the interfacial adhesion between Si and polymers is poor, leading to easy detachment of polymer film. In addition, a smooth polymer film with a low surface roughness can be coated and transferred to the substrate. The temperature during the transfer process was critical to the film transfer and the film transfer was not perfect below 100 °C and it was optimized at 120 °C.

The morphology of polymer films is critical to the device performances and the surface morphology of a transferred yellow film was analyzed with an atomic force microscope to compare the surface roughness of spin-coated and stamp transferred films (Fig. 1). Mean surface roughness of spin-coated film was 0.4 nm with a peak to valley value of 9 nm, while the transferred film showed a mean surface roughness of 0.5 nm and a peak to valley value of 6 nm. There was little difference of the mean surface roughness between spin-coated and stamp transferred films and they showed similar morphology even though some spikes were observed in spin-coated films. The transfer printed polymer film was transferred from Si substrate which has a smooth surface, resulting in the low surface

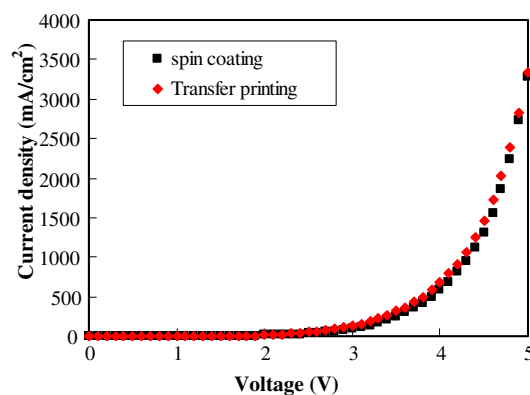
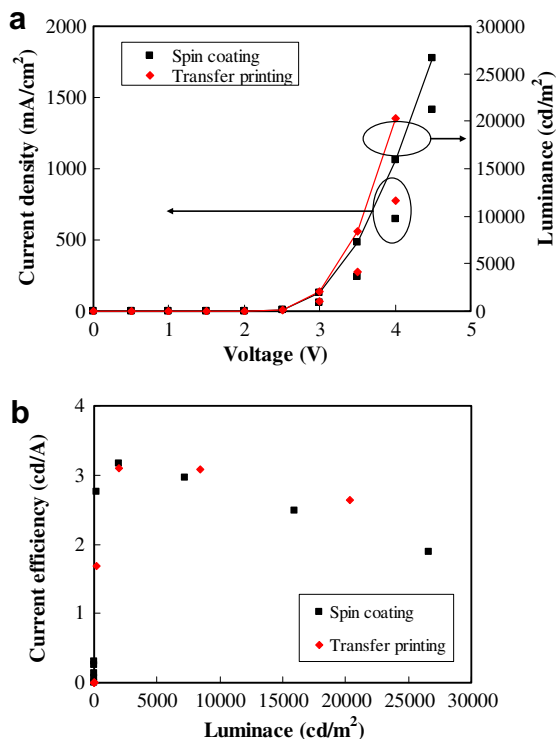


Fig. 2. Current density-voltage curves of hole only devices of spin-coated and stamp transfer printed yellow polymers.

roughness. This indicates that the film morphology of spin-coated polymer film is not affected by the stamp transfer printing process. A smooth surface film morphology was maintained during processing. Therefore, it can be expected that device performances may not be degraded by the stamp transfer process.

To study the effect of the stamp transfer process on device performances, the device performances of hole only devices of the yellow polymer fabricated by a spin-coating process and the stamp transfer process were compared. Fig. 2 shows current density-voltage curves of the hole only devices of the yellow polymer. The current density of the yellow device fabricated by the stamp transfer process was not decreased compared with that of the spin-coated devices. The current density was rather increased by 20%. The small increase of current density in the transfer printed device may be due to intimate interface formation between PEDOT:PSS and yellow polymer during transfer printing process at 120 °C. The interfacial contact can be improved because of pressure and heat applied during the transfer printing process [5]. Considering the similar film morphology of spin-coated and transfer printed films, the high current density of transfer printed films is due to improved hole injection rather than efficient electron injection. The interface between PEDOT:PSS and the



**Fig. 3.** Current density-voltage-luminance curves of spin-coated and stamp transfer printed yellow devices. (a) Current density-voltage-luminance, (b) current efficiency-luminance.

yellow polymer may be influenced by the film-forming process and the hole injection was different [9].

Fig. 3 compares device performances of yellow polymer devices prepared by the spin-coating process and the stamp transfer printing process. The stamp transfer printing process was better than the spin-coating process in terms of current density as expected from the hole only device data. Hole injection was efficient in the stamp transfer printed device, resulting in high current density in the stamp transfer printed device. Luminance was also high in the stamp transfer printed device due to high current density.

Current efficiency was also improved in the stamp transfer printed device. Although maximum current efficiency was similar in the two devices prepared by the different process, efficiency roll-off was serious in the spin-coated device, resulting in a high efficiency at high luminance in the stamp transfer printed device. The high efficiency of the stamp transfer printed device may be due to good interfacial contact between PEDOT:PSS and the yellow polymer. In our previous work about the device performances of laser transferred PLEDs, the use of high energy laser irradiation increased the current efficiency of PLEDs. At high laser dose, the temperature was high and additional pressure by laser contributed to the high efficiency. Similarly, the pressure and heat applied during the transfer process of polymers might enhanced the interfacial contact between the transferred polymer and the hole transport layer.

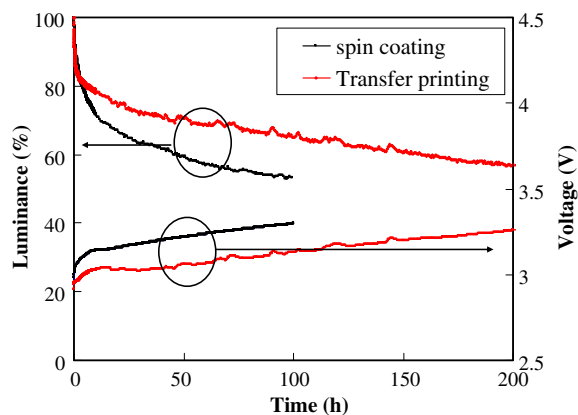


**Fig. 4.** Lifetime curves of spin-coated and stamp transfer printed yellow devices.

The lifetime of the stamp transfer printed and spin-coated devices was also compared and it is shown in Fig. 4. The lifetime was measured at a constant current density of 40 mA/cm<sup>2</sup>. The lifetime of the stamp transfer printed device was much better than that of the spin-coated device. The lifetime may depend on the interface considering the similar surface roughness and the similar efficiency at the lifetime test condition. Intimate interface formation by the stamp transfer process may be responsible for the improved lifetime of the stamp transfer printed device. The low voltage rise during lifetime measurement supports this explanation. The voltage rise typically depends on the internal resistance increase during driving which is originated from the interface [10]. Therefore, the low voltage rise during measurements implies that the increased lifetime of the stamp transfer printed device is due to good interfacial contact between PEDOT:PSS and the yellow polymer.

To clarify the origin of the improved lifetime in the stamp transferred device, the lifetime of the spin-coated device with and without stamp pressing was compared. The lifetime data of the two devices are shown in Fig. 5. The lifetime of the spin-coated device was almost doubled after pressing stamp on the spin-coated yellow film. This

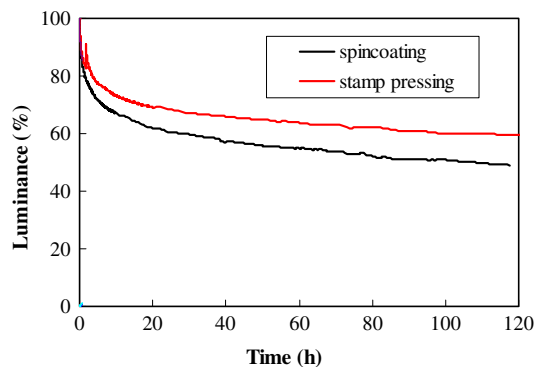


**Fig. 5.** Lifetime curves of spin-coated devices with and without stamp pressing.

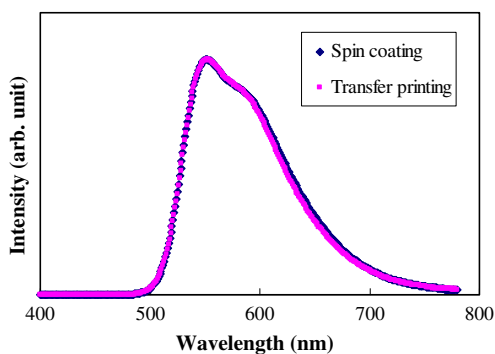


**Fig. 6.** Electroluminescence spectra of spin-coated and stamp transfer printed devices.

indicates that the stamp press process at 120 °C is responsible for the enhanced lifetime in the stamp transfer printed device. Improved interfacial contact by the stamp press process may contribute to the improved lifetime. Therefore, it can be concluded that the stamp transfer printing process is better than the spin-coating process in terms of device performances.

EL spectra of the spin-coated and the stamp transfer printed devices are shown in Fig. 6. The two devices showed the same spectra, indicating that the film coating process did not greatly affect the emission behavior of the yellow devices.

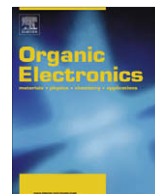
In conclusion, the device performances of the stamp transfer printed device were better than that of the spin-coated device. In particular, the lifetime of yellow devices were greatly improved by using the stamp transfer printing process. Therefore, it can be expected that the stamp transfer printing method can be effectively used as a film coating method of polymers in organic electronic devices.

### Acknowledgement

This work was supported by the Korea Research Foundation Grant funded by the Korean Government (MOEHRD, Basic Research Promotion Fund) (KRF-2007-331-D00124).

### References

- [1] T.R. Hebner, C.C. Wu, D. Marcy, M.H. Lu, J.C. Sturm, *Appl. Phys. Lett.* 72 (1998) 1998.
- [2] J. Bharathan, Y. Yang, *Appl. Phys. Lett.* 72 (1998) 2660.
- [3] S.C. Chang, J. Liu, J. Bharathan, Y. Yang, J. Onohara, J. Kido, *Adv. Mater.* 11 (1999) 734.
- [4] M.C. Suh, B.D. Chin, M.H. Kim, T.M. Kang, S.T. Lee, *Adv. Mater.* 15 (2003) 1254.
- [5] J.Y. Lee, S.T. Lee, *Adv. Mater.* 16 (2004) 51.
- [6] Y.N. Xia, G.M. Whitesides, *Annu. Rev. Mater. Sci.* 28 (1998) 153.
- [7] B.D. Gates, Q.B. Xu, M. Stewart, D. Ryan, C.G. Willson, G.M. Whitesides, *Chem. Rev.* 105 (2005) 1171.
- [8] L. Chen, P. Degenaar, D.D.C. Bradley, *Adv. Mater.* 20 (2008) 1679.
- [9] J.Y. Lee, *J. Ind. Eng. Chem.* 14 (2008) 792.
- [10] T. Chu, Y. Lee, O.K. Song, *Appl. Phys. Lett.* 91 (2007) 223509.



## Flexible, plastic transistor-based chemical sensors

Mark E. Roberts, Stefan C.B. Mannsfeld, Randall M. Stoltenberg, Zhenan Bao\*

Department of Chemical Engineering, Stanford University, Stauffer III, 381 North-South Mall, Stanford, CA 94305-5025, USA

### ARTICLE INFO

#### Article history:

Received 19 September 2008

Received in revised form 2 December 2008

Accepted 2 December 2008

Available online 11 December 2008

#### PACS:

70

#### Keywords:

Organic transistor

Sensor

Flexible

Patterning

### ABSTRACT

Flexible, plastic chemical sensors were fabricated using a thin polymer gate dielectric layer and polymer electrodes patterned via selective wetting directly on the surface of the organic semiconductor film. Low-voltage transistors based on DDFTF with PEDOT:PSS electrodes had a mobility as high as  $0.05 \text{ cm}^2/\text{Vs}$  with an on-off ratio of  $1.2 \times 10^4$  on ITO/PET substrates. These devices demonstrated stable operation in water with sensor characteristics similar to those reported on rigid silicon substrates, with sub-ppm detection for cysteine and 2,4,6-trinitrobenzene (TNB).

© 2008 Elsevier B.V. All rights reserved.

Recent progress in organic materials has given a great deal of promise to plastic electronics, especially for organic light-emitting diodes (OLEDs) [1] and radio-frequency identification cards (RFIDs) [2–4]. The rapid progress of the field has been, in part, due to improvements in fabrication processes and new material design, with noticeable improvements in electronic properties for the semiconducting [5–7], conducting [8] and insulating [9–12] components. Recently, organic field-effect transistors (OTFTs) have gained considerable attention with the demonstration of potentially scalable patterning processes [13–18] and improved semiconductor and gate insulator performance, laying the groundwork for low-power circuits [11] and devices [19].

Due to the versatility of chemical synthesis, organic materials have a niche application in chemical sensors based on OTFTs [20], in which the semiconductor functions simultaneously as the active transport layer and the sensing component. Functional derivatives of organic semiconductors have already demonstrated utility in chemical and biological sensors based upon the ability to impart specific

functionality to direct the interaction with target analytes [21,22]. However, most devices used a rigid, planar substrates and required high operating voltages. The development of low-cost, disposable sensors for environmental monitoring, health diagnostics or detection of chemical warfare agents requires incorporation of simple processing on inexpensive, large area substrates. The ability to detect chemical species in water adds another degree of versatility to OTFT sensors, allowing for in situ measurements with these applications for non-volatile species. For example, detection of amino acid concentrations in situ could have a profound impact on disease detection and prevention [23], while the ability to monitor munitions disposal is important for maintaining safe water supplies [24]. In this report, we combine the fundamental advantages of organic materials for the demonstration of flexible, transparent chemical sensors based on plastic thin-film transistors in aqueous solutions.

Our OTFT sensors are fabricated using organic and polymeric materials with simple processing on a conductive indium tin oxide (ITO) film on polyethylene terephthalate (PET) substrates. These devices were operable at low bias in vapor and liquid solutions enabled by the use of a

\* Corresponding author. Tel.: +1 650 723 2419.

E-mail address: [zbao@stanford.edu](mailto:zbao@stanford.edu) (Z. Bao).

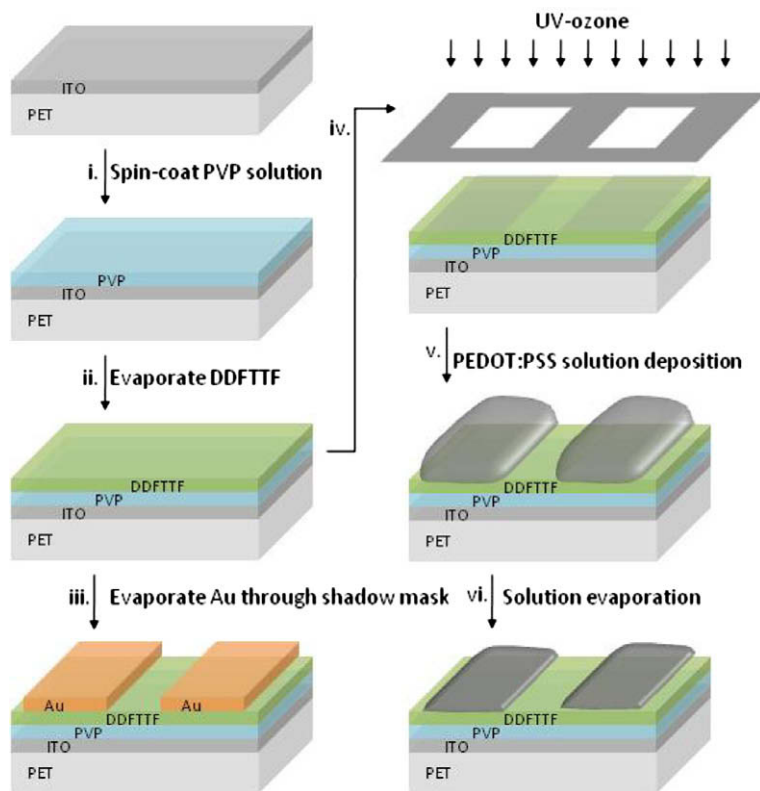


**Fig. 1.** Fabrication scheme for flexible sensors with gold and PEDOT:PSS electrodes. (i) A 35 nm PVP–HDA film is deposited via spin-coating on ITO/PET. (ii) 30 nm DDFTTF is thermally evaporated on the PVP–HDA films. (iii) Gold electrodes are deposited through a shadow mask. (iv) DDFTTF surface is modified with UV-ozone through a shadow mask. (v) PEDOT:PSS solution is selectively patterned on the UV-ozone treated areas. (vi) The solvent is removed in vacuum leaving conductive polymer electrodes.

cross-linked gate dielectric layer [9]. Additionally, we show the chemical sensing performance of these devices is comparable to that of OTFTs fabricated on rigid, planar substrates, with detection of cysteine and trinitrobenzene (TNB) down to 100 parts per billion.

The fabrication scheme for the flexible OTFTs is shown in Fig. 1. A previously reported polymer dielectric film, [9] poly(4-vinylphenol) (PVP) cross-linked with 4,4'-(hexafluoroisopropylidene)diphthalic anhydride (HDA), was deposited via spin-coating directly on the ITO surface at 3000 rpm and cured at 100 °C for 2 h, resulting in a film with a thickness of 35 nm and a capacitance of 115 nF/cm<sup>2</sup>. Fig. 2B shows the atomic force micrograph (AFM) of the PVP–HDA surface with a surface roughness of 2.6 nm, moderately rougher than that reported on a planar surface. DDFTTF, an organic semiconductor demonstrating long-term stability in water, was thermally deposited on the cross-linked polymer film at a rate of 0.2–0.3 Å/s and a substrate temperature of 105 °C to a thickness of 30 nm. Top-contact electrodes were deposited on the semiconductor surface using two methods. Gold (40 nm) was deposited via thermal evaporation (1.0 Å/s) and PEDOT:PSS was deposited via selective wetting.

The surface energy of the organic semiconductor surface can be considerably modified as shown by a decrease in water contact angle (First Ten Angstroms FTA200 equipped with a CCD camera) upon UV-ozone exposure.

Without any treatment, the DDFTTF surface is very hydrophobic (112°), due to the vertically-aligned, densely-packed alkyl chains. After treating the organic semiconductor surface with UV-ozone for 12 min, the water contact angle decreases substantially from 112° to 23° (shown in Supporting information, figure S1), due to the complete removal of the alkyl chains. Using X-ray photoelectron spectroscopy (SSI S-Probe Monochromatized XPS Spectrometer, Al(kα) radiation (1486 eV)), we showed that a dodecyl silane monolayer is completely removed from a silicon oxide surface after 12 min (Supporting information figure S2).

The unique contrast in surface energy is the premise for the deposition of poly(3,4-ethylenedioxythiophene) poly(styrenesulfonate) (PEDOT:PSS) [25] via selective wetting. Immediately after UV-ozone exposure, the substrate with a patterned DDFTTF surface (with features varying from 50 μm to 400 μm) is briefly held in a solution vortex [26] of PEDOT:PSS (Baytron P, 1.2–1.4% aqueous solution, Bayer Corp.) diluted with water and ethylene glycol (EG) at a ratio of 47:47:6, 90:0:10, or 50:50:0 (Baytron P:water:EG). As the substrate is withdrawn from the solution, the contrast in surface energy results in the deposition of PEDOT:PSS solution on the regions previously exposed to UV-ozone. The substrates are then placed on a hot plate at 90 °C for 1 h to dry the film. The addition of ethylene glycol is known to lead to a significant increase



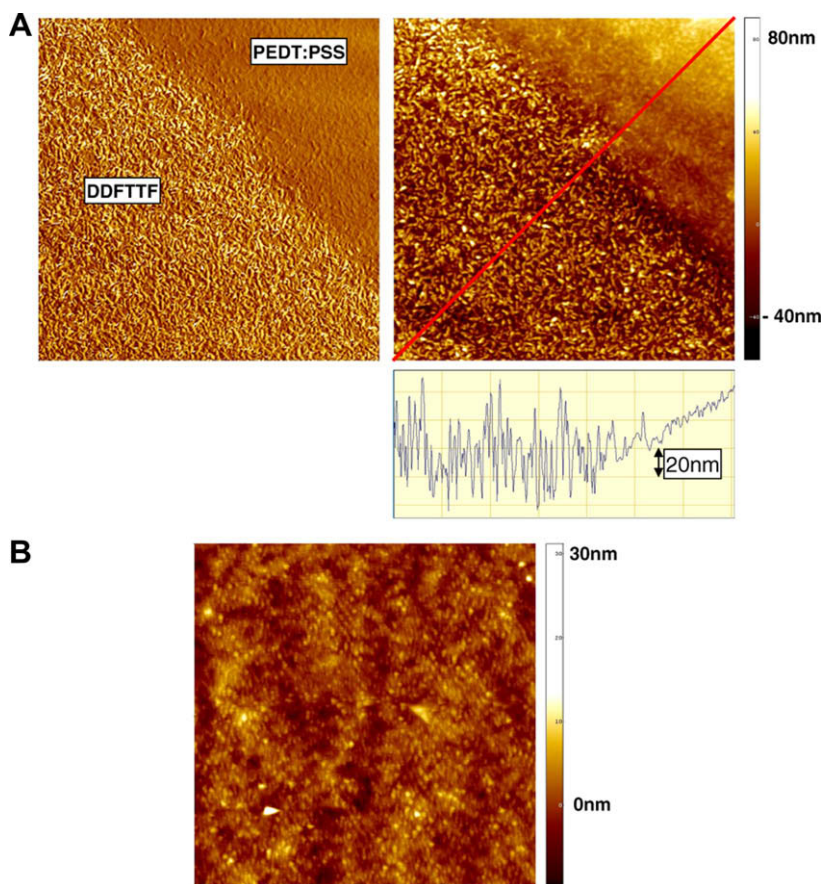


**Fig. 2.** (A) AFM images ( $10 \times 10 \mu\text{m}^2$ , phase left, height right) of the top-contact PEDOT:PSS electrode interface with DDFTTF. The line profile (red line in height image) shows good conformity of the PEDOT:PSS electrodes that are actually smoother than the top surface of the DDFTTF film. (B) AFM ( $10 \times 10 \mu\text{m}^2$ , height) of the PVP-HDA surface on an ITO/PET substrate.

in the conductivity of PEDOT:PSS films [27]. We found that ethylene glycol can either be directly added to the PEDOT:PSS formulation as described above or the sample can be subsequently treated by dipping it into ethylene glycol. In the latter case, the significant surface energy contrast between DDFTTF and the already deposited PEDOT:PSS electrodes leads to an exclusive wetting of the ethylene glycol on the PEDOT:PSS electrodes (Supporting information, figure S4). Both treatments resulted in a reduction of the surface resistivity of the PEDOT:PSS electrodes by several orders of magnitude (compared to untreated PEDOT:PSS electrodes) to values as low as  $20 \Omega/\text{sq}$ .

Atomic force micrographs (AFM) (Digital Instruments Nanoscope IV operated in tapping mode ( $\sim 350$  kHz frequency, Si tip)) images of the PEDOT:PSS electrodes on the DDFTTF surface are shown in Fig. 2A. The PEDOT:PSS makes a good, conformal contact with the surface of the DDFTTF film (see line profile, red line in height image), partially filling the pores on the top surface of the DDFTTF film. The resultant PEDOT:PSS electrode surface is therefore significantly smoother than the top surface of the DDFTTF film.

Aside from the top-contact gold electrodes, the resultant devices shown in Fig. 3 are both flexible and transparent, highlighting the advantageous properties of organic

materials. Fig. 3C and D show optical micrographs of PEDOT:PSS electrodes patterned on the semiconductor surface. While the DDFTTF surface was patterned with UV-ozone using a shadow mask with channel lengths ( $L$ ) of  $50 \mu\text{m}$  and  $100 \mu\text{m}$ , and respective channel widths ( $W$ ) of  $1 \text{ mm}$  and  $2 \text{ mm}$  for a  $W/L$  ratio of 20, the final electrodes had a  $W/L$  ratio ranging between 4 and 6 for  $L = 50$  and  $100 \mu\text{m}$ . As the solvent (water and ethylene glycol) evaporated, the polymer in solution was drawn to the center leaving slight remnants along the periphery of the UV-ozone treated regions while maintaining the defined  $L$ , shown by the light extensions of the electrodes in the images. The lighter regions of the electrodes, however, were not conductive. The feature size can potentially be reduced by stamping hydrophobic masks [28], for example, using a PDMS elastomeric template for dimensions down to  $10 \mu\text{m}$  [29].

5,5'-Bis-(7-dodecyl-9H-fluoren-2-yl)-2,2'-bithiophene, DDFTTF, was chosen for the semiconductor layer based on its proven stability in ambient and water [9], thin-film transistor characteristics, and long alkyl side chains that promote molecular packing and water stability. Previously, we showed that thin evaporated films of DDFTTF grow perpendicular to the substrate with highly two-dimensional films promoted by the interactions between the alkyl side

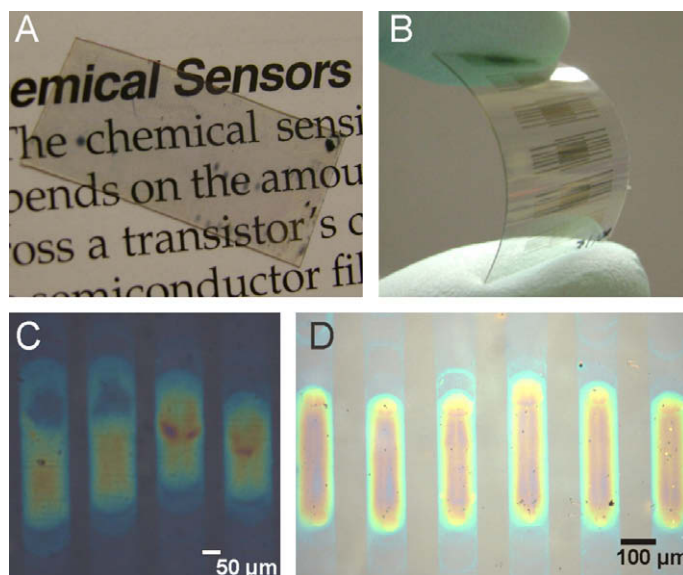


**Fig. 3.** Digital photograph of an OTFT with PEDOT:PSS electrodes on black and white text (A) and a flexed OTFT with gold electrodes (B); optical micrographs of OTFTs with PEDOT:PSS electrodes with 50  $\mu\text{m}$  (C) and 100  $\mu\text{m}$  (D) channels. Panel C shows the device on a dark surface while D shows the device on a white surface, illustrating the transparency. Note that the electrodes are invisible when the light is focused on the substrate.

chains [30–32]. Additionally, it is well known that the charge transport occurs within the first 5 nm (in proximity to the dielectric) [33], therefore, the gentle UV-ozone surface modification of the film should not affect the transport properties, as shown in the following section.

OTFTs with top-contact gold and PEDOT:PSS were electrically characterized in ambient and water to determine their suitability for sensing in water environments. By incorporating a thin, cross-linked polymer gate dielectric, we were able to operate at gate and source-drain biases below 1 V. The OTFTs fabricated with gold electrodes ( $W/L = 20$ ) on DDFTF showed a mobility of  $0.06 \text{ cm}^2/\text{Vs}$  with an on-off ratio of  $4 \times 10^3$ . The rough ITO surface, and correspondingly rough dielectric surface, lead to the decreased electrical performance compared to using rigid, planar substrates. OTFTs fabricated with PEDOT:PSS electrodes ( $W/L = 4\text{--}6$ ) performed comparable to those with gold electrodes with a mobility of  $0.05 \text{ cm}^2/\text{Vs}$  with an on-off ratio of  $1.2 \times 10^4$ . Although the performance of the two systems was quite similar, the OTFTs with PEDOT electrodes had a lower on-current due to the shorter electrode width from the solution deposition process. A slight increase in leakage current was observed for OTFTs on ITO/PET (3 nA at 1 V) as compared to devices on planar silicon substrates (0.2 nA at 1 V), both of which are much less than the source-drain current. The influence of bending on the OTFT performance for devices fabrication with small molecule organic semiconductors and polymer dielectrics has been reported previously [9,34,35], and we expect similar mechanical properties for these sensors.

Electrical characterization in water is performed by placing a droplet of deionized water across the entire electrode (channel) region. It was critical to reduce the source-drain bias ( $V_{\text{DS}}$ ) to  $-0.6 \text{ V}$  in order to limit the ionic conduction through water. The transfer characteristics of the OTFT

with gold electrodes are shown in Fig. 4A in ambient (black) and water (grey). The influence of water on the electronic properties is similar to that reported in a previous report, with a slight increase in the mobility ( $0.12 \text{ cm}^2/\text{Vs}$ ), positive threshold shift, and a reduction in the on-off ratio due to the finite ionic current through water. The output characteristics under water are shown in Fig. 4D. As mentioned above, a slight leakage current is observed as a result of using a thin insulating layer on a rough electrode surface. Similar plots for the OTFT with PEDOT:PSS electrodes are shown in Fig. 4C and D. Interestingly, only a small change in transfer characteristics is observed when exposing these devices to water. Other than an increase in the off-current, as previously discussed, and a marginal increase in mobility, the characteristics are nearly identical. This is most likely due to the fact that the semiconductor was previously exposed to water during the PEDOT:PSS deposition process.

We demonstrated chemical sensing by adding a small volume of analyte solution to a droplet of water spanning the source and drain electrodes. Based on the sensitivity to various analytes in a previous report, we investigated the influence of cysteine, trinitrobenzene (TNB), and pH on the OTFT performance. In the sensing trials, the source-drain and gate electrodes are continuously biased at  $-0.6 \text{ V}$  (in the saturation regime), and a droplet of analyte solution is added after current stabilized (approx. 30–60 s). The relative drain current change,  $\Delta I_{\text{DS}} = I_{\text{DS}}/I_{\text{DS}-0}$  ( $I_{\text{DS}-0}$  is the drain current baseline before the analyte addition) is plotted versus time for each analyte system. We observed similar  $\Delta I_{\text{DS}}$  responses on the flexible ITO/PET substrates as we previously observed on silicon for cysteine solutions and pH [9], which was performed on OTFTs with PEDOT:PSS electrodes.

Top-contact OTFTs with PEDOT:PSS electrodes were covered in water (5  $\mu\text{l}$ ) and biased according to the condi-

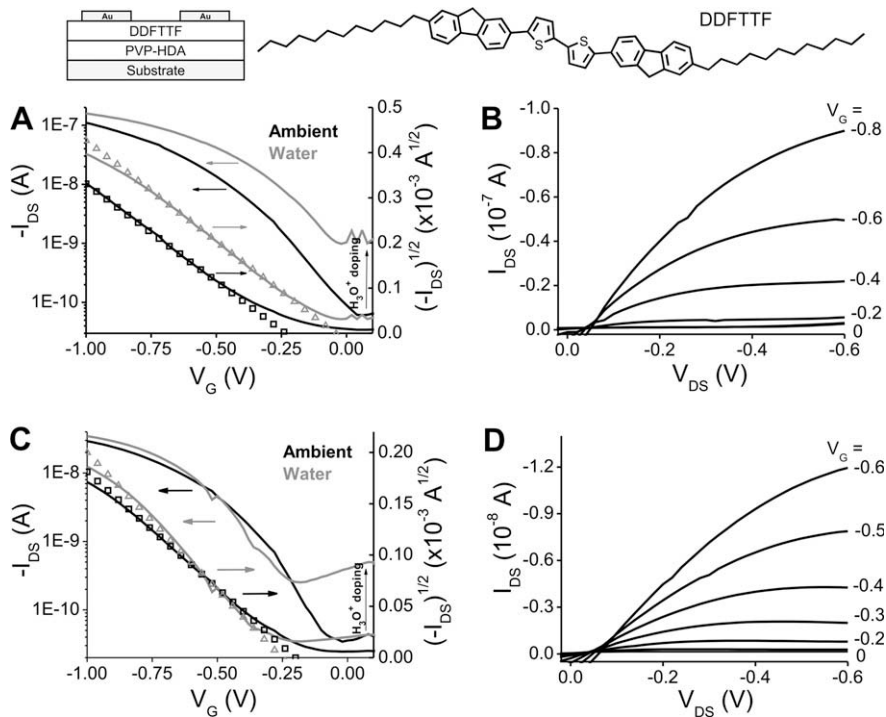


**Fig. 4.** (A) Semi-log plot of the transfer characteristics ( $I_{DS}$  versus  $V_G$ ) for the OTFT on ITO/PET with 35 nm PVP-HDA, 30 nm DDFTF and gold electrodes in ambient (black) and under water (grey).  $I_{DS}^{1/2}$  versus  $V_G$  is also plotted on the right axis. (B) Output characteristics ( $I_{DS}$ – $V_{DS}$ ) for the device in (A) under water. (C) Log plot of transfer characteristics with PEDOT:PSS electrodes in ambient (black) and under water (grey) with the square root shown on the right axis. (D) Output characteristics for device in (C) under water. The structure of a top-contact OTFT with the structure of DDFTF is shown above.

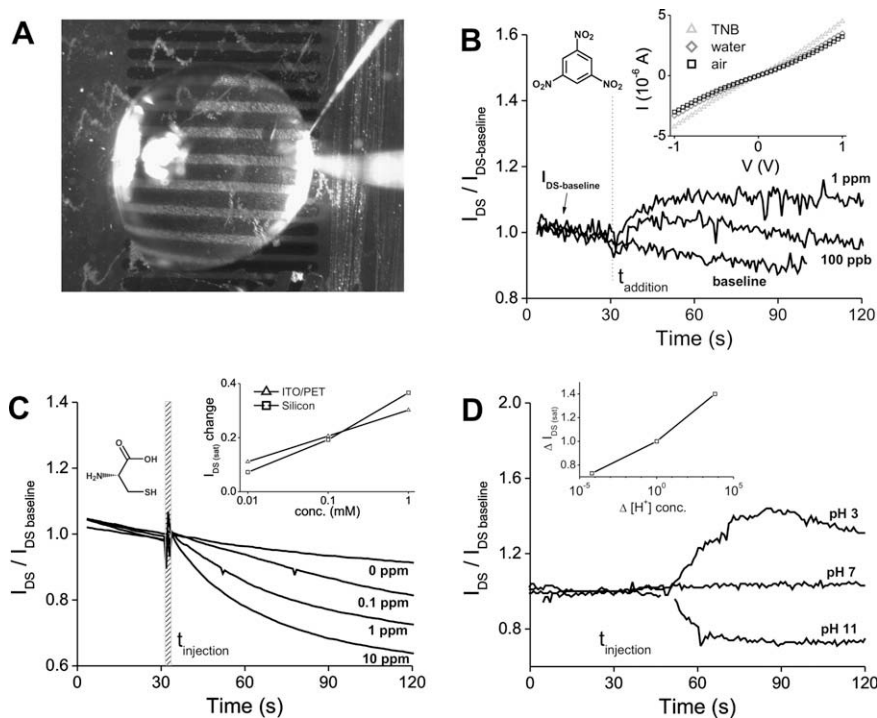


**Fig. 5.** (A) Optical micrograph of an OTFT under operation in water. (B)  $\Delta I_{DS}$  of an OTFT with PEDOT:PSS electrodes when exposed to solutions of TNB with concentrations as low as 100 ppb, (inset) resistive current of PEDOT electrodes in air, water, and 100 ppb TNB solution. (C)  $\Delta I_{DS}$  ( $I_{DS}/I_{DS\text{baseline}}$ ) when exposed to solutions of cysteine with various concentrations, (inset) relative saturation current change with concentration for OTFTs fabricated on silicon and ITO/PET substrates. (D)  $\Delta I_{DS}$  with solution pH on ITO/PET substrates with PEDOT:PSS electrodes, (inset)  $\Delta I_{DS}$  as a function of change in  $[H^+]$  concentration.

tions described. Fig. 5A shows the droplet of water spanning the channel region. After establishing a baseline, 2  $\mu\text{l}$  of 300 ppb TNB was added to the droplet, and an increase in  $I_{\text{DS}}$  was observed. The same procedure was done using 3 parts per million (ppm) TNB, and the composite current characteristics are shown in Fig. 5B in the form of  $\Delta I_{\text{DS}}$  versus time. A higher degree of noise relative to the signal is observed due to the contact between the gold wire probes and the soft, conducting polymer electrodes. Previously, we observed a decrease in current when the OTFTs (silicon substrates and gold electrodes) were exposed to TNB; however, with the polymer electrodes we observed an increase in current. To explain this, we measured the resistive current of the electrodes in water and in the saturated (300 ppb) TNB solution. Indeed, the conductivity of the electrodes increases by an average of 31% in the TNB solution due to a charge transfer between the analyte and conducting polymer [36,37], indicating, in this case, that a change in contacts plays a major role. Therefore, when using electrode materials, such as conducting polymers, that can dope and de-dope under specific solution conditions, it is important to consider the influence of the analyte on the electrode conductivity. In fact, the use of polymer doping/de-doping can be used to fabricate organic electrochemical transistors [38].

We also investigated the influence of pH on the polymer electrode conductivity since the conductivity has been shown to vary with acidity [39] or alkalinity [40]. However, we observed a change in resistive current of less than 3% when exposing the polymer electrode to solutions of pH 3 (based on HCl) and pH 11 (based on NaOH). Therefore, the  $\Delta I_{\text{DS}}$  response was similar for OTFTs fabricated with gold and PEDOT:PSS electrodes (Fig. 5D). The inset shows a plot of  $\Delta I_{\text{DS}}$  versus change in hydronium ion,  $\text{H}^+$ , concentration. It is important to note that the parasitic current between the S-D electrodes is negligible for the acidic or basic solutions under the bias conditions applied [9].

Fig. 5C shows the drain current response to solutions of cysteine with concentrations ranging from 0.1 ppm to 10 ppm. For comparison, the inset of Fig. 5C shows the concentration dependent OTFT drain current change ( $I_{\text{DS}}$  at saturation minus  $I_{\text{DS}}$  of the baseline, divided by  $I_{\text{DS}}$  of the baseline) for plastic and rigid substrates.

With the demonstration of chemical sensing using organic thin-film transistors fabricated on flexible substrates, we have taken a step toward the realization of low-cost, disposable sensors. In our fabrication process, we maintain the requirements of low input power and device stability in air and water environments. Our fabrication process relies on the simplicity of solution methods with the ability to deposit a polymer insulating layer and patterned polymer electrodes from solution without damaging the organic semiconductor or plastic substrate. However, consideration must be given to the choice of electrode material, which can potentially influence the OTFT response toward certain analytes.

## Acknowledgement

M.E.R. acknowledges the NASA GSRP fellowship. Z.B. acknowledges the NSF-sponsored Center for Polymer Inter-

face Macromolecular Assemblies (CPIMA), NSF DMR Solid State Chemistry and NSF-EXP on sensors.

## Appendix A. Supplementary material

Supplementary data associated with this article can be found, in the online version, at doi:10.1016/j.orgel.2008.12.001.

## References

- [1] R.H. Friend, R.W. Gymer, A.B. Holmes, J.H. Burroughes, R.N. Marks, C. Taliani, D.D.C. Bradley, D.A. Dos Santos, J.L. Bredas, M. Logdlund, W.R. Salaneck, *Nature* 397 (1999) 121.
- [2] P.F. Baude, D.A. Ender, M.A. Haase, T.W. Kelley, D.V. Muires, S.D. Theiss, *Applied Physics Letters* 82 (2003) 3964.
- [3] S. Steudel, K. Myny, V. Arkhipov, C. Deibel, S. De Vusser, J. Genoe, P. Heremans, *Nature Materials* 4 (2005) 597.
- [4] B.K. Crone, A. Dodabalapur, R. Sarpeshkar, A. Gelperin, H.E. Katz, Z. Bao, *Journal of Applied Physics* 91 (2002) 10140.
- [5] A.R. Murphy, J.M.J. Frechet, *Chemical Reviews* 107 (2007) 1066.
- [6] J.E. Anthony, *Chemical Reviews* 106 (2006) 5028.
- [7] Z. Bao, J. Locklin, *Organic Field-Effect Transistors*, Taylor and Francis Group, Boca Raton, FL, 2007.
- [8] K.S. Lee, T.J. Smith, K.C. Dickey, J.E. Yoo, K.J. Stevenson, Y.L. Loo, *Advanced Functional Materials* 16 (2006) 2409.
- [9] M.E. Roberts, S.C.B. Mannsfeld, N. Queralto, C. Reese, J. Locklin, W. Knoll, Z. Bao, *Proceedings of the National Academy of Sciences of the United States of America* 105 (2008) 12134.
- [10] M.H. Yoon, H. Yan, A. Facchetti, T.J. Marks, *Journal of the American Chemical Society* 127 (2005) 10388.
- [11] H. Klauk, U. Zschieschang, J. Pflaum, M. Halik, *Nature* 445 (2007) 745.
- [12] M.-H. Yoon, A. Facchetti, T.J. Marks, *Proceedings of the National Academy of Sciences of the United States of America* 102 (2005) 4678.
- [13] A.L. Briseno, S.C.B. Mannsfeld, M.M. Ling, S.H. Liu, R.J. Tseng, C. Reese, M.E. Roberts, Y. Yang, F. Wudl, Z.N. Bao, *Nature* 444 (2006) 913.
- [14] J.A. Rogers, Z. Bao, K. Baldwin, A. Dodabalapur, B. Crone, V.R. Raju, V. Kuck, H. Katz, K. Amundson, J. Ewing, P. Drzaic, *Proceedings of the National Academy of Sciences of the United States of America* 98 (2001) 4835.
- [15] H. Sirringhaus, T. Kawase, R.H. Friend, T. Shimoda, M. Inbasekaran, W. Wu, E.P. Woo, *Science* 290 (2000) 2123.
- [16] T. Someya, T. Sekitani, S. Iba, Y. Kato, H. Kawaguchi, T. Sakurai, *Proceedings of the National Academy of Sciences of the United States of America* 101 (2004) 9966.
- [17] M.L. Chabiny, W.S. Wong, A.C. Arias, S. Ready, R.A. Lujan, J.H. Daniel, B. Krusor, R.B. Apte, A. Salleo, R.A. Street, *Proceedings of the IEEE* 93 (2005) 1491.
- [18] P. Andersson, D. Nilsson, P.O. Svensson, M.X. Chen, A. Malmstrom, T. Remonen, T. Kugler, M. Berggren, *Advanced Materials* 14 (2002) 1460.
- [19] J.Y. Lee, J.H. Kwon, H.K. Chung, *Organic Electronics* 4 (2003) 143.
- [20] L. Torsi, A.J. Lovinger, B. Crone, T. Someya, A. Dodabalapur, H.E. Katz, A. Gelperin, *Journal of Physical Chemistry B* 106 (2002) 12563.
- [21] J. Huang, J. Miragliotta, A. Becknell, H.E. Katz, *Journal of the American Chemical Society* 129 (2007) 9366.
- [22] L. Torsi, G.M. Farinola, F. Marinelli, M.C. Tanese, O.H. Omar, L. Valli, F. Babudri, F. Palmisano, P.G. Zamboni, F. Naso, *Nature Materials* 7 (2008) 412.
- [23] K.S. McCully, *American Journal of Clinical Nutrition* 86 (2007) 1563S.
- [24] J.C. Pennington, D. Gunnison, D.W. Harrelson, J.M. Brannon, M. Zakikhani, T.F. Jenkins, J.U. Clarke, C.A. Hayes, T. Myers, E. Perkins, D. Ringelberg, D.M. Townsend, H. Fredrickson, J.H. May, *Natural Attenuation of Explosives in Soil and Water Systems at Department of Defense Sites: Interim Report*, US Army Corps of Engineers, 1999.
- [25] A.L. Briseno, M. Roberts, M.M. Ling, H. Moon, E.J. Nemanick, Z.N. Bao, *Journal of the American Chemical Society* 128 (2006) 3880.
- [26] S.C.B. Mannsfeld, A. Sharei, S. Liu, M.E. Roberts, I. McCulloch, M. Heeney, Z. Bao, *Advanced Materials* 20 (2008) 4044.
- [27] X. Crispin, S. Marciniak, W. Osikowicz, G. Zotti, A.W.D. Van, F. der Gon, M. Louwet, L. Fahlman, F. Groenendaal, W.R. De Schryver, L.

- Salaneck, *Journal of Polymer Science Part B-Polymer Physics* 41 (2003) 2561.
- [28] J.L. Wilbur, A. Kumar, E. Kim, G.M. Whitesides, *Advanced Materials* 6 (1994) 600.
- [29] A.L. Briseno, M. Roberts, M.M. Ling, H. Moon, E.J. Nemanick, Z. Bao, *Journal of the American Chemical Society* 128 (2006) 3880.
- [30] D.M. DeLongchamp, M.M. Ling, Y. Jung, D.A. Fischer, M.E. Roberts, E.K. Lin, Z. Bao, *Journal of the American Chemical Society* 128 (2006) 16579.
- [31] Y. Quan, S.C.B. Mannsfeld, M.L. Tang, M. Roberts, M.F. Toney, D.M. DeLongchamp, Z. Bao, *Chemistry of Materials* 20 (2008) 2763.
- [32] T.J. Shin, H. Yang, M.M. Ling, J. Locklin, L. Yang, B. Lee, M.E. Roberts, A.B. Mallik, Z. Bao, *Chemistry of Materials* 19 (2007) 5882.
- [33] G. Horowitz, *Journal of Materials Research* 19 (2004) 1946.
- [34] Y.G. Seol, J.G. Lee, N.E. Lee, *Organic Electronics* 8 (2007) 513.
- [35] Y.G. Seol, H.Y. Noh, S.S. Lee, J.H. Ahn, N.E. Lee, *Applied Physics Letters* 93 (2008) 013305.
- [36] A. Arena, N. Donato, G. Pioggia, G. Rizzo, G. Saitta, *Microelectronics Journal* 37 (2006) 1384.
- [37] H. Peisert, M. Knupfer, F. Zhang, A. Petr, L. Dunsch, J. Fink, *Applied Physics Letters* 83 (2003) 3930.
- [38] J.T. Mabeck, G.G. Malliaras, *Analytical and Bioanalytical Chemistry* 384 (2006) 343–353.
- [39] T.P. Nguyen, S.A.d. Vos, *Applied Surface Science* 221 (2004) 330.
- [40] C.H.L. Weijtens, V. van Elsbergen, M.M. de Kok, S.H.P.M. de Winter, *Organic Electronics* 6 (2005) 97.



# Fabrication of high efficiency and color stable white organic light-emitting diodes by an alignment free mask patterning

Kyoung Soo Yook, Soon Ok Jeon, Chul Woong Joo, Jun Yeob Lee \*

Department of Polymer Science and Engineering, Dankook University, Jukjeon-dong, Suji-gu, Yongin-si, Gyeonggi-do, Seoul 448-701, Republic of Korea

## ARTICLE INFO

### Article history:

Received 9 November 2008

Received in revised form 17 December 2008

Accepted 20 December 2008

Available online 3 January 2009

### PACS:

85.60.jb

### Keywords:

White organic light-emitting diodes

Color stability

High efficiency

Alignment free mask patterning

## ABSTRACT

Small molecule based white organic light-emitting diodes were fabricated by using an alignment free mask patterning method. A phosphorescent red/green emitting layer was patterned by a metal mask without any alignment and a blue phosphorescent emitting layer was commonly deposited on the patterned red/green emitting layer. A white emission could be obtained due to separate emission of red/green and blue emitting layers. A maximum current efficiency of 30.7 cd/A and a current efficiency of 26.0 cd/A at 1000 cd/m<sup>2</sup> were obtained with a color coordinate of (0.39, 0.45). In addition, there was little change of emission spectrum according to luminance because of balanced red/green and blue emissions.

© 2009 Elsevier B.V. All rights reserved.

## 1. Introduction

White organic light-emitting diodes (WOLEDs) have attracted great attention from many researchers for their application as a display and a general lighting. WOLEDs have advantages over red, green and blue patterned device such as a simple process and the ease of fabrication. However, WOLEDs suffer from low efficiency, color shift at high luminance and poor color stability.

There have been many studies to develop WOLEDs with a high efficiency and a good color stability. A red, green and blue stacked structure [1–9] and a single layer emitting structure doped with red, green and blue dopants were reported [10–13]. The stack structure has a merit of high efficiency and good color stability, while the single layer emitting structure has a problem of poor color stability even though high efficiency can be obtained. Other than the stacked and single layer mixed structures, a color converting structure has also been developed to get white

emission using a blue emitting layer and color converting materials [14,15]. Another method to realize white devices is to use a single white emitting material which can emit red, green and blue colors [16–18].

In the case of common WOLED structures, it was difficult to manage the light emission from each color because RGB materials are included in a single layer or in a single stack structure. In addition, color stability could not be obtained because there was an exciton movement or charge leakage between emitting layers depending on the luminance of the device [1]. These problems can be overcome by designing a device structure with separated RGB or RB regions [19].

A combination of RGB separate emission and a diffuse film was effective to get white emission and white color could be easily controlled by managing the luminance of each RGB pixel. However, each RGB pixel had to be precisely patterned to get controlled white emission. The RGB patterning by a fine metal mask after mask and substrate alignment was required. Although a high efficiency and controlled light emission could be obtained from the device, the device fabrication process was complicated due to mask alignment process.

\* Corresponding author. Tel./fax: +82 31 8005 3585.

E-mail address: [leej17@dankook.ac.kr](mailto:leej17@dankook.ac.kr) (J.Y. Lee).

In this work, a simple device fabrication method which can achieve controlled white emission without any mask alignment process was developed. A separate emission without any mask alignment can be achieved by a device structure with a patterned red/green layer and a common blue layer. The common blue layer would be stacked on the patterned red/green emitting layer in some region and it will exist as a blue single layer in the region without the red/green layer. The blue layer can play a role of hole blocking layer of the red/green emitting layer and the device performances of red/green and blue emitting layers can be separately managed. Three color devices could be fabricated by the method and stable white device performances were demonstrated from three color white devices.

## 2. Experimental

One pixel in this work was patterned by metal mask and it had red and blue emitting units. Red emitting region had a stack structure of indium tin oxide (ITO, 150 nm)/poly-3,4-ethylenedioxythiophene:polystyrenesulfonate (PEDOT:PSS, 60 nm)/N, N'-di(1-naphthyl)-N,N'-diphenylbenzidine (NPB, 10 nm)/4,4',4''-tris(N-carbazolyl)triphenylamine (TCTA, 10 nm)/N, N'-dicarbazolyl-3,5-benzene (mCP, 10 nm)/TCTA:3-phenyl-4-(1'-naphthyl)-5-phenyl-1,2,4-triazole (TAZ): iridium(III) tris(2-phenylpyridine) (Ir(ppy)<sub>3</sub>): iridium(III) bis(1-phenylquinoline) acetylacetonate (Ir(pq)<sub>2</sub>-acac) (20 nm, 10%, 1%)/2-diphenylphosphorylspirofluorene (SPPO1): iridium(III) bis(4,6-(di-fluorophenyl)-pyridinato-N,C2') picolinate (Flrpic) (30 nm, 15%)/4,7-diphenyl-1,10-phenanthroline (Bphen, 5 nm)/tris(8-hydroxyquinoline) aluminum (Alq<sub>3</sub>, 20 nm)/LiF(1 nm)/Al(200 nm). Blue emitting region had a structure of ITO/PEDOT:PSS(60 nm)/NPB(10 nm)/TCTA(10 nm)/mCP(10 nm)/SPPO1:Flrpic(30 nm, 15%)/Bphen(5 nm)/Alq<sub>3</sub>(20 nm)/LiF(1 nm)/Al(200 nm). Pixel size was 2 mm by 2 mm and the open width of stripe type metal mask was controlled to investigate the effect of the emitting area of red/green and blue colors on the device performances of pixel divided white devices. Two devices with different relative emitting area were fabricated. Relative emitting areas of red/green to blue were 1:1 (device I) and 2:1 (device II). Current density–voltage–luminance characteristics and electroluminescence (EL) spectra of PHOLEDs were measured with Keithley 2400 source measurement unit and CS 1000 spectrophotometer.

## 3. Results and discussion

It is required to use hole blocking type blue phosphorescent emitting layer to get high efficiency and pure red/green emission in red/green emitting layer [20]. Therefore, a new electron transport type blue phosphorescent host material based on spirofluorene and phosphine oxide was synthesized. The 2-(diphenylphosphoryl)spirofluorene (SPPO1) was synthesized by the reaction of diphenylphosphorylchloride with 2-bromospirofluorene followed by oxidation with H<sub>2</sub>O<sub>2</sub>. The SPPO1 had a triplet bandgap of 2.8 eV and the highest occupied molecular orbital (HOMO) level of 6.5 eV. The HOMO level was deep enough for effective

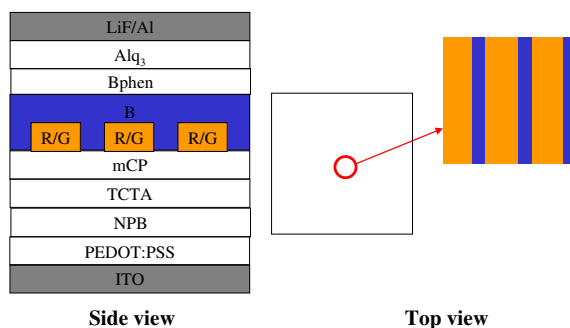


Fig. 1. Schematic diagram of the pixel structure.

hole blocking and the triplet energy of SPPO1 was wide enough for efficient energy transfer to Flrpic with a triplet bandgap of 2.6 eV. Therefore, the Flrpic doped SPPO1 layer can play a role of hole blocking layer on red/green emitting layer. Schematic diagram of the pixel structure is shown in Fig. 1. The relative area of the red/green emitting region was 50% in device I, while it was 66% in device II.

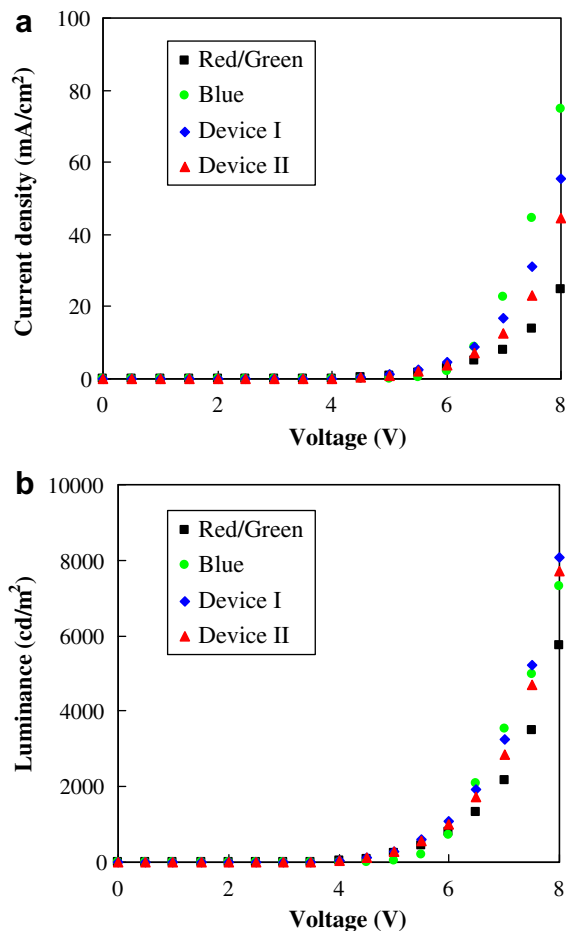


Fig. 2. Current density–voltage and luminance–voltage curves of red/green, blue and white devices. (a) Current density–voltage and (b) luminance–voltage.

Standard devices with red/green emitting layer and blue emitting layer were also fabricated in addition to the white device with divided red/green and blue pixel region. Fig. 2 shows the current efficiency–voltage and luminance–voltage curves of red/green, blue and two white devices. The current density was high in the blue device, while red/green device showed the lowest current density. The low current density in the red/green device can be explained by the thickness of red emitting layer. Total thickness of the emitting layer in the red/green device was 50 nm compared with 30 nm of the blue device, resulting in low current density. The white devices showed an intermediate current density value of red/green and blue devices. The current density was high in the device with large area for blue emission because of high current density in the blue device. The luminance of the devices also followed the same trend as current density.

Quantum efficiency and current efficiency of the red/green, blue and white devices are shown in Fig. 3. The red/green device with blue emitting layer stacked on red/green emitting layer showed a quantum efficiency of 12.6% and a current efficiency of 28 cd/A at 1000 cd/m<sup>2</sup>. Compared with the red standard device without the blue emitting layer, the efficiency was not degraded. The similar efficiency of the red/green device may be due to hole blocking properties of the SPPO1 with the HOMO level of

6.5 eV. The blue standard device showed a quantum efficiency of 13% and a current efficiency of 29 cd/A at 1000 cd/m<sup>2</sup>. The SPPO1 can be a good host material for Flrpic because of a wide triplet bandgap of 2.8 eV and a wide singlet bandgap of 3.8 eV. An exothermic energy transfer can be induced by using the SPPO1 host and a high quantum efficiency of 12% was obtained. The white device showed a little lower quantum efficiency value than red/green and blue devices. A maximum current efficiency of 30.7 cd/A and a current efficiency of 26 cd/A at 1000 cd/m<sup>2</sup> were achieved in the white device II. Relative area of the red/green emitting region to blue emitting region in the white pixel affected the efficiency of the white device and high efficiency was observed in the device II with larger red/green emitting area compared with blue emitting area. This is due to a rather large efficiency roll-off and high current density of the blue device. Local current density is high in the blue emitting region due to high current density through blue emitting layer (Fig. 2). The blue emitting region contributes to the efficiency of the white device and the luminance of the blue emitting region is relatively high compared with that of red emitting region. Therefore, the luminance of the blue emitting region is higher than 1000 cd/m<sup>2</sup> even at 1000 cd/m<sup>2</sup> white emission in the pixel. In the case of the blue emission, a rather large efficiency roll-off was observed, leading to relatively low quantum efficiency in the white device. The quantum efficiency was increased as the relative area of blue emitting region was decreased because of less contribution of the efficiency roll-off behavior on the white emitting characteristics.

Fig. 4 compares EL spectra of red/green, blue and white devices. The red/green device showed a red/green emission with little blue emission from the blue emitting layer stacked on the red/green emitting layer. This indicates that most excitons are generated inside the red/green emitting layer and the blue emitting layer does not contribute to the red/green light emission. The blue layer just acts as a hole blocking layer even though there is a little hole leakage through Flrpic in the blue emitting layer. The HOMO level of SPPO1 is suitable for hole blocking and holes cannot be injected from red/green emitting layer to SPPO1 layer. Therefore, red/green emission with little blue emission

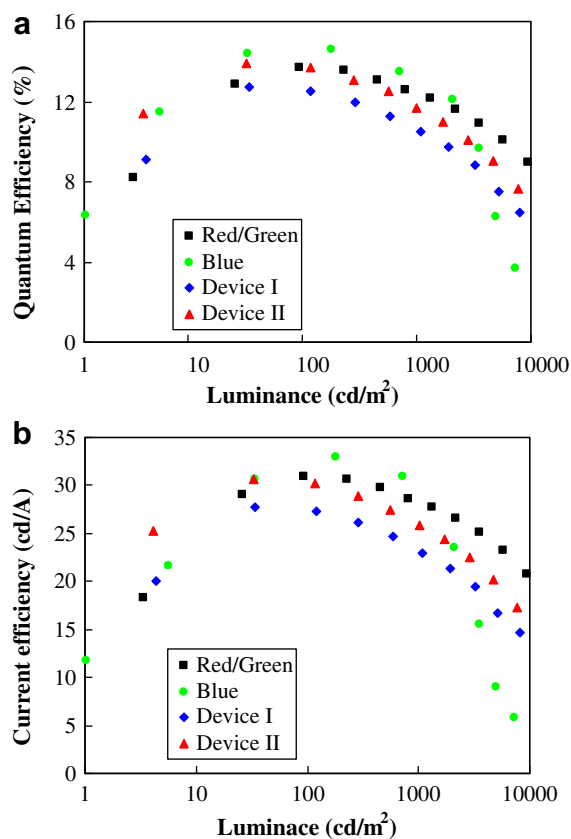


Fig. 3. Quantum efficiency and current efficiency of red/green, blue and white devices. (a) Quantum efficiency–luminance and (b) current efficiency–luminance.

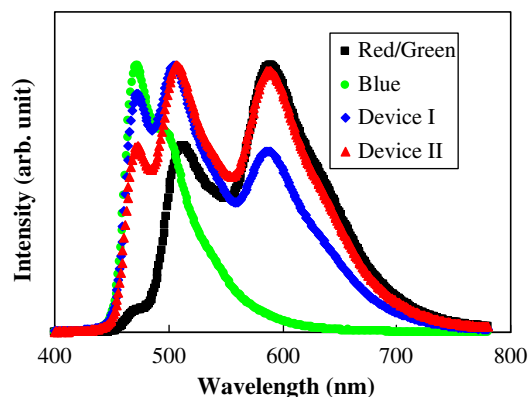
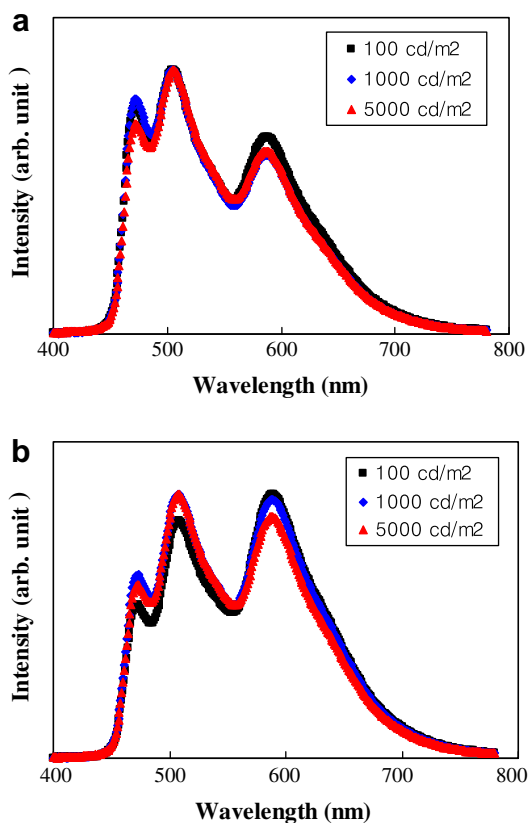


Fig. 4. Electroluminescence spectra of red/green, blue and white devices.





**Fig. 5.** Electroluminescence spectra of white organic light-emitting diodes according to luminance. (a) Device I and (b) device II.

was observed from the red/green emitting layer. In the case of blue device, only blue emission from FIrpic doped SPPO1 layer was observed. The blue device showed a peak maximum at 474 nm and a strong shoulder at 499 nm which is overlapped with green emission peak of the red/green device. The white device showed both red/green and blue emissions because it had red/green emitting region and blue emitting region. The relative intensity of the red/green and blue emissions were dependent on the relative area of the red/green and blue emitting region and the blue emission was strong in the device with large area for blue emission. Color coordinate of device I was (0.33, 0.43), while the color coordinate of device II was (0.38, 0.45). More blue emission was observed in device I due to large blue emitting area.

One merit of using the patterned pixel structure for white light emission is the color stability through independent red/green and blue emissions. The red/green and blue emissions are separate, which makes it easy to keep good color stability in the device. Fig. 5 shows the EL spectra of device I and device II according to luminance. The EL

spectra were not greatly changed within the luminance range from 100 to 5000  $\text{cd/m}^2$ . The white device with the patterned pixel structure does not have the problem of exciton leakage or charge leakage through the interface between emitting layers in common stacked white devices. Detrapping of charges in a single layer white device is also not observed in this patterned pixel structure, resulting in constant EL spectra irrespective of luminance. The color coordinate of the device I was (0.35, 0.44) at 100  $\text{cd/m}^2$  and it was (0.34, 0.44) at 5000  $\text{cd/m}^2$ . The color coordinate was kept stable even at 10,000  $\text{cd/m}^2$  and it was (0.35, 0.45). Similar data were obtained in the device II and the color coordinate was changed from (0.40, 0.45) to (0.38, 0.45) by changing luminance from 100 to 5000  $\text{cd/m}^2$ . It was (0.39, 0.46) at 10,000  $\text{cd/m}^2$ .

#### 4. Conclusions

In summary, a white device with patterned red/green and blue region inside a pixel was effectively fabricated by using a fine metal mask without any alignment. Red/green and blue emissions were independently controlled in a single pixel and good color stability was observed. A high current efficiency of 30.7  $\text{cd/A}$  was achieved in the white device with a color coordinate of (0.39, 0.45).

#### References

- [1] Y. Sun, N.C. Giebink, H. Kanno, B.W. Ma, M.E. Thompson, S.R. Forrest, *Nature* 440 (2006) 908.
- [2] B.W. D'Andrade, S.R. Forrest, *Adv. Mater.* 16 (2005) 1585.
- [3] G. Schwartz, M. Pfeiffer, S. Reineke, K. Walzer, K. Leo, *Adv. Mater.* 19 (2007) 3672.
- [4] G. Schwartz, S. Reineke, K. Walzer, K. Leo, *Appl. Phys. Lett.* 92 (2008) 053311.
- [5] S.H. Kim, J. Jang, J.Y. Lee, *Appl. Phys. Lett.* 91 (2007) 123509.
- [6] Y. Wang, Y. Hua, X. Wu, L. Zhang, Q. Hou, S. Yin, M.C. Petty, *Appl. Phys. Lett.* 92 (2008) 123504.
- [7] C. Ho, M. Lin, W. Wong, W. Wong, C.H. Chen, *Appl. Phys. Lett.* 92 (2008) 083301.
- [8] K.S. Yook, S.O. Jeon, C.W. Joo, J.Y. Lee, *Appl. Phys. Lett.* 92 (2008) 073302.
- [9] K.S. Yook, J.Y. Lee, *Appl. Phys. Lett.* 92 (2008) 193308.
- [10] M. Granstrom, O. Inganäs, *Appl. Phys. Lett.* 68 (1996) 147.
- [11] P.I. Shih, C.F. Shu, Y.L. Tung, Y. Chi, *Appl. Phys. Lett.* 88 (2006) 251110.
- [12] J. Kido, H. Shionoya, K. Nagai, *Appl. Phys. Lett.* 67 (1995) 2281.
- [13] G. Tu, Q. Zhou, Y. Cheng, L.X. Wang, D.G. Ma, F.S. Wang, *Appl. Phys. Lett.* 85 (2004) 2172.
- [14] B.C. Krummacher, V. Choong, M.K. Mathai, S.A. Choulis, F. So, F. Jermann, T. Fiedler, M. Zachau, *Appl. Phys. Lett.* 88 (2006) 123506.
- [15] A. Duggal, J. Shiang, C. Heller, D. Foust, *Appl. Phys. Lett.* 80 (2002) 3470.
- [16] J.X. Jiang, Y.H. Xu, W. Yang, R. Guang, Z.Q. Liu, H.Y. Zhen, Y. Cao, *Adv. Mater.* 18 (2006) 1769.
- [17] F.-I. Wu, X.-H. Yang, D. Neher, R. Dodda, Y.-H. Tseng, C.-F. Shu, *Adv. Funct. Mater.* 17 (2007) 1085.
- [18] X. Yang, Z. Wang, S. Madakuni, J. Li, G.E. Jabbour, *Adv. Mater.* 20 (2008) 2405.
- [19] J.Y. Lee, J.H. Kwon, H.K. Chung, *Org. Electron.* 4 (2003) 143.
- [20] M.H. Kim, M.W. Song, S.T. Lee, H.D. Kim, J.S. Oh, H.K. Chung, *SID Symp. Dig. Tech. Papers* 37 (2006) 135.



## Oxidised carbon nanotubes as solution processable, high work function hole-extraction layers for organic solar cells

Ross A. Hatton<sup>a,\*</sup>, N.P. Blanchard<sup>b</sup>, Li Wei Tan<sup>b</sup>, Gianluca Latini<sup>b</sup>, Franco Cacialli<sup>c</sup>, S. Ravi P. Silva<sup>b</sup>

<sup>a</sup> Department of Chemistry, The University of Warwick, Coventry, CV4 7AL, UK

<sup>b</sup> Nanoelectronics Centre, Advanced Technology Institute, University of Surrey, Guildford, Surrey, GU2 7XH, UK

<sup>c</sup> Department of Physics and Astronomy, University College London, Gower Street, London, WC1E 6BT, UK

### ARTICLE INFO

#### Article history:

Received 21 November 2008

Received in revised form 15 December 2008

Accepted 18 December 2008

Available online 3 January 2009

#### PACS:

84.60.Jt

73.50.Pz

85.60.Bt

73.22.-f

73.30.+y

78.30.Na

#### Keywords:

Organic solar cell

Organic photovoltaic

Carbon nanotube

Electrode

### ABSTRACT

For efficient hole-extraction in solution processed organic solar cells the transparent indium-tin oxide (ITO) electrode is invariably pre-coated with a thin layer of the high work function conducting polymer poly(3,4-ethylenedioxythiophene) doped with poly(styrene-sulfonate). Herein we show that thin films of partially oxidised multi-wall and single-wall carbon nanotubes are equally effective at facilitating hole-extraction in efficient (~2.7%) bulk-heterojunction organic solar cells based on poly(3-hexylthiophene) (P3HT): [6,6]-phenyl-C<sub>61</sub> butyric acid methyl ester (PCBM) blends. Crucially, in contrast to PEDOT:PSS, deposition is from aqueous solutions of low acidity (pH 6–7) ensuring compatibility with ITO and other emerging conducting oxides. Furthermore, thin oxidised carbon nanotube films offer greater transparency in the near-infrared as compared to PEDOT:PSS films of comparable thickness. The functionality of these nano-structured films is demonstrated in relatively large area devices (~0.35 cm<sup>2</sup>) and the performance rationalised based on measurements of the electronic structure and morphology.

© 2009 Elsevier B.V. All rights reserved.

### 1. Introduction

Organic solar cells (OSCs) [1] have strong potential as a low cost path to harvesting electrical energy from sunlight and in recent years a great deal of progress has been made in the search for low cost, transparent and flexible substrate electrodes for this application [2,3]. One particularly promising material system is that of carbon nanotube (CNT) films, which can be prepared by filtration [3a–f], densification of nanotube yarns [4a,b] or spraying [5], although it is yet to be seen which processing technology will dominate. Whilst the electrical conductivity of these

films is far below the axial conductivity of individual CNTs it is now approaching that of commercial ITO glass for comparable transparency (i.e. <100 Ω/sq at >80% transparency) [3f]. With the exception of the pioneering work of Zhang et al. [4], which pertains to the densification of dry CNT yarns, all other processing methods involve deposition from relatively dilute dispersions typically achieved using a surfactant to de-bundle and solubilise the CNTs without damaging their highly conductive graphitic structure. In the context of OSC applications optimal performance is only realised when the CNT electrode is coated with a thin layer of the high work function [6] conducting polymer poly(3,4-ethylenedioxythiophene) doped with poly(styrenesulfonate) (PEDOT:PSS) which reduces the sheet resistance [3d] and planarizes [3e] the porous CNT film.

\* Corresponding author. Tel.: +44 (0) 24761 50874.

E-mail address: [ross.hatton@warwick.ac.uk](mailto:ross.hatton@warwick.ac.uk) (R.A. Hatton).

OSCs fabricated on CNT electrodes without PEDOT:PSS were reported by Lagemaat et al. to exhibit inferior open-circuit voltage ( $V_{oc}$ ) and short-circuit current density ( $J_{sc}$ ) as compared to devices employing PEDOT:PSS [5]. Notably, the work function of the pristine CNTs in that work, whilst comparable to ITO glass, was lower than that of PEDOT:PSS. Consequently, optimal alignment of the electrode Fermi level with the highest occupied molecular orbital (HOMO) of the adjacent donor material was unlikely to be realised.

Thin films of PEDOT:PSS are widely regarded as efficient hole-extracting layers (HELs) in OSCs, combining a high work function, good optical transparency, high electrical conductivity and ease of processing from solution [6,7]. The primary drawback of PEDOT:PSS is its acidity, which is believed to etch the surface of ITO liberating oxygen and metal ions which contaminate the adjacent photoactive organic layer to the detriment of device performance [8a–c]. In this paper we show that thin films of both multi-wall and single wall carbon nanotubes (MWCNTs and SWCNTs, respectively) that have been extensively oxidised via acid treatment to render them soluble in water, are as effective as PEDOT:PSS for hole-extraction in efficient archetypal OSCs based on poly(3-hexylthiophene) (P3HT): [6,6]-phenyl- $C_{61}$  butyric acid methyl ester (PCBM) blends supported on ITO glass. The monochromatic internal quantum efficiency of OSCs employing PEDOT:PSS in conjunction with P3HT:PCBM photoactive layers is reported to be as high as ~90% at optimum wavelengths [7a] making this material system an excellent benchmark against which other HELs can be compared [9]. Importantly, in this study both PEDOT:PSS and acid oxidised CNT films were supported on ITO glass to ensure that the bulk conductivity of the transparent electrode was the same in all devices. Care was also taken to ensure that the different HELs were of comparable transparency across the range of wavelengths over which P3HT-PCBM absorbs light (400–675 nm) [7b] and that the photoactive layer thickness was the same in all devices. In this way differences in the performance of OSCs employing different HELs could be decoupled from variations in the transparency and conductivity of the substrate electrode and rationalised solely in terms of their respective electronic structure and morphology.

## 2. Experimental

MWCNT (>90 wt.%) and SWCNT (>90 wt.%) grown by chemical vapour deposition were obtained commercially (Nanocyl) and used as received. Stable dispersions of SWCNTs and MWCNTs in de-ionized water were prepared by ultrasonically dispersing CNT in a 3:1 mixture of concentrated sulphuric and nitric acids for ten minutes. The mixture was refluxed at 130 °C for 60 min or 25 min for MWCNT and SWCNT respectively, before diluting with HPLC grade de-ionized water. The very low pH of the resulting solution destabilizes the CNTs causing them to flocculate. To accelerate this process the dispersion was centrifuged and the acid supernatant decanted off. The remaining solid was repeatedly washed with de-ionized

water over a 50 nm polycarbonate filter until the washings were pH 6–7. Before allowing the oxidised nanotubes to dry the entire filter paper was submerged in a small quantity of de-ionized water whereupon they spontaneously disperse to form a concentrated dispersion. The resulting dispersion was centrifuged to remove residual aggregates. In order to determine the actual CNT loadings in solution a sample of known volume was completely dried and weighed. The resulting black solutions required no further preparative treatment and were stable for >6 months.

CNTs were characterized using a Philips CM200 ST transmission electron microscope (TEM) with a LaB<sub>6</sub> filament and 200 kV accelerating voltage. Transmission spectra were obtained using a UV-Vis Varian Cary 5000 UV-Vis-NIR spectrometer. The XPS measurements were carried out in an Omicron multi-probe system, with a base pressure in the  $10^{-10}$  mbar range. The analysis chamber was equipped with a ThermoVG XRE32 twin anode X-ray source and an Omicron EA 125 electron energy analyser. The XPS was measured using the Mg k (1256.3 eV) anode of the source operated at 300 W with a 6mm circular diameter analyser entrance slit and electron pass energy of 20 eV. The zero of the binding energy scale of the XPS is such that the Au 4  $f_{7/2}$  peak is at  $83.9 \pm 0.1$  eV. Field-emission scanning electron microscopy imaging was conducted with a Zeiss SUPRA 55-VP using an accelerating voltage of 500–600 V. Atomic force microscope (AFM) measurements were made using a Dimension 3100 AFM under ambient conditions. Raman scattering spectra were obtained using a Renishaw Raman Scope 1000 and laser excitation wavelength of 785 nm. Kelvin probe measurements performed in air were referenced to freshly cleaved highly orientated pyrolytic graphite (HOPG). Thick CNT films (>1 micron) were used for the work function measurements to ensure no contribution from the underlying substrate. Sheet resistance measurements of o-CNT and PEDOT:PSS films were made on glass microscope slides of comparable roughness and hydrophilicity to ITO glass using the four point probe method.

Devices were fabricated on ITO coated glass (PsiOTec) with a nominal sheet resistance of  $15 \Omega \text{ sq}^{-1}$ . The ITO substrates were cleaned using a three stage ultrasonic cleaning procedure: toluene; an aqueous solution of Decon-90; and acetone. Immediately prior to use the ITO substrates were oxygen plasma treated. o-SWCNT or o-MWCNT films were prepared by the drop-then-spin method with a spin speed of 2250 r.p.m. onto clean ITO substrates followed by heating at 120 °C in air for 20 min to remove residual water. The drop-then-spin method, which is widely used for PEDOT:PSS, ensures a high degree of uniformity of large areas. Conductive grade (1 S/cm) 1.3 wt% dispersion of PEDOT (0.5 wt.%) : PSS (0.8 wt.%) in water was spin cast at 6000 rpm prior to baking at 120 °C for 20 min in air. Poly(3-hexylthiophene): [6,6]-phenyl- $C_{61}$  butyric acid methyl ester blends in dichlorobenzene with loadings  $20 \text{ mg ml}^{-1}$  each were spin cast onto substrates at 600 r.p.m. and allowed to dry in an open Petri-dish in a nitrogen filled glove-box for 20 min. The P3HT:PCBM coated substrates were heated at 110 °C in a nitrogen atmosphere for 10 min to remove residual solvent before transferring to a vacuum system. The thickness of

the P3HT:PCBM layer was measured directly using a Dektak profilometer to be 210–230 nm. The electron extracting electrode, comprising a 10 nm calcium layer followed by 80 nm aluminum was deposited at  $<10^{-5}$  mbar with deposition rates of  $0.1 \text{ nm s}^{-1}$  and  $0.3\text{--}4 \text{ nm s}^{-1}$ , respectively. The thickness of the evaporated layers was monitored using a calibrated quartz crystal microbalance. The photoactive device area was  $\sim 35 \text{ mm}^2$ . Devices were tested using an Oriel solar simulator under AM 1.5 G spectral illumination of  $100 \text{ mW cm}^{-2}$  (1 sun). The output power of the simulator was measured using an NREL calibrated silicon reference cell. All measurements were made in the air immediately after device fabrication.

### 3. Results and discussion

Treatment of CNTs using nitric [10] or hydrochloric acid [10,11] under relatively mild conditions is an established method for removing metal catalyst particles without altering CNT dimensions. Conversely, sulphuric acid is known to shorten CNTs via scission of the sidewalls and ends and so is not normally used as part of a purification procedure [12]. Both of these treatments introduce oxygen containing groups at pre-existing or new defect sites, which – crucially for the current application – help to increase the solubility in water. When nitric and sulphuric acids are used together at elevated temperature (70–130 °C), oxidation and chopping proceed rapidly, decorating the CNT ends and sidewalls with a high concentration of oxygen containing groups which render the CNTs highly soluble in water and alcohols. In this work the oxidation procedure has been optimised to strike a balance between achieving stable concentrated dispersions of CNTs via surface oxidation and the requirement to maintain the integrity of the tubular structure.

Acid oxidation of CNTs is known to result in the formation of oxygen containing moieties, including CO– (e.g. alcohol, ether), C=O (e.g. aldehyde, ketone) and COO– (e.g. carboxylic acid, ester) [13]. Using X-ray photoelectron spectroscopy (XPS) (Fig. 1) and high-resolution transmission electron microscopy (HRTEM) (Supporting information) we have studied the effect of the acid treatment described herein on MWCNTs with diameters  $\sim 10 \text{ nm}$ . The relative proportions of these groups based on atomic percentages determined from peak fitting to the C1s XPS peak are 5:4:8, making COO– the most abundant moiety. From this data it is possible to estimate the COO– density to be  $3\text{--}4 \text{ nm}^{-2}$ , or  $7.3 \times 10^{20}$ – $9.7 \times 10^{20}$  sites/g of MWCNTs, which is in excellent agreement with the value of  $7.6 \times 10^{20}$  sites/g determined by titration of acid oxidised MWCNTs with NaOH. [14] Furthermore, only the outer 2–3 layers were appreciably modified by the acid treatment – determined by HRTEM (Supporting information) – and so the oxygen containing moieties are essentially confined to the MWCNT surface.

In SWCNTs all constituent atoms are located at the CNT surface and so defects formed in the side walls tend to propagate, chopping the SWCNT into shorter lengths [12,15a,b]. As a result the oxygen containing groups are believed to be concentrated at the ends of acid oxidised SWCNTs [12,15a,b]. The increased susceptibility of SWCNTs to oxidation required that the oxidation time be reduced from 60 min for MWCNTs to 25 min for SWCNTs. After treatment with acid there was no trace of residual metal catalyst using energy dispersive X-ray analysis. To probe the effect of acid oxidation on the SWCNTs Raman scattering (Fig. 2) was employed in conjunction with HRTEM (Supporting information).

In the low frequency region of the Raman spectrum radial breathing modes (RBM) in resonance with the laser photon frequency can be probed to obtain information about the tube diameters present [16]. In this case there are numerous peaks, some of which appear as shoulders on more intense neighbours corresponding to contributions from SWCNTs of different radii. The relationship between SWCNT diameter ( $d_t$ ) and the RBM frequency is

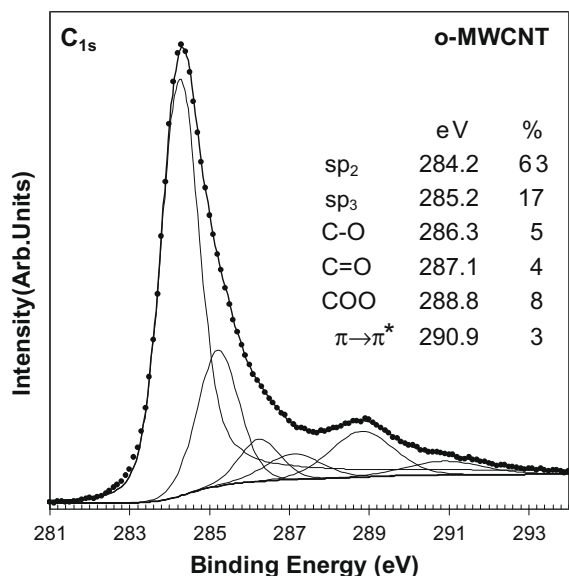


Fig. 1. C1s XPS spectrum of o-MWCNT. Dots correspond to experimental data points and dashed/solid lines are fitting to curves.

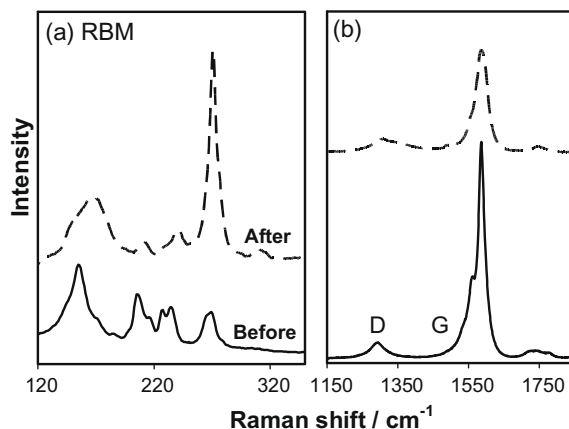


Fig. 2. Raman spectra of single-walled carbon nanotubes before and after acid oxidation using 785 nm laser excitation.

given by  $d_c(\text{nm}) \sim 223.7 \text{ cm}^{-1}/\omega_{\text{RBM}}$  from which the diameter range present is estimated to be 0.8–1.5 nm [16]. Using a Kataura plot [17], which relates the SWCNT diameter to the electronic transition energies calculated using the first-neighbour tight binding method, it is possible to assign o-SWCNT diameters in the ranges 0.8–1.1 nm and 1.2–1.5 nm to semiconducting and metallic respectively. Assuming a transfer integral of 2.9 eV and a carbon-carbon distance of 0.142 nm, the energy gap between the valence and conduction bands ( $E_g$ ) in the semiconducting SWCNTs present ranges between  $\sim 0.8$ –1.0 eV. Notably the Raman modes of metallic tubes are broadened by the interaction with free electrons, whilst the lines for semiconducting tubes should have a Lorentzian profile, making the latter easier to resolve. Such a large diameter distribution is not unexpected for SWCNTs grown by chemical vapour deposition (CVD) since the CNT diameter is to a large extent determined by the catalyst size, which is difficult to control on the nanometre scale. Upon acid oxidation some RBM peaks increase in intensity whilst others decrease. These changes can be attributed to changes in the degree of bundling and inter-tube contact area and/or the effect of chemical functionalisation which cause tubes with different radii to come into resonance with the laser photon frequency whilst others move away [18].

Raman scattering is also an effective probe of disorder in  $\text{sp}^2$  carbons such as graphene [19] and CNTs. The band characteristic of well ordered graphite ( $E_{2g} \sim 1582 \text{ cm}^{-1}$ ) is split into a number of components in the spectrum of CNTs due to their cylindrical symmetry [18]. Disorder appears as a broad band at  $\sim 1300 \text{ cm}^{-1}$  (D-band) and is activated by any change in the periodicity of the  $\text{sp}^2$  network such as missing carbon atoms or surface functionality resulting from chemical treatment. In Fig. 2 it is evident that the relative intensity of the D band is fractionally increased, broadened and up-shifted upon acid oxidation consistent with a decrease in structural order resulting from the incorporation of oxygen containing moieties into the  $\text{sp}^2$  lattice. The G band is also slightly up-shifted consistent with previous reports pertaining to the effective of electronegative functionality on the Raman spectra of SWCNTs [20]. Throughout the remainder of this paper, SWCNTs and MWCNTs acid treated according to the protocol reported herein will be abbreviated as o-SWCNT and o-MWCNT, respectively.

An important property of CNTs for OSC and OLED applications is their work function, since the difference between the CNT Fermi level and the relevant energy level of charge carriers in an adjacent organic semiconductor sets the barrier for injection or extraction. Table 1 gives the work function of o-SWCNT, o-MWCNT, PEDOT:PSS and ITO glass

cleaned according to the procedure described herein, measured using the Kelvin probe method. These measurements are referenced to freshly cleaved HOPG [21]. Importantly, since the Kelvin Probe method measures the spatial average of the work function, the values for o-MWCNT and o-SWCNT given in Table 1 were made on relatively thick ( $>1 \mu\text{m}$ ) films supported on non-conducting glass substrates, ensuring that the underlying substrate did not contribute to the measurement. Notably, the work function of the same films supported on ITO glass was identical to that on plain glass, verifying the credibility of the measurement [22].

The work function of PEDOT:PSS coated ITO glass is entirely consistent, within the experimental error, with that recently reported in the literature [23]. The work function of o-MWCNT is  $\sim 0.5$  eV higher than that of HOPG (4.475 eV) [21] and of untreated MWCNTs [13]. We consider that such a large increase is due to modification of the CNT surface potential by the high density of electronegative oxygen containing moieties which decorate the outermost layers only, since MWCNTs are essentially metallic in nature [13] and the inner walls remain intact. The work function of o-SWCNTs ( $\sim 5.06$  eV) is slightly higher than that reported for untreated SWCNT (4.7–4.9 eV) [13,24]. However, since in SWCNTs all constituent atoms are located at the CNT surface the interpretation of the increase in work function is more complex than in the case of o-MWCNTs. We attribute the observed increase in work function to a lowering of the Fermi level in the semi-conducting SWCNTs due to p-type doping by the electronegative oxygen containing moieties formed upon acid treatment.

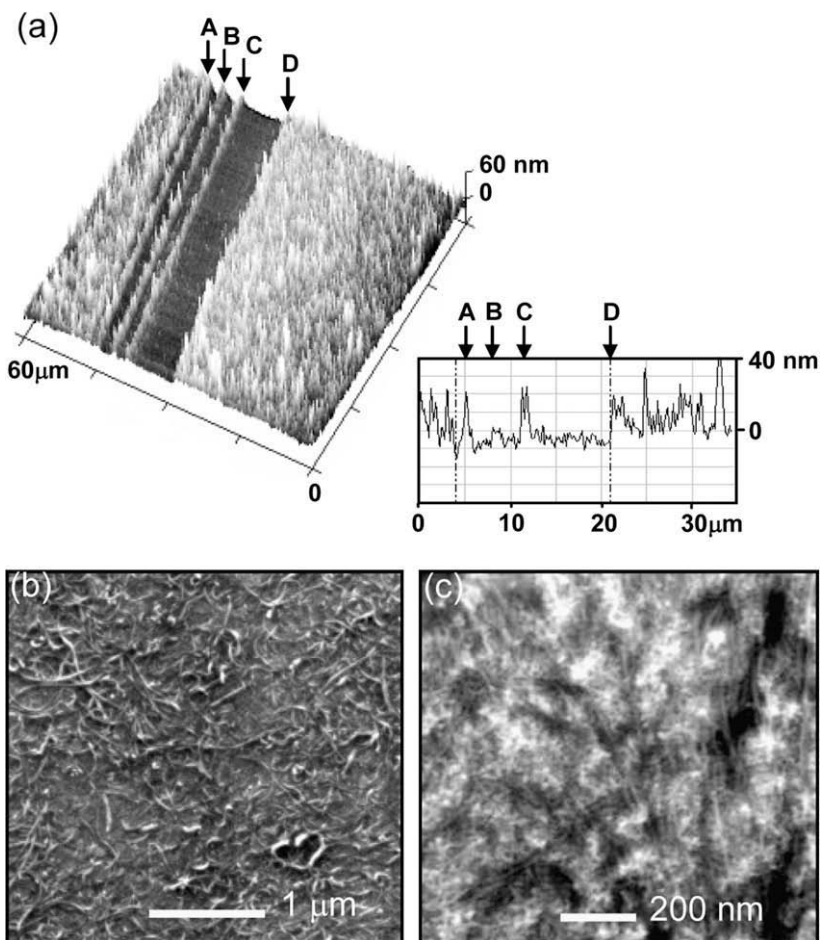
For application in OSCs thin films of o-SWCNTs and o-MWCNTs were prepared by the drop-then-spin casting method onto ITO glass from  $2.7 \text{ mg ml}^{-1}$  dispersions. The nanotube film thicknesses – determined by the dispersion concentration and spin speed – were selected to ensure that their transparency, thickness and conductivity was comparable to that of PEDOT:PSS films typically used in OSCs. The film thickness was measured directly using an AFM by carefully scoring films with a moist probe without scratching the underlying ITO (Fig. 3a). Notably, from the cross-section it is evident that the narrow strips between channels (A and C) have the same peak-to-peak roughness as the step edge of the widest channel (D), evidence that nanotubes are removed by the probe rather than displaced to the edges which would otherwise artificially increase the step height at the edge of the channel. The effective thickness of both films, based on the peak-to-peak roughness, was  $\sim 30$  nm. SEM images of o-SWCNT and o-MWCNT films drop and spin cast onto ITO glass are shown in Fig. 3b and c. These images are representative of a number of measurements at different sites on a number of different samples, from which it can be concluded that the films are uniform and relatively dense because the distinctive polycrystalline surface of the underlying ITO glass is not evident. Upon close inspection it is clear that both films comprise dense mats of entangled individual CNTs, with the difference in density reflecting the difference in nanotube dimensions.

Fig. 4a shows the transparency of the PEDOT:PSS, o-MWCNT and o-SWCNT coated ITO glass substrates. In all

**Table 1**

Summary of work function measurements made of commercial ITO (100 nm) on glass, PEDOT:PSS ( $\sim 45$  nm) on ITO glass, and thick films ( $>1 \mu\text{m}$ ) of o-SWCNT and o-MWCNT films on plain glass using the Kelvin probe method referenced to freshly cleaved HOPG [21].

	ITO glass	PEDOT:PSS	MWCNT (oxidised)	SWCNT (oxidised)
$\phi/\text{eV} \pm 0.04 \text{ eV}$	4.73	4.94	5.07	5.06



**Fig. 3.** (a) AFM image of a scored o-MWCNT film on ITO glass, with associated cross-section. SEM images of o-MWCNT (b) and o-SWCNT (c) films on ITO glass respectively. All films were prepared by drop-then-spin casting from  $2.7 \text{ mg ml}^{-1}$  dispersions.

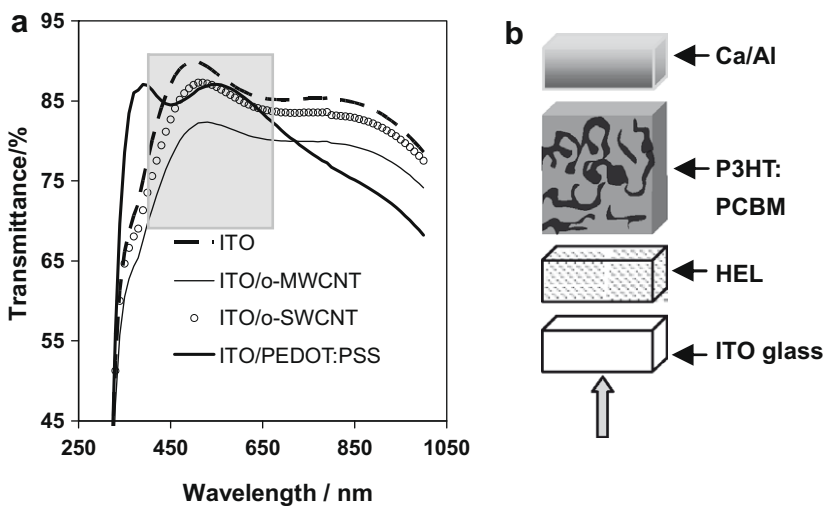


**Fig. 4.** (a) Transmittance of ITO glass and ITO glass coated with thin films of o-SWCNT ( $\sim 30 \text{ nm}$ ), o-MWCNT ( $\sim 30 \text{ nm}$ ) or PEDOT:PSS ( $\sim 45 \text{ nm}$ ); (b) Exploded schematic of OSC structure.

cases the substrates were illuminated from the glass side, as is the case in an OSC. The highlighted region is that over which P3HT:PCBM absorbs light, from which it can be seen that, to a good approximation, the same photon flux is incident on the photo-active layer in all devices. It is clear from Fig. 4 that the oxidised CNT films have greater transparency at near infra-red wavelengths ( $>700$  nm) at which a significant proportion of the terrestrial solar spectrum is located. This would prove to be a distinct advantage for the growing body of photoactive materials that harvest light in the near infrared, although this is not the case for P3HT:PCBM.

With improvements in the recorded efficiency of OSCs, the requirement to measure these values accurately has become increasingly important. A number of leading research groups have highlighted common sources of error when measuring device efficiency [25,26]. Arguably the greatest potential source of error relates to the accurate measurement of device area owing to shadowing [25] and edge effects [26] particularly when the device area is very small. The vast majority of reports in the literature pertain to devices with areas  $\leq 0.1$  cm<sup>2</sup>. In this study we have taken care to minimise these errors by both increasing the device area to  $\sim 0.35$  cm<sup>2</sup> and by masking off the edges of the device with a mat black mask to minimise edge effects. Furthermore, the calcium/aluminium electron extracting electrode was deposited using a rotating substrate stage to eliminate shadow effects. Devices were tested under standard test conditions of 100 mW cm<sup>-2</sup> AM1.5 G irradiance using an NREL traceable calibrated silicon solar cell.

In order to draw meaningful conclusions from a direct comparison of the performance of OSCs employing different hole-extracting electrodes it is critical to have knowledge of any difference in the thickness or roughness of the photoactive organic layer between cells employing different electrodes. The thickness of the photoactive layer can depend on properties of the substrate surface such as hydrophilicity and surface roughness particularly when deposited using the spin coating method. In this case the thicknesses of the P3HT:PCBM films deposited under identical conditions on ITO, ITO/PEDOT:PSS, ITO/o-MWCNT and ITO/o-SWCNT were  $246 \pm 15$  nm. A thickness variation of  $\pm 15$  nm across different samples with the same substrate electrode is consistent with that previously reported by Li et al. [27] using identical deposition procedure. The peak-to-valley roughness of P3HT:PCBM films deposited using the slow dry method employed herein is known to be  $\sim 100$  nm, which corresponds to  $\sim 50\%$  of the mean film thickness [27]. The peak-to-valley roughness of P3HT:PCBM films deposited on PEDOT:PSS, o-SWCNT and o-MWCNT films in this work was  $\sim 100$  nm, and fractionally smaller,  $\sim 70$  nm, on the virgin ITO glass substrate. This small difference, combined with the fact that these features are much smaller than the wavelength of visible light, make it unlikely that any significant differences in device performance can be attributed to variations in the extent to which light is scattered by the reflective back contact.

The OSCs employing a PEDOT:PSS HEL at the interface between the ITO electrode and bulk-heterojunction exhibit increased open circuit voltage ( $V_{oc}$ ), short circuit current

( $J_{sc}$ ) and fill factor ( $FF$ ) as compared to ITO alone (Fig. 5:  $V_{oc} = 0.61$  V vs. 0.57–0.60 V;  $J_{sc} = 6.8$ –7.3 mA cm<sup>-2</sup> vs. 6.3–6.6 mA cm<sup>-2</sup>;  $FF = 0.61$ –0.62 vs. 0.5–0.55). The  $V_{oc}$  of devices employing o-MWCNT or o-SWCNT HELs was identical to that of devices using PEDOT:PSS and fractionally larger than in devices employing plasma cleaned ITO glass alone.

Whilst the factors that determine  $V_{oc}$  in OSCs are not yet fully understood this result indicates that  $V_{oc}$  is weakly dependent on the positive contact (cathode) work function and that the optimal value lies between that of ITO (4.73 eV) and PEDOT:PSS (4.94 eV) which correlates with the ionisation energy of P3HT (4.65–4.85 eV) [28]. Interestingly, in the simplest case where the vacuum level is aligned across the interface (i.e. in the Schottky-Mott limit) there would be a modest barrier ( $\geq 0.2$  eV) to hole-extraction by o-MWCNTs and o-SWCNTs, which would be expected to deteriorate device performance as compared to OSCs employing PEDOT:PSS or plasma cleaned ITO alone. Clearly, this is not the case and so the simplistic assumption of vacuum level alignment across the interface between oxidised CNTs and P3HT is unlikely to be valid. In cases where the work function of the HEL is higher than the ionisation energy of P3HT and when the former has accessible states above the Fermi level (as in the case of o-MWCNTs and metallic o-SWCNTs) ground state charge transfer from the HOMO of P3HT to the HEL is expected [29]. The effect of such charge transfer across the interface would be to pin the electrode Fermi level close to the P3HT HOMO level [29], thus removing any energy barrier to hole extraction that would otherwise exist across interfaces with o-SWCNT or o-MWCNT. The implication for device performance of such an interaction would be an insensitivity of  $V_{oc}$  to the work function of the hole-extracting electrode for HELs having work functions equal to or greater than the ionisation energy of P3HT, which is observed to be the case.

In bulk-heterojunction OSCs free carriers are generated throughout the light absorbing organic layer and so charge carrier extraction is primarily driven by the built-in

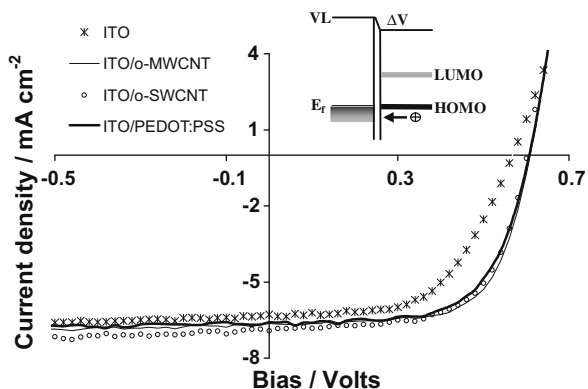


Fig. 5. Typical current-voltage characteristics of OSCs incorporating various HELs at the ITO/P3HT:PCBM interface under one sun (AM1.5 G) irradiance. Inset: Schematic energy level diagram depicting pinning of the Fermi level of o-MWCNT and o-SWCNT to the HOMO of P3HT as a result of a ground state charge transfer interaction.

electric field that results from asymmetry in the anode and cathode work functions. The fact that in all devices the  $J_{sc}$  changes very little as the electric field is increased beyond the maximum built-in potential by an applied bias of up to 0.5 V (i.e. in the 3rd quadrant response) is evidence that in all cases the field is sufficient to sweep out the photogenerated carriers to the external circuit. The  $J_{sc}$  in devices utilizing ITO glass alone was consistently lower than those using o-MWCNT, o-SWCNT or PEDOT:PSS HELs. Khodabakhsh et al. [30] have previously shown that the  $J_{sc}$  in discrete heterojunction OSCs increases as the work function of the hole-extracting electrode approaches the ionisation energy of the donor material. The observation of a larger  $J_{sc}$  in OSCs incorporating o-SWCNT, o-MWCNT and PEDOT:PSS as compared to ITO glass only is therefore consistent with improved alignment between the Fermi level of the electrode (in this case the HEL modified ITO glass) and the HOMO of P3HT. The fractionally lower  $J_{sc}$  in cells incorporating o-MWCNTs as compared to PEDOT:PSS can be attributed to the lower transparency across the part of the solar spectrum that P3HT:PCBM absorbs (400–700 nm) [7b]. However, in narrower band gap devices, which harvest a greater proportion of the near infrared spectrum, this disadvantage would be off-set.

The high and comparable shunt resistance (defined as the gradient of the  $JV$  characteristic at  $J_{sc}$ ) of all the device structures reported herein is compelling evidence that the incorporation of o-CNT layers does not increase leakage due to filamentary short circuits. The primary advantage of incorporating an o-CNT or PEDOT:PSS HEL is the large (~50%) reduction in cell series resistance (defined as the gradient of the  $JV$  characteristic at  $J = 0 \text{ mA cm}^{-2}$ ) as compared to those using plasma-cleaned ITO glass only. The sheet resistance of the ~30 nm thick o-MWCNT and o-SWCNT films supported on plain glass was found to be very high and comparable to that of the ~45 nm thick films of PEDOT:PSS:  $\sim 10^7 \Omega \text{ sq}^{-1}$ . Such a high sheet resistance is consistent with the very low film thickness utilised (~30 nm) and disruption of the pi-conjugation in the CNT walls as a result of acid treatment. Consequently, the observed reduction in device series resistance cannot result from an increase in the conductivity of the electrode due to the presence of the o-CNT or PEDOT:PSS layers. It can also be assumed that the resistance to transport through the photoactive layer and ITO electrode is the same in all device structures and so the observed reduction in device series resistance must be attributed to a difference in contact resistance. In the context of OSCs the interaction between the photoactive organic layer and the supporting substrate electrode is a weak van der Waals type interaction and so the difference in contact resistance may be correlated with a difference in molecular conformation at the interface. Conjugated molecules including polythiophenes [31] are known to adopt a parallel orientation with respect to the graphitic wall of CNTs a configuration that would be expected to minimise the contact resistance, although in this instance the nature of the interaction is complicated by the presence of surface bound oxygen containing moieties. The low series resistance and high shunt resistance in devices incorporating CNTs results in a high  $F.F.$  (o-MWCNT ~0.64, o-SWCNT ~0.63), comparable to that uti-

lising PEDOT:PSS (0.61–0.62) and, to our knowledge, the largest  $F.F.$  for an OSC employing CNTs in any capacity [2c,3b,4,5,32a–c]. Importantly, the power conversion efficiency in devices employing o-SWCNT and o-MWCNT films is identical to that achieved using PEDOT:PSS films: ~2.7%.

MWCNTs are essentially metallic in nature having a small but finite density of states at the Fermi level [13]. Consequently they are equally capable of conducting both electrons and holes and so offer predictable functionality as reliable high work function nano-wires, simplifying the interpretation of functionality as well as design in a device context. Conversely, the electronic structure of o-SWCNTs is more complex than that of o-MWCNTs primarily due to the presence of both semi-conducting and metallic SWCNTs, which co-exist in bulk samples regardless of the method of synthesis. From the spread of Raman active radial breathing modes (Fig. 2) it is evident that the sample comprises a distribution of SWCNT diameters with  $E_g \sim 0.8$ –1.0 eV. The result is a complex multi-level energy structure of metallic and semiconducting o-SWCNT. Clearly, from the performance of devices incorporating o-SWCNTs this complexity is not disadvantageous. A possible explanation is that the Fermi level in the semiconducting o-SWCNT is close to the valance band edge due to p-type doping by oxygen defects, enabling holes to move easily between metallic and semiconducting o-SWCNTs. This does not however rule out the possibility of significantly better performance should the type selection of the SWCNT be more precise.

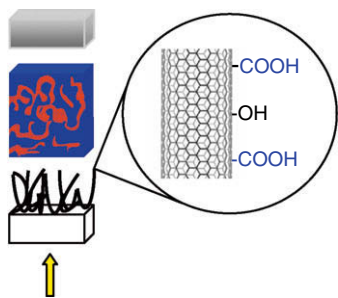
#### 4. Conclusion

In conclusion we have shown that thin films of extensively oxidised single wall and multi-wall carbon nanotubes can be utilised as high work function, solution processable hole-extraction layers in efficient OSCs. An important advantage over PEDOT:PSS – the most widely used hole-extraction layer in OSCs – is that they are processed from a pH neutral aqueous dispersion, reducing the likelihood of adverse chemical reaction with conducting oxide electrodes. Furthermore, absorption measurements show that films of acid oxidised carbon nanotubes of comparable thickness to PEDOT:PSS offer greater transparency at near infra-red wavelengths over which a significant portion of the terrestrial solar spectrum is located. As such we have demonstrated that extensively oxidised carbon nanotubes are a new tool in electrode design for low cost OSCs pointing the way to the realisation of wholly carbon nanotube based conformable hole-extracting electrodes in OSCs.

#### Table of contents

Thin films of extensively oxidised single-wall and multi-wall carbon nanotubes offer a path to efficient hole-extraction in state-of-the-art solution processed organic solar cells, as high work function solution processable hole-extraction layers with the advantages of low acidity and high transparency in the near infra-red.





## Acknowledgements

The authors would like to thank Dr S. J. Henley for recording the Raman spectra and Dr. V. Stolojan for the HRTEM study. The authors would also like to thank Dr. J.D. Carey, Professor J. Shannon, Dr. M. Shkonov and Dr. H. Shiozawa for helpful discussions. This research was supported by the Royal Academy of Engineering and United Kingdom Engineering and Physical Science Research Council.

## Appendix A. Supplementary data

Supplementary data associated with this article can be found, in the online version, at [doi:10.1016/j.orgel.2008.12.013](https://doi.org/10.1016/j.orgel.2008.12.013).

## References

- [1] (a) B.C. Thompson, J.M.J. Fréchet, *Angew. Chem. Int. Ed.* 47 (2008) 58–77;  
(b) S.R. Forrest, *MRS Bulletin* 30 (2005) 28–32.
- [2] (a) J.-Y. Lee, S.T. Connor, Y. Cui, P. Peumans, *Nano Lett.* 8 (2008) 689–692;  
(b) P.A. Levermore, L.C. Chen, X.H. Wang, R. Das, D.D.C. Bradley DDC, *Adv. Mater.* 19 (2007) 2379;  
(c) J.B. Wu, H.A. Becerril, Z.N. Bao, Z. Liu, Y. Chen, P. Peumans, *Appl. Phys. Lett.* 92 (2008) 263302.
- [3] (a) A.D. Pasquier, H.E. Unalan, A. Kanwal, S. Miller, M. Chhowalla, *Appl. Phys. Lett.* 87 (2005) 203511;  
(b) Z. Wu, Z. Chen, X. Du, J.M. Logan, J. Sippel, M. Nikolou, K. Kamaras, J.R. Reynolds, D.B. Tanner, A.F. Hebard, A.G. Rinzler, *Science* 305 (2004) 1273;  
(c) C.M. Aguirre, S. Auvray, S. Pigeon, R. Izquierdo, P. Desjardins, R. Martel, *Appl. Phys. Lett.* 88 (2006) 183104;  
(d) M.W. Rowell, M.A. Topinka, M.D. McGehee, H.J. Prall, G. Dennler, N.S. Sariciftci, L.B. Hu, G. Gruner, *Appl. Phys. Lett.* 88 (2006) 233506;  
(e) D. Zhang, K. Ryu, X. Liu, E. Polikarpov, J. Ly, M.E. Tompson, C. Zhou, *Nano. Lett.* 6 (2006) 1880;  
(f) G. Gruner, *J. Mater. Chem.* 16 (2006) 3533.
- [4] (a) M. Zhang, S. Fang, A.A. Zakhidov, S.B. Lee, A.E. Aliev, C.D. Williams, K.R. Atkinson, R.H. Baughman, *Science* 309 (2005) 1215;  
(b) R. Ulbricht, X. Jiang, S. Lee, K. Inoue, M. Zhang, S. Fang, R. Baughman, A. Zakhidov, *Phys. State Solid B.* 243 (2006) 3528.
- [5] J. van de Lagemaat, T.M. Barnes, G. Rumbles, S.E. Shaheen, T.J. Coutts, C. Weeks, I. Levitsky, J. Peltola, P. Glatkowski, *Appl. Phys. Lett.* 88 (2006) 233503.
- [6] T.M. Brown, J.S. Kim, R.H. Friend, F. Cacialli, R. Daik, W.J. Feast, *Appl. Phys. Lett.* 75 (1999) 1679.
- [7] (a) P. Schilinsky, C. Waldauf, C.J. Brabec, *Appl. Phys. Lett.* 81 (2002) 3885;  
(b) Y. Kim, S. Cook, S.M. Tuladhar, S.A. Choulis, J. Nelson, J.R. Durrant, D.D.C. Bradley, M. Giles, I. McCulloch, C.-S. Ha, M. Ree, *Nat. Mater.* 5 (2006) 197.
- [8] (a) M.P. de Jong, L.J. van Ijendoorn, M.J.A. de Voigt, *Appl. Phys. Lett.* 77 (2000) 2255;  
(b) K.W. Wong, H.L. Yip, Y. Luo, K.Y. Wong, W.M. Lau, K.H. Low, H.F. Chow, Z.Q. Gao, W.L. Yeung, C.C. Chang, *Appl. Phys. Lett.* 80 (2002) 2788;  
(c) T.P. Nguyen, S.A. De Vos, *Surf. Sci.* 221 (2004) 330.
- [9] V. Shrotriya, G. Li, Y. Yao, C.-W. Chu, Y. Yang, *Appl. Phys. Lett.* 88 (2006) 073508.
- [10] C.A. Furtado, U.J. Kim, H.R. Gutierrez, L. Pan, E.C. Dickey, P.C. Eklund, *J. Am. Chem. Soc.* 126 (2004) 6095.
- [11] A.R. Harutyunyan, B.K. Pradhan, J.P. Chang, G. Chen, P.C. Eklund, *J. Phys. Chem. B.* 106 (2002) 8671.
- [12] J. Liu, A.G. Rinzler, H. Dai, J.H. Hafner, R.K. Bradley, P.J. Boul, A. Lu, T. Iverson, K. Shelimov, C.B. Huffman, F.J. Rodríguez-Macias, Y.-S. Shon, T.R. Lee, D.T. Colbert, R.E. Smalley, *Science* 280 (1998) 1253.
- [13] H. Ago, T. Kugler, F. Cacialli, W.R. Salaneck, M.S.P. Shaffer, A.H. Windle, R.H. Friend, *J. Phys. Chem. B.* 103 (1999) 8116.
- [14] B.C. Satishkumar, A. Govindaraj, J. Mofokeng, G.N. Subbanna, C.N.R. Rao, *J. Phys. B.* 29 (1996) 4925.
- [15] (a) B. Wu, J. Zhang, Z. Wei, S. Cai, Z. Liu, *J. Phys. Chem. B.* 105 (2001) 5075;  
(b) G.A. Forrest, A.J. Alexander, *J. Phys. Chem. C.* 111 (2007) 10792.
- [16] (a) Chase, P.C. Eklund, K.A. Williams, S. Fang, K.R. Subbaswamy, M. Menon, A. Thess, R.E. Smalley, G. Dresselhaus, M.S. Dresselhaus, *Science* 275 (1997) 187;  
(b) M. Milnera, J. Kürti, M. Hulman, H. Kuzmany, *Phys. Rev. Lett.* 84 (2000) 1324.
- [17] H. Kataura, Y. Kumazawa, Y. Maniwa, I. Umezumi, S. Suzuki, Y. Ohtsuka, Y. Achiba, *Synth. Met.* 103 (1999) 2555.
- [18] M.S. Dresselhaus, G. Dresselhaus, R. Saito, A. Jorio, *Phys. Rep.* 409 (2005) 47.
- [19] A.C. Ferrari, J.C. Meyer, V. Scardaci, C. Casiraghi, M. Lazzeri, F. Mauri, F. S. Piscanec, D. Jiang, K.S. Novoselov, S. Roth, A.K. Geim, *Phys. Rev. Lett.* 97 (2006) 187401.
- [20] (a) A.M. Rao, P.C. Eklund, S. Bandow, A. Thess, R.E. Smalley, *Nature* 388 (1997) 257;  
(b) U.J. Kim, C.A. Furtado, X. Liu, G. Chen, P.C. Eklund, *J. Am. Chem. Soc.* 127 (2005) 15437.
- [21] W.N. Hansen, G.J. Hansen, *Surf. Sci.* 481 (2001) 172.
- [22] S.R. Day, R.A. Hatton, M.A. Chesters, M.R. Willis, *Thin Solid Films* 410 (2002) 159.
- [23] G. Winroth, G. Latini, D. Credgington, L.Y. Wong, L.L. Chua, P.K.H. Ho, F. Cacialli, *Appl. Phys. Lett.* 92 (2008) 103308.
- [24] (a) P. Liu, Q. Sun, F. Zhu, K. Liu, K. Jiang, L. Liu, Q. Li, S. Fan, *Nano. Lett.* 8 (2008) 647;  
(b) S. Suzuki, C. Bower, Y. Watanabe, O. Zhou, *Appl. Phys. Lett.* 76 (2000) 4007.
- [25] V. Shrotriya, G. Li, Y. Yao, T. Moriarty, K. Emery, Y. Yang, *Adv. Funct. Mater.* 16 (2006) 2016.
- [26] A. Cravino, P. Schilinsky, C.J. Brabec, *Adv. Funct. Mater.* 17 (2007) 3906.
- [27] G. Li, V. Shrotriya, J. Huang, Y. Yao, T. Moriarty, K. Emery, Y. Yang, *Nat. Mater.* 4 (2005) 864.
- [28] (a) M. Onoda, K. Tada, H. Nakayama, *J. Appl. Phys.* 86 (1999) 2110;  
(b) A.J. Cascio, J.E. Lyon, M.M. Beerbom, R. Schlaf, Y. Zhu, S.A. Jenekhe, *Appl. Phys. Lett.* 88 (2006) 062104;  
(c) Y. Sohn, J.T. Stuckless, *Chem. Phys. Lett.* 436 (2007) 228.
- [29] (a) Z.E. Oooi, R. Jin, J. Huang, Y.F. Loo, A. Sellinger, J.C. de Mello, *J. Mater. Chem.* 18 (2008) 1644;  
(b) A. Crispin, X. Crispin, M. Fahlman, M. Berggren, W.R. Salaneck, *Appl. Phys. Lett.* 89 (2006) 213503;  
(c) C. Tengstedt, W. Osikowicz, W.R. Salaneck, I.D. Parker, C.-H. Hsu, M. Fahlman, *Appl. Phys. Lett.* 88 (2006) 053502.
- [30] S. Khodabakhsh, B.M. Sanderson, J. Nelson, T.S. Jones, *Adv. Funct. Mater.* 16 (2006) 95.
- [31] (a) T. Hamano, J. Kikuchi, A. Ikeda, K. Nobusawa, *Org. Lett.* 8 (2006) 5489;  
(b) Y. Kanai, J.C. Grossman, *Nano Lett.* 8 (2008) 908.
- [32] (a) S. Berson, R. de Bettignies, S. Bailly, S. Guillerez, B. Joussetme, *Adv. Funct. Mater.* 17 (2007) 3363;  
(b) A.J. Miller, R.A. Hatton, S.R.P. Silva, *Appl. Phys. Lett.* 89 (2006) 133117;  
(c) S. Chaudhary, H. Lu, A.M. Müller, C.J. Bardeen, M. Ozhan, *Nano Lett.* 7 (2007) 1973.



# Bottom gate organic thin-film transistors fabricated by ultraviolet transfer embossing with improved device performance

Shi Jingsheng, Mary B. Chan-Park, Chang Ming Li\*

School of Chemical and Biomedical Engineering, Nanyang Technological University, 70 Nanyang Drive, Singapore 637457, Singapore

## ARTICLE INFO

### Article history:

Received 12 November 2008

Received in revised form 20 December 2008

Accepted 20 December 2008

Available online 3 January 2009

### PACS:

73.40.Cg

73.40.Sx

73.61.Ph

### Keywords:

Organic field-effect transistors

Organic thin-film transistors

UV embossing

Transfer embossing

Dielectric-semiconductor interface

Cross-linking

Printable

Large-area

Flexible

## ABSTRACT

Ultraviolet transfer embossing is optimized to fabricate bottom gate organic thin-film transistors (OTFTs) on flexible plastic substrates, achieving significant improved device performance ( $\mu = 0.01\text{--}0.02\text{cm}^2/\text{Vs}$ ; on/off ratio =  $10^4$ ) compared with the top gate OTFTs made previously by the same method ( $\mu = 0.001\text{--}0.002\text{cm}^2/\text{Vs}$ ; on/off ratio =  $10^2$ ). The performance improvement can be ascribed to the reduced roughness of the dielectric-semiconductor interface ( $R_{\text{rms}} = 0.852\text{nm}$ ) and thermally cross-linked PVP dielectric which leads to reduced gate leakage current and transistor off current in the bottom-gated configuration. This technique brings an alternative great opportunity to the high-volume production of economic printable large-area OTFT-based flexible electronics and sensors.

© 2009 Elsevier B.V. All rights reserved.

## 1. Introduction

Organic thin-film transistors (OTFTs) are receiving increasing interest in the area of printed low-cost and large-area electronics on flexible substrates for applications such as electronic paper, solar panels and flexible sensors [1–3]. To lower the cost of organic electronics, it is important to develop fabrication processes that do not rely on clean room and that are compatible with solution processable dielectric materials and organic semiconductors [4]. Cold welding methods, both subtractive and additive, developed by Forrest's group [1,5,6] are capable to

transfer metallic patterns on submicrometer scale by applying high pressure to form metallic bonds at the conformal contact area. In the additive cold welding method, a strike layer for facilitating the bonding process requires a gentle etching or simple sputtering process to be removed. Inkjet printing is an alternative technique to photolithography that has recently reached submicron scale resolution [7]; this process, however, requires a chemically modified ink to fabricate ultra-hydrophobic electrodes and post-printing sintering at a high temperature to increase the conductivity of the electrodes. Screen printing and micro contact printing ( $\mu\text{CP}$ ) have been actively investigated by different research groups [8], but these techniques are limited to low resolution of  $\sim 20\text{ }\mu\text{m}$ . Nanotransfer printing (nTP), developed by rogers' research group as advances of

\* Corresponding author. Tel./fax: +65 67904485.

E-mail address: [ECMLi@ntu.edu.sg](mailto:ECMLi@ntu.edu.sg) (C.M. Li).

$\mu$ CP, offers a better resolution ( $\sim 100$  nm) comparing to  $\mu$ CP [9,10]. The process utilizes the surface chemistry or noncovalent forces between the receiving surface and transferred metal to form the source and drain electrodes in OTFTs [11,12].

Our lab has previously demonstrated a fast and efficient OTFT fabrication process employing ultraviolet (UV) transfer embossing at room temperature with a resolution ( $\sim 2$   $\mu$ m) comparable to lithography process [13]. UV transfer embossing is fast, does not require clean room and can achieve small micron-resolution. The embossing template fabrication itself does require clean fabrication conditions, but once it is made, it may be used repeatedly to produce OTFTs under less stringent conditions. However, our previous top gate devices, regardless of using P3HT or poly(3,3''-didodecyl quaterthiophene) (PQT-12) (see [Supplementary material](#)) as organic semiconductors, have relatively low device performance of mobility ( $\mu$ ) of 0.001–0.002  $\text{cm}^2/\text{Vs}$  and on/off ratio of  $10^2$  [13]. The poor performance is attributed principally to the roughness between the PVP dielectric and the semiconductor; this is propagated from the relatively rough PET substrate surface through the thin semiconductor film. The high roughness at the dielectric-semiconductor interface significantly perturbs the structure of the semiconductor and forms many electron traps. Further, the top-gated configuration, which requires deposition of the organic semiconductor prior to deposition of the poly(4-vinylphenol) (PVP) dielectric, prevents thermal cross-linking of the dielectric since that

would damage the underlying semiconductor (the typical cross-link temperature for PVP is above  $150$   $^\circ\text{C}$ , which would degrade the semiconductor [14]), with the consequence of high leakage current through the dielectric layer.

In this letter we report our optimization of the UV transfer embossing process by fabricating bottom gate devices with a resolution of  $\sim 2$   $\mu$ m which exhibit much improved device performance. Bottom gate devices allow deposition of PVP dielectric before semiconductor deposition. Fig. 1 shows a schematic illustration of the fabrication process for bottom gate devices by our UV transfer embossing process.

## 2. Experimental

The UV embossing resin was a mixture of epoxy bisphenol-A diacrylate (Ebecryl 600), dipropylene glycol diacrylate (SR 508) and trimethylolpropane triacrylate (SR 351) with weight ratio of 12:5:3 diluted (50 wt%) in isobutylmethylketone (IBMK). Ebecryl 600 was supplied by UCB chemicals and SR 508 and SR 351 were supplied by Sartomer. Our UV resin mixture offers a fast curing response, good adhesion and superior cured film strength. This formulation was chosen also because the contact between UV resin and PVP thin-film was good enough for the deposition of UV resin on PVP via spin-coating. PVP and methylated poly(melamine-co-formaldehyde) (MPMF, used as PVP cross-linking agent) with weight ratio of 4:1 were dissolved in dimethyl formamide (DMF) to give a 8 wt% solu-

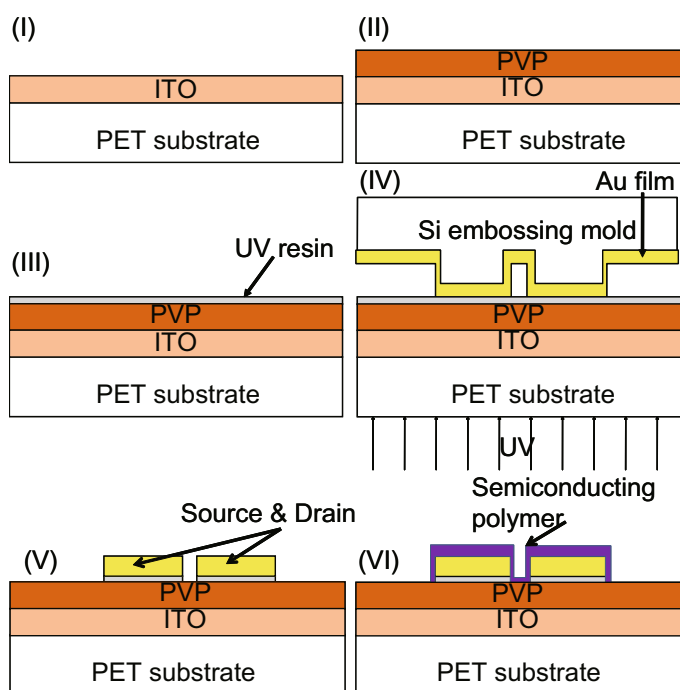


**Fig. 1.** Schematic illustration of the UV transfer embossing process in fabrication of bottom gate devices: (I) ITO coated PET films are cleaned in detergent, (II) PVP with MPMF is spin-coated on top of ITO and cross-linked in an oven followed with  $\text{O}_2$  plasma treatment, (III) UV resin is spin-coated on PVP, (IV) Si embossing mold and UV resin coated substrate are brought into contact and exposed to UV light, (V) source and drain electrodes are transferred onto PVP after demolding and (VI) semiconducting polymer is drop-coated to complete device fabrication.

tion. The solution was filtered with a polytetrafluoroethylene (PTFE) syringe filter with 0.2  $\mu\text{m}$  pore size. The embossing template was fabricated, passivated and coated with Au film in the same manner as reported in our previous work [13].

Poly(ethylene terephthalate) (PET) films coated with indium tin oxide (ITO) supplied by Sigma–Aldrich were cleaned by sonication in detergent. ITO served as the transistor gate electrode. The PVP solution was spin-coated onto the ITO coated PET substrate at 500 rpm for 3 min. The dielectric layer was then cross-linked in air at 200  $^{\circ}\text{C}$  for 2 h. For high-volume production, PVP dielectric could also be sufficiently cross-linked at 200  $^{\circ}\text{C}$  for 15 min as it turns insoluble in acetone and chlorobenzene. Since reduced cross-linking time is critical for the mass production, we conducted this process and successfully fabricated proper transistor devices.  $\text{O}_2$  plasma treatment at power of 400 w and  $\text{O}_2$  pressure of 200 m Torr were applied to PVP dielectric for 10 s. UV resin was then spin-coated onto the PVP thin-film at 3000 rpm for 2 min. The UV resin coated substrate was immediately brought into contact with a gold coated embossing template and exposed to UV light through the transparent substrate, ITO gate electrode and PVP thin-film. After removal of the template, the adhered gold patterns formed source and drain electrodes. The whole construct was rinsed with ethanol or isopropyl alcohol to remove the uncured UV resin. The transistor channel formed after removal of the uncured UV resin which is in the uncontacted areas and inhibited from curing by oxygen. The fabrication process was completed by drop coating of PQT-12 solution in chlorobenzene and annealing at 125  $^{\circ}\text{C}$  for 15 min in a vacuum oven.

### 3. Results and discussion

$\text{O}_2$  plasma treatment is a key step for the successful transfer of electrodes onto the hydrophobic PVP surface. Fig. 2a and b shows transferred gold electrodes on PVP thin-film without (a) and with (b)  $\text{O}_2$  plasma treatment. Without plasma treatment, the gold electrodes were only partially transferred. It is known that  $\text{O}_2$  plasma treatment can activate a surface, make it hydrophilic and greatly improved the adhesion of cured UV resin to the PVP, which was necessary for the gold electrodes to remain on the construct after removal of the UV embossing template. Fig. 2c and d shows micrographs of water droplets on untreated and plasma-activated PVP surfaces. The  $\text{O}_2$  plasma treatment reduces the water contact angle from  $76 \pm 1^{\circ}$  to  $19 \pm 2^{\circ}$ .

The transfer embossed electrodes were characterized by high resolution scanning electron microscope (HR-SEM) and atomic force microscope (AFM). Fig. 3a shows the top view of the gap between two patterned electrodes on PVP dielectric film. The measured length of the gap, which is the channel length of the transistor device, is  $3.0 \pm 0.1 \mu\text{m}$  and the ratio between the length of the gap and roughness of the electrodes is estimated to be 30:1, resulting in a roughness of around 100 nm. The relatively high roughness is believed to arise from the mechanical breakage in the Au film at the edge of the mold during demolding. Fig. 3b shows a 3D AFM image of the patterned electrodes, focusing on the gap between two electrodes. The measured gap of  $3.0 \pm 0.3 \mu\text{m}$  in length between the two electrodes was obtained. These results indicate that the technology described in this work is capable of achieving a resolution as low as  $\sim 3 \mu\text{m}$ .

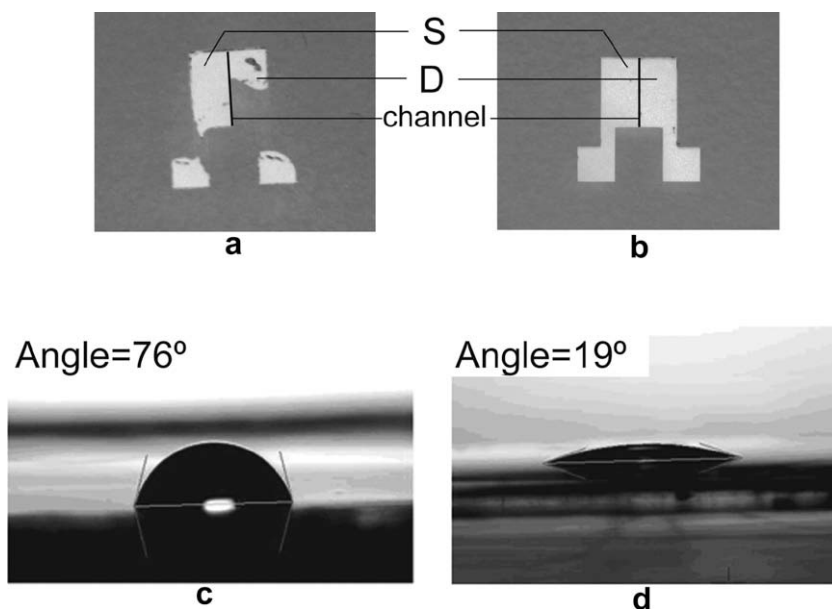


**Fig. 2.** (a) Incomplete transfer of source and drain electrodes without plasma activation, (b) intact source and drain electrodes transferred onto plasma-activated PVP, (c) water contact angle of PVP surface without plasma activation and (d) water contact angle of PVP surface with brief plasma activation. (S, source electrode in transistor device; D, drain electrode in transistor device; channel, a line indicating the position of transistor channel).

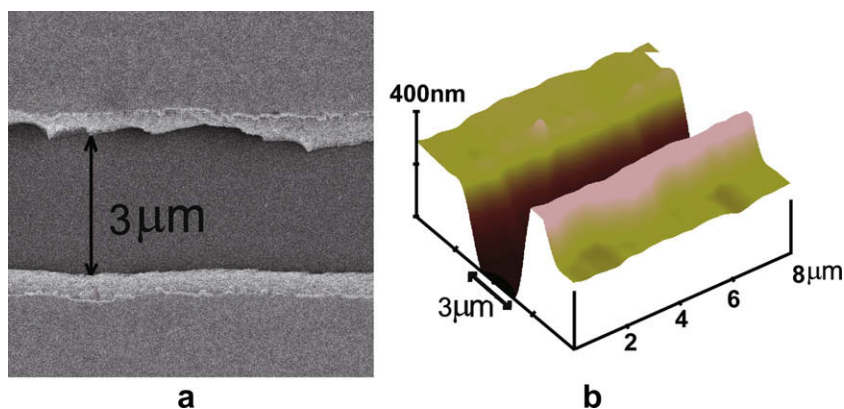


Fig. 3. (a) High resolution SEM image of a gap between two electrodes and (b) AFM image of a gap between two electrodes.

The device performance of OTFT fabricated by this transfer embossing technology was measured in air using an Agilent 5270B parameter analyzer with a cascade probe station. Fig. 4a shows a representative drain current versus drain voltage ( $I_d$ - $V_d$ ) curve and Fig. 4b shows the transfer characteristics ( $I_d$ - $V_g$ ) curve. The devices achieved a much better performance than the prior top gate devices we have

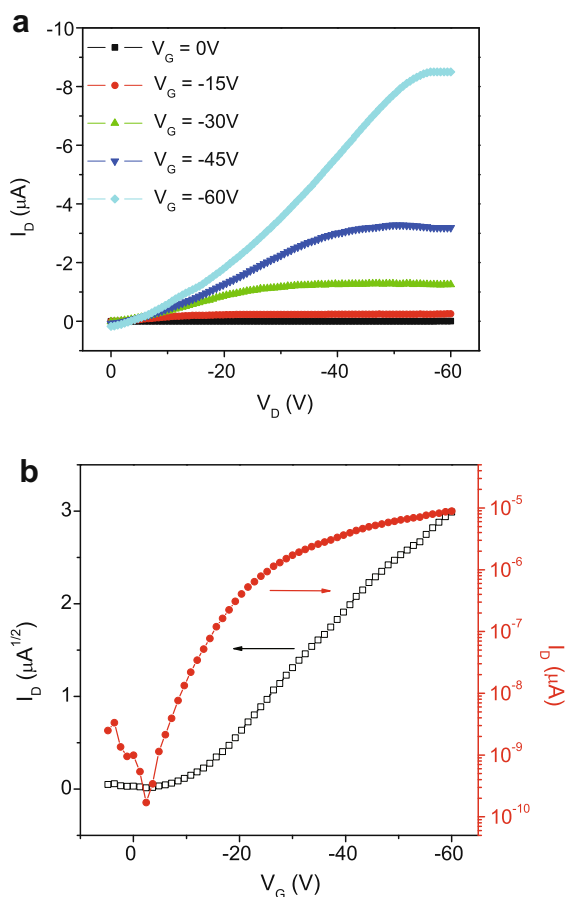


Fig. 4. (a) Output and (b) transfer characteristics of bottom gate OTFTs fabricated by UV transfer embossing.

reported. The calculated carrier mobility ranged from 0.01–0.02  $\text{cm}^2/\text{Vs}$  in the saturation regime, which is more than 1 order of magnitude higher than our previous top gate devices [13]; the on/off ratio reached as high as  $10^4$ , which is 2 orders of magnitude higher than that in our previous report [13].

The electrical properties at the interface of transfer embossed Au electrode/semiconducting polymer was studied with standard TLM method [15]. The total contact to contact resistance ( $R_{\text{total}}$ ) can be divided into sheet resistance ( $R_{\text{sh}}$ ) in the channel and the contact resistance ( $R_c$ ) at the electrodes. At low drain voltage [15],

$$R_{\text{total}} = R_{\text{sh}} + R_c = \frac{L}{W\mu C_i(V_G - V_T)} + R_c,$$

and by normalizing resistance with channel width [16],

$$R_{\text{total}}W = \frac{L}{\mu C_i(V_G - V_T)} + R_cW,$$

where  $W$ ,  $\mu$ ,  $L$ ,  $C_i$ ,  $V_G$  and  $V_T$  are channel width, charge mobility, channel length, capacitance per unit area of dielectric layer, gate voltage and threshold voltage, respectively. The width-normalized contact resistance can be evaluated at  $L=0$ . Devices with four different channel

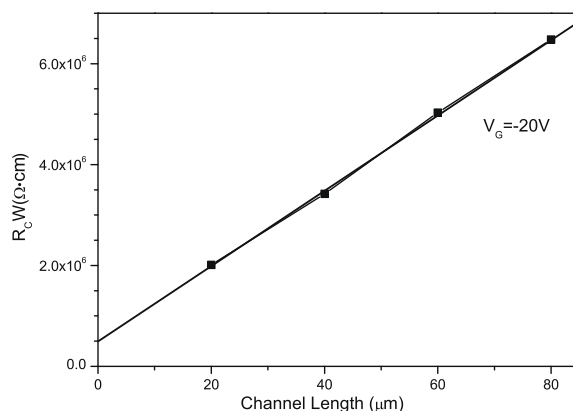
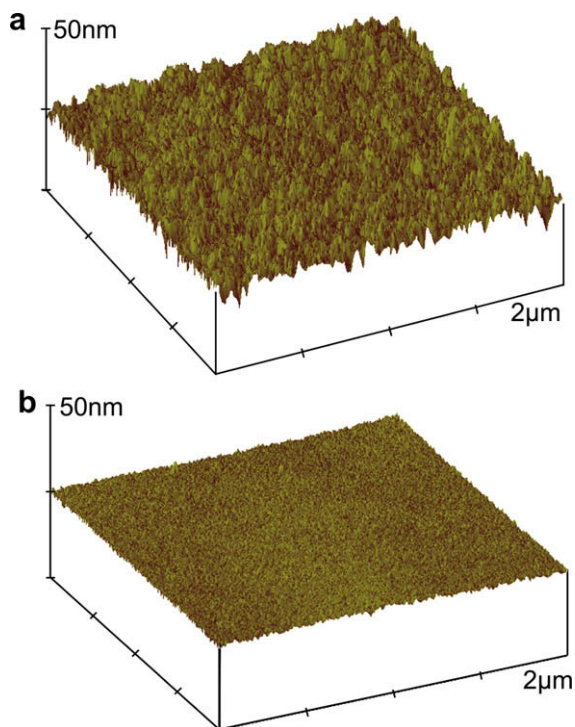


Fig. 5. Plot of width normalized total contact to contact resistance as a function of channel length to obtain contact resistance values.



**Fig. 6.** AFM morphology of (a) ITO coated PET substrate and (b) cross-linked PVP.

lengths were fabricated and tested. Fig. 5 shows the plot of width normalized  $R_{\text{total}}$  as a function of  $L$ . A straight line is fitted to four corresponding total contact to contact resistances. The interception between the fitting line and Y axis gives a width normalized contact resistance of around 500 K $\Omega$  cm when  $V_G = -20$  V. The moderate contact resistance is believed to be caused by the roughness produced at the demolding step.

To investigate the cause of the improvement in charge carrier mobility, atomic force microscopy (AFM) was used to study the dielectric-semiconductor interface. Fig. 6a and b shows the surface morphology of ITO coated PET substrate and cross-linked PVP, respectively. The root mean square roughness ( $R_{\text{rms}}$ ) of ITO coated PET substrate was 3.7 nm. With proper spin-coating parameters for the PVP thin-film,  $R_{\text{rms}}$  of the dielectric surface was reduced to 0.9 nm. It is well-known that the mobility in OTFTs is affected by morphology and grain size of the semiconductor film [17]. The semiconductor film morphology is in turn partly driven by the substrate surface [18]. Therefore, substrate roughness, to some extent, determines the quality of interface and further affects transistor characteristics [19,20]. In our earlier top gate devices, the PET substrate showed a regular ripple-like morphology ( $R_{\text{rms}} = 6.7$  nm), which was a typical surface morphology of a polymer substrate. The spin-coated semiconductor film was very thin and closely conformed to this morphology; the roughness of semiconductor film only reduced modestly to  $R_{\text{rms}} = 4.4$  nm [13]. In the present bottom-gated configuration, the PVP film is thick enough (800–1000 nm) to cover

up the rough surface of the ITO film and produce a very smooth ( $R_{\text{rms}} = 0.9$  nm) dielectric interface. We propose that the increased mobility is a consequence of this significant roughness reduction at the dielectric-semiconductor interface.

The bottom gate device structure makes it possible to cross-link the PVP thin-film at high temperature without affecting the quality of semiconductor layer, which is deposited after PVP has been cross-linked. Generically, cross-linking of polymer systems enhances mechanical strength and stiffness and increases the resistance to solvents [21,22]. In our experiments, PVP thermally cross-linked with MPMF also shows high solvent resistance to chlorobenzene and, as a result of the cross-linking process, the gate leakage current is reduced below nA scale and the off current is as low as 0.1 nA, leading to the increase of on/off ratio. These results agree well with others' reports in which leakage current through PVP cross-linked with the proper amount of MPMF is more than two orders of magnitude lower than uncross-linked PVP film [23] and transistor off current is found to decrease by 2 orders of magnitude with prolonged cross-linking time [24]. Based on our optimized process, real, commercially interesting OTFT applications such as low-cost, large-area sensor systems become feasible.

#### 4. Conclusions

In summary, our UV transfer embossing process is optimized by using bottom-gated configuration so that the resulting OTFT has greatly improved mobility and on/off ratio of 0.01–0.02 cm<sup>2</sup>/Vs and 10<sup>4</sup>, respectively. The bottom-gated configuration permits thermal cross-linking of the PVP dielectric and hence lower gate leakage current and off current. The increased mobility is proposed to result from significant roughness reduction at the dielectric-semiconductor interface. The improved OTFT performance makes this technique feasible for medium performance and/or disposable applications such as electronic paper and large-area environmental sensors.

#### Acknowledgement

This work was financially supported by Singapore A\* STAR Grant No. 052 117 0031.

#### Appendix A. Supplementary data

Supplementary data associated with this article can be found, in the online version, at [doi:10.1016/j.orgel.2008.12.012](https://doi.org/10.1016/j.orgel.2008.12.012).

#### References

- [1] S.R. Forrest, Nature 428 (6986) (2004) 911.
- [2] H.E. Katz, A.J. Lovinger, J. Johnson, C. Kloc, T. Siegrist, W. Li, Y.Y. Lin, A. Dodabalapur, Nature 404 (6777) (2000) 478.
- [3] R.F. Service, Science 278 (5337) (1997) 383.
- [4] C.W. Sele, T. von Werne, R.H. Friend, H. Sirringhaus, Adv. Mater. 17 (8) (2005) 997.
- [5] C. Kim, P.E. Burrows, S.R. Forrest, Science 288 (5467) (2000) 831.

- [6] C. Kim, M. Shtein, S.R. Forrest, *Appl. Phys. Lett.* 80 (21) (2002) 4051.
- [7] Y.Y. Noh, N. Zhao, M. Caironi, H. Sirringhaus, *Nat. Nanotechnol.* 2 (12) (2007) 784.
- [8] R. Parashkov, E. Becker, T. Riedl, H.H. Johannes, W. Kowalsky, *Proc. IEEE*. 93 (7) (2005) 1321.
- [9] P. Cosseddu, A. Bonfiglio, *Appl. Phys. Lett.* 88 (2) (2006) 023506.
- [10] E. Menard, M.A. Meitl, Y. Sun, J.-U. Park, D.J.-L. Shir, Y.-S. Nam, S. Jeon, J.A. Rogers, *Chem. Rev.* 107 (4) (2007) 1117.
- [11] Y.-L. Loo, D.V. Lang, J.A. Rogers, J.W.P. Hsu, *Nano Lett.* 3 (7) (2003) 913.
- [12] S.-H. Hur, D.-Y. Khang, C. Kocabas, J.A. Rogers, *Appl. Phys. Lett.* 85 (23) (2004) 5730.
- [13] J. Zhang, C.M. Li, M.B. Chan-Park, Q. Zhou, Y. Gan, F. Qin, B. Ong, T. Chen, *Appl. Phys. Lett.* 90 (2007) 243502.
- [14] D. Fichou, *Handbook of Oligo- and Polythiophenes*, Wiley-VCH, Weinheim, 1999.
- [15] S. Luan, G.W. Neudeck, *J. Appl. Phys.* 72 (2) (1992) 766.
- [16] J. Zaumseil, K.W. Baldwin, J.A. Rogers, *J. Appl. Phys.* 93 (10) (2003) 6117.
- [17] J. Veres, S. Ogier, G. Lloyd, D. de Leeuw, *Chem. Mater.* 16 (2004) 4543.
- [18] R.J. Kline, M.D. McGehee, M.F. Toney, *Nat. Mater.* 5 (3) (2006) 222.
- [19] L.-L. Chua, J. Zaumseil, J.-F. Chang, E.C.W. Ou, P.K.H. Ho, H. Sirringhaus, R.H. Friend, *Nature* 434 (7030) (2005) 194.
- [20] D. Knipp, R.A. Street, A.R. Volkel, *Appl. Phys. Lett.* 82 (22) (2003) 3907.
- [21] L.E. Nielsen, *J. Macromol. Sci. Polym. Rev.* 3 (1) (1969) 69.
- [22] M. Halik, H. Klauk, U. Zschieschang, G. Schmid, W. Radlik, W. Weber, *Adv. Mater.* 14 (23) (2002) 1717.
- [23] G.H. Kim, S.M. Yoon, C.A. Kim, K.H. Baek, I.K. You, S.Y. Kang, S.D. Ahn, K.S. Suh, *J. Korean Phys. Soc.* 49 (3) (2006) 1239.
- [24] D.K. Hwang, K. Lee, J.H. Kim, S. Im, J.H. Park, E. Kim, *Appl. Phys. Lett.* 89/9 (2006).



# The structural composite effect of Au–WO<sub>3</sub>–Al interconnecting electrode on performance of each unit in stacked OLEDs

H.M. Zhang<sup>a,b,1</sup>, Wallace C.H. Choy<sup>a,\*</sup>, Y.F. Dai<sup>b</sup>, D.G. Ma<sup>b</sup>

<sup>a</sup> Department of Electrical and Electronic Engineering, The University of Hong Kong, Pokfulam Road, Hong Kong

<sup>b</sup> State Key Laboratory of Polymer Physics and Chemistry, Changchun Institute of Applied Chemistry, Chinese Academy of Sciences, Changchun 130022, China

## ARTICLE INFO

### Article history:

Received 22 September 2008

Received in revised form 30 December 2008

Accepted 1 January 2009

Available online 6 January 2009

### PACS:

85.60.Jb

78.60.Fi

73.61.Ng

### Keywords:

Stacked OLEDs

Intermediate electrode

High transmission

High efficiency

## ABSTRACT

In this article, we report the effects of the thickness of metal and oxide layers of the Al/WO<sub>3</sub>/Au interconnecting structure on the electrical and optical characteristics of the upper and bottom units of the two-unit stacked organic-light-emitting-devices (OLEDs). It is found that light emission performance of the upper unit is sensitive to the transmittance of semitransparent Al/WO<sub>3</sub>/Au structure, which can be improved by changing the thickness of each layer of the Al/WO<sub>3</sub>/Au structure. It is important to note that the introduction of WO<sub>3</sub> between Al and Au significantly enhances the current efficiency of both the upper and bottom units with respect to that of the corresponding Al/Au structure without WO<sub>3</sub>. In addition, the emission spectra of both the upper and bottom units are narrower than that of the control device due to microcavity effect. Our results indicate that the Al/WO<sub>3</sub>/Au interconnecting structure is a good candidate for fabricating independently controllable high efficiency stacked OLEDs.

© 2009 Elsevier B.V. All rights reserved.

## 1. Introduction

Independently controllable and dependently controllable stacked organic-light-emitting-device (OLED) structures have been widely studied to improve the emission efficiency [1–6,8,9]. Each OLED unit of the independent controllable stacked OLEDs can be individually biased and operated. The performance of the stacked OLEDs strongly depends on the carrier conduction into the emissive units. For independently controllable stacked OLEDs, the interconnecting electrode plays a special role for OLED performances because the electrode has the dual functions of hole injection for the upper OLED unit and electron injection for the bottom unit simultaneously. Thus, serious at-

tempts have been put on exploring high performance interconnecting electrodes. To realize the role, the interconnecting electrode generally utilizes structures based on thin semitransparent metal layer or transparent indium-tin oxide (ITO), such as, Mg:Ag/indium zinc oxide [6] and Cs:BCP/indium-tin oxide(ITO) [7], apart from LiF/Ca/Ag and LiF/Al/Au [8,9]. ITO might cause damage to the underlying organic thin films because it is usually deposited by means of magnetron sputtering process. Metal electrodes can contribute to good carrier injection when the Fermi level can match with the highest occupied molecular orbit (HOMO) and the lowest unoccupied molecular orbit (LUMO) of the organic material for hole and electron injection, respectively. However, the transmittance of metal is generally low which may cause problems. Therefore, it is urgent to develop new connecting layers.

In this article, we shall discuss the effects of the Al/WO<sub>3</sub>/Au interconnecting electrode. The interconnecting

\* Corresponding author. Tel.: +852 2857 8485; fax: +852 2559 8738.

E-mail address: [chchoy@eee.hku.hk](mailto:chchoy@eee.hku.hk) (W.C.H. Choy).

<sup>1</sup> Currently visiting the University of Hong Kong.



electrode can be proved to be an efficient interconnecting structure for uses in high efficiency stacked OLEDs with good transmission and to improve the color purity. We will investigate the effects of the thickness of each metal and oxide layers of the interconnecting structure on the electrical and optical properties of each unit in the stacked OLEDs. To ease the study, the two-units of the stacked OLEDs are identical which are integrated by Al/WO<sub>3</sub>/Au and Al/Au connecting layers as detailed in next section. Each unit in the stacked OLEDs can be independently biased.

## 2. Experiment

Fig. 1 shows the schematic diagram of the independently controllable stacked OLEDs (Device A) and control OLED (Device B) used in this study. The structure of Device A is ITO /MoO<sub>3</sub> (8 nm)/4,4'-N,N'-bis[N-(1-naphthyl)-N-phenyl-amino]biphenyl (NPB) (50 nm)/(tris (8-hydroxyquinoline) aluminum(III) (Alq<sub>3</sub>):C545T (30 nm)/Alq<sub>3</sub> (30 nm)/LiF(1 nm)/Al/WO<sub>3</sub>/Au/MoO<sub>3</sub> (5 nm)/NPB (50 nm)/Alq<sub>3</sub>:C545T (30 nm)/Alq<sub>3</sub> (30 nm)/LiF (1 nm)/Al(140). Device B is ITO/MoO<sub>3</sub> (8 nm) /NPB (50 nm)/Alq<sub>3</sub>:C545T (30 nm)/Alq<sub>3</sub> (30 nm)/LiF (1 nm)/Al (150 nm). All devices were fabricated on indium-tin oxide (ITO) coated glass with a sheet resistance of 15 Ω/□ and the thermally deposited LiF/Al was used as cathode. ITO substrate was cleaned and then treated by UV ozone. The deposition was carried out at a pressure less than  $3 \times 10^{-4}$  Pa without vacuum breaks. The organics and metal oxide were evaporated at the rate of 0.2–0.3 nm/s, and the metal of Au was evaporated at the rate of 0.1 nm/s and Al at the rate of 0.8–1 nm/s. The OLEDs had an emissive area of 16 mm<sup>2</sup>. The current density–voltage–luminance (J–V–L) characteristics were measured by using a computer controlled sourcemeter (Keithley 2400) and multimeter (Keithley 2000) with a calibrated silicon photodiode. The electroluminescence (EL) spectra were measured by JY SPEX CCD3000 spectrometer. All the measurements were carried out in ambi-

ent atmosphere at room temperature. Al/WO<sub>3</sub>/Au structures with different thicknesses of Al, WO<sub>3</sub> and Au were also deposited on glass substrates for transmission studies.

## 3. Results and discussion

Fig. 2 depicts J–V–L characteristics and current efficiency of the upper unit of the stacked OLEDs with various thicknesses of Al, Au and WO<sub>3</sub> layers as the interconnecting electrode. It can be seen that the current injection generally increases when the total thickness of metal layers (Al and Au) increases. However, inserting WO<sub>3</sub> layer between the Al and Au layers make the current injection decrease as shown in Fig. 2a. The current injection of the device with Al/WO<sub>3</sub>/Au (2 nm/3 nm/16 nm) is lower than that of the device with Al/Au (2 nm/16 nm). When the thickness of WO<sub>3</sub> is further increased, hole injection enhances due to the modifying effect of the oxide layer on the Al layer which is similar to the case reported by Lee [10]. They used C<sub>60</sub> as the adjacent buffer layer of Al layer for improving hole injection in OLEDs. Despite that the total metal thickness of the OLED with Al/WO<sub>3</sub>/Au (2 nm/3 nm/16 nm) is the thicker than that of the OLED with Al/WO<sub>3</sub>/Au (1 nm/5 nm/14 nm) (see Fig. 2a), the carrier injection of the device with Al/WO<sub>3</sub>/Au (1 nm/5 nm/14 nm) is higher than that of the devices with Al/WO<sub>3</sub>/Au (2 nm/3 nm/16 nm). This is attributed to the increase of the oxide thickness. For example, at  $J = 100$  mA/cm<sup>2</sup>, the driving voltages of OLEDs with Al/WO<sub>3</sub>/Au structures of (1 nm/5 nm/14 nm), (2 nm/3 nm/16 nm), and (2 nm/3 nm/15 nm) are 13.9, 14, and 14.5 V, respectively.

Fig. 2b shows the brightness–efficiency–current density plots of the upper unit of Device A. At any current density, the brightness of the OLEDs with various Al/WO<sub>3</sub>/Au structures is higher than that of the corresponding Al/Au OLEDs. For example, at current density of 20 mA/cm<sup>2</sup>, the brightness reaches 2700 cd/m<sup>2</sup> for Al/WO<sub>3</sub>/Au (2 nm/3 nm/16 nm) OLED, which is larger than 2033 cd/m<sup>2</sup> for Al/Au (2 nm/16 nm) OLEDs and close to 2752 cd/m<sup>2</sup> for the control OLED. By using Al/WO<sub>3</sub>/Au (1 nm/5 nm/14 nm) structure, the brightness increases to 2900 cd/m<sup>2</sup> at current density of 20 mA/cm<sup>2</sup>, this means that the current efficiency is further improved. The inset of Fig. 2b shows the current efficiency versus current density of the OLEDs with various Al/WO<sub>3</sub>/Au and Al/Au structures as well as the control device. The maximal current efficiency are 14.6 cd/A (for the OLED with Al/WO<sub>3</sub>/Au thicknesses = 1 nm/5 nm/14 nm, respectively), 14.3 cd/A (2 nm/3 nm/15 nm), 13.2 cd/A (2 nm/3 nm/16 nm), 12.6 cd/A (1 nm/5 nm/17 nm), and 11 cd/A (the OLED with Al/Au thickness = 2 nm/16 nm, respectively), and 10.9 cd/A (2 nm/17 nm). It is clearly observed that the current efficiency of the upper unit of the Al/WO<sub>3</sub>/Au OLEDs is greater than that of the control device as well as the upper unit of Al/Au OLEDs with same Al and Au thicknesses. One of the reasons of the lower current efficiency of the upper unit of Al/Au OLEDs is due to the low optical transmittance which will be discussed below.

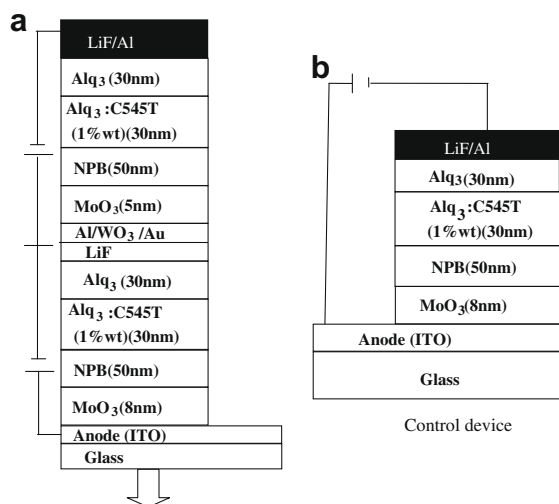
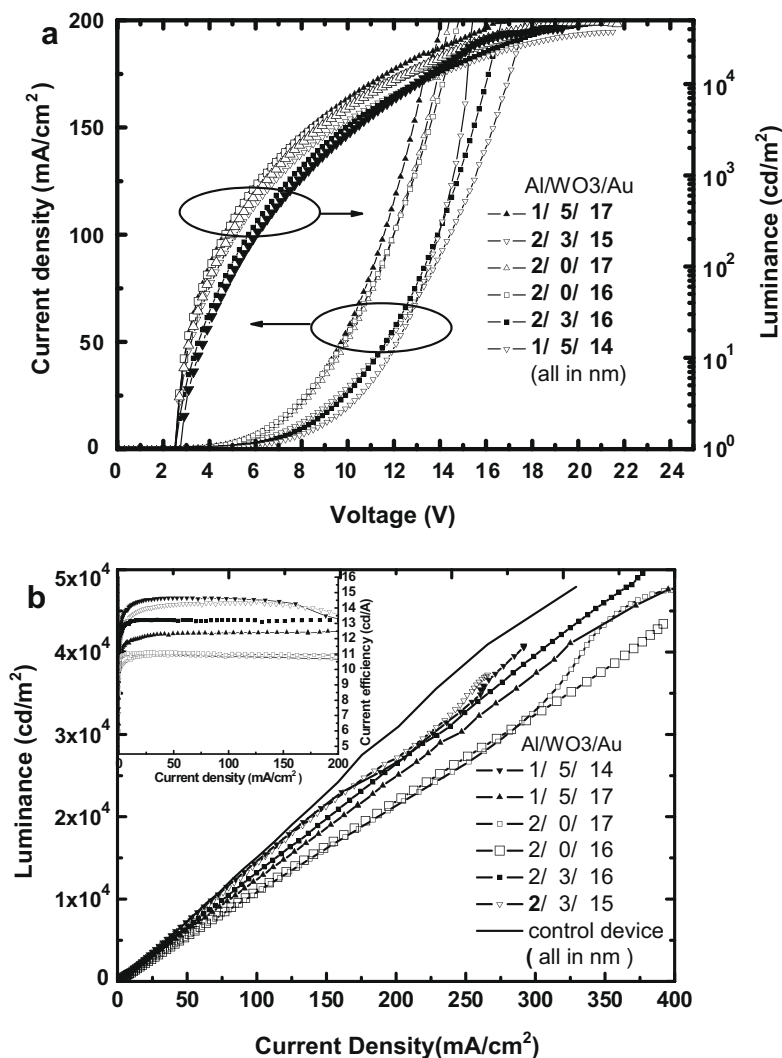
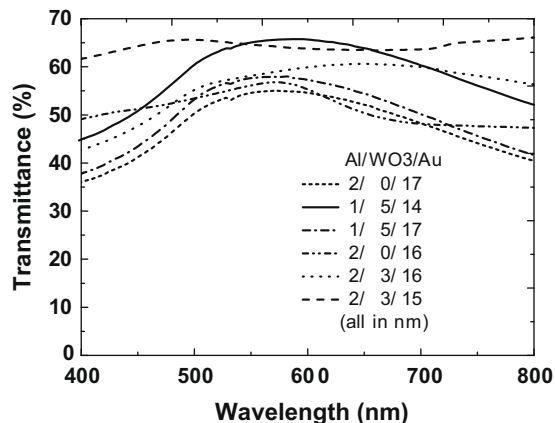


Fig. 1. Schematic diagram of the independently controllable stacked OLED (Device A) and control OLED (Device B).



**Fig. 2.** (a) Current density–brightness–voltage characteristics of the upper unit of the Al/WO<sub>3</sub>/Au and Al/Au stacked OLEDs. (b) Current density–brightness characteristics of the upper unit of the Al/WO<sub>3</sub>/Au and Al/Au stacked OLEDs and the control OLED. The inset show the current density–current efficiency characteristics of the upper OLED unit of the Al/WO<sub>3</sub>/Au and Al/Au stacked OLEDs and the control OLED.

To achieve efficient light emission from the upper unit in the stacked device, the intermediate connecting layers shall have high enough transmission and low absorption [11,12]. Here we study the transmittance of Al/WO<sub>3</sub>/Au/MoO<sub>3</sub> as depicted in Fig. 3. The results clearly indicate that the transmittance of the Al/WO<sub>3</sub>/Au structure is indeed enhanced with respect to the corresponding Al/Au structure without WO<sub>3</sub>. One of the possible reasons is the improvement of transmission of the opaque metallic structure through the coupling of the SP modes to radiative modes [13,14]. It has been reported that coupling of SP modes can occur by inserting an insulating layer between two metal films to form metal/insulator/metal [15] which can enhance the radiation. These results are important for improving of device performance. For the upper unit, the light will propagate through the interconnecting structure and bottom unit before emitting to the outside environment from the ITO glass, the increase of the transmittance



**Fig. 3.** Transmittance spectra of various thicknesses Al/WO<sub>3</sub>/Au and Al/Au.

of the interconnecting structure results in improvement of brightness. Although the introduction of thin  $\text{WO}_3$  layer reduces the injection current, the improvement of the brightness not only overcomes the reduction but also enhances the emission efficiency. The maximal power efficiency of upper units of the Al/ $\text{WO}_3$ /Au stacked OLEDs reaches about 11 lm/W, when that of the Al/Au stacked OLEDs is 9 lm/W and the efficiency of the control device is 8.9 lm/W. In addition, the structure Al/ $\text{WO}_3$ /Au is similar to a capacitor structure. Since a layer of  $\text{WO}_3$  between Al and Au layers serves as a dielectric layer. There is no direct contact between the Au and Al; thus the positive charge exists on the positive anode and the negative exists on the cathode. These results indicate that both Al/Au and Al/ $\text{WO}_3$ /Au are excellent dependently interconnecting electrodes for upper emitting unit in stacked OLEDs and the introduction of  $\text{WO}_3$  further improve the performance of the stacked OLEDs. Consequently, the metal/oxide/metal structures

can serve useful interconnecting structures for improving the stacked OLEDs performance.

Regarding the bottom unit of the stacked OLEDs, Fig. 4 shows the J–V–L characteristics and current efficiency. The thin  $\text{WO}_3$  oxide has no obvious influence on the current injection of the bottom devices. The driving voltage of the bottom OLED with Al/Au structure of (2 nm/16 nm), Al/ $\text{WO}_3$ /Au structures of (2 nm/3 nm/16 nm), and (1 nm/5 nm/17 nm) at  $J = 100 \text{ mA/cm}^2$  are 12.1, 12.1, and 12.7 V, respectively (see Fig. 4a). It is interesting to note that the current efficiency and brightness of corresponding devices are improved as shown in the inset of Fig. 4b. For example, at current density of  $20 \text{ mA/cm}^2$ , the brightness is  $3354 \text{ cd/m}^2$  for Al/ $\text{WO}_3$ /Au (2 nm/3 nm/16 nm) OLEDs, which is higher than  $3019 \text{ cd/m}^2$  for the corresponding Al/Au (2 nm/16 nm) OLEDs and  $2752 \text{ cd/m}^2$  for the control device. The maximal current efficiency the devices are 16.7 cd/A (Al/ $\text{WO}_3$ /Au thicknesses = 2 nm/3 nm/16 nm), 14.3 cd/A (2 nm/3 nm/

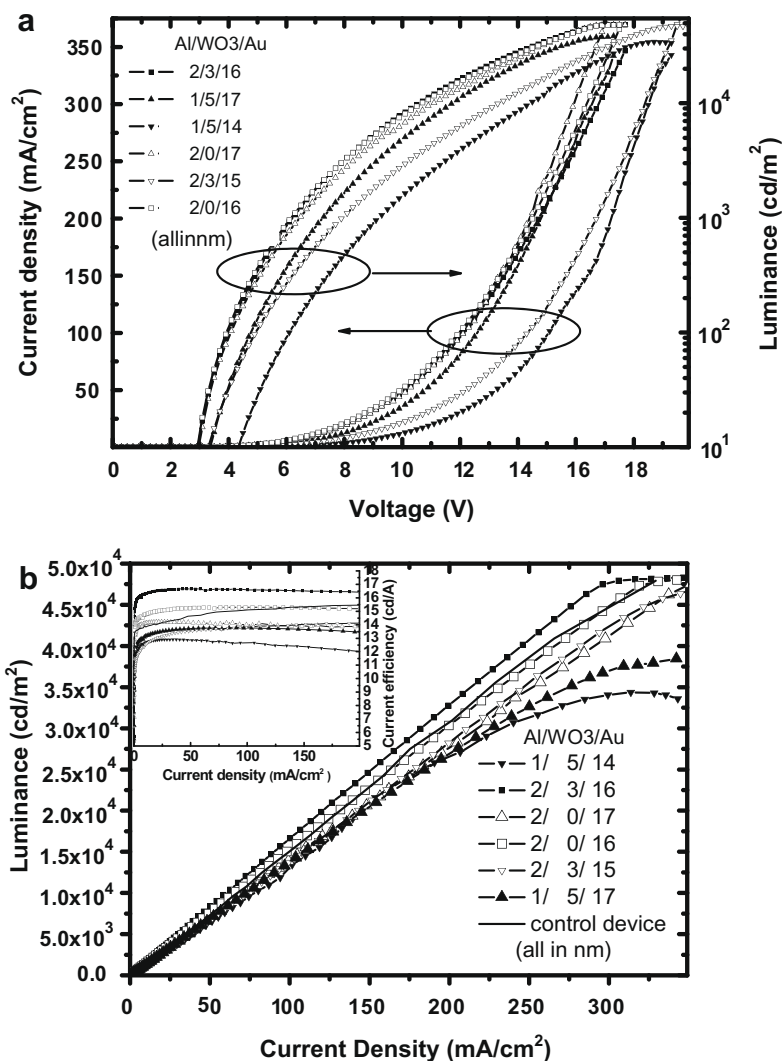


**Fig. 4.** (a) Current density–brightness–voltage characteristics of the bottom units of the Al/ $\text{WO}_3$ /Au and Al/Au stacked OLEDs. (b) Current density–brightness characteristics of the bottom units of the Al/ $\text{WO}_3$ /Au and Al/Au stacked OLEDs and the control OLED. The inset show the current density–current efficiency characteristics of the bottom units of the Al/ $\text{WO}_3$ /Au and Al/Au stacked OLEDs and the control OLED.

15 nm), 13.8 cd/A (1 nm/5 nm/17 nm), 12.9 cd/A (1 nm/5 nm/14 nm), 15.3 cd/A (Al/Au thicknesses = 2 nm/16 nm), and 14.2 cd/A (2 nm/17 nm). The current efficiency of the bottom device depends on the thickness of the oxide layer and the metal layers. In addition, with the same metal thickness, the current efficiency (16.7 cd/A) of stacked OLEDs with the interconnecting electrode of Al (2 nm)/WO<sub>3</sub> (3 nm)/Au (16 nm) has been improved compared to the current efficiency (15.3 cd/A) of stacked OLEDs with the interconnecting electrode of the Al/Au (2 nm/16 nm) device, which should be attributed to microcavity effect enhancement and the transmittance improvement of Al/WO<sub>3</sub>/Au (2 nm/3 nm/16 nm) OLEDs (see Fig. 4b). However, the current efficiency of the Al/WO<sub>3</sub>/Au OLEDs with structure of (1 nm/5 nm/17 nm) and (1 nm/5 nm/14 nm) are lower than that of the Al/Au (2 nm/16 nm) structure which indicate that the increase of the Al thickness favors the electron injection. It has been reported that the electron injection at the organic/metal contact is mainly controlled by the work function [16,17]. The Al in the interconnecting structure, which has lower work function, provides the electron injection for the bottom unit. One can modify the thickness of each metal and oxide layer to fulfill the performance of a particular OLED design.

Due to the utilization of semitransparent interconnecting layer, the microcavity effect exists in upper and bottom units of the stacked OLEDs. Fig. 5a and b shows the EL spectra from upper units of Al/WO<sub>3</sub>/Au (2 nm/3 nm/16 nm) and Al/Au (2 nm/16 nm) OLEDs, Fig. 5c and d shows that from bottom units. All devices emit green color with the peak at about 526 nm, but both the bottom and upper units of Al/WO<sub>3</sub>/Au OLEDs show narrower EL spectrum than that of the Al/Au OLED. The full-width at half-maximum (FWHM) of the upper and bottom units of Al/WO<sub>3</sub>/Au OLED are 43 and 40 nm respectively, and that of Al/Au OLED 52 and 50 nm respectively, which is narrower than 69 nm of the one-unit control device. Obviously, the narrowing phenomenon is due to the microcavity effect, and the utilization of WO<sub>3</sub> between Al and Au, indicating that the Al/WO<sub>3</sub>/Au possesses the more effective microcavity optical confinement role [18] than the Al/Au which should be favor in the improvement of device efficiency. Furthermore, it can be seen that the microcavity effect does not produce any significant angular dependence in the emission spectrum for both bottom and upper units of the Al/WO<sub>3</sub>/Au stacked OLEDs, although the emissive spectra of the upper units of the both OLEDs slightly red shift and widen at 50° as shown in Fig. 5a and b.

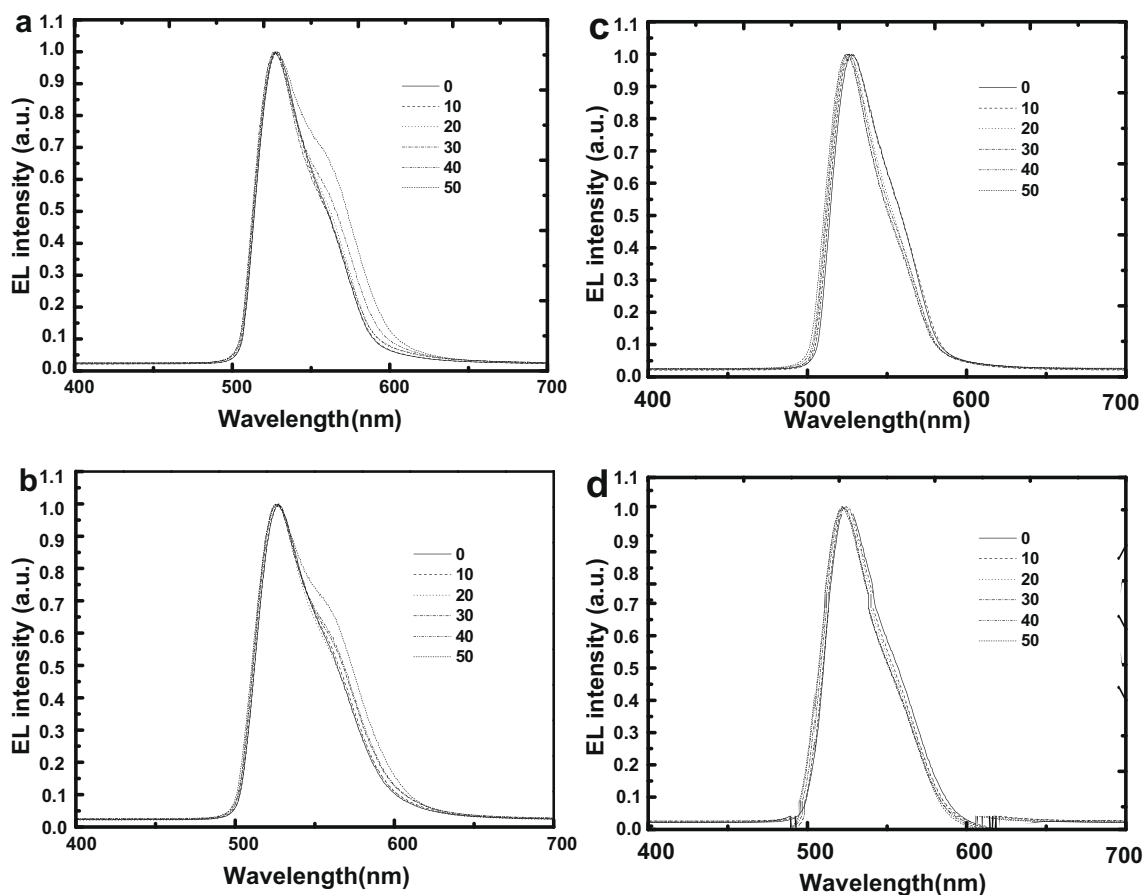


**Fig. 5.** EL spectra of device respectively, from the upper units of (a) Al/WO<sub>3</sub>/Au (2 nm/3 nm/16 nm) stacked OLEDs and (b) Al/Au (2 nm/16 nm) stacked OLEDs as well as the bottom unit of (c) Al/WO<sub>3</sub>/Au (2 nm/3 nm/16 nm) stacked OLEDs and (d) Al/Au (2 nm/16 nm) stacked OLEDs with various viewing angles.

#### 4. Conclusion

An independently external bias interconnecting structure for improving the efficiency of both the upper and bottom units of stacked OLEDs has been reported and discussed. The connecting structure is composed of a thin metal oxide sandwiched between Al and Au layers. Our results show that the utilization of metal oxide between Al and Au significantly improves the transmittance of the interconnecting structures, and thus the device efficiency. The spectra of both the upper and bottom emitting unit are also narrow down compared to the control device. Besides the angular dependence of spectrum caused by microcavity effect is not significant. The concept of introducing oxide layer between metal layers can be applied to other metal multilayered structures. By adjusting the thickness of each layer of the interconnecting structures, one can tailor the performance of the top and bottom units of the stacked OLEDs to meet the special requirement. Furthermore, such interconnecting layered structure can be easily fabricated by simple thermal evaporation, and can be easily applied the structures for fabricating real-time color-tunable stacked OLEDs for realizing high-resolution, independently addressable, stacked red–green–blue pixels in color displays.

#### Acknowledgement

We acknowledge the support of the grant (#14300.324.01) from the Research Grant Council of the Hong Kong Special Administrative Region, China.

#### References

- [1] Z. Shen, P.E. Burrows, V. Bulovic, S.R. Forrest, M.E. Thompson, *Science* 276 (1997) 2009.
- [2] P.E. Burrows, G. Gu, V. Bulovic, Z. Shen, S.R. Forrest, M.E. Thompson, *IEEE Trans. Electron Dev.* 44 (1997) 1188; S. Tanaka, C. Hosakawa, US Patent No. 6,107 (22 August 2000) 734.
- [3] P.E. Burrows, S.R. Forrest, S.P. Sibley, M.E. Thompson, *Appl. Phys. Lett.* 69 (1996) 2959.
- [4] H.M. Zhang, W.C.H. Choy, *J. Phys. D* 41 (2008) 105108.
- [5] C.C. Chang, J.F. Chen, S.W. Hwang, C.H. Chen, *Appl. Phys. Lett.* 87 (2005) 253501.
- [6] G. Gu, G. Parthasarathy, P. Tian, P.E. Burrows, S.R. Forrest, *J. Appl. Phys.* 86 (1999) 4076.
- [7] T. Matsumoto, T. Nakada, J. Endo, K. Mori, N. Kavamura, A. Yokoi, J. Kido, in: *Proceedings 2003 Society for Information Display (SID) International Symposium*, Baltimore, MD, 2003, p. 979.
- [8] J.X. Sun, X.L. Zhu, H.J. Peng, M. Wong, H.S. Kwok, *Org. Electron.* 8 (2007) 305.
- [9] J.X. Sun, X.L. Zhu, H.J. Peng, M. Wong, H.S. Kwok, *Appl. Phys. Lett.* 87 (2005) 093504.
- [10] J.Y. Lee, *Appl. Phys. Lett.* 88 (2006) 073512.
- [11] G. Gu, G. Parthasarathy, P.E. Burrows, P. Tian, I.G. Hill, A. Kahn, S.R. Forrest, *J. Appl. Phys.* 86 (1999) 4067.
- [12] P.E. Burrows, G. Gu, S.R. Forrest, E.P. Vicenzi, T.X. Zhou, *J. Appl. Phys.* 87 (2000) 3080.
- [13] R. Dragila, B. Luther-Davies, S. Vukovic, *Phys. Rev. Lett.* 55 (1985) 1117.
- [14] X.W. Chen, W.C.H. Choy, S. He, P.C. Chui, *Opt. Express* 15 (2007) 7083.
- [15] G.J. Kovacs, G.D. Scott, *Phys. Rev. B* 16 (1977) 1297.
- [16] M.Y. Chan, S.L. Lai, M.K. Fung, C.S. Lee, S.T. Lee, *J. Appl. Phys.* 95 (2004) 5397.
- [17] M.Y. Chan, S.L. Lai, M.K. Fung, S.W. Tong, C.S. Lee, S.T. Lee, *Appl. Phys. Lett.* 82 (2003) 1784.
- [18] V. Bulović, V.B. Khalfin, G. Gu, P.E. Burrows, *Phys. Rev. B* 58 (1998) 3730.



## Small-molecule vacuum processed melamine-C<sub>60</sub>, organic field-effect transistors

Mihai Irimia-Vladu<sup>a,\*</sup>, Nenad Marjanovic<sup>b</sup>, Marius Bodea<sup>c</sup>, Gerardo Hernandez-Sosa<sup>d</sup>, Alberto Moutaigne Ramil<sup>b</sup>, Reinhard Schwödauer<sup>a</sup>, Siegfried Bauer<sup>a</sup>, Niyazi Serdar Sariciftci<sup>e</sup>, Frank Nüesch<sup>f</sup>

<sup>a</sup> Department of Soft Matter Physics, Johannes Kepler University, Altenberger Strasse Nr. 69, 4040 Linz, Austria

<sup>b</sup> plastic electronic GmbH, Rappetsederweg Nr. 28, 4040 Linz, Austria

<sup>c</sup> Institute of Applied Physics, Johannes Kepler University, Altenberger Strasse Nr. 69, 4040 Linz, Austria

<sup>d</sup> Institute of Semiconductor and Solid State Physics, Johannes Kepler University, Altenberger, Strasse Nr. 69, 4040 Linz, Austria

<sup>e</sup> Linz Institute for Organic Solar Cells (LIOS), Physical Chemistry, Johannes Kepler University, Altenberger Strasse Nr. 69, 4040 Linz, Austria

<sup>f</sup> Laboratory for Functional Polymers, Empa Swiss Federal Laboratories for Materials Testing and Research, Überlandstrasse Nr. 129, CH-8600 Dübendorf, Switzerland

### ARTICLE INFO

#### Article history:

Received 13 November 2008

Received in revised form 29 December 2008

Accepted 1 January 2009

Available online 19 January 2009

#### PACS:

68.35.bt

68.37.Ps

68.55.at

72.80.Sk

73.40.Qv

#### Keywords:

Organic field effect transistors

Vacuum deposition

Small molecule semiconductor

Small molecule dielectric

Roll to roll production

### ABSTRACT

The transfer of benchtop knowledge into large scale industrial production processes represents a challenge in the field of organic electronics. Large scale industrial production of organic electronics is envisioned as roll to roll (R2R) processing which nowadays comprises usually solution-based large area printing steps. The search for a fast and reliable fabrication process able to accommodate the deposition of both insulator and semiconductor layers in a single step is still under way. Here we report on the fabrication of organic field effect transistors comprising only evaporable small molecules. Moreover, both the gate dielectric (melamine) and the semiconductor (C<sub>60</sub>) are deposited in successive steps without breaking the vacuum in the evaporation chamber. The material characteristics of evaporated melamine thin films as well as their dielectric properties are investigated, suggesting the applicability of vacuum processed melamine for gate dielectric layer in OFETs. The transistor fabrication and its transfer and output characteristics are presented along with observations that lead to the fabrication of stable and virtually hysteresis-free transistors. The extremely low price of precursor materials and the ease of fabrication recommend the evaporation processes as alternative methods for a large scale, R2R production of organic field effect transistors.

© 2009 Elsevier B.V. All rights reserved.

### 1. Introduction

Macroelectronic devices, such as flexible or conformable displays, smart cards, sensors etc. are impelling the emerging field of organic electronics [1,2]. Materials employed in such applications include small molecule semi-

conductors, as used for example in current organic light emitting diode displays (OLEDs) as well as polymeric organic semiconductors that have proven to be favorable in organic solar cells [3]. Advantageously, these soluble materials offer the possibility to be processed by cost-efficient roll-to-roll (R2R) printing technologies [4,5]. As has been demonstrated in the packaging industry, R2R processing is also compatible with vapor deposition methods that generally apply not only for small organic molecules [6] but also for polymers [7].

\* Corresponding author. Tel.: +43 732 2468 9293; fax: +43 732 2468 9273.

E-mail address: [Mihai.Irimia-Vladu@jku.at](mailto:Mihai.Irimia-Vladu@jku.at) (M. Irimia-Vladu).

While small molecules can be purified to a high degree, polymers and solvents are more likely to present impurities. Solution based processing may require extensive cleaning steps, to avoid contamination of the devices with ionic impurities [8]. In the field of organic field-effect transistors (OFETs), such impurities may give rise to unwanted ionic electret effects, causing bias stress degradation or hysteresis in transfer characteristics [9]. Though the hysteresis in the transfer characteristics of OFETs may be used as an advantage in non-volatile memory elements [10,11], it is detrimental in transistors designed for integrated organic circuits and sensors [12]. Therefore alternative routes for production of key components in OFETs are desirable. These include not only the deposition of the active semiconductor material, but also the fabrication of the insulating dielectric layer [7]. Advantageously, small molecule evaporable materials allow fabrication to be pursued by vapor deposition only [13], enabling therefore high purity production of organic electronic devices. Importantly, small molecule materials allow the forming of well defined interfaces between the organic semiconductor and the organic dielectric when growth conditions are optimized. Consequently, thermal oxide growth and wet chemical steps which are used in classical inorganic semiconductor technology would no longer be required. Moreover, since there are no dangling bonds, the organic-organic interface in such devices may also provide for low interface trap densities in comparison to inorganic-inorganic interfaces like the ones present in silicon-metal oxide-semiconductor transistors [14]. As a result, vacuum processed small molecule OFETs may represent a viable alternative route for the R2R processing of organic electronics [6].

Here we report on vacuum processed small molecule OFETs with vacuum evaporated melamine as gate dielectric and  $C_{60}$  as semiconductor material. We describe the vacuum evaporation of melamine, the structural and dielectric properties of the evaporated melamine thin film dielectrics, the fabrication of the vacuum processed small molecule OFETs and their electrical characterization.

The first synthesis of 1,3,5-triazine-2,4,6-triamine (*i.e.*  $C_3H_6N_6$ ) can be traced back to the German scientist Justus von Liebig, who first synthesized the material in 1834 by heating an intimate mixture of ammonium chloride and potassium thiocyanate [15]. He called the fusion product melamine. Perceived initially as an expensive chemical, melamine attracted significant commercial interest one century later, for applications including fabric impregnation, adhesives and moulding powders containing cellulosic fibers, fillers and pigments. The reaction of melamine with formaldehyde to produce a thermosetting resin firmly established the industrial interest towards the duroplasts. Nowadays, melamine represents one of the most common molecular units of our daily life owing to its excellent chemical stability, low fabrication cost and simple synthesis route. In addition, melamine possesses a considerable number of attractive properties, like excellent optical transmission; very good fire and abrasion resistance; excellent chemical inertness including stability to heat, light, moisture and various chemicals attack. All these features pushed melamine as a front runner in applications including cross-linking additives for coatings of

automotive and household parts; flame retardant additives for foams in furniture and mattresses; various moulded plastic wares; laminates for kitchen cabinets, floors and table tops; concrete plasticizers; resins for textile and paper finishing and others [16]. However, despite intensive academic interest shown in the second part of the last century towards elucidating the electronic and structural properties of melamine [17–19], no report has surfaced to date with respect to the suitability of melamine for large scale industrial production of electronic devices.

Melamine crystallizes in monoclinic crystal structure in which each molecule is linked to its neighbours by eight hydrogen bonds [18,20–23]. Melamine crystals have a melting point of 350 °C and start sublimating at a temperature greater than 270 °C in a vacuum of  $10^{-5}$  torr, the recrystallized product consisting of melamine and possibly a series of fused products of pyrolysis referred elsewhere as melam (*i.e.*  $C_6H_9N_{11}$ ), melem (*i.e.*  $C_6H_6N_{10}$ ) and melon (*i.e.*  $C_6H_3N_9$ ) [19,24]. Melon is the final condensate obtained during the melamine pyrolysis and was recently investigated by several groups for the inexpensive route of fabrication of carbon nitride (*i.e.*  $C_3N_4$ ) [24,25]. The above mentioned thermal behaviour therefore recommends melamine as a suitable material for the deposition of the dielectric layer in fully evaporated organic field effect transistors.

## 2. Experimental

Transistors are built on  $1.5 \times 1.5$  cm glass substrates. Melamine is evaporated through a square mask on top of an evaporated aluminium stripe acting as gate electrode for the transistor. After the evaporation of the organic semiconductor layer, the transistors are placed on top of a patterned mask and aluminium is used to define the source and drain electrodes. All the aluminium electrodes (gate, source and drain) are 60 nm thick. For the batches built on Cr/Au gate electrodes, the thickness of the two successively evaporated metal layers was 10 nm and 50 nm, respectively. The ITO gate electrodes for the batches featuring this gate material were patterned by etching the ITO glass with “aqua regia” (*i.e.* an aqueous etching solution containing 36% hydrochloric acid, 65% nitric acid, and water in the volume ratio 0.92:0.08:1). Melamine was purchased from Aldrich Inc. and purified by two successive recrystallizations in a glass tube in an open furnace. The closed side of the tube was inserted in the furnace heated at 300 °C and the open end connected to a vacuum pump and a pressure of  $10^{-2}$  bar established. The low fractions of melamine impurities evaporated first and were drained into vacuum and the rest of the material condensed at the end of the tube exiting the furnace. The recrystallization was repeated one more time in order to increase the purity of the material. We observed that the quality of the transistors built from precursor material recrystallized more than twice was no different to that of the transistors produced from the twice-recrystallized material. Attempts to build transistors from the “as received material” proved successful in the sense that transistor behaviour was observed in both output and transfer curves, however the evaporation of

melamine was marred by an unsteady sublimation rate at fixed temperature, presumably due to the evolution of ammonia containing impurities. The organic materials were evaporated successively in the same vacuum typically of  $1 \times 10^{-6}$  bar in an EDWARDS High Vacuum (Manor Royal, Crawley, Sussex), from crucibles containing melamine and  $C_{60}$ . The distance measured from the plane of the crucible holder to the one of the sample holder during the evaporation of the organic layers was always 15 cm in this work. We observed that altering this distance had a great influence on the quality of the melamine layer condensed on the substrate. Higher distances (up to 25 cm in total) offered a much better dielectric behaviour of the melamine layer in terms of breakthrough voltage, but also a considerably higher film roughness leading therefore to undesired transistor characteristics like more pronounced hysteresis, higher threshold voltage and modest on-off ratio. All the transistor samples within this work that were built on glass

substrates have gone through a post-production heat treatment at temperatures in the range of 100 to 125 °C, on hot plate in glove box under nitrogen. The transistor samples prepared on  $1.5 \times 1.5$  cm PET foils have been treated at 80 °C for four hours under the same environmental conditions. The channel length  $L$  of the OFETs is 100  $\mu\text{m}$  and the channel width  $W$  is 1 mm. The area of the overlapping top and bottom electrodes of the MIM capacitor built for the dielectric measurements is 6.25  $\text{mm}^2$ . The electrical characterization of all transistor batches was performed in inert environment (*i.e.* nitrogen filled glove box). The dielectric measurements of the MIM capacitor were performed in a sample chamber under argon gas, without any prior heat treatment of the melamine sample after thermal evaporation. For the steady state current-voltage measurements, an Agilent E5273A instrument was employed, whereas a Novocontrol Alpha Analyzer was used for the dielectric spectroscopy investigation. For both the

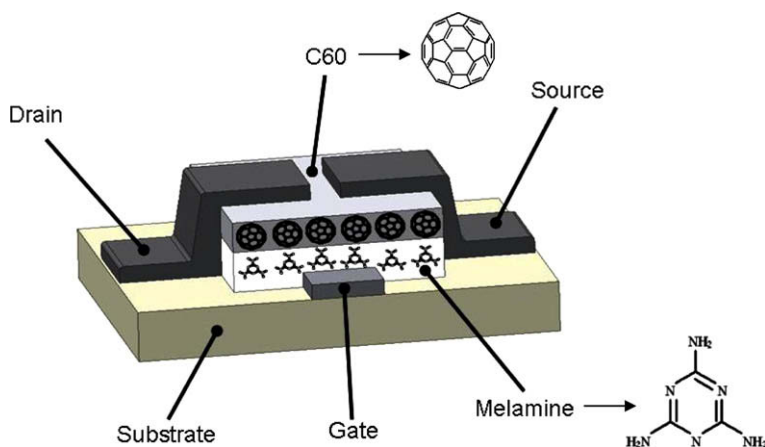


**Fig. 1.** Schematic of the vapor deposited melamine- $C_{60}$  OFET. The inset displays the schematic of the small molecules melamine and  $C_{60}$ .

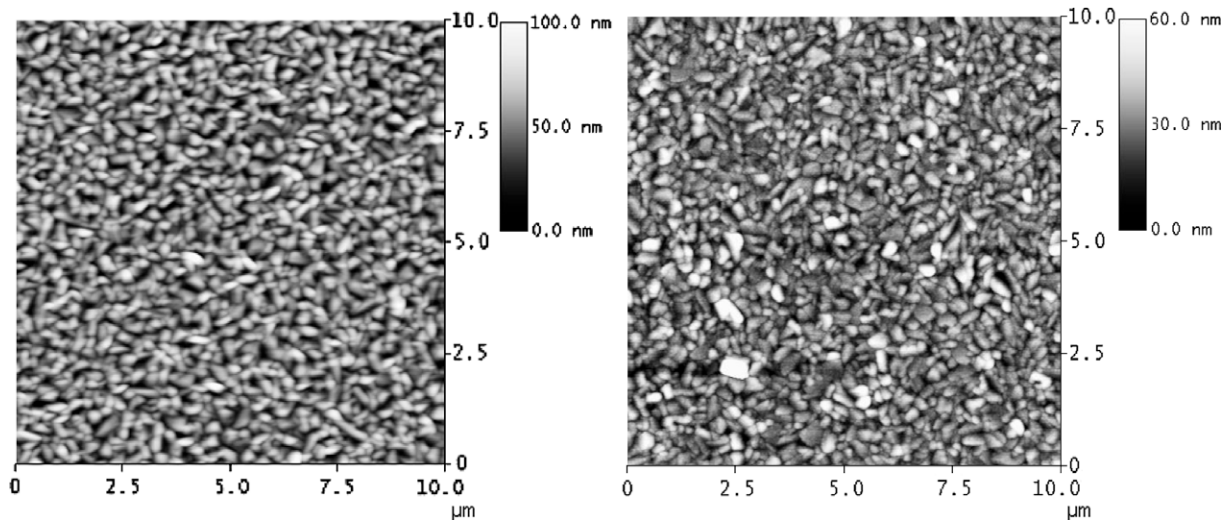


**Fig. 2.** AFM image of a 1.25  $\mu\text{m}$  thick melamine film (a) and 75 nm thick  $C_{60}$  film on the top of melamine (b).



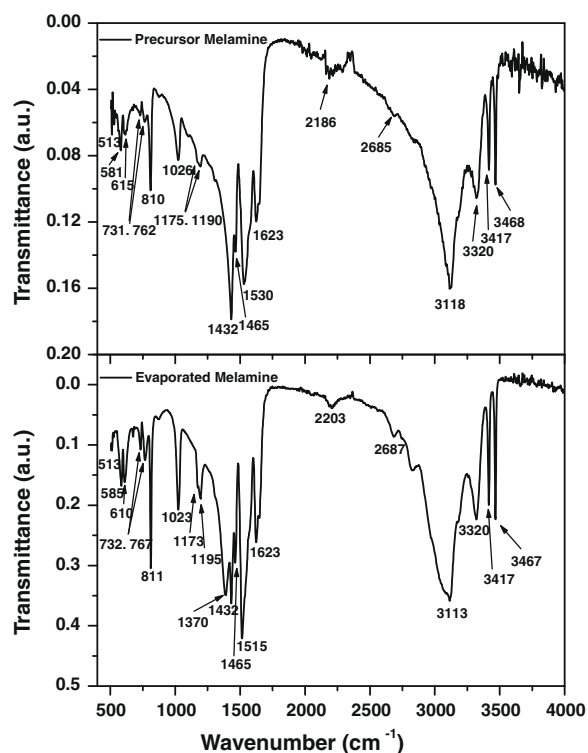


**Fig. 3.** FTIR spectra of precursor melamine (a) and evaporated melamine (b); the peaks are labelled according to literature data summarized in Table 1.

**Table 1**

Observed FTIR peaks of melamine and their corresponding assignment in literature. Schneider and Schrader list only the intensity of the observed vibrations but do not link them to any particular mode [18].

Observed peaks (this work) [cm <sup>-1</sup> ]	Literature reported peaks [cm <sup>-1</sup> ]	Vibrational mode assignment	References
~3468	~3464–3471	Free NH stretching	[17,18,22]
~3417	~3416–3421	Interchain H bonded NH stretching	[17,18,22]
~3320	~3320–3333	Interacting NH groups	[17,18,22]
~3113–3118	~3120–3130	Interacting NH groups	[18,22]
~2685–2687	~2684	Mixed mode of free N–H stretching and side-chain out-of-plane C–N bending	[17]
~2186–2203	~2193	Mixed mode of NH <sub>2</sub> rocking and ring breathing	[17]
~1623	~1626–1660	NH <sub>2</sub> bending CN ring distortion	[17] [22]
~1515–1530	~1531–1550	CN stretch + NH rocking + NH scissor NH <sub>2</sub> bending Side chain asymmetric CN stretching	[23] [18,22] [17,23]
~1465	~1465–1469	Side-chain CN breathing	[17,18]
~1432	~1434–1438	CN ring stretching	[17,18,23]
~1370	~1338	CN ring stretch in Melam type structure	[27]
~1173–1195	~1164–1195	NH <sub>2</sub> rocking NH rocking + CN stretch	[17,18] [23]
~1023–1026	~1022–1033	CN ring breathing CN stretch + NH rocking	[17,18] [23]
~810–811	~811–813	CN ring bending	[17,22]
~731–767	~730–780	CN wagging + CN torsion + NH torsion CN ring bending	[23] [17,18]
~610–615	~619–620	CN wagging + CN torsion + NH wagging + NH torsion	[23]
~581–585	~581–582	NH <sub>2</sub> wagging CN ring bending	[17,18] [17,18]
~505–513	~518	CN ring bending + CN rocking Side-chain in-plane CN bending	[23] [17]

transfer and the output characteristics, a sweep rate of 66 mV s<sup>-1</sup> was employed, and the instrument featured a timing of 1 s for each of the hold, delay and step delay times respectively. For the calculation of the electron mobility in the OFETs, an experimentally measured value of capacitance per unit area ( $C_{od} = 3.85$  nF/cm<sup>2</sup>) was employed. For the calculation of interface trap state density, the transistor displayed in this work in Fig. 7a–b was inserted in the measurement cell for dielectric measurements and the capacitance vs. voltage measurements performed with the Novocontrol Alpha Analyzer. The measurement was performed connecting the electrical wires to the bottom gate and to only one of the top electrodes, neglecting the finite influence of the nearby floating top electrode for the calculation of the interface trap density of states. An active area of 1.2 mm<sup>2</sup> for the metal-insulator-semiconductor-metal (MIS) structure was considered, as well as a value for the capacitance per unit area of the dielectric insulator ( $C_{od} = 3.85$  nF/cm<sup>2</sup>). Implementing during the measurement the active area of the measured structure and considering the corresponding value of depletion capacitance offered by the instrument, a depletion capacitance per unit area ( $C_{dep} = 3.3$  nF/cm<sup>2</sup>) was used to compute the calculation for the interface trap density of states, and a value of subthreshold swing ( $S = 4$  V/dec) extracted from the ratio of the derivatives of gate voltage to logarithm of source-drain current [26]. The FTIR measurements were performed on a BRUKER OPTICS (EQUINOX 55) attenuated total reflection spectrometer with all analyzed samples in KBr pellet mode. Precursor powder (collected after the second

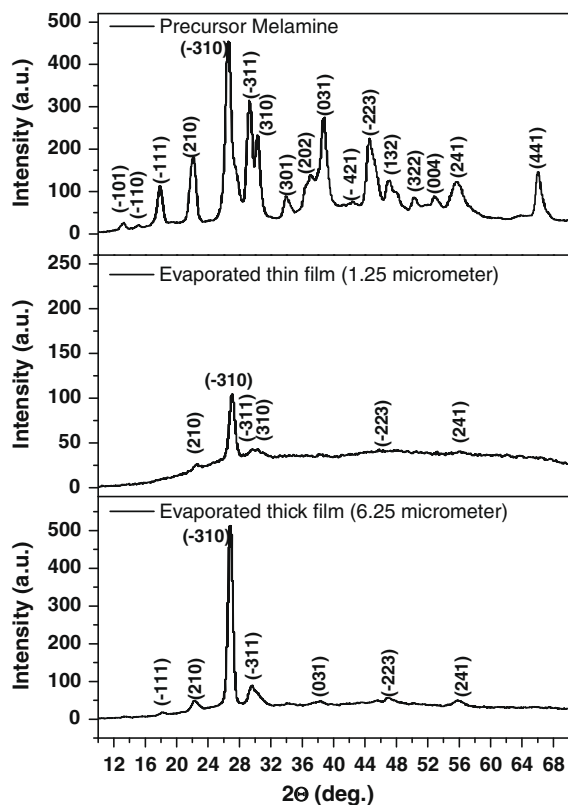


**Fig. 4.** X-ray diffraction spectra of precursor melamine (a) and evaporated melamine (b) and (c): The bottom graph displays a five times thicker evaporated film. The corresponding crystallographic planes are labelled according to the pattern in a standard card.

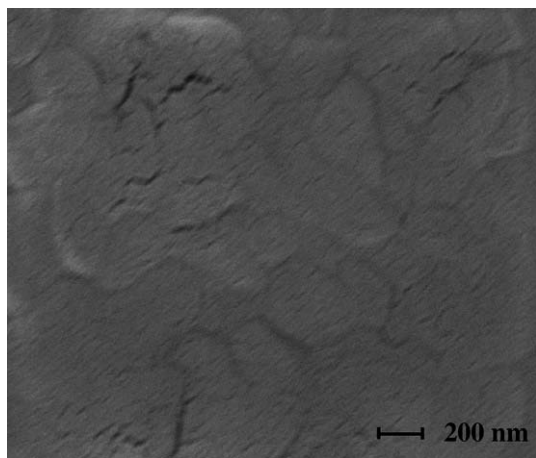


**Fig. 5.** SEM image of a region in the melamine film (1.25  $\mu\text{m}$  thick) displaying nanometer size cracks.

recrystallization) was mixed with KBr, whereas evaporated melamine was vacuum deposited on the surface of a pure KBr pellet. SEM measurements were performed on Zeiss-Cross Beam Series, scanning electron microscope on 1.25  $\mu\text{m}$  thick samples thermally evaporated on glass slides

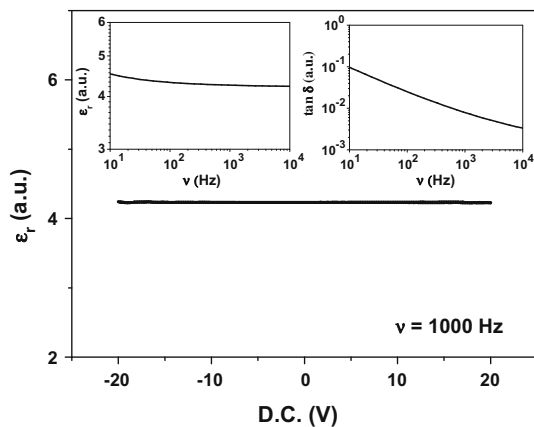


**Fig. 6.** Relative permittivity as a function of applied voltage for 600 nm thick evaporated melamine film in MIM configuration with evaporable aluminium electrodes; the top inserts represent the loss angle and relative permittivity spectra as a function of applied frequency in the range of 10 kHz to 10 Hz.

with no heat treatment performed after the deposition. A thin layer of 5 nm Au layer was thermally evaporated on the top of melamine thin film to avoid charging of the dielectric during the SEM scanning. X-ray diffractograms were obtained using a Bruker AXS X-ray diffractometer ( $\text{Cu K}\alpha$ ), on precursor powder (two times recrystallized) and thin films of 1.25 and 6.25  $\mu\text{m}$ , respectively, which were thermally evaporated on glass slides, with no heat-treatment following thermal evaporation of melamine. Topographical surface investigations were performed by analyzing the Atomic Force Microscope (AFM) images of the surface of the samples obtained from a Digital Instruments Dimension 3100 microscope working in tapping mode. As in the case of SEM measurements, the samples were not submitted to heat treatment at the end of melamine deposition. Thickness measurements of the melamine and  $\text{C}_{60}$  layers were initially performed with the aid of the AFM microscope and all the values reported here confirmed by a Dektak profilometer.

### 3. Results and discussion

#### 3.1. Structural and dielectric characterization of melamine

In this work we used no solution processing; instead both types of small molecules (*i.e.* melamine and  $\text{C}_{60}$ ) have been successively evaporated without interrupting the vacuum in the evaporation chamber. A schematic of both melamine and  $\text{C}_{60}$  small molecules is displayed, as an inset of Fig. 1 showing schematically a fully evaporated OFET structure. Fig. 2a and Fig. 2b show atomic force microscopy (AFM) images of 1.25  $\mu\text{m}$  thick melamine films evaporated on aluminium electrodes and 75 nm thick  $\text{C}_{60}$  films deposited on top of the evaporated melamine, respectively. The melamine grains are of elongated shape and randomly oriented. Most of the grains have lengths ranging from 350 to 700 nm, and the width is around 150 nm. The surface of the film displays a considerable peak-to-valley ratio in the range of 60 nm and an average root-mean-square

(RMS) roughness equal to 15 nm. The  $C_{60}$  layer built on top of the melamine film shows randomly oriented grains with no clearly defined shape. The surface of the  $C_{60}$  film displays a somewhat reduced roughness as compared to the melamine film; the peak-to-valley ratio and RMS values are situated in the range of 40 and 10 nm respectively.

Further analysis of the evaporated material was performed by means of Fourier transform infrared spectroscopy (FTIR) and X-ray diffraction (XRD). For the two investigations, 1.25  $\mu\text{m}$  thick melamine films have been evaporated on KBr pellets and glass slides, respectively. The FTIR spectra of the precursor and evaporated melamine are displayed in Fig. 3a and b, respectively, and the characteristic peaks are assigned in very good agreement to the literature data summarized in Table 1 [17,22,23]. It is interesting to point out the vibrational peak centered at  $\sim 1370\text{ cm}^{-1}$  which is not characteristic to the melamine crystal structure reported elsewhere [17,18,22,23]. Lotsch and Schnick attribute this peak to the  $\nu(\text{C-N})$  vibrational mode in melam-type structures [27]. However, in our work despite repeated FTIR characterization, we were not able to observe the other type of vibration (*i.e.*  $\delta(\text{NH})$  centered at  $\sim 1250\text{ cm}^{-1}$ ), which the above mentioned group further attributed to melam. This may be due to the transitory nat-

ure of melam which is a low-temperature de-amination product of melamine, formed upon linking of two molecules of melamine and the subsequent release of one mole of ammonia [19,27,28].

The melamine structure of the evaporated film is also confirmed by the X-ray diffraction pattern of the precursor powder and evaporated thin films, respectively (see Fig. 4a–c). The X-ray pattern of the precursor melamine powder is in excellent agreement with data published elsewhere, and the planes are indexed conforming to the pattern available in the standard card (No. 24-1654) of the instrument [20,24,25,27–31]. In agreement with observations of Jahromi and Moosheimer [31], we also presume that melamine grows in a columnar fashion originating from various nucleation centers distributed randomly on the substrate (*i.e.* aluminium stripe). Fig. 4c displays a five-fold thicker evaporated film with respect to the one shown in Fig. 4b and shows that the thin evaporated films are preferentially oriented as compared to the precursor powder. Scanning electron microscopy analysis of a 1.25  $\mu\text{m}$  thick evaporated melamine film on glass slide (Fig. 5) revealed the presence of nanometer size cracks in some regions of the film. The cracking, however, was sporadic and there were extensive crack-free regions of at

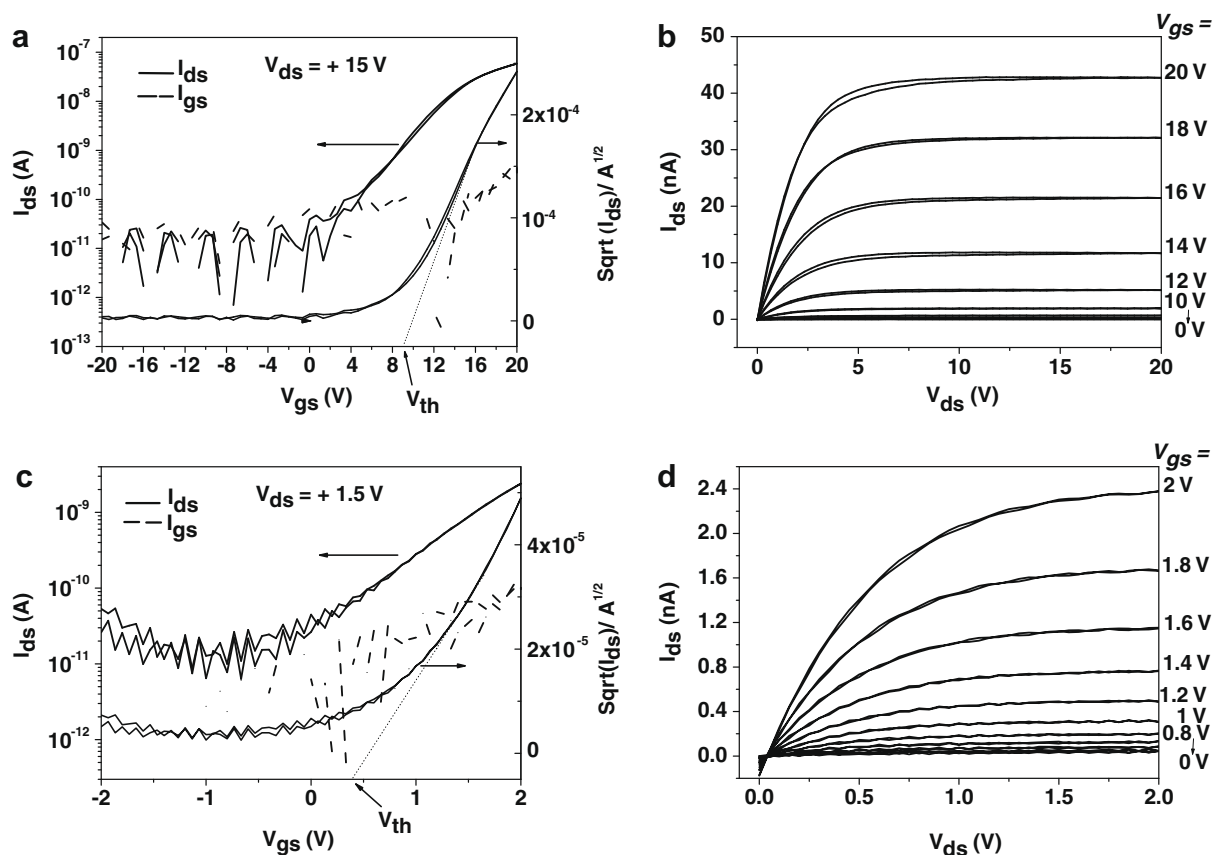


**Fig. 7.** Transfer and output characteristics of a transistors featuring 1.5  $\mu\text{m}$  melamine and 75 nm  $C_{60}$  with 60 nm thick top and bottom aluminium electrodes acting as gate and source/drain respectively (a), (b); Transfer and output characteristics of a transistor displaying 400 nm melamine and 75 nm  $C_{60}$ , with 60 nm thick aluminium top and bottom electrodes acting as gate and source/drain respectively (c), (d). Both  $I_{ds}$  and  $I_{gs}$  current values are displayed on the left axis in transfer characteristics. All transistors were subjected prior to the measurement to a heat-treatment in glove box, under nitrogen, at a temperature of 125  $^{\circ}\text{C}$  for one hour.

least  $100 \mu\text{m}^2$ . The variation in the amount of cracking throughout and between samples could be attributed to differences in thickness between different regions of the evaporated films, since the induced stresses during the thermal cooling stage of the film at the end of evaporation may vary with film thickness. The presence of such cracks could be therefore responsible for the high leakage currents observed during the transistor characterization of some of the fabricated devices within different batches.

The dielectric spectrum of a 600 nm thick evaporated melamine film in a metal-insulator-metal (MIM) configuration is displayed in Fig. 6. The applied voltage bias across the MIM structure was in the range of  $-20 \text{ V}$  to  $+20 \text{ V}$  and the scanned frequency spanned between 10 kHz and 10 Hz. The dielectric response of the measured sample is independent of the applied voltage and virtually dispersion free in the range of frequencies measured. In the range of frequencies investigated, a dielectric constant of 4.25 for the evaporated thin film of melamine has been measured.

### 3.2. Transfer and output characteristics of small-molecule transistors

Fig. 7 displays the transfer and output characteristics of melamine- $\text{C}_{60}$  transistors that are entirely grown by vapor deposition. We observed that for thicknesses of the dielectric material in the range of  $1 \mu\text{m}$  to  $1.5 \mu\text{m}$ , the transistors are stable and reproducible, offering a change in the source to drain current in excess of 3 orders of magnitude and leakage between 2 to 3 orders of magnitude lower than the driven current. Noteworthy, our best performing device working at 15 V, displayed more than 4 orders of magnitude on-off ratio and a leakage over 3 orders of magnitude below the source-drain current. On the other side of the scale, a thin melamine layer of only 400 nm acts as a gate dielectric in a transistor working at only 2 V and featuring 2 orders of magnitude on-off ratio, with an acceptable leakage current of more than one order of magnitude below the source-drain current. We also observed that heating the devices on the top of a hot plate at a temperature of  $100\text{--}125 \text{ }^\circ\text{C}$  for one hour further improves the transistor characteristics: the hysteresis vanishes, the leakage current decreases substantially, and the on-off ratio improves sometimes up to one order of magnitude when compared to the “as-fabricated” devices. We propose that the reason for this improvement rests in the finite diffusion of melamine molecules that arrests melamine film cracks. Some of the devices displaying an initial leakage within one order of magnitude below the drive current could be transformed in valuable devices after heat treatment, ultimately displaying leakages in excess of two orders of magnitude below the source-drain current. Thirty transistor batches with an aluminium gate in a bottom gate configuration were deposited on glass substrates, with four to six fabricated devices per batch. The measured transistors were subsequently subjected to the heat treatment exemplified above. The typical electron mobility calculated in the saturation regime for the heat treated transistors like the ones exemplified in Fig. 7a–d lies between 0.1 and  $0.3 \text{ cm}^2/\text{Vs}$ , averaged over samples produced in the same batch. The method employed for the mobility calculations

was reported elsewhere [26]. The electron mobility range and the transistor characteristics in this work correlate well with typical mobilities in OFETs featuring  $\text{C}_{60}$  as organic semiconductor layer [32–34]. It is worth mentioning that these transistor characteristics are obtained on a rough dielectric layer as depicted in the AFM pictograms. The considerable roughness of the dielectric films is responsible for a late opening of the devices (*i.e.* high and positive threshold voltage, evidenced by the transfer graphs) as well as low mobility and relatively modest on-off ratio, since it is expected that at low positive gate voltages, the electric charges are trapped in the valleys where the potential energy is minimized [12]. The calculation of the interface trap density of states is performed with the aid of the relation [14]:

$$S = \frac{kT}{q} \ln 10 \left( 1 + \frac{C_{dep} + C_{it}}{C_{od}} \right) \quad (1)$$

where  $S$  is the subthreshold swing,  $C_{dep}$  is the depletion capacitance per unit area measured from independent  $C(V)$  measurements,  $C_{od}$  is the insulator capacitance per unit area and  $C_{it}$  is the capacitance contribution per unit area of the charged interface traps, the latter being in fact expressed as:

$$C_{it} = q^2 D_{it} \quad (2)$$

with  $D_{it}$  the interface trap density of states and  $q$  the elementary charge.

Performing the calculations for the particular case of the device shown in Fig. 7a–b, one obtains for  $D_{it}$  a value of  $1.5 \times 10^{12} \text{ cm}^{-2} (\text{eV})^{-1}$ . Furthermore, considering typical trap energies of 0.2 eV below the conduction band edge of  $\text{C}_{60}$ , this would correlate with a value of interface trap density  $N_{it} = 3 \times 10^{11} \text{ cm}^{-2}$ , very close with similar values reported for organic-organic interfaces featuring pentacene as a semiconductor [14]. Various other transistor batches were produced on Cr/Au, Cu and indium-tin-oxide (ITO) as gate material and the devices were completed with Al for the source and drain electrodes. We observed that the characteristics of the transistors featuring ITO and Cr/Au as gate electrodes lie within the batch-to-batch variation and are very similar to the ones featuring Al gate. However regarding the copper gate, the transistors showed significantly lower on-off ratio as well as pronounced hysteresis which may be due to the strong interaction between copper and amino moieties, a fact observed in our previous work and also by others [7,35–36]. In another embodiment, an ordinary xerographic foil ( $1.5 \times 1.5 \text{ cm}$ ) of polyethylene terephthalate (PET) was used as a substrate on which an aluminium stripe was evaporated and the OFET was built in a similar way to the samples fabricated on glass substrate, resulting in a device displaying similar transistor characteristics.

## 4. Conclusion

In summary, we have developed organic field effect transistors having both the insulator and the semiconductor layers consisting of small evaporable molecules *i.e.* melamine and buckminsterfullerene, respectively. The characteristics of the transistors are stable and reproduc-

ible even several months after fabrication and the method offers the versatility to produce devices displaying adjustable operation voltage. The fabrication route substantiates further the vacuum evaporation method as suitable for large scale industrial processing (roll-to-roll production) of organic field effect transistors.

### Acknowledgements

The authors thank Prof. Jeffrey W. Fergus (Auburn University, Alabama, USA), Prof. Helmut Sitter, Dr. Gebhard Matt, Angela Vlad, Mujeeb Ullah, Pablo Jimenez-Manero and Heide Piglmayer-Brezina, for fruitful discussions and help during experimental design and/or measurements. Thanks are also conveyed to Narendhiran Pari (Auburn University, Alabama, USA) and Dr. Santhana Eswaramoorthy (Northwestern University, Illinois, USA) for help provided in obtaining valuable literature data. This work has been financially supported by the Austrian Science Foundation “FWF” within the National Research Network NFN on Organic Devices (S09712-N08, S09706-N08 and S9711-N08).

### References

- [1] S.R. Forrest, *Nature* 428 (2004) 911.
- [2] H. Sirringhaus, M. Ando, *MRS Bull.* 33 (7) (2008) 676.
- [3] C.J. Brabec, N.S. Sariciftci, J.C. Hummelen, *Adv. Funct. Mater.* 11 (1) (2001) 15.
- [4] F. So, J. Kido, P. Burrows, *MRS Bull.* 33 (7) (2008) 663.
- [5] T. Sekitani, Y. Noguchi, U. Zschieschang, H. Klauk, T. Someya, *Proc. Nat. Acad. Sci. USA* 105 (13) (2008) 4976.
- [6] Plastic electronic GmbH, patent applications pending (2007 and 2008).
- [7] M. Irimia-Vladu, N. Marjanovic, A. Vlad, A. Montaigne Ramil, G. Hernandez-Sosa, R. Schwödäuer, S. Bauer, N.S. Sariciftci, *Adv. Mater.* 20 (20) (2008) 3887.
- [8] M. Egginger, M. Irimia-Vladu, R. Schwödäuer, A. Tanda, I. Frischauf, S. Bauer, N.S. Sariciftci, *Adv. Mater.* 20 (2008) 1018.
- [9] L.S. McCarty, G.M. Whitesides, *Angew. Chem. Int. Ed.* 47 (12) (2008) 2188.
- [10] Th.B. Singh, N. Marjanovic, G.J. Matt, N.S. Sariciftci, R. Schwödäuer, S. Bauer, *Appl. Phys. Lett.* 85 (2004) 5409.
- [11] Th.B. Singh, N. Marjanovic, N.S. Sariciftci, R. Schwödäuer, S. Bauer, *IEEE Trans. Dielect. Electr. Insulation* 13 (5) (2006) 1082.
- [12] J. Lancaster, D.M. Taylor, P. Sayers, H.L. Gomes, *Appl. Phys. Lett.* 90 (2007) 103513.
- [13] S.A. DiBenedetto, D. Frattarelli, M.A. Ratner, A. Facchetti, T.J. Marks, *J. Am. Chem. Soc.* 130 (24) (2008) 7528.
- [14] M. Zirkel, A. Haase, A. Fian, H. Schön, C. Sommer, G. Jakopic, G. Leising, B. Stadlober, I. Graz, N. Gaar, R. Schwödäuer, S. Bauer-Gogonea, S. Bauer, *Adv. Mater.* 19 (17) (2007) 2241.
- [15] J. von Liebig, *Ann. Pharm.* 10 (1834) 1.
- [16] Borealis A.G. website, <<http://www.borealisgroup.com>>.
- [17] W.J. Jones, W.J. Orville-Thomas, *Trans. Faraday Soc.* 55 (1959) 203.
- [18] J.R. Schneider, B. Schrader, *J. Mol. Struct.* 29 (1975) 1.
- [19] H. May, *J. Appl. Chem.* 9 (1959) 340.
- [20] E.W. Hughes, *J. Am. Chem. Soc.* 63 (1941) 1737.
- [21] D. Larson, D.C. Cromer, *J. Chem. Phys.* 60 (1) (1974) 185.
- [22] R.J. Meier, J.R. Maple, M.-J. Hwang, A.T. Hagler, *J. Phys. Chem.* 99 (1995) 5445.
- [23] M.P. Fernandez-Liencre, A. Navarro, J.J. Lopez-Gonzales, M. Fernandez-Gomez, J. Tomkinson, G.J. Kearley, *Chem. Phys.* 266 (2001) 1.
- [24] D.L. Yu, J.L. He, Z.Y. Liu, B. Xu, D.C. Li, Y.J. Tian, *J. Mater. Sci.* 43 (2008) 689.
- [25] L.D. Yao, F.Y. Li, J.X. Li, C.Q. Jin, R.C. Yu, *Phys. State Solid (a)* 202 (14) (2005) 2679.
- [26] C.R. Newman, C. Daniel Frisbie, D.A. da Silva Filho, J.-L. Bredas, P.C. Ewbank, K.R. Mann, *Chem. Mater.* 16 (2004) 4436.
- [27] B. Lotsch, W. Schnick, *Chem. Eur. J.* 13 (2007) 4956.
- [28] B. Juergens, E. Irran, J. Senker, P. Kroll, H. Mueller, W. Schnick, *J. Am. Chem. Soc.* 125 (2003) 10288.
- [29] R.S. Rajeev, S.K. De, A.K. Bhowmick, B. Gong, S. Bandyopadhyay, *J. Adhes. Sci. Technol.* 16 (14) (2002) 1957.
- [30] H.A. Ma, X. Jia, Q.L. Cui, Y.W. Pan, P.W. Zhu, B.B. Liu, H.J. Liu, X.C. Wang, J. Liu, G.T. Zou, *Chem. Phys. Lett.* 368 (2003) 668.
- [31] S. Jahromi, U. Moosheimer, *Macromolecules* 33 (2000) 7582.
- [32] R.C. Haddon, A.S. Perel, R.C. Morris, T.T.M. Palstra, A.F. Hebard, *Appl. Phys. Lett.* 67 (1995) 121.
- [33] S. Kobayashi, T. Takenobu, S. Mori, A. Fujiwara, Y. Iwasa, *Appl. Phys. Lett.* 82 (2003) 4581.
- [34] Th.B. Singh, N. Marjanovic, G.J. Matt, S. Gunes, N.S. Sariciftci, A. Montaigne Ramil, A. Andreev, H. Sitter, R. Schwödäuer, S. Bauer, *Org. Electron.* 6 (2005) 105.
- [35] R.V. Plank, N.J. DiNardo, J.M. Vohs, *Phys. Rev. B* 55 (16) (1997) R10241.
- [36] K.K. Lee, J.M. Vohs, N.J. DiNardo, *Surf. Sci. Lett.* 420 (1999) L115.



## High efficiency polymer solar cells with wet deposited plasmonic gold nanodots

Ji Hwang Lee<sup>a</sup>, Jong Hwan Park<sup>b</sup>, Jong Soo Kim<sup>a</sup>, Dong Yun Lee<sup>b</sup>, Kilwon Cho<sup>a,b,\*</sup>

<sup>a</sup> School of Environmental Science and Engineering, Pohang University of Science and Technology, Pohang 790-784, Republic of Korea

<sup>b</sup> Department of Chemical Engineering, Pohang University of Science and Technology, Pohang 790-784, Republic of Korea

### ARTICLE INFO

#### Article history:

Received 27 October 2008

Received in revised form 24 December 2008

Accepted 2 January 2009

Available online 18 January 2009

#### PACS:

73.20.Mf

73.50.Pz

78.67.Bf

#### Keywords:

Organic solar cell

Surface plasmon

Gold nanodot

Layer-by-layer deposition

Bulk heterojunction

### ABSTRACT

We report the enhanced performance of poly(3-hexylthiophene)/[6,6]-phenyl-C<sub>61</sub> butyric acid methyl ester (P3HT/PCBM) bulk heterojunction solar cells with wet deposited interfacial gold nanostructures on their indium tin oxide (ITO) surfaces. To produce localized surface plasmons at the ITO surfaces, gold nanostructures were fabricated through the layer-by-layer deposition of gold nanorods onto the ITO substrates and transformed into nanodots through a thermally induced shape transition. The incorporation of plasmonic gold nanodots on the ITO surface was found to result in an increase in the power conversion efficiency from 3.04% to 3.65%, which is due to the presence of the resulting plasmon field.

© 2009 Elsevier B.V. All rights reserved.

### 1. Introduction

Organic solar cells have recently been intensively investigated with the aim of increasing their efficiency [1–7]. In particular, devices containing blends of poly(3-hexylthiophene) (P3HT) and [6,6]-phenyl-C<sub>61</sub>-butyric acid methyl ester (PCBM) have been widely studied and have consistently been reported to produce efficiencies over 4% [2–4]. The recent development of metal nanoparticles with surface plasmon excitation has been used to further improve the performance of both silicon and organic solar cell devices [8–14]. Metallic nanoparticles are well known for their strong interactions with visible light, which arise

because of the localized surface plasmon resonances (LSPR) of the collective oscillations of the conduction electrons within the particles. Excitation of LSPR within metal nanoparticles can create strong near-field electromagnetic fields and far-field propagating waves that enhance the light absorption and photocurrent of organic photovoltaic devices [11–14]. Recent studies have shown that hybrid organic photovoltaic devices with metal particles incorporated in the photo-active region have enhanced light absorption and photocurrent [13,14]. However, the power conversion efficiency (PCE) in these cases might be restricted by exciton quenching with nonradiative energy transfer and the differences between the electronic properties of the metal nanoparticles and the conjugated molecules in the hybrid material. In contrast, this undesirable quenching does not occur in interfacial metallic nanostructures between poly(3,4-ethylene dioxythiophene):poly(styrenesulfonate) (PEDOT:PSS) and indium tin

\* Corresponding author. Address: Department of Chemical Engineering, Pohang University of Science and Technology, Pohang, 790-784, Republic of Korea. Tel.: +82 54 279 2270; fax: +82 54 279 8298.

E-mail address: [kwcho@postech.ac.kr](mailto:kwcho@postech.ac.kr) (K. Cho).

oxide (ITO) substrates. Previous attempts to fabricate gold and silver nanostructures have used physical deposition techniques [11–13]. Wet chemistry approaches provide particularly efficient methods for the fabrication of well-dispersed metallic nanostructures with control over the size, shape, and density of particles [16,20,27]. There have been no previous studies of the effects of plasmon excitation in bulk heterojunction polymer solar cells containing interfacial gold nanoparticles fabricated with simple wet chemistry method rather than vacuum deposition.

In this study, we report a simple method for the fabrication of interfacial gold nanostructures through the thermally-induced shape transformation of anisotropic gold nanoparticles on ITO substrates, and investigate how the resulting surface plasmons affect the optical properties of the conjugated polymer and the PCE of bulk heterojunction polymer solar cells. These results are useful for understanding the role of surface plasmons in the performance of organic photovoltaic devices.

## 2. Experimental

For the fabrication of the photovoltaic devices, a multilayer film of gold nanorods was prepared by the layer-by-layer electrostatic assembly approach, and the particle density of the gold nanorods on the ITO substrate was controlled by varying the number of deposition cycles [15,18]. The resulting films were annealed at 400 °C for 5 min to remove the insulating polyelectrolyte layers. In the wet chemistry approach, gold nanorods can be synthesized using the seed-mediated growth method described by Nikoobakht and El-Sayed [16]. First, the gold nanorods are capped with a bilayer of cetyltrimethyl ammonium bro-

mid, which is positively charged [15,16]. The positively charged surfaces of the gold nanorods are then converted to negatively charged surfaces by exposing them to 1 mM poly(sodium-4-styrenesulfonate) (PSS) polyelectrolyte solution. In the gold nanorod deposition, positively charged 10 mM linear polyethyleneimine (PEI) is used as an adhesive layer on the ITO substrate. After the ITO substrate has been modified with PEI, repeated depositions of PSS-coated gold nanorods and PEI result in the formation of gold nanorod multilayer films on the ITO substrate. The conductive ITO film deposited with gold nanostructures was measured by using a scanning electron microscopy (SEM, Hitachi 4800). Optical spectra were acquired using Cary 5000 UV–vis spectrometer (Varian) and photoluminescence (PL) spectra were recorded by using the front face geometry of P3HT films by a spectrofluorometer (Jasco FP-6500) with the 500 nm excitation wavelength.

In order to investigate the effect of surface plasmons on the performance of P3HT/PCBM bulk heterojunction polymer solar cells, an active layer composed of 1 wt% P3HT (Rieke Metals)/PCBM (Nano-C) blend (1:0.8) in chlorobenzene was spin cast onto PEDOT:PSS (Baytron P AI 4083) coated ITO substrates with gold nanodots and treated at 150 °C for 10 min. The devices were completed by evaporation of a metal top electrode (LiF/Al), as shown schematically in the inset of Fig. 4a. For comparison, the control devices were also fabricated under the same experimental procedures with those of gold nanodots. Current density–voltage ( $J$ – $V$ ) characteristics were measured under AM 1.5 solar illumination (with reference to a standard Si cell calibrated with NREL) at an intensity of 100 mW/cm<sup>2</sup> with an Oriel 1 kW solar simulator by using a programmable Keithley 4200 measurement source under inert nitrogen

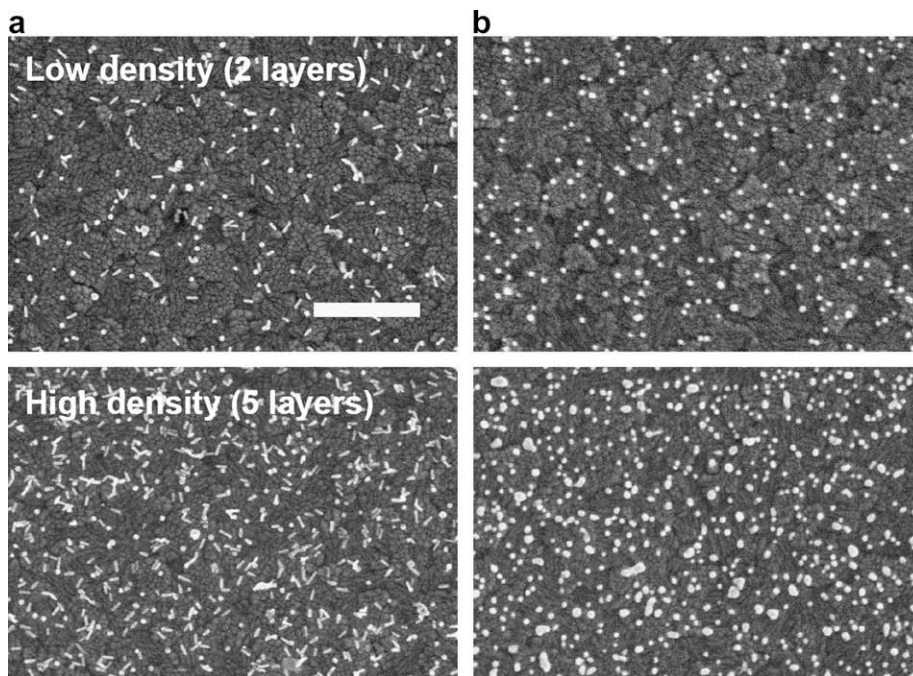


**Fig. 1.** SEM images showing (a) gold nanorods and (b) thermally transformed gold nanodots on ITO substrates. Top: low density (two layers), bottom: high density (five layers). The scale bar is 500 nm.

gas. The incident photon to current conversion efficiency (IPCE) as a function of wavelength was measured with a photomodulation spectroscopic setup (model Merlin, Oriel).

### 3. Results and discussion

Fig. 1 clearly shows the difference in the particle density of the gold nanorod multilayer films between the case of two layers of deposited gold nanorods (low density) and the case of five layers of gold nanorods (high density). Most of the gold nanorods are present in isolation with a few aggregates. Fig. 1a and b show a sequence of SEM images of gold nanorods changing their shape during thermal heating at 400 °C for 5 min. Thermally-transformed gold nanodots with an average size of 30 nm are then present uniformly on the ITO substrate. These SEM results confirm that the initially anisotropic nanorods have been converted into isotropic particles. The changes in the structure of the gold nanorods occur via diffusion of surface atoms from the regions of high curvature at the ends of the nanorods toward the straight cylindrical faces because of the structural instability of gold nanorods [17,18]. This trend is in agreement with changes in the shape of the UV–vis spectrum, in which a single plasmon band centered near 530 nm is present after heating instead of the two distinct plasmon bands in the original spectrum (Fig. 2).

Fig. 3a shows the absorption spectra of P3HT thin films on PEDOT:PSS-coated quartz substrates with and without gold nanodots, and the inset in Fig. 3a shows the absorption difference,  $\Delta A$  ( $A_{\text{sample}} - A_{\text{P3HT}}$ ). Because of the lack of distinct features in the absorption spectrum of the thick P3HT film on the gold nanodots, which is attributed to the high extinction coefficient of P3HT, a relatively thin 20 nm P3HT film was spin cast onto the quartz substrate instead of the ITO substrate. Since the plasmon region of the gold nanodots matches the absorption spectrum of P3HT, the absorbance of P3HT with gold nanodots in-

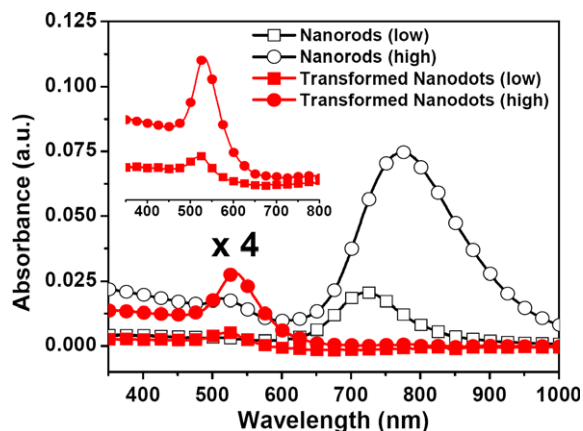


Fig. 2. UV–vis spectra of the gold nanorods (black, empty) and thermally transformed gold nanodots (red, filled) with low (square) and high (circle) particle density on ITO substrates. The inset shows the enlarged UV–vis spectra of the thermally transformed gold nanodots. (For interpretation of the references to colour in this figure legend, the reader is referred to the web version of this article.)

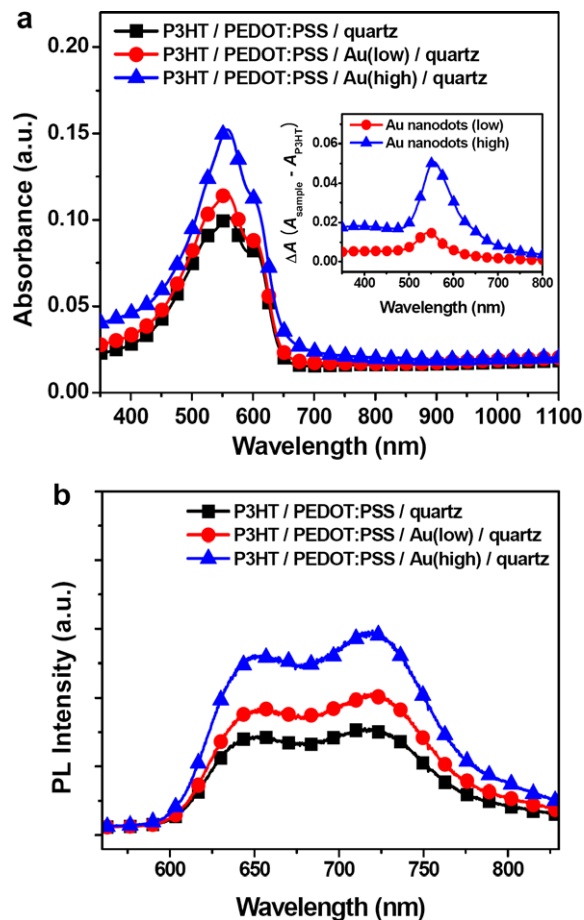
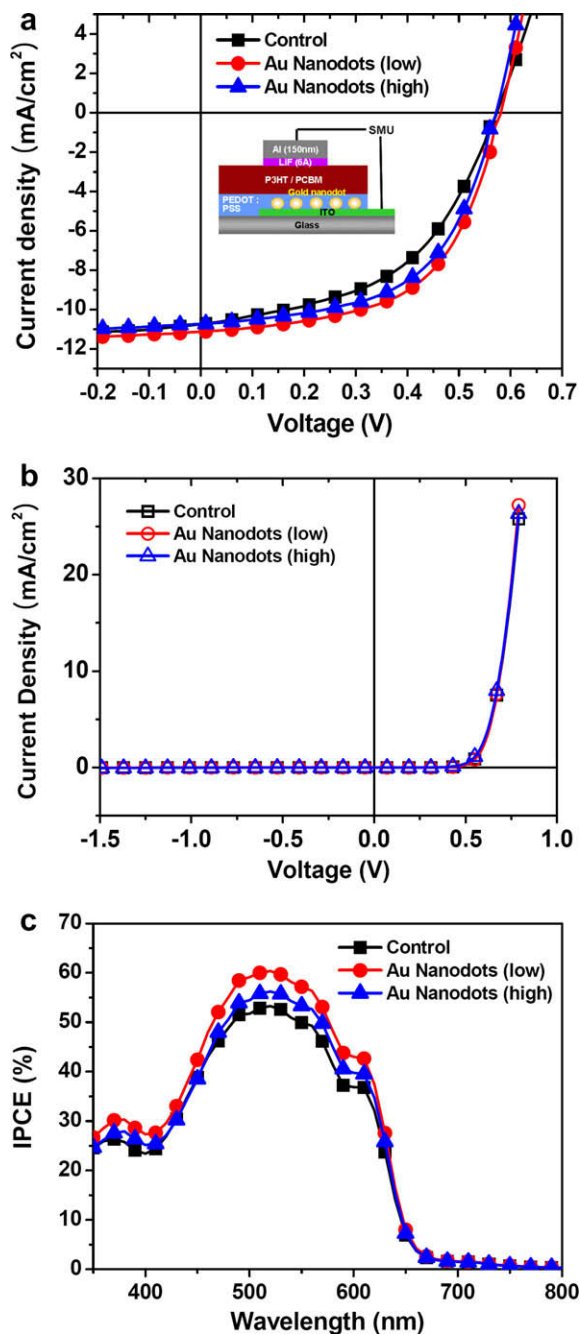


Fig. 3. (a) Optical absorption spectra and (b) PL spectra of P3HT thin films for P3HT/PEDOT:PSS/Au/quartz structures. The inset in (a) shows the differential absorption  $\Delta A$  ( $A_{\text{sample}} - A_{\text{P3HT}}$ ) spectra of the samples.

creases with the gold nanodot particle density. As a result, the differential absorption spectrum shown in the inset of Fig. 3a is very similar to the absorption spectrum of gold nanodots shown in the inset of Fig. 2, and the differential absorbance increases with the gold nanodot density. The weaker P3HT absorbance in the plasmon region is overwhelmed by the stronger plasmon excitation, which results in a profile similar to the surface plasmon band shapes.

The PL spectra of the same samples at room temperature are shown in Fig. 3b. The intensity of the PL spectrum of the P3HT film with gold nanodots is significantly stronger than that of the P3HT film without gold nanodots. The surface plasmons on the metal surface create a far-field propagating wave that penetrates into the P3HT layer via the excitation of surface plasmon resonances in the vicinity of the gold nanoparticles [9,19,20,27]. The large enhancement of the PL with increases in the gold nanodot density indicates that the propagating plasmon field results in an increase in the radiative relaxation of electronic states in the conjugated polymer. It is therefore clear that the PL enhancement of P3HT arises from the strong coupling between the excitonic state of P3HT and the plasmonic field





**Fig. 4.**  $J$ - $V$  characteristics of polymer solar cells with and without gold nanodots (a) under illumination with  $100 \text{ mW/cm}^2$  AM1.5 simulated light, (b) in the dark, and (c) IPCE spectra of these devices. A schematic diagram of the bulk heterojunction solar cell device with gold nanodots is shown in the inset in (a).

of the gold nanodots, which is due to the propagating oscillation of the surface plasmon dipole.

The  $J$ - $V$  characteristics under illumination of these solar cells with and without a layer of interfacial gold nanodots are shown in Fig. 4a, and a summary of their performance is given in Table 1. An enhanced efficiency was observed for the device with interfacial gold nanodots. A highest

**Table 1**  
Summary of device characteristics.

	$J_{sc}$ (mA/cm <sup>2</sup> )	$V_{oc}$ (V)	FF	PCE (%)
P3HT/PCBM control	10.74	0.57	0.50	3.04
With gold nanodots (low density)	11.13	0.58	0.57	3.65
With gold nanodots (high density)	10.74	0.57	0.56	3.43

PCE of 3.65% with an open-circuit voltage ( $V_{oc}$ ) of 0.58 V, a short-circuit current density ( $J_{sc}$ ) of  $11.13 \text{ mA/cm}^2$ , and a fill factor (FF) of 0.57 was obtained for the device with a low density of gold nanodots. The IPCE data follow the same trend (Fig. 4c). The results demonstrated a substantial enhancement over the entire excitation spectral range, in which the improved IPCE was mainly observed from 500 nm to 600 nm. This agrees with the improved light harvesting via plasmon excitation of gold nanodots. Fig. 4b shows the corresponding  $J$ - $V$  curves of these devices in the dark. This lack of change in the  $J$ - $V$  curves in the dark strongly indicates that the total series resistance of the diode devices is unchanged by incorporation of interfacial gold nanodots. Fig. 4a and b provide further evidence that the significant change in  $J$ - $V$  curve shape under illumination will therefore primarily originate from a change in bulk resistance of active layer under the plasmon-field interaction, not a change in sheet resistance of the electrode with metal nanoparticles.

According to the Mie theory [19], the total Mie extinction is a sum of contribution from absorption and scattering components associated with surface plasmon mode of the particles. For small gold particles unlike silver ones, the total extinction cross section consists of a large absorption and small scattering cross section. Thus, the transmission of incident light in proximate gold nanodots is largely absorbed than forward scattered at resonance condition. Because of the strong near-field absorption and far-field scattering characteristics of gold nanoparticles, there is competition between the loss of transmitted photon energy and the enhancement of incident light intensity coupling by a far-field scattering plasmon wave [19,20,24]. For this reason,  $J_{sc}$  changes negligibly from  $10.74 \text{ mA/cm}^2$  to  $11.13 \text{ mA/cm}^2$ .

However, the enhancement of the PCE from 3.04% to 3.65% on the addition of a low particle density of gold nanodots is a consequence of an increase in FF. This result suggests that the improved FF results from the efficient charge transfer of excitons in P3HT because of the presence of the surface plasmon field. Several mechanisms by which localized surface plasmon fields can enhance the relaxation processes of excited-state excitons have been proposed as the possible interpretations of the plasmon effect [19–23]. When the strong coupling between a surface plasmon and an exciton occurs, the surface plasmon can shorten the excitonic lifetime and modify the dynamic properties of excited state excitons, which mean that the excitons do not have time to find their minima in the excitonic materials. According to these interpretations, the intense electromagnetic field of plasmon can increase the population of

'hot' exciton, the exciton with excess thermal energy being necessary to overcome the coulombic attraction of the initially generated radical pairs, in the P3HT films due to the acceleration of the radiative relaxation of P3HT exciton at plasmon resonant energy. Recently, Ohkita et al. [25] reported that this 'hot' exciton has a high probability of dissociation into free polarons for efficient charge separation. It was suggested that an increase of 'hot' exciton of P3HT might result in the enhanced charge dissociation yield without geminate recombination losses. Therefore, the plasmon-field interaction at resonant energies may be sufficient to facilitate the relaxation processes of P3HT electronic states for participating in the efficient charge dissociation, for which there is kinetic competition between geminate recombination to ground and charge dissociation. This model is supported by our results for the plasmon effect in P3HT/PCBM blend films, which implies that strong coupling between the plasmon and excitonic systems results in efficient charge dissociation at the excitation energies that overlap with those of the surface plasmon oscillations.

On the other hand, when there is a high particle density of gold nanodots, the randomly distributed gold nanoparticles generate 'hot-spots' due to their dipole-dipole electromagnetic interactions [26,27]. These hot-spots generate new hybridized plasmons below the surface plasmon frequency that complicate the propagation of the electromagnetic field into the active layer. Despite the stronger propagating plasmon field of gold nanodots with a high particle density, the excitons of P3HT cannot interact efficiently with the plasmon, resulting in a lower efficiency than that of the low particle density sample.

#### 4. Conclusions

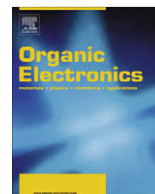
In conclusion, we have demonstrated that thermally-transformed gold nanodots deposited on the ITO substrate with the layer-by-layer technique enhance the far-field propagating plasmon field via surface plasmon excitation. The PCE was found to be increased from 3.04% to 3.65% by the incorporation of the plasmonic gold nanostructures because of the presence of the plasmon field proximate to the gold nanodots. These results suggest that the strong coupling between the organic excitons and plasmons of the gold nanostructures results in more efficient charge transfer in the bulk heterojunction blend. These results can contribute to our understanding of plasmonic interactions between conjugated polymers and metal nanostructures in polymer solar cells, and related experiments are under way.

#### Acknowledgements

This work was supported by a Grant (M108K0010008K1501-00810) from the Center for Nanostructured Materials Technology under the 21st Century Frontier R&D Program and Creative Research Initiative (CRI)-Acceleration Research Program (R17-2008-029-01000-0) of the Ministry of Education, Science and Technology.

#### References

- [1] C.J. Brabec, N.S. Sariciftci, J.C. Hummelen, *Adv. Funct. Mater.* 11 (2001) 15.
- [2] G. Li, V. Shrotriya, J.S. Huang, Y. Yao, T. Moriarty, K. Emery, Y. Yang, *Nat. Mater.* 4 (2005) 864.
- [3] M.D. Irwin, D.B. Buchholz, A.W. Hains, R.P.H. Chang, T.J. Marks, *Proc. Natl. Acad. Sci.* 105 (2008) 2783.
- [4] J.Y. Kim, K. Lee, N.E. Coates, D. Moses, T. Nguyen, M. Dante, A.J. Heeger, *Science* 317 (2007) 222.
- [5] J.S. Kim, J.H. Park, J.H. Lee, J. Jo, D.-Y. Kim, K. Cho, *Appl. Phys. Lett.* 91 (2007) 112111.
- [6] Y. Kinoshita, R. Takenaka, H. Murata, *Appl. Phys. Lett.* 92 (2008) 243309.
- [7] J.B. Xia, N. Masaki, M. Lira-Cantu, Y. Kim, K.J. Jiang, S. Yanagida, *J. Am. Chem. Soc.* 130 (2008) 1258.
- [8] M. Westphalen, U. Kreibitz, J. Rostalski, H. Lüth, D. Meissner, *Sol. Energy Mater. Sol. Cells* 61 (2000) 97.
- [9] D. Derkacs, S.H. Lim, P. Matheu, W. Mar, E.T. Yu, *Appl. Phys. Lett.* 89 (2006) 093103.
- [10] R.B. Konda, R. Mundle, H. Mustafa, O. Bamiduro, A.K. Pradhan, U.N. Roy, Y. Cui, A. Burger, *Appl. Phys. Lett.* 91 (2007) 191111.
- [11] A.J. Morfa, K.L. Rowlen, T.H. Reilly III, M.J. Romero, J. Van de Lagemaat, *Appl. Phys. Lett.* 92 (2008) 013504.
- [12] S.-S. Kim, S.-I. Na, J. Jo, D.-Y. Kim, Y.-C. Nah, *Appl. Phys. Lett.* 93 (2008) 073307.
- [13] B.P. Rand, P. Peumans, S.R. Forrest, *J. Appl. Phys.* 96 (2004) 7519.
- [14] K. Kim, D.L. Carroll, *Appl. Phys. Lett.* 87 (2005) 203113.
- [15] A. Gole, C.J. Murphy, *Chem. Mater.* 17 (2005) 1325.
- [16] B. Nikoobakht, M.A. El-Sayed, *J. Phys. Chem. A* 107 (2003) 3372.
- [17] H. Petrova, J.P. Juste, I. Pastoriza-Santos, G.V. Hartland, L.M. Liz-Marzán, P. Mulvaney, *Phys. Chem. Chem. Phys.* 8 (2006) 814.
- [18] X. Hu, T. Wang, S. Dong, *J. Colloid Interface Sci.* 316 (2007) 947.
- [19] J.R. Lakowicz, *Anal. Biochem.* 337 (2005) 171.
- [20] W.A. Murray, W.L. Barnes, *Adv. Mater.* 19 (2007) 3771.
- [21] J. Bellessa, C. Bonnand, J.C. Plenat, J. Mugnier, *Phys. Rev. Lett.* 93 (2004) 036404.
- [22] J. Lee, P. Hernandez, J. Lee, A.O. Govorov, N.A. Kotov, *Nat. Mater.* 6 (2007) 291.
- [23] E.C. Le Ru, P.G. Etchegoin, J. Grand, N. Félidj, J. Aubard, G. Lévi, *J. Phys. Chem. C* 111 (2007) 16076.
- [24] J.R. Cole, N.J. Halas, *Appl. Phys. Lett.* 89 (2006) 153120.
- [25] H. Ohkita, S. Cook, Y. Astuti, W. Duffy, S. Tierney, W. Zhang, M. Heeney, I. McCulloch, J. Nelson, D.D.C. Bradley, J.R. Durrant, *J. Am. Chem. Soc.* 130 (2008) 3030.
- [26] P. Etchegoin, L.F. Cohen, H. Hartigan, R.J.C. Brown, M.J.T. Milton, J.C. Gallop, *Chem. Phys. Lett.* 383 (2004) 577.
- [27] M. Pelton, J. Aizpurua, G. Bryant, *Laser & Photon. Rev.* 2 (2008) 136.



## Effect of active layer thickness on environmental stability of printed thin-film transistor

Min Hee Choi<sup>a</sup>, Seung Hoon Han<sup>a</sup>, Sun Hee Lee<sup>a</sup>, Dong Joon Choo<sup>a</sup>, Jin Jang<sup>a,\*</sup>, Soon Ki Kwon<sup>b</sup>

<sup>a</sup>Advanced Display Research Center, Kyung Hee University, Seoul 130-701, Republic of Korea

<sup>b</sup>School of Nano and Advanced Materials and Engineering Research Institute, Gyeong Sang University, Jinju 660-701, Republic of Korea

### ARTICLE INFO

#### Article history:

Received 4 October 2008

Received in revised form 4 January 2009

Accepted 8 January 2009

Available online 16 January 2009

#### PACS:

05.65.+b

31.70.Hq

72.80.Le

#### Keywords:

Organic TFT

Stability

TIPS pentacene

### ABSTRACT

We have studied the effect of active layer thickness on the performance and environmental stability of the 6,13-bis(triisopropylsilylethynyl) pentacene (TIPS pentacene) thin-film transistor. The organic thin-film transistors (OTFTs) were fabricated by inkjet printing using a solution based TIPS pentacene. To get thick organic semiconductor, the surface of gate insulator was treated with *n*-octyltrichlorosilane (OTS-C<sub>8</sub>) before jetting. The on-currents of the OTFT with ~1 μm active layer decreases a little in air, but the OTFT with 0.05 μm TIPS pentacene shows a significant degradation in drain currents.

© 2009 Elsevier B.V. All rights reserved.

Organic thin-film transistors (OTFTs) are of increasing interest for low cost, large-area electronic applications such as active-matrix displays, electronic paper and flexible microelectronics [1–3]. Among solution processed organic semiconductors, thiophene and pentacene derivatives exhibit good TFT performance. However, device stability under air should be improved to apply printed OTFTs to flexible displays.

The lifetime of the OTFTs having no passivation layer is usually short when they are exposed to ambient air due to the interaction of organic semiconductor with oxygen and moisture [4]. It results in the degradation of TFT performance. Therefore, in order to achieve OTFTs with long lifetime, the OTFTs should be protected from the environmental moisture and oxygen [5]. The studies on

the environmental stability of OTFTs indicate that some specific gases such as moisture and oxygen affect the TFT performance significantly.

In this paper, we report the environmental stability of unpassivated OTFT made of the 6,13-bis(triisopropylsilylethynyl) pentacene (TIPS pentacene) using inkjet printing. The on-currents of the OTFT with ~1 μm active layer degrade a little in air, but the OTFT with 0.05 μm TIPS pentacene shows a significant degradation in drain currents. The thick active layer has a self-passivation effect by intrinsic organic semiconductor even though the surface region is affected by H<sub>2</sub>O or O<sub>2</sub>, leading to keep the on-currents in air.

We used a piezoelectric type of Litrex Corp. 80.L equipment with spectra SE-128 printing head for inkjet printing [6]. The printer has an optical module which can inspect the substrate condition and analyze the volume, velocity and angle deviation of in-flight drops. We have optimized the parameters in order to make stable droplets with good

\* Corresponding author. Tel.: +82 2 961 0270; fax: +82 2 961 9154.

E-mail address: [jjang@khu.ac.kr](mailto:jjang@khu.ac.kr) (J. Jang).

repeatability and to remove satellite drops before printing onto the substrate.

Fig. 1a shows the schematic cross-sectional view of a bottom contact TIPS pentacene OTFT used in the present work. As gate electrode, AlN<sub>d</sub> (100 nm) was deposited on polyethylenephthalate (PEN) substrate and patterned by photolithography. The gate insulator, photo-definable poly(4-vinylphenol) (P-PVP) having a dielectric constant of 3.6 and 450 nm thickness, was spin coated from the P-PVP precursor, and then developed after UV exposure. Then, the sample was cured in a vacuum oven to harden the pattern [7]. An Au layer (50 nm) was deposited on

the gate insulator and patterned as source/drain electrodes. The W/L, ratio of channel width to channel length, of the OTFTs was fixed to 236 μm/6 μm for all the OTFTs studied in this work.

To define a TFT region in a pixel and to keep the organic semiconductor inside of the TFT region, a bank was formed by poly(vinylalcohol) (PVA). Then, we treated the gate dielectric surface with O<sub>2</sub> plasma to make it clean and hydrophilic. Finally, TIPS pentacene was inkjet printed using the overlap jetting at 90 °C [8]. After printing, the OTFT substrate was cooled down to 26 °C with the cooling rate of ~0.5 °C/min. Measurement of the TFT performances were carried out at room temperature under ambient air and the sample was stored in ambient air.

It is found that boiling point of the solvent is important because the drying time upon jetting affects the structure of organic semiconductor [9]. Note that it increases with increasing boiling point. Therefore, cyclohexanol (viscosity of 41 cP) was mixed to 1,2,4-trichlorobenzene (viscosity of ~1 cP) and then more uniform TIPS pentacene layer could be achieved [10]. The boiling points for cyclohexanol and trichlorobenzene are 160 and 214 °C, respectively. And the sample was treated by *n*-octyltrichlorosilane (OTS-C<sub>8</sub>) to make hydrophobic surface before TIPS pentacene printing. The surface energy of PVP dielectric decreases sufficiently by OTS-C<sub>8</sub> treatment, and thus printed drops could not spread out on the PVP surface, leading to a thick active layer. The thickness of the TIPS pentacene was changed between 50 nm and 1000 nm by increasing the drop number from 15 to 60 and surface treatment as well. Fig. 1b and c shows the cross-sectional view of FIB images of TIPS pentacene on the channel, from which the thickness can be decided.

Fig. 2 shows the optical image of a TIPS pentacene TFT before and after printing. The inkjet printed TIPS pentacene OTFT using mixed solvent shows more uniform layer in the channel [10]. But the optical images are very different between the two; the films of thin and thick TIPS pentacenes. The TFT channel is transparent for thin TFT as shown in Fig. 2b and the thick one is black as can be seen in Fig. 2c.

Fig. 3 shows the transfer characteristics of the TIPS pentacene TFT by inkjet printing [8]. The thin TIPS pentacene TFT on plastic exhibited an on/off current ratio of ~10<sup>5</sup>, a threshold voltage of 1 V, a gate voltage swing of 1.6 V/dec. and a field-effect mobility of 0.006 cm<sup>2</sup>/Vs in the saturation region. On the other hand, the thick TIPS pentacene TFT on plastic exhibited an on/off current ratio of ~10<sup>6</sup>, a threshold voltage of -1 V, a gate voltage swing of 0.8 V/decade and a field-effect mobility of 0.02 cm<sup>2</sup>/Vs in the saturation region.

It is found that the performance of the TFT using a mixed solvent is worse than that using a single aromatic solvent. Note that aromatic solvents have π-π stacking showing relatively good electrical conduction because TIPS pentacene has π-electron conjugated segments. Therefore, when we dissolve the TIPS pentacene in aromatic solvent, electric conduction in TIPS pentacene is enhanced as a result of π-π interaction. However, when we used cyclohexanol solvent, non-aromatic solvent, the solvent molecules solvate non-conjugated segments of polymer and thus films with lower electrical conduction are obtained. Note

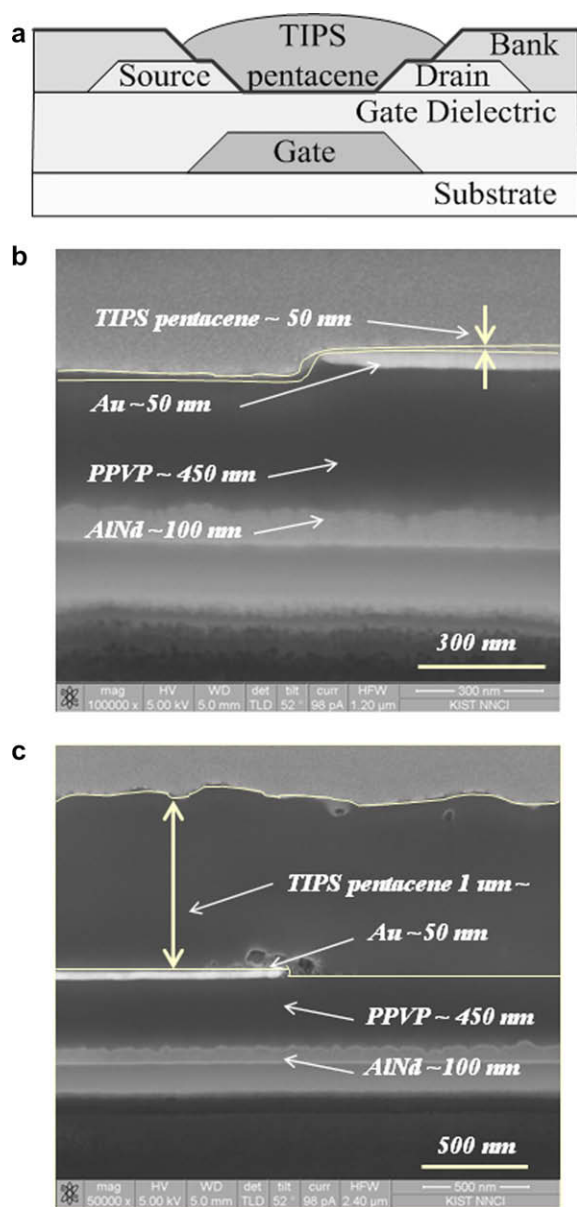
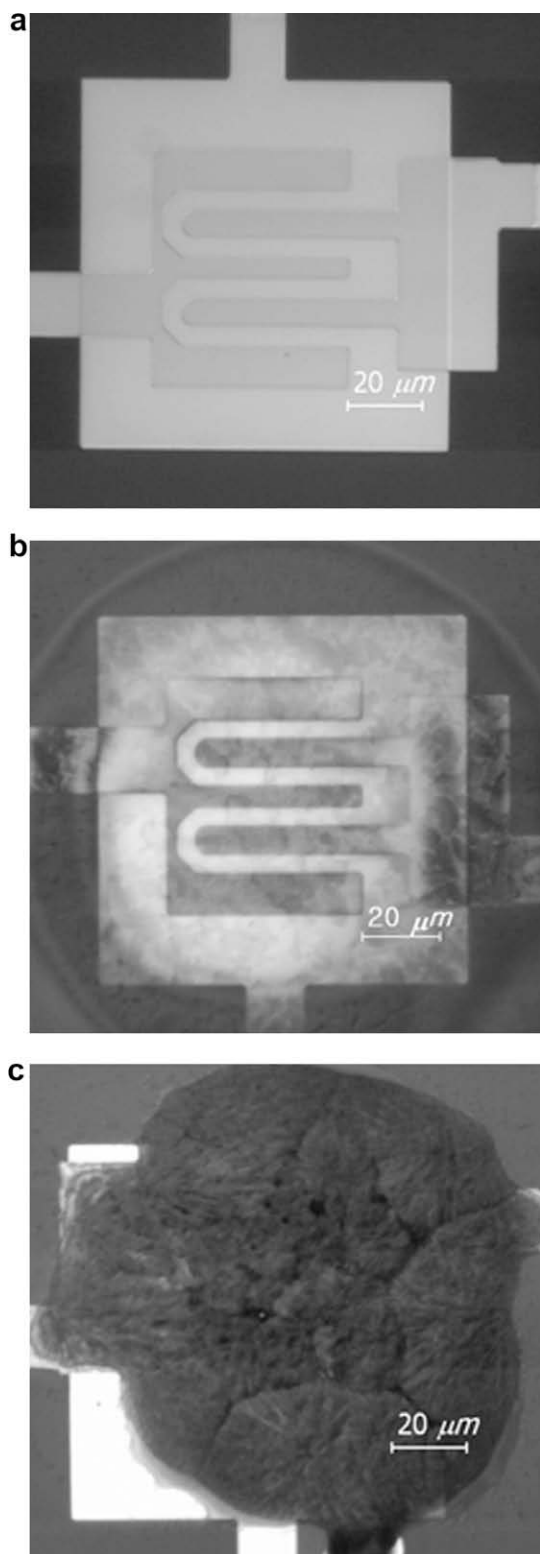
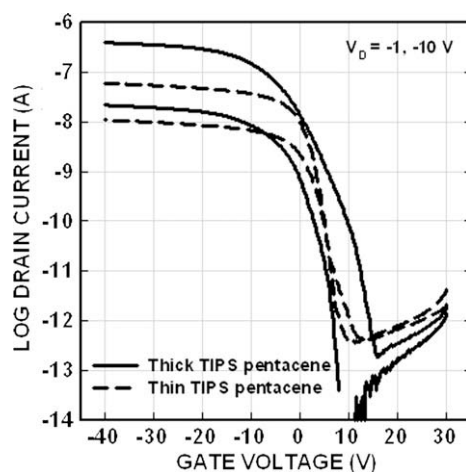


Fig. 1. A cross-sectional view of an OTFT studied in the present work (a); FIB image of thin TIPS pentacene TFT (b); thick TIPS pentacene TFT (c) on the channel region.



**Fig. 2.** Optical images of TIPS pentacene TFTs on the channel regions: before printing of TIPS pentacene (a); after thin TIPS pentacene jetting (b); after thick TIPS pentacene jetting (c).



**Fig. 3.** The transfer characteristics of the thin and thick TIPS pentacene TFTs printed by overlapping method.

that we used the mixed solvent of cyclohexanol and trichlorobenzene so that the performances of OTFTs are not as good as before [6]. The non-aromatic solvent, cyclohexanol, can deteriorate the OTFT performance even though the uniformity can be improved by adding it.

Fig. 4 shows the performances of the TIPS pentacene TFTs before and after 1400 h in ambient air using thin (a,b) and thick (c,d) active layers; transfer (a,c) and output characteristics (b,d). The thin TIPS pentacene TFT shows the drop in currents over the whole region. Its performance after 1400 h exhibited an on/off current ratio of  $\sim 10^5$ , a threshold voltage of 2 V, gate voltage swing of 0.6 V/decade and field-effect mobility of  $0.0016 \text{ cm}^2/\text{Vs}$  in the saturation region. The turn-on-voltage ( $V_{\text{on}}$ ) shifts to the negative direction and field-effect mobility decreases significantly.

It is found that  $\text{H}_2\text{O}$  trapping is more significant than  $\text{O}_2$  doping under ambient air and  $\text{O}_2$  effect is dominant over  $\text{H}_2\text{O}$  trapping in dry air [11]. The  $\text{H}_2\text{O}$  absorbed by exposure to ambient air creates new trapping sites for the carriers. Therefore,  $\text{H}_2\text{O}$  absorbed by exposure to ambient air decreases the electrical conductivity of TIPS pentacene TFT. The overall drop of the drain currents after air exposure appears to be due mainly to the  $\text{H}_2\text{O}$  absorption in organic semiconductor.

For the thick TIPS pentacene, formed by using OTS- $\text{C}_8$ , the TFT exhibited an on/off current ratio of  $\sim 10^6$ , a threshold voltage of 2 V, a gate voltage swing of 2.0 V/decade and a field-effect mobility of  $0.015 \text{ cm}^2/\text{Vs}$  in the saturation region as shown in Fig. 4c. The on-current shows almost no change in ambient air even though a large shift in  $V_T$  from  $-1 \text{ V}$  to 2 V. The significant increase of off-current ( $I_{\text{off}}$ ) can be seen for thick TIPS pentacene TFT after long exposure to air because of  $\text{O}_2$  doping effect into the TIPS pentacene layer. Increase of the subthreshold slope can be seen together with  $V_T$  shift. We compared the output characteristics of the OTFTs before and after long time exposure to air. A thin TIPS pentacene TFT shows a significant decrease in currents as shown in Fig. 4b, but the TFT with a thick TIPS pentacene shows a little increase in the drain currents as shown in Fig. 4d. However, the ohmic contact behavior

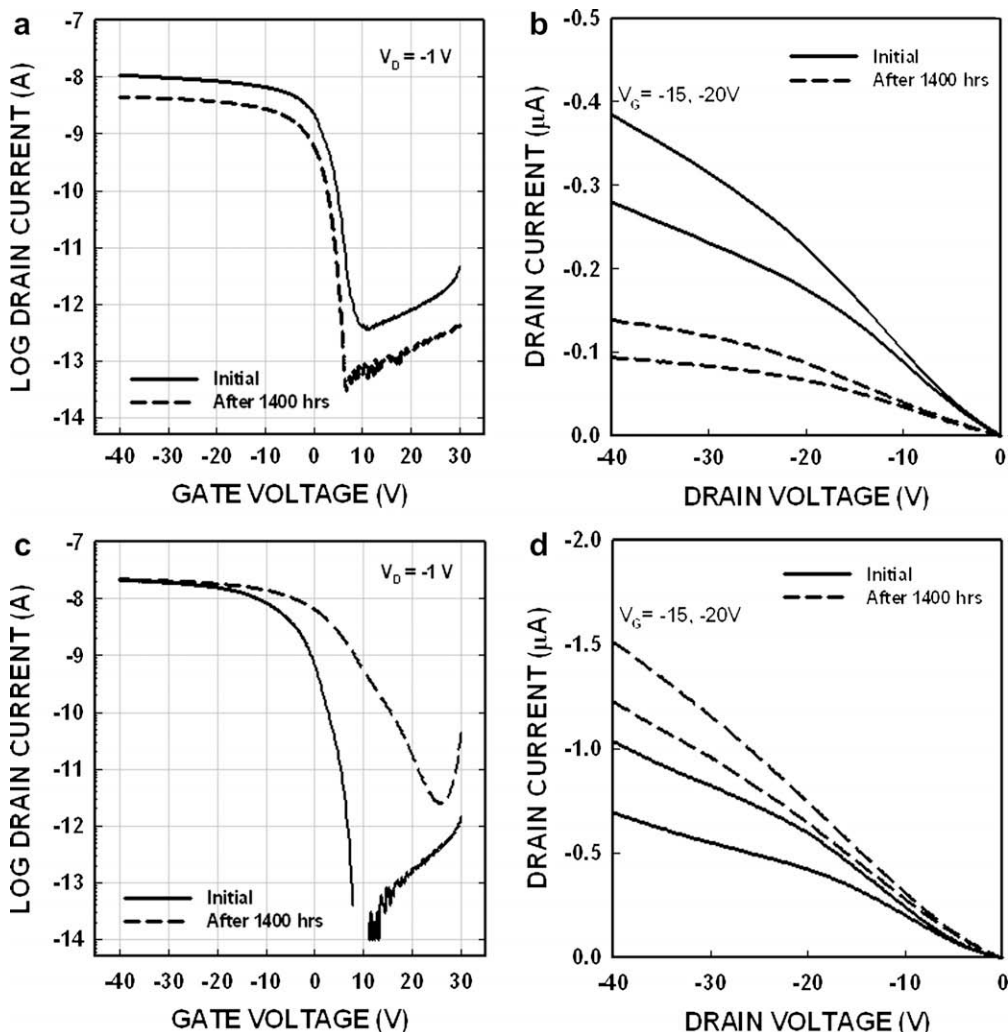


Fig. 4. The degradations of the TIPS pentacene TFTs using thin (a,b) and thick (c,d) layers before and after 1400 hours in ambient air; transfer (a,c) and output (b,d) characteristics.

seems to be not much different before and after the degradation in air. Therefore, it is concluded that the degradation in the drain currents is due to the bulk effect.

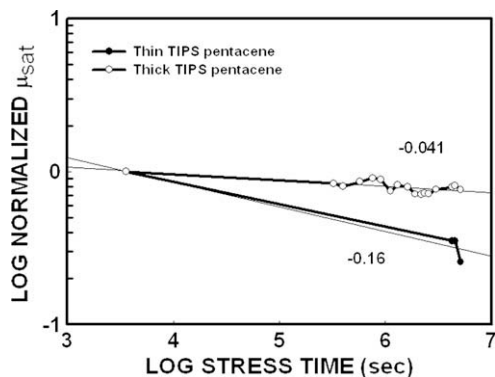


Fig. 5. The degradation in the field-effect mobility in the saturation region for both OTFTs in log-log scale.

The drain current ( $I_D$ ) decreases and threshold voltage increases with time ( $t$ ) in ambient air and the time dependence of field-effect mobility ( $\mu_{fe}$ ) can be described as

$$\mu_{fe} = \mu_{fe0} t^\alpha \quad (1)$$

where  $\mu_{fe0}$  is the field-effect mobility in air at  $t = 1$  s and the constant  $\alpha$  is the slope obtained from the plot of  $\log \mu_{fe}$  versus  $\log t$ .

Fig. 5 shows the data indicating the plots of the  $\mu_{fe}$  versus lifetime ( $t$ ) in log-log scale. From the slope, the TFT with a thick TIPS pentacene exhibited the  $\alpha$  of  $-0.041$ , and that for the TFT with  $0.05 \mu\text{m}$  active-layer  $-0.16$ . On the other hand, that for the TFT with vacuum-deposited pentacene shows  $-0.78$  [5]. Therefore, it is concluded that the environmental stability depends strongly on the thickness of active layer. The thick active layer protects the channel region against  $\text{O}_2$  and  $\text{H}_2\text{O}$  adsorptions from ambient air. Note that the absorption of  $\text{H}_2\text{O}$  and  $\text{O}_2$  in the active layer, especially in the channel region, degrades the TFT performance significantly.

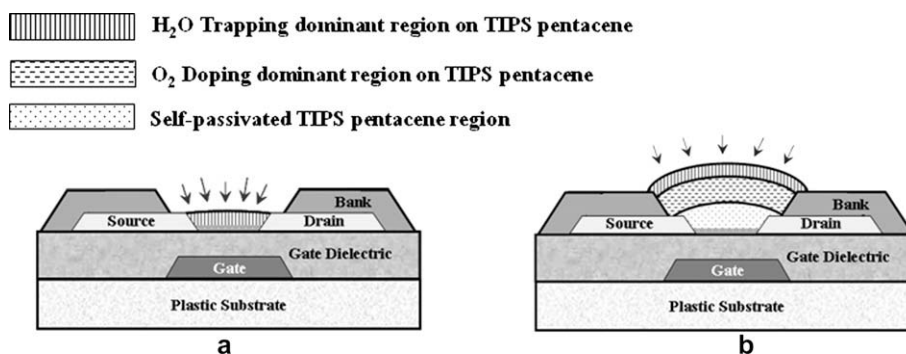


Fig. 6. Cross-sectional views of the TIPS pentacene TFT channels dividing 2 and 4 regions using thin (a) and thick (b) TIPS pentacene layers, respectively.

Fig. 6 shows a model explaining the degradation of drain currents of OTFT with thin (a) and thick (b) active layers. The active layer can be divided into 2 for thin and 4 sub-layers for thick active-layers. These are channel and H<sub>2</sub>O trapping dominant regions for a thin active layer as shown in Fig. 6a. The H<sub>2</sub>O absorbed by exposure to ambient air affects the whole channel region. On the other hand, the thick organic semiconductor can be divided into 4 sub-layers; channel, intrinsic pentacene, O<sub>2</sub> doping dominant and H<sub>2</sub>O trapping dominant regions as shown in Fig. 6b.

Thick TIPS pentacene has a H<sub>2</sub>O trapped region on the surface, as the case in the thin TIPS pentacene TFT. The middle region just beneath the H<sub>2</sub>O trapped one appears to be O<sub>2</sub> doping dominant region because O<sub>2</sub> can diffuse deeper than H<sub>2</sub>O [11], and the region between the O<sub>2</sub> doping and channel regions is intrinsic organic semiconductor layer having a high resistivity. This can be a passivation layer to protect the channel layer from vapor and O<sub>2</sub> diffusion.

As shown in Fig. 4c, the on-currents are quite stable due to self-passivation effect. But the  $V_T$  shift increases the currents in the subthreshold region. These variations are attributed to the influence of the O<sub>2</sub> doping region. Note that the width of accumulation by gate bias decreases with increasing bias potential.

In conclusion, we have studied the effects of active layer thickness on the performance and environmental stability of the TIPS pentacene TFT. The OTFT was fabricated by ink-jet printing using a TIPS pentacene solution. The OTFT with a thin active layer shows the decreases in transfer charac-

teristics because of the H<sub>2</sub>O diffuses into the whole active layer, but the OTFT with thick active layer exhibited a little change in on-currents because the channel can be protected from air and O<sub>2</sub> diffusion by a thin intrinsic organic semiconductor between channel and O<sub>2</sub> doped sub-layer.

#### Acknowledgment

This work was supported by a Grant from the Knowledge Economy, Korea.

#### References

- [1] K. Nomoto, N. Hirai, N. Yoneya, N. Kawashima, M. Noda, M. Wada, J. Kasahara, *IEEE Trans. Electron Devices* 52 (2005) 1519.
- [2] C.D. Dimitrakopoulos, D.J. Mascaro, *IBM J. Res. Dev.* 45 (2001) 11.
- [3] D.M. deLeeuw, G.H. Gelinck, T.C.T. Geuns, van Veenendaal, E. Cantore, E. Huisman, *Tech. Dig. Int. Electron Devices Meet.* 293 (2002).
- [4] Y.W. Wang, J.L. Cheng, Y.K. Wang, T.H. Hu, J.C. Ho, C.C. Lee, T.F. Lei, C.F. Yeh, *Thin Solid Films* 467 (2004) 215.
- [5] S.H. Han, J.H. Kim, S.M. Cho, S.H. Lee, D.J. Choo, M.H. Oh, J. Jang, *Appl. Phys. Lett.* 88 (2006) 073519.
- [6] S.H. Lee, M.H. Choi, S.H. Han, D.J. Choo, S.K. Kwon, J. Jang, *Organic Electronics* 9 (2008) 721.
- [7] S.H. Lee, D.J. Choo, S.H. Han, J.H. Kim, Y.R. Son, J. Jang, *Appl. Phys. Lett.* 90 (2007) 033502.
- [8] D.H. Song, M.H. Choi, J.Y. Kim, J. Jang, *Appl. Phys. Lett.* 90 (2007) 053504.
- [9] J.F. Chang, B. Sun, D.W. Breiby, M.M. Nielsen, H. Shringhaus, *Chem. Mater.* 16 (2006) 4772.
- [10] M.H. Choi, S.H. Lee, S.H. Han, Y.H. Kim, D.J. Choo, J. Jang, *SID Symposium Digest* 39 (2008) 440.
- [11] Oana D. Jurchescu, J. Baas, T.M. Palstra, *Appl. Phys. Lett.* 87 (2005) 052102.



## Flexible light-emitting three-terminal device with color-controlled emission

Sung Heum Park<sup>a,b</sup>, Shinuk Cho<sup>a</sup>, Jae Kwan Lee<sup>a</sup>, Kwanghee Lee<sup>a,b,\*</sup>, Alan J. Heeger<sup>a,b,\*</sup>

<sup>a</sup> Center for Polymer and Organic Solids, University of California at Santa Barbara, Santa Barbara, CA 93106, USA

<sup>b</sup> Heeger Center for Advanced Materials, Gwangju Institute of Science and Technology (GIST), Gwangju 500-712, South Korea

### ARTICLE INFO

#### Article history:

Received 14 October 2008

Received in revised form 6 January 2009

Accepted 8 January 2009

Available online 22 January 2009

#### PACS:

72.80 Le

78.60 Fi

85.60 Jb

#### Keywords:

Flexible devices

Light-emitting three-terminal device

Colortunable devices

Polymer light-emitting diode

### ABSTRACT

A new architecture for flexible light-emitting devices with color-controlled emission is described. The various layers in these novel three-terminal devices are fabricated by casting soluble conjugated polymers from solution. The light-emitting three-terminal device (LET) can be described as comprising two polymer light-emitting diodes (LEDs) connected back-to-back with an internal common electrode. By controlling the bias voltages between the common buried electrode and the two outer electrodes, the LET can be turned on/off, and the emission color can be switched and modulated. Thus, the LET architecture provides a route to flexible displays that can be fabricated by printing technology with pixels that are color-switchable and color-tunable.

© 2009 Elsevier B.V. All rights reserved.

### 1. Introduction

High information content displays for future applications must be lower in cost, thinner, lighter and mechanically flexible. These demanding features are required to enable paper-like, portable “roll-up” and disposable displays [1–3]. Moreover, since such displays must have a device structure that is sufficiently simple to be compatible with low-cost manufacturing, it is important to reduce the number and complexity of circuit elements by integrating multiple functions into the components within each pixel.

We report here that we have successfully demonstrated a new architecture for flexible polymer-based, three-terminal devices with all layers cast from solution. The light emitting three-terminal device (LET) can be described as comprising two polymer light-emitting diodes (LEDs) connected back-to-back with an internal common electrode. By controlling the bias voltages between the common buried electrode and the two outer electrodes, the device can be turned on/off, and the emission color can be switched and modulated.

Plastic electronic devices made from semiconducting and metallic polymers offer a number of potential advantages, including lightweight, flexibility, and fabrication by printing/coating methods that enable low-cost manufacturing [4–6]. Moreover, multifunctional devices have been demonstrated, including light-emitting transistors [7,8], light-emitting solar cells (LESCs) [9] and light-emitting photo-diodes [10].

\* Corresponding authors. Address: Center for Polymer and Organic Solids, University of California at Santa Barbara, Santa Barbara, CA 93106, USA.

E-mail addresses: [klee@gist.ac.kr](mailto:klee@gist.ac.kr) (K. Lee), [ajhe1@physics.ucsb.edu](mailto:ajhe1@physics.ucsb.edu) (A.J. Heeger).



The pixels within high information content active matrix electroluminescent displays require two main functions: light generation from a LED and on/off switching by a field-effect transistor (FET). Full color is obtained by dividing each pixel into three sub-pixels which emit red, green and blue, respectively. Demonstration of a flexible three-terminal light emitting device that can be turned on/off and color-controlled by applied voltages is, therefore, of interest.

Voltage controlled color change has been demonstrated by using polymer blends [11] or multilayer stacks [12,13] for EL, or by using voltage controlled thermochromism [14]. Vertical-type color-controlled light emitting devices (CCLEDs) have been demonstrated using independently stacked electrode and emitting layers [15,16]. Light emitting transistors were shown to function as an LED and a transistor in series [17,18].

Vertical-type CCLEDs are particularly interesting because the emission of each emitting layer can be controlled independently, thereby maximizing display resolution with high color purity. In addition, they also exhibit a high aperture ratio for light-emission compared with a device having a narrow light emitting region [7,18]. In spite of such advantages, however, known vertical-type CCLEDs are hard to consider as components for next generation flexible displays because of the inflexibility of their components and the relative complexity of fabrication (vapor deposition of many layers of small molecule organic semiconductors). With the LET described in here, we have successfully addressed the challenge of creating flexible CCLEDs fabricated by solution processing.

## 2. Results and discussion

### 2.1. LET structure

Fig. 1 shows the structure of the LET together with the molecular structures and the electronic structures of the component materials. The LET is equivalent to two polymer LEDs connected back-to-back with poly(3,4-ethylenedioxythiophene)-poly(styrene sulfonate), PEDOT:PSS, as the internal common electrode. The first diode with structure Al/poly [2-(4-(3',7'-dimethyloctyloxy)-phenyl)-p-phenylenevinylene](P-PPV)/PEDOT:PSS (Bottom) emits green light. The second diode with structure PEDOT:PSS/poly(2-methoxy, 5-(2-ethyl-hexoxy)-1,4-phenylene vinylene) (MEH-PPV)/Al (Top) emits orange-red light. The function of the PEDOT:PSS layer is analogous to that of the polyaniline network layer in the polymer grid triode (PGT) [19,20]. Since the PEDOT:PSS electrode is continuous, there is no direct current path between the two outer electrodes. Thus, the LET described here is equivalent to two back-to-back diodes in contrast to the polymer grid triode (the latter can, in principle, exhibit gain).

Three different conducting materials were used as electrodes, each with a different work function: Al ( $\sim 4.3$  eV), Ba:Al ( $\sim 2.7$  eV) and PEDOT:PSS ( $\sim 5.2$  eV) (see Fig. 1b). Semitransparent Al with a thickness of 10 nm is used as a low work function metal for injecting electrons into the bottom PLED, while Ba:Al (100 nm) is used for injecting electrons into the top PLED. The high work function semitransparent PEDOT:PSS conducting polymer is used as the internal anode for hole injection into both the top and bottom PLEDs. Because the Al electrode is grounded, the Ba:Al

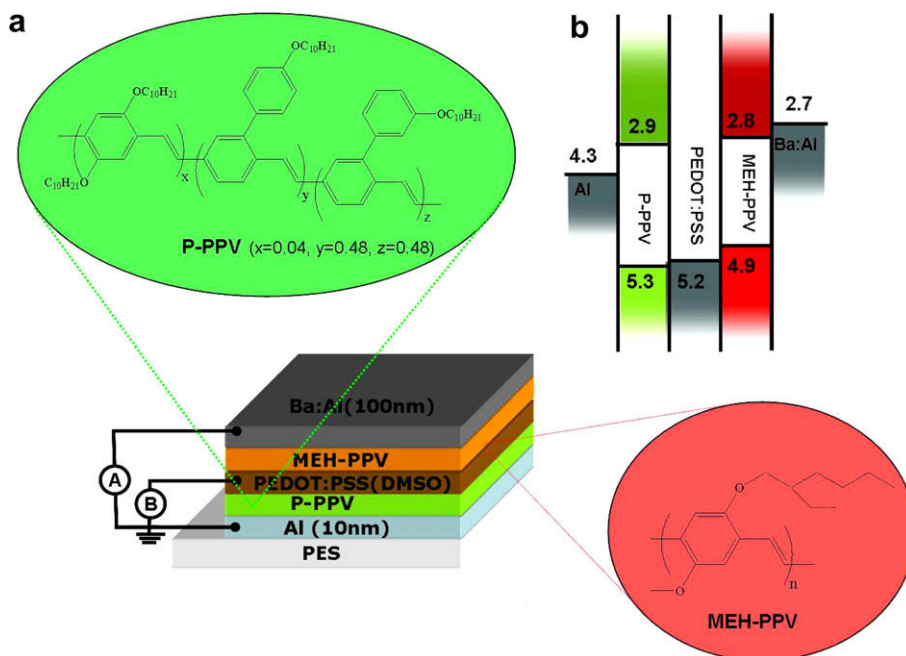


**Fig. 1.** (a) Schematic of the device cross-section: the device consists of two polymer light emitting diodes, Al/P-PPV/PEDOT:PSS and PEDOT:PSS/MEH-PPV/Ba:Al, connected back-to-back. The P-PPV diode emits green light; the MEH-PPV diode emits red-orange light. (b) Energy level diagram.

and PEDOT:PSS electrodes can also be switched to perform either the functions of anode or cathode under different applied bias conditions.

The water-soluble PEDOT:PSS layer enables the fabrication of the multilayered device architecture. Because P-PPV and MEH-PPV are insoluble in water and PEDOT:PSS is insoluble in organic solvents, the various layers remain intact with no intermixing. The emission from MEH-PPV in the top LED must pass through the PEDOT:PSS layer and the P-PPV layer; the former is semitransparent and the absorption edge of the latter is at a photon energy above that of the emission from MEH-PPV. Earlier work has demonstrated that P-PPV shows high luminous intensity in single devices using Al as the cathode material [21,22].

The semitransparent Al electrode (thickness of  $\sim 10$  nm) was deposited on a polyethersulfone (PES) substrate by thermal evaporation in a vacuum of about  $5 \times 10^{-7}$  Torr. The P-PPV was spin-cast (2000 rpm) from solution [1 wt.% in chlorobenzene (CB)] on top of the Al electrode, and baked at  $80^\circ\text{C}$  for 60 min in a glove box. Because the P-PPV film is hydrophobic, we have deposited a thin layer of  $\text{TiO}_x$  [23–25] onto the P-PPV film before depositing hydrophilic PEDOT:PSS layer. The dilute  $\text{TiO}_x$  precursor solution was spin-cast onto the P-PPV emitting layer at 6000 rpm for only 5 s and the PEDOT:PSS solution was immediately dropped onto the  $\text{TiO}_x$  film. Since a continu-

ous film of  $\text{TiO}_x$  is not typically formed under such spin-casting conditions, the  $\text{TiO}_x$  (amphiphilic) acts principally as a “glue” that assures adhesion between the P-PPV (hydrophobic) and PEDOT:PSS (hydrophilic) layers.

Highly conductive PEDOT:PSS (Baytron PH 500) solution mixed with DMSO solvent [26] was dropped on the  $\text{TiO}_x$ -treated P-PPV film without substrate spinning and then baked at  $30^\circ\text{C}$  for 3 h. This results in higher conductivity for PEDOT:PSS (the extended annealing at  $30^\circ\text{C}$  increases the degree of crystallinity of PEDOT:PSS). The MEH-PPV solution was spin-cast on top of the PEDOT:PSS layer. Finally, Ba (10 nm):Al(100 nm) was deposited by thermal evaporation in a vacuum of about  $5 \times 10^{-7}$  Torr.

Since the LET has three-terminals, there are three different current pathways:  $I_1$ ,  $I_2$  and  $I_3$  as shown Fig. 2a.  $I_1$  is the current between the PEDOT:PSS and Al electrode,  $I_2$  is the current between the PEDOT:PSS and Ba:Al electrode, and  $I_3$  is the current between the Ba:Al and Al electrode.  $I_1$ ,  $I_2$  and  $I_3$  are determined by the electric field (E-field) generated by the combination of  $V_A$  voltage (Ba:Al to Al electrode) and  $V_B$  voltage (PEDOT:PSS to Al electrode). In the zero-bias condition shown in the energy diagram of Fig. 2b, the E-field in each layer results from the difference between the work functions of the two neighboring electrodes ( $E_G$  for P-PPV and  $E_R$  for MEH-PPV). We assume

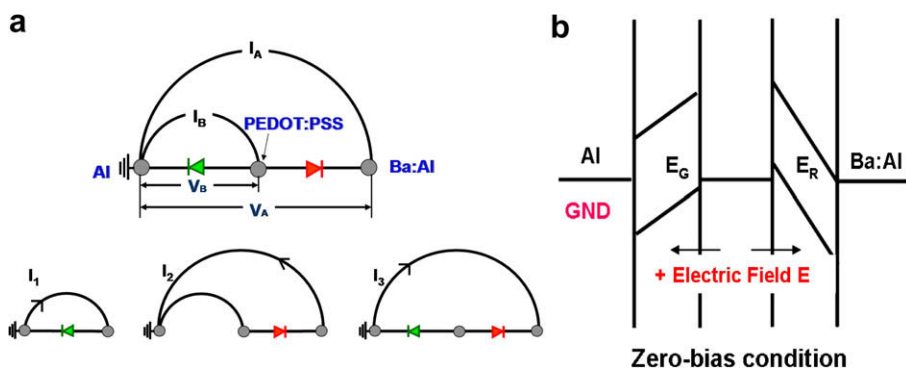


**Fig. 2.** (a) Schematic of current paths in the device.  $I_1$ ,  $I_2$  and  $I_3$  represent the hole currents between the PEDOT:PSS and Al electrode, PEDOT:PSS and Ba:Al electrode, and Ba:Al and Al electrode, respectively. (b) Energy band diagram for zero-bias condition.

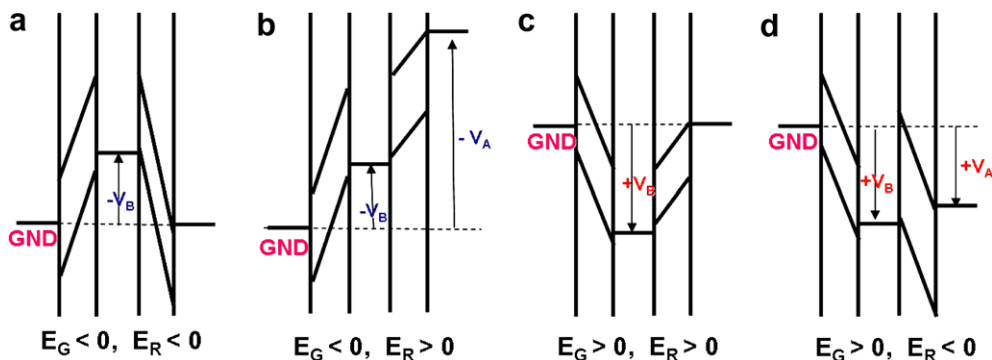


**Fig. 3.** Energy band diagram for different bias conditions (see text).

the direction of E-field as positive from PEDOT:PSS to both outside electrodes.

Fig. 3 shows four different combinations of  $E_G$  and  $E_R$  in the device. Fig. 3a represents zero (or small) bias; Fig. 3a is similar to Fig. 2b in that both diodes are in reverse bias. Under the conditions described by Fig. 3b, the first diode is back-biased while the second diode is forward biased. In Fig. 3c, both diodes are in forward bias. In Fig. 3d, the first diode is in forward bias and the second diode is in reverse bias.

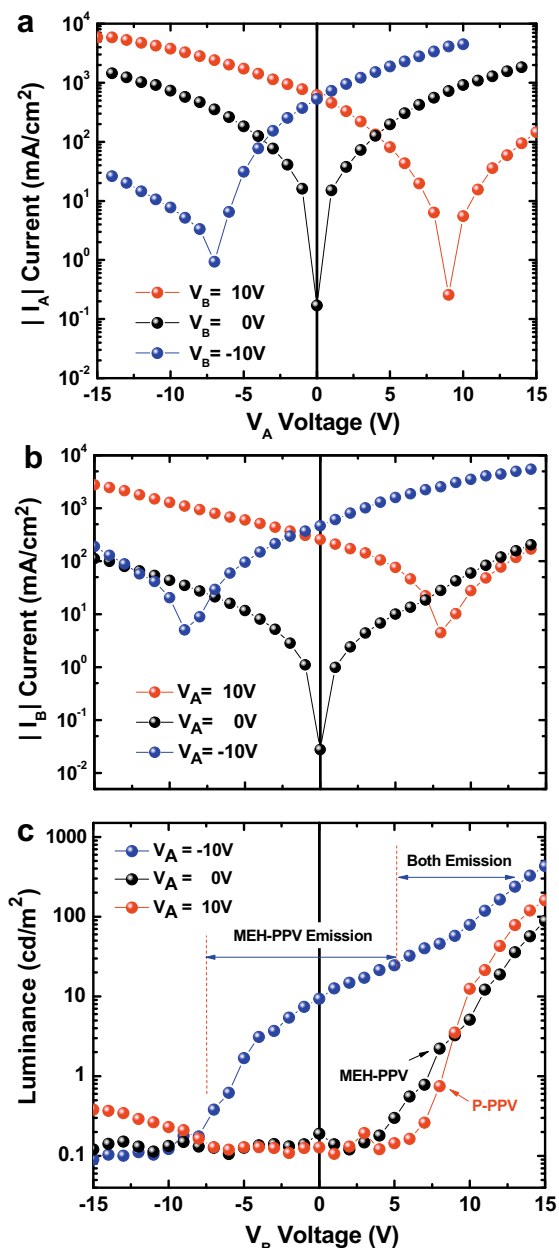


Fig. 4. Current-density versus voltage and luminance versus voltage curve characteristics under different combination of  $E_G$  and  $E_R$  electric field.  $I_A$  and  $V_A$  indicate the current and voltage between the Al and Ba:Al electrode and  $I_B$  and  $V_B$  between the PEDOT:PSS and Al electrode.

## 2.2. LET performance

This device operating concept described above is verified by the measurements of current density ( $I$ ) – voltage ( $V$ ) characteristics at various external biases. A plot of  $I_A$  (current from Al to Ba:Al, see Fig. 2a) versus  $V_A$  voltage under various  $V_B$  is shown in Fig. 4a. For  $V_B = 0$ , the  $I$ – $V$  curve exhibits general PLED characteristics except symmetric curve shape [27]. The current increases with increasing voltage. Control of the  $I_A$ – $V_A$  characteristics by the application of  $V_B$  is shown in Fig. 4a. With  $V_B = 10$  V (red line),  $I_A$  is negative below  $V_A < 9$  V and  $I_A \neq 0$  even for  $V_A = 0$  V. In contrast, when  $V_B$  is biased at  $-10$  V (blue line),  $I_A$  is positive above  $V_A > -7$  V and current flows even at  $V_A = 0$  V.

This tendency is also observed in the control of the  $I_B$ – $V_B$  (current and voltage from Al to Ba:Al, see Fig. 2 a) characteristics by the application of  $V_A$  in Fig. 4b. For  $V_A = 10$  V (red line),  $I_B$  is negative below  $V_B < 8$  V and  $I_B \neq 0$  even for  $V_A = 0$  V. In contrast, when  $V_A$  is biased at  $-10$  V (blue line),  $I_B$  is positive above  $V_B > -9$  V and current flows even at  $V_B = 0$  V.

Since  $I_A$  is determined by the combination of  $V_A$  and  $V_B$  ( $E_G$  and  $E_R$ ), these current behaviors can be understood by the comparison of the energy level diagrams shown in Fig. 3a–d. For  $V_B = 10$  V and  $V_A < 9$  V in Fig. 4a, both  $E_G$  and  $E_R$  are positive (corresponding to Fig. 3c). Consequently holes are injected from PEDOT:PSS to Ba:Al. This corresponds to  $I_A < 0$  because Ba:Al is the anode. For  $V_B = -10$  V and  $V_A > -7$  V in Fig. 4a, therefore, both  $E_G$  and  $E_R$  are negative (corresponding to Fig. 3a).

On the other hand,  $I_B$  has two current pathways,  $I_1$  and  $I_2$  (see Fig. 2a). Thus holes from PEDOT:PSS can be injected to Al [ $I_1$ ] and Ba:Al [ $I_2$ ]. For  $V_A = -10$  V and  $V_B > -9$  V in Fig 4b, the holes are injected from PEDOT:PSS to Ba:Al (corresponding to Fig. 3b). Under high  $+V_B$ , especially, the holes are injected from PEDOT:PSS to both Al and Ba:Al. This corresponds to the same E-field configuration shown in Fig. 3c. For  $V_A = 10$  V and  $V_B < 9$  V in Fig. 4b, holes are withdrawn at PEDOT:PSS from Ba:Al. This hole injection from Ba:Al is caused by the strongly reversed bias  $E_R$  (see Fig 3a). Under these conditions,  $I_B < 0$ . When  $V_B$  increases from negative to positive, the negative  $I_B$  current decreases. Moreover, when  $V_B > 9$  V,  $E_G > 0$  (corresponding to Fig 3d) and holes are injected from PEDOT:PSS to Al. Therefore  $I_B$  changes sign from negative to positive. These experimental results are fully consistent with the device operating concept shown in the energy diagrams of Fig. 3a–d. The data clearly indicate that one can not only control  $I_A$  by controlling  $V_B$  at fixed  $V_A$ , but also  $I_B$  by controlling  $V_A$  at fixed  $V_B$ .

## 2.3. Color switching

Since the energy barrier corresponding to the difference between the workfunction of PEDOT:PSS and the LUMO levels of two emitting polymers is much higher than those of PEDOT:PSS and the HOMO levels, electron injection from the PEDOT:PSS layer into the emitting layers is inhibited [27]; i.e. the device can usually emit the light under positive  $E_G$  or positive  $E_R$ .

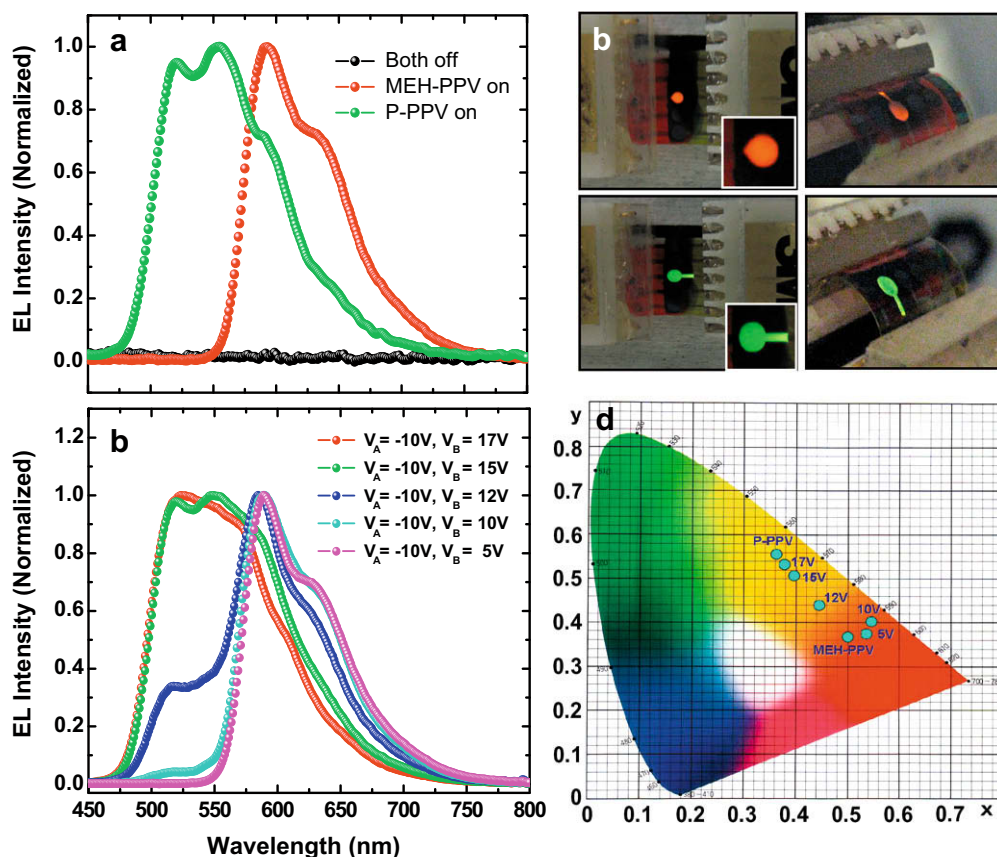


**Fig. 5.** (a) Electroluminescent spectra of the device for various  $V_A$  and  $V_B$  combinations. The emission spectrum can be switched from that of P-PPV to that of MEH-PPV. (b) Photos of color switching from the LET. The LET fabricated on PES is flexible. (c) EL spectra for various  $V_B$  at fixed  $V_A$  voltage. The EL spectra are dramatically changed for different  $V_B$ . (d) Evolution of color coordinates. The chromaticity coordinates on a CIE diagram can be changed from  $x = 0.5, y = 0.37$  to  $x = 0.37, y = 0.5$  by controlling the  $V_A$  and  $V_B$  voltage.

Because both  $E_C$  and  $E_R$  can be changed in both sign and magnitude by the combination of  $V_A$  and  $V_B$ , the device can function as a color switch. Fig. 4c shows the luminance ( $L_B$ ) – voltage ( $V_B$ ) characteristics at various external  $V_A$  biases. For  $V_A = 10$  V (red line) and  $V_B = 10$  V ( $E_R < 0, E_C > 0$ ) in Fig. 4c, holes are injected into the P-PPV layer and electrons are injected into the P-PPV layer from Al. Consequently the device emits light from the P-PPV layer. For  $V_A = -10$  V (blue line) and  $V_B = 0$  V ( $E_R > 0, E_C < 0$ ), however, holes are injected from PEDOT:PSS into MEH-PPV and electrons are injected into MEH-PPV from Ba:Al. Thus the device emits light from MEH-PPV layer. Since the emission of each layer is governed by a combination of both  $I_A$  and  $I_B$  currents, the calculation of luminous efficiency defined by luminance intensity for injected current is non-trivial. Here, for simplicity, we use the current  $I_B$  as the basis for calculating the luminous efficiency. For  $V_B = 15$  V, the luminous efficiency was 0.05 cd/A for the P-PPV layer and 0.03 cd/A for the MEH-PPV layer.

Fig. 5a shows the electroluminescent spectra of the device with various combinations of  $V_A$  and  $V_B$ . When  $E_C > 0$  and  $E_R < 0$  ( $V_A = 10$  V and  $V_B = 10$  V), the LET exhibits the typical green emission of P-PPV. However,

when  $E_C < 0$  and  $E_R > 0$  ( $V_A = -10$  V and  $V_B = 0$  V), the emission color switches to orange-red corresponding to that of MEH-PPV. The LET does not emit under  $E_C < 0$  and  $E_R < 0$ .

Fig. 5b directly illustrates the color switching with color photos obtained by varying  $V_A$  and  $V_B$  (orange-red color or green color from a single LET). In addition, since the device consists of ductile metals and polymers layer fabricated on top of the plastic PES substrate, the LET is flexible (total device thickness of  $\sim 200$   $\mu\text{m}$ ).

Interestingly, for  $E_C > 0$  and  $E_R > 0$ , the device can emit both colors simultaneously and the intensity of each color can be controlled by varying  $V_B$  and  $V_A$ . Because the emission color can be changed continuously by varying the ratio of emission from MEH-PPV and P-PPV (see the blue line in Fig. 4c), the LET can function as a color-tunable device. The EL spectra of the device for various  $V_B$  at fixed  $V_A$  are shown in Fig. 5c. The spectra change dramatically for different  $V_B$ . As a consequence, the color of the device gradually changes continuously from orange-red to green. The corresponding chromaticity coordinates on a CIE (Commission Internationale de l'Éclairage) 1931 diagram, see Fig. 5d, change from  $x = 0.5, y = 0.37$  to  $x = 0.37, y = 0.5$ .

### 3. Conclusion

We have successfully demonstrated a flexible, light emitting and color-switchable polymer-based three-terminal devices. The LET functions as a color switch and a color modulator. By varying the bias voltages between the common internal electrode and the two outer electrodes, the LET can be turned on/off, the emission color can be switched, and the color (and brightness) can be modulated. Moreover, the multilayer LET structure can be fabricated with each layer cast from solution.

### Acknowledgement

The research was supported by a grant from Samsung Advanced Institute of Technology. S. H. Park was partially supported by the Korea Research Foundation funded by the Korean Government (KRF-2007-357-D00076).

### References

- [1] S.R. Forrest, *Nature* 428 (2004) 911.
- [2] T. Sekitani, M. Takamiya, Y. Noguchi, S. Nakano, Y. Kato, T. Sakurai, T. Someya, *Nature* 6 (2007) 413.
- [3] D.J. Gundlach, *Nature* 6 (2007) 173.
- [4] R.H. Friend, R.W. Gymer, A.B. Holmes, J.H. Burroughes, R.N. Marks, C.D. Taliani, D.C. Bradley, D.A. Dos Santos, J.L. Bredas, M. Logdlund, W.R. Salaneck, *Nature* 397 (1999) 121.
- [5] G. Gustafsson, Y. Cao, G.M. Treacy, F. Klavetter, N. Colaneri, A.J. Heeger, *Nature* 357 (1992) 477.
- [6] A.J. Heeger, *Rev. Mod. Phys.* 73 (2001) 681.
- [7] J.S. Swensen, C. Soci, A.J. Heeger, *Appl. Phys. Lett.* 87 (2005) 2535111.
- [8] Z. Xu, S.H. Li, L. Ma, G. Li, Y. Yang, Y. Shi, J. Liu, Y. Yang, *Appl. Phys. Lett.* 91 (2007) 092911.
- [9] H. Kim, J.Y. Kim, S.H. Park, Y. Jin, J. Kim, H. Suh, K. Lee, *Appl. Phys. Lett.* 86 (2005) 1835021.
- [10] G. Yu, C. Zhang, A.J. Heeger, *Appl. Phys. Lett.* 64 (1994) 1540.
- [11] C.D. Müller, A. Falcou, N. Reckefuss, M. Rojahn, V. Wlederlrm, P. Rudatl, H. Frohne, O. Nuyken, H. Becker, K. Meerholz, *Nature* 42 (2003) 829.
- [12] S. Yang, Z. Wang, Z. Xu, Y. Hou, X. Xu, *Chem. Phys.* 274 (2001) 267.
- [13] J. Kalinowski, P.Di. Marco, M. Cocchi, V. Fattori, N. Camaioni, J. Duff, *Appl. Phys. Lett.* 68 (1996) 2317.
- [14] S.H. Park, J.Y. Kim, H.J. Kim, K. Lee, *J. Korean phys. Soc.* 46 (2005) 1049.
- [15] Z. Shen, P.E. Burrow, V. Bulovic, S.R. Forrest, M.E. Thompson, *Science* 276 (1997) 2009.
- [16] P.E. Burrow, S.R. Forrest, S.P. Sibley, M.E. Thompson, *Appl. Phys. Lett.* 69 (1996) 2959.
- [17] C.W. Chu, C.W. Chen, S.H. Li, E.H.E. Wu, Y. Yang, *Appl. Phys. Lett.* 86 (2005) 2535031.
- [18] M. Muccini, *Nature Mater.* 5 (2006) 605.
- [19] Y. Yang, A.J. Heeger, *Nature* 372 (1994) 344.
- [20] J. EcElvain, A.J. Heeger, *J. Appl. Phys.* 80 (2006) 4755.
- [21] Y. Zhang, J. Peng, W. Gao, K. Yang, Y. Cao, *Synth. Met.* 152 (2005) 253.
- [22] H. Becker, H. Spreitzer, W. Kreuder, E. Kluge, H. Schenk, I. Parker, Y. Cao, *Adv. Mater.* 12 (2000) 42.
- [23] J.Y. Kim, K. Lee, N.E. Coates, D. Moses, T.Q. Nguyen, M. Dante, A.J. Heeger, *Science* 317 (2007) 222.
- [24] J.Y. Kim, S.H. Kim, H.H. Lee, K. Lee, W. Ma, X. Gong, A.J. Heeger, *Adv. Mater.* 18 (2006) 572.
- [25] K. Lee, J.Y. Kim, S.H. Park, S.H. Kim, S. Cho, A.J. Heeger, *Adv. Mater.* 19 (2007) 2445.
- [26] J.Y. Kim, J.H. Jung, D.E. Lee, J. Joo, *Synth. Met.* 126 (2002) 311.
- [27] I.D. Parker, *J. Appl. Phys.* 75 (1994) 1656.



## High-performance C<sub>60</sub> and picene thin film field-effect transistors with conducting polymer electrodes in bottom contact structure

Yumiko Kaji<sup>a</sup>, Ryoji Mitsuhashi<sup>a</sup>, Xuesong Lee<sup>a</sup>, Hideki Okamoto<sup>b</sup>, Takashi Kambe<sup>c</sup>, Naoshi Ikeda<sup>c</sup>, Akihiko Fujiwara<sup>d</sup>, Minoru Yamaji<sup>e</sup>, Kenji Omote<sup>f</sup>, Yoshihiro Kubozono<sup>a,\*</sup>

<sup>a</sup> Research Laboratory for Surface Science, Okayama University, Okayama 700-8530, Japan

<sup>b</sup> Department of Chemistry, Okayama University, Okayama 700-8530, Japan

<sup>c</sup> Department of Physics, Okayama University, Okayama 700-8530, Japan

<sup>d</sup> Japan Advanced Institute of Science and Technology, Ishikawa 923-1292, Japan

<sup>e</sup> Department of Chemistry and Chemical Biology, Gunma University, Kiryu 376-8515, Japan

<sup>f</sup> Ideal Star Inc., Sendai 989-3204, Japan

### ARTICLE INFO

#### Article history:

Received 26 November 2008

Received in revised form 6 January 2009

Accepted 7 January 2009

Available online 18 January 2009

#### PACS:

81.05.Lg

73.61.Ph

73.61.Wp

#### Keywords:

Organic thin film transistors

Conducting polymer electrodes

Bottom contact structure

C<sub>60</sub>

Picene

### ABSTRACT

C<sub>60</sub> and picene thin film field-effect transistors (FETs) in bottom contact structure have been fabricated with poly(3,4-ethylenedioxythiophene): poly(styrenesulfonate) (PEDOT:PSS) electrodes for a realization of mechanical flexible organic FETs. The C<sub>60</sub> thin film FETs showed *n*-channel enhancement-type characteristics with the field-effect mobility  $\mu$  value of 0.41 cm<sup>2</sup> V<sup>-1</sup> s<sup>-1</sup>, while the picene thin film FET showed *p*-channel enhancement-type characteristics with the  $\mu$  of 0.61 cm<sup>2</sup> V<sup>-1</sup> s<sup>-1</sup>. The  $\mu$  values recorded for C<sub>60</sub> and picene thin film FETs are comparable to those for C<sub>60</sub> and picene thin film FETs with Au electrodes.

© 2009 Elsevier B.V. All rights reserved.

## 1. Introduction

Mechanical flexibility is one of the most important advantages in organic thin film FETs from viewpoints of next-generation ubiquitous electronics. For a realization of flexible FET devices, C<sub>60</sub> and pentacene thin film FETs with many kinds of plastic substrates and polymer dielectrics have been investigated during a past decade [1–4]. Furthermore, in addition to plastic substrates and polymer gate dielectrics, source/drain/gate contact electrodes are

indispensable to be replaced from conventional metal to conducting polymers for a complete mechanical flexibility.

Several studies on transport characteristics for organic thin film FETs with conducting polymers have been performed so far [5–9]. Cosseddu et al. recently reported ambipolar transport in C<sub>60</sub>/pentacene FET with representative conducting polymer, poly(ethylenedioxythiophene)/poly(styrenesulfonate) (PEDOT:PSS), electrodes on poly(ethylene terephthalate) (PET) substrate fabricated by use of soft lithography (micro contact printing) technique [9]. Actually, the ambipolar FET characteristics with the *n*-channel  $\mu$  value of  $3.5 \times 10^{-4}$  cm<sup>2</sup> V<sup>-1</sup> s<sup>-1</sup> and *p*-channel  $\mu$  value of 0.01 cm<sup>2</sup> V<sup>-1</sup> s<sup>-1</sup> are observed in this device.

\* Corresponding author. Tel.: +81 86 251 7850; fax: +81 86 251 7903.  
E-mail address: [kubozono@cc.okayama-u.ac.jp](mailto:kubozono@cc.okayama-u.ac.jp) (Y. Kubozono).

The  $n$ -channel  $\mu$  value originating from  $C_{60}$  thin films was lower by three orders of magnitude than those for standard  $C_{60}$  FETs with Au electrodes on  $SiO_2/Si$  and parylene/PET substrates [4,10–12].

Furthermore, the best  $\mu$  value among  $p$ -channel organic thin film FETs with conducting polymer electrodes fabricated in bottom contact structure was at most  $0.01 \text{ cm}^2 \text{ V}^{-1} \text{ s}^{-1}$ , which was realized in pentacene thin film FET with PEDOT:PSS electrodes [8], although the very high  $\mu$  value of  $0.05\text{--}0.3 \text{ cm}^2 \text{ V}^{-1} \text{ s}^{-1}$  is exceptionally reported by Halik et al. [6]; very recently the high  $\mu$  value of  $0.2 \text{ cm}^2 \text{ V}^{-1} \text{ s}^{-1}$  is realized in pentacene thin film FET with PEDOT:PSS-coated Au electrodes in bottom contact structure [13]. On the other hand, the best  $\mu$  value in top contact structure was  $0.3\text{--}0.7 \text{ cm}^2 \text{ V}^{-1} \text{ s}^{-1}$ , which was also realized in pentacene thin film FET with PEDOT:PSS electrodes [8,9]. Therefore, the  $\mu$  values in bottom contact structure are still low in comparison with that in top contact structure. For a design of complementary MOS (CMOS) integrated circuit with mechanical flexibility,  $n$ -channel and  $p$ -channel organic thin film FETs with conducting polymer electrodes are required with the high  $\mu$  value in bottom contact structure.

In this study, we have fabricated and characterized the  $C_{60}$  and the new aromatic hydrocarbon, picene, thin film FETs with PEDOT:PSS electrodes in bottom contact structure. First, we expected a high  $n$ -channel  $\mu$  value for  $C_{60}$  thin film FET with PEDOT:PSS electrodes fabricated by use of an air-controlled dispensing system. Second, we expected a high  $p$ -channel  $\mu$  value for picene thin film FET with PEDOT:PSS electrodes because a very high  $\mu$  value of  $1.0\text{--}3.2 \text{ cm}^2 \text{ V}^{-1} \text{ s}^{-1}$  was recently recorded in picene thin film FET with Au electrodes in top contact structure [14,15]. As a consequence, we have realized the high  $\mu$  value of  $0.41$  and  $0.61 \text{ cm}^2 \text{ V}^{-1} \text{ s}^{-1}$  for  $C_{60}$  and picene thin film FETs with PEDOT:PSS electrodes, respectively, in bottom contact structure.

## 2. Experimental

Device structures of  $C_{60}$  and picene thin film FETs with PEDOT:PSS electrodes are shown in Fig. 1a. Commercially available  $C_{60}$  (Matsubo Co.; purity of 99.98%) and picene synthesized by ourselves [14] were used for fabrication

of FET devices;  $^1\text{H}$  NMR spectrum (not shown) of picene showed no impurity. Commercially available  $Si/SiO_2$  are cleaned and treated to form hydrophobic surface according to procedures described elsewhere [12], and heavily doped Si was used as gate electrode in FET devices. Thickness of  $SiO_2$  was  $400 \text{ nm}$  and capacitance per area  $C_0$  was  $8.63 \times 10^{-9} \text{ F cm}^{-2}$ . Source/drain electrodes of PEDOT:PSS were formed on gate dielectric by use of an air-controlled dispensing system (Musashi Engineering Co.: SHOTMASTER 300). Two commercially available PEDOT:PSS reagents (Baytron PH500 and Baytron PHCV4, H. C. Stark GmbH) were used for the formation of PEDOT:PSS electrodes; in this letter, PEDOT:PSS (Baytron PH500) and PEDOT:PSS (Baytron PHCV4) are represented as PEDOT:PSS-A and PEDOT:PSS-B, respectively. The granule size is reported to be larger in PEDOT:PSS-B ( $200\text{--}500 \text{ nm}$ ) than PEDOT:PSS-A ( $20\text{--}60 \text{ nm}$ ). Finally,  $C_{60}$  or picene thin films with thickness of  $50 \text{ nm}$  were formed on these substrates.

## 3. Results and discussion

The photos of the  $C_{60}$  and picene FETs with PEDOT:PSS-A electrodes on  $Si/SiO_2$  substrate are shown in Fig. 1a. The FET parameters of  $\mu$ , on-off ratio and threshold voltage  $V_{TH}$  are determined from the transfer curves ( $I_D^{1/2}\text{--}V_G$  plots at  $V_{DS} = 100 \text{ V}$ ) in saturation regime, which are measured in forward-measurement mode (forward transfer curve) and the reverse measurement mode (reverse transfer curve); the parameters are determined for picene thin film FET from the transfer curve ( $|I_D|^{1/2}\text{--}|V_G|$  plots at  $V_{DS} = -100 \text{ V}$ ). The  $C_{60}$  thin film FET was annealed from  $353$  to  $393 \text{ K}$  at  $20 \text{ K}$  step for each  $18 \text{ h}$  under  $10^{-6}$  Torr, after transferring the device from evaporation chamber to measurement vessel, so that  $O_2$  and  $H_2O$  are removed from channel region, and then the FET characteristics were measured under vacuum of  $10^{-6}$  Torr at  $300 \text{ K}$ . On the other hand, the characteristics of picene thin film FET were measured at  $300 \text{ K}$  under vacuum of  $10^{-6}$  Torr and under  $500$  Torr of  $O_2$  without any annealing.

Fig. 1b and c show output and transfer characteristics of  $C_{60}$  FET with source/drain PEDOT:PSS-A electrodes on  $Si/SiO_2$  substrate measured under  $10^{-6}$  Torr of vacuum at  $300 \text{ K}$  after an annealing up to  $393 \text{ K}$ . Typical  $n$ -channel enhancement-type output curves are observed in  $C_{60}$  FET

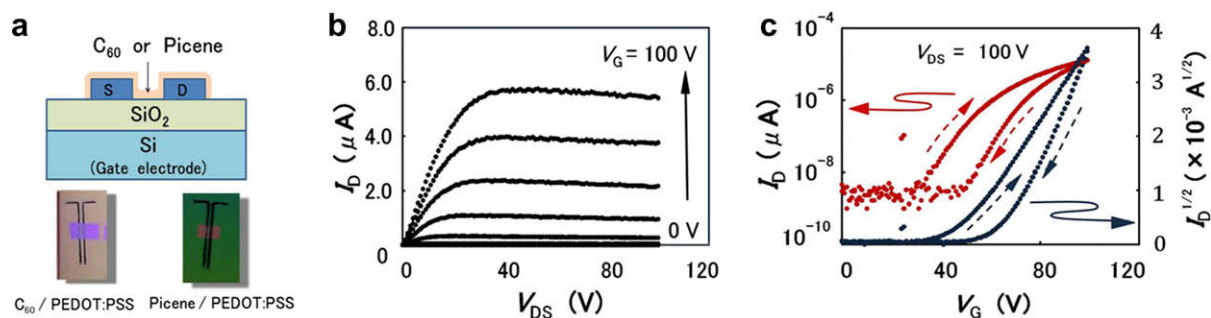


**Fig. 1.** (a) Device structure (bottom contact type) of  $C_{60}$  and picene thin film FETs with PEDOT:PSS electrodes on gate dielectrics. Photos of these devices are also shown. (b) Output and (c) transfer curves measured at  $300 \text{ K}$  under vacuum of  $10^{-6}$  Torr after annealing up to  $393 \text{ K}$  for  $C_{60}$  FET with PEDOT:PSS-A electrodes. For  $C_{60}$  FET with PEDOT:PSS-A electrodes shown in Fig. 1, channel length and width are  $370 \mu\text{m}$  and  $3.3 \text{ mm}$ , respectively.

device (Fig. 1b). The  $\mu$ , on-off ratio and  $V_{TH}$  and were  $0.13 \text{ cm}^2 \text{ V}^{-1} \text{ s}^{-1}$ ,  $1.3 \times 10^7$  and 47 V, respectively, for the forward transfer curve (Fig. 1c), while their values were  $0.29 \text{ cm}^2 \text{ V}^{-1} \text{ s}^{-1}$ ,  $1.3 \times 10^7$  and 66 V for the reverse transfer curve (Fig. 1c). The  $\mu$  value,  $0.29 \text{ cm}^2 \text{ V}^{-1} \text{ s}^{-1}$ , is larger by three orders of magnitude than that,  $3.5 \times 10^{-4} \text{ cm}^2 \text{ V}^{-1} \text{ s}^{-1}$ , reported by Cosseddu et al. [9] and it is comparable to those,  $0.08\text{--}0.55 \text{ cm}^2 \text{ V}^{-1} \text{ s}^{-1}$ , for the standard  $\text{C}_{60}$  FET with Au electrodes on  $\text{Si}/\text{SiO}_2$  [4,10–12]. The high  $V_{TH}$  value suggests an existence of large trap states in mid-gap position between highest occupied molecular orbital (HOMO) and lowest unoccupied molecular orbital (LUMO), which are formed in interface between  $\text{C}_{60}$  and  $\text{SiO}_2$  gate dielectric. On the other hand, the relatively high  $\mu$  values obtained in this FET suggest very small shallow trap states in the interface.

A hysteresis between forward and reverse transfer curves is observed, as seen from Fig. 1c. Nevertheless, it is important to say that the hysteresis found in the transfer curve (e.g. Fig. 1c) obtained by data acquisition at 300 K under  $10^{-6}$  Torr after an annealing of the FET device at 353–393 K under  $10^{-6}$  Torr is smaller than that in the transfer curve (not shown) measured at 300 K under  $10^{-6}$  Torr without any annealing. Recently, we investigated air and  $\text{O}_2$ -exposure effects on FET characteristics of  $p$ -channel FET device with thin films of picene [14,15]. These investigations clarified that the hysteresis is closely associated with  $\text{H}_2\text{O}$  introduced into channel region. Therefore, the hysteresis observed in transfer curve of  $\text{C}_{60}$  FET with PEDOT:PSS-A electrodes may also be associated with  $\text{H}_2\text{O}$ . As seen from Fig. 2a, the  $\mu$  value in  $\text{C}_{60}$  FET with PEDOT:PSS-A increases rapidly by the annealing above 350 K whose temperature is consistent with the critical temperature where the hysteresis decreases rapidly in transfer

curves (not shown). As a consequence, we can present the scenario that a reduction of  $\text{H}_2\text{O}$ -induced trap states by the annealing of device under vacuum produces both the decrease of hysteresis and the increase in  $\mu$ .

The output characteristics (Fig. 1b) show a smooth carrier injection from source electrode to  $\text{C}_{60}$  thin films because linear (Ohmic)  $I_D\text{--}V_{DS}$  plots are observed in low  $V_{DS}$  region. This suggests an existence of small barrier height or Ohmic contact between PEDOT:PSS-A and  $\text{C}_{60}$  thin films. As seen from Fig. 2b, the work function,  $\phi_m$ , of PEDOT:PSS was determined to be 5.2 eV (Fermi level  $\varepsilon_F$  of  $-5.2$  eV) from the onset energy of photoemission (not shown), whose value is close to that, 5.1 eV, of Au [16]. Since the LUMO and HOMO levels of  $\text{C}_{60}$  are  $-3.6$  eV and  $-6.0$  eV, respectively [17], this energy diagram predicts a large carrier injection barrier height for  $n$ -channel conduction owing to the large energy difference (1.6 eV) between  $\varepsilon_F$  of PEDOT:PSS-A and LUMO level. Nevertheless, such a large carrier injection barrier height was not observed in the output characteristics. This suggests that the junction between PEDOT:PSS-A and  $\text{C}_{60}$  thin films is largely deviated from the electronic structure expected in pure metal-semiconductor junction. This result may be caused by charge transfer, formation of electric dipole and orbital hybridization at the interface between  $\text{C}_{60}$  and PEDOT:PSS. Thus, the use of PEDOT:PSS-A electrodes led to smooth carrier injection as well as high  $\mu$  value in  $\text{C}_{60}$  thin film FET.

The output and transfer characteristics of  $\text{C}_{60}$  FETs with PEDOT:PSS-B electrodes were measured under the same conditions as those in  $\text{C}_{60}$  FET with PEDOT:PSS-A electrodes. The  $\mu$ , on-off ratio and  $V_{TH}$  were  $0.07 \text{ cm}^2 \text{ V}^{-1} \text{ s}^{-1}$ ,  $1.3 \times 10^7$  and 35 V, respectively, for forward transfer curve, and  $0.41 \text{ cm}^2 \text{ V}^{-1} \text{ s}^{-1}$ ,  $1.2 \times 10^7$  and 73 V for reverse transfer curve in  $\text{C}_{60}$  FET with PEDOT:PSS-B, which are measured at 300 K after annealing up to 393 K. These values are almost the same values as those for  $\text{C}_{60}$  FET with PEDOT:PSS-A. As a consequence, the difference in granule size between PEDOT:PSS-A and B never affected the FET characteristics. The values of  $\mu$ , on-off ratio and  $V_{TH}$  for  $\text{C}_{60}$  FETs fabricated in this study are listed in Table 1.

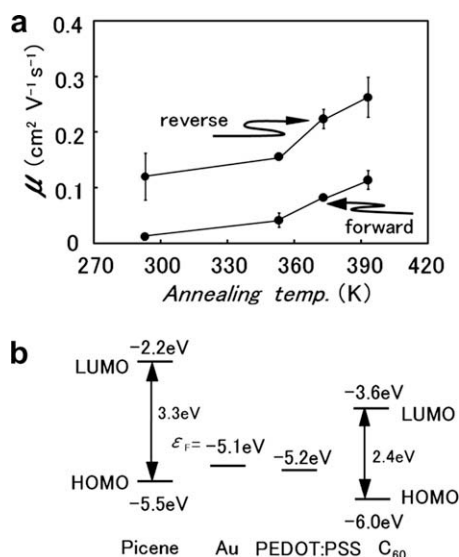


**Fig. 2.** (a) Plots of  $\mu$  as a function of annealing temperature in  $\text{C}_{60}$  FET with PEDOT:PSS-A electrodes; the values correspond to the average ones for two devices measured. (b) Energy diagram of Au, PEDOT:PSS,  $\text{C}_{60}$  and picene. The  $\phi_m$  was 5.2 eV for both electrodes of PEDOT:PSS-A and PEDOT:PSS-B.

**Table 1**

FET parameters in  $\text{C}_{60}$  FET with PEDOT:PSS electrodes.

Annealing temp. (K)	$\mu$ ( $\text{cm}^2 \text{ V}^{-1} \text{ s}^{-1}$ )	On-off ratio	$V_{TH}$ (V)
<i>Forward (PEDOT:PSS-A)<sup>a</sup></i>			
Non-annealing	0.01	$8.9 \times 10^5$	55
353	0.04	$2.7 \times 10^6$	58
373	0.08	$7.6 \times 10^6$	50
393	0.11	$1.5 \times 10^7$	42
<i>Reverse (PEDOT:PSS-A)<sup>a</sup></i>			
Non-annealing	0.12	$7.4 \times 10^5$	87
353	0.16	$2.5 \times 10^6$	79
373	0.22	$7.3 \times 10^6$	71
393	0.26	$1.4 \times 10^7$	62
<i>Forward (PEDOT:PSS-B)</i>			
393	0.07	$1.3 \times 10^7$	35
<i>Reverse (PEDOT:PSS-B)</i>			
393	0.41	$1.2 \times 10^7$	73

<sup>a</sup> The values of  $\text{C}_{60}$  FET with PEDOT:PSS-A electrodes correspond to the average ones for two devices measured. The annealing time is 18 h.



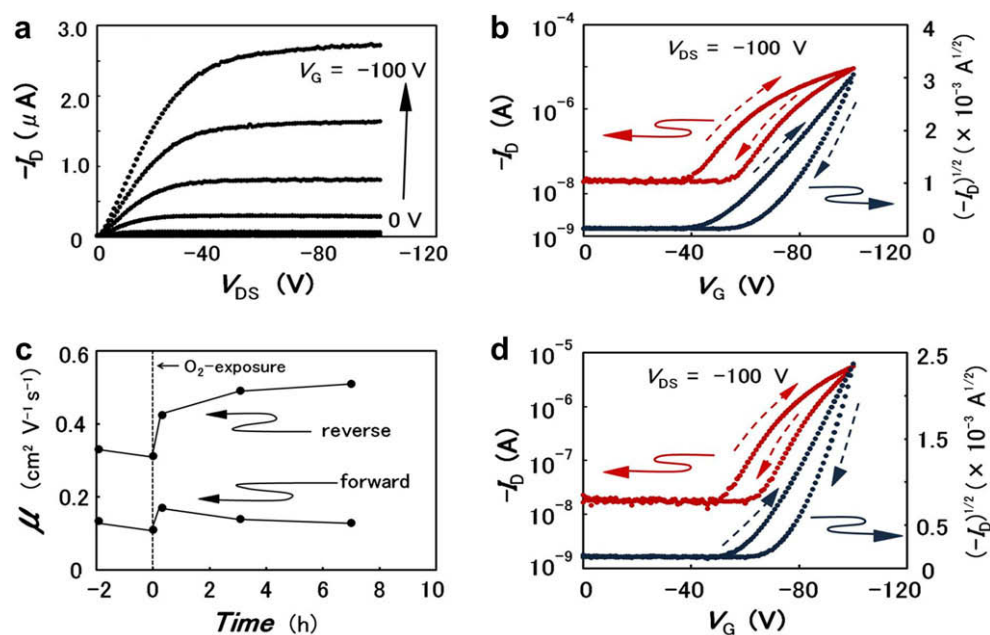


**Fig. 3.** (a) output and (b) transfer curves measured at 300 K under vacuum of  $10^{-6}$  Torr, and (c)  $O_2$ -exposure time dependence of  $\mu$  in picene thin film FET with PEDOT:PSS-A electrodes. (d) Transfer curves for picene thin film FET with PEDOT:PSS measured under 500 Torr of  $O_2$ ; the  $O_2$ -exposure time is 7 h. For picene thin film FET with PEDOT:PSS-A electrodes shown in Fig. 3, channel length and width are 300  $\mu\text{m}$  and 2 mm, respectively.

Fig. 3a and b show the output and transfer curves for picene thin film FET with PEDOT:PSS-A electrodes fabricated in bottom contact structure. The curves were measured at 300 K under vacuum of  $10^{-6}$  Torr after a dynamical pumping under vacuum of  $10^{-6}$  Torr for 60 h. The output curves show typical *p*-channel enhancement-type FET characteristics. The transfer curve shows a large hysteresis between the forward and reverse curves, in the same manner as the picene thin film FET with Au electrodes fabricated in top contact structure [14,15]. The hysteresis originates from the existence of  $H_2O$  in the channel region of thin films [14]. The  $\mu$ , on-off ratio and  $V_{\text{TH}}$  are determined from the forward transfer curve to be  $0.13 \text{ cm}^2 \text{ V}^{-1} \text{ s}^{-1}$ , 510 and 50 V, respectively, while those are determined from the reverse transfer curve to be  $0.44 \text{ cm}^2 \text{ V}^{-1} \text{ s}^{-1}$ , 470 and 73 V. The  $\mu$  values are larger than those ( $0.11 \text{ cm}^2 \text{ V}^{-1} \text{ s}^{-1}$  for forward curve and  $0.27 \text{ cm}^2 \text{ V}^{-1} \text{ s}^{-1}$  for reverse curve) under vacuum reported previously for the picene FET with Au electrodes in top contact structure [14]. This result suggests a smooth hole injection based on a lowering of the contact resistance by replacement of Au to PEDOT:PSS electrode [14,15]. Furthermore, the fact that we have never observed the FET operation in picene thin film FET device with Au electrodes fabricated in the bottom contact structure supports more smooth hole injection from PEDOT:PSS electrode to picene thin films than from Au electrode.

The energy difference between  $\varepsilon_{\text{F}}$  of PEDOT:PSS ( $-5.2 \text{ eV}$ ) and HOMO level of picene thin film ( $-5.5 \text{ eV}$ ) is 0.3 eV [14] whose value is slightly smaller than that, 0.4 eV, between  $\varepsilon_{\text{F}}$  ( $-5.1 \text{ eV}$ ) of Au and the HOMO level (Fig. 2b). Since the slight difference is not likely to be responsible for the difference of efficiency of hole injection, we may expect the factors such as the charge transfer, for-

mation of electric dipole and hybridization of orbitals as an origin for the smooth carrier injection from PEDOT:PSS electrode, instead of the direct energy mismatch with HOMO level of picene thin films.

After a dynamical pumping of the picene FET under vacuum of  $10^{-6}$  Torr at 323 K for 18 h, 500 Torr of  $O_2$  gas was introduced into the measurement vessel. As seen from Fig. 3c, before an introduction of  $O_2$  gas, the  $\mu$  values were 0.11 and  $0.31 \text{ cm}^2 \text{ V}^{-1} \text{ s}^{-1}$ , respectively, for the forward and the reverse transfer curves. After an introduction of  $O_2$  gas, the  $\mu$  increases drastically to  $0.17 \text{ cm}^2 \text{ V}^{-1} \text{ s}^{-1}$  for the forward transfer curve and  $0.42 \text{ cm}^2 \text{ V}^{-1} \text{ s}^{-1}$  for the reverse transfer curve within a few minutes. The  $\mu$  value for the reverse transfer curve increased up to  $0.51 \text{ cm}^2 \text{ V}^{-1} \text{ s}^{-1}$  at 7 h after the  $O_2$  gas exposure, while the  $\mu$  value determined from the forward transfer curve a little reduces from the maximum value ( $0.17 \text{ cm}^2 \text{ V}^{-1} \text{ s}^{-1}$ ); the transfer curves are shown in Fig. 3d. The values of  $\mu$  in picene FETs fabricated in this study are listed in Table 2, together with the on-off ratio and  $V_{\text{TH}}$  values.

As seen from Table 2, the  $V_{\text{TH}}$  values were 61 and 81 V for the forward and reverse transfer curves at 7 h after  $O_2$ -exposure, respectively. These values slightly decrease in comparison with the values of 71 V (forward transfer curve) and 83 V (reverse transfer curve) before  $O_2$ -exposure. Thus, the enhancement of  $\mu$  and the reduction of  $V_{\text{TH}}$  by  $O_2$ -exposure is found in the picene thin film FET with PEDOT:PSS electrodes in bottom contact structure. The increase in  $\mu$  is already reported in picene thin film FET with Au electrodes in top contact structure [14,15], but it should be noticed that the decrease in  $V_{\text{TH}}$  by  $O_2$ -exposure has not yet been reported. The decrease in  $V_{\text{TH}}$  observed for picene thin film FET with PEDOT:PSS

**Table 2**  
FET parameters in picene FET with PEDOT:PSS-A electrodes.

O <sub>2</sub> -exposure time (h) <sup>a</sup>	$\mu$ (cm <sup>2</sup> V <sup>-1</sup> s <sup>-1</sup> )	On-off ratio	V <sub>TH</sub> (V)
<i>Forward</i>			
-1.9	0.13	$2.2 \times 10^2$	72
0.0	0.11	$1.9 \times 10^2$	71
0.3	0.17	$3.1 \times 10^2$	69
3.1	0.14	$3.4 \times 10^2$	63
7.0	0.13	$3.7 \times 10^2$	61
<i>Reverse</i>			
-1.9	0.33	$1.9 \times 10^2$	82
0.0	0.31	$1.6 \times 10^2$	83
0.3	0.42	$3.1 \times 10^2$	80
3.1	0.49	$3.0 \times 10^2$	80
7.0	0.51	$3.8 \times 10^2$	81

<sup>a</sup> The O<sub>2</sub>-exposure time of -1.9 h refers to 1.9 h before O<sub>2</sub>-exposure. The O<sub>2</sub>-exposure time, 0.0 h, means just before O<sub>2</sub>-exposure.

electrodes in bottom contact structure suggests that not only shallow trap states in picene thin films are affected by O<sub>2</sub> gas but also middle trap states are affected. The quick response of this picene thin film FET for O<sub>2</sub> gas exposure may open a way for an application toward flexible and portable O<sub>2</sub> gas sensor.

The highest  $\mu$  values for picene thin film FET with PEDOT:PSS electrodes was 0.61 cm<sup>2</sup> V<sup>-1</sup> s<sup>-1</sup> for the reverse transfer curve (not shown), recorded for another device which was stored in air for one week. The  $\mu$  value of 0.61 cm<sup>2</sup> V<sup>-1</sup> s<sup>-1</sup> is comparable to that, 0.3–0.7 cm<sup>2</sup> V<sup>-1</sup> s<sup>-1</sup>, for pentacene thin film FET with PEDOT:PSS electrodes in top contact structure [8]. The  $\mu$  value of 0.61 cm<sup>2</sup> V<sup>-1</sup> s<sup>-1</sup> is higher by a factor of 60 than that, 0.01 cm<sup>2</sup> V<sup>-1</sup> s<sup>-1</sup>, for the previous standard pentacene thin film FETs with PEDOT:PSS electrodes in bottom contact structure [8,9]. Furthermore, this value is higher by a factor of two than the best  $\mu$  value, 0.3 cm<sup>2</sup> V<sup>-1</sup> s<sup>-1</sup>, for pentacene thin film FET with PEDOT:PSS electrodes in bottom contact structure reported by Halik et al. [6].

#### 4. Conclusion

We have fabricated high-performance C<sub>60</sub> and picene thin film FETs with PEDOT:PSS electrodes in bottom contact structure. The best  $\mu$  values in this study were 0.41 cm<sup>2</sup> V<sup>-1</sup> s<sup>-1</sup> in *n*-channel C<sub>60</sub> thin film FET and 0.61 cm<sup>2</sup> V<sup>-1</sup> s<sup>-1</sup> in *p*-channel picene thin film FET. The  $\mu$  value of 0.41–0.61 cm<sup>2</sup> V<sup>-1</sup> s<sup>-1</sup> is the best record in organic thin film FETs with conducting polymer electrodes fabricated in bottom contact structure [5–9]. Here it should be noted that the V<sub>TH</sub> value of C<sub>60</sub> and picene thin film FETs with PEDOT:PSS electrodes are very high (>40 V). For a reduction of V<sub>TH</sub>, it is important to modify the interface be-

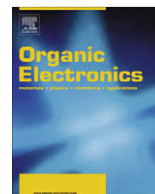
tween gate dielectrics and active layers to reduce the trap states in mid-gap position. This is the next important study in a development of high-performance organic thin film FET with conducting polymer electrodes. In this study, we have used Si/SiO<sub>2</sub> substrate for the C<sub>60</sub> and picene thin film FETs. However, for the realization of complete flexible organic FET devices, the plastic substrate and polymer gate dielectric must be used in addition to the conducting polymer electrodes. Since we have already fabricated high-performance C<sub>60</sub> thin film FET with PET substrate and parylene gate dielectric [4], the C<sub>60</sub> and picene thin film FETs with plastic substrate and polymer gate dielectric as well as conducting polymer electrodes may be easily fabricated in the next step. This study shows that the practical CMOS integrated circuits can be designed with C<sub>60</sub> and picene as active layers and PEDOT:PSS for electrodes.

#### Acknowledgement

The authors appreciate to Naoko Kawaski for her helpful assistance. This work was partly supported by a Grant-in-Aid (18340104) and Kyoto-Advanced Nano technology Network from MEXT, Japan.

#### References

- [1] Y. Kato, S. Iba, R. Teramoto, T. Sekitani, T. Someya, H. Kawaguchi, T. Sakurai, *Appl. Phys. Lett.* 84 (2004) 3789.
- [2] Y. Kubozono, T. Nagano, Y. Haruyama, E. Kuwahara, T. Takayanagi, K. Ochi, A. Fujiwara, *Appl. Phys. Lett.* 87 (2005) 143506.
- [3] Y. Noguchi, T. Sekitani, T. Someya, *Appl. Phys. Lett.* 89 (2006) 253507.
- [4] Y. Kubozono, S. Haas, W.L. Kalb, P. Joris, F. Meng, A. Fujiwara, B. Batlogg, *Appl. Phys. Lett.* 93 (2008) 033316.
- [5] H. Sirringhaus, T. Kawase, R.H. Friend, T. Shimoda, M. Inbasekaran, W. Wu, E.P. Woo, *Science* 290 (2000) 2123.
- [6] M. Halik, H. Klauk, U. Zschieschang, G. Schmid, W. Radlik, W. Weber, *Adv. Mater. (Weinheim, Ger.)* 14 (2002) 1717.
- [7] M. Lefenfeld, G. Blanchet, J.A. Rogers, *Adv. Mater. (Weinheim, Ger.)* 15 (2003) 1188.
- [8] D. Li, L.J. Guo, *Appl. Phys. Lett.* 88 (2006) 063513.
- [9] P. Cosseddu, A. Bonfiglio, I. Salzmann, J.P. Rabe, N. Koch, *Org. Electron.* 9 (2008) 191.
- [10] R.C. Haddon, A.S. Perel, R.C. Morris, T.T.M. Palstra, A.F. Hebard, R.M. Fleming, *Appl. Phys. Lett.* 67 (1995) 121.
- [11] S. Kobayashi, T. Takenobu, S. Mori, A. Fujiwara, Y. Iwasa, *Appl. Phys. Lett.* 82 (2003) 4581.
- [12] T. Kanbara, K. Shibata, S. Fujiki, Y. Kubozono, S. Kashino, T. Urisu, M. Sakai, A. Fujiwara, R. Kumashiro, K. Tanigaki, *Chem. Phys. Lett.* 379 (2003) 223.
- [13] K. Hong, S.Y. Yang, C. Yang, S.H. Kim, D. Choi, C.E. Park, *Org. Electron.* 9 (2008) 864.
- [14] H. Okamoto, N. Kawasaki, Y. Kaji, Y. Kubozono, A. Fujiwara, M. Yamaji, *J. Am. Chem. Soc.* 130 (2008) 10470.
- [15] Naoko Kawasaki, Yoshihiro Kubozono, Hideki Okamoto, Akihiko Fujiwara, and Minoru Yamaji, *Appl. Phys. Lett.*, in press.
- [16] T. Nagano, M. Tsutsui, R. Nouchi, N. Kawasaki, Y. Ohta, Y. Kubozono, N. Takahashi, A. Fujiwara, *J. Phys. Chem. C* 111 (2007) 7211.
- [17] N. Hayashi, H. Ishii, Y. Ouchi, K. Seki, *J. Appl. Phys.* 92 (2002) 3784.



# Carrier-density and field-dependent charge-carrier mobility in organic semiconductors with correlated Gaussian disorder

M. Bouhassoune<sup>a</sup>, S.L.M. van Mensfoort<sup>b,c</sup>, P.A. Bobbert<sup>a,\*</sup>, R. Coehoorn<sup>b,c</sup>

<sup>a</sup> Group Polymer Physics and Eindhoven Polymer Laboratories, Eindhoven University of Technology, P.O. Box 513, NL-5600 MB Eindhoven, The Netherlands

<sup>b</sup> Department of Applied Physics, Eindhoven University of Technology, P.O. Box 513, 5600 MB Eindhoven, The Netherlands

<sup>c</sup> Philips Research Laboratories, High Tech Campus 4, NL-5656 AE Eindhoven, The Netherlands

## ARTICLE INFO

### Article history:

Received 22 November 2008

Received in revised form 5 January 2009

Accepted 8 January 2009

Available online 18 January 2009

### PACS:

72.20.Ee

72.80.Le

73.61.Ph

### Keywords:

Hopping mobility

Gaussian disorder

Correlated disorder

Poole-Frenkel law

Hole-only device

Poly-phenylene-vinylene

## ABSTRACT

Recently, it has been demonstrated that for organic semiconductors with a Gaussian density of states (DOS) and with on-site energies that are spatially uncorrelated the hopping mobility of charge-carriers can be strongly carrier-density-dependent (extended Gaussian disorder model, EGDM). In the literature, it has been argued that for some materials, the on-site energies are actually spatially correlated. In this paper, we develop a full description of the mobility in a correlated Gaussian DOS (extended correlated disorder model, ECDM), using a master-equation method. We show that the mobility is less strongly carrier-density-dependent than in the EGDM, but that the field dependence is more pronounced. The field dependence is found to be described by a Poole-Frenkel factor, as has been deduced from empirical analyses of experimental data, but only in a limited field range. As an example of an application, we present a comparison between analyses of the current–voltage–temperature  $J(V,T)$  characteristics of a poly-phenylene-vinylene (PPV) based hole-only device using the EGDM and the ECDM. For both cases, excellent fits can be obtained, but with the EGDM a more realistic value of the intersite distance is found than in the case of the ECDM. We view this as an indication that site-energy correlations do not play an important role in PPV.

© 2009 Elsevier B.V. All rights reserved.

## 1. Introduction

The interest in electronic devices based on disordered semiconducting organic materials is rapidly increasing. Important applications are organic light-emitting diodes (OLEDs) [1,2] organic field-effect transistors [3], and organic photo-voltaic devices [4]. It is of crucial importance to understand the charge-carrier transport in these materials in order to design and synthesize appropriate materials and to improve the efficiency and lifetime of devices. Many investigations have addressed the mobility  $\mu$  of charge-carriers in these materials, since this is one of the important parameters controlling the performance of devices.

Charge transport in polymers and organic small-molecule materials occurs by thermally assisted tunneling – hopping – between localized molecular states. In several studies, the dependence of  $\mu$  on temperature  $T$  and electric-field  $E$ , due to this hopping process, has been investigated [5–10]. BäSSLer and co-workers introduced a model with an uncorrelated Gaussian distribution of the random energies of hopping sites, which became known as the “Gaussian disorder model” (GDM). They found a temperature dependence of the mobility of the form  $\mu \propto \exp[-(T_0/T)^2]$  and a Poole-Frenkel behavior  $\mu \propto \exp[\gamma\sqrt{E}]$  for the electric-field dependence in a rather limited range of electric-fields [5,6]. Gartstein and Conwell argued that in order to obtain a Poole-Frenkel behavior in a broad range of electric-fields, as observed in time-of-flight mobility measurements, it is necessary to assume correlation

\* Corresponding author.

E-mail address: [p.a.bobbert@tue.nl](mailto:p.a.bobbert@tue.nl) (P.A. Bobbert).

between the site energies, leading to what is now known as the “correlated disorder model” (CDM) [7]. Indeed, their simulations, which assume static fluctuations of the site energies due to the interaction of a charge-carrier with permanent and induced dipoles, show that the concept of correlation between the energies of spatially close sites leads to an extended range of validity of the Poole-Frenkel law [7]. Dunlap et al. developed a one-dimensional analytical model with correlations caused by randomly oriented dipoles, which yields a Poole-Frenkel  $E$  dependence of  $\mu$  in agreement with time-of-flight measurements of molecularly doped polymers [8]. An extension of this model to three dimensions was developed by Novikov et al. [9]. Apart from dipoles, long-range thermal fluctuations in the molecular geometries of a polymer were suggested as a possible cause for correlation in the disorder [10]. Recently, it has also been suggested that the Poole-Frenkel dependence on the electric-field is caused by carrier heating [11]. In an early study the assumption of a Poole-Frenkel field dependence of the hole mobility appeared to lead to a good description of the current-voltage  $J(V)$  characteristics of hole-only devices of PPV (poly-phenylene vinylene)-based polymers [12].

In organic field-effect transistors, where the carrier-density is relatively high (up to on average 0.01–0.1 carriers per site), a dependence of the mobility on the charge-carrier-density  $p$  was taken into account in the modeling [13]. In sandwich-type hole-only devices containing, e.g., PPV-based or polyfluorene-based polymers used in OLEDs, the carrier-densities are typically much smaller, viz.  $10^{-5}$ – $10^{-4}$  carriers per site, except in a thin region near the anode interface. Nevertheless, it was concluded during the last few years that it is also for such devices and in OLEDs important to take the dependence of  $\mu$  on  $p$  into account [14–16]. By changing the thickness of the polymer layer it was demonstrated that by only assuming a dependence of  $\mu$  on  $E$  of the Poole-Frenkel type it is not possible to fit the  $J(V)$  characteristics of hole-only devices with different thicknesses without changing the fit parameters, but that a consistent set of fits can be obtained by assuming a dependence of  $\mu$  on  $p$  [15,16]. Several theoretical and computational approaches were employed to describe this carrier-density dependence of the mobility [10,17–19]. From a numerical solution of the master-equation within the GDM for the occupation probabilities of an array of hopping sites Pasveer et al. obtained a dependence of  $\mu$  on  $T$ ,  $E$ , and  $p$  that was shown to lead to excellent agreement of calculated and measured  $J(V,T)$  characteristics of hole-only devices of PPV-based polymers [18]. We call this the “extended” Gaussian disorder model (EGDM), in order to indicate that the carrier-density dependence of the mobility is taken into account. It was found that only at high voltages and low temperatures the dependence of  $\mu$  on  $E$  plays a role.

Pasveer and co-workers concluded that it is not necessary to assume correlations in the site energies in order to obtain for the PPV-based hole-only devices studied agreement with measured  $J(V)$  characteristics. However, this does not yet prove that the site energies are uncorrelated, as it has not yet been established whether the experiments performed are sufficiently sensitive to the

occurrence of correlations. In this paper, we first provide the required theoretical basis for addressing this question, viz. by deriving from master-equation calculations and percolation theory (Section 2) a full description of the temperature, electric-field and carrier-density dependence of the mobility (Section 3). To be definite, we will consider correlated disorder as caused by random dipoles, since this is the most commonly accepted model. We show that the carrier-density dependence of the mobility is weaker than in the EGDM, but that the field dependence is stronger. As an application of our results, we re-analyse in Section 4 the  $J(V)$  characteristics of the PPV-based hole-only devices studied already in Ref. [18] within this extended version of the CDM (“ECDM”), by making use of a drift-diffusion device model. For the device considered, a very good description of the  $J(V)$  characteristics can also be obtained within the ECDM, but with a much smaller intersite distance than obtained within the description using the EGDM. In Section 5 a summary and conclusions are given.

## 2. Methods

As in Ref. [18], we determine the charge-carrier mobility  $\mu$  of carriers on an array of hopping sites, representing a disordered semiconducting organic material, by considering the master-equation for the mean-field occupation probabilities of these sites:

$$\sum_{j \neq i} [W_{ij} p_i (1 - p_j) - W_{ji} p_j (1 - p_i)] = 0. \quad (1)$$

Here  $p_i$  is the time-averaged probability that site  $i$  is occupied by a charge-carrier and  $W_{ij}$  is the transition rate for hopping from site  $i$  to  $j$ . The factors  $1 - p_i$  account for the fact that only one carrier can occupy a site, due to the high Coulomb penalty for the presence of two or more carriers at the same site. We assume hopping of carriers from site to site as a thermally assisted tunneling process and coupling to a system of acoustical phonons, leading to the Miller-Abrahams transition rates [20]:

$$W_{ij} = \begin{cases} v_0 \exp[-2\alpha R_{ij} - \beta(\epsilon_j - \epsilon_i)] & \epsilon_j \geq \epsilon_i, \\ v_0 \exp[-2\alpha R_{ij}] & \epsilon_j < \epsilon_i, \end{cases} \quad (2)$$

where  $\beta \equiv 1/k_B T$ , with  $k_B$  the Boltzmann constant;  $v_0$  is an intrinsic rate,  $R_{ij} \equiv |\mathbf{R}_j - \mathbf{R}_i|$ , with  $\mathbf{R}_i$  and  $\mathbf{R}_j$  the site positions;  $\alpha$  is the inverse localization length of the localized wave functions under consideration and  $\epsilon_i$  is the on-site energy of site  $i$ . The energy differences in Eq. (2) are supposed to contain a contribution  $-eER_{ij,x}$  due to an electric-field  $E$  applied in the  $x$  direction, where  $e$  is the charge of the carriers.

As in Ref. [18] we solve Eq. (1) by an iteration procedure comparable to the one proposed by Yu et al. [10], starting from the zero-field Fermi-Dirac distribution. We take a regular cubic lattice of sites with lattice constant  $a$  and periodic boundary conditions. For the inverse localization length we take the same value as in Ref. [18]:  $\alpha = 10/a$ . The effect of changing  $\alpha$  is predominantly a change of the prefactor of the mobility, which is not a matter of concern here, and a slight change in the temperature dependence of the mobility. We refer to Ref. [19] for a more detailed dis-

discussion of the role of  $\alpha$ . For very low temperatures, it is known that variable-range hopping becomes important in conjugated polymers [21], i.e. hopping events further than to the nearest neighbor take place. We verified that for the temperature range considered in the present paper it is sufficient to take into account hops not further than to the third nearest neighbor, corresponding to a maximum distance of  $\sqrt{3}a$ . Once Eq. (1) has been solved, the carrier mobility can be obtained from

$$\mu = \frac{\sum_{ij} W_{ij} p_i (1 - p_j) R_{ij,x}}{N E}, \quad (3)$$

with  $N$  the number of charge-carriers in the system.

In order to obtain a density of states with a selected standard deviation  $\sigma$  and with spatially correlated on-site energies, we take the energy on each site equal to the electrostatic energy resulting from a distribution of randomly oriented dipole moments of equal magnitude,  $d$ , on all other sites. It is well-known that this procedure leads to a distribution of energies that is to a good approximation Gaussian [22,23], with a width proportional to  $d$ . The energy on site  $i$  is thus given by the expression

$$\varepsilon_i = - \sum_{j \neq i} \frac{e \mathbf{d}_j (\mathbf{R}_j - \mathbf{R}_i)}{\varepsilon |\mathbf{R}_j - \mathbf{R}_i|^3}, \quad (4)$$

where the summation is over all sites  $j$  in a cube centered around site  $i$  and of a size equal to that of the simulation box, and where  $\varepsilon$  is the permittivity. For large inter-site distances  $R$ , the correlation function between the energies of different sites has the form [9]

$$C(R) \equiv \langle \varepsilon_i \varepsilon_j \rangle \propto \frac{a}{R} \sigma^2, \quad (5)$$

where  $\langle \dots \rangle$  denotes an ensemble average.

For large values of the disorder parameter  $\hat{\sigma} \equiv \sigma/k_B T$  it was not always possible to obtain a converged solution of Eq. (1) for small fields. We found that for such cases accurate results can be obtained from a numerical percolation approach. For Miller–Abrahams transition rates, the mobility can then be obtained by considering the conductivity of a random-resistor network with a conductance  $G_{ij}$  between each pair of hopping sites, given by [24]

$$G_{ij} = \frac{e^2}{k_B T} v_0 \exp(-s_{ij}), \quad (6)$$

with

$$s_{ij} = 2\alpha R_{ij} + \frac{|\varepsilon_i - \varepsilon_F| + |\varepsilon_j - \varepsilon_F| + |\varepsilon_i - \varepsilon_j|}{2k_B T}, \quad (7)$$

where  $\varepsilon_F$  is the Fermi energy. We first determine numerically the exponent of the critical percolation conductance,  $s_c$ , i.e. the value of the exponent  $s$  such that the bonds with  $s_{ij} < s_c$  just form a percolating network between one side of a simulation box and the other. We then replace all bonds with a conductance  $G_c = (e^2/k_B T) \exp(-s_c)$ , evaluate the conductivity, and from that the mobility. We found that at moderate values of  $\hat{\sigma}$  the mobility evaluated in this way agrees, after multiplication with an overall “geometrical” factor [24], very accurately with the low-field mobility as calculated within the master-equation approach, when-

ever the latter approach converged. For large values of  $\hat{\sigma}$ , for which we could not obtain convergence of the latter approach, this percolation approach is also expected to give accurate results. A similar numerical percolation approach was successfully applied to the case of an (uncorrelated) exponential distribution of site energies [25].

### 3. Temperature, electric-field, and carrier-density dependence of the mobility

We calculated the mobility for various values of  $\hat{\sigma}$  as a function of the carrier-density and the electric-field, using the master-equation and percolation method discussed in Section 2, employing sufficiently large arrays such that finite-size effects could be neglected. For the master-equation approach array sizes up to  $50 \times 50 \times 50$  were used and for the percolation approach sizes up to  $100 \times 100 \times 100$ . Averages were taken over a sufficiently large number of different disorder configurations, such that  $\mu$  was obtained with an accuracy better than 10%.

In Fig. 1a, we display the carrier-density dependence of the mobility in the zero-field limit for various values of  $\hat{\sigma}$ , in units of  $\mu_0 \equiv a^2 v_0 e / \sigma$ , as calculated within the ECDM. Only for  $\hat{\sigma} = 2, 3$ , and 4 we were able to obtain converged results for the master-equation approach. A geometrical factor of 0.12 brings the results obtained with the percolation approach on top of the master-equation results for these values of  $\hat{\sigma}$ . We expect the percolation results multiplied with this geometrical factor to be accurate for the entire range of values of  $\hat{\sigma}$  studied. We note that in OLEDs the carrier-densities can be situated in the entire range for which the results are given. In Fig. 1b, we display the corresponding results obtained within the EGDM, as calculated in Ref. [18] with the master-equation approach. At low carrier-densities, the dependence of the mobility on  $\hat{\sigma}$  is for the ECDM weaker than for the EGDM, in agreement with studies in the low-density limit for the GDM [6] and the CDM [9]. We observe that for the ECDM also the dependence on the carrier-density is weaker than for the EGDM. Roughly, the difference can be modeled as a change in  $\hat{\sigma}$ .

In Fig. 2a, we display the mobility calculated within the ECDM as a function of  $E^{1/2}$ , at a relatively low carrier-density,  $p = 10^{-5}/a^3$  (main panel), and a relatively high carrier-density,  $p = 0.05/a^3$  (inset). The field is expressed in units of  $\sigma/(ea)$ . For a typical organic semiconductor, with  $\sigma = 0.1$  eV and  $a = 1$  nm, a voltage of 10 V applied across a 100 nm thick device leads to an average reduced field  $E_{\text{red}} \equiv eaE/\sigma = 1$ . In agreement with previous studies of the CDM [7,8] we find indeed a Poole–Frenkel (PF) behavior  $\mu \propto \exp[\gamma\sqrt{E}]$ , but only in a limited range of intermediate electric-fields. At very small fields the PF behavior has to break down since  $\mu$  should be an even function of  $E$  around  $E = 0$  with a first derivative equal to zero at  $E = 0$ . Indeed, we find at very small fields a deviation from the PF behavior. At very large fields only energetically downhill hops occur and all curves collapse onto a  $\mu \propto 1/E$  dependence. This regime is found to set in around  $E_{\text{red}} = 1$ . In Fig. 2b, we give for the same carrier-densities the mobility as calculated within the EGDM, displayed as a function of  $E$ . In agreement with general theoretical considerations of

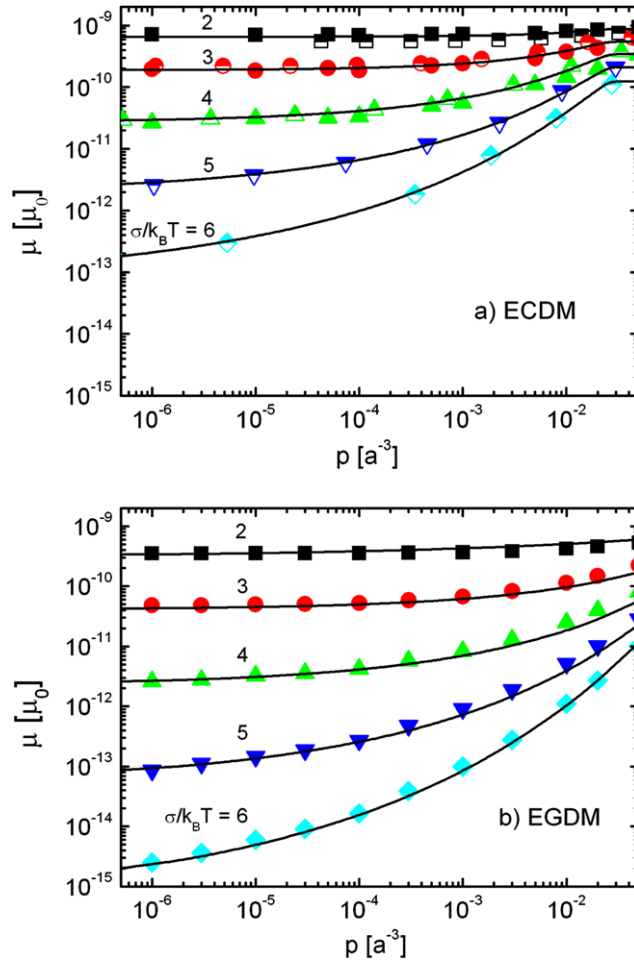


**Fig. 1.** Dependence of the mobility on the charge-carrier-density at vanishing electric-field for (a) the ECDM, calculated with the master-equation approach (filled symbols) and the percolation approach (half-filled symbols), and (b) the EGDM (only master-equation approach, Ref. [18]). The curves correspond to the parameterization given for the ECDM in the present paper (the flattening of the parameterization at high densities is discussed in the Appendix) and given for the EGDM in Ref. [18].

Gaussian disorder with algebraically decaying correlation functions [8] ( $\propto 1/R^p$ , leading to  $\ln \mu \propto E^{p/(p+1)}$ ), the field dependence obtained from the EGDM is of the form  $\ln \mu \propto E$  for a broad range of fields ( $p = \infty$ ). The transition to the high-field  $\mu \propto 1/E$  regime sets in at a significantly higher reduced field than for the ECDM, in particular for small carrier-densities.

In order to make applications of the master-equation results within a drift-diffusion device model possible, we have developed an empirical parameterization scheme for the mobility. First, separate expressions for the mobility in the low-field regime ( $E_{\text{red}} \lesssim 1$ ) and in the high-field regime ( $E_{\text{red}} \gtrsim 1$ ) are established. Subsequently, these expressions are combined, yielding a fully general expression for the mobility function  $\mu(T, p, E)$ .

In the low-field regime, the mobility can be written as

$$\mu_{\text{low}}(T, p, E) = \mu_0(T)g(T, p)f(T, E, p), \quad (8)$$

with  $\mu_0(T)$  the mobility in the zero-carrier-density limit and zero-field limit, and with  $g$  and  $f$  dimensionless mobility enhancement functions. The function  $g(T, p)$  gives the

carrier-density induced enhancement of the zero-field mobility with respect to the value in the zero-carrier-density limit. The function  $f(T, E, p)$  gives the field-induced enhancement of the mobility with respect to the mobility at zero field. In the low carrier-density (Boltzmann) limit, the zero-field mobility is only dependent on the temperature, as in the EGDM, and is for the range  $2 \leq \hat{\sigma} \leq 6$  to a good approximation given by

$$\mu_0(T) = \mu_0 c_1 \exp(-0.29 \hat{\sigma}^2), \quad (9)$$

where the fit constant  $c_1 = 1.0 \times 10^{-9}$  is of the order of the exponential factor describing the wavefunction overlap between two neighbor molecules,  $\exp(-2\alpha a) = \exp(-20) = 2.06 \times 10^{-9}$ . For the disorder parameter range studied, the temperature dependence given by Eq. (9) coincides approximately with the temperature dependence  $\mu \propto \exp[-0.42 \hat{\sigma}^2]$  obtained in Ref. [18] for the EGDM, after shifting  $\hat{\sigma}$  by approximately  $-1.2$ . Effectively, the energy-level landscape is thus, for a given value of  $\sigma$ , smoother than in the EGDM. This is a result of the correlated nature of the energy-level landscape in the ECDM: close to each

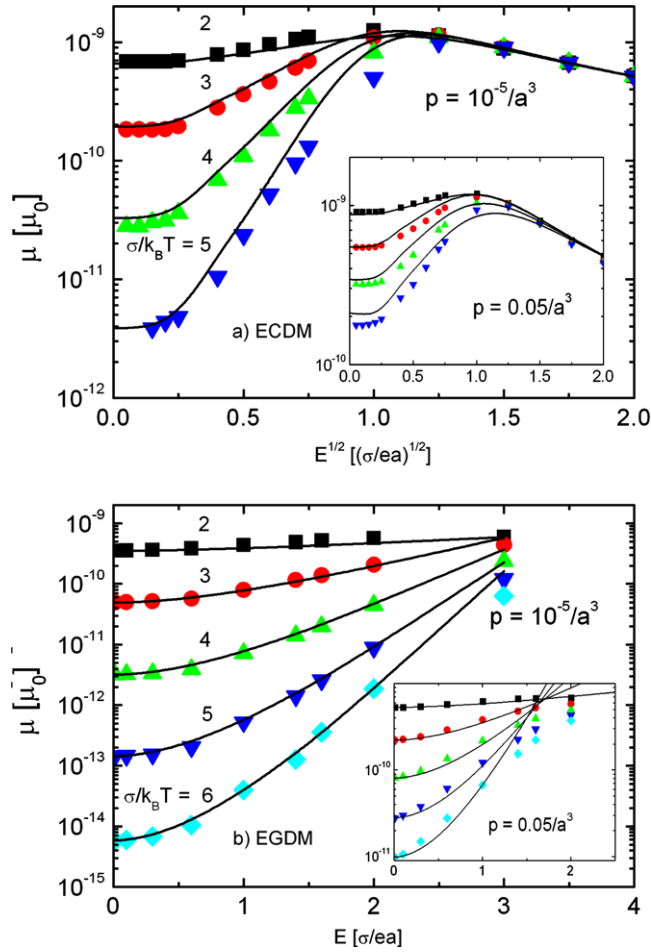


**Fig. 2.** Dependence of the mobility on the electric-field at a low (main panel) and high (inset) carrier-density, calculated with the master-equation approach, for (a) the ECMD and (b) the EGDM. The curves correspond to the parameterization given for the ECMD in the present paper and given for the EGDM in Ref. [18].

occupied state many low-lying states are present, to which hopping processes that contribute significantly to the conductivity can take place. In the Appendix, a phenomenological parameterization for the functions  $g(T,p)$  and  $f(T,E,p)$  is given. The density-dependent function  $g$  is quite similar to that obtained earlier for the EGDM. The field-dependent function  $f$  describes the mobility in the three transport regimes indicated already briefly above.

In the high-field regime, the mobility-determining hops are all “down-hill”, so that the mobility is not anymore dependent on the degree of disorder and on the temperature. The mobility is then described by

$$\mu_{\text{high}}(p, E) = c_2 \frac{av_0}{E} (1 - pa^3) = \frac{c_2}{E_{\text{red}}} \mu_0 (1 - pa^3), \quad (10)$$

with  $c_2 = \exp(-2\alpha a)$ . For the parameters used in this study,  $c_2 = \exp(-20) = 2.06 \times 10^{-9}$ . The  $(1 - pa^3)$  factor is included in order to describe for high carrier-densities in a phenomenological way the inhibiting effect of the occupation of final states on the mobility.

A description of the mobility at any field, including the region around  $E_{\text{red}} = 1$ , is obtained by joining the expres-

sions given above for low- and high-fields using the phenomenological expression

$$\mu(T, p, E) = \left( (\mu_{\text{low}}(T, p, E))^{q(\hat{\sigma})} + (\mu_{\text{high}}(p, E))^{q(\hat{\sigma})} \right)^{1/q(\hat{\sigma})}, \quad (11)$$

with

$$q(\hat{\sigma}) = \frac{2.4}{1 - \hat{\sigma}}. \quad (12)$$

As can be seen from the drawn lines in Figs. 1a and 2a, this parameterization is very satisfactory, for the parameter range studied. We note that the parameterization of the electric-field dependence was not only optimized for the low and high carrier-densities for which the results are given in Fig. 2a, but also for master-equation results for a range of intermediate carrier-densities. The parameterization of the results for the EGDM can be found in Ref. [18] and is indicated by the drawn lines in Figs. 1b and 2b. An important difference between the parameterization for the two models is that the electric-field dependence of the ECMD comes in via a factor  $f(T,E,p)$  that depends both on  $T$  and  $p$ , whereas for the case of the EGDM it comes in via a factor  $f(T,E)$  that is independent of the

carrier-density  $p$ . In particular, the electric-field dependence of the ECDM decreases with increasing carrier-density. The reason for this is that in the case of correlated disorder broad “valleys” of energetically low-lying sites exist that gradually fill up with increasing carrier-density. Hence, the electric-field needed for escape of the carriers with the highest energy in each valley decreases with increasing carrier-density.

It is of interest to compare the field dependence of the mobility obtained from the master-equation method with the results of an analytic scaling analysis carried out by Parris et al. [26]. These authors focused on the PF regime. In that regime, the mobility is assumed to be due to the rate of certain critical forward hops. It is assumed that the backward hop rate can already be neglected. The authors considered the typical critical (rate-determining) hop distance and hop energy (thermal activation energy). Within a somewhat simplifying summary of their approach, it may be stated that they argued that a spatial correlation between the on-site energies, obeying Eq. (5), gives rise to an effective  $-1/R$  dependence of the energies of sites at distance  $R$  from the low-energy sites in the tail of the Gaussian DOS at which most carriers are located. The application of an electric-field decreases the depth of this potential well as experienced by forward hops, due to the additional potential proportional to  $-R$ . This leads to a decrease of the escape time and hence to an increase of the conductivity. Eq. (15) in Ref. [26] gives the resulting analytic expression for the electric-field dependence of the mobility<sup>1</sup>

$$\mu = \mu_0 \exp(\hat{\sigma}^{3/2} \sqrt{2E_{\text{red}}}). \quad (13)$$

Within the PF regime and in the zero-carrier-density limit, our parameterization (Eq. (A.6) with  $h(E_{\text{red}}) = 1$ ) approaches for  $E_{\text{red}} \gg 1$  and  $\hat{\sigma} \gg 1$  the field dependence given by Eq. (13). However, in the field range within which PF behavior is found,  $0.16 < E_{\text{red}} < 0.8$ , and for a more extended range of disorder parameters, the full form of Eq. (A.6) provides a much better description of the actual mobility function.

At very small fields, the PF behavior breaks down as a result of the fact that the conductivity is then not only determined by the rate of forward hops, but also by a non-negligible rate of backward hops. We find that the mobility in the very-small-field (vsf) regime is well described by the expression

$$\mu_{\text{vsf}} \propto \frac{\exp\left(\frac{ed_0E}{k_B T}\right) - \exp\left(-\frac{ed_0E}{k_B T}\right)}{E}, \quad (14)$$

with  $d_0 \approx 4 \times a$  for the entire  $\hat{\sigma}$ -range studied. In particular for large disorder ( $\hat{\sigma} > 4$ ) and small carrier-densities ( $p = 10^{-5}/a^3$ ), the agreement between Eq. (14) and the parameterization given by Eqs. ((A.6), (A.8), and (A.9)) is excellent. We view this as an indication that the critical hop distance, which within the theory for the PF regime given in Ref. [26] goes to infinity with decreasing field, actually converges to

a fairly large but fixed finite value, which is within a factor of order unity equal to  $d_0$ . Due to the presence of the field the thermal activation energy for forward (backward) hopping to sites at a distance  $d_0$  decreases (increases) by an energy  $ed_0E$ . The two terms in the numerator of Eq. (14) are proportional to the contributions to the average carrier velocity from forward and backward hopping carriers.

#### 4. Application to a PPV-based hole-only device

As an example of an application we consider the question whether the ECDM is able to describe the  $J(V)$  characteristics of the PPV-based hole-only sandwich-type devices studied in Ref. [18] as successfully as the EGDM. We perform our analysis for a device based on poly[4'-(3,7-dimethyloctyloxy)-1,1'-biphenylene-2,5-vinylene] (NRS-PPV), with a layer thickness of  $L = 560$  nm, sandwiched in between an indium tin oxide (ITO) electrode used as anode and an evaporated gold electrode used as cathode. In Ref. [18] it was shown that the  $J(V)$  characteristics of this device, measured at 298, 272, 252, and 233 K, can be well described within the EGDM, using a drift-only device model and assuming excellent charge-carrier injection (no injection barrier at the ITO injecting contact). The lattice constant  $a$  and the standard deviation  $\sigma$  of the Gaussian DOS were treated as fitting parameters and an optimal fit was obtained with  $a = 1.8$  nm and  $\sigma = 0.14$  eV. Here, we re-analyse these experimental data for PPV-based devices by (i) employing the EGDM within a model that goes beyond the model used in Ref. [18] by also taking the diffusion contribution to the current density into account and by allowing for a built-in voltage  $V_{\text{bi}}$  between the two electrodes, and by (ii) carrying out a similar analysis using the ECDM.

The drift–diffusion method used is described in detail in Ref. [27] for the case of the EGDM. Within this method, the diffusion coefficient is calculated from the mobility using the generalized Einstein equation, taking the effects of a finite carrier-density into account. Only a modest modification of the method, in order to include the field and density dependence of the function  $f(T, E, p)$  in Eq. (8), was needed to make it suitable in conjunction with the ECDM. As in

**Table 1**

Optimal combinations of materials parameters used for fitting the  $J(V)$  characteristics of a NRS-PPV hole-only device with a thickness  $L = 560$  nm at four different temperatures, with a mobility as predicted by the ECDM and the EGDM, and a temperature dependence given by Eq. (15). The bold numbers indicate the parameter combination for which the best overall fit was obtained, and for which the fit results are shown in Fig. 3a and b.

ECDM			
$a$ [nm]	$\sigma$ [eV]	$\mu_0$ [m <sup>2</sup> /Vs]	$C$
0.8	0.10	$1.1 \times 10^{-8}$	0.56
0.6	0.11	$1.3 \times 10^{-8}$	0.46
0.4	0.14	$3.8 \times 10^{-8}$	0.33
<b>0.3</b>	<b>0.18</b>	<b><math>3.8 \times 10^{-7}</math></b>	<b>0.27</b>
0.2	0.22	$0.6 \times 10^{-5}$	0.25
EGDM			
3.2	0.085	$1.3 \times 10^{-8}$	0.77
2.7	0.093	$1.6 \times 10^{-8}$	0.67
<b>1.8</b>	<b>0.14</b>	<b><math>2.5 \times 10^{-7}</math></b>	<b>0.44</b>
1.2	0.20	$0.9 \times 10^{-4}$	0.41

<sup>1</sup> We believe that Eq. (15) in Ref. [26] contains a sign error of the argument under the exponential function and we have corrected this in Eq. (13).



Ref. [18], we assume that the ITO anode is a perfect injector. The injection barriers for holes at the anode and cathode are  $\varphi_1 = 0$  and  $\varphi_2 = eV_{bi}$ . The carrier-densities at the electrode interfaces  $i = 1, 2$  are obtained under the assumption of local thermal equilibrium at the electrode planes, so that they are equal to the thermal-equilibrium density within a Gaussian DOS, with the Fermi energy  $\varepsilon_F = -\varphi_i$  (with  $\varepsilon_F$  defined with respect to the top of the Gaussian DOS). Like in Ref. [18], we take the relative dielectric constant of the polymer equal to  $\varepsilon_r = 3$ . For both models, the temperature dependence of the mobility in the zero field and zero density limit has the form

$$\mu_0(T) = \mu_0^* \exp[-C(\sigma/k_B T)^2], \quad (15)$$

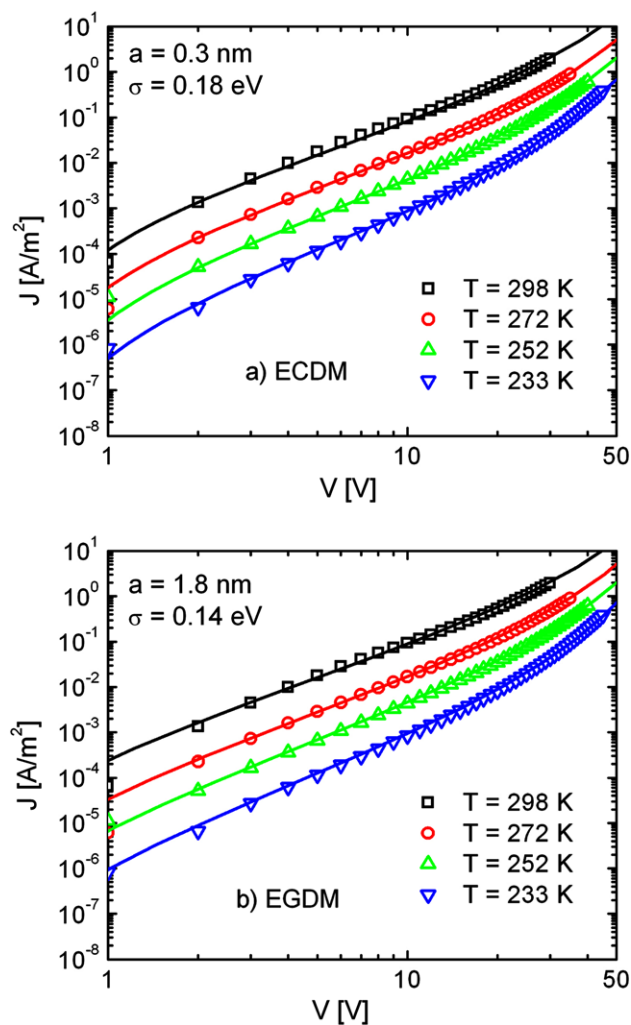
as discussed already in Section 3 (Eq. (9) for the ECDM).

Table 1 gives for selected values of the inter-site distance  $a$  the parameters  $\sigma$ ,  $\mu_0^*$ , and  $C$  for which optimal fits were obtained using the ECDM and EGDM. The combinations of fit parameters that yielded the best overall fit are

given in bold numbers. The corresponding values of the fitted built-in voltage  $V_{bi}$  were 1.7 and 1.1 V for the ECDM and EGDM, respectively. These values of  $V_{bi}$  are larger than would be expected on the basis of the small difference between the vacuum work functions of ITO and Au. This is indicative of the occurrence of important organic–metal interactions at the polymer/Au interface, as have been revealed earlier for many other organic/metal interfaces [28].

For the ECDM and EGDM parameter combinations for which the best fits were obtained the corresponding fits are displayed in Fig. 3a and b, respectively. It may be seen that both with the ECDM and the EGDM excellent fits to the measured  $J(V)$  characteristics can be obtained. We note that within both models the mobility at any temperature is described using only three parameters, viz.  $a$ ,  $\sigma$  and  $\mu_0$ , each with a clear physical meaning.

The optimal fit values of  $a$  as obtained from the ECDM and EGDM are very different, viz. 0.3 and 1.8 nm, respectively. The value of  $a$  found for the ECDM may be



**Fig. 3.** Experimental current–voltage characteristics (symbols) at various temperatures for a NRS-PPV hole-only device with a thickness  $L = 560$  nm, and best fits (lines) with (a) the ECDM mobility and (b) the EGDM mobility model, using the parameters given in Table 1 (bold numbers) and with the built-in voltage  $V_{bi}$  as given in the main text.

considered as unrealistically small, in view of the fact that in NRS-PPV the use of side-branches is expected to give rise to a larger typical distance between neighboring polymer chains. Furthermore, intra-chain hopping between the rather long conjugated segments is also expected to be associated with a larger  $a$ -parameter. The distance between two subsequent monomer units is equal to approximately 0.7 nm, and the conjugation length is believed to be at least five monomer units. This suggests that in the PPV-derivative studied correlations between the site energies are insignificant. The comparison between the values obtained for  $\sigma$  and  $C$  does not change this point of view. For  $\sigma$ , the optimal values obtained from the ECDM and EGDM are very similar, viz. 0.18 and 0.14 eV, respectively, each with an uncertainty of  $\pm 0.03$  eV.<sup>2</sup> For  $C$ , the values that yield the best fits ( $C = 0.27$  for the ECDM and  $C = 0.44$  for the EGDM) are both very close to the values predicted within each model ( $C = 0.29$  for the ECDM and  $C = 0.42$  for the EGDM). We note that we have treated  $C$  as a free parameter upon making the fits. The reason is that different values of  $C$  can be found in literature, both for the (E)CDM [9], as well as for the (E)GDM [6,19]. Also, the precise value of the inverse localization length  $\alpha$  (for which we have assumed  $\alpha = 10/a$ ) can have some influence on the value of  $C$  [19].

We envisage that more certainty about the validity of the analysis given above can be obtained by extending this work to a series of devices with a wide range of layer thicknesses and by investigating the consistency of the analysis using the results of transient experiments (e.g. dark injection, admittance or time-of-flight experiments).

## 5. Summary and conclusions

In summary, using a master-equation and percolation approach, we have extended the correlated disorder model (CDM) to include the dependence of the mobility on the charge-carrier-density, in addition to the dependence of the charge-carrier mobility on temperature and electric-field. This leads to what we have called the extended correlated disorder model (ECDM). In this model, the on-site energies and the correlation in these energies are assumed to follow from the interaction of the charge-carriers with randomly oriented dipoles. We have provided an accurate parameterization of these dependencies that can be used in device studies of disordered semiconducting materials, such as small-molecule semiconductors and conjugated polymers.

As an application of our results, we modeled the  $J(V)$  characteristics of a hole-only device of a conjugated PPV-based polymer (NRS-PPV), measured at various temperatures, by solving a drift–diffusion equation with a mobility and diffusion coefficient as obtained from the ECDM and as obtained from the previously investigated extended Gaussian disorder model (EGDM). We found that both with the ECDM and the EGDM excellent fits between the calculated and measured  $J(V)$  characteristics can be obtained. The

most remarkable distinction between the two sets of optimal fit parameters is an observed large (factor  $\sim 5$ ) difference between the effective lattice parameter  $a$ . We view the more realistic intersite distance found using the EGDM ( $a \approx 1.8$  nm) compared to the value found using the ECDM ( $a \approx 0.3$  nm) as a first indication that in the PPV-derivative studied correlations between the site energies are absent or play a minor role. The parameterizations for the ECDM given in the present paper may be used to investigate the possible role of correlations in other conjugated polymers and small-molecule semiconductors.

## Acknowledgments

The authors thank Dr. S.V. Novikov for very interesting discussions and useful suggestions. The work is part of the research program of the “Stichting voor Fundamenteel Onderzoek der Materie (FOM)”, which is financially supported by the “Nederlandse Organisatie voor Wetenschappelijk Onderzoek (NWO)”. The work was also supported by NanoNed, a National Nanotechnology Program coordinated by the Dutch Ministry of Economic Affairs. The computations were made possible by support from NCF (Dutch National Computer Facilities).

## Appendix Carrier-density, and electric-field dependence of the mobility in the low-field regime

In the low-field regime ( $E_{\text{red}} \equiv eaE/\sigma \lesssim 1$ ), the mobility is expressed in the form given by Eq. (8). Using the numerical data shown in Fig. 1a for the range  $2 \leq \hat{\sigma} \leq 6$ , and inspired by Refs. [8,18,19], we parameterize the carrier-density-dependent mobility-enhancement function as follows

$$g(T, p) = \exp[(0.25\hat{\sigma}^2 + 0.7\hat{\sigma})(2pa^3)^\delta] \quad \text{for } pa^3 < 0.025, \quad (\text{A.1})$$

$$g(T, p) = g(T, 0.025a^{-3}) \quad \text{for } pa^3 \geq 0.025, \quad (\text{A.2})$$

with

$$\delta \equiv 2.3 \frac{\ln(0.5\hat{\sigma}^2 + 1.4\hat{\sigma}) - 0.327}{\hat{\sigma}^2} \quad (\text{A.3})$$

Eq. (A.1) describes the increase of the mobility with increasing carrier-density. This effect becomes significant when the carrier-density is not anymore in the Boltzmann regime. Defining the cross-over density,  $p_{\text{cross-over}}$ , as the density at which the mobility is enhanced by a factor of 2, it follows from Eq. (A.1) that to a good approximation

$$p_{\text{cross-over,ECDM}} = \frac{1}{2} a^{-3} \exp\left(-\frac{\hat{\sigma}^2}{2.3}\right) \quad (\text{A.4})$$

Within the EGDM, the (exact) expression for the cross-over density is [19]

$$p_{\text{cross-over,EGDM}} = \frac{1}{2} a^{-3} \exp\left(-\frac{\hat{\sigma}^2}{2}\right) \quad (\text{A.5})$$

The basic assumption made in the derivation of the latter expression (Eq. (13) in Appendix A of Ref. [19]) is that at the cross-over density the carriers that contribute to the mobility still occupy predominantly states within the tail of the Gaussian density of states (DOS), so that only hops

<sup>2</sup> The results obtained for less-ideal  $a - \sigma$  combinations, given in Table 1, show how an uncertainty in  $\sigma$  is correlated to an uncertainty in  $a$ .

that involve a large increase in energy, towards a rather high effective transport level, contribute significantly to the mobility. Our calculations show that this assumption is not strictly true anymore for the ECDM.

At very high carrier-densities, the calculations reveal a weakening of the density dependence, and even a small decrease. We have not attempted to make a detailed fit to the density dependence of the mobility in this transport regime. Instead, we have introduced a cutoff carrier-density,  $p_{\text{cutoff}} = 0.025/a^3$ , above which the mobility is taken to be constant (Eq. (A.2)). We note that above densities of approximately 0.01–0.1 per site, the precision of the methods used is expected to be somewhat lowered due to the neglect of the long-range part of the Coulomb interaction [29]. For applications to single-layer OLEDs, such as discussed in Section 4, this uncertainty is in practice of little importance, as in such devices high carrier-densities occur only in very thin regions near one or both electrodes. Even a relatively large uncertainty in the (high) conductivity of the organic layers in these thin regions is of little influence on the calculated  $J(V)$  characteristics.

The field-dependent mobility-enhancement function  $f(T, E_{\text{red}}, p)$  is expressed in terms of the reduced field,  $E_{\text{red}}$ . Within the low-field regime, we distinguish two sub-regimes. In the very-small-field regime, defined as  $0 \leq E_{\text{red}} < 0.16 \equiv E_{\text{red}}^*$ , forward and backward hops contribute to the mobility. For larger fields, the presence of the electric-field makes the (negative) contribution to the mobility from backward hops already insignificant. In the main text we have called this the Poole-Frenkel (PF) regime. The mobility-enhancement function is then parameterized as

$$f(T, E_{\text{red}}, p) = \exp \left[ h(E_{\text{red}}) (1.05 - 1.2(pa^3)^{r(\hat{\sigma})}) (\hat{\sigma}^{3/2} - 2) \right. \\ \left. (\sqrt{1 + 2E_{\text{red}}} - 1) \right], \quad (\text{A.6})$$

with

$$r(\hat{\sigma}) = 0.7\hat{\sigma}^{-0.7}, \quad (\text{A.7})$$

and  $h(E_{\text{red}}) = 1$ . Within the very-low-field regime, the derivative of the mobility with respect to the field should vanish at zero field. This is accomplished in a phenomenological way by using Eq. (A.6) with

$$h(E_{\text{red}}) = \frac{4}{3} \frac{E_{\text{red}}}{E_{\text{red}}^*} \text{ for } E_{\text{red}} \leq E_{\text{red}}^*/2, \quad (\text{A.8})$$

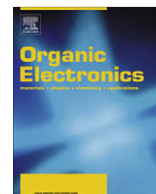
and

$$h(E_{\text{red}}) = \left[ 1 - \frac{4}{3} \left( \frac{E_{\text{red}}}{E_{\text{red}}^*} - 1 \right)^2 \right] \text{ for } E_{\text{red}}^*/2 \leq E_{\text{red}} \leq E_{\text{red}}^*. \quad (\text{A.9})$$

The function  $h(E_{\text{red}})$  is continuous and differentiable for all values of  $E_{\text{red}}$ , so that also  $f(T, E_{\text{red}}, p)$  and  $\mu(T, p, E_{\text{red}})$  are continuous and differentiable.

## References

- [1] C.W. Tang, S.A. van Slyke, Appl. Phys. Lett. 51 (1987) 913.
- [2] J.H. Burroughes, D.D.C. Bradley, A.R. Brown, R.N. Marks, K. Mackay, R.H. Friend, P.L. Burns, A.B. Holmes, Nature (London) 347 (1990) 539.
- [3] A.R. Brown, C.P. Jarrett, D.M. de Leeuw, M. Matters, Synth. Met. 88 (1997) 37.
- [4] G. Yu, J. Gao, J.C. Hummelen, F. Wudl, A.J. Heeger, Science 270 (1995) 1789.
- [5] L. Pautmeier, R. Richert, H. Bässler, Synth. Met. 37 (1990) 271.
- [6] H. Bässler, Phys. Stat. Sol. (b) 175 (1993) 15.
- [7] Y.N. Gartstein, E.M. Conwell, Chem. Phys. Lett. 245 (1995) 351.
- [8] D.H. Dunlap, P.E. Parris, V.M. Kenkre, Phys. Rev. Lett. 77 (1996) 542.
- [9] S.V. Novikov, D.H. Dunlap, V.M. Kenkre, P.E. Parris, A.V. Vannikov, Phys. Rev. Lett. 81 (1998) 4472.
- [10] Z.G. Yu, D.L. Smith, A. Saxena, R.L. Martin, A.R. Bishop, Phys. Rev. Lett. 84 (2000) 721.
- [11] Y. Preezant, N. Tessler, Phys. Rev. B 74 (2006) 235202.
- [12] P.W.M. Blom, M.J.M. de Jong, M.G. van Munster, Phys. Rev. B 55 (1997) R656.
- [13] M.C.J.M. Vissenberg, M. Matters, Phys. Rev. B 57 (1998) 12964.
- [14] C. Tanase, E.J. Meijer, P.W.M. Blom, D.M. de Leeuw, Phys. Rev. Lett. 91 (2003) 216601; C. Tanase, P.W.M. Blom, D.M. de Leeuw, Phys. Rev. B 70 (2004) 193202.
- [15] P.W.M. Blom, C. Tanase, D.M. de Leeuw, R. Coehoorn, Appl. Phys. Lett. 86 (2005) 092105.
- [16] S.L.M. van Mensfoort, S.I.E. Vulto, R.A.J. Janssen, R. Coehoorn, Phys. Rev. B 78 (2008) 085208.
- [17] Y. Roichman, N. Tessler, Synth. Met. 135 (2003) 443.
- [18] W.F. Pasveer, J. Cottaar, C. Tanase, R. Coehoorn, P.A. Bobbert, P.W.M. Blom, D.M. de Leeuw, M.A.J. Michels, Phys. Rev. Lett. 94 (2005) 206601.
- [19] R. Coehoorn, W.F. Pasveer, P.A. Bobbert, M.A.J. Michels, Phys. Rev. B 72 (2005) 155206.
- [20] A. Miller, E. Abrahams, Phys. Rev. 120 (1960) 745.
- [21] H.C.F. Martens, I.N. Huela, I. Romijn, H.B. Brom, W.F. Pasveer, M.A.J. Michels, Phys. Rev. B 67 (2003) 121203.
- [22] S.V. Novikov, A.V. Vannikov, JETP 79 (1994) 482.
- [23] R.H. Young, Philos. Mag. B 72 (1995) 435.
- [24] V. Ambegaokar, B.I. Halperin, J.S. Langer, Phys. Rev. B 4 (1971) 2612.
- [25] S.D. Baranovskii, O. Rubel, P. Thomas, Thin Solid Films 487 (2005) 2.
- [26] P.E. Parris, D.H. Dunlap, V.M. Kenkre, Phys. Stat. Sol. (b) 218 (2000) 47.
- [27] S.L.M. van Mensfoort, R. Coehoorn, Phys. Rev. B 78 (2008) 085207.
- [28] A. Kahn, N. Koch, W. Gao, J. Polym. Sci. B 41 (2003) 2529.
- [29] J. Zhou, Y.C. Zhou, J.M. Zhao, C.Q. Wu, X.M. Ding, X.Y. Hou, Phys. Rev. B 75 (2007) 153201.



# Exciton sensitive microscopy of anthracene monolayers on Si(1 1 1)

Niemma M. Buckanie, Frank-J. Meyer zu Heringdorf\*

Universität Duisburg-Essen, FB Physik and Center for Nanointegration Duisburg-Essen (CeNIDE), Lotharstrasse 1, 47057 Duisburg, Germany

## ARTICLE INFO

### Article history:

Received 29 April 2008

Received in revised form 14 January 2009

Accepted 14 January 2009

Available online 22 January 2009

### PACS:

71.35.Cc

79.60.Dp

68.37.Xy

### Keywords:

Anthracene

Photoemission microscopy

Two photon photoemission

## ABSTRACT

Thin anthracene films were studied with photoemission electron microscopy, using both a Hg discharge lamp and a femtosecond Ti:Sapphire laser for generation of the photoelectrons. In threshold photoemission, under illumination of the surface with the Hg lamp, anthracene islands appear dark due to the high work function of anthracene. Under illumination with frequency doubled femtosecond laser pulses ( $\lambda = 400$  nm) two photon photoemission takes place, and the anthracene islands each exhibit a characteristic brightness. We find that the brightness of the islands in two photon photoemission (2PPE) is modulated by the  $S_1$ -exciton in anthracene that serves as the intermediate state in 2PPE. Whenever the  $\vec{b}$ -axis of the unit cell within a particular anthracene island is aligned with the in-plane component of the electric field of the laser pulses, the island exhibits a maximal two photon photoemission yield. Based on exciton sensitive microscopy we find that the orientation of molecules in each island is different and that the anthracene film as a whole is textured.

© 2009 Elsevier B.V. All rights reserved.

## 1. Introduction

The technological improvements of organic light emitting devices (OLEDs) [1] have been very rapid in recent years, with the first applications in flat-panel displays already on the market [2]. Light that is emitted from such OLED displays originates from exciton states inside the emissive organic layer. Light is emitted whenever the exciton's electron and hole recombine. Accordingly, the wavelength of the device is determined by the energy of the exciton. Furthermore, the molecular ordering, the grain size distribution, and grain boundaries in the active layers play a crucial role for transport of the charge carriers into the recombination zone and affect the efficiency of the recombination process. The morphology and composition of the films will thus ultimately limit the device's performance [3].

Some of the organic semiconductors that have successfully been used in blue OLEDs are anthracene ( $C_{14}H_{10}$ ) and

its derivatives [4–6]. Anthracene is a polycyclic aromatic hydrocarbon that consists of three linearly fused aromatic rings. In our previous work we have studied the growth of anthracene on Si(111) [7] and demonstrated that under suitable deposition conditions, large and textured anthracene films could be grown. In contrast, here we address the interplay of the morphology of monolayer thin anthracene films with electronic excitations of the molecule. Anthracene exhibits several excitonic states that are closely linked to the crystal lattice. Studying of the interplay of morphology and excitons in anthracene will provide a better understanding of the underlying OLED action in anthracene and add to our knowledge of excited electronic states in polyacenes in general. The lowest energy exciton in bulk anthracene is a singlet state with an excitation energy of  $E \approx 3.1$  eV [8]. In the present work we use femtosecond laser pulses with a wavelength appropriate to excite the singlet exciton in monolayer thin anthracene films, and we use nonlinear photoemission microscopy (PEEM) to directly image the occupied singlet exciton in individual anthracene islands. The contrast in PEEM is in this case based on a two photon photoemission (2PPE)

\* Corresponding author.

E-mail addresses: [niemma.buckanie@uni-due.de](mailto:niemma.buckanie@uni-due.de) (N.M. Buckanie), [meyerzh@uni-due.de](mailto:meyerzh@uni-due.de) (F.-J. Meyer zu Heringdorf).

process, as the photon energy of the  $\lambda = 400$  nm fs-laser pulses is not sufficient for threshold photoemission from the highest occupied molecular orbital (the ionization potential of bulk anthracene is 5.65 eV [9]).

First attempts to understand the nature of the 2PPE process in anthracene were already performed in the 1960s [10] with spatially averaging 2PPE spectroscopy in anthracene bulk crystals, and the singlet exciton was identified as the responsible intermediate state. The 2PPE process is since then believed to originate from a two-exciton excitation that decays into a free electron. Exploitation of the 2PPE process in PEEM to directly observe the exciton in a heterogeneous and polycrystalline film, however, has not been attempted until now.

## 2. Experimental

The 2PPE PEEM experiments were performed in the ultra high vacuum (UHV) spectroscopic photoemission electron microscope (ELMITEC PEEM III), located at the University of Duisburg-Essen. The microscope is equipped with a cooling option and allows the *in-situ* growth of anthracene thin films inside the microscope. The high vapor pressure of anthracene ( $\sim 10^{-7}$  mbar at RT [11]) requires a growth temperature well below room temperature ( $T \approx -40$  °C). During annealing to room temperature after growth, anthracene re-evaporates from the surface, and accordingly, all images shown here were recorded at the low deposition temperature.

Anthracene (Sigma–Aldrich, zone-refined, 99%) was deposited from a resistively heated ceramic crucible after degassing of the source material for several days. The high vapor pressure of anthracene required differential pumping of the evaporator to sustain UHV conditions during and in between the experiments.

Si samples were cut from a precision oriented Si(111) wafer, and were wiped with ethanol before mounting into the sample holder. After transfer to UHV they were degassed for at least 3–4 h at  $T \sim 500$  °C and were then repeatedly flash-annealed to  $T \sim 1250$  °C to thermally desorb the protective oxide. For the anthracene deposition the samples were cooled to about  $T \approx -40$  °C. The temperature was monitored with a thermocouple.

For threshold photoemission experiments, an ordinary Hg discharge lamp was used. For the 2PPE experiments, however, a light source with a higher photon density is needed. Femtosecond laser pulses with a pulse energy of about 9 nJ and a pulse duration of 20 fs [12] were generated by a  $\lambda = 800$  nm Ti:Sapphire laser oscillator (FEMTO-LASERS GmbH [13]). The repetition rate was 80 MHz.

The laser pulses were frequency doubled in a beta-barium-borate (BBO) crystal to yield blue light with a wavelength of  $\lambda = 400$  nm, i.e., a photon energy that matches one of the exciton energies of anthracene.

As the fs-pulses must pass through a UHV-window to reach the sample, correction of the dispersion of the pulses by two prisms [14] is mandatory. In the PEEM, we obtain  $\lambda = 400$  nm pulses with a pulse duration of  $\tau < 40$  fs, as verified by a second order interferometric pump-probe auto-correlation trace. Details of the femtosecond laser setup are published elsewhere [15].

To adjust the laser intensity, a  $\lambda/2$ -plate in combination with a Brewster polarizer was used. A second  $\lambda/2$ -plate provides control over the polarization of the pulses. Fig. 1 illustrates the definition of the polarization direction of the laser pulses with respect to the PEEM sample geometry. Due to the grazing incidence geometry of  $\phi = 74^\circ$  of the light on the sample surface, different polarizations of the laser pulses translate into electrical field components at the sample surface as follows: during the interaction of s-polarized pulses with the surface, the electric field vector  $\vec{E}$  lies completely in the surface plane. In p-polarization, the electric field of the laser pulses is parallel to the optical table and during interaction with the surface, the electric field vector has a component in the surface plane and a component perpendicular to the surface as well [16]. An important fact to consider during PEEM experiments on organic materials is the possibility of light-induced film damage [17]. Interestingly, we find that under illumination with 400 nm laser pulses the films remain stable for hours.

## 3. Results and discussion

We have previously studied the growth dynamics of anthracene thin films on Si(111) with PEEM [7]. During deposition, a covalently bound layer of flat lying molecules is formed on the surface [18]. Subsequent layers grow on top of this initial layer and form fractal-shaped islands with a fractal dimension of  $d \approx 1.6$ , indicating a diffusion limited aggregation [19] growth mechanism. It is remarkable that despite the low deposition temperatures fractals with a diameter of several tens of micrometers can be observed. As the growth dynamics, the islands shapes, and the islands sizes are similar to the case of pentacene on Si [20,17], one expects that – as in the case of pentacene – the molecules in higher layers stand upright.

Panels (a) and (b) of Fig. 2 show PEEM images of a two molecular layer high anthracene island under illumination with different light sources and compares the image con-

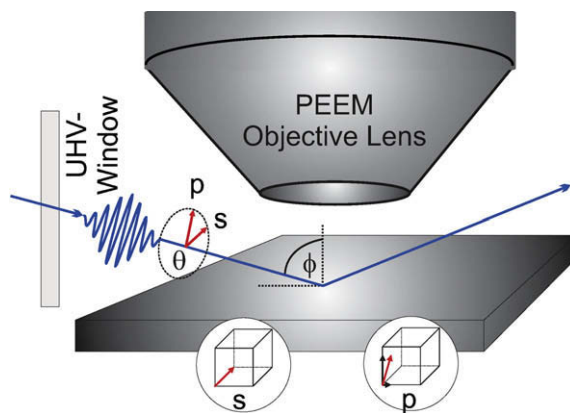


**Fig. 1.** The orientation of the laser beam relative to the objective lens of the PEEM for the 2PPE experiment and the definition of the relevant angles. The incidence angle of the laser beam on the surface is  $\phi$ . The polarization angle is  $\theta$ . In s-polarization, the electric field vector of the laser lies completely in the surface plane. In p-polarization, the electric field-vector has an in-plane and an out-of-plane component.

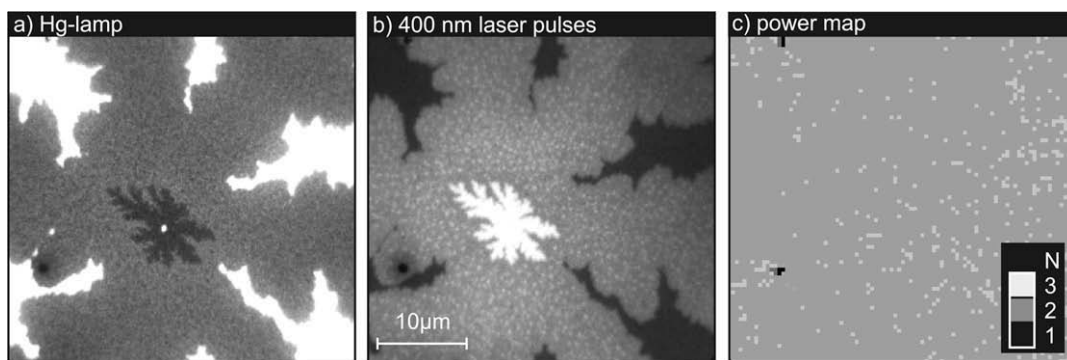


**Fig. 2.** (a) An anthracene island with the nucleating second layer imaged by the Hg discharge lamp. (b) The same island after illumination with the blue pulsed laser  $E = 3.1$  eV. (c) The determination of the emission exponent (EP) for each pixel results in a power map. The black spot that can be found on the lower left in each image resembles a damaged region on the multichannel plate of the PEEM.

trast obtained with threshold photoemission to the 2PPE case. In Fig. 2a the Hg discharge lamp was used to illuminate the sample. The layer of flat lying molecules separating the islands is over exposed, while the first and second layer of standing-up anthracene molecules appear dark, with weak contrast. We speculate that during the formation of the first layers the surface dipole varies and thus causes the observed reduction of the brightness for higher layers. If the surface is illuminated with  $\lambda = 400$  nm fs-laser pulses, the situation is completely different, as displayed in panel (b) of Fig. 2. Here, the layer of flat lying molecules appears darker than higher layers. Also, the brightness of the islands increases with the film thickness.

To investigate the photoemission process, we record the photoelectron yield  $Y$  as a function of the laser intensity  $I$ , that is expected to follow a power law [21]:

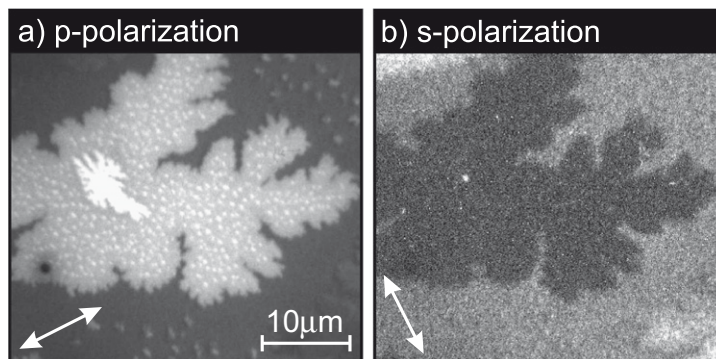
$$Y \sim I^N, \quad (1)$$

where  $N$  reflects the order of the photoemission process and is a measure of how many photons are needed to generate one photoelectron. For a 2PPE process,  $N = 2$  is expected. Furthermore, to verify that the order of the photoemission mechanism is homogeneous throughout the observed area on the surface, we record images at different laser intensities and determine  $N$  for every pixel of

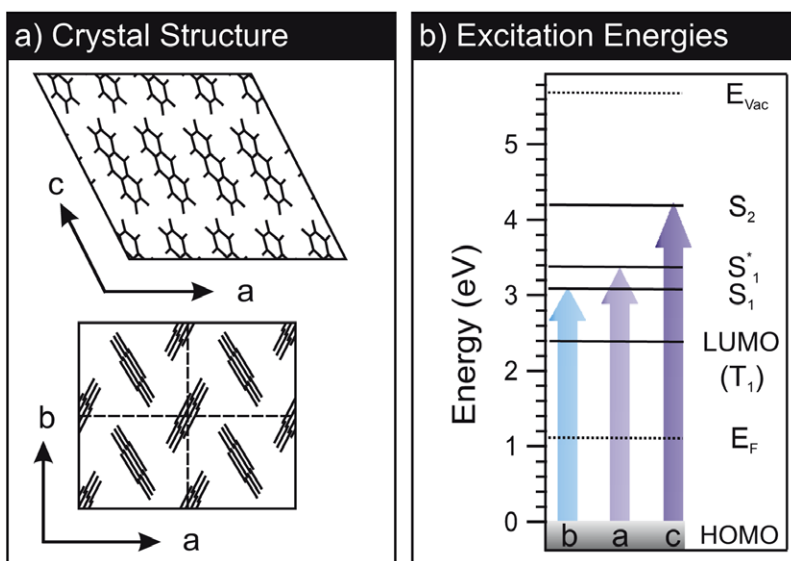
the image. The resulting power map [22] in panel (c) of Fig. 2 displays the value of  $N$  as a function of the film's morphology. Except some noise (and a burnt spot in the imaging channel plate), no morphological features of panel (b) are visible in panel (c) and we find  $N = 2$  for all areas of the surface. We conclude that we indeed observe a 2PPE process in all areas on the surface and that – based on the photon energy of the laser pulses of 3.1 eV – the anthracene singlet exciton is the intermediate state for the 2PPE process in the bright islands.

Fig. 3 shows two images of the same anthracene island under different polarization of the laser pulses (see Fig. 1 for a definition of the polarization directions). In panel (a) of Fig. 3, the surface is illuminated with p-polarized laser pulses. The monolayer-height island is bright, and even a  $10 \mu\text{m}$  large second layer island is visible. Also, many small islands exist that can be found on both the substrate and the larger islands. These islands nucleate from the residual gas during the measurement, as the cooling is still running, the sample temperature is still decreasing, and the vacuum in the chamber is only slowly recovering from the higher anthracene partial pressure during the deposition.

In panel (b) of Fig. 3 the surface is shown under illumination with s-polarized laser pulses. In comparison to



**Fig. 3.** Two images of the identical anthracene island recorded with (a) p-polarized and (b) s-polarized laser pulses. The gray scale of the two images has been adjusted to obtain maximum contrast. The arrows at the bottom left of the panels indicate the direction of the in-plane component of the exciting electric field vector of the laser pulses.



**Fig. 4.** (a) Sketch of the orientation of anthracene molecules within the unit cell [23] and (b) the exciton energies for optical excitation in the principal directions of the unit cell [24]. Letters (a)–(c) represent excitations along the three unit cell vectors from (a).

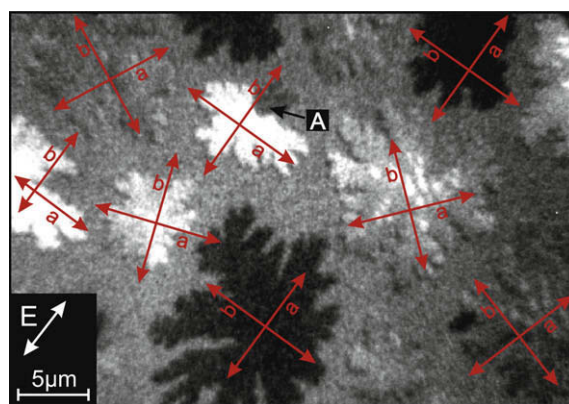
panel (a), in which the same area on the surface is displayed, the contrast is inverted: the island is now dark and the second layer on top of the island is hardly visible.

Fig. 4 shows the orientation of anthracene molecules within the unit cell and the energetic levels of the excitons in the principal directions of the crystal lattice for bulk anthracene, with data from the literature [23,24]. In the bulk, anthracene forms monoclinic crystals [25] with two molecules per unit cell (Fig. 4a). The angle between the  $\vec{a}$ - and the  $\vec{b}$ -axis is  $\gamma = 90^\circ$  and the molecules form a herringbone stacking where the long axis of the molecules is almost aligned with the  $\vec{c}$ -axis. That the molecules stand up on the surface [7] implies that the  $\vec{a}$ - and  $\vec{b}$ -axis lie within the surface plane, while the  $\vec{c}$ -axis sticks out of the surface. More precisely, the  $\vec{c}$ -axis stands perpendicularly on the  $\vec{b}$ -axis and forms the monoclinic angle of  $\beta = 124.7^\circ$  [26] with the  $\vec{a}$ -axis.

The exciton levels for bulk anthracene are sketched in Fig. 4b. The first singlet exciton  $S_1$  is located at  $E = 3.1$  eV [27], which matches exactly the photon energy of the laser pulses in our experiments. The  $S_1$  exciton, however, can only be excited by an electric field that is aligned with the  $\vec{b}$ -axis of the anthracene unit cell [28]. Excitation with fields aligned with the  $\vec{a}$ - or  $\vec{c}$ -axis would require light with an energy of  $E = 3.3$  eV [29] or  $E = 4.2$  eV ( $S_2$ -exciton) [28], respectively. Obviously, as the photon energy of our illumination source is insufficient to create an excitation along the  $\vec{a}$ - or the  $\vec{c}$ -axis, only the  $S_1$  exciton can be excited by the laser pulses. As such excitation requires an electric field along the  $\vec{b}$ -axis, the island brightness in PEEM is a measure of the projection of the exciting electric field of the laser pulse on the  $\vec{b}$ -axis of the island. By the knowledge of the polarization of the laser pulses, one can thus determine the orientation of the  $\vec{b}$ -axis within the unit cell and from this conclude the azimuthal orientation of each island. This is a powerful *in-situ* method for the determina-

tion of the orientation of molecules in textured anthracene films.

Fig. 5 shows an image of several anthracene islands under illumination with p-polarized laser pulses. The islands display different brightnesses that vary from black to white and go through different gray levels. The brightness, however, is homogeneous throughout each island, and inhomogeneities of the brightness within one island are caused exclusively by nucleation of higher layers on top of the islands, or by coalescence of islands of different orientations, as in marked as feature "A" in Fig. 5. Using our



**Fig. 5.** Determination of the molecular orientation of individual anthracene islands. The in-plane component of the electric field of the laser pulse that was used to record the image is indicated at the lower left. Various orientations of the in-plane component of the electric field vector of the laser pulses were used to determine the orientation of the unit cell vectors for the islands. In all islands, the molecules are standing up on the surface. Feature A marks a grain boundary between two islands with different orientations that was formed by coalescence of two anthracene islands during growth.

argument that the photoemission yield reflects the projection of the electric field vector on the  $\vec{b}$ -axis of the crystal, we conclude that the islands are mono crystalline and that within each island the orientation of the molecules is the same, while the molecular orientation differs from island to island. For the brightest islands the orientation of the molecules is such that the  $\vec{b}$ -axis of the unit cell is aligned with the in-plane component of the exciting electric field. If, on the other hand, the  $\vec{b}$ -axis of the crystal and the in-plane component of the exciting electric field are perpendicular to each other, the islands appear black. In Fig. 5 the orientations of the unit cells of the anthracene island is displayed as an overlay. We will now describe how the orientation of the  $\vec{b}$ -axis of the unit cell – as plotted in the overlay of Fig. 5 – can be determined from the polarization dependence of each anthracene island.

Fig. 6 shows the 2PPE yield of a selected anthracene island as a function of the polarization angle  $\theta$  of the laser pulses. To explain the polarization dependence of the yield curve, we have to consider three contributions. First, we have to consider the number of photons that are absorbed by the sample under our experimental conditions. This number varies with both the polarization angle  $\theta$ , and the (fixed) incidence angle of the light on the surface  $\phi \approx 74^\circ$ . As can be easily calculated from the dielectric function of Si,  $\phi$  is close to the Brewster angle of Si, and depending on the polarization of the laser pulses, a big portion of the light is simply reflected. The reflectivity reaches its maximum for s-polarization, because in this case the entire electric field lies within the sample surface. As a result, the integral intensity of images recorded with s-polarized light is always lower than the intensity of images recorded with other polarizations. Because for p-polarization ( $\theta = 0$ ) the Brewster reflectivity is low, the 2PPE yield is high. During any variation of the polarization angle  $\theta$ , the 2PPE yield decreases, and images recorded with p-polarized laser pulses have the highest intensity of all. To properly obtain the orientation of the  $\vec{b}$ -axis of the unit cells within the anthracene islands, we correct the measured

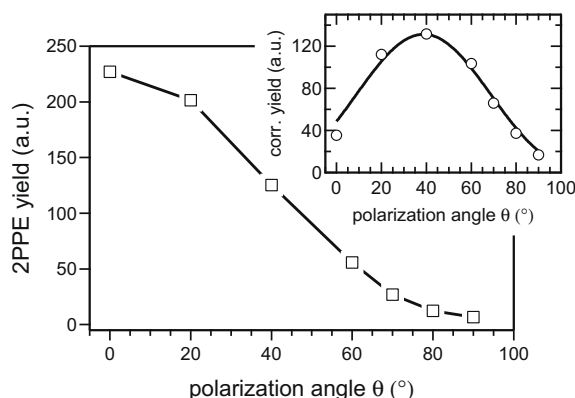


**Fig. 6.** The typical dependence of the 2PPE yield as a function of the polarization of the laser pulses. Inset: the same curve after proper background subtraction. The maximum of the curve in the inset indicates the situation where the angle  $\alpha$  between in-plane component of the exciting laser field and the  $\vec{b}$ -axis of the anthracene island is zero.

2PPE yield by subtracting the measured background intensity of the area between the islands (the 2PPE signal of the disordered layer of flat-lying molecules) from the island intensity. The result of a proper background subtraction of the island photoemission yield of Fig. 6 is shown in the inset of Fig. 6.

Second, again caused by the grazing incidence geometry, both the in-plane component and the out-of-plane component of the electric-field of the laser pulses are a function of the polarization angle  $\theta$ . For a surface in the  $(y, z)$  plane, we obtain for the projection of the electric field of the laser pulses into the  $(y, z)$  plane, i.e., for the in-plane component of the electric field vector

$$\vec{E}_{proj}(\theta, \phi) \sim (0, -\sin(\phi) \cdot \cos(\theta), \sin(\theta)). \quad (2)$$

In this notation, the  $x$ -axis is perpendicular to the substrate surface.

The third contribution to the 2PPE signal originates from the information of interest, namely the projection of the in-plane component of the electric field, as given in Eq. (2) on the  $\vec{b}$ -axis of the crystal. We obtain a maximum of the 2PPE yield, whenever the in-plane component  $\vec{E}_{proj}$  of the electric field of the laser pulses is – for a particular island – aligned with the  $\vec{b}$ -axis of the anthracene unit cell. In the other extreme, when the in-plane component of  $\vec{E}_{proj}$  is parallel to the  $\vec{a}$ -axis of the crystal (i.e., oriented perpendicularly to the  $\vec{b}$ -axis), we obtain no 2PPE signal at all.

Within this simple model, the expected photoemission signal of an anthracene island on the surface can be estimated by the knowledge of the polarization angle  $\theta$ , by the fixed incident angle  $\phi = 74^\circ$  for the projection of the laser pulses onto the surface plane, and by the angle  $\alpha$  for the projection of  $\vec{E}_{proj}$  on the  $\vec{b}$ -axis of the anthracene island. This last projection can be expressed by the scalar product  $\vec{E}_{proj} \cdot \vec{e}_b$ , where  $\vec{e}_b = (0, \cos(\alpha), \sin(\alpha))$  is a unit vector along the  $\vec{b}$ -axis of the unit cell of the anthracene island. We obtain for the 2PPE yield

$$I_{2PPE} = (E_0 \cdot (\sin(\alpha) \cdot \sin(\theta) - \cos(\theta) \cdot \sin(\phi) \cdot \cos(\alpha)))^4 \quad (3)$$

with  $E_0$  as a proportionality factor for the electric field amplitude. The inset of Fig. 6 shows the measured and background-subtracted 2PPE intensity of a one molecular layer high island (as points) with a fitted intensity curve (solid line) that is calculated using Eq. (3) with  $\alpha$  and  $E_0$  as the only free parameters. The agreement between the fit and the data points is excellent. For the particular island shown in Fig. 6, the fit of the corrected data points indicates a maximum for  $\alpha = 40^\circ$ , which allows the determination of the absolute orientation of the  $\vec{b}$ -axis of the unit cell of the anthracene island.

To analyze the distribution of the azimuthal orientation of the islands with respect to the substrate we will now perform a statistical analysis of the angle  $\alpha$  for a larger number of islands. For this purpose, small anthracene islands were grown, and for every pixel of each island the orientation of the  $\vec{b}$ -axis was determined by the procedure explained above. Each island was then assigned the average orientation angle  $\alpha$ , where the spread of the values throughout each island was used to estimate the accuracy of the method. Fig. 7 shows a histogram of the number of



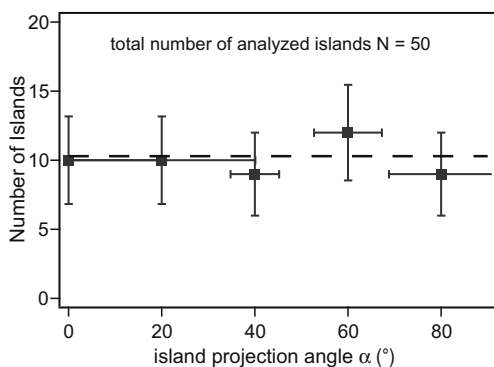


**Fig. 7.** The distribution of the number of anthracene islands that exhibit a particular projection angle  $\alpha$  after a fit with Eq. (3) of the background subtracted 2PPE data. The error bars in the x-direction are obtained from the average uncertainty of the fit of Eq. (3) for every pixel of the island. Error bars in the y-direction represent the standard deviation.

islands that exhibit a particular orientation. The featureless and homogeneous distribution curve indicates that the azimuthal orientation of the islands on the surface is completely random. Apparently, the molecular orientation in the islands is not at all influenced by the 3-fold symmetry of the Si(111) surface. The same behavior has also been observed with low energy electron diffraction for the slightly longer but similar molecule pentacene. The azimuthal degree of freedom for the islands to orient on the surface is caused by the flat-lying wetting layer of molecules that in both cases, pentacene and anthracene, lies below the fractal-shaped islands [7,20] and shields the growing layer from the substrate [30].

We will now discuss the azimuthal orientation of anthracene unit cells in higher layers with respect to the orientation of the unit cells in the layers below them. The second layer island in Fig. 3a is representative of many islands that we analyzed. In all cases, the polarization behavior, i.e., the angle  $\alpha$ , of the second layer is identical to the polarization behavior of the first layer islands on which the second layer islands are nucleated. Apparently, as the  $\vec{b}$ -axis is aligned in the same way in the first and second layer, the higher layers form an epitaxial relation with the layers below them. Such concept of an epitaxial relationship can, however, not be extended to the interaction between the anthracene islands and the substrate. As was already shown in Fig. 7, the orientation of the first layer islands with respect to the substrate is completely random.

#### 4. Conclusion

Anthracene films deposited on Si(111) appear dark in regular threshold photoemission with a Hg discharge lamp, caused by the high ionization potential of the films. In 2PPE PEEM, however, anthracene islands appear in different shades of gray, depending on the polarization of the laser pulses. The contrast in 2PPE PEEM is caused by the coupling of our  $\lambda = 400$  nm laser pulses to the  $S_1$ -exciton of the anthracene islands. The excitation of the  $S_1$  state, however, is only possible with electric fields that are aligned

with the  $\vec{b}$ -axis of the anthracene unit cell. Together with our previous PEEM studies of the anthracene growth dynamics [7], we conclude that anthracene islands on Si(111) – after a chemisorbed interfacial layer of flat-lying molecules is formed – consist of standing up molecules wherein the  $\vec{a}$ - and the  $\vec{b}$ -axis of the monoclinic anthracene unit cell is aligned within the surface plane.

The selectivity of 2PPE PEEM to the  $S_1$ -exciton, i.e., the  $\vec{b}$ -axis of the anthracene unit cell, forms the basis of a novel exciton-based contrast mechanism in 2PPE PEEM and provides a powerful *in-situ* technique for the determination of the orientation of molecules in textured anthracene films. Such information is usually not attainable with regular threshold photoemission. An important issue to be taken into consideration in the interpretation of our results, is a modification of the  $S_1$ -exciton level that may be caused by differences of the film's crystallographic properties compared to anthracene bulk. The  $S_1$ -excitation energy used in this work represents the bulk exciton value and a slight change of the energy of the  $S_1$ -exciton is not important for the interpretation of our results, as long as the exciton can be excited by  $\lambda = 400$  nm laser pulses. Using tunable fs laser sources in combination with PEEM, i.e., by using fs amplifiers and optical parametrical oscillators to generate the illuminating light, one could perform a spatially resolved *in-situ* determination of the energetics of the  $S_1$ -exciton in heterogeneous anthracene films.

Exciton sensitive PEEM shows, that the islands are randomly oriented, but that the second layer of anthracene islands has a perfect epitaxial relationship with the first layer. This implies that if one managed to build devices consisting of single anthracene islands, or if it was possible to control the orientation of the islands in the first layer, OLEDs that emit polarized light might become possible.

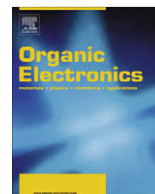
In conclusion, 2PPE PEEM is an excellent technique to directly perform microscopy on excitons in thin films, if the photon energy of the laser matches the energy of the exciton of interest. While optical transmission measurements can be used to obtain similar information [31], the use of visible light in a transmission geometry is not surface sensitive and is usually performed in a less controlled environment. In contrast, here we used femtosecond laser pulses in 2PPE PEEM and demonstrated the capability to perform exciton-sensitive microscopy on molecular monolayers in a UHV environment, with video rate and even during growth. Using the combination of PEEM and femtosecond laser pulses in a pump-probe setup will provide the possibility to study exciton dynamics in single anthracene islands as a function of their size and height and will offer new insight into the interplay of the exciton dynamics and the morphological features of an organic thin film. Such investigations are currently under way.

#### Acknowledgements

We are thankful to M. Horn-von Hoegen for fruitful discussions. Financial support from the Deutsche Forschungsgemeinschaft through SFB616 "Energy Dissipation at Surfaces" is gratefully acknowledged.

## References

- [1] C.W. Tang, S.A. VanSlyke, *Applied Physics Letters* 51 (1987) 913.
- [2] <<http://www.oled.at>>, Samsung 40 inch oled tv, 20 October 2006, <<http://www.oled.at/oledtv.htm>>.
- [3] C.D. Dimitrakopoulos, A.R. Brown, A. Pomp, *Journal of Applied Physics* 80 (1996) 2501.
- [4] S.-K. Kwon, J. Heo, J.-W. Park, Y.-H. Kim, H.-Y. Oh, S.-T. Kim, *SID Symposium Digest of Technical Papers* 36 (2005) 835.
- [5] C.A. Landis, S.R. Parkin, J.E. Anthony, *Japanese Journal of Applied Physics* 44 (2005) 3921.
- [6] H. Tang, Y. Li, X. Wang, W. Wang, R. Sun, *Semiconductor Science and Technology* 22 (2007) 287.
- [7] N.M. Buckanie, F.-J. Meyer zu Heringdorf, *Surface Science* 601 (2007) 1701.
- [8] Y.H. Meyer, R. Astier, J.M. Leclercq, *The Journal of Chemical Physics* 56 (1972) 801.
- [9] L.E. Lyons, G.C. Morris, *Journal of the Chemical Society* (1960) 5192.
- [10] M. Pope, H. Kallmann, J. Giachino, *The Journal of Chemical Physics* 42 (1965) 2540.
- [11] G.R. Johnston, L.E. Lyons, *Australian Journal of Chemistry* 23 (1970) 1571.
- [12] L. Xu, G. Tempea, A. Poppe, M. Lenzner, C. Spielmann, F. Krausz, A. Stingl, K. Ferencz, *Applied Physics B* 65 (1997) 151.
- [13] Femtolasers-GmbH, Femtosecond technology, 31 October 2006, <<http://www.femtolasers.com>>.
- [14] J.D. Kafka, T. Baer, *Optics Letters* 12 (1987) 401.
- [15] F.-J. Meyer zu Heringdorf, L. Chelaru, S. Möllenbeck, D. Thien, M. Horn-von Hoegen, *Surface Science* 601 (2007) 4700.
- [16] L.I. Chelaru, M. Horn-von Hoegen, D. Thien, F.-J. Meyer zu Heringdorf, *Physical Review B* 73 (2006) 115416.
- [17] F.-J. Meyer zu Heringdorf, M. Reuter, R. Tromp, *Applied Physics A* 78 (2004) 787.
- [18] K. Okamura, Y. Hosoi, Y. Kimura, H. Ishii, M. Niwano, *Applied Surface Science* 237 (2004) 439.
- [19] T. Witten, L. Sander, *Physical Review Letters* 47 (1981) 1400.
- [20] F. Meyer zu Heringdorf, M. Reuter, R. Tromp, *Nature* 412 (2001) 517.
- [21] M. Aeschlimann, C.A. Schmittenmaer, H.E. Elsayed-Ali, R.J.D. Miller, J. Cao, Y. Gao, D.A. Mantell, *The Journal of Chemical Physics* 102 (1995) 8606.
- [22] G.H. Fecher, O. Schmidt, Y. Hwu, G. Schönhense, *Journal of Electron Spectroscopy* 126 (2002) 77.
- [23] K. Hummer, P. Puschnig, C. Ambrosch-Draxl, *Physical Review B* 67 (2003) 184105.
- [24] A.S. Davydov, *Theory of Molecular Excitons*, Plenum Press, NewYork, 1971.
- [25] S.W.H. Bragg, *Proceedings of the Physical Society* 34 (1921) 167.
- [26] J. Robertson, *Reviews of Modern Physics* 30 (1958) 155.
- [27] C.L. Braun, *Physical Review Letters* 21 (1968) 215.
- [28] M. Kobayashi, K.-I. Mizuno, A. Matsui, *Journal of the Physical Society of Japan* 58 (1989) 809.
- [29] M. Schwoerer, H.C. Wolf, *Organische Molekulare Festkoerper*, Wiley-VCH, 2005.
- [30] P. Kury, K. Roos, D. Thien, S. Möllenbeck, D. Wall, M. Horn-von Hoegen, F.-J. Meyer zu Heringdorf, *Organic Electronics* 9 (2008) 461.
- [31] J. Vrijmoeth, R.W. Stok, R. Veldman, W.A. Schoonveld, T.M. Klapwijk, *Journal of Applied Physics* 83 (1998) 3816.



# An ambipolar low band gap material based on BODIPY and EDOT

Fatih Algi<sup>a,\*</sup>, Atilla Cihaner<sup>b,\*</sup>

<sup>a</sup>Laboratory of Organic Materials (LOM), Çanakkale Onsekiz Mart University, TR-17100 Çanakkale, Turkey

<sup>b</sup>Chemistry Group, Faculty of Engineering, Atılım University, TR-06836 Ankara, Turkey

## ARTICLE INFO

### Article history:

Received 28 November 2008

Received in revised form 19 January 2009

Accepted 23 January 2009

Available online 3 February 2009

### PACS:

82.45.Wx

62.72.up

### Keywords:

Electropolymerization

Ethylendioxythiophene (EDOT)

BODIPY

## ABSTRACT

A novel donor–acceptor type conducting polymer based on BODIPY dye as acceptor and EDOT units as donor parts is synthesized electrochemically. The unique combination of BODIPY and EDOT units provides an ambipolar (n- and p-doping processes) low band gap material (**4**). This is the first example of p–n junction in an organic  $\pi$ -conjugated material where BODIPY unit is incorporated directly in the main chain. Furthermore, the polymer film exhibits electrochromic behavior upon p-doping: a color change from light violet (neutral) to indigo (oxidized).

© 2009 Elsevier B.V. All rights reserved.

## 1. Introduction

Organic  $\pi$ -conjugated materials, in particular polymers, have attracted considerable attention due to their low cost, easy processing, compatibility and tunable intrinsic properties (electronic, optical, conductivity and stability) offered by the structural design [1,2]. One of the best ways [3] to manipulate the electronic structure is combining an appropriate electron-donating moiety with an electron acceptor. This donor–acceptor strategy in the design of  $\pi$ -conjugated materials did not only allow a fine tuning of highest occupied molecular orbital (HOMO) and lowest unoccupied molecular orbital (LUMO) energy levels, band gap ( $E_g$ ) and absorption–emission spectra of the system [4–9], but also provided access to a variety of advanced technological applications in the field of sensors [10–12], nonlinear optics [13], molecular electronics [14–16], photovoltaics [17–21],

light emitting diodes (LEDs) [22–25], field effect transistors (FETs) [26–29], displays and electrochromics [30–34].

On the other hand, 4,4-difluoro-4-bora-3a,4a-diaza-s-indacene (BODIPY) dyes have found diverse use as fluorescent switches, chemosensors, artificial light harvesters, etc. due to their intriguing properties (i.e. absorption in the visible region, sharp fluorescence, thermal and photostability) [35,36]. Considering the fact that the intriguing features and the rich chemistry of BODIPY could be amplified to create viable combinations with polymerizable electroactive units, it was assumed that these materials hold promise for new applications in material science. Recently, from our endeavours in this regard, we have been able to show that a switchable multielectrochromic material which gave fast response to external stimulus could be obtained from a dithienylpyrrole bearing BODIPY unit in the backbone (**1**) (Fig. 1) [37]. Furthermore, copolymers derived from **3** represented environmentally robust electroactive materials that have multielectrochromic behaviors [38]. It is also noteworthy that BODIPY dyes can be used to enhance the nonlinear optical properties of some copolymers [39].

In an effort to extend our work [34,40–42] to the design and synthesis of BODIPY based materials, we herein wish

\* Corresponding authors. Tel.: +90 2862180018/1860; fax: +90 2862180533 (F. Algi), tel.: +90 3125868304; fax: +90 3125868091 (A. Cihaner).

E-mail addresses: [falgi@comu.edu.tr](mailto:falgi@comu.edu.tr) (F. Algi), [cihaner@atilim.edu.tr](mailto:cihaner@atilim.edu.tr) (A. Cihaner).

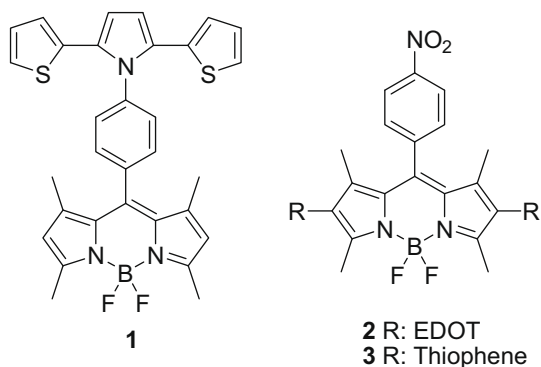


Fig. 1. BODIPY based compounds 1–3.

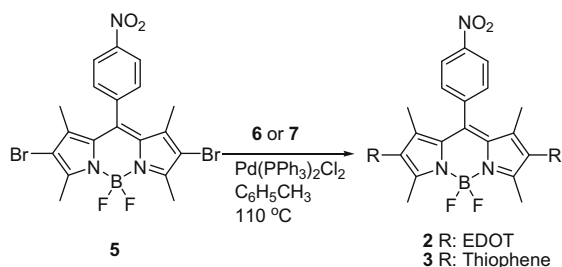
to report the synthesis and characterization of a donor–acceptor type system, **2**, consisting of BODIPY as the central acceptor unit and 3,4-ethylenedioxythiophene (EDOT) as the donor parts. EDOT was the choice as donor part due to its low oxidation potential which minimized the detrimental effect of high polymerization potentials such as the degradation of the polymer film. It is of worth to note that this unique system (**2**) provided an ambipolar [43,44] low band gap [45–55] material (**4**) by electrochemical polymerization. To the best of our knowledge, this is the first example of p–n junction in an organic  $\pi$ -conjugated material where BODIPY unit is incorporated directly in the main chain. Furthermore, the comparison of **2** with thiophene analogue **3**, and spectro-electrochemical properties of the polymer film **4** were presented.

## 2. Results and discussion

### 2.1. Synthesis and redox behavior of **2**

The syntheses of **2** and **3** were based on Stille coupling reactions of dibromo BODIPY **5** [38] with 2-(trimethylstannyl)-3,4-ethylenedioxythiophene (**6**) and 2-(trimethylstannyl)thiophene (**7**), respectively, as outlined in Scheme 1. The characterization of compounds was based on  $^1\text{H}$ ,  $^{13}\text{C}$  NMR and FTIR spectral data along with the combustion analysis.

First, the redox behavior of **2** was determined and compared to that of **3** in order to elaborate the effect of donor part in the system. Cyclic voltammetry studies revealed that both **2** and **3** exhibited amphoteric redox behaviors. As shown in Fig. 2, **2** and **3** had irreversible anodic peaks



Scheme 1. Synthesis of **2** and **3**.

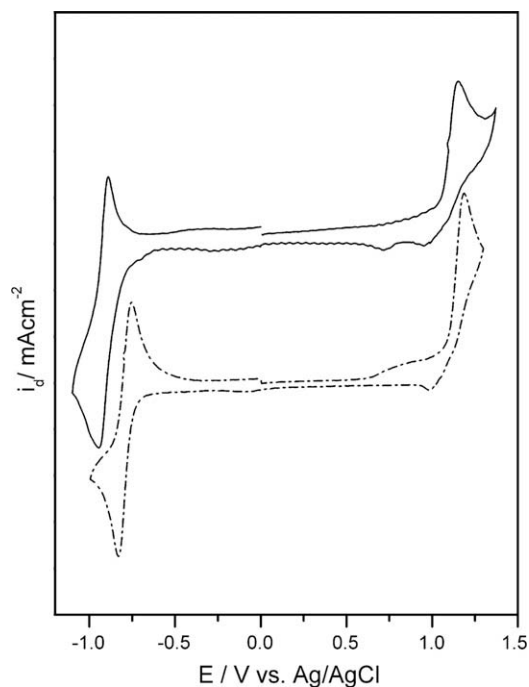


Fig. 2. Cyclic voltammogram of **2** (—) and **3** (-·-·-) in DCM/TBAH (0.1 M) at 20 °C, scan rate of 100 mV/s, Pt disk working electrode.

at 1.14 and 1.19 V, respectively, ascribed to the oxidation of the external units. As expected, **2** has somewhat lower oxidation potential than **3** due to the electron rich nature of EDOT units when compared to thiophene.

On the other hand, reversible reduction waves for the formation of radical anion of the central BODIPY units in **2** and **3** were observed in the negative side of the voltammograms at  $E_{\text{red}}^0 = -0.92$  and  $-0.79$  V, respectively [57,58]. These results suggested that the interaction between BODIPY and external units in the donor–acceptor system was in line with the electronic nature of the donor parts, since electron rich EDOT units made the reduction of BODIPY in compound **2** more difficult when compared to **3**. This interaction was also reflected by the electronic absorption spectra, which showed a bathochromic shift along with some widening of the absorption band of BODIPY (Fig. 3).

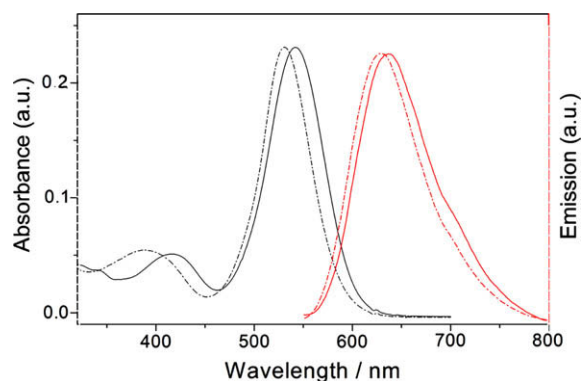
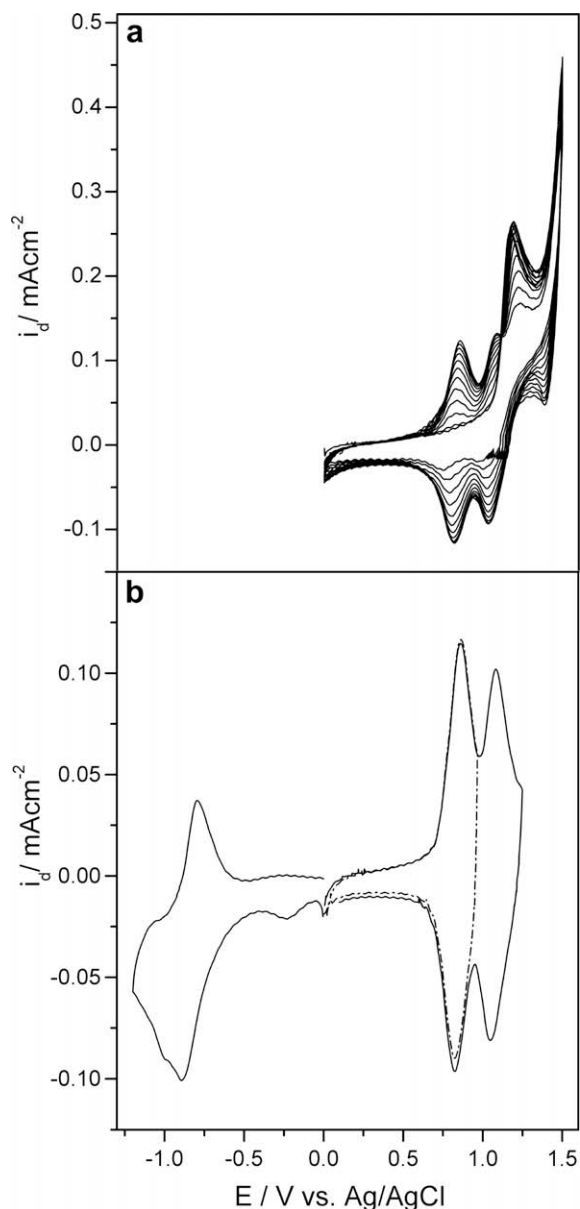
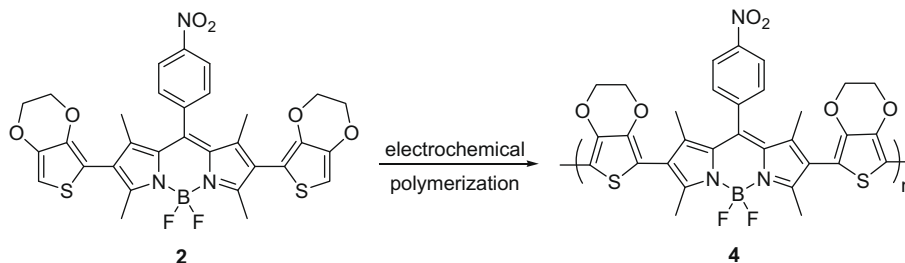


Fig. 3. Electronic absorption and emission spectra of **2** (solid line) ( $\lambda_{\text{ex}} = 540$  nm) and **3** (dash-dot-dash line) ( $\lambda_{\text{ex}} = 530$  nm) in DCM.



**Fig. 4.** (a) Repeated scan electropolymerization of **2** and (b) cyclic voltammogram of n- and p-doped polymer film of **4** in DCM/TBAH (0.1 M) at 20 °C, scan rate of 100 mV/s, Pt disk working electrode.



**Scheme 2.** Electrochemical polymerization of **2** to give **4**.

Furthermore, the emission of both compounds was also shifted to near infrared region.

## 2.2. Electropolymerization of **2**

Next, the electrochemical polymerization of the compounds was investigated. Unfortunately, all of our attempts to get the corresponding polymer film from a solution of **3** under various conditions have failed [38]. To our delight, however, the growth of a conducting polymer film on the surface of the electrode was achieved with **2** to give **4** by repetitive anodic scans which provided a gradual increase in the current density (Fig. 4a). The as-prepared polymer film was electrochemically characterized in a monomer-free electrolyte solution (Scheme 2).

Cyclic voltammogram of the polymer film exhibited two reversible and well-defined redox couples with half peak potentials ( $E_{ox}^0$ ) at +0.86 and +1.08 V (Fig. 4b). The linearity between the value of peak currents and the scan rates ( $I$ - $V$  curve) revealed a nondiffusional redox process of a well-adhered electroactive polymer film (Fig. 5). Apart from p-doping process, the polymer film was also highly active in n-doping process with a half peak potential of -0.84 V arising from the BODIPY unit which was directly conjugated with the donor parts.

It is noteworthy that the band gap ( $E_g$ ) of the polymer was found to be 1.33 eV from the onset of redox waves in the voltammogram (Fig. 4b) that made **4**, a good candidate for device applications.

## 2.3. Electro-optical properties of the polymer **4**

The electro-optical properties of the polymer film were examined by recording the changes upon doping process. First of all, the polymer film was electrodeposited on ITO electrode by repeated cyclic polymerization after which the thickness of the polymer film could be increased in each cycle without deactivation of the electrode surface. The as-prepared polymer film was switched between its redox states several times in monomer-free electrolyte solution to equilibrate the redox behavior after washing with DCM to remove the unreacted monomers and/or oligomeric species.

The polymer film **4** had a broad absorption band centered at 596 nm ( $\pi$ - $\pi^*$  transition) with a shoulder at

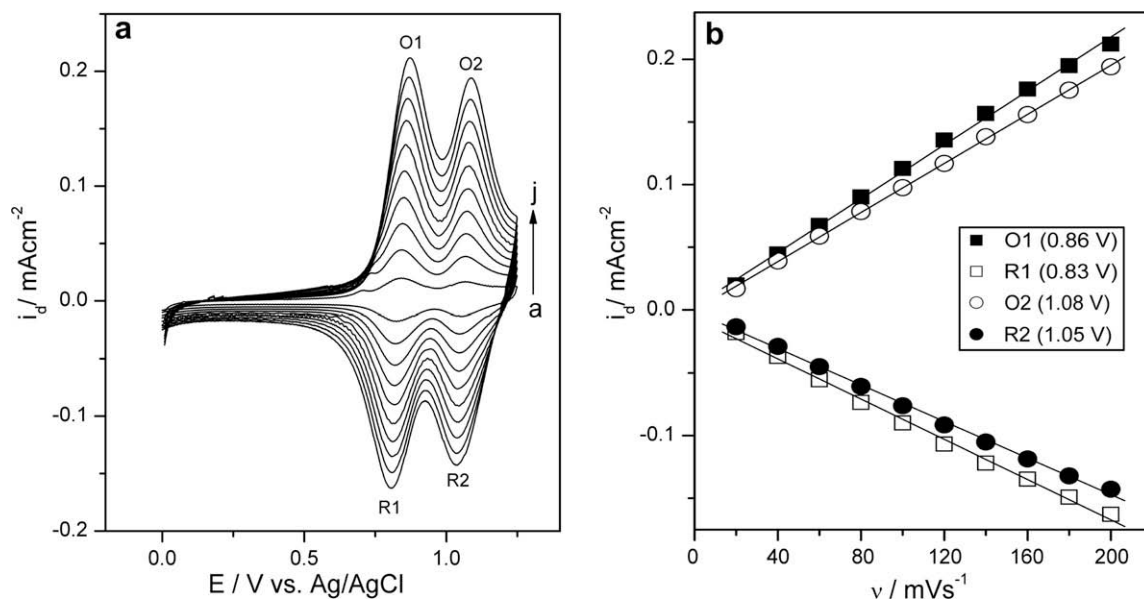


**Fig. 5.** (a) Scan rate dependence of the polymer film in 0.1 M TBAH/DCM at different scan rates, a: 20 mV/s; b: 40 mV/s; c: 60 mV/s; d: 80 mV/s; e: 100 mV/s; f: 120 mV/s; g: 140 mV/s; h: 160 mV/s; i: 180 mV/s; j: 200 mV/s. (b) Relationship of anodic and cathodic current peaks as a function of scan rate for **4** in 0.1 M TBAH/DCM.

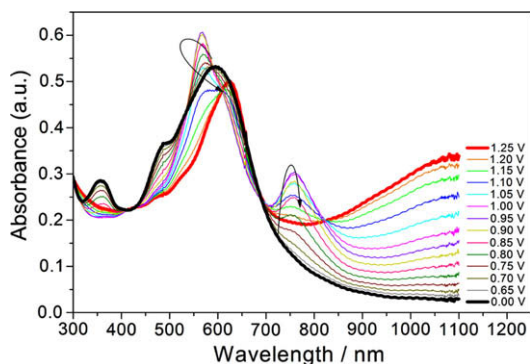


**Fig. 6.** UV-vis absorption spectra of **4** on ITO at various applied potentials between 0.0 and +1.25 V in 0.1 M TBAH/DCM.

490 nm in the neutral state (0.0 V) (Fig. 6). The UV-vis spectrum of **4** covers the whole visible region (400–930 nm) and from the onset of the end of this broad absorption band (930 nm), a band gap of 1.33 eV, which is in agreement with the  $E_g$  value obtained from the CV data (1.33 eV), was calculated for **4**.

However, it was noted that the absorption band at 596 nm shifted to a high energy level (567 nm) with a concomitant increase in intensity upon p-doping process and a new absorption band appeared at 759 nm due to the polaron formation (Fig. 6). Further oxidation shifted the  $\pi$ - $\pi^*$  transition band at 567–623 nm, which confirms the presence of BODIPY units in the polymer backbone since BODIPY units in donor-acceptor system has a band at 542 nm, and the intensity of bipolaron band (1100 nm) increased whereas the polaron band disappeared. During the p-doping process, the polymer film **4** exhibited electrochromic behavior: a color change from light violet (neutral) to indigo (oxidized).

### 3. Conclusion

In summary, a novel donor-acceptor type polymer based on BODIPY dye as acceptor and EDOT units as donor parts was synthesized electrochemically. This unique combination of BODIPY and EDOT units provided an ambipolar (n- and p-doping processes) material (**4**) which had a low band gap 1.33 eV. To our best knowledge, this is the first example of p-n junction in an organic  $\pi$ -conjugated material where BODIPY unit is incorporated directly in the main chain. Furthermore, the polymer film exhibited electrochromic behavior upon p-doping: a color change from light violet (neutral) to indigo (oxidized). Considering the fact that the intriguing features and the rich chemistry of BODIPY can be amplified to create a huge number of viable combinations, these materials hold promise for new applications in photovoltaics, LEDs, ambipolar field effect transistors, p-n junction and so forth. Efforts to get solution processable variants of **4** are currently underway in our laboratories and the results will be reported in due course.

### 4. Experimental

#### 4.1. General

All chemicals were purchased from Aldrich and used without any further purification. About 0.1 M tetrabutylammonium hexafluorophosphate (TBAH) dissolved in freshly distilled dichloromethane (DCM) was used as electrolyte solution. A platinum disk (0.02 cm<sup>2</sup>) and a platinum wire were used as working and counter electrodes, respectively, as well as Ag/AgCl in 3 M NaCl(aq) solution as a reference. Repeated electropolymerization was used to obtain polymer films and then the coated working electrode was

washed with DCM to remove unreacted monomers. In order to elaborate the electrochemical behavior of the polymer film, the coated working electrode was transferred in monomer-free electrolyte solution of 0.1 M TBAH/DCM. Indium–tin oxide (ITO, Delta Tech. 8–12  $\Omega$ , 0.7 cm  $\times$  5 cm) electrodes were used to investigate the electro-optical properties of the polymer film. In spectro-electrochemical studies, a platinum wire as counter electrode and a Ag wire as a pseudo-reference electrode (calibrated externally using 5 mM solution of ferrocene/ferrocenium couple) were used. To obtain reproducible data in electroanalytical and optical studies, the polymer films coated on Pt and/or ITO electrodes were switched between redox states several times by equilibrating the redox behavior.

NMR spectra were recorded on a Bruker NMR Spectrometer (DPX-400) in  $\text{CDCl}_3$ . Electroanalytical measurements were performed using a Gamry PCI4/300 potentiostat–galvanostat. The electro-optical spectra were monitored on a Hewlett–Packard 8453A diode array spectrometer. The syntheses of **5** were described elsewhere [38]. Organostannanes **6** and **7** were obtained from the reactions of EDOT and/or thiophene, respectively, with BuLi and trimethyltin chloride in THF by following a literature procedure [56].

#### 4.2. Representative procedure for the synthesis of **2** and **3**

To argon degassed solution of **5** (0.27 g, 0.51 mmol) and stannyl compound (**6** and/or **7**, 1.01 mmol) in dry toluene (40 mL) was added Pd( $\text{PPh}_3$ ) $\text{Cl}_2$  (0.07 g, 20% mmol) and the mixture was heated under reflux until all the starting materials were consumed (TLC). The flask was cooled and the solvent was removed under reduced pressure. The residue was filtered through a short pad of silica gel by eluting with hexane– $\text{CH}_2\text{Cl}_2$  (1:1, v/v) to give the product (**2** and/or **3**).

**1,3,5,7-tetramethyl-8-(4-nitro-phenyl)-2,6-bis(2-(3,4-ethylenedioxythienyl)-4,4-difluoroboradiaindacene (2):** 0.245 g (0.36 mmol), 71% yield, red solid, M.p. 77–79  $^\circ\text{C}$ ;  $^1\text{H}$  NMR (400 MHz,  $\text{CDCl}_3$ )  $\delta$ /ppm: 8.34 (d,  $J = 8.5$  Hz, 2H), 7.59 (d,  $J = 8.5$  Hz, 2H), 6.38 (s, 2H), 4.18 (bs, 8H), 2.57 (s, 6H), 1.33 (s, 6H);  $^{13}\text{C}$  NMR (100 MHz,  $\text{CDCl}_3$ )  $\delta$ /ppm: 157.0, 148.4, 142.0, 141.5, 140.9, 138.8, 138.7, 129.8, 124.4, 121.4, 107.5, 99.7, 64.6, 64.4, 39.3, 23.3; FTIR/ $\text{cm}^{-1}$ : 675, 728, 777, 854, 886, 905, 971, 1010, 1068, 1177, 1230, 1313, 1361, 1384, 1437, 1529, 2873, 2922, 2991, 3107; UV–vis ( $\lambda_{\text{max}}$ , nm): 417, 542; Anal. Calcd. for  $\text{C}_{31}\text{H}_{26}\text{BF}_2\text{N}_3\text{O}_6\text{S}_2$ : C, 57.33; H, 4.03; N, 6.47; S, 9.87. Found: C, 57.28; H, 4.01; N, 6.45; S, 9.80.

**1,3,5,7-tetramethyl-8-(4-nitro-phenyl)-2,6-bis(2-thienyl)-4,4-difluoroboradiaindacene (3):** 0.187 g (0.35 mmol), 68% yield, dark red solid, M.p. 201–202  $^\circ\text{C}$ ;  $^1\text{H}$  NMR (400 MHz,  $\text{CDCl}_3$ )  $\delta$ /ppm: 8.40 (d,  $J = 8.5$  Hz, 2H), 7.60 (d,  $J = 8.5$  Hz, 2H), 7.37 (d,  $J = 5.2$  Hz, 2H), 7.09 (dd,  $J = 5.2$ – $3.2$  Hz, 2H), 6.86 (d,  $J = 3.2$  Hz, 2H), 2.61 (s, 6H), 1.36 (s, 6H);  $^{13}\text{C}$  NMR (100 MHz,  $\text{CDCl}_3$ )  $\delta$ /ppm: 156.7, 148.5, 142.0, 140.0, 139.0, 133.6, 130.5, 129.7, 128.8, 127.9, 127.3, 126.3, 124.5, 38.7, 13.2; FTIR/ $\text{cm}^{-1}$ : 690, 731, 842, 907, 1008, 1095, 1174, 1203, 1230, 1317, 1345, 1390, 1437, 1514, 1540, 2854, 2922, 2960, 3074; UV–vis ( $\lambda_{\text{max}}$ , nm): 388, 531; Anal. Calcd. for  $\text{C}_{27}\text{H}_{22}\text{BF}_2\text{N}_3\text{O}_2\text{S}_2$ : C, 60.79; H, 4.16;

N, 7.88; S, 12.02. Found: C, 60.73; H, 4.15; N, 7.82; S, 11.92.

#### Acknowledgement

We gratefully acknowledge the financial support from the Scientific and Technical Research Council of Turkey (TUBITAK).

#### References

- [1] S.R. Forrest, Nature 428 (2004) 911.
- [2] C. Reese, M. Roberts, M.-M. Ling, Z. Bao, Mater. Today 7 (2004) 20.
- [3] Y. Lee, S. Sadki, B. Tsuie, P. Schottland, J.R. Reynolds, Synth. Met. 119 (2001) 77.
- [4] X. Xu, S. Chen, G. Yu, C. Di, H. You, D. Ma, Y. Liu, Adv. Mater. 19 (2007) 1281.
- [5] Y. Zhu, A.P. Kulkarni, S.A. Jenekhe, Chem. Mater. 17 (2005) 5225.
- [6] C.-T. Chen, J.-S. Lin, M.V.R.K. Moturu, Y.-W. Lin, W. Yi, Y.-T. Tao, C.-H. Chen, Chem. Commun. 16 (2005) 3980.
- [7] M. Heeney, W. Zhang, D.J. Crouch, M.L. Chabiny, S. Gordeyev, R. Hamilton, S.J. Higgins, I. McCulloch, P.J. Skabara, D. Sparrowe, S. Tierney, Chem. Commun. 18 (2007) 5061.
- [8] C.J. Du Boris Jr., F. Larmat, D.J. Irvin, J.R. Reynolds, Synth. Met. 199 (2001) 321.
- [9] H.A.M. Mullekom, J.A.J.M. Vekemans, E.E. Havinga, E.W. Meijer, Chem. Eur. J. 4 (1998) 1235.
- [10] O.R. Miranda, C.-C. You, R. Phillips, I.-B. Kim, P.S. Ghosh, U.H.F. Bunz, V.M. Rotello, J. Am. Chem. Soc. 129 (2007) 9856.
- [11] A.M. Buono, I. Immediata, P. Rizzo, G.J. Guerra, J. Am. Chem. Soc. 129 (2007) 10992.
- [12] S.H. Lee, S.K. Kim, J.H. Jung, J.S. Kim, J. Org. Chem. 70 (2005) 9288.
- [13] S.J. Chung, M. Rumi, V. Alain, S. Barlow, J.V. Perry, S.R. Marder, J. Am. Chem. Soc. 127 (2005) 10844.
- [14] M. Palma, J. Levin, V. Lemaure, A. Liscio, V. Palermo, J. Cornil, Y. Geerts, M. Lehmann, P. Samori, Adv. Mater. 18 (2006) 3313.
- [15] X. Chen, Y.-M. Jeon, J.-W. Jang, L. Qin, F. Huo, W. Wei, C.A. Mirkin, J. Am. Chem. Soc. 130 (2008) 8166.
- [16] T.-L. Coi, K.-H. Lee, W.-J. Joo, S. Lee, T.-W. Lee, M.Y. Chae, J. Am. Chem. Soc. 129 (2007) 9842.
- [17] L. Schmidt-Mende, A. Fechtenkotter, K. Mullen, E. Moons, R.H. Friend, J.D. Mackenzie, Science 293 (2001) 1119.
- [18] A. Liscio, G. De Luca, F. Nolde, V. Palermo, K. Müllen, P. Samori, J. Am. Chem. Soc. 130 (2008) 780.
- [19] J.M.J. Fréchet, B.C. Thompson, Angew. Chem. Int. Ed. 47 (2008) 58.
- [20] Z.E.X. Dance, M.J. Ahrens, A.M. Vega, A.B. Ricks, D.W. McCamant, M.A. Ratner, M.R. Wasielewski, J. Am. Chem. Soc. 130 (2008) 830.
- [21] D.P. Hagberg, J.-H. Yum, H. Lee, F. De Angelis, T. Marinado, K.M. Karlsson, R. Humphry-Baker, L. Sun, A. Hagfeldt, M. Grätzel, Md.K. Nazeeruddin, J. Am. Chem. Soc. 130 (2008) 6259.
- [22] A. Goel, M. Dixit, S. Chaurasia, A. Kumar, R. Raghunandan, P.R. Maulik, R.S. Anand, Org. Lett. 10 (2008) 2553.
- [23] N.C. Greenham, S. Moratti, D.D.C. Bradley, R.H. Friend, A.B. Holmes, Nature 365 (1993) 628.
- [24] R.H. Friend, R.W. Gymer, A.B. Holmes, J.H. Burroughes, R.N. Marks, C. Taliani, D.D.C. Bradley, D.A. Dos Santos, J.L. Bredas, M. Logdlund, W.R. Salaneck, Nature 397 (1999) 121.
- [25] E.J.W. List, R. Guentner, P.S. De Freitas, U. Scherf, Adv. Mater. 14 (2002) 374.
- [26] M. Muccini, Nat. Mater. 5 (2006) 605.
- [27] P. Gao, D. Beckmann, H.N. Tsao, X. Feng, V. Enkelmann, W. Pisula, K. Müllen, Chem. Commun. (2008) 1548.
- [28] H. Usta, A. Facchetti, T.J. Marks, J. Am. Chem. Soc. 130 (2008) 8580.
- [29] C. Yang, J.Y. Kim, S. Cho, J.K. Lee, A.J. Heeger, F. Wudl, J. Am. Chem. Soc. 130 (2008) 6444.
- [30] G. Sonmez, C.K.F. Shen, Y. Rubin, F. Wudl, Angew. Chem. Int. Ed. 43 (2004) 1498.
- [31] G. Sonmez, H.B. Sonmez, C.K.F. Shen, W. Robert, Y. Rubin, F. Wudl, Macromolecules 38 (2005) 669.
- [32] P.M. Beaujuge, S. Ellinger, J.R. Reynolds, Adv. Mater. 20 (2008) 2772.
- [33] G.E. Gunbas, A. Durmus, L. Toppare, Adv. Funct. Mater. 18 (2008) 2026.
- [34] A. Cihaner, F. Algi, Adv. Funct. Mater. 18 (2008) 3583.
- [35] A. Loudet, K. Burgess, Chem. Rev. 107 (2007) 4891.
- [36] R. Ulrich, R. Ziessel, A. Harriman, Angew. Chem. Int. Ed. 46 (2007) 2.
- [37] A. Cihaner, F. Algi, Electrochim. Acta 54 (2008) 786.

- [38] A. Cihaner, F. Algi, *React. Funct. Polym.* 69 (2009) 62.
- [39] M. Zhu, L. Jiang, M. Yuan, X. Liu, C. Ouyang, H. Zheng, X. Yin, Z. Zuo, H. Liu, Y.J. Li, *Polym. Sci.: Part A: Polym. Chem.* 46 (2008) 7401.
- [40] F. Algi, A. Cihaner, *Tetrahedron Lett.* 49 (2008) 3530.
- [41] A. Cihaner, F. Algi, *Electrochim. Acta* 54 (2008) 665.
- [42] A. Cihaner, F. Algi, *Electrochim. Acta* 53 (2008) 2574.
- [43] Z.H. Li, M.S. Wong, Y. Tao, H. Fukutani, *Org. Lett.* 9 (2007) 3659.
- [44] R. Blanco, R. Gómez, C. Seoane, J.L. Segura, E. Mena-Osteritz, P. Bäuerle, *Org. Lett.* 9 (2007) 2171.
- [45] F. Wudl, M. Kobayashi, A.J. Heeger, *J. Org. Chem.* 49 (1984) 3382.
- [46] J. Roncali, *Chem. Rev.* 97 (1997) 173.
- [47] T.A. Skotheim, R.L. Elsenbaumer, J.R. Reynolds, *Handbook of Conducting Polymers*, second ed., Marcel Dekker Inc., New York, 1998.
- [48] M. Pfeiffer, K. Leo, X. Zhou, J.S. Huang, M. Hofmann, A. Wernera, J. Blochwitz-Nimoth, *Org. Electron.* 4 (2003) 89.
- [49] Y.A. Udum, A. Durmus, G.E. Gunbas, L. Toppare, *Org. Electron.* 9 (2008) 501.
- [50] M.S. Taylor, T.M. Swager, *Angew. Chem. Int. Ed.* 46 (2007) 8480.
- [51] J.P. Nietfeld, C.L. Heth, S.C. Rasmussen, *Chem. Commun.* (2008) 981.
- [52] L.B. Groenendaal, F. Jonas, D. Freitag, H. Pielartzik, J.R. Reynolds, *Adv. Mater.* 12 (2000) 481.
- [53] J. Rault-Berthelot, E. Raoult, *Adv. Mater. Opt. Electron.* 10 (2000) 267.
- [54] J. Rault-Berthelot, E. Raoult, F. Le Floch, *J. Electroanal. Chem.* 546 (2003) 29.
- [55] M. Turbiez, P. Frère, M. Allain, C. Videlot, J. Ackermann, J. Roncali, *Chem. Eur. J.* 11 (2005) 3742.
- [56] F. Wang, M.S. Wilson, R.D. Rauh, P. Schottland, B.C. Thompson, J.R. Reynolds, *Macromolecules* 33 (2000) 2083.
- [57] A. Burghart, H. Kim, M.B. Welch, L.H. Thoresen, J. Reibenspies, K. Burgess, F. Bergström, L.B.-Å. Johansson, *J. Org. Chem.* 64 (1999) 7813.
- [58] R.Y. Lai, A.J. Bard, *J. Phys. Chem. B* 107 (2003) 5036.





## Effect of fabrication process on the microstructure and the efficiency of organic light-emitting diode

Wei-Chun Lin<sup>a</sup>, Yu-Chin Lin<sup>a</sup>, Wei-Ben Wang<sup>b</sup>, Bang-Ying Yu<sup>a</sup>, Shin-ichi Iida<sup>c</sup>, Miyako Tozu<sup>c</sup>, Mao-Feng Hsu<sup>b</sup>, Jwo-Huei Jou<sup>b</sup>, Jing-Jong Shyue<sup>a,d,\*</sup>

<sup>a</sup> Research Center for Applied Sciences, Academia Sinica, Taipei 115, Taiwan, ROC

<sup>b</sup> Department of Materials Science and Engineering, National Tsing Hua University, Hsin-Chu 300, ROC

<sup>c</sup> Analysis Laboratory, ULVAC-PHI, Inc., Chigasaki 253-8522, Japan

<sup>d</sup> Department of Materials Science and Engineering, National Taiwan University, Taipei 106, ROC

### ARTICLE INFO

#### Article history:

Received 22 October 2008

Received in revised form 23 December 2008

Accepted 23 January 2009

Available online 3 February 2009

#### PACS:

81.70.Jb

85.60.Jb

85.65.+h

#### Keywords:

Organic light-emitting diode

C60 cluster ion beam

X-ray photoelectron spectrometry (XPS)

Secondary ion mass spectrometry (SIMS)

### ABSTRACT

Small molecular organic light-emitting diodes (OLEDs) can be fabricated by spin-coating and thermo-evaporation of organic materials. In this work, X-ray photoelectron spectrometry (XPS) and secondary ion mass spectrometry (SIMS) are used to examine the microstructure of emissive layers in organic LEDs prepared with different technique using *in situ* C<sub>60</sub><sup>+</sup> sputtering. It is found that the Ir-containing guest molecule is enriched at the bottom-interface and a concentration gradient results from spin-coating while the opposite molecular distribution is observed with thermo-evaporation. Such a difference in microstructure affects the carrier-injection and carrier-transportation and is key to the dramatic difference (~3.5×) in the efficiency of the resultant OLED devices.

© 2009 Elsevier B.V. All rights reserved.

## 1. Introduction

The fabrication of small molecular organic light-emitting diodes (OLEDs) can be categorized into wet- and dry-processes that consist of spin-coating and thermo-evaporation of organic materials, respectively. Typically, dry-processed devices exhibit much higher efficiency [1–5] but wet-process also draws great attention for easier fabrication. Recently, emissive layers (ELs) of highly efficient green OLEDs were fabricated with a bis[5-methyl-7-trifluoromethyl-5H-benzo(c)(1,5)naphthyridin-6-one]iridium(picolate) ((CF<sub>3</sub>BNO)<sub>2</sub>IrPLA) guest in a 4-4'-bis(car-

bazol-9-yl)biphenyl (CBP) host using these two techniques. While keeping other fabrication procedures the same, it was found that devices with the EL prepared via the wet-process yield much higher (70 lm W<sup>-1</sup>) efficiency than the dry-process counterpart (21 lm W<sup>-1</sup>) [6]. The reason to this enhancement in efficiency with wet-process needs to be examined.

Because of the high molecular weight and low decomposition temperature of the (CF<sub>3</sub>BNO)<sub>2</sub>IrPLA, it is considerably more difficult to evaporatively deposit than CBP. As a result, it is accepted that the concentration of the materials in the deposited film can be different from that of the evaporation source. In addition, during the sublimation, the vapor pressures of the molecules change with time so that the ratio of the molecules in the deposited film could change with the film thickness. In contrast, spin-coating

\* Corresponding author. Address: Research Center for Applied Sciences, Academia Sinica, Taipei 115, Taiwan, ROC. Tel.: +866 2 2789 8000x69.

E-mail address: [shyue@gate.sinica.edu.tw](mailto:shyue@gate.sinica.edu.tw) (J.-J. Shyue).

consists of drying a homogeneous solution so that homogeneous thin-film is expected. However, there is no direct evidence of the assumed distribution of molecules due to a lack of appropriate analytical techniques.

Due to its high sensitivity, XPS and SIMS are the most common techniques for studying the surface of materials. Combined with *in situ* ion sputtering, the depth-distribution of elements close to the surface can be profiled. Mono-atomic argon sputtering is the most accepted technique for removing surface contaminants and obtaining information about the depth-distribution of a species within a sample. However, this erosion technique is known to cause severe damage to organic samples and cannot be used to analyze organic materials [7]. Recently, buckminsterfullerene ( $C_{60}$ ) ion guns were used to sputter materials away for studying surface compositions [7]. Molecular dynamics (MD) calculations suggested that  $C_{60}^+$  ions are more efficient in removing material [8] and leaving behind a relatively thin damage layer [9] than monoatomic ions. Experimental results have also confirmed the reduction in surface damage using  $C_{60}^+$  sputtering compared with  $Ar^+$  sputtering [10]. The application of  $C_{60}^+$  profiling to thick organic films is further extended by concurrently applying a low-energy  $Ar^+$  ion beam [11].

Although it is found that this analysis technique causes comparable damage to inorganic specimens [12] and the damage to the specimens is fluence-dependent [13], it provides a direct method for analyzing the distribution of materials in organic electronics with high depth resolution and is adopted in this work to examine the microstructure of ELs prepared with different method. It is found that the chemical composition of the EL-blend is non-homogeneous. In particular, spin-coating yields significant phase segregation as a function of depth. The Ir-containing guest molecule was found to be enriched at the bottom-interface. For a thermally-evaporated EL, the molecular distribution was the opposite of that obtained with spin-coating. Such a graded microstructure as a result of a different fabrication process dramatically affects the charge-injection and charge-transportation [14–22]; hence, the efficiency is up to  $3.5\times$  higher with a spin-coated EL.

## 2. Experimental

### 2.1. Fabrication of EL films

In the wet-process (spin-coating),  $(CF_3BNO)_2IrPLA$  doped (16%) CBP solution was prepared by dissolving the materials in dimethoxyethane at  $80^\circ C$ . The resultant well-mixed solution was then spin-coated at 6000 rpm under nitrogen. In the dry-process (thermo-evaporation), the resultant solution prepared above was slowly dried at  $70^\circ C$  under vacuum to obtain the deposition source. This pre-mixed material was then vapor-deposited at  $2 \times 10^{-3}$  Pa.

### 2.2. ToF-SIMS measurements

The experiments were performed with a PHI TRIFT IV ToF-SIMS system. The pulsed primary ion source was  $Bi_3^{2+}$

operated at 30 kV (4 nA DC) with  $100 \mu m \times 100 \mu m$  rastering area at an incident angle of  $35^\circ$ . A flooding electron beam (28 V) was used for charge compensation. A Wien-filtered  $C_{60}^+$  sputter gun was operated at 10 kV, 3.2 nA with an incident angle of  $42^\circ$  and rastered on an area of  $1.5 mm \times 1.5 mm$ .

### 2.3. XPS measurements

The experiments were performed with a PHI 5000 VersaProbe (Chigasaki, Japan) XPS system. A micro-focused (25 W,  $100 \mu m$ )  $Al-K\alpha$  X-ray was used, and the take-off angle of the photoelectron was  $45^\circ$ . A dual-beam charge neutralizer (7 V  $Ar^+$  and 30 V flooding electron beam) was used for charge compensation. The  $Ar^+$  sputter source was operated at 0.2 kV, 300 nA with an incident angle of  $45^\circ$ . The  $C_{60}^+$  ion source was operated at 10 kV, 10 nA with an incident angle of  $70^\circ$ . Both ion beams were simultaneously rastered over an area of  $2 mm \times 2 mm$ .

The surface potential was measured with a Veeco InnoVa (Woodbury, NY) atomic force microscope using a conductive 75 kHz cantilever in the lift-mode. The magnitude of the AC on the tip is 2 V. The dipole moment was calculated with Gaussian 03 revision D.02 using the B3LYP density function theory (DFT). The LANL2DZ basis set was employed for Ir atoms, and the 6-31G\* basis set was employed for all other atoms.

## 3. Results and discussion

Using concurrent *in situ*  $C_{60}^+$  and  $Ar^+$  sputtering in XPS, Fig. 1 shows the elemental depth profile of ELs prepared with both dry- and wet-processes. In general, the intensity of Ir and C decreased with sputter time and the intensity of In increased with sputter time, indicating that the EL was removed and the ITO exposed. It is clear that the EL prepared via the dry-process is slightly thicker than via the wet-process. The integration of signal intensity throughout the sputtering revealed comparable amounts of Ir in both samples. Therefore, the EL prepared with the dry-process has a similar amount of Ir-compound compared with that prepared with the wet-process. In other word, the change

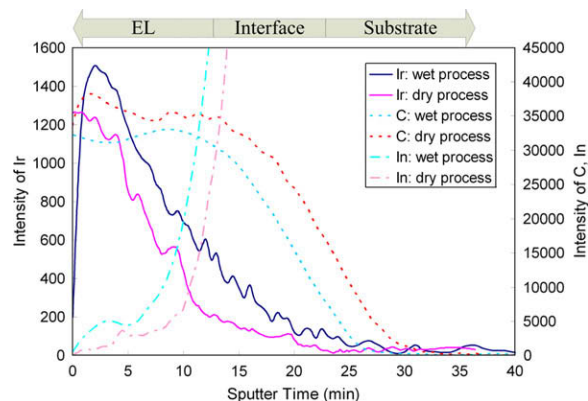
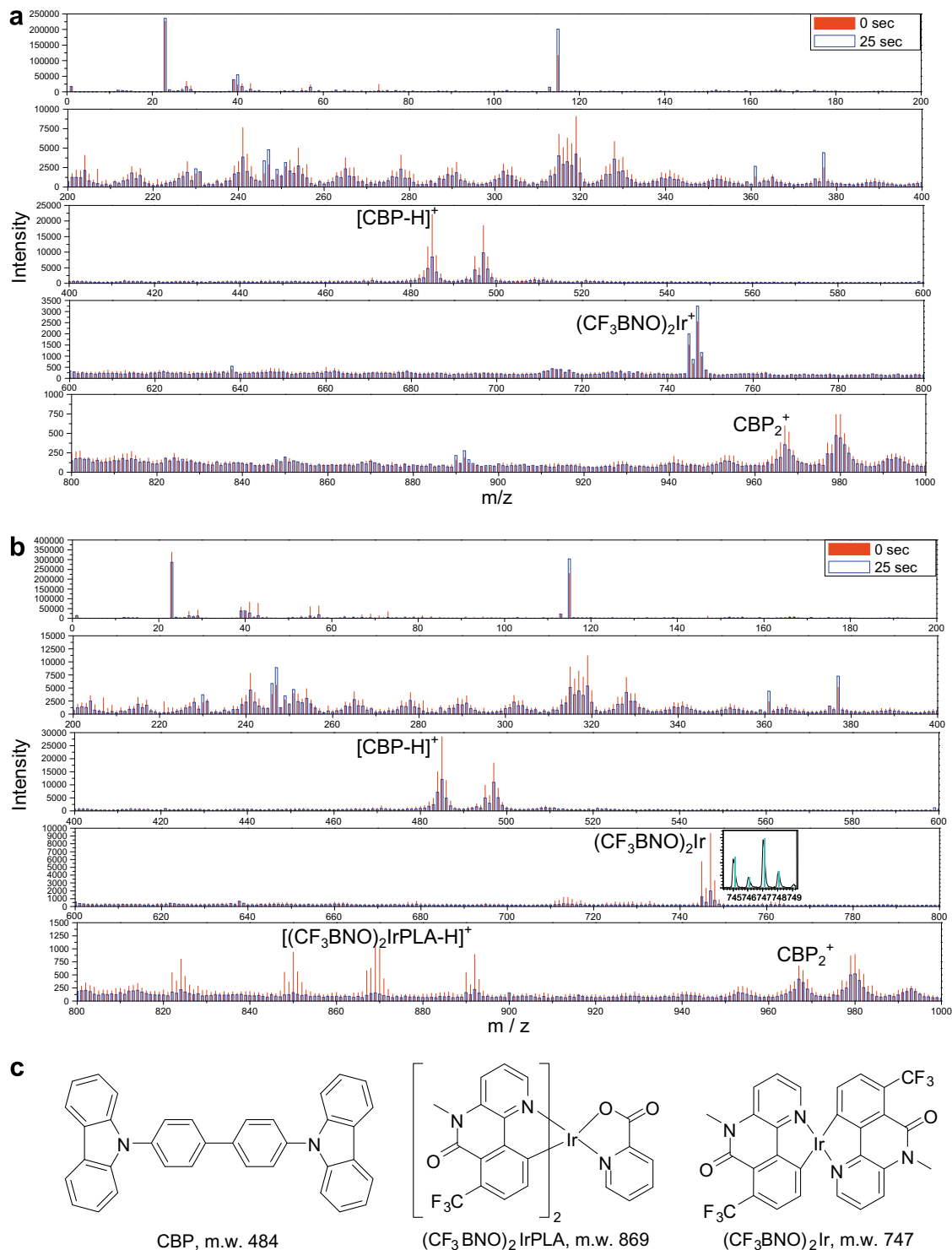


Fig. 1. XPS elemental depth profiles of emissive layers prepared with thermo-evaporation (dry-process) and spin-coating (wet-process).

in overall chemical composition due to the evaporation process is insignificant because the evaporated film and

the evaporation source, whose composition is identical to the spin-coated film, have comparable Ir-content.



**Fig. 2.** Positive ion spectra of (a) spin-coated emissive layer and (b) thermo-evaporated emissive layer after sputtering by  $C_{60}^+$  for 0 and 25 s. The enlarged pattern near  $m/z = 747$  shows the spectra with the isotopic ratio of Ir. (c) Molecular structures and fragments observed in SIMS.

Comparing the slopes of the Ir and C intensity, the steeper Ir signal of the thermo-evaporated specimen indicated that the concentration of Ir-compound is higher at the top surface. This concentration gradient could be explained by the evaporation process. Since the  $(\text{CF}_3\text{BNO})_2\text{IrPLA}$  has a higher sublimation point than CBP, the initial vapor pressure of  $(\text{CF}_3\text{BNO})_2\text{IrPLA}$  is lower. In addition, as the evaporation source losses CBP preferentially and the temperature increases during the continuous heating of the evaporation source, the relative vapor pressure of  $(\text{CF}_3\text{BNO})_2\text{IrPLA}$  increases, so the concentration of  $(\text{CF}_3\text{BNO})_2\text{IrPLA}$  is higher at the end of the evaporation process. As the result, the Ir concentration is higher at the out-most surface.

In contrast, the Ir intensity of the spin-coated specimen increased dramatically at an early stage of the profiling then decreased as the film was removed by ion sputtering. Furthermore, the Ir intensity was higher near the bottom-interface compared with the thermo-evaporated specimen. Therefore, it can be concluded that the concentration of  $(\text{CF}_3\text{BNO})_2\text{IrPLA}$  is higher at the bottom-interface and significantly lower at the top-most surface. Such a change in composition could be explained by the polarity of the molecules.

Although the wet-process consists of drying a homogeneous solution of  $(\text{CF}_3\text{BNO})_2\text{IrPLA}$  and CBP, the dipole moments of  $(\text{CF}_3\text{BNO})_2\text{IrPLA}$  and CBP are 8.5502 and 0.0022 Debye, as calculated using the density function theory (DFT). Since the substrate is polar (PEDOT:PSS coated ITO or bare ITO), the polar Ir-guests diffuse toward the bottom-interface during the drying, and non-polar CBPs migrate to the air interface. The segregation of molecules at the nano-scale thus occurs during the drying process. Similar infiltration of Ir-guest into PEDOT:PSS is reported before [23]. To further confirm the microstructure of the host-guest mixture in ELs prepared with different methods, time-of-flight SIMS (ToF-SIMS) was also used to analyze the specimen. This allowed for an examination of whether the sputtering caused damage to the remaining surface, generating artifacts in the XPS depth profile.

Fig. 2 shows secondary positive ion spectra of ELs prepared with the wet- and dry-processes, and the specimens were sputtered with  $\text{C}_{60}^+$  ions for 0 s (as-prepared EL) and 25 s (about 10 nm of the EL was removed by the ion beam at this stage). The pattern at  $m/z = 747$  matches with the natural isotopic ratio of the Ir-complex (inset in Fig. 2b) and the pattern at  $m/z = 485, 747, 869$  and  $870$  can be assigned to the  $[\text{CBP-H}]^+$ ,  $[(\text{CF}_3\text{BNO})_2\text{Ir}]^+$  fragment,  $[(\text{CF}_3\text{BNO})_2\text{IrPLA}]^+$  and  $[(\text{CF}_3\text{BNO})_2\text{IrPLA-H}]^+$ , respectively. Comparing the spectra before and after  $\text{C}_{60}^+$  ion sputtering, the overlapping pattern indicates that the damage to the molecular structure due to  $\text{C}_{60}^+$  ion sputtering is negligible. The only difference observed at different sputter stages is the relative intensity of peaks related to CBP and  $(\text{CF}_3\text{BNO})_2\text{IrPLA}$ , due to the difference in molecular ratios at different depths of the EL.

It has generally been believed that due to the high molecular-weight and low decomposition temperature, the Ir-containing guest does not easily deposit via thermo-evaporation. The major concern was that the molecular concentration of the evaporated film would be

different from its source. In addition, thermo-decomposition of molecules could occur during the evaporation process, and the EL could contain decomposed fragments that degrade its efficiency. However, comparing the SIMS spectra of ELs prepared using different methods (Fig. 2), the pattern is almost identical aside from the difference in relative intensity associated with ratios of host to guest molecules. Because the spin-coating would not alter the molecular structure or overall ratio, this result indicates that thermo-evaporated EL contains identical molecules to that of the evaporative source, and the Ir-guest was not decomposed during the evaporation. Therefore, the change in the device performance cannot be simply explained by the difficulty in depositing the Ir-guest.

Fig. 3 shows the intensity of  $[\text{CBP-H}]^+$ ,  $[(\text{CF}_3\text{BNO})_2\text{Ir}]^+$  fragment as a function of sputter time. Similar to the elemental depth-profile in XPS (Fig. 1), the enrichment of Ir-guest near the outer surface is observed with the dry-process while the amount of Ir-guest is higher near the bottom-interface with the wet-process. Moreover, the total intensity from the Ir-fragment throughout the sputtering is comparable for ELs prepared using different methods. This result confirms that the overall ratio of CBP and  $(\text{CF}_3\text{BNO})_2\text{IrPLA}$  is similar in the ELs prepared via different process.

In addition to the distribution of molecules along the depth of the EL, the planar distribution is another important factor in understanding its microstructure. Scanning electrical potential microscopy (SEPM) is used to analyze the planar distribution of the work-function. Because the work-function of CBP and  $(\text{CF}_3\text{BNO})_2\text{IrPLA}$  is 6.0 and 5.1 eV, respectively, planar segregation of materials would yield clear contrasts in the SEPM image. However, the SEPM images (Supporting Information) reveal a weak contrast on the order of mV. This result indicates that the distribution of CBP and  $(\text{CF}_3\text{BNO})_2\text{IrPLA}$  is rather uniform on the surface and the different fabrication processes do not significantly affect the planar distribution of materials.

Since the overall composition is similar for both process and the planar distribution of molecules is also similar, the dramatic difference in the device performance ( $70 \text{ lm W}^{-1}$  and  $21 \text{ lm W}^{-1}$  for wet- and dry-process, respectively [6]) can only be attributed to the difference in the microstructure.

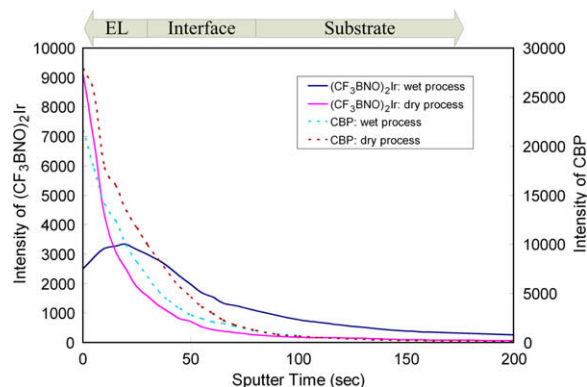
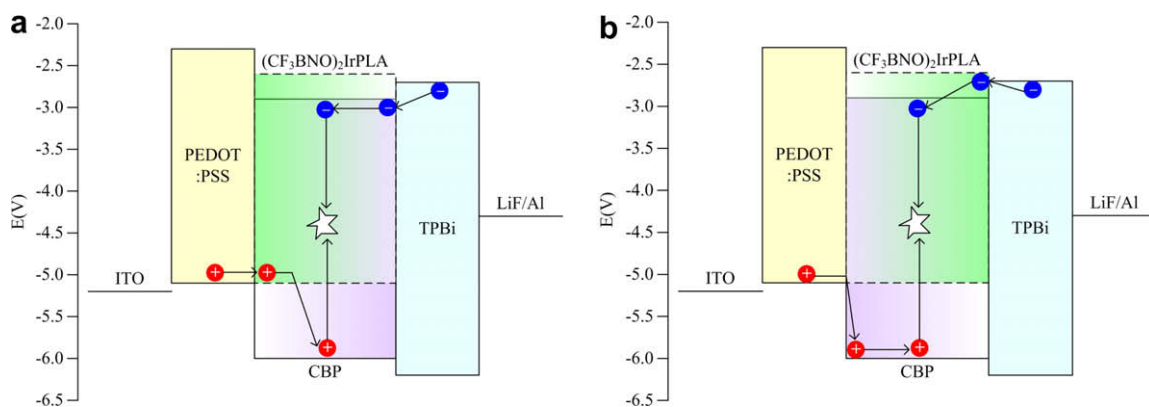


Fig. 3. ToF-SIMS depth profiles of emissive layers prepared with thermo-evaporation (dry-process) and spin-coating (wet-process).



**Fig. 4.** Energy diagram and the route of charge carriers of OLED with EL prepared with (a) wet-process and (b) dry-process. The shade of CBP and  $(\text{CF}_3\text{BNO})_2\text{IrPLA}$  indicates its relative concentration.

ture of the EL along the vertical axis, *i.e.* the depth-distribution of Ir-guest in the CBP-host. Fig. 4 shows the energy diagram of the OLED device and the route of charge-carrier that generates excitons in the host. Considering the HOMO of PEDOT:PSS,  $(\text{CF}_3\text{BNO})_2\text{IrPLA}$ , CBP, and TPBi, the enriched  $(\text{CF}_3\text{BNO})_2\text{IrPLA}$  near HTL in a spin-coated EL makes the hole easier to inject to the EL through the HOMO of the Ir-guest and can be considered as an alternative channel for hole transportation in the EL [18]. As a result, the observed turn-on voltage of spin-coated EL (3.5 V) is lower than thermo-evaporated EL (4.6 V). In addition, the hopping distance of the holes increases as the concentration of  $(\text{CF}_3\text{BNO})_2\text{IrPLA}$  decreases during the transportation toward the cathode so that holes are trapped and confined in the EL [19]. As the result, the device efficiency of a spin-coated EL is much higher ( $\sim 3.5\times$ ) than a thermo-evaporated EL.

Similarly, considering the LUMO of PEDOT:PSS,  $(\text{CF}_3\text{BNO})_2\text{IrPLA}$ , CBP, and TPBi, the graded EL also helps the electron injection to the CBP-rich interface, and the electron transport gradually decreases during the movement toward the  $(\text{CF}_3\text{BNO})_2\text{IrPLA}$ -rich interface, hence the electrons are also trapped in the EL. This enhancement in carrier-injection and carrier-transportation favors carrier-recombination in the EL and is the key to its high efficiency.

Notably, the molecular distribution of the EL prepared with the dry-process is opposite that of the wet-process. Since the energy barriers for hole-injection into CBP is higher than that for  $(\text{CF}_3\text{BNO})_2\text{IrPLA}$ , the hole injection into EL is comparatively suppressed due to the deficiency of  $(\text{CF}_3\text{BNO})_2\text{IrPLA}$  near the interface. Meanwhile, from the viewpoint of electron-injection, electrons would hardly inject into the enriched  $(\text{CF}_3\text{BNO})_2\text{IrPLA}$  because its injection barrier is higher than that of CBP. The impeded carrier-injection would then result in fewer carriers in the EL. In addition, because of the change in chemical composition, the hopping distance of carriers decreases during transportation so that they are not trapped in the EL. As the result, there will be lower carrier-recombination in the EL, hence fewer excitations, and a dramatic change in the efficiency results.

## 4. Conclusion

XPS and ToF-SIMS are used to study the microstructure of the emissive layer in an organic light-emitting diode with *in situ*  $\text{C}_{60}^+$  ion sputtering. The  $\text{C}_{60}^+$  ion sputtering has been confirmed here to cause no appreciable damage to the molecular structure of the remaining materials. It is also found that the wet-process (spin-coating) yields an EL with a significant variation in Ir-guest distribution along the depth, *i.e.* enriched Ir-guest near the bottom and deficient Ir-guest near the outer surface. For the dry-process (thermo-evaporation), the distribution of molecules is opposite to that observed with the wet-process. Such graded EL structure changes the transportation properties of charge carriers and is the key to the high-efficiency of the OLED.

## Acknowledgements

Sponsorship by Academia Sinica and Taiwan National Science Council through Grant number 97-2113-M-001-015- and 97-2120-M-002-014-.

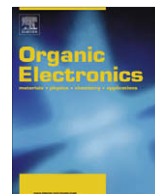
## Appendix A. Supplementary material

Supplementary data associated with this article can be found, in the online version, at [doi:10.1016/j.orgel.2009.01.013](https://doi.org/10.1016/j.orgel.2009.01.013).

## References

- [1] J.S. Huang, T. Watanabe, K. Ueno, Y. Yang, *Adv. Mater.* 19 (2007) 739.
- [2] S. Watanabe, N. Ide, J. Kido, *Jpn. J. Appl. Phys.* 46 (2007) 1186–1188.
- [3] M.H. Tsai, Y.H. Hong, C.H. Chang, H.C. Su, C.C. Wu, A. Matoliukstyte, J. Simokaitiene, S. Grigalevicius, J.V. Grazulevicius, C.P. Hsu, *Adv. Mater.* 19 (2007) 862.
- [4] E.L. Williams, K. Haavisto, J. Li, G.E. Jabbour, *Adv. Mater.* 19 (2007) 197.
- [5] J.-H. Jou, C.-C. Chen, Y.-C. Chung, M.-F. Hsu, Ching-HsuanWu, S.-M. Shen, M.-H. Wu, W.-B. Wang, Y.-C. Tsai, C.-P. Wang, J.-J. Shyue, *Adv. Func. Mater.* 18 (2008) 121–126.
- [6] J.-H. Jou, M.-F. Hsu, W.-B. Wang, C.-L. Chin, S.-Z. Chen, C.-T. Chen, Y.-C. Chung, C.-C. Chen, C.-P. Liu, C.-J. Wang, S.-M. Shen, M.-H. Wu, W.-C. Chang, W.-C. Chen, H.-Y. Chen, *Chem. Mater.*, submitted for publication.

- [7] Y.-Y. Chen, B.-Y. Yu, W.-B. Wang, M.-F. Hsu, W.-C. Lin, Y.-C. Lin, J.-H. Jou, J.-J. Shyue, *Anal. Chem.* 80 (2008) 501–505.
- [8] B. Czerwinski, R. Samson, B.J. Garrison, N. Winograd, Z. Postawa, *Vacuum* 81 (2006) 167–173.
- [9] Z. Postawa, B. Czerwinshi, M. Szewczyk, E.J. Smiley, N. Winograd, B.J. Garrison, *Anal. Chem.* 75 (2003) 4402.
- [10] B.-Y. Yu, Y.-Y. Chen, W.-C. Lin, Y.-C. Lin, J.-J. Shyue, *Appl. Surf. Sci.* 255 (2008) 2490–2493.
- [11] B.-Y. Yu, Y.-Y. Chen, W.-B. Wang, M.-F. Hsu, S.-P. Tsai, W.-C. Lin, Y.-C. Lin, J.-H. Jou, C.-W. Chu, J.-J. Shyue, *Anal. Chem.* 80 (2008) 3412–3415.
- [12] Y.-Y. Chen, Y.-C. Lin, B.-Y. Yu, W.-C. Lin, J.-J. Shyue, *Analyst* (2009), doi:10.1039/B814729A.
- [13] A.G. Shard, P.J. Brewer, F.M. Green, I.S. Gilmore, *Surf. Interface Anal.* 39 (2007) 294–298.
- [14] G.T. Lei, L.D. Wang, Q. Yong, *Jpn. J. Appl. Phys.* 43 (2004) L1226–L1228.
- [15] A. Gusso, D.G. Ma, I.A. Hummelgen, M.G.E. da Luz, *J. Appl. Phys.* 95 (2004) 2056–2062.
- [16] Y. Bai, M.A. Khan, W.Q. Zhu, X.Y. Jiang, Z.L. Zhang, *Displays* 29 (2008) 365–368.
- [17] C.W. Chen, T.Y. Cho, C.C. Wu, H.L. Yu, T.Y. Luh, *Appl. Phys. Lett.* 81 (2002) 1570–1572.
- [18] C.-H. Wu, P.-I. Shih, C.-F. Shu, Y. Chi, *Appl. Phys. Lett.* 92 (2008) 233303.
- [19] D. Ma, C.S. Lee, S.T. Lee, L.S. Hung, *Appl. Phys. Lett.* 80 (2002) 3641–3643.
- [20] A.B. Chwang, R.C. Kwong, J.J. Brown, *Appl. Phys. Lett.* 80 (2002) 725–727.
- [21] Y. Shao, Y. Yang, *Appl. Phys. Lett.* 83 (2003) 2453–2455.
- [22] Y. Shao, Y. Yang, *Adv. Func. Mater.* 15 (2005) 1781–1786.
- [23] W.-C. Lin, W.-B. Wang, Y.-C. Lin, B.-Y. Yu, Y.-Y. Chen, M.-F. Hsu, J.-H. Jou, J.-J. Shyue, *Org. Electron.* (2009), doi:10.1016/j.orgel.2009.02.012.



# Synthesis, photoluminescence and electroluminescence properties of iridium complexes with bulky carbazole dendrons

Noriaki Iguchi, Yong-Jin Pu, Ken-ichi Nakayama, Masaaki Yokoyama, Junji Kido\*

Department of Organic Device Engineering, Yamagata University, 4-3-16, Jōnan, Yonezawa, Yamagata 992-8510, Japan

## ARTICLE INFO

### Article history:

Received 17 December 2008

Received in revised form 26 January 2009

Accepted 26 January 2009

Available online 5 February 2009

### PACS:

61.66.Hq

78.55.Kz

78.60.Fi

33.50.Dq

33.50.j

### Keywords:

Phosphorescence

Dendrimer

Iridium complex

Solution process

Organic light-emitting device

## ABSTRACT

We synthesized solution-processable iridium complexes having bulky carbazole dendrons, *fac*-tris[2-(3-(3,5-bis(3,6-di-*n*-butylcarbazol-9-yl)phenyl)phenyl)pyridine]iridium (III) (mCP)<sub>3</sub>Ir and *fac*-bis[2-(3-(3,5-bis(3,6-di-*n*-butylcarbazol-9-yl)phenyl)phenyl)pyridine][2-(3-(3,5-di(4-pyridyl)phenyl)phenyl)pyridine]iridium (III) (mCP)<sub>2</sub>(bpp)Ir. Photoluminescence quantum efficiencies (PLQEs) of (mCP)<sub>3</sub>Ir and (mCP)<sub>2</sub>(bpp)Ir in their diluted solutions were 91% and 84%, respectively. They showed high PLQEs of 49% for (mCP)<sub>3</sub>Ir and 29% for (mCP)<sub>2</sub>(bpp)Ir even in a neat film. The triplet exciton energy level of the dendronized ligand (2.8 eV), 2-[3-(3,5-bis(3,6-di-*n*-butylcarbazol-9-yl)phenyl)]pyridine **10**, and the dendron (2.9 eV), 3,5-bis(3,6-di-*n*-butylcarbazol-9-yl)benzene **7**, are enough higher than that of the core complex Ir(ppy)<sub>3</sub> (2.6 eV). External quantum efficiency (EQE) of single layer light-emitting device with (mCP)<sub>2</sub>(bpp)Ir was much higher than that of (mCP)<sub>3</sub>Ir because of better affinity of (mCP)<sub>2</sub>(bpp)Ir to cathode metal. When an electron transporting and hole-blocking material was used, the EQEs of double layer devices were dramatically improved to 8.3% for (mCP)<sub>3</sub>Ir and 5.4% for (mCP)<sub>2</sub>(bpp)Ir at 100 cd/m<sup>2</sup>.

© 2009 Elsevier B.V. All rights reserved.

## 1. Introduction

Organic light-emitting devices (OLEDs) have attracted a great attention because of their potentials for next generation of flat panel displays and general lighting [1]. Solution processes such as ink-jet printing are considered to have an advantage of low cost over the vacuum process for manufacturing of large area displays or lighting.

As solution-processable materials, phosphorescent iridium dendrimer complexes have recently been reported [2]. The phosphorescent dendrimers have well-defined structures, and can be purified by general purification technique. In contrast, structural defects in polymers cannot be removed and those defects could result in poor device

stability. The phosphorescent dendrimer consists of an emitting central core and surrounding dendrons. These dendrons have roles of transporting charge carriers and suppressing intermolecular interactions between emitting iridium cores, which cause photoluminescence quenching in a neat film [3]. In addition, solubility of the dendrimer metal complexes are generally better than that of the conventional metal complexes. One of the requirements for dendron is to possess the higher triplet excited energy level than that of core complex Ir(ppy)<sub>3</sub> (2.6 eV) not to quench triplet emission from the core complex.

We previously reported on high electroluminescence efficiency of carbazole-substituted phosphorescent dendrimer complex (mCP)<sub>3</sub>Ir in solution-processed OLED [4]. In this paper, we discuss the synthesis detail of (mCP)<sub>3</sub>Ir and another novel dendrimer complex (mCP)<sub>2</sub>(bpp)Ir (Chart 1), which has carbazole dendrons in two of three ligands. The ligand has a 4-pyridine-substituted dendron to

\* Corresponding author.

E-mail address: [kid@yz.yamagata-u.ac.jp](mailto:kid@yz.yamagata-u.ac.jp) (J. Kido).

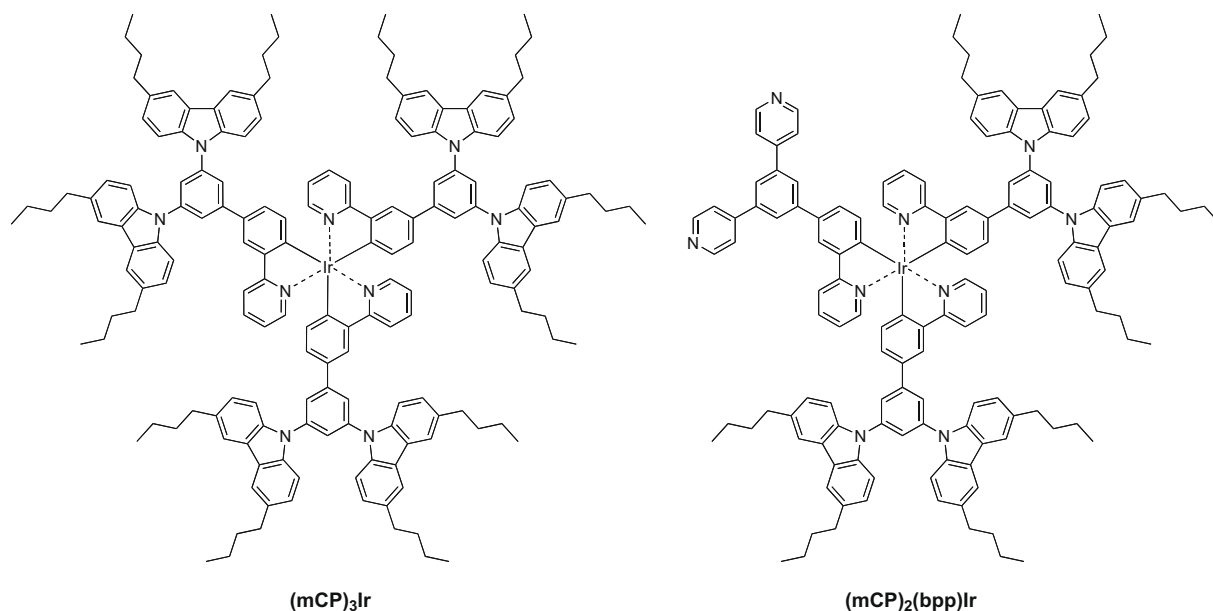


**Chart 1.** Chemical structure of (mCP)<sub>3</sub>Ir and (mCP)<sub>2</sub>(bpp)Ir.

improve electron injection from cathode metal [5]. Suppression of concentration-quenching and efficient exciton confinement by the bulky dendrons having higher triplet energy than that of Ir(ppy)<sub>3</sub> were studied. The energy level of the dendrimers and solution-processed OLED properties are also reported.

## 2. Results and discussion

### 2.1. Synthesis and thermal properties

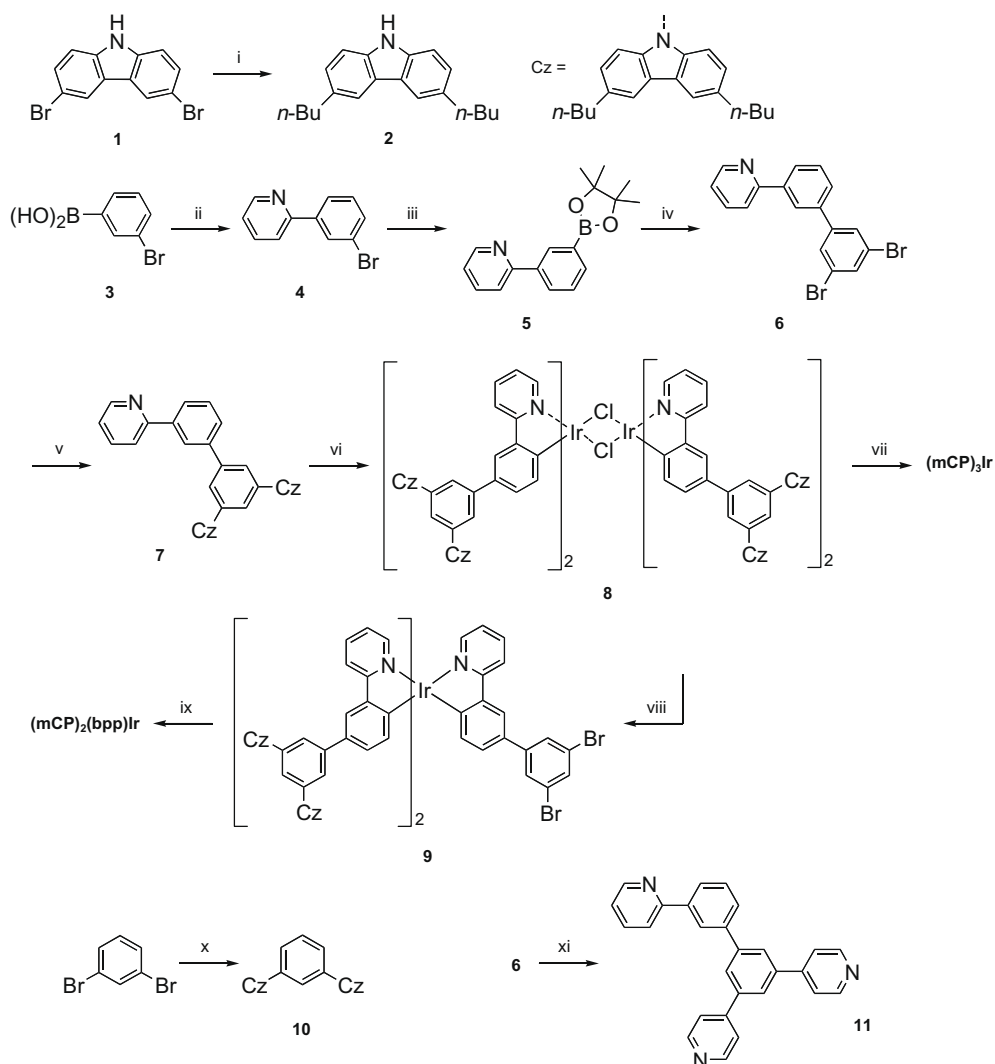
Scheme 1 shows synthetic schemes of (mCP)<sub>3</sub>Ir and (mCP)<sub>2</sub>(bpp)Ir. Alkyl carbazole **2** was synthesized by palladium catalyzed Suzuki coupling reaction with *n*-butylboronic acid and dibromocarbazole **1**. 3-Bromophenylboronic acid **3** selectively reacted with 2-bromopyridine to give 2-(3-bromophenyl)pyridine **4**, and corresponding boronic ester **5** was given by palladium catalyzed borylation of **4**. Carbazole attached ligand **7** was obtained by palladium catalyzed C–N coupling with **2** and dibromo compound **6** [2j]. The dendrimers were prepared from the two step of complexation [6]. First, a mixture of iridium chloride trihydrate and excess of **7** afforded dichloro bridged dimer complex **8**. Second, the dimer **8** was clacked by the ligand **7** with silver trifluoromethane sulfonate to give a homoleptic dendrimer complex (mCP)<sub>3</sub>Ir [2g]. Pyridine-substituted heteroleptic dendrimer complex (mCP)<sub>2</sub>(bpp)Ir was synthesized by Suzuki coupling with 4-pyridylboronic acid pinacol ester and dibromo complex **9**, which was obtained by the clacking of the dimer **8** with another phenylpyridine compound **6**. Carbazole dendron **10** and pyridine substituted ligand **11** were synthesized for photoluminescence (PL) measurement. The two dendrimer complexes were fully characterized by <sup>1</sup>H NMR, matrix-assisted laser desorption/ionization time-of-flight (MALDI) mass spectrometry (MS), and elemental analysis.

The dendrimers showed high thermal stability. The 5% weight loss temperature (*T*<sub>d5%</sub>) was 468 °C for (mCP)<sub>3</sub>Ir and 445 °C for (mCP)<sub>2</sub>(bpp)Ir, compared with 400 °C of Ir(ppy)<sub>3</sub>. This improvement of the thermal stability may result from the protection of core complex by outer bulky dendrons. Glass transition was not observed in differential scanning calorimetry (DSC) measurement in 50–335 °C.

### 2.2. Photophysical properties

The UV–visible absorption and PL spectra of the Ir complexes are shown in Fig. 1. The strong absorption ranging from 250 nm to 360 nm of the dendrimers are ascribed to the singlet  $\pi$ – $\pi^*$  transitions of the dendronized phenylpyridine ligand, and the weak absorption around 360–500 nm comes from metal-to-ligand charge transfer (MLCT) transitions [7]. The absorption of (mCP)<sub>2</sub>(bpp)Ir around 250–360 nm are weaker than that of (mCP)<sub>3</sub>Ir, because the number of carbazole dendron unit of (mCP)<sub>2</sub>(bpp)Ir is smaller than that of (mCP)<sub>3</sub>Ir. Photoluminescence spectra of the two dendrimers and Ir(ppy)<sub>3</sub> were nearly identical, which show that the substitution of the dendrons to the *m*-position of 2-phenylpyridine ligand does not affect the emission characteristics of the Ir(ppy)<sub>3</sub> core complex [2j]. Photoluminescence quantum efficiencies (PLQEs) of the dendrimers in the neat film are important parameter to estimate the dendrimer's shielding effect to the core (Table 1) [8]. PLQEs of the toluene solution and the 2 or 15 wt% doped PMMA films were measured by using an integrating sphere system under 325 nm excitation. In the diluted solutions, all complexes showed high PLQE, 91% for (mCP)<sub>3</sub>Ir and 84% for (mCP)<sub>2</sub>(bpp)Ir, which are comparable to 85% of Ir(ppy)<sub>3</sub>. This result demonstrated that the dendron is optically inert and does not affect the emission efficiency of Ir(ppy)<sub>3</sub> core. In the 2 wt% doped films, all of them showed high PLQEs as well: 90%





**Scheme 1.** Synthetic procedure of (mCP)<sub>3</sub>Ir, (mCP)<sub>2</sub>(bpp)Ir, **10**, and **11**: (i) *n*-butylboronic acid, Pd(PPh<sub>3</sub>)<sub>4</sub>, P(*t*-Bu)<sub>3</sub>, K<sub>2</sub>CO<sub>3</sub> aq., toluene, N<sub>2</sub>, 85 °C, (ii) 2-bromopyridine, Pd(PPh<sub>3</sub>)<sub>4</sub>, K<sub>2</sub>CO<sub>3</sub> aq., THF, N<sub>2</sub>, reflux, (iii) bis(pinacolato)diboron, KOAc, PdCl<sub>2</sub>(dppf), N<sub>2</sub>, DMF, 85 °C, (iv) 1,3,5-tribromobenzene, Pd(PPh<sub>3</sub>)<sub>4</sub>, Na<sub>2</sub>CO<sub>3</sub> aq., EtOH, toluene, N<sub>2</sub>, reflux, (v) **2**, Pd<sub>2</sub>(dba)<sub>3</sub>, P(*t*-Bu)<sub>3</sub>, NaO-*t*-Bu, toluene, N<sub>2</sub>, reflux, (vi) IrCl<sub>3</sub>·3H<sub>2</sub>O, H<sub>2</sub>O, 2-ethoxyethanol, N<sub>2</sub>, 130 °C, (vii) **7**, CF<sub>3</sub>SO<sub>3</sub>Ag, diglyme, N<sub>2</sub>, 130 °C, (viii) **6**, CF<sub>3</sub>SO<sub>3</sub>Ag, diglyme, N<sub>2</sub>, 130 °C, (ix) 4-pyridylboronic acid pinacol ester, Pd(PPh<sub>3</sub>)<sub>4</sub>, K<sub>2</sub>CO<sub>3</sub> aq., EtOH, toluene, N<sub>2</sub>, reflux, (x) **2**, Pd<sub>2</sub>(dba)<sub>3</sub>, P(*t*-Bu)<sub>3</sub>, NaO-*t*-Bu, toluene, N<sub>2</sub>, reflux, (xi) **6**, 4-pyridylboronic acid pinacol ester, Pd(PPh<sub>3</sub>)<sub>4</sub>, Na<sub>2</sub>CO<sub>3</sub> aq., EtOH, toluene, N<sub>2</sub>, reflux.

for (mCP)<sub>3</sub>Ir, 86% for (mCP)<sub>2</sub>(bpp)Ir, and 95% for Ir(ppy)<sub>3</sub> [9]. In the 15 wt% doped film, Ir(ppy)<sub>3</sub> showed a very low PLQE of 15% because of severe concentration-quenching effect. On the other hand, the dendrimers exhibited much higher PLQEs of 49% for (mCP)<sub>3</sub>Ir and 29% for (mCP)<sub>2</sub>(bpp)Ir even in the neat films. These results showed that these dendron substituents are partially effective to suppress concentration-quenching in a neat film of an iridium complex. There are two reasons why concentration-quenching happened even after the substitution of the dendrons. First, these dendrimers are facial isomers, therefore a some space around pyridyl groups of Ir(ppy)<sub>3</sub> core are opened and the three dimensional structure of the dendrimer complexes is like a hemisphere [8b]. There are spatial rooms for the core complex of the dendrimers to contact each other. Second, the substituted dendrons are

not enough large to suppress the interaction between the core complexes completely. Adachi et al. reported that an average distance between iridium complexes in a doped film critically influenced on PLQE [10]. Förster type energy transfer between Ir(ppy)<sub>3</sub> cores through an overlap of the emission and the absorption causes a decrease of neat film PLQY. If the average distance between iridium complexes is shorter than Förster radius, a strong quenching occurs. The stronger quenching of (mCP)<sub>2</sub>(bpp)Ir in the neat film than that of (mCP)<sub>3</sub>Ir is due to the shorter average distance between the cores derived from a less number of bulky carbazole dendron of (mCP)<sub>2</sub>(bpp)Ir than that of (mCP)<sub>3</sub>Ir. More branched and larger dendrons and their dense substitution to the core complexes are desirable to achieve the more effective suppression of concentration-quenching [2j,8].

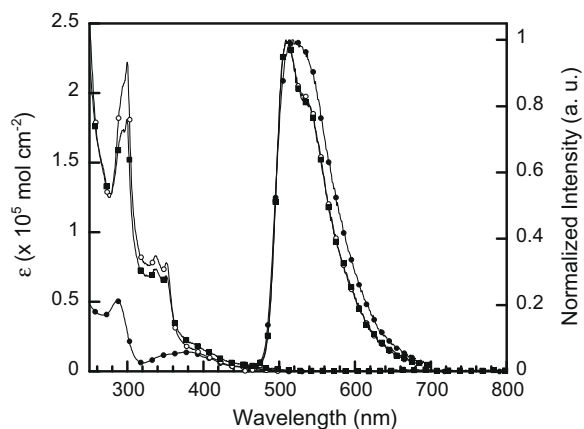


**Fig. 1.** UV-visible and PL spectra (excited at 400 nm) of Ir(ppy)<sub>3</sub> (closed circle), (mCP)<sub>3</sub>Ir (open circle) and (mCP)<sub>2</sub>(bpp)Ir (closed square) at room temperature in chloroform solution.

**Table 1**

PLQEs of the dendrimer complexes in a solution and film.

Compound	$\Phi_{\text{sol}}^{\text{a}}$ (%)	$\Phi_{2\text{wt}\% \text{ film}}^{\text{b}}$ (%)	$\Phi_{\text{neat film}}$ (%)	$(\Phi_{\text{sol}} - \Phi_{\text{film}})/\Phi_{\text{sol}}$ (%)
(mCP) <sub>3</sub> Ir	91	90	49	46
(mCP) <sub>2</sub> (bpp)Ir	84	86	29	65
Ir(ppy) <sub>3</sub>	85	95	15 <sup>c</sup>	82

<sup>a</sup> Toluene solution ( $2.0 \times 10^{-6}$  mol/L).

<sup>b</sup> 2 wt% Doped PMMA film.

<sup>c</sup> 15 wt% Doped PMMA film.

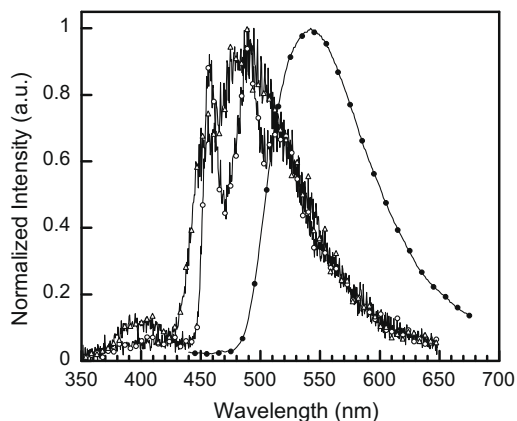


**Fig. 2.** Phosphorescence spectra of Ir(ppy)<sub>3</sub> (closed circle), **7** (open circle), and **10** (open triangle) in a neat film (Ir(ppy)<sub>3</sub>): at room temperature, excited at 400 nm; **7** and **10**: at 4 K, excited at 337 nm.

The triplet exciton energy level ( $T_1$ ) of the dendron determined by the edge at shorter wavelength side of phosphorescence spectrum at 4 K well supported the exciton confinement of the emitting core.  $T_1$  of the dendronized ligands, 2.8 eV of **7** and 2.9 eV of **10**, are higher than 2.6 eV of Ir(ppy)<sub>3</sub> (Fig. 2).  $T_1$  of **11** was not able to determined because its film was crystallized at 4 K, but the life time of photoluminescence of 2 wt% Ir(ppy)<sub>3</sub> in the film of

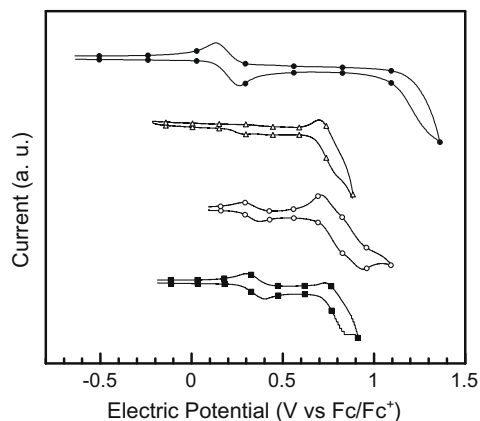


**Fig. 3.** Cyclic voltammograms of Ir(ppy)<sub>3</sub> (closed circle), **10** (open triangle), (mCP)<sub>3</sub>Ir (open circle), (mCP)<sub>2</sub>(bpp)Ir (closed square) (100 mV/s, 0.1 M *n*-Bu<sub>4</sub>NBF<sub>4</sub>, 1 mM dichloromethane, working electrode: Pt, counter electrode: Pt, reference electrode: Ag/Ag<sup>+</sup>).

**11** showed single exponential decay, indicating that the  $T_1$  level of **11** was high enough to confine the energy of Ir(ppy)<sub>3</sub> core.

### 2.3. Electrochemical properties

Ionization potential ( $I_p$ ) of the compounds was measured by ultraviolet photoelectron spectroscopy.  $I_p$  of (mCP)<sub>3</sub>Ir and (mCP)<sub>2</sub>(bpp)Ir were 5.5 eV and 5.6 eV, respectively, and these are lower than 5.9 eV of **10**, and slightly larger than 5.3 eV of Ir(ppy)<sub>3</sub>. These results suggest that highest occupied molecular orbital (HOMO) level of the dendrimers are derived from Ir(ppy)<sub>3</sub> core rather than carbazole dendron, and those higher HOMO level than that of Ir(ppy)<sub>3</sub> are due to the electron withdrawing effect of the dendron to the Ir core complex [11]. In cyclic voltammetry measurements, the dendrimers, (mCP)<sub>3</sub>Ir and (mCP)<sub>2</sub>(bpp)Ir, showed two redox waves in anodic scan. The first redox at 0.20–0.34 V is ascribed to the redox of Ir(ppy)<sub>3</sub> core, and the second at 0.75–0.79 V is ascribed to the redox of carbazole dendron (Fig. 3). These results demonstrated that these dendrimers have independent two energy levels corresponding to the Ir(ppy)<sub>3</sub> core and the dendron, respectively, and these two  $\pi$  systems are not fully conjugated. Lowest unoccupied molecular orbital (LUMO) level of (mCP)<sub>3</sub>Ir, (mCP)<sub>2</sub>(bpp)Ir and Ir(ppy)<sub>3</sub>, estimated by the energy gap and HOMO level, were 2.7 eV, 2.8 eV and 2.6 eV, respectively. LUMO level of the dendron **10** was 2.5 eV, higher than that of Ir(ppy)<sub>3</sub>.

### 2.4. OLED performance

Single layer devices with the configuration of ITO/poly(3,4-ethylenedioxythiophene)(PEDOT): poly(styrene sulfonic acid) (PSS) (40 nm)/(mCP)<sub>3</sub>Ir or (mCP)<sub>2</sub>(bpp)Ir (120 nm)/LiF (1 nm)/Al (100 nm) and double layer devices with the configuration of ITO/PEDOT: PSS (40 nm)/(mCP)<sub>3</sub>Ir or (mCP)<sub>2</sub>(bpp)Ir (60 nm)/bis-4,6-(3,5-di-3-pyridylphenyl)-2-methylpyrimidine (B3PYMPM) [5d] (60 nm)/LiF (1 nm)/Al (100 nm) were fabricated. Electroluminescence

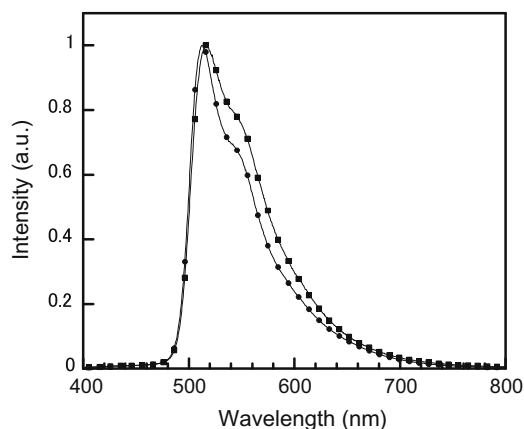


**Fig. 4.** Electroluminescence spectra of (mCP)<sub>3</sub>Ir (closed circle) and (mCP)<sub>2</sub>(bpp)Ir (closed square) in the double layer devices.

spectra of double layer devices were shown in Fig. 4. These spectra were identical to the photoluminescence spectra and the spectra of single layer devices. Higher driving voltages of (mCP)<sub>2</sub>(bpp)Ir than those of (mCP)<sub>3</sub>Ir in current density are probably due to the larger hole injection barrier to the HOMO level of dipyriddyphenyl dendron compared with the barrier to the HOMO level of dicarbazolyphenyl dendron (Fig. 5). Hole injection barriers from PEDOT: PSS to the HOMO levels of these dendrimers are quite small compared with electron injection barriers from aluminum to the LUMO levels. Therefore, hole current should be dominant in single layer devices. However, in contrast to the result of the current density – voltage plots of the single layer device, (mCP)<sub>2</sub>(bpp)Ir in the single layer device showed lower driving voltages than that of (mCP)<sub>3</sub>Ir in the luminance – voltage plots. As well as the luminance, external quantum efficiencies (EQEs) of the single layer device with (mCP)<sub>2</sub>(bpp)Ir were much higher than those of (mCP)<sub>3</sub>Ir (Fig. 6). EQE at 100 cd/m<sup>2</sup> with (mCP)<sub>2</sub>(bpp)Ir was 0.23%, and that with (mCP)<sub>3</sub>Ir was 0.014%. This improvement showed that the pyridine groups of (mCP)<sub>2</sub>(bpp)Ir are effective

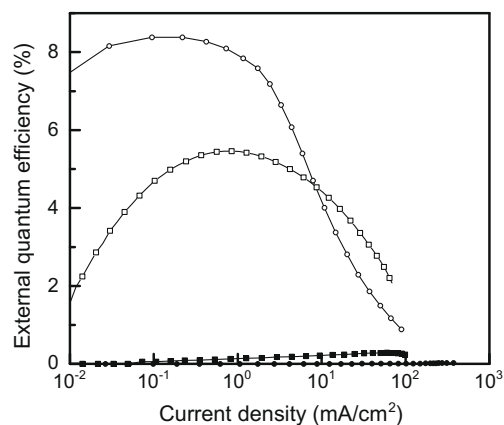


**Fig. 6.** EQE – current density plots of single layer devices of (mCP)<sub>3</sub>Ir (closed circle) and (mCP)<sub>2</sub>(bpp)Ir (closed square), and double layer devices of (mCP)<sub>3</sub>Ir (open circle) and (mCP)<sub>2</sub>(bpp)Ir (open square).

to the better electron injection from cathode metal to the dendrimer because of their better affinity to LiF of cathode [5e].

The double layer devices were fabricated using B3PYMPM as an electron transporting and hole-blocking material on the dendrimer emitting layer. The current density increased and driving voltages decreased compared with the single layer devices due to the improved electron injection by the electron transporting layer (ETL). Especially, their efficiencies were drastically improved to 8.3% for (mCP)<sub>3</sub>Ir and 5.4% for (mCP)<sub>2</sub>(bpp)Ir at 100 cd/m<sup>2</sup>. These high efficiencies resulted from improved charge recombination by the efficient hole block of B3PYMPM layer, whose HOMO and LUMO levels are 6.8 eV and 3.2 eV, respectively. These drastic improvements of efficiencies by ETL also supported that the current of the single layer devices was hole dominant. The higher efficiency of (mCP)<sub>3</sub>Ir than that of (mCP)<sub>2</sub>(bpp)Ir is derived from the higher PLQE of (mCP)<sub>3</sub>Ir. The roll-off of EQE in high current density region in double layer devices may be because of

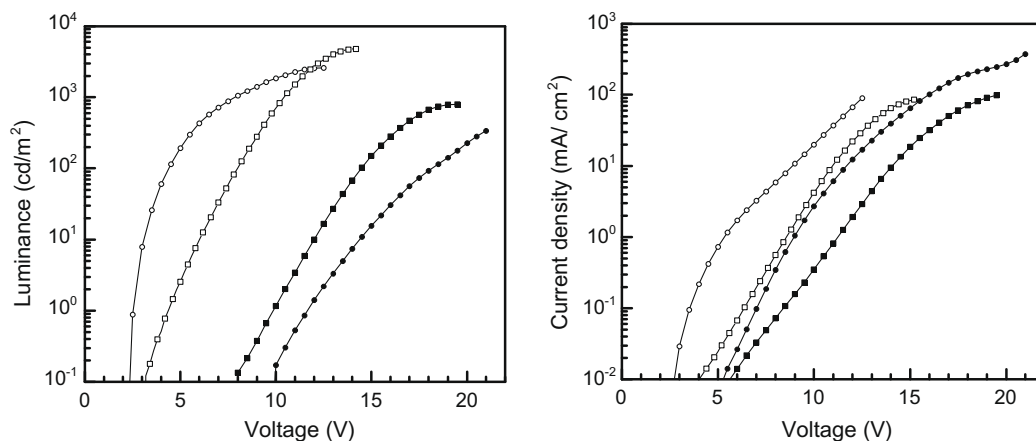


**Fig. 5.** Luminance – voltage (left) and current density – voltage (right) plots of single layer devices of (mCP)<sub>3</sub>Ir (closed circle) and (mCP)<sub>2</sub>(bpp)Ir (closed square), and double layer devices of (mCP)<sub>3</sub>Ir (open circle) and (mCP)<sub>2</sub>(bpp)Ir (open square).

imbalance of injected electrons and holes. This carrier imbalance is caused by electron leakage to PEDOT: PSS layer through the dendrimer complex layer that is why an insertion of interlayer having electron blocking property between PEDOT: PSS and the dendrimer layer would be necessary to improve EQE and its roll-off behavior.

### 3. Conclusions

We synthesized solution-processable iridium complexes (mCP)<sub>3</sub>Ir and (mCP)<sub>2</sub>(bpp)Ir having bulky carbazole dendrons. The dendrimers exhibited still high PLQEs, 49% for (mCP)<sub>3</sub>Ir and 29% for (mCP)<sub>2</sub>(bpp)Ir even in the neat films. T<sub>1</sub> level of the dendronized ligand and the dendron are enough higher than that of the core complex Ir(ppy)<sub>3</sub>. The EQE of single layer light-emitting device with (mCP)<sub>2</sub>(bpp)Ir was much higher than that of (mCP)<sub>3</sub>Ir because of better affinity of (mCP)<sub>2</sub>(bpp)Ir to LiF of cathode. The EQEs of double layer devices with ETL were dramatically improved to 8.3% for (mCP)<sub>3</sub>Ir and 5.4% for (mCP)<sub>2</sub>(bpp)Ir at 100 cd/m<sup>2</sup>.

### 4. Experimental

NMR spectra were recorded on a JEOL ECX-400 400 MHz spectrometer. UV–visible spectra were recorded on a Shimadzu UV3150 spectrometer and photoluminescence spectra were recorded on a Horiba Jobin Yvon Fluoromax-2 spectrofluorometer. Ionization potentials were measured by Riken Keiki AC-3. Mass spectra were recorded on a JEOL JMS-K9 for electron impact-ionization (EI) or an Applied Biosystems Voyager DE-PRO for matrix-assisted laser desorption/ionization time-of-flight (MALDI-TOF) from dithranol (DITH) in linear or reflection mode. Elemental analyses were carried out in the Elemental Analysis Service, Yamagata University. Gel permeation chromatography was carried out using Nippon Bunseki Kogyo LC-9204 with JAIGEL 2H and 2.5H columns. Thermal gravimetric analysis was performed on a SII thermogravimetric analyzer TG / DTA 6200. Glass transition temperatures were measured on a Perkin Elmer differential scanning calorimeter Diamond DSC. Electrochemistry was performed on ALS / H CH Instruments Electrochemical analyzer 660B. All measurements were made at room temperature on samples dissolved in dry dichloromethane with 0.1 M tetrabutylammonium tetrafluoroborate as a supporting electrolyte. The dry dichloromethane was purchased from Kanto Kagaku Co. The solutions were deoxygenated with argon. A platinum working electrode, platinum wire counter electrode and Ag/Ag<sup>+</sup> reference electrode was used. The ferrocene/ferricenium couple was used as an internal standard. All potentials are quoted relative to ferrocene / ferricenium couple. Ir(ppy)<sub>3</sub> film for PL measurement were deposited under  $2 \times 10^{-5}$  Pa to give a thickness of about 80 nm. Films for PL and PLQE measurement were obtained by spin-coating on quartz substrate from 1,2-dichloroethane solution with a concentration of 25 g/L at 1000 rpm for 30 s to give a thickness of about 130 nm. For PLQE measurement in solution, Ir(ppy)<sub>3</sub> was dissolved in toluene at the concentration of  $1 \times 10^{-5}$  mol/L, and the dendrimers

were dissolved in toluene at the concentration of  $2 \times 10^{-6}$  mol/L. Their PLQE was measured using an integrating sphere of Hamamatsu Photonics A10094 with a xenon lamp at 325 nm at room temperature. The integrating sphere was purged with nitrogen during measurements. On preparing OLEDs, PEDOT: PSS was spin-coated as an anode buffer layer on pre-cleaned ITO substrate. On the top of PEDOT: PSS layer, dendrimers were spin-coated from 1,2-dichloroethane solutions. B3PYMPM was deposited on the top of the dendrimer layer under  $5.8 \times 10^{-5}$  Pa. Finally, electron injection layer, LiF and Al cathode were successively deposited under  $2.4 \times 10^{-3}$  Pa. Luminance measurements were carried out with a Konica Minolta CS200 luminance meter and electroluminescence spectra were taken by Hamamatsu Photonics PMA-11 optical multi-channel analyzer at room temperature.

**3,6-Dibutylcarbazole (2):** A mixture of 3,6-dibromocarbazole (**1**) (13.3 g, 40.9 mmol), potassium carbonate (28.2 g, 204 mmol), *n*-butylboronic acid (10.0 g, 98.1 mmol), tetrakis(triphenylphosphine)palladium(0) (0.238 g, 0.206 mmol), tri-*tert*-butylphosphine (0.30 ml, 1.2 mmol), deionized water (65 ml), toluene (175 ml) was heated at 85 °C under nitrogen for 24 h. After being allowed to cool to room temperature, the organic layer was extracted with diethyl ether and washed with deionized water, dried over anhydrous sodium sulfate. The solvents were completely removed to give white solid and purified by column chromatography over silica gel with chloroform–*n*-hexane (0:1–1:1) as eluent to give white solid of **2** (6.85 g, 60%). (Found: C, 86.95; H, 7.41; N, 5.35. C<sub>20</sub>H<sub>25</sub>N requires C, 87.09; H, 7.57; N, 5.35%; *d*<sub>H</sub>(400 MHz, CDCl<sub>3</sub>) 1.24 (6H, t, *J* 7.3, 2 × CH<sub>2</sub>CH<sub>2</sub>CH<sub>2</sub>CH<sub>3</sub>), 1.62–1.69 (4H, m, 2 × CH<sub>2</sub>CH<sub>2</sub>CH<sub>2</sub>CH<sub>3</sub>), 1.92–1.97 (4H, m, 2 × CH<sub>2</sub>CH<sub>2</sub>CH<sub>2</sub>CH<sub>3</sub>), 3.01 (4H, t, *J* 7.5, 2 × CH<sub>2</sub>CH<sub>2</sub>CH<sub>2</sub>CH<sub>3</sub>), 7.50 (2H, d, *J* 8.2, ArH), 7.65 (2H, d, *J* 8.2, ArH), 8.18 (2H, s, ArH), 11.2 (H, s, NH). *d*<sub>C</sub>(100 MHz, CDCl<sub>3</sub>) 14.2, 22.6, 34.7, 35.9, 110.4, 119.7, 123.6, 126.6, 134.0, 138.4. *m/z* [EI] 380 (M<sup>+</sup>).

**2-(3-Bromophenyl)pyridine (4):** A mixture of 3-bromophenylboronic acid (**3**) (3.00 g, 14.9 mmol), 2-bromopyridine (3.03 ml, 29.9 mmol), tetrakis(triphenylphosphine)palladium(0) (0.695 g, 0.601 mmol), potassium carbonate (4.11 g, 29.8 mmol), deionized water (15 ml), tetrahydrofuran (40 ml) was heated at reflux under nitrogen for 24 h. After being allowed to cool to room temperature, the organic layer was extracted with diethyl ether and washed with deionized water, dried over anhydrous sodium sulfate. The solvents were completely removed to give brown oil and purified by column chromatography over silica gel with chloroform–*n*-hexane (1:1) as eluent to give light yellow oil. The oil was distilled under 90 °C, 50 mmHg to give light yellow oil of **2** (2.01 g, 58%). (Found: C, 56.71; H, 3.41; N, 5.75. C<sub>11</sub>H<sub>8</sub>BrN requires C, 56.44; H, 3.44; N, 5.98%; *d*<sub>H</sub>(400 MHz, DMSO-*D*<sub>6</sub>) 7.67 (1H, t, *J* 6.7, ArH), 7.73 (1H, t, *J* 7.8, ArH), 7.90 (1H, d, *J* 8.2, ArH), 8.17 (1H, t, *J* 7.8, ArH), 8.29 (1H, d, *J* 7.8, ArH), 8.35 (1H, d, *J* 8.7, ArH), 8.55 (1H, s), 8.95 (1H, d, *J* 5.5, ArH). *d*<sub>C</sub>(100 MHz, DMSO-*D*<sub>6</sub>) 122.1, 123.9, 125.0, 126.9, 130.6, 132.5, 133.2, 139.0, 142.4, 151.2, 155.7. *m/z* [EI] 233: (M<sup>+</sup>).

**2-[3-((4,4,5,5-Tetramethyl)-1,3,2-dioxaborolan-2-yl)phenyl]pyridine (5):** A mixture of **4** (1.00 g, 4.27 mmol), bis(pina-

colato)diboron (1.19 g, 4.70 mmol), [1,1-bis(diphenylphosphino)ferrocene]dichloropalladium(II) dichloromethane complex (1:1) (0.105 g, 0.128 mmol), potassium acetate (1.26 g, 12.8 mmol), *N,N*-dimethylformamide (20 ml) was heated at 85 °C under nitrogen for 18 h. After being allowed to cool to room temperature, the solvent was completely removed. The residue was purified by column chromatography over silica gel with chloroform–ethyl acetate (1:1) as eluent to give **5** (0.860 g, 86%) as a white crystal. (Found: C, 72.45; H, 7.26; N, 4.90.  $C_{17}H_{20}BNO_2$  requires C, 72.62; H, 7.17; N, 4.98%);  $d_H$ (400 MHz, DMSO- $D_6$ ) 1.65 (12H, s, 4 ×  $CH_3$ ), 7.69 (1H, t, *J* 6.2, ArH), 7.83 (1H, t, *J* 7.5, ArH), 8.05 (1H, d, *J* 7.3, ArH), 8.20 (1H, t, *J* 7.0, ArH), 8.28 (1H, d, *J* 8.2, ArH), 8.50 (1H, d, *J* 8.2, ArH), 8.75 (1H, s, ArH), 8.99 (1H, d, *J* 5.0, ArH). *m/z* [EI] 281 ( $M^+$ ).

2-[3-(3,5-Dibromophenyl)phenyl]pyridine (**6**): A mixture of **5** (2.33 g, 8.29 mmol), 1,3,5-tribromobenzene (7.84 g, 24.9 mmol), tetrakis(triphenylphosphine)palladium(0) (0.387 g, 0.335 mmol), sodium carbonate (1.15 g, 10.8 mmol), deionized water (5.5 ml), ethanol (5 ml), toluene (20 ml) was heated at reflux under nitrogen for 26 h. After being allowed to cool to room temperature, the organic layer was extracted with diethyl ether and washed with deionized water, dried over anhydrous sodium sulfate. The solvent was completely removed. The residue was purified by column chromatography over silica gel with chloroform as eluent to give **6** (2.64 g, 82%) as a white crystal. (Found: C, 52.42; H, 2.62; N, 3.54.  $C_{17}H_{11}Br_2N$  requires C, 52.48; H, 2.85; N, 3.60%);  $d_H$ (400 MHz, DMSO- $D_6$ ) 7.71 (1H, t, *J* 6.2, ArH), 7.92 (1H, t, *J* 7.9, ArH), 8.10 (1H, d, *J* 6.8, ArH), 8.18 (1H, s, ArH), 8.23 (1H, t, *J* 7.7, ArH), 8.32 (2H, s, ArH), 8.47 (2H, d, *J* 8.1, ArH), 8.66 (1H, s, ArH), 9.01 (1H, d, *J* 4.5, ArH).  $d_C$ (100 MHz,  $CDCl_3$ ) 120.9, 122.7, 123.5, 125.9, 127.1, 127.8, 129.3, 129.6, 132.9, 137.1, 139.1, 140.4, 144.8, 150.0, 157.0. *m/z* [EI] 389 ( $M^+$ ).

2-[3-{3,5-Bis(3,6-dibutylcarbazol-9-yl)phenyl}phenyl]pyridine (**7**): A mixture of **2** (2.53 g, 9.05 mmol), **6** (1.47 g, 3.77 mmol), tris(dibenzylideneacetone)dipalladium(0) (0.0934 g, 0.102 mmol), tri-*tert*-butylphosphine (0.210 ml, 0.867 mmol), sodium *tert*-butoxide (1.45 g, 15.1 mmol), toluene (180 ml) was heated at reflux under nitrogen for 36 h. After being allowed to cool to room temperature, the organic layer was extracted with diethyl ether and washed with deionized water, dried over anhydrous sodium sulfate. The solvent was completely removed and purified by column chromatography over silica gel with chloroform as eluent to give white brown solid **7** (2.32 g, 78%). (Found: C, 86.25; H, 8.90; N, 4.99.  $C_{57}H_{59}N_3$  requires C, 85.97; H, 9.02; N, 5.01%);  $d_H$ (400 MHz, DMSO- $D_6$ ) 1.23 (12H, t, *J* 7.5, 4 ×  $CH_2CH_2CH_2CH_3$ ), 1.65–1.67 (8H, m, 4 ×  $CH_2CH_2CH_2CH_3$ ), 1.94–1.96 (8H, m, 4 ×  $CH_2CH_2CH_2CH_3$ ), 3.05 (8H, t, *J* 7.5, 4 ×  $CH_2CH_2CH_2CH_3$ ), 7.58 (4H, d, *J* 8.1, ArH), 7.66 (1H, t, *J* 4.7, ArH), 7.84 (4H, d, *J* 8.2, ArH), 7.94 (1H, t, *J* 7.7, ArH), 8.09 (1H, s, ArH), 8.16 (1H, t, *J* 6.8, ArH), 8.26 (1H, d, *J* 7.7, ArH), 8.35 (4H, s, ArH), 8.40–8.45 (3H, m, ArH), 8.48 (1H, d, *J* 7.7, ArH), 8.81 (1H, s, ArH), 8.96 (1H, d, *J* 4.6, ArH). *m/z* [EI] 786: ( $M^+$ ).

*fac*-Bis[2-{3-(3,5-bis(3,6-di-*n*-butylcarbazol-9-yl)phenyl)phenyl}pyridine]iridium(III) (**9**): A mixture of **7** (3.43 g, 4.36 mmol), iridium chloride trihydrate (0.638 g,

1.81 mmol), deionized water (30 ml), 2-ethoxyethanol (125 ml) was heated (oil bath temperature: 130 °C) under nitrogen for 25 h. After being allowed to cool to room temperature, deionized water was added and filtrated. Then aqueous potassium carbonate (0.33 M, 30 ml) was added and sonicated for 5 min and washed with deionized water. The solvent was completely removed and purified by column chromatography over silica gel to remove the residual ligand with dichloromethane–*n*-hexane (4:1) as eluent to give ocherous solid (2.38 g). A mixture of the obtained chloro-bridged dimer (2.38 g), **6** (0.774 g, 1.99 mmol), silver trifluoromethanesulfonate (0.204 g, 0.794 mmol), diglyme 100 ml was heated (sand bath temperature: 130 °C) under nitrogen for 6.8 day. After being allowed to cool to room temperature, purified by column chromatography over silica gel with dichloromethane–*n*-hexane (3:4) as eluent to give brown oil. The oil was distilled under 110 °C, 50 mmHg. The solvent was completely removed and purified by gel permeation chromatography with 1,2-dichloroethane as eluent to give **9** (0.543 g, 14%) as a yellow solid. (Found: C, 73.14; H, 5.91; N, 4.55.  $C_{131}H_{126}Br_2IrN_7$  requires C, 73.17; H, 5.91; N, 4.56%);  $d_H$ (400 MHz,  $CD_2Cl_2$ ) 0.91 (24H, t, *J* 6.3, 8 ×  $CH_2CH_2CH_2CH_3$ ), 1.20–1.50 (16H, m, 8 ×  $CH_2CH_2CH_2CH_3$ ), 1.50–1.80 (16H, m, 8 ×  $CH_2CH_2CH_2CH_3$ ), 2.76 (16H, t, *J* 6.1, 8 ×  $CH_2CH_2CH_2CH_3$ ), 6.80–7.10 (6H, m, ArH), 7.10–7.30 (10H, m, ArH), 7.30–8.10 (38H, m, ArH). [MALDI: DITH] (*m/z*) 2149.49 ( $MH^+$ ).

3,5-Bis(3,6-dibutylcarbazol-9-yl)benzene (**10**): A mixture of **2** (0.306 g, 1.10 mmol), 1,3-dibromobenzene (0.055 ml, 0.458 mmol), tris(dibenzylideneacetone)dipalladium(0) (0.0114 g, 0.0124 mmol), tri-*tert*-butylphosphine (0.025 ml, 0.11 mmol), sodium *tert*-butoxide (0.176 g, 1.83 mmol), toluene (20 ml) was heated at reflux under nitrogen for 24 h. After being allowed to cool to room temperature, the organic layer was extracted with diethyl ether and washed with deionized water, dried over anhydrous sodium sulfate. The solvent was completely removed and purified by column chromatography over silica gel with chloroform–*n*-hexane (2:1) and with chloroform–*n*-hexane (0:1 to 1:1) as eluent to give colorless oil **10** (0.262 g, 90%). (Found: C, 87.41; H, 8.26; N, 4.31.  $C_{46}H_{52}N_2$  requires C, 87.29; H, 8.28; N, 4.43%);  $d_H$ (400 MHz, DMSO- $D_6$ ) 1.18 (12H, t, *J* 7.3, 4 ×  $CH_2CH_2CH_2CH_3$ ), 1.56–1.66 (8H, m, 4 ×  $CH_2CH_2CH_2CH_3$ ), 1.88–1.95 (8H, m, 4 ×  $CH_2CH_2CH_2CH_3$ ), 3.01 (8H, t, *J* 7.5, 4 ×  $CH_2CH_2CH_2CH_3$ ), 7.54 (4H, d, *J* 8.2, ArH), 7.72 (4H, d, *J* 8.6, ArH), 7.98–8.05 (3H, m, ArH), 8.20 (1H, t, *J* 8.0, ArH), 8.30 (4H, s, ArH).  $d_C$ (100 MHz,  $CDCl_3$ ) 14.3, 22.6, 34.7, 35.9, 109.6, 119.9, 123.8, 124.8, 125.2, 126.9, 131.1, 135.0, 139.4, 139.9. *m/z* [EI] 634: ( $M^+$ ).

2-[3-{3,5-Di(4-pyridyl)phenyl}phenyl]pyridine (**11**): A mixture of **6** (0.500 g, 1.29 mmol), 4-(4,4,5,5-tetramethyl-1,3,2-dioxaborolan-2-yl)pyridine (0.792 g, 3.86 mmol), tetrakis(triphenylphosphine)palladium(0) (0.120 g, 0.104 mmol), sodium carbonate (0.355 g, 3.35 mmol), deionized water (1.7 ml), ethanol (2.3 ml), toluene (9.3 ml) was heated at reflux under nitrogen for 19 h. After being allowed to cool to room temperature, the organic layer was extracted with diethyl ether and tetrahydrofuran. The extracted fraction was washed with deionized water, dried

over anhydrous sodium sulfate. The solvent was completely removed and purified by column chromatography over silica gel with ethyl acetate–methanol (10:3) as eluent to give white solid **11** (0.380 g, 76%). (Found: C, 84.24; H, 4.79; N, 10.87.  $C_{27}H_{19}N_3$  requires C, 84.13; H, 4.97; N, 10.90%);  $d_H$ (400 MHz, DMSO- $D_6$ ) 7.97 (1H, t,  $J$  5.0, ArH), 7.98 (1H, t,  $J$  7.7, ArH), 8.22–8.35 (6H, m, ArH), 8.45–8.58 (5H, m, ArH), 8.82 (1H, s, ArH), 9.02 (5H, d,  $J$  5.9, ArH).  $d_C$ (100 MHz,  $CDCl_3$ ) 121.0, 122.1, 122.7, 125.0, 126.2, 126.8, 126.9, 128.0, 129.7, 137.1, 140.0, 140.5, 140.9, 143.3, 148.0, 150.0, 150.7, 157.2.  $m/z$  [EI] 386: ( $M^+$ ).

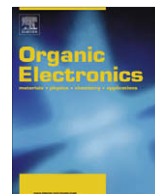
(mCP) $_3$ Ir: A mixture of **7** (0.300 g, 0.381 mmol), iridium chloride trihydrate (0.0561 g, 0.159 mmol), deionized water (2.7 ml), 2-ethoxyethanol (12 ml) was heated (oil bath temperature: 130 °C) under nitrogen for 24 h. After being allowed to cool to room temperature, deionized water was added and filtrated. Then aqueous potassium carbonate (0.35 M, 5.8 ml) was added and sonicated for 5 min and washed with deionized water. After it was dried, the crude product was directly used for next step without further purification. A mixture of the obtained chloro-bridged dimer (0.262 g), **7** (0.434 g, 0.552 mmol), silver trifluoromethanesulfonate (0.0491 g, 0.191 mmol), diglyme 5.0 ml was heated (sand bath temperature: 130 °C) under nitrogen for 64 h. After being allowed to cool to room temperature, dichloromethane was added and the solution was washed with brine and deionized water, dried over anhydrous sodium sulfate. The solvent was completely removed and purified by column chromatography over silica gel with dichloromethane–*n*-hexane (1:2) as eluent to give (mCP) $_3$ Ir (0.174 g, 43%) as a yellow solid. (Found: C, 80.52; H, 7.05; N, 5.01.  $C_{171}H_{174}IrN_9$  requires C, 80.62; H, 6.88; N, 4.95%);  $d_H$ (400 MHz,  $CD_2Cl_2$ ) 1.23 (36H, t,  $J$  7.2,  $12 \times CH_2CH_2CH_2CH_3$ ), 1.30–1.50 (24H, m,  $12 \times CH_2CH_2CH_2CH_3$ ), 1.50–1.80 (24H, m,  $12 \times CH_2CH_2CH_2CH_3$ ), 2.76 (24H, t,  $J$  7.5,  $12 \times CH_2CH_2CH_2CH_3$ ), 6.97 (3H, t,  $J$  6.1, ArH), 7.03 (3H, d,  $J$  7.3, ArH), 7.17–7.28 (15H, m, ArH), 7.44–7.55 (12H, d, ArH), 7.57 (3H, d,  $J$  6.1, ArH), 7.63–7.71 (8H, m, ArH), 7.86–8.50 (24H, m, ArH).  $d_C$ (100 MHz,  $CD_2Cl_2$ ) 13.8, 22.5, 34.5, 35.7, 109.7, 119.36, 119.37, 119.6, 122.0, 122.5, 122.8, 123.6, 126.8, 128.6, 131.4, 134.9, 136.8, 137.7, 139.5, 140.1, 145.0, 145.5, 147.5, 162.0, 166.0. [MALDI: DITH] ( $m/z$ ) 2545.8: ( $MH^+$ ).

(mCP) $_2$ (bpp)Ir: A mixture of **9** (0.400 g, 0.186 mmol), 4-(4,4,5,5-tetramethyl-1,3,2-dioxaborolan-2-yl)pyridine (0.305 g, 1.49 mmol), tetrakis(triphenylphosphine)palladium(0) (0.0174 g, 0.0151 mmol), potassium carbonate (0.0668 g, 0.483 mmol), deionized water (0.24 ml), ethanol (18 ml), toluene (35 ml) was heated at reflux under nitrogen for 62.5 h. After being allowed to cool to room temperature, purified by column chromatography over silica gel with chloroform–methanol (20:1) as eluent to give ochreous solid. The solid was purified by gel permeation chro-

matography with 1,2-dichloroethane as eluent to give (mCP) $_2$ (bpp)Ir (0.316 g, 79%) as a yellow solid. (Found: C, 78.73; H, 6.52; N, 5.80.  $C_{141}H_{134}IrN_9$  requires C, 78.88; H, 6.29; N, 5.87%);  $d_H$ (400 MHz,  $CD_2Cl_2$ ) 0.92 (24H, t,  $J$  7.3,  $8 \times CH_2CH_2CH_2CH_3$ ), 1.30–1.45 (16H, m,  $8 \times CH_2CH_2CH_2CH_3$ ), 1.60–1.75 (16H, m,  $8 \times CH_2CH_2CH_2CH_3$ ), 2.75 (16H, t,  $J$  4.1,  $8 \times CH_2CH_2CH_2CH_3$ ), 6.91–7.08 (6H, m, ArH), 7.14–7.30 (11H, m, ArH), 7.42–7.82 (21H, m, ArH), 7.84–8.12 (20H, m, ArH), 8.64 (4H, d,  $J$  5.5, ArH). [MALDI: DITH] ( $m/z$ ) 2146.91 ( $MH^+$ ).

## References

- [1] (a) F. So, J. Kido, P.L. Burrows, MRS Bulletin 33 (2008) 663; (b) R.F. Service, Science 16 (2005) 1762.
- [2] (a) J. Ding, J. Lü, Y. Cheng, Z. Xie, L. Wang, X. Jing, F. Wang, Adv. Funct. Mater. 18 (2008) 2754; (b) B.-L. Li, Y.-M. He, Q.-H. Fan, Dalton Trans. (2007) 2048; (c) B. Liang, L. Wang, Y. Xu, H. Shi, Y. Cao, Adv. Funct. Mater. 17 (2007) 3580; (d) J. Ding, J. Gao, Y. Cheng, Z. Xie, L. Wang, D. Ma, X. Jing, F. Wang, Adv. Funct. Mater. 16 (2006) 575; (e) Y. You, C.-G. An, D.-S. Lee, J.-J. Kim, S.Y. Park, J. Mater. Chem. 16 (2006) 4706; (f) S.-C. Lo, G.J. Richards, J.P.J. Markham, E.B. Namdas, S. Sharma, P.L. Burn, I.D.W. Samuel, Adv. Funct. Mater. 15 (2005) 1451; (g) N. Cumpstey, R.N. Bera, P.L. Burn, I.D.W. Samuel, Macromolecules 38 (2005) 9564; (h) T. Tsuzuki, N. Shirasawa, T. Suzuki, S. Tokito, Jpn. J. Appl. Phys. 44 (2005) 4151; (i) T.D. Anthopoulos, M.J. Frampton, E.B. Namdas, P.L. Burn, I.D.W. Samuel, Adv. Mater. 16 (2004) 557; (j) S.-C. Lo, E.B. Namdas, P.L. Burn, I.D.W. Samuel, Macromolecules 36 (2003) 9721; (k) J.P.J. Markham, S.-C. Lo, S.W. Magennis, P.L. Burn, I.D.W. Samuel, Appl. Phys. Lett. 80 (2002) 2645.
- [3] (a) P.L. Burn, S.-C. Lo, I.D.W. Samuel, Adv. Mater. 19 (2007) 1675; (b) S.-C. Lo, P.L. Burn, Chem. Rev. 107 (2007) 1097.
- [4] N. Iguchi, Y.-J. Pu, K. Nakayama, J. Kido, J. Photopolym. Sci. Technol. 20 (2007) 73.
- [5] (a) S.-J. Su, D. Tanaka, Y.-J. Li, H. Sasabe, T. Takeda, J. Kido, Org. Lett. 10 (2008) 941; (b) H. Sasabe, E. Gonmori, T. Chiba, Y.-J. Li, D. Tanaka, S.-J. Su, T. Takeda, Y.-J. Pu, K. Nakayama, J. Kido, Chem. Mater. 20 (2008) 5951; (c) H. Sasabe, T. Chiba, S.-J. Su, Y.-J. Pu, K. Nakayama, J. Kido, Chem. Commun. (2008) 5821; (d) D. Tanaka, H. Sasabe, Y.-J. Li, S.-J. Su, T. Takeda, J. Kido, Jpn. J. Appl. Phys. 46 (2007) L10; (e) T. Oyamada, H. Yoshizaki, H. Sasabe, C. Adachi, Chem. Lett. 33 (2004) 1034.
- [6] A.B. Tamayo, B.D. Alleyne, P.I. Djurovich, S. Lamansky, I. Tsyba, N.N. Ho, R. Bau, M.E. Thompson, J. Am. Chem. Soc. 125 (2003) 7377.
- [7] E.B. Namdas, A. Ruseckas, I.D.W. Samuel, J. Phys. Chem. B 108 (2004) 1570.
- [8] (a) S.-C. Lo, R.N. Bera, R.E. Harding, P.L. Burn, I.D.W. Samuel, Adv. Mater. 18 (2008) 3080; (b) S.-C. Lo, T.D. Anthopoulos, E.B. Namdas, P.L. Burn, I.D.W. Samuel, Adv. Mater. 17 (2005) 1945.
- [9] The PLQE of Ir(ppy) $_3$  is reasonable as compared with the value in the following literature: A. Endo, K. Suzuki, T. Yoshihara, S. Tobita, M. Yahiro, C. Adachi, Chem. Phys. Lett. 460 (2008) 155.
- [10] Y. Kawamura, J. Brooks, J.J. Brown, H. Sasabe, C. Adachi, Phys. Rev. Lett. 96 (2006) 017404.
- [11] K. Dedeian, P.I. Djurovich, F.O. Garces, C. Carlson, R.J. Watts, Inorg. Chem. 30 (1991) 1685.



# Unipolar nonvolatile memory devices with composites of poly(9-vinylcarbazole) and titanium dioxide nanoparticles

Byungjin Cho, Tae-Wook Kim, Minhyeok Choe, Gunuk Wang, Sunghoon Song, Takhee Lee \*

Department of Materials Science and Engineering, Gwangju Institute of Science and Technology, Gwangju 500-712, Republic of Korea

## ARTICLE INFO

### Article history:

Received 11 November 2008

Received in revised form 31 January 2009

Accepted 1 February 2009

Available online 8 February 2009

### PACS:

73.61.Ph

84.37.+q

85.35.-p

### Keywords:

Nonvolatile unipolar memory

Filamentary conduction

Poly(9-vinylcarbazole)

Titanium dioxide nanoparticles

## ABSTRACT

Organic-based devices with an  $8 \times 8$  array structure using titanium dioxide nanoparticles ( $\text{TiO}_2$  NPs) embedded in poly(9-vinylcarbazole) (PVK) film exhibited bistable resistance states and a unipolar nonvolatile memory effect.  $\text{TiO}_2$  NPs were a key factor for realizing the bistability and the concentration of  $\text{TiO}_2$  NPs influenced ON/OFF ratio. From electrical measurements, switching mechanism of PVK: $\text{TiO}_2$  NPs devices was closely associated with filamentary conduction model and it was found that the OFF state was dominated by thermally activated transport while the ON state followed tunneling transport. PVK: $\text{TiO}_2$  NPs memory devices in  $8 \times 8$  array structure showed a uniform cell-to-cell switching, stable switching endurance, and a high retention time longer than  $10^4$  s.

Crown Copyright © 2009 Published by Elsevier B.V. All rights reserved.

## 1. Introduction

Several types of organic electronics, including organic light emitting diodes, transistors, solar cells, and nonvolatile memory devices, have attracted considerable attention due to a variety of advantages such as printability, flexibility, low processing cost, and easy fabrication [1–4]. Among these organic electronics, organic memory devices have been investigated as a promising alternative to the conventional semiconductor-based nonvolatile memory devices [5–10]. In particular, organic memory devices employing nanoparticles in the active memory materials have been extensively studied due to easily controllable processing factors such as different kinds of particles, particle size, and concentration of particles [11–13]. Much research has been done to construct organic memory devices with

high specifications including highly reproducible electrical characteristics, a large ON/OFF ratio, and a long retention time by optimizing these processing factors [11–14]. Bozano et al. showed that different types of nanoparticles (NPs) in hybrid organic–inorganic switching devices could tune the memory performance parameters such as threshold voltages and the ON/OFF ratio [14]. As compared with the organic memory devices with metallic NPs, relatively few studies have been conducted on the organic memory devices containing semiconducting NPs [15,16]. Memory devices with the hybrid organic–semiconducting NPs composites have been particularly attractive due to their unique advantages of low cost, inert chemical properties, and feasibility of various chemical compositions [15,16]. Li et al. reported data for bistability and operating mechanisms of memory devices fabricated with core/shell-type CdSe/ZnS NPs and chemically self-assembled ZnO NPs [15,16]. However, the detailed memory performances such as cell-to-cell uniformity, distribution of threshold voltages, and endurance cycles, which must be considered

\* Corresponding author. Tel.: +82 62 9702313; fax: +82 62 9702304.

E-mail address: [tlee@gist.ac.kr](mailto:tlee@gist.ac.kr) (T. Lee).

for realistic memory device application, have not been thoroughly investigated.

In this study, we report on the operation and performance of unipolar resistive switching devices involving titanium dioxide nanoparticles ( $\text{TiO}_2$  NPs) embedded in a poly(9-vinylcarbazole) (PVK) matrix layer in an  $8 \times 8$  cross-bar array structure. The switching mechanism and the charge transport were studied by electrical measurements. The statistical distribution of the ON and OFF states in the  $8 \times 8$  cell array was investigated to quantify cell-to-cell uniformity. Endurance cycle and retention tests were also performed to evaluate the performance of the memory devices.

## 2. Experimental

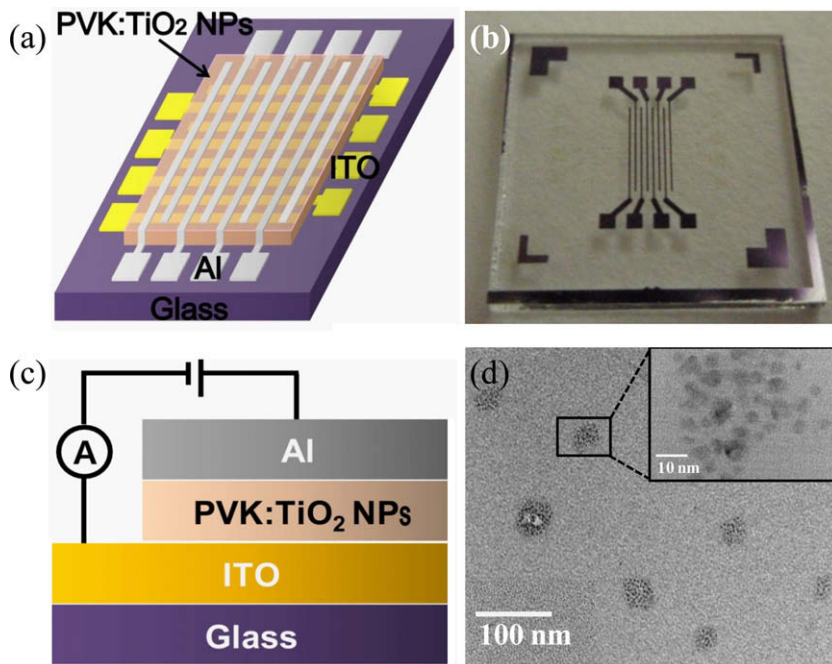
Organic memory devices using  $\text{TiO}_2$  NPs embedded in poly(9-vinylcarbazole) (PVK) in the  $8 \times 8$  cross-bar array structure were fabricated on indium tin oxide (ITO) (sheet resistance of  $\sim 8 \Omega/\square$ ) on glass substrates. ITO-coated glass substrates were pre-cleaned with a typical ultrasonic cleaning process. ITO electrodes with 8 line patterns of  $100 \mu\text{m}$  line-width were prepared as bottom electrodes (Fig. 1) by conventional photolithography and a subsequent etching process. PVK (molecular weight  $\sim 1,100,000$ ) and  $\text{TiO}_2$  NPs (anatase 5 nm) were used to make a mixture (PVK: $\text{TiO}_2 = 200:1, 150:1, 100:1, 10:1$ , and  $1:1$  solution volume ratios) of PVK solution (5 mg/ml) and  $\text{TiO}_2$  NPs solution (2 mg/ml) dissolved in 1,2-dichloroethane. The PVK: $\text{TiO}_2$  NPs solution was spin-coated at 4000 rpm for 40 s in a  $\text{N}_2$ -filled glove box and the thickness of the resulting film was measured to be  $\sim 60$  nm (for the case of PVK: $\text{TiO}_2 = 150:1$  volume ratio). To improve film

uniformity and remove residual solvent from the film, a baking process was performed on a hotplate in the  $\text{N}_2$ -filled glove box at  $150^\circ\text{C}$  for 2 min. Then, Al (100 nm thick) electrodes were deposited using an e-beam evaporator at a pressure of  $\sim 10^{-7}$  torr. Fig. 1a shows a schematic of the ITO/PVK: $\text{TiO}_2$  NPs/Al memory devices in the  $8 \times 8$  cross-bar array structure. An optical image of the fabricated memory devices is displayed in Fig. 1b. Fig. 1c shows a schematic cross-sectional view, illustrating the PVK: $\text{TiO}_2$  NPs composite layer sandwiched between ITO and Al. Aggregates of  $\text{TiO}_2$  NPs, having a diameter of 20–40 nm, were found within PVK matrix and the size of individual  $\text{TiO}_2$  NP was found as 3 to 7 nm as shown in the inset of Fig. 1d. As the PVK: $\text{TiO}_2$  NPs volume ratio changed from 200:1 to 1:1 (i.e., the  $\text{TiO}_2$  NPs concentration was increased), stronger aggregation of NPs was observed.

## 3. Results and discussion

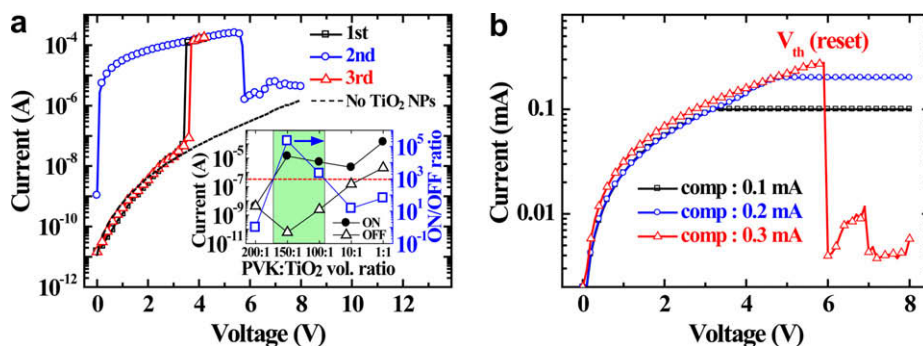
### 3.1. Switching characteristics

Fig. 2a shows current–voltage ( $I$ – $V$ ) characteristics of a memory cell in the  $8 \times 8$  cross-bar array devices consisting of the ITO/PVK: $\text{TiO}_2$  NPs (volume ratio 150:1)/Al structure. As the voltage was swept to a positive bias, the memory device exhibited an abrupt increase of current by three orders of magnitude near 3.4 V (set voltage), indicating an electrical resistance transition from a high resistance state (OFF state) to a low resistance state (ON state) (1st sweep). When the applied bias was higher than the set voltage, the device still remained in the ON state until 5.7 V (reset voltage). Beyond the reset voltage, a sharp decrease in the current occurred, showing a negative differential resistance



**Fig. 1.** (a) Schematic and (b) optical image of ITO/PVK: $\text{TiO}_2$  NPs/Al memory devices in an  $8 \times 8$  array structure. (c) Schematic of the cross-sectional view of ITO/PVK: $\text{TiO}_2$  NPs/Al structure. (d) TEM image of a composite film with PVK: $\text{TiO}_2$  NPs volume ratio of 150:1.





**Fig. 2.** (a)  $I$ - $V$  characteristics of a ITO/PVK:TiO<sub>2</sub> NPs (volume ratio of 150:1)/Al memory device (line + symbol curves) and ITO/PVK/Al device without TiO<sub>2</sub> NPs (dashed line). The inset shows ON and OFF currents (left axis) and ON/OFF ratio (right axis) measured at 0.5 V as a function of PVK:TiO<sub>2</sub> NPs volume ratio. (b) Turn-off process as a function of compliance current.

(NDR) behavior (2nd sweep). The NDR phenomenon has been reported elsewhere in other polymer-based memory devices [11,17]. The current beyond the NDR region ( $>5.7$  V) appeared to continue on a trend extending from OFF state. When the  $I$ - $V$  characteristics were measured again (3rd sweep), the device exhibited an almost equivalent track of the current that was shown during the 1st sweep, indicating a rewritable memory effect. Therefore, the device could be set from OFF to ON (writing) by applying a voltage slightly higher than the set voltage and reset from ON to OFF (erasing) by a voltage beyond the NDR region. In this system, the switching can be achieved by successive application of voltages of the same polarity, which is typical unipolar memory effect. From the  $I$ - $V$  characteristics described above, two different resistances at the same voltage could be obtained below the set voltage and remained stable even after the power was turned off, indicating the nonvolatile memory effect. However, devices made with just PVK without TiO<sub>2</sub> NPs showed no resistive switching behavior (dashed line in Fig. 2a). These effects clearly demonstrate that TiO<sub>2</sub> NPs play an important role in the electrical bistability phenomenon.

To investigate the role of TiO<sub>2</sub> NPs in the bistable switching, we performed  $I$ - $V$  measurements on devices with different TiO<sub>2</sub> NPs concentration. The ON and OFF state currents measured at 0.5 V are plotted as a function of PVK:TiO<sub>2</sub> NPs volume ratio, as shown in the inset of Fig. 2a (left axis). It can be seen clearly that the OFF current gradually increased with increasing TiO<sub>2</sub> NPs concentration while the ON current remained nearly constant regardless of TiO<sub>2</sub> NPs concentration. These different concentration-dependent features between ON and OFF currents eventually resulted in the large variation in the ON/OFF ratios, as summarized in the inset of Fig. 2a (right axis). Especially, NPs concentrations in the range from  $\sim 150:1$  to  $100:1$  volume ratio was observed to realize organic memory devices with high ON/OFF ratio more than three orders of magnitude. Therefore, the TiO<sub>2</sub> NPs concentration can be a critical factor for determining ON/OFF ratio, one of the key parameters of the memory operation. Contrary to OFF currents, ON currents show relatively little variation regardless of TiO<sub>2</sub> NPs concentration. It reveals that high current states are attributed to the introduction of TiO<sub>2</sub> NPs.

Specifically, the conduction process of ON state is consistent with the filamentary conduction model [18]. The model invokes the formation of filaments in the PVK polymer, exhibiting ohmic conduction without thermal activation. The fracture of the filaments is probably a consequence of Joule heating, raising the temperature of a part of the filament. The Joule heating effect gives rise to atomic reorganization. In our device, the filamentary paths are not only made by defects or structural disorder within the PVK polymer. TiO<sub>2</sub> NPs also become involved in formation of the filamentary paths. Growth of the filamentary paths may occur mainly in the localized region where TiO<sub>2</sub> NPs are distributed. TiO<sub>2</sub> NPs serve as one element source of materials which constitute the high conducting paths. It is reasonable to assume that the filament consists of TiO<sub>2</sub> NPs and some kind of defect within the PVK. Note that others have reported the bistability switching in PVK materials [19]. However the electrode materials, device structures, PVK layer thickness, and charge conduction behavior are different from our devices [20], which may explain different switching properties.

PVK is well known as a hole transporting material [21]. Some reports on polymer memory devices using PVK or PVK composite with NPs suggested that holes can serve as major carriers to cause the memory effect [19,22]. Furthermore, hole injection barrier of PVK is much lower than electron injection barrier because of the relatively high highest occupied molecular orbital (HOMO) energy level of PVK. Thus, holes will be the major charge carriers responsible for the memory effect. PVK mainly functions as matrix where filamentary paths are formed.

Fig. 2b shows the turn-off process as a function of compliance current. Once the ON state was formed, the OFF state could be obtained only when enough compliance current was applied to the devices. The turn-off process of the memory devices could be triggered only by the appropriate compliance current. In Fig. 2b, the device did not turn to the OFF state if the compliance current was set at 1 mA or 2 mA, but it successfully turned to the OFF state when the compliance current was set larger than 3 mA. A similar compliance dependency of the turn-off process has been reported for the case of memory devices with the Al/PVK/Al structure previously [19]. Our device showed considerable noise fluctuations beyond the NDR region. The noise

might have been closely related with rupturing and regrowing of conducting filaments inside the PVK polymer on the filament model [18]. The number of mobile carriers and their mobility would have provoked noise fluctuations. The considerable noise fluctuations generally occurred within the NDR region which displayed a gradual decrease of current [18,23], whereas the noise of our devices appeared after the NDR region (Fig. 2b). Note that some reports suggested that the bistability of the organic nonvolatile memory devices is attributed to the effect of an interfacial oxide layer such as  $\text{Al}_2\text{O}_3$  [24,25]. In order to minimize the possible effect of the thin native oxide, the Al top electrode was deposited on the composite film with a delay time as small as possible. In addition, to minimize  $\text{O}_2$  and  $\text{H}_2\text{O}$  effects, all electrical measurements were performed in a nitrogen filled glove box.

To obtain further information about the switching characteristics of the devices, we examined the correlation between the set current (current at the set voltage) and the reset current (current at the reset voltage). As shown in Fig. 3, we found that the reset current gradually increased as increasing the set current. This correlation between reset and set currents can also be used to understand the mechanism of memory operation associated with the filamentary conduction model [19,26]. It is expected that the higher set current will form stronger filaments. On the other hand, if the stronger filaments are formed, it is hard to break the filamentary current path, and thus the higher reset current should be expected.

### 3.2. Charge transport mechanism

The charge transport mechanism was studied by temperature-variable  $I$ - $V$  measurements in a vacuum pressure of  $\sim 10^{-3}$  torr. Fig. 4 is the Arrhenius plot of the ON and OFF state currents in the temperature range from 150 to 300 K. The ON and OFF currents were read at 2 V while the temperature was swept at a speed of 2 K/min. The OFF current can be explained by a thermally activated transport with an activation energy of  $\sim 66$  meV. In contrast, the ON current was almost temperature-independent, exhibiting negligible activation energy of  $\sim 3$  meV. It was found that the log-log plot of the ON current clearly exhibited the form of  $I$ - $V$ , indicating ohmic characteristics (Fig. 4 inset). These features of the ON current are mainly attributed to charge

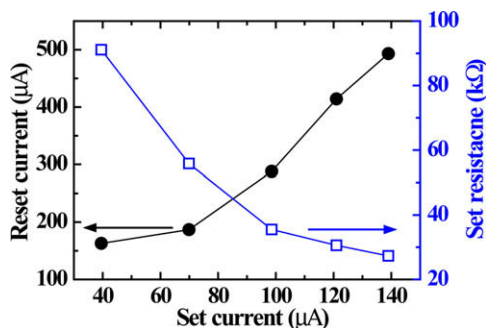


Fig. 3. Reset current (left axis) and set resistance (right axis) as a function of set current for a ITO/PVK:TiO<sub>2</sub> NPs (volume ratio of 150:1)/Al memory device.

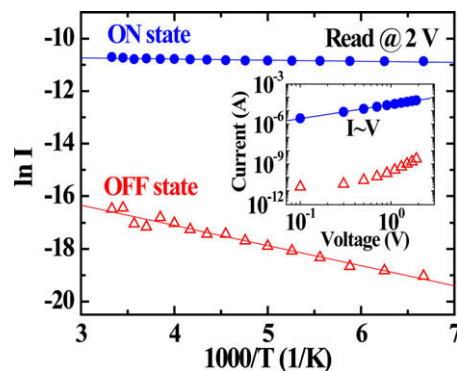


Fig. 4. Arrhenius plot of ON and OFF currents at temperature range from 150 to 300 K for a ITO/PVK:TiO<sub>2</sub> NPs (volume ratio of 150:1)/Al device. The inset shows the log-log plot of  $I$ - $V$  characteristics in the voltage range of 0 to 2 V at 300 K.

tunneling through filamentary paths induced by high electric field [18,24,27]. Consequently, bistable resistance switching of PVK:TiO<sub>2</sub> NPs devices accompanies the change of charge conduction mechanism from thermally activated transport (OFF state) into tunneling transport (ON state).

### 3.3. Memory performance

For practical memory device applications, the cell-to-cell uniformity of memory array devices is critical. Fig. 5 shows the cumulative probability data of ITO/PVK:TiO<sub>2</sub> NPs/Al memory devices, exhibiting a good cell-to-cell uniformity. Our memory devices have a narrow distribution in both the ON and OFF states. Particularly, the OFF state showed less variable resistance due to the insulating property of the PVK polymer. The statistical distribution of both the set and reset threshold voltages was obtained from repetitive sweeping operation of a single cell, as shown in the inset of Fig. 5. Both distributions of the set and reset threshold voltages were fitted with Gaussian functions with  $3\sigma$  (three standard deviations), shown as black curves in the inset. The set voltages were mainly distributed from 2.5 to 4 V, and the reset voltages ranged widely from 5 to

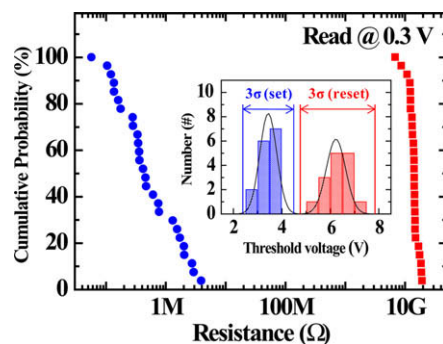
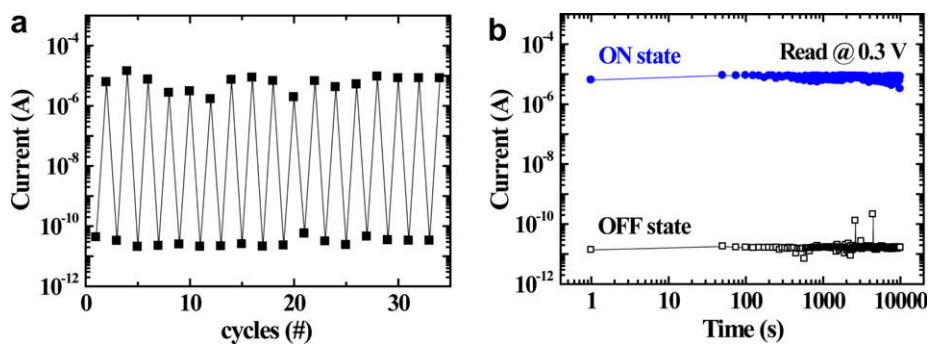


Fig. 5. A cumulative probability data set of ITO/PVK:TiO<sub>2</sub> NPs (volume ratio of 150:1)/Al memory devices, exhibiting a good cell-to-cell uniformity. The inset shows the distribution of set and reset threshold voltages from repetitive sweep cycles from a single working cell. Both distributions were fitted with Gaussian functions with  $3\sigma$  (three standard deviations), shown as black curves in the inset.



**Fig. 6.** (a) Endurance cycles obtained by repetitive sweeping and (b) retention time characteristics of the two resistance states under 0.3 V constant voltage stress.

7.5 V, showing a difference of  $\sim 1$  V. Thus, the distribution of each threshold voltage was fairly separated enough to be utilized for potential memory application. The substantial distribution of switching voltages is especially important for determining the operative voltages of resistance-based memory devices which can be definitely distinguished between the OFF and ON state.

The performance evaluation of the memory devices was checked by endurance and retention tests. Fig. 6a shows the sweep endurance of the PVK:TiO<sub>2</sub> NPs memory devices. The initial state for the device was OFF, and, after sweeping by 4.3 V, the ON state was achieved. The state of the devices (ON or OFF) could be determined by measuring the current at a read voltage of 0.3 V. Two stable resistance states with a high ON/OFF ratio were achieved, which can provide improved information storage ability by precise control over the ON and OFF states. In addition, the retention test result is shown in Fig. 6b. The PVK:TiO<sub>2</sub> NPs memory devices presented reasonably good retention characteristics for  $10^4$  s without significant current degradation, maintaining an ON/OFF ratio of over  $10^5$ . However, the formed filamentary paths will become gradually weak. It indicates that the device cannot keep the ON state any more after a long time.

#### 4. Conclusions

In summary, we demonstrated unipolar nonvolatile resistive switching devices with an  $8 \times 8$  array structure based on composites of PVK and TiO<sub>2</sub> NPs. The TiO<sub>2</sub> NP induced the bistability and its concentration within PVK was a critical factor to control ON/OFF ratio. From electrical characterizations, the switching was mainly governed by the filamentary conduction mechanism and the transport accompanied the change from thermally activated transport (OFF state) into tunneling transport (ON state). The PVK:TiO<sub>2</sub> NPs memory devices showed uniform cell-to-cell switching, stable endurance, and good retention, which feature a potential application for nonvolatile memory devices.

#### Acknowledgements

This work was supported by the National Research Laboratory (NRL) Program of the Korea Science and Engineer-

ing Foundation (KOSEF), the Program for Integrated Molecular System at GIST, and System IC 2010 project of Korea Ministry of Knowledge Economy.

#### References

- [1] S.H. Park, Y. Jin, J.Y. Kim, S.H. Kim, J. Kim, H. Suh, K. Lee, *Adv. Funct. Mater.* 17 (2007) 3063.
- [2] Y. Chen, G.-Y. Jung, D.A.A. Ohlberg, X. Li, D.R. Stewart, J.O. Jeppesen, K.A. Nielsen, J.F. Stoddart, R.S. Williams, *Nanotechnology* 14 (2003) 462.
- [3] J.Y. Kim, K. Lee, N.E. Coates, D. Moses, T.-Q. Nguyen, M. Dante, A.J. Heeger, *Science* 317 (2007) 222.
- [4] J. Ouyang, C.-W. Chu, C.R. Szmanda, L. Ma, Y. Yang, *Nat. Mater.* 3 (2004) 918.
- [5] K. Galatsis, K. Wang, Y. Botros, Y. Yang, Y.-H. Xie, J.F. Stoddart, R.B. Kaner, C. Ozkan, J. Liu, M. Ozkan, C. Zhou, K.W. Kim, *IEEE Circ. Dev. Mag.* 22 (2006) 12.
- [6] J.C. Scott, L.D. Bozano, *Adv. Mater.* 19 (2007) 1452.
- [7] E.Y.H. Teo, Q.D. Ling, Y. Song, Y.P. Tan, W. Wang, E.T. Kang, D.S.H. Chan, C. Zhu, *Org. Electron.* 7 (2006) 173.
- [8] J. Chen, D. Ma, *J. Appl. Phys.* 100 (2006) 034512.
- [9] F. Verbakel, S.C.J. Meskers, R.A.J. Janssen, H.L. Gomes, A.J.M. van den Biggelaar, D.M. de Leeuw, *Org. Electron.* 9 (2008) 829.
- [10] B.C. Das, A.J. Pal, *Org. Electron.* 9 (2008) 39.
- [11] R.J. Tseng, J. Huang, J. Ouyang, R.B. Kaner, Y. Yang, *Nano Lett.* 5 (2005) 1077.
- [12] D.T. Simon, M.S. Griffo, R.A. DiPietro, S.A. Swanson, S.A. Carter, *Appl. Phys. Lett.* 89 (2006) 133510.
- [13] Y. Song, Q.D. Ling, S.L. Lim, E.Y.H. Teo, Y.P. Tan, L. Li, E.T. Kang, D.S.H. Chan, C. Zhu, *IEEE Electron. Dev. Lett.* 28 (2007) 107.
- [14] L.D. Bozano, B.W. Kean, M. Beinhoff, K.R. Carter, P.M. Rice, J.C. Scott, *Adv. Funct. Mater.* 15 (2005) 1933.
- [15] F. Li, T.W. Kim, W. Dong, Y.H. Kim, *Appl. Phys. Lett.* 92 (2008) 011906.
- [16] F. Li, D.I. Son, S.M. Seo, H.M. Cha, H.J. Kim, B.J. Kim, J.H. Jung, T.W. Kim, *Appl. Phys. Lett.* 91 (2007) 122111.
- [17] L.D. Bozano, B.W. Kean, V.R. Deline, J.R. Salem, J.C. Scott, *Appl. Phys. Lett.* 84 (2004) 607.
- [18] G. Dearnaley, A.M. Stoneham, D.V. Morgan, *Rep. Prog. Phys.* 33 (1970) 1129.
- [19] Y.-S. Lai, C.-H. Tu, D.-L. Kwong, J.S. Chen, *Appl. Phys. Lett.* 87 (2005) 122101.
- [20] Y.-S. Lai, C.-H. Tu, D.-L. Kwong, J.S. Chen, *IEEE Electron. Dev. Lett.* 27 (2006) 451.
- [21] Q.D. Ling, S.L. Lim, Y. Song, C.X. Zhu, D.S.H. Chan, E.T. Kang, K.G. Neoh, *Langmuir* 23 (2007) 312.
- [22] D.-I. Son, J.-H. Kim, D.-H. Park, W.K. Choi, F. Li, J.H. Ham, T.W. Kim, *Nanotechnology* 19 (2008) 055204.
- [23] G. Dearnaley, D.V. Morgan, A.M. Stoneham, *J. Non-Cryst. Solids* 4 (1970) 593.
- [24] M. Cölle, M. Büchel, D.M. de Leeuw, *Org. Electron.* 7 (2006) 305.
- [25] F. Verbakel, S.C.J. Meskers, R.A.J. Janssen, *Appl. Phys. Lett.* 91 (2007) 192103.
- [26] W. Guan, S. Long, Q. Liu, M. Liu, W. Wang, *IEEE Electron. Dev. Lett.* 29 (2008) 434.
- [27] H.S. Majumdar, J.K. Baral, A. Laiho, J. Ruokolainen, O. Ikkala, R. Österbacka, *Adv. Mater.* 18 (2006) 2805.



## Efficiency analysis of organic light-emitting diodes based on optical simulation

Benjamin C. Krummacher<sup>a</sup>, Stefan Nowy<sup>b</sup>, Jörg Frischeisen<sup>b</sup>, Markus Klein<sup>a</sup>, Wolfgang Brütting<sup>b,\*</sup>

<sup>a</sup> OSRAM Opto Semiconductors, OLED-Lighting, Leibnizstr. 4, D-93055 Regensburg, Germany

<sup>b</sup> Experimental Physics IV, University of Augsburg, 86135 Augsburg, Germany

### ARTICLE INFO

#### Article history:

Received 3 November 2008

Received in revised form 30 January 2009

Accepted 2 February 2009

Available online 11 February 2009

#### Keywords:

Organic light-emitting diode

Quantum efficiency

Optical simulation

### ABSTRACT

In spite of huge progress in improving the internal quantum efficiency of organic light-emitting diodes (OLEDs), these devices still suffer from poor light out-coupling. Loss mechanisms are for example waveguiding in the organic layers and the substrate as well as the excitation of surface plasmons at metallic electrodes. Their relative strength and the mutual dependence on the OLED structure have been studied both experimentally and by numerical simulation. Here, we consider the impact of the radiative quantum efficiency of the emitter material on predictions of light extraction from OLEDs. Competing processes resulting in non-radiative recombination of charge carriers usually reduce the emitter quantum efficiency in a real device. We show that optical simulation leads to erroneous conclusions when neglecting these competing processes. Furthermore, we demonstrate a method, which allows determining both the radiative quantum efficiency and the charge recombination factor via simulation based analysis of experimental data. This analysis of device efficiency is applied on a set of red-emitting electrophosphorescent devices.

© 2009 Elsevier B.V. All rights reserved.

### 1. Introduction

Organic solid state lighting technology is on the verge of creating commercial applications in the lighting sector. The possibility of producing a flat large area lighting panel drives the development of creative products and opens exciting fields of application. However, one evident drawback is still the low light out-coupling efficiency of organic light-emitting diodes (OLEDs). The external device efficiency is significantly reduced by various optical loss channels. Considering a conventional coplanar bottom-emitting OLED based on an ITO coated glass substrate a major part of the generated radiant power is lost to thin film waveguided modes (or ITO/organic waveguided modes), surface plasmon polariton modes of the metal cathode and sub-

strate waveguided modes. Furthermore a small fraction of the generated radiation is absorbed by the materials of the different layers.

The modification of the substrate surface directed towards the ambient environment is a basic approach to increase external device efficiency. Diffuse layers (i.e. scattering particles in a transparent matrix [1–4]), microstructured films (e.g. microlens arrays [5]) or roughened substrates [6] are well-known techniques for this purpose. Application of a diffusor or sandblasting the substrate are low cost approaches which could be used in future mass production.

Although, external device efficiency could be increased by such methods, substrate surface modification cannot be utilized, when a reflecting off-state appearance of the bottom-emitting OLED is desired. The optimum configuration of such a device differs from the one of a device with substrate surface modification: Maximum light has to be directed into the light escape cone of the substrate in the

\* Corresponding author.

E-mail addresses: [benjamin.krummacher@osram-os.com](mailto:benjamin.krummacher@osram-os.com) (B.C. Krummacher), [wolfgang.brueetting@physik.uni-augsburg.de](mailto:wolfgang.brueetting@physik.uni-augsburg.de) (W. Brütting).

case of a non modified substrate. On the other side maximum radiant power has to be coupled from the thin film stack into the substrate when using substrate surface modification. Here, we neglect aspects regarding the target emission color (e.g. there is a wavelength dependence of the enhancement factor of light out-coupling, which leads to a change in emission color after applying the substrate surface modification [7]).

Recently, we have studied optical loss mechanisms and the light extraction efficiencies of OLEDs by means of a dipole model [8]. We have shown that experimental data on the angular dependent emission spectra of green bottom-emitting OLEDs are in excellent agreement with optical simulations. Furthermore, we have demonstrated the influence of different device parameters, like organic layer thicknesses and the position of the emission layer, on the coupling of the emitting dipoles to different optical channels in an OLED. In this article we consider the impact of the radiative quantum efficiency of the emitter material on predictions of external device efficiency obtained from optical simulation in more detail. The radiative quantum efficiency  $q$  of an emitting dye is defined as the quantum efficiency in an unbounded space filled by the dye and its host. Non-radiative recombination of charge carriers, e.g. by bimolecular recombination processes or interaction with charge carriers, reduces the value of  $q$ . The intention of this paper is twofold: First we will demonstrate that optical simulations neglecting the impact of these competing processes on  $q$  lead to erroneous results not only in terms of the total amount of light extracted from an OLED, but also concerning the optimal device architecture to achieve this. Secondly, we will show that even if the radiative quantum efficiency of an emitter material is not known beforehand, it can be extracted by an analysis of experimental data based on optical simulation.

## 2. Method

### 2.1. Experimental

The structure of the red-emitting electrophosphorescent OLEDs used for this study was 113 nm indium tin oxide (ITO)/203 nm hole transporting layer (HTL)/10 nm electron blocking layer (EBL)/7 nm emission layer (EML)/10 nm hole blocking layer (HBL)/electron transporting layer (ETL)/200 nm Ag-cathode (see Fig. 1). The thickness of the ETL was varied in the range from 48 to 110 nm. The peak wavelength of the photoluminescence spectrum of the red-emitting phosphorescent dye was 593 nm.

The ETL and HTL were doped by materials improving electron and hole transport, respectively. The diodes were fabricated as follows: The organic stack was deposited on ITO coated glass substrates (refractive index 1.52) using standard evaporation technique from crucibles. The evaporation rate was 1 Å/s at a base pressure of  $10^{-7}$  mbar. Following evaporation of the Ag-cathode, the devices were encapsulated with a glass lid and getter. The ETL and its dopant, the HTL and its dopant, and the matrix of the EML and its red dye were applied by co-evaporation. The active area of the OLEDs was 4 mm<sup>2</sup>. Additionally single layers were deposited on silicon substrates. To ensure

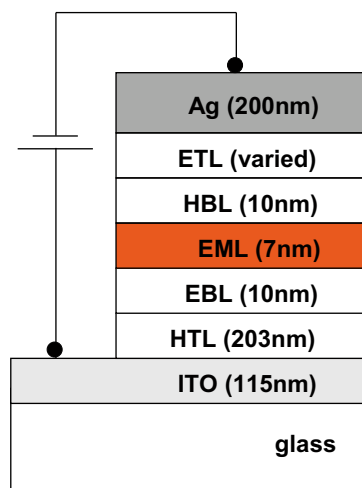


Fig. 1. Structure of the red-emitting electrophosphorescent OLEDs used in this study. The thickness of the ETL has been varied in the range between 48 and 110 nm.

accurate optical simulation, the complex index of refraction of the samples as a function of wavelength was determined by means of standard spectral ellipsometry for all organic layers.

The current density–voltage ( $j$ – $V$ ) characteristics of the devices used in this study were measured by means of a Keithley 238 as current source and a Keithley 6514 as voltmeter. The experimental  $j$ – $V$  characteristics of the devices with thinnest (48 nm) and thickest (110 nm) ETL are plotted in Fig. 2. Both characteristics do not differ significantly, which can be attributed to appropriate n-doping. As will be shown below, the optical properties of the device are strongly affected by the thickness variation of the n-doped ETL, while there is almost no change in the electrical properties of the diode.

In order to collect both directly emitted light and light coupled from the active layers into the substrate, the bottom-emitting OLEDs with planar substrate (4 mm<sup>2</sup> active area) was coupled to the center of a glass hemisphere (diameter 25 mm, refractive index 1.52) by using a refrac-

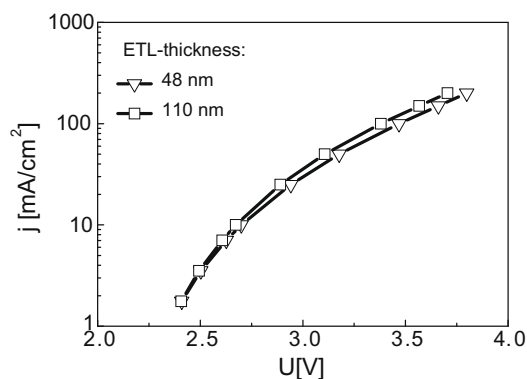


Fig. 2. Current density vs. voltage characteristics of devices with ETL thickness of 48 and 110 nm.

tive index matching gel obtained from Cargille Laboratories. The configuration effectively makes the emission angle in glass equal to the emission angle in air. Thus nearly all photons hit the surface of the glass hemisphere at normal incidence. This allows the measurement of the OLED emission within the substrate at angles exceeding the critical angle of total internal reflection between glass and air [9,10]. The emission of the OLED equipped with the glass hemisphere was measured in an integrating sphere, which was connected to a fiber spectrometer (Instrument Systems CAS 140B). The Commission Internationale de l'Éclairage (CIE) color coordinates related to the measured spectra of the different devices are given in Table 1. Additionally, the graph in Fig. 3 shows the external quantum efficiency as a function of current density as obtained from the measurements of the device with 72 nm ETL in the integrating sphere.

## 2.2. Optical modeling

The optical modeling of OLEDs must consider near-field phenomena and the photonic mode density due to the use of thin organic films. Traditional device simulation is based on the dipole model developed by Chance, Prock and Silbey (CPS) for molecular fluorescence and energy transfer near interfaces [11,12]. This model was extended to the near-field optics of OLEDs by various authors [13–17], where an exciton within the OLED is modeled as a point dipole driven by the reflected electromagnetic waves inside a microcavity.

The simulations presented in this work are also based on this traditional approach of emissive dipoles. The dipoles, embedded in the multilayer stack of an OLED, are treated as forced damped harmonic oscillators [13,14]

$$\frac{d^2 p}{dt^2} + \omega_0^2 p = \frac{e^2}{m} E_r - b_0 \frac{dp}{dt}, \quad (1)$$

where  $p$  is the electric dipole moment,  $\omega_0$  is the resonant angular frequency in the absence of damping,  $m$  is the effective mass,  $e$  the electric charge,  $E_r$  is the reflected electric field at the dipole position and  $b_0$  is the radiative decay rate in the absence of any interfaces. Both the dipole and the reflected field oscillate with the same complex frequency  $\Omega = \omega - ib/2$  as:

$$p = p_0 \exp(-i\Omega t) \quad \text{and} \quad E_r = E_0 \exp(-i\Omega t) \quad (2)$$

where  $\omega$  and  $b$  are the frequency and decay rate in the presence of interfaces. Then the modified decay rate is obtained as:

**Table 1**

CIE color coordinates related to the emission measured in an integrating sphere. The devices were operated at a current density of 7.5 mA/cm<sup>2</sup>.

ETL thickness (nm)	CIE x	CIE y
48	0.612	0.387
56	0.612	0.386
64	0.613	0.385
72	0.614	0.384
98	0.616	0.383
110	0.617	0.380

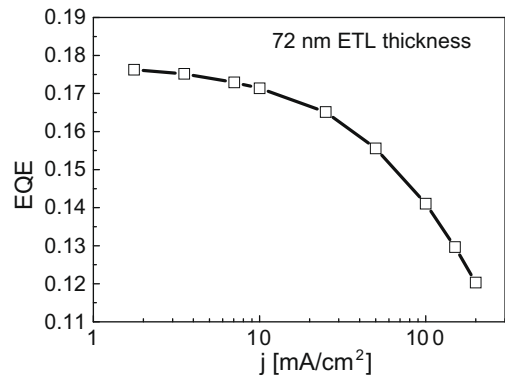


**Fig. 3.** Plot of the measured external quantum efficiency as a function of current density for the device with an ETL thickness of 72 nm.

$$b = b_0 + \frac{e^2}{m\omega p_0} \text{Im}(E_0). \quad (3)$$

This equation shows that the change of the decay rate inside the microcavity is determined by the magnitude of the reflected electric field at the position of the emitting dipole. It is calculated using the Hertz vector and solving the Helmholtz equation by an expansion into plane waves (for details see e.g. Lukosz et al. [18]). Thereby all layers in this multilayer stack are treated as infinite in two dimensions, having a certain thickness in the third direction. The interface between two layers is assumed sharp and without roughness. Using a transfer matrix method the Fresnel coefficients are calculated by taking the optical constants and thicknesses of the different layers of the OLED stack into account, as well as the position of the dipoles within the OLED, which is assumed to be sharp as well. The modified decay rate for arbitrary dipole orientation can then be expressed as a combination of parallel and perpendicular contributions  $b_{\parallel}$  and  $b_{\perp}$ , respectively, which are calculated numerically by integrating over all in-plane wave vector values of  $k_x$  from 0 to  $\infty$  (for details see Chance et al. or Barnes [12,14]). Thereby the radiative quantum efficiency of the emitter (denoted as  $q$ ) enters as a material parameter. Finally the orientation of the dipoles (parallel or perpendicular to the substrate, weighted 2:1 for isotropic dipole orientation) yielding

$$b_{\text{iso}} = \frac{2}{3} b_{\parallel} + \frac{1}{3} b_{\perp} \quad (4)$$

and the emission spectrum of the emitter is taken into account. As a result we obtain a polychromatic power dissipation spectrum, i.e. the contribution of modes with in-plane wave vector component  $k_x$  to the spontaneous emission decay rate of the dipoles at each wavelength. (An example of such a power dissipation spectrum for a green fluorescent device calculated by this method can be found in our recent publication [8].)

The power dissipation spectra can be split up into four regions depending on the magnitude of the in-plane wave vector component  $k_x$  as compared to the vacuum wavelength  $\lambda$  and the (effective) refractive index  $n$  of the medium, where the produced radiation is traveling. Region 1

with  $k_x < 2\pi n_{\text{air}}/\lambda$  represents the light which can leave the OLED directly ('direct emission'). Region 2, where  $2\pi n_{\text{air}}/\lambda < k_x < 2\pi n_{\text{glass}}/\lambda$  is valid, denotes the amount of light which is emitted to the glass substrate and is trapped there due to total internal reflection ('emission to substrate'). For even larger values of  $k_x$  the radiation of the dipoles does no longer reach the glass substrate but is waveguided in the organic layers and the adjacent ITO electrode ('waveguiding', region 3) with  $2\pi n_{\text{glass}}/\lambda < k_x < 2\pi n_{\text{ITO+org}}/\lambda$ , where  $n_{\text{ITO+org}}$  denotes an effective refractive index of the ITO and organic layers taken together. Finally, for  $k_x > 2\pi n_{\text{ITO+org}}/\lambda$ , the emitting dipoles couple to surface plasmon polaritons (SPPs) traveling at the organic–cathode interface ('plasmons', region 4). We note that, in principle, waveguided modes and SPPs (apart from very small distances between the emitting dipoles and the metal electrodes ( $\leq 25$  nm) not being relevant here) contribute to an enhancement of the spontaneous emission decay rate, although it is usually not possible to extract the energy contained in these modes [8]. Integrating over the different regions in the polychromatic power dissipation spectrum leads to the amount of power coupled into the different modes. Additionally the transmission of the generated light (i.e. 'direct emission' + 'emission to substrate') through the OLED stack is calculated from the optical constants and thickness of each layer with a transfer matrix method. Thus by comparing the internal and the transmitted power of these two modes, the total amount of light absorbed in the OLED stack is determined.

To confirm the outcome of the simulations the power dissipation spectra can be compared to the experimental angular emission spectra of the OLEDs, optionally with the distinction between s- and p-polarization. This has been done in Ref. [8] for a green bottom-emitting device and is thus not shown here.

### 3. Results and discussion

#### 3.1. Effect of the radiative quantum efficiency

In this section we discuss the impact of the radiative quantum efficiency of the emitter material  $q$  on predictions of the external quantum efficiency of organic light-emitting diodes. In general the optical performance of OLEDs depends on several factors. For example, the layer thicknesses mainly have an influence on the waveguided modes, whereas the location of the emission zone (i.e. in terms of the model: *the location of the dipole layer*) determines the fraction of power dissipated by the waveguided modes and the fraction coupled to surface plasmon polaritons (SPPs) [8]. Simulations of the red-emitting OLEDs described above have been performed using the model presented in Section 2.2. Here the emission zone was assumed to be located at the interface between EML and HBL. This can be concluded from the excellent hole transporting properties of the host material used for the EML. Furthermore the free emitter spectrum is needed as input for the simulations. Here, we define the free emitter spectrum as the emission spectrum of the emitter in an unbounded space filled with the material(s) forming the EML. The free emitter spectrum has been extracted from

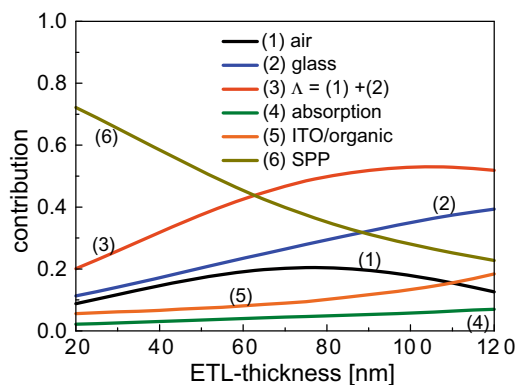


**Fig. 4.** Plots of the relative contributions of the different optical loss channels as a function of the ETL thickness. The data was obtained from simulation, where the radiative quantum efficiency was set to  $q = 1$ .

the electroluminescence spectrum emitted in the direction perpendicular to the substrate by applying optical simulation on the measured data.<sup>1</sup> The computed contributions of the different loss channels as a function of ETL thickness are plotted in the graph of Fig. 4. The radiative quantum efficiency  $q$  was set to be one in the calculations, i.e. the presence of processes resulting in non-radiative recombination of electrons and holes was neglected. The variation of the ETL thickness not only influences the waveguided modes (plots (2) and (5) in Fig. 4), but the dipole layer position with respect to the cathode as well. This leads to changes in the contribution of the SPP losses (6). The coupling to SPPs is reduced drastically as the dipole layer moves further away from the cathode. At the same time the fraction of ITO/organic waveguided light (5) increases. Furthermore, the total amount of absorbed light (4) increases with increasing ETL thickness. As all other layer thicknesses have been kept constant, this is mostly due to the absorbing n-dopant of the ETL. The direct emission into air (1) shows a maximum at 75 nm ETL thickness. The amount of light coupled from the active layers into air and substrate (3) has its maximum at 105 nm ETL thickness. This configuration has to be chosen if optimum efficiency based on substrate surface modification is desired. However, we have already shown in another article that the optimal dipole layer position also depends on the radiative quantum efficiency  $q$  [8]. We will discuss the role of  $q$  in more detail in the following.

The radiative quantum efficiency  $q$  of an electroluminescent dye is defined as the quantum efficiency of electroluminescence in an unbounded space filled by the dye and its host. Competing processes resulting in non-radiative recombination of charge carriers reduce the radiative quantum efficiency. Possible competing processes include impurity quenching [19], triplet–polaron annihilation [20] or triplet–triplet annihilation [21]. The importance of the latter two is evident from the current–density

<sup>1</sup> To obtain the free emitter spectrum we first simulated the zero degree emission from the OLED using a white spectrum (constant intensity over all wavelengths) and subsequently divided the outcome by the measured EL-spectrum.

dependent roll-off of the external quantum efficiency shown in Fig. 3.

The radiative quantum efficiency is given by:

$$q = k_r / (k_r + \sum k_{nr}) \quad (5)$$

where  $k_r$  is the radiative decay rate in an unbounded emitter material and  $\sum k_{nr}$  is the sum of the decay rates of all competing processes. In the optical cavity formed by an OLED device the radiative decay rate and the spatial distribution of the emitted radiation can be altered (see Section 2.2), if a fundamental mode of the system is resonant with the free emission spectrum [8,15]. (Please note, that in the terminology used here, waveguided modes and SPPs are not considered as non-radiative, because the exciton is *a priori* generating radiation – even though, it is hard to get that radiation out of the device.) Hence, the fraction of radiative decay in the OLED cavity can differ from the value  $q$  in the unbounded emitter space. This effective fraction of radiative decay in the EML of the device is given by:

$$q_{\text{eff}} = \frac{k_r^*}{k_r^* + \sum k_{nr}} \rightarrow q_{\text{eff}}(q) = \frac{q}{q + \frac{k_r}{k_r^*}(1-q)} \quad (6)$$

where  $k_r^*$  is the radiative decay rate determined by the boundary conditions of the electromagnetic field in the optical cavity. Such cavity effects on the radiative quantum efficiency are well explored for emitting dipoles in the vicinity of metal surfaces [11,12,22], but only rarely discussed in the context of OLEDs [16,23]. In many cases, device simulations assume  $q$  to be just a multiplicative factor, which is first taken to be unity and then scaled to match the measured external quantum efficiency of a device. As we will show below, this approach leads to erroneous results when the position of the emitter in the OLED cavity is varied.

Considering the layer structure of the red-emitting OLEDs described above,  $q_{\text{eff}}$  as a function of the ETL thickness is plotted for different values of the radiative quantum efficiency  $q$  in Fig. 5. The effective radiative quantum efficiency  $q_{\text{eff}}$  is significantly enhanced for smaller values of the ETL thickness. The enhancement is higher for lower values of the radiative quantum efficiency  $q$ . Fig. 6a shows

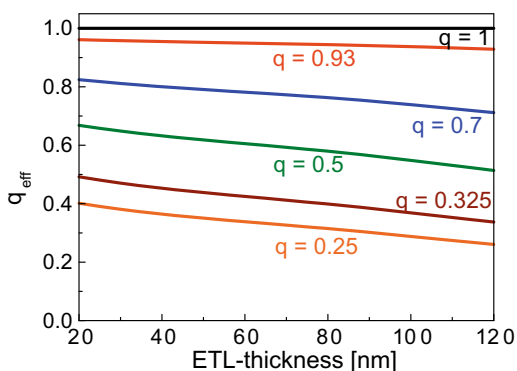


Fig. 5. Effective fraction of radiative decay in the emission layer as a function of layer thickness for different values of the radiative quantum efficiency  $q$ .

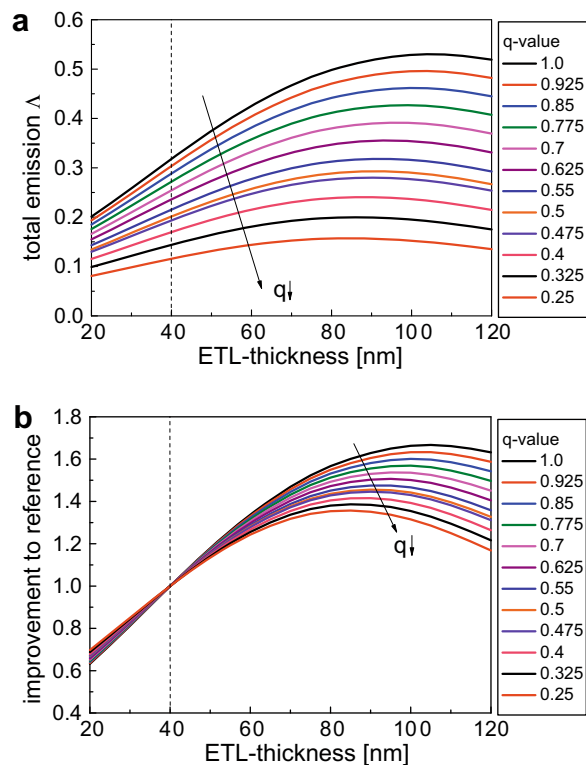


Fig. 6. (a) Plot of the generated light coupled from the active layers to the outside world (total emission  $A = \text{air} + \text{glass}$ ). The data was obtained by simulation assuming different values of  $q$ . (b)  $A$  as a function of ETL thickness normalized on the values at 40 nm ETL thickness. The plot gives the efficiency improvement in comparison to the reference device with 40 nm ETL.

the corresponding simulation results for the amount of light  $A$  coupled from the active layers to the outside world (i.e. the sum of the direct emission and the substrate waveguided light).  $A$  corresponds to the power fraction of all excitons generated in the emission layer which can leave the device. It can be seen, that both the values of  $A$  and the progression of the maxima depend on  $q$ . The ETL thickness, where the maximum of light accessible by substrate surface modification is located in each curve, increases for higher values of  $q$ . For a given value of  $q$  the location of this maximum is given by the trade-off between effective radiative rate and SPP losses, which are both dependent on the distance between the emission zone and the metal cathode (compare the curves in Fig. 5 to plot (6) in Fig. 4). Additionally the data shown in Fig. 6a has been normalized to the values for an ETL thickness of 40 nm (Fig. 6b), which was taken as reference configuration. Hence, the data of Fig. 6b give the improvement of  $A$  in comparison to the reference configuration. Again the achievable improvement depends on the radiative quantum efficiency  $q$ . Higher improvement can be obtained based on higher values of  $q$ , but at the same time the optimum device configuration moves to larger ETL thickness. This, however, implies that neither the optimum ETL thickness nor the achievable efficiency improvement of  $A$  can be predicted based on optical simulation alone, if the



radiative quantum efficiency  $q$  is not known beforehand, which is usually the case for new or undisclosed emitter systems.

White-emitting OLEDs usually comprise two or more emitting layers. Consequently exact simulation based prediction of emission color (or change in emission color) of such a device is challenging without knowledge of the radiative quantum efficiencies of the individual emitting components, since the resulting white spectrum relies on the effective decay rate of the different emitters. However, optical simulation may be used to obtain the radiative quantum efficiency from experimental data as will be shown in the following section.

### 3.2. Device analysis based on optical simulation

In this section we apply the above mentioned methodology to determine both the radiative quantum efficiency and the charge recombination factor via simulation based analysis of external quantum efficiencies of a series of devices with different ETL thickness.

The light generated by the red-emitting OLEDs and coupled from the active layers into the substrate has been measured by placing the devices equipped with a glass hemisphere into an integrating sphere. The external quantum efficiency (EQE) of this configuration is derived from the measurements of the light output and applied current:

$$\eta_{\text{EQE}} = N_{\text{ph}}/N_e \quad (7)$$

where  $N_{\text{ph}}$  is the number of photons emitted by the device divided by the number of electrons injected,  $N_e$ . When the measured *quantum* efficiency is brought in correlation with simulation results, one should keep in mind that the prediction of  $\Delta$  based on our model is a *power* contribution. However, the color of the emission detected in the integrating sphere is almost not affected by the variation of the ETL thickness of the red-emitting devices (Table 1), i.e. there is only little redistribution of the emission spectrum. Hence, the following equation can be used to fit the measurements of the EQE as a function of ETL thickness  $d$ :

$$\eta_{\text{EQE}}(d) = \gamma \cdot \eta_{\text{s/t}} \cdot q_{\text{eff}}(q) \cdot \eta_{\text{out}} = \gamma \cdot \eta_{\text{s/t}} \cdot \Delta_q(d), \quad (8)$$

where  $\gamma$  is the efficiency with which electrons and holes combine to form excitons (charge recombination factor),  $\eta_{\text{out}}$  is the light extraction efficiency,  $\eta_{\text{s/t}}$  is the fraction of excitons that is formed in a spin state capable of radiating (for phosphorescent materials such as the red-emitting dye of the considered devices this is unity) and  $q_{\text{eff}}$  is the effective quantum efficiency depending on  $q$  as discussed above. In principle, fitting Eq. (8) to the experimental thickness variation allows to extract both  $q$  and  $\gamma$ . We note that the charge recombination factor might change with the thicknesses of the layers and applied bias, however, as we only change the thickness of the n-doped ETL, which has almost no influence on the  $j$ - $V$  characteristics (see Fig. 2), it seems reasonable to assume the same value of  $\gamma$  for all layer thicknesses.

The measured external quantum efficiency as a function of ETL thickness is plotted in Fig. 7. The devices were

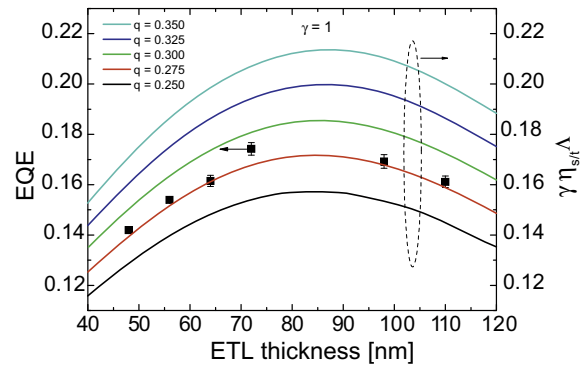


**Fig. 7.** Black squares: measured external quantum efficiency as a function of ETL thickness (device operation at current density of 7.5 mA/cm<sup>2</sup>). The error bars represent the standard deviation resulting from the measurements of several devices with the same ETL thickness. Solid lines: corresponding simulations for different quantum efficiencies  $q$  with a fixed charge recombination factor  $\gamma = 1$ .

operated at a current density of 7.5 mA/cm<sup>2</sup> when performing the measurements in the integrating sphere. Additionally five plots of the fit-function given in Eq. (8) are shown in the same graph, where only the quantum efficiency  $q$  is varied and the charge recombination factor is kept fixed as  $\gamma = 1$ . As the EQE scales linearly with the charge recombination factor and as  $\gamma$  can not be higher than one we can conclude from Fig. 7 that the quantum efficiency of the emitter must be at least  $q = 0.275$  or higher.

As discussed above,  $q$  determines the curve progression, i.e. the position of the maximum. Thus assuming a higher value for  $q$  can lead to a better correlation with the experimental data, but requires a charge recombination factor smaller than one (see Eq. (8)). This is shown in Fig. 8 for different combinations of  $q$  and  $\gamma$ . From this figure we conclude that the quantum efficiency  $q$  for this red phosphorescent emitter is about  $(33 \pm 5)\%$ . Still higher values of  $q$  result in a mismatch of the curve progression, which can not be scaled by the linear factor  $\gamma$ . The best fit result (red solid line in Fig. 8) is obtained for  $q = 0.325$  and

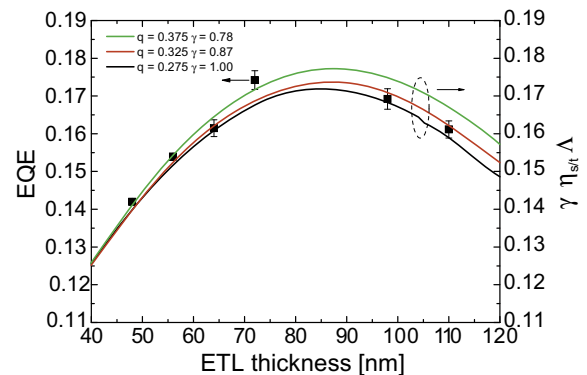


**Fig. 8.** Black squares: measured external quantum efficiency as a function of ETL thickness (same data as in Fig. 7). Solid lines: corresponding simulations for different combinations of quantum efficiency  $q$  and charge recombination factor  $\gamma$  (see Eq. (8)).

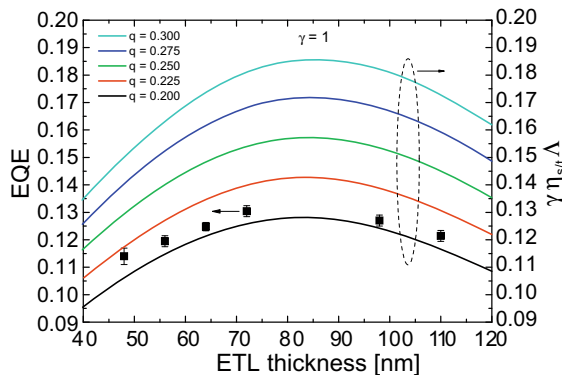


**Fig. 9.** Black squares: measured external quantum efficiency as a function of ETL thickness (device operation at current density of  $150 \text{ mA/cm}^2$ ). Solid lines: corresponding simulations for different quantum efficiencies  $q$  with a fixed charge recombination factor  $\gamma = 1$ .

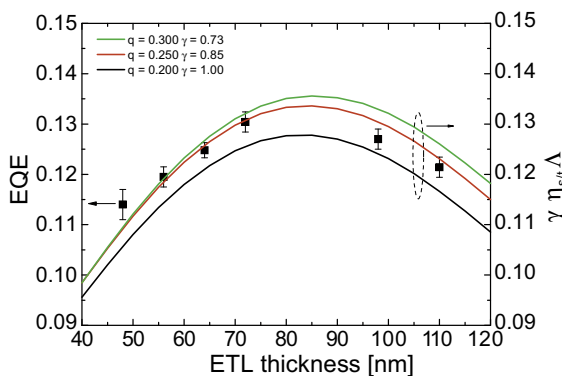


**Fig. 10.** Black squares: measured external quantum efficiency as a function of ETL thickness (same data as in Fig. 9). Solid lines: corresponding simulations for different combinations of quantum efficiency  $q$  and charge recombination factor  $\gamma$  (see Eq. (8)).

$\gamma = 0.87$ . For an accurate determination of both  $q$  and  $\gamma$  for sure, more experimental data points are required. However, our method, combining simulations and experimentally derived EQE, shows that a simultaneous determination of both quantities is possible.

Next, we confirm our method by ‘adjusting’ a lower value of the radiative quantum efficiency. As can be seen in Fig. 3, device efficiency decreases with increasing current density. This is expected due to the enhancement of triplet–polaron and triplet–triplet annihilation at higher values of current density, i.e. the rate of competing non-radiative processes is enhanced by increasing the operational current density. The graph in Fig. 9 shows the external quantum efficiency as a function of ETL thickness as derived from the measurements of the devices operated at a high current density of  $150 \text{ mA/cm}^2$ . Again, first the simulation results for  $\gamma = 1$  are shown, yielding a lower limit of  $q$  of at least 0.20. The adaption to the curve progression is shown in Fig. 10. The best fit of the experimental data in the case of  $j = 150 \text{ mA/cm}^2$  is obtained for  $q = 0.25$  and  $\gamma = 0.85$ . (Again the value of  $\gamma$  should be taken only as an estimate.) Compared to the above case this low-

er radiative quantum efficiency reflects the expected enhancement of non-radiative recombination at higher current density, resulting in a lower EQE (Fig. 3). Our method therefore demonstrates the ability to extract the quantum efficiency of an emitter embedded inside an OLED even for different current densities.

#### 4. Summary and conclusion

In conclusion we have discussed the impact of the radiative quantum efficiency of the emitter material on predictions of the external quantum efficiency of organic light-emitting diodes. We have shown that simulation based prediction of external efficiency (or efficiency improvement) is not possible without knowledge of  $q$ . Moreover, not only does the value of EQE depend on this quantity, but also the optimum position of the emission zone for achieving the highest light extraction efficiency. For a given value of  $q$  the location of the maximum is given by the trade-off between effective radiative rate and other losses like SPPs or waveguided modes, which are both dependent on the distance between the emission zone and the metal cathode. Furthermore, simulation based prediction of the resulting emission color (or change in emission color) of devices with several emitting layers is challenging without knowledge of the radiative quantum efficiencies of the individual emitting components.

In turn we have demonstrated that both the radiative quantum efficiency of an emitter inside an OLED stack and the charge recombination factor can be determined via simulation based analysis of experimental data. This analysis of device efficiency was successfully applied on a set of red-emitting electrophosphorescent devices.

#### Acknowledgements

The authors would like to thank Dr. Britta Götz for fruitful discussion and support and Daniel Setz for processing of simulation data and performing measurements. Furthermore the authors would like to thank the German Federal Ministry of Education and Research (BMBF) for funding part of this work under contract FKZ 13N8995 (OPAL).

#### References

- [1] T. Nakamura, N. Tsutsumi, N. Juni, H. Fujii, *J. Appl. Phys.* 96 (2004) 6016.
- [2] J.J. Shiang, A.R. Duggal, *J. Appl. Phys.* 95 (5) (2004) 2880.
- [3] J.J. Shiang, T. Faircloth, A.R. Duggal, *J. Appl. Phys.* 95 (5) (2004) 2889.
- [4] C. Gärditz, R. Paetzold, D. Buchhauser, R. Bathelt, G. Gieres, C. Tschamber, A. Hunze, K. Heuser, A. Winnacker, J.R. Niklas, J. Amelung, D. Kunze, *SPIE Conf. Proc.* 5937 (2005) 94–105.
- [5] H.J. Peng, Y.L. Ho, C.F. Qiu, M. Wong, H.S. Kwok, *SID Int. Symp. Digest* 158 (2004).
- [6] M. Scheffel, A. Hunze, J. Birnstock, J. Blässing, W. Rogler, G. Wittmann, A. Winnacker, in: *European Conference on Organic Electronics and Related Phenomena '01*, Proceedings, vol. 158, 2001.
- [7] B. Krummacher, M. Mathai, V. Choong, S.A. Choulis, F. So, A. Winnacker, *J. Appl. Phys.* 100 (2006) 054702.
- [8] S. Nowy, B.C. Krummacher, J. Frischeisen, N.A. Reinke, W. Brütting, *J. Appl. Phys.* 104 (2008) 123109.
- [9] M.H. Lu, J.C. Sturm, *J. Appl. Phys.* 91 (2002) 595.
- [10] V. Bulovic, V.B. Khalfin, G. Gu, P.E. Burrows, D.Z. Garbuzov, S.R. Forrest, *Phys. Rev. B* 58 (1998) 3730.

- [11] R.R. Chance, A. Prock, R. Silbey, *J. Chem. Phys.* 60 (7) (1974) 2744–2748.
- [12] R.R. Chance, A. Prock, R. Silbey, *Adv. Chem. Phys.* 37 (1978) 1–65.
- [13] L. Novotny, *J. Opt. Soc. Am. A* 14 (1) (1997) 91–104.
- [14] W.L. Barnes, *J. Mod. Opt.* 45 (4) (1998) 661–699.
- [15] J.A.E. Wasey, W.L. Barnes, *J. Mod. Opt.* 47 (4) (2000) 725–741.
- [16] L.H. Smith, J.A.E. Wasey, I.D.W. Samuel, W.L. Barnes, *Adv. Funct. Mater.* 15 (11) (2005) 1839–1844.
- [17] K. Celebi, T.D. Heidel, M.A. Baldo, *Opt. Exp.* 15 (4) (2007) 1762–1772.
- [18] W. Lukosz, W. Kunz, *J. Opt. Soc. Am.* 67 (1977) 1615.
- [19] M. Pope, C.E. Swenberg, *Electronic Processes in Organic Crystals and Polymers*, Oxford University Press, 1992.
- [20] N.C. Giebink, B.W. D'Andrade, M.S. Weaver, P.B. Mackenzie, J.J. Brown, M.E. Thompson, S.R. Forrest, *J. Appl. Phys.* 103 (2008) 044509.
- [21] M.A. Baldo, C. Adachi, S.R. Forrest, *Phys. Rev. B* 62 (2000) 10967–10977.
- [22] K.H. Drexhage, *Prog. Opt.* 12 (1974) 163–232.
- [23] H. Becker, S.E. Burns, R.H. Friend, *Phys. Rev. B* 56 (1997) 1893–1905.



# Environmental and operational stability of solution-processed 6,13-bis(triisopropyl-silylethynyl) pentacene thin film transistors

Sung Kyu Park<sup>a,\*</sup>, Devin A. Mourey<sup>b,c</sup>, Jeong-In Han<sup>a</sup>, John E. Anthony<sup>d</sup>, Thomas N. Jackson<sup>b,e</sup>

<sup>a</sup> Information Display Research Center, Korea Electronics Technology Institute, Sungnam, Kyunggi, Republic of Korea

<sup>b</sup> Center for Thin Film Devices, and Materials Research Institute, Penn State University, University Park, PA 16802, USA

<sup>c</sup> Department of Material Science Engineering, Penn State University, 121 Elect Engineering East, University Park, PA 16802, USA

<sup>d</sup> Department of Chemistry, University of Kentucky, Lexington, KY 40506, USA

<sup>e</sup> Department of Electrical Engineering, Penn State University, University Park, PA 16802, USA

## ARTICLE INFO

### Article history:

Received 10 November 2008

Received in revised form 6 February 2009

Accepted 10 February 2009

Available online 20 February 2009

### PACS:

73.40.-c

73.61.Ph

### Keywords:

Organic thin film transistor

Printed electronics

Stability

## ABSTRACT

We report operational and environmental stability of solution-processed organic thin film transistors (OTFTs) using the small molecule organic semiconductor 6,13-bis(triisopropyl-silylethynyl) pentacene (TIPS-pentacene). Typical drop-cast TIPS-pentacene OTFTs show strong molecular ordering and relatively stable characteristics with air and illumination compared to vapor-deposited pentacene OTFTs. For short channel length devices, TIPS-pentacene OTFTs undergo significant degradation with bias-stress, possibly due to operation at large drive currents and large local power dissipation as well as built-in charges in the channel area.

© 2009 Elsevier B.V. All rights reserved.

## 1. Introduction

Although a great deal of improvement has been achieved in vapor phase and solution-processed OTFTs [1–5], organic transistors still have the significant shortcoming of performance degradation due to environmental and operational instability of the organic active layer [6,7]. Extensive research efforts have been focused on synthesizing organic semiconductor materials with environmental and operational stability, high mobility, and good current modulation, in addition to improving OTFT performance by device engineering and optimizing processing conditions [8–10]. Because electronic applications of OTFTs may require good stability in threshold voltage and mobility, the factors that limit operational and environmental

stability of devices must be understood and controlled along with the factors that limit device performance.

Many studies have investigated the stability of OTFTs fabricated from vapor-deposited polycrystalline pentacene and solution-coated polymers [11–13]. Previous reports have shown that ambient O<sub>2</sub> may degrade pentacene TFT performance by oxidation of the pentacene molecule, while water and other polar molecules can generate traps at grain boundaries, which reduce mobility and current modulation, and cause threshold voltage changes [11,12]. Large operational power density, combined with exposure to an air ambient, has also led to performance degradation of bias-stressed OTFTs [14].

## 2. Experimental

In this report, both the operational and environmental contributions to stability of solution-processed 6,13-bis(triisopropyl-silylethynyl) pentacene (TIPS-pentacene)

\* Corresponding author.

E-mail address: [skpark@keti.re.kr](mailto:skpark@keti.re.kr) (S.K. Park).

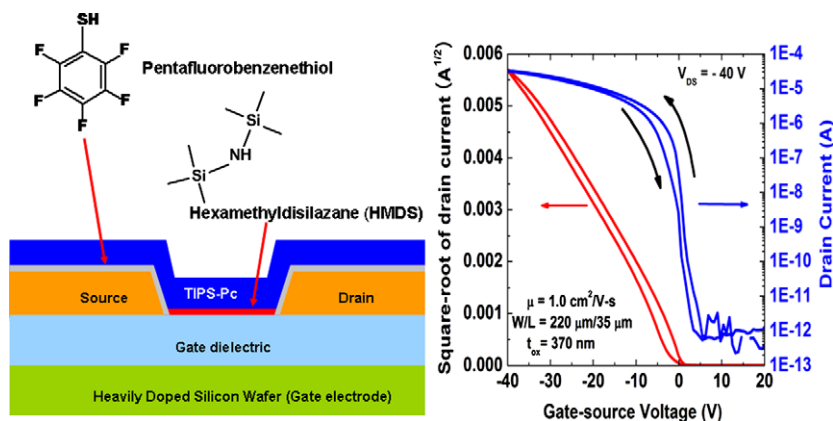


Fig. 1. Cross-sectional image and typical  $I_D$ - $V_{GS}$  characteristics of fabricated TIPS-pentacene OTFTs from 1 wt% toluene solution ( $L = 35 \mu\text{m}$ ,  $W = 220 \mu\text{m}$ ).

OTFTs are investigated. The TIPS-pentacene OTFTs in this study were fabricated on thermally oxidized, heavily doped silicon wafers with gold source and drain electrodes. Self assembled monolayers (SAMs) of pentafluorobenzenethiol (PFBT, Aldrich) and hexamethyldisilazane (HMDS, Aldrich) were formed on the Au source/drain electrodes and gate dielectric, respectively, to modify surface energy, film wetting, and contact characteristics [5]. TIPS-pentacene active layers were deposited from 1–2 wt% solutions by drop-casting in a solvent-rich ambient. Best results were obtained using toluene or chlorobenzene, yielding devices with best mobility of more than  $1.2 \text{ cm}^2/\text{V s}$  and strong molecular ordering in the organic thin films [5]. After fabrication, TIPS-pentacene OTFTs were exposed to air with and without illumination, or stored in vacuum for periods of up to four weeks. To simplify comparison, the devices in these studies were fabricated on a substrate which was then divided into several pieces for the different environmental experiments. Fig. 1 shows the cross-section image of the fabricated OTFT and  $\log(I_D)$  versus  $V_{GS}$  characteristics for  $V_{DS} = -40 \text{ V}$ . Typically, the turn-on position of the original devices are more positive than usual for these devices. It is not fully understood but we believe somewhat impurity related charges in organic semiconductor and interface charges in gate dielectric may be related to those devices.

### 3. Results and discussion

As shown in Fig. 2, over time all devices showed threshold voltage shifts towards normally-on devices, along with increases in sub-threshold slope. The addition of illumination increased the magnitude of these shifts. Devices stored under a vacuum without illumination for the same period showed little change in threshold voltage or sub-threshold slope. The normal humidity and illumination used in the experiments was 30–50% RH and 400–600 lux, respectively. In air and dark conditions, the devices typically showed slightly decreased mobility and increased (that is, more depletion mode) threshold voltages and sub-threshold slopes while maintaining almost same saturation current. With exposure to air and illumination the devices showed an increase in drain current and sub-threshold slope, with a larger (more positive) shift of threshold voltage compared to devices operated under air exposure in the dark. Similar to vapor-deposited pentacene, it appears that the combination of oxygen and light leads to degradation of charge transport possibly by introducing traps or defects inside film from oxygen doping effects and inducing oxidation of molecules.

For an operational stability test, a bias-stress was applied to TIPS-pentacene OTFTs and their electrical characteristics were measured. The application of 30 V for  $V_{GS}$

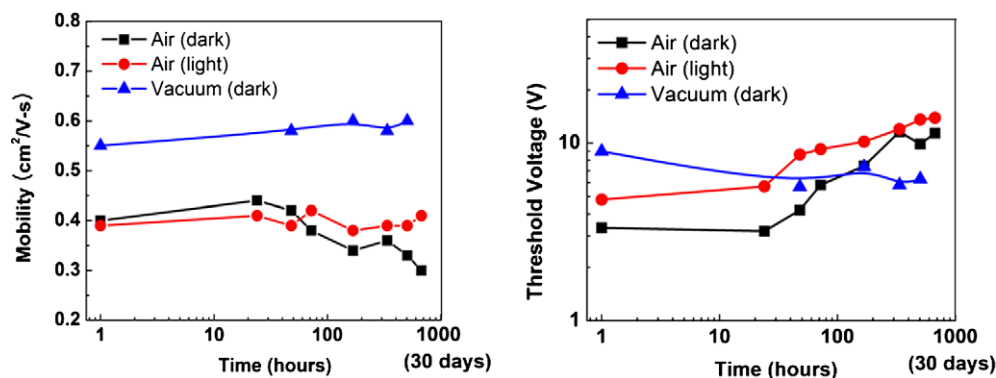


Fig. 2. Typical self life-test results of TIPS-pentacene OTFTs from 1 wt% toluene solution with environmental conditions ( $L = 20 \mu\text{m}$ ,  $W = 220 \mu\text{m}$ ).

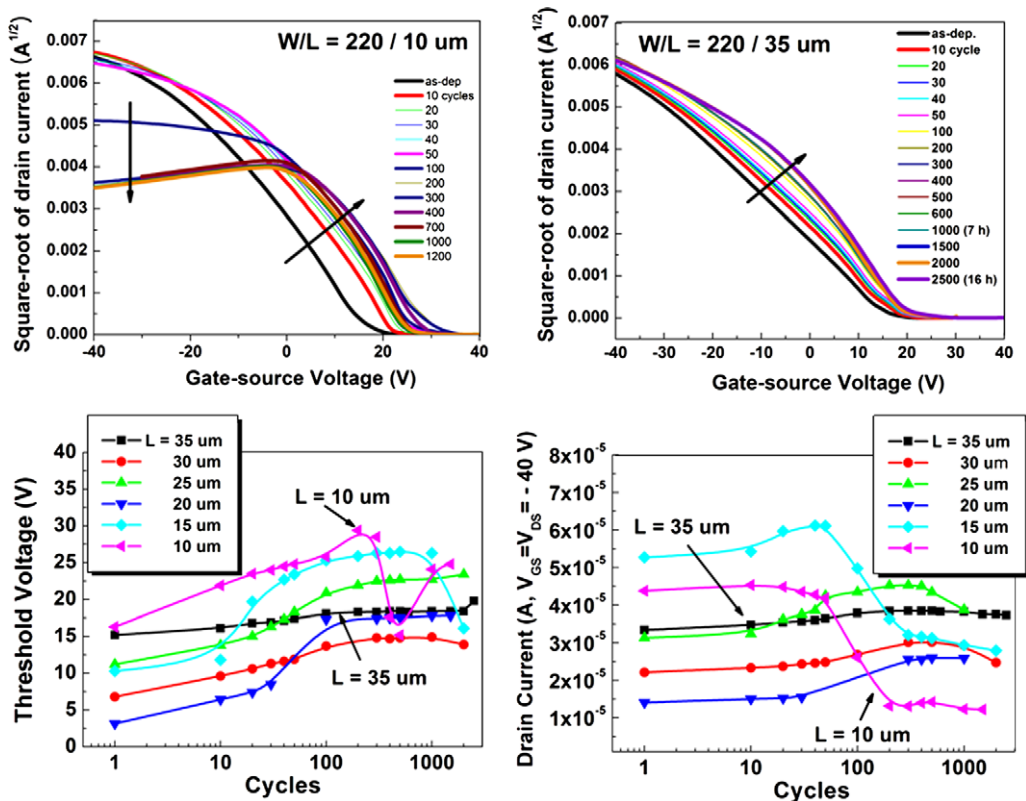


Fig. 3. (a) Typical repeated cycling test ( $L = 10, 35 \mu\text{m}$ ,  $W = 220 \mu\text{m}$ ) and (b) channel length dependent repeated cycling test results of TIPS-pentacene OTFTs from 1 wt% toluene ( $W = 220 \mu\text{m}$ ).

and  $-40 \text{ V}$  for  $V_{DS}$  for more than 2000 s led to a slight increase and fluctuation in the OTFT off current. For the corresponding on current test,  $-40 \text{ V}$  was applied for both  $V_{GS}$  and  $V_{DS}$  and the current behavior was measured as a function of time. The on current was quite stable and only small positive shifts in threshold voltage, with little or no change in mobility, sub-threshold slope, or on/off current ratio, was observed. As a second test, the  $I_D$ - $V_{GS}$  characteristics of devices with air plus illumination exposure were repeatedly measured. For this test, devices were repeatedly stressed by measuring the  $I_D$ - $V_{GS}$  characteristics in saturation for up to 2000 cycles (about 14 h) with no delay of reverse bias between scans. For these tests the drain voltage was set to  $-40 \text{ V}$  and the gate voltage was swept from  $-40$  to  $40 \text{ V}$ . Relatively long channel ( $>20 \mu\text{m}$ ) OTFTs had changes with operation similar to, but greater than, devices with only environmental exposure. Shifts were observed in the threshold voltage and the sub-threshold slope, but little or no change was observed in mobility and current on/off ratio.

Fig. 3 illustrates the results for the repeated cycling test, including the results from channel length dependent cycling testing. As shown in Fig. 3a, shorter channel length devices had somewhat greater shifts in threshold voltage and also showed a decrease in mobility and a significant current drop with repeated cycling. As expected, the largest changes in threshold voltage and drain current were observed in the shortest channel devices which have the

highest drain currents per unit channel area. When  $V_{DS}$  of  $-1 \text{ V}$  was applied during the cycling test, the current and threshold voltage degradation of the shorter channel devices were much more limited but we could still observe slight degradation of the device's performance. The drain current and threshold voltage degradation appears to be partially related to operation at large drive currents and may be related to large local power dissipation at source contact. In addition to the contact-related effects, built-in gate charge which is naturally influenced more in shorter

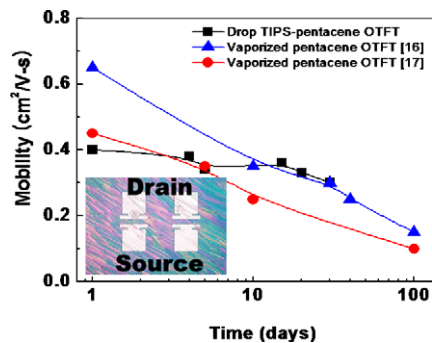


Fig. 4. Comparison of self life-test results for air exposed TIPS-pentacene OTFTs from 1 wt% toluene solution ( $L = 20 \mu\text{m}$ ,  $W = 220 \mu\text{m}$ ) with reference data.

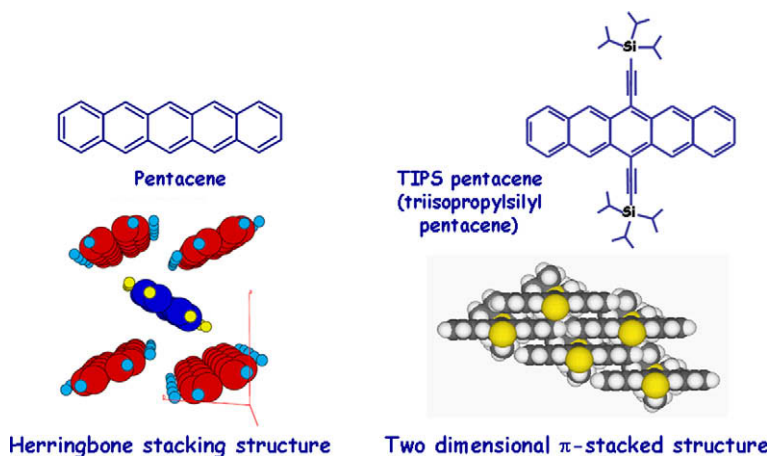


Fig. 5. Molecular and stacking structure of vapor-deposited pentacene and solution-processed TIPS-pentacene.

channel devices also may be related to the more degradation of current and threshold voltage in those devices. As Kagan et al. [14] pointed out, device scaling using thinner gate dielectric may be helpful to reduce the operational power, resulting in improvement of operational stability.

Fig. 4 compares the environmental stability of solution-processed TIPS-pentacene OTFTs (this study) and literature results for vapor-deposited pentacene OTFTs. Inset of this figure is the optical micrograph of solution deposited TIPS-pentacene OTFTs used in this experiment. Because contact effects tend to dominate over other degradation effects in shorter channel devices, relatively long channel devices ( $>20\ \mu\text{m}$ ) were used for this comparison to minimize the contact effects. Compared to literature results [16,17] for vapor-deposited pentacene OTFTs (channel lengths of 100 and  $30\ \mu\text{m}$ , respectively), solution-processed TIPS-pentacene OTFTs typically show improved mobility stability with time for air exposure conditions. Most of results for the environmental stability test of vapor-deposited pentacene without encapsulation layer typically have shown the mobility degradation of more than 30% in air ambient over 4 weeks [11,16–19]. Previous investigations have shown pentacene oxidation at the central aromatic ring may be one of the pathways for degradation of pentacene OTFTs.

As shown in Fig. 5, in TIPS-pentacene, the functional groups at the 6 and 13 positions of the TIPS-pentacene molecule may hinder this oxidation, resulting in relatively stable mobility in air ambient. Another possibility for the increased air stability could be due to the different crystal structure of TIPS-pentacene. Pentacene in vapor-deposited thin films packs in a herringbone stacking with molecular backbone spacing of  $\sim 4\ \text{\AA}$  which is larger than the spacing for 2-dimensional  $\pi$  stacked solution deposited TIPS-pentacene ( $\sim 3.5\ \text{\AA}$ ) [8]. The larger spacing may allow moisture or oxygen to diffuse into crystal more easily, resulting in poorer stability. These stability results are in marked contrast to the simple thin film stability tests performed by Maliakal and co-workers [15], which showed solution-cast TIPS-pentacene films to be an order of magnitude less stable than vapor-deposited pentacene films. The differ-

ence may be explained by the poor molecular ordering in the films studied earlier, which UV-vis studies showed to be amorphous. We demonstrate here that highly crystalline films [5] of solution-cast TIPS-pentacene are in fact somewhat more stable than vapor-deposited pentacene films.

#### 4. Conclusion

In summary, environmental and operational stability tests of solution-processed TIPS-pentacene OTFTs with a variety of exposure ambient and operation conditions were performed. The results demonstrate that solution-processed TIPS-pentacene OTFTs can have more stable device characteristics with both environmental exposure and device operation than is typically observed for vapor-deposited pentacene OTFTs. In addition to recent researches regarding improvement of operational and environmental stability of OTFTs including device scaling [14], passivation layer on organic semiconductors [20], top-gate structures [21], and blending polymer with small molecular organic semiconductors [22], the stability in mobility and current on/off ratio found in this study is encouraging for the use of TIPS-pentacene and similar OTFTs in low-cost and large-area electronic applications.

#### References

- [1] H. Klauk, M. Halik, U. Zschieschang, G. Schmid, W. Radlik, J. Appl. Phys. 92 (2002) 5259–5263.
- [2] Y.-Y. Lin, D.J. Gundlach, S. Nelson, T.N. Jackson, IEEE Electron. Dev. Lett. 18 (1997) 606–608.
- [3] Ali Afzali, Christos D. Dimitrakopoulos, Tricia L. Breen, J. Am. Chem. Soc. 124 (2002) 8812–8813.
- [4] N.S. Stutmann, E. Smits, H. Wondergem, C. Tanase, P. Blom, P. Smith, D.D. Leeuw, Nature Mater. 4 (2005) 601–607.
- [5] S.K. Park, D.A. Mourey, J.E. Anthony, T.N. Jackson, Appl. Phys. Lett. 91 (2007) 063514–063516.
- [6] C. Goldmann, D.J. Gundlach, B. Batlogg, Appl. Phys. Lett. 88 (2006) 063501–063503.
- [7] Z. Zhu, J.T. Mason, R. Dieckmann, G.G. Malliaras, Appl. Phys. Lett. 81 (2001) 24–26.
- [8] John E. Anthony, James S. Brooks, David L. Eaton, Sean R. Parkin, J. Am. Chem. Soc. 123 (2001) 9482–9483.

- [9] D.J. Gundlach, Y.-Y. Lin, T.N. Jackson, S.F. Nelson, D.G. Schlom, *IEEE Electron. Dev. Lett.* 18 (1997) 87–89.
- [10] D.J. Gundlach, J.E. Royer, S.K. Park, S. Subramanian, L.C. Teague, B.H. Hamadani, O.D. Jurchescu, A.J. Moad, O. Kirillov, C.A. Richter, J.G. Kushmerick, L.J. Richter, T.N. Jackson, J.E. Anthony, *Nature Mater.* 7 (2008) 216–222.
- [11] Yong Qiu, Yuanchuan Hu, Guifang Dong, Liduo Wang, Junfeng Xie, Yaning Ma, *Appl. Phys. Lett.* 83 (2003) 1644–1646.
- [12] G. Gu, M.G. Kane, J.E. Doty, A.H. Firester, *Appl. Phys. Lett.* 87 (2005) 243512–243514.
- [13] Hany Aziz, Zoran Popovic, Shuang Xie, Ah-Mee Hor, Nan-Xing Hu, Carl Tripp, *Appl. Phys. Lett.* 72 (1998) 756–758.
- [14] C.R. Kagan, A. Afzali, T.O. Graham, *Appl. Phys. Lett.* 86 (2005) 193505–193507.
- [15] Ashok Maliakal, Krishnan Raghavachari, Howard Katz, Edwin Chandross, Theo Siegrist, *Chem. Mater.* 16 (2004) 4980–4984.
- [16] W.J. Kim, W.H. Koo, S.J. Jo, C.S. Kim, H.K. Baika, *J. Vac. Sci. Technol. B* 23 (2005) 2357–2361.
- [17] Hagen Klauk, Ute Zschieschang, Jens Pflaum, Marcus Halik, *Nature* 445 (2007) 745–749.
- [18] F. De Angelis, S. Cipolloni, L. Mariucci, G. Fortunato, *Appl. Phys. Lett.* 88 (2006) 193508.
- [19] J.A. Merio, C.R. Newman, C.P. Geriach, T.W. Kelley, D.V. Muryres, S.E. Fritz, M.F. Toney, C.D. Frisbie, *J. Am. Chem. Soc.* 127 (2005) 3997.
- [20] M. Kawasaki, S. Imazeki, M. Ando, Y. Sekiguchi, S. Hirota, S. Uemura, T. Kamata, *IEEE Electron. Dev. Lett.* 53 (2006) 435.
- [21] N. Choi, D. Kim, H. Seo, C. Kim, H. Kang, M. Kim, I. Chung, *Jpn. J. Appl. Phys.* 46 (2007) 1333.
- [22] J. Kang, N. Shin, D.Y. Jang, V.M. Prabhu, D.Y. Yoon, *J. Am. Chem. Soc.* 130 (2008) 12273.





# High efficiency fluorescent white organic light-emitting diodes with red, green and blue separately monochromatic emission layers

Zhiqiang Zhang, Qi Wang, Yanfeng Dai, Yipeng Liu, Lixiang Wang, Dongge Ma\*

State Key Laboratory of Polymer Physics and Chemistry, Changchun Institute of Applied Chemistry, Chinese Academy of Sciences, Graduate School of Chinese Academy of Sciences, Changchun 130022, PR China

## ARTICLE INFO

### Article history:

Received 16 September 2008

Received in revised form 4 February 2009

Accepted 10 February 2009

Available online 20 February 2009

### PACS:

81.07.Pr

73.40.Vz

85.30.De

### Keywords:

White organic light-emitting diodes

Fluorescence

Separated emissive layers

## ABSTRACT

Highly efficient fluorescent white organic light-emitting diodes (WOLEDs) have been fabricated by using three red, green and blue, separately monochromatic emission layers. The red and blue emissive layers are based on 4-(dicyanomethylene)-2-tert-butyl-6-(1,1,7,7-tetramethyljulolidin-4-yl-vinyl)-4H-pyran (DCJTB) doped *N,N'*-di(naphthalene-1-yl)-*N,N'*-diphenyl-benzidine (NPB) and *p*-bis(*p*-*N,N*-diphenyl-amino-styryl) benzene (DSA-ph) doped 2-methyl-9,10-di(2-naphthyl) anthracene (MADN), respectively; and the green emissive layer is based on tris(8-hydroxyquinoline)aluminum (Alq<sub>3</sub>) doped with 10-(2-benzothiazolyl)-2,3,6,7-tetrahydro-1,1,7,7-tetramethyl-1H,5H,1[H-(1)-benzopyropyrano(6,7-8-*i,j*)quinolizin-1]-one (C545T), which is sandwiched between the red and the blue emissive layers. It can be seen that the devices show stable white emission with Commission International de L'Éclairage coordinates of (0.41, 0.41) and color rendering index (CRI) of 84 in a wide range of bias voltages. The maximum power efficiency, current efficiency and quantum efficiency reach 15.9 lm/W, 20.8 cd/A and 8.4%, respectively. The power efficiency at brightness of 500 cd/m<sup>2</sup> still arrives at 7.9 lm/W, and the half-lifetime under the initial luminance of 500 cd/m<sup>2</sup> is over 3500 h.

© 2009 Elsevier B.V. All rights reserved.

## 1. Introduction

White organic light-emitting diodes (WOLEDs) are of considerable interest in recent years due to their potential applications in full color displays, backlight for liquid crystal displays and solid-state lighting sources [1–3]. For the application in solid-state lighting sources, high efficiency and long operation lifetime are required. Phosphorescent WOLEDs generally are more efficient due to its demonstrated potential for achieving 100% internal emission efficiency by employing the participation of triplet emission [4–10]. However, in comparison with fluorescent WOLEDs, phosphorescent WOLEDs typically have shorter operational lifetime [10]. Also, because of the short operational lifetimes of blue electro-phosphorescent devices, the color

stability of all-phosphor-doped WOLEDs is limited. Therefore, the development of all-fluorescent WOLEDs with high efficiency and long lifetime is very important.

However, the fabrication of high efficiency all-fluorescent WOLEDs is still difficult due to the waste of the triplet excitons formed from the majority of recombination events [11–13]. To fully achieve optimum efficiency and color rendition from different fluorescent emission molecules in WOLEDs, besides developing more efficient electro-fluorescent host and guest materials, some effective new architectural approaches seem to be rather important [14,15]. In this letter, we achieved high performance fluorescent WOLEDs by introducing three red, green and blue fluorescent emission layers, separately [9,16]. The red, green and blue fluorescent dopants, respectively, are doped in three separate hosts, and it is found that the introduction of the thin green emission layer between the red and blue emission layers significantly improves the efficiency and spectral color due to the effective control

\* Corresponding author. Tel.: +86 431 85262357; fax: +86 431 85262873.

E-mail address: [mdg1014@ciac.jl.cn](mailto:mdg1014@ciac.jl.cn) (D. Ma).

of the location of the exciton recombination zone. By optimization, the resulting WOLEDs emit a maximum power efficiency of 15.9 lm/W and show current efficiency of 20.8 cd/A. The color rendering index (CRI) reaches 84. At the initial brightness of 500 cd/m<sup>2</sup>, the lifetime is over 3500 h.

## 2. Experimental procedures

The resulting WOLEDs were fabricated on a cleaned glass substrate precoated with, 180 nm-thick, 10 Ω/sq, indium-tin-oxide (ITO). The optimized device in this study was ITO/copper phthalocyanine (CuPc) (15 nm)/N,N-di(naphthalene-1-yl)-N,N'-diphenyl-benzidine (NPB)(80 nm)/NPB:0.5 wt% 4-(dicyanomethylene)-2-tert-butyl-6-(1,1,7,7-tetramethyljulolidin-4-yl-vinyl)-4H-pyran (DCJTb) (20 nm)/tris(8-hydroxyquinoline) aluminum (Alq<sub>3</sub>):0.5 wt% 10-(2-benzothiazolyl)-2,3,6,7-tetrahydro-1,1,7,7-tetramethyl-1H,5H,1[H-(1)-benzopyrroprano(6,7-8-i,j)quinolizin-1]-one (C545T)(3 nm)/2-methyl-9,10-di(2-naphthyl) anthracene (MADN):0.8 wt% *p*-bis(*p*-N,N-diphenyl-amino-styryl) benzene (DSA-ph)(40 nm)/bis(2-methyl-8-quinolinolato-N1,O8)-(1,1'-biphenyl-4-olato) aluminum (BALq<sub>3</sub>) (10 nm)/LiF/Al. To demonstrate the role of the thin green emissive layer, the device of ITO/CuPc (15 nm)/NPB (80 nm)/NPB:0.5 wt% DCJTb (20 nm)/MADN:0.8 wt% DSA-ph (40 nm)/BALq<sub>3</sub> (10 nm)/LiF/Al was fabricated and the devices with different green layer thicknesses were also studied for comparison. In the devices, the CuPc, NPB and BALq<sub>3</sub> were used as hole-injecting, hole-transporting, and hole-blocking/electron-transporting layers, respectively. The DCJTb, C545T and DSA-ph were red, green and blue dopants, respectively. The ITO coated glass was used as the anode and the stacked LiF/Al as the cathode. All layers were prepared by thermal evaporation in a high-vacuum system with pressure of less than 3 × 10<sup>-4</sup> Pa without breaking the vacuum. The evaporation rates were monitored by a frequency counter, and calibrated using a Dektak 6 M profiler. The current–luminance–voltage characteristics were mea-

sured by using a Keithley source measurement unit (Keithley 2400 and Keithley 2000) with a calibrated silicon photodiode. The devices are encapsulated in nitrogen glove box. The device area is 5 × 5 mm<sup>2</sup>. Fig. 1 shows the energy level diagram of the studied devices.

## 3. Discussion and results

Fig. 2a shows the normalized electro-luminescent spectra of the device with green emissive layer at different driving voltages. Three separate peaks, respectively, at 453, 515 and 590 nm, corresponding to the emissions from DSA-ph, C545T and DCJTb, are clearly observed. The EL spectra show stable and high quality white light emission. There is nearly no color shift with the bias voltages as the Commission Internationale de L'Eclairage (CIE) coordinates are (0.42, 0.41) at 7 V and (0.41, 0.42) at 11 V, and the color rendering indexes (CRI) are 82 and 84, respectively, at 7 V and 11 V. This apparent resistance to the color change under the different voltages well indicates the balanced charge carrier injection and transport for exciton recombination in the three separate emissive regions. Obviously, the designed device structure is greatly effective to obtain stable white emission. Fig. 2b gives a 2-in. WOLED lighting panel, showing better illumination quality. Although the device without green emissive layer also shows white emission, as the EL spectra at different voltages shown in Fig. 2c, the EL spectrum includes two peaks with 460 nm and 570 nm, which are from DSA-ph and DCJTb, respectively, and the CRI is low, only 74.

The most importance is that the introduction of the thin green layer also significantly improves the device EL performance. Fig. 3a and b displays the current density–luminance–voltage characteristics of the devices with and without green emissive layer in forward direction. The current efficiency, power efficiency, quantum efficiency and current density characteristics of the devices with and without green emissive layer are plotted in the inset of

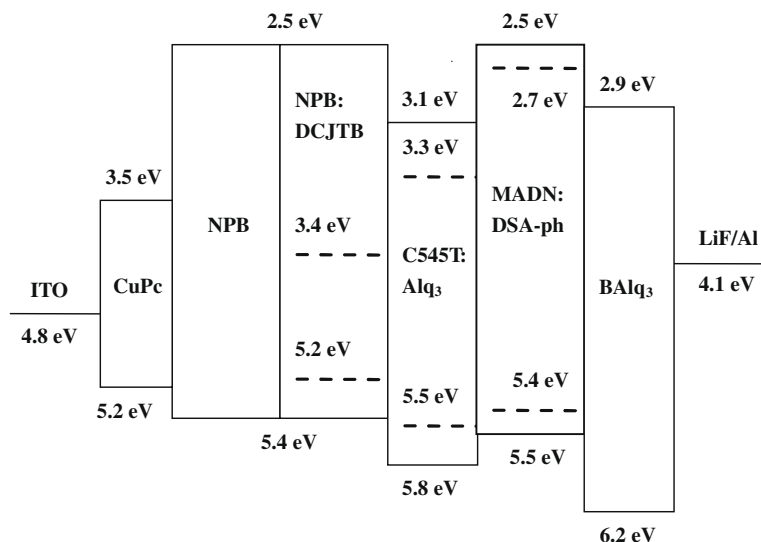
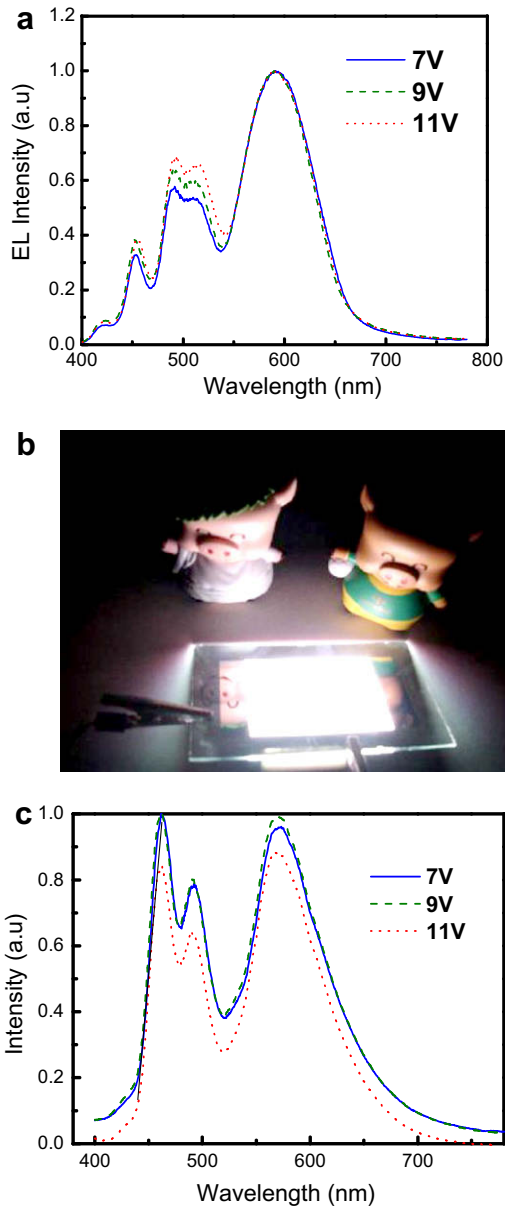


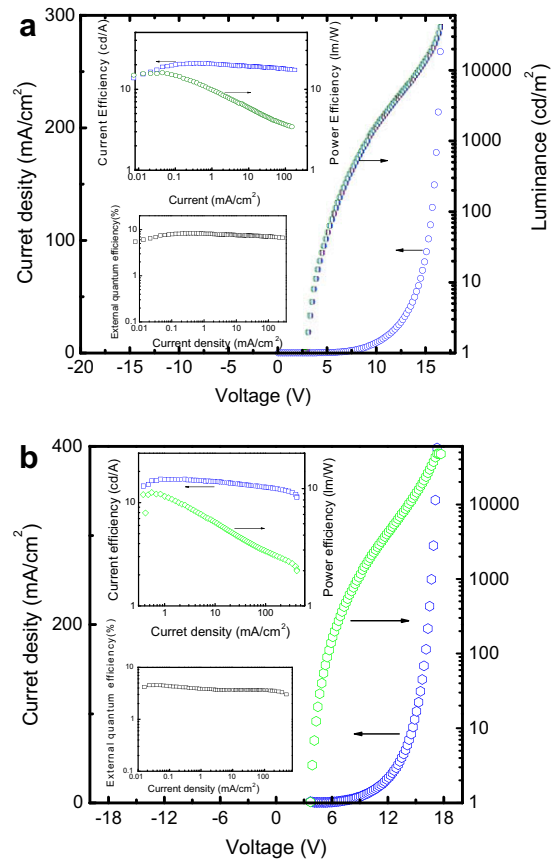
Fig. 1. Energy level diagram of the fabricated white OLED.

Fig. 3a and b, respectively. For the case of device with green emissive layer, the turn-on voltage (defined as the voltage at the luminance of  $1 \text{ cd/m}^2$ ) is 2.9 V. The maximum luminance reaches  $45000 \text{ cd/m}^2$  at the current density of  $270.0 \text{ mA/cm}^2$  and 16 V. At 9 V bias, the luminance reaches  $1000 \text{ cd/m}^2$ , which is a typical value for lighting purposes. The maximum current efficiency, power efficiency and quantum efficiency arrive at  $20.8 \text{ cd/A}$ ,  $15.9 \text{ lm/W}$  and  $8.4\%$ , respectively. At a luminance of  $1000 \text{ cd/m}^2$ , the device emits a current efficiency of  $19.4 \text{ cd/A}$ , showing a

power efficiency of  $6.8 \text{ lm/W}$  ( $7.8\%$  quantum efficiency). However, the device without green emissive layer emits



**Fig. 2.** (a) Normalized EL spectra of the device with green emissive layer at different driving voltages. (b) Two-inch fabricated WOLED lighting panel. (c) Normalized EL spectra of the device without green emissive layer at different driving voltages (For interpretation of the references in colour in this figure legend, the reader is referred to the web version of this article.).



**Fig. 3.** Current density–luminance–voltage characteristics of the devices with (a) and without (b) green emissive layer in forward direction. The inset gives the current efficiency, power efficiency, quantum efficiency and current density characteristics of the devices with and without green emissive layer (For interpretation of the references in colour in this figure legend, the reader is referred to the web version of this article.).

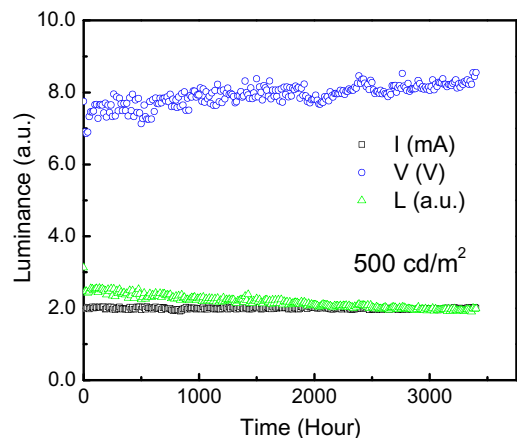


**Fig. 4.** Lifetime measurement of the resulting WOLEDs. The stability is measured with an initial luminance of  $500 \text{ cd/m}^2$  at a constant current density of  $2 \text{ mA}$ .

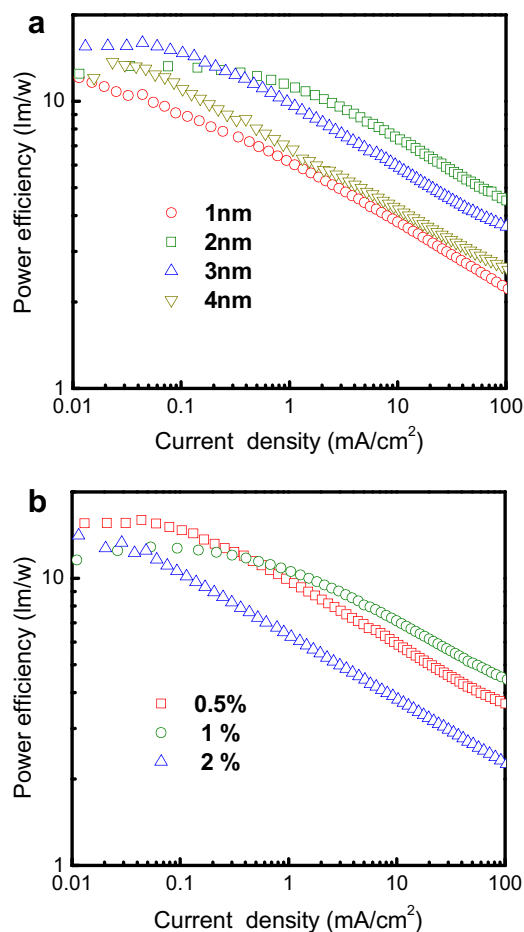


**Fig. 5.** Power efficiency as a function of current density in devices with different thicknesses of green emissive layer (a) and different concentrations of C545T in green emissive layer (b) (For interpretation of the references in colour in this figure legend, the reader is referred to the web version of this article).

the luminance of 25,000  $\text{cd/m}^2$  at the current density of 270.0  $\text{mA/cm}^2$ . The maximum current efficiency, power efficiency and quantum efficiency are 16.9  $\text{cd/A}$ , 9.3  $\text{lm/W}$  and 4.5%, respectively. At the luminance of 1000  $\text{cd/m}^2$ , the power efficiency reduces to 5.7  $\text{lm/W}$ . Obviously, the utilization of the proper green emissive layer enhances the EL efficiency. Especially, the reduction in efficiency at higher luminance is greatly suppressed, as shown in Fig. 3.

Furthermore, the white device with green emissive layer also exhibits good stability. Fig. 4 shows the result of the lifetime measurement of the resulting white device.

The lifetime measurement was made at room temperature after setting the initial luminance of the device at 500  $\text{cd/m}^2$ . The half-lifetime under the initial brightness of 500  $\text{cd/m}^2$  is over 3500 h. The whole improvement in the performances of the resulting WOLEDs should be related to the utilization of the reasonable device structure.

Actually, the thickness of the C545T doped  $\text{Alq}_3$  layer and concentration of C545T in  $\text{Alq}_3$  also have larger effect on the device performances. Fig. 5a and b shows the power efficiency as a function of current density in devices with different thicknesses of green emissive layer and different concentrations of C545T in green emissive layer, respectively. It is clearly seen that 2–3 nm thick C545T: $\text{Alq}_3$  layer and less than 1% concentration of C545T in  $\text{Alq}_3$  lead to the higher EL efficiency. Table 1 summarizes the efficiency and lifetime results in the context of what has been published for all-fluorescent white OLEDs. It can be seen that the unique three-emissive layer structure with proper energy level match not only makes our white OLED high efficiency and luminance, but more importantly, also results in our white OLED showing longer lifetime with respect to other reported white OLEDs based on all-fluorescent organics [9,13,16].

It is clearly found that the introduction of the proper green emissive layer C545T doped  $\text{Alq}_3$  between the red emissive layer and the blue emissive layer greatly enhances the EL efficiency and CRI. This could be well explained by the energy level diagram shown in Fig. 1. Obviously, the energy positions of the highest occupied molecular orbital (HOMO) and the lowest unoccupied molecular orbital (LUMO) of  $\text{Alq}_3$  determine the tuning role in the transport and recombination of the injected electrons and holes in emissive regions. The injected holes from anode ITO will be transported into DCJTb doped NPB emissive layer across the CuPc hole injection layer and the NPB hole transport layer, and due to the block role of the thin  $\text{Alq}_3$  layer, some holes will remain in the DCJTb doped NPB layer and the some will be injected into the DSA-ph doped MADN blue emissive layer across the C545T doped  $\text{Alq}_3$  green emissive layer, and finally are blocked in the blue emissive layer by the  $\text{BALq}_3$  layer. Relatively, the injected electrons from the LiF/Al cathode will be injected into the C545T doped  $\text{Alq}_3$  green emissive layer across the  $\text{BALq}_3$  and the DSA-ph doped MADN blue emissive layers, and these electrons will be accumulated in the green emission region because of the blocking role of NPB. If so, the holes in the blue emissive region will recombine with the electrons in the blue DSA-ph molecules as the electrons transport across the blue emissive region, and finally leading to the emission of blue DSA-ph molecules, whereas the electrons blocked in the C545T doped  $\text{Alq}_3$

**Table 1**

Summary of efficiency and lifetime of all-fluorescent white OLEDs published in literatures and this work.

	Power efficiency ( $\text{lm/W}$ )	Current efficiency ( $\text{cd/A}$ )	Lifetime (h)	Reference
1	11.4 (100 $\text{cd/m}^2$ )	20.8 (100 $\text{cd/m}^2$ )	Over 3500 (500 $\text{cd/m}^2$ )	This work
2	6.0 (10 $\text{mA/cm}^2$ )	10.9 (10 $\text{mA/cm}^2$ )	100 (5000 $\text{cd/m}^2$ )	[17]
3	9.5 (100 $\text{cd/m}^2$ )	10.6 (100 $\text{cd/m}^2$ )		[18]
4	17.1 (100 $\text{cd/m}^2$ )	17.6 (100 $\text{cd/m}^2$ )	61 (500 $\text{cd/m}^2$ )	[13]

green emissive region will be trapped by the C545T molecules and recombine with the trapped holes in the C4545T molecules as the holes are transported across the C545T doped Alq<sub>3</sub> layer, resulting in the green emission. Furthermore, due to the low LUMO of DCJTb and the high LUMO of NPB, some electrons in the C545T doped Alq<sub>3</sub> green emissive region will be directly injected into the DCJTb molecules and recombine with the trapped holes in DCJTb from NPB, finally leading to the red emission of the DCJTb molecules. Clearly, the transport of the electrons and holes in the emissive layers is well tuned by the thin C454T doped Alq<sub>3</sub> layer.

#### 4. Conclusions

We have demonstrated highly efficient fluorescent white organic light-emitting diodes composed of three separate fluorescent emission layers. The introduction of the thin C545T doped Alq<sub>3</sub> layer between the red and blue emission layers well controls the location of the exciton formation regions. The sequence of red, green and blue emission layers and the refined control of the exciton recombination region have been shown to significantly improve the EL performances of the fabricated WOLEDs. The WOLEDs emit a maximum power efficiency of 15.9 lm/W and show a maximum current efficiency of 20.8 cd/A. The color rendering index (CRI) reaches 84. At the initial brightness of 500 cd/m<sup>2</sup>, the lifetime is over 3500 h.

#### Acknowledgements

The authors thank the Hundreds Talents program of Chinese Academy of Sciences, the National Science Fund for Distinguished Young Scholars of China (50325312), the Foundation of Jilin Research Council (20050517,

20080337), Foundation of Changchun Research Council (2007GH06), Science Fund for Creative Research Groups of NSFC (20621401) and Ministry of Science and Technology of China (863 Program No. 2006AA03A161, 973 Program No. 2009CB930603, 973 Program No. 2009CB623604) for the support of this research. Prof. Lixiang Wang thanks NSFC (50633040) for financial support.

#### References

- [1] J. Kido, K. Nagai, K. Okutama, *Appl. Phys. Lett.* 64 (1994) 815.
- [2] B.W. D' Andrade, S.R. Forrest, *Adv. Mater. (Weinheim, Ger.)* 16 (2004) 1585.
- [3] F. So, J. Kido, P. Burrows, *MRS Bull.* 33 (2008) 663.
- [4] B.W. D' Andrade, R.J. Holmes, S.R. Forrest, *Adv. Mater. (Weinheim, Ger.)* 16 (2004) 624.
- [5] Y. Sun, N.C. Giebink, H. Kanno, B. Ma, M.E. Thompson, S.R. Forrest, *Nature (London)* 440 (2006) 908.
- [6] G. Schwartz, K. Fehse, M. Pfeiffer, K. Walzer, K. Leo, *Appl. Phys. Lett.* 89 (2006) 083509.
- [7] H. Kanno, R.J. Holmes, Y. Sun, S.K. Cohen, S.R. Forrest, *Adv. Mater. (Weinheim, Ger.)* 18 (2006) 339.
- [8] E.L. Williams, K. Haavisto, J. Li, G.E. Jabbour, *Adv. Mater. (Weinheim, Ger.)* 19 (2007) 197.
- [9] Y. Sun, S.R. Forrest, *Appl. Phys. Lett.* 91 (2007) 263503.
- [10] G. Schwartz, M. Pfeiffer, S. Reineke, K. Walzer, K. Leo, *Adv. Mater. (Weinheim, Ger.)* 19 (2007) 3672.
- [11] G. Cheng, Y. Zhang, Y. Zhao, Y. Lin, C. Ruan, S. Liu, T. Fei, Y. Ma, Y. Cheng, *Appl. Phys. Lett.* 89 (2006) 043504.
- [12] J.H. Jou, M.H. Wu, C.P. Wang, Y.S. Chiu, P.H. Chiang, H.C. Hu, R.Y. Wang, *Org. Electron.* 8 (2007) 735.
- [13] M.H. Ho, T.M. Chen, P.C. Yeh, S.W. Hwang, C.C. Chen, *Appl. Phys. Lett.* 91 (2007) 233507.
- [14] J.H. Jou, C.C. Chen, Y.C. Chung, M.F. Hsu, C.H. Wu, S.M. Shen, M.H. Wu, W.B. Wang, Y.C. Tsai, C.P. Wang, J.J. Shyue, *Adv. Funct. Mater.* 4 (2008) 121.
- [15] J.H. Jou, S.M. Shen, C.C. Chen, Y.C. Chung, C.J. Wang, M.F. Hsu, W.B. Wang, M.H. Wu, C.J. Yang, C.P. Liu, *Proc. SPIE* 6999 (2008) 69992S.
- [16] Y. Sun, S.R. Forrest, *Org. Electron.* 9 (2008) 994.
- [17] Y.C. Tsai, J.H. Jou, *Appl. Phys. Lett.* 89 (2006) 243521.
- [18] J.H. Jou, C.J. Wang, Y.P. Lin, Y.C. Chung, P.H. Chiang, M.H. Wu, C.P. Wang, C.L. Lai, C. Chang, *Appl. Phys. Lett.* 92 (2008) 223504.



## Efficient organic solar cells with polyfluorene derivatives as a cathode interfacial layer

Seok-In Na<sup>a</sup>, Seung-Hwan Oh<sup>a</sup>, Seok-Soon Kim<sup>b</sup>, Dong-Yu Kim<sup>a,\*</sup>

<sup>a</sup> Heeger Center for Advanced Materials, Department of Materials Science and Engineering, Gwangju Institute of Science and Technology, 1 Oryong-Dong, Buk-Gu, Gwangju 500-712, South Korea

<sup>b</sup> School of Materials Science and Chemical Engineering, Kunsan National University, Kunsan, Chonbuk 753-701, South Korea

### ARTICLE INFO

#### Article history:

Received 17 December 2008

Received in revised form 11 February 2009

Accepted 12 February 2009

Available online 20 February 2009

#### PACS:

71.20.Rv

72.80.Le

73.50.Pz

73.61.Ph

79.60.Jv

#### Keywords:

Organic solar cells

Bulk-heterojunction

Water-soluble conjugated polymers

Cathode modification

### ABSTRACT

Use of a polyfluorene derivative (WPF-oxy-F) as the cathode interfacial layer was investigated for low-cost and high-efficiency organic solar cells (OSCs) based on poly(3-hexylthiophene) (P3HT) and 1-(3-methoxycarbonyl)-propyl-1-phenyl-(6,6)C<sub>61</sub> (PCBM). Insertion of the WPF-oxy-F interfacial layer between the P3HT/PCBM active layer and the metal cathode increased overall power conversion efficiency from 2.95% to 3.77% primarily due to the improved open circuit voltage and enhanced fill factor, resulting from a reduction of the metal work-function through the introduction of WPF-oxy-F.

Crown Copyright © 2009 Published by Elsevier B.V. All rights reserved.

## 1. Introduction

Conjugated polymer-based organic solar cells (OSCs) have received significant attention because they are a cost-efficient and flexible power source. As a result, OSCs have undergone considerable development and the organic syntheses and fabrication methods used in their production have been significantly improved [1–11]. Among the available polymer solar cell systems, poly(3-hexylthiophene) (P3HT) and 1-(3-methoxycarbonyl)-propyl-1-phenyl-(6,6)C<sub>61</sub> (PCBM) blends have efficiencies of up to 4–5%; however, further improvement in efficiency is required for practical applications [9–11].

Typically, P3HT and PCBM based bulk-heterojunction (BHJ) solar cells have a sandwich-like structure consisting of an indium tin oxide (ITO) anode, a photoactive layer, and an Al metal cathode. Here, to achieve high-performance OSCs, the interface between the electrode and active layer must be an Ohmic contact to minimize the contact resistance and to maximize the open circuit voltage ( $V_{oc}$ ) [12,13]. A preferred and simple method to enhance the contact between the electrode and the active layer is modification of the electrode by insertion of a buffer layer. For example, the insertion of poly(3,4-ethylenedioxythiophene):poly(styrenesulfonate) (PEDOT:PSS) between the ITO anode and active layer is commonly used in OSCs to enhance hole collection and increase  $V_{oc}$  [14]. In the case of cathode modification, it was suggested that a thin LiF layer improves cell efficiency through the formation of an interfacial dipole that reduces the

\* Corresponding author. Tel.: +82 62 970 2319; fax: +82 62 970 2304.  
E-mail address: [kimdy@gist.ac.kr](mailto:kimdy@gist.ac.kr) (D.-Y. Kim).

work-function of Al for better electron collection [15]. However, LiF is not an ideal interfacial layer in polymer-based cells for the following reasons: the LiF layer must be very thin (<1.2 nm) [15], which is difficult to achieve; and, vapor deposition of LiF in a vacuum is not well-suited for use in high-throughput roll-to-roll manufacturing, which is the most significant advantage of polymer-based cells [16].

Recently, the use of metal oxides, such as TiO<sub>x</sub> and ZnO, as an efficient buffer layer led to significantly enhanced cell efficiency [17–19], and OSCs with SAM-modified ZnO showed dramatic improvements in efficiency, mostly due to enhancements in  $V_{oc}$  and fill factor (FF) resulting from the formation of a favorable interfacial dipole [12,13]. In particular, Zhang et al. demonstrated that a solution-processed poly(ethylene oxide) (PEO) layer can form internal dipoles at the active layer/Al interface, resulting in enhanced the power conversion efficiency (PCE) and  $V_{oc}$  [16]. This organic-based interfacial layer that can be created using a simple solution-based process may be desirable for the realization of low-cost and high-efficiency OSCs. However, until very recently, only a few approaches for an organic-based interfacial layer in OSCs have been reported and, to date, insertion of an organic-based cathode interfacial layer into P3HT/PCBM-based OSCs has not been achieved.

The aim of the present study was to realize a low-cost and high-efficiency organic solar cell by insertion of an organic-based cathode interfacial layer into the cell using a simple solution-based process. We investigated the use of a water-soluble polyfluorene derivative (WPF-oxy-F) as the cathode interfacial layer in polymer solar cells, which was synthesized using a palladium-catalyzed Suzuki coupling reaction [20]. Herein, we demonstrate that simply by spin-coating the WPF-oxy-F, the overall power conversion efficiency of solar cells was increased, mainly resulting from the enhanced  $V_{oc}$  and FF.

## 2. Experimental

The structure of the solar cell and the chemical structure of the WPF-oxy-F are presented schematically in Fig. 1. To fabricate the OSCs, glass substrates coated with ITO (Samsung Corning Co., Ltd.) having a sheet resistance

of  $\sim 10 \Omega/\text{sq}$  were cleaned and PEDOT:PSS (Baytron P VPAI 4083) was spin-coated onto ITO followed by drying at 120 °C for 10 min, with a thickness of  $\sim 20$  nm. A solution of 30 mg of P3HT (Rieke Metals) and 15 mg of PCBM (Nano-C) in 2 ml of chlorobenzene was then spin-coated on top of the PEDOT:PSS layer, forming the active layer with a thickness of  $\sim 80$  nm. The WPF-oxy-F, dissolved in methanol at a concentration of 1 mg/ml, was spin-coated onto the active layer. Finally, aluminum (100 nm) was thermally evaporated on the WPF-oxy-F layer in a vacuum at  $10^{-6}$  Torr. For comparison, solar cells without the WPF-oxy-F layer were also fabricated using experimental procedures identical to those used to make the cells with the WPF-oxy-F layer. Photocurrent–voltage ( $I$ – $V$ ) measurements were performed using a Keithley 4200 instrument under 100 mW/cm<sup>2</sup> illumination from a 1 kW Oriel solar simulator with an AM 1.5 G filter in a N<sub>2</sub>-filled glove box. A calibrated silicon reference solar cell certified by the National Renewable Energy Laboratory (NREL) was used to confirm the measurement conditions.

## 3. Results and discussion

First, we investigated the effect of the WPF-oxy-F layer and its thickness on the performance of OSCs without thermal annealing of the active layers. A reference cell containing only Al and cells with a WPF-oxy-F layer spin-coated at either 6000, 4000, or 2000 rpm were fabricated. The thicknesses of WPF-oxy-F layers spin-coated at various speeds were as follows:  $\sim 3$  nm at 6000 rpm,  $\sim 4$  nm at 4000 rpm, and  $\sim 6$  nm at 2000 rpm. The photocurrent density–voltage ( $J$ – $V$ ) characteristics of the cells with a WPF-oxy-F layer are shown in Fig. 2, and detailed information on  $V_{oc}$ , short-circuit current density ( $J_{sc}$ ), FF, and PCE, calculated from the  $J$ – $V$  curves in Fig. 2a, is presented in Table 1. As shown in Fig. 2b,  $V_{oc}$  values in all cells with a WPF-oxy-F layer were increased by 110 mV.  $V_{oc}$  was relatively constant at  $\sim 0.68$  V, independent of the thickness of the WPF-oxy-F layer, while FF and  $J_{sc}$  were slightly reduced as the thickness of the WPF-oxy-F layer increased. Thus, the cell with the WPF-oxy-F layer that was spin-coated at 6000 rpm had the highest efficiency. Furthermore, compared with the efficiency of the reference cell, the efficiency of each cell with a WPF-oxy-F layer was dramatically enhanced.

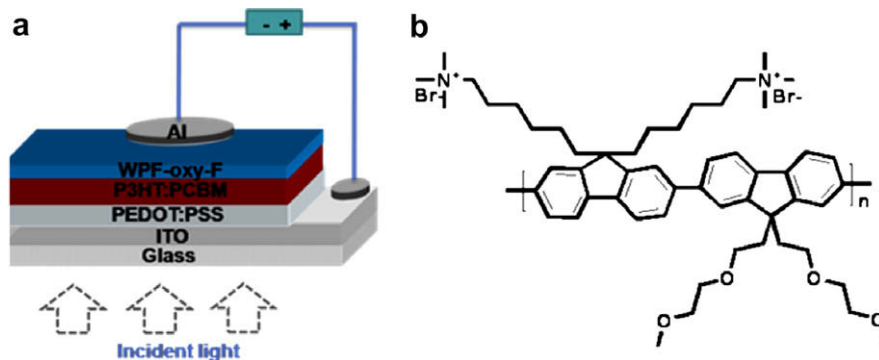
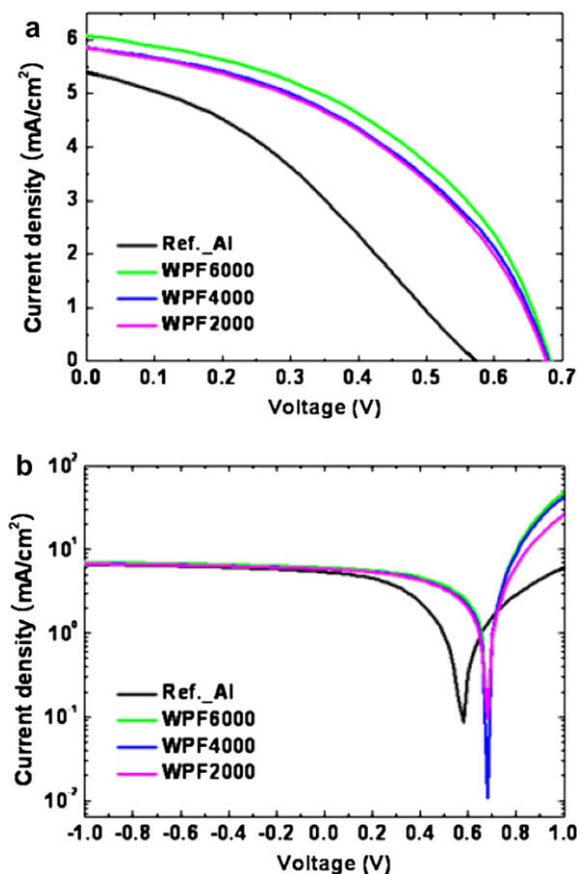


Fig. 1. (a) Structure of the organic solar cell with a WPF-oxy-F layer. (b) The chemical structure of the WPF-oxy-F polyfluorene derivative.



**Fig. 2.** Current density–voltage ( $J$ – $V$ ) curves (a) and  $J$ – $V$  curves plotted on a log scale (b) of the organic solar cells with WPF-oxy-F layers of variable thickness and of the reference cell.

These results could be explained by a reduction of the metal work-function through the introduction of the WPF-oxy-F layer, leading to better electron transport and collection [12,16,21]. However, the overall cell performance was relatively poor due to the absence of thermal annealing of the active layer. Although annealing-free systems would be more suitable for the realization of flexible and large-area OSCs [6], at the present time, the annealing procedure seems to be needed for high-efficiency OSCs.

To obtain detailed information about the function of the WPF-oxy-F buffer layer in cells, cells with and without the WPF-oxy-F spin-coated at 6000 rpm were compared under illumination and in the dark, as shown in Fig. 3. In addition, to further improve the relatively low cell performance

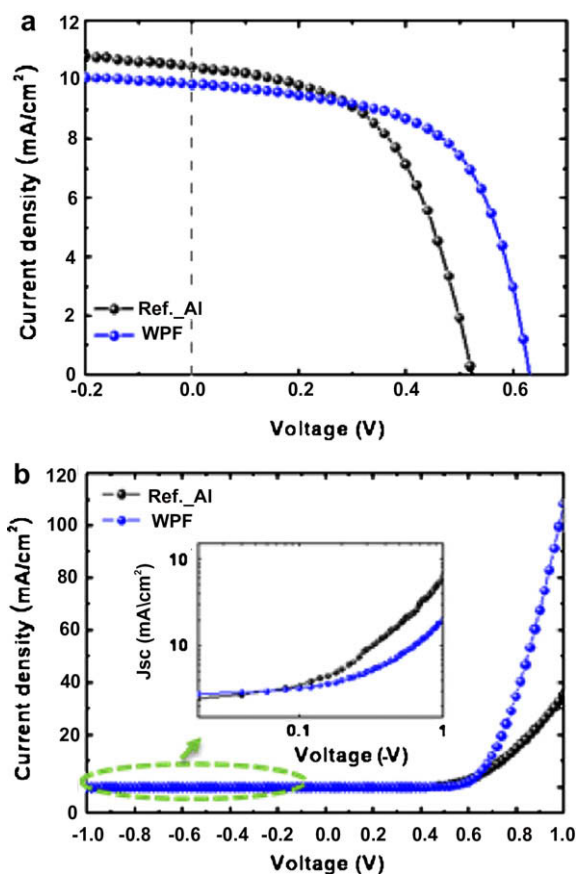


**Fig. 3.**  $J$ – $V$  characteristics (a) and  $J$ – $V$  curves measured in the dark (b) of organic solar cells with and without WPF-oxy-F. The inset shows the dark  $J$ – $V$  curves for the negative-voltage region, plotted on a log–log scale.

shown in Fig. 2, a heat treatment to the as-prepared active layers was applied at 110 °C for 10 min in nitrogen ambient [7,8]. As demonstrated in Fig. 3a, the performance characteristics of the reference cell were as follows:  $V_{oc}$ , 0.52 V;  $J_{sc}$ , 10.45 mA/cm<sup>2</sup>; FF, 54.3%; and, PCE, 2.95%. In contrast, the performance characteristics of the cell with the WPF-oxy-F were:  $V_{oc}$ , 0.63 V;  $J_{sc}$ , 9.86 mA/cm<sup>2</sup>; FF, 60.7%; and, PCE, 3.77%. Compared with cell performance without a heat treatment to the as-prepared active layers, the cell performances with the heat treatment were all enhanced except for  $V_{oc}$ . The decrease in  $V_{oc}$  after thermal annealing was attributed to enhanced crystallinity of the P3HT polymer film. In fact, it is demonstrated that the enhancement in P3HT crystallinity resulting from heat

**Table 1**

Photovoltaic parameters and efficiencies of organic solar cells with WPF-oxy-F layers of variable thickness compared with the reference cell. The averages for photovoltaic parameters of each cell are given in parentheses with mean variation.

	$V_{oc}$ (V)	$J_{sc}$ (mA/cm <sup>2</sup> )	FF (%)	PCE (%)
Ref._Al	0.57 (0.56 ± 0.02)	5.40 (5.2 ± 0.5)	35.4 (34 ± 2)	1.09 (1.0 ± 0.2)
WPF6000	0.68 (0.67 ± 0.01)	6.09 (6.1 ± 0.1)	45.6 (46 ± 2)	1.89 (1.9 ± 0.1)
WPF4000	0.68 (0.67 ± 0.01)	5.87 (6.0 ± 0.2)	44.1 (44 ± 1)	1.76 (1.8 ± 0.1)
WPF2000	0.68 (0.67 ± 0.01)	5.85 (5.7 ± 0.3)	43.7 (42 ± 2)	1.74 (1.6 ± 0.2)



treatment induced an upward shift of the highest occupied molecular orbital (HOMO) level of the P3HT polymer, ultimately leading to a reduction in  $V_{oc}$  [22]. However, the difference in  $V_{oc}$  between the reference cell and the cell with the WPF-oxy-F was still maintained, irrespective of the heat treatment. Here, the increase in  $V_{oc}$  that results from introduction of the WPF-oxy-F interfacial layer can be tightly linked to the reduction of the metal work-function. For better studies, we directly investigated a change of the Al work-function by using a Kelvin probe (KP 6500 Digital Kelvin probe, McAllister Technical Services. Co., Ltd.), which can detect the contact potential difference ( $V_{CPD}$ ) and the work-function difference ( $\Delta\Phi = e \times V_{CPD}$ , where  $e$  is the electron charge between the probe and the sample). In fact, the  $V_{CPD}$  of Al/Glass underneath the WPF-oxy-F was 1.407 V, while the  $V_{CPD}$  of Al/Glass showed 1.288 V. It means that the  $\Phi$  of Al with the WPF-oxy-F layer was reduced by 0.119 eV compared with the  $\Phi$  of Al, which is consistent with the enhanced  $V_{oc}$  of the cell with the WPF-oxy-F layer. Thus, it is believed that the WPF-oxy-F layer effectively induces an interfacial dipole pointing away from the metal surface that reduces the work-function of Al [12,16,23–25].

The reduction of the Al work-function could help electron transport from the active layer to the cathode, resulting in a lower interface resistance and a higher FF [12,16]. In fact, the series resistance ( $R_s$ ) of the OSC with WPF-oxy-F, calculated from the inverse slope near  $V_{oc}$  in the  $J$ - $V$  curves shown in Fig. 3b, was decreased to  $\sim 29\%$  compared with that of the reference cell. In addition, in the inset of

Fig. 3b, the OSC with the WPF-oxy-F had a smaller leakage current at a negative-voltage. This result indicates that the WPF-oxy-F layer is both an efficient shield for the P3HT/PCBM active layer from the physical damage caused by hot Al atoms and an efficient buffer layer that reduces hole-electron recombination loss at the P3HT/Al interface [18,21]. From these results, it is clear that the enhanced efficiency shown in Fig. 3a, especially improved  $V_{oc}$  and FF, originated from a reduction of the metal work-function through the introduction of the WPF-oxy-F layer, leading to better electron transport and collection [12,16].

Another objective of the use of an organic-based interfacial layer in the OSCs is to enable the replacement of low-work-function and highly reactive metals such as Ca and Ba as well as the replacement of LiF. Thus, we fabricated several identical OSCs that varied only in their respective cathode. The performances of the OSCs with Al, LiF/Al, Ca/Al, and WPF-oxy-F/Al as cathodes are compared in Fig. 4. Compared with efficiencies of the reference cell with Al, the efficiencies of cells with LiF, Ca, and WPF-oxy-F were all enhanced, and in cells with LiF, Ca, and WPF-oxy-F, most of the increase in the cell efficiency comes from the enhanced FF and  $V_{oc}$ , as shown in Fig. 4c and d, respectively. As demonstrated in Fig. 4, the overall photovoltaic characteristics of the cell with the WPF-oxy-F were comparable to those of cells with LiF and Ca, indicating that the WPF-oxy-F has a similar function in the solar cell as LiF and Ca. In addition, the qualitative similarity of the photovoltaic characteristics shown in Fig. 4 indicates the possibility to substitute the LiF or Ca with the WPF-

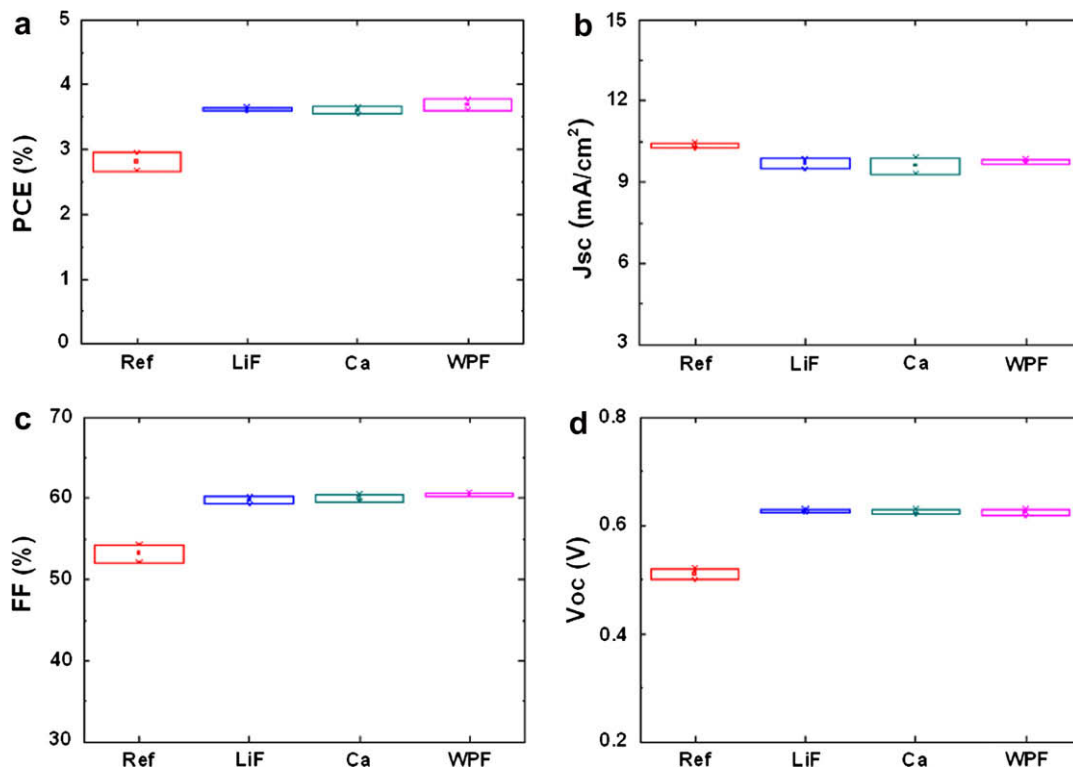


Fig. 4. Comparison of the performance (a) PCE, (b)  $J_{sc}$ , (c) FF, (d)  $V_{oc}$  of the solar cells with Al, LiF/Al, Ca/Al, and WPF-oxy-F/Al.

oxy-F. Furthermore, when considering the simplicity of depositing a WPF-oxy-F layer, it is believed that the WPF-oxy-F is better suited than LiF or Ca for fabrication of low-cost and high-efficiency photovoltaic cells.

#### 4. Conclusion

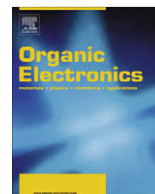
In conclusion, we demonstrated that the polyfluorene derivative (WPF-oxy-F) can be used as an efficient cathode interfacial layer for low-cost and high-efficiency OSCs based on P3HT and PCBM. Introduction of the WPF-oxy-F layer increased cell efficiency from 2.95% to 3.77%, resulting from a reduction in the metal work-function for better electron transport at the active layer/Al interface. Furthermore, the overall photovoltaic characteristics of the cell with the WPF-oxy-F were comparable to those of cells with LiF and Ca, indicating that the WPF-oxy-F shows potential as a practical replacement for LiF or Ca. The organic-based interfacial layer fabricated using a simple solution process will advance the realization of low-cost and high-efficiency OSCs. More detailed studies on the relationship between the performance of OSCs with stable and high work-function metals, such as Ag and Au, and water-soluble polyfluorene derivatives with different internal dipoles are currently underway.

#### Acknowledgements

This work was financially supported by the Heeger Center for Advanced Materials (HCAM), the Bioluminescence Research Center at GIST, the Ministry of Education of Korea through Brain Korea 21 (BK21) program, the Korea Science and Engineering Foundation (KOSEF) through the National Research Lab Program funded by the Korea government (MEST) (M10500000077-06J0000-07710), and the Korea Science and Engineering Foundation (KOSEF) NCRC Grant funded by the Korea government (MEST) (R15-2008-006-02001-0).

#### References

- [1] N.S. Sariciftci, L. Smilowitz, A.J. Heeger, F. Wedl, *Science* 258 (1992) 1474.
- [2] C.J. Brabec, N.S. Sariciftci, J.C. Hummelen, *Adv. Funct. Mater.* 11 (2001) 15.
- [3] K. Kawano, R. Pacios, D. Poplavskyy, J. Nelson, D.D.C. Bradley, J.R. Durrant, *Sol. Energy Mater. Sol. Cells* 90 (2006) 3520.
- [4] M.-G. Kang, M.-S. Kim, J. Kim, L.J. Guo, *Adv. Mater.* 20 (2008) 4408.
- [5] S.-I. Na, S.-S. Kim, J. Jo, D.-Y. Kim, *Adv. Mater.* 20 (2008) 4061.
- [6] A. Pivrikas, P. Stadler, H. Neugebauer, N.S. Sariciftci, *Org. Electron.* 9 (2008) 775.
- [7] Y. Kim, S.A. Choulis, J. Nelson, D.D.C. Bradley, S. Cook, J.R. Durrant, *Appl. Phys. Lett.* 86 (2005) 063502.
- [8] S.-S. Kim, S.-I. Na, J. Jo, G. Tae, D.-Y. Kim, *Adv. Mater.* 19 (2007) 4410.
- [9] W. Ma, C. Yang, X. Gong, K. Lee, A.J. Heeger, *Adv. Funct. Mater.* 15 (2005) 1617.
- [10] G. Li, V. Shrotriya, J. Huang, Y. Yao, T. Moriarty, K. Emery, Y. Yang, *Nature Mater.* 4 (2005) 864.
- [11] S.-I. Na, S.-S. Kim, J. Jo, S.-H. Oh, J. Kim, D.-Y. Kim, *Adv. Funct. Mater.* 18 (2008) 3956.
- [12] H.-L. Yip, S.K. Hau, N.S. Baek, A.K.-Y. Jen, *Appl. Phys. Lett.* 92 (2008) 193313.
- [13] H.-L. Yip, S.K. Hau, N.S. Baek, H. Ma, A.K.-Y. Jen, *Adv. Mater.* 20 (2008) 2376.
- [14] F. Zhang, M. Johansson, M.R. Andersson, J.C. Hummelen, O. Inganäs, *Adv. Mater.* 14 (2002) 662.
- [15] C.J. Brabec, S.E. Shaheen, C. Winder, N.S. Sariciftci, *Appl. Phys. Lett.* 80 (2002) 1288.
- [16] F. Zhang, M. Ceder, O. Inganäs, *Adv. Mater.* 19 (2007) 1835.
- [17] J.Y. Kim, S.H. Kim, H.-H. Lee, K. Lee, W. Ma, X. Gong, A.J. Heeger, *Adv. Mater.* 18 (2006) 572.
- [18] A. Hayakawa, O. Yoshikawa, T. Fujieda, K. Uehara, S. Yoshikawa, *Appl. Phys. Lett.* 90 (2007) 163517.
- [19] J. Gilot, I. Barbu, M.M. Wienk, R.A.J. Janssen, *Appl. Phys. Lett.* 91 (2007) 113520.
- [20] S.-H. Oh, S.-I. Na, Y.-C. Nah, D. Vak, S.-S. Kim, D.-Y. Kim, *Org. Electron.* 8 (2007) 773.
- [21] Q. Wei, T. Nishizawa, K. Tajima, K. Hashimoto, *Adv. Mater.* 20 (2008) 2211.
- [22] K. Vandewal, A. Gadisa, W.D. Oosterbaan, S. Bertho, F. Banishoeb, I.V. Severen, L. Lutsen, T.J. Cleij, D. Vanderzande, J.V. Manca, *Adv. Funct. Mater.* 18 (2008) 2064.
- [23] H. Ishii, K. Sugiyama, E. Ito, K. Seki, *Adv. Mater.* 11 (1999) 605.
- [24] B. de Boer, A. Hadjipour, M.M. Mandoc, T. van Woudenberg, P.W.M. Blom, *Adv. Mater.* 17 (2005) 621.
- [25] C.J. Brabec, V. Dyakonov, J.S. Parisi, N.S. Sariciftci, *Organic Photovoltaics-Concepts and Realization*, Springer-Verlag, Berlin 2003.



## Letter

# Photogenerated charge carrier transport and recombination in polyfluorene/fullerene bilayer and blend photovoltaic devices

Bekele Homa, Mattias Andersson, Olle Inganäs\*

Biomolecular and Organic Electronics, IFM, Center of Organic Electronics, Linköping University, S-5813 Linköping, Sweden

## ARTICLE INFO

## Article history:

Received 30 May 2008

Received in revised form 14 November 2008

Accepted 22 November 2008

Available online 25 December 2008

## PACS:

72.20.Jv

72.80.Le

72.80.Rj

## Keywords:

Polymer photovoltaics

Electrical transport

Photogeneration

## ABSTRACT

Using extraction of photogenerated charge carriers by linearly increasing voltage (photo-CELIV), we investigated two key transport parameters in photovoltaic materials based on the donor APFO-3 and acceptor PCBM: the mobility and lifetime of photogenerated charge carriers, in bilayers of varying geometry and in blends with various acceptors loading. We find that mobility depends strongly on delay time for shorter delay time in all devices. The observed recombination kinetics is found to be monomolecular. The mean lifetime of charge carriers is 2–3  $\mu\text{s}$  in blends and is slightly greater than 4  $\mu\text{s}$  in bilayer devices. In addition, the implications of mobility and lifetime values on the collection efficiency of the devices are presented.

© 2008 Elsevier B.V. All rights reserved.

## 1. Introduction

Organic solar cells have become a center of attention because they are considered to be a potential low cost renewable energy sources [1–3]. There are several challenges to be overcome to realize this potential in practical devices. Among the challenges, increasing power conversion efficiency is paramount. In general the overall efficiency of organic solar cells is influenced by four main processes; absorption (creation of bound electron-hole pairs (excitons)), charge generation (dissociation of exciton to free carriers), recombination and/or collection of carriers to their respective electrodes [1].

Recently conversion efficiency above 6% was reported [4]. This remarkable improvement of polymer solar cells was reached by using conjugated polymer–fullerene heterojunctions (HJ) and improved device architecture in a

tandem cell. A doubling of the efficiency of organic solar cells was also achieved by folding two planar cells, similar or spectrally different, towards each other [5]. In HJ solar cells the photogenerated excitons dissociate at the donor/acceptor interface via an ultrafast electron transfer from the donor (polymer) to the acceptor [6]. In order to dissociate, excitons must be created within the exciton diffusion length from the interface. There are two categories of HJ solar cells, bilayer HJ and bulk HJs. Bulk HJ solar cells have interpenetrating donor/acceptor interface, which provides large interface area for exciton dissociation and hence increase free carrier generation compared to bilayer HJ. On the other hand, numerical simulations show that collection efficiency of charge carriers is higher in bilayers [7], while still the overall efficiency is better in bulk heterojunctions.

In studies using transient optical spectroscopy, the different neutral and charged species formed by photoexcitation of bulk heterojunctions of APFO3 and PCBM have been followed during the ps– $\mu\text{s}$  time interval after excitation. A full kinetic model has been proposed, where geminate

\* Corresponding author.

E-mail address: [ois@ifm.liu.se](mailto:ois@ifm.liu.se) (O. Inganäs).

recombination is an important loss mechanism at long times [8]. It is desirable to follow the fate of these charge carriers as we enter the time slot where electrical transport can be directly followed. This is our ambition in the present study. Collection efficiency and loss through recombination of free carriers are controlled by the mobility of free carriers. Therefore, better knowledge of mobility and carrier lifetime will certainly help further improvement of efficiency of polymer solar cells.

In this work we report the mobility and lifetime of photogenerated carriers in donor/acceptor blends with various compositions, and in donor/acceptor bilayer photovoltaic devices and their significance for conversion efficiency. We used the photo-CELIV technique [9], which enables determination of mobility and recombination rate of free carriers simultaneously. The donor polymer used was APFO-3 (poly [2,7-(9,9-dioctyl-fluorene)-alt-5, 5-(4',7'-di-2 thienyl-2',1',3-benzo-thiadiazole)]). The acceptors are PCBM ([6,6]-phenyl-C<sub>61</sub>-butyric acid methyl ester) in blends and C<sub>60</sub> in bilayer.

## 2. Experimental

Devices studied in this work are bilayers and blends with a configuration of ITO/APFO-3/C<sub>60</sub>/Al and ITO/(APFO-3:PCBM) blend/Al, respectively. Solutions of APFO-3:PCBM blend in chloroform with a PCBM content of 80%, 60%, 40% and 0% (pure APFO-3) with concentrations 75 mg/ml, 40 mg/ml, 25 mg/ml and 15 mg/ml were spin coated on pre cleaned glass substrate coated with ITO. Then aluminum was thermally evaporated on the film in a vacuum chamber at a pressure of  $2.6 \times 10^{-6}$  mbar, to complete the device fabrication. Bilayer devices were made the same way as that of pure polymer devices, except C<sub>60</sub> was thermally evaporated on top of the polymer in a vacuum chamber at  $5.2 \times 10^{-6}$  mbar prior to aluminum deposition. The thicknesses of the active layers vary from sub 100 nm to 200 nm. The areas of the active layers were 4–5 mm<sup>2</sup>.

The technique used in this study was photo-CELIV, which employs excitation of charge carriers by absorbed laser light followed by extraction of carriers by linearly increasing voltage [9]. Generated carriers either undergo recombination or are collected by the built in electric field at the junction between electrode and active material. If the built in electric field is fully compensated, the only means through which the generated carrier concentration decays is recombination. These charges, which are created and forced to stay in the layer by an offset field, can then be extracted by linearly increasing voltage.

The devices were illuminated from the ITO side by a 3–5 ns pulse of a Nd: YAG laser at 530 nm excitation wavelength. After a given delay time the reverse bias, triangular shaped voltage pulse, with a slope of  $A = 2 \times 10^5$  V/s was applied by a digital function generator (Stanford Research DS 345) by connecting aluminum to the positive terminal and ITO to negative terminal. An offset voltage of 0.4–0.7 V was used. The delay time between laser light and onset of extraction was varied by a Tti TGP110 10 MHz Pulse generator. The transients were recorded by a digital

storage oscilloscope (Tektronix TDS 340A) for different delay times using a 50 Ω load resistance.

From the transients, the mobility and carrier concentration with varied delay time were calculated. The mobility of carriers is related to the time at which the extraction current reaches its maximum by Eq. (1) [9]:

$$\mu = \frac{2d^2}{3At_{\max}^2 \left(1 + 0.36 \frac{\Delta j}{j(0)}\right)} \quad (1)$$

where  $A$  is the increasing speed of extraction voltage,  $d$  is the thickness of the active layer,  $j(0)$  the displacement current density between the electrodes,  $\Delta j$  is the maximum conductive current density ( $\Delta j = j_{\max} - j(0)$ ), and  $t_{\max}$  the time at which the transient reaches maximum. The displacement current density is  $j(0) = \frac{\varepsilon_0 A}{d}$ , where  $\varepsilon_0$  is permittivity of the material. The photo generated charge carrier concentration for the different delay times were calculated by integrating the conduction current over the extraction time given by Eq. (2).

$$n = \frac{1}{ed} \int_0^T (j(t) - j(0)) dt \quad (2)$$

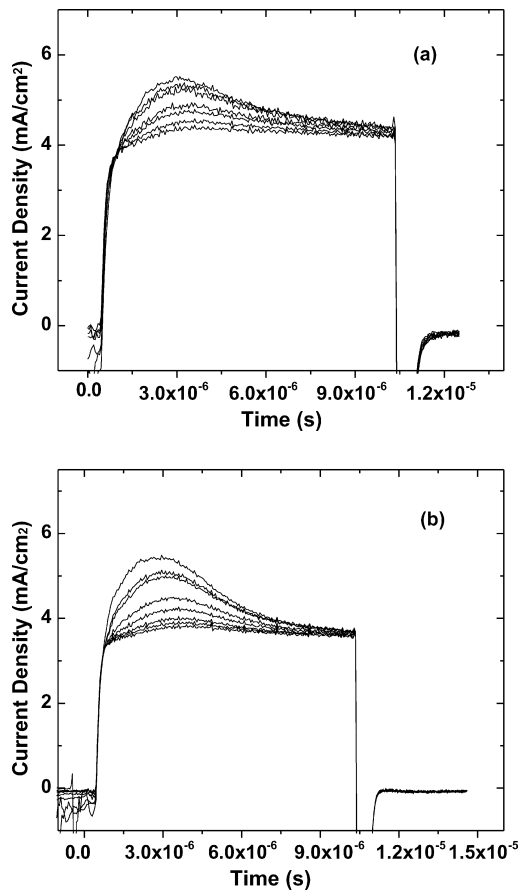
## 3. Results

Fig. 1 shows transient curves obtained from photo-CELIV measurements; (a) bilayer and (b) blend of 1:4 weight ratios APFO-3:PCBM. The extraction current decreases as delay time is increased for all devices. The time at which the maximum of extraction is reached also increased with increasing delay time. The mobility calculated using Eq. (1) for various delay times are displayed in Fig. 2a for bilayer and b for blends of different compositions of APFO-3 and PCBM. Calculated concentration of carriers versus delay time is plotted and shown in Fig. 3a and b. The curves are fitted to exponential decay of the form given by Eq. (3):

$$n(t) = n(0)e^{-\frac{t}{\tau}} + n_1 \quad (3)$$

where  $n_1$  is the concentration of carriers that remain in the layer in the given extraction time,  $n(0)$  is the concentration of carrier with delay time close to zero.  $\tau$  is the mean lifetime of photogenerated carriers. Table 1 shows the average mean lifetime of several devices and, by a rough estimation, the minimum thickness a carrier can traverse with the slowest mobility driven by the weakest built in field, where the field is estimated by the applied voltage.

Accurate measurements of both mobility and concentration are affected by offset voltage and thickness measurement. The offset voltage, applied to compensate the built in potential, was not exactly equal to the built in potential. The difference between the offset voltage and built in potential will extract carriers, which will result in significant photo current prior to the application of the triangular pulse. The thicknesses of devices were calculated from displacement current given by taking the approximate value 3 for the dielectric constant of the material. They were also measured mechanically by profilometer (DekTak 3030) and the values of both measurements agree well. However, inevitable error in measuring thickness due to



**Fig. 1.** Photo-CELIV transients of (a) APFO-3/C<sub>60</sub> bilayer device (b) APFO-3:PCBM (1:4) ratio blend at different delay times. The extraction current decreases from shorter delay time to longer delay time.

roughness affects the absolute concentration and mobility values, but does not affect the variation of mobility and concentration as a function of delay time.

#### 4. Discussion

The charge transport mechanism in disordered organic systems depends upon the morphology, order, and molecular structure. In such systems the energy distribution of the HOMO (highest occupied molecular orbital) and the LUMO (lowest unoccupied molecular orbital) levels can be well approximated by a Gaussian distribution [10] as in Eq. (4) where  $\sigma$  is the standard deviation energy levels.

$$g(E) = \frac{1}{\sqrt{2\pi}\sigma} \exp\left(-\frac{E^2}{2\sigma^2}\right) \quad (4)$$

Charge carriers transport in such system is via hopping transport between localized states, in which carriers have to hop from one localized state to another following the Miller-Abraham hopping rate given in Eq. (5),

$$v_{ij} = v_0 \exp(-2\gamma R_{ij}) \begin{cases} \exp\left(-\frac{\varepsilon_j - \varepsilon_i}{kT}\right), & \varepsilon_j > \varepsilon_i \\ 1, & \varepsilon_j < \varepsilon_i \end{cases} \quad (5)$$

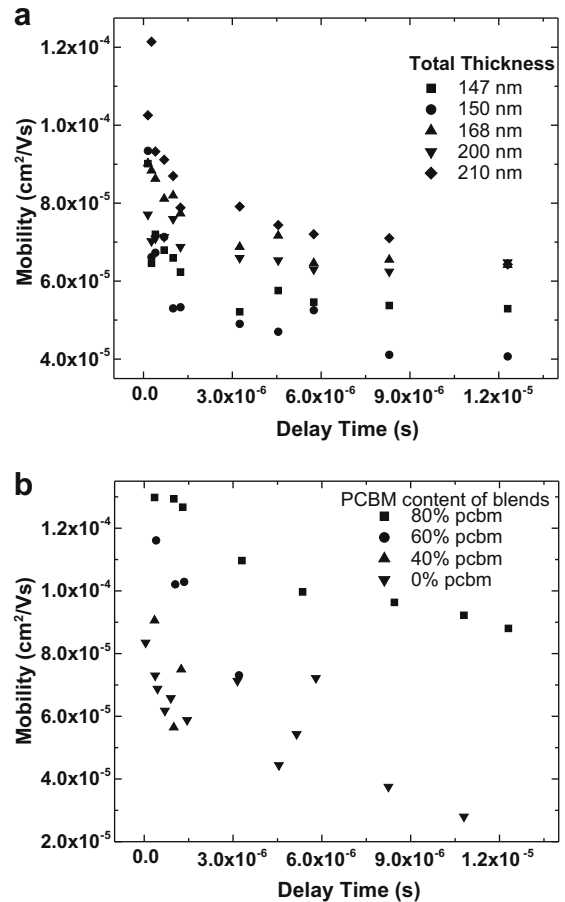


**Fig. 2.** (a) Photo-CELIV mobility versus delay time of (a) bilayer devices with different thickness of polymer films and (b) for blend devices. The thickness C<sub>60</sub> in bilayer is 45 nm for all devices.

where  $v_{ij}$  is the hopping rate between sites  $i$  and  $j$  with energies  $\varepsilon_i$  and  $\varepsilon_j$ . The first exponential in Eq. (5) describes the electronic wave function overlap and the second describes a Boltzmann factor for sites upward in energy. Carriers need to absorb thermal energy, which amounts to energy difference of the two sites  $j$  and  $i$  for an upward jump. The rate for downward movement is only limited by the first exponential term, i.e. only the spatial disorder controls the downward jump.

The decrease in mobility as indicated in Fig. 2a is attributed to the relaxation of carriers toward the tail of the density of states (DOS). Carriers that are excited to higher energy have higher mobility or higher probability to move, compared to those in the lower energy states in the distribution. The disordered nature of the material gives a high density of traps to which carriers continue to relax, until they eventually recombine with opposite carriers.

The extraction current is negligible in the dark, implying the density of intrinsic charge carrier density is so small that it cannot be detected with this experiment. All the carriers extracted are photogenerated which means that both carrier types are extracted. In all devices

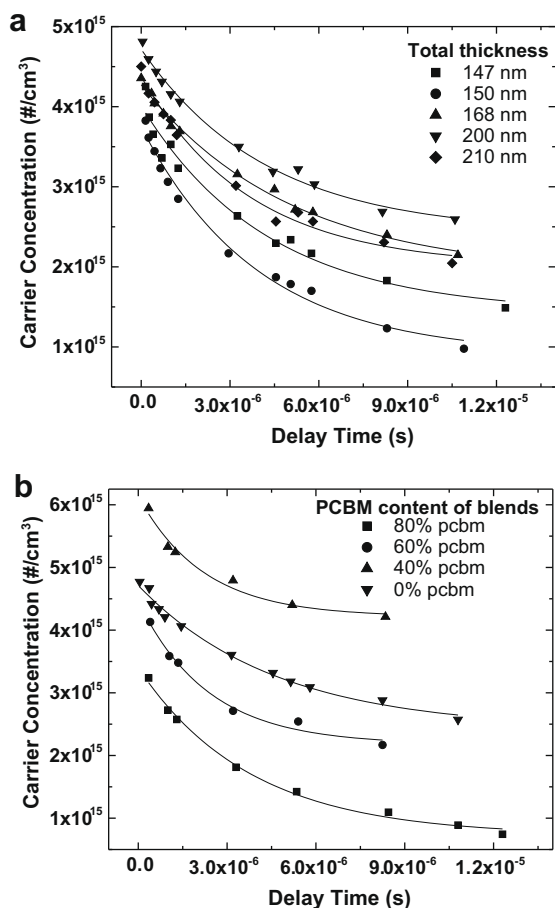


**Fig. 3.** Charge carrier concentration plotted versus delay time (a) bilayer devices (b) different composition of APFO-3:PCBM blends. The solid lines in both (a) and (b) are the curve fits using Eq. (2).

**Table 1**

Mean lifetime of charge carriers and extraction depth by built in field.

Devices	Mean life time ( $\tau$ ) (s)	$\mu \times \tau \times E$ (nm)
Pure	$(2.3 \pm 0.7) \times 10^{-6}$	61
Bilayer	$(4.1 \pm 0.6) \times 10^{-6}$	91
Blend (80% PCBM)	$(2.7 \pm 0.4) \times 10^{-6}$	110
Blend (60% PCBM)	$(2.3 \pm 0.5) \times 10^{-6}$	94
Blend (40% PCBM)	$(2.2 \pm 0.6) \times 10^{-6}$	90

investigated only one peak is observed, which indicates that the mobility of electron and hole are comparable or else very different. From mathematical considerations, there needs to be a factor  $\approx 3$  in difference between the electron and hole mobility, in order to observe two resolved peaks in geometries and under measurement conditions pertinent to samples resembling well functioning solar cells. In reality the peaks usually are less well defined and so the required difference is probably larger still. Furthermore, the mobility range possible to observe with a CELIV pulse is about three orders of magnitude in the relevant samples, due to RC- and signal amplitude effects,

which means that the actual window for observing both mobilities is rather limited. More often than not, it is thus the case that only one extraction peak is observed. It is not possible to ascertain if it is one or both mobilities, neither which one, that should be associated with the peak.

By examining mobility values obtained through other means, and based on some general assumptions regarding different measurement techniques [11,12], we infer that it should be possible to make an APFO-3:PCBM blend sample of suitable thickness and suitable stoichiometry so as to observe two resolved mobility peaks in CELIV. Since this has proved difficult, another possibility is to use a bilayer to determine which peak it is that is observed. If a suitable excitation wavelength is selected so that almost all carrier generation in a photo-CELIV experiments occurs in the polymer layer, a systematic variation of the layer thicknesses could give the desired information. Unfortunately, the reported electron mobilities [13] in  $C_{60}$  are so high that manageable thicknesses have almost no effect on the peak position. Moreover, it can be argued that density of electrons and holes are equal. For equal number of both carriers, the decay of carrier density may follow the Eq. (6), which depends linearly and nonlinearly on concentration  $n$  [14]:

$$\frac{dn}{dt} = -(An + Bn^2) \quad (6)$$

where  $A$  is the monomolecular recombination coefficient, describing recombination through defects (traps). The recombination rate is directly proportional to the density of carriers.  $B$  is the coefficient of describing the direct radiative or non-radiative recombination of an electron in LUMO to holes in HOMO, which is therefore a bimolecular process and hence proportional to the square of the carrier density.

Clearly, both types of recombination can happen at the same time, but depending on the intrinsic properties of the material, one may be the dominant process. For instance, if a material has low trap density and high charge density bimolecular outweighs the monomolecular recombination. On the other hand, if a material has high trap density and low concentration of carriers, monomolecular recombination dominates. In line with the above argument, the results displayed in Fig. 3 show that the recombination type is predominantly monomolecular type, which is the result of the disordered nature of the material i.e., high trap density.

The mean lifetime in bilayer structures is longer compared to pure and blend materials (see Table 1). This is because the photogenerated carriers generated at the interface, stay apart for a longer time in the different materials (polymer and  $C_{60}$ ) by internal electric field, which is oriented in one direction, whereas in blends the orientation of junctions is quite random and therefore the internal electric field does not induce cumulative barriers to carriers. The result in Table 1 shows the minimum distance that carriers can traverse during their lifetime driven by internal field. It can therefore be concluded that in sub 100 nm thick devices carrier collection is not a limiting factor.

## 5. Conclusion

Photo-CELIV technique has been used to investigate mobility and lifetime of photo generated charge carriers in blend and bilayer structures of photovoltaic devices. It is found that the mobility decreases very fast for shorter delay time and slower for longer delay time in all blends and bilayer devices. This decrease in mobility is ascribed to the relaxation of carriers to lower energy states in the distribution of energy states. Monomolecular recombination is found to be dominant in all APFO-3 based devices with acceptors used here, which is attributed to intrinsic energetic and spatial disorder of the material. The mean lifetime of photogenerated carriers is longer in bilayer structures as a result of a built in barriers at bilayer interface. Finally, the overall efficiency of sub 100 nm devices is not significantly limited by the collection of charge carriers.

## Acknowledgments

We would like to thank Fengling Zhang for her assistance in device fabrication. One of the authors (Bekele Homa) acknowledges the financial support from the International Program in the Physical Sciences (IPPS) of Uppsala University, Sweden. These investigations were financially

supported by the Center of Organic Electronics (COE) at Linköping University, Sweden, financed by the Strategic Research Foundation SSF.

## References

- [1] Privikas, N.S. Sarciftci, G. Juska, R. Osterbacka, Progress in photovoltaic, Res. Appl. 15 (2007) 677–696.
- [2] C.J. Brabec, N.S. Sariciftci, J.C. Hummelen, Adv. Funct. Mater. 11 (2001) 15.
- [3] J. Nelson, Science 293 (2001) 1059–1060.
- [4] J.Y. Kim, K. Lee, N.E. Coates, D. Moses, Th.Q. Nguyen, M. Dante, A.J. Heeger, Science 317 (2007) 222–225.
- [5] K. Tvingstedt, V. Andersson, F.L. Zhang, O. Inganäs, Appl. Phys. Lett. 91 (2007) 123514.
- [6] D. Moses, J. Wang, G. Yu, A.J. Heeger, Phys. Rev. Lett. 80 (12) (1998).
- [7] A. Marsh, C. Groves, N.C. Greenham, J. App. Phys. 101 (2007) 083509.
- [8] D. Swati, T. Pascher, M. Maiti, K.G. Jespersen, T. Kesti, F.L. Zhang, O. Inganäs, A. Yartsev, V. Sundström, J. Am. Chem. Soc. 129 (27) (2007) 8466–8472.
- [9] A.J. Mozer, N.S. Sariciftci, L. Lutsen, D. Vanderzande, R. Osterbacka, M. Westerling, G. Juska, Appl. Phys. Lett. 86 (2005) 112104.
- [10] H. Bassler, Phys. Status Solidi B 175 (1993) 15.
- [11] L.M. Andersson, F.L. Zhang, O. Inganäs, Appl. Phys. Lett. 89 (2006) 142111.
- [12] L. Mattias Andersson, Fengling Zhang, Olle Inganäs, Appl. Phys. Lett. 91 (2007) 071108.
- [13] T. Singh, H. Yang, B. Plochberger, L. Yang, H. Sitter, H. Neugebauer, N. Sariciftci, Phys. Status Solidi B 244 (2007) 3845–3848.
- [14] J. Szymkowski, J. Phys. D: Appl. Phys. 40 (2007) 3352–3357.



## Letter

# Soluble pentacene thin-film transistor using a high solvent and heat resistive polymeric dielectric with low-temperature processability and its long-term stability

Kyoseung Sim<sup>a</sup>, Youngill Choi<sup>a</sup>, Hyojoong Kim<sup>a</sup>, Sungwoo Cho<sup>b</sup>, Sung Cheol Yoon<sup>c</sup>, Seungmoon Pyo<sup>a,\*</sup>

<sup>a</sup> Department of Chemistry, Konkuk University, Seoul 143-701, Republic of Korea

<sup>b</sup> Nano Practical Application Center, Daegu 704-801, Republic of Korea

<sup>c</sup> Korea Research Institute of Chemical Technology, Daejeon 305-343, Republic of Korea

## ARTICLE INFO

## Article history:

Received 28 August 2008

Accepted 22 December 2008

Available online 3 January 2009

## PACS:

68.55ag

68.55aj

## Keywords:

Organic thin film transistors

Soluble pentacene

Polyimide

Gate dielectric

## ABSTRACT

Solution processable organic thin-film transistors (OTFTs) were fabricated using 6,13-bis(triisopropyl-silylethynyl) pentacene (TIPS-pentacene) and low-temperature processable polyimide gate dielectric. The TIPS-pentacene OTFT with the dielectric was found to have a field-effect mobility of 0.15 cm<sup>2</sup>/Vs, which is comparable to that of OTFT with an inorganic dielectric. The OTFTs with the polyimide dielectric did not show any significant performance degradation as time passed. A field-effect mobility of the OTFTs in 60 days was found to be almost identical to that of pristine OTFT. The combination of TIPS-pentacene and our polyimide gate dielectric can be one of the potential candidates for the fabrication of stable OTFTs for large-area flexible electronics.

© 2009 Elsevier B.V. All rights reserved.

During the past decades organic thin-film transistors (OTFTs) have attracted tremendous attention as a component for flexible display such as organic light emitting devices (OLEDs) [1], e-paper [2] and radiofrequency identification devices [3] due to their good compatibility with commercially available flexible substrates, low-temperature processability and flexible controllability of their electronic properties. Pentacene is one of the most promising and widely investigated organic semiconductors for OTFTs as an active layer. Field-effect mobility of pentacene OTFTs was found to be as high as 1.0 cm<sup>2</sup>/Vs at room temperature [4,5], which is already in the level of conventional hydrogenated amorphous silicon based field-effect transistors. But, pentacene thin-film was usu-

ally obtained using a vapor deposition method, which is not suitable for the fabrication of large-area flexible device because its solubility in conventional organic solvents is limited and thus solution process can not be employed.

One of the effective approaches to solve such problem is to design soluble semiconductor with same or even better charge transport properties than pentacene. Several soluble semiconductors have been proposed for the fabrication of OTFTs by many research groups [6–14]. Among them 6,13-bis(triisopropyl-silylethynyl) pentacene (TIPS-pentacene) has attracted huge attention for the fabrication of OTFTs since it is highly soluble in organic solvent and face-to-face stacking in crystalline form is optimal for  $\pi$ -orbital overlap [6]. However, OTFTs with TIPS-pentacene reported so far were fabricated using inorganic gate dielectric such as surface modified silicon dioxide [7–11], which

\* Corresponding author. Tel.: +82 2 450 3397; fax: +82 2 3436 5382.

E-mail address: [pyosm@konkuk.ac.kr](mailto:pyosm@konkuk.ac.kr) (S. Pyo).



is not suitable for the fabrication of flexible devices which requires solution processes.

Poly(4-vinylphenol) (PVP) is one of representative polymeric gate dielectrics for OTFTs and their characteristic has been studied extensively by many research groups [15–17]. However, the PVP can be damaged by the organic solvents such as dichlorobenzene and toluene used to dissolve TIPS-pentacene for solution processes. That is, when the TIPS-pentacene thin-film was formed on top of the PVP by drop-, spin- or dip-coating method, there is a possibility for the surface of the PVP to be roughened and/or swollen by the good solvent. In addition, thin-film formation of cross-linked PVP requires high temperature around 200 °C [15–17]. Therefore, it is necessary to use a low-temperature processable polymeric gate dielectric with a high chemical resistance to organic solvent for flexible electronic devices. In addition, it should be thermally stable enough to endure the heat generated during device fabrication and operation. In this letter, we report long-term stable TIPS-pentacene OTFTs with a polyimide gate dielectric, which is a well-known class of material with a high chemical and thermal stability and good electrical properties. For comparison, we have fabricated TIPS-pentacene OTFTs with a cross-linked PVP. In addition, we have investigated a long-term stability of the TIPS-pentacene OTFTs as a function of time.

TIPS-pentacene was prepared based on the procedures reported by Anthony et.al. and purified several times by using re-crystallization and column chromatography [6]. Polyimide gate dielectric (BTDA-DADM), which is not soluble in *o*-dichlorobenzene that was used as a solvent for TIPS-pentacene, was prepared via two synthetic routes reported elsewhere [18]. As a first step polyimide precursor, poly(amic acid), was prepared through a conventional polycondensation reaction from 1, 2, 3, 4-butanetetracarboxylic dianhydride (BTDA) and 4, 4-diaminodiphenyl methane (DADM).

Subsequently, the obtained poly(amic acid) was converted directly to its corresponding polyimide by a chemical imidization. Fig. 1 shows the chemical structure of TIPS-pentacene (a) and BTDA-DADM (b). The geometry of OTFTs for all electrical characterizations was a bottom gated top-contact as shown in Fig. 1c. Photo-lithographically patterned indium tin oxide on a glass substrate was used as a gate electrode and was cleaned by the following process; sonication in detergent, deionized water, acetone and isopropanol in that order for 15 min at room temperature. Prior to deposition of gate dielectric, the ITO/glass substrate was further cleaned using UV ozone. The BPDA-DADM in *N*-methylpyrrolidone (NMP) solution was spin-coated on top of the gate electrodes and then soft-baked at 90 °C for 1 min on a hot plate in air. The film was baked further at 175 °C for 1 h in vacuum (ca.  $10^{-2}$  torr) oven to remove completely the residual solvent. Although the post baking temperature can be lowered down to 125 °C, we employed 175 °C in order to directly compare with cross-linked PVP which was post-baked at 175 °C in this study. The thickness was controlled to about 220 nm. The active layer was prepared by blending a polymeric binder, poly( $\alpha$ -methyl styrene) (0.1 wt%), and TIPS-pentacene (0.1 wt%) in *o*-dichlorobenzene. Although the active layer can be formed by simple solution processes such as spin-coating and drop-coating, drop coating method was used in this study since it gives better molecular ordering and device performance than the other [7]. The active layer was drop-coated using a long syringe needle at room temperature and then was baked at 90 °C for 1 h in vacuum oven to evaporate the solvent thoroughly. TIPS-pentacene OTFTs were then completed by thermally evaporating 60 nm-thick source and drain gold electrodes on top of the active layer through a shadow mask. The channel

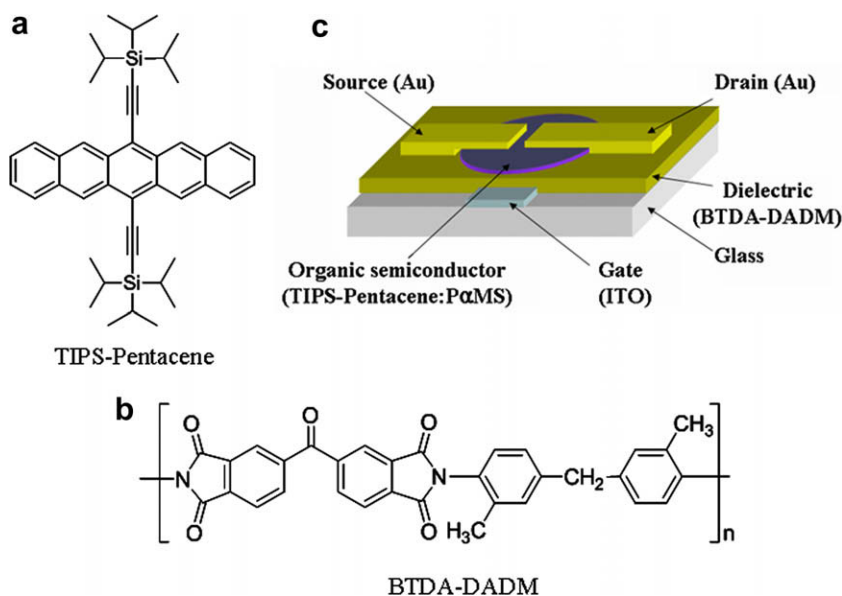


**Fig. 1.** Chemical structure of (a) 6,13-bis(triisopropyl-silylethynyl) pentacene (TIPS-Pentacene), (b) BTDA-DADM prepared through a conventional polycondensation reaction from 1, 2, 3, 4-butanetetracarboxylic dianhydride (BTDA) and 4, 4-diaminodiphenyl methane (DADM) and (c) geometry of TIPS-pentacene OTFTs with BTDA-DADM gate dielectric.

length ( $L$ ) and width ( $W$ ) are  $50\ \mu\text{m}$  and  $3\ \text{mm}$ , respectively. The thickness of the gate dielectric and active layer was determined using a surface profiler (AMBIOS XP-100). Optical microscopy (OM) image was taken with an OLYMPUS BX51. The output (for drain current vs drain voltage,  $I_{ds}$  vs  $V_{ds}$ ) and transfer (for drain current vs gate voltage,  $I_{ds}$  vs  $V_{gs}$ ) characteristics curves of the OTFTs were measured using an HP4145B semiconductor analyzer in air without any encapsulation.

The output curves of the TIPS-pentacene OTFTs with the BTDA-DADM gate dielectric at  $V_{gs}$  (from  $0\ \text{V}$  to  $-40\ \text{V}$  with a step of  $-10\ \text{V}$ ) were shown in Fig. 2a. It showed typical  $p$ -type characteristics with a clear transition from linear to saturation behavior. At a given  $V_{gs}$ ,  $I_{ds}$  initially increased linearly with small negative  $V_{ds}$  and then saturates due to a pinch-off of the accumulation layer located in the interface between TIPS-pentacene and BTDA-DADM. The inset of Fig. 2a shows OM image of channel region of the device and it was found that the active layer was bridged well between source and drain electrodes. Fig. 2b shows its corresponding transfer characteristic curve, where  $V_{gs}$  is swept from  $+20$  to  $-40\ \text{V}$  and  $V_{ds}$  is set at  $-30\ \text{V}$ . The field-effect mobility ( $\mu$ ) is extracted from the plot of  $\sqrt{I_{ds}}$  versus  $V_{gs}$  in a saturation regime based on the following equation:

$$I_{ds} = \frac{WC_i}{2L} \mu (V_{gs} - V_{Th})^2$$

where  $I_{ds}$  is the drain current,  $W$  and  $L$  are, respectively, the channel width and length.  $V_{gs}$  and  $V_{Th}$  are the gate voltage and the threshold voltage, respectively.  $C_i$  is the capacitance per unit area of the dielectric layer which was measured by using metal-dielectric-metal device and was found to be  $125\ \text{pF}/\text{mm}^2$ .  $V_{Th}$  of the device in the saturation regime was determined from the plot of the square root of the drain current ( $\sqrt{I_{ds}}$ ) and the gate voltage ( $V_{gs}$ ) by extrapolating the measured data to  $I_{ds} = 0$ . The inverse subthreshold swing ( $ss$ ), which is a measure of how sharply the device transits from the off to the on state, is given by  $ss = \left[ \frac{d \log(I_{ds})}{dV_{gs}} \right]^{-1}$ .

The calculated  $\mu$  and  $V_{Th}$  for the OTFT were  $0.15\ \text{cm}^2/\text{Vs}$  and  $-2.7\ \text{V}$ , respectively. The value of  $ss$  and current modulation ratio ( $I_{ON}/I_{OFF}$ ) were  $0.7\ \text{V}/\text{dec}$ ,  $1.46 \times 10^6$ , respectively. The extracted performance parameters of the TIPS-pentacene OTFTs with the BTDA-DADM gate dielectric were comparable to that of OTFTs with silicon dioxide gate

dielectric [10]. This indicates that BTDA-DADM is good gate dielectric for the fabrication of OTFTs based on soluble semiconductor including TIPS-pentacene.

In addition, we have fabricated TIPS-pentacene OTFT with a cross-linked PVP (inset of Fig. 3a) as a gate dielectric using the same process described above in order to compare the performance of TIPS-pentacene OTFT with the BTDA-DADM gate dielectric. The cross-linked PVP gate dielectric solution was prepared by dissolving PVP (10 wt%) and poly(melamine-co-formaldehyde) methylated (5 wt%) as a cross-linking agent in propylene glycol monomethyl ether acetate (PGMEA), and stirred vigorously for 2 h to give homogenous solution. Prior to its deposition to the substrate, the solution was filtered by a PTFE membrane filter with a pore size of  $0.20\ \mu\text{m}$ . The solution was spin-coated and soft-baked at  $90\ ^\circ\text{C}$  for 1 min on a hot plate in air and baked further at  $175\ ^\circ\text{C}$  for 1 h in vacuum (ca.  $10^{-2}$  torr) oven.  $C_i$  of the cross-linked PVP dielectric layer was found to be  $61\ \text{pF}/\text{mm}^2$ . The output and transfer curves of the TIPS-pentacene OTFTs at various gate and drain voltages were shown in Fig. 3a and b, respectively. The calculated  $\mu$  and  $V_{Th}$  for the OTFTs were  $1.07 \times 10^{-3}\ \text{cm}^2/\text{Vs}$  and  $-2.4\ \text{V}$ , respectively. The value of  $ss$  and current modulation ratio ( $I_{ON}/I_{OFF}$ ) were  $1.91\ \text{V}/\text{dec}$ ,  $1.23 \times 10^4$ , respectively. Overall performance of TIPS-pentacene OTFTs with the BTDA-DADM was better than that of OTFTs with the cross-linked PVP. It may be due to the better interface formation between TIPS-pentacene and BTDA-DADM gate dielectric since the insoluble polyimide, BTDA-DADM, is stronger than cross-linked PVP in a *o*-dichlorobenzene used as a solvent to dissolve TIPS-pentacene.

In order to investigate long-term stability of the TIPS-pentacene OTFTs with the BTDA-DADM, we measured their electrical properties as time passed: right after fabrication, after 2, 4, 10, 30 and 60 days. The OTFTs were stored in a specially designed box which was slightly vacuumed (550 torr) in order to control their exposure condition precisely. The electrical measurement for the OTFTs was carried out in ambient condition at room temperature. Fig. 4a shows transfer characteristic curves of the OTFTs as a function of time. They are almost identical to each other except for small change of  $I_{OFF}$  and  $|V_{Th}|$  as time passed. Fig. 4b–d shows  $\mu$ ,  $ss$ ,  $I_{ON}$ ,  $I_{OFF}$ ,  $|V_{Th}|$  plotted as a function of a time. The performance parameters of the

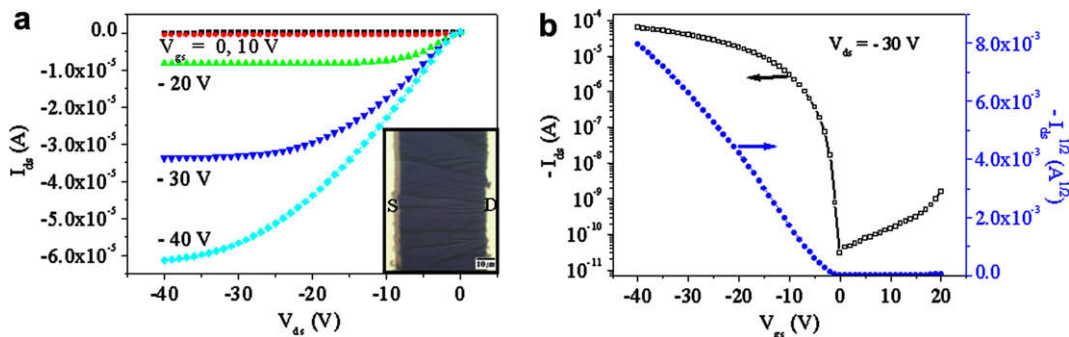


**Fig. 2.** Electrical characteristics of the TIPS-Pentacene OTFTs with BTDA-DADM gate dielectric right after fabrication. Output curves (a) were recorded by sweeping  $V_{ds}$  from  $0$  to  $40\ \text{V}$  with a step of  $-10\ \text{V}$  and transfer curves (b) were recorded by sweeping  $V_{gs}$  from  $20$  to  $-40\ \text{V}$  at a fixed  $V_{ds} = -30\ \text{V}$  (left y-axis, logarithmic scale; right y-axis, square root of  $I_{ds}$ ). Inset: Optical microscope image of channel region the OTFTs.

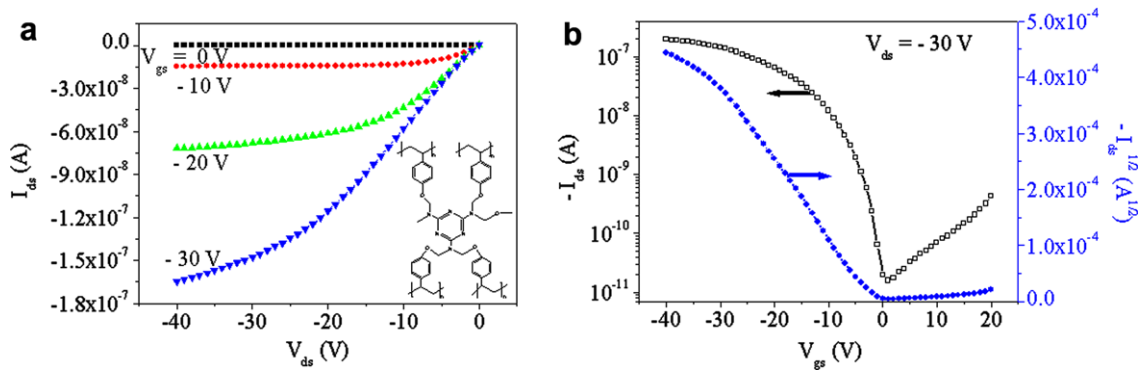


**Fig. 3.** Electrical characteristics of the TIPS-Pentacene OTFTs with cross-linked PVP right after fabrication. Output curves (a) were recorded by sweeping  $V_{ds}$  from 0 to  $-40$  V with a step of  $-10$  V and transfer curves (b) were recorded by sweeping  $V_{gs}$  from 20 to  $-40$  V at a fixed  $V_{ds} = -30$  V (left y-axis, logarithmic scale; right y-axis, square root of  $I_{ds}$ ).

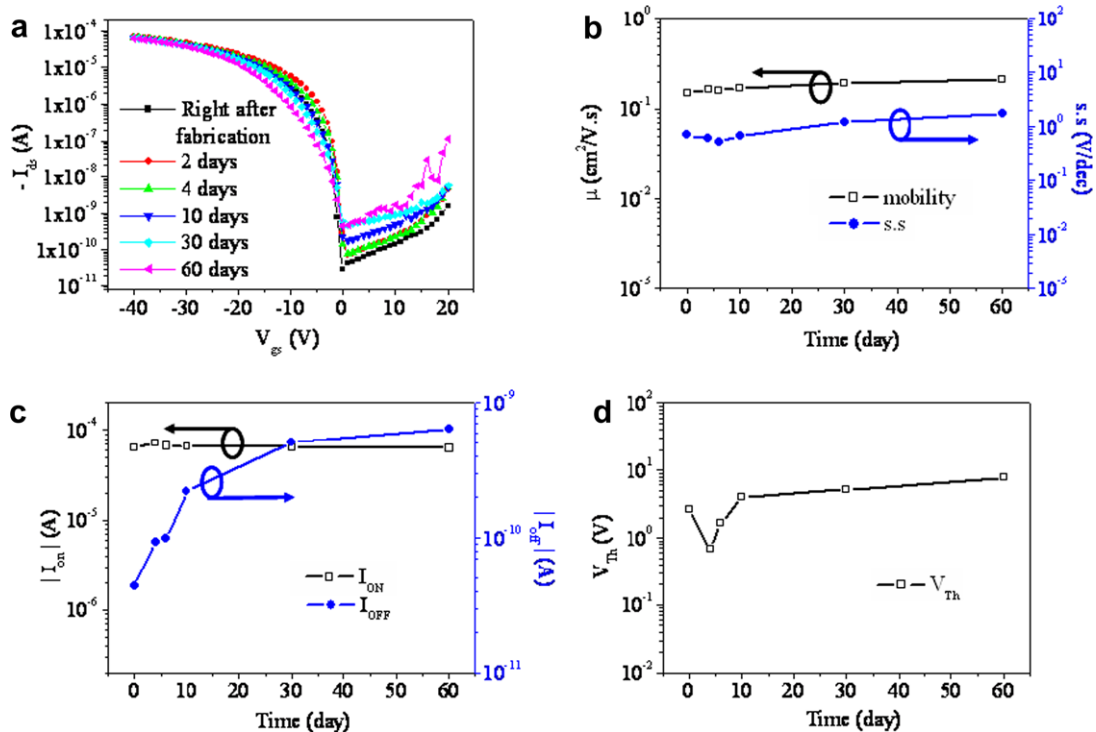


**Fig. 4.** (a) Transfer curves of the TIPS-Pentacene OTFTs with BTDA-DADM gate dielectric as time passed: right after fabrication, after 2, 4, 10, 30 and 60 days. The transfer curves were recorded by sweeping  $V_{gs}$  from 20 to  $-40$  V at a fixed  $V_{ds} = -30$  V. The plot of field-effect mobility (left y-axis) and subthreshold swing (right y-axis) (b),  $I_{ON}$  (left y-axis) and  $I_{OFF}$  (right y-axis) (c), and threshold voltage (d) as a function of time.

OTFTs are extracted from the transfer characteristic curves with a fixed  $V_{ds}$  ( $V_{ds} = -30$  V) in a saturation regime. The  $\mu$  and  $ss$  value of the OTFTs did not show any significant change up to 60 days (Fig. 4b). The  $\mu$  of the OTFTs right after fabrication was  $0.15 \text{ cm}^2/\text{Vs}$  and it increased gradually as time passed and was found to be  $0.21 \text{ cm}^2/\text{Vs}$  in 60 days. We believe that the slightly improved  $\mu$  may be due to crystalline structure formation as time passed by

self-organization at room temperature, which was also observed soluble acene OTFTs [19]. The  $ss$  value for the OTFTs was around  $0.7 \text{ V}/\text{dec}$  up to 10 days and it increased to  $1.69 \text{ V}/\text{dec}$  in 60 days. However, any significant change was not observed as time passed. As shown in Fig. 4c and d, the  $I_{OFF}$  of the OTFTs was increased from  $4.4 \times 10^{-11}$  (right after fabrication) to  $6.4 \times 10^{-10}$  (after 60 days) although their  $I_{ON}$  was not changed at all.  $|V_{Th}|$  of OTFTs in-

creases from 2.67 V (right after fabrication) to 7.8 V (after 60 days) as time passed. This indicates that as time passed the interface between TIPS-pentacene and the gate dielectric was slightly damaged by moisture and oxygen from device storage environment. This behavior was also observed for pentacene OTFTs which was exposed to moisture and oxygen [20,21]. However, compared to the pentacene OTFTs with silicon dioxide gate dielectric, the performance of our TIPS-pentacene OTFTs with the BTDA-DADM gate dielectric showed much better performance stability.

In conclusion, we report a fabrication of TIPS-pentacene OTFTs using a low-temperature processable polyimide gate dielectric and an investigation on their long-term stability. The calculated  $\mu$ , *s.s.*, current modulation ratio ( $I_{ON}/I_{OFF}$ ) and  $V_{Th}$  for the pristine OTFTs with BTDA-DADM were 0.15 cm<sup>2</sup>/Vs, 0.7 V/dec,  $1.46 \times 10^6$  and  $-2.7$  V, respectively. The performance is comparable to that of TIPS-Pentacene OTFTs with silicon dioxide gate dielectric and better than that of TIPS-Pentacene OTFTs with cross-linked PVP. In addition, we found that the performance of the TIPS-Pentacene OTFTs with the BTDA-DADM could be maintained for long period of time without any significant performance degradation. This study reveals that the combination of TIPS-pentacene and our polyimide gate dielectric, BTDA-DADM, can be one of the potential candidates for the fabrication of stable OTFTs for large-area flexible electronics.

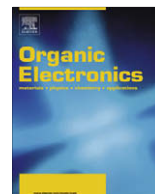
### Acknowledgements

This study was supported by KOSEF through EPB Center (R11-2008-052-03003). This work was also supported by a grant from the Fundamental R&D Program for Core Tech-

nology of Materials funded by the Ministry of Commerce, Industry and Energy.

### References

- [1] B.W. D'Andrade, J.J. Brown, *Appl. Phys. Lett.* 88 (2006) 192908.
- [2] R. Winnieff, *Nature* 394 (1998) 225.
- [3] P.F. Baude, D.A. Ender, M.A. Haase, T.W. Kelley, D.V. Muires, S.D. Theiss, *Appl. Phys. Lett.* 82 (2003) 3964.
- [4] A.L. Briseno, S.C.B. Mannsfeld, M.M. Ling, S.H. Liu, R.J. Tseng, C. Reese, M.E. Roberts, Y. Yang, F. Wudl, Z.N. Bao, *Nature* 444 (2006) 913.
- [5] S.W. Park, J.M. Hwang, J.M. Choi, D.K. Hwang, M.S. Oh, J.H. Kim, S. Im, *Appl. Phys. Lett.* 90 (2007) 153512.
- [6] J.E. Anthony, J.S. Brooks, D.L. Eaton, S.R. Parkin, *J. Am. Chem. Soc.* 124 (2001) 9482.
- [7] S.K. Park, T.N. Jackson, J.E. Anthony, D.A. Mourey, *Appl. Phys. Lett.* 91 (2007) 063514.
- [8] R.L. Headrick, S. Eo, F. Sansoz, J.E. Anthony, *Appl. Phys. Lett.* 92 (2008) 063302.
- [9] C.D. Sheraw, T.N. Jackson, D.L. Eaton, J.E. Anthony, *Adv. Mater.* 15 (2003) 2009.
- [10] W. Lee, D. Kim, Y. Jang, J. Cho, M. Hwang, Y. Park, Y. Kim, J. Han, K. Cho, *Appl. Phys. Lett.* 90 (2007) 132106.
- [11] Y. Li, Y. Wu, Z. Prostran, S. Gardner, B.S. Ong, *Chem. Mater.* 19 (2007) 418.
- [12] J. Kwon, J. Seo, S. Shin, K. Kim, D. Choi, B. Kang, H. Kang, B. Ju, *IEEE Trans. Elec. Dev.* 55 (2008) 500.
- [13] D. Zander, N. Hoffmann, K. Lmimouni, S. Lenfant, C. Petit, D. Vuillaume, *Microelectron. Eng.* 80 (2005) 394.
- [14] S.H. Chan, H.K. Lee, Y.M. Wang, N.Y. Fu, X.M. Chen, Z.W. Cai, H.N.C. Wong, *Chem. Commun.* 1 (2005) 66.
- [15] M. Halik, H. Klauk, U. Zschieschang, T. Kriem, G. Schmid, W. Radlik, *Appl. Phys. Lett.* 81 (2002) 289.
- [16] S. Scheinert, G. Paasch, M. Schrodner, H.-K. Roth, S. Sensfub, *J. Appl. Phys.* 92 (2002) 330.
- [17] H. Klauk, M. Halik, U. Zschieschang, F. Eder, G. Schmid, C. Dehm, *Appl. Phys. Lett.* 82 (2003) 4175.
- [18] S. Pyo, H. Son, M. Yi, *J. Mater. Res.* 20 (2005) 931.
- [19] W. Lee, J. Lim, D. Kim, J. Cho, Y. Jang, Y. Kim, J. Han, K. Cho, *Adv. Func. Mater.* 18 (2008) 560.
- [20] S.H. Han, J.H. Kim, J. Jang, S.M. Cho, M.H. Oh, S.H. Lee, D.J. Choo, *Appl. Phys. Lett.* 88 (2006) 073519.
- [21] H. Jung, T. Lim, Y. Choi, M. Yi, J. Won, S.M. Pyo, *Appl. Phys. Lett.* 92 (2008) 163504.



## Letter

## Buffer layer formation in organic photovoltaic cells by self-organization of poly(dimethylsiloxane)s

Shimpei Yamakawa<sup>a</sup>, Keisuke Tajima<sup>a</sup>, Kazuhito Hashimoto<sup>a,b,\*</sup><sup>a</sup> Department of Applied Chemistry, School of Engineering, The University of Tokyo, 7-3-1 Hongo, Bunkyo-ku, Tokyo 113-8656, Japan<sup>b</sup> HASHIMOTO Light Energy Conversion Project, ERATO, Japan Science and Technology Agency (JST), Japan

## ARTICLE INFO

## Article history:

Received 10 November 2008

Received in revised form 15 December 2008

Accepted 18 December 2008

Available online 3 January 2009

## PACS:

73.61.Ph

## Keywords:

Self-organization

Interfacial buffer layer

Organic photovoltaic cells

Block copolymers

## ABSTRACT

A surface-segregated thin layer of poly(dimethylsiloxane)-*block*-poly(methylmethacrylate) (PDMS-*b*-PMMA) formed by self-organization during spin-coating was utilized as an interfacial buffer layer in organic photovoltaic cells. X-ray photoelectron spectroscopy revealed that PDMS-*b*-PMMA mixed into the coating solution spontaneously accumulated at the surface of the active layer due to the low surface energy of PDMS. The introduction of the PDMS-*b*-PMMA layer in bulk-heterojunction cells of poly(3-hexylthiophene):[6,6]-phenyl C<sub>61</sub>-butyric acid methyl ester resulted in an improvement of the power conversion efficiency (PCE) of the cells from 3.05% to 3.56% on average. The highest PCE of 3.86% was achieved with 0.4 mg ml<sup>-1</sup> of PDMS-*b*-PMMA. These results indicate that the PDMS-*b*-PMMA layer formed by self-organization provides a facile and versatile approach to improve the photovoltaic performance, possibly by suppressing charge carrier recombination at the organic/metal interface.

© 2009 Elsevier B.V. All rights reserved.

Control of charge carrier transport at heterointerfaces in multilayer structures is one of the most important issues in the improvement of organic photovoltaic cells (OPVs). It has been reported that insertion of buffer layers between the organic layer and the electrodes improves the device performance. To date, inorganic materials such as LiF [1,2], TiO<sub>x</sub> [3–5], ZnO [6–8], and the like [9–12], and organic materials such as naphthalene tetracarboxylic anhydride [13], poly(3,4-ethylenedioxythiophene):poly(styrene sulfonate) (PEDOT:PSS) [2,14,15] among others [16] have been employed for this purpose. However, the deposition of the buffer layers requires performance of multi-step processes, these processes being either dry (vacuum evaporation) or wet (repeated coating using an orthogonal solvent), which could detract from the advantage of the ease of fabrication of OPVs. Recently, we proposed a new con-

cept of utilizing self-organized surface-segregated layers [17] for the buffer layers in OPVs. In this method, a small amount of a low surface energy material (i.e., a fluoroalkyl-attached fullerene compound) is mixed into the solution used to form the active layers. During the spin-coating, the low surface energy material becomes segregated at the liquid–air interface driven by the total energy minimization of the system. The photovoltaic device performance was improved by the introduction of the fluoroalkyl fullerene compound, which was attributed to surface dipole formation at the organic/metal interface.

In this work, we report on the use of a conventional low surface energy material for spontaneous buffer layer formation: poly(dimethylsiloxane) (PDMS). Analogous to fluoroalkyl-attached fullerene compounds, poly(dimethylsiloxane)-*block*-poly(methyl methacrylate) (PDMS-*b*-PMMA) can form surface-segregated layers during the solution coating processes due to the low surface energy of the PDMS block, while the PMMA block makes the polymer solid and thus easy to handle. Green et al. reported that in the structure of silicon solar cells known as MINP

\* Corresponding author. Address: Department of Applied Chemistry, School of Engineering, The University of Tokyo, 7-3-1 Hongo, Bunkyo-ku, Tokyo 113-8656, Japan.

E-mail address: [hashimoto@light.t.u-tokyo.ac.jp](mailto:hashimoto@light.t.u-tokyo.ac.jp) (K. Hashimoto).

devices [18–20], surface passivation by means of an ultrathin SiO<sub>2</sub> layer disposed under the metal contacts prevents charge recombination at the semiconductor/metal interface and thereby improves the open-circuit voltage ( $V_{OC}$ ). Furthermore, in organic light emitting diodes, insertion of a SiO<sub>2</sub> buffer layer blocks hole transport [21], resulting in enhancement of brightness and efficiency. Keeping this interfacial passivation with SiO<sub>2</sub> in mind, we can expect a similar effect in OPVs by using very thin layers of PDMS, which can prevent reverse hole flow and consequently improve the efficiency of solar cells. In addition, PDMS would provide wider range of solubility in common solvents compared to the fluorocarbon compounds, which could be advantageous for designing various molecules having the surface segregation property.

The OPV cells used in this study were fabricated as follows. ITO-coated glass substrates (Geomatech, Japan,  $10 \Omega \square^{-1}$ ) were sequentially washed by sonication in detergent, water, acetone, isopropanol and water for 20 min, and were finally exposed to UV-ozone for 5 min. The ITO-coated substrates were then coated with a 50 nm layer of PEDOT:PSS (Battron P, H.C. Starck) by spin-coating, followed by baking at 150 °C for 5 min under a N<sub>2</sub> atmosphere. A bulk-heterojunction layer was spin-cast onto the PEDOT:PSS layer at a coating speed of 500 rpm for 60 s from a chlorobenzene solution containing 10 mg ml<sup>-1</sup> of poly(3-hexylthiophene) (P3HT, Rieke Metals, USA), 6.5 mg ml<sup>-1</sup> of [6,6]-phenyl C<sub>61</sub>-butyric acid methyl ester (PCBM, Frontier Carbon Corp., Japan) and 0.0–1.0 mg ml<sup>-1</sup> of PDMS-*b*-PMMA ( $M_n = 8000$  for PDMS and  $M_n = 4000$  for PMMA,  $M_w/M_n = 1.09$ , Polymer Source, Canada). Finally, 60 nm of Al was thermally deposited on top of the organic layer under a vacuum of  $\sim 10^{-4}$  Pa. After the cathode deposition, the devices were annealed at 150 °C for 30 min under a N<sub>2</sub> atmosphere. The active area of the devices was defined by a photo mask as 0.06 cm<sup>2</sup>. The *I*-*V* characteristics of the OPV devices were measured under irradiation of simulated solar light (PEC-L11, Pecell Technologies, Inc., Japan). The photovoltaic parameters were obtained by taking the averages of four devices. The light intensity was calibrated with a standard silicon solar cell with a filter (BS520, Bunkou Keiki, Japan) to 100 mW cm<sup>-2</sup>. X-ray photoelectron spectra (XPS) were measured using a JPS-90SX (Nihon Denshi, Japan). Film thickness was measured by surface profilometry (Dektak 6M, ULVAC, Japan).

Fig. 1 shows the results of XPS measurements performed on the spin-coated films of P3HT:PCBM with different PDMS-*b*-PMMA concentrations. The sample surfaces were repeatedly etched away using an Ar<sup>+</sup> beam in the sample chamber of an XPS instrument. Fig. 1a and b shows the signal intensities of silicon and indium, respectively, as functions of the etching durations. Before the etching, silicon peaks can be seen for each sample, superimposed on the spectrum of PDMS-*b*-PMMA (Fig. 1a). For the samples with 0.1 mg ml<sup>-1</sup> and 0.4 mg ml<sup>-1</sup> of PDMS-*b*-PMMA, heights of the silicon peaks are considerably decreased after etching for 5 s. These results indicate that most of the silicon exists in the region extending to less than ca. 1.5 nm from the surface when the concentration of PDMS-*b*-PMMA is lower than 0.4 mg ml<sup>-1</sup>, assuming an etching rate of 0.3 nm (see below). When the concentration of PDMS-*b*-PMMA was in-

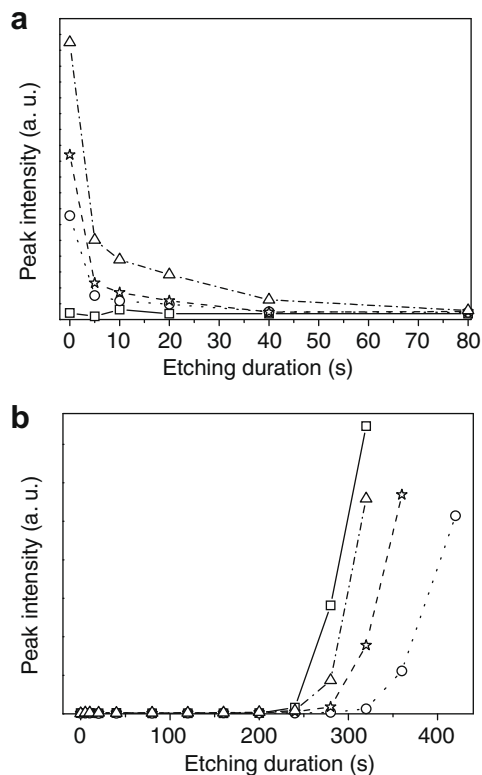


Fig. 1. XPS depth profiles of (a) Si 2p<sub>3/2</sub> and (b) In 3d<sub>5/2</sub> on the surface of an organic layer spin-cast from a chlorobenzene solution of 10 mg ml<sup>-1</sup> of P3HT and 6.5 mg ml<sup>-1</sup> of PCBM mixed with 0.0 mg ml<sup>-1</sup> (squares), 0.1 mg ml<sup>-1</sup> (circles), 0.4 mg ml<sup>-1</sup> (stars) or 1.0 mg ml<sup>-1</sup> (triangles) of PDMS-*b*-PMMA.

creased to 1.0 mg ml<sup>-1</sup>, the silicon peak is reduced to one-third after etching for 5 s and almost disappears after 40 s, indicating that PDMS-*b*-PMMA covers the surface and also exists in a region extending ca. 12 nm from the surface, assuming the same etching rate (see below). These results of the depth profiling clearly show that PDMS-*b*-PMMA mixed into the active layer solution was segregated at the air/organic interface spontaneously during the spin-coating because of its low surface energy.

The addition of PDMS-*b*-PMMA in the solutions also affected the film thickness of active layer, measured by surface profilometry as shown in Fig. 2. The active layer was 70 nm thick without PDMS-*b*-PMMA, while it became ca. 1.5 times thicker with 0.1 mg ml<sup>-1</sup> of PDMS-*b*-PMMA. This thickness difference is obvious in optical density of the active layers. With a higher concentration of PDMS-*b*-PMMA (0.3–1.0 mg ml<sup>-1</sup>), the thickness returns to ca. 70 nm. The XPS depth profile of indium peak intensity (Fig. 1b) gives the rate of Ar<sup>+</sup> beam etching as ca. 0.3 nm s<sup>-1</sup> and also supports the thickness change of the organic films when mixed with PDMS-*b*-PMMA. This tendency of the film thickness change was observed in four different series of the experiments. The reason for this complex change in the film thickness is not clear, but the presence of PDMS-*b*-PMMA in the solution might cause a change in the factors such as solution viscosity, solvent drying rate or wet-

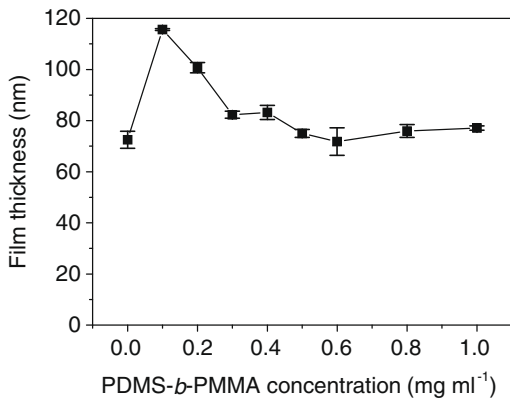


Fig. 2. Film thickness of the active layers on ITO substrates measured by surface profilometry.

tability that could work competitively to determine the film thickness.

Fig. 3 shows the performances of OPVs with various concentrations of PDMS-*b*-PMMA. For the device without PDMS-*b*-PMMA added to the solution, a short-circuit current ( $I_{SC}$ ) of  $8.31 \pm 0.08 \text{ mA cm}^{-2}$ , a  $V_{OC}$  of  $0.57 \pm 0.01 \text{ V}$  and a fill factor (FF) of  $65.1 \pm 1.3\%$  were shown, resulting in a power conversion efficiency (PCE) of  $3.05 \pm 0.09\%$ . When  $0.1 \text{ mg ml}^{-1}$  of PDMS-*b*-PMMA was added to the solution, FF dropped slightly to  $62.4 \pm 0.8\%$ , while  $I_{SC}$  re-

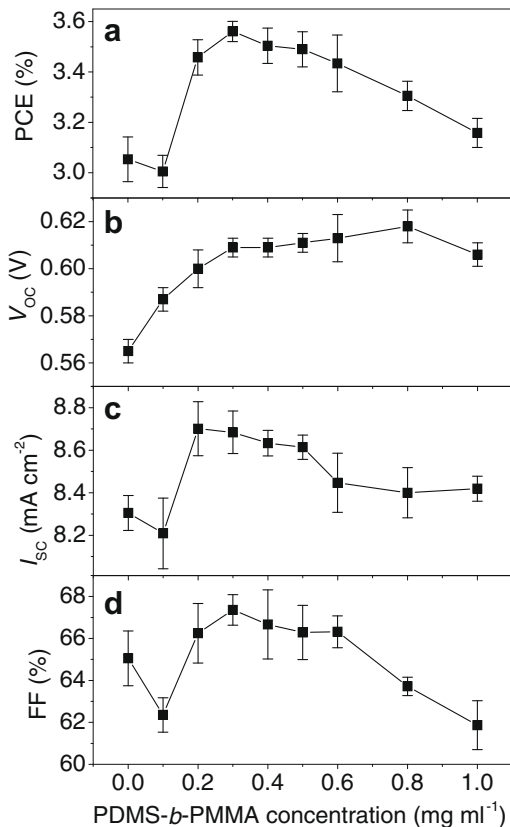


Fig. 3. (a) PCE, (b)  $V_{OC}$ , (c)  $I_{SC}$ , and (d) FF under  $100 \text{ mW cm}^{-2}$  AM1.5 irradiation plotted as functions of the PDMS-*b*-PMMA concentration.

mained around  $8.2 \pm 0.2 \text{ mA cm}^{-2}$  and  $V_{OC}$  increased to  $0.59 \pm 0.01 \text{ V}$ . The decrease in FF observed for  $0.1 \text{ mg ml}^{-1}$  of PDMS-*b*-PMMA might be attributed to the thick active layer (116 nm), compared with the film without PDMS-*b*-PMMA (73 nm), as shown in Fig. 2. Since the optimum thickness for this device parameter is around 73 nm, the thicker active layer could cause the recombination of charges in the bulk-heterojunction films and therefore deterioration of FF. When more than  $0.1 \text{ mg ml}^{-1}$  of PDMS-*b*-PMMA was added to the solution,  $I_{SC}$  and FF first increased and peaked around  $0.3 \text{ mg ml}^{-1}$  and then gradually decreased, while  $V_{OC}$  continuously increased up to ca.  $0.62 \text{ V}$ . As the result, the optimum parameters were achieved with  $0.3 \text{ mg ml}^{-1}$  of PDMS-*b*-PMMA for which average values of PCE,  $V_{OC}$ ,  $I_{SC}$  and FF of  $3.56 \pm 0.04\%$ ,  $0.61 \pm 0.00 \text{ V}$ ,  $8.68 \pm 0.10 \text{ mA cm}^{-2}$  and  $67.4 \pm 0.7\%$ , respectively, were observed. The highest PCE of 3.86% was achieved with  $0.4 \text{ mg ml}^{-1}$  PDMS-*b*-PMMA and  $V_{OC}$  of  $0.60 \text{ V}$ ,  $I_{SC}$  of  $9.61 \text{ mA cm}^{-2}$  and FF of 67.0% in a different trial (Fig. 4). Since the active layer thickness did not change at this concentration of PDMS-*b*-PMMA (Fig. 2), this enhancement of the device performance can be attributed to the improved interfacial charge transport between the organic layer and the metal electrode.

For comparison, a commonly used buffer layer, LiF, was vacuum deposited on the P3HT:PCBM layer and used for the photovoltaic devices. The highest PCE of 3.19% was achieved in the device with 0.5 nm of LiF with  $V_{OC}$  of  $0.58 \text{ V}$ ,  $I_{SC}$  of  $8.69 \text{ mA cm}^{-2}$  and FF of 63.4%. The improvement of the performance was more significant with PDMS-*b*-PMMA than with LiF. Along with the easy preparation in the single solution process, the PDMS-*b*-PMMA layer has a great advantage compared to the other buffer layers deposited by dry processes.

The detailed mechanisms occurring in the buffer layers are still unclear and several mechanisms have been proposed such as dipole-layer formation, protecting the organic layer surface from evaporated metals, or interfacial passivation preventing charge recombination [2,13–15]. In the current case, PDMS-*b*-PMMA itself does not have strong molecular dipole unlike the fluoroalkyl-attached fullerene compound, therefore the origin of the improvement is not likely the energy matching at the interface.

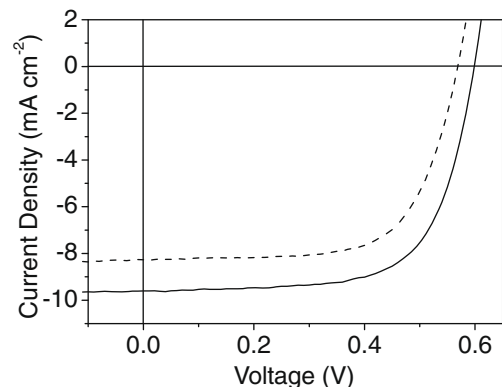
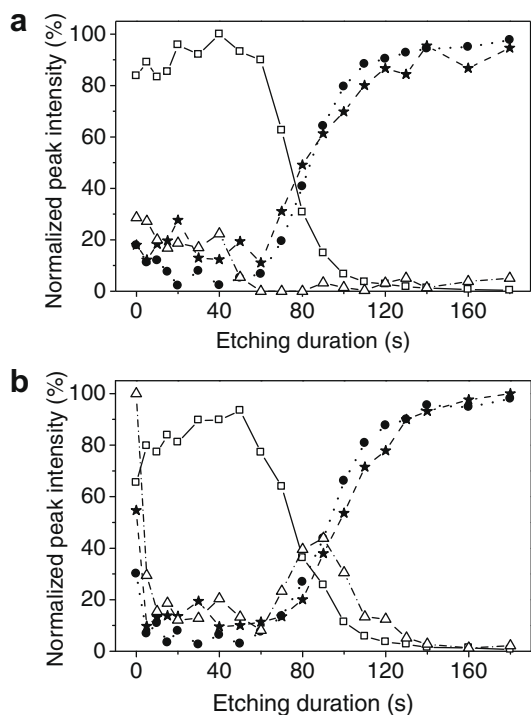


Fig. 4. The  $I$ - $V$  curves of the OPVs under  $100 \text{ mW cm}^{-2}$  AM1.5 irradiation, showing the highest PCE with  $0.4 \text{ mg ml}^{-1}$  PDMS-*b*-PMMA (solid line) and without PDMS-*b*-PMMA (dashed line).



**Fig. 5.** XPS depth profiles of Al (squares), C (circles), S (stars) and Si (triangles) for the (a) P3HT:PCBM/Al and (b) P3HT:PCBM/PDMS-*b*-PMMA/Al layers.

To investigate the possibility of the protecting effect by PDMS-*b*-PMMA from the evaporated metal, the XPS depth profile was performed on the P3HT:PCBM films coated with vacuum deposited Al with and without  $1.0 \text{ mg ml}^{-1}$  of PDMS-*b*-PMMA added in the solutions (Fig. 5). The intensities are normalized to the maximum signal intensity of each atom. In both samples, as the etching proceed from the surface, Al peak start to decrease and C and S peaks start to increase at the interface. After 120 s etching, Al peaks were completely disappeared and intensities of C and S peaks became constant. Si peak is detected between the Al and the organic layers (i.e. appearance of C and S) when PDMS-*b*-PMMA was used (Fig. 5b). This showed that PDMS-*b*-PMMA formed a buffer layer at the interface between Al electrode and the organic layer as expected. The comparison of the detection limit of Al between the films indicated that the depth of Al penetration into the films was almost the same in each sample (approximately 10 nm). These results suggested that there was no detectable protecting effect of the PDMS-*b*-PMMA layer from the penetration of Al into the organic films. Another possible role of the PDMS-*b*-PMMA layer is provision of an interfacial passivation effect similar to the case of silicon solar cells with an ultra thin layer of SiO<sub>2</sub> passivation layers [18–20]. PDMS-*b*-PMMA is an electronically inert material and could reduce the number of charge recombination sites at the interface between the aluminum cathode and organic active layers, resulting in improvement of the device performance. Because of the insulation property of PDMS-*b*-PMMA, adding an excessive amount (0.6–1.0  $\text{mg ml}^{-1}$ ) of PDMS-*b*-PMMA results in excessively thick

passivation layers (more than 3 nm) being formed that hinder electron transport from the organic layer to the aluminum electrode and therefore degrades  $I_{\text{SC}}$  and FF.

Finally, it is worth to note that silicone compounds similar to PDMS-*b*-PMMA are often used as lubricants in many apparatuses and therefore may easily contaminate the materials. In fact, we observed similar Si accumulation on the surface by XPS even without adding PDMS-*b*-PMMA when we used a plastic disposable syringe with a rubber gasket for the sample preparation. Considering the fact that even a small amount of PDMS-*b*-PMMA may affect the device performance, one should take extra care in avoiding the contaminations in order to observe consistent device results.

In conclusion, we have demonstrated that PDMS-*b*-PMMA mixed into the active layer solution spontaneously formed a buffer layer in OPV devices. Addition of the proper amount of PDMS-*b*-PMMA improves the OPV performance, while the performance was decreased when an excessive amount was added. The highest PCE of 3.86% was achieved for the OPV device with  $0.4 \text{ mg ml}^{-1}$  of PDMS-*b*-PMMA as a self-organized layer. The approach reported herein will provide a facile and versatile way to control the interface between semiconducting materials and metal electrodes in various organic electronic devices.

#### Acknowledgements

We thank Mr. Qingshuo Wei and Mr. Motoshi Nakamura for helpful discussions.

#### References

- [1] E. Ahlswede, J. Hanisch, M. Powalla, Appl. Phys. Lett. 90 (2007) 163504.
- [2] S.K.M. Jonsson, E. Carlegrim, F. Zhang, W.R. Salaneck, M. Fahlman, Jpn. J. Appl. Phys. Part 1 44 (2005) 3695.
- [3] J.Y. Kim, S.H. Kim, H.H. Lee, K. Lee, W.L. Ma, X. Gong, A.J. Heeger, Adv. Mater. 18 (2006) 572.
- [4] A. Hayakawa, O. Yoshikawa, T. Fujieda, K. Uehara, S. Yoshikawaa, Appl. Phys. Lett. 90 (2007) 163512.
- [5] S.J. Yoon, J.H. Park, H.K. Lee, O.O. Park, Appl. Phys. Lett. 92 (2008) 143504.
- [6] H.-L. Yip, S.K. Hau, N.S. Baek, H. Ma, A.K.-Y. Jen, Adv. Mater. 9999 (2008).
- [7] H.-L. Yip, S.K. Hau, N.S. Baek, A.K.-Y. Jen, Appl. Phys. Lett. 92 (2008) 193313.
- [8] J. Gilot, I. Barbu, M.M. Wienk, R.A.J. Janssen, Appl. Phys. Lett. 91 (2007) 113520.
- [9] V. Shrotriya, G. Li, Y. Yao, C.W. Chu, Y. Yang, Appl. Phys. Lett. 88 (2006) 073508.
- [10] G. Li, C.W. Chu, V. Shrotriya, J. Huang, Y. Yang, Appl. Phys. Lett. 88 (2006) 3.
- [11] M.D. Irwin, B. Buchholz, A.W. Hains, R.P.H. Chang, T.J. Marks, Proc. Natl. Acad. Sci. USA 105 (2008) 2783.
- [12] Z.A. Tan, C.H. Yang, E.J. Zhou, X. Wang, Y.F. Li, Appl. Phys. Lett. 91 (2007) 023509.
- [13] K. Suemori, T. Miyata, M. Yokoyama, M. Hiramoto, Appl. Phys. Lett. 85 (2004) 6269.
- [14] C.J. Brabec, S.E. Shaheen, C. Winder, N.S. Sariciftci, P. Denk, Appl. Phys. Lett. 80 (2002) 1288.
- [15] F. Zhang, M. Ceder, O. Inganäs, Adv. Mater. 19 (2007) 1835.
- [16] A.W. Hains, T.J. Marks, Appl. Phys. Lett. 92 (2008) 023504.
- [17] Q.S. Wei, T. Nishizawa, K. Tajima, K. Hashimoto, Adv. Mater. 20 (2008) 2211.
- [18] A.W. Blakers, M.A. Green, Appl. Phys. Lett. 39 (1981) 483.
- [19] M.A. Green, A.W. Blakers, Sol. Cells 8 (1983) 3.
- [20] M.A. Green, A.W. Blakers, J. Shi, E.M. Keller, S.R. Wenham, IEEE Trans. Electron Dev. 31 (1984) 679.
- [21] Z.B. Deng, X.M. Ding, S.T. Lee, W.A. Gambling, Appl. Phys. Lett. 74 (1999) 2227.





## Letter

# Measurement of the lowest unoccupied molecular orbital energies of molecular organic semiconductors

Peter I. Djurovich<sup>a</sup>, Elizabeth I. Mayo<sup>b</sup>, Stephen R. Forrest<sup>c,\*</sup>, Mark E. Thompson<sup>a</sup>

<sup>a</sup> Department of Chemistry, University of Southern California, Los Angeles, California 90089, USA

<sup>b</sup> Global Photonic Energy Corporation, 20 Trading Post Way, Medford Lake, New Jersey 08055, USA

<sup>c</sup> Departments of Electrical Engineering and Computer Science, Physics, and Materials Science and Engineering, University of Michigan, 4080 Fleming administration building, 503 Thompson street, Ann Arbor, Michigan 48109-1340, USA

## ARTICLE INFO

## Article history:

Received 12 November 2008

Received in revised form 21 December 2008

Accepted 28 December 2008

Available online 4 January 2009

## Keywords:

Organic

Energy levels

Lowest unoccupied molecular orbital

## ABSTRACT

The lowest unoccupied molecular orbital (LUMO) energies of a variety of molecular organic semiconductors have been evaluated using inverse photoelectron spectroscopy (IPES) data and are compared with data determined from the optical energy gaps, electrochemical reduction potentials, and density functional theory (DFT) calculations. A linear fit to the electrochemical reduction potential (relative to an internal ferrocene reference) vs. the LUMO energy determined by IPES gives a slope and intercept of  $-1.19 \pm 0.08$  eV/V and  $-4.78 \pm 0.17$  eV, respectively, and  $0.92 \pm 0.04$  and  $-0.44 \pm 0.11$  eV, respectively, based on the DFT calculated LUMO energies. From these fits, we estimate the LUMO and exciton binding energies of a wide range of organic semiconductors.

© 2009 Elsevier B.V. All rights reserved.

## 1. Introduction

As the field of organic electronics continues to mature, designing high performance devices requires that the frontier energies of molecular semiconductors be accurately determined. For example, the energy of the highest occupied molecular orbital (HOMO) of molecular thin films can be determined with reasonable accuracy (with an error of typically  $\pm 0.2$  eV) [1] using ultraviolet photoelectron spectroscopy (UPS). Furthermore, the lowest unoccupied molecular orbital (LUMO) can also be determined from inverse photoelectron spectroscopy (IPES), which allows for a direct measurement of the electron affinity [2,3]. The transport gap ( $E_t$ ) of these materials is then taken as the difference between the HOMO and the LUMO energy levels. In practice, the LUMO energy is often inaccurately defined as the HOMO energy plus the optical energy gap ( $E_{opt}$ ), referred to here as the “optical LUMO”, where  $E_{opt}$  corresponds to the energy of the long wavelength edge of

the exciton absorption band. While  $E_{opt}$  can be measured to within  $\pm 0.05$  eV, the value of  $E_t$  can exceed this by as much 0.5–1.0 eV due to the exciton binding energy [4]. Additionally, lower energy transitions into intermediate states can lead to an underestimation of both  $E_{opt}$  and  $E_t$ , and consequently, the LUMO energy. This incomplete picture has led to confusion about charge carrier injection, the role of heterojunction interfaces in determining energy transfer, and charge transport in organic materials. Unfortunately, the consistent use of UPS and IPES can be both time consuming and complex, with differences in measurement conditions resulting in variations in measured energies for the same material [1]. In practice, therefore, indirect methods have been employed to estimate the HOMO and LUMO energies of organic solids, leading to further confusion in the interpretation and comparisons of these various results.

Rather than use data from optical and UPS measurements to locate the LUMO energy, a common alternative is to use results from electrochemical measurements. In principle, the LUMO energy can be determined from the electrochemical reduction potential ( $E_{red}$ ), a process analo-

\* Corresponding author. Tel.: +1 734 647 1147; fax: +1 734 763 0085.  
E-mail address: [stevefor@umich.edu](mailto:stevefor@umich.edu) (S.R. Forrest).

gous to charge injection in organic films. However,  $E_{\text{red}}$  must be adjusted to account for the differing dielectric media in which the measurements are performed. Nevertheless,  $E_{\text{red}}$  measured for organic compounds have been shown to depend linearly on their electron affinities in the gas phase [5,6]. The use of  $E_{\text{red}}$  to determine LUMO energies was originally applied to conjugated oligomers, and has recently been extended to include small molecular weight materials [7,8]. One drawback to this approach is the need to establish an electrochemical reference potential to vacuum. The ferrocenium/ferrocene ( $\text{Fc}^+/\text{Fc}$ ) couple with a potential of 4.80 eV relative to vacuum, is commonly used for this purpose [9]. Alternatively, aluminum

*tris*-8,hydroxyquinolate ( $\text{Alq}_3$ ) has recently been shown to be a useful electrochemical reference with a potential of  $-2.30$  V with respect to  $\text{Fc}^+/\text{Fc}$  [10]. The LUMO energy of  $\text{Alq}_3$  is found to be  $2.25 \pm 0.25$  eV measured by IPES [11]. Implicit in all of these methods is a linear dependence between  $E_{\text{red}}$  and IPES measured values with a slope equal to unity. However, we recently reported a relationship between the HOMO energy (measured by UPS) and the oxidation potential ( $E_{\text{ox}}$ ) of molecular organic semiconductors [12] that had a linear dependence with a slope of 1.4. The slope was found to be determined, in part, by image forces between the electronic orbital distribution and the metal electrode immersed in a dielectric solution.

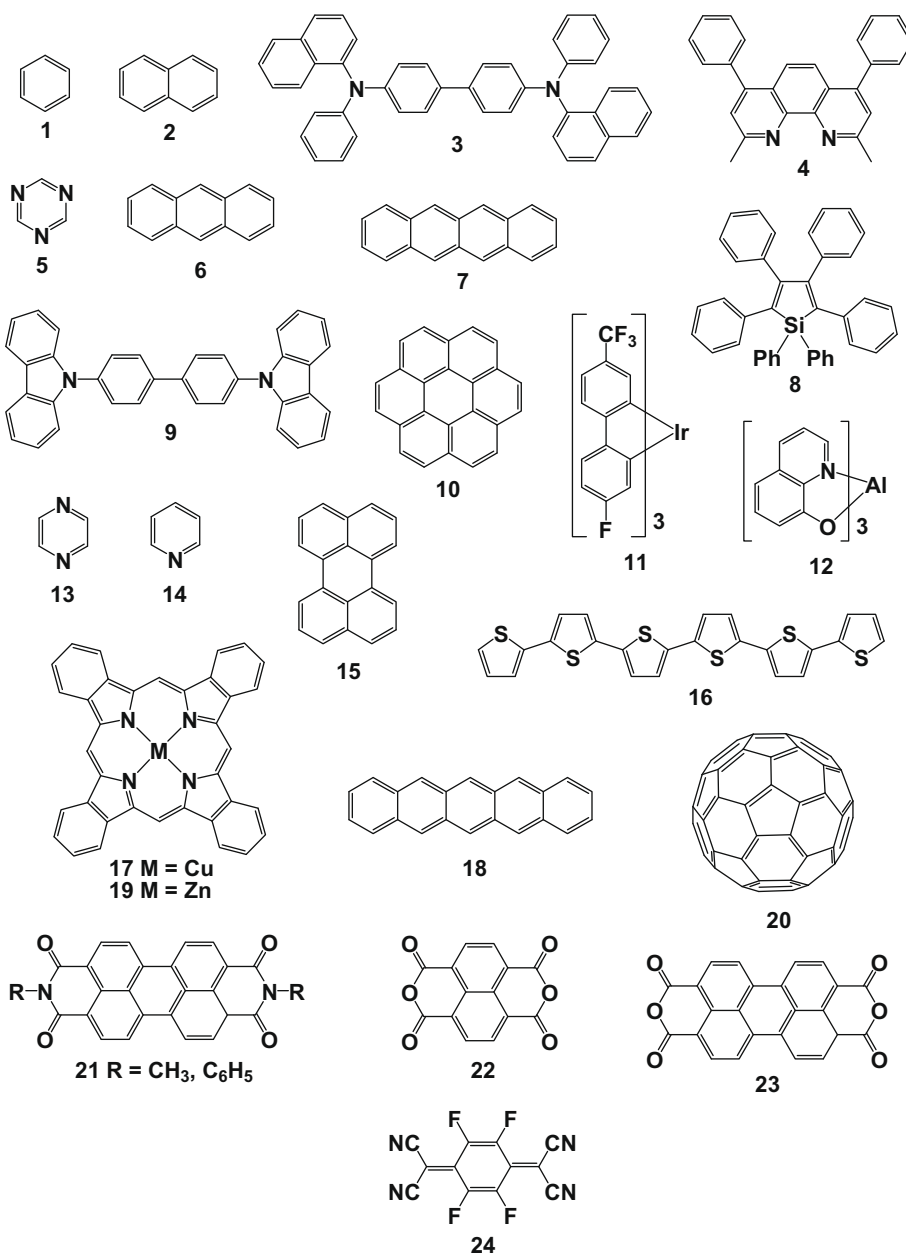


Fig. 1. Molecular structures for the compounds listed in Table 1.

Here, we present the interrelationships between the LUMO energies of a variety of molecular organic semiconductors measured by several techniques. These correlations allow us to evaluate the accuracies and advantages of the various methods, and to extract a relationship between the exciton binding energy and the energy gap.

The electron affinities for 24 compounds shown in Fig. 1 are presented in Table 1. Included in the table are LUMO and HOMO energies obtained from IPES and UPS, the optical energy gap, the optical LUMO (UPS plus  $E_{\text{opt}}$ ), the electrochemical reduction potential, and the LUMO energies obtained from electron density functional theory (DFT) calculations. The LUMO energies obtained by IPES span a range of approximately 5 eV, and include both organic compounds and inorganic complexes. The criteria used to select compounds for Table 1 is that both IPES and reversible reduction energies were available. The errors are  $\pm 0.2$  eV for UPS, and  $\pm 0.35$  eV for IPES data. The values do not account for ambiguities in some reports of IPES data taken from the peak maxima, as opposed to others that report the peak onset of the spectra. The use of the peak onset data can lower the IPES values by several 100 meV, an issue that is addressed in detail by Krause et al. [13]. The optical energy gap is estimated from the low energy edge of the absorption band of the lowest energy exciton manifold, preferably where the normalized absorption and fluorescence spectra intersect. This value has an error of  $\pm 0.05$  eV. To determine the optical LUMO values, data were

taken from UPS measurements which give a direct measure of the HOMO energy. Reduction potentials are either taken from literature values, or measured using cyclic voltammetry vs. a  $\text{Fc}^+/\text{Fc}$  reference. A correction was applied to literature values recorded in acetonitrile (0.40 V) or dimethylformamide (0.45 V) vs. a standard calomel electrode (SCE) for comparison purposes [14].

A plot of the transport gap, determined from the difference between the LUMO and HOMO energies measured by photoelectron spectroscopic methods (IPES and UPS, respectively), and the optical gap for the materials in Table 1 is shown in Fig. 2. A linear fit to the data gives a slope and intercept of  $1.39 \pm 0.15$  and  $-0.46 \pm 0.38$  eV, respectively, with a correlation coefficient of  $r^2 = 0.80822$ . The slope indicates that, as the energy gap increases, the exciton binding energy ( $E_{\text{BE}}$ ) increases as well, with a minimum of approximately  $E_{\text{BE}} = 0.25$  eV for  $E_{\text{t}} = 2$  eV, to  $E_{\text{BE}} = 1.5$  eV at  $E_{\text{t}} = 6$  eV (i.e.  $E_{\text{BE}} = 0.3(E_{\text{t}} - 1)$  eV). These values fall within the range of independent measurements of the binding energy, determined either from peak-to-peak [4] or peak onset [13] UPS–IPES data, and also correspond to behavior commonly observed in inorganic semiconductors. In that case, the material polarizability (and hence permittivity,  $\epsilon$ ) decreases with increasing band gap. Then, since  $E_{\text{BE}} \sim 1/\epsilon$ , we expect to see a linear increase in binding energy with band gap, as observed here for organic semiconductors. We caution, however, that the charge density and distribution, which depend on molecular size, influence the binding

**Table 1**  
Frontier orbital (LUMO and HOMO) energies for a series of molecular organic semiconductor compounds measured by different methods.

Compound	IPES LUMO (eV)	Ref.	UPS HOMO (eV)	Ref.	$E_{\text{opt}}$ (eV)	Ref.	Optical LUMO (eV)	$E_{\text{red}}$ (V)	Ref.	DFT (eV)
1 Benzene	-0.4	[19]	-7.58	[18]	4.68	[20]	-2.90	-3.87	[21]	+0.09
2 Naphthalene	-1.1	[22]	-6.4	[18]	4.00	[20]	-2.4	-2.93	[6]	-0.96
3 NPD	-1.52	[23]	-5.30	[12]	3.12	<sup>a</sup>	-2.18	-2.8	<sup>a</sup>	-1.13
4 BCP	-1.56	[24]	-6.5	[24,25]	3.43	<sup>a</sup>	-3.07	-2.53	<sup>a</sup>	-1.30
5 s-Triazine	-1.58	[26]	-	-	-	-	-	-2.47	[27]	-1.57
6 Anthracene	-1.7	[22]	-5.70	[18]	3.25	[20]	-2.45	-2.36	[6]	-1.63
7 Tetracene	-1.8	[22]	-5.10	[18]	2.51	[28]	-2.52	-1.95	[6]	-2.07
8 Silole-Ph <sub>6</sub>	-1.85	[11]	-6.19	[11]	2.97	[11]	-3.22	-2.43	[11]	-1.35 <sup>b</sup>
9 CBP	-1.9	[29]	-6.1	[29]	3.46	<sup>a</sup>	-2.64	-2.75	<sup>a</sup>	-1.25
10 Coronene	-1.9	[22]	-5.52	[18]	2.90	[30]	-2.62	-2.48	[31]	-1.41
11 Ir(FF-ppy) <sub>3</sub>	-1.9	[29]	-5.9	[29]	2.56 <sup>c</sup>	[32]	-3.34	-2.24	[32]	-1.97
12 Alq <sub>3</sub>	-1.96	[23]	-5.65	[12]	2.75	[33]	-2.90	-2.30	[10]	-1.74
13 Pyrazine	-2.08	[26]	-	-	-	-	-	-2.56	[27]	-1.42
14 Pyridine <sup>d</sup>	-2.18	[26]	-	-	-	-	-	-3.06	[27]	-0.61
15 Perylene	-2.5	[22]	-5.2	[18]	2.83	[30]	-2.37	-2.10	[6]	-1.90
16 a-6T	-2.57	[4]	-5.3	[34]	2.43	[35]	-2.87	-2.18	[36]	-2.18
17 CuPc	-2.65 <sup>e</sup>	[37]	-4.82	[37]	1.80	[38]	-3.02	-1.29	[39]	-2.76
18 Pentacene	-2.8	[40]	-4.85	[18]	2.06	[41]	-2.78	-1.76	[6]	-2.38
19 ZnPc	-3.3	[42]	-5.28	[42]	1.82	[43]	-3.46	-1.31	[44,45]	-2.76
20 C <sub>60</sub>	-3.5	[46]	-6.17	[47]	1.95	[48]	-4.22	-0.86	[49]	-3.23
21 Me/Ph-PTCDI	-3.95 <sup>f</sup>	[37]	-6.6	[37]	2.35	[50]	-4.25	-1.0 <sup>g</sup>	[51]	-3.45
22 NTCDA	-4.02	[24]	-7.97	[24]	3.54	[52]	-4.43	-0.82	[53]	-3.99
23 PTCDA	-4.10 <sup>h</sup>	[37]	-6.95	[37]	2.20	[54]	-4.75	-	-	-3.91
24 F <sub>4</sub> -TCNQ	-5.24	[42,55]	-8.34	[42,55]	2.94	<sup>a</sup>	-5.40	+0.13	[56]	-5.25

<sup>a</sup> This work.

<sup>b</sup> A value of -1.60 eV is given in Ref. [11].

<sup>c</sup> Estimated from the onset of the emission spectrum.

<sup>d</sup> Pyridine binds strongly to the substrate surface through nitrogen, Ref. [57] making the IPES value unreliable. For this reason, pyridine was not included in the plots shown in Figs. 2–4.

<sup>e</sup> A value of 3.3 eV is given in Ref. [4].

<sup>f</sup> A value of 4.4 eV is given in Ref. [58].

<sup>g</sup> Value is for Ph-PTCDI.

<sup>h</sup> A value of 4.6 eV is given in Ref. [23].

energy and must also be considered in a full analysis of the energy gap.

A plot of the optical LUMO (equal to  $|E_{\text{opt}} + \text{HOMO}|$ ) vs. LUMO energies measured via IPES is shown in Fig. 3. A linear fit to the data gives a slope and intercept of  $1.14 \pm 0.16$  and  $1.19 \pm 0.52$  eV, respectively, with a correlation coefficient of  $r^2 = 0.72019$ . The slope is consistent with an increase in the exciton binding energy with increasing electron affinity. For linear acenes, this increase has also been attributed to larger electron-hole Coulombic interactions in smaller  $\pi$ -systems [15]. The relatively poor correlation coefficient is a consequence of two distinct regions apparent in the plot. A linear correlation exists for compounds with optical LUMO energies greater than 4.0 eV,

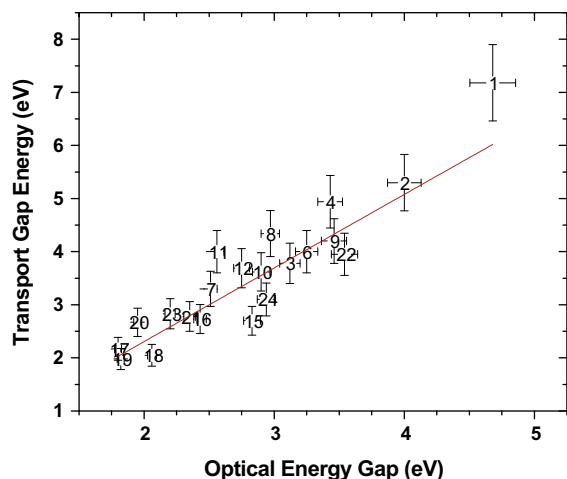


**Fig. 2.** Optical gap energy vs. transport gap energy. The transport gap is the energy (the lowest unoccupied molecular orbital measured by IPES minus the highest occupied molecular orbital measured by UPS) derived from data given in Table 1. A linear fit to the data is shown.

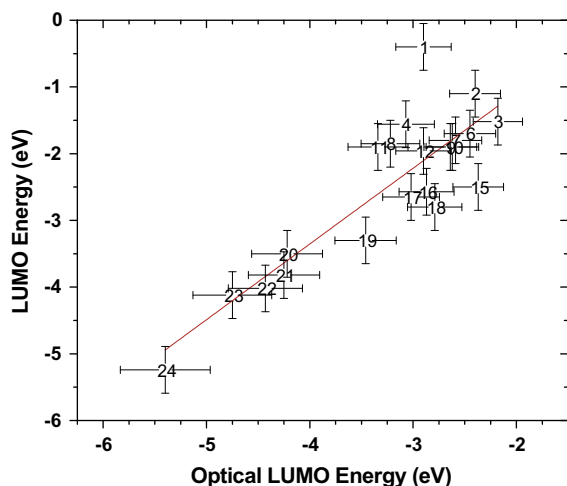


**Fig. 3.** Optical LUMO energy vs. LUMO energy measured by IPES. The optical LUMO is the difference between the HOMO energy (from UPS) and the optical gap energy.

whereas the data show considerable scatter for compounds with higher energies. Some of the variability can be ascribed to ambiguities in assigning the energy of the HOMO–LUMO gap from optical data. For example, we note that compounds such as benzene, BCP, and  $\text{Ir}(\text{ff-ppy})_3$  (compounds 1, 4, and 11) have weak optical transitions at energies lower than their strong ( $>1000 \text{ M}^{-1} \text{ cm}^{-1}$ ) absorption bands. For these compounds,  $E_{\text{opt}}$  does not represent a transition to an orbital involved in electron capture, and hence,  $E_{\text{opt}}$  may underestimate the actual transport gap. This is in contrast to the other materials studied here.

A plot of LUMO energies determined from IPES data vs. the reduction energy,  $E_{\text{red}}$ , is given in Fig. 4. A linear fit to the data presented gives a slope and intercept of  $-1.19 \pm 0.08$  eV/V and  $4.78 \pm 0.17$  eV, respectively, with a correlation coefficient of  $r^2 = 0.92140$ . The value of the intercept is in agreement with that commonly assumed for the  $\text{Fc}^+/\text{Fc}$  reference energy relative to vacuum (4.80 eV). The slope implies that compounds with large transport energy gaps are slightly destabilized as neat solids relative to the fluid dielectric medium used to perform the electrochemical measurements. The correlation coefficient is markedly higher than that from Fig. 3, and indicates that reduction potentials are more strongly correlated with the actual LUMO energies, particularly for compounds with large transport gaps.

The dependence of IPES measured LUMOs on LUMO energies obtained from DFT calculations is shown in Fig. 5. A linear fit to the data gives a slope and intercept of  $0.92 \pm 0.04$  and  $0.44 \pm 0.11$  eV, respectively, with a correlation coefficient of  $r^2 = 0.95067$ . This result is a consequence of the correlations shown by DFT calculations with gas phase electron affinities [16,17]. Since the LUMO energies from DFT calculations are equivalent to values in the gas phase, the near unity value for the slope in Fig. 5 implies that there is relatively constant polarization energy for these materials in the solid state [18]. The quality of the fit indicates that DFT calculations can provide a

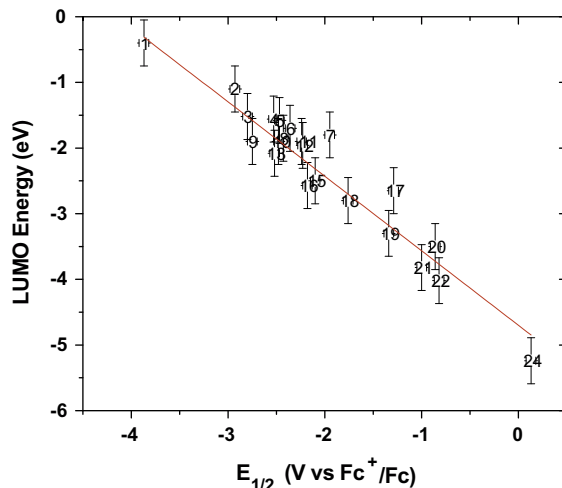


**Fig. 4.** Plot of the reduction potential vs. LUMO energy determined by IPES. A linear fit to the data is shown.

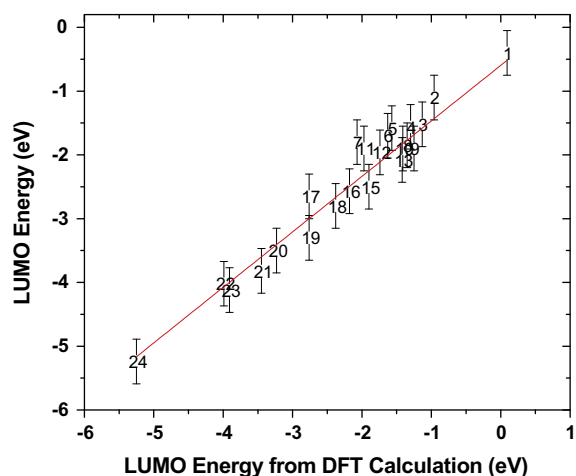


Fig. 5. LUMO energy calculated by DFT methods vs. LUMO energy determined by IPES. A linear fit to the data is shown.

reliable estimate for LUMO energies of organic solids where the needed experimental data are not available.

In summary, the correlations of IPES data with other methods currently used to estimate the LUMO energies of organic solids demonstrate several strengths and weaknesses among the various approaches. While the optical LUMO data can give a reasonable estimate for the LUMO energy for many compounds in the solid state in cases where the exciton binding energy is known, care must be taken to ensure that the lowest energy value of  $E_{\text{opt}}$  represents the appropriate HOMO–LUMO transition. Uncritical use of this method for some materials can give LUMO energies that can significantly differ from the true LUMO energy. The strong correlation between  $E_{\text{red}}$  and IPES shows that solution electrochemistry provides a satisfactory means to estimate the LUMO energy in the solid state. For compounds where it is difficult to obtain  $E_{\text{red}}$  values, use of the LUMO energy derived from DFT calculations also gives an accurate estimate of the transport level.

## 2. Experimental

The absorption spectra of NPD, BCP, CBP and  $F_4$ -TCNQ were recorded in dichloromethane solvent using a Hewlett–Packard 4853 diode array spectrometer. Cyclic voltammetry and differential pulse voltammetry were performed using an EG&G potentiostat/galvanostat model 28. Anhydrous DMF (Aldrich) was used as the solvent under a nitrogen atmosphere, and 0.1 M tetra(*n*-butyl)ammonium hexafluorophosphate was used as the supporting electrolyte. A Pt wire acted as the counter electrode, Ag wire was used as the pseudo-reference electrode, and the working electrode was glassy carbon. The working electrode was 0.2 cm in diameter by 1.5 cm long. The redox potentials are based on values measured from differential pulse voltammetry and are reported relative to an internal ferrocenium/ferrocene reference. Electrochemical reversibility was determined using cyclic voltammetry. The solutions contained only micro-molar concentrations of the sample solutes to prevent shifts in oxidation potential

due to concentration effects, and the voltage between the working and counter electrodes was swept at a scan rate of 100 mV/s. DFT calculations were performed structures that were geometry optimized at a B3LYP level using either 6–31 G\* (hydrocarbons) or LACVP\*\* (organometallics) basis sets using the Titan software package (Wavefunction, Inc.).

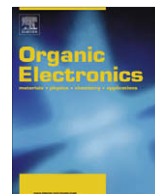
## Acknowledgements

The authors thank the Air Force Office of Scientific Research and Universal Display Corp. for partial financial support of this work.

## References

- [1] S.M. Tadayyon, H.M. Grandin, K. Griffiths, L.L. Coatsworth, P.R. Norton, H. Aziz, Z.D. Popovic, *Organic Electronics* 5 (2004) 199–205.
- [2] K. Seki, K. Kanai, *Molecular Crystals and Liquid Crystals* 455 (2006) 145–181.
- [3] D. Cahen, A. Kahn, *Advanced Materials* 15 (2003) 271–277.
- [4] I.G. Hill, A. Kahn, Z.G. Soos, R.A. Pascal, *Chemical Physics Letters* 327 (2000) 181–188.
- [5] E.S. Chen, E.C.M. Chen, N. Sane, L. Talley, N. Kozanecki, S. Shulze, *Journal of Chemical Physics* 110 (1999) 9319–9329.
- [6] R.S. Ruoff, K.M. Kadish, P. Boulas, E.C.M. Chen, *Journal of Physical Chemistry* 99 (1995) 8843–8850.
- [7] J.L. Bredas, R. Silbey, D.S. Boudreaux, R.R. Chance, *Journal of the American Chemical Society* 105 (1983) 6555–6559.
- [8] A.P. Kulkarni, C.J. Tonzola, A. Babel, S.A. Jenekhe, *Chemistry of Materials* 16 (2004) 4556–4573.
- [9] J. Pommerehne, H. Vestweber, W. Guss, R.F. Mahrt, H. Bassler, M. Porsch, J. Daub, *Advanced Materials* 7 (1995) 551–554.
- [10] J.D. Anderson, E.M. McDonald, P.A. Lee, M.L. Anderson, E.L. Ritchie, H.K. Hall, T. Hopkins, E.A. Mash, J. Wang, A. Padias, S. Thayumanavan, S. Barlow, S.R. Marder, G.E. Jabbour, S. Shaheen, B. Kippelen, N. Peyghambarian, R.M. Wightman, N.R. Armstrong, *Journal of the American Chemical Society* 120 (1998) 9646–9655.
- [11] X.W. Zhan, C. Risko, F. Amy, C. Chan, W. Zhao, S. Barlow, A. Kahn, J.L. Bredas, S.R. Marder, *Journal of the American Chemical Society* 127 (2005) 9021–9029.
- [12] B.W. D'Andrade, S. Datta, S.R. Forrest, P. Djurovich, E. Polikarpov, M.E. Thompson, *Organic Electronics* 6 (2005) 11–20.
- [13] S. Krause, M.B. Casu, A. Scholl, E. Umbach, *New Journal of Physics* 10 (2008) 085001.
- [14] N.G. Connelly, W.E. Geiger, *Chemical Reviews* 96 (1996) 877–910.
- [15] K. Hummer, C. Ambrosch-Draxl, *Physical Review B* 71 (2005) 081202.
- [16] A. Modelli, L. Mussoni, D. Fabbri, *Journal of Physical Chemistry A* 110 (2006) 6482–6486.
- [17] J.C. Rienstra-Kiracofe, G.S. Tschumper, H.F. Schaefer, S. Nandi, G.B. Ellison, *Chemical Reviews* 102 (2002) 231–282.
- [18] N. Sato, K. Seki, H. Inokuchi, *Journal of the Chemical Society-Faraday Transactions 2* (77) (1981) 1621–1633.
- [19] R. Dudde, B. Reihl, A. Otto, *Journal of Chemical Physics* 92 (1999) 3930–3934.
- [20] S.L. Murov, I. Carmichael, G.L. Hug, *Handbook of Photochemistry*, 2nd ed., Marcel Dekker, New York, 1993.
- [21] J. Mortensen, J. Heinze, *Angewandte Chemie-International Edition in English* 23 (1984) 84–85.
- [22] K.H. Frank, P. Yannoulis, R. Dudde, E.E. Koch, *Journal of Chemical Physics* 89 (1988) 7569–7576.
- [23] I.G. Hill, A. Kahn, J. Cornil, D.A. dos Santos, J.L. Bredas, *Chemical Physics Letters* 317 (2000) 444–450.
- [24] C.K. Chan, E.G. Kim, J.L. Bredas, A. Kahn, *Advanced Functional Materials* 16 (2006) 831–837.
- [25] I.G. Hill, A. Kahn, *Journal of Applied Physics* 86 (1999) 4515–4519.
- [26] K.H. Frank, R. Dudde, E.E. Koch, *Chemical Physics Letters* 132 (1986) 83–87.
- [27] J.E. O'Reilly, P.J. Elving, *Journal of the American Chemical Society* 94 (1972) 7941–7949.
- [28] J.W. Sidman, *Journal of Chemical Physics* 25 (1956) 122–124.
- [29] Y. Wang, W.Y. Gao, S. Braun, W.R. Salaneck, F. Amy, C. Chan, A. Kahn, *Applied Physics Letters* 87 (2005) 193501.

- [30] N. Nijegorodov, R. Mabbs, W.S. Downey, *Spectrochimica Acta Part A-Molecular and Biomolecular Spectroscopy* 57 (2001) 2673–2685.
- [31] B.S. Jensen, V.D. Parker, *Journal of the American Chemical Society* 97 (1975) 5211–5217.
- [32] V.V. Grushin, N. Herron, D.D. LeCloux, W.J. Marshall, V.A. Petrov, Y. Wang, *Chemical Communications* (2001) 1494–1495.
- [33] R. Ballardini, G. Varani, M.T. Indelli, F. Scandola, *Inorganic Chemistry* 25 (1986) 3858–3865.
- [34] H. Fujimoto, U. Nagashima, H. Inokuchi, K. Seki, H. Nakahara, J. Nakayama, M. Hoshino, K. Fukuda, *Journal of Chemical Physics* 89 (1988) 1198–1199.
- [35] R.S. Becker, J.S. deMelo, A.L. Macanita, F. Elisei, *Journal of Physical Chemistry* 100 (1996) 18683–18695.
- [36] K. Meerholz, J. Heinze, *Electrochimica Acta* 41 (1996) 1839–1854.
- [37] D.R.T. Zahn, G.N. Gavrila, M. Gorgoi, *Chemical Physics* 325 (2006) 99–112.
- [38] J.M. Assour, S.E. Harrison, *Journal of the American Chemical Society* 87 (1965) 651–652.
- [39] D.W. Clack, N.S. Hush, I.S. Woolsey, *Inorganica Chimica Acta* 19 (1976) 129–132.
- [40] F. Amy, C. Chan, A. Kahn, *Organic Electronics* 6 (2005) 85–91.
- [41] A.F. Prikhotko, A.F. Skorobogotko, L.I. Tsikora, *Optics and Spectroscopy-USSR* 26 (1969) 115–120.
- [42] W.Y. Gao, A. Kahn, *Organic Electronics* 3 (2002) 53–63.
- [43] P.G. Seybold, M. Gouterman, *Journal of Molecular Spectroscopy* 31 (1969) 1–13.
- [44] A. Giraudeau, A. Louati, M. Gross, J.J. Andre, J. Simon, C.H. Su, K.M. Kadish, *Journal of the American Chemical Society* 105 (1983) 2917–2919.
- [45] T. Nyokong, Z. Gasyna, M.J. Stillman, *Inorganic Chemistry* 26 (1987) 548–553.
- [46] R. Schwedhelm, L. Kipp, A. Dallmeyer, M. Skibowski, *Physical Review B* 58 (1998) 13176–13180.
- [47] N. Sato, Y. Saito, H. Shinohara, *Chemical Physics* 162 (1992) 433–438.
- [48] H. Ajie, M.M. Alvarez, S.J. Anz, R.D. Beck, F. Diederich, K. Fostiropoulos, D.R. Huffman, W. Kratschmer, Y. Rubin, K.E. Schriver, D. Sensharma, R.L. Whetten, *Journal of Physical Chemistry* 94 (1990) 8630–8633.
- [49] S.A. Lerke, B.A. Parkinson, D.H. Evans, P.J. Fagan, *Journal of the American Chemical Society* 114 (1992) 7807–7813.
- [50] K. Puech, H. Frob, M. Hoffman, K. Leo, *Optics Letters* 21 (1996) 1606–1608.
- [51] S.K. Lee, Y.B. Zu, A. Herrmann, Y. Geerts, K. Mullen, A.J. Bard, *Journal of the American Chemical Society* 121 (1999) 3513–3520.
- [52] H. Yamaguchi, K. Kitano, K. Toyoda, H. Baumann, *Spectrochimica Acta Part A-Molecular and Biomolecular Spectroscopy* 38 (1982) 261–263.
- [53] E.V. Pykhtina, N.P. Glukhoedov, I.E. Kardash, A.N. Pravednikov, *Zhurnal Fizicheskoi Khimii* 52 (1978) 1217–1219.
- [54] U. Gomez, M. Leonhardt, H. Port, H.C. Wolf, *Chemical Physics Letters* 268 (1997) 1–6.
- [55] W.Y. Gao, A. Kahn, *Applied Physics Letters* 79 (2001) 4040–4042.
- [56] R.C. Wheland, J.L. Gillson, *Journal of the American Chemical Society* 98 (1976) 3916–3925.
- [57] D.B. Dougherty, J. Lee, J.T. Yates, *Journal of Physical Chemistry B* 110 (2006) 11991–11996.
- [58] N. Sato, H. Yoshida, K. Tsutsumi, *Journal of Electron Spectroscopy and Related Phenomena* 88 (1998) 861–865.



## Letter

Supersonic molecular beams deposition of  $\alpha$ -quaterthiophene: Enhanced growth control and devices performancesT. Toccoli<sup>a,\*</sup>, M. Tonzzer<sup>a,b,\*</sup>, P. Bettotti<sup>c</sup>, N. Coppedè<sup>a</sup>, S. Larcheri<sup>c</sup>, A. Pallaoro<sup>a</sup>, L. Pavese<sup>c</sup>, S. Iannotta<sup>a,d</sup><sup>a</sup> IFN-CNR Trento Division, Institute of Photonics and Nanotechnology Via Alla Cascata 56/C, 38100 Povo di Trento, Italy<sup>b</sup> TASC INFN-CNR National Laboratory S. S. 14 km 163, 5, I-34012 Basovizza, Italy<sup>c</sup> Laboratorio Nanoscienze, Dipartimento di Fisica, Università di Trento, Via Sommarive 14, I-38050 Povo Trento, Italy<sup>d</sup> IMEM-CNR, Istituto Materiali per Elettronica e Magnetismo Parco Area delle Scienze, 37/a 43100 Parma, Italy

## ARTICLE INFO

## Article history:

Received 7 August 2008

Received in revised form 24 December 2008

Accepted 30 December 2008

Available online 6 January 2009

## PACS:

68.55.A—nucleation and growth

85.30.—z semiconductor devices

85.30.Tv field effect devices

## Keywords:

Seeded supersonic beams

Oligothiophenes

Organic field effect transistor

Morphology

## ABSTRACT

The alpha-quaterthiophene is widely considered an interesting material for the realization of organic electronics and opto-electronics. Compared to other oligothiophenes, the performances of transistors based on this compound are limited by its kind of growth on the typical materials used for device realization. Here we show that via seeded supersonic beams we can lead to a nice improvement of both morphological and electrical properties of the film grown, through a better control of the initial state of the precursor in the vapor phase. Using the high kinetic energy achievable in the supersonic beams, we increase the dimensions of the grains and the coalescence of different islands, limiting the grain boundary formation. As consequence, the performance of the realized field effect transistors is enhanced of one order of magnitude.

© 2009 Elsevier B.V. All rights reserved.

Small molecules are widely considered an interesting and viable way to understand the intrinsic properties and the processes involved in charge and energy transport in semiconductor conjugated polymers [1]. These are key issues in the fabrication of improved, reliable, and efficient devices both for electronics and electro-optics [2]. In particular, oligothiophenes are an appealing class of compounds for their high stability to oxidation processes [3] and for their high degree of flexibility in “molecular engi-

neering”. On the other hand major difficulties arise from the solid state packing of this class of molecules, where lack of control on structure, morphology and grain boundaries formation reduces the efficiency of the charge transport [4] limiting the performances of the organic devices [5].

The processes that control the thin films formation depend on the delicate balances between molecule–molecule and molecule–surface interactions [6], which regulate the kind of growth (Frank van der Merwe, Volmer–Weber, Stransky–Krastanov) [7]. Nevertheless for the feeble nature of the forces involved in the formation of molecular solids and for the large number of polymorphs and orientations possible in the organics [8,9], it is hard to have a good control on growth. The objective of our work is to improve

\* Corresponding authors. Address: CNR-FBK Trento Division, Institute of Photonics and Nanotechnology Via Alla Cascata 56/C, 38100 Povo di Trento, Italy. Tel.: +39 0461314250; fax: +39 0461314875 (T. Toccoli).

E-mail addresses: [toccoli@science.unitn.it](mailto:toccoli@science.unitn.it) (T. Toccoli), [matteo.tonzzer@cnr.it](mailto:matteo.tonzzer@cnr.it) (M. Tonzzer).

the performances of devices, field effect transistor (FET) in particular, improving the control on the molecular assembling.

Starting from these problematic and knowing the different works that have shown the importance of the state (in terms of translational, rovibrational and momentum) of the molecules in the processes involving their collision and the energy transfer with the surface [10], we have proposed a new approach to grow organic thin films, based on seeded supersonic beams [11]. Supersonic beams give, indeed, the possibility to control the energetic state in terms of kinetic energy ( $E_k$ ), momentum and internal degree of freedom of the impinging particles, by setting the initial working conditions such as the source nozzle dimensions, the temperature and pressure of the reservoir, etc. Seeding the vapors of the organic semiconductors in a lighter carrier gas (He in our experiments) that defines the conditions of the free jet expansion, makes it possible to control the final state of the seeded molecules [12]. During the supersonic expansion, the internal degrees of freedom of the molecules undergo a strong cooling process while the kinetic energy can be increased, from the few hundreds of meV of an effusive source, up to several eV by varying the degree of seeding [11]. For this reason supersonic molecular beam deposition (SuMBD) allows to overcome some of the difficulties inherent to the available techniques for the growth of films of organic molecules.

Here we show the results achieved in the growth of quaterthiophene ( $\alpha$ -4T) on  $\text{SiO}_x/\text{Si}$  for the realization of organic field effect transistors by SuMBD. The  $\alpha$ -4T molecules on this kind of surface typically present a 3D growth that strongly limits the performances in devices [13]. We will see that varying the  $E_k$  of the impinging molecules, it is possible to modify the growth of the  $\alpha$ -4T, improving its morphology. To verify the importance of  $E_k$ , we selected two different regimes of growth: the first one where the seeded  $\alpha$ -4T molecules have an average  $E_k$  of 3.0 eV and the second one where their  $E_k$  is in the order of 7.5 eV. We have characterized the obtained films by atomic force microscopy to optimize the growth processes and to understand the effect of the kinetic energy of the impinging molecules in the thin film growth. We then used these films to build FETs in top contact configuration. Thus we are able to correlate the films morphology to the devices performances showing that a fine control on the state of the molecules can improve the characteristic of our transistors.

The experimental apparatus and the method used to realize the seeded supersonic beams of  $\alpha$ -4T are described elsewhere [11]. It essentially consists of: two stages/chambers differentially pumped high vacuum apparatus, a hyperthermal source placed in the first chamber, an ultra high vacuum deposition chamber and a time of flight mass spectrometer (ToF-MS) used to verify the purity of the materials, to determine the energetic properties of the seeded molecules, and to determine the molecular flux. The ionization of the molecules/atoms in the beam is obtained with the 4th harmonic of a Nd:YAG laser (266 nm/4.66 eV). The  $\alpha$ -4T was grown on highly doped silicon ( $n^{++}$ ) wafers covered with 50 nm thermally grown silicon oxide, cleaned in hot (325 K) isopropyl alcohol,

treated with ozone for 30 min, and then outgassed at 455 K for 12 h in ultra high vacuum. All the depositions were performed at room temperature (298 K) with a flux of about 0.2 nm/min. XRD spectra was collected in Bragg-Brentano geometry with a Panalytical X'Pert Pro diffractometer. We used a Cu anode with wavelength of 1.5406 Å. The step size was 0.05° ( $2\Theta$ ) and the average time was 60 s/step. Topographic characterization of the films has been performed by AFM microscopy in air, using a Smena SFC050 scanning head by NT-MDT. Depending on the sample, measurements have been carried out in semi-contact mode AFM (using NSG11 silicon cantilevers by NT-MDT) or in contact mode (using CSG10 Au-coated silicon cantilever by NT-MDT).

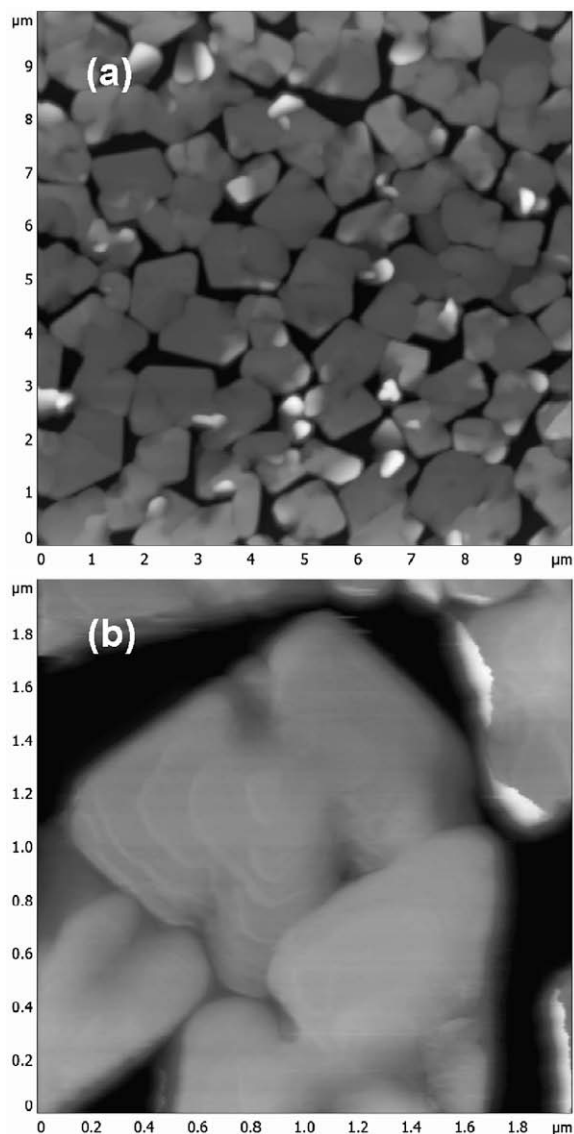


**Fig. 1.** AFM topographic images of a film grown on  $\text{SiO}_x/\text{Si}$  with impinging molecules having 3.0 eV of  $E_k$ . (a) Image  $10 \times 10 \mu\text{m}^2$  acquired in semi-contact mode; (b) detail of a grain ( $2 \times 2 \mu\text{m}^2$ ) acquired in contact mode.



Fig. 1 shows the typical morphology of our films grown on  $\text{SiO}_x/\text{Si}$  using 3.0 eV of  $E_k$ . In particular, Fig. 1a reports a large area ( $10 \times 10 \mu\text{m}^2$ ) where it is possible to recognize the kind of growth of the films. Two aspects are clear: the 3D (Volmer-Weber) growth and the crystallinity of the films. The first one is recognizable from the aspect of the grains that are developed in height presenting sharp walls. This is more evident when the thin films growth is stopped with a nominal thickness lower than the monolayer (ML). In this case, the islands produced from the nucleation of the  $\alpha - 4T$  molecules, typically present a height of about 5 nm (about 3 MLs) leaving uncovered most of the underneath surface. When increasing the coverage, we observe both a growing of the islands surface and height. The coalescence of the islands starts when the nominal thickness of the films is of about 50 nm. In these conditions the average islands height is about 100 nm, indicating that  $\sim 50\%$  of the surface is uncovered by the molecules. When the growth is carried out further, the islands begin to join together up to the point of forming a “polycrystalline” film, whose thickness is already several layers (Fig. 1a). This growth results to be different respect to the case of pentacene growth by SuMBD in which, in similar conditions, we observe the starting formation of islands of one molecule in height and their coalescence without the formation of the second layer [14]. For pentacene films about 50 nm thick, we find  $1\text{--}2 \mu\text{m}^2$  terraced grains that completely cover the surface [15].

The shape of the grains gives us the information relative to the crystallinity of films grown with this  $E_k$ . In fact, the islands present a polygonal form typical of ordered structure (crystal), with an average size of the grain of  $2\text{--}3 \mu\text{m}^2$  and no preferential direction of growth. In this situation the main problem in the FET realization is related to the poor interconnection between the different islands and the consequent need to increase the thickness of the film. This limits the device’s performances. If we compare this kind of morphology with the morphology reported in literature growing the  $\alpha - 4T$  molecules on the same surface in similar conditions [13,16], we see that in our case the grains seem to be more regular and with a larger size. This effect is probably related to the increased energy of the impinging molecules (3.0 eV in respect to about 150 meV of a thermal evaporation) that, in our case, allows their better rearrangement.

The growth is completely different in the case of impinging molecules having  $E_k = 7.5$  eV. Fig. 2 shows the typical morphology obtained in this case. The islands present really different shapes and dimensions. On the large area (Fig. 2a) we observe that typically the films are formed by elongated terraced islands with dimensions in some cases larger than  $10 \mu\text{m}$ . At the same time, the ratio between the covered surface and the islands’ height increases, thus realizing more homogenous films with less grain boundaries. The high  $E_k$  achievable in this case is able to partially overcome the low affinity between the  $\alpha - 4T$  and the surface, leading to formation of these structures. Also in this case, starting the characterization from the sub-monolayer growth, we observe the difficulty of the  $\alpha - 4T$  molecules to cover completely the  $\text{SiO}_x/\text{Si}$  surface. Going into detail (Fig. 2b) we observe that the grains present the terraced structure typical

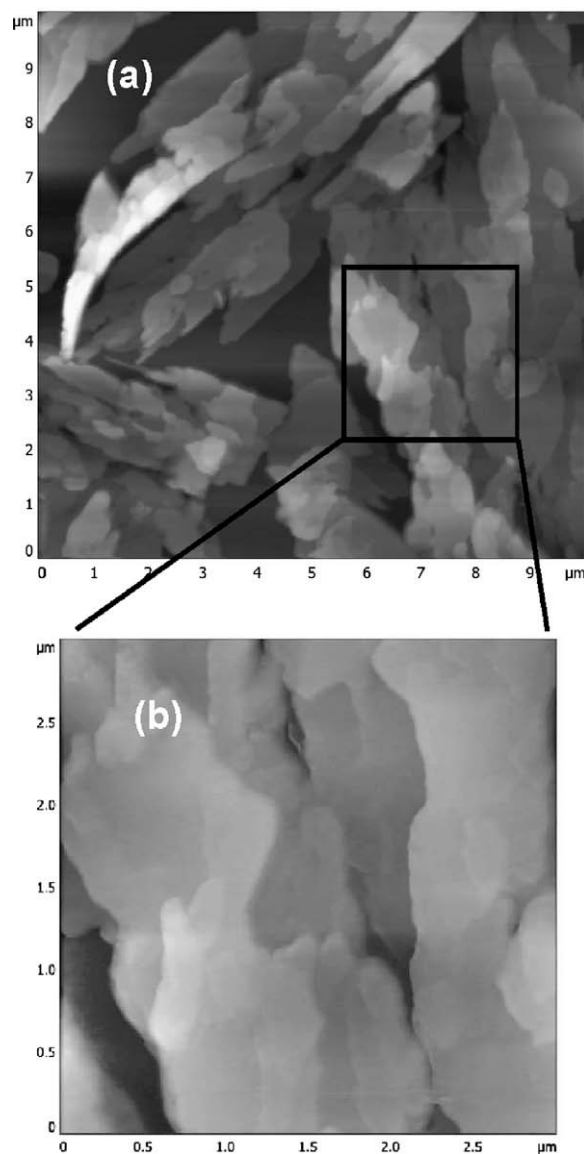


Fig. 2. AFM topographic images of a film grown with impinging molecules having  $E_k = 7.5$  eV. (a) Image  $10 \times 10 \mu\text{m}^2$ ; (b) zoom on a few grains (region indicated by the black square,  $3 \times 3 \mu\text{m}^2$ ). Both images have been acquired in contact mode AFM.

of a layered morphology with steps of one molecule in height. With respect to the steps visible on the top of the islands in the low  $E_k$  films the lateral size of these terraces present a large surface. This indicates a better rearrangement of the molecules giving rise to a more ordered structure. A similar situation was found for pentacene growth at different  $E_k$  of the impinging molecules, where the effect of higher  $E_k$  is an increase of the lateral size of the terraces [15]. This kind of growth indicates that, by increasing the kinetic energy of the impinging molecules, we are able to modify the preferred growth of the  $\alpha - 4T$  molecules, thus having the possibility to realize films with a prevalent layer plus island growth. This gives the possibility to decrease the number of grain boundaries that, for devices realization, is

an important point in order to improve their performances. To confirm that the films grown at higher kinetic energy are more ordered with a larger grain size, we made a structural characterization by X-ray diffraction. Fig. 3 shows the XRD spectra of two samples grown at low (black) and high (grey, orange online) energy, respectively, 3.0 and 7.5 eV. The films have the same nominal thickness determined by a quartz microbalance. Both spectra show the same peak positions: 5.8°, 11.6°, 17.5°, 23.4°, 35.3°, 41.5° and 47.7°. All of them confirm, in both cases, the structure of the low temperature phase of  $\alpha$ -4T [17]. The right panel of Fig. 3a shows a detail of the 008 reflection, rescaled to show the difference between the two spectra. Comparing the peaks line shapes we note that the full width at half maximum for the films grown at high  $E_k$  is narrower (0.208°) with respect to that grown at low  $E_k$  (0.233°). This confirms the indication that the typical crystal size of the high energy grown films is larger with respect to that of the films grown at low  $E_k$  and is in agreement with the observation of AFM micrographs, reflecting an improved order of the film.

We have realized a series of top contact field effect transistors to confirm that the growth by SuMBD permits to obtain films with better optical [18], morphological and electrical characteristics, due to the control achievable on the energetic state of the precursor. The devices (length  $L = 30 \mu\text{m}$ ; width  $W = 200 \mu\text{m}$ ) have been realized on the thickest films previously characterized by AFM, by depositing the 30 nm gold contacts (source and drain) through a shadow mask. The electrical characterization was performed in a probe station equipped with an Agilent 4156 C source meter. Making devices on films previously charac-

terized by AFM could limit their performances, but our objective is the correlation of the electrical performances with the growth conditions and the morphological-structural properties.

Fig. 4 shows the typical transfer characteristics in saturation (Fig. 4a) and in the linear (Fig. 4b) regimes of our  $\alpha$ -4T FETs in the case of films grown at low  $E_k$  (grey line, orange online) and in the case of films grown at high  $E_k$  (black line, blue online). From these curves, we can evaluate the electrical properties that characterize our devices [19].

In particular, in the linear regime, the drain current  $I_D$  can be written as:

$$I_D = \frac{WC_j\mu_{FE}}{L} \left( V_G - V_T - \frac{V_D}{2} \right) V_D \quad (1)$$

where  $L$  is the channel length and  $W$  the channel width,  $C_j$  is the capacitance for unit area of the dielectric,  $V_T$  is the threshold voltage, and  $\mu_{FE}$  is the field effect mobility. We can therefore calculate the mobility in the linear regime from the slope of the curve obtained by plotting  $I_D$  versus  $V_G$  for sufficient low  $V_D$ . The threshold voltage in this case is determined as the intercept ( $I_D = 0$ ) for the slope of  $I_D$ . In the saturation regime, the drain current saturates and can be modeled by the following equation:

$$I_D = \frac{WC_j\mu_{FE}}{2L} (V_G - V_T)^2 \quad (2)$$

In the saturation regime,  $\mu_{FE}$  can be calculated from the slope of the plot of  $\sqrt{|I_D|}$  versus  $V_G$ , and, in the same way,  $V_T$  can be calculated as the intercept ( $I_D = 0$ ) of the slope

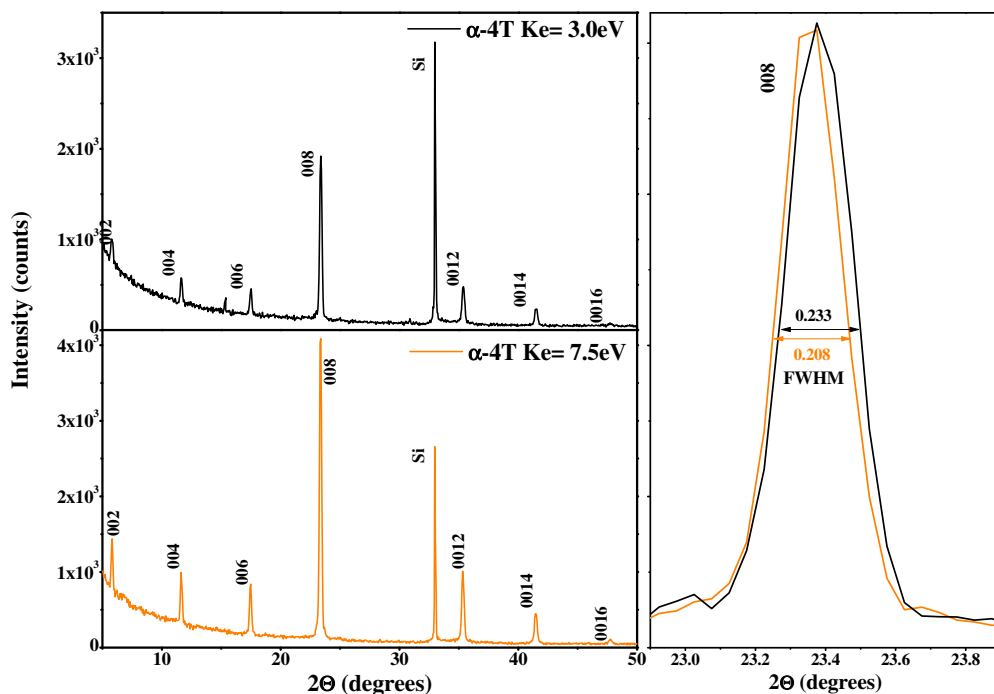
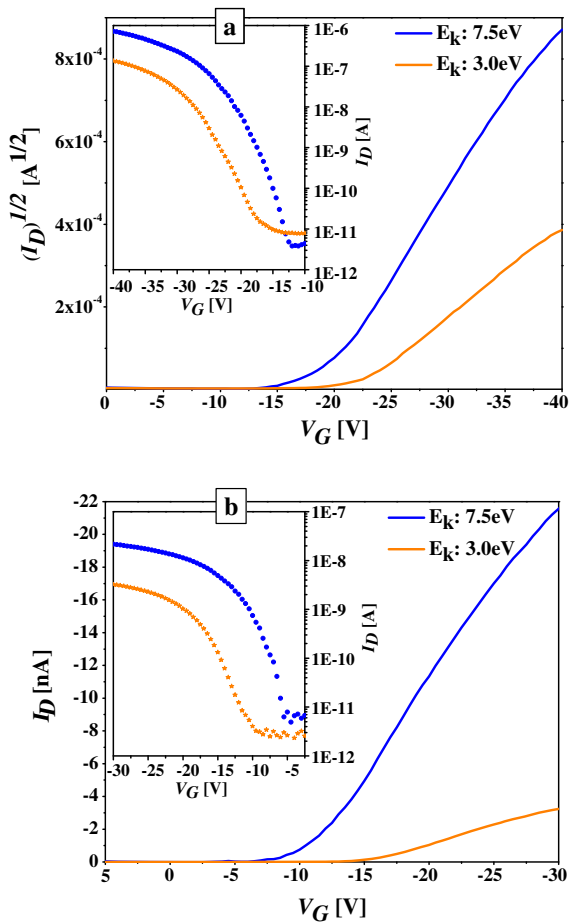


Fig. 3. XRD spectra of two samples grown at 3.0 eV (top left) and 7.5 eV (bottom left, orange online), respectively. At right a zoom on the 008 reflection, comparing in detail the width of the peak in both spectra. (For interpretation of the references to colour in this figure legend, the reader is referred to the web version of this article.)



**Fig. 4.** Transfer curves of a low  $E_k$  grown sample (nominal thickness about 100 nm) (grey, orange online) and a high  $E_k$  grown sample (nominal thickness about 100 nm) (black, blue online). The curves are compared both in (a) saturate ( $V_D = -41$  V) and (b) linear regime ( $V_D = -1$  V). The inset shows the transconductance of the same devices in both regimes. (For interpretation of the references to colour in this figure legend, the reader is referred to the web version of this article.)

of  $\sqrt{|I_D|}$  versus  $V_G$ . From the semilogarithmic plot of  $I_D$  versus  $V_G$  we extracted the  $I_{on}$  over  $I_{off}$  ratio and the subthreshold slope. The typical values obtained for our devices, grown at the different  $E_k$ , are reported in Table 1.

Fig. 4 and Table 1 give us the information about the strong impact of the growth conditions on the perfor-

**Table 1**

Main working parameters of the devices fabricated. The first two columns show the low  $E_k$  sample values, while the last two columns refer to the high  $E_k$  sample.

	$E_k = 3.0$ eV		$E_k = 7.5$ eV	
	$V_D = -1$ V	$V_D = -41$ V	$V_D = -1$ V	$V_D = -41$ V
$V_T$ [V]	-15.9	-22.5	-11.2	-16.0
$I_{ON}/I_{OFF}$	$1.1 \times 10^3$	$1.6 \times 10^4$	$8 \times 10^4$	$1.8 \times 10^5$
$S_T$ slope [V dec $^{-1}$ ]	2.0	2.5	0.98	1.66
$\mu$ [cm $^2$ V $^{-1}$ s $^{-1}$ ]	$0.75 \times 10^{-3}$	$1.7 \times 10^{-3}$	$3.8 \times 10^{-3}$	$1.22 \times 10^{-2}$

mances of the devices. Indeed FETs grown at low  $E_k$  have characteristics in terms of mobility, threshold voltage,  $I_{on}/I_{off}$  ratio and subthreshold slope comparable with the majority of  $\alpha - 4T$  transistors reported in literature [20]. This is a first good result considering the absence of optimization in our realization processes. However, if we compare these results with those obtained for the growth at 7.5 eV of  $E_k$ , we see the great advantage given by the growth method that we have developed. The extracted mobility for these devices (about  $1.2 \cdot 10^{-2}$  V cm $^{-1}$  s $^{-1}$ ) is about one order of magnitude larger with respect to the first one and the performances of these transistors are better or comparable to the best ones reported in literature [21–23].

We have investigated the correlation of the observed enhanced mobility with the structure/morphology of the films and in particular the average grain size of the crystallites composing the film grown. In Fig. 5 we plotted the field effect mobility measured for samples as a function of the mean grain size calculated from their AFM images. It appears evident that there is a linear dependence, showing that the improved transport properties of the films grown at high energy come from increasing grain size and hence from the consequent decrease of grain boundaries, as previously reported [24,25].

As a conclusion, we have shown that the growth dynamics of organic thin films starting from the vapor phase are governed by a delicate equilibrium between the molecule/molecule and the molecule/surface interactions and for this reason are also strongly dependent on the energetic state of the precursors. It can be obtained, and above all determined, by using the free jet expansion and the supersonic beam technique, thus improving the organic material growth. The key factor is the high kinetic energy achievable with this technique (up to 15 eV for the  $\alpha - 4T$  seeded in  $H_2$ ) by the impinging molecules. When colliding with the surface, the kinetic energy of the seeded molecules is rearranged among the different degrees of freedom and partially converted into energy  $E_k$

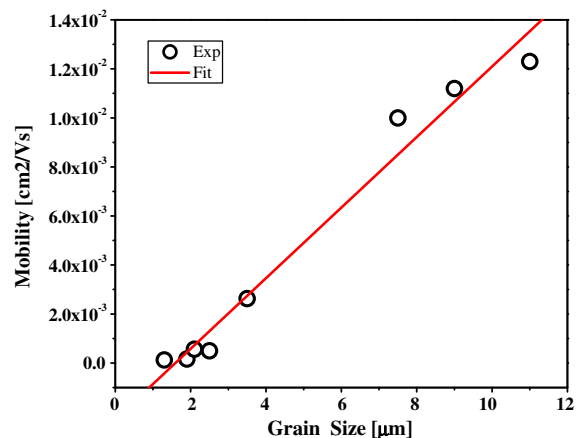


**Fig. 5.** Graph reporting the field effect mobility of some devices as a function of the grain size of the film they were fabricated on. It is quite clear the linear dependency.

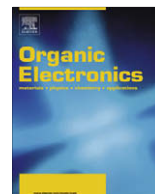
parallel to the surface via a complex mechanism involving inelastic molecule–molecule and molecule–surface energy transfer processes [10]. It is reasonable to assume, by extending consolidated growth models [5,26], that molecules with higher  $E_k$  diffuse over longer distances before aggregating or being captured by preformed molecular islands. The total amount of energy exchange at the surface is quite relevant to modify locally the physical–chemical processes occurring but definitely too small to produce any change of the sample temperature, in the order of 10 pW for  $\text{cm}^2$ . The final effect, as we have shown for the  $\alpha - 4T$ , is an increase in grain size while increasing the kinetic energy and an enhancement of the order inside the grain. The better morphology in terms of order and limiting of grain boundaries gives also the possibility to grow devices with better performances. The electrical characteristics of our FETs obtained at 3.0 eV are comparable to the ones of transistors realized with the same materials but with different techniques. However, in the case of transistors obtained on films grown at 7.5 eV the performances are similar to the state of the art but without using any optimization processes. The SuMBD is a very promising technique to fabricate devices with better performance and stability and opens interesting perspectives in the realization of FET sensors based on oligothiophene derivatives.

### Acknowledgments

We are grateful to C. Corradi, M. Pola, A. Rossi and M. Mazzola for their precious technical support and C. Armellini for the XRD spectra. This work was made possible through the financial support of Provincia Autonoma di Trento Project FOTOMINA, the financial support of the Fondazione CARITRO Project CELTIC and of the Italian Ministry of Education, University and Research (MIUR)—FIRB program projects: SYNERGY (RBNE03S7XZ).

### References

- [1] A.R. Murphy, J.M.J. Fréchet, *Chem. Rev.* 107 (2007) 066.
- [2] A. Facchetti, *Mater. Today* 10 (2007) 28.
- [3] K. Takimiya, Y. Kunugi, T. Otsubo, *Chem. Lett.* 36 (2007) 578.
- [4] C. Reese, Z. Bao, *Mater. Today* 10 (2007) 20.
- [5] R. Ruiz, D. Choudhary, B. Nickel, T. Toccoli, K.C. Chang, A.C. Mayer, P. Clancy, J.M. Blakely, R.L. Headrick, S. Iannotta, G.G. Malliaras, *Chem. Mater.* 16 (2004) 4497.
- [6] F. Schreiber, *Phys. Stat. Sol. A* 210 (2004) 1037.
- [7] J.A. Venables, G.D.T. Spiller, M. Hanbucken, *Rep. Prog. Phys.* 47 (1984) 399.
- [8] T. Kakudate, N. Yoshimoto, Y. Saito, *Appl. Phys. Lett.* 90 (2007) 081903.
- [9] N. Coppedè, T. Toccoli, A. Pallaoro, F. Siviero, K. Walzer, M. Castriota, E. Cazzanelli, S. Iannotta, *J. Phys. Chem. A* 111 (2007) 12550.
- [10] F.O. Goodman, H.Y. Wachman, *Dynamics of Gas Surface Scattering*, Academic, New York, 1976.
- [11] S. Iannotta, T. Toccoli, *J. Polym. Sci. B* 41 (2003) 2501.
- [12] P. Milani, S. Iannotta, *Synthesis of Nanophase Materials by Cluster Beam Deposition*, Springer, Berlin, 1999.
- [13] J. Ackermann, C. Vidélot, P. Dumas, A. El Kassmi, R. Guglielmetti, V. Safarov, *Org. Electron.* 5 (2004) 213.
- [14] Y. Wu, T. Toccoli, N. Koch, E. Iacob, A. Pallaoro, P. Rudolf, S. Iannotta, *Phys. Rev. Lett.* 98 (2007) 076601.
- [15] T. Toccoli, A. Pallaoro, N. Coppedè, S. Iannotta, F. De Angelis, L. Mariucci, G. Fortunato, *Appl. Phys. Lett.* 88 (2006) 132106.
- [16] A. Sassella, M. Campione, A. Papagni, C. Goletti, G. Bussetti, P. Chiaradia, V. Marcon, G. Raos, *Chem. Phys.* 325 (2006) 193.
- [17] T. Siegrist, C. Kloc, R.A. Laudise, H.E. Katz, R.C. Haddontr, *Adv. Mater.* 10 (1998) 379.
- [18] S. Iannotta, T. Toccoli, F. Biasioli, A. Boschetti, M. Ferrari, *Appl. Phys. Lett.* 76 (2000) 1845.
- [19] C.D. Dimitrakopoulos, P.R.L. Malenfant, *Adv. Mater.* 14 (2002) 99.
- [20] P. Wolfer, C. Müller, P. Smitha, M.A. Baklar, N. Stingelin-Stutzmann, *Synth. Met.* 157 (2007) 827.
- [21] S.E. Fritz, S. Mohapatra, B.T. Holmes, A.M. Anderson, C.F. Prendergast, C.D. Frisbie, M.D. Ward, M.F. Toney, *Chem. Mater.* 19 (2007) 1355.
- [22] A. Hoppe, T. Balster, T. Muck, V. Wagner, *Phys. Stat. Sol. A* 205 (2008) 612.
- [23] C. Vidélot-Ackermann, J. Zhang, J. Ackermann, H. Brisset, Y. Didane, P. Raynal, A. El Kassmi, F. Fages, *Current Appl. Phys.* 9 (2009) 26.
- [24] G. Horowitz, M.E. Hajlaoui, *Adv. Mater.* 12 (2000) 1046.
- [25] R. Matsubara, N. Ohashi, M. Sakai, K. Kudo, M. Nakamura, *Appl. Phys. Lett.* 92 (2008) 242108.
- [26] J.G. Amar, F. Family, *Phys. Rev. Lett.* 74 (1995) 2066.



## Letter

## All-polymer thin film transistors on patterned elastomeric substrates

Hyewon Kang, Tae-il Kim, Keon-kook Han, Hong H. Lee \*

*School of Chemical and Biological Engineering, Seoul National University, Seoul 151-744, Republic of Korea*

## ARTICLE INFO

*Article history:*

Received 17 March 2008

Received in revised form 19 December 2008

Accepted 16 January 2009

Available online 25 January 2009

## PACS:

77.84.Jd

81.16.Nd

81.16.Rf

85.40.Hp

*Keywords:*

Organic thin film transistor

All-polymer TFTs

Poly(dimethylsiloxane)

PDMS

Soft TFTs

Ethyl cellulose

Micromolding in capillaries

## ABSTRACT

A patterned soft elastomeric substrate is utilized for fabricating an all-polymer thin film transistor (TFT). With a polymer solution for the source/drain electrodes, it is difficult to form a well defined narrow channel. The problem is resolved with the aid of a micromolding technique and the patterned substrate. When the all polymer TFT is subjected to bending, the polymer gate dielectric is the layer that experiences the most stress. This stress problem, which can lead to device failure, can be relieved to an extent by introducing a small fraction of ethyl cellulose to the polymer dielectric. The effects of the ethyl cellulose content on the device performance are not significant.

© 2009 Elsevier B.V. All rights reserved.

Organic thin film transistors (TFTs) based on conjugated polymers [1,2] have received much attention for a number of reasons. Low cost fabrication of the device afforded by solution processibility [3] is one major reason. Flexible devices and its application to flexible displays is another.

The substrates typically used for flexible devices and displays are polymers [4–7], metal foils [8], and thin glasses [9]. However, polymeric substrates such as polyethylene terephthalate (PET) are favored because they have less mechanical, thermal, or electrical problems that are associated with metal foils and thin glasses. All-polymer flexible transistors have been fabricated with poly(3-hexylthiophene) (P3HT) semiconductor and PET substrate [5–7]. Not often used as a polymeric substrate is an elasto-

mer such as poly(dimethylsiloxane) (PDMS). A flat PDMS substrate was used for an organic transistor with rubrene monocrystalline semiconductor and metal electrodes [10]. The PDMS slab was also used to laminate a fabricated circuit on PET for better flexibility [11]. An elastomer has many advantages over a plastic substrate, such as crack and scratch protection, and easy recovery from any deformation. In all-solution processing that is typically employed in fabricating all-polymer transistor, the most demanding patterning task is to form a well defined narrow channel, in particular with a polymer solution that is used for forming the source/drain electrodes such as poly(3,4-ethylenedioxythiophene) poly(styrenesulfonate) (PEDOT:PSS) or polyaniline (PANI). Various techniques have been utilized to define the transistor channel with these polymer solutions. These include photolithography [12], ink-jet printing [13], stamping [14], and dewetting

\* Corresponding author.

E-mail address: [honghlee@snu.ac.kr](mailto:honghlee@snu.ac.kr) (H.H. Lee).

[15]. Photolithography requires many processing steps and the solvent used in resist development is detrimental to organics. It is not surprising, therefore, that the performance of the device fabricated on PET with photolithography is not good [6,7]. Ink-jet printing and stamping usually do not lead to good resolution mainly due to smearing problem. To overcome the problem, a polyimide film was patterned as a blocking layer on a glass substrate with photolithography [13]. Dewetting [15] on a prepatterned silicon dioxide partition on a silicon substrate, which is in turn treated with a self-assembled monolayer (SAM), was also used to define the channel. It is desirable in defining the channel with the polymer solution on a flexible substrate to avoid photolithography, which can be accomplished with the use of a prepatterned PDMS substrate. In addition to the advantages offered by PDMS as a substrate, it is rather straightforward to produce a well defined narrow channel by a molding technique with PDMS, which is an excellent molding material.

Often unrecognized in flexible transistor is that the gate dielectric layer is most susceptible to mechanical failure such as cracking when the device is subjected to stress as in bending. The flexibility of a layer is inversely proportional to  $t^3$  where  $t$  is the layer thickness. The dielectric layer is generally much thicker than the other layers. Moreover, in our system, the dielectric layer covers the whole device area. In contrast, all the other layers are present as stripes or islands. Therefore, the flexibility of the dielectric layer is essentially equivalent to that of the device.

In this letter, we present a technique for forming a well defined narrow channel with an electrode-forming polymer solution and an elastomeric substrate for flexible, all-polymer TFT. We also present a method for making the device more stress-tolerant by introducing a ductile material to the dielectric layer. The device performance does not change much with increasing content of the added material.

The polymer TFT (PTFT) considered in this work is a top gate transistor. Illustrated schematically in Fig. 1a are the processing steps in fabricating the device. The patterned PDMS (Dow corning, Sylgard 184) substrate was prepared from a master mold that had been made by conventional photolithographic method with a channel length of 65  $\mu\text{m}$  and a width of 3 mm. As shown in the figure, the two hollow channels are to be filled with PEDOT:PSS to form the source and drain, thereby defining the transistor channel. After a oxygen plasma treatment to make the PDMS surface hydrophilic, the technique of micromolding in capillaries (MIMIC) [16] was used to fill the channels by placing droplets of PEDOT:PSS at the inlets of the channels. A flat PET film was placed on the prepatterned PDMS substrate to induce capillarity. After drying for 30 min at 60  $^\circ\text{C}$ , the top plate was removed, which showed no residue of PEDOT:PSS. The semiconductor layer of P3HT was shaped by drop casting a 0.3 wt% regioregular P3HT (Aldrich Co.,  $M_w = 87,000$ ) solution in toluene onto the source-drain pattern [20]. For the gate dielectric, poly(methylmethacrylate) (PMMA) (Aldrich Co.,  $M_w = 350,000$ ) was used instead of poly(hexaethyl methacrylate) (PHEMA), which is known to be a better dielectric

[17] than PMMA with P3HT, because of the solvent compatibility problem discussed later. Onto the spin-coated and dried dielectric layer, PEDOT:PSS was dropped for the gate electrode. It was then dried for 30 min at 60  $^\circ\text{C}$ . All the processing steps were carried out in open air.

Shown in Fig. 1b is an optical microscopy image of the channel formed by the MIMIC technique with prepatterned PDMS substrate. The source and drain electrodes of PEDOT:PSS (dark shade) are seen to be clearly separated from each other by the protruding PDMS wall (light shade). Although the channel length in this study is 65  $\mu\text{m}$  (top image of Fig. 1b), it can be made smaller with the technique. The smallest feature size that can be patterned with PDMS mold is about 0.5  $\mu\text{m}$  when the aspect ratio is larger than unity [18]. The bottom images of Fig. 1b show various channel lengths patterned by MIMIC technique with PEDOT. While the smallest channel size is 35  $\mu\text{m}$ , fabrication of smaller channel should be possible with this technique.

The transistor with PDMS substrate invariably failed to function unless the substrate was handled very carefully. The PDMS substrate is very flexible and readily deforms. This deformation causes the device failure, the deformation leading to fracture of the layers constituting the transistor. The fracture should occur in the dielectric layer for two reasons. The first is that all the other layers are present in stripes or islands whereas the dielectric layer blankets the whole device area. These stripes and islands can withstand strains far in excess of the fracture strain [19–21] whereas a blanket layer is subject to the usual fracture strain. The other reason is that the dielectric layer is usually the thickest layer in the stacked layer configuration of thin film transistor. The flexibility of a layer is inversely proportional to  $Et^3$  where  $E$  is Young's modulus and  $t$  is the layer thickness [22]. Since the Young's moduli for all the polymers in the TFT are similar in magnitude, the dielectric layer is least flexible and stiffest.

To relieve this fracture problem, we chose to add a ductile polymer to PMMA and use that blend as the dielectric layer. Although a rubber [23] or ductile polymer [24] mixed with PMMA and a solution treatment [25] of PMMA were also used to increase the ductility, these involved either material synthesis [23,24] or an elaborate solution treatment [25]. Therefore, a ductile polymer of ethyl cellulose (Aldrich Co.) was used. According to the manufacturer, ethyl cellulose dissolves in a solvent mixture of 80% toluene and 20% ethanol. PMMA does dissolve in this solvent mixture whereas PHEMA does not, which is the reason why PMMA was chosen in place of PHEMA. When the ratio of ethyl cellulose to PMMA exceeds 3/7, a phase separation takes place. Therefore, the ratios of 3/7, 2/8, and 1/9 were tested for enhancing the ductility of the dielectric layer. In all experiments, PMMA and ethyl cellulose were dissolved in the mixed solvent to 10% by weight.

The mechanical and electrical characteristics of the transistor as affected by the addition of ethyl cellulose are summarized in Table 1. The critical bending radius in the last column of the table is the radius of curvature above which the off current increases dramatically. It is noted in this regard that the thickness of PDMS sheet and that of dielectric layer are approximately 3 mm and 1  $\mu\text{m}$ , respectively. The electrical characteristics of the devices that

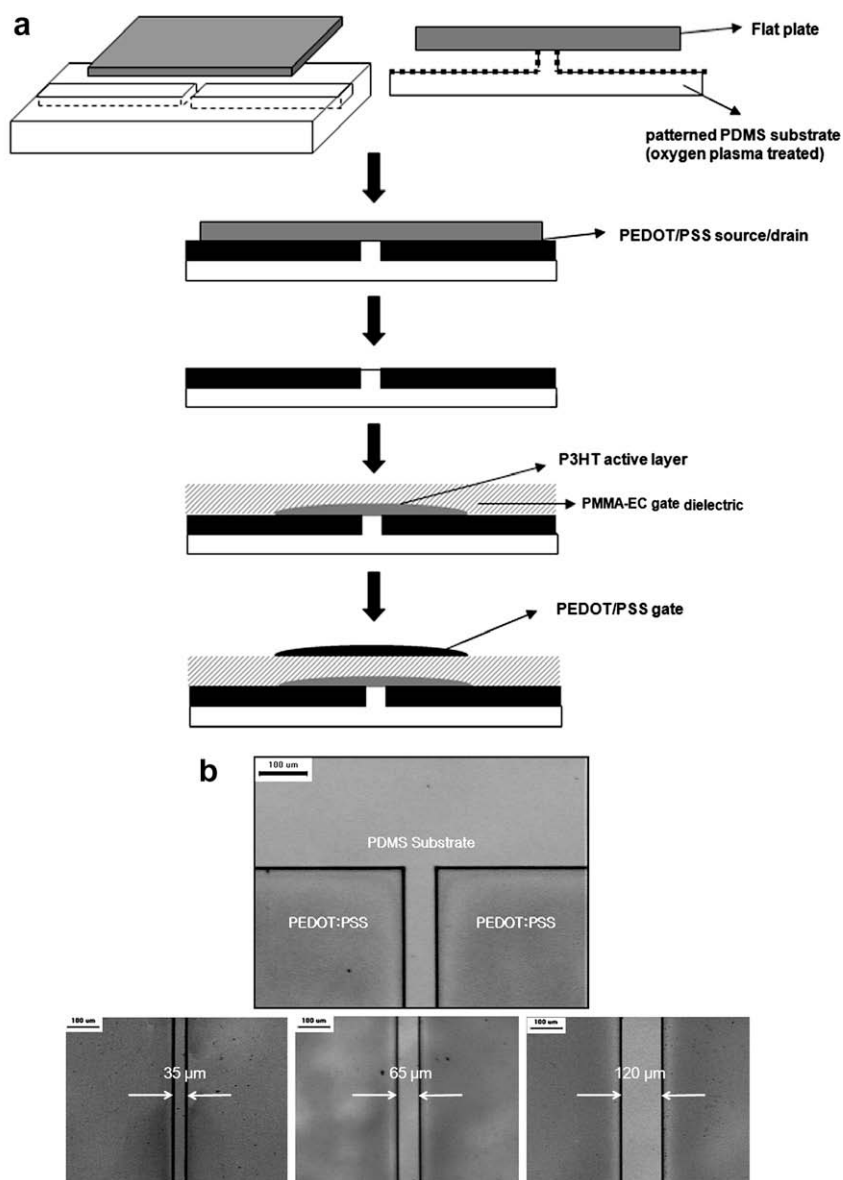


**Fig. 1.** (a) Schematic illustration of fabrication procedure of soft, all-polymer TFT. (b) Optical microscope image of the source-drain pattern prepared by MIMIC. Darker areas are PEDOT:PSS source-drain electrodes and lighter area including the center line separating the electrodes is PDMS substrate.

**Table 1**

Electrical characteristics and critical bending radii of soft, all-polymer TFTs. The TFTs were prepared with different mixing ratios of PMMA and ethyl cellulose (EC). The capacitance was measured at  $10^5$  Hz and  $-20$  V.

Dielectric	Capacitance (nF/cm <sup>2</sup> )	Mobility (cm <sup>2</sup> /Vs)	Threshold voltage (V)	On/off ratio	Critical bending radius (cm)
PMMA 10%	7.5	Not meaningful			Device failure
PMMA 9% + EC 1%	3.4	$2.3 \times 10^{-3}$	-17	$1.5 \times 10^2$	1.0
PMMA 8% + EC 2%	2.6	$2.8 \times 10^{-3}$	-15	$3.6 \times 10^2$	0.9
PMMA 7% + EC 3%	2.2	$2.5 \times 10^{-3}$	-13	$2.8 \times 10^2$	0.8

were fabricated with pure PMMA dielectric were not meaningful because of abnormally high off current, which were on order of  $10$ – $10^2$  nA and therefore the on–off ratios were less than 10 in some cases. Toluene that is a solvent of PMMA can also dissolve P3HT. Therefore there would

be a damage problem during spin-coating of the dielectric layer. However, the mixed solvent of toluene and ethanol becomes very viscous when PMMA and EC are dissolved in the solvent and thus the dissolution becomes much less of a problem. A value for the critical bending radius is not

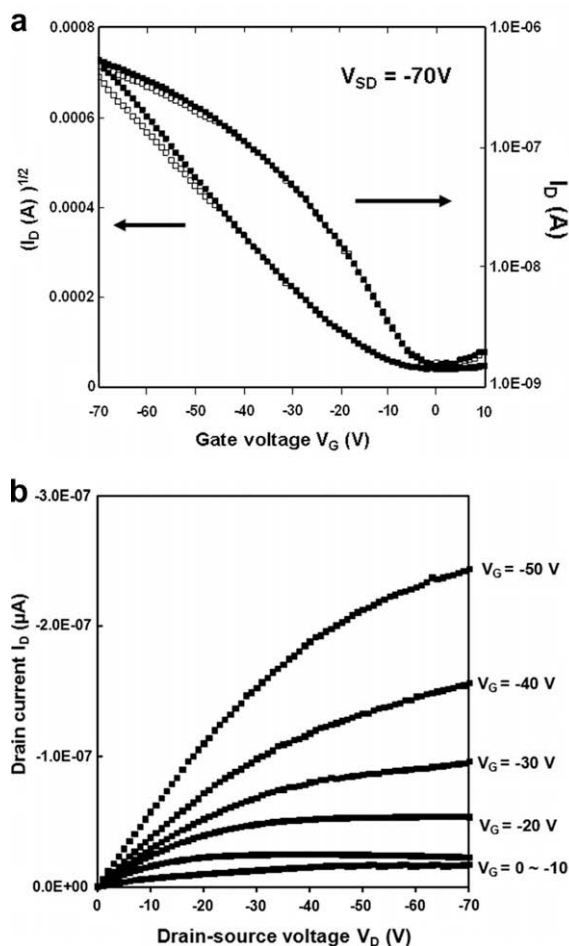


**Fig. 2.** Electrical characteristics of soft, all-polymer TFT. Gate dielectric is PMMA and ethyl cellulose content is 20%. Channel width is 3  $\mu\text{m}$  and channel length is 65  $\mu\text{m}$ . Thickness of dielectric layer is about 1  $\mu\text{m}$ . Gate leakages before and after bending were 1.48 and 1.57 nA. (a) Electrical transfer characteristics of the device before (dark rectangles) and after (open rectangles) the bending. Drain voltage is  $-70\text{ V}$ . (b) Electrical output characteristics of the device at various gate voltages.

listed for the device with no ethyl cellulose in the first row of the table because the handling involved in trying to bend the PDMS invariably led to device failure and the device characteristics were not meaningful due to high off current. The addition of ethyl cellulose (EC) allowed for the determination of the critical bending radius. The maximum solubility of EC in the mixed solvent of toluene and ethanol is 5% by weight. The content of EC was varied from 1% to 3% because the electrical characteristics were the best for EC content of 2%. The capacitance of pure PMMA layer was 7.5  $\text{nF}/\text{cm}^2$  but when the EC content was 1%, it decreased to 3.4  $\text{nF}/\text{cm}^2$ . The capacitance decreased with increasing EC content. As given in the table, the critical bending radius is 1 cm for 10% EC, decreasing down to 0.8 cm for 30% EC. In general, the capacitance decreases with increasing EC content. As apparent from the table, the device performance is not significantly affected by the addition up to EC content of 30%. The mobility in the

table was obtained in the saturation regime [26] from the transfer characteristics of the device at the source-drain voltage of  $-70\text{ V}$ . It is noted in this regard that the device performance with EC addition is better than that reported in the literature for all-polymer transistors [5–7].

The device characteristics before and after device bending are of interest, which are shown in Fig. 2. The transfer characteristics show that there is not much difference between the device before (dark rectangles) and that after (open rectangles) the bending. The EC content in the dielectric layer was 20%. The output characteristics of the device are shown in Fig. 2b. When the performance of device was compared with that reported on all polymer transistors on flexible substrates [5–7] the on-off current ratio is about the average but the mobility is better.

In summary, a soft, all-polymer TFTs have been fabricated on a patterned elastomeric substrate of PDMS. Because of the soft and shape-changing nature of the substrate, the TFT easily fails to function unless the substrate is handled carefully. It has been found that the failure is caused by the fracture of the gate dielectric layer. By introducing a small amount of ductile polymer to the polymer dielectric, the device can be made flexible without causing the device failure. When a polymer solution is used as the electrode material, it is difficult to form a well defined narrow channel. With the micromolding technique of MIMIC [16] and the prepatterned substrate, the channel can be defined as small as possible without any smearing problems that are associated with a liquid source. The results presented here should be useful for low cost, flexible electronics.

## References

- [1] F. Garrier, R. Hajlaoui, A. Yassar, P. Srivastava, *Science* 265 (1994) 1684.
- [2] H. Sirringhaus, N. Tessler, R.H. Friend, *Science* 280 (1998) 1741.
- [3] H. Sirringhaus, *Adv. Mater.* 17 (2005) 2411.
- [4] L. Zhou, A. Wang, S.C. Wu, J. Sun, S. Park, T.N. Jackson, *Appl. Phys. Lett.* 88 (2006) 083502.
- [5] M.S. Lee, H.S. Kang, H.S. Kang, J. Joo, A.J. Epstein, J.Y. Lee, *Thin Solid Films* 477 (2005) 169.
- [6] T. Mäkelä, S. Jussila, H. Kosonen, T.G. Bäccklund, H.G.O. Sandberg, H. Stubb, *Synth. Met.* 153 (2005) 285.
- [7] T.G. Bäccklund, H.G.O. Sandberg, R. Österbacka, H. Stubb, T. Mäkelä, S. Jussila, *Synth. Met.* 148 (2005) 87.
- [8] M.N. Troccoli, A.J. Roudbari, T.K. Chuang, M.K. Hatalis, *Solid-State Electron.* 50 (2006) 1080.
- [9] A. Plichta, A. Weber, A. Habeck, in: *MRS Spring Meeting, Symposium H*, vol. 769. Materials Research Society, San Francisco, CA, USA, 2003.
- [10] V.C. Sundar, J. Zaumseil, V. Podzorov, E. Menard, R.L. Willett, T. Someya, M.E. Gershenson, J.A. Rogers, *Science* 303 (2004) 1644.
- [11] Y.L. Loo, T. Someya, K.W. Baldwin, Z. Bao, P. Ho, A. Dodabalapur, H.E. Katz, J.A. Rogers, *Proc. Natl. Acad. Sci. USA* 99 (2002) 10252.
- [12] M. Halik, H. Klauk, U. Zschieschang, T. Kriem, G. Schmid, W. Radlik, K. Wussov, *Appl. Phys. Lett.* 81 (2002) 289.
- [13] H. Sirringhaus, T. Kawase, R.H. Friend, T. Shimoda, M. Inbasekaran, W. Wu, E.P. Woo, *Science* 290 (2000) 2123.
- [14] D. Li, L.J. Guo, *Appl. Phys. Lett.* 88 (2006) 063513.
- [15] J.Z. Wang, Z.H. Zheng, H.W. Li, W.T.S. Huck, H. Sirringhaus, *Nat. Mater.* 3 (2004) 171.
- [16] Y. Xia, G.M. Whitesides, *Angew. Chem. Int. Ed.* 37 (1998) 550.
- [17] J. Park, S.Y. Park, S.O. Shim, H. Kang, H.H. Lee, *Appl. Phys. Lett.* 85 (2004) 3283.
- [18] H. Kang, J. Lee, J. Park, H.H. Lee, *Nanotechnology* 17 (2006) 197.
- [19] S.P. Lacour, S. Wagner, Z. Huang, Z. Suo, *Appl. Phys. Lett.* 82 (2003) 2404.
- [20] D.S. Gray, J. Tien, C.S. Chen, *Adv. Mater.* 16 (2004) 393.



- [21] T. Someya, Y. Kato, T. Sekitani, S. Iba, Y. Noguchi, Y. Murase, H. Kawaguchi, T. Sakurai, Proc. Natl. Acad. Sci. USA 102 (2005) 12321.
- [22] D. Suh, S.-J. Choi, H.H. Lee, Adv. Mater. 17 (2005) 1554.
- [23] P.A. Lovell, J. McDonald, D.E.J. Sanders, R.J. Young, Polymer 34 (1993) 61.
- [24] K. Arai, J. Mater. Sci. Jpn. 28 (1991) 264.
- [25] M. Kawagoe, J. Qiu, M. Morita, S. Nunomoto, J. Mater. Sci. 31 (1996) 4553.
- [26] R.F. Pierret, Semiconductor Device Fundamentals, Addison Wesley, 1996.



## Letter

# Calculation of ionization potential of amorphous organic thin-films using solvation model and DFT

Pabitra K. Nayak, N. Periasamy \*

Department of Chemical Sciences, Tata Institute of Fundamental Research, Homi Bhabha Road, Colaba, Mumbai 400005, India

## ARTICLE INFO

## Article history:

Received 26 October 2008

Received in revised form 16 January 2009

Accepted 23 January 2009

Available online 3 February 2009

## PACS:

31.15ap

31.15E

73.61Ph

## Keywords:

Density functional theory

Polarizable continuum model

Ionization potential

Ultraviolet photoemission spectroscopy

Organic thin-film

## ABSTRACT

Density functional theory and polarizable continuum model are used to calculate ionization potential of thin-films of 12 organic molecules. Computed values are compared with experimental values obtained from ultraviolet photoemission spectroscopy. The excellent correlation shows that it is possible to determine the ionization potential of organic molecules in solid-state within  $\pm 0.15$  eV of the experimental value. This method is useful for chemists in designing molecules for organic electronics.

© 2009 Elsevier B.V. All rights reserved.

## 1. Introduction

Organic electronics has attracted much attention in recent research activity in molecules and materials. Organics based light emitting devices (OLEDs), solar cells (OSC), and field effect transistors (FET) are important devices under development in electronic industry. In organic semiconductor devices, thin solid films of organic molecules are used as active or passive functional layers. Information about the charge (electron or hole) carrier levels in organic thin-films, and relative energy levels with respect to electrodes are needed in understanding and fabricating the devices. For example, in OLEDs multiple layers of organic thin-films are used [1]. Carrier injection and transport occurs in HOMO or LUMO levels of organic material. The difference in the energy levels at the interface of the layers

determines the flow of carrier and formation of excitons (excited state of molecule). A method to calculate these energy levels of organic solids will be highly useful for a synthetic chemist in designing the structure of organic molecules for organic electronics.

Energy levels and properties of isolated organic molecules can be calculated theoretically. Energy levels and properties in solid thin-film are usually different from those of isolated molecule, due to interaction among the molecules in the solid-state. A method is required to modify the energy levels calculated theoretically for isolated molecules to obtain a value appropriate for solid films.

Ultraviolet photoemission spectroscopy (UPS) is one of the frequently used techniques to determine the vertical ionization potentials in solids [2]. This gives the HOMO level of solid films. The ionization potentials of organic solids determined by UPS were compared with experimental and computational values for isolated molecules [3–6]. Not

\* Corresponding author. Tel.: +91 22 22782383; fax: +91 22 22804610.  
E-mail address: [peri@tifr.res.in](mailto:peri@tifr.res.in) (N. Periasamy).

surprisingly, there is a big offset between the values for molecules in gas phase and solid-state. There have been attempts to bridge this offset by appropriate theoretical models [7,8]. For example, Lee and Han used the crystal structure data and molecular cluster model in the DFT calculation, which is successful for a sufficiently large cluster of CuPc ( $n = 6$ ).

In this letter, a method is described to determine the ionization potential of large organic molecules in solid-state using DFT method and polarizable continuum model. The polarizable continuum model [9,10] has been very successful in calculating realistic values of energy properties of molecules in liquid-like condensed phase. We show that the computationally determined ionization potentials for twelve organic molecular solids agree well with the experimental values, validating the proposed method. A novel feature of our method is that no experimental data for the molecule, other than the molecular structure, is used.

## 2. Methods of computation

Twelve organic molecules, for which experimental values of ionization potential of solid films are known, were chosen for this study. Density functional theory (DFT) was used in all the calculations using Gaussian 03 [11]. The DFT method used here is based on the hybrid B3LYP func-

tional [12]. The geometries of all the molecules were optimized at 6-31G (d) basis functions. Molecular cavity for polarizable continuum model (PCM), was built using united atom topological model [13], i.e. by putting a sphere around each atom except hydrogen. Hydrogen atoms are enclosed in the sphere of the atom to which they are bonded.

The molecule in solid was considered as solvated by the molecules of its own type. The solvent in the PCM calculation is defined by the dielectric constant, the number of solvent molecules in unit volume and radius of the molecule. Following methods were used to obtain these values. The dielectric constant,  $\epsilon$  was obtained by Clausius–Mossotti equation

$$\frac{\epsilon - 1}{\epsilon + 2} = \frac{4\pi}{3} \frac{\rho}{M} N_A \alpha$$

where  $\rho$ ,  $M$ ,  $N_A$  and  $\alpha$  are the density of material, molecular mass, Avogadro number and the electronic polarizability, respectively.  $\rho N_A / M$  is reciprocal of the molecular volume. Molecular volume was obtained at 6-31G (d) level (tight option was taken in all the calculation for better accuracy). Isotropic polarizability (at zero frequency) of molecules was calculated for the optimized geometry of molecules at 6-31G (d) level. Radius of the molecule is defined as radius of a sphere which has equivalent volume of the concerned molecule.

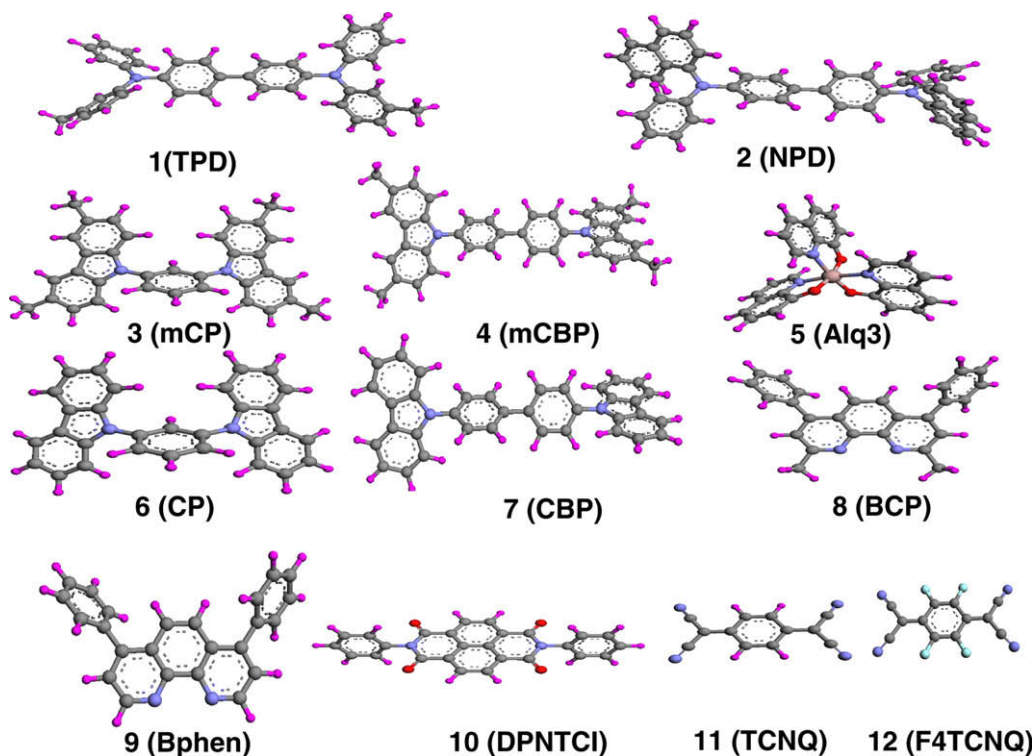


**Fig. 1.** Geometry optimized structure of molecules used in this study. 1: *N,N'*-bis(3-methylphenyl)-*N,N'*-diphenyl-[1,1'-biphenyl]-4,4'-diamine (TPD); 2: *N,N'*-bis-(1-naphthyl)-*N,N'*-diphenyl-[1,1'-biphenyl]-4,4'-diamine (NPD); 3: *N,N'*-bis(3,6-dimethyl carbazoyl)-3,5-benzene (mCP); 4: 4,4'-*N,N'*-bis(3,6-dimethylcarbazoyl)biphenyl (mCBP); 5: Tris(8-hydroxyquinolate)aluminium(III) (Alq<sub>3</sub>); 6: 4,4'-*N,N'*-bis-carbazoyl-biphenyl (CBP); 7: *N,N'*-dicarbazoyl-3,5-benzene (CP); 8: 4,7-diphenyl-1,10-phenanthroline (BCP); 9: 2,9-dimethyl-4,7-diphenyl-1,10-phenanthroline (Bphen); 10: *N,N'*-diphenyl-1,4,5,8-naphyl-tetracarboxyl-diimide (DPNTCI); 11: 7,7,8,8-tetracyano-p-quinodimethane (TCNQ); 12: 2,3,5,6-tetrafluoro-7,7,8,8-tetracyano-p-quinodimethane (F4TCNQ).

Single point energy calculation of the molecule was calculated at 6-311++G(d,p) level with PCM. The single positive state with the same molecular geometry of the molecule is also calculated using same basis set and PCM. The difference in energies gave the vertical ionization potential in the solid-state. Single point calculation of the molecule is also done without PCM, which gives the gas phase ionization potential.

### 3. Results and discussion

Fig. 1 shows the geometry optimized structures of 12 organic molecules, which are commonly used in organic electronics for different purposes. This series of molecules were chosen in such a way that they cover a wide range of ionization potential. Some molecules like TPD and NPD are used as hole transporting material in OLED, molecules like Alq<sub>3</sub>, BCP are used as hole blocking material, molecule like TCNQ and F4TCNQ are used as p-doping material.

In organic powder/thin-film samples, the organic molecule can be considered as 'solvated' by the molecules of its own type. Hence, it is more realistic that calculation of the ionization potential of the molecule in thin-film takes into account 'solvation' due to the presence of other molecules.

But it is not possible to include an assembly of molecules in DFT calculation. Instead, a continuum solvent model can be considered to represent the surrounding molecules. Here, the solvent is modeled as an isotropic, continuous dielectric that surrounds a spherical or non-spherical 'solute' cavity. In this way, polarizable continuum model (PCM) [10] provides an efficient way to include the 'solvent' effect for the calculation of ionization potential.

Organic molecular solids are generally polycrystalline or amorphous. In amorphous solids, molecules are oriented randomly. Though there is a degree of anisotropy in polarizability at the molecular level, it has little effect in determining the bulk dielectric property of the amorphous organic solid [14]. The isotropic polarizability, used in the calculation of dielectric constant, is the algebraically averaged value of  $\alpha_{xx}$ ,  $\alpha_{yy}$  and  $\alpha_{zz}$ . Dielectric constants ( $\epsilon$ ) obtained from the calculation, for the organic solids, are listed in Table 1. It may be noted that the calculated values for TPD and Alq<sub>3</sub> agree well with the experimental values:  $4.2 \pm 0.2$  [15] and  $3.0 \pm 0.3$  [5], respectively. Table 1 also shows other values (number of molecules in 1000 Å<sup>3</sup> and radius of the molecule) used as inputs for the PCM calculation. All the values were calculated as described earlier. Though experimental values for some molecules are known, the calculated values were used, so that calculation

**Table 1**

Calculated values for dielectric constant, radius of the molecule, IP in gas phase and IP in solid using PCM and experimental IP values of solid films using UPS.

Compound	Dielectric constant ( $\epsilon$ )	Molecules in 1000 Å <sup>3</sup>	Radius of 'solvent' molecule (Å)	IP from gas phase calculation (eV)	IP from calculation with PCM (eV)	IP by UPS (eV) @@	Refs. for IP by UPS
(1) TPD	3.74	1.621	5.278	6.00	5.19	5.10, <u>5.20</u>	[4,16]
(2) NPD	4.21	1.599	5.350	6.05	5.20	<u>5.20</u> , 5.30, 5.40	[17–19]
(3) mCP	3.28	1.742	5.156	6.59	5.78	5.61	[18]
(4) mCBP	3.13	1.340	5.628	6.39	5.67	5.76	[18]
(5) Alq <sub>3</sub>	2.69	1.780	5.118	6.63	5.82	5.65, <u>5.80</u> , 5.93	[18–20]
(6) CBP	3.68	1.751	5.144	6.65	5.80	6.0	[19]
(7) CP	2.91	1.853	5.050	6.89	6.02	5.98	[18]
(8) BCP	2.91	2.049	4.883	7.43	6.56	6.50	[19,21]
(9) Bphen	3.47	2.632	4.490	7.65	6.66	6.4, <u>6.7</u>	[22,23]
(10) DPNTCI	3.48	2.380	4.656	8.42	7.44	7.40	[4]
(11) TCNQ	3.76	3.860	3.954	9.17	7.66	7.70	[16]
(12) F4TCNQ	3.75	3.592	4.051	9.55	8.01	8.34	[24]

@@ Values that are underlined are used in the plot shown in Fig. 2.

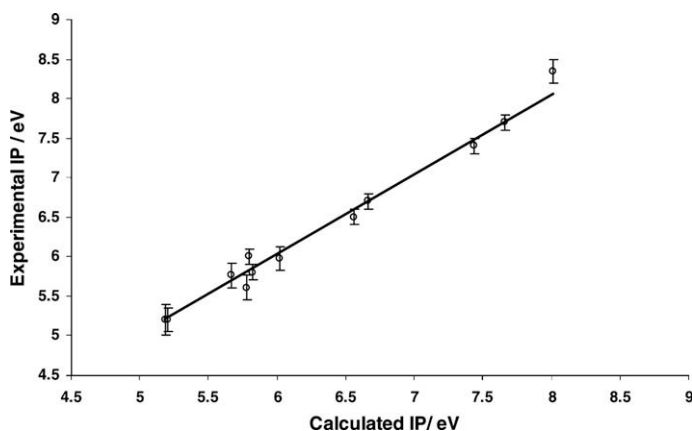


**Fig. 2.** The correlation of calculated ionization potential using PCM with experimental ionization potential of 12 molecules in solid-state.

can be done for any new molecule without reference to the experimental value.

Vertical ionization potential (IP) is the energy difference between the neutral molecule and positively charged molecule while keeping the molecular geometry of the two states remains same. Therefore, in order to get the vertical ionization potential in the calculation, identical molecular geometries were used for both neutral and charged state. Table 1 shows the calculated values of IP. Experimental values reported for these molecules are also shown.

Fig. 2 shows a plot between calculated and experimental value of ionization potential. The plot shows an excellent linear correlation. The slope of the fitted line is 1.004 with the intercept value of 0. This correlation shows that it is possible to determine the ionization potential of organic molecules in solid-state within error bar ( $\pm 0.15$  eV) of the experimental value. Table 1 also shows values of IP for isolated molecule in gas phase. The large difference between IP values of isolated molecule and solid-state shows that the solvation effect on the value of IP is very substantial.

The method described here is more appropriate for amorphous films because molecular orientational details are ignored as if the molecules in the solid film are in a liquid-like environment. Irrespective of this limitation, it is highly useful for a synthetic chemist to estimate IP values of solid films of organic molecules before actual synthesis.

#### 4. Conclusions

A method is described for theoretical calculation of realistic ionization potential of organic molecules in solid-state using the DFT method and polarizable continuum model. In this method, no experimental data is required other than the molecular structure. This method will be useful

to design molecules for organic electronics with a good estimation of the ionization potentials in the solid-state.

#### References

- [1] J. Shinar, *Organic Light-Emitting Devices*, Springer-Verlag, New York, 2003.
- [2] A. Rajagopal, C.I. Wu, A. Kahn, *J. Appl. Phys.* 83 (1998) 2649.
- [3] N. Sato, K. Seki, H. Inokuchi, *J. Chem. Soc., Faraday Trans.* 77 (1981) 1621.
- [4] K. Sugiyama, D. Yoshimura, T. Miyamae, T. Miyazaki, H. Ishii, Y. Ouchi, K. Seki, *J. Appl. Phys.* 83 (1998) 4928.
- [5] R.L. Martin, J.D. Kress, I.H. Campbell, D.L. Smith, *Phys. Rev. B: Condens. Matter* 61 (2000) 15804.
- [6] D.K. Slattery, C.A. Linkous, N.E. Gruhn, J.C. Baum, *Dyes Pigments* 49 (2001) 21.
- [7] X. Zhan, C. Risko, F. Amy, C. Chan, W. Zhao, Stephen Barlow, A. Kahn, J. Brédas, S.R. Marder, *J. Am. Chem. Soc.* 127 (2005) 9021.
- [8] S.U. Lee, Y.-K. Han, *J. Mol. Struct.: Theochem* 672 (2004) 231.
- [9] J. Tomasi, B. Mennucci, R. Cammi, *Chem. Rev.* 105 (2005) 2999.
- [10] S. Miertus, E. Scrocco, J. Tomasi, *Chem. Phys.* 55 (1981) 117.
- [11] M.J. Frisch et al, *Gaussian 03, Revision C.02*, Gaussian, Inc., Wallingford, CT, 2004.
- [12] C.J. Cramer, *Essentials of Computational Chemistry*, Wiley, England, 2003.
- [13] V. Barone, M. Cossi, J. Tomasi, *J. Chem. Phys.* 107 (1997) 3210.
- [14] K. Yamada, A. Saiki, H. Sakaue, S. Shingubara, T. Takahagi, *Jpn. J. Appl. Phys.* 40 (2001) 4829.
- [15] Y.S. Lee, J. Park, J.S. Choi, *J. Korean Phys. Soc.* 42 (2003) 294.
- [16] R.J. Murdey, W.R. Salaneck, *Jpn. J. Appl. Phys.* 44 (2005) 3751.
- [17] S.T. Lee, Y.M. Wang, X.Y. Hou, C.W. Tang, *Appl. Phys. Lett.* 74 (1999) 670.
- [18] B.W.D. Andrade, S. Datta, S.R. Forrest, P. Djurovich, E. Polikarpov, M.E. Thompson, *Org. Electron.* 6 (2005) 11.
- [19] I.G. Hill, A. Kahn, *J. Appl. Phys.* 86 (1999) 4515.
- [20] A. Schmidt, M.L. Anderson, N.R. Armstrong, *J. Appl. Phys.* 78 (1995) 5619.
- [21] B.P. Rand, J. Li, J. Xue, R.J. Holmes, M.E. Thompson, S.R. Forrest, *Adv. Mater.* 17 (2005) 2714.
- [22] M.Y. Chan, S.L. Lai, K.M. Lau, C.S. Lee, S.T. Lee, *Appl. Phys. Lett.* 89 (2006) 163515.
- [23] M. Pfeiffer, S.R. Forrest, K. Leo, M.E. Thompson, *Adv. Mater.* 14 (2002) 1633.
- [24] W. Gao, A. Kahn, *Org. Electron.* 3 (2002) 53.



## Letter

## Polymer solar cells based on inkjet-printed PEDOT:PSS layer

Seung Hun Eom<sup>a</sup>, S. Senthilarasu<sup>a</sup>, Periyayya Uthirakumar<sup>b</sup>, Sung Cheol Yoon<sup>c,\*</sup>, Jongsun Lim<sup>c</sup>, Changjin Lee<sup>c</sup>, Hyun Seok Lim<sup>c</sup>, J. Lee<sup>d</sup>, Soo-Hyoung Lee<sup>a,\*</sup>

<sup>a</sup>School of Semiconductor and Chemical Engineering, Research Center of Industrial Technology, Chonbuk National University, Jeonju 561-756, Republic of Korea

<sup>b</sup>Department of Semiconductor Science and Technology, Semiconductor Physics Research Center, Chonbuk National University, Jeonju 561-756, Republic of Korea

<sup>c</sup>Advanced Materials Division, Korea Research Institute of Chemical Technology, Daejeon 305-600, Republic of Korea

<sup>d</sup>Jeonju Center, Korea Basic Science Institute, Jeonju 561-756, Republic of Korea

## ARTICLE INFO

## Article history:

Received 11 November 2008

Received in revised form 19 January 2009

Accepted 23 January 2009

Available online 10 February 2009

## PACS:

84.60.Jt

85.60.Bt

82.35.Cd

## Keywords:

Polymer solar cell

Inkjet printing

PEDOT:PSS

## ABSTRACT

In this article, we have demonstrated solar cell performance of the inkjet-printed PEDOT:PSS layer and the roles of additives in device efficiency. The newly proposed PEDOT:PSS inks with additives of glycerol and surfactant show the improved surface morphology and high conductivity resulting in the enhanced photovoltaic performance. Using the optimized ink formulation of PEDOT:PSS, we have demonstrated a 3.16% efficient solar cell with an inkjet printing.

© 2009 Elsevier B.V. All rights reserved.

## 1. Introduction

During the past decade, there has been an intensive search for cost-effective photovoltaics [1–3]. As an alternative to inorganic solar cells, polymer solar cells could provide a significant cost reduction since their low temperature processing may allow for the printing of large area solar cells on flexible substrates at low fabrication cost [4]. Progress in the field of polymer solar cells is rapid [5,6]. The performance of polymer solar cells has been improved by using new materials [7], new structures [8] and new techniques in devices. Recently, several printing techniques have been used to fabricate various polymer based organic devices. Among them, inkjet printing is a commonly used technique for the controlled deposition of

solutions of functional materials in specific locations on a substrate. It facilitates easy and fast deposition of polymer films over a large area. Moreover, it may be suitable for the large scale production of various electronic devices. In addition, inkjet printing is very promising because the polymer devices can be fabricated easily, due to their compatibility with various substrates and already complete patterning. Inkjet printing has been extensively used in the fields of polymer light emitting diodes (LEDs), and thin film transistors (TFT) [9–12]. Inkjet printing technology has also been used for fabricating polymer:fullerene bulk heterojunction solar cells, but not many results have been reported. Aernouts et al. developed polymer solar cells with an active layer of P3HT:PCBM using inkjet printing [13]. Steirer group recently reported inkjet-printed thin film electrodes for polymer.

Poly(3,4-ethylenedioxythiophene) doped with poly(4-styrenesulfonate) (PEDOT:PSS) has attracted much attention and has been widely used as an antistatic coating

\* Corresponding authors. Tel.: +82 63 270 2435; fax: +82 63 270 2306.

E-mail addresses: [yoonsch@kriict.re.kr](mailto:yoonsch@kriict.re.kr) (S.-C. Yoon), [shlee66@chonbuk.ac.kr](mailto:shlee66@chonbuk.ac.kr) (S.-H. Lee).

material, as electrodes for capacitors or photodiodes, and as a hole transport layer in organic LEDs during the last decade [14–17]. PEDOT:PSS is optically transparent and easily processed using simple coating methods such as spin-coating [18–20]. Many researchers reported on the conductivity modification of PEDOT:PSS by adding several additives such as polyols, metals and different solvents [21–23]. The increase in conductivity of the PEDOT:PSS improves characteristics such as electromagnetic radiation shielding and electrical transport. In spite of such a potential use of PEDOT:PSS, few studies dealing with a PEDOT:PSS printing technique have been reported. Steirer et al. only reported inkjet-printed thin film electrodes of PEDOT:PSS for polymer solar cells [24].

In this paper, we report on the performance of bulk heterojunction polymer solar cells with an inkjet-printed PEDOT:PSS layer. The morphological and electrical studies and device performance of the inkjet-printed PEDOT:PSS layer in polymer solar cells are discussed in this article.

**Table 1**

Formulation details of the PEDOT:PSS inks with additives.

Inks	PEDOT:PSS (g)	Glycerol		EGBE	
		g	wt.%	g	wt.%
1	7.194	–	–	–	–
2	7.194	0.431	6	–	–
3	7.194	0.431	6	0.014	0.2
4	7.194	0.431	6	0.028	0.4

## 2. Experimental

PEDOT:PSS was purchased from Bayer (Baytron P Al 4083) and used alone, as well as mixed with additives of glycerol and ethylene glycol butyl ether (EGBE) to make inks for printing. (Details are given in Table 1.) The polymer solar cell device was fabricated with a configuration of indium tin oxide (ITO)/PEDOT:PSS/P3HT:PCBM/LiF-Al. Patterned ITO glass was cleaned with chloroform, acetone and isopropyl alcohol using an ultrasonication method, and then treated with an O<sub>2</sub>-plasma. After solvent cleaning, the PEDOT:PSS thin films were coated by using inkjet printing (UJ2100, Unijet, Korea) and dried for 20 min at 140 °C. An active layer of P3HT:PCBM (mixed solution of 1:0.7 wt.%) was cast on top of the PEDOT:PSS film by spin-coating and dried for 1 h at 50 °C in a nitrogen atmosphere. To complete the device, LiF was evaporated on the active layer to about 0.7 nm thicknesses, and then Al evaporated to about 150 nm thicknesses under vacuum (10<sup>-6</sup> torr). This device was encapsulated to measure the solar cell performance. The current versus voltage (*I*–*V*) characteristics of the solar cell devices in the dark and under white light illumination were measured with an AM 1.5G solar simulator (300 W, Newport, USA) and 100 mW/cm<sup>2</sup> conditions, adjusted with a standard PV reference cell (2 × 2 cm, a monocrystalline silicon solar cell, calibrated at NREL, Colorado, USA) with a Keithley 2400 source-measure unit. In order to avoid the underestimation of the area of the devices due to cross conduction of

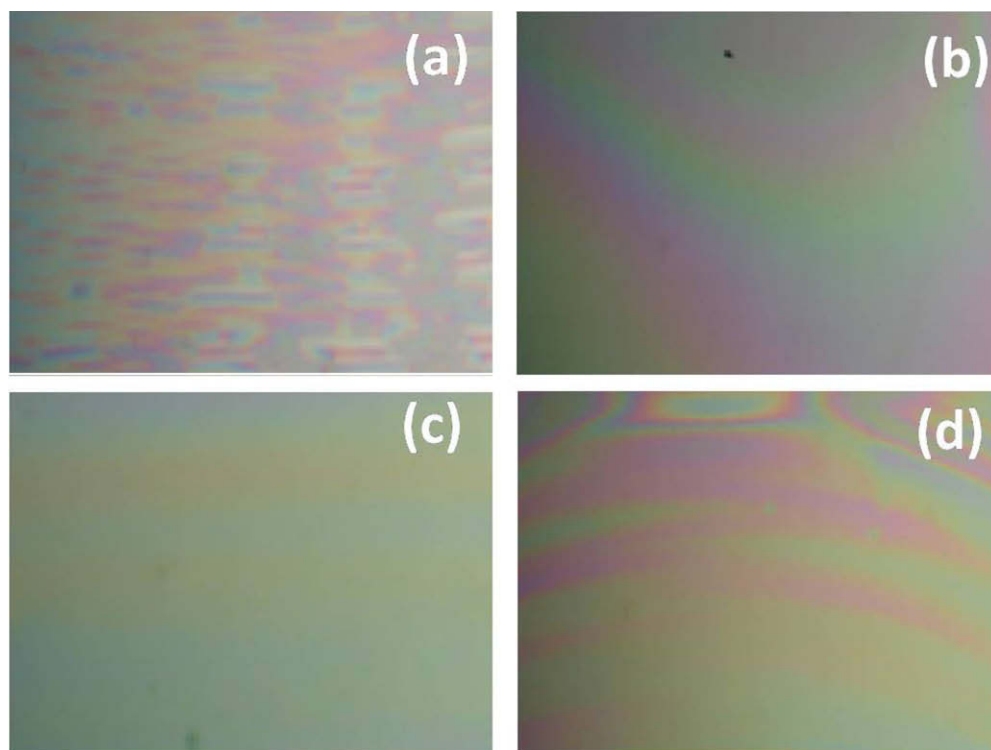


**Fig. 1.** Polarization microscope images of inkjet-printed PEDOT:PSS films (a) without additives (pure PEDOT:PSS): ink 1, with (b) glycerol (6 wt.%): ink 2, (c) glycerol (6 wt.%), and EGBE (0.2 wt.%): ink 3, (d) glycerol (6 wt.%) and EGBE (0.4 wt.%): ink 4.

a highly conducting PEDOT:PSS used in this study, we used a black mask fitted to the active area ( $3 \times 3$  mm) of the device [25,26]. The surface topography and morphology of the inkjet-printed PEDOT:PSS thin films were analyzed using polarization microscopy (JEOL-2010), surface profiler (SNU Precision SIS3747) and atomic force microscopy (AFM, VECCO, 613R1). All the characterizations were performed at room temperature.

### 3. Results and discussion

Polarization microscopy images of the inkjet-printed PEDOT:PSS films were completed to examine film morphology and thickness uniformity at the millimeter length scale (Fig. 1). As shown in Fig. 1a, the surface of the inkjet-printed films appeared non-uniform for PEDOT:PSS ink

without any additives (ink 1 in Table 1). It appears to be composed of discontinuous clusters which do not stick to ITO substrates. The PEDOT:PSS accumulates in the center of the substrate due to spreading and wetting on the substrate and the drying behavior of the inkjet-printed films. The surface anchoring forces want to align the PEDOT:PSS parallel to the bottom surface and perpendicular to the top surface of the film. The elastic forces work against the resulting vertical distortions of the director field. Inkjet-printed PEDOT:PSS film with 6 wt.% glycerol (ink 2) gives better uniformity than film from ink 1 as shown in Fig. 1b. The colors shown in the images are due to the Newton colors of thin films which depend on the thickness of the film. Fig. 1c shows an image of PEDOT:PSS film with glycerol 6 wt.% and 0.2 wt.% EGBE added (ink 3). This ink had the best uniform film thickness and density. This

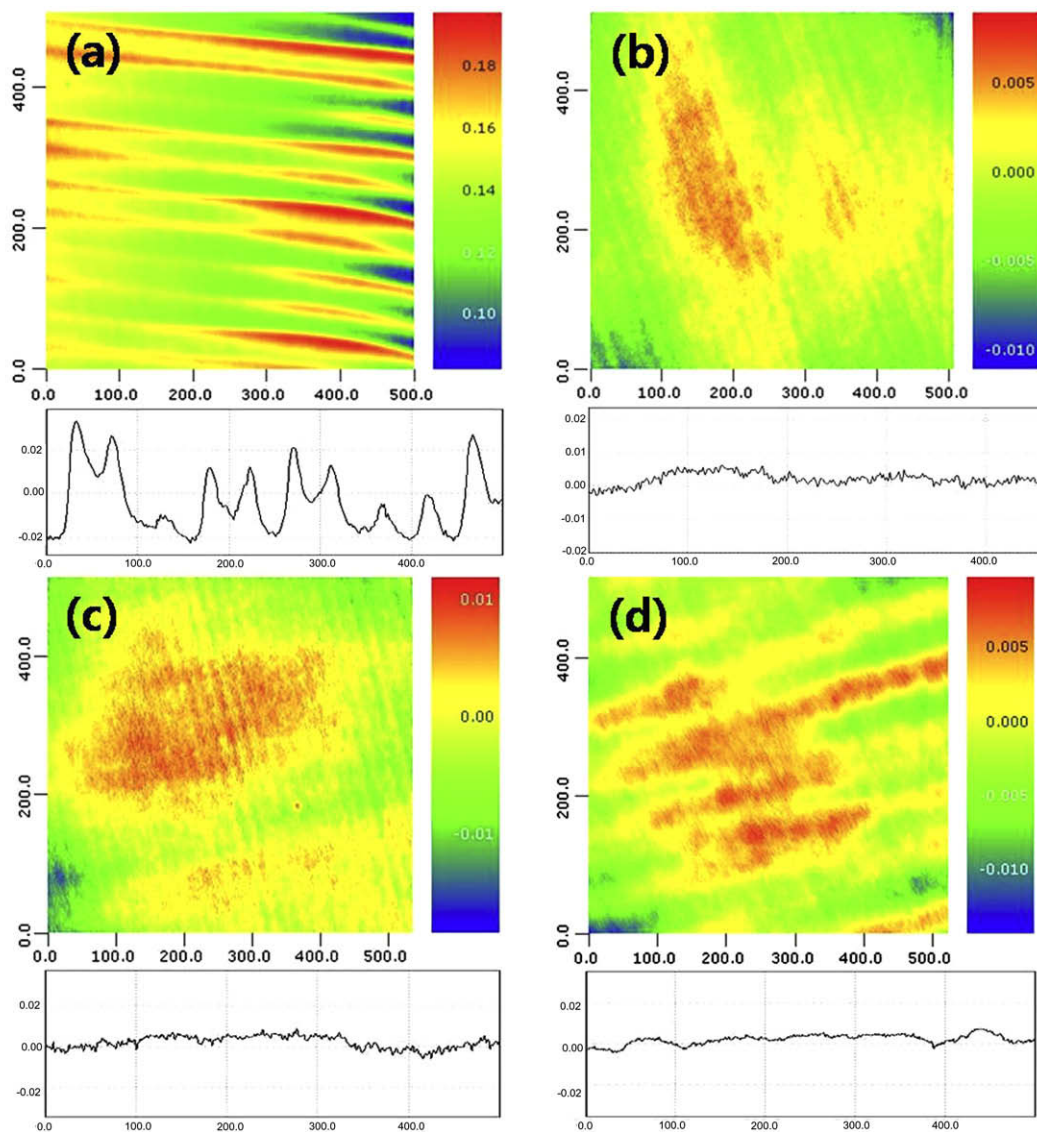


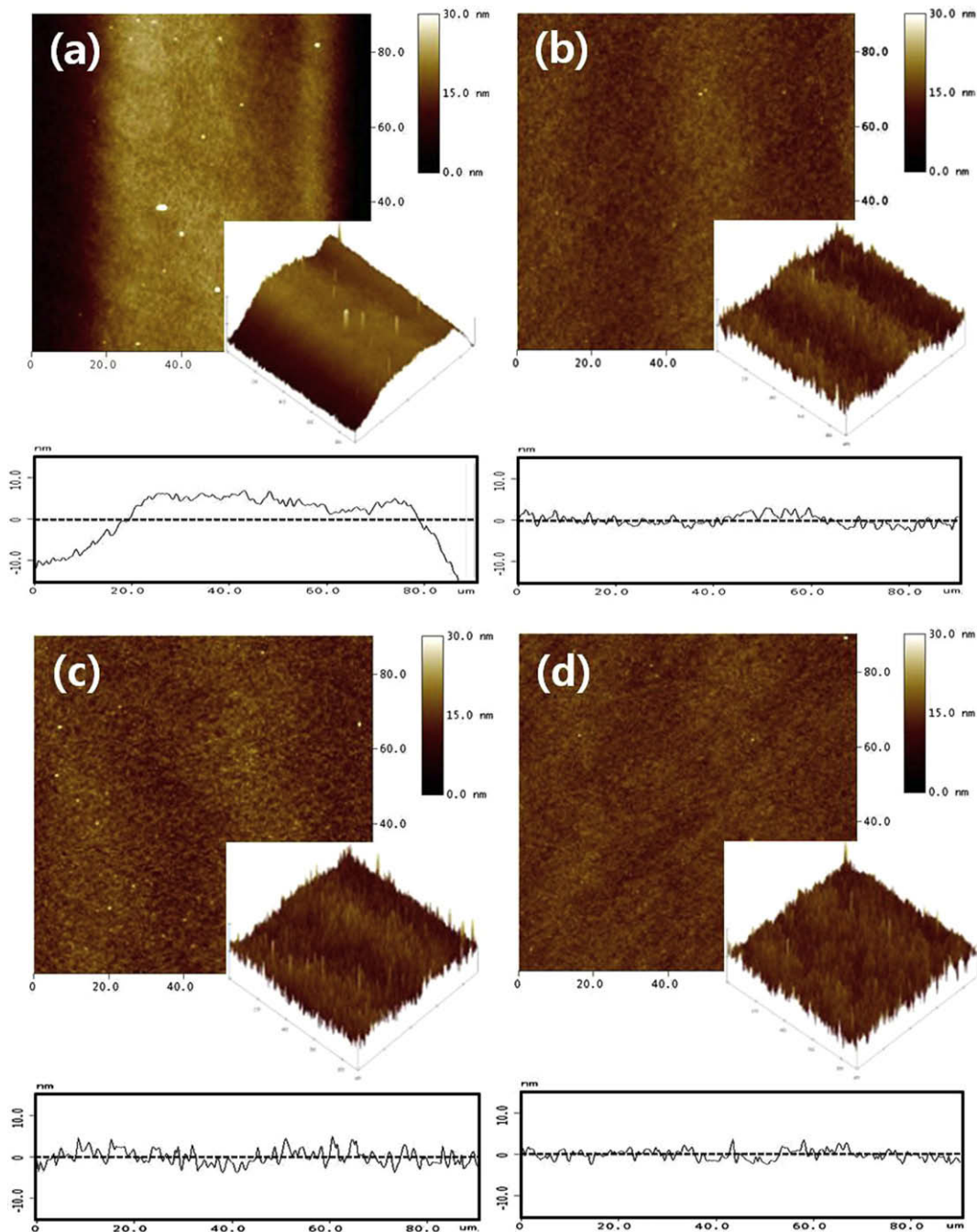
**Fig. 2.** Surface profile images of inkjet-printed PEDOT:PSS films (a) without additives (pure PEDOT:PSS): ink 1, with (b) glycerol (6 wt.%): ink 2, (c) glycerol (6 wt.%), and EGBE (0.2 wt.%): ink 3, (d) glycerol (6 wt.%), and EGBE (0.4 wt.%): ink 4.



may be due to the EGBE surfactant in the dispersion which minimizes the interfacial tension between the PEDOT:PSS and glycerol, allowing the pitch size (distance between individual droplets from the inkjet head) to be smaller than the droplet diameter. When the EGBE ratio is increased to 0.4 wt.%, the formation of the film seems to be disturbed, and film uniformity decreases as shown in Fig. 1d.

Fig. 2 shows the surface profile images of inkjet-printed PEDOT:PSS films without and with additives. A significant

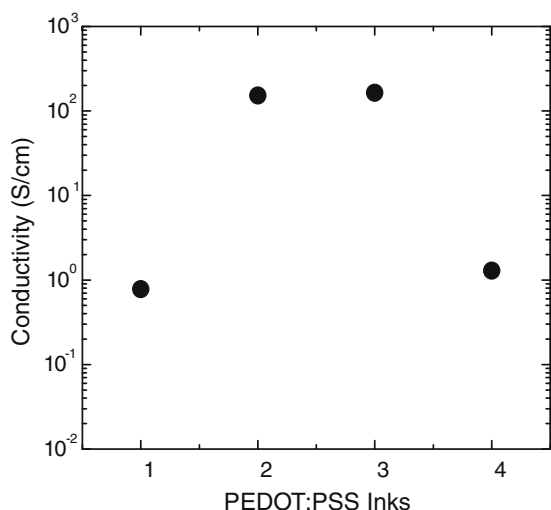
distinction in the film surface profile was observed in inkjet-printed PEDOT:PSS films. The surface profile image of the inkjet-printed PEDOT:PSS film without any additives (ink 1 in Table 1) shows significantly rough surface in 500  $\mu\text{m}$  length scale. The surface roughness was dramatically improved in the inkjet-printed PEDOT:PSS film with adding 6 wt.% glycerol (ink 2). With adding of additional EGBE surfactant of 0.2–0.4 wt.% (ink 3 and 4), the surface roughness were slightly changed and smoother surface



**Fig. 3.** AFM images of inkjet-printed PEDOT:PSS films (a) without additives (pure PEDOT:PSS): ink 1, with (b) glycerol (6 wt.%): ink 2, (c) glycerol (6 wt.%), and EGBE (0.2 wt.%): ink 3, (d) glycerol (6 wt.%) and EGBE (0.4 wt.%): ink 4.

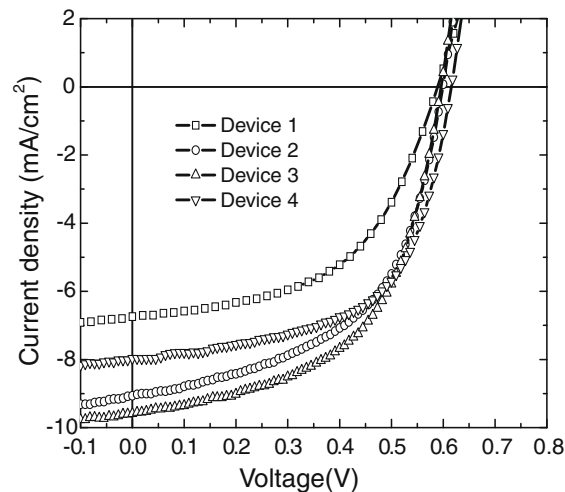
profiles were obtained. The surface morphology was further studied with AFM. Fig. 3 represents the AFM images of the inkjet-printed PEDOT:PSS films without and with additives in different amounts. Similarly with a surface profile result, the inkjet-printed PEDOT:PSS film from ink 1 without any additives shows relatively rough surface morphology with an rms roughness of 6.67 nm. The AFM images of the inkjet-printed PEDOT:PSS films from ink 2 and ink 3 with additives provide significantly reduced roughness profiles with similar rms roughness values of 1.64 and 1.63 nm. The rms roughness of inkjet-printed PEDOT:PSS film from ink 4 was slightly reduced up to 1.36 nm. A non-uniform surface roughness and profile, especially in the PEDOT:PSS film without additives (ink 1), may affect the interfaces between PEDOT:PSS and the photoactive layer, and therefore the performance of the inkjet-printed solar cell devices [9].

Fig. 4 shows the conductivity results of the PEDOT:PSS films with and without additives. The conductivity was enhanced in the inkjet-printed PEDOT:PSS film by the addition of 6 wt.% glycerol (ink 2) and with further addition of 0.2 wt.% EGBE (ink 3). The conductivity of PEDOT:PSS increased from  $7.82 \times 10^{-1}$  to  $1.52 \times 10^2$  S/cm for PEDOT:PSS by adding 6 wt.% glycerol and to  $1.64 \times 10^2$  S/cm by adding 0.2 wt.% EGBE. However, the conductivity decreases to  $1.28 \times 10^0$  S/cm when EGBE is increased to 0.4 wt.%. The addition of glycerol to the aqueous PEDOT:PSS dispersion is known to enhance the conductivity of the thin films by several orders of magnitude, depending on its concentration [27]. The conductivity of the PEDOT:PSS is strongly dependent on the film morphology and its chemical structure. F. Zhang et al. recently reported that PEDOT:PSS with glycerol shows higher performance in solar cells than pure PEDOT:PSS film due to the swelling and aggregation of colloidal PEDOT-rich particles that ultimately facilitate conduction in the film [36]. Several reports show that the dramatic effect of glycerol as a



**Fig. 4.** Conductivity measurements for inkjet-printed PEDOT:PSS films (1) without additives ( $7.82 \times 10^{-1}$  S/cm), with (2) glycerol (6 wt.%) ( $1.52 \times 10^2$  S/cm), (3) glycerol (6 wt.%) and EGBE (0.2 wt.%) ( $1.64 \times 10^2$  S/cm), (4) glycerol (6 wt.%) and EGBE (0.4 wt.%) ( $1.28 \times 10^0$  S/cm).

processing additive is due to the reorganization and stabilization of the PEDOT and PSS chains during subsequent thermal annealing of the films by a plasticizing effect [28–35]. In our study, the addition of glycerol and surfactant EGBE may also affect the morphology and physical structures of inkjet-printed PEDOT:PSS film. Here, we propose a hypothesis to explain the basic principles of molecular interactions between the surfactant, glycerol and the PEDOT:PSS film. Normally PEDOT:PSS film originates from a core-shell type framework, as shown in Fig. 2d, where PSS molecules are located around the PEDOT units through ionic interaction. Similarly, upon addition of glycerol, the polar functionality (–OH) in the glycerol molecule might directly interact with cationic species of PEDOT. Probably stronger ionic interactions between the glycerol and PEDOT are responsible for the highly conductive network formation in glycerol added PEDOT:PSS, when compared to PSS and PEDOT in pure PEDOT:PSS film. A mild repulsive force may be exerted between the PSS and glycerol units. The level of conductive network formation is further extended by an incorporation of 0.2 wt.% EGBE surfactant, which has both a polar alcoholic (–OH) group and a non-polar alkyl group (butyl) at the other end. However, with a higher weight percentage of EGBE surfactant, the conductive network formation is significantly suppressed by the formation of hydrophobic areas. The alkyl group in the EGBE surfactant aggregates along with PSS units to form hydrophobic domains that will decrease the surface poten-



**Fig. 5.** Current-density versus voltage ( $J$ - $V$ ) characteristics of solar cells with different inkjet-printed PEDOT:PSS layers in the dark and under simulated AM1.5 illumination of  $100 \text{ mW/cm}^2$ .

**Table 2**

Summary of solar cell device characteristics with different inkjet-printed PEDOT:PSS layers.

Devices	Voc (V)	Jsc ( $\text{mA/cm}^2$ )	FF (%)	EFF (%)
1	0.589	6.746	52.63	2.09
2	0.599	9.063	53.70	2.92
3	0.595	9.593	55.28	3.16
4	0.615	7.972	59.06	2.90

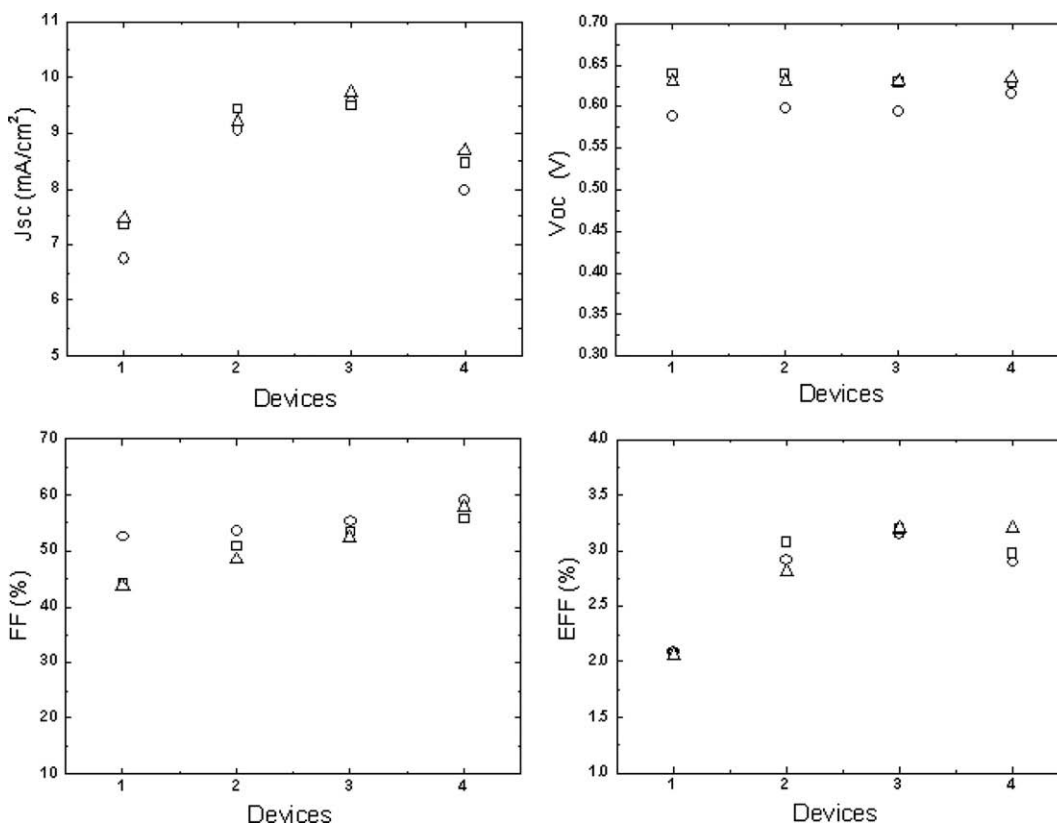


Fig. 6. Photovoltaic characteristics of three solar cell devices by inkjet printing of PEDOT:PSS inks prepared in the different batches.

tial of the PEDOT:PSS film in order to reduce conductivity. The work is still underway to find an exact mechanism.

To study the effect of additives on solar cell device performance, polymer bulk heterojunction solar cells (device 1–4) from different PEDOT:PSS inks (inks 1–4 as shown in Table 1) have been fabricated in the configuration of ITO/PEDOT:PSS inks/P3HT:PCBM/LiF-Al by inkjet printing. Current-density versus voltage ( $J$ – $V$ ) characterization has been performed in the dark and under simulated illumination as shown in Fig. 5. The resulting characteristics are shown in Table 2. Without any additives (device 1), the device performance was very poor showing low power conversion efficiency (EFF), circuit current density (Jsc) and fill factor (FF). This is due to the roughness surface profile as indicated in surface morphology results and low conductivity of PEDOT:PSS layer. The Jsc, FF and EFF of the device 2 from inkjet-printed PEDOT:PSS with glycerol were more than that of the pure PEDOT:PSS (device 1). Especially, Jsc was dramatically enhanced in device 2. This enhancement in the Jsc as well as device efficiency may be due to the improvement of the surface morphology and the improved charge collection by increased conductivity of the PEDOT:PSS with glycerol compared with pure PEDOT:PSS [37,38]. This may also be explained by the swelling and aggregation of colloidal PEDOT-rich particles which form a highly conductive network in the films [36,39]. The device performance (device 3) further improved with the addition of 0.2 wt.% EGBE surfactant from

2.92% to 3.16% in efficiency. Jsc and FF values were also enhanced in device 3. The conductivity of PEDOT:PSS film in this device is almost the same as glycerol added to PEDOT:PSS (device 2), but the surface roughness is optimal compared to other films. When the amount of EGBE in the PEDOT:PSS film is increased from 0.2 to 0.4 wt.%, it decreases the conductivity of the film, therefore efficiency and Jsc decrease in device 4.

In order to investigate the reproducibility of solar cell devices with inkjet-printed PEDOT:PSS layers, we have prepared several solar cell devices from inkjet-printed PEDOT:PSS inks in the different batches and their solar cell properties were measured. Fig. 6 shows the photovoltaic characteristics of three solar cell devices. All devices show good reproducibilities in Voc, Jsc, FF and efficiency. The best solar cell performance was obtained in device 3.

#### 4. Conclusion

We have demonstrated solar cell performance of the inkjet-printed PEDOT:PSS layer and the roles of additives in device performance. We have used glycerol and EGBE surfactant as additives to improve the surface morphology and conductivity of PEDOT:PSS inks. The newly proposed ink formulation of PEDOT:PSS increases the photovoltaic performance such as Jsc, FF and efficiency of inkjet-printed PEDOT:PSS resulting in a reliable print head with optimum wetting, spreading and drying. Using the newly developed

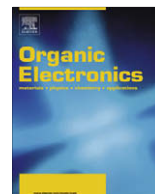
ink formulation of PEDOT:PSS (ink 3) with glycerol and optimized EGBE surfactant, we have demonstrated a 3.16% efficient and reliable solar cell with an inkjet-printed PEDOT:PSS layer (device 3). This high photovoltaic performance indicates the potential of inkjet printing for the mass production of organic photovoltaics.

### Acknowledgement

This work was supported by Ministry of Commerce, Industry and Energy (MOCIE) under Grant No. 200701-0041.

### References

- [1] N.S. Sariciftci, L. Smilowitz, A.J. Heeger, F. Wudl, *Science* 258 (1992) 1474.
- [2] J.J.M. Halls, C.A. Walsh, N.C. Greenham, E.A. Marseglia, R.H. Friend, S.C. Moratti, A.B. Holmes, *Nature* 376 (1995) 498.
- [3] G. Yu, J. Gao, J.C. Hummelen, F. Wudl, A.J. Heeger, *Science* 270 (1995) 1789.
- [4] C.J. Brabec, J.A. Hauch, P. Schilinsky, C. Waldauf, *MRS Bull.* 30 (2005) 50.
- [5] C.J. Brabec, N.S. Sariciftci, J.C. Hummelen, *Adv. Funct. Mater.* 11 (2001) 15.
- [6] P. Schilinsky, C. Waldauf, C.J. Brabec, *Appl. Phys. Lett.* 81 (2002) 3885.
- [7] M. Svensson, F. Zhang, S.C. Veenstra, W.J.H. Verhees, J.C. Hummelen, J.M. Kroon, O. Inganäs, M.R. Andersson, *Adv. Mater. (Weinheim, Ger.)* 15 (2003) 988.
- [8] M. Granström, K. Petritsch, A.C. Arias, A. Lux, M.R. Andersson, R.H. Friend, *Nature (London)* 395 (1998) 257.
- [9] Claudia N. Hoth, Stelios A. Choulis, Pavel Schilinsky, Christoph J. Brabec, *Adv. Mater.* 19 (2007) 3973.
- [10] H. Sirringhaus, T. Kawase, R.H. Friend, T. Shimoda, M. Inbasekaran, W. Wu, E.P. Woo, *Science* 290 (2000) 2133.
- [11] H. Sirringhaus, T. Kawase, R.H. Friend, *Mater. Res. Bull.* 26 (2001) 539.
- [12] J. Bharathan, Y. Yang, *Appl. Phys. Lett.* 72 (1998) 2660.
- [13] T. Aernouts, T. Aleksandrov, C. Girotto, J. Genoe, J. Poortmans, *Appl. Phys. Lett.* 92 (2008) 033306.
- [14] G. Heywang, F. Jonas, *Adv. Mater.* 4 (1992) 116.
- [15] Q. Pei, G. Zucacafrello, M. Ahlskog, O. Inganäs, *Polymer* 35 (1994) 1347.
- [16] S. Garreau, G. Louarn, S. Lefrant, J.P. Buisson, G. Froyer, *Synth. Met.* 101 (1999) 312.
- [17] L. Groenendaal, F. Jonas, D. Freitag, H. Pielartzik, J.R. Reynolds, *Adv. Mater.* 12 (2000) 481.
- [18] A.N. Aleshin, R. Kiebooms, A.J. Heeger, *Synth. Met.* 101 (1999) 369.
- [19] A.N. Aleshin, R. Kiebooms, R. Menon, A.J. Heeger, *Synth. Met.* 90 (1997) 61.
- [20] P. Buvat, P. Hourquebie, *Synth. Met.* 101 (1999) 17.
- [21] H. Yamato, K. Kai, M. Ohwa, T. Koshiba, W. Wernet, *Synth. Met.* 83 (1996) 125.
- [22] Y. Cao, J. Qiu, P. Smith, *Synth. Met.* 69 (1995) 187.
- [23] A.G. MacDiarmid, A.J. Epstein, *Synth. Met.* 65 (1994) 103.
- [24] K.X. Steirer, J.J. Berry, M.O. Reese, M.F.A.M. van Hest, A. Miedaner, M.W. Liberatore, R.T. Collins, D.S. Ginley, *Thin Solid Films* 517 (2009) 2781.
- [25] J. Park, H.-J. Koo, B. Yoo, K. Yoo, K. Kim, W. Choi, N.-G. Park, *Sol. Energy Mater. Sol. Cells* 91 (2007) 1749.
- [26] A. Cravino, P. Schilinsky, C.J. Brabec, *Adv. Funct. Mater.* 17 (2007) 3906.
- [27] J. Huang, P.F. Miller, J.S. Wilson, A.J. de Mello, J.C. de Mello, D.D.C. Bradley, *Adv. Funct. Mater.* 15 (2005) 290.
- [28] A.M. Nardes, M. Kemerink, R.A.J. Janssen, J.A.M. Bastiaansen, N.M.M. Kiggen, B.M.W. Langeveld, A.J.J.M. van Breemen, M.M. de Kok, *Adv. Mater.* 19 (2007) 1196.
- [29] S. Timpanaro, M. Kemerink, F.J. Touwslager, M.M. de Kok, S. Schrader, *Chem. Phys. Lett.* 394 (2004) 339.
- [30] J.Y. Kim, J.H. Jung, D.E. Lee, J. Joo, *Synth. Met.* 126 (2002) 311.
- [31] F.J. Touwslager, N.P. Willard, D.M. de Leeuw, *Synth. Met.* 135 (2003) 53.
- [32] L.A.A. Pettersson, S. Ghosh, O. Inganäs, *Organ. Electron.* 3 (2002) 143.
- [33] S.K.M. Jönsson, W.R. Salaneck, M. Fahlman, *J. Electron. Spectrosc. Relat. Phenom.* 137–140 (2004) 805.
- [34] J. Ouyang, C.-W. Chu, F.-C. Chen, Q. Xu, Y. Yang, *Adv. Funct. Mater.* 15 (2005) 203.
- [35] X. Crispin, F.L.E. Jakobsson, A. Crispin, P.C.M. Grim, P. Anderson, A. Volodin, C. van Haesendonck, M. van der Auweraer, W.R. Salaneck, M. Berggren, *Chem. Mater.* 18 (2006) 4354.
- [36] F. Zhang, M. Johansson, M.R. Andersson, J.C. Hummelen, O. Inganäs, *Adv. Mater.* 14 (2002) 662.
- [37] W.H. Kim, A.J. Ma kinen, N. Nikolov, R. Shashidhar, H. Kim, Z.H. Kafafi, *Appl. Phys. Lett.* 80 (2002) 3844.
- [38] Sung-Ho Jin, B. Vijaya Kumar Naidu, Han-Soo Jeon, Sung-Min Park, Jin-Soo Park, Sung Chul Kim, Jae Wook Lee, Yeong-Soon Gal, *Sol. Energy Mater. Sol. Cells* 91 (2007) 1187.
- [39] H.J. Snaith, H. Kenrick, M. Chiesa, R.H. Friend, *Polymer* 46 (2005) 2573.



## Letter

## Improvement in the on/off ratio of a vertical-type metal-base organic transistor by heat treatment in air

Ken-ichi Nakayama<sup>a,b,\*</sup>, Shin-ya Fujimoto<sup>b</sup>, Masaaki Yokoyama<sup>b</sup><sup>a</sup> Graduate School of Science and Engineering, Yamagata University, 4-3-16 Jonan, Yonezawa, Yamagata 992-8510, Japan<sup>b</sup> Graduate School of Engineering, Osaka University, 2-1 Yamadaoka, Suita, Osaka 565-0871, Japan

## ARTICLE INFO

## Article history:

Received 27 November 2008

Received in revised form 8 January 2009

Accepted 3 February 2009

Available online 11 February 2009

## PACS:

85.30.De

73.61.Ph

81.40.Rs

73.40.Vz

## Keywords:

Organic transistor

Vertical-type transistor

On/off ratio

## ABSTRACT

The on/off ratio of a vertical-type metal-base organic transistor was significantly improved by subjecting it to heat treatment in air. The heat treatment of the collector layer and the base electrode reduced the off current that is mainly due to leakage current between the base and the collector, resulting in a considerable decrease in the off current. As a result, a high on/off ratio greater than  $10^5$  was achieved, in addition to the low-voltage and high current operation of the vertical-type organic transistor.

© 2009 Elsevier B.V. All rights reserved.

## 1. Introduction

Organic transistors have been extensively studied and are expected to be used for producing flexible displays and low-cost radio frequency identification systems [1–4]. Most studies conducted on organic transistors have focused on organic field-effect transistors (OFETs) having “lateral” structures. In these structures, the channel carriers flow along the plane of the organic semiconductor film. Further, the channel length in these structures, which is determined by the fine patterning technique commonly employed, can be reduced to less than several microns only by expensive techniques such as lithography.

Recently, several researchers have proposed different types of organic transistors that have a “vertical” structure. In such structures, channel carriers flow across the thin film in a direction perpendicular to the substrate. Therefore, the channel length in this case corresponds to the thickness of the film and can be easily reduced to less than one micron. In order to achieve enhanced transistor performance, for example, high current modulation, low-voltage operation, and high frequency response, it is important to have a short channel length. Thus far, several types of vertical transistors have been proposed; for example, organic static induction transistors with a striped central electrode [5–7], vertical organic triodes [8–10], vertical transistors made of organic–inorganic hybrid materials [11–13], and polymer space-charge-limited transistors [14,15].

We have recently proposed a metal-base organic transistor (MBOT), which is a promising vertical-type organic transistor [16,17]. This transistor has a simple structure

\* Corresponding author. Address: Graduate School of Science and Engineering, Yamagata University, 4-3-16 Jonan, Yonezawa, Yamagata 992-8510, Japan.

E-mail address: [nakayama@yz.yamagata-u.ac.jp](mailto:nakayama@yz.yamagata-u.ac.jp) (K. Nakayama).

in the form of organic/metal/organic layers. The middle electrode of the MBOT can be fabricated by techniques other than the fine patterning technique; further, the MBOT has a high current modulation of over 100 mA/cm<sup>2</sup> and low-voltage operation of the order of several volts.

Generally, vertical-type transistors have a low on/off ratio because their short channel length tends to increase the leakage current. The on/off ratio of the proposed MBOT was also reported to be low (around 100). However, we have already reported a slight improvement in the on/off ratio by exposing the device to air [18]; this improvement was accompanied by a decrease in the on current. In this study, we propose an efficient method for decreasing the leakage (off) current; this method involves subjecting only the collector semiconductor layer and the base electrode to heat treatment in air. By this method, the off current is reduced significantly without a decrease in the on current, resulting in a very high on/off ratio.

## 2. Experimental

In this study, the transistor device with a simple layered structure (Fig. 1) was fabricated by vacuum evaporation. The first organic layer (collector layer) of *N,N'*-dimethyl-3,4,9,10-perylene tetracarboxylic diimide (Me-PTC) (Dainichiseika Color and Chemicals Manufacturing Co., Ltd.) with a thickness of 500 nm and an aluminum layer (base electrode) with a thickness of 20 nm were deposited successively on a clean indium tin oxide (ITO) glass substrate that was subjected to ultrasonic cleaning in acetone, methanol and deionized water. At this stage, the two layers were subjected to heat treatment at 150 °C in air. Next, the remaining layers, i.e., the second organic layer of C<sub>60</sub> (100 nm) and the emitter electrode layer of Ag (30 nm) were deposited.

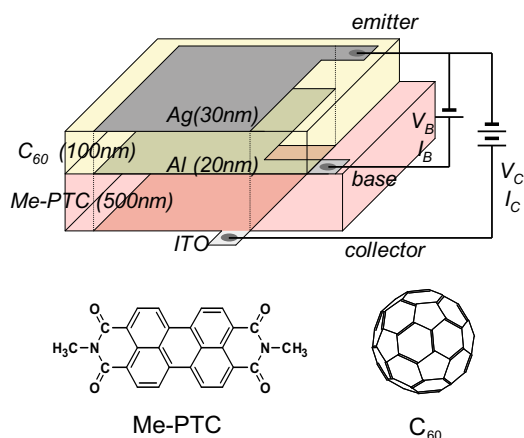


**Fig. 1.** Structure of metal-base organic transistors and the system for measurement of transistor performance. Both collector voltage ( $V_C$ ) and base voltage ( $V_B$ ) were applied with the emitter electrode negatively biased.

using a common emitter circuit (Fig. 1) with two source-measure units (Keithley Instruments Inc., model 236) under vacuum ( $10^{-1}$  Pa) at room temperature. The collector voltage ( $V_C$ ) was applied between the collector and emitter electrodes, and the base voltage ( $V_B$ ) was applied between the emitter and base electrodes; in both these cases, the emitter was negatively biased. The current amplification factor ( $h_{FE}$ ) is defined as the ratio of the change in the collector current ( $I_C$ ) to that in base current ( $I_B$ ) induced by applying the input voltage ( $V_B$ ). The HOMO level of the organic semiconductor was measured by photoelectron yield spectroscopy (Sumitomo Heavy Industries, PYS-201), and the HOMO–LUMO gap was estimated from the absorption spectrum.

## 3. Results and discussion

The output current ( $I_C$ ) was increased by the application of base voltage ( $V_B$ ), and  $h_{FE}$  exceeded unity; therefore, the device functions effectively as an MBOT. Fig. 2 shows the effect of the time for which the layers were subjected to heat treatment on the on and off currents at  $V_C = 5$  V, where the on and off currents are the  $I_C$  at  $V_B = 3$  and  $V_B = 0$  V, respectively. For the heat treatment time equal to zero (no heat treatment), a large off current was observed, and the on/off ratio remained around 100. The off current decreased significantly as the heat treatment time increased and subsequently, it decreased by approximately three orders of magnitude within several hours of heat treatment. In contrast, the on current decreased by only a slight amount. As a result, the on/off ratio increased with increasing heat treatment time and attained a maximum value of  $3 \times 10^5$ . Such a high on/off ratio of a vertical-type organic transistor is desirable and comparable to that of lateral-type OFETs.

Fig. 3 shows the current modulation characteristics of the device subjected to heat treatment for 2 h ( $V_C = 3, 5$  and 7 V). Those of the device without heat treatment are also shown ( $V_C = 5$  V). Fig. 3a shows the  $I_C$ – $V_B$  curves at various values of  $V_C$ . From the figure, it is clearly observed that the output collector current ( $I_C$ ) was modulated by the input base voltage ( $V_B$ ) by five orders of magnitude. It should be noted that a large current density of over 100 mA/cm<sup>2</sup> was obtained at a low operation voltage, that is, when  $V_C = 5$  V and  $V_B = 2$  V. The current amplification factors ( $h_{FE}$ ) for these modulations are shown in Fig. 3b. The value of  $h_{FE}$  reached around 140 at  $V_C = 7$  V and  $V_B = 2.5$  V, which indicates that small input base current is amplified to large output collector current. This low-voltage operation of the transistor is attributed to its vertical structure with a very short channel length. The fact that the  $I_C$ – $V_B$  curves are coincident for various values of  $V_B$  suggests that the output current reaches a saturation point as  $V_C$  increases. Such a saturation of the output current, similar to that observed in OFETs, is also a desirable but uncommon feature of vertical-type organic transistors. Furthermore, the decrease of leakage current by the heat treatment resulted in high reproducibility and stability in the fabrication of MBOTs.

The decrease in the off current by heat treatment in air can be explained by the suppression of electron injection from the base electrode. The operation mechanism of the

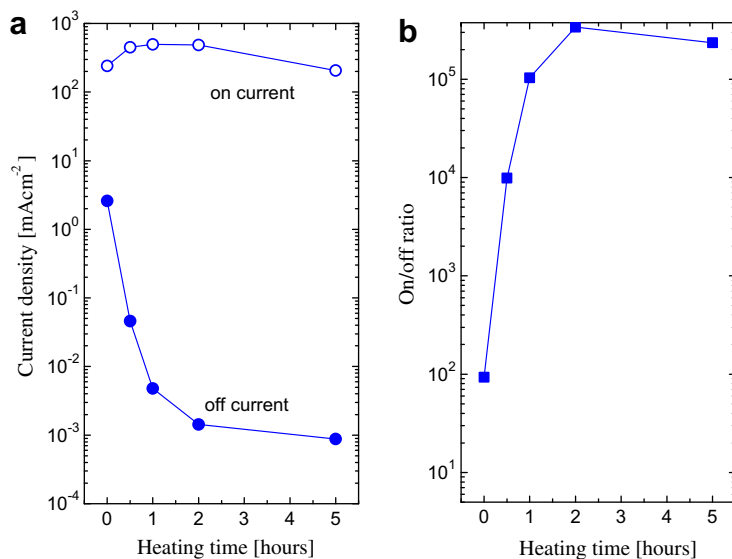


Fig. 2. Dependence of (a) on and off currents and (b) on/off ratio on the heat treatment time at  $V_C = 5$  V and  $V_B = 3$  V.

MBOT is explained with the help of a schematic energy diagram shown in Fig. 4a. The real energy level of each layer is illustrated in Fig. 4b. To explain its operation, we propose the following mechanism of electron transmission through the base electrode [16,17]. The electrons injected from the emitter on applying  $V_B$  are transmitted across the thin base electrode with a high probability and are collected on the

ITO electrode through the Me-PTC layer. This mechanism induces high current modulation of  $I_C$  for a small increase in  $I_B$ , namely, current amplification. In the off state, there is no potential difference between the emitter and base because  $V_B = 0$ . Therefore, the major component of the off current is regarded as the leakage current from the base to the collector. Furthermore, this component is attributed to the flow of electrons from the base electrode because

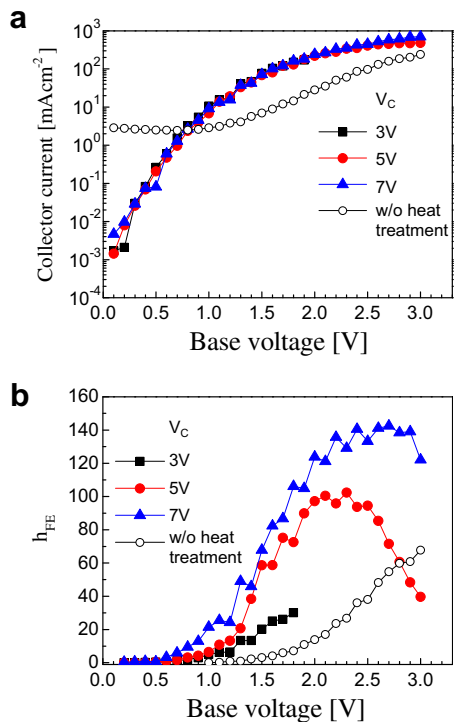


Fig. 3. Modulation characteristics of the MBOT subjected to optimized heat treatment (150 °C for 2 h) and without heat treatment; (a)  $I_C$ - $V_B$  curves and (b)  $h_{FE}$ - $V_B$  curves.

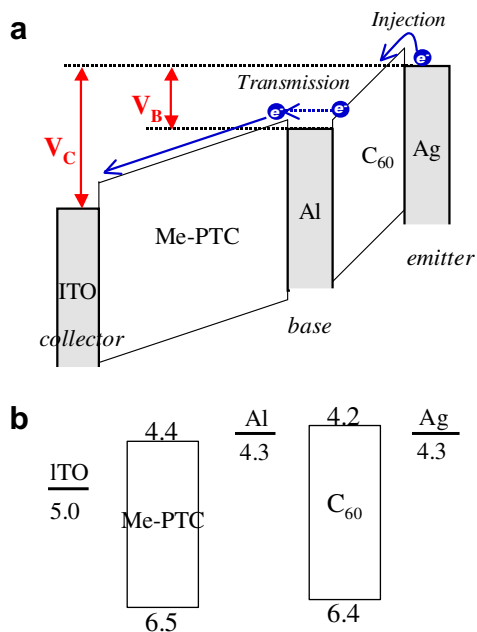


Fig. 4. (a) Energy diagram of MBOT during its operation. The emitted electrons pass through the base electrode with high probability. The off current ( $I_C$  at  $V_B = 0$ ) corresponds to the current of the electrons injected from the base electrode to the Me-PTC layer. (b) HOMO and LUMO levels of the organic semiconductors, and work function of each electrode.

Me-PTC is a well-known n-type semiconductor [19–21]. Thus, it is concluded that heat treatment of the device in air suppresses the current due to electron injection at the Me-PTC/Al interface, causing a decrease in the off current. In fact, two-terminal  $I$ - $V$  curves between the base and collector indicated clear decrease of current after the heat treatment.

The current saturation that occurs with increasing  $V_C$ , as shown in Fig. 3b, can also be explained by the above mentioned mechanism. In the proposed mechanism, the number of electrons injected from the emitter depends only on  $V_B$ , and the collector voltage  $V_C$  facilitates the collection of these carrier electrons by the collector electrode. Therefore,  $I_C$  is expected to saturate when the upper limit of the current due to the injected electrons is reached. In the present study, the ideal current modulation observed is also believed to be attributed to the decrease in the additional leakage current. This behavior also suggests that  $V_C$  has no effect on the electron injection at the emitter interface; that is, the electric flux lines between the emitter and collector are completely separated by the base electrode.

To further investigate the effect of heat treatment, we performed some additional experiments. We tried heat treating only the Me-PTC layer before depositing the base electrode on it. However, this technique did not decrease the off current, which indicates that the heat treatment did not alter the bulk transport properties of Me-PTC. In addition, no significant change was observed in HOMO and LUMO levels of the Me-PTC film. Therefore, change in the morphology or energy levels of the film was excluded as a possible cause of the decrease in the off current, and this decrease was concluded to be attributed to the Me-PTC/Al interface. Such a heat treatment including aluminum associates us with some oxidation process. However, the in-plane resistance of the base electrode was maintained at several hundred ohms and did not increase by heat treatment, which suggests that even after the heat treatment, the base electrode functions effectively. From all these results, we speculated that the heat treatment forms some oxidation layer mainly at the Me-PTC/Al interface, and this layer efficiently blocks electron injection into Me-PTC. It was an interesting observation that this layer did not block the electrons emitted from the emitter. However, the exact mechanism of electron transmission through the base electrode is still unclear and requires further investigation.

#### 4. Conclusion

In conclusion, we successfully decreased the leakage (off) current by subjecting the collector layer and base

electrode to heat treatment in air and therefore realized a vertical-type MBOT with a very high on/off ratio while maintaining high current and low-voltage operation. The fact that this method also improves stability and reproducibility of the fabrication of MBOTs has encouraged us to further elucidate the operation mechanism systematically.

#### Acknowledgements

This study was partially supported by the New Energy and Industrial Technology Development Organization (NEDO), PRESTO program of the Japan Science and Technology agency (JST), and the Konica–Minolta Imaging Foundation.

#### References

- [1] G.H. Gelinck, H.E.A. Huitema, E. Van Veenendaal, E. Cantatore, L. Schrijnemakers, J. Van der Putten, T.C.T. Geuns, M. Beenhakkers, J.B. Giesbers, B.H. Huisman, E.J. Meijer, E.M. Benito, F.J. Touwslager, A.W. Marsman, B.J.E. Van Rens, D.M. De Leeuw, *Nat. Mater.* 3 (2004) 106.
- [2] L.S. Zhou, A. Wanga, S.C. Wu, J. Sun, S. Park, T.N. Jackson, *Appl. Phys. Lett.* 88 (2006) 083502.
- [3] P.F. Baude, D.A. Ender, M.A. Haase, T.W. Kelley, D.V. Muires, S.D. Theiss, *Appl. Phys. Lett.* 82 (2003) 3964.
- [4] E. Cantatore, T.C.T. Geuns, G.H. Gelinck, E. van Veenendaal, A.F.A. Gruijthuijsen, L. Schrijnemakers, S. Drews, D.M. de Leeuw, *IEEE J. Solid-State Circ.* 42 (2007) 84.
- [5] K. Kudo, M. Iizuka, S. Kuniyoshi, K. Tanaka, *Thin Solid Films* 393 (2001) 362.
- [6] Y. Watanabe, H. Iechi, K. Kudo, *Appl. Phys. Lett.* 89 (2006) 233509.
- [7] K. Fujimoto, T. Hiroi, K. Kudo, M. Nakamura, *Adv. Mater.* 19 (2007) 525.
- [8] L.P. Ma, Y. Yang, *Appl. Phys. Lett.* 85 (2004) 5084.
- [9] C.Y. Yang, T.M. Ou, S.S. Cheng, M.C. Wu, S.Y. Lin, I.M. Chan, Y.J. Chan, *Appl. Phys. Lett.* 89 (2006) 183511.
- [10] S.H. Li, Z. Xu, L.P. Ma, C.W. Chu, Y. Yang, *Appl. Phys. Lett.* 91 (2007) 083507.
- [11] M.S. Meruvia, I.A. Hummelgen, M.L. Sartorelli, A.A. Pasa, W. Schwarzacher, *Appl. Phys. Lett.* 84 (2004) 3978.
- [12] M.S. Meruvia, I.A. Hummelgen, *Adv. Funct. Mater.* 16 (2006) 459.
- [13] C.G. Feng, M.D. Yi, S.Y. Yu, I.A. Hummelgen, T. Zhang, D.G. Ma, J. Nanosci. Nanotechnol. 8 (2008) 2037.
- [14] Y.C. Chao, H.F. Meng, S.F. Horng, *Appl. Phys. Lett.* 88 (2006) 223510.
- [15] Y.C. Chao, H.F. Meng, S.F. Horng, C.S. Hsu, *Org. Electron.* 9 (2008) 310.
- [16] S. Fujimoto, K. Nakayama, M. Yokoyama, *Appl. Phys. Lett.* 87 (2005) 133503.
- [17] K. Nakayama, S. Fujimoto, M. Yokoyama, *Appl. Phys. Lett.* 88 (2006) 153512.
- [18] K. Yutani, K. Nakayama, M. Yokoyama, *Mol. Cryst. Liquid Cryst.* 444 (2006) 197.
- [19] P.R.L. Malenfant, C.D. Dimitrakopoulos, J.D. Gelorme, L.L. Kosbar, T.O. Graham, A. Curioni, W. Andreoni, *Appl. Phys. Lett.* 80 (2002) 2517.
- [20] S. Tatemichi, M. Ichikawa, T. Koyama, Y. Taniguchi, *Appl. Phys. Lett.* 89 (2006) 112108.
- [21] K. Nakayama, M. Hiramoto, M. Yokoyama, *J. Appl. Phys.* 87 (2000) 3365.





## Letter

## Novel in-line method for patterned deposition of conductive structures

T. Fischer<sup>a,\*</sup>, U. Hahn<sup>b</sup>, M. Dinter<sup>b</sup>, M. Bartzsch<sup>b</sup>, G. Schmidt<sup>b</sup>, H. Kempa<sup>b</sup>, A.C. Huebler<sup>b</sup><sup>a</sup> Printed Systems GmbH, 09120 Chemnitz, Germany<sup>b</sup> Institute for Print and Media Technology, Chemnitz University of Technology, 09126 Chemnitz, Germany

## ARTICLE INFO

## Article history:

Received 27 October 2008

Received in revised form 5 February 2009

Accepted 10 February 2009

Available online 20 February 2009

## PACS:

72.80.Je

81.65.cf

85.30.tv

## Keywords:

Printed electronics

Printing technologies

Surface patterning

Organic field-effect transistor

## ABSTRACT

We report on a novel method for patterned deposition of conductive polymers, which is derived from and fully compatible with fast in-line printing methods. The method is aimed at improving resolution, homogeneity and edge sharpness of printed conductive structures for applications in the field of printed electronics. The surface energy of a foil substrate, which has been increased by means of corona treatment, was reduced in selected areas through contact with materials that have suitable surface properties and can be patterned at micrometer scale (i.e. printing plates). A conductive fluid was sprayed onto the chemically heterogeneous surface. The fluid accumulated at areas with higher surface energy. After the drying process, the conductive polymer structures were used as source/drain contacts for the preparation of OFETs.

© 2009 Elsevier B.V. All rights reserved.

## 1. Introduction

In recent years, considerable progress has been made in the relatively new field of printed electronics. Conductive, semiconductive and insulating functional polymers were successfully formulated as inks and applied in a patterned way by means of mass printing methods, like offset, flexographic and gravure printing. On the basis of these technologies, all-printed, fully polymeric electronic devices (transistors, inverters, ring oscillators) were realised in a continuous process at a process speed of approx. 1 m/s, [1,2]. The printed conductive structures, however, have a limited resolution and the layer morphology is not optimal especially with offset printing [3]. In order to enhance the performance of polymer electronic devices, research currently focuses on new technological approaches that improve layer homogeneity and reduce structure sizes. A

major challenge is to guarantee the compatibility of new technological approaches with the continuity of conventional printing and the utilised materials. Moreover, material availability and processability are important issues [4].

Various approaches and methods for the preparation of patterns on surfaces which are pre-structured in terms of surface tension (so-called wetting structuring) have been described. The increasing demand for miniaturisation of structure sizes led to the development of complex technologies, like microcontact printing ( $\mu$ CP) [5–7]. One aspect of  $\mu$ CP, the transfer of PDMS oligomers during contact between PDMS stamp and substrate, is discussed from various perspectives in the literature [8–11]. In [11] a method for applying low-molecular siloxane oligomers with PDMS stamps to a substrate is presented. This method was used for the preparation of a TFT (thin film transistor). Another interesting method is plasma mask technology for surface structuring of polymers [12]. However, reasonable integration of the above mentioned methods into a conventional printing process seems impossible, because contact times of several minutes [11] or complex cleaning

\* Corresponding author. Tel.: +49 371 531 32445; fax: +49 371 530 460 700.

E-mail address: [thomas.fischer@printed-systems.de](mailto:thomas.fischer@printed-systems.de) (T. Fischer).

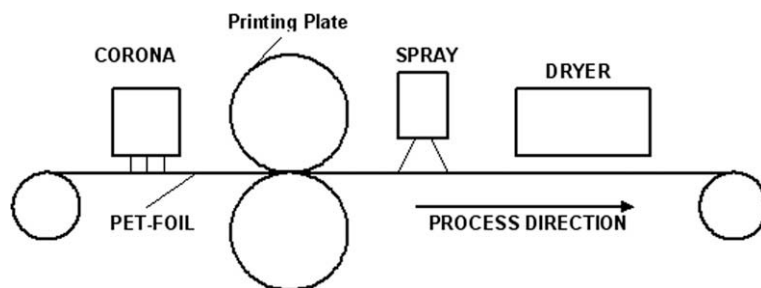


Fig. 1. Wetting structuring – process scheme.

procedures [13] are necessary. The method described in [14] uses ink jet printing for applying droplets of an aqueous dispersion of PEDOT/PSS to a  $\text{SiO}_2/\text{n}^+\text{-Si}$  substrate. Electron beam lithography, vacuum deposition and lift-off processes were used to apply hydrophobic self-assembled monolayers (SAMs) of fluorodecyltrichlorosilane (FDTS) to the raised areas of the  $\text{SiO}_2$  substrate surface. When PEDOT/PSS droplets hit the hydrophobic areas, the liquid dewetted into two parts, which were employed as source/drain electrodes in field-effect transistors. The width of the raised  $\text{SiO}_2$  structures to which FDTS was applied determined the channel length. Channel lengths down to 500 nm have been realised.

## 2. Experimental

In conventional printing processes, surface activation by corona is usually employed to improve wetting behaviour of foil substrates. Corona treatment results in areas with different surface energies. In the simplest case, these differences result from the fact that only parts of the substrate are corona-treated while others remain untreated. This can be done by either turning the corona on and off or by partial treatment of the web with segmented corona electrodes. The usual area treatment, however, fails in continuous processes where the surface energy has to be modified at micrometer scale in running direction and perpendicular to it.

The process presented here is based on contact between a surface-modified foil substrate with the surface of a non-inked printing plate processed with a reduced light detacking (UVC) time of 5 min, as for instance used in flexographic printing (Flint Group nyloflex® FAH). The partial reduction of the surface energy by contact requires the structuring of the printing plate in printing and non-printing areas. In flexographic printing the printing elements are raised. Contact with the foil substrate and, thus, reduction of the surface energy only takes place at raised areas. After contact between printing plate surface and corona-treated foil, which shall be termed “wetting structuring”, the surface of the foil has areas of different wetting behaviour. The surface energy of the polymer formulation is adapted by adding a mixture of surfactants (about 0.03% by weight) in order to match the foil areas having a high surface energy. The conductivity of the dried layer is improved by adding glycerol (15% by weight).

When these formulations are applied to the substrate it is mainly the high surface energy areas that are wetted.

Table 1  
Functional layers – OFET.

Functional layer	Material	Layer thickness [μm]	Application process
Substrate	PET foil	50	
Source/drain	PEDOT:PSS	0.1	Spraying
Semiconductor	F8T2	0.05	Spin coating
Dielectric	Cytop/Luxprint 8153	10	Spin coating
Gate	PEDOT:PSS	1	Dispensing

The amount of liquid that is applied per unit area is a crucial factor for the preparation of homogenous polymer structures with defined outlines. Only exact dosing guarantees that a pinhole-free, sufficiently thick layer is applied and non-image areas are not wetted. Preparatory experiments showed that spraying via nozzle is a suitable method for the precise application of a functional polymer liquid. A two fluid nozzle with a nozzle diameter of 0.4 mm producing a spray with a Sauter mean diameter of approx. 8 μm was chosen. The PET foil Melinex 401 with a thickness of 50 μm was used as substrate. The surface energy of the foil was increased from 47 to approx. 60 mN/m by means of corona pre-treatment (system by Arcotec GmbH) on a laboratory printing press. The layout of the flexographic printing plate consisted of source/drain structures for transistors and connecting lines, which allow for more complex functions (e.g. inverters). The channel

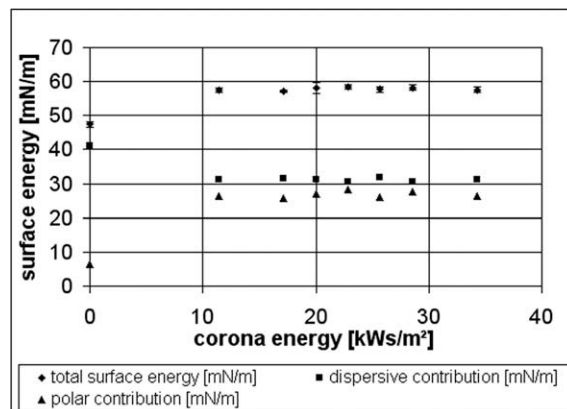
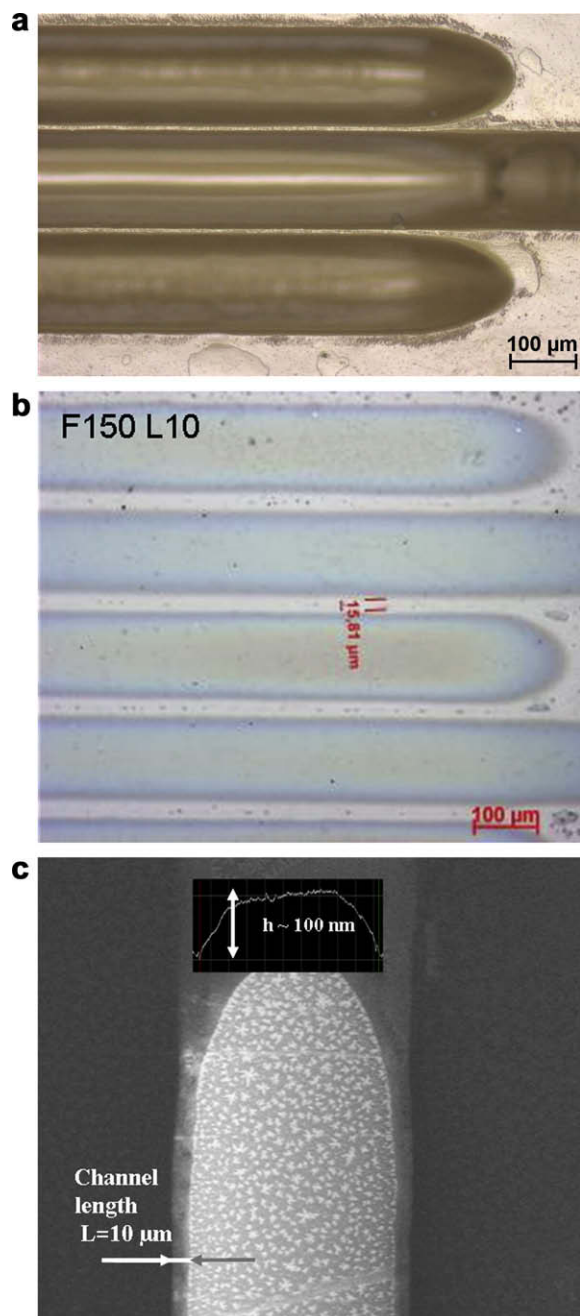
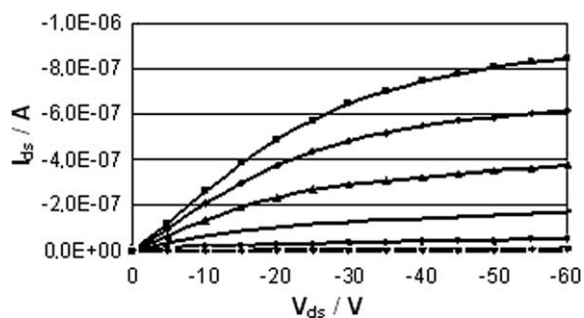


Fig. 2. Surface energy of corona-treated PET foil (contact angle measurement: sessile drop; calculation method: Owens–Wendt).

lengths on the printing plate were 10  $\mu\text{m}$ . The formulation of the conducting function polymer PEDOT:PSS in aqueous dispersion (Baytron P, now Clevios P, by H.C. Starck GmbH, Germany) was sprayed onto the wetting-structured foil surface in order to prepare source/drain structures for field-effect transistors. The process is explained in Fig. 1. The other layers of the top-gate transistors were applied by means of spin coating or dispensing. Table 1 provides



**Fig. 3.** (a) Flexographic printing form with source/drain layout: finger width  $F = 150 \mu\text{m}$ ; channel length  $L = 10 \mu\text{m}$ , (b) PEDOT:PSS structures after spraying and drying, (c) SEM micrograph + profile scan of one line shown in (b).



**Fig. 4.** OFET output characteristics ( $V_{GS} = 0$  to  $-60$  V).

an overview of the utilised materials, layer thicknesses and application methods.

### 3. Results and discussion

Corona treatment increases the surface energy of PET foil from 47 to approx. 60 mN/m. Fig. 2 shows the characteristics of the surface energy depending on the corona energy. The corona energy is defined as the energy that is applied to the substrate in order to modify its surface energy. It is determined by the generator power, the speed of the foil web and the width of the electrodes, i.e. the width of the corona discharge. Under the given conditions – web speed 0.5 m/s and width of the corona discharge 35 mm – the surface energy of the foil reaches a state of saturation at a corona dose of  $>10 \text{ kW/s/m}^2$ . Contact with the flexographic printing plate results in a reduction of the surface energy of the foil (dispersive contribution) at the contact points. The difference in surface energy between contact and non-contact areas is 12 mN/m. The surface energy of the aqueous PEDOT:PSS dispersion is adjusted to guarantee wetting of the non-contact areas, i.e. areas with a higher surface energy, on the foil (cf. Fig. 3b). The PEDOT:PSS formulation is sprayed onto the foil immediately after wetting structuring. Drying is realized in a hot air stream adjusting a PET surface temperature of 130  $^{\circ}\text{C}$  for 20 s. The SEM micrograph in Fig. 3c shows a profile scan of one finger of a source/drain structure with a channel length of 10  $\mu\text{m}$  and a cross section height of the finger of approx. 100 nm. The surface roughness ( $R_a$ ) is low, approx. 10 nm. Typical output characteristics of an OFET which is based on these source/drain structures with a channel length of 10  $\mu\text{m}$  and a channel width of 2.5 mm is shown in Fig. 4. Mobility is  $4 \times 10^{-4} \text{ cm}^2/\text{Vs}$  and on/off ratio 275.

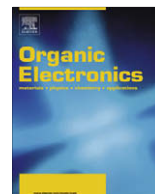
### 4. Conclusions

A new approach for the preparation of conducting polymer structures by means of a continuous process was presented. Very thin, homogenous layers with low roughness were produced. The minimum channel length of 10  $\mu\text{m}$  is determined by the limited resolution of the used printing plate. There is a difference in channel length between Fig. 3b ( $\sim 15 \mu\text{m}$ ) and Fig. 3c ( $\sim 10 \mu\text{m}$ ) due to the limited depth of field of the light microscope used for Fig. 3b.

Challenges are the durability of the printing plate surface, as there is a decrease in homogeneity of the surface energy reduction regarding the contact area when using the same plate for several times, and the spraying parameters, which have to be adjusted in order to achieve very small structure sizes and channel lengths. Other substrates, pre-treatment methods, like atmospheric pressure plasma (plasma spot), application methods for conducting polymers, like dipping or blading, and the combination with other functional materials in OFETs will be tested in order to further improve the technology.

## References

- [1] Zielke et al, Applied Physics Letters 87 (2005) 123508.
- [2] A.C. Huebler et al, Organic Electronics 8 (2007) 480–486.
- [3] K. Reuter et al, Progress in Organic Coatings 58 (2007) 312–315.
- [4] G. Schmidt et al, SPIE Optics and Photonics 2006 – Organic Field-Effect Transistors V (2006) 6336.
- [5] A.D. Payne, P.G. Clem, Journal of Electroceramics 3 (2) (1999) 163–172.
- [6] S.H. Choi, B.Z. Newby, Langmuir 19 (2003) 7427–7435.
- [7] A.A. Darhuber, S.M. Troian, S.M. Miller, S. Wagner, Journal of Applied Physics 87 (11) (2000) 7768–7775.
- [8] D.J. Graham, D.D. Price, B.D. Ratner, Langmuir 18 (2002) 1518–1527.
- [9] K. Glasmästar, J. Gold, A.S. Andersson, D.S. Sutherland, B. Kasemo, Langmuir 19 (2003) 5475–5483.
- [10] X. Wang, M. Östblom, T. Johansson, O. Inganäs, Thin Solid Films 449 (2004) 125–132.
- [11] A.L. Briseno, M. Roberts, M.M. Ling, H. Moon, E.J. Nemanick, Z. Bao, Journal of American Chemical Society 128 (2006) 3880–3881. <http://pubs.acs.org>.
- [12] M. Müller, V. Sciaratta, C. Oehr, Vakuum in Forschung und Praxis 15 (1) (2003) 19–22.
- [13] Z. Yang, A.M. Belu, A. Liebmann-Vinson, H. Sugg, A. Chilkoti, Langmuir 16 (2000) 7482–7492.
- [14] J.Z. Wang et al, Synthetic Metals 146 (2004) 287–290.



## All-solution-processed inverted polymer solar cells on granular surface-nickelized polyimide

Yu-Sheng Hsiao<sup>a</sup>, Chih-Ping Chen<sup>b</sup>, Ching-Hsun Chao<sup>c</sup>, Wha-Tzong Whang<sup>a,\*</sup>

<sup>a</sup> Department of Materials Science and Engineering, National Chiao Tung University, Hsinchu 300, Taiwan, ROC

<sup>b</sup> Material and Chemical Research Laboratories, Industrial Technology Research Institute, Hsinchu 300, Taiwan, ROC

<sup>c</sup> Department of Materials Science and Engineering, Mingdao University, Chang-Hwa, Taiwan, ROC

### ARTICLE INFO

#### Article history:

Received 14 December 2008

Received in revised form 22 January 2009

Accepted 23 January 2009

Available online 3 February 2009

#### Keywords:

All-solution-process

Inverted polymer solar cells

PEDOT/PSS

### ABSTRACT

In this study, we prepared all-solution-processed inverted polymer solar cells (PSCs) incorporating two solution-processed electrodes – surface-nickelized polyimide films (NiPI films) as cathodes and high-conductivity poly(3,4-ethylenedioxythiophene)/poly(styrene-sulfonate) (PEDOT:PSS) films as anodes – and an active layer with a bulk heterojunction morphology of poly(3-hexylthiophene) (P3HT) and [6,6]-phenyl-C<sub>61</sub>-butyric acid methyl ester (PCBM). The granular Ni thin films, which exhibited good adhesion and high-conductivity (ca. 2778 S cm<sup>-1</sup>) on the polyimide (PI) substrates and possessed a work function different from that of pure Ni metal (WF, 5.4 eV). Using ultraviolet photoelectron spectroscopy, we determined that the WF of the NiPI films was ca. 3.9 eV. Prior to the coating of the photoactive layer, the surface of the NiPI films were treated with titanium(diisopropoxide)bis(2,4-pentanedionate) (TIPD) solution to facilitate the deposition of high-quality active layer and further as a hole blocking layer. The solution processed anodes (solvent-modified PEDOT:PSS films) were further coated and subjected to mild oxygen plasma treatment on the active layer. Short exposure (5 s) to the plasma improved the quality of the surface of the active layer for PEDOT:PSS deposition. These inverted PSCs on flexible granular NiPI films provided a power conversion efficiency of 2.4% when illuminated under AM 1.5 conditions (100 mW cm<sup>-2</sup>). The phenomenon of light absorption enhancement in those inverted PSCs was observed as indicated in reflective UV–vis, haze factor and external quantum efficiency (EQE) responses. The resulting fill factor (FF) of 0.43 is still significantly lower than the FF of 0.64 for standard devices. When compared to the planar structure, the improvement of absorbance of light and good haze factors was obtained for granular structure which suggests NiPI as a better back contact electrode through enhancing the light trapping and scattering in inverted PSCs.

© 2009 Elsevier B.V. All rights reserved.

### 1. Introduction

Polymer solar cells (PSCs) have recently received considerable attention because of their low cost, light weight, high flexibility, and solution-processability. The power conversion efficiency (PCE) of PSCs has been improved to 5% under AM 1.5G conditions [1–4] when using a bulk heterojunction (BHJ) structure comprising a blended film of

poly(3-hexylthiophene) (P3HT) as the donor and [6,6]-phenyl-C<sub>61</sub>-butyric acid methyl ester (PCBM) as the acceptor. In addition to their improved device efficiency [1–5] and lifetime [6,7], PSCs possessing inverted structures have also been investigated to further reduce production costs and to facilitate high-throughput production [8–22]. Among inverted PSCs, two major structures are studied most frequently. One employs modified layers located between the active layer and the electrodes to change the energy level of the whole device, i.e., the roles of the indium tin oxide (ITO) material (as the cathode) and the metal

\* Corresponding author. Tel.: +886 35 731873; fax: +886 35 724727.  
E-mail address: [wthagang@mail.nctu.edu.tw](mailto:wthagang@mail.nctu.edu.tw) (W.-T. Whang).

electrode (as anode) are different from those of standard PSCs systems [ITO (anode)/PEDOT:PSS/active layer/metal (cathode)] (Fig. 1A). For this inverted system, in which the roles of the electrodes are exchanged, the use of solution processing methods results in enhanced efficiency from the collocation of appropriate energy levels for the electron- and hole-collection layers [8–14]; in addition, a roll-to-roll suited module would be achieved when introducing an inject-printed metal as the anode (Fig. 1B). The second type of inverted PSC possessing a layer sequence has great promise for use as a cost-efficient roll-to-roll suited module, i.e., starting with the metallic electron contact on a plastic substrate [16–23]. The active layer is coated on the metal layer, followed by the PEDOT:PSS layer, which forms the transparent hole contact. In this inverted system, the roles of the anode and cathode are similar to those in standard cells, but the processing method employed to build the PSCs is different (Fig. 1C). Moreover, the preparation of this second type of inverted PSC would presumably provide higher efficiency and lower device fabrication costs when using ITO-free materials. Another advantage when using this inverted PSC system [22,23] with high topographical variations of metals is that it would lead to an imposed topography on the photovoltaic device; it could also be used to couple light into the film, increasing the optical length in the device. Based on these previous studies, we suspected that combining the technologies for all-solution processing with the high topographical variations of the metal and the high-conductivity of PEDOT:PSS would allow us to obtain ITO-free inverted PSCs for high-throughput production on flexible substrates.

Recently, polyimide (PI) films have become generally used components for flexible electronic devices because they exhibit high glass transition temperatures, low surface roughnesses, low coefficients of thermal expansion (CTE), and high chemical resistance under typical fabrica-

tion conditions. Surface-metallized PIs have been developed widely using various metals, including Ag, Cu, and Ni [24–27]. In a previous study [26], we developed an all-solution method for fabricating thin granular Ni films on PI (NiPI) with high adhesion and conductivity (ca.  $2778 \text{ S cm}^{-1}$ ). These NiPI films are readily fabricated through alkaline hydrolysis to open the imide rings of the pristine PI film, followed by ion exchange with Ni ions and their subsequent reduction on the PI (Fig. 2A–E).

In this paper, we report the fabrication of all-solution-processed inverted PSCs featuring NiPI as the cathode material (back contact electrode) on flexible substrates; these devices have the following configuration: PI/Ni (cathode)/titanium(diisopropoxide)bis(2,4-pentanedionate (TIPD))/P3HT:PCBM/PEDOT:PSS (anode). From the many reports describing the insertion of a buffer layer between the cathode and the active layer to improve device performances [4,28–30], we chose the solution-processable TIPD as the buffer layer in this study because Tan et al. [30] demonstrated that the TIPD interface dramatically reduces the degree of interface resistance between the cathode and the active layer. Furthermore, because the energy level of the lowest unoccupied molecular orbital (LUMO) of TIPD is ca. 3.9 eV, we suspected that it would be easy to transport electrons to the NiPI film [work function (WF) = 3.9 eV]. In addition, we developed a low-temperature fabrication process (<150 °C) to obtain high-conductivity PEDOT:PSS films in these inverted ITO-free PSCs. We readily obtained these high-conductivity PEDOT:PSS films (ca.  $283 \text{ S cm}^{-1}$ ) through spin-coating of a solvent (methoxyethanol, ME) onto pre-coated PEDOT:PSS films [31]; this method appears to be more suitable for plastic substrates because it does not require a very high-temperature (>150 °C) to remove any polyalcohol [32–37] and, thereby, decreases the likelihood of destroying the active layer. Based on the previous report, [31] the sheet resistance of PEDOT:PSS electrode (a distance effect for PED-

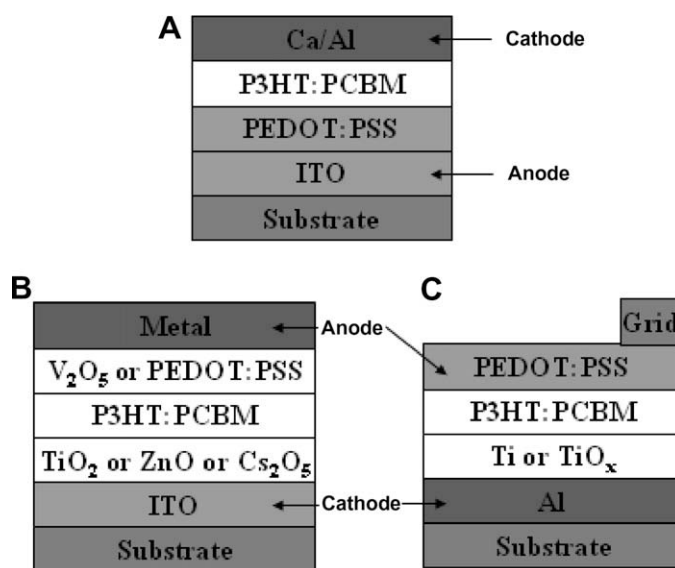


**Fig. 1.** Architectures of polymer solar cells: (A) standard, (B) inverted (in terms of the roles of the electrodes), and (C) inverted (in terms of the alternative processing structure).

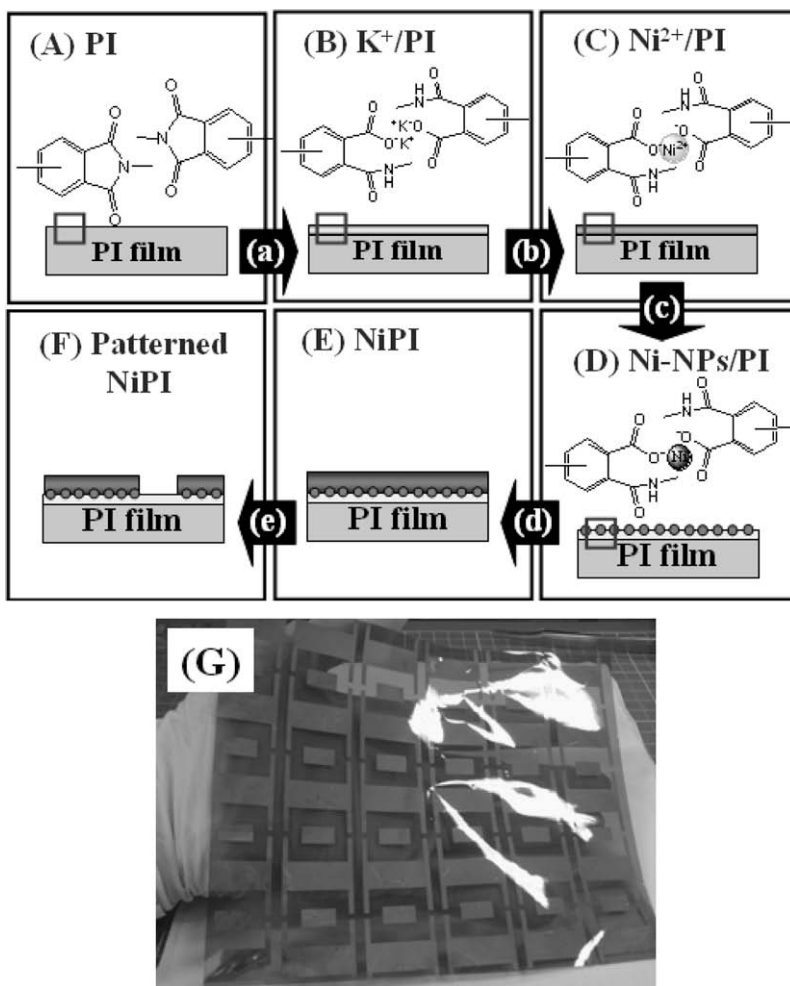


**Fig. 2.** Flow chart for the formation of the patterned NiPI film. (A) PI: pristine polyimide; (B)  $K^+$ /PI:  $K^+$ /PAA layer on PI film; (C)  $Ni^{2+}$ /PI:  $Ni^{2+}$ /PAA layer on PI film; (D) Ni-NPs/PI: Ni-NPs/PAA layer on PI film; (E) NiPI: Ni/PAA layer on PI film; (F) Patterned NiPI: patterned Ni/PAA layer on PI film; (G) photograph of the patterned NiPI. (a) Alkaline hydrolysis to open imide rings; (b) cation-exchange reaction leading to the incorporation of  $Ni^{2+}$  ions; (c) reduction of  $Ni^{2+}$  ions by aqueous  $NaBH_4$ ; (d) Ni electroless plating using an EN solution; (e) patterning of Ni through photolithography.

OT:PSS based ITO-free PSC devices) increased as the area of the device increasing, and hence decreased the device performance. The low conductivity of the PEDOT:PSS electrode is actually limited for larger area cells. Therefore, we further deposited a Au grid (thickness at 100 nm) onto the PEDOT:PSS films to efficiently collect holes and efficiently increase the sheet conductivity of the transparent electrode.

## 2. Experimental

### 2.1. Nickelized polyimide films (cathodes and substrates)

The process for the direct all-wet-chemical treatment of Ni-coated conductive films was performed according to the procedure outlined in Fig. 2A–F. The PI films were synthesized from pyromellitic dianhydride (PMDA; from TCI) and 4,4'-diaminodiphenylether (ODA, 98%; from Aldrich); the experimental details for fabricating the PI and nickelized PI films are available elsewhere [26]. Briefly, the PI films

were first immersed in 5 M aqueous KOH at 25 °C for 7 min and then rinsed with deionized water. Next, the  $K^+$  counterions associated with the opened imide rings on the surface of the PI films were exchanged with  $Ni^{2+}$  ions through immersion in 50 mM aqueous nickel sulfate at 25 °C for 5 min, followed by rinsing with deionized water. The surface  $Ni^{2+}$  ions were then reduced in aqueous  $NaBH_4$  (0.2 g/100 ml deionized water) at 25 °C for 5 min to form Ni nanoparticles on the PI surface (Ni-NPs/PI films), which were then rinsed with deionized water. The Ni NP-seeded PI films were immersed in an electroless nickel bath (EN solution) at 50 °C for 8 min to form thin Ni layers on the PI films (NiPI). The EN solution was prepared from a 4:1 (v/v) mixture of a Ni stock solution [nickel sulfate (40 g l<sup>-1</sup>), sodium citrate (20 g l<sup>-1</sup>), and lactic acid (10 g l<sup>-1</sup>) in deionized water] and a DMAB solution (1 g l<sup>-1</sup> in deionized water). A cartoon representation and a photograph of the patterned NiPI are presented in Fig. 2F and G, respectively. The NiPI films have long-term air stability in the atmosphere. Prior to the deposition of

the photoactive layer, the NiPI films were cleaned with organic solvents.

## 2.2. Active-layer materials

Because of the large differences in the values of the contact angles and surface energies of Ni and PI surfaces (Table 1), the solution-processable titanium chelate TIPD (from Aldrich) was pre-coated as the cathode buffer layer on the patterned NiPI film surfaces to facilitate the fabrication of high-quality active layers. Next, a blend [1:0.8 (w/w), 17 mg ml<sup>-1</sup> in dichlorobenzene (DCB)] of P3HT (Rieke Met. Inc.) and PCBM was stirred overnight in DCB, filtered through a 0.2 μm poly(tetrafluoroethylene) (PTFE) filter, and then spin-coated (500 rpm, 60 s) on top of the NiPI films.

## 2.3. High-conductivity PEDOT:PSS films (anodes)

The high-conductivity PEDOT:PSS anodes were prepared using a two-step method [31]. In the first step, a 95:5 (w/w) mixture of PEDOT:PSS solution (HC V4; from H. C. Starck) and dimethyl sulfoxide (DMSO; from Aldrich) was filtered through a 0.45 μm filter prior and then deposited (spin-coating at 4000 rpm in the air) onto the active layers with a mild oxygen plasma exposure for 5 s (plasma cleaner PDC-32G, Harrick Scientific, Ossining, NY) at a thickness ca. 50 nm. In the second step, the surface-modifying solvent, ME, was spin-coated onto the pristine PEDOT:PSS films at 3000 rpm, which were then dried at 100 °C for 5 min inside a glove box. The device was completed by coating a 100 nm-thick layer of Au as a metal grid and a mask to improve hole-collection and define the active area, respectively. The cell was then encapsulated using UV-curing glue (Nagase, Japan). The active area of each photovoltaic (PV) cell was 0.036 cm<sup>2</sup>. Fig. 4A displays the architecture of the inverted ITO-free polymer/fulerene solar cells.

## 2.4. Instrumentation

The NiPI films were transferred within 3 min of their formation into the sample-loading chamber of an ultraviolet photoelectron spectroscopy (UPS) system. UPS (VG ESCA-

**Table 1**

Contact angles and surface energies obtained after performing the inverted fabrication process.

Sample	H <sub>2</sub> O	C <sub>2</sub> H <sub>4</sub> I <sub>2</sub>	Surface energy (mJ m <sup>-2</sup> )
PI	75.5	41.1	39.1
NiPI	104.9	38.0	58.4
TNiPI	87.0	33.6	46.6
PTNiPI	108.2	60.6	37.0
PTNiPI <sup>a</sup>	55.8	32.7	47.4
HCV4	48.0	29.5	52.1

PI: Pristine polyimide film.

NiPI: Ni/PI film obtained after annealing at 150 °C for 30 min.

TNiPI: Sample obtained after depositing TIPD solution on the NiPI and then annealing at 70 °C for 5 min.

PTNiPI: Sample obtained after depositing the P3HT:PCBM film on the TNiPI and then annealing at 140 °C for 15 min.

HCV4: Sample obtained after depositing the PEDOT:PSS film on the glass substrate and then annealing at 100 °C for 5 min.

<sup>a</sup> After mild air plasma treatment for 5 s.

Lab 250, HeI *hν* = 21.2 eV) spectra were recorded at a sample bias of -5.0 V to observe the secondary electron cutoff, from which the work function could be derived from the width of the Fermi edge of a Au substrate. XPS spectra were recorded using a VG Scientific Microlab 350 spectrometer operated in the constant analyzer energy mode with a pass energy of 50 eV and Mg · Kα (1253.6 eV) radiation as the excitation source (with normal emission detected). The sheet resistances of the PEDOT:PSS films were measured using a four-point probe; the average of the measured values is reported. The transmittance spectra were recorded using an HP8453 UV-vis spectrometer. Contact angles and surface energies were measured and calculated using the geometric mean approximation (GMA) and a FTA-200 dynamic contact analyzer operated with H<sub>2</sub>O and CH<sub>2</sub>I<sub>2</sub> as the two standard liquids. The crystalline phase of samples was characterized using a BEDE D1 grazing incidence X-ray diffractometer (GIXRD) and Cu · Kα radiation. The incident angle of the X-ray beam was fixed at 0.5°. The surface morphologies and phase changes of the PEDOT:PSS films were analyzed using a VEECO DICP-II atomic force microscope (AFM) operated in the tapping mode (Si tips on Si cantilevers having a spring constant of 2 N m<sup>-1</sup> and a set point of ca. 0.8–0.9) in the air. A JEOL JSM-6500F scanning electron microscope (SEM) was employed to investigate the thicknesses of the PEDOT:PSS films. Samples for transmission electron microscopy (TEM) analysis were prepared through microtoming with a Leica Ultracut Uct apparatus into 90 nm-thick slices that were placed onto a 200-mesh carbon-coated Cu TEM grid (Agar Sci., Inc.). TEM images were recorded using a JEOL-2010 transmission electron microscope and an internal charge-coupled device (CCD) camera. Current-voltage (*I*-*V*) curves of the PSC devices were measured using a computer-controlled Keithley 2400 source measurement unit (SMU) equipped with a Peccell solar simulator under AM 1.5 illumination (100 mW cm<sup>-2</sup>). The spectral irradiance data of the light source was similar to the AM 1.5G solar spectrum (spectral mismatch <5% in the range 350–800 nm). The illumination intensity was calibrated using a standard Si photodiode detector equipped with a KG-5 filter. All of these measurements were performed under an ambient atmosphere at room temperature. All of these inverted PSCs are identified by "PTXNiPI-X", the first number denoting to the incorporating different concentrations of TIPD (wt%), the follow number denoting to the thermal annealing time (min). The absorption spectra were recorded using a Hitachi U-4100 UV-vis spectrometer with the integrating sphere. The planar and granular substrates were characterized by optical spectrometry (MFS-530 commercialized by Hong-Ming Technology): the total and scattered reflectivity have been measured and the haze factors (*H<sub>R</sub>*(λ)) have been calculated for each of the substrates according to the equation, *H<sub>R</sub>*(λ) = *R*scat(λ)/*R*tot(λ), and these optical measurements have been performed in air.

## 3. Results and discussion

To examine the feasibility of using NiPI as the cathode (back contact electrode), we used UPS to determine that



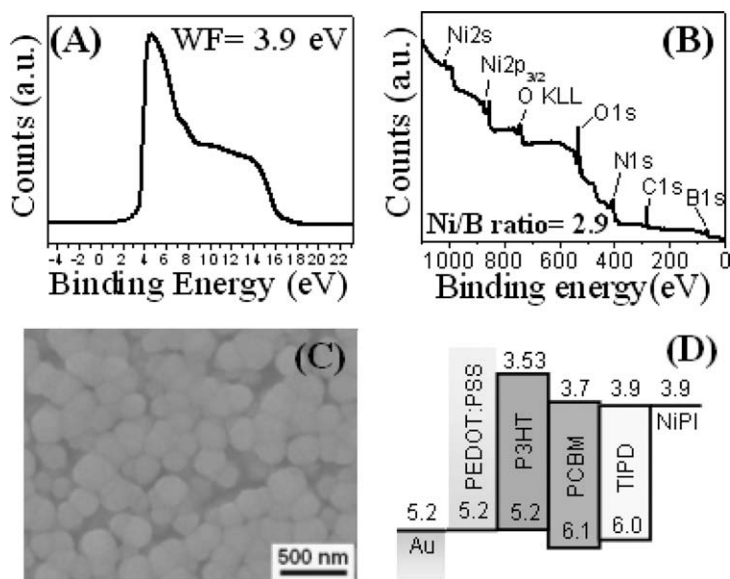


**Fig. 3.** (A) Photoelectron spectrum of NiPI film. (B) XPS spectrum of NiPI surface. (C) SEM image of NiPI surface. (D) Schematic representation of the energy levels of an ITO-free inverted PSC on PI.

the WF of the surface-nickelized PI (NiPI) was 3.9 eV, i.e., it differs from that of pure Ni (Fig. 3A) [38]. Because this value is lower than that of the Al cathode (ca. 4.2 eV), it appeared suitable for application as the back contact electrode in inverted PSCs. To understand why there was a difference in the WFs of NiPI and pure Ni, we performed an XPS survey and then obtained the Ni/B ratio of NiPI (ca. 2.9) by using the Shirley method to estimate the peak areas of the atom contents on the NiPI surface in Fig. 3B. According to previous reports [26,27] and the results of this XPS analysis, in addition to a small amount of oxygen (representing native oxides or  $B_2O_3$ ) formed on the NiPI surface, we suspect that the Ni–B component, which arose from the use of dimethylamine borane (DMAB) as the reductant in the Ni electroless deposition process, was responsible for the WF of the NiPI film to differ from that of pure Ni. The SEM image in Fig. 3C reveals that the granular NiPI consisted of fine particles (ca. 200–300 nm) with a continuous and interconnected network. Fig. 3D provides a schematic energy level diagram. The WF of NiPI allows efficient electron transfer from the LUMO of PCBM. Based on the previously report [30], the TIPD layer could improve the electron collection and reduce the interface resistance between the active layer and the metal cathode. From the view of energy level, the WF of TIPD matches the transport levels of the respective charge carriers for efficient charge transferring, however, other effects like oxide layers, dipole layers or the interface morphology of the photoactive layer might affect the charge injection. Table 1 summarizes the contact angle (CA) and surface energy (SE) data. On the surface of patterned NiPI, the difference in the  $H_2O$  contact angles of PI (CA =  $75.5^\circ$ ) and Ni (CA =  $104.9^\circ$ ) was dramatic. We attempted to improve the device performance through solvent annealing (slow drying) with DCB, a solvent with a high-boiling-point, to enhance the degree of microcrystalline lamellar stacking in the solid state packing of the ac-

tive layer [39]. We found, however, that the slow drying process had a negative effect on the quality of the P3HT:PCBM film when using the patterned NiPI as the substrate. After spin-coating the P3HT:PCBM solution onto the patterned NiPI film, droplets of P3HT:PCBM tended to aggregate on the Ni surface through slow growth and the thickness of the active layer became non-uniform. To overcome this problem, we pre-coated the TIPD onto the NiPI surface. The TIPD-modified, patterned NiPI film, which we refer to as TNiPI, had a contact angle of  $87.0^\circ$ ; therefore, droplets of the P3HT:PCBM solution covered the TNiPI surface more completely, resulting in uniform P3HT:PCBM films that we name PTNiPI.

Because of the large variation in the values of CA of P3HT:PCBM and PEDOT:PSS (Table 1), the deposition of PEDOT:PSS on the highly hydrophobic P3HT:PCBM surface requires a preliminary treatment process to ensure wettability and adhesion. Chaudhary et al. [40] demonstrated that short exposure (5 s) to Ar plasma can effectively tailor the wettability of P3HT:PCBM layers for subsequent deposition of single-wall carbon nanotubes (SWNT) from an aqueous solution. In our present study, oxygen plasma treatment was more convenient than Ar plasma treatment; therefore, we subjected our PTNiPI film to a short (5 s exposure) oxygen plasma treatment to facilitate the deposition of PEDOT:PSS on the active layer. The oxygen plasma-treated PTNiPI film exhibited values of CA and SE of ca.  $55.8^\circ$  and  $47.4 \text{ mJ m}^{-2}$ , respectively, similar to those of the PEDOT:PSS film. To determine the influence of the 5 s oxygen plasma treatment on the surface of the active layer, we analyzed the performance of standard PSC structures (glass/ITO/PEDOT:PSS/P3HT:PCBM/Ca/Al) formed with and without plasma treatment. The variation in the PCE was less than ca. 0.1%, arising mostly from a slight loss in the current density; the values of  $V_{oc}$  and the fill factor (FF) were unaffected, as revealed by the  $I$ – $V$  characteristics

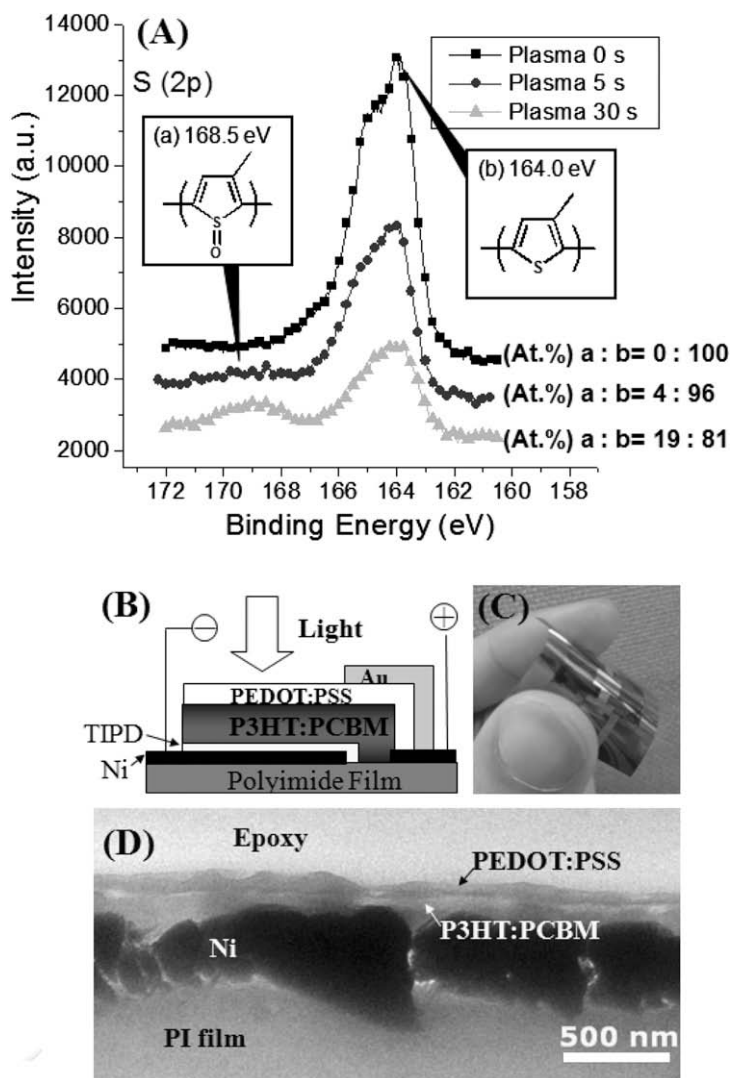


**Fig. 4.** (A) S(2p) core level spectra of P3HT:PCBM film (1:0.8 w/w) with plasma treatment for various seconds. (B) Architecture of an inverted PSC featuring an inverted sequence on NiPI as the back contact electrode. (C) Optical image of an inverted PSC on NiPI. (D) TEM cross-sectional image of an inverted PSC on NiPI. Scale bars, 500 nm.

**Table 2**

Sheet resistances and conductivities of PEDOT:PSS, ITO, and NiPI films.

Sample	Film thickness (nm)	Transmittance at 550 nm (%)	Sheet resistance <sup>c</sup> ( $k\Omega \text{ sq}^{-1}$ )	Conductivity <sup>c</sup> ( $S \text{ cm}^{-1}$ )
H	90 <sup>a</sup>	96.7	22.00	5
HD	45 <sup>a</sup>	96.9	1.310	170
HDM	45 <sup>a</sup>	96.4	0.785	283
ITO	200 <sup>a</sup>	89.6	0.007	7143
NiPI	300 <sup>b</sup>	–	0.012	2778

H: Thin film of PEDOT:PSS (HCV4) on the glass substrate.

HD: Thin film obtained from a mixture of HCV4 (95 wt%) and DMSO (5 wt%) on the glass substrate.

HDM: ME-modified HD thin film on the glass substrate.

<sup>a</sup> Film thickness identified using SEM.

<sup>b</sup> Film thickness identified using TEM.

<sup>c</sup> Values determined using a four-probe point.

(Table 3). The treatment of oxygen plasma might predominantly destroy the P3HT phase, but not the PCBM phase. As the consequence, the electron injection interface might still be working for standard cell. However, this may significant effect the anode interface. To investigate if and how the effect through oxygen plasma treatment, we employed XPS measurements to quantitative determine the thiophene defects through oxygen plasma treatment (Fig. 4A). The S(2p) core level spectra showed that there were 96% thiophene (at 164 eV) preserved and only 4% thiophene defects (at 168.5 eV) were observed through 5 s oxygen plasma treatment on the active layer surface. In the inverted geometry, this would lead to a destruction of the anode interface; however the effect is not significant as a result of XPS spectra.

To apply PSCs in an economical roll-to-roll-suited mod-  
ule, the major requirement to reduce the cost of produc-

**Table 3**  
Performance of PSCs under AM 1.5 illumination ( $100 \text{ mW cm}^{-2}$ ).

Sample	Structure	$J_{sc}$ ( $\text{mA cm}^{-2}$ )	$V_{oc}$ (V)	FF	PCE (%)
Standard <sup>a</sup>	Standard	9.2	0.64	0.63	3.7
Standard-p <sup>a</sup>	Standard	8.8	0.63	0.64	3.6
PT1NiPI-5 <sup>b</sup>	Inverted	8.3	0.58	0.26	1.2
PT3NiPI-5 <sup>b</sup>	Inverted	9.0	0.54	0.29	1.4
PTONiPI-15 <sup>b</sup>	Inverted	5.4	0.43	0.25	0.6
PT1NiPI-15 <sup>b</sup>	Inverted	9.2	0.59	0.37	2.0
PT3NiPI-15 <sup>b</sup>	Inverted	9.3	0.60	0.43	2.4
PT7NiPI-15 <sup>b</sup>	Inverted	5.2	0.61	0.35	1.1
PT15NiPI-15 <sup>b</sup>	Inverted	4.4	0.59	0.24	0.6

Standard: Standard PSC structure without plasma treatment.  
Standard-p: Standard PSC structure with plasma treatment on the active layer.

<sup>a</sup> Active area =  $0.04 \text{ cm}^2$ .

<sup>b</sup> Active area =  $0.036 \text{ cm}^2$ .

tion is substitution of a cheap material in place of the ITO electrode. In a previous report, Zimmermann et al. [18] constructed an ITO-free PSC module that comprised PSCs on metal-coated plastic substrates with an inverted layer sequence. Based on their module concept, we examined the solution processing of NiPI, our surface-nickelized PI film, as the cathode/substrate and the high-conductivity PEDOT:PSS as the anode for the all-solution processing of PSCs (Fig. 4B). Fig. 4B–D presents the structure, optical and TEM images of the inverted PSC cell on NiPI. Although the TIPD layer was too thin to identify, the cross-sectional TEM image of the device clearly indicates the presence of individual layers without interlayer mixing (Fig. 4D). The PSCs had the following device structure: PI/Ni ( $385 \text{ nm} \pm 77 \text{ nm}$ )/TIPD/P3HT:PCBM ( $100 \text{ nm}$ )/PEDOT:PSS ( $45 \text{ nm}$ ).

The conductivity of NiPI and ITO were  $2778$  and  $7143 \text{ S cm}^{-1}$ , respectively (Table 2). The resistive loss of NiPI could be ignored for small cell device. Nonetheless, NiPI layer is actually limited for larger area cells similar to the ITO based devices. To form a transparent conducting anode, we employed the low-temperature processing of high-conductivity PEDOT:PSS. When processing with a polyalcohol, the conductivity of PEDOT:PSS films can be enhanced for their application in PSCs. Although adding a polyalcohol would obviously decrease the sheet resistance of the PEDOT:PSS films, higher processing temperatures ( $>140 \text{ }^\circ\text{C}$ ) and longer thermal treatment times are necessary to remove the high-boiling-point ( $>200 \text{ }^\circ\text{C}$ ) additive [32–37], which may damage the P3HT/PCBM blends in our inverted structure. Herein, we selected DMSO and ME as solvents to investigate their ability to enhance the conductivity of PEDOT:PSS at low processing temperatures. The pristine PEDOT:PSS film (H; HC V4 from H. C. Starck) had the lowest conductivity ( $5 \text{ S cm}^{-1}$ ). When we added 5 wt% DMSO into this pristine PEDOT:PSS aqueous solution, the conductivity of the HD film was enhanced to  $170 \text{ S cm}^{-1}$ . Furthermore, consistent with our results from a previous study [31], surface solvent-treatment of HD films with ME (HDM) led to a dramatic increase in the conductivity of the PEDOT:PSS to  $283 \text{ S cm}^{-1}$  and a corresponding processing temperature lower than that required for the polyalcohol system.

If transparent electrodes are to be used in PV devices, they must have high transparency in the visible region. Thicker PEDOT:PSS films will lead to transmittance and vertical conductivity problems. We observed that the transmittances of the thin PEDOT:PSS films ( $<100 \text{ nm}$ ) of H, HD, and HDM on glass (each ca. 96%) were better than that of ITO (ca. 89.6%; Table 2). From a comparison of the electrical conductivities of ITO (same as the anode of a standard cell), and NiPI, we observed that the highest conductivity of PEDOT:PSS (HDM) was enhanced to  $283 \text{ S cm}^{-1}$  with a order less than ITO and NiPI. We suspect that combining a suitable metal grid (such as a metal grating or random metal nanowire mesh) with HDM film may be compatible with the future development of flexible PSCs [41,42].

Because TIPD was present as an ultrathin layer on NiPI (Fig. 4D), it was necessary for us to determine the thickness of P3HT:PCBM on the highly topographically variant NiPI to obtain the optimized parameters for these inverted PSCs, because the effect of a thinner active layer (higher speed of coating of the P3HT:PCBM solution) on the imposed topography of the anode would increase the risk of creating short circuits (i.e., lower the efficiency of the device) [22]. If the P3HT:PCBM solution was spin-coated on TNiPI for 700 rpm, the thinner active layer film on the imposed topography of anode would increase the risk of creating short circuits to lower the efficiency of the device. As the result of the device performance and the TEM cross-sectional image, the minimum active layer film thickness was suggested to be ca. 200 nm. Thus, under the optimal conditions for spin-coating of the P3HT:PCBM solution onto TNiPI (500 rpm), we investigated the concentrations with respect to the thickness of the TIPD layer of the whole devices. Prior to the coating of the photoactive layer, the TIPD layers were treated at the temperature of  $80 \text{ }^\circ\text{C}$  and  $160 \text{ }^\circ\text{C}$  for 5–30 min to investigate the temperature effect of the TIPD film without a superimposed effect of the active layer. Similar cell performances were obtained as the temperature and annealing condition change. First, to understand the thermal stability of the TIPD-coated devices, we examined the device performances after employing various thermal annealing times. Table 3 summarizes the device performance under AM 1.5 illumination at an intensity of  $100 \text{ mW cm}^{-2}$ . The device formed using an interfacial layer of 3.75 wt% TIPD (PT3NiPI-5) and a short thermal annealing time (5 min;  $140 \text{ }^\circ\text{C}$ ), exhibited poor performance:  $V_{oc} = 0.54 \text{ V}$ ;  $J_{sc} = 9.0 \text{ mA cm}^{-2}$ ,  $\text{FF} = 0.29$ ;  $\text{PCE} = 1.4\%$ . After increasing the thermal annealing time at  $140 \text{ }^\circ\text{C}$  to 15 min, the values of  $V_{oc}$ ,  $J_{sc}$ , and FF all increased, thereby improving the value of PCE to 2.4%. When TIPD was incorporated at 1.88 wt% (PT1NiPI-15), we obtained similar results, i.e., improved performance after longer periods of thermal treatment; after thermal annealing for 15 min, the values of  $V_{oc}$ ,  $J_{sc}$ , FF, and PCE were 0.59 V,  $9.2 \text{ mA cm}^{-2}$ , 0.37, and 2.0%, respectively. Consistent with previous results, this TIPD-coated NiPI was stable to thermal annealing at  $140 \text{ }^\circ\text{C}$  for several minutes. We suspect that this TIPD-coated NiPI would be more suitable than the corresponding ITO/PET system [43,44] for long-time high-temperature annealing.

To compare the performance of devices incorporating different concentrations of TIPD (0.94, 1.88, 3.75, 7.5, and 15 wt%), we performed AFM measurements to determine the underlying mechanism of TIPD incorporation on NiPI. We observed interesting morphologies with high topographical variations for the pristine NiPI and TIPD-coated NiPI surfaces (Fig. 5). After coating with TIPD at 0.94, 3.75, and 15 wt%, the root-mean-square roughness (Rms) changed from 33.8 nm for pristine NiPI to 24.6, 24.3, and 25.3 nm, respectively. Thus, coating with different TIPD concentrations did not have a significant effect on the value of the Rms. Furthermore, in the phase image of NiPI, the topographical variations of granular Ni films were expressed as a darker edge effect (Fig. 5b). After coating TIPD onto NiPI, we expected the phase changes to be more obvious at the darker edges of the granular NiPI. The previous study have been reported [17] that charge collection could

be enhanced by using a thin layer of Ti/TiO<sub>x</sub> on top of the Al electrode; in the absence of this Ti compound coating, the oxide formed on Al blocked charge transport. For our TIPD systems, even a small amount of oxygen (representing native oxides or B<sub>2</sub>O<sub>3</sub>) formed on the NiPI surface (Fig. 3B), we suspected that a higher concentration of the coating TIPD solution (3.75 wt%) would be more effective at enabling charge collection in the inverted cells than would a coating of 0.94 wt%. From an analysis of the PSCs' performances, we found that higher concentrations of TIPD led to improved PCE, presumably because a more uniform TIPD layer on NiPI enhanced electron transport to the anode (Fig. 5c–f). Increasing the concentration of TIPD from 3.75 to 15 wt% decreased the current density, which led to poorer performance. Based on the similar values of  $V_{oc}$  of the PT3NiPI-15, PT7NiPI-15, and PT15NiPI-15 devices (Table 3 and Fig. 6), it appears that exceeding the critical con-

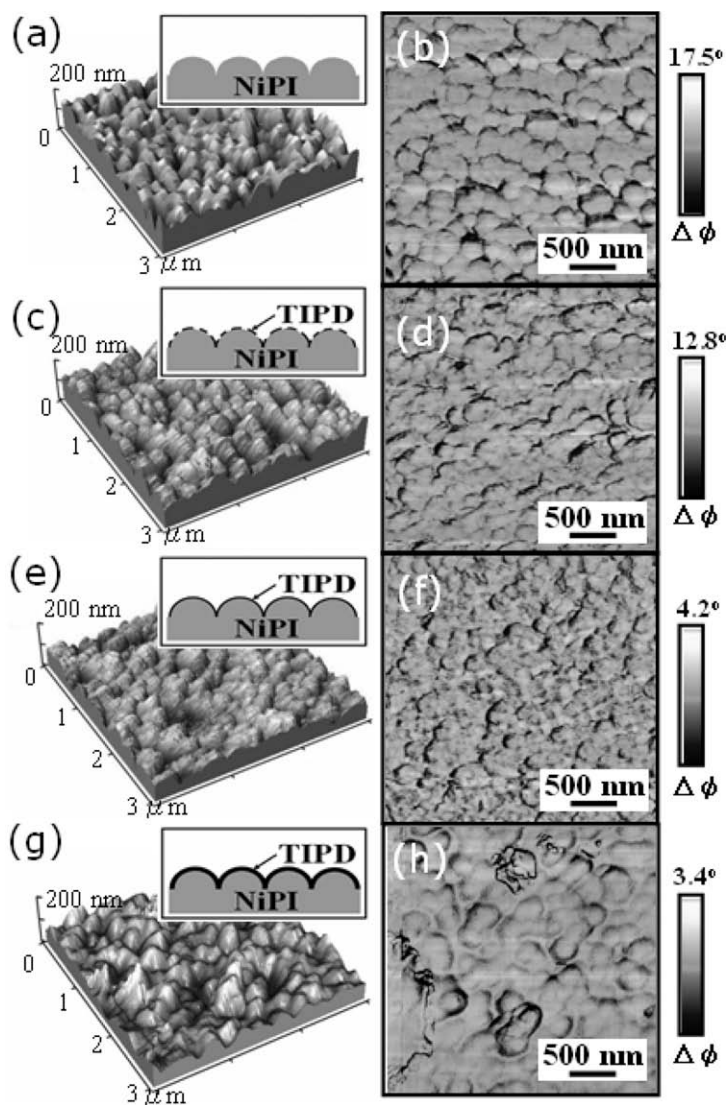


**Fig. 5.** (a, c, e, g) Topographies (including cartoon representations) and (b, d, f, h) phase images of NiPI and TIPD-modified NiPI films. (a, b) NiPI: pristine NiPI film; (c, d) TONiPI: TIPD (0.94 wt%) on NiPI film; (e, f) T3NiPI: TIPD (3.75 wt%) on NiPI film; (g, h) T15NiPI: TIPD (15 wt%) on NiPI film. Scale bars, 500 nm.

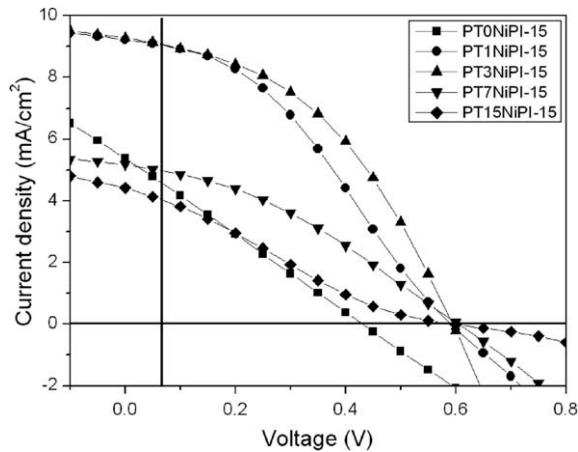


**Fig. 6.** *I*–*V* characteristics of inverted PSCs under AM 1.5 illumination ( $100 \text{ mW cm}^{-2}$ ).

centration of TIPD (3.75 wt%) led to a lower variation of the angles in the phase images (cf. Fig. 5g and h), which would block the degree of electron transport to NiPI and, thereby, decrease the current density.

Roman et al. [23] have reported that the light-trapping effects from active layers on the periodic Al metal nanostructures, and those structures could further enhance PSCs performance. Comparing the dimension of the granu-

lar NiPI with the Al grating structure, the NiPI films were believed to have the same effect in PSCs. To complement the observed degree of light confinement in whole devices, herein, we performed reflective UV–vis, reflection haze factor ( $H_R$ ) [45] and external quantum efficiency (EQE) measurements of overall inverted PSCs process of the plane AlPI and the granular NiPI films. Fig. 7A and B showed the SEM image of planar AlPI and granular NiPI films, respectively. In the reflective UV–vis spectra of absorbance, Fig. 7C represents that the granular NiPI films were well-adapted to improve the light-trapping in 200 nm thick P3HT:PCBM cells. Based on the previous reports, [46,47] the refractive indices of PEDOT:PSS and P3HT:PCBM were 1.1–1.6 and 1.6–2.2, respectively, in the range 400–800 nm. The higher  $H_R$  was obtained from rougher NiPI structure through reflective haze factor measurements (Fig. 8A). The total internal reflection could occur where light travels from a P3HT:PCBM film with a higher refractive index to the PEDOT:PSS film with a lower refractive index. The absorption, haze factor and EQE analysis, Figs. 7C–E, C–f and 8A show that there were more light absorptions in granular NiPI of devices (PT3NiPI device) than the planar structures of electrode (PT3AlPI device) in the range of wavelengths 400–650 nm. The beam of light scattering on the granular NiPI shows better light confinements than planar AlPI of devices. Therefore, a light trapping effect were presumed by the NiPI layer in the range 400–800 nm, hence the EQE of P3HT devices show enhance-

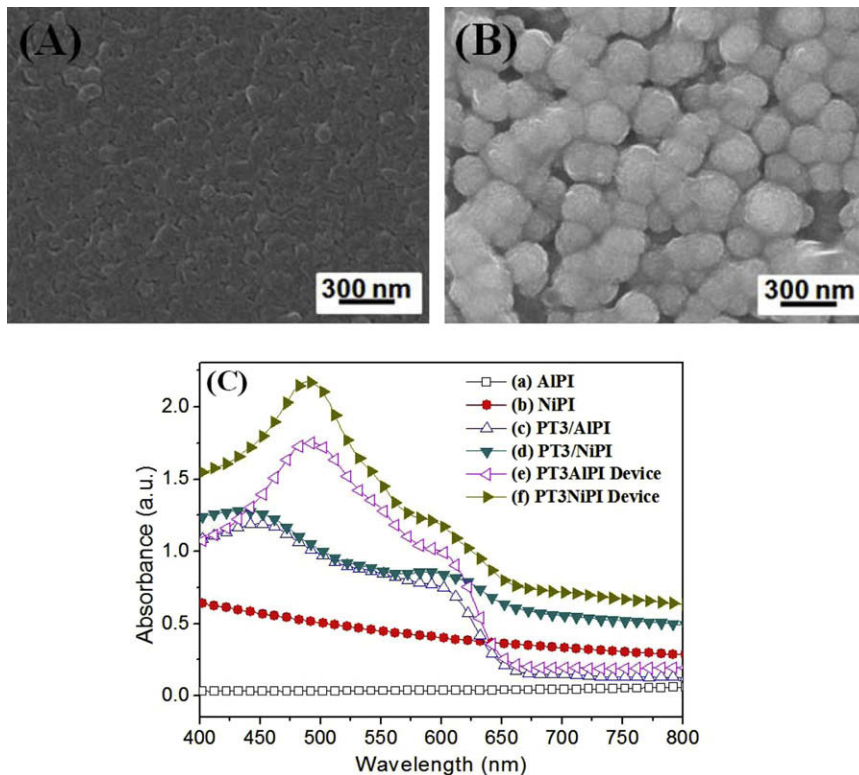


**Fig. 7.** SEM images (top-view) of different structure of cathodes. (A) AlPI: planar AlPI, (B) NiPI: granular NiPI. (C) Reflective UV–vis spectra of films on different structures of cathodes. (a) AlPI: planar AlPI, (b) NiPI: granular NiPI, (c) PT3/AlPI: P3HT:PCBM/TIPD(3.75 wt%)/AlPI, (d) PT3/NiPI: P3HT:PCBM/TIPD(3.75 wt%)/NiPI, (e) PT3AlPI device: PEDOT:PSS/PT3/AlPI, (f) PT3NiPI device: PEDOT:PSS/PT3/NiPI.

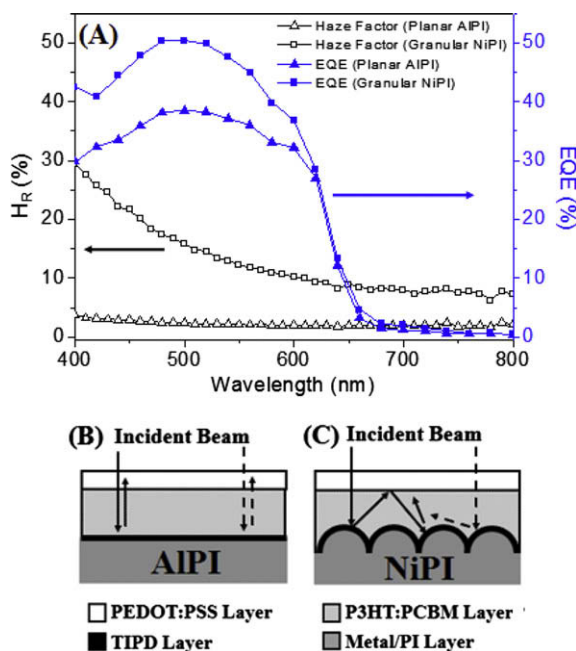


**Fig. 8.** (A) Reflection haze factors for different structure of cathodes and the EQE spectra of inverted PSCs on different structure of cathodes. Cartoon representations for inverted PSCs illuminated on different structure of cathodes. (B) Planar AlPI, (C) granular NiPI.

ment in the range 400–620 nm (Fig. 8A). Although different materials of cathodes may cause to the different device performance, in this study, the comparison of haze factors and EQE results, give some information of optical path length enhancement in the active layer. The Rms of coated photoactive was ca. 5.6 nm and its surface roughness was smoother than NiPI substrate (Rms  $\sim$  33.8 nm). The cross-sectional TEM image showed the thickness of the photoactive layer was ca. 200 nm and the granular NiPI film can actually be well covered by the photoactive layer. The thin film architecture of device suggests that the variation in the film thickness would not be a problem for charge carrier extraction. As shown in Fig. 8B and C, the cartoon illustration summarized the representations of light-reflection and light-scattering properties in PSCs, and the schematic representations can be presumed that, in the active layer, rougher NiPI would induce better of light trapping than planar AlPI.

#### 4. Conclusions

We have developed a procedure for the all-solution processing of inverted PSCs on PI substrates. In this approach, the solution processing led to the chemical formation of granular Ni thin films with high-conductivity (ca.  $2777.8 \text{ S cm}^{-1}$ ) and a suitable WF for use as back contact cathodes in PSCs. We used a TIPD solution to modify the surface energy of the patterned NiPI film prior to further P3HT:PCBM coating. An analysis of the values of PCE revealed that a suitable concentration of the TIPD coating led to improved PV performance. After performing a mild

oxygen plasma treatment for 5 s on the P3HT:PCBM surface, the active layer was appropriately modified for further coating with PEDOT:PSS. Moreover, we further investigated the low-temperature fabrication of high-conductivity PEDOT:PSS films by employing DMSO and ME as additives; using this approach, we obtained a high-conductivity (ca.  $283.1 \text{ S cm}^{-1}$ ) HDM film after thermal treatment at just  $100^\circ\text{C}$  for 5 min. The ITO-free inverted PSCs incorporating HDM films as anodes and TNiPI as the modified layer/cathodes exhibited high performance, with the PCE reaching 2.4% under AM 1.5 illumination ( $100 \text{ mW cm}^{-2}$ ). Although the deposition of Au grids (thickness at 100 nm) was helpful for decreasing the distance effect of PEDOT:PSS layer (hole-collection), the FF of 0.43 is still significantly lower than the FF of 0.64 for standard devices. It was believed that higher conductivity of NiPI films and PEDOT:PSS films still need for further improving the device performance. As the results of the absorption, haze factor and EQE responses, the granular NiPI was presumed to be a better electrode/substrate through enhancing the light scattering and trapping in inverted PSCs.

#### Acknowledgement

We thank the National Science Council (Project NSC 97-2221-E-009-012-MY3), ROC, for financial support.

#### References

- [1] J.Y. Kim, S.H. Kim, H.H. Lee, K. Lee, W. Ma, X. Gong, A.J. Heeger, *Adv. Mater.* 18 (2006) 572.
- [2] S.S. Kim, S.I. Na, J. Jo, G. Tae, D.Y. Kim, *Adv. Mater.* 19 (2007) 4410.
- [3] J.Y. Kim, K. Lee, N.E. Coates, D. Moses, T.Q. Nguyen, M. Dante, A.J. Heeger, *Science* 317 (2007) 222.
- [4] M.D. Irwin, D.B. Buchholz, A.W. Hains, R.P.H. Chang, T.J. Marks, *Proc. Natl. Acad. Sci. USA* 105 (2008) 2783.
- [5] C.P. Chen, S.H. Chan, T.C. Chao, C. Ting, B.T. Ko, *J. Am. Chem. Soc.* 130 (2008) 12828.
- [6] X. Yang, J. Loos, S.C. Veenstra, W.J.H. Verhees, M.M. Wienk, J.M. Kroon, M.A.J. Michels, R.A.J. Janssen, *Nano Lett.* 5 (2005) 579.
- [7] F.C. Krebs, K. Norrman, *Prog. Photovolt: Res. Appl.* 15 (2007) 697.
- [8] M.S. White, D.C. Olson, S.E. Shaheen, N. Kopidakis, D.S. Ginley, *Appl. Phys. Lett.* 89 (2006) 143517.
- [9] C. Waldauf, M. Morana, P. Denk, P. Schilinsky, K. Coakley, S.A. Choulis, C.J. Brabec, *Appl. Phys. Lett.* 89 (2006) 233517.
- [10] G. Li, C.W. Chu, V. Shrotriya, J. Huang, Y. Yang, *Appl. Phys. Lett.* 88 (2006) 253503.
- [11] H.H. Liao, L.M. Chen, Z. Xu, G. Li, Y. Yang, *Appl. Phys. Lett.* 92 (2008) 173303.
- [12] R. Steim, S.A. Choulis, P. Schilinsky, C.J. Brabec, *Appl. Phys. Lett.* 92 (2008) 093303.
- [13] T. Ameri, G. Dennler, C. Waldauf, P. Denk, K. Forberich, M.C. Scharber, C.J. Brabec, K. Hingerl, *J. Appl. Phys.* 103 (2008) 084506.
- [14] B.Y. Yu, A. Tsai, S.P. Tsai, K.T. Wong, Y. Yang, C.W. Chu, J.J. Shyue, *Nanotechnology* 19 (2008) 255202.
- [15] S.K. Hau, H.L. Yip, O. Acton, N.S. Baek, H. Ma, A.K.Y. Jen, *J. Mater. Chem.* 18 (2008) 5113.
- [16] T. Nyberg, *Synth. Met.* 140 (2004) 281.
- [17] M. Glatthaar, M. Niggemann, B. Zimmermann, P. Lewer, M. Riede, A. Hinsch, J. Luther, *Thin Solid Films* 491 (2005) 298.
- [18] B. Zimmermann, M. Glatthaar, M. Niggemann, M.K. Riede, A. Hinsch, A. Gombert, *Sol. Energy Mater. Sol. Cells* 91 (2007) 374.
- [19] K. Tvingstedt, O. Inganäs, *Adv. Mater.* 19 (2007) 2893.
- [20] V. Kažukauskas, M. Pranaitis, F. Kajzar, M. Glatthaar, A. Hinsch, *Mol. Cryst. Liquid Cryst.* 484 (2008) 373.
- [21] J. Kim, D.Y. Khang, J.H. Kim, H.H. Lee, *Appl. Phys. Lett.* 92 (2008) 133307.
- [22] K. Tvingstedt, N.K. Persson, O. Inganäs, *Appl. Phys. Lett.* 91 (2007) 113514.

- [23] L.S. Roman, O. Inganäs, T. Granlund, T. Nyberg, M. Svensson, M.R. Andersson, J.C. Hummelen, *Adv. Mater.* 12 (2000) 189.
- [24] K. Akamatsu, S. Ikeda, H. Nawafune, *Langmuir* 19 (2003) 10366.
- [25] S. Ikeda, H. Yanagimoto, K. Akamatsu, H. Nawafune, *Adv. Funct. Mater.* 17 (2007) 889.
- [26] Y.S. Hsiao, W.T. Whang, S.C. Wu, K.R. Chuang, *Thin Solid Films* 516 (2008) 4258.
- [27] Y. Matsumura, Y. Enomoto, M. Sugiyama, K. Akamatsu, H. Nawafune, *J. Mater. Chem.* 18 (2008) 5078.
- [28] A. Hayakawa, O. Yoshikawa, T. Fujieda, K. Uehara, S. Yoshikawa, *Appl. Phys. Lett.* 90 (2007) 163517.
- [29] F. Zhang, M. Ceder, O. Inganäs, *Adv. Mater.* 19 (2007) 1835.
- [30] Z. Tan, C. Yang, E. Zhou, X. Wang, Y. Li, *Appl. Phys. Lett.* 91 (2007) 023509.
- [31] Y.S. Hsiao, W.T. Whang, C.P. Chen, Y.C. Chen, *J. Mater. Chem.* 18 (2008) 5948.
- [32] S.K.M. Jönsson, J. Brigerson, X. Crispin, G. Greczynski, W. Osikowicz, A.W. Denier van der Gon, W.R. Salaneck, M. Fahlman, *Synth. Met.* 10361 (2003) 1.
- [33] B.D. Martin, N. Nikolov, S.K. Pollack, A. Saprigin, R. Shashidhar, F. Zhang, P.A. Heiney, *Synth. Met.* 142 (2004) 187.
- [34] J. Ouyang, Q. Xu, C.W. Chu, Y. Yang, G. Li, J. Shinar, *Polymer* 45 (2004) 8443.
- [35] J. Ouyang, C.W. Chu, F.C. Chen, Q. Xu, Y. Yang, *Adv. Funct. Mater.* 15 (2005) 203.
- [36] J. Hung, P.F. Miller, J.S. Wilson, A.J. de Mello, J.C. de Mello, D.D.C. Bradley, *Adv. Funct. Mater.* 15 (2005) 290.
- [37] A.M. Nardes, M. Kemerink, M.M. de Kok, E. Vinken, K. Maturova, R.A.J. Janssen, *Org. Electron.* 9 (2008) 727.
- [38] H.L. Skriver, N.M. Rosengaard, *Phys. Rev. B* 46 (1992) 7157.
- [39] G. Li, V. Shrotriya, Y. Yao, J. Huanga, Y. Yang, *J. Mater. Chem.* 17 (2007) 3126.
- [40] S. Chaudhary, H. Lu, A.M. Müller, C.J. Bardeen, M. Ozkan, *Nano Lett.* 7 (2007) 1973.
- [41] T. Aernouts, P. Vanlaeke, W. Geens, J. Poortmans, P. Heremans, S. Borghs, R. Mertens, R. Andriessen, L. Leenders, *Thin Solid Films* 451 (2004) 22.
- [42] J.Y. Lee, S.T. Connor, Y. Cui, P. Peumans, *Nano Lett.* 8 (2008) 689.
- [43] J. Huang, X. Wang, Y. Kim, A.J. de Mello, D.D.C. Bradley, J.C. de Mello, *Phys. Chem. Chem. Phys.* 8 (2006) 3904.
- [44] S.I. Na, S.S. Kim, J. Jo, D.Y. Kim, *Adv. Mater.* 20 (2008) 1.
- [45] V. Terrazzoni-Daudrix, J. Guillet, X. Niquille, A. Shah, R. Morf, A. Tishchenko, V. Brioude, O. Parriaux, D. Fischer, *Mat. Res. Soc. Symp. Proc.* 769 (2003) H6.14.1.
- [46] F. Monestier, J.-J. Simon, P. Torchio, L. Escoubas, F. Flory, S. Bailly, R. de Bettignies, S. Guillerez, C. Defranoux, *Sol. Energy Mater. Sol. Cells* 91 (2007) 405.
- [47] L.A.A. Pettersson, S. Ghosh, O. Inganäs, *Org. Electron.* 3 (2002) 143.



# Influence of side chain symmetry on the performance of poly(2,5-dialkoxy-*p*-phenylenevinylene): fullerene blend solar cells

Sachetan M. Tuladhar<sup>a,\*</sup>, Marc Sims<sup>a,b</sup>, Stelios A. Choulis<sup>a,c</sup>, Christian B. Nielsen<sup>d</sup>, Wayne. N. George<sup>d</sup>, Joachim H.G. Steinke<sup>d</sup>, Donal D.C. Bradley<sup>a</sup>, Jenny Nelson<sup>a,\*</sup>

<sup>a</sup> Department of Physics, Imperial College London, Prince Consort Road, London SW7 2AZ, UK

<sup>b</sup> DuPont Displays Inc., 6780 Cortona Drive, Santa Barbara, California 93101, USA

<sup>c</sup> Department of Mechanical Engineering and Materials Science and Engineering, Cyprus University of Technology, 3603 Limassol, Cyprus

<sup>d</sup> Department of Chemistry, Imperial College London, London SW7 2AY, UK

## ARTICLE INFO

### Article history:

Received 14 October 2008

Received in revised form 6 February 2009

Accepted 9 February 2009

Available online 20 February 2009

### Keywords:

DialkoxyPPV

Fullerene

Side chain symmetry

Bulk heterojunction

Organic photovoltaic

Cells

Charge transport

## ABSTRACT

We report on studies of poly-(2,5-dihexyloxy-*p*-phenylenevinylene) (PDHeOPV), a symmetric side-chain polymer, as a potential new donor material for polymer:fullerene blend solar cells. We study the surface morphology of blend films of PDHeOPV with PCBM, the transport properties of the blend films, and the performance of photovoltaic devices made from such blend films, all as a function of PCBM content. In each case, results are compared with those obtained using the asymmetric side chain polymer, poly[2-methoxy-5-(3,7-dimethyloctyloxy)-1,4-phenylenevinylene] (MDMO-PPV), in order to investigate the influence of polymer side chain symmetry on solar cell performance. AFM images show that large PCBM aggregates appear at lower PCBM content (50 wt.% PCBM) for PDHeOPV:PCBM than for MDMO-PPV:PCBM (67 wt.% PCBM) blend films. Time-of-Flight (ToF) mobility measurements show that charge mobilities depend more weakly on PCBM content in PDHeOPV:PCBM than in MDMO:PPV:PCBM, with the result that at high PCBM content the mobilities in PDHeOPV:PCBM are significantly lower than in MDMO:PPV:PCBM blend films, despite the higher mobilities in pristine PDHeOPV compared to pristine MDMO-PPV. Photovoltaic devices show significantly lower power conversion efficiency (~0.93%) for PDHeOPV:PCBM (80 wt.% PCBM) blend films than for MDMO-PPV:PCBM (2.2% at 80 wt.% PCBM) blends. This is attributed to the relatively poor transport properties of the PDHeOPV:PCBM blend, which limit the optimum thickness of the photoactive layer in PDHeOPV:PCBM blend devices. The behaviour is tentatively attributed to a higher tendency for the symmetric side-chain polymer chains to aggregate, resulting in poorer inter-action with the fullerene and poorer network formation for charge transport.

© 2009 Elsevier B.V. All rights reserved.

## 1. Introduction

The performance of bulk heterojunction solar cells based on the blend of a conjugated polymer and a fullerene derivative is critically dependent on the nano- and micro-scale morphology of the thin solution-processed semicon-

ductor blend layer [1–6]. In several systems it has been observed that optimum device performance is achieved for blend films that feature a certain degree of phase separation (~10 nm length scale). This positive effect of phase segregation is attributed to improved charge transport or light harvesting as a result of increased crystallinity of components [7] and to a reduction in bimolecular [8] or geminate [9] charge recombination with less intimate phase mixing. Large scale (>100 nm) phase segregation, on the other hand, leads to poor device performance due to the limited interfacial area available for charge

\* Corresponding authors. Tel.: +4402075946679 (S.M. Tuladhar); tel.: +4402075947581 (J. Nelson).

E-mail addresses: [s.tuladhar@imperial.ac.uk](mailto:s.tuladhar@imperial.ac.uk) (S.M. Tuladhar), [nelson@imperial.ac.uk](mailto:nelson@imperial.ac.uk) (J. Nelson).



separation [10]. Control of the microstructure of the active layer is therefore critical for the optimisation of photovoltaic device performance.

One means by which the blend morphology can be controlled is through the self-organising nature of the molecular components used, for instance, the degree of crystallinity of the polymer or fullerene [7] or the interaction energy between the components [11]. In the case of conjugated polymers, polymer chain packing is known to be influenced by the length and nature of the polymer side chains. In particular, symmetric side chains in poly-*p*-phenylenevinylene (PPV) polymers are known to lead to more rigid chain conformations and a higher degree of chain aggregation than asymmetric chains [12,13]. A recent study by Blom and co-workers [14,15] has shown that hole transport in blend films of a symmetrically substituted PPV polymer with PCBM is insensitive to composition, in contrast to blend films of the widely studied asymmetrically substituted polymer poly[2-methoxy-5-(3',7'-dimethyloctyloxy)-1-4-phenylene vinylene] (MDMO-PPV) with PCBM, suggesting that side chain symmetry can affect blend film morphology. In this paper, we investigate the influence of the polymer donor side chain symmetry on the morphology of PPV polymer:PCBM blend films, on charge transport in the blend films and on the behaviour of the corresponding bulk heterojunction photovoltaic devices. We select two alternative dialkoxy-*p*-phenylenevinylene polymers as the donor material, the symmetrically substituted polymer 2,5-dihexyloxy-*p*-phenylenevinylene (PDHeOPV) and the asymmetrically substituted polymer MDMO-PPV. We show that the symmetrically substituted polymer leads to larger scale phase separation and poorer device performance, and that the differences in device performance are correlated both to the different degree of phase segregation and to a very different dependence of the electron and hole transport properties of the blend films on PCBM content. The results demonstrate the critical influence of polymer phase behaviour on bulk heterojunction performance.

## 2. Experimental

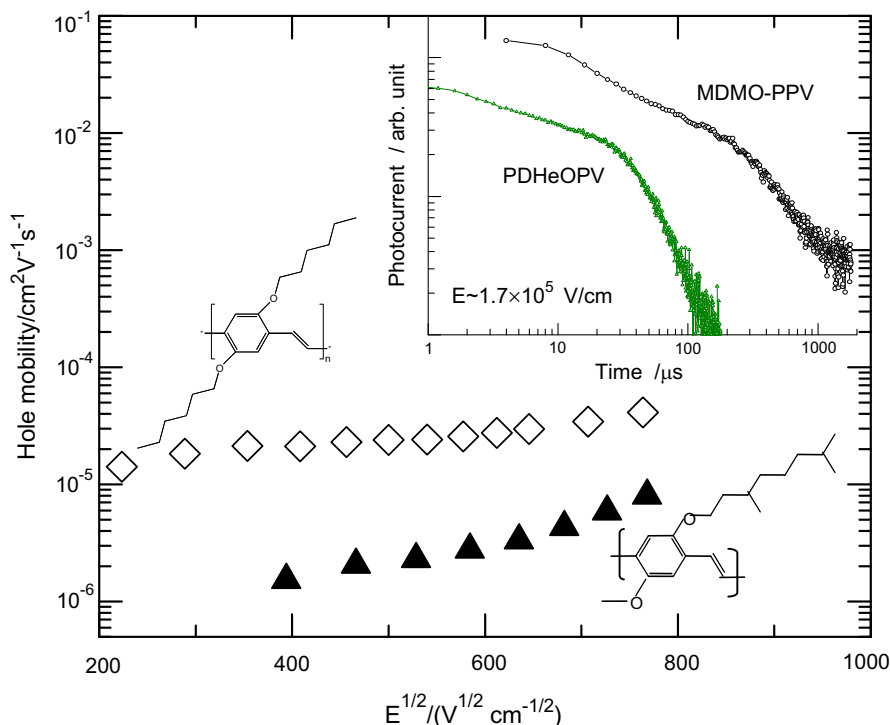
The PDHeOPV polymer (number average molecular weight  $\sim 25$  kDa (approximately 82 repeat units)) was prepared as detailed in Ref. [16]. For atomic force microscopy (AFM, Burleigh Instruments) and photoluminescence (PL, FluoroMax-3, Jobin-Yvon) measurements, blend films of thickness  $\sim 50$  nm were spin coated from chlorobenzene solution onto indium tin oxide (ITO) coated glass substrates coated with a  $\sim 70$  nm layer of polystyrene sulphate doped poly(ethylenedioxythiophene) (PEDOT:PSS). This sample structure was used in order to simulate conditions in the solar cell as closely as possible, since it is known that substrate influences phase segregation. Devices for time-of-flight (ToF) mobility measurements were made by spin coating films of pristine PDHeOPV and blend films of PDHeOPV:PCBM blends containing 0, 20, 33, 50, 67 and 75 wt.% PCBM from chlorobenzene solutions onto indium tin oxide (ITO) coated glass substrates. Pristine films of PDHeOPV (92 mg/ml) and blend

films of PDHeOPV:PCBM containing 20 (18 mg/ml), 33 (30 mg/ml), 50 (45 mg/ml), 67 (60 mg/ml) and 75 (67 mg/ml) wt.% PCBM were spin-coated on to ITO at spin speeds of 2000, 1800, 1500, 1500 and 1000 rpm, respectively. The ToF devices were then completed by thermal evaporation of a shadow masked, aluminum top contact ( $\sim 100$  nm), at a typical pressure of  $10^{-6}$  mbar. Film thicknesses were measured with a Sloan Dektak<sup>TM</sup> surface profilometer. Hole mobility values were obtained by analysis of ToF photocurrent transients as described in Ref. [17]. Bulk heterojunction solar cells with the sandwich structure ITO/PEDOT:PSS (70–75 nm)/X/Al were fabricated where X was a blend layer of either PDHeOPV or MDMO-PPV with a varying weight fraction of PCBM. All devices were illuminated through the semitransparent ITO electrode with AM1.5G light from a filtered Xe lamp at an intensity of  $100$  mW/cm<sup>2</sup>.

## 3. Results and discussions

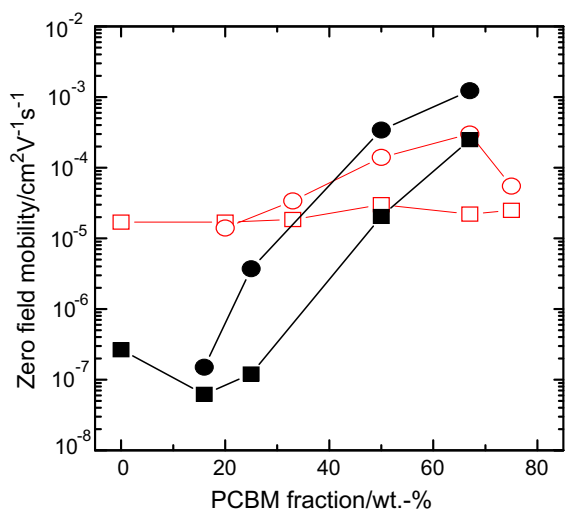
The electric field dependence of hole mobility of PDHeOPV and MDMO-PPV at room temperature is shown in Fig. 1. The data for both samples follow the Poole-Frenkel form, generally found in a wide range of disordered materials [18]. The hole mobility of symmetrically substituted PDHeOPV ( $\sim 10^{-5}$  cm<sup>2</sup>/Vs) at low fields is about an order of magnitude higher than the hole mobility of the asymmetrically substituted MDMO-PPV ( $\sim 10^{-6}$  cm<sup>2</sup>/Vs). This is also true of the hole mobility of other symmetrically substituted dialkoxy-poly-*p*-phenylene vinylenes, even those with longer side chains [16]. The higher low field mobility for the symmetrically than for the asymmetrically substituted PPVs thus implies that the nature of chain packing is important in determining the hole-transporting characteristics of these materials. This is reflected in the ToF photocurrent transients shown in the inset to Fig. 1. The photocurrent transients of PDHeOPV films exhibit relatively non-dispersive behaviour (characterised by the pronounced knee in the transient when plotted on double logarithmic axes) in comparison to MDMO-PPV at similar fields. Weak dependence of hole mobility on electric field, such as that seen for PDHeOPV in Fig. 1, is often correlated with low energetic disorder and non-dispersive charge transport [19].

Fig. 2 shows the zero-field electron and hole mobilities in PDHeOPV:PCBM blend films as a function of PCBM content, obtained by extrapolation of Poole-Frenkel fits to the field dependent mobility data. The zero-field ToF mobility of holes and electrons in MDMO-PPV:PCBM blend films [20] are also presented as a function of PCBM content in the same plot for comparison. Whilst both electron and hole mobility increase continuously with increasing PCBM content from 16 to 67 wt.% PCBM in the case of MDMO-PPV:PCBM blend films, leading to a net increase of two to four orders of magnitude, the zero-field electron and hole mobilities of PDHeOPV:PCBM blends are relatively insensitive to PCBM content. The mild increase in electron mobility with PCBM content in PDHeOPV:PCBM blends can be attributed to improved electron percolation with PCBM network formation. A similar weak dependence of hole mobility on PCBM content was observed previously for an-



**Fig. 1.** The electric field dependent ToF hole mobility at room temperature in pristine PDHeOPV (open diamonds) and MDMO-PPV (filled triangles) films of thicknesses 1.2 and 1.6  $\mu\text{m}$ , respectively. The inset shows the structure of the respective polymers and the ToF photocurrent transients for PDHeOPV, MDMO-PPV samples plotted on double logarithmic axes at similar electric field  $\sim 1.7 \times 10^5$  V/cm.

other symmetrically substituted dialkoxy PPV polymer [14]. Although the strong dependence of charge transport on PCBM content observed for MDMO-PPV:PCBM blend films has not been unambiguously explained, the influence



**Fig. 2.** Zero-field electron (circles) and hole mobilities (squares) in (a) PDHeOPV:PCBM and (b) MDMO-PPV:PCBM blends as a function of PCBM concentration. Open symbols represent PDHeOPV:PCBM and filled symbols MDMO-PPV:PCBM blends.

of PCBM on polymer chain packing is thought to be relevant [6,20].

The very different composition dependence of charge carrier mobilities in PDHeOPV:PCBM blends compared to MDMO-PPV:PCBM may result from different polymer chain conformations. Symmetric side chain polymers are expected to assume more rigid conformations [12] and therefore the PDHeOPV chain morphology may be less strongly affected by the presence of PCBM than MDMO-PPV with its asymmetric side chains and tendency to form ring-like structures [13]. This difference may be enhanced by the fact that the side chains in MDMO-PPV are branched while those in PDHeOPV are linear. The observation of phase segregation at 50 wt.% PCBM in PDHeOPV:PCBM blends while none is seen in MDMO-PPV:PCBM until  $\sim 67$  wt.% [3,21] is consistent with the hypothesis that the more rigid, symmetrically substituted PDHeOPV polymer chains have a stronger tendency to aggregate than the asymmetrically substituted MDMO-PPV chains, and consequently are less strongly affected by the presence of PCBM.

Fig. 3 shows the photoluminescence spectra (480 nm excitation) for PDHeOPV:PCBM blend films as a function of PCBM content. The PL of PDHeOPV is increasingly quenched with the addition of PCBM up to a content of 70–80 wt.% PCBM, consistent with photoinduced charge transfer in these composite films. The PL spectra of the PDHeOPV:PCBM blend films exhibit well resolved vibronic structure and resemble the spectra of pristine PDHeOPV [16], at all PCBM contents. In contrast, it has been shown

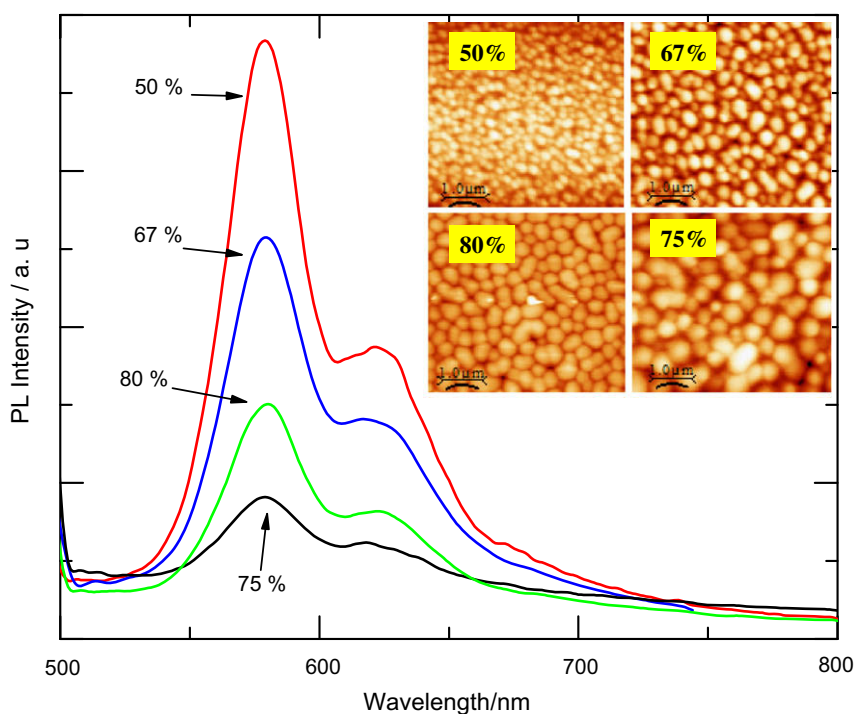


**Fig. 3.** PL spectra from PDHeOPV:PCBM blend films as a function of PCBM weight percentage for excitation at 480 nm. The inset shows the AFM phase images of the PDHeOPV:PCBM blend films of 80, 75, 67 and 50 wt.% PCBM.

that the PL spectra of MDMO-PPV:PCBM blend films become structureless with increasing PCBM content, completely losing the red shoulder seen in the PL spectrum of pristine MDMO-PPV at PCBM contents greater than 30 wt.% [3]. This again suggests that the morphology of the blend film made from the symmetrically substituted polymer will be quite different from that of the blend made from the asymmetrically substituted polymer.

As a further probe of morphology, the PDHeOPV:PCBM blend films were studied with atomic force microscopy (AFM) as a function of PCBM content. Fig. 3 (inset) shows the height images obtained by AFM for composite PDHeOPV:PCBM films ( $\sim 50$  nm) for four different compositions. Whilst the surface roughness of pristine films of both PDHeOPV and PCBM films is low (root-mean-square roughness,  $z_{\text{RMS}} < 1$  nm), the PDHeOPV:PCBM blend films are rough ( $z_{\text{RMS}} \geq 10$  nm) and exhibit separate domains of diameter  $> 100$  nm, with both surface roughness and domain size increasing with PCBM content. These roughness values and domain sizes are much larger than those observed for MDMO-PPV:PCBM blend films at similar PCBM content ( $z_{\text{RMS}} < 1$  nm, domain size 60–80 nm at 80 wt.% PCBM [3,10] compared to  $z_{\text{RMS}} \sim 12$  nm, domain size 500 nm for PDHeOPV:PCBM). Larger domains may lead to a lower efficiency of exciton dissociation, depending on the purity of the domains observed. The height fluctuations of the PDHeOPV:PCBM blend films thus account for a significant fraction of the total thickness of the thin films used to make devices, as discussed below.

Photovoltaic devices were made from PDHeOPV:PCBM blends containing 50, 67, 75 and 80 wt.% PCBM. The high-

est EQE was obtained at 80 wt.% PCBM. To optimise device structure, device performance was then studied as a function of blend film thickness for the composition (80 wt.% PCBM). Film thickness was varied from 50 to 240 nm by changing either solution concentration or the rate of spin coating. For all devices, blend films were spin coated on to PEDOT:PSS layers (70–75 nm thick) and finished with Al top contacts. A similar series of MDMO-PPV:PCBM de-

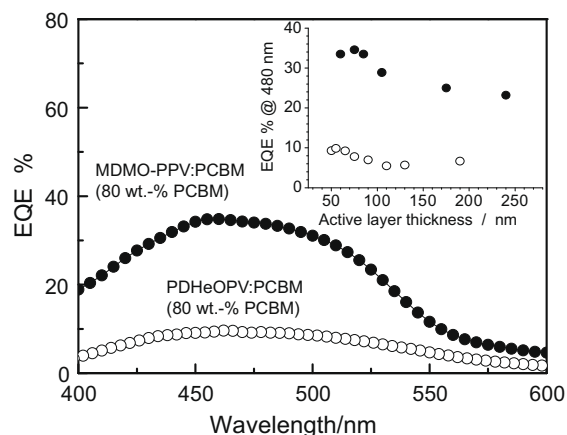


**Fig. 4.** External quantum efficiency (EQE) spectra for PDHeOPV:PCBM (80 wt.% PCBM) and MDMO-PPV:PCBM (80 wt.% PCBM) blend devices with photoactive layer film thicknesses of 55 nm and 75 nm, respectively. The inset shows the EQE of both blends with various photoactive layer thicknesses at an excitation wavelength of 480 nm.

vices was made for comparison and the resulting EQE spectra are depicted in Fig. 4. The data clearly show that the EQE of the devices based on PDHeOPV:PCBM is substantially lower than that of MDMO-PPV:PCBM based devices, across the thicknesses range. The EQE shows a maximum 35% for the MDMO-PPV:PCBM device with a 75 nm thick active layer while for the PDHeOPV:PCBM devices, the lowest thickness studied (50–55 nm) produced the highest EQE (~10%). Good quality devices with thinner active layers could not be made, probably due to defects such as pinholes in the active layer.

The value of the optimum active layer thickness in a bulk heterojunction solar cell is determined by the competition between light absorption and charge carrier mobility. Given that the optical absorption of the two polymers is similar, the lower optimum thickness for PDHeOPV:PCBM than for MDMO-PPV:PCBM is consistent with the lower electron and hole mobilities of the former blend.

Fig. 5 shows a plot of the photovoltaic parameters, the short circuit current density,  $J_{sc}$ , open circuit voltage,  $V_{oc}$ , power conversion efficiency  $\eta$  and fill factor FF for the series of PDHeOPV:PCBM (80 wt.% PCBM) devices with different active layer thickness in comparison with those for a series of MDMO-PPV:PCBM (80 wt.% PCBM) devices.

The dependence of  $J_{sc}$  on active layer thickness for PDHeOPV:PCBM and MDMO-PPV:PCBM blend devices resembles that of the EQE with an optimum at 55 nm for PDHeOPV:PCBM and at 75 nm for MDMO-PPV:PCBM, after which  $J_{sc}$  tends to decrease with increasing thickness as a result of the competition between transport and recombination, as discussed above. In the case of MDMO-PPV:PCBM blend devices  $J_{sc}$  shows a broad local minimum around ~100 nm which can be attributed to optical interference and is expected theoretically [22]. Similar structure is also visible in the case of PDHeOPV:PCBM blend films.

Open-circuit voltages were comparable for the two blend types (~0.7–0.8 V) and relatively insensitive to film thickness, as previously observed [23,24]. However, a fall-off in both  $V_{oc}$  and fill factor with reducing thickness for the thinnest PDHeOPV:PCBM blend devices suggests shunt losses possibly due to non-uniformities in film thickness.

The highest power conversion efficiencies are found for the device thicknesses that led to the highest  $J_{sc}$ , i.e. 55 nm ( $\eta = 0.93\%$ ) in the case of PDHeOPV:PCBM blend devices and 75 nm ( $\eta = 2.2\%$ ) in the case of MDMO-PPV:PCBM blend devices, in good agreement with previous results for solar cells based on same materials [10]. The inferior performance of PDHeOPV:PCBM devices compared to MDMO-PPV:PCBM is likely to result from the lower photon to electron conversion efficiency, resulting both from the lower mobility (enhancing recombination) and the relatively large domain size (possibly reducing exciton dissociation efficiency) relative to MDMO-PPV:PCBM. In addition, the relatively high surface roughness (~10 nm) is likely to limit the performance of thinner devices through charge leakage along shunt paths between the electrodes.

#### 4. Conclusions

Polymer:PCBM blend films and devices were made using dialkoxyPPV polymers with symmetric (PDHeOPV) and asymmetric (MDMO-PPV) side chains and their transport and photovoltaic properties were studied. The effects of PCBM content and active layer thickness on PDHeOPV:PCBM blend photovoltaic device parameters were also examined. We have optimised the active layer thickness for PDHeOPV:PCBM and MDMO-PPV:PCBM blend solar cells and found efficiency maxima of 0.93% at 55 nm for PDHeOPV:PCBM and 2.2% at 75 nm for MDMO-PPV:PCBM devices. The maximum EQE for PDHeOPV:PCBM blend devices was found to be about 10% in the range of

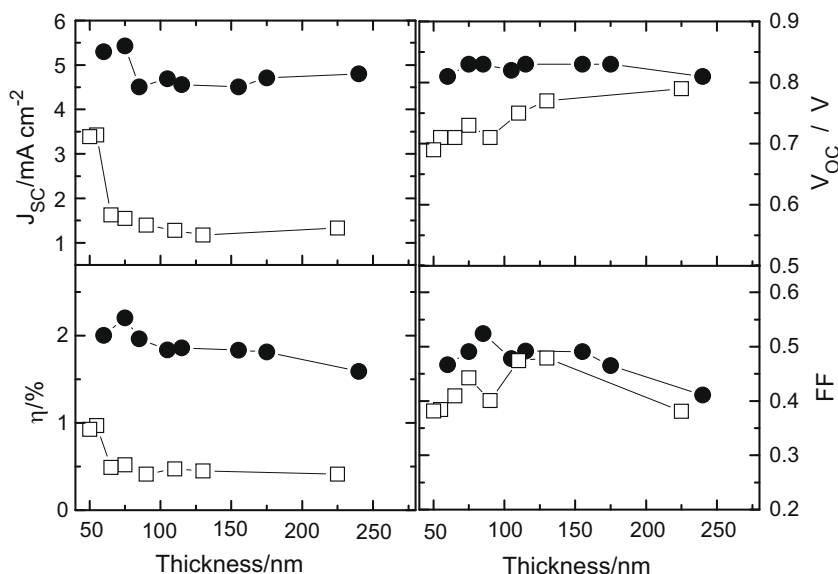


Fig. 5. Photovoltaic parameters  $V_{oc}$ ,  $J_{sc}$ , FF and  $\eta$  as a function of active layer thickness for ITO/PEDOT:PSS/PDHeOPV:PCBM (80 wt.% PCBM)/Al (filled squares) and ITO/PEDOT:PSS/MDMO-PPV:PCBM (80 wt.% PCBM)/Al (filled circles) devices.

420–520 nm compared to about 34% for MDMO-PPV:PCBM blend devices.

AFM images show that the surface morphology is different for PDHeOPV:PCBM and for MDMO-PPV:PCBM blend films and that the morphology is affected differently by blend composition in the two cases. For example, phase segregation is observed at 50 wt.% PCBM in PDHeOPV:PCBM blends while none is seen in MDMO-PPV:PCBM until ~67 wt.%. The poorer device performance for PDHeOPV:PCBM than for MDMO-PPV:PCBM can be attributed to the more phase-segregated morphology and poorer transport properties, which in turn limit the thickness of the PDHeOPV:PCBM active layer that can be used for efficient device performance. Furthermore, the strong positive effect of PCBM addition on the hole transport properties observed in MDMO-PPV:PCBM blends was not observed in the case PDHeOPV:PCBM; the mechanism requires further investigation but the different morphology of the blend films is likely to be a factor. Thus it appears that the choice of the symmetric or asymmetric side chains has a clear influence on the blend morphology and transport properties within the blend, and should be taken into consideration in the design of new conjugated polymer materials for photovoltaic applications.

### Acknowledgements

We thank James Kirkpatrick and Panagiotis Keivanidis for helpful discussions. This work was supported by BP Solar (OSCEP Project) and the UK Engineering and Physical Sciences Research Council (EP/E036341, Materials for Energy Supply programme).

### References

- [1] M. Campoy-Quiles, T. Ferenczi, T. Agostinelli, P.G. Etchegoin, Y. Kim, T.D. Anthopoulos, P.N. Stavrinou, D.D.C. Bradley, J. Nelson, *Nature Materials* 7 (2008) 158–164.
- [2] H. Hoppe, N.S. Sariciftci, *Journal of Materials Research* 19 (2004) 1924–1945.
- [3] J.K.J. van Duren, X.N. Yang, J. Loos, C.W.T. Bulle-Lieuwma, A.B. Sieval, J.C. Hummelen, R.A.J. Janssen, *Advanced Functional Materials* 14 (2004) 425–434.
- [4] J. Peet, J.Y. Kim, N.E. Coates, W.L. Ma, D. Moses, A.J. Heeger, G.C. Bazan, *Nature Materials* 6 (2007) 497–500.
- [5] C. Melzer, E.J. Koop, V.D. Mihailetschi, P.W.M. Blom, *Advanced Functional Materials* 14 (2004) 865–870.
- [6] V.D. Mihailetschi, L.J.A. Koster, P.W.M. Blom, C. Melzer, B. de Boer, J.K.J. van Duren, R.A.J. Janssen, *Advanced Functional Materials* 15 (2005) 795–801.
- [7] C. Muller, T.A.M. Ferenczi, M. Campoy-Quiles, J.V. Frost, D.D.C. Bradley, P. Smith, N. Stingelin-Stutzmann, J. Nelson, *Advanced Materials* 20 (2008) 3510–3515.
- [8] W.J.E. Beek, M.M. Wienk, R.A.J. Janssen, *Advanced Functional Materials* 16 (2006) 1112–1116.
- [9] D. Veldman, O. Ipek, S.C.J. Meskers, J. Sweelssen, M.M. Koetse, S.C. Veenstra, J.M. Kroon, S.S. van Bavel, J. Loos, R.A.J. Janssen, *Journal of the American Chemical Society* 130 (2008) 7721–7735.
- [10] S.E. Shaheen, C.J. Brabec, N.S. Sariciftci, F. Padinger, T. Fromherz, J.C. Hummelen, *Applied Physics Letters* 78 (2001) 841–843.
- [11] C.M. Björström, K.O. Magnusson, E. Moons, *Synthetic Metals* 152 (2005) 109–112.
- [12] M. Bresselge, I. Van Severen, L. Lutsen, P. Adriaensens, J. Manca, D. Vanderzande, T. Cleij, *Thin Solid Films* 511 (2006) 328–332.
- [13] M. Kemerink, J.K.J. van Duren, P. Jonkheijm, W.F. Pasveer, P.M. Koenraad, R.A.J. Janssen, H.W.M. Salemink, J.H. Wolter, *Nano Letters* 3 (2003) 1191–1196.
- [14] V.D. Mihailetschi, J. Wildeman, P.W.M. Blom, *Physical Review Letters* 94 (2005) 126602–126605.
- [15] P.W.M. Blom, V.D. Mihailetschi, L.J.A. Koster, D.E. Markov, *Advanced Materials* 19 (2007) 1551–1566.
- [16] S.M. Tuladhar, M. Sims, J. Kirkpatrick, R.C. Maher, A.J. Chatten, D.D.C. Bradley, J. Nelson, P.G. Etchegoin, C.B. Nielsen, P. Massiot, W.N. George, Joachim H.G. Steinke, *Physical Review B* 79 (2009) 035201.
- [17] T. Kreouzis, D. Poplavskyy, S.M. Tuladhar, M. Campoy-Quiles, J. Nelson, A.J. Campbell, D.D.C. Bradley, *Physical Review B* 73 (2006).
- [18] P.M. Borsenberger, E.H. Magin, M. Vanderauweraer, F.C. Deschryver, *Physica Status Solidi A-Applied Research* 140 (1993) 9–47.
- [19] H. Bassler, *Physica Status Solidi B-Basic Research* 175 (1993) 15–56.
- [20] S.M. Tuladhar, D. Poplavskyy, S.A. Choulis, J.R. Durrant, D.D.C. Bradley, J. Nelson, *Advanced Functional Materials* 15 (2005) 1171–1182.
- [21] T. Fromherz, F. Padinger, D. Gebeyehu, C. Brabec, J.C. Hummelen, N.S. Sariciftci, *Solar Energy Materials and Solar Cells* 63 (2000) 61–68.
- [22] F. Braun, Ph.D. Thesis (2007), University of London, UK.
- [23] C.J. Brabec, A. Cravino, D. Meissner, N.S. Sariciftci, M.T. Rispens, L. Sanchez, J.C. Hummelen, T. Fromherz, *Thin Solid Films* 403 (2002) 368–372.
- [24] V.D. Mihailetschi, P.W.M. Blom, J.C. Hummelen, M.T. Rispens, *Journal of Applied Physics* 94 (2003) 6849–6854.



## Effect of Co permeation on spin polarized transport in a Co/organic semiconductor (OSC) structure

Yubin Zhang<sup>a</sup>, Junfeng Ren<sup>b</sup>, Jie Lei<sup>a</sup>, Shijie Xie<sup>a,C,\*</sup>

<sup>a</sup>School of Physics, Shandong University, Jinan 250100, China

<sup>b</sup>College of Physics and Electronics, Shandong Normal University, Jinan 250014, China

<sup>c</sup>State Key Laboratory of Crystal Materials, Shandong University, Jinan 250100, China

### ARTICLE INFO

#### Article history:

Received 17 November 2008

Received in revised form 5 February 2009

Accepted 10 February 2009

Available online 20 February 2009

#### PACS:

85.75.-d

72.25.Dc

71.38.Ht

73.30.+y

#### Keywords:

Organic spintronics

Magnetic doped interface

Spin injection and transport

### ABSTRACT

Co atoms will permeate into the soft organic material to form a magnetic permeated sub-layer (MPS) during the fabrication of an organic spin device, such as Co/OSC/LSMO. We considered the OSC as a two-sublayer structure of MPS and pristine OSC, and then established a dynamic spin-diffusion equation to study the effect of MPS on the spin current polarization and the magnetoresistance of the device. It was found that the MPS will change the spin transport due to its different spin-flip time and mobility from that in the pristine OSC. The splitting of spin-flip times will be favorable to the spin polarization transport. Mobility of spin polarons in the MPS will be reduced due to the scattering of the Co atoms, which will weaken the spin polarization. For a given device, effect of the thickness of the MPS on the spin polarization is discussed. Finally, we calculated the magnetoresistance of a Co/OSC/LSMO device. A theoretical result which is consistent with the experimental data was obtained.

© 2009 Elsevier B.V. All rights reserved.

### 21. Introduction

Organic semiconductors (OSCs) are a class of functional materials that have attracted considerable attention during the last decades. They have revolutionized important technological applications including large-area electronics, owing to their processing and performance advantages compared with conventional semiconductors for low-cost or large-area device applications [1–3]. Recently, another application of OSCs as spin transport materials has been found. Their soft lattice structure and capability of reconstructing the structure provide an opportunity to form a good interface with ferromagnetic metal (FM) or half-metal contacts, reducing the probability

of spin scattering at the interface. In addition, the spin-orbit coupling and hyperfine interaction are very weak in the OSCs, so that the electron spin-diffusion length of an OSC is expected to be much longer than that of a usual inorganic material [4]. A new field called organic spintronics is emerging out and attracting the attention of both physical scientists and chemical scientists [5–7,15]. In 2002, Dediu's group firstly reported spin injection into a thin film of conjugated organic material sexithienyl ( $T_6$ ) on a nanostructured planar hybrid junction  $La_{0.7}Sr_{0.3}MnO_3/T_6/La_{0.7}Sr_{0.3}MnO_3$  (LSMO) at room temperature [5]. The spin-diffusion length in  $T_6$  they observed is about 200 nm at room temperature. Xiong et al. have also observed spin injection and transport in a  $La_{0.7}Sr_{0.3}MnO_3/Alq_3/Co$  organic spin valve. The measured magnetoresistance can be as high as 40% at low temperature [6]. Majumdar et al. have observed as much as 80% magnetoresistance (MR) at 5 K and 1.5% MR at room

\* Corresponding author. Address: School of Physics, Shandong University, Jinan 250100, China. Tel.: +86 531 8837035 8321.

E-mail address: [xsj@sdu.edu.cn](mailto:xsj@sdu.edu.cn) (S. Xie).

temperature in the structure of  $\text{La}_{0.67}\text{Sr}_{0.33}\text{MnO}_3/\text{poly 3-hexylthiophene}/\text{Co}$  organic spin valve [7]. On the theoretical side, Yu et al. studied the influence of weak magnetic field for spin transport process in magnet/polymer/magnet structures [8]. Xie et al. suggested a model for  $\text{Re}_{1-x}\text{Sr}_x\text{MnO}_3/\text{polymer}$  structure and studied the spin density distribution of the system from the Su–Schrieffer–Heeger-like Hamiltonian [9]. They indicated that the carriers in OSCs contain spin polarons and spinless bipolarons. We used the spin-dependent diffusion model [8,10–12] of the electrochemical potential and studied the spin polarized injection and transport in the structure of FM/OSC hetero junction and FM/OSC/FM trilayers [13,14]. By supposing that polarons and bipolarons coexist in OSCs with a given proportion  $r$ , we found that spin polarons are the dominant carriers of the spin polarized current. Further considering the polaron–bipolaron transition, we found that spinless bipolarons will affect the spin polarization of the OSC device [16], which is different from the case in a normal inorganic semiconductor.

Otherwise, the permeation of metal atoms into OSC in a metal/organic semiconductor interface had been exposed experimentally [17–20]. And it might be a prevalent phenomenon due to the thermal evaporation technique, which made it easy that the metal atoms diffuse from an electrode into the soft OSC layer. Recently, people predicted the existence of MPS in the Co/OSC interface in a spin valve [6,21,27,30], but the effect of MPS on the spin injection and transport was not explicit. The investigation of Co doped  $\text{Alq}_3$  [22] has indicated that it will result in superparamagnetic behavior, but the investigation on a magnetic doped inorganic semiconductor (for example, Co doped ZnO [23]) implied that magnetic impurities can result in the ferromagnetism if the concentration of magnetic impurity is high enough. Thus the influence of the magnetic impurities of MPS on the spin injection and transport may be crucial.

Among all the experimental investigation, Xiong et al. revealed the interfacial characteristics between the ferromagnetic electrode (Co) and the organic layer [6]. They predicted that a magnetic permeated region exists in the organic layer, which has a width of up to 100 nm. It was suggested that transport channel is composed of two sublayers: one with a thickness of up to 100 nm immediately attached to the Co electrode that contains Co inclusions; and the other of pristine deposited  $\text{Alq}_3$  attached to the LSMO electrode. Xiong et al. assumed that the injected carriers through the Co/OSC interface reached the pristine sublayer without any losing of spins. In other words, they neglected the decay of spin in the MPS. In fact, the magnetic atoms in the MPS may influence the spin transport in two main aspects: mobility and spin-flip time of a spin carriers or polarons. In this paper, basing on the drift-diffusion model, we calculate the current polarization and magnetoresistance of a Co/ $\text{Alq}_3$  device. We will focus on the influence of magnetic permeation on the spin transport in an OSC layer. Section 2 will provide a description of the model and the derivation of relevant formulae, numerical results will be presented and discussed in Section 3, and the conclusions will be drawn in Section 4.

## 2. Model and method

We consider an organic device Co/Co +  $\text{Alq}_3$ / $\text{Alq}_3$ /LSMO referring to the experimental fabrications [6] as shown in Fig. 1, where Co +  $\text{Alq}_3$  means the MPS. Spin polarized carriers are injected from the Co electrode into the Co +  $\text{Alq}_3$  layer ( $0 < x \leq x_0$ ). They transport under a driving field from the MPS (Co +  $\text{Alq}_3$  layer) to the pristine  $\text{Alq}_3$  layer and then finally into the right LSMO electrode. Here we will investigate the transport of carriers in the OSC (Co +  $\text{Alq}_3$ / $\text{Alq}_3$ ). We suppose that Co electrode and the Co +  $\text{Alq}_3$  layer have the same magnetic orientation with different magnetization intensities. When spin polarized electrons are injected into the organic layer, they will evolve into spin polarons as described elsewhere. Here we neglect the possible formation of bipolarons from a pair polarons, although it has been predicated that spinless bipolarons may affect the current polarization to some extent [16]. As a polaron has particle-like characteristic, whose transport may be described by the classical diffusion equation. Firstly, the mobility of polarons will be different in the MPS from that in the pristine OSC due to the additional scattering from the magnetic impurity atoms [26].

$$\mu(x) = \frac{1}{a + bN_m(x)}, \quad (1)$$

where  $N_m(x)$  means the magnetic impurity density,  $a$  and  $b$  the parameters related to temperature and the fabrication conditions. It indicates that the mobility of polarons in MPS is position dependent because of the nonuniform permeation of the impurity atoms. Secondly, in the MPS the spin-flip time  $\tau_{\uparrow\downarrow}$  (from spin-up to spin-down) will be different from  $\tau_{\downarrow\uparrow}$  (from spin-down to spin-up) due to the effect of the magnetization of the impurity atoms, which should also be dependent on the impurity density,

$$\tau_{\uparrow(\downarrow)\uparrow}(x) = \tau_0 \pm cN_m(x), \quad (2)$$

where  $\tau_0$  means a spin-flip time of a polaron in the pristine OSC,  $c (>0)$  is a constant parameter. It indicates spin-up polarons take a longer time to reverse its spin than spin-down ones.

Now let us consider the transport behavior of the spin polarons in the device. Based on the drift-diffusion model [24,25], the evolution of the densities of polarons  $n_{\uparrow(\downarrow)}$  are written as,

$$\frac{\partial n_{\uparrow(\downarrow)}}{\partial t} = \frac{1}{e} \text{div} \vec{j}_{\uparrow(\downarrow)} \pm \left( \frac{n_{\downarrow}}{\tau_{\downarrow\uparrow}} - \frac{n_{\uparrow}}{\tau_{\uparrow\downarrow}} \right), \quad (3)$$

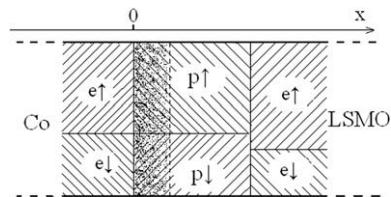


Fig. 1. A schematic diagram of the “Co/MPS/OSC/LSMO” structure.

where  $-e$  is the electron charge.  $\vec{j}_{\uparrow(\downarrow)}$  is the current density of spin-up (down) polarons, which can be described by:

$$\vec{j}_{\uparrow(\downarrow)} = \sigma_{\uparrow(\downarrow)} \vec{E} + eD \nabla n_{\uparrow(\downarrow)}, \quad (4)$$

where  $\sigma_{\uparrow(\downarrow)} = en_{\uparrow(\downarrow)}\mu$  is the conductivity of polarons with up (down) spin.  $\vec{E}$  is the applied external electric field.  $D$  and  $\mu$  are the diffusion coefficient and mobility of polarons which obey Einstein relation  $D/\mu = k_B T/e$ , where  $k_B$  is Boltzmann constant and  $T$  the temperature. We neglect the spin dependence of the diffusion coefficients and mobilities of polarons in present investigation.

Substituting Eq. (4) into Eq. (3), we finally obtain the evolution equations for spin polarons along the  $x$ -direction,

$$\frac{\partial n_{\uparrow(\downarrow)}}{\partial t} = D \frac{\partial^2 n_{\uparrow(\downarrow)}}{\partial x^2} + \left( \mu E + \frac{\partial D}{\partial x} \right) \frac{\partial n_{\uparrow(\downarrow)}}{\partial x} + \left( \frac{\partial \mu}{\partial x} E + \mu \frac{\partial E}{\partial x} \right) n_{\uparrow(\downarrow)} \pm \left( \frac{n_{\uparrow}}{\tau_{\uparrow 1}} - \frac{n_{\downarrow}}{\tau_{\downarrow 1}} \right). \quad (5)$$

### 3. Results and discussion

The investigation of spin transport through the MPS and the pristine OSC sublayer is performed based on Eq. (5). We set the initial and boundary conditions as  $n_{\uparrow}(x=0^+, t=0) = 3.5 \times 10^{16} \text{ cm}^{-3}$  and  $n_{\downarrow}(x=0^+, t=0) = 1.5 \times 10^{16} \text{ cm}^{-3}$ . This assumption may be rational for Co contact (the spin polarization in cobalt is about 0.4) if we neglect the spin-flip at the interface due to the so-called self adjusting capability of organic materials [6,9]. We choose parameters in the pristine OSC as follow:  $\mu_0 = 1.0 \times 10^{-7} \text{ cm}^2/\text{Vs}$  and  $\tau_0 = 2.7 \times 10^{-3} \text{ s}$  [27]. All the other parameter values are listed in the caption of the corresponding figures. To simple the calculation, we suppose the density of impurity in the MPS is uniform with  $N_m(x) = N_m(x \leq L_{\text{MPS}})$ , where  $L_{\text{MPS}}$  is the thickness of the MPS, which gives a constant mobility and spin-flip time as  $\mu(x) = \mu_1$  and  $\tau_{\uparrow(\downarrow)} = \tau_0 \pm \Delta\tau$  in the MPS, where  $\Delta\tau \geq 0$ . We take a numerical calculation by a driving electric field  $E = 3.0 \times 10^4 \text{ v/cm}$ , which is supposed to be uniform along the MPS and OSC layer. It should be pointed out that the current density along the whole system should obey conservation law. For the total drift current density  $j = e(n_{\uparrow} + n_{\downarrow})\mu E$ , a constant assumption of the deriving field means that product  $\mu(n_{\uparrow} + n_{\downarrow})$  is constant along the whole system. However, either mobility  $\mu$  or the total charge distribution  $(n_{\uparrow} + n_{\downarrow})$  may be changeable in space.

When a deriving field is switched on, spin polarized charge will be injected into the organic layers from the ferromagnetic electrode. After a long-time evolution from Eq. (5), we obtain that the system will reach a steady state and in this case the spin distribution is time-independent, i.e.,  $\partial n_{\uparrow(\downarrow)}/\partial t|_{t \rightarrow \infty} = 0$ . However, the spin polarization is position dependent, which may be reflected by the density of polarons defined as,

$$P(x) = (n_{\uparrow} - n_{\downarrow})/(n_{\uparrow} + n_{\downarrow}). \quad (6)$$

If the MPS was not considered, it was obtained that the spin polarization decays exponentially in the OSC as described elsewhere [16,25]. As there is a MPS in a real organic spin device, which is reflected in present model,

the spin polarization will be different from that in a pristine OSC due to the effect of two factors: the spin-flip time and the mobility of polarons in the MPS.

Firstly, let us consider the effect of spin-flip time on the spin polarization. As the magnetization of the MPS comes from the permeated Co clusters or atoms, we suppose that the magnetization of the MPS is less than that of the Co electrode, which asks  $\Delta\tau \leq P_0\tau_0$ , where  $P_0 = 0.4$  is the spin polarization of Co at Fermi level [29]. The distribution of spin polarization with different spin-flip time in the MPS is shown in Fig. 2, in which  $\tau_0 = 2.7 \times 10^{-3} \text{ s}$  and  $\Delta\tau = 0.0, 0.1\tau_0, 0.3\tau_0$ , and  $0.38\tau_0$ , respectively. It is found that the spin polarization decays slowly in the MPS, but in the pristine OSC it decays rapidly with an exponential form. We also note that the spin polarization in the MPS is related to the spin-flipping time. A large splitting of  $\tau_{ss'}$  or  $\Delta\tau$  will result in a high spin polarization, where  $s$  and  $s'$  denote the different spin orientation. It can be understood as follow: If  $\Delta\tau = 0$ , the probability of a spin from up to down is equal to that from down to up. As the amount of spin-flipping from  $s$  to  $s'$  is proportional to  $n_s/\tau_{ss'}$ , the system will finally reach a spin degenerate state with  $n_{\uparrow} = n_{\downarrow}$  or  $P(+\infty) = 0$ . If  $\Delta\tau \neq 0$ , however, the situation will be different. The flipping probability of a spin from up to down is always smaller than that from down to up. Therefore, the system will exist in a spin non-degenerate state with  $n_{\uparrow} > n_{\downarrow}$ . In present parameters,  $\Delta\tau = 0.4\tau_0$  means that the MPS has the same characteristic as the Co electrode and it keeps a maximum spin polarization unchanged. If  $\Delta\tau < 0.4\tau_0$ , the injected polarons in the MPS will experience a spin evolution and finally reach a dynamic equilibrium with  $P(+\infty) \neq 0$ .

Then we consider the effect of the mobility of polarons on the spin polarization, which is shown in Fig. 3. As the mobility is smaller in the MPS than that in the OSC due to the additional scattering of Co on polarons, we give the results of  $\mu_1 = \mu_0, 0.8\mu_0$ , and  $0.4\mu_0$ , respectively in Fig. 3. It is found that the effect of mobility is related to the spin-flip time. In the case of a large splitting of the spin-flip time, for example  $\Delta\tau = 0.35\tau_0$  as shown in

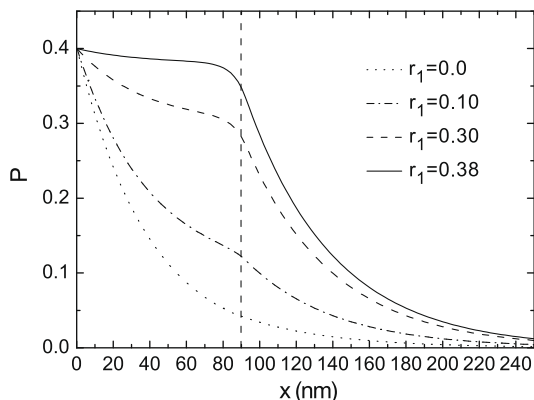


**Fig. 2.** Distribution of spin polarization with different spin-flip time  $\Delta\tau = r_1\tau_0$  in the MPS. The dotted, dash-dotted, dashed, and solid lines indicate  $r_1 = 0.0, 0.1, 0.3$ , and  $0.38$ , respectively. The other parameters are  $\mu = \mu_0 = 1.0 \times 10^{-7} \text{ cm}^2/\text{Vs}$ ,  $\tau_0 = 2.7 \times 10^{-3} \text{ s}$ ,  $\mu_1 = 0.8\mu_0$ , and  $L_{\text{MPS}} = 90 \text{ nm}$ .



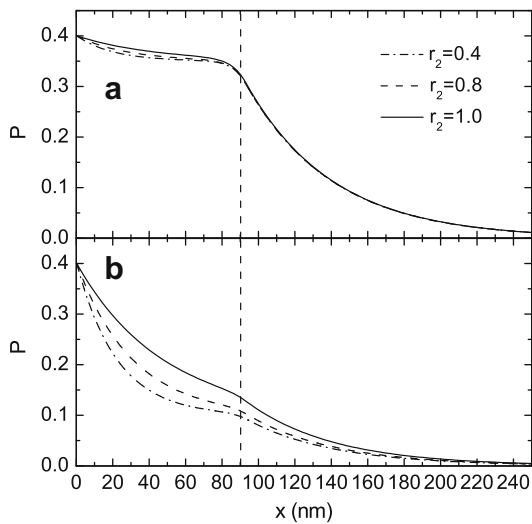


**Fig. 3.** Distribution of spin polarization with different polaron mobility in the MPS. (a)  $\Delta\tau = 0.35\tau_0$ , (b)  $\Delta\tau = 0.1\tau_0$ . The solid, dashed, and dash-dotted lines are for  $\mu_1 = \mu_0$ ,  $0.8\mu_0$ , and  $0.4\mu_0$ , respectively. The other parameters are same as those in Fig. 2.

Fig. 3a, the effect of mobility on spin polarization is not apparent. But in the case of a small splitting of the spin-flip time, for example  $\Delta\tau = 0.1\tau_0$  as shown in Fig. 3b, the spin polarization will have an apparent decrease with the mobility. As the thickness of the MPS is limited, a small mobility means that a polaron will experience a long time to move through the MPS, which means that the polaron has a long time to reverse its spin in this layer. Therefore, the spin polarization will become small in the MPS. It also predicates that a small mobility in the MPS is not favorable for the transport of spin.

It has been reported that the thickness of the MPS may distribute from a few nanometers to nearly one hundred nanometers upon the concrete preparation of a device [6,21,30]. Except for the spin-flip time and the mobility of a polaron, the thickness of the MPS will also affect the current spin polarization of the device. Here we consider a device with a preparation thickness of the OSC layer (MPS + pristine layer)  $L = L_{\text{MPS}} + L_{\text{p-OSC}}$ . A deep permeation means a large  $L_{\text{MPS}}$  and so a small  $L_{\text{p-OSC}}$ . Dependence of the spin polarization on the thickness of the MPS with a large splitting of spin-flip time is shown in Fig. 4, in which  $L = 160$  nm and  $L_{\text{MPS}} = 0, 5, 50,$  and  $90$  nm, respectively.  $L_{\text{MPS}} = 0$  means that there is not any permeation of Co atoms. In this case, it is found that the spin polarization decays exponentially as  $\exp(-x/\lambda)$ , where  $\lambda$  is the spin-diffusion length [25]. For a shallow permeation, for example  $L_{\text{MPS}} = 5$  nm, the spin polarization keeps nearly the same as that with no permeation. It is also found that, for a shallow permeation, the polarized polarons could not conserve its spin orientation when it reaches the right side of the OSC layer as the polarization  $P(L)$  is nearly zero. But in the case of a deep permeation, for example  $L_{\text{MPS}} = 90$  nm, a much change will take place for the spin polarization. It has a slow decay both in the MPS and the pristine OSC. Most importantly, the polarons will keep a large spin

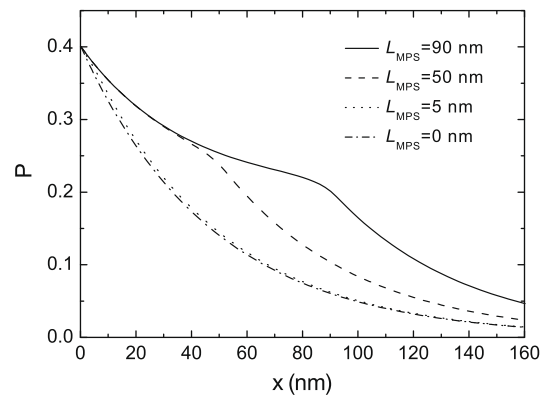


**Fig. 4.** Distribution of spin polarization with the thickness ( $L_{\text{MPS}}$ ) of MPS. The solid, dashed, dotted, and dash-dotted lines indicate  $L_{\text{MPS}} = 90, 50, 5,$  and  $0$  nm, respectively. The parameters are  $\mu_1 = 0.8\mu_0$ ,  $\Delta\tau = 0.2\tau_0$ , and  $L = 160$  nm, the other parameters are same as those in Fig. 2.

polarization  $P(L) = 0.05$ , which means that a spin polarized current will appear in a Co/OSC/LSMO device if there is a deep permeation of Co.

Finally we calculate the magnetoresistance of a spin valve Co/OSC/LSMO. Let  $P_1 = P(L)$  be the spin polarization of polarons at the OSC side near the OSC/LSMO interface, and  $P_2$  the spin polarization of LSMO at Fermi level. Magnetoresistance  $\Delta R/R$  is given by the Julliere formula [6,28]

$$\frac{\Delta R}{R} = \frac{R_{\text{AP}} - R_{\text{P}}}{R_{\text{AP}}} = \frac{2P_1P_2}{1 + P_1P_2} = \frac{2P_1}{1 + P_1}, \quad (7)$$

where we suppose that the detecting contact LSMO is 100% polarized, i.e.,  $P_2 = 1$ . The results with different thickness of OSC layer are shown in Fig. 5. The dotted line is the result that there is no any Co permeation ( $L_{\text{MPS}} = 0$ ). The solid line is the result that there is a MPS with a thickness of  $L_{\text{MPS}} = 90$  nm. Apparently, the theoretical calculation is quite consistent to the experimental data [6] if a deep permeation layer is considered. It is found that the permeation of Co is seriously important to the magnetoresistance

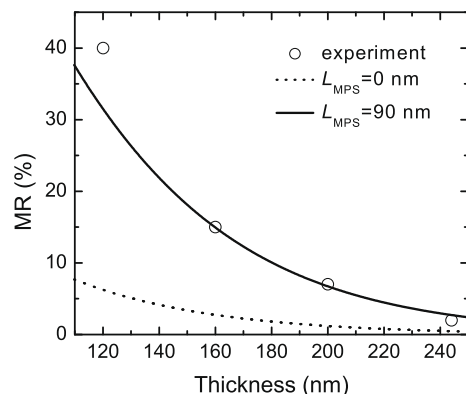


**Fig. 5.** The GMR value of Co/MPS/OSC/LSMO device with the different thickness of the OSC layer. The circles are for the experimental data [6], the dotted and solid lines for  $L_{\text{MPS}} = 0$  and  $90$  nm, respectively. The parameters are  $\mu_1 = 0.8\mu_0$  and  $\Delta\tau = 0.35\tau_0$ . The other parameters are same as those in Fig. 2.

of a spin device. The existence of a Co permeation layer especially a deep permeation one will be favorable to a large magnetoresistance of a device.

#### 4. Summary

In summary, we investigated the effect of a magnetic permeated sublayer on the spin transport in a Co/OSC/LSMO device. We established a dynamic spin-diffusion equation and calculated the spin polarization and the magnetoresistance. It was found that, due to the permeation of magnetic atoms or the appearance of the MPS, the spin transport in the MPS will be adjusted with both the spin-flip time and the mobility of polarons. The spin-flip time from spin-up to down and that from spin-down to up will split due to the magnetization of MPS, which will result in a slow decay of spin polarization. As the mobility of polarons is reduced due to the additional scattering of the permeated Co atoms, the spin polarization will be weakened. For a given device, we discussed the effect of different permeation thickness on the spin polarization. Finally, we calculated the magnetoresistance of a Co/OSC/LSMO device. A theoretical result which is consistent with the experimental data was obtained. It was found that the permeation of Co is seriously important for the current polarization of the device. A deep permeation will be favorable to a large magnetoresistance of the device.

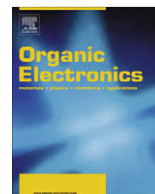
#### Acknowledgments

The authors would like to acknowledge the financial support from the National Basic Research Program of China (Grant No. 2009CB929204) and the National Natural Science Foundation of the People's Republic of China (Grant Nos. 10874100 and 10747143).

#### References

- [1] I.H. Campbell, D.L. Smith, *Solid State Phys.* 55 (2001) 1.  
 [2] R.H. Friend, R.W. Gymer, A.B. Holmes, et al, *Nature* 397 (1999) 121.

- [3] D. Voss, *Nature* 407 (2000) 442.  
 [4] S.A. Wolf, D.D. Awschalom, R.A. Buhrman, J.M. Daughton, S. von Molnár, M.L. Roukes, A.Y. Chtchelkanova, D.M. Treger, *Science* 294 (2001) 1488.  
 [5] V. Dediu, M. Murgia, F.C. Matocotta, C. Taliani, S. Barbanera, *Solid State Commun.* 122 (2002) 181.  
 [6] Z.H. Xiong, Di Wu, Z. Vally Vardeny, Jing Shi, *Nature* 427 (2004) 821.  
 [7] Sayani Majumdar, R. Laiho, P. Laukkanen, I.J. Väyrynen, Himadi S. Majumdar, R. Österbacka, *Appl. Phys. Lett.* 89 (2006) 122114.  
 [8] Z.G. Yu, M.A. Berding, S. Krishnamurthy, *Phys. Rev. B* 71 (2005) 060408R.  
 [9] S.J. Xie, K.H. Ahn, D.L. Smith, A.R. Bishop, A. Saxena, *Phys. Rev. B* 67 (2003) 125202.  
 [10] D.L. Smith, R.N. Silver, *Phys. Rev. B* 64 (2001) 045323.  
 [11] P.P. Ruden, D.L. Smith, *J. Appl. Phys.* 95 (2004) 4898.  
 [12] Z.G. Yu, M.A. Berding, S. Krishnamurthy, *J. Appl. Phys.* 97 (2005) 024510.  
 [13] J.F. Ren, J.Y. Fu, D.S. Liu, L.M. Mei, S.J. Xie, *J. Appl. Phys.* 98 (2005) 074503.  
 [14] J.F. Ren, J.Y. Fu, D.S. Liu, L.M. Mei, S.J. Xie, *J. Phys.: Condens. Matter* 17 (2005) 2341.  
 [15] A. Saxena, T. Castan, A. Planes, M. Porta, Y. Kishi, T.A. Lograsso, D. Viehland, M. Wuttig, M. De Graef, *Phys. Rev. Lett.* 92 (2004) 197203.  
 [16] Yubin Zhang, Junfeng Ren, Guichao Hu, Shijie Xie, *Org. Electron.* 9 (2008) 687.  
 [17] S.T. Lee, Z.Q. Gao, L.S. Hung, *Appl. Phys. Lett.* 75 (1999) 1404.  
 [18] C. Chao, K. Chuang, S. Chen, *Appl. Phys. Lett.* 69 (1996) 2894.  
 [19] Junqing Zhao, Shijie Xie, Shenghao Han, Zhiwei Yang, Lina Ye, Tianlin Yang, *Synth. Metal.* 114 (2000) 251.  
 [20] A.R. Schlatmann, D. Wilms Floet, A. Hilberer, F. Garten, P.J.M. Smulders, T.M. Klapwijk, G. Hadziioannou, *Appl. Phys. Lett.* 69 (1996) 1764.  
 [21] F.J. Wang, C.G. Yang, Z. Vally Vardeny, X.G. Li, *Phys. Rev. B* 75 (2007) 245324.  
 [22] Shinichi Tanabe, Shinji Miwa, Masaki Mizuguchi, Teruya Shinjo, Yoshishige Suzuki, Masashi Shiraishi, *Appl. Phys. Lett.* 91 (2007) 063123.  
 [23] Eun-Cheol Lee, K.J. Chang, *Phys. Rev. B* 69 (2004) 085205.  
 [24] Yuriy V. Pershin, Vladimir Privman, *Phys. Rev. Lett.* 90 (2003) 256602.  
 [25] Z.G. Yu, M.E. Flatté, *Phys. Rev. B* 66 (2002) 235302.  
 [26] M.B. Prince, *Phys. Rev.* 92 (1953) 681.  
 [27] S. Pramanik, C.-G. Stefanita, S. Bandyopadhyay, N. Harth, K. Garre, M. Cahay, [arxiv:cond-mat/0508744](https://arxiv.org/abs/cond-mat/0508744).  
 [28] M. Julliere, *Phys. Lett. A* 54 (1975) 225.  
 [29] R.J. Soulen Jr., J.M. Byers, M.S. Osofsky, B. Nadgorny, T. Ambrose, S.F. Cheng, P.R. Broussard, C.T. Tanaka, J. Nowak, J.S. Moodera, A. Barry, J.M.D. Coey, *Science* 282 (1998) 85.  
 [30] Yaohua Liu, Shannon M. Watson, Taegweon Lee, Justin M. Gorham, Howard E. Katz, Julie A. Borchers, Howard D. Fairbrother, Daniel H. Reich, [arxiv:0810.0289](https://arxiv.org/abs/0810.0289).



## Organic field-effect transistors for biosensing applications

S.M. Goetz<sup>a,\*</sup>, C.M. Erlen<sup>a</sup>, H. Grothe<sup>b</sup>, B. Wolf<sup>b</sup>, P. Lugli<sup>a</sup>, G. Scarpa<sup>a</sup>

<sup>a</sup> *Institute for Nanoelectronics, TU München, Arcisstr. 21, DE-80333 Munich, Germany*

<sup>b</sup> *Heinz-Nixdorf-Lehrstuhl für Medizinische Elektronik, TU München, Arcisstr. 21, DE-80333 Munich, Germany*

### ARTICLE INFO

#### Article history:

Received 24 August 2008

Received in revised form 10 February 2009

Accepted 12 February 2009

Available online 25 February 2009

#### PACS:

72.80.Le

73.40.Gk

87.85.fk

#### Keywords:

Polymer semiconductors

Organic thin film transistor (otft, ofet)

P3HT

Gate dielectric leakage currents

Tunneling effects

Biosensors

### ABSTRACT

Organic field-effect transistors (OFETs) with regioregular poly(3-hexylthiophene) (P3HT) have been designed and fabricated aiming at the lowest possible working point (i.e. the adjusted values of gate voltage and drain–source voltage) for the use as sensor in electrolytes. Using thermally grown silicon dioxide with a thickness of 45 nm it has been possible to dramatically lower the gate potential. Even around one volt the channel current and its modulation are still large enough for detection with simple operational amplifiers.

The experimental results indicate a strong dependence of the transistor performance on the solvent used for spin coating the organic film. A theoretical analysis based on an analytical model allowed us to relate the different behavior of the transistor to their mobility, which is in turn dependent on the density of traps. In the context of this paper the leakage currents – as a non-zero gate current – have been analyzed. The observed gate leakage currents of the electrode structures themselves as well as of the complete transistors can be well described by Fowler's and Nordheim's field enhanced tunneling.

© 2009 Elsevier B.V. All rights reserved.

## 1. Introduction

Molecular electronics have been standing in the spotlight of semiconducting materials research for several decades now. Oligo- and polymers seem to offer a way out of the energy dissipating and cost intensive fabrication technologies needed for silicon-based electronics. On the other side, the high sensitivity of the organic molecules to physical and chemical influences seems to open a unique application niche in the sensing field [1–5]. One crucial obstacle in the use of organic transistors is the low mobility of charge carriers in these films and consequently the huge ratio between driving voltage and modulated current which leads to a high vulnerability to noise effects.

If one considers medical and biosensing applications, the currently common voltage levels are not fulfilling the safety requirements in those fields. In many cases – for example when device areas are in contact with ionic solutions – unwanted electrochemical reactions of the molecules could no longer be prevented. The measured signals would therefore be affected by large errors, which would hinder the proper operation of the devices. In the case of cell signal studies, high voltages can disturb ion concentration gradients and induce action potentials. For defining the proper working point of a field-effect transistor, i.e. the adjusted values of gate voltage and drain–source voltage, a suitable range of the current–voltage curves is required. This is typically chosen by applying a constant drain–source voltage and a constant gate voltage at high values of the transistor transconductance (constant voltage mode). Environmental influences acting as gating potential result in corresponding changes of the drain current. Changes in the drain–source current (as sensor output

\* Corresponding author. Fax: +49 89 289 25337.

E-mail addresses: [sgoetz@tum.de](mailto:sgoetz@tum.de), [goetz@gsma.de](mailto:goetz@gsma.de) (S.M. Goetz), [scarpa@tum.de](mailto:scarpa@tum.de) (G. Scarpa).

URL: <http://www.nano.ei.tum.de> (G. Scarpa).

signal) can eventually be converted into voltages and amplified.

One solution to the above mentioned problems involves the enhancement of the current density in the field-effect transistor channel. In recent years great progress has been achieved in the chemical design of competitive active materials [6]. As the identified limiting factor for the carrier mobility has been identified in the hopping process between molecules in the disordered organic films, ordering has proven a successful way [7,8].

A second strategy focused on tailoring the electric field between the gate electrode and the semiconducting layer which is responsible for carrier accumulation. The nature of the insulating material has therefore become an important issue. Assuring high fields at low voltages is achieved in traditional semiconductor technology via the use of *high-k* dielectrics [9–13]. One central drawback is the fact that the expensive *high-k* layer preparation outweighs the simple and cheap deposition methods of organic semiconductors. As the growth processes of these insulators are carried out often at high temperatures [14] or in wet surrounding [11], it is at the moment not clear if they will be a reasonable way to reduce the operating voltage of organic transistor devices. The biocompatibility of *high-k* materials is also an important question. For example barium, widely used in BZT [9] layers, is known to act as an ion channel inhibitor [15]. Lead ions in the alternative compound PZT are also well-known to be poisonous [16]. Toxic side-effects of self-assembling monolayers for gate dielectrics have not been investigated to a satisfying extend. A second problem of the latter mentioned molecules for any use in biochemical applications is their solubility in typical organic fluids [11], which hinders their biochemical application.

In using classical established insulating materials such as SiO<sub>2</sub>, higher electric fields have been achieved by thinning the oxide layer separating the gating electrode and the channel. A dramatic increase of leakage currents is the expected consequence [17,18]. Unfortunately, a clear analysis of the gate currents in organic thin-film transistors (OTFTs) is still missing.

It is worth mentioning that stability problems related to the use of a silicon dioxide insulating layer in sensors can lead to a slow and widely monotonic shift of the threshold voltages [19–21]. The amount of drifting is not only dependent on the material [22], but also very intensely on the deposition process [23,20]. Meanwhile those effects can be side-stepped very elegantly by taking into account the drift with theoretical models [21,24,25] that have even been applied to real-time compensation systems [26]. In this context also a separation of the sensor as a disposable and the read-out as well as compensation circuitry appears reasonable. Mechanical damage in long-term use, e.g. flaking or crumbling, can be prevented quite effectively by covering the dielectric surface with very thin Si<sub>3</sub>N<sub>4</sub>-layers grown by CVD.

We designed and fabricated organic field-effect transistors based on thin silicon dioxide dielectric layers showing the possibility to lower the driving voltages to ranges suitable for in vitro biosensing applications and evaluate the leakage currents in the complete devices. Parallel to the

experimental investigation, we have carried out a theoretical analysis of the transport phenomena in our OTFTs. Such study allows us to extract valuable information about the operation of the device.

## 2. Structure fabrication

The field-effect transistor devices have been fabricated on two-inch boron-doped silicon wafers (with a doping level around 10<sup>18</sup> cm<sup>-3</sup>, conductivity ≈10,000 S/m, obtained from Si-Mat, Landsberg). A bottom-gate bottom-contact structure was used in this work (see the inset of Fig. 2). The use of silicon substrates is justified by considering that silicon CMOS electronics can be used for processing the biosensors' signal.

Initially the wafers have been treated with a full two-step RCA cleaning procedure. On the ⟨100⟩-surface a 45 nm thick silicon dioxide layer was grown in a dry oxidation process at 1000 °C. The back side of the wafers was etched using hydrofluoric acid (HF). Afterwards the source/drain electrode structures were patterned by lift-off on the silicon dioxide dielectric layer in an optical lithography step. A 4 nm titanium sticking layer was followed by a gold coating with a height of about 46 nm deposited by RF-sputtering. The resulting pattern of each transistor was an interdigitated electrode structure (10 mm<sup>2</sup>), half of that area building the source/drain contacts (see Fig. 1). The silicon dioxide surface has explicitly not been treated by silanisation or similar methods, but was left hydrophilic. The values for the channel length *L* were chosen between 10 μm and 100 μm.

The active organic semiconductor (regioregular poly(3-hexylthiophene), P3HT, Sigma-Aldrich) was used as received and spun out of toluene and chloroform (both with

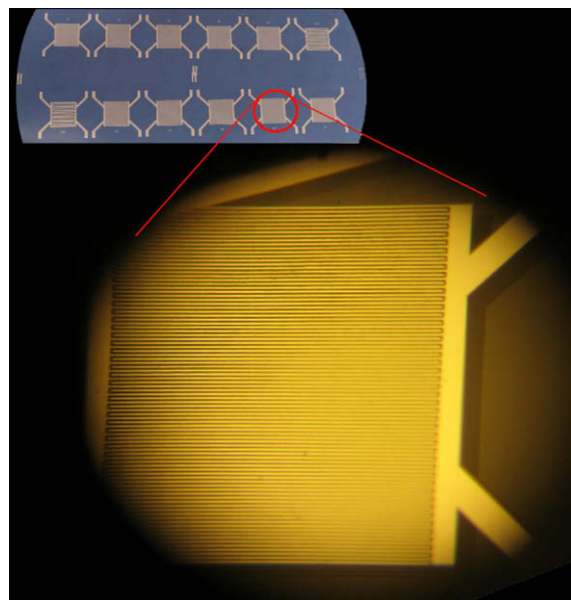


Fig. 1. Layout of the used gold structure for the source/drain electrodes.

a concentration higher than 99.5%), respectively, with a mass relation of 1 to 100.

The films (1000 rpm for 20 s) were deposited onto the wafers under nitrogen atmosphere and no other thermal treatment was applied. An Agilent 4156B parameter analyzer was used to probe the devices. All measurements took place at room temperature in normal atmosphere.

### 3. Experiments

In the following the input characteristics (drain current vs. gate voltage for varying drain–source voltages) as well as the output characteristics (drain current vs. drain–source voltage for varying gate voltages) of various transistors will be analyzed. In addition to such standard measurements, the leakage current across the oxide layer will also be investigated, as it constitutes an important limiting factor for biosensing applications.

#### 3.1. Transistor performance

The field-effect mobility for positive charge carriers of the processed transistors differed between toluene and chloroform solutions, as is well known in the literature [27]. The devices spun with P3HT from the halogenic solvent reached mobility values around  $10^{-3}$  cm<sup>2</sup>/Vs, whereas the toluene samples stayed behind with approximately  $2 \times 10^{-4}$  cm<sup>2</sup>/Vs. These values were extremely constant throughout all samples. Such mobility values have been extracted from the transfer characteristics of the P3HT transistors in the standard way [28].

As the surface of the silicon dioxide was not treated separately, nearly all transistors showed a positive threshold voltage of about +5 V. The described devices displayed a clearly conducting channel already at a zero gate voltage.

Thus, one is allowed to choose a low working point for measurements of current modulations.

The latter is an optimal method for lowering the operating voltage of transistor-based sensor devices.

Fig. 2 shows the output characteristic of an exemplary organic field-effect transistor with P3HT as the semiconductor layer spun out of toluene and the used structure as an inset. The channel length was  $20 \mu\text{m}$  with a ratio of  $W/L = 13350$ . Consistent with previous findings [29], the drain current and the on/off ratio (calculated from the highest on-current and the lowest off-current from the transfer curve) become higher when the channel length is reduced. For the produced devices the current could be controlled over a bandwidth of nearly four decades with a voltage range within 10 volts. The logarithmic transfer curves shown in Fig. 3 stems from a P3HT transistor spun out of toluene with a channel length of  $50 \mu\text{m}$  and a ratio of  $W/L = 2100$ . Compared with the device characteristics shown in Fig. 2 the lower drain current values and on/off ratio are in agreement with the difference in the geometrical dimensions.

#### 3.2. Analysis of leakage currents

The most important fact preventing the use of thin dielectric layers in organic field-effect transistors are leakage currents through the insulator [30]. Nevertheless, a thorough study of the underlying mechanisms is rarely performed. A suitable model could open the way for estimating the exact influence of the insulator's thickness on the leakage behavior, thus helping to design low-voltage transistors and sensors. The dominating effect for leakage currents of the present samples is expected to be a field-assisted tunneling through the oxide between source/drain and gate contacts.

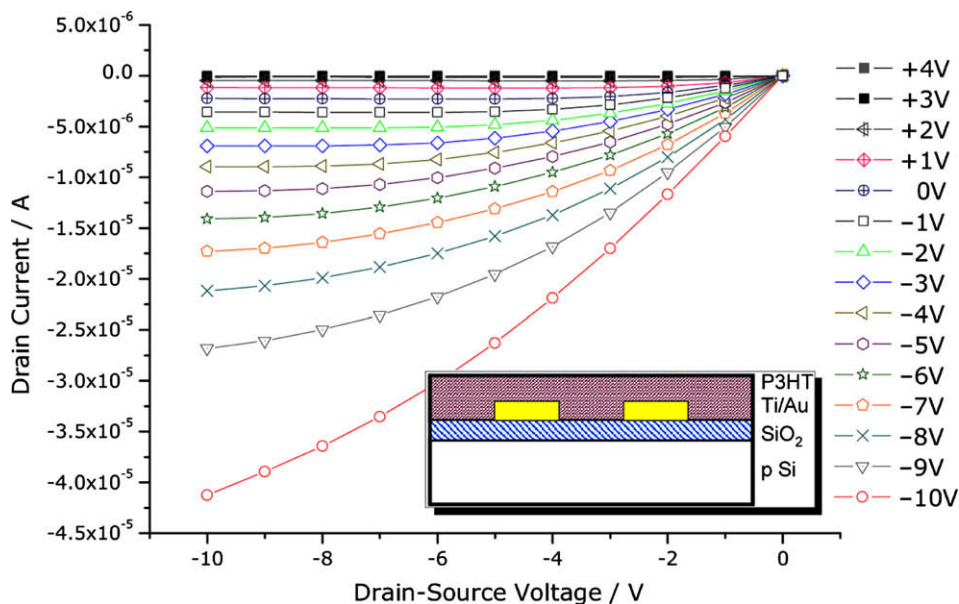


Fig. 2. Output characteristics of an OFET with P3HT spun out of toluene with a channel length of  $20 \mu\text{m}$  and  $W/L = 13350$  on  $45 \text{ nm}$  silicon dioxide, the structure of the transistor samples is presented schematically in the inset.

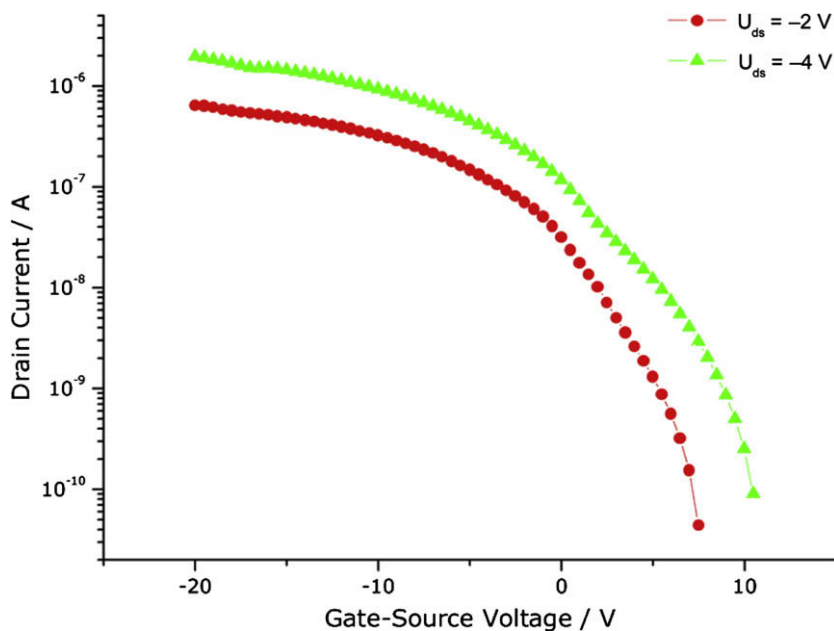


Fig. 3. Transfer behavior of an P3HT transistor with  $L = 50$  nm and  $W/L = 2100$  spun out of toluene.

The leakage current between the bottom gate and the source/drain contacts has been measured with and without the presence of the polymer. The results are displayed in Fig. 5. To show the relatively low current of devices without the polymer layer, the y axis is shown with a log scale. For this measurement, the silicon dioxide surface has also explicitly not been treated by silanisation or by other methods to avoid undefined surface properties. The source and drain contacts have been shorted and biased against the bottom gate electrode. After spin-coating the

P3HT layer, the edge of all 2" wafers has been cleaned with acetone to ensure that no direct ohmic paths to the back gate exist along the P3HT film. Apart from this the semiconductor layer fully covers the substrate. Fig. 6 displays the gate current of the gold source/drain structure fully covered with P3HT, together with the fitting curve (see next section).

In the very detailed work by Jia et al. [31], leakage currents have been reduced by lithographically patterning the P3HT so it is only present in the channel area. In their re-

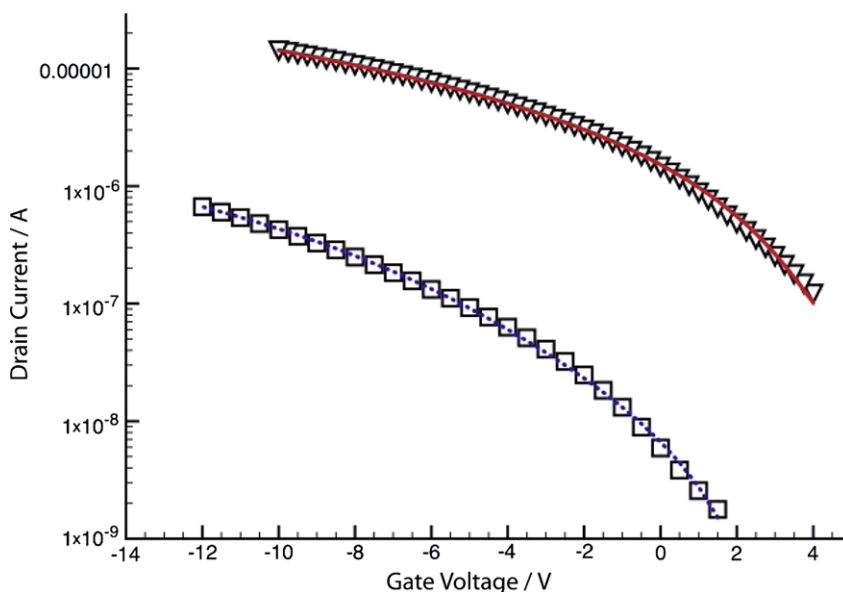


Fig. 4. Fitted subthreshold characteristics of two P3HT devices. Symbols denote experimental data while lines represent model calculations. The upper (lower) curves belong to a device fabricated with chloroform (toluene) solvent.

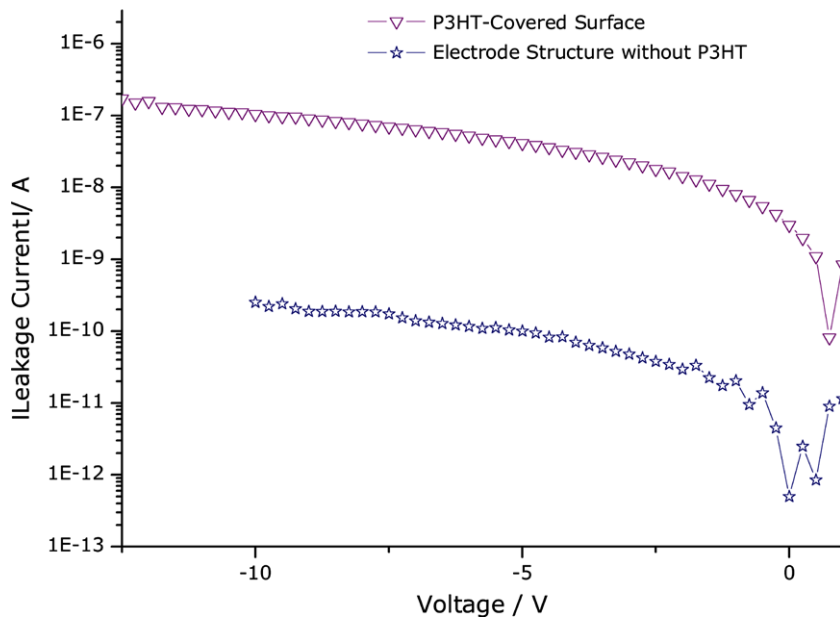


Fig. 5. Leakage currents between the source/drain electrodes and the back gate of the structure itself without an active layer and of the complete transistor.

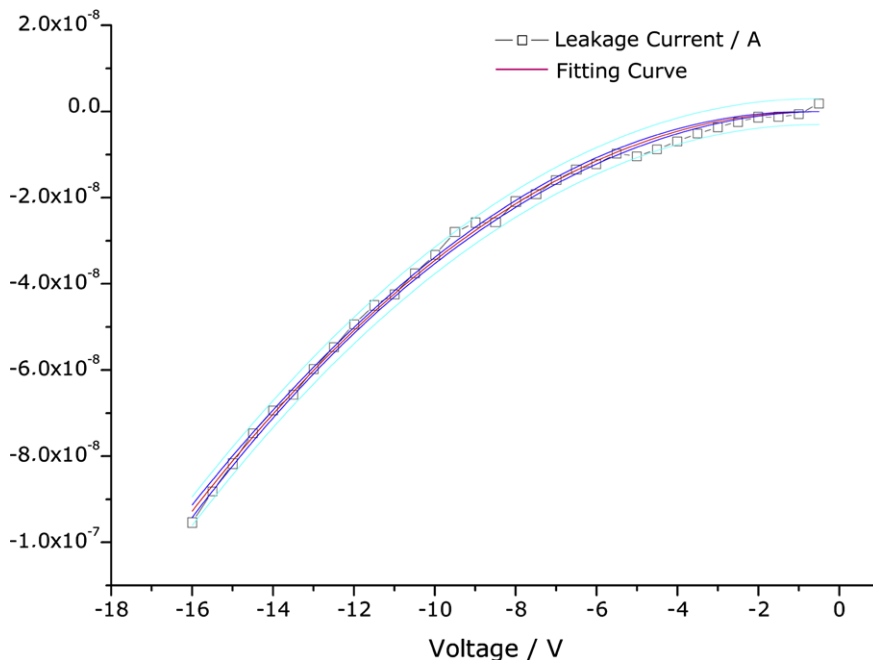


Fig. 6. Leakage current through the thermally grown silicon oxide with a thickness of 45 nm and the fitted formula (1) with the 0.95 side bands around for the error values as solid lines in blue color. In this case the surface of the 2" wafer was fully covered with P3HT.

sults however the leakage currents already of the unpatterned P3HT structures strongly influenced the shape of the  $I$ - $V$  characteristic, although the thermally grown silicon dioxide dielectric layer was 100 nm thick. In our case the distortion on the output characteristics for low drain-source voltages was much lower, although the dielectric layer is among the thinnest used with such a large device area. This may be partly an effect caused by

the cleaning treatments they applied prior to the P3HT solution coating, which we explicitly avoided here.

#### 4. Theoretical analysis

The theoretical analysis focuses on the influence of trap states on the current-voltage characteristics as well as on

the leakage current through the gate at almost zero drain–source bias.

#### 4.1. Analysis of trap states

Our analysis is based both on finite element drift–diffusion simulations (Dessis, Synopsis) and analytic transistor models that account for the influence of trap states on the current–voltage characteristics of the OTFTs. By fitting the sub-threshold characteristics, the approximate energy and density of trap levels can be determined. Details of the models can be found elsewhere [32]. In the following we will compare our model against the experimental characteristics of our set of organic transistors and extract relevant trap parameters. As traps reflect the quality of fabrication process and materials, such parameters are valuable information in performance benchmarking and device optimization.

Chloroform and toluene related films do not only show differences in obvious properties such as color shading. We observed that the fabrication process with chloroform solvent yields higher mobility over a wide variety of tested devices. This behavior has already been reported in [6] and was related to the influence of the solvent on the formation of semi-crystalline regions in the semiconductor [7,27,33]. As an example Yang et al. determined via X-ray diffraction analysis that P3HT films from chloroform solution have a higher tendency to form ordered fibrillar networks without sharp boundaries. In the following, we investigate whether the general mobility trend is related to the presence of trap states. The transfer characteristics of two randomly chosen representative chloroform and toluene P3HT OTFTs are therefore fitted using our model. The resulting curves are shown in Fig. 4. We are able to precisely reproduce the experimental data using the parameters given in Table 1.

In our derivation, the traps are assumed to populate the semiconductor–insulator interface with a density  $N_{At}$ . Their energy  $E_{At}$  is located somewhere between the Fermi level  $E_F$  and the valence band energy  $E_v$ . Generally, the obtained trap densities and energies are within the expected range [34,35]. Our results indicate that the device with inferior mobility (toluene) also exhibits a substantially higher trap density. The traps are additionally located closer to the valence band which increases their effectiveness. This agrees with the notion that less ordered films possess more structural defects which act as trapping centers and reduce the effective mobility [34].

**Table 1**  
Results for exemplary subthreshold analysis.

Solvent	Chloroform	Toluene
$W/L$	2100	510
$\mu(\text{cm}^2/(\text{Vs}))$	$7.2 \times 10^{-4}$	$3.5 \times 10^{-4}$
$V_0$ (V)	4.6	–4
$E_{At}$ (eV)	0.22	0.12
$N_{At}$ ( $\text{cm}^{-2}$ )	$7.7 \times 10^{11}$	$3.9 \times 10^{12}$

**Table 2**  
Results for leakage analysis.

Scenario	$A$ ( $\text{A}/\text{V}^2$ )	$B$ (V)
Without active layer	$(1.87 \pm 0.10) \times 10^{-13}$	$(3.44 \pm 0.62)$
Fully covered surface	$(3.92 \pm 0.10) \times 10^{-10}$	$(3.13 \pm 0.13)$

#### 4.2. Theoretical analysis of leakage currents

In an ideal case, leakage currents should be dominated by tunneling effects. When neglecting thermal effects and barrier lowering mechanisms of the contacting material, the Fowler–Nordheim-tunneling can be simply described by the following approximation [36,37]:

$$I = AU^2 \cdot \exp\left(-\frac{B}{|U|}\right) \quad (1)$$

where  $I$  is the current,  $U$  the potential difference across the insulating layer and  $A$ ,  $B$  are constants left as fitting parameters (the physical meaning of those constants is described in [36]). All the experimental curves have been evaluated using such model. The results are reported in Table 2.

The scenario *without active layer* represents the leakage current through the oxide, while the *fully covered surface* describes the case in which the organic layer was spun onto the whole wafer removing only the outermost areas (at wafer edges) to prevent paths to the bottom gate as mentioned before. Whereas the second parameter  $B$  varies only within a small interval between the two cases,  $A$  shows a variation of more than two orders of magnitude. The  $A$  parameter in Eq. (1) is proportional to the contact cross section area. Since the gate contact extends over the whole wafer, the presence of P3HT effectively increases the overall contact area by a factor 400.

In addition, we believe that the P3HT layer leads to an enhanced tunneling probability, related to a higher electric field under the P3HT than under the gold contact, and to the presence of the LUMO orbital providing a resonant channel for the tunneling process that in turn induces the presence of electrons in the P3HT. A confirmation of this condition can be seen in the data shown in Fig. 7, depicting the standard I–V characteristics of an OTFT (upper panel) together with an enlargement of the low drain-to-source bias region. In such region a positive current is observed at high negative gate bias (evidenced by the circle in the lower panel of Fig. 7), which is a direct signature of the presence of electrons at the interface to the oxide. Tunneling of holes from the side of the semiconductor into the gate contact is excluded, since the energy barrier seen by the holes lays approximately 3 eV above that for the electrons. The present model can only take into account those effects roughly as an increased effective contact area, thus in the coefficient  $A$ . Further experimental and theoretical work for better understanding those processes is in progress.

## 5. Conclusion

In this paper, we demonstrated the possibility to reduce the driving voltages of OTFTs with a bottom contact config-



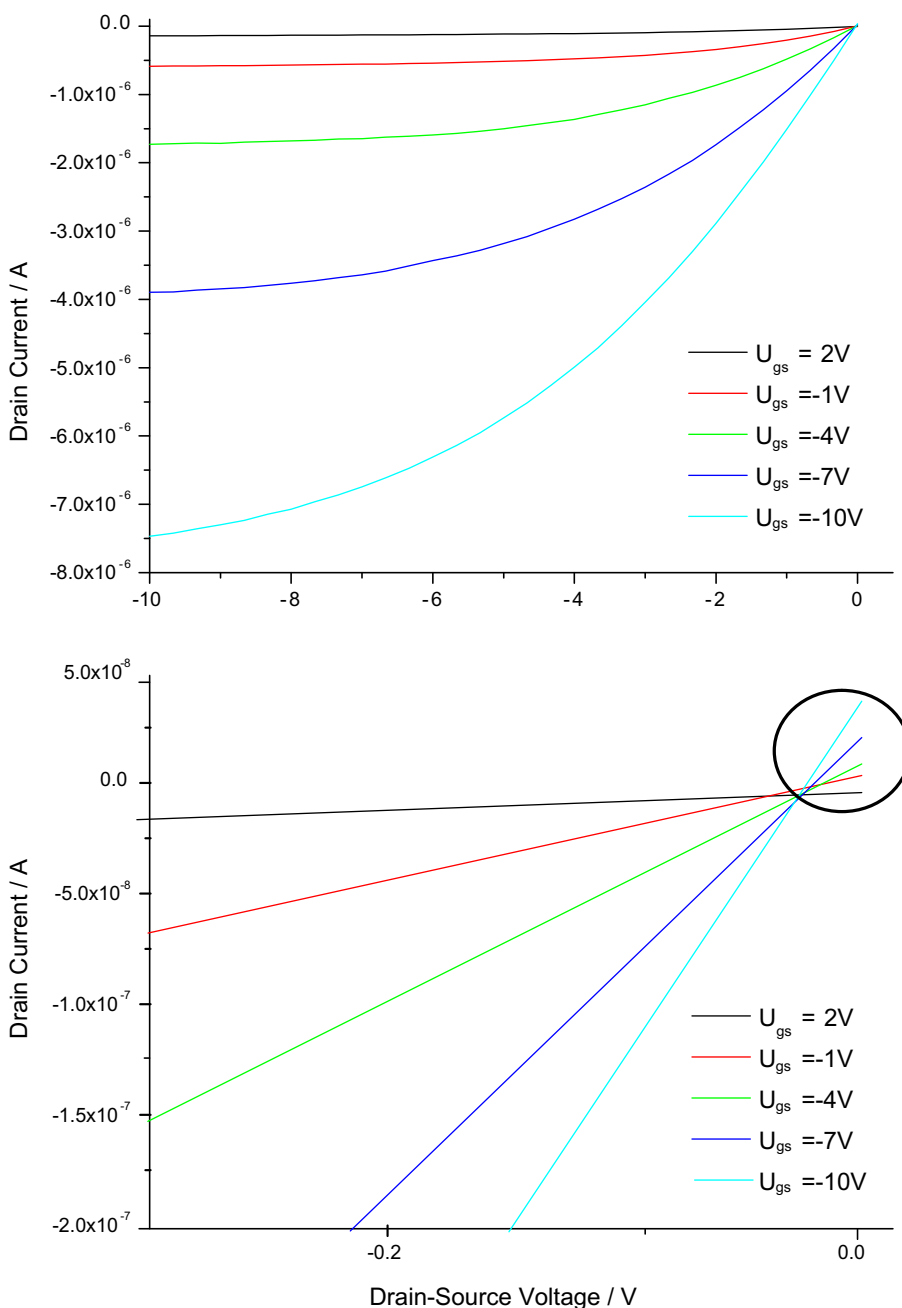


**Fig. 7.** Graph of the output curves from a 20 μm transistor with the same geometry as in Fig. 2. The full area of the 2" wafer was covered with P3HT. The displayed intersection region of the single curves around  $V_{ds} = 0$  V shows already the worst observed distortion of the output characteristics during the study. Nevertheless it is still confined to a very sharp area.

uration by reducing the thickness of the dielectric layer. The values reached for the transistor working point are now compatible with in vitro biosensing applications in order to avoid unwanted electrochemical reactions as well as action potentials of attached cells.

A preliminary test on biocompatibility was performed by the authors with L929 cells from culture. The untreated poly(3-hexylthiophene) showed a positive result after

48 h. All negative reference samples behaved as they were supposed to. Further results will be published later.

First test measurements in electrolytes have shown that the performance of the transistors did not deteriorate. We are currently studying the influence of different solutions on the performance of the devices.

The leakage currents of these devices have been analyzed by means of a field assisted tunneling model based

on the Fowler–Nordheim-formula. The increased leakage currents in the presence of the polymer has been explained in terms of an increased number of electronic states available at one side of the oxide layer with respect to the case in which only the metal contacts are there. The influence of tunneling through thinner oxide layers can be clearly seen. The data extracted from the subthreshold analysis indicate not only that the choice of solvent, which is used during spin coating, influences the observed mobility. Good mobility also coincides with a reduced density of traps.

A comparison with classical biosensors shows that the driving voltages and the modulated current values are within the specification of the required purposes.

## Acknowledgement

The authors would like to thank Prof. Doris Schmitt-Landsiedel and Prof. Walter Hansch for kindly providing access to their fabrication and characterization infrastructure. This work was supported by the cluster of excellence *Nanosystems Initiative Munich* (nim).

## References

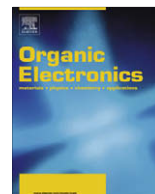
- [1] J.T. Mabeck, G.G. Malliaras, Chemical and biological sensors based on organic thin-film transistors, *Analytical and Bioanalytical Chemistry* 384 (2006) 343–353.
- [2] M. Kaempgen, A. Roth, Transparent and flexible carbon nanotube/polyaniline pH sensor, *Journal of Electroanalytical Chemistry* 586 (2006) 72–76.
- [3] M.C. Tanese, D. Fine, A. Dodabalapur, L. Torsi, Interface and gate bias dependence responses of sensing organic thin-film transistors, *Biosensors and Bioelectronics* 21 (2005) 782–788.
- [4] Y. Sakurai, H.-S. Jung, T. Shimanouchi, T. Inoguchi, S. Morita, R. Kuboi, K. Natsukawa, Novel array-type gas sensors using conducting polymers, and their performance for gas identification, *Sensors and Actuators B* 83 (2002) 270–275.
- [5] M.G.H. Meijerink, D.J. Strike, N.F. de Rooij, M. Koudelka-Hep, Reproducible fabrication of an array of gas-sensitive chemoresistors with commercially available polyaniline, *Sensors and Actuators B* 68 (2000) 331–334.
- [6] C.D. Dimitrakopoulos, D.J. Mascaro, Organic thin-film transistors: a review of recent advantages, *IBM Journal of Research and Development* 45 (1) (2001) 11–27.
- [7] H.G.O. Sandberg, G.L. Frey, M.N. Shkunov, H. Sirringhaus, R.H. Friend, M.M. Nielsen, C. Kumpf, Ultrathin regioregular poly(3-hexylthiophene) field-effect transistors, *Langmuir* 18 (26) (2002) 10176–10182.
- [8] G. Wang, J. Swensen, D. Moses, A.J. Heeger, Increased mobility from regioregular poly(3-hexylthiophene) field-effect transistors, *Journal of Applied Physics* 93 (10) (2003) 6137–6141.
- [9] C.D. Dimitrakopoulos, S. Purushothaman, J. Kyriassis, A. Callegari, J.M. Shaw, Low-voltage organic transistors on plastic comprising high-dielectric constant gate insulators, *Science* 283 (5403) (1999) 822–824.
- [10] C. Batic, H. Jansen, A. Campitelli, S. Borghs, Ta<sub>2</sub>O<sub>5</sub> as gate dielectric material for low-voltage organic thin-film transistors, *Organic Electronics* 3 (2002) 65–72.
- [11] L.A. Majewski, R. Schroeder, M. Grell, One-volt organic transistor, *Advanced Materials* 17 (2) (2005) 192–196.
- [12] M.-H. Yoon, A. Facchetti, T.J. Marks, From the cover: sigma-pi molecular dielectric multilayers for low-voltage organic thin-film transistors, *PNAS* 112 (13) (2005) 4678–4682.
- [13] H. Klauk, U. Zschieschang, J. Pflaum, M. Halik, Ultralow-power organic complementary circuits, *Nature* 445 (2007) 745–748.
- [14] G.D. Wilk, R.M. Wallace, J.M. Anthony, High- $\kappa$  gate dielectrics: current status and materials properties considerations, *Journal of Applied Physics* 89 (10) (2001) 5243–5275.
- [15] J. Argibay, M. Ildefonse, C. Ojeda, O. Rougier, Y. Tourneur, Inhibition by Ba of background current and its modifications by carbachol in frog atrium, *Journal of Molecular and Cellular Cardiology* 15 (11) (1983) 785–788.
- [16] P.B. Hammond, Exposure of humans to lead, *Annual Review of Pharmacology and Toxicology* 17 (1977) 197–214.
- [17] M.D. Austin, S.Y. Chou, Fabrication of 70 nm channel length polymer organic thin-film transistors using nanoimprint lithography, *Applied Physics Letters* 81 (23) (2002) 4431–4433.
- [18] L.A. Majewski, R. Schroeder, M. Grell, Organic field-effect transistors with ultrathin gate insulator, *Synthetic Metals* 144 (2004) 97–100.
- [19] P. Bergveld, Thirty years of ISFETOLOGY: what happened in the past 30 years and what may happen in the next 30 years, *Sensors and Actuators B* 88 (2003) 1–20.
- [20] P. Woias, L. Meixner, P. Fröstl, Slow pH response effects of silicon nitride ISFET sensors, *Sensors and Actuators B* 48 (1998) 501–504.
- [21] R.P. Buck, Kinetics and drift of gate voltages for electrolyte-bathed chemically sensitive semiconductor devices, *IEEE Transactions on Electron Devices* 29 (1) (1982) 108–115.
- [22] C. Batic, G. Borghs, Organic thin-film transistors as transducers for (bio)analytical applications, *Analytical and Bioanalytical Chemistry* 384 (2006) 354–365.
- [23] P.A. Hammond, D. Ali, D.R.S. Cumming, Design of a single-chip pH sensor using a conventional 0.6- $\mu$ m CMOS Process, *IEEE Sensors Journal* 4 (6) (2004) 706–712.
- [24] J. Kakalios, R.A. Street, W.B. Jackson, Stretched-exponential relaxation arising from dispersive diffusion of hydrogen in amorphous silicon, *Physical Review Letters* 59 (9) (1987) 1037–1044.
- [25] S. Jamasb, S. Collins, R.L. Smith, A physical model for drift in pH ISFETs, *Sensors and Actuators B* 49 (1998) 146–155.
- [26] P.A. Hammond, D.R.S. Cumming, Performance and system-on-chip integration of an unmodified CMOS ISFET, *Sensors and Actuators B* 111–112 (2005) 254–258.
- [27] H. Yang, T. Shin, L. Yang, K. Cho, C. Ryu, Z. Bao, Effect of mesoscale crystalline structure on the field-effect mobility of regioregular poly(3-hexylthiophene) in thin-film transistors, *Advanced Functional Materials* 15 (4) (2005) 671–676.
- [28] S.M. Sze, *Physics of Semiconductor Devices*, second ed., John Wiley & Sons, New York, 1981.
- [29] H. Jia, S. Gowrisanker, G.K. Pant, R.M. Wallace, B.E. Gnade, Effect of poly(3-hexylthiophene) film thickness on organic thin film transistor properties, *Journal of Vacuum Science and Technology A* 24 (4) (2006) 1228–1232.
- [30] M. Raja, G. Lloyd, N. Sedghi, S.J. Higgins, W. Eccleston, Critical considerations in polymer thin-film transistor (TFT) dielectrics, *Proceedings of the Materials Research Symposium* 725 (2002) 6.5.1–6.5.6.
- [31] H. Jia, G.K. Pant, E.K. Gross, R.M. Wallace, B.E. Gnade, Gate induced leakage and drain current offset in organic thin film transistors, *Organic Electronics* 7 (2007) 16–21.
- [32] P. Lugli, C. Erlen, A. Pecchia, F. Brunetti, L. Latessa, A. Bolognesi, G. Csaba, G. Scarpa, A. Di Carlo, The simulation of molecular and organic devices: a critical review and a look at future developments, *Applied Physics A* 87 (3) (2007) 593–598, and references therein.
- [33] Z. Bao, A. Dodabalapur, A.J. Lovinger, Soluble and processable regioregular poly(3-hexylthiophene) for thin film field-effect transistor applications with high mobility, *Applied Physics Letters* 69 (26) (1996) 4108–4110.
- [34] A. Bolognesi, M. Berlocchi, M. Manenti, A. Di Carlo, P. Lugli, K. Lmimouni, C. Dufour, Effects of grain boundaries, field dependent mobility and interface trap states on the electrical characteristics of pentacene thin film transistors, *IEEE Transactions on Electronic Devices* 51 (12) (2004) 1997–2003.
- [35] S. Scheinert, G. Paasch, Fabrication and analysis of polymer field-effect transistors, *Physica Status Solidi A* 201 (2004) 1263–1301.
- [36] R.H. Fowler, L. Nordheim, Electron emission in intense electric fields, *Proceedings of the Royal Society of London* 119 (1928) 173–181.
- [37] H.A. Kramers, *Wellenmechanik und halbzahlige Quantisierung*, *Zeitschrift für Physik A* 39 (1926) 828–840.



ELSEVIER

Contents lists available at ScienceDirect

## Organic Electronics

journal homepage: [www.elsevier.com/locate/orgel](http://www.elsevier.com/locate/orgel)

## Migration of small molecules during the degradation of organic light-emitting diodes

Wei-Chun Lin<sup>a</sup>, Wei-Ben Wang<sup>b</sup>, Yu-Chin Lin<sup>a</sup>, Bang-Ying Yu<sup>a</sup>, Ying-Yu Chen<sup>a</sup>,  
Mao-Feng Hsu<sup>b</sup>, Jwo-Huei Jou<sup>b</sup>, Jing-Jong Shyue<sup>a,c,\*</sup>

<sup>a</sup> Research Center for Applied Sciences, Academia Sinica, 128 Section 2, Academia Road, Taipei 115, Taiwan, ROC

<sup>b</sup> Department of Materials Science and Engineering, National Tsing Hua University, Taipei 106, Taiwan, ROC

<sup>c</sup> Department of Materials Science and Engineering, National Taiwan University, Hsin-Chu 300, Taiwan, ROC

## ARTICLE INFO

## Article history:

Received 24 September 2008

Received in revised form 2 December 2008

Accepted 17 February 2009

Available online 27 February 2009

## PACS:

81.70.Jb

85.60.Jb

85.65.+h

## Keywords:

Organic light-emitting diode

Degradation

Migration

C60 cluster ion beam

X-ray photoelectron spectrometry (XPS)

## ABSTRACT

Degradation process of organic light-emitting diodes (OLEDs) is examined directly by X-ray photoelectron spectroscopy with *in situ* high-energy C<sub>60</sub><sup>+</sup> and low-energy Ar<sup>+</sup> co-sputtering. It is proven that this analytical technique clearly indicates the elemental depth profile of as-prepared OLED device (Al/LiF/2,2',2''-(1,3,5-benzinetriyl)-tris(1-phenyl-1-*H*-benzimidazole) (TPBi)/4,4'-bis(carbazol-9-yl)biphenyl:bis(3,5-difluoro-2-(2-pyridyl)-phenyl-(2-carboxypyridyl) iridium (III) (CBP:Flrpic)/poly(ethylenedioxythiophene): poly(styrene sulfonic acid) (PEDOT:PSS)/ITO). Devices operated for different durations are subjected to this profiling technique for studying the change of elemental distribution. In addition to some of the accepted degradation mechanisms, it is observed that small TPBi molecules migrate towards the ITO anode under a direct driving voltage while retaining its original structure. It is also observed that oxygen diffused into the device through the Al cathode and along the Al–organic interface. Molecules with high stereo-hindrance may have less degradation due to the electron migration.

© 2009 Elsevier B.V. All rights reserved.

### 1. Introduction

Over the past two decades, organic light-emitting diodes (OLEDs) have drawn considerable attention as a potential technology for flat panel displays [1–3]. One of the basic requirements in any emissive device is providing adequate stability to ensure a sufficiently long lifetime. In the development of long lifetime devices, a variety of degradation models have been proposed [4].

In general, the degradation of OLEDs can be ascribed to three independent mechanisms: (i) dark-spot degradation,

(ii) catastrophic failure, and (iii) intrinsic degradation [4]. Dark-spot degradation is caused by environmentally induced electrode degradation and can be suppressed by proper encapsulation. Catastrophic failure is the result of the development of electrical shorts across the device and can be alleviated by proper substrate cleaning and adequate control over the fabrication process. On the other hand, although significant works on understanding the intrinsic reason have been reported, a fully consistent mechanism is still lacking and limits the progress of OLED development.

Currently, it is accepted to divide intrinsic degradation into five mechanisms: (i) morphological instability, (ii) unstable cationic aluminum tris(8-hydroxyquinoline) (Alq<sub>3</sub>), (iii) indium migration, (iv) mobile ionic impurities, and (v) immobile positive charge accumulation [4]. Exper-

\* Corresponding author. Address: Research Center for Applied Sciences, Academia Sinica, 128 Section 2, Academia Road, Taipei 115, Taiwan, ROC. Tel.: +886 2 2789 8000/69.

E-mail address: [shyue@gate.sinica.edu.tw](mailto:shyue@gate.sinica.edu.tw) (J.-J. Shyue).

imentally, these mechanisms have been proposed by studying the lifetimes of different devices [4–6]. Therefore, this observation has been indirect. Recently, degradation has been directly studied using a peel-off technique [7] and cross-sectional scanning electron microscopy [8]. However, the depth-resolution and the information regarding chemical composition measured in these means is not sensitive enough to yield a complete picture of the true degradation mechanism.

X-ray photoelectron spectroscopy (XPS) is one of the most common techniques for studying the surface of materials due to its high surface sensitivity and the wealth of elemental and molecule information. When combined with *in situ* ion sputtering, the depth distribution of materials close to the surface can be profiled with nanometer resolution as well. Monoatomic argon sputtering is the most accepted technique for both removing surface contaminants and acquiring information on the depth distribution of a species within a sample. However, this erosion technique is known to cause severe damage to organic samples and cannot be used to analyze organic materials [9].

Recently, buckminsterfullerene ( $C_{60}$ ) ions have been used to sputter materials away in order to study surface composition. Molecular dynamics (MD) calculations suggest that  $C_{60}^+$  ions are more efficient than monoatomic ions in removing material [10] and leaving behind a relatively thin damaged layer [11]. Experimental result also confirmed a reduction in surface damage when using  $C_{60}^+$  sputtering compared with  $Ar^+$  sputtering [12]. The application of  $C_{60}^+$  profiling for thick organic films is further extended by applying a secondary low-energy  $Ar^+$  ion beam concurrently [13]. Although it is found that this analysis technique causes comparable damage to inorganic specimens [14], it provides a direct method for analyzing the distribution of materials in organic electronics with high depth-resolution and is adopted in this work in the attempt to study the degradation processes of OLED.

## 2. Experimental

### 2.1. Fabrication of OLED devices

Details on the fabrication and properties of the OLED devices can be found elsewhere [15]. In short, a hole-transporting layer (HTL) consisting of poly(ethylenedioxythiophene): poly(styrene sulfonic acid) (PEDOT:PSS, 35 nm), Baytron® P VP Al 4083, PEDOT:PSS ~1:4.5) was spin-coated on a 125 nm-thick indium tin oxide (ITO) glass. A light emissive layer (EL, 40 nm) comprising a 4,4'-bis(carbazol-9-yl)biphenyl (CBP) molecular host doped with 14 wt% bis(3,5-difluoro-2-(2-pyridyl)-phenyl-(2-carboxypyridyl) iridium (III) (Flrpic) was spin-coated on the HTL. On the EL, an electron-transporting layer (ETL, 32 nm) consisting of 2,2',2''-(1,3,5-benzinetriyl)-tris(1-phenyl-1-*H*-benzimidazole) (TPBi) was then thermal-evaporated. Finally, an additional electron injection layer (EIL, 0.7 nm) of LiF and the Al cathode (150 nm) were evaporated on the ETL. The luminescence area is 2 mm × mm and each chip contains 4 devices separated by 2 mm.

### 2.2. XPS measurements

The experiments were performed with a PHI 5000 VersaProbe (Chigasaki, Japan) XPS system. Micro-focused (25 W, 100 μm) Al K $\alpha$  X-ray was used and the take-off angle of the photoelectron was 45°. Throughout data acquisition, the X-ray and acceptance lens of the analyzer was rastering over an area of 500 μm × 500 μm and centered at the center of luminescence area of the device. A dual-beam charge neutralizer (7 V  $Ar^+$  and 30 V flooding electron beam) was used for charge compensation. The  $Ar^+$  sputter source was operated at 0.2 kV, 300 nA with an incident angle of 45°. The  $C_{60}^+$  ion source was operated at 10 kV, 10 nA with an incident angle of 70°. Both ion beams were rastered over an area of 2 × 2 mm at the same time. The beam currents were measured with the target current on an Au foil and were stable for at least two weeks of continuous operation. Between each profile, reference devices on the same chip were profiled to ensure the steady sputtering condition and to eliminate chip-to-chip variation. This experimental design also allows the direct comparison between degraded device and as-prepared referencing device.

## 3. Results and discussion

Fig. 1a shows the elemental depth profile of the as-prepared (reference) OLED device using *in situ*  $C_{60}^+$  and  $Ar^+$  sputtering concurrently in the XPS. At the top-most surface, oxidized Al (as in  $Al_2O_3$ ) is observed, as Al is known to be easily oxidized in the air. At the bottom of the Al layer, O is also observed. The O 1s binding energy in this region (180–220 min) is 532.4 eV (Fig. 1b), which is close to the oxygen in the top-most  $Al_2O_3$  layer. In addition, two Al 2p peaks are observed at 72.7 and 75.4 eV (Fig. 1c) that indicate  $Al^0$  and  $Al^{3+}$ , respectively. In comparison, oxygen is not observed on identical organic layers that do not have the Al cathode so that the oxygen source cannot be attributed to the adsorption [13]. It can be therefore concluded that oxygen diffuses through the interface of the Al cathode and the organic layers; hence both sides of the Al cathode are oxidized. Right below the oxidized layer of the Al metal, traces of Li and F at ~1:1 ratio are observed.

Below the inorganic layers, TPBi and CBP layers that have different C to N ratios are observed. Although the C concentration is slightly higher than the value expected due to carbon implantation from the  $C_{60}^+$  beam, the difference between TPBi and CBP is still observable. Trace amount of Ir is also observed at the CBP layer, indicating that the Flrpic dye is mainly confined in the CBP layer; hence the host-guest EL structure is evident. Following with the EL, S is observed, indicating the HTL layer, which consists of PEDOT:PSS. At the interface of EL and HTL, the Ir signal extends slightly deeper into the HTL than N. This result suggests that some Flrpic-dye from the EL infiltrates into the HTL. Finally, below the HTL, ITO and glass substrate are observed. It is noteworthy that although the total thickness of the organic layer is thinner than that of inorganic layer, the time required to remove the organic layer is longer. The apparent slower sputtering rate of organic

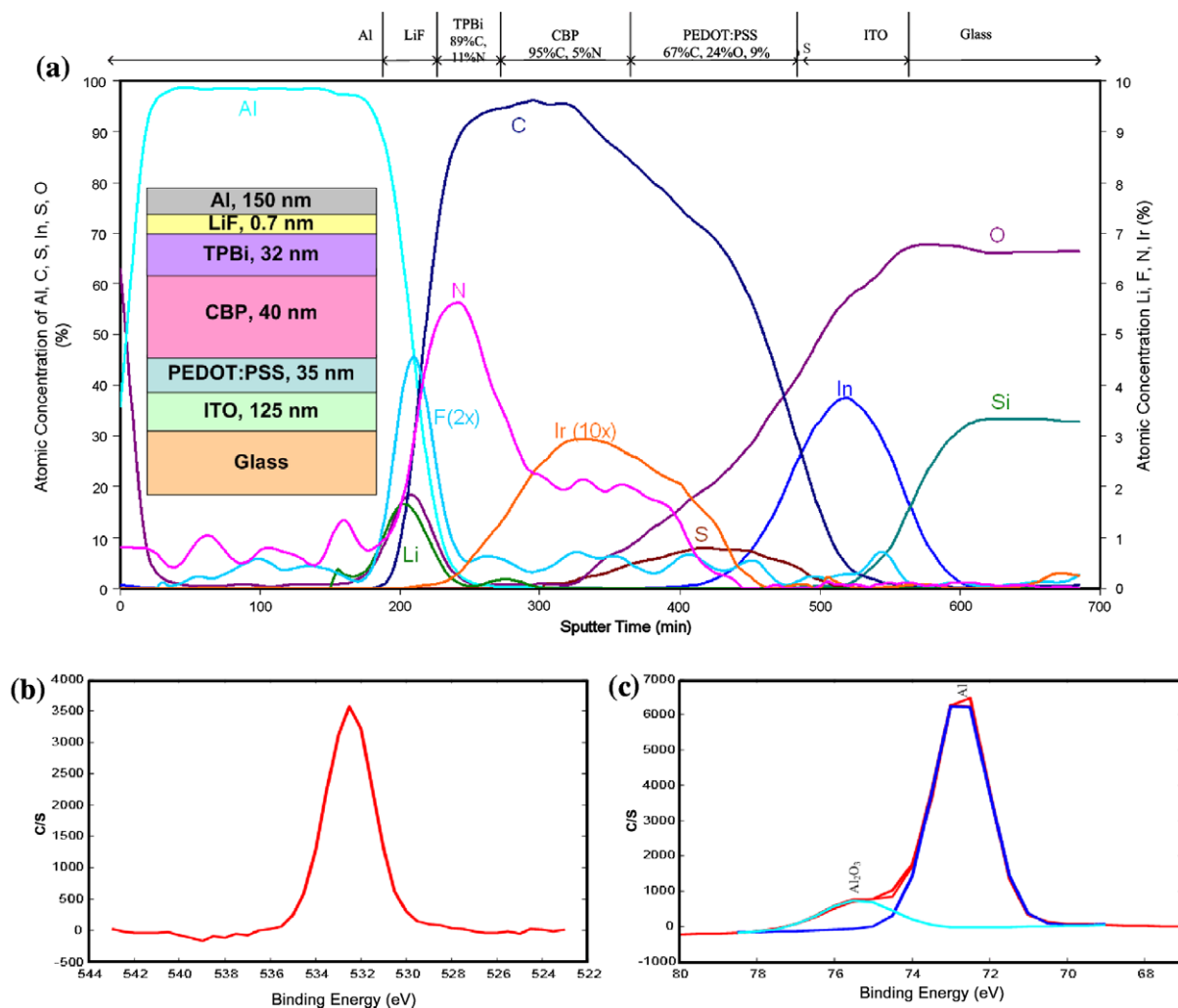


**Fig. 1.** (a) XPS elemental depth profiles of as-prepared (reference) OLED device. (b) O 1s spectrum extracted from 180 to 200 min. (c) Al 2p spectrum extracted from 180 to 200 min.

layer maybe be attributed to ion-induced cross-linking of organic molecule [16].

The depth profile correctly reflects the multilayer structure of the referencing OLED device. Therefore, it can be concluded that such a profiling technique is suitable for profiling the OLED device. To study the degradation of the OLED device, as-deposited devices are operated at a constant 5 V forward bias for 15 min, 1, 3, 6, and 12 h and are subject to depth profiling. Fig. 2a shows the depth profile of the device after operating for 12 h in an ambient environment.

It is clear that a significant portion of the Al cathode is oxidized showing increased oxygen concentration throughout the Al layer. Therefore, the organic layer appears later in the sputtering because the sputtering rate of  $\text{Al}_2\text{O}_3$  is lower than that of Al. In addition, Al diffused into the organic layer. Based on the binding energy of the Al 2p peak, both  $\text{Al}^0$  and  $\text{Al}^{3+}$  are observed (350–500 min, Fig. 2b). Such results suggest that electron migration of Al may have occurred. In addition, the LiF signal indicates

that  $\text{Li}^+$  migrated into the Al cathode and  $\text{F}^-$  diffused slightly into both Al and the organic layer.

In the organic layers, all the profiles are more diffused than that of the reference device; thus, it is evident that the interface is broadened by the electrical current. By examining the elemental profile more closely, it is obvious that the change in the C to N ratio is less clear in the ETL/EL interface than that in the reference device (Fig. 2c). The increase of N ratio in the EL region indicates that the N-rich ETL (TPBi, 11% N) diffuses into the EL (CBP, 5% N). Nevertheless, the N 1s doublet at 398 and 400 eV due to the non-planar TPBi structure [9] is still observed (350–500 min, Fig. 2d). Note that the peak at 400 eV is stronger than that at 398 eV due to the overlap with the N in CBP. Therefore, it can be concluded that the TPBi is not decomposed and the whole molecule migrates into the EL under the electric current.

Similarly, the change in atomic ratio is also observed in the N to S ratio in the EL/HTL interface and the S to In ratio in the HTL/ITO interface. In addition, trace amounts of C

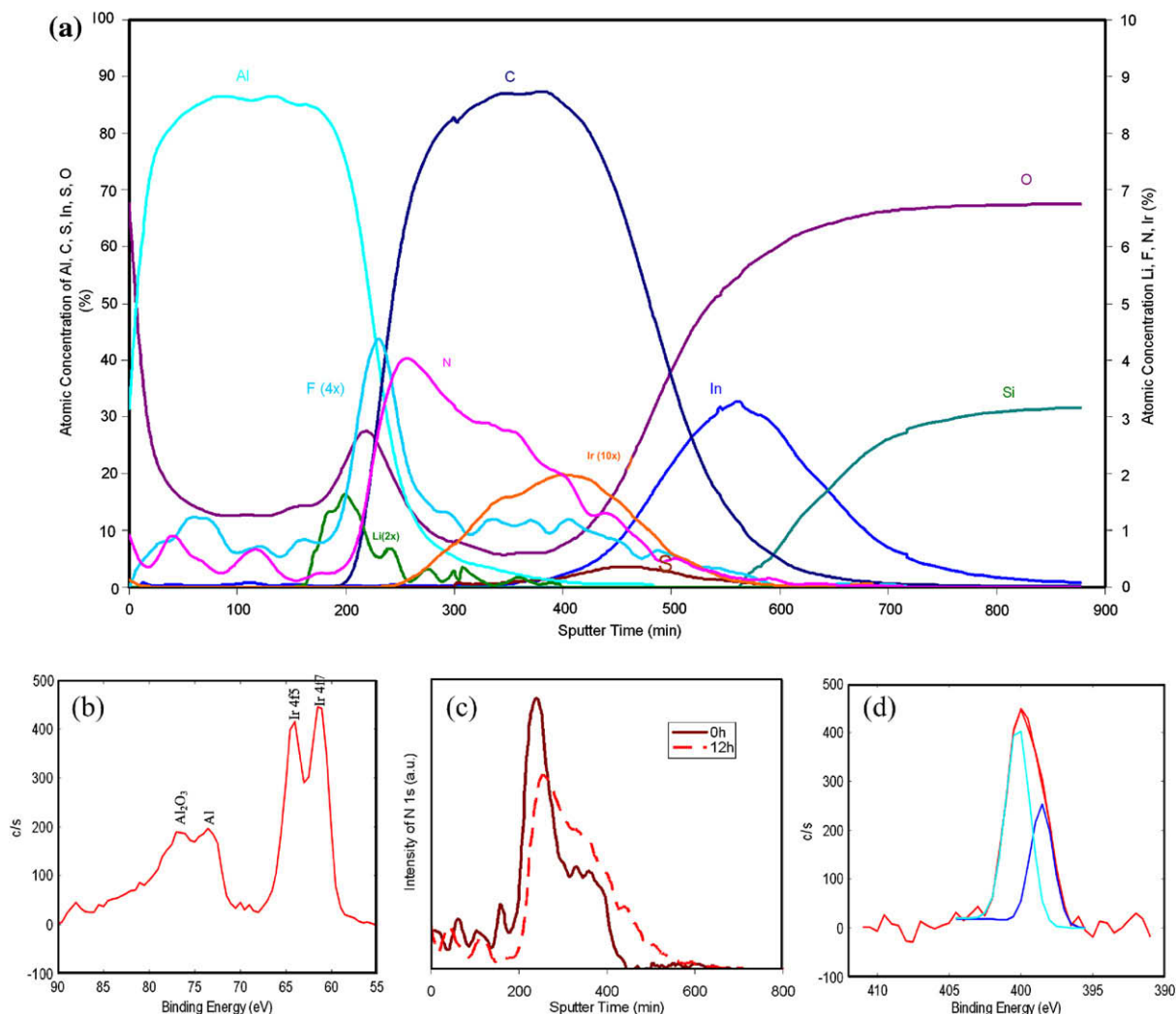


**Fig. 2.** (a) XPS elemental depth profiles of OLED device aged at 5 V forward bias for 12 h. (b) Ir 4f and Al 2p spectra of aged device extracted between 350 and 500 min. (c) N distribution before (solid line) and after operation for 12 h (broken line). (d) N 1s spectrum of aged device extracted between 350 and 500 min.

and N are observed deep in the ITO layer (600–700 min) where no S is observed in the same region. These results indicate that the TPBi and/or CBP migrate into the ITO anode through the PEDOT:PSS layer while the polymeric HTL does not migrate into the ITO. As the small-molecular organics migrate into the ITO layer and possibly In diffused into the organic layer, the thickness of the In-containing layer increases; thus the time required to remove the ITO layer becomes longer.

In order to obtain information on the progress of degradation, similar profiles are acquired after the device is operated for 15 min, 1, 3, and 6 h (Fig. 3). After 15 min of operation, most of the profiles remain unchanged. However, the change in the N to C ratio reflects that the interface between TPBi and CBP is less sharp than that in the reference device. As time progresses, the N intensity at the Al-TPBi interface decreases while the N intensity in CBP increases. It is clear that the migration of TPBi into CBP starts immediately after applying voltage.

It is reported that, although the efficiency is lower, a device using Al complexes as hole-blocking-layers yields longer device lifetime than that by employing TPBi [17]. This difference in lifetime can be explained by molecule migration. Al complexes are ball-shaped molecules that have higher stereo-hindrance than that of planar TPBi. Therefore, under a similar driving force, it is easier for TPBi to migrate through the pores of amorphous organic materials. It is also reported that using inorganic silicate nanodots in the HTL, the lifetime increases [18]. Since the silicate is crystalline, the dense structure acts as a blockade to small molecules, thus molecular migration is suppressed and the lifetime increased.

After 1 h operation, the thickness of the surface  $\text{Al}_2\text{O}_3$  layer increases significantly, indicating that oxidation of the Al cathode occurs. Nevertheless, besides oxidation of the Al cathode and continuous migration of TPBi into CBP, there is no other change in the device at this stage of aging. At 3 h, a considerable amount of oxygen diffuses

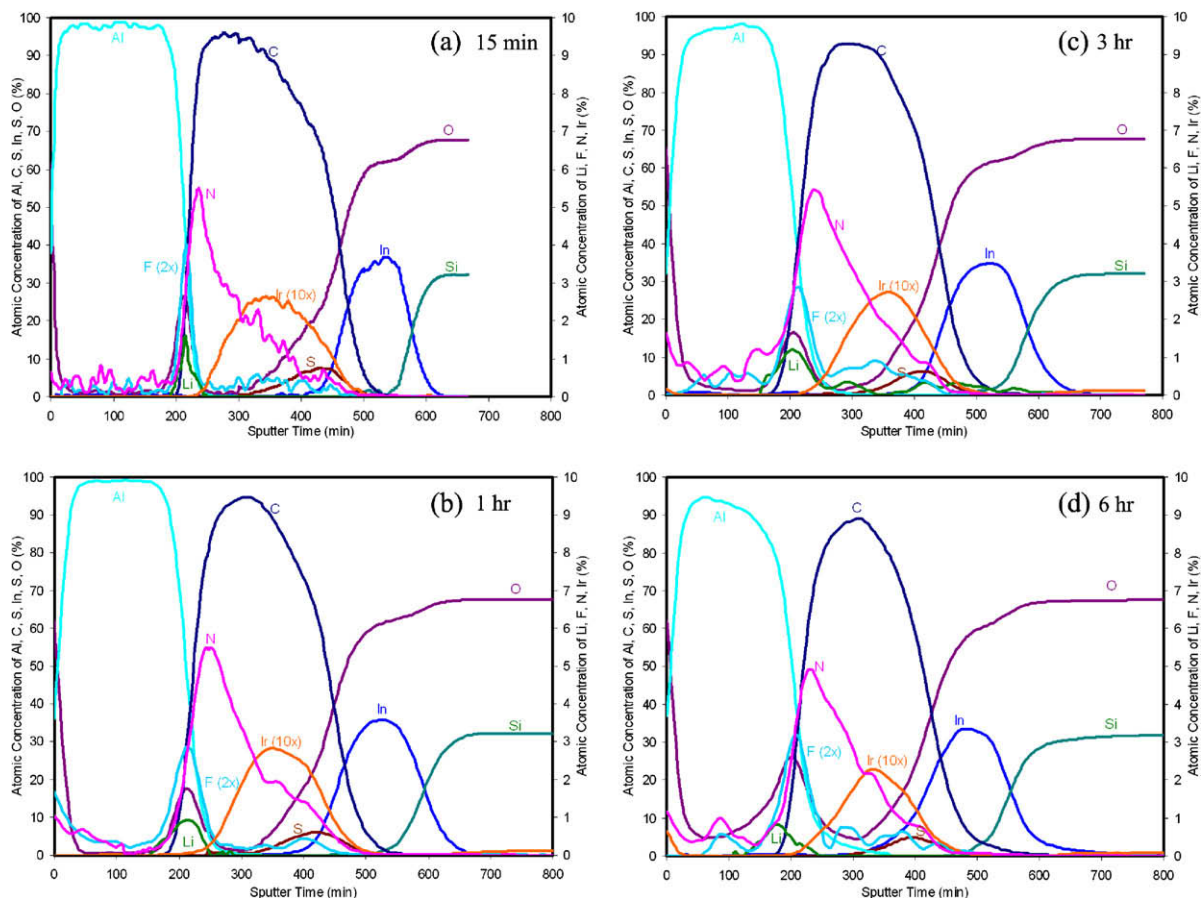


Fig. 3. XPS elemental depth profiles of OLED devices aged at 5 V forward bias for different times.

into the Al cathode from the surface and diffusion of Li into the cathode is observed. A trace amount of Al atoms is also observed in the organic layer, indicating the occurrence of electron-migration of the Al atoms.

At 6 h, a significant amount of oxygen is observed at the interface of the cathode and the organic layer. The oxygen concentration is higher at the Al-organic interface than on the outer surface at this point. This result suggests that oxygen diffuses into the organic layer through the interface. Even though diffusion through the interface is observed later than that through the Al cathode, the diffusion rate through the interface is actually higher; the oxygen has to diffuse through a distance of 500  $\mu\text{m}$  to reach the analyzing region while only 150 nm is required through the Al layer. This result confirms the hypothesis that device degradation is caused by oxygen diffusion along the interface [19]. In addition, at this stage, the migration of Li into Al and organic materials into ITO is clear.

#### 4. Conclusion

Using *in situ* co-sputtering of high-energy  $\text{C}_{60}^+$  and low-energy  $\text{Ar}^+$  in XPS, OLED devices (Al/LiF/TPBi/CBP:Flrpic/PEDOT:PSS/ITO) operated for different times are profiled to study the degradation process. As soon as the device is

under voltage bias, the TPBi molecules in the ETL start to migrate toward the ITO anode. Eventually, small organic molecules migrate all the way down to the ITO layer. Nevertheless, the molecular structure of TPBi appears unchanged during this migration. As the device is not encapsulated, oxygen diffuses into the device through the Al cathode and along the Al/TPBi interface, and the diffusion rate is faster through the interface than that through the Al layers. Meanwhile, while F appears to be stationary, Li diffuses into the Al cathode and Al diffuses into organic layers.

#### Acknowledgement

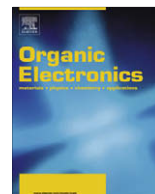
Sponsorship by Academia Sinica and Taiwan National Science Council through Grant number 96-2113-M-001-012-MY2 and 96-2120-M-002-018.

#### References

- [1] P.L. Burn, S.C. Lo, I.D.W. Samuel, *Adv. Mater.* 19 (2007) 1675.
- [2] J. Kido, M. Kimura, K. Nagai, *Science* 267 (1995) 1332.
- [3] W. D'Andrade, S.R. Forrest, *Adv. Mater.* 16 (2004) 1585.
- [4] H. Aziz, Z.D. Popovic, *Chem. Mater.* 16 (2004) 4522.
- [5] T.-Y. Chu, Y.-H. Lee, O.-K. Song, *Appl. Phys. Lett.* 91 (2007) 223509.
- [6] Y. Luo, H. Aziz, Z.D. Popovic, G. Xu, *J. Appl. Phys.* 101 (2007) 034510.
- [7] H.J. Shin, M.C. Jung, J. Chung, K. Kim, J.C. Lee, S.P. Lee, *Appl. Phys. Lett.* 89 (2006) 063503.

- [8] R. Czerw, D.L. Carroll, H.S. Woo, Y.B. Kim, J.W. Park, *J. Appl. Phys.* 96 (2004) 641.
- [9] Y.-Y. Chen, B.-Y. Yu, W.-B. Wang, M.-F. Hsu, W.-C. Lin, Y.-C. Lin, J.-H. Jou, J.-J. Shyue, *Anal. Chem.* 80 (2008) 501.
- [10] B. Czerwinski, R. Samson, B.J. Garrison, N. Winograd, Z. Postawa, *Vacuum* 81 (2006) 167.
- [11] Z. Postawa, B. Czerwinshi, M. Szewczyk, E.J. Smiley, N. Winograd, B.J. Garrison, *Anal. Chem.* 75 (2003) 4402.
- [12] B.-Y. Yu, Y.-Y. Chen, W.-C. Lin, Y.-C. Lin, J.-J. Shyue, *Appl. Surf. Sci.* 255 (2008) 2490.
- [13] B.-Y. Yu, Y.-Y. Chen, W.-B. Wang, M.-F. Hsu, S.-P. Tsai, W.-C. Lin, Y.-C. Lin, J.-H. Jou, C.-W. Chu, J.-J. Shyue, *Anal. Chem.* 80 (2008) 3412.
- [14] Y.-Y. Chen, Y.-C. Lin, B.-Y. Yu, W.-C. Lin, J.-J. Shyue, *Analyst* (2009), doi:10.1039/b814729a.
- [15] J.-H. Jou, W.-B. Wang, M.-F. Hsu, C.-P. Liu, C.-C. Chen, C.-J. Wang, Y.-C. Tsai, J.-J. Shyue, S.-C. Hu, C.-C. Chiang, H. Wang, *PIERS Online* 4 (2008) 351.
- [16] A.G. Shard, P.J. Brewer, F.M. Green, I.S. Gilmore, *Surf. Interface Anal.* 39 (2007) 294.
- [17] R.C. Kwong, M.R. Nugent, L. Michalski, T. Ngo, K. Rajan, Y.-J. Tung, M.S. Weaver, T.X. Zhou, M. Hack, M.E. Thompson, S.R. Forrest, J.J. Brown, *Appl. Phys. Lett.* 81 (2002) 162.
- [18] J.-H. Jou, C.-C. Chen, Y.-C. Chung, M.-F. Hsu, Ching-Hsuan Wu, S.-M. Shen, M.-H. Wu, W.-B. Wang, Y.-C. Tsai, C.-P. Wang, J.-J. Shyue, *Adv. Funct. Mater.* 18 (2008) 121.
- [19] M. Schaer, F. Nüesch, D. Berner, W. Leo, L. Zuppiroli, *Adv. Funct. Mater.* 11 (2001) 116.





## Topographical and morphological aspects of spray coated organic photovoltaics

Claudia N. Hoth<sup>a,b,\*</sup>, Roland Steim<sup>a,c</sup>, Pavel Schilinsky<sup>a</sup>, Stelios A. Choulis<sup>d</sup>, Sandro F. Tedde<sup>e</sup>, Oliver Hayden<sup>e</sup>, Christoph J. Brabec<sup>a,\*</sup>

<sup>a</sup> Konarka Technologies GmbH, Landgrabenstr. 94, D-90443 Nürnberg, Germany

<sup>b</sup> Department of Energy and Semiconductor Research, University of Oldenburg, D-26129 Oldenburg, Germany

<sup>c</sup> Light Technology Institute, University of Karlsruhe (TH), D-76131 Karlsruhe, Germany

<sup>d</sup> Department of Mechanical Engineering and Materials Science and Engineering, Cyprus University of Technology, 3603 Limassol, Cyprus

<sup>e</sup> Siemens AG, Corporate Technology, CT MM1, Günther-Scharowsky-Str. 1, D-91058 Erlangen, Germany

### ARTICLE INFO

#### Article history:

Received 2 December 2008

Received in revised form 13 February 2009

Accepted 14 February 2009

Available online 23 February 2009

#### PACS:

81.15.Rs

72.40

84.60.Jt

82.35.Cd

72.80.Le

72.80.Rj

#### Keywords:

Spray coating

Photovoltaics

Solar cells

Polymers

Fullerenes

P3HT

### ABSTRACT

Herein we discuss the topographical and nanomorphological aspects of spray deposited organic photovoltaics. We show that the solvent properties have a massive impact on the topography, but less on the nanomorphology formation of composites based on the electron donor poly(3-hexylthiophene) (P3HT) and the electron acceptor [6,6]-phenyl C61 butyric acid methyl ester (PCBM). An adapted solvent mixture consisting of ortho-dichlorobenzene (oDCB) and 1,3,5-trimethylbenzene (mesitylene) allows us to demonstrate spray coated organic photovoltaic devices with 3.1% power conversion efficiency (PCE). Moreover, we show that spray coating is a feasible technology to deposit all solution processable layers of organic solar cells, including the hole transporting layer poly(3,4-ethylene dioxythiophene) doped with polystyrene sulphonic acid (PEDOT:PSS) as well and demonstrate fully spray coated devices with 2.7% PCE.

© 2009 Elsevier B.V. All rights reserved.

Organic photovoltaics (OPVs) are of increasing interest as new materials for future light-activated energy sources. OPVs have the virtue of being lightweight and flexible and could open up many new applications due to their easy processing offering the potential for low fabrication cost [1]. A variety of approaches have been used to deposit or-

ganic semiconductors based on the nature of those materials. The commonly applied technique is the solution-processed deposition, such as spin coating, doctor blading [2] or printing, which are evaluated as one of the future key technologies opening up completely new applications and markets for photovoltaics [1]. Printing technologies such as screen printing [3], gravure, offset, micro-contact and inkjet printing [4] are attractive candidates to utilize a low-cost OPV roll to roll production.

At present, bulk heterojunction (BHJ) structures based on blends of polymer donor and a highly soluble fullerene

\* Corresponding authors. Address: Konarka Technologies GmbH, Landgrabenstr. 94, D-90443 Nürnberg, Germany (C.N. Hoth).

E-mail addresses: [choth@konarka.com](mailto:choth@konarka.com) (C.N. Hoth), [cbrabec@konarka.com](mailto:cbrabec@konarka.com) (C.J. Brabec).

derivative as acceptor have been the material system with the highest reported power conversion efficiencies (PCE) [5] and the demonstration of solar cells with 5% PCE under calibrated AM 1.5 conditions have been regarded as an important milestone to prove the technology's potential [6]. Among other technologies, spray coating [7] was recently reported as an elegant coating technique for the fabrication of BHJ devices. Recently, Vak et al. showed that spray coating the active layer from chlorobenzene solutions gives highly efficient devices [8]. Furthermore, Green et al. presented spray deposited poly(3-hexylthiophene) (P3HT): [6,6]-phenyl C61 butyric acid methyl ester (PCBM) films from a variety of common organic solvents with different boiling points [9].

In this communication, we investigate spray coating as a production technique for depositing the active layer in organic BHJ solar cells. We specifically investigate the film formation, surface topography and the morphology of spray coated mono- and bilayers based on pristine solvents compared to mono- and bilayers based on multiple solvent systems. Furthermore, we studied the impact of the ink formulation and specifically the solvent properties such as vapor pressure, boiling point, viscosity and surface tension on the topography, nanomorphology

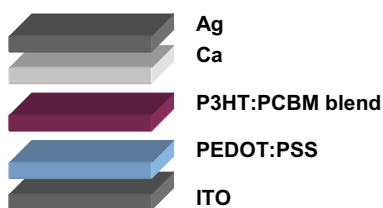


**Fig. 1.** Device architecture of a solar cell ITO/PEDOT:PSS/P3HT:PCBM blend/Ca/Ag under study.

**Table 1**  
Solvent properties.

Solvent	Vapor pressure at 20 °C (mm Hg)	Boiling point (°C)	Surface tension (dynes cm <sup>-1</sup> )	Viscosity at 25 °C (mPa)
Chlorobenzene	11.70	132	33.0	0.76
ortho-Dichlorobenzene	1.20	180	37.0	1.32
Mesitylene	1.86	165	28.8	1.04

**Table 2**  
Measured values of ink properties with appropriate random errors, thickness of spray coated active layer and rms roughness.

Ink formulation	Surface tension (dynes cm <sup>-1</sup> )	Contact angle on PEDOT:PSS (°)	Kinematic viscosity (m <sup>2</sup> s <sup>-1</sup> )	Active layer thickness mono/bi (nm)	RMS roughness mono/bi (nm)
P3HT:PCBM in chlorobenzene ( <b>IF1</b> )	29.5 ± 0.1	9.7 ± 0.2	1.8 ± 0.02	250/400	67.9/46.0
P3HT:PCBM in oDCB/mesitylene ( <b>IF2</b> )	28.0 ± 0.3	7.7 ± 0.2	2.4 ± 0.2	250/400	24.1/51.7

and device performance of spray coated photoactive P3HT:PCBM films. In detail, we show that a mixture of high and low boiling solvent, in our case 68% ortho-dichlorobenzene (oDCB) and 32% 1,3,5-trimethylbenzene (mesitylene) allows to produce spray coated organic solar cells with AM 1.5 calibrated PCE of over 3.1%. Interestingly, the large surface roughness of the films does not seem to impact the device performance. Moreover, we show that spray coating is a feasible technology to deposit all solution processable layers of organic solar cells, including poly(3,4-ethylene dioxythiophene) doped with polystyrene sulphonic acid (PEDOT:PSS) as well and demonstrate fully spray coated cells with a PCE of 2.7%. The device performance of spray coated films is demonstrated based on the common device configuration glass/ITO/doctor bladed or spray coated PEDOT:PSS/spray coated active layer/Ca/Ag, depicted in Fig. 1.

In the spray coating technique, organic thin films are generated stepwise. Single droplets are deposited by the transfer gas pressure with a high velocity onto the substrate. Spray coated films are formed via droplets, drying immediately when hitting the surface of the substrate. This is very different to most conventional printing technologies such as inkjet printing [4], where the film formation is based on the spreading of droplets and combining with adjacent droplets, forming a liquid bulk that dries during vaporization of the organic solvents. To achieve rapid drying, the semiconductor ink must fulfill certain requirements, which are primarily defined by the solvent properties, such as boiling point, vapor pressure, viscosity and surface tension, as presented in Table 1. In this study, the ink is processed at ambient conditions and is not heated during the spray deposition. To be compatible with the nozzle of the airbrush, the viscosity needs to be rather low at room temperature. High viscous inks require higher temperatures to decrease the viscosity and adapt the fluid properties on the airbrush setup. If the nozzle-to-substrate distance is constant, inks with too low drying rates the liquid droplets are immediately pushed sideways by the pressure gas of the airbrush, resulting in non-uniform wetting. On the other hand, organic solvents with too high evaporation rates, at a certain nozzle-to-substrate distance the spray deposited droplets may be dry prior to reaching the substrate surface and a film deposition is inhibited. According to this, we studied two ink formulations differing in the drying behaviour. The first ink formulation is based on pristine chlorobenzene (**IF1**) and features a low boiling point and high vapor pressure resulting in rapid drying. The low surface tension for the blended semiconductor solutions guarantees decent wettability, which is also indicated by the small contact angle, represented in

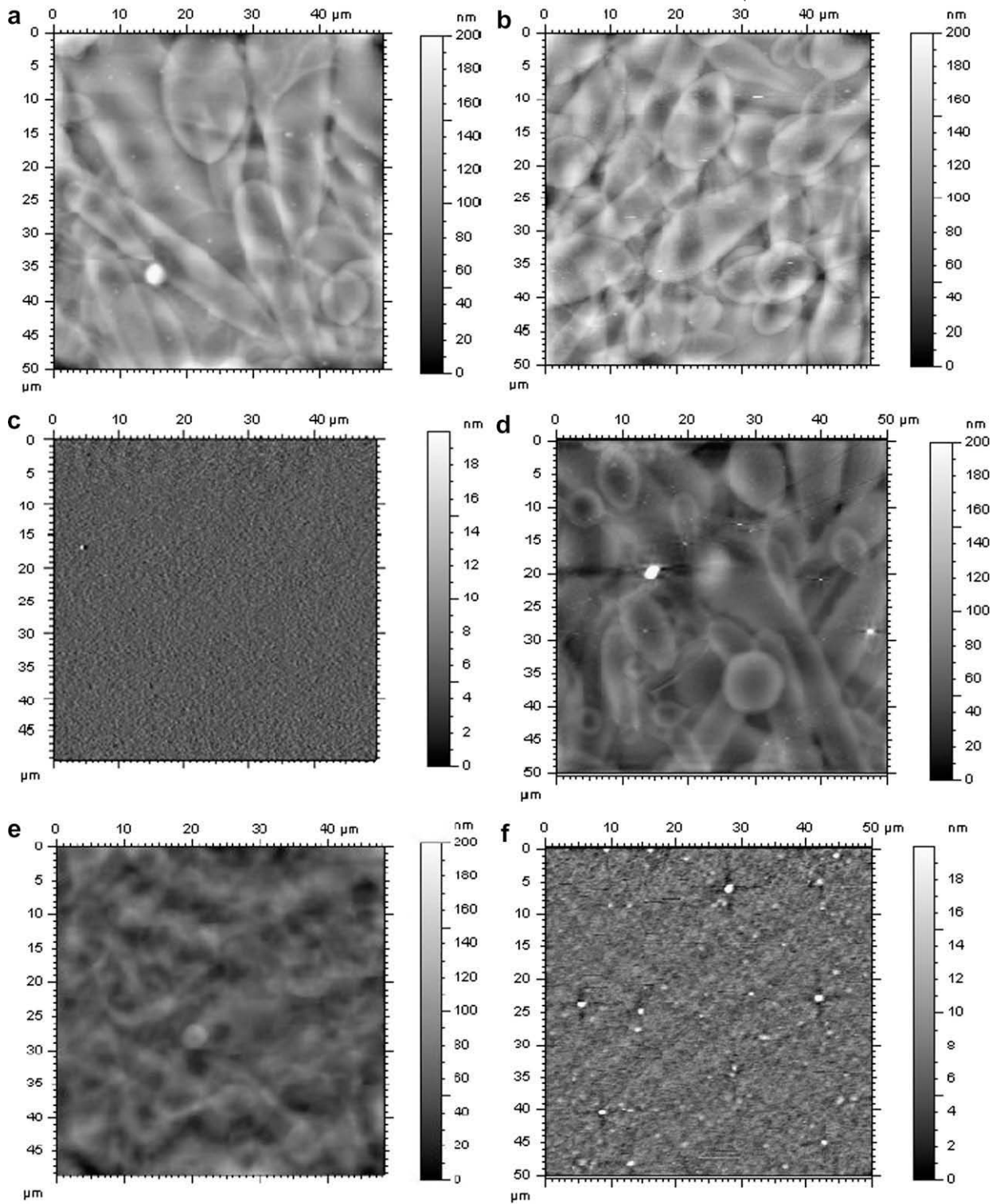


**Fig. 2.** AFM images representing the surface topographies of the devices under study. (a) Chlorobenzene (IF1), spray coated monolayer. (b) Chlorobenzene (IF1), spray coated bilayer. (c) Chlorobenzene (IF1), doctor bladed reference, rms 3.3 nm. (d) oDCB/mesitylene (IF2), spray coated monolayer. (e) oDCB/mesitylene (IF2), spray coated bilayer. (f) oDCB/mesitylene (IF2), doctor bladed reference, rms 4.1 nm.

**Table 2.** The second ink formulation is based on 68% oDCB and 32% mesitylene organic solvents (IF2) showing higher

boiling points and lower vapor pressures for a slow drying. The surface tension of the blend solution and the low

contact angle again guarantee good wettability. More details on the development of ink formulation **IF2** can be found elsewhere [4].

The atomic force microscope (AFM) images of the mono- and bilayer spray coated P3HT:PCBM films on doctor bladed PEDOT:PSS substrates are presented in Fig. 2. Due to the high surface roughness and to better reveal the film topography, the height scale is chosen to be 200 nm for all spray deposited layers. For both ink formulations, the spray coated films demonstrate a significantly larger grain size and higher roughness compared to doctor bladed layers. Single dried droplets are identified and indicate a stepwise film formation. Considering **IF1** spray deposited active layers (Fig. 2a and b), the monolayer (Fig. 2a) exhibits an rms roughness of 67.9 nm, whereas the rms roughness of the bilayer sprayed film (Fig. 2b) could be reduced to 46.0 nm due to smaller droplet sizes while depositing the film in two steps (bilayer). In this study, the thickness of mono- and bilayers for both ink formulations was adjusted to 250 and 400 nm, respectively. The overall film thickness can be varied by the spraying time interval, the droplet size and the flow rate. To obtain a 400 nm thickness for bilayer sprayed films, the flow volume per time was slightly reduced compared to monolayers, resulting in smaller droplets. Otherwise, by using the same spraying parameter as for monolayers, the film thickness would be doubled. With this spray coating setup it was not possible to obtain equal film thicknesses of 250 nm for both, mono- and bilayers without altering the spraying parameters nozzle distance and ink flow rate as well as solution concentrations significantly. This modification would lead to entirely different processing conditions for mono- and bilayers, which prevent a fair comparison between **IF1** and **IF2**. Therefore, we set the film thickness to 250 nm for monolayers and 400 nm for bilayers. We achieved the same film thickness for **IF1** and **IF2**, measured by both AFM, as well as optical absorption measurement (Fig. S3). The lower surface roughness for **IF1** bilayers is explained by the smaller droplets. Spraying the second layer, the droplets fill the gaps produced by the first sprayed layer and thus, the overall surface roughness is reduced. The doctor bladed reference film is shown in Fig. 2c and provides a completely different topography with very smooth layer and little grain sizes resulting in an rms roughness of only 3.3 nm.

The spray deposited monolayer based on **IF2** (Fig. 2d) demonstrates a considerably lower rms roughness of 24.1 nm compared to the monolayer from **IF1**. Using identical nozzle-to-substrate distances for both ink formulations but decreased ink flow rates for **IF2** over **IF1**, the dried droplets based on **IF2** show a smaller diameter and a more circular shape. The lower rms roughness can be related to the improved wetting behaviour of **IF2** due to the low surface tension of the component mesitylene which results in an overall decreased surface tension of the P3HT:PCBM-**IF2** and a lower contact angle on doctor bladed PEDOT:PSS. Regarding the **IF2** spray deposited bilayer (Fig. 2e) with its rms roughness of 51.7 nm, the surface topography indicates significant differences in the film formation compared to **IF1** bilayers (Fig. 2b). While the AFM image of the **IF1** bilayer clearly exhibits individu-

ally dried droplets from two sequential steps, the film formation of the **IF2** bilayer (Fig. 2e) is dominated by the film forming dynamics, where the second layer partially redissolves the first layer. This difference in the surface topography between the **IF1** bilayer and **IF2** bilayer is attributed to the differences in boiling points and, more important, to distinct vapor pressures by almost a factor 10. According to the higher vapor pressure and thus, faster drying condition, the spray deposition of a second **IF1** layer will not influence/reorder and redissolve the first **IF1** layer as much as the second **IF2** layer, since all deposited droplets are dried at their impact. This is also consistent with Fig. 2b showing clear dried droplets and a sequential film formation of the **IF1** bilayer. While spraying a second **IF2** layer on top of a first layer, leads to a reordering and mixing between the two layers due to a lower drying rate of **IF2** and therefore, the droplets contain higher solvent residual at their impact. This reorganization does affect the film quality and the morphology which is in good accordance with the AFM image in Fig. 2e showing a more blended structure of the two successive deposited layers. If the droplets are not dry at all or too wet at their impact, spray coating as a deposition method is not capable, since the droplets would not adhere to the substrate, but rather pushed sideways due to the transfer gas pressure. The doctor bladed reference film based on **IF2** is demonstrated in Fig. 2f with observably smaller grain sizes and rms roughness is calculated to be 4.1 nm. The AFM analysis of the spray coated films indicates significant distinctions in the surface topography compared to doctor bladed films. In the next paragraph, we will discuss whether differences in film topography can be related to differences in nanomorphology and device performance.

The nanomorphology of mono- or bilayer spray coated films was investigated by analyzing the device performance of organic solar cells. The cells were fabricated in an identical manner using either **IF1** or **IF2** as organic solvents for the spray deposition of the P3HT:PCBM active layer on doctor bladed PEDOT:PSS (see Section 1). A statistical analysis of the solar cell device parameters under AM 1.5 illumination can be found in the supplementary information (Fig. S1). The **IF2** monolayer (Fig. 2d) is formed by depositing smaller droplets yielding a more uniform film with decreased rms roughness (Table 2) and a lower pinhole density. Correspondingly, the shunt is reduced while the fill factor (*FF*) and open circuit voltage (*V<sub>oc</sub>*) increase, as also indicated by the representative current–voltage (*J–V*) behaviour under illumination shown in Fig. 3b. A better molecular distribution of PCBM within the P3HT domains and the improved intermixing of the first and second spray deposited layer for the **IF2** bilayer are indicated by a reduced reverse bias dependence of the photocurrent and results in significant better charge transport properties (Fig. 3).

For a detailed investigation of the morphology, the current–voltage behaviour of representative solar cell devices is analyzed [10].

$$J = J_0 \left( e^{\frac{-q(V - JR_S)}{nkT}} - 1 \right) + \frac{V - JR_S}{R_p} + J_{light} \quad (1)$$

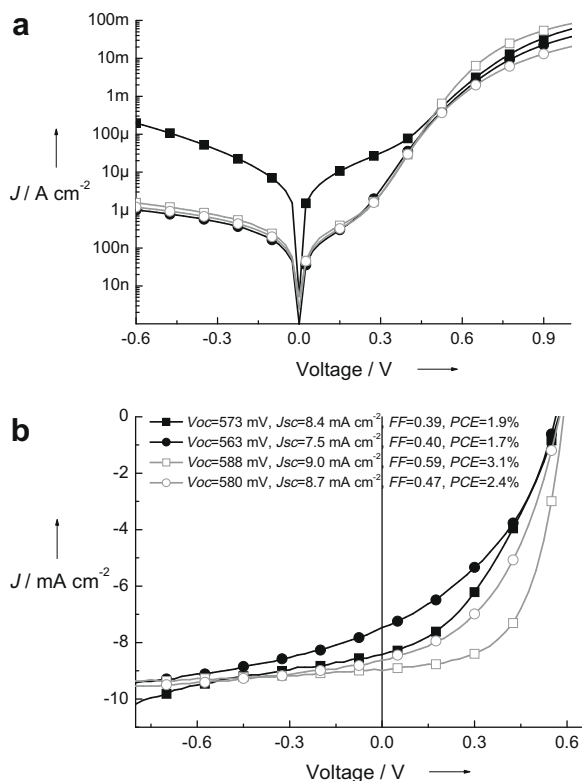


**Fig. 3.** Current density–voltage ( $J$ – $V$ ) characteristics of the devices under study: chlorobenzene (**IF1**) monolayer (black squares), chlorobenzene (**IF1**) bilayer (black dots), oDCB/mesitylene (**IF2**) monolayer (grey open squares) and oDCB/mesitylene (**IF2**) bilayer (grey open dots). (a) Representative dark  $J$ – $V$  characteristics in a semi-logarithmic representation in the voltage range revealing the opening of the diode. (b)  $J$ – $V$  curves under AM 1.5 illumination with  $100\text{ mW cm}^{-2}$ .

The above equation represents the  $J$ – $V$  characteristics of a solar cell according to a standard replacement circuit as demonstrated elsewhere [10], where  $J$  reveals the measured current density throughout the device,  $J_0$  shows the reverse current of the diode (saturation current),  $V$  the applied voltage,  $R_s$  and  $R_p$  the serial and parallel resistances,  $J_{light}$  the photogenerated current of the device,  $e$  evidences the natural exponential function and  $q$  the elementary charge [10]. The diode ideality factor  $n$  represents the opening of the diode, which is the recombination at the interfaces between the donor and acceptor material. Therefore  $n$  correlates with the number of distributed interfaces within the blend [11] and reflects the morphology of the blend. The dark  $J$ – $V$  curves (Fig. 3a) between 0 and the built in potential  $V_{BI}$  are characteristic for the diode behaviour of the solar cells, as defined by the ideality factor  $n$  and saturation current  $J_0$ . Variations in the absolute values of  $n$  are related to different morphologies, where  $n = 1$  is representative for a bilayer system and  $n = 2$  represents an intimate mixing of the donor with the acceptor throughout the bulk. Values larger than 2 indicate more complex carrier recombination mechanisms. From the dark  $J$ – $V$  characteristics between 0.3 and 0.6 V (Fig. 3a) all fabricated devices reveal, within the accuracy of the

analysis method, similar values for  $n$  in the range of 1.6–1.9 which are typical values for polythiophene:PCBM blend devices. The dark  $J$ – $V$  curve of **IF1** spray coated monolayer (Fig. 3a, black squares) solar cell exhibits a huge limitation in the shunt and can therefore not be simulated with this model. The **IF1** spray deposited bilayer (Fig. 3a, black dots) and the doctor bladed equivalent (not shown) indicate similar values within the certainty of the fit of  $n = 1.8 \pm 0.1$  and  $1.9 \pm 0.05$ , respectively. Comparing the dark  $J$ – $V$  characteristics of **IF2** based spray deposited devices (Fig. 3a, grey curves) with their doctor bladed equivalent (Fig. S2a), the differences are also within the certainty of the fit, namely  $n = 1.8 \pm 0.1$  for the mono- and bilayer and  $n = 1.6 \pm 0.05$  for the doctor bladed (dark  $J$ – $V$  curve of doctor bladed device, see Supplementary information, Fig. S2a). For both solvents we can not measure a significant difference in the ideality factor between a spray coated and doctor bladed devices. Typically such an observation is explained by a rather comparable distribution of the donor and acceptor interface throughout the bulk of the heterojunction. Even though the similar ideality factors are not a direct proof for identical nanomorphologies, our experience on several material systems showed good correlation between ideality factor and morphology [10,11]. In contrast, there is a significant variation in the charge carrier extraction between the various spray coated solar cells (Fig. 3b) and doctor bladed devices (Fig. S2b). That variation is correlated to differences in the mobility–lifetime product as clearly seen by the simulations. The low  $\mu\tau$ -product goes hand-in-hand with the lower fill factors for spray coated devices as discussed in more detail below. The AFM images show clear distinctions in the topography (Fig. 2). Furthermore, the dark  $J$ – $V$  characteristics distinguish significantly in the series resistance  $R_s$  (Fig. 3a). Independent of the ink formulation, the monolayers demonstrate a lower  $R_s$  than the spray coated bilayers due to the lower film thickness for the monolayers. In addition, the dark  $J$ – $V$  characteristics exhibit low leakage currents for the **IF1** bilayer (Fig. 3a, black dots), the **IF2** monolayer (Fig. 3a, grey open squares) and **IF2** bilayer (Fig. 3a, grey open dots), whereas the dark  $J$ – $V$  curve of the monolayer based on **IF1** (Fig. 3a, black squares) reveals an atypical shape, low currents in forward direction and high leakage current in reverse bias indicating decreased bottom contact selectivity. The diagram in Fig. 3b summarizes the  $J$ – $V$  characteristics under AM 1.5 illumination with  $100\text{ mW cm}^{-2}$ . A clear difference in the device performance is visible comparing **IF1** with **IF2** devices. The **IF1** monolayer device (Fig. 3b, black squares) exhibits a  $V_{oc}$  of 573 mV, a short circuit current density ( $J_{sc}$ ) of  $8.4\text{ mA cm}^{-2}$ , a  $FF$  of 0.39 resulting in 1.9% PCE. The bilayer device based on **IF1** (Fig. 3b, black dots) shows the lowest solar cell parameters with  $V_{oc} = 563\text{ mV}$ ,  $J_{sc} = 7.5\text{ mA cm}^{-2}$ ,  $FF$  of 0.40 and a PCE of 1.7%. The strong limitation in  $FF$  for **IF1** devices is attributed to a reduced extraction of the charge carriers. In contrast, the **IF2** spray deposited devices perform significantly better, with a  $V_{oc}$  of 588 mV,  $J_{sc}$  of  $9.0\text{ mA cm}^{-2}$ , a high  $FF$  of 0.59 for the monolayer (Fig. 3b, grey squares). This corresponds to a power conversion efficiency of 3.1%. The bilayer based on **IF2** (Fig. 3b, grey dots) features similar performance,

$V_{oc} = 580$  mV,  $J_{sc} = 8.7$  mA cm<sup>-2</sup>, but shows the main limitation in *FF* with 0.47 corresponding to a PCE of 2.4%. Comparing the shape of the *J-V* characteristics under illumination, there is an obvious distinction in the curve progression. Clearly, bilayer devices have lower *FF* due to the larger  $R_s$ . Moreover, a difference due to the mobility-lifetime ( $\mu\tau$ ) product can be seen. The photogenerated carriers are field driven [10], therefore a product of internal field and  $\mu\tau$  smaller than the film thickness will lead to a loss in photocurrent. At larger external negative bias the field for the carriers is large enough to be completely extracted, which can be seen for all illuminated *J-V* curves showing the same photocurrent at bias around -0.6 V. The monolayer of **IF2** (Fig. 3b, grey squares) shows a nearly constant photocurrent for voltages < 0.2 V. The thicker bilayer devices of **IF2** (Fig. 3b, grey dots) are affected by a  $\mu\tau$  limitation, and it needs reverse bias of -0.3 V to extract all photogenerated carriers. The monolayer of **IF1** (Fig. 3b, black squares) shows also a lower photocurrent at 0 V than at -0.3 V, while the bilayer (Fig. 3b, black dots) shows a complete extraction only at -0.6 V. Monolayer devices with a thickness of 250 nm are much weaker field dependent than thicker bilayer devices. In good agreement with earlier reports [5], the more slowly dried **IF2** films have a larger  $\mu\tau$ -product, sufficient to extract all carriers under  $J_{sc}$  conditions.

Fig. 4a represents the *J-V* behaviour of a fully spray coated device, comprising a 60 nm spray deposited PEDOT:PSS layer on top of ITO and a subsequent spray deposited P3HT:PCBM based on **IF2** (monolayer with 250 nm P3HT:PCBM film thickness; these parameters resulted in the most efficient spray coated active layer device). The fully spray deposited solar cell exhibits a decent device performance (Fig. 4a),  $V_{oc}$  of 560 mV,  $J_{sc}$  of 9.1 mA cm<sup>-2</sup> and a *FF* of 0.52. This corresponds to a power conversion efficiency of 2.7% for a fully spray coated device. Comparing the **IF2** monolayer reference solar cell device (grey open squares in Fig. 3) with the “fully sprayed” device comprising a spray deposited PEDOT:PSS and a spray coated P3HT:PCBM (*J-V* behaviour is shown in Fig. 4a), a clear difference of the device performance is visible, which can be attributed to the spray deposited PEDOT:PSS. The fully sprayed solar cell (see Fig. 4a) indicates a 5% lower  $V_{oc}$  (560 mV) compared to the **IF2** monolayer device with doctor bladed PEDOT:PSS, grey squares in Fig. 3b (588 mV), whereas the  $J_{sc}$  is in the same range (9.0 mA/cm<sup>2</sup> for **IF2** monolayer and 9.1 mA/cm<sup>2</sup> for fully sprayed solar cell). Comparing the *FF* of both devices, there is a clear distinction between the **IF2** monolayer reference and the fully sprayed solar cell device, namely 0.59 and 0.52, respectively. This lower *FF* for the fully sprayed solar cell is attributed to the spray deposited PEDOT:PSS due to higher surface roughness (rms = 20.7 nm) and higher leakage current, while same low  $R_s$ . Fig. 4b shows the AFM image of the PEDOT:PSS film with rms roughness of 20.7 nm and Fig. 4c reveals a reference doctor bladed PEDOT:PSS film with rms roughness of 3.7 nm. A significantly larger droplet size is observed for PEDOT:PSS spray coated films compared to spray deposited P3HT:PCBM layers. This larger droplet size is attributed to the higher surface tension of the water based PEDOT:PSS solution compared to the

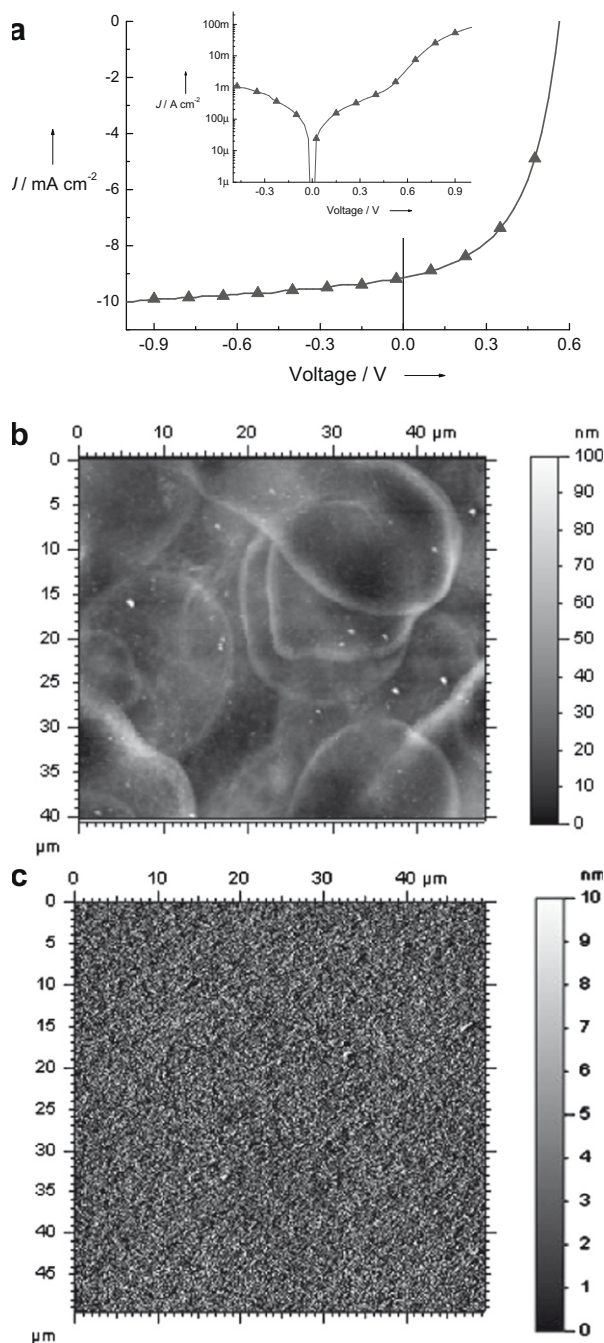


**Fig. 4.** Fully spray deposited solar cell with spray coated PEDOT:PSS and spray coated P3HT:PCBM. (a) *J-V* characteristics under AM 1.5 illumination with 100 mW cm<sup>-2</sup>. The inset shows the dark *J-V* curve in a semi-logarithmic plot; (b) surface topography of a spray deposited PEDOT:PSS film and (c) surface topography of a reference doctor bladed PEDOT:PSS film.

P3HT:PCBM solution where smaller drop sizes can be created.

In this study, an alternative method is presented to deposit P3HT:PCBM blend and PEDOT:PSS to produce high efficiency devices. We discussed the topographical and

the nanomorphological aspects between a spray deposited mono- and bilayer based on a pristine solvent compared to a multiple solvent system. The AFM images in Fig. 2 indicate significant topographical differences between spray deposited and doctor bladed films. A  $J$ - $V$  analysis (Fig. 3a) revealed similar ideality factors of mono- and bilayer spray coated films over doctor bladed ones indicating similar interface between the donor and acceptor in the BHJ, but differences in the charge carrier extraction between spray coated solar cells among themselves (Fig. 3b) and doctor bladed devices. The solvent properties such as boiling point, vapor pressure, viscosity and surface tension have a massive impact on the topography as shown by the AFM analysis. An optimized spray coating formulation is found with **IF2**, which allows to spray deposit films with outstanding high carrier transport properties, directly comparable to high qualitatively doctor bladed films. This resulted in an enhanced device performance with 3.1% PCE for spray coated polymer:fullerene based solar cells. Interestingly to note that the nearly 10 times higher surface roughness of **IF2** spray coated compared to doctor bladed films does not negatively influence the device performance. Moreover, we show that spray coating is a feasible technology to deposit among others also the PEDOT:PSS film without affecting the device parameters adversely. The high photovoltaic performance of 2.7% PCE for fully sprayed cells proves the outstanding potential of spray coating as a novel manufacturing method for organic electronics.

## 1. Experimental section

The devices were built on transparent indium tin oxide (ITO) coated glass substrates, purchased from TFD. The glass was cleaned for 10 min in acetone and another 10 min in isopropyl alcohol using an ultrasonic bath and finally with an ozone treatment lasting 10 min. A thin 60 nm layer of poly(3,4-ethylene dioxythiophene) doped with polystyrene sulphonic acid (PEDOT:PSS) was deposited by doctor blading on top of the ITO bottom electrode. For our devices the Baytron PH, comprising a PEDOT:PSS ratio of 1:2.5 by weight, purchased from H.C. Starck was used. After the PEDOT:PSS doctor blading step, the samples were stored in inert atmosphere for at least 2 h. For spray deposited PEDOT:PSS layers, the Baytron PH dispersion was diluted with deionized water in a ratio of 1:3. The thickness of the spray deposited PEDOT:PSS film was measured to be 60 nm. In comparison to doctor bladed PEDOT:PSS, the spray deposited PEDOT:PSS on ITO was used as prepared for the spray deposition of the P3HT:PCBM. The photoactive layer consists of 1.5 w% P3HT blended with fullerene PCBM in a 1:0.8 weight ratio and dissolved in pristine chlorobenzene or ortho-dichlorobenzene/mesitylene solvent mixture. The deposition of the active layer by spray coating was performed with an airbrush system in ambient surroundings with 3 bar pressure. For the fabrication of bilayers, no additional drying procedure among mono- and bilayer deposition was applied, despite the delay of 2 min needed by the setup between the two successive spray deposited films. On top of the active layer, an

additional Ca–Ag top electrode was deposited by physical vapor deposition to complete the bulk heterojunction solar cell. Prior to evaporation of the top electrode, all devices were subjected to a thermal treatment at 140 °C for 10 min. For efficiency evaluation the device area was defined by the overlap between the underlying ITO and the top electrode. Solar cells with an active area of typically 20 mm<sup>2</sup> were studied. The current density–voltage ( $J$ - $V$ ) characteristics were assessed with a source measurement unit SMU 2400 from Keithley under nitrogen atmosphere. For illumination a Steuernagel Solarsimulator was used providing an AM 1.5G spectra at 0.1 W cm<sup>-2</sup>. AFM images of the thermally annealed spray coated films were recorded on glass substrates coated with a 60 nm PEDOT:PSS layer with a NanoSurf easyScan 2 operating under ambient conditions in contact mode. Measurements were performed using a pointprobe-plus silicon-SPM cantilever. Surface tensions and contact angles were measured with a Krüss easy drop tool. The kinematic viscosity of the two blend formulations was determined at room temperature with a micro Ubbelohde capillary viscosimeter from Schott.

## Acknowledgement

We would like to acknowledge Professor Jürgen Parisi for valuable discussions.

## Appendix A. Supplementary data

Supplementary data associated with this article can be found, in the online version, at [doi:10.1016/j.orgel.2009.02.010](https://doi.org/10.1016/j.orgel.2009.02.010).

## References

- [1] C.J. Brabec, J.A. Hauch, P. Schilinsky, Christoph Waldauf, MRS Bulletin 30 (2005) 50.
- [2] P. Schilinsky, C. Waldauf, C.J. Brabec, Adv. Funct. Mater. 16 (2006) 1669.
- [3] S.E. Shaheen, R. Radspinner, N. Peyghambarian, G.E. Jabbour, Appl. Phys. Lett. 79 (2001) 2996.
- [4] C.N. Hoth, S.A. Choulis, P. Schilinsky, C.J. Brabec, Adv. Mater. 19 (2007) 3973.
- [5] (a) Y. Kim, S. Cook, S.M. Tuladhar, S.A. Choulis, J. Nelson, J.R. Durrant, D.D.C. Bradley, M. Giles, I. McCulloch, C.S. Ha, M. Ree, Nature Mater. 5 (2006) 197; (b) W. Ma, C. Yang, X. Gong, K. Lee, A.J. Heeger, Adv. Funct. Mater. 18 (2006) 572; (c) G. Li, V. Shrotriya, J. Huang, Y. Yao, T. Moriarty, K. Emery, Y. Yang, Nature Mater. 4 (2005) 864; (d) S. Curran, D.L. Carroll, Org. Lett. 7 (2005) 5749.
- [6] NREL Certificate Konarka, 5.24% under AM1.5 spectrum, November 2006.
- [7] (a) T. Ishikawa, M. Nakamura, K. Fujita, T. Tsutsui, Appl. Phys. Lett. 84 (2004) 2424; (b) X.L. Mo, T. Mizokuro, H. Mochizuki, N. Tanigaki, T. Hiraga, Jpn. J. Appl. Phys., Part 1 44 (2005) 656.
- [8] D. Vak, S. Kim, J. Jo, S. Oh, S. Na, J. Kim, D. Kim, Appl. Phys. Lett. 91 (2007) 081102.
- [9] R. Green, A. Morfa, A.J. Ferguson, N. Kopidakis, G. Rumbles, S.E. Shaheen, Appl. Phys. Lett. 92 (2008) 033301.
- [10] (a) C. Waldauf, P. Schilinsky, J.A. Hauch, C.J. Brabec, Thin Solid Films 451–452 (2004) 503–507; (b) P. Schilinsky, C. Waldauf, J.A. Hauch, C.J. Brabec, J. Appl. Phys. 95 (2004) 5.
- [11] C. Waldauf, M.C. Scharber, P. Schilinsky, J.A. Hauch, C.J. Brabec, J. Appl. Phys. 99 (2006) 04503.



# Highly branched green phosphorescent tris-cyclometalated iridium(III) complexes for solution-processed organic light-emitting diodes

Wei-Sheng Huang<sup>a</sup>, Chia-Wei Lin<sup>a</sup>, Jiann T. Lin<sup>b,\*</sup>, Jen-Hsien Huang<sup>c</sup>, Chih-Wei Chu<sup>c</sup>, Ying-Hsien Wu<sup>d</sup>, Hong-Cheu Lin<sup>a,\*</sup>

<sup>a</sup> Department of Materials Science and Engineering, National Chiao Tung University, Hsinchu, Taiwan, ROC

<sup>b</sup> Institute of Chemistry, Academia Sinica, Taipei, Taiwan, ROC

<sup>c</sup> Department of Chemical Engineering, National Taiwan University, Taipei, Taiwan, ROC

<sup>d</sup> Electro-optical Engineering and Graduate Institute of Electronics Engineering, National Taiwan University, Taipei, Taiwan, ROC

## ARTICLE INFO

### Article history:

Received 14 October 2008

Received in revised form 28 November 2008

Accepted 24 February 2009

Available online 3 March 2009

### PACS:

78.60-Fi

### Keywords:

Iridium complexes

Dendrimers

Phosphorescence

Organic light-emitting diodes

## ABSTRACT

A series benzimidazole-based dendritic complexes of iridium dendrimers containing Fréchet-type dendrons with peripheral fluorenyl surface groups have been synthesized. These iridium dendrimers are green-emitting with high phosphorescence quantum yield, and can be spin-coated as films of good quality. From cyclic voltammograms (CV), high onset potentials at 1.42–1.58 V due to the peripheral fluorene group were observed. Device from a second generation dendrimer **17** with structure of ITO/PEDOT:PSS/CBP: 20 wt% **17**/TPBI/LiF/Al (PEDOT:PSS = poly(ethylene dioxythiophene): polystyrenesulfonate and CBP = bis(*N*-carbazolyl)biphenyl) has the best performance: maximum external quantum efficiency of 13.58% and maximum current efficiency of 45.7 cd/A. Space-charge-limited current (SCLC) flow technique was used to measure the mobility of charge carriers in the blend films of the compounds in CBP. Blend films of higher generation dendrimers have lower hole mobility, albeit with higher device efficiencies.

© 2009 Elsevier B.V. All rights reserved.

## 1. Introduction

Since Tang and coworkers reported electroluminescent devices based on tris(8-hydroxyquinoline) aluminum (Alq<sub>3</sub>) in 1987, organic light-emitting diodes (OLEDs) have attracted great attention [1]. In recent years, there are increasing numbers of solution-processed OLED devices fabricated from fluorescent polymers or dendrimers [2]. However, the devices exhibit only low efficiencies in most cases. A lot of efforts have been directed to phosphorescent materials in order to improve device efficiencies [3]. Because both singlet and triplet excitons can be harvested, theoretical 100% internal quantum efficiency is possible

to be achieved in electrophosphorescent devices [4]. However, intermolecular interaction frequently leads to quenching of excited states and reduces the performance of OLEDs, fabricated via either vacuum deposition or solution-processing.

An ideal approach to suppress intermolecular interaction and retain high emission quantum yields is to use bulky and/or rigid peripheries to encapsulate the emitting core, i.e., dendritic approach [5,6]. Indeed, dendritic LEDs (DLEDs) using electrophosphorescent iridium dendrimers as emitters were reported to exhibit high luminous efficiency even without any host. For example, a maximum external quantum efficiency (EQE) of 13% and a maximum luminous efficiency of 34.7 cd A<sup>-1</sup> were reported for green light-emitting iridium dendrimers with benzimidazole-based ligands containing carbazolyl dendrons [7]. Similarly, a high EQE value of 13.6% (30 lm/W, 47 cd/A, 110 cd/m<sup>2</sup>) was also achieved on a host-free DLED based on a dendrimer with a

\* Corresponding authors. Fax: +886 2 27831237 (J.T. Lin); +886 3 5724727 (H.-C. Lin).

E-mail addresses: [jtlin@chem.sinica.edu.tw](mailto:jtlin@chem.sinica.edu.tw) (J.T. Lin), [linhc@cc.nctu.edu.tw](mailto:linhc@cc.nctu.edu.tw) (H.-C. Lin).



*fac*-tris(2-phenylpyridyl)iridium(III) core [8]. Possibly due to the presence of void space and the insulating linkages inside a dendrimer, the carrier mobility generally decreases as the dendrimer generation increases [9]. Consequently, the dendrimers are commonly doped in host materials, such as bis(*N*-carbazolyl)biphenyl (CBP) [10], in order to improve the device efficiency. Red- [11], green- [7,12], and blue-emitting [13] DLEDs have been fabricated to demonstrate very promising efficiencies. It is worthy to note that besides encapsulation, dendrons surrounding the phosphorescent core also allow one to tether with suitable surface groups for enhancing the solubility of the dendrimer to facilitate spin-coating of the film [14], or tether with carrier-transport units for improving charge transporting [11,15].

Previously we synthesized a series of phosphorescent cyclometalated iridium complexes containing benzoimidazole-based ligands [16]. High performance DLEDs based on the complexes were fabricated via vacuum deposition. In a recent report we extended our study to Fréchet-type dendritic benzoimidazole ligands [17], and electroluminescent (EL) devices with good efficiencies can be achieved by solution-processing. In an attempt to further enlarge the size of Fréchet-type dendron, we tethered periphery with a fluorene moiety which was beneficial to raising the solubility and reducing the intermolecular interactions [12b]. Furthermore, fluorene moiety is also possible to assist in carrier hopping [18]. In this paper, we report the first- and second-generation cyclometalated iridium dendrimer, in which Fréchet-type benzyl ether-based dendrons were tethered with peripheral alkylated fluorenyl groups. DLEDs fabricated from these dendrimers by spin-coating technique will also be discussed.

## 2. Experimental

### 2.1. Characterization

The  $^1\text{H}$  NMR spectra were recorded on a Bruker AMX400 spectrometer. FAB-mass spectra were collected on a JMS-700 double focusing mass spectrometer (JEOL, Tokyo, Japan) with a resolution of 3000 for low resolution and 8000 for high resolution (5% valley definition). For FAB-mass spectra, the source accelerating voltage was operated at 10 kV with a Xe gun, using 3-nitrobenzyl alcohol as the matrix. MALDI-mass spectra were collected on a Voyager DE-PRO (Applied Biosystem, Houston, USA) equipped with a nitrogen laser (337 nm) and operated in the delayed extraction reflector mode. Elemental analyses were performed on a Perkin–Elmer 2400 CHN analyzer. Cyclic voltammetry experiments were performed with a BHI-621B electrochemical analyzer. All measurements were carried out at room temperature with a conventional three-electrode configuration consisting of a platinum working electrode, an auxiliary electrode, and a nonaqueous Ag/AgNO<sub>3</sub> reference electrode. The  $E_{1/2}$  values were determined as  $1/2(E_p^a + E_p^c)$ , where  $E_p^a$  and  $E_p^c$  are the anodic and cathodic peak potentials, respectively. The solvent used was CH<sub>2</sub>Cl<sub>2</sub> and the supporting electrolyte was 0.1 M tetrabutylammonium hexafluorophosphate. Electronic absorption spectra were obtained on a Cary 50 Probe UV–visible spectrometer.

Emission spectra were recorded in deoxygenated solutions at 298 K by a JASCO FP-6500 fluorescence spectrometer. The emission spectra were collected on samples with o.d.  $\sim 0.1$  at the excitation wavelength. UV–visible spectra were checked before and after irradiation to monitor any possible sample degradation. Emission maxima were reproducible within 2 nm. Luminescence quantum yields ( $\Phi_{em}$ ) were calculated relative to Ir(ppy)<sub>3</sub> ( $\Phi_{em} = 0.40$  in toluene) [19]. Luminescence quantum yields were taken as the average of three separate determinations and were reproducible within 10%. Luminescence lifetimes were determined on an Edinburgh FL920 time-correlated pulsed single-photon-counting instrument. Samples were degassed via freeze–thaw–pump cycle at least three times prior to measurements. Samples were excited at 337 nm from a nitrogen pulsed flashlamp with 1 ns FWHM pulse duration transmitted through a Czerny–Turner design monochromator. Emission was detected at 90° via a second Czerny–Turner design monochromator onto a thermoelectrically cooled red-sensitive photomultiplier tube. The resulting photon counts were stored on a microprocessor-based multichannel analyzer. The instrument response function was profiled using a scatter solution and subsequently deconvoluted from the emission data to yield an undisturbed decay. Nonlinear least square fittings of the decay curves were performed with the Levenburg–Marquardt algorithm and implemented by the Edinburgh Instruments F900 software. The reported values represent the average of at least three readings.

### 2.2. Light-emitting devices fabrication

A layer of 70 nm thick poly(ethylenedioxythiophene):poly(styrene-sulfonic acid) (PEDOT:PSS) (Baytron PVP CH 8000) films was spin-coated on pre-cleaned ITO-coated glass substrates as the hole injection layer and then baked at 100 °C in air for 1 h. Next, the film of CBP containing iridium dendrimer or the neat iridium film (thickness at  $\sim 45$  nm for **16** and **18**,  $\sim 70$  nm for **17** and **19**, respectively) as the emitter was spin-coated using dichloroethane as the solvent (concentration: 10 mg mL<sup>-1</sup> for the host and  $\times$  wt% Ir dendrimer as the guest) at a spin rate of 2800 rpm (revolution per min.). Then, a electron-transporting and hole blocking 1,3,5-tris(*N*-phenylbenzimidazol-2-yl)benzene (TPBI) film of 40 nm thick was vacuum deposited in a vacuum chamber less than  $2.5 \times 10^{-5}$  torr. Finally, the device was completed by thermal deposition of a LiF/Al (1 nm/120 nm) cathode.

### 2.3. Hole-only devices fabrication

The hole-only devices in this study consists of a 20 wt% of **16** (or **17–19**) in CBP blend thin film sandwiched between transparent indium tin oxide (ITO) anode and metal cathode. Before device fabrication, the ITO glasses ( $1.5 \times 1.5$  cm<sup>2</sup>) were ultrasonically cleaned in detergent, de-ionized water, acetone and isopropyl alcohol before the deposition. After routine solvent cleaning, the substrates were treated with UV ozone for 15 min. Then a modified ITO surface was obtained by spin-coating a layer of poly(ethylene dioxythiophene): polystyrenesulfonate

(PEDOT:PSS) (~30 nm). After baking at 130 °C for 1 h, the substrates were then transferred into a nitrogen-filled glove box. The active layer was spin coated (spin rate = 2800 rpm; spin time = 45 s) on top of PEDOT:PSS and then dried in covered glass Petri dishes. The film thickness of the active layer was measured to be 55, 50, 50 and 50 nm, for **16**, **17**, **18** and **19**, respectively. Subsequently, a 20 and 100 nm thick of MoO<sub>3</sub> and aluminum was thermally evaporated under vacuum at a pressure below  $6 \times 10^{-6}$  torr through a shadow mask. The active area of the device was 0.12 cm<sup>2</sup>.

### 3. Materials

Chemicals and solvents were reagent grades and purchased from Aldrich, Acros, TCI, and Lancaster Chemical Co. Solvents were dried by standard procedures. All reactions and manipulations were carried out under N<sub>2</sub> with the use of standard inert atmosphere and Schlenk techniques. Solvents were dried by standard procedures. All column chromatography was performed by using silica gel (230–400 mesh, Macherey-Nagel GmbH & Co.) as the stationary phase in a column which is 25–35 cm in length and 2.5 cm in diameter.

#### 3.1. 9,9-Dihexyl-9H-fluorene-2-carbaldehyde (**1**)

2-Bromo-9,9-dihexyl-9H-fluorene (20.2 g, 48.9 mmol) was dissolved in 100 mL of dry THF and the solution was cooled to –78 °C. *n*-Butyl lithium in hexane (1.6 M, 30.5 mL, 48.9 mmol) was added dropwise over a period of 30 min. The mixture was allowed to warm to –20 °C in the next 1 h, and 3.8 mL of dry DMF was added. The mixture was stirred at room temperature for 12 h. The reaction was quenched with water and the solution was extracted with diethyl ether. The combined organic extracts were washed with brine solution, dried over MgSO<sub>4</sub>, and evaporated to dryness. The residue was purified by column chromatography using a mixture of CH<sub>2</sub>Cl<sub>2</sub> and hexanes (1:1) as the eluent to afford a white solid (13.4 g, 75%). <sup>1</sup>H NMR (CDCl<sub>3</sub>, 400 MHz, ppm): δ 10.04 (s, 1H, CHO), 7.85 (s, 1H), 7.83–7.80 (m, 2H), 7.76–7.74 (m, 1H), 7.37–7.33 (m, 3H), 2.00–1.97 (m, 4H, CH<sub>2</sub>), 1.07–0.97 (m, 12H, CH<sub>2</sub>), 0.75 (t, *J* = 7.2 Hz, 6H, CH<sub>3</sub>), 0.56–0.53 (m, 4 H, CH<sub>2</sub>).

#### 3.2. 4-(9,9-Dihexyl-9H-fluorene-2-yl)benzaldehyde (**2**)

4-Bromobenzaldehyde (9.25 g, 50 mmol), 9,9-dihexyl-9H-fluorene-2-yl-boronic acid (22.5 g, 1.2 equiv.), Na<sub>2</sub>CO<sub>3</sub> (12.0 g, 2 equiv.), and Pd(OAc)<sub>2</sub> (112 mg, 0.01 equiv.) were dissolved in a mixture of 30 mL of acetone and 35 mL of water. The mixture was stirred at room temperature for 16 h. The reaction was then quenched by pouring the solution into water and the desired compound was extracted with diethyl ether. The collected organic extracts were collected, dried over anhydrous MgSO<sub>4</sub>. Filtration and removal of the solvent provided a white solid. It was purified by column chromatography using a mixture of dichloromethane and hexanes (1:1) as the eluent to give a yellow oil in 73% yield (16.0 g). <sup>1</sup>H NMR (CDCl<sub>3</sub>,

400 MHz, ppm): δ 10.06 (s, 1H, CHO), 7.97 (d, *J* = 8.4 Hz, 2H, C<sub>6</sub>H<sub>4</sub>), 7.82 (d, *J* = 8.4 Hz, 2H, C<sub>6</sub>H<sub>4</sub>), 7.78 (d, *J* = 8.0 Hz, 1H, fluorene), 7.75–7.73 (m, 1H, fluorene), 7.62–7.60 (m, 2H, fluorene), 7.38–7.30 (m, 3H, fluorene), 2.04–1.99 (m, 4H, CH<sub>2</sub>), 1.12–1.04 (m, 12H, CH<sub>2</sub>), 0.75 (t, *J* = 7.2 Hz, 6H, CH<sub>3</sub>), 0.68–0.66 (m, 4H, CH<sub>2</sub>).

#### 3.3. (9,9-Dihexyl-9H-fluorene-2-yl)methanol (**3**)

Compound **1** was dissolved in 40 mL of THF and 40 mL of methanol. Sodium borohydride (2 equiv.) was added slowly to the above solutions in portions, and the solution was allowed to stir for 24 h. The reaction was quenched by pouring the solution into water and the desired compound was extracted with diethyl ether. The organic extracts were collected and dried over anhydrous MgSO<sub>4</sub>. Filtration and removal of the solvent provided a white solid. It was purified by column chromatography using a mixture of dichloromethane and hexanes (1:1) as the eluent to afford a white powder in 75% yield. <sup>1</sup>H NMR (CDCl<sub>3</sub>, 400 MHz, ppm): δ 7.67–7.64 (m, 2H), 7.32–7.25 (m, 5H), 4.75 (s, 2H, OCH<sub>2</sub>), 1.96–1.91 (m, 4H, CH<sub>2</sub>), 1.11–1.00 (m, 12H, CH<sub>2</sub>), 0.75 (t, *J* = 7.2 Hz, 6H, CH<sub>3</sub>), 0.61–0.55 (m, 4H, CH<sub>2</sub>).

#### 3.4. 4-(9,9-Dihexyl-9H-fluorene-2-yl)phenyl)methanol (**4**)

Compound **4** was synthesized by the same procedure as illustrated for compound **3** except that compound **1** was used instead of compound **2**. The compound was isolated as a white solid in 75% yield. <sup>1</sup>H NMR (CDCl<sub>3</sub>, 400 MHz, ppm): δ 7.77–7.73 (m, 2H, fluorene), 7.69 (d, *J* = 8.4 Hz, 2H, C<sub>6</sub>H<sub>4</sub>), 7.59–7.57 (m, 2H), 7.48 (d, *J* = 8.4 Hz, 2H, C<sub>6</sub>H<sub>4</sub>), 7.39–7.31 (m, 3H, fluorene), 4.74 (d, *J* = 2.0 Hz, 2H, OCH<sub>2</sub>) 1.99–1.96 (m, 4H, CH<sub>2</sub>), 1.09–1.01 (m, 12H, CH<sub>2</sub>), 0.73 (t, *J* = 7.2 Hz, 6H, CH<sub>3</sub>), 0.66–0.64 (m, 4H, CH<sub>2</sub>).

#### 3.5. 2-(Bromomethyl)-9,9-dihexyl-9H-fluorene (**5**)

A mixture of compound **3** (1.82 g, 5.0 mmol) and triphenylphosphine (1.1 equiv.) was dissolved in THF (15 mL) and cooled to 15 °C. *N*-bromosuccinimide (1.1 equiv.) was added all at once. The reaction was stirred for additional 10 min and immediately quenched by cold water. The solids formed were extracted into dichloromethane. The organic extracts were collected, washed with brine, and dried over anhydrous MgSO<sub>4</sub>. After filtration and removal of the solvent, the crude product was further purified by column chromatography on a silica gel column using a mixture of CH<sub>2</sub>Cl<sub>2</sub> and hexanes (1:5 by volume) as the eluent to afford the pure compound as a white solid in 85% yield. <sup>1</sup>H NMR (CDCl<sub>3</sub>, 400 MHz, ppm): δ 7.67–7.61 (m, 2H, fluorene), 7.36–7.30 (m, 5H, fluorene), 4.59 (s, 2H, CH<sub>2</sub>Br), 1.98–1.90 (m, 4H, CH<sub>2</sub>), 1.12–1.05 (m, 12H, CH<sub>2</sub>), 0.75 (t, *J* = 7.2 Hz, 6H, CH<sub>3</sub>), 0.59–0.50 (m, 4H, CH<sub>2</sub>).

#### 3.6. 2-(4-(Bromomethyl)phenyl)-9,9-dihexyl-9H-fluorene (**6**)

Compound **6** was synthesized by the same procedure as illustrated for compound **5** except that compound **3** was used instead of compound **4**. The product was isolated as

a white solid in 76% yield.  $^1\text{H}$  NMR ( $\text{CDCl}_3$ , 400 MHz, ppm):  $\delta$  7.73 (d,  $J = 8.0$  Hz, 1H, fluorene), 7.70 (d,  $J = 7.2$  Hz, 1H, fluorene), 7.62 (d,  $J = 8.4$  Hz, 2H,  $\text{C}_6\text{H}_4$ ), 7.54 (dd,  $J = 8.0$  Hz and 1.6 Hz, 1H, fluorene), 7.51 (d,  $J = 1.2$  Hz, 1H, fluorene), 7.47 (d,  $J = 8.4$  Hz, 2H,  $\text{C}_6\text{H}_4$ ), 7.34–7.28 (m, 3H, fluorene), 4.55 (s, 2H,  $\text{CH}_2\text{Br}$ ), 1.99–1.96 (m, 4H,  $\text{CH}_2$ ), 1.09–1.01 (m, 12H,  $\text{CH}_2$ ), 0.73 (t,  $J = 7.2$  Hz, 6H,  $\text{CH}_3$ ), 0.66–0.64 (m, 4H,  $\text{CH}_2$ ).

### 3.7. (3,5-Bis((9,9-dihexyl-9H-fluoren-2-yl)methoxy)phenyl)methanol (**7**)

A mixture of 3,5-dihydroxybenzyl alcohol (2.80 g, 20 mmol), potassium carbonate (6.67 g, 40 mmol), compound **5** (2.1 equiv.), and 18-crown-6-ether (0.52 g, 0.2 mmol) in acetone (30 mL) was heated to reflux for 48 h. After being cooled, water was added and the solution was extracted with dichloromethane. The organic extracts were collected, washed with brine, and dried over anhydrous  $\text{MgSO}_4$ . After filtration and removal of the solvent, the crude product was further purified by column chromatography using a mixture of  $\text{CH}_2\text{Cl}_2$  and hexanes (1:1 by volume) as the eluent. The product was isolated as a white solid in 70% yield.  $^1\text{H}$  NMR ( $\text{CDCl}_3$ , 400 MHz, ppm):  $\delta$  7.67 (d,  $J = 8.0$  Hz, 4H, fluorene), 7.37–7.28 (m, 10H, fluorene), 6.64 (d,  $J = 2.0$  Hz, 2H,  $\text{C}_6\text{H}_3$ ), 6.62 (t,  $J = 2.0$  Hz, 1H,  $\text{C}_6\text{H}_3$ ), 5.10 (s, 4H,  $\text{OCH}_2$ ), 4.62 (s, 2H,  $\text{OCH}_2$ ), 1.95–1.91 (m, 8H,  $\text{CH}_2$ ), 1.12–0.97 (m, 24H,  $\text{CH}_2$ ), 0.74 (t,  $J = 7.2$  Hz, 12H,  $\text{CH}_3$ ), 0.64–0.56 (m, 8H,  $\text{CH}_2$ ).

### 3.8. (3,5-Bis(4-(9,9-dihexyl-9H-fluoren-2-yl)benzyloxy)phenyl)methanol (**8**)

Compound **8** was synthesized by the same procedure as illustrated for compound **7** except that **5** was used instead of **6**. The product was isolated as a white solid in 70% yield.  $^1\text{H}$  NMR ( $\text{CDCl}_3$ , 400 MHz, ppm):  $\delta$  7.74–7.68 (m, 4H, fluorene), 7.67 (d,  $J = 8.4$  Hz, 4H,  $\text{C}_6\text{H}_4$ ), 7.56–7.49 (m, 4H, fluorene), 7.47 (d,  $J = 8.4$  Hz, 4H,  $\text{C}_6\text{H}_4$ ), 7.33–7.25 (m, 6H, fluorene), 6.67 (d,  $J = 2.0$  Hz, 2H,  $\text{C}_6\text{H}_3$ ), 6.60 (t,  $J = 2.0$  Hz, 1H,  $\text{C}_6\text{H}_3$ ), 5.07 (s, 4H,  $\text{OCH}_2$ ), 4.61 (s, 2H,  $\text{OCH}_2$ ), 1.95–1.91 (m, 8H,  $\text{CH}_2$ ), 1.12–0.97 (m, 24H,  $\text{CH}_2$ ), 0.74 (t,  $J = 7.2$  Hz, 12H,  $\text{CH}_3$ ), 0.64–0.56 (m, 8H,  $\text{CH}_2$ ).

### 3.9. Compound **9**

Compound **9** was synthesized by the same procedure as illustrated for compound **5** except that compound **3** was used instead of compound **7**. The product was isolated as a white solid in 70% yield.  $^1\text{H}$  NMR ( $\text{CDCl}_3$ , 400 MHz, ppm):  $\delta$  7.68 (d,  $J = 8.4$  Hz, 4H, fluorene), 7.41–7.25 (m, 10H, fluorene), 6.66 (d,  $J = 2.0$  Hz, 2H,  $\text{C}_6\text{H}_3$ ), 6.62 (t,  $J = 2.0$  Hz, 1H,  $\text{C}_6\text{H}_3$ ), 5.09 (s, 4H,  $\text{OCH}_2$ ), 4.39 (s, 2H,  $\text{OCH}_2$ ), 1.95–1.91 (m, 8H,  $\text{CH}_2$ ), 1.09–1.00 (m, 24H,  $\text{CH}_2$ ), 0.74 (t,  $J = 7.2$  Hz, 12H,  $\text{CH}_3$ ), 0.56–0.53 (m, 8H,  $\text{CH}_2$ ).

### 3.10. Compound **10**

Compound **10** was synthesized by the same procedure as illustrated for compound **5** except that compound **3** was used instead of compound **8**. The product was isolated

as a white solid in 72% yield.  $^1\text{H}$  NMR ( $\text{CDCl}_3$ , 400 MHz, ppm):  $\delta$  7.74–7.69 (m, 4H, fluorene), 7.67 (d,  $J = 8.4$  Hz, 4H,  $\text{C}_6\text{H}_4$ ), 7.56–7.54 (m, 4H, fluorene), 7.51 (d,  $J = 8.4$  Hz, 4H,  $\text{C}_6\text{H}_4$ ), 7.34–7.26 (m, 6H, fluorene), 6.67 (d,  $J = 2.0$  Hz, 2H,  $\text{C}_6\text{H}_3$ ), 6.61 (t,  $J = 2.0$  Hz, 1H,  $\text{C}_6\text{H}_3$ ), 5.09 (s, 4H,  $\text{OCH}_2$ ), 4.43 (s, 2H,  $\text{OCH}_2$ ), 1.99–1.95 (m, 8H,  $\text{CH}_2$ ), 1.11–1.03 (m, 24H,  $\text{CH}_2$ ), 0.73 (t,  $J = 7.2$  Hz, 12H,  $\text{CH}_3$ ), 0.67–0.63 (m, 8H,  $\text{CH}_2$ ).

### 3.11. 4-(1-Phenyl-1H-benzo[d]imidazol-2-yl)phenol (**11**)

*N*-Phenyl-*o*-phenylenediamine (9.21 g, 50 mmol), and 4-hydroxybenzaldehyde (6.10 g, 50 mmol) were dissolved in 40 mL of 2-methoxyethanol. The mixture was heated to reflux for 48 h. After cooling, the deposited solids were filtered, washed with dichloromethane, and dried under vacuum to give the desired product (5.1 g, 35%).  $^1\text{H}$  NMR ( $\text{DMSO}-d_6$ , 400 MHz, ppm):  $\delta$  7.71 (d,  $J = 7.6$  Hz, 1H), 7.57–7.51 (m, 3H), 7.36 (d, 7.6 Hz, 2H), 7.32 (d,  $J = 8.4$  Hz, 2H), 7.26 (t,  $J = 7.2$  Hz, 1H), 7.20 (t, 7.2 Hz, 1H), 7.11 (d,  $J = 8.0$  Hz, 1H), 6.68 (d, 8.4 Hz, 2H). FABMS:  $m/z$  287.2 ( $\text{M}+\text{H}$ ) $^+$ . Anal. Calcd for  $\text{C}_{19}\text{H}_{14}\text{N}_2\text{O}$ : C, 79.70; H, 4.93; N, 9.78. Found: C, 79.29; H, 5.04; N, 9.58.

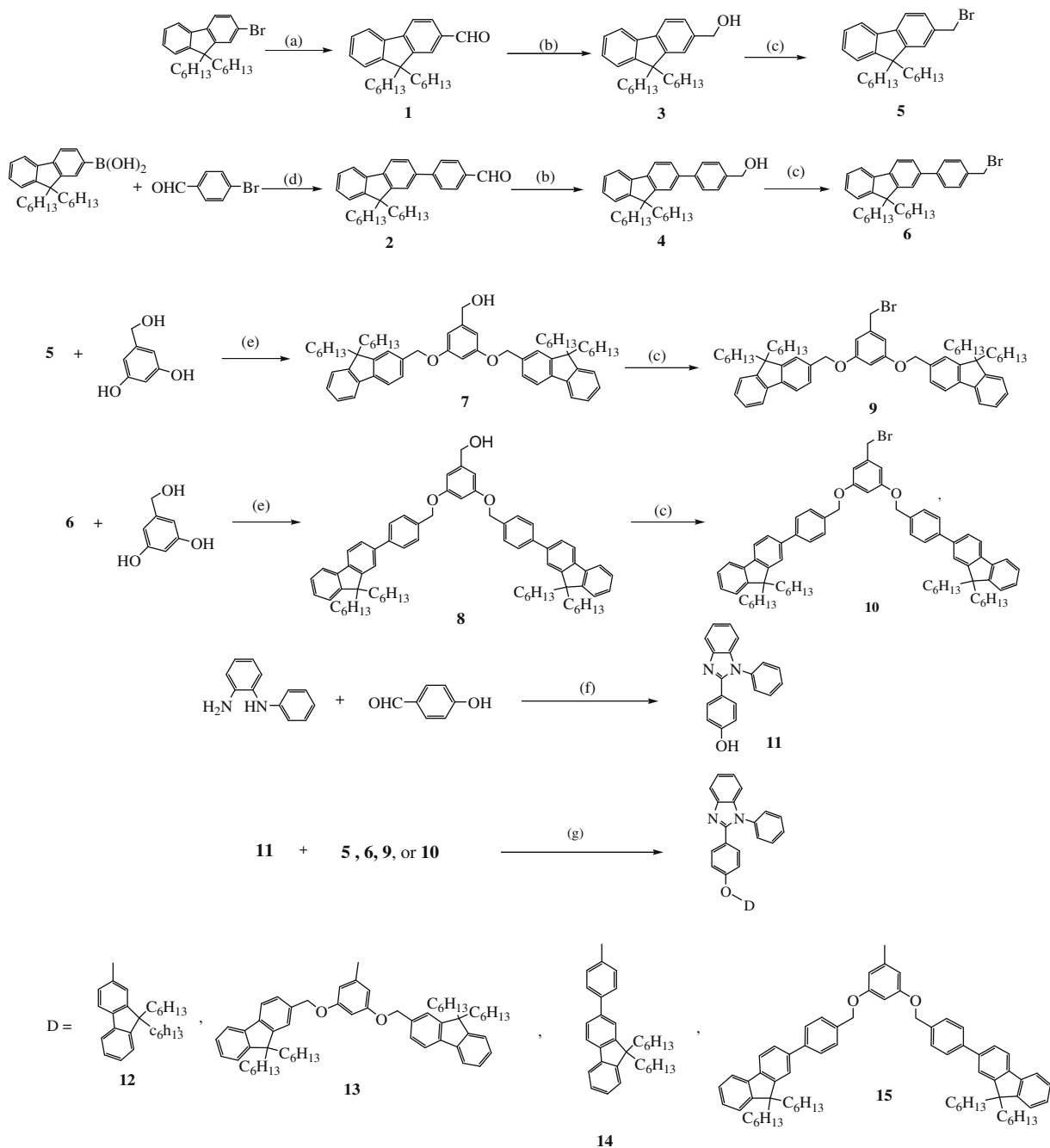
Ligands **12**, **13**, **14**, and **15** were synthesized by similar procedures, as described below for compound **12**. Compound **11** (0.73 g, 2.5 mmol),  $\text{K}_2\text{CO}_3$  (0.35 g, 2.5 mmol), and compound **5** (1.06 g, 2.5 mmol) were dissolved in 30 mL of DMF. The mixture was heated at 100 °C for 24 h. After cooling, the reaction was quenched with water and the mixture was extracted with dichloromethane. The organic extracts were collected, washed with brine, and dried over anhydrous  $\text{MgSO}_4$ . After filtration and removal of the solvent, the crude product was further purified by column chromatography using a mixture of  $\text{CH}_2\text{Cl}_2$  and hexanes (3:1 by volume) as the eluent to provide **12** as a white solid in 73% yield.  $^1\text{H}$  NMR ( $\text{CDCl}_3$ , 400 MHz, ppm):  $\delta$  7.84 (d,  $J = 8.0$  Hz, 1H), 7.67 (d,  $J = 8.4$  Hz, 2H,  $\text{C}_6\text{H}_4$ ), 7.55–7.43 (m, 5H), 7.35–7.27 (m, 8H), 7.20 (d,  $J = 8.0$  Hz, 2H), 6.92 (d,  $J = 8.4$  Hz, 2H,  $\text{C}_6\text{H}_4$ ), 5.10 (s, 2H,  $\text{OCH}_2$ ), 1.94–1.90 (m, 4H,  $\text{CH}_2$ ), 1.10–1.00 (m, 12H,  $\text{CH}_2$ ), 0.74 (t,  $J = 7.2$  Hz, 6H,  $\text{CH}_3$ ), 0.60–0.58 (m, 4H,  $\text{CH}_2$ ). FABMS:  $m/z$  633.3 ( $\text{M}+\text{H}$ ) $^+$ . Anal. Calcd for  $\text{C}_{45}\text{H}_{48}\text{N}_2\text{O}$ : C, 85.40; H, 7.64; N, 4.43. Found: C, 85.24; H, 7.79; N, 4.35.

**13**: White solid. Yield = 75%.  $^1\text{H}$  NMR ( $\text{CDCl}_3$ , 400 MHz, ppm):  $\delta$  8.14 (d,  $J = 8.0$  Hz, 1H), 7.68–7.60 (m, 8H), 7.54–7.46 (m, 3H), 7.38–7.18 (m, 13H), 6.89 (d,  $J = 8.4$  Hz, 2H), 6.67 (d,  $J = 2.0$  Hz, 2H,  $\text{C}_6\text{H}_3$ ), 6.62 (t,  $J = 2.0$  Hz, 1H,  $\text{C}_6\text{H}_3$ ), 5.09 (s, 4H,  $\text{OCH}_2$ ), 4.99 (s, 2H,  $\text{OCH}_2$ ), 1.94–1.86 (m, 8H,  $\text{CH}_2$ ), 1.09–0.99 (m, 24H,  $\text{CH}_2$ ), 0.73 (t,  $J = 7.2$  Hz, 12H,  $\text{CH}_3$ ), 0.65–0.54 (m, 8H,  $\text{CH}_2$ ). FABMS:  $m/z$  1101.9 ( $\text{M}+\text{H}$ ) $^+$ . Anal. Calcd for  $\text{C}_{78}\text{H}_{88}\text{N}_2\text{O}_3$ : C, 85.05; H, 8.05; N, 2.54. Found: C, 85.15; H, 8.22; N, 2.60.

**14**: White solid. Yield = 56%.  $^1\text{H}$  NMR ( $\text{CDCl}_3$ , 400 MHz, ppm):  $\delta$  7.84 (d,  $J = 8.0$  Hz, 1H), 7.72 (d,  $J = 8.0$  Hz, 1H), 7.69 (d,  $J = 7.2$  Hz, 1H), 7.65 (d,  $J = 8.0$  Hz, 2H), 7.55–7.45 (m, 9H), 7.31–7.28 (m, 6H), 7.22–7.18 (m, 2H), 6.91 (d,  $J = 8.8$  Hz, 2H), 5.09 (s, 2H,  $\text{OCH}_2$ ), 1.99–1.96 (m, 4H,  $\text{CH}_2$ ), 1.09–1.01 (m, 12H,  $\text{CH}_2$ ), 0.73 (t,  $J = 6.8$  Hz, 6H,  $\text{CH}_3$ ), 0.66–0.64 (m, 4H,  $\text{CH}_2$ ). FAB MS:  $m/z$  709.5 ( $\text{M}+\text{H}$ ) $^+$ . Anal. Calcd for  $\text{C}_{51}\text{H}_{52}\text{N}_2\text{O}$ : C, 86.40; H, 7.39; N, 3.95. Found: C, 86.54; H, 7.40; N, 3.67.

**15**: White solid. Yield = 56%.  $^1\text{H}$  NMR ( $\text{CDCl}_3$ , 400 MHz, ppm):  $\delta$  8.02 (d,  $J = 8.0$  Hz, 1H), 7.71–7.61 (m, 10H), 7.55–7.47 (m, 12H), 7.34–7.27 (m, 9H), 7.20 (d,  $J = 8.4$  Hz, 1H),

6.92 (d,  $J = 8.4$  Hz, 2H), 6.67 (d,  $J = 2.0$  Hz, 2H,  $\text{C}_6\text{H}_3$ ), 6.62 (t,  $J = 2.0$  Hz, 1H,  $\text{C}_6\text{H}_3$ ), 5.11 (s, 4H,  $\text{OCH}_2$ ), 4.43 (s, 2H,  $\text{OCH}_2$ ), 1.99–1.96 (m, 8H,  $\text{CH}_2$ ), 1.09–1.01 (m, 24H,  $\text{CH}_2$ ),



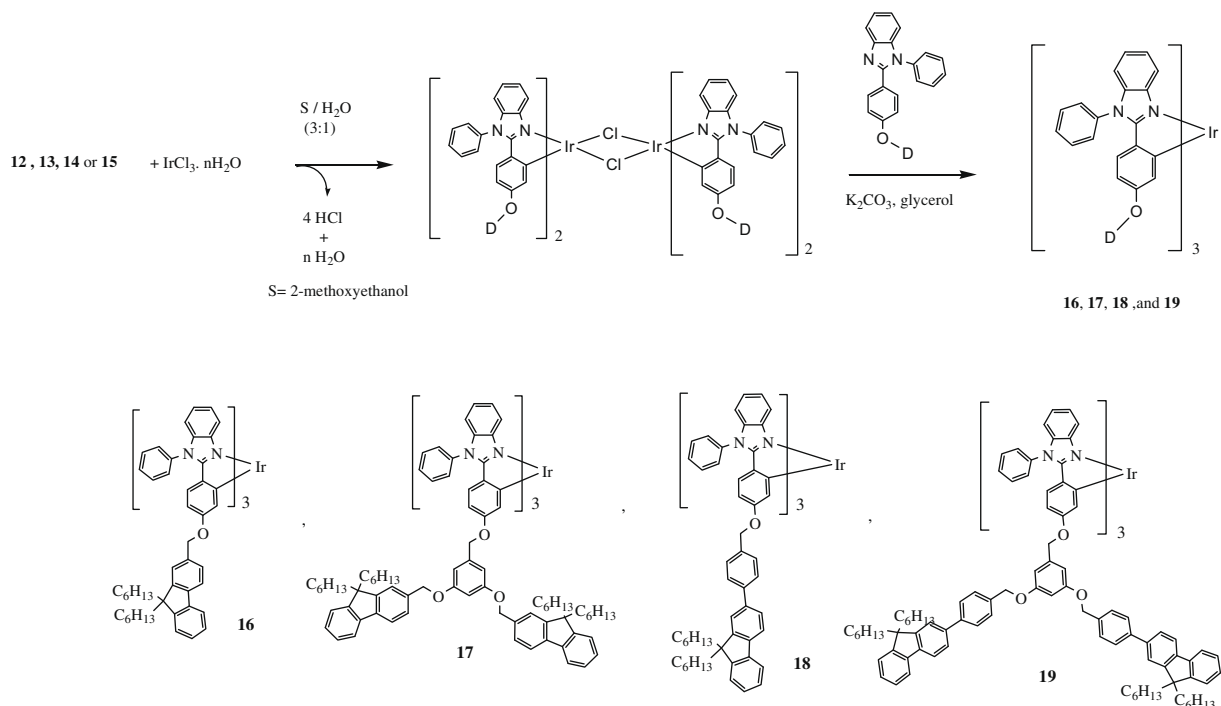
(a) (i) BuLi, THF,  $-78^\circ\text{C}$ , (ii) DMF (iii)  $\text{H}^+$ ; (b)  $\text{NaBH}_4$ , THF: MeOH = 1: 1, rt, 16h; (c) NBS,  $\text{PPh}_3$ , THF, rt, 20 min; (d)  $\text{Pd}(\text{OAc})_2$ , acetone,  $35^\circ\text{C}$ , 16 h; (e)  $\text{K}_2\text{CO}_3$ , 18-crown-6-ether, acetone, reflux, 24h; (f) 2-methoxyethanol, reflux, 16 h; (g)  $\text{K}_2\text{CO}_3$ , DMF,  $100^\circ\text{C}$ , 16 h.

**Scheme 1.** Synthesis of the dendritic ligands.

0.73 (t,  $J = 7.2$  Hz, 12H, CH<sub>3</sub>), 0.66–0.64 (m, 8H, CH<sub>2</sub>). FAB-MS:  $m/z$  1253.8 (M+H)<sup>+</sup>. Anal. Calcd for C<sub>90</sub>H<sub>96</sub>N<sub>2</sub>O<sub>3</sub>: C, 86.22; H, 7.72; N, 2.23. Found: C, 85.88; H, 7.58; N, 2.00.

Tris-Ir complexes **16**, **17**, **18**, **19** were synthesized by similar procedures, as described below for **16**. To a flask

containing IrCl<sub>3</sub> · 3H<sub>2</sub>O (176 mg, 0.50 mmol) and **12** (1.10 g, 1.0 mmol) was added a 3:1 mixture of 2-ethoxyethanol and water (25 mL). The mixture was refluxed for 48 h. After cooling, the reaction was quenched by water, and the mixture was filtered and washed with diethyl



**Scheme 2.** Synthesis of dendritic iridium complexes.

**Table 1**  
Physical data of the compounds.

cpd	$\lambda_{\text{abs}}$ (log $\epsilon$ ), <sup>a</sup> (nm)	$\lambda_{\text{em}}(\Phi_p)$ in solution nm (%)	$\lambda_{\text{em}}^c(\Phi_p)$ in film nm (%)	$\tau_r^d$ , $\mu\text{s}$	$\tau_r^e$ , $\mu\text{s}$	$E_{\text{ox}}^f(\Delta E_p)$ , mV	$E_g^g$ , eV	HOMO <sup>h</sup> , eV	LUMO <sup>i</sup> , eV
<b>12</b>	275 (4.63), 307 (4.73)	354 <sup>a</sup>				1580	3.64	6.11	2.47
<b>13</b>	273 (4.82), 306 (4.67)	355 <sup>a</sup>				1520	3.64	6.05	2.41
<b>14</b>	308 (4.69)	356 <sup>a</sup>				1420	3.64	5.95	2.31
<b>15</b>	282 (4.90), 314 (4.70)	357 <sup>a</sup>				1420	3.64	5.95	2.31
(G0) <sub>3</sub> Ir <sup>j</sup>	298 (4.6), 313 (4.6), 375 (4.1), 410 (3.8), 453 (3.5)	517 (45)	534 (15)	1.07	2.37	370 (76)	2.90	4.95	2.0
<b>16</b>	268 (4.66), 308 (4.69), 374 (3.96), 407 (3.74), 432 (3.57)	512 <sup>b</sup> (55)	529 (16)	1.46	1.78	394 (63)	2.90	4.92	2.0
<b>17</b>	271 (4.87), 306 (4.64), 366 (3.88), 427 (3.34)	512 <sup>b</sup> (63)	525 (30)	1.46	2.31	397 (76)	2.90	4.92	2.0
<b>18</b>	292 (4.60), 317 (4.69), 356 (3.99), 420 (3.34)	513 <sup>b</sup> (65)	522 (17)	1.05	1.78	413 (93)	2.90	4.94	2.0
<b>19</b>	296 (4.83), 312 (4.77), 354 (3.77), 407 (3.07)	519 <sup>b</sup> (74)	523 (33)	1.02	1.37	414 (124)	2.90	4.94	2.0

<sup>a</sup> Measured in CH<sub>2</sub>Cl<sub>2</sub> at 298 K at a concentration of 10<sup>-5</sup> M.  $\epsilon$  is the absorption coefficient.

<sup>b</sup> Recorded in toluene solutions at 298 K. Excitation wavelength was 410 nm for all compounds. Quantum yield was measured in toluene relative to *fac*-Ir(ppy)<sub>3</sub> ( $\Phi_p = 0.40$ ).

<sup>c</sup> Neat-film data measured at 298 K. PL quantum efficiencies in films were measured in an integrating sphere.

<sup>d</sup> Measured in toluene solutions at 298 K.

<sup>e</sup>  $\tau_r = \tau/\Phi_p$ .

<sup>f</sup> Oxidation potential reported is adjusted to the potential of ferrocene ( $E_{1/2} = 270$  mV vs. Ag/AgNO<sub>3</sub>) which was used as an internal reference. Conditions of cyclic voltammetric measurements: platinum working electrode; Ag/AgNO<sub>3</sub> reference electrode. Scan rate: 100 mV/s. Electrolyte: tetrabutylammonium hexafluorophosphate.

<sup>g</sup>  $E_g$ : bandgap.  $E_g$  was obtained from the absorption spectra.

<sup>h</sup> HOMO level were calculated from CV potentials using ferrocene as a standard [HOMO = 4.8 + ( $E_{\text{ox}} - E_{\text{Fc}}$ )].

<sup>i</sup> LUMO derived via equation,  $E_g = \text{HOMO} - \text{LUMO}$ .

<sup>j</sup> Ref. [7].

ether to give  $\mu$ -chloro-bridged Ir(III) dimer. One equiv. of  $\mu$ -chloro-bridged Ir(III) dimer was mixed with 2.5 equiv. of  $K_2CO_3$ , 2.0 equiv. of **12**, and glycerol (5.0 mL) in a flask. The mixture was heated at 190 °C for 24 h. After cooling, the reaction was quenched with water and the mixture was extracted with dichloromethane. The combined extracts were then washed with brine, dried over  $MgSO_4$ , filtered, and dried under vacuum. The crude product was isolated by column chromatography using a mixture of  $CH_2Cl_2$  and *n*-hexane (1:1 by volume) as the eluent.

**16**: Yellow solid. Yield = 56%.  $^1H$  NMR ( $CDCl_3$ , 400 MHz, ppm):  $\delta$  7.57–7.45 (m, 21H), 7.28–7.24 (m, 12H), 7.18 (d,  $J = 8.0$  Hz, 3H), 7.06–7.02 (m, 6H), 6.81 (t,  $J = 6.4$  Hz, 3H), 6.72 (s, 3H), 6.60 (d,  $J = 8.4$  Hz, 3H), 6.39 (d,  $J = 8.0$  Hz, 3H), 6.21 (d,  $J = 8.4$  Hz, 3H), 4.87 (d,  $J = 12.0$  Hz, 3H,  $OCH_2$ ), 4.79 (d,  $J = 12.0$  Hz, 3H,  $OCH_2$ ), 1.90–1.86 (m, 12H,  $CH_2$ ), 1.04–0.97 (m, 36H,  $CH_2$ ), 0.74 (t,  $J = 7.2$  Hz, 18H,  $CH_3$ ), 0.60–0.56 (m, 12H,  $CH_2$ ). MADLI-TOF:  $m/z$  2087.5 ( $M+H$ )<sup>+</sup>. Anal. Calcd for  $C_{135}H_{141}N_6O_3Ir$ : C, 86.22; H, 7.72; N, 2.23. Found: C, 85.97; H, 7.42; N, 2.20.

**17**: Yellow solid. Yield = 15%.  $^1H$  NMR ( $CDCl_3$ , 400 MHz, ppm):  $\delta$  7.63–7.56 (m, 18H), 7.52 (t,  $J = 7.5$  Hz, 9H), 7.41 (d,  $J = 8.0$  Hz, 3H), 7.30–7.26 (m, 30H), 7.00–6.94 (m, 6H), 6.79 (t,  $J = 7.2$  Hz, 3H), 6.57–6.54 (m, 12H), 6.30 (s, 3H), 6.04 (s, 3H), 4.95 (s, 12H,  $OCH_2$ ), 4.74 (d,  $J = 12.0$  Hz, 3H,  $OCH_2$ ), 4.68 (d,  $J = 12.0$  Hz, 3H,  $OCH_2$ ), 1.92–1.88 (m, 24H,  $CH_2$ ), 1.06–0.97 (m, 72H,  $CH_2$ ), 0.71–0.67 (m, 36H,  $CH_3$ ), 0.58–0.53 (m, 24H,  $CH_2$ ). MADLI-TOF:  $m/z$  3494.8 ( $M+H$ )<sup>+</sup>. Anal. Calcd for  $C_{234}H_{261}N_6O_9Ir$ : C, 80.44; H, 7.53; N, 2.41. Found: C, 80.21; H, 7.33; N, 2.25.

**18**: Yellow solid. Yield = 40%.  $^1H$  NMR ( $CDCl_3$ , 400 MHz, ppm):  $\delta$  7.67–7.63 (m, 6H), 7.52–7.46 (m, 12H), 7.41 (d,  $J = 7.6$  Hz, 3H), 7.40–7.32 (m, 9H), 7.32–7.28 (m, 9H), 7.24–7.22 (m, 9H), 7.00 (t,  $J = 7.6$  Hz, 3H), 6.92 (d,  $J = 7.6$  Hz, 3H), 6.75 (t,  $J = 7.6$  Hz, 3H), 6.66 (d,  $J = 2.4$  Hz, 3H), 6.53 (d,  $J = 8.4$  Hz, 3H), 6.28 (d,  $J = 8.4$  Hz, 3H), 6.22 (dd,  $J = 8.4$  and 2.4 Hz, 3H), 4.77 (d,  $J = 12.0$  Hz, 3H,  $OCH_2$ ), 4.74 (d,  $J = 12.0$  Hz, 3H,  $OCH_2$ ), 1.88–1.80 (m, 12H,  $CH_2$ ), 1.10–1.02 (m, 36H,  $CH_2$ ), 0.72 (t,  $J = 7.2$  Hz, 18H,  $CH_3$ ), 0.66–0.63 (m, 12H,  $CH_2$ ). MADLI-TOF:  $m/z$  2316.4 ( $M+H$ )<sup>+</sup>. Anal. Calcd for  $C_{153}H_{153}N_6O_3Ir$ : C, 79.34; H, 6.66; N, 3.63. Found: C, 78.97; H, 6.33; N, 3.35.

**19**: Yellow solid. Yield = 10%.  $^1H$  NMR ( $CDCl_3$ , 400 MHz, ppm):  $\delta$  7.74–7.69 (m, 12H), 7.65–7.60 (m, 12H), 7.57–7.50 (m, 21H), 7.45–7.42 (m, 15H), 7.36–7.28 (m, 21H), 6.98–6.92 (m, 6H), 6.88–6.83 (m, 3H), 6.71–6.64 (m, 6H), 6.54–6.45 (m, 15H), 4.95 (s, 12H,  $OCH_2$ ), 4.74 (d,  $J = 12.0$  Hz, 3H,  $OCH_2$ ), 4.68 (d,  $J = 12.0$  Hz, 3H,  $OCH_2$ ), 1.92–1.88 (m, 24H,  $CH_2$ ), 1.06–0.97 (m, 72H,  $CH_2$ ), 0.71–0.67 (m, 36H,  $CH_3$ ), 0.58–0.53 (m, 24H,  $CH_2$ ). MADLI-TOF:  $m/z$  3951.3 ( $M+H$ )<sup>+</sup>. Anal. Calcd for  $C_{270}H_{285}N_6O_9Ir$ : C, 82.09; H, 7.27; N, 2.13. Found: C, 81.71; H, 7.23; N, 2.25.

## 4. Results and discussion

### 4.1. Syntheses

Bouveault's synthesis [20] and palladium-catalyzed Suzuki reaction [21] were used to prepare two aldehydes, 9,9-dihexyl-9H-fluorene-2-carbaldehyde (**1**), and 4-(9,9-

dihexyl-9H-fluorene-2-yl)benzaldehyde (**2**) (Scheme 1). Reduction of **1** and **2** with  $NaBH_4$  gave the benzyl alcohol **3** and **4** in ~80% yield, which was then treated with *N*-bromosuccinimide and triphenylphosphine to form the benzyl bromides, **5** and **6** [4]. Reaction of compound **5** (or **6**) with 3,5-dihydroxybenzyl alcohol provides compound **7** (or **8**) containing two fluorene branches. Similar to the synthesis

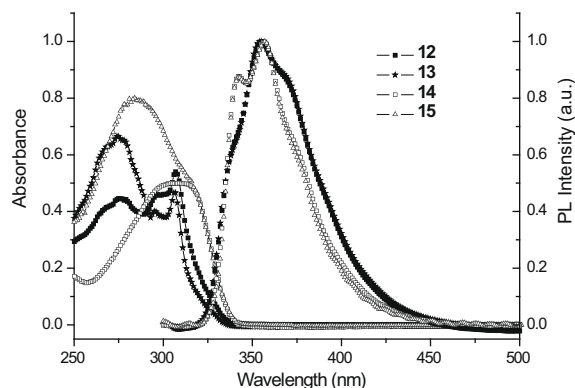


Fig. 1. The absorption spectra and PL of **12**–**15** in  $CH_2Cl_2$  solution.

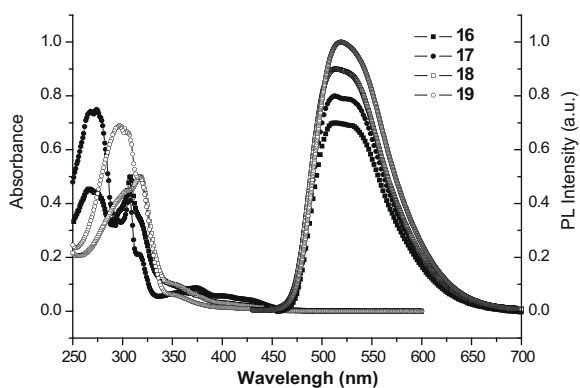


Fig. 2. The absorption spectra of **16**–**19** measured in  $CH_2Cl_2$  solution and the normalized PL spectra of **16**–**19** measured in toluene.

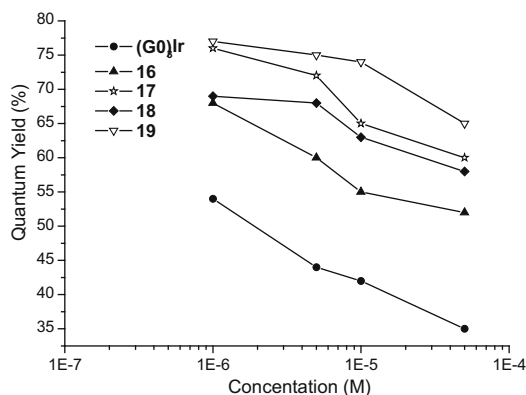


Fig. 3. The variation of quantum yields for  $(G0)_3Ir$ , and **16**–**19** in different concentration in toluene.

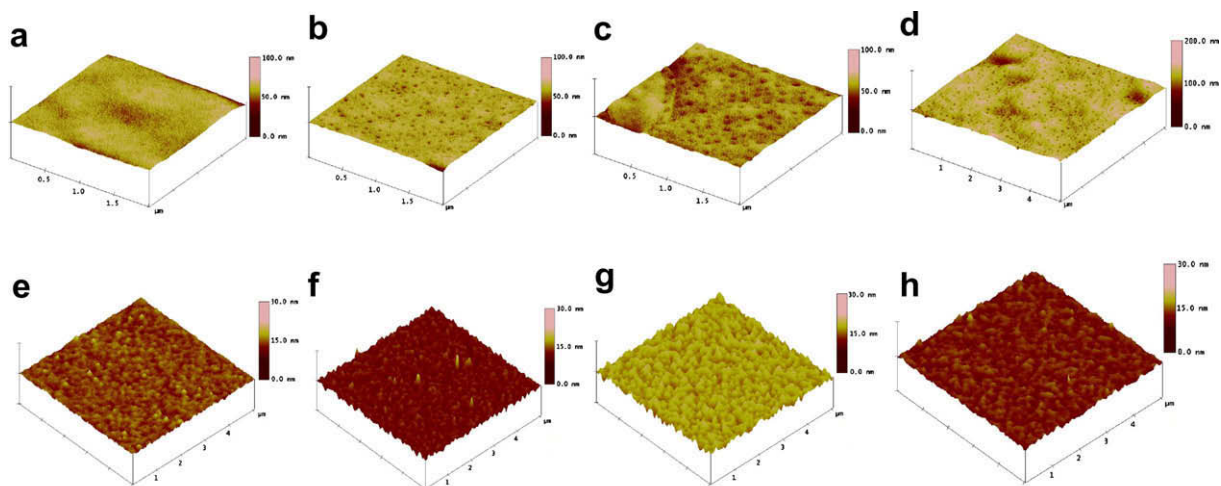


Fig. 4. AFM images from spin-casting films: blend film of CBP: 20 wt% **16** (a); **17** (b); **18** (c); **19** (d) and neat film of **16** (e); **17** (f); **18** (g); **19** (h).

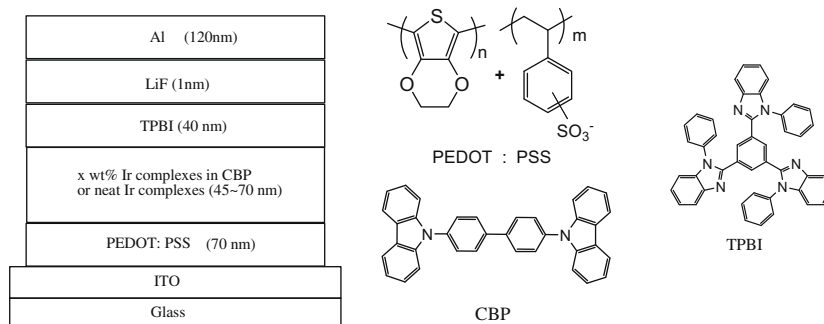
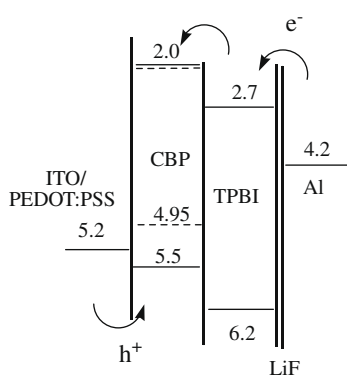


Fig. 5. The configuration of EL devices and the molecular structures of the compounds used.



----- energy levels of iridium complexes (**16-19**)

Fig. 6. Relative energy levels of the compounds utilized in DLEDs.

of **5** from **3**, compounds **7** and **8** can be converted to **9** and **10**, respectively. Compound **11**, prepared from *N*-phenyl-*o*-phenylenediamine and 4-hydroxybenzaldehyde, was then allowed to react with **5**, **6**, **9**, and **10**, respectively, using

Williamson ether synthesis to form dendritic benzoimidazole ligands **12-15** in 30–90% yields. The preparation of tris-cyclometalated iridium complexes **16-19** involved a two-step synthesis (see Scheme 2): (1) reaction of  $\text{IrCl}_3 \cdot 3\text{H}_2\text{O}$  with dendritic ligands **12-15** to form a chloro-bridged dimer intermediate; (2) reaction of the dimer with additional **12-15** in glycerol at 190 °C. Only the facial (*fac*) isomer was isolated for **16-19**, as evidenced from the NMR spectra.

#### 4.2. Optical properties

The photophysical data of compounds **12-19** are summarized in Table 1. The absorption spectra and photoluminescence (PL) spectra of compounds **12-15** and **16-19** are shown in Figs. 1 and 2, respectively. Absorption bands at  $\sim 310$  nm ( $\epsilon \sim 10^4\text{--}10^5 \text{ M}^{-1} \text{ cm}^{-1}$ ) are  $\pi\text{-}\pi^*$  transition characteristic of the benzoimidazolyl moiety, and those at  $\sim 275$  nm ( $\epsilon \sim 10^4\text{--}10^5 \text{ M}^{-1} \text{ cm}^{-1}$ ) can be attributed to  $\pi\text{-}\pi^*$  the transition of the peripheral fluorene. Besides the  $\pi\text{-}\pi^*$  transition bands of the ligands, the dendritic iridium complexes **16-19** also exhibit weak absorption bands in the range of  $\sim 350\text{--}450$  nm due to metal-to-ligand charge transfer transitions,  $^1\text{MLCT}$  and  $^3\text{MLCT}$ .

The dendritic ligands **12–15** emit in the violet-purple region ( $\lambda_{em} \sim 355$  nm) in  $\text{CH}_2\text{Cl}_2$ . Because of non-conjugated nature between the iridium center and the dendron, all dendritic iridium complexes emit green light both in toluene solution and neat film state ( $\lambda_{em} = 510\text{--}529$  nm), similar to their non-dendronized congener,  $(\text{GO})_3\text{Ir}$  [7]. The solution PL quantum yields (0.55–0.74 in toluene) of **16–19** compared favorably with that (0.45 in toluene) of the non-dendronized congener,  $(\text{GO})_3\text{Ir}$  [7], indicating that the encapsulation indeed more effectively suppresses triplet–triplet annihilation of the emitting core. The phosphorescent lifetimes (1.02–1.46  $\mu\text{s}$ ) of these complexes fall into the range of prototype non-dendronized tris-cyclo-metalated iridium complexes [19]. Apparently, the incorporation of flexible alkyl group or ether linkage does not lead to facile non-radiative decay pathways. The encapsulation efficiency increases as the surface group becomes bulkier (i.e.,  $\Phi_{\text{PL}}(\mathbf{18}) > \Phi_{\text{PL}}(\mathbf{16})$  and  $\Phi_{\text{PL}}(\mathbf{19}) > \Phi_{\text{PL}}(\mathbf{17})$ ), or the generation of the dendron increases (i.e.,  $\Phi_{\text{PL}}(\mathbf{17}) > \Phi_{\text{PL}}(\mathbf{16})$  and  $\Phi_{\text{PL}}(\mathbf{19}) > \Phi_{\text{PL}}(\mathbf{18})$ ). Similar to the quantum yields of the solutions, the trend retains in the film state. The studies of concentration quenching on **16–19** and non-encapsulated complex  $(\text{GO})_3\text{Ir}$  further witness the merit of encapsulation from the dendron, that is, the solution quantum yield of  $(\text{GO})_3\text{Ir}$  decreases more rapidly than **16–19** as the concentration increases from  $10^{-6}$  M to  $5 \times 10^{-4}$  M (see Fig 3). Compared to the solution state in Table 1, there is a significant drop of PL quantum yields in the solid film state ( $\Phi_{\text{PL}} = 0.15\text{--}0.33$ ). This is consistent with concentration quenching observed in the toluene solution (*vide supra*). Similar behavior was also reported in other phosphorescent dendrimers [5]. No

emission from the peripheral fluorene was noticed, indicating that energy transfer from the peripheral fluorene to the iridium center may occur, or there exists inner filter effect. We found that excitation at the  $^1\text{MLCT}$  band ( $\sim 410$  nm) of **17** in the film state led to phosphorescent emission of higher intensity by 2.0–2.5 times compared to excitation at the peripheral fluorene (250–300 nm). Therefore, the energy transfer from the dendron to the iridium center is not likely to be the main cause of the increased quantum yields in the larger dendrimers. This is in contrast to  $\text{Irpic}$  (iridium(III) bis[[4,6-difluorophenyl]pyridinato- $N,C^2$ ]-3-hydroxypicolinate) derivatives with  $N,N'$ -dicarbazolyl-3,5-benzene-based dendrons [22], which were described to have efficient singlet–singlet and triplet–triplet energy transfer from the dendron to the iridium center.

#### 4.3. Film morphology

Good thin film quality is prerequisite for good performance of OLEDs. Therefore, AFM was used to examine the morphology of the spin-casting films for these complexes. All compounds can be fabricated as good-quality films by spin-coating technique. Fig. 4 shows the AFM images of the spin-coating films (45–70 nm thick), obtained from iridium complexes **16–19**, on plasma treated indium tin oxide (ITO) substrates. The root mean square (RMS) surface roughness of neat film in **16–19** was found to be 0.489, 1.055, 1.287, and 0.667 nm, respectively. The blend films of CBP with 20 wt% of **16–19** had slightly larger RMS surface roughness at 1.175, 0.741, 2.264, and 3.121 nm, respectively.

**Table 2**  
EL data of DLEDs with different composition in the emitting layer.

Emitting-layer	$V_{\text{on}}$ , V	max. $L$ (at $V$ ), $\text{cd}/\text{m}^2$	max. $\eta_{\text{ext}}$ , %	max. $\eta_{\text{c}}$ , $\text{cd}/\text{A}$	max. $\eta_{\text{p}}$ , $\text{lm}/\text{W}$	$J = 20 \text{ mA}/\text{cm}^2; J = 100 \text{ mA}/\text{cm}^2$				$\lambda_{\text{em,max}}$ (fwhm), nm	CIE, $x,y$	
						$L$ (at $V$ ) $\text{cd}/\text{m}^2$	$\eta_{\text{ext}}$ , %	$\eta_{\text{c}}$ , $\text{cd}/\text{A}$	$\eta_{\text{p}}$ , $\text{lm}/\text{W}$			
<i>Blend film</i>												
20 wt% <b>16</b> (4.65 mmol)	4.0	14005 (16.0)	9.8	33.8	21.2	3534 (11.6); 10,954 (14.4)	5.7; 3.2	19.5; 11.2	5.3; 2.4	516 (74)	0.29, 0.62	
20 wt% <b>17</b> (2.77 mmol)	5.0	16229 (16.0)	13.6	45.8	20.6	6926 (8.7); 15,711 (12.5)	10.4; 4.7	35.1; 15.7	12.7; 3.9	514 (72)	0.27, 0.61	
40 wt% <b>17</b> (5.54 mmol)	5.5	6321 (20.0)	9.4	33.0	9.4	3766 (16.2); –	5.2; –	18.4; –	3.5; –	520 (76)	0.30, 0.62	
20 wt% <b>18</b> (4.20 mmol)	5.0	19217 (20.0)	8.28	27.9	13.48	3395 (12.5); 10,396 (18.1)	5.04; 3.10	17.0; 10.5	5.1; 2.4	520 (74)	0.31, 0.61	
20 wt% <b>19</b> (2.45 mmol)	6.0	13,876 (18.0)	9.0	31.1	15.0	4025 (11.5); 10,830 (14.8)	5.8; 3.2	15.0; 20.1	5.5; 2.3	514 (72)	0.28, 0.62	
40 wt% <b>19</b> (4.91 mmol)	8.0	5814 (20.0)	8.6	26.5	7.6	3073 (15.8); –	5.0; –	31.1; –	3.1; –	514 (72)	0.28, 0.61	
<i>Neat film</i>												
<b>16</b>	3.0	4895 (10.0)	3.6	11.4	10.3	1735 (6.0); 4375 (8.6)	2.7; 1.4	8.7; 4.4	4.5; 1.6	516 (76)	0.30, 0.58	
<b>17</b>	3.0	993 (10.5)	7.1	23.1	14.5	990 (10.3); 502 (16.9)	1.5; 0.15	5.0; 0.5	1.5; 0.1	516 (74)	0.30, 0.60	
<b>18</b>	3.0	5711 (11.5)	4.6	13.7	12.3	1964 (5.8); 4340 (8.2)	3.3; 1.5	10.0; 4.4	5.5; 1.7	516 (76)	0.30, 0.57	
<b>19</b>	5.0	1235 (13.5)	5.0	16.6	9.5	1013 (10.2); 1081 (15.8)	1.5; 0.33	5.1; 1.1	1.6; 0.22	512 (70)	0.26, 0.60	

$V_{\text{on}}$ , turn-on voltage, at a brightness of  $1 \text{ cd}/\text{m}^2$ ;  $L$ , luminance;  $V$ , voltage;  $\eta_{\text{ext}}$ , external quantum efficiency;  $\eta_{\text{c}}$ , current efficiency;  $\eta_{\text{p}}$ , power efficiency; fwhm, full width at half-maximum, max., maximum.



#### 4.4. Electrochemical studies

The electrochemical properties of the ligands (**12–15**) and the complexes (**16–19**) were studied by cyclic voltammetric (CV) method, and the electrochemical data are summarized in Table 1. All ligands show an irreversible oxidation wave with an onset potential at 1.42–1.58 V vs. Ag/AgNO<sub>3</sub>, which is characteristic of the peripheral fluorene group. Besides the irreversible oxidation wave of the ligands, a quasi-reversible one-electron oxidation wave attributed to the oxidation of the iridium(III) was detected in the range of ~0.39–0.41 mV vs. Ag/AgNO<sub>3</sub>. The negligible influence of the dendrons on the oxidation potential of the iridium center is likely due to non-conjugated nature of the spacer between the dendron and the iridium center. No reduction waves up to -2.0 V were detected in these iridium dendrimers. The HOMO (highest occupied molecular orbital) energy levels of compounds **12–19** were calculated from cyclic voltammogram in comparison with ferrocene (4.8 eV) [23]. The thus obtained HOMO levels, (~6.0 eV for **12–15** and ~4.95 eV for **16–19**) in combination with the optical bandgaps which were derived from the optical edges of absorption spectra, were used to calculate the LUMO (lowest unoccupied molecular orbital) energy levels [24]. Both HOMO and LUMO data are collected in Table 1.

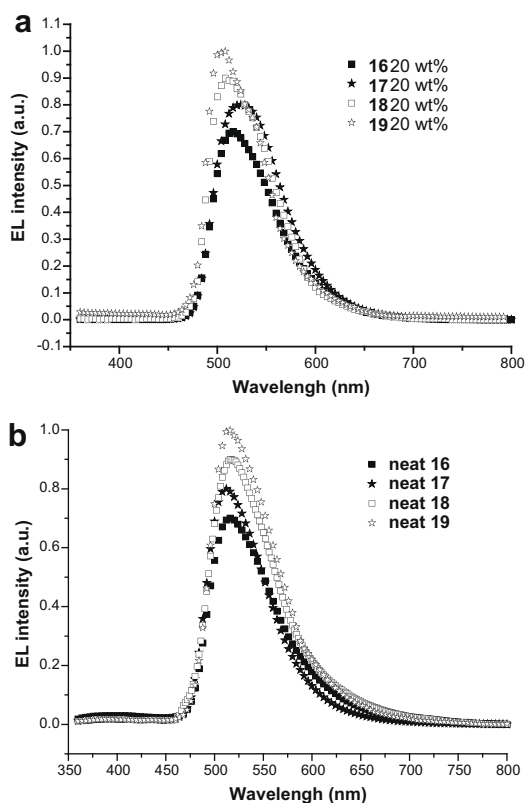


Fig. 7. EL spectra at a driving voltage of 12 V of DLEDs containing (a) **16–19** doped with CBP, (b) **16–19** neat film.

#### 4.5. Electroluminescent properties

Electroluminescent (EL) devices of bilayered configuration, ITO/PEDOT:PSS/neat **16–19** or *x* wt% of dopant **16–19** in CBP (45–70 nm)/TPBI (40 nm)/LiF (1 nm)/Al (120 nm), were fabricated via spin-coating technology (see Fig. 5). Spin-coating technology was used for device fabrication except for the vacuum deposition of TPBI (the electron-transporting and hole-blocking layer). The LED devices without the use of TPBI will not be discussed because the efficiency dropped at least two orders in both cases. The energy band structures of the devices are shown in Fig. 6, and the performance data are presented in Table 2. The EL spectra are shown in Fig. 7. All devices emitted green light and the EL spectra were superimposed with the PL spectra. The absence of emission from CBP suggests that either energy transfer from CBP to the complexes is complete or the trapping of electrons and holes by the complexes is efficient.

Although neat films of good quality can be obtained by spin-coating technique (*vide supra*), the devices using the neat films of the complexes have efficiencies far from ideal: the maximum external quantum efficiencies are lower than 7.1%. The following four factors are probably responsible for the low device efficiencies: (1) T–T annihilation

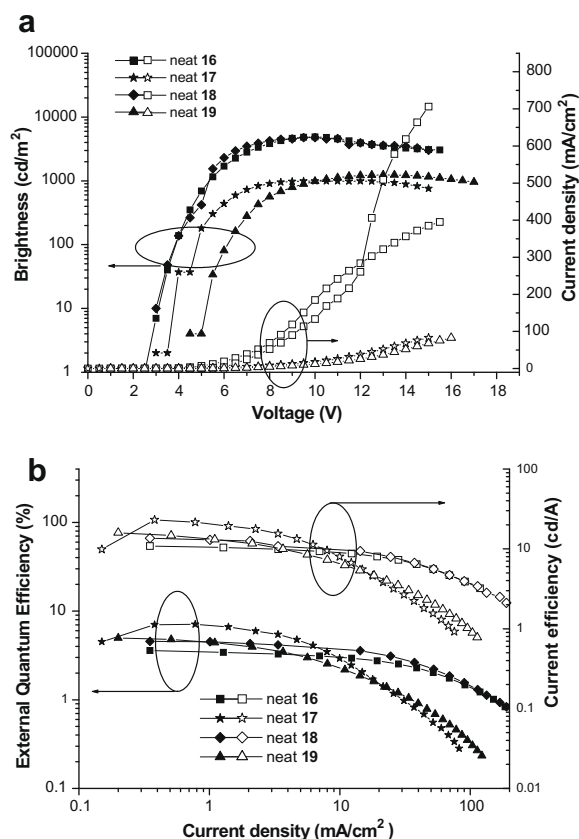
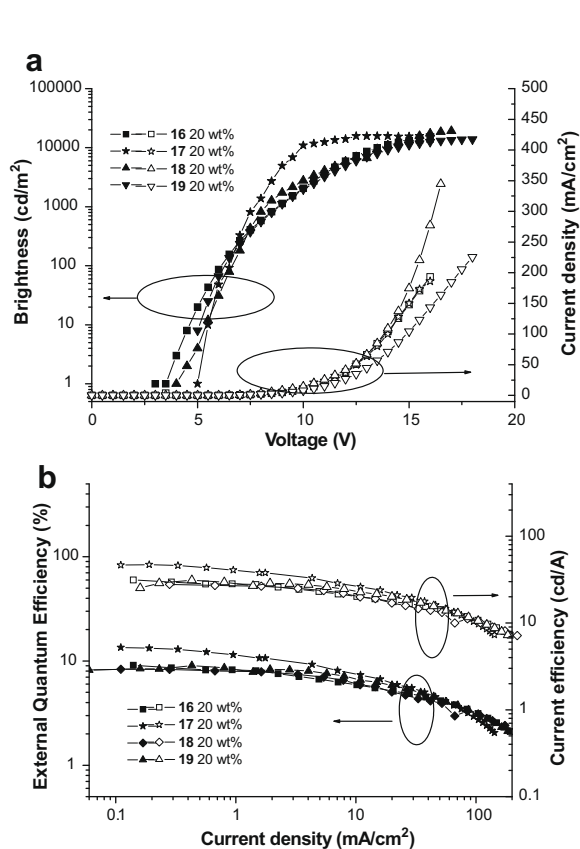


Fig. 8. The electro-optical characteristic of DLEDs containing neat **16–19** (a) brightness and current density as a function of voltage, and (b) current efficiency and EQE as a function of current density.

lation due to the high concentration of the guest; (2) the large energy gap between PEDOT:PSS and the HOMO level of peripheral fluorenyl group which hampers the hole injection into the emitting layer; (3) inefficient carrier mobility of the dendrons; (4) quenching of phosphorescence via energy transfer from the iridium center to the dendron due to small gap ( $\sim 1000\text{ cm}^{-1}$ ) between the triplet energies of the two. For example, **15** ( $E_T$  (77 K, toluene) = 2.55 eV; **10**,  $E_T$  (77 K, toluene) = 2.53 eV; **16**,  $E_T$  (77 K, toluene) = 2.34 eV. The current–voltage–brightness ( $I$ – $V$ – $L$ ) characteristic and the EQEs and current efficiency vs. current density for the devices based on neat films of **16**–**19** are shown in Fig. 8. DLEDs based on **17** and **19** exhibit much lower current density and brightness. Our observations are consistent with previous report illustrating that the carrier mobility decreases as the dendrimer generation increases [9]. The  $I$ – $V$ – $L$  characteristic and the EQEs and current efficiency vs. current density of DLEDs containing CBP doped with complexes **16**–**19** are shown in Fig. 9. Among them, the best efficiencies were found to be  $\eta_{\text{ext,max}} = 9.8\%$ , 13.6%, 8.3%, and 9.0%, and  $\eta_{\text{c,max}} = 33.8$ , 45.8, 27.9, and 31.1 cd/A for the devices with 4.65, 2.77, 4.20, and 2.45 mol% of **16**, **17**, **18**, and **19**, respectively. The significant drop of device efficiencies at dopant concentrations above 40% for all the complexes is likely due to T–T annihilation. The best device performance was

achieved at a lower dopant concentrations (mol%) for the devices based on the second-generation dendrimers (**17** and **19**) compared to the devices based on the first-generation dendrimers (**16** and **18**), which may be attributed to the inefficient carrier conductivity of the fluorene-containing dendrons. Inefficient carrier conductivity of the dendron is evident from the  $I$ – $V$  plots (Fig. 10) of **16** (first generation dendrimer) and **19** (second generation dendrimer) at different doping concentrations: the current decreases as the doping concentration increases at the same driving voltage. Though the current density of **18**-based device was higher than that of **19**-based device, **16**- and **17**-based devices were found to have comparable current density, where the conductivity might be affected by the film morphology. Nevertheless, the efficiency of the device increases as the generation of the dendrimer increases, i.e., **17** > **16** and **19** > **18**. Arylamine-based dendrimers with stilbene dendrons were also reported to have better device efficiency and inferior carrier mobility as the generation increases [9]. It was suggested that the increased spacing of hopping sites in the bulkier dendrimers inhibited transport of majority charge carriers and resulted in a reduction of the mobility. The influence of the dendron on the device efficiency may also be accounted by the same token in our



**Fig. 9.** The electro-optical characteristic of DLEDs containing  $x$  wt% **16**–**19** in CBP: (a) brightness and current density as a function of voltage; (b) current efficiency and EQE as a function of current density.

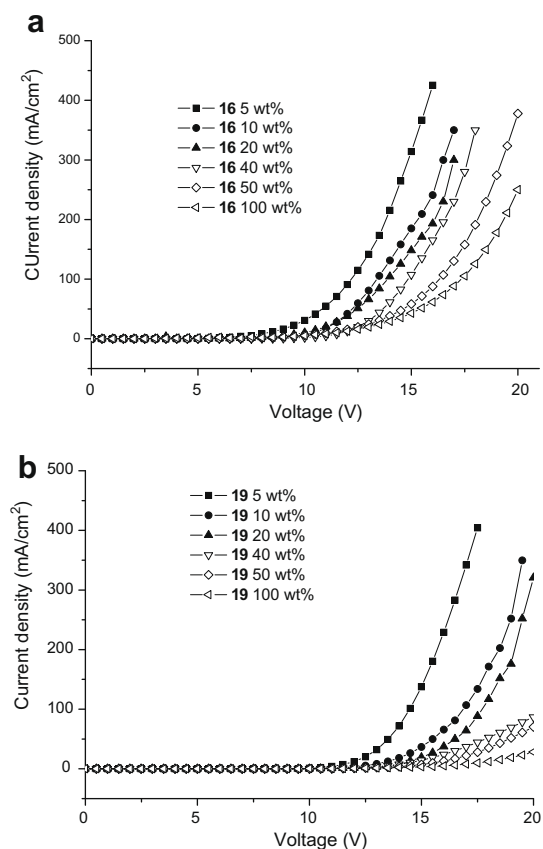


**Fig. 10.** The electro-optical characteristic of current–voltage ( $I$ – $V$ ) curves in DLEDs containing CBP with various dopant ratios of (a) compound **16** and (b) compound **19**.

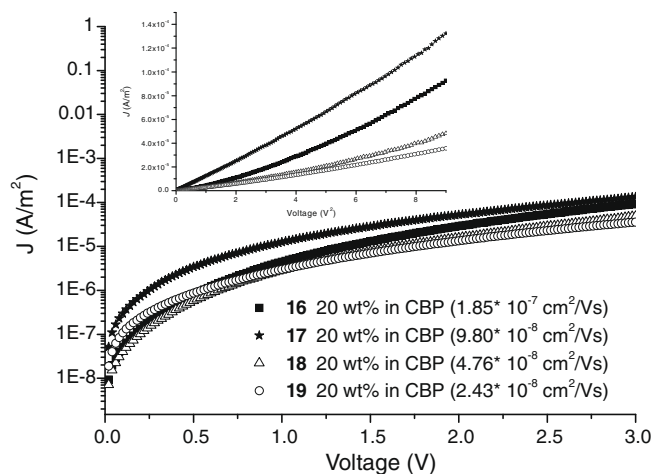


Fig. 11. The current–voltage ( $J$ – $V$ ) plots of hole-only devices with 20 wt% of **16**–**19** in CBP. Insert is the  $\log J$ – $V^2$  curves.

case. It is interesting to note that neat film devices also behave similarly (see Fig. 11).

#### 4.6. Hole mobility properties

Space-charge-limited current (SCLC) flow technique was used to measure the mobility of charge carriers in the films [25]. In spite of the ambipolar carrier-transporting characteristic of CBP [26], no discernible currents were detected for the blend film of CBP with the compounds synthesized in electron-only devices, indicating that the electron mobility was negligible in the film. This is consistent with the poor performance of DLEDs without the presence of TPBI (*vide supra*). In comparison, from the hole-only devices the hole mobilities can be determined precisely by fitting the dark current vs. voltage ( $J$ – $V$ ) curves for single carrier devices to SCLC model [27–28]. The dark current is given by  $J = 9\epsilon_0\epsilon_r\mu V^2/8L^3$  [29], where  $\epsilon_0\epsilon_r$  is the permittivity of the dendrimer,  $\mu$  is the carrier mobility, and  $L$  is the device thickness. From the capacitance–voltage measurements we have obtained a relative dielectric constant  $\epsilon_r$  of 0.65, 1.81, 1.30, 1.98 for the blend film of 20 wt% of **16**, **17**, **18**, and **19** in CBP, respectively. Therefore, the hole mobilities were calculated to be  $1.85 \times 10^{-7}$ ,  $9.80 \times 10^{-8}$ ,  $4.76 \times 10^{-8}$ , and  $2.43 \times 10^{-8}$   $\text{cm}^2/\text{Vs}$  for the blend films of **16**, **17**, **18** and **19**, respectively. These observations are consistent with the lower current density measured for DLEDs based on larger dendrimers, i.e., device of **17** < device **16** and device **19** < device **18** (*vide supra*). The lower hole mobility of the larger dendrimers (**17** and **19**) is likely due to increased spacing of hopping sites [9]. The better efficiencies of the devices for the larger dendrimers may be stemmed from the increased waiting time of charge carriers which will increase the probability of recombination, similar to that reported for triarylamine-cored distyrylbenzene-based dendrimers [9]. The device based on the neat film has a lower efficiency than that based on the CBP blend film, which may also be attributed to the non-conductivity of the former, and the very narrow exciton recombination region near the interface between

the neat film and TPBI. Compared with the iridium complexes encapsulated with benzyl ether dendrons we reported earlier [17], the hole mobilities of the dendrimers in this study appear to be  $\sim$ one order lower. The hole mobilities of the previous dendrimers were measured to be  $2.7 \times 10^{-6}$ , and  $9.2 \times 10^{-7}$   $\text{cm}^2/\text{Vs}$  for the 20 wt% CBP blend films of (**G1**)<sub>3</sub>Ir (first generation dendrimer) and (**G2**)<sub>3</sub>Ir (second generation dendrimer), respectively. Possibly the larger fluorene moiety increases spacing of hopping sites and results in a reduction of the mobility (*vide supra*). The somewhat lower device efficiencies in this study may be due to the less balanced hole and electron mobilities (the electron mobility of TPBI is  $\sim 10^{-5}$   $\text{cm}^2/(\text{Vs})$  [30]).

## 5. Conclusions

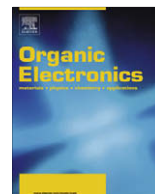
In conclusion, we have synthesized a series of benzoimidazole-based dendritic complexes of iridium dendrimers containing Fréchet-type dendrons with peripheral fluorenyl surface groups. These iridium dendrimers emit green light with high PL quantum yields, and can be spin-cast as films of good quality. The electroluminescent devices fabricated by the spin-coating technique have high-performance of electro-optical properties. One of the devices with the structure of ITO/PEDOT:PSS/CBP: **17** (20 wt%)/TPBI/LiF/Al has a maximum EQE of 13.58% and a maximum current efficiency of 45.7 cd/A. The high HOMO level of the peripheral fluorenyl surface group leads to a larger turn on voltage. EL devices based on the dendrimers of higher generation have a lower current density because of the slower carrier mobility of the higher generation dendrimer. However, EL devices from dendrimers of higher generation exhibit higher EQEs and current efficiencies.

## Acknowledgments

We thank the Academia Sinica, National Chiao Tung University and the National Science Council for supporting this work.

## References

- [1] C.W. Tang, S.A. VanSlyke, *Appl. Phys. Lett.* 51 (1987) 913.
- [2] (a) P.W. Wang, Y.J. Liu, C. Devadoss, P. Bharathi, J.S. Moore, *Adv. Mater.* 8 (1996) 237;  
(b) M. Halim, J.N.G. Pillow, I.D.N. Samuel, P.L. Burn, *Adv. Mater.* 11 (1999) 371;  
(c) A.W. Freeman, S.C. Koene, P.R.L. Malenfant, M.E. Thomson, J.M.J. Fréchet, *J. Am. Chem. Soc.* 122 (2000) 12385;  
(d) A. Adronov, J.M.J. Fréchet, *Chem. Commun.* (2000) 1701;  
(e) J.M. Lupton, I.D.W. Samuel, R. Beavington, M.J. Frampton, P.L. Burn, H. Bässler, *Phys. Rev. B* 63 (2001) 5206.
- [3] (a) H.Z. Xie, M.W. Liu, O.Y. Wang, X.H. Zhang, C.S. Lee, L.S. Hung, S.T. Lee, P.F. Teng, H.L. Kwong, H. Zheng, C. Che, *Adv. Mater.* 13 (2001) 1245;  
(b) J. Ostrowski, M.R. Robinson, A.J. Heeger, G.C. Bazan, *Chem. Commun.* (2002) 784;  
(c) J.-P. Duan, P.-P. Sun, C.-H. Cheng, *Adv. Mater.* 15 (2003) 224;  
(d) Y.-J. Su, H.-L. Huang, C.-L. Li, C.-H. Chien, Y.-T. Tao, P.-T. Chou, S. Datta, R.-S. Liu, *Adv. Mater.* 15 (2003) 884;  
(e) A.B. Tamayo, B.D. Alleyne, P.I. Djurovich, S. Lamansky, I. Tsyba, N.N. Ho, R. Bau, M.E. Thompson, *J. Am. Chem. Soc.* 125 (2003) 7377;  
(f) W. Lu, B.-X. Mi, M.C.W. Chan, Z. Hui, N. Zhu, S.-T. Lee, C.-M. Che, *Chem. Commun.* (2002) 206;  
(g) B.W. D'Andrade, J. Brooks, V. Adamovich, M.E. Thompson, S.R. Forrest, *Adv. Mater.* 14 (2002) 1032;  
(h) Y. Ma, H. Zhang, J. Shen, C.-M. Che, *Synth. Met.* 94 (1998) 245;  
(i) Y. Ma, C.-M. Che, H.-Y. Chao, X. Zhou, W.H. Chan, J. Shen, *Adv. Mater.* 11 (1999) 852.
- [4] (a) M.A. Baldo, D.F. O'Brien, Y. You, A. Shoustikov, S. Sibley, M.E. Thompson, S.R. Forrest, *Nature* 395 (1998) 151;  
(b) M.A. Baldo, D.F. O'Brien, M.E. Thompson, S.R. Forrest, *Phys. Rev. B* 60 (1999) 14422;  
(c) C. Adachi, M.A. Baldo, M.E. Thompson, S.R. Forrest, *J. Appl. Phys.* 90 (2001) 5048.
- [5] T.D. Anthopoulos, M.J. Frampton, E.B. Namdas, P.L. Burn, I.D.W. Samuel, *Adv. Mater.* 16 (2004) 557.
- [6] S.-C. Lo, N.A.H. Male, J.P.J. Markham, S.W. Magennis, P.L. Burn, I.D.W. Samuel, *Adv. Mater.* 14 (2002) 975.
- [7] J. Ding, J. Gao, Y. Cheng, Z. Xie, L. Wang, D. Ma, X. Jing, F. Wang, *Adv. Funct. Mater.* 16 (2006) 575.
- [8] S.-C. Lo, T.D. Anthopoulos, E.B. Namdas, P.L. Burn, I.D.W. Samuel, *Adv. Mater.* 17 (2005) 1945.
- [9] (a) J.M. Lupton, I.D.W. Samuel, R. Beavington, P.L. Burn, H. Bässler, *Adv. Mater.* 13 (2001) 258;  
(b) J.M. Lupton, I.D.W. Samuel, R. Beavington, M.J. Frampton, P.L. Burn, H. Bässler, *Phys. Rev. B* 63 (2001) 155206.
- [10] P.L. Burn, S.-C. Lo, I.D.W. Samuel, *Adv. Mater.* 19 (2007) 1675.
- [11] (a) G. Zhou, W.-Y. Wong, B. Yao, Z. Xie, L. Wang, *Angew. Chem., Int. Ed.* 46 (2007) 1149;  
(b) B. Liang, L. Wang, Y. Xu, H. Shi, Y. Cao, *Adv. Funct. Mater.* 17 (2007) 3580.
- [12] (a) J.P.J. Markham, S.-C. Lo, S.W. Magennis, P.L. Burn, I.D.W. Samuel, *Appl. Phys. Lett.* 80 (2002) 2645;  
(b) R.N. Bera, N. Cumpstey, P.L. Burn, I.D.W. Samuel, *Adv. Funct. Mater.* 17 (2007) 1149.
- [13] S.-C. Lo, G.J. Richard, J.P.J. Markham, E.B. Namdas, S. Sharma, P.L. Burn, I.D.W. Samuel, *Adv. Funct. Mater.* 15 (2005) 1451.
- [14] (a) T.D. Anthopoulos, J.P.J. Markham, E.B. Namdas, J.R. Lawrence, I.D.W. Samuel, S.-C. Lo, P.L. Burn, *Org. Electron.* 4 (2003) 71;  
(b) N. Cumpstey, R.N. Bera, P.L. Burn, I.D.W. Samuel, *Macromolecules* 38 (2005) 9564.
- [15] (a) T. Suzuki, N. Shirasawa, T. Suzuki, S. Tokito, *Jpn. J. Appl. Phys.* 44 (2005) 4151;  
(b) S.-C. Lo, E.B. Namdas, C.P. Shipley, J.P.J. Markham, T.D. Anthopoulos, P.L. Burn, I.D.W. Samuel, *Org. Electron.* 7 (2006) 85.
- [16] W.-S. Huang, J.T. Lin, C.-H. Chien, Y.-T. Tao, S.-S. Sun, Y.-S. Wen, *Chem. Mater.* 16 (2004) 2480.
- [17] W.-S. Huang, J.T. Lin, H.-C. Lin, *Org. Electron.* 9 (2008) 557.
- [18] (a) C.-C. Wu, T.-L. Liu, W.-Y. Hung, Y.-T. Lin, K.-T. Wong, R.-T. Chen, Y.M. Chen, Y.-Y. Chieh, *J. Am. Chem. Soc.* 125 (2003) 3710;  
(b) C.-C. Wu, Y.-T. Lin, K.-T. Wong, R.-T. Chen, Y.-Y. Chieh, *Adv. Mater.* 16 (2004) 61;  
(c) C.-C. Wu, T.-L. Liu, Y.-T. Lin, W.-Y. Hung, T.-H. Ke, *Appl. Phys. Lett.* 85 (2004) 1172;  
(d) C.-C. Wu, W.-G. Liu, W.-Y. Hung, T.-L. Liu, K.-T. Wong, Y.-Y. Chieh, R.-T. Chen, T.-H. Hung, T.-C. Chao, Y.-M. Chen, *Appl. Phys. Lett.* 87 (2005) 052103.
- [19] A. Tsuboyama, H. Iwakaki, M. Furugori, T. Mukaide, J. Kamatani, S. Igawa, T. Moriyama, S. Miura, T. Takiguchi, S. Okada, M. Hoshino, K. Ueno, *J. Am. Chem. Soc.* 125 (2003) 12971.
- [20] (a) L. Bouveault, *Bull. Soc. Chim. Fr.* 31 (1994) 1306;  
(b) J.D. Einhorn, *J. Org. Chem.* 49 (1984) 1078;  
S.M. Denton, A. Wood, *Synlett* (1999) 55.
- [21] L. Liu, Y. Zhang, B. Xin, *J. Org. Chem.* 71 (2006) 3994.
- [22] T.-H. Kwon, M.K. Kim, J. Kwon, D.-Y. Shin, S.J. Park, C.-L. Lee, J.-J. Kim, J.-I. Hong, *Chem. Mater.* 19 (2007) 3673.
- [23] J. Pommerehne, H. Vestweber, W. Guss, R.F. Mahrt, H. Bässler, M. Porsch, J. Daub, *Adv. Mater.* 7 (1995) 551.
- [24] (a) B.E. Koene, D.E. Loy, M.E. Thompson, *Chem. Mater.* 10 (1998) 2235;  
(b) M. Thelakkat, H.-W. Schmidt, *Adv. Mater.* 10 (1998) 219.
- [25] D. Hertel, H. Bässler, *ChemPhysChem* 9 (2008) 666.
- [26] H. Kanai, S. Ichinosawa, Y. Sato, *Syn. Met.* 91 (1997) 195.
- [27] P.W.M. Blom, M.J.M. De Jong, M.G. Van Munster, *Phys. Rev. B* 55 (1997) R656.
- [28] D.H. Dunlap, P.E. Parris, V.M. Kenkre, *Phys. Rev. Lett.* 77 (1996) 542.
- [29] W.D. Gill, *J. Appl. Phys.* 43 (1972) 5033.
- [30] Y. Li, M.K. Fung, Z. Xie, S.-T. Lee, L.-S. Hung, J. Shi, *Adv. Mater.* 14 (2002) 1317.



## Photoreactive $\pi$ -conjugated star-shaped molecules for the organic field-effect transistor

Mai Ha Hoang<sup>a</sup>, Min Ju Cho<sup>a</sup>, Dae Cheol Kim<sup>a</sup>, Kyung Hwan Kim<sup>a</sup>, Ji Won Shin<sup>b</sup>,  
Mi Yeon Cho<sup>b</sup>, Jin-soo Joo<sup>b</sup>, Dong Hoon Choi<sup>a,\*</sup>

<sup>a</sup> Department of Chemistry, Advanced Materials Chemistry Research Center, Korea University, 5 Anam-dong, Sungbuk-gu, Seoul 136-701, South Korea

<sup>b</sup> Department of Physics, Korea University, Seoul 136-701, South Korea

### ARTICLE INFO

#### Article history:

Received 29 August 2008

Received in revised form 25 December 2008

Accepted 24 February 2009

Available online 3 March 2009

#### PACS:

72.80.Le

85.30.Tv

82.35.x

61.10.Nz

#### Keywords:

Photoreactive

Organic field-effect transistor

Star-shaped molecule

Carrier mobility

### ABSTRACT

A number of semiconducting organic molecules capable of wet processing exhibit high carrier mobility and current modulation. In this work, we synthesized photopatternable  $\pi$ -conjugated star-shaped molecules and characterized their physical properties. The solubility of the synthesized molecules is very good for solution processing. The synthesized organic semiconducting multi-branched molecules are capable of photopatterning by virtue of photopolymerization of the reactive pentadienyl end groups. The transistor devices using these molecules provided a field-effect mobility of  $1.3(\pm 0.2) \times 10^{-3}$ – $3.7(\pm 0.5) \times 10^{-3} \text{ cm}^2 \text{ V}^{-1} \text{ s}^{-1}$  as well as a high current on/off ratio ( $I_{\text{on/off}} > 10^3$ ) and a low threshold voltage. In the case of the photoreactive star-shaped conjugated molecule HP2P, it was found that field-effect mobility was maintained even after the photocrosslinking process. This result can be used in the design of photopatternable semiconductor molecules for thin-film transistor electronic applications.

© 2009 Elsevier B.V. All rights reserved.

## 1. Introduction

There has been growing interest in  $\pi$ -conjugated systems over the last several years due to their unique semiconducting and electro-optical properties and because of their potential applications in different electronic devices, such as organic field-effect transistor devices (OFETs) [1,2] and organic photovoltaic devices (OPVs) [3,4]. Among the various types of soluble organic semiconducting materials, star-shaped crystalline molecules have been attractive for synthesis because of their strong potential advantages. Compared with the linear organic conjugated

oligomers and polymers currently used in OFETs, these molecules have a number of advantages including the ability to demonstrate multifunctionality in one molecule [5,6]. The synthesis of  $\pi$ -conjugated star-shaped molecules raises the possibility of creating thiophene derivatives that are fully tethered to the aromatic core. Furthermore, the solubility problem in conjugated linear oligothiophene is resolved under dendritic architecture [7,8]. Recently, the authors demonstrated some star-shaped molecules showing good solubilities, film-forming properties, and reasonably high field-effect carrier mobilities [9].

The development of OFETs has generated a great deal of interest in solution-processible organic semiconductors, which can combine high charge transport mobility, stability, and patternability [10]. However, the carrier mobility of the linear thiophene-based liquid crystalline molecule

\* Corresponding author. Tel.: +82 2 3290 3140; fax: +82 2 924 3141.  
E-mail address: [dhchoi8803@korea.ac.kr](mailto:dhchoi8803@korea.ac.kr) (D.H. Choi).

was observed to decrease after the photocrosslinking reaction due to the disruption of the preferred anisotropic molecular packing. [10]. In this work, the authors report the design of a new class of hole transporting semiconductor materials incorporating photoreactive end groups, which can undergo a photopolymerization without a photoinitiator. In this instance, the core of the molecule is designed to have conjugative connecting properties, which will be discussed later. The photopolymerizable 1,4-pentadien-3-yl group at the periphery was used because of its ability to undergo photopolymerization. [11,12]. Ultraviolet (UV) radiation ( $\lambda = 254\text{--}270\text{ nm}$ ) at room temperature is effective in inducing photopolymerization, forming cross-links between the reactive units, which results in the formation of insoluble 2-D or 3-D polymer networks.

## 2. Experiment

### 2.1. Material

All commercially available starting reagents or reactants were purchased from Aldrich or Acros Organics Co. and used without further purification unless otherwise stated. All solvents used in this study were freshly dried under the standard distillation method.

Compounds **4** [13], **9** [14], and **11** [9] were prepared according to the procedures in the literature. Compounds **1** [15,16], **2** [16,17] were also synthesized using similar methods that have been reported in the literature. Compound **7** was prepared using the reaction between penta-1,4-dien-3-ol and succinic anhydride in the presence of 4-dimethylaminopyridine and triethylamine in a quantitative yield.

### 2.2. Synthesis

#### 2.2.1. 5'-((Tert-butyl dimethylsilyloxy)methyl)-2,2'-bithiophene-5-carbaldehyde, **3**

A solution of compound **2** (31.0 g, 100 mmol) in tetrahydrofuran (THF, 200 mL) was cooled to  $-78\text{ }^{\circ}\text{C}$  in an acetone/dry ice bath. *N*-Butyllithium (105 mmol, 42 mL, 2.5 M in hexane) was added through a syringe over 10 min. The temperature of the reaction mixture was slowly raised to  $-30\text{ }^{\circ}\text{C}$  and was maintained for 1 h. Next, *N,N*-dimethylformamide (DMF, 9.0 mL, 120 mmol) was added through a syringe over 5 min. The mixture was allowed to stir at room temperature for 2 h and then was quenched with an aqueous ammonium acetate solution. The organic layer was separated and the aqueous phase was extracted with ether. The combined organic layer was condensed and the residue was purified with silica-gel column chromatography using chloroform/hexane (1/15 v/v) and then crystallized in methanol to afford 24.7 g of solid: yield 73%.

$^1\text{H NMR}$  (400 MHz,  $\text{CDCl}_3$ ):  $\delta$ (ppm) 9.85 (s, 1H), 7.65 (d,  $J = 4.0\text{ Hz}$ , 1H), 7.21 (d,  $J = 4.0\text{ Hz}$ , 1H), 7.20 (d,  $J = 4.0\text{ Hz}$ , 1H), 6.86 (d,  $J = 4.0\text{ Hz}$ , 1H), 4.86 (s, 2H), 0.94 (s, 9H), 0.13 (s, 6H).

Anal. Calcd for  $\text{C}_{16}\text{H}_{22}\text{O}_2\text{S}_2\text{Si}$ : C, 56.76; H, 6.55; found: C, 56.96; H, 6.52.

#### 2.2.2. 1,2,4,5-Tetrakis((*E*)-2-(5'-((*tert*-butyldimethylsilyloxy)methyl)-2,2'-bithiophen-5-yl)vinyl)benzene, **5**

A solution of potassium *tert*-butoxide (2.6 g, 23 mmol) in 50 mL of THF was added to a mixture of octaethyl benzene-1,2,4,5-tetrayltetrakis(methylene) tetrphosphonate (3.4 g, 5.0 mmol), 5'-((*tert*-butyldimethylsilyloxy)methyl)-2,2'-bithiophene-5-carbaldehyde **3** (7.8 g, 23 mmol), and 50 mL of THF over 10 min under magnetic stirring. The mixture was allowed to stir at room temperature overnight. Then, ethanol (200 mL) was added to the reaction mixture. The resultant precipitate was filtered and washed with methanol and then purified with silica-gel column chromatography using chloroform/hexane (1/2 v/v). After that, it was crystallized in THF/methanol to afford 4.4 g of red-yellow solid: yield 62%.

$^1\text{H NMR}$  (400 MHz,  $\text{CDCl}_3$ ):  $\delta$ (ppm) 7.65 (s, 2H), 7.18 (d,  $J = 16.0\text{ Hz}$ , 4H), 7.13 (d,  $J = 16.0\text{ Hz}$ , 4H), 7.07 (d,  $J = 4.0\text{ Hz}$ , 4H), 7.05 (d,  $J = 4.0\text{ Hz}$ , 4H), 7.01 (d,  $J = 4.0\text{ Hz}$ , 4H), 6.82 (d,  $J = 4.0\text{ Hz}$ , 4H), 4.86 (s, 8H), 0.95 (s, 36H), 0.13 (s, 24H).

Anal. Calcd for  $\text{C}_{74}\text{H}_{94}\text{O}_4\text{S}_8\text{Si}_4$ : C, 62.75; H, 6.69, found: C, 62.61; H, 6.70.

#### 2.2.3. (5',5'',5''',5''''-(1*E*,1'*E*,1''*E*,1'''*E*)-2,2',2'',2''''-(Benzene-1,2,4,5-tetrayl)tetrakis(ethene-2,1-diyl)tetrakis(2,2'-bithiophene-5',5'-diyl))tetramethanol, **6**

Compound **5** (2.83 g, 2.0 mmol) was dissolved in 50 mL of THF. Dilute hydrochloric acid (6.0 mL, 0.75 N) was added and the mixture was stirred at room temperature for 3 h. Triethylamine (6.0 mmol) was added to neutralize the acid; then, 100 mL of water was added slowly to precipitate out the product. The product was collected by filtration, washed, and dried *in vacuo* to give a quantitative yield.

Anal. Calcd for  $\text{C}_{50}\text{H}_{38}\text{O}_4\text{S}_8$ : C, 62.60; H, 3.99, found: C, 63.01; H, 4.14.

#### 2.2.4. 1'',1',1-(5',5'',5''''-(1*E*,1'*E*,1''*E*)-2,2',2''-(5'-((*E*)-2-(5'-((4-((*Z*)-Hexa-1,4-dien-3-yloxy)-4-oxobutanoyloxy)methyl)-2,2'-bithiophen-5-yl)vinyl)benzene-1,2,4-triyl)tris(ethene-2,1-diyl)tris(2,2'-bithiophene-5',5'-diyl))tris(methylene) 4-tributanedioate, **8 (HBAP)**

To a solution of **6** (0.96 g, 1.0 mmol) and **7** (0.92 g, 5.0 mmol) in 50 mL of dichloromethane (DCM)/THF (1:3), 4-(dimethyl-amino)pyridinium *p*-toluenesulfonate (DPTS) (1.32 g, 4.5 mmol) was added; the mixture was allowed to stir at room temperature under nitrogen atmosphere for 15 min. *N,N'*-Dicyclohexylcarbodiimide (DCC, 0.93 g, 4.5 mmol) was then added and the mixture was allowed to stir at  $40\text{ }^{\circ}\text{C}$  for 5 days. The reaction mixture was filtered and the filtrate was concentrated under a reduced pressure. The crude product was then purified by silica-gel column chromatography (eluent; ethyl acetate/ $\text{CHCl}_3 = 1:10\text{ v/v}$ ) to afford 1.03 g of a red solid: yield 63%.

$^1\text{H NMR}$  (400 MHz,  $\text{CDCl}_3$ ):  $\delta$ (ppm) 7.62 (s, 2H), 7.18 (d,  $J = 16.0\text{ Hz}$ , 4H), 7.13 (d,  $J = 16.0\text{ Hz}$ , 4H), 7.07 (d,  $J = 4.0\text{ Hz}$ , 4H), 7.05 (d,  $J = 4.0\text{ Hz}$ , 4H), 7.01 (d,  $J = 4.0\text{ Hz}$ , 4H), 6.99 (d,  $J = 4.0\text{ Hz}$ , 4H), 5.82 (m, 8H), 5.72 (t, 4H), 5.27 (m, 16H), 5.25 (s, 8H), 2.7 (s, 16H).

$^{13}\text{C NMR}$  (100 MHz,  $\text{CDCl}_3$ ):  $\delta$ (ppm) 172.16, 171.28, 142.42, 139.16, 136.99, 136.50, 135.07, 134.88, 129.47,

127.90, 125.64, 124.74, 124.42, 123.67, 117.85, 75.71, 61.13, 29.49, 29.31.

Anal. Calcd for  $C_{86}H_{78}O_{16}S_8$ : C, 63.60; H, 4.84, found: C, 63.64; H, 4.78.

2.2.5. (5',5''-(1E,1'E)-2,2'-(2,5-Dibromo-1,4-phenylene)-bis(ethene-2,1-diyl)bis(2,2'-bithiophene-5',5'-diyl))bis(methylene)bis(oxy)bis(tert-butyltrimethylsilane), **10**

A solution of potassium *tert*-butoxide (0.78 g, 7.0 mmol) in 20 mL of THF was added to a mixture of **9** (1.6 g, 3.0 mmol) and **3** (2.37 g, 7.0 mmol), and 50 mL of THF was added over 10 min under magnetic stirring. The mixture was stirred at room temperature overnight. The same work-up procedure was employed for preparing **5**. The authors obtained 1.81 g (yield 67%) of a pure red solid.

$^1H$  NMR (400 MHz,  $CDCl_3$ ):  $\delta$ (ppm) 7.80 (s, 2H), 7.14 (d,  $J = 16.0$  Hz, 2H), 7.09 (d,  $J = 16.0$  Hz, 2H), 7.07 (d,  $J = 4.0$  Hz, 4H), 7.05 (d,  $J = 4.0$  Hz, 4H), 7.01 (d,  $J = 4.0$  Hz, 4H), 6.82 (d,  $J = 4.0$  Hz, 4H), 4.85 (s, 4H), 0.95 (s, 18H), 0.13 (s, 12H).

Anal. Calcd for  $C_{40}H_{48}Br_2O_2S_4Si_2$ : C, 53.08; H, 5.35, found: C, 53.67; H, 5.31.

2.2.6. (5',5''-(1E,1'E)-2,2'-(2,5-Bis((E)-2-(5'-hexyl-2,2'-bithiophen-5-yl)vinyl)-1,4-phenylene)bis(ethene-2,1-diyl)bis(2,2'-bithiophene-5',5'-diyl))bis(methylene)bis(oxy)bis(tert-butyltrimethylsilane), **12**

Compound **10** (0.9 g, 1.0 mmol), **11** (0.69 g, 2.5 mmol), and tri-*o*-tolylphosphine (30 mg, 0.1 mmol) were dissolved in 50 mL DMF and then tributylamine (0.6 mL, 2.5 mmol) was added. After 10 min,  $Pd(OAc)_2$  (45 mg, 0.2 mmol) was added and the mixture was stirred at 95 °C overnight. Then, water (200 mL) was added to the reaction mixture. The resultant precipitate was filtered and washed with methanol. It was purified with silica-gel column chromatography using chloroform/hexane (1/2 v/v) and then crystallized in THF/methanol to afford 0.7 g of red solid: yield 54%.

$^1H$  NMR (400 MHz,  $CDCl_3$ ):  $\delta$ (ppm) 7.65 (s, 2H), 7.18 (d,  $J = 16.0$  Hz, 4H), 7.13 (d,  $J = 16.0$  Hz, 4H), 7.07 (d,  $J = 4.0$  Hz, 4H), 7.05 (d,  $J = 4.0$  Hz, 4H), 7.01 (d,  $J = 4.0$  Hz, 4H), 6.82 (d,  $J = 4.0$  Hz, 2H), 6.68 (d,  $J = 4.0$  Hz, 2H), 4.86 (s, 4H), 2.80 (t, 4H), 1.69 (t, 4H), 1.34 (m, 12H), 0.95 (s, 18H), 0.90 (t, 6H), 0.13 (s, 12H).

Anal. Calcd for  $C_{72}H_{86}O_2S_8Si_2$ : C, 66.72; H, 6.69, found: C, 67.06; H, 7.05.

2.2.7. (5',5''-(1E,1'E)-2,2'-(2,5-Bis((E)-2-(5'-hexyl-2,2'-bithiophen-5-yl)vinyl)-1,4-phenylene)bis(ethene-2,1-diyl)bis(2,2'-bithiophene-5',5'-diyl))dimethanol, **13**

Compound **12** (0.65 g, 0.5 mmol) was dissolved in 30 mL of THF. Dilute hydrochloric acid (3.0 mL, 0.75 N) was added and the mixture was stirred at room temperature for 3 h. The same work-up procedure was employed for preparing **6** to give a quantitative yield.

$^1H$  NMR (400 MHz,  $CDCl_3$ ):  $\delta$ (ppm) 7.65 (s, 2H), 7.18 (d,  $J = 16.0$  Hz, 4H), 7.13 (d,  $J = 16.0$  Hz, 4H), 6.97–7.09 (m, 12H), 6.90 (d,  $J = 4.0$  Hz, 2H), 6.68 (d,  $J = 4.0$  Hz, 2H), 4.82 (s, 4H), 2.80 (t, 4H), 1.69 (t, 4H), 1.34 (m, 12H), 0.90 (t, 6H).

Anal. Calcd for  $C_{50}H_{38}O_4S_8$ : C, 67.50; H, 5.48, found: C, 66.55; H, 5.22.

2.2.8. 1,1'-(5',5''-(1E,1'E)-2,2'-(2,5-Bis((E)-2-(5'-hexyl-2,2'-bithiophen-5-yl)vinyl)-1,4-phenylene)bis(ethene-2,1-diyl)bis(2,2'-bithiophene-5',5'-diyl))bis(methylene) 4-di(penta-1,4-dien-3-yl) dibutanedioate, **14 (HB2P)**

DPTS (0.35 g, 1.2 mmol) was added to a solution of **13** (0.53 g, 0.5 mmol) and **7** (0.22 g, 1.2 mmol) in 40 mL of DCM/THF (1:1); the mixture was allowed to stir at room temperature under nitrogen atmosphere for 15 min. DCC (0.25 g, 1.2 mmol) was then added and the mixture was stirred at room temperature overnight. The same work-up procedure was employed for preparing **8**. The authors obtained 0.64 g (yield 92%) of a pure red solid.

$^1H$  NMR (400 MHz,  $CDCl_3$ ):  $\delta$ (ppm) 7.61 (s, 2H), 7.17 (d,  $J = 16.0$  Hz, 4H), 7.11 (d,  $J = 16.0$  Hz, 4H), 7.07 (d,  $J = 4.0$  Hz, 4H), 7.05 (d,  $J = 4.0$  Hz, 4H), 7.01 (d,  $J = 4.0$  Hz, 4H), 6.98 (d,  $J = 4.0$  Hz, 4H), 6.68 (d,  $J = 4.0$  Hz, 2H), 5.82 (m, 4H), 5.72 (t, 2H), 5.27 (m, 8H), 5.25 (s, 4H), 2.80 (t, 4H), 2.7 (s, 8H), 1.69 (t, 4H), 1.34 (m, 12H), 0.90 (t, 6H).

$^{13}C$  NMR (100 MHz,  $CDCl_3$ ):  $\delta$ (ppm) 171.92, 171.04, 145.78, 142.30, 141.18, 138.99, 137.32, 136.67, 136.17, 134.84, 134.77, 134.69, 134.56, 129.22, 127.68, 127.57, 125.56, 124.91, 124.85, 124.49, 124.35, 124.26, 124.03, 123.66, 123.42, 75.48, 60.90, 31.58, 30.23, 29.27, 29.09, 28.78, 22.59, 14.1.

Anal. Calcd for  $C_{78}H_{78}O_8S_8$ : C, 66.92; H, 5.62, found: C, 66.53; H, 5.56.

### 2.3. Instrumental analysis

$^1H$  NMR spectra were recorded on a Varian Mercury NMR 400 MHz spectrometer using deuterated chloroform (Cambridge Isotope Laboratories, Inc.). Elemental analyses were performed using an EA1112 elemental analyzer (Thermo Electron Corp.). Thermal properties were studied under a nitrogen atmosphere on a Mettler DSC 821<sup>e</sup> instrument and a TGA50 (Heating rate of 5 °C/min under  $N_2$ ). Fourier transform infrared (FT-IR) spectra were recorded using a Perkin-Elmer 783 infrared spectrophotometer (sample on KBr window). The redox properties of the star-shaped molecules were examined using cyclic voltammetry (Model: EA161 eDAQ). Thin films were coated on a platinum plate using chloroform as a solvent. The electrolyte solution employed was 0.10 M tetrabutylammonium hexafluorophosphate ( $Bu_4NPF_6$ ) in a freshly dried MC. The Ag/AgCl and Pt wire (0.5 mm in diameter) electrodes were used as the reference and counter electrode, respectively. The scan rate was 50 mV/s.

The X-ray diffraction (XRD) experiment was performed at varying temperatures using the synchrotron radiation (1.542 Å) of the 3C2 beam line at the Pohang Synchrotron Laboratory, Pohang, Korea. The film samples were fabricated by drop-casting on a silicon wafer, followed by drying at 70 °C under vacuum (solvent: chloroform, solution concentration: 10 mg/mL). The measurements were obtained in a scanning interval of  $2\theta$  between 1° and 40°.

Atomic force microscopy (AFM, Digital Instruments Multimode equipped with a nanoscope IIIa controller) operating in tapping mode with a silicon cantilever was used to characterize the surface morphologies of the samples. The film samples were fabricated by spin-coating (1500 rpm) on silicon wafer followed by drying at 60 °C

under vacuum (solvent: chloroform, solution concentration: 10 mg/mL).

Absorption spectra of the samples in a film and solution state (chloroform, concentration  $1 \times 10^{-5}$  mol/L) were obtained using a UV–vis spectrometer (HP 8453, photodiode array type) in the wavelength range of 190–1100 nm. To study absorption behavior, the films of the two molecules were fabricated on quartz substrates: The solution (1 wt%) of each molecule in chloroform (**HB4P**) and monochlorobenzene (**HB2P**) was spin-coated onto the quartz glass. The films were dried overnight under vacuum.

#### 2.4. OFET fabrication

Bottom-contact OFET devices were fabricated using the gold source and drain electrodes, which were thermally evaporated using the conventional method. P-doped polycrystalline silicon was used as a gate electrode; its 300-nm bare and surface-modified  $\text{SiO}_2$  layer was used as a gate dielectric insulator. The deposition of a self-assembled monolayer (SAM) with octyltrichlorosilane (OTS) on the

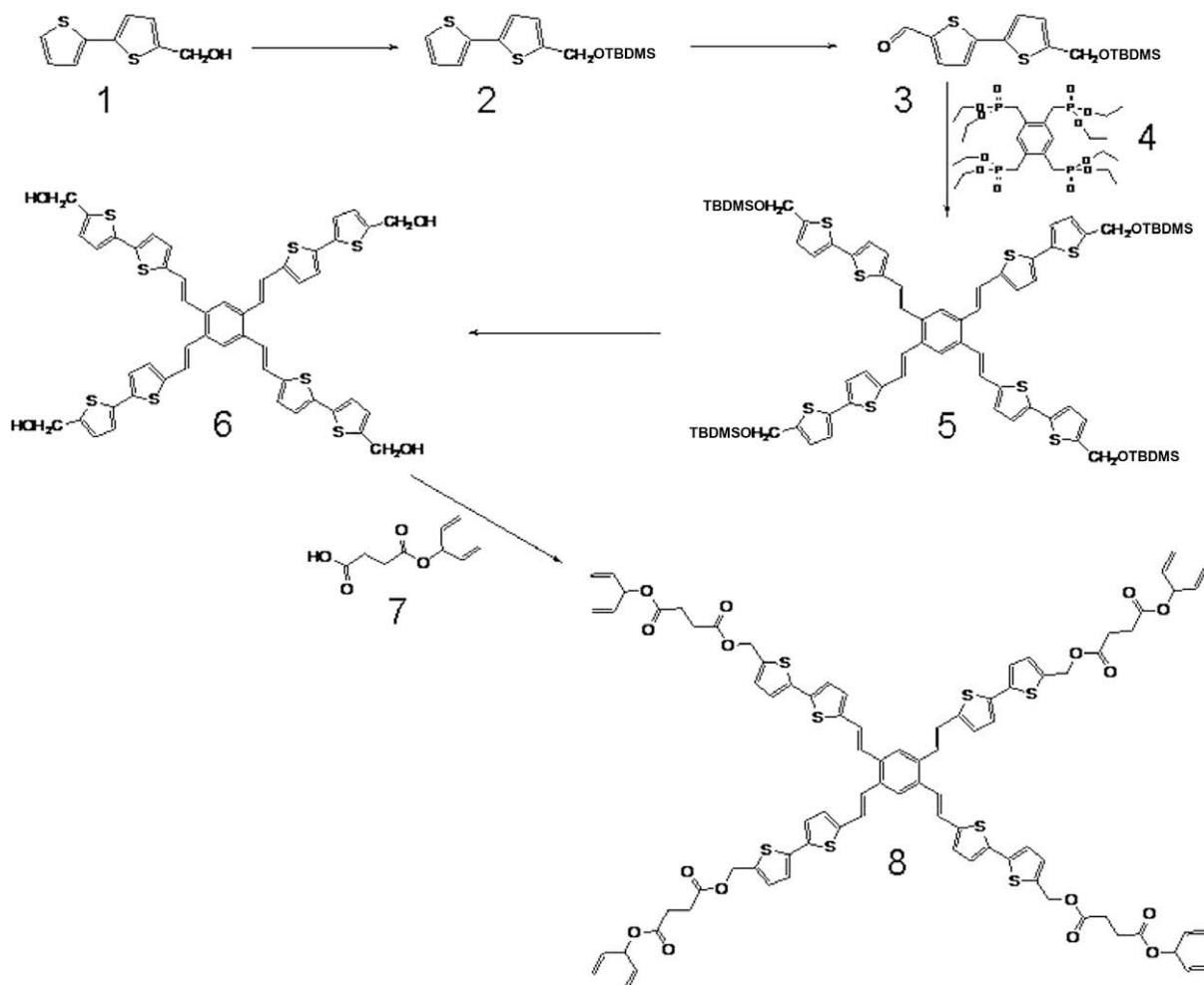
$\text{SiO}_2$  gate dielectric was performed according to the method in the literature [18].

The gold was deposited onto the untreated and OTS-treated  $\text{SiO}_2$  surface via thermal evaporation. The current–voltage ( $I$ – $V$ ) characteristics of the OTFTs were measured under vacuum below  $10^{-2}$  Torr using a Keithley 237 SMU. A wire bonder (Kunche & Sona 4524) was used for electrical contact from the Au electrodes to a chip carrier for the OTFTs. Field-effect mobility in cross-linked organic semiconducting films was measured by exposure to the films under UV light ( $\lambda = 254$  nm,  $I = 40.64$  mW/cm<sup>2</sup>) for 5 min at room temperature.

### 3. Results and discussion

#### 3.1. Synthesis

The authors report the easy, high-yield synthesis of new photopolymerizable p-type thiophene-based star-shaped semiconducting molecules. In Scheme 1, **5** was prepared by the Horner–Emmons coupling of [1,2,4,5-tetra-(dieth-



Scheme 1. Synthetic route of **8** (**HB4P**).



oxy-phosphorylmethyl)-benzyl]-phosphonic acid diethyl ester and 5'-((tert-butyldimethylsilyloxy)methyl)-2,2'-bithiophene-5-carbaldehyde. After deprotecting TBDMS, the esterification of **6** and 4-oxo-4-(penta-1,4-dien-3-yloxy)butanoic acid **7** produces **HB4P** in a good yield (63%). **HB4P** came to have four pentadienyl reactive groups in each arm.

However, in Scheme 2, the Horner–Emmons coupling of tetraethyl (2,5-dibromo-1,4-phenylene)bis(methylene)diphosphonate and 5'-((tert-butyldimethylsilyloxy)methyl)-2,2'-bithiophene-5-carbaldehyde produces **10**. The Heck coupling reaction was then used to attach 5-hexyl-5'-vinyl-2,2'-bithiophene for the synthesis of **12**. The same method was employed for preparing **HB2P**.

The identity and purity of the synthetic materials were confirmed by  $^1\text{H}$  NMR,  $^{13}\text{C}$  NMR, and elemental analysis. They were found to have good self-film-forming properties and to be well-soluble in various organic solvents such as chloroform, dichloromethane, ethyl acetate, chlorobenzene, and tetrahydrofuran.

Furthermore, computer calculations using the AM1 theoretical model incorporated into the Spartan program ('06) were performed to determine the minimum energy conformations for **HB4P** and **HB2P** [19]. Such calculations have been found reliable for the determination of geometrical shapes in cruciform molecules. The optimized geometrical structures of the two molecules are illustrated in Fig. 1. The shapes of the molecules are expected to be quite similar. **HB4P** is likely to have randomly oriented photoreactive peripheral moieties. It is interesting to note why they have a low degree of crystallization during cooling, which will be discussed in Section 3.6. In particular, **HB2P** has two hexyl peripheral groups with a zig-zag extended confor-

mation, which can be interdigitated due to molecular interaction.

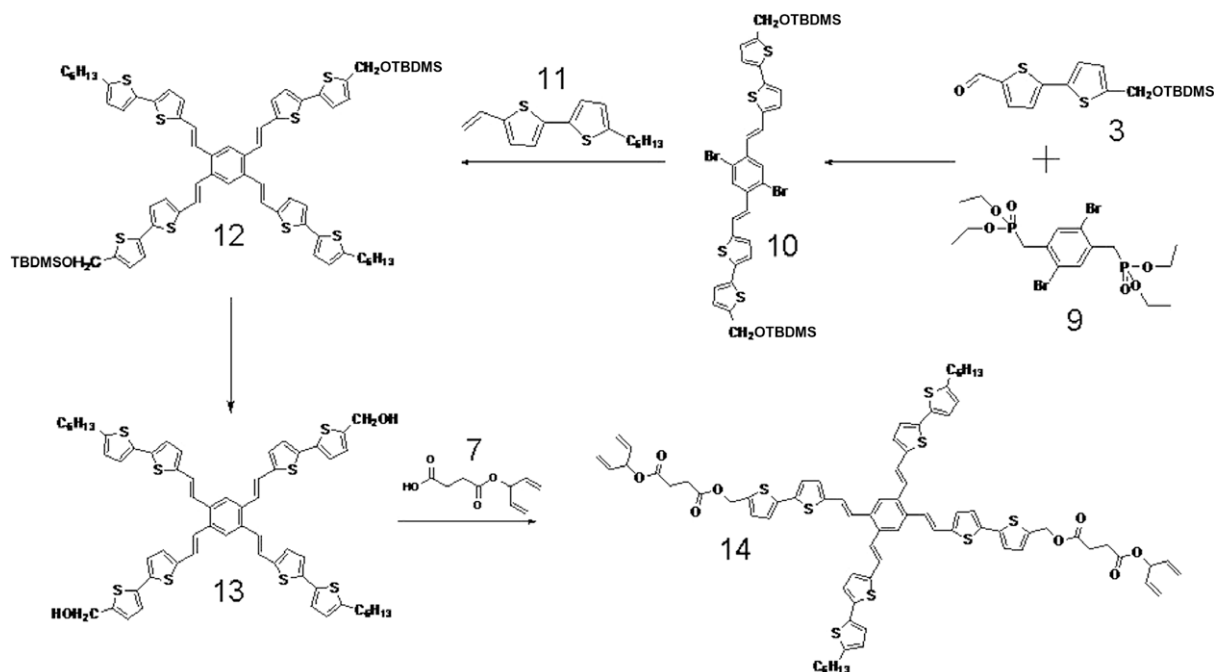
### 3.2. Thermal analysis

When employing the photopolymerizable star-shaped molecules for OFET applications, their thermal stabilities and dynamic behaviors are emphasized for device fabrication. The thermal properties of the molecules were characterized by differential scanning calorimetry (DSC) and thermogravimetric analysis (TGA). DSC measurement was performed at a heating (cooling) scan rate of  $5\text{ }^\circ\text{C}/\text{min}$  under nitrogen with the highest temperature limited to be below the decomposition temperature (Fig. 2). **HB4P** and **HB2P** displayed distinct melting temperatures at  $76\text{ }^\circ\text{C}$  and  $142\text{ }^\circ\text{C}$ , respectively. **HB4P** and **HB2P** exhibited distinct isotropic-to-crystalline transitions at  $58\text{ }^\circ\text{C}$  and  $116\text{ }^\circ\text{C}$  during cooling cycles, respectively. On comparison of the crystalline and melting points of **HB4P**, **HB2P**, and 1,2,4,5-tetrakis((E)-2-(5'-hexyl-2,2'-bithiophen-5-yl)vinyl)benzene [9], the authors determined that the hexyl peripheral groups play a key role in increasing the crystallinity due to the presence of 2-D lamella ordering.

### 3.3. Confirmation of photocrosslink

#### 3.3.1. FT-IR spectroscopy

An FT-IR investigation was carried out to confirm that photopolymerization had occurred between the diene units. Fig. 3 shows FT-IR spectra of the **HB4P** and **HB2P** film before and after UV exposure ( $\lambda = 254\text{ nm}$ ,  $I = 40.64\text{ mW}/\text{cm}^2$ ). The characteristic absorption bands at  $932$ ,  $993$ ,  $1150$ ,  $1640$ , and  $1737\text{ cm}^{-1}$ , which can be unambiguously



Scheme 2. Synthetic route of **14** (**HB2P**).

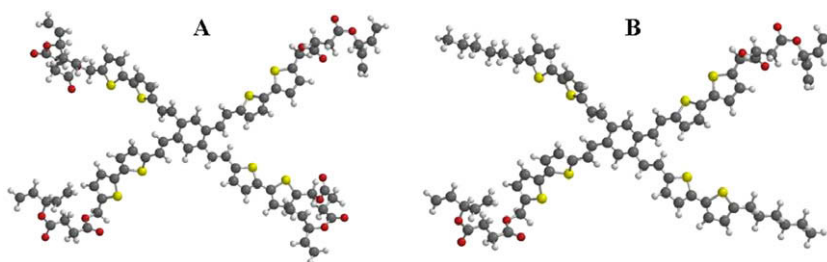


Fig. 1. Optimized geometries of molecules. (A) **HB4P** and (B) **HB2P**.

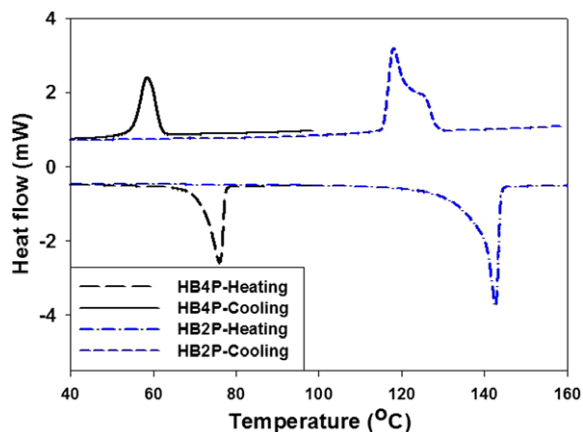


Fig. 2. Thermal properties of **HB4P** and **HB2P** molecules.

assigned to the diene photoreactive groups, are labeled in Fig. 3. Clear evidence for polymerization was demonstrated by the disappearance of the stretching band of the C=C bond at  $1641\text{ cm}^{-1}$ . The difference spectrum shows a differential line shape at  $\sim 1737\text{ cm}^{-1}$ , corresponding to a spectral shift of the C=O transition of the diene groups as a result of cross-linking. This shift occurs because the transition is inductively coupled to the double bond, which breaks during polymerization. The decrease in intensity of the =CH wag transitions at  $993$  and  $932\text{ cm}^{-1}$  further verified cross-linking.

### 3.3.2. Solubility test

Approximate 100-nm-thick films of **HB4P** and **HB2P** were spin-coated on the quartz glass and annealed at proper temperatures. The films were exposed to UV light ( $\lambda = 254\text{ nm}$ ,  $I = 40.64\text{ mW/cm}^2$ ) for 10 min. No photoiniti-

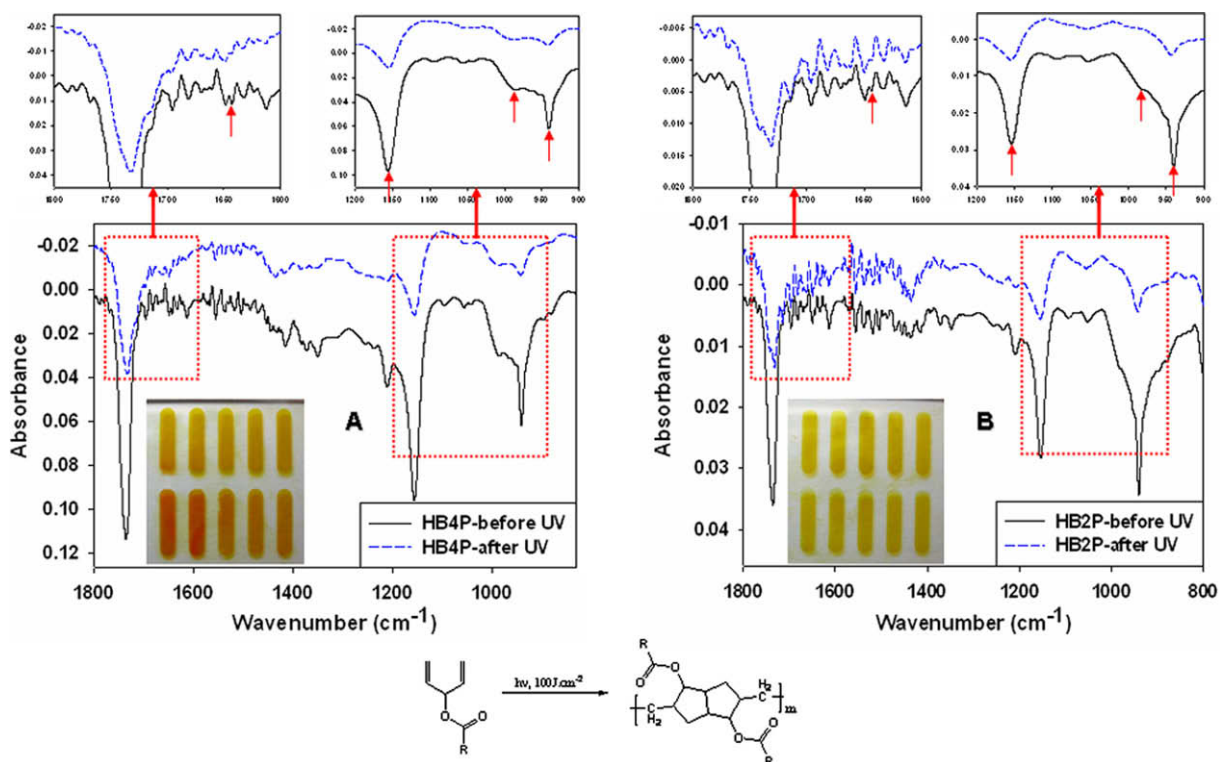


Fig. 3. FT-IR spectra before and after UV expose of molecules. (A) **HB4P** and (B) **HB2P**.

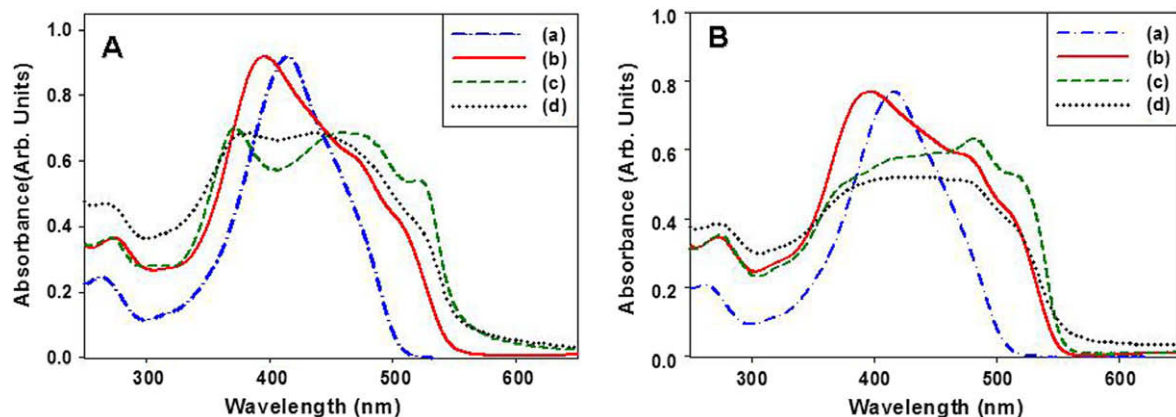


Fig. 4. UV-vis absorption spectra of **HB4P** (A) and **HB2P** (B). (a) Solution, (b) pristine film, (c) annealed film, (d) annealed and UV exposure.

ator was used. The exposed films were immersed into chloroform for 60 s. The partially polymerized regions of the film were washed away. The thickness decreased about ~10% after washing, indicating that only a small amount of the material is removed. This confirms conclusively that insoluble networks were formed in the film of our two molecules predominantly. Furthermore, the patterning processes were carried out using a photo mask. The photo-patterned images of UV-crosslinked films after washing unexposed parts were also showed as an inset in Fig. 3.

### 3.4. Optical properties

The absorption spectra of the samples in chloroform and thin films were obtained (Fig. 4). Similar absorption maxima of **HB4P** and **HB2P** in solution state are located at 415 and 416 nm, respectively. A drastic spectral change is observed in the film states of these molecules, which is attributed to a high degree of intermolecular interaction. For instance, in the film state after annealing, the absorption spectrum is significantly red-shifted with vibronic transitions; this shift may be due to the formation of an ordered structure with an intermolecular  $\pi$ -stacking. The difference between the HOMO–LUMO gaps in solution and film states provides useful information for understanding intermolecular interactions. The difference in the HOMO–LUMO gaps results from the difference in the intramolecular conjugation through the core. The larger difference (0.20 and 0.22 eV) in **HB2P** and **HB4P** imply a higher de-

gree of intermolecular interaction in the film states (Table 1).

### 3.5. Electrochemical analysis

Electrochemical characterization of these molecules revealed that their oxidation is reversible, which is a necessary condition for a stable FET active material. The values of the ionization potential match well with the work function of a gold electrode. Cyclic voltammograms (CV) were recorded on a film sample and the potentials were obtained relative to an internal ferrocene reference ( $\text{Fc}/\text{Fc}^+$ ). These CV scans in the range of  $-2.0$ – $+2.0$  V (vs  $\text{Ag}/\text{AgCl}$ ) show quasi-reversible oxidation peaks. Unfortunately, the reduction behaviors were irreversible; therefore, accurate estimation of HOMO and LUMO energies was not possible. To determine the LUMO levels, the oxidation potential in CV was combined with the optical energy band gap ( $E_g^{\text{opt}}$ ) resulting from the absorption edge in the absorption spectrum. HOMO and LUMO levels of the two molecules in solution state and film state before and after UV exposure are shown in Table 1. These levels indicate that the molecules behave as a p-type semiconductor.

### 3.6. X-ray diffraction analysis

To study the crystallinity and preferred orientations of the star-shaped molecules, XRD was performed at varying temperatures. The star-shaped molecular layers in **HB2P**

Table 1  
Optical absorption and cyclic voltammetry analysis data of **HB4P** and **HB2P**.

Sample	Adsorption				Energy levels								
	Solution		Film		Solution			Film					
	$\lambda_{\text{max}}$ (nm)	$\lambda_{\text{cut off}}$ (nm)	$\lambda_{\text{cut off}}$ (nm)		HOMO (eV)	LUMO (eV)	$\Delta E_g$ (eV)	Before UV			After UV		
			Before UV	After UV				HOMO (eV)	LUMO (eV)	$\Delta E_g$ (eV)	HOMO (eV)	LUMO (eV)	$\Delta E_g$ (eV)
<b>HB4P</b>	415	506	555	559	–5.21	–2.76	2.45	–5.14	–2.91	2.23	–5.23	–3.01	2.22
<b>HB2P</b>	416	507	552	556	–5.17	–2.72	2.45	–5.17	–2.92	2.25	–5.22	–2.99	2.23

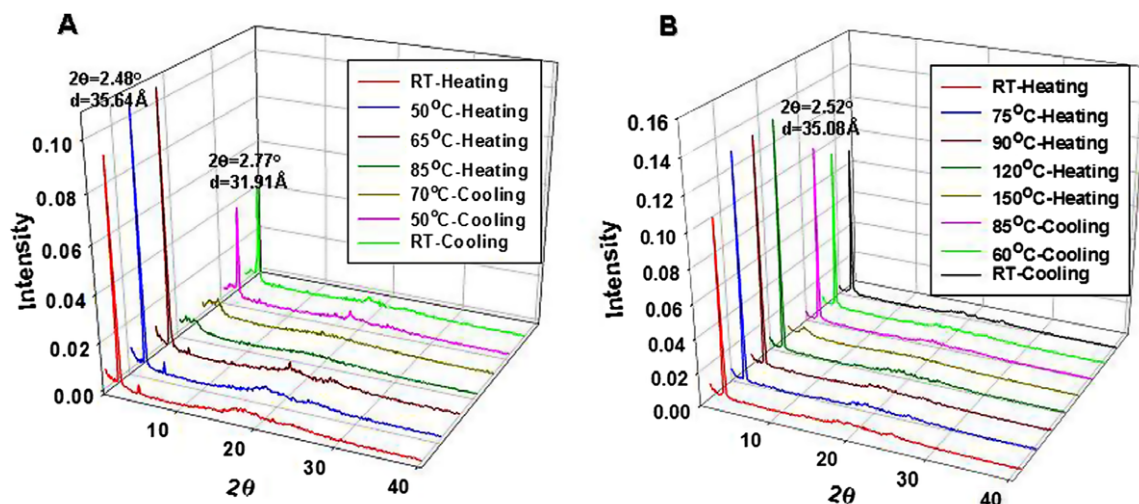


Fig. 5. Temperature dependence of X-ray diffraction patterns of molecules. (A) **HB4P** and (B) **HB2P**.

must be associated with the layered stacking properties brought about by the terminal alkyl groups, which are already known to induce long-range lamella ordering. The X-ray diffraction scans of **HB4P** and **HB2P** films annealed at different temperatures reveal the temperature at which the highest crystalline order is achieved (Fig. 5). In the film samples, the preferred orientation is clearly indicated by the high reflection intensity of the peaks at about 35 Å ((100) reflection) and the ambiguous presence of peaks in the 3–5 Å ((010) reflection) region, as seen in the X-ray diffractograms. The former spacing corresponds to the edge-to-edge transverse packing of the peripheral arms and the latter to a  $\pi$ - $\pi$  stacked distance with a  $\pi$ -electron cloud overlap. This result implies that most of the crystallites in these molecules are preferentially oriented along the (100)-axis in the plane. **HB4P** showed a smaller degree of lamella ordering during cooling, while **HB2P** exhibited comparable diffraction peaks during cooling. It implies that the hexyl peripheral groups enhance the intermolecular ordering to improve the crystallinity in **HB2P**.

In the case of **HB4P**, the layer distance before annealing is approximately 35.64 Å ( $2.48^\circ$ ). However, after annealing, the distance is reduced to 31.91 Å ( $2.77^\circ$ ). A possible explanation could be related to the fact that during cooling, some molecules are forced to adopt a slightly closer packing arrangement. In contrast, in the case of **HB2P**, the layer distances before and after annealing remain constant. This phenomenon could be explained by the role of hexyl group of **HB2P**. Usually long alkyl peripheral groups can interact between themselves by van der Waals interaction, which induce highly packed crystalline structure even at room temperature.

Aside from using the vacuum evaporation technique, it is difficult to achieve high crystallinity for the films of organic molecules. However, in the solution-processed films in this study, significantly high crystalline properties and the preferential orientation of the ordered molecular domains were found in the samples.

Fig. 6 showed X-ray diffraction patterns of **HB4P** and **HB2P** before and after UV exposure. **HB4P** showed a large

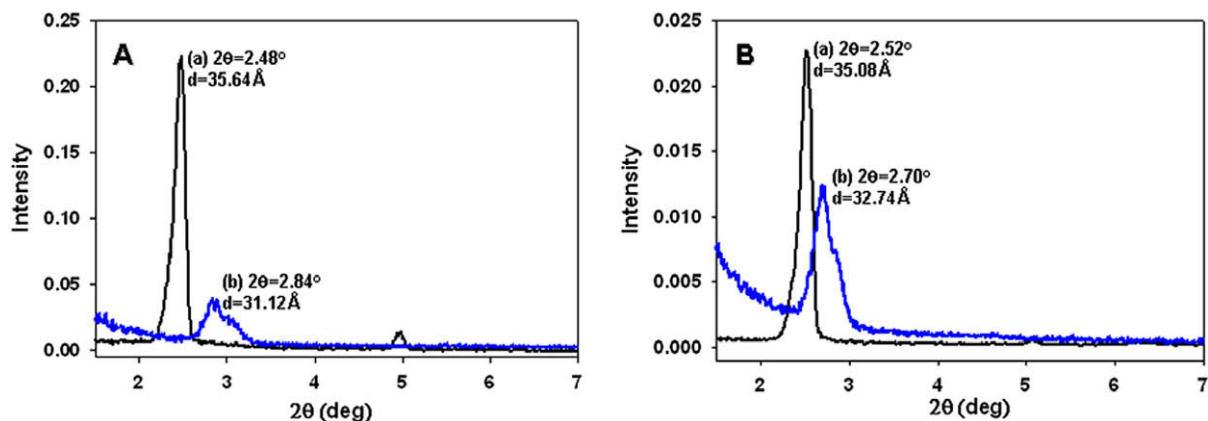


Fig. 6. X-ray diffraction patterns of molecules. (A) **HB4P** and (B) **HB2P**. (a) Before and (b) after UV exposure.

decrease of lamella ordering after UV exposure. The layer distance before UV exposure is approximately 35.64 Å (2.48°). However, after exposure, the distance was reduced to 31.12 Å (2.77°). The d-spacing decrements after polymerization occur as a result of conformation changes such as changes in the tilt angle and the extent of their interdigitation, resulted in closer packing arrangement. The full width at half maximum (FWHM) also increased from 0.15 Å before UV exposure to 0.42 Å after UV exposure. In addition, the degree of crystallization was also decreased after UV exposure. This phenomenon might be due to disruption of the molecular ordering significantly.

In the case of **HB2P**, with a higher packed crystalline structure, the layer distance only slightly reduced from 35.08 Å (2.52°) before UV exposure to 32.74 Å (2.70°) after UV exposure. FWHM also increased from 0.15 Å before UV exposure to 0.31 Å after UV exposure. The degree of crystallinity determined by integration of diffraction peak, maintained constantly even after UV exposure. In comparison with **HB4P**, **HB2P** showed a smaller decrease of lamella ordering after UV crosslinking. It implies that the hexyl peripheral groups enhance the intermolecular interaction of the star-shaped conjugated structure, which can relatively prevent disruption of molecular ordering during the crosslinking.

### 3.7. Optical and atomic force microscopic study of molecules

By using a hot-stage optical microscope (Mettler Co.), the crystalline shape of the molecules was observed at different temperatures under crossed polarizers from room temperature to their melting points. Fig. 6 shows the crystalline structures of **HB4P** and **HB2P** after inducing crystallization. Under the same magnification ( $\times 200$ ), the crystallites of **HB2P** are significantly bigger than those of **HB4P**.

Further study of film morphology was obtained by AFM (Fig. 7). The solutions of the molecules **HB4P** and **HB2P** were spin-coated on a silicon wafer and annealed at their crystalline points (58 °C and 116 °C, respectively). The images of the molecules are quite similar; however, the crystals of **HB2P** are significantly bigger than those of **HB4P** due to the presence of intermolecular ordering.

In **HB2P**, the crystallite size was observed to be larger than that of **HB4P**, which is consistent with the optical microscope results. The optical spectroscopy and AFM micrographs results could provide indirect evidence of the strong intermolecular interaction and preferred molecular orientation of these molecules in the crystalline film, particularly for **HB2P**. In addition to the long-range molecular structural organization confirmed by the X-ray study, the AFM micrographs display well-resolved surface structures on the dielectric layer.

### 3.8. Properties of OFET made from star-shaped molecules

Bottom-contact OFET devices were fabricated using gold source and drain electrodes which were thermally evaporated using the conventional method. A 400-nm-thick film of the semiconductor was deposited by drop-casting a 2 wt% solution of **HB4P** in chloroform or **HB2P** in monochlorobenzene. To achieve optimal performance, the OFET devices made of **HB4P** and **HB2P** were further annealed at 65 °C and 115 °C, respectively, for 30 min. The output characteristics showed very good saturation behaviors and clear saturation currents that were quadratic to the gate bias (Figs. 8 and 9). The saturated field-effect mobilities,  $\mu_{\text{FET}}$ , can be calculated from the amplification characteristics by using the classical equations describing field-effect transistors [20]. The mobility values obtained by measuring different devices are listed in Table 2 (Fig. 10).

The transistor devices of **HB4P** and **HB2P** after annealing provided a field-effect mobility of  $1.3(\pm 0.2) \times 10^{-3}$ – $3.7(\pm 0.5) \times 10^{-3} \text{ cm}^2 \text{ V}^{-1} \text{ s}^{-1}$  as well as a high current on/off ratio and a low threshold voltage ( $V_{\text{th}} < -15 \text{ V}$ ). Compared to **HB4P**, **HB2P** showed higher mobility. This molecule exhibited a carrier mobility of  $3.7(\pm 0.5) \times 10^{-3} \text{ cm}^2 \text{ V}^{-1} \text{ s}^{-1}$  for a 10- $\mu\text{m}$  channel length device, with the current on/off ratio higher than  $10^3$  and a threshold voltage of  $-16 \text{ V}$ . The best mobility obtained was  $6.0(\pm 0.2) \times 10^{-3} \text{ cm}^2 \text{ V}^{-1} \text{ s}^{-1}$ ; however, it is not reproducible. When using the bare  $\text{SiO}_2$  gate insulator, the mobilities were much lower than those with the OTS-treated  $\text{SiO}_2$  (Table 2).

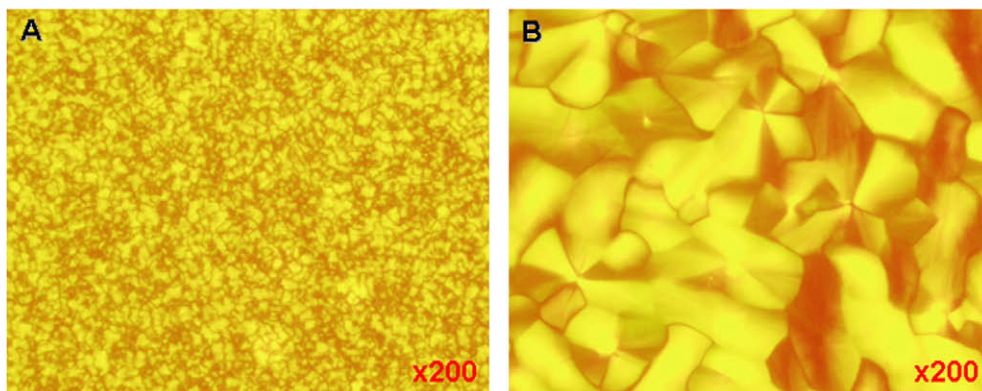


Fig. 7. Optical micrographs of two molecules. (A) **HB4P** and (B) **HB2P**.

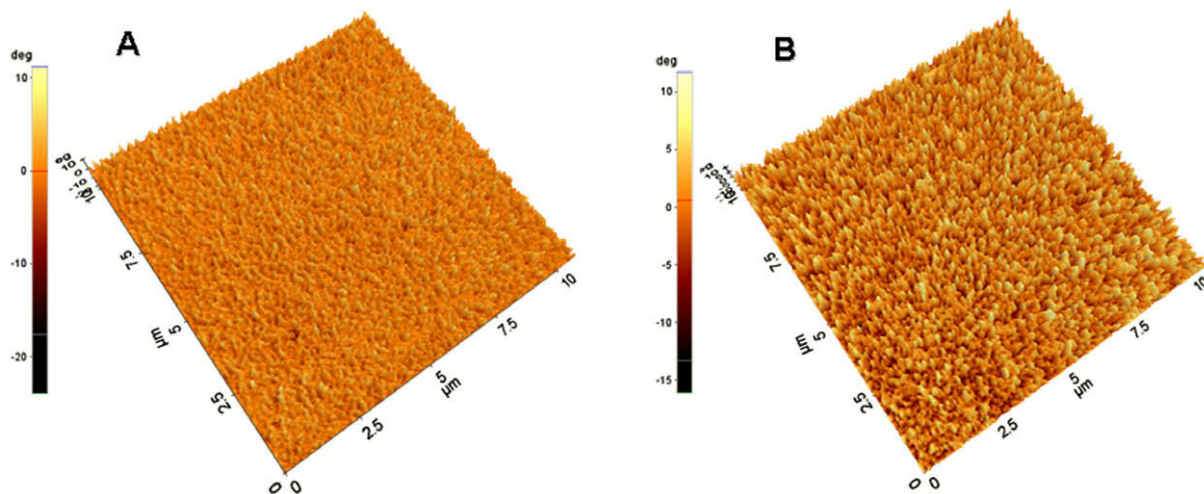


Fig. 8. AFM topographic images of two molecules. (A) HB4P and (B) HB2P.

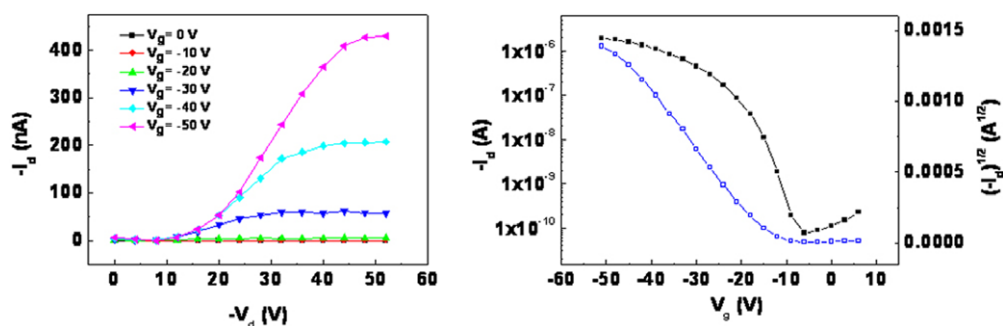


Fig. 9. Output (left) and transfer (right) characteristics of the OFET made by the drop-casting of HB4P from chloroform solution, annealed at 65 °C for 30 min.

Table 2

Physical properties of the two molecules and device performance of the OFETs.

Sample	$T_c$ (°C)	$T_m$ (°C)	$\lambda_{max}^{abs}$ (nm)	$\lambda_{max}^{em}$ (nm)	on SiO <sub>2</sub>		OTS treated SiO <sub>2</sub>		OTS treated SiO <sub>2</sub> /UV exposure	
					$\mu_{max}$ (cm <sup>2</sup> V <sup>-1</sup> s <sup>-1</sup> )	$I_{on/off}$	$\mu_{max}$ (cm <sup>2</sup> V <sup>-1</sup> s <sup>-1</sup> )	$I_{on/off}$	$\mu_{max}$ (cm <sup>2</sup> V <sup>-1</sup> s <sup>-1</sup> )	$I_{on/off}$
HB4P	58	76	415	528(570)	$5.7(\pm 0.5) \times 10^{-4}$	$>10^3$	$1.3(\pm 0.2) \times 10^{-3}$	$>10^4$	$3.4(\pm 0.5) \times 10^{-4}$	$>10^3$
HB2P	116	142	416	518(557)	$5.4(\pm 0.5) \times 10^{-4}$	$>10^3$	$3.7(\pm 0.5) \times 10^{-3}$	$>10^3$	$3.6(\pm 0.5) \times 10^{-3}$	$>10^3$

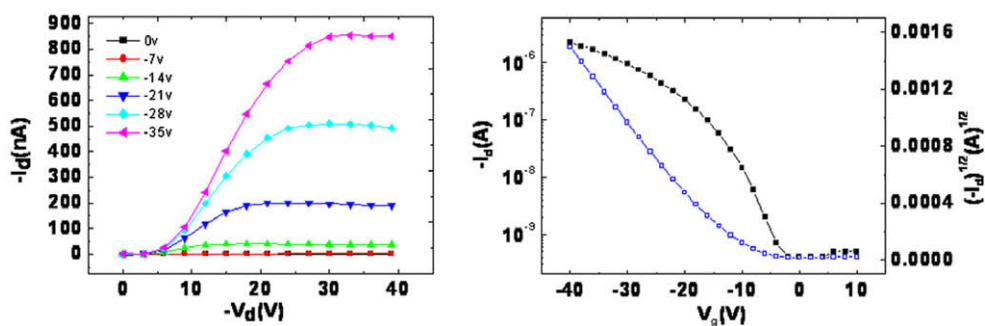


Fig. 10. Output (left) and transfer (right) characteristics of the OFET made by the drop-casting of HB2P from monochlorobenzene solution, annealed at 115 °C for 30 min.

As mentioned above, **HB2P** showed a more compact structure on the surface with bigger crystallites. It is thought that the highly packed crystalline molecules on the dielectric layer help the carrier transport by producing good connection behavior. As observed in X-ray analysis, it is assumed that the hexyl peripheral groups and lamella ordering induce higher intermolecular interaction and preferred molecular orientation, leading to increased carrier mobility.

In previous reports about photopolymerizable linear organic semiconductors, the reduction in charge transport was observed. Field-effect mobility in cross-linked films was reduced approximately 10-fold [10]. This phenomenon was explained by suggesting a reduced degree of molecular ordering induced by cross-linking. During the formation of polymer main chains, some molecules are forced to adopt a slightly closer packing arrangement randomly, whereas others are “pulled away” to accommodate these structural changes. As a result, there is a broader distribution of molecular axis angles with respect to the director, and consequently, a lower degree of  $\pi$ -orbital overlap between the adjacent aromatic cores.

However, in the case of the star-shaped conjugated molecule **HB2P**, the field-effect mobility in cross-linked films was well maintained. As discussed in Section 3.6, a possible explanation could be related to the strong intermolecular interaction of the star-shaped conjugated structure, which could arrest the molecular axis under push-pull force during the cross-linking and is accompanied by a high degree of lamella ordering in two directions. Thus, a star-shaped molecular structure seems to be a suitable design for photopatternable semiconductor molecules in practical electronic applications.

#### 4. Conclusion

This work provides the first demonstration of working field-effect transistor devices fabricated from novel, solution-processible, photopolymerizable, star-shaped conjugated molecules. These compounds have a good solubility and application to soluble processing. The patterning process was carried out by photopolymerization of the reactive diene end groups, creating an insoluble network. Dendritic molecules bearing pentadiene groups can be photopolymerized without a photoinitiator, which can behave as a charge trap. The maximum field-effect mobility of annealed **HB2P** was found to be approximately  $3.7(\pm 0.5) \times 10^{-3} \text{ cm}^2 \text{ V}^{-1} \text{ s}^{-1}$  with a current on/off ratio

higher than  $10^3$ . It was also found that **HB2P** exhibited great persistency of field-effect mobility even after photopolymerization, which suggests that the patternable process is feasible for the fabrication of OTFT array device structures. This result can be applied to the design of photoreactive semiconductor molecules for practical electronic applications. Although the measurement and the device fabrication were not fully optimized in this study, the field-effect mobility showed promise for future studies. Further studies to improve the charge mobility ( $\mu$ ) and current on/off ratio are now in progress.

#### Acknowledgements

This research work was supported by 21st century Frontier Research Program (2008) and LG-display Co. Ltd. (2008). Particularly, M.J. Cho acknowledges the financial support by the Seoul R&BD Program (2008–2009).

#### References

- [1] S.A. Ponomarenko, E.A. Tatarinova, A.M. Muzafarov, S. Kirchmeyer, L. Brassat, A. Mourran, M. Moeller, S. Setayesh, D. De Leeuw, *Chem. Mater.* 18 (2006) 4101.
- [2] N. Yoshimoto, J. Hanna, *J. Mater. Chem.* 13 (2003) 1004.
- [3] R. De Bettignies, Y. Nicolas, P. Blanchard, E. Levillain, J.-M. Nunzi, J. Roncali, *Adv. Mater.* 15 (2003) 1939.
- [4] S. Roquet, A. Cravino, P. Leriche, O. Alévêque, P. Frère, J. Roncali, *J. Am. Chem. Soc.* 128 (2006) 3459.
- [5] S.A. Ponomarenko, S. Kirchmeyer, A. Elschner, B.-H. Huisman, A. Karbach, D. Drechsler, *Adv. Funct. Mater.* 13 (2003) 591.
- [6] Y. Sun, K. Xiao, Y. Liu, J. Wang, J. Pei, G. Yu, D. Zhu, *Adv. Funct. Mater.* 15 (2005) 818.
- [7] J. Cremer, P. Bäuerle, *J. Mater. Chem.* 16 (2006) 874.
- [8] A.R. Murphy, J.M.J. Frechet, *Chem. Rev.* 107 (4) (2007) 1066.
- [9] K.H. Kim, Z. Chi, M.J. Cho, J.-I. Jin, M.Y. Cho, S.J. Kim, J.-S. Joo, D.H. Choi, *Chem. Mater.* 19 (2007) 4925.
- [10] I. McCulloch, W. Zhang, M. Heeney, C. Bailey, M. Giles, D. Graham, M. Shkunov, D. Sparrowe, S. Tierney, *J. Mater. Chem.* 13 (2003) 2436.
- [11] A.E.A. Contoret, S.R. Farrar, M. O'Neill, J.E. Nicholls, G.J. Richards, S.M. Kelly, A.W. Hall, *Chem. Mater.* 14 (2002) 1477.
- [12] M.P. Aldred, A.J. Eastwood, S.M. Kelly, P. Vlachos, A.E.A. Contoret, S.R. Farrar, B. Mansoor, M. O'Neill, W.C. Tsoi, *Chem. Mater.* 16 (2004) 4928.
- [13] H. Meier, M. Fettes, *Tetrahedron Lett.* 41 (2000) 1535.
- [14] J. Blum, M. Zimmerman, *Tetrahedron* 28 (2) (1972) 275.
- [15] K. Kazuhiko, S. Hiroshi, S. Takeo, *Tetrahedron Lett.* 33 (42) (1992) 6327.
- [16] Y. Wei, Y. Yang, J.-M. Yeh, *Chem. Mater.* 8 (1996) 2659.
- [17] C. Zhang, C. Wang, L.R. Dalton, H. Zhang, W.H. Steier, *Macromolecules* 34 (2001) 253–261.
- [18] D.H. Lee, D. Kim, T. Oh, K. Cho, *Langmuir* 20 (2004) 8124.
- [19] M.J.S. Dewar, E.G. Zebisch, E.F. Healy, J.J.P. Stewart, *J. Am. Chem. Soc.* 107 (1985) 3902.
- [20] J.A. Merlo, C.R. Newman, C.P. Gerlach, T.W. Kelley, D.V. Muires, S.E. Fritz, M.F. Toney, C.D. Frisbie, *J. Am. Chem. Soc.* 127 (2005) 3997.



# A highly efficient tris-cyclometalated iridium complex based on phenylphthalazine derivative for organic light-emitting diodes

Yuan Fang<sup>a</sup>, Bihai Tong<sup>b</sup>, Sujun Hu<sup>c</sup>, Shuanjin Wang<sup>a</sup>, Yuezhong Meng<sup>a</sup>, Junbiao Peng<sup>c</sup>, Biao Wang<sup>a,\*</sup>

<sup>a</sup> State Key Laboratory of Optoelectronic Materials and Technologies, Institute of Optoelectronic and Functional Composite Materials, Sun Yat-Sen University, Guangzhou 510275, China

<sup>b</sup> Institute of Molecular Engineering and Applied Chemistry, Anhui University of Technology, Maanshan 243002, China

<sup>c</sup> Institute of Polymer Optoelectronic Materials and Devices, South China University of Technology, Guangzhou 510640, China

## ARTICLE INFO

### Article history:

Received 11 December 2008

Received in revised form 20 February 2009

Accepted 21 February 2009

Available online 1 March 2009

### PACS:

72.80.Ga

78.60.Fi

85.60.Jb

### Keywords:

Tris-cyclometalated iridium(III) complex

Organic light-emitting diodes

Phosphorescence

Carbazole

Phenylphthalazine derivative

## ABSTRACT

A novel ligand 9-(4-(4-chlorophenyl)phthalazin-1-yl)-9H-carbazole (HCPC) was designed and prepared, and the corresponding tris-cyclometalated iridium(III) complex Ir(CPC)<sub>3</sub> was readily synthesized by the reaction of the ligand with IrCl<sub>3</sub> · 3H<sub>2</sub>O at 80 °C for 20 h. A highly efficient organic light-emitting device using this complex as a dopant was obtained. The device fabricated by solution process showed a maximum luminance of 2948 cd/m<sup>2</sup> at a current density of 115.6 mA/cm<sup>2</sup> and a maximum external quantum efficiency of 20.2% at 0.18 mA/cm<sup>2</sup>.

© 2009 Elsevier B.V. All rights reserved.

## 1. Introduction

Organic light-emitting diodes (OLEDs) have attracted great attention in the past decades because of their potential advantages in full-color displays [1]. As phosphorescent dopants in the emitting layers, heavy metal complexes, such as iridium(III), platinum(II), osmium(II), and ruthenium(II) complexes, can harvest both singlet and triplet excitons for emission and hence lead to efficient OLEDs with the internal quantum efficiency potentially as high as 100% [2–5]. By reason of the theoretical limit from simple classical optics, the external quantum efficiency is confined to ~20% [6]. An external quantum efficiency of 19.2%

ph/el at a current density of 0.55 mA/cm<sup>2</sup> was achieved by using tris(2-phenylpyridine) iridium(III) (Ir(ppy)<sub>3</sub>) as a dopant [7]. Kang et al. reported the efficient OLEDs based on Ir(2-(1-cyclohexenyl)pyridine)<sub>3</sub> with a maximum external quantum efficiency of 18.7% [8]. Most of reported highly efficient OLEDs were achieved by vacuum deposition technique, and yet solution process owning low cost and convenience advantages is expected to be important to OLEDs for large-area displays [9]. A solution processed OLEDs with an external quantum efficiency of 13.3% at 6.3 mA/cm<sup>2</sup> has been prepared by adopting a neutral osmium(II) complex other than iridium complexes [10].

Recently, we have reported the red device using tris-(1-(2,6-dimethylphenoxy)-4-(4-chlorophenyl)phthalazine) iridium(III) as a dopant by solution process with internal quantum efficiency of nearly 100% [11]. Mi et al. reported

\* Corresponding author. Tel./fax: +86 20 84115692.

E-mail address: [wangbiao@mail.sysu.edu.cn](mailto:wangbiao@mail.sysu.edu.cn) (B. Wang).



efficient and thermally stable OLEDs using tris(1,4-bis(phenyl) phthalazine) iridium(III) [12]. Based on these works, it is found that the ligands which have the structure of an  $sp^2$ -hybrid N-atom adjacent to the chelating N-atom, such as phenylpyridazine and phenylphthalazine derivatives [13], are beneficial for iridium(III) complexes due to the shorter bonding length and the stronger bonding strength between the chelating N-atom and Ir-atom, compared with these analogues which have a C-atom instead of the non-chelating N-atom. It is well known that carbazole-based compounds have been widely used as the host materials for OLEDs due to their high triplet energy and good hole-transporting ability. In addition, there are many reports about the integrations of carbazole modules and iridium(III) complexes which possess the dual functions of light emission and hole transportation [14–20].

In this article, we introduce carbazole unit into a phenylphthalazine derivative to get a novel ligand 9-(4-(4-chlorophenyl)phthalazin-1-yl)-9H-carbazole (HCPC). The ligand can bond to the Ir-atom more strongly, which leads to efficient mixing of the singlet and triplet excited states [12], and the incorporation of carbazole unit is beneficial to improve the charge balance in the electroluminescent (EL) process and enhance thermal stability [21–25]. The corresponding tris-cyclometalated iridium complex  $\text{Ir}(\text{CPC})_3$  is synthesized by the reaction of the ligand with  $\text{IrCl}_3 \cdot 3\text{H}_2\text{O}$  at 80 °C for 20 h, directly. The thermal, photo-physical and electrochemical properties of the complex are studied, and the performance of OLEDs fabricated by solution process is investigated.

## 2. Experimental

### 2.1. General information

The solvents were purified by routine procedures and distilled under an atmosphere of dry nitrogen before use. All reagents, unless otherwise specified, were purchased from Aldrich and were used as received. The original compound 1-chloro-4-(4-chlorophenyl)phthalazine was prepared according to the procedure previously reported [26].  $^1\text{H}$  NMR spectra were recorded on a Varian Inova500NB spectrometer using  $\text{CDCl}_3$  as solvent. Elemental analyses of carbon, hydrogen, and nitrogen were performed on a Vario EL microanalyzer. Thermal gravimetric analysis (TGA) was performed under a flow of nitrogen at a heating rate of 10 °C/min with a Perkin-Elmer Pyris Diamond TG/DTA thermal analyzer. Differential scanning calorimetry (DSC) was performed on a Netzsch DSC-200PC instrument at a heating rate of 10 °C/min. Photoluminescence (PL) spectra were measured with a Shimadzu RF-5301PC fluorescence spectrophotometer. Luminescence lifetime was determined on an Edinburgh FL920 time-correlated pulsed single-photon-counting instrument. UV–vis absorption spectra were recorded on a Shimadzu UV-2501 PC spectrophotometer. PL quantum yield was measured at room temperature in an argon prepurged tetrahydrofuran (THF) solution and compared with quinine sulfate in 1.0 N  $\text{H}_2\text{SO}_4$  ( $\Phi_{\text{PL}} = 0.546$ ) as a standard [27]. Electron ionization (EI) mass spectrum were recorded on a Shimadzu GC-MS-QP2010 PLUS mass spectrometer, and electron

spray ionization (ESI) mass spectra on a Thermo LCQ DECA XP mass spectrometer. Cyclic voltammetry (CV) was performed with a Solartron SI 1287 voltammetric analyzer. It was conducted at room temperature in a typical three-electrode cell with a working electrode (Pt disk), a reference electrode (saturated calomel electrode), and a counter electrode (Pt wire) under a nitrogen atmosphere at a sweeping rate of 100 mV/s in a solution of 0.1 M tetra-*n*-butylammonium hexafluorophosphate ( $\text{Bu}_4\text{NPF}_6$ ) in anhydrous  $\text{CH}_2\text{Cl}_2$ . Each oxidation potential was calibrated with that of ferrocene.

### 2.2. Synthesis of 9-(4-(4-chlorophenyl)phthalazin-1-yl)-9H-carbazole (HCPC)

A 60.5% suspension of sodium hydride (1.0 g, 25 mmol) in paraffin oil was added slowly to a solution of carbazole (4.18 g, 25 mmol) in anhydrous dimethylformamide (70 mL) under nitrogen as a protective gas. After stirred for 1 h at room temperature, this mixture was added dropwise to a solution of 1-chloro-4-(4-chlorophenyl)phthalazine (6.88 g, 25 mmol) in anhydrous dimethylformamide (70 mL) with an ice bath. Then the mixture was stirred at room temperature for 12 h. After reaction, the resulting mixture was poured into water and extracted with chloroform. The extracts were combined, washed with brine, dried over anhydrous magnesium sulfate, and filtered. Then the solvent was evaporated. The product thus obtained was purified by silica gel column chromatography using chloroform as the eluent to give a yellow solid. Yield: 78%. mp: 191–193 °C.  $^1\text{H}$  NMR ( $\text{CDCl}_3$ ):  $\delta$  8.22–8.18 (t, 3H), 7.96–7.92 (t, 1H), 7.88–7.84 (d,  $J = 8.6$  Hz, 2H), 7.82–7.78 (t, 1H), 7.76–7.72 (d, 1H), 7.65–7.61 (d,  $J = 8.6$  Hz, 2H), 7.4–7.33 (m, 4H), 7.29–7.26 (d, 2H). EI-MS ( $m/z$ ): 404 (100%), 405 (68%), 406 (43%), 407 (23%).

### 2.3. Synthesis of $\text{Ir}(9-(4-(4\text{-chlorophenyl})\text{phthalazin-1-yl})\text{-9H-carbazole})_3 [\text{Ir}(\text{CPC})_3]$

9-(4-(4-Chlorophenyl)phthalazin-1-yl)-9H-carbazole (0.408 g, 1.00 mmol) was dissolved in 2-ethoxyethanol (12 mL) in a 25 mL round-bottom flask. Iridium trichloride hydrate (0.1 g, 0.284 mmol) and water (4 mL) were then added to the flask. The mixture was stirred under nitrogen at 80 °C for 20 h and then cooled to room temperature. The precipitate formed in the mixture was collected and washed with methanol, ether and dried. The product thus obtained was purified by silica gel column chromatography using dichloromethane as the eluent to give a red solid. Yield: 34%.  $^1\text{H}$  NMR ( $\text{CDCl}_3$ ):  $\delta$  8.98–8.95 (d,  $J = 8.7$  Hz, 1H), 8.30–8.27 (d,  $J = 8.7$  Hz, 1H), 7.90–7.86 (t, 1H), 7.82–7.78 (d,  $J = 7.5$  Hz, 1H), 7.70–7.67 (d,  $J = 7.7$  Hz, 1H), 7.53–7.48 (t, 1H), 7.23–7.20 (d,  $J = 8.5$  Hz, 1H), 7.20–7.19 (d,  $J = 2.3$  Hz, 1H), 7.13–7.09 (dd,  $J = 8.5, 2.3$  Hz, 1H), 6.92–6.88 (t, 1H), 6.65–6.60 (t, 1H), 6.55–6.52 (d,  $J = 8.2$  Hz, 1H), 6.47–6.43 (t, 1H), 6.00–5.92 (m, 2H). ESI-MS ( $m/z$ ):  $[\text{M}^+ + \text{H}]$  Calcd. for  $\text{C}_{78}\text{H}_{46}\text{N}_9\text{Cl}_3\text{Ir}$  1404.26 (29%), 1405.23 (30%), 1406.25 (97%), 1407.25 (82%), 1408.21 (100%), 1409.21 (74%), 1410.20 (44%), 1411.23 (22%). Found 1404.25 (33%), 1405.25 (30%), 1406.25 (100%), 1407.25 (82%), 1408.24(99%), 1409.25 (68%), 1410.25 (46%),

1411.24 (24%). Anal. Calcd. For  $C_{78}H_{45}N_9Cl_3Ir$ : C, 66.59; H, 3.22; N, 8.96. Found: C, 66.21; H, 3.45; N, 8.81%.

#### 2.4. OLED fabrication and measurements

The indium tin oxide (ITO) glass substrate was washed in turn with a substrate-cleaning detergent, deionized water, acetone, and ethanol for 15 min, under ultrasonic condition, and finally treated with ozone for about 20 min. Poly(3,4-ethylenedioxythiophene) doped with poly(styrene sulfonic acid) (PEDOT) (Baytron P4083, Bayer AG) in water was spin-coated at a rate of 3000 rpm on the ITO substrate and dried by baking in air at 120 °C for 10 h. Then the solution of poly(vinylcarbazole) (PVK,  $M_w = 81,800$ ) (68 wt%) blended with 2-tert-butylphenyl-5-biphenyl-1,3,4-oxadiazole (PBD) (30 wt%) and  $Ir(CPC)_3$  (2 wt%) in chloroform was spin-coated at a rate of 1300 rpm on top of the PEDOT layer. The assembly was transferred into a deposition chamber with a base pressure of  $3 \times 10^{-6}$  Torr, a film of 1,3,5-tris(N-phenylbenzimidazol-2-yl)-benzene (TPBI) was evaporated onto the polymer layer. Finally, the Ba and Al layers were evaporated. Current density–voltage–luminance data were collected using a Keithley 236 source measurement unit and a calibrated silicon photodiode. External quantum efficiency was obtained by measuring the total light output in all directions in an integrating sphere (IS080, Labsphere). Luminance and luminous efficiency were measured by a silicon photodiode and calibrated using a PR-705 photometer (Photo Research).

### 3. Results and discussion

#### 3.1. Synthesis and characterization

The synthetic procedures of the ligand and the complex are shown in Scheme 1. The cyclometalating ligand HCPC was prepared from 1-chloro-4-(4-chlorophenyl)phthalazine reacted with carbazole by an alkali of NaH in a polar solvent. Cl-atom on phthalazine has been replaced by carbazole unit, but Cl-atom on benzene ring did not take part in reaction due to low activity.

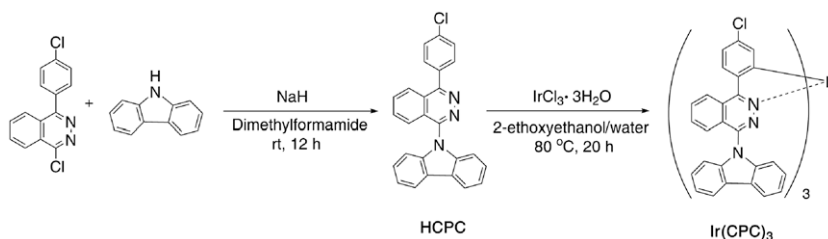
The complex  $Ir(CPC)_3$  was synthesized by a simple procedure. HCPC reacted with  $IrCl_3 \cdot 3H_2O$  directly formed the tris-cyclometalated iridium complex  $Ir(CPC)_3$  at 80 °C for 20 h. Generally, the synthesis of tris-cyclometalated iridium(III) complexes is in need of Ir(III) organic complexes, such as  $(C^{\wedge}N)_2Ir(O^{\wedge}O)$ ,  $(C^{\wedge}N)_2Ir(\mu-Cl)_2Ir(C^{\wedge}N)_2$  or  $Ir(O^{\wedge}O)_3$  ( $C^{\wedge}N$  = cyclometalating ligand,  $O^{\wedge}O$  =  $\beta$ -diketonate anion),

reacted with excessive free cyclometalating ligand precursors at high temperature [28]. We believe this special reaction is relative to the strong bonding strength and the small steric hindrance between the ligand and the centric Ir-atom. Research on the mechanism of this reaction is currently underway. The complex was also characterized by  $^1H$  NMR spectroscopy. The spectra indicate the facial isomer is formed, because three ligands surrounding the iridium atom are magnetically equivalent [29].

#### 3.2. Thermal, absorption, photophysical and electrochemical properties

The thermal properties of the complex were characterized with TGA and DSC under a nitrogen stream. The TGA data reveal that the 5% weight-reduction temperature of  $Ir(CPC)_3$  is 444 °C. In comparison, the analogous complex  $Ir(MPCPPZ)_3$  which contains 2,6-dimethylphenoxy group instead of carbazole commences decomposition at 388 °C [11]. So, the introduction of carbazole unit can observably improve the thermal stability of the complex. The DSC curve shows no crystallization and melting peaks, and it is revealed that the complex is amorphous. The absorption and photoluminescence spectra of  $Ir(CPC)_3$  in dichloromethane at room temperature are shown in Fig. 1. The absorption spectra show broad bands from 270 to 600 nm, and the most intense bands between 270 and 330 nm are attributed to the spin allowed  $\pi-\pi^*$  transitions from the cyclometalating ligand. The absorption bands around 350–470 nm can be assigned to the spin-allowed metal-ligand charge transfer band ( $^1MLCT$ ). The absorption features at the lowest energy ( $\lambda > 470$  nm) are attributed to the formally spin-forbidden  $^3MLCT$  transition. Upon irradiation with 400 nm light, the complex gives a strong photoluminescence in dichloromethane at 615 nm. The PL quantum yield of  $Ir(CPC)_3$  in THF at room temperature is 0.46. The emission decay curve of  $Ir(CPC)_3$  in solid state is shown in Fig. 2. The lifetime of  $Ir(CPC)_3$  shows double exponentials as 0.182 and 0.837  $\mu s$ , respectively. Because long lifetime will give rise to the emission saturation and elevate the triplet–triplet annihilation, the suitable lifetime of Ir(III) complex ( $\sim 0.1$ –3  $\mu s$ ) is beneficial to improve the efficiency of OLEDs [30].

The electrochemical properties of  $Ir(CPC)_3$  were examined by cyclic voltammetry. The complex showed reversible oxidation processes during the anodic scan in dichloromethane solution, but no clear reduction peak was observed. The highest occupied molecular orbital (HOMO) and the lowest unoccupied molecular orbital



Scheme 1. Synthesis of  $Ir(CPC)_3$ .

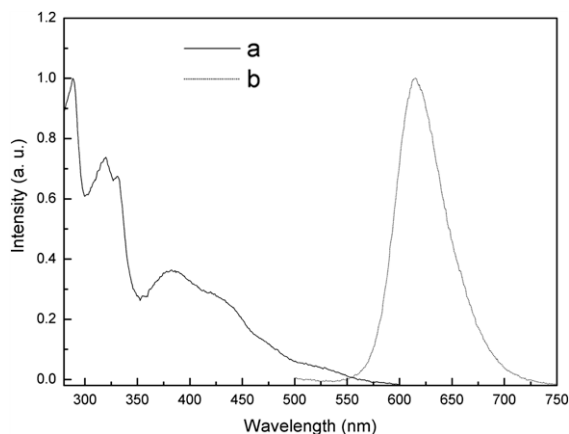


Fig. 1. UV-vis absorption (a) and photoluminescence (b) spectra of Ir(CPC)<sub>3</sub>.

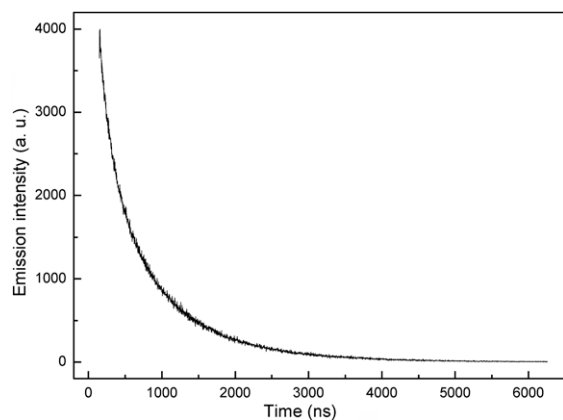


Fig. 2. Emission decay curve of Ir(CPC)<sub>3</sub> in solid state.

(LUMO) energy levels of Ir(CPC)<sub>3</sub> are  $-5.35$  eV and  $-3.15$  eV, estimated by using the oxidation potential and UV-vis absorption spectrum edge. Because its HOMO level is above that of the hosts ( $-5.8$  eV for PVK,  $-6.2$  eV for PBD) and its LUMO level is below that of the hosts ( $-2.2$  eV for PVK,  $-2.6$  eV for PBD), the complex can function as trap for both electrons and holes [31].

### 3.3. Electroluminescent properties

For studying EL properties of the complex, the OLEDs using Ir(CPC)<sub>3</sub> as a dopant was fabricated by solution process with the following structure: ITO/PEDOT(45 nm)/2 wt% Ir(CPC)<sub>3</sub>+ 68 wt% PVK+ 30 wt% PBD (80 nm)/TPBI(30 nm)/Ba(4 nm)/Al(100 nm). PEDOT was used as a hole-injecting material. PVK and PBD were selected as the host material and the electron transport material, respectively. TPBI acted as both a hole-blocker and an electron-transporter. Fig. 3 shows the general structure of the device and the molecular structures of the compounds used in the device.

The device has a maximum emission at 620 nm (Fig. 4), and the fine vibronic structure of the EL spectra leads us to conclude that EL emission originates from a mixed

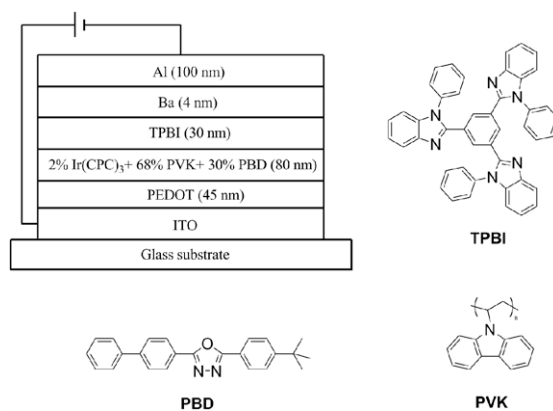


Fig. 3. General structure for the device and molecular structures of the relevant compounds.

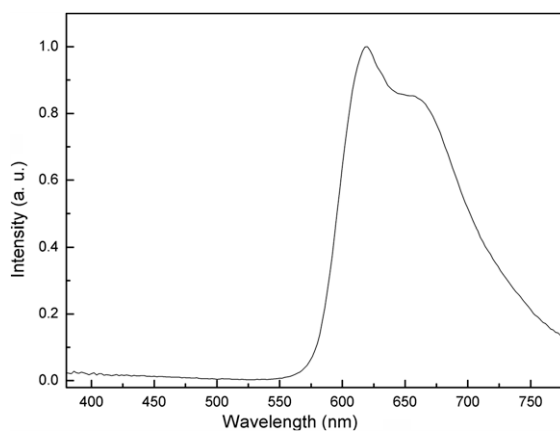


Fig. 4. Electroluminescence spectra of the device.

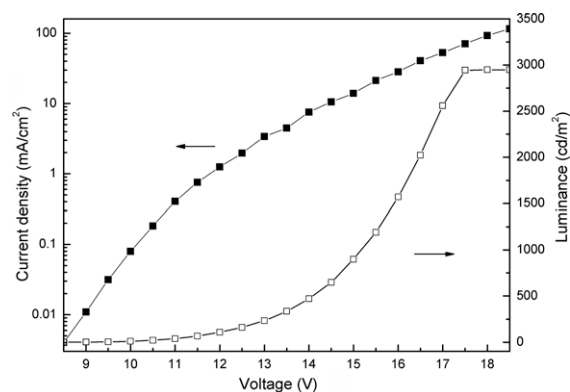
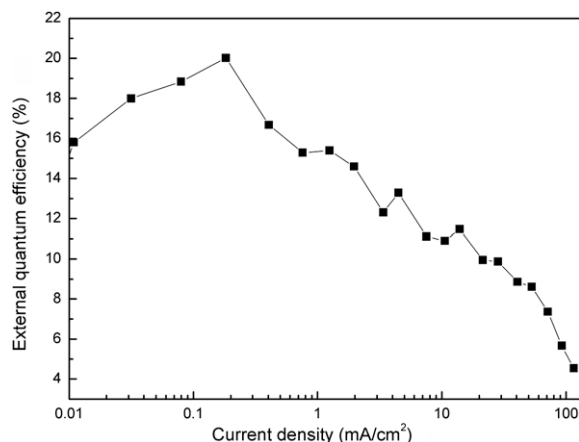


Fig. 5. Current density–voltage–luminance curves of the device.

<sup>3</sup>MLCT/<sup>3</sup> $\pi$ - $\pi^*$  state [30]. The Commission Internationale de L'Eclairage (CIE) coordinate is (0.65, 0.33) at a driving voltage of 12 V. No emission from the PVK–PBD blend is detected, which implies that the energy transfer from the blend to Ir(CPC)<sub>3</sub> is efficient under electrical excitation.

As shown in Fig. 5, the device gives a maximum luminance of 2948 cd/m<sup>2</sup> at a current density of



**Fig. 6.** External quantum efficiency vs. current density curve of the device.

115.6 mA/cm<sup>2</sup>. A maximum external quantum efficiency of 20.2% corresponding to a luminous efficiency of 11.3 cd/A is obtained at a current density of 0.18 mA/cm<sup>2</sup>. To the best of our knowledge, it is one of the highest reported efficiencies for red-emission OLEDs. Such an outstanding performance can be explained by the high PL quantum yield of Ir(CPC)<sub>3</sub> ( $\Phi_{PL} = 0.46$ ), which is higher than those of other known high-performance iridium(III) complexes, such as Ir(ppy)<sub>3</sub> ( $\Phi_{PL} = 0.40$ ) and Ir(piq)<sub>3</sub> (piq = 1-phenylisoquinolino) ( $\Phi_{PL} = 0.26$ ) [7,30]. The rigid ligand can significantly reduce the non-radiative transition. Moreover, the hole-transporting carbazole unit in the complex can improve the charge-balance properties in the EL process [21–23]. Compared to other OLEDs fabricated by vacuum deposition, this solution processed device has more advantages for large-area displays, such as low cost, simple preparation.

However, the efficiency roll-off, mostly due to triplet-triplet annihilation of phosphor-bound excitons, is severe at high current density as shown in Fig. 6. An external quantum efficiency of 10.9% is obtained at a current density of 10.6 mA/cm<sup>2</sup>. When the current density increases to 92.7 mA/cm<sup>2</sup>, the external quantum efficiency is 5.7% with a decrease of 47.7%. We believe this poor result arises from unstable thin-film morphology probably induced by the planar structure of the cyclometalating ligand, which tends to cause aggregation of molecules at high current density and then leads to excited-state intermolecular interactions.

#### 4. Conclusions

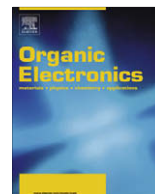
In summary, we synthesized a new tris-cyclometalated iridium(III) complex by the reaction of 9-(4-(4-chlorophenyl)phthalazin-1-yl)-9H-carbazole with IrCl<sub>3</sub> · 3H<sub>2</sub>O at 80 °C for 20 h. The device using the complex at 2 wt% doping concentration exhibited excellent performance. A maximum external quantum efficiency of 20.2% corresponding to a luminous efficiency of 11.3 cd/A at a current density of 0.18 mA/cm<sup>2</sup> and a maximum luminance of 2948 cd/m<sup>2</sup> at 115.6 mA/cm<sup>2</sup> were obtained. The optimization to the device for suppressing efficiency roll-off at high current density is in progress.

#### Acknowledgements

This work was supported by the National Natural Science Foundation of China (10732100, 10572155), Guangdong Science and Technology Bureau (2006A11001002), and the Ministry of Education PRC Special Scientific Research Fund for Doctor Subjects in Colleges and Universities (20060558070).

#### References

- [1] R.H. Friend, R.W. Gymer, A.B. Holmes, J.H. Burroughes, R.N. Marks, C. Taliani, D.D.C. Bradley, D.A.D. Santos, J.L. Brédas, M. Löglund, W.R. Salaneck, *Nature* 397 (1999) 121.
- [2] M.A. Baldo, S. Lamansky, P.E. Burrows, M.E. Thompson, S.R. Forrest, *Appl. Phys. Lett.* 75 (1999) 4.
- [3] P.-T. Chou, Y. Chi, *Chem. Eur. J.* 13 (2007) 380.
- [4] Y. Chi, P.-T. Chou, *Chem. Soc. Rev.* 36 (2007) 1421.
- [5] C.S.K. Mak, A. Hayer, S.I. Pascu, S.E. Watkins, A.B. Holmes, A. Köhler, R.H. Friend, *Chem. Commun.* (2005) 4708.
- [6] G. Gu, D.Z. Garbuzov, P.E. Burrows, S. Venkatesh, S.R. Forrest, M.E. Thompson, *Opt. Lett.* 22 (1997) 396.
- [7] M. Ikai, S. Tokito, Y. Sakamoto, T. Suzuki, Y. Taga, *Appl. Phys. Lett.* 79 (2001) 156.
- [8] D.M. Kang, J.-W. Kang, J.W. Park, S.O. Jung, S.-H. Lee, H.-D. Park, Y.-H. Kim, S.C. Shin, J.-J. Kim, S.-K. Kwon, *Adv. Mater.* 20 (2008) 2003.
- [9] Y.-H. Niu, Y.-L. Tung, Y. Chi, C.-F. Shu, J.H. Kim, B. Chen, J. Luo, A.J. Carty, A.K.-Y. Jen, *Chem. Mater.* 17 (2005) 3532.
- [10] Y.-M. Cheng, G.-H. Lee, P.-T. Chou, L.-S. Chen, Y. Chi, C.-H. Yang, Y.-H. Song, S.-Y. Chang, P.-I. Shih, C.-F. Shu, *Adv. Funct. Mater.* 18 (2008) 183.
- [11] B. Tong, Q. Mei, S. Wang, Y. Fang, Y. Meng, B. Wang, *J. Mater. Chem.* 18 (2008) 1636.
- [12] B.X. Mi, P.F. Wang, Z.Q. Gao, C.S. Lee, S.T. Lee, H.L. Hong, X.M. Chen, M.S. Wong, P.F. Xia, K.W. Cheah, C.H. Chen, W. Huang, *Adv. Mater.* 21 (2009) 339.
- [13] Z.Q. Gao, B.X. Mi, H.L. Tam, K.W. Cheah, C.H. Chen, M.S. Wong, S.T. Lee, C.S. Lee, *Adv. Mater.* 20 (2008) 774.
- [14] K.A. Knights, S.G. Stevenson, C.P. Shipley, S.-C. Lo, S. Olsen, R.E. Harding, S. Gambino, P.L. Burn, I.D.W. Samuel, *J. Mater. Chem.* 18 (2008) 2121.
- [15] E.B. Namdas, A. Ruseckas, I.D.W. Samuel, S.-C. Lo, P.L. Burn, *Appl. Phys. Lett.* 86 (2005) 091104.
- [16] S. Bettington, M. Tavasli, M.R. Bryce, A. Beeby, H.A. Attar, A.P. Monkman, *Chem. Eur. J.* 13 (2007) 1423.
- [17] H. Zhen, C. Jiang, W. Yang, J. Jiang, F. Huang, Y. Cao, *Chem. Eur. J.* 11 (2005) 5007.
- [18] J. Jiang, C. Jiang, W. Yang, H. Zhen, F. Huang, Y. Cao, *Macromolecules* 38 (2005) 4072.
- [19] Z. Liu, M. Guan, Z. Bian, D. Nie, Z. Gong, Z. Li, C. Huang, *Adv. Funct. Mater.* 16 (2006) 1441.
- [20] T. Tsuzuki, N. Shirasawa, T. Suzuki, S. Tokito, *Jpn. J. Appl. Phys.* 44 (2005) 4151.
- [21] W.-Y. Wong, C.-L. Ho, Z.-Q. Gao, B.-X. Mi, C.-H. Chen, K.-W. Cheah, Z. Lin, *Angew. Chem. Int. Ed.* 45 (2006) 7800.
- [22] C.-L. Ho, W.-Y. Wong, Z.-Q. Gao, C.-H. Chen, K.-W. Cheah, B. Yao, Z. Xie, Q. Wang, D. Ma, L. Wang, X.-M. Yu, H.-S. Kwok, Z. Lin, *Adv. Funct. Mater.* 18 (2008) 319.
- [23] C.-L. Ho, W.-Y. Wong, Q. Wang, D. Ma, L. Wang, Z. Lin, *Adv. Funct. Mater.* 18 (2008) 928.
- [24] S.J. Lee, J.S. Park, K.-J. Yoon, Y.-I. Kim, S.-H. Jin, S.K. Kang, Y.-S. Gal, S. Kang, J.Y. Lee, J.-W. Kang, S.-H. Lee, H.-D. Park, J.-J. Kim, *Adv. Funct. Mater.* 18 (2008) 3922.
- [25] J. Ding, J. Gao, Y. Cheng, Z. Xie, L. Wang, D. Ma, X. Jing, F. Wang, *Adv. Funct. Mater.* 16 (2006) 575.
- [26] B. Constantin, D. Mircea, *Heterocycl. Commun.* 9 (2003) 641.
- [27] J.N. Demas, G.A. Groshy, *J. Phys. Chem.* 75 (1971) 991.
- [28] A.B. Tamayo, B.D. Alleyne, P.I. Djurovich, S. Lamansky, I. Tsyba, N.N. Ho, R. Bau, M.E. Thompson, *J. Am. Chem. Soc.* 125 (2003) 7377.
- [29] M.G. Colombo, T.C. Brunold, T. Riedener, H.U. Güdel, M. Förtsch, H. Bürgi, *Inorg. Chem.* 33 (1994) 545.
- [30] A. Tsuboyama, H. Iwawaki, M. Furugori, T. Mukaide, J. Kamatani, S. Igawa, T. Moriyama, S. Miura, T. Takiguchi, S. Okada, M. Hoshino, K. Ueno, *J. Am. Chem. Soc.* 125 (2003) 12971.
- [31] D.R. Whang, Y. You, S.H. Kim, W.-I. Jeong, Y.-S. Park, J.-J. Kim, S.Y. Park, *Appl. Phys. Lett.* 91 (2007) 233501.



## 2-Mercaptobenzothiazolate complexes of rare earth metals and their electroluminescent properties

Marina A. Katkova\*, Vasilii A. Ilichev, Alexey N. Konev, Irina I. Pestova, Georgy K. Fukin, Mikhail N. Bochkarev

G.A. Razuvaev Institute of Organometallic Chemistry of RAS, Tropinina 49, Nizhny Novgorod 603950, Russia

### ARTICLE INFO

#### Article history:

Received 1 December 2008

Received in revised form 17 February 2009

Accepted 21 February 2009

Available online 3 March 2009

#### PACS:

78.60.Fi

85.60.Jb

#### Keywords:

Rare earth complexes

2-Mercaptobenzothiazolate

Electroluminescence

Non-doped OLED

### ABSTRACT

We have demonstrated the electroluminescent (EL) properties of 2-mercaptobenzothiazolate complexes of rare earth metals  $[\text{Ln}(\text{mbt})_3]$ ,  $\text{Ln} = \text{Y}, \text{Sm}, \text{Eu}, \text{Gd}, \text{Tb}, \text{Dy}, \text{Tm}$ ] using simple non-doped two-layer organic light emitting diode with the configuration of indium tin oxide/*N,N'*-bis(3-methylphenyl)-*N,N'*-diphenylbenzidine/ $\text{Ln}(\text{mbt})_3/\text{Yb}$ . It was found that 2-mercaptobenzothiazolate complexes have highly efficient intra-energy transfer from the singlet to the triplet state of the ligand, and then to the excited state of the central lanthanide ions. Thus  $\text{Y}(\text{mbt})_3$  and  $\text{Gd}(\text{mbt})_3$  exhibit the broad ligand-centered emission with maximum near 600 nm and  $\text{Dy}(\text{mbt})_3$ ,  $\text{Tb}(\text{mbt})_3$  and  $\text{Tm}(\text{mbt})_3$  complexes exhibit pure sharp emission bands from the intra f–f transitions of lanthanide ions  $\text{Tb}^{3+}$ :  $^5\text{D}_4 \rightarrow ^7\text{F}_6$  (492 nm),  $^5\text{D}_4 \rightarrow ^7\text{F}_5$  (547 nm),  $^5\text{D}_4 \rightarrow ^7\text{F}_4$  (589 nm),  $^5\text{D}_4 \rightarrow ^7\text{F}_3$  (624 nm);  $\text{Dy}^{3+}$ :  $^4\text{F}_{9/2} \rightarrow ^6\text{H}_{13/2}$  (575 nm) and  $\text{Tm}^{3+}$ :  $^3\text{H}_4 \rightarrow ^3\text{H}_6$  (795 nm).

© 2009 Elsevier B.V. All rights reserved.

### 1. Introduction

The rare earth metals are unique elements which fascinating luminescent properties lead to an outstanding role in light conversion technologies [1]. In the past decade, the main attention was focused on the application of lanthanide complexes as electroluminescent materials for organic light emitting diodes (OLED) [2,3]. One of the most important problems in this field is a selection of suitable ligands which would provide high efficiency of emission of the metal ions. Up to now the basic research are focused on the lanthanide  $\beta$ -diketonate complexes and its analogues which are limited in terms of practical applications by their poor photo and electro stability [4,5]. Recently, we have proposed the homoleptic 2-mercaptobenzothiazolate

complexes of rare earth metals  $\text{Ln}(\text{mbt})_3$  ( $\text{Ln} = \text{Y}, \text{La}, \text{Sm}, \text{Eu}, \text{Gd}, \text{Tb}, \text{Er}, \text{Tm}$ ) as a new class of luminescent materials [6]. The 2-mercaptobenzothiazolate ligands in these complexes are bonded to the metal atom in  $\eta^2$ -fashion via nitrogen and terminal sulfur atoms forming the chelating structure. These complexes exhibit at 77 K ligand-centered bands of fluorescence (at 395 nm) and phosphorescence (at 550 nm) and weak emission of lanthanide ions (Eu or Tb). Due to the phosphorescence – an emission from the lowest excited electronic triplet state to the electronic singlet ground state – these complexes can be formalized as the triplet emitters. It is well known that the triplet emitters based on metal–organic complexes have attracted significant attention [7]. Nowadays many research groups have focused on the development of efficient light emitting phosphorescent materials based on iridium, platinum, osmium, and ruthenium complexes [7–12]. However, the little attention in this area has been given to the rare earth complexes,

\* Corresponding author. Tel.: +7 831 4624021; fax: +7 831 4627487.  
E-mail address: [marina@iomc.ras.ru](mailto:marina@iomc.ras.ru) (M.A. Katkova).

meanwhile the rare earth complexes are characterized by highly efficient intra-energy conversion from the ligand singlet to the triplet, and then to the excited state of the central metal ion in the case of lanthanide [1]. The lanthanide ions may be luminescent, either fluorescent ( $\text{Pr}^{3+}$ ,  $\text{Nd}^{3+}$ ,  $\text{Ho}^{3+}$ ,  $\text{Er}^{3+}$ ,  $\text{Yb}^{3+}$ ) or phosphorescent ( $\text{Sm}^{3+}$ ,  $\text{Eu}^{3+}$ ,  $\text{Gd}^{3+}$ ,  $\text{Tb}^{3+}$ ,  $\text{Dy}^{3+}$ ,  $\text{Tm}^{3+}$ ) or have no f–f transition ( $\text{La}^{3+}$  and  $\text{Lu}^{3+}$ ) [13]. So the rare earth complexes may offer to give phosphorescent materials with emission properties in OLED technology.

In this work, we describe the electroluminescent properties of 2-mercaptobenzothiazolate complexes of rare earth metals and their utility in simple two-layer non-doped OLED devices. The prepared devices consisted of exclusively vacuum deposited layers using ITO glass as the anode, *N,N'*-bis(3-methylphenyl)-*N,N'*-diphenylbenzidine (TPD) as the hole-transporting layer,  $\text{Ln}(\text{mbt})_3$  as the electron-transport/emission layers and Yb as the cathode.

## 2. Experimental section

### 2.1. General

All manipulations were carried under vacuum using standard Schlenk techniques. The lanthanide complexes  $\text{Ln}[\text{N}(\text{SiMe}_3)_2]_3$  [14],  $[(\text{Me}_3\text{Si})_2\text{N}]_3\text{Tb}(\mu\text{-Cl})\text{Li}(\text{THF})_3$  [15] and  $\text{Ln}(\text{mbt})_3$  (Ln = Y, Gd, Sm, Eu, Tb, Er, Tm) [6] were synthesized according to the published procedure. Commercial 2-mercaptobenzothiazole (Aldrich) was used without additional purification. IR spectra were obtained on a Perkin Elmer 577 spectrometer and recorded from 4000 to  $450\text{ cm}^{-1}$  as a Nujol mull on KBr plates.

### 2.2. Synthesis

#### 2.2.1. Tris(benzothiazole-2-thialato-*N,S*)-dysprosium [ $\text{Dy}(\text{mbt})_3$ ]

The compound was prepared similarly to other  $\text{Ln}(\text{mbt})_3$  complexes [6]. To a solution of  $\text{Dy}[\text{N}(\text{SiMe}_3)_2]_3$  (283 mg, 0.44 mmol) in THF (5 ml) was added a solution of 2-mercaptobenzothiazole (221 mg, 1.32 mmol) in THF (10 ml). The reaction mixture was stirred for 45 min at room temperature and the solvent was evaporated under vacuum. The solid residue was washed with toluene and the beige powder of  $\text{Dy}(\text{mbt})_3$  was dried under vacuum. Yield: 280 mg, 95%.  $\text{C}_{21}\text{DyH}_{12}\text{N}_3\text{S}_6$  (661.25): calcd. C 38.14, H 1.83, Dy 24.58; found: C 38.11, H 1.87, Dy 24.52. IR (Nujol,  $\text{cm}^{-1}$ ): 3050 (w), 1597 (w), 1446 (br), 1321 (m), 1247 (m), 1078 (s), 1035 (s), 1013 (s), 753 (s), 727 (w), 708 (br), 670 (m), 606 (w).

#### 2.2.2. Tris(benzothiazole-2-thialato-*N,S*)-bis(tetrahydrofuran)-terbium tetrahydrofuran solvate [ $\text{Tb}(\text{mbt})_3(\text{THF})_2(\text{THF})$ ]

To a solution of  $\text{Tb}[\text{N}(\text{SiMe}_3)_2]_3$  (156 mg, 0.24 mmol) in THF (20 ml) was added a solution of 2-mercaptobenzothiazole (121 mg, 0.72 mmol) in THF (20 ml). The reaction mixture was stirred for 15 min at 12 °C and then was placed in a freezer for 2 days. The beige crystals suitable for X-ray analysis of  $[\text{Tb}(\text{mbt})_3(\text{THF})_2](\text{THF})$  was separated by filtration, washed with toluene, and dried under vacuum. Yield: 78 mg, 37%.  $\text{C}_{33}\text{H}_{36}\text{N}_3\text{O}_3\text{S}_6\text{Tb}$  (873.99): calcd. C 45.35, H 4.15, Tb 18.18; found: C 45.31, H 4.19, Tb 18.13. IR (Nujol,  $\text{cm}^{-1}$ ): 3054 (w), 1597 (w), 1445 (br), 1321 (m), 1248 (m),

**Table 1**

The details of crystallographic, collection and refinement data for  $[\text{Tb}(\text{mbt})_3(\text{THF})_2](\text{THF})$  and  $\text{Tb}(\text{mbt})_4\text{Li}(\text{DME})_3$ .

	$[\text{Tb}(\text{mbt})_3(\text{THF})_2](\text{THF})$	$\text{Tb}(\text{mbt})_4\text{Li}(\text{DME})_3$
Empirical formula	$\text{C}_{33}\text{H}_{36}\text{N}_3\text{O}_3\text{S}_6\text{Tb}$	$\text{C}_{40}\text{H}_{46}\text{LiN}_4\text{O}_6\text{S}_8\text{Tb}$
Formula weight	873.93	1101.15
Temperature (K)	100(2)	100(2)
Wavelength (Å)	0.71073	0.71073
Crystal system, space group	Triclinic, P-1	Tetragonal, $\text{P4}(3)2(1)2$
Unit cell dimensions		
<i>a</i> (Å)	9.8468(4)	23.3235(4)
<i>b</i> (Å)	10.8274(4)	23.3235(4)
<i>c</i> (Å)	16.2886(6)	35.4438(7)
$\alpha$ (°)	86.5250(10)	90
$\beta$ (°)	89.6150(10)	90
$\gamma$ (°)	86.8510(10)	90
Volume (Å <sup>3</sup> )	1730.79(11)	19280.9(6)
<i>Z</i> , calculated density (Mg/m <sup>3</sup> )	2, 1.677	16, 1.517
Absorption coefficient (mm <sup>-1</sup> )	2.444	1.861
<i>F</i> (000)	880	8928
Crystal size (mm)	0.17 × 0.15 × 0.07	0.14 × 0.14 × 0.13
$\theta$ range for data collection (°)	2.33–26.50	2.54–26.00
Limiting indices	–12 ≤ <i>h</i> ≤ 11, –13 ≤ <i>k</i> ≤ 13, –20 ≤ <i>l</i> ≤ 15	–28 ≤ <i>h</i> ≤ 28, –28 ≤ <i>k</i> ≤ 28, –43 ≤ <i>l</i> ≤ 43
Reflections collected/unique [ <i>R</i> <sub>int</sub> ]	10,736/7097 [0.0141]	167,220/18,835 [0.1954]
Completeness to $\theta = 26.50$	98.9%	99.2%
Absorption correction	Semi-empirical from equivalents	Semi-empirical from equivalents
Max. and min. transmission	0.8475 and 0.6814	0.7940 and 0.7807
Refinement method	full-matrix least-squares on <i>F</i> <sup>2</sup>	full-matrix least-squares on <i>F</i> <sup>2</sup>
Data/restraints/parameters	7097/0/415	18,835/3/1009
Goodness-of-fit on <i>F</i> <sup>2</sup>	1.026	0.974
Final <i>R</i> indices [ <i>I</i> > 2σ( <i>I</i> )]	<i>R</i> <sub>1</sub> = 0.0246, <i>wR</i> <sub>2</sub> = 0.0582	<i>R</i> <sub>1</sub> = 0.0564, <i>wR</i> <sub>2</sub> = 0.1017
<i>R</i> indices (all data)	<i>R</i> <sub>1</sub> = 0.0307, <i>wR</i> <sub>2</sub> = 0.0599	<i>R</i> <sub>1</sub> = 0.0937, <i>wR</i> <sub>2</sub> = 0.1121
Largest diff. peak and hole (eÅ <sup>-3</sup> )	1.171 and –0.782	2.011 and –0.563

1080 (s), 1027 (s), 1012 (s), 860 (br), 751 (s), 727 (m), 706 (br), 670 (m), 606 (w).

### 2.2.3. Tris(1,2-dimethoxyethane-*O,O'*)-lithium-tetra(benzothiazole-2-thiolato-*N,S*)-terbium [Tb(mbt)<sub>4</sub>Li(DME)<sub>3</sub>]

Solution of 2-mercaptobenzothiazole (121 mg, 0.72 mmol) in 5 ml DME was added to a solution of [(Me<sub>3</sub>Si)<sub>2</sub>N]<sub>3</sub>Tb(μ-Cl)Li(THF)<sub>3</sub> (215 mg, 0.24 mmol) in 5 ml DME. The reaction mixture was stirred for 45 min at room temperature and then was placed in a freezer for 2 days. The formed beige crystals were separated by decantation, washed with toluene and dried in vacuum to give 140 mg (53%) of Tb(mbt)<sub>4</sub>Li(DME)<sub>3</sub>. C<sub>40</sub>H<sub>46</sub>LiN<sub>4</sub>O<sub>6</sub>S<sub>8</sub>Tb (1101.23): calcd. C 43.63, H 4.21, Tb 14.43; found: C 43.61, H 4.19, Tb 14.46. IR (Nujol, cm<sup>-1</sup>): 3054 (w), 1597 (w), 1445 (br), 1321 (m), 1248 (m), 1080 (s), 1027 (s), 1012 (s), 998 (m), 751 (s), 727 (m), 706 (br), 670 (m), 606 (w).

### 2.3. X-ray crystallography study

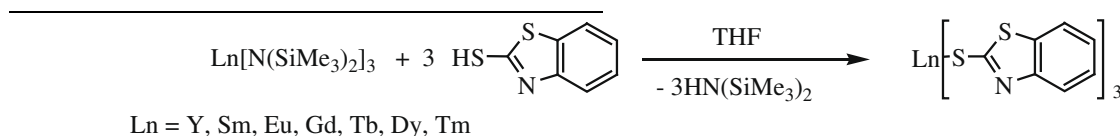
The X-ray diffraction data were collected on a SMART APEX diffractometer (graphite-monochromated, MoKα-

emission layer were fabricated (Fig. 1). A commercial ITO on glass substrate with 100 Ω/sq. was used as anode material (Merck Balzers) and commercial Yb metal (Sigma-Aldrich) as cathode material. The constituent organic (20 nm) and metal (150 nm) layers were deposited using thermal vacuum evaporation (at a base pressure of approximately 10<sup>-6</sup> mbar) of commercial grade TPD and Yb metal, freshly synthesized Ln(mbt)<sub>3</sub> (Ln = Y, Gd, Sm, Eu, Dy, Tb, Er, Tm). The active area of the devices was a circle with ∅ 8 mm. The EL spectra and current–voltage luminescence characteristics were measured with an Ocean Optics USB-2000 fluorimeter and a computer controlled TEC-23 power supply under ambient conditions.

## 3. Results and discussion

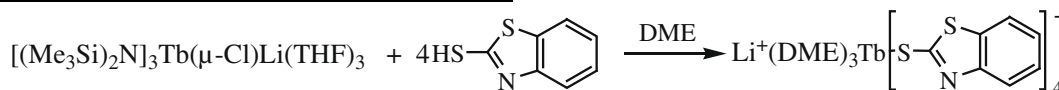
### 3.1. Synthesis and structure

The 2-mercaptobenzothiazolate lanthanide complexes Ln(mbt)<sub>3</sub> (Ln = Y, Sm, Eu, Gd, Tb, Dy, Tm) for investigation of their electroluminescent properties were synthesized from the corresponding Ln[N(SiMe<sub>3</sub>)<sub>2</sub>]<sub>3</sub> and 2-mercaptobenzothiazole, using a previously developed method [6].



radiation, φ-ω-scan technique, λ = 0.71073 Å). The intensity data were integrated by SAINT program [16]. SADABS [17] was used to perform area-detector scaling and absorption corrections. The structures were solved by direct methods and were refined on F<sup>2</sup> using all reflections with SHELXTL package [18]. All non-hydrogen atoms were refined anisotropically. H-atoms in [Tb(mbt)<sub>3</sub>(THF)<sub>2</sub>](THF) were found from Fourier synthesis and refined isotropically except for the H-atoms of THF molecules in the Er-complex, which were placed in calculated positions and refined in the “riding-model”. Details of crystallographic, collection and refinement data for [Tb(mbt)<sub>3</sub>-

For preparation of the terbium complex in crystalline form suitable for X-ray investigation the modified method was used: diluted THF solution of Tb[N(SiMe<sub>3</sub>)<sub>2</sub>]<sub>3</sub> was added slowly to a diluted solution of 2-mercaptobenzothiazole at reduced temperature. Another type of terbium 2-mercaptobenzothiazolate has been obtained using the ate-complex [(Me<sub>3</sub>Si)<sub>2</sub>N]<sub>3</sub>Tb(μ-Cl)Li(THF)<sub>3</sub> as the starting reagent. Predictably the treatment of it with 2-mercaptobenzothiazole in DME resulted in a formation of Tb(mbt)<sub>4</sub>Li(DME)<sub>3</sub> which was isolated from a reaction clear solution in 53% yield as colorless crystals soluble in THF and DME.



(THF)<sub>2</sub>](THF) and Tb(mbt)<sub>4</sub>Li(DME)<sub>3</sub> are shown in the Table 1.

### 2.4. Device fabrication

OLED devices were prepared in a vacuum system with different evaporation chambers for different types of organic and metal layers (cluster-tool) [19]. The simple non-doped two-layer devices ITO/TPD/Ln(mbt)<sub>3</sub>/Yb, consisting of triphenylamine derivative (TPD) as a hole transport layer, and 2-mercaptobenzothiazolate complex of rare earth metal Ln(mbt)<sub>3</sub> as an electron transport and

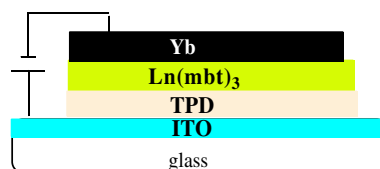
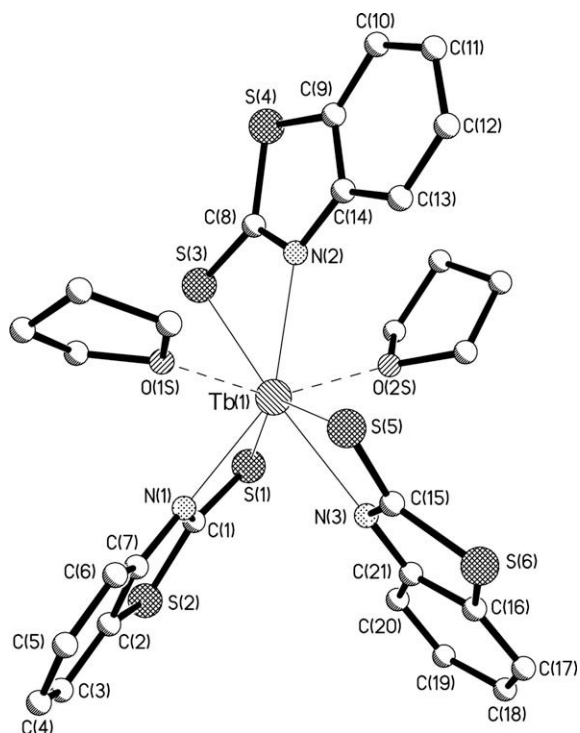
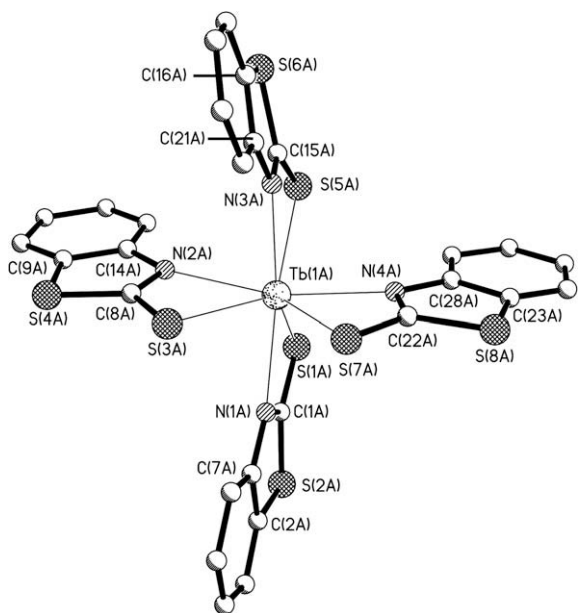


Fig. 1. Structure of the OLEDs.



**Fig. 2.** Molecular structure of  $[\text{Tb}(\text{mbt})_3(\text{THF})_2](\text{THF})$ . Solvate THF molecular is omitted for clarity.



**Fig. 3.** Molecular structure of  $\text{Tb}(\text{mbt})_4\text{Li}(\text{DME})_3$ .  $\text{Li}(\text{DME})_3$  cation is omitted for clarity.

Molecular structures of the complexes are shown in Figs. 2 and 3, selected structural parameters are listed in Table 2.

X-ray single crystal structure analysis has revealed that the  $[\text{Tb}(\text{mbt})_3(\text{THF})_2](\text{THF})$  is isostructural to the previ-

**Table 2**  
Selected bond lengths (Å) and angles (°) for  $\text{Tb}(\text{mbt})_3(\text{THF})_2$ .

	[Tb(mbt) <sub>3</sub> (THF) <sub>2</sub> ](THF)	Tb(mbt) <sub>4</sub> Li(DME) <sub>3</sub>	
		A	B
<i>Distances</i>			
Tb(1)–O(2S)	2.382(1)	–	–
Tb(1)–O(1S)	2.451(1)	–	–
Tb(1)–N(1)	2.443(2)	2.506(4)	2.504(4)
Tb(1)–N(2)	2.501(2)	2.484(4)	2.470(4)
Tb(1)–N(3)	2.542(2)	2.482(5)	2.468(4)
Tb(1)–N(4)	–	2.466(5)	2.464(4)
Tb(1)–S(1)	2.8850(5)	2.875(2)	2.875(1)
Tb(1)–S(3)	2.8319(5)	2.896(2)	2.892(1)
Tb(1)–S(5)	2.8390(5)	2.890(2)	2.850(1)
Tb(1)–S(7)	–	2.860(2)	2.881(1)
S(1)–C(1)	1.703(2)	1.714(6)	1.692(6)
S(2)–C(2)	1.742(2)	1.742(6)	1.720(7)
S(2)–C(1)	1.754(2)	1.761(6)	1.761(6)
S(3)–C(8)	1.722(2)	1.695(6)	1.697(6)
S(4)–C(8)	1.740(2)	1.763(5)	1.697(6)
S(4)–C(9)	1.741(2)	1.744(2)	1.712(6)
S(5)–C(15)	1.710(2)	1.675(6)	1.685(5)
S(6)–C(16)	1.739(2)	1.709(7)	1.733(6)
S(6)–C(15)	1.756(2)	1.795(6)	1.765(6)
S(7)–C(22)	–	1.695(6)	1.699(6)
S(8)–C(23)	–	1.735(6)	1.678(6)
S(8)–C(22)	–	1.783(6)	1.771(6)
N(1)–C(1)	1.324(3)	1.308(7)	1.310(7)
N(1)–C(7)	1.394(3)	1.402(7)	1.359(7)
N(2)–C(8)	1.320(3)	1.329(7)	1.318(7)
N(2)–C(14)	1.392(3)	1.390(7)	1.391(7)
N(3)–C(15)	1.312(3)	1.306(8)	1.330(7)
N(3)–C(21)	1.399(3)	1.380(7)	1.399(7)
N(4)–C(22)	–	1.296(8)	1.318(7)
N(4)–C(28)	–	1.438(7)	1.370(7)
<i>Angles</i>			
N(1)Tb(1)S(1)	59.25(4)	58.67(11)	59.22(11)
N(2)Tb(1)S(3)	59.58(4)	58.66(11)	58.68(10)
N(3)Tb(1)S(5)	58.92(4)	58.90(12)	59.34(10)
N(4)Tb(1)S(7)	–	58.96(12)	59.23(10)
N(1)C(1)S(1)	122.6(2)	122.4(4)	125.8(5)
N(2)C(8)S(3)	121.8(2)	122.7(4)	122.8(4)
N(3)C(15)S(5)	122.7(2)	126.3(4)	122.9(4)
N(4)C(22)S(7)	–	123.7(4)	123.7(4)

ously reported  $[\text{Eu}(\text{mbt})_3(\text{THF})_2](\text{THF})$  and  $[\text{Er}(\text{mbt})_3(\text{THF})_2](\text{THF})$  [6]. The molecules of  $[\text{Tb}(\text{mbt})_3(\text{THF})_2](\text{THF})$  have distorted dodecahedral arrangement with the bidentate coordination mode of mbt ligands. The difference between Tb(1)–S(N) and Eu(1)–S(N) or Er(1)–S(N) distances are close to the difference in their ionic radii of the metals whereas the geometric parameters of mbt ligands in the complexes are practically the same. Four-membered metalocycle TbSCN is planar. The mercaptobenzothiazolate  $\text{Tb}(\text{mbt})_4\text{Li}(\text{DME})_3$  is ate-complex, containing  $[\text{Tb}(\text{mbt})_4]^-$  anion and  $\text{Li}(\text{DME})_3^+$  counterion. In a crystal there are two independent types of the molecules, which negligibly differ to each other by geometry of the anionic fragments. One of the types is presented in Fig. 3. Four bidentate mbt ligands form a distorted Tb-centered dodecahedron. Its structure and geometric parameters is similar to that of  $[\text{Nd}(\text{mbt})_4]$  in the complex  $[\text{K}(15\text{-crown-5})_2][\text{Nd}(\text{mbt})_4]$  [20] and virtually coincide with those of respective fragment in  $[\text{Tb}(\text{mbt})_3(\text{THF})_2](\text{THF})$ . It should be noted that solvent plays the important role in formation, structure and properties of the complexes. To



gain more insight into the problem we calculated the shielding of central metal atom by ligand solid angle approach (*G*-parameter) [21]. The *G*-parameter in  $[\text{Tb}(\text{mbt})_3(\text{THF})_2](\text{THF})$  (88.6(2)%) noticeably exceeds the analogous value in  $\text{Tb}(\text{mbt})_4$  anion (83.7(2)%). In the molecule of  $[\text{Tb}(\text{mbt})_3(\text{THF})_2](\text{THF})$  only two THF ligands coordinate the Tb cation whereas the third THF molecule remains free in crystalline space. Each intersphere THF ligand shields 12–13% space at the Tb atom and consequently there is no room in coordination sphere for the third THF molecule. At the same time, the hypothetical  $\text{Tb}(\text{mbt})_3$  complex (free of coordinated THF) would have too low value of *G*-parameter, 62.8(2)%. Thus the coordination of two THF molecules stabilizes  $[\text{Tb}(\text{mbt})_3(\text{THF})_2](\text{THF})$  complex and influences on his structure. The different situation is observed in  $\text{Tb}(\text{mbt})_4\text{Li}(\text{DME})_3$ . The value of *G*-parameter of DME molecules in rare earth complexes is 29.9(6)%. The additionally coordination of DME should increase the shielding of central metal up to 113% that is impossible. Thus, despite the fact that DME is a strongly coordinated solvent, there is insufficient room about the Tb atom to accommodate the DME molecule. In

other words, non-bonding ligand–ligand interactions in coordination sphere of Tb prevent the intersphere solvation of the lanthanide atom.

### 3.2. EL properties

To follow up on the discovery of electroluminescent properties of these complexes we fabricated the simple non-doped two-layer OLEDs with the structures of ITO/TPD/Ln(mbt)<sub>3</sub>/Yb. It should be noted that all these devices do not reveal the emission according the fluorescence component at 395 nm. Predictably as Y<sup>3+</sup> have 4f<sup>0</sup> electronic configuration the device based on Y(mbt)<sub>3</sub> exhibits the broad peak centered at 600 nm (Fig. 4), which is contributed to phosphorescent emission at 550 nm. As it is shown in Fig. 4, the gadolinium complex, due to the stability of the half-filled 4f<sup>7</sup> shell configuration in Gd<sup>3+</sup> ion, demonstrates the broad emission band centered at 640 nm. Note that the device based on the complex with heavy and strong paramagnetic gadolinium ion exhibit the higher luminance than the device based on the complex with diamagnetic yttrium ion. In contrast, Dy(mbt)<sub>3</sub>, Tb(mbt)<sub>3</sub> and Tm(mbt)<sub>3</sub>

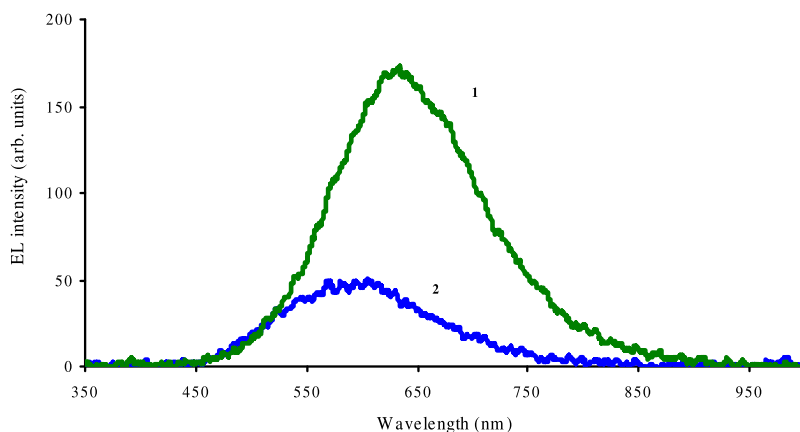


Fig. 4. EL spectra of the devices with different emitting layers ITO/TPD/Gd(mbt)<sub>3</sub>/Yb (1), and ITO/TPD/Y(mbt)<sub>3</sub>/Yb (2) obtained at 12 V.

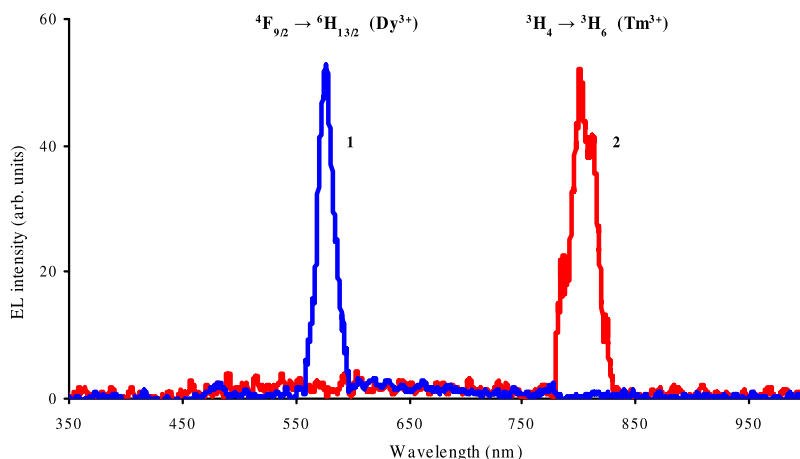
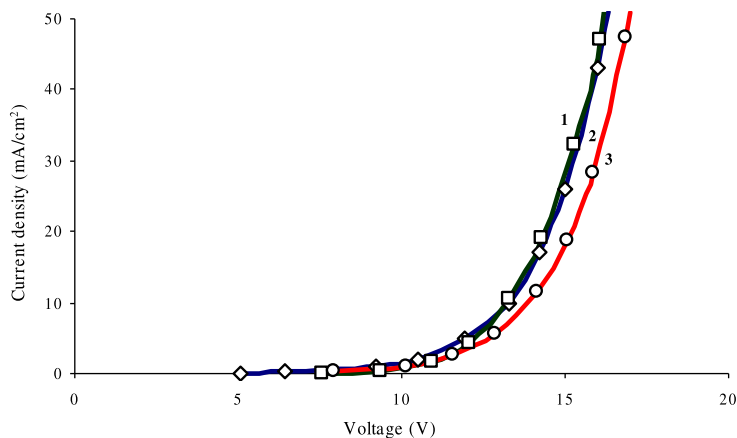
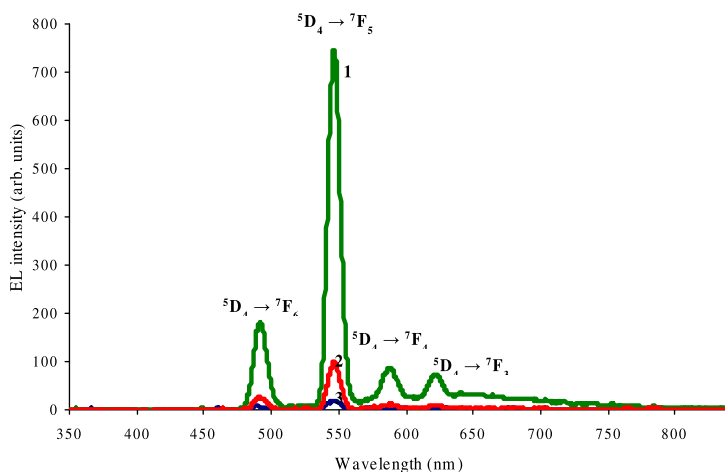


Fig. 5. EL spectra of the devices with different emitting layers ITO/TPD/Dy(mbt)<sub>3</sub>/Yb (1), and ITO/TPD/Tm(mbt)<sub>3</sub>/Yb (2) obtained at 12 V.



**Fig. 6.** Current density as a function of operating voltage for OLED devices ITO/TPD/Tb(mbt)<sub>3</sub>/Yb (1), ITO/TPD/Eu(mbt)<sub>3</sub>/Yb (2), and ITO/TPD/Sm(mbt)<sub>3</sub>/Yb (3).



**Fig. 7.** EL spectra of the devices with different emitting layers ITO/TPD/Tb(mbt)<sub>3</sub>/Yb (1), ITO/TPD/[Tb(mbt)<sub>3</sub>(THF)<sub>2</sub>](THF)/Yb (2), and ITO/TPD/Tb(mbt)<sub>4</sub>Li(DME)<sub>3</sub>/Yb (3) obtained at 12 V.

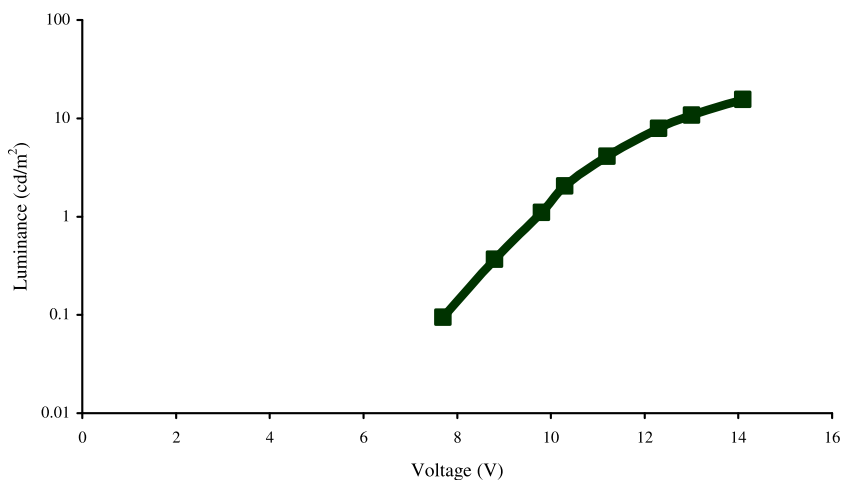


**Fig. 8.** Luminance as a function of operating voltage for OLED devices ITO/TPD/Tb(mbt)<sub>3</sub>/Yb.

complexes exhibit only sharp emission bands from the intra f–f transitions of lanthanide ions  $\text{Tb}^{3+}$ :  $^5\text{D}_4 \rightarrow ^7\text{F}_6$  (492 nm),  $^5\text{D}_4 \rightarrow ^7\text{F}_5$  (547 nm),  $^5\text{D}_4 \rightarrow ^7\text{F}_4$  (589 nm),  $^5\text{D}_4 \rightarrow ^7\text{F}_3$  (624 nm);  $\text{Dy}^{3+}$ :  $^4\text{F}_{9/2} \rightarrow ^6\text{H}_{13/2}$  (575 nm) and  $\text{Tm}^{3+}$ :  $^3\text{H}_4 \rightarrow ^3\text{H}_6$  (795 nm). (Figs. 5 and 7) Unfortunately, EL devices based on  $\text{Sm}(\text{mbt})_3$  or  $\text{Eu}(\text{mbt})_3$  turned out the luminescence though their current–voltage ( $I$ – $V$ ) characteristics are quite similar to that of  $\text{Tb}(\text{mbt})_3$  (Fig. 6).

Compared to the previous results [6] of the photoluminescence of these complexes the EL spectra have a red shift which can be attributed to the solvent influence (for PL) or to the congregated molecular state (for EL). It is well known that as a model system, the undoped OLEDs directly based on the molecular properties of emitting material in which both the singlet and triplet states are populated by excitation. The fact that an emission from the singlet state is not observed in EL spectra is resulted from the efficient intersystem crossing from the singlet to the triplet excited state for all of these complexes. For lack of emission from the triplet to the ground state in the case of Tb, Dy, Tm, Sm and Eu complexes suggests subsequent efficient crossing from the triplet to the emissive and non-emissive intra

f levels of these lanthanide ions. Furthermore, the pure metal-centered emission of Tb, Dy and Tm also confirms this statement.

Comparing the luminescent characteristics of the EL devices based on  $\text{Tb}(\text{mbt})_3$ ,  $[\text{Tb}(\text{mbt})_3(\text{THF})_2](\text{THF})$  and  $[\text{Tb}(\text{mbt})_4][\text{Li}(\text{DME})_3]$  we have found that emission intensity of the first complex is significantly higher than that of two latter compounds (Fig. 7). One of plausible explanation of it is decreased thermal stability of THF and Li containing compounds, which partially decompose at sublimation during the OLED device fabrication. Moreover OLED device ITO/TPD/ $\text{Tb}(\text{mbt})_3$ /Yb displays significant improvements in EL performance compared with the devices based on another Ln( $\text{mbt})_3$  complexes. Fig. 8 presents the luminance–voltage ( $L$ – $V$ ) characteristic of this device, Fig. 9 shows the current efficiency (in cd/A), and Fig. 10 shows the power efficiency (in lm/W) vs. the current density. It is found that even for the device which is not yet optimized, the green emission appears when the bias is above 7.7 V, and at 12 V the current efficiency of 0.16 cd/A is achieved. Note that the efficiency decreases slowly with an increase of the current

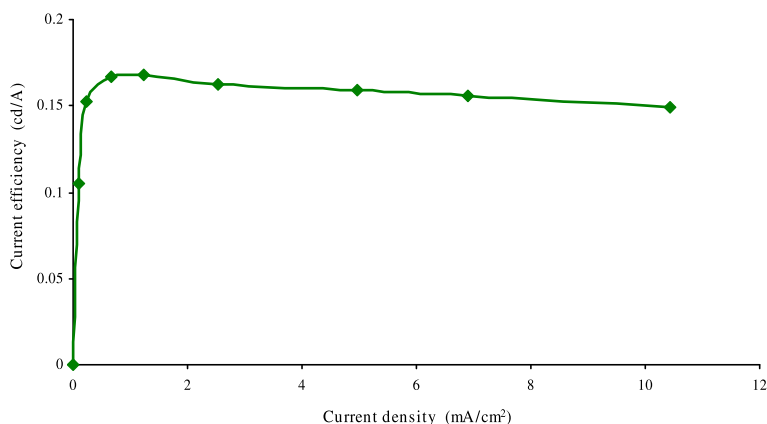


Fig. 9. Current efficiency vs. current density for OLED devices ITO/TPD/ $\text{Tb}(\text{mbt})_3$ /Yb.

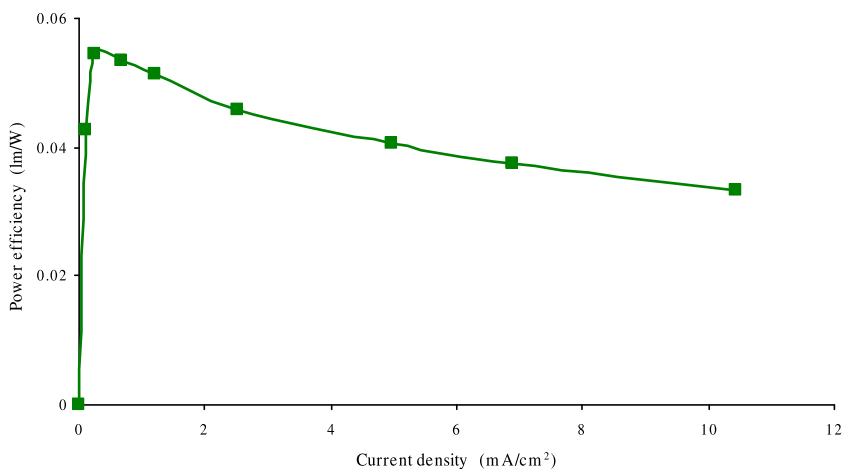


Fig. 10. Power efficiency vs. current density for OLED devices ITO/TPD/ $\text{Tb}(\text{mbt})_3$ /Yb.

density, suggesting that the device based on  $\text{Tb}(\text{mbt})_3$  demonstrates the rather high stability in a current than lanthanide  $\beta$ -diketonate complexes. This gives the ground to consider 2-mercaptobenzothiazolate lanthanide complexes as a promising material for design of efficient OLED.

#### 4. Conclusions

In summary, we report for the first time the EL properties of 2-mercaptobenzothiazolate complexes of rare earth metals with the non-doped simple OLEDs of configuration ITO/TPD/Ln(mbt)<sub>3</sub>/Yb. Depending on the nature of the rare earth metal in the complexes, emission wavelengths span from the broad visible spectrum considering the ligand-centered phosphorescence to the sharp emission bands from the intra f–f transitions of lanthanide ions. This suggests that 2-mercaptobenzothiazolate complexes have highly efficient intra-energy transfer from the singlet to the triplet state of the ligand, and then to the excited state of the central lanthanide ions, to give phosphorescent materials with emission properties which may be tuned specifically for optimum performance in OLED technology.

#### 5. Supplementary material

Crystallographic data for the structural analysis have been deposited with the Cambridge Crystallographic Data Center, CCDC nos. 710983 and 710984 for  $[\text{Tb}(\text{mbt})_3(\text{THF})_2](\text{THF})$  and  $\text{Tb}(\text{mbt})_4\text{Li}(\text{DME})_3$ . This material can be obtained upon request to CCDC, 12 Union Road, Cambridge, CB2 1EZ, UK ([www.ccdc.cam.ac.uk](http://www.ccdc.cam.ac.uk); email: [deposit@ccdc.cam.ac.uk](mailto:deposit@ccdc.cam.ac.uk)).

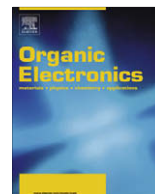
#### Acknowledgments

This work was supported by the Grant of Federal Agency on Sciences and Innovations of Russian Federation

(project No. 02.513.11.3207) and the Russian Foundation of Basic Research (Grant Nos. 04-03-32093a and 06-03-32728a).

#### References

- [1] J.C.G. Bunzli, C. Piguet, *Chem. Soc. Rev.* 34 (2005) 1048.
- [2] J. Kido, Y. Okamoto, *Chem. Rev.* 102 (2002) 2357.
- [3] M.A. Katkova, A.G. Vitukhnovsky, M.N. Bochkarev, *Russ. Chem. Rev.* 74 (2005) 1089.
- [4] A. de Bettencourt-Dias, *Dalton Trans.* (2007) 2229.
- [5] R.C. Evans, P. Douglas, C.J. Winscom, *Coord. Chem. Rev.* 250 (2006) 2093.
- [6] M.A. Katkova, A.V. Borisov, G.K. Fukin, E.V. Baranov, A.S. Averyushkin, A.G. Vitukhnovsky, M.N. Bochkarev, *Inorg. Chim. Acta* 359 (2006) 4289.
- [7] H. Yersin (Ed.), *Highly Efficient OLEDs with Phosphorescent Materials*, Wiley-VCH, Weinheim, 2008, p. 438.
- [8] B. Ma, P.I. Djurovich, M. Yousufuddin, R. Bau, M.E. Thompson, *J. Phys. Chem. C* 112 (2008) 8022.
- [9] C. Borek, K. Hanson, P.I. Djurovich, M.E. Thompson, K. Aznavour, R. Bau, Y. Sun, S.R. Forrest, J. Brooks, L. Michalski, J. Brown, *Angew. Chem. Int. Ed.* 46 (2007) 1109.
- [10] D. Wasserberg, S.C.J. Meskers, R.A.J. Janssen, *J. Phys. Chem. A* 111 (2007) 1381.
- [11] A. Endo, K. Suzuki, T. Yoshihara, S. Tobita, M. Yahiro, C. Adachi, *Chem. Phys. Lett.* 460 (2008) 155.
- [12] R. Meerheim, S. Scholz, S. Olthof, G. Schwartz, S. Reineke, K. Walzer, K. Leo, *J. Appl. Phys.* 104 (2008) 014510.
- [13] J.C.G. Bunzli, *Acc. Chem. Res.* 39 (2006) 53.
- [14] D.C. Bradley, J.S. Chotra, F.A. Hart, *J. Chem. Soc. Dalton Trans.* (1973) 1021.
- [15] H.X. Li, Z.G. Ren, Y. Zhang, W.H. Zhang, J.P. Lang, Q. Shen, *J. Am. Chem. Soc.* 127 (2005) 1122.
- [16] Bruker SAINTPlus Data Reduction and Correction Program v. 6.02a, Bruker AXS, Madison, Wisconsin, USA, 2000.
- [17] G.M. Sheldrick, SADABS v. 2.01, Bruker/Siemens Area Detector Absorption Correction Program, Bruker AXS, Madison, Wisconsin, USA, 1998.
- [18] G.M. Sheldrick, SHELXTL v. 6.12, Structure Determination Software Suite, Bruker AXS, Madison, Wisconsin, USA, 2000.
- [19] M.A. Katkova, V.A. Ilichev, A.N. Konev, M.A. Batenkin, I.I. Pestova, A.G. Vitukhnovsky, M.N. Bochkarev, *Appl. Surf. Sci.* 254 (2008) 2216.
- [20] M. Roger, T. Arliguie, P. Thuéry, M. Ephritikhine, *Inorg. Chem.* 47 (2008) 3863.
- [21] I.A. Guzei, M. Wendt, *Dalton Trans.* (2006) 3991.



## Donor acceptor type neutral state green polymer bearing pyrrole as the donor unit

Selin Celebi, Abidin Balan, Bugra Epik, Derya Baran, Levent Toppare \*

Department of Chemistry, Middle East Technical University, 06531 Ankara, Turkey

### ARTICLE INFO

#### Article history:

Received 31 December 2008

Received in revised form 17 February 2009

Accepted 22 February 2009

Available online 3 March 2009

#### PACS:

82.45.Wx

68.55.Ln

72.80.Le

78.20.Jq

85.60.Pg

#### Keywords:

Green polymer

Doping

Conducting polymer

Electrochromism

Electrochromic Devices

### ABSTRACT

A new neutral state green polymer, poly (2,3-bis(4-tert-butylphenyl)-5,8-di(1H-pyrrol-2-yl) quinoxaline) (PTBPPQ) was synthesized and its potential use as an electrochromic material was investigated. Spectroelectrochemistry studies showed that polymer reveals two distinct absorption bands as expected for a donor–acceptor type polymer, at 408 and 745 nm. In addition, polymer has excellent switching properties with satisfactory optical contrasts and very short switching times. Outstanding optical contrast in the NIR region and stability make this polymer a great candidate for many applications. It should be noted that PTBPPQ is one of the few examples of neutral state green polymeric materials with superior switching properties. Hence, PTBPPQ can be used as a green polymeric material for display technologies.

© 2009 Elsevier B.V. All rights reserved.

## 1. Introduction

Conjugated polymers have attracted a great attention after their discovery [1], since these materials can be used as active layers in polymer light emitting diodes [2], sensors [3], batteries [4], artificial noses and muscles [5], transistors [6] and electrochromic devices [7]. Electrochromism is defined as the reversible and visible change in the transmittance and/or reflectance of a material caused by an applied voltage [8,9]. First studies in the field of electrochromism were on inorganic materials such as tungsten oxide (WO<sub>3</sub>) and iridium dioxide (IrO<sub>2</sub>) [10]. Inorganic materials lack color tuning and require use of relatively high voltages to operate devices. Organic compounds such

as conducting polymers became great candidates for electrochromic devices. As regards to the advantages of conducting polymers; high optical contrasts [11], short switching time [12,13], processability [14], fine tuning of the band gap via structure modification [15], and more importantly low applied voltages [16] are worth to mention.

Due to the extended delocalization of  $\pi$  electrons along the polymer backbone, an optical absorption band in the visible region of the electromagnetic spectrum occurs. The insertion of an anion or a cation occurs when the redox processes generate charge carriers on the conjugated backbone [17]. One of the method of increasing stability of the doping process is to incorporate donor–acceptor (D–A) units into the polymer backbone. Moreover, D–A method is also used for reducing the band gap energy [18–20]. While electron donor group raises the HOMO energy and lowers the oxidation potential, electron acceptor group

\* Corresponding author. Tel.: +90 3122103251; fax: +90 3122103200.  
E-mail address: [toppare@metu.edu.tr](mailto:toppare@metu.edu.tr) (L. Toppare).

lowers the energy of conduction band (LUMO) hence; reduction occurs easily [21–23].

Several pyrrole derivatives were employed in the field of electrochromism, such as; the use of modified pyrrole [16], in situ synthesis of pyrrole [24–27], and use of pyrrole in donor acceptor type polymers. Up to date there are few studies where pyrrole has been used as the donor/acceptor unit [28]. In our previous studies, quinoxaline derivatives [29–31] were efficiently used as the acceptor unit. Ethylenedioxythiophene (EDOT) and thiophene derivatives were used as the donor units for those studies. Pyrrole was rarely used as the donor unit with a quinoxaline acceptor unit in D–A type polymers [32,33].

There are a number of electrochromic polymers reflecting red and blue color in their neutral states [34,35] whereas few studies have been reported related to polymers reflecting green color [36–38]. In order to have red or blue color in reduced state, the materials have to absorb at only one dominant wavelength. On the contrary, for a green color, there should exist at least two simultaneous absorption bands in the red and blue regions of the visible spectrum where these bands should be controlled with the same applied potential.

Here we report the synthesis of a newly designed donor–acceptor type polymer. The unique polymer bears pyrrole as the donor unit. The polymer, namely 2,3-bis(4-tert-butylphenyl)-5,8-di(1H-pyrrol-2-yl)quinoxaline, revealed higher optical contrast in near IR region and faster switching time compare to 2,3-bis(4-tert-butylphenyl)-5,8-(2,3-dihydrothieno[3,4-b][1,4]dioxin-7yl)quinoxaline (TBPEQ) [30] and (2,3-bis(4-tert-butylphenyl)-5,8-bis(4-hexylthiophen-2-yl)quinoxaline) (HTQ) [31].

## 2. Experimental

### 2.1. Materials

All chemicals were purchased from Aldrich except anhydrous tetrahydrofuran (THF) which was purchased from Acros. 4,7-Dibromobenzo[1,2,5]thiadiazole [39], 3,6-dibromo-1,2-phenylenediamine [40], benzoin [41], benzyl [41], 1,2-bis(4-tert-butylphenyl)-2-hydroxyethanone [42], 1,2-bis(4-tert-butylphenyl)ethane-1,2-dione [42], 5,8-dibromo-2,3-diphenylquinoxaline [43], tert-butyl pyrrole-1-carboxylate [44], *N*-(tert-butoxycarbonyl)-2-(trimethylstannyl)pyrrole [44] were synthesized according to previously described methods. Electropolymerization was performed with a Voltalab 50 potentiostat in a three-electrode cell consisting of platinum wire or Indium Tin Oxide (ITO) coated glass as the working electrodes, platinum wire as the counter electrode, and an Ag wire as the pseudo reference electrode. Electrodeposition was performed from a 0.1 M solution of tetrabutylammonium perchlorate (TBAPC) at a scan rate of 100 mV/s for 15 cycles. UV–Vis–NIR spectra were recorded on a Varian Cary 5000 spectrophotometer at a scan rate of 2000 nm/min. <sup>1</sup>H and <sup>13</sup>C NMR spectra were recorded in CDCl<sub>3</sub> on Bruker Spectrospin Avance DPX-400 Spectrometer. Colorimetry measurements were performed via Minolta CS-100 Spectrophotometer.

### 2.2. Monomer synthesis

#### 2.2.1. 5,8-Bis[*N*-(tert-butoxycarbonyl)-2-pyrrolyl]2,3-bis(4-tert-butylphenyl) quinoxaline

5,8-Dibromo-2,3-bis(4-tert-butylphenyl) quinoxaline (550 mg, 1.0 mmol), and *N*-(tert-butoxycarbonyl)-2-(tributylstannyl)pyrrole (2.29 g, 5.0 mmol) were dissolved in anhydrous THF (150 ml) and purged with argon for 30 min. Then, dichlorobis(triphenyl phosphine)-palladium(II) (75 mg, 0.068 mmol) was added at room temperature under argon atmosphere. The mixture was refluxed for 3 days. Solvent was evaporated under vacuum and the crude product was purified by column chromatography on neutral alumina (eluent DCM:hexane, 2:1 v/v) to obtain 456 mg (63%) of 5,8-bis[*N*-(tert-butoxycarbonyl)-2-pyrrolyl]2,3-bis(4-tert-butylphenyl) quinoxaline. <sup>1</sup>H NMR (CDCl<sub>3</sub>, δ): 0.9 (s, 18 H), 1.22 (s, 18 H), 6.26 (t, 2H, *J* = 6.4 Hz), 6.32 (d, 2H, *J* = 7.0 Hz), 7.22 (d, 4 H, *J* = 8.8 Hz), 7.43 (d, 4 H, *J* = 8.4 Hz), 7.48 (q, 2 H, *J* = 3 Hz), 7.66 (s, 2 H). <sup>13</sup>C NMR (CDCl<sub>3</sub>, δ): 152.0, 151.2, 149.8, 139.0, 136.1, 133.3, 131.5, 129.7, 128.0, 125.1, 123.0, 115.0, 110.4, 83.0, 34.7, 31.2, 27.2.

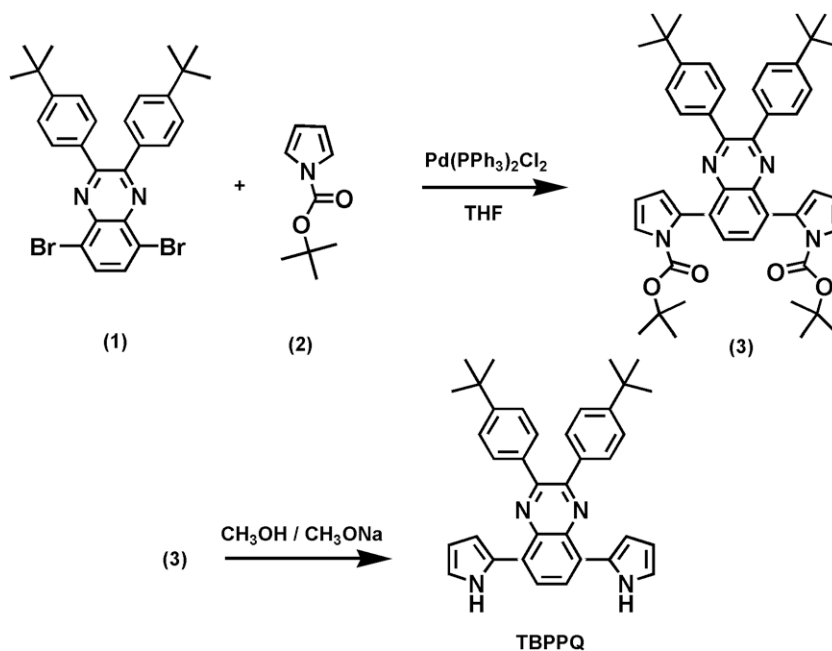
#### 2.2.2. 5,8-Bis [2-pyrrolyl] 2,3-bis(4-tert-butylphenyl) quinoxaline (TBPPQ)

5,8-Bis [*N*-(tert-butoxycarbonyl)-2-pyrrolyl] 2,3-bis(4-tert-butylphenyl) quinoxaline (350 mg, 0.48 mmol) was dissolved in 60 ml methanol. About 120 mg Na, (5.2 mmol) was added and the reaction mixture was heated under reflux for 24 h. The solvent was evaporated and the residue was treated with water and extracted with dichloromethane. The organic extracts were dried over MgSO<sub>4</sub>, the solvent was evaporated and the residue chromatographed on a column with silica gel using hexane:DCM (2:1 v/v) as eluent. In the second fraction 180 mg (72%) of product TBPPQ isolated. <sup>1</sup>H NMR (CDCl<sub>3</sub>, δ): 1.31 (s, 18 H), 6.27 (m, 2H), 6.82(m, 2H), 6.90 (m, 2H), 7.35 (d, 4 H, *J* = 8.4 Hz), 7.41 (d, 4 H, *J* = 8.8 Hz), 8.00 (s, 2 H), 11.93 (s, 2 H). <sup>13</sup>C NMR (CDCl<sub>3</sub>, δ): 152.7, 151.4, 138.0, 136.4, 131.4, 129.7, 126.3, 125.8, 125.7, 119.7, 109.5, 107.7, 35.1, 31.6. MS: *m/e* 525 (M<sup>+</sup>). IR (drift) *v*: 1084, 1112, 1392, 1473, 1608, 2962, 3350 cm<sup>-1</sup>

## 3. Results and discussion

### 3.1. Monomer synthesis

The reagent 2,1,3-benzothiadiazole was brominated in the presence of a HBr/Br<sub>2</sub> mixture (95%) and reduced with an excess amount of NaBH<sub>4</sub> to give 3,6-dibromo-1,2-phenylenediamine as pale yellow solid. The purified compound was condensed with 1,2-bis(4-tert-butylphenyl)ethane-1,2-dione in ethanol to afford 5,8-dibromoquinoxaline. In order to achieve *N*-(tert-butoxycarbonyl)-2-(tributylstannyl)pyrrole (2), pyrrole was *N*-protected by using di-tert-butyl dicarbonate (Boc)<sub>2</sub>O and reacted with tri-*n*-butylstannyl chloride after lithiation at the 2 position. Deprotection of pyrrole substituents in (3) after coupling reaction between (1) and (2) resulted in donor acceptor type monomer TBPPQ (Scheme 1).



**Scheme 1.** Synthetic route of monomer.

### 3.2. Electropolymerization

The potentiodynamic electropolymerization of monomer on ITO was performed in a 0.1 M TBAPC and  $1 \times 10^{-2}$  M TBPPQ solution applying potentials between 0.0 V and +1.0 V at a scan rate of 100 mV/s via multiple scan voltammetry. Due to the poor solubility of the monomer in acetonitrile (ACN), a mixture of ACN and dichloromethane (DCM) (95/5, v/v) was chosen as the solvent. The representative electrochemical growth revealing electroactivity of monomer TBPPQ and formation of corresponding insoluble polymer are given in Fig. 1. Polymerization was repeated on a Pt (1 cm  $\times$  1 cm) elec-

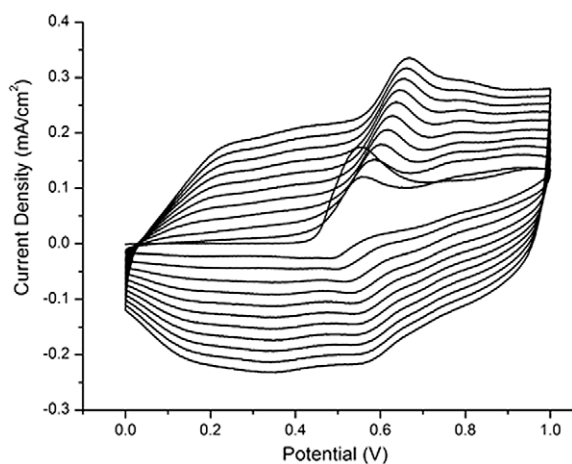


**Fig. 1.** Repeated potential scan electropolymerization of TBPPQ ( $10^{-2}$  M) at 100 mV/s in 0.1 M TBAPC in DCM/ACN (5/95, v/v) on ITO electrode vs Ag wire after 40 cycles.

trode to obtain a 20  $\mu$  thick free standing film for conductivity measurement ( $10^{-2}$  S/cm). The monomer oxidation potential was observed at 0.54 V (0.27 V vs Fc/Fc<sup>+</sup>), which is quite lower than the oxidation potentials of either of pyrrole, TBPEQ and HTQ. This observation can be attributed to a more effective D–A match. After the first cycle, an oxidation peak at 0.23 V and its reverse cathodic peak at 0.13 V appeared. These values are also quite lower than those for polypyrrole and PHTQ and comparable with PTBPEQ. A direct relation between current response and scan rate was observed for polymer film which proved that the film was well adhered on the electrode surface and electroactive (Fig. 2). The TBPPQ was coated on Pt wire potentiodynamically over 40 cycles from a 0.01 M monomer and 0.1 M TBAPC DCM/ACN (5/95, v/v) solution.

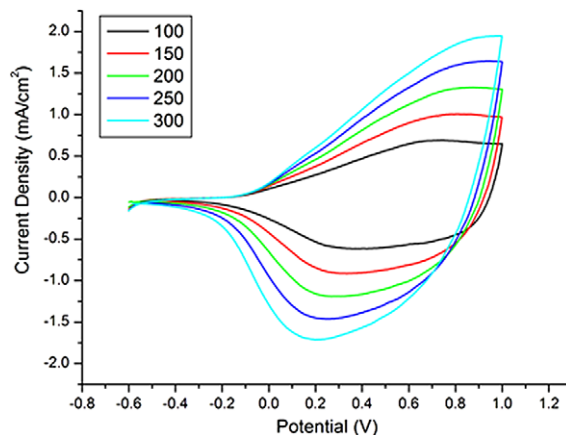


**Fig. 2.** Scan rate dependence of PTBPPQ film on Pt vs Ag wire in 0.1 M TBAPC/ACN (a) 100, (b) 150, (c) 200, (d) 250, (e) 300 mV/s.

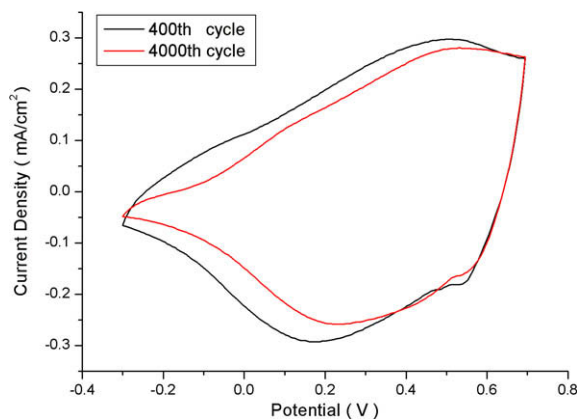


**Fig. 3.** Switching ability of PTBPPQ on ITO coated glass slide vs Ag wire in 0.1 M TPAPC/PC with a 200 mV/s scan rate at  $-0.5$  V and  $+1.0$  V.

Anodic and cathodic peak currents revealed a linear relationship as a function of scan rate for polymer film, indicating that electrochemical processes are not diffusion limited and reversible even at high scan rates [45,17].

The long-term switching stability is a severe requirement for electrochromic polymers due to their potential uses in numerous commercial applications, especially smart windows [46]. To investigate this characteristic, PTBPPQ film was deposited on ITO electrode with repeated scanning in TBAPC/DCM/ACN. The polymer film was washed with ACN to remove unreacted monomer, later cycled for 4000 times with a scan rate of 200 mV/s in 0.1 M TBAPC/propylenecarbonate (PC). The overall charge involved in the electrochemical process was calculated. Once the polymer electrochemical equilibration has been reached after 400 cycles, PTBPPQ showed 13% decrease upon cycling for 4000 times (Fig. 3).

### 3.3. Spectroelectrochemistry

Spectroelectrochemical studies were performed in order to monitor in situ optical changes upon doping. Spectral changes were recorded by UV–Vis–NIR spectrophotometer in a monomer free, 0.1 M TBAPC/ACN solution while varying the applied potential between  $-0.5$  V and  $+1.1$  V. Generally, donor acceptor type polymers show two distinct absorption maxima due to high energy and low energy  $\pi-\pi^*$  transitions [47]. As a donor acceptor polymer, PTBPPQ showed these absorption maxima due to the transitions from pyrrole based valence band to its antibonding counterpart as well as to the substituent localization narrow conduction band [48]. In order to achieve green color these absorption bands should be observed in the visible region at around 400 nm and 700 nm. PTBPPQ showed  $\pi-\pi^*$  transitions centered at 408 nm and 745 nm. As doping proceeds, formation of charge carriers leads to new absorption bands at 1100 nm and 1480 nm while absorptions for the neutral state are decreasing. This change represents the formation of polaron and bipolaron bands respectively [49]. The band gap of the polymer is 1.25 eV which was calculated from the onset of the second  $\pi-\pi^*$  transition. This value is in good agreement with values reported for the polymers having the same acceptor unit, with EDOT and 3-hexylthiophene as the donor units (PTBPEQ: 1.18 eV and PHTQ: 1.75 eV) [30,31]. Spectroelectrochemical studies for the polymer film showed that the color of the film changed from saturated green (Y:464, x:0.301, y:0.401) to brownish green (Y:492, x:0.309, y:0.358) during oxidation (Fig. 4). Coloration efficiency is the ratio between the injected/ejected charge per unit area of the electrode and the change in the optical density at a dominant wavelength. Coloration efficiency of the PTBPPQ was found to be  $85 \text{ cm}^2 \text{ C}^{-1}$  at 100% full switch at 408 nm.

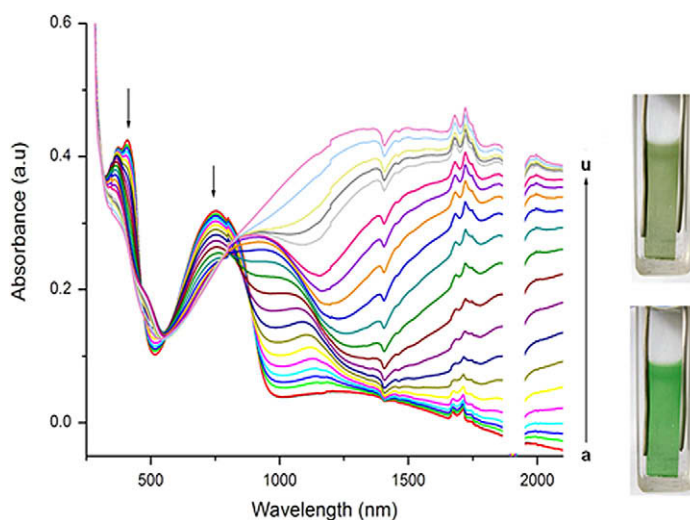


**Fig. 4.** Spectroelectrochemistry of PTBPPQ film on ITO-coated glass slide in a monomer free, 0.1 M TBAPC/ACN electrolyte–solvent couple at applied potentials (V) vs Ag wire: (a)  $-0.5$ , (b)  $-0.4$ , (c)  $-0.3$ , (d)  $-0.2$ , (e)  $-0.1$ , (f) 0.0, (g) 0.1, (h) 0.15, (i) 0.2, (j) 0.25, (k) 0.3, (l) 0.35, (m) 0.4, (n) 0.45, (o) 0.5, (p) 0.6, (q) 0.7, (r) 0.8, (s) 0.9, (t) 1.0, and (u) 1.1.



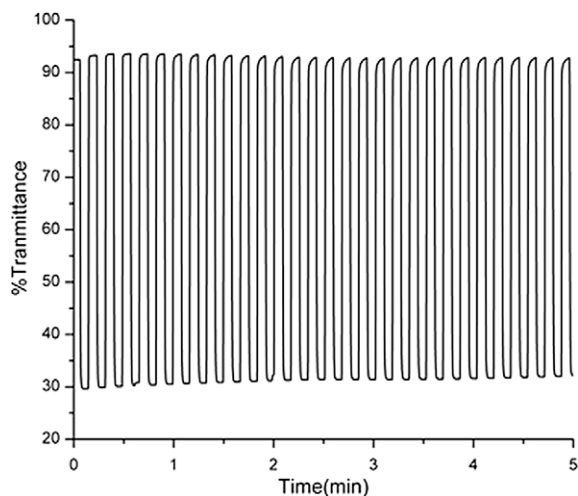


Fig. 5. Electrochromic switching, percent transmittance change monitored at 1480 nm for PTBPPQ in 0.1 M TBAPC/ACN.

### 3.4. Kinetic studies

In order to determine switching time and percent transmittance change ( $\Delta T\%$ ) of the polymer between neutral and oxidized states, it was polymerized on ITO coated glass slides. The polymer film was stepped between  $-0.5$  V and  $1.1$  V with a switching interval of 5 s in 0.1 M TBAPC/ACN while recording percent transmittance as a function of time (Fig. 5). PTBPPQ film showed 21% optical contrast at 408 nm and a 12% optical contrast at 745 nm. In the NIR region it showed a remarkable contrast of 65% which confirmed that it can be used for near-IR applications. A square-wave potential step method was used to calculate switching time. The polymer achieved 95% of its optical contrast in 0.6 s at 408 nm. At 745 nm, which corresponds to the second  $\pi$ - $\pi^*$  transition, switching time recorded as 0.3 s. In the near-IR region (1480 nm), polymer film showed a remarkably fast switching time of less than 0.2 s [50–52]. Kinetic studies for polymer film showed that PTBPPQ has not only a comparable optical contrast, but also faster switching times compare to its competitors, PTBPEQ [30] and PHTQ [31].

## 4. Conclusion

A novel pyrrole substituted quinoxaline monomer was synthesized via Stille coupling reaction. Monomer was electrochemically polymerized to investigate its potential use as a neutral state green electrochromic material. The polymer revealed high optical contrast in NIR region with excellent switching properties, and stability. PTBPPQ was shown to be one of the few examples of neutral state green polymeric materials in literature. Stability and very fast switching times make this neutral state green polymer a robust candidate for the completion of RGB color space. Considering these advanced properties, many quinoxaline derivatives can be utilized in the polymer backbone for synthesis of new superior polymers to be used in electrochromic devices.

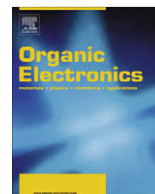
## Acknowledgments

We thank METU and TUBA for financial support.

## References

- [1] H. Shirakawa, E.J. Louis, A.G. MacDiarmid, C.K. Chinag, A.J. Heeger, *Chem. Commun.* 16 (1977) 578–580.
- [2] S. Osman, M. Senol, *Org. Electron.* 10 (1) (2009) 18–26.
- [3] D.T. McQuade, A.E. Pullen, T.M. Swager, *Chem. Rev.* 100 (2000) 2537–2574.
- [4] C. Lungenschmied, G. Dennler, H. Neugebauer, N.S. Sariciftci, T. Meyer, A. Meyer, *Sol. Energ. Mat. Sol. C* 91 (2007) 379–384.
- [5] G.G. Wallace, G.M. Spinks, L.A.P. Kane-Maguire, P.R. Teasdale, *Conductive Electroactive Polymers: Intelligent Materials Systems*, second ed., CRC Press LLC, New York, 2003.
- [6] N. Stutzman, R.H. Friend, H. Sirringhaus, *Science* 299 (2003) 299–384.
- [7] R. Schwendeman, R. Hickman, G. Sonmez, P. Schottland, K. Zong, D.M. Welsh, J.R. Reynolds, *Chem. Mater.* 14 (2002) 3119–3122.
- [8] A.A. Argun, P.H. Aubert, B.C. Thompson, I. Schwendeman, C.L. Gaupp, J. Hwang, N.J. Pinto, D.B. Tanner, A.G. MacDiarmid, J.R. Reynolds, *Chem. Mater.* 16 (23) (2004) 4401–4412.
- [9] M.M. Verghese, M.K. Ram, H. Vardhan, B.D. Malhotra, S.M. Ashraf, *Polymer* 38 (7) (1997) 1625–1629.
- [10] W.C. Dautremont-Smith, *Displays* 3 (1) (1982) 3–22.
- [11] S.A. Sapp, G.A. Sotzing, J.R. Reynolds, *Chem. Mater.* 10 (8) (1998) 2101–2108.
- [12] A. Kumar, D.M. Welsh, M.C. Morvant, F. Piroux, K.A. Abboud, J.R. Reynolds, *Chem. Mater.* 10 (3) (1998) 896–902.
- [13] L.B. Groenendaal, G. Zotti, P.H. Aubert, S.M. Waybright, J.R. Reynolds, *Adv. Mater.* 15 (11) (2003) 855–879.
- [14] G. Sonmez, H.B. Sonmez, C.K.F. Shen, R.W. Jost, Y. Rubin, F. Wudl, *Macromolecules* 38 (3) (2005) 669–675.
- [15] I. Schwendeman, R. Hickman, G. Sonmez, P. Schottland, K. Zong, D. Welsh, J.R. Reynolds, *Chem. Mater.* 14 (7) (2002) 3118–3122.
- [16] G. Sonmez, I. Schwendeman, P. Schottland, K. Zong, J.R. Reynolds, *Macromolecules* 36 (3) (2003) 639–647.
- [17] G. Sonmez, H. Meng, Q. Zhang, F. Wudl, *Adv. Func. Mater.* 13 (9) (2003) 726–731.
- [18] H.A.M. van Mullekom, J.A.J.M. Vekemans, E.E. Havinga, E.W. Meijer, *Mater. Sci. Eng. R32* (1) (2001) 1–40.
- [19] G.E. Gunbas, A. Durmus, L. Toppare, *Adv. Funct. Mater.* 18 (14) (2008) 2026–2030.
- [20] P.M. Beaujuge, S. Ellinger, J.R. Reynolds, *Nature Materials* 7 (10) (2008) 795–799.
- [21] M. Heeney, W. Zhang, D.J. Crouch, M.L. Chabinyc, S. Gordeyev, R. Hamilton, S.J. Higgins, I. McCulloch, P.J. Skabara, D. Sparrow, S. Tierney, *Chem. Commun.* 47 (2007) 5061–5063.
- [22] C.J. Du Boris, F. Larmat, D.J. Irvin, J.R. Reynolds, *Synth. Met.* 199(1–3) (2001) 321–322.
- [23] H.A.M. Mullekom, J.A.J.M. Vekemans, E.E. Havinga, E.W. Meijer, *Chem. Eur. J.* 4 (7) (1998) 1235–1243.
- [24] S. Tarkuc, E. Sahmetlioglu, C. Tanyeli, I.M. Akhmedov, L. Toppare, *Electrochim. Acta* 51 (25) (2006) 5412–5419.
- [25] S. Tarkuc, E. Sahmetlioglu, C. Tanyeli, I.M. Akhmedov, L. Toppare, *Sensors and Actuators B: Chemical* B121 (2) (2007) 622–628.
- [26] B. Yigitsoy, S. Varis, C. Tanyeli, I.M. Akhmedov, L. Toppare, *Thin Solid Films* 515 (7–8) (2007) 3898–3904.
- [27] E. Sahin, E. Sahmetlioglu, I.M. Akhmedov, C. Tanyeli, L. Toppare, *Org. Electron.* 7 (2006) 351–362.
- [28] G.A. Sotzing, J.L. Reddinger, A.R. Katritzky, J. Soloducho, R. Musgrave, J.R. Reynolds, *Chem. Mater.* 9 (1997) 1578–1587.
- [29] G.E. Gunbas, A. Durmus, L. Toppare, *Adv. Mater. (Weinheim, Germany)* 20(4) (2008) 691–695.
- [30] F. Ozyurt, E.G. Gunbas, A. Durmus, L. Toppare, *Org. Electron.* 9 (2008) 296–302.
- [31] Y.A. Udum, A. Durmus, G.E. Gunbas, L. Toppare, *Org. Electron.* 9 (2008) 501–506.
- [32] H.A.M. van Mullekom, J.A.J.M. Vekemans, E.W. Meijer, *Chem. Eur. J.* 4 (7) (1998) 1235–1243.
- [33] C. Kitamura, S. Tanaka, Y. Yamashita, *Chem. Mater.* 8 (1996) 570–578.
- [34] S.R. Tseng, S.Y. Li, H.F. Meng, Y.H. Yu, C.M. Yang, H.H. Liao, S.F. Horng, C.S. Hsu, *Org. Electron.* 9 (3) (2008) 279–284.
- [35] A. Balan, G. Gunbas, A. Durmus, L. Toppare, *Chem. Mater.* 20 (24) (2008) 7510–7513.

- [36] G. Sonmez, C.K.F. Shen, F. Rubin, F. Wudl, *Angew. Chem. Int. Ed.* 43 (12) (2004) 1498–1502.
- [37] A. Durmus, G.E. Gunbas, P. Camurlu, L. Toppare, *Chem. Commun.* 31 (2007) 3246–3248.
- [38] P.M. Beaujuge, S. Ellinger, R. Reynolds, *Adv. Mater.* 20 (14) (2008) 2772–2776.
- [39] A.B. Da Silveria Neto, A. Lopes Sant'Ana, G. Ebeling, S.R. Goncalves, E.V.U. Costa, H. F. Quina, J. Dupont, *Tetrahedron* 61(46) (2005) 10975–10982.
- [40] Y. Tsubata, T. Suzuki, T. Miyashi, Y. Yamashita, *J. Org. Chem.* 57 (25) (1992) 6749–6755.
- [41] A.I. Vogel, in: B.S. Furniss, A.J. Hannaford, P.W.G. Smith, A.R. Tatchell (Eds.), *Vogel's Textbook of Practical Organic Chemistry*, fifth ed., Longman Scientific & Technical, England, 1989.
- [42] G.Y. Han, P.F. Han, J. Perkins, H.C. McBay, *J. Org. Chem.* 46 (23) (1981) 4695–4700.
- [43] C. Chen, Y. Wei, J. Lin, M.V.R.K. Moturu, W. Chao, Y. Tao, C. Chen, *J. Am. Chem. Soc.* 128 (34) (2006) 10992–10993.
- [44] H. Salman, Y. Abraham, S. Tal, S. Meltzman, M. Kapon, N. Tessler, S. Speiser, Y. Eichen, *Eur. J. Org. Chem.* 11(2005) 2207–2212.
- [45] A. Kumar, D.M. Welsh, M.C. Morvant, F. Piroux, K.A. Abboud, J.R. Reynolds, *Chem. Mater.* 10 (3) (1998) 896–902.
- [46] H.W. Heuer, R. Wehrmann, J. Kirchmeyer, *Adv. Func. Mater.* 12 (2) (2002) 89–94.
- [47] U. Salzner, M.E. Kose, *J. Phys. Chem. B.* 106 (36) (2002) 9221–9226.
- [48] A. Berlin, G. Zotti, S. Zecchin, G. Schiavon, B. Vercelli, A. Zanelli, *Chem. Mater.* 16 (19) (2004) 3667–3676.
- [49] J.L. Bredas, R.R. Chance, R. Silbey, *Phys. Rev. B* 26 (10) (1982) 5843–5854.
- [50] J. Tarabek, P. Rapta, E. Jaehne, D. Ferse, H.J. Adler, M. Maumy, L. Dunsch, *Electrochim. Acta* 50 (7–8) (2005) 1643–1651.
- [51] L. Dunsch, N. Andreas, P. Rapta, *Fresenius J. Anal. Chem.* 367 (4) (2000) 314–319.
- [52] A. Cirpan, A.A. Argun, C.R.G. Grenier, B.D. Reeves, J.R. Reynolds, *J. Mater. Chem.* 13 (10) (2003) 2422–2428.



## Interface electronic structures of organic light-emitting diodes with WO<sub>3</sub> interlayer: A study by photoelectron spectroscopy

Min Jung Son<sup>a</sup>, Sehun Kim<sup>a,\*</sup>, Soonnam Kwon<sup>b</sup>, Jeong Won Kim<sup>c,\*</sup>

<sup>a</sup> Department of Chemistry and School of Molecular Science (BK 21), Korea Advanced Institute of Science and Technology, Daejeon 305-701, Republic of Korea

<sup>b</sup> Department of Materials chemistry, Sejong Campus, Korea University 339-700, Republic of Korea

<sup>c</sup> Korea Research Institute of Standards and Science, 1 Doryong-dong, Daejeon 305-340, Republic of Korea

### ARTICLE INFO

#### Article history:

Received 2 December 2008

Received in revised form 9 February 2009

Accepted 19 February 2009

Available online 3 March 2009

#### PACS:

73.20.-rj

73.30.+y

79.60.-i

#### Keywords:

Tungsten oxide

Hole injection layer

OLED

Photoelectron spectroscopy

### ABSTRACT

The energy level alignment and chemical reaction at the interface between the hole injection and transport layers in an organic light-emitting diode (OLED) structure has been studied using in-situ X-ray and ultraviolet photoelectron spectroscopy. The hole injection barrier measured by the positions of the highest occupied molecular orbital (HOMO) for *N,N'*-bis(1-naphthyl)-*N,N'*-diphenyl-1,1'-biphenyl-4,4'-diamine (NPB)/indium tin oxide (ITO) was estimated 1.32 eV, while that with a thin WO<sub>3</sub> layer inserted between the NPB and ITO was significantly lowered to 0.46 eV. This barrier height reduction is followed by a large work function change which is likely due to the formation of new interface dipole. Upon annealing the WO<sub>3</sub> interlayer at 350 °C, the reduction of hole injection barrier height largely disappears. This is attributed to a chemical modification occurring in the WO<sub>3</sub> such as oxygen vacancy formation.

© 2009 Elsevier B.V. All rights reserved.

### 1. Introduction

OLEDs (organic light-emitting diodes) are display devices composed of multiple organic layers that create light by electron-hole recombination. The improvement of OLED performance has been achieved by controlling the charge carrier injection and transport passing through each layer. The inorganic/organic interfacial contact in OLEDs is important to charge injection and transport characteristics since the choice of interlayer structure has a large influence on the electron/hole injection efficiency. For instance, by adopting ultrathin metal oxides such as SiO<sub>2</sub>, WO<sub>3</sub>, MoO<sub>3</sub>, and V<sub>2</sub>O<sub>5</sub> layers between the anode and the hole transport layer (HTL), the OLED performance could be largely enhanced [1–5].

Among them, tungsten trioxide (WO<sub>3</sub>) is lately drawing strong attention as a promising hole injection layer (HIL) since it has a very high work function (~6.2 eV) and is highly transparent in visible region [6]. The bulk structure of WO<sub>3</sub> has various phases at different temperatures. It is monoclinic at temperatures from 17 °C to 330 °C, orthorhombic from 330 °C to 740 °C, and tetragonal above 740 °C [7]. J. Meyer et al. reported that an OLED using the WO<sub>3</sub> layer exhibited a largely reduced operation voltage and its power efficiency was improved by about twice compared to the OLED without the WO<sub>3</sub> layer [6]. In addition, Li et al. reported that after thermal annealing WO<sub>3</sub> buffer layer at 450 °C, the structure of WO<sub>3</sub> was changed from amorphous to crystalline phase and consequently WO<sub>3</sub> further enhanced the device performance at the WO<sub>3</sub> thickness of 1.0 nm [8]. Also many other reports have shown that the WO<sub>3</sub> interlayer adopted as an HIL improved the device efficiency [9,10]. However, the mechanism for

\* Corresponding authors. Tel.: +82 42 868 5761 (J.W. Kim).

E-mail addresses: [sehun-kim@kaist.ac.kr](mailto:sehun-kim@kaist.ac.kr) (S. Kim), [jeongwonk@kriss.re.kr](mailto:jeongwonk@kriss.re.kr) (J.W. Kim).

this improvement is not clearly understood yet at the film interface level. Therefore the elucidation of the interfacial electronic structures between anode and organic semiconductor is necessary for understanding and further improving the device performance.

In this paper, we will show ultraviolet photoelectron spectroscopy (UPS) studies of the *N,N'*-bis-(1-naphyl)-*N,N'*-diphenyl-1,1'-biphenyl-4,4'-diamine (NPB)/indium tin oxide (ITO) interface, and the structure of a thin  $\text{WO}_3$  layer inserted between the NPB and ITO anode. We have studied the change in the electronic structures and the energy level alignment at each interface. Also, to investigate the structural and chemical changes of  $\text{WO}_3$  upon the annealing, X-ray photoelectron spectroscopy (XPS) is applied.

## 2. Experimental

The part of OLED structures used here were NPB/ $\text{WO}_3$  on ITO substrate, in which the NPB,  $\text{WO}_3$ , and ITO covered glass substrate were used as HTL, HIL, and anode, respectively. ITO coated glass had been cleaned by chemicals and undergone a UV ozone treatment before insertion into a chamber. After each deposition of a target film, the sample was transferred to an analysis chamber without exposing to air.  $\text{WO}_3$  layers were prepared below  $2.0 \times 10^{-7}$  Torr by thermal evaporation of  $\text{WO}_3$  powder (99.99% purity) in a crucible wound with W filament for heating. NPB film was also deposited similar way. The film thickness was controlled by a quartz crystal microbalance. The typical deposition rate was 0.1 Å/s. To investigate the influence of the  $\text{WO}_3$  structural change on the interface, the  $\text{WO}_3$  film was annealed in ultra high vacuum (UHV) at 350 °C for 15 min ( $P = 2.0 \times 10^{-8}$  Torr) and subsequently cooled down to room temperature. The heating temperature was measured by a thermocouple connected to the sample.

The experiments were performed in an UHV system consisting of a sample preparation chamber and analysis chamber. The UPS spectra were recorded on VG ESCALAB 220i system with a hemispherical electron energy analyzer using a HeI (21.2 eV) gas discharge lamp. And the samples were biased to  $-10$  and  $-5$  V for the measurement of secondary cutoff region and near Fermi level ( $E_F$ , binding energy = 0), respectively. For XPS measurement, a Mg  $K_{\alpha}$  (1253.6 eV) radiation was used as the excitation source. The XPS and UPS spectra were collected under normal emission.

A fitting procedure was performed on the W 4f spectra using an XPS curve fitting program. Each W 4f emission peak was fit with a doublet of Voigt functions with a constant branching ratio (0.75) and a spin-orbit splitting (2.12 eV) between  $4f_{7/2}$  and  $4f_{5/2}$ .

## 3. Results and discussion

Fig. 1 shows the UPS spectra of secondary cutoff for work function measurement, valence band region, and the zooming in near  $E_F$  region, respectively as a function of NPB thickness on ITO film. Upon the adsorption of NPB, the film work function gradually decreases to 4.08 eV at the NPB thickness of 2 nm in Fig. 1a. The total work function change measures 0.74 eV possibly due to the formation of interface dipole between NPB and ITO [11,12]. The NPB/ITO interface spectra in Fig. 1b clearly show a series of characteristic peaks for the valence band structure of NPB at 9.1, 7.0, and 4.0 eV as the NPB thickness increases. Those peak positions are in good agreement with the previous results for the molecular orbitals of the NPB film [13–15]. In particular, the highest occupied molecular orbital (HOMO) is mainly localized on the N-nonbonding orbitals. As shown in the near  $E_F$  region of

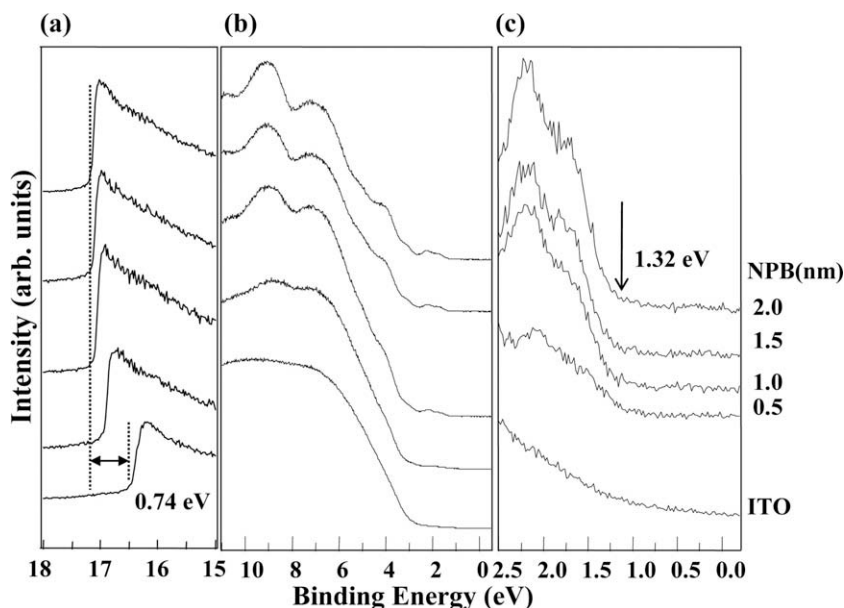


Fig. 1. UPS spectra as a function of NPB thickness on ITO substrates. (a) Secondary cutoff region, (b) valence band region and (c) near  $E_F$  region (arrow in graph: hole injection barrier height).

Fig. 1c, the HOMO level of NPB moves slightly to the high binding energy side as the layer thickens. This movement of the HOMO peak is not due to the charging of the NPB films, since a time-dependent measurement of UPS spectra does not show any change with irradiation time. Rather than that, the initial shift of the HOMO position is related to molecular orientation change and interface dipole formation at submonolayer regime. This means there is no serious misleading in determination of peak positions upto this film thickness. The hole injection barrier height, estimated by the difference between the onset of HOMO energy and the Fermi level ( $E_F$ ), is 1.32 eV at the 2 nm thickness. This value is readily in the range of previously reported results [1,5].

In the UPS spectra of  $WO_3$ /ITO interface in Fig. 2b, the increase of the  $WO_3$  layer thickness clearly shows new emission features at 4.5 and 6.4 eV. These peaks are attributed to O 2p-derived band (4.5 eV) and O 2p-W 5d hybridized states (6.4 eV), respectively [16]. Another weak feature near  $E_F$  in Fig. 2c is attributed to W 5d band, which is originated from imperfect stoichiometry of  $WO_3$  [16,17]. For  $WO_3$  layer thicker than 1.5 nm, the valence band region does not show any peak changes or new emission features. Since thicker  $WO_3$  films showed worse electrical performance [8], we concluded that the saturated behaviour in terms of UPS spectra at the  $WO_3$  thickness of 1.5 nm is a good choice for the platform for the following NPB deposition. Moreover, the work function of the  $WO_3$  film already reaches a high value of 6.26 eV at the thickness of 1.5 nm. When NPB is deposited on the  $WO_3$ /ITO layer, the secondary cutoff moves toward high binding energy by about 1.50 eV (Fig. 2a). The valence band spectra show different binding energies for NPB at 8.4, 6.3, and 3.3 eV in Fig. 2b.

The overall energy shift by 0.7 eV toward the low binding energy side is observed in comparison with NPB/ITO case in Fig. 1b. In case of  $MoO_3$ , Lee et al. observed a gap state at 0.15 eV for 0.1 and 0.3 nm of NPB on  $MoO_3$  in HOMO region [5]. But there is no such new emission peak in NPB/ $WO_3$ /ITO film in Fig. 2c. The most remarkable change is the hole injection barrier height of NPB, which is largely decreased to 0.46 eV by the insertion of  $WO_3$  layer (Fig. 2c). The origin of this result will be discussed in Fig. 6. In addition we could observe the barrier height of 0.24 eV at the  $WO_3$ /ITO interface.

As mentioned before, the  $WO_3$  has various bulk phases at different temperatures and its structure transformation influences the electrical properties of an OLED film [8]. To investigate any change of interfacial electronic structure of  $WO_3$  due to high temperature treatment, UHV annealing was performed at 350 °C for 15 min after 1.5 nm of  $WO_3$  deposition on ITO. As shown in the Fig. 3a, the total shift of the secondary cutoff position of NPB on the annealed  $WO_3$  is 0.59 eV. Fig. 3b shows that the valence band spectra of  $WO_3$  and NPB/ $WO_3$  become broadened and overall peaks are largely attenuated by the annealing of  $WO_3$  film. On the other hand, the very small peak close to the  $E_F$  on  $WO_3$  gains intensity upon annealing. Since this peak is attributed to W 5d state [16,17], its intensity increase means the partial reduction of W atoms. This change is consistent with W 4f core level spectra, as discussed below. In addition, the hole injection barrier for the annealed  $WO_3$  is decreased to 0.06 eV in Fig. 3c. However, the energy difference between the HOMO of NPB (2 nm) and the  $E_F$  is increased to 1.50 eV. In addition, other high binding peaks are shifted back to 9.5, 7.4, and 4.4 eV in comparison with those in Fig. 2b.

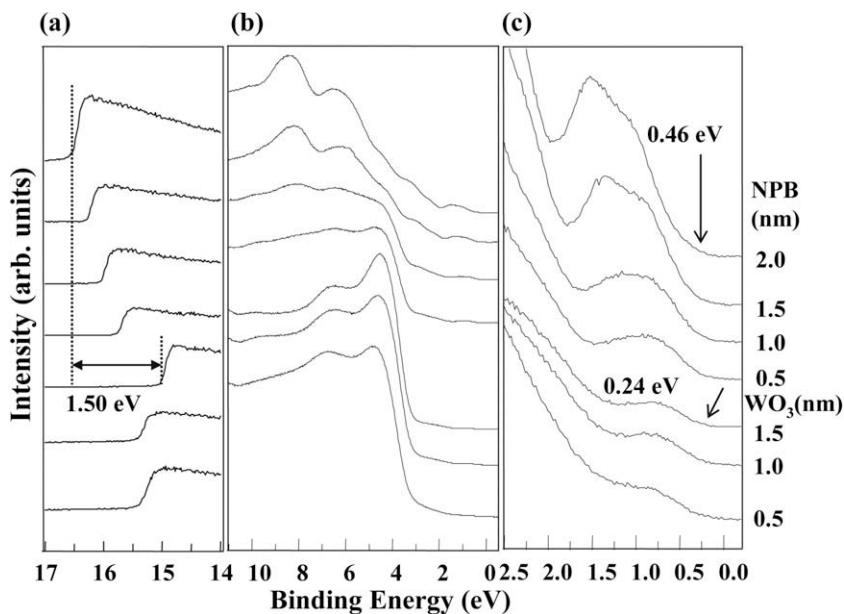
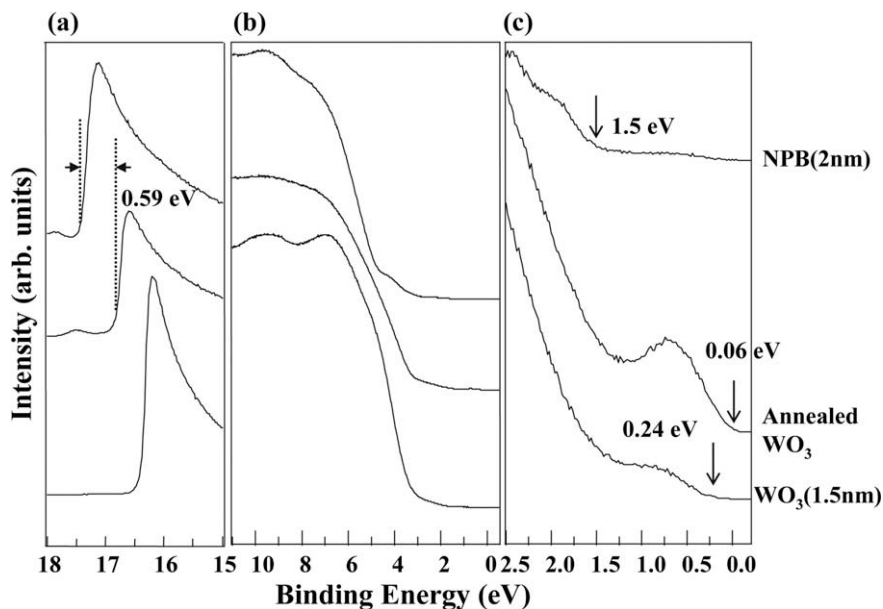
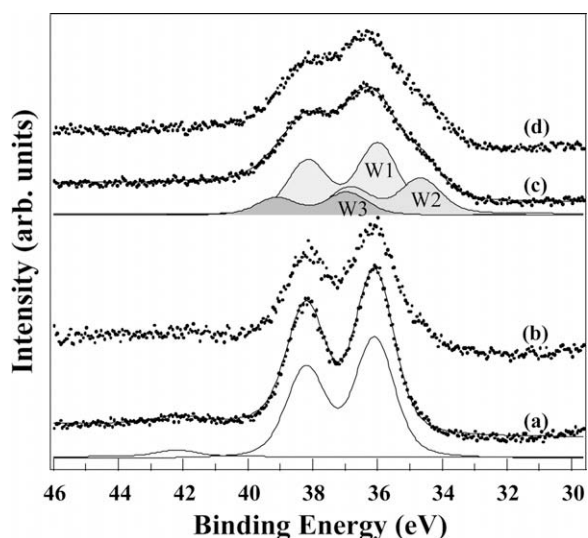


Fig. 2. UPS spectra of NPB/ $WO_3$ /ITO interface. (a) Secondary cutoff region, (b) valence band region and (c) near  $E_F$  region (arrows in graph: whole injection barrier heights).



**Fig. 3.** UPS spectra for  $WO_3$  films on ITO before and after annealing, and 2 nm of NPB on the annealed  $WO_3$ . (a) Secondary cutoff region, (b) valence band region and (c) near  $E_F$  region (arrows in graph: hole injection barrier heights).

To look into the reason for the above changes induced by the  $WO_3$  interlayer, we carried out XPS experiments. Fig. 4 shows the XPS core level spectra of W 4f for different multilayer films. As prepared by thermal deposition in Fig. 4a, the W 4f spectrum presents a sharp doublet peak at 36.09 eV ( $4f_{7/2}$ ) and a broad  $5p_{3/2}$  core level peak approximately at 42 eV. These peak positions have been assigned to the  $WO_3$  compound in  $W^{6+}$  chemical state [16–20]. When NPB film is deposited on the  $WO_3$  layer, the W 4f peak shape and position do not change at all,



**Fig. 4.** XPS core level spectra of W 4f peak and their peak fittings for (a)  $WO_3/ITO$ , (b) NPB/ $WO_3/ITO$ , (c) annealed  $WO_3/ITO$ , and (d) NPB/annealed  $WO_3/ITO$  interfaces.

but its intensity is slightly attenuated as shown in Fig. 4b. After annealing the  $WO_3$  film under UHV, the W 4f peak becomes broad with a clear shoulder on the low binding energy side in Fig. 4c. In similar way, the  $5p_{3/2}$  peak area can be regarded negligible in fitting the spectra hereafter. The W 4f peak is fitted by three different components at the  $4f_{7/2}$  binding energies of 35.98 (W1), 34.66 (W2), and 36.93 eV (W3). This spectral change and peak decomposition upon the annealing are consistent with the previous study where the  $WO_3$  film is annealed in UHV at high temperatures or exposed to synchrotron beam radiation [16,17]. The peak position for the W1 component remains at the same position for the  $W^{6+}$  of the  $WO_3$  as before annealing. On the other hand, the new species W2 indicates reduced W atoms in  $WO_{3-x}$ . This is also confirmed by the decrease of O 1s intensity after annealing (not shown here). The third component W3 has been attributed to the inhomogeneities in barrier height on the surface [17,21]. The defect formation on the surface or at the  $WO_3/ITO$  interface leads to the charge localization, so the barrier height inhomogeneities increase because the photoelectrons become difficult to be emitted from the surface. A common defect in  $WO_3$  film is oxygen vacancy, which induces negative charge accumulation in order to compensate the electronegative oxygen ion vacancy. Such charge makes up a donor-like level below conduction band minimum, which forms a  $E_F$  at a different position. This is why the W3 is located at the higher binding energy than that for  $W^{6+}$ .

Upon the deposition of NPB molecules even on the annealed  $WO_3$ , the W 4f does not show any change in Fig. 4d. This and the above result in Fig. 4b mean that there are no chemical reactions between NPB and  $WO_3$  layers whether the  $WO_3$  film is annealed or not. These results present that the existence of oxygen vacancies and conse-

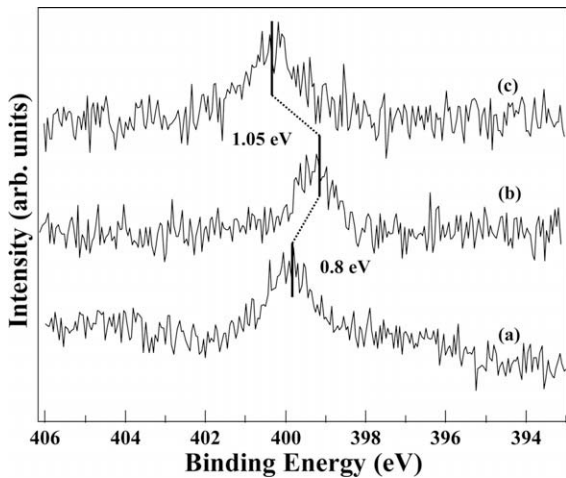


Fig. 5. XPS core level spectra of N 1s for (a) NPB/ITO, (b) NPB/WO<sub>3</sub>/ITO, (c) NPB/annealed WO<sub>3</sub>/ITO interfaces.

quent formation of WO<sub>3-x</sub> component are not related with chemical reaction between NPB and annealed WO<sub>3</sub>.

Specifically, due to the annealing-induced reduction WO<sub>3-x</sub> species have relatively low electronegativity compared with WO<sub>3</sub> state, thus, the charge density is expected to increase at the NPB. Therefore the reduction of tungsten significantly causes the charge redistribution of the interface dipole between NPB and annealed WO<sub>3</sub> layer.

To further investigate how the annealed WO<sub>3</sub> layer affects the electronic structure of NPB, we performed XPS measurement of N 1s core level. The N 1s core level peaks for three different films with NPB layer are shown in Fig. 5. The N 1s peak for NPB film on ITO surface is located at 399.89 eV in Fig. 5a. But its position on the WO<sub>3</sub>/ITO in Fig. 5b is shifted to 399.09 eV without any change in peak shape. When the NPB is deposited on annealed WO<sub>3</sub> in

Fig. 5c, the N 1s peak moves back to 400.14 eV by the shift of 1.05 eV (Fig. 5b and c). This binding energy shift is almost same as the valence band energy shift of about 1.1 eV as already shown in Fig. 3b. These remarkable changes demonstrate the rearrangement of electronic charge between NPB and annealed WO<sub>3</sub> due to the formation of new chemical states such as WO<sub>3-x</sub>.

From the above experimental results, the interfacial energy level diagrams are summarized in Fig. 6. The average value for the work functions of ITO surfaces used here is 4.82 eV. In the energy level alignment diagram at the NPB/ITO interface, the barrier height for the hole injection, corresponding to the energy difference between the HOMO of NPB and the  $E_F$  of the ITO, is 1.32 eV in Fig. 6a. However, the NPB/WO<sub>3</sub>/ITO interface shows a different vacuum level ( $E_{vac}$ ) and a small hole injection barrier because the WO<sub>3</sub> interlayer has a large work function (6.0–6.5 eV) in Fig. 6b. When NPB is deposited on the WO<sub>3</sub>/ITO, the WO<sub>3</sub> is suggested to draw charge from the NPB because the NPB is relatively strong electron donor. Therefore there forms an additional dipole layer between NPB and WO<sub>3</sub> as well as WO<sub>3</sub>/ITO interface. Due to the large  $E_{vac}$  shift, the HOMO level of NPB also moves near to the  $E_F$  level. Therefore the hole injection barrier is remarkably reduced to 0.46 eV by the insertion of WO<sub>3</sub> layer between NPB and ITO. This demonstration was supported by binding energy shifts of valence band and N 1s core level, respectively, in Figs. 2 and 5. In case of NPB/WO<sub>3</sub>/ITO interface, the total up shift of HOMO level in Fig. 6a and b is 0.86 eV which is comparable to the N 1s binding energy shift from NPB/ITO to NPB/WO<sub>3</sub>/ITO interfaces in Fig. 5. From this energy level alignment we can conclude that the thin WO<sub>3</sub> layer plays a strong role in reducing the total barrier height for hole injection. Therefore this is the main reason for the reduction of the operation voltage and high power efficiency in the organic electroluminescence by WO<sub>3</sub> inter-layer [6].

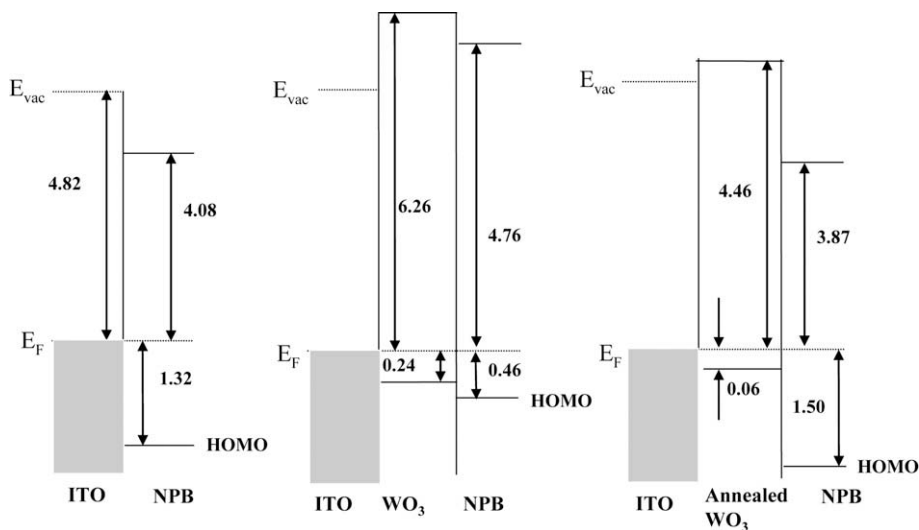


Fig. 6. Schematics of energy level alignment diagrams at the interfaces (a) NPB/ITO, (b) NPB/WO<sub>3</sub>/ITO, and (c) NPB/WO<sub>3</sub> (after annealing)/ITO interfaces from UPS.

In case of annealed WO<sub>3</sub> film, the net barrier height for hole injection is increased to 1.50 eV in Fig. 6c. As mentioned before, this result was due to the redistribution of electron charge at the interface between annealed WO<sub>3</sub> and NPB. The annealing of WO<sub>3</sub> layer produces various chemical states due to the oxygen vacancy formation. This nonstoichiometric WO<sub>3-x</sub> formation upon annealing is supported by the increased intensity of W 5d band in Fig. 3c, and the appearance of W2 and W3 species in Fig. 4c. On consequence, the work function of the WO<sub>3</sub> surface is reduced and the  $E_{\text{vac}}$  level of NPB is shifted back toward the  $E_{\text{F}}$  level. By the modification of energy level at the interface, the HOMO energy level of NPB is pulled down. Therefore annealed WO<sub>3</sub> would not improve the hole injection at the interfaces under the present scheme. The previous report argued that a high temperature annealing (450 °C) in air brings out a better performance in OLED characteristics [8]. The reason was explained by a positive structural change, which was in favor of electrical conduction. However, its actual enhancement in  $I$ – $V$  curves was marginal probably due to a small change in work function (0.27 eV). Thus, the device performance will be determined by the various factors such as interface energy level alignment shown here and electrical conductivity of films.

An exact interpretation of structural change of ultrathin (1.5 nm) WO<sub>3</sub> film upon annealing is far from practical. However, from previous literatures where thick films (>100 nm) undergo marginal change in structure up to 400 °C annealing [17–19,22], one can assume that the structural change is not severe, as a relatively low-temperature annealing at 350 °C has been performed here. If a strong structural change took place upon the 350 °C annealing, the intensities of substrate In 3d and/or W 4f core levels would change significantly. But such changes were not observed in this experiment. Instead, relatively low-temperature annealing at 350 °C in UHV brings out stoichiometric change of the WO<sub>3</sub> film and possibly micro-crystallization.

#### 4. Conclusion

We have shown by photoelectron spectroscopy that with a thin WO<sub>3</sub> layer inserted between the NPB and ITO films, the hole injection barrier height was significantly lowered from 1.32 eV to 0.46 eV. This phenomenon is followed by a large work function change which is likely due to the formation of new interface dipole layer. This result explains well the reduction of the operation voltage and enhancement in power efficiency observed in OLEDs with WO<sub>3</sub> interlayer. Upon UHV annealing of the WO<sub>3</sub>

interlayer at 350 °C, the hole injection barrier was largely increased back to 1.50 eV. When the WO<sub>3</sub> layer is annealed, an oxygen vacancy is formed and various chemical states of tungsten oxide are generated. Therefore, the stoichiometry and defects inside the tungsten oxide film largely influence the energy level alignment at the NPB/WO<sub>3</sub> interface.

#### Acknowledgement

This work was supported by the Brain Korea 21 project (BK21) and KOSEF grant funded by MEST (No. R01-2006-000-10920-0), Korea Research Foundation Grant (No. KRF-2005-070-C00063), and Korea Research Foundation Grant (No. KRF-2006-312-C00565).

#### References

- [1] X.M. Ding, L.M. Hung, L.F. Cheng, Z.B. Deng, X.Y. Hou, C.S. Lee, S.T. Lee, *Appl. Phys. Lett.* 76 (2000) 2704.
- [2] S.W. Cho, K.-H. Yoo, K. Jeong, C.-N. Whang, Y. Yi, M. Noh, *Appl. Phys. Lett.* 91 (2007) 052102.
- [3] H. You, Y. Dai, Z. Zhang, D. Ma, *J. Appl. Phys.* 101 (2007) 026105.
- [4] Z.B. Deng, X.M. Ding, S.T. Lee, W.A. Gambling, *Appl. Phys. Lett.* 74 (1999) 2227.
- [5] H. Lee, S.W. Cho, K. Han, P.E. Jeon, C.-N. Whang, K. Jeong, K. Cho, Y. Yi, *Appl. Phys. Lett.* 93 (2008) 043308.
- [6] J. Meyer, S. Hamwi, T. Bulow, H.-H. Johannes, T. Riedl, W. Kowalsky, *Appl. Phys. Lett.* 91 (2007) 113506.
- [7] Erik Lassner, Wolf-Dieter Schubert, *Tungsten: Properties, Chemistry, Technology of the Element, Alloys, and Chemical Compounds*, Kluwer Academic, New York, 1999.
- [8] J. Li, M. Yahiro, K. Ishida, H. Yamada, K. Matsushige, *Synth. Met.* 151 (2005) 141.
- [9] C.-C. Chang, S.-W. Hwang, C.H. Chen, J.F. Chen, *Jpn. J. Appl. Phys.* 43 (2004) 6418.
- [10] K.S. Yook, S.O. Jeon, C.W. Joo, J.Y. Lee, *Appl. Phys. Lett.* 93 (2008) 013301.
- [11] Q.T. Le, F. Nüesch, L.J. Rothberg, E.W. Forsythe, Y. Gao, *Appl. Phys. Lett.* 75 (1999) 1357.
- [12] P. He, S.D. Wang, W.K. Wong, C.S. Lee, S.T. Lee, *Appl. Phys. Lett.* 79 (2001) 1561.
- [13] B. Lu, H.J. Zhang, H.Y. Li, S.N. Bao, P. He, *Phys. Rev. B* 68 (2003) 125410.
- [14] L.S. Liao, L.F. Cheng, X.H. Sun, N.B. Wong, C.S. Lee, S.T. Lee, *Chem. Phys. Lett.* 370 (2003) 425.
- [15] R.Q. Zhang, C.S. Lee, S.T. Lee, *J. Chem. Phys.* 112 (2000) 8614.
- [16] G. Hollinger, R.M. Duc, A. Deneuville, *Phys. Rev. Lett.* 37 (1976) 1564.
- [17] F. Bussolotti, L. Lozzi, M. Passacantando, S. La Rosa, S. Santucci, L. Ottaviano, *Surf. Sci.* 538 (2003) 113.
- [18] L. Lozzi, L. Ottaviano, M. Passacantando, S. Santucci, C. Cantalini, *Thin Solid Films* 391 (2001) 224.
- [19] T.G.G. Maffei, D. Yung, L. LePennec, M.W. Penny, R.J. Copley, E. Comini, G. Sberveglieri, S.P. Wilks, *Surf. Sci.* 601 (2007) 4953.
- [20] F.J. Himpsel, J.F. Morar, F.R. McFeely, R.A. Pollack, G. Hollinger, *Phys. Rev. B* 30 (1984) 7236.
- [21] R. Cimino, A. Giarante, K. Horn, M. Pedio, *Surf. Sci.* 331 (1995) 534.
- [22] G.R. Jafari, A.A. Saberi, R. Azimirad, A.Z. Moshfegh, S. Rouhani, *J. Stat. Mech.* (2006) P09017.





## Crystal structure and charge-transport properties of *N*-trimethyltriindole: Novel p-type organic semiconductor single crystals

Eva M. García-Frutos<sup>a</sup>, Enrique Gutierrez-Puebla<sup>a</sup>, M. Angeles Monge<sup>a</sup>, Rafael Ramírez<sup>a</sup>, Pedro de Andrés<sup>a</sup>, Alicia de Andrés<sup>a</sup>, Rafael Ramírez<sup>b</sup>, Berta Gómez-Lor<sup>a,\*</sup>

<sup>a</sup> Instituto de Ciencia de Materiales de Madrid, CSIC, Cantoblanco, E-28049 Madrid, Spain

<sup>b</sup> Departamento de Física, Escuela Politécnica Superior, Universidad Carlos III de Madrid, Avenida Universidad 30, 28911, Madrid, Spain

### ARTICLE INFO

#### Article history:

Received 12 January 2009

Received in revised form 19 February 2009

Accepted 21 February 2009

Available online 3 March 2009

#### PACS:

71.20.Rv

72.20.Ee

72.80.Le

#### Keywords:

Hole transport

Organic semiconductor

Single crystals

### ABSTRACT

We report on a new p-type organic semiconductor single crystal, 5,10,15-trimethyl-10,15-dihydro-5*H*-diindolo[3,2-*a*:3',2'-*c*]carbazole (*N*-trimethyltriindole). This molecule crystallizes forming a highly ordered columnar structure in which stacked molecules are situated at two alternating distances (3.53 Å and 3.68 Å) along the column as determined by single crystal X-ray diffraction analysis. These short intermolecular distances between adjacent units, make this system an ideal candidate for charge-transport processes along the stacks.

Relevant parameters for transport (i.e. internal reorganization energies, transfer integral) have been estimated by DFT calculations at a 6-311G(d,p)/B3LYP level of theory. As a double check for the transfer integral, the electronic band structure of a one-dimensional stack of molecules has been computed. The electronic properties of this material have been studied both theoretically and experimentally. Its HOMO value is found to coincide with Au work function ( $\Phi_{\text{Au}} = 5.1$  eV), thus low barriers are expected for hole injection from gold electrodes. The hole mobility of this material has been predicted theoretically considering a hopping-type mechanism for the charge-transport and determined experimentally at the space charge limited current (SCLC) regime of the current–voltage measurements. Both theoretical and experimental values are in good agreement. The high hole mobility ( $\mu_{\text{min}} = 0.4$  cm<sup>2</sup> V<sup>-1</sup> s<sup>-1</sup>) of this material points towards its useful application in the organic electronics arena. *N*-Trimethyltriindole single crystals constitute an essential model to study transport properties of triindole-based materials and to design new derivatives with improved electronic performance.

© 2009 Elsevier B.V. All rights reserved.

## 1. Introduction

The field of organic electronics has experienced in a few years a rapid development moving from a basic research level to the construction of molecule-based devices that are already commercially viable [1]. These devices have in common that their performance depend on how efficiently the charge carriers are injected and transported in the different organic active layers. Therefore, important

advances achieved in this field have been connected to the enhancement of the charge carrier mobility of the organic molecules. However the incorporation of organic molecules in the electronic devices shows still serious stability and processability limitations. At this stage one of the main needs is to find new stable organic semiconducting materials.

In the quest for new molecular conducting systems, two-dimensional polycyclic aromatics (with extended  $\pi$ -conjugated systems) are among the best candidates. This type of molecules tend to form highly ordered structures due to self-assembly facilitated by strong  $\pi$ – $\pi$ -interactions, paving the way for increased charge mobility in

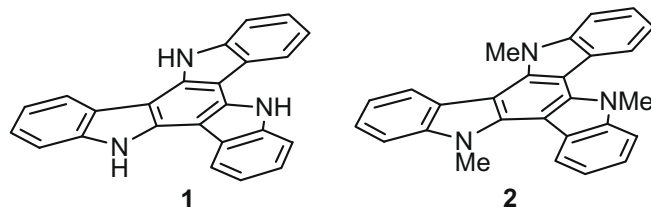
\* Corresponding author. Fax: +34 91 3349031.

E-mail address: [bgl@icmm.csic.es](mailto:bgl@icmm.csic.es) (B. Gómez-Lor).

the bulk of the material as the result of a favorable intermolecular  $\pi$ -orbital overlap. In close relation with the supramolecular order, the highest charge carrier mobility is usually obtained in organic single crystals [2]. Furthermore, organic single crystals offer an excellent opportunity to investigate structure-properties relationships and to elucidate charge-transport mechanism in organic materials [3]. In response to this need a large effort is being made to find new classes of crystalline charge carrier transport organic materials, even if the realization of devices based in single crystal implies important technological challenges [4].

In this context we became interested on the electron-rich 10,15-dihydro-5*H*-diindolo[3,2-*a*:3',2'-*c*]carbazole (triindole, **1**). This molecule can be formally considered as an extended  $\pi$ -system in which three carbazole units share an aromatic ring (Scheme 1). The particular relation of this polycyclic aromatic system to the well known hole transporter carbazole [5], together with its  $\pi$ -extended structure render triindoles attractive candidates for organic electronics. Curiously, in contrast with its all carbon analogue truxene [6,7] this platform has been very scarcely studied in the context of molecular electronics [8]. We have found that triindole-based discotic liquid crystals exhibit high charge mobility values ( $\mu \sim 0.03 \text{ cm}^2 \text{ V}^{-1} \text{ s}^{-1}$ ) in the mesophases since they combine its inherent donor character with the supramolecular organization typical of disc-like mesogens [9]. Additionally, we have recently reported that it is possible to optimize the electronic as well as the self assembly properties of this platform through functionalization of its peripheral positions [10].

In this paper we describe the synthesis, crystal structure, and the electronic properties of *N*-trimethyltriindole (**2**) (Scheme 1) a molecule that crystallizes forming a highly ordered columnar structure, with short intermolecular distances between adjacent units within the stacks yielding a high hole mobility system. The electronic properties of this material have been studied both theoretically and experimentally. Quantum mechanical calculations have been performed to investigate the electronic structure and to determine relevant parameters for charge-transport such as internal reorganization energies and hole transfer integral. The hole mobility of this material has been predicted theoretically considering a hopping-type mechanism for the charge-transport and determined experimentally at the space charge limited current (SCLC) regime of the current–voltage measurements. Both theoretical and experimental values are in good agreement.



Scheme 1.

## 2. Results and discussion

### 2.1. Synthesis and molecular properties

The synthesis of *N*-methyltriindole (**2**) was straightforward by deprotonation of triindole (**1**) with *n*-BuLi and trapping of the trianion with MeI. The thermal stability of **2** has been determined by thermal gravimetric analysis (TGA) and differential scanning calorimetry (DSC), this material is thermally stable up to 400 °C (see Supplementary Material, Fig. S1). In order to estimate the value of the HOMO level, the electron-donating nature and redox stability of **2**, cyclic voltammetry has been performed. Compound **2** shows two reversible oxidation waves at 761 mV and 1370 mV vs. Ag/Ag<sup>+</sup> in the accessible potential window of the solvent (CH<sub>2</sub>Cl<sub>2</sub>) reflecting its oxidation to a stable cation radical and subsequent generation of further oxidized species. From the first oxidation process an HOMO energy value of  $-5.11 \text{ eV}$  can be estimated for **2**. This value matches very well with the work function of gold ( $\Phi_{\text{Au}} = 5.1 \text{ eV}$ ) and therefore low barriers are expected for hole injection (see Supplementary Material, Fig. S2).

The electronic properties of **2** have also been studied by UV–vis absorption (Fig. 1). The absorption spectrum of a  $10^{-5} \text{ M}$  solution of **2** in CHCl<sub>3</sub> shows the maximum absorption at 3.89 eV (319 nm) and the lowest transition at 3.35 eV (370 nm). From this lowest transition a HOMO–LUMO energy gap 3.35 eV can be estimated [11].

In order to determine the effect of chemical oxidizing agents on the molecular electronic levels of this molecule (doping), the oxidation of **2** with trifluoroacetic acid (TFA) has been monitored by UV–vis spectroscopy. TFA has been extensively used as a one-electron oxidant to generate radical cations [12], even though there is controversy about how the oxidation actually occurs [13]. Thus, addition of 10 equivalents of (TFA) to a  $10^{-5} \text{ M}$  CHCl<sub>3</sub> solution of **2**, increases the intensity of the 3.06 eV band (Fig. 1) while the intensity of the bands corresponding to the neutral species decreases. This absorption band is related to oxidized molecules, whose gap between HOMO and LUMO energy levels has therefore varied by about 0.3 eV. For concentrations of oxidant above 20 equivalents two new bands can be distinguished around 3.17 and 1.72 eV corresponding to further oxidized species.

### 2.2. Crystal structure

Long needle-like hexagonal colorless crystals of **2** suitable for single crystal X-ray analysis were obtained from

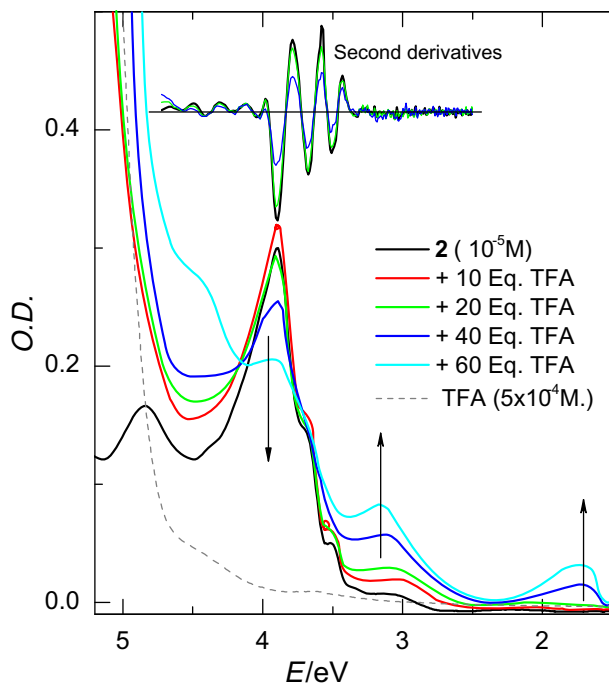


**Fig. 1.** Evolution of the UV-vis absorption of **2** in  $\text{CHCl}_3$  as a function of TFA content. The spectrum in dashed line corresponds to a  $5 \times 10^{-4}$  M of TFA in chloroform and is the origin of the steep optical density (O.D.) increase above 4 eV as the TFA content increases. The upper inset shows the second derivatives of the neutral solution and two oxidized stages.

slow evaporation of an  $\text{CH}_2\text{Cl}_2$ :acetone (3:1) solution. X-ray analysis indicates that the triindole core is slightly twisted, with the three peripheral rings bending ( $\sim 8^\circ$ ) out of the plane of the central aromatic ring (Fig. 2). The

methyl groups are slightly out of the molecular plane in an all-*syn* conformation [ $\delta$  (C5-C4-N1-C9):  $-18.5^\circ$ ].

Compound **2** crystallizes in *R*-3 space group, forming stacks along the crystallographic *c*-axis (Fig. 3). Each stack

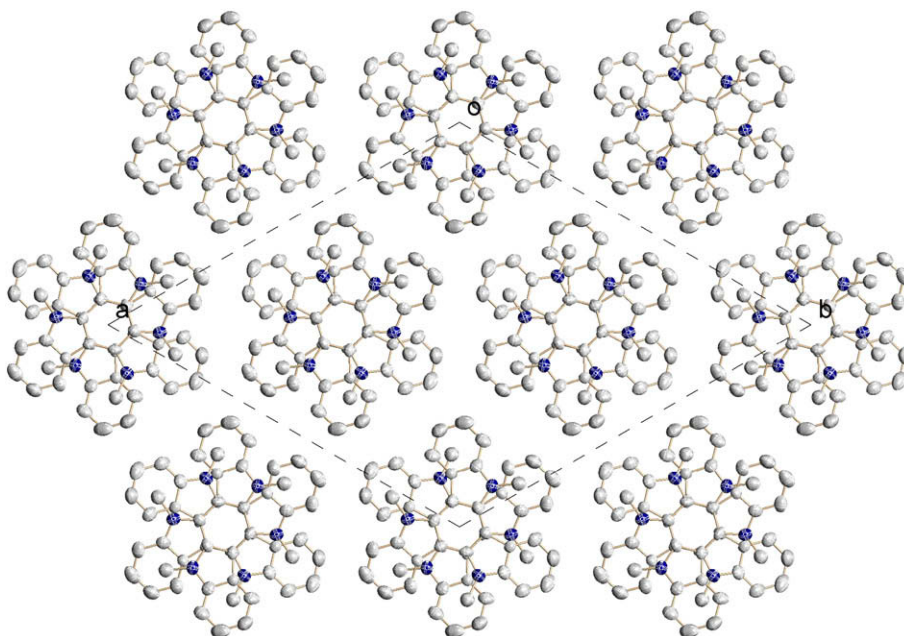


**Fig. 2.** ORTEP representation of **2**.

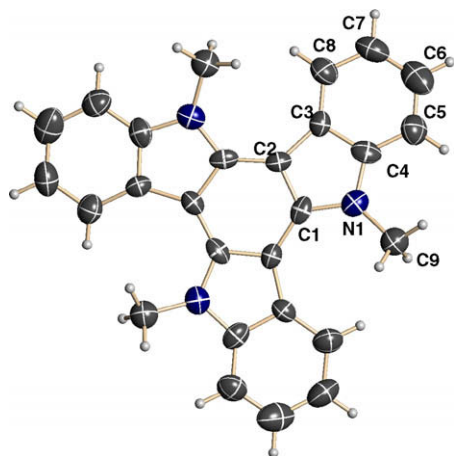


Fig. 3. View of the unit cell along the *c*-axis of **2**.

is surrounded by six neighbouring stacks that interact only through weak Van der Waals forces.

Within the stacks the molecules are oriented face-to-face in an alternate arrangement, one molecule rotated  $60^\circ$  with respect to the next molecular unit, being the central aromatic rings perfectly superimposable. Such a perfect cofacial arrangement between aromatics is rarely observed since repulsive interactions involving approaching  $\pi$ -electron clouds are generally minimized through parallel displacement resulting normally in an offset stack [14]. The triindole units are situated at two different distances that alternate along the column reflecting the steric hindrance by the methyl groups. The centroid–centroid distance of the central aromatic rings of two adjacent molecules are  $3.53 \text{ \AA}$  ( $d_S$ ) and  $3.68 \text{ \AA}$  ( $d_L$ ) respectively (Fig. 4).

The short intermolecular distances between adjacent units observed experimentally by X-ray analysis, as well as the easy reversible oxidation of *N*-trimethyltriindole make this system an ideal candidate for charge-transport studies along the stacks.

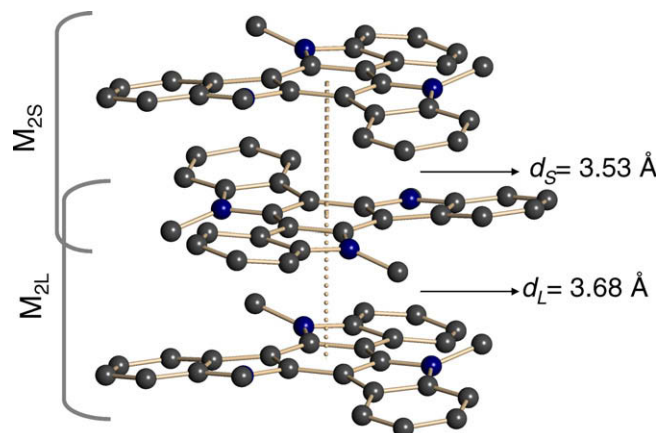


Fig. 4. Side view of the *N*-trimethyltriindole stacks displaying the two different intermolecular distances.

### 2.3. Electronic structure calculations

Quantum mechanical methods have been used to analyze the electronic structure, the equilibrium geometry and the electronic density distribution of neutral and oxidized (+1) molecules in order to determine important parameters for charge-transport (internal reorganization energies and hole transfer integral) and estimate the hole mobility of this compound.

The electronic structure of a single *N*-trimethyltriindole molecule **2** both in its neutral (M) and charged state (M<sup>+</sup>) have been optimized by density functional calculations (DFT) at a 6-311G(d,p)/B3LYP level of theory. The obtained optimized molecular structure of **2** compares well with the experimental structure derived from the X-ray data, the largest difference between theory and experiment being found in the dihedral angles that measure the deviation of the methyl groups from the molecular plane [ $\delta$  (C5–C4–N1–C9):  $-18.5^\circ$  (exp.),  $-25.3^\circ$  (calc.)]. This is probably due to the lack of intermolecular steric effects (packing effects) in the geometry optimization of the isolated molecule [15].

The energies of the HOMO and LUMO levels have been derived from the DFT calculations of the neutral molecule M. The HOMO level is found at  $-5.01 \text{ eV}$ , in good agreement with the value obtained from cyclic voltammetry ( $-5.11 \text{ eV}$ ). In contrast the predicted HOMO–LUMO gap ( $4.25 \text{ eV}$ ) results larger than the value obtained experimentally by UV–vis spectroscopy ( $3.35 \text{ eV}$ ).

The Mulliken analysis of the electronic charge distribution of **2** is displayed in Fig. 5a. The largest negative net charge ( $-0.55 e$ ) is found at the N positions, while the largest positive net charge ( $0.22 e$ ) is found at the three C atoms of the central benzene ring that are bonded to the N atoms. Carbon atoms with partial positive and negative charge alternate in the central aromatic ring, resulting in a charge distribution that is probably responsible for the perfect columnar arrangement observed in the solid state. Thus a close inspection of the crystal packing shows that the experimental configuration of the closest neighbouring

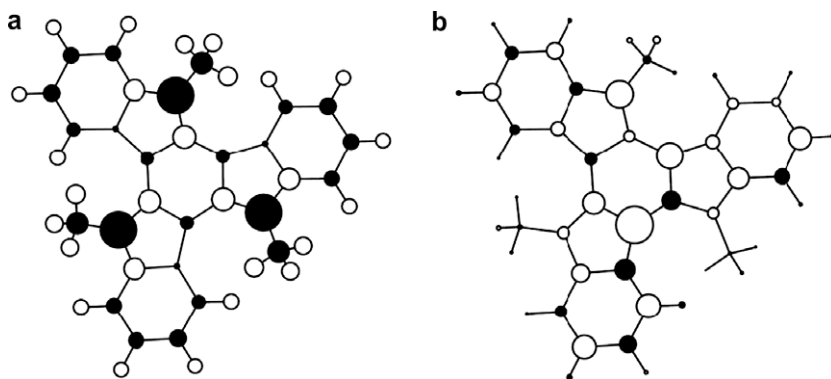


**Fig. 5.** (a) Mulliken population analysis of the electronic charge density at the atomic centers of M. The size of the circles is proportional to the calculated net charge. Black solid circles represent negative charge while empty circles are associated to the positive charges. (b) Mulliken population analysis of the spin density at the atomic centers of  $M^+$ . The size of the circles is proportional to the calculated spin density.

molecules (Fig. 4), results in the approach of atoms with partial charges of opposite sign.

We have performed a Mulliken population analysis of the spin density of the oxidized molecule  $M^+$  (Fig. 5b). The largest spin density is located on one of the nitrogen positions and on the C atom of the central aromatic ring in para to the former nitrogen (approximately 0.26 e). However extensive delocalization of the unpaired electron density on all the atomic centers can be observed explaining the stability of the cation radical as revealed from the easy reversible oxidation of *N*-trimethyltriindole.

The geometry optimization of *N*-trimethyltriindole in its cationic state,  $M^+$ , shows a molecular distortion due to the Jahn–Teller coupling between the electronic and vibrational degrees of freedom. This coupling originates from the fact that the HOMO of *N*-trimethyltriindole is a two-fold degenerated electronic state that belongs to the irreducible representation *E* of the  $C_3$  point group. The analysis of the Jahn–Teller distortion shows that specific C–C and C–N bonds in  $M^+$  become larger or smaller than in the neutral state, M. Interestingly, enlargement of bonds in  $M^+$  correlate with the presence of in-phase bonding amplitudes in the HOMO of the neutral molecule M, while shortening of bonds in  $M^+$  are related to the presence of nodal planes in the HOMO of M. This behaviour is illustrated in Fig. 6, where we compare one of the *E* components of the HOMO for the neutral molecule M (Fig. 6a), with the Jahn–Teller distortion of  $M^+$  (Fig. 6b) by presenting, for those bond distances with largest variation, the difference between the equilibrium values found in  $M^+$  and M.

#### 2.4. Hole mobility calculations

At room temperature, the hole mobility of organic semi-conducting materials is often described by a hopping process [16], where the transport mechanism between neighbouring molecules can be formulated as a hole transfer by the equation



where M and  $M^+$  play the role of electron donor and electron acceptor molecules, respectively.

The hole-transfer rate,  $k_t$ , can be approximated by the Marcus electron-transfer theory [17] with the equation

$$k_t = \frac{4\pi^2}{h} \frac{1}{\sqrt{4\pi K_B T}} t^2 \exp\left(-\frac{\lambda}{4K_B T}\right) \quad (2)$$

where  $h$  and  $K_B$  are Planck's and Boltzmann's constants,  $T$  is the temperature,  $t$  is the electronic transfer integral between the donor and acceptor molecules, and  $\lambda$  is the reorganization energy for hole transfer between both molecules. Therefore the transport process, is determined by two important molecular parameters: the internal reorganization energy ( $\lambda$ ) which needs to be small for an efficient charge-transport and the intermolecular hole transfer integral ( $t$ ) which describes the strength of the electronic coupling between adjacent molecules [16].

The reorganization energy for hole transfer,  $\lambda$ , is the sum of two contributions,  $\lambda_1 + \lambda_2$ , that are defined as

$$\lambda_1 = E_0(M^+) - E_0(M) \quad (3)$$

$$\lambda_2 = E_1(M) - E_1(M^+) \quad (4)$$

where  $E_0(M^+)$  and  $E_0(M)$  represent the energies of the neutral molecule at the cation geometry and at the optimal ground-state geometry respectively.  $E_1(M)$  and  $E_1(M^+)$  represent the energy of the charged state at the neutral geometry and optimal cation geometry, respectively.

Using the DFT optimized molecular configurations for M and  $M^+$  we found the values  $\lambda_1 = 123$  meV and  $\lambda_2 = 113$  meV, giving an estimate for the  $\lambda$  value for hole transport in this molecule of 236 meV.

The hopping integral for intermolecular hole transfer,  $t$ , can be estimated from the energy splitting between the electronic level HOMO,  $e_H$ , and the HOMO-1,  $e_{H-1}$ , taken from the closed-shell configuration of the neutral state of a dimer  $M_2$  by the relation

$$t = \frac{e_H - e_{H-1}}{2} \quad (5)$$

The value of the transfer integral  $t$  depends strongly on the molecular configuration of the dimer. As shown in Fig. 4, in the crystal of *N*-trimethyltriindole two alternating  $M_{2S}$  and  $M_{2L}$  dimer configurations can be observed. The electronic structure of both *N*-trimethyltriindole dimers

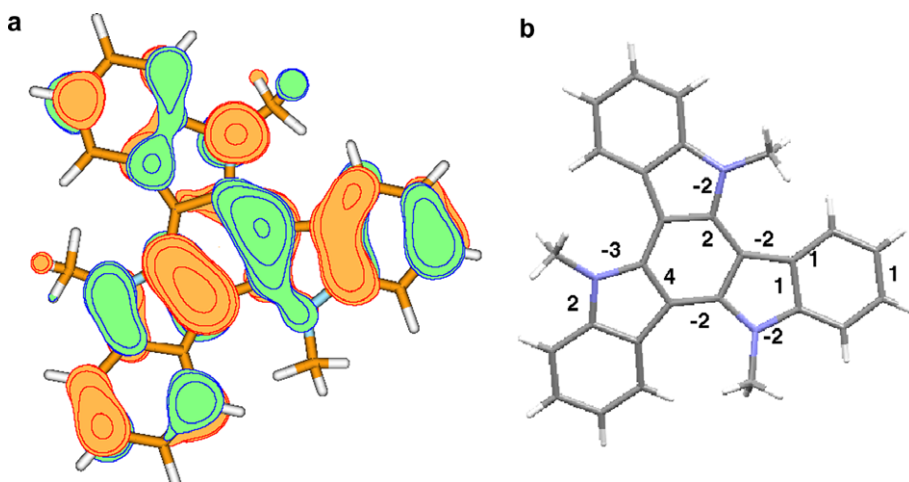


**Fig. 6.** (a) Isosurface representation for the HOMO wavefunction of **2** in its neutral state M. Only one component of the two-fold degenerate *E* molecular orbital is shown. The interval between contour lines is  $25 \times 10^{-8} \text{ \AA}^{-3/2}$ . (b) Changes in the bond distances in pm (0.01 Å) found for the optimized structure of *N*-trimethyltriindole in its cationic state, *M*<sup>+</sup>, with respect to the neutral state M. Only distances modified by more than 1 pm are shown. The Jahn–Teller coupling is responsible for this structural change.

has been studied by DFT in order to obtain the value of the transfer integral for both configurations. However in a crystal the charge mobility will be most likely controlled by the smaller value of the transfer integral, corresponding to the *M*<sub>2L</sub> configuration.

Fig. 7 shows the value of *t* as derived from the optimized *M*<sub>2L</sub> configuration (solid line) vs the separation between the molecular units, as well as the results obtained by using the experimental *M*<sub>2L</sub> dimer configuration found in the crystal structure (dashed line). Both sets of results show very similar behaviour. However the optimized structure provides values for the transfer integral, *t*, slightly smaller than the derived from the experimental dimer configuration. This is probably related to the larger deviation from planarity found in the optimized structure

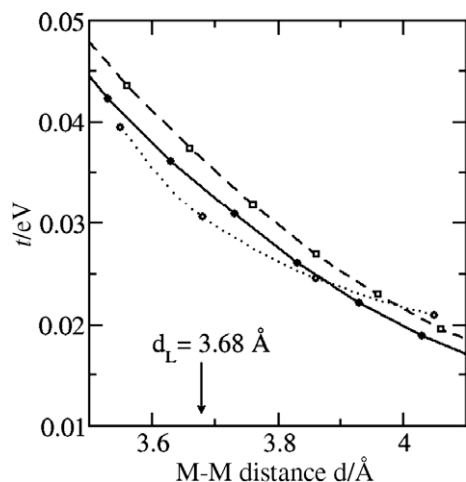


**Fig. 7.** Comparison of the evolution of the hole transfer integral, as a function of the distance, calculated for the optimized structure of the triindole dimer *M*<sub>L</sub> (solid line), the experimental structure of the dimer *M*<sub>L</sub> (dashed line) and a one-dimensional stack of triindole units (dotted line).

when compared with the experimental one, due to the lack of packing effects.

The transfer integral, *t*, depends on the geometrical parameters and plays an important role in our theoretical predictions. Therefore, we double checked the value of *t* performing a band structure calculation for a stack of molecules forming a quasi-1D crystal (Fig. 4). From these calculations the transfer integral has been obtained as half of the bandwidth. Fig. 7 (dotted line) displays *t* vs. the distance *d*<sub>L</sub>. Taking into account the approximations involved in the model, the agreement with our previous calculations based on localized basis and a different prescription for exchange and correlation is remarkable.

The calculated values of *t* and  $\lambda$  allows us to derive the transfer rate of holes, *k*<sub>t</sub>, as a function of temperature from the Marcus expression in Eq. (2). For the purpose of estimating the hole-transfer rate we have taken the value of *t* corresponding to the optimized dimer geometry at the experimental intermolecular distance of 3.68 Å (*t* = 34 meV).

By considering the expression for the diffusion coefficient associated to a one-dimensional jumping process.

$$D = K_B d_L^2 \quad (6)$$

the hole mobility,  $\mu$ , can then be obtained from the following expression

$$\mu = eD/kT \quad (7)$$

where *e* is the electron charge. At 300 K we obtain a transfer rate, *k*<sub>t</sub>, of  $4 \times 10^{12} \text{ s}^{-1}$  and a corresponding hole mobility of  $0.21 \text{ cm}^2 \text{ V}^{-1} \text{ s}^{-1}$ .

## 2.5. Electrical measurements

The electrical conductivity of *N*-trimethyltriindole crystals was measured along the crystallographic *c*-axis, which coincides with the longest direction of the needle-like single crystals, in a two contact configuration by gluing a sin-

gle crystal with silver paint to two gold electrodes (distance between electrodes 2 mm). A value of  $\sigma = 2 \times 10^{-7} \text{ Ohm}^{-1} \text{ cm}^{-1}$  at 298 K has been obtained (Fig. 8a).

Upon exposure to different oxidizing vapours,  $\text{HNO}_3$  or trifluoroacetic acid (TFA), the conductivity increases several orders of magnitude depending on the oxidation time (Fig. 8b). External oxidation would remove electrons from the HOMO level of *N*-trimethyltriindole increasing the hole density (doping) explaining the observed variations of the conductivity. Non-linearity in the  $I$ - $V$  curves was detected for heavily oxidized crystals. The observed complex  $I$ - $V$  behaviour, which could not be analysed straightforwardly with the usual conduction mechanisms, is probably related to deficiencies of the contacts regarding their stability and the control of the oxidation effects on the interfaces. However an ohmic behaviour of the resistance is evidenced for as grown crystals, as well as for lightly oxidized crystals,

for applied voltages up to 800 V. Both as grown and oxidized crystals, show a temperature activated conductivity (90–500 K) indicating the predominance of a polaron hopping mechanism in this system as invoked in the previously shown theoretical calculations

Because of the relatively high conductivity of the crystals, in order to measure the mobility, we needed to obtain the high electric field regime and therefore to shrink the distance between the electrodes. Also, to reduce possible problems arising from silver paint contacts and from deficient crystal–gold interfaces, several single crystals were grown directly on a glass substrate with previously deposited Cr/Au electrodes (distance between electrodes 200  $\mu\text{m}$ ). This configuration allowed us to measure the high field  $I$ - $V$  characteristics and to observe the space charge limited current (SCLC) regime. The results for as grown crystals are shown in Fig. 9. Trace (a) is the measured current which shows the ohmic behaviour at low voltages (dashed line). This observation indicates that non-linearities due to Schottky barriers at the interfaces are negligible as a result of the good alignment of the work function of the gold electrode with the HOMO level of the

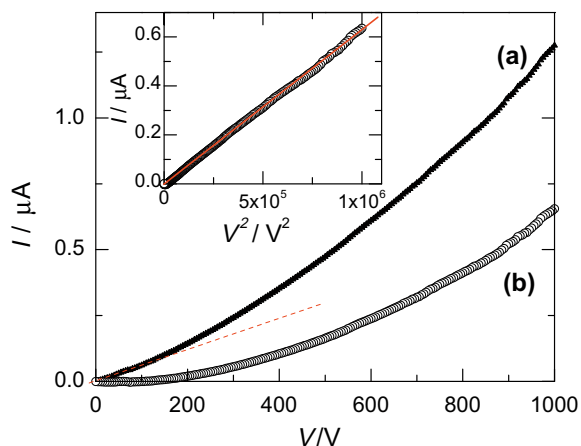


Fig. 9. (a)  $I$ - $V$  curve of the as grown crystals. The dashed line corresponds to the ohmic part. (b) Non linear part of the current. The upper inset shows the  $V^2$  dependence of the current.

*N*-trimethyltriindole. By subtracting this ohmic contribution from the measured current we obtain trace (b). The  $I$ - $V^2$  plot (inset) evidences the typical behaviour of the space charge limited current (SCLC) regime where the Mott–Gurney equation [18] applies:

$$J = \frac{9\varepsilon_0\varepsilon\mu V^2}{8L^3} \quad (8)$$

$J$  is the measured current density,  $\varepsilon_0$  is the vacuum permittivity,  $\varepsilon$  is the relative dielectric constant of the material (we have used the commonly estimated value for organic materials of 3),  $\mu$  is the charge mobility,  $L$  is the distance between the contact electrodes and  $V$  is the applied voltage. In this configuration several crystals are connecting the gold electrodes. Therefore, in order to calculate the current density  $J$ , the section for conduction has been estimated from the resistance in the linear regime and the resistivity previously determined for an isolated crystal.

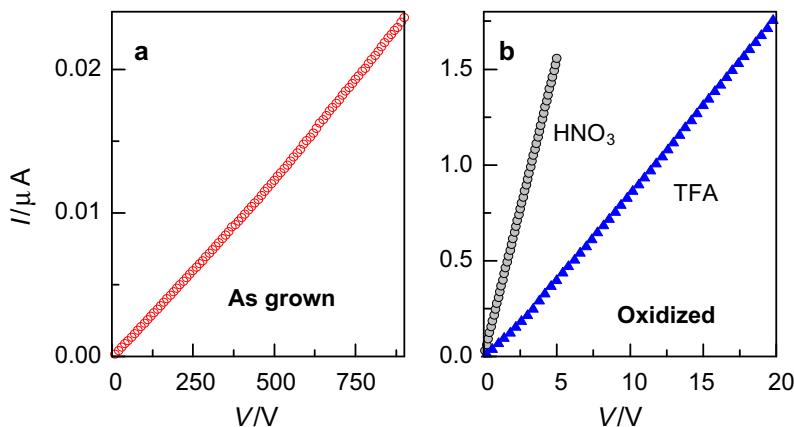


Fig. 8. (a)  $I$ - $V$  measurements at room temperature of as grown crystals and (b) of crystals lightly oxidized upon exposure to  $\text{HNO}_3$  and TFA vapours for 10 min.

Although our measurements are performed on pure single crystals, it is likely that shallow traps play a role, therefore the Mott–Gurney law is only expected to provide a lower limit for the mobility ( $\mu_{min}$ ). The linear fit on the  $I-V^2$  curve, gives a value of  $\mu_{min} = 0.4 \text{ cm}^2 \text{ V}^{-1} \text{ s}^{-1}$ , in reasonable agreement with the value predicted by our calculations using the Marcus electron-transfer theory ( $\mu = 0.21 \text{ cm}^2 \text{ V}^{-1} \text{ s}^{-1}$ ).

### 3. Conclusion

In summary, the positive synergy between molecular structure (electron-rich, extended  $\pi$ -system) and bulk arrangement (close packing, efficient intermolecular  $\pi$ -orbital overlap) results in the construction of a novel high hole mobility crystalline material.

The title molecule crystallizes forming a highly ordered columnar structure, with short intermolecular distances between adjacent units, favouring the charge-transport along the stacks and resulting in the high measured mobility ( $0.4 \text{ cm}^2 \text{ V}^{-1} \text{ s}^{-1}$ ). The structure and electronic states, as well as the relevant parameters governing the charge-transport, as internal reorganization energies, transfer integral and hole mobility, have been calculated. This theoretical analysis agrees well with our experiments and supports the interpretation of our results.

This single crystalline material fulfils many conditions for a good organic hole transport in the construction of devices namely: (i) its HOMO value almost coincides with the Au work function, (ii) its mobility is high, (iii) the conductivity can be increased by several orders of magnitude by doping, and (iv) its energy gap lies above the visible range which is necessary for combining it with optical active materials in order not to absorb the visible excitation or emission energies.

The interesting electrical properties obtained for this material along with the synthetic versatility of this platform make heptacyclic triindoles promising candidates in the search for new tunable organic semiconductors. *N*-Trimethyltriindole single crystals constitute an indispensable model to study transport properties of this new type of compounds and in the design of new triindole derivatives with optimal semiconductor properties.

## 4. Experimental section

### 4.1. Synthesis and characterization of 5,10,15-trimethyl-10,15-dihydro-5H-diindolo[3,2-a:3',2'-c]carbazole (**2**) [19]

To a stirred solution of **1** (170 mg, 0.5 mmol) in THF (3 mL) at  $-80^\circ\text{C}$  was added *n*-BuLi (2.0 M pentane, 110  $\mu\text{L}$ , 1.78 mmol). The reaction was stirred for 1 h ( $-78^\circ\text{C} \rightarrow -10^\circ\text{C}$ ). Then, methyl iodide (153  $\mu\text{L}$ , 2.46 mmol) was added and the mixture was stirred for 1 h. The mixture was diluted with  $\text{CH}_2\text{Cl}_2$  and washed with water and with saturated aqueous NaCl solution, dried ( $\text{Na}_2\text{SO}_4$ ) and evaporated. The residue was triturated with acetone to give **2** as a white solid (149 mg, 77 %): mp  $> 230^\circ\text{C}$ ;  $^1\text{H}$  NMR (300 MHz,  $\text{CDCl}_3$ )  $\delta$  8.44 (d,  $J = 8.1 \text{ Hz}$ , 3 H), 7.57 (d,  $J = 7.5 \text{ Hz}$ , 3 H), 7.45 (t,  $J = 7.4 \text{ Hz}$ ,

3 H), 7.34 (t,  $J = 8.0 \text{ Hz}$ , 3 H), 4.43 (s, 9 H);  $^{13}\text{C}$  NMR ( $\text{CDCl}_3$ , 50 MHz)  $\delta$  141.93, 139.06, 122.89, 122.79, 121.74, 119.62, 109.66, 102.55, 35.92; FAB-MS  $m/z$  (%) 387 ( $\text{M}^+$ , 49), 307 (36), 154 (100). HR MS (FAB) calcd. for.  $\text{C}_{27}\text{H}_{21}\text{N}_3$  387.1735, found 387.1737.

### 4.2. Cyclic voltammetry measurements and determination of the HOMO energy value

Cyclic voltammetric (CV) experiments were performed on an Epsilon Electrochemical Analyzer in a three electrode cell (Pt working electrode) at room temperature, under nitrogen atmosphere. Electrochemical measurements were performed in a millimolar  $\text{CH}_2\text{Cl}_2$  solution of **2** containing 0.1 M of recrystallized supporting electrolyte tetra-*n*-butylammonium hexafluorophosphate (TBAPF<sub>6</sub>). Potentials were measured against Ag/AgCl as reference electrode. A large area coiled Pt wire was used as a counter electrode. The measurement was calibrated using a ferrocene/ferrocenium redox system as an internal standard by adding a equimolar amount of ferrocene and then measuring the complete voltamogram.

The HOMO energy value for **2** was calculated from the first oxidation potential value with respect to ferrocene, based on the value of  $-4.8 \text{ eV}$  for Fc with respect to zero vacuum level. This value is obtained from the calculated value of  $-4.6 \text{ eV}$  for the standard electrode potential ( $E^\circ$ ) using a normal hydrogen electrode (NHE) [20] on the zero vacuum level and the value of 0.2 V for Fc vs. NHE [21].

### 4.3. UV-vis spectrometry

UV-vis spectrometry analyses were performed in a Varian-Cary 4000 spectrophotometer.

### 4.4. X-ray structure determinations

Colorless crystals of **2** showing well defined faces were mounted on a Bruker Smart CCD diffractometer equipped with a normal focus, 2.4 kW sealed-tube X-ray source ( $\text{MoK}\alpha$  radiation,  $\lambda = 0.71067 \text{ \AA}$ ) operating at 50 kV and 20 mA. Data were collected over a hemisphere of the reciprocal space by a combination of three exposure sets. Each exposure of 10 s covered  $0.3^\circ$  in  $\omega$  over the range  $2^\circ < \theta < 28^\circ$ . The first 100 frames were recollected at the end of the data collection to monitor crystal decay. The intensities were corrected for Lorentz and polarization effects. The structures were solved by the Multan and Fourier methods.

Crystal dimensions:  $0.30 \times 0.20 \times 0.20 \text{ mm}^3$ , unit cell dimensions  $\mathbf{a} = 21.4897(11)$ ,  $\mathbf{c} = 7.2102(5) \text{ \AA}$ ,  $\gamma = 120(0)^\circ$ ,  $\mathbf{V} = 2883.6(3) \text{ \AA}^3$ ,  $\mathbf{Z} = 6$ , hexagonal, *R*-3 space group,  $\rho$  calcd.  $1.339 \text{ Mg/m}^3$ . **2** was refined anisotropically  $R1(\text{F}) = 0.0912$  for observed data ( $I > 2\sigma(I)$ ),  $R1(\text{F}) = 0.1185$  for all data;  $\text{GOF}(\text{F}^2) = 1.11$ .

Most of the calculations were carried out with SMART [22] software for data collection and reduction, and SHELXTL [23] for structure solution and refinements of **2**. CCDC 670066 contains the supplementary crystallographic data for **2**. These data can be obtained free of charge via [www.ccdc.cam.ac.uk/conts/retrieving.html](http://www.ccdc.cam.ac.uk/conts/retrieving.html) (or from the



Cambridge Crystallographic Data Centre, 12 Union Road, Cambridge CB21EZ, UK; (fax: +44 1223 336 033; or e-mail: deposit@ccdc.cam.ac.uk).

#### 4.5. Theoretical methods and computational details

The electronic structure of a single *N*-trimethyltriindole molecule, both for its neutral (M) and charged (M<sup>+</sup>) states, as well as the electronic structure of *N*-trimethyltriindole dimers (M<sub>2</sub>) have been studied using the Gaussian program package [24]. The ground state geometries have been optimized by density functional theory (DFT) with the B3LYP functional to approximate the exchange and correlation energy [25] and the standard 6-311G(d,p) basis set [26]. Optimization of the neutral molecule M has been performed by applying constraints compatible with the C<sub>3</sub> point group symmetry, while for the cationic state, M<sup>+</sup>, no symmetry constraints were imposed. For dimer configurations, we have optimized the ground state geometry by constraining the point symmetry of the dimer to the S<sub>6</sub> group, which is the symmetry observed in the *N*-trimethyltriindole crystal.

To compute the electronic band structure of a one-dimensional stacking of *N*-trimethyltriindole monomers density functional theory [27] was used within the generalized-gradient approximation [28] with a plane-waves basis set and norm-conserving pseudopotentials. Band structure calculations for the quasi-1D crystal have been performed using the CASTEP code [29]. Periodic boundary conditions are used to fill the space by repeating a basic unit cell. A kinetic energy cutoff of 30 Ry has been used to define the number of plane-waves in the basis, and the Brillouin zone has been sampled with four points equally spaced along the  $\Gamma$ -X direction [30]. Norm-conserving pseudopotentials have been chosen because their good performance to describe molecules and materials made with N, C and H atoms.

A rhombohedral unit cell is constructed including 102 atoms representing two molecules separated by  $d_s$  and oriented face-to-face as previously described. On the plane of the dimer the unit cell is defined by fixed length vectors ( $a = b = 25 \text{ \AA}$ ,  $60^\circ$ ), while in the perpendicular direction we optimize the distance between unit cells ( $c = d_s + d_L$ ,  $90^\circ$ ). All atoms, and the  $c$  distance, are allowed to relax until forces and stresses are below 0.2 eV/Å and 0.3 GPa respectively. The symmetry group P-3 (C3 1-1) has been imposed throughout the optimization. The resulting geometry is comparable to the experimental one, predicting a slightly shorter inner distance between molecules ( $d_s = 3.51 \text{ \AA}$ , 0.5% off from the experimental value) and a larger value on the outer side ( $d_L = 3.86 \text{ \AA}$ , 5% off). In this cell, lateral interactions between long threads for molecules are negligible.

#### 4.6. Electrical measurements

DC electrical conductivity was measured along the crystallographic  $c$ -axis which coincides with the long edge of the needle-like single crystals using a Keithley 2410 1100 V sourcemeter for current measurements and power

supply. The typical cross section of the crystals is  $0.1 \times 0.1 \text{ mm}^2$  and their length is up to 10 mm.

To perform resistance measurements in wide temperature ranges, it was necessary to maintain only one end of the crystal glued to the sample holder of the cryostat. The other end was only attached to the Pt wire. First attempts to measure the resistance gluing both ends to the sample holder result in the breaking of the crystal due to the different expansion coefficients of both materials.

#### Acknowledgements

This work was supported by the MCyT projects MAT 2006-60822, MAT 2005-3866, CTQ2007-65683/BQU, FIS2006-12117-C04-03, and consolider-ingenio CSD2006-0015 and NANOSELECT. E.M.G.F. thanks the CSIC for a post-doctoral contract (Program I3P).

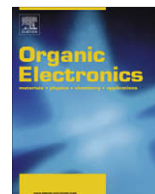
#### Appendix A. Supplementary data

Supplementary data associated with this article can be found, in the online version, at doi:10.1016/j.orgel.2009.02.016.

#### References

- [1] (a) H. Klauk, Organic Electronics, Wiley-VCH, Weinheim, 2006; (b) K. Müllen, U. Scherf, Organic Light-Emitting Devices. Synthesis, Properties and Applications, Wiley-VCH, Weinheim, 2006.
- [2] (a) Mobilities up to  $18 \text{ cm}^2/\text{V s}$  and  $35 \text{ cm}^2/\text{V s}$  have been reported for rubrene and pentacene single crystals respectively J. Takeya, M. Yamagishi, Y. Tominari, R. Hirahara, Y. Nakazawa, T. Nishikawa, T. Kawase, T. Shimoda, S. Ogawa, Appl. Phys. Lett. 90 (2007) 102120; (b) O.D. Jurchescu, J. Baas, T.T.M. Palstra, Appl. Phys. Lett. 84 (2004) 3061–3063.
- [3] (a) E.G. Kim, V. Coropceanu, N. Gruhn, R. Sánchez, R. Snoeberger, A. Matzger, J.L. Brédas, J. Am. Chem. Soc. 129 (2007) 8546–8553; (b) M. Mas-Torrent, P. Hadley, S.T. Bromley, X. Ribas, J. Tarrés, M. Mas, E. Molins, J. Veciana, C. Rovira, J. Am. Chem. Soc. 126 (2004) 8546–8553; (c) C. Reese, Z. Bao, J. Mater. Chem. 16 (2006) 329–333; (d) V. Podzorov, E. Menard, A. Borissov, V. Kiryukhin, J.A. Rogers, M.E. Gershenson, Phys. Rev. Lett. 93 (2004) 086602.
- [4] (a) V.C. Sundar, V. Zaumseil, V. Podzorov, E. Menard, R.L. Willet, T. Someya, E. Gershenson, J.A. Rogers, Science 303 (2004) 1644–1646; (b) A.L. Briseno, S.C.B. Mannsfeld, M.M. Ling, S. Liu, R.J. Tseng, C. Reese, M.E. Roberts, Y. Yang, F. Wudl, Z. Bao, Nature 444 (2006) 913–917.
- [5] (a) Carbazole-based compounds have been extensively studied due to their ability to transport holes N. Blouin, M. Leclerc, Acc. Chem. Res. 41 (2008) 1110–1119; (b) Y. Song, Ch. Di, Z. Wei, T. Zhao, W. Xu, Y. Liu, D. Zhang, D. Zhu, Chem. Eur. J. 14 (2008) 4731–4740; (c) N. Drolet, J.-F. Morin, N. Leclerc, S. Wakim, Y. Tao, M. Leclerc, Adv. Funct. Mater. 15 (2005) 1671–1682; (d) J.V. Grazulevicius, P. Strohriegel, J. Pielichowski, K. Pielichowski, Prog. Polym. Sci. 28 (2003) 1297–1353; (e) Y. Wu, Y. Li, S. Gardner, B.S. Ong, J. Am. Chem. Soc. 127 (2005) 614–618.
- [6] (a) J.-L. Wang, Z.-M. Tang, Q. Xiao, Q.-F. Zhou, Y. Ma, J. Pei, Org. Lett. 10 (2008) 17–20; (b) J.-L. Wang, J. Yan, Z.-M. Tang, Q. Xiao, Y. Ma, J. Pei, J. Am. Chem. Soc. 130 (2008) 9952–9962; (c) B. Gómez-Lor, E. González-Cantalapiedra, M. Ruiz, O. de Frutos, D.J. Cárdenas, A. Santos, A.M. Echavarren, Chem. Eur. J. 10 (2004) 2601–2608; (d) L. Sanguinet, J.C. Williams, Z. Yang, R.J. Twieg, G. Mao, K.D. Singer, G. Wiggers, R.G. Petschek, Chem. Mater. 18 (2006) 4259–4269.
- [7] Mobilities up to  $1.03 \times 10^{-3} \text{ cm}^2 \text{ V}^{-1} \text{ s}^{-1}$  have been measured in truxene-based OFETs Y. Sun, K. Xiao, Y. Liu, J. Wang, J. Pei, D. Zhu, Adv. Funct. Mater. 15 (2005) 818–822.

- [8] (a) Triindole-based emissive materials W.-Y. Lai, Q.-Y. He, R. Zhu, Q.-Q. Chen, W. Huang, *Adv. Funct. Mater.* 18 (2008) 265–276;  
(b) P.A. Levermore, R. Xia, W. Lai, X.H. Wang, W. Huang, D.D.C. Bradley, *J. Phys. D: Appl. Phys.* 40 (2007) 1896–1901.
- [9] (a) Triindole-based discotic liquid crystals B. Gómez-Lor, B. Alonso, A. Omenat, J.L. Serrano, *Chem. Commun.* (2006) 5012–5014;  
(b) M. Talarico, R. Termine, E.M. García-Frutos, A. Omenat, J.L. Serrano, B. Gómez-Lor, A. Golemme, *Chem. Mater.* 20 (2008) 6589–6591.
- [10] E.M. García-Frutos, B. Gómez-Lor, *J. Am. Chem. Soc.* 190 (2008) 9173–9177.
- [11] It should be noted that, although this is a common approximation, this band does not necessarily corresponds to the transition between the lowest vibrational states of the ground state and first excited molecular configuration.
- [12] (a) A. Alberti, B. Ballarin, M. Guerra, D. Macciantelli, A. Mucci, F. Parenti, L. Schenetti, R. Seeber, C. Zanardi, *Chem. Phys. Chem.* 4 (2003) 1216–1225;  
(b) Upon oxidation of with TFA as a one electron oxidant, we have previously succeeded in oxidizing a triindol-based cyclophane obtaining a highly stable crystalline dimeric radical cation suitable for X-ray analysis B. Gómez-Lor, G. Hennrich, B. Alonso, A. Monge, E. Gutierrez-Puebla, A.M. Echavarren, *Angew. Chem. Int. Ed.* 45 (2006) 4491–4494.
- [13] (a) R. Rathore, C. Zu, S.V. Lindeman, J.K. Kochi, *J. Chem. Soc., Perkin Trans. 2* (2000) 1837–1840;  
(b) L. Ebersson, F. Radner, *Acta Chem. Scand.* 52 (1998) 114–130.
- [14] (a) C.A. Hunter, K.R. Lawson, J. Perkins, C.J. Urch, *J. Chem. Soc., Perkin Trans. 2* (2001) 651–669;  
(b) M.L. Waters, *Curr. Opin. Chem. Biol.* 6 (2002) 736–741.
- [15] This effect has already been observed in other systems. See for example S.T. Bromley, M. Mas-Torrent, P. Hadley, C. Rovira, *J. Am. Chem. Soc.* 126 (2004) 6544–6545.
- [16] V. Coropceanu, J. Cornil, D.A. da Silva Filho, Y. Oliver, R. Silbey, J.-L. Brédas, *Chem. Rev.* 107 (2007) 926–952.
- [17] R.A. Marcus, *Rev. Mod. Phys.* 43 (1993) 599–610 (and references therein).
- [18] M.A. Lampert, P. Mark, *Current Injection in Solids*, Academic Press, New York, 1970.
- [19] The synthesis of this compound has been previously reported through a multistep procedure J. Bergman, N. Eklund, *Tetrahedron* 36 (1980) 1439–1443.
- [20] G. Gritzner, J. Kuta, *Pure Appl. Chem.* 56 (1984) 461–466.
- [21] A.J. Bard, L.R. Faulkner, *Electrochemical Methods – Fundamentals and Applications*, Wiley, New York, 1980.
- [22] Software for the SMART system, V.5.04, Bruker-Siemens Analytical X-ray Instruments, Inc., Madison, WI, USA, 1998.
- [23] G.M. Sheldrick, SHELXL97, Program for Crystal Structure Refinement, University of Göttingen, Germany, 1997.
- [24] M.J. Frisch, G.W. Trucks, H.B. Schlegel, et al., *Gaussian Inc.*, Pittsburgh, PA, 2003.
- [25] (a) A.D. Becke, *Phys. Rev. A* 38 (1988) 3098–3100;  
(b) C. Lee, W. Yang, R.G. Parr, *Phys. Rev. B* 37 (1988) 785–789;  
(c) S.H. Vosko, L. Wilk, M. Nusair, *Can. J. Phys.* 58 (1980) 1200–1211.
- [26] R. Krishnan, J.S. Binkley, R. Seeger, J.A. Pople, *J. Chem. Phys.* 72 (1980) 650–654.
- [27] R.M. Martin, *Electronic Structure*, Cambridge University Press, Cambridge, 2004.
- [28] J.P. Perdew, K. Burke, M. Ernzerhof, *Phys. Rev. Lett.* 77 (1996) 3865–3868.
- [29] (a) S.J. Clark, M.D. Segall, C.J. Pickard, P.J. Hasnip, M.J. Probert, K. Refson, M.C. Payne, *Z. Kristallogr.* 220 (2005) 567–570;  
[b] *Materials Studio 4.3*. <<http://www.accelrys.com>>.
- [30] (a) R. Ramirez, M.C. Bohm, *Int. J. Quantum Chem.* 30 (1986) 391–411;  
(b) R. Ramirez, M.C. Bohm, *Int. J. Quantum Chem.* 34 (1988) 571–594.



# Synthesis, characterization and high-efficiency blue electroluminescence based on coumarin derivatives of 7-diethylamino-coumarin-3-carboxamide

Tianzhi Yu<sup>a,\*</sup>, Peng Zhang<sup>a</sup>, Yuling Zhao<sup>b</sup>, Hui Zhang<sup>a</sup>, Jing Meng<sup>a</sup>, Duowang Fan<sup>a</sup>

<sup>a</sup> Key Laboratory of Opto-Electronic Technology and Intelligent Control, Lanzhou Jiaotong University, Ministry of Education, 88 West Anning Road, Lanzhou, Gansu 730070, China

<sup>b</sup> School of Chemical and Biological Engineering, Lanzhou Jiaotong University, Lanzhou 730070, China

## ARTICLE INFO

### Article history:

Received 19 August 2008

Received in revised form 3 February 2009

Accepted 24 February 2009

Available online 12 March 2009

### PACS:

78.60.Fi

85.60.Jb

78.66.Qn

### Keywords:

Photoluminescence

Electroluminescence

Coumarin derivative

Blue dopant

## ABSTRACT

A novel tripodal compound, tris[2-(7-diethylamino-coumarin-3-carboxamide)ethyl]amine (tren-C), and a model compound, N-butyl-7-(diethylamino)-coumarin-3-carboxamide, were synthesized and characterized by elemental analysis, infrared and <sup>1</sup>H NMR spectra. The structure of the model compound was characterized by single crystal X-ray crystallography. The electroluminescence devices of ITO/2-TNATA (5 nm)/NPB (40 nm)/CBP: tren-C or model compound (wt%, 30 nm)/Bu-PBD (30 nm)/LiF (1 nm)/Al (100 nm) were fabricated and characterized. The EL spectra of the devices comprising vacuum vapour-deposited films using tren-C as a dopant are similar to the PL spectrum of tren-C in chloroform solutions. At the concentration of 0.5 wt% tren-C, a blue-emitting OLED with an emission peak at 464 nm, a maximum external quantum efficiency (EQE) of 1.39% and a maximum luminous efficiency of 2 cd/A at the current density of 20 mA/cm<sup>2</sup>, and a maximum luminance of 1450 cd/m<sup>2</sup> at 12 V are achieved.

© 2009 Elsevier B.V. All rights reserved.

## 1. Introduction

Coumarins are an important class of naturally occurring and synthetic compounds, which have been extensively investigated for electronic and photonic applications [1–6], such as fluorescence probe, charge-transfer agents, solar energy collectors, and nonlinear optical properties due to their high emission yield, excellent photo-stability, extended spectral range, good solubility and their relative ease of synthesis. As emitting materials, their fluorescent wavelength and the fluorescence quantum yield strongly depend on the nature, the position of the substituent and also on the rigidity of the molecule [7–10]. Moreover, for each derivative the fluorescence wavelength, the fluores-

cence quantum yield and other photophysical properties exhibit strong solvent effect. Since Tang et al. [11] first used 3-(2-benzothiazolyl)-7-diethylaminocoumarin (coumarin 6) as an electroluminescent (EL) material successfully, coumarin dyes have attracted much interest owing to their potential application in organic light-emitting diodes (OLEDs). However, coumarin dyes are easily suffered from self-quenching in solid state due to interaction and aggregation with its neighboring compounds. As a result, they were always used as guest that doped in host materials with optimized transport and luminescent properties in organic electroluminescence field [11–15]. This guest–host doped emitter system can not only obtain rather high-efficiency, but also enhance the device operational stability by transferring the electrogenerated exciton to the highly emissive and stable dopant site thus minimizing its possibility for nonradiative decay [16]. Prior work on guest–host doped

\* Corresponding author. Tel.: +86 931 4956935; fax: +86 931 4938756.  
E-mail address: [ytz823@hotmail.com](mailto:ytz823@hotmail.com) (T. Yu).

emitter systems, most of them were involved with the green fluorescent dopants such as coumarin 6, coumarin 545 and coumarin 545T. Apart from the commercial coumarin dyes directly using as highly fluorescent dopants, many efforts have been devoted to explore new EL materials [17–23]. To add steric spacers to minimize dye–dye interaction at high dopant concentration, Chen and coworkers rigidized the alkylamino donor moiety via cyclization to the julolidine ring to develop new coumarin 545 analogues (C-545P, C-545 TB) and fabricated efficient green OLEDs [17,21]. Swanson and coworkers [18] incorporated diphenylamine replacing diethylamine in 7-position of coumarin ring to obtained coumarin 6 and coumarin 7 analogues (C-6S and C-7S), which efficiency and stability are superior to their commercial dialkylamino analogues. Suzuki and coworkers [22] reported a new coumarin red dopant and bright red OLEDs (max. luminance, 5600 cd/m<sup>2</sup>), though the efficiency of the device was not shown. Fujiwara et al. [20] prepared a series of symmetrical biscoumarin blue dyes, in which the same coumarin chromophores were combined through aromatic ring bridges, to overcome the stability of the blue dyes at the vacuum deposition in the EL device production process, and they investigated the EL devices using these blue dyes as a dopant. Zhang et al. [23] reported the photoluminescent and electroluminescent properties of a new amide-type coumarin derivative, this compound in solution state and in PVK matrix exhibited blue emission, and the doped double-layer device displayed brighter pure blue emission with the low turn-on voltage at 6.3 V and high external quantum efficiency of 0.8%. Compared with green coumarin dyes, there were few OLEDs using red and blue coumarin dyes as guest–host doped emitter.

Recently, we have synthesized a new tripodal compound in which three fluorophores, 7-diethylamino-coumarin moiety, were incorporated into tris(2-aminoethyl)amine (tren) to form tris[2-(7-diethylamino-coumarin-3-carboxamide)ethyl]amine (tren-C) (Scheme 1). The strategies for designing the tripodal compounds with coumarin fluoro-

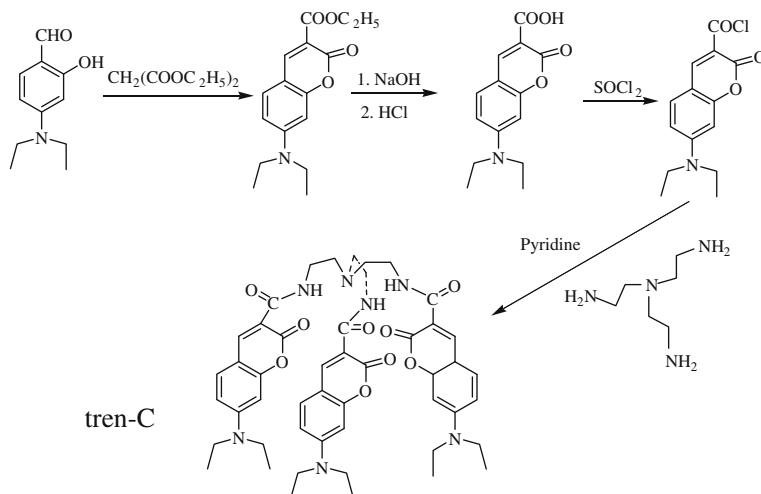
phores are: To attach three coumarin fluorophores onto the terminal amido groups of tren is expected to separate the coumarin fluorophores each other, keeping the optical properties of the molecule identical to the pristine coumarin fluorophore. Another reason is to increase the spatial extent of the molecule and reduce the interactions such as aggregation and dye self-quenching between the numerous terminal groups. To verify the conception, in the present paper *N*-butyl-7-(diethylamino)-coumarin-3-carboxamide as the model compound was synthesized and the performance of the electroluminescent devices doped with the compound and tren-C was compared.

## 2. Experimental details

### 2.1. Materials and methods

4-(*N,N'*-diethylamino) salicylaldehyde from Zhejiang Huadee Dyestuff Chemical Co., Ltd. (China) was recrystallized from ethanol. Tris(2-aminoethyl)amine (tren) was purchased from Fluka. Thionyl chloride was freshly distilled prior to use. Butylamine was bought from Shanghai No. 3 Chemical Reagent Factory (China). 4,4'-bis(9-carbazolyl)biphenyl (CBP), 2-(4-biphenyl)-5-(4-*tert*-butylphenyl)-1,3,4-oxadiazole (Bu-PBD), 4,4',4''-tris-*N*-naphthyl-*N*-phenylamino-triphenylamine (2-TNATA) and *N,N'*-bis(naphthyl)-*N,N'*-diphenyl-1,1'-biphenyl-4,4'-diamine (NPB) were purchased from Electro-Light Technology Corp., Beijing. The other solvents were analytical grade reagents.

IR spectra (400–4000 cm<sup>-1</sup>) were measured on a Shimadzu IRPrestige-21 FT-IR spectrophotometer. <sup>1</sup>H NMR spectra were obtained on Unity Varian-500 MHz. UV–vis absorption and photoluminescent spectra were recorded on a Shimadzu UV-2550 spectrometer and on a Perkin-Elmer LS-55 spectrometer, respectively. The cyclic voltammogram was performed on a Model CHI660 Electrochemical Analyzer (CH instruments, Austin, TX). The electroluminescent spectra were measured on a Hitachi MPF-4 spectrometer.



Scheme 1. Synthetic route for tren-C.

### 2.3. Synthesis and characterization of tris[2-(7-diethylamino-coumarin-3-carboxamide)ethyl]-amine (tren-C)

The synthetic route was shown in Scheme 1. The intermediates, ethyl 7-(diethylamino)-coumarin-3-carboxylate and 7-(diethylamino)-coumarin-3-carboxylic acid, were obtained as previously described [24].

7-(Diethylamino)-coumarin-3-carboxylic acid (6 g, 0.023 mol) was dissolved in 50 ml of dichloromethane, and then thionyl chloride (10 ml) was dropped stepwise under ice bath. The mixture was refluxed for 10 h. The resulting solution was evaporated to dryness under reduced pressure and the residue was dispersed in dry toluene (20 ml). After elimination of the solvent under reduced pressure, and the process was repeated twice. The residue was dried under vacuum.

7-(Diethylamino)-coumarin-3-carbonyl chloride (1.4 g, 5 mmol) was dissolved in anhydrous pyridine (10 ml) and added with stirring to a solution of tris(2-aminoethyl)amine (0.2 g, 1.36 mmol) in anhydrous pyridine (10 ml). After 5 h at room temperature, the resulting mixture was poured into 100 ml water and extracted with chloroform (3 × 50 ml). The organic phase was washed with water (2 × 50 ml) and dried over anhydrous MgSO<sub>4</sub>. After filtering, the filtrate was evaporated to dryness under reduced pressure. The crude was purified by chromatography on silica gel using chloroform/methanol (1:24, v/v) as the eluent to give a white powder (0.52 g, 42.7%). mp. 116–118 °C. IR: 3348 (N–H), 2970, 2930, 2870, 2816 (C–H, aliphatic), 1701 (C=O, lactone), 1635 (C=O, amide), 1620, 1585, 1512 cm<sup>-1</sup>; <sup>1</sup>H NMR (CDCl<sub>3</sub>, TMS): 8.97 (s, 3H, 4-H), 8.62 (s, 3H, NH), 7.38 (d, 3H, 5-H), 6.60 (d, 3H, 6-H), 6.42 (s, 3H, 8-H), 3.58 (d, 6H, CONH–CH<sub>2</sub>), 3.44–3.39 (m, 12H, 7-N–CH<sub>2</sub>), 2.88 (t, 6H, N–CH<sub>2</sub>), 1.23 (t, 18H, CH<sub>3</sub>).

### 2.4. Synthesis and characterization of N-butyl-7-(diethylamino)-coumarin-3-carboxamide

The model compound, N-butyl-7-(diethylamino)-coumarin-3-carboxamide, was obtained from 7-(diethylamino)-coumarin-3-carbonyl chloride and butylamine following a procedure similar to that described for tren-C. The crude was purified by chromatography on silica gel using ethyl acetate/petroleum(1:5, v/v). Yield: 60.5% m.p. 107–109 °C. IR (KBr pellet, cm<sup>-1</sup>): 3336 (N–H), 3043 (aryl–CH), 2969, 2929, 2866 (alkyl–CH), 1697 (C=O, lactone), 1644 (C=O, amide), 1617, 1582, 1525, 1509, 1377, 1133. <sup>1</sup>H NMR (CDCl<sub>3</sub>, δ, ppm): 8.77 (s, 1H, NH), 8.71 (s, 1H, 4-H), 7.42 (d, 1H, 5-H), 6.65 (d, 1H, 6-H), 6.51 (s, 1H, 8-H), 3.48–3.41 (m, 2H, CONH–CH<sub>2</sub>), 3.48–3.41 (m, 4H, 7-N–CH<sub>2</sub>), 1.60 (m, 2H, CH<sub>2</sub>), 1.42 (m, 2H, CH<sub>2</sub>), 1.24 (m, 6H, CH<sub>3</sub>), 0.95 (t, 3H, CH<sub>3</sub>). Anal. Calc. for C<sub>18</sub>H<sub>24</sub>N<sub>2</sub>O<sub>3</sub> (%): C, 68.33; H, 7.65; N, 8.85. Found: C, 68.40; H, 7.61; N, 8.79.

### 2.5. Crystallography

Suitable single crystal of the model compound was obtained from methanol solution. The diffraction data were collected with a Bruker Smart Apex CCD area detector using a graphite monochromated Mo K $\alpha$  radiation ( $\lambda = 0.71073 \text{ \AA}$ ) at 20 °C. The structure was solved by using the program SHELXL and Fourier difference techniques, and refined by full-matrix least-squares method on  $F^2$ . All hydrogen atoms were added theoretically.

### 2.6. OLEDs fabrication

The multilayer OLEDs were fabricated by vacuum-deposition method. ITO-coated glass with a sheet resistance  $R_{\square} \sim 20 \Omega/\square$  was cut into 3 cm × 3 cm plates and etched

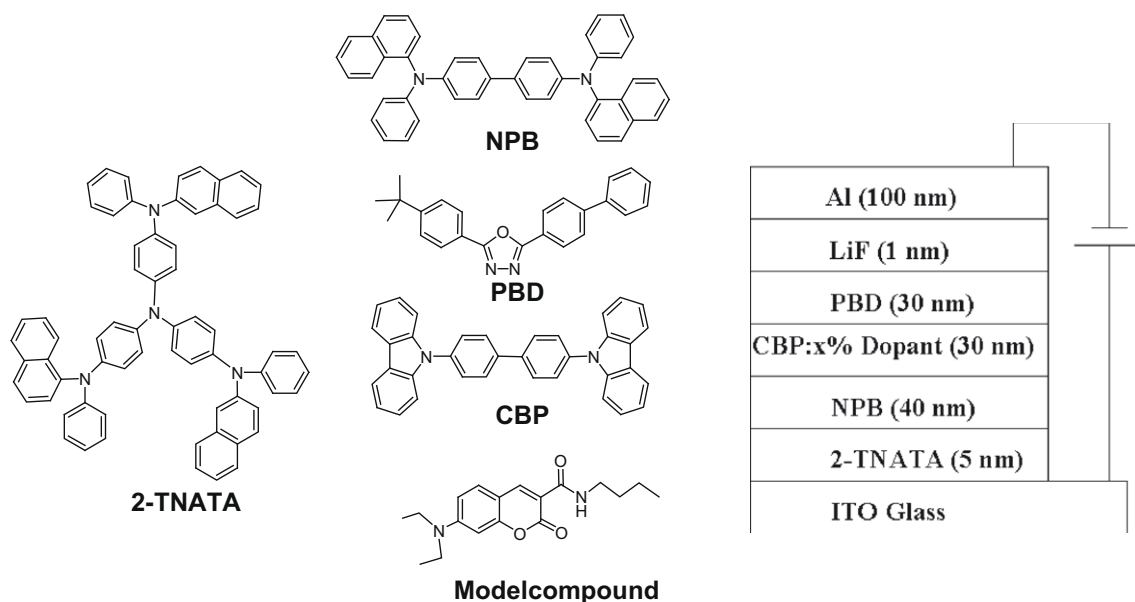


Fig. 1. The molecular structures of materials and the structure of EL device.

in dilute hydrochloric acid for 20 min. Then the ITO substrates were routinely cleaned by ultrasonic treatment in solvents and then cleaned by exposure to an UV-ozone ambient. All organic layers were sequentially deposited without breaking vacuum ( $2 \times 10^{-4}$  Pa). Thermal deposition rates for organic materials, LiF and Al were  $\sim 2$ ,  $\sim 1$  and  $10 \text{ \AA/s}$ , respectively. The active area of the devices was  $12 \text{ mm}^2$ . The EL spectra and Commission Internationale de l'Eclairage (CIE) coordinates were measured on a Hitachi MPF-4 fluorescence spectrometer. The characterization of brightness–current–voltage ( $B$ – $I$ – $V$ ) were measured with a 3645 DC power supply combined with a 1980A spot photometer and were recorded simultaneously. All measurements were done in the air at room temperature without any encapsulation.

The molecular structures of the materials and the structure of devices used in this work are shown in Fig. 1. Tren-C: CBP and Model compound: CBP were employed as the emitters, 2-TNATA, NPB, and PBD were used as hole injection, hole transport and electron transport materials, respectively. LiF was used as the electron-injection layer.

### 3. Results and discussion

#### 3.1. Synthesis

Preparation of the compound tren-C was performed in four steps from 4-(diethylamino)-2-hydroxybenzaldehyde by means of Knoevenagel condensation with diethyl malonate as the key step (Scheme 1). The hydrolysis of ethyl 7-(diethylamino)-coumarin-3-carboxylate was easily realized by alkaline hydrolysis followed by acidification to afford 7-(diethylamino)-coumarin-3-carboxylic acid. Subsequent treatment with thionyl chloride led to the intermediate 7-(diethylamino)-coumarin-3-carbonyl chloride that then reacted with tris(2-aminoethyl)amine (tren) to afford the final compound tren-C in 42.7% yield. 7-(diethylamino)-coumarin-3-carbonyl chloride reacted with butylamine to give the model compound, *N*-butyl-7-(diethylamino)-coumarin-3-carboxamide in 60.5% yield.

When 7-(diethylamino)-coumarin-3-carboxamide was incorporated into the tris(2-aminoethyl)amine (tren), a tripod compound was obtained which shows a three-dimensional space. Three coumarin fluorophores were attached to an apical N atom through the isolating chains

and formed a cage cavity. The molecular design concept of this work was to realize the absence of significant interactions between the three coumarin fluorophore groups in the tripod tren-C and compel them to emit simultaneously. Moreover, it will reduce the interactions such as crystallization and aggregation of the molecules due to the three-dimensional space to prevent the dye self-quenching. In addition, the tripod tren-C has a flexible structure characteristic, therefore the host molecule can enter into the cage cavity of the guest tren-C when forming emitting layer. It can avoid the occurrence of phase segregation.

#### 3.2. X-ray crystal structure of the model compound

The crystal structure and packing diagram of the model compound are given in Figs. 2 and 3, respectively. Crystal data:  $\text{C}_{18}\text{H}_{24}\text{N}_2\text{O}_3$ ,  $M = 316.39$ , monoclinic, crystal dimensions  $0.37 \times 0.22 \times 0.07 \text{ mm}$ , space group  $C2/c$ ,  $a = 22.603$  (6)  $\text{\AA}$ ,  $b = 9.002$  (4)  $\text{\AA}$ ,  $c = 18.276$  (5)  $\text{\AA}$ ,  $\beta = 109.532$  (7),  $\lambda = 0.71073 \text{ \AA}$ ,  $T = 187(2) \text{ K}$ ,  $U = 3505$  (2)  $\text{\AA}^3$ ,  $Z = 8$ ,  $D_c = 1.199 \text{ g cm}^{-3}$ ,  $\mu = 0.082 \text{ mm}^{-1}$ . Reflections (8691) measured, 3083 unique ( $R_{\text{int}} = 0.0392$ ), 211 refined parameters, transmission factors 0.9942 and 0.9705. The final discrepancy factors were  $R_1 = 0.1037$ ,  $wR_2 = 0.2715$ , good-

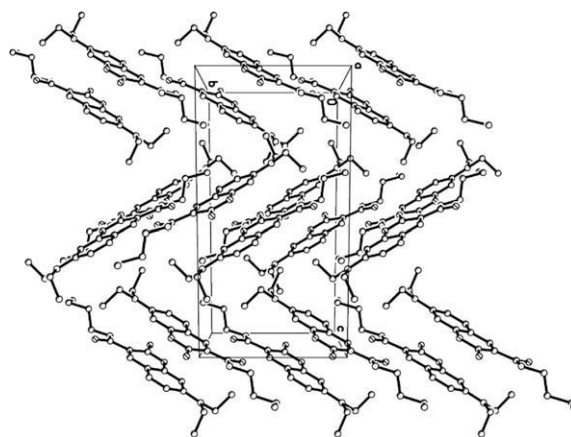


Fig. 3. Three-dimensional packing diagram of the model compound, H atoms are omitted for clarity.

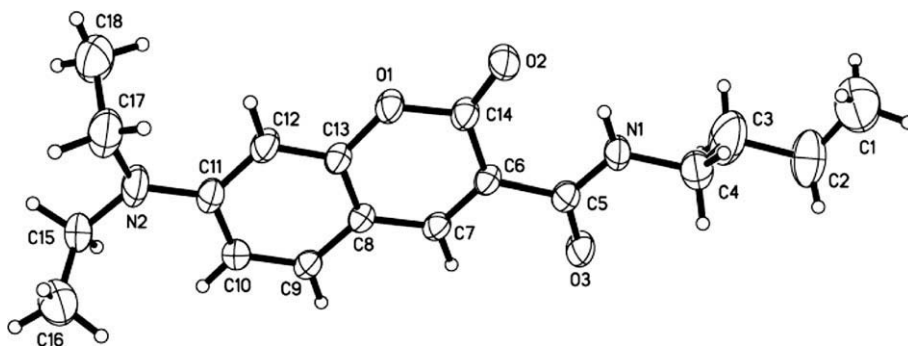


Fig. 2. Crystal structure of the model compound.

ness-of-fit  $S = 1.054$  on  $F^2$ , largest difference peak and hole 0.392 and  $-0.271 \text{ e}\text{\AA}^{-3}$ . CCDC reference number 716852.

There is an intermolecular  $\pi$ - $\pi$  stacking between the model compound molecules in crystal lattice as shown in Fig. 3. The interplanar distance is approximately 3.468 Å, it is the rather short  $\pi$ - $\pi$  interaction and possibly plays a role in the radiationless quenching of the fluorescent emission.

### 3.3. UV-vis absorption and photoluminescence spectra

Fig. 4 shows UV-vis absorption and photoluminescent spectra of tren-C in the solution of dichloromethane and solid state. It is clear that tren-C exhibits two observable peaks at ca. 257 and 415 nm in the absorption spectrum. The absorption bands of tren-C were blue-shifted obviously compared to that of its precursor, 7-diethylamino-coumarin-3-carboxylic acid (DCCA), which exhibits two peaks in the absorption spectrum at 261 and 432 nm [24], but a similarity in absorption spectral shape between tren-C and DCCA is observed. The similarity can be attributed to the commonality of the center core (i.e., 7-diethylamino-coumarin-3-carbonyl). From the molecular structures of tren-C and DCCA, it can be seen that they have the same electron-donor groups (diethylamino group) at 7-position and different electron-acceptor groups (imide for tren-C and carboxyl for DCCA) at the 3-position. Clearly, the efficiency of electron-acceptance of the latter is slightly higher. Furthermore, contrasted with the absorption spectrum of 7-diethylamino-coumarin which exhibits two peaks at 256 and 376 nm [25], the longer wavelength band of tren-C is red-shifted to 415 nm due to the fluorophores bearing an electron-acceptance group in 3-position, but the absorption spectral shapes of them are markedly alike in dichloromethane solution, which displayed a rather weak band at shorter wavelength followed by a intense band at longer wavelength. From above comparison, it was clearly indicated that three fluorophores in tren-C are independent units and no interactions each other.

In addition, the absorption band at 415 nm corresponds to the lowest unoccupied molecular orbital level of tren-C, and it has a significant influence on the characteristic emission spectra, so the PL spectra of tren-C was selected

at 415 nm as the excitation wavelength. The maximum optical absorption edge of tren-C is at ca. 450 nm, the optical bandgap energy ( $E_g$ ) is calculated to be 2.78 eV.

Tren-C has different PL spectra in the solid state and in the solution of dichloromethane ( $1 \times 10^{-5} \text{ mol/l}$ ) (Fig. 4). Tren-C exhibits bright green emission with the peak at 519 nm in the solid state, whereas the photoluminescence of tren-C in dichloromethane has blue emission with the peak at 464 nm, and it was found that the PL spectrum in the solid state is much broader than that in dichloromethane solution and the full width at halfmaximum (fwhm) are 65 nm for the former and 40 nm for the latter, respectively. The results are suggested that the compound in the solid state has more intermolecular interaction than that in solution situation, and thus may lead to change of the emission band.

Fig. 5 shows the photoluminescent behaviors of tren-C doped in poly(methyl methacrylate) (PMMA). Mixed systems of tren-C with PMMA were prepared by dissolving the compound with a certain weight ratios into acetone. The samples for spectroscopy were fabricated by spin-coating the acetone solutions onto clean quartz substrates. It was illustrated that the emission spectral features of the compound in the tren-C/PMMA systems change with the weight ratios of the compound and PMMA. It is noticed that the emission located at 463 nm increases gradually with increasing the weight ratio and reaches a maximum at about concentration of 0.5 wt% the compound. When the concentration was higher than 0.5 wt%, the fluorescence emission was decreasing, and the emission band was broadening and bathochromically shifted. Noteworthy, when the concentration exceeded 2 wt%, an additional emission band appeared at around 520 nm, which corresponds to the emission in the solid state. Moreover, as the concentration exceeded 10 wt%, we can find that the emission band at 463 nm disappeared and the emission band at 520 nm reserved. The results show that the fluorescence intensity is intensively quenched by concentration of the compound, so it was found that a self-quenching was occurred. On the other hand, the shape of emission spectra is intensively affected by the intermolecular interaction, thus may lead to

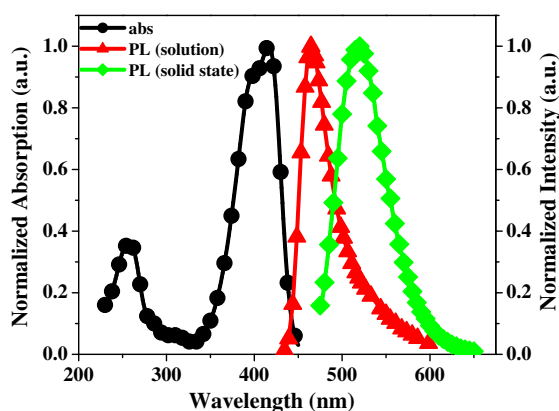


Fig. 4. UV-vis absorption and photoluminescent spectra of tren-C in the solution of chloroform ( $1.0 \times 10^{-5} \text{ mol/l}$ ) and solid states.

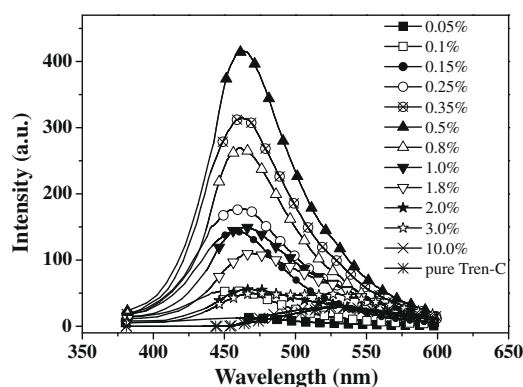


Fig. 5. The PL spectra of the thin film of tren in the tren-C/PMMA system ( $C_{\text{PMMA}} = 10 \text{ mg/ml}$ ,  $\lambda_{\text{ex}} = 416 \text{ nm}$ ).

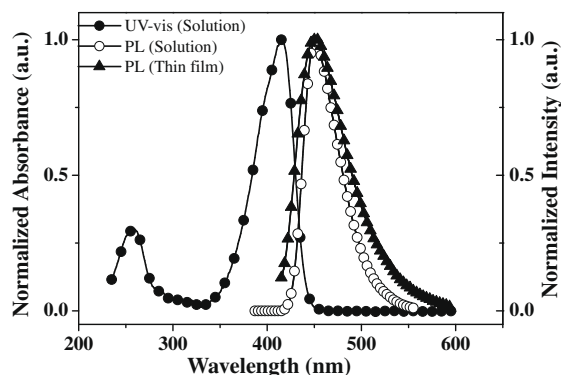


Fig. 6. Normalized UV-vis absorption spectrum and PL spectra of the model compound.

change of the emission band with increasing the weight ratios.

Fig. 6 shows the UV-vis absorption spectrum and PL spectra of the model compound in the solution of dichloromethane ( $1 \times 10^{-5}$  mol/l $^{-1}$ ) and in thin film. It is clear that the model compound exhibits two observable bands at about 257 and 415 nm, which is similar to that of tren-C. The PL spectra of the compound in thin film with the emission peak at 451 nm is identical with that in the solution of dichloromethane, but the former is much broader than the latter.

### 3.4. Electrochemical properties and OLED performance

The electrical property of tren-C was first investigated using the cyclic voltammetry (CV), from which the highest occupied molecular orbital (HOMO) level of tren-C was determined. The HOMO level is related to the hole injection/transporting property of tren-C. Tren-C was dissolved in dichloromethane with tetra-*n*-butylammonium tetrafluoroborate (0.1 mol/l) as the electrolyte. A platinum working electrode and a saturated Ag/AgCl reference electrode were used. Ferrocene was used for potential calibration. Fig. 7 shows the cyclic voltammogram of tren-C and ferrocene reference material. The oxidation onset at

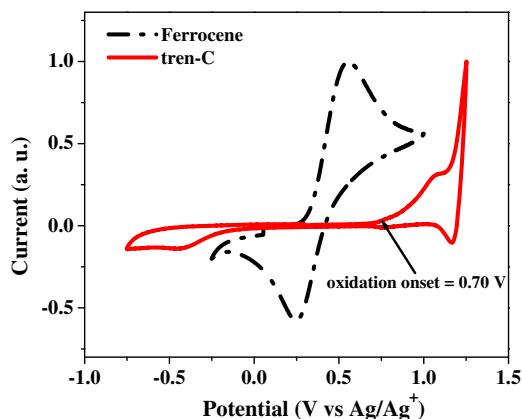


Fig. 7. Cyclic voltammograms of the ferrocene (dotted line) and tren-C (solid line) (scan rate: 10 mV/s, solvent: dichloromethane).

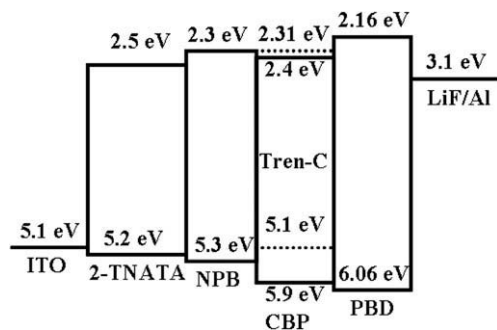


Fig. 8. The energy-level diagram of the blue-emitting device.

0.70 V was clearly observed in the CV curve of tren-C. In the CV curve of ferrocene, the oxidation peak and the reductive peak were observed at 0.55 and 0.25 V, respectively, then the  $E_{1/2}$  (Fc/Fc $^{+}$ ) is 0.40 V. From the oxidation onset of tren-C, the HOMO of tren-C is determined to be  $-5.10$  eV regarding the energy level of ferrocene/ferrocenium as  $-4.80$  eV [26]. Then the LUMO of tren-C is calculated to be  $-2.32$  eV.

The device with the configuration of ITO/2-TNATA (5 nm)/NPB (40 nm)/CBP: tren-C ( $x$  wt%, 30 nm)/PBD

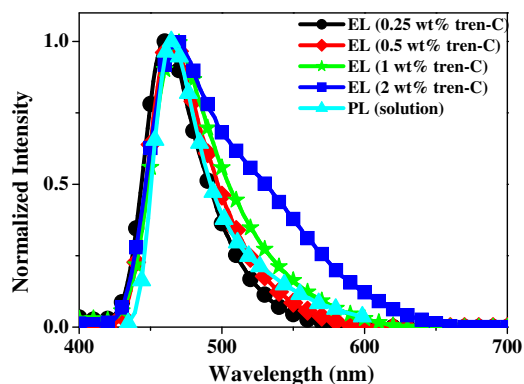


Fig. 9. EL spectra of different tren-C concentrations in the device and PL spectrum of tren-C in dichloromethane.

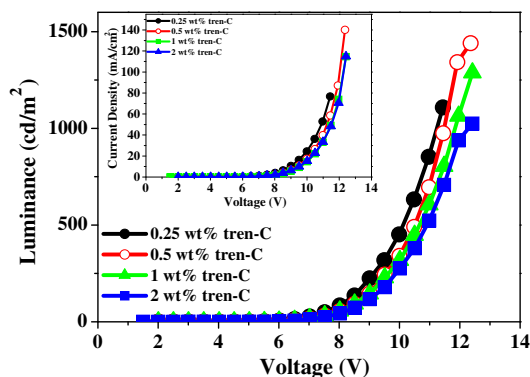


Fig. 10. The luminance versus voltage and current density versus voltage (inset) curves of the devices with different dopant concentrations.



**Table 1**

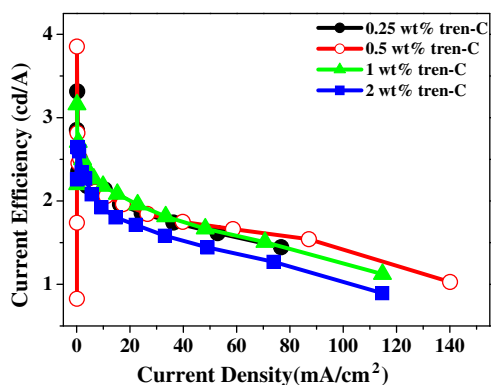
EL performances of the tren-C doped devices.

Entry (wt%)	Maximum efficiency (cd/A)	Efficiency at 20 mA/cm <sup>2</sup>	Maximum external quantum efficiency (EQE)	CIE <sub>x,y</sub>
0.25	3.32 @ 0.20 mA/cm <sup>2</sup>	1.89	2.81%	(0.132, 0.124)
0.5	3.85 @ 0.10 mA/cm <sup>2</sup>	1.89	2.85%	(0.134, 0.161)
1.0	2.71 @ 0.63 mA/cm <sup>2</sup>	1.99	1.56%	(0.149, 0.225)
2.0	2.65 @ 0.23 mA/cm <sup>2</sup>	1.75	1.25%	(0.193, 0.295)

(30 nm)/LiF (1 nm)/Al (100 nm) and the corresponding HOMO-LUMO energy levels are depicted in Fig. 8. From the energy diagram, the strong hole trapping can be expected due to the lower HOMO level of tren-C than that of CBP. On the other hand, little variation in LUMO level between tren-C and CBP allows electron easier to inject into tren-C. Moreover, it is clear that NPB and PBD can act as substantial electron-blocking and hole-blocking layers, respectively. As a result, effective electron-hole pairs confinement in the emission layer can be expected.

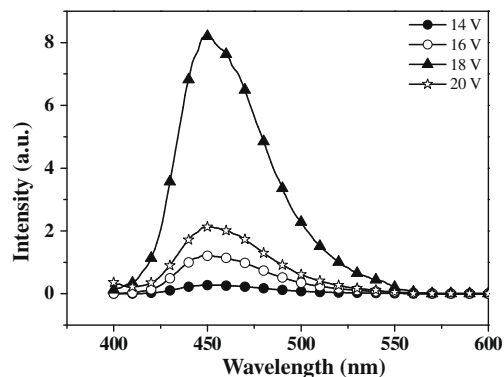
Fig. 9 shows the EL spectra of the device with tren-C doped at concentrations of 0.25, 0.5, 1 and 2 wt%. All devices exhibit blue emissions with the maximum peaks at ca. 464 nm. The EL spectra are identical to the PL spectrum of tren-C in dichloromethane solution. Such results indicate that these emissions take place from the tren-C molecules. As shown in Fig. 9, it can be seen that the EL spectral width broadens gradually with tren-C dopant concentrations in CBP host increase, this suggests that there is slight interaction between tren-C molecules as increase of the dopant concentration.

Fig. 10 shows the luminance–current density–voltage characteristics of the devices for various concentrations of tren-C molecules. It can be seen that the increasing doped concentrations suppressing the luminance and current density of the devices, indicating that strong charge trapping occurred in present device structures. Table 1 summarized the performances of the devices with various tren-C doping concentrations in CBP host. The 0.5 wt% tren-C doped device has maximum efficiency of 2 cd/A at 20 mA/cm<sup>2</sup>, which has a blue color with a CIE<sub>x,y</sub> of (0.134, 0.161). From the results, it is indicated that there is an optimal doping concentration of tren-C.



**Fig. 11.** Current efficiency–current density characteristics of the doped devices with various dopant concentration.

It is obvious that the optimal tren-C concentration in the CBP host is 0.5 wt%, and the 0.5 wt% tren-C doped device showed maximum luminance was 1450 cd/m<sup>2</sup> at 12 V. Fig. 11 shows the relationship between current efficiency and the current density in the devices with various tren-C doping concentrations. It is shown that all doped devices have higher efficiencies at low current densities, and then the efficiencies fall off fleetly at higher current densities. The above finding indicates that the electron hole recombination may not be effective under high current density, revealing that the present host, CBP, might not be an optimal host material. The present device performance could be further improved by substituting other host candidates.



**Fig. 12.** EL spectra of the device with ITO/2-TNATA (5 nm)/NPB (40 nm)/CBP: Model compound (1.5 wt%, 30 nm)/PBD (30 nm)/LiF (1 nm)/Al (100 nm) at different applied voltages.

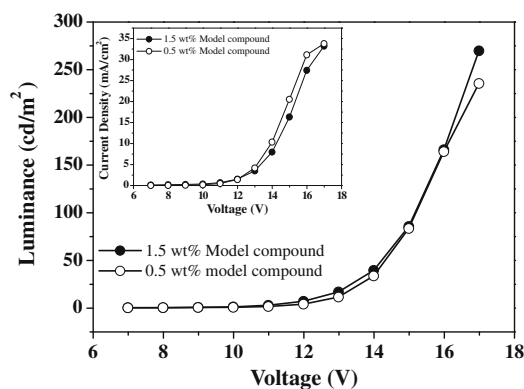


**Fig. 13.** The luminance versus voltage and current density versus voltage (inset) curves of the devices doped the model compound with different concentrations.

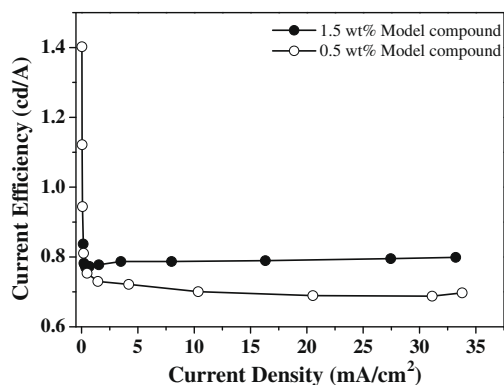


**Fig. 14.** Current efficiency–current density characteristics of the devices doped the model compound with different concentrations.

To compare the performance of the devices doped with tren-C, the devices with the model compound doped at concentrations of 0.5 and 1.5 wt% were fabricated. Fig. 12 shows the EL spectra of the device with concentration of 1.5 wt% the model compound at different driving voltages. The EL spectrum is almost identical to the PL spectrum of the model compound thin film, a bright blue emission at 451 nm was observed. The representative current–luminance–voltage characteristics of the device doped the model compound with different concentrations are depicted in Fig. 13. The devices show a turn-on voltage about 10 V. At the doped concentration of 1.5 wt%, the luminance reaches as high as 270 cd/m<sup>2</sup> at 17 V. The 1.5 wt% model compound doped device has a maximum efficiency of 0.8 cd/A at 20 mA/cm<sup>2</sup>, which has a blue color with a CIE<sub>x,y</sub> of (0.141, 0.084) (Fig. 14).

From above results, we can find that the performance of the tren-C doped devices is superior to that of the model compound doped devices.

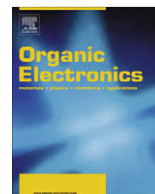
In conclusion, we designed and prepared a new tripodal compound, tris[2-(7-diethylamino-coumarin-3-carboxamide)ethyl]amine (tren-C), which exhibits different colors emission in a solid states and solutions. The doped devices fabricated from tren-C doped in CBP show the blue emissions with the maximum peaks at ca. 464 nm and have the EL spectra identical to the PL spectrum of tren-C in dichloromethane. The ITO/2-TNATA (5 nm)/NPB (40 nm)/CBP: tren-C (0.5 wt%, 30 nm)/PBD (30 nm)/LiF (1 nm)/Al (100 nm) device displayed the pure brighter blue emission, a maximum external quantum efficiency (EQE) of 1.39%, a maximum luminous efficiency of 2 cd/A at the current density of 20 mA/cm<sup>2</sup>, and maximum luminance of 1450 cd/m<sup>2</sup>.

## Acknowledgements

This work was supported by the National Natural Science Foundation of China (Grant 60776006) and ‘Qing Lan’ talent engineering funds (QL-05-23A) by Lanzhou Jiaotong University, and also supported by the Program for Changjiang Scholars and Innovative Research Team in University (IRT0629).

## References

- [1] R.P. Haugland, Handbook of Fluorescent Probes and Research Chemicals. Eugene (OR): Molecular Probes, 1994–1996.
- [2] H. Schwander, P. Hendrix, in: Y.S. Yamamoto (Ed.), Ullmann’s Encyclopedia of Industrial Chemistry, fifth ed., vol. A11, Weinheim, VCH, 1988, p. 280.
- [3] O.S. Wolfbeis, E. Koller, P. Hochmuth, Bull. Chem. Soc. Jpn. 58 (1985) 731.
- [4] U. Tripathy, P.B. Bisht, J. Chem. Phys. 125 (2006) 144502.
- [5] S.L. Gilat, A. Adronov, J.M.J. Fréchet, Angew. Chem. Int. Ed. 38 (1999) 1422.
- [6] T. Hiroshi, O. Yoshio, I. Juzo, I. Masato, T. Atsushi, Jpn. Kokai Tokkyo Koho, CODEN: JKXXAF JP 02126241 A2 19900515 (1990) Heisei.
- [7] H. Ammar, S. Fery-Forgues, R. E1 Gharbi, Dyes and Pigments 57 (2003) 259.
- [8] K. Azuma, S. Suzuki, S. Uchiyama, T. Kajiro, T. Santa, K. Imai, Photochem. Photobiol. Sci. 2 (2003) 443.
- [9] T.Z. Yu, Y.L. Zhao, X.S. Ding, D.W. Fan, L. Qian, W.K. Dong, J. Photochem. Photobiol. A: Chem. 188 (2007) 245.
- [10] T.Z. Yu, Y.L. Zhao, D.W. Fan, J. Mol. Struct. 791 (2006) 18.
- [11] C.W. Tang, S.A. VanSlyke, C.H. Chen, J. Appl. Phys. 65 (1989) 3610.
- [12] W.M. Su, W.L. Li, Z.R. Hong, M.T. Li, T.Z. Yu, B. Chu, B. Li, Z.Q. Zhang, Z.Z. Hu, Appl. Phys. Lett. 87 (2005) 213501.
- [13] T. Tsutsui, S.B. Lee, K. Fujita, Appl. Phys. Lett. 85 (2004) 2382.
- [14] X.Z. Jiang, R.A. Register, K.A. Killeen, M.E. Thompson, F. Pschenitzka, T.R. Hehner, J.C. Sturm, J. Appl. Phys. 91 (2002) 6717.
- [15] M. Uchida, C. Adachi, T. Koyama, Y. Taniguchi, J. Appl. Phys. 86 (1999) 1680.
- [16] S.A. VanSlyke, P.S. Bryan, C.W. Tang, in: R.H. Manch, H.E. Gumlich (Eds.), The 8th International Workshop on EL’96, Inorganic and Organic EL’96, Berlin, p. 195.
- [17] M.T. Lee, C.K. Yen, W.P. Yang, H.H. Chen, C.H. Liao, C.H. Tsai, C.H. Chen, Org. Lett. 6 (2004) 1241.
- [18] S.A. Swanson, G.M. Wallraff, J.P. Chen, W.J. Zhang, L.D. Bozano, K.R. Carter, J.R. Salem, R. Villa, J.C. Scott, Chem. Mater. 15 (2003) 2305.
- [19] C.T. Chen, C.L. Chiang, Y.C. Lin, L.H. Chan, C.H. Huang, Z.W. Tsai, C.T. Chen, Org. Lett. 5 (2003) 1261.
- [20] M. Fujiwara, N. Ishida, M. Satsuki, S. Suga, J. Photopolym. Sci. Technol. 15 (2002) 237.
- [21] C.H. Chen, C.W. Tang, Appl. Phys. Lett. 79 (2001) 3711.
- [22] M. Mitsuya, T. Suzuki, T. Koyama, H. Shirai, Y. Taniguchi, Appl. Phys. Lett. 77 (2000) 3272.
- [23] H.P. Zheng, R.F. Zhang, F. Wu, W.J. Tian, J.C. Shen, Synth. Met. 100 (1999) 291.
- [24] H. Zhang, T.Z. Yu, Y.L. Zhao, D.W. Fan, L.L. Chen, Y.Q. Qiu, L. Qian, K. Zhang, C.H. Yang, Spectrochim. Acta Part A: Mol. Biomol. Spectrosc. 69 (2008) 1136.
- [25] H. Turki, S. Abid, S. Fery-Forgues, R.E. Gharbi, Dyes and Pigments 73 (2007) 311.
- [26] J. Pommerehne, H. Vestweber, W. Guss, R.F. Mahrt, H. Bässler, M. Porsch, J. Daub, Adv. Mater. 7 (1995) 551.



# High temperature carrier mobility as an intrinsic transport parameter of an organic semiconductor

K.K. Tsung, S.K. So \*

Department of Physics and Centre for Advanced Luminescence Materials, Hong Kong Baptist University, Kowloon Tong, Hong Kong, China

## ARTICLE INFO

### Article history:

Received 17 January 2009

Received in revised form 20 February 2009

Accepted 21 February 2009

Available online 3 March 2009

### PACS:

72.80.Le

72.20.Ee

73.50.Bk

### Keywords:

NPB

Charge transport

Organic semiconductor

High temperature limit of carrier mobility

## ABSTRACT

The high temperature limit of hole mobility ( $\mu_\infty$ ) in *N,N'*-diphenyl-*N,N'*-bis(1-naphthyl)(1,1'-biphenyl)-4,4'-diamine (NPB) has been studied by time-of-flight technique. The effect of dopants on  $\mu_\infty$  was also investigated. It was found that the  $\mu_\infty$  is independent of the nature of dopants. The common  $\mu_\infty$  can be applied to estimate the full temperature dependence of zero-field mobility ( $\mu_0$ ), if  $\mu_0$  at one temperature is known. We demonstrate this concept by predicting the room temperature  $\mu_0$  of NPB-doped with copper phthalocyanine (CuPc). The mobility prediction of CuPc-doped-NPB was then verified by the classic work of Hoesterey and Letson [D.C. Hoesterey, G.M. Letson, J. Phys. Chem. Solids 24 (1963) 1609].

© 2009 Elsevier B.V. All rights reserved.

## 1. Introduction

Charge carrier transport behaviors in organic semiconductors have been intensively studied by both industry and academia for many years [1,2]. The interests in studying organic materials are driven by their applications in optoelectronic devices including e.g. organic light emitting diodes, thin film transistors and photovoltaic cells [3–5]. To date, carrier mobility measurement has emerged to be a key technique for the characterization of organic material [6]. In addition, the measurement of mobility provides a means of examining carrier transport inside organic semiconductors. Generally, measuring the room temperature carrier mobility ( $\mu_{RT}$ ) is the first step to characterize transport behaviors of an organic material. However,  $\mu_{RT}$  can be easily affected by dopants (intrinsic or extrinsic) and defects inside the material. Therefore,  $\mu_{RT}$  is clearly not the

best parameter to describe the intrinsic transport properties of the organic materials.

Below, we demonstrate that the high temperature limit of carrier mobility ( $\mu_\infty$ ) is a better parameter for quantifying the charge transport properties of an organic material because it is less sensitive to the presence of dopants and defects. Previous reports suggested that  $\mu_\infty$  can be utilized to estimate transport parameters such as the average inter-site distance ( $a$ ), the localization length ( $L$ ) with the relation [7,8]:

$$\mu_\infty = \frac{ea^2v_0}{\sigma} \exp(-2a/L) \quad (1)$$

In Eq. (1),  $e$  is the electron charge,  $v_0$  is the attempt-to-escape frequency. But the value of  $v_0$ , which is ranged between  $10^{-12}$  and  $10^{-14} \text{ s}^{-1}$ , is a big uncertainty. The practical use of  $\mu_\infty$  is still not very evident.

In this study, we measure  $\mu_\infty$  of *N,N'*-diphenyl-*N,N'*-bis(1-naphthyl)(1,1'-biphenyl)-4,4'-diamine (NPB) by time-of-flight (TOF) technique. NPB is widely used in

\* Corresponding author. Tel.: +852 3411 7038; fax: +852 3411 5813.  
E-mail address: [skso@hkbu.edu.hk](mailto:skso@hkbu.edu.hk) (S.K. So).

OLEDs as a hole transporter. It possesses trap-free hole-transporting property, excellent film forming ability, and chemically stability [9]. Hence, the research on the intrinsic hole-transporting properties of NPB is of clear importance. The effect of dopants on  $\mu_{\infty}$  of NPB will be examined. Furthermore, knowledge of  $\mu_{\infty}$  allows us to estimate the full temperature dependence of zero-field mobility ( $\mu_0$ ), if  $\mu_0$  at one temperature is known. We demonstrate this concept by doping NPB with copper phthalocyanine (CuPc).

## 2. Experimental

All TOF samples had a structure of indium-tin-oxide (ITO)/undoped-NPB or doped-NPB(7–10  $\mu\text{m}$ )/CuPc(100 nm)/Al(15 nm). Table 1, second column, shows the chemical structures of the host (NPB) and the dopants. All doped samples are represented with the notation NPB:X, where X is the name of the dopant. The full names of all dopants are spelt out in Table 1. Doping was achieved by thermal co-evaporation of the two materials (i.e. NPB and dopant) on

**Table 1**

Hole transport parameters of pristine and doped-NPB. The chemical structures of the host/dopants, and their energy levels are shown in the second and third columns, respectively.

Sample	Chemical structure of host/dopant	LUMO/HOMO[eV][10–15]	$\mu_h$ at $F = 0.29$ MV/cm and RT [ $\text{cm}^2/\text{Vs}$ ]	$\mu_0$ at RT [ $\text{cm}^2/\text{Vs}$ ]	$\mu_{\infty}$ [ $\text{cm}^2/\text{Vs}$ ]	$\sigma$ [meV]	$\Sigma$
NPB		–2.5/–5.5	$6.6 \times 10^{-4}$	$3.0 \times 10^{-4}$	$1.7 \times 10^{-2}$	75	1.3
NPB:ADN <sup>a</sup>		–2.6/–5.8	$6.1 \times 10^{-4}$	$2.9 \times 10^{-4}$	$1.5 \times 10^{-2}$	74	1.4
NPB:tBu-PBD <sup>b</sup>		–2.5/–6.1	$4.7 \times 10^{-4}$	$1.5 \times 10^{-4}$	$1.2 \times 10^{-2}$	74	1.6
NPB:BCP <sup>c</sup>		–3.0/–6.5	$6.2 \times 10^{-4}$	$2.3 \times 10^{-4}$	$1.4 \times 10^{-2}$	77	0.7
NPB:DCM1 <sup>d</sup>		–3.1/–5.3	$1.0 \times 10^{-4}$	$1.4 \times 10^{-5}$	$1.5 \times 10^{-2}$	100	1.8
NPB:DCM2 <sup>e</sup>		–3.1/–5.3	$1.5 \times 10^{-4}$	$1.5 \times 10^{-5}$	$1.5 \times 10^{-2}$	98	1.6
NPB:CuPc <sup>f</sup>		–3.5/–5.2	–	$4.2 \times 10^{-7}$ [fitted]	–	121 [fitted]	–

<sup>a</sup> ADN: 9, 10-di(2-naphthyl) anthracene.

<sup>b</sup> tBu-PBD: 2-(4-biphenyl)-5-(4-*tert*-butylphenyl)-1,3,4-oxadiazole.

<sup>c</sup> BCP: 2,9-dimethyl-4,7-diphenyl-1,10-phenanthroline.

<sup>d</sup> DCM1: 4-(dicyanomethylene)-2-methyl-6-(*p*-dimethylaminostyryl)-4H-pyran.

<sup>e</sup> DCM2: 4-(dicyanomethylene)-2-methyl-6-[2-(2,3,6,7-tetra-hydro-1H,5H-benzo[*ij*] quinolizin-8-yl)vinyl]-4H-pyran.

<sup>f</sup> CuPc: copper phthalocyanine.

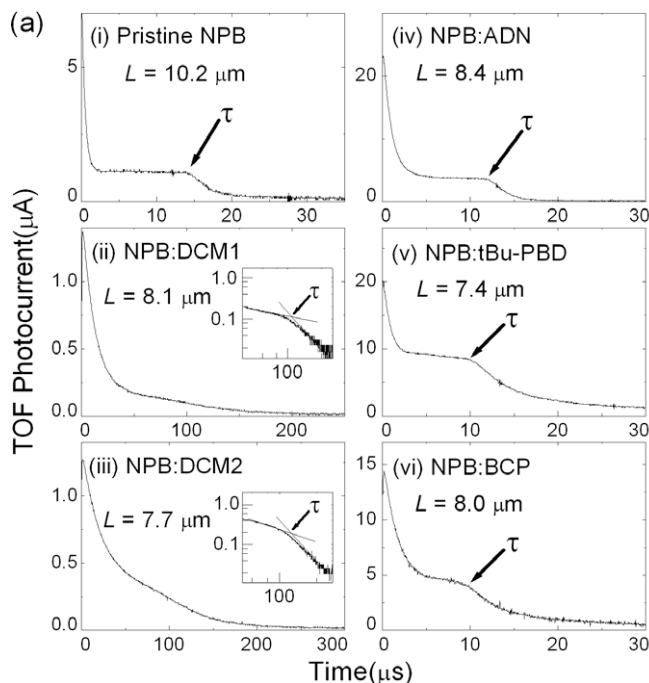
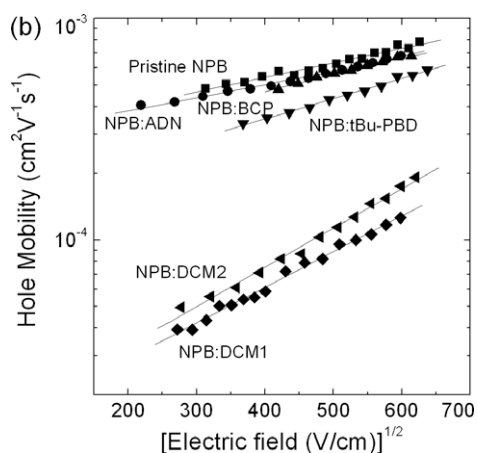


**Fig. 1a.** Typical time-of-flight transients for (i) Pristine NPB, (ii) NPB:DCM1 (iii) NPB:DCM2 (iv) NPB:ADN and (v) NPB:tBu-PBD (vi) NPB:BCP under an applied field of 0.14 MV/cm at room temperature. In (ii) and (iii), the insets show the log–log plots. The film thicknesses  $L$  are also shown.

ITO under a pressure of about  $10^{-6}$  Torr. The coating rate for NPB and the dopants were fixed at 9.85 and 0.15 Å/s, respectively. So, the doping concentration was fixed at 1.5% by volume. Three of the dopants, ADN, tBu-PBD, and BCP were chosen to act as hole scatterers in NPB because they possess low-lying highest occupied molecular orbitals (HOMO) relative to the HOMO of NPB (Table 1, third column) [10–13]. The other three dopants, DCM1, DCM2, and CuPc were chosen as hole traps in NPB because they have high-lying HOMO relative to NPB [14,15]. During hole mobility measurement, the sample was reverse-biased. A nitrogen pulsed laser ( $\lambda = 337.1$  nm) was irradiated on the semi-transparent Al/organic interface to generate electron-hole pairs. Since CuPc has strong absorption at 337.1 nm, over 90% of the incident photons were absorbed by the CuPc layer [16]. A dc power supply was used to provide the bias voltage for hole detection. Free holes are drifted towards the negatively biased anode.

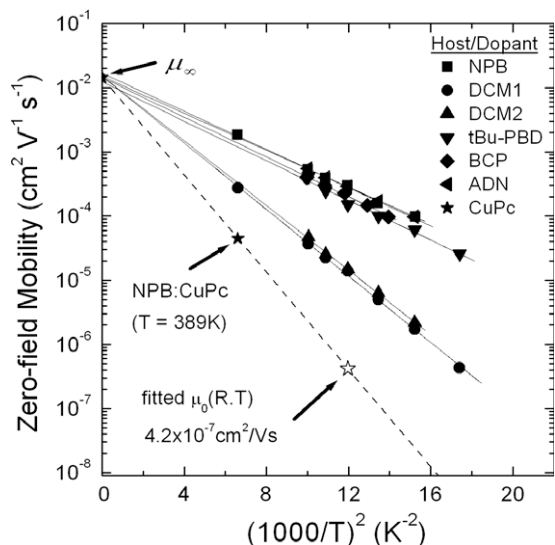
### 3. Results and discussion

Fig. 1a shows the representative TOF hole transients for pristine NPB and doped-NPB at room temperature and an applied electric field strength ( $F$ ) of 0.14 MV/cm. The hole transit time ( $\tau$ ) can be determined at the instant at which the plateau drops abruptly in the TOF signal. Pristine NPB exhibits non-dispersive hole transport with a very well-defined plateau region. Similarly, when NPB is doped with scatterers (i.e. ADN, tBu-PBD, and BCP), the plateau region is still evident for the extraction of  $\tau$ . When NPB is doped with traps (i.e. DCM1/2), the plateau region in the TOF signal is less evident. However,  $\tau$  can be defined from the



**Fig. 1b.** Hole mobilities of NPB and doped-NPB at room temperature. Solid lines are the best linear fits to the data.

inserted log–log plots of Fig. 1a(ii) and (iii). For CuPc-doped-NPB, the TOF signals were very dispersive.  $\tau$  cannot be determined at room temperature. This observation will be discussed later. Once the transit time is determined, the hole mobilities can be evaluated by  $\mu_h = L^2/(V \cdot \tau)$  where  $L$  is the thickness of the sample and  $V$  is the applied voltage [6]. Fig. 1b shows the hole mobilities for doped and pristine NPB at room temperature. A plot of  $\mu(F,T)$  vs  $\sqrt{F}$  generally yields a straight line. Extrapolation of this line to  $F=0$  results in  $\mu_0$ . Table 1, fifth column summarizes all  $\mu_0$  at room temperature. Subsequently, the experiment was re-



**Fig. 2.** The zero-field mobilities  $\mu_0$  vs  $(1000/T)^2$  for NPB (■) and doped-NPB. For a doped sample, the data are labeled with the name of the dopant. Solid lines are best linear fits to the data sets.  $\mu_\infty$  can be extracted from the y-intercept of these plots. For NPB:CuPc, only one data point labeled with the filled star symbol (★) can be determined from TOF signals at 389 K. The open star symbol (☆) is the extrapolated  $\mu_0$  of NPB:CuPc at room temperature (290 K).

peated at different temperatures to investigate the dependence of  $\mu_0$  on  $T$ . Fig. 2 shows the temperature dependences of  $\mu_0$  for pristine and doped-NPB. The temperature dependent mobility data were then analyzed by the Gaussian disorder model (GDM) [17]. The essence of the GDM can be embodied in the following equation for the carrier mobility:

$$\mu(F, T) = \mu_\infty \exp \left[ - \left( \frac{2\sigma}{3kT} \right)^2 \right] \exp \left\{ C \left[ \left( \frac{\sigma}{kT} \right)^2 - \Sigma^2 \right] F^2 \right\} \quad (2)$$

In Eq. (2),  $\mu_\infty$  is the high temperature limit of carrier mobility,  $\sigma$  is the energetic disorder,  $\Sigma$  is the positional disorder,  $T$  is the absolute temperature,  $k$  is the Boltzmann constant,  $F$  is the applied electric field, and  $C$  is a fitting constant. Generally,  $\ln(\mu_0) \sim -\frac{1}{T^2}$  as predicted by Eq. (2). For a particular sample,  $\mu_\infty$  and  $\sigma$  can be extracted from the y-intercept and the slope of this plot, respectively (Table 1, sixth and seventh columns). For pristine NPB, the extracted  $\mu_\infty$  and  $\sigma$  were about  $1.7 \times 10^{-2} \text{ cm}^2/\text{Vs}$  and 75 meV, respectively. From Fig. 1b, we see that charge scatterers (i.e. ADN, tBu-PBD, BCP) have little effects on hole mobilities or  $\mu_0$  in NPB. As a result, the temperature dependent  $\mu_0$  for undoped-NPB and NPB-doped with charge scatterers have almost overlapping data. In contrast, charge traps (i.e. DCM1, DCM2, CuPc) severely hinder hole mobilities in NPB. The reduction of  $\mu_0$  is more than one order down for NPB:DCM1 or NPB:DCM2 compared to the pristine case at room temperature (Table 1, fifth column). Irrespective of the nature of the dopant, we note that all samples appear to have a common y-intercept, i.e.  $\mu_\infty$ , from Fig. 2 (Table 1, sixth column). The mean value of

$\mu_\infty = 1.5 \pm 0.3 \times 10^{-2} \text{ cm}^2/\text{Vs}$  remain almost the same as the pristine case. This suggests that  $\mu_\infty$  is independent of the nature of dopants. At  $T \rightarrow \infty$ , it is expected that charge carriers gain sufficient thermal energy to overcome all energetic barriers which are formed by the dopant molecules. Hence, the  $\mu_\infty$  should not be affected by the presence of dopant molecules.

Below, we employ this common  $\mu_\infty$  to estimate the full temperature dependence of  $\mu_0$  for NPB:CuPc. When CuPc was doped into NPB, the mobile holes are severely trapped by CuPc molecule. This explains why the TOF transient for NPB:CuPc was very dispersive as shown in Fig. 3a. Subsequently, the temperature of the sample was increased. Non-dispersive signals with well-defined plateau regions were observed at  $T = 389 \text{ K}$ . An example is shown in Fig. 3b. Fig. 3 shows  $\mu_h$  ( $T = 389 \text{ K}$ ) of NPB:CuPc at different electric fields.  $\mu_0$  ( $T = 389 \text{ K}$ ) can be extracted from the y-intercept of this plot. This data point is shown with a “star” symbol (★) in Fig. 2. The full temperature dependence of  $\mu_0$ , however, still cannot be obtained experimentally. To obtain a full temperature dependence of  $\mu_0$ , we fit a straight line to  $\mu_\infty$  and  $\mu_0$  ( $T = 389 \text{ K}$ ) as shown in the dashed line in Fig. 2. With this fitted line, we can extrapolate the value of  $\mu_0$  at room temperature to be  $4.2 \times 10^{-7} \text{ cm}^2/\text{Vs}$  (open “star” symbol, ☆ in Fig. 2). The energetic disorder,  $\sigma$  can also be evaluated from the slope of the fitting line ( $= -\frac{4\sigma^2}{9(1000)^2 k^2}$ ), and the value is about 121 meV. These extrapolations concur with the expectations that  $\mu_h$  should be strongly reduced when deep traps (trap depth  $\sim 300 \text{ meV}$  for CuPc-doped into NPB) are introduced into NPB. The overlap between the HOMO of CuPc molecules and the upper part of the density of state of NPB would broaden the hopping transport manifold and lead to an increase in the energetic disorder [18]. The overall hole transport properties of NPB are summarized in Table 1.

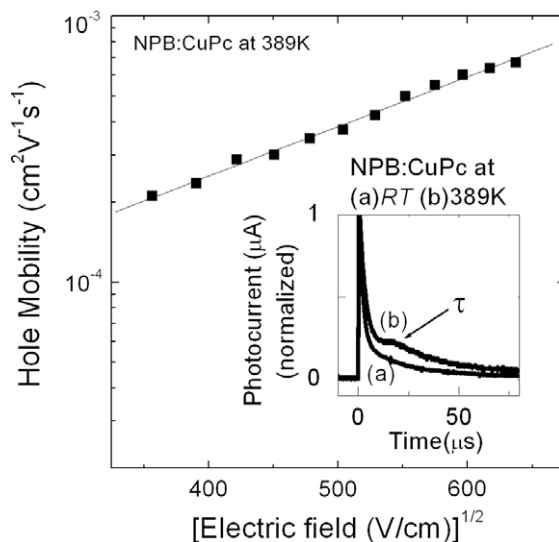


**Fig. 3.** Hole mobilities of NPB:CuPc at 389 K. Typical TOF transients of (a) NPB:CuPc at room temperature (RT), (b) NPB:CuPc at 389 K under an applied field of 0.2 MV/cm.

The mobility extrapolation of NPB:CuPc can be cross-examined by the classic work of Hoesterey and Letson (H&L) which was originally developed for organic crystals [19]. The formalism is based on discrete trap energy and devoid of the effects of disorder. They proposed that in the presence of traps, the mobility is given by:

$$\mu_{\text{trap}}(c) = \mu_{\text{trap-free}} f^{-1} = \mu_{\text{trap-free}} \left[ 1 + c \exp\left(\frac{E_t}{kT}\right) \right]^{-1} \quad (3)$$

where  $f$  is a trapping factor reflecting the transit time spent by a carrier in traps,  $\mu_{\text{trap-free}}$  is the trap-free mobility,  $c$  is the doping concentration,  $k$  is the Boltzmann constant, and  $E_t$  is the trap depth, i.e. the energy level difference between host and trap [18]. The validity of Eq. (3) has been demonstrated in small organic molecules [20,21]. Besides affecting the mobility, the presence of traps also affect the energetic disorder. From the well-known GDM and Eq. (3), the effective energetic disorder parameter ( $\sigma_{\text{eff}}$ ), which is the width of the cumulative density of states (DOS) in the presence of traps, can be described by [22]:

$$\left(\frac{\sigma_{\text{eff}}}{\sigma}\right)^2 = 1 + \left(\frac{3kT}{2\sigma}\right)^2 \left[ \ln(c) + \frac{E_t}{kT} \right] \quad \text{for } c \left[ \exp\left(\frac{E_t}{kT}\right) \right] \geq 1 \quad (4)$$

where  $\sigma$  is the intrinsic energetic disorder (i.e. the width of the intrinsic DOS in the absence of traps). Below, we employ Eqs. (3) and (4) to cross-examine the transport parameters extrapolated from Fig. 2 for NPB:CuPc.

For NPB:CuPc, substituting the known values of  $c \sim 0.015$ ,  $E_t \sim (5.5-5.2)\text{eV} = 0.3\text{eV}$ ,  $\mu_{\text{trap-free}}$  ( $\mu_0$  of NPB)  $\sim 3 \times 10^{-4}\text{cm}^2/\text{Vs}$ , and  $\sigma$  (NPB)  $\sim 75\text{meV}$  into Eqs. (3) and (4). It yields a  $\mu_{\text{trap}}$  of  $1.2 \times 10^{-7}\text{cm}^2/\text{Vs}$  ( $\mu_0$  of NPB:CuPc) and a  $\sigma_{\text{eff}}$  (NPB:CuPc) of 129 meV at room temperature. The computed results from the work of H&L only deviate with our mobility extrapolation ( $4.2 \times 10^{-7}\text{cm}^2/\text{Vs}$ ) within half an order and agree to our energetic disorder extrapolation (121 meV). Exact agreement is not expected between the computed results [by Eqs. (3) and (4)] and our extrapolated results in Fig. 2 as there is an uncertainty in  $E_t$  of at least  $\sim 0.1\text{eV}$  due to uncertainties in the HOMO values of NPB and CuPc. However, this agreement shows that  $\mu_{\infty}$  can be used to estimate the full temperature dependence of  $\mu_0$ .

#### 4. Conclusion

In conclusion, when dopants were introduced into NPB, the measured mobilities were reduced compared to the

intrinsic values, especially for the cases of trapping. However, the values of the  $\mu_{\infty}$  remain nearly the same as the pristine case. This indicates that  $\mu_{\infty}$  is indeed an intrinsic property of organic semiconductor, irrespective of the nature of dopants. The application of the common  $\mu_{\infty}$  for mobility extrapolation was demonstrated from the case of NPB:CuPc. The results generally agree to the classic work of Hoesterey and Letson.

#### Acknowledgements

Support of this research by the Research Committee of Hong Kong Baptist University under Grant No. FRG/06-07/II-73 and the Research Grant Council of Hong Kong under Grant No. HKBU210608E is gratefully acknowledged.

#### References

- [1] P.W.M. Blom, M.C.J.M. Vissenberg, Mater. Sci. Eng. R 27 (2000) 53.
- [2] J. Cornil, J.-L. Brédas, J. Zaumseil, H. Sirringhaus, Adv. Mater. 19 (2007) 1791.
- [3] L.S. Hung, C.H. Chen, Mater. Sci. Eng. R 39 (2002) 143.
- [4] G. Horowitz, Adv. Mater. 10 (1998) 365.
- [5] J. Xue, S. Uchida, B.P. Rand, S.R. Forrest, Appl. Phys. Lett. 84 (2004) 3013.
- [6] (a) S.K. So, S.C. Tse, K.L. Tong, J. Display Technol. 3 (2007) 225; (b) Y. Shirota, H. Kageyama, Chem. Rev. 107 (2007) 953.
- [7] H.C.F. Martens, P.W.M. Blom, H.F.M. Schoo, Phys. Rev. B 61 (2000) 7489.
- [8] N.I. Craciun, J. Wildeman, P.W.M. Blom, Phys. Rev. Lett. 100 (2008) 056601.
- [9] S.C. Tse, S.W. Tsang, S.K. So, J. Appl. Phys. 100 (2006) 063708.
- [10] Y. Hamada, H. Kanno, T. Tsujioka, H. Takahashi, T. Usuki, Appl. Phys. Lett. 75 (1999) 1682.
- [11] J. Shi, C.W. Tang, Appl. Phys. Lett. 80 (2002) 3201.
- [12] J. Kalinowski, M. Cocchi, P.D. Marco, W. Stampor, G. Giro, V. Fattori, J. Phys. D 33 (2000) 2379.
- [13] R.J. Holmes, S.R. Forrest, T. Sajoto, A. Tamayo, P.I. Djurovich, M.E. Thompson, J. Brooks, Y.J. Tung, B.W. D'Andrade, M.S. Weaver, R.C. Kwong, J.J. Brown, Appl. Phys. Lett. 87 (2005) 243507.
- [14] J. Lam, T.C. Gorjanc, Y. Tao, M. D'lorio, J. Vac. Sci. Technol. A 18 (2000) 593.
- [15] G. Parthasarathy, P.E. Burrows, V. Khalfin, V.G. Kozlov, S.R. Forrest, Appl. Phys. Lett. 72 (1998) 2138.
- [16] A.T. Davidson, J. Chem. Phys. 77 (1982) 168.
- [17] H. Bässler, Phys. Status Solidi B 175 (1993) 15.
- [18] (a) H.H. Fong, K.C. Lun, S.K. So, Chem. Phys. Lett. 353 (2002) 407; (b) K.L. Tong, S.W. Tsang, K.K. Tsung, S.C. Tse, S.K. So, J. Appl. Phys. 102 (2007) 093705.
- [19] D.C. Hoesterey, G.M. Letson, J. Phys. Chem. Solids 24 (1963) 1609.
- [20] A. Fleissner, H. Schmid, C. Melzer, H. Seggern, Appl. Phys. Lett. 91 (2007) 242103.
- [21] U. Wolf, H. Bässler, P.M. Borsenberger, W.T. Gruenbaum, Chem. Phys. 222 (1997) 259.
- [22] I.I. Fishchuk, A.K. Kadashchuk, A. Vakhnin, H. Bässler, B. Souharce, U. Scherf, Phys. Rev. B 73 (2006) 115210.



## *p*-Doped *p*-phenylenediamine-substituted fluorenes for organic electroluminescent devices

Zhi Qiang Gao<sup>a,d,\*</sup>, Ping Fan Xia<sup>b</sup>, Pik Kwan Lo<sup>b</sup>, Bao Xiu Mi<sup>a,d,1</sup>, Hoi Lam Tam<sup>a,c</sup>, Man Shing Wong<sup>a,b,\*</sup>, Kok Wai Cheah<sup>a,c</sup>, Chin H. Chen<sup>e</sup>

<sup>a</sup> Centre for Advanced Luminescence Materials, Hong Kong Baptist University, Kowloon Tong, Hong Kong, SAR China

<sup>b</sup> Department of Chemistry, Hong Kong Baptist University, Kowloon Tong, Hong Kong, SAR China

<sup>c</sup> Department of Physics, Hong Kong Baptist University, Kowloon Tong, Hong Kong, SAR China

<sup>d</sup> Institute of Advanced Materials, Nanjing University of Posts and Telecommunications, Nanjing, China

<sup>e</sup> Display Institute, Microelectronics and Information Systems Research Center, National Chiao Tung University, Hsinchu, Taiwan

### ARTICLE INFO

#### Article history:

Received 22 November 2008

Received in revised form 19 December 2008

Accepted 24 February 2009

Available online 12 March 2009

#### PACS:

78

#### Keywords:

Fluorene

*p*-Phenylenediamine

Hole injection material

Organic electroluminescent devices

Hole transporting materials

### ABSTRACT

Two novel *p*-phenylenediamine-substituted fluorenes have been designed and synthesized. Their applications as hole injection materials in organic electroluminescent devices were investigated. These materials show a high glass transition temperature and a good hole-transporting ability. It has been demonstrated that the 2,3,5,6-tetrafluoro-7,7,8,8-tetracyanoquinodimethane (F4-TCNQ) doped *p*-phenylene-diamine-substituted fluorenes, in which F4-TCNQ acts as *p*-type dopant, are highly conducting with a good hole-transporting property. The organic light emitting devices (OLEDs) utilizing these F4-TCNQ-doped materials as a hole injection layer were fabricated and investigated. The pure Alq<sub>3</sub>-based OLED device shows a current efficiency of 5.2 cd/A at the current density of 20 mA/cm<sup>2</sup> and the operation lifetime is 1500 h with driving voltage increasing only about 0.7 mV/h. The device performance and stability of this hole injection material meet the benchmarks for the commercial requirements for OLED materials.

© 2009 Elsevier B.V. All rights reserved.

### 1. Introduction

Organic semiconductors have been intensively studied as active materials in various electronic and optoelectronic devices because of the low cost, ability to tune the functional/material properties by means of chemical structural modifications, ease of fabrication, and feasibility for flexible devices [1]. In addition, the high absorptivity in the visible range of organic semiconductors offers the possibility

to prepare a thin-film for photovoltaic cells (OPV) and photodetectors [2]. Hence, in the past decade, these materials have been intensively studied as alternative active materials in various electronic and optoelectronic devices. Recently, enormous progresses have been made in tailoring properties of organic semiconductors through chemical structure modification [3]. Organic semiconductors are generally in the form of undoped amorphous state when used as carrier transporters in thin-film optoelectronic devices. However, the inherent low charge mobility of organic semiconductors resulting from the hopping transport in disordered organic thin-films often gives rise to a high operating voltage. For example, the hole mobility in amorphous organic thin-films is in the range of 10<sup>-3</sup>–10<sup>-5</sup> cm<sup>2</sup> v<sup>-1</sup> s<sup>-1</sup>, which is about 1000 times lower than that of the amorphous Si thin-film. To improve the

\* Corresponding authors. Address: Department of Chemistry, Centre for Advanced Luminescence Materials, Hong Kong Baptist University, Kowloon Tong, Hong Kong, SAR China. Tel.: +852 3411 7069; fax: +852 3411 7348.

E-mail address: [mswong@hkbu.edu.hk](mailto:mswong@hkbu.edu.hk) (M.S. Wong).

<sup>1</sup> Present address: Institute of Advanced Materials, Nanjing University of Posts and Telecommunications, Nanjing, China



conductivity of organic semiconductors, doping concepts have been adopted from their inorganic counterparts. Similar to the conventional doping in inorganic semiconductors, the basic concept of doping in organic semiconductor is to add a strong electron-donor or electron-acceptor which either transfer an electron to the lowest unoccupied molecular orbital (LUMO) of a host molecule to produce a free electron (*n*-type doping) or remove an electron from the highest occupied molecular orbital (HOMO) of a host molecule to generate a free hole (*p*-type doping) [4]. In this concept, by matching the LUMO/HOMO of the dopant to the HOMO/LUMO of the organic semiconductor, the Fermi level of the organic semiconductor can be successfully shifted towards the transport states, and hence, the organic devices will be beneficial from reducing ohmic losses, lowering carrier injection barriers and increasing the built-in potential of Schottky- or *p*-*n*-junctions [5]. The organic optoelectronic device with a hole transporting layer (HTL) doped with *p*-type dopant such as 2,3,5,6-tetrafluoro-7,7,8,8-tetracyanoquinodimethane (F4-TCNQ), and an electron transporting layer (ETL) doped with *n*-type dopant such as alkali metal atoms are widely reported, and the device structure is known as *p*-*i*-*n* [6]. Currently, *p*-*i*-*n* organic light emitting devices (OLED) [7] and *p*-*i*-*n* OPV [8] are two of the hot topics in the organic optoelectronic devices due to the improved ohmic contact and electrical conductivity in the devices. For instance, a very low-operation-voltage multilayered OLED with high efficiency has been achieved by combining a thick F4-TCNQ doped 4,4',4''-tris(*N,N*-diphenylamino)-triphenylamine (TDATA) as a HTL with a thin undoped buffer layer [9]. This OLED exhibits a turn-on voltage of 2.5 V at a luminance of 1 cd/m<sup>2</sup> and an operating voltage of 3.4 V at a luminance of 100 cd/m<sup>2</sup> for pure tris-(8-hydroxyquinoline) aluminum (Alq<sub>3</sub>) device without dopant emitter. Most recently, a *p*-*i*-*n* white OLED reached a high efficiency of 23.3 lm/W [10]; and a *p*-*i*-*n* red phosphorescent OLED obtained an external quantum efficiency of 12.4% with extremely high lifetime of about 1 × 10<sup>7</sup> h [11]. Among the *p*-doped hole transporting systems, F4-TCNQ is the state-of-art dopant, and most of the host materials for *p*-doping are based on the wide bandgap amorphous hole transporting materials with triphenylamine unit, such as 4,4',4''-tris-*N*-naphthyl-*N*-phenylamino-triphenylamine (TNATA), *N,N,N',N'*-tetrakis-(4-methoxyphenyl)benzidine (MeO-TPD) [7a], 4,4',4''-tris(3-methylphenyl-phenyl-amino)triphenylamine (m-MTDA-TA) [7b]. Low bandgap metal phthalocyanines can also be efficiently doped with F4-TCNQ. However, phthalocyanines are not well suited for OLEDs due to their small energy gap between HOMO and LUMO levels of phthalocyanines, which leads to re-absorption and electron injection from the emitting layer to the HTL [12]. Other type of materials that can be doped with F4-TCNQ are very rarely reported. In the practical point of view, device stability is an important issue that governs the key factor to realize the success of commercialization. In order to achieve the practically targeted stability, organic semiconductors with high thermal stability are necessary to be developed. Fluorene derivatives have been received considerable attention as potential candidates for the ac-

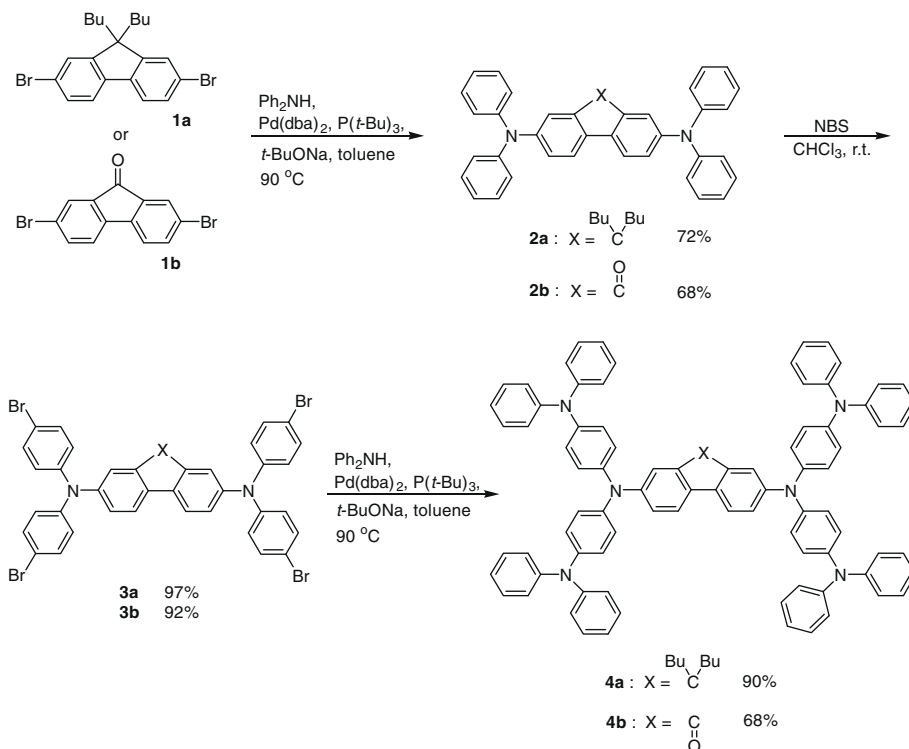
tive materials in OLED due to their good chemical stability and high luminescence over the past decade [13]. By attaching appropriate functional substituent, fluorene derivatives can act as a HTL [14], or an ETL [15], or a deep-blue emitting material (EM) [16] in OLEDs. To the best of our knowledge, there is no report on the applications of fluorene derivatives as a *p*-doping host in OLEDs. In this contribution, we have designed and synthesized two new *p*-phenylenediamine-substituted fluorenes for the hole injection application. It is anticipated that these materials show a high glass transition temperature (*T*<sub>g</sub>) and a good hole transport ability because of the highly thermally stable nature of fluorene and phenylenediamine moieties as well as the good hole transporting property of phenylenediamine functional group. We have demonstrated that controlled *p*-type doping system using F4-TCNQ as a dopant can be extended to materials with a fluorene core which was found to be efficient and stable in application of OLED devices. It has been shown that high conductivities can be achieved through doping with F4-TCNQ in these two derivatives. On the other hand, for good device performance, the ionization potential of the host also plays an important role. The lower the ionization potential of the host, the better is the performance. The best Alq<sub>3</sub>-based OLED device using such a host material doped with F4-TCNQ as a hole injection layer (HIL) shows an efficiency of 5.2 cd/A and operation lifetime of 1500 h at 20 mA/cm<sup>2</sup>, with the driving voltage increasing about 0.7 mV/h. This material with the best performance can be used to replace the currently employed triphenylamine based HIL materials.

## 2. Results and discussion

### 2.1. Synthesis and characterization

Scheme 1 shows the synthetic route utilized to prepare *p*-phenylenediamine-substituted fluorenes, **4a** and **4b**. 2,7-dibromofluorene derivatives **1a** and **1b** were prepared according to the literature procedures [16a]. Double amination of 2,7-dibromofluorene derivatives **1a** and **1b** with two equivalent of diphenylamine in the presence of Pd(OAc)<sub>2</sub>:2P(*o*-tolyl)<sub>3</sub> as a catalyst afforded the corresponding diamination product **2a** and **2b** in 72% and 68% yield, respectively. Bromination of diphenylamino end-capped fluorene derivatives **2a** and **2b** with NBS in chloroform yielded tetrabromo-substituted intermediates **3a** and **3b** in excellent yields. Palladium catalyzed amination of **3a** and **3b** with diphenylamine afforded the desired *p*-phenylenediamine-substituted fluorene derivatives in good yields. All the newly synthesized hole injection materials were fully characterized with <sup>1</sup>H NMR, <sup>13</sup>C NMR, MALD-TOF HRMS, and elemental analysis and found to be in good agreement with their structures. The detail procedures are shown in experimental section. These fluorene derivatives were purified by the flash column chromatography and degassed under vacuum before used for deposition.

Table 1 summarizes the physical properties measured by the corresponding techniques. As determined by differential scanning calorimeter and thermal gravimetric ana-



**Scheme 1.** Synthesis of *p*-phenylenediamine-substituted fluorene derivatives **4a** and **4b**.

**Table 1**

Summaries of physical measurements of **4a** and **4b**.

	Absorption band/nm <sup>a</sup>	$E_{1/2}^{\text{oxd}}/\text{V}^b$	$E_p^{\text{red}}/\text{V}^b$	HOMO/eV <sup>c</sup>	LUMO eV <sup>d</sup>	$T_g/^\circ\text{C}^e$	$T_{\text{dec}}/^\circ\text{C}^f$
<b>4a</b>	309/354/394	0.39, 0.52, 0.86	−1.00	−5.07	−2.16	126	521
<b>4b</b>	314/348/400	0.48, 0.58, 0.89	−1.27	−5.16	−2.34	146	590

<sup>a</sup> Measured in  $\text{CHCl}_3$ .

<sup>b</sup>  $E_{1/2}^{\text{oxd}}$  (or  $E_p^{\text{red}}$ ) vs. SCE estimated by CV method using platinum disc electrode as a working electrode, platinum wire as a counter electrode, and SCE as a reference electrode with an agar salt bridge connecting to the oligomer solution and ferrocene was used as an external standard,  $E_{1/2}(\text{Fc}/\text{Fc}^+) = 0.50 \text{ V}$  vs. SCE).

<sup>c</sup> Determined by ultraviolet photoemission spectroscopy using Surface Analyzer model AC-2.

<sup>d</sup> LUMO = HOMO – Optical Bandgap.

<sup>e</sup> Determined by differential scanning calorimeter with a heating rate of  $10 \text{ } ^\circ\text{C min}^{-1}$  under  $\text{N}_2$ .

<sup>f</sup> Determined by thermal gravimetric analyzer with a heating rate of  $10 \text{ } ^\circ\text{C min}^{-1}$  under  $\text{N}_2$ .

lyzer with a heating rate of  $10 \text{ } ^\circ\text{C min}^{-1}$  under  $\text{N}_2$ , both fluorene derivatives possess a high glass transition temperature ( $T_g$ ),  $> 125 \text{ } ^\circ\text{C}$  and thermal decomposition temperature ( $T_{\text{dec}}$ ),  $> 520 \text{ } ^\circ\text{C}$ , respectively. Such high  $T_g$  values are superior to most of the commonly used hole transporting materials (i.e.  $T_g$  of 4,4',4''-tris(*N*-(2-naphthyl)-*N*-(phenylamino)triphenylamine (2T-NATA) =  $110 \text{ } ^\circ\text{C}$ ) [17]. It is well-known that the higher the  $T_g$  of a material, the better is the morphological stability of an organic thin-film. Hence, high morphological stability is anticipated using these materials as a hole transporting material in an OLED application.

Cyclic voltammetry (CV) was carried out in a three-electrode cell set-up with 0.1 M of  $\text{Bu}_4\text{NPF}_6$  as a supporting electrolyte in  $\text{CH}_2\text{Cl}_2$  to examine the electrochemical properties of these molecules. All the potentials reported are referenced to  $\text{Fc}/\text{Fc}^+$  standard and the results are tabulated

in Table 1. These fluorene derivatives exhibit a low first reversible one-electron anodic redox wave corresponding to phenylenediamine oxidation with  $E_{1/2}^{\text{oxd}1}$  at 0.39–0.48 V and followed by a reversible one-electron and two-electron anodic redox waves with  $E_{1/2}^{\text{oxd}2}$  at 0.52–0.58 V and  $E_{1/2}^{\text{oxd}3}$  at 0.86–0.89 V, respectively. Such a facile first electrochemical oxidation of phenylenediamine moiety suggests a very low first ionization potential of the materials which was confirmed by the estimated HOMO level around  $-5.1 \text{ eV}$  as determined by ultraviolet photoemission spectroscopy. The low HOMO level make them feasible to be removed an electron to generate a free hole upon doped with a strong electron-acceptor. On the other hand, these fluorene derivatives also exhibit an irreversible cathodic wave with  $E_{1/2}^{\text{red}1}$  at  $-1.00$  to  $-1.27 \text{ eV}$ , which corresponds to the formation of the radical anion on the fluorene/fluorone core.

## 2.2. Charge-transfer complex of **4** and F4-TCNQ

Due to the strong electron-donating nature of **4** and the strong electron-accepting property of F4-TCNQ, **4** and F4-TCNQ can interact to form a charge-transfer (CT) complex via partial electron transfer upon mixing with which free carriers would be generated as depicted in Fig. 1. There are two possible reaction routes for one-electron transfer between electron-donor **4** and electron-acceptor F4-TCNQ, as shown in Fig. 1. Assuming that there is only one route dominates the one-electron transfer process, the reaction between **4** (represented as *D*) and F4-TCNQ (represented as *A*) can be written as [18]:



where,  $E_{1A}$  and  $E_{1D}$  are the first reduction potential of the electron-acceptor and the first oxidation potential of the electron-donor, respectively. Thus the equilibrium constant (*K*) for electron transfer can be given:

$$\log K = \log \left[ \frac{[D^+][A^-]}{[D][A]} \right] = \frac{E_{1A} - E_{1D}}{0.059} \quad (2)$$

Using  $E_{1D}$  of 0.39 and 0.48 V for **4a** and **4b** from Table 1, respectively and  $E_{1A}$  of 0.568 V for F4-TCNQ [19], the reaction constants of  $K_{4a-F4-TCNQ}$  and  $K_{4b-F4-TCNQ}$  obtained were  $10^{3.02}$  and  $10^{1.49}$ , respectively. With such large positive values, the corresponding reactions for one-electron transfer between **4** and F4-TCNQ are likely to occur. The occurrence of such electron transfer reactions are also reflected in the UV–Vis absorption spectra as shown in Fig. 2. Upon addition of F4-TCNQ, new bands/peaks at longer wavelengths appear in the solution mixture as compared to the spectra of their pure solutions. In the **4a** and **4b** absorption spectra, there are no absorption above 700 nm, while the mixture of F4-TCNQ with **4a** and **4b** show additional strong absorption peaks around 760 and 870 nm, which are attributed to the absorption of anion radical of F4-TCNQ [20]. Concomitantly, the absorption intensity of F4-TCNQ decreases dramatically

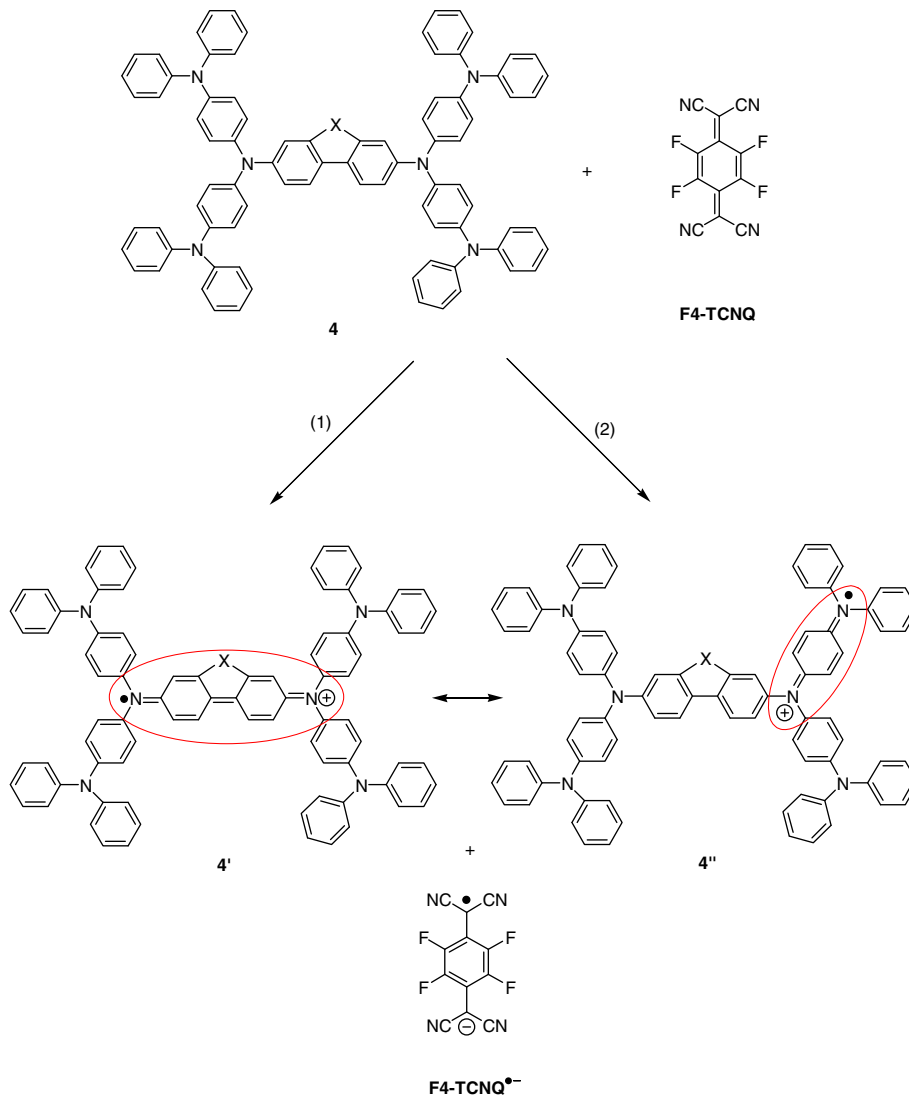
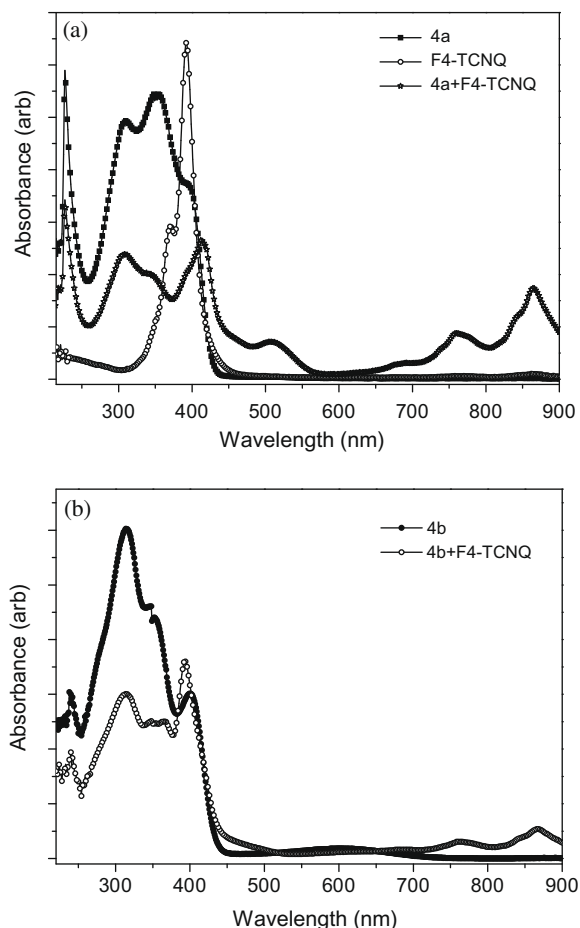


Fig. 1. Possible reaction mechanism for electron-donor **4** and electron-acceptor F4-TCNQ.

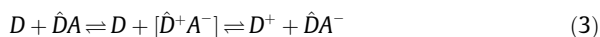


**Fig. 2.** (a) UV-Vis absorption of **4a** ( $10^{-5}$  M), F4-TCNQ ( $10^{-5}$  M) and **4a** ( $10^{-5}$  M) + F4-TCNQ ( $10^{-5}$  M) in DCM and (b) UV-Vis absorption of **4b** ( $10^{-5}$  M) and **4b** ( $10^{-5}$  M) + F4-TCNQ ( $10^{-5}$  M) in DCM.

in the solution mixture. This illustrates that the charge transfer (CT) complex is formed between **4a** (and **4b**) and F4-TCNQ which also implies that these materials doped with F4-TCNQ would form a good *p*-type system. In addition, the charge transfer band of F4-TCNQ doped **4a** system was about 10 times higher than that of F4-TCNQ doped **4b** system, suggesting a more efficient charge transfer between F4-TCNQ and **4a** than F4-TCNQ and **4b**. This may explain the better hole conduction in the **4a** doped with F4-TCNQ thin-film shown in the next section.

### 2.3. *p*-Type doping properties in thin-films

From a chemical point of view, in amorphous thin-films, the *p*-type doping of a hole transporting molecules *D* by electron-acceptor molecules *A* is determined by a mass action law (In this case, *D* concentration is much higher than *A* concentration):



Here, *D* is a random matrix molecule and  $\hat{D}$  is the matrix molecule adjacent to the electron-acceptor, which is sup-

posed to give the electron to the acceptor in the initial charge transfer step, this is exactly the reaction shown in Fig. 1 and Eq. (1). Thus, the intermediate state  $[\hat{D}^+A^-]$  is a local charge transfer state, where the charges may be bound by different interactions and form a kind of complex. The final state is assumed to be unbound, i.e. the matrix molecule that carries the positive charge is so far away from the ionized acceptor that it does not feel the Coulomb interaction. In such a situation, the positive charge can move by hopping and the density of  $D^+$  can be associated with the hole density *p*. If a very strong electron-acceptor is used and the initial charge transfer (first step of reaction (3)) is complete, the hole density will be governed by the second step of reaction (3). The problem of the generation of free carriers is not only about the Coulomb attraction between two molecules with opposite charge. It is about the difference in the total energy between the following two states: (a) a matrix with a certain density of charged acceptors with holes bound to the acceptors and (b) the same matrix with mobile holes. Here, all kind of structural relaxation and quantum chemical reorganization processes have to be considered [21]. In our case, it could be thought or assumed that the F4-TCNQ acceptors could react with the host molecules in a great extent or even completely because of the energetically favorable reaction and the small electron-acceptor concentration. Therefore, the free hole density in the doping system shall be only controlled by the dissociation of the intermediate state  $[\hat{D}^+A^-]$ . In other words, besides the high tendency for electron transfer from electron-donor to electron-acceptor, another important factor that influences the conductivity of the doped system is the status of the intermediate  $[\hat{D}^+A^-]$ : the easier the dissociation, the higher conductivity is the doped system.

In order to study the hole transporting properties of **4a** and **4b** without or with doping, we fabricated hole-only devices with the structure of ITO/**4a** and **4b** with 0% or 1.5% F4-TCNQ (60 nm)/NPB (10 nm)/Al (where NPB = *N,N'*-bis-(1-naphthyl)-*N,N'*-diphenyl-1,1'-biphenyl-4,4'-diamine). *N,N'*-bis-(1-naphthyl)-*N,N'*-diphenyl-1,1'-biphenyl-4,4'-diamine). For comparison, the 2T-NATA hole-only devices with and without F4-TCNQ were fabricated simultaneously. The *I*-*V* measurements were carried out on these devices and the results are shown in Fig. 3. It is clearly indicated that the F4-TCNQ doped films of **4a**, **4b** and 2T-NATA exhibit significantly higher current as compared to their undoped counterparts, demonstrating high conductivity in the doped films. In the F4-TCNQ doped systems, **4a**-based film shows a greater improvement in conductivity with about 2–3 orders of magnitude increase in hole current with respect to the undoped film. It is important to note that the current densities of F4-TCNQ doped **4a**, **4b**, and 2T-NATA hole-only devices at 3 V are 135, 6.6 and 51.8 mA/cm<sup>2</sup>, respectively. These findings are consistent with the HOMO data determined which indicate that the HOMO level of **4a** is lower than that of **4b** and 2T-NATA, as shown in Table 1. In addition, the absorption spectra in the doping system indicate that the degree of charge transfer in **4a**/F4-TCNQ system is higher than that of **4b**/F4-TCNQ system due to the lower HOMO of **4a**. Therefore, F4-TCNQ doped **4a** film showed higher hole conductivity than those of F4-TCNQ doped **4b** and 2T-NATA

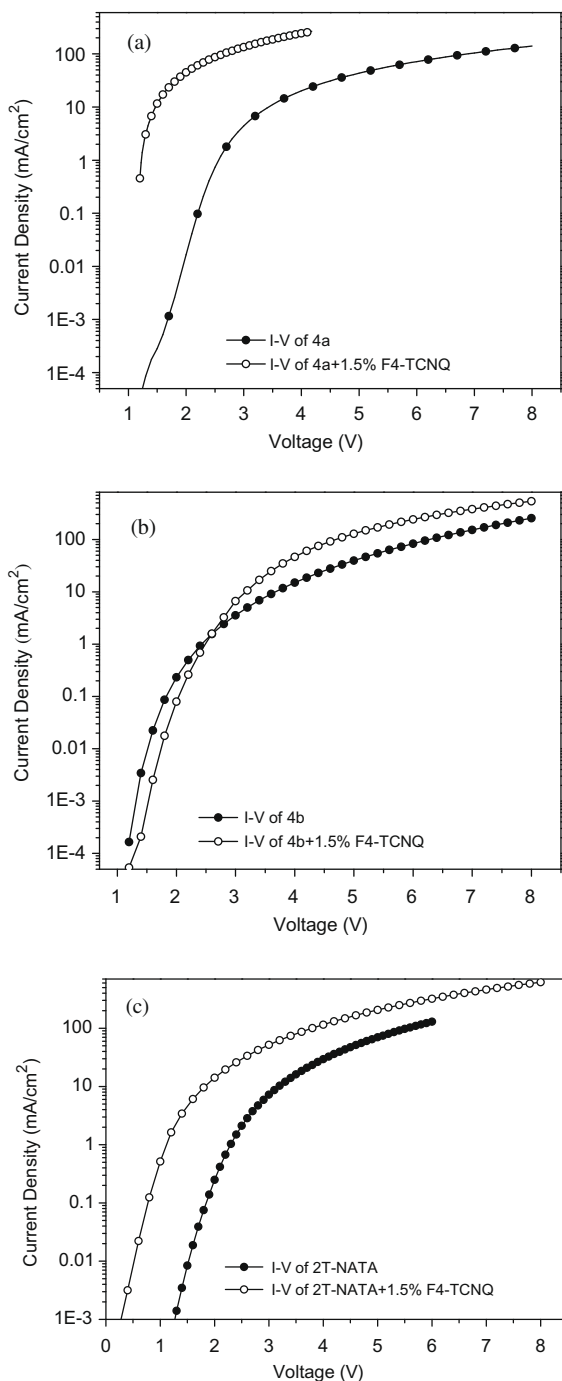


**Fig. 3.** I–V characteristics of (a) **4a**, (b) **4b**, and (c) 2T-NATA hole-only devices with and without F4-TCNQ.

films. As a result, **4a** is anticipated to be a better candidate for the *p*-type doping host material than 2T-NATA.

#### 2.4. Application in OLED devices

Encapsulated OLED devices with a sheet desiccant inside a glass cover were fabricated using F4-TCNQ doped

**4a** and **4b** as a HIL. The device structure is ITO/**4a** or **4b**:1.5% F4-TCNQ (150 nm)/NPB (10 nm)/Alq<sub>3</sub> (60 nm)/LiF (1 nm)/Al. The performance of the devices was tested and the *I–V–B* characteristics are shown in Table 2 and Fig. 4. The operation lifetimes were measured at a constant current of 20 mA/cm<sup>2</sup>. The lifetime was recorded after a 10-h burn-in. For comparison, the OLED using 2T-NATA doped with F4-TCNQ as a HIL was also fabricated and tested under the same conditions. The results are summarized in Table 2.

Due to the doping of HIL, a high luminance is achieved at low voltage which results in a high power efficiency even though a comparatively thick HTL (160 nm in thickness) is used. For the **4a**-based device, the turn-on voltage, defined as the bias at a brightness of 1 cd/m<sup>2</sup>, is only 2.7 V. At 20 mA/cm<sup>2</sup>, the device driving voltage is 6.0 V and current efficiency is 5.2 cd/A as compared to the commonly used 2T-NATA doped with F4-TCNQ as a HIL, the driving voltage is 6.7 V with a current efficiency of 4.5 cd/A at the same current density. These results indicate that **4a** is a superior material for the HIL in OLED. For **4b**-based device, it shows a slightly higher driving voltage which agrees with its relatively inferior hole transporting properties in F4-TCNQ doped thin-film and a shorter lifetime. Fig. 5 shows the stability curve of **4a**-based device to its half brightness. As shown in the figure that such an OLED device has an operation lifetime of 1500 h at 20 mA/cm<sup>2</sup>, and the driving voltage increasing is about 0.7 mV/h. This result demonstrates that our material **4a** is a very useful and stable *p*-type dopant host for the use of OLEDs and has a great potential for practical applications.

### 3. Experimental

#### 3.1. Synthesis

**2a.** A mixture of 2,7-dibromo-9,9-bis(*n*-butyl)fluorene, **1a** (4.36 g, 10.0 mmol), diphenylamine (3.72 g, 22.0 mmol), palladium(II) acetate (0.11 g, 0.5 mmol), tri-(*o*-tolyl)phosphine (0.30 g, 1.0 mmol) and sodium *tert*-butoxide (2.88 g, 30.0 mmol) in dry toluene (50 mL) was stirred under a nitrogen atmosphere at 110 °C for 24 h. After cooling to room temperature, the reaction mixture was poured into a saturated aqueous solution of ammonium chloride and extracted with dichloromethane (3 × 60 mL). The combined organic extract was washed with water and dried over anhydrous Na<sub>2</sub>SO<sub>4</sub>. Evaporation of volatiles gave a brown solid, which was separated by silica gel column chromatography using petroleum ether/dichloromethane as a gradient eluent affording **2a** in 72% yield (4.4 g) as a white solid. <sup>1</sup>H NMR (400 MHz, CDCl<sub>3</sub>, δ) 7.47 (d, *J* = 8.0 Hz, 2H), 7.22–7.25 (m, 8H), 7.07–7.13 (m, 10H), 6.97–7.01 (m, 6H), 1.73–1.77 (m, 4H), 1.02–1.10 (m, 4H), 0.72 (t, *J* = 7.6 Hz, 6H), 0.64–0.67 (m, 4H). <sup>13</sup>C NMR (100 MHz, CDCl<sub>3</sub>, δ) 152.0, 148.0, 146.4, 136.2, 129.1, 123.7, 123.6, 122.3, 119.7, 119.4, 54.9, 39.7, 26.1, 22.9, 13.9. MS (MALDI-TOF) *m/z* 612.8 (*M*<sup>+</sup>).

**2b.** The synthetic procedure for **2a** was followed using 2,7-dibromofluorenone, **1b** (3.38 g, 10.0 mmol), Ph<sub>2</sub>NH (3.72 g, 22.0 mmol), *t*-BuONa (2.88 g, 30.0 mmol), Pd(OAc)<sub>2</sub>

**Table 2**  
Summaries of OLED Performance.

Device <sup>a</sup>	HIL	Turn On/V <sup>b</sup>	V <sub>20</sub> /V	CE <sub>20</sub> /cd/A <sup>c</sup>	Lifetime <sub>20</sub> /h <sup>d</sup>
I	2T-NATA	2.7	6.7	4.5	1600
II	<b>4a</b>	2.7	6.0	5.2	1500
III	<b>4b</b>	3.1	7.6	3.4	1100

<sup>a</sup> Device I: ITO/2T-NATA:1.5%F4-TCNQ(150 nm)/NPB(10 nm)/Alq<sub>3</sub>(60 nm)/LiF(1 nm)/Al. Device II: ITO/**4a**:1.5%F4-TCNQ(150 nm)/NPB(10 nm)/Alq<sub>3</sub>(60 nm)/LiF(1 nm)/Al. Device III: ITO/**4b**:1.5%F4-TCNQ(150 nm)/NPB(10 nm)/Alq<sub>3</sub>(60 nm)/LiF(1 nm)/Al.

<sup>b</sup> Turn on is the voltage to show 1 cd/m<sup>2</sup> luminance.

<sup>c</sup> CE<sub>20</sub> refers to the current efficiency under 20 mA/cm.

<sup>d</sup> Lifetime<sub>20</sub> presents the lifetime at constant driven-current of 20 mA cm.

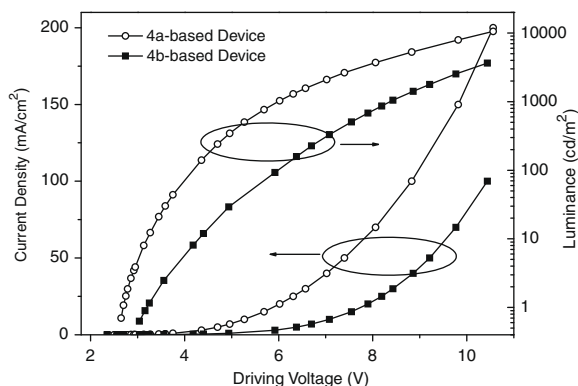


**Fig. 4.** I–V–B characteristic of **4a**- and **4b**-based OLED devices.

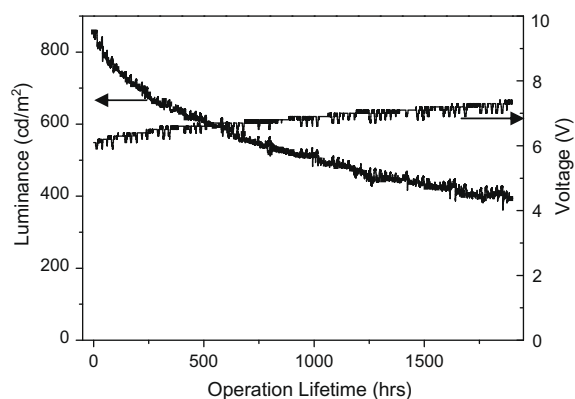


**Fig. 5.** Operation lifetime of **4a**-based OLED device.

(0.11 g, 0.5 mmol), P(*o*-tolyl)<sub>3</sub> (0.30 g, 1.0 mmol) and dry toluene (50 mL). The product was purified by silica gel column chromatography using petroleum ether/dichloromethane as a gradient eluent affording 3.48 g (68%) of **2b** as a dark red solid. <sup>1</sup>H NMR (400 MHz, CDCl<sub>3</sub>, δ) 7.24 (d, *J* = 2.0 Hz, 2H), 7.14–7.19 (m, 10H), 6.94–7.04 (m, 14H). <sup>13</sup>C NMR (100 MHz, CDCl<sub>3</sub>, δ) 193.3, 148.1, 147.0, 137.9, 135.7, 129.4, 128.5, 124.5, 123.4, 120.3, 119.3. HRMS (MALDI-TOF) Calc. for C<sub>37</sub>H<sub>26</sub>N<sub>2</sub>O: 514.2040. Found: 514.2041.

**3a.** A mixture of **2a** (4.28 g, 7.0 mmol) and NBS (5.0 g, 28.0 mmol) in 50 mL of CHCl<sub>3</sub> were stirred at room temperature for 4 h. Evaporation of solvent under vacuum re-

sulted in a yellow solid that was adsorbed on silica gel and purified by flash column chromatography using dichloromethane/petroleum ether mixture as eluent affording **3a** in 97% yield (6.30 g) as a white solid. <sup>1</sup>H NMR (400 MHz, CDCl<sub>3</sub>, δ) 7.49 (d, *J* = 8.0 Hz, 2H), 7.34 (d, *J* = 8.8 Hz, 8H), 7.02 (d, *J* = 2.0 Hz, 2H), 6.97 (m, 10H), 1.75–1.79 (m, 4H), 1.02–1.10 (m, 4H), 0.72 (t, *J* = 7.2 Hz, 6H), 0.61–0.69 (m, 4H). <sup>13</sup>C NMR (100 MHz, CDCl<sub>3</sub>, δ) 152.3, 146.6, 145.6, 136.6, 132.2, 125.1, 123.6, 120.1, 119.3, 115.2, 55.0, 39.6, 26.1, 22.9, 14.0. MS (MALDI-TOF) *m/z* 928.1 (M<sup>+</sup>).

**3b.** The above procedure for **3a** was followed using **2b** (3.4 g, 6.6 mmol) and NBS (4.71 g, 26.5 mmol). The crude product was purified by silica gel flash column chromatography using dichloromethane/petroleum ether mixture as eluent affording **3b** in 92% yield (5.04 g) as a dark purple solid. <sup>1</sup>H NMR (400 MHz, CDCl<sub>3</sub>, δ) 7.37 (d, *J* = 8.8 Hz, 8H), 7.28–7.30 (m, 4H), 7.11 (dd, *J* = 2.0, 8.0 Hz, 4H), 6.94 (d, *J* = 8.8 Hz, 8H). <sup>13</sup>C NMR (100 MHz, CDCl<sub>3</sub>, δ) 192.7, 147.4, 145.6, 138.6, 135.8, 132.6, 129.0, 125.8, 120.8, 119.6, 116.4. MS (MALDI-TOF) *m/z* 829.9 (M<sup>+</sup>).

**4a.** A dried 250 mL two-necked flask containing the solution of **3a** (4.64 g, 5.0 mmol), Ph<sub>2</sub>NH (4.06 g, 24.0 mmol), *t*-BuONa (2.88 g, 30.0 mmol), Pd(dba)<sub>2</sub> (116 mg, 0.2 mmol), tri-*tert*-butylphosphine (40 mg, 0.2 mmol) and 70 mL of dry toluene was heated at 90 °C overnight with good stirring under N<sub>2</sub>. After cooling to room temperature, the purple-blue mixture was poured into a saturated aqueous solution of ammonium chloride and extracted twice with toluene. The combined organic layers were washed with brine, dried over anhydrous magnesium sulfate and evaporated under vacuum. The residue was rapidly eluted through silica gel column using toluene/hexane (4:1) to give crude product, which was further purified by crystallization from EtOAc/EtOH affording 5.44 g (85% yield) of **4a** as a light-yellow solid. <sup>1</sup>H NMR (400 MHz, C<sub>6</sub>D<sub>6</sub>, δ) 7.35–7.38 (m, 4H), 7.21 (dd, *J* = 1.6, 8.0 Hz, 2H), 7.12–7.16 (m, 24H), 7.00–7.08 (m, 24H), 6.83 (t, *J* = 7.6 Hz, 8H), 1.70–1.73 (m, 4H), 0.94–1.07 (m, 4H), 0.84–0.91 (m, 4H), 0.63 (t, *J* = 7.6 Hz, 6H). <sup>13</sup>C NMR (100 MHz, C<sub>6</sub>D<sub>6</sub>, δ) 152.5, 148.4, 147.1, 143.7, 143.0, 136.5, 129.5, 125.9, 125.0, 124.2, 123.7, 122.7, 120.4, 119.4, 55.2, 40.0, 26.5, 23.2, 14.1. HRMS (MALDI-TOF) calc. for C<sub>93</sub>H<sub>80</sub>N<sub>6</sub>: 1281.6471. Found: 1281.6514. Anal. Calc. for C<sub>93</sub>H<sub>80</sub>N<sub>6</sub>: C 87.15, H 6.29, N 6.56. Found: C 87.30, H 6.19, N 6.40.

**4b.** The general amination procedure was followed using **3b** (2.1 g, 2.53 mmol), Ph<sub>2</sub>NH (2.06 g, 12.2 mmol),

Pd(dba)<sub>2</sub> (58.7 mg, 0.1 mmol), P(*t*-Bu)<sub>3</sub> (20.2 mg, 0.1 mmol), *t*-BuONa (1.46 g, 15.2 mmol) and toluene. The crude product was purified by silica gel flash column chromatography (toluene/hexane) and then by crystallization from THF/CH<sub>3</sub>OH affording 2.03 g (68% yield) of **4b** as a red solid. <sup>1</sup>H NMR (400 MHz, C<sub>6</sub>D<sub>6</sub>, δ) 7.68 (d, *J* = 2.0 Hz, 2H), 7.09–7.13 (m, 18H), 7.02–7.06 (m, 16H), 6.93–6.98 (m, 16H), 6.89 (d, *J* = 8.0 Hz, 2H), 6.83 (t, *J* = 7.2 Hz, 8H). <sup>13</sup>C NMR (100 MHz, C<sub>6</sub>D<sub>6</sub>, δ) 192.7, 148.6, 148.2, 144.0, 142.2, 137.9, 136.4, 129.6, 127.6, 125.9, 125.5, 124.5, 123.0, 120.6, 118.6. HRMS (MALDI-TOF) calc. for C<sub>85</sub>H<sub>62</sub>N<sub>6</sub>O: 1182.4980; Found: 1182.4988. Anal. Calc. for C<sub>85</sub>H<sub>62</sub>N<sub>6</sub>O: C 86.27, H 5.28, N 7.10; found: C 86.14, H 5.17, N 7.02.

### 3.2. Device fabrication

OLED and hole-only devices were fabricated using a vacuum thermal evaporation chamber with a base pressure of  $1 \times 10^{-6}$  Torr. All the materials were deposited in one pump-down. Two shadow masks were used to define the deposition areas for organic and metal cathode, respectively. The *I*-*V* characteristics of hole-only devices were measured with a computer-controlled DC power supply at room temperature in open air. OLED devices were encapsulated with sheet desiccant under dry N<sub>2</sub> atmosphere before measurements. The luminance of OLEDs was measured with PR650 spectrophotometer and a KETHLEY 236 source meter. The lifetime of OLED device was recorded by a homemade lifetime measurement system at constant current mode. The ionization potential (or HOMO) of a thin-film was measured by ultraviolet photoemission spectroscopy using Surface Analyzer model AC-2.

### 4. Conclusions

In summary, we have designed and synthesized two new *p*-phenylenediamine-substituted fluorenes, **4a** and **4b** which possess a high glass transition temperature and a good hole transport ability. The *p*-type doping properties of these materials were studied using F4-TCNQ as a *p*-type dopant in hole-only device. Furthermore, the mechanism in the doping system was discussed and some insights were highlighted. The OLED device with a HIL utilizing **4a/4b** doped with F4-TCNQ were fabricated and characterized. The pure Alq<sub>3</sub>-based device using **4a** doped with F4-TCNQ as a HIL shows an operation lifetime of 1500 h at 20 mA/cm<sup>2</sup>, and the driving voltage increasing about 0.7 mV/h. These results suggest that **4a** is a useful and stable hole injection material for OLEDs which shows a great potential for practical applications.

### Acknowledgements

This work is supported by Guangdong-HK ITF (GHP/057/05), Research Grants Council of Hong Kong, Earmarked

Research Grant HKBU 202507, Nanjing University of Posts and Telecommunications Grant NY207162 and Natural Science Foundation of Jiangsu High Education under Grant 08KJB430011.

### References

- [1] C.D. Dimitrakopoulos, P.R.L. Malenfant, *Adv. Mater.* 14 (2002) 99.
- [2] (a) P. Peumans, A. Yakimov, S.R. Forrest, *J. Appl. Phys.* 93 (2003) 3693; (b) S. Günes, H. Neugebauer, N.S. Sariciftci, *Chem. Rev.* 107 (2007) 1324.
- [3] (a) T.P.I. Saragi, T. Spehr, A. Siebert, T. Fuhrmann-Lieker, J. Salbeck, *Chem. Rev.* 17 (2007) 1011; (b) A. Gadisa, W. Mammo, L.M. Andersson, S. Admassie, F. Zhang, M.R. Andersson, O. Inganäs, *Adv. Func. Mater.* 17 (2007) 3836.
- [4] (a) C.K. Chan, E.-G. Kim, J.-L. Bredas, A. Kahn, *Adv. Funct. Mater.* 16 (2006) 831; (b) Z.Q. Gao, B.X. Mi, G.Z. Xu, Y.Q. Wan, M.L. Gong, K.W. Cheah, C.H. Chen, *Chem. Commun.* (2008) 117.
- [5] M. Pfeiffer, K. Leo, X. Zhou, J.S. Huang, M. Hofmann, A. Werner, J. Blochwitz-Nimoth, *Org. Electron.* 4 (2003) 89.
- [6] K. Walzer, B. Maennig, M. Pfeiffer, K. Leo, *Chem. Rev.* 107 (2007) 1233.
- [7] (a) J.S. Huang, M. Pfeiffer, A. Werner, J. Blochwitz, K. Leo, S. Liu, *Appl. Phys. Lett.* 80 (2002) 139; (b) G. He, M. Pfeiffer, K. Leo, *Appl. Phys. Lett.* 85 (2004) 3911.
- [8] B. Maennig, J. Drechsel, D. Gebeyehu, P. Simon, F. Kozlowski, A. Werner, F. Li, S. Grundmann, S. Sonntag, M. Koch, K. Leo, M. Pfeiffer, H. Hoppe, D. Meissner, N.S. Sariciftci, I. Riedel, V. Dyakonov, J. Parisi, *Appl. Phys. A* 79 (2004) 1.
- [9] X. Zhou, M. Pfeiffer, J. Blochwitz, A. Werner, A. Nollau, T. Fritz, K. Leo, *Appl. Phys. Lett.* 78 (2001) 410.
- [10] G. Schwartz, M. Pfeiffer, S. Reineke, K. Walzer, K. Leo, *Adv. Mater.* 19 (2007) 3672.
- [11] R. Meerheim, K. Walzer, M. Pfeiffer, K. Leo, *Appl. Phys. Lett.* 89 (2006) 061111.
- [12] X. Zhou, J. Blochwitz, M. Pfeiffer, A. Nollau, T. Fritz, K. Leo, *Adv. Funct. Mater.* 11 (2001) 310.
- [13] P. Chen, G. Yang, T. Liu, T. Li, M. Wang, W. Huang, *Polym. Int.* 55 (2006) 473.
- [14] (a) K.-F. Shao, Y.-F. Li, L.-M. Yang, X.-J. Xu, G. Yu, Y.-Q. Liu, *Chem. Lett.* 34 (2005) 1604; (b) Z.H. Li, M.S. Wong, H. Fukutani, Y. Tao, *Chem. Mater.* 17 (2005) 5032.
- [15] (a) L. Oldridge, M. Kastler, K. Müllen, *Chem. Commun.* (2006) 885; (b) Z.H. Li, M.S. Wong, Y. Tao, H. Fukutani, *Org. Lett.* 9 (2007) 3659.
- [16] (a) Z.H. Li, M.S. Wong, Y. Tao, J.P. Lu, *Chem. Eur. J.* 11 (2005) 3285; (b) Z.Q. Gao, Z.H. Li, P.F. Xia, M.S. Wong, K.W. Cheah, C.H. Chen, *Adv. Funct. Mater.* 17 (2007) 3194; (c) T.-C. Chao, Y.-T. Lin, C.-Y. Yang, T.S. Hung, H.-C. Chou, C.-C. Wu, K.-T. Wong, *Adv. Mater.* 17 (2005) 992; (d) P.A. Levermore, R. Xia, W. Lai, X.H. Wang, W. Huang, D.D.C. Bradley, *J. Phys. D: Appl. Phys.* 40 (2007) 1896.
- [17] Y. Shirota, H. Kageyama, *Chem. Rev.* 107 (2007) 953.
- [18] R.C. Wheland, *J. Am. Chem. Soc.* 98 (1976) 3926.
- [19] Notes: At Ref [4b], the first reduction potential of F4-TCNQ was measured as 0.61 V vs. Ag/AgCl electrode in saturated KCl solution, where the potential of reference electrode itself is 0.200 V. According to the SCE potential of 0.242, the first reduction potential of F4-TCNQ vs. SCE is calculated as: 0.61 + 0.200 – 0.242 = 0.568 V.
- [20] L.R. Melby, R.J. Harder, W.R. Hertlbr, W. Mahler, R.E. Benson, W.E. Mochel, *J. Am. Chem. Soc.* 84 (1962) 3374.
- [21] B. Kramer (Ed.), *Advances in Solid State Physics*, vol. 39, Vieweg, Braunschweig, Wiesbaden, 1999, pp. 77–90.

enhancing processability and increasing the quantum efficiency. The bulky functional alkyl groups are expected to reduce aggregation of the perylene derivatives as is the case in conjugated polymers [12]. The successful synthesis of the 3,4,9,10-tetra-(12-alkoxycarbonyl)-perylene molecule reported here is a practical implementation of the aforementioned theories resulting in a product with improved solubility and reduced aggregation.

The two-photon-absorption (TPA) properties of derivatives of perylene have been scarcely investigated [13–16] and yet are extremely useful for potential applications in two-photon-pumped frequency up conversion lasers [14], TPA optical limiters [17], three-dimensional optical storage, three-dimensional photo polymerisation, photodynamic therapy, micro fabrication and microlithography [18–23]. The synthesis of new nonlinear optical (NLO) materials is fundamental in the development of optoelectronic technologies [24]. The open-aperture Z-scan is a convenient and quick experimental method for analysis of nonlinear optical properties of materials [25] and has been successfully applied in this paper.

Herein is presented the synthesis, characterisation and optical limiting properties of the novel 3,4,9,10-tetra-(12-alkoxycarbonyl)-perylene. The parent molecule was chosen as 3,4,9,10-perylene-tetracarboxylic-dianhydride (PTCDA) an archetypal molecule whose basic properties have been studied for more than a decade [26]. In addition, in this paper, we demonstrate the useful nonlinear optical property of this dye.

## 2. Experimental

### 2.1. Synthesis

A 95% yield of 3,4,9,10-tetra-(12-alkoxycarbonyl)-perylene was produced by refluxing 1 g of PTCDA in a 5:1 1-iodododecane ( $\text{CH}_3(\text{CH}_2)_{11}\text{I}$ ) and 1-dodecanol ( $\text{CH}_3(\text{CH}_2)_{11}\text{OH}$ ) mix over 5 g of potassium carbonate ( $\text{K}_2\text{CO}_3$ ) at 110 °C for 7 days (see Scheme 1). The product was dissolved in chloroform and the  $\text{K}_2\text{CO}_3$  filtered out. The chloroform was extracted, followed by a filtration yielding a golden yellow product which was dried in a vacuum oven at 60 °C. The compound was characterised by  $^1\text{H}$ NMR,  $^{13}\text{C}$ NMR, FTIR, mass spectroscopy and chemical analysis to confirm the product. The sharp  $^1\text{H}$ NMR peaks obtained are indicative of very high material purity.

$^1\text{H}$  NMR (400 MHz,  $\text{CDCl}_3$ ):  $\delta$  0.89 (t, 12H,  $\text{CH}_3$ ), 1.44 (m, 72H, 9( $\text{CH}_2$ )), 1.50 (m, 8H, O–C– $\text{CH}_2$ ), 4.33 (t, 8H, O–C– $\text{CH}_2$ ), 8.05 (d, 4H, CH), 8.30 (d, 4H, CH).  $^{13}\text{C}$  NMR (100 MHz,  $\text{CDCl}_3$ ) 14.2, 22.7, 26.0, 28.6, 29.3, 29.5, 29.6, 29.7, 31.9, 66.6, 121.4, 128.9, 1129.1, 130.4, 133.1, 168.5. FTIR (NaCl):  $\nu$  = 2954.0, 2919.4, 2850.3, 1731.9, 1719.6, 1584.5, 1471.9,

1292.2, 1279.5, 1173.5, 747.2  $\text{cm}^{-1}$ . MS 1100. Anal. Calc. for  $\text{C}_{72}\text{H}_{108}\text{O}_8$ : C 78.50%, H 9.88%, (M, 1100) Found: 77.54.0%, 9.81%, ( $\text{M}^+$ , 1100)].

### 2.2. Characterisation

The  $^1\text{H}$ NMR spectra were recorded on a Bruker Avance III 400 spectrometer with a proton resonance of 400.23 MHz.  $^{13}\text{C}$ NMR were recorded on a Bruker Avance III 400 spectrometer with a C resonance of 100.65 MHz, tip angle of 30°, an acquisition time of 0.5 s and a relaxation delay of 1 s. Tetramethoxysilane (TMS) was used as the internal reference with deuterated chloroform ( $\text{CDCl}_3$ ) as the NMR solvent. A Micromass LCT Orthogonal Acceleration TOF Electrospray mass spectrometer was used to determine the molecular weight of the compound. The FTIR spectra were taken on a Nicolet NEXUS FTIR spectrometer in the transmission mode. UV–Vis absorption was recorded on a CARY 6000i UV–Vis–NIR spectrophotometer. The fluorescence was carried out on a PerkinElmer LS55 Luminescence Spectrometer. Thermal responses were studied using PerkinElmer Thermo gravimetric Analyser Pyris TGA and PerkinElmer Pyris Diamond DSC. Structural studies were carried out on a Nanoscope 111a AFM machine, a Hitachi S-4300 Field Emission microscope operating in high vacuum mode for HRSEM images and a Jeol 2100 Transmission Electron Microscope.

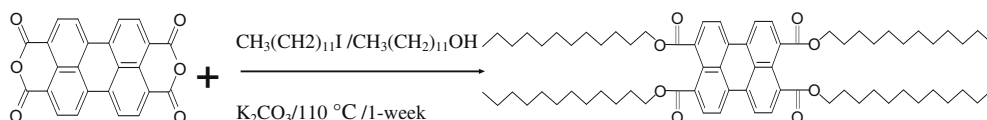
### 2.3. Nonlinear optical measurement

The Z-scan technique is a well-known method applicable to study the nonlinear optical properties of materials, including nonlinear absorption, scattering or refraction [25]. A standard open-aperture Z-scan system [24,27] was used to measure the nonlinear extinction (NLE) coefficients, as well as the optical limiting properties of 3,4,9,10-tetra-(12-alkoxycarbonyl)-perylene at 1  $\text{g cm}^{-3}$  chloroform solution concentration. The experiment was performed using 6 ns pulses from a Q-switched Nd:YAG laser. The laser, operating at its second harmonic, 532 nm, with a pulse repetition rate of 10 Hz, was spatially filtered to remove higher-order modes, and tightly focused with a 9 cm focal length lens. In order to enhance NLO response, all samples were tested in 1 cm quartz cells [27,28].

## 3. Experimental results and discussion

### 3.1. Solubility

The Hildebrand solubility parameter is chosen as a measure of solubility since its solvent spectrum includes the



**Scheme 1.** Chemical reaction for the synthesis of 3,4,9,10-tetra-(12-alkoxycarbonyl)-perylene from PTCDA.



complete solvent range and most solubility scales can be easily related to it. The Hildebrand solubility parameter,  $\delta$ , of a material is given by the square root of the cohesive energy density as in Eq. (1) [29,30].

$$\delta = \sqrt{\left(\frac{\Delta E}{V}\right)} \quad (1)$$

The cohesive energy density is the energy  $\Delta E$  needed to remove a molecule from its nearest neighbours per unit volume  $V$  of the moved molecule. The enthalpy of mixing of a solution,  $\Delta H_{mix}$ , can then be calculated from Eq. (2),

$$\Delta H_{mix} = V_{mix}(\delta_1 - \delta_2)\Phi_1\Phi_2 \quad (2)$$

where  $V_{mix}$  is the total volume of is mixing,  $\delta_1$  is the Hildebrand solubility parameter of the solvent,  $\delta_2$  is the Hildebrand solubility parameter of the solute,  $\Phi_1$  and  $\Phi_2$  are the respective solvent and solute volume fractions [30]. A good solution is formed at zero enthalpy of mixing and this occurs when the solute and solvent Hildebrand solubility parameters are the same, hence the chemistry adage “Like dissolves like”.

At room temperature, the parent molecule in the synthesis PTCDA, was found to be best soluble in NMP,  $\delta = 23.1$  (MPa)<sup>1/2</sup> and weak or partially soluble in both pyridine  $\delta = 21.7$  (MPa)<sup>1/2</sup> and DMSO  $\delta = 26.4$  (MPa)<sup>1/2</sup> [31]. These results suggest a Hildebrand solubility parameter for PTCDA as  $(23 \pm 2)$  (MPa)<sup>1/2</sup>. PTCDA is therefore best soluble in polar aprotic solvents. Previous studies have shown that PTCDA is insoluble or poorly soluble in organic solvents [32]. The solvents which minimize the enthalpy of mixing for PTCDA are generally harsh and toxic therefore not preferred for use in device fabrication due to the inherently low solubility, the production of PTCDA based devices is mostly by thermal evaporation with extremely high expenses. The synthesis of 3,4,9,10-tetra-(12-alkoxycarbonyl)-perylene from PTCDA adds 12-C chain alkyl groups to the peri-positions of the perylene core making it easily soluble at room temperature in most common organic solvents like chloroform  $\delta = 18.7$  (MPa)<sup>1/2</sup>, dichloromethane  $\delta = 20.2$  (MPa)<sup>1/2</sup>, tetrahydrofuran  $\delta = 18.5$  (MPa)<sup>1/2</sup> and toluene  $\delta = 18.3$  (MPa)<sup>1/2</sup> [31]. This improvement in solubility makes device fabrication in solution possible by such methods as spin coating, dipping and/or casting which are less expensive relative to thermo sublimation. The soluble product can also be easily blended with polymers in such cases as the production of optoelectronic devices where bulky heterojunctions are made from intimate mixtures of donors and acceptors, as is the case in organic photovoltaic cells, so reducing the chance of exciton recombination. The improvement in solubility can be attributed to the introduction of the alkoxycarbonyl groups which reduce the interaction between the perylene rings.

### 3.2. Linear optical properties

Dilute solutions of 3,4,9,10-tetra-(12-alkoxycarbonyl)-perylene have an intense yellowish-green colour and show a bright emission when exposed to ordinary light.

Fig. 1 shows the normalized absorption and fluorescence spectra of 3,4,9,10-tetra-(12-alkoxycarbonyl)-perylene in chloroform. The spectra are strongly structured

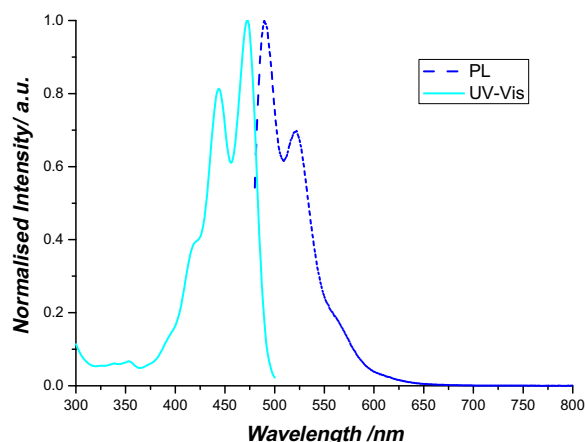
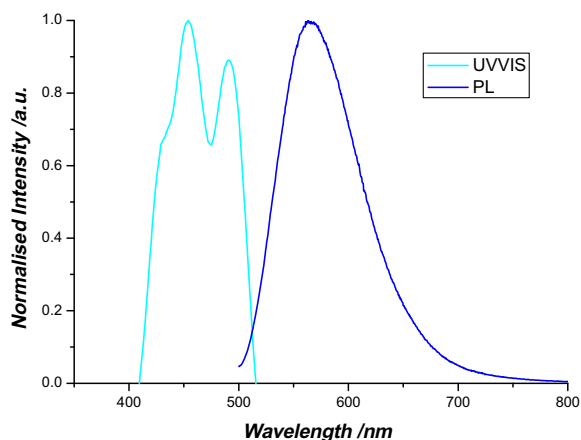


Fig. 1. Normalized absorption and fluorescence spectra of 3,4,9,10-tetra-(12-alkoxycarbonyl)-perylene in chloroform.

with peak wavelengths for absorption and fluorescence at 472 and 489 nm, respectively, resulting in a narrow Stokes's shift of 17 nm. A second absorption peak occurs at 444 nm with a shoulder occurring at 417 nm. This structure is similar to the perylene ring progression of  $\pi-\pi^*$   $S_0-S_1$  or  $S_1-S_0$  transitions [7]. The fluorescence spectrum is a close mirror image of the absorption spectra but with different relative intensities. Previous studies on similar materials of the form 3,4,9,10-tetra-(*n*-alkoxycarbonyl)-perylene where  $2 \leq n \leq 10$  showed similar spectra confirming that the perylene core has a greater influence on the absorption and emission rather than the alkyl chain length [7,33,34]. In fact, this observation is consistent independent of the position of substitution in all perylene derivatives, be it peri-, bay- or at the N-atom in perylene imides [3,33]. The absorption and emission peaks remain the same independent of solvent, as is the case for relative peak intensities, but the actual intensities decrease in the order dichloromethane, chloroform, toluene and tetrahydrofuran. The peak integrals for absorption increased linearly with wavelength and were proportional to the concentration. The energy difference between peaks is 0.16 eV, about the same (0.15 eV) as that of the benzene ring stretch oscillation of perylene [35]. This suggests that the dilute series absorbances are controlled by monomeric absorption. No shift in the peak wavelengths was observed for concentration dependent UV-Vis in the individual solvents. The photoluminescence excitation spectra resembled the absorption spectra in solution.

Fig. 2 shows the normalized absorption and fluorescence of a spin cast film of the compound from a chloroform solution. Both spectra are very broad, unstructured and bathochromically shifted compared to the spectra of the monomeric solution. This red shift and broadening are due to fluorescence emanating from excimers owing to the different energetic environments [36]. For absorption, the trend is attributed to additional interactions between individual molecules and their surroundings, much stronger in the solid phase than in monomeric solution. Evidence of aggregation in thin films of perylene derivatives usually occurs in the form of an additional absorption



**Fig. 2.** Normalized absorption and fluorescence spectra of 3,4,9,10-tetra-(12-alkoxycarbonyl)-perylene spin cast onto glass from a chloroform solution.

peak around 570 nm [37]. The absence of this absorption peak in the case of 3,4,9,10-tetra-(12-alkoxycarbonyl)-perylene is possibly due to lack of dimmers or higher aggregates as a result of steric hindrance by the bulky alkyl chains. For the emission spectra, there is no corresponding band in the absorption spectra thus the mirror symmetry exhibited in solution is lost. The formation of excimers in thin films is highly likely as the distance between adjacent molecules is much shorter than in solution.

The optical band gap was determined by applying the Tauc relation [38,39], given in Eq. (3), to the optical absorption edge of the thin film of 3,4,9,10-tetra-(12-alkoxycarbonyl)-perylene,

$$Ahv = (hv - E_g)^n \quad (3)$$

where  $A$  is the absorbance,  $E_g$  is the band gap corresponding to a specific absorption in the thin film,  $h\nu$  is the photon energy and  $n$  has the values 1/2, 2, 3/2, and 3, respectively for allowed direct, allowed indirect, and forbidden indirect transitions materials. An extrapolation of absorbance to zero on the straight line section of the plot of absorbance squared versus photon energy (Fig. 3.), was used to determine the optical band gap as 3.81 eV. The exciton energy,  $E_{ex}$ , 2.63 eV, determined from  $E_{ex}(\text{eV}) = 1240/\lambda_{max}$ , gives 1.2 eV as the exciton binding energy for the 3,4,9,10-tetra-(12-alkoxycarbonyl)-perylene. This suggests Frenkel type excitons and consequently a small dielectric constant for the material conclusive also from the dielectric constants of the solvents in which it readily dissolves. This result is consistent with previous findings on the exciton binding energies of small molecule or oligomeric organic semiconductors [40].

The results of a concentration dependence fluorescence study are shown in Fig. 4 on a logarithmic scale. An initial study using a 10 mm × 10 mm cuvette revealed a deviation from linearity at high concentrations. This would normally be attributed to some complex processes like aggregation or some equivalent effect. Rickard et al. have shown that the deviation is due to the inner filter effect and re-absorption [41]. The inner filter effect is attributed

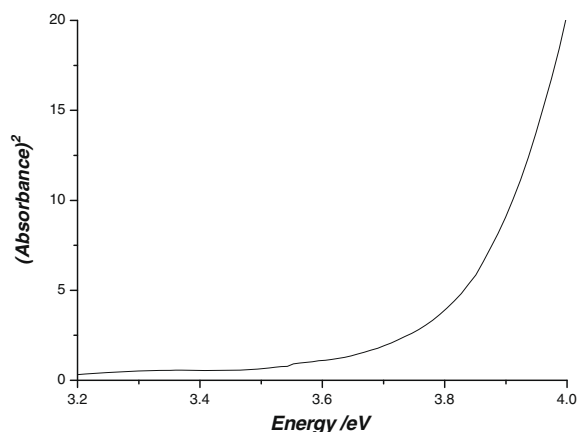


**Fig. 3.** Van Tauc plot of absorbance squared vs. photon energy for determination of the band gap energy of 3,4,9,10-tetra-(12-alkoxycarbonyl)-perylene by extrapolation to zero absorbance.

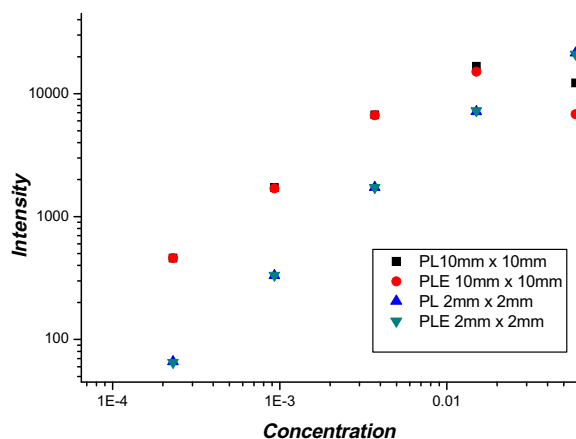


**Fig. 4.** Concentration dependent photoluminescence, PL, and photoluminescence excitation, PLE, results of 3,4,9,10-tetra-(12-alkoxycarbonyl)-perylene in chloroform, showing the response to cuvette path length.

to the instrument, where light absorbed by the cuvette's edge will fluoresce but the detector is not able to detect the fluorescence. Re-absorption occurs where the fluorescence emission and absorption spectra overlap as shown in the region just below 500 nm in Fig. 1. The use of a smaller path length cuvette reduces the two effects and more so re-absorption. A second study using a 2 mm × 2 mm micro-cuvette showed linearity over the whole range of concentrations and so suggesting absence of or reduced aggregation or equivalent effects.

### 3.3. Thermal responses

Fig. 5 shows the TGA and its first derivative (DTGA) curves for 3,4,9,10-tetra-(12-alkoxycarbonyl)-perylene performed in an air environment at a scan rate of 10 °C/min. The 3,4,9,10-tetra-(12-alkoxycarbonyl)-perylene is thermally stable up to 300 °C in air which is very good for normal everyday operations. The onset of the weight loss begins around 300 °C and is completed at 557 °C with

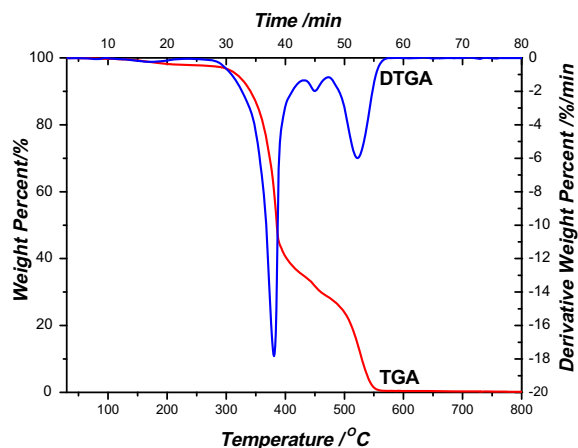


Fig. 5. The thermal response TGA and its derivative DTGA of 3,4,9,10-tetra-(12-alkoxycarbonyl)-perylene at 10 °C/min in air.

100% weight loss. This trend is similar to that of perylene, the aromatic core for 3,4,9,10-tetra-(12-alkoxycarbonyl)-perylene. The first and second endothermic peaks at 300 and 450 °C, respectively can therefore be attributed to the destruction of the perylene core, the third endothermic peak at 521 °C corresponds to of any remaining organics. In some perylene imides, the alkyl group on the diimide nitrogen is lost between 416 and 513 °C [3,42].

The melting point for 3,4,9,10-tetra-(12-alkoxycarbonyl)-perylene was determined using DSC to be at 80 °C (Fig. 6). This is much lower than that of the parent molecules PTCDA which is above 200 °C. Introduction of alkyl chains to the aromatic perylene core lowers the melting temperature independent of the position to which the chain is added [3,7]. The low melting point implies that boiling water can be used to achieve melting. The liquid crystalline phase is absent in the DSC trace, normally present in similar 3,4,9,10-tetra-(*n*-alkoxycarbonyl)-perylene for  $2 \leq n \leq 9$ . Previous studies [7] have shown that these 3,4,9,10-tetra-(*n*-alkoxycarbonyl) perylenes form liquid crystals for  $n = 2$  to  $n = 9$  with the  $n = 10$  showing no liquid crystalline phase just like the  $n = 12$  being reported here.

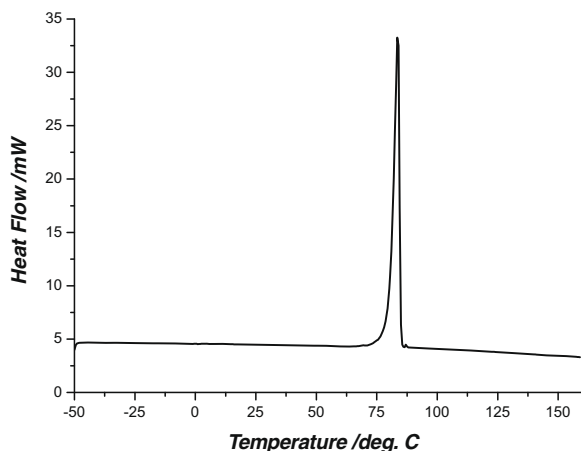


Fig. 6. A DSC trace of 3,4,9,10-tetra-(12-alkoxycarbonyl)-perylene.

This gives partial support for the reduced aggregation behavior. The molecular volume is much smaller for shorter C-chains than for longer ones, thus the higher molecular volume due to long chains is unfavorable for stacking.

### 3.4. Morphology

Dilution series of 3,4,9,10-tetra-(12-alkoxycarbonyl) perylene in chloroform were spin cast and drop cast onto glass, ITO and Si(111) substrates for structural studies using scanning electron microscopy (SEM) and contact mode atomic force microscopy (AFM). As shown in Fig. 7, the AFM micrographs of spin cast solutions on respective substrates indicate clusters less than 7 nm in height. Compared to drop cast samples, the clusters in the spin cast films are less coalescent whereas extended coalescence is observed in drop cast films. This trend was also confirmed by SEM (Fig. 8).

In drop cast films, the coalescence increases with concentration as does the height of the clusters. Two possibilities are pertinent to the formation of clusters, they are either formed dynamically during film formation or they already exist in solution. Further studies are currently underway to investigate this trend. Transmission electron microscopy (TEM) studies have revealed nanoparticles less than 100 nm in diameter as source of the clusters (Fig. 9).

### 3.5. Optical limiting

The NLE coefficient,  $\beta_{\text{eff}}$ , for the 3,4,9,10-tetra-(12-alkoxycarbonyl)-perylene solution in chloroform was measured by the open aperture Z-scan method at 532 nm. The incident laser pulsed energy used in the Z-scan measurement was altered from 0.10 to 0.32 mJ. The corresponding on-focus beam intensity varied from 0.68 to 1.91 GW cm<sup>-2</sup>. All Z-scans performed in this experiment

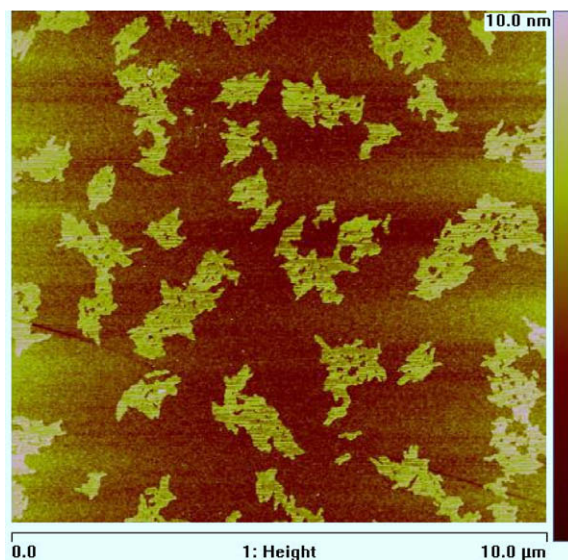
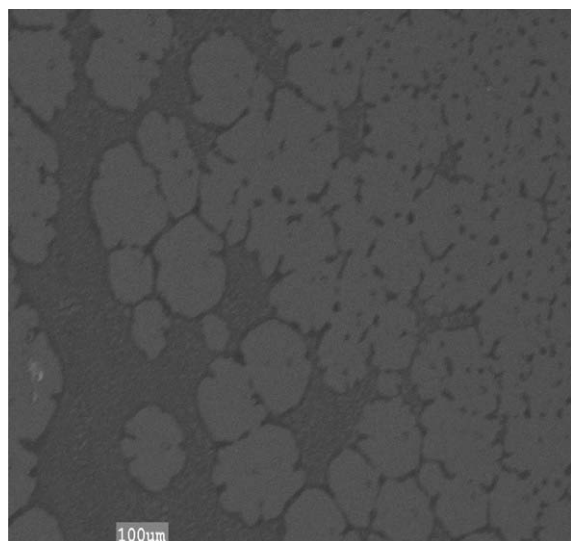
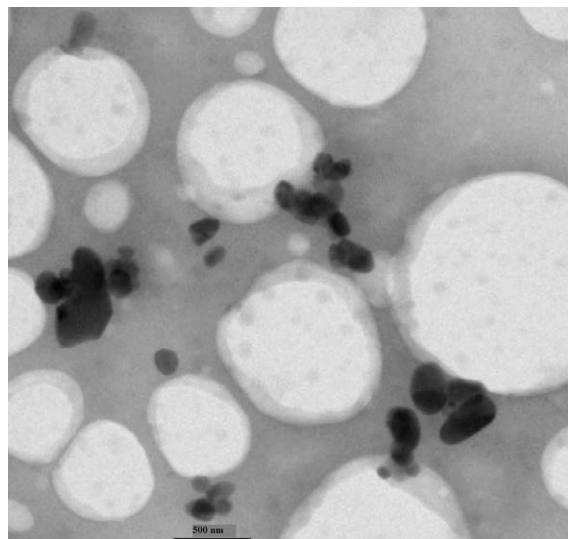


Fig. 7. An AFM micrograph of 3,4,9,10-tetra-(12-alkoxycarbonyl)-perylene spin cast from a chloroform solution at 4500 rpm for 30s onto a Si wafer.



**Fig. 8.** An SEM micrograph of 3,4,9,10-tetra-(12-alkoxycarbonyl)-perylene spin cast from a chloroform solution at 4500 rpm for 30 s onto a Si wafer.



**Fig. 9.** A TEM micrograph of 3,4,9,10-tetra-(12-alkoxycarbonyl)-perylene drop cast from a chloroform solution onto a silicon nitride TEM grid.

showed a reduction in the transmission about the focus of the lens, indicating the optical limiting property.

As evident in the Z-scan signature shown in Fig. 10, the depth of reduction changes along with the variation of the on-focus intensity. The  $\beta_{\text{eff}}$  were deduced from the Z-scan data by curve fitting theory based on an intensity dependent extinction coefficient [25]. The linear and NLO results for the 3,4,9,10-tetra-(12-alkoxycarbonyl)-perylene solution are summarized in Table 1.

The nonlinear transmission has an apparent discontinuity, corresponding to the limiting threshold. The transmission keeps roughly constant when the energy fluence is below the threshold. When the incident fluence exceeds

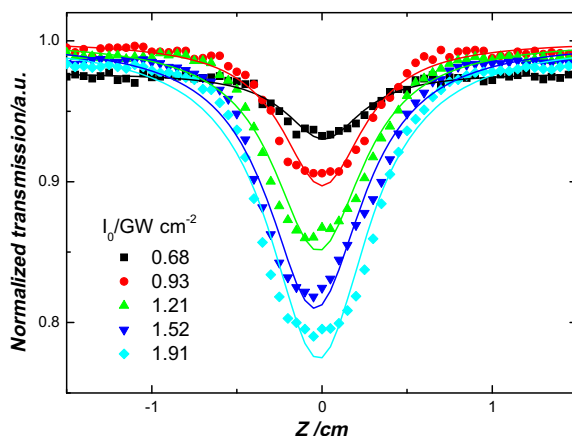


**Fig. 10.** Z-scan signature of a  $1 \text{ g cm}^{-3}$  chloroform solution of 3,4,9,10-tetra-(12-alkoxycarbonyl)-perylene.

**Table 1**  
Summary of typical NLO results for 3,4,9,10-tetra-(12-alkoxycarbonyl)-perylene.

Conc. [mg/mL]	Transmission [%]	$\alpha_0$ [ $\text{cm}^{-1}$ ]	$\beta_{\text{eff}}$ [ $\text{cm W}^{-1}$ ]	$\text{Im}\{\chi^{(3)}\}$ [esu]
1	95.6	0.045	$(3.0 \pm 0.6)e^{-10}$	$(11 \pm 2)e^{-14}$

the threshold, the transmission reduces significantly. The optical limiting trace of the 3,4,9,10-tetra-(12-alkoxycarbonyl)-perylene solutions is analogous to that of SWNT dispersions, resulting from the thermally-induced nonlinear scattering [27,28]. Therefore, it is believable that the optical limiting for the 3,4,9,10-tetra-(12-alkoxycarbonyl)-perylene solutions is largely due to the nonlinear scattering, as is implied by both the evident limiting threshold and the strong scattering signal observed at 532 nm whose response is shown in Fig. 11.

Referring to the nonlinear scattering mechanism of SWNT dispersions [27,28,43,44], the scattering centres in the perylene solutions may arise from the formation of the solvent bubbles and/or the vapor bubbles, resulting from the sublimation of the nanoparticles by the aggregation of the 3,4,9,10-tetra-(12-alkoxycarbonyl)-perylene molecules (see Fig. 9). Nevertheless, we cannot rule out the contribution of TPA to the optical limiting response, but the contribution should be very restricted since (1) the wavelength of the incident beam 532 nm is far away from the TPA resonant wavelength of the perylene solutions [15,17] and (2) the nanosecond incident pulses are inferior for the TPA-induced optical limiting [45,46]. In addition, the excited state absorption, such as reverse saturable absorption or saturable absorption could have influence on the nonlinear responses of the perylene solutions. However, such nonlinear absorption effects can be suppressed when nonlinear scattering becomes significant since the increased scattering cross section results in the reduced absorption cross section [47,48]. Although, the optical limiting efficiency of the 3,4,9,10-tetra-(12-alkoxycarbonyl)-perylene solutions is lower to the present laser source, it is expected that the perylene solutions would

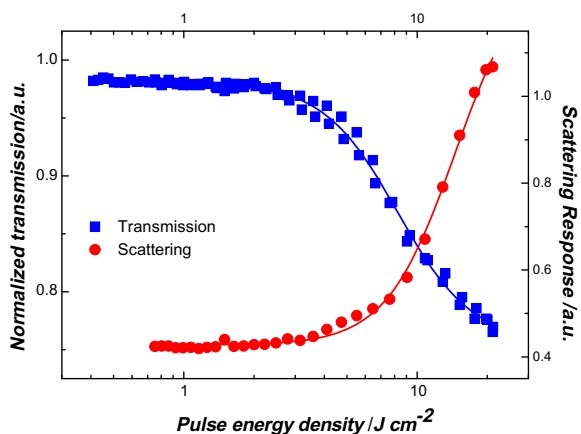


**Fig. 11.** Evidence of limiting threshold from optical limiting trace and the scattering response of 3,4,9,10-tetra-(12-alkoxycarbonyl)-perylene.

be effective to attenuate the laser beam with shorter picosecond or femtosecond pulses and suitable wavelength in the near infrared [9,45].

### 3.6. Chemical Stability

The reproducibility of all results from fresh samples to samples aged up to 24 months in all experiments described in this paper are evidence of the chemical stability of the 3,4,9,10-tetra-(12-alkoxycarbonyl)-perylene.

## 4. Conclusions

The 3,4,9,10-tetra-(12-alkoxycarbonyl)-perylene dye offers both chemical and thermal stability, strongly absorbs and fluoresces in the blue section of the UV–Vis range with the added benefits that it can be processed in solution and its bulky alkyl chains hamper aggregation. In addition, the molecule is optically limiting with a high absorption cross section. The solubilisation exhibited by the molecule is due to the alkyl chains and makes the molecule desirable for polymer blending or film casting thus reducing the cost of device fabrication. These results have opened a window for ongoing investigations regarding a wide variety of possible optoelectronic applications.

## Acknowledgements

The authors wish to acknowledge financial support from Science Foundation Ireland (SFI). J.W. thanks the Irish Research Council for Science, Engineering and Technology (IRCSET) for his postdoctoral research fellowship.

## References

- [1] M.M. Shi, H.Z. Chen, J.Z. Sun, J. Ye, M. Wang, *Chemical Communications* 14 (2003) 1710.
- [2] L. Schmidt-Mende, A. Fechtenkötter, K. Müllen, E. Moons, R.H. Friend, J.D. MacKenzie, *Science* 293 (2001) 1119.
- [3] X. Zhang, Y. Wu, J. Li, F. Li, M. Li, *Dyes and Pigments* 76 (2008) 810.
- [4] U. Haas, C. Thalacker, J. Adams, J. Fuhmann, S. Reithmüller, U. Beginn, U. Ziener, M. Möller, R. Dobra, F. Würthner, *Journal of Materials Chemistry* 13 (2003) 767.

- [5] Y. Ma, C. Wang, Y. Zhao, Y. Yu, C. Han, X. Qui, Z. Shi, *Supramolecular Chemistry* 19 (3) (2007) 141.
- [6] C.M. Aguirre, S. Auvray, S. Pigeon, R. Izquierdo, P. Desjardins, R. Matel, *Applied Physics Letters* 88 (2006) 183104-1.
- [7] S. Benning, H.S. Kitzerow, H. Bock, M.F. Archard, *Liquid Crystals* 27 (2000) 901.
- [8] P. Schouwink, G. Gadret, R.F. Mahrt, *Chemical Physics Letters* 341 (2001) 213.
- [9] A. Herrmann, K. Müllen, *Chemistry Letters* 35 (9) (2006) 978.
- [10] J.L. Bredas, J.P. Calbert, D.A. Filho, J. Cornil, *Proceedings of the National Academy of Sciences* 99 (9) (2002) 5804.
- [11] T. Hassheider, S.A. Benning, H.S. Kitzerow, M.F. Archard, H. Bock, *Angewandte Chemie International Edition* 40 (11) (2001) 2060.
- [12] C.L. Gettinger, A.J. Heeger, J.M. Drake, D.J. Pine, *Journal of Physical Chemistry* 101 (1994) 1673.
- [13] L. De Boni, C.J.L. Constantino, L. Misoguti, R.F. Aroca, S.C. Zilio, C.R. Mendonca, *Chemical Physics Letters* 371 (2003) 744.
- [14] B. Gao, C. Lu, J. Xu, F. Meng, Y. Cui, H. Tian, *Chemistry Letters* 35 (12) (2006) 1416.
- [15] D.S. Correa, S.L. Olivieara, L. Misoguti, S.C. Zilio, R.F. Aroca, C.J.L. Constantino, C.R. Mendonca, *Journal of Physical Chemistry* (2006) 6433.
- [16] K.D. Belfield, M.V. Bondar, F.E. Hernandez, O.V. Przhosnka, *Journal of Physical Chemistry C* 112 (2008) 5618.
- [17] S.L. Oliveira, D.S. Correa, L. Misoguti, C.J.L. Constantino, R.F. Aroca, S.C. Zilio, C.R. Mendonca, *Advanced Materials* 17 (2005) 1890.
- [18] D.A. Parthenopolous, P.M. Rentzepis, *Science* 245 (1989) 843.
- [19] W. Denk, J.H. Strickler, W.W. Webb, *Science* 248 (1990) 73.
- [20] R.H. Kohler, J. Cao, W.R. Zipfel, W.W. Webb, M.R. Hanson, *Science* 276 (1997) 2039.
- [21] S. Kawata, H. Sun, T. Tanaka, K. Takada, *Nature* 412 (2001) 697.
- [22] K.D. Belfield, X. Ren, E.W. Van Stryland, D.J. Hagan, V. Dubikovskiy, E.J. Mesiak, *Journal of the American Chemical Society* 122 (2000) 1217.
- [23] K.D. Belfield, K.J. Schafer, Y. Liu, J. Liu, X. Ren, E.W. Van Stryland, *Journal of Physical Organic Chemistry* 13 (2000) 837.
- [24] S.M. O'Flaherty, S.V. Hold, M.J. Cook, T. Torres, Y. Chen, M. Hanack, W.J. Blau, *Advanced Materials* 15 (2003) 9.
- [25] M. Sheik-Bahae, A.A. Said, T.H. Wei, D.J. Hagan, E.W. Van Stryland, *IEEE Journal of Quantum Electronics* QE-26 (1990) 760.
- [26] S. Heutz, A.J. Ferguson, G. Rumbles, T.S. Jones, *Organic Electronics* 3 (2002) 119.
- [27] J. Wang, W.J. Blau, *Journal of Physical Chemistry C* 112 (2008) 298.
- [28] J. Wang, W.J. Blau, *Applied Physics B: Laser and Optics* 91 (2008) 521.
- [29] J.H. Hildebrand, J.S. Prausnitz, R.L. Scott, *Regular and Related Solution: The Solubility of Gases, Liquids and Solids*, Van Nostrand Reinhold Company, New York, USA, 1970 (Chapter 6, App. 5).
- [30] S.F. Sun, *Physical Chemistry of Macromolecules: Basic Principles and Issues*, John Wiley and Sons Inc., New York, USA, 1994 (Chapter 4).
- [31] A.F.M. Barton, *Handbook of Solubility Parameters and Other Cohesive Parameters*, CRC Press, Boca Raton, Florida, USA, 1983.
- [32] W. Huang, D.Y. Yan, Q.H. Lu, Y. Huang, *European Polymer Journal* 39 (6) (2003) 1099.
- [33] D. Markovitsi, H. Ringsdorf, *Molecular Crystals and Liquid Crystals* 293 (1997) 123.
- [34] H. Langals, *Helvetica Chimica Acta* 88 (2005) 1309.
- [35] K. Arkers, R. Aroca, A.M. Hor, R. Loufy, *Journal of Physical Chemistry* 91 (1987) 2954.
- [36] B. Stevens, M.I. Ban, *Trans. Faraday Society* 60 (1964) 1515.
- [37] C. Kohl, T. Weil, J. Qu, K. Mullen, *Chemistry – A European Journal* 10 (2004) 5297.
- [38] J. Tauc, R. Grigorovici, A. Vancu, *Physica Status Solidi* 15 (1966) 627.
- [39] I. Seguy, P. Jolinat, P. Destreul, J. Farence, R. Many, H. Bock, J. Ip, T.P. Nguyen, *Journal of Applied Physics* 89 (2001) 5442.
- [40] M. Knupfer, *Journal of Applied Physics* A 77 (2003) 623.
- [41] D. Rickard, S. Giordani, W.J. Blau, J.N. Coleman, *Journal of Luminescence* 128 (2008) 31.
- [42] W. Shin, H. Jeong, M.K. Kim, S. Jin, M.R. Kim, J.K. Lee, J.W. Lee, Y. Gal, *Journal of Materials Chemistry* 16 (2006) 384.
- [43] L. Vivien, P. Lançon, D. Riehl, F. Hache, E. Anglaret, *Carbon* 40 (2002) 1789.
- [44] Y. Chen, Y. Lin, Y. Liu, J. Doyle, N. He, X.D. Zhuang, J.R. Bai, W.J. Blau, *Journal of Nanoscience and Nanotechnology* 7 (2007) 168.
- [45] L.W. Tutt, T.F. Boggess, *Progress in Quantum Electronics* 17 (1993) 299.
- [46] J. Wang, W.J. Blau, *Journal of Optics A: Pure and Applied Optics* 11 (2009) 024001.
- [47] J. Wang, W.J. Blau, *Chemical Physics Letters* 465 (2008) 265.
- [48] I.M. Belousova, N.G. Mironova, M.S. Yur'ev, *Optics and Spectroscopy* 94 (2003) 86.

phosphorescent materials have to be adopted in the WOLEDs to improve the efficiency and to realize pure white emission.

In this work, a deep blue phosphorescent emitting material, tris(3,5-difluoro-4-cyanophenyl)pyridine iridium (FCNIr), was used as a blue emitter in WOLEDs. A pure white emission with a color coordinate of (0.29, 0.31) and a high current efficiency of 28 cd/A was demonstrated by using the deep blue phosphorescent dopant and red/green phosphorescent materials.

## 2. Experimental

A device configuration of indium tin oxide (ITO, 150 nm)/poly-3,4-ethylenedioxythiophene:polystyrene-sulfonate (PEDOT:PSS, 60 nm)/N,N'-di(1-naphthyl)-N,N'-diphenylbenzidine (NPB, 30 nm)/N,N'-dicarbazolyl-3,5-benzene (mCP, 10 nm)/mCP:FCNIr( $x$  nm, 15% doping)/4,4',4''-tris(N-carbazolyl)triphenylamine (TCTA):1,3,5-tris(N-phenylbenzimidazole-2-yl)benzene (TAZ):iridium(III) tris(2-phenylpyridine) ( $\text{Ir}(\text{ppy})_3$ ):iridium(III) bis(2-phenylquinoline) acetylacetonate ( $\text{Ir}(\text{pq})_2\text{acac}$ ) (30- $x$  nm)/4,7-diphenyl-1,10-phenanthroline (Bphen, 20 nm)/LiF(1 nm)/Al(200 nm) was used to fabricate all phosphorescent pure white color WOLEDs. The doping concentration of  $\text{Ir}(\text{ppy})_3$  and  $\text{Ir}(\text{pq})_2\text{acac}$  was 10% and 0.7%. The relative ratios of TCTA and TAZ in red:green emitting layers were 75:25 and the thickness of the blue emitting layer ( $x$ ) was varied as 10, 15, 20 nm. Three devices were named as device I, device II and device III respectively. In addition, device IV with TCTA between the NPB and mCP hole transport layer was also fabricated. Chemical structures and device structures of WOLEDs fabricated in this work are shown in Fig. 1. TCTA, TAZ, mCP, Bphen and NPB were supplied from Dongyang Creditech Co. after purification by sublimation and FCNIr was synthesized according to the procedure reported in our previous

work [12].  $\text{Ir}(\text{ppy})_3$  and  $\text{Ir}(\text{pq})_2\text{acac}$  were products of Gracel Display Co. and they were sublimed twice. Electroluminescence (EL) characteristics and EL spectra of WOLEDs were measured with Keithley 2400 source measurement unit and CS 1000 spectroradiometer. Voltage sweep method was used to measure current density–voltage–luminance characteristics of the WOLEDs. Data were collected at an interval of 0.5 V. The EL spectra and luminance were obtained after calibration of the spectroradiometer and EL spectra were normalized to compare relative intensity of the red, green and blue emissions.

## 3. Results and discussion

A pure white device for display application should have red, green and blue peaks and a WOLED with red, green and blue three colors was fabricated. A deep blue emitting material is strongly required to achieve pure white color in WOLEDs. However, there have been few materials available to get pure blue emission [11]. One of the deep blue materials which can be used in WOLEDs is FCNIr [11,12]. The material can emit deep blue color because of wide bandgap of FCNIr. The strong electron withdrawing F and CN substituents in the phenyl unit of the FCNIr lowers the highest occupied molecular orbital (HOMO) of the material, leading to a wide triplet bandgap of 2.8 eV for deep blue emission. A quantum efficiency of 9% with a color coordinate of (0.15, 0.16) was obtained [11]. Therefore, it is suitable as a deep blue emitter in the WOLEDs to get pure white emission. A stack structure of blue/red:green was used to realize three color peaks in the WOLEDs. A mixed host of TCTA:TAZ was used as a host in the red:green emitting layer and common  $\text{Ir}(\text{ppy})_3$  and  $\text{Ir}(\text{pq})_2\text{acac}$  were used as dopant materials. The red/green layer was stacked on the mCP blue emitting layer to balance holes and electrons in the light-emitting layer.

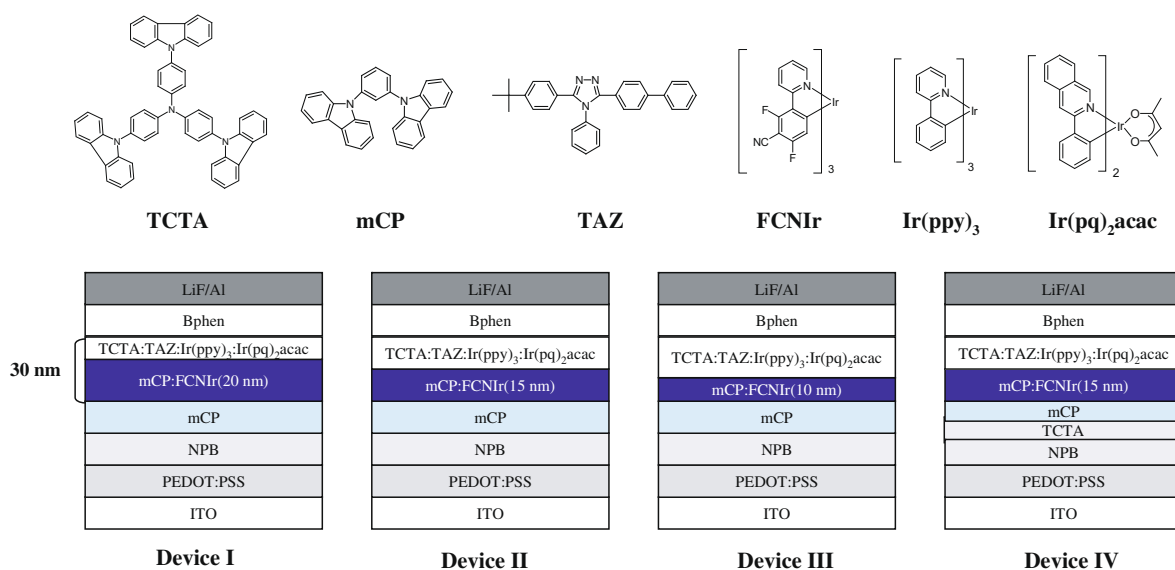


Fig. 1. Chemical structures of materials and device structures of WOLEDs fabricated in this work.

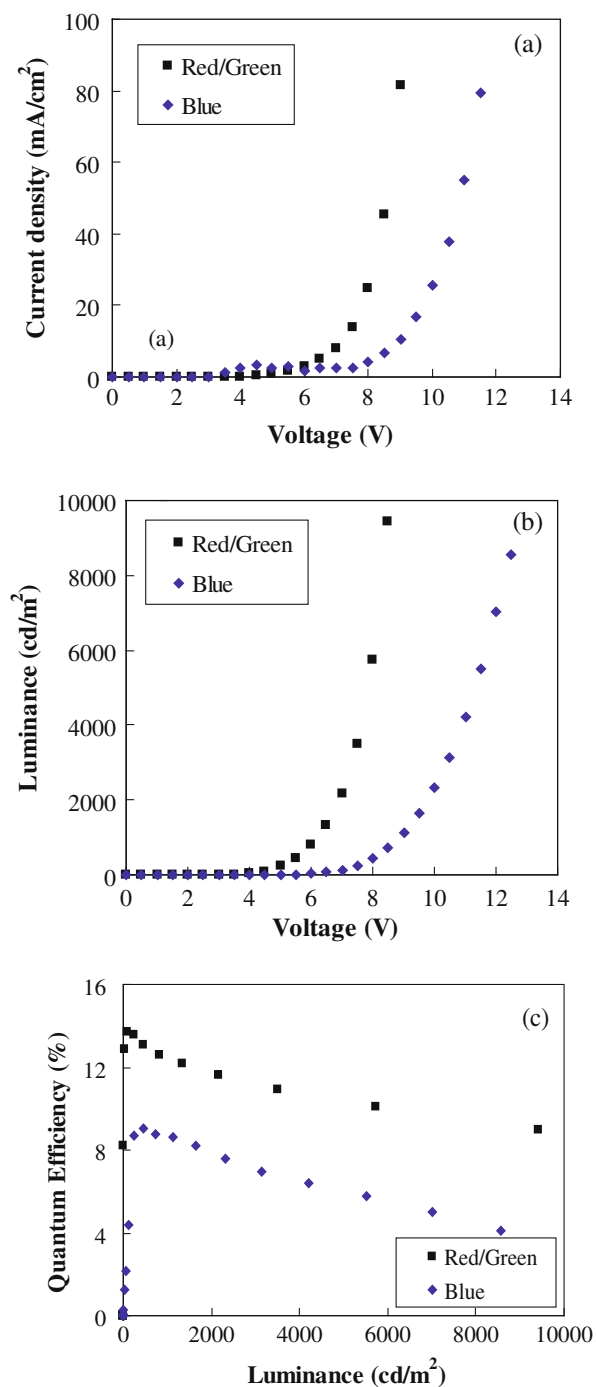


Fig. 2. Current density–voltage–luminance curves of red:green and blue single layer devices. (a) Current density–voltage, (b) luminance–voltage and (c) quantum efficiency–luminance.

Fig. 2 shows current density–voltage–luminance curves of the blue and red/green devices. The blue device had an optimized device configuration of ITO/N,N'-diphenyl-N,N'-bis-[4-(phenyl-m-tolyl-amino)-phenyl]-biphenyl-4,4'-diamine(DNTPD, 60 nm)/NPB(20 nm)/mCP(10 nm)/mCP:FCNir(30 nm)/Bphen(20 nm)/LiF(1 nm)/Al(100 nm)

and the red/green device had a device structure of ITO/PEDOT:PSS(60 nm)/NPB(20 nm)/TCTA(10 nm)/TCTA:TAZ:Ir(ppy)<sub>3</sub>:Ir(pq)<sub>2</sub>acac(30 nm)/Bphen(20 nm)/LiF(1 nm)/Al(100 nm). High current density and luminance were observed in the red:green device, while the blue device showed lower current density and luminance than the blue device. The low current density of the blue device is due to poor electron injection from electron transport layer to the mCP emitting layer as can be seen in the energy level diagram of the in Fig. 3. In addition, the use of DNTPD with relatively low conductivity compared with PEDOT:PSS is also responsible for the low current density. In the case of red:green device with a mixed host structure, hole and electron injection are favored as reported in our early work [13]. The deep blue device showed a quantum efficiency of 9% [11], while the red/green device showed a quantum efficiency of 13% in the optimized device structure.

Fig. 4 shows current density–voltage–luminance curves of the three peak WOLEDs. The thickness of the whole emitting layer was fixed at 30 nm and the thickness of the blue emitting layer was controlled from 10 to 20 nm. The current density of the WOLEDs was greatly dependent on the thickness of the blue and red:green emitting layers. The device III with 10 nm thick blue emitting layer showed the highest current density, while the device I with 20 nm thick blue emitting layer showed the lowest current density. As the thickness of the blue emitting layer increased, the current density was decreased. The low current density in the device with thick blue emitting layer is due to low electron mobility of the mCP layer. Electron transport in the FCNir doped mCP layer is limited because of electron trapping by the FCNir dopant. There is a LUMO level difference of 0.4 eV between the mCP and the FCNir (Fig. 3), resulting in significant electron trapping by the FCNir as reported previously [11]. In addition, the low mobility of the mCP host is also responsible for the low current density in the WOLED with thick blue emitting layer [14]. Compared with the FCNir doped mCP layer, the red:green doped TCTA:TAZ layer is advantageous in terms of hole and electron transport. Relative composition of the TCTA and TAZ in the mixed host was 75:25 and the mixed host can form a percolation path for holes and electrons [15]. As the hole transport through TCTA and electron transport through TAZ are efficient at the host composition, high current density was obtained in the device III. In addition, device IV with TCTA interlayer exhibited higher current density than device II without TCTA interlayer due to

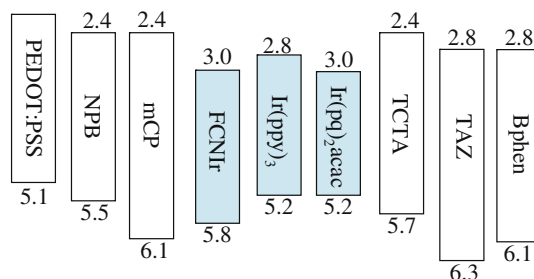
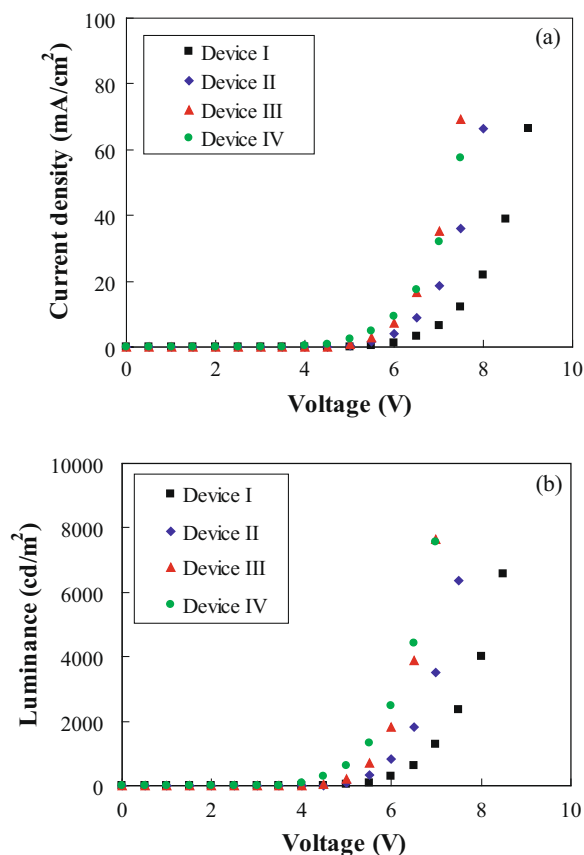


Fig. 3. Energy level diagram of the materials used in this work.



**Fig. 4.** Current density–voltage–luminance curves of WOLEDs according to the thickness of blue emitting layer. Device I (20 nm), device II (15 nm), device III (10 nm) and device IV (15 nm). (a) current density–voltage and (b) luminance–voltage.

facilitated hole injection. The HOMO level gap between the NPB and mCP is 0.6 eV and the insertion of the TCTA can reduce the energy barrier, enhancing the hole density in the emitting layer.

The luminance of the WOLEDs also followed the same tendency as the current density. As the luminance of OLEDs depends on the current density and the recombination efficiency in the device [16], the device with the thick red:green emitting layer showed higher luminance than other devices. The highest luminance was obtained in the device IV due to high current density and high recombination efficiency which will be shown in Fig. 5. The driving voltage at 1000 cd/m<sup>2</sup> was 5.3 V in the device IV.

The quantum efficiency and the current efficiency of the WOLEDs were plotted against luminance in Fig. 5. The device III showed high quantum efficiency, while the device II and the device I showed rather low quantum efficiency values. The high quantum efficiency in the device III can be explained by the relative contribution of the blue emission to the red/green emission. As can be seen in the electroluminescence spectra of the WOLEDs in Fig. 6, the red/green intensity was increased in the device with thick red/green emitting layer. The quantum efficiency of the blue single layer device was 9% and the quantum efficiency

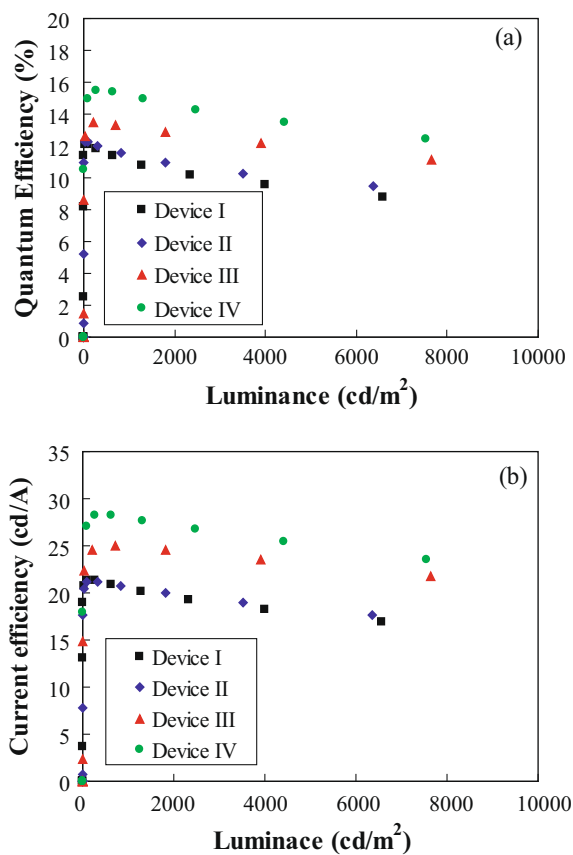


**Fig. 5.** Quantum efficiency and current efficiency of WOLEDs with different blue emitting layer thicknesses. Device I (20 nm), device II (15 nm), device III (10 nm) and device IV (15 nm). (a) Quantum efficiency–luminance, (b) current efficiency–luminance and (c) power efficiency–luminance.

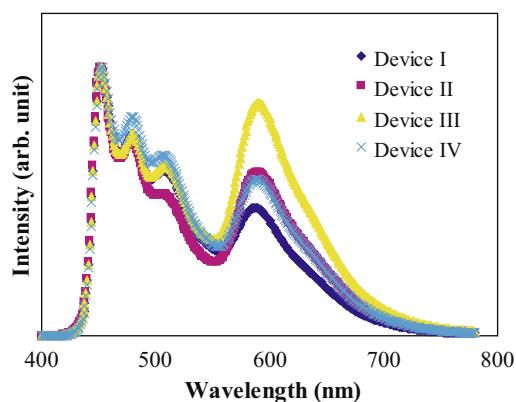


**Fig. 6.** Electroluminescence spectra of WOLEDs with different blue emitting layer thicknesses. Device I (20 nm), device II (15 nm), device III (10 nm) and device IV (15 nm).

of red/green single layer device was 14%. Therefore, the increase of the red/green intensity resulted in the improvement of the quantum efficiency. Current efficiency of the WOLEDs was also high in the WOLED with thick red/green



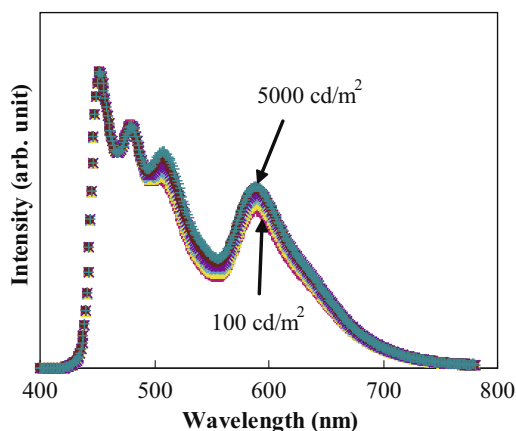


Fig. 7. Electroluminescence spectra of the device IV WOLED with TCTA interlayer according to the luminance.

emitting layer. The current efficiency of the device III was 25 cd/A with a color coordinate of (0.35, 0.34) and the current efficiency of the device II was 21 cd/A with a color coordinate of (0.30, 0.30). The combination of the high efficiency deep blue device and red/green mixed host device improved the current efficiency of the pure white WOLEDs. The efficiency of the WOLEDs was further enhanced by using the TCTA inserted hole transport layer and a high current efficiency of 28 cd/A with a color coordinate of (0.29, 0.31) was obtained in the device IV. The TCTA layer improved the hole injection and the charge balance was enhanced, leading to better efficiency. The efficiency value is better than any other current efficiency value reported in the pure white WOLEDs. The power efficiency was also improved by the TCTA layer and a high power efficiency 18.1 lm/W was obtained in the white device IV.

Fig. 6 shows the electroluminescence (EL) spectra of three WOLEDs fabricated in this work. Sharp emission peaks from the red, green and blue phosphorescent emitters are observed from the WOLEDs even though relative intensity of the peaks depended on the device structure. The blue emission was strong in the device I with 20 nm thick blue layer and red/green emission was strong in the device III with 10 nm thick blue layer. The thickness of the emitting layer affected the relative intensity of blue and red/green emission.

The EL spectra of the WOLEDs were monitored according to the luminance and the EL spectra are shown in Fig. 7. The spectrum change of the device IV with TCTA interlayer was plotted representatively. The luminance of the device IV was changed from 100 to 5000 cd/m<sup>2</sup>. There was little

change of emission spectrum within the luminance range investigated and the color coordinate of (0.29, 0.31) was changed into (0.30, 0.33) at high luminance. The shift of the color coordinate was less than 0.02 from 100 to 5000 cd/m<sup>2</sup>. Similar results were obtained in other devices. The good color stability of the WOLEDs may be due to hole blocking properties of TAZ and electron blocking properties of mCP. The charge blocking properties of the host materials may limit the charge leakage and exciton diffusion at high luminance.

#### 4. Conclusions

In summary, a high efficiency pure white WOLED was developed by using a deep blue phosphorescent emitting material. A high efficiency of 28 cd/A and a pure white color coordinate of (0.29, 0.31) were obtained from the all phosphorescent pure white WOLED. The combination of mCP and TCTA:TAZ mixed host was effective to improve the efficiency of the WOLEDs.

#### Acknowledgement

This work was partially supported by the GRRC program of Gyeonggi province [2008–66968, Materials development for high efficiency organic solid state lighting], grant No. RTI04-01-02 from the Regional Technology Innovation Program of the Ministry of Knowledge Economy (MKE), MKE/ITEP [10028439-2008-21], MKE/ITEP [10016748-2007] and 2008 research funds supplied by the Strategic Research Institute, Dankook University.

#### References

- [1] J. Kido, M. Kimura, K. Nagai, *Science* 267 (1995) 1332.
- [2] J.Y. Lee, J.H. Kwon, H.K. Chung, *Org. Electron.* 4 (2003) 143.
- [3] Y. Sun, N.C. Giebink, H. Kanno, B. Ma, M.E. Thompson, S.R. Forrest, *Nature* 440 (2006) 908.
- [4] K.S. Yook, J.Y. Lee, *Appl. Phys. Lett.* 92 (2008) 193308.
- [5] Y. Sun, S.R. Forrest, *Appl. Phys. Lett.* 91 (2007) 263503.
- [6] E.L. Williams, K. Haavisto, J. Li, G.E. Jabbour, *Adv. Mater.* 19 (2007) 197.
- [7] S.H. Kim, J. Jang, J.Y. Lee, *Appl. Phys. Lett.* 91 (2007) 123509.
- [8] B.W. D'Andrade, R.J. Holmes, S.R. Forrest, *Adv. Mater.* 16 (2004) 624.
- [9] B.W. D'Andrade, S.R. Forrest, *Adv. Mater.* 16 (2005) 1585.
- [10] G. Schwartz, S. Reineke, K. Walzer, K. Leo, *Appl. Phys. Lett.* 92 (2008) 053311.
- [11] K.S. Yook, S.O. Jeon, C.W. Joo, J.Y. Lee, *Org. Electron.* 10 (2008) 170.
- [12] S.H. Kim, J. Jang, S.J. Lee, J.Y. Lee, *Thin Solid Films* 517 (2008) 722.
- [13] S.H. Kim, J. Jang, J.Y. Lee, *Appl. Phys. Lett.* 91 (2007) 083511.
- [14] R.J. Holmes, S.R. Forrest, Y.-J. Tung, R.C. Kwong, J.J. Brown, S. Garon, M.E. Thompson, *Appl. Phys. Lett.* 82 (2003) 2422.
- [15] S.H. Kim, J. Jang, J.Y. Lee, *J. Appl. Phys.* 103 (2007) 054502.
- [16] J.Y. Lee, *J. Ind. Eng. Chem.* 14 (2008) 676.

[12,13], FIr6-based PHOLEDs show deeper blue emissions than FIrpic-based devices, and therefore are more advantageous for lighting and display applications. However, the higher triplet energy ( $T_1$ ) of FIr6 than that of FIrpic (2.72 eV vs. 2.62 eV) [11] makes it even more challenging to efficiently generate and confine excitons on the phosphor molecules. Also note that the deeper blue emission of FIr6-based devices leads to an approximately 20% lower photopic sensitivity by the human eyes compared to that of FIrpic devices.

Recently we have shown that external quantum efficiencies ( $\eta_{EQE}$ ) up to 18% can be achieved in FIr6-based PHOLEDs by using the hole transport material of 1,1-bis-(di-4-tolylaminophenyl)cyclohexane (TAPC,  $T_1 = 2.87$  eV) [14]. Furthermore, we employed a dual-emissive-layer (D-EML) structure using *p*-bis(triphenylsilyl)benzene (UGH2) and *N,N'*-dicarbazolyl-3,5-benzene (mCP) as the host materials for FIr6 in the two adjacent emissive layers to maximize the exciton formation on FIr6 molecules, and applied the *p-i-n* device structure with highly conductive charge injection/transport layers to lower the device operating voltage. As a result, a high power efficiency of  $\eta_p = 25$  lm/W at a luminance of  $L = 100$  cd/m<sup>2</sup> was demonstrated, which was only slightly reduced to  $\eta_p = 20$  lm/W at  $L = 1000$  cd/m<sup>2</sup> [15].

Here, we compare performance of FIr6-based D-EML PHOLEDs with three different electron transport materials, bathocuproine (BCP), 4,7-diphenyl-1,10-phenanthroline (BPhen), and tris[3-(3-pyridyl)mesityl]borane (3TPYMB) [16–19], and study the effect of doping alkaline metals (Li and Cs) [20] into these charge transport materials. We show that  $\eta_{EQE} = 20\%$  and maximum  $\eta_p = 36$  lm/W can be achieved in devices with 3TPYMB as the electron transport material and 3TPYMB:Cs as the electron injection layer. The high efficiencies are attributed to the high triplet energy of 3TPYMB,  $T_1 = 2.95$  eV [19], compared to 2.5 eV for BCP and BPhen [16,17], as well as the increased conductivities due to alkaline doping.

## 2. Experimental

Glass substrates precoated with an indium tin oxide (ITO) anode (sheet resistance  $\sim 20 \Omega/\square$ ) were degreased in detergent and de-ionized water, and cleaned with ultrasonic baths of acetone and isopropanol consecutively for 15 min each. The substrates were then exposed to an ultraviolet-ozone ambient for 15 min immediately before being loaded into a high-vacuum thermal evaporation system (background pressure  $\sim 3 \times 10^{-7}$  Torr), where all the organic and metal layers were deposited successively without breaking the vacuum.

The schematic energy level diagram of the D-EML *p-i-n* deep-blue PHOLEDs [15] and the molecular structures of FIr6 and the three electron transport materials are shown in Fig. 1 (energy levels are taken from the literature) [11,13,21,22]. The D-EML structure composed of 4 wt% FIr6 doped mCP (7 nm thick) and 25 wt% FIr6 doped UGH2 (15 nm thick) layers was used to maximize the exciton generation within the broadened charge recombination zone [15]. TAPC serves as the hole transporting/

electron blocking layer (HTL), whereas an undoped layer of BCP, BPhen, or 3TPYMB was used as the electron transporting/hole blocking layer (ETL). The thicknesses of both HTL and ETL were  $x$  nm with  $x$  varying from 5 to 20. A (40- $x$ ) nm thick *N,N'*-diphenyl-*N,N'*-bis(3-methylphenyl)-[1,1'-biphenyl]-4,4'-diamine (MeO-TPD) layer doped with 2 mol% tetrafluoro-tetracyanoquinodimethane (F<sub>4</sub>-TCNQ) was used as the *p*-type hole injection layer (HIL) [21], whereas Li or Cs was doped into the ETL material to serve as the *n*-type electron injection layer (EIL), whose thickness was also (40- $x$ ) nm. As a comparison, “conventional”, i.e. non-*p-i-n* type, devices were also fabricated, which did not contain the *p*- and *n*-doped charge injection layers. The thicknesses of HTL and ETL in the conventional devices were both 40 nm.

For the alkaline doping of the electron transport materials, lithium metal was used as the Li source, whereas cesium carbonate (Cs<sub>2</sub>CO<sub>3</sub>), which decomposes during thermal evaporation to generate cesium atoms ( $2\text{Cs}_2\text{CO}_3 \rightarrow 4\text{Cs} + \text{O}_2\uparrow + 2\text{CO}_2\uparrow$ ) [23], was used as the Cs source. The cathode consisting of a 0.5 nm thick layer of LiF followed by a 50 nm thick Al was deposited through an in situ shadow mask, forming active device area of 4 mm<sup>2</sup>. 3TPYMB, mCP, UGH2, and FIr6 were purchased from Luminescence Technology Corp., and used as obtained without further purification.

Luminance ( $L$ )–current density ( $J$ )–voltage ( $V$ ) measurements were carried out in ambient using an Agilent 4155C semiconductor parameter analyzer and a calibrated Newport silicon detector. The luminance was calibrated using a Konica Minolta LS-100 luminance meter assuming Lambertian emission pattern. Electroluminescence (EL) spectra were taken using an Ocean Optics HR4000 high-resolution spectrometer. The luminous, power, and external quantum efficiencies ( $\eta_L$ ,  $\eta_p$ , and  $\eta_{EQE}$ , respectively) were derived based on the recommended methods [24]. The conductivities of nominally undoped or alkaline doped electron transport materials were obtained from the ohmic regions of the  $J$ - $V$  characteristics of 100 nm thick films sandwiched between two Al electrodes.

## 3. Results and discussions

### 3.1. Conventional devices with different ETLs

Fig. 2 shows the comparison of  $\eta_{EQE}$  of three conventional devices with different ETLs. The layer thicknesses and ETL materials for these devices are summarized in Table 1. A maximum  $\eta_{EQE} = 14\%$  is achieved at a current density of  $J < 10^{-2}$  mA/cm<sup>2</sup> in device A with BCP as the ETL, compared to the maximum of  $\eta_{EQE} = 16\%$  in device B with a BPhen ETL, which is obtained at  $J \approx 0.1$  mA/cm<sup>2</sup>. In device C which uses 3TPYMB as the ETL,  $\eta_{EQE}$  is substantially higher than in the other two devices, and reaches a maximum of 20%. This is the highest  $\eta_{EQE}$  ever reported for deep-blue PHOLEDs without any particular light extraction enhancement mechanism. As the light extraction efficiency in these planar-type OLEDs is generally believed to be 20% [2,25] (although there have been recent evidences that it could be slightly higher [10]), this suggests that the internal

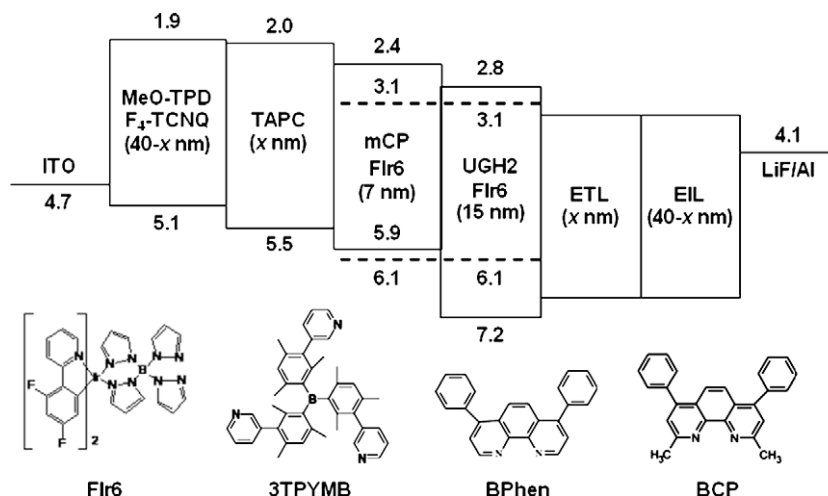


**Fig. 1.** Schematic energy level diagram of the dual-emissive-layer (D-EML) *p-i-n* phosphorescent organic light-emitting devices (PHOLEDs) and molecular structures of the deep-blue phosphor (Flr6) and the three different electron transporting materials used (BCP, BPhen, and 3TPYMB).

quantum efficiency ( $\eta_{EQE}$ ) could be very close to 100% in device C.

Among the most important properties for an ETL in a PHOLED are the electron mobility ( $\mu_e$ ), the energy levels of the highest occupied and lowest unoccupied molecular orbitals (HOMO and LUMO, respectively), and the triplet energy. The electron mobility affects the charge balance in the device, hence the location of the charge recombination zone. The HOMO and LUMO energies affect the hole blocking and electron injection properties, respectively, at the ETL/EML interface, whereas the triplet energy of the ETL significantly impacts the exciton confinement within the EML. As BCP and BPhen have similar HOMO/LUMO (6.5/3.0 eV) [18] and  $T_1$  (2.5 eV) [16,17], the higher  $\eta_{EQE}$  of device B compared to that of device A should be attributed to the more balanced charge injection due to the

higher  $\mu_e$  of BPhen than that of BCP ( $\sim 10^{-4}$  cm<sup>2</sup>/V s vs.  $\sim 10^{-6}$  cm<sup>2</sup>/V s) [18,26] (the hole mobility of the TAPC HTL is  $\sim 10^{-2}$  cm<sup>2</sup>/V s) [27]. However, charge balance cannot be used to explain the higher  $\eta_{EQE}$  in device C compared with device B, as the electron mobility of 3TPYMB ( $\mu_e \sim 10^{-5}$  cm<sup>2</sup>/V s) [19] is approximately one order of magnitude lower than that of BPhen. The different efficiencies of these two devices should therefore be attributed to the much higher  $T_1 = 2.95$  eV of 3TPYMB [19] enabling better confinement of triplet exciton in the EML, although the 0.3 eV lower HOMO of 3TPYMB (6.8 eV) [19] than that of BCP/BPhen (6.5 eV) also results in more effective hole blocking at the EML/ETL interface. The electroluminescence (EL) spectra of these three devices as shown in the inset of Fig. 2 (measured at 1 mA/cm<sup>2</sup>) are very similar. The minor differences in the relative intensities of the multiple vibronic peaks are possibly due to the different optical properties of the three ETLs as well as the slightly different position of the recombination zone. The peak luminous efficiency ( $\eta_L$ ) of device C reached 36 cd/A, com-

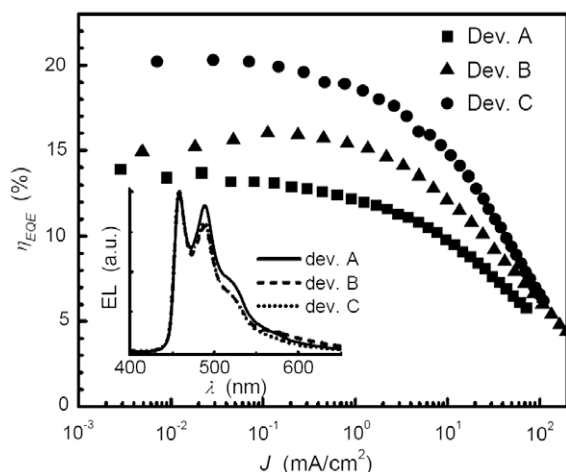


**Fig. 2.** External quantum efficiencies ( $\eta_{EQE}$ ) of conventional deep-blue PHOLEDs with different electron transporting materials: BCP (device A), BPhen (device B), and 3TPYMB (device C). (Inset) Electroluminescent (EL) spectra of these three devices.

**Table 1**

List of thicknesses and materials of charge injection and transport layers of dual-emissive-layer (D-EML) OLEDs. The general device structure is ITO/HIL/HTL/D-EML/ETL/EIL/LiF/Al, where HIL = hole injection layer, HTL = hole transport layer, ETL = electron transport layer, and EIL = electron injection layer. The D-EML consists of mCP:4 wt%Flr6 (7 nm) and UGH2:25 wt%Flr6 (15 nm) for all devices.

Device	HIL <sup>a</sup>	HTL <sup>b</sup>	ETL	EIL
A	–	40 nm	40 nm, BCP	–
B	–	40 nm	40 nm, BPhen	–
C	–	40 nm	40 nm, 3TPYMB	–
D	20 nm	20 nm	20 nm, BPhen	20 nm, BPhen:Li
E	30 nm	10 nm	10 nm, BPhen	30 nm, BPhen:Li
F	30 nm	10 nm	10 nm, BPhen	30 nm, BPhen:Cs
G	20 nm	20 nm	40 nm, 3TPYMB	–
H	20 nm	20 nm	20 nm, 3TPYMB	20 nm, 3TPYMB:Li
I	30 nm	10 nm	10 nm, 3TPYMB	30 nm, 3TPYMB:Cs

<sup>a</sup> MeO-TPD:F<sub>4</sub>-TCNQ (2 mol%).

<sup>b</sup> TAPC.

**Table 2**

Comparison of the turn-on voltage ( $V_T$ , defined as the drive voltage at 0.1 cd/m<sup>2</sup>), drive voltage at 100 cd/m<sup>2</sup> ( $V_{100}$ ), external quantum efficiency ( $\eta_{EQE}$ ), luminous efficiency ( $\eta_L$ ), power efficiency ( $\eta_P$ ), and CIE coordinates of various devices. See Table 1 for detailed device structures.

Device	ETL/dopant	$V_T, V_{100}$ (V)	$\eta_{EQE}$ (%) (at peak)	$\eta_L$ (cd/A) (at peak)	$\eta_P$ (lm/W) (at peak, 100 cd/m <sup>2</sup> )	CIE (x, y) (at 1 mA/cm <sup>2</sup> )
B	BPhen/none	3.4, 4.5	16 ± 1	30 ± 2	25, 21 ± 2	(0.19, 0.27)
D	BPhen/Li	3.2, 4.3	17 ± 1	35 ± 2	25, 25 ± 2	(0.16, 0.28)
F	BPhen/Cs	3.1, 3.7	17 ± 1	35 ± 2	29, 28 ± 2	(0.18, 0.30)
C	3TPYMB/none	3.7, 4.7	20 ± 1	36 ± 2	30, 23 ± 2	(0.15, 0.25)
H	3TPYMB/Li	3.3, 4.4	20 ± 1	41 ± 2	32, 28 ± 2	(0.16, 0.27)
I	3TPYMB/Cs	3.0, 3.8	20 ± 1	41 ± 2	36, 32 ± 2	(0.16, 0.28)

pared to 26 and 30 cd/A for the BCP and BPhen based devices, respectively, even though device C showed the highest deep-blue color purity with CIE coordinates of (0.15, 0.25) (also see Table 2 for various device characteristics of devices B and C).

### 3.2. *p-i-n* devices with BPhen ETL/EIL

We have shown previously [15] that the operating voltages of the deep-blue D-EML PHOLEDs can be significantly reduced by employing the *p-i-n* device structure [20] that incorporates highly conductive *p*- and *n*-doped charge injection layers to reduce the total resistance of the organic layers and enhance charge injection from the electrodes. In that work [15], we used BPhen doped with Li as the *n*-type EIL and a thin, nominally undoped BPhen layer was sandwiched between the doped BPhen layer and the EMLs as the ETL. Here we further studied the effect of different ETLs and different alkaline (Li or Cs) doping in the EIL on performance of the *p-i-n* deep-blue PHOLEDs. For devices with BPhen:Li as the EIL, as shown in Fig. 3a, when the layer thickness of the undoped BPhen ETL as well as the TAPC HTL is reduced from 20 nm (device D) to 10 nm (device E), the current at a given voltage ( $V > 4$  V) is improved by approximately an order of magnitude. However, as shown in Fig. 3b,  $\eta_L$  is drastically reduced from 35 cd/A (device D) to 11 cd/A (device E). When Cs is used instead of Li as the dopant in BPhen, with a 10 nm thick undoped BPhen layer, the PHOLED (device F) has slightly higher current injection than device E as

shown in Fig. 3a. This could be attributed to the difference in the electrical conductivity of the doped EILs. As summarized in Table 3, the conductivity of BPhen:Cs (with a weight ratio of 15:1, corresponding to a molar ratio of 1:0.2) is measured to be  $\sigma = (6 \pm 2) \times 10^{-6}$  S/cm, approximately doubling that of BPhen:Li (with the same weight ratio), although both are approximately four orders of magnitude higher than that of undoped BPhen. More importantly, however, device F has essentially the same  $\eta_L$  as device D as shown in Fig. 3b, although a further reduction of the undoped BPhen layer thickness to 5 nm also leads to a substantial reduction in  $\eta_L$  (data not shown here). The efficiency drop for very thin ETLs can be attributed to the diffusion of the alkaline dopants from the EIL to the EBL/EML interface or even into the EML where they act as luminescence quenching centers for excitons in the EML. The results here also suggest that Cs has a lower diffusivity than Li, consistent with the apparent difference in their atomic sizes [20]. While device F has almost identical  $\eta_L$  as device D, the thinner undoped HTL/ETL in device F (10 nm vs. 20 nm) leads to a reduction of device operating voltage, therefore an increase in  $\eta_P$  by approximately 15%, from a maximum of 25 lm/W [15] to 29 lm/W (also see the comparison of device parameters summarized in Table 2). The EL spectra of Li and Cs doped *p-i-n* PHOLEDs are slightly different, and the CIE coordinates are shifted from (0.16, 0.28) for device D to (0.18, 0.30) for device F, possibly due to the different optical properties of BPhen:Li and BPhen:Cs and/or shift of recombination zone toward HTL with a higher conductivity of BPhen:Cs [28].

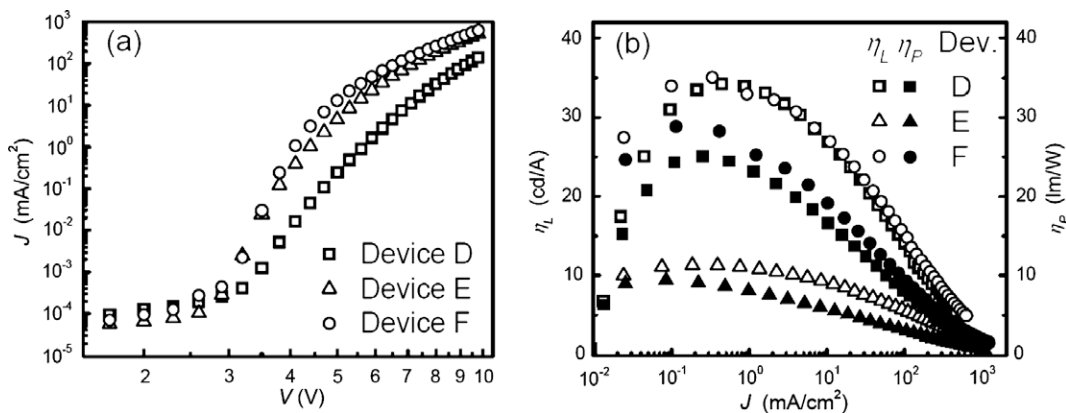


**Fig. 3.** Device characteristics of three *p-i-n* devices (D, E, and F) using BPhen as the electron transporting/injection material: (a) Current density ( $J$ )–voltage ( $V$ ) characteristics, and (b) luminous ( $\eta_L$ , open symbols) and power ( $\eta_P$ , filled symbols) efficiencies. BPhen:Li is used as the electron injection layer in devices D and E, whereas BPhen:Cs is used for device F. The undoped BPhen layer thickness is 20 nm for device D, and 10 nm for devices E and F.

**Table 3**

Conductivities of pure and alkaline doped BPhen and 3TPYMB films.

ETL	Dopant	Weight ratio of ETL:dopant	Molar ratio of ETL:dopant	Conductivity (S/cm)
BPhen	None	–	–	$(4 \pm 1) \times 10^{-10}$
	Li	15:1	1:1	$(3 \pm 1) \times 10^{-6}$
	Cs	15:1	1:0.2	$(6 \pm 2) \times 10^{-6}$
3TPYMB	None	–	–	$(2 \pm 1) \times 10^{-13}$
	Li	15:1	1:1.8	$(2 \pm 1) \times 10^{-6}$
	Cs	15:1	1:0.3	$(4 \pm 2) \times 10^{-6}$

### 3.3. *p-i-n* devices with 3TPYMB ETL/EIL

We also measured the electrical conductivities of undoped and alkaline doped 3TPYMB films. As listed in Table 3, while the conductivity of pure 3TPYMB,  $\sigma = 2 \times 10^{-13}$  S/cm, is much lower than that of pure BPhen ( $\sigma = 4 \times 10^{-10}$  S/cm), the conductivities of Li or Cs doped 3TPYMB (with the same weight ratio of ETL:dopant = 15:1) are very similar to those of doped BPhen films, on the order of  $10^{-6}$  S/cm. Although we have not carried out a complete study of the doping concentration dependence, it appears that Cs doped 3TPYMB films can also achieve approximately twice higher conductivities than the Li-doped films.

To understand the effect of alkaline doped 3TPYMB EILs on device efficiencies, we fabricated two *p-i-n* devices with Li (device H) or Cs (device I) doped 3TPYMB EIL as well as a *p-i-i* device with a 40 nm thick undoped 3TPYMB ETL but no EIL (device G). Similar to BPhen based devices, a 20 nm thick undoped 3TPYMB ETL is used for Li-doped EIL (device H), which is reduced to 10 nm in device I with Cs doping. It is apparent from Fig. 4a that device I has the best charge injection due to the high conductivity of 3TPYMB:Cs and the very thin undoped ETL layer. The external quantum efficiencies of these three devices, however, are nearly identical with maximum  $\eta_{EQE} = 20\%$ , as shown in Fig. 4b. This suggests that the apparent difference in charge balance for these three devices does not affect exciton generation/recombination appreciably. This, in

fact, is consistent with the superior exciton confinement/charge blocking provided by the TAPC and 3TPYMB charge transport layers. The large HOMO level offset ( $\Delta E \sim 0.7$  eV) between FIr6 and 3TPYMB provides sufficient confinement of holes in the EML so that those holes injected into the EML will ultimately recombine with electrons injected from the ETL. In addition, the high triplet energy of 3TPYMB ensures negligible loss of excitons created in the EML regardless whether the position of the recombination zone, which is determined by charge balance, is close to the EML/ETL interface or not. The power efficiencies of these three 3TPYMB-based devices, however, do show appreciable differences due to the differences in device operating voltages. The peak  $\eta_p$  for device G, H, and I are 29, 32, and 36 lm/W, respectively. Device I especially has a very low turn-on voltage of 3.0 V, and needs a bias of 3.8 and 4.3 V to achieve a luminance of 100 and 1000 cd/m<sup>2</sup>, respectively. The CIE coordinates of these three devices remain at approximately (0.16, 0.28).

Note that typically for a planar-type OLED, only about 20% of the overall emission can escape the device in the forward viewing directions, while the rest is trapped in the glass substrate and in the ITO and organic layers as wave-guiding modes [2,25]. While there have been active research in enhancing the light extraction efficiencies in OLEDs [4,29], here we simply attached a near-hemispherical lens (BK-7 plano-convex lens, diameter 25.4 mm and height 9.5 mm) to the glass substrate of device I using

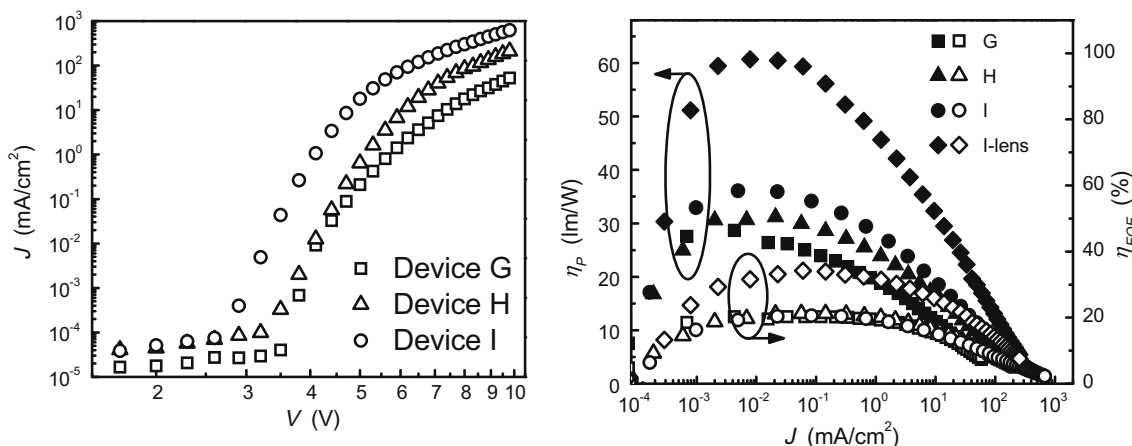


**Fig. 4.** Device characteristics of three devices (G, H, and I) using 3TPYMB as the electron transporting/injection material: (a) Current density ( $J$ )–voltage ( $V$ ) characteristics and (b) power ( $\eta_p$ , filled symbols) and external quantum ( $\eta_{EQE}$ , open symbols) efficiencies versus luminance ( $L$ ). Device G is a *p-i-i* type device with a 40 nm thick undoped 3TPYMB ETL, whereas the other two are *p-i-n* devices with Li (device H) or Cs (device I) doped 3TPYMB EIL. See Table 1 for detailed device structures. The total power and external quantum efficiencies of device I with a near-hemispherical lens attached to the light-emitting surface were also shown (labeled as “I-lens”).

refractive index matching gel ( $n = 1.517$ ). As shown in Fig. 4b, attaching the macrolens to device I (labeled as I-lens) leads a maximum  $\eta_{EQE} = (34 \pm 2)\%$ , or approximately 70% enhanced compared to the device without the macrolens, which is in general agreement with previous reports [30]. The power efficiency of device I with the lens attached reaches a maximum of  $\eta_P = (61 \pm 4)$  lm/W at  $L \approx 10$  cd/m<sup>2</sup>, slightly reducing to  $(57 \pm 3)$  lm/W at  $L = 100$  cd/m<sup>2</sup> and  $(44 \pm 2)$  lm/W at  $L = 1000$  cd/m<sup>2</sup>. With more complicated optical designs to achieving 2.3 times enhancement in light extraction [29], power efficiencies up to 80 lm/W could be achieved in the FIr6-based deep-blue PHOLEDs.

#### 4. Conclusions

We have shown that the efficiencies of FIr6-based deep-blue PHOLEDs significantly depend on the properties of the electron transport and injection materials. A maximum  $\eta_{EQE} = 20\%$  was achieved using an ETL of 3TPYMB, substantially higher than those of similar devices with BCP or BPhen as the ETL, respectively. This is attributed to the nearly perfect charge and exciton confinement provided by the 3TPYMB as the ETL and the counterpart HTL of TAPC. We also showed that alkaline doping (Li and Cs) in the 3TPYMB ETL can effectively increase its conductivity by several orders of magnitude, similar to the effect in the more widely studied BPhen ETL. Incorporation of such doped layers in *p-i-n* devices led to significantly improved charge injection and lower device drive voltage. As a result, peak power efficiency of 36 lm/W and a turn-on voltage of only 3.0 V were achieved for these deep-blue PHOLEDs with CIE coordinates of (0.16, 0.28). The efficiencies were further improved to the maxima of  $\eta_{EQE} = 34\%$  and  $\eta_P = 61$  lm/W by attaching a near-hemispherical lens to the light-emitting surface of the glass substrate, and  $\eta_P$  has the potential to be further improved to up to 80 lm/W by using more complicated optical designs to enhance the light extraction.

#### Acknowledgements

This work was supported by the US Department of Energy Solid State Lighting Program (Award # DE-FC26-06NT42855). S.-H.E. also acknowledges a fellowship from Samsung SDI. Co., Ltd.

#### References

- [1] M.A. Baldo, D.F. O'Brien, Y. You, A. Shoustikov, S. Sibley, M.E. Thompson, S.R. Forrest, *Nature* 395 (1998) 151.
- [2] C. Adachi, M.A. Baldo, M.E. Thompson, S.R. Forrest, *J. Appl. Phys.* 90 (2001) 5048.
- [3] M. Ikai, S. Tokito, Y. Sakamoto, T. Suzuki, Y. Taga, *Appl. Phys. Lett.* 79 (2001) 156.
- [4] B.W. D'Andrade, S.R. Forrest, *Adv. Mater.* 16 (2004) 1585.
- [5] S.R. Forrest, *Nature* 428 (2004) 911.
- [6] R.J. Holmes, S.R. Forrest, Y.-J. Tung, R.C. Kwong, J.J. Brown, S. Garon, M.E. Thompson, *Appl. Phys. Lett.* 82 (2003) 2422.
- [7] S. Tokito, T. Iijima, Y. Suzuki, H. Kita, T. Tsuzuki, F. Sato, *Appl. Phys. Lett.* 83 (2003) 569.
- [8] D. Tanaka, Y. Agata, T. Takeda, S. Watanabe, J. Kido, *Jpn. J. Appl. Phys.* 46 (2007) L117.
- [9] J. Lee, N. Chopra, S.-H. Eom, Y. Zheng, J. Xue, F. So, *Appl. Phys. Lett.* 93 (2008) 123306.
- [10] N. Chopra, J. Lee, Y. Zheng, S.-H. Eom, J. Xue, F. So, *Appl. Phys. Lett.* 93 (2008) 143307.
- [11] X. Ren, J. Li, R.J. Holmes, P.I. Djurovich, S.R. Forrest, M.E. Thompson, *Chem. Mater.* 16 (2004) 4743.
- [12] J. Li, P.I. Djurovich, B.D. Alleyne, M. Yousufuddin, N.N. Ho, J.C. Thomas, J.C. Peters, R. Bau, M.E. Thompson, *Inorg. Chem.* 44 (2005) 1713.
- [13] R.J. Holmes, B.W. D'Andrade, S.R. Forrest, X. Ren, J. Li, M.E. Thompson, *Appl. Phys. Lett.* 83 (2003) 3818.
- [14] Y. Zheng, S.-H. Eom, N. Chopra, J. Lee, F. So, J. Xue, *Appl. Phys. Lett.* 92 (2008) 223301.
- [15] S.-H. Eom, Y. Zheng, N. Chopra, J. Lee, F. So, J. Xue, *Appl. Phys. Lett.* 93 (2008) 133309.
- [16] M.A. Baldo, S.R. Forrest, *Phys. Rev. B* 62 (2000) 10958.
- [17] Q. Xin, W.L. Li, W.M. Su, T.L. Li, Z.S. Su, B. Chu, B. Li, *J. Appl. Phys.* 101 (2007) 044512.
- [18] M.Y. Chan, C.S. Lee, S.L. Lai, M.K. Fung, F.L. Wong, H.Y. Sun, K.M. Lau, S.T. Lee, *J. Appl. Phys.* 100 (2006) 094506.
- [19] D. Tanaka, T. Takeda, T. Chiba, S. Watanabe, J. Kido, *Chem. Lett.* 36 (2007) 262.
- [20] K. Walzer, B. Maennig, M. Pfeiffer, K. Leo, *Chem. Rev.* 107 (2007) 1233.
- [21] G. He, M. Pfeiffer, K. Leo, M. Hofmann, J. Birnstock, R. Pudzich, J. Salbeck, *Appl. Phys. Lett.* 85 (2004) 3911.
- [22] J. Kalinowski, M. Cocchi, D. Virgili, V. Fattori, J.A.G. Williams, *Adv. Mater.* 19 (2007) 4000.
- [23] Y. Li, D.-Q. Zhang, L. Duan, R. Zhang, L.-D. Wang, Y. Qiu, *Appl. Phys. Lett.* 90 (2007) 012119.
- [24] S.R. Forrest, D.D.C. Bradley, M.E. Thompson, *Adv. Mater.* 15 (2003) 1043.
- [25] N.C. Greenham, R.H. Friend, D.D.C. Bradley, *Adv. Mater.* 6 (1994) 491.
- [26] S. Naka, H. Okada, H. Onnagawa, T. Tsutsui, *Appl. Phys. Lett.* 76 (2000) 197.
- [27] P.M. Borsenberger, L. Pautmeier, R. Richert, H. Bassler, *J. Chem. Phys.* 94 (1991) 8276.
- [28] M.K. Mathai, V.-E. Choong, S.A. Choulis, B. Krummacker, F. So, *Appl. Phys. Lett.* 88 (2006) 243512.
- [29] Y. Sun, S.R. Forrest, *Nat. Photonics* 2 (2008) 483.
- [30] M.-H. Lu, J.C. Sturm, *Appl. Phys. Lett.* 78 (2001) 1927.

present to prevent the excess water from ALD process to penetrate into PVP which (ii) being highly hygroscopic can be loaded with significant amount of water which can then be released into P3HT.

To solve this problem, here we propose an enhanced sealing architecture by adding a stopping layer against water penetration under the PVP/ $\text{Al}_2\text{O}_3$  stack. The additional layer has to satisfy the following requirements: it has to be compact and non polar, in order to avoid water diffusion, and it has to be integrated in the existing process, without destroying the previously deposited layer (P3HT) and without being destroyed by the deposition of the subsequent layers.

To address these constraints we adopt a PVP-based cross-linkable layer. Such material has been previously used as gate insulator for all-organic field effect transistors by Facchetti and coworkers [15]. They showed that cross-linked PVP is insoluble in common organic solvents and it has better insulating properties than normal PVP, suggesting that the cross-linked polymer is more compact and pin-hole free.

## 2. Experimental details

Devices are based on a bottom contact structure using highly p-doped Si as common gate electrode and 130 nm of thermally grown  $\text{SiO}_2$  as gate insulator. Platinum source and drain contacts have been realized by means of a standard photolithographic process on the oxide surface (Microfab, Bremen). Devices with channel lengths ranging from 3 to 18  $\mu\text{m}$  have been used (channel width 15 mm). The oxide surface has been carefully cleaned with chloroform and acetone and then plasma polished for 10 min. Immediately after the cleaning process, the  $\text{SiO}_2$  surface has been functionalized by exposure to dimethyl-dichlorosilane vapors, in order to maximize the mobility and reduce the hysteresis [16]. Solution of Regio-Regular poly-(3-hexylthiophene) (MW = 33 kDa) in toluene ( $5 \text{ mg ml}^{-1}$ ) was filtered through a 0.45  $\mu\text{m}$  pore size PTFE membrane and finally spin coated at 4000 rpm on the substrate, achieving a thickness of about 30 nm. Samples were then cured at 110  $^\circ\text{C}$  for 20 min in high vacuum ( $p = 10^{-5}$  mbar) in order to remove any trace of solvents.

According to the process reported in [15] the cross-linked layer was obtained as follows: a solution of PVP (MW = 11 kD) in anhydrous tetrahydrofuran (THF) ( $4 \text{ mg ml}^{-1}$ ) was mixed with 1,6-bis(trichlorosilyl)-hexane ( $9 \mu\text{l ml}^{-1}$  in anhydrous THF) in a 1:1 by volume solution. The blend was then spun (5000 rpm) on the P3HT film. Even though THF is not a very good solvent for P3HT, in order to minimize its interaction with the P3HT film, we put in rotation the spin coater *before* dropping the THF-based solution. When P3HT films were compact and smooth, they withstood this step without experiencing any sizeable dissolution.

A thermal curing treatment was finally performed (110–120  $^\circ\text{C}$ , 20 min in high vacuum). At this stage the cross-linking agent reacts with OH groups on the PVP so that PVP chains are  $\sigma$ -bonded to a siloxane network [15].

Glassware for solutions containing the cross-linking agent have been derivatized by exposure to dimethyl-dichlorosilane vapors prior to use, since 1,6-bis(trichlorosilyl)-hexane is quite moisture sensitive.

As OH groups are consumed during the cross-linking process, the final layer is apolar, and therefore can act as water stopping layer, and is insoluble and therefore can easily sustain the subsequent deposition of PVP from ethyl acetate (MW = 20 kDa, solution 1 mg/ml spun at 6000 rpm). Solvents, dimethyl-dichlorosilane, PVP, 1,6-bis(trichlorosilyl)-hexane (Aldrich) were used as received without further purification.

Finally, the capping structure was completed by the deposition of  $\text{Al}_2\text{O}_3$  by ALD according to the experimental details reported in our previous paper [14].

To summarize, the capping layer is now composed of three thin films: (i) cross-linked PVP, which is deposited directly on the P3HT and acts as water stopping layer; (ii) PVP which provides the  $-\text{OH}$  groups to act as TMA stopping layer; (iii) atomic layer deposited  $\text{Al}_2\text{O}_3$  which is the actual capping layer (Fig. 1).

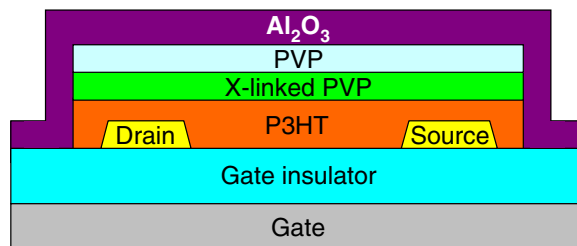


Fig. 1. Cross section of the device capped with the three-layer structure.

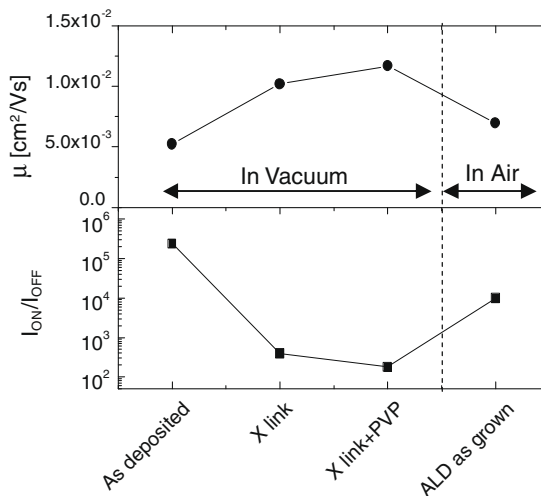


Fig. 2. Trend of the mobility and  $I_{\text{ON}}/I_{\text{OFF}}$  ratio during the process (channel length 18  $\mu\text{m}$ ). The first three points are measured in vacuum, the last point in ambient atmosphere. The effect of the process on the mobility is marginal and the final value is close to the value measured in the uncapped devices (as deposited). On the contrary, the  $I_{\text{ON}}/I_{\text{OFF}}$  ratio drops after the deposition of the cross-linked PVP before improving after the ALD growth and it finally stabilizes around  $10^4$ . Note that the  $I_{\text{ON}}/I_{\text{OFF}}$  ratio has been calculated as the ratio between the current driven at  $V_G = -30 \text{ V}$  and the current at  $V_G = 0 \text{ V}$ .

### 3. Results and discussion

We monitored the electrical characteristics of the devices step by step throughout the whole capping process, in order to evaluate the impact of each single stage on the performance of the devices. In *high vacuum* the uncapped devices showed mobilities between  $0.5 \times 10^{-2}$  and  $0.8 \times 10^{-2} \text{ cm}^2/\text{Vs}$  with on/off ratio close to  $10^6$ . After the deposition and the cross-linking of PVP, the  $I_{\text{ON}}/I_{\text{OFF}}$  ratio drops between  $10^2$  and  $10^3$  while the mobility is less affected (Fig. 2). The reduction of the  $I_{\text{ON}}/I_{\text{OFF}}$  ratio is probably due to residual unreacted  $-\text{OH}$  groups on PVP chains. The subsequent deposition of PVP does not modify the mobility or the on/off ratio.

Finally the sample is capped by  $\text{Al}_2\text{O}_3$ . From now on, all electrical measurements are performed in *ambient air*. While the mobility decreases slightly, the on/off ratio reaches values around  $10^4$ , with an improvement of more than one order of magnitude with respect to the previous stage (Fig. 2). It is likely that during the ALD growth, some TMA molecules reach the cross-linked PVP layer, reacting

and consuming the residual  $-\text{OH}$  groups responsible for the P3HT doping.

We realized, capped and tested a total of 33 devices on different substrates in the same ALD run. We found that for all the tested devices the mobility was marginally affected by the capping process. Regarding the  $I_{\text{ON}}/I_{\text{OFF}}$  ratio, a certain dispersion was observed, ranging from less than  $10^2$  to  $10^4$ , with a majority of devices (55%) in the range  $10^2$ – $10^3$ . From now on, we focus on the best performing samples with on/off ratio greater than  $10^3$ , which represent about the 30% of the devices tested.

Fig. 3 compares transfer characteristics (right) and external characteristics (left) measured in air in samples capped with PVP +  $\text{Al}_2\text{O}_3$  and capped with cross-linked-PVP + PVP +  $\text{Al}_2\text{O}_3$ . In order to better compare the *off* current in the two structures, transfer characteristics are shown in a logarithmic scale. It is clear that the *off* current is reduced by about two orders of magnitude in the “three-layers” structure, if compared to the PVP +  $\text{Al}_2\text{O}_3$  structure. This demonstrates that the cross-linked layer is really effective as barrier against water diffusion.

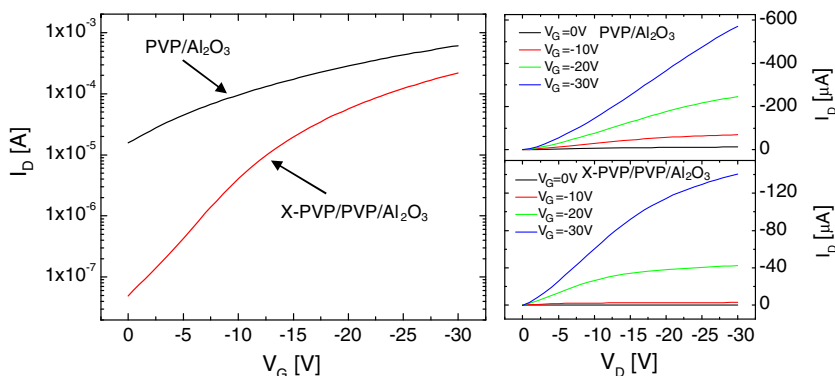


**Fig. 3.** Comparison between the performances obtained from the different capping structures (measurements performed in air, channel length 3  $\mu\text{m}$ ). The sample with the cross-linked PVP layer shows an improvement of the on/off ratio of about two orders of magnitude and a better saturation of the drain current with respect to the sample capped with PVP/ $\text{Al}_2\text{O}_3$ .

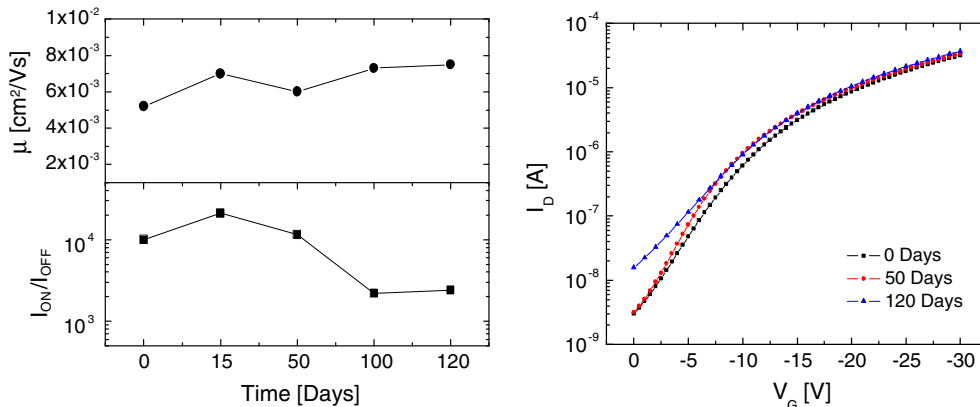


**Fig. 4.** Left, trend of the mobility and  $I_{\text{ON}}/I_{\text{OFF}}$  ratio as a function of time for the three-layer capped device (channel length 18  $\mu\text{m}$ ). Right, evolution of transfer characteristics curves of the same device.



By comparing the external characteristics we realize that the saturation of the drain current is improved in the sample with the cross-linked PVP with respect to the sample capped with PVP/ $\text{Al}_2\text{O}_3$ . This is due to the reduced doping which improves the channel pinch-off at the drain side.

Finally, we tested the performances of the capped devices over some months, in order to prove the robustness and the long term stability of the capping layer. Graph in Fig. 4 (left) shows the trend of the mobility and  $I_{\text{ON}}/I_{\text{OFF}}$  ratio measured in ambient atmosphere as a function of time. After almost two months from the deposition the  $I_{\text{ON}}/I_{\text{OFF}}$  ratio is still very high in the range of  $10^4$ , comparable to the value measured just after the ALD growth. In the following 60 days the on/off ratio diminishes but maintains a value larger than  $10^3$ . The mobility does not change significantly over the whole period that we monitored, remaining between  $0.6 \times 10^{-2}$  and  $0.8 \times 10^{-2} \text{ cm}^2/\text{Vs}$ .

Fig. 4 (right) shows the evolution of transfer characteristics measured on the same device ( $L = 18 \mu\text{m}$ ) in ambient atmosphere. The curves measured in the device just after the ALD growth (0 days) and after 50 days are practically coincident, while after 120 days a marginal increase of the off current can be noticed.

#### 4. Conclusions

To conclude, we have developed a three-layers structure for the effective encapsulation of P3HT based TFT. The structure is comprised of an ALD deposited  $\text{Al}_2\text{O}_3$  layer, and of two spin-cast films acting as stopping layers for  $\text{Al}_2\text{O}_3$  precursors: PVP against TMA and cross-linked PVP against water. With respect to our previous two-layer structure [14], this latter layer provides a dramatic improvement of the  $I_{\text{ON}}/I_{\text{OFF}}$  ratio, which reaches values between  $10^3$  and  $10^4$  in ambient atmosphere. Encapsulated devices have shown ambient stability in excess of a few months.

#### Acknowledgements

The authors are grateful to G. Tallarida and M. Alia (MDM CNR-INFM, Italy) for collaboration in devices realization, to S. Masci for careful bonding of devices and to P. Trigilio for collaboration in devices characterization. The financial support of Project "Proteo" (Fondazione Cariplo) is also gratefully acknowledged.

#### References

- [1] S. Hoshino, M. Yoshida, S. Uemura, T. Kodzasa, N. Takada, T. Kamata, K. Yase, *Journal of Applied Physics* 95 (2004) 5088.
- [2] D. Li, E.J. Borkent, R. Nortrup, H. Moon, H. Katz, Z. Bao, *Applied Physics Letters* 86 (2005) 042105.
- [3] C.R. Kagan, A. Afzali, T.O. Graham, *Applied Physics Letters* 86 (2005) 193505.
- [4] B.S. Ong, Y. Wu, Y. Li, P. Liu, H. Pan, *Chemistry – A European Journal* 14 (2008) 4766.
- [5] S.H. Han, J.H. Kim, J. Jang, S.M. Cho, M.H. Oh, S.H. Lee, D.J. Choo, *Applied Physics Letters* 88 (2006) 073519.
- [6] H. Jung, T. Lim, Y. Choi, M. Yi, J. Won, S. Pyo, *Applied Physics Letters* 92 (2008) 163504.
- [7] T. Sekitani, T. Someya, *Japanese Journal of Applied Physics* 46 (2007) 4300.
- [8] S. Koul, Y. Vygranenko, F. Li, A. Sazonov, A. Nathan, *Material Research Society Symposium Proceedings* 871E (2005) 19.4.1.
- [9] H. Jeon, K. Shin, C. Yang, C.E. Park, S.-H.K. Park, *Applied Physics Letters* 93 (2008) 163304.
- [10] S.-H.K. Park, J. Oh, C. Hwang, J. Lee, Y.S. Yang, H.Y. Chu, *Electrochemical and Solid-State Letters* 8 (2005) H21.
- [11] W. Kim, W. Koo, S. Jo, C. Kim, H. Baik, J. Lee, S. Im, *Applied Surface Science* 252 (2005) 1332.
- [12] S. Meyer, S. Sellner, F. Schreiber, H. Dosch, G. Ulbricht, M. Fischer, B. Gompf, J. Pflaum, *Material Research Society Symposium Proceedings* (2007) 965 E.
- [13] S. Sellner, A. Gerlach, F. Schreiber, M. Kelsch, N. Kasper, H. Dosch, S. Meyer, J. Pflaum, M. Fischer, B. Gompf, *Advanced Materials* 16 (2004) 1750.
- [14] S. Ferrari, L. Fumagalli, D. Natali, F. Perissinotti, E. Peron, M. Sampietro, *Organic Electronics* 8 (2007) 407.
- [15] M.-H. Yoon, H. Yan, A. Facchetti, T.J. Marks, *Journal of the American Chemical Society* 127 (2005) 10388.
- [16] J. Veres, S. Ogier, G. Lloyd, D. De Leeuw, *Chemistry of Materials* 16 (2004) 4543.

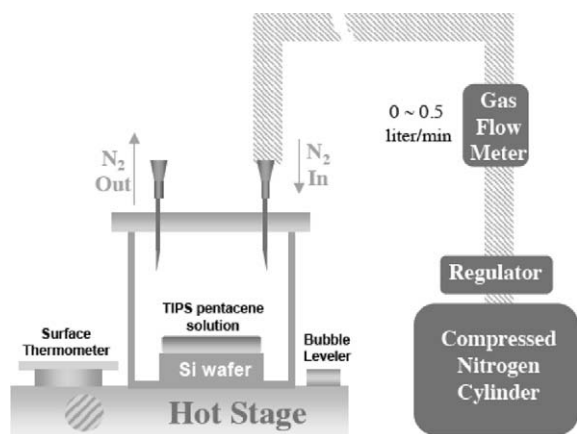


Fig. 1. The design of controlled solution process system.

pentacene [7], rubrene [8], and pentacene [9–11]. Headrick et al. with a four-channel transistor configuration and hollow-pen deposition method, measured the hole mobility of polycrystalline TIPS pentacene films along the hollow-pen writing direction and its vertical direction [7]. On the other hand, by using transient photoconductivity technique, Ostroverkhova et al. studied TIPS pentacene single crystals, and estimated the mobility anisotropy of  $a$ – $b$  plane to be  $3.5 \pm 0.6$  [12].

In this work, besides suggesting a maximum anisotropic ratio of 10 in solution-processed TIPS pentacene thin films, which was supported by Headrick's work [7], our results demonstrated a unique example of systematic study on charge-transport anisotropy in single-crystal textured TIPS pentacene films by using direct mobility measurement. Furthermore, information about the molecular alignments in crystalline TIPS pentacene thin films was collected from electron and polarized light microscopy, which revealed frequent twinning across the  $(1\bar{2}0)$  planes that are the lateral facets for single crystalline domains in the TIPS pentacene films. The  $[210]$  direction is close to one of the two  $\pi$ – $\pi$  stacking directions in TIPS pentacene unit cell, and was identified as an excellent pathway for hole transport in solution-processed TIPS pentacene thin films.

Most importantly, we exhibited the potential of controlled solution deposition in fabricating single-crystal textured TIPS pentacene films with adjustable morphologies, which may be transferable to the studies of other solution-processible organic molecular semiconductors. The controlled solution deposition system (Fig. 1) allowed us to study in detail the effect of grain size [4], thermal cracking [13], and crystal orientation (this work) on the charge transport of TIPS pentacene thin films.

## 2. Experimental

### 2.1. Materials

6,13 bis(triisopropylsilylethynyl) pentacene (TIPS pentacene) was in the form of dark-blue needle-shaped crystals, prepared through a one-step reaction from 6,13 pentacenequinone [5].

### 2.2. X-ray diffraction

X-ray diffraction of TIPS pentacene films on the silicon wafer was performed with a Rigaku Miniflex and a Brukers D8. Both one-dimension ( $2\theta$  vs. intensity) and two-dimension diffraction results (diffraction pattern) were obtained and compared with simulated data from Cerius<sup>2</sup>, which is a molecular modeling platform commercially available from Accelrys.

### 2.3. Polarized light microscopy

A Nikon OptiPhot2-POL polarized optical microscope, equipped with Spot RT Color 2.2.1 CCD camera (Diagnostic Instruments, Inc.), was used for taking polarized optical micrographs of solution-processed TIPS pentacene thin films.

### 2.4. TEM

TEM and selected area electron diffraction (SAED) experiments were conducted on a Philips CM12, working at 120 kV. Electron diffraction pattern were obtained with spot size 6 or 7, and compared with simulations from Cerius<sup>2</sup> (intensity factor 10, and accelerating voltage 120 kV).

### 2.5. Transistor fabrication and characterization

TIPS pentacene thin films were fabricated in the controlled solution-process chamber (Fig. 1). The silicon wafers used in this study were heavily arsenide-doped and the insulator layer was thermally grown silicon dioxide of 200 nm thickness. About 100 nm-thick gold electrodes (source and drain) were thermally evaporated through a laser-machined shadow mask. Transistor characteristics were measured with a Keithley 4200 or HP 4145 semiconductor parameter analyzer and an Alessi-3200 probe station. Transistor characterization was conducted at room temperature in dark. Both transfer ( $I_d$ – $V_g$ ) and output ( $I_d$ – $V_d$ ) characteristics were tested five times for each transistor. The  $I_d$ – $V_d$  curves were obtained upon sweeping gate voltage  $V_g$  from  $-40$  to  $0$  V, and then varying the source–drain voltage from  $-40$  to  $0$  V. The  $I_d$ – $V_g$  curves were collected with the gate voltage increase from  $-60$  to  $20$  V at a constant  $V_d$  of  $-40$  V. Saturation mobility was then extracted from the slope of the transfer curve  $V_g$ – $(I_d)^{1/2}$ , according to the equation  $I_d = \mu WC_i (V_g - V_T)^2 / 2L$ , where  $W$  and  $L$  are channel width and length respectively,  $C_i$  the specific capacitance in the insulator layer,  $V_T$  the threshold voltage, and  $\mu$  the saturation mobility.  $W$  and  $L$  were about 300 and 25  $\mu\text{m}$ .

## 3. Results and discussion

In the controlled solution deposition system, [4] temperature control of the deposition chamber was achieved with a hot stage and surface thermometer. Nitrogen gas was released from a compressed gas cylinder through a flow meter (Key Instruments), which monitored and regulated the nitrogen gas flow ( $0$ – $0.5$  l/min). The nitrogen gas

flowed in and out of the system through syringe needles, to provide an oxygen-free environment, and to vary the solvent evaporation rate in a systematic manner. Droplets of TIPS pentacene solutions (0.1–1 wt% in bromobenzene or toluene) were placed on a pre-cleaned [13] Si substrate (2000 Å thermally oxidized SiO<sub>2</sub>) inside the deposition chamber, and allowed to dry in minutes or hours depending on the nitrogen flushing rate and deposition temperature.

The acene planes in TIPS pentacene are known to take an “edge-on” orientation in thin films on glass and amorphous carbon substrates [5,14,15]. X-ray diffraction of TIPS pentacene films on glass yielded a sharp (001) peak at 1.683 nm [5]. Here we studied the molecular orientation of TIPS pentacene films fabricated with the controlled deposition chamber on an oxidized Si wafer. In both 1-D and 2-D out-of-plane X-ray diffraction, strong reflections of lattice spacing (001), (002), and (003) were visible (Fig. 2). These results and further in-plane X-ray diffractions suggested that, in the thin films fabricated with the controlled solution deposition chamber, the TIPS pentacene molecules arranged with the same “edge-on” orientation on SiO<sub>2</sub> substrates. In other words, the TIPS pentacene films on oxidized Si wafers fabricated with the controlled solution process had [001] projection as the top view, identical to the case with amorphous carbon substrates in TEM and electron diffraction experiments [14,15]. TEM experiments revealed that in these solution-processed films, the long axis of the needle-shaped TIPS pentacene grains was parallel to [210], and the short axis was close to [1 $\bar{2}$ 0] [14,15].

At relatively low nitrogen flushing rates (0–0.04 l/min) and proper temperatures (from room temperature to 90 °C), TIPS pentacene thin films with well ordered textures could be fabricated over relatively large areas (up to several square millimeters) (Fig. 3a), using the controlled solution deposition system [4]. If the deposition temperature was close enough (~90 °C) to the previously reported solid-to-solid structural phase transition temperature (124 °C), [14] numerous crystallographic facets along (120) would uniformly appear in single crystalline TIPS pentacene domains (Fig. 3b). Similar (120) facets were frequently observed under bright-field TEM in TIPS pentacene

thin films briefly annealed above the phase transition temperature (124 °C) (Fig. 3c and d). More importantly, these (120) facets provided unambiguous evidences of frequent twinning between the large grains (with typical grain widths  $W_C$  of microns to hundred microns) of the solution-processed TIPS pentacene films (Fig. 3b–d). Fig. 3e is a simplified crystal modeling top view of these solution-processed TIPS pentacene films, showing the different characteristic crystallographic planes and axes.

It is necessary to point out that deposition conditions for generating (120) facets (i.e. 90–130 °C) only served the purpose to understand the molecular orientations in TIPS pentacene thin films. Deposition temperatures for the active layer of actual devices were significantly lower (10–50 °C), in order to avoid the effect of thermal faceting or cracking, which has been shown to reduce the effective mobility by up to several times [13].

A top-contact thin film transistor configuration was used throughout this study (Fig. 4a). TIPS pentacene films were solution-cast from 0.1 to 1 wt% bromobenzene or toluene solution with the controlled solution process system [4] at relatively low temperatures (10–50 °C) and very low (0–0.04 l/min) nitrogen flushing rates. Generally five transfer and output characteristics measurements were performed on each transistor, which had standard deviations of 5–20% of the average mobility.

Fig. 4b shows an optical image of an actual device layout in top view. On top of the Si wafer, the crystalline TIPS pentacene films had a central nucleus (Fig. 4b); the needle-shaped grains stretched out in different directions and meet the later-deposited gold source–drain channel array at various  $\theta$  angles (Fig. 4c). Here the angle between [210] (the long axis of TIPS pentacene grains) and the channel direction was defined as  $\theta$  (Fig. 4c). The fabricated TIPS pentacene films in Fig. 4 had thicknesses of ~150 nm according to atomic force microscopy experiments. Representative transfer (Fig. 4d) and output (Fig. 4e) characteristics of these TIPS pentacene thin film transistors are shown as a function of the  $\theta$  angle, demonstrating a strong orientation-dependence of effective mobility. Noticeably, non-linear  $I_{ds}$ – $V_{ds}$  responses at low  $V_{ds}$  region were mainly observed in devices with low  $\theta$  angle (e.g.  $\theta = 20^\circ$  in Fig. 4e). This may be explained by the facts that channel

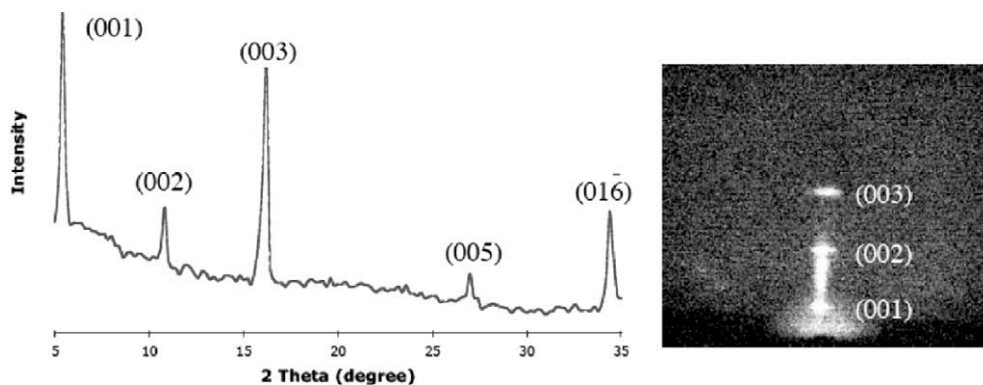
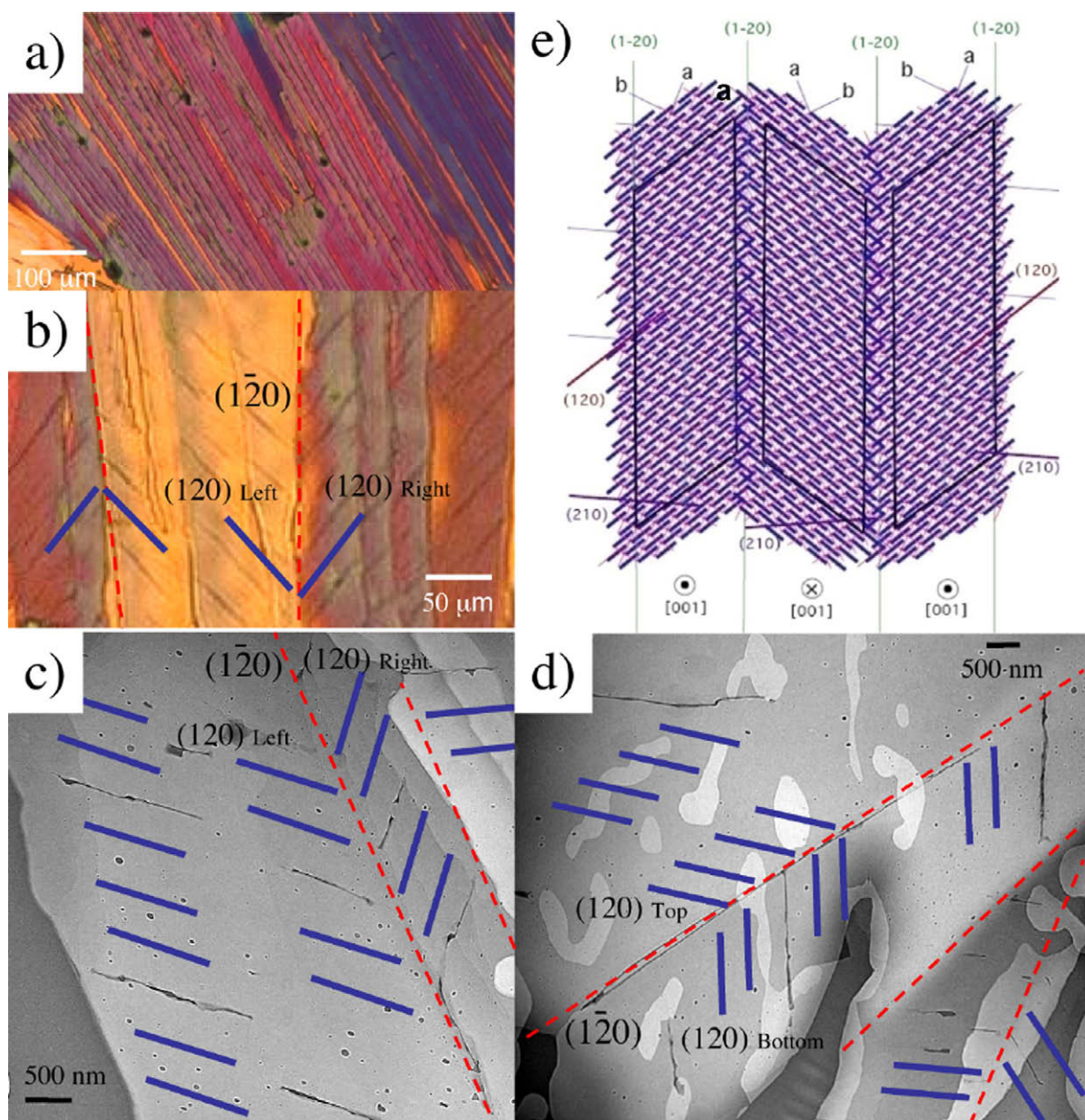


Fig. 2. Two- and one-dimensional out-of-plane X-ray diffraction results of TIPS pentacene films fabricated with the controlled deposition chamber in Fig. 1.



**Fig. 3.** (a) At very low nitrogen flushing rates (0–0.04 l/min) and proper temperatures (room temperature to 90 °C), TIPS pentacene thin films with well ordered texture could be fabricated over a relatively large area (up to several millimeter by several millimeter) by using the controlled solution deposition system [4]. (b) If the deposition temperature was close enough ( $\sim 90$  °C) to the previously reported solid-to-solid structural phase transition temperature (124 °C), [14] numerous crystallographic facets along (120) could be uniformly seen in a single crystalline TIPS pentacene domain. (c, d) Similar (120) facets were frequently observed under bright-field TEM in TIPS pentacene thin films briefly annealed above the solid-to-solid structural phase transition temperature (124 °C). These (120) facets provided unambiguous evidences of frequent twinning along [210] in large grain (grain width  $W_G$  of microns to hundred microns) solution-processed TIPS pentacene films. (e) A simplified crystal modeling top view of the solution-processed TIPS pentacene films shows different crystallographic planes and axes.

resistance is made up of contact and channel resistance; contact resistance is relatively constant for devices in this work as they have similar grain width, while channel resistance is orientation-dependent and will sharply decrease as the  $\theta$  angle decreases. In addition, we found that threshold voltage and on/off ratio did not change dramatically as a function of crystal orientation. In Fig. 4d, as the  $\theta$  angle increased, the threshold voltages increased by only a cou-

ple of volts (from 0.2 to about  $-2$  V), and the on/off ratios decreased slightly (from  $10^6$  to  $10^{5.5}$ ).

Several sets of these  $\theta$  angle dependent mobilities were obtained, which showed similar anisotropic trends to the 10-transistor data set presented in Fig. 5a, on the top right quadrant (0–90°) of a 360° pole figure. The other three quadrants of the pole figure (90–360°) were symmetrically plotted with the experimental fit of the data in the first

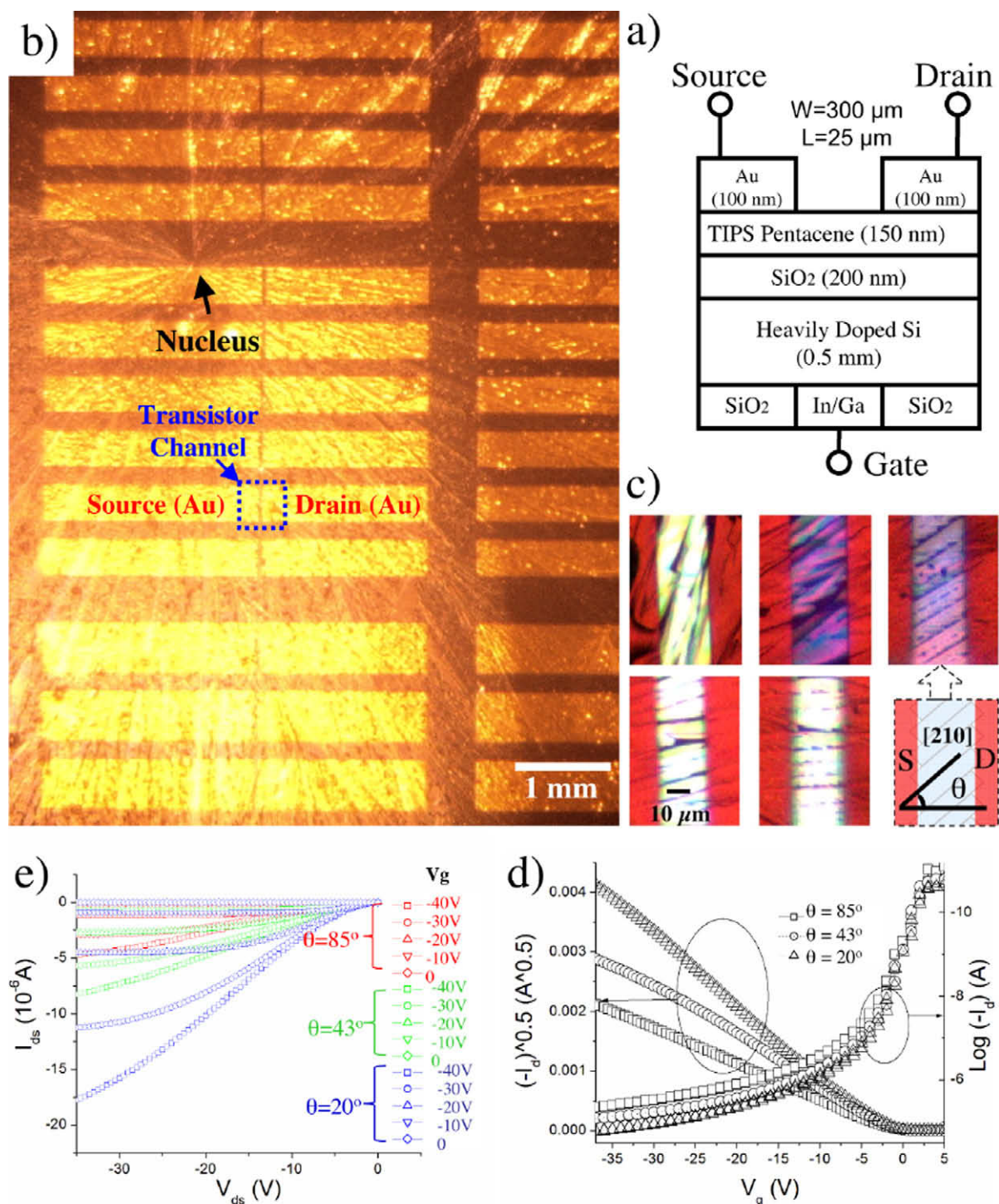


**Fig. 4.** (a) A not-to-scale schematic of the top-contact thin film transistor configuration used in this study. (b) An optical image of an actual device layout in top view. On top of the Si/SiO<sub>2</sub> wafer, TIPS pentacene films had a central nucleus. (c) Needle-shaped grains stretched out to different directions and the later-deposited gold source–drain channel array met the grains at various  $\theta$  angles. Here the angle between [210] (long axis of TIPS pentacene grains) and channel direction was defined as  $\theta$ . (d, e) Typical transfer and output characteristics of TIPS pentacene thin films as a function of crystal orientation.

quadrant, due to the film symmetry. As the  $\theta$  angle increased, the effective hole mobility decreased by up to ten-fold (from 0.04 to 0.004 cm<sup>2</sup>/V s in Fig. 5a).

It has been argued theoretically that TIPS pentacene crystals should be essentially two-dimensional in their band structures due to the  $\pi$ – $\pi$  stacking along both the

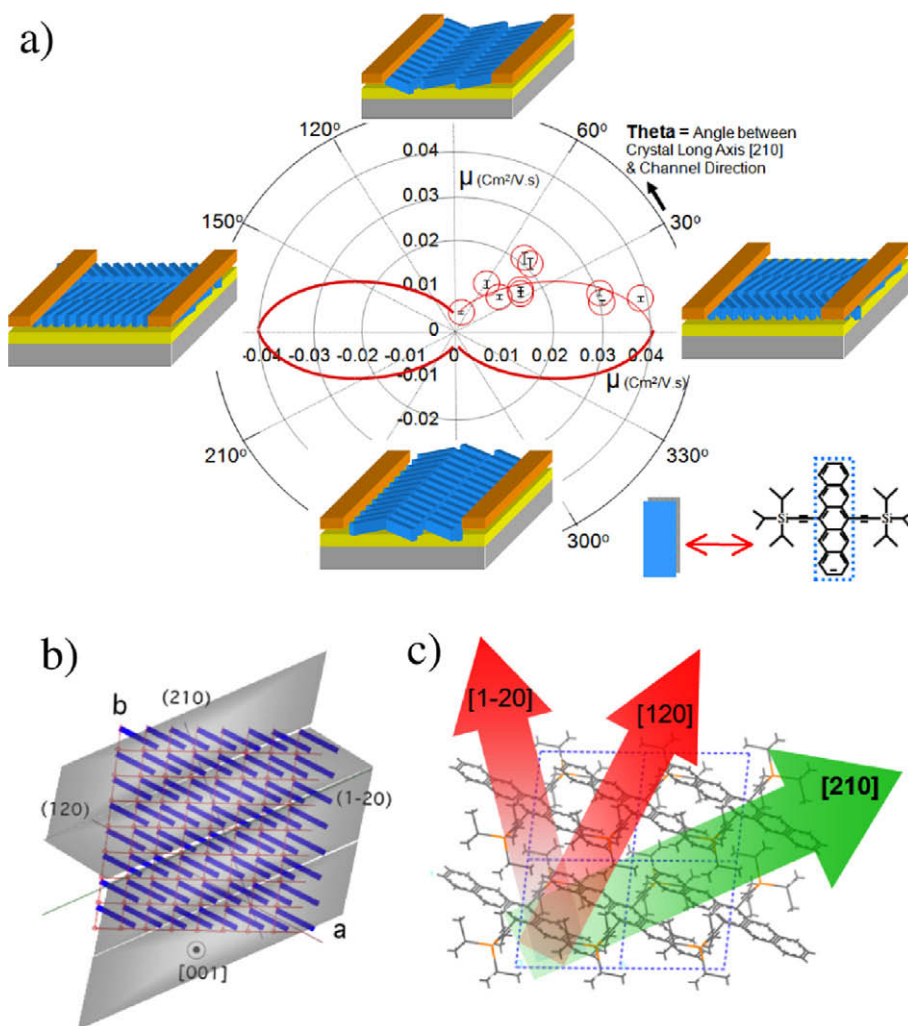


**Fig. 5.** (a) The experimental results of the  $\theta$  angle dependent charge carrier mobility were presented on the top right quarter (0–90°) of the 360° pole figure. The other three quarters of the pole figure (90–360°) were symmetrically plotted with the experimental fit of the data in the first quarter, based on the film symmetry. TIPS pentacene molecules were over-magnified and simplified as plates (underneath source/drain electrodes) in the device cartoons to show the relative positions of twin boundaries and regular grain boundaries. (b, c) Because of a combination of good  $\pi$ – $\pi$  stacking and low boundary density, [210] is the best charge carrier pathway in large grain solution-processed TIPS pentacene thin films. The needle-grain-textured TIPS pentacene films with frequent twinning across [210] (b) were plotted against the relative positions of important crystallographic planes and axes (b and c).

“ $a$ ” and “ $b$ ” directions (Fig. 5b and c) [16,17]. However, the frequent twinning across the  $(1\bar{2}0)$  lateral facets and grain boundaries (Fig. 3b–e) in a typical solution-processed TIPS pentacene thin film significantly limited the charge transport along the  $[1\bar{2}0]$  direction, which was the short axis of the needle-shaped TIPS pentacene grains and close to the  $[010]$  axis (Figs. 3 and 5). In contrast, the  $[210]$  direction (the long axis of the needle-shaped TIPS pentacene grains) is close to the  $[100]$  axis. Because of a combination of good  $\pi$ – $\pi$  stacking and low boundary density, the  $[210]$  direction was found to be the best charge carrier pathway in these solution-processed TIPS pentacene thin films (Fig. 5b and c).

Occasionally single grain TIPS pentacene crystals (with grain widths  $W_G > 25 \mu\text{m}$ , or the channel length) occupied the whole channel ( $300 \mu\text{m}$  by  $25 \mu\text{m}$ ), with  $[210]$  axis

perpendicular to the channel direction. This was actually very similar to the case with  $\theta$  close to  $90^\circ$  in Fig. 4c, but without grain boundaries in channel. These “single-crystal” transistors with  $\theta \sim 90^\circ$  were found to have large mobilities, nearly equivalent to those with  $\theta = 0$ – $10^\circ$ . This agreed well with the two-dimensional  $\pi$ – $\pi$  stacking crystal structure of TIPS pentacene (Fig. 5c), and confirmed that the strong anisotropic (10:1) charge-transport behavior of solution-processed TIPS pentacene films is essentially due to their grain geometry and boundary distribution.

Most importantly, the controlled solution deposition system (Fig. 1) was shown to yield relatively uniform, adjustable morphologies of single-crystal textured TIPS pentacene films. With the controllable nitrogen flow and chamber temperature, fine tuning of the resultant film morphology becomes possible, which can potentially lead

to both enhanced performance reproducibility and better understanding of the structure–property relationships in small-molecule solution-processible organic semiconductors.

From the micrograph in Fig. 3, some crystallographic discontinuities or additional defects beyond the regular and twin boundaries were visible, possibly representing internal fractures and cleavage planes, or perhaps merged boundary facets generated during crystal growth. Therefore, the crystal orientation-dependent mobility illustrated in Fig. 5 may actually represent combined influences of these extra structural complexities as well as the more obviously conceived crystal structure anisotropy and grain boundaries. Precise determination of the actual impact of these extra structural complexities on charge-transport is beyond the scope of this paper and has been partially addressed elsewhere [13]. In addition, micrographs in Figs. 3 and 4 occasionally demonstrated tiny circular particles on top of, or inside the crystallographically well defined grains. Some of these particles were previously reported as a second layer (or islands) of TIPS pentacene crystals on top of the bottom films [7]. However, we cannot rule out the possibilities of impurity inclusions and heterogeneous nucleation, which may be resulted from the slow crystallization process. Since the TIPS pentacene transistors with systematically varied crystal orientations are likely to suffer from this effect equally, we do not expect the overgrown TIPS pentacene crystals or slight film irregularities to significantly interfere with the trend of anisotropic charge transport illustrated in Fig. 5.

It needs to be pointed out that some of the structural analysis in this work, such as crystallographic planes and directions of grain boundaries and cracks, were presented previously in the context of TIPS pentacene films with similar crystal orientation angles ( $\theta \sim 30^\circ$ ) but systematically varied grain widths (1.5–33  $\mu\text{m}$ ) [4]. However, according to our knowledge, the correlation of charge-transport mobility and TIPS pentacene grain boundaries have not been reported as a function of crystal orientation in films with uniform grain widths, and this is the key focus of the current work (with grain width  $W_G$  of  $\sim 10 \mu\text{m}$ ). In addition, although the controlled solution deposition method was already used previously [4] to generate TIPS pentacene films with systematically varied grain sizes, this paper is aimed to reveal the optimal deposition conditions for fabricating films with large grains but different crystal orientations ( $\theta = 0\text{--}90^\circ$ ). For example, the gas flushing rates used in Ref. [4] were varied between 0 and 0.5 l/min, while the films studied in this work were fabricated with a very slow nitrogen flow speed ( $<0.04$  l/min). Through the temperature control in this work, the TIPS pentacene twin boundaries were conveniently identified in large grain TIPS pentacene crystalline films with optical microscopy and associated with charge-transport anisotropy, which was not achieved in Ref. [4].

Compared to the mobility anisotropy measurements in Ref. [7], the key advantages of this work are three-fold. (1) The measurements in Ref. [7] were performed on films deposited with a hollow-pen, which generated grain sizes with large variations, while the films tested in this work were fabricated with a controlled solution casting method

that yielded a consistent grain width of about 10  $\mu\text{m}$ . Grain sizes of TIPS pentacene grains have a large effect on charge-transport, [4] and the effect of grain size should be removed in order to precisely determine the charge-transport anisotropy. (2) The channel length and width in this work (25 and 300  $\mu\text{m}$ ) were significantly smaller than those in Ref. [7] (75 and 1000  $\mu\text{m}$ ). The reduced channel area significantly minimized the effect of crystal orientation variation within the same transistor channel. In other words, the estimation of crystal orientation angle in this work was much more accurate. (3) With the controlled solution deposition, it is now possible to generate the data set in Fig. 5 with as many as 10 different crystal orientation angles, while the four-channel electrode array in Ref. [7] only provided mobility comparison between two orientations (hollow-pen writing pathway and its vertical direction).

We notice that the mobilities achieved in this work were considerably smaller than those reported previously [18]. The measured hole mobilities of TIPS pentacene crystals are strongly dependent on the impurity level, substrate treatment, deposition methods, and other factors. The focus of this work is on the crystal orientation-dependent charge transport, instead of achieving the highest mobility possible. Some of the requirements for generating TIPS pentacene grains with uniform grain widths but different orientations may be even contradictory to the ones for achieving the highest mobility. For example, no surface treatment was performed on the silicon dioxide substrate in this study. A very slow crystallization is beneficial for crystal orientation study, but may lead to higher impurity levels. In this work, no efforts were made to maximize the measured mobility values, which could be the reason for the relatively low mobilities observed.

#### 4. Conclusions

In summary, a controlled solution process system with variable deposition temperatures and nitrogen gas flow rates was used to fabricate active layers of TIPS pentacene thin film transistors with relatively large grains ( $W_G \sim 10 \mu\text{m}$ ) and different crystal orientations. Acene planes of TIPS pentacene crystals took an “edge-on” orientation on the oxidized Si wafer substrates, and one of the  $\pi$ – $\pi$  stacking directions was close to [210] – the long axis of the needle-shaped TIPS pentacene grains. Frequent twinning across the ( $1\bar{2}0$ ) planes was evidenced by both optical and transmission electron microscopy. A maximum charge-transport anisotropic ratio of 10 was measured upon systematically changing the  $\theta$  angle (i.e. the angle between [210] and the source–drain direction). Our results also demonstrate the possibilities of controlled solution deposition in fabricating single-crystal textured TIPS pentacene films with uniform and adjustable morphologies, which may be applicable to the studies of other solution-processible organic molecular semiconductors.

#### Acknowledgement

The authors thank the Office of Naval Research and the National Science Foundation for financial supports (DMR-

0084304 and DMR-6518079). TEM studies and electrical characterizations were conducted in the Electron Microbeam Analysis Laboratory and Solid State Electronics Laboratory at the University of Michigan at Ann Arbor.

## References

- [1] W.S. Hu, Y.T. Tao, Y.J. Hsu, D.H. Wei, Y.S. Wu, *Langmuir* 21 (2005) 2260.
- [2] A. Troisi, G. Orlandi, *J. Phys. Chem. B* 109 (2005) 1849.
- [3] K. Hummer, C. Ambrosh-Draxl, *Phys. Rev. B* 72 (2005) 205205.
- [4] J. Chen, C.K. Tee, M. Shtein, J.E. Anthony, D.C. Martin, *J. Appl. Phys.* 103 (2008) 114513.
- [5] J.E. Anthony, J.S. Brooks, D.L. Eaton, S.R. Parkin, *J. Am. Chem. Soc.* 123 (2001) 9482.
- [6] J. Chen, S. Subramanian, S.R. Parkin, M. Siegler, K. Gallup, C. Haughn, D.C. Martin, J.E. Anthony, *J. Mater. Chem.* 18 (2008) 1961.
- [7] R.L. Headrick, S. Wo, F. Sansoz, J.E. Anthony, *Appl. Phys. Lett.* 92 (2008) 063302.
- [8] V.C. Sundar, J. Zaumseil, V. Podzorov, E. Menard, R.L. Willett, T. Someya, M.E. Gershenson, J.A. Rogers, *Science* 303 (2004) 1644.
- [9] J.Y. Lee, S. Roth, Y.W. Park, *Appl. Phys. Lett.* 88 (2006) 252106.
- [10] X.L. Chen, A.J. Lovinger, Z. Bao, J. Sapjeta, *Chem. Mater.* 13 (2001) 1341.
- [11] M.L. Swiggers, G. Xia, J.D. Slinker, A.A. Gorodetsky, G.G. Malliaras, R.L. Headrick, B.T. Weslowski, R.N. Shashidhar, C.S. Dulcey, *Appl. Phys. Lett.* 79 (2001) 1300.
- [12] O. Ostroverkhova, D.G. Cooke, F.A. Hegmann, R.R. Tykwinski, S.R. Parkin, J.E. Anthony, *Appl. Phys. Lett.* 89 (2006) 192113.
- [13] J. Chen, C.K. Tee, C. Shaw, M. Shtein, D.C. Martin, J.E. Anthony, *J. Polym. Sci.: Polym. Phys.* 44 (2006) 3631.
- [14] J. Chen, J.E. Anthony, D.C. Martin, *J. Phys. Chem. B* 110 (2006) 16397.
- [15] J. Chen, J.E. Anthony, D.C. Martin, *J. Mater. Res.* 22 (2007) 1701.
- [16] A. Troisi, G. Orlandi, J.E. Anthony, *Chem. Mater.* 17 (2005) 5024.
- [17] R.C. Haddon, X. Chi, M.E. Itkis, J.E. Anthony, D.L. Eaton, T. Siegrist, C.C. Mattheus, T.T.M. Palstra, *J. Phys. Chem. B* 106 (2002) 8288.
- [18] S.K. Park, T.N. Jackson, J.E. Anthony, D.A. Mourey, *Appl. Phys. Lett.* 91 (2007) 063514.



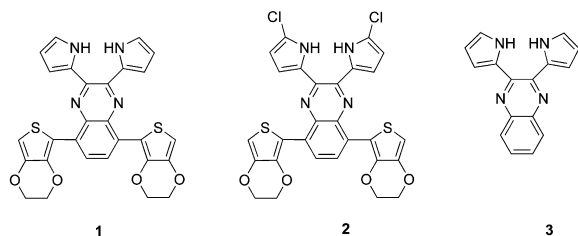


Chart 1. The structures of 1, 2 and 3.

(red–green–blue, RGB) has remained elusive. The problem was that the green polymeric electrochromics should have at least two absorption bands (blue and red) in their neutral state and these bands should also deplete simultaneously during oxidation [24] and it has been difficult to control both absorption bands by the application of a voltage pulse. Fortunately, a real advance on polymeric electrochromics came in the year 2004 by the work of Wudl and Sonmez et al. which brought all the problem to a close by designing hybrid materials in which electron rich (donor) and electron poor (acceptor) units were combined [24,25]. Nevertheless, the examples of neutral state green polymeric materials have still been very rare [26–30] and the newer ones are welcome.

During the course of a programme aimed at the synthesis and applications of novel photo- and electro-active materials [31–33], we have recently reported that the donor–acceptor systems which were based on thiophene and/or EDOT units as donor parts and 2,1,3-benzoselenadiazole as acceptor part, respectively, provided neutral state green polymeric electrochromic material [34]. In this paper, we wish to report the synthesis and properties of a novel and highly stable neutral state green polymeric electrochromic material which is based on 5,8-bis(2,3-dihydrothieno[3,4-b][1,4]dioxin-5-yl)-2,3-di(1H-pyrrol-2-yl)quinoxaline, **1** [35–37] (Chart 1). Although the synthesis of **1** was previously reported by Anzenbacher et al., to our best knowledge, no attention has been paid to the electrochromic properties of its polymer **P1**. **P1** has an ambipolar character (n- and p-doping process) and it exhibits a green color in the neutral state and a highly transmissive blue color in the oxidized state, which is a quite important feature for RGB applications. Furthermore, the optical, electronic and electrochromic properties of **P1** were discussed in comparison with the precedent analogues **P4–P6** [27,28].

## 2. Results and discussion

### 2.1. Electropolymerization

In order to elaborate the redox behavior of **1**, cyclic voltammetry studies were carried out in 0.1 M tetrabutylammonium hexafluorophosphate (TBAH)/dichloromethane (DCM) solution. As depicted in Fig. 1, **1** showed an irreversible peak ( $E_{m,a}^{\text{ox}} = 0.85$  V vs Ag/AgCl) during anodic scan. On the other hand, during the cathodic scan, a reversible reduction peak with a half peak potential ( $E_{1/2}^{\text{red}}$ ) of  $-1.39$  V (vs Ag/AgCl) was observed for stable radical anion formation.

For **1**, new reversible redox couples and concomitant increase in the current intensities were observed during

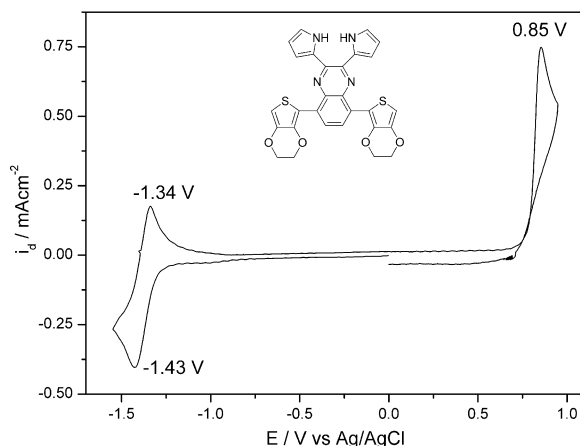


Fig. 1. Cyclic voltammogram of  $1.0 \times 10^{-3}$  M **1** in 0.1 M TBAH/DCM at 100 mV/s.

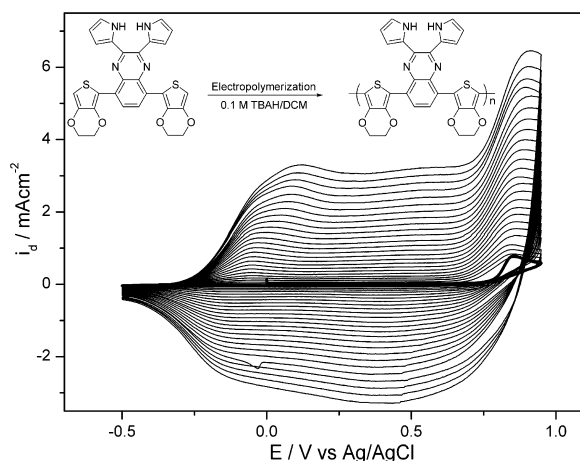
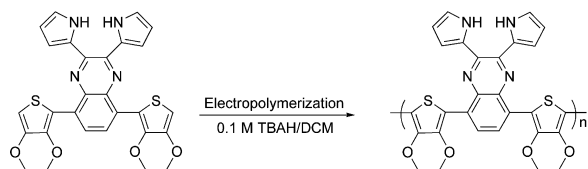


Fig. 2. Electropolymerization of  $1.0 \times 10^{-3}$  M **1** in 0.1 M TBAH/DCM at 100 mV/s by potential scanning to give **P1**.

the repetitive anodic potential scan in 0.1 M TBAH/DCM solution when it was clipped at 0.95 V (Fig. 2). This clearly indicated the formation of an electroactive polymer film on the electrode surface. After electrodeposition, we were delighted to note that the as-prepared polymer was green in the neutral state.

However, at this stage it was tempting to think that the polymerization of **1** might proceed in two different ways, since two different heterocyclic rings (EDOT and pyrrole) which generally exhibited distinct oxidation potentials were available for oxidative polymerization. In order to reveal that the polymerization preceded exclusively through the EDOT units, two similar systems were taken into account: **2** [35–37] where the oxidative polymerization through pyrrole rings was precluded by the presence of chlorine atoms, and **3** [35–37], where the oxidative polymerization, if possible yet, is only feasible through pyrrole rings, since EDOT units were eliminated from the structure.

It was reported that **2** could give the corresponding conducting material electrochemically through EDOT units [35–37]. On the other hand, it was noted that **3** did not polymerize alone to yield a polymer film [35–37]. Undoubt-



**Scheme 1.** Electrochemical polymerization of **1** to give **P1**.

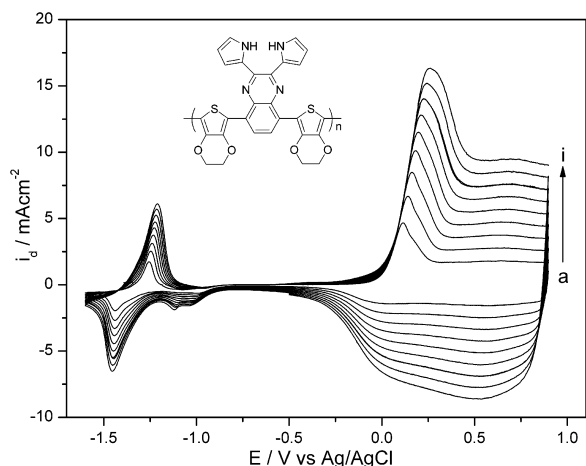


**Fig. 3.** Cyclic voltammograms of n- and p-doped **P1** film in 0.1 M TBAH/ACN at a scan rate of (a) 50, (b) 75, (c) 100, (d) 125, (e) 150, (f) 175, (g) 200, (h) 225 and (i) 250 mV/s.

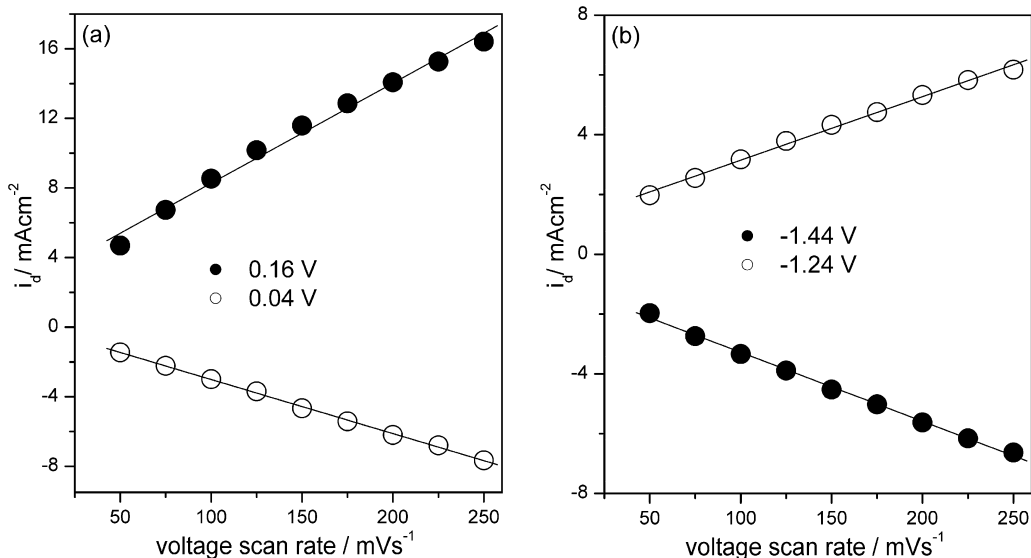
edly, these results suggested that the electrochemical polymerization of **1** proceeded through EDOT units to give **P1** (Scheme 1).

The redox behavior of the polymer film was investigated in monomer-free electrolyte solution containing 0.1 M TBAH/DCM. **P1** has an ambipolar (n- and p-doping

process) character and it exhibited single and well-defined reversible redox couples during p-doping at  $E_{1/2}^{\text{ox}} = 0.10$  V (Fig. 3). The peak currents were linearly proportional to the scan rates which indicated a non-diffusional redox process and well-adhered electroactive polymer film (Fig. 4). The n- and p-doping processes take place much easier for **P1** when compared to **P4** (Table 1).

On the other hand, **P1** also exhibited a true n-doping behavior which mainly took place in the acceptor (quinoxaline) parts of the polymer chain (Fig. 3). The polymer film has a stable and well-defined reversible n-doping process with a half peak potential ( $E_{p,1/2}^{\text{red}}$ ) of  $-1.34$  V and the peak currents were intensified linearly as a function of scan rate indicating that redox couple was non-diffusion-controlled.

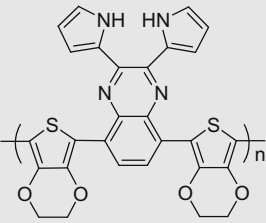
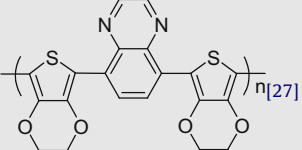
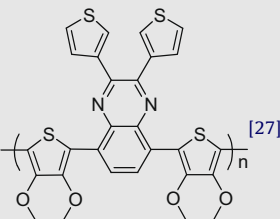
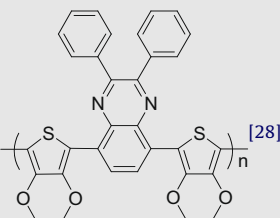
It is noteworthy to mention that n- and p-doping processes with the same material make it an excellent candidate for battery, supercapacitor and light-emitting diode applications [8]. Of special interest, the characteristic feature of electrochemical capacitors is the shape of cyclic voltammogram which should ideally be a rectangle with wide potential window. In order to probe the utility of **P1** film as a capacitor, it was cycled as a function of scan rate. As illustrated in Fig. 5, the flat current response was observed even after high scan rates, indicating a fast charge (doping)/discharge (dedoping) process. It was also noted that the polymer film exhibited perfect stability under multiple cycle between 0.0 and 1.0 V at a scan rate of 200 mV/s since no appreciable changes in the shape of the voltammogram was observed after a thousand of scans (Fig. 6). The stability upon switching or cycling is also crucially important feature for such materials to be amenable for practical and commercial applications. The stability of polymer film was recorded between neutral and oxidized states by potential scanning at a scan rate of 200 mV/s. After thousand of cycles, no appreciable change was observed in the redox response of **P1** which unambiguously showed that it is highly robust and/or stable (Fig. 6). These intriguing features pave the way of utilizing **P1** in



**Fig. 4.** Relationship of anodic and cathodic current peaks as a function of scan rate for (a) p- and (b) n-doped **P1** film in 0.1 M TBAH/ACN.

**Table 1**

The structures and properties of quinoxaline based polymers P1, P4–P6.

Polymers	$E_m^{ox}/V$	$E_{p,1/2}^{ox}/V$	$E_{p,1/2}^{red}/V$	$\lambda_{max}/nm$	$E_g/eV^a$
 <p><b>P1</b></p>	0.85	0.1	−1.34	334 427 746	1.25
 <p><b>P4</b>[27]</p>	0.73 <sup>*</sup>	0.2 <sup>*</sup>	−1.45 <sup>*</sup>	410 660	1.40
 <p><b>P5</b>[27]</p>	0.85 <sup>*</sup>	−0.03 <sup>*</sup>	−1.41 <sup>*</sup>	405 780	1.20
 <p><b>P6</b>[28]</p>	1.01 <sup>*</sup>	0.17 <sup>*</sup>	−1.35 <sup>*</sup>	448 732	1.01

<sup>a</sup> Estimated with respect to optical data.<sup>\*</sup> Estimated from the corresponding references.

supercapacitors as either cathode or anode electrode material with broad potential window.

## 2.2. Electrochemistry

The electro-optical properties of the polymer film were investigated using the changes in electronic absorption spectra under a voltage pulse. Before p-doping process, the polymer film was initially neutralized at −0.5 V. It is noteworthy that **P1** is unique since it has shown three well-defined absorption maxima at 334 nm (3.60 eV), 427 nm (2.90 eV) and 746 nm (1.66 eV) in the neutral state (Fig. 7), and all the other analogues, **P4–P6** have shown only two absorption bands (see Table 1). The deep valleys (at 353 and 507 nm) among the three absorption bands of **P1** control the hue and brightness of the green color [24]. Estimated differences in transmittance of the bands (at 334, 427 and 746 nm) with respect to these deep valleys

were found to be 2.7%, 14.2%, 25% for 353 nm and 16.2%, 27.8%, 38.6% for 507 nm. These values are quite enough to get the green color with various hue.

Although three sets of band gap ( $E_g$ ) values can be calculated from the onset of the low energy end of three  $\pi-\pi^*$  transition bands (at 334, 427 and 746 nm) for green **P1** as 3.58, 2.54 and 1.25 eV, respectively, it is evident that  $E_g$  is 1.25 eV which was also supported by either cyclic (1.20 eV) or differential pulse voltammetry (1.17 eV) (Fig. 8a–c). It is also reasonable to assume that the  $E_g$  of **P1** from the optical study is 1.25 eV which is quite lower than that of **P4** and in well-agreement with the all other analogues (Table 1).

Upon oxidation, the polymer film exhibited a color change from green to transparent sky blue. It is of worth noting that the color change from green to sky blue is a quite significant trait in electrochromic devices and/or displays along with the green color of the neutral state.

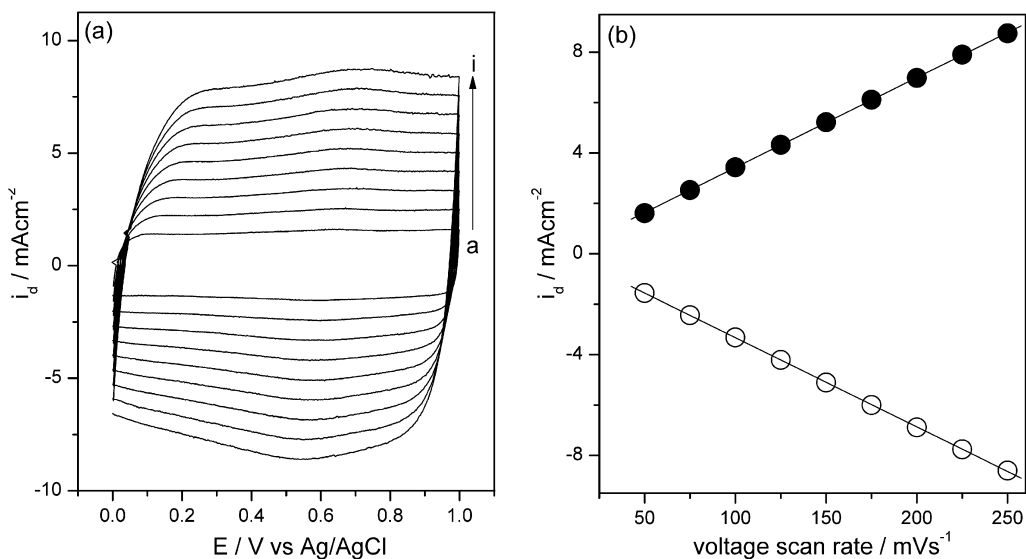


**Fig. 5.** (a) Capacitance effect of P1 film by cyclic voltammetry at a scan rates of (a) 50, (b) 75, (c) 100, (d) 125, (e) 150, (f) 175, (g) 200, (h) 225 and (i) 250 mV/s. (b) Relationship of anodic (●) and cathodic (○) current peaks as a function of scan rate for P1 film in 0.1 M TBAH/ACN.

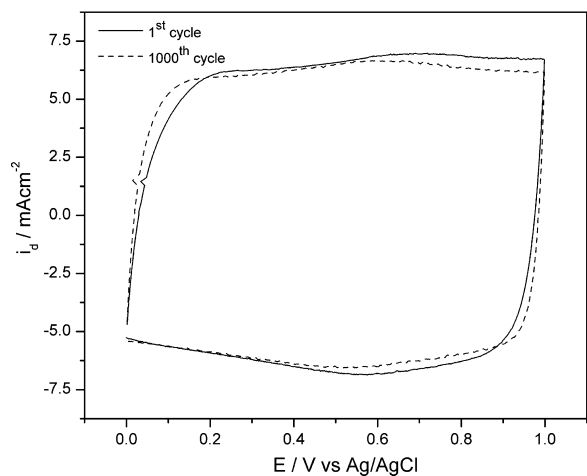


**Fig. 6.** Stability of P1 film by cyclic voltammetry at a scan rates of 200 mV/s in 0.1 M TBAH/ACN between 0.0 and 1.0 V.

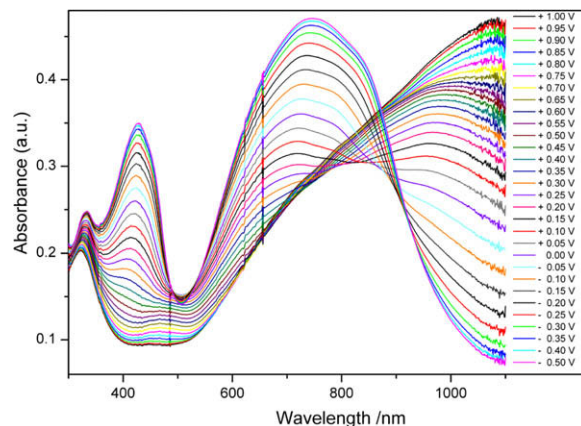


**Fig. 7.** Electronic absorption spectra of P1 ( $11 \text{ mC/cm}^2$ ) on ITO in 0.1 M TBAH/ACN at various applied potentials between  $-0.5$  and  $1.0$  V.

At low doping levels, the intensities of the three  $\pi-\pi^*$  transition bands of **P1** decreased simultaneously and a new absorption band around 1080 nm started to intensify due to the polaron formation in Fig. 7. Upon further oxidation, the absorption band at 334 nm reached the minimum intensity and the bands at 427 and 746 nm diminished completely. The percentage transmittance changes ( $\Delta\%$ ) between the neutral (at  $-0.5$  V) and oxidized states (at 1.0 V) were found to be 7.3% for 334 nm, 36.4% for 427 nm, 19.2% for 746 nm and 49.9% for 1080 nm.

The promising true n-doping behavior of **P1** film was also confirmed by the changes in the electronic absorption spectra during reduction (Fig. 9). When the polymer film was reduced, its color changed from green to gray-purple

(Fig. 10) and the three  $\pi-\pi^*$  transition bands began to decrease simultaneously and new absorption bands started to intensify at 345, 496, 541 and 984 nm with a concomitant appearance of four isosbestic points (377, 457, 618 and 922 nm). This indicated that only two phases did coexist during the process (n-doping).

**P1** film was found to be one of the most promising polymers bearing three absorption bands and durable n- and p-doping processes. Furthermore, the robustness and the stability of the system suggest that **P1** is an excellent candidate for electrochromic devices and optical displays. The transmittance changes (optical contrast) was measured as a function of switching time of 10, 5, 2 and 1 s via square-wave potential methods between  $-0.5$  and  $1.0$  V. As shown in Fig. 11, the variation changes in the optical contrast at 334, 427 and 746 nm are 1.7%, 3.8% and 0.1%, respectively, as the switching time is increased from 10 to 1 s. This

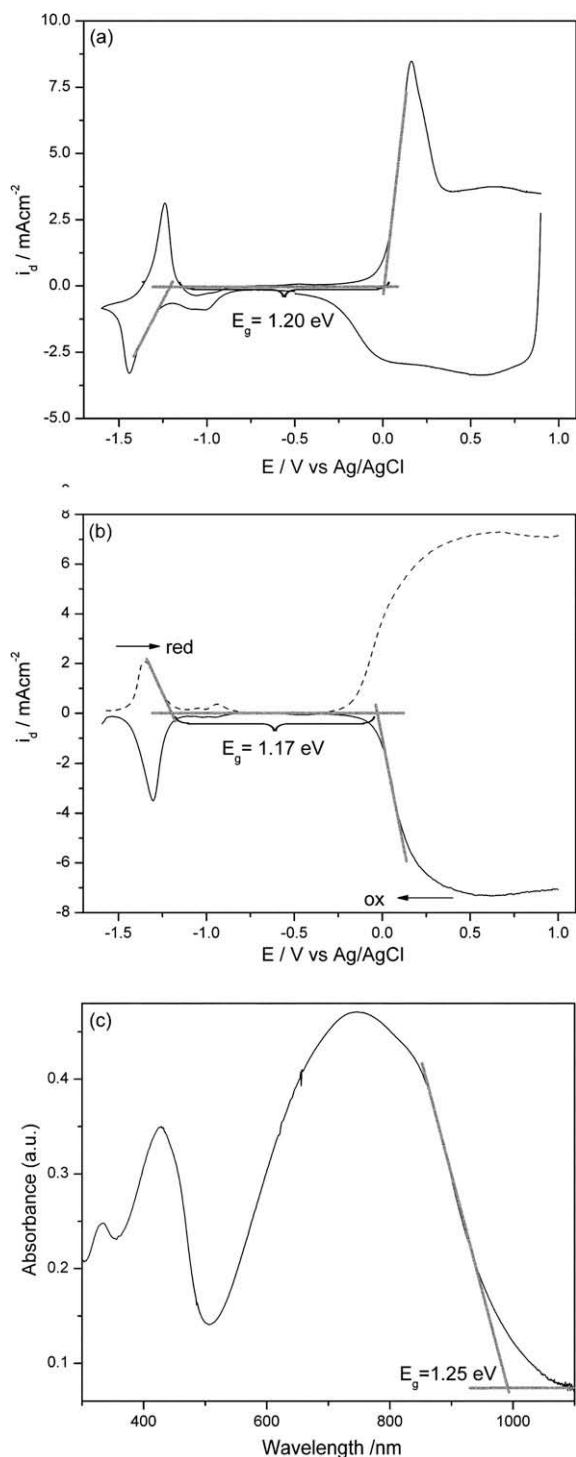


**Fig. 8.** (a) Cyclic voltammetry, (b) differential pulse voltammetry, and (c) electronic absorption spectrum of P1 at  $-0.5$  V (at neutral state) in 0.1 M TBAH/ACN.

result clearly indicates that **P1** gave response in a very short time with no appreciable change in the optical contrast values, when it was switched for p-doping process.

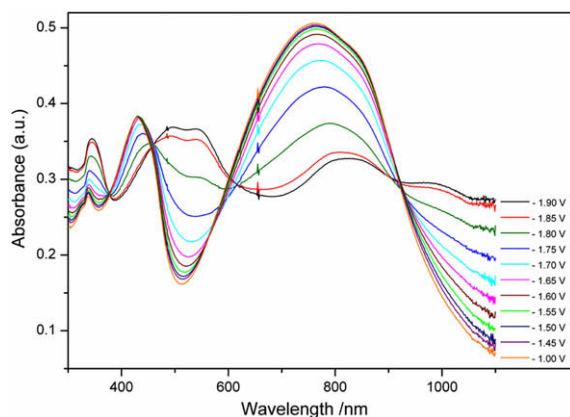


**Fig. 9.** Electronic absorption spectra of P1 ( $11 \text{ mC/cm}^2$ ) on ITO in 0.1 M TBAH/ACN at various applied potentials between  $-1.00$  and  $-1.90$  V.

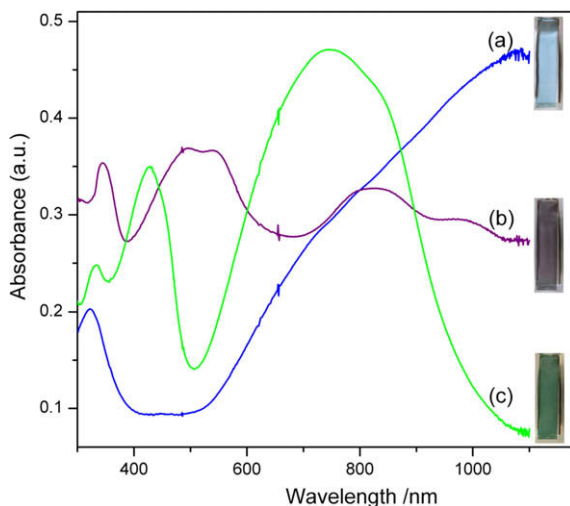


**Fig. 10.** Electronic absorption spectra and the color of P1 on ITO in 0.1 M TBAH/ACN at  $-0.5$  V (at neutral state),  $-1.9$  V (at reduced state) and  $1.0$  V (at oxidized state).

### 3. Conclusion

In summary, a new and highly stable neutral state green polymeric electrochromic based on quinoxaline (acceptor) and EDOT (donor) units, **P1**, was synthesized electrochemically and the intriguing features were described. **P1** is green in the neutral state and it exhibits three well-defined absorption bands. Furthermore, **P1** has a narrow band gap (1.17 eV). The n- and p-doping processes suggest that **P1** is one of the promising neutral state green polymers and it can be used in supercapacitors as either cathode or anode electrode material. Apart from the stability and the robustness of the polymer film, **P1** shows multi-electrochromic behavior; gray-purple in the reduced form and highly transmissive blue color in the oxidized state. Further work along these lines is currently underway in our laboratories and the results will be reported in due time.

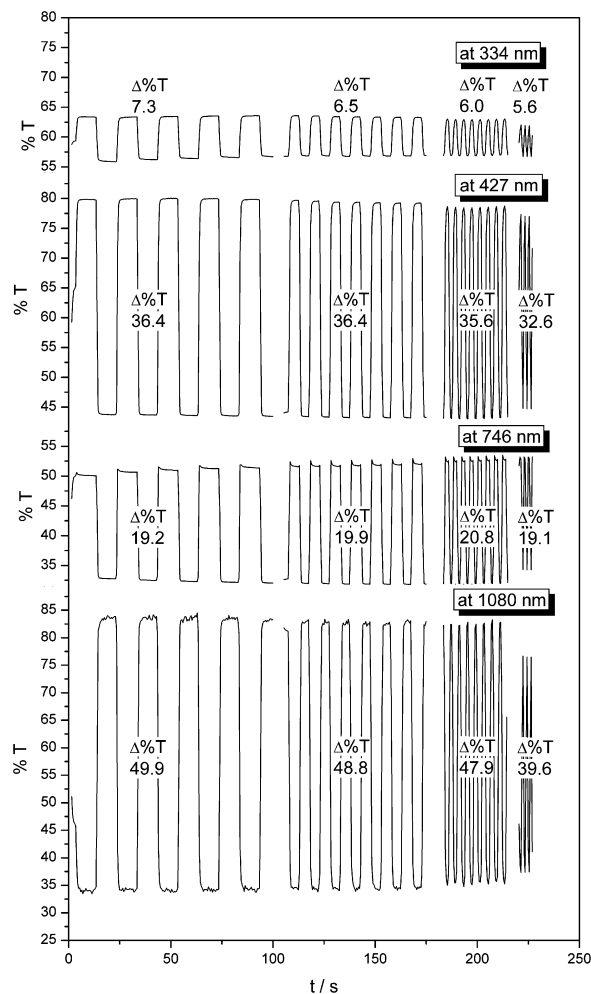


**Fig. 11.** Chronoabsorptometry experiments for P1 on ITO in 0.1 M TBAH/ACN while the polymer was switched between  $-0.5$  and  $1.0$  V with a switching time order of 10, 5, 2 and 1 s.

## 4. Experimental

### 4.1. General

All chemicals were purchased from Aldrich Chemical. 0.1 M tetrabutylammonium hexafluorophosphate (TBAH) dissolved in freshly distilled dichloromethane (DCM) and acetonitrile (ACN) was used as electrolyte solution. A platinum disk ( $0.02 \text{ cm}^2$ ) and a platinum wire were used as working and counter electrodes, respectively, as well as Ag/AgCl in 3 M NaCl(aq) solution as a reference. Repetitive cycling or constant potential electrolysis was used to obtain the polymer films. Electro-optical properties were investigated by using an indium–tin oxide (ITO, Delta Tech. 8–12  $\Omega$ ,  $0.7 \text{ cm} \times 5 \text{ cm}$ ) electrode as well as a platinum wire as counter electrode and a Ag wire as a pseudo-reference electrode (calibrated externally using 5 mM solution of ferrocene/ferrocenium couple). In order to equilibrate the redox behavior of the polymer film and to obtain repeated results, the coated polymer films were switched between their neutral

and oxidized states several times before electroanalytical and optical studies. Electroanalytical measurements were performed using a Gamry PCI4/300 potentiostat–galvanostat. The electro-optical spectra were monitored on a Hewlett–Packard 8453A diode array spectrometer. Photographs of the polymer films were taken by using a Canon (PowerShot A75) digital camera. 5,8-bis(2,3-dihydrothieno[3,4-b][1,4]dioxin-5-yl)-2,3-di(1H-pyrrol-2-yl)quinoxaline (**1**) was synthesized according to the literature [35–37].

## Acknowledgements

We gratefully acknowledge the financial support from the Scientific and Technical Research Council of Turkey (TUBITAK).

## References

- [1] D.N. Buckley, L.D. Burke, *J. Chem. Soc., Faraday Trans. 1* 71 (1975) 1447.
- [2] D.N. Buckley, L.D. Burke, J.K. Mukahy, *J. Chem. Soc., Faraday Trans. 1* 72 (1976) 1896.
- [3] L.D. Burke, T.A.M. Thomey, D.P. Whelan, *J. Electroanal. Chem.* 107 (1980) 201.
- [4] W.C. Dautremont-Smith, *Displays* 3 (1982) 3.
- [5] C.G. Granqvist, *Sol. Energy Mater. Sol. Cells* 60 (2000) 201.
- [6] C.G. Granqvist, E. Avendano, A. Azens, *Thin Solid Films* 442 (2003) 201.
- [7] E. Avendano, L. Berggren, G.A. Niklasson, C.G. Granqvist, A. Azens, *Thin Solid Films* 496 (2006) 30.
- [8] T.A. Skotheim, J.R. Reynolds (Eds.), *Handbook of Conducting Polymers—conjugated Polymers: Processing and Applications*, CRC Press Taylor and Francis Group, 2007.
- [9] T.A. Skotheim, J.R. Reynolds (Eds.), *Handbook of Conducting Polymers—conjugated Polymers: Synthesis, Properties and Characterization*, CRC Press Taylor and Francis Group, 2007.
- [10] I. Schwendeman, R. Hickman, G. Sonmez, P. Schottland, K. Zong, D. Welsh, J.R. Reynolds, *Chem. Mater.* 14 (2002) 3118.
- [11] H. Meng, D. Tucker, S. Chaffins, Y. Chen, R. Helgeson, B. Dunn, F. Wudl, *Adv. Mater.* 15 (2003) 146.
- [12] A. Pennisi, F. Simone, G. Barletta, G. Di Marco, L. Lanza, *Electrochim. Acta* 44 (1999) 3237.
- [13] R. Rauh, *Electrochim. Acta* 44 (1999) 3165.
- [14] R.G. Mortimer, *Chem. Soc. Rev.* 26 (1997) 147.
- [15] D.R. Rosseinsky, R.J. Mortimer, *Adv. Mater.* 13 (2001) 783.
- [16] K. Bange, T. Gambke, *Adv. Mater.* 2 (1990) 10.
- [17] J.H. Burroughes, D.D.C. Bradley, A.R. Brown, R.N. Marks, K. Mackay, R.H. Friend, P.L. Burns, A.B. Holmes, *Nature* 347 (1990) 539.
- [18] A. Kraft, A.C. Grimsdale, A.B. Holmes, *Angew. Chem. Int. Ed.* 37 (1998) 402.
- [19] P. Chandrasekhar, B.J. Zay, G.C. Birur, S. Rawal, E.A. Pierson, L. Kauder, T. Swanson, *Adv. Funct. Mater.* 12 (2002) 95.
- [20] S.R. Forrest, *Nature* 428 (2004) 911.
- [21] C. Reese, M. Roberts, M.-M. Ling, Z. Bao, *Mater. Today* 7 (2004) 20.
- [22] G.A. Sotzing, J.R. Reynolds, P.J. Steel, *Chem. Mater.* 8 (1996) 882.
- [23] L.B. Groenendaal, J. Friedrich, D. Freitag, H. Pielartzik, J.R. Reynolds, *Adv. Mater.* 12 (2000) 481.
- [24] G. Sonmez, C.K.F. Shen, Y. Rubin, F. Wudl, *Angew. Chem. Int. Ed. Engl.* 43 (2004) 1498.
- [25] G. Sonmez, H.B. Sonmez, C.K.F. Shen, R.W. Jost, Y. Rubin, F. Wudl, *Macromolecules* 38 (2005) 669.
- [26] A. Durmus, G.E. Gunbas, P. Camurlu, L. Toppare, *Chem. Commun.* (2007) 3246.
- [27] A. Durmus, G.E. Gunbas, L. Toppare, *Chem. Mater.* 19 (2007) 6247.
- [28] A. Durmus, G.E. Gunbas, L. Toppare, *Adv. Mater.* 20 (2008) 691.
- [29] G.E. Gunbas, A. Durmus, L. Toppare, *Adv. Funct. Mater.* 18 (2008) 2026.
- [30] P.M. Beaujuge, S. Ellinger, J.R. Reynolds, *Adv. Mater.* 20 (2008) 2772.
- [31] A. Cihaner, F. Algi, *Electrochim. Acta* 53 (2008) 2574.
- [32] A. Cihaner, F. Algi, *J. Electroanal. Chem.* 614 (2008) 101.
- [33] F. Algi, A. Cihaner, *Tetrahedron Lett.* 49 (2008) 3530.
- [34] A. Cihaner, F. Algi, *Adv. Funct. Mater.* 18 (2008) 3583.
- [35] D. Aldakov, P. Anzenbacher Jr., *Chem. Commun.* (2003) 1394.
- [36] D. Aldakov, P. Anzenbacher Jr., *J. Am. Chem. Soc.* 126 (2004) 4752.
- [37] P. Anzenbacher Jr., K. Jursikova, D. Aldakov, M. Marquez, R. Pohl, *Tetrahedron* 60 (2004) 11163.

panels, and various cheap mass products, notably electronic paper and radio-frequency identification (RFID) tags [9–12]. The most mature memory cell structure for use in digital integrated circuit (IC) applications consists of a single field-effect-transistor (FET) that includes a binary information storage element and acts as a memory-cell addressing switch. The data sensing mode of single-FET memory structures renders them robust against read current distortions to the storage mechanism; an important advantage over their two-terminal contenders (i.e. cross-point resistive memories where parasitic leakage currents in a passive array can affect the reading process) [13,14]. In memory transistors, the storage element is incorporated in between the channel and the gate electrode. It can be placed in two readily discernible physical states that modulate the channel conductivity enabling data to be read electrically by sensing the current level of the transistor. Various storage elements based on: (1) charge injection and trapping in inorganic dielectrics [15], organic dielectrics [16] or nanoparticles [17], (2) ferroelectric polarization of dielectrics [18] as well as (3) proton motion and trapping in dielectrics [19] have been investigated as alternatives to the conventional polysilicon floating-gate of the transistor based Flash memories. In the case of high-density Si-based ICs, an aggressive reduction of the physical thickness of the gate dielectric storage element is required for scaling the size of the FET memory cell beyond 20 nm. On the other hand, single-FET memory structures with large feature sizes and thick storage elements compatible with organic electronic processing may be further exploited in emerging large-area low-performance logic circuit applications on flexible substrates.

In this direction, we recently proposed a simple approach for producing proton storage elements that can be reliably incorporated into the gate dielectric of inorganic and/or organic transistors [20]. Basically, a proton memory device utilizes the motion of protons within the gate dielectric of a Metal–Insulator–Semiconductor (MIS) transistor, and presents the benefit to be programmed at much lower voltages than charge-trapping memory devices, thus offering a better alternative for low-power consumption [21,22]. Our approach is based on solution-processed polymeric materials and enables the manipulation of the storage element properties simply via formulation or/and chemical synthesis. Realization of non-volatile memory devices is achieved using a stacked structure consisted of a proton-conducting polymeric layer (PCL) based on a tungsten heteropolyacid and poly(methyl methacrylate) (PMMA), and a proton-trapping polymeric layer (PTL) based on PMMA containing amine proton trapping sites, as depicted in Fig. 1 in the case of a MIS-type capacitor. Application of a positive voltage to the gate electrode with the substrate connected to ground (“Write” operation) allows for the dissociation of neutral (n) sites of the PCL into anions (–) and protons (+), motion and trapping of protons in the PTL. This induces a negative flat-band voltage shift of the capacitor C–V characteristics (Fig. 1). A subsequent negative voltage moves back the trapped protons leading to the reformation of neutral sites within the PCL (“Erase” operation).

The concept of using a PCL/PTL stack for the realization of non-volatile proton memory devices is quite simple and

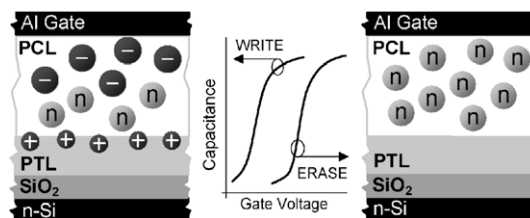


**Fig. 1.** Schematic illustrating the structure and the operation principle of a non-volatile bistable MIS memory device with a molecular-based proton storage element consisting of a proton-conducting polymeric layer (PCL) and a proton-trapping polymeric layer (PTL) bi-layer stacked structure.

many materials are possible candidates. The materials' selection is primarily guided by requirements of memory performance and process integration compatibility that strongly depend on the physicochemical properties of the candidate materials. In the present paper, we provide a more detailed analysis of the relationship between the material properties and electrical performance of the PCL/PTL stack reported in our previous communication [20]. Particular emphasis is placed on the thermal processing conditions and their optimization to avoid undesirable phenomena like reactions within the PCL and inter-mixing of the PCL and PTL. Moreover, based on a combination of UV spectroscopy studies and transient current experiments, a comprehensive picture about the protons involved in the memory effect and their motion through the PCL is presented. Finally, the write characteristics and scalability prospects of molecular proton memory devices are examined in terms of the physical properties of generic PCL/PTL bi-layer stacked structures.

## 2. Experimental

The PCL consists of a PMMA film containing molecules of 12-tungstophosphoric acid ( $\text{H}_3\text{PW}_{12}\text{O}_{40}$ ; here referred as HPW), whereas the PTL is a PMMA film with embedded 2-aminoanthracene (AA) molecules. Details on materials' preparation are reported in [20]. UV–vis spectra were acquired on a Perkin–Elmer Lambda 40 spectrophotometer. Fourier transform infrared spectroscopy (FTIR) transmittance spectra were collected on a Bruker, Tensor 27 spectrometer using 128 scans at  $4\text{ cm}^{-1}$  resolution. The thicknesses of the polymeric layers were measured using an Ambios Technology XP-2 profilometer.

The devices examined consist of MIS structures with a PCL fabricated by spin coating of a HPW/PMMA solution onto an n-type silicon substrate pre-coated with a 3.5 nm-thick  $\text{SiO}_2$  layer. The thickness of the PCL is about 270 nm. The gate electrode ( $9 \times 10^{-4}\text{ cm}^2$  area) is made of aluminum deposited by e-beam evaporation and defined by conventional optical lithography and metal etching. Further details on device structure and fabrication can be found in [20]. Proton motion in the HPW/PMMA layer was investigated by monitoring the time evolution of the gate current for various gate voltages. All measurements were carried out using a HP4140B pA meter/DC voltage source under ambient conditions in a light-free probe station.

### 3. Results and discussion

#### 3.1. Material characterization

The thermal processing conditions of the HPW/PMMA film (PCL) may have a significant negative impact on the material chemical stability and subsequently on the proton motion, if the strong Brønsted acid used (HPW), participates in undesirable acid catalysed or redox [23] reactions with the polymer matrix promoted by temperature. In order to investigate possible reactions of the HPW molecules with the PMMA matrix, especially under thermal treatment, the HPW/PMMA films were monitored by means of FTIR spectroscopy. As depicted in Fig. 2, where the effect of thermal treatment temperature on the HPW/PMMA films at a fixed time (5 min) is presented, no significant changes in HPW and PMMA peak widths and positions were observed for  $T \leq 120^\circ\text{C}$  indicating that up to that temperature no reaction between HPW and PMMA takes place inside the film (at least not to the extent that could be detectable with the FTIR spectrometer). In contrast, for  $T \geq 130^\circ\text{C}$  substantial changes can be detected in the PMMA-related-FTIR peaks. These data point out possible formation of glutaric anhydride through the acid-catalyzed hydrolysis of PMMA by HPW in presence of water (derived from the atmosphere) and the subsequent dehydration of the poly(methacrylic acid) formed [24,25]. The changes in FTIR peaks that support the hypothesis of the anhydride formation are the following: (a) decrease of the broad O–H absorption peak at  $\sim 3500\text{ cm}^{-1}$ ; (b) decrease of the carbonyl peak at  $1732\text{ cm}^{-1}$  characteristic of PMMA, and simultaneous appearance of twin carbonyl peaks at  $1802$  and  $1761\text{ cm}^{-1}$  characteristics of the anhydride; (c) appearance of the C–O–C peak at  $1020\text{ cm}^{-1}$ . On the other hand, the FTIR peaks of the  $[\text{PW}_{12}\text{O}_{40}]^{3-}$  anion attributed to (a) the asymmetric stretching of the P–O<sub>a</sub> bond ( $1081\text{ cm}^{-1}$ ), (b) the asymmetric stretching of the W–O<sub>d</sub> bond ( $981\text{ cm}^{-1}$ ), (c) the asymmetric stretching of the W–O<sub>b</sub>–W bridge ( $898\text{ cm}^{-1}$ ) and (d) the asymmetric stretching of the W–O<sub>c</sub>–W bridge ( $820\text{ cm}^{-1}$ ) where O<sub>a–d</sub> are different oxygen atoms of the HPW structure [26–30],

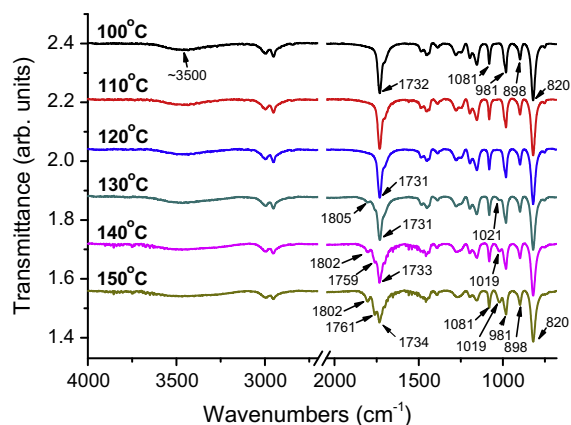


**Fig. 2.** FTIR spectra showing the effect of the thermal treatment temperature on the HPW/PMMA film. The duration of all thermal treatments was 5 min. Solution: HPW/PMMA 5/5% (w/w).

are not affected by this reaction, indicating therefore, that only the protons of the HPW molecules participate in the aforementioned reaction with PMMA whereas the anions of the HPW molecules remain unaffected.

Continuing in this direction, the effect of the thermal treatment duration on the HPW/PMMA film composition was also studied by FTIR spectroscopy at  $120^\circ\text{C}$ . As shown in Fig. 3, for up to 60 min duration of the thermal treatment no significant change in the FTIR peaks was detected. Two small shoulders appear first at  $1021$  and  $1802\text{ cm}^{-1}$ , which can be barely observed for the 60 min thermal treatment, indicating that such a reaction would evolve for higher annealing times as it is indeed observed in Fig. 3. As a result, it was concluded that the thermal treatment at  $120^\circ\text{C}$  of the HPW/PMMA film should not be extended for longer than 60 min, in order to avoid undesirable PMMA reactions and thus alteration of the device performance.

On the other hand, the possible undesirable intermixing of the two layers (PCL and PTL) had to be addressed, since the same solvent is used for both layers. It is well known that the thermally treated PMMA films dissolve very slowly in organic solvents, due to the reduction of the film free volume during the treatment and the better packing of the polymer chains. For that reason, PMMA is used as a positive resist, where the unexposed film areas dissolve much more slowly than the exposed regions in selected solvents [31]. In order to investigate whether undesirable intermixing occurs under the conditions of our experiments, we monitored possible changes in intensity of the characteristic HPW peak at  $266\text{ nm}$  induced by the coating of a PMMA layer on top of the HPW/PMMA layer (Fig. 4). In this study the lower layer (HPW/PMMA) was first treated thermally at  $120^\circ\text{C}$  for a duration ranging from 10 to 60 min (taking into account the results of the previous FTIR analysis). As shown in Fig. 4, after a thermal treatment at  $120^\circ\text{C}$  for 60 min of the HPW/PMMA layer the subsequent coating of the PMMA layer on top of it causes only a minor ( $\sim 5\%$ ) decrease in HPW concentration. Such a decrease could be attributed to the dissolution of the HPW molecules located near the surface of the HPW/PMMA layer. In contrast, for

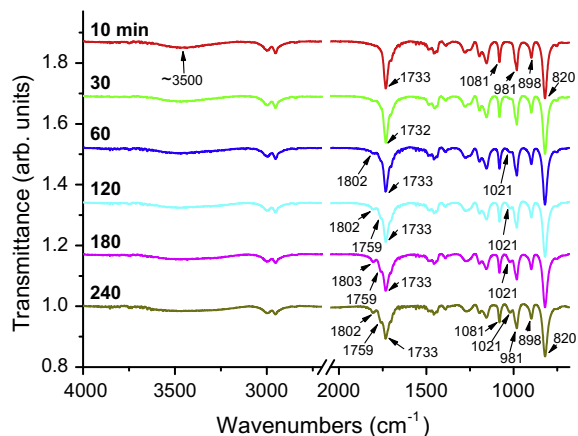


**Fig. 3.** FTIR spectra showing the effect of the duration of the  $120^\circ\text{C}$  thermal treatment on the HPW/PMMA film. Solution: HPW/PMMA 5/5% (w/w).



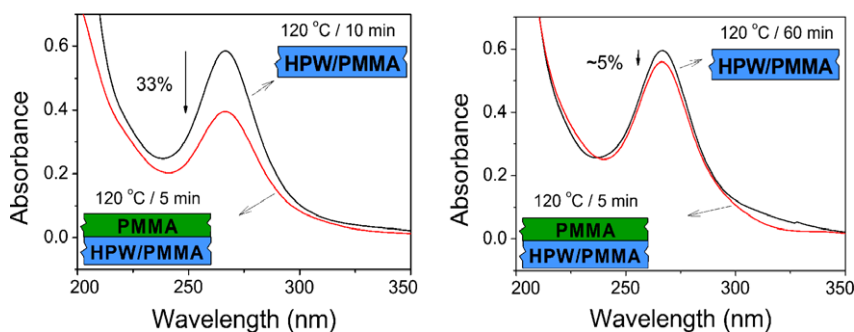


**Fig. 4.** UV spectra showing the change of the characteristic HPW peak at 266 nm of the HPW/PMMA layer induced by the coating of a PMMA layer on top of it. The lower layer (HPW/PMMA) was treated thermally at 120 °C for two different durations: 10 and 60 min. The upper layer (PMMA) was treated thermally at 120 °C for 5 min in both cases. Solutions: PMMA 5% (w/w) and HPW/PMMA 5/5% (w/w).

thermal treatments of the HPW/PMMA layer at 120 °C for 10 and 30 min 33% and 29% decrease in HPW concentration was observed respectively (data for the 10 min case are presented in Fig. 4), indicating solvent penetration to the bottom layer and intermixing of the two layers. Consequently, the thermal treatment selected for the HPW/PMMA film was 120 °C for 60 min as it fulfilled both requirements to prevent reactions between HPW and PMMA and to avoid intermixing in the bi-layer structures. The above thermal treatment was also applied to the other films (AA/PMMA and PMMA) used in this study in order to have comparable PMMA packing in all the films.

The concentration of the HPW molecules within the HPW/PMMA layer annealed at 120 °C for 60 min was determined by applying the Lambert–Beer law ( $A = \epsilon c l$ ) to the characteristic HPW peak at 266 nm. In a typical experiment using the absorbance of this 266 nm peak ( $A_{266} = 0.5303$ ), a film thickness,  $l$ , of 346 nm (measured by profilometry), and the molar absorptivity of HPW at 266 nm obtained from literature ( $\epsilon_{266} = 4.85 \times 10^4 \text{ M}^{-1} \text{ cm}^{-1}$ ; [32–34]), the HPW concentration in the film is found to be equal to  $0.316 \text{ mol l}^{-1}$  ( $1.903 \times 10^{20}$  molecules  $\text{cm}^{-3}$ ). Given that the size of the HPW molecules is approximately 1 nm, the above HPW concentration value corresponds to an average distance between the molecules of ca. 1 nm, for a close packing arrangement of HPW molecules within the PMMA matrix. The mass density of the HPW-embedded matrix,  $\rho$ , can be expressed as:  $\rho = (n_{\text{HPW}} M_{\text{HPW}}/N_A) [(c_m + 1)/c_m]$ . Here,  $n_{\text{HPW}}$  is the concentration of the HPW molecules within the HPW/PMMA layer,  $N_A$  is the Avogadro number,  $M_{\text{HPW}} = 2880.17 \text{ g/mol}$  the molecular weight of HPW and  $c_m = m_{\text{HPW}}/m_{\text{matrix}}$  the relative mass concentration of HPW molecules and matrix material. Thus, for the PCL layer under investigation (i.e., an HPW-embedded PMMA matrix with equal weights of HPW and PMMA,  $c_m = 1$ ), the extracted HPW concentration of  $n_{\text{HPW}} = 1.903 \times 10^{20}$  molecules  $\text{cm}^{-3}$  is found to correspond to an HPW/PMMA mass density  $\rho$  of about  $1.82 \text{ g cm}^{-3}$  (to be compared with the given mass density of PMMA matrix  $\rho_{\text{PMMA}} = 1.19 \text{ g cm}^{-3}$  at 25 °C [35]). Finally, regarding the protons inside the film, in the general case of an HPW-embedded PMMA matrix, the number of dissociated protons per HPW molecule, which are expected to attach to the PMMA basic sites, i.e. the ester oxygens

[36], is expected to range between zero (case of no dissociation) and three (case of complete dissociation). In our case, the dissociation of HPW in low basicity solvents or matrices (as PMMA) is expected to be one proton per HPW molecule [37].

### 3.2. Electrical characterization

Fig. 5 shows typical transient gate current vs time ( $I-t$ ) characteristics of the MIS device. For clarity, the applied gate voltage ( $V_G$ ) during current measurements is also indicated. A constant  $V_G$  (ranging from 1 to 5 V) was applied (bias on) for 10 min to the gate electrode and then abruptly switched off (bias off). The time dependence of the induced polarization ( $t \leq 600 \text{ s}$ ) and depolarization ( $t > 600 \text{ s}$ ) currents is plotted in Fig. 5a and b, respectively (note that the recorded polarization and depolarization currents have opposite directions).

For the 1 V  $V_G$  regime (Fig. 5a), the current decays with time and vanishes after about 250 s, while for higher  $V_G$  values it reaches a quasi steady state that expresses a non-ohmic leakage current  $I_L$  of 0.4, 1.8, 4 and 7 pA for the 2, 3, 4, and 5 V regimes, respectively (see inset of Fig. 5a). Based on our previous capacitance–voltage investigations [20], we attribute the observed polarization current decays to the mobile protons of the HPW/PMMA layer, which migrate and accumulate toward the lower edge of this layer under application of positive  $V_G$ . The counter anions stay in a region close to the upper edge of HPW/PMMA layer forming a symmetric charge distribution around the center of the HPW/PMMA layer. In principle, for ion-blocking electrodes, one expects the contribution from ionic current after a potential step to vanish after sufficiently long times (i.e., when the total number of ions that contributes to the current, for a given polarization, is close to the electrodes). The low leakage current levels,  $I_L$ , detected for  $V_G \geq 2 \text{ V}$  (Fig. 5a) seems most likely to be due to electrons that flow from the Si substrate to the Al gate electrode. Such an electron flow would involve tunnelling through the thin oxide barrier and hopping between localized states in the HPW/PMMA layer and therefore, could result in non-linear  $I_L-V_G$  characteristics in agreement with our observations (inset of Fig. 5a). It is pointed out that  $I_L$  must be considered in any estimation

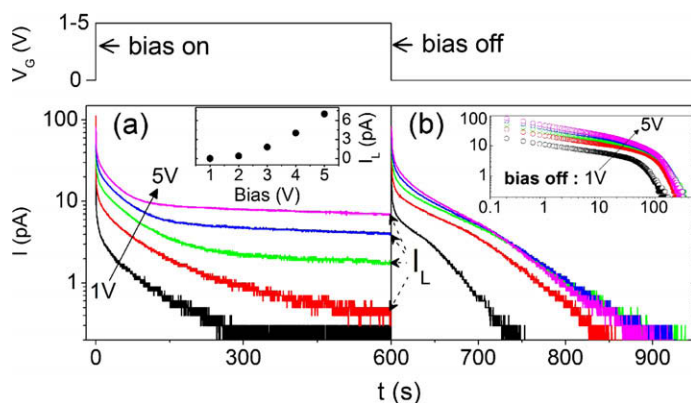


**Fig. 5.** Polarization (a) and depolarization (b) transient currents after the displayed bias steps. The inset (a) shows the displayed leakage current  $I_L$  as a function of the applied bias, and the inset (b) plots the depolarization currents in logarithmic time scale.

of the migrated protonic charge,  $Q$ , by direct integration of the polarization current. In our case (Fig. 5a), the leakage current is subtracted from the total measured current before integration [38]:  $Q = \int_0^{t_{\text{steady}}} [I(t) - I_L] dt$ .  $Q$  calculations allow extraction of the number density of proton carriers,  $n_p$ , that contribute to the current ( $n_p = Q/qV$ , with  $q$  the absolute electronic charge and  $V$  the volume of the HPW/PMMA layer).

Further information on the transport behaviour of protons can be gained by examining the depolarization current curves presented in Fig. 5b. After the gate voltage is cut off at  $t = 600$  s, the protons that were accumulated close to the lower edge of HPW/PMMA layer will move back toward the counter anions restoring thus, the equilibrium state of the unbiased device. Plotting the depolarization current in a logarithmic time scale (inset in Fig. 5b), an almost polarization-independent characteristic time for the return to equilibrium (ca. 300 s) is found, for  $V_G \geq 2$  V. Such behaviour can be exploited for long-refresh volatile memory applications [20]. During depolarization, it is believed that the migration of protons is governed by the proton concentration gradient in the HPW/PMMA layer initially established during the polarization regime. Regardless of the exact nature of proton transfer mechanism, the total amount of proton's charge that accumulates close to the lower edge of the HPW/PMMA layer should also contribute to the depolarization current, in the absence of any permanent trapping of the migrated proton. In this case, an equal magnitude of the integrated current for each polarization/depolarization experiment should take place (i.e., area of  $I(t) - I_L$  curves in Fig. 5a = area of the corresponding  $I(t)$  curves in Fig. 5b), in agreement with our integrated current vs  $V_G$  results depicted in Fig. 6. The resulting proton density,  $n_p$ , normalized to the maximum estimated value,  $n_p^{\text{max}}$ , is shown in the inset of Fig. 6.  $n_p^{\text{max}}$  is the value expected if each HPW molecule gives one mobile proton (i.e.,  $n_p^{\text{max}} = \text{HPW concentration within PMMA}$ , ca.  $1.9 \times 10^{20} \text{ cm}^{-3}$ , see Section 3.1). As depicted, the number of migrated protons in the sample gradually increases with  $V_G$  and exhibits a trend to saturation ( $n_p \sim 3.8 \times 10^{17} \text{ protons/cm}^3$  for  $V_G = 5$  V). The latter result indicates that only 2 protons per 1000 HPW molecules contribute to

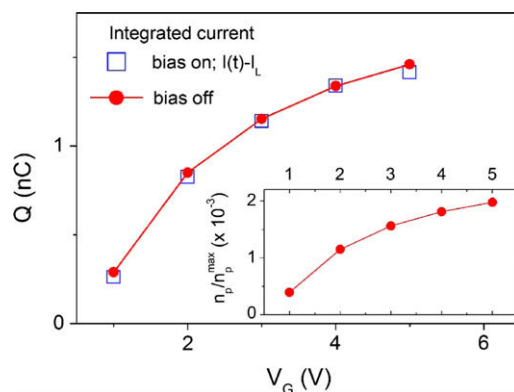


**Fig. 6.** Migrated protonic charge,  $Q$ , calculated by direct integration of the polarization (bias on; after the subtraction of the leakage current) and the depolarization currents (bias off). The inset shows the extracted ratio of the number proton density  $n_p$  and the maximum proton density  $n_p^{\text{max}}$  vs applied gate voltage  $V_G$ .

the current under full polarization conditions (saturation regime) and thereby, reveals that the main part of the dissociated protons is mainly immobile.

The polarization  $I-t$  curves can also be used to obtain information about proton conductivity ( $\sigma_{dc}$ ) and mobility ( $\mu$ ) and therefore, to estimate the number of protons ( $n_p$ ) that contribute to the current according to:  $\sigma_{dc} = n_p q \mu$ . In the case of  $V_G = 1$  V where no leakage current flows across the sample, the extracted  $\sigma_{dc}$  and  $\mu$  values are  $5.0 \times 10^{-13} \text{ S cm}^{-1}$  and  $2.8 \times 10^{-10} \text{ cm}^2 \text{ V}^{-1} \text{ s}^{-1}$ , respectively [20]. We find that about  $1.1 \times 10^{16} \text{ cm}^{-3}$  protons/cm<sup>3</sup> contribute to the current under 1 V polarization. This  $n_p$  value is comparable to that previously extracted by the integrated current method at  $V_G = 1$  V ( $n_p \sim 7.4 \times 10^{16} \text{ protons/cm}^3$ , see inset of Fig. 6).

### 3.3. Write characteristics and scalability prospects of molecular proton memories

This section treats the performance of a generic molecular proton memory. In particular, it examines the write

characteristics of the device depicted in Fig. 1 from a material perspective of its bi-layer storage element (i.e. PCL/PTL). The memory window, the write time and the write voltage of this type of memory device are successively discussed in terms of PCL/PTL material features such as the proton mobility and the mobile proton concentration in the PCL as well as the PCL and PTL thicknesses.

### 3.3.1. Memory window

By neglecting the finite size of protons and counter ions, we can express the symmetric effective proton and anion charges per unit area that develop under complete polarization close to the lower and upper edges of the PCL as:  $Q_{\text{proton}} = |Q_{\text{anion}}| = n_p q d$ , with  $d$  being the thickness of the PCL. Hence, in the case of the MIS device, the maximum magnitude of the induced negative flat band voltage shift,  $\Delta V_{\text{FB}}(-)$ , due to the accumulation of protons at the lower edge of the PCL can be expressed as:

$$\Delta V_{\text{FB}} = -\frac{n_p q d^2}{\epsilon_i} \quad (1)$$

where  $\epsilon_i$  is the dielectric constant of the PCL. In Fig. 7, the resulting  $|\Delta V_{\text{FB}}(-)|$  is plotted as a function of the thickness of the PCL with the mobile proton number density,  $n_p$ , as a parameter and an assumed effective relative dielectric constant of 3.9 [20]. By increasing the mobile proton density the thickness of the PCL must decrease in order to maintain a constant memory window. For  $n_p$  values of 0.1, 0.5, 1 and  $5 \times 10^{17} \text{ cm}^{-3}$ , the estimated thickness of the PCL for a constant memory window of about 3.5 V is close to 270, 120, 85 and 40 nm, respectively.

### 3.3.2. Write time

By assuming in the case of an initial uniform charge distribution that the protons have moved a distance  $d/2$  on average before reaching a PCL layer edge, the magnitude of the write time can be estimated according to [20]:

$$\tau = \frac{d}{2E\mu} \quad (2)$$

where  $E$  is the “write” electric field. Fig. 8a depicts write time estimations as a function of the applied electric field

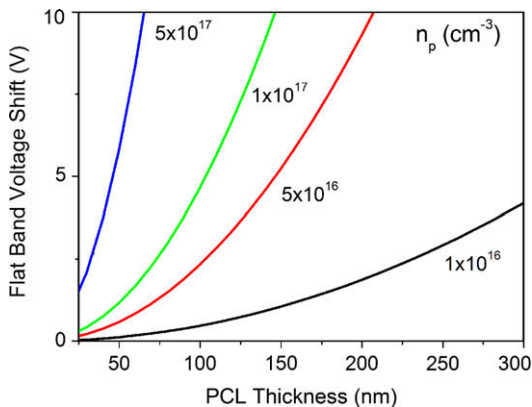


Fig. 7. Flat band voltage estimations for complete polarization as a function of the HPW/PMMA thickness for different densities of mobile protons.

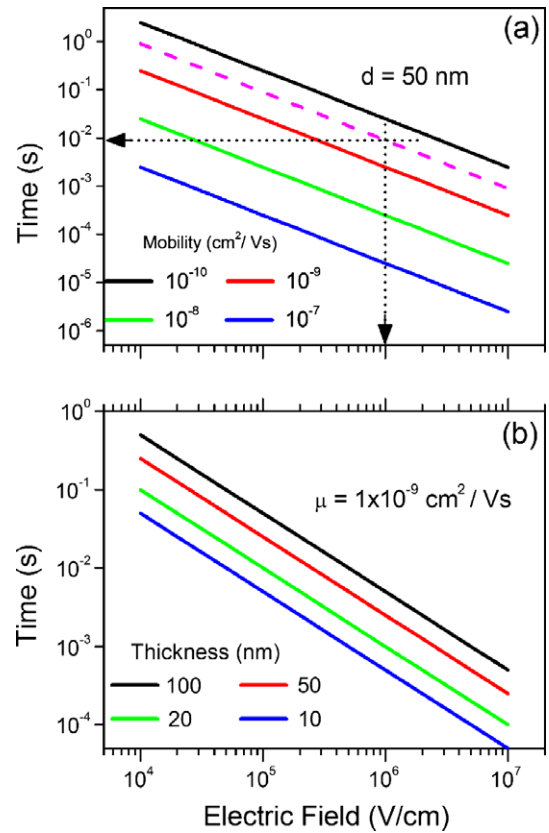
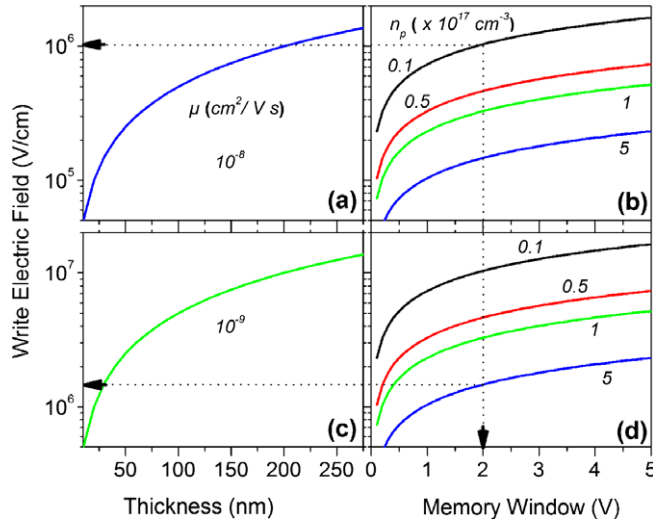
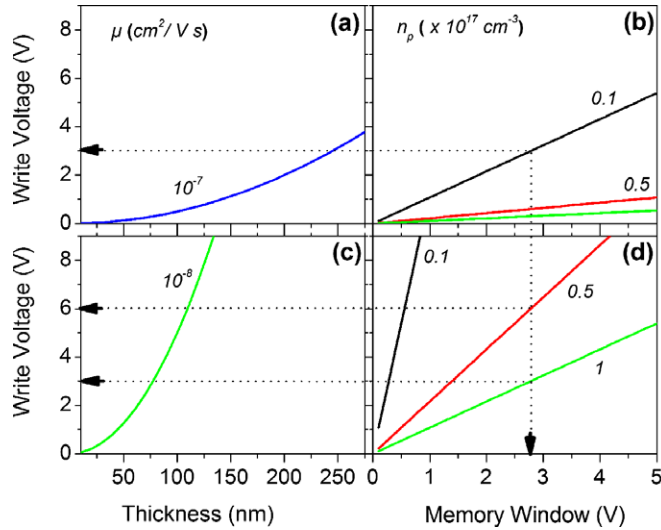


Fig. 8. Write time estimations for complete polarization as a function of the applied write electric field for: (a) different proton mobilities and constant thickness of the PCL; (b) different PCL thicknesses and constant proton mobility.

for different mobility values and constant thickness of the PCL. In the case of 50 nm PCL thickness, the experimentally extracted  $\mu$  value of  $2.8 \times 10^{-10} \text{ cm}^2 \text{ V}^{-1} \text{ s}^{-1}$  for the HPW/PMMA layer (dashed curve) affords write times of around 10 ms at a write electric field as low as 1 MV/cm. Shorter write times are attainable by decreasing further the thickness of the PCL layer (Fig. 8b); in such a case, attention should be drawn to maintain a detectable memory window, as the latter is proportional to the thickness of the PCL for a given effective protonic charge per unit area,  $Q_{\text{proton}}$ . For the case of 1 ms write time, Fig. 9 connects the write electric field and the resulting memory window with the physical properties of the PCL (i.e., the proton mobility,  $\mu$ , the proton number density,  $n_p$ , and the layer thickness,  $d$ ). A PCL with material features:  $\mu = 10^{-8} \text{ cm}^2 \text{ V}^{-1} \text{ s}^{-1}$ ,  $n_p = 10^{16} \text{ cm}^{-3}$  and a thickness of about 200 nm can induce a memory window of 2 V under application of a write electric field of  $\sim 1 \text{ MV/cm}$  for 1 ms, Fig. 9a and b. By decreasing the proton mobility (case of Fig. 9c and d), the thickness ( $d$ ) and the proton number density ( $n_p$ ) must decrease and increase, respectively ( $d$  to  $\sim 30 \text{ nm}$  and  $n_p$  to  $\sim 5 \times 10^{17} \text{ cm}^{-3}$ ), in order to maintain the write characteristics of the device (i.e., a write time of 1 ms, a write electric field in the 1 MV/cm regime, and a memory window of 2 V).



**Fig. 9.** Write electric field vs memory window estimations for complete polarization under 1 ms write time, for different physical properties of the PCL (i.e., proton mobility, proton density and thickness).



**Fig. 10.** Write voltage vs memory window estimations in the limit  $d_{PTL} \ll d_{PCL}$ , for complete polarization under 1 ms write time, for different physical properties of the PCL.

### 3.3.3. Write voltage

Ignoring the work function difference between the semiconductor substrate and the metal gate electrode, the write voltage,  $V_w$ , can be expressed as:  $V_w = E d_{total}$ , where  $d_{total}$  represents the total physical thickness of the PCL/PTL stack (i.e.,  $d_{total} = d_{PTL} + d_{PCL}$ ). In the limit  $d_{PTL} \ll d_{PCL}$  (e.g., in the case of a PTL made by a small number of monolayer containing basic sites),  $V_w$  can be approximated under complete polarization (i.e., full write) through a combination of the previous relations of the memory window ( $\Delta V_{FB}$ ) and write time ( $\tau$ ), i.e. Eqs. (1) and (2), such as:

$$V_w = \frac{\epsilon_i \Delta V_{FB}}{2n_p q \mu \tau} = \frac{d^2}{2\mu\tau} \quad (3)$$

In Fig. 10, in an analogous way to Fig. 9, the overall write characteristics of the device (i.e., the write voltage and the resulting memory window) for 1 ms pulsed time are plotted as a function of the physical properties of the PCL. A PCL with  $\mu = 10^{-7} \text{ cm}^2 \text{ V}^{-1} \text{ s}^{-1}$ ,  $n_p = 10^{16} \text{ cm}^{-3}$  and  $d_{PCL} \sim 245 \text{ nm}$  leads to a memory window of about 2.8 V under an applied write voltage of 3 V for 1 ms (Fig. 10a and b). As depicted in Fig. 10c and d, for lower proton mobility ( $10^{-8} \text{ cm}^2 \text{ V}^{-1} \text{ s}^{-1}$ ) the layer thickness has to decrease to  $\sim 75 \text{ nm}$ , while the proton density must increase to  $10^{17} \text{ cm}^{-3}$ , in order to maintain the write characteristics of the memory device (i.e.  $V_w/\tau = 3 \text{ V}/1 \text{ ms}$ ,  $\Delta V_{FB} = 2.8 \text{ V}$ ). Note that, an intermediate decrease (increase) of the thickness (proton density) of the PCL to 110 nm ( $5 \times 10^{16} \text{ cm}^{-3}$ )

requires a twofold increase of the write voltage, i.e. from 3 to 6 V, to conserve a memory window of 2.8 V for a write time of 1 ms.

It should be here emphasized that the write voltage scalability of a proton memory device with equal PCL and PTL thicknesses can be approximated under complete polarization (i.e., full write), and for proton trapping in a region close to PTL/PCL interface, through the relation:

$$V_w = \frac{\epsilon_i \Delta V_{FB}}{n_p q \mu \tau} = \frac{d^2}{4 \mu \tau} \quad (4)$$

In such a case the thickness  $d$  corresponds to the total PCL and PTL thicknesses. For example, a PCL with  $\mu = 10^{-7} \text{ cm}^2 \text{ V}^{-1} \text{ s}^{-1}$ ,  $n_p = 2 \times 10^{16} \text{ cm}^{-3}$  and  $d_{\text{PCL}} = 175 \text{ nm}$  on the top of a PTL of equal thickness (175 nm) leads to a memory window of about 2.8 V under an applied write voltage of 3 V for 1 ms. From the above discussion it is clear that a proton memory device using a PCL with appropriate proton mobility ( $\mu$ ) and density ( $n_p$ ) does not require an aggressive scaling in PCL and PTL thicknesses for low-voltage operation.

#### 4. Conclusions

Physicochemical and transient current experiments have been conducted on stacked bilayer structures consisted of a proton conducting layer (PCL) and a proton trapping layer (PTL) for the development of molecular proton memory. FTIR investigation of the effect of the thermal processing parameters (temperature and duration) on the HPW/PMMA layer (PCL) resulted in the successful prevention of two undesirable phenomena: (a) the reaction between HPW and PMMA matrix inside the PCL, and (b) the intermixing of the PCL and PTL layers. By means of UV spectroscopy, the concentration of the HPW molecules within the HPW/PMMA layer is estimated to approximately  $1.9 \times 10^{20}$  HPW molecules  $\text{cm}^{-3}$ . Transient current measurements on MIS devices allowed the determination of the concentration of mobile protons within the HPW/PMMA layer as well as an estimation of the proton mobility. The extracted proton density of  $\sim 3.8 \times 10^{17}$  protons/ $\text{cm}^3$  under full polarization conditions corresponds to only 2 mobile protons per  $\sim 1000$  HPW molecules, indicating that the main part of the dissociated protons which are attached to polymer basic sites is mainly immobile. Finally, the analysis of a generic molecular proton memory revealed that several material features of the PCL/PTL bilayer stacked structure should affect the write characteristics of this type of memory device. Our calculations point out the dependence of the device memory window, write

time and write voltage on the proton mobility, the mobile proton concentration and the PCL and PTL thicknesses.

#### References

- [1] G.W. Burr, B.N. Kurdi, J.C. Scott, C.H. Lam, K. Gopalakrishnan, R.S. Shenoy, IBM J. Res. Dev. 52 (2008) 449.
- [2] R. Waser, M. Aono, Nat. Mater. 6 (2007) 833.
- [3] J.A. Hutchby, R. Cavin, V. Zhirnov, J.E. Brewer, G. Bourianoff, Computer 41 (2008) 28.
- [4] S.K. Lai, IBM J. Res. Dev. 52 (2008) 529.
- [5] C.D. Dimitrakopoulos, P.R.L. Malenfant, Adv. Mater. 14 (2002) 99.
- [6] J.M. Sun, J.Q. Liu, D.B. Zhu, J. Mater. Chem. 15 (2005) 53.
- [7] T.B. Singh, N.S. Sariciftci, Annu. Rev. Mater. Res. 36 (2006) 199.
- [8] L. Fortuna, M. Frasca, M. Gioffre, M. La Rosa, N. Malagnino, A. Marcellino, D. Nicolosi, L. Occhipinti, F. Porro, G. Sicurella, E. Umana, R. Vecchione, IEEE Circuits Syst. Mag. 8 (3) (2008) 6.
- [9] J.A. Rogers, Z. Bao, K. Baldwin, A. Dodabalapur, B. Crone, V.R. Raju, V. Kuck, H. Katz, K. Amundson, J. Ewing, P. Drzaic, Proc. Natl. Acad. Sci. 98 (2001) 4835.
- [10] S.R. Forrest, Nature 428 (2004) 911.
- [11] G.G. Malliaras, R. Friend, Phys. Today 58 (4) (2005) 53.
- [12] J.A. Dodabalapur, Mater. Today 9 (4) (2006) 24.
- [13] J.C. Scott, L.D. Bozano, Adv. Mater. 19 (2007) 1452.
- [14] Qi-Dan Linga, Der-Jang Liaw, Chunxiang Zhu, Daniel Siu-Hung Chan, En-Tang Kang, Koon-Gee Neoh, Prog. Polym. Sci. 33 (2008) 917.
- [15] K.-T. Park, J.-S. Sel, J. Choi, Y. Song, C. Kim, K. Kim, IEEE Trans. Electron. Dev. 55 (2008) 404.
- [16] G. Gelinck, Nature 445 (2007) 268.
- [17] J. De Blauwe, IEEE Trans. Nanotechnol. 1 (2002) 72.
- [18] T.P.-C. Juan, C.-Y. Chang, J.Y.-M. Lee, IEEE Electron. Dev. Lett. 27 (2006) 217.
- [19] K. Vanheusden, W.L. Warren, R.A.B. Devine, D.M. Fleetwood, J.R. Schwank, M.R. Shaneyfelt, P.S. Winokur, Z.J. Lemnios, Nature 386 (1997) 587.
- [20] E. Kapetanakis, A.M. Douvas, D. Velessiotis, E. Makarona, P. Argitis, N. Glezos, P. Normand, Adv. Mater. 20 (2008) 4568.
- [21] C.Z. Zhao, J.F. Zhang, G. Groeseneken, R. Degraeve, J.N. Ellis, C.D. Beech, IEEE Electron. Lett. 37 (2001) 716.
- [22] Betty Prince, Emerging Memories – Technologies and Trends, Kluwer Academic Publishers, 2002 (Chapter 3).
- [23] I.V. Kozhevnikov, Chem. Rev. 98 (1998) 171.
- [24] D.H. Grant, N. Grassie, Polymer 1 (1960) 125.
- [25] M. Freluche, I. Iliopoulos, M. Milléquant, J.J. Flat, L. Leibler, Macromolecules 39 (2006) 6905.
- [26] C. Rocchiccioli-Deltcheff, M. Fournier, R. Franck, R. Thouvenot, Inorg. Chem. 22 (1983) 207.
- [27] R. Thouvenot, M. Fournier, R. Franck, C. Rocchiccioli-Deltcheff, Inorg. Chem. 23 (1984) 598.
- [28] M.T. Pope, A. Müller, Angew. Chem. Int. Ed. Engl. 30 (1991) 34.
- [29] E. Papaconstantinou, Chem. Soc. Rev. 18 (1989) 1.
- [30] A.M. Douvas, E. Makarona, N. Glezos, P. Argitis, J.A. Mielczarski, E. Mielczarski, ACS Nano 2 (2008) 733.
- [31] A. Kokkinis, E.S. Valamontes, D. Goustouridis, T. Ganetsos, K. Beltsios, I. Raptis, Microelectron. Eng. 85 (2008) 93.
- [32] D.A. Dimotikali, Ph.D. Thesis, Athens University, 1989, p. 59.
- [33] G.M. Varga, E. Papaconstantinou, M.T. Pope, Inorg. Chem. 9 (1970) 662.
- [34] E. Papaconstantinou, M.T. Pope, Inorg. Chem. 9 (1970) 667.
- [35] <[http://en.wikipedia.org/wiki/Polymethyl\\_methacrylate](http://en.wikipedia.org/wiki/Polymethyl_methacrylate)>.
- [36] J. March, in: Advanced Organic Chemistry: Reactions, Mechanisms and Structure, 4th ed., Wiley, New York, 1992, pp. 250–252.
- [37] R.S. Drago, J.A. Dias, T.O. Maier, J. Am. Chem. Soc. 119 (1997) 7702.
- [38] P. Kohn, K. Schröter, T. Thurn-Albrecht, Phys. Rev. Lett. 99 (2007) 086104.

to passivate inorganic surface traps as well as mediate forward charge transfer to reduce back recombination at the interface leading to much improved fill factors and photocurrent densities [8]. These improvements have led to efficiencies as high as 4.9% while maintaining good ambient device stability. This is important because the encapsulation process can be potentially performed under ambient conditions which will lead to reduced fabrication costs. However, the devices in our previous studies have been based on vacuum deposited Ag as anode which is not as ideal in terms of simplicity for large area, roll-to-roll processing.

In this letter, we investigate the possibility of utilizing a spraycoating process for the deposition of Ag-NPs as the anode electrode in inverted solar cells. These spraycoated Ag electrodes show good performance and similar ambient device stability when compared to the ones fabricated using the conventional vacuum deposition process. Devices were also fabricated onto flexible ITO substrates to demonstrate the feasibility of making flexible solar cells closer to the ideal large area, roll-to-roll processing.

To fabricate the inverted solar cells, ITO-coated glass substrates ( $15 \Omega/\square$ ) and ITO-coated plastic substrates ( $60 \Omega/\square$ ) (Bayview Optics) were cleaned with detergent, de-ionized water, acetone, and isopropyl alcohol. A thin layer of ZnO nanoparticles ( $\sim 50$  nm), synthesized using the method described by Beek et al. [9], was spin-coated onto ITO-coated glass. The  $C_{60}$ -SAM was then deposited as previously reported [7]. Afterward, a chlorobenzene (CB) solution of poly(3-hexylthiophene) (P3HT) (Rieke Metals) and [6,6]-phenyl  $C_{61}$ -butyric acid methyl ester (PCBM) (American Dye Source) (60 mg/ml) with a weight ratio of (1:0.6) was spin-coated onto the ZnO modified layer to achieve a thickness of ( $\sim 210$  nm) and annealed at  $160^\circ\text{C}$  for 10 min in an argon glovebox. After annealing, PEDOT:PSS was spin-coated multiple times and annealed for 10 min at  $120^\circ\text{C}$  in air between subsequent spincoating steps onto the active layer to achieve a thickness of  $\sim 150$  nm. The silver electrode was vacuum deposited (100 nm) at a pressure of  $1 \times 10^{-6}$  torr or spraycoated on top of PEDOT:PSS to complete the device. For the spraycoating, a solution of Ag-NPs (NanoMas: contents of 25% Ag-NPs, 25–60% dodecane, 0–50% cyclohexane, 0–20% terpinol) was diluted in 1:40 (v:v) in hexane. An airbrush spraycoater is used to spray the dilute solution onto a masked device (7 mm) at a distance of 6 cm with a spray pressure of 15 psi using  $N_2$  as the gas. This is repeated until the desired number of coats is achieved. Spraycoating the Ag-NPs leads to extremely rough films which make measuring the exact thickness difficult, but the film thickness as measured by a profilometer is in the range of  $\sim 1$ – $2 \mu\text{m}$ . The devices coated with the Ag-NPs electrode were then annealed at  $120^\circ\text{C}$  for 5 min in air as suggested by NanoMas to promote the nanoparticle interconnectivity. The unencapsulated solar cells were tested under ambient conditions using a Keithley 2400 SMU and an Oriel Xenon lamp (450 W) with an AM1.5 filter. A mask was used to define the device illumination area to minimize photocurrent generation from the edge of the electrodes [10,11]. The light intensity was calibrated to  $100 \text{ mW}/\text{cm}^2$  using a calibrated silicon solar cell with a KG5 filter which has been

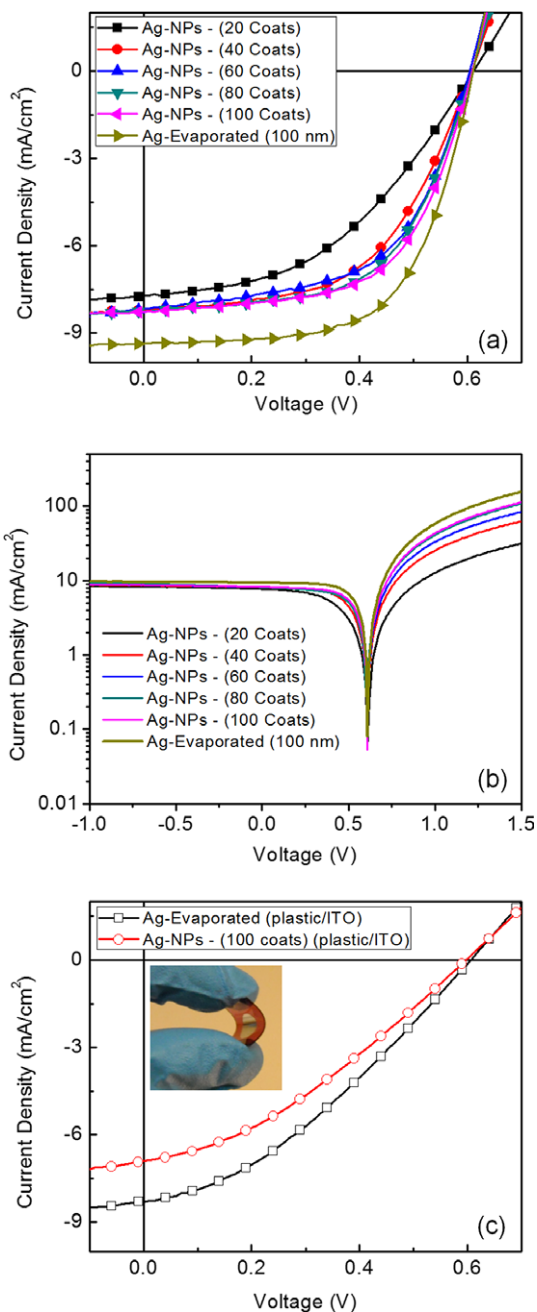


**Fig. 1.** (a) Illuminated  $J$ - $V$  characteristics of inverted ZnO NP/ $C_{60}$ -SAM/P3HT:PCBM bulk heterojunction solar cells fabricated on glass/ITO by spraycoating Ag-NPs (from 20–100 coats) or evaporating Ag as the anode electrode. (b) Plot of  $\log(J)$ - $V$  characteristics of inverted ZnO NP/ $C_{60}$ -SAM/P3HT:PCBM bulk heterojunction solar cells fabricated on glass/ITO by spraycoating Ag-NPs (from 20–100 coats) or evaporating Ag as the anode electrode. (c) Illuminated  $J$ - $V$  characteristics of devices fabricated on flexible ITO substrates by spraycoating Ag-NPs and evaporating Ag as the anode electrode. Inset: photograph of flexible inverted spraycoated electrode solar cell.

previously standardized at the National Renewable Energy Laboratory.

The spraycoating technique has been previously demonstrated by others for the deposition of the active layers

[12,13] as well as PEDOT:PSS-based electrodes [14] in polymer solar cells. The spraycoating process has many variables that can be controlled including the solution viscosity, spray pressure, the spray distance from sample, spray time and number of spray coats which can affect the formation of the final coating of the film. In this study, most of these variables are held constant except for the number of coating layers. The number of coats (from 20 to 100) of the Ag-NPs was systematically studied to explore the effect on device performance.

The illuminated  $J$ - $V$  characteristics of the devices fabricated by different number of coating layers of Ag-NPs are compared to vacuum deposition of Ag in Fig 1a and b. With a coating of 20, the diode characteristics are poor, but are improved as the number of coatings increase. Table 1 summarizes the average device performance of these spraycoated electrodes to the ones prepared by vacuum

deposition. Devices with a coating of 20 show a low short circuit current ( $J_{sc}$ ), fill factor (FF), and power conversion efficiency (PCE) of 7.71 mA/cm<sup>2</sup>, 44.5%, and 2.10%, respectively. The photocurrent increases with increasing coating layers but saturates to ~8.3 mA/cm<sup>2</sup> at 100 coats. However, the FF dramatically improves from 44.5% with a coating of 20–54.2% with a coating of 40 and further improves to 59.6% with a coating of 100. This leads to an average PCE of ~3.00% by spraying 100 coats of the Ag-NPs. The device series resistance of the different number of coats was estimated at 1.5 V showing a resistance of 26.1  $\Omega$  cm<sup>2</sup> with 20 coats. Increasing the number of coats show lowering of the device series resistance eventually saturating around ~7  $\Omega$  cm<sup>2</sup> with 100 coats. This resistance is still higher than the evaporated Ag which had a resistance of ~5  $\Omega$  cm<sup>2</sup>. Overall, the vacuum deposited Ag devices had higher performances in  $J_{sc}$ , FF, and PCE of 9.34 mA/cm<sup>2</sup>,

**Table 1**

Average device performance of inverted ZnO NP/C<sub>60</sub>-SAM/P3HT:PCBM bulk heterojunction solar cells fabricated on glass/ITO and plastic/ITO substrates by either vacuum deposition of Ag or spraycoating of Ag-NPs as the anode electrode. Average was obtained from multiple device tests. Sheet resistance of vacuum deposited Ag and different spraycoated Ag-NPs electrodes.

Electrode deposition	$V_{oc}$ (V)	$J_{sc}$ (mA/cm <sup>2</sup> )	FF (%)	PCE (%)	$R_s$ ( $\Omega$ cm <sup>2</sup> )	Ag sheet resistance ( $\Omega/\square$ )
Vacuum	0.61	9.34	62.2	3.55	5.0	0.51
Vacuum (plastic)	0.61	8.31	34.3	1.73	42.0	–
Spraycoat (20 coats)	0.61	7.71	44.5	2.10	26.1	–
Spraycoat (40 coats)	0.61	8.19	54.2	2.70	13.3	7.55
Spraycoat (60 coats)	0.61	8.16	56.6	2.79	9.7	3.47
Spraycoat (80 coats)	0.61	8.24	58.1	2.92	7.2	1.84
Spraycoat (100 coats)	0.61	8.26	59.6	3.00	7.0	0.71
Spraycoat (100 coats) (plastic)	0.60	6.90	34.0	1.40	51.6	–

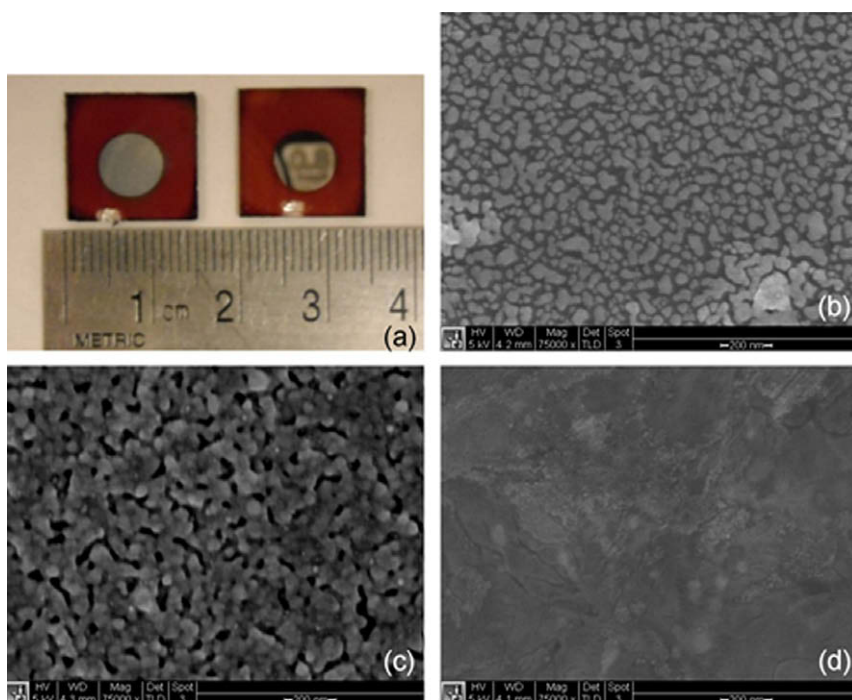


**Fig. 2.** (a) Photograph of polymer solar cells using an Ag spraycoated electrode with 100 coats (left) and Ag evaporated electrode (right) on ITO/glass substrates. SEM images of (b) spraycoated Ag-NPs (20 coats) after annealing at 120 °C for 5 min; (c) spraycoated Ag-NPs (100 coats) after annealing 120 °C for 5 min; (d) 100 nm evaporated Ag. Scale bar: 200 nm.

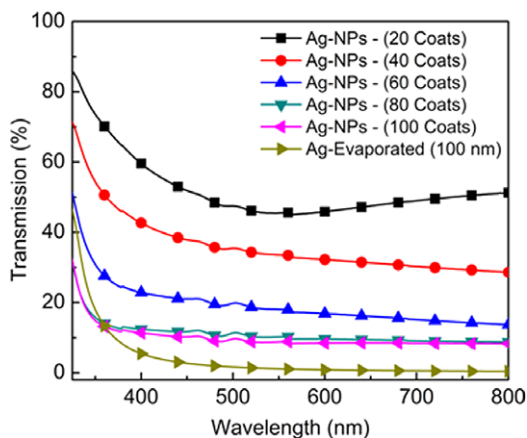


**Fig. 3.** UV-Vis transmission spectrum of spraycoated Ag-NPs electrodes from 20 to 100 coats compared to a 100 nm Ag evaporated electrode on glass substrates.

62.2% and 3.55%, respectively. Fig 2a shows two devices, one of which is fabricated using the spraycoating technique (100 coats) and the other is by vacuum deposition (100 nm). The spraycoated electrode with 100 coats shows similar device series resistance and fill factor compared to the evaporated electrode, however a 0.55% lower PCE mainly from the lower  $J_{sc}$  in the spraycoated electrode devices is unaccounted for.

To understand the reason for this difference in efficiency the spraycoated and evaporated electrodes were characterized by measuring the sheet resistance using the four-point probe technique, transmission by UV-Vis spectroscopy and surface morphology by scanning electron microscopy (SEM). Table 1 shows the sheet resistance of the Ag electrodes as measured by four-point probe. A sheet resistance was not able to be measured on the electrode with 20 coats which is attributed to the poor nanoparticle interconnectivity in forming a film as can be seen in the SEM image in Fig 2b. As a note, even the devices fabricated using 20 coats had poor stability and performance degraded rapidly after multiple  $I-V$  scans. Increasing to 40 coats a sheet resistance of  $7.55 \Omega/\square$  was obtained and the performance of devices after multiple  $I-V$  scans was stable. Further increasing the coating to 100 lead to a sheet resistance of  $0.71 \Omega/\square$  which is comparable to the evaporated electrode ( $0.51 \Omega/\square$ ). This reduced sheet resistance is the main reason for the improvement in device fill factor in the spraycoated electrode devices. The minimized sheet resistance improves the device series resistance in both the 100 coats and evaporated Ag film which leads to similar fill factors. However, this does not explain the reason for the difference in photocurrent density between the 100 spray coat and Ag evaporated electrode. The transmission spectrum measured by UV-Vis of the spraycoated and evaporated electrodes are shown in Fig 3. At the P3HT absorbance peak ( $\sim 550$  nm), the spraycoated electrode with 20 coats has a transparency of  $\sim 45\%$ . Increasing the number of coats to 80 and 100 reduces the transmission to  $\sim 12\%$  and  $\sim 9\%$ , respectively which is still much higher than the transparency of evaporated Ag film ( $\sim 1\%$ ). Fig 2c

and d shows the SEM images of the Ag-NPs film by spraycoating 20 coats, 100 coats and the Ag evaporated film. The 100 coat film shows a much denser aggregation and interconnection of the Ag-NPs compared to the 20 coat film which explains the reduced sheet resistance. However, even the 100 coat film show many voids which is the reason for the higher transparency and higher sheet resistance compared to the Ag evaporated film which does not have these voids. One potential reason for the difference in photocurrent is the higher transmission in the 100 coat films compared to the Ag evaporated films which reduces the potential for light to be reflected back into the active layer from the electrode to increase absorption.

The spraycoating procedure was used to fabricate solar cells on flexible plastic ITO substrates which were compared to evaporated Ag electrodes. The illuminated  $J-V$  characteristics are shown in Fig 1c. Devices with the spraycoated electrode on the plastic substrate show a lower  $J_{sc}$ , FF and PCE of  $6.90 \text{ mA}/\text{cm}^2$ , 34.0% and 1.40%, respectively compared to the evaporated electrode which had a  $J_{sc}$ , FF and PCE of  $8.31 \text{ mA}/\text{cm}^2$ , 34.3% and 1.73%, respectively. The lower performance especially in fill factor compared to the ITO/glass substrates is due to the lower transparency of the flexible ITO substrate as well as the higher sheet resistance [15]. The unencapsulated devices stored in ambient for 21 days also show that the device with Ag-NPs electrodes have similar stability as previously reported with the Ag evaporated electrodes [6].

In conclusion, the performance of inverted solar cells using spraycoated Ag-NPs has been systematically studied showing that the number of coating layers can affect its final device performance. With higher number of coating layers, a better nanoparticle interconnectivity and morphology is achieved which reduces the sheet resistance and transparency of the Ag electrode leading to improved fill factor and device performances of  $\sim 3.00\%$ . This efficiency is lower than the evaporated Ag film which is attributed to the higher transmission of light due to a rougher and less dense Ag-NPs film which leads to a reduction of photocurrent. Furthermore, spraycoating of the Ag electrode onto flexible ITO substrates devices shows a performance of  $\sim 1.40\%$ . The ability to use a non-vacuum technique to deposit the electrode in polymer solar cells is important for large area, flexible, roll-to-roll production of low-cost solar cells.

## Acknowledgements

This work was supported by the National Science Foundation's NSF-STC program under Project No. DMR-0120967 and the DOE "Future Generation Photovoltaic Devices and Process" program under Project No. DE-FC36-08G018024/A000. A.K.-Y.J. thanks the Boeing-Johnson Foundation for financial support. S.K.H. and H.L.Y. thank the Intel Foundation Ph.D. Fellowship.

## References

- [1] W.L. Ma, C.Y. Yang, X. Gong, K. Lee, A.J. Heeger, Adv. Funct. Mater. 15 (2005) 1617.



- [2] G. Li, V. Shrotyriya, J.S. Huang, Y. Yao, T. Moriarty, K. Emery, Y. Yang, *Nat. Mater.* 4 (2005) 864.
- [3] J. Peet, J.Y. Kim, N.E. Coates, W.L. Ma, D. Moses, A.J. Heeger, G.C. Bazan, *Nat. Mater.* 6 (2007) 497.
- [4] M.S. White, D.C. Olson, S.E. Shaheen, N. Kopidakis, D.S. Ginley, *Appl. Phys. Lett.* 87 (2006) 143517.
- [5] C. Waldauf, M. Morana, P. Denk, P. Schilinsky, K. Coakley, S.A. Choulis, C.J. Brabec, *Appl. Phys. Lett.* 89 (2006) 233517.
- [6] S.K. Hau, H.L. Yip, N.S. Baek, J. Zou, K. O'Malley, A.K.Y. Jen, *Appl. Phys. Lett.* 92 (2008) 253301.
- [7] S.K. Hau, H.L. Yip, H. Ma, A.K.Y. Jen, *Appl. Phys. Lett.* 93 (2008) 233304.
- [8] S.K. Hau, H.L. Yip, O. Acton, N.S. Baek, H. Ma, A.K.Y. Jen, *J. Mater. Chem.* 18 (2008) 511.
- [9] W.J.E. Beek, M.M. Wienk, M. Kemerink, X. Yang, R.A.J. Janssen, *J. Phys. Chem. B* 109 (2005) 9505.
- [10] A. Cravino, P. Schilinsky, C.J. Brabec, *Adv. Funct. Mater.* 17 (2007) 3906.
- [11] M.-S. Kim, M.-G. Kang, L.J. Guo, J. Kim, *Appl. Phys. Lett.* 92 (2008) 133301.
- [12] D. Vak, S.-S. Kim, J. Jo, S.-H. Oh, S.-I. Na, J. Kim, D.-Y. Kim, *Appl. Phys. Lett.* 91 (2007) 081102.
- [13] R. Green, A. Morfa, A.J. Ferguson, N. Kopidakis, G. Rumbles, S.E. Shaheen, *Appl. Phys. Lett.* 92 (2008) 033301.
- [14] Y.-F. Lim, S. Lee, D.J. Herman, M.T. Lloyd, J.E. Anthony, G.G. Malliaras, *Appl. Phys. Lett.* 93 (2008) 19330.
- [15] B. Maennig, J. Drechsel, D. Gebeyehu, P. Simon, F. Kozlowski, A. Werner, F. Li, S. Grundmann, S. Sonntag, M. Koch, K. Leo, M. Pfeiffer, H. Hoppe, D. Meissner, N.S. Sariciftci, I. Riedel, V. Dyakonov, J. Parisi, *Appl. Phys. A* 79 (2004) 1.

Great efforts have been made to address this problem by optimizing thin-film morphology to improve the charge transport and suppress recombination [12–15]. Moreover, the bulk heterojunction structure based on organic small-molecule dyes could be formed through donor–acceptor (D–A) co-deposition [16–19]. However, the carrier recombination rate in such type of mixed layer remains at a very high level [20].

In this paper, a multisteped (MS) structure of a device made from a CuPc:C<sub>60</sub> heterojunction materials system is introduced. Through simultaneous dynamic alteration of the relative deposition rates of the two kinds of materials, the C<sub>60</sub> content in the device ascends from the anode to the cathode, while that of CuPc descends from the anode to the cathode, which seems similar to the graded junction solar cell design for inorganic solar cells [22–24]. However, in organic solar cells, only Sullivan et al. [17], Drees et al. [13], and Koeppe et al. [5] have made similar structures by other methods. Sullivan et al. produced a five-layered device based on the CuPc/C<sub>60</sub> materials system where the CuPc:C<sub>60</sub> composition varies from purely donor to purely acceptor via three mixed layers of increasing acceptor concentration, which are 25%, 50%, and 75% [17]. Drees et al. propelled the interdiffusion of an initial MEH-PPV/C<sub>60</sub> bilayer by simple heat treatment to obtain a bulk heterojunction with a concentration gradient of donor and acceptor [13]. Koeppe et al. used a pyrrolidinofullerene compound with chelating pyridyl groups (PyF) that can interact with the Zn atom in the Zn-phthalocyanine (ZnPc) molecule in the bilayer solar cell, which may also induce a similar molecular architecture [5]. These devices all exhibit good photovoltaic performance, but its causes were discussed

from the aspect of mixed film morphology only. Based on this concept, we envisioned MS device as a different approach to obtain a high photovoltaic performance. Thus, the effect of different sizes of concentration gradients of donor and acceptor on the solar cell performance is further discussed. Also, the optimization mechanism based on the theory of excitonic solar cells [6] is investigated to better understand the potential advantages of both bilayer heterojunction cell and homogeneously mixed cell in this structure.

Several devices with three different structures were designed for comparison (Fig. 1 inset). These are as follows:

- A: ITO/CuPc (30 nm)/C<sub>60</sub> (30 nm)/TPBI (6 nm)/Al (80 nm);
- B: ITO/CuPc:C<sub>60</sub> (MS, 60 nm)/TPBI (6 nm)/Al (80 nm); and
- C: ITO/CuPc:C<sub>60</sub> (1:1,60 nm)/TPBI (6 nm)/Al (80 nm).

Among them, A is the bilayer heterojunction device (standard device), B is the MS device, and C is the 1:1 homogeneously mixed device. The CuPc:C<sub>60</sub> (1:1) homogeneously mixed device is chosen owing to the fact that the total CuPc content is the same as that of C<sub>60</sub> in the MS layers, and could thus be used to compare with these MS devices as the extreme case without the gradient. The 2,2,2-(1,3,5-benzenetriyl)tris-[1-phenyl-1H-benzimidazole] (TPBI) layer in each device acts as an exciton blocking layer.

Glass/indium tin oxide (ITO) substrate with a sheet resistance of 20 Ω/sq was cleaned in an ultrasonic bath using detergent water, de-ionized water, acetone, and ethanol in

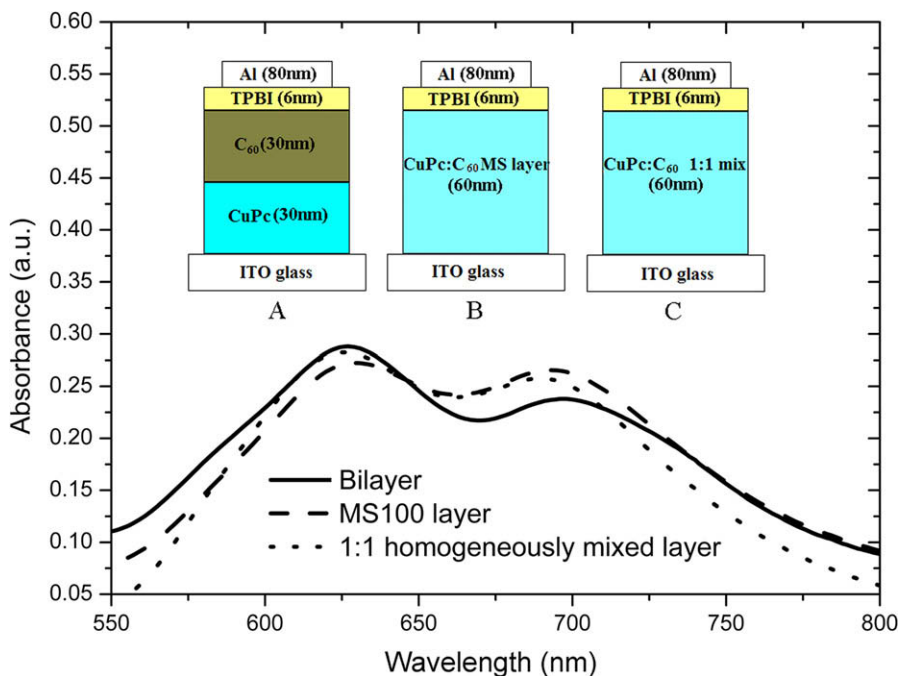


**Fig. 1.** Absorption spectra of CuPc/C<sub>60</sub> bilayer, MS100 layer, and 1:1 homogeneously mixed layer deposited on quartz substrates. Inset: schematic of the PV devices investigated. A is the bilayer heterojunction device (standard device); B is the MS device; and C is the 1:1 homogeneously mixed device.

turn for 15 min. Afterwards, it was treated in an ultraviolet-ozone chamber (UVO) then coated with layers of 30 nm CuPc, 30 nm C<sub>60</sub>, and 6 nm TPBI through thermal evaporation in a high-vacuum chamber especially designed for organic materials. In circumstances where the vacuum conditions are not broken, the substrate was moved into the vacuum chamber particularly for metals to be coated with an 80 nm Al layer. This eventually becomes the standard device. The MS layers could be produced through dynamic alteration of the relative deposition rates of the two kinds of materials evaporated simultaneously. The thicknesses of the MS films were all controlled at 60 nm and there were a total of 10 steps in the MS system. Take MS100 for example, in which the CuPc concentration was gradually decreased from 100% in the first step to 0 in the last step. The preparation process is detailed as follows. First, the initial deposition rates of CuPc and C<sub>60</sub> were respectively controlled at 0.5 Å/s and 0 Å/s. In the former 30 nm, every time the deposition layer thickness increased by 6 nm, the deposition rate of C<sub>60</sub> increased by 0.1 Å/s, whereas that of CuPc maintained the initial value. When the rates of these two reached 1:1 (both 0.5 Å/s), the layer thickness was just 30 nm. In the latter 30 nm, the deposition rate of C<sub>60</sub> was kept at 0.5 Å/s, whereas that of CuPc was gradually decreased from 0.5 Å/s to 0 Å/s by the same alteration speed maintained by C<sub>60</sub> before. Other MS layers were all similarly prepared following these steps in addition to the different relative deposition rates in order to make different concentrations. We believed that the rate changes between steps were so

small that the concentration gradients in the MS system approached that of a diffusive method. The active area of the cell was  $2 \times 2 \text{ mm} = 0.04 \text{ cm}^2$ , and the *J*-*V* curve of the cell was measured on a computer-controlled Keithley 2000 current meter. The solar simulator YSS-50A (Yamashita DESO) was at a light intensity of  $100 \text{ mW/cm}^2$  (AM1.5G). The measuring processes used in this study were performed under vacuum conditions at room temperature.

Three kinds of MS devices were fabricated similar to the structure of the cell B shown in the inset of Fig. 1. Fig. 2a shows the detailed stepped distributions of CuPc and C<sub>60</sub> in their photoactive layers. Since all their CuPc concentration decreased from 100% in the first step to 0 in the last step and the major difference lies in the position of the step when the CuPc concentration reached 50%, they are exhibited as MS100 a/b/c, respectively. As shown in Fig. 2a, the distributions of concentration gradients in the bulk of the MS100 b/c layers are asymmetrical while that of the MS100 a is symmetrical around the center of the layer. Their characteristics are summarized in Table 1. We observe that all their *V*<sub>oc</sub> displays the same value. However, the short-circuit current (*J*<sub>sc</sub>) and fill factor (FF) of the MS100 a device are both the highest among the three. It is suggested that the centrosymmetrical distributions of concentration gradients in the MS100 a film might help the balance of hole and electron transport on both sides. Later, we will lay emphasis on an MS system of this kind.

Fig. 1 shows the absorption spectrogram of the photoactive layers of the standard device, the MS100 device, and

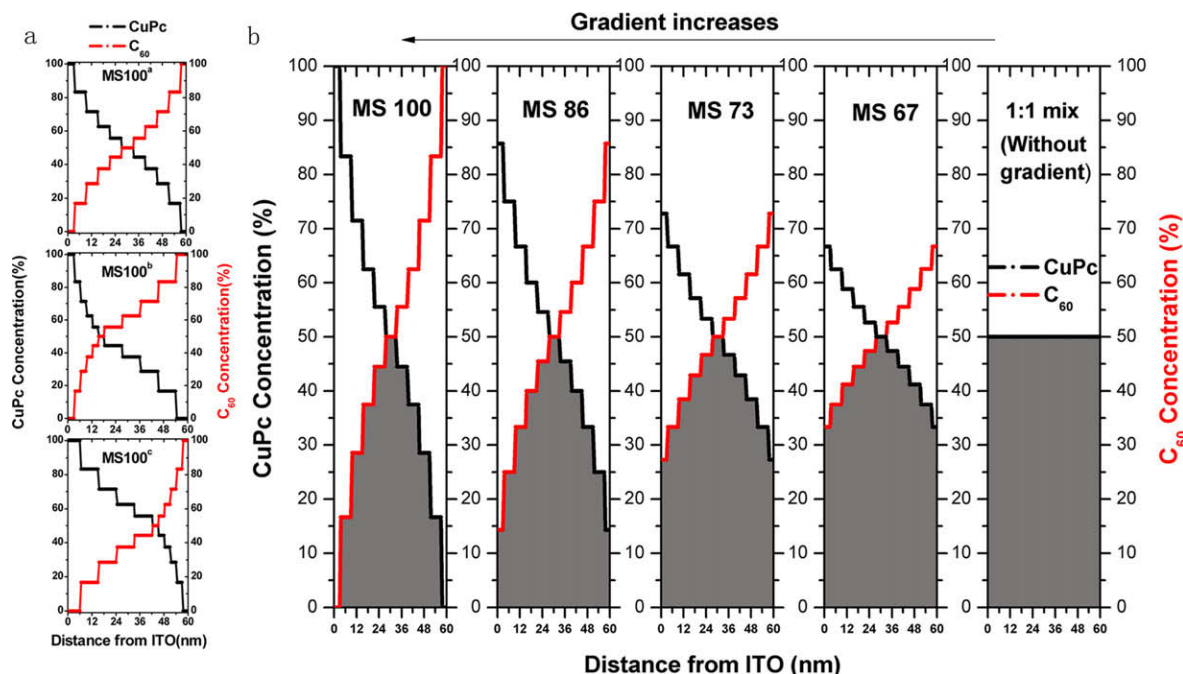


**Fig. 2.** Stepped distributions of CuPc and C<sub>60</sub> concentration in (a) three kinds of MS layers with different symmetries of concentration gradients of donor-acceptor; (b) a series of MS layers with the same symmetries but different sizes of concentration gradients and 1:1 homogeneously mixed film. The shadow denotes the apparent effective CS interfacial area in the film. When two substances blend, the apparent interfacial area depends on the surface area of the substance of less content. In this paper, we use the material content to stand for its approximate surface area. Of all these MS layers, the former half contains less C<sub>60</sub> and the latter half contains less CuPc, thus the apparent effective CS interfacial area is as shown in the shadow.

**Table 1**

Photocurrent–voltage characteristics of organic thin-film PV devices investigated under 100 mW/cm<sup>2</sup> AM1.5G illumination. Each cell has the common parts, that is, ITO as the anode contact and TPBI (6 nm)/Al (80 nm) as the cathode.

Device	$V_{oc}$ (V)	$J_{sc}$ (mA/cm <sup>2</sup> )	FF	$\eta_p$ (%)
A CuPc/C <sub>60</sub>	0.50	3.95	0.60	1.19
B MS100 <sup>a</sup>	0.52	9.17	0.45	2.15
MS86	0.49	9.26	0.42	1.94
MS73	0.46	10.25	0.40	1.88
MS67	0.45	9.90	0.40	1.78
C CuPc:C <sub>60</sub> (1:1)	0.40	8.78	0.41	1.44
D MS100 <sup>b</sup>	0.52	7.82	0.37	1.51
MS100 <sup>c</sup>	0.52	8.05	0.44	1.84

<sup>a</sup> MS100 a.

<sup>b</sup> MS100 b.

<sup>c</sup> MS100 c.

the 1:1 homogeneously mixed device. The pure CuPc film has two peaks centered at wavelengths of 620 and 695 nm; the longer wavelength peak is dominant in the gas phase or dilute solution, and the shorter wavelength feature results from molecular aggregation [21]. We observe that the absorbance of the MS100 layer within the absorption wave band of aggregation CuPc is slightly lower than that of the CuPc/C<sub>60</sub> bilayer even though their photoactive materials content are the same. This suggests that the MS100 structure could also inhibit molecular aggregation as a homogeneously mixed structure does, which may lead to reduced carrier transport in the film [19]. However, compared with the standard device (3.95 mA/cm<sup>2</sup>), the  $J_{sc}$  of both the MS100 device and the 1:1 homogeneously mixed device has increased tremendously (Table 1). We suggest that the structural advantages of the MS device

over the standard device lie in the D–A interpenetrating networks morphology and increased charge-separation (CS) interface area, which seems similar to the mixed device. Actually, as evident in Fig. 2b, the apparent effective CS interfacial area in the MS100 layer seems smaller than that of 1:1 homogeneously mixed film. However, the  $J_{sc}$  of the MS100 device reaches 9.17 mA/cm<sup>2</sup>, which is even higher than the aforementioned device (8.78 mA/cm<sup>2</sup>). Thus, aside from the increased CS interfacial area, there must be other plausible reasons behind the increase in  $J_{sc}$  of the MS100 device. Moreover, we observe a minimal increase in the  $V_{oc}$  of the MS100 device and a decrease in the  $V_{oc}$  of CuPc:C<sub>60</sub> (1:1) homogeneously mixed device as compared with the standard device. It seems that the MS100 structure takes the advantages of both a bilayer heterojunction cell (limited by exciton dissociation) and a homogeneously mixed cell (limited by carrier transport).

To understand the effect of concentration gradients of donor and acceptor on the device performance, we prepared a series of four MS devices similar to the MS100 device with different sizes of concentration gradients, where CuPc concentration gradually decreased from 100%, 86%, 73%, and 67% in the first step to 0, 14%, 27%, and 33% in the last step, respectively, as indicated in Fig. 2b (MS100/86/73/67, respectively). Thus, according to the sizes of concentration gradients: MS100 > MS86 > MS73 > MS67 > 1:1 mixed layer. Fig. 3 shows the current density–voltage ( $J$ – $V$ ) characteristics as a function of the sizes of concentration gradients. Interestingly,  $V_{oc}$  increases as the gradient increases, despite the fact that the electrodes and photoactive materials of these devices are the same. Although there are no direct experimental data that could explain such result, the features of exciton solar cells proposed

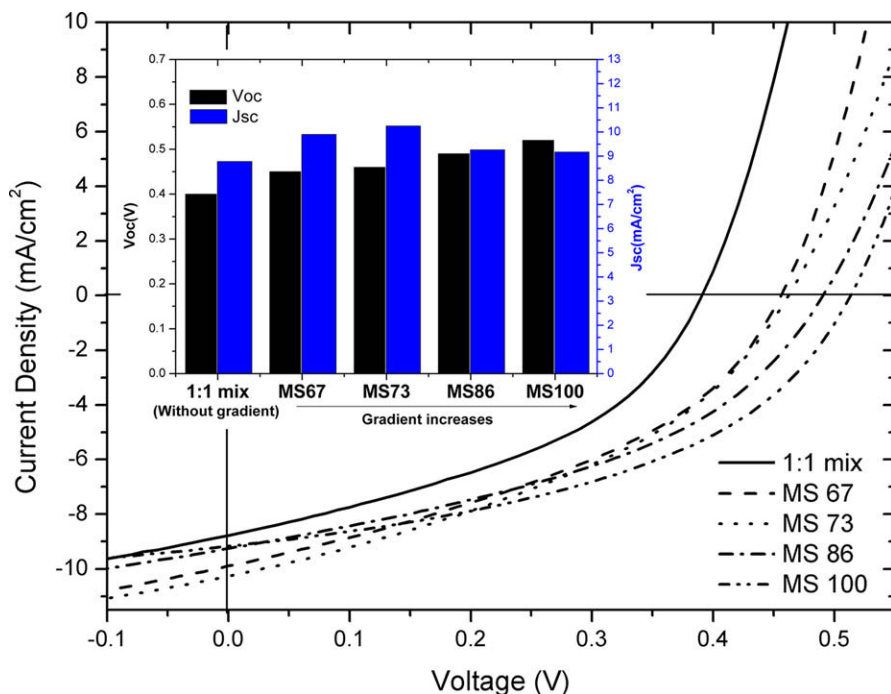


**Fig. 3.**  $J$ – $V$  curves of the devices with the photoactive layers in Fig. 2b under 100 mW/cm<sup>2</sup> AM1.5G illumination. Inset:  $V_{oc}$  vs.  $J_{sc}$  as a function of the sizes of concentration gradients.

by Gregg [6] are adopted. Generally speaking, the  $V_{oc}$  of a solar cell is a function of both the built-in electrical potential energy differences ( $\Phi_{bi}$ ) and the photoinduced chemical potential energy differences ( $\nabla\mu_{hv}$ ) across the cell [6]. According to the expression for the chemical potential energy gradient  $\nabla\mu_{hv} = kT/n(x)\nabla n(x)$ , where  $n(x)$  is the concentration of charge carriers, and  $k$  and  $T$  are Boltzmann's constant and absolute temperature, respectively, the MS device may introduce an extra  $\nabla\mu_{hv}$  because the concentration gradient of donor and acceptor may form a decreasing gradient of "excitons queue" from the center of the photoactive layer to each side. Moreover, the higher concentration gradient of charge carriers (proportional to  $\nabla\mu_{hv}$ ) may produce a higher value of  $\nabla\mu_{hv}$ , which could enhance the  $V_{oc}$  as well. Therefore, the increase in  $V_{oc}$  can be attributed to the increase in  $\nabla\mu_{hv}$ .

Introducing a concentration gradient will also contribute to the improved photogenerated charge carrier transport and a higher gradient may result in a higher  $J_{sc}$  [22–24] because  $\Phi_{bi}$  and  $\nabla\mu_{hv}$  are equivalent forces that drive the current flow of all electronic devices [6]. On the other hand, as shown in Fig. 2b, when the concentration gradient is higher, the apparent effective CS interfacial area seems smaller, which may lead to fewer photogenerated charges and hence a lower  $J_{sc}$ . Based on these two factors, the  $J_{sc}$  displays a different trend from  $V_{oc}$  as shown in Fig. 3. At the extreme case with zero gradient, as the CuPc:C<sub>60</sub> (1:1) homogeneously mixed device, the  $V_{oc}$  and the  $J_{sc}$  are both the lowest. As the gradient is increased, probably owing to the more favorable effect of improved photogenerated charge carrier transport, the  $J_{sc}$  increases at MS67, and then peaks at MS73. A further increase of the gradient leads to a fall in current, probably due to the smaller CS interfacial area and fewer photogenerated charges. However, the FF follows a similar trend to the  $V_{oc}$ . This may result from the reduced resistances across the devices, consistent with improved charge transport due to the increased gradients. Consequently, the MS100 device exhibits the best performance, with  $\eta_p = 2.15\%$  at 1 sun.

According to the expression for the  $\nabla\mu_{hv}$ , when the temperature, pressure, and the concentration of charge carriers are identified, the chemical potential has the only determined value [6]. In the present devices, although the MS100 structure induced a larger  $\nabla\mu_{hv}$ , the  $V_{oc}$  is still a severe limitation probably due to a smaller  $\Phi_{bi}$  at the CuPc/C<sub>60</sub> interface. We note that the highest occupied molecular orbital (HOMO) level of H<sub>2</sub>Pc (5.24 eV) [25] is slightly larger than that of CuPc (5.05 eV) [26]. If CuPc was replaced with H<sub>2</sub>Pc, which may exhibit a similar  $\nabla\mu_{hv}$  due to the similar concentration gradient of charge carriers in the device but a larger  $\Phi_{bi}$  due to the larger HOMO, the  $V_{oc}$  is expected to enhance in addition to  $J_{sc}$ . Indeed, by using H<sub>2</sub>Pc, we observe an increase in the  $V_{oc}$  from 0.52 to 0.54 V as well as the enhancement of  $J_{sc}$  (9.98 mA/cm<sup>2</sup>). Compared with the standard H<sub>2</sub>Pc/C<sub>60</sub> bilayer device, both  $J_{sc}$  and  $V_{oc}$  have been improved simultaneously and the resulting  $\eta_p$  reaches 2.42%. Our results give further space for changing the  $\nabla\mu_{hv}$  or  $\Phi_{bi}$  to improve the efficiency of the MS100 structure.

In sum, we have produced an MS device by dynamic alteration of the relative deposition rates of CuPc and C<sub>60</sub>.

Its  $V_{oc}$  still maintains a high value even though its  $J_{sc}$  is more than twice that of the conventional bilayer device. The multidirectional experiments conducted in this study indicate that the improved photovoltaic performance is possibly due to a high  $\nabla\mu_{hv}$  produced by the concentration gradient of donor and acceptor in addition to a large CS interface in the photoactive layer. Finally, the  $\eta_p$  has been increased from 1.19% of the simple CuPc/C<sub>60</sub> bilayer device to 2.15% of the MS100 device with the largest gradient. By replacing CuPc with H<sub>2</sub>Pc, which can produce a larger  $\Phi_{bi}$  when interacted with C<sub>60</sub>, both  $J_{sc}$  and  $V_{oc}$  have been improved simultaneously and the  $\eta_p$  reaches 2.42%. These results highlight the potential of a co-deposition technique and well-defined structures, wherein through the careful design of co-deposition methods, solar cells improvement based on small molecules could be further achieved.

## Acknowledgments

This research was supported by the National Science Foundation of the People's Republic of China, under Grant Nos. 50673003, 50833001, 309001.

## References

- [1] C.W. Tang, Appl. Phys. Lett. 48 (1986) 183.
- [2] N.S. Sariciftci, L. Smilowitz, A.J. Heeger, F. Wudl, Science 258 (1992) 1474.
- [3] N.S. Sariciftci, D. Braun, C. Zhang, V.I. Srdanov, A.J. Heeger, G. Stucky, F. Wudl, Appl. Phys. Lett. 62 (1993) 585.
- [4] Z.R. Hong, B. Maennig, R. Lessmann, M. Pfeiffer, K. Leo, P. Simon, Appl. Phys. Lett. 90 (2007) 203505.
- [5] R. Koeppel, N.S. Sariciftci, P.A. Troshin, R.N. Lyubovskaya, Appl. Phys. Lett. 87 (2005) 244102.
- [6] B.A. Gregg, J. Phys. Chem. B 107 (2003) 4688.
- [7] C.J. Brabec, N.S. Sariciftci, J.C. Hummelen, Adv. Funct. Mater. 11 (2001) 15.
- [8] G. Yu, J. Gao, J.C. Hummelen, F. Wudl, A.J. Heeger, Science 270 (1995) 1789.
- [9] J.J.M. Halls, C.A. Walsh, N.C. Greenham, E.A. Marseglia, R.H. Friend, S.C. Moratti, A.B. Holmes, Nature 376 (1995) 498.
- [10] G. Yu, A.J. Heeger, J. Appl. Phys. 78 (1995) 4510.
- [11] M. Granström, K. Petritsch, A.C. Arias, A. Lux, M.R. Andersson, R.H. Friend, Nature 395 (1998) 257.
- [12] A. Pivrikas, N.S. Sariciftci, G. Juška, R. Österbacka, Prog. Photovoltaics: Res. Appl. 15 (2007) 677.
- [13] M. Drees, R.M. Davis, J.R. Hefflin, J. Appl. Phys. 97 (2005) 036103.
- [14] C.R. McNeill, S. Westenhoff, C. Groves, R.H. Friend, N.C. Greenham, J. Phys. Chem. C 111 (2007) 19153.
- [15] S. Miller, G. Fanchini, Y.-Y. Lin, C. Li, C.-W. Chen, W.-F. Su, M. Chhowalla, J. Mater. Chem. 18 (2008) 306.
- [16] P. Peumans, S. Uchida, S.R. Forrest, Nature 425 (2003) 158.
- [17] P. Sullivan, S. Heutz, S.M. Schultes, T.S. Jones, Appl. Phys. Lett. 84 (2004) 1210.
- [18] B.P. Rand, J. Xue, S. Uchida, S.R. Forrest, J. Appl. Phys. 98 (2005) 124902.
- [19] S. Uchida, J. Xue, B.P. Rand, S.R. Forrest, Appl. Phys. Lett. 84 (2004) 4218.
- [20] B.P. Rand, J. Genoe, P. Heremans, J. Poortmans, Prog. Photovoltaics: Res. Appl. 15 (2007) 659.
- [21] O.E. Sielcken, M.M. van Tilborg, M.F.M. Roks, R. Hendriks, W. Drenth, R.J.M. Nolte, J. Am. Chem. Soc. 109 (1987) 4261.
- [22] B.T. Boiko, G.S. Khripunov, V.B. Yurchenko, H.E. Ruda, Sol. Energy Mater. Sol. Cells 45 (1997) 303.
- [23] F. Smole, J. Furlan, J. Appl. Phys. 72 (1992) 5964.
- [24] S. Sinharoy, M.O. Patton, T.M. Valko, V.G. Weizer, Prog. Photovoltaics: Res. Appl. 10 (2002) 427.
- [25] M. Hiramoto, H. Fujiwara, M. Yokoyama, J. Appl. Phys. 72 (1992) 3781.
- [26] A. Kahn, N. Koch, W. Gao, J. Polym. Sci. Part B: Polym. Phys. 41 (2003) 2529.

surrounding the channel width effect has been carried out in field effect transistors based on metal oxide silicon [10], poly-crystalline silicon [11], or hydrogenated amorphous silicon [12] and thus the channel width effects on the OTFT's performance are not well known at the present time.

This work focuses on the three issues as follows: (1) thin film study of 6,13-bis(triisopropyl-silylethynyl)-pentacene (TIPS-pentacene) with semiconducting polymer binder (poly-triarylamine, PTAA) in order to impose a function as forming a good interfacial contact between the organic semiconductor (OSC) and the source/drain electrodes; (2) employing two kinds of metals, one with a low work function (Ag) and the other with a high work function (Au), in order to compare the function of metallurgy for low cost devices; and (3) a structural study of the channel dimension in order to optimize the device parameters effectively and to obtain good performance of the device characteristics.

## 2. Experimental

Fig. 1c shows a schematic diagram of the OTFT structure where an insulator layer of silicon dioxide ( $\text{SiO}_2$ ) is thermally grown on top of a heavy doped p-type Si wafer to act as the gate contact. A highly doped p-type Si wafer was used both as a substrate and as a gate electrode for the bottom-contact structure. Initially, the gate insulator, for most of the devices, was thermally grown to a thickness of 100 nm. Sequentially, a 200 nm-thick source-drain Au and Ag contacts were fabricated on top of the insulator

by a thermal evaporation method (DOV Co., Ltd) to give the channel widths in the range of 500–2500  $\mu\text{m}$ , and the channel length of 100  $\mu\text{m}$  using a shadow mask. Particularly, the source-drain interdigitatd finger (SDIF) type electrode were employed in our device configuration since this SDIF pattern permits the use of printing and other techniques for fabricating display backplanes that are not capable of attaining the fine resolution limits of standard silicon processing using photolithography. Next, the TIPS-pentacene mixed with PTAA were deposited by a drop casting from a 2 wt% solution of TIPS-pentacene in monochlorobenzene. Fig. 1a and b exhibit the molecular structures of TIPS-pentacene and PTAA, respectively. In our sample, PTAA was employed as a dopant and TIPS-pentacene was used as a host material. Also, in order to improve device performance, polymer binder, PTAA was employed to fabricate OTFT device with organic soluble TIPS-pentacene for decreasing the injection barrier from the metal electrode to the OSC and used as a hole conductor between the OSC and source-drain contacts for reducing the surface dipoles [13]. Here, TIPS-pentacene was synthesized following the procedure reported by our previous study [14]. PTAA was synthesized by following the literature method and a modified method [15–18]. All reactions were performed under an argon atmosphere unless otherwise stated. Finally, after coating the OSC, the device was annealed using a hotplate at 110  $^\circ\text{C}$  for 1 min.

The optical absorption spectra of the host-guest (TIPS-pentacene-PTAA) system film was obtained using UV spectrometry (Ultraviolet–visible, UV-vis, HP 8453, PDA, type  $\lambda = 190\text{--}1100\text{ nm}$ ). The surface morphology of the OSC lay-

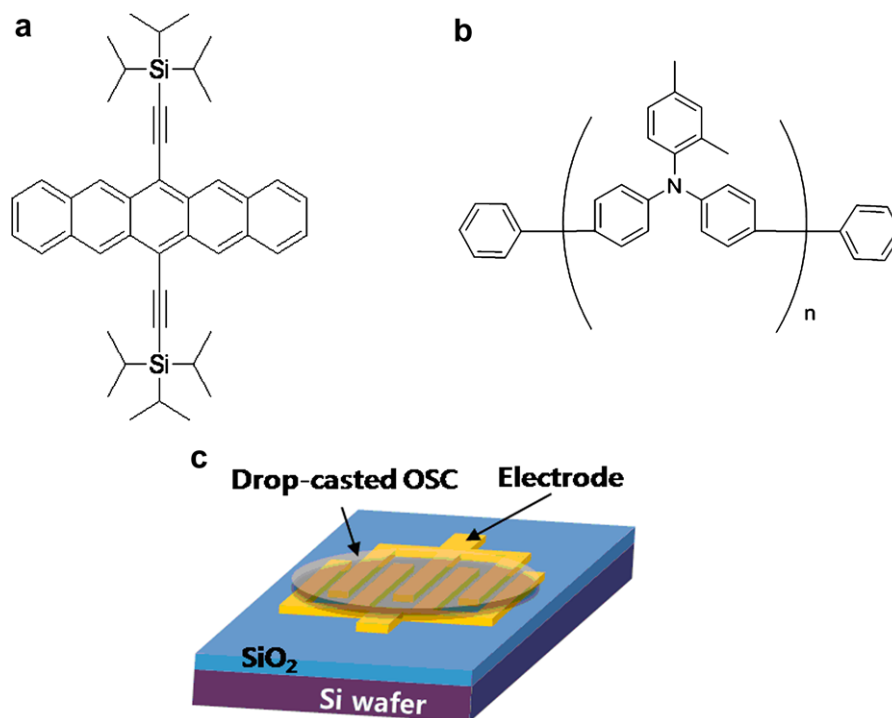


**Fig. 1.** The molecular structure of (a) TIPS-pentacene, (b) PTAA and (c) the schematic geometry of the OTFT on heavy doped silicon wafer with SDIF bottom contacts varying the  $W/L$  ratio from 25 down to 5 (channel length: 100  $\mu\text{m}$ ).

ers was observed using an AFM (XE-100 system). The transistor characteristics were measured using a Keithley SCS/4200 in a dark box.

### 3. Result and discussion

Fig. 2a shows the optical absorption spectra of the host-guest (TIPS-pentacene-PTAA) system film. Each spin-coated thin film (1 wt% solution) was formed by using the monochlorobenzene solvent. OSC films with 1:1 or 10:1 weight ratio mixture of TIPS-pentacene and PTAA were measured individually before and after the annealing process, as shown in Fig. 2a. The spectrum of TIPS-penta-

cene shows the crystalline properties, confirmed by the baseline floating phenomenon. When preparing the thin film without polymer binder, the quality of the surface of OSC was not well defined. Whereas, after mixing PTAA with a proper concentration, we could obtain much better film forming property. Therefore, the OSC was prepared with TIPS-pentacene and PTAA for improving film forming properties in a large area using the host-guest system, which produces a better film condition than the OSC without the polymer binder. Additionally, as it can be observed from the spectrum of Fig. 2a, the crystalline properties of the OSC film with 1:1 (TIPS-pentacene:PTAA) is not relatively lower than that with 1:10 (TIPS-pentacene:PTAA).

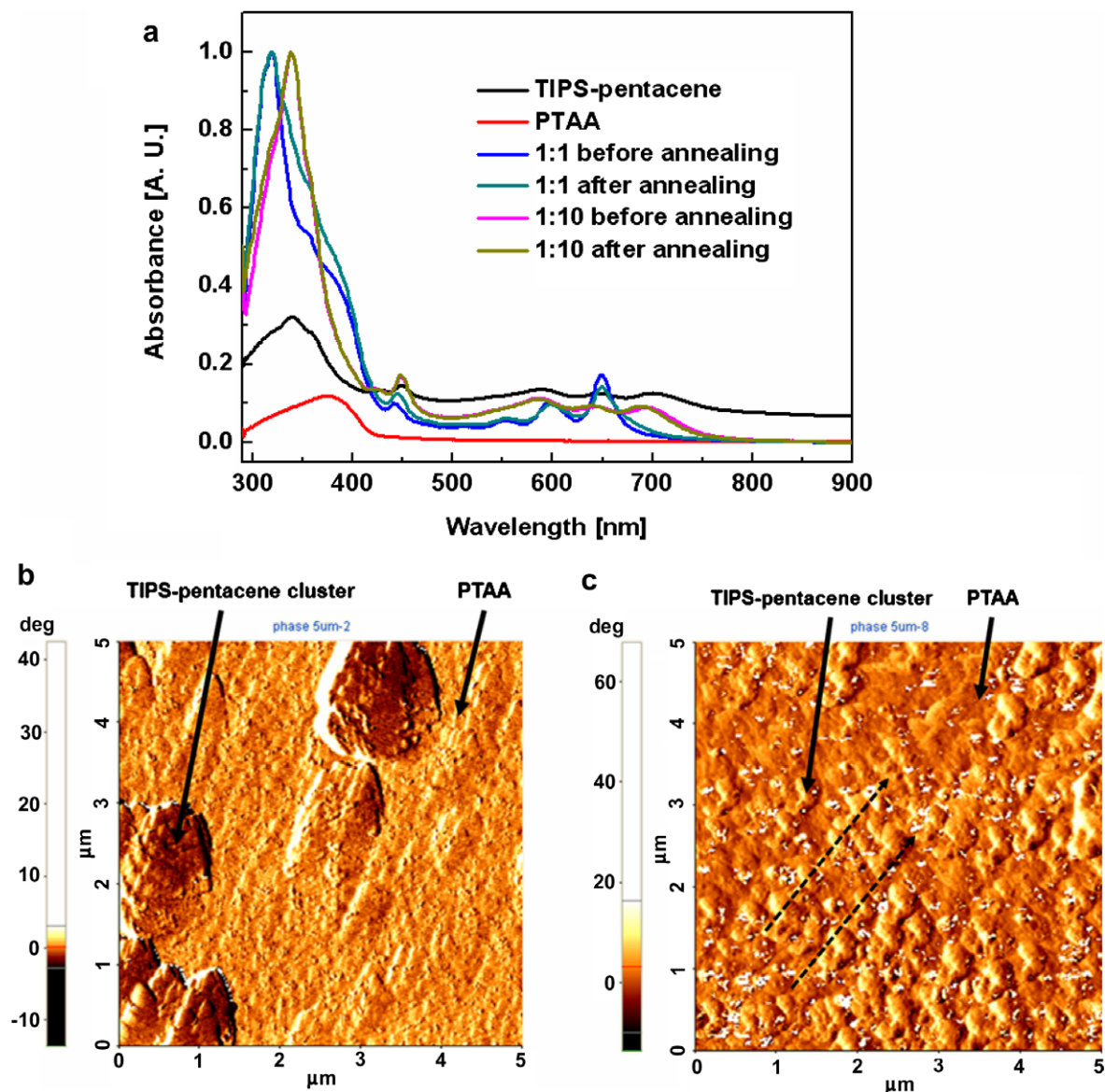


**Fig. 2.** (a) UV-vis spectra of thin films of spin-coated TIPS-pentacene (black), PTAA (red), OSC (TIPS-pentacene: PTAA = 1:1) film before annealing (blue), OSC (TIPS-pentacene: PTAA = 1:1) film after annealing (dark cyan), OSC (TIPS-pentacene: PTAA = 10:1) film before annealing (magenta), and OSC (TIPS-pentacene: PTAA = 10:1) film after annealing (dark yellow), individually. AFM images of OSC films for 1:1 (b) and 10:1 (c) weight ratio mixture of TIPS-pentacene and PTAA, respectively, after annealing. Scan size: 5 μm × 5 μm. (For interpretation of the references to color in this figure legend, the reader is referred to the web version of this article.)

Fig. 2b and c shows AFM (atomic force microscope) images of the OSC films for 1:1 and 10:1 weight ratio mixtures of TIPS-pentacene and PTAA after annealing, respectively. Bright areas in the images indicate higher values of the film thickness. Fig. 2b is a topographic image of the OSC film with 1:1 (TIPS-pentacene: PTAA) that shows discontinuous  $\sim 1 \mu\text{m}$ -TIPS-pentacene clusters, while Fig. 2c is the OSC film with 10:1 (TIPS-pentacene: PTAA) that shows continuous OSC film with regularly formed 20–30 nm-TIPS-pentacene clusters. It was clearly seen that the surface film showed straight line without any preferential orientation (dotted arrow in inset of Fig. 2c). Although good film has been obtained using the polymer binder, as shown in Fig. 2a, the TIPS-pentacene cluster can be a cause of poor carrier field effect mobility due to interference with the flowing carriers in the active channel. Therefore, the OSC (i.e., 10:1 weight ratio mixture of the TIPS-pentacene

and PTAA) film, formed by drop casting a 2 wt% solution in monochlorobenzene, was prepared. As smaller concentration of polymer binder is used, the preferential orientation of TIPS-pentacene molecules is sustained on the surface of the blend film.

Fig. 3a and c shows the output characteristics of OTFTs with  $L = 100 \mu\text{m}$  and  $W = 2500 \mu\text{m}$ . The gate voltage ( $V_G$ ) was increased in a stepwise manner from 0 V to  $-40$  V for OTFTs with different electrodes of Au and Ag, respectively. Obviously, the output confirms typical characteristics of p-type OTFTs working in an accumulation mode. Fig. 3a and c shows that the drain-source current ( $I_{DS}$ ) also saturates at an increasingly higher drain-source voltage ( $V_{DS}$ ) with increasing  $V_G$ . However, the data in Fig. 3a and c shows that the linear and saturation regimes for each curve cannot be clearly distinguished, especially at high values of the gate bias,  $V_G$ , and when there is a lack of sat-

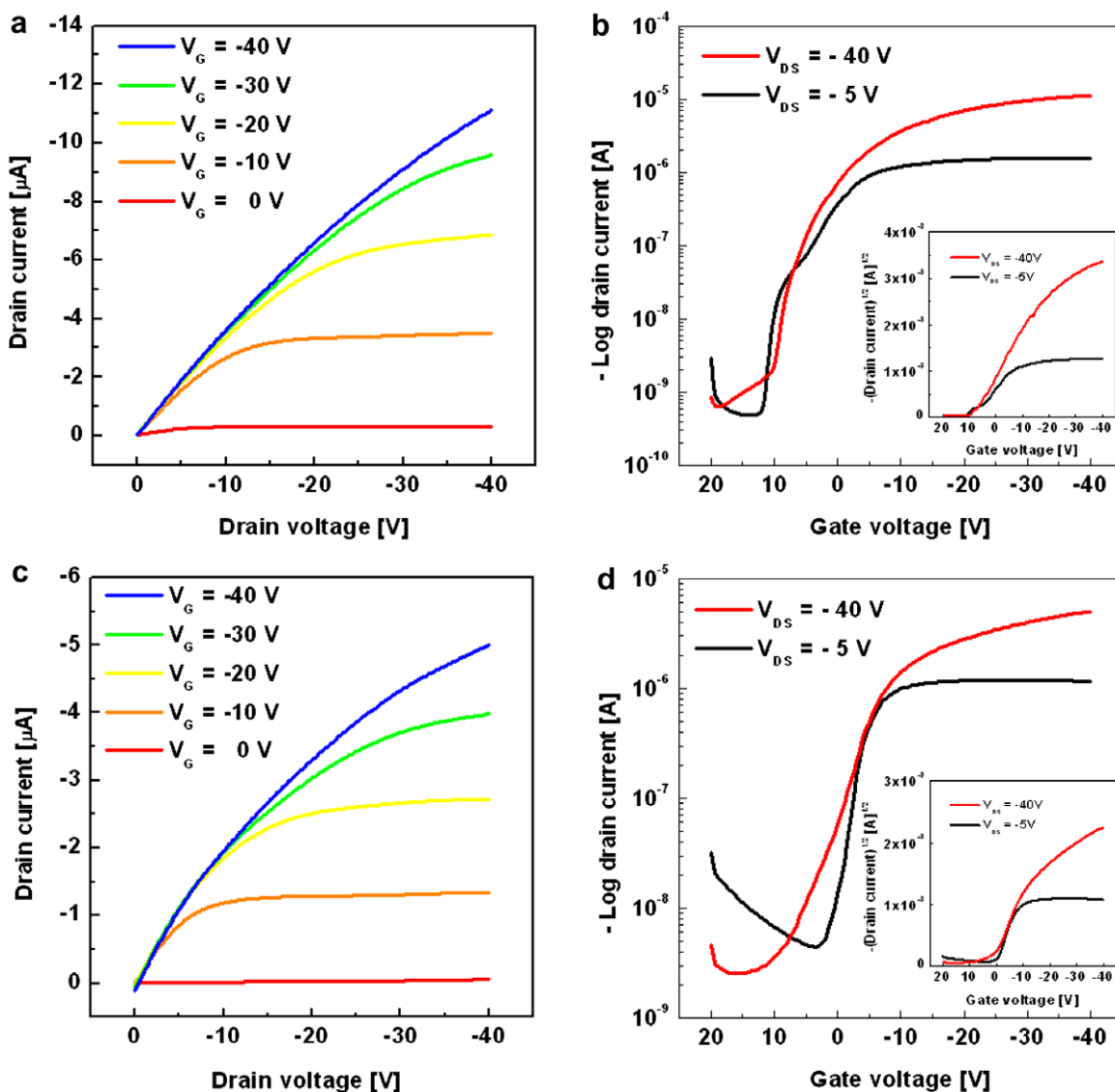


Fig. 3. Output characteristics  $I_{DS}$  vs.  $V_{DS}$  for OTFTs with different electrodes of Au (a) and Ag (c). Transfer characteristics  $-\log(I_{DS})$  vs.  $V_G$  and  $-\sqrt{I_{DS}}$  vs.  $V_G$  (inset) measured for an OTFT ( $W/L = 2500 \mu\text{m}/100 \mu\text{m}$ ) with Au contact (b) and Ag contact (d), respectively.



uration in  $I_{DS}$ . We believe this phenomenon, similar to the ‘punch-through effect’ [19] for the metal-oxide-semiconductor field effect transistor (MOSFET), which is caused by space charge limiting current [20], is preventing saturation.

Fig. 3b and d shows graphs of  $-\log(I_{DS})$  against  $V_G$  with their insets,  $-\sqrt{I_{DS}}$  vs.  $V_G$ , for Au and Ag contacts, respectively. For each device, the carrier field effect mobility and the threshold voltage ( $V_T$ ) were extracted in the linear ( $V_{DS} = -5$  V) and saturation ( $V_{DS} = -40$  V) regimes at a  $V_G$  of  $-40$  V, where the results are shown in Fig. 4. Additionally, OTFTs with a channel length of  $100 \mu\text{m}$  and a channel width range from  $500$  to  $2500 \mu\text{m}$  were fabricated for different electrodes. However, all devices, regardless of their channel widths, exhibited a current on/off ratio between  $10^4$  and  $10^5$  for Au contacts, and between  $10^3$  and  $10^4$  for Ag contacts.

The data in Fig. 4 represent average values of device parameters such as field effect mobility and  $V_T$  when using

Au and Ag electrodes. Here, we measured at least four devices to average the parameters for these plots.

In order to explore the effects of different source-drain electrodes on the performance of OTFTs, two kinds of electrodes having different work-functions were employed. Fig. 4 shows the transistor parameters of devices with Au and Ag electrode materials as source-drain contacts. It also shows the variation of carrier mobility and  $V_T$  as functions of the channel width  $W$  for devices with constant channel length  $L = 100 \mu\text{m}$ . The decreasing behaviors of carrier mobilities in both saturation and linear regimes with increase in channel width are observed from Fig. 4a and b, where the saturation mobility depended much more on the channel width than the linear mobility. Moreover, with increasing the channel width from  $500 \mu\text{m}$  to  $2500 \mu\text{m}$ ,  $V_T$  is increased, as shown in Fig. 4c and d. These results, variation of carrier mobility and  $V_T$  as function of channel width, are in good agreement with previously reported work using inorganic TFT [11,12].

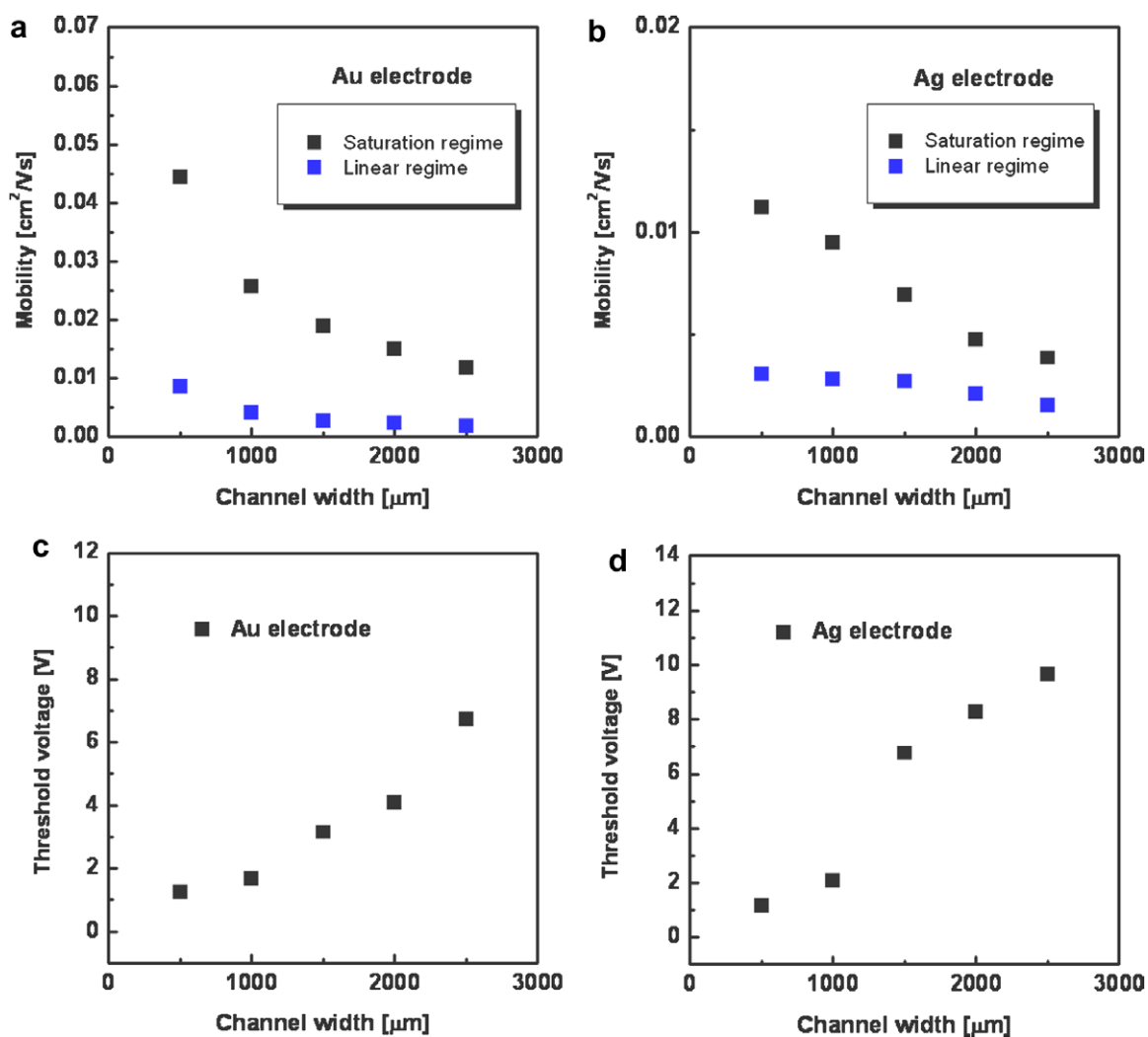


Fig. 4. Carrier field effect mobilities of Au contact (a) and Ag contact (b), and threshold voltage of Au contact (c) and Ag contact (d), extracted from the transfer characteristics. The channel widths range from  $500$  to  $2500 \mu\text{m}$ ; the channel length is  $100 \mu\text{m}$  in all cases. The carrier mobilities were extracted at a  $V_G$  of  $-5$  V and  $-40$  V, respectively.

The field effect mobility increases with decreasing channel width, while  $V_T$  increases with increasing channel width in the saturation ( $V_{DS} = -40$  V) and linear ( $V_{DS} = -5$  V) regimes. Here, the  $I_{DS}$  of the devices increases with increasing channel width [10] since the transistor channel width to length ratio, which means larger  $I_{DS}$ , is proportional to the larger channel width. Although  $I_{DS}$  increases with increasing channel width [21], saturation and linear mobility reduce with increasing channel width since  $V_T$  increases. This, in turn, results not only in a significant increase in  $V_T$  but also in its pronounced channel width dependency.

#### 4. Conclusion

In summary, in order to enhance device performance, TIPS-pentacene was employed as a host materials and a small amount of PTAA was used as a guest material. The host-guest system gave improved and uniform film formation in a large area, and helped the TIPS-pentacene to form a stronger binding between the source/drain electrodes onto the dielectric layer. Additionally, the devices were fabricated using different electrodes such as Au and Ag. Maximum saturation mobilities of  $5.44 \times 10^{-2}$  and  $1.33 \times 10^{-2}$  cm<sup>2</sup>/Vs for OTFTs were obtained using Au and Ag contacts, respectively. From these results, it can be predicted that Ag-based devices would be expected to provide dramatic reductions in cost and to significantly improve the device performance upon full optimization. Finally, experimental observations showed that the field effect mobility depends on  $V_T$ . Although the field effect mobility values should increase as  $I_{DS}$  is proportionally increased, by increasing channel width, decrease in mobility were observed since  $V_T$  also increased.

#### Acknowledgements

This work was supported by the National Research Laboratory (NRL, No. R0A-2007-000-20111-0) Program of the Ministry of Education, Science and Technology (Korea Sci-

ence and Engineering Foundation, KOSEF), the KOSEF grant funded by the Korea Ministry of Education, Science and Technology (MEST) (No. R11-2007-045-01003-0) and the KRF Grant funded by the Korean Government (MOEHRD) (KRF-2007-511-D00099). Particularly, D.H. Choi acknowledges the financial support by 21<sup>st</sup> Century Frontier Research Program (2008–2009).

#### References

- [1] R. Rotzoll, S. Mohapatra, V. Olariu, R. Wenz, M. Grigas, K. Dimmler, O. Shchekin, A. Dodabalapur, *Appl. Phys. Lett.* 88 (2006) 123502.
- [2] K. Tsukagoshi, J. Tanabe, I. Yagi, K. Shigeto, K. Yanagisawa, *J. Appl. Phys.* 99 (2006) 064506.
- [3] L. Zhou, A. Wang, S.-C. Wu, J. Sun, S. Park, T.N. Jackson, *Appl. Phys. Lett.* 88 (2006) 083502.
- [4] T. Someya, Y. Kato, T. Sekitani, S. Iba, Y. Noguchi, Y. Murase, H. Kawaguchi, T. Sakurai, *Proc. Natl. Acad. Sci. USA* 102 (2005) 12321.
- [5] J.H. Kwon, S.H. Lee, B.K. Ju, *J. Appl. Phys.* 101 (2007) 104515.
- [6] H. Sirringhaus, T. Kawase, R.H. Friend, T. Shimoda, M. Inbasekaran, W. Wu, E.P. Woo, *Science* 290 (2000) 2123.
- [7] G. Leising, B. Stadlober, U. Haas, A. Haase, C. Pfalinger, H. Gold, G. Jakopic, *Microelectron. Eng.* 83 (2006) 831.
- [8] G.P. Crawford, *Flexible Flat Panel Displays*, John Wiley & Sons Ltd., 2005 (Chapter 21), p. 409.
- [9] C.R. Kagan, P. Andry, *Thin-film Transistors*, Marcel Dekker Inc., 2003. Part I, p. 43.
- [10] Y.R. Ma, K.L. Wang, *IEEE Trans. Electron Dev.* ED-29 (1982) 1825.
- [11] Y.-C. Wu, T.-C. Chang, P.-T. Liu, C.-S. Chen, C.-H. Tu, H.-W. Zan, Y.-H. Tai, C.-Y. Chang, *IEEE Trans. Electron Dev.* 52 (2005) 2343.
- [12] A.T. Hatzopoulos, N. Arpatzianis, D.H. Tassis, C.A. Dimitriadis, F. Templier, M. Oudwan, G. Kamarinos, *IEEE Trans. Electron Dev.* 54 (2007) 1265.
- [13] N. Koch, J. Ghijsen, A. Elschner, R.L. Johnson, J.-J. Pireaux, J. Schwartz, A. Kahn, *Appl. Phys. Lett.* 82 (2003) 70.
- [14] J.H. Kwon, J.H. Seo, S.I. Shin, K.H. Kim, D.H. Choi, I.B. Kang, H. Kang, B.K. Ju, *IEEE Trans. Electron Dev.* 55 (2008) 500.
- [15] Z. Yu, S. Tan, Z. Yuan, Y. Zou, B. Fan, Y. Li, *J. Mater. Sci.* 42 (2007) 1325.
- [16] C.-G. Wu, Y.-C. Lin, C.-E. Wu, P.-H. Huang, *Polymer* 46 (2005) 3748.
- [17] J. Veres, S. Ogier, S. Leeming, B. Brown, D. Cupertino, *Mater. Res. Soc. Symp. Proc.* 708 (2002) BB 8.7.1.
- [18] J.H. Kwon, S.I. Shin, K.H. Kim, M.J. Cho, K.N. Kim, D.H. Choi, B.K. Ju, *Appl. Phys. Lett.* 94 (2009) 013506.
- [19] B.G. Streetman, S. Banerjee, *Solid State Electronic Devices*, fifth ed., Prentice Hall, New Jersey, 2000, p. 192.
- [20] J.G. Lee, Y.G. Seol, N.-E. Lee, *Thin Solid Films* 515 (2006) 805.
- [21] J.H. Kwon, J.H. Seo, S.I. Shin, B.K. Ju, *J. Phys. D-Appl. Phys.* 42 (2009) 065105.

poorer electrical/thermal stability [14] compared to metals. Metal nanoparticle (NP) based inks are more often used to demonstrate solution-based, highly conductive pathways and contacts, generally obtained by sintering via annealing at relatively low temperatures [15,16], or else by laser [17] or microwave [18] treatment. These conductive metals have for example been used in the production of thin-film transistors (TFTs), where they serve as source and drain electrodes [19]. Their deposition on top of organic semiconductors, however, is challenging because organic materials are damaged either by the temperatures required for sintering the NPs or by the solvent dissolving the underlying layer. Most of the research has thus focused on the production of bottom-contact devices, where ink-jet printing has been used to pattern lines on the substrates, either glass, silicon or plastic foils. In this way, the constraints on the process are not severe, since the sintering temperature and solvent choice are only limited by the substrate.

The deposition of metal NPs on top of organic semiconductors requires, then, to overcome these two limitations. Recently, Sekitani et al. produced top contact TFTs with a silver solution deposited directly onto the surface of organic semiconductor films using a subfemtoliter ink-jet printer [20]. Noguchi et al. showed that it is important to deposit small volumes of a silver ink on top of the organic material in order to limit the degradation of the transistor performance caused by a large amount of solvent [21]. Their work shows that reducing the volume of each droplet makes it possible to manufacture TFTs with characteristics comparable to those with vacuum evaporated top contacts. Nevertheless, this deposition method is not easily applicable to organic solar cells, where the need for a fast deposition technique able to cover large area contacts is contradictory to the precise deposition of well aligned, micron-scale droplets. An attempt to produce solar cells with an inkjet printed silver top contact can be found in the work by Eom et al., albeit for devices with a limited performance [22]. In this work, we spray coat a Ag NP film followed by sintering at low temperatures to achieve a solution processed and patterned metal contact deposited directly on top of the organic device, yielding solar cells with efficiencies very close to those with evaporated top contacts [23].

Spray coating is a well established technique in graphic arts, industrial coatings, and painting. In spray coating systems, the ink is atomized at the nozzle by pressure or ultrasounds and then directed toward the substrate by a gas flow. A random distribution of tiny droplets then land on the surface producing either a full wet layer, in the case of large flow rates, or depositions characterized by sparse arrangements of dots that dry independently, in the case of reduced flow rates [11]. The key advantage of the technique is the ability to cover relatively large areas by the superposition of femtoliter-size droplets, characterized by a fast drying time on the order of  $\mu\text{s}$  [24,25]. As a consequence, the impact of the solvent on the underlying layer is reduced as compared to other solution based deposition techniques, considering that subsequent droplets are deposited on top of dried droplets rather than directly on the underlying layer.

In this study, we deposited a silver nanoparticle ink (25 wt% silver ( $\varnothing = 5 \text{ nm}$ ) in cyclohexane, NanoMas Technologies, Inc.) using a commercially available airbrush (Badger 200 NH) powered by  $\text{N}_2$  gas to spray a 0.5 cm wide pattern of droplets characterized by volume on the order of femtoliters, as deduced from a statistical analysis performed on sparse depositions. Standard settings included gas pressure of 20 psi and an airbrush-substrate distance of approximately 10 cm. We achieved a uniform coverage of the complete sample by moving the airbrush across the substrate ( $1.25 \text{ cm} \times 1.25 \text{ cm}$ ) and patterned the deposition by simple shadow masking.

In order to define the optimal temperature and time conditions to obtain highly conductive contacts, we first investigated the behavior of the material on glass substrates. With the airbrush, we sprayed a 200–400 nm thick film on pre-cleaned samples (acetone and isopropanol, 10 min each in ultrasonic bath) between two indium-tin oxide (ITO) stripes, the latter to provide an easy contact for probes. We first probed and connected the structure to a parameter analyzer (Agilent 4156C) and only then put the samples in contact with a pre-heated hot plate at a fixed temperature. The resistance of the silver pads was then recorded versus time for a period of 10 min. We corrected the curve to the final resistivity ( $\rho$ ) of each sample, calculated via  $\rho = R_{\square} \cdot d$ , where  $R_{\square}$  is the sheet resistance, evaluated at room temperature with a four probe station (FPP 5000 Veeco Instruments Inc.), and  $d$  is the average thickness of the deposition (Dektak V 200-Si profilometer). This was done to eliminate the geometry and temperature dependence of the resistance measurements. The results are plotted in Fig. 1 for a range of temperatures between 100 °C and 180 °C along with the resistivity of 100 nm ITO and 100 nm evaporated Ag.

The resistivity of the films dropped rapidly to  $10^2 \mu\Omega \text{ cm}$ , by several orders of magnitude, after a critical annealing time, which depends on the annealing temperature. An annealing time of the order of a few seconds is sufficient for annealing temperatures above 150 °C. The resistivity of the layer typically saturates at values around 40–100  $\mu\Omega \text{ cm}$ . Interestingly, these values are close to those obtained with the evaporated Ag layer (24  $\mu\Omega \text{ cm}$ ): the higher final resistivity of the sprayed depositions could be explained by their roughness, with peak-to-valley

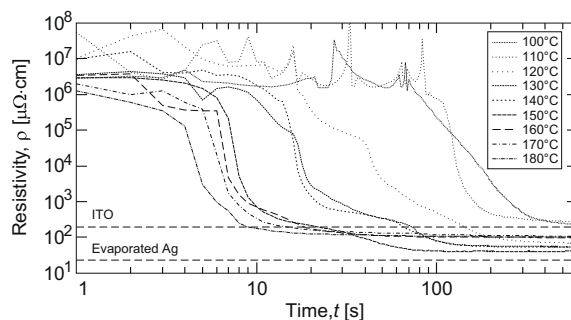


Fig. 1. Resistivity ( $\rho$ ) of Ag nanoparticles during sintering recorded versus time,  $t$ . Measured values of  $\rho$  for ITO and vacuum evaporated Ag are reported as reference.

values in the order of a few tens of nanometers, and the presence of voids inside the layer. The calculation of resistivity was performed on the average thickness for these samples, while the minimum thickness greatly impacts the electrical performance of the layer.

The curves in Fig. 1 show a two step profile, revealing a two phase characteristic of the sintering process [19]. In order to understand this, we should recall that the NP solution is composed of Ag NPs capped by a functional group that prevents their aggregation and allows them to be dispersed in the solvent. After the deposition, the solvent evaporates leaving an agglomerate of NPs still capped by the functional group, which insulate them from each other. The resistivity of the layer at this stage is extremely large ( $10^6$ – $10^8 \mu\Omega \text{ cm}$ ). The first step of the thermal treatment thus removes the thin capping layer and allows for direct contact between NPs, creating conductive percolating paths: curves show a sudden change in the resistivity at this point when the layers also become reflective. However, the conduction is still restrained by the limited contact between the NPs. The second step is then the effective sintering process, where the Ag NPs coalesce together into larger aggregates, resulting in a highly conductive film [19,26]. The process is activated at temperatures as low as  $100^\circ\text{C}$  indicating a high surface energy of the NPs owing to their small size [27]. From this analysis we can deduce that the two fundamental characteristics of an ink suitable for a top contact are the presence of functional groups that evaporate or decompose at low temperatures ( $<150^\circ\text{C}$ ) and an average size of the NPs limited to values in the nanometer range ( $<10 \text{ nm}$ ). From scanning electron microscopy (SEM, Fig. 2) imaging of the top surface, performed on the samples treated at  $100^\circ\text{C}$ ,  $140^\circ\text{C}$  and  $180^\circ\text{C}$ , it is clear that the increase of the sintering temperature is concomitant with an increase of agglomerate size.

Fig. 3 plots the annealing time for the layer to reach a threshold resistivity of  $\rho_t = 1 \text{ m}\Omega \text{ cm}$  as well as the final resistivity  $\rho$  after the 10 min sintering treatment, both versus the applied temperature. The temperature dependence of the time to reach the threshold  $\rho_t$  follows a simple Arrhenius relation, as expected from a thermally-induced process. The data points can be fitted with an exponential law, represented by the equation:

$$t = t_i + t_0 \cdot e^{-E_a/kT_s} \quad (1)$$

where  $k$  is Boltzmanns constant and  $T_s$  is the sintering temperature. The initial delay  $t_i = 3.0 \text{ s}$ , calculated from

$$\frac{\partial^2 T}{\partial x^2} = \frac{\rho c}{k} \frac{\partial T}{\partial t} \quad (2)$$

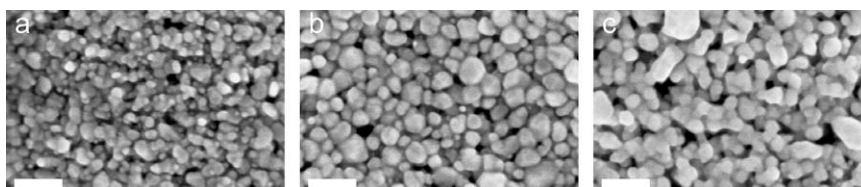


Fig. 2. Scanning electron micrographs of Ag nanoparticle layers annealed at (a)  $100^\circ\text{C}$ , (b)  $140^\circ\text{C}$  and (c)  $180^\circ\text{C}$  show that the increase of the sintering temperature is concomitant with an increase of agglomerate size. The white scale bars represent  $100 \text{ nm}$ .

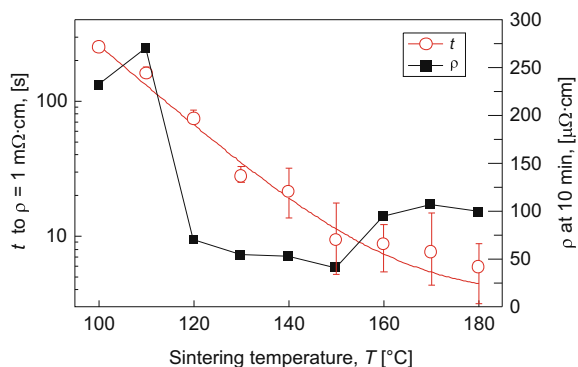


Fig. 3. Time,  $t$ , to reach a threshold resistivity,  $\rho_t$ , of  $1 \text{ m}\Omega \text{ cm}$  and  $\rho$  of the samples at 10 min sintering versus the applied temperature. The red curve shows the exponential fit using Eq. (1). (For interpretation of the references to colour in this figure legend, the reader is referred to the web version of this article.)

has been introduced to consider the time needed to heat the top surface of the glass substrate (thickness =  $0.7 \text{ mm}$ ) to 95% of the final temperature. The activation energy  $E_a$  required by the NPs can be calculated from Eq. (1) as  $0.211 \text{ eV}$ . The time needed to reach the threshold  $\rho_t$  is almost halved for every  $10^\circ\text{C}$  increment of the applied temperature, resulting in a drop from  $254 \text{ s}$  at  $100^\circ\text{C}$  to less than  $6 \text{ s}$  at  $180^\circ\text{C}$ . The final  $\rho$  after the 10 min treatment shows that temperatures as low as  $100^\circ\text{C}$  are sufficient to achieve conductive contacts. Nevertheless, the resistivity of the films treated with temperatures below  $120^\circ\text{C}$  is higher than that of ITO and thus not favorable as a top contact. The resistivity plot shows a minimum at  $150^\circ\text{C}$ : at higher temperatures the NPs sinter into domains that become large enough that voids are introduced between neighboring domains (*cf.* Fig. 2c), thus limiting the conductivity.

At  $150^\circ\text{C}$  the film resistance reaches saturation after 120 s, an interval that is shorter than the typical annealing conditions for organic solar cells based on poly(3-hexyl thiophene) (P3HT) and (6,6)-phenyl C61-butyric acid methyl ester (PCBM) mixture. Post annealing treatments are often performed at temperatures in the range of  $130$ – $150^\circ\text{C}$  for time intervals in the range of 5–10 min. Since our standard post-production annealing conditions for P3HT:PCBM organic solar cells consist of 300 s at  $150^\circ\text{C}$ , our process already satisfies the requirement for the sintering of the top contact, without the need to introduce further thermal treatments.

Silver is characterized by a work function of  $-4.3 \text{ eV}$  that shifts towards  $-5.0 \text{ eV}$  for silver oxide [28]. This shift

should be taken into account when employing NPs, since their large surface-to-volume ratio renders them extremely sensitive to oxidation. The work function makes Ag more suitable as a hole collecting rather than as an electron collecting contact. The ideal structure in order to use Ag as a top contact is therefore a reverse structure, as demonstrated by White et al. [28]. Among the different reverse structures suggested [28–31], the one comprising a thin zinc oxide (ZnO) NP film between ITO and the active layer as a cathode is attractive because it can be processed from solution [28,32]. On top of the active layer, a thin film of PEDOT:PSS is usually spin coated [29,30,33,32], producing at the same time a hole-selective interlayer, a protection for the active layer and a smooth surface for a silver top contact. Since the HOMO level of PEDOT:PSS is positioned at  $-5.1$  eV from the vacuum level, it is clear that an oxidation of silver during the deposition is not detrimental to the functioning of the contact, but rather improves the ohmic contact between the two materials.

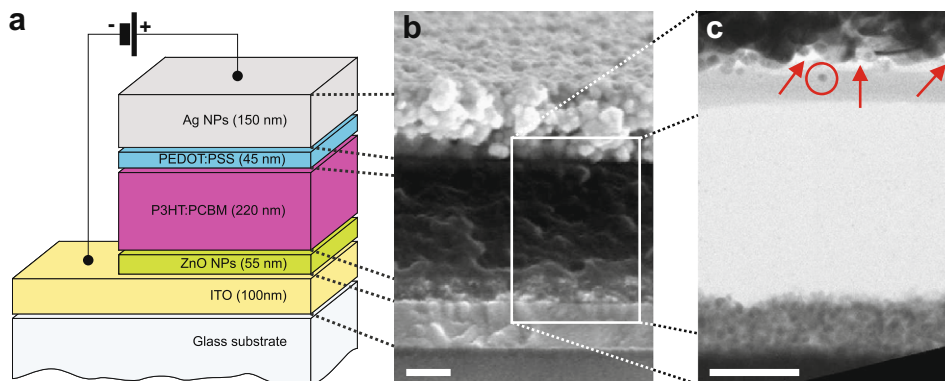
Devices have been produced according to the steps previously introduced in an all-solution process on top of patterned ITO-glass samples (Merck Display Technologies, ITO thickness 100 nm, sheet resistance  $<20 \Omega/\square$ ).

Samples were first cleaned by detergent, de-ionized water, acetone and isopropyl alcohol in an ultrasonic bath. A dispersion of ZnO NPs in acetone was spin coated in air on the samples to produce a 55 nm thick layer. After a 10 min annealing step on a hot plate at  $150^\circ\text{C}$ , samples were brought in a nitrogen glovebox for the deposition of the active layer. A solution of P3HT (Rieke Metals) and PCBM (Solenne) dissolved in *ortho*-dichlorobenzene (oDCB) in a 1:1 ratio with a concentration of 30 mg/ml was prepared and stirred for 24 h at  $50^\circ\text{C}$ . Spin coating was performed at 1000 rpm for 60 s (resulting thickness: 250 nm) and then samples were allowed to dry under a petri-dish, according to the “slow drying” method [34,35]. The hydrophobic surface of the P3HT:PCBM layer was rendered hydrophilic with a short oxygen-plasma treatment (6 s; oxygen pressure: 0.26 Torr; power: 100 W). The PEDOT:PSS (H.C. Starck, Baytron P VPAI4083) layer was spin coated in air at 3000 rpm for 60 s, to produce a 46 nm thick layer. Samples were then transferred again in a  $\text{N}_2$  glovebox, where a thermal treatment to

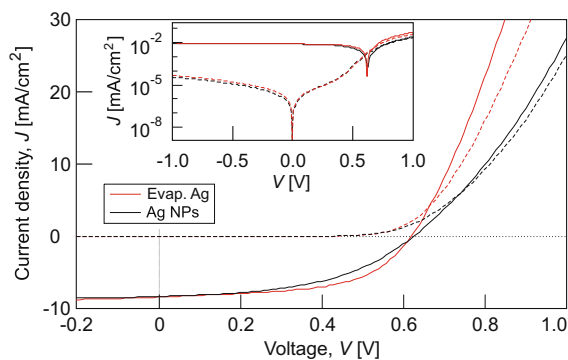
remove the excess water was performed at  $120^\circ\text{C}$  for 10 min. Samples were then fixed on a sample holder and covered with a shadow mask. With the previously mentioned settings the top contact was sprayed, resulting in 8 devices per sample with an active area of  $3 \text{ mm}^2$ . Samples were then finalized with the sintering step ( $150^\circ\text{C}$  for 5 min).

Fig. 4 shows the layer structure and the thicknesses of each layer, together with two cross sections of the device performed with SEM and transmission electron microscopy (TEM), the latter on a sample prepared by focused ion beam (FIB) lift-out technique. A CVD glass layer and a sputtered Au layer are deposited on the area of interest in order to protect the specimen during the FIB wedge milling. The TEM analyses are performed with a FEI Tecnai (F30) FEG transmission microscope operating at 200 kV. From the SEM scan we can observe once more that the top Ag NP contact is not a fully sintered bulk Ag film, but is characterized by a merging of NPs into domains which allow a much higher conductivity compared to non treated NPs. Similar conclusions can be made for the ZnO layer in that it is also an agglomerate of NPs rather than a uniform, continuous layer. Concerning the solvent damage, the TEM scan shows that the spray deposition of cyclohexane does not dissolve the PEDOT:PSS layer and that the interface between PEDOT:PSS and the active material is clearly preserved. The TEM scan reveals the presence of voids between the PEDOT:PSS layer and the Ag NPs, indicated by arrows, reducing the electrical contact between the two layers. Moreover, single particles or clusters are found in the PEDOT:PSS layer, highlighted by the circle, confirming the role of PEDOT:PSS as buffer layer that prevents the diffusion of Ag to the active layer, where it would act as quenching center for charge carriers as well as excitons.

The photovoltaic characteristics were measured in a  $\text{N}_2$  atmosphere using an Agilent 4156C parameter analyzer and under  $100 \text{ mW}/\text{cm}^2$  AM1.5 simulated illumination using a LOT-Oriel Group Europe solar simulator with a 1000 W Xenon arc lamp fitted with AM 1.5D filters. Calibration was performed by a KG3 band pass filter and a calibrated Si photodetector. The current density vs. voltage ( $J$ - $V$ ) curves of the produced solar cells are



**Fig. 4.** (a) Structure, (b) SEM and (c) FIB/TEM cross sections of the inverted polymer solar cell with a spray coated Ag top contact. The white scale bars represent 100 nm. The arrows indicate voids between PEDOT:PSS and the Ag NPs, while the circle highlights a NP embedded within the PEDOT:PSS layer.



**Fig. 5.** The current density-voltage characteristics of solar cells produced with either an evaporated (red) or spray-coated (black) Ag top contact in the dark (dashed curves) or under 100 mW/cm<sup>2</sup> AM1.5 simulated illumination (solid curves). The inset graph shows a semi-log plot of the same devices in dark. (For interpretation of the references to colour in this figure legend, the reader is referred to the web version of this article.)

reported in Fig. 5. The red curve represents an evaporated Ag top contact reference device, while the black line is the sample with the solution processed Ag top contact. The reference device shows performances in line with the values reported in literature [28,32]. The solution processed Ag top contact cell is characterized by a slightly higher series resistance as indicated by lower current values at biases >0.7 V.

The higher series resistance affects the fill factor (*FF*), reduced from 53% (evaporated) to 48% (solution processed). This could be due to the voids at the interface between the Ag layer and PEDOT:PSS observed with FIB/TEM (cf. Fig. 4c), which may increase the contact resistance between the two layers. A high short circuit current ( $J_{sc}$ ) is extracted from the contacts (9 mA/cm<sup>2</sup> for the evaporated and 8.3 mA/cm<sup>2</sup> for the solution processed), and the open circuit voltage ( $V_{oc}$ ) reaches values as high as 620 mV. The attained final power conversion efficiency (*PCE*) of the cell with solution processed Ag is 2.5%, close to that of the reference cell with evaporated Ag (2.9%), showing that this solution processed top contact is well suited for the production of organic solar cells.

In conclusion, a Ag NP based ink was sprayed on a thin PEDOT:PSS layer deposited on top of the active layer of a P3HT:PCBM film in a reverse structure, in which a sintered layer of solution-processed ZnO acts as cathode and a solution-processed bi-layer of PEDOT:PSS and sintered Ag NPs acts as anode. The whole process was performed at room pressure from solutions and with temperatures below 150 °C and, apart from the ITO patterning, did not require any lithographic step. The devices showed efficiency similar to control devices produced with the same structure and an evaporated Ag top contact. Spray coating, the deposition technique used in this work, offers the ability to cover relatively large areas by the superposition of femtoliter-size droplets, reducing the impact of the solvent on the underlying layer as compared to other solution based deposition techniques. Moreover, this technique is easily scalable to large areas by proper choice of the atomizing pattern or by coupling several nozzles in arrays, making it possible to scale this method to a high-through-

put roll-to-roll deposition, virtually without limits in the achievable area.

## Acknowledgements

The authors would like to thank Dr. David Cheyns (IMEC v.z.w.) for the SEM scans, Dr. Paola Favia (IMEC v.z.w.) for the FIB/TEM scans and Dr. Heidi Van den Rul (Hasselt University and Division IMOMEC, IMEC v.z.w.) for providing the ZnO NPs.

The research was (partly) performed in the framework of the IWT SBO-Project 060843 “PolySpec” funded by the Institute for the Promotion of Innovation by Science and Technology in Flanders (IWT).

## References

- [1] J. Peet, J.Y. Kim, N.E. Coates, W.L. Ma, D. Moses, A.J. Heeger, G.C. Bazan, *Nat. Mater.* 6 (2007) 497.
- [2] J.Y. Kim, K. Lee, N.E. Coates, D. Moses, T.-Q. Nguyen, M. Dante, A.J. Heeger, *Science* 317 (2007) 222.
- [3] B.C. Thompson, J.M.J. Fréchet, *Angew. Chem. Int. Edit.* 47 (2008) 58.
- [4] B.P. Rand, J. Genoe, P. Heremans, J. Poortmans, *Prog. Photovoltaics* 15 (2007) 659.
- [5] T. Aernouts, T. Aleksandrov, C. Girotto, J. Genoe, J. Poortmans, *Appl. Phys. Lett.* 92 (2008) 033306.
- [6] C.N. Hoth, S.A. Choulis, P. Schilinsky, C.J. Brabec, *Adv. Mater.* 19 (2007) 3973.
- [7] S.E. Shaheen, R. Radspinner, N. Peyghambarian, G.E. Jabbour, *Appl. Phys. Lett.* 79 (2001) 2996.
- [8] F.C. Krebs, J. Alstrup, H. Spanggaard, K. Larsen, E. Kold, *Sol. Energy Mater. Sol. Cells* 83 (2004) 293.
- [9] P. Schilinsky, C. Waldauf, C.J. Brabec, *Adv. Funct. Mater.* 16 (2006) 1669.
- [10] D. Vak, S.-S. Kim, J. Jo, S.-H. Oh, S.-I. Na, J. Kim, D.-Y. Kim, *Appl. Phys. Lett.* 91 (2007) 081102.
- [11] C. Girotto, B.P. Rand, J. Genoe, P. Heremans, *Sol. Energy Mater. Sol. Cells* 93 (2009) 454.
- [12] R. Green, A. Morfa, A.J. Ferguson, N. Kopidakis, G. Rumbles, S.E. Shaheen, *Appl. Phys. Lett.* 92 (2008) 033301.
- [13] Y.-F. Lim, S. Lee, D.J. Herman, M.T. Lloyd, J.E. Anthony, G.G. Malliaras, *Appl. Phys. Lett.* 93 (2008) 193301.
- [14] E. Vitoratos, S. Sakkopoulos, E. Dalas, N. Paliatsas, D. Karageorgopoulos, F. Petraki, S. Kennou, S.A. Choulis, *Org. Electron.* 10 (2009) 61.
- [15] P. Buffat, J.-P. Borel, *Phys. Rev. A* 13 (1976) 2287.
- [16] Y. Wu, Y. Li, B.S. Ong, P. Liu, S. Gardner, B. Chiang, *Adv. Mater.* 17 (2005) 184.
- [17] S.H. Ko, H. Pan, C.P. Grigoropoulos, C.K. Luscombe, J.M.J. Fréchet, D. Poulikakos, *Appl. Phys. Lett.* 90 (2007) 141103.
- [18] J. Perelaer, B. de Gans, U.S. Schubert, *Adv. Mater.* 18 (2006) 2101.
- [19] D. Huang, F. Liao, S. Molesa, D. Redinger, V. Subramanian, *J. Electrochem. Soc.* 150 (2003) G412.
- [20] T. Sekitani, Y. Noguchi, U. Zschieschang, H. Klauk, T. Someya, *Proc. Natl. Acad. Sci. USA* 105 (2008) 4976.
- [21] Y. Noguchi, T. Sekitani, T. Yokota, T. Someya, *Appl. Phys. Lett.* 93 (2008) 043303.
- [22] S.H. Eom, S. Senthilarasu, P. Uthirakumar, C.-H. Hong, Y.-S. Lee, J. Lim, S.C. Yoon, C. Lee, S.-H. Lee, *Sol. Energy Mater. Sol. Cells* 92 (2008) 564.
- [23] Note added in review: A similar procedure has been developed concerning the large area deposition of Ag nanoparticles on a polymer solar cell: S.K. Hau, H.L. Yip, K. Leong, A.K.-Y. Jen, *Org. Electron.* (2009), doi:10.1016/j.orgel.2009.02.019.
- [24] R.D. Deegan, O. Bakajin, T.F. Dupont, G. Huber, S.R. Nagel, T.A. Witten, *Nature* 389 (1997) 827.
- [25] G. Guena, C. Poulard, M. Voue, J. De Coninck, A.M. Cazabat, *Colloid Surf. A - Physicochem. Eng. Asp.* 291 (2006) 191.
- [26] K.-S. Chou, K.-C. Huang, H.-H. Lee, *Nanotechnology* 16 (2005) 779.
- [27] D. Kim, J. Moon, *Electrochem. Solid State Lett.* 8 (2005) J30.
- [28] M.S. White, D.C. Olson, S.E. Shaheen, N. Kopidakis, D.S. Ginley, *Appl. Phys. Lett.* 89 (2006) 143517.
- [29] M. Glatthaar, M. Niggemann, B. Zimmermann, P. Lewer, M. Riede, A. Hinsch, J. Luther, *Thin Solid Films* 491 (2005) 298.

- [30] C. Waldauf, M. Morana, P. Denk, P. Schilinsky, K. Coakley, S.A. Choulis, C.J. Brabec, *Appl. Phys. Lett.* 89 (2006) 233517.
- [31] G. Li, C.W. Chu, V. Shrotriya, J. Huang, Y. Yang, *Appl. Phys. Lett.* 88 (2006) 253503.
- [32] S.K. Hau, H.-L. Yip, N.S. Baek, J. Zou, K. O'Malley, A.K.Y. Jen, *Appl. Phys. Lett.* 92 (2008) 253301.
- [33] T. Ameri, G. Dennler, C. Waldauf, P. Denk, K. Forberich, M.C. Scharber, C.J. Brabec, K. Hingerl, *J. Appl. Phys.* 103 (2008) 084506.
- [34] G. Li, V. Shrotriya, J. Huang, Y. Yao, T. Moriarty, K. Emery, Y. Yang, *Nat. Mater.* 4 (2005) 864.
- [35] G. Li, Y. Yao, H. Yang, V. Shrotriya, G. Yang, Y. Yang, *Adv. Funct. Mater.* 17 (2007) 1636.

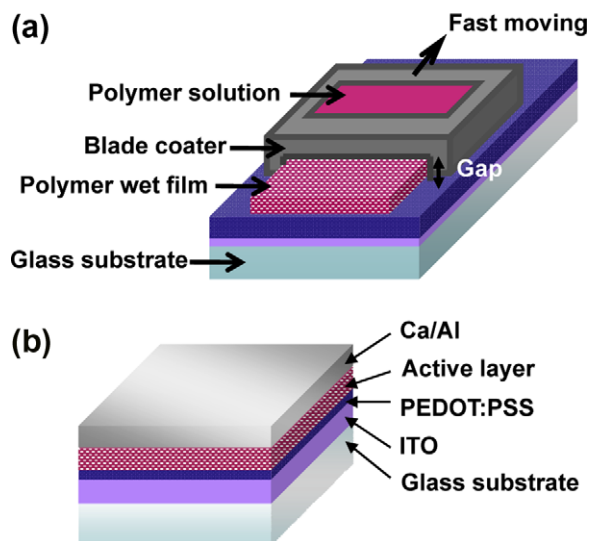


**Fig. 1.** (a) Schematic working principle of blade coating. The polymer wet film is formed by moving the blade coater. The thickness of polymer wet film is defined by the gap of the blade coater. (b) The schematic device structure of the bulk hetero-junction cells.

structured by printing in organic solar cells, blade coating for large area fabrication has been proved to be the better way [6]. The film thickness by blade coating can be reduced to nanometer scale by carefully controlling the fabrication parameters such as the solution concentration, the blade gap, and the blade coating speed. Recently we verified the feasibility of blade coating for high-efficiency polymer light-emitting diodes [8]. Unlike spin coating, the area can be easily scaled up and the material usage is almost 100% in blade coating. In this work, blade coating is applied to poly(3-hexylthiophene) (P3HT) and (6,6)-phenyl-C61-butyric acid methyl ester (PCBM) blend in the toluene solution which has a lower boiling point (110 °C) and is less toxic. High efficiency is achieved from toluene solution without the slow solvent evaporation process.

Fig. 1a shows the schematic working principle of blade coating. The thickness of the wet polymer film is defined by the gap. The polymer dry film thickness is tuned by the polymer concentration in solution and the gap of the blade coater. The polymer wet film is deposited by dragging the blade coater at a certain speed about 15 cm/s. We first focus on solar cells with P3HT:PCBM blend dissolved in toluene. Device performances are compared for

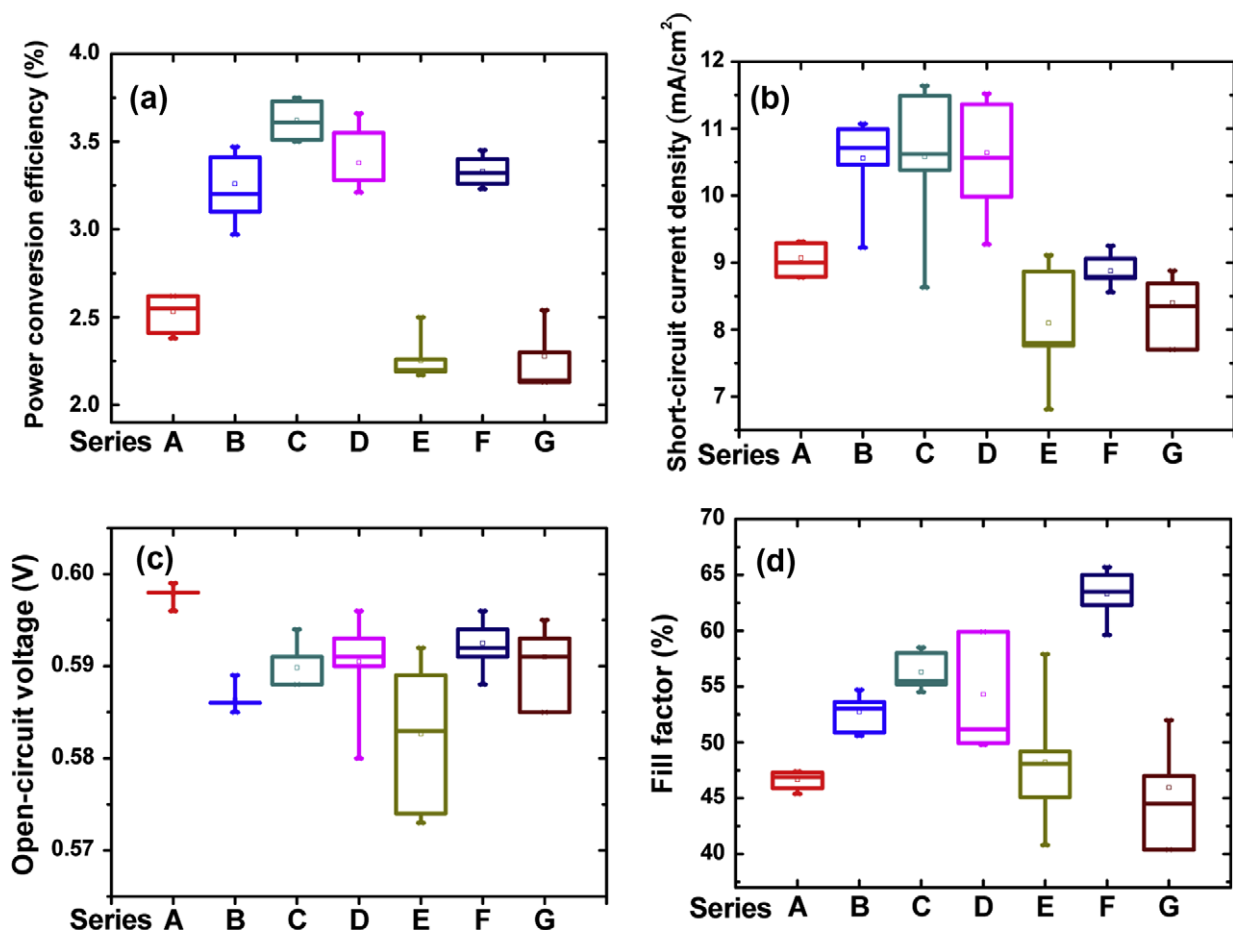


**Fig. 2.** Statistical results of the seven series of devices: (a) the power conversion efficiency, (b) the short-circuit current, (c) the open-circuit voltage and (d) the fill factor. The horizontal lines in the box denote the 25th, 50th, and 75th percentile values. The error bars denote the 5th and 95th percentile values. The open square inside the box denotes the mean value.



different coating methods including spin coating, blade coating, blade coating on a hot plate, as well as blade and spin coating. For the blade and spin coating the polymer wet film is deposited by blade coating which is followed by spinning until the dry film is formed. In all cases the weight ratio of P3HT and PCBM is 1:1. The device structure is ITO/PEDOT:PSS/P3HT:PCBM/Ca/Al shown in Fig. 1b. ITO is indium tin oxide and PEDOT:PSS is poly-(3,4-ethylenedioxythiophene):poly-(styrenesulfonate) (Baytron PVP Al 4083). A 40 nm PEDOT:PSS layer is spin coated on a patterned ITO substrate and baked at 200 °C in nitrogen for 15 min.

Seven series of devices with six devices in each are made to study the different coating processes with different solvents statistically. Among them, five series are made with toluene solution to compare the coating processes, including spin coating (series A), blade coating (series B), blade coating on a hot plate at 60 °C (series C), as well as blade and spin coating (series D). In addition, the devices with the PEDOT:PSS layer by blade coating at 100 °C and P3HT:PCBM by blade and spin coating from toluene solution is made to study the feasibility of bladed PEDOT:PSS layer (series G). The other two series made from two conventional high boiling point solvents, chlorobenzene (series E) and dichlorobenzene (series F), are compared with those from toluene by blade and spin coating. After coating all the P3HT:PCBM layers are annealed at 140 °C for 20 min in nitrogen. The Ca(35 nm)/Al(100 nm) cathode is deposited by thermal evaporation. The active area of the device is 0.04 cm<sup>2</sup>. All the devices are packaged in the glove box and measured in the ambient environment. The power conversion efficiency is measured by the solar simulator (PEC-L11, Peccell Technologies) under AM1.5G irradiation. The incident photon-to-electron conversion efficiency (IPCE) is measured by the spectral response measurement system (SR300, Optosolar GMBH). The morphology of P3HT:PCBM is monitored by atomic force microscope (AFM, Dimension 3100, Digital Instruments).

Fig. 2 shows the statistical results of the seven series of devices. Among the series based on toluene solution (series A, B, C, D, and G), the series of devices by blade coating have the higher efficiencies except the series with bladed the PEDOT:PSS layer. Because the open-circuit voltages  $V_{oc}$  are about the same, the high performances of series B, C, and D result from the high short-circuit currents  $J_{sc}$  and fill factor. Among the series by blade and spin coating (series D, E, and F), the series of devices from toluene solution and dichlorobenzene have the higher performances. While the  $J_{sc}$  of series E and series F are about the same, the high performance of series F results from the relatively high fill factor. For further discussion, the best devices in each series are chosen to show the advanced device properties.

Fig. 3a shows the current–voltage ( $J$ – $V$ ) curves of five devices in toluene solution made by different active layer coating processes. The short-circuit currents  $J_{sc}$  made by blade coating (device B, C, and D) are larger than that of the device made by conventional spin coating (device A). Using blade coating the  $J_{sc}$  increases from 9.3 mA/cm<sup>2</sup> with spin coating to 11.5 mA/cm<sup>2</sup>. The fill factor rises from 47% to 55% and the open-circuit voltage  $V_{oc}$  remains the same. The efficiency, which is proportional to  $J_{sc}$ ,  $V_{oc}$ , and fill fac-

tor as a whole, is improved from 2.6% (device A) by spin coating to 3.8% (device C) by blade coating on a hot plate.

It is believed that in order to get a high efficiency in bulk hetero-junction polymer solar cell the microscopic morphology of the active layer needs to be well controlled to achieve an ordered structure by certain annealing processes such as slow solvent evaporation [1] and postproduction heat treatment [2,9]. Such annealing promotes molecular self-organization and makes the polymer chains more ordered in its domains. In spin coating for low boiling point solvents such as toluene (110 °C), high volatility leads to the fast drying of the active layer and may limit the self-assembly as well as the power conversion efficiency. However, the polymer films made by blade coating could be more ordered than those by spin coating due to the fact that the polymer chains are relatively free to move in the absence of centrifugal force. Therefore even without the slow drying process the donors and acceptors quickly

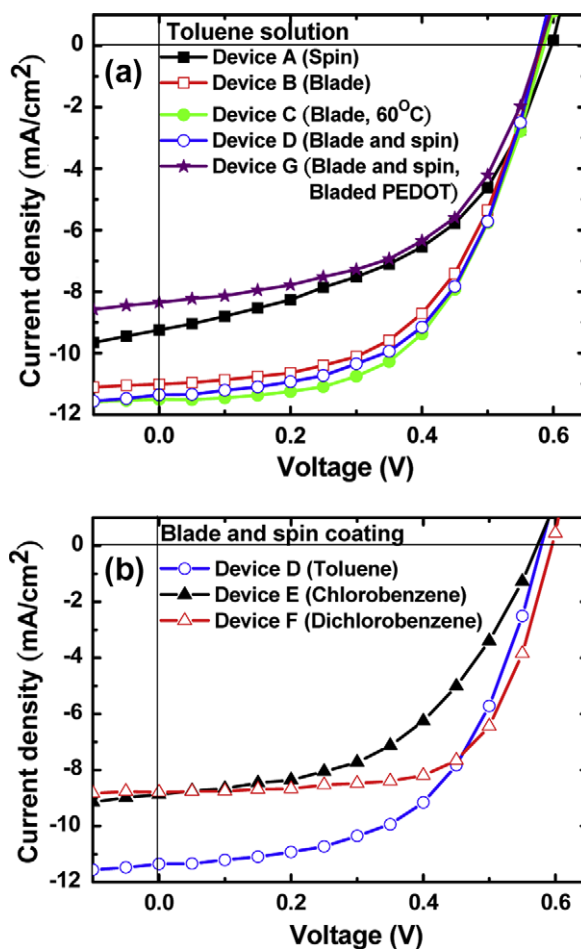


Fig. 3. Current–voltage ( $J$ – $V$ ) relations of the devices in this work. (a) Devices made by spin coating (device A, solid square), blade coating (device B, empty square), blade coating at 60 °C (device C, solid circle), and blade and spin coating (device D, empty circle) in toluene solution, blade and spin coating with bladed PEDOT:PSS (device G, solid star). (b) Devices made by blade and spin coating in toluene solution (device D, empty circle), chlorobenzene solution (device E, solid triangle), and dichlorobenzene solution (device F, empty triangle).

**Table 1**

Performance of bulk hetero-junction solar cells in this work.

Label	$J_{sc}$ (mA/cm <sup>2</sup> )	$V_{oc}$ (V)	Fill factor (%)	PCE (%)	Thickness (nm)
A. (Toluene) spin	9.25	0.59	47	2.6	223
B. (Toluene) blade	11.07	0.59	53	3.5	412
C. (Toluene) blade at 60 °C	11.49	0.59	55	3.8	304
D. (Toluene) blade and spin	11.36	0.58	55	3.7	245
E. (Chlorobenzene) blade and spin	8.87	0.57	49	2.5	345
F. (Dichlorobenzene) blade and spin	8.79	0.60	66	3.5	242
G. (Toluene) blade and spin with bladed PEDOT:PSS (120 nm)	8.35	0.59	52	2.5	245

self-assemble into the desired ordered and interpenetrating morphology during the blade coating process. We speculate that the quick assembly occurs at the beginning of the blade coating because the device made by blade and spin coating (device D) shows high efficiency as well. Interestingly, device B, C, and D have different film thickness but similar performances. High efficiency is maintained for device B with 412 nm thickness probably because pure

blade coating with neither heating nor spinning give the highest freedom to chain motions and the most ordered morphology. In short, the blade coating method allows an ordered polymer morphology in a fast drying solution like toluene. In addition, the result of the device with the bladed PEDOT:PSS and blade and spin coated P3HT:PCBM layer is also shown in Fig. 3a. The efficiency of device G is 2.5% with  $J_{sc}$  of 8.35 mA/cm<sup>2</sup>,  $V_{oc}$  of 0.59 V, and fill factor

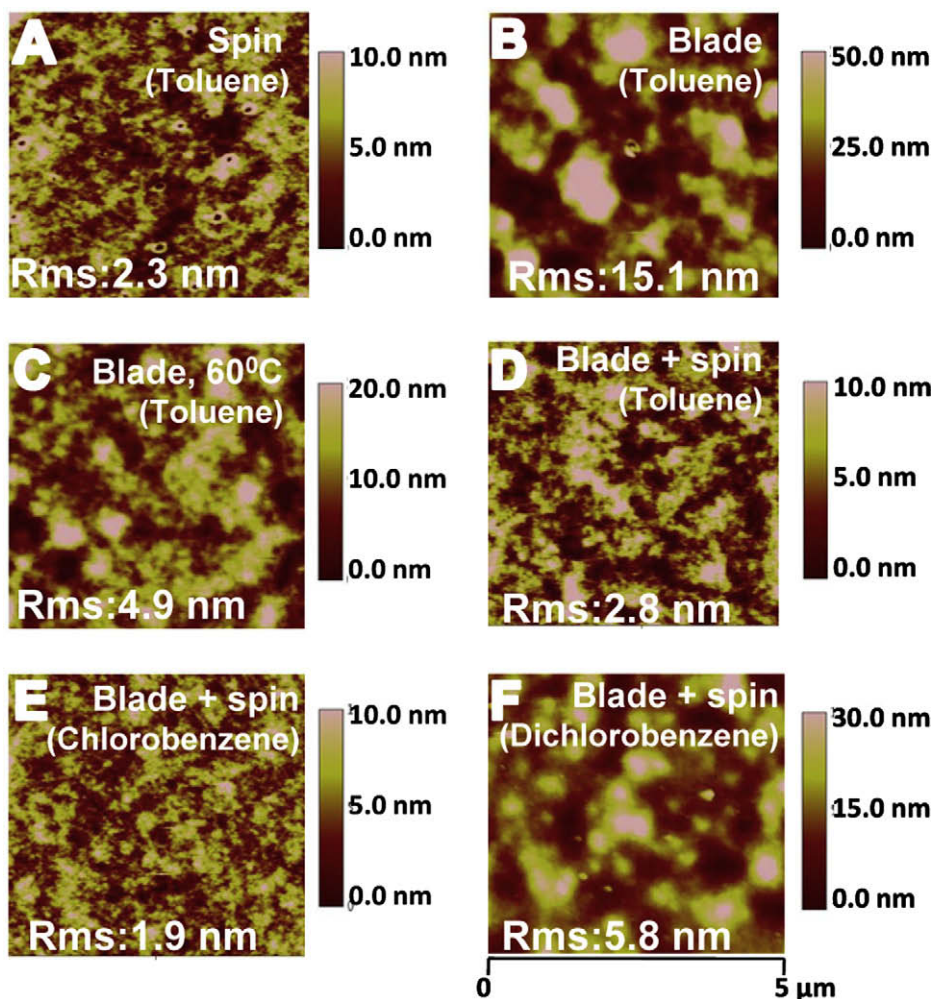


**Fig. 4.** AFM images of the devices in this work. P3HT:PCBM thin film made by: (a) spin coating, (b) blade coating, (c) blade coating at 60 °C, (d) blade and spin coating and (e) blade and spin coating in chlorobenzene solution, (f) blade and spin coating in dichlorobenzene solution. The P3HT:PCBM films in (a)–(d) are made in toluene solution.

of 52%. The relative low performance of device G results from the thick PEDOT:PSS film (120 nm), which causes high series resistance. It is difficult for us to reduce the PEDOT:PSS film thickness now because we use the PEDOT:PSS solution from H. C. Stark without any further dilution. The concentration needs to be lowered without sacrificing the conductivity to get the normal film thickness (40 nm). More experiments need to be done to optimize the PEDOT:PSS layers by blade coating. Nevertheless, such device shows the feasibility of all blade coated devices with very low cost and high throughput in mass production.

Now we turn to different solvent systems. Two devices are made by conventional high boiling points solvents chlorobenzene (device E) and dichlorobenzene (device F). Fig. 3b shows the results of the devices by the fast-drying blade and spin process with different solvents. There is no slow solvent evaporation in the fabrication process. The power conversion efficiencies are 2.5% in the device from chlorobenzene solution (device E) and 3.5% in that

from dichlorobenzene solution (device F). The  $J_{sc}$  are both about  $8.8 \text{ mA/cm}^2$ , which is significantly smaller than  $J_{sc}$  of  $11.4 \text{ mA/cm}^2$  in device D from toluene. Interestingly high boiling point solvents give higher  $J_{sc}$  for spin coating but smaller  $J_{sc}$  for blade coating. There are probably more P3HT/PCBM interfaces in toluene solution than those in chlorobenzene and dichlorobenzene solutions, resulting in more efficient exciton dissociation. It is remarkable that the fill factor of dichlorobenzene solution is 66%, much higher than 55% for toluene and 49% for chlorobenzene. Dichlorobenzene has the highest boiling point among the three solvents. The highest fill factor in dichlorobenzene solution may result from the highest carrier mobility due to the enhanced self-assembly of P3HT taking place during the relatively slow drying in spinning. The device performances are summarized in Table 1.

The AFM images of the devices are shown in Fig. 4. The root-mean-square roughness are 2.3 nm for device A, 15.1 nm for device B, 4.9 nm for device C, 2.8 nm for device D, 1.9 nm for device E, and 5.8 nm for device F. The different root-mean-square values are attributed to the different fabrication processes with different solvents. Neat P3HT layers by any process would be very rough ( $15 \pm 3 \text{ nm}$ ) due to the fact that the polymer chains have the trend to form crystallization, and the neat PCBM could not even form thick films by blade coating. We think that the devices with high efficiency (device B, C, D, and F) have stronger self-organization than those with low efficiency (device A and E). Higher surface roughness corresponds to higher degree of self-organization. [10,11] However, there is no clear evidence for the correlation between self-organization and device efficiency. Nevertheless, we speculate that device B by blade coating shows clear self-organization, implying ordered structures within each component. Therefore, the carrier mobility is high and the power conversion efficiency is high as well even with a thick film of 412 nm. The clear self-organizations in device C and device F also could be seen due to their relative high roughness. Interestingly, the roughness of device D by blade and spin coating is just slightly higher than that of device A only by spin coating, but the efficiency of device D is still much higher. This may be due to the ordered structure occurred at the beginning of blade coating, combined with thicker film thickness by blade coating. As for the low efficiency devices such as device A and device E, the films are relatively smooth. The images show that the self-organization could be achieved within the short drying time by blade coating.

Fig. 5a shows the absorption spectra of the P3HT and PCBM blend films deposited by different methods and solutions. The IPCE for all devices are shown in Fig. 5b. Despite of the different morphologies there is no significant variations among the absorption spectra. So the differences in the device performances must come from the exciton dissociation and carrier transport processes. The IPCE values appear similar in all the devices except that of device G and show slightly difference at about 600 nm. However, the  $J_{sc}$  values show much difference among the devices. In principle the measured  $J_{sc}$  should be proportional to the product of the IPCE and the illuminating spectrum, integrated over all wavelengths. We may attribute the incon-

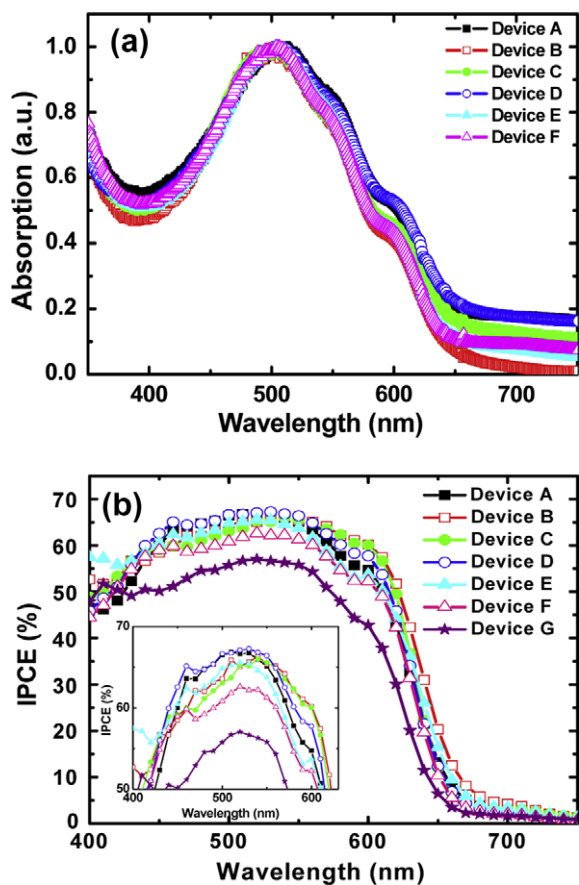


Fig. 5. (a) The absorption spectra of the devices and (b) the incident photon to current efficiency (IPCE) in this work. The inset shows the IPCE from 400 nm to 600 nm for clarity. Devices made by spin coating (device A, solid square), blade coating (device B, empty square), blade coating at  $60^\circ\text{C}$  (device C, solid circle), and blade and spin coating (device D, empty circle) in toluene solution. Devices made by blade and spin coating in chlorobenzene solution (device E, solid triangle), and in dichlorobenzene solution (device F, empty triangle), as well as blade and spin coating with bladed PEDOT:PSS (device G, solid star).

sistency between IPCE and  $J_{sc}$  values to the different spectral-mismatch factors of the different light sources.[6]

In conclusion we develop the blade coating method to fabricate bulk hetero-junction polymer solar cells with decent power conversion efficiency of 3.8%. The active layer is deposited in toluene solution, which is less toxic than the conventional chlorobenzene and dichlorobenzene solution optimized for spin coating. In sharp contrast to spin coating there is almost no material waste in blade coating. Moreover, this method can be easily scaled up to large sizes as meters and can be applied in a future roll-to-roll fashion for high volume production.

### Acknowledgement

This work is supported by the National Science Council of Taiwan under Grant No. NSC96-2120-M-007-007 and NSC96-2112-M-009-036.

### References

- [1] G. Li, V. Shrotriya, J. Huang, Y. Yao, T. Moriarty, K. Emery, Y. Yang, *Nat. Mater.* 4 (2005) 864.
- [2] W.L. Ma, C.Y. Yang, X. Gong, K. Lee, A.J. Heeger, *Adv. Funct. Mater.* 15 (2005) 1617.
- [3] C.N. Hoth, P. Schilinsky, S.A. Choulis, C.J. Brabec, *NanoLetters* 8 (2008) 2806.
- [4] S.E. Shaheen, R. Radspinner, N. Peyghambarian, G.E. Jabbour, *Appl. Phys. Lett.* 79 (2001) 2996.
- [5] K.X. Steirer, M.O. Reese, B.L. Rupert, N. Kopidakis, D.C. Olson, R.T. Collins, D.S. Ginley, *Sol. Energy Mater. Sol. Cells* 93 (2009) 447.
- [6] P. Schilinsky, C. Waldauf, C.J. Brabec, *Adv. Funct. Mater.* 16 (2006) 1669.
- [7] S.-S. Kim, S.-I. Na, J. Jo, G. Tae, D.-Y. Kim, *Adv. Mater.* 19 (2007) 4410.
- [8] S.R. Tseng, K.C. Lee, H.F. Meng, S.F. Horng, *Appl. Phys. Lett.* 93 (2008) 153308.
- [9] K. Kim, J. Liu, M.A.G. Namboothiry, D.L. Carrll, *Appl. Phys. Lett.* 90 (2007) 163511.
- [10] Y. Zhao, Z. Xie, Y. Qu, Y. Geng, L. Wang, *Appl. Phys. Lett.* 90 (2007) 043504.
- [11] X. Yang, J. Loos, S.C. Veenstra, W.J. Verhees, M.M. Wienk, J.M. Kroon, M.A.J. Michels, R.A.J. Janssen, *NanoLetters* 5 (2005) 579.

microscopy images were taken in a Jeol JSM-6460 LV scanning microscope. The sample was metalized with gold-palladium alloy in a Denon Desk II metallizer. The infrared spectra were measured in a FT-IR Perkin-Elmer Spectrum BX model equipped with a DTGS detector.

## 2.1. Synthesis

The synthesis of monomers (Fig. 1) was carried out by Ullmann coupling according to literature procedures [9].

### 2.1.1. *N,N,N',N'*-tetra-*p*-tolyl-4,4'-diaminodiphenylmethane [1]

In a hermetically sealed glass bottle, 5 ml of dry and degassed toluene were mixed with 4-iodotoluene (5.25 g, 24 mmoles), 4,4'-diaminodiphenylmethane (1.2 g, 6 mmoles), CuI (0.080 g, 0.4 mmol), 1,10-phenanthroline (0.081 g, 0.4 mmol) and potassium *tert*-butoxide (4 g, 36 mmoles). The mixture was sealed, and then heated at 120 °C in a sand bath for 50 h in an argon atmosphere with vigorous stirring. After finishing the reaction, 10 ml of toluene was added, the whole mixture was filtered and the solid was washed with three aliquots of 10 ml of toluene. All the liquid fractions were combined and the solution was dried in a rotary evaporator. The solid was purified twice by chromatography in a silica gel column (1.5 × 20 cm, Merck 60, 0.040–0.06 mm grain) with hexane/cyclohexane (2:1) as solvent. The elution was monitored by TLC in silica plates (Merck 60) with the same solvent mixture, using standards of the initial reagents. The product was collected after the elution of the 4-iodotoluene and, by evaporation, yielded a white powder. Yield: 20%. Pf: 184–187 °C. *m/z* (%) = 558 [M<sup>+</sup>] (100). Calculated theoretical mass: 558 g/mol.

### 2.1.2. *N,N,N',N'*-tetraphenyl-4,4'-diaminodiphenylmethane [2]

In a hermetically sealed glass bottle, 5 ml of dry and degassed toluene were mixed with iodobenzene (5 g, 24 mmoles), 4,4'-diaminodiphenylmethane (1.2 g, 6 mmoles), CuI (0.080 g, 0.4 mmol), 1,10-phenanthroline (0.081 g, 0.4 mmol), potassium *tert*-butoxide (4 g, 36 mmoles). The mixture was sealed, and then heated at 120 °C in a sand

bath for 50 h in an argon atmosphere with vigorous stirring. After finishing the reaction, 10 ml of toluene was added, the whole mixture was filtered and the solid was washed with three aliquots of 10 ml of toluene. All the liquid fractions were combined and the solution was dried in a rotary evaporator. The solid was purified twice by chromatography in a column of silica gel (1.5 × 20 cm, Merck 60, 0.040–0.06 mm grain). Elution solvent was a gradient starting with a mixture of hexane/cyclohexane (1:1) and finishing with hexane/cyclohexane/toluene (1:1:0.25). The elution was monitored by TLC in silica plates (Merck 60) with the final elution mixture, using standards of the initial reagents (*R<sub>f</sub>* of the product was 0.75) and, by evaporation, yields a white powder. Yield: 23%. *m/z* (%) = 502.10 [M<sup>+</sup>] (100). Calculated theoretical mass: 502 g/mol.

### 2.1.3. *N,N'*-diphenyl-*N,N'*-ditolyl-4,4'-diaminodiphenylmethane [3]

In a hermetically sealed glass bottle, 5 ml of dry and degassed toluene were mixed with *N*-phenyl-*N*-tolylamine (2 g, 10 mmoles), 4,4'-diiododiphenylmethane (2 g, 4.7 mmoles), CuI (0.03 g, 0.15 mmol), 1,10-phenanthroline (0.03 g, 0.15 mmol), potassium *tert*-butoxide (4 g, 36 mmoles). The mixture was sealed, and then heated at 120 °C in a sand bath for 50 h in an argon atmosphere with vigorous stirring. After finishing the reaction, 10 ml of toluene was added, the whole mixture was filtered and the solid was washed with three aliquots of 10 ml of toluene. All the liquid fractions were combined and the solution was dried in a rotary evaporator. The solid was purified twice by chromatography in a column of silica gel (1.5 × 20 cm, Merck 60, 0.040–0.06 mm grain) with hexane/cyclohexane (2:1) as solvent. The elution was monitored by TLC in silica plates (Merck 60) with the same solvent mixture, using standards of the initial reagents (*R<sub>f</sub>* of the product was 0.50) and, by evaporation, yields a white powder. Yield: 23%. *m/z* (%) = 530 [M<sup>+</sup>] (100). Calculated theoretical mass: 530 g/mol.

## 2.2. Electrochemical characterization

Electrolysis and cyclic voltammeteries were performed in a conventional three-electrode electrochemical cell. A mixture of MeCN/Toluene 1:4 was used as electrolysis solvent and TBAPF<sub>6</sub> 0.1 M as supporting electrolyte [10]. The working electrode was either indium-doped tin oxide covered glasses (ITO glasses, VisionTeK Systems, Ltd., UK) or a 0.5 mm diameter platinum disc (99.99% purity). A plate of pure gold was used as counterelectrode, and a standardized (ferrocene/ferrocenium<sup>+</sup> couple in acetonitrile [11]) double junction electrode of Ag/Ag<sup>+</sup> in acetonitrile was used as reference. The platinum electrode was polished with 1% alumina powder (1 μm) in water over a piece of cloth, cleaned in an ultrasonic bath with absolute ethanol and dried in air. All redox potentials are referred to NHE.

## 2.3. Electropolymerization of [2]

The electropolymerization of [2] was performed potentiostatically on ITO covered glasses of a 10<sup>-2</sup> M solution in

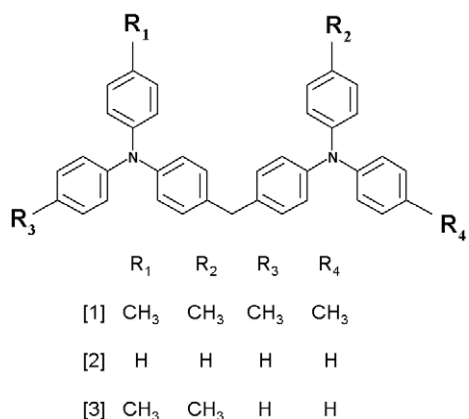


Fig. 1. Chemical formula of species involved in this study.

electrolysis solvent. A constant potential of 1500 mV was applied for 10 min and then reduced to 0 mV until the current dropped to less than 1% of the initial value. The electrode was washed with the solvent mixture in order to eliminate the rest of [2] and then with ethanol to remove the remaining supporting electrolyte. The film was characterized by FT-IR and SEM, and showed no TBAPF<sub>6</sub> crystals.

#### 2.4. Spectroelectrochemistry

An ITO covered glass with a film about 0.5 μm thick was placed in a 1 cm path-length quartz cell filled with electrolysis solution without [2]. The spectrum was obtained at the selected potential after the final current dropped to less than 1% of the initial value and the absorbance remained stable.

#### 2.5. Characterization by infrared spectroscopy

Samples were prepared on ITO covered glasses of 1 × 3 cm. The film was deposited on a subarea of 1 × 2 cm. Three films were prepared for 0.5, 1 and 1.5 h of electrolysis. The adhered polymers were reduced at 0 mV until the current dropped to less than 1% of the initial value. After this treatment, the electrode was placed in the electrolysis solution free of [2] and it was cycled for 1 h between 0 and 1500 mV at 50 mV/s in order to make sure that there was no monomer occluded in the films. The samples were removed from the cell at the reduced state (uncolored), then washed with ethanol to eliminate the rest of TBAPF<sub>6</sub>, and dried in air. These film-covered glasses were scraped with a spatula and mixed with BrK in a mortar to prepare transparent tablets for FT-IR analysis.

### 3. Results

The cyclic voltammetry of [1] showed a remarkable similarity to the voltammogram of tri-p-tolylamine (TTA). Only one quasireversible wave was observed at  $E^{1/2} = 1150$  mV (1130 mV in TTA) with  $\Delta E = 90$  mV. The UV-vis spectrum of oxidized [1] was very similar to that reported for TTA, although it stayed stable only for a few minutes (Fig. S1, see Supplementary material). Absorption bands in the NIR were not observed for the transient specie. On the contrary, a complex process was observed in the first voltammogram of a solution of [2], which was very similar to triphenylamine (TPA), with an oxidation wave at 1370 mV and reduction waves around 1020 and 1130 mV [12] (Fig. 2a). The different height and shape of the current peaks suggests that a coupled chemical process, in which the oxidized specie participates, follows the redox reaction. In the successive cycles, two new reversible waves were observed at  $E^{1/2} = 1030$  mV and 1150 mV, with the characteristic shape of an adsorbed species redox process [13]. In order to verify this assignment, the Pt electrode was rinsed with clean solvent and immersed in new electrolysis solution without [2]. The voltammogram of this sample showed the disappearance of the wave at 1370 mV and the permanence of the recently formed peaks (Fig. 2b). SEM pictures of ITO electrodes show that the deposited film completely

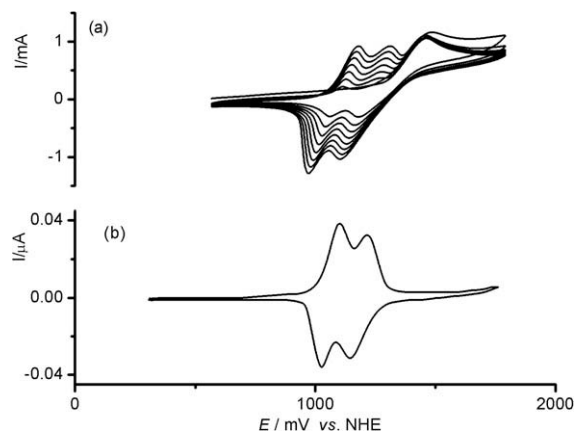


Fig. 2. (a) Cyclic voltammetry of [2] (0.01 M) in electrolysis solution. Scan rate: 25 mV/s. (b) Cyclic voltammetry of electrodeposited film on ITO glass in electrolysis solution (free of [2]).

covers the electrode with a homogenous texture (Fig. S2, see Supplementary material).

The infrared spectrum of the electropolymerized film material (p-[2] from now on) showed substantial differences with its molecular precursor [2]. The last one presented bands at 690 and 750 cm<sup>-1</sup>, associated with the five adjacent CH out-of-plane bending in the terminal phenyl rings. These two bands are remarkably diminished in the film spectrum, in which a new band appears at 815 cm<sup>-1</sup>. This band, which is characteristic of the para-substitution in benzene, is not present in the spectrum of [2] (Fig. S3, see Supplementary material).

Fig. 3 shows the evolution of the film UV-vis spectrum with potential, as it oxidizes from 0 to 1500 mV. Three successive bands are observed at 360, 485, and 760 nm. As it can be seen in the inset image (absorption at these three wavelengths), the band at 360 nm corresponds to the

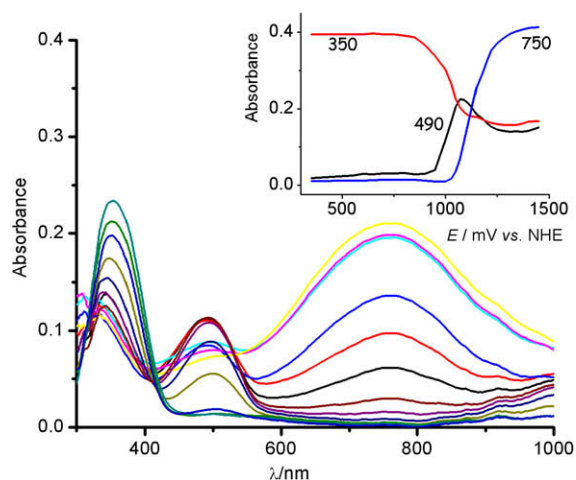


Fig. 3. Spectroelectrochemistry of p-[2] deposited on ITO glass. Potentials varied from 0 to 1500 mV. Inset shows absorbance as a function of voltage for 350, 490 and 750 nm. Data was extracted from the spectroelectrochemical experiment.

reduced form of the film, the one at 485 nm to the singly oxidized form, and the one at 760 nm to the fully oxidized film.

In order to estimate the molar absorptivity of singly oxidized TPB fragments in the film, a potential step experiment from 1030 to 0 mV was carried out. In that potential range, the signal at 485 nm was sufficiently high to be distinguished from the base noise (although it was as low as to diminish the errors of Lambert–Beer's law deviations), whereas the band at 760 nm (two electron oxidation) was not observed. The film's absorbance was plotted against the charge accumulated from the start of the potential step to a given time  $t_i$ . A strongly non-linear relationship (sigmoid) was obtained, thus we concluded that it is not possible to obtain a reliable measurement of the molar absorptivity.

Fig. S4, see Supplementary material shows the spectrum of the oxidized p-[2] film (at 1030 mV) between 400 and 2000 nm (solvent mixture NIR cutoff). We observed an intense band at 1470 nm (besides the one at 485 nm), which we assigned to the intervalence charge transfer corresponding to the TPB fragments in p-[2].

In order to evaluate the electrochromic response, a series of potential pulses were applied to the film. We observed that when increasing the potential from 0 to 1500 mV the time to reach 95% of absorbance at 760 nm was 100 s. When repeating the experience with potential steps from 0 to 1000 mV and measuring the absorbance at 490 nm this time was 130 s. Notice that these times are slower than in polymer films with greater delocalization [14]. After 1 h of applying pulses to the film, the absorbance steps at 490 and 760 nm dropped less than 5% when changing from neutral to fully oxidized species (Fig. 4).

#### 4. Discussion

Although it is not possible to assign the structure of the electrogenerated p-[2] exactly, a qualitative analysis of the experimental results can be used to make some useful inferences.

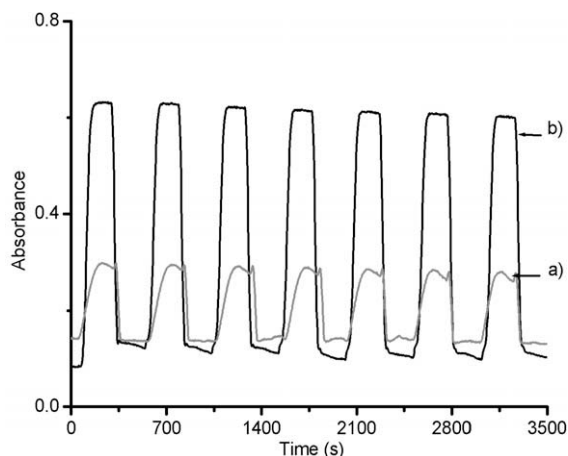


Fig. 4. (a) Absorbance at 490 nm when rising from 0 to 1000 mV, and (b) Absorbance at 750 nm from 0 to 1500 mV.

Previous studies on polymerization of arylamines have demonstrated that, when these molecules are oxidized, they form dimeric [12,15] or polymeric [10] species through the para-position (whenever it is not substituted). In the case of the aniline oxidation, for instance, position 4 of one molecule is bound to the nitrogen of another one, generating a conductive polymer that adheres to the electrode [16,17]. It has been observed on studies made on the triphenylamine oxidation [12] that two radicals  $\text{TPA}^+$  rapidly react to yield tetraphenylbenzidine (TPB). Its formation can be verified in the cyclic voltammogram of TPA either by means of the appearance of new redox peaks corresponding to the generated species, or by spectroelectrochemistry where the electronic transitions corresponding to TPB are also seen. The polymerization of arylamines that are interconnected by bridges containing double and triple bonds [18] and by electron donor-acceptor structures [19] has also been studied. They all follow the same polymerization pattern through para-positions and form films that remain adhered at the electrodes.

In our case, it is reasonable to assume that linear polymerization is a necessary previous step at the early stages of the film growth. At the beginning of the process, a pair of phenyl rings from two independent molecules of [2] probably reacts to start a dimer, eventually forming a benzidine chain separated by methylene groups. It has been reported that linear polymers of arylamines (comparable to our case) are soluble in intermediate polarity solvents like chloroform and toluene [20]. In our case, the presence of soluble and colored substances was observed during electrolysis in the neighborhood of the electrode. The same happened with the electropolymerization of [3] which was only able to form linear arrangements and did not form any film at the electrode (Fig. S5, see Supplementary material). We then infer that the insoluble species that form the film cannot be only linear, but may come from the interweaving of previously formed linear chains, after polymerization of the remaining free phenyl as a cross linker between them.

It is observed from the IR spectrum of the film that the bands at  $750$  and  $690\text{ cm}^{-1}$  originally present in [2] diminish their intensity in p-[2]. The vibration band at  $815\text{ cm}^{-1}$  suggests that the polymer presents rings with substitutions in para-. This fact has already been described in the case of electropolymerization of TPA [10]. Then, in the case of [2], polymerization might lead to the structure shown in Fig. 5.

Note that neither the bands at  $750$  and  $690\text{ cm}^{-1}$  disappear completely, nor the band at  $815\text{ cm}^{-1}$  reaches its maximum height as compared to the IR spectrum of [1] (a full para-substituted model compound). The vibration pattern in the IR spectrum is independent of the oxidation time used in the film growing and also of the time of voltammetry cycling after the film was already formed (in the absence of [2]). This indicates that the substitution pattern in p-[2] is the same at any film stage and, once it is deposited, its reoxidation would not increase the substitution in para- of the remaining (and free) phenyls. Consequently, the polymer precipitation freezes the reactivity of the unreacted phenyl groups, virtually preventing the film from obtaining further interweaving.

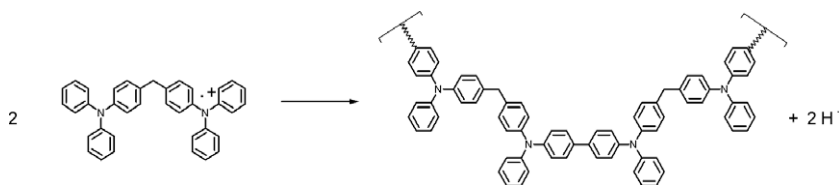


Fig. 5. Proposed reaction for electropolymerization of [2].

Molecules that present two electronically connected redox sites show intervalence charge transfer phenomena when they are in certain oxidation states. According to the degree of electronic interaction between these sites, intervalence compounds have been classified by Robin and Day in three classes [21–24]. In Class I compounds, both redox centers have different chemical surroundings and the valence is located in one of them at any time scale. In Class II, both redox centers present small structural differences although the valence is still located in one of them at the vibrational time scale ( $10^{-12}$  s). In Class III, the valence is delocalized as much in the time scale of the vibrations as in the spatial distribution of electron density. In Classes II and III, the greater electronic interaction shows up by the appearance of an electronic transition called intervalence charge transfer, and by a disturbance in the redox potentials compared to the isolate fragments (i.e. without electronic interaction). Although the original classification applies to inorganic extended solid compounds, organic radicals with two electroactive sites can also be classified using this criterion [25–28].

In the case of [1], the cyclic voltammetry and the UV–vis spectrum show a remarkable similarity to TTA [29], suggesting that the arylamine fragments that compose [1] would behave independently. This is consistent with the absence of intervalence band in the NIR. So, we can infer that [1] is a Class I intervalence compound. The uncoupling phenomena observed between redox centers can be associated with the fragment that connects arylamines. The presence of a tetrahedral methylene carbon allows adjacent phenyl rings (pertaining to different triarylamine) to take a space conformation so that the planes containing them are  $90^\circ$  rotated to each other. This conformation diminishes repulsion energy between phenyls due to hydrogen neighboring, and induces a symmetry that prevents the  $\pi$ -orbital interaction [30]. This fact derives in each redox site being not sensitive to the other, and therefore, polymerization from triarylamine to benzidine in one side of the molecule would not electronically disturb the capacity of the other site to react in the same way and efficiency.

It has been previously reported [18] that branching in arylamine polymers is a less likely event than the formation of linear chains. Cationic radicals lying in the backbone of the polymer are more delocalized than the terminal ones, thus diminishing the charge at the reactive position. As a consequence, polymerization via terminal arylamines should be preferable (and faster) because the terminal cation is more reactive. This argument also suggests that the linear chains of [2] formed during the early

stages of polymerization correspond to Fig. 6a and not to Fig. 6b because the first one is the faster process, as it does not involve any of the arylamines that already participate in benzidines (a much less reactive cation).

High amounts of disconnected benzidines would also be responsible for the slow electrochromic response in comparison with other published arylamine polymers. The absence of delocalization may produce electronic hopping, being the preferred charge transport mechanism between isolated benzidines in the film and there would be no conduction through electronic bands.

The relationship between electronic coupling and the twist degree between adjacent arylamine fragments in substituted TPB analogs has been previously reported [30]. The presence of methyl groups in positions 2 and 6 twists the rotation planes of adjacent rings, interrupting the  $\pi$ -conjugation along the molecule. This phenomenon is translated both in a substantial change in the UV–vis spectra (including the intervalence band) and in the separation of successive redox potentials ( $\Delta E$ ), another indication of coupling. The UV–vis spectra of TPB fragments in p-[2] in their mixed valence state (Fig. S4, see Supplementary material) showed remarkable similarity with specie 4 of Ref. [30] in which the whole molecule is coplanar and highly coupled. Although the small  $\Delta E$  makes p-[2] comparable to the less coupled TPB examples (species 5a and 5b in Ref. [30], the most twisted ones), we think that this indication of coupling is not reliable because the matrices that contain the electroactive species are different (solid film versus solution). Thus, we think that the TPB fragments that are comprised in the film of p-[2] are planar and that

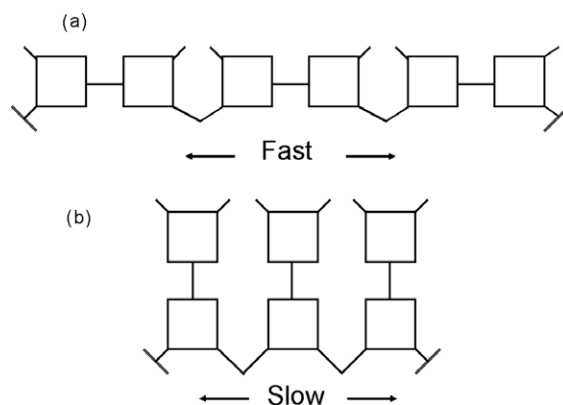


Fig. 6. (a) More efficient polymerization mechanism proposed, (b) slower possibility.



the arylamine coupling is the same as that observed in specie 4 of Ref. [30].

## 5. Conclusions

In the present work, an electrochromic film formed by cross linked phenylbenzidines was synthesized by electrochemical methods. This synthesis is much simpler than a multi-step polymerization approach. The film remained stable during the oxidation/reduction cycling. Its high insolubility in several solvents (hexane, cyclohexane, toluene, dichloromethane, acetonitrile, methanol, ethanol and water) makes it useful in layered devices production because it allows using spin coating mixtures without any risk of dissolution. The suggested polymerization pattern would allow the introduction of diverse substituents (donors, acceptors, ionophores) through covalent unions with unsubstituted phenyls, which would allow its use in fields like optoelectronics, manufacture of electrochromic devices and sensors, etc. We are also working on the chemical modification of the methylene spacer in order to explore the effect of different bridges in adhesive and electronic properties.

## Acknowledgements

We are grateful to Mireille Perec for helping in preliminary FT-IR measurement, Fernando Fungo and Luis Otero for helpful discussions and manuscript revision, and INQUIMAE staff for technical support. ARP is a staff member of CONICET. CLR is a recipient of a doctoral scholarship from CONICET.

## Appendix A. Supplementary material

Supplementary data associated with this article can be found, in the online version, at [doi:10.1016/j.orgel.2009.03.019](https://doi.org/10.1016/j.orgel.2009.03.019).

## References

- [1] O. Nuyken, S. Jungermann, V. Wiederhorn, E. Bacher, K. Meerholz, *Monatshfte für Chem.* 137 (2006) 811.
- [2] Yasuhiko Shirota, *J. Mater. Chem.* 10 (2000) 1.
- [3] M. Holzapfel, C. Lambert, *J. Phys. Chem. C* 112 (2008) 1227.
- [4] C.W. Tang, S.A. Van Slyke, *Appl. Phys. Lett.* 51 (1987) 913.
- [5] J. Xu, Y. Zhang, J. Hou, Z. Wei, S. Pu, J. Zhao, Y. Du, *Eur. Polymer J.* 42 (2006) 1154.
- [6] H.Z. Chen, Y.D. Jin, R.S. Xu, B.X. Peng, H. Desseyn, J. Janssens, P. Heremans, G. Borghs, H.J. Geise, *Synth. Met.* 139 (2003) 529.
- [7] C. Belot, C. Filiatre, L. Guyard, A. Foissy, M. Knorr, *Electrochem. Commun.* 7 (2005) 439.
- [8] H. Shirikawa, E.J. Louis, A.G. MacDiarmid, C.K. Chiang, A.J. Heeger, *J. Chem. Soc. Chem. Commun.* (1977) 578.
- [9] N.M. Patil, A.A. Kelkar, R.V. Chaudhari, *J. Mol. Cat. A: Chem.* 223 (2004) 45.
- [10] A. Petr, C. Kvarnstrom, L. Dunsch, A. Ivaska, *Synth. Met.* 108 (2000) 245.
- [11] I. Noviantri, K. Brown, D.S. Leming, *J. Phys. Chem. B* 103 (1999) 6713.
- [12] E.T. Seo, R.F. Nelson, J.M. Fritsch, L.S. Marcoux, D.W. Leedy, R.N. Adams, *J. Am. Chem. Soc.* 88 (15) (1966) 3498.
- [13] A.J. Bard, L.R. Faulkner, *Electrochemical Methods*, John Wiley & Sons Inc., 1980.
- [14] J. Natera, L. Otero, L. Sereno, F. Fungo, *Macromolecules* 40 (2007) 4456.
- [15] K.Y. Chiu, T.X. Su, J.H. Li, T.H. Lin, G.S. Liou, S.H. Cheng, *J. Electroanal. Chem.* 575 (2005) 95.
- [16] F.F. Runge, *Poggendorfs Ann. Physik u. Chem.* 31 (1834) 513.
- [17] J. Fritzsche, *J. für Prakt. Chem.* 20 (1840) 454.
- [18] C. Lambert, G. Nöll, *Synth. Met.* 139 (2003) 57.
- [19] L. Otero, L. Sereno, F. Fungo, Y.L. Liao, C.Y. Lin, K.T. Wong, *Chem. Mater.* 18 (2006) 3495.
- [20] J.M. Son, T. Mori, K. Ogino, H. Sato, *Macromolecules* 32 (1999) 4849.
- [21] M.B. Robin, P. Day, *Adv. Inorg. Chem. Radiochem.* 10 (1967) 247.
- [22] G.C. Allen, N.S. Hush, *Prog. Inorg. Chem.* 8 (1967) 357.
- [23] C. Creutz, *Prog. Inorg. Chem.* 30 (1983) 1.
- [24] R.J. Crutchley, *Adv. Inorg. Chem.* 41 (1994) 273.
- [25] C. Lambert, G. Nöll, *J. Am. Chem. Soc.* 121 (1999) 8434.
- [26] C. Lambert, G. Nöll, *J. Schelter, Nat. Mater.* 1 (2002) 69.
- [27] V. Coropceanu, C. Lambert, G. Nöll, J.L. Bredas, *Chem. Phys. Lett.* 373 (2003) 153.
- [28] V. Coropceanu, N.E. Gruhn, S. Barlow, C. Lambert, J.C. Durivage, T.G. Bill, G. Nöll, S.R. Marder, J.L. Bredas, *J. Am. Chem. Soc.* 126 (2004) 2727.
- [29] S. Granick, D.L. Michaelis, *J. Am. Chem. Soc.* 62 (1940) 2241.
- [30] P.J. Low, M.A.J. Paterson, A.E. Goeta, D.S. Yufit, J.A.K. Howard, J.C. Cherryman, D.R. Tackleyb, B. Brown, *J. Mater. Chem.* 14 (2004) 2516.

operation temperature [14], film crystallinity and electrode structure [15] on electric fatigue were systematically studied and fatigue recovery was observed in fatigued films after a long-time rest [16]. However, ferroelectric polymers are semi-crystalline with coexistence of amorphous and crystalline phases and thus have more complicated morphology than inorganic ferroelectrics. All these experimental results mentioned above originated from microscopic measurements and were the complicated average of fatigue in thousands of ferroelectric domains. To reveal the mechanism of polarization fatigue, it is necessary to characterize fatigue from microscopic viewpoint. In this paper, we tried to understand polarization fatigue from SPM-based experimental observations.

## 2. Experimental

Copolymer films were spin-coated on electrode-deposited glass slides from a 5.0% by weight solution of 78/22 P(VDF-TrFE) in butanone. The films had a thickness of  $\sim 800$  nm and were annealed at  $142$  °C for 6 h to increase their crystallinity. Both top Au and bottom Al electrodes were vacuum deposited. The top electrodes had a round shape with a thickness of 15 nm and a diameter of 1.0 mm.

The simultaneous measurements of microscopic surface vibrations and macroscopic polarization–voltage ( $P$ – $V$ ) hysteresis loops were performed by an integration of a home-made sawyer–Tower circuit and a scanning probe microscope (SPM, Ultraobjective, SIS, Germany), as shown in Fig. 1. An AC driving signal and a DC driving signal were superposed by an additional circuit SUM and were applied onto ferroelectric films. The switching current through sampling resistance  $R$  was recorded by an oscilloscope OSC, the integration of which resulted in macroscopic  $P$ – $V$  loops. Thus we could get the value of remanent polarization ( $P_r$ ) at different fatigue stages, which would be used to characterize macroscopic electric fatigue. Voltage-excited local vibrations were detected by SPM's probe, which was located at a fixed position on a sample surface. SPM

worked in a tapping mode and the probe was made of silicon with resonance frequency of 75.6 kHz. When the amplitude of the applied voltage was lower than that of the coercive voltage (for the films used in our experiments, this value was about 40 V), the detected local vibrations were linearly dependent on the driving voltage. However, when the amplitude of driving voltage had exceeded that of the coercive voltage, though local vibrations could still be observed, these vibrations were no longer linearly dependent on the driving voltage. In a driving cycle, dual vibration peaks had been induced and these nonlinear vibrations were caused by ferroelectric switching [17]. Local butterfly loops could be obtained by plotting these nonlinear vibrations as a function of driving voltage. With this integration system, we observed the evolution of local vibrations and macroscopic  $P$ – $V$  loops during fatigue process. Polymer films were fatigued by applying an alternating triangular voltage with amplitude of 100 V, high enough to cause ferroelectric switching, and frequency of 500 Hz. The fatigue process was interrupted at precalculated intervals to conduct measurements of macroscopic  $P$ – $V$  loops and local vibrations.

## 3. Results

Typical SPM morphology of a well-grown P(VDF-TrFE) films is shown in Fig. 2. Film surface was covered with lamellar crystallites with dimensions of  $\sim 500$  nm length and  $\sim 120$  nm width. In this paper local vibrations at two certain locations were characterized by SPM: one was just on the crystallites, as indicated by solid squares in Fig. 2, the other was at the boundaries between crystallites, as indicated by solid circles.

Firstly, we reported the dependence of local piezoelectricity on electric fatigue. A bipolar triangular driving voltage with amplitude of  $70 V_{pp}$  (lower than the coercive voltage) and frequency of 5.0 Hz was applied to the sample after a given switching cycle and the voltage-excited vibration was detected by SPM. The typical result is shown in Fig. 2. Local vibration (Fig. 2b) of virgin sample displayed a linear dependence on driving voltage with a peak-to-peak vibration displacement of  $\sim 2.36$  nm. With the increased fatigue cycles, vibration amplitude gradually decreased. After  $2.30 \times 10^5$  cycles (curve c), the peak-to-peak displacement decreased to  $\sim 1.66$  nm, but local vibration still showed a linear dependence on driving voltage. However, after  $1.28 \times 10^6$  cycles (curve d), vibration amplitude induced by driving voltage was so small that it was hard to be distinguished from noise.

Macroscopic fatigue rate was determined by the decrease of  $P_r$ . Microscopic fatigue rate was characterized according to the attenuation of local piezoelectric coefficient  $d_{33}$ , which was defined as:

$$d_{33} = A_{pp}/V_{pp} \quad (1)$$

where  $A_{pp}$  was the peak-to-peak vibration amplitude in nanometer, excited by a voltage with peak-to-peak amplitude  $V_{pp}$ . According to both definitions we could study electric fatigue at different characteristic locations (crystallites and boundaries in this paper).

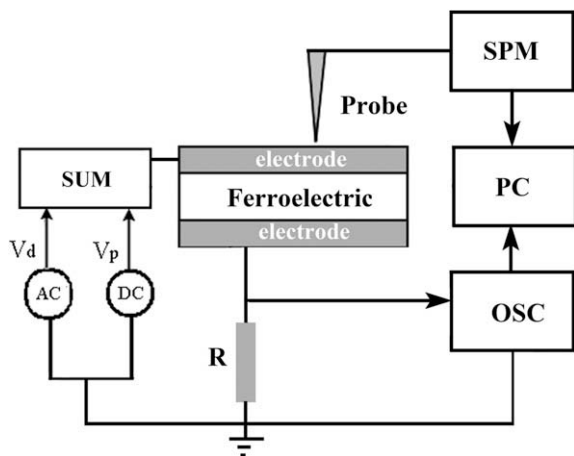
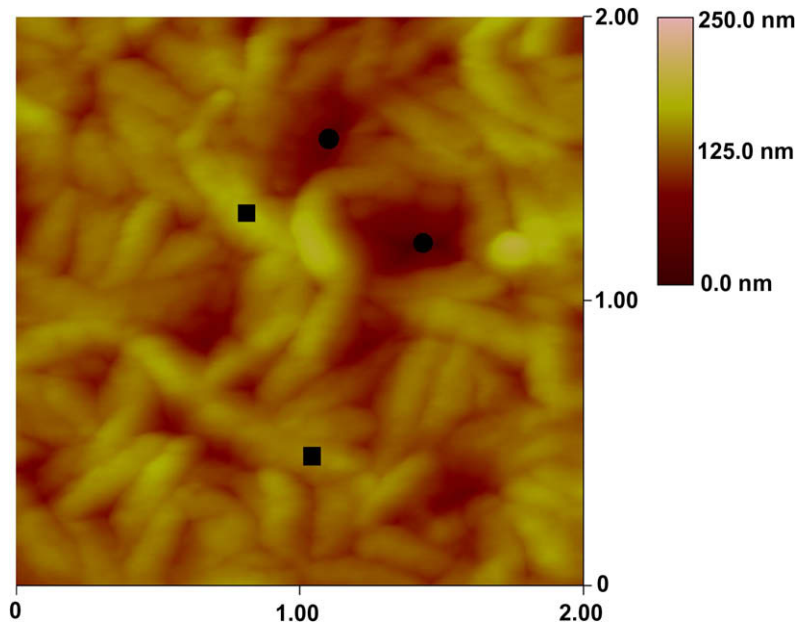
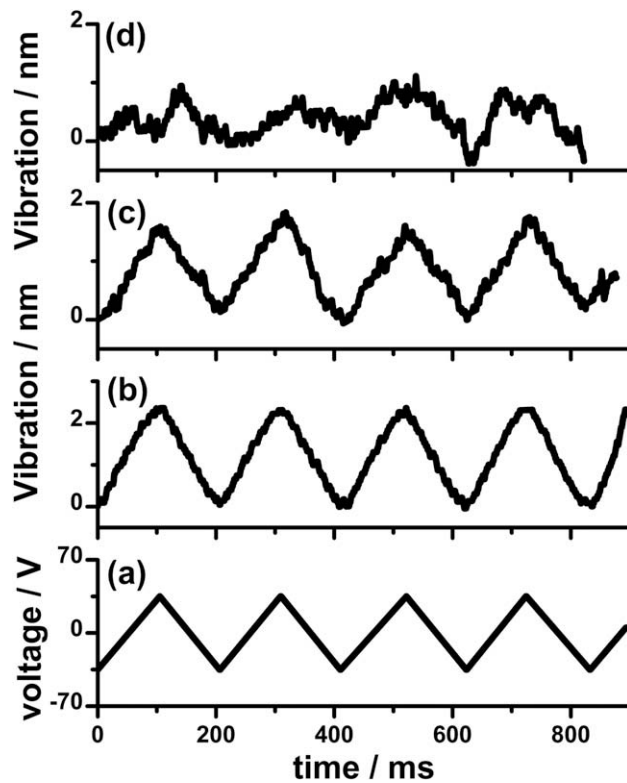


Fig. 1. Schematic diagram for the simultaneous measurements of local vibrations and macroscopic  $P$ – $V$  loops.



**Fig. 2.** SPM morphology of a well-grown P(VDF-TrFE) film, which was obtained on film surface without top electrode. Several spots are marked to indicate the possible sampling locations to be used for microscopic observations: crystallites are indicated by solid squares and boundaries between crystallites are indicated by solid circles.



**Fig. 3.** Local vibrations detected by the SPM's probe at the boundaries between crystallites. Curve (a) indicates the driving voltage with amplitude of 70 V<sub>pp</sub> and frequency of 5.0 Hz. Curve (b) indicates the voltage-driven local vibrations before fatigue and curves (c) and (d) indicate recorded local vibrations after (c)  $2.30 \times 10^5$  and (d)  $1.28 \times 10^6$  fatigue cycles.

In Fig. 4 a typical experimental result of local electric fatigue on crystallites is shown. For comparison, macroscopic fatigue rate was also plotted. It was very clear that the attenuation of local vibration amplitude was much slower than the decrease of macroscopic Pr. Two kinds of local fatigue processes were observed on crystallites. From Fig. 4a, it can be seen that with the increase of fatigue cycles, local vibration amplitude measured on crystallites also gradually decreased, though the local fatigue rate was slower than the macroscopic fatigue rate obtained from the decrease of Pr. For example, after  $1.86 \times 10^7$  fatigue cycles, macroscopic Pr decreased to 52.6% of its original values, while local vibration amplitude only decreased to 86.4% of its original value. Interestingly, in Fig. 4b, we observed a nearly unchanged local vibration, though macroscopic Pr had decreased to 70% of its original value after  $4 \times 10^7$  cycles in our experimental observation. Both phenomena were observed just on crystallites.

In Fig. 5 a typical fatigue characteristic observed at the boundaries between crystallites is shown. Again, for comparison, macroscopic fatigue rate defined by the decrease of Pr with fatigue cycles was plotted. Different from the slow decrease of local vibration amplitude observed on crystallites, local vibration amplitude measured at boundaries greatly decreased with fatigue cycles and the local fatigue rate was much faster than macroscopic rate from the decrease of Pr (Fig. 5a, compare the black curve with the blue one). For example, after  $3.8 \times 10^5$  fatigue cycles, macroscopic Pr only attenuated to 86.3% of its original value, while local vibration amplitude had decreased to 48.4% of its original value. We observed this fast attenuation of local vibration amplitude at all boundaries between crystallites. However, at some boundaries, with the further increase of fatigue cycles, we observed a surprising increase of local vibrations, though the macroscopic Pr continuously decreased, as indicated by the red curve shown in Fig. 5a. At this boundary, the local vibration amplitude firstly decreased to 34.6% of its original value after  $6.8 \times 10^5$  fatigue cycles, then, with the continuous increase of fatigue cycles, local vibration amplitude began to increase and rapidly

reached double of its original value after  $9.4 \times 10^6$  cycles and finally remained at this value until the end of our experimental observation. In fact, after local vibration amplitude began to increase abnormally, the voltage-excited local vibration was no more linearly dependent on the applied voltage but showed a rounded shape, as shown in Fig. 5b. A simple quadratic relationship could be used to well fit such a local vibration with respect to the applied voltage.

If an alternating voltage with amplitude larger than that of coercive voltage of ferroelectric films was applied to the sample, ferroelectric switching would occur when the voltage reached the value of coercive voltage. Ferroelectric switching would result in the occurrence of dual-peak vibrations and then local butterfly loops. A typical dual peak vibration is shown in Fig. 6a. Local butterfly loops could be obtained by plotting local vibration as a function of driving voltage, as shown in Fig. 6b. By this means the evolution of local butterfly loops at different fatigue levels could also be used as a characteristic to evaluate fatigue process.

Macroscopic  $P$ - $V$  loops and microscopic butterfly loops were simultaneously recorded during fatigue process. Both kinds of loops were measured by a poling voltage with amplitude of 80 V and frequency of 1.0 Hz. In this experiment, at each sampling point, three measurements were conducted: macroscopic  $P$ - $V$  loop, measured by Sawyer-Tower circuit, and local butterfly loop on a given crystallite and local butterfly loop at a given boundary, measured by SPM. The evolution of both kinds of loops with increased fatigue cycles is shown in Fig. 7.

Before fatigue, the film showed a  $P$ - $V$  loop with a rectangle shape (Fig. 7a1), which implied high crystallinity from macroscopic viewpoint. The local butterfly loop on the crystallite (Fig. 7b1) exhibited a relatively sharp ferroelectric switching. However, the local loop obtained at the boundary showed a rounded shape with a wide distribution of ferroelectric switching from 30 to 70 V.

With the increase of fatigue cycles, macroscopic loops gradually became rounded and the remanent polarization

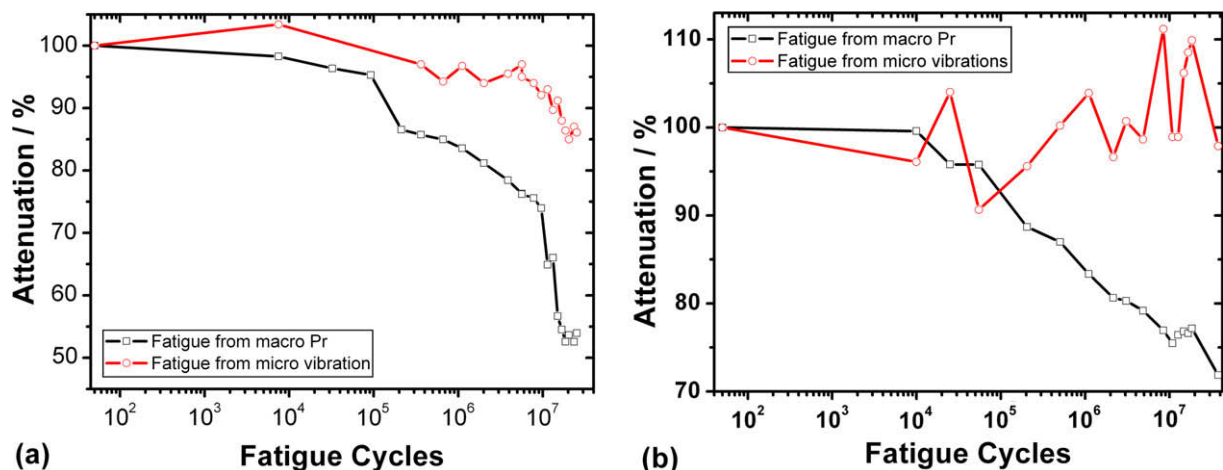
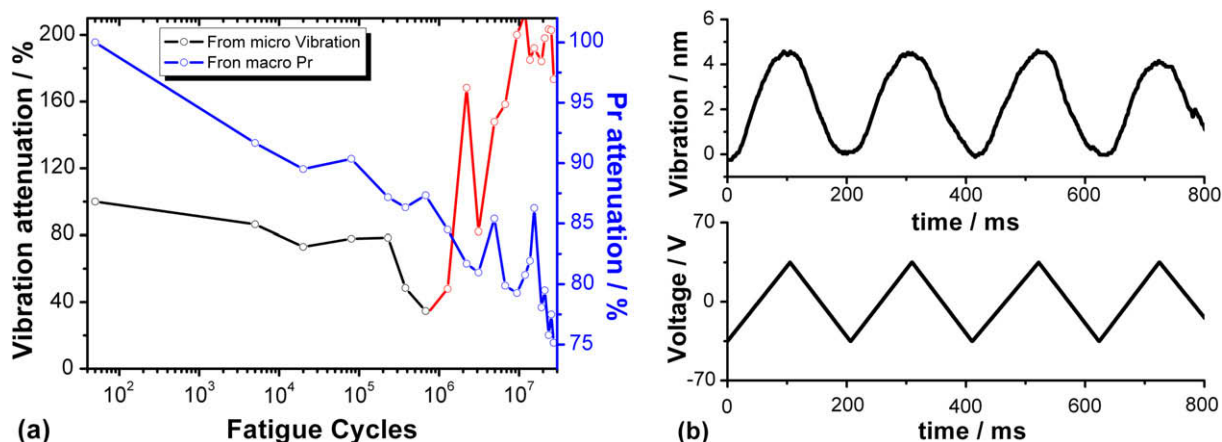
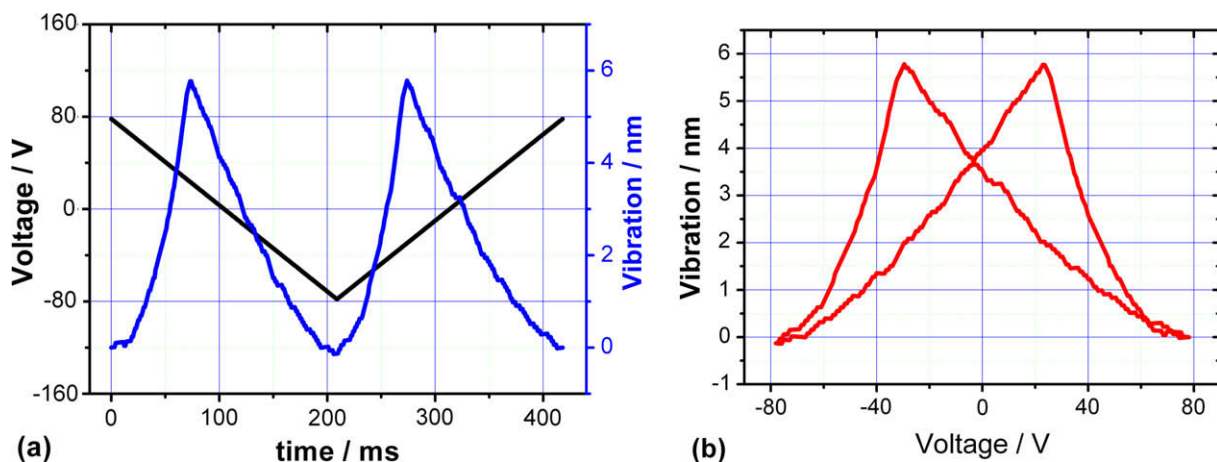


Fig. 4. Polarization fatigue characterized by the attenuation of macroscopic Pr of the whole film (black curves) and local  $d_{33}$  just on crystallites (red curves). (For interpretation of the references to colour in this figure legend, the reader is referred to the web version of this article.)



**Fig. 5.** (a) Dependence of polarization fatigue on fatigue cycles and (b) voltage-excited local vibration after  $1.19 \times 10^7$  fatigue cycles. Local vibration was measured at the boundaries between crystallites. In Fig. 5a, electric fatigue is characterized by the attenuation of macroscopic Pr (blue curve) and local  $d_{33}$  (black and red curves). In Fig. 5b, the lower curve shows the applied triangular voltage with amplitude of  $70 V_{pp}$  and frequency of 5.0 Hz and the upper curve shows the local vibrations. (For interpretation of the references to colour in this figure legend, the reader is referred to the web version of this article.)



**Fig. 6.** (a) Local dual-peak vibrations and (b) the local butterfly loop. In Fig. 6a, the black curve indicates a whole cycle of the applied voltage with amplitude of  $156.0 V_{pp}$  and frequency of 2.4 Hz and the blue curve indicates the voltage-excited local vibration. The film had been fatigued by  $2.20 \times 10^5$  cycles.

Pr decreased from the original value of  $0.091 C/m^2$  (a1) to  $0.074 C/m^2$  (a2) and  $0.057 C/m^2$  (a3), corresponding to fatigue cycles of  $2.00 \times 10^5$  (a2) and  $1.60 \times 10^7$  (a3). Local butterfly loops also revealed some interesting changes. For the loops obtained on crystallites, with increased fatigue cycles, ferroelectric switching became smoother and smoother, the change in film thickness decreased from 5.86 nm (b1), 5.3 nm (b2) to 3.3 nm (b3). For loops observed at boundaries, the change in film thickness decreased with increased cycles from 5.3 nm (c1) to 4.4 nm (c2), as was the same as that observed on crystallites; however, at some boundaries we also observed an abnormal increase of film thickness with further fatigue cycles (9.5 nm in Fig. 3c) and local butterfly loop displayed a slim shape (that is to say, for a given voltage, the change in film thickness due to ferroelectric switching was almost similar as that due to piezoelectricity) at such a situation. We should emphasize again that this slim loop was only observed at

few boundaries. Such a slim loop was very similar to that observed from electron-irradiated P(VDF-TrFE) films [18]. Different from relaxor ferroelectric behavior in electron-irradiated P(VDF-TrFE) films, in our experiments, the slim loops were only observed in microscopic measurements and macroscopic  $P$ - $V$  loops still showed large hysteresis.

#### 4. Discussions

Compared to inorganic ferroelectrics, ferroelectric polymers have more complicated morphology with coexistence of crystalline phase and amorphous phase. Macroscopic fatigue characterization in ferroelectric polymers was only a complicated average of fatigue characteristic from microscopic structures, such as crystallites, amorphous phase and boundaries between crystallites. To understand fatigue mechanism, it is necessary to distinguish different contributions from different microscopic structures. The changes

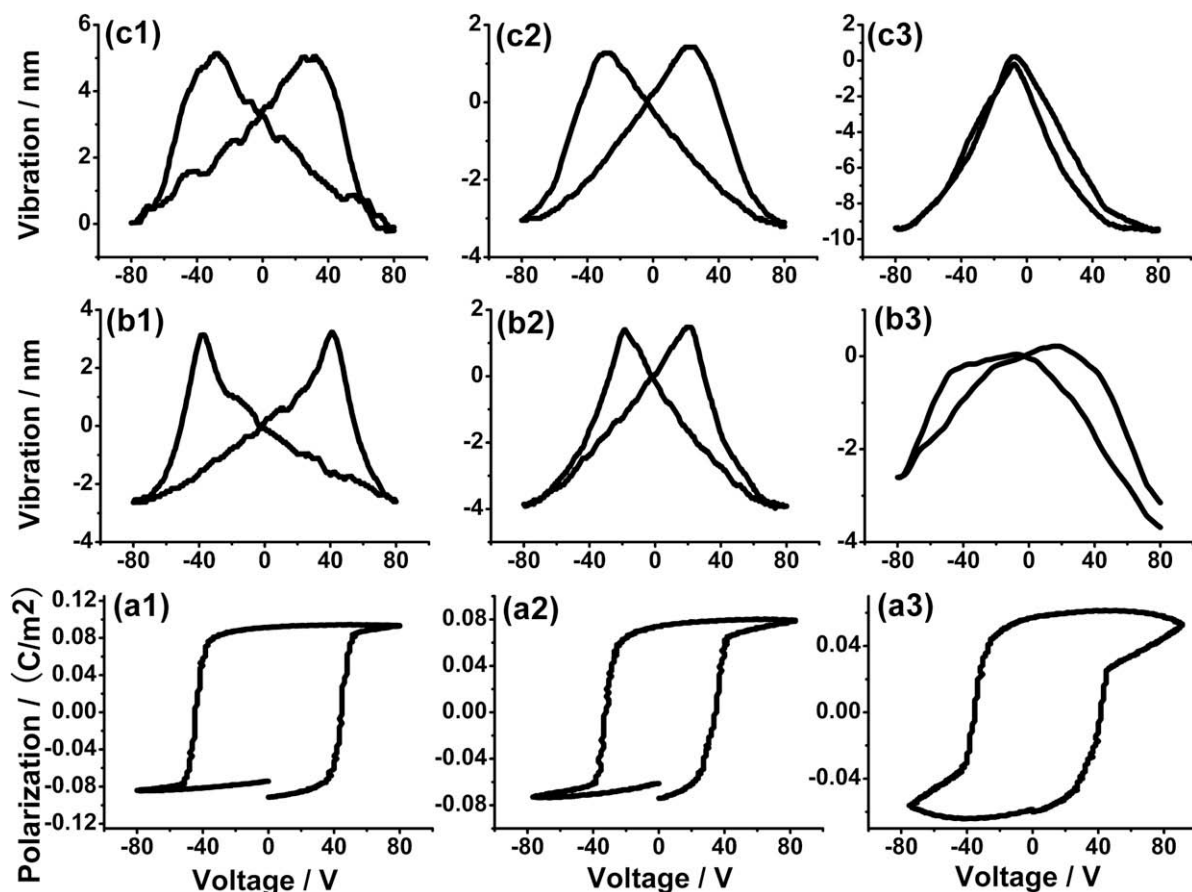


**Fig. 7.** The evolution of (a) macroscopic  $P$ - $V$  loops measured by Sawyer–Tower circuit and local butterfly loops obtained (b) on the crystallite and (c) at the boundary between crystallites with increased fatigue cycles. Loops a1, b1 and c1 were measured before the sample was fatigued. Loops a2, b2 and c2 were measured after  $2.00 \times 10^9$  fatigue cycles and loops a3, b3 and c3 were measured after  $1.60 \times 10^7$  cycles.

of local piezo- and ferro-electricity with increased fatigue cycles are measured in our experiments. Here we will make some discussions on our microscopic fatigue characterization.

#### 4.1. About our characterization technique of microscopic fatigue

AFM is well known for its excellent lateral resolution down to an atomic scale. The lamellar crystallites of P(VDF-TrFE) are known to be about several tens of nanometers thick [19], and considerably larger in the other two directions (by electron microscopy it has been found that the crystallites can have lateral size up to 3  $\mu\text{m}$  [20]), and these crystallites are known to be oriented with their large dimensions perpendicular to the surface [21]. So the local vibrations, detected by SPM, are not averaged properties of several adjacent structures in the directions parallel to sample plane, but vibrations on a single crystallite or just at one boundary. However, films used in this paper are about 800 nm thick, so it should be a complicated combination of crystallites, boundaries and even amorphous phase in the direction normal to the film plane, that is to say, the observed local vibrations are most likely the

integrated results of all these local structures (crystallites, boundaries and amorphous phase) along film-thickness direction. However, in our microscopic measurements, we do observe the shape difference of local butterfly loops on crystallites and at boundaries (Fig. 7). It should not be an occasional observation because we have detected similar results on several films. We still cannot understand why we observe such a difference, though it seems to imply that local vibrations are more sensitive to the structure near the surface. Further work should be done to give a reasonable explanation. Also to distinguish the different contributions of crystallites, boundaries and amorphous phase to electric fatigue, it is necessary to prepare ultrathin ferroelectric polymer films to make sure that only one structure exists along the direction normal to film plane. Langmuir–Blodgett technique should be preferable to get such a high-quality ultrathin film. In this paper we only put forward a possible method to characterize local electric fatigue.

#### 4.2. About the origination of electric fatigue

Many macroscopic experiments have been conducted on ferroelectric fatigue in polymers [9–16]. All these experimental observations seem to imply the charge effect on

fatigue. In fact, trapped charge is a crucial factor in fatigue origination of inorganic ferroelectrics [8]. With increased switching cycles, more and more charges are injected into ferroelectrics through electrodes and trapped at the boundaries between crystallites and captured by the defects in crystallites and especially in amorphous phase. These trapped charges in ferroelectrics inhibit the reversal of electric dipoles and thus induce polarization fatigue. So fatigue in polymers should depend on voltage profile, electrode structure, film morphology (crystallinity and defects) and so on. Our previous work reported the effect of film crystallinity on ferroelectric fatigue and found the well-grown P(VDF-TrFE) films show a much better fatigue endurance than films with low crystallinity [22], as was due to the amorphous phase in low-crystallinity films that had more defects and could trap more charges.

In this paper, local fatigue observed on crystallites shows a slower rate than macroscopic fatigue rate from the whole film, while local vibration amplitude at boundaries show a much faster attenuation, though at some boundaries we observe an abnormal increase of vibration amplitude at deep fatigue state. This can be well understood according to fatigue mechanism mentioned above. In the study of ferroelectricity in polymers, Eisenmenger, et al. [23] proposed an opinion that space charges would prefer to be trapped at boundaries between crystallites. Furthermore, from the lamella model the boundaries between crystallites should consist of most of amorphous phase with much lower crystallinity [24]. So more charges can be accumulated at boundaries, as results in the worse fatigue endurance. However, we have to emphasize again that here we have only considered the structures on surface or near the surface and not the complicated combination along film-thickness direction. We believe that space charges are captured preferentially by defects and boundaries on surface or subsurface and then by these structures in the film.

#### 4.3. About the slim butterfly loops

In the measurements of local butterfly loops, especially at some boundaries, we observed slim loops (Fig. 7 curves b3, c3) in deeply fatigued films, though macroscopic  $P$ - $V$  loops still show large hysteresis. Zhang, et al. [18] attributed the slim hysteresis loops in electron-irradiated P(VDF-TrFE) films to the formation of relaxor ferroelectric: electron irradiation broke up polarization domain in normal ferroelectric copolymer into nanopolar regions. In our fatigue researches, for the whole ferroelectric films, it is hard to transfer normal ferroelectric polymer into relaxor ferroelectric only by millions of ferroelectric switching which can only inject a finite number of charges into ferroelectric. However, a much large local charge density can be expected at some local areas, especially at some boundaries which have lower crystallinity and more defects. So it is very possible that such local areas can possess part of relaxor ferroelectric behaviors and show slim loops. But in our present work we still have not observed such a relaxor-like behavior on any of crystallites, as may be due to the limited fatigue cycles and much high crystallinity.

#### 4.4. About the abnormal increase of vibration amplitude

In this paper we characterize both microscopic fatigue processes according to the attenuation of local vibration amplitude and macroscopic fatigue according to the decrease of  $P_r$ . It is usually believed that voltage-excited surface vibration in ferroelectric polymers originates from the dimensional effect, which is linearly dependent on driving voltage, and the electrostriction, which is proportional to the square of the applied voltage. For normal ferroelectric polymers, vibrations induced by electrostriction effect can be negligible. Macroscopic measurements have already approved that piezoelectric coefficient has a linear dependence on spontaneous polarization in ferroelectric polymers [25,26]. So the voltage-excited local vibration amplitude can be regarded as a measurement of local polarization at the certain location and the attenuation of local vibrations can be used to compare with macroscopic decrease of  $P_r$ .

In deeply fatigued films, we observe an abnormal increase of vibration amplitude at some of boundaries between crystallites, which is no more linearly dependent on the driving voltage and can be fitted according to a simple quadratic relationship with respect to the voltage ( $V$ ). However, it must be emphasized that such large local vibrations are not only dependent on  $V^2$ , but also determined by the polarity of this voltage. The voltage-excited vibrations have the same frequency as driving voltage. This is very different from the effect of electrostriction, which is defined only by  $V^2$  and the vibration frequency due to electrostriction should double the frequency of driving voltage. It is regarded that the abnormal increase of vibration amplitude in fatigued films should be the combined action of dimensional effect, electrostriction and the interaction between the applied electric field and trapped charges. In this paper, we still cannot evaluate to what extent these three parts contribute to our experimental observations.

### 5. Conclusion

In this paper we characterized electric fatigue in ferroelectric polymers from the macroscopic decrease of remanent polarization and the microscopic attenuation of vibration amplitude measured on crystallites and at boundaries between crystallites. Experimental results indicated that local crystallites had much better fatigue endurance than the boundaries had. At few boundaries we observed an abnormal increase of local vibration amplitude at deep fatigue state, which was assumed to be due to the combined action of dimensional effect, electrostriction and the interaction between the applied electric field and trapped charges.

### Acknowledgments

This work was supported by National Natural Science Foundation of China (No. 10804020), Specialized Research Fund for the Doctoral Program of Higher Education of China (No. 200802461088) and Shanghai Leading Academic Discipline Project (B113).

## References

- [1] S. Ducharme, J. Reece, C.M. Othon, R.K. Rannow, *IEEE Trans. Device Mater. Reliab.* 5 (2005) 720.
- [2] T.J. Reece, S. Ducharme, A.V. Sorokin, M. Poulsen, *Appl. Phys. Lett.* 82 (2003) 142.
- [3] K.N.N. Unni, R. Bettignies, S. Dabos-Seignon, J.M. Nunzi, *Appl. Phys. Lett.* 85 (2004) 1823.
- [4] A. Matsumoto, S. Horie, H. Yamada, K. Matsushige, S. Kuwajima, K. Ishida, *Appl. Phys. Lett.* 90 (2007) 202906.
- [5] L. Zhang, S. Ducharme, J. Li, *Appl. Phys. Lett.* 91 (2007) 172906.
- [6] T.T. Wang, J.M. Herbert, A.M. Glass, *The Application of Ferroelectric Polymers*, Blackie and Son, Glasgow, 1988.
- [7] A.V. Bune, V.M. Fridkin, S. Ducharme, L.M. Blinov, S.P. Palto, A.V. Sorokin, S.G. Yudin, A. Zlatkin, *Nature* 391 (1998) 874.
- [8] A.K. Tagantsev, I. Stolichnov, E.L. Colla, N. Setter, *J. Appl. Phys.* 90 (2001) 1387.
- [9] L.L. Guy, A. Limbong, Z. Zheng, D.K. Das-Gupta, *IEEE Trans. Dielectr. Electr. Insul.* 7 (2000) 489.
- [10] F. Fang, W. Yang, M.Z. Zhang, *J. Appl. Phys.* 101 (2007) 044902.
- [11] S. Nozaki, K. Ishida, A. Matsumoto, S. Horie, S. Kuwajima, H. Yamada, K. Matsushige, *Thin Solid Films* 516 (2008) 2450.
- [12] S. Horie, K. Ishida, S. Kuwajima, K. Kobayashi, H. Yamada, K. Matsushige, *Jpn. J. Appl. Phys.* 47 (2008) 1259.
- [13] G. Zhu, Z. Zeng, L. Zhang, X. Yan, *Appl. Phys. Lett.* 89 (2006) 102905.
- [14] G. Zhu, Z. Zeng, L. Zhang, X. Yan, *J. Appl. Polym. Sci.* 107 (2008) 3945.
- [15] G. Zhu, Z. Zeng, Q. Zhang, X. Yan, R. Liu, *J. Appl. Phys.* 103 (2008) 084125.
- [16] Z. Zeng, G. Zhu, R. Liu, Q. Zhang, X. Yan, *Microelectron. Eng.* 85 (2008) 2187.
- [17] G. Zhu, Z. Zeng, L. Zhang, X. Yan, J. Li, *J. Polym. Sci. B* 44 (2006) 3282.
- [18] Q.M. Zhang, V. Bharti, X. Zhao, *Science* 280 (1998) 2101.
- [19] K. Koga, H. Ohigashi, *J. Appl. Phys.* 59 (1986) 2142.
- [20] M.G. Broadhurst, G.T. Davis, J.E. McKinney, R.E. Collines, *J. Appl. Phys.* 49 (1978) 4992.
- [21] Y. Tajitsu, H. Ogura, A. Chiba, T. Furukawa, *Jpn. J. Appl. Phys.* 26 (1987) 554.
- [22] Z. Zeng, G. Zhu, L. Zhang, X. Yan, *Chin. J. Polym. Sci.* 27 (2009) 1.
- [23] M. Momes, E. Bihler, W. Eisenmenger, *IEEE Trans. Electr. Insul.* 24 (1989) 461.
- [24] M.G. Broadhurst, G.T. Davis, J.E. McKinney, R.E. Collins, *J. Appl. Phys.* 49 (1978) 4992.
- [25] T. Furukawa, J.X. Chen, K. Suzuki, Y. Takashina, M. Date, *J. Appl. Phys.* 56 (1984) 829.
- [26] C. Park, Z. Ounaies, K.E. Wise, J.S. Harrison, *Polymer* 45 (2004) 5417.



(on-grid) energy production lies somewhere in the future. There have been relatively few reports on large scale fabrication of polymer solar cells that explore the full potential of R2R processing [11–14] and common to all of them is that they employ indium-tin-oxide (ITO) as the transparent electrode. In one example a rigid cost-analysis based on the materials and effort consumed was made showing the actual cost [14]. This study underlined that polymer solar cells can conceivably be made at low cost but that this is not automatically granted and that this will only come at an effort. In addition any large scale commercial future for polymer solar cells is unlikely to be shared with ITO. In the latter case ITO accounted for ~30% of the overall module cost [14]. The commercially available substrates with ITO (rigid and flexible) are exclusively obtained via a vacuum coating step where the ITO is applied. A valiant cause is thus not only to alleviate the need for ITO but also the need for vacuum coating steps in the process as these add unnecessarily to the cost. It is not a simple matter to avoid the use of ITO as the process technology for polymer solar cells has evolved and matured to its current level with ITO and it is nearly implicit that the device illumination is through (the transparent) substrate that has ITO as the transparent conductor. One line of research simply replace the ITO with high conductivity PEDOT:PSS [15] or with a metallic grid or a thin metal with an overlayer of PEDOT:PSS [16–18] and otherwise employ a normal device geometry. Other methods either employ an inverted geometry or illumination through the back electrode [19]. Neither of the reported attempts however avoids the use of a vacuum coating step nor do they present full R2R compatibility with all solution processing. An additional desire is the possibility to process the devices entirely in the ambient atmosphere. While large scale processing can be envisaged in an inert and clean room environments the aim is to find the simplest process conditions to minimise the cost.

In this report a fully R2R compatible process to complete polymer solar cell modules is presented with processing of all five layers from solution on virtually any flexible substrate. The device geometry is inverted and there is no requirement for transparency of the substrate. The process is compatible with most polymer bulk heterojunction mixtures and is exemplified here using P3HT-PCBM as the active material.

## 2. Experimental

### 2.1. Materials

Poly(3-hexylthiophene) was prepared according to the McCullough route [20] and the purified material had a regioregularity >97% and  $M_n = 18,700$ ,  $M_w = 36,600$ ,  $M_p = 33,900$ , PD = 1.9. [60]PCBM was purchased from Solenne BV with a purity of 99%. Silver nanoparticles with an average diameter of  $100 \pm 15$  nm as determined by light scattering were used for slot-die coating the non-transparent back electrode as the first layer. Zinc oxide nanoparticles (ZnO np) were prepared and stabilized with methoxyethoxyacetic acid (MEA) as described earlier [21]. The thermocleavable solvent WS-1 was obtained as described in the

literature [22,23]. PEDOT:PSS was purchased as a screen printing paste from Agfa (Orgacon EL-P 5010, www.agfa.com). The silver electrode was purchased from Dupont as a screen printing paste (Dupont PV410, www.dupont.com). The PEN substrate was obtained from Dupont and had a thickness of 130 micron and a roll width of 305 mm. The material was used as received. Cold lamination with a mechanical protection layer was carried out after completion of the device on top of the silver back electrodes, using a 25  $\mu\text{m}$  thick Fasson overlaminating polyester material from Avery Dennison.

### 2.2. Ink formulations

#### 2.2.1. Silver back electrode ink

Silver nanoparticles ( $100 \pm 15$  nm) were dispersed in a 1:1 mixture of triethyleneglycolmonomethylether and ortho-xylene. The final concentration of silver nanoparticles was 25% (w/v) and used directly for printing after formulation.

#### 2.2.2. ZnO nanoparticle ink

A stock solution containing ZnO nanoparticles (5 g) in chlorobenzene stabilized with MEA (20% w/w) was mixed with WS-1 (20 mL) and evaporated at 70 °C for 30 min. The slightly turbid WS-1 solution of MEA stabilized ZnO nanoparticles was diluted with ortho-xylene (80 mL) and mixed well before filtering through a 0.45 micron Teflon filter. The final clear colourless solution was 50 mg mL<sup>-1</sup> in ZnO and was used directly for coating. The solution is stable for several weeks with the exclusion of moisture from the atmosphere.

#### 2.2.3. The P3HT-PCBM ink

P3HT (2.2 g) was dissolved in 1,2-dichlorobenzene (50 mL) at 90 °C with stirring for 3 h. PCBM (2.0 g) was added and the mixture was stirred for an additional 1 h at 90 °C. The mixture was then cooled and CHCl<sub>3</sub> (50 mL) was added. The final solution was 22 mg mL<sup>-1</sup> in P3HT and 20 mg mL<sup>-1</sup> in PCBM. The solution was allowed to stand at room temperature for 2 h before use. This repository time allows for aggregation that was found to be beneficial during coating. The ink was stable for several days at room temperature.

#### 2.2.4. The PEDOT:PSS and silver grid front electrode

A commercially available screen printing formulation (Agfa EL-P 5010) was diluted with isopropanol 10:5 (w/w) and stirred for 1 h using a large magnetic stirring bar. The best viscosity for the coating was found to be around 200 mPa s. The final viscosity was reached by adding a small amount of isopropanol. The final mixture was typically 10:6 (w/w). The solution was stable for several days at room temperature. The silver ink for screen printing the silver grid front electrode was used as received.

### 2.3. R2R processing

The R2R coating was carried out on a BC30 basecoater from Solarcoating Machinery GmbH (Germany). All coating

was performed with tension control on the web using the coating roller to drive the web at fixed speed. The system comprised: unwinder, corona treater (Arcotec), double roller edge guiding system (BST), double sided web cleaning unit (TekNek), tension roller, coating roller, ink jet printer for labelling (Domino), drier (1 m length), cooling roller, tension roller, speed monitoring roller and rewinder. The temperature and relative humidity during all the coating experiments described here were respectively,  $20 \pm 1$  °C and  $35 \pm 5\%$ rh.

### 2.3.1. Slot-die coating of the silver back electrode

The silver ink was slot-die coated at a web roll speed of  $0.9 \text{ m min}^{-1}$  and was dried in the hot air oven at  $130$  °C. The web was cleaned using adhesive rollers on both the front and backside of the web (TekNek). In order for the final silver to adhere better to the PEN surface a corona treatment was employed (1070 W) in conjunction with antistatic removal. This gave a highly reflective smooth and non-transparent silver back electrode (Fig. 1).

The electrode stuck well to the PEN and had a typical sheet resistance of  $0.01 \text{ } \Omega \text{ square}^{-1}$ . The pattern for the device structure has been presented earlier [11,13].

### 2.3.2. Slot-die coating of ZnO

The ZnO ink (Section 2.2.2) was slot-die coated with a web speed of  $0.7 \text{ m min}^{-1}$  and drying at  $130$  °C. The ZnO film was slightly opaque and insoluble in common organic solvents after the drying step. The position of the ZnO layer was off-set 1 mm with respect to the silver line allowing for later contact to be made to the silver bottom electrode that was prepared in Section 2.3.1. The serial connection between the individual cells of the module is shown in Fig. 2. The wet thickness of the layer was  $16 \text{ } \mu\text{m}$  and the

dry thickness of the layer was  $140 \text{ nm}$ . The coating of the ZnO is shown in Fig. 3.

### 2.3.3. Slot-die coating of P3HT-PCBM

The P3HT-PCBM ink (Section 2.2.3) was slot-die coated at a web speed of  $0.4 \text{ m min}^{-1}$ . The drying temperature was  $130$  °C. The wet thickness of the layer was  $17 \text{ } \mu\text{m}$  and the dry thickness of the layer was  $600 \text{ nm}$ . The coating of P3HT-PCBM is shown in Fig. 3.

### 2.3.4. Slot-die coating of PEDOT:PSS

The PEDOT:PSS solution was slot-die coated at a web speed of  $0.2 \text{ m min}^{-1}$ . It was necessary to wet the surface of the P3HT-PCBM layer with isopropanol immediately prior to coating 4 cm before the coating meniscus. Otherwise the PEDOT:PSS solution does not wet the surface of the P3HT-PCBM film. Drying at  $130$  °C yielded a dark blue semitransparent PEDOT:PSS film. The optical transmission of the PEDOT:PSS was  $>10\%$  in the range of wavelengths from  $350$  to  $750 \text{ nm}$  and  $>15\%$  in the range of wavelengths from  $375$  to  $650 \text{ nm}$  with a maximum of  $20\%$  at  $450 \text{ nm}$ . The sheet resistivity of the PEDOT:PSS layer was typically  $75\text{--}78 \text{ } \Omega \text{ square}^{-1}$  and the devices were functional at this point. To achieve a good extraction of carriers it was found necessary to apply a silver grid front electrode.

### 2.3.5. Sheet-fed screen printing of the silver front electrode grid

The silver front electrode grid was printed through a  $120$  mesh screen with the grid pattern. The printing speed was  $525 \text{ mm s}^{-1}$  and the sheets with the wet print were loaded into a rack. The time between printing and drying was kept as short as possible and was typically less than

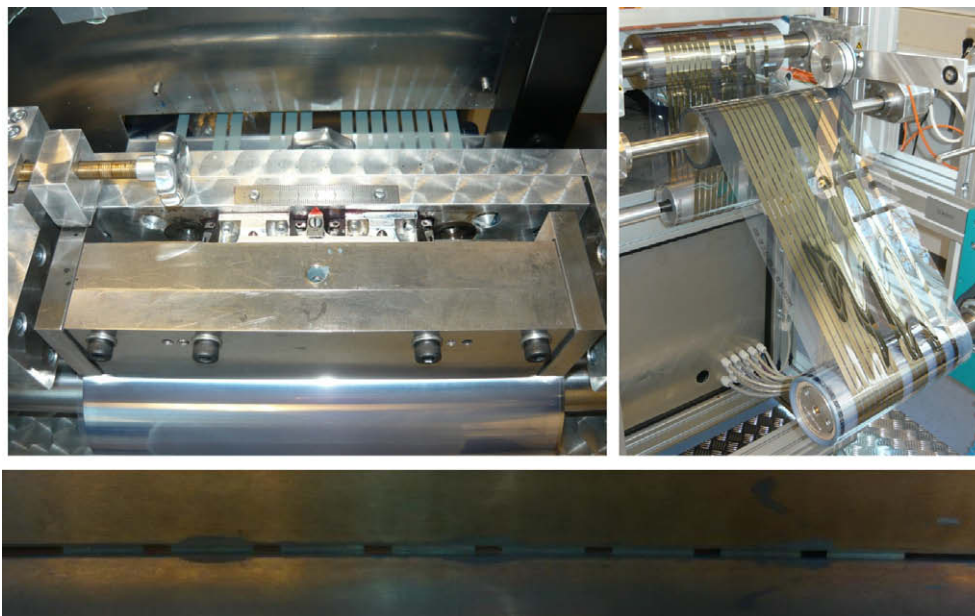


**Fig. 1.** Slot-die coating of the silver back electrode onto PEN. The wet print that has an opaque green colour is seen behind the slot-die coating head (top right). The dried and highly reflective silver back electrode is shown on the rewinding side (top right). The menisci during coating of the eight stripe module is also shown. (For interpretation of the references to colour in this figure legend, the reader is referred to the web version of this article.)

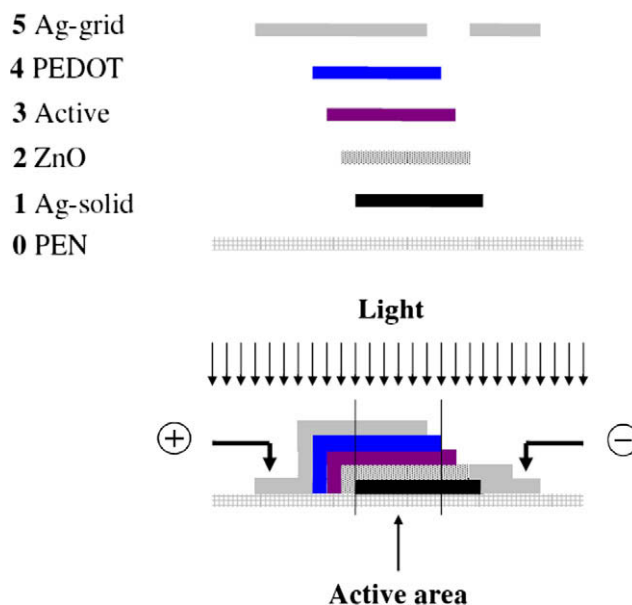


**Fig. 2.** Schematic cross section of the device showing the order of the layers and their juxtaposition. With each coating cycle the position of the layer was shifted 1 mm to the left (on the figure). The device comprising 1 stripe is shown.

10 min for the first print. Batches of 40 sheets were processed each time. The rack was then loaded into a hot air oven preset at 140 °C. Upon introduction the temperature in the oven drops due to the heat capacity of the rack and the rack was left in the oven for 10 min during which time a temperature of 140 °C was reached after about 5 min. The devices were then removed from the oven and were cooled in air.

#### 2.4. Device testing

The devices were either characterised as prepared or cold laminated with a 25  $\mu\text{m}$  PET film using an acrylic adhesive. Electrical contacts were made with alligator clips and electrical measurements of the IV-characteristics were carried out with a Keithley 2400 source-measure unit. Solar simulation was carried out using a KHS575 solarkonstant from Steuernagel Lichttechnik GmbH (Germany). The luminous intensity at the sample position was calibrated using a precision radiometer from Eppley laboratories and monitored continuously during measurements using a CM4 high temperature pyranometer from (Kipp&Zonen). The emission spectrum of the solar simulator was monitored using an optical spectrum analyzer from Avantes. The solar simulator was for the duration of the experiments Class AAA. The conditions for the devices were 1000  $\text{W m}^{-2}$ , AM1.5G,  $72 \pm 2$  °C and a relative humidity of  $35 \pm 2\%$ rh.

### 3. Results and discussion

#### 3.1. The need for new processing methods

One of the great promises of polymer and organic photovoltaics is the possibility for preparing the solar cell

using commonly available materials at temperatures around room temperature under ambient conditions. Most scientific reports have concentrated on preparation of devices under inert conditions in a glovebox on small glass substrates using spin coating as the film forming technique. In addition evaporated metal electrodes are used almost exclusively. There are few reports that employ processing in air and avoid the use of vacuum deposited metal electrodes [8,11,13,14,21]. From a technological point of view the vacuum deposition of a metal electrode in large volume using R2R methods is feasible and not viewed as a hindrance. It is however very attractive if the same coating equipment can be employed for processing all layers in the solar cells and particularly attractive if vacuum coating steps can be avoided. In addition a device geometry that does not necessitate the need for a transparent substrate is also viewed as an advantage as it will allow for the polymer solar cells to be processed onto virtually any substrate surface (provided that the substrate can withstand the solvents and process conditions). The current state-of-the-art has evolved around transparent bottom electrodes and rigid glass substrates and it is thus a significant challenge to find a new device geometry that outperforms (or even approaches) the current state of the art. It is however clear that a significant research effort has to be directed towards finding methods that deviates from the current state-of-the-art while solving some of the pertinent problems. Even if this implies a sacrifice in performance it should be viewed as a valiant cause.

#### 3.2. All solution, all air R2R processing of OPV

It is possible to process devices entirely from solution on ITO substrates using an inverted device geometry whereby the transparent front ITO electrode becomes

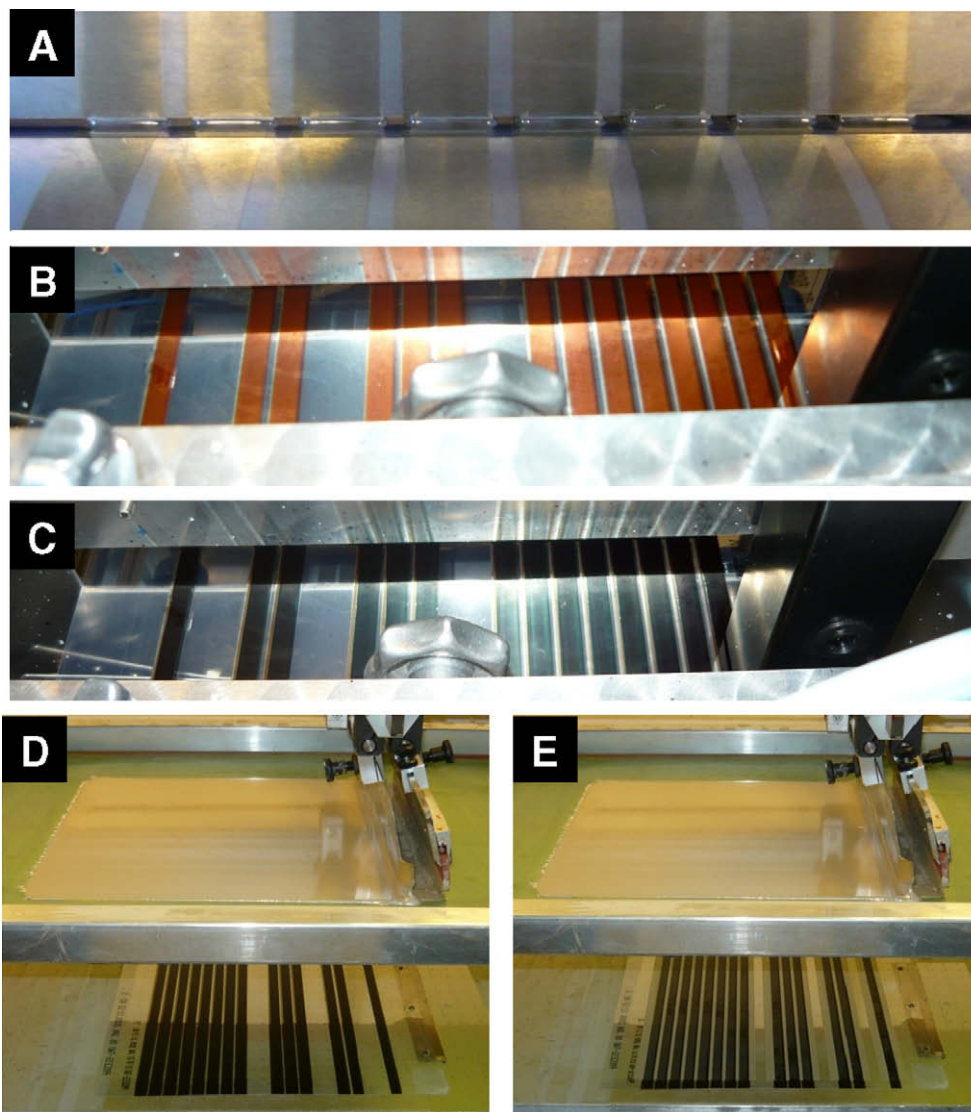


**Fig. 3.** The menisci during slot-die coating of ZnO (A). The ZnO stripes are shifted 1 mm to the right with respect to the underlying silver pattern (top). The wet layer during coating of P3HT-PCBM (B) and PEDOT:PSS (C) are shown just after the slot-die coating head. Sheet-fed screen printing of the silver front electrode grid before (D) and after the printing (E).

the electron accepting electrode (the cathode) and the metallic back electrode becomes the hole accepting electrode (the anode). This has some advantages in terms of device stability as the metals used for the back electrode can be less reactive towards water and oxygen in the atmosphere. This approach has been followed in a series of papers where ZnO nanoparticles [24–27] are processed onto the ITO. The ZnO nanoparticles are excellent for transporting electrons and block hole transport while being highly transparent. The use of ITO in combination with ZnO gives a highly transparent electrode that allows for illumination of the active layer and such a device does not require the back electrode to be transparent [11]. It is however possible to have semi-transparency of the device since PEDOT:PSS can be used as the back electrode on its own or in conjunction with a conducting

printed metal grid structure. This was shown earlier to be possible with all solution, all air R2R processed modules that gave quite a good device performance. The typical performance was well in excess of 1% for large area devices (120 cm<sup>2</sup>) and up to 2.3% for devices with small areas (4.8 cm<sup>2</sup>) using P3HT:PCBM as the active layer [13]. The account however employed the use of ITO and had to make use of a thick PEDOT:PSS layer to avoid that the solvents in the silver metal paste electrode destroyed the active layer. Back illumination was possible but at the expense of performance that was about 5 times lower than front face illumination [13]. There have so far been no convincing reports of an all-solution processable transparent anode/cathode couple. In order to reach the objectives of not using ITO or vacuum coating the semi-transparent back electrode structure presented earlier

[13] could be used in conjunction with a non transparent electrode thus sacrificing performance while gaining in processing ease.

### 3.3. Choice of substrate, materials, device structure and performance

Polyethyleneternaphthalate (PEN) was chosen as the device substrate. While the material presents excellent transparency it is not strictly needed in this experiment since the bottom electrode is non-transparent.

The bottom electrode was chosen as a solution processable silver electrode. Highly reflective electrodes can be prepared in this manner by slot-die coating the silver nanoparticle solution from a mixture of triethyleneglycol-monomethylether and ortho-xylene as shown in Fig. 1. This electrode had excellent conductivity and sheet resistivities as low as  $0.01 \Omega \text{ square}^{-1}$  were typically observed. By use of corona treatment the silver stuck quite firmly to the surface of the PEN and was insoluble allowing for subsequent solution processing of the next layers in the stack. It was found crucial to prewash the silver layer using isopropanol immediately before slot-die coating of the ZnO layer. In the first experiments this step was not performed and it gave rise to poor operating voltage for the devices (Fig. 4). The isopropanol pre-washing enables good wetting of the subsequent ZnO ink solution and possibly also removes some impurities on the surface of the silver electrode. After slot-die coating the ZnO layer and drying, the layer was insoluble and slot-die coating of P3HT:PCBM proceeded in the same manner as reported earlier [13]. The PEDOT:PSS layer was slot-die coated using prewashing with isopropanol and gave functional devices after drying. The sheet resistivity of the PEDOT:PSS is however too high for efficient extraction of the current from the large area devices. Each stripe has a nominal active area of  $15 \text{ cm}^2$ . The silver grid front electrode was printed using screen printing of silver grid lines with a width of 0.2 mm and a spacing of 1 mm. This gave an open aperture of 80%. The transmission of the PEDOT:PSS electrode was 15–20% in the range of wavelengths where P3HT:PCBM absorbs

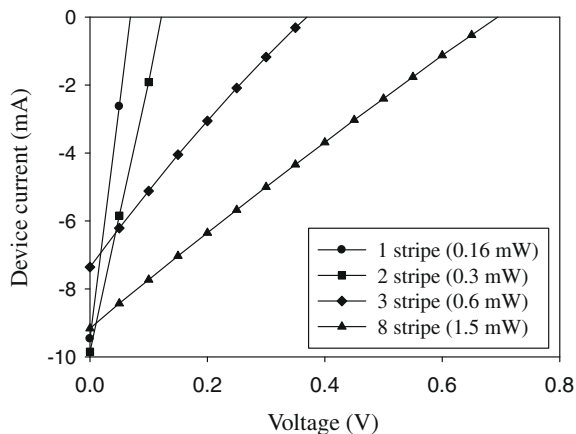


Fig. 4. IV-curves and maximum power output for the 1, 2, 3 and 8 stripe modules without careful pre-washing using isopropanol and fast drying of the silver grid electrode ( $1000 \text{ W m}^{-2}$ , AM1.5G).

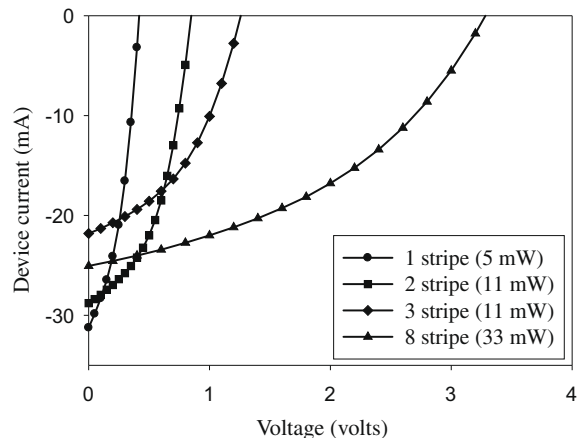


Fig. 5. IV-curves for the 1, 2, 3 and 8 stripe modules with careful pre-washing using isopropanol and fast drying of the silver grid electrode ( $1000 \text{ W m}^{-2}$ , AM1.5G).

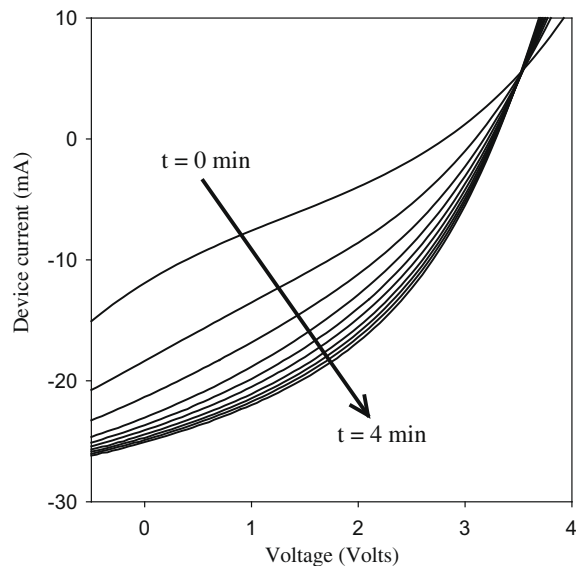


Fig. 6. Maturation of the IV-curve for an 8 stripe device during light soaking. Initially the device presents a poor fill factor with an inflection point reminiscent of a transport barrier ( $1000 \text{ W m}^{-2}$ , AM1.5G).

meaning that the effective transmission of light to the active layer was 12–16%. After completion of the devices they were screened for function and the functional modules were cold laminated using a 25 micron PET layer with an acrylic resin. The device performance was in the 0.2–0.3% range for the active layer for the best devices after light soaking (Fig. 5) using an incident light intensity of  $1000 \text{ W m}^{-2}$  (AM1.5G). It is noteworthy that these devices consistently gave a relatively poor performance when freshly prepared and after light soaking without UV-filtering they gradually improved as shown in Fig. 6.

### 3.4. Comparison with the state-of-the-art

All of the objectives that served as motivation for this work were successfully met. The process described here allows for full R2R processing of complete polymer solar cell

modules on both transparent and non-transparent substrates. The process only employs solution coating of five stacked layers and does not involve vacuum steps nor is ITO used in the device. The material used as the active layer is the well known P3HT:PCBM system that has been documented to give around 3.5% power conversion efficiency under idealized conditions when taking an average of many devices [28]. The performance obtained here for significantly larger devices is about ten times lower. To make a fair comparison and seek for possible means to improve the device performance it is reasonable to compare with the performance obtained for a similarly prepared device with the same inverted device geometry. When preparing the same device by replacing the bottom silver electrode with ITO a performance of up to 1.78% PCE ( $1000 \text{ W m}^{-2}$ , AM1.5G) for an 8-stripe module [13] as compared to 0.27% PCE obtained for the 8-stripe device reported here. However, the earlier report [13] employed illumination through ITO and the higher performance is ascribed to more efficient light access to the active layer. A direct comparison is also possible since the earlier report employed the same grid electrode as back electrode. In this report the grid electrode is employed as front electrode. A comparison of the earlier result employing illumination through the printed grid electrode which allow for direct comparison with the results obtained here show that a similar performance has been reached in this experiment and that the device within reasonable error presents the expected performance. The earlier report had a slightly higher  $V_{oc}$  and a better fill factor. The low performance obtained here is thus most rationally ascribed to a poor front electrode that transmits the light poorly due to both shadow loss of the grid and poor transmission of the PEDOT:PSS electrode. The shadow loss from the grid electrode amounts to 20% and while it can be anticipated that it can be improved to maybe only 10% this will not lead to the most significant improvement. It is possible to prepare PEDOT:PSS with a much better transmission at the expense of a higher sheet resistivity and an optimum must in that case be found between the highly conducting metal grid structure and the poorer conducting PEDOT:PSS layer. In the case here the choice of a thick poorly transmitting PEDOT:PSS electrode was however necessary for device function. Thinner PEDOT:PSS electrodes were found to lead to short circuited devices. The reason for this has been found to be the solvents in the metal paste employed for printing the silver grid electrode. When the wet print of the silver grid is applied the solvents readily diffuse through the PEDOT:PSS layer and into the active layer leading to short circuit of the devices. By application of a thicker PEDOT:PSS and fast drying it was possible to prepare functional devices. There is thus little room for improving the process presented here and new material combinations must be found allowing for a more transparent composite grid electrode that can still be processed from solution without destroying the underlying layers.

### 3.5. Future directions

One possible solution to the electrode transparency problem in the process described here that comprise a

non-transparent bottom electrode is to employ materials for the active layer that is not soluble after processing. In this process the bottom electrode and the ZnO layer were insoluble after processing while the P3HT:PCBM layer was not. Some materials exist that do allow for solubility switching after processing. The most successful class so far has been the thermocleavable materials [29–36] that have enabled the preparation of very stable devices while performance have been somewhat poor. This has improved recently where a PCE of up to 1.5% has been reported for devices prepared on rigid glass using native polythiophene [34]. In addition multilayer processing has been demonstrated for tandem cells prepared with thermocleavable materials without the use of orthogonal solvents [35]. One limitation of the thermocleavable materials is that they need to be heated to a temperature of around 200 °C in order to achieve insolubility. This is not possible for common polymer materials such as PET or even PEN as employed here. PEN endure higher processing temperatures than PET and that was also one of the reasons for employing PEN in this study. While PET melts at temperatures much above 140 °C PEN does withstand temperatures as high as 200 °C briefly but it was found that the material shrinks significantly in a direction perpendicular to the web making the registration of the printed pattern with subsequent processing of layers impossible. It should be noted that the use of PET substrates in conjunction with thermocleavable materials have been demonstrated with processing temperatures as low as 140 °C [14] with a sacrifice in processing time. In the latter case thermocleavage for 4 h was found to be necessary to achieve insolubility. Such a long processing time is clearly impractical in a roll-to-roll process. There are methods to lower the temperature of thermocleavage such as acid catalysis in conjunction with THP ether sidegroups [37] and there are also precursor routes to conjugated polymers [38–40]. There would thus seem to be a significant challenge in either obtaining a low cost substrate that readily allows for processing of thermocleavable materials without shrinkage or the development of a solution processable transparent high conductivity cathode that does not employ ITO.

## 4. Conclusions

In this work a process is presented that offer full roll-to-roll processing of polymer solar cells on flexible substrates entirely from solution. A device comprising five layers was prepared employing slot-die coating for the first four layers and screen printing for the last layer. The process does not involve the use of ITO and no vacuum steps are involved. In addition the illumination of the device is through the top electrode enabling the use of non-transparent substrates. While the process efficiently met all the objectives set out and solves many of the problems currently encountered in the attempts to upscale and transfer the polymer solar cell technology to industry, there is a sacrifice in performance due to poor light transmission of the PEDOT:PSS-silver grid composite electrode. This poor transmission was due to a requirement for a thick PED-

OT:PSS layer that served the purpose of enabling printing of a silver grid electrode involving solvents that damage the active layer which consisted of P3HT:PCBM. A comparison with the state-of-the-art in an identical geometry with a transparent bottom electrode showed that the device was working properly and the decreased performance was due to the poor optical transmission of the composite PEDOT:PSS-silver grid electrode. Possible means to improve the process through usage of thermocleavable materials that allow for processing using a larger variety of solvents were identified while these have a requirement for a low cost thermally stable substrate.

## Acknowledgements

This work was supported by the Danish Strategic Research Council (DSF 2104-05-0052 and 2104-07-0022). Jan Alstrup and Ole Hagemann are thanked for technical support. Keith Rollins from Teijin Dupont is gratefully acknowledged for providing the PEN material for the purpose of this work. The method for manufacture of polymer solar cells described in this work is known as ProcessTwo.

## References

- [1] B.C. Thompson, J.M.J. Fréchet, *Angew. Chem. Intl. Ed.* 47 (2008) 58–77.
- [2] M. Jørgensen, K. Norrman, F.C. Krebs, *Sol. Energy Mater. Sol. Cells* 92 (2008) 686–714.
- [3] F.C. Krebs, *Sol. Energy Mater. Sol. Cells* 93 (2009) 394–412.
- [4] W. Ma, C. Yang, X. Gong, K. Lee, A.J. Heeger, *Adv. Funct. Mater.* 15 (2005) 1617.
- [5] X. Yang, J. Loos, S.C. Veenstra, W.J.H. Verhees, M.M. Wienk, J.M. Kroon, M.A.J. Michels, R.A.J. Janssen, *Nanoletters* 5 (2005) 579–583.
- [6] F.C. Krebs, H. Spanggaard, *Chem. Mater.* 17 (2005) 5235–5237.
- [7] F.C. Krebs, K. Norrman, *Prog. Photovolt. Res. Appl.* 15 (2007) 697–712.
- [8] F.C. Krebs, *Sol. Energy Mater. Sol. Cells* 92 (2008) 715–726.
- [9] E.A. Katz, S. Gevorgyan, M.S. Orynbayev, F.C. Krebs, *Eur. Phys. J. Appl. Phys.* 36 (2006) 307–311.
- [10] J.A. Hauch, P. Schilinsky, S.A. Choulis, R. Childers, M. Biele, C.J. Brabec, *Sol. Energy Mater. Sol. Cells* 92 (2008) 727–731.
- [11] F.C. Krebs, *Sol. Energy Mater. Sol. Cells* 93 (2009) 465–475.
- [12] L. Blankenburg, K. Schultheis, H. Schache, S. Sensfuss, M. Schrödner, *Sol. Energy Mater. Sol. Cells* 93 (2009) 476–483.
- [13] F.C. Krebs, S.A. Gevorgyan, J. Alstrup, *J. Mater. Chem.*, doi:10.1039/B823001C.
- [14] F.C. Krebs, M. Jørgensen, K. Norrman, O. Hagemann, J. Alstrup, T.D. Nielsen, J. Fyenbo, K. Larsen, J. Kristensen, *Sol. Energy Mater. Sol. Cells* 93 (2009) 422–441.
- [15] B. Winther-Jensen, F.C. Krebs, *Sol. Energy Mater. Sol. Cells* 90 (2006) 123–132.
- [16] T. Aernouts, P. Vanlaeke, W. Geens, J. Poortmans, P. Heremans, S. Borghs, R. Mertens, R. Andriessen, L. Leenders, *Thin Solid Films* 451–452 (2004) 22–25.
- [17] K. Tvingsstedt, O. Inganäs, *Adv. Mater.* 19 (2007) 2893–2897.
- [18] M. Strange, D. Plackett, M. Kaasgaard, F.C. Krebs, *Sol. Energy Mater. Sol. Cells* 92 (2008) 805–813.
- [19] B. Zimmermann, M. Glatthaar, M. Niggemann, M.K. Riede, A. Hinsch, A. Gombert, *Sol. Energy Mater. Sol. Cells* 91 (2007) 374–378.
- [20] R.D. McCullough, R.D. Lowe, M. Jayaraman, D.L. Anderson, *J. Org. Chem.* 58 (1993) 904–912.
- [21] F.C. Krebs, Y. Thomann, R. Thomann, J.W. Andreasen, *Nanotechnology* 19 (2008) 424013.
- [22] M. Jørgensen, O. Hagemann, J. Alstrup, F.C. Krebs, Thermo-cleavable solvents for printing of conjugated polymers: application in polymer solar cells, *Sol. Energy Mater. Sol. Cells* 93 (2009) 413–421.
- [23] F.C. Krebs, M. Jørgensen, Decomposable vehicles in printing or coating compositions, WO2007118850 A1 (filing date 13.04.2007).
- [24] H. Womelsdorf, W. Hoheisel, G. Passing, Nanopartikeläres, redispersierbares Fällungsoxid German Patent Specification 19907704 A1, 1999 (filing date: 23.02.1999).
- [25] H. Womelsdorf, W. Hoheisel, G. Passing, Process for producing nanoparticulate, redispersible zinc oxide gels European Patent Specification 1157064 B1 (filing date: 11.02.2000).
- [26] H. Womelsdorf, W. Hoheisel, G. Passing, Nanoparticulate, redispersible zinc oxide gels US Patent Specification 6,710,091 B1 (patent date: 23.03.2004).
- [27] W.J.E. Beek, M.M. Wienk, M. Kemerink, X. Yang, R.A.J. Janssen, *J. Phys. Chem. B* 109 (2005) 9505–9516.
- [28] M.K. Riede, K.O. Sylvester-Hvid, M. Glatthaar, N. Keegan, T. Ziegler, B. Zimmermann, M. Niggemann, A.W. Liehr, G. Willeke, A. Gombert, *Prog. Photovolt.: Res. Appl.* 16 (2008) 561–576.
- [29] J.S. Liu, E.N. Kadnikova, Y.X. Liu, M.D. McGehee, J.M.J. Fréchet, *J. Am. Chem. Soc.* 126 (2004) 9486–9487.
- [30] M. Bjerring, J.S. Nielsen, N.C. Nielsen, F.C. Krebs, *Macromolecules* 40 (2007) 6012–6013.
- [31] M. Bjerring, J.S. Nielsen, A. Siu, N.C. Nielsen, F.C. Krebs, *Sol. Energy Mater. Sol. Cells* 92 (2008) 772–784.
- [32] J.W. Andreasen, M. Jørgensen, F.C. Krebs, *Macromolecules* 40 (2007) 7758–7762.
- [33] H.P. Jakobsen, J.W. Andreasen, K. Norrman, F.C. Krebs, *Thin Solid Films* 516 (2008) 2203–2212.
- [34] S.A. Gevorgyan, F.C. Krebs, *Chem. Mater.* 20 (2008) 4386–4390.
- [35] O. Hagemann, M. Bjerring, N.C. Nielsen, F.C. Krebs, *Sol. Energy Mater. Sol. Cells* 92 (2008) 1327–1335.
- [36] M.H. Petersen, S.A. Gevorgyan, F.C. Krebs, *Macromolecules* 41 (2008) 8986–8994.
- [37] X. Han, X. Chen, S.A. Holdcroft, *Adv. Mater.* 19 (2007) 1697–1702.
- [38] L.H. Nguyen, S. Günes, H. Neugebauer, N.S. Sariciftci, F. Banishoeib, A. Henckens, T. Cleij, L. Lutsen, D. Vanderzande, *Sol. Energy Mater. Sol. Cells* 90 (2006) 2815–2828.
- [39] F. Banishoeib, P. Adriaenssens, S. Berson, S. Guillerez, O. Douheret, J. Manca, S. Fourier, T.J. Cleij, L. Lutsen, D. Vanderzande, *Sol. Energy Mater. Sol. Cells* 91 (2007) 1026–1034.
- [40] F. Banishoeib, A. Henckens, S. Fourier, G. Vanhooyland, M. Breselge, J. Manca, T.J. Cleij, L. Lutsen, D. Vanderzande, L.H. Nguyen, H. Neugebauer, N.S. Sariciftci, *Thin Solid Films* 516 (2008) 3978–3988.

memory device, comprising a conjugated polymer coating a CNT transistor irradiated with UV light at 365 nm, provided an ON/OFF ratio of ca. 4 at a value of  $V_{GS}$  of 4 V, but with a retention time of over 16 h [5].

It appears that commercially viable TFT memory devices exhibiting high ON/OFF current ratios and long retention times (particularly when the gate voltage is turned off) are difficult to prepare. Approaches toward improving device performances while simplifying their fabrication processes are, therefore, necessary for the development and application of future commercial memory devices.

Bulk heterojunctions [10], in which n-type (e.g., fullerene) and p-type (e.g., conjugated polymer) materials are intimately mixed on the nanometer scale to form interpenetrated networks, have been adopted recently to achieve efficient photoinduced charge generation and separation [11,12]. On the other hand, semiconductor nanocrystal quantum dots (QDs) have also been used in such organic optoelectronic devices as solar cells [13] and light-emitting diodes (LEDs) [14]. Recently, the first bulk heterojunction photoresponsive OTFT memory device incorporating P3HT and CdSe QDs by our group was reported to have an ON/OFF ratio of ca.  $10^2$ ; because the CdSe QDs served as trap centers, the memory effect of the device was maintained for 1 h—even without a gating voltage [15].

Type-I core/shell structured QDs, in which the conduction and valence bands of the shell material are higher and lower, respectively, than the corresponding values of the core material, feature a quantum well structure that can confine both holes and electrons in the core [16]. Hence, the quantum well structure of such QDs enhances their electroluminescence (EL) in LED applications [17].

In this paper, we report bulk heterojunction polymer TFT memory devices exhibiting long retention times and high ON/OFF ratios that we fabricated using quantum well-structured QDs comprising CdSe cores and ZnSe shells (CdSe@ZnSe). To the best of our knowledge, this system is the first to employ a quantum well structure to enhance the memory effect of polymer TFTs.

## 2. Experiment

### 2.1. Materials

Regioregular poly(3-hexylthiophene) was obtained from Rieke Metals and used as received. Cadmium acetate dihydrate [ $\text{Cd}(\text{OAc})_2 \cdot 2\text{H}_2\text{O}$ ] was obtained from Fisher Chemicals. Selenium (Se, 99.999%) and hexadecylamine (HDA, tech. 90%) were obtained from Aldrich. Trioctylphosphine oxide (TOPO, 98%), *n*-octylphosphonic acid (OPA, 98%), and trioctylphosphine (TOP, tech. 90%) were purchased from Alfa Aesar. Zinc stearate was obtained from J.T. Baker. The solvents heptane, toluene, methyl alcohol, and chloroform (HPLC-grade) were obtained from commercial sources.

TOPO-capped CdSe and CdSe@ZnSe QDs were synthesized using a modification of a procedure reported previously [18,19]: A mixture of  $\text{Cd}(\text{OAc})_2 \cdot 2\text{H}_2\text{O}$  (105 mg), HDA (1.39 g), OPA (225 mg), and TOPO (1.95 g) was heated in a 25-ml three-neck flask at 270 °C under an argon flow to obtain a colorless, clear solution. At this temperature,

the Se solution (100 mg in 2.4 ml TOP) was injected rapidly. The growth temperature was maintained at 270 °C for 100 s and then the reaction mixture was cooled to room temperature. The CdSe QDs were collected as powders after their precipitation with MeOH. A colloidal solution of the CdSe QDs (ca. 20 mg) in heptane (4 ml) was heated in a 25-ml three-neck flask under an argon flow. After addition of TOPO (2.5 mg) and HDA (1.5 mg), the mixture was heated at ca. 190 °C to completely remove the heptane. Zinc stearate (316 mg) was dissolved in toluene (2.5 ml) at ca. 60 °C. After cooling to room temperature, the resulting 0.2 M solution was mixed with TOP (2.5 ml) and Se (39.48 mg). This mixture was injected via syringe pump (0.085 ml/min) into the reaction flask containing the CdSe QDs at ca. 190 °C. After the addition was complete, the crystals were annealed at 190 °C for an additional 1 h. The CdSe@ZnSe QDs were collected as powders after their precipitation with MeOH.

### 2.2. Device fabrication and measurement

A solution of P3HT in  $\text{CHCl}_3$  was blended with a solution of the QDs in  $\text{CHCl}_3$ ; the P3HT/QD composite weight ratio was 1:0.1. The P3HT and P3HT/QD TFT devices were fabricated in a bottom-gate configuration. An n+ silicon wafer ( $<0.005 \Omega \text{ cm}$ ) was used as the substrate and gate; 900-Å thermal  $\text{SiO}_2$  (capacitance:  $38.4 \text{ nF/cm}^2$ ) was the gate insulator; a photolithographically patterned Au/Cr layer (thickness: 600/50 Å) functioned as the source and drain electrodes ( $W = 1000 \mu\text{m}$ ;  $L = 10 \mu\text{m}$ ). Octadecyltrichlorosilane (OTS) was deposited by immersing the substrate in 1 mM heptane solution for 10 min; the substrates were rinsed with heptane and isopropanol, followed by drying with  $\text{N}_2$ . The P3HT and P3HT/QD films (thickness: ca. 60 nm) were deposited through spin-coating and then they were annealed at 150 °C for 5 min inside a glove box under  $\text{N}_2$  atmosphere. The samples were then transferred to a cryogenic probe station (VFFTP4, Lakeshore). The performance of each device was measured under vacuum ( $<1 \times 10^{-5}$  torr) in the dark using a Hewlett–Packard 4156C semiconductor parameter analyzer. The devices were illuminated under vacuum using a tungsten halogen lamp ( $2.75 \text{ mW/cm}^2$ ).

### 2.3. Characterization

TEM images were obtained using an FEI Tecnai Spirit TWIN apparatus operated at 120 keV. For TEM analysis, the devices were placed into 1% HF solution; after the active layers had floated to the solution surface, they were transferred to the TEM grid. A Hitachi U-4100 spectrophotometer was used to obtain optical absorption spectroscopy in the UV–vis range; a Hitachi F-4500 FL spectrophotometer was employed to obtain photoluminescence spectra.

## 3. Results and discussion

To discern the effect that the ligands on the QDs had on the performance of the memory devices, we investigated



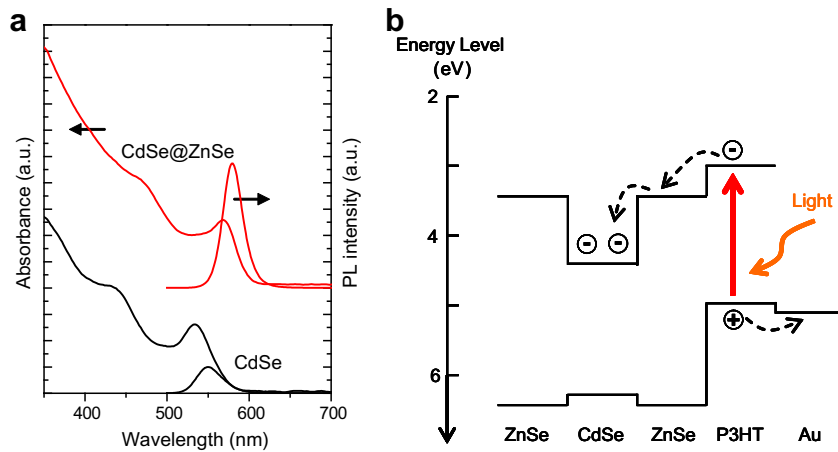


**Fig. 1.** (a) Absorption and photoluminescence spectra of the CdSe and CdSe@ZnSe QDs. (b) Energy level diagram for the CdSe and ZnSe bulk materials, P3HT, and the electrode materials.

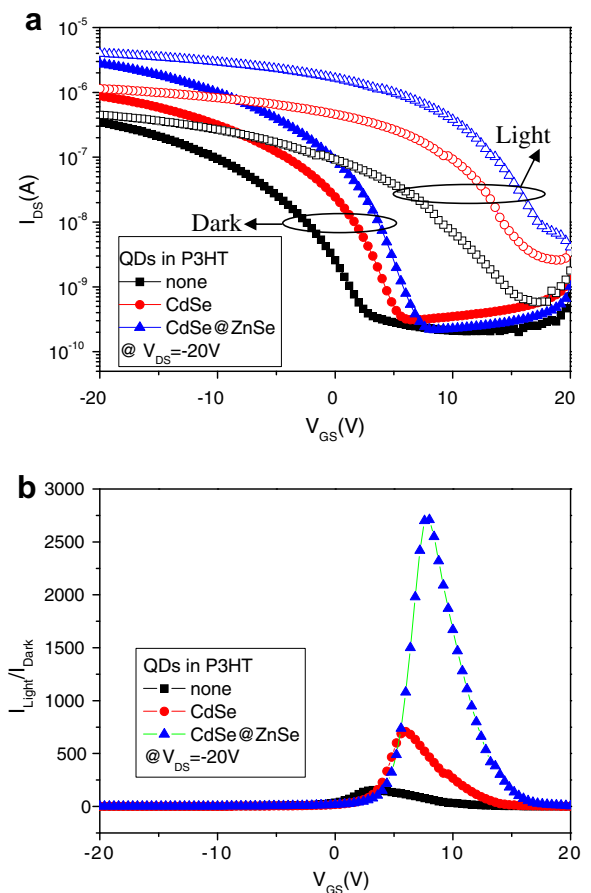
trioctylphosphine oxide (TOPO) as the ligand because TOPO-capped CdSe QDs feature large barriers that prevent electron tunneling into P3HT and better dispersion than pyridine-capped CdSe QDs in P3HT (see Fig. S1, Supplementary material).

Fig. 1a presents the UV–vis and photoluminescence (PL) spectra of CdSe and CdSe@ZnSe QDs that we prepared from the same concentrations in toluene. The first excitonic absorption peak of the CdSe QDs appeared at ca. 540 nm, suggesting an average particle size of ca. 2.85 nm [20], which is consistent with the dimensions obtained from transmission electron microscopy (TEM) image analyses. The presence of the ZnSe shell caused a red shift in the absorption spectrum and enhanced the PL intensity.

Fig. 1b displays a schematic energy level diagram of the CdSe and ZnSe bulk materials, P3HT, and Au electrodes [21,22]. Because the lowest unoccupied molecular orbital (LUMO) and the highest occupied molecular orbital (HOMO) of P3HT lie above the conduction band (CB) and valence band (VB) edges of the CdSe and ZnSe materials, respectively, the P3HT–ZnSe interface forms an offset band heterojunction; in contrast, the CdSe core and ZnSe shell form a type-I heterojunction. When illuminated, excitons were generated in the QDs and P3HT, charge separation occurred at the P3HT–QDs interface, and then electrons and holes were transferred into the QDs and P3HT, respectively [23]. The work function of Au (5.1 eV) matched the HOMO of P3HT (4.9 eV); therefore, an Ohmic contact formed for hole injection, resulting in hole-only transport in the P3HT/QD TFTs.

Fig. 2a displays the transfer curves (drain-to-source voltage,  $V_{DS} = -20$  V) of the P3HT-only and P3HT/QD (including CdSe and CdSe@ZnSe) bulk heterojunction TFTs in the dark and under white light ( $2.75 \text{ mW/cm}^2$ ). All of the devices exhibited the characteristic behavior of p-channel field-effect transistors. The hole mobility  $\mu_h$  was obtained using the following equation [24]:

$$I_{DS} = \frac{W}{2L} \mu_h C (V_{GS} - V_{th})^2 \quad (1)$$



**Fig. 2.** (a) Transfer characteristics ( $V_{DS} = -20$  V) of TFTs incorporating P3HT-only, P3HT/CdSe, and P3HT/CdSe@ZnSe blend films and operated in the dark and under white light ( $2.75 \text{ mW/cm}^2$ ). (b) Relative  $I_{\text{light}}/I_{\text{dark}}$  ratios of the transfer characteristics of the drain current in the dark and under white light.

where  $V_{th}$  is the threshold voltage,  $W$  is the channel width,  $L$  is the channel length,  $C$  is the gate oxide capacitance per

unit area, and  $V_{GS}$  is the gate voltage. In the saturation regime, the hole mobilities of the P3HT-only, P3HT/CdSe QD, and P3HT/CdSe@ZnSe QD devices were  $4 \times 10^{-4}$ ,  $8 \times 10^{-4}$ , and  $3 \times 10^{-3} \text{ cm}^2 \text{ V}^{-1} \text{ s}^{-1}$ , respectively. Since the HOMO of the P3HT is much higher than the VB of CdSe QDs, this energy difference constitutes a larger energy barrier that prevents holes transferring from P3HT to CdSe QDs [25]. Thus, incorporation of the CdSe and CdSe@ZnSe QDs into the P3HT enhanced the hole mobility of the devices slightly, owing to the fact that it is possible that the QDs reduced the density of traps in the polymer [the concentration of the QDs in the P3HT film was 10% (w/w)]. The hole mobility of each of these three composites was lower than that reported recently for pure P3HT (ca.  $10^{-2}$  to  $10^{-3} \text{ cm}^2 \text{ V}^{-1} \text{ s}^{-1}$ ) [26]. Note, however, that several factors, such as the molecular weight of the P3HT, its methods of preparation and purification, the channel dimensions, and the substrate treatment conditions, can influence the characteristics of a TFT device. The values of  $V_{th}$  of the P3HT-only, P3HT/CdSe QD, and P3HT/CdSe@ZnSe QD devices were 0.8, 3.4, and 3.8 V, respectively; i.e., those of the blended devices shifted to more-positive values, indicating the existence of a permanent electric field at the interface. The increase in the drain current of the polymer/QD blends under illumination resulted from accumulation of the majority carriers (holes) inside the active layer; these holes tended to drift toward the drain electrode, whereas the electrons will stay in the QDs or the insulator layer. It is well-known that the properties of the interface between the insulator and the semiconductor can critically influence the device performance. When the OTFT is illuminated, the electrons are attracted to the interface with the gate dielectric by a positive gate voltage; they are then trapped either in the dielectric layer or at the interface. Acceptor-like traps, when the traps are filled by electrons, leads to a positive threshold voltage. After turning the light off, electron detrapping under a negative gate bias indicates a returning to the initial state.

Fig. 2b present plots of the ratio  $I_{light}/I_{dark}$  versus  $V_{GS}$ . We obtained the ratio  $I_{light}/I_{dark}$  from the transfer curves of the drain current for samples either in the dark or irradiated under white light ( $2.75 \text{ mW/cm}^2$ ). The  $I_{light}/I_{dark}$  ratio depends on the gate bias for a given drain bias; it decreases as the gate bias is applied above or below the switch-on voltage. In the depletion regime, the maximum  $I_{light}/I_{dark}$  ratios for the P3HT-only, P3HT/CdSe, and P3HT/CdSe@ZnSe devices were  $1.6 \times 10^2$ ,  $7.1 \times 10^2$ , and  $2.7 \times 10^3$ , respectively; i.e., the photosensitivity of the P3HT/CdSe@ZnSe device was higher than that of the P3HT-only and P3HT/CdSe devices. Because the switch-on voltages, which were defined by the maximum  $I_{light}/I_{dark}$  ratios, for the P3HT/CdSe and P3HT/CdSe@ZnSe devices were 5.6 and 8 V, respectively (Fig. 2b), we chose to operate these two devices at a value of  $V_{GS}$  of 5 V for our subsequent time-response studies.

Fig. 3a displays the evolution of the normalized drain current for the P3HT/CdSe and P3HT/CdSe@ZnSe devices at values of  $V_{DS}$  and  $V_{GS}$  of  $-20$  and  $5$  V, respectively, after they were subject to a light of  $2.75 \text{ mW/cm}^2$  with a duration of  $100$  s. At the onset of illumination, the drain currents of both the P3HT/CdSe and P3HT/CdSe@ZnSe

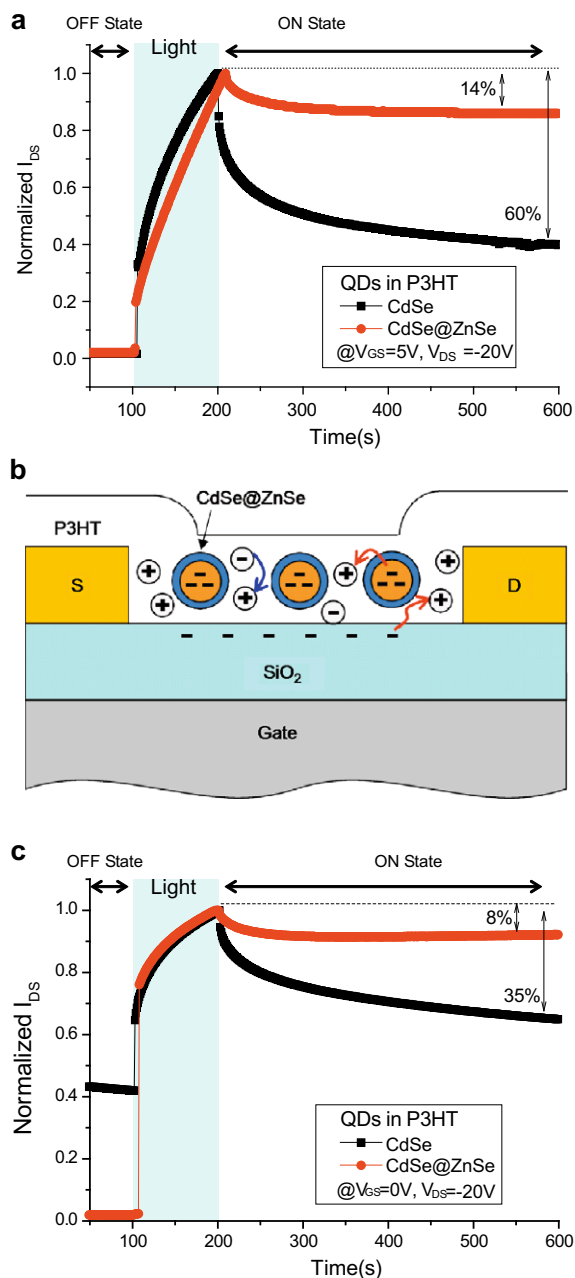


**Fig. 3.** Time responses of the normalized drain currents of the P3HT/CdSe and P3HT/CdSe@ZnSe devices ( $V_{DS} = -20$  V) illuminated by a light of  $2.75 \text{ mW/cm}^2$  with a duration of  $100$  s at values of  $V_{GS}$  of (a)  $5$  and (c)  $0$  V. (b) Schematic representation of the relaxation processes within the bulk heterojunction P3HT/CdSe@ZnSe active layers in TFT devices. Red: slow decay process; blue: fast decay process. (For interpretation of the references to colour in this figure legend, the reader is referred to the web version of this article.)

devices increased dramatically, and then dropped off to form plateaus when light is turned off. After the light had been turned off for  $400$  s, the drain current of the P3HT/CdSe@ZnSe device had decreased by  $14\%$ , compared with a corresponding loss of  $60\%$  for the P3HT/CdSe device. We suspect that the mechanism underlying this behaviors

involved two relaxation processes: (i) rapid decay corresponding to the recombination of closely spaced charge carriers and (ii) slow decay resulting from the recombination of well-separated carriers [27] (Fig. 3b). The slow decay might be manifested by the fact that, in a heterojunction device, the spatially separated holes and electrons will move differently—the holes drifting toward the channel and then reaching the drain electrode, the electrons mostly confined in the QDs and at the P3HT-SiO<sub>2</sub> interface. After the light was turned off, the devices existed in a non-equilibrium state; some of the photogenerated holes presumably recombined with some residual electrons that were not confined in QDs, causing a reduction in the drain current, eventually reaching a metastable state. Because the coverage of the CdSe QDs surfaces by TOPO was only ca. 55% [21], the ZnSe shell layer between the CdSe core and the P3HT polymer in the P3HT/CdSe@ZnSe devices resulted in an additional tunneling barrier that prevented the electrons from tunneling back to P3HT, leading to a smaller decrease in the drain current and a larger retention time relative to those of the CdSe QDs devices, as indicated by the slope of the drain currents at 600 s.

Because low power consumption is an important feature for non-volatile memory applications, it is preferable to operate optoelectronic memory devices in the absence of a gate voltage. Fig. 3c displays the evolution of the normalized drain currents at values of  $V_{DS}$  and  $V_{GS}$  of  $-20$  and  $0$  V, respectively, for the devices subjected to a light of  $2.75$  mW/cm<sup>2</sup> with a duration of  $100$  s. After turning off the light, the P3HT/CdSe@ZnSe and P3HT/CdSe devices exhibited losses of  $8$  and  $35\%$ , respectively, of their ON state currents, with ON/OFF ratios of  $36$  and  $1.5$ , respectively. Therefore, we conclude that Type-I heterojunction core/shell QDs are more suitable than homogenous QDs for memory applications both with and without applied gate voltages.

Fig. 4 presents TEM images of the CdSe and CdSe@ZnSe QDs dispersed in the P3HT matrix at a P3HT-to-QD weight ratio of  $1:0.1$ . The bright appearance of the P3HT regions relative to dark QD regions in the contrast image was probably due to the large difference in their respective electron densities. The CdSe QDs were distributed rather homogeneously in the P3HT matrix; we suspect that the lower homogeneity of the P3HT/CdSe@ZnSe film was due to a loss of TOPO coverage during the growth of the shell. The TEM images in the insets to Fig. 4 reveal that the CdSe and CdSe@ZnSe QDs had average sizes of ca.  $2.9$  and  $4.3$  nm, respectively. The ZnSe shell thickness was ca.  $0.7$  nm, i.e., slightly larger than the critical penetration length of electrons (ca.  $0.5$  nm) [21].

To determine the optimal operating conditions, we fabricated  $10$  devices from three independently prepared P3HT/CdSe@ZnSe films; the optimal ON/OFF ratio was greater than  $1000$  at a value of  $V_{GS}$  of  $10$  V. Fig. 5 reveals that the P3HT/CdSe@ZnSe devices exhibited a high ON/OFF ratio of  $2700$  at a value of  $V_{GS}$  of  $10$  V—without any noticeable decay after the light had been turned off for  $8000$  s. This result indicates that incorporating core/shell QDs into a conjugated polymer significantly extends the lifetime of the memory states of the resulting polymer TFTs. Moreover, the inset to Fig. 5 also displays the

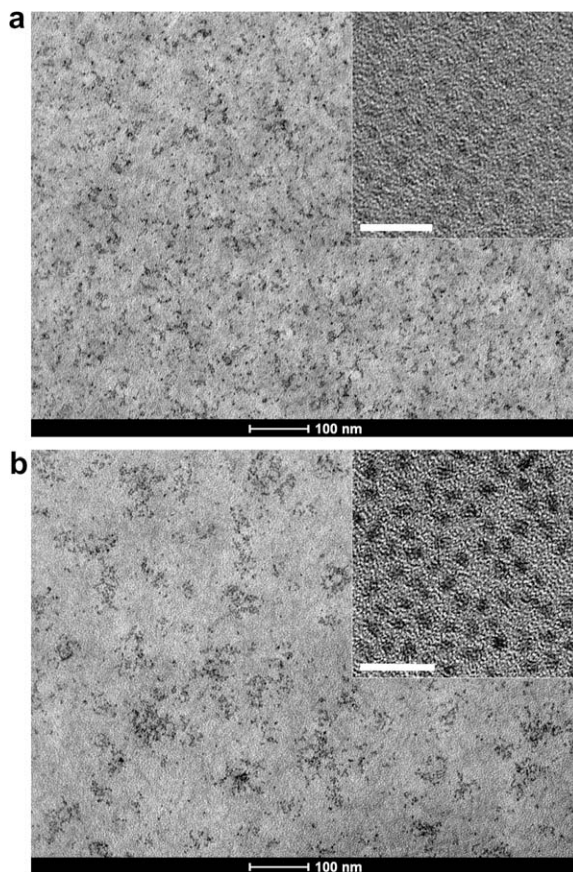


Fig. 4. TEM images of (a) the CdSe QDs and (b) the CdSe@ZnSe QDs dispersed in the P3HT matrix. Insets: TEM images of the CdSe and CdSe@ZnSe QDs (scale bar:  $20$  nm).

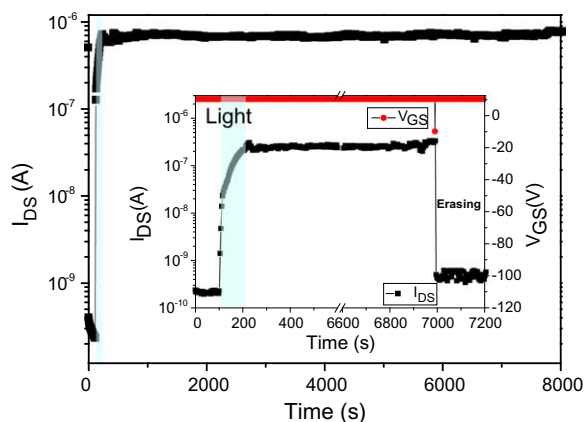


Fig. 5. Time response of the value of  $I_{DS}$  of the P3HT/CdSe@ZnSe device at  $V_{GS} = 10$  V and  $V_{DS} = -20$  V illuminated by a light of  $2.75$  mW/cm<sup>2</sup> with a duration of  $100$  s. Inset: Time response of the P3HT/CdSe@ZnSe device after a negative gate voltage pulse ( $V_{GS} = -10$  V) was applied at  $7000$  s to erase the memory.

dynamic responses of the optical programming and electrical erasing of the P3HT/CdSe@ZnSe device. The ON state current could be erased effectively when using a single

pulse of the gate voltage ( $-10$  V) for a short duration (1 s). When this negative pulse gate bias was applied, the Fermi level of CdSe and ZnSe modulated up towards the conduction band, thereby reducing the barrier height. As a result of the decrease in the barrier height, electron jump back into the P3HT and recombine with hole. Thus, we suspect that the trapped electrons were induced by the electric field to move out of the QDs and recombine with the holes to reform the OFF state. Based on this protocol of operation, it was possible for us to program the P3HT/CdSe@ZnSe device optically and then erase it electrically.

#### 4. Summary

In summary, we have examined the optoelectronic properties and memory effects of polymer TFTs incorporating P3HT/CdSe and P3HT/CdSe@ZnSe QDs as an active layer. After illumination, the presence of the quantum well-structured core/shell CdSe@ZnSe quantum dots in the P3HT film substantially enhanced the ON/OFF ratio to 2700, maintaining this value for 8000 s without noticeable decay. This fabrication approach opens up the possibility of improving the memory performance of polymeric materials prepared at low cost using simple processes.

#### Acknowledgements

We thank the National Science Council of Taiwan for funding (NSC 97-2120-M-009-006) and (NSC97-2218-E009-004).

#### Appendix A. Supplementary material

Supplementary data associated with this article can be found, in the online version, at [doi:10.1016/j.orgel.2009.03.011](https://doi.org/10.1016/j.orgel.2009.03.011).

#### References

- [1] S. Dutta, K.S. Narayan, *Adv. Mater.* 16 (2004) 2151.
- [2] J. Borghetti, V. Derycke, S. Lenfant, P. Chenevier, A. Filoramo, M. Goffman, D. Vuillaume, J.P. Bourgoin, *Adv. Mater.* 18 (2006) 2536.
- [3] J.P. Bourgoin, J. Borghetti, P. Chenevier, V. Derycke, A. Filoramo, L. Goux, M.F. Goffman, S. Lyonnais, K. Nguyen, G. Robert, S. Streiff, J.M. Bethoux, H. Happy, G. Dambrine, S. Lenfant, D. Vuillaume, *Proc. Int. Electron. Dev. Meeting* (2006) 435.
- [4] C. Anghel, V. Derycke, A. Filoramo, S. Lenfant, B. Giffard, D. Vuillaume, J.-P. Bourgoin, *Nano Lett.* 8 (2008) 3619.
- [5] A. Star, Y. Lu, K. Bradley, G. Grüner, *Nano Lett.* 4 (2004) 1587.
- [6] L. Hu, Y.L. Zhao, K. Ryu, C. Zhou, J.F. Stoddart, G. Grüner, *Adv. Mater.* 20 (2008) 939.
- [7] S. Dutta, K.S. Narayan, *Phys. Rev. B: Condens. Matter Mater. Phys.* 68 (2003) 125208.
- [8] K.S. Narayan, M. Rao, R. Zhang, P. Maniar, *Appl. Phys. Lett.* 88 (2006) 243507.
- [9] Y. Shi, H. Tantang, C.W. Lee, C.H. Weng, X. Dong, L.J. Li, P. Chen, *Appl. Phys. Lett.* 92 (2008) 103310.
- [10] (a) N.S. Sariciftci, L. Smilowitz, A.J. Heeger, F. Wudl, *Science* 258 (1992) 1474; (b) G. Yu, J. Gao, J.C. Hummelen, F. Wudl, A.J. Heeger, *Science* 270 (1995) 1789.
- [11] N. Marjanovic, T.B. Singh, G. Dennler, S. Gunes, H. Neugebauer, N.S. Sariciftci, R. Schwodiauer, S. Bauer, *Org. Electron.* 7 (2006) 188.
- [12] S.M. Mok, F. Yan, H.L.W. Chan, *Appl. Phys. Lett.* 93 (2008) 023310.
- [13] W.U. Huynh, J.J. Dittmer, A.P. Alivisatos, *Science* 295 (2002) 2425.
- [14] M. Gao, B. Richter, S. Kirstein, *Adv. Mater.* 9 (1997) 802.
- [15] C.C. Chen, M.Y. Chiu, J.T. Sheu, K.H. Wei, *Appl. Phys. Lett.* 92 (2008) 143105.
- [16] X. Peng, M.C. Schlamp, A.V. Kadavanich, A.P. Alivisatos, *J. Am. Chem. Soc.* 119 (1997) 7019.
- [17] (a) J. Lim, S. Jun, E. Jang, H. Baik, H. Kim, J. Cho, *Adv. Mater.* 19 (2007) 1927; (b) Z. Tan, F. Zhu, J. Xu, A.Y. Wang, J.D. Dixon, L. Li, Q. Zhang, S.E. Mohoney, J. Ruzyllo, *Nano Lett.* 7 (2007) 3803; (c) M.T. Harrison, S.V. Kershaw, A.L. Rogach, A. Kornowski, A. Eychmuller, H. Weller, *Adv. Mater.* 12 (2000) 123.
- [18] H. Skaff, K. Sill, T. Emrick, *J. Am. Chem. Soc.* 126 (2004) 11322.
- [19] P. Reiss, J. Bleuse, A. Pron, *Nano Lett.* 2 (2002) 781.
- [20] W.W. Yu, L. Qu, W. Guo, X. Peng, *Chem. Mater.* 15 (2003) 2854.
- [21] J. Bleuse, S. Carayon, P. Reiss, *Physica E* 21 (2004) 331.
- [22] S. Cho, J. Yuen, J.Y. Kim, K. Lee, A.J. Heeger, *Appl. Phys. Lett.* 90 (2007) 063511.
- [23] N.C. Greenham, X. Peng, A.P. Alivisatos, *Phys. Rev. B* 54 (1996) 17628.
- [24] G. Horowitz, *Adv. Mater.* 10 (1998) 365.
- [25] Z.X. Xu, V.A.L. Roy, P. Stallinga, M. Muccini, S. Toffanin, H.F. Xiang, C.M. Che, *Appl. Phys. Lett.* 90 (2007) 223509.
- [26] R.J. Kline, M.D. McGehee, E.N. Kadnikova, J. Liu, M.J. Frechet, *Adv. Mater.* 15 (2003) 1519.
- [27] K.S. Narayan, N. Kumar, *Appl. Phys. Lett.* 79 (2001) 1891.

to interface contact barrier [6,7] and irregular deposition or poor morphology of the semiconductor film around the already patterned source and drain contacts [8–10].

In an OTFT device, either one or both of the above described effects can be operational. Therefore, it is not only important to identify the dominant effect but also to understand the actual device operation mechanism for enhancing the device performance. The methods for investigating these mechanisms are based on experimental techniques such as potentiometry studies [10–14] and innovative device structures [15]. Potentiometry studies on an operating device are able to reveal the voltage drops around the source and drain electrodes that are cumulative of voltage drop due to the metal-semiconductor contact barrier and disordered region in the vicinity of the metal electrodes [10–14]. Alternative device structure like a combination of top and bottom contact configuration, as proposed by Yoshida et al. [15], is also an important experimental tool to describe the device operation mechanism.

Due to the complexity involved in the transistor operation, it is often difficult to identify the actual physical mechanisms that have significant impact on the device characteristics, solely by a simple analysis of the experimental data based on analytical models. These analytical models can predict the overall device behavior, but are often unable to identify the underlying microscopic behavior. In this respect, two-dimensional physics-based numerical simulation has proven to be of great help not only in understanding the detailed microscopic processes in the interior of the device, but also in enhancing the possibility of the investigations of those physical quantities that would otherwise be difficult to obtain [16–18]. Such examinations lead to the analysis of the cause of the non-ideal performance of the device behavior and its optimization towards obtaining the best electrical characteristics, for e.g. contact resistance [19–21]. Towards these goals, in this article, we build on the previous efforts by combining detailed device simulation with experiments to systematically identify the reasons for the large differ-

ence in device performance of top and bottom contact device structures. It is also our goal to obtain a calibrated standard and established simulation tool which can then be used to design devices further.

## 2. Experimental and device simulation procedure

### 2.1. Experimental procedure

A highly doped (1 0 0) n++ silicon wafer with 200 nm thick thermally grown oxide acts as a gate electrode for both top and bottom contact devices. A measurement of impedance of n++ Si/SiO<sub>2</sub>/aluminum structure yields capacitance of the oxide gate dielectric  $C_i = 1.65 \times 10^{-8}$  F cm<sup>-2</sup>.

For bottom contact devices, the source and drain electrodes (Ti (5 nm)/Au (40 nm)) are defined through photolithography and lift off methods, while for top contact devices, gold electrodes are deposited through a shadow mask. The channel length ( $L$ ) for both top and bottom contact devices is 30 μm and their widths ( $W$ ) are 1 and 3.6 mm, respectively. Pentacene films with thicknesses of 50 nm are deposited by thermal evaporation at the rate of 0.03–0.04 nm/s at substrate temperature of 65 °C. The transistor characteristics were measured using a Keithley 4200 semiconductor characterization system.

### 2.2. Corrections to the measured data

In order to obtain a comparative nature of the device characteristics of the top and bottom contact device structures, we first made preliminary corrections on the measured transistor characteristics, which are based on the gate leakage and metal-semiconductor contact resistance. The method of correction for the gate leakage currents and metal-semiconductor contact resistance is described in the Sections 2.2.1 and 2.2.2, respectively. These corrections to the measured device data for both the top contact and bottom contact devices are shown in Fig. 1.

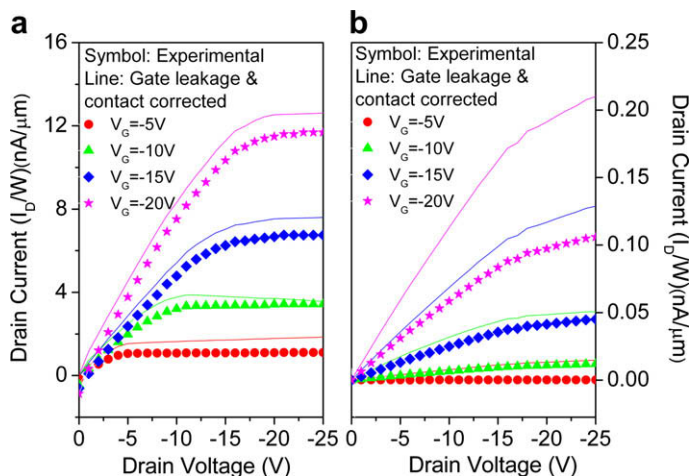


**Fig. 1.** Output curves for (a) top contact device and (b) bottom contact device. The 'symbol' represents the as-measured data and the 'line' represents the data corrected for gate leakage and contact resistance. The pentacene thickness is 50 nm and  $L = 30$  μm.

### 2.2.1. Correction for the gate leakage currents

In the output curves, it was observed that for all the gate voltages, at  $V_D = 0$ , the drain current is not zero. The offset in drain current is attributed to the gate leakage currents, which are often substantial in OTFTs because OTFTs require a large gate field in order to induce enough charge to attain a reasonable conductance.

Zeitsoff et al. [22] and Shih et al. [23] demonstrated through physically based simulations, a correction to the device characteristics in the presence of gate leakage in MOSFETs having a thin or high dielectric constant insulator layer. They show that by following a common practice of accounting for the gate leakage current as having equal proportion from source and drain, the error can be reduced to 3–10% at high values of  $V_G$ . Therefore, at time of measuring transistor characteristics, we simultaneously measured gate and added half of the gate leakage current to the drain current at each gate voltage. In spite of the correction, we reason that we may still have 3–10% error in the corrected drain currents, especially at high gate voltages and low drain voltages. After correction, it was found that there is no drain offset and the drain current at zero drain voltage is zero. Additionally, there is an increase in the drain current by approximately 3% after correcting for the gate leakage currents.

### 2.2.2. Correction for the metal-semiconductor contact resistance

In order to correct the device characteristics for the metal-semiconductor contact resistance, we consider an equivalent circuit model for a transistor with additional source and drain contact resistances ( $R_s$  and  $R_D$ ), respectively, as described in Refs. [3] and [24]. Due to the presence of contact resistances, the applied voltages (gate voltage  $V_G$  and drain voltage  $V_D$ ) will not represent the actual drop in the channel, but are modulated due to the voltage drop across the contact resistances [3,24]. In such a case, assuming  $R_s = R_D$ , the drain current ( $I_D$ ) corrected for the contact resistance are according to Refs. [3,24].

The total parasitic resistance,  $R_p$ , is sum of  $R_s$  and  $R_D$ . To estimate the  $R_p$ , the method of transmission line (TLM)

[3,25] is used Eq. (1), where  $R_{ON} (=V_D/I_D)$  at different  $V_G$  is estimated for several channel lengths. The intercept of the straight line fit of  $R_{ON}W$  vs.  $L$  curve at  $L = 0$  gives the value of  $R_p$  [3,25].

$$R_{ON} = \frac{V_D}{I_D} = \frac{L}{\mu WC_i(V_G - V_T)} + R_p$$

$$\text{OR } R_{ON}W = \frac{L}{\mu C_i(V_G - V_T)} + R_p W \quad (1)$$

where  $\mu$  and  $V_T$  are mobility and threshold voltage, respectively. This data is represented in Fig. 2 for the top and bottom contact devices. Once, the total parasitic resistance is determined (half at both source and drain), it can be used to correct the drain currents to their equivalent values in a device with no metal-semiconductor contact resistance [3,24]. These curves are then used for further analysis, and also for comparison with simulations, in which the contacts are considered ohmic.

The contact resistance corrected field effect mobility and the threshold voltage for the OTFT can also be extracted by plotting the inverse of the slope of Eq. (1) at different gate voltages. The slope of the resultant plot thus determines the contact corrected mobility, while the  $x$ -axis intercept obtains the corrected threshold voltage.

### 2.2.3. Device simulation procedure

A two-dimensional device simulator ATLAS (Silvaco) is used for numerical simulations. The simulator predicts the electrical characteristics associated with a specified physical structure and bias conditions by solving systems of Poisson's equation and continuity equation which are a set of coupled, partial differential equations given for holes by Eqs. (2) and (3) below:

$$\varepsilon \nabla^2 \psi = -pq \quad (2)$$

$$\frac{\partial p}{\partial t} = \frac{1}{q} \nabla \cdot J_p + G_p - R_p \quad (3)$$

where  $\varepsilon$  is the dielectric constant,  $\psi$  is the potential,  $p$  is the local hole density,  $q$  is the fundamental electronic charge,  $G_p$  is the charge generation rate,  $R_p$  is the charge recombina-

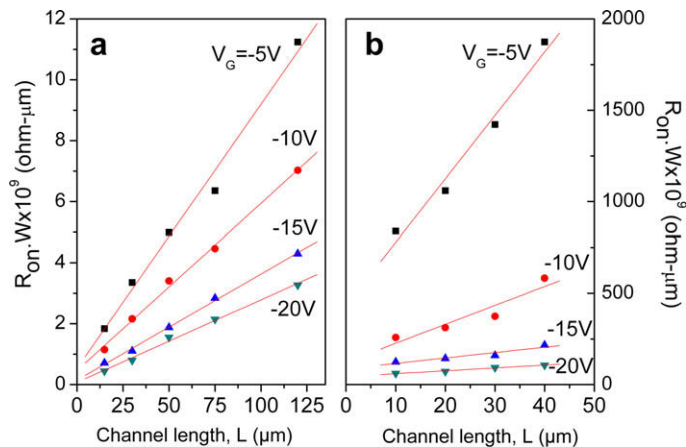


Fig. 2. Plot of  $R_{ON}W$  as a function of channel length for (a) top contact device and (b) bottom contact devices. The gate voltage is varied from –5 to –25 V in –5 V steps.

tion rate, and  $J_p$  is the current density which is given considering its drift and diffusion components by Eq. (4):

$$J_p = q p \mu_p F + q D_p \nabla p \quad (4)$$

where  $\mu_p$  is the mobility of holes,  $F$  is the local electric field, and  $D_p$  is the hole diffusion coefficient. This simulator was primarily developed for silicon devices and, therefore, its applicability to organic materials is limited. However, the simulator can still predict the qualitative device characteristics correctly, as demonstrated by available literature [18,26–29] on simulation of organic devices.

The bandgap of pentacene is taken as an average of values reported in literature, 2.2 eV [30–35], electron affinity ( $E_A$ ) as 2.8 eV [31–35], density of both conduction and valence band states as  $2 \times 10^{21} \text{ cm}^{-3}$  [31–35] and dielectric constant as four [31–35]. The acceptor doping concentration is estimated according to procedure defined in Ref. [36] and taken as  $3 \times 10^{16} \text{ cm}^{-3}$ ; furthermore, even if the doping density is varied by two orders of magnitude, the transistor characteristics show only a minor change. The work function of the source, drain and gate metal is assumed to be 5.0 eV.

The simulation of the experimental output and transfer curves after correcting for gate leakage and contact resistance of the top contact devices was performed with the input parameters as described above. However, we observed a mismatch between the experimental and simulated curves. In the output curves, the experimental drain currents were lower than the simulated values at all the gate voltages, whereas in the transfer curves, experimental drain currents were lower than the simulated currents above the threshold voltage and higher in the sub-threshold region. Thus, additional simulation parameters related to traps were included to calibrate the simulation.

The mismatch between the experimental and simulated curves could at first be attributed to the difference in the measured threshold voltages and those extracted from the simulated curves. The threshold voltage for the simulated curves was 0.8 V, whereas the experimentally obtained value is  $-3.2$  V. This, difference in threshold voltage can be removed by including a positive interface charge of approximately  $q \times 3 \times 10^{11} \text{ C-cm}^{-2}$  ( $q$  is charge of an electron) at insulator/pentacene interface. The match above the threshold region is nearly perfect with the above mentioned fixed charge, but in the sub-threshold region of the transfer curves, the experimental drain currents are still higher than that simulated. This discrepancy is subsequently resolved by including interface acceptor traps of the concentration  $2 \times 10^{12} \text{ cm}^{-2} \text{ eV}^{-1}$  at an energy level of 0.52 eV from the valence band edge.

With these set of calibration data, the simulator predicts the electrical behavior of a top contact device. With this as the basis of simulations, the paper then discusses additional features that need to be incorporated to calibrate a bottom contact device.

### 3. Results and discussion

We begin by comparing device characteristics in the top and bottom contact configurations, fabricated and

measured according to method described in Section 2.2. In both cases, the gate is at the bottom and the two configurations differ in the order the semiconductor and the source/drain contacts are placed on the gate/insulator substrate. For comparison, the dotted curves in Fig. 1 depict the as measured output characteristics of (a) top and (b) bottom contact device at various gate voltages ( $V_G$ ); the channel length ( $L$ ) is  $30 \mu\text{m}$  and pentacene thickness is 50 nm in these devices. Clearly, the drain currents per unit width in top contact devices are higher, for example at  $V_G = -20$  V, by two orders of magnitudes as compared to bottom contact devices. This difference is further characterized by extraction of field effect mobility from detailed output and transfer curves.

From the as measured curves, the extracted field effect mobility for top and bottom contact devices are  $0.125 \text{ cm}^2/\text{Vs}$  and  $1.74 \times 10^{-3} \text{ cm}^2/\text{Vs}$ , respectively, in the saturation region. Similarly, in the linear region, we determined the hole mobility for top and bottom contact devices as  $0.085 \text{ cm}^2/\text{Vs}$  and  $1.44 \times 10^{-3} \text{ cm}^2/\text{Vs}$ , respectively. From these measurements, whether based on linear or saturation region, the field effect mobility measured in the top contact configuration is significantly greater than that in bottom contact device. In addition, the mobilities extracted from the saturation region in either configurations, top or bottom, is slightly greater than that in the linear region.

First we examine the cause of difference in mobilities extracted from linear and saturation region, and then focus on the reasons for differences in the top and bottom contact devices. These differences could first be ascribed to the gate leakage and, especially, contact resistance, which are important in the linear region. Therefore, both these corrections to the measured data are made according to the method described in Section 2.2, after which the mobilities are again extracted. The metal-semiconductor contact resistance ( $R_p$ ) value at a gate voltage is extracted from the  $R_{\text{ON}}W$  vs.  $L$  plot, (as described in Section 2.2), and is shown in Fig. 2a and b for the top and the bottom contact devices, respectively.

The corrected output characteristics, at a gate voltage for both device configurations are also included in Fig. 1, as solid lines. Following this correction, the mobility of holes from the linear region, and corresponding threshold voltage of the device is also estimated according to the method defined in Section 2.2. This correction yields an effective mobility of  $0.14 \text{ cm}^2/\text{Vs}$  and  $3.2 \times 10^{-3} \text{ cm}^2/\text{Vs}$  for the top and bottom contact devices, respectively, and the corresponding  $V_T$  are  $-3.2$  V and  $-8.5$  V. Hence, after correction, the hole mobilities are similar from both saturation and linear region, but still the mobility in bottom contact configuration is poor in comparison to that in top contact configuration.

Since the corrected mobility value of the bottom contact devices does not increase significantly, it suggests that the contact resistance is not the only reason for the deterioration of the mobility in bottom contact configuration. We therefore investigate the difference in mobilities in the two geometries by simulating the impact of possible structural differences on transistor characteristics.

### 3.1. Simulation of top and bottom contact devices under normal conditions

A top contact device differs from a bottom contact device in that in the former, source/drain current passes through the thickness of the semiconductor (although very thin in comparison to the channel length) and that the bulk conduction could be slightly higher. In order to identify the possible variations in the device characteristics due to the device configuration in top and bottom contact devices, we simulated the device characteristics in both the structures with identical pentacene thickness and material parameters, according to details in Section 2.2. Corresponding to the case of channel length as 30  $\mu\text{m}$ , pentacene thickness as 50 nm and hole mobility in pentacene as  $0.14 \text{ cm}^2/\text{Vs}$  (the same as that extracted for the top contact device), the output characteristics of the top and bottom contact devices are simulated. As expected, the output curves of top and bottom contact devices overlay on each other, implying that neither the current flow through the thickness of pentacene nor bulk current can justify lower effective field effect mobility in bottom contact configuration.

Effectively, the simulation clarifies that the device structure by itself is not a major factor for the lower mobility of the bottom contact devices. The other factors which may be responsible for the observed differences could depend upon the differences in the manner that two devices are fabricated.

### 3.2. Effect of unfilled region at the edges near the source and drain contacts

In the bottom contact devices, source and drain contacts are deposited first and then the pentacene layer is deposited. In this case, it is possible that a shadow cast by metal during evaporation of pentacene could lead to unfilled corners at the source/drain contacts, which in turn could result in lower effective device mobility. We modelled this possibility in our simulations by introducing a vacuum layer of  $50 \text{ nm} \times 45 \text{ nm}$  at the edge near the source and drain contacts, as illustrated in Fig. 3a for a bottom contact configuration. The mobility of the pentacene is taken as  $0.14 \text{ cm}^2/\text{Vs}$ , which is equal to the corrected mobility value of the top contact devices. This attempt is made in order to find out whether the introduction of the vacuum layer in bottom contact devices would lead to a lower effective device mobility in the simulated transistor characteristics than the top contact devices.

Fig. 3b illustrates that the simulated drain currents in the bottom contact device with the unfilled region and without the unfilled region at the source and drain contact edges are only slightly different. It is clear that the drain currents simulated on the assumption of unfilled region at the contact edges cannot match with the experimental curves, which are also depicted in Fig. 3b (dotted line).

In order to gain insight into device operation of this device, we study the current flowlines in the pentacene

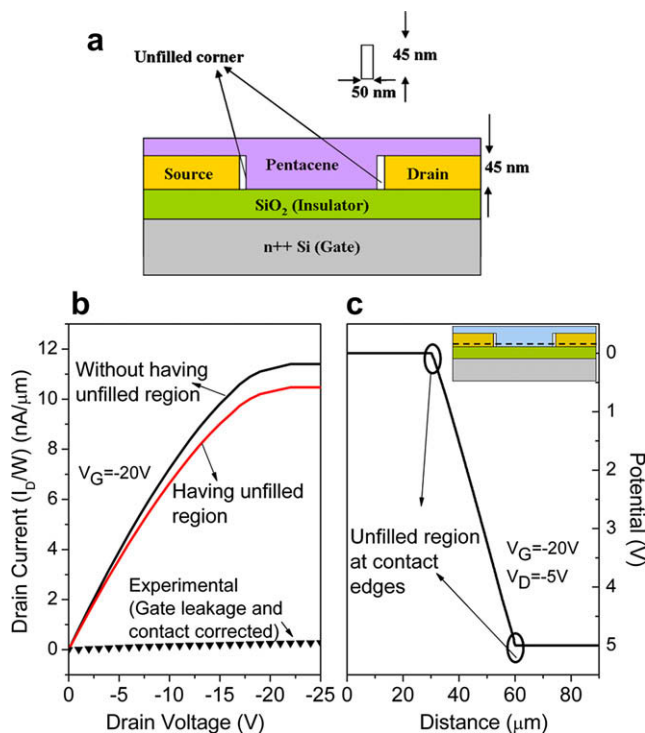


**Fig. 3.** (a) Schematic diagram of the bottom contact device showing unfilled region of  $50 \text{ nm} \times 45 \text{ nm}$  near the source and drain contact edges. The thickness of the source and drain contacts is 45 nm, (b) comparison of the output curves of bottom contact devices with and without having the unfilled region at the source and drain contact edges at  $V_G = -20 \text{ V}$  and (c) potential profiles above source and drain contacts for different mobilities of the low-mobility-region at  $V_G = -20 \text{ V}$ ,  $V_D = -5 \text{ V}$ . Source, drain and channel lie between 0–30  $\mu\text{m}$ , 60–90  $\mu\text{m}$  and 30–60  $\mu\text{m}$ , respectively. (The pentacene thickness is 50 nm and  $L = 30 \mu\text{m}$ . The mobility of the rest of the pentacene is taken as  $0.14 \text{ cm}^2/\text{Vs}$ .)



film for the device without the unfilled region (Fig. 4a) and with (Fig. 4b) the unfilled region near the contact edges at the gate voltage of  $-20$  V and drain voltage of  $-5$  V. As expected, for a device with no unfilled region adjacent to source and drain (Fig. 4a), the current between source and drain is confined in few tens of nanometers above the dielectric. The remaining portion of the source and drain contacts are inconsequential in current injection. However, when an unfilled region of size  $45\text{ nm} \times 50\text{ nm}$  (as in Fig. 3a) is introduced in the same device, no longer can current be injected from the sides of the metal contact. In this case, as shown in Fig. 4b, on the introduction of the unfilled region at contact edges, the current starts injecting/extracting from the top surface of the source/drain contacts. An expanded view in Fig. 4c illustrates that the current injected from the top surface of the source contact traverses through the pentacene film adjacent to the unfilled region, reaches the insulator interface and then is extracted from the top surface of the drain electrode (see Fig. 4d). In their study of surface potential profile in the bottom contact devices, Li et al. [20] also studied a similar case where they modelled the region adjacent to the contacts as low-mobility-region and observed that injection/extraction process involves top surface of the contacts.

The injection/extraction process causes a small potential drop across the unfilled region, which is depicted

through a potential profile across the channel region, taken  $1\text{ nm}$  above the dielectric interface (represented through a dashed horizontal line in the inset of Fig. 3c). Across this horizontal line, source lies between  $0\text{--}30\text{ }\mu\text{m}$  and the drain lies between  $60\text{--}90\text{ }\mu\text{m}$ , and the pentacene film lies between  $30\text{--}60\text{ }\mu\text{m}$ . Due to the involvement of top surface of the contacts, there is a small decrease in the drain current for the device having the unfilled region, unlike the case without having the unfilled region, where the injection/extraction takes place only from a very thin region of the contacts adjacent to the insulator (Fig. 4a).

Based on the above results, it is clear that the unfilled region at the source and drain contact edge cannot explain the large difference in the behavior of top and bottom contact devices. Therefore, as another possibility, we study the effect of pentacene morphology around the source and drain contacts to further examine the cause for inferior performance of bottom contact devices.

### 3.3. Effect of pentacene morphology at the contact edge and on source/drain contacts

In the top contact devices, the pentacene film is deposited on the dielectric layer, whereas, in the bottom contact device, since contacts are made first, a part of pentacene film deposits on the contact metal. Therefore,

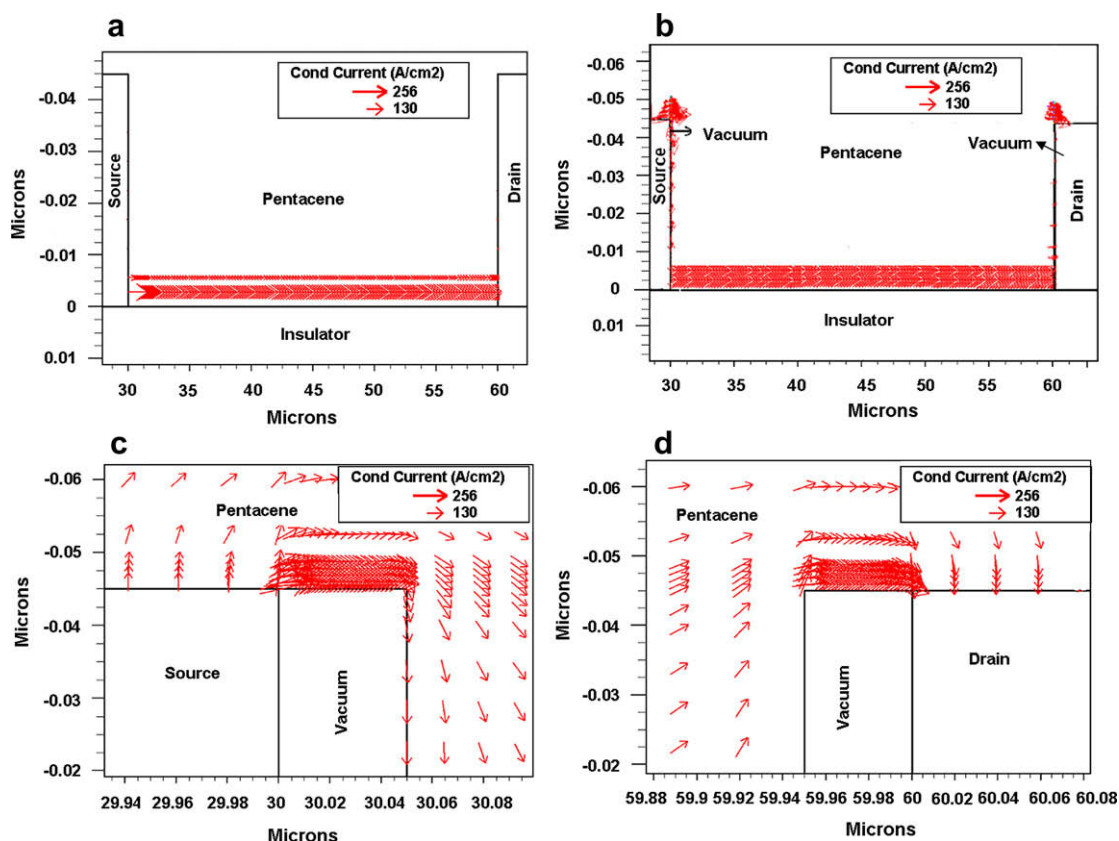


**Fig. 4.** Schematic diagram for the current flow path in pentacene film in a bottom contact device (a) without an unfilled corner adjacent to the source and drain contacts and (b) with an unfilled corner adjacent to the source and drain contacts. Expanded view of the current flow path in pentacene film with an unfilled region (modelled as vacuum layer) adjacent to (c) the source contact and (d) the drain contact.

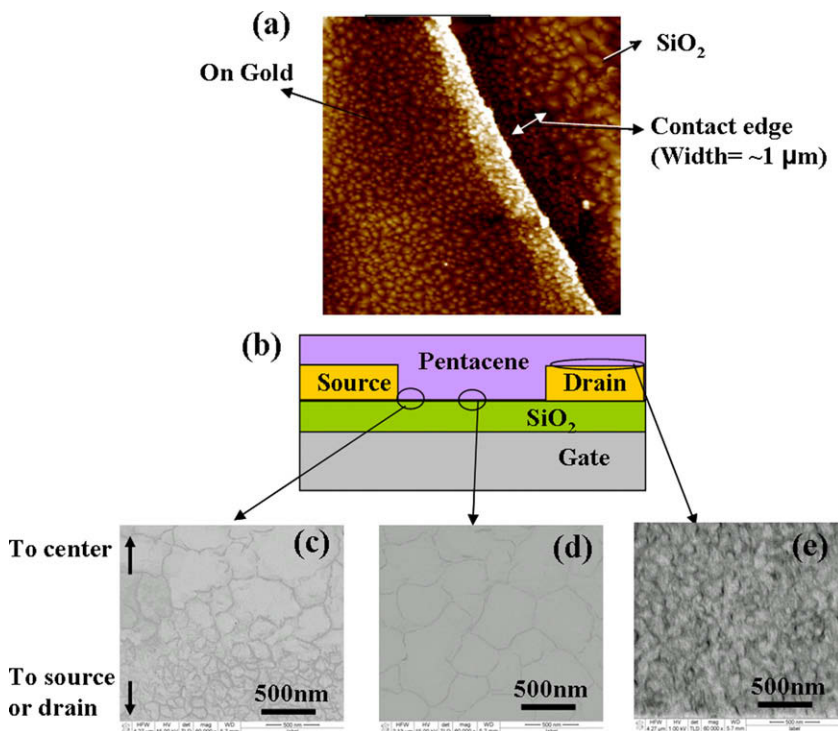


**Fig. 5.** (a) Atomic force micrograph of pentacene on gold and SiO<sub>2</sub> (Image size = 6 μm × 6 μm), (b) schematic of the bottom contact device showing different region of pentacene morphology. Scanning electron micrograph of pentacene on gold contact (c) near gold contact edge on SiO<sub>2</sub>, (d) far away from gold contact edge on SiO<sub>2</sub> and (e) on gold contacts.

the morphology of pentacene film in the vicinity of metal in the bottom contact devices could be different.

Fig. 5 contains the image of pentacene film deposited in a bottom contact geometry, and the different regions are pictorially represented in Fig. 5b. Based on atomic force microscopy (AFM) (Fig. 5a) and scanning electron microscopy (SEM) (Fig. 5c–e) images, change in the morphology of pentacene film (50 nm thick) on gold and SiO<sub>2</sub> can be clearly seen. Fig. 5a, which is an AFM image near the step caused by gold contacts, clearly shows two distinct regions. The grain size adjacent to the gold contact is comparatively smaller than the grain size in the channel region away from the contact. This is further illustrated by SEM images of pentacene film in the channel region near metal contact (Fig. 5c; notice the orientation of the image), in the middle of the channel (Fig. 5d), and on gold contacts (Fig. 5e). The micrographs depict a marked change in the morphology of pentacene film grown in the three regions. The large grain structure far away from the source/drain contact edges changes into a small grain structure as one move closer to the edge of the channel, near the gold electrodes. On SiO<sub>2</sub>, the average grain size is 0.57 μm and on the source and drain contacts, the grain size is 0.15 μm. As represented in Fig. 5a, the effect of the gold contact in reducing the grain size permeates upto a distance of 1.0 μm.

The reason for the different morphology is attributed to the difference in surface energies of metal and dielectric layers [8,9,37]. When pentacene is deposited on a metal surface, the back bone of the pentacene molecule is at-

tracted to the metal leading to a lying down configuration of pentacene molecules. While on SiO<sub>2</sub>, low surface energy causes the pentacene molecules to stand vertically. Near the source/drain contact edges, pentacene molecules tend to have both lying down and standing mode leading to poor packing and poor molecular ordering [8,9,37].

In order to understand the consequences of morphological differences in device characteristics, we modelled this small grain size region by assigning it a lower mobility value as compared to rest of the pentacene. Fig. 6a is a schematic diagram illustrating this low-mobility-region near the source and drain contact edges and above the contacts in a bottom contact device. The width of this low-mobility-region on the insulator is 1 μm, as determined from Fig. 5a. Fig. 6b depicts the output curves (at  $V_G = -20$  V) as a function of the various low values of mobility in this region. The bulk mobility value of the remaining pentacene is taken as 0.14 cm<sup>2</sup>/Vs, as before. It is clear from Fig. 6b that the drain current decreases in proportion to the reduction in mobility of the low-mobility-region. The combined effect of bulk mobility as 0.14 cm<sup>2</sup>/Vs and this low-mobility-region on the effective device mobility value extracted from output characteristics is illustrated in Fig. 6c. From Fig. 6c, it is observed that the extracted device mobility in the saturation region forms almost a linear relationship with the mobility value of the low-mobility-region.

The reason for such a behavior could again be understood by examining the charge injection/extraction process. In Fig. 4b, introducing an unfilled region forced the current injection from the top of the contact (and similarly

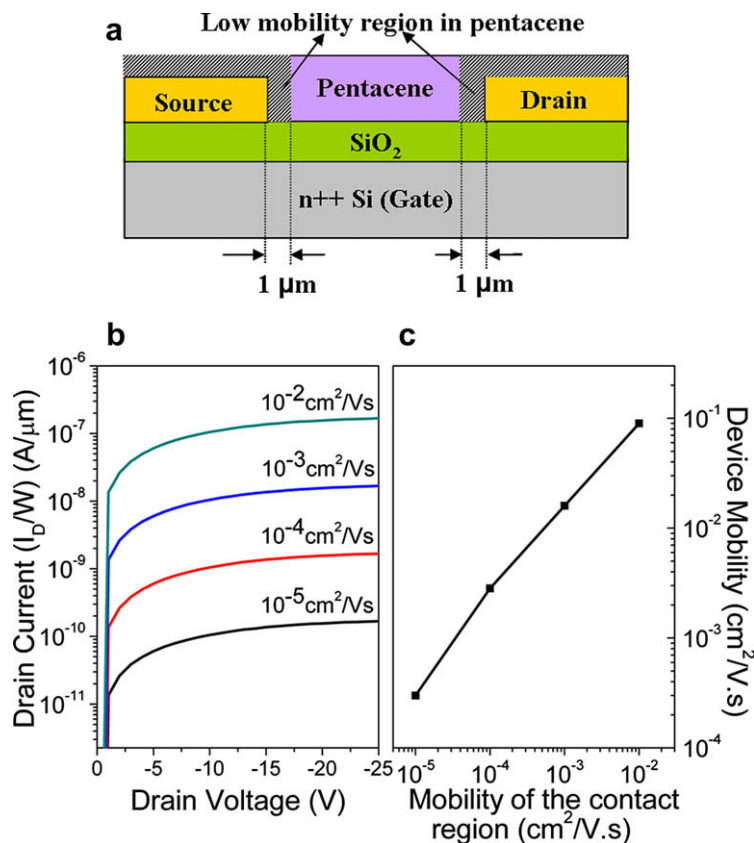


**Fig. 6.** (a) Schematic of the 1 μm wide low-mobility-region near the source and drain contact edges and above the contacts in bottom contact devices, (b) output curves plotted for different mobility values of the low-mobility-region adjacent to and above the source and drain contacts and (c) extracted mobility of the device for different mobility values of the low-mobility-region adjacent to and above the source and drain contacts. (The pentacene thickness is 50 nm and  $L = 30$  μm. The mobility of the rest of the pentacene is taken as  $0.14$  cm<sup>2</sup>/Vs).

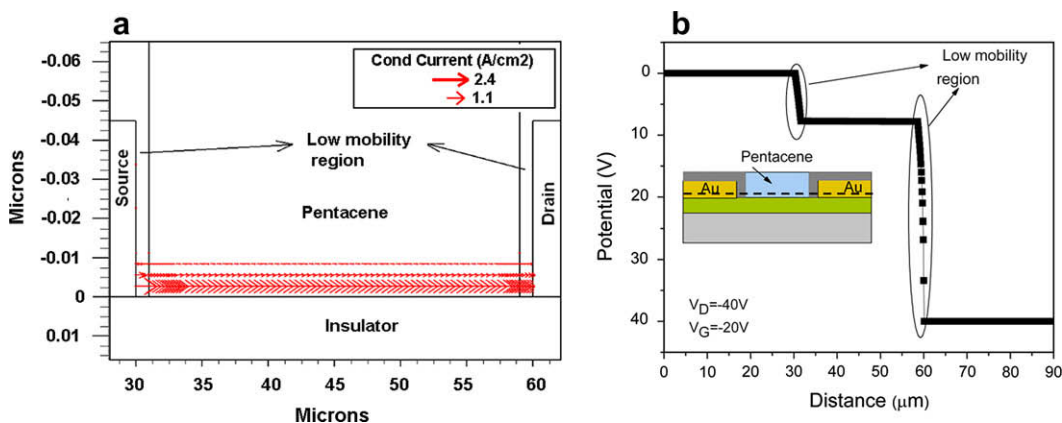


**Fig. 7.** (a) Schematic diagram for the path of the current flow in pentacene film (line with the arrow) in a bottom contact device having a low-mobility-region adjacent to and above the source and drain contacts and (b) surface potential profile 1 nm above the dielectric surface (source, drain and channel lie between 0–30 μm, 60–90 μm and 30–60 μm, respectively). The mobility of low-mobility-region is  $1 \times 10^{-4}$  cm<sup>2</sup>/Vs at  $V_G = -40$  V and  $V_D = -20$  V. (The pentacene thickness is 50 nm and  $L = 30$  μm. The mobility of the rest of the pentacene is taken as  $0.14$  cm<sup>2</sup>/Vs).

for the current collection at the drain). However, on introducing a low-mobility-region all around the metal contact forces the current injection and extraction again to the lower region of metal contacts (within 5 nm region from

the insulator), as illustrated in Fig. 7a, forcing the current to pass through the low-mobility-region. Due to this, a large potential drop is expected to take place in the low-mobility-region at the contact edges.

Fig. 7b shows the potential profile between the source and drain contacts at 1 nm above the dielectric interface (along a horizontal dashed line in the inset of Fig. 7b), for the mobility value of the low-mobility-region as  $1 \times 10^{-4} \text{ cm}^2/\text{Vs}$ . Clearly, almost all the applied potential is accommodated in the low-mobility-region at the contact edge, forcing its effect on the overall device characteristics. As a result, the apparent field effect mobility value is much lower compared to the bulk mobility value of  $0.14 \text{ cm}^2/\text{Vs}$ . The apparent mobility values are in fact very close to the mobility value of the contact edge, which shows that this region becomes dominant in determining the overall device characteristics. Also, the voltage drop near the drain is much higher than that at the source, which is reflective of the depletion region near the drain in the saturation region. The reports on surface potential studies in the bottom contact devices through Kelvin probe force microscopy or electrostatic force microscopy revealed a large potential

drop near the source and drain contacts, attributed to poor morphology of pentacene near the metal contact edges [10–14]. These simulations further confirm this phenomenon, emphasizing the importance of the morphology of the pentacene films near the contact edges and on the source and drain contacts. Improvement of the morphology of pentacene at the contact edges by the surface treatments or by using polymer electrodes could significantly increase the device mobility values [9,37,38]. In short, based on these simulations, we determine that the possible cause of differences observed in bottom and top contact devices could be due to differences in pentacene morphology leading to low-mobility-regions near the contacts.

### 3.4. Low-mobility-region in the top contact devices

In a top contact device, since the pentacene is deposited first, its morphology in the channel region is not expected

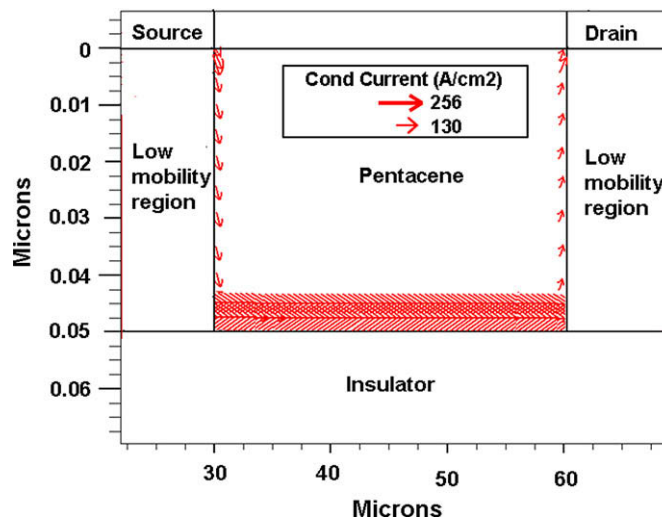


Fig. 8. Schematic diagram for the path of the current flow in pentacene film (line with the arrow) in a top contact device having a low-mobility-region under the source and drain contacts.

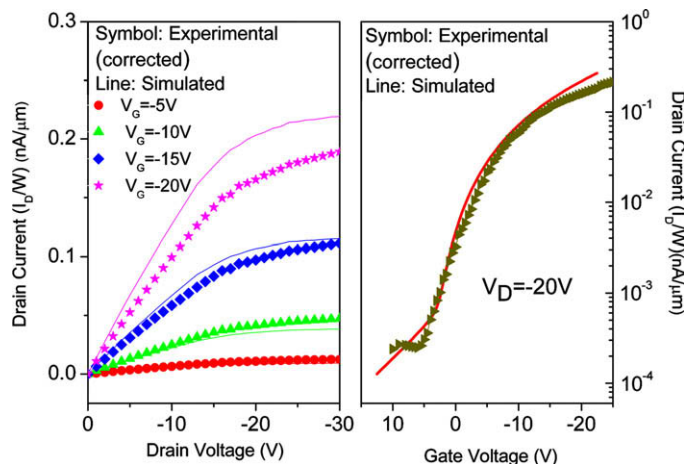


Fig. 9. Comparison of the experimental (gate leakage and contact corrected) and the simulated (a) output and (b) transfer curves. The mobility of the low-mobility-region is  $1.5 \times 10^{-4} \text{ cm}^2/\text{Vs}$  and bulk mobility of pentacene is  $0.14 \text{ cm}^2/\text{Vs}$ . Pentacene thickness is 50 nm and  $L = 30 \text{ μm}$ .

to be different from the contact region. However, due to metal diffusion into the pentacene may reorganize the morphology of pentacene under the contact which in turn causes the mobility of pentacene below the electrodes to be lower than the bulk mobility [39,40]. Therefore, to make a comparison with the bottom contact devices, we also evaluated the effect of the low-mobility-region under the source and drain contacts in the top contact devices. As an extreme case, a low-mobility-region, with mobility value of  $1 \times 10^{-3} \text{ cm}^2/\text{Vs}$ , is located across the full thickness of pentacene. Still, we do not observe any significant change in the device behavior between with or without low-mobility-layer cases. The reason for this can be understood from Fig. 8 illustrating the current flow path in a top contact device. In this case the charge is injected from the side/corner of the contacts, bypassing the low-mobility-region (Fig. 8). Thus top contact devices would be less susceptible to morphological variations caused by the presence of metal.

### 3.5. Comparison with the experimental device behavior

On the basis of the above discussion, we determine that the cause of the low mobility of the bottom contact devices in comparison to top contact devices is due to the poor morphology/domain structure of pentacene at contact edges and on gold source and drain contacts. While the bulk mobility of holes in pentacene may be  $0.14 \text{ cm}^2/\text{Vs}$ , we determine that introducing a low-mobility-region of mobility value  $1.5 \times 10^{-4} \text{ cm}^2/\text{Vs}$  in the bottom contact devices yields a good comparison with the measured data, as shown in Fig. 9a (output curves) and Fig. 9b (transfer curves).

## 4. Conclusions

The difference in the drain currents and mobility values of the top and bottom contact devices is not inherent to the device configuration, but is a result of the manner in which bottom contact devices are fabricated. The pentacene film near the source/drain contact edges and on the contacts exhibits poor morphology as compared to the film far away from the contacts. This region is modelled as a low-mobility-region with a mobility value of  $1.5 \times 10^{-4} \text{ cm}^2/\text{Vs}$  as compared to the mobility value of  $0.14 \text{ cm}^2/\text{Vs}$  for the rest of pentacene film. The low-mobility-region incurs most of the potential drop due to which the extracted mobility from the bottom contact devices becomes significantly lower than the top contact devices. A reasonable matching of the experimental curves with the simulated curves is obtained on substituting the above described mobility values in the bottom contact devices.

Also, first calibration of simulator was achieved for a top contact device (details in Section 2). Finally, by including special considerations of low-mobility-regions

in a bottom contact device, the simulation tool is further calibrated for use in design of devices.

## References

- [1] S.F. Nelson, Y.-Y. Lin, D.J. Gundlach, T.N. Jackson, Appl. Phys. Lett. 72 (1998) 1854.
- [2] P.V. Necliudov, M.S. Shur, D.J. Gundlach, T.N. Jackson, Solid-State Electron. 47 (2003) 259.
- [3] D.J. Gundlach, L. Zhou, J.A. Nichols, T.N. Jackson, P.V. Necliudov, M.S. Shur, J. Appl. Phys. 100 (2006) 024509.
- [4] R.A. Street, A. Salleo, Appl. Phys. Lett. 81 (2002) 2887.
- [5] Y. Roichman, N. Tessler, Appl. Phys. Lett. 80 (2002) 151.
- [6] P.G. Schroeder, C.B. France, J.B. Park, B.A. Parkinson, J. Phys. Chem. B 107 (2003) 2253.
- [7] N. Koch, J. Ghijsen, R.L. Johnson, J. Schwartz, J.-J. Pireaux, A. Kahn, J. Phys. Chem. B 106 (2002) 4192.
- [8] J.H. Kang, X.Y. Zhu, Appl. Phys. Lett. 82 (2003) 3248.
- [9] I. Kymissis, C.D. Dimitrakopoulos, S. Purushothaman, IEEE Trans. Electron. Dev. 48 (2001) 1060.
- [10] K.S. Lee, T.J. Smith, K.C. Dickey, J.E. Yoo, K.J. Stevenson, Y.-L. Loo, Adv. Funct. Mater. 16 (2006) 2409.
- [11] K. Sheshadri, C.D. Frisbie, Appl. Phys. Lett. 78 (2001) 993.
- [12] K.P. Puntambekar, P.V. Pesavento, C.D. Frisbie, Appl. Phys. Lett. 83 (2003) 5539.
- [13] L. Burgi, H. Sirringhaus, R.H. Friend, Appl. Phys. Lett. 80 (2002) 2913.
- [14] L. Burgi, T.J. Richards, R.H. Friend, H. Sirringhaus, J. Appl. Phys. 94 (2003) 6129.
- [15] M. Yoshida, S. Uemura, S. Hoshino, N. Takada, T. Kodzasa, T. Kamata, Jpn. J. Appl. Phys. 44 (2005) 3715.
- [16] M.A. Alam, A. Dodabalapur, M.R. Pinto, IEEE Trans. Electron. Dev. 44 (1997) 1332.
- [17] S. Scheinert, G. Paasch, Phys. Status Solidi A 201 (2004) 1263.
- [18] D. Gupta, N. Jeon, S. Yoo, Org. Electron. 9 (2008) 1026.
- [19] I.G. Hill, Appl. Phys. Lett. 87 (2005) 163505.
- [20] T. Li, P.P. Ruden, I.H. Campbell, D.L. Smith, J. Appl. Phys. 93 (2003) 4017.
- [21] T. Li, J.W. Balk, P.P. Ruden, I.H. Campbell, D.L. Smith, J. Appl. Phys. 91 (2002) 4312.
- [22] P.M. Zeitzoff, C.D. Young, G.A. Brown, Y. Kim, IEEE Electron. Dev. Lett. 24 (2003) 275.
- [23] K.W. Shih, R. Rios, P. Packan, K. Mistry, T. Abbott, in: IEEE Electron. Dev. Meeting, IEDM, (2001) p. 13.3.1.
- [24] D. Natali, L. Fumagalli, M. Sampietro, J. Appl. Phys. 101 (2007) 014501.
- [25] J. Zaumseil, K.W. Baldwin, J.A. Rogers, J. Appl. Phys. 93 (2003) 6117.
- [26] S. Schienert, G. Paasch, T. Lindler, Synth. Met. 137 (2003) 1451.
- [27] S. Schienert, G. Paasch, M. Schrodner, J. Appl. Phys. 92 (2002) 330.
- [28] A. Bolognesi, A.D. Carlo, P. Lugli, Appl. Phys. Lett. 81 (2002) 4646.
- [29] S. Cherian, C. Donley, D. Mathine, L. LaRussa, W. Xia, N. Armstrong, J. Appl. Phys. 96 (2004) 5638.
- [30] M. Pope, C.E. Swenberg, Electronic Processes in Organic Crystals and Polymers, Oxford University Press, New York, 1999.
- [31] E.A. Silinich, V.Čápek, Organic Molecular Crystals, Their Electronic States, New York, 1980.
- [32] E.A. Silinich, A. Klimkåns, S. Larsson, V. Čápek, Chem. Phys. 198 (1995) 311.
- [33] L. Sebastian, G. Weiser, H. Bässler, Chem. Phys. 61 (1981) 125.
- [34] D. Gupta, Effect of Pentacene Thickness in Organic Thin Film Transistors: Measurements and Simulations in Top and Bottom Contact Devices' Ph.D. Dissertation, Dept. Mater. Met. Eng., Indian Institute of Technology, Kanpur, July, 2007.
- [35] K. Hummer, C.A. Draxl, Phys. Rev. B 72 (2005) 205205.
- [36] G. Horowitz, F. Deloof, F. Garnier, R. Hajlaoui, M. Hmyene, A. Yassar, Synth. Met. 54 (1993) 435.
- [37] C. Bock, D.V. Pham, U. Kunze, D. Käfer, G. Witte, Ch. Wöll, J. Appl. Phys. 100 (2006) 114517.
- [38] M.S. Xu, M. Nakamura, M. Sakai, K. Kudo, Adv. Mater. 19 (2007) 371.
- [39] P.V. Pesavento, K.P. Puntambekar, C.D. Frisbie, J.C. McKeen, P.P. Ruden, J. Appl. Phys. 99 (2006) 94504.
- [40] M. Nakamura, N. Goto, N. Ohashi, M. Sakai, K. Kudo, Appl. Phys. Lett. 86 (2005) 122112.

junctions consisting of PEDOT:PSS and InZnO have been rarely reported so far. In this research, we investigated the  $I$ - $V$  characteristics of ITO/PEDOT:PSS/InZnO devices for two sets of samples. The first set is composed of PEDOT:PSS as-prepared, while the second set is composed of PEDOT:PSS irradiated by UV light source. Following that, the electronic, structure, and morphological changes of the PEDOT:PSS films were analyzed using ultraviolet photoelectron spectroscopy (UPS), X-ray photoelectron spectroscopy (XPS) and atomic force microscopy (AFM). The effect of storage on the electrical properties of the fabricated devices is also reported.

## 2. Experiment

The substrates used for the fabrication of the devices were  $2 \times 2 \text{ cm}^2$  glass plates coated with 100 nm layer of indium tin oxide (ITO). The substrates were cleaned following standard procedure. Next, a 300 nm thick PEDOT:PSS layer was then deposited by multiple spin-coating. After each spin-coating, the PEDOT:PSS layer was baked at  $130^\circ\text{C}$  for 10 min in air. PEDOT:PSS (Baytron P Al 4083) was purchased from Starck. In our experiment, two sets of four samples each were prepared in the same way. In the first set, PEDOT:PSS films on glass substrates were irradiated for 10 min by UV light source (output power density of  $4 \text{ W/cm}^2$ ) with emission centered at 355 nm (referred to as: UV-exposed devices). The second set of samples is composed of PEDOT:PSS on glass substrates without UV irradiation (referred to as: un-exposed devices). The InZnO thin films (80 nm) fabricated by rf magnetron sputtering at room temperature were deposited on top of PEDOT:PSS through a shadow mask. The active area of the devices is shown in Fig. 1. The current–voltage characteristics of the fabricated devices were measured by an Agilent 4156C semiconductor parameter analyzer in laboratory atmosphere at room temperature and under dark condition. After the first measurements, the samples were stored in normal laboratory environment in a Vacuum Desiccator. All the measurements were repeated on the stored samples after 30 days. We used a monochromatic Al  $K\alpha$  source (1486.6 eV) for XPS analysis. The binding energy was calibrated with the core-level spectrum of Au 4f. UPS spectra were obtained, using HeI radiation (40.8 eV) from a He-resonance lamp. Surface morphology was investigated by AFM (Model SPI-3800, SII).

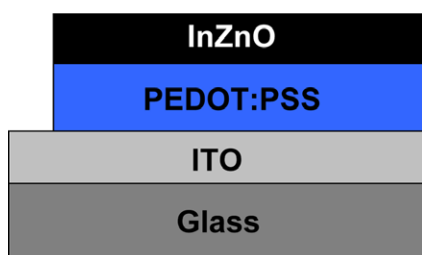


Fig. 1. Schematic representation of the device structure.

## 3. Results and discussion

The  $I$ - $V$  characteristics of UV-exposed and un-exposed devices are shown in Fig. 2. Each curve represents the average value of four samples. The  $I$ - $V$  characteristics of un-exposed devices are shown in Fig. 2a and that of UV-exposed devices are shown in Fig. 2b. Also shown in the figures are the  $I$ - $V$  characteristics measured after 30 days on the same samples. It can be seen from Fig. 2a that the  $I$ - $V$  characteristics of the un-exposed devices show asymmetrical non-linear behavior. The current does not show any linear dependence with voltage even in the low voltage region (see inset). In the case of UV-exposed devices, a linear region is seen at low voltages (see inset) indicating an ohmic conduction mechanism. This implies that the work function of PEDOT:PSS (4.8–5.3 eV [14]) is close to that of InZnO electrode (5.2 eV [15]).

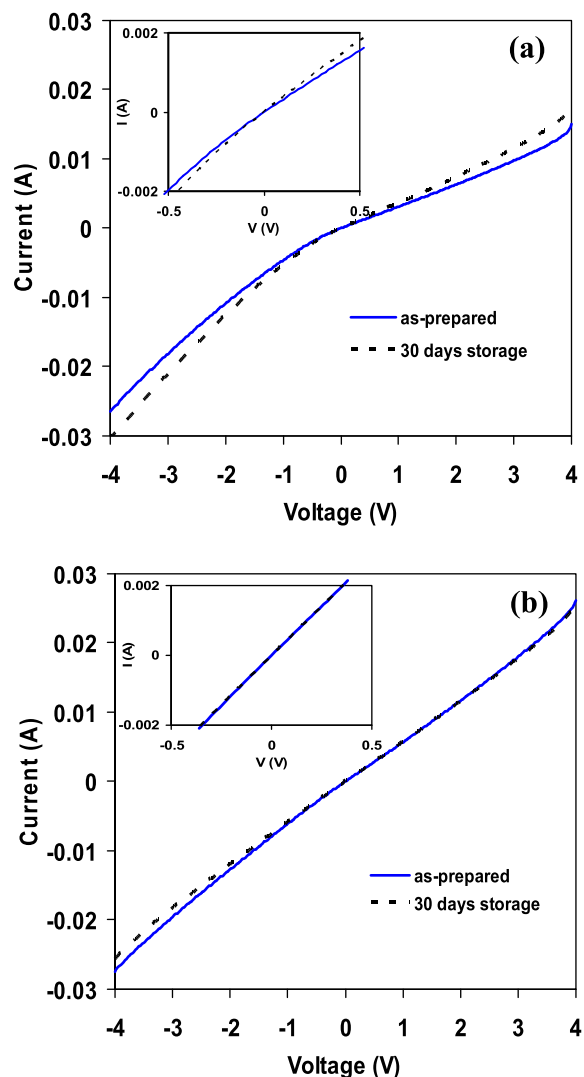


Fig. 2. Current–voltage characteristics for as-prepared and stored samples: (a) un-exposed devices and (b) UV-exposed devices.

The  $I$ - $V$  characteristics measured after one month of storage show no significant degradation of the devices, which demonstrates the excellent stability of these organic/metal junctions. The excellent stability is most likely due to the storage in the Vacuum Desiccator, which prevents interaction of the environment and because of PEDOT:PSS is an air-stable material [16]. We see a slight deviation between the measured data before and after storage, this deviation is more pronounced in the case of un-exposed devices as it appears in Fig. 2a. However, it is difficult to draw firm conclusions regarding the observed results, because we were able to find some samples (before averaging) with excellent reproducibility (not shown here). An additional factor that can affect the durability of organic/metal contact is the degradation of the metal electrodes. This degradation appears mainly after the first measurement [17] or after performing several consecutive sweeps in the forward and backward direction [18]. Fig. 3 shows the  $I$ - $V$  measurements of UV-exposed devices taken from 20 consecutive forward and backward sweeps. Identical  $I$ - $V$  responses are obtained, the data points fall on top of each other, showing that there is no sign of deterioration after consecutive sweeps. We performed the sweeps between  $\pm 2$  V in order to verify the stability of the electrodes and prevent the degradation of our devices for further studies.

Fig. 4 shows the  $I$ - $V$  characteristics of the samples with and without UV treatment superimposed on the same axes. The un-exposed film was more electrically resistive than the exposed one. In the case of UV-exposed devices, the  $I$ - $V$  characteristics exhibit better response than that obtained with un-exposed devices. In the forward bias, the magnitude of the current at any voltage was higher and the devices show a linear  $I$ - $V$  behavior. The plot is linear over a potential range of approximately 8 V. It is well known that local joule heating reduces the contact resistance between conducting polymer and metal electrodes.

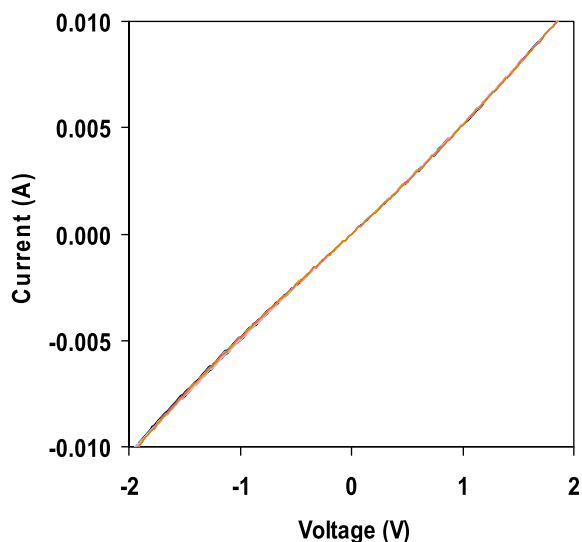


Fig. 3. Current–voltage measurements out of 20 consecutive sweeps of UV-exposed devices stored in a Vacuum Desiccator for 30 days.

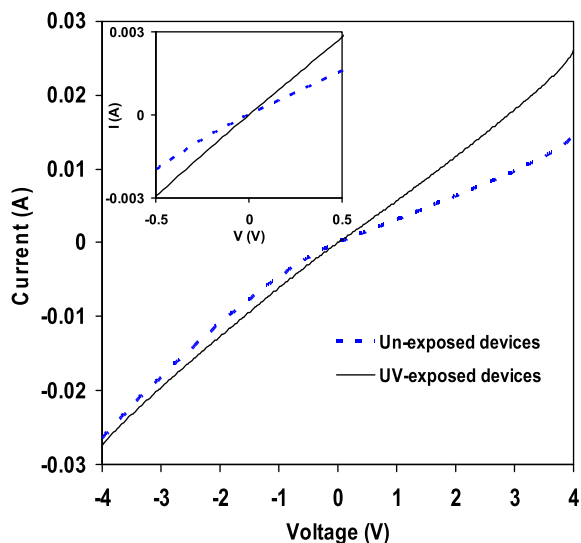


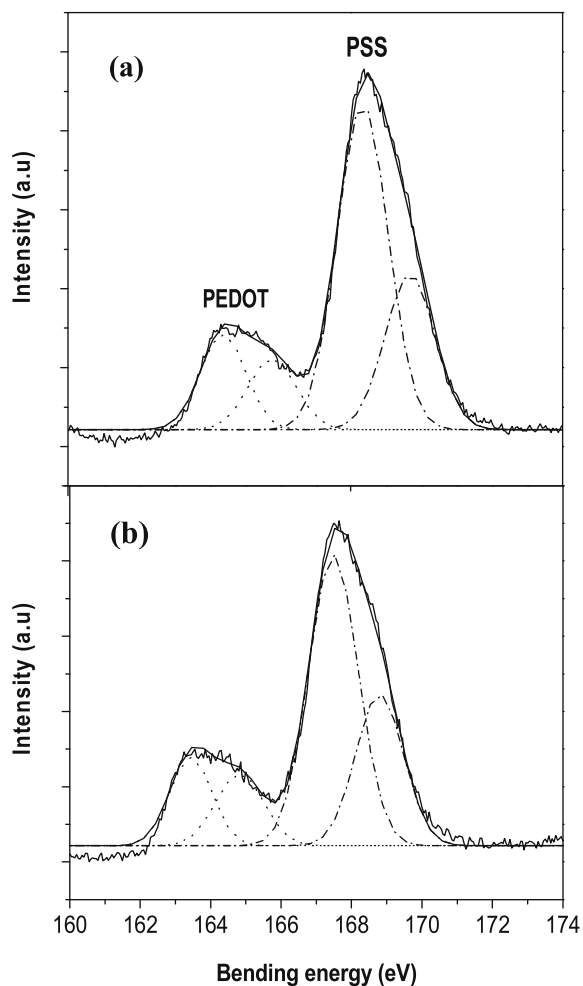
Fig. 4. Comparison of  $I$ - $V$  characteristics of UV-exposed and un-exposed devices.

Since Joule heating occurs at the interface region during electrical measurement, both the physical and chemical properties of the interface region could be altered. Our devices based on PEDOT:PSS/InZnO contact did not show any thermal degradation due to current injection during operation. After several sweeps (Fig. 3) and within the applied voltage range, current performance without noticeable degradation is notable. We found no evidence for significant Joule heating in our devices, which indicates good thermal contact between the thin polymer film and metal electrode. We suggest that the linear  $I$ - $V$  curve obtained with UV-exposed devices is mainly due to the changes in the work function of PEDOT:PSS layer induced by UV irradiation.

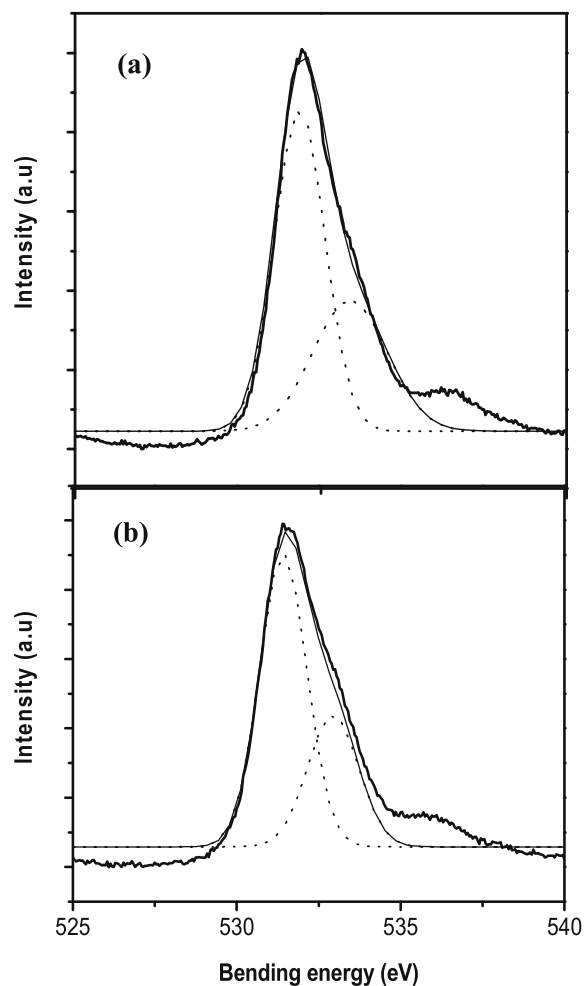
We employed XPS and UPS to determine the origin of the conductivity enhancement. The changes in work function of PEDOT:PSS films with and without UV treatment are obtained from UPS (Table 1). The work function of as-prepared film was 4.89 eV and that of UV-treated film was 5.07 eV. The XPS spectra for S2p and O1s with curve fitting results obtained on samples with and without UV treatment are shown in Figs. 5 and 6, respectively. For S2p, four peaks were clearly resolved. Curve fitting analysis shows that the lower binding energy peaks at 164.3 and 165.7 eV correspond to the sulfur atom of PEDOT. The two decomposed peaks at 169.5 and 168.5 eV are due to neutral and ionic sulfur in the PSS dopant [19,20]. The S2p doublet, which could not be resolved in these mea-

Table 1  
Surface stoichiometry and work function of PEDOT:PSS samples with and without UV treatment.

Sample	S2p	O1s	C1s	Work function (eV)
As-prepared	10.3%	22.5%	67.2%	4.89
UV-treated	9.8%	23.2%	67%	5.07



**Fig. 5.** XPS spectra of S2p for as-prepared PEDOT:PSS (a) and PEDOT:PSS after UV irradiation (b).



**Fig. 6.** XPS spectra of O1s for as-prepared PEDOT:PSS (a) and PEDOT:PSS after UV irradiation (b).

measurements, was fitted by a single peak. For O1s, two peaks were resolved. A shoulder at 533.3 eV with high binding energy corresponding to the oxygen atoms of the PEDOT chain, and a strong peak at 531.7 eV with lower binding energy arising from the  $\text{SO}_3\text{H}$  and  $\text{SO}_3\text{Na}$  units of the PSS chains [21]. The chemical composition of PEDOT:PSS surface was calculated based on the core level peak areas and their relative sensitivity factors. The results are shown in Table 1. As is evident from the spectra of S2p and O1s and the films composition analysis (Table 1), the UV treatment does not induce any significant changes in the core level features of PEDOT:PSS films. However, we found that the binding energies of all core levels have been shifted to lower binding energies. The binding energy of sulfur, oxygen and carbon (not shown here) shifted by 0.9, 0.4 and 0.7 eV, respectively. This suggests that the change in work function is not primarily due to chemical changes in the films. Instead, we suggest that the reason for this change is to be found in morphological changes induced by the UV irradiation. In order to see the differences of morphologies of our samples, we investigated the AFM images of

as-prepared and UV-treated films. From the AFM images of both samples, we could not find significant difference on surface morphology except slight reduction in degree of surface roughness (Table 2). Reduced root mean square (RMS) surface roughness and the increase of electrical conductivity of the film by UV treatment support the conformational change of PEDOT:PSS films observed by Lee et al. [4]. Such changes in surface structure most probably change the surface dipole structure and thereby influence the measured binding energies [22]. The trend in device performance could be explained by the observed changes in the work function of the PEDOT:PSS layer.

In order to examine if InZnO electrode played a role in the improved stability of our devices, a set of ITO/PEDOT:PSS/Al samples were fabricated in the same conditions and tested. The  $I$ - $V$  curves of ITO/PEDOT:PSS/Al are shown in Fig. 7. When ITO and Al are used as anode and cathode, respectively, the  $I$ - $V$  characteristics change, becoming asymmetric with a rectification value around 20 at 1.5 V. The difference in the work function values (in vacuum) of the Al electrode ( $\sim 4.3$  eV [23]) and PEDOT:PSS introduces



**Table 2**

RMS roughness, average roughness, and mean height of as-prepared and UV-treated samples measured by AFM.

Sample	RMS (nm)	Average roughness (nm)	Mean height (nm)
As-prepared	2.46	1.97	20.04
UV-treated	2.15	1.80	14.20

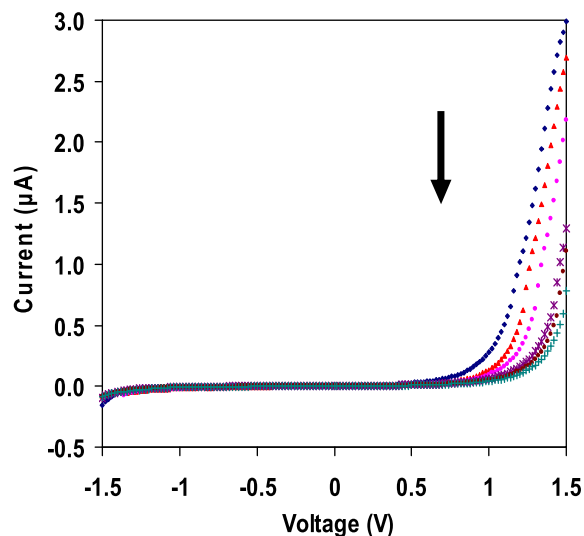


Fig. 7.  $I$ - $V$  characteristics of ITO/PEDOT:PSS/Al. The arrow shows the direction of repeated  $I$ - $V$  sweeps.

a built-in potential that can be seen in the  $I$ - $V$  characteristics of ITO/PEDOT:PSS/Al, where at low forward bias the intrinsic field is opposing the charge injection until around 0.75 V. After the first sweep, the current gradually decreased, indicating that the Al electrode was immediately deteriorated. The overall current values have decreased by almost 300% causing a reduction in the rectification ratio. AFM was used to investigate the electrodes before and after voltage application. A smooth and defect-free surface was observed for the un-operated Al-electrode (Fig. 8a). After bias application, some blisters were seen on the Al contact over the active area of the device (Fig. 8b). It is well known that poly(4-styrenesulfonate) (PSS) of PEDOT:PSS has strong acidic characteristics and can be corrosive to the electrode. Thus, the Al electrode damage under voltage might be due to the highly acidic property of the PSS. The InZnO electrode does not show any blisters even after applying high voltage and repeated measurements (Fig. 8b). For the operated InZnO electrode surface, a smooth and crack-free layer is observed. The InZnO films before and after voltage application show a RMS roughness of 4.95 and 1.43 nm, respectively. The improvement of surface morphology of operated InZnO electrode may be due to the chemical interaction between PEDOT:PSS and InZnO under voltage, or the trapped moisture during measurement gets electrolyzed as the bias is applied and the gases are released causing the change in the surface morphology of InZnO film.

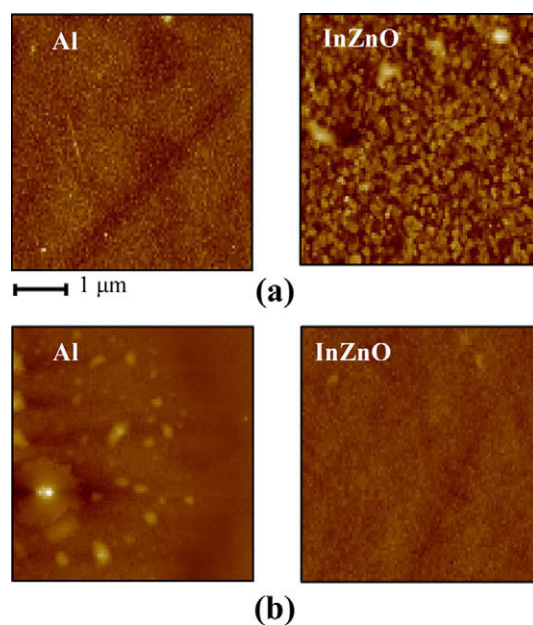


Fig. 8. AFM images of Al and InZnO electrodes: (a) before application of voltage and (b) after application of voltage.

#### 4. Summary

The effects of UV irradiation on the work function of PEDOT:PSS films have been investigated in this study. Based on the UPS, XPS, and AFM measurements, it was found that UV irradiation leads to an increase in the work function and the enhancement of electrical conductivity of PEDOT:PSS films, resulting from the morphological change in the polymer chain of PEDOT:PSS. The UV-exposed devices show an ohmic contact over a large potential range. We also studied the effect of storage on the electrical properties of ITO/PEDOT:PSS/InZnO devices. No significant changes of electrical characteristics have been found after storing the devices for a period of 30 days. AFM investigations show no blistering of InZnO contacts in devices on application of voltage. InZnO contacts may provide a good solution to develop reliable and low resistance ohmic contacts.

#### Acknowledgements

This work was supported by the Korea Science and Engineering Foundation (KOSEF) grant funded by the Korea government (MOST) (No. R0A-2007-000-10044-0(2007)).

#### References

- [1] H. Shirakawa, E.J. Louis, A.G. MacDiarmid, C.K. Chiang, A.J. Heeger, *J. Chem. Soc. Chem. Commun.* 16 (1977) 578.
- [2] H. Hoppe, N.S. Sariciftci, *J. Mater. Res.* 19 (2004) 1924.
- [3] J. Shinar, *Organic Light-Emitting Devices: A Survey*, Springer-Verlag, New York, 2004.
- [4] Y.J. Lin, F.M. Yang, C.Y. Huang, *Appl. Phys. Lett.* 91 (2007) 092127.
- [5] M. Nakano, A. Tsukazaki, R.Y. Gunji, K. Ueno, A. Ohtomo, T. Fukumura, M. Kawasaki, *Appl. Phys. Lett.* 91 (2007) 142113.
- [6] P.Y. Emelie, E. Cagin, J. Siddiqui, J.D. Phillips, C. Fulk, J. Garland, S. Sivananthan, *J. Electron. Mater.* 36 (2007) 841.
- [7] Y.J. Lin, *J. Appl. Phys.* 103 (2008) 063702.

- [8] J. Ficker, *J. Appl. Phys.* 94 (2003) 2638.
- [9] J. Steiger, S. Karg, R. Schmechel, H. von Seggern, *Synth. Met.* 122 (2001) 49.
- [10] Y. Qui, Y. Hu, G. Dong, L. Wang, J. Xie, Y. Ma, *Appl. Phys. Lett.* 83 (2003) 1644.
- [11] T. Minami, *MRS Bull.* 38 (2000) 25.
- [12] J. Cui, A. Wang, N.L. Edleman, J. Ni, P. Lee, N.R. Armstrong, T.J. Marks, *Adv. Mater.* 13 (2001) 1476.
- [13] B. Yaglioglu, Y. Huang, H. Yeom, D.C. Paine, *Thin Solid Films* 496 (2006) 89.
- [14] C. Scott, G. Malliaras, W.D. Chen, J. Breach, J. Salem, P. Brock, S. Sachs, C. Chidsey, *Appl. Phys. Lett.* 74 (1999) 1510; G. Greczynski, T. Kugler, M. Keil, W. Osikowicz, M. Fahlman, W.R. Salaneck, *J. Electron. Spectrosc., Relat. Phenom.* 121 (2001) 1; A.J. Makenin, I.G. Hill, R. Shashindhar, N. Nikolov, Z.H. Kafafi, *Appl. Phys. Lett.* 79 (2001) 557; N. Koch, A. Kahn, J. Ghijsen, J.J. Pireaux, J. Schwartz, R.L. Johnson, A. Elschner, *Appl. Phys. Lett.* 82 (2003) 70.
- [15] B.J. Cui, A. Wang, N.L. Edleman, J.N. Lee, N.R. Armstrong, T.J. Marks, *Adv. Mater.* 13 (2001) 1476.
- [16] L. Groenendaal, F. Jonas, D. Freitag, H. Pielartzik, J.R. Reynolds, *Adv. Mater.* 12 (2000) 481.
- [17] K.S. Kang, H.K. Lim, K.Y. Cho, K.J. Han, J.W. Kim, *J. Phys. D: Appl. Phys.* 41 (2008) 1.
- [18] G. Pham, T.U. Kampen, I. Thurzo, M. Friedrich, D.R. Zahn, *Appl. Surf. Sci.* 542 (2003) 212.
- [19] S.J. Wang, H.H. Park, *J. Electroceram.* 18 (2007) 161.
- [20] G. Greczynski, T. Kugler, M. Keil, W. Osikowicz, M. Fahlman, W.R. Salaneck, *J. Electron. Spectrosc., Relat. Phenom.* 121 (2001) 1.
- [21] S.K.M. Jonsson, J. Brigerson, X. Crispin, G. Greczynski, W. Osikowicz, A.W. Denier van der Gon, W.R. Salaneck, M. Fahlman, *Synth. Met.* 139 (2003) 1.
- [22] Y.J. Lin, F.M. Yang, C.S. Lin, *J. Appl. Phys.* 102 (2007) 103702.
- [23] H.B. Michaelson, *J. Appl. Phys.* 48 (1977) 4729.

tional buffer layer or poly(ethylenedioxythiophene) doped with poly(styrenesulfonate) (PEDOT:PSS) being considered to have several latent issues such as chemical reaction with ITO anodes [9,10] efforts to replace PEDOT:PSS with metal-oxide semiconductors are currently receiving an increased attention. In the area of organic light-emitting diodes (OLED), which already perceived the beneficial role of these metal-oxide semiconductors as buffer layers or as part of multilayer electrodes, tungsten oxides ( $\text{WO}_3$ ) have also been recognized as important buffer layers with a good hole-injecting property [11–13]. In spite of its significance in OLEDs, its application as an anodic buffer layer in organic solar cells was relatively limited. Chan et al. [14] used  $\text{WO}_3$  as an anodic buffer on ITO in vacuum-deposited copper phthalocyanine ( $\text{CuPc}$ )/ $\text{C}_{60}$  solar cells, and Janssen et al. [15] used it as a part of intermediate electrode in their hybrid tandem cells consisting of BHJ bottom cells and  $\text{CuPc}/\text{C}_{60}$  top cells in which  $\text{WO}_3$  functioned also as a buffer for  $\text{CuPc}/\text{C}_{60}$  cells. Recently Tao et al. [16], have employed  $\text{WO}_3$  as a buffer layer in solution-processed P3HT:PCBM BHJ cells, but their devices were in so-called inverted geometry where  $\text{WO}_3$  layer is grown on top of P3HT:PCBM films. It is noted that the fact that a buffer layer works in vacuum-deposited cells or in inverted-geometry BHJ cells does not necessarily mean it will work also in bulk-heterojunction (BHJ) cells of conventional geometry in which active layers are deposited on top of the buffer by solution processing. (i) because the fabrication compatibility is not always guaranteed and, moreover, (ii) because its presence can influence the properties of BHJ active layers such as molecular ordering and phase separation, all of which carry important implications for operation of BHJ cells. In this work, we explore thermally-evaporated  $\text{WO}_3$  layer as an anodic buffer in the popular P3HT:PCBM-60 BHJ cells in their conventional non-inverted geometry with a special attention paid to the film properties of thermally-evaporated  $\text{WO}_3$  layers in context of their effect on the properties of BHJ active layers as well as device performance.

## 2. Experimental

Thin films of  $\text{WO}_3$  (Alfa Aesar) were thermally evaporated in high vacuum ( $2 \times 10^{-6}$  Torr) onto ITO films on glass substrates or onto 30 nm-thick PEDOT:PSS layers (Baytron P AI 4083, H.C. Starck, Inc.) spun on those ITO films.

After deposition of  $\text{WO}_3$  layers, samples were transferred to a nitrogen-filled glove box, where the BHJ layers were spin-coated at 700 rpm for 60 s from a solution of P3HT:PCBM-60 (17 mg/mL, 1:0.9 by volume) in dichlorobenzene [1]. Devices without buffer layers or those with a buffer layer consisting only of 30 nm-thick PEDOT:PSS layers were also fabricated for comparison experiments. Annealing was done at 110 °C for 10 min on a hot plate. Then the samples were re-loaded into the chamber for deposition of Ca electrodes that are capped with Al. Schematic diagram for overall device structure is presented in Fig. 1. The active area  $A$  of the fabricated devices was in the range of 0.05–0.10  $\text{cm}^2$ . Photovoltaic measurement was done using the illumination from 150 W solar simula-

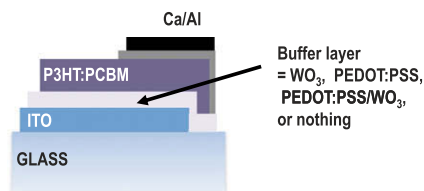


Fig. 1. [Color online] Schematic device structure of organic solar cells under study.

tor (ABET technologies) with AM1.5G filters. Irradiance was measured each time using a Si photodiode the response of which was cross-checked with the calibrated reference cell. Throughout the fabrication and photovoltaic measurement, samples were not exposed to ambient air to avoid any potential contamination or degradation.

## 3. Results and discussion

### 3.1. Film properties of $\text{WO}_3$

#### 3.1.1. Film morphologies and surface properties of $\text{WO}_3$ films

In order for buffer layers for ITO to work effectively, it is often desired to form a smooth and uniform layer when being deposited onto ITO surface. According to the atomic force microscopy (AFM) images shown in Fig. 2a, deposition of thin  $\text{WO}_3$  layer (10 nm) on ITO was shown to yield a highly smooth surface with the RMS roughness as small as 0.88 nm. This RMS roughness is comparable to that of PEDOT:PSS (=0.81 nm) spun on ITO and much smaller than that of bare ITO surface (=2.8 nm). Such smoothing effect of  $\text{WO}_3$  is expected to reduce the chance of direct shorts and local high fields and thus to help prevent leakage current and formation of defects that can possibly be induced by those [17]. Fig. 2b presents the X-ray diffraction (XRD) pattern of both 20 nm- and 60 nm-thick  $\text{WO}_3$  films grown on  $\text{SiO}_2$ . No crystalline peaks are observed except for a

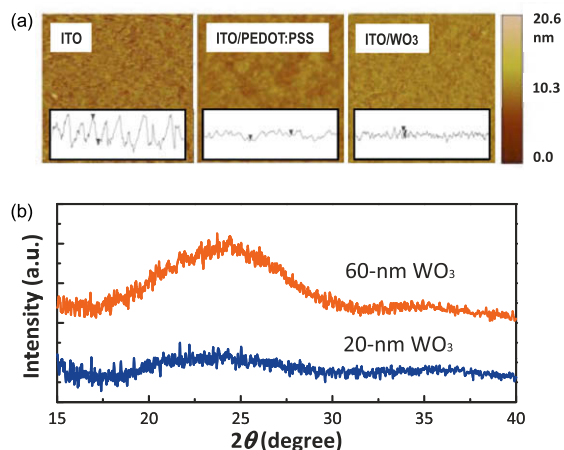


Fig. 2. [Color online] (a) AFM images of the surface and cross sectional profile of ITO, PEDOT:PSS on ITO, and  $\text{WO}_3$  on ITO. (Tapping mode,  $3 \times 3 \mu\text{m}^2$  scan size). (b) X-ray diffraction patterns of 20 nm and 60 nm-thick  $\text{WO}_3$  thin films evaporated on  $\text{SiO}_2/\text{Si}$  wafer.

broad feature near  $23^\circ$ , and thus  $\text{WO}_3$  films under study can be regarded amorphous. From the perspectives of large-area fabrication of organic devices or similar systems involving (semi)conductive oxide materials, being amorphous is regarded important, provided that it can yield a device performance that is sufficient for each target application, because it can reduce the chance of spatial non-uniformity which can often occur in polycrystalline materials with limited grain sizes [18].

In addition to the film morphologies, the surface energy of the film onto which photoactive layers will be deposited is often of interest because it is known that it can play a subtle but important role in growth of ordered films as well as in wetting properties. Results for contact angle measurement of a bare ITO substrate or those having  $\text{WO}_3$  or PEDOT:PSS layers are presented in Fig. 3a, and it can be easily seen that  $\text{WO}_3$  surface is more hydrophobic than the bare ITO or PEDOT:PSS-coated surfaces. Surface energy for each case was calculated using Young–Dupre equation [19] with the contact angles measured for deionized (DI)-water and diiodomethane liquid, and it is estimated to be 64.0, 72.4, and 47.6 mJ/m<sup>2</sup>, respectively, for bare ITO (plasma-treated), PEDOT:PSS on ITO, and  $\text{WO}_3$ (10 nm) on ITO. Note that there were several reports suggesting that hydrophobic surfaces or those treated by self-assembled monolayer (SAM) promote an ordered growth of P3HT films [20–22], although it appears there are several other factors that can affect the growth of P3HT [23,24]. It was also reported, although the physical origin was not clearly identified, that performance in inverted-geometry OPV cells with  $\text{Cs}_2\text{CO}_3$  buffer layers (for bottom cathodes) correlates inversely with the surface energy of the buffer layers [6]. As shown in Fig. 3b, we were also able to observe that P3HT films grown on  $\text{WO}_3$  layers exhibit the slightly higher ordering than those grown on ITO or PEDOT:PSS. The tendency of P3HT to organize with a higher degree of ordering is expected to improve the mobility of P3HT films. In an effort to study the effect of buffer layer on the carrier mobility of P3HT films, we have

measured the current density ( $J$ )–voltage ( $V$ ) characteristics of hole-only devices in a geometry of ITO/PEDOT:PSS/P3HT ( $70 \pm 6$  nm)/Au and ITO/ $\text{WO}_3$  (15 nm)/P3HT ( $70 \pm 6$  nm)/Au (see the inset of Fig. 3b). One can easily see from the log–log plots of  $J$ – $V$  characteristics (at  $V > \sim 1$ ) that both types of devices (four devices each) follow the typical  $V^2$ -dependence of space-charge-limited current (SCLC) given by [25]:

$$J = \frac{9}{8} \epsilon_0 \epsilon_r \mu \frac{V^2}{d^3} \quad (1)$$

in which  $\epsilon_0$  is the permittivity of vacuum,  $\epsilon_r$  the relative dielectric constant,  $\mu$  the mobility, and  $d$  the active layer thickness. In addition, one can note in the plot that  $\text{WO}_3$ -based devices exhibited a better device-to-device reproducibility than PEDOT:PSS-based devices. Using Eq. (1) and the Y-cut of the apparent linear fit for log–log plot in each case, the hole mobility values of the P3HT films on PEDOT:PSS and  $\text{WO}_3$  are extracted to be  $(1.0 \pm 0.3) \times 10^{-4} \text{ cm}^2/\text{V s}$  and  $(2.4 \pm 0.6) \times 10^{-4} \text{ cm}^2/\text{V s}$ , respectively, with  $\epsilon_r$  of 3.0 [26]. Such improvement in carrier mobility is known to be beneficial for OPV device performance by reducing bias-dependent recombination as it effectively increases the mean free path of photogenerated-carriers [27] or by decreasing the possibility of space-charge build-up [28].

### 3.1.2. Electronic properties of $\text{WO}_3$ films

Current density ( $J$ )–voltage ( $V$ ) characteristics of a device in a structure of ITO/ $\text{WO}_3$  ( $70 \pm 10$  nm)/Al is presented in Fig. 4a. It is observed that  $J$ – $V$  exhibits a linear relation-

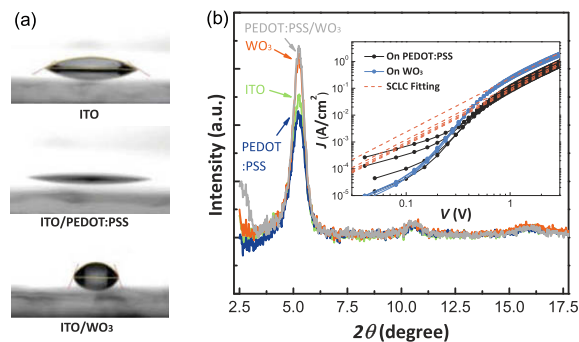


**Fig. 3.** [Color online] (a) Contact angle measurement of ITO,  $\text{WO}_3$  on ITO, and PEDOT:PSS on ITO surfaces for DI-water. (b) X-ray diffraction patterns of P3HT films grown on various buffer layers under study. Inset: Current density ( $J$ )–voltage ( $V$ ) characteristics of hole-only devices in a geometry of ITO/ $X$ /P3HT ( $70 \pm 6$  nm)/Au with  $X$  being  $\text{WO}_3$  (15 nm; blue) or PEDOT:PSS (black). Fitting curves using the equation for space-charge limited current [SCLC; Eq. (1)] are shown as red dashed lines for each case. (For interpretation of the references to colour in this figure legend, the reader is referred to the web version of this article.)

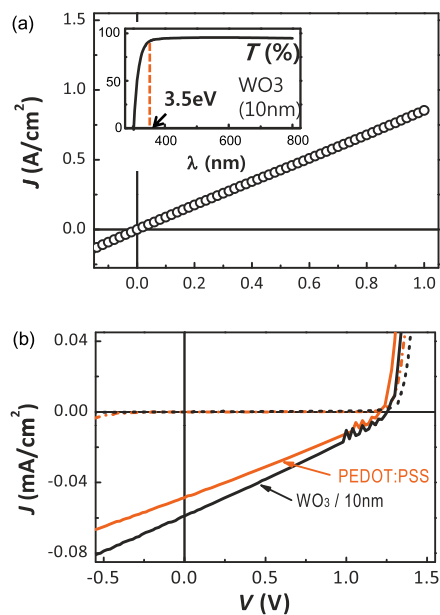


**Fig. 4.** [Color online] (a) Electrical characteristics of ITO/ $\text{WO}_3$  (70 nm)/Al device. (b) Electrical characteristics of ITO/ $x$ /P3HT/Ca/Al [ $x = \text{WO}_3$  (black) or PEDOT:PSS/ $\text{WO}_3$  (red)] under illumination (solid) and in dark (dashed). Inset in (a): Optical transmission spectrum of 10 nm-thick  $\text{WO}_3$  films. (For interpretation of the references to colour in this figure legend, the reader is referred to the web version of this article.)

ship throughout the voltage range applied. Such linear relationship is consistent with the fact that some transition metal oxides such as  $V_2O_5$ ,  $MoO_3$ , and  $WO_3$  are *p*-doped semiconductors as prepared when they are grown by thermal evaporation, due to the presence of impurities and different oxidation states, etc. [29]. From its slope, the conductivity of  $WO_3$  films used in this study is estimated to be  $(6 \pm 1) \times 10^{-6}$  S/cm, which is comparable to that of doped *p*-type organic semiconductors used in *pin*-type OLEDs [30]. This level of conductivity will be large enough to ensure the series resistance owing to insertion of a  $WO_3$  layer to be negligible unless it is too thick.

Another important parameter would be the effective work function of the anode system, because  $V_{OC}$  tends to correlate with the work function of an anode for a given cathode in BHJ type cells [6] although it can be influenced by a combination of several other factors. Moreover, the energy level of the anode system should provide cells with efficient pathways for carrier collection with no, or if any, negligible energy barrier. According to the previous reports, the work function of  $WO_3$ , or  $\Phi_{WO_3}$  can range from 4.7 to 6.4 eV depending on film preparation conditions [13,16,31,32]. To estimate  $\Phi_{WO_3}$  of the layer used in the present study, we have investigated the light and dark characteristics of devices based on single active layers in a geometry of ITO/X/P3HT/Ca/Al with X being  $WO_3$  (10 nm) or PEDOT:PSS as shown in Fig. 4b. In such single-layer structure Malliaras et al. showed that the built-in voltage  $V_{bi}$ , or  $|\Phi_{anode} - \Phi_{cathode}|/e$  correlates with the compensation voltage  $V_0$  at which the current density values under dark and illuminated conditions become equal [33]. From Fig. 4b,  $V_0$  is found to be 1.26 V for a  $WO_3$ -based device and 1.22 V for a PEDOT:PSS-based device, respectively. Since these devices have the same kind of active layers and cathode structures, the observed small difference in  $V_0$  indicates that  $\Phi_{WO_3}$  can be approximated to the work function of PEDOT:PSS or  $\Phi_{PEDOT}$ , which is known to be about 5.1–5.2 eV [4]. Using the optical energy gap of  $WO_3$  films measured by UV/vis transmission spectrum (see the inset of Fig. 4a), the approximate energy diagram ignoring band bending at interfaces is summarized as shown in the inset of Fig. 5.

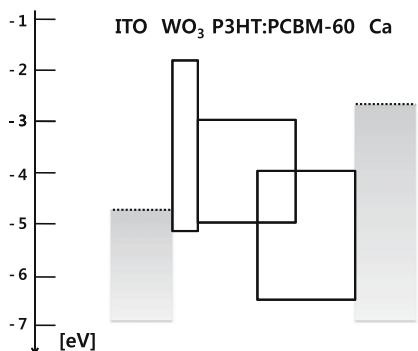


**Fig. 5.** (a) Schematic energy diagram of the OPV cells under study. Band bending and a formation of interface dipoles, etc. could be possible but are ignored in this diagram. Values are given in unit of electron volt with respect to the vacuum level.

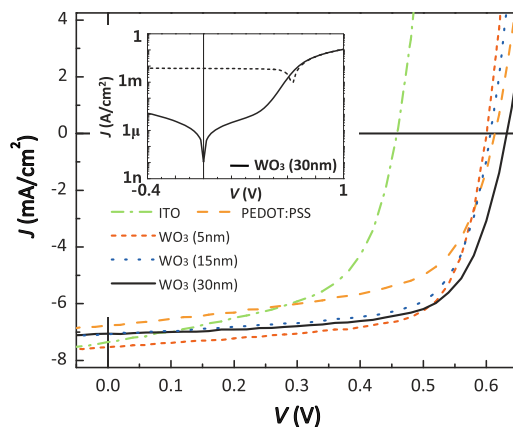


**Fig. 6.** [Color online] Current density–voltage ( $J$ – $V$ ) characteristics under illumination of simulated AM1.5G ( $100 \text{ mW/cm}^2$ ) for (a) fabricated P3HT:PCBM organic solar cells without buffer layers (green, dash dot) or with buffer layers of PEDOT:PSS (orange, dash), 5 nm-thick  $WO_3$  (red, short dash), 15 nm-thick (blue, dot)  $WO_3$ , or 30 nm-thick  $WO_3$  (black, solid) films. The inset shows the semi-logarithmic plot for  $J$ – $V$  characteristics of the cell with 30 nm-thick  $WO_3$  films for both dark (solid) and illumination (short dash) cases. The device with 30 nm-thick  $WO_3$  films was fabricated in a separate batch. (For interpretation of the references to colour in this figure legend, the reader is referred to the web version of this article.)

### 3.2. Photovoltaic properties of organic solar cells with $WO_3$ buffer layers

The current density ( $J$ )–voltage ( $V$ ) characteristics of OPV cells measured under the simulated AM 1.5G illumination ( $100 \text{ mW/cm}^2$ ) are presented in Fig. 6 for solar cells made in a structure of ITO/buffer layer (=x)/P3HT:PCBM-60/Ca/Al in which x is  $WO_3$  (5 nm, 15 nm, or 30 nm), PEDOT:PSS (30 nm), or nothing. The best device with x of 5 nm-thick  $WO_3$  exhibited the PCE of 3.1% [3.0%] and FF of 0.69 [0.69], while the best device fabricated in the same batch without buffer or with x of PEDOT:PSS exhibited the PCE and FF of 1.9% and 0.56 and 2.5% and 0.60, respectively. The best device with x of 30 nm-thick  $WO_3$ , which was fabricated in a separate batch, exhibited the PCE and FF of 3.1% and 0.70, respectively. The fact that the cell performance does not show a significant dependence on the thickness of  $WO_3$  layers may be beneficial in optimizing the optical/electrical structure of OPV cells. For example, one can vary the thickness of  $WO_3$  layers (at least up to a few tens of nanometers) without a significant compromise in cell electrical properties until the optical absorption by active layers is maximized with the help of multilayer thin-film optics [34] as in the work by Kim et al. [35] in which  $TiO_x$  buffer layers function also as an optical spacer for such purpose.

The effect of  $WO_3$  on PV performance is presented in a statistical sense in Fig. 7 showing the box graph for photovoltaic parameters obtained in total of 90 devices fabricated in five independent batches. One can note that  $WO_3$ -based devices exhibit improvement in FF,  $V_{OC}$ , and efficiency over ITO-based cells, and in FF and efficiency over PEDOT:PSS-based cells, with a significantly better batch-to-batch consistency. Recalling the correlation of

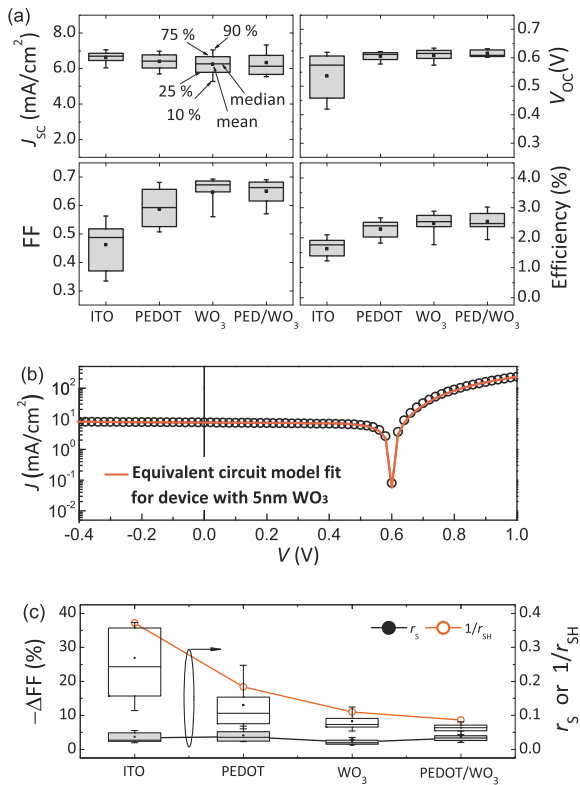


**Fig. 7.** [Color online] (a) Statistical box graph for  $J_{sc}$ ,  $V_{oc}$ , FF, and efficiency for total of 90 devices (13 of ITO, 27 of PEDOT:PSS, 32 of  $WO_3$ , and 18 of PEDOT/ $WO_3$ -based cells) over five independent batches. Thickness of  $WO_3$  ranges between 5 and 30 nm. (b) Current density–voltage ( $J$ – $V$ ) characteristics (black, open circle) and its fitting curve (red, solid) under equivalent circuit model in which  $n = 1.85$ ,  $J_0 = 27 \text{ nA/cm}^2$ ,  $R_{sh} A = 1000 \Omega \text{ cm}^2$ , and  $R_s A = 1.0 \Omega \text{ cm}^2$ . (c) The average values of the normalized series resistance  $r_s$  and a reciprocal of shunt resistance  $1/r_{sh}$ , and the statistical box graph for the relative decrease in fill factors in% ( $\equiv -\Delta FF$ ) due to each of  $r_s$  (shaded) and  $r_{sh}$  (clear). The points for  $r_s$  are behind the box graph because  $-\Delta FF$  due to  $r_s$  follows approximately  $\sim r_s$  itself. To estimate the decrease in FF due to  $r_{sh}$ , the diode ideality factor  $n$  of 2.0 was assumed. Lines in graph (c) are guide to eyes and bear no physical meaning. (For interpretation of the references to colour in this figure legend, the reader is referred to the web version of this article.)

$V_{oc}$  value in a BHJ cell with the work function of its anode [6], the  $V_{oc}$  values observed in  $WO_3$ -based devices that are larger than those of ITO based devices can be attributed to the work function of  $WO_3$  layers that is larger than that of ITO ( $\sim 4.7 \text{ eV}$ ) [4], as described in Section 3.1. On the other hand, short-circuit current density  $J_{sc}$  showed a relatively wide device-to-device and batch-to-batch variation, possi-

bly due to the local variation in the active layer thickness resulting from the low-speed spin-coating process.

Note that common enhancement in  $WO_3$ -based devices over buffer-free or PEDOT:PSS-based devices is the consistently high FF values. Most of the FF values that are being reported for the P3HT:PCBM cells employing PEDOT:PSS buffer layer are typically in the range of 0.5–0.6 except for a few notable cases [2]. For comparison's sake, FF values in  $MoO_3$ - or  $V_2O_5$ -based cells were reported to be about 0.59–0.62 and were virtually same as that of PEDOT:PSS-based cells [8], and those in devices using  $NiO_x$  buffer layer were as high as 0.69 [4]. As can be seen in Table 1,  $MoO_3$ ,  $V_2O_5$ ,  $NiO_x$ , and  $WO_3$  all have LUMO levels that can provide a significant energy barrier for electrons in PCBM so that chances of electron recombination can be suppressed near anodes. However, it is noted that the surface roughness values of  $MoO_3$  and  $V_2O_5$  is much larger than those of  $NiO_x$  and  $WO_3$  layers. Since the local high electric fields due to the roughness of buffer or electrode layers are likely to increase a chance of bias-dependent carrier recombination [27], one may consider that the large FF values found in  $WO_3$ - and  $NiO_x$ -based devices come partly from their smooth surface morphologies.

The fill factor of solar cells can be influenced (i) by the voltage drop due to the non-zero series resistance  $R_s$  that results from contact resistance and limited bulk transport properties; and (ii) by the current leakage resulting from either the presence of electrical shunt paths or voltage-dependent carrier recombination both of which can be conveniently modeled as a finite shunt resistance  $R_{sh}$  [36]. The effect of these parasitic resistances on FF can be quantified using normalized series and shunt resistances,  $r_s$  and  $r_{sh}$ , which are defined by  $R_s A |J_{sc}| / V_{oc}$  and  $R_{sh} A |J_{sc}| / V_{oc}$ , respectively [36]. Fig. 7b shows that the  $J$ – $V$  characteristics of the P3HT:PCBM cells under study can be reasonably modeled by the simple equivalent circuit model (ECM) shown in Ref. [36] which consists of (i) a diode characterized by the reverse saturation current density  $J_0$  and the diode ideality factor  $n$ , (ii) a dc current source, and (iii)  $R_{sh}$  and  $R_s$ . The closed and open circles in Fig. 7c present the mean values of  $r_s$  and  $1/r_{sh}$  extracted for each type of the cells under study (illuminated case) under the ECM, respectively, and the box graphs with [without] shades present the statistics for the relative decrease in FF due to  $R_s$  [ $R_{sh}$ ] which was analyzed using the formula given in Refs. [36–38].

One can note that it is the relatively large shunt resistance of  $WO_3$ -based cells that resulted in most of the improvement in FF. On the other hand,  $R_s$  and its effect on FF do not show much variation both for the type of buffer layers and for different batches and samples.

**Table 1**  
Comparison of metal oxide buffer layers used on ITO electrodes in OPVs.

	$MoO_3$	$V_2O_5$	$NiO_x$	$WO_3$
LUMO/HOMO (eV)	2.3/5.3	2.4/4.7	1.8/5.0–5.4	1.6/5.1
RMS roughness (nm) <sup>a</sup>	7.2	3.7	1.5	0.88
Deposition method/crystallinity	Thermal/NA	Thermal/NA	Pulsed laser dep./crystalline	Thermal/amorphous
Refs.	[8]	[8]	[4]	This work

<sup>a</sup> Measured for  $\sim 10 \text{ nm}$ -thick films.

Under illumination, low  $R_{sh}$  is related to a recombination of photogenerated-carriers unless it is limited by the current leakage through local shorts [27]. Irwin et al. pointed out that the energy offset between the LUMO levels of  $NiO_x$  layer and PCBM-60 layers can prevent unwanted electron captures at anodes in their  $NiO_x$ -based cells [4]. The LUMO of  $WO_3$  being approximately 1.6 eV as described in Section 3.1, it is also expected to provide a sufficient energy barrier at LUMO levels, as in the  $NiO_x$  case, for electrons that are present in PCBM-60 molecules near the anode, considering that the LUMO of PCBM-60 is around 4.0 eV [4]. Another factor that can influence carrier recombination is the carrier mobility  $\mu$  of each active layer because the mean free path, or the characteristic distance over which a carrier can travel before it recombines at a given voltage, is proportional to the carrier mobility [27]. Therefore, the relatively high hole mobility (and thus long mean free path) observed in P3HT films grown on  $WO_3$  layers may also be linked to the improvement in FF in  $WO_3$ -based cells, as discussed in Section 3.1. Low recombination of photo-generated carriers will be important also in ensuring the large open-circuit voltage, because too small  $r_{sh}$  or non-linear voltage-dependence of recombination can decrease  $V_{OC}$  as well as fill factor [27,36,37].

#### 4. Conclusions

In summary, we demonstrated that a thin layer of  $WO_3$  can enhance the photovoltaic performance of P3HT:PCBM-60 solar cells when it is inserted between the anode and active layers. It was shown that  $WO_3$  layers thermally evaporated on ITO form uniform amorphous films with the RMS roughness of 0.88 nm and a relatively low surface energy and that P3HT films grown on  $WO_3$  films have a higher degree of ordering and larger hole mobility than those grown on PEDOT:PSS films. It was shown that  $WO_3$  layers thermally evaporated on ITO form uniform amorphous films with the RMS roughness of 0.88 nm and with a relatively low surface energy. Analysis using electrical characteristic of ITO/ $WO_3$  (70 nm)/Al indicates that  $WO_3$  layers under study can be regarded as doped semiconductors so that Ohmic injection from a conductor to  $WO_3$  is easily realized. Near-ideal, high shunt-resistance OPV characteristics was consistently observed in cells with  $WO_3$  layers, leading to fill factor values often as high as 0.67–0.70 and  $V_{OC}$  values that are comparable to PEDOT:PSS-based cells and are larger than ITO-based cells. Such improvement is considered to originate partly from the HOMO level of  $WO_3$  that matches relatively well with that of P3HT and thus allows for efficient hole collection from P3HT as in the case of PEDOT:PSS and at the same time from its LUMO level that provides a sufficient energy barrier for photogenerated electrons in PCBM-60 and thus prevents them from being recombined near the anode. The smoothness of  $WO_3$  layers and the improved hole mobility of P3HT films grown on  $WO_3$  are also expected to benefit OPV cells by reducing the chance of bias-dependent carrier recombination. Considering that  $WO_3$  films presented in this work are amorphous, the work shown here can potentially lead to scalable OPV technologies. In

addition, as  $WO_3$  films can be prepared by a simple thermal evaporation, the results shown here may get easily extended to a tandem-cell structure employing  $WO_3$  layer as a part of intermediate electrodes [15] for high efficiency OPV cells [11].

#### Acknowledgements

This work was supported by the Korea Research Foundation Grant funded by the Korean Government (MOEHRD, Basic Research Promotion Fund) (No. KRF-2007-511-D00100) and by the Korea Energy Management Corporation (KEMCO) under the New and Renewable Energy R&D Grant (No. 2008-N-PV08-02). The work of D. Gupta was supported by the Brain Korea 21 Project 2008, School of Information Technology, KAIST.

#### References

- [1] G. Li, V. Shrotriya, J. Huang, Y. Yao, T. Moriarty, K. Emery, Y. Yang, *Nat. Mater.* 4 (2005) 864.
- [2] J.Y. Kim, K. Lee, N.E. Coates, D. Moses, T.Q. Nguyen, M. Dante, A.J. Heeger, *Science* 317 (2007) 222.
- [3] S. Yoo, W.J. Potscavage, B. Domercq, J. Kim, J. Holt, B. Kippelen, *Appl. Phys. Lett.* 89 (2006) 233516.
- [4] M.D. Irwin, B. Buchholz, A.W. Hains, R.P.H. Chang, T.J. Marks, *PNAS* 105 (2008) 2783.
- [5] P. Peumans, S.R. Forrest, *Appl. Phys. Lett.* 79 (2001) 126.
- [6] H.-H. Liao, L.-M. Chen, Z. Xu, G. Li, Y. Yang, *Appl. Phys. Lett.* 92 (2008) 173303.
- [7] H. Frohne, S.E. Shaheen, C.J. Brabec, D.C. Müller, N.S. Sariciftci, K. Meerholz, *Chem. Phys. Chem.* 2002 (2002) 795.
- [8] V. Shrotriya, G. Li, C.-W. Chu, Y. Yang, *Appl. Phys. Lett.* 88 (2006) 073508.
- [9] M.P. de Jong, L.J. van Ijzendoorn, M.J.A. de Voigt, *Appl. Phys. Lett.* 77 (2000) 2255.
- [10] C. Ionescu-Zenetti, A. Mechler, S.A. Carter, R. Lal, *Adv. Mater.* 16 (2004) 385–389.
- [11] S.Y. Ryu, J.H. Noh, B.H. Hwang, C.S. Kim, S.J. Jo, J.T. Kim, H.S. Hwang, H.K. Baik, H.S. Jeong, C.H. Lee, S.Y. Song, S.H. Choi, S.Y. Park, *Appl. Phys. Lett.* 92 (2008) 023306.
- [12] J. Li, M. Yahiro, K. Ishida, H. Yamada, K. Matsushige, *Synthetic Met.* 151 (2005) 141.
- [13] J. Meyer, S. Hamwi, T. Buelow, H.-H. Johannes, T. Riedl, W. Kowalsky, *Appl. Phys. Lett.* 91 (2007) 113506.
- [14] M.Y. Chan, C.S. Lee, S.L. Lai, M.K. Fung, F.L. Wong, H.Y. Sun, K.M. Lau, S.T. Lee, *J. Appl. Phys.* 100 (2006) 094506.
- [15] A.G.F. Janssen, T. Riedl, S. Hamwi, H.-H. Johannes, W. Kowalsky, *Appl. Phys. Lett.* 91 (2007) 073519.
- [16] C. Tao, S. Ruan, G. Xie, X. Kong, L. Shen, F. Meng, C. Liu, X. Zhang, W. Dong, W. Chen, *Appl. Phys. Lett.* 94 (2009) 043311.
- [17] G. Liu, J.B. Kerr, S. Johnson, *Synthetic Met.* 144 (2004) 1.
- [18] K. Nomura, H. Ohta, A. Takagi, T. Kamiya, M. Hirano, H. Hosono, *Nature* 432 (2004) 488–492.
- [19] K.-X. Ma, C.-H. Ho, F. Zhu, T.-S. Chung, *Thin Solid Films* 371 (2000) 140–147.
- [20] K.-M. Chang, C.-H. Lin, S.-S. Huang, *ECS Trans.* (2008) 43–49.
- [21] H. Sirringhaus, N. Tessler, R.H. Friend, *Science* 280 (1998) 1741.
- [22] R.J. Kline, M.D. McGehee, M.F. Toner, *Nat. Mater.* 5 (2006) 222.
- [23] M. Surin, Ph. Leclere, R. Lazzaroni, J.D. Yuen, G. Wang, D. Moses, A.J. Heeger, S. Cho, K. Lee, *J. Appl. Phys.* (2006) 033712.
- [24] H. Sirringhaus, P.J. Brown, R.H. Friend, M.M. Nielsen, K. Bechgaard, B.M.W. Langeveld-Voss, A.J.H. Spiering, R.A.J. Janssen, E.W. Meijer, P. Herwig, D.M. de Leeuw, *Nature* 401 (1999) 685.
- [25] M.A. Lampert, P. Mark, *Current Injection in Solids*, Academic Press, NY, 1970.
- [26] P. Kumar, S. Chand, S. Dwivedi, M.N. Kamalasanan, *Appl. Phys. Lett.* 90 (2007) 023501.
- [27] P. Schilinsky, C. Waldauf, J. Hauch, C.J. Brabec, *J. Appl. Phys.* 95 (2004) 2816.
- [28] V.D. Mihailetschi, H. Xie, B. Boer, L.J.A. Koster, P.W.M. Blom, *Adv. Funct. Mater.* 16 (2006) 699.
- [29] C.-W. Chu, S.-H. Li, C.-W. Chen, V. Shrotriya, Y. Yang, *Appl. Phys. Lett.* 87 (2005) 193508.

- [30] X. Zhou, J. Blochwitz, M. Pfeiffer, A. Nollau, T. Fritz, K. Leo, *Adv. Funct. Mater.* 11 (2001) 310.
- [31] K. Miyake, H. Kaneko, M. Sano, N. Suedomi, *J. Appl. Phys.* 55 (1984) 2747–2753.
- [32] Gy. Vida, V.K. Josepovits, M. Gyoer, P. Deak, *Microsc. Microanal.* 9 (2003) 337.
- [33] G.G. Malliaras, J.R. Salem, P.J. Brock, J.C. Scott, *J. Appl. Phys.* 84 (1998) 1583–1587.
- [34] L.A.A. Pettersson, L.S. Roman, O. Inganas, *J. Appl. Phys.* 86 (1999) 487.
- [35] J.Y. Kim, S.H. Kim, H.-H. Lee, K. Lee, W. Ma, X. Gong, A.J. Heeger, *Adv. Mater.* 18 (2006) 572.
- [36] S. Yoo, B. Domercq, B. Kipplen, *J. Appl. Phys.* 97 (2005) 103706.
- [37] M.A. Green, *Solar Cells*, Prentice-Hall, NJ, 1982.
- [38] To estimate the effect of  $r_{sh}$  on FF, the diode ideality factor  $n$  of 2.0 was assumed. In fact, the error associated with this assumption falls within  $\sim\pm 10\%$  when  $n$  varies between 1.5 and 2.5.



In this paper, we report on small-molecule-based, efficient WOLEDs with a high CRI, that can be fabricated by combining a solution process and a vacuum deposition process. We employed a double-emitting layer (DEL) structure in a phosphorescent WOLED device, whereby one emitting layer is fabricated in a solution process (emitting layer I) and the other emitting layer is fabricated by vacuum deposition (emitting layer II). Emitting layer I consists of three materials: a hole-transporting host, blue phosphorescent guest, and green phosphorescent guest. Emitting layer II, on the other hand, consists of a hole-blocking host and red phosphorescent guest. Emitting layer II acts to block holes and emit red light in the DEL device to obtain a white emission. We found that using this combined process is an easy way to obtain efficient WOLEDs with high CRIs, since double emitting layers distribute the emission region within the device. Furthermore, we measured the transient phosphorescence behavior, which is important information to discuss the energy transfer mechanism in WOLED, by using very short electrical pulses.

## 2. Experimental

The selection of host material for the emitting layer is one of the most critical issues in the solution process for small-molecule-based WOLEDs. In this study, we used 2,2-bis(4-carbazolyl-9-ylphenyl)adamantane (Ad-Cz) as the host material, which has solubility to organic solvents, high  $T_g$  ( $\sim 160^\circ\text{C}$ ), carrier-transport ability, and high  $T_1$  [17]. There are two types of phosphorescent WOLEDs with high CRI; one includes three phosphorescent guests and the other includes blue fluorescent guest and two phosphorescent guests [5,8,9,18,19]. We selected the former type not only to obtain high efficiency but also to discuss the energy transfer mechanism of triplet exciton in WOLED. Three phosphorescent guests we relied on are the previously reported iridium(III)bis(4',6'-difluorophenylpyridinato)tetrakis(1-pyrazolyl)borate [Flr6], *fac* tris(2-phenylpyridine) iridium (III) [Ir(ppy)<sub>3</sub>] and tris[1-phenylisoquinolino-C2,N] iridium (III) [Ir(piq)<sub>3</sub>]. Two WOLED devices were developed, one having a single emitting layer (SEL) and the other having a DEL. The OLEDs were produced on a glass substrate coated with a 200-nm-thick indium-tin-oxide (ITO) layer having a sheet resistance of 10  $\Omega$ /square. Prior to fabrication of the organic layers, the substrate was cleaned with ultra-purified water and organic solvents, and treated with a UV-ozone ambient. The OLEDs were fabricated as follows. Poly(3,4-ethylenedioxythiophene)/poly(styrenesulfonic acid) (PEDOT/PSS; Baytron P CH8000) as a hole injection layer was spin-coated from a water solution onto the ITO substrate and dried in air at 180  $^\circ\text{C}$  for 1 h. The first emitting layer of the SEL and DEL devices, which consisted of Ad-Cz and Ir complexes, was spun onto the PEDOT/PSS layer from a 0.5 wt.% tetrahydrofuran solution. The emitting layer of the SEL device has four different materials (Ad-Cz (79.4 wt.%), Flr6 (20 wt.%), Ir(ppy)<sub>3</sub> (0.2 wt.%), and Ir(piq)<sub>3</sub> (0.4 wt.%)). The film thickness of emitting layer is about 40 nm. Moreover, a 5-nm-thick *p*-bis(triphenylsilyl)benzene (UGH2) layer is formed by vacuum deposition to act

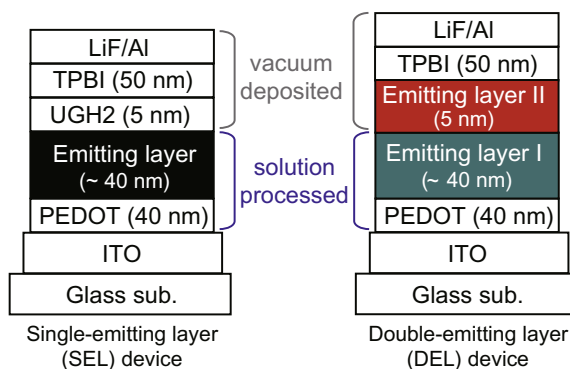
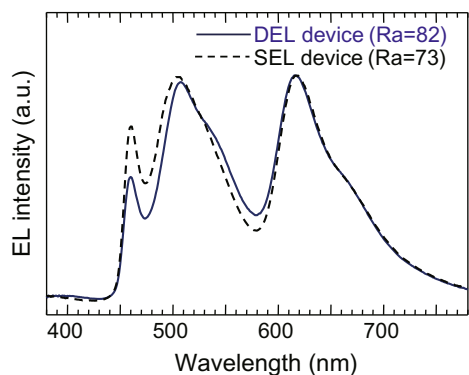


Fig. 1. Device structure of SEL and DEL devices.

as an electron-transporting and hole-blocking layer, since Ad-Cz is a hole-transporting host [17]. The film thickness of the UGH2 layer is very thin, which is adjusted to obtain high power efficiency ( $\eta_p$ ). With the increase of the thickness of UGH2 layer, the lower  $\eta_p$  is obtained due to the low carrier mobility of UGH2 [20]. On the other hand, emitting layer I of the DEL device has three different materials (Ad-Cz (79.8 wt.%), Flr6 (20 wt.%), Ir(ppy)<sub>3</sub> (0.2 wt.%)). The film thickness of emitting layer I is about 40 nm. The 5-nm-thick emitting layer II is formed by co-depositing 0.8 wt.%-Ir(piq)<sub>3</sub> with UGH2. The reason why the guest concentrations of Ir(piq)<sub>3</sub> in both devices are different will be described in the next section. After formation of the hole-blocking layer of SEL device or emitting layer II of the DEL device, a 50-nm-thick 1,3,5-tris(*N*-phenylbenzimidazol-2-yl)benzene (TPBI) was deposited as the electron-transporting layer. Finally, a 0.5-nm-thick LiF layer and 100-nm-thick Al layer were deposited as the cathode. Device configurations used in this experiment are shown in Fig. 1. The devices were encapsulated using a UV-epoxy resin and a glass cover within a nitrogen atmosphere, after cathode formation. The electroluminescent (EL) spectra and luminance were measured with a spectroradiometer (Minolta CS-1000). A digital source meter (Keithley 2400) and a desktop computer were used to operate the devices. We assumed that the emissions from the OLED device were isotropic, such that the luminance was Lambertian, and calculated the external quantum efficiency from the luminance, current density, and EL spectra.

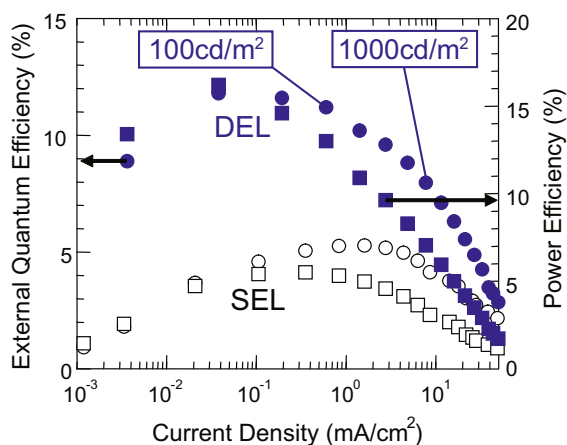
## 3. Results and discussion

Fig. 2 shows the electroluminescence spectra of the SEL and DEL devices at a current density of 10 mA/cm<sup>2</sup>. The CIE coordinates and CRI values for the emissions from the SEL device are respectively (0.42, 0.42) and 69 at 0.1 mA/cm<sup>2</sup> and (0.36, 0.40) and 73 at 10 mA/cm<sup>2</sup>, whereas they are (0.38, 0.47) and 82 at 0.1 mA/cm<sup>2</sup>, and (0.38, 0.43) and 82 at 10 mA/cm<sup>2</sup> for the DEL device. We also fabricated the another SEL device, where the guest concentrations in emitting layer are similar to that of DEL device (Ad-Cz (79.0 wt.%), Flr6 (20 wt.%), Ir(ppy)<sub>3</sub> (0.2 wt.%), and Ir(piq)<sub>3</sub> (0.8 wt.%)). However, the white emission was not obtained, e.g., the CIE coordinates of the device was (0.55, 0.38) at



**Fig. 2.** EL spectra for two different WOLED devices at current density of  $10 \text{ mA/cm}^2$ . One device (SEL) had a single emitting layer and the other had two emitting layers (DEL). The CRI values of these devices are also shown.

$10 \text{ mA/cm}^2$ . Although, the guest concentration of  $\text{Ir}(\text{piq})_3$  varies slightly, we decided that it is suitable to compare the performance of white light-emitting SEL device with that of DEL device as proposed in experimental section. The external quantum efficiencies ( $\eta_{\text{ext}}$ ) of the two WOLED devices are plotted as a function of current density in Fig. 3.  $\eta_{\text{ext}}$  of the SEL device was about 6%, whereas it was 11.7% for the DEL device. The maximum  $\eta_{\text{p}}$  of the DEL device was  $16 \text{ lm/W}$ , which is relatively high compared with the previously reported value for solution-processed WOLEDs [9]. This improvement can be explained by the distribution of the emission region within the two emitting layers. In both devices, a high density of Ad-Cz excitons are formed at the Ad-Cz/UGH2 interface, and phosphorescence occurs through host-guest energy transfer [17]. The emitting region of the SEL device becomes narrow, resulting in a lower  $\eta_{\text{ext}}$  due to the unconfinement of triplet energy in the light-emitting region. The  $T_1$  energy of TPBI is  $2.58 \text{ eV}$ , which is smaller than that of Flr6 [21]. Thus, it is expected that the triplet excitons diffuse to the TPBI layer through the thin UGH2 layer [18,22]. In contrast, the emitting region of



**Fig. 3.** External quantum efficiency and power efficiency vs. current density for the two WOLED devices.

the DEL device is distributed as a result of doping  $\text{Ir}(\text{piq})_3$  in the UGH2 layer, and this enables the confinement of triplet energy in the light-emitting region compared to SEL device.

To understand the distribution mechanism of the emitting region, we examined the transient decay of electroluminescence by applying an electrical pulse with a pulse width of  $100 \text{ ns}$  to the DEL device [23]. It is usually difficult to operate the OLEDs by the duration of  $100 \text{ ns}$  input voltage [24]. However, we prepared the specialized pulse generator which can apply the voltage of about  $30 \text{ V}$  with a pulse width of  $100 \text{ ns}$ . By synchronizing the pulse generator with the streak camera (C4334, Hamamatsu) in cycle of  $500 \mu\text{s}$ , the few microsecond range transient phenomena can be observed. For comparison, transient decays in three other single doped OLEDs, each doped with one of the three phosphorescent guests (Flr6,  $\text{Ir}(\text{ppy})_3$  and  $\text{Ir}(\text{piq})_3$ ) was also examined. Fig. 4a shows the transient decays of the OLEDs and (b) summarizes the electroluminescence lifetimes ( $\tau$ ) of each phosphorescent guest in the single doped OLEDs. The triplet lifetimes of each guest were estimated from the fitting lines, as illustrated in the figure. The measured  $\tau$  values of Flr6,  $\text{Ir}(\text{ppy})_3$ , and  $\text{Ir}(\text{piq})_3$  were  $2.0 \mu\text{s}$ ,  $1.4 \mu\text{s}$ , and  $1.0 \mu\text{s}$ , respectively. There are small differences in  $\tau$  between the previously reported photoluminescent values and the current electroluminescent ones [25,26]. However, the correlation is quite similar; that is,  $\tau$  of Flr6 is the longest, and  $\tau$  of  $\text{Ir}(\text{piq})_3$  is the shortest. A detailed discussion about the difference in  $\tau$  value between estimated from photoluminescence and estimated from electroluminescence will be described elsewhere.

Here, we discuss the emission mechanism in the DEL device, on the basis of the estimated  $\tau$  of each phosphorescent guest. Fig. 4c shows the transient decay for each phosphorescent guest. The triplet lifetimes of Flr6,  $\text{Ir}(\text{ppy})_3$  and  $\text{Ir}(\text{piq})_3$  were taken from their emission peaks centered at  $\lambda = 460, 520, \text{ and } 620 \text{ nm}$ , respectively. The lifetimes of Flr6 and  $\text{Ir}(\text{ppy})_3$  decrease to  $1.1 \mu\text{s}$ , which is similar to  $\tau$  of  $\text{Ir}(\text{piq})_3$  in the single doped OLEDs. These results suggest that the Flr6 and  $\text{Ir}(\text{ppy})_3$  emissions are primarily quenched by energy transfer to  $\text{Ir}(\text{piq})_3$ , as illustrated in Fig. 4d [5]. Therefore, the distribution mechanism of the emitting region is dominated by energy transfer between phosphorescent guests, as illustrated by the arrows in Fig. 4d, and not dominated by the direct charge trapping by  $\text{Ir}(\text{piq})_3$  in the UGH2 layer [17]. The emission mechanism in the DEL device can be summarized as follows. First, carrier recombination occurs at the Ad-Cz/UGH2 interface, and singlet and triplet excited states of Ad-Cz are generated. Next, energy transfer from the singlet exciton of the Ad-Cz to Flr6 occurs via Förster energy transfer [27], and energy transfer from the triplet exciton of the Ad-Cz to Flr6 occurs via Förster and/or Dexter energy transfer, since the guest concentration of Flr6 is significantly higher than those of other guests in the DEL device. Therefore, the transfer processes originate from the excitation of Flr6. Accordingly, energy is transferred from Flr6 to both  $\text{Ir}(\text{ppy})_3$  and  $\text{Ir}(\text{piq})_3$ , and in addition, energy might be transferred from  $\text{Ir}(\text{ppy})_3$  to  $\text{Ir}(\text{piq})_3$ . The energy transfer between phosphorescent guests in the DEL device leads to the emitting region becoming distributed and a decrease

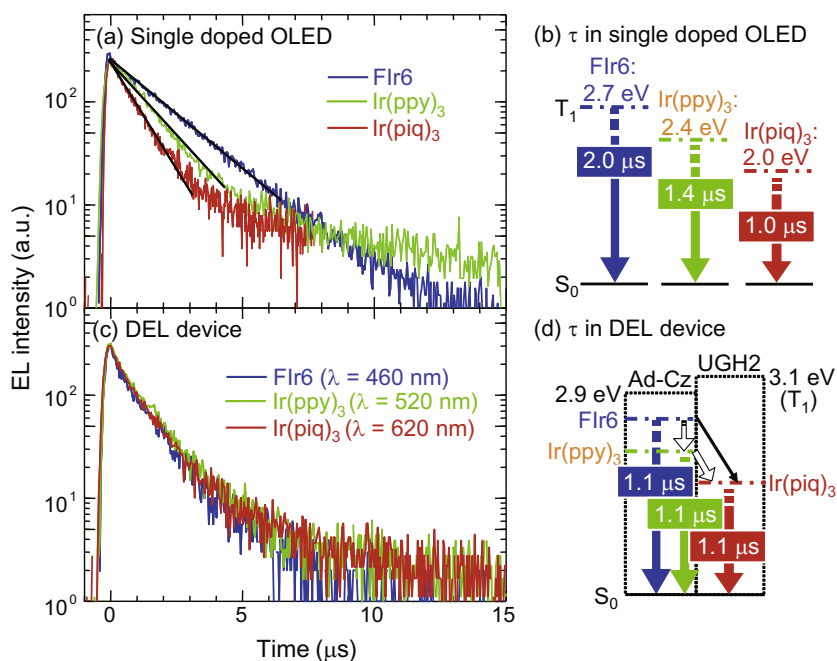


**Fig. 4.** Transient electroluminescent decay for Flr6, Ir(ppy)<sub>3</sub>, and Ir(piq)<sub>3</sub> in single doped OLED devices (a) and DEL device (c). The transient decays of each phosphorescent guest are distinguished by their colors. The estimated phosphorescence lifetimes of emitters in the single doped OLED devices and DEL device are summarized in (b) and (d), respectively. The energy transfer pathways between Flr6, Ir(ppy)<sub>3</sub>, and Ir(piq)<sub>3</sub> in the DEL device is also shown in (d).

**Table 1**

Selected WOLED architectures with their corresponding performance characteristics. All the WOLEDs are based on phosphorescent dye and have a high CRI.

Architecture	Fabrication process	$\eta_{\text{ext}}$ [%]	$\eta_{\text{p}}$ [lm/W]	CIE	CRI	Refs.
DEL device	Solution + deposition	12	16.2	(0.38, 0.43)	82	This work
Triple-doped emissive layer (polymer based)	Solution	14.4	9.5	(0.34, 0.47)	77	[9]
Triple-doped emissive layer	Deposition	12	26	(0.43, 0.45)	82	[5]
Three kinds of single-doped emissive layer	Deposition	16.6	32	(0.38, 0.39)	80	[8]

in the possible diffusion path of the triplet excitons of Flr6 to TPBI layer.

Table 1 compares the performances of our structure and previously reported phosphorescent WOLEDs with high CRIs. The fabrication methods are also compared. The fabrication process of vacuum-deposited WOLEDs tends to be complicated, since at least three phosphorescent guests in WOLED are essential to obtain high CRI. On the other hand, the fabrication process of our solution processed and vacuum-deposited WOLED is much easier. The guest concentration of three kinds of molecules (one host and two guests) in one emitting layer can be easily controlled by solution process. Moreover, the fabrication process of the other emitting layer is one time co-evaporation, which is similar to that of conventional POLEDs. The  $\eta_{\text{p}}$  of our devices is lower than that of the vacuum-deposited WOLEDs. However, it is significantly higher than that of the polymer-based device fabricated by solution process. Thus, small-molecule-based WOLEDs likely have more potential than polymer-based ones. The problem we have to consider here is that it might be difficult to fabricate high-efficient, SEL WOLEDs with a solution process due to the lack of suitable host materials. Most host materials suitable for

solution-processed WOLEDs are unipolar, which makes the emitting region narrow. The DEL structure, however, distributes the emitting region, and it enables efficient, high CRI WOLEDs to be easily fabricated.

#### 4. Summary

We succeeded in demonstrating a highly efficient, high CRI WOLED with a double-emitting layer, wherein one emitting layer is fabricated in a solution process and the other is fabricated by vacuum deposition. The device had a maximum power efficiency of 16 lm W<sup>-1</sup> and CIE coordinates that varied from (0.38, 0.47) at 0.1 mA/cm<sup>2</sup> to (0.38, 0.43) at 10 mA/cm<sup>2</sup>, with CRI = 82. By distributing the emitting region with the double-emitting layer, the confinement of triplet energy in the light-emitting region was achieved. The distribution mechanism of the emitting region was investigated by measuring the electroluminescent transient decays of the phosphorescent guests in the WOLED. The results clearly demonstrate that the distribution mechanism is energy transfer between phosphorescent guests.

**References**

- [1] E.L. Williams, K. Haavisto, J. Li, G.E. Jabbour, *Adv. Mater.* 19 (2007) 197.
- [2] Y. Sun, N.C. Giebink, H. Kanno, B.W. Ma, M.E. Thompson, S.R. Forrest, *Nature (London)* 440 (2006) 908.
- [3] J.H. Seo, J.H. Seo, J.H. Park, Y.K. Kim, J.H. Kim, G.W. Hyung, K.H. Lee, S.S. Yoon, *Appl. Phys. Lett.* 90 (2007) 203507.
- [4] S. Tokito, T. Iijima, T. Tsuzuki, F. Sato, *Appl. Phys. Lett.* 83 (2003) 2459.
- [5] B.W. D'Andrade, R.J. Holmes, S.R. Forrest, *Adv. Mater.* 16 (2004) 624.
- [6] B.W. D'Andrade, S.R. Forrest, *Adv. Mater.* 16 (2004) 1585.
- [7] M. Cocchi, J. Kalinowski, D. Virgili, V. Fattori, S. Develay, J.A.G. Williams, *Appl. Phys. Lett.* 90 (2007) 163508.
- [8] Y. Sun, S.R. Forrest, *Appl. Phys. Lett.* 91 (2007) 263503.
- [9] H.B. Wu, J.H. Zou, F. Liu, L. Wang, A. Mikhailovsky, G.C. Bazan, W. Yang, Y. Cao, *Adv. Mater.* 20 (2008) 696.
- [10] H. Kanno, R.J. Holmes, Y. Sun, S.K. Cohen, S.R. Forrest, *Adv. Mater.* 18 (2006) 339.
- [11] S.H. Kim, J. Jang, J.Y. Lee, *Appl. Phys. Lett.* 91 (2007) 123509.
- [12] H. Kim, Y. Byun, R.R. Das, B.K. Choi, P.S. Ahn, *Appl. Phys. Lett.* 91 (2007) 093512.
- [13] N. Rehmman, D. Hertel, K. Meerholz, H. Becker, S. Heun, *Appl. Phys. Lett.* 91 (2007) 103507.
- [14] H.M. Liu, P.F. Wang, J. He, C. Zheng, X.H. Zhang, S.L. Chew, C.S. Lee, J. Chang, S.T. Lee, *Appl. Phys. Lett.* 92 (2008) 023301.
- [15] I. Tanaka, M. Suzuki, S. Tokito, *Jpn. J. Appl. Phys.* 42 (2003) 2737.
- [16] M. Suzuki, S. Tokito, F. Sato, T. Igarashi, K. Kondo, T. Koyama, T. Yamaguchi, *Appl. Phys. Lett.* 86 (2005) 103507.
- [17] H. Fukagawa, K. Watanabe, T. Tsuzuki, S. Tokito, *Appl. Phys. Lett.* 93 (2008) 133312.
- [18] Y. Sun, N.C. Giebink, H. Kanno, B. Ma, M.E. Thompson, S.R. Forrest, *Nature* 440 (2006) 908.
- [19] G. Schwartz, M. Pfeiffer, S. Reineke, K. Walzer, K. Leo, *Adv. Mater.* 19 (2007) 3672.
- [20] R.J. Holmes, B.W. D'Andrade, S.R. Forrest, X. Ren, J. Li, M.E. Thompson, *Appl. Phys. Lett.* 83 (2003) 3818.
- [21] H. Fukagawa, unpublished data.
- [22] M.A. Baldo, D.F. O'Brien, M.E. Thompson, S.R. Forrest, *Phys. Rev. B* 60 (1999) 14422.
- [23] M.A. Baldo, M.E. Thompson, S.R. Forrest, *Nature* 403 (2000) 750.
- [24] Z.Y. Xie, T.C. Wong, L.S. Hung, S.T. Lee, *Appl. Phys. Lett.* 80 (2002) 1477.
- [25] A. Tsuboyama, H. Iwawaki, M. Furugori, T. Mukaide, J. Kamatani, S. Igawa, T. Moriyama, S. Miura, T. Takiguchi, S. Okada, M. Hoshino, K. Ueno, *J. Am. Chem. Soc.* 125 (2003) 12971.
- [26] A. Endo, K. Suzuki, T. Yoshihara, S. Tobita, M. Yahiro, C. Adachi, *Chem. Phys. Lett.* 460 (2008) 155.
- [27] Y. Kawamura, J. Brooks, J.J. Brown, H. Sasabe, C. Adachi, *Phys. Rev. Lett.* 96 (2006) 017404.

for LEDs based on a green phosphorescent dendrimer [15]. However, the influence of the film morphology on the photophysical and electronic properties is still unexplored and a better understanding of how these properties are affected by the processing conditions is now required for further improvements in the device performance.

In this paper, we investigate the effects of thermal annealing on the photophysical properties of a conjugated dendrimer film. The structure of the first generation dendrimer is shown in the inset of Fig. 1. It consists of a bisfluorene core with two *n*-hexyl groups attached to the 9-position of each of the fluorenyl moieties, and first generation phenylene dendrons with 2-ethylhexyloxy surface groups attached to the 7-position of the fluorenyl groups. Previous studies have shown that this fluorescent dendrimer exhibits good hole mobility of  $\sim 10^{-4}$  cm<sup>2</sup>/Vs at a field of 0.55 MV/cm [23,24] and makes fluorescent blue LEDs with an external quantum efficiency of 1.2% [25]. Recently, this dendrimer has been successfully incorporated into one and two-photon pumped lasers [22,26]. The photophysical properties of poly(fluorene)s are strongly influenced by film morphology [8] and hence it was of interest to determine whether blue emissive fluorescent dendrimers behave in a similar way. Our results show that thermal annealing affects the absorption and photoluminescence (PL) spectra of the dendrimer film but does not significantly modify the PL efficiency and lifetime, singlet–singlet exciton annihilation, or ASE threshold. Spectroscopic ellipsometry measurements indicate that the film becomes birefringent on annealing, the bisfluorene chromophores preferentially adopting an orientation in the plane of the film. This study demonstrates that thermal annealing strongly modifies the molecular rearrangement within the dendrimer film but has only a mild effect on the photophysical properties. Thus annealing provides an efficient way to finely tune the emission colour of the dendrimer film without a strong decrease in PLQY and ASE threshold.

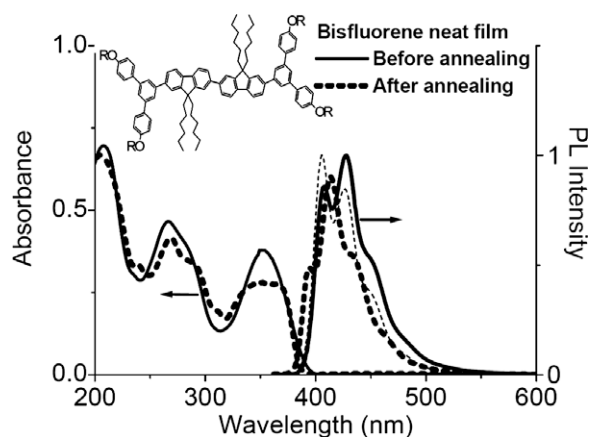


**Fig. 1.** Absorption and steady state PL spectra of a neat film of the bisfluorene-cored dendrimer before (solid line) and after (dotted line) thermal annealing. PL spectra are normalized according to the measured PLQY values. The PL spectrum of the dendrimer in THF is also shown (dashed line). The chemical structure of the dendrimer is shown in the inset (R = 2-ethylhexyl).

## 2. Experimental

Neat bisfluorene-cored dendrimer films were deposited onto precleaned quartz substrates by spin-coating from chloroform at concentrations in the range 10–20 mg/mL. The films were annealed at 100 °C for 1 h with the sample under a vacuum ( $8 \times 10^{-5}$  mbar) to prevent any oxidation effects. Absorption spectra were measured using a Varian model 300 absorption spectrophotometer. PL measurements were performed in 180 nm thick films. Time integrated PL spectra were recorded by a Jobin Yvon Fluoromax 2 fluorimeter. Film PLQYs were determined with an integrating sphere under flowing nitrogen atmosphere [27]. The samples were excited at 325 nm by a helium–cadmium laser with a power of nearly 0.2 mW. Time resolved PL measurements were carried out by using 100 fs light pulses at 330 nm for excitation with a repetition rate of 5 kHz and a synchroscan Hamamatsu streak camera for detection. The excitation spot size corresponding to the full-width at half maximum was determined by using a beam profiler to be 200  $\mu$ m. These measurements were carried out at room temperature and the samples were placed in a vacuum chamber with a pressure lower than  $8 \times 10^{-5}$  mbar. In order to characterize the spectral line narrowing by ASE, films were photoexcited with the same 100 fs excitation pulses. The energy of the pulses was adjusted using a set of neutral density filters. The excitation light was shaped into a stripe of length approximately 1 mm and width 30  $\mu$ m and focused near the edge of the film. The spatial uniformity of the pump intensity was checked with a beam profiler. The light emitted from the waveguide edge was then detected with an optical fiber connected to an Ocean Optics CCD spectrometer.

Variable-angle spectroscopic ellipsometry (VASE) measurements were carried out to measure the refractive index and the extinction coefficient of the films. The ellipsometric  $\Psi$  and  $\Delta$  data were acquired in the reflection mode using a J.A. Woollam, Inc. M-2000DI system, and analyzed by means of the WVASE32<sup>®</sup> data analysis software. The incidence angle was typically varied from 45° to 75° across a wavelength range from 190 to 1700 nm. The wide range of angles used allowed the path length of the probe beam inside the sample to be changed. In addition, some angles were chosen in order to ensure that, at several wavelengths,  $\Delta$  was close to 90°, as it increases sensitivity in the data analysis [28]. Parameter correlation was further reduced by analyzing simultaneously VASE data from several samples with significantly different film thicknesses [29] within the range 50–180 nm, and by fitting normal incidence intensity transmittance spectra in addition to the  $\Psi$  and  $\Delta$  data [30].

An air-film-substrate model was assumed, with the interface between the film and the substrate being abrupt and no film surface roughness. The dielectric function of the films was described using a Kramers–Kronig consistent parametric functional model, with the absorption bands in the imaginary part of the dielectric function being modelled using a sum of Gaussian oscillator functions. The optical constants of the substrates were determined independently by performing VASE measurements on bare substrates. For both as-deposited and annealed films, isotropic and uniaxial

models were constructed. In the case of the pristine samples, both types of models produced nearly identical dispersion relations, with the uniaxial model providing only a modest improvement to the fit quality. In contrast, it was found that, following annealing, only a uniaxial model, with the optical axis perpendicular to the plane of the films, could yield a close fit to the experimental data.

### 3. Results and discussion

The film absorption and the steady state PL spectra of the bisfluorene-cored dendrimer before and after annealing are shown in Fig. 1. Peaks at 267 nm and 350 nm are observed in the absorption spectrum of the film before annealing, arising from, to a first approximation, the biphenyl moieties within the dendrons and the bis(phenylfluorene) chromophoric unit. That is, although the core is defined as the bis(fluorene) unit the first two phenyl groups of the dendrons are attached in such a manner that they are part of the delocalised  $\pi$ -electron pathway of the main chromophoric unit. The *meta* linkages around the branching phenyl of the dendrons limits the electron delocalisation, and hence the phenyl units that have the surface groups attached are not part of the main chromophoric unit. The annealing unusually induced a blue-shift of the PL spectrum by 15 nm. We also observed that the annealed film shows a blue shift as compared to solution, which suggests a twisting of the bisfluorene core out of planarity with the benzene ring of the dendron or an increase of the dihedral angle between fluorene units. The decrease in PL intensity of the (0,0) transition relative to the (0,1) transition in the annealed film arises simply from the fact that the short wavelengths of the emission spectra overlap more strongly with the absorption spectrum. It is important to note that annealing the dendrimer film does not give rise to the “greenish” emission that is often observed in polyfluorenes on annealing [31]. The PLQY of the bisfluorene dendrimer film before and after annealing was measured to be  $92 \pm 5\%$  [32] and  $83 \pm 4\%$ , respectively. The film PLQY before thermal treatment is close to that measured in solution which indicates that concentration quenching of the PL does not occur in the solid state. It should be noted that annealing the samples for a further 12 h did not cause more changes in the photophysical properties of the film, which indicates that a thermal treatment of 1 h is sufficient to induce these morphological effects.

Fig. 2 shows the excitation density dependence of the PL kinetics in the film before and after annealing. The PL kinetics at low excitation densities are described satisfactorily by a single exponential decay yielding a PL lifetime constant  $\tau_{\text{ph}}$  of 730 and 660 ps in films before and after the annealing respectively. The radiative and non-radiative decay rates, denoted  $k_{\text{R}}$  and  $k_{\text{NR}}$ , were then calculated by combining the following equations:  $\text{PLQY} = k_{\text{R}}\tau_{\text{ph}}$  and  $1/\tau_{\text{ph}} = k_{\text{R}} + k_{\text{NR}}$ . We found, in both samples,  $k_{\text{R}} = 1.3 \times 10^9 \text{ s}^{-1}$ . There is an increase in  $k_{\text{NR}}$ , from  $1.1 \pm 0.6 \times 10^8 \text{ s}^{-1}$  for the pristine film to  $2.6 \pm 0.6 \times 10^8 \text{ s}^{-1}$  for the annealed film, but the key point is that the PLQY remains very high in both cases.

At excitation densities higher than  $5 \times 10^{17} \text{ cm}^{-3}$ , the decays become faster and strongly deviate from a single

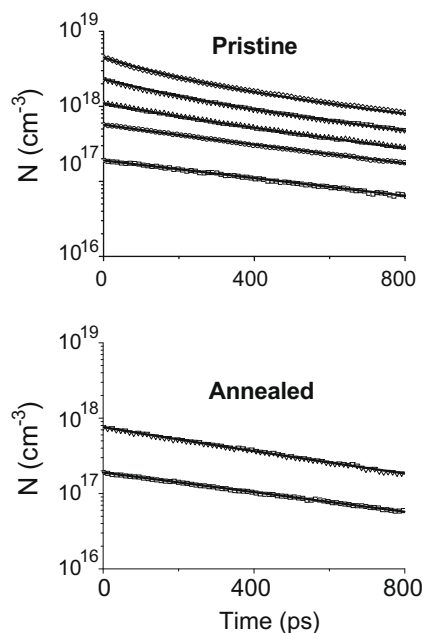


Fig. 2. Emission decay curves measured in the window 395–495 nm under various laser excitation densities of the films before and after thermal annealing. Solid lines are the fits obtained with a single exponential:  $I(t) = I_0 \exp(-t/\tau_{\text{ph}})$  for the curve obtained at the lowest excitation density and with Eq. (1) for the other decays.

exponential. This behaviour is due to singlet–singlet exciton annihilation [33,34]. In the case of a time independent annihilation rate  $\gamma$ , the density of singlet excitons  $N(t)$  which is directly proportional to the PL intensity can be described as:

$$N(t) = \frac{N_0 \exp(-kt)}{1 + \frac{\gamma}{k} N_0 [1 - \exp(-kt)]} \quad (1)$$

where  $N_0$  is the exciton density just after the laser pulse excitation and  $k = 1/\tau_{\text{ph}}$  is the decay rate of excitations in the absence of annihilation. Fig. 2 shows the best fits obtained with  $\gamma$  values of  $4.5 \pm 0.9 \times 10^{-10} \text{ cm}^3 \text{ s}^{-1}$  and  $5.5 \pm 1.5 \times 10^{-10} \text{ cm}^3 \text{ s}^{-1}$  in the films before and after annealing, respectively. The fact that the PL decays at different excitation intensities can be fitted with time independent  $\gamma$  values indicates that the annihilation process is diffusion controlled and that exciton diffusion is three-dimensional. The two  $\gamma$  values are within experimental error and show that no substantial change in exciton diffusivity occurs upon thermal annealing. It is interesting to note that the  $\gamma$  value for the dendrimer film is two orders of magnitude smaller than that reported in poly(9,9-dioctylfluorene) [35], which demonstrates that addition of the dendrons strongly reduces the exciton diffusivity. Energy transfer of singlet excitons in fluorescent materials occurs by Förster type dipole–dipole interactions. This mechanism depends on the average centre-to-centre spacing distance between adjacent emitters  $R$  and its rate is proportional to  $R^{-6}$  [36]. The dendrons attached to the bisfluorene-cored dendrimer emitter cause an increase in the intermolecular spacing between the emitting moieties

which modifies the diffusion constant of the singlet excitons. In contrast, the charge carrier mobility of the dendrimer and poly(9,9-dioctylfluorene) are similar [24]. A possible explanation is that charge transport through films is controlled by traps, whereas the exciton diffusion takes place over much shorter distances and is not affected by these traps. The fact that the charge mobility of the bisfluorene-cored dendrimer and poly(9,9-dioctylfluorene) are similar but the annihilation constant in the dendrimer is lower suggests that dendrimers may be attractive for high brightness blue LEDs. The lower exciton annihilation is particularly interesting in applications such as lasers and optical amplifiers [37–39].

The annihilation constant is related to the diffusion constant in the three-dimensional case by the relation:  $\gamma = 4\pi R_a D$ , where  $R_a$  is the annihilation radius. We assume that  $R_a$  is the same as an average distance between chromophores, which was estimated to be 17.4 Å for the bisfluorene-cored dendrimer from its molecular weight using a uniform film density of 1.1 g/cm<sup>3</sup> measured by neutron reflectivity (data not shown) and assuming the molecules to be hard spheres. The diffusion constant was calculated to be  $D = 2 \times 10^{-4}$  cm<sup>2</sup> s<sup>-1</sup> leading to a 3D diffusion length, defined as  $L_d = (3D\tau_{ph})^{1/2}$ , equal to 6 nm.

Fig. 3 shows the emission spectra collected at various pump excitation energies in the neat bisfluorene-cored dendrimer film before and after annealing. When the pump pulse energy was lower than 1.2 nJ, a broad PL spectrum characteristic of spontaneous emission and similar to that shown in Fig. 1 was detected with the emission from the annealed film blue-shifted relative to the unannealed. The shape of the spectrum was found not to be dependent on the pump excitation density for low pump energies. As the pump pulse energy was increased above 1.2 nJ, a substantial reduction in the full-width at half maximum (FWHM) of the spectra for both films was observed. Increasing the pump level above this threshold results in a gradual spectral narrowing of the emission band from a FWHM of 53 nm to a FWHM of 6 nm centered at 421 nm for the pristine film. The spectral line narrowing observed here is due to ASE [40–44]. Spontaneously emitted photons were waveguided in the structure and amplified by stimulated emission due to the population inversion. ASE is generally observed where the net gain, (after taking account of absorption and the scattering losses) is highest. The ASE peak is slightly red-shifted with respect to the fluorescence maximum because re-absorption losses decrease towards longer wavelengths. The ASE peak in the annealed film is 11 nm blue-shifted relative to that measured in pristine films, which is consistent with the shift observed in the steady state PL spectrum. However, no significant difference in the ASE threshold and linewidths was observed. Waveguide modelling shows cut off thicknesses for the TE<sub>0</sub> and TM<sub>0</sub> modes of 70 nm and 100 nm which indicate that both modes are waveguided in the 180 nm thick films. Because the film thickness is much higher than the cutoff thicknesses, we can exclude the changes in refractive indexes upon annealing as a possible reason for the blue-shift of the ASE spectrum [44]. These measurements can be used to compare directly the threshold densities for ASE and singlet–singlet exciton annihilation, which are

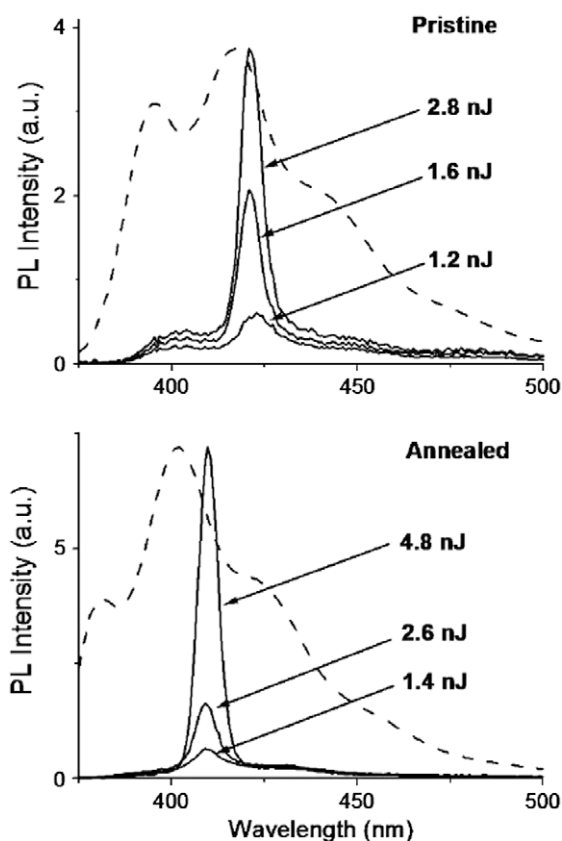
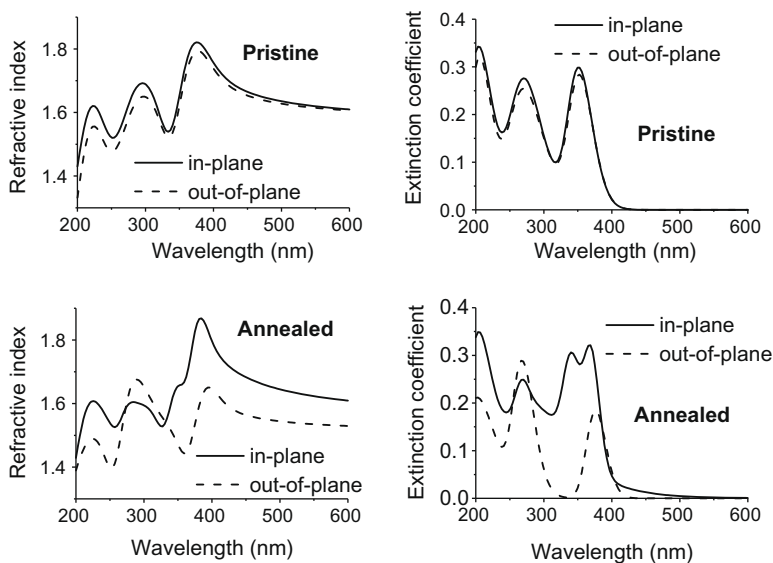


Fig. 3. Photoluminescence ASE spectra collected from the edge of a 30  $\mu\text{m} \times 1$  mm stripe in the bisfluorene-cored dendrimer films before and after annealing and at different light pump energies. The dotted lines correspond to the PL steady state spectra.

$5 \times 10^{17}$  cm<sup>-3</sup> and  $1.5 \times 10^{18}$  cm<sup>-3</sup>, respectively. The threshold for ASE is generally higher than the laser threshold due to the absence of feedback, and hence the fact that the threshold for ASE is lower than for singlet–singlet exciton annihilation means lasing without exciton annihilation should be obtained using a bisfluorene dendrimer as a gain medium. These results confirm the fact that light-emitting fluorescent dendrimers are promising materials for optical amplifiers and lasers.

To gain further insights into the effects of the thermal annealing, the optical constants of the films were measured before and after annealing using VASE. Fig. 4 shows the dispersion curves of the refractive index and extinction coefficient for light polarised with its electric field in the plane of the film and for light polarised perpendicular to the film (out-of-plane). The pristine film before annealing was found to be very close to isotropic, which implies no significant orientation of the molecules. In contrast, we observed in the annealed film a measurable optical uniaxial anisotropy in addition to a redistribution of the oscillator strengths in the absorption spectra. In the absorption region of the bisfluorene core between 330 and 400 nm the ordinary (in-plane) refractive index  $n_o$  and extinction coefficient  $k_o$  are higher than the extraordinary (out-of-plane) index  $n_e$  and coefficient  $k_e$ . Thus, in this region, the peak values of  $n_o$  and  $n_e$  vary, respectively, from 1.82 and 1.79



**Fig. 4.** Refractive index and extinction coefficient of the pristine and annealed films for light polarised with its electric field in the plane of the film and for light polarisation perpendicular to the film (out-of-plane).

before annealing to 1.87 and 1.65, following annealing. As the transition dipole moment for the lowest energy electronic transition in polyfluorenes is polarised along the long molecular axis [45], this optical anisotropy indicates that the bisfluorene chromophores are preferentially oriented in the plane of the film (that is, parallel to the substrate surface). Quantitative information about molecular orientation can be obtained from the measurement of the ratio  $k_e/k_o$  and the angular distribution  $d_{\pi\theta}$ , defined as [46]:

$$d_{\pi\theta} = \frac{1}{1 + \frac{k_e}{2k_o}} \quad (2)$$

where  $\theta$  refers to the polar angle in between the molecular axis and the normal to the film. For a uniform molecular distribution,  $d_{\pi\theta} = 2/3$  is expected, whilst a value close to 1 should be obtained in the case of a strongly uniaxial film. In the case of the pristine samples, we find  $k_e/k_o$  at the peak wavelength of the bisfluorene core transition to be 0.95, giving  $d_{\pi\theta} = 0.68$ , therefore close to  $2/3$ , as expected for a nearly isotropic film. Following annealing, the dispersion relation of  $k_o$  shows two maxima in this spectral region. Thus, in this case, we have calculated  $k_e/k_o$  at both peak wavelengths, and then averaged the results, giving  $k_e/k_o = 0.25$ . This gives  $d_{\pi\theta} = 0.89$ , which is much closer to 1, indicating substantial alignment. If all the molecules pointed in the same direction this would imply they were at an angle of  $71^\circ$  to the normal to the film. Whilst of course there will be a distribution of orientations, Ref. [46] suggests this procedure as a way of visualising molecular orientation.

An increase in the optical anisotropy upon annealing has been previously reported in films of conjugated polymers [47,48]. In contrast,  $k_e$  is larger than  $k_o$  in the absorption region of the biphenyl dendrons between 270 and 300 nm, which suggests a preferential alignment of the dendrons perpendicular to the substrate.

During the thermal annealing, bisfluorene dendrimers tend to rearrange themselves to minimize the energy of the film. Ellipsometry data show that the bisfluorene cores re-orient upon annealing to lie preferentially in the plane parallel to the substrate. However, the rigid dendrons and surface groups have less ability to move or relax due to steric hindrance. Reorientation of the bisfluorene core upon annealing is likely to increase the dihedral angle between the branching phenyl and the fluorenyl groups of the core, therefore, excitations in the annealed films would be more localised on the bisfluorene core, which would explain the blue-shift of the PL and ASE spectra. Finally, we note that the PLQY, lifetime and ASE threshold are not modified after annealing, which indicate that the formation of close contacts between bisfluorene cores remains inhibited and that even first generation dendrons are extremely effective in preventing core–core interactions.

#### 4. Conclusion

Annealed films of a bisfluorene-cored dendrimer show a 15 and 11 nm blue-shift of the PL and ASE peaks respectively relative to pristine films. Variable-angle spectroscopic ellipsometry measurements show that the refractive index and extinction coefficient become anisotropic after annealing with larger optical constants observed for light polarisation in the plane of the film than the corresponding out-of-plane values in the absorption region of the bisfluorene core. This anisotropy indicates that in annealed films the bisfluorene cores are preferentially oriented parallel to the substrate. This molecular rearrangement however did not change the fluorescence efficiency, singlet–singlet exciton annihilation rate, and threshold for ASE, which are important properties for organic LEDs and lasers. In addition, our results give a means of fine-tuning the colour of dendrimer lasers and LEDs



without any significant losses in their efficiencies. Possible control of the ordinary and extraordinary refractive indexes in annealed conjugated dendrimer films might also be an interesting opportunity for fabricating photonic structures such as microcavity LEDs. It is worth noting that this work provides the first evidence of the effect of film morphology on the optoelectronic properties of fluorescent dendrimers. Importantly, the size of these morphological effects is much lower than those typically observed in conjugated polymers such as poly[2-(2'-ethylhexyloxy)-5-methoxy-1,4-phenylenevinylene] or polyfluorenes, suggesting that dendrimers might have the advantage of much lower sensitivity to processing.

## References

- [1] J.H. Burroughes, D.D.C. Bradley, A.R. Brown, R.N. Marks, K. Mackay, R.H. Friend, P.L. Burn, A.B. Holmes, *Nature* 347 (1990) 539.
- [2] G. Gustafsson, Y. Cao, G.M. Treacy, F. Klavetter, N. Colaneri, A.J. Heeger, *Nature* 357 (1992) 477.
- [3] R.H. Friend, R.W. Gymer, A.B. Holmes, J.H. Burroughes, R.N. Marks, C. Taliani, D.D.C. Bradley, D.A. Dos Santos, J.L. Brédas, M. Logdlund, W.R. Salaneck, *Nature* 397 (1999) 121.
- [4] I.D.W. Samuel, G. Rumbles, C.J. Collison, S.C. Moratti, A.B. Holmes, *Chem. Phys.* 227 (1998) 75.
- [5] T.-Q. Nguyen, V. Doan, B.J. Schwartz, *J. Chem. Phys.* 110 (1999) 4068.
- [6] T.-Q. Nguyen, R.C. Kwong, M.E. Thompson, B.J. Schwartz, *Appl. Phys. Lett.* 76 (2000) 2454.
- [7] T.-Q. Nguyen, I.B. Martini, J. Liu, B.J. Schwartz, *J. Phys. Chem. B* 104 (2000) 237.
- [8] A.J. Cadby, P.A. Lane, H. Mellor, S.J. Martin, M. Grell, C. Giebeler, D.D.C. Bradley, M. Wohlgenannt, C. An, Z.V. Vardeny, *Phys. Rev. B* 62 (2000) 15604.
- [9] W.J. Mitchell, P.L. Burn, R.K. Thomas, G. Fragneto, J.P.J. Markham, I.D.W. Samuel, *J. Appl. Phys.* 95 (2004) 2391.
- [10] A.R. Inigo, H.C. Chiu, W. Fann, Y.S. Huang, U. Ser Jeng, T.L. Lin, C.-H. Hsu, K.-Y. Peng, S.-A. Chen, *Phys. Rev. B* 69 (2004) 075201.
- [11] J. Liu, T.F. Gou, Y. Shi, Y. Yang, *J. Appl. Phys.* 89 (2001) 3668.
- [12] J. Liu, Y. Shi, L. Ma, Y. Yang, *J. Appl. Phys.* 88 (2000) 605.
- [13] J. Liu, T.F. Guo, Y. Yang, *J. Appl. Phys.* 91 (2002) 1595.
- [14] M. Halim, J.N.G. Pillow, I.D.W. Samuel, P.L. Burn, *Adv. Mater.* 11 (1999) 371.
- [15] S.-C. Lo, N.A.H. Male, J.P.J. Markham, S.W. Magennis, P.L. Burn, O.V. Salata, I.D.W. Samuel, *Adv. Mater.* 14 (2002) 975.
- [16] S.-C. Lo, T.D. Anthopoulos, E.B. Namdas, P.L. Burn, I.D.W. Samuel, *Adv. Mater.* 17 (2005) 1945.
- [17] A.W. Freeman, C.K. Shannon, P.R.L. Malenfant, M.E. Thompson, J.M.J. Fréchet, *J. Am. Chem. Soc.* 122 (2000) 12385.
- [18] Y. Shirota, Y. Kuwabara, H. Inada, T. Wakimoto, H. Nakada, Y. Yonemoto, S. Kawami, K. Imai, *Appl. Phys. Lett.* 65 (1993) 807.
- [19] W.Y. Wong, C.L. Ho, Z.Q. Gao, B.X. Mi, C.H. Chen, K.W. Cheah, Z. Lin, *Angew. Chem.* 118 (2006) 7694.
- [20] J.R. Lawrence, G.A. Turnbull, I.D.W. Samuel, G.J. Richards, P.L. Burn, *Opt. Lett.* 29 (2004) 869.
- [21] J.R. Lawrence, E.B. Namdas, G.J. Richards, P.L. Burn, I.D.W. Samuel, *Adv. Mater.* 19 (2007) 3000.
- [22] J.C. Ribierre, G. Tsimimis, S. Richardson, G.A. Turnbull, I.D.W. Samuel, H.S. Barcena, P.L. Burn, *Appl. Phys. Lett.* 91 (2007) 081108.
- [23] J.P.J. Markham, T.D. Anthopoulos, I.D.W. Samuel, G.J. Richards, P.L. Burn, C. Im, H. Bässler, *Appl. Phys. Lett.* 81 (2002) 3266.
- [24] S. Gambino, I.D.W. Samuel, H. Barcena, P.L. Burn, *Org. Electron.* 9 (2008) 220.
- [25] J.P.J. Markham, E.B. Namdas, T.D. Anthopoulos, I.D.W. Samuel, G.J. Richards, P.L. Burn, *Appl. Phys. Lett.* 85 (2004) 1463.
- [26] G. Tsimimis, J.C. Ribierre, A. Ruseckas, H.S. Barcena, G.J. Richards, G.A. Turnbull, P.L. Burn, I.D.W. Samuel, *Adv. Mater.* 20 (2008) 1940.
- [27] N.C. Greenham, I.D.W. Samuel, G.R. Hayes, R.T. Phillips, R.R. Kessener, S.C. Moratti, A.B. Holmes, *Chem. Phys. Lett.* 241 (1995) 89.
- [28] P.G. Snyder, M.C. Rost, G.H. Bu-Abbud, J.A. Woollam, *J. Appl. Phys.* 60 (1986) 3293.
- [29] C.M. Herzinger, B. Johs, W.A. McGahan, J.A. Woollam, W. Paulson, *J. Appl. Phys.* 83 (1998) 3323.
- [30] B. Johs, R.H. French, F.D. Kalk, W.A. McGahan, J.A. Woollam, in: F. Abeles (Ed.), *Optical Interference Coatings*, SPIE, vol. 2253, 1994, p. 1098.
- [31] J.W. List, R. Guentner, P. Scanducci de Freitas, U. Scherf, *Adv. Mater.* 14 (2002) 374.
- [32] J.C. Ribierre, A. Ruseckas, I.D.W. Samuel, H.S. Barcena, P.L. Burn, *J. Chem. Phys.* 128 (2008) 204703.
- [33] A. Suna, *Phys. Rev. B* 1 (1970) 1716.
- [34] I. Sokolik, R. Priestley, A.D. Walsler, R. Dorsinville, C.W. Tang, *Appl. Phys. Lett.* 69 (1996) 4168.
- [35] M.A. Stevens, C. Silva, D.M. Russell, R.H. Friend, *Phys. Rev. B* 63 (2001) 165213.
- [36] T. Förster, *Discuss. Faraday Soc.* 27 (1959) 7.
- [37] N. Tessler, *Adv. Mater.* 11 (1999) 363.
- [38] I.D.W. Samuel, G.A. Turnbull, *Chem. Rev.* 107 (2007) 1272.
- [39] D. Amarasinghe, A. Ruseckas, G.A. Turnbull, I.D.W. Samuel, *IEEE J. Quant. Electron.*, in press.
- [40] F. Hide, M.A. Diaz-Garcia, B.J. Schwartz, M.R. Anderson, Q.B. Pei, A.J. Heeger, *Science* 273 (1996) 1835.
- [41] M.D. McGehee, R. Gupta, S. Veenstra, E.K. Miller, M.A. Diaz Garcia, A.J. Heeger, *Phys. Rev. B* 58 (1998) 7035.
- [42] G.J. Denton, N. Tessler, M.A. Stevens, R.H. Friend, *Adv. Mater.* 9 (1997) 547.
- [43] C. Zenz, W. Graupner, S. Tasch, G. Leising, K. Müllen, U. Scherf, *Appl. Phys. Lett.* 71 (1997) 2566.
- [44] A.K. Sheridan, G.A. Turnbull, A.N. Safonov, I.D.W. Samuel, *Phys. Rev. B* 62 (2000) 11929.
- [45] S.M. King, H.L. Vaughan, A.P. Monkman, *Chem. Phys. Lett.* 440 (2007) 268.
- [46] D. McBranch, I.H. Campbell, D.L. Smith, J.P. Ferraris, *Appl. Phys. Lett.* 66 (1995) 1175.
- [47] K.H. Yim, R. Friend, J.S. Kim, *J. Chem. Phys.* 124 (2006) 184706.
- [48] J.M. Winfield, C.L. Donley, J.S. Kim, *J. Appl. Phys.* 102 (2007) 063505.

Ovchinnikov et al. and Cao et al. have separately synthesized an organic ferromagnet called *poly-BIPO*, which can be obtained by replacing the H atom of polyacetylene alternately with a heterocycle containing an unpaired electron which we call a side radical, as schematically shown in the central part of Fig. 1. The main zigzag chain consists of carbon atoms with  $\pi$  itinerant electrons. There exists anti-ferromagnetic coupling between the spin of  $\pi$ -electron along the main chain and the residual spin of the side radical. From an extended SSH + Heisenberg (SSH=Su-Schrieffer-Heeger) model, one obtains that the system will have the lowest energy when the spins of side radical forms a ferromagnetic order [11–13]. Recently, several designs of organic ferromagnetic device have been proposed theoretically and some interesting phenomena such as spin filtering and spin-current rectification are predicted [14–16].

At present, most investigations on an organic polymer ferromagnet are limited to ground state properties of the system. In reality, external stimulations including photo-excitation, magnetic field or temperature etc may drive the magnetic molecule deviate from ground state. Several experiments have revealed the underlying function of spin excited states in electron transport through a magnetic molecule. For example, Petukhov et al. gave an evidence of spin excited states existing in a molecular magnet based on electron paramagnetic resonance (EPR) measurements [17]; Heersche et al. observed a complete current suppression and negative differential conductance in a single  $Mn_{12}$  molecular magnetic device, which is believed to have a relation with the spin excited states of the molecule [6]. For organic ferromagnet *poly-BIPO*, the spin excited state means that the ferromagnetic order of radical spins is destroyed owing to the spin flipping, which induces the magnetic molecule to a high-energy state. As the radical spins are correlated with the  $\pi$ -electrons in the main chain, it is expected that the spin excited state will affect the  $\pi$ -electron transport along the main chain. In this paper, we construct a metal/organic ferromagnet/metal (M/O/M) device and then investigate the spin-polarized transport when the organic ferromagnetic molecule is in different spin excited states. The paper is organized as follows: The model and formula are described in Section 2. In Section 3, we give the numerical calculation and the results are analyzed. Finally, in Section 4, a summary is given.

## 2. Model and method

As shown in Fig. 1, an organic ferromagnetic device M/O/M is modeled as a quasi-one-dimensional chain. The

central organic ferromagnetic molecule is connected with two noninteracting semi-infinite one-dimensional metallic chains. The complete Hamiltonian is written as,

$$H = H_{OF} + H_l + H_r + H_{coup} + H_E \quad (1)$$

The first term is the Hamiltonian of organic ferromagnetic molecule [12,13],

$$H_{OF} = - \sum_{n,s} [t_0 - \alpha(u_{n+1} - u_n)] (c_{n,s}^+ c_{n+1,s} + c_{n+1,s}^+ c_{n,s}) + \frac{K}{2} \sum_n (u_{n+1} - u_n)^2 + J_f \sum_n \delta_{n,o} \vec{S}_{nR} \cdot \vec{S}_n + U \sum_n c_{n,\uparrow}^+ c_{n,\uparrow} c_{n,\downarrow}^+ c_{n,\downarrow} + V \sum_{n,s,s'} c_{n,s}^+ c_{n,s} c_{n+1,s'}^+ c_{n+1,s'} \quad (2)$$

where  $t_0$  is the hopping integral of  $\pi$ -electrons along the main chain with a uniform lattice.  $\alpha$  stands for the electron-lattice coupling parameter and  $u_n$  the lattice displacement at site  $n$ .  $K$  is the elastic constant of the lattice atoms, and  $c_{n,s}^+$  ( $c_{n,s}$ ) denotes the creation (annihilation) operator of an electron at site  $n$  with spin  $s$ . The third term in Eq. (2) describes the correlation between spin  $\vec{S}_n$  of  $\pi$ -electron and residual spin  $\vec{S}_{nR}$  of radical  $R$ . It is assumed that the side radicals are connected with the odd sites of the main chain, which is denoted by  $\delta_{n,o}$ . Coupling constant  $J_f$  is assumed to be positive (anti-ferromagnetic coupling). We use mean-field approximation to treat the radical spin  $\vec{S}_{nR}$  as  $\langle S_{nR}^z \rangle$ , where  $\langle \dots \rangle = \langle G | \dots | G \rangle$  is the average with respect to the ground state  $|G\rangle$ . Then the third term can be written as  $\frac{J_f}{2} \sum_n \delta_{n,o} \langle S_{nR}^z \rangle \cos \theta_{nR} (c_{n,\uparrow}^+ c_{n,\downarrow} - c_{n,\downarrow}^+ c_{n,\uparrow})$  and  $\theta_{nR}$  the radical spin orientation at site  $n$  (angle with  $-z$  axis). The last two terms describe the  $e$ - $e$  (electron-electron) interactions between  $\pi$ -electrons under the extended Hubbard model. As spin coulomb drag effect may exist between spin-up and spin-down electrons and affect the spin-polarized current during transport [18,19], it is very necessary to take the consideration of the interactions among electrons. So far, many theoretical techniques can deal with  $e$ - $e$  interactions, for example, mean-field approximation, perturbation, full coulomb interactions [20,21] and density matrix renormalization group (DMRG) calculation etc [22–24]. As the first step of our investigation, in this paper, we will just adopt the simple mean-field approximation to deal with the Hubbard term. Its validity will be discussed in the later summary.

$H_{l(r)}$  is the Hamiltonian of the left (right) electrode, which is a semi-infinite metal chain,

$$H_{l(r)} = \sum_{m,s} \varepsilon_{l(r)} a_{m,s}^+ a_{m,s} + \sum_{m,s} t_{l(r)} (a_{m,s}^+ a_{m+1,s} + h.c.) \quad (3)$$

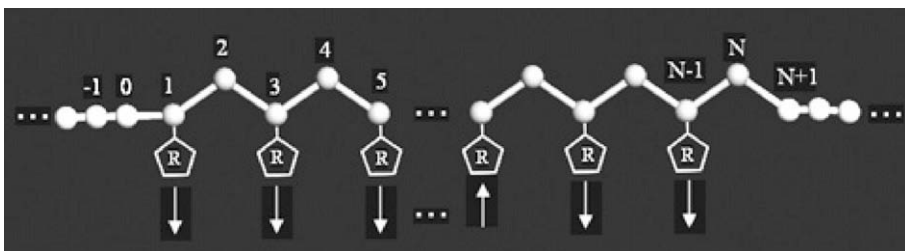


Fig. 1. Simplified structure of a metal/*poly-BIPO*/metal nanojunction. The arrows indicate the spin orientation of radical spins.

where  $\varepsilon_{l(r)}$  is on-site energy of a metal atom comparing to that of a carbon atom and  $t_{l(r)}$  the transfer integral of adjacent sites.  $a_{m,s}^+$  ( $a_{m,s}$ ) is the creation (annihilation) operator of an electron in electrodes.

The coupling between the electrodes and the molecule is assumed to take place only at the nearest connecting atoms at the interfaces,

$$H_{coup} = \sum_s t_{lM}(a_{0,s}^+ c_{1,s} + h.c.) + \sum_s t_{rM}(c_{N,s}^+ a_{N+1,s} + h.c.) \quad (4)$$

$t_{l(r)M}$  is the interfacial coupling, which is simplified by neglecting the spin-dependent scattering at the interfaces.  $N$  is the total number of the sites in the organic ferromagnetic interlayer.

The last term is the contribution of driving field  $E$  arising from the bias voltage  $V$  between the two electrodes,

$$H_E = - \sum_{n,s} |e|E \left[ \left( n - \frac{N+1}{2} \right) a + u_n \right] c_{n,s}^+ c_{n,s} + \sum_n |e|E \left[ \left( n - \frac{N+1}{2} \right) a + u_n \right] \quad (5)$$

with  $e$  being the electronic charge and  $a$  the lattice constant. The first term is the electric potential energy of electrons of all sites and the second term is the electric potential energy of lattice ions. It is assumed that the field is uniform along the whole molecule chain and  $E = V / [(N-1)a]$ . This linear treatment is suitable for the case that the bias applied on the molecule is not too large.

For the M/OF/M device, the current measured at the right electrode is contributed by both the spin-conserving scattering and spin-flip scattering. As the spin-orbit coupling and hyperfine interaction in an organic material are usually very weak, they will result in a large spin relaxation length [1,25]. In this work, we neglect the spin-flip scattering during the transport. Then the spin-dependent current can be calculated with Landauer-Büttiker formula,

$$I_s(V) = \frac{e}{h} \int_{-\infty}^{+\infty} T_{ss}(E,V) [f(E - \mu_l) - f(E - \mu_r)] dE \quad (6)$$

where  $f(E - \mu_{l(r)}) = 1 / \{1 + \exp[(E - \mu_{l(r)}) / k_B T]\}$  is the Fermi function and  $\mu_{l(r)} = E_F \pm eV/2$  is the chemical potential of the left (right) electrode with Fermi energy  $E_F$ .

The spin-conserving transmission coefficient  $T_{ss}(E,V)$  can be obtained from Lattice Green Function through Fish-Lee relation [26]  $T_{ss}(E,V) = \text{Tr}[\Gamma_l G_{ss}(E,V) \Gamma_r G_{ss}^+(E,V)]$ , where  $G_{ss}(E,V) = \frac{1}{E - H_{OF}^s - H_{elec}^s - \sum_i - \sum_r}$  with  $\Sigma_l(\Sigma_r)$  being the self-energy operators due to the coupling with left (right) electrode.  $H_{OF}^s$  and  $H_{elec}^s$  correspond to the electron Hamiltonian with spin  $s$  in Eqs. (2) and (5).  $\Gamma_{r(l)}$  denotes the broadening matrix which is related to self energy with  $\Gamma_{r(l)} = i[\sum_{r(l)} - \sum_{r(l)}^+]$ .

The calculation is performed as follows: we firstly solve the electronic eigenequation of an isolated *poly*-BIPO molecule. By minimizing the total energy, the lattice and the electronic structures of an isolated *poly*-BIPO molecule can be obtained self-consistently. Then we use Green's function formula to calculate the transmission probability of spin  $s$ , and the spin-dependent current is obtained from Eq. (6).

In order to investigate the spin-polarized transport properties of the M/OF/M sandwiched device, we define the spin polarization (SP) of the current as,

$$P = \frac{I_{\uparrow} - I_{\downarrow}}{I_{\uparrow} + I_{\downarrow}} \quad (7)$$

In the calculation, the parameters are chosen as follows [12,15]: For the organic ferromagnet,  $t_0 = 2.5$  eV,  $\alpha = 4.1$  eV/Å,  $K = 21.0$  eV/Å<sup>2</sup>,  $J = J_f/t_0 = 0.8$ . As the mean-field approximation is only valid in the case of weak  $e$ - $e$  interactions, we choose  $U = 1.0$  eV and  $V = U/3$ . In ground state, the radical spin is supposed to be  $\langle S_{nR}^z \rangle = -\frac{1}{2}$ ,  $\theta_{nR} = 0$ . For the electrodes,  $\varepsilon_{l(r)}$ ,  $t_l = t_r = 2.5$  eV,  $E_F = 1.55$  eV. The interfacial coupling is taken as  $t_{lM} = t_{rM} = 1.0$  eV.

### 3. Results and discussion

We firstly consider the ground state and spin excited state of an isolated *poly*-BIPO chain. In ground state, the radical spins form a ferromagnetic order. There exists an antiferromagnetic SDW of  $\pi$ -electrons in the main chain [11]. The SDW is depicted in Fig. 2, where the SDW order parameter is defined as  $s_n = (-1)^{n+1} (n_{n\uparrow} - n_{n\downarrow}) \cdot n_{ns} = \sum_{\mu} |Z_{\mu,n,s}|^2$  is the electronic charge density of spin  $s$  at site  $n$  and  $Z_{\mu,n,s}$  the eigenvector obtained by solving Schrödinger equation of Hamiltonian  $H_{OF}^s$ . A spin excited state means that there is one or several radical spins flipped. For example, if a radical spin at site  $n_0$  is excited from  $\theta_{n_0R} = 0$  to  $\theta_{n_0R} = \pi$ , we obtain a single-spin excited state. In this case, the SDW of the molecule will be destroyed and a localized spin defect around site  $n_0$  appears in the main chain. As shown in Fig. 2, the defect has a width of about  $5 \sim 7a$ , which depends on the electron-lattice coupling constant. In the meantime, the appearance of an excited state will result in the change of the electronic states and the energy levels from that of the ground state. It is found that LUMO (lowest unoccupied molecular orbital) of spin-up electrons will departure from the Fermi level and the case is opposite for spin-down ones. Both spin-up and spin-down electronic states near the Fermi level tend to be weakly localized. It is expected that these variations due to spin

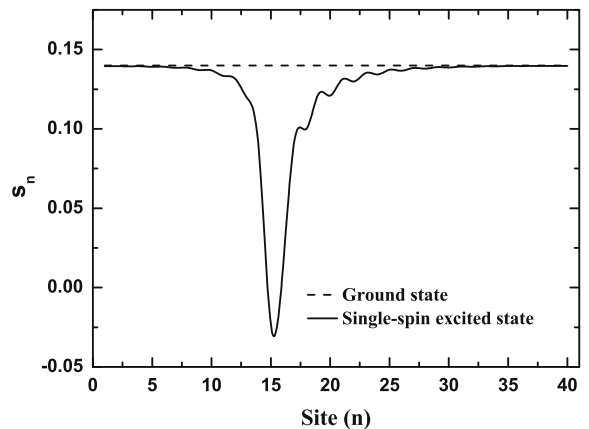


Fig. 2. SDW in the ground state and a single-spin excited state.

excitations will seriously affect the conductance and current polarization of such a spin device.

If two or more radical spins are excited, it is found that they will attract each other to form a coupled spin excitation, which will be lower in energy than separated ones. With the increasing of the number of excited radical spins, the system will lay in a high spin excited state in energy. We define the excited energy as,

$$\Delta E(m) = E(m) - E_0 \quad (8)$$

Here  $E(m)$  denotes the total energy of system when there are  $m$  radical spins being excited, and  $E_0$  the ground state. Fig. 3 shows the dependence of  $\Delta E(m)$  on the number of the excited radical spins. It is found that spin excitation energy increases with the number of excited spins. We note that when  $m > m_0 = 8$ , the excitation energy keeps nearly unchanged. The reason is that the ferromagnetic molecule is degenerate with  $\langle S_{nR}^z \rangle = \pm 1/2$ . When  $m > m_0$ , the excited zone of the system forms a stable domain and excitation energy only exists in the domain walls.

In the following, we investigate the electron transport properties of a *poly*-BIPO device in different spin excited states. Firstly, we consider the effect of spin excitations on total current through the device. The result is shown in Fig. 4. We see that, at a fixed bias voltage  $V = 0.5$  V, the total current decreases apparently with the number of excited spins. This current suppression effect on the transport of high spin state has been found in single molecular magnets experimentally [6]. It is predicated that such an organic ferromagnetic device can realize a controllable charge transport. In present parameters, a current suppression ratio  $\gamma = -(I_{ex} - I_g)/I_g = 34\%$  is obtained for only one single-spin excitation. Especially, if the molecule lay in a high-energy excited state, it is found that the current may disappear, which means that the device may have a function of a conductance switch.

It has been found that the ferromagnetic molecule has spin-filter function in ground state. Now we consider the spin-polarized transport property through the device when the molecule is excited. A spin excitation may appear either at the interface of M/OF/M or in the interior of the molecule, which has a little difference of about 0.025 eV

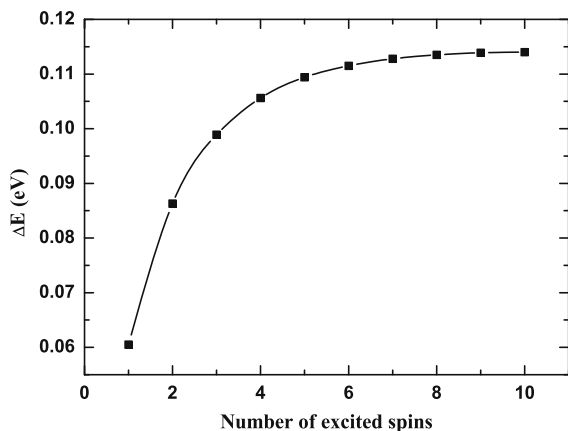


Fig. 3. Dependence of spin excitation energy  $\Delta E$  on the number of excited radical spins.

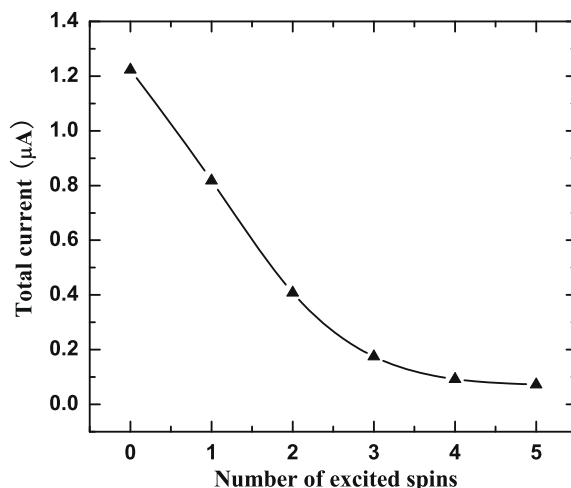


Fig. 4. Dependence of total current on the number of excited radical spins at  $V = 0.5$  V.

in energy for a single-spin excitation. Here, we only consider the case of low spin excited states, i.e. there is a single-spin excitation or a double-spin excitation. The results are shown in Fig. 5 for the dependence of SP on the external bias. It is found that the SP has a little decrease whether the spin excitation is at the interface or in the interior. There is no much difference for the case of a double-spin and a single-spin excitation.

To understand the effect of spin excitations on SP, we fix bias  $V = 0.5$  V and calculate the dependence of SP on the number of excited radical spins. The result is shown in Fig. 6. It is found that, if the number of excited spins is less ( $m \leq 3$  in present case), the decreasing of SP is  $m$  not apparent. In this case, the device can serve as a spin function with a high spin polarization. However, if the number of the excited spins is close to half of the total radical spins, it is found that the SP will decrease to near zero, which means that the spin-up electrons and the spin-down

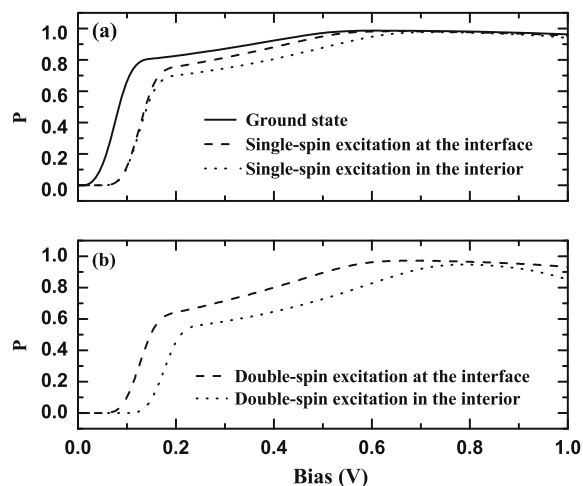


Fig. 5. Calculated spin polarization as the function of bias voltage. (a) Single-spin excitation. (b) Double-spin excitation.

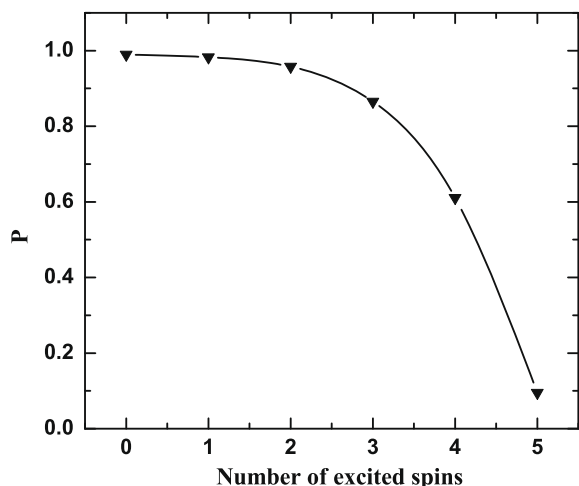


Fig. 6. Current spin polarization as a function of the number of excited radical spins at  $V = 0.5$  V.

electrons have the same probability to tunnel through the molecule. Of course, such a spin excitation needs a high energy as indicated in Fig. 3. Therefore, an M/OF/M device is stable to serve a spin filter.

To give the explanation of total current suppression in Fig. 4 and SP modulation effect in Fig. 6, we depict the spin-dependent transmission coefficient at a fixed bias  $V = 0.5$  V with the number of excited radical spins from  $m = 0$  to  $m = 5$ . The results are shown in Fig. 7. When there is no spin excitation in the system, it is found that only the transmission peak of spin-up LUMO lies in the conducting region  $[-0.25$  V,  $+0.25$  V]. In this case, the current is contributed mainly by spin-up electrons and so the SP through the device is nearly 100%. With the exciting of the radical spins, the peak corresponding to the spin-up LUMO is moving away from conducting region gradually. As no (or not apparent) any other transmission enter the conducting region all the time, so the conductance decreases. At a high

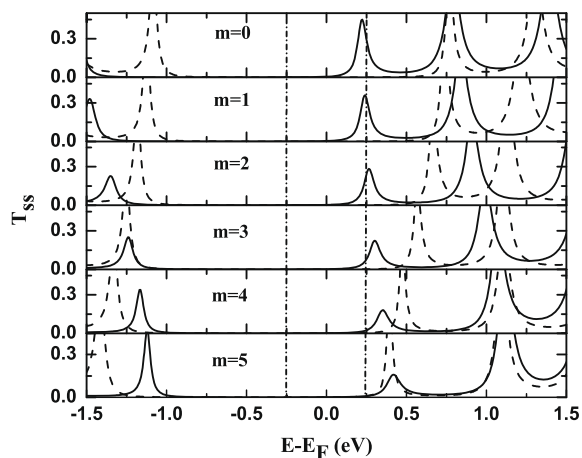


Fig. 7. Spin-dependent transmission coefficient at  $V = 0.5$  V in different spin excited states.

spin excited state, for example  $m = 5$ , the transmission becomes nearly zero in the conducting region, so there is no current in this case. From Fig. 7 we also note that the transmission strengths become weaker and weaker with the number of excited radical spins. It is because the electronic states near the Fermi level tend to be weakly localized with the appearance of excited spin defect.

As stated above, spin excitations can affect the conductance and the current polarization of an M/OF/M device. However, the investigation also shows that a low-energy excitation could not destroy the SP and the device can serve a SP function. To give a further understanding, we consider the effect of temperature on the SP as thermal fluctuation may make the radical spins to deviate from the ferromagnetic ground state. It is supposed that the angle  $\theta_{nR} \in [0, \theta_0]$  of radical spin  $\vec{S}_{nR}$  is randomly valued and obeys a uniform distribution. Here  $\theta_0$  means the strength of thermal perturbation, which is related to temperature through a simple Boltzmann relation  $\Delta\varepsilon \approx k_B T/2$ , where  $\Delta\varepsilon$  denotes the energy difference per site freedom between states at a distribution  $\{\theta_{nR}\}$  and the ground state of the system. We firstly calculate the order parameter  $\langle s_n \rangle$  of the molecule. It is found that the order parameter will decrease with temperature. In present work, the order parameter will decrease to nearly zero when temperature is higher than the critical value  $T = T_c \approx 360$  K, which is close to the experimental value [7]. It means that the magnetism of the molecule will vanish beyond the critical point. Then we investigate the behavior of SP in different temperature. The results are shown in Fig. 8, where the inset gives the dependence of SP on temperature at a fixed bias  $V = 0.5$  V. From it we see that, although there is a decreasing of the SP with the temperature, the current through the device is still apparently spin polarized if temperature is not too high. In present parameters, the current can keep a high spin polarization when temperature is less than 280 K. However, when temperature approaches the critical point, the SP drops rapidly and becomes very small when temperature is beyond the critical point.

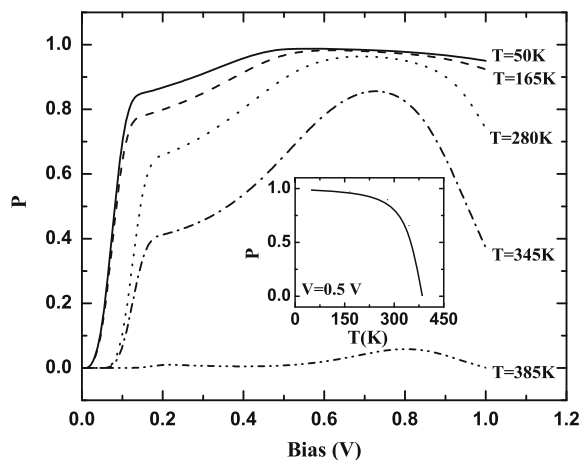


Fig. 8. Current spin polarization as a function of bias voltage in different temperatures. The inset is the dependence of current spin polarization on temperature at  $V = 0.5$  V.

#### 4. Summary

In summary, spin excited states in organic ferromagnet *poly*-BIPO are investigated to study the spin transport in an organic metal/*poly*-BIPO/metal device under a finite temperature. The picture of spin excited state is elucidated by calculating the SDW along the molecular chain and the spin excited energy. A localized defect of SDW appears when a spin excited state forms. The spin excited energy increases with the number of excited spins and keeps nearly unchanged when the number of excited spins is over a certain value. Then the spin-dependent transport through a metal/*poly*-BIPO/metal device is investigated. It is found that a suppression of the total current may take place when the magnetic molecule is in a spin excited state, which predicts a conductance switch function of the device. It is also found that a low spin excited state has little effect on SP and the device may still function as a spin filter. The intrinsic mechanism is explained by calculating the spin-dependent transmission in different spin excited states. The temperature effect on the spin-polarized transport is studied. The current can keep a high spin polarization when temperature is not too high. The result indicates that the device may serve as a stable spin filter. Finally, it should be mentioned about the validity of the  $e$ - $e$  interactions adopted in present work. Usually Hubbard model is considered to be the simplest one to treat  $e$ - $e$  interactions, although it is only valid in a narrow-band system. In organic semiconductors, Hubbard model is widely adopted, and the strength of Hubbard  $U$  is considered to be widely distributed from 1.0 to 11.0 eV [27]. A strong  $e$ - $e$  interaction will seriously affect the electronic structure of the system and so the spin current polarization. For example, a spin-polarized ground state may be obtained in the case of large  $U$ . As the first step to understand the spin current polarization in an organic device, in present work, we only considered the case of a weak Hubbard interaction. The effect of  $e$ - $e$  interactions was mainly reflected in the structure of the electronic energy levels of the system, which will affect the transmission probability of spin-up and spin-down electrons to some extent. In the further work, we will try to consider the effect of  $e$ - $e$  interactions on the ferromagnetic ground state and the spin drag effect with a more effective technique beyond the mean-field approximation.

#### Acknowledgements

The authors would like to acknowledge the financial support from the National Basic Research Program of China (Grant No. 2009CB929204) and the National Natural Science Foundation of the People's Republic of China (Grant Nos. 10874100, 10747143, and 10847151).

#### References

- [1] V. Dediu, M. Murgia, F.C. Matocota, C. Taliani, S. Barbanera, *Solid State Commun.* 122 (2002) 181.
- [2] V. Podzorov, E. Menard, A. Borisov, V. Kiryukhin, J.A. Rogers, M.E. Gershenson, *Phys. Rev. Lett.* 93 (2004) 086602.
- [3] M.P.S. Wenjie Liang, Marc Bockrath, Jeffrey R. Long, H. Park, *Nature* 417 (2002) 725.
- [4] S.A. Wolf, D.D. Awschalom, R.A. Buhrman, J.M. Daughton, S. von Molnar, M.L. Roukes, A.Y. Chtchelkanova, D.M. Treger, *Science* 294 (2001) 1488.
- [5] Z.H. Xiong, D. Wu, Z. Vally Vardeny, J. Shi, *Nature* 427 (2004) 821.
- [6] H.B. Heersche, Z. De Groot, J.A. Folk, H.S.J. Van der Zant, *Phys. Rev. Lett.* 96 (2006) 206801.
- [7] Y.V. Korshak, T.V. Medvedeva, A.A. Ovchinnikov, V.N. Spector, *Nature* 326 (1987) 370.
- [8] Y. Cao, P. Wang, Z. Hu, S. Li, L. Zhang, J. Zhao, *Synth. Met.* 27 (1988) 625.
- [9] J.M. Manriquez, G.T. Yee, R.S. McLean, A.J. Epstein, J.S. Miller, *Science* 252 (1991) 1415.
- [10] N.P. Raju, T. Savrin, V.N. Prigodin, K.I. Pokhodnya, J.S. Miller, A.J. Epstein, *J. Appl. Phys.* 93 (2003) 6799.
- [11] Z. Fang, Z.L. Liu, K.L. Yao, *Phys. Rev. B* 49 (1994) 3916.
- [12] Z. Fang, Z.L. Liu, K.L. Yao, Z.G. Li, *Phys. Rev. B* 51 (1995) 1304.
- [13] S.J. Xie, J.Q. Zhao, J.H. Wei, S.G. Wang, L.M. Mei, S.H. Han, *Europhys. Lett.* 50 (2000) 635.
- [14] W.Z. Wang, *Phys. Rev. B* 73 (2006) 235325.
- [15] G.C. Hu, Y. Guo, J.H. Wei, S.J. Xie, *Phys. Rev. B* 75 (2007) 165321.
- [16] G.C. Hu, K.L. He, A. Saxena, S.J. Xie, *J. Chem. Phys.* 129 (2008) 234708.
- [17] K. Petukhov, S. Hill, N.E. Chakov, K.A. Abboud, G. Christou, *Phys. Rev. B* 70 (2004) 054426.
- [18] I. D'Amico, G. Vignale, *Phys. Rev. B* 62 (2000) 4853.
- [19] G. Vignale, *Phys. Rev. B* 71 (2005) 125103.
- [20] C.Q. Wu, X. Sun, *Phys. Rev. Lett.* 59 (1987) 831.
- [21] S.J. Xie, L.M. Mei, *Phys. Rev. B* 10 (1992) 6169.
- [22] M.B. Lepetit, G.M. Pastor, *Phys. Rev. B* 56 (1997) 4447.
- [23] Z.G. Yu, A. Saxena, A.R. Bishop, *Phys. Rev. B* 56 (1997) 3697.
- [24] Z. Shuai, J.L. Brédas, *Phys. Rev. B* 58 (1998) 15329.
- [25] S. Pramanik, C.G. Stefanita, S. Patibandla, S. Bandyopadhyay, K. Garre, N. Harth, M. Cahay, *Nat. Nanotechnol.* 2 (2007) 216.
- [26] Z.M. Zeng, J.F. Feng, Y. Wang, X.F. Han, W.S. Zhan, X.G. Zhang, Z. Zhang, *Phys. Rev. Lett.* 97 (2006) 106605.
- [27] W. Barford, R.J. Bursill, Richard W. Smith, *Phys. Rev. B* 66 (2002) 115205.

processing, including ink-jet printing, screen printing [23], soft lithography [24,25], laser-assisted patterning [26,27], contact printing [28], and self-organization processes [29–33]. Among these methods, self-organization has great potential for use in the fabrication of high-throughput, low-cost electronics without degrading their OTFT performances. For example, Bao et al. [29] reported a micro-contact printing ( $\mu$ CP) method for transferring low-molecular-weight siloxane oligomers from PDMS stamps to pattern organic poly(3-hexylthiophene) (P3HT) and poly(vinyl phenol) (PVP) materials via selective wetting/dewetting to fabricate regions with and without oligomers [29]; nevertheless, the interface of the channel region was only the bare surface, lacking a modification layer. Many authors have determined that modification layers present between the dielectric and organic active material are necessary to improve the interfacial adhesion and the film's crystallinity, thereby providing more-stable devices exhibiting higher carrier mobilities [10]. During the preparation of this manuscript, two research groups published self-organization processes featuring the treatment of two modification layers on silicon oxide surfaces [32,33]. Minari et al. [32] reported a surface presenting phenyl-terminated SAMs as channel regions and hexamethyldisilazane (HMDS) units covering the rest of the surface. Small organic molecules that had been drop-cast from toluene solutions were selectively crystallized on the phenyl-presenting SAM regions. Kim et al. [33] coated a hydrophobic fluoropolymer film onto silicon dioxide and then modified the channel regions with HMDS. A soluble pentacene derivative was then self-deposited from a xylene solution onto the channel areas. Although these two initial studies [32,33] appear to have several advantages over simple mono-modification treatment [29–31] the authors studied the patterning of semiconductors in nonpolar solvents only; they did not explore the use of other materials (e.g., conducting polymers, organic gate dielectrics) or other polar and nonpolar solvents. In addition, the origins of the self-organization processes were considered to occur mostly through differences in the water contact angles of the substrates inducing the hydrophilic/hydrophobic properties; there remains much room to provide a more appropriate explanation of these phenomena.

In this study, we developed a new system for the self-patterning of two types of SAMs on silicon dioxide surfaces, with HMDS forming channel regions and octyltrichlorosilane (OTS) covering the remaining areas. We prepared these patterns readily using traditional photolithography processes. In addition to investigating several organic and inorganic semiconductors, we also processed the conducting polymers from aqueous solutions and employed organic gate dielectric materials. We explain the self-patterning phenomena in terms of surface energy differences – rather than the previously reported simple hydrophilic/hydrophobic water contact angle theory.

## 2. Experimental section

Materials: PVP ( $M_w = 20,000$ ), PMF ( $M_w = 511$ ), OTS, HMDS, chlorobenzene, toluene, propylene glycol mono-

methyl ether acetate (PGMEA),  $\text{CH}_2\text{Cl}_2$ , hexane, and acetone were purchased from Sigma–Aldrich and used without further purification. Regioregular P3HT was purchased from Aldrich and purified through Soxhlet extractions with hexane and  $\text{CH}_2\text{Cl}_2$  to remove low-molecular-weight chains. 13,6-*N*-sulfinylacetamidopentacene (NSFAAP) and zinc acetate were also obtained commercially from Aldrich and used directly. Poly(9,9-dioctylfluorene-*alt*-bithiophene) (F8T2) was purchased from American Dye Source. The PEDOT:PSS water solution (AI4083) was purchased from Bayer.

Device fabrication: We prepared the substrate using the self-patterning process presented in Fig. 1. We employed a silicon wafer presenting thermally grown  $\text{SiO}_2$  ( $d = 100$  nm) as the substrate. The source and drain (S/D) Pt/Ti (50 nm/2 nm) electrodes having channel widths and lengths of 1000 and 10  $\mu\text{m}$ , respectively, were prepared using a photolithography/Pt–Ti deposition/lift-off (acetone) process. The entire device surface was treated with HMDS vapor and then cured at 150 °C for 0.5 h, and then the channel regions of the device were covered with photoresist using conventional photolithography processing. The remaining region not covered with the photoresist was treated through  $\text{O}_2$  plasma bombardment and then treated with OTS vapor then cured at 100 °C for 0.5 h. Finally, the photoresist was removed to provide a substrate presenting HMDS in the channel regions and OTS over the remaining areas.

Electrical Measurements: All TFT devices arrays in this study, each containing 20 devices were fabricated. To ensure accuracy of data that were collected, we measured at least 10 devices for each array and no significant (<10%) variations were observed from device to device. All *I*–*V* measurements of our OTFT devices were recorded at room temperature under ambient conditions using an Agilent 4156C semiconductor parameter analyzer. The thicknesses of the corresponding films were determined through cross-sectional scanning electron microscopy (SEM). The surface energies of the various SAM surfaces were determined through contact angle measurements using a FACE contact-angle meter (Kyowa Kaimenkagaku Co.) and distilled water and  $\text{CH}_2\text{I}_2$  as probe liquids.

## 3. Results and discussion

We employed various solutions of organic and inorganic materials to examine the scope of this self-patterning method; Fig. 2 presents their chemical structures. After depositing a drop of the semiconductor solution [P3HT (5 mg) in dichlorobenzene (1 mL)] onto the HMDS/OTS-presenting S/D electrode-patterned substrate and then decanting the substrate to remove the large droplet, we found that some small droplets remained adhered to the HMDS regions. After the solvent had dried, the resulting films were isolated with finely featured shapes on the HMDS region. Thus, using this approach, we fabricated a bottom gate, bottom contact configuration of the patterned P3HT-OTFT. Fig. 3a displays an optical micrograph of the with uniformly patterned P3HT-OTFT device array. A magnified image of the P3HT-OTFT single device (Fig. 3b)

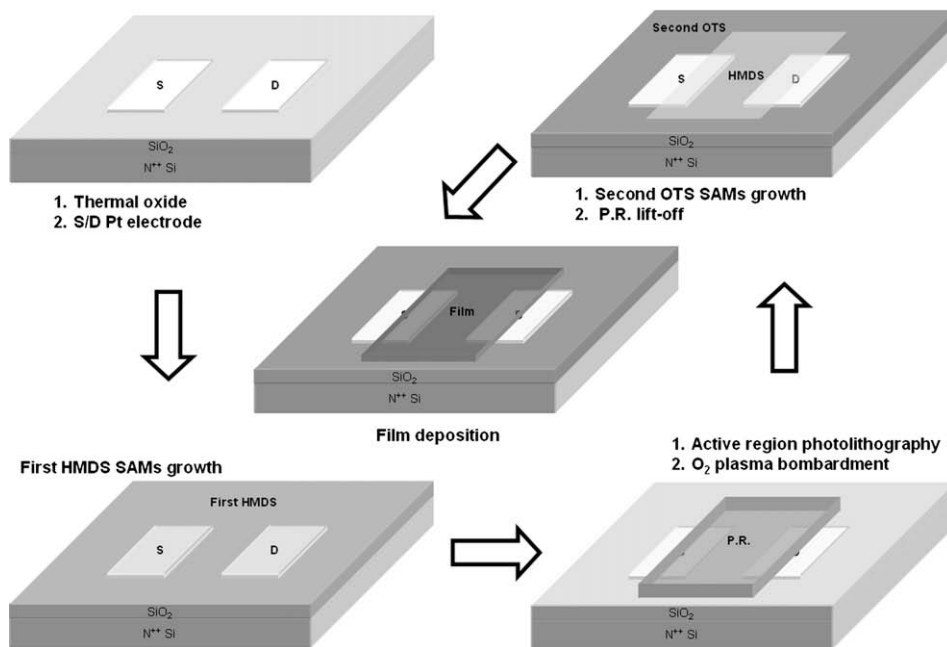


Fig. 1. Schematic procedure used for the self-patterning of OTFTs.

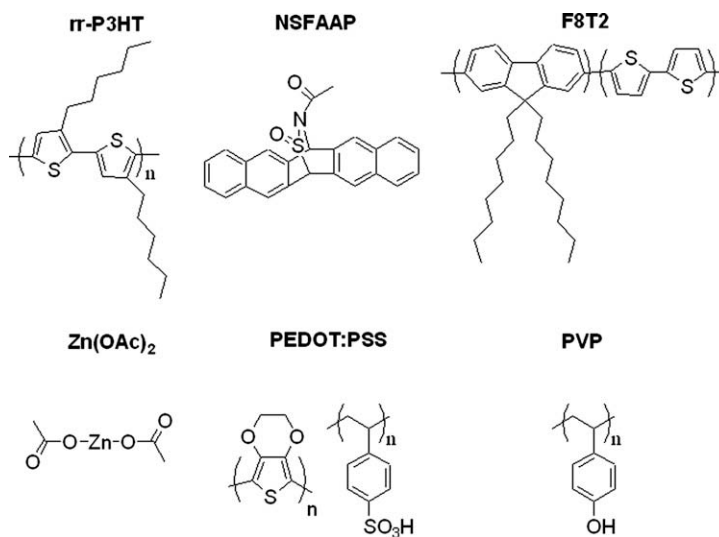


Fig. 2. Chemical structures of the materials used to prepare the patterned organic and inorganic films.

reveals rectangular features ( $250\ \mu\text{m} \times 300\ \mu\text{m}$ ). In addition, when we used the HMDS/OTS-presenting substrate lacking any S/D electrodes, we formed films of the organic conductor poly(3,4-ethylenedioxythiophene) doped with poly(styrene sulfonic acid) (PEDOT:PSS) from an aqueous solution (Fig. 3c) and of poly(vinyl phenol) (PVP), a commonly used dielectric layer, from a propylene glycol methyl ether acetate (PGMEA) solution (Fig. 3d); these polymers were also well defined in the desired regions, with their films exhibiting uniformly striped rectangular featured having areas of  $100\ \mu\text{m} \times 1000\ \mu\text{m}$ . Thus, a series of materials could be self-patterned using HMDS/

OTS substrates through solution processing with a wide range of solvents.

We used an energy dispersive spectrometer (EDS) to analyze the surfaces of the patterned P3HT-OTFT devices to determine whether any residues or contaminants existed outside the active region after performing the solution deposition process. Before taking SEM photographs, we deposited a thin Pt film to make the substrate conductive. So the Pt signals were observed at both regions. Fig. 4 presents EDS spectra recorded over an active P3HT region and over a P3HT-free region. P3HT has the chemical formula  $\text{C}_{10}\text{H}_{14}\text{S}$ ; we found S and C atom signal distributions



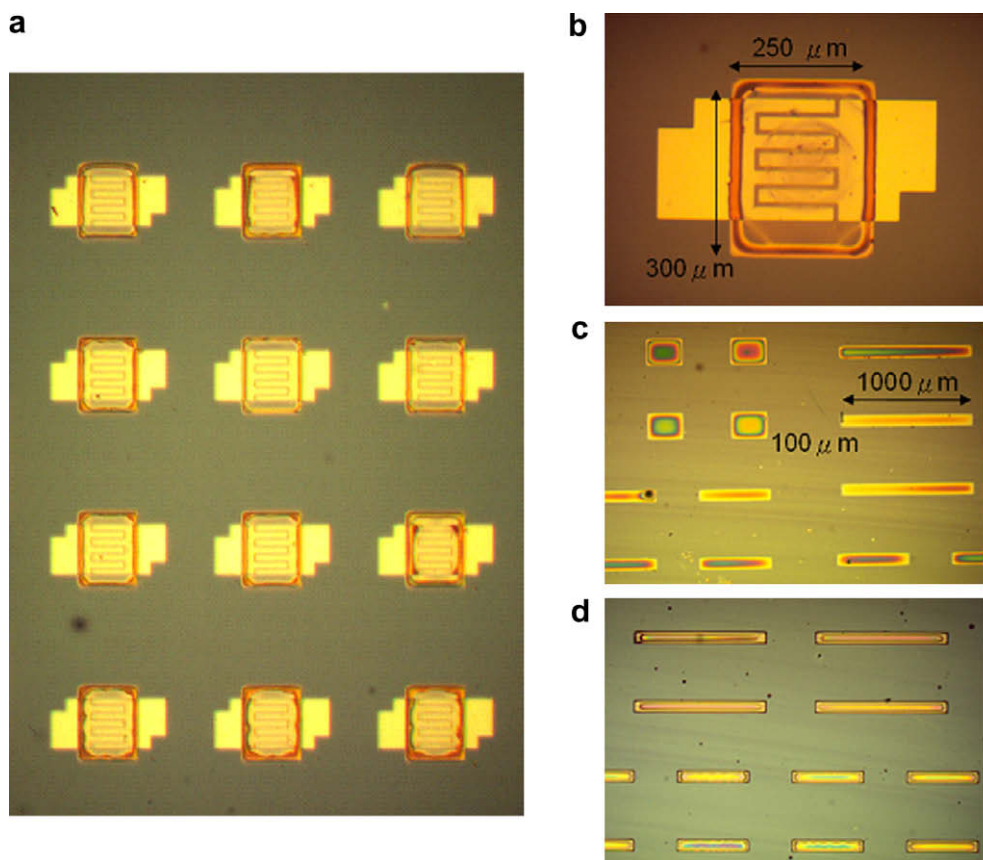


**Fig. 3.** Optical micrographs of silicon substrates presenting (a) a P3HT-OTFT array, (b) a single P3HT-OTFT device, (c) a PEDOT:PSS array, and (d) a PVP self-patterned array.

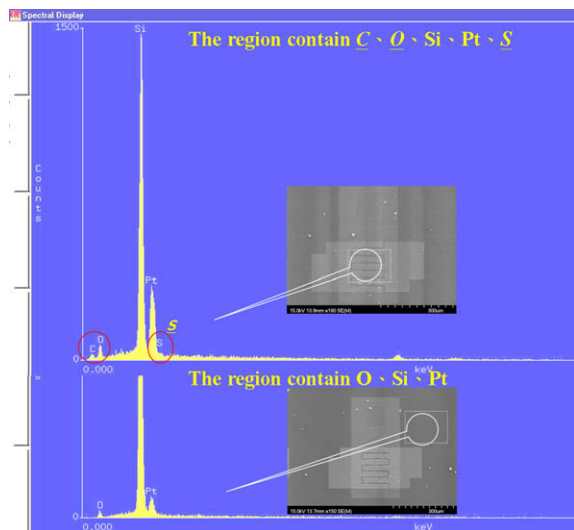


**Fig. 4.** SEM images and EDS spectra of a P3HT-OTFT device prepared using the self-patterning method.

in the EDS profile of active region, as well as O, Si, and Pt atom signals representing the  $\text{SiO}_2$  substrate and the S/D Pt electrodes. In contrast, the EDS profile recorded away

from the HMDS region, i.e., the region presenting OTS, reveals signals only for O, Si, and Pt atoms, suggesting that no or non-sufficient P3HT residues or other organic contaminants were present in this area.

In addition to rr-P3HT, we also employed two other organic semiconductors – poly(9,9-dioctylfluorene-*alt*-bithiophene) (F8T2; 20 mg in 1 mL of  $\text{CHCl}_3$ ), 13,6-*N*-sulfinylacetamidopentacene (NSFAAP; 15 mg in 1 mL of  $\text{CHCl}_3$ ) – and one inorganic semiconductor (ZnO precursor solution; zinc acetate-to-ethanolamine molar ratio, 1:1; mixture concentration, 0.375 M in 2-methoxyethanol) to prepare OTFTs using the HMDS/OTS substrates. Again, we found that all of the resulting films exhibited isolated, fine feature shapes located in the HMDS regions, thereby providing bottom gate, bottom contact configurations for their patterned OTFTs. Moreover, we prepared corresponding controlled non-patterned P3HT-OTFT devices to compare their off currents with those of the patterned devices. Fig. 5 presents the electronic characteristics of the OTFT devices; we determined the transfer characteristics of P3HT, F8T2, and pentacene devices by operating the devices at a value of  $V_{ds}$  of  $-40$  V and values of  $V_G$  ranging from  $+40$  to  $-40$  V and of ZnO device by operating at a value of  $V_{ds}$  of 20 V and values of  $V_G$  ranging from  $-10$  to 60 V. We define the carrier mobility ( $\mu$ ) and the threshold voltage  $V_{th}$  using Eq. (1):

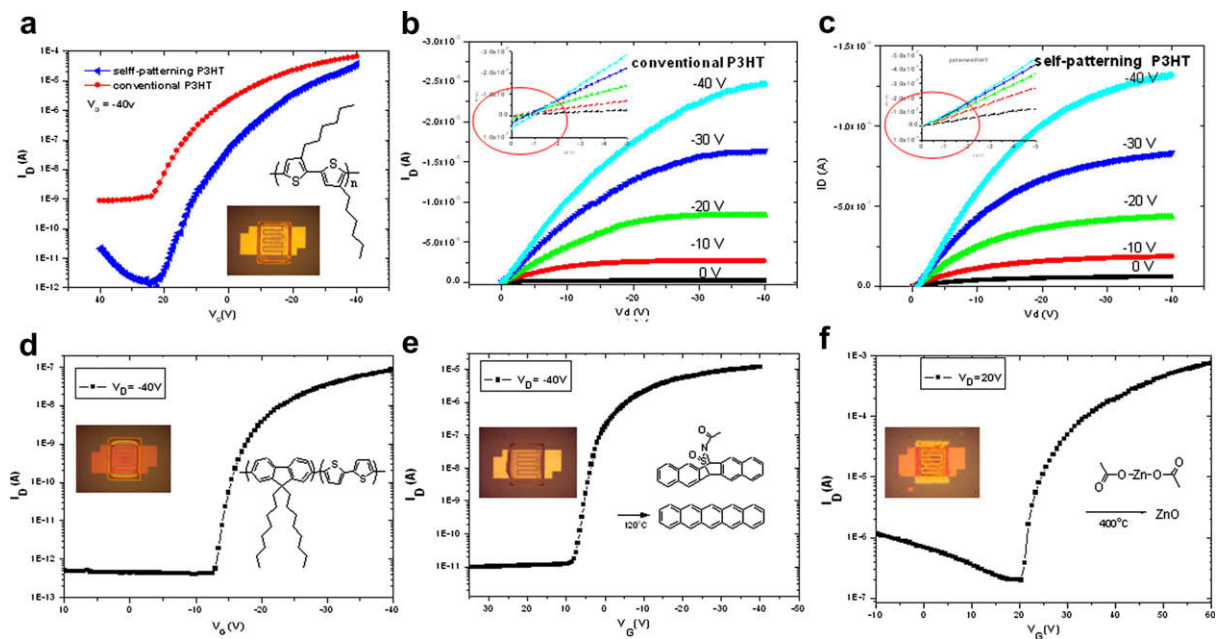


**Fig. 5.** (a) Transfer curves and (b and c) output curves of P3HT devices prepared on non-patterned and self-patterned semiconductor films. (d–f) Transfer curves of the (d) F8T2, (e) pentacene precursor, and (f) ZnO TFT devices.

$$\sqrt{I_{D,SAT}} = \sqrt{\frac{W\mu C_{ox}}{2L}}(V_G - V_{th}) \quad (1)$$

where  $I_{D,sat}$  is the saturated drain current,  $C_{ox}$  is the gate capacitance per unit area,  $W$  and  $L$  are the conducting channel width and length, respectively, and  $V_G$  is the applied gate voltage. We extracted the mobilities from the slopes of the linear plots of the square root of the drain current versus the gate voltage. The transfer curve of the non-patterned P3HT-OTFT device (Fig. 5a) exhibited an off current of  $10^{-9}$  A. The on/off ratio, the mobility, and the threshold voltage were  $8.9 \times 10^4$ ,  $3.2 \times 10^{-2} \text{ cm}^2 \text{ V}^{-1} \text{ s}^{-1}$ , and 8 V, respectively. For the patterned P3HT-OTFT device (also presented in Fig. 5a), the on/off ratio improved dramatically from  $8.9 \times 10^4$  to  $3.8 \times 10^7$ , with the off current decreasing from  $10^{-9}$  to  $10^{-12}$  A. We suspect that the off current was suppressed effectively as a result of self-patterning. The mobility of the patterned P3HT device decreased only slightly (to  $2.6 \times 10^{-2} \text{ cm}^2 \text{ V}^{-1} \text{ s}^{-1}$ ) relative to that of the non-patterned device ( $3.2 \times 10^{-2} \text{ cm}^2 \text{ V}^{-1} \text{ s}^{-1}$ ). The differences of mobilities caused by patterning of P3HT layer was also found by Jia et al. [17] Fig. 5b and c present the  $I_D$ - $V_D$  output characteristics of the non-patterned and self-patterned P3HT-OTFTs, respectively; the insets provide the drain current ( $I_D$ ) offset, defined as the value of  $I_D$  at various gate biases, when the drain voltage was zero [18]. Ideally, the value of the  $I_D$  offset would be zero when  $V_D$  is zero. For the non-patterned device (Fig. 5b inset), the value of the  $I_D$  offset increased when higher gate voltages were applied; the  $I_D$ - $V_D$  output curve in the linear region was clearly distorted. On the other hand, the  $I_D$ - $V_D$  output curve of the patterned device exhibited an ideal  $I_D$  offset (Fig. 5c inset), thanks to the patterning effect of the semiconductors. Note that

NSFAAP is transformed into pentacene through thermally degradation, and that ZnO films are formed from zinc acetate during high temperature annealing. Fig. 5d–f display the transfer curves of the F8T2, pentacene, and ZnO TFTs, respectively. The on/off ratio, mobility, and threshold voltage of the F8T2 device were  $2 \times 10^5$ ,  $2.1 \times 10^{-5} \text{ cm}^2 \text{ V}^{-1} \text{ s}^{-1}$ , and -5 V, respectively; for the pentacene-containing device, these values were  $7 \times 10^6$ ,  $3.5 \times 10^{-2} \text{ cm}^2 \text{ V}^{-1} \text{ s}^{-1}$ , and 7 V, respectively; for the ZnO-based device, they were  $3 \times 10^3$ ,  $0.31 \text{ cm}^2 \text{ V}^{-1} \text{ s}^{-1}$ , and 5 V, respectively. Thus, all of these OTFT devices exhibited moderate to good electrical characteristics after performing self-patterning, suggesting that this method has great potential for application to the preparation of large-area, low-cost organic electronic devices.

To determine the origins of the self-patterning effect, we determined the surface energies of the SAM-treated dielectrics by measuring their contact angles for distilled water and  $\text{CH}_2\text{I}_2$  as probe liquids and employing the geometric mean Eq. (2) [34]:

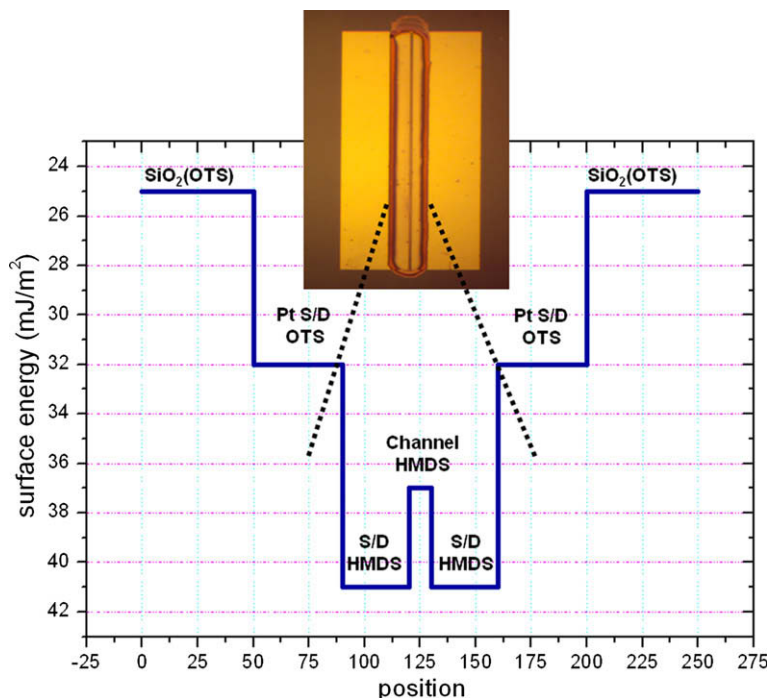
$$(1 + \cos \theta)\gamma_{pl} = 2(\gamma_s^d \gamma_{pl}^d)^{1/2} + 2(\gamma_s^p \gamma_{pl}^p)^{1/2} \quad (2)$$

where  $\gamma_s$  and  $\gamma_{pl}$  are the surface energies of the sample and probe liquid, respectively, and the superscripts  $d$  and  $p$  represent the dispersion and polar components of the surface energy, respectively. Table 1 summarizes the contact angles and surface energies of our various SAM-modified surfaces. The surface energies of the active regions (HMDS on  $\text{SiO}_2$ :  $37.4 \text{ mJ m}^{-2}$ ; HMDS on Pt:  $40.7 \text{ mJ m}^{-2}$ ) of the P3HT-OTFT devices were higher than those of the non-active regions (OTS on  $\text{SiO}_2$ :  $24.5 \text{ mJ m}^{-2}$ ; OTS on Pt:  $31.9 \text{ mJ m}^{-2}$ ). Because the surface energy is related to the absorbance of the surface, a surface having a high surface energy more readily absorbs the contacting liquid. Fig. 6

**Table 1**

Contact angles and surface energies of various SAM-modified surfaces.

Surface treatment	Contact angle		Surface energy (dispersion component) $\gamma_s^d$ (mJ m <sup>-2</sup> )	Surface energy (polar component) $\gamma_s^p$ (mJ m <sup>-2</sup> )	Surface energy (substrate) $\gamma_s$ (mJ m <sup>-2</sup> )
	Water(°)	CH <sub>2</sub> I <sub>2</sub> (°)			
Bare SiO <sub>2</sub>	61.5	53.9	32.1	14.6	46.7
Bare SiO <sub>2</sub> + HMDS	74.8	59.4	28.9	8.5	37.4
Bare SiO <sub>2</sub> + O <sub>2</sub> plasma	25.2	43.1	38.0	32.0	70.0
Bare SiO <sub>2</sub> + O <sub>2</sub> plasma + OTS	98.2	69.6	23.1	1.5	24.5
Bare Pt	86.9	40.8	37.2	1.6	40.8
Bare Pt + HMDS	85.2	41.9	38.6	2.1	40.7
Bare Pt + O <sub>2</sub> plasma	87.6	35.8	41.7	1.2	42.8
Bare Pt + O <sub>2</sub> plasma + OTS	95.0	56.0	30.9	1.0	31.9

**Fig. 6.** Surface energy diagram for the OTFT devices.

presents the surface energies of the HMDS/OTS-treated surfaces with S/D Pt electrodes (stripe pattern;  $W = 500 \mu\text{m}$ ,  $L = 10 \mu\text{m}$ ) as well as their relative locations. We observe that the contacting liquids more readily adhere to the HMDS surface with its higher surface energy than to the OTS surface with its lower surface energy. When we placed a drop of P3HT in dichlorobenzene onto the device substrate's surface, the droplet selectively wetted/adhered to the HMDS regions and dewetted the OTS regions. After decanting the substrate, the remaining P3HT solution was located (adhered) only on the areas of higher surface energy. As the solvent was evaporated, the P3HT film formed in the desired areas with confined features. The use of contacting liquids of other organic and inorganic semiconductors in either CHCl<sub>3</sub> or methoxyethanol, of PEDOT:PSS in aqueous solutions, and of PVP in PGMEA solution was also compatible with this method.

We note that both the HMDS- and OTS-SiO<sub>2</sub> surfaces possessed large water contact angles, i.e., the surfaces are

hydrophobic; therefore, aqueous solutions should not adhere to them at all. Indeed, several researchers have reported self-organization processes in which HMDS-SiO<sub>2</sub> [32] and OTS-SiO<sub>2</sub> [30,31] act as dewetting regions. In our case, however, the two HMDS- and OTS-SiO<sub>2</sub> surfaces provided a unique patterning platform for successful solution processing using a wide range of solvents. Therefore, the simple hydrophilic/hydrophobic interactions cannot explain our wetting phenomena. We believe that the surface energy interactions – considering the differences in surface energy of the two SAMs – is more suitable for explaining this self-patterning phenomenon.

#### 4. Conclusions

In summary, we have developed a solution-processable self-patterning method using a two-phase SAM-modified silicon dioxide surface for the deposition of a variety of

organic and inorganic materials from both organic and aqueous solutions. The resulting films were self-patterned in the desired regions with well-defined feature shapes. From analyses of substrates presenting S/D electrodes, all of our self-patterned TFT devices exhibited moderate to good electronic characteristics. This method has great potential for application to the fabrication of large-area, low-cost, fully-solution-processed electronics when combined with mature photolithographic technology for mass production. Surface energy interaction explains this self-patterning phenomenon more suitably than does a simple hydrophilic/hydrophobic interaction.

### Acknowledgments

The authors thank the Ministry of Economic Affairs (8351A11410) and the National Science Council (NSC97-2218-E-009-005) of the Republic of China for financially supporting this research.

### References

- [1] H. Sirringhaus, T. Kawase, R.H. Friend, T. Shimoda, M. Inbasekaran, W. Wu, E.P. Woo, *Science* 290 (2000) 2123.
- [2] L.-L. Chua, J. Zaumseil, J.-F. Chang, E.C.W. Ou, P.K.H. Ho, H. Sirringhaus, R.H. Friend, *Nature* 434 (2005) 194.
- [3] B. Crone, A. Dodabalapur, Y.-Y. Lin, R.W. Filas, Z. Bao, A. LaDuca, R. Sarpeshkar, H.E. Katz, W. Li, *Nature* 403 (2000) 521.
- [4] J.H. Burroughes, D.D.C. Bradley, A.R. Brown, R.N. Marks, K. Mackay, R.H. Friend, P.L. Burns, A.B. Holmes, *Nature* 347 (1990) 539.
- [5] A. Afzali, C.D. Dimitrakopoulos, T.O. Graham, *Adv. Mater.* 15 (2003) 2066.
- [6] A. Afzali, C.D. Dimitrakopoulos, T.L. Breen, *J. Am. Chem. Soc.* 124 (2002) 8812.
- [7] C.D. Dimitrakopoulos, P.R.L. Malenfant, *Adv. Mater.* 14 (2002) 99.
- [8] G. Horowitz, *Adv. Mater.* 10 (1998) 365.
- [9] A. Facchetti, *Mater. Today* 10 (3) (2007) 28.
- [10] S. Kobayashi, T. Nishikawa, T. Takenobu, S. Mori, T. Shimoda, T. Mitani, H. Shimotani, N. Yoshimoto, S. Ogswa, Y. Iwasa, *Nat. Mater.* 3 (2004) 317.
- [11] W.-Y. Chou, H.-L. Cheng, *Adv. Func. Mater.* 14 (2004) 811.
- [12] S.-Z. Weng, W.-S. Hu, C.-H. Kuo, Y.-T. Tao, L.-J. Fan, Y.-W. Yang, *Appl. Phys. Lett.* 89 (2006) 172103.
- [13] Y. Wu, P. Liu, B.S. Ong, T. Srikumar, N. Zhao, G. Botton, S. Zhu, *Appl. Phys. Lett.* 86 (2005) 142102.
- [14] S. Natalie, R.H. Friend, H. Sirringhaus, *Science* 299 (2003) 1881.
- [15] R. Parashkov, E. Becker, S. Hartmann, G. Ginev, D. Schneider, H. Krautwald, T. Dobbertin, D. Metzendorf, F. Brunetti, C. Schildknecht, A. Kammoun, M. Brandes, T. Riedl, H. Johannes, W. Kowalsky, *Appl. Phys. Lett.* 82 (2003) 4579.
- [16] Y.H. Kim, S.M. Han, W. Lee, M.K. Han, Y.U. Lee, J.I. Han, *Appl. Phys. Lett.* 91 (2007) 042113.
- [17] H. Jia, E.K. Gross, R.M. Wallace, B.E. Gnade, *Org. Electron.* 8 (2007) 44.
- [18] H. Jia, G.K. Pant, E.K. Gross, R.M. Wallace, B.E. Gnade, *Org. Electron.* 7 (2006) 16.
- [19] S.H. Han, J.H. Kim, J. Jang, S.M. Cho, M.H. Oh, S.H. Lee, D.J. Choo, *Appl. Phys. Lett.* 88 (2006) 73519.
- [20] L. Zhou, S. Park, B. Bai, J. Sun, S. Wu, T.N. Jackson, S. Nelson, D. Freeman, Y. Hong, *IEEE Dev. Lett.* 26 (2005) 640.
- [21] Y. Wang, H. Cheng, Y. Wang, T. Hu, J. Ho, C. Lee, T. Lei, C. Yeh, *Thin Solid Films* 491 (2005) 305.
- [22] J.S. Lewis, M.S. Weaver, *IEEE J. Selected Topics Quantum Electron.* 10 (2004) 45.
- [23] D.A. Pardo, G.E. Jabbour, N. Peyghambarian, *Adv. Mater.* 12 (2000) 1249.
- [24] Z. Bao, J.A. Rogers, H.E. Katz, *J. Mater. Chem.* 9 (1999) 1895.
- [25] M.L. Chabinyc, A. Salleo, Y. Wu, P. Liu, B.S. Ong, M. Heeney, I. McCulloch, *J. Am. Chem. Soc.* 126 (2004) 13928.
- [26] D.G. Lidzey, M. Voigt, C. Giebeler, A. Buckley, J. Wright, K. Bohlen, J. Fieret, R. Allott, *Org. Electron.* 6 (2005) 221.
- [27] H. Kobayashi, T. Shimoda, H. Kiguchi, *World Pat. WO* 99/46961, 1999.
- [28] C. Kim, P.E. Burrows, S.R. Forrest, *Science* 288 (2000) 831.
- [29] A.L. Briseno, M. Robert, M.M. Ling, H. Moon, E.J. Nemanick, Z. Bao, *J. Am. Chem. Soc.* 123 (2006) 3880.
- [30] H.Y. Choi, S.H. Kim, J. Jang, *Adv. Mater.* 16 (2004) 732.
- [31] A. Salleo, A.C. Arias, *Adv. Mater.* 19 (2007) 3540.
- [32] T. Minari, M. Kano, T. Miyadera, S.D. Wang, Y. Aoyagi, M. Seto, T. Nemoto, S. Isoda, K. Tsukagoshi, *Appl. Phys. Lett.* 92 (2008) 173301.
- [33] S.H. Kim, D. Choi, D.S. Chung, C. Yang, J. Jang, C.E. Park, S.H.K. Park, *Appl. Phys. Lett.* 93 (2008) 113306.
- [34] F.M. Fowkes, in: R.L. Patrick (Ed.), *Treatise on Adhesion and Adhesives*, vol. 1, Marcel Dekker, New York, 1967, p. 352.

Television System Committee (NTSC) blue color standard (0.14, 0.08).

It is extremely difficult to produce highly efficient blue light emitters with long device life-times because, with a wide band gap, their electronic levels are likely to be mismatched with the highest occupied molecular orbital (HOMO) and lowest unoccupied molecular orbital (LUMO) levels of the other OLED layers such as the hole transporting layer (HTL) and the electron transporting layer (ETL). These differences between the electronic levels result in a mismatched carrier balance of electrons and holes, and a low EL efficiency and short life-time.

Many types of blue light emitting derivatives of diaryl-anthracene [16], di(styryl)arylene [17], fluorene [18], pyrene [19], and fluoranthene [20] have been intensively investigated, and attempts have been made to improve their EL properties. The commercial product 4,4-bis(2,2-diphenylvinyl)-1,1-biphenyl (DPVBi) [17] has a low glass transition temperature ( $T_g$ ) of 64 °C [17b], undergoes recrystallization after long operation, and has a shorter device life-time than green and red light emitters. Another well known blue compound, 2-methyl-9,10-di(2'-naphthyl)anthracene (MADN) [21], has a high  $T_g$ , a longer life-time and better CIE<sub>x,y</sub> coordinates than DPVBi; however, MADN has low luminance efficiency, which reduces its utility in full color displays. Thus, much research is being directed at developing a new high efficiency blue light emitter.

Cheng and coworkers reported pyrene derivatives with color coordinates of (0.15, 0.11) and a maximum external quantum efficiency (EQE) of 5.2% [22], and Jenekhe and coworkers described oligoquinoline derivatives with a very high EQE (6.56%) and color coordinates of (0.15, 0.16) [23].

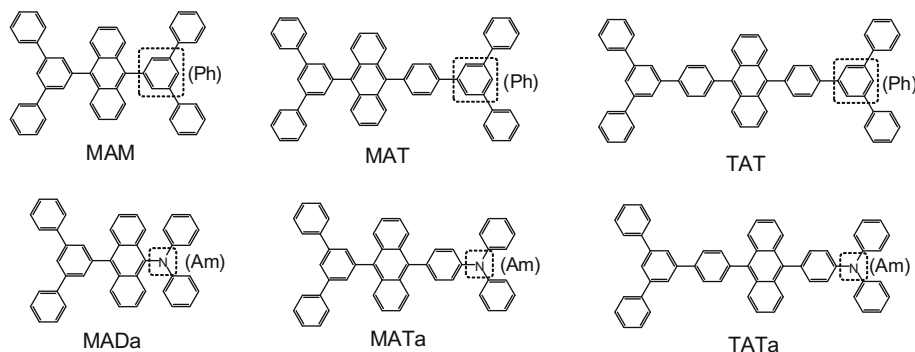
Highly efficient synthetic blue light emitters with an anthracene core and *m*-terphenyl or triphenylbenzene side groups have recently been reported [24,25]. The synthesized compounds are 10-bis(3',5'-diphenylphenyl)anthracene (MAM), 9-(3',5'-diphenylphenyl)-10-(3''',5'''-diphenylbiphenyl-4''-yl) anthracene (MAT), and 9,10-bis(3'',5''-diphenylbiphenyl-4''-yl)anthracene (TAT) (Scheme 1).

An aromatic ring in the meta rather than the para position was selected because the former has a shorter conjugation length; this is advantageous because it reduces the *y*-CIE coordinate value of the emitter [26]. In addition, the introduction of a bulky and non-planar side group prevents  $\pi$ - $\pi^*$  stacking interactions, which leads to the

formation of more reliable amorphous films [22,27]. This is expected to have a positive effect on the life-time of operating OLED devices. Furthermore, the absolute PL quantum efficiency of the *m*-terphenyl group is 0.29 [28], which is higher than that of the more commonly used naphthalene group (0.21) [29], so an increase in EL efficiency is expected. Interestingly, as the photoluminescence efficiency of the side groups has increased, the performance of the synthesized blue light emitters has also improved substantially. In particular, TAT had a higher PL fluorescence quantum efficiency (QE) than MADN, and had a  $T_g$  more than 30 °C that of MADN. Its color coordinates (0.156, 0.088) meet the NTSC blue standard, and it exhibits an excellent EQE value (7.18%) about twice that of MADN; these are the best reported results for non-doping deep-blue fluorescence OLED emitter [25]. Thus, large variations in device efficiency have been found for compounds with the same core but different side groups, confirming the importance of the latter.

In this study, a phenyl group (Ph) in three synthetic blue light emitters reported in a previous study was changed to an amine group (Am) to produce three new emitting compounds. Thus, three types of organic compound with asymmetric structure were synthesized by substituting an *m*-terphenyl group with a diphenylamine group, and a triphenylbenzene group with a triphenylamine group. This gave rise to the synthetic compounds 10-(3,5-diphenylphenyl)-*N,N*-diphenylanthracen-9-amine (MADa), 4-(10-(3,5-diphenylphenyl)anthracen-9-yl)-*N,N*-diphenylaniline (MATa), and 4-(10-(3',5'-diphenylbiphenyl-4-yl)anthracen-9-yl)-*N,N*-diphenylaniline (TATa), where M, A, T, Da and Ta denote *m*-terphenyl, anthracene, triphenylbenzene, diphenylamine, and triphenylamine, respectively (Scheme 1). It was hypothesized that addition of an amine unit [12] commonly contained by other highly efficient blue dopants could increase the luminance efficiency of the three synthesized compounds. In addition, the bulky side group could prevent interactions between molecules, and potentially enhance the formation of more reliable amorphous films. The syntheses was also undertaken to address one of the biggest issues with blue light emitters, namely that of increasing device life-time.

The thermal, electrochemical and spectroscopic properties of the synthesized materials were characterized using differential scanning calorimetry (DSC), thermogravimetric



**Scheme 1.** Chemical structures of the synthesized materials.

analysis (TGA), cyclic voltammetry (CV), atomic force microscopy (AFM), and UV–visible and photoluminescence (PL) spectroscopy. Multi-layered EL devices were fabricated using the materials as non-doped emitting layers.

## 2. Experimental

### 2.1. General Information

$^1\text{H}$  nuclear magnetic resonance (NMR) spectra were recorded on Bruker Avance 300 and Avance 500 spectrometers. Fourier transform infrared spectroscopy (FT-IR) spectra were recorded on a Thermo Electron Nicolet IR-200 spectrometer. Fast atom bombardment (FAB<sup>+</sup>) and positive electron impact (EI<sup>+</sup>) spectra were recorded on a JEOL, JMS-AX505WA, HP5890 series II mass spectrometer. The optical absorption spectra were obtained with a HP 8453 UV–VIS–NIR spectrometer. Crystals of MATa and TATA were obtained from THF/hexane at room temperature, sealed in glass capillaries under nitrogen, and mounted in a diffractometer. The ground state geometries were fully optimized using density functional theory (DFT) [32] with the B3LYP hybrid functional at the basis set level of 6-31G\*. All calculations were performed using Gaussian 03 software [32c] on a PowerLeader workstation. Atomic force microscopy (AFM) imaging was performed in air using a PicoScan system (Molecular Imaging) equipped with a 5 × 5 μm scanner. Magnetic-ac(Mac) mode (a non-contact mode) was used for all the AFM images. The melting temperatures ( $T_m$ ), glass transition temperatures ( $T_g$ ), and degradation temperatures ( $T_d$ ) of the compounds were measured by differential scanning calorimetry (DSC) under a nitrogen atmosphere using a DSC2910 differential calorimeter (TA Instruments), and thermogravimetric analysis (TGA) was performed using a SDP-TGA2960 (TA Instruments). The redox potentials of the compounds were determined by cyclic voltammetry (CV) using an EG&G 362 electrochemical workstation with a scanning rate of 50–200 mV/s. The synthesized materials were dissolved in *N,N*-dimethylformamide (DMF) with 0.1 M tetrabutylammonium tetrafluoroborate as the electrolyte. We used a platinum working electrode and a saturated Ag/AgNO<sub>3</sub> reference electrode. Ferrocene was used for potential calibration and for reversibility criteria. A Perkin Elmer luminescence spectrometer LS50 (Xenon flash tube) was used for photo- and electro-luminescence spectroscopy, and to determine the fluorescence quantum yields ( $\phi_F$ ) [30]:

$$\Phi_{F(A)} = \Phi_{F(\text{ref})} \times \frac{PL_A}{UV_A} \times \frac{UV_{\text{ref}}}{PL_{\text{ref}}} \times \left( \frac{\eta_A}{\eta_{\text{ref}}} \right)^2 \quad (1)$$

where  $\phi_{F(\text{ref})} = 1.00$  (relative PL quantum efficiency ( $\phi_F$ ) of MADN in ethanol solution);  $\phi_{F(A)}$  is relative  $\phi_F$  in ethanol solution of synthesized materials;  $PL_A$  and  $PL_{\text{ref}}$  are the integrated emission intensities of the sample and the standard, respectively;  $UV_A$  and  $UV_{\text{ref}}$  are the absorbances of the sample and the standard at the excitation wavelength, respectively; and  $\eta_A$  and  $\eta_{\text{ref}}$  are the refractive indexes of the corresponding solutions (pure solvents were assumed).

The diffraction experiments were carried out on a Rigaku R-AXIS RAPID diffractometer equipped with a Mo-K $\alpha$

and Control Software using the RAPID AUTO at 293 ( $\pm 2$ ) °C. Empirical absorption corrections were applied automatically. The structures were solved with direct methods and refined with a full-matrix least-squares technique using the SHELXS v. 5.1 programs [33]. The space groups were determined from the systematic absences and their correctness was confirmed by successful solution and refinement of structures. Anisotropic thermal parameters were refined for all the non-hydrogen atoms. The hydrogen atoms were added in idealized position and refined with isotropic displacement.

For the EL devices, all organic layers were deposited under 10<sup>−6</sup> torr at a deposition rate of 1 Å/s, to give an emitting area of 4 mm<sup>2</sup>. The LiF and aluminum layers were subsequently deposited under the same vacuum conditions. The current–voltage (*I*–*V*) characteristics of the fabricated EL devices were obtained using a Keithley 2400 electrometer. The light intensities were determined using a Minolta CS-1000A. OLED device was encapsulated for life-time with glass-lid under the nitrogen.

### 2.2. Single crystal X-ray diffraction data

(MATa): Empirical formula: C50 H35N, formula weight: 649, temperature: 293(2)K, wavelength: 0.71073 Å, crystal system, space group: monoclinic, *P*2(1)/*c*, unit cell dimensions:  $a = 10.468(2)$  Å,  $b = 19.184(4)$  Å,  $c = 17.903(4)$  Å,  $\alpha = 90^\circ$ ,  $\beta = 100.70(3)^\circ$ ,  $\gamma = 90^\circ$ , volume: 3532.7(12) Å<sup>3</sup>, *Z*, calculated density: 1.04, 1.321 Mg/m<sup>3</sup>, absorption coefficient: 0.093 mm<sup>−1</sup>, *F*(0 0 0): 1456, crystal size: 0.109 × 0.138 × 0.276 mm,  $\theta$  range for data collection: 3.14–27.47°, limiting indices:  $-13 < h < 13$ ,  $-24 < k < 20$ ,  $-23 < l < 23$ , reflections collected/unique: 5934/5934 [*R*(int) = 0.0000], completeness to  $\theta = 27.48$ : 99.0%, refinement method: full-matrix least-squares on *F*<sup>2</sup>, data/restraints/parameters: 8019/0/460, goodness-of-fit on *F*<sup>2</sup>: 0.825, final *R* indices [*I* > 2 $\sigma$ (*I*): *R*1 = 0.0695, *wR*2 = 0.1994, *R* indices (all data): *R*1 = 0.1882, *wR*2 = 0.2943.

(TATA): Empirical formula: C56 H39N, formula weight: 725, temperature: 293(2) K, wavelength: 0.71073 Å, crystal system, space group: triclinic, *P*1̄, unit cell dimensions:  $a = 9.900(2)$  Å,  $b = 14.436(3)$  Å,  $c = 17.901(4)$  Å,  $\alpha = 103.22(3)^\circ$ ,  $\beta = 104.72(3)^\circ$ ,  $\gamma = 107.03(3)^\circ$ , volume: 2235.1(8) Å<sup>3</sup>, *Z*, calculated density: 0.66, 1.349 Mg/m<sup>3</sup>, absorption coefficient: 0.097 mm<sup>−1</sup>, *F*(0 0 0): 940, crystal size: 0.108 × 0.189 × 0.394 mm,  $\theta$  range for data collection: 3.11–27.48°, limiting indices:  $-12 < h < 12$ ,  $-18 < k < 18$ ,  $-22 < l < 23$ , reflections collected/unique: 22145/10099 [*R*(int) = 0.0913], completeness to  $\theta = 27.48$ : 98.5%, refinement method: full-matrix least-squares on *F*<sup>2</sup>, data/restraints/parameters: 10099/0/559, goodness-of-fit on *F*<sup>2</sup>: 0.917, Final *R* indices [*I* > 2 $\sigma$ (*I*): *R*1 = 0.1072, *wR*2 = 0.2756, *R* indices (all data): *R*1 = 0.2556, *wR*2 = 0.3674.

### 2.3. Synthesis

#### 2.3.1. Synthesis of compound 1

Bromobenzene (30 mL, 0.28 mol) was added in 300 mL of dry THF solution and stirred at −78 °C, then 1.6 M *n*-BuLi

(260 mL) was added. Next, isopropoxy-4,4,5,5-tetramethyl-1,3,2-dioxaborolane (87 mL, 0.42 mol) was added to the reaction mixture after 30 min. After the reaction had finished, the reaction mixture was extracted with diethyl ether and water. The organic layer was dried with anhydrous  $\text{MgSO}_4$  and filtered. The mixture was evaporated. The residue was purified by column chromatography with  $\text{CHCl}_3$ :*n*-hexane (1:1) eluent to afford colorless solution (compound **1**) (50 g, 87%).  $^1\text{H}$  NMR (500 $\text{CDCl}_3$ ,  $\delta$ ): 7.81 (d, 2H), 7.41 (t, 1H), 7.33 (t, 2H), 1.30 (s, 12H),  $\text{EI}^+$ -Mass: 204.

### 2.3.2. Synthesis of compound 2

Compound **1** (32 g, 155 mmol), 1,3,5-tribromobenzene (20 g, 62 mmol), and  $\text{Pd}(\text{PPh}_3)_4$  (3.57 g, 3.1 mmol) were added to 300 mL of dry THF solution, then 2 M  $\text{K}_2\text{CO}_3$  solution (50 mL) was added to reaction mixture. The mixture was heated to 65 °C for 5 h under nitrogen. After the reaction finished, the reaction mixture was extracted with diethyl ether and water. The organic layer was dried by anhydrous  $\text{MgSO}_4$  and filtered. The solution was evaporated. The product was isolated by silicagel column chromatography using  $\text{CHCl}_3$ :*n*-hexane (1:19) eluent to afford white solid (compound **2**) (12 g, 62.4 %)  $^1\text{H}$  NMR (300 $\text{CDCl}_3$ ,  $\delta$ ): 7.70 (s, 3H), 7.60 (d, 4H), 7.46 (t, 4H), 7.36 (t, 2H),  $\text{EI}^+$ -Mass: 310.

### 2.3.3. Synthesis of compound 3

Compound **2** (12 g, 38.7 mmol) was added in 300 mL of dry THF solution and stirred at –78 °C, then 1.6 M *n*-BuLi (36 mL) was added. Next, isopropoxy-4,4,5,5-tetramethyl-1,3,2-dioxaborolane (12 mL, 58 mmol) was added to the reaction mixture after 30 min. After the reaction had finished, the reaction mixture was extracted with diethyl ether and water. The organic layer was dried with anhydrous  $\text{MgSO}_4$  and filtered. The mixture was evaporated. The precipitate was filtered and washed with an excess of methanol. The yellowish powder was purified by using column chromatography with  $\text{CHCl}_3$ :*n*-hexane (1:1) eluent to afford white solid (compound **3**) (13 g, 94%).  $^1\text{H}$  NMR (500 $\text{CDCl}_3$ ,  $\delta$ ): 8.03 (s, 2H), 7.90 (s, 1H), 7.69 (d, 4H), 7.44 (t, 4H), 7.35 (t, 2H), 1.37 (s, 12H)  $\text{EI}^+$ -Mass: 356.

### 2.3.4. Synthesis of compound 4

Compound **3** (3 g, 8.4 mmol), 9-bromoanthracene (2.37 g, 9.25 mmol),  $\text{Pd}(\text{OAc})_2$  (0.190 g, 0.85 mmol), and (cyclohexyl) $_3\text{P}$  (0.22 g, 0.85 mmol) were added toluene (150 mL) solution, then tetraethylammonium hydroxide (20 wt%) 10 mL was added to the reaction mixture. The mixture was heated to 110 °C for 2 h under nitrogen. After the reaction had finished, the reaction mixture was extracted with chloroform and water. The organic layer was dried with anhydrous  $\text{MgSO}_4$  and filtered. The solution was evaporated. The residue was re-dissolved in  $\text{CHCl}_3$  and added to methanol. The precipitate was filtered and washed with methanol. The yellowish powder was purified by using column chromatography with  $\text{CHCl}_3$ :*n*-hexane (1:5) eluent to afford a beige solid (compound **4**) (3.1 g, 90.9 %).  $^1\text{H}$  NMR (500 $\text{CDCl}_3$ ,  $\delta$ ): 8.53 (s, 1H), 8.06 (d, 2H), 8.01 (t, 1H), 7.83 (d, 2H), 7.74 (m, 4H), 7.68 (d, 2H), 7.46 (m, 6H), 7.36 (m, 4H),  $\text{Fab}^+$ -Mass: 406.

### 2.3.5. Synthesis of compound 5

Compound **4** (2 g, 4.92 mmol) and NBS (0.98 g, 5.5 mmol) were added to 150 mL of  $\text{CHCl}_3$  solution. The mixture was heated to 60 °C for 30 min under nitrogen. After the reaction had finished, solution was evaporated. The residue was re-dissolved in acetone and added to methanol. The precipitate was filtered and washed with methanol to get compound **5** of yellowish color. (2.3 g, 96.4 %).  $^1\text{H}$  NMR (500 $\text{CDCl}_3$ ,  $\delta$ ): 8.64 (d, 2H), 8.02 (t, 1H), 7.82 (d, 2H), 7.74 (m, 4H), 7.62 (d, 2H), 7.60 (m, 2H), 7.44 (m, 8H),  $\text{Fab}^+$ -Mass: 486.

### 2.3.6. Synthesis of MAMA

Compound **5** (1 g, 2.06 mmol), diphenylamine (0.51 g, 3.0 mmol), *t*-BuONa (0.58 g, 6.18 mmol), and  $\text{Pd}_2(\text{dba})_3$  (0.05 g, 0.6 mmol) were added to dried toluene solvent (150 mL), then (t-Bu) $_3\text{P}$  was added into the reaction mixture. The mixture was heated to 110 °C for 1 h under nitrogen. After the reaction mixture cooled, it was then acidified with 1 N HCl solution, and extracted with  $\text{CHCl}_3$ . The organic layer was dried by anhydrous  $\text{MgSO}_4$  and filtered. The solution was evaporated. The residue was dissolved in  $\text{CHCl}_3$  and added to acetone. The precipitate was filtered and washed with acetone. The dark yellow residue was purified by column chromatography with  $\text{CHCl}_3$ :*n*-hexane (1:1) eluent to afford yellowish-green solid (MAMA) (0.9 g, 76.5%).  $^1\text{H}$  NMR (500 $\text{CDCl}_3$ ,  $\delta$ ): 8.21 (d, 2H), 8.03 (s, 1H), 7.88 (d, 2H), 7.75 (q, 6H), 7.47 (t, 4H), 7.36 (m, 6H), 7.17 (m, 8H), 6.89 (t, 2H),  $^{13}\text{C}$  NMR (500 $\text{CDCl}_3$ ,  $\delta$ ): 147.96, 142.04, 140.94, 139.91, 136.61, 137.48, 131.63, 130.62, 129.41, 129.28, 129.11, 127.87, 127.55, 126.73, 125.77, 125.36, 124.64, 121.41, 120.46,  $\text{Fab}^+$ -Mass: 574, FI-IR (KBr,  $\text{cm}^{-1}$ ): 3061 (s, C–H stretch), 3032 (s), 1589 (m, C=C aromatic), 1496 (m), 1275 (m, C–N stretch), 751 (s, meta-sub aromatic), 694 (m, 1,3,5-sub aromatic).

### 2.3.7. Synthesis of compound 6

4-Bromo-N,N-diphenylaniline (8 g, 24.7 mmol) was added in 300 mL of dry THF solution and stirred at –78 °C, then 1.6 M *n*-BuLi (31 mL) was added. Next, isopropoxy-4,4,5,5-tetramethyl-1,3,2-dioxaborolane (10.3 mL, 50 mmol) was added to the reaction mixture after 30 min. After the reaction had finished, the reaction mixture was extracted with diethyl ether and water. The organic layer was dried with anhydrous  $\text{MgSO}_4$  and filtered. The mixture was evaporated. The residue was purified by column chromatography with EA:*n*-hexane (1:1) eluent to afford colorless solution (compound **6**) (5.0 g, 54.6%).  $^1\text{H}$  NMR (500 $\text{CDCl}_3$ ,  $\delta$ ): 7.87 (d, 2H), 7.22 (m, 4H), 7.10 (m, 6H), 6.97 (t, 2H), 1.32 (s, 12H),  $\text{EI}^+$ -Mass: 372.

### 2.3.8. Synthesis of MATA

Compound **5** (1.5 g, 3.1 mmol), compound **6** (1.26 g, 3.4 mmol),  $\text{Pd}(\text{OAc})_2$  (0.145 g, 0.65 mmol), and (cyclohexyl) $_3\text{P}$  (0.16 g, 0.65 mmol) were added toluene (200 mL) solution, then tetraethylammonium hydroxide (20 wt%) 10 mL was added to the reaction mixture. The mixture was heated to 110 °C for 5 h under nitrogen. After the reaction had finished, the reaction mixture was extracted with chloroform and water. The organic layer was dried with anhydrous  $\text{MgSO}_4$  and filtered. The solution

was evaporated. The residue was re-dissolved in  $\text{CHCl}_3$  and added to acetone. The precipitate was filtered and washed with acetone. The yellowish powder was purified by using column chromatography with  $\text{CHCl}_3$ :*n*-hexane (1:3) eluent to afford a greenish-yellow solid (MATa) (1.2 g, 59.6 %).  $^1\text{H}$  NMR (500 $\text{CDCl}_3$ ,  $\delta$ ): 8.02 (s, 1H), 7.87 (m, 4H), 7.74 (t, 6H), 7.46 (t, 4H), 7.34 (m, 18H), 7.08 (t, 2H),  $^{13}\text{C}$  NMR(500 $\text{CDCl}_3$ ,  $\delta$ ): 148.02, 147.40, 142.02, 141.04, 140.36, 137.43, 136.85, 132.81, 132.34, 130.34, 130.20, 129.61, 129.31, 129.10, 127.81, 127.54, 127.34, 127.24, 125.45, 125.26, 124.92, 123.32,  $\text{Fab}^+$ -Mass: 649, FI-IR (KBr,  $\text{cm}^{-1}$ ): 3059 (s, C–H stretch), 3031 (s), 1589 (m, C=C aromatic), 1497 (m), 1275 (m, C–N stretch), 761 (s, meta-sub aromatic), 670 (m, 1,3,5-sub aromatic).

### 2.3.9. Synthesis of compound 7

Compound **3** (8 g, 22.5 mmol), 1,4-dibromobenzene (50 g, 212 mmol), and  $\text{Pd}(\text{PPh}_3)_4$  (1.3 g, 1.125 mmol) were added to THF (400 mL) solution, then 2 M  $\text{K}_2\text{CO}_3$  solution (50 mL), which was dissolved in  $\text{H}_2\text{O}$ , was added to the reaction mixture. The mixture was heated to 65 °C for 4 h under nitrogen. After the reaction finished, the reaction mixture was extracted with diethyl ether and water. The organic layer was dried by anhydrous  $\text{MgSO}_4$  and filtered. The solution was evaporated. The product was isolated by silicagel column chromatography using  $\text{CHCl}_3$ :*n*-hexane (1:10) eluent to afford white solid (compound **7**) (5 g, 57.7%).  $^1\text{H}$  NMR (500 $\text{CDCl}_3$ ,  $\delta$ ): 7.79 (s, 1H), 7.73 (s, 2H), 7.68 (d, 4H), 7.60 (d, 2H), 7.56 (d, 2H), 7.48 (t, 4H), 7.39 (t, 2H),  $\text{Fab}^+$ -Mass: 385.

### 2.3.10. Synthesis of compound 8

Compound **7** (3 g, 7.8 mmol), anthracen-9-ylboronic acid (1.55 g, 7.0 mmol),  $\text{Pd}(\text{OAc})_2$  (0.175 g, 0.78 mmol), and  $(\text{cyclohexyl})_3\text{P}$  (0.20 g, 0.78 mmol) were added toluene (150 mL) solution, then tetraethylammonium hydroxide (20 wt%) 10 mL was added to the reaction mixture. The mixture was heated to 110 °C for 2 h under nitrogen. After the reaction had finished, the reaction mixture was extracted with chloroform and water. The organic layer was dried with anhydrous  $\text{MgSO}_4$  and filtered. The solution was evaporated. The residue was re-dissolved in  $\text{CHCl}_3$  and added to methanol. The precipitate was filtered and washed with methanol. The yellowish powder was purified by using column chromatography with  $\text{CHCl}_3$ :*n*-hexane (1:5) eluent to afford a beige solid (compound **8**) (2.8 g, 82.8 %).  $^1\text{H}$  NMR (500 $\text{CDCl}_3$ ,  $\delta$ ): 8.52 (s, 1H), 8.07 (d, 2H), 7.96 (s, 2H), 7.93 (d, 2H), 7.86 (s, 1H), 7.77 (t, 6H), 7.55 (d, 2H), 7.50 (m, 6H), 7.39 (m, 4H),  $\text{Fab}^+$ -Mass: 483.

### 2.3.11. Synthesis of compound 9

Compound **8** (2 g, 4.14 mmol), NBS (0.89 g, 5 mmol) were added to 150 mL of  $\text{CHCl}_3$  solution. The mixture was heated to 60 °C for 30 min under nitrogen. After the reaction had finished, solution was evaporated. The residue was re-dissolved in acetone and added to methanol. The precipitate was filtered and washed with methanol to get compound **9** of yellowish color. (2.3 g, 98.8 %).  $^1\text{H}$  NMR (500 $\text{CDCl}_3$ ,  $\delta$ ): 8.64 (d, 2H), 7.95 (s, 2H), 7.93 (d, 2H), 7.86 (s, 1H), 7.76 (t, 6H), 7.61 (t, 2H), 7.52 (m, 6H), 7.42 (m, 4H),  $\text{Fab}^+$ -Mass: 562.

### 2.3.12. Synthesis of TATA

Compound **9** (1.74 g, 3.1 mmol), compound **6** (1.26 g, 3.4 mmol),  $\text{Pd}(\text{OAc})_2$  (0.145 g, 0.65 mmol), and  $(\text{cyclohexyl})_3\text{P}$  (0.16 g, 0.65 mmol) were added toluene (200 mL) solution, then tetraethylammonium hydroxide (20 wt%) 10 mL was added to the reaction mixture. The mixture was heated to 110 °C for 5 h under nitrogen. After the reaction had finished, the reaction mixture was extracted with chloroform and water. The organic layer was dried with anhydrous  $\text{MgSO}_4$  and filtered. The solution was evaporated. The residue was re-dissolved in  $\text{CHCl}_3$  and added to acetone. The precipitate was filtered and washed with acetone. The yellowish powder was purified by using column chromatography with  $\text{CHCl}_3$ :*n*-hexane (1:3) eluent to afford a greenish-yellow solid (TATA) (1.2 g, 59.6 %).  $^1\text{H}$  NMR (500 $\text{CDCl}_3$ ,  $\delta$ ): 7.98 (s, 2H), 7.95 (d, 2H), 7.87 (d, 3H), 7.78 (t, 6H), 7.60 (d, 2H), 7.51 (t, 4H), 7.74(m, 6H), 7.34(m, 6H), 7.30(m, 6H), 7.08(t, 2H),  $^{13}\text{C}$  NMR(500 $\text{CDCl}_3$ ,  $\delta$ ): 148.03, 147.39, 142.70, 142.26, 141.38, 140.43, 138.67, 137.37, 136.72, 132.82, 132.34, 132.12, 130.34, 130.12, 129.62, 129.12, 127.83, 127.62, 127.56, 127.35, 127.20, 125.53, 125.45, 125.35, 125.23, 124.92, 123.32,  $\text{Fab}^+$ -Mass: 726, FI-IR (KBr,  $\text{cm}^{-1}$ ): 3058 (s, C–H stretch), 3032 (s), 1592 (m, C=C aromatic), 1391 (m), 1275 (m, C–N stretch), 764 (s, meta-sub aromatic), 671 (m, 1,3,5-sub aromatic).

## 3. Results and discussion

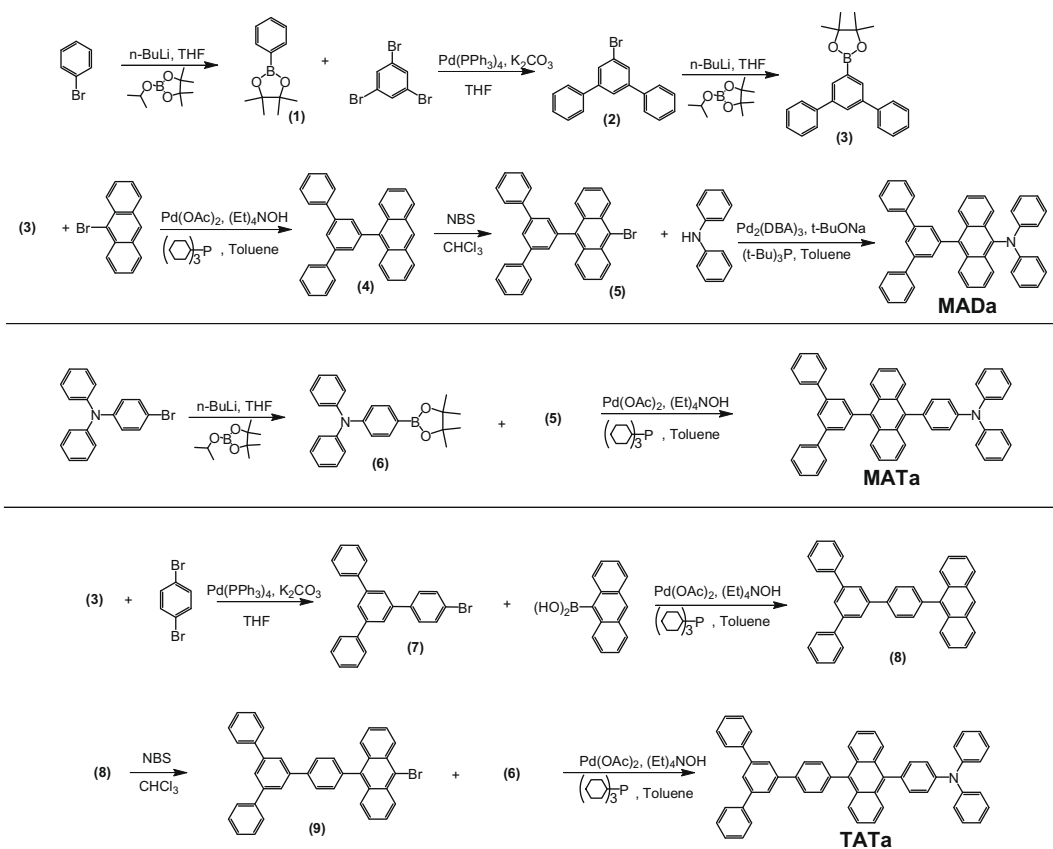
### 3.1. Synthesis and optical properties

**Scheme 1** shows the chemical structures of the synthesized compounds, which were purified by using silica column chromatography and re-crystallization to produce very pure powders that were characterized by NMR, FT-IR and FAB mass spectrometry analysis (overall yields: 50–60%).

The synthetic routes to the three compounds are shown in **Scheme 2**. Boration and metal aryl–aryl coupling reactions were used in all syntheses. As the bulky side groups 5-bromo-[1,13,1]terphenyl (compound **2**) and 5-(*p*-bromophenyl)-[1,13,1]terphenyl (compound **7**) are substituted with halogens, it was easy to couple them with anthracene by using the metal-catalyzed aryl–aryl coupling reaction. Thus, the side groups can be incorporated in other core molecular structures. Asymmetrical compounds have the disadvantage of being generally difficult to separate from the many compounds created at the time of synthesis. However, the asymmetric compounds in this study were synthesized with relative ease and high yield using a combination of compounds **2** and **7**; this should be of considerable value to asymmetric compounds research involving functional organic materials.

The UV and PL spectra of the synthesized compounds in  $\text{CHCl}_3$  solution and in thin films are shown in **Table 1**. In solution, MATa and TATA had a  $\text{UV}_{\text{max}}$  of 398 nm and a blue  $\text{PL}_{\text{max}}$  of about 475 nm. However, MADA had a  $\text{UV}_{\text{max}}$  of 428 nm and a  $\text{PL}_{\text{max}}$  of 509 nm, indicating a red shift of about 35 nm relative to MATa and TATA. The PL spectra of the compounds in thin films, fabricated by vacuum





Scheme 2. Synthetic routes of MADA, MAMA and TATA.

Table 1

Optical, electrical and thermal properties of the synthesized compounds and MADN.

	$\text{UV}_{\text{max}}^a$ (nm)	$\text{PL}_{\text{max}}^a$ (nm)	Solution $\varphi_F^b$	$\text{UV}_{\text{max}}^c$ (nm)	$\text{PL}_{\text{max}}^c$ (nm)	FWHM (nm)	HOMO (eV)	LUMO (eV)	$E_g$ (eV)	$T_g$ ( $^\circ\text{C}$ )	$T_m$ ( $^\circ\text{C}$ )	$T_d$ ( $^\circ\text{C}$ )
MADa	428	509	0.92	441	498	63	5.44	2.82	2.62	125	271	374
MATa	398	474	0.76	403	463	57	5.35	2.48	2.87	130	305	427
TATa	398	476	1.02	403	463	56	5.37	2.50	2.87	139	272	479
MADN	398	436	1.00	405	447	60	5.5 <sup>d</sup>	2.5 <sup>d</sup>	3.0 <sup>d</sup>	120 <sup>d</sup>	255 <sup>d</sup>	397 <sup>d</sup>

<sup>a</sup>  $\text{CHCl}_3$  Solution ( $1.00 \times 10^{-5}$  M).<sup>b</sup> Relative  $\varphi_F$  in ethanol solution (Ref. [30]).<sup>c</sup> Film on glass (500 nm).<sup>d</sup> Ref. [21].

deposition, showed that MATa and TATA had a  $\text{PL}_{\text{max}}$  in the blue region at 463 nm, and MADa had a  $\text{PL}_{\text{max}}$  at 498 nm, the latter again representing a red shift of about 35 nm. All three synthesized compounds showed a PL wavelength that was red shifted 10 nm in solution compared to the film. Since there is a  $\pi$ - $\pi^*$  interaction between molecules in a film, this state typically shows red shifts relative to molecules in solution. The amine unit in the synthesized compounds created a dipole within the molecule and with the solvent, which in solution may have resulted in the red shift in the PL spectrum. In a previous study, PL spectra of MAM, MAT and TAT without the amine unit showed normal red shifts in the film relative to in solution [25].

To accurately interpret the EL efficiency of the compounds, their relative PL quantum efficiencies ( $\text{QEs}(\varphi_F)$ ) in solution were measured [30] using the method described in the Section 2. The QE of the reference material (MADN) was set at 1.00, and the relative QE of the synthesized compounds was measured. All the compounds showed high PL QE values: MADa (0.92), MATa (0.76), and TATA (1.02). A more accurate QE comparison was possible for MATa and TATA because they had identical spectra and  $\text{PL}_{\text{max}}$ . TATA (side group, triphenylbenzene) had a higher QE than MATa (side group, *m*-terphenyl) because the QE of triphenylbenzene is higher than that of *m*-terphenyl; this result emphasizes the importance of the side group [25].

### 3.2. Electrochemical properties and electronic energy levels

The HOMO values of the synthesized compounds were determined using cyclic voltammetry (CV). Based on these analyses, all three compounds were found to have an electrochemical stability greater than 50 cycles. The energy band gaps and HOMO and LUMO levels of MADa, MATa, and TATa were estimated by CV and analysis of the absorption edge using a plot of  $(hv)$  vs.  $(ahv)^2$ , where  $a$ ,  $h$ , and  $v$  are absorbance, Plank's constant, and the frequency of light. The results of these analyses are summarized in Table 1. The band gaps of MADa, MATa, and TATa were 2.62, 2.87, and 2.87 eV, respectively, and the HOMO values for MADa, MATa, and TATa were 5.44, 5.35, and 5.37 eV, respectively.

These HOMO values were different from the HOMO values of other anthracene derivatives, 5.5–5.6 eV, that do not

include an amine unit, such as MADN [21,25,31]. In particular, MATa and TATa had HOMO values about 0.2 eV higher than that for MAT and TAT, and MADa had a HOMO value 0.1 eV higher than that of MAM [25]. Molecular calculation was performed to interpret these results.

The HOMO and LUMO electron densities of MADa, MATa, TATa, and TAT were determined by DFT/B3LYP/6-31G<sup>\*</sup> calculations using Gaussian 03 software [32] (Fig. 1).

Fig. 1 shows the molecular structures of MADa, MATa, TATa and TAT in the ground state, and the HOMO and LUMO electron density distributions. Fig. 2 shows the single crystal structure of MATa and TATa. Unfortunately, THF molecule was found together for the TATa single crystal because it was incorporated into the TATa crystal. The calculated structures of MATa and TATa were found to be very similar to the actual single crystal structure, indicating that molecular calculation is very accurate.

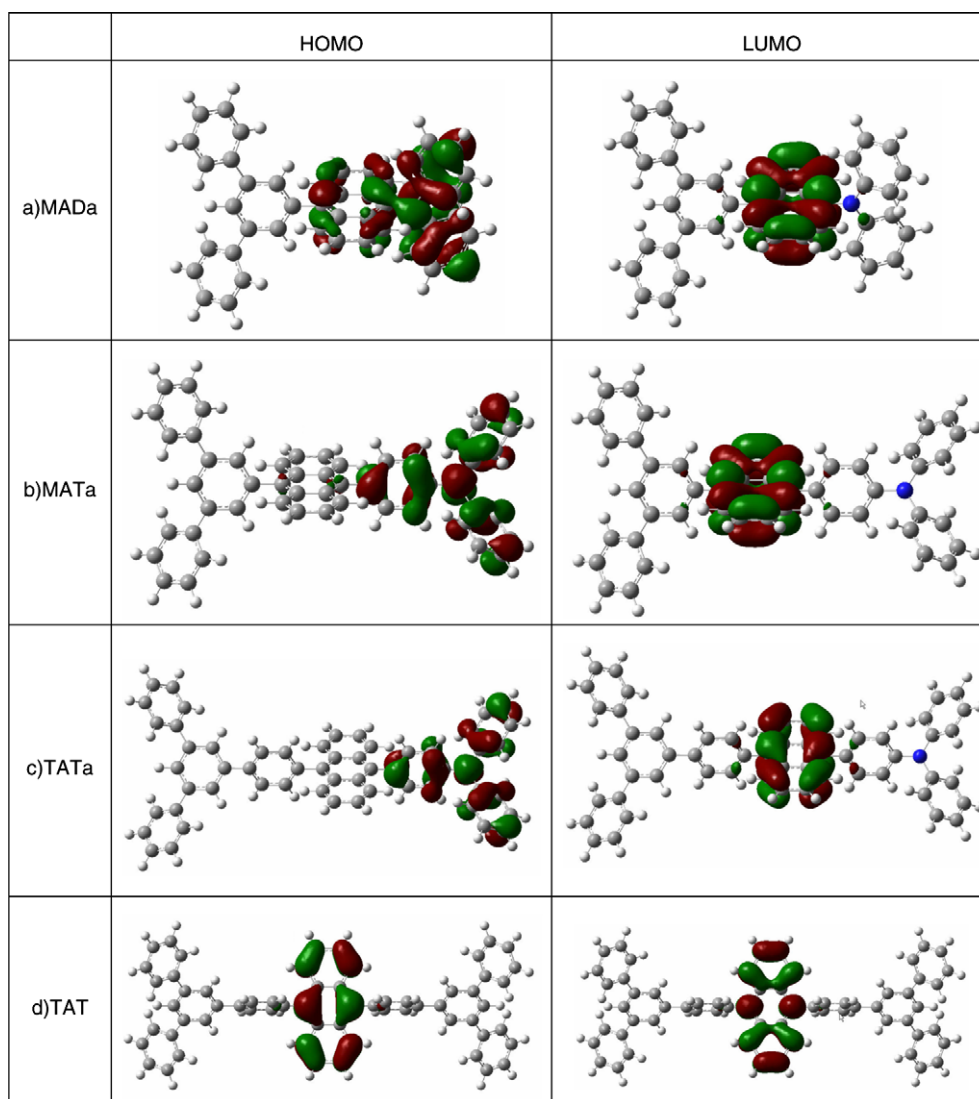


**Fig. 1.** HOMO and LUMO electronic density distributions of (a) MADa, (b) MAMa, (c) TATa, and (d) TAT calculated at the DFT/B3LYP/6-31G<sup>\*</sup> for optimization and Time Dependent DFT (TDDFT) using Gaussian 03.

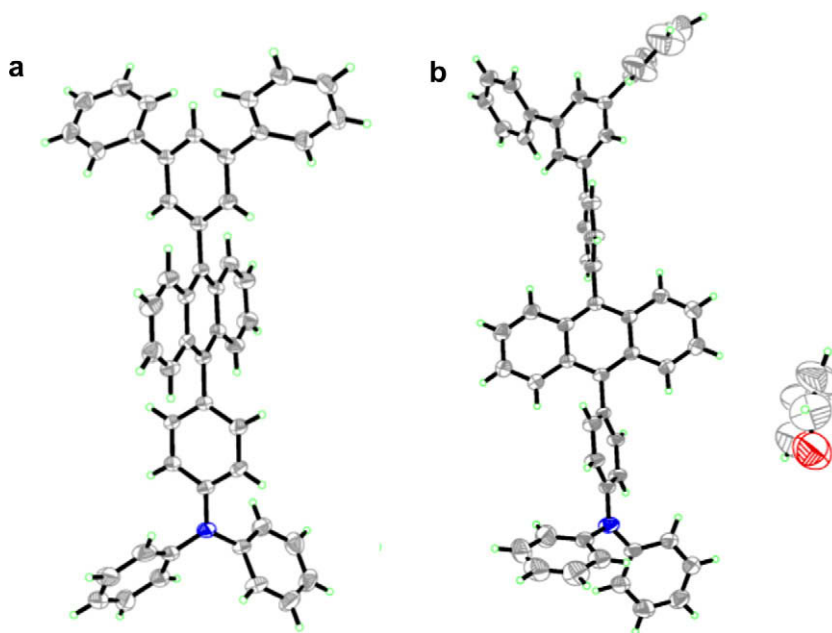


Fig. 2. The crystal structures of (a) MATa and (b) TATa.

The HOMO electron distributions of the four compounds were substantially different (Fig. 1). The HOMO electrons of MATa and TATa were in the triphenylamine unit, while those of TAT were in the anthracene moiety. This indicates that the triphenylamine unit is more easily oxidized as it has more electrons.

Moreover, from the structure obtained by molecular calculation, the phenyl unit incorporated at the 9th and 10th positions of anthracene has a torsion angle of about 90, which allows the anthracene unit and the side group to form independent conjugation systems. Consequently, the HOMO shapes of MATa, TATa, and TAT are different.

The HOMO electron distribution of MADa was present in both the anthracene and diphenyl amine groups. The torsion angle (C–C–N–C) between anthracene and the diphenylamine groups was about 138. Thus, conjugation in MADa between the anthracene and diphenylamine units was possible. The LUMO electron density of all four compounds was found to occur in the electron deficient anthracene unit. Calculation of each HOMO value for the anthracene and triphenylamine compound, triphenylamine, had a HOMO value approximately 0.3 eV higher than anthracene [34]. Thus, MATa and TATa (which have HOMO electrons in the triphenylamine unit, where electrons are comparatively more abundant than in anthracene) had relatively higher HOMO energy levels (5.35 and 5.37 eV, respectively) than TAT (5.54 eV) [25]. For MADa, where the HOMO electron is distributed at both the anthracene and amine groups, the HOMO value was intermediate (5.44 eV).

### 3.3. Thermal properties

We carried out DSC analyses to determine the thermal properties of the synthesized molecules (see Table 1).

A high  $T_g$  value indicates that the morphology of the material will not easily be changed by the high temperatures generated during the operation of OLED devices, and is closely correlated with long OLED device life-times [27,35]. MADa, MATa and TATa all had  $T_g$  values above 120 °C. TATa had a  $T_g$  value above 139 °C, which is twice that of DPVBi (64 °C) and much higher than that of MADN (120 °C). The degradation temperature ( $T_d$ ) of MADa, MATa, and TATa, measured at the 5% weight loss point, was 374, 427, and 479 °C respectively. TATa had the highest  $T_d$  (479°C), indicating it has the greatest heat stability.

To investigate the morphological stabilities of TATa and MADN, we prepared thin films (50 nm) of these materials by vapor deposition on glass substrates, and determined their surface morphologies before and after annealing at 100 °C for 6 h under a nitrogen atmosphere by using AFM.

Fig. 3 shows the surface immediately after vacuum deposition (Fig. 3a), after storage for 6 h at room temperature under air (Fig. 3b), and after storage for 6 h at 100 °C under nitrogen (Fig. 3c).

Immediately after deposition, the RMS roughnesses of TATa and MADN were 0.21 nm and 0.42 nm, respectively, indicating that the film surface characteristics of TATa are superior to those of MADN, probably due to the amine unit allowing dipole formation within the molecules. Organic molecules in OLED devices are very sensitive to oxygen and moisture, and this directly affects the device lifetime. The stability of the deposited films to moisture and oxygen was assessed by exposing the film to air for 6 h, at which time the RMS had increased relative to the RMS immediately after deposition (Fig. 3b). The RMS values for MADN (1.22 nm) and TATa (0.41 nm) represented an increase of three and two times, respectively, relative to the RMS immediately following deposition. The RMS for TATa (0.41 nm) was similar to that of MADN immediately

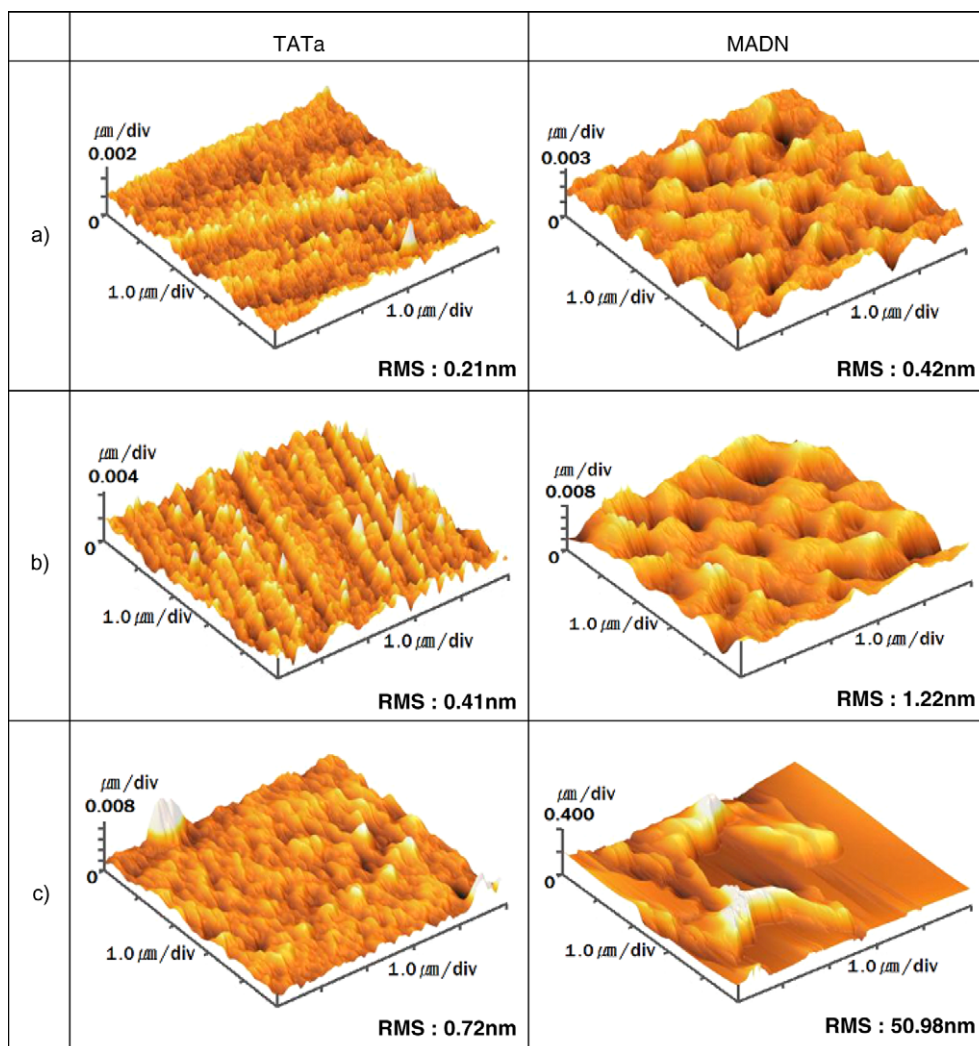


**Fig. 3.** AFM images of TATa and MADN: (a) immediately following deposition, (b) following storage at room temperature under air for 6 h, and (c) following storage at 100 °C under nitrogen for 6 h.

after vapor deposition, indicating that it has excellent surface characteristics. The organic film in an OLED device can be degraded by heat resulting from device operation, and this is directly related to the life-time of the device. The MADN film had an RMS value of 50.98 nm after 6 h at 100 °C under nitrogen (Fig. 3c), which was more than 40 times that immediately after vapor deposition. For TATa, almost no damage to the film was evident (RMS = 0.72 nm). Consequently, devices using TATa as the emitting layer would be expected to have a longer life-time than those using MADN.

### 3.4. Electroluminescence properties

We fabricated EL devices using the synthesized compounds in the following configuration: ITO/4,4',4''-tris(N-(2-naphthyl)-N-phenyl-amino)-triphenylamine (2-TNATA) (60 nm)/N,N'-bis(naphthalen-1-yl)-N,N'-bis(phenyl)benzidine (NPB) (15 nm)/synthesized emitting materials

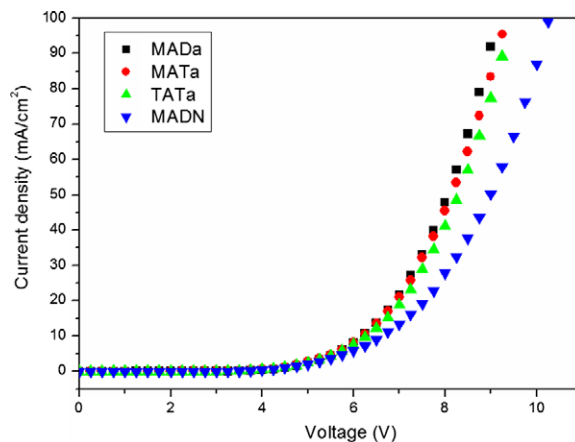


**Fig. 4.** Current density–voltage characteristics of ITO/2-TNATA (60 nm)/NPB (15 nm)/MADa (■) or MATa (●) or TATa (▲) or MADN (▼) (30 nm)/Alq<sub>3</sub> (30 nm)/LiF (1 nm)/Al (200 nm) devices.

(30 nm)/8-hydroxyquinoline aluminum ( $\text{Alq}_3$ ) (30 nm)/LiF (1 nm)/Al (200 nm). We compared the EL properties of these devices with those of a standard device: ITO/2-TNATA (60 nm)/NPB (15 nm)/MADN (30 nm)/ $\text{Alq}_3$  (30 nm)/LiF (1 nm)/Al (200 nm).

Fig. 4 shows the  $I$ - $V$  characteristics of the four devices. Devices with MADa, MATa, or TATa as the emitting layer had better  $I$ - $V$  characteristics than the device with MADN as the emitting layer. This is likely to be due to highly efficient carrier injection compared to the MADN device, due to the effect of the narrower band gap.

The EL performances of the devices with a current density of 10  $\text{mA}/\text{cm}^2$  are summarized in Table 2. Although the

device that used MADa as the emitting layer was highly efficient (10.3  $\text{cd}/\text{A}$ ), it had a bluish-green color coordinate of (0.199, 0.152). The device with MATa as the emitting layer had a performance of 4.67  $\text{cd}/\text{A}$  and an EQE of 4.69%, while the device with TATa had a performance of 6.07  $\text{cd}/\text{A}$  and an EQE of 6.19%. The CIE values for the MATa and TATa devices were (0.151, 0.177) and (0.149, 0.177), respectively. Thus the efficiency of the TATa device was higher than that of the MATa device, this is identical to the PL QE result. In comparison to MAM, MAT, and TAT only composed of phenyl group in side part [25], MADa, MATa, and TATa that include amine group in molecules showed increase in  $\text{cd}/\text{A}$  and  $\text{lm}/\text{W}$  and reduction of EQE.

**Table 2**

EL performances of multi-layered devices with the structure ITO/2-TNATA (60 nm)/NPB (15 nm)/emitting layer (30 nm)/ $\text{Alq}_3$  (30 nm)/LiF (1 nm)/Al (200 nm) at 10  $\text{mA}/\text{cm}^2$ .

Blue EMLs	$E_{L\text{-max}}$ (nm)	FWHM (nm)	Voltage (V)	Brightness ( $\text{cd}/\text{m}^2$ )	CIE ( $x, y$ )	Luminance efficiency ( $\text{cd}/\text{A}$ )	Power efficiency ( $\text{lm}/\text{W}$ )	External quantum efficiency (%)
MADa	497	63	6.27	1030	0.199, 0.512	10.3 ( $\pm 0.40$ )	5.68 ( $\pm 0.10$ )	4.18 ( $\pm 0.20$ )
MATa	464	57	6.27	467	0.151, 0.177	4.67 ( $\pm 0.30$ )	2.59 ( $\pm 0.05$ )	4.69 ( $\pm 0.10$ )
TATa	465	56	6.26	607	0.149, 0.177	6.07 ( $\pm 0.30$ )	3.37 ( $\pm 0.05$ )	6.19 ( $\pm 0.20$ )
MADN	454	62	6.71	286	0.171, 0.138	2.86 ( $\pm 0.20$ )	1.48 ( $\pm 0.05$ )	3.18 ( $\pm 0.20$ )

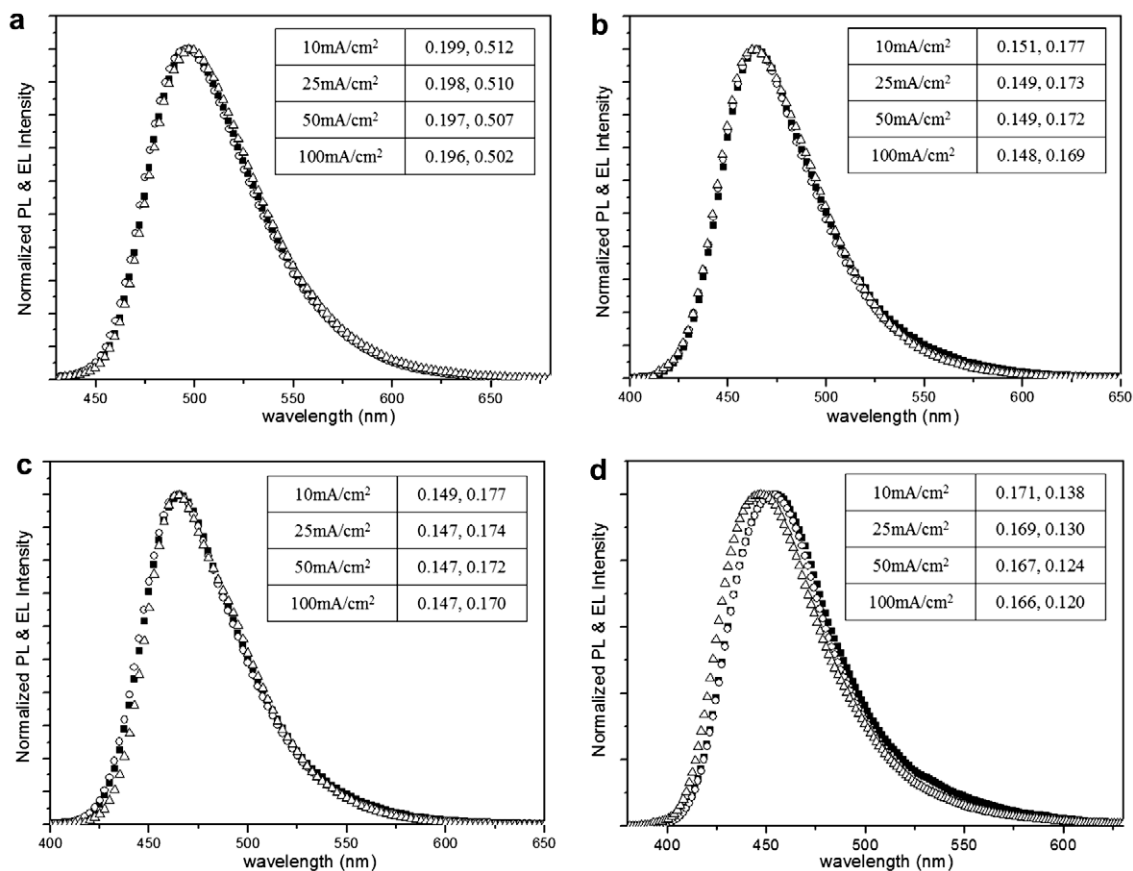


**Fig. 5.** Normalized PL ( $\Delta$ ) and EL 10  $\text{mA}/\text{cm}^2$ : ( $\blacksquare$ ) 100  $\text{mA}/\text{cm}^2$ : ( $\circ$ ) spectra of MAMa (a), MATa (b), TATa (c), and MADN (d). Inset:  $\text{CIE}_{x,y}$  values of EL devices according to current densities.

Increase in cd/A and lm/W resulted from reduction in the energy-barrier between inside layers of device due to the formation of relatively narrow band-gap by the intermolecular dipole caused by amine group. As a result, easier movement of hole and electron brings lower operating voltage and higher cd/A and lm/W. However, since sensing effect of photon differs according to the wavelength during EQE measurement, narrow band-gap is thought to have caused bathochromic shift of EL spectrum and reduction in EQE. Although the CIE value of the TATa device was slightly different from that of the MADN device, its luminance efficiency and power efficiency were more than two times that of the latter device (2.86 cd/A, 1.48 lm/W). The TATa device also had an excellent FWHM value (56 nm) despite its asymmetric structure. This value was lower than for MADN (62 nm) because the bulky side group effectively prevented  $\pi$ - $\pi$  stacking interactions between molecules.

The EL spectra for current densities of 10 mA/cm<sup>2</sup> and 100 mA/cm<sup>2</sup>, as well as the PL spectra, are shown in Fig. 5.

Agreement between the EL and PL spectra indicates that the emitting zone of the device was inside the emitting layer, and not at the interface between the layers. In addition, the EL spectra as a function of current density of MAMa, MATa, and TATa were identical, but that of MADN was slightly different.

Based on the CIE<sub>x,y</sub> values at 100 mA/cm<sup>2</sup> and 10 mA/cm<sup>2</sup>, the TATa device was especially the same unlike the MADN device, indicating stable CIE characteristics with variable current density. (Fig. 5 inset) Among synthesized compounds, life-time of TATa which showed the best EL efficiency in this series was measured under initial luminance of 500 cd/m<sup>2</sup> as shown in Fig. 6. Its life-time was more than twice that of MADN, which can be explained by the more stable morphology of TATa.

Fig. 7 shows the EL spectra of devices using MADa, TATa, or TAT [25] as the emitting layer. Although the layer included the same core moieties, the EL maxima changed according to the side group. This finding suggests that changing the side group mainly affected the HOMO elec-

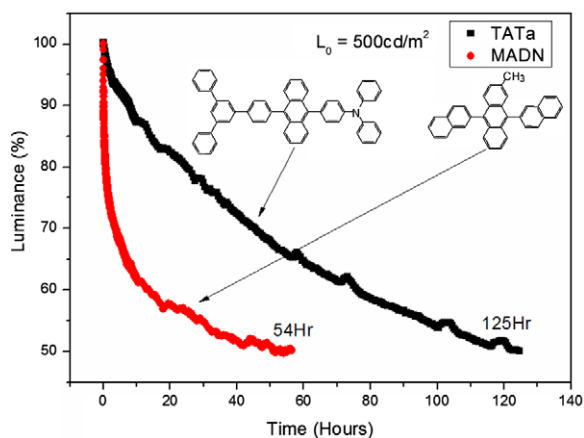


Fig. 6. Life-time comparison of ITO/2-TNATA (60 nm)/NPB (15 nm)/TATa (■) or MADN (●) (30 nm)/Alq<sub>3</sub> (30 nm)/LiF (1 nm)/Al (200 nm) devices ( $L_0 = 500$  cd/m<sup>2</sup>, under nitrogen).

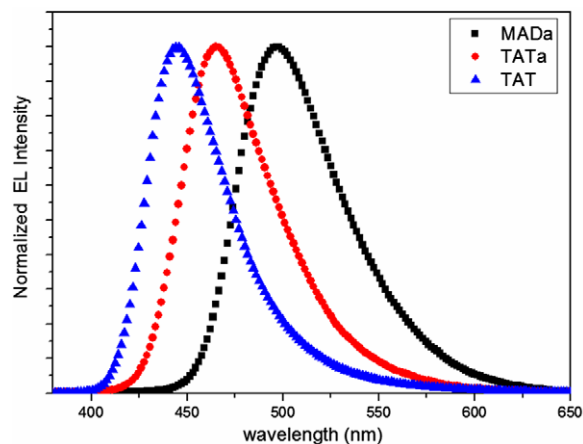


Fig. 7. Normalized EL spectra of ITO/2-TNATA (60 nm)/NPB (15 nm)/MADa (■) or TATa (●) or TAT (▲) (30 nm)/Alq<sub>3</sub> (30 nm)/LiF (1 nm)/Al (200 nm) devices at 10 mA/cm<sup>2</sup>.

tron density distribution and the HOMO level, as well as the band gap in this series.

#### 4. Conclusions

New OLED blue emitters (MADa, MATa, and TATa) were synthesized with bulky side groups asymmetrically substituted at the anthracene core.

The frontier orbital of HOMO and the band gap could be changed by varying the side groups, and thus the PL and EL spectra were easily changed even though the core remained the same.

TATa synthesized by asymmetric coupling of the bulky side groups triphenylbenzene and triphenylamine to anthracene had a high  $T_g$  (139 °C) and better surface morphology than MADN in a thin film. As a result, the OLED devices constructed using TATa as the blue emitting layer had a luminance efficiency of 6.07 cd/A and power efficiency of 3.37 lm/W (more than twice the levels obtained for the MADN device), as well as a high EQE (6.19%). Moreover, the TATa device had a life-time more than twice that of the MADN device.

#### Acknowledgement

This work was supported by the Korea Science and Engineering Foundation (KOSEF) grant funded by the Korea government (2009-0080199). This study was supported by a grant from the Fundamental R&D Program for Core Technology of Materials funded by the Ministry of Knowledge Economy (MKE), Republic of Korea. This study was supported by a grant from the Strategy Project funded by the Ministry of Knowledge Economy (MKE), Republic of Korea.

#### References

- [1] C.W. Tang, S.A. Van Slyke, Appl. Phys. Lett. 51 (1987) 913.
- [2] M.A. Baldo, M.E. Thompson, S.R. Forrest, Nature 403 (2000) 750.
- [3] C.C. Wu, Y.T. Lin, K.T. Wong, R.T. Chen, Y.Y. Chien, Adv. Mater. 16 (2004) 61.

- [4] P.L. Burn, S.C. Lo, I. D.W. Samuel, *Adv. Mater.* 19 (2007) 1675.
- [5] K.C. Wu, P.J. Ku, C.S. Lin, H.T. Shih, F.I. Wu, M.J. Huang, J.J. Lin, I.C. Chen, C.H. Cheng, *Adv. Funct. Mater.* 18 (2008) 67.
- [6] Y.S. Yao, Q.X. Zhou, X.S. Wang, Y. Wang, B.W. Zhang, *J. Mater. Chem.* 16 (2006) 3512.
- [7] B.J. Jung, J.I. Lee, H.Y. Chu, L.M. Do, J.M. Lee, H.K. Shim, *J. Mater. Chem.* 15 (2005) 2470.
- [8] T. Tsuzuki, S. Tokito, *Adv. Mater.* 19 (2007) 276.
- [9] M. Cocchi, D. Virgili, V. Fattori, D.L. Rochester, J.A.G. Williams, *Adv. Funct. Mater.* 17 (2007) 285.
- [10] K.T. Kamtekar, C. Wang, S. Bettington, A.S. Batsanov, I.F. Perepichka, M.R. Bryce, J.H. Ahn, M. Rabinal, M.C. Petty, *J. Mater. Chem.* 16 (2006) 3823.
- [11] C.H. Chen, F.I. Wu, C.F. Shu, C.H. Chien, Y.T. Tao, *J. Mater. Chem.* 14 (2004) 1585.
- [12] (a) M.T. Lee, C.H. Liao, C.H. Tsai, C.H. Chen, *Adv. Mater.* 17 (2005) 2493;  
(b) Z.Q. Gao, B.X. Mi, C.H. Chen, K.W. Cheah, Y.K. Cheng, W.S. Wen, *Appl. Phys. Lett.* 90 (2007) 123506.
- [13] S.K. Kim, Y.I. Park, I.N. Kang, J.W. Park, *J. Mater. Chem.* 17 (2007) 4670.
- [14] Y.I. Park, J.H. Son, J.S. Kang, S.K. Kim, J.H. Lee, J.W. Park, *Chem. Commun.* (2008) 2143.
- [15] T. Arakane, M. Funahashi, H. Kuma, K. Fukuoka, K. Ikeda, H. Yamamoto, F. Moriwaki, C. Hosokawa, *SID Dig.* (2006) 37.
- [16] J. Shi, C.W. Tang, *Appl. Phys. Lett.* 80 (2000) 3201.
- [17] (a) C. Hosokawa, H. Higashi, H. Nakamura, T. Kusumoto, *Appl. Phys. Lett.* 67 (1995) 3853;  
(b) S. Wang, W.J. Oldham Jr., R.A. Hudack Jr., G.C. Bazan, *J. Am. Chem. Soc.* 122 (2000) 5695.
- [18] A. Saitoh, N. Yamada, M. Yashima, K. Okinaka, A. Senoo, K. Ueno, D. Tanaka, R. Yashiro, *SID Dig.* (2004) 150.
- [19] C.C. Yeh, M.T. Lee, M.T.H.H. Chen, C.H. Chen, *SID Dig.* (2004) 788.
- [20] R.C. Chiechi, R.J. Tseng, F. Marchioni, Y. Yang, F. Wudl, *Adv. Mater.* 18 (2006) 325.
- [21] S.W. Wen, M.T. Lee, C.H. Chen, *J. Display Technol.* 1 (2005) 90.
- [22] K.C. Wu, P.J. Ku, C.S. Lin, H.T. Shin, F.I. Wu, M.J. Huang, J.J. Lin, I.C. Chen, C.H. Cheng, *Adv. Funct. Mater.* 18 (2008) 67.
- [23] C.J. Tonzola, A.P. Kulkarni, A.P. Gifford, W. Kaminsky, S.A. Jenekhe, *Adv. Funct. Mater.* 17 (2007) 863.
- [24] S.K. Kim, J.W. Park, K.S. Kim, C.K. Choi, S.D. Lee, S.W. Kim, *SID Dig.* (2007) 879.
- [25] S.K. Kim, B. Yang, Y. Ma, J.H. Lee, J.W. Park, *J. Mater. Chem.* 18 (2008) 3376.
- [26] (a) M. Sonntag, P. Strohrriegel, *Chem. Mater.* 16 (2004) 4736;  
(b) F. Terenziani, C.L. Droumaguet, C. Katan, O. Mongin, M. Blanchard-Desce, *Chem. Phys. Chem.* 8 (2007) 723;  
(c) T. Ahn, M.S. Jang, H.K. Shim, D.H. Hwang, T. Zyung, *Macromolecules* 32 (1999) 3279.
- [27] K. Danel, T.H. Huang, J.T. Lin, Y.T. Tao, C.H. Chuen, *Chem. Mater.* 14 (2002) 3860.
- [28] B.I. Berlman (Ed.), *Handbook of Fluorescence Spectra of Aromatic Molecules*, vol. 2, Academic press, New York, 1971. p. 473.
- [29] C.A. Parker, T.A. Joyce, *Trans. Faraday Soc.* 62 (1966) 2785.
- [30] H.S. Joshi, R. Jamshidi, Y. Tor, *Angew. Chem. Int. Ed.* 18 (1999) 38.
- [31] (a) Y.H. Kim, S.K. Kwon, D.S. Yoo, M.F. Rubner, M.S. Wrington, *Chem. Mater.* 9 (1997) 2699;  
(b) T.H. Liu, W.J. Shen, B. Balaganesan, C.K. Yen, C.Y. Iou, H.H. Chen, C.H. Chen, *Synth. Met.* 137 (2003) 1033;  
(c) M.X. Yu, J.P. Duan, C.H. Lin, C.H. Chung, Y.T. Tao, *Chem. Mater.* 14 (2002) 3958.
- [32] (a) C. Lee, W. Yang, R.G. Parr, *Phys. Rev. B* 37 (1988) 785;  
(b) A.D. Becke, *J. Chem. Phys.* 56 (1993) 48;  
(c) M.J. Frisch et al., *GAUSSIAN 03*, Revision B.05, Gaussian, Inc., Pittsburgh, PA, 2003.
- [33] *SHELXTL, Reference Manual*, Version 5.1, Bruker AXS Inc., Madison, WI, 1998.
- [34] B. Yang, S.K. Kim, H. Xu, H. Zhang, C. Gu, F. Shen, C. Wang, D. Liu, X. Liu, M. Hanif, S. Tang, W. Li, F. Li, J. Shen, J.W. Park, Y. Ma, *Chem. Phys. Chem.* 9 (2008) 2601.
- [35] H. Aziz, Z.D. Popovic, *Chem. Mater.* 16 (2004) 4522.

(EML) improved the device efficiency [20]. Poly(9,9'-dioctylfluorene-co-*N*-(4-butylphenyl)diphenylamine) (TFB) was used as the interlayer, where it was spin-coated onto the PEDOT:PSS layer and then thermally treated above the glass transition temperature ( $T_g$ ), followed by spin-rinsing with an organic solvent to obtain insoluble TFB interlayer. The interlayer can bring about significant improvement of efficiency [20–27], lifetime [23–25], and lowering turn-on voltage [20,21,24–27].

It is, however, often observed that the insertion of the hole-transporting interlayer causes severe reduction of current density. Chin et al. reported that the current reduction could be understood in terms of the thicker interlayer, since the introduction of a thin ( $\sim 10$  nm) interlayer increased in current of the device [24]. Harding et al. studied of various combinations of interlayer-polymers and light-emitting polymers (LEPs). They found that the interlayers alter the hole injection property in PLEDs in spite of their highest occupied molecular orbital (HOMO) levels very similar to the LEPs [26]. Whereas, we attribute the current reduction to thermal treatment above  $T_g$ . According to the study of Lee et al. a thermal treatment at elevated temperature reduced the hole mobility of interlayer-polymers and thus reduced the hole current in the EML, which resulted in lower device efficiency [23]. It is expected that hole transport layers (HTL) formed without the thermal treatment above  $T_g$  bring about improvement in the performance of PLEDs.

We have reported that a polymer thin film preparation technique, evaporative spray deposition using ultradilute solution (ESDUS) has enabled preparing an organic thin film from highly diluted solutions at a concentration of 1 ppm, and fabricating PLEDs [28], organic photovoltaics [29], and organic field-effect transistors [30]. In addition, this method has been exhibited that a successive polymer layer can be deposited without damaging the proceeding polymer layer using a same organic solvent for each layer deposition [31,32]. Therefore, it is enable to construct polymer bilayer structure with a bottom layer prepared in various conditions.

In this report, we have successfully achieved a significant improvement in the performance of bilayer PLEDs prepared by ESDUS using HTL annealed below  $T_g$  as compared with that of PLEDs having the interlayer that was formed by the thermal treatment above  $T_g$ .

## 2. Experimental

### 2.1. Materials

We used two typical conjugated polymers for PLEDs, poly(9,9'-dioctylfluorene-co-*N*-(4-butylphenyl)diphenylamine) (TFB;  $M_w = 267,000$ ) and poly(9,9'-dioctylfluorene-*alt*-benzothiadiazole) (F8BT;  $M_w = 69,000$ ) supplied from Sumitomo Chemical Co., Ltd., without further purification. The chemical structures of these polymers are shown in Fig. 1a. The energy band gap of each polymer was estimated from the absorption spectra edge at the thin polymer films using UV-VIS-NIR spectrophotometer (UV-3150, Shimadzu). The ionization potential of each

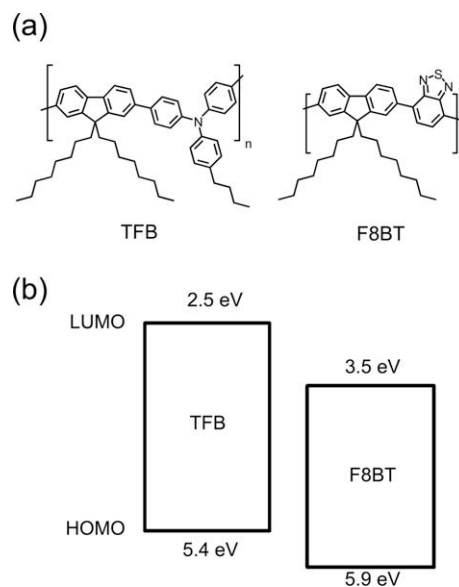


**Fig. 1.** (a) Chemical structures of TFB and F8BT. (b) The highest occupied molecular orbital (HOMO) and the lowest unoccupied molecular orbital (LUMO) levels of TFB and F8BT.

material was determined by photoemission spectroscopy (AC-2, Rikenkeiki). The energy level diagram, which is derived from the ionization potentials and the optical band gaps of the polymers, is shown in Fig. 1b. The HOMO levels of the TFB and the F8BT are 5.4 eV and 5.9 eV, and the lowest unoccupied molecular orbital (LUMO) levels are 2.5 eV and 3.5 eV, respectively.

### 2.2. Device fabrication

A thin film of PEDOT:PSS (P VP Al 4083, H. C. Starck) (40 nm) was spin-coated as an anode buffer layer on transparent electrode, indium tin oxide (ITO), followed by drying at 120 °C for 5 min on a hot plate in atmosphere. Prior to PEDOT:PSS deposition, the ITO-coated glass substrates were cleaned in an ultrasonic bath with detergent, deionized water, acetone, and ethanol, and were treated with UV-ozone. For single-layer devices, 100 nm thick F8BT layer was formed as an EML on top of the PEDOT:PSS layer by a spin-coating from mixed-xylene solution (device A) or by ESDUS from tetrahydrofuran (THF) solution (device B). For interlayer devices (device C and G), TFB was spin-coated from mixed-xylene solution onto the PEDOT:PSS layer and then annealed at 180 °C ( $>T_g$  of TFB) for 1 h in a  $N_2$  glove box. To prevent mixing of the interlayer with the EML, the soluble part of TFB was removed by a spin-rinsing with mixed-xylene. In this manner, 20 nm-thick interlayer was obtained. F8BT was then spin-coated as the EML onto the interlayer with 85 nm. For ESDUS bilayer devices (device D, E, F and H), TFB was spin-coated as a HTL (40 nm) onto the PEDOT:PSS layer and then annealed at 130 °C for device D and H, 180 °C for device E and 230 °C for device F for 20 min in the glove box. F8BT was then deposited as the EML (65 nm) directly onto the TFB layer using ESDUS from THF solution. All F8BT layers



**Table 1**

Fabrication conditions of PLEDs in this study. Device A and B are single-layer devices, device C and G are interlayer devices and device D, E, F, H are ESDUS bilayer devices.

Device	IL <sup>a</sup> or HTL <sup>b</sup> (TFB)			EML <sup>c</sup> (F8BT)		Cathode
	Thickness (nm)	Annealing temperature (°C)	Preparation method	Thickness (nm)	Preparation method	
A	–	–	–	100	Spincoat	LiF/Al
B	–	–	–	100	ESDUS	LiF/Al
C	20	180 <sup>d</sup>	Spincoat	85	Spincoat	LiF/Al
D	40	130 <sup>e</sup>	Spincoat	65	ESDUS	LiF/Al
E	40	180 <sup>e</sup>	Spincoat	65	ESDUS	LiF/Al
F	40	230 <sup>e</sup>	Spincoat	65	ESDUS	LiF/Al
G	20	180 <sup>d</sup>	Spincoat	85	Spincoat	Ca/Al
H	40	130 <sup>e</sup>	Spincoat	65	ESDUS	Ca/Al

<sup>a</sup> IL: interlayer.

<sup>b</sup> HTL: hole transport layer.

<sup>c</sup> EML: emitting layer.

<sup>d</sup> For 1 h.

<sup>e</sup> For 20 min.

were annealed at 80 °C for 20 min in the glove box. Finally, cathodes were deposited at pressures less than  $10^{-4}$  Pa; a cathode buffer layer of LiF (1.0 nm) for device A to F or Ca (10 nm) for device G and H was thermally deposited in a vacuum evaporator, followed by an Al (100 nm) electrode through a shadow mask to obtain active areas of  $2 \times 2$  mm<sup>2</sup>. Devices with Ca/Al electrode were encapsulated in the glove box before measurements. The fabrication conditions of device A–H were listed in Table 1.

For hole only devices, 170 nm-thick TFB was spin-coated onto the PEDOT:PSS and then annealed at 80 °C, 130 °C, 180 °C and 230 °C for 20 min in the glove box. Au cathode was thermally deposited to ensure no injection of electrons into the LUMO of the TFB.

### 2.3. Measurements and characterization

The current–voltage–luminescence (*L–J–V*) characteristics were measured using a source measure unit (Keithley 238) and using a luminance meter (BM-5A, Topcon). The electroluminescence (EL) spectra were measured using a multi-channel analyzer (PMA-11, Hamamatsu Photonics). The external quantum efficiency (EQE) and the power efficiency (PE) were calculated from the *L, J, V* and EL spectrum of each device. The thickness and the surface roughness of the polymer films were determined using an atomic force microscopy (AFM) (Nanopics 100, SII). A differential scanning calorimeter (DSC) (Q100, TA Instruments) was used to determine the  $T_g$  of the TFB sample studied in this research at a rate of 10 °C min<sup>-1</sup>. The  $T_g$  was determined by the second heating scans.

## 3. Results and discussion

### 3.1. The comparison of single-layer devices prepared by spin-coating or ESDUS

On comparison of device performance of the single layered spin-coating device (device A) and ESDUS device (device B), the *L–J–V* characteristics were almost comparable as shown in Fig. 2. Leakage current in device B was higher at the low voltage region below turn-on. Root mean square

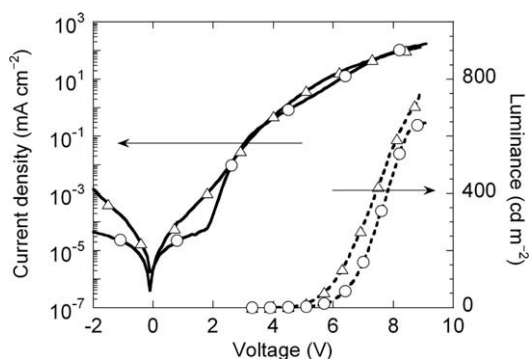


**Fig. 2.** The luminance–current density–voltage characteristics for single-layer devices composed of F8BT layer prepared by spin-coating (device A; circles) and by ESDUS (device B; up-pointing triangles). Solid lines and dashed lines represent the current density–voltage characteristics and the luminance–voltage characteristics, respectively.

roughness ( $R_{rms}$ ) of the F8BT film prepared by ESDUS, which was examined using an AFM, was higher ( $R_{rms} = 8.2$  nm, in the scale of  $20 \mu\text{m} \times 20 \mu\text{m}$ ) than that of one prepared by spin-coating ( $R_{rms} = 0.5$  nm, in the scale of  $20 \mu\text{m} \times 20 \mu\text{m}$ ). The heterogeneity represented by the roughness would cause the leak-current at low-voltage regions though the light emission of two devices is homogeneous.

### 3.2. Improvement in the PLEDs performance using HTL without thermal treatment above $T_g$

Fig. 3a and b shows the *L–J–V* characteristics for device A, C and D. The current in interlayer devices (device C) was much lower than that of single-layer devices (device A), but the turn-on voltage for luminance ( $>1$  mcd m<sup>-2</sup>) of device C is almost identical to that of device A. Yang et al. reported that the residual thickness of the interlayer-polymer and the characteristics of the underlying PEDOT:PSS [22]. They proposed that the formation of the insoluble polymer layer is due to the binding of individual chains at the surface of PEDOT:PSS. The molecular weight of the

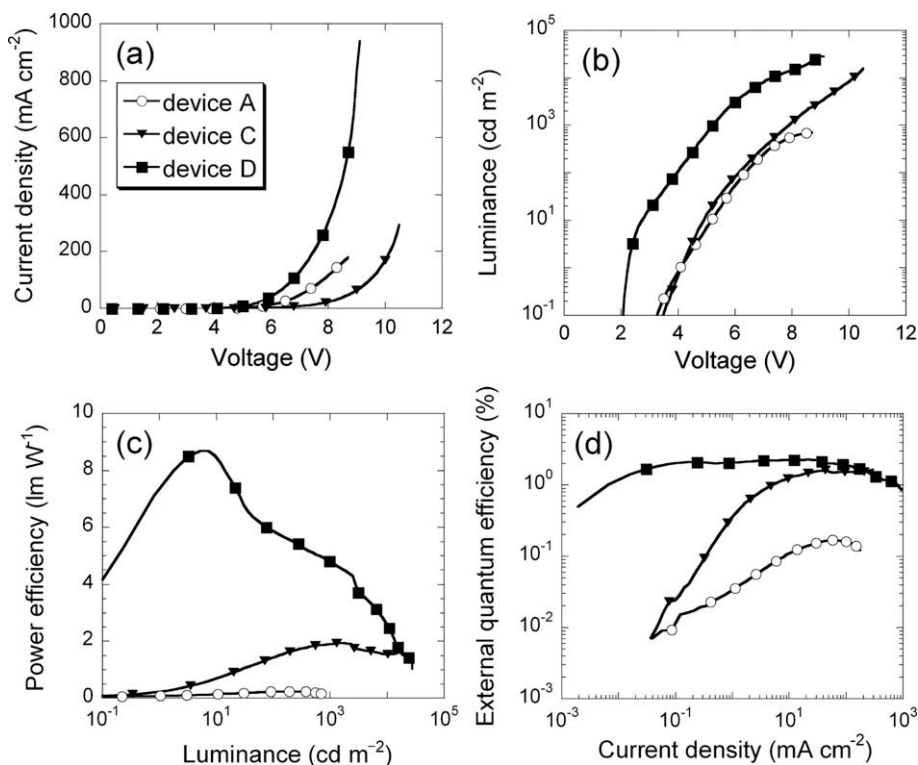


**Fig. 3.** (a) The current density–voltage characteristics, (b) the luminance–voltage characteristics, (c) the power efficiency–current density characteristics and (d) the external quantum efficiency–current density characteristics for the single-layer device prepared by spin-coating (device A; opened circles), the interlayer device (device C; closed down-pointing triangles) and the ESDUS bilayer device (device D; closed squares).

TFB used in this research is so high that the thickness of the interlayer would be relatively thicker. The resulting current density of interlayer devices was lower than that of single-layer devices. On the other hand, the current density of ESDUS bilayer devices (device D) having thicker TFB layer (40 nm) than device C was significantly higher than that of device A and C. In addition, the turn-on voltage was 1.2 V lower and the luminance of device D was markedly enhanced, so that the PEs of device D were improved significantly through the whole luminance region as shown in Fig. 3c. In particular, the maximum PE of device D showed 8.7 lm W<sup>-1</sup> and surpassed other devices (PE<sub>MAX</sub> of device A = 0.24 lm W<sup>-1</sup>, PE<sub>MAX</sub> of device C = 1.9 lm W<sup>-1</sup>). These higher current and lower turn-on voltage of device D would be caused by improvement in hole injection and transport in the device due to the insertion of TFB layer as HTL, which has a high hole mobility [33,34] and a low ionization potential (5.4 eV) creating the stepped electronic profile [21,27] between PEDOT:PSS (5.2 eV) and F8BT (5.9 eV). Fig. 3d shows the EQE–J characteristics for the PLEDs. The maximum EQE of device D was improved drastically (2.3%) as compared with that of device A (0.17%) and C (1.6%). The enhancement of the EQEs of device D at low-current region is especially notable, therefore, the EQEs of device D tended to be a constant (about 2%) through the wide current region. While, those of device A and C showed a gradual increase as current density was getting higher.

The gradual increase in EQEs of device A can be explained mainly by a carrier imbalance at low voltage region due to the injection barrier difference at the anode and the cathode, and a shift of the carrier recombination site. Generally conjugated polymers exhibit different mobilities for holes and electrons, and the electric field dependence of each mobility is also quite different. In single-layer PLEDs, the carrier recombination site should be located close to an electrode where the less mobile carrier is injected. The emission would be quenched by a non-radiative energy transfer near an electrode surface, causing low EQE. As the electric field is getting higher, the mobility difference between electrons and holes often becomes smaller due to different electric field dependence [35–37]. The recombination site would extend away from the electrode, reducing non-radiative energy transfer [38,39]. In the case of device A, the recombination process should occur at a PEDOT:PSS/F8BT interface since F8BT is a good electron transport material [40].

The steep rise in the EQEs of device D at the low-current region and the following plateau indicate the charge injection and transport to be balanced at lower electric field, and the balance to be maintained through the wide range. These tendencies can be understood as has been discussed in bilayer organic LEDs [4,41–44], i.e., the blocking of carriers at the organic/organic interface prevents the majority carriers from reaching the opposite electrode without forming excitons, and accumulation of them causes a

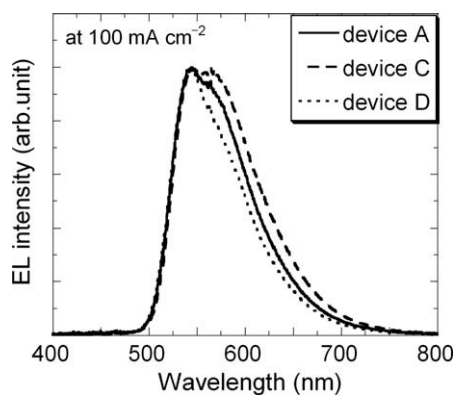


**Fig. 4.** The electroluminescence spectra for the single-layer device prepared by spin-coating (device A; solid line), the interlayer device (device C; dashed line) and the ESDUS bilayer device (device D; dotted line) driving at  $100 \text{ mA cm}^{-2}$ .

redistribution of the electric field within the device, which promotes injection of the minority carriers, and the recombination zone is away from the electrode.

As shown by the EL spectra of device A, C and D driving at  $100 \text{ mA cm}^{-2}$  in Fig. 4, we could see the F8BT emission (peaking at 544 nm) from these devices. Similarly the shoulder at 575 nm of device C and D became stronger and weaker relatively to the main peak, respectively. We attribute shift in EL spectrum of device C to the formation of an exciplex at TFB/F8BT heterojunctions [45,46]. However, the weaker shoulder of the EL spectrum for device D cannot be explained only by the formation of the exciplex. The difference among spectra of device A, device C and device D should be ascribed to interference effects between the emission directly out of the active layer and the reflection at the metal electrode since the location of the emission zone has changed due to the position of the TFB/F8BT interface [47–49]. In device C, the recombination zone might be located away from the PEDOT:PSS due to the insertion of interlayer, preventing the exciton quenching by PEDOT:PSS, and it also contributes to the improvement in the EQEs of device C [20].

However, the gradual increase of the EQEs of device C suggests that the carrier balance was not as good as device D in spite of the interlayer insertion. Another interlayer device composed of TFB (interlayer)/F8BT (ESDUS) showed much lower current and gradual increase in EQEs as device C. Therefore, the difference between device C and D would be caused by the annealing temperature for TFB layer.

### 3.3. The influence of the annealing temperature for HTL on PLEDs characteristics

We studied the effect of the higher annealing temperature for TFB layer on the performance of bilayer PLEDs. Fig. 5 shows the  $L$ - $J$ - $V$  and the EQE- $J$  characteristics of ESDUS bilayer devices with TFB layer annealed at various temperatures (device D, E and F). The current density and luminance were reduced as the thermal treatment temperature of TFB layer increased from  $130^\circ\text{C}$  to  $230^\circ\text{C}$  regardless of having the same thickness and structure as shown

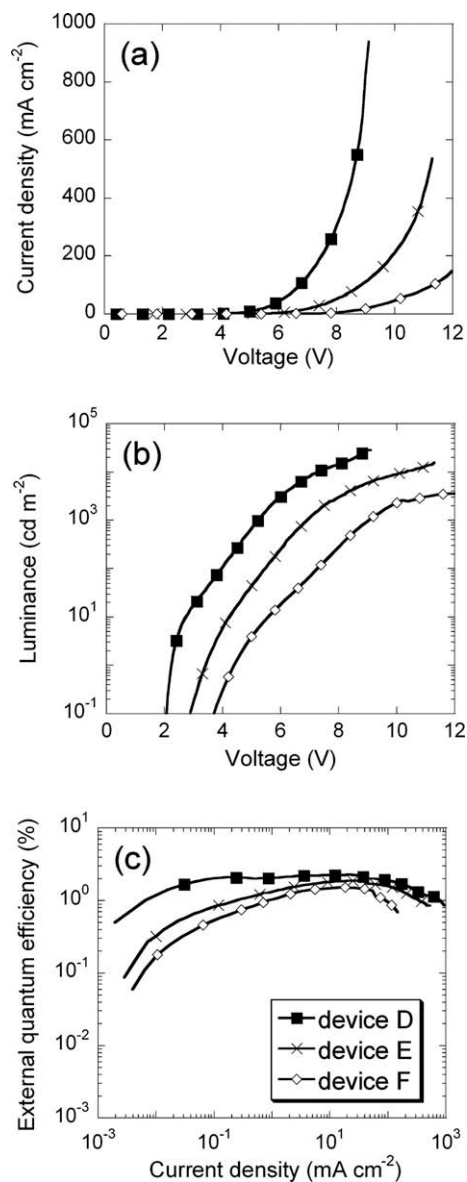


**Fig. 5.** (a) The current density–voltage characteristics, (b) the luminance–voltage characteristics, (c) the external quantum efficiency–current density characteristics for ESDUS bilayer devices with TFB layer annealed at  $130^\circ\text{C}$  (device D; closed squares),  $180^\circ\text{C}$  (device E; crosses) and  $230^\circ\text{C}$  (device F; opened diamonds).

in Fig. 5a and b. The maximum EQE of device E and F were 1.9% and 1.5%, respectively, and lower than that of device D (2.3%). The EQEs of device E and F in the low-current region significantly reduced and showed a gradual increase with current density as shown in Fig. 5c. We consider that the inferior performance of the bilayer PLEDs with TFB annealed at higher temperature would be caused a decrease in hole current since the insertion of TFB as HTL brought about the improvement in carrier balance of electron-rich F8BT devices.

To investigate the change of hole current as a function of the annealing temperature of TFB layer, we fabricated hole

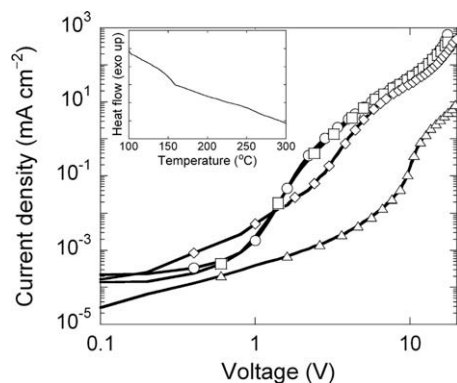


**Fig. 6.** The current density–voltage characteristics for hole only devices; ITO/PEDOT:PSS/TFB (170 nm)/Au, whose TFB layer was annealed at 80 °C (circles), 130 °C (squares), 180 °C (diamonds) and 230 °C (triangles). The inset shows differential scanning calorimetry curve of TFB used in this research.

only devices of ITO/PEDOT:PSS/TFB (170 nm)/Au structure. Fig. 6 shows the  $J$ – $V$  characteristics of the hole only devices with TFB layer annealed at various temperatures. The plots of the devices annealed at 80 °C and 130 °C were almost identical, although, the hole current decreased as the thermal treatment temperature increased from 130 °C to 230 °C. Furthermore, it is remarkable that the turn-on voltages for hole injection became large when annealing temperature exceeded in 180 °C. According to a DSC measurement, the  $T_g$  of TFB used in this study is determined 156.0 °C as shown in the inset of Fig. 6. We consider that the thermal treatment above  $T_g$  of TFB would induce the degradation of hole injection property. Therefore, interlayers should be damaged the intrinsic nature of the interlayer-polymers as a good hole transporting material, since they are annealed above the  $T_g$  and rinsed with a organic solvent, and the insoluble residue of them remains as interlayers. The preparation process of interlayers, which needs the thermal treatment above  $T_g$ , would also affect the current reduction of PLEDs with interlayers apart from the thickness of interlayers and the interlayer–LEP combination. We suppose that the interlayer in this study would not greatly improve in hole injection and transport of device C.

But it remains open now what problems arise by thermal treatment above  $T_g$ . No changes in surface morphology, absorption and ionization potential were observed in TFB films annealed at 80 °C, 130 °C, 180 °C and 230 °C. As shown by other reports, absorption and photoluminescence, vibrational transitions, redox energy levels and the surface potential of interlayers is almost identical to those of “bulk” polymer layers [20,22]. It is required that the investigation into the interface of PEDOT:PSS/TFB.

We fabricated another ESDUS bilayer device having thinner TFB layer (20 nm) without the thermal treatment above  $T_g$ . The  $L$ – $J$ – $V$  characteristics were found to be almost identical to those of device D. It is well known for conventional small-molecule-base OLEDs, the device characteristics are not sensitive to thickness of a hole transporting layer because most of applied electric field is concentrated on an electron transporting layer [50,51]. The device characteristics independent of the TFB thickness in the

ESDUS devices suggests that the interlayer thickness should not be a major issue for the inferior performance in the interlayer devices but the thermal degradation of TFB would be the most important.

#### 3.4. The electron-rich devices having a cathode with lower work function on the bilayer PLEDs

We fabricated more electron-rich devices by applying the Ca/Al cathode to interlayer devices (device G) and ESDUS bilayer devices (device H). Fig. 7a and b shows the  $L$ – $J$ – $V$  characteristics of device G and H. On comparison between ESDUS bilayer devices (device D and H), the current and luminance of the Ca/Al cathode devices (device H) showed the rapid rise at much lower voltage than those of the LiF/Al cathode devices (device D), so that the PEs of device H were much higher throughout the luminance region, and exhibited 12 lm W<sup>−1</sup> in the maximum as shown in Fig. 7c. On the other hand, in the interlayer devices, the PEs of the more electron-rich devices (device G) showed inferior PE<sub>MAX</sub> of 1.3 lm W<sup>−1</sup> where device C showed 1.9 lm W<sup>−1</sup>, though the current and luminance of device G showed rise as compared with device C.

Fig. 7d shows the EQE– $J$  characteristics of device G and H. The EQEs of device H with the ESDUS bilayer structure showed the flat tendency at the wide range of the current density and the maximum EQE of device H was 2.3%, which was same value to that of device D. The EL spectrum of device H was identical to the F8BT emission without the TFB emission, being almost identical to that of device D. The EQE is the ratio of the number of photons coming out of a device to the number of charge carriers injected into it, and EQE is given by  $\text{EQE} = \gamma \eta_r \phi_f \eta_{\text{ext}}$  using the charge-balance factor  $\gamma$ , the efficiency of production for singlet excitons  $\eta_r$ , the quantum efficiency of fluorescence  $\phi_f$ , and the extraction efficiency of light from the device  $\eta_{\text{ext}}$  [52]. Almost same value of EQEs of device D and H suggests that the ESDUS bilayer devices would attain the  $\gamma$  value close to 1.0 assuming that the value of  $\eta_r$ ,  $\phi_f$  and  $\eta_{\text{ext}}$  is constant. Therefore, these observations indicate that electrons are effectively blocked at the TFB/F8BT interface and the carrier balance is maintained despite using more electron-rich cathode in the ESDUS bilayer devices. On the other hand, the EQEs of device G decreased as compared with device C and the maximum EQE reduced to 0.91%, which results in the severe decrease in PEs of device G. The reduction of EQEs of the more electron-rich devices suggests that the interlayer is not working as an efficient electron blocking layer, which was reported by Harding et al. [26], despite the large difference of LUMO level between TFB and F8BT (1.0 eV). Probably due to the thin thickness of the interlayer and/or the degree of intermixing at TFB/F8BT interface, the interlayer composed of TFB exhibits the inefficient electron blocking.

Interlayers are easy to be formed and certainly useful for improvement in EQE of PLEDs to keep the carrier recombination zone away from the PEDOT:PSS and to enhance the hole injection compared with single-layer devices, although, they cannot act as strong carrier blocking layers. The further development would be brought for PLEDs by forming more effective polymer heterojunction.

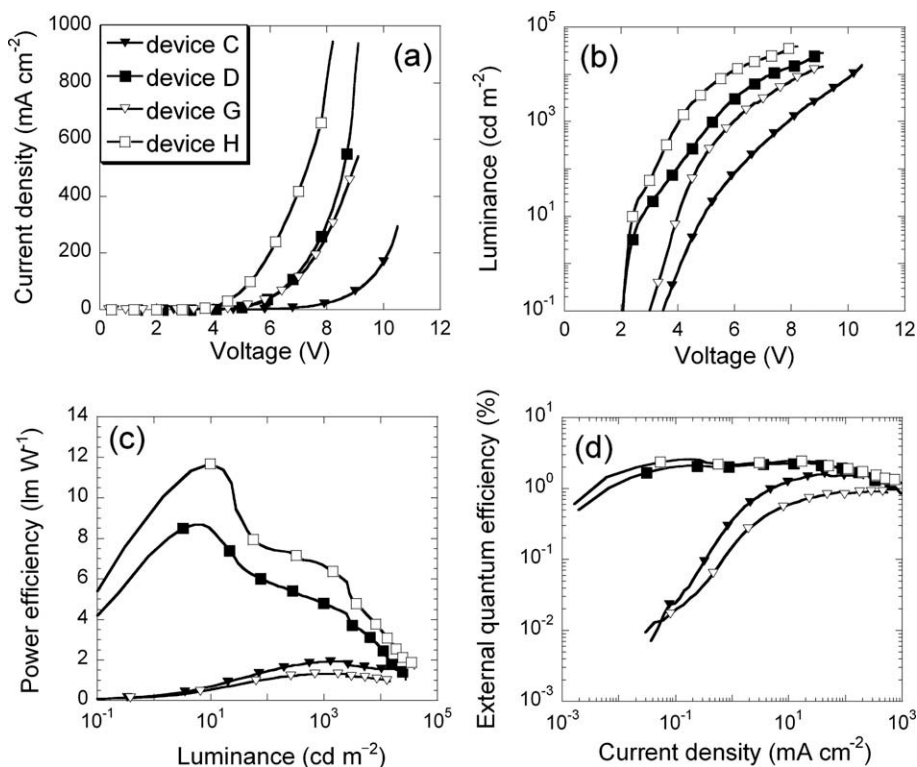


**Fig. 7.** (a) The current density–voltage characteristics, (b) the luminance–voltage characteristics, (c) the power efficiency–current density characteristics and (d) the external quantum efficiency–current density characteristics for the interlayer device with LiF/Al cathode (device C; closed down-pointing triangles), the ESDUS bilayer device with LiF/Al cathode (device D; closed squares), the interlayer device with Ca/Al cathode (device G; opened down-pointing triangles) and the ESDUS bilayer device with Ca/Al cathode (device H; opened squares).

#### 4. Conclusions

We have successfully achieved a significant improvement in the performance of bilayer PLEDs by introducing TFB as HTL without thermal treatment above  $T_g$  through the stack of EML using ESDUS. Comparison with characteristics of devices having the TFB annealed at various temperatures indicates that the thermal treatment above  $T_g$  induces the degradation of hole injection, and that thermal treatment temperature for HTL can vary the carrier balance of bilayer PLEDs. The higher current and lower turn-on voltage, and therefore the higher power efficiency can be achieved in the ESDUS bilayer PLEDs which do not require a severe annealing for HTL formation. On the other hand, interlayers which are often used for PLEDs are formed through the thermal treatment above  $T_g$ . Some studies have been reported that the thickness of interlayers and the interlayer-LEP compatibility were discussed for inferior device performance in their PLEDs. The thermal degradation would be the major factor for inferior performance in the interlayer devices.

The EQEs of the ESDUS bilayer devices showed the constant value through the wide current region even in the more electron-rich condition, whereas, those of the interlayer devices showed lower and a gradual increasing tendency. These observations suggest that electrons are effectively blocked at the TFB/F8BT interface in ESDUS

bilayer devices but the electron block of the interlayer is not as effective.

It is required the degradation of polymers by thermal treatment above  $T_g$  is taken into consideration in case of constructing bilayer PLEDs. The multilayer structure has been proved to be quite effective for improvement of device performance in small molecule-based OLEDs. The further improvement in PLEDs would be also brought by more effective processes which do not require any procedure inducing degradation of the materials. Cross-linkable polymers could be one of promising candidates in order to insolubilize the bottom layer without thermal treatment. ESDUS method would be another.

#### Acknowledgments

We would like to express sincere thanks to Prof. Tetsuo Tsutsui for helpful discussions, and Sumitomo Chemical Co., Ltd. for supplying the TFB and F8BT available for our use. This work was supported by a grant from the Global-Center of Excellence in Novel Carbon Resource Sciences, Kyushu University and by KAKENHI (21350102).

#### References

- [1] C.W. Tang, S.A. VanSlyke, Organic electroluminescent diodes, Appl. Phys. Lett. 51 (1987) 913–915.

- [2] C. Adachi, T. Tsutsui, S. Saito, Confinement of charge carriers and molecular excitons within 5-nm-thick emitter layer in organic electroluminescent devices with a double heterostructure, *Appl. Phys. Lett.* 57 (1990) 531–533.
- [3] N.C. Greenham, S.C. Moratti, D.D.C. Bradley, R.H. Friend, A.B. Holmes, Efficient light-emitting diodes based on polymers with high electron affinities, *Nature* 365 (1993) 628–630.
- [4] X. Zhang, S.A. Jenekhe, Electroluminescence of multicomponent conjugated polymers. 1. Roles of polymer/polymer interfaces in emission enhancement and voltage-tunable multicolor emission in semiconducting polymer/polymer heterojunctions, *Macromolecules* 33 (2000) 2069–2082.
- [5] H. Yan, B.J. Scott, Q. Huang, T.J. Marks, Enhanced polymer light-emitting diode performance using a crosslinked-network electron-blocking interlayer, *Adv. Mater.* 16 (2004) 1948–1953.
- [6] A.C. Morteani, P.K.H. Ho, R.H. Friend, C. Silva, Electric field-induced transition from heterojunction to bulk charge recombination in bilayer polymer light-emitting diodes, *Appl. Phys. Lett.* 86 (2005) 163501-1–163501-3.
- [7] A. Charas, H. Alves, L. Alcácer, J. Morgado, Use of cross-linkable polyfluorene in the fabrication of multilayer polyfluorene-based light-emitting diodes with improved efficiency, *Appl. Phys. Lett.* 89 (2006) 143519-1–143519-3.
- [8] M. Granström, K. Petritsch, A.C. Arias, A. Lux, M.R. Andersson, R.H. Friend, Lamination fabrication of polymeric photovoltaic diodes, *Nature* 395 (1998) 257–260.
- [9] T.-F. Guo, S. Pyo, S.-C. Chang, Y. Yang, High performance polymer light-emitting diodes fabricated by a low temperature lamination process, *Adv. Funct. Mater.* 11 (2001) 339–343.
- [10] C.M. Ramsdale, J.A. Barker, A.C. Arias, J.D. MacKenzie, R.H. Friend, N.C. Greenham, The origin of the open-circuit voltage in polyfluorene-based photovoltaic devices, *J. Appl. Phys.* 92 (2002) 4266–4270.
- [11] K.-H. Yim, Z. Zheng, Z. Liang, R.H. Friend, W.T.S. Huck, J.-S. Kim, Efficient conjugated-polymer optoelectronic devices fabricated by thin-film transfer-printing technique, *Adv. Funct. Mater.* 18 (2008) 1012–1019.
- [12] L. Chen, P. Degenaar, D.D.C. Bradley, Polymer transfer printing: application to layer coating, pattern definition, and diode dark current blocking, *Adv. Mater.* 20 (2008) 1679–1683.
- [13] A. Elschner, F. Bruder, H.-W. Heuer, F. Jonas, A. Karbach, S. Kirchmeyer, S. Thurm, R. Wehrmann, PEDT/PSS for efficient hole-injection in hybrid organic light-emitting diodes, *Synth. Met.* 111–112 (2000) 139–143.
- [14] F. Huang, H. Wu, D. Wang, W. Yang, Y. Cao, Novel electroluminescent conjugated polyelectrolytes based on polyfluorene, *Chem. Mater.* 16 (2004) 708–716.
- [15] W. Ma, P.K. Iyer, X. Gong, B. Liu, D. Moses, G.C. Bazan, A.J. Heeger, Water/methanol-soluble conjugated copolymer as an electron-transport layer in polymer light-emitting diodes, *Adv. Mater.* 17 (2005) 274–277.
- [16] X. Gong, S. Wang, D. Moses, G.C. Bazan, A.J. Heeger, Multilayer polymer light-emitting diodes: white-light emission with high efficiency, *Adv. Mater.* 17 (2005) 2053–2058.
- [17] F. Huang, Y.-H. Niu, Y. Zhang, J.-W. Ka, M.S. Liu, A.K.-Y. Jen, A conjugated, neutral surfactant as electron-injection material for high-efficiency polymer light-emitting diodes, *Adv. Mater.* 19 (2007) 2010–2014.
- [18] S.-H. Oh, D. Vak, S.-I. Na, T.-W. Lee, D.-Y. Kim, Water-soluble polyfluorenes as an electron injecting layer in PLEDs for extremely high quantum efficiency, *Adv. Mater.* 20 (2008) 1624–1629.
- [19] S.-R. Tseng, S.-C. Lin, H.-F. Meng, H.-H. Liao, C.-H. Yeh, H.-C. Lai, S.-F. Horng, C.-S. Hsu, General method to solution-process multilayer polymer light-emitting diodes, *Appl. Phys. Lett.* 88 (2006) 163501-1–163501-3.
- [20] J.-S. Kim, R.H. Friend, I. Grizzi, J.H. Burroughes, Spin-cast thin semiconducting polymer interlayer for improving device efficiency of polymer light-emitting diodes, *Appl. Phys. Lett.* 87 (2005) 023506-1–023506-3.
- [21] S.A. Choulis, V.-E. Choong, M.K. Mathai, F. So, The effect of interfacial layer on the performance of organic light-emitting diodes, *Appl. Phys. Lett.* 87 (2005) 113503-1–113503-3.
- [22] X.H. Yang, F. Jaiser, B. Stiller, D. Neher, F. Galbrecht, U. Scherf, Efficient polymer electrophosphorescent devices with interfacial layers, *Adv. Funct. Mater.* 16 (2006) 2156–2162.
- [23] T.-W. Lee, M.-G. Kim, S.Y. Kim, S.H. Park, T.-S. Oh, Hole-transporting interlayers for improving the device lifetime in the polymer light-emitting diodes, *Appl. Phys. Lett.* 89 (2006) 123505-1–123505-3.
- [24] B.D. Chin, N.S. Kang, J.-W. Yu, S.M. Jo, J.Y. Lee, Role of the interfacial layer in the efficiency and lifetime of polymeric light emitting devices, *J. Appl. Phys.* 102 (2007) 024506-1–024506-7.
- [25] L. Duan, B.D. Chin, N.C. Yang, M.-H. Kim, H.D. Kim, S.T. Lee, H.K. Chung, Multilayer blue polymer light-emitting devices with spin-coated interlayers, *Synth. Met.* 157 (2007) 343–346.
- [26] M.J. Harding, D. Poplavskyy, V.-E. Choong, A.J. Campbell, F. So, Effects of solution-processed polymer interlayers on hole injection and device performance of polymer light-emitting diodes, *Org. Electron.* 9 (2008) 183–190.
- [27] S.A. Choulis, V.-E. Choong, A. Patwardhan, M.K. Mathai, F. So, Interface modification to improve hole-injection properties in organic electronic devices, *Adv. Funct. Mater.* 16 (2006) 1075–1080.
- [28] K. Fujita, T. Ishikawa, T. Tsutsui, Novel method for polymer thin film preparation: spray deposition of highly diluted polymer solutions, *Jpn. J. Appl. Phys.* 41 (2002) L70–L72.
- [29] T. Ishikawa, M. Nakamura, K. Fujita, T. Tsutsui, Preparation of organic bulk heterojunction photovoltaic cells by evaporative spray deposition from ultradilute solution, *Appl. Phys. Lett.* 84 (2004) 2424–2426.
- [30] K. Sagane, M. Shakutsui, T. Tsutsui, K. Fujita, Polymer field effect transistors of F8T2 prepared by evaporative spray deposition using ultradilute solution technique, *J. Photopolym. Sci. Technol.* 21 (2008) 193–196.
- [31] T. Ishikawa, K. Fujita, T. Tsutsui, Small-area deposition of light emission polymer by evaporative spray deposition from ultradilute solution technique, *Jpn. J. Appl. Phys.* 44 (2005) 6292–6294.
- [32] M. Shakutsui, K. Fujita, T. Tsutsui, Improvement in polymer light-emitting diode performance using polymer heterojunction structure prepared by evaporative spray deposition from ultradilute solution, *Jpn. J. Appl. Phys.* 45 (2006) L790–L792.
- [33] M. Redecker, D.D.C. Bradley, M. Inbasekaran, W.W. Wu, E.P. Woo, High mobility hole transport fluorene-triarylamine copolymers, *Adv. Mater.* 11 (1999) 241–246.
- [34] R.U.A. Khan, D. Poplavskyy, T. Kreuzis, D.D.C. Bradley, Hole mobility within arylamine-containing polyfluorene copolymers: a time-of-flight transient-photocurrent study, *Phys. Rev. B* 75 (2007) 035215-1–035215-14.
- [35] L. Bozano, S.A. Carter, J.C. Scott, G.G. Malliaras, P.J. Brock, Temperature- and field-dependent electron and hole mobilities in polymer light-emitting diodes, *Appl. Phys. Lett.* 74 (1999) 1132–1134.
- [36] L. Bozano, S.E. Tuttle, S.A. Carter, P.J. Brock, Temperature-dependent recombination in polymer composite light-emitting diodes, *Appl. Phys. Lett.* 73 (1998) 3911–3913.
- [37] G.G. Malliaras, J.C. Scott, The roles of injection and mobility in organic light emitting diodes, *J. Appl. Phys.* 83 (1998) 5399–5403.
- [38] G.G. Malliaras, J.C. Scott, Numerical simulations of the electrical characteristics and the efficiencies of single-layer organic light emitting diodes, *J. Appl. Phys.* 85 (1999) 7426–7432.
- [39] P.W.M. Blom, H.C.F. Martens, H.E.M. Schoo, M.C.J.M. Vissenberg, J.N. Huiberts, Performance of a polymer light-emitting diode with enhanced charge carrier mobility, *Synth. Met.* 122 (2001) 95–98.
- [40] A.J. Campbell, D.D.C. Bradley, H. Antoniadis, Dispersive electron transport in an electroluminescent polyfluorene copolymer measured by the current integration time-of flight method, *Appl. Phys. Lett.* 79 (2001) 2133–2135.
- [41] A.R. Brown, D.D.C. Bradley, J.H. Burroughes, R.H. Friend, N.C. Greenham, P.L. Burn, A.B. Holmes, A. Kraft, Poly(p-phenylenevinylene) light-emitting diodes: enhanced electroluminescent efficiency through charge carrier confinement, *Appl. Phys. Lett.* 61 (1992) 2793–2795.
- [42] D.V. Khramtchenkov, H. Bässler, V.I. Arkhipov, A model of electroluminescence in organic double-layer light-emitting diodes, *J. Appl. Phys.* 79 (1996) 9283–9290.
- [43] B.K. Crone, P.S. Davids, I.H. Campbell, D.L. Smith, Device model investigation of bilayer organic light emitting diodes, *J. Appl. Phys.* 87 (2000) 1974–1982.
- [44] B. Ruhstaller, S.A. Carter, S. Barth, H. Riel, W. Riess, J.C. Scott, Transient and steady-state behavior of space charges in multilayer organic light-emitting diodes, *J. Appl. Phys.* 89 (2001) 4575–4586.
- [45] A.C. Morteani, A.S. Dhoot, J.-S. Kim, C. Silva, N.C. Greenham, C. Murphy, E. Moons, S.C. Jeremy, H. Burroughes, R.H. Friend, Barrier-free electron-hole capture in polymer blend heterojunction light-emitting diodes, *Adv. Mater.* 15 (2003) 1708–1712.
- [46] A.C. Morteani, R.H. Friend, C. Silva, Electronic processes at semiconductor polymer heterojunctions, in: K. Müllen, U. Scherf (Eds.), *Organic Light Emitting Devices: Synthesis, Properties and Applications*, Wiley-VCH, Weinheim, 2006, pp. 35–94.

- [47] T. Granlund, L.A.A. Pettersson, M.R. Anderson, O. Inganäs, Interference phenomenon determines the color in an organic light emitting diode, *J. Appl. Phys.* 81 (1997) 8097–8104.
- [48] X. Jiang, P. Herguth, T. Sassa, A.K.-Y. Jen, Efficient green polymer light-emitting diodes with microcavity effect in electroluminescence spectrum but constant quantum efficiency, *J. Appl. Phys.* 96 (2004) 3553–3555.
- [49] D.J. Pinner, R.H. Friend, N. Tessler, The use of electrical pulses to study the physics of bilayer organic light-emitting diodes, *J. Appl. Phys.* 97 (2004) 014504-1–014504-3.
- [50] F. Röhlfing, T. Yamada, T. Tsutsui, Electroabsorption spectroscopy on tris-(8-hydroxyquinoline) aluminum-based light emitting diodes, *J. Appl. Phys.* 86 (1999) 4978–4984.
- [51] S.J. Martin, G.L.B. Verschoor, M.A. Webster, A.B. Walker, The internal electric field distribution in bilayer organic light emitting diodes, *Org. Electron.* 3 (2002) 129–141.
- [52] C. Adachi, T. Tsutsui, Molecular LED: design concept of molecular materials for high-performance OLED, in: J. Shinar (Ed.), *Organic Light-Emitting Devices: A Survey*, Springer-Verlag, New York, 2004, pp. 43–69.

would degrade significantly during operation, thus limit their practical applications. In order to overcome this problem and obtain efficient WPLEDs with high color quality and long-term stability, an alternative approach is to use efficient deep-blue polymer as both host material and blue emitter to fabricate multiple dopants all-polymer WPLEDs. So far, polyfluorenes (PFs) and its derivatives are the most frequently used deep-blue polymer for WPLEDs although their luminous efficiency is typically between 1 and 2  $\text{cd A}^{-1}$ , making the efficiency of WPLEDs based on these polymers rarely exceed 10  $\text{cd A}^{-1}$  [15]. Therefore, it is expected that the efficiency of all-polymer WPLEDs can be significantly enhanced if more efficient blue emitter be used in these devices.

In this paper, we report realization of efficient WPLEDs with good color quality based on blending of fluorescent polymers with RGB emission covering the entire visible spectrum. The polymers used here include, a newly synthesized efficient deep-blue emitting polyfluorene derivative named poly[(9,9-bis(4-(2-ethylhexyloxy)phenyl)-+ fluorene)-co-(3,7-dibenzothiophene-S,S-dioxide10)] (PPF-3,7SO10) [19], a green light-emitting poly[2-(4-(3',7'-dimethyloctyloxy)-phenyl)-*p*-phenylenevinylene] (P-PPV) and an orange-red light-emitting 2-methoxy-5-(2'-ethylhexyloxy)-1, 4-phenylenevinylene (MEH-PPV), respectively. Optimized device shows a peak luminous efficiency of 14.0  $\text{cd A}^{-1}$  and a peak power efficiency of 7.6  $\text{lm W}^{-1}$ , with a CIE of (0.33, 0.35) at a current density of 10  $\text{mA cm}^{-2}$ .

## 2. Experimental details

The device structure in this study is indium tin oxide (ITO)/PEDOT:PSS/PPF-3,7SO10 (100 wt%):P-PPV (*x* wt%):MEH-PPV (*y* wt%)/Ba/Al, where PEDOT:PSS is poly(ethylendioxythiophene):poly(styrene sulfonic acid), purchased from H. C. Starck, Inc., while the polymers PPF-3,7SO10, P-PPV and MEH-PPV were synthesized in our laboratory and the chemical structures of these materials show in Fig. 1. The devices were fabricated following a well-established procedure. First, a 40 nm film of PEDOT:PSS (Baytron P4083) was spin coated on a precleaned ITO substrate and baked to dry in a vacuum oven at 80 °C for 12 h. The poly-

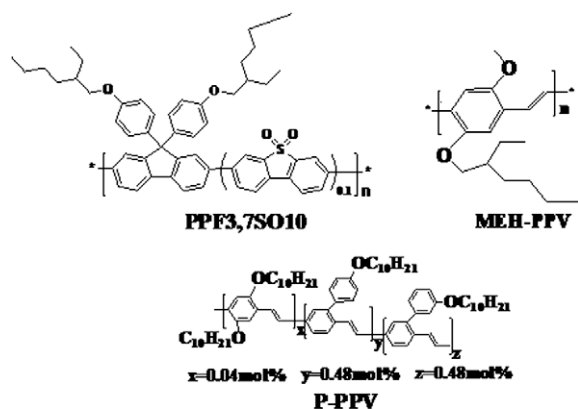


Fig. 1. The chemical structures of PPF-3,7SO10, P-PPV and MEH-PPV device.

mer blend consisting of PPF-3,7SO10, P-PPV and MEH-PPV were spin coated from toluene solution, resulting in an emissive layer of 80 nm (as determined by a profiler, Tencor Alfa-Step 500). Finally, 4 nm barium and 120 nm aluminum layer were evaporated with a shadow mask at a base pressure of  $3 \times 10^{-4}$  Pa. The thickness of the evaporated cathodes was monitored by a quartz crystal thickness/ratio monitor (Model:STM-100/MF, Sycon). The overlapping area between the cathode and anode defined a pixel size of 19  $\text{mm}^2$ . Except for the deposition of the PEDOT:PSS layers, all of the fabrication processes were carried out inside a controlled atmosphere of nitrogen dry-box (Vacuum Atmosphere Co.) containing less than 10 ppm oxygen and moisture. Current density (*j*)-voltage (*V*)-luminance (*L*) data was collected using a Keithley 236 source meter and a calibrated silicon photodiode. The EL spectra and CIE coordinate was recorded using PR-705 SpectraScan spectrophotometer (Photo Research), while the color rendering index (CRI) was calculated following the CIE publication released in 1974 [19]. After the devices were annealed atop of a hotplate at high temperature (120–200 °C) for 2–12 h, spectral stability of EL upon thermal annealing were performed in atmosphere by a PR-705 SpectraScan spectrophotometer soon after cooling down to room temperature. The stability of the white emitting PLEDs was studied in atmosphere by applying a constant current stress with an initial luminance of 1500  $\text{cd m}^2$ . Before annealing in atmosphere and stress test, the PLEDs were encapsulated with a UV-cured epoxy resin.

## 3. Results and discussion

For the monochromatic devices based on MEH-PPV (red), P-PPV (green), and PPF-3,7SO10 (blue), peak LE of 2.5  $\text{cd A}^{-1}$ , 22.2  $\text{cd A}^{-1}$  and 5.1  $\text{cd A}^{-1}$  were recorded, which corresponded to external quantum efficiencies (EQE) of 2.5%, 9.0% and 6.1%, respectively. The 1931 CIE coordinate of the RGB devices were (0.61, 0.39), (0.46, 0.52), and (0.16, 0.16), respectively. While keeping in mind the CIE coordinates of the primary RGB color system adopted by National Television System Committee (NTSC) for color TV are (0.67, 0.33) (R), (0.21, 0.71) (G) and (0.14,

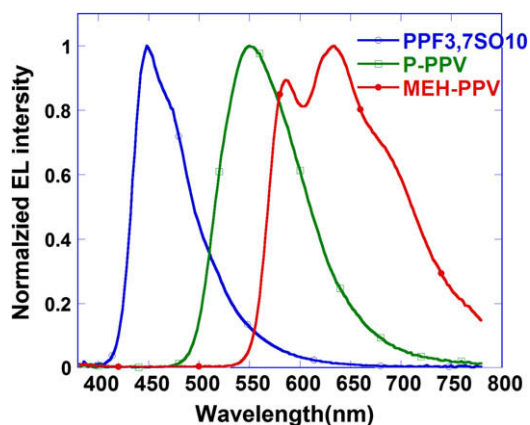


Fig. 2. EL spectra of PPF-3,7SO10, P-PPV and MEH-PPV device.



0.08) (B), it can be clearly seen that the blue emitter match the NTSC best. Also, as shown in Fig. 2, the emission of the monochromatic devices based on the RGB emitters covers the entire visible light spectrum. It is expected that white emission can be realized if emission of each color is carefully balanced.

To obtain white emission with good color quality, a series of devices with various doping concentrations and ratios were fabricated and evaluated, and their device performance was summarized in Table 1. Depending on the doping concentration, devices were referred to as device A1–device D1, with structure like ITO/PEDOT:PSS/PPF-3,7SO10 (100 wt%):P-PPV ( $x$  wt%) and MEH-PPV ( $y$  wt%)/Ba/Al, in which  $x$  vary within 0.5–1.0,  $y$  within 0.2–0.5. As seen from the normalized EL spectra of devices (Fig. 3a), three intense peaks around 450 nm 482 nm and 573 nm were clearly observed, which can be assigned to the emission from PPF-3,7SO10 and MEH-PPV, respectively. Since there is considerable overlap between the EL peak of P-PPV (550 nm) and the shoulder of PPF3, 7SO10 (Fig. 2), the former is merged and could not be seen very clearly in Fig. 3a. Device B1 (with a blend ratio of 100:0.8:0.5 between the RGB emitters) exhibit the most balanced RGB emission, with a CIE coordinate of (0.341, 0.348), very close to the equi-energy white point (0.333, 0.333). Consistent with our previous study on the blue emitter [20], there is a considerable enhancement in LE and EQE for the white emission PLEDs when a thin layer of PVK was inserted at the anode side to facilitate hole injection and transport. The devices with PVK as anode buffer layer were denoted as device A2–D2 and their performances were also included in Table 1 for comparison. Similar to its analog device B1, device B2 had a CIE coordinate of (0.331, 0.353) also very close to the equal-energy point as device B1.

It is interesting to consider the origin of the efficient white emission from this system. Two independent excitation mechanisms may occur: energy transfer from the fluorescent host to the guest materials and charge trapping at the emitter sites [5,21]. As can be seen in Fig. 4a, there is significant overlap between the PL spectrum of PPF-

3,7SO10 and the absorption of P-PPV and MEH-PPV (large overlap between the PL spectrum of P-PPV and absorption of MEH-PPV is also observed, not shown here), implying effective energy transfer from PPF-3,7SO10 to P-PPV and MEH-PPV, or from P-PPV to MEH-PPV could readily take place. However, upon blending with other emitting species, charge trapping at the low band gap emitting sites may also occur. Comparison of PL spectra (Fig. 3b) from the emitting layers with the EL spectra (Fig. 3a) of the devices reveals that the EL spectra have a much higher contribution from the narrow band gap red/green emitters, indicating that charge trapping is the dominant process [5,10]. As shown in Fig. 4b, the HOMO energy levels for PPF-3,7SO10, P-PPV and MEH-PPV are  $-5.6$  eV,  $-5.3$  eV and  $-4.9$  eV, respectively, while the lowest unoccupied molecular orbital (LUMO) are  $-2.8$  eV,  $-2.9$  eV and  $-2.9$  eV, respectively. That is, the HOMO level of the low band gap emitters is above (closer to vacuum level) that of the host, while at the same time, the LUMO level of the guest is below (deeper from vacuum level) that the host. Therefore, when charge carriers are injected from electrodes, simultaneous excitation of the green and red emitting polymers via direct charge trapping could occur as this is energetically favored [22].

Fig. 5 shows the typical current density–luminance–voltage ( $J$ – $L$ – $V$ ) characteristics and luminous efficiency–power efficiency–current density ( $LE$ – $PE$ – $J$ ) characteristics of device B1 and device B2. For device B1, a maximal luminous efficiency of  $8.7$  cd A $^{-1}$  was observed at a current density of  $5.5$  mA cm $^{-2}$  (5.4 V) with a luminance of  $484$  cd m $^{-2}$ , while a maximal power efficiency  $5.6$  lm W $^{-1}$  was reached at  $1.2$  mA cm $^{-2}$  (4.5 V). It is important to note that the turn-on voltage (defined as the voltage at which a luminance of  $1$  cd m $^{-2}$  is reached) of device is as low as  $3.0$  V, which is very helpful to reduce power consumption and obtain high power efficiency. With increasing current density, the device retains high efficiency. For example, at a current density of  $120$  mA cm $^{-2}$ , the LE is  $7.0$  cd A $^{-1}$ , only 20 % roll-off from its peak, corresponding to a luminance of  $8480$  cd m $^{-2}$ . As shown in Fig. 5, for device B2, a maximal LE of  $14.0$  cd A $^{-1}$  and a maximal EQE of 6.9%

**Table 1**

Devices performance for WPLEDs at different doping ratio and device structure.

Device performances							
Device	Composition	Max LE	Max EQE	Max PE	CIE <sup>d</sup>	CCT	CR <sup>d</sup>
	PPFSO10:P-PPV:MEH-PPV	[cd A] <sup>a</sup>	[%] <sup>b</sup>	[lm W] <sup>c</sup>			
A1	100:0.5:0.5	7.4	3.7	4.5	0.307, 0.340	3811	59
B1	100:0.8:0.5	8.7	4.3	5.6	0.341, 0.348	5357	72
C1	100:1.0:0.2	8.1	4.1	4.7	0.341, 0.395	5252	69
D1	100:1:0.8	8.0	4	4.5	0.476, 0.457	2817	43
A2	100:0.5:0.5	12.5	6.2	5.3	0.383, 0.413	4179	70
B2	100:0.8:0.5	14.0	6.9	7.6	0.331, 0.353	5955	79
C2	100:1.0:0.2	12.6	6.3	6	0.304, 0.363	6641	77
D2	100:1:0.8	13.5	6.7	7.2	0.424, 0.412	3297	63

Device structure of A1–D1:ITO/PEDOT:PSS/EML/Ba/Al.

Device structure of A2–D2:ITO/PEDOT:PSS/PVK/EML/Ba/Al.

<sup>a</sup> Maximal front viewing luminous efficiency in cd A $^{-1}$ .

<sup>b</sup> Maximal external quantum efficiency in %.

<sup>c</sup> Maximal front viewing power efficiency in lm W $^{-1}$ .

<sup>d</sup> Observer: 2°; obtained at 10 mA cm $^{-2}$ .

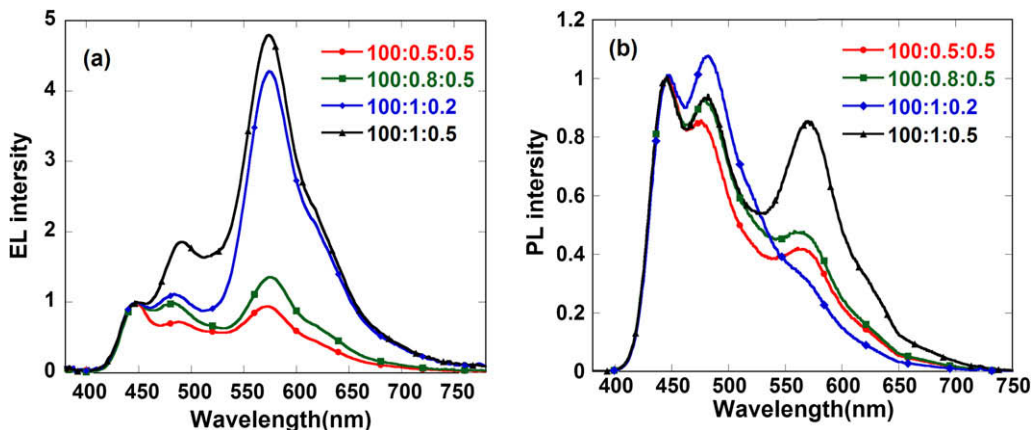


Fig. 3. (a) The EL spectra of the devices with different blend ratio (PPF3,7SO10:P-PPV:MEH-PPV), and (b) the PL spectra from the same emitting layers. The device structure for the devices is ITO/PEDOT:PSS/PPF3,7SO10:(x%)P-PPV:(y%)MEH-PPV/Ba/Al (device: A1–D1). The EL spectra were obtained at a current density of  $10 \text{ mA cm}^{-2}$ .

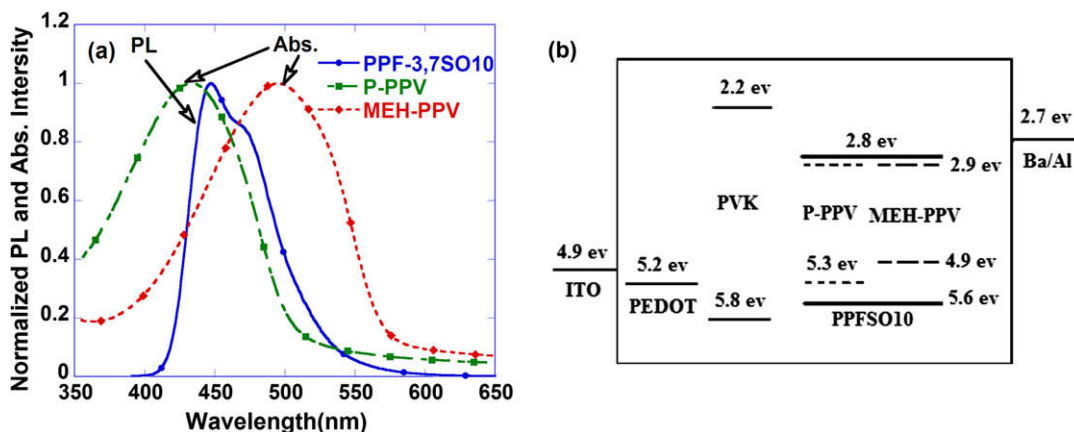


Fig. 4. (a) The PL spectra of PPF-3,7SO10 and the absorption spectrum of the green emitter P-PPV and red emitter MEH-PPV, and (b) energy diagram of devices.

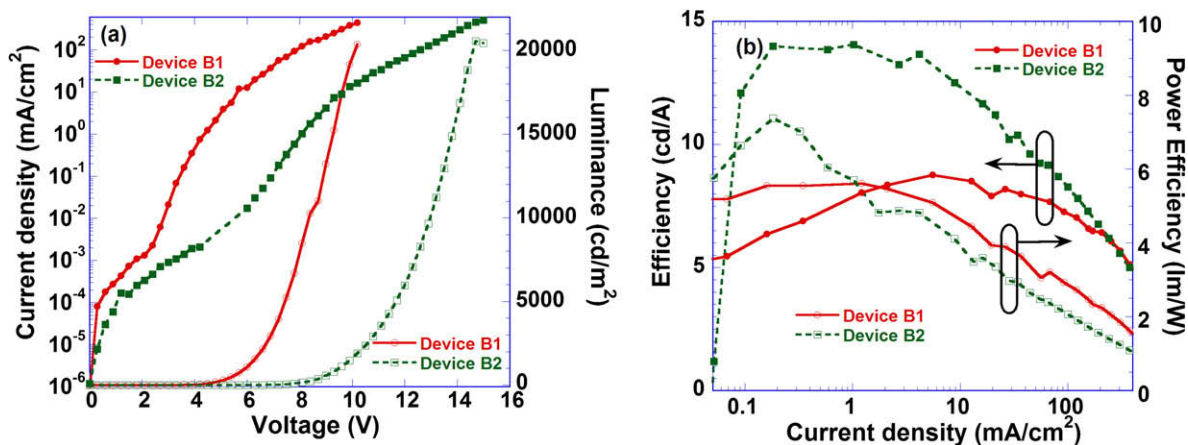
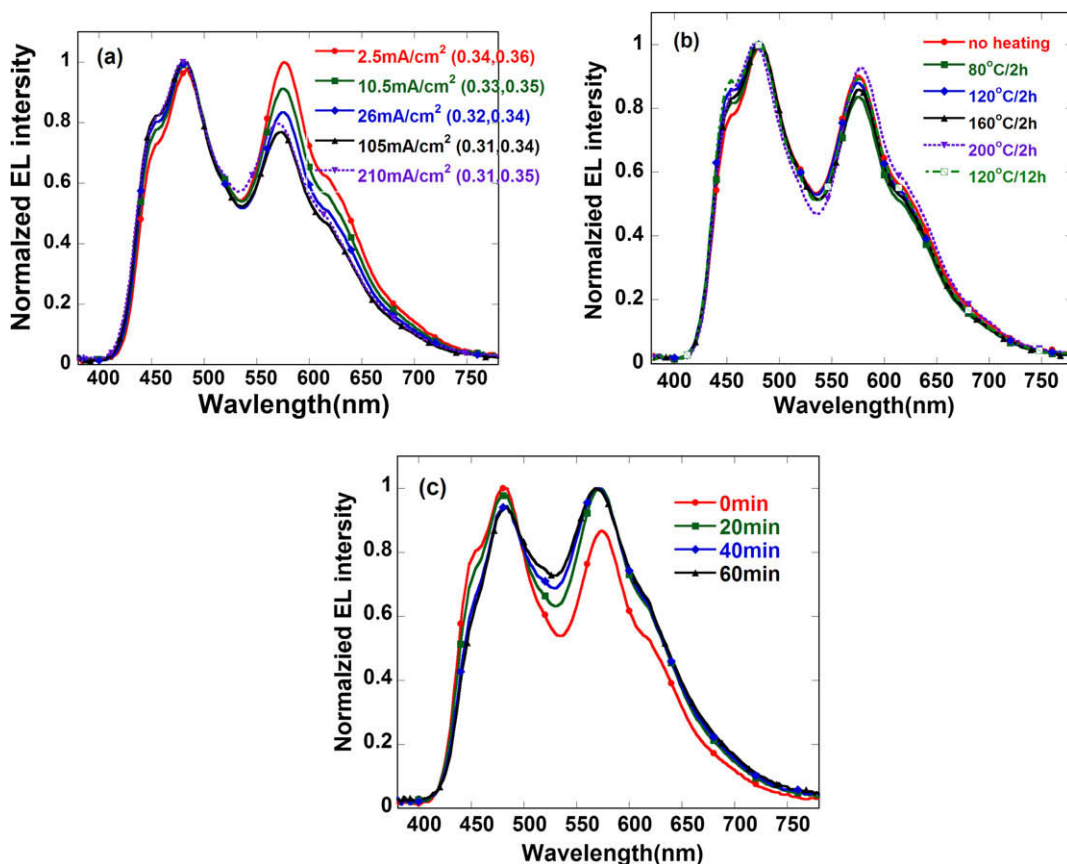


Fig. 5. The current density–luminance–voltage ( $J$ – $L$ – $V$ ) (a) and luminous efficiency–power efficiency–current density ( $LE$ – $PE$ – $J$ ) (b) characteristics of device B1 and B2.



**Fig. 6.** The EL spectra of the device B2 at different current density (a), annealed at different temperatures and hours (b) and under continuous operation at an initial luminance of  $1500 \text{ cd m}^{-2}$  (c).

can be obtained at a current density of  $1.0 \text{ mA cm}^{-2}$  (the maximal power efficiency  $7.6 \text{ lm W}^{-1}$  was reached at  $0.18 \text{ mA cm}^{-2}$ ). It exhibited a turn-on voltage of  $5.7 \text{ V}$  and a maximum brightness of  $20546 \text{ cd m}^{-2}$  at  $454 \text{ mA cm}^{-2}$ . At a luminance of practical applications for solid-state lighting (SSL) application, for example,  $1000 \text{ cd m}^{-2}$ , good forward viewing LE and PE values are maintained:  $12.5 \text{ cd A}^{-1}$ ,  $3.7 \text{ lm W}^{-1}$  at  $8.9 \text{ mA cm}^{-2}$  and  $9.6 \text{ V}$  for device B2. As shown in Table 1, most of the white emission devices had appropriate color temperature (as measured as correlated color temperature (CCT) within 2500–6500 K and relative higher color rendering index (CRI) suitable for solid-state lighting. At a current density of  $10 \text{ mA cm}^{-2}$ , the CRI were 72 and 79 for device B1 and device B2, respectively, representing a good color quality for white lighting source.

Spectral stability upon change of current density, thermal annealing and stress was also studied. When the current density varied from  $2.5 \text{ mA cm}^{-2}$  to  $210 \text{ mA cm}^{-2}$ , as shown in Fig. 6a, the emission color of a typical device B2 did not change much, which is important for illumination. And the CIE coordinates of the white light emission showed a slight change from (0.31, 0.35) to (0.34, 0.36), still close to the white equivalent-energy point of (0.33, 0.33). Fig. 6b showed the EL spectra of device B2 annealed at 80, 120, 160 and  $200^\circ\text{C}$  for 2 h, and  $120^\circ\text{C}$  for 12 h,

respectively. It is important to note that the emission color remained nearly unchanged even high temperature was applied, in consistent with what was found in our previous report on the blue emitter [19]. Moreover, the evolution of spectral stability under continuous stress was also carried out with an initial luminance of  $1500 \text{ cd m}^{-2}$  for device B2. As revealed in Fig. 6c, there is no obvious change with variation of the operating time up to 60 min. Thus, the device B2 represented a good spectral stability upon operational stress, indicating good device stability can be obtained in this white system. It is important to note that, much longer lifetime can be expected if the initial luminance be set as a typical luminance of  $100 \text{ cd m}^{-2}$  and a more reliable encapsulation technology was used.

#### 4. Conclusions

In summary, we report white polymer light-emitting devices with both high efficiency and good color quality, stability based on a newly synthesized efficient blue emitting polymer which dually functions as host material and blue emitter, with appropriate blending ratio with two typical electroluminescent polymers, green emitting P-PPV and orange–red emitter MEH–PPV. Optimized device shows a peak LE of  $14.0 \text{ cd A}^{-1}$  (corresponding to an EQE of 6.9%) with a CIE of (0.33, 0.35) at a current density of

10 mA cm<sup>-2</sup>. Furthermore, our devices are characterized by very good color quality, both in term of color rendering index (~79) and color temperature 2800–6600 K), suitable for solid-state lighting applications. Upon change of current density, continuous operation and annealing at high temperature, the EL spectra shows negligible change, indicating good device stability can be obtained in this system.

### Acknowledgements

The authors are grateful to the Natural Science Foundation of China (Project No. 2009CB623602 and U0634003) for financial support.

### References

- [1] B. Hu, F. Karasz, J. Appl. Phys. 93 (2003) 1995.
- [2] Q.J. Sun, J.H. Hou, C.H. Yang, Y.F. Li, Y. Yang, Appl. Phys. Lett. 89 (2006) 153501.
- [3] Q.L. Niu, Y.H. Xu, J.B. Peng, J. Lumin. 126 (2007) 531.
- [4] Y.H. Xu, J.B. Peng, J.X. Jiang, W. Xu, W. Yang, Y. Cao, Appl. Phys. Lett. 87 (2005) 193502.
- [5] H.B. Wu, J.H. Zou, F. Liu, A. Mikhailovsky, G.C. Bazan, W. Yang, Y. Cao, Adv. Mater. 20 (2008) 696.
- [6] Y. Zhang, F. Huang, Y. Chi, A.K.-Y. Jen, Adv. Mater. 20 (2008) 1565.
- [7] F. Huang, P.-I. Shih, C.-F. Shu, Y. Chi, A.K.-Y. Jen, Adv. Mater. 21 (2009) 361.
- [8] D. An, J.H. Zou, H.B. Wu, J.B. Peng, W. Yang, Y. Cao, Org. Electron. 10 (2009) 299.
- [9] Y.H. Xu, R.Q. Yang, J.B. Peng, A. Milhailovski, Y. Cao, T.-Q. Nguyen, G.C. Bazan, Adv. Mater. 21 (2009) 584.
- [10] X. Gong, W. Ma, J.C. Ostrowski, G.C. Bazan, D. Moses, A.J. Heeger, Adv. Mater. 16 (2004) 615.
- [11] G. Tu, Q. Zhou, Y. Cheng, L. Wang, D. Ma, X. Jing, F. Wang, Appl. Phys. Lett. 85 (2004) 2172.
- [12] M. Mazzeo, D. Pisignano, F. Della Sala, J. Thompson, R.I.R. Blyth, G. Gigli, R. Cingolani, G. Sotgiu, G. Barbarella, Appl. Phys. Lett. 82 (2003) 334.
- [13] Q.J. Sun, B.H. Fan, Z.A. Tan, C.H. Yang, Y.F. Li, Y. Yang, Appl. Phys. Lett. 88 (2006) 163510.
- [14] Y.H. Xu, J.B. Peng, Y.Q. Mo, Q. Hou, Y. Cao, Appl. Phys. Lett. 86 (2005) 163502.
- [15] X. Gong, S. Wang, D. Moses, G.C. Bazan, A.J. Heeger, Adv. Mater. 17 (2005) 2053.
- [16] J. Liu, Q.G. Zhou, Y.X. Cheng, Y.H. Geng, L.X. Wang, D.G. Ma, X.B. Jing, F.S. Wang, Adv. Mater. 17 (2005) 2974.
- [17] J. Liu, Z.Y. Xie, Y.X. Cheng, Y.H. Geng, L.X. Wang, X.B. Jing, F.S. Wang, Adv. Mater. 19 (2007) 531.
- [18] J. Liu, Y.X. Cheng, Z.Y. Xie, Y.H. Geng, L.X. Wang, X.B. Jing, F.S. Wang, Adv. Mater. 20 (2008) 1357.
- [19] "Method of measuring and specifying colour rendering properties of light sources". Publication CIE no. 13.2, Bureau Central de la CIE, Paris, 1974.
- [20] J. Liu, J.H. Zou, W. Yang, H.B. Wu, C. Li, B. Zhang, J.B. Peng, Y. Cao, Chem. Mater. 20 (2008) 4499.
- [21] B.W. D'Andrade, R.J. Holmes, S.R. Forrest, Adv. Mater. 16 (2004) 624.
- [22] X. Gong, J.C. Ostrowski, D. Moses, G.C. Bazan, A.L. Heeger, Adv. Funct. Mater. 13 (2003) 439.

the electrical conductance of the semi-conductor channel and thus distinguishes two logic states, the ON or OFF states of the channel current for memory function [3,5]. Because spontaneous polarization directly controls channel conductance, neither the ferroelectric cell capacitance nor the requirement of a high polarization are determining factors in the device operation potentially beneficial for high density as well as low-power consumption. Furthermore, utilization of organic and polymeric semi-conducting channels turned out beneficial in FeFET for low cost, flexible memory, including vacuum deposited pentacene [6–8], poly(3-hexylthiophene) (P3HT) [9] and poly[2-methoxy, 5-(2'-ethyl-hexyloxy)-*p*-phenylene-vinylene] (MEH-PPV) [3].

For the successful non-volatile ferroelectric memory, high ON/OFF ratio at zero gate voltage should be guaranteed for distinct data recognition. In principle both ON and OFF source–drain current strongly depend upon the charge density of semi-conducting layer in contact with gate insulator at each polarization state. An imperfect ferroelectric gate insulator with many structural defects often results in the leakage current between gate and drain electrode usually larger than that between source and drain one at OFF state, which leads to high OFF current and low ON/OFF ratio in the device. In fact, a thin film of semi-crystalline PVDF and PVDF-TrFE contains many defects arising from crystalline grain–grain mismatch and trapped residual solvent in the film. One way to overcome the problem is obviously to introduce a ferroelectric gate insulator thick enough to minimize the leakage current. The method is; however, not effective because it dramatically increases operating gate voltage required for polarization switching of PVDF-TrFE with relatively large coercive electric field of approximately 50 MV/m. The selection of a proper solvent that can give rise to very dense thin PVDF-TrFE film was another way to reduce the gate leakage. Viscous cyclohexanone has been successfully employed for low operation voltage FeFET with PVDF-TrFE gate insulator [9].

Insertion of an additional interlayer between PVDF-TrFE and gate electrode has been proposed for controlling the leakage [10]. In particular a polymeric interlayer would be beneficial because it forms easily on a substrate based on spin coating and provides a good interface with PVDF-TrFE. We have recently employed 200 nm thick poly(4-vinylphenol) (PVP) and poly(melamine-*co*-formaldehyde) film known as a good dielectric layer for OTFTs into a FeFET with single crystal 6,13-bis(tri-isopropylsilyl)ethynyl pentacene (TIPS-PEN) semi-conducting layer [11]. The sufficiently low OFF current was obtained of approximately  $10^{-11}$  A which guaranteed high ON/OFF ratio with very reliable data retention property. More detailed study was also performed to understand the role of PVP interlayer in both metal-ferroelectric-insulator-semiconductor (MFIS) and FeFET architectures [12]. We found that PVP in the MFIS effectively prevented the shifting of the *C*–*V* hysteresis curve toward the negative bias voltage. The recent work by Lim et al. has also shown that a PVP layer was successfully incorporated in a FeFET with ZnO semi-conducting layer [13]. In spite of the studies with PVP for improving the performance of FeFETs with PVDF-TrFE, only

few work has been devoted to systematic approaches to address fundamental issues including interfacial energy with a ferroelectric layer, surface roughness, dielectric properties and film thickness of an interlayer for minimizing both gate leakage current and operating voltage.

There are in general several factors to be considered when one designs a polymeric interlayer incorporated with PVDF-TrFE. First of all, a firm interface should be obtained between a polymer interlayer and PVDF-TrFE. Good miscibility of poly(methylmethacrylate) (PMMA) with PVDF-TrFE insures the solid and firm interface with surface energy matched with each other [14]. Secondly, a polymeric interlayer should be chemically and thermally resistive to remain stable upon the spin coating and subsequent thermal annealing of a thin PVDF-TrFE layer. A cross-linkable polymer would be one of the candidates for satisfying the requirement. Finally an interlayer with high dielectric constant needs in principle to be used for low operating voltage. We do not; however, have many design rules in this aspect because most of polymer interlayers fall into less than 10 in their dielectric constants.

In this contribution, we employ a new type of polymeric interlayer to systematically investigate the effect of interlayer thickness on FeFETs with ferroelectric PVDF-TrFE. Upon consideration of the aforementioned requirements, we chose an interlayer of a poly(styrene-*random*-methylmethacrylate) copolymer (P(*S-r*-MMA)) containing benzocyclobutene (BCB) as a cross-linking agent. The cross-linkable P(*S-r*-MMA) which has been used for surface modification of self assembled block copolymers [15] is easily spin coated on a substrate with well controlled film thickness ranging from even a few to tens of nanometers. In addition, simple cross-linking of a film by thermal baking provides excellent chemical resistance against various organic solvents. Our study shows that gate–drain leakage current is effectively shielded with a P(*S-r*-MMA) layer of the thickness greater than approximately 25 nm in a bottom gate FeFET containing ca. 350 nm thick PVDF-TrFE layer.

## 2. Experimental

### 2.1. Materials

A P(*S-r*-MMA) used as an insulating layer in the study was anionically polymerized with a lithium initiator. The random copolymer contains 45% of PS moiety with reactive 4-vinylbenzocyclobutene (~3 mole%). Molecular weight ( $M_n$ ) and polydispersity index (PDI) were characterized by typical size-exclusion chromatography (SEC) of 30,000 g/mol and 1.3, respectively. A poly(vinylidene fluoride-*co*-trifluoroethylene) (PVDF-TrFE) with 27.5 wt% TrFE was kindly supplied by MSI Sensor PA, USA. The melting ( $T_m$ ) and Curie ( $T_c$ ) temperature of the polymer are 150 and 80 °C, respectively. Pentacene (purity = 99%) was purchased from Aldrich Chem. Co.

### 2.2. Interlayer preparation

Thin P(*S-r*-MMA) films were spin coated from the solutions in toluene onto either Boron doped Si substrate or Al

electrode with various concentrations. The films were controlled in thickness ranging from 5 to 30 nm. The cross-linked networks were formed when the films were subsequently heated at 250 °C for 15 min under a nitrogen atmosphere. In this study, the films with six different thicknesses were prepared, denoted to P(S-*r*-MMA)1 to 6 in Table 1. The thickness measured by an ellipsometry (Gaertner Scientific Co., USA) is listed in Table 1.

### 2.3. Capacitor and Fe-FET fabrication

Thin PVDF-TrFE films with the thickness of approximately 250 and 350 nm were formed on the P(S-*r*-MMA) interlayers by spin coating (spin rate of 2000 rpm for 1 min) from a 3 to 5 wt% solution in methylethylketone (MEK) for capacitors and FeFET devices, respectively. The films were subsequently annealed at 135 °C for 2 h for enhancing the degree of crystallinity. Metal/PVDF-TrFE/P(S-*r*-MMA)/metal capacitors were made with a highly Boron doped Si substrate as the bottom electrode. Aluminum top electrodes were thermally evaporated on polymer films using a shadow mask with holes of 200 μm in diameter under a pressure of  $7.5 \times 10^{-7}$  torr and rate of 1 Å/s. Metal/P(S-*r*-MMA)/metal capacitors were also prepared for characterization of the thin interlayer films. Capacitance–voltage measurements were performed using HP4284A at 1 MHz. Ferroelectric properties were obtained using a virtual ground circuit (Radiant Technologies Precision LC unit).

Fabrication of a FeFET memory with pentacene active layer channel starts with the formation of a bilayered PVDF-TrFE/P(S-*r*-MMA) gate dielectric consecutively spin coated on a heavily Boron doped Si gate electrode. Pentacene channel and source/drain Au films were sequentially patterned on the gate insulators through shadow mask on the substrate at room temperature by thermal evaporation in a vacuum chamber at a base pressure of  $9.0 \times 10^{-7}$  torr. The deposition rates were fixed at 0.3 Å/s for the pentacene, and at 1 Å/s for Au electrodes. The pentacene and the Au films were 60 and 100 nm thick, respectively. The pentacene channel length and width were 50 μm and 200 μm, respectively. The schematic of a pentacene FeFET device with bilayered PVDF-TrFE/P(S-*r*-MMA) gate insulator is shown with the detailed chemical structures of the components in Fig. 1. The electrical properties of the devices were recorded using semiconductor systems (E5270B, HP4284A, Agilent Technologies). All measurements were done in metallic shielded box at room temperature in air.

**Table 1**

Characteristics of thin P(S-*r*-MMA) interlayer films.

Samples	Thickness (nm)	RMS (nm)	Capacitance (pF)	Dielectric constant
P(S- <i>r</i> -MMA)1	5.23	0.598	111.73	2.10
P(S- <i>r</i> -MMA)2	11.28	0.569	56.48	2.29
P(S- <i>r</i> -MMA)3	15.09	0.432	43.42	2.44
P(S- <i>r</i> -MMA)4	19.68	0.442	33.18	2.35
P(S- <i>r</i> -MMA)5	25.06	0.555	27.85	2.51
P(S- <i>r</i> -MMA)6	29.15	0.446	21.94	2.36

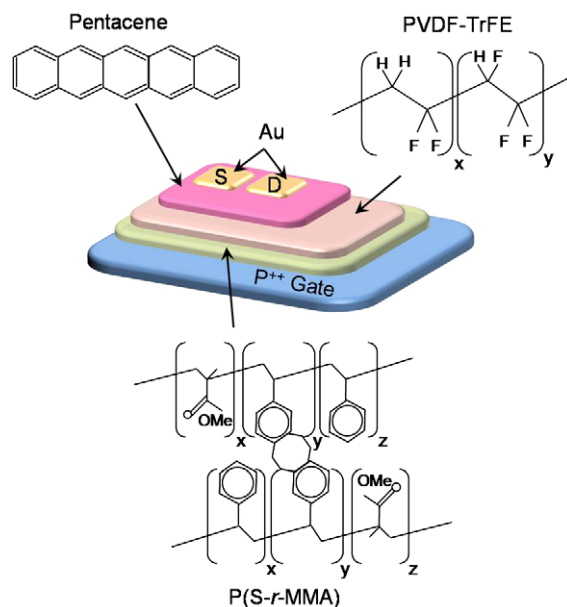


**Fig. 1.** Schematic of a bottom gate FeFET with pentacene active layer and bilayered PVDF-TrFE/P(S-*r*-MMA) gate dielectric.

### 2.4. Measurement and characterization

Tapping Mode Atomic Force Microscope(TM-AFM, Nanoscope IV.Digital Instrument) was used to examine the surface morphologies of P(S-*r*-MMA) and PVDF-TrFE films. Both initial and final morphologies of pentacene on PVDF-TrFE were also characterized by AFM and Field Emission Scanning Electron Microscope (FESEM) (Jeol 2000). The crystalline structure of PVDF-TrFE was characterized by 2 dimensional (2D) Grazing-Incidence X-ray Diffraction (GIXD). The GIXD was performed on the 4C2 beam line at the Pohang Accelerator Laboratory in Korea (incidence angle: 0.09°–0.15°). Monochromatized X-rays ( $\lambda = 0.1608$  nm) under vacuum and the full range of available incidence angles are used. The scattered beam intensity was recorded with an SCX: 4300-165/2 CCD detector (Princeton Instruments). 2D GIXD patterns we obtained in the range  $0 < q_z < 2.33 \text{ \AA}^{-1}$ ,  $0 < q_{xy} < 2.33 \text{ \AA}^{-1}$  ( $q = 4\pi \cdot \sin\theta/\lambda$  with  $z$  perpendicular and  $xy$  parallel to the substrate).

## 3. Results and discussion

First of all, we characterized thin film properties of P(S-*r*-MMA) interlayers with different film thickness. All films are very smooth and their root mean square (RMS) roughness values range from 0.43 to 0.59 nm with the standard deviation of 0.07 nm, regardless of the film thickness as shown in Table 1. The capacitance values measured from metal/P(S-*r*-MMA)/metal capacitors are also listed in Table 1. In addition, the relative dielectric constants of the interlayers were calculated, based on the contact area and film thickness in Table 1. One can easily notice that the capacitance values are almost inversely proportional to the film thickness within experimental uncertainty, giving rise to

dielectric constants all similar for the films. The dielectric constant values of P(S-*r*-MMA) samples are between 2.1 and 2.5 and their average value is 2.34 with the standard deviation 0.139. Compared with the dielectric constants of PS, PMMA and BCB of approximately 2.5 [16], 2.6 [17] and 2.7 [18] at 1 MHz, respectively, the values we obtained from the random copolymers are slightly lower. Our interlayers turn out to be well controlled in thickness with fairly constant surface and dielectric properties.

The microdomain and crystalline molecular structures of a thin PVDF-TrFE film were visualized on a P(S-*r*-MMA)<sub>2</sub> with FE-SEM and GIXD in Fig. 2a and b, respectively. The PVDF-TrFE film annealed at 135 °C for 2 h clearly exhibits the characteristic needle-like crystalline domains randomly organized with the length and width of approximately 200 and 40 nm, respectively, as shown in Fig. 2a. The crystalline structure of the film by 2D GIXD in Fig. 2b shows an intensified reflection on the meridian arising from the preferred (1 1 0) crystals aligned along the film surface normal with the polymer chains lying on the surface, consistent with our previous results obtained on Al or Si substrates [19,20]. The ordered (1 1 0) reflection

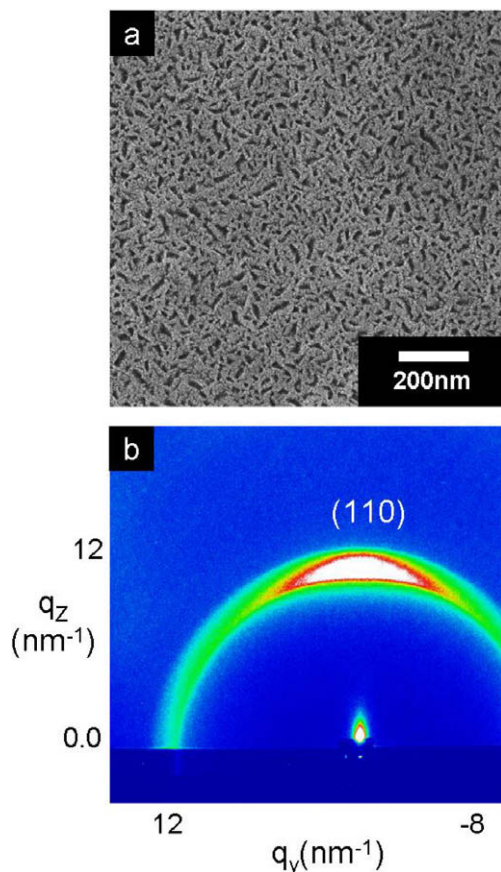


**Fig. 2.** (a) A FESEM image (b) a 2D GIWAXD pattern of ca. About 250 nm thick PVDF-TrFE film spin coated and subsequently annealed at 135 °C for 2 h on 10 nm thick P(S-*r*-MMA) layer. The characteristic needle-like crystalline microdomains are well developed on the interlayer with the length and width of approximately 200 and 40 nm, respectively. The preferentially aligned (1 1 0) reflection is apparent on the meridian in (b).

on the meridian is again desirable for polarization switching upon electric field, allowing the effective rotation of *b*-axis, polarization axis around chain backbone. PVDF-TrFE films on the other interlayers also exhibit the similar micro and molecular structures. The data indicate that ferroelectric PVDF-TrFE microdomains are also well developed with the proper crystalline orientation to polarization switching on our P(S-*r*-MMA) interlayers.

The ferroelectric polarization behavior of a 250 nm thick PVDF-TrFE film was characterized using typical polarization-applied voltage (*P*-*V*) hysteresis loop on P(S-*r*-MMA) interlayer with different film thickness as shown in Fig. 3a. A capacitor of the PVDF-TrFE film spin coated and subsequently annealed at 135 °C for 2 h on highly Boron doped Si electrode without an interlayer shows a typical square-like and symmetrical hysteresis loop, resulting in a remanent polarization,  $P_r$ , of approximately 7  $\mu\text{C}/\text{cm}^2$  and a coercive Voltage,  $V_c$  of 11.9 V, when sweep voltage is applied above  $\pm 30$  V as shown in Fig. 3a (black squares). Incorporation of an interlayer requires higher sweep voltage for the saturation of PVDF-TrFE polarization, giving rise to the increase of the apparent coercive voltage with the thickness of an interlayer as displayed in Fig. 3a. The  $P_r$  values of the capacitors with the hysteresis loops fully saturated remain almost same as approximately 7  $\mu\text{C}/\text{cm}^2$  irrespective of interlayer thickness.

A capacitor with bilayered PVDF-TrFE/P(S-*r*-MMA) with the architecture of metal-insulator-ferroelectric-metal (MIFM) is treated as two independent and individual capacitors connected in series similar to the previous works by others [13,21,22]. In particular a PVDF-TrFE film we prepared is in pristine unpoled state just like a dielectric one at the beginning. In this condition, the voltage applied should be shared with our interlayer according to the series model, giving rise to the increase of the apparent coercive voltage as observed in our experiment. It should be noted that the effective coercive voltage applied only to the PVDF-TrFE film is supposed to be same regardless of the interlayers. Each capacitor takes the part of the voltage applied proportional to film thickness and inversely proportional to dielectric constant. In our cases, at least  $\pm 30$  V should be exerted on a 250 nm thick PVDF-TrFE layer for full polarization saturation. The total voltage applied in a bilayered capacitor should therefore, increase linearly with the thickness of interlayer. In addition, the relatively low 2.5 dielectric constant of P(S-*r*-MMA), compared to that of PVDF-TrFE ( $\sim 10$ ), makes the sweep voltage higher than  $\pm 90$  V even with 30 nm thick interlayer. In fact, a plot of the apparent  $V_c$  as a function of the interlayer thickness clearly displays a linear relation as shown in Fig. 3b. The ferroelectric properties of the capacitors including coercive voltage and remnant polarization are also summarized in Table 2. In our experiments; however, the effective coercive voltage also slightly increases with the interlayer thickness. The reason may be due to the leakage current in the interlayer. We speculate that at the voltage close to the breakdown one of an interlayer, there must be some leakage current which again influences the polarization of PVDF-TrFE. In addition, the polarization behavior of a PVDF-TrFE layer different on an interlayer from on metal surface without the interlayer may result

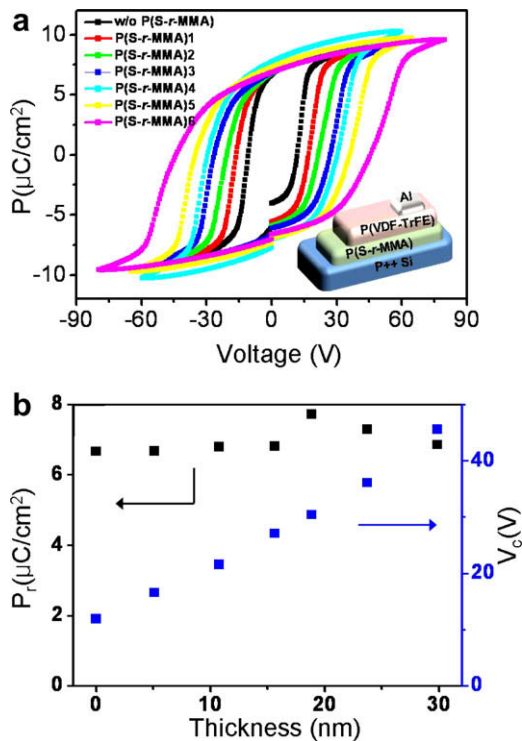


**Fig. 3.** (a) Polarization vs. applied voltage ( $P$ - $V$ ) hysteresis loops of metal/250 nm thick PVDF-TrFE/P(S-r-MMA)/metal capacitors with different P(S-r-MMA) interlayers. The inset shows a schematic of a capacitor. (b) Plots of remanent polarization ( $P_r$ ) (left hand side) and coercive voltage ( $V_c$ ) (right hand side) as a function of the P(S-r-MMA) interlayer thickness in the capacitors.

in the increase of the effective  $V_c$  due to the complicated PVDF-TrFE/interlayer interfacial properties containing surface charges, defects and residual solvent molecules and so on.

A pentacene FeFET with single layered PVDF-TrFE film clearly exhibits the hysteresis of source-drain current ( $I_{\text{DS}}$ ) as a function of gate voltage due to the ferroelectric PVDF-TrFE gate dielectric layer as shown in Fig. 4a. The sharp increase of  $I_{\text{DS}}$  with negative bias gate voltage was attributed to excess holes accumulated in the pentacene layer in particular at the vicinity of the interface between pentacene and PVDF-TrFE layer. When gate voltage became back to zero,  $I_{\text{DS}}$  still remains at the value saturated with the gate voltage of  $-40$  V due to the non-volatility of H-F dipoles in PVDF-TrFE film. The subsequent applica-

tion of positive gate voltage on the device gradually switches the H-F dipoles with H atoms pointing to pentacene layer, giving rise to the rapid decrease of  $I_{\text{DS}}$ . The non-volatility of polarization again makes the current remaining same even after the removal of the positive voltage as shown in Fig. 4a.

The ON and OFF current were obtained of approximately  $1.28 \times 10^{-7}$  and  $5.83 \times 10^{-9}$  A, respectively, leading to the ON/OFF bistability ratio of approximately 20 as shown in both Fig. 4a and Table 2. The lower ON current in our device than a typical bottom gate pentacene OTFT with  $\text{SiO}_2$  gate dielectric ( $\sim 10^{-5}$  A) arose from the roughened crystalline surface of PVDF-TrFE layer directly in contact with pentacene, consistent with our recent results observed in a FeFET with single crystal TIPS-PEN as an active layer [11]. On the other hand, the OFF current in our device is much higher than that observed in a pentacene OTFT we prepared in our laboratory ( $\sim 10^{-11}$  A). In addition, the single crystal TIPS-PEN FeFET displayed the OFF current of approximately  $10^{-11}$  when 200 nm thick PVP interlayer was employed. The high OFF current did not arise from the pentacene channel between source and drain electrode but from the leakage current between gate and drain electrode.

The gate current simultaneously measured with the source-drain current hysteresis arises from both H-F dipole switching which corresponds to peaks and leakage during accumulation and depletion cycle as shown in the inset of Fig. 4a. The leakage becomes significant with gate voltage and becomes as large as approximately  $5 \times 10^{-8}$  A. This value is smaller than ON source-drain current observed ( $\sim 1.28 \times 10^{-7}$  A), which implies that ON current is mainly attributed to the channel current arising from holes accumulated in the pentacene layer. The OFF current is, on the other hand, apparently dominated by the large gate leakage, as observed in Fig. 4a.

In order to gain the insight of the high OFF current in the pentacene FeFET, we investigated the cross-section of a 200 nm thick PVDF-TrFE film spin coated and subsequently annealed at  $135^\circ\text{C}$  by FE-SEM in Fig. 4b. As noticed, there exist many pin holes which arise from the crystalline defects as well as residual solvent in the film. The origin of the defective microstructure is currently under investigation. It is; however, apparent that the defective film structure gave rise to the high OFF current of the FeFET mainly originated from the leakage current between gate and drain electrode.

The incorporation of P(S-r-MMA) interlayer between gate electrode and PVDF-TrFE film significantly influences

**Table 2**  
Device performances of FeFETs and MFIM Capacitors with P(S-r-MMA) interlayers.

Samples	$P_r$ ( $\mu\text{C}/\text{cm}^2$ )	$V_c$ (V)	$I_{\text{on}}$ (A)	$I_{\text{off}}$ (A)	$I_{\text{on}}/I_{\text{off}}$	Mobility ( $\text{cm}^2/\text{V s}$ )
w/o P(S-r-MMA)	6.67	11.9	1.28E-07	5.83E-09	$10^{1.34}$	0.0065
P(S-r-MMA)1	6.68	16.6	8.07E-08	1.20E-09	$10^{2.28}$	0.0065
P(S-r-MMA)2	6.79	21.6	1.42E-07	1.18E-09	$10^{2.46}$	0.0065
P(S-r-MMA)3	6.82	27.1	1.28E-07	5.05E-10	$10^{2.6}$	0.0066
P(S-r-MMA)4	7.72	30.4	1.06E-07	1.90E-10	$10^{2.98}$	0.0061
P(S-r-MMA)5	7.29	36.1	1.25E-07	5.34E-11	$10^{3.58}$	0.0064
P(S-r-MMA)6	6.86	45.6	9.20E-08	7.09E-11	$10^{3.16}$	0.0066



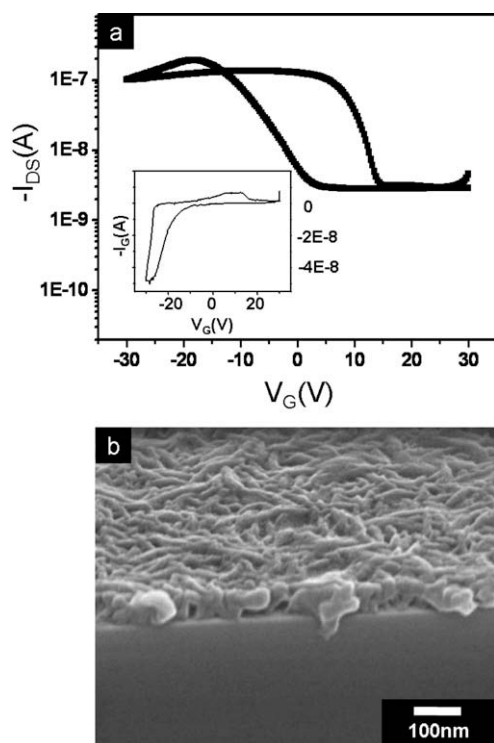


**Fig. 4.** (a) Transfer characteristic curve ( $I_{DS}$ – $V_G$ ) of a pentacene FeFET with ca. 350 nm thick PVDF-TrFE gate insulator at  $V_D = -5$  V. The inset displays  $I_G$ – $V_G$  curve simultaneously obtained with the transfer curve. (b) A FESEM image of a thin PVDF-TrFE film with the thickness of approximately 200 nm annealed at 135 °C for 2 h on Si substrate.

OFF current in pentacene FeFETs, depending upon interlayer thickness as shown in Fig. 5a. To avoid the experimental error due to uneven pentacene evaporation, all devices with the different interlayers were fabricated in a same batch and the ON and OFF current of a FeFET memory were averaged with 4 sets of samples. It should be noted that the  $I_{DS}$  hysteresis curves in Fig. 5a are the representative ones with the different interlayers. The gate voltage is generally swept from 40 to  $-40$  V in double mode with which gate voltage is swept twice from positive to negative value to confirm the bistability of the drain current. One can easily notice that OFF current becomes significantly lowered with the interlayer with a certain thickness while ON current remains all similar at approximately  $1 \times 10^{-7}$  A, which indicates that the interlayer indeed shields the gate leakage current present in bare PVDF-TrFE layer. A plot of ON and OFF current as a function of the interlayer thickness in Fig. 5b clearly displays that OFF current gradually decreases with interlayer thickness and reaches at approximately  $10^{-11}$  A when the interlayer becomes thicker than 25 nm. The OFF currents we chose for comparison as a function of the interlayer thickness was the values at  $V_g$  equal to 0, the condition for non-volatility of the data. The reduction of OFF source–drain current with the interlayers apparently results in the improvement of data bistability characterized with the ratio of ON to OFF current. For instance the ON/OFF current ratio of approximately 20 in a FeFET without an interlayer was signifi-

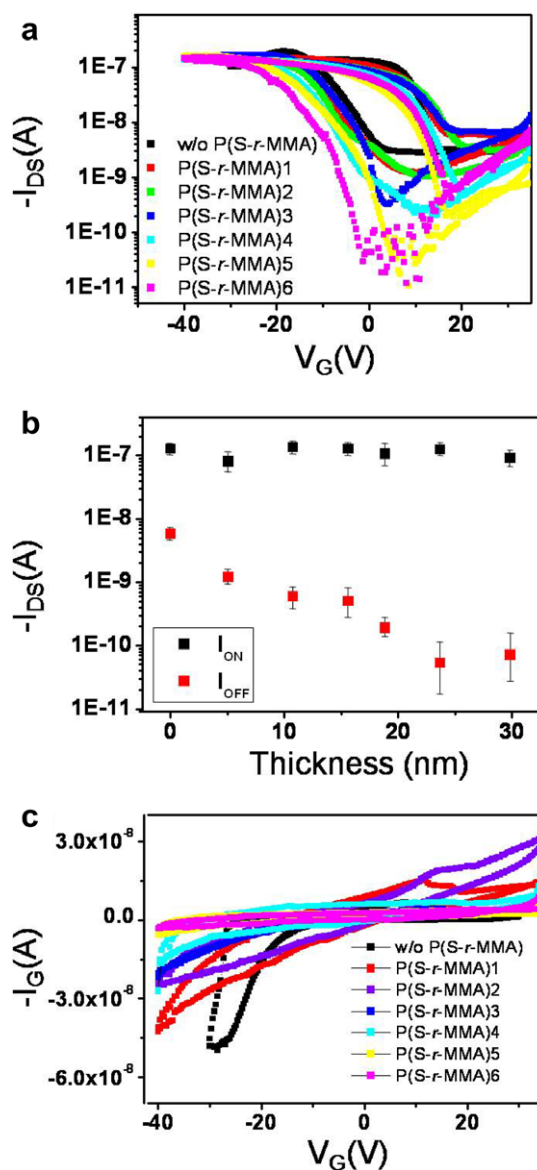


**Fig. 5.** (a) Transfer characteristic curves ( $I_{DS}$ – $V_G$ ) at  $V_D = -5$  V of pentacene FeFETs with six different P(S-r-MMA) interlayers. The transfer curve of the FeFET without P(S-r-MMA) layer (Fig. 4a) is also plotted for comparison. (b) Plots of ON and OFF current as a function of the P(S-r-MMA) interlayer thickness. While ON current remains all similar, OFF current gradually decreases with the interlayer film thickness up to approximately 25 nm. (c)  $I_G$ – $V_G$  curves of the FeFETs simultaneously obtained with the transfer curves show that gate leakage current becomes significantly reduced with the thickness of the interlayer.

cantly enhanced to the value greater than 1000 with 25 nm thick interlayer. Detailed ON and OFF current information with different P(S-r-MMA) interlayers is also shown in Table 2.

The reduction of OFF source–drain current with the interlayers is also confirmed with the gate currents simultaneously obtained with the hysteresis curves in Fig. 5c. As expected, the gate current remarkably decreases with the thickness of P(S-r-MMA) interlayers. In particular the gate

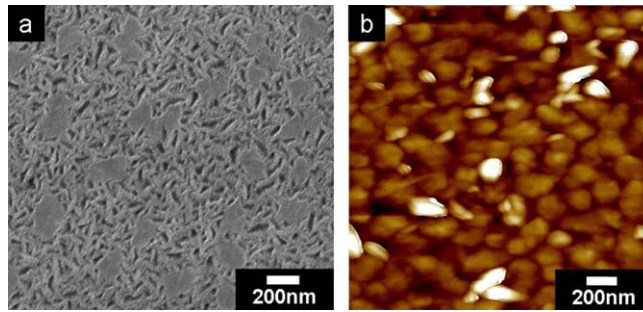


**Fig. 6.** (a) A FESEM image of pentacene layer deposited on PVDF-TrFE film with 1 nm nominal thickness exhibits non-spherical pentacene domains grown on randomly ordered needle-like crystal domains of the PVDF-TrFE layer. (b) An AFM image of ca. 60 nm thick pentacene layer grown on a PVDF-TrFE film shows both pentacene grains with approximately 200 nm in size and unusually protuberant ones.

leakage of a FeFET with P(S-*r*-MMA)6 becomes negligible with the gate voltage sweep of  $\pm 40$  V and does not contribute to the OFF source–drain current any more. The OFF current observed now mainly arises from the pentacene channel current in depletion mode in our experimental set up.

It is noteworthy that the coercive voltages observed in MFM capacitors are not the same as the turn-on gate voltages in the transistors. For instance, the apparent  $V_c$  of a capacitor with 250 nm thick PVDF-TrFE/P(S-*r*-MMA)6 is approximately 45 V while the turn-on voltage of 350 nm thick PVDF-TrFE/P(S-*r*-MMA)6 is 40 V. A transistor with PVDF-TrFE has shown very complicated device behavior such as flat band shift depending on the majority carrier type of organic semiconductors [5]. Furthermore, the insertion of an interlayer renders it more difficult to fully understand the device performance. The difference of coercive voltage between MFIM and transistor structure is one of those unsolved issues. Although it is obvious that turn-on voltage of a ferroelectric transistor is directly proportional to coercive field of the ferroelectric layer, the voltage does not coincide with the coercive voltage of a capacitor in particular when an interlayer is inserted.

The field effect mobility of a FeFET was calculated from the slope of  $I_{DS}$  vs. gate voltage ( $V_G$ ) in Fig. 5a, using an equation suitable for linear regime of drain current–voltage due to the application of a low source–drain voltage ( $V_{DS}$ ) of  $-5$  V in our device. The equation is given by  $I_{DS} = (W/2L)C_i\mu[2(V_G - V_T)V_{DS} - V_{DS}^2]$ , where  $W$  and  $L$  are the width and length of channel and  $C_i$ ,  $\mu$ , and  $V_T$  correspond to the capacitance per unit area of either PVDF-TrFE or P(S-*r*-MMA)/PVDF-TrFE gate insulator, the field effect mobility and threshold voltage, respectively [23]. The hole mobility values with the different interlayers are all similar of approximately  $0.006 \text{ cm}^2/\text{V s}$  which is much smaller than a typical value of a bottom gate, top contact pentacene OTFT with oxide gate dielectric ( $0.5\text{--}1 \text{ cm}^2/\text{V s}$ ). The similar field effect mobilities irrespective of the interlayers imply that the variation of OFF current observed with the interlayers was not ascribed to the pentacene active layer. The lower field effect mobility in our FeFET device may arise from the rough surface of a semi-crystalline PVDF-TrFE film with the needle-like microdomains shown in Fig. 2a as reported by Stadlober et al. [24]. The rough surface of a PVDF-TrFE film was confirmed by RMS roughness

of approximately 2.3 nm, measured and averaged from several AFM images.

In order to examine the effect of the rough PVDF-TrFE surface on pentacene layer formation, we monitored the early stage deposition of pentacene layer on a PVDF-TrFE film annealed at  $135^\circ\text{C}$  for 2 h. A pentacene layer with 1 nm nominal thickness deposited on the PVDF-TrFE film clearly exhibits non-circular shape pentacene domains sporadically distributed with approximately 200 nm in size as shown in Fig. 6a. These anisotropic pentacene domains at early stage of deposition are all observed with P(S-*r*-MMA) interlayers beneath PVDF-TrFE. All 60 nm thick pentacene films used for the FeFET devices with the interlayers show a unique surface morphology in which approximately 200 nm pentacene grains are closely packed with characteristic protruding peaks as evidenced in Fig. 6b. Both small grains and the unusual peaks developed from the initial anisotropic domains may result in the relatively low hole mobility of the devices. More detailed understanding of the crystalline pentacene structure is under investigation.

#### 4. Conclusion

Our results demonstrated that new P(S-*r*-MMA) films were successfully utilized as interlayers between ferroelectric PVDF-TrFE layer and gate electrode for bottom gate pentacene FeFET memory devices. Both chemically and thermally resistive interlayers were beneficial not only for forming thin and uniform PVDF-TrFE films with the characteristic ferroelectric domain well developed but also more importantly for reducing gate leakage current in the devices, leading to both low OFF source–drain current and high ON/OFF current ratio. In particular such a low OFF current of approximately  $10^{-11}$  A was obtained with the P(S-*r*-MMA) interlayers thicker than 25 nm, giving rise to the ON/OFF current ratio greater than  $10^3$  which was improved two orders of magnitude larger than that without an interlayer at operating sweep voltage of  $\pm 40$  V.

#### Acknowledgements

This project was supported by The National Research Program for the 0.1 Terabit Non-Volatile Memory Develop-

ment and “SYSTEM2010” project sponsored by Korea Commerce, Industry and Energy and Samsung Electronics, Co., Ltd. This work was supported by the Second Stage of Brain Korea 21 Project in 2006 and the Korea Science and Engineering Foundation (KOSEF) grant funded by the Korea government (MOST) (No. R11-2007-050-03001-0) DAPA and ADD.

## References

- [1] J.C. Scott, L.D. Bozano, *Adv. Mater.* 19 (2007) 1452–1463.
- [2] K. Asadi, D.M. de Leeuw, B. de Boer, P.W.M. Blom, *Nat. Mater.* 7 (2008) 547–550.
- [3] R.C.G. Naber, C. Tanase, P.W.M. Blom, G.H. Gelinck, A.W. Marsman, F.J. Touwslager, S. Setayesh, D.M. de Leeuw, *Nat. Mater.* 4 (2004) 243–248.
- [4] A.J. Lovinger, *Science* 220 (1983) 1115–1121.
- [5] C.A. Nguyen, P.S. Lee, S.G. Mhaisalkar, *Org. Electron.* 8 (2007) 415–422.
- [6] W. Choi, S.H. Noh, D.K. Hwang, J.M. Choi, S. Jang, E. Kim, S. Im, *Electrochem. Solid-State Lett.* 11 (2008) H47–H50.
- [7] K.N.N. Unni, R. de Bettingnies, S.D. Seignou, J.M. Nulzi, *Appl. Phys. Lett.* 85 (2004) 1823–1825.
- [8] C.A. Nguyen, S.G. Mhaisalkar, J. Ma, P.S. Lee, *Org. Electron.* 9 (2008) 1087–1092.
- [9] R.C.G. Naber, B. de Boer, P.W.M. Blom, D.M. de Leeuw, *Appl. Phys. Lett.* 87 (2005) 203509.
- [10] S.L. Miller, P.J. McWhorter, *J. Appl. Phys.* 72 (1992) 5999–6010.
- [11] S.J. Kang, I. Bae, Y.J. Park, T.H. Park, J. Sung, S.C. Yoon, K.H. Kim, D.H. Choi, C. Park, *Adv. Funct. Mater.*, in press.
- [12] C.W. Choi, A.A. Prabu, Y.M. Kim, S. Yoon, K.J. Kim, C. Park, *Appl. Phys. Lett.* 93 (2008) 182902.
- [13] S.H. Noh, W. Choi, M.S. Oh, D.K. Hwang, K. Lee, S. Im, S. Jang, E. Kim, *Appl. Phys. Lett.* 90 (2007) 253504.
- [14] B.R. Hahn, O. Herrmann-Schönherr, J.H. Wendorff, *Polymer* 28 (1987) 201–208.
- [15] D.Y. Ryu, K. Shin, E. Drockenmuller, C.J. Hawker, T.P. Russel, *Science* 308 (2005) 236–238.
- [16] J. Brandrup, E.H. Immergut, E.A. Grulke, A. Abe, D.R. Bloch, *Polymer Handbook*, fourth ed., J. Wiley & Sons, New York, 1999.
- [17] M. Estrada, I. Mejia, A. Cerdeira, B. Iñiguez, *Solid-State Electron.* 52 (2008) 53–59.
- [18] D. Burdeaux, P. Townsend, J. Carr, P. Garrou, *J. Electron. Mater.* 19 (1990) 1357–1366.
- [19] Y.J. Park, S.J. Kang, C. Park, E. Woo, K. Shin, K.J. Kim, *Appl. Phys. Lett.* 90 (2007) 222903.
- [20] Y.J. Park, S.J. Kang, C. Park, K.J. Kim, H.S. Lee, M.S. Lee, U. Chung, I.J. Park, *Appl. Phys. Lett.* 88 (2006) 242908.
- [21] S.H. Lim, A.C. Rastogi, S.B. Desu, *J. Appl. Phys.* 96 (2004) 5673–5682.
- [22] H. Ishiwara, *J. Semicon. Tech. Sci.* 1 (2001) 1–14.
- [23] R.S. Muller, T.I. Kamins, *Device Electronics for Integrated Circuits*, third ed., J. Wiley & Sons, New York, 2003.
- [24] B. Stadlober, M. Zirkl, M. Beutl, G. Leising, S. Bauer-Gogonea, S. Bauer, *Appl. Phys. Lett.* 86 (2005) 242902.

in the application of computer desktop visualization in which bright saturated colors are widely used, adding a white sub-pixel may not be as efficient as in the video application. Moreover, if the size of each sub-pixel is kept the same, adding additional sub-pixel will reduce the display's resolution. On the contrary, if the display's resolution is kept the same, the sub-pixel's size has to be reduced to accommodate the additional sub-pixel. In this work, we present a novel method to characterize the display performance over the whole color space, and we introduce a color usage frequency to simulate real world images. By adjusting the color usage frequency, the advantage of the white sub-pixel can be clearly deduced.

## 2. Color matching

Since there are three different types of the retinal receptors in human eyes that provide the photopic vision, in principle, any arbitrary color can be reproduced by three primary colors [17]. In a RGB display, any color within the triangle enclosed by the red, green, and blue primary colors can be reproduced (Fig. 1), and the color matching is unique. The following equations give the amount of each primary needed to produce a color at a certain luminance:

$$m_1 = \frac{\left(\frac{1}{y_2} - \frac{1}{y_3}\right) \frac{x}{y} - \left(\frac{1}{y} - \frac{1}{y_3}\right) \frac{x_2}{y_2} - \left(\frac{1}{y_2} - \frac{1}{y}\right) \frac{x_3}{y_3}}{\left(\frac{1}{y_2} - \frac{1}{y_3}\right) \frac{x_1}{y_1} + \left(\frac{1}{y_3} - \frac{1}{y_1}\right) \frac{x_2}{y_2} + \left(\frac{1}{y_1} - \frac{1}{y_2}\right) \frac{x_3}{y_3}} m$$

$$m_2 = \frac{\left(\frac{1}{y_3} - \frac{1}{y_1}\right) \frac{x}{y} - \left(\frac{1}{y} - \frac{1}{y_1}\right) \frac{x_3}{y_3} - \left(\frac{1}{y_3} - \frac{1}{y}\right) \frac{x_1}{y_1}}{\left(\frac{1}{y_2} - \frac{1}{y_3}\right) \frac{x_1}{y_1} + \left(\frac{1}{y_3} - \frac{1}{y_1}\right) \frac{x_2}{y_2} + \left(\frac{1}{y_1} - \frac{1}{y_2}\right) \frac{x_3}{y_3}} m \quad (1)$$

$$m_3 = \frac{\left(\frac{1}{y_1} - \frac{1}{y_2}\right) \frac{x}{y} - \left(\frac{1}{y} - \frac{1}{y_2}\right) \frac{x_1}{y_1} - \left(\frac{1}{y_1} - \frac{1}{y}\right) \frac{x_2}{y_2}}{\left(\frac{1}{y_2} - \frac{1}{y_3}\right) \frac{x_1}{y_1} + \left(\frac{1}{y_3} - \frac{1}{y_1}\right) \frac{x_2}{y_2} + \left(\frac{1}{y_1} - \frac{1}{y_2}\right) \frac{x_3}{y_3}} m$$

where  $m$  and  $(x, y)$  is the amount and chromaticity coordinates of the color to be produced,  $m_1, m_2, m_3$  and  $(x_1, y_1), (x_2, y_2), (x_3, y_3)$  are the required amounts and chromaticity coordinates of the three primaries, respectively.

With the additional freedom induced by the fourth primary, the color matching becomes not unique. For example, for a color located inside the triangle enclosed by the

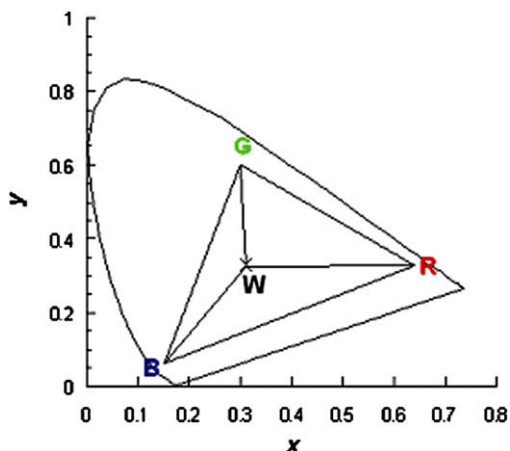


Fig. 1. CIE coordinates of R, G, B, and W primaries.

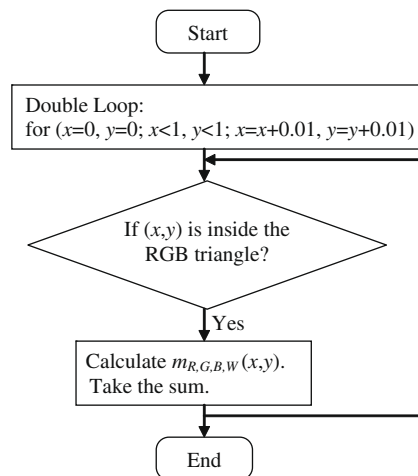
green, blue, and white, it could be produced either by red, green, and blue without white, or by green, blue, and white without red. Furthermore, if all the four primaries are used, the solution becomes infinite. To simplify the calculation and take full advantage of the white emitter, we divide the large triangle formed by the primary R, G, and B into three small triangles formed by the primary W with other primaries as illustrated in Fig. 1. Any color will be reproduced by the vertexes of the small triangle where the color is located inside. By this simple color matching scheme, the white emitter is utilized at the maximum rate.

## 3. Uniform luminance color space

To characterize the display performance, the traditional method is to calculate the efficiency of the display at 200 cd/m<sup>2</sup> white. However, in a four primary color display with white emitter, characterizing the display at the white point will not be sufficient. For example, if the color coordinates of the white emitter is right at the  $D_{65}$  white position, the display's efficiency will be equal to that of the white emitter, regardless of the efficiencies of the other three primary colors. To characterize the display in a way close to that under actual operation, we present uniform luminance color space, in which all the color points in the color space have a luminance of 200 cd/m<sup>2</sup>, and we characterize the display's performance all over the whole color space, not limited only to the white point. The process of characterization is listed in Scheme 1. For every reproducible color point, we calculate the amount of each primary required for the full color pixel to emit 200 cd/m<sup>2</sup> light at that color point. After all the values are obtained, the average luminance of each primary in the uniform luminance color space is given by the following equations:

$$\bar{m}_{R,G,B,W} = \frac{\sum_i m_{R,G,B,W}^i}{\sum_i} \quad (2)$$

where  $i$  is the index of the reproducible colors, and  $m$  is the luminance of each primary.



Scheme 1.

**Table 1**

Device structures and CIE coordinates of PLEDs emitting red, green, blue and white lights.

Primary	Device structure	CIE	HDTV CIE
R	ITO/PEDOT:PSS/PVK/PFO:PBD:Ir(DMFPq) <sub>2</sub> acac(2%)/PFN/Ba/Al	(0.665, 0.319)	(0.640, 0.330)
G	ITO/PEDOT:PSS/P-PPV/Ba/Al	(0.368, 0.588)	(0.300, 0.600)
B	ITO/PEDOT:PSS/PVK/PPF28505/Ba/Al	(0.16, 0.08)	(0.150, 0.060)
W	ITO/PEDOT/PVK:OXD-7:Firpic:Ir(piq)/Ba/Al	(0.329, 0.362)	(0.313, 0.329)

#### 4. PLED devices

To simulate the display's performance, we fabricated polymer OLEDs (PLEDs) emitting R, G, B and W lights whose device structures are listed in Table 1. Their current density ( $J$ )–bias ( $V$ )–luminance ( $L$ ) characteristics are shown in Fig. 2, and the external quantum efficiency (EQE)– $J$  characteristics are shown in the inset. Detailed descriptions of device making have been reported elsewhere [13,14,18,19]. The CIE chromaticity coordinates of the R, G, B and W primaries for high definition television (HDTV) are also included in Table 1 for comparison [17,20]. Since the chromaticity coordinates of the PLEDs are very close to those of HDTV ones, in the following sections, our calculations will be carried out based on the real electroluminescent (EL) characteristics of the devices and the CIE coordinates of HDTV primary colors.

#### 5. Display structures

To find out the performance of the display based on the fabricated devices, we assume a full color pixel consisting of 3 or 4 sub-pixels in the planar configuration in which the sub-pixels are laid side by side. As mentioned early, adding a fourth sub-pixel will alter the display's structure. If the size of each sub-pixel is kept the same, the display resolution will lose 25% by adding the fourth sub-pixel. If we keep the display resolution intact, the sub-pixel size has to be reduced by 25% as shown in Fig. 3. In the following calculations comparing the performances between the RGB display and the RGBW display, we will assume the

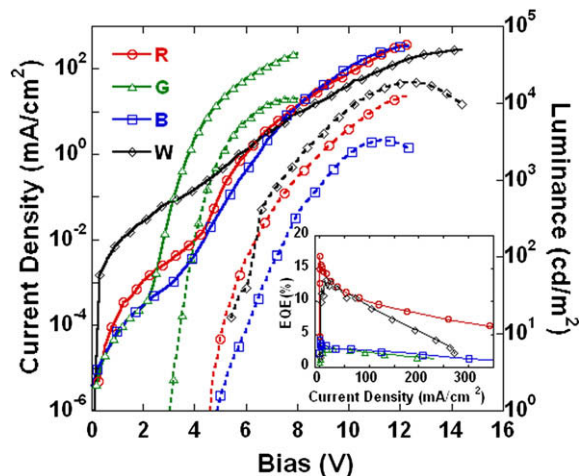


**Fig. 2.** Current density ( $J$ ) (solid lines)–operation voltage ( $V$ )–luminance ( $L$ ) (dot lines) characteristics of R, G, B, and W PLEDs. Inset: external quantum efficiency (EQE)– $J$  characteristics.

display resolution is the same for both displays. As a result, if the size of the full color pixel is set to  $100\ \mu\text{m} \times 100\ \mu\text{m}$ , and each sub-pixel has the same size, the sub-pixel size is  $33.3\ \mu\text{m} \times 100\ \mu\text{m}$  for the RGB panel, and  $25\ \mu\text{m} \times 100\ \mu\text{m}$  for the RGBW panel. To simplify the calculation, the aperture ratio is set to 100%. The actual luminance of each sub-pixel is first obtained in the uniform luminance color space following the process described in Section 3. Then, the luminous efficiency, the pixel power, and the power efficiency of the full color pixel are calculated based on the performance of the primary color devices shown in Fig. 2.

#### 6. Results

The actual luminance of each sub-pixel in the uniform luminance color space is listed in Table 2 as well as the characteristics of the full color pixel in both the RGB panel and the RGBW panel. As shown, the RGBW display with the luminous efficiency of 8.05 cd/A and the power efficiency

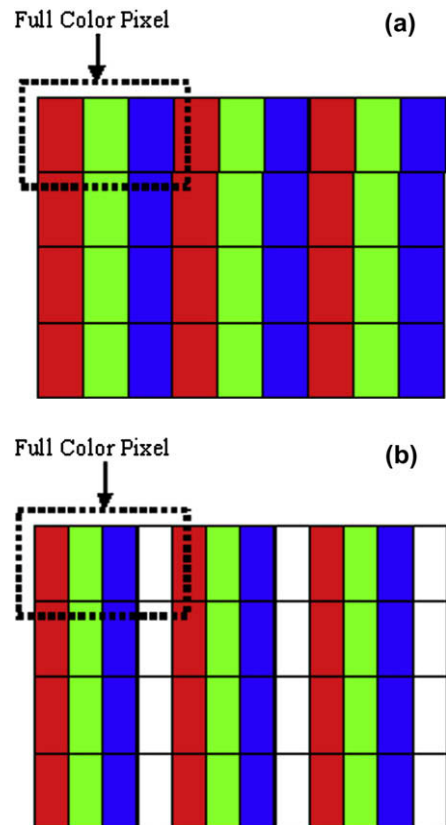


**Fig. 3.** (a) A full color pixel in RGB display. (b) A full color pixel in RGBW display.

**Table 2**

The characteristics of the full color pixel in both the RGB display and the RGBW display in the uniform luminance color space.

Method	Performance	R	G	B	W	Full pixel
RGB	Areal luminance (cd/m <sup>2</sup> )	72	110	18	–	200
	Actual luminance (cd/m <sup>2</sup> )	217	329	54	–	600
	Luminous efficiency (cd/A)	8.45	8.25	2.56	–	6.91
	Pixel power (μW)	0.56	0.56	0.48	–	1.60
	Power efficiency (lm/W)	4.05	6.16	1.18	–	3.93
RGBW	Areal luminance (cd/m <sup>2</sup> )	57	58	13	72	200
	Actual luminance (cd/m <sup>2</sup> )	228	232	52	288	800
	Luminous efficiency (cd/A)	8.43	7.69	2.57	13.1	8.05
	Pixel power (μW)	0.44	0.31	0.34	0.36	1.45
	Power efficiency (lm/W)	4.02	5.90	1.19	6.34	4.33

of 4.33 lm/W, is more efficient than the RGB one with the luminous efficiency of 6.91 cd/A and the power efficiency of 3.93 lm/W. In addition, it takes less pixel power in the RGBW display (1.45 μW) to produce 200 cd/m<sup>2</sup> light than that in the RGB displays (1.60 μW). The efficiency improvement and the power consumption reduction are due to the high performance of the white emitter, since the emission of the W sub-pixel accounts for 36% of the full color pixel's luminance in the uniform luminance color space. At the required luminance of 288 cd/m<sup>2</sup>, the luminous efficiency and the power efficiency of the white emitter are as high as 13.1 cd/A and 6.34 lm/W, respectively. However, if the efficiency of the white emitter is low, the RGBW display may not possess any advantage in terms of power efficiency in comparison with the RGB display. We recalculated the RGBW display's efficiency by varying the white emitter's efficiency while fixing the efficiencies of the red, green, and blue emitters. The result shows that only when the white emitter's efficiency is larger than 4.46 lm/W, the RGBW display becomes more power efficient than the RGB display (Fig. 4a).

In the RGB display, the most used primary color is green, since the human eyes are most sensitive to the green color. Apparently, increasing the green emitter's efficiency will improve the display's efficiency. Recently, the power efficiency of the green OLED has reached 102 lm/W at 100 cd/m<sup>2</sup> [21]. At such high green emitter's efficiency, without a high efficient white emitter, the RGBW display will not be as power efficient as the RGB display. To find out the minimum efficiency of the W sub-pixel required for the RGBW display to be as efficient as the RGB display, we fixed the efficiencies of the red and the blue emitters, and varied the green emitter's efficiency to carry out the simulation. The result is plotted in Fig. 4b. The curve illustrates that the white emitter's efficiency has to keep up with the green emitter's efficiency to ensure the RGBW display's power efficiency. For the currently highest green emitter with the power efficiency of 102 lm/W, the white emitter's efficiency has to reach 8.32 lm/W. It is worth noting that when the green emitter's efficiency increases from 1 to 25 lm/W, the white emitter's efficiency has to go from 1.3 to 7.1 lm/W to catch up. However, at the high efficiency region, when the green emitter's efficiency increases from 25 to 120 lm/W, the white emitter's efficiency only goes from 7.1 to 8.4 lm/W. It reveals that, in order for the RGB display to be as efficient as the RGBW display, the power efficiency requirement for the green emitter is much higher than the requirement for the white

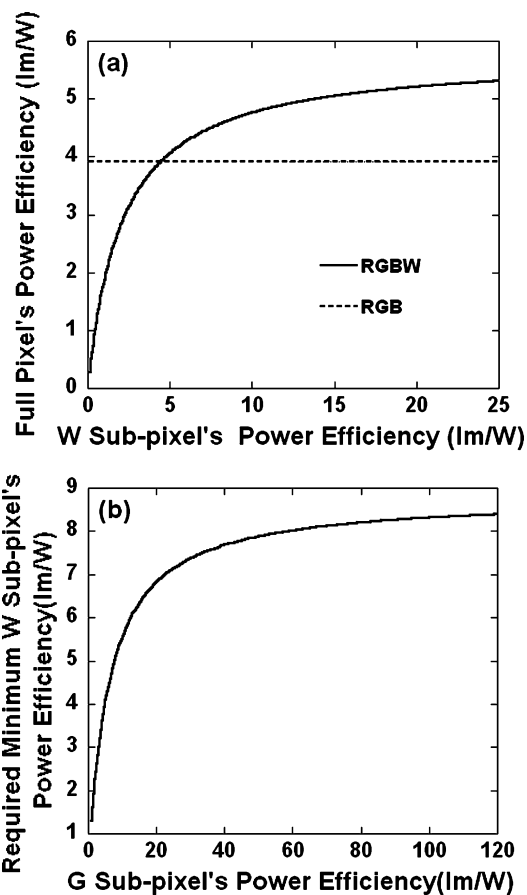


**Fig. 4.** (a) The dependence of the full color pixel's power efficiency in the RGBW display on the white emitter's power efficiency with fixed R, G, and B sub-pixels' efficiencies. (b) The minimum efficiency of the W sub-pixel required for the RGBW display to be as efficient as the RGB display at various green sub-pixel's efficiency.

emitter in the RGBW display in order for the RGBW display to be as efficient as the RGB display. The said feature allows for utilizing low efficient green emitter in RGBW display while achieving high display efficiency.

## 7. Color usage frequency

The OLED team in Eastman Kodak Company has sampled more than 13,000 digital images to find out that the

most prevalent colors in nature are unsaturated colors around the white point [3]. Lacking their resources, we introduce a color usage frequency  $f$  taking the form of a Gaussian distribution into the uniform luminance color space to simulate the nature colors:

$$f_i = \exp \left[ -\frac{(x_i - x_W)^2 + (y_i - y_W)^2}{0.043/\alpha} \right] \quad (3)$$

where  $f_i$  is the color usage frequency,  $(x_W, y_W)$  is the CIE coordinates of HDTV white located at (0.313, 0.329), and  $\alpha$  is the normalization non-negative factor defined by the boundary conditions. We use the blue primary usage frequency to set the boundary conditions as follows:

$$\begin{aligned} f_W &= 1 \\ f_B &= 10^{-\alpha} f_W \end{aligned} \quad (4)$$

Fig. 5a illustrates the color usage frequency with  $\alpha = 1$ , i.e.  $f_B = 10\%$ , while Fig. 5b shows the color usage frequency with  $\alpha = 10$ . As the value of  $\alpha$  increases, the color usage frequency approaches the probability of color usage in nature images [3]. When  $\alpha$  takes the value of zero, all the reproducible colors have the same probability of usage, which simulates the color usages in the application of computer desktop visualization in which bright saturated colors are widely used. After the color usage frequency is introduced, the average luminance of each primary in the uniform luminance color space is modified into the following equation:

$$\bar{m}_{R,G,B,W} = \frac{\sum f_i \times m_{R,G,B,W}^i}{\sum f_i} \quad (5)$$

The characterizations of a full color pixel in both the RGB and the RGBW displays were carried out in the uniform luminance color space coupled with the color usage frequency. The average luminance of each primary was calculated with different  $\alpha$  value and shown in Fig. 6a. In the RGBW display, the contribution of white emitter grows from 43% to 67% of the total luminance as  $\alpha$  increases from 1 to 10, while the contribution of the other three primaries steadily decreases, especially R and B primaries. With  $\alpha$  increasing, the usage frequency of the saturated colors becomes lower. As a result, the average luminance contributions of R, G, and B primaries decrease from 23.5%, 28.2%, and 5.3%, to 8.9%, 21.7%, and 2.7% of the total luminance, respectively, when  $\alpha$  grows from 1 to 10. In the RGB display, G primary makes the most contributions to the total luminance. As  $\alpha$  increases, the average luminance of G primary also increase while the luminance of the other two primaries drop, which means the RGB display mostly depends on the G primary in displaying natural images.

The dependence of a full color pixel's power efficiency on the color usage frequency in both the RGB and the RGBW displays is shown in Fig. 6b. As revealed in Fig. 6a, when  $\alpha$  is large, the luminance of the RGBW display depends mostly on W sub-pixel. Therefore, the efficiency of the white emitter plays a critical role in the full color pixel's efficiency. Shown in Fig. 6b, the full color pixel's power efficiency in the RGBW display rises rapidly with the increase of  $\alpha$ . It reaches 6.4 lm/W at  $\alpha = 10$  from 4.8 lm/W at  $\alpha = 1$ . In the simulation, the white emitter has a high effi-

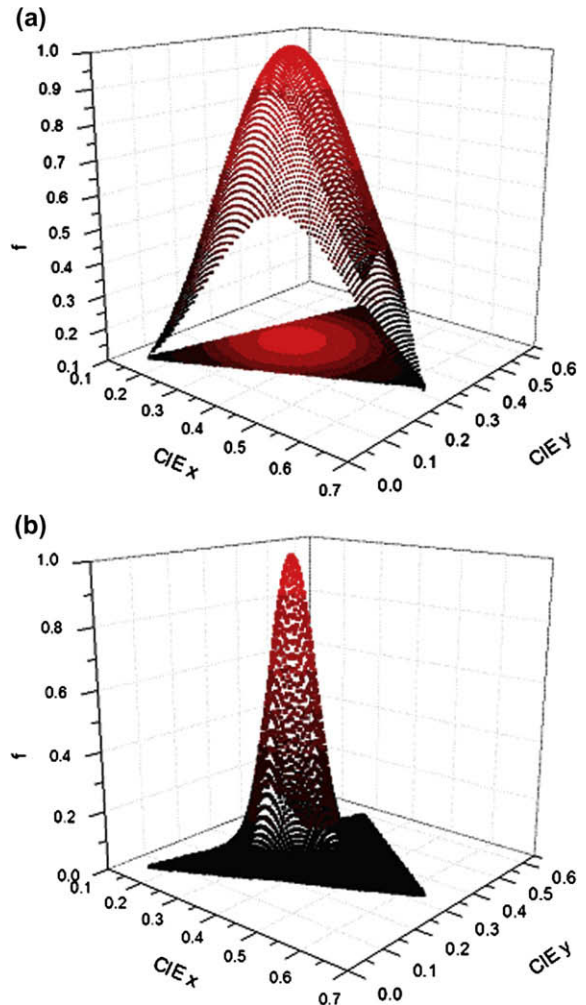
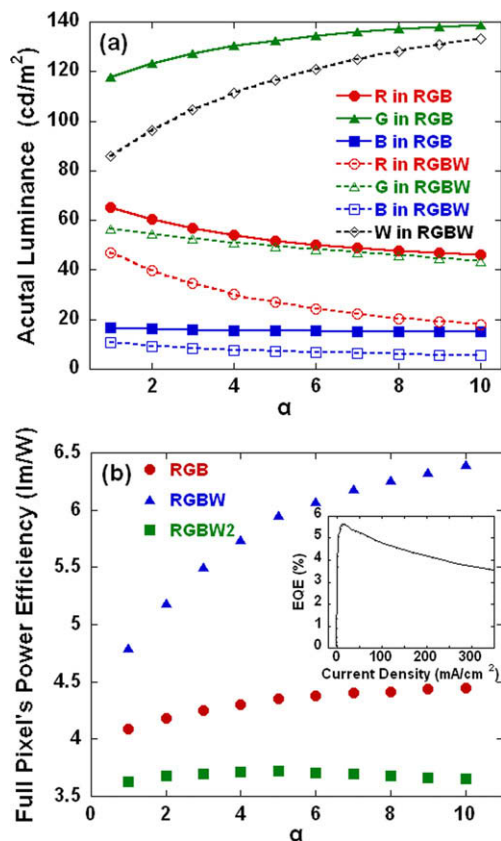


Fig. 5. The color usage frequency with (a)  $\alpha = 1$  and (b)  $\alpha = 10$ .

ciency illustrated in Fig. 2. For comparison, another white emitter with the configuration of ITO/PEDOT:PSS/PVK/PFO-poss/Ir(Bu-ppy)<sub>3</sub>:(Piq)<sub>2</sub>Ir(acaF)/Ba/Al was fabricated and utilized as W primary in the RGBW display denoted as RGBW2. Detailed descriptions of device fabrication could be found in Ref. [7]. The EQE-J characteristics of the device are shown in the inset of Fig. 6b. The power efficiency of a full color pixel in the RGBW2 display dependent on  $\alpha$  was as well calculated and plotted in Fig. 6b. For RGBW2 display, although the full color pixel's power efficiency increases from 3.63 to 3.72 lm/W as  $\alpha$  increases from 1 to 5, it begins to drop thereafter, and falls to 3.65 lm/W when  $\alpha$  reaches 10. The power efficiency's drop at large  $\alpha$  value is attributed to the low white emitter's efficiency. Since the full color pixel's efficiency in the RGBW display is mostly determined by the white emitter's EL performance at large  $\alpha$  value, the more contribution of the W sub-pixel, the more power consumption of the full color pixel if the white emitter has a low efficiency, which leads to the reduction of the power efficiency. For the RGB display, the full pixel's power efficiency is not seriously



**Fig. 6.** (a) The average luminance of each primary in the RGBW display and the RGB display with different  $\alpha$ . (b) The power efficiencies of a full color pixel in the RGB and the RGBW displays with different  $\alpha$ . Inset of (b): EQE- $J$  characteristics of the white PLED in RGBW2.

affected by the color usage frequency. It only changes from 4.09 to 4.45 lm/W as  $\alpha$  goes from 1 to 10. The difference of the full pixel's power efficiency between the RGBW and the RGB displays becomes larger as  $\alpha$  increases. Thus, by utilizing highly efficient white emitters, the RGBW display will be much more energy efficient than the RGB display for video applications. As the simulation revealed, in the RGBW display, video applications transfer the huge luminance requirements from R, G, and B primaries to W primary. Therefore, if the white emitter has a long lifetime, the RGBW display will have a long lifetime limited only by the white emitter.

## 8. Summary

In summary, the performances of the flat panel displays utilizing PLEDs with both RGB sub-pixels and RGBW sub-pixels layouts were analyzed theoretically and experimentally. A simple color matching scheme was applied to maximize the usage of the white sub-pixel. Uniform luminance color space was introduced to better characterize

the display performance than the traditional single white point characterization. In the uniform luminance color space, the RGBW sub-pixel display will be more energy efficient than the RGB display, when the power efficiency of the white emitter reaches a threshold determined by the green emitter's efficiency. To simulate the real natural images, the color usage frequency with Gaussian distribution was adopted in the calculation. As the color usage frequency distribution gets closer to that in the real images, the full color pixel's power efficiency of the RGBW display is more dependent on the EL performance of the white emitter. In order for the RGBW display to be more energy efficient than the RGB display with the same red, green, and blue emitters, a highly efficient white emitter is necessary.

## Acknowledgements

This research was supported by the National Basic Research Program of China (973 Program 2009CB623602 and 2009CB623604), the National Natural Science Foundation of China (U0634003) and the Science Foundation of Educational Commission of Hubei Province of China (Q20091204).

## References

- [1] C.W. Tang, S.A. VanSlyke, *Appl. Phys. Lett.* 51 (1987) 913.
- [2] J.H. Burroughes, D.D.C. Bradley, A.R. Brown, R.N. Marks, K. Mackay, R.H. Friend, P.L. Burns, A.B. Holmes, *Nature* 347 (1990) 539.
- [3] G. Rajeswaran, S. Van Slyke, in: Eighth Annual Display Search US FPD Conference, March 21–23, Loews Coronado Bay Resort, San Diego, 2006.
- [4] J.P. Spindler, T.K. Hatwar, Michael E. Miller, Andrew D. Arnold, M.J. Murdoch, P.J. Kane, J.E. Ludwicki, S.A. Van Slyke, *SID Digest* 36 (2005) 36.
- [5] C.H.B. Elliott, T.L. Credelle, M.F. Higgins, *SID Digest* 5 (2005) 26.
- [6] F. Robert, *Science* 310 (2005) 1762.
- [7] Y. Xu, J. Peng, J. Jiang, W. Xu, W. Yang, Y. Cao, *Appl. Phys. Lett.* 87 (2005) 193502.
- [8] B.W. D'Andrade, S.R. Forrest, *Adv. Mater.* 16 (2004) 1585.
- [9] X. Gong, S. Wang, D. Moses, G.C. Bazan, A.J. Heeger, *Adv. Mater.* 17 (2005) 2053.
- [10] J. Jiang, Y. Xu, W. Yang, R. Guan, Z. Liu, H. Zhen, Y. Cao, *Adv. Mater.* 18 (2006) 1769.
- [11] J. Huang, G. Li, E. Wu, Q. Xu, Y. Yang, *Adv. Mater.* 18 (2006) 114.
- [12] N. Tomoyuki, H. Kunimasa, F. Keiichi, O. Hirofumi, *SID Digest* 38 (Bk. 2) (2007) 1018.
- [13] H. Wu, J. Zou, F. Liu, L. Wang, A. Mikhailovsky, G.C. Bazan, W. Yang, Y. Cao, *Adv. Mater.* 20 (2008) 696.
- [14] Y. Xiong, W. Xu, C. Li, B. Liang, L. Zhao, J. Peng, Y. Cao, J. Wang, *Org. Electron.* 9 (2008) 533.
- [15] J. Wang, G. Yu, *Proc. SPIE* 5632 (2005) 32.
- [16] K. Mitsuhiro, H. Koji, A. Reo, K. Isamu, M. Ryoko, Y. Hirokazu, Y. Tetsuro, O. Atsushi, S. Yukio, T. Shoji, Y. Jiro, S. Tatsuya, T. Shinichiro, U. Tetsuo, *SID Digest* 35 (2004) 1017.
- [17] R.W.G. Hunt (Ed.), *Measuring Colour*, second ed., Ellis Horwood, New York, 1992.
- [18] L. Wang, B. Liang, F. Huang, J. Peng, Y. Cao, *Appl. Phys. Lett.* 89 (2006) 151115.
- [19] J. Liu, J. Zou, W. Yang, H. Wu, C. Li, B. Zhang, J. Peng, Y. Cao, *Chem. Mater.* 20 (2008) 4499.
- [20] C. Poynton, *Digital Video and HDTV*, Morgan Kaufmann, San Francisco, 2003.
- [21] S.-J. Su, T. Chaiba, T. Takeda, J. Kido, *Adv. Mater.* 20 (2008) 2125.



convenient chromaticity-tuning they afford. However, the use of multiple dopants in either a single layer or multi-layer stack is complicated by the different energy transfer efficiencies involving the host and different dopants in the system, which can lead to significant imbalance in the white emission and current/brightness-dependent color changes [1]. These problems can be substantially mitigated by use of a single dopant which emits over a broad spectral range as is the case with materials which exhibit both monomer and excimer emission. Excimers usually lack a bound ground state and therefore color mixing from another dopant can be feasible to optimize white light emission without complications from inter-dopant energy transfer [1,4]. Further, the use of broad-band emitters simplifies chromaticity tuning, and reduces the number of device layers, processing steps and cost.

White/near-white electrophosphorescence due to combined monomer and excimer emission from “FPt” complexes [e.g., (2-(4',6'-difluorophenyl)pyridinato-N,C<sup>2'</sup>)(2,4-pentanedionato)platinum(II)] has been first reported by Thompson, Forrest and co-workers [4]. The peak power efficiency obtained for devices featuring singly-doped FPt2:CBP films was 2.5 lm/W; improvement to 4.4 lm/W and balanced white was obtained by doubly-doping CBP with both the FPt1 complex and a blue iridium phosphor (Flrpic), attaining a maximum CRI of 78. More recently, Williams, Cocchi, Kalinowski and co-workers have reported the synthesis [10] and electrophosphorescent properties [11] of cyclometalated platinum (II) complexes (PtL<sup>2</sup>Cl), featuring N<sup>2</sup>C<sup>2</sup>N-coordinated terdentate ligands based on 1,3-dipyridylbenzene. Optimized WOLEDs fabricated from this material in an intricate device architecture produced a CRI of 90 and external quantum efficiency of 6.5% [11]. The emission was assigned to monomer emission of the PtL<sup>2</sup>Cl molecule, triplet excimer emission of the PtL<sup>2</sup>Cl: PtL<sup>2</sup>Cl dimer, as well as a PtL<sup>2</sup>Cl: *m*-MTDATA exciplex (heteromolecular dimer) emission, where *m*-MTDATA = 4,4',4''-tris(*N*-(3-methylphenyl)-*N*-phenylamino)triphenylamine. Further variation and optimization of device structure from the same dopant has allowed these researchers to obtain an external quantum of 15.5% and color coordinates close to that of an incandescent lamp (0.43, 0.43) [12]. Other notable research on electrophosphorescence from Pt(II) complexes has been reported by Chang et al. utilizing pyridyl azolate-based chelates, attaining maximum external quantum and power efficiencies of 5.9% and 6.4 lm/W, respectively, for the best dopant and attaining color tunability by varying the dopant concentration [13]. The luminescence in this work [13] has been assigned to metal-metal-to-ligand charge transfer in excimers and oligomers. In general, these literature precedents of Pt(II) complexes have shown rather strong sensitivity of device performance to the device structure (necessitating addition of exciton- and charge-blocking layers [11–15]) and color tuning by controlling the excimer/monomer ratio. However, the operational stability suggested by the roll-off of device efficiency and color metrics at higher brightness, voltage, and current density is generally inferior in devices based on such Pt(II) square planar complexes [4,11–15] compared to those known for Ir(III) cyclometalated octahedral complexes [1].

Here, we report an investigation of photoluminescence (PL) and electroluminescence (EL) of singly-doped thin films and OLEDs based on a new electrophosphorescent dopant, Pt(ftp)<sub>2</sub> = bis[3,5-bis(2-pyridyl)-1,2,4-triazolato]platinum(II). We investigate the effect of Pt(ftp)<sub>2</sub> concentration in the common OLED host 4,4'-bis(carbazol-9-yl)triphenylamine (CBP) on the PL properties of the thin films as well as the EL properties of OLEDs utilizing a basic device architecture. The overall results of this work suggest an excellent potential for OLEDs based on Pt(ftp)<sub>2</sub> to overcome the aforementioned inferior operational stability of devices based on other Pt(II) complexes while retaining the facile color-tuning advantage.

## 2. Experimental

### 2.1. Materials synthesis and characterization

Pt(ftp)<sub>2</sub>, a new metal-organic phosphorescent material, was synthesized by refluxing two equivalents of 3,5-bis(2-pyridyl)-1,2,4-triazole with one equivalent of *cis*-bis(benzonitrile)dichloroplatinum(II) in pyridine/acetone under a nitrogen ambient for three days. The insoluble product was washed with acetonitrile and diethyl ether and dried overnight under vacuum. The material was subsequently purified by sublimation. The complex exhibits poor solubility in common organic solvents, which precluded standard spectroscopic and chromatographic characterization methods. However, single crystals were successfully grown from a dichloromethane/methanol mixed solvent to form poorly-diffracting long orange needles. X-ray diffraction identified the formula as Pt(ftp)<sub>2</sub> based on X-ray intensity data measured on a Bruker SMART APEX CCD area detector system equipped with an Oxford Cryosystems 700 Series Cryostream cooler, a graphite monochromator, and a Mo K $\alpha$  fine-focus sealed tube ( $\lambda = 0.71073 \text{ \AA}$ ). The data frames were integrated with the Bruker SAINT-PLUS software package. The data were corrected for absorption effects using the multi-scan technique (SADABS). The structure was solved and refined using the Bruker SHELXTL software package. Room temperature photoluminescence (PL) and photoluminescence excitation (PLE) of neat and various doped films of Pt(ftp)<sub>2</sub> were measured using a calibrated PTI QuantaMaster Model QM-4 scanning spectrofluorometer. The excitation and emission spectra were corrected for the wavelength-dependent lamp intensity and detector response, respectively. All films were deposited by thermal evaporation/co-evaporation using a computer-controlled Trovato system. The doped thin films in the PL and EL experiments have different doping levels as only a general correlation for the variation of the excimer/monomer emission trends vs. the doping concentration was sought.

### 2.2. Device fabrication and characterization

Organic light emitting diodes with the structure: glass/ITO/NPB (40 nm)/*x*% Pt(ftp)<sub>2</sub>:CBP (25 nm)/TPBI (30 nm)/Mg:Ag, 1:10, (200 nm) were fabricated by sequential thermal evaporation. Prior to device fabrication the glass/ITO substrates were cleaned by sonication in acetone then methanol for 15 min, and afterward subjected to an oxy-

gen plasma treatment for ITO surface conditioning. A Photo Research PR650 camera integrated with a Keithley 2420 source-measure unit via LabView was used for quantitative electro-optical characterization. The software is also commercially available from Photo Research Inc., and reports all of the pertinent data: radiometric, photometric, CIE, CRI and color temperature. Both the PR650 and the Keithley 2420 are factory calibrated. All measurements were performed at room temperature and only the forward uncoupled light was measured.

### 3. Results and discussion

Fig. 1 represents the molecular structure of  $\text{Pt}(\text{ptp})_2$  obtained by X-ray crystallography. Although the X-ray diffraction data show significant disorder in the non-coordinated pyridine ring of each ptp ligand, the  $\text{PtN}_4$  coordination geometry is determined accurately showing a bidentate  $\mu_2$ - $N,N'$ - coordination mode from the nitrogen atom of the other pyridine ring and the nitrogen atom in the 1-position of the triazolate moiety to the platinum(II) center. The Pt(II) pyridyltriazolate square-planar units

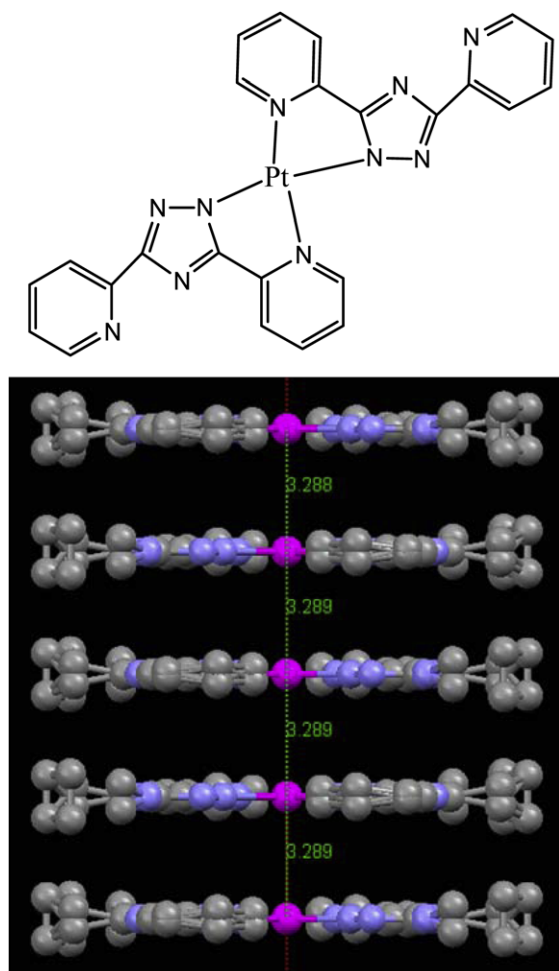


Fig. 1. Molecular structure (top) and packing diagram (bottom) of  $\text{Pt}(\text{ptp})_2$  as determined by single crystal X-ray diffraction.

stack into infinite chains with relatively strong  $\text{Pt}(\text{II}) \cdots \text{Pt}(\text{II})$  intermolecular interactions extended in columnar one-dimensional chains. These intermolecular forces belong to the general category of closed-shell “metallophilic interactions” known for multiple classes of molecular materials, including  $d^8$  and  $d^{10}$  complexes, which have been ascribed to correlation effects that are strengthened by relativistic effects [16]. Detailed structural refinement and improvement thereof using solid-state density-functional quantum mechanical computations are in progress and, upon completion, will be reported. Overall, the X-ray structure confirms that  $\text{Pt}(\text{ptp})_2$  is a non-organometallic/non-cyclometalated square-planar complex with no C–Pt bonds, and that it exhibits intermolecular interactions that warrant formation of fully-overlapped excimer units. The desired advantages of the design include the symmetry of the coordination sphere, which facilitates formation of fully-overlapped excimers, and the extended  $\pi$  system (six aromatic rings total), which renders the molecule an excellent antenna with visible absorptions. The homoleptic nature of the  $\text{Pt}(\text{N}^{\wedge}\text{N})_2$  coordination sphere in  $\text{Pt}(\text{ptp})_2$  is distinctly different from the heterolytic  $\text{Pt}(\text{C}^{\wedge}\text{N})(\text{O}^{\wedge}\text{O})$  or  $\text{Pt}(\text{N}^{\wedge}\text{C}^{\wedge}\text{N})\text{Cl}$  coordination spheres in the aforementioned most efficient Pt(II) complexes used in the OLED literature thus far. None of these literature precedents has exhibited the symmetric overlap of adjacent square planar complexes in dimeric units or stacked chains as that seen in the structure of  $\text{Pt}(\text{ptp})_2$ .

Room temperature photoluminescence (PL) and photoluminescence excitation (PLE) of neat  $\text{Pt}(\text{ptp})_2$  films as well CBP films doped with different percentages of  $\text{Pt}(\text{ptp})_2$  (i.e., films in their device formats) are presented in Fig. 2. The PLE maxima for all doped films correspond

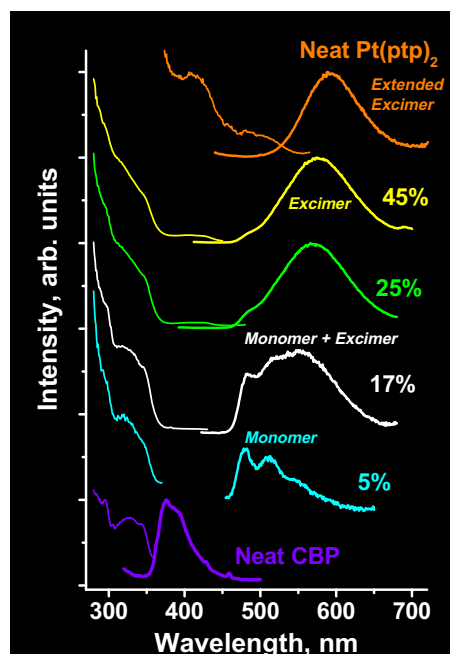


Fig. 2. Thin film photoluminescence excitation (thinner curve) and photoluminescence (thicker curve) spectra of neat CBP,  $\text{Pt}(\text{ptp})_2$  and different volume percentages  $\text{Pt}(\text{ptp})_2$  in CBP.

to the 340 nm excitation of CBP, thus indicating a common excitation pathway involving energy transfer from the host to the dopant; direct excitation is seen only as weak shoulders in the PLE for only the two highest-doped films. These weak PLE features are similar to those in the neat film (Fig. 2). The absence of CBP emission in the spectra of the doped films suggests that the energy transfer is complete in all cases; note that the PLE of neat Pt(otp)<sub>2</sub> overlaps with the entire emission profile of CBP. These PL and PLE data of x% Pt(otp)<sub>2</sub>:CBP thin

films suggest that the excitation mechanism in OLEDs employing this material system as the emissive layer will be dictated by the host instead of the dopant; i.e., primarily host excitons will form upon electrical excitation and direct excitation/recombination on the dopant will be negligible up to ~25% doping levels (above which direct excitation starts to contribute but only as a minor route). Neat films exhibit no or hardly detectable electro-luminescence in the device structure used in this work. With increasing doping levels in the in x% Pt(otp)<sub>2</sub>:CBP

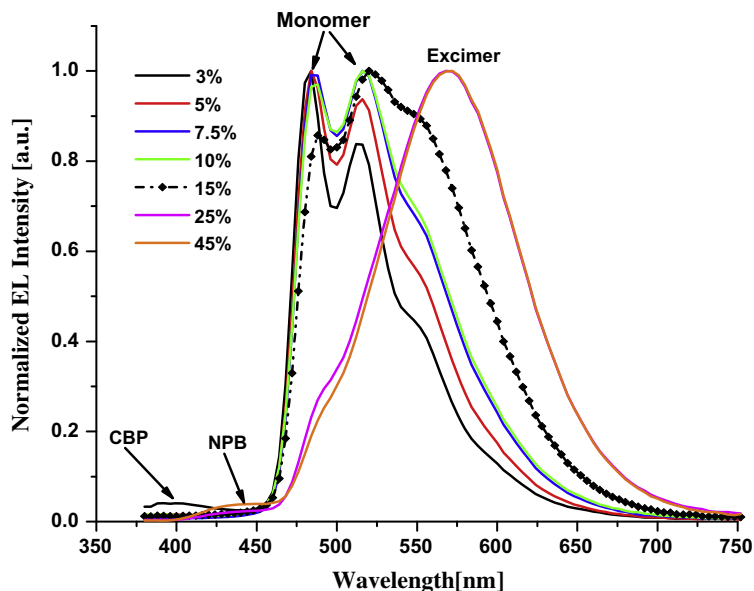


Fig. 3. Electroluminescence spectra of different volume percentages Pt(otp)<sub>2</sub> in CBP.

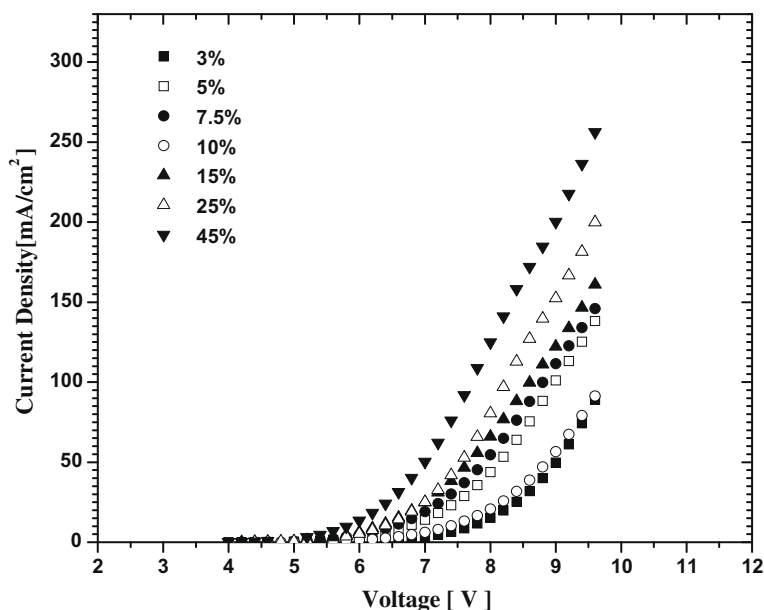


Fig. 4. Current–voltage curves for devices with different dopant concentration.

thin films, the spectral character of the PL red-shifts, and progressively changes from monomer- to excimer-dominated emission. This result is consistent with an increase in the number of pairs of  $\text{Pt}(\text{ptp})_2$  molecules with the separation required for excimer formation as the dopant concentration increases. The neat film exhibits PL maximum that is further red-shifted from the excimer band

in doped films, which we assign to formation of extended excimers in the neat material but localized excimers in the doped films. A careful inspection of the PL data in Fig. 2 suggests a red shift in the excimer band at high concentration levels. While it is difficult to ascertain the crystal structure of aggregates in doped films, it is known from the published literature for molecular

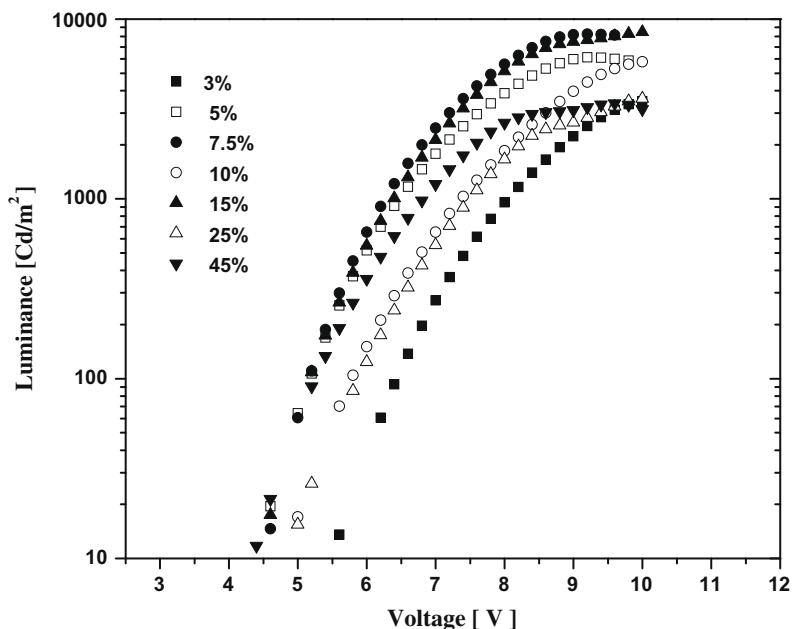


Fig. 5. Luminance–voltage curves for devices with different dopant concentration.

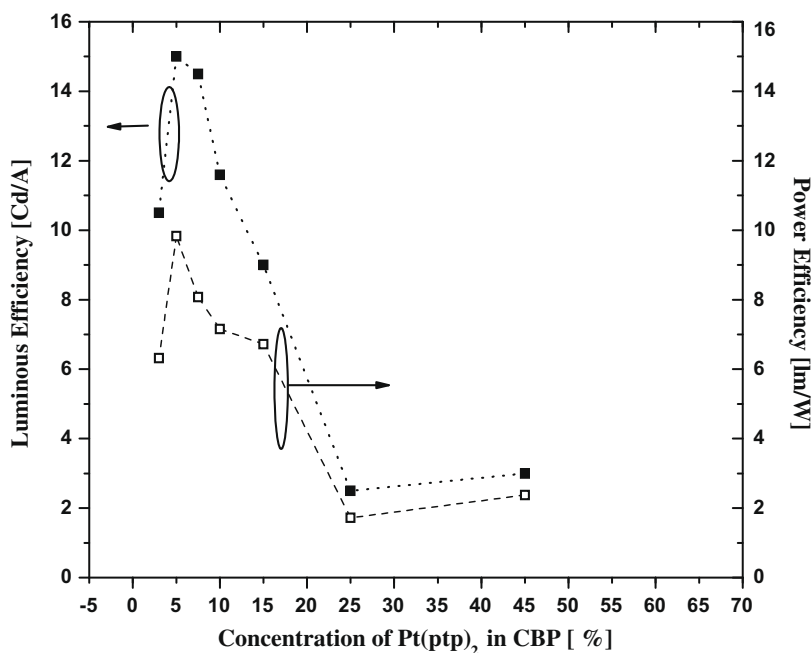


Fig. 6. Peak luminous efficiency (solid squares) and power efficiency (open squares) as a function of  $\text{Pt}(\text{ptp})_2$  doping percent.

excimers (best-established for pyrene) that a greater overlap between the two planar monomer units results in a red shift in the excimer emission band [17], suggesting increased overlap of the planar monomer units that constitute the excimeric luminophore upon increasing the doping concentration.

Similar to the photoluminescence, a shift from monomer- to excimer-dominated emission with increasing dopant concentration is observed in the electroluminescence, as the normalized spectra in Fig. 3 show. The CBP emission in the spectrum of the sample doped at 3% suggests that this doping level is insufficient for optimal energy transfer

from the host to the dopant. We interpret the NPB shoulder in the electroluminescence of the samples doped at 25% and 45% to mean that the carrier mobility associated with the dopant is strongly influencing the carrier transport properties of the emissive layer, and thus the extent of the recombination zone. As Fig. 4 shows, a decrease in the electrical threshold voltage and an increase in the current at a given voltage generally accompanies the dopant concentration increase. The luminance as a function of voltage dependence is shown in Fig. 5. In the 5–15 doping percent range, the average brightness was  $\sim 7200$   $\text{cd/m}^2$  at 9 V. We expect that the incorporation of hole injecting and/

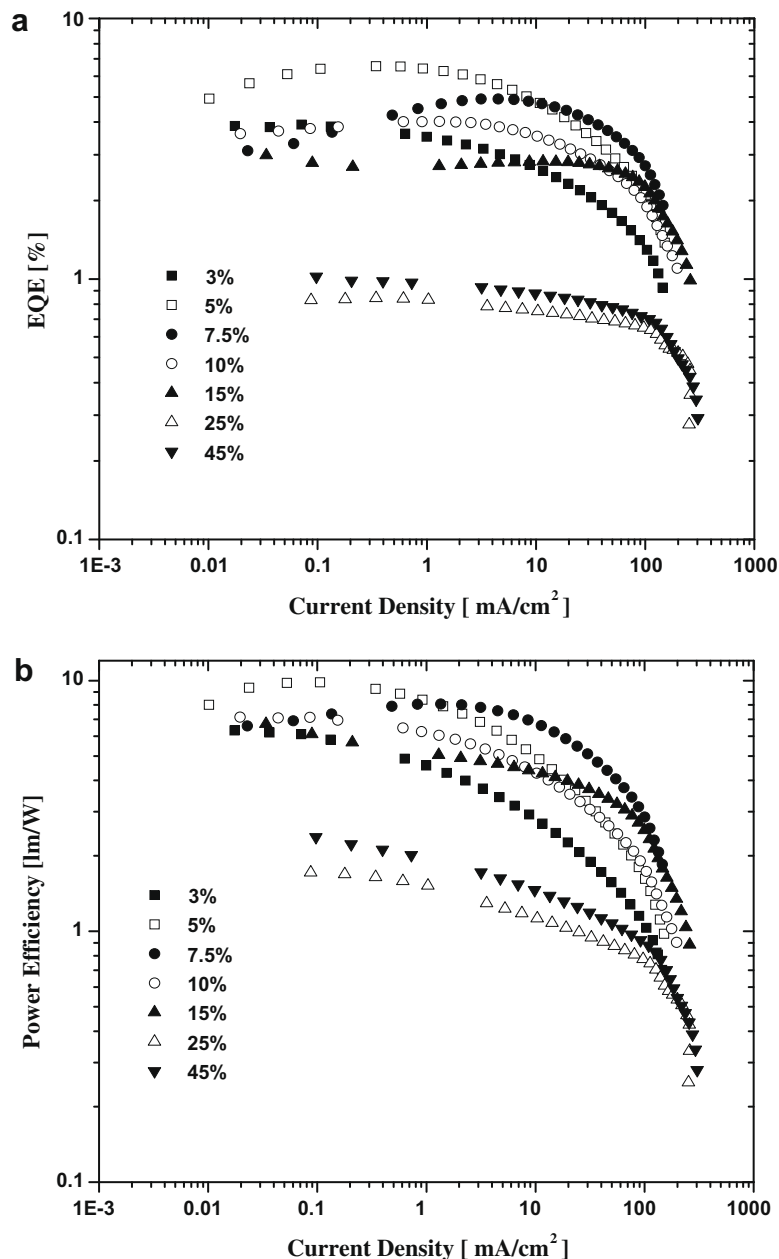


Fig. 7. External quantum efficiency (a) and power efficiency (b) as a function of current density.

or electron-blocking layers into the device structure might lower the turn-on voltages seen. A doping concentration of 5% produced peak luminous and power efficiencies of 15 cd/A and 9.8 lm/W, respectively. Interestingly, the power efficiency at high luminance was higher for the 7.5% device, decreasing from a peak value of 8.07 lm/W only to 7.29 lm/W at 1000 cd/m<sup>2</sup>; the EQE likewise de-

creased from 4.91% only to 4.89%. The dependence of the luminous and power efficiencies on doping concentration for the full series of devices studied in this work is presented in Fig. 6. As Figs. 7 and 8 show, the reduction in power efficiency and external quantum efficiency parameters under high current, brightness, and voltage conditions is relatively moderate compared to the sharp reduction in

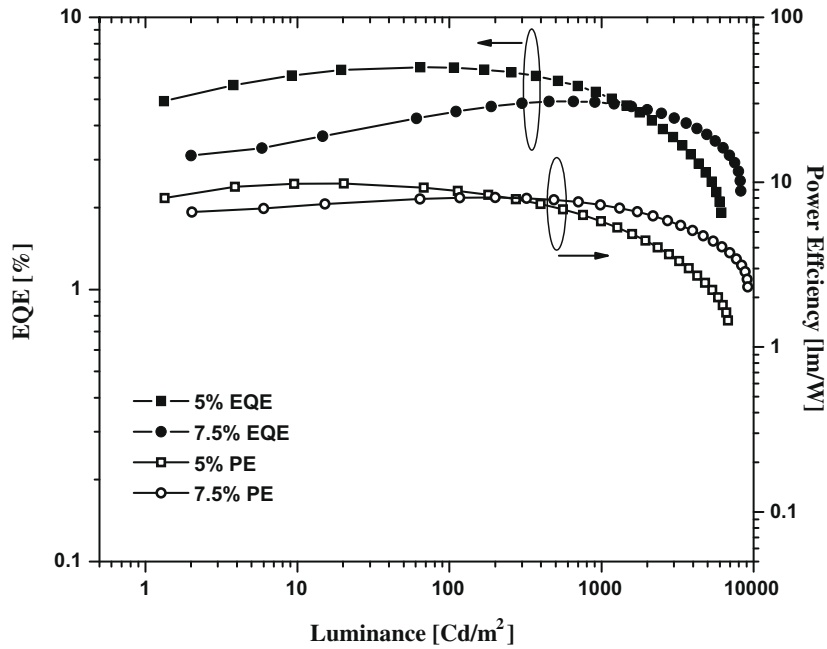


Fig. 8. External quantum efficiency and power efficiency as a function of luminance for devices doped at 5% and 7.5%.

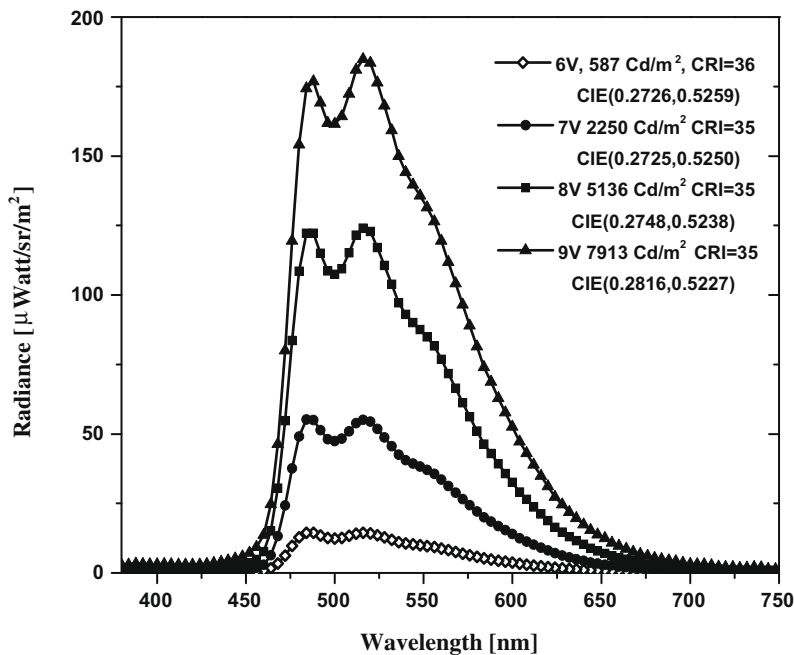


Fig. 9. Electroluminescence spectra as a function of drive voltage. For the device doped at 7.5%.

**Table 1**Summary of electro-optical parameters showing peak values as well as values at 1000 cd/m<sup>2</sup>.

Pt(PTP) <sub>2</sub> Doping (%)	PE <sub>peak</sub> (lm/W)	PE <sub>1000</sub> (lm/W)	EQE <sub>peak</sub> (%)	EQE <sub>1000</sub> (%)	Brightness Cd/m <sup>2</sup>	CIE <sub>peak</sub> (x, y)	CIE <sub>1000</sub> (x, y)	CRI <sub>peak</sub>	CRI <sub>1000</sub>	V <sub>T</sub>
3	6.32	2.47	3.92	2.46	3480	(0.229,0.4956)	(0.2246,0.4723)	26	27	5
5	9.83	5.81	6.55	5.32	6130	(0.2485,0.517)	(0.2454,0.5136)	27	30	4
7.5	8.07	7.29	4.91	4.89	8250	(0.2739,0.5264)	(0.2721,0.5255)	36	35	4.2
10	7.16	4.27	4.03	3.53	6170	(0.276,0.5133)	(0.2681,0.5091)	38	35	4.4
15	6.72	4.26	2.98	2.82	8470	(0.3334,0.5363)	(0.3258,0.5333)	45	41	4.2
25	1.72	0.87	0.84	0.69	3620	(0.469,0.5076)	(0.4184,0.5177)	47	51	4
45	2.38	1.13	1.02	0.79	3390	(0.4622,0.5092)	(0.4359,0.5102)	51	56	4

efficiency that characterizes typical electrophosphorescent devices.

Fig. 9 is representative of the CIE and CRI dependence on drive voltage. For this dopant concentration (7.5%) the color rendering index is 36 at 6 V and 35 at 10 V. The electroluminescence spectral features are essentially voltage-independent and, as Fig. 9 depicts, the ratio of monomer to excimer emission is essentially constant for the voltage range used in this study; i.e., we see little or no evidence of preferential saturation of monomer compared to excimer excited states with increased device current, or vice versa. In general all of the devices in this work exhibited better color stability than that reported for other square planar Pt(II) complexes [4,11–15]. The CRI increased with doping concentration and the maximum value obtained was 56. To the naked eye the emission appeared to be white with a green hue. Table 1 is a summary of the pertinent electro-optical performance metrics for OLEDs based on Pt(PTP)<sub>2</sub> in this work, showing both peak values as well as values at 1000 cd/m<sup>2</sup>. This luminance level is deemed an appropriate reference level for OLEDs by the US Department of Energy [18], although device performance data at this high luminance level is rarely seen in the published literature for electrophosphorescent OLEDs. The overall data in Table 1 and Fig. 8 show that OLEDs based on Pt(PTP)<sub>2</sub> in this work exhibit remarkably insignificant roll-off in performance metrics at this high luminance, albeit to a different extent in devices with different doping levels. We expect this general device stability to improve upon further optimization of the device architecture.

#### 4. Conclusion

In summary, we have demonstrated near-white electrophosphorescence with moderately high external power efficiencies (10 lm/W) in a basic OLED architecture with a singly-doped emissive layer based on a new homoleptic Pt(II) complex. The shift of emission wavelength with dopant concentration affords some degree of chromaticity tuning. It is expected that device structures which include hole injection and/or electron blocking layers will result in improved external efficiencies, as such approaches increased the efficiency of singly-doped devices based on other Pt(II) complexes by nearly an order of magnitude [14,15] vs. an

earlier generation of devices that employed a similar device structure to the one used herein [4]. Similarly, inclusion of a deep-blue fluorescent emitter and/or engineering device structures with different emission regions of Pt(PTP)<sub>2</sub> monomer and excimer emission are expected to yield a more balanced white EL than what has been attained in this work.

#### Acknowledgement

This work is supported by the US Department of Energy under contract DE-FC26-06NT 42859.

#### References

- [1] (a) C. Adachi, M.A. Baldo, M.E. Thompson, S.R. Forrest, *J. Appl. Phys.* 90 (2001) 5048; (b) H. Yersin, *Top. Curr. Chem.* 1 (2004) 241; (c) B.W. D'Andrade, S.R. Forrest, *Adv. Mater.* 16 (2004) 1585; (d) Y. Sun, N.C. Giebink, H. Kanno, B. Ma, M.E. Thompson, S.R. Forrest, *Nature* (2006) 908.
- [2] J. Kido, M. Kimura, K. Nagai, *Science* 267 (1995) 1332.
- [3] B.W. D'Andrade, S.R. Forrest, *J. Appl. Phys.* 94 (2003) 3101.
- [4] B.W. D'Andrade, J. Brooks, V. Adamovich, M.E. Thompson, S.R. Forrest, *Adv. Mater.* 14 (2002) 1032.
- [5] J. Kido, K. Hongawa, K. Okuyama, K. Nagai, *Appl. Phys. Lett.* 64 (1994) 815.
- [6] B. Hu, F.E. Karasz, *J. Appl. Phys.* 93 (2003) 1995.
- [7] J. Feng, F. Li, W.B. Gao, S.Y. Liu, Y. Liu, Y. Wang, *Appl. Phys. Lett.* 78 (2001) 3947.
- [8] J. Feng, Y. Liu, F. Li, Y. Wang, S.Y. Liu, *Opt. Quant. Electron* 35 (2003) 259.
- [9] J. Thompson, R.I.R. Blyth, M. Mazzeo, M. Anni, G. Gigli, R. Cingolani, *Appl. Phys. Lett.* 79 (2001) 560.
- [10] S.J. Farley, D.L. Rochester, A.L. Thompson, J.A.K. Howard, J.A. Gareth Williams, *Inorg. Chem.* 44 (2005) 9690.
- [11] J. Kalinowski, M. Cocchi, D. Virgili, V. Fattori, J.A.G. Williams, *Adv. Mater.* 19 (2007) 4000.
- [12] M. Cocchi, J. Kalinowski, D. Virgili, V. Fattori, S. Develay, J.A.G. Williams, *Appl. Phys. Lett.* 90 (2007) 163508.
- [13] S.-Y. Chang, J. Kavitha, S.-W. Li, C.-S. Hsu, Y. Chi, Y.-S. Yeh, P.-T. Chou, G.-H. Lee, A.J. Carty, Y.-T. Tao, C.-H. Chien, *Inorg. Chem.* 45 (2006) 137.
- [14] E.L. Williams, K. Haavisto, K.J. Li, G.E. Jabbour, *Adv. Mater.* 19 (2007) 197.
- [15] V. Adamovich, J. Brooks, A. Tamayo, A.M. Alexander, P.I. Djurovich, B.W. D'Andrade, C. Adachi, S.R. Forrest, M.E. Thompson, *New J. Chem.* 26 (2002) 1171.
- [16] P. Pykkö, *Chem. Rev.* 97 (1997) 597.
- [17] F.M. Winnik, *Chem. Rev.* 93 (1993) 587.
- [18] Multi-Year Program Plan FY'09-FY'15, Solid-State Lighting Research and Development, US Department of Energy, March 2009.

between the energy levels of CBP and the red triplet dopants usually results in direct charge trapping within the emitting layer (EML). Therefore, red phosphorescent devices based on CBP often require high operation voltages and provide unsatisfactory PEs. To break free from these constraints, several attempts have been made recently to use host materials possessing narrower band gaps [28–30] or bipolar characteristics [31–33] to improve the charge injection and electroluminescence (EL) performance of red phosphorescent OLEDs. Nevertheless, the PEs of the red electrophosphorescence remain far below those reported for blue- or green-emitting devices [3,20–27].

In this paper, we report the fabrication of efficient red phosphorescent OLEDs incorporating the bipolar host 2,7-bis(diphenylphosphoryl)-9-[4-(*N,N*-diphenylamino)phenyl]-9-phenylfluorene (POAPF) doped with the efficient red-emitting phosphor Os(fptz)<sub>2</sub>(PPh<sub>2</sub>Me)<sub>2</sub> (fptz = 3-trifluoromethyl-5-pyridyl-1,2,4-triazole); Fig. 1 presents their chemical structures. This charge-neutral osmium complex has been used previously as a phosphor in red-emitting devices displaying high EQEs [22,34]. The relatively low oxidation potential of Os(fptz)<sub>2</sub>(PPh<sub>2</sub>Me)<sub>2</sub>, however, results in severe charge trapping in devices using CBP as the host, resulting in high driving voltages and unsatisfactory PEs. POAPF, which contains an electron-rich triphenylamine group and an electron-deficient bis(diphenylphosphoryl)fluorene unit [35–37], has recently been developed as a host material exhibiting bipolar characteristics [38] that not only provide suitable frontier orbital energies for facile hole- and electron-injection but also improve the balance of charge flux in the emission layer. Moreover, the triplet energy ( $E_T$ ) of POAPF is estimated to be 2.72 eV – a value that is sufficiently high for POAPF to act as a host material for red, green, and even blue phosphorescent emitters. Indeed, blue phosphorescent OLEDs based on POAPF doped with FIrpic can exhibit high values of EQE and PE [38]. We expected that POAPF could also be utilized as a host for the red-emitting Os(fptz)<sub>2</sub>(PPh<sub>2</sub>Me)<sub>2</sub>, thereby improving charge injection and enhancing charge balance to result in highly efficient red phosphorescent devices.

## 2. Experimental

The bipolar host molecule POAPF [38] and the red phosphorescent emitter Os(fptz)<sub>2</sub>(PPh<sub>2</sub>Me)<sub>2</sub> [22] were prepared using previously reported procedures. The hole-

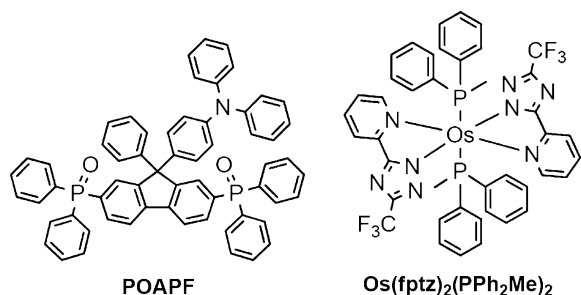


Fig. 1. Chemical structures of POAPF and Os(fptz)<sub>2</sub>(PPh<sub>2</sub>Me)<sub>2</sub>.

transport material 4,4'-bis(3-methylphenylphenylamino)biphenyl (TPD), the conventional host material CBP, and the electron-transport material 4,7-diphenyl-1,10-phenanthroline (BPhen) were all purchased from LumTec Corp. and used without further purification.

The oxidation and reduction potentials were measured, respectively, in anhydrous CH<sub>2</sub>Cl<sub>2</sub> and anhydrous DMF, containing 0.1 M TBAPF<sub>6</sub> as the supporting electrolyte, at a scan rate of 50 mV/s against a Ag/Ag<sup>+</sup> (0.01 M AgNO<sub>3</sub>) reference electrode, with ferrocene as the internal standard. The onset potentials were determined from the intersection of two tangents drawn at the rising current and background current of the cyclic voltammogram.

The EL devices were fabricated through vacuum deposition (10<sup>−6</sup> torr) of the materials onto ITO glass (sheet resistance: 25 Ω/square). All of the organic layers were deposited at a rate of 1.0 Å/s. The cathode was completed through thermal deposition of LiF (15 Å; deposition rate: 0.1 Å/s) and then capping with Al metal (100 nm) through thermal evaporation (deposition rate: 4.0 Å/s). The current–voltage–luminance relationships of the devices were measured using a Keithley 2400 source meter and a Newport 1835C optical meter equipped with an 818ST silicon photodiode. The EL spectrum was obtained using a Hitachi F4500 spectrofluorimeter.

## 3. Results and discussion

Fig. 2 presents the current density–voltage ( $I$ – $V$ ) characteristics of the hole-only devices having the configuration indium tin oxide (ITO)/TPD (30 nm)/host material (30 nm)/TPD (30 nm)/Al (100 nm) and the electron-only devices having the configuration ITO/BPhen (30 nm)/host material (30 nm)/BPhen (30 nm)/LiF (15 Å)/Al (100 nm). Here, “host material” refers to either the bipolar host POAPF or the conventional host CBP. Because of the high LUMO energy level (−2.20 eV) of TPD in the hole-only devices and the low HOMO energy level (−6.40 eV) of BPhen in the electron-only devices, injections of electrons and holes were prohibited in the hole- and electron-only devices, respectively; accordingly, the measured  $I$ – $V$  characteristics were dominated by holes and electrons, respectively. Fig. 2 reveals that the POAPF-based devices exhibited lower turn-on voltages and higher current densities than did the CBP-based devices under the same bias.

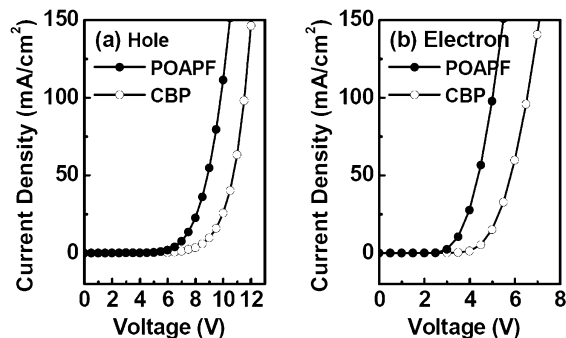


Fig. 2. Current density–voltage ( $I$ – $V$ ) curves of (a) hole- and (b) electron-only devices.



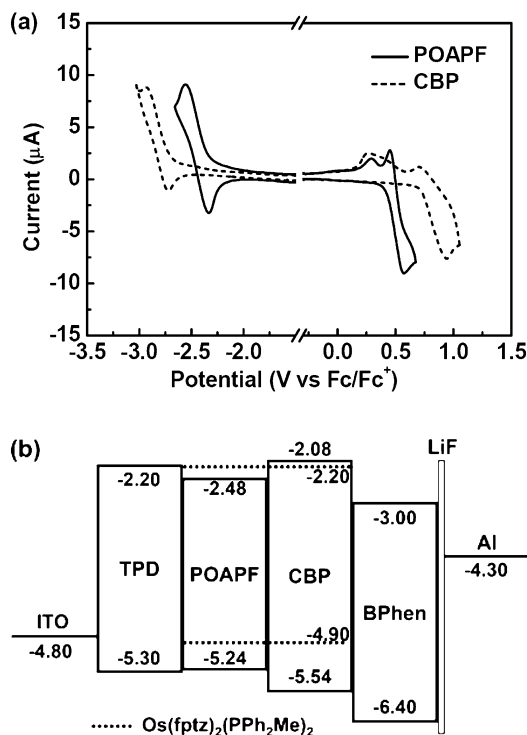


Fig. 3. (a) Cyclic voltammograms of POAPF and CBP, recorded at a scan rate of 50 mV/s. (b) Energy level diagram of the red phosphorescent devices.

The reduced driving voltages in the POAPF-based devices may be due to the decrease in barrier heights for hole- and electron-injection from the charge transport layers (CTLs) to POAPF.

To further understand the improved injection of holes and electrons in the POAPF-based devices, we employed cyclic voltammetry (CV) to estimate the HOMO and LUMO energy levels of POAPF and CBP (Fig. 3a), using a three-electrode cell with ferrocene as the internal standard. Because of its triphenylamine donor unit, POAPF exhibits a lower onset of its oxidation potential (0.44 V) relative to that of CBP (0.74 V). On the other hand, the onset of the reduction potential of POAPF (−2.32 V), originating from its bis(diphenylphosphoryl)fluorene unit, is significantly less negative than that of CBP (−2.72 V). On the basis of these onset values for oxidation and reduction, we estimated the HOMO and LUMO energy levels of POAPF (−5.24 and −2.48 eV, respectively) and CBP (−5.54 and −2.08 eV, respectively) relative to ferrocene (4.80 eV below the vacuum) as a reference [39]. According to the energy level diagram in Fig. 3b, the hole-injection barrier from TPD and the electron-injection barrier from BPhen to the POAPF layer were both considerably lower than those to the CBP layer. As a result, the presence of POAPF facilitates hole- and electron-injection, as observed in the hole- and electron-only measurements (*vide supra*).

Using POAPF as the host material, we fabricated red OLEDs in the configuration ITO/TPD (30 nm)/R-EML (30 nm)/BPhen (30 nm)/LiF (15 Å)/Al (100 nm), where

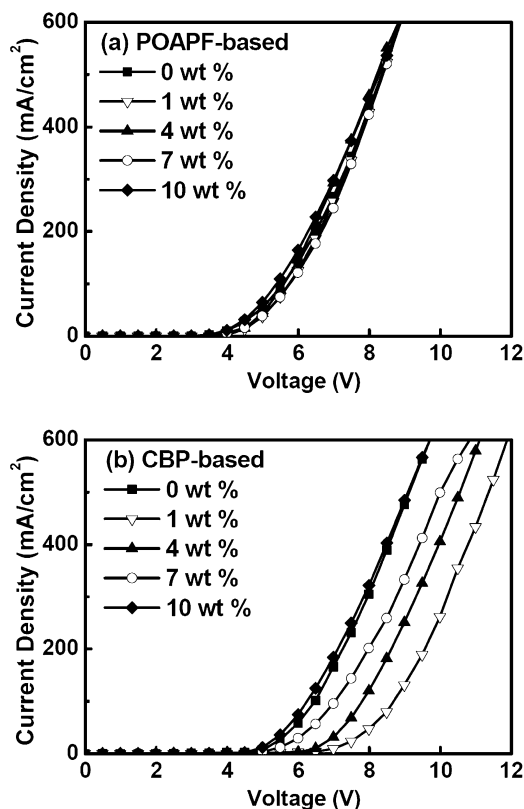


Fig. 4. *I*–*V* characteristics of devices incorporating (a) POAPF and (b) CBP as hosts at various doping concentrations.

TPD and BPhen were employed as hole- and electron-transporting layers, respectively, and R-EML refers to the POAPF layer doped with various concentrations of Os(fptz)<sub>2</sub>(PPh<sub>2</sub>Me)<sub>2</sub>. For comparison, we also fabricated reference devices incorporating CBP as the host. Fig. 4 depicts the *I*–*V* characteristics of these red-emitting OLEDs. As expected, the POAPF-based devices exhibited significantly higher current densities than did the CBP-based devices under the same bias. The *I*–*V* characteristics of the POAPF-based devices underwent no apparent changes when we increased the doping concentration of Os(fptz)<sub>2</sub>(PPh<sub>2</sub>Me)<sub>2</sub> from 0 to 10 wt%. This phenomenon can be explained by considering the energy level diagram of the devices (Fig. 3b). Because the HOMO energy level of Os(fptz)<sub>2</sub>(PPh<sub>2</sub>Me)<sub>2</sub> is merely 0.34 eV higher than that of POAPF, it behaves as a less-effective trapping sites for holes; meanwhile, because the LUMO energy level of Os(fptz)<sub>2</sub>(PPh<sub>2</sub>Me)<sub>2</sub> is 0.28 eV above that of POAPF, electrons injected from the BPhen layer into the POAPF layer are mostly transported through the POAPF layer without being trapped in the osmium phosphor. Thus, varying the concentration of Os(fptz)<sub>2</sub>(PPh<sub>2</sub>Me)<sub>2</sub> in the EML should not significantly alter the degree of charge injection in POAPF-based devices. On the other hand, the current density of the CBP-based devices exhibited a strong dependence on the doping concentration. Because the HOMO energy level of Os(fptz)<sub>2</sub>(PPh<sub>2</sub>Me)<sub>2</sub> is 0.64 eV higher than that of CBP, holes can potentially be trapped at

**Table 1**  
Device performance.

Device	Red		White
	POAPF	CBP	POAPF
Turn-on voltage [V] <sup>a</sup>	2.3	3.5	2.2
Max. EQE [%]	19.9	13.2	18.4
Max. LE [cd/A]	32.8	21.4	34.5
Max. PE [lm/W]	34.5	13.4	43.9
Voltage [V] <sup>b</sup>	3.7	5.1	3.0
EQE [%] <sup>b</sup>	18.6	13.1	14.9
LE [cd/A] <sup>b</sup>	30.6	21.1	27.9
PE [lm/W] <sup>b</sup>	26.1	13.1	29.5
EL $\lambda_{\text{max}}$ [nm] <sup>c</sup>	616	616	472, 498, 612
CIE, $x$ and $y$ <sup>c</sup>	(0.64, 0.36)	(0.64, 0.36)	(0.38, 0.34)

<sup>a</sup> Recorded at 1 cd/m<sup>2</sup>.

<sup>b</sup> Recorded at 1000 cd/m<sup>2</sup>.

<sup>c</sup> At 5 V.

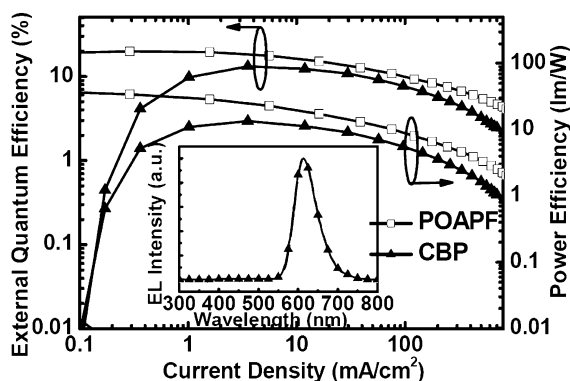


**Fig. 5.** EQE and PE of 7 wt% Os(fptz)<sub>2</sub>(PPh<sub>2</sub>Me)<sub>2</sub>-doped POAPF- and CBP-based devices plotted with respect to the current density. Inset: EL spectra (applied voltage: 5 V) of the POAPF- and CBP-based devices.

Os(fptz)<sub>2</sub>(PPh<sub>2</sub>Me)<sub>2</sub> at low doping concentrations. When the concentration of the osmium phosphor was increased, we attribute the resulting increased hole-injection efficiency to direct charge injection from the hole-transporting layer (HTL) into Os(fptz)<sub>2</sub>(PPh<sub>2</sub>Me)<sub>2</sub>. Accordingly, employing POAPF as the host for Os(fptz)<sub>2</sub>(PPh<sub>2</sub>Me)<sub>2</sub> significantly reduced the degree of charge trapping within the EML.

The optimal performances of both the POAPF- and CBP-based devices occurred at a doping concentration of 7 wt%. Table 1 lists the key characteristics of these red electrophosphorescent devices. The POAPF-based red-emitting device had a relatively low turn-on voltage of 2.3 V (corresponding to 1 cd/m<sup>2</sup>) and, at a practical brightness of 1000 cd/m<sup>2</sup>, its driving voltage was merely 3.7 V. These

values are much lower than those of the CBP-based device (3.5 and 5.1 V, respectively). We ascribe the reduced driving voltage of the POAPF-based device to facile hole/electron-injections and less-effective charge trapping within this bipolar host. Fig. 5 presents the EQE and PE profiles plotted with respect to the current density. The POAPF-based device exhibited a maximum EQE of 19.9% (at a luminance of 96 cd/m<sup>2</sup>) – 1.5 times greater than that of its CBP-based counterpart (13.2%). These values reveal that the presence of the bipolar host material resulted in balanced charge fluxes within the EML and, therefore, a high EQE. Notably, the PE of the POAPF-based device (34.5 lm/W) was 2.5 times higher than that of its CBP-based counterpart (13.4 lm/W). We attribute this large enhancement in device performance to the substantially lower driving voltage and improved charge balance within the POAPF-based device. In addition to its highly efficient device performance, the POAPF-based OLED displayed a less-problematic efficiency roll-off at higher luminance. The efficiencies remained fairly high (18.6% and 26.1 lm/W) at a practical luminance of 1000 cd/m<sup>2</sup>. Our POAPF-based red-emitting device possesses superior EL performance, particularly in terms of its PE (Table 2), relative to those of previously reported red electrophosphorescent OLEDs [29,31,32,34]. Both the POAPF- and CBP-based devices emitted saturated red light (each main peak at 616 nm) and Commission Internationale de L'Eclairage (CIE) coordinates of (0.64, 0.36) at 5 V (inset to Fig. 5).

To further utilize the superior host properties of POAPF, we fabricated white light-emitting devices – featuring red emission from Os(fptz)<sub>2</sub>(PPh<sub>2</sub>Me)<sub>2</sub> and complementary blue/green emission from Flrpic – having the configuration ITO/TPD (30 nm)/R-EML ( $x$  nm)/B-EML (30– $x$  nm)/BPhen (30 nm)/LiF (15 Å)/Al (100 nm). Here, we used POAPF as the bipolar host material for both the red EML [R-EML; doped with 7 wt% Os(fptz)<sub>2</sub>(PPh<sub>2</sub>Me)<sub>2</sub>] and the blue EML (B-EML; doped with 7 wt% Flrpic); the total thickness of these dual emission layers was fixed at 30 nm in each device. To realize white light emission from such composite emission systems, we adjusted the thickness ratio at various compositions to achieve appropriate fractions of excitons for both triplet emitters. Fig. 6 reveals an increase in the blue emission intensity relative to red emission upon decreasing the thickness of the R-EML. We obtained white emission when the thicknesses of the R-EML and B-EML were 1 and 29 nm, respectively. This white-emitting device also exhibited a low turn-on voltage (2.2 V) and an applicable luminance of 1000 cd/m<sup>2</sup> at merely 3.0 V (Fig. 7a); its maximum EQE reached 18.4% at a luminance of 90 cd/m<sup>2</sup>. As a result of the low driving voltage, the PE reached as high as 43.9 lm/W (Fig. 7b). Even when the luminance

**Table 2**  
Performance of red electrophosphorescent devices.

Host	Dopant	Max. EQE [%]	Max. PE [lm/W]	CIE ( $x$ , $y$ )	Ref.
POAPF	Os(fptz) <sub>2</sub> (PPh <sub>2</sub> Me) <sub>2</sub>	19.9	34.5	(0.64, 0.36)	This study
(ppy) <sub>2</sub> Ir(acac)	Ir(piq) <sub>3</sub>	9.2	11.0	(0.65, 0.35)	[29]
D2ACN	Mpq <sub>2</sub> Iracac	10.8	13.0	(0.66, 0.34)	[31]
<i>o</i> -CzOXD	Ir(piq) <sub>2</sub> acac	18.5	11.5	(0.68, 0.32)	[32]
TFTPA	Os(fptz) <sub>2</sub> (PPh <sub>2</sub> Me) <sub>2</sub>	18.0	25.2	(0.64, 0.36)	[34]

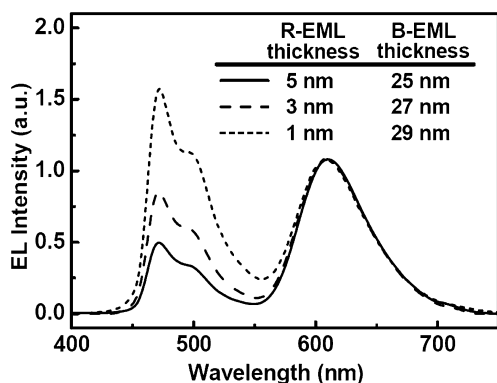


Fig. 6. EL spectra of dual-emission devices (applied voltage: 5 V) incorporating various thicknesses of their R-EML and B-EML.

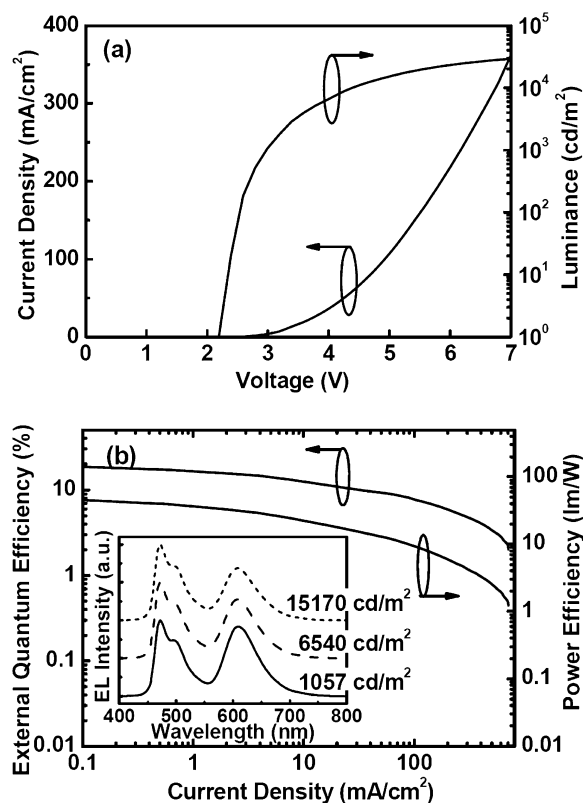


Fig. 7. Plots of (a) current density and luminance with respect to the voltage and (b) EQE and PE with respect to the current density for the white light-emitting device. Inset: EL spectra recorded at various luminances.

was 1000  $\text{cd/m}^2$ , the EL efficiencies remained high (14.9% and 29.5  $\text{lm/W}$ ). The EL efficiency of this white electrophosphorescence is among the highest values ever reported for white light-emitting diodes [12,40,41]. The EL spectra of this device revealed a virtually stable white color emission (inset to Fig. 7b). The CIE coordinates shifted slightly from (0.40, 0.34) at a luminance of 1057  $\text{cd/m}^2$  to (0.38, 0.34) at 15,170  $\text{cd/m}^2$ ; nevertheless, the color coordinates remained in the white light region.

## 4. Conclusion

We have realized highly efficient red electrophosphorescence in OLEDs incorporating the bipolar host POAPF doped with the red-emitting osmium phosphor  $\text{Os}(\text{fptz})_2(\text{PPh}_2\text{Me})_2$ . The bipolar characteristics of POAPF resulted in the red-emitting devices exhibiting very low driving voltages and achieving EL efficiencies as high as 19.9% and 34.5  $\text{lm/W}$  – the highest performance of any red phosphorescent OLED reported to date – with a saturated red emission located at CIE coordinates of (0.64, 0.36). In addition, we used POAPF to fabricate a white light-emitting device possessing a dual EML configuration; it also exhibited satisfying efficiencies (18.4% and 43.9  $\text{lm/W}$ ). The white emission remained stable, with the CIE coordinates shifting slightly from (0.40, 0.34) at a luminance of 1057  $\text{cd/m}^2$  to (0.38, 0.34) at 15,170  $\text{cd/m}^2$ . The performance of these phosphorescent devices makes them very attractive materials for potential commercial applications.

## Acknowledgment

We thank the National Science Council for financial support.

## References

- [1] M.A. Baldo, D.F. O'Brien, Y. You, A. Shoustikov, S. Sibley, M.E. Thompson, S.R. Forrest, *Nature* 395 (1998) 151.
- [2] M.A. Baldo, S. Lamansky, P.E. Burrows, M.E. Thompson, S.R. Forrest, *Appl. Phys. Lett.* 75 (1999) 4.
- [3] S. Lamansky, P. Djurovich, D. Murphy, F. Abdel-Razzaq, H.E. Lee, C. Adachi, P.E. Burrows, S.R. Forrest, M.E. Thompson, *J. Am. Chem. Soc.* 123 (2001) 4304.
- [4] C. Adachi, M.A. Baldo, M.E. Thompson, S.R. Forrest, *J. Appl. Phys.* 90 (2001) 5048.
- [5] E.L. Williams, K. Haavisto, J. Li, G.E. Jabbour, *Adv. Mater.* 19 (2007) 197.
- [6] S. Watanabe, N. Ide, J. Kido, *Jpn. J. Appl. Phys.* 46 (2007) 1186.
- [7] M. Ikai, S. Tokito, Y. Sakamoto, T. Suzuki, Y. Taga, *Appl. Phys. Lett.* 79 (2001) 156.
- [8] S.J. Yeh, M.F. Wu, C.T. Chen, Y.H. Song, Y. Chi, M.H. Ho, S.F. Hsu, C.H. Chen, *Adv. Mater.* 17 (2005) 285.
- [9] M.H. Tasi, H.W. Lin, H.C. Su, T.H. Ke, C.C. Wu, F.C. Fang, Y.L. Liao, K.T. Wong, C.I. Wu, *Adv. Mater.* 18 (2006) 1216.
- [10] D. Tanaka, H. Sasabe, Y.J. Li, S.J. Su, T. Takeda, J. Kido, *Jpn. J. Appl. Phys.* 46 (2007) L10.
- [11] S.J. Su, T. Chiba, T. Takeda, J. Kido, *Adv. Mater.* 20 (2008) 2125.
- [12] S.J. Su, E. Gonmori, H. Sasabe, J. Kido, *Adv. Mater.* 20 (2008) 4189.
- [13] C.W. Tang, S.A. VanSlyke, *Appl. Phys. Lett.* 51 (1987) 913.
- [14] C.W. Tang, S.A. VanSlyke, C.H. Chen, *J. Appl. Phys.* 65 (1989) 3610.
- [15] M.A. Baldo, M.E. Thompson, S.R. Forrest, *Nature* 403 (2000) 750.
- [16] T. Fuhrmann, J. Salbeck, *MRS Bull.* 28 (2003) 354.
- [17] B.W. D'Andrade, R.J. Holmes, S.R. Forrest, *Adv. Mater.* 16 (2004) 624.
- [18] B.W. D'Andrade, S.R. Forrest, *Adv. Mater.* 16 (2004) 1585.
- [19] H. Kanno, R.J. Holmes, Y. Sun, S. Kena-Cohen, S.R. Forrest, *Adv. Mater.* 18 (2006) 339.
- [20] A. Tsuboyama, H. Iwawaki, M. Furugori, T. Mukaide, J. Kamatani, S. Igawa, T. Moriyama, S. Miura, T. Takiguchi, S. Okada, M. Hoshino, K. Ueno, *J. Am. Chem. Soc.* 125 (2003) 12971.
- [21] C.H. Yang, C.C. Tai, I.W. Sun, *J. Mater. Chem.* 14 (2004) 947.
- [22] Y.L. Tung, S.W. Lee, Y. Chi, Y.T. Tao, C.H. Chien, Y.M. Cheng, P.T. Chou, S.M. Peng, C.S. Liu, *J. Mater. Chem.* 15 (2005) 460.
- [23] C.L. Li, Y.J. Su, Y.T. Tao, P.T. Chou, C.H. Chien, C.C. Cheng, R.S. Liu, *Adv. Funct. Mater.* 15 (2005) 387.
- [24] D.K. Rayabarapu, B.M.J.S. Paulose, J.P. Duan, C.H. Cheng, *Adv. Mater.* 17 (2005) 349.
- [25] Y.L. Tung, S.W. Lee, Y. Chi, L.S. Chen, C.F. Shu, F.I. Wu, A.J. Carty, P.T. Chou, S.M. Peng, G.H. Lee, *Adv. Mater.* 17 (2005) 1059.
- [26] S. Takizawa, Y. Sasaki, M. Akhtaruzzaman, H. Echizen, J. Nishida, T. Iwata, S. Tokito, Y. Yamashita, *J. Mater. Chem.* 17 (2007) 841.

- [27] C.L. Ho, W.Y. Wong, Z.Q. Gao, C.H. Chen, K.W. Cheah, B. Yao, Z. Xie, Q. Wang, D. Ma, L. Wang, X.M. Yu, H.S. Kwok, Z. Lin, *Adv. Funct. Mater.* 18 (2008) 319.
- [28] T. Tsuzuki, Y. Nakayama, J. Nakamura, T. Iwata, S. Tokito, *Appl. Phys. Lett.* 88 (2006) 243511.
- [29] T. Tsuzuki, S. Tokito, *Adv. Mater.* 19 (2007) 276.
- [30] T.J. Park, W.S. Jeon, J.J. Park, S.Y. Kim, Y.K. Lee, J. Jang, J.H. Kwon, R. Pode, *Appl. Phys. Lett.* 92 (2008) 113308.
- [31] W.Y. Hung, T.C. Tsai, S.Y. Ku, L.C. Chi, K.T. Wong, *Phys. Chem. Chem. Phys.* 10 (2008) 5822.
- [32] Y. Tao, Q. Wang, C. Yang, Q. Wang, Z. Zhang, T. Zou, J. Qin, D. Ma, *Angew. Chem. Int. Ed.* 47 (2008) 8104.
- [33] Y. Tao, Q. Wang, Y. Shang, C. Yang, L. Ao, J. Qin, D. Ma, Z. Shuai, *Chem. Commun.* (2009) 77.
- [34] C.H. Wu, P.I. Shih, C.F. Shu, Y. Chi, *Appl. Phys. Lett.* 92 (2008) 233303.
- [35] A.B. Padmaperuma, L.S. Sapochak, P.E. Burrows, *Chem. Mater.* 18 (2006) 2389.
- [36] S.O. Jeon, K.S. Yook, C.W. Joo, J.Y. Lee, *Appl. Phys. Lett.* 94 (2009) 013301.
- [37] F.M. Hsu, C.H. Chien, P.I. Shih, C.F. Shu, *Chem. Mater.* 21 (2009) 1017.
- [38] F.M. Hsu, C.H. Chien, C.-F. Shu, C.H. Lai, C.C. Hsieh, K.W. Wang, P.T. Chou, submitted for publication.
- [39] J. Pommerehne, H. Vestweber, W. Guss, R.F. Mahrt, H. Bässler, M. Porsch, J. Daub, *Adv. Mater.* 7 (1995) 551.
- [40] Y. Sun, S.R. Forrest, *Appl. Phys. Lett.* 91 (2007) 263503.
- [41] G. Schwartz, M. Pfeiffer, S. Reineke, K. Walzer, K. Leo, *Adv. Mater.* 19 (2007) 3672.

hand, the pyridine group is classically well-known to have electron affinity rather than hole and coordination ability with metal cation.

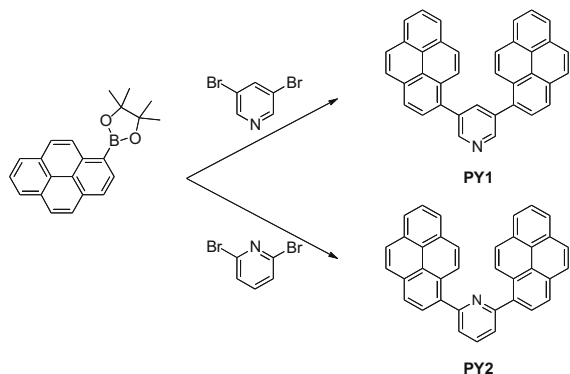
## 2. Results and discussion

### 2.1. Synthesis and thermal properties

Pyrene derivatives were readily synthesized by the Pd(0)-catalyzed Suzuki-Miyaura cross-coupling reaction of two equivalent of pyrene-1-boronic acid pinacol ester with 3,5-dibromopyridine for **PY1** and with 2,6-dibromopyridine for **PY2** (Scheme 1). The compounds were purified by train sublimation, and were characterized by  $^1\text{H}$ - and  $^{13}\text{C}$ -NMR, mass spectrometry, and elemental analysis. The details of synthesis and characterization are available in the supporting information. These pyrene oligomers are thermally stable. Thermogravimetric analysis (TGA) of the compounds showed that they had high thermal stability with 5% weight loss occurring at temperatures greater than 400 °C. Glass transition temperatures were 107 °C for **PY1** and 99 °C for **PY2**, determined by differential scanning calorimetry (DSC) measurement (Table 1).

### 2.2. Photophysical properties

UV-vis absorption and photoluminescence (PL) spectra of the pyrene oligomers in the solid state were measured for the vacuum deposited films on quartz (Fig. 1). PL spec-



**Scheme 1.** Synthesis of the dipyrenylpyridines. Condition: Pd(PPh<sub>3</sub>)<sub>4</sub>, K<sub>2</sub>CO<sub>3</sub>, EtOH, H<sub>2</sub>O, toluene, 80 °C, 12 h.

**Table 1**

Thermal and optical properties of the compounds.

	$T_g^a$ (°C)	$T_{d5\%}^b$ (°C)	UV <sup>c</sup> (nm)	PL <sup>c</sup> (nm)	PLQE <sup>d</sup> (%)	$E_g^e$ (eV)	$I_p^f$ (eV)	$E_a^g$ (eV)
<b>PY1</b>	107	417	246, 282, 351 (241, 286, 355) <sup>d</sup>	389 (483) <sup>d</sup>	75	3.09	5.99	2.90
<b>PY2</b>	99	440	246, 282, 352 (244, 286, 361) <sup>d</sup>	398 (493) <sup>d</sup>	66	3.00	5.94	2.94

<sup>a</sup> Glass transition temperature.

<sup>b</sup> Decomposition temperature at 5 wt% loss.

<sup>c</sup> Chloroform solution.

<sup>d</sup> Neat film.

<sup>e</sup> Estimated from onset of UV absorption of the neat film.

<sup>f</sup> Measured by Riken-keiki AC-3.

<sup>g</sup>  $E_g - I_p$ .

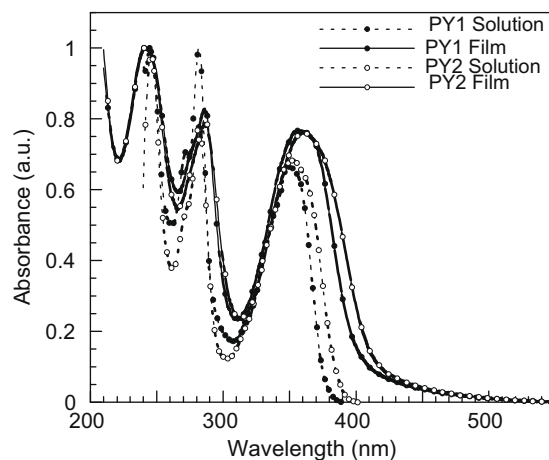


**Fig. 1.** UV spectra of **PY1** and **PY2**.

tra showed 70–95 nm of large red shift compared with those of the chloroform solutions due to their excimer formation, which is typical for the emission from pyrene derivatives in the solid state. Absolute PL quantum efficiency of the film ( $F_{\text{film}}$ ) was determined by using an integrating sphere system under argon atmosphere. A high  $F_{\text{film}}$  of 75% was found for **PY1**, which is one of the highest among the electroluminescent small molecules ever reported. The other compound also exhibited relatively high  $F_{\text{film}}$  of 66% for **PY2**. The  $F_{\text{film}}$  of **Alq<sub>3</sub>** determined in the same condition was 22%, which is consistent with the value previously reported [8]. The reason of high  $F_{\text{film}}$  might be related with less quenching through vibrational mode due to their rigid structure and small structural difference between ground state and excited state, or less self absorption due to small overlap between the absorption and the emission spectrum of the neat film.

### 2.3. Electrochemical and electron-transporting properties

Ionization potential ( $I_p$ ), estimated by photoelectron spectrometer surface analyzer [9,10], was 5.99 eV for **PY1** and 5.94 eV for **PY2**, and electron affinity ( $E_a$ ), estimated by the difference of optical band gap, was 2.90 eV for **PY1** and 2.94 eV for **PY2**. The two pyrene derivatives showed no difference in their electronic energy state derived from their molecular structure. Charge mobilities of

the pyrenes were measured by time of flight (TOF) method. **PY1** and **PY2** showed partially nondispersive photocurrent (Figs. S1 and S2). The electron mobility were estimated to be  $9.4 \times 10^{-5} \text{ cm}^2 \text{ V}^{-1} \text{ s}^{-1}$  for **PY1**,  $1.7 \times 10^{-4} \text{ cm}^2 \text{ V}^{-1} \text{ s}^{-1}$  for **PY2** at  $6.4 \times 10^4 \text{ V/cm}$ , which are higher than that of **Alq<sub>3</sub>**,  $1.7 \times 10^{-6} \text{ cm}^2 \text{ V}^{-1} \text{ s}^{-1}$ , determined in the same experimental condition (Fig. 2). For comparison, electron mobilities of smaller  $\pi$ -conjugated analogues, 3,5-difluorenylpyridine (**FL1**), and 2,6-difluorenylpyridine (**FL2**) shown in Fig. 3, were measured. **FL1** showed dispersive photocurrent (Fig. S3) and much lower electron mobility of

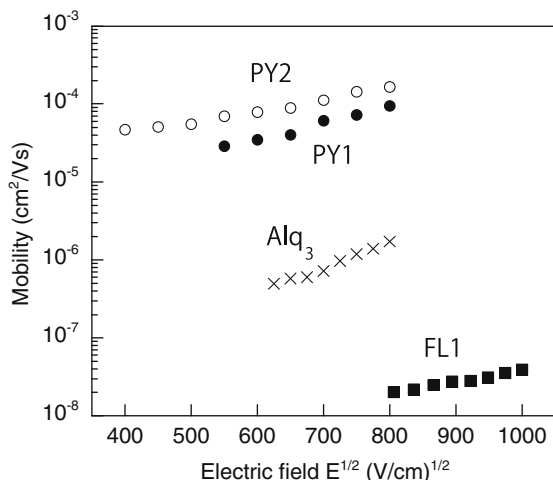


Fig. 2. Electron mobility measured by time of flight (TOF) method.

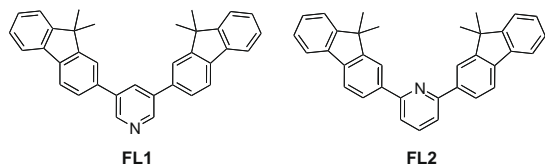


Fig. 3. Chemical structure of the fluorenylpyridines, **FL1** and **FL2**.

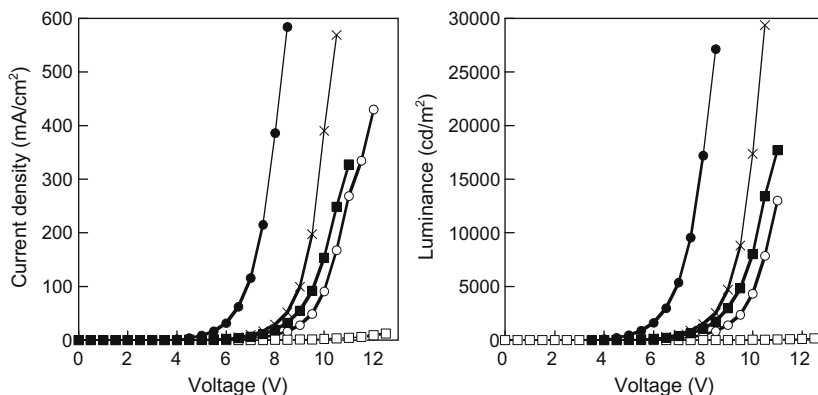


Fig. 4. Current density–voltage plots (left) and luminance–voltage plots (right) of the OLED: **PY1** (closed circle), **PY2** (open circle), **FL1** (closed square), **FL2** (open square), and **Alq<sub>3</sub>** (cross).

$10^{-8} \text{ cm}^2 \text{ V}^{-1} \text{ s}^{-1}$  and that of **FL2** was not measurable. These results demonstrated that much faster electron mobility of the pyrenylpyridines than that of **Alq<sub>3</sub>** is due to their  $\pi$ -conjugated pyrene moieties and the  $\pi$ - $\pi$  stacking.

#### 2.4. OLED performance

The two pyrenes, **PY1** and **PY2**, showed no large difference in ionization potential, electron affinity, and electron mobility, and generally, those three parameters are regarded as important parameters for OLED. However, they showed a considerable difference in OLED performance as an electron-transporting material. OLEDs with the configuration of ITO/NPD (40 nm)/**Alq<sub>3</sub>** (30 nm)/ETL (**Alq<sub>3</sub>**, **PY1**, **PY2**, **FL1**, or **FL2**) (30 nm)/LiF (0.5 nm)/Al (100 nm) were fabricated to examine the electron-transporting materials (Fig. 4 and Table 2). Driving voltages at 100 cd/m<sup>2</sup> for **PY1** was 2.6 V lower than that for **PY2**, and even 1.8 V lower than that for **Alq<sub>3</sub>**. Power efficiency,  $\eta_p$  (lm/W), for **PY1** was higher than that for **Alq<sub>3</sub>**. Power efficiency  $\eta_p$  (lm/W) is more practically important in terms of energy consumption rather than current efficiency  $\eta_c$  (cd/A) or  $\eta_e$  external quantum efficiency (%). Higher performance observed for **PY1** compared with **PY2** cannot be explained in terms of their electronic properties such as ionization potential, electron affinity, and electron mobility because those are similar in the two compounds. We therefore assume that the barrier height for the electron injection from Al cathode through LiF to **PY1** must be lower than that to **PY2**.

The mechanisms of the improvement of electron injection by the thin LiF interlayer have been discussed [11]. Li ion in LiF is expected to be reduced to Li metal by the thermally activated Al during vacuum deposition process, and interact with electron-transporting materials as an electron donor [12]. In such cases, steric hindrance of the organic materials should affect the reaction, and the bulky pyrene group substituted on 2,6-position of the pyridine ring may prevent coordination to Li. In contrast, the nitrogen atom of the pyridine ring of **PY2** is available for the coordination to Li. Such steric effect was also observed

**Table 2**

Voltage and efficiencies at 100 cd/m<sup>2</sup> (at 1000 cd/m<sup>2</sup> in parentheses) of the OLED devices.

	Voltage (V)	$\eta_p^a$ (lm/W)	$\eta_c^b$ (cd/A)	$\eta_e^c$ (%)
<b>PY1</b>	4.0 (5.6)	3.8 (2.9)	4.9 (5.2)	1.5 (1.6)
<b>PY2</b>	6.6 (8.6)	2.2 (1.8)	4.6 (5.0)	1.4 (1.5)
<b>FL1</b>	5.8 (7.9)	3.0 (2.2)	5.5 (5.5)	1.7 (1.7)
<b>FL2</b>	11.8 (n. d.)	0.34 (n. d.)	1.3 (n. d.)	0.40 (n. d.)
<b>Alq<sub>3</sub></b>	5.6 (7.6)	2.9 (2.2)	5.2 (5.3)	1.6 (1.6)

<sup>a</sup> Power efficiency.

<sup>b</sup> Current efficiency.

<sup>c</sup> External quantum efficiency.

for **FL1** and **FL2**. **FL1**, having substituents at 3 and 5 positions, also showed lower driving voltage than **FL2**, in which the positions of the substituents at the pyridine ring are at 2 and 6 positions. Efficiencies of the device with **FL1** were as high as those with **Alq<sub>3</sub>** and better than those of **PY2**, although the electron mobility of **FL1** is much smaller than that of **PY2** and **Alq<sub>3</sub>**. These results suggest that the electron injection from cathode is an important process determining driving voltage. In particular, specific affinity of the electron-transporting materials with cathode metal or metal halide is dominant to determine the barrier height for the electron injection. To take a close look at the injection process, electron only devices with the configuration of ITO/BCP (10 nm)/ETL (**Alq<sub>3</sub>**, **PY1**, or **PY2**) (100 nm)/LiF (0.5 nm)/Al (100 nm) were fabricated, where BCP was used as hole blocking layer (Fig. 5). **PY2** showed much smaller current density than that of **Alq<sub>3</sub>** and **PY1**. These results also support that the barrier height for the electron injection from Al to **PY2** is high, compared with **Alq<sub>3</sub>** and **PY1**. However, in contrast to the current density–voltage characteristics of the OLED device (Fig. 4), **Alq<sub>3</sub>** showed higher current density than that of **PY1** in the electron only device. Probably, in the OLED device with **PY1**, better hole injection from NPD to **PY1** was achieved, and the holes

were consumed in recombination with electron, which contributed to the increase of whole current density. In terms of the ionization potentials, **PY1** and **Alq<sub>3</sub>** have almost same barrier height for the hole injection from NPD, which are 0.44 and 0.38 eV, respectively. The better hole injection from NPD to **PY1** than that to **Alq<sub>3</sub>** could be considered to be resulted from a better molecular contact between the pyrene group of **PY1** and the naphthalene group of NPD.

In the design of ETL materials, their *chemical affinity* with cathode metal or metal halide is more important than their *electron affinity*, and their electron mobility is not necessary to be very high compared with **Alq<sub>3</sub>**.

### 3. Experimental

#### 3.1. Measurement

The <sup>1</sup>H-NMR spectra were measured in deuterated solvents with JEOL ECX 400 MHz spectrometers. Elemental analyses were carried out in the Elemental Analysis Service, Yamagata University, Japan. Mass spectra were obtained by a JEOL JMS-K9 mass spectrometer. Thermal gravimetric analysis was performed on a SII EXSTAR 6000 and TGA/DTA 62000. Differential scanning calorimetry (DSC) was performed on a Perkin–Elmer Diamond DSC7. Ionization potentials were measured with Photoelectron Spectrometer Surface Analyzer (RIKEN KEIKI AC-3). UV–visible absorption spectra were recorded as solutions in chloroform or film on quartz with a Shimadzu UV-3150 spectrometer. PL spectra were recorded using a Jobin Yvon Fluoromax-2 fluorometer. PL quantum efficiencies were measured with integral sphere system Hamamatsu C9920-01 under nitrogen. Electrochemistry was performed using a BAS Electrochemical Analyzer 660B. All measurements were made at room temperature on samples dissolved in dry benzonitrile or THF with 0.1 M tetra-*n*-butylammonium tetrafluoroborate as the electrolyte. The sample concentration was 1 mM, and a platinum working electrode, platinum counter electrode in 0.1 M tetra-*n*-butylammonium tetrafluoroborate in the same solvent as used for the sample, and an Ag/0.1 M AgNO<sub>3</sub> in acetonitrile reference electrode were used. The scan rate was 100 mV/s. The solutions were deoxygenated with argon. The ferricenium/ferrocene couple was used as standard. All potentials are quoted relative to the ferricenium/ferrocene couple. The EL devices were fabricated on indium tin oxide (ITO) coated glass substrates, ultrasonicated sequentially in detergent, methanol, 2-propanol, and acetone and exposed under UV–ozone ambient for 20 min. NPD, Alq<sub>3</sub>, BCP or ETL materials were deposited by thermal evaporation under 2 × 10<sup>−4</sup> Pa. Lithium fluoride and aluminum were finally deposited under 1 × 10<sup>−3</sup> Pa as a cathode through a shadow mask, and its active area is 5 × 5 mm<sup>2</sup>. Layer thickness calibration was performed using Dektak 3 surface profilometer. The EL spectra were measured on a Hamamatsu photonic multichannel analyzer PMA-11. The current–voltage (*I*–*V*) characteristics and luminance were measured using a Keithley 2400 Source Meter and Konika

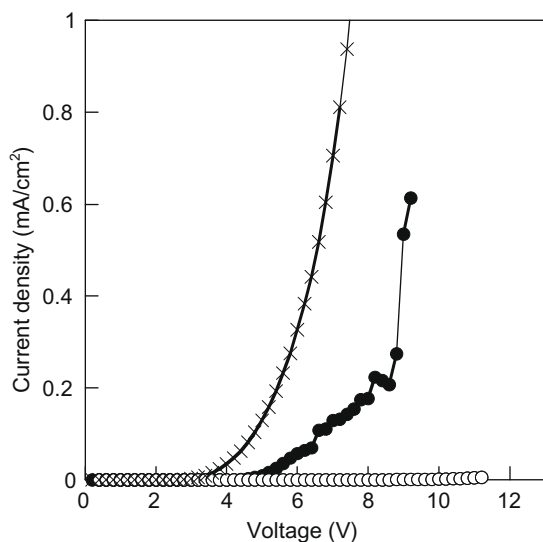


**Fig. 5.** Current density–voltage plots of the electron only device of **PY1** (closed circle), **PY2** (opened circle), and **Alq<sub>3</sub>** (cross).

Minolta CS-200, respectively. External quantum efficiencies were calculated assuming Lambertian emission pattern and considering all spectral features in the visible.

### 3.2. Materials

Pyrene-1-boronic acid was purchased from TCI-Japan. 3,5-Dibromopyridine was purchased from Aldrich. 2,6-Dibromopyridine was purchased from Acros. 2-(4,4,5,5-Tetramethyl-1,3,2-dioxaborolan-2-yl)-9,9-dimethylfluorene was synthesized according to the literature.

### 3.3. PY1

A mixture of pyrene-1-boronic acid (2.17 g, 8.82 mmol), 3,5-dibromopyridine (0.95 g, 4.0 mmol), tetrakis(triphenylphosphine)palladium(0) (0.46 g, 0.40 mmol), potassium carbonate (3.32 g, 24.0 mmol), water (12 ml), ethanol (40 ml), and toluene (80 ml) was degassed and placed under nitrogen, and then heated at 80 °C for 12 h. The mixture was allowed to cool to room temperature and then chloroform was added. The organic layer was washed with water, dried over magnesium sulfate, and filtered. The solvent was removed and the residue was purified by column chromatography over silica using a chloroform as eluent to give a pale yellow solid (1.54 g, 3.21 mmol, 80%). The product was purified again by train sublimation.  $^1\text{H-NMR}$  (400 MHz,  $\text{CDCl}_3$ , TMS, ppm) 9.04 (2H, d,  $J = 2.1$  Hz), 8.32–8.20 (9H, m), 8.14–8.10 (8H, m), 8.05 (2H, t,  $J = 7.7$  Hz).  $^{13}\text{C-NMR}$  (100 MHz,  $\text{CDCl}_3$ , TMS, ppm) 149.77, 139.46, 136.61, 133.31, 131.44, 131.31, 130.89, 128.82, 128.32, 128.01, 127.77, 127.35, 126.27, 125.57, 125.24, 125.04, 124.89, 124.80, 124.40. EI-MS ( $m/z$ ) calcd. 479.57; found 480. Elemental analysis calcd. for  $\text{C}_{37}\text{H}_{21}\text{N}$ : C, 92.67; H, 4.41; N, 2.92; found: C, 92.58; H, 4.26; N, 2.96.

### 3.4. PY2

A mixture of pyrene-1-boronic acid (2.17 g, 8.82 mmol), 2,6-dibromopyridine (0.95 g, 4.0 mmol), tetrakis(triphenylphosphine)palladium(0) (0.46 g, 0.40 mmol), potassium carbonate (3.32 g, 24.0 mmol), water (12 ml), ethanol (40 ml), and toluene (80 ml) was degassed and placed under nitrogen, and then heated at 80 °C for 12 h. The mixture was allowed to cool to room temperature and then chloroform was added. The organic layer was washed with water, dried over magnesium sulfate, and filtered. The solvent was removed and the residue was purified by column chromatography over silica using a chloroform: *n*-hexane mixture (1:1) as eluent to give a pale yellow solid (1.05 g, 2.19 mmol, 55%). The product was purified again by train sublimation.  $^1\text{H-NMR}$  (400 MHz,  $\text{CDCl}_3$ , TMS, ppm) 8.62 (2H, d,  $J = 9.5$  Hz), 8.37 (2H, d,  $J = 7.6$  Hz), 8.30 (2H, d,  $J = 7.7$  Hz), 8.23–8.08 (11H, m), 8.03 (2H, t,  $J = 7.5$  Hz), 7.85 (2H, d,  $J = 7.7$  Hz).  $^{13}\text{C-NMR}$  (100 MHz,  $\text{CDCl}_3$ , TMS, ppm) 159.52, 136.57, 135.98, 131.46, 131.43, 130.94, 128.75, 127.99, 127.92, 127.87, 127.46, 126.02, 125.35, 125.12, 125.07, 125.04, 124.90, 124.89, 124.02. EI-MS ( $m/z$ ) calcd. 479.57; found 479. Elemental analysis calcd. for  $\text{C}_{37}\text{H}_{21}\text{N}$ : C, 92.67; H, 4.41; N, 2.92; found: C, 92.61; H, 4.33; N, 2.93.

### 3.5. FL1

A mixture of 2-(4,4,5,5-tetramethyl-1,3,2-dioxaborolan-2-yl)-9,9-dimethylfluorene (2.8 g, 8.8 mmol), 3,5-dibromopyridine (0.95 g, 4.0 mmol), tetrakis(triphenylphosphine)palladium(0) (0.46 g, 0.40 mmol), potassium carbonate (3.32 g, 24.0 mmol), water (12 ml), ethanol (40 ml), and toluene (80 ml) was degassed and placed under nitrogen, and then heated at 80 °C for 12 h. The mixture was allowed to cool to room temperature and then chloroform was added. The organic layer was washed with water, dried over magnesium sulfate, and filtered. The solvent was removed and the residue was purified by column chromatography over silica using a chloroform as eluent to give a white solid (1.76 g, 3.80 mmol, 95%). The product was purified again by train sublimation.  $T_g$  88 °C.  $T_{d5\%}$  360 °C.  $I_p$  6.4 eV.  $E_g$  3.59 eV.  $^1\text{H-NMR}$  (400 MHz,  $\text{CDCl}_3$ , TMS, ppm) 8.89 (2H, d,  $J = 2.3$  Hz), 8.15 (1H, t,  $J = 2.1$  Hz), 7.86 (2H, d,  $J = 8.2$  Hz), 7.80–7.77 (2H, m), 7.71 (2H, d,  $J = 1.4$  Hz), 7.65 (2H, dd,  $J = 7.7, 1.8$  Hz), 7.49–7.47 (2H, m), 7.40–7.34 (4H, m), 1.57 (12H, s). EI-MS ( $m/z$ ) calcd. 463.61; found 464. Elemental analysis calcd. for  $\text{C}_{35}\text{H}_{29}\text{N}$ : C, 90.67; H, 6.30; N, 3.02; found: C, 90.97; H, 6.36; N, 3.07.

### 3.6. FL2

A mixture of 2-(4,4,5,5-tetramethyl-1,3,2-dioxaborolan-2-yl)-9,9-dimethylfluorene (2.8 g, 8.8 mmol), 3,5-dibromopyridine (0.95 g, 4.0 mmol), tetrakis(triphenylphosphine)palladium(0) (0.46 g, 0.40 mmol), potassium carbonate (3.32 g, 24.0 mmol), water (12 ml), ethanol (40 ml), and toluene (80 ml) was degassed and placed under nitrogen, and then heated at 80 °C for 12 h. The mixture was allowed to cool to room temperature and then chloroform was added. The organic layer was washed with water, dried over magnesium sulfate, and filtered. The solvent was removed and the residue was purified by column chromatography over silica using a toluene:*n*-hexane mixture (2:3) as eluent to give a white solid (1.48 g, 3.19 mmol, 80%). The product was purified again by train sublimation.  $T_g$  84 °C.  $T_{d5\%}$  340 °C.  $I_p$  6.3 eV.  $E_g$  3.33 eV.  $^1\text{H-NMR}$  (400 MHz,  $\text{CDCl}_3$ , TMS, ppm) 8.25 (2H, d,  $J = 1.3$  Hz), 8.16 (2H, dd,  $J = 8.1, 1.8$  Hz), 7.87–7.75 (7H, m), 7.49–7.47 (2H, m), 7.40–7.33 (4H, m), 1.59 (12H, s). EI-MS ( $m/z$ ) calcd. 463.61; found 464. Elemental analysis calcd. for  $\text{C}_{35}\text{H}_{29}\text{N}$ : C, 90.67; H, 6.30; N, 3.02; found: C, 90.74; H, 6.36; N, 3.02.

## Appendix A. Supplementary data

Supplementary data associated with this article can be found, in the online version, at [doi:10.1016/j.orgel.2009.04.020](https://doi.org/10.1016/j.orgel.2009.04.020).

## References

- [1] T. Urabe, T. Sasaoka, K. Tatsuki, J. Takaki, SID Int. Symp. Dig. Tech. (2007) 161.
- [2] R.F. Service, Science 310 (2005) 1762.



- [3] (a) G. Hughes, M.R. Bryce, *J. Mater. Chem.* 15 (2005) 94;  
(b) A.P. Kulkarni, C.J. Tonzola, A. Babel, S.A. Jenekhe, *Chem. Mater.* 16 (2004) 4556;  
(c) P. Stroehriegel, J.V. Grazulevicius, *Adv. Mater.* 14 (2002) 1439.
- [4] C.W. Tang, S.A. VanSlyke, *Appl. Phys. Lett.* 51 (1987) 913.
- [5] L.S. Hung, C.W. Tang, M.G. Mason, *Appl. Phys. Lett.* 70 (1997) 152.
- [6] G.F. He, O. Schneider, D.S. Qin, X. Zhou, M. Pfeiffer, K. Leo, *J. Appl. Phys.* 95 (2004) 5773.
- [7] (a) T. Oyamada, H. Sasabe, C. Adachi, S. Murase, T. Tominaga, C. Maeda, *Appl. Phys. Lett.* 86 (2005) 33503;  
(b) T. Matsushima, C. Adachi, *Appl. Phys. Lett.* 89 (2006) 253506.
- [8] H. Mattoussi, H. Murata, C.D. Merritt, Y. Iizumi, J. Kido, Z.H. Kafafi, *J. Appl. Phys.* 86 (1999) 2642.
- [9] Model AC-3, Riken Keiki Co., Ltd.
- [10] In cyclic voltammetry, no redox peaks appeared between 1.5 and  $-2.5$  V vs.  $\text{Ag}/\text{Ag}^+$  in benzonitrile or THF with Pt or glassy carbon working electrode.
- [11] (a) J.M. Zhao, Y.Q. Zhan, S.T. Zhang, X.J. Wang, Y.C. Zhou, Y. Wu, Z.J. Wang, X.M. Ding, X.Y. Hou, *Appl. Phys. Lett.* 84 (2004) 5377;  
(b) K. Ihm, T.-H. Kang, K.-J. Kim, C.-C. Hwang, Y.-J. Park, K.-B. Lee, B. Kim, C.-H. Jeon, C.-Y. Park, K. Kim, Y.-H. Tak, *Appl. Phys. Lett.* 83 (2004) 2949.
- [12] (a) Q.T. Le, L. Yan, Y. Gao, M.G. Mason, D.J. Giesen, C.W. Tang, *J. Appl. Phys.* 87 (2000) 375;  
(b) M.G. Mason, C.W. Tang, L.-S. Hung, P. Raychaudhuri, J. Madathil, D.J. Giesen, L. Yan, Q.T. Le, Y. Gao, S.-T. Lee, L.S. Liao, L.F. Cheng, W.R. Salaneck, D.A.d. Santos, J.L. Bredas, *J. Appl. Phys.* 89 (2001) 2756;  
(c) C.-I. Wu, G.-R. Lee, T.-W. Pi, *Appl. Phys. Lett.* 87 (2005) 212108.

P3HT is still under development, and it is uncertain whether the specialized film-forming techniques for achieving high mobility in P3HT OTFTs will be compatible with the to-be-determined manufacturing process. Therefore, it is important that more options for controlling the P3HT morphology to obtain high field-effect mobility are available, so that the commercial applications of the P3HT OTFTs can be facilitated.

In this study, we explore the plausibility of manipulating the morphology of P3HT films with a post-casting solvent–vapor exposure treatment (vapor annealing) to achieve high field-effect mobility in P3HT OTFTs. Vapor annealing has been shown to enhance the crystallization and thus improves the carrier mobility of P3HT molecules in bulk-heterojunction solar cells, but its effects on P3HT-based OTFTs have not been reported [12]. We analyze the film morphology and the OTFT characteristics resulting from exposing P3HT films to unsaturated and saturated solvent vapor conditions, based on which we determine the vapor annealing conditions that achieve optimal OTFT characteristics. We also characterize the lifetime of the OTFT devices, a property important to practical use, as a function of the vapor annealing condition, and we then demonstrate encapsulation methods capable of sufficiently extending the lifetime.

## 2. Materials and methods

P3HT (regioregular ratio 98.5%, molecular weight 87 k) was purchased from Sigma–Aldrich Co. and used as received. The substrates were p-type heavily-doped silicon wafers with a 200 nm thermal oxide capping layer that was used as the gate dielectric. The OTFTs used in this study were bottom-gate, bottom-contact devices, and the fabrication process is as follows. First, the SiO<sub>2</sub> gate dielectric was treated with octadecyltrichlorosilane (OTS) to form a self-assembled monolayer (SAM) [9]. Second, a 100 nm gold layer was thermally evaporated through a shadow mask onto the substrates to form the source and drain electrodes, whose channel length/width (*L*/*W*) was 100 μm/1500 μm. Third, a P3HT layer was spin-coated from a 1 wt% dichlorobenzene (DCB) solution at 800 rpm to complete the devices. Conditions of the various solvent–vapor annealing treatments applied to the P3HT film are as follows. For the control, the P3HT film was spun to dry for 60 s, followed by a 30 min bake at 130 °C. The unsaturated solvent–vapor annealing treatment consisted of the following steps: (1) spin-cast a P3HT film with a 30 s spin, when it was partially dry, (2) transfer the film to a partially sealed volume maintained at 25 °C, which was controlled so that the film was dried after 10 min, (3) bake the film at 130 °C for 30 min. The saturated solvent–vapor annealing treatment was similar except that the partially dried P3HT films were placed in a fully sealed volume filled with saturated DCB vapor, where it was stored for 60 min before being retrieved. All steps of the fabrication process were performed in a nitrogen-filled glove box. The *I*–*V* characteristics of the devices were measured in air using a Keithley 4200-SCS Semiconductor Characterization System. The mobility values reported were effective mobility that neglected the effects of con-

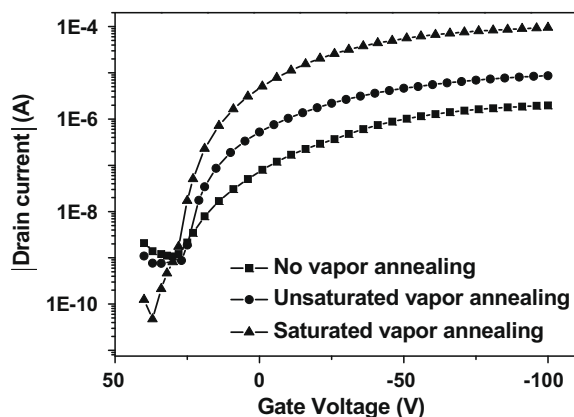


Fig. 1. Transfer characteristics of the P3HT OTFTs made with different vapor annealing conditions, measured at a source-drain bias of 60 V.

tact resistance. The morphology of the P3HT films was observed using a Nanoscope 3D Controller Atomic Force Microscope (AFM) (Digital Instruments) operated at the tapping mode and a X-ray diffraction graph was observed using Rigaku TTRAXIII X-ray diffractometer (XRD).

## 3. Results and discussion

The saturated and unsaturated solvent–vapor annealing treatments improved the field-effect mobility of the P3HT OTFTs in two distinct manners, as shown in Fig. 1 and Table 1. With unsaturated annealing (which results in slow drying), the mobility increased by ~9 folds, from 0.0013 to up to 0.012 cm<sup>2</sup>/V s. With saturated annealing, however, a drastic increase in the mobility occurred, raising the mobility to 0.11 cm<sup>2</sup>/V s. With unsaturated vapor annealing, the increase in the mobility was found to result from enhanced crystallization of the P3HT molecules, as can be seen in the AFM micrographs in Fig. 2 and in the XRD patterns in Fig. 3. The AFM micrographs show that fiber-like features, which are characteristic of crystalline P3HT [7,8], were indistinct in the unannealed samples but were significantly more defined and larger in size upon unsaturated vapor annealing. Similarly, the XRD pattern of the unsaturated-vapor-annealed samples shows an increase in the intensity of the peak corresponding to the (1 0 0) lattice plane of the P3HT crystal unit cell. The observed effects of solvent–vapor annealing in this stage were similar to what have been reported for P3HT-containing bulk-heterojunction photovoltaic cells and P3HT thin films, i.e., enhanced crystallization and increased hole mobility [8,12]. It should be noted that the rather high and positive threshold voltages of the devices are due to the p-doping effects of H<sub>2</sub>O/O<sub>2</sub> from air as well as the low capacitance of the thick SiO<sub>2</sub>/OTS gate insulator, and are characteristic of P3HT OTFTs with similar insulator materials. [4,5,9,13]

With saturated solvent–vapor annealing treatment, a change in the appearance of the P3HT films accompanied the drastic increase in the mobility. Upon saturated annealing (prior to the final bake), the films started to reflow as they fully absorbed the solvent vapor, and because of the greater affinity of P3HT to itself and to the gold con-

**Table 1**

Electrical characteristic of P3HT OTFTs made with different vapor annealing conditions.

	Mobility ( $\text{cm}^2/\text{V s}$ )	On/off ratio	Threshold voltage (V)
No vapor annealing	0.0013	$1.5 \times 10^4$	22
Unsaturated solvent annealing	0.012	$6.7 \times 10^4$	28
Saturated vapor annealing	0.11	$1.9 \times 10^6$	18

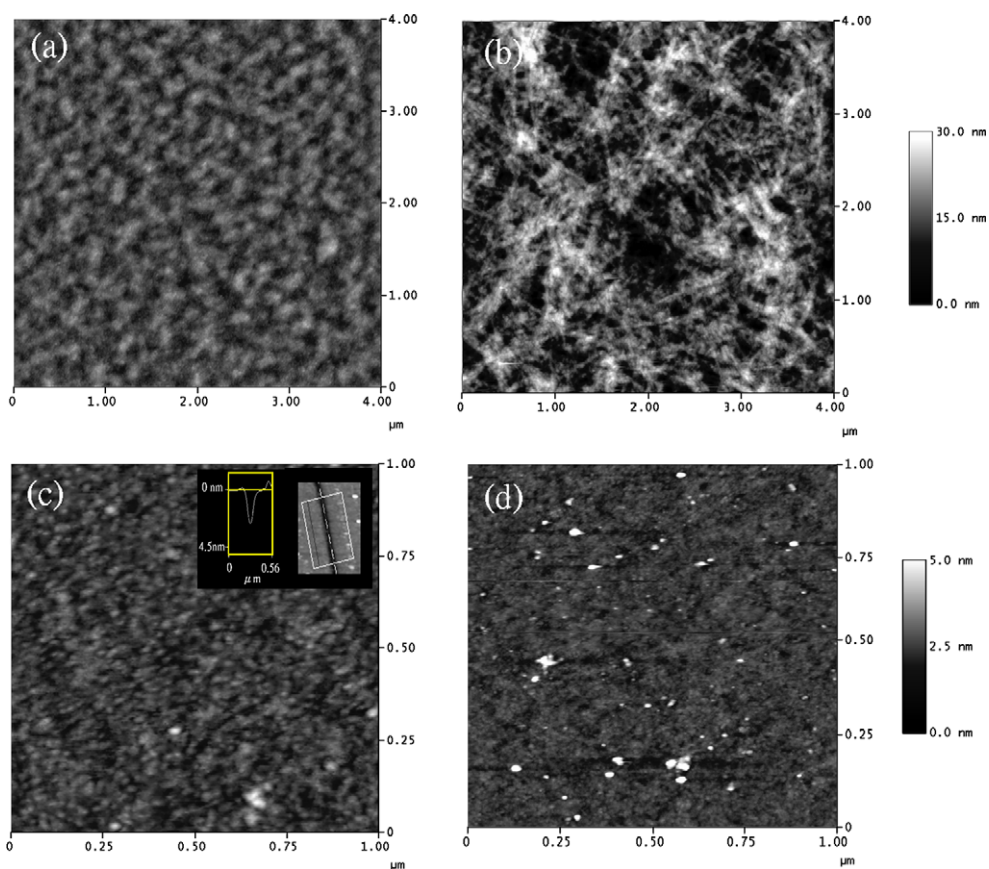


**Fig. 2.** AFM topography images of P3HT films: (a) without solvent vapor annealing, (b) annealed in unsaturated solvent vapor, and (c) annealed with saturated solvent vapor (reflowed); inset: a scan showing the thickness of the reflowed film, where the scan was made over a scraped line through the film. (d) AFM topography image of the  $\text{SiO}_2$ -OTS surface.

tacts than to the  $\text{SiO}_2$ -OTS surface of the FET channel area, the P3HT films reflowed out of the FET channels into a few isolated drops on the large gold contact pads in the non-device area, leaving the FET channels free of visible P3HT film. A schematic drawing illustrating this process is given in Fig. 4. Despite showing no visible P3HT film, the FET channels did retain a thin layer of P3HT that was  $\sim 2$  nm in thickness as determined by AFM (see Fig. 2c inset), which corresponded to 2–3 monolayers; moreover, the FET characteristics of the reflowed devices (Fig. 5) showed that the thin P3HT layer was functional as the semiconductor layer. The normal FET function of the thin P3HT layer was consistent with the knowledge that charge transport in OTFTs proceeds mostly via the 1–2 monolayers of the organic semiconductor adjacent to the gate dielectric. The mechanism that resulted in the high mobility of the re-

flowed P3HT may be that the reflow motion caused the P3HT chains to extend horizontally along the surface, so that charges were better able to transport along the chains (intramolecular charge transport) rather than across the chains (intermolecular charge transport) (see Fig. 4). This mechanism may be similar to that of the dip coating technique reported by Cho et al. and Wang et al. [4,5], where the dipping motion applied to coat P3HT films helped to extend the P3HT chains along the surface, producing 2–3-monolayer P3HT thin films with similarly high FET mobility. Consistent with the fibril/grain-like crystal morphology observed for the dip-coated P3HT films, the surface of the reflowed films also appeared to consist of small fibrils and grains, as can be seen by comparing the AFM images of the reflowed P3HT layer and the  $\text{SiO}_2$ -OTS surface (on which the P3HT layer was coated) in

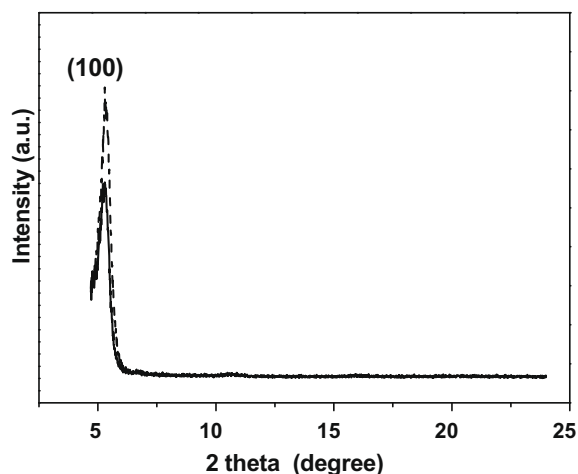


**Fig. 3.** X-ray diffraction patterns of P3HT films before (solid line) and after (dotted line) unsaturated vapor annealing.

Fig. 2c and d). In terms of uniformity of the OTFTs produced by the reflow process, the uniformity in the mobility was slight better than that of the pristine devices on

$1.5 \times 2.0 \text{ cm}^2$  square substrates with 10 devices: The standard deviation was 10% of the average mobility for the reflowed device, as opposed to 14% for the non-reflowed devices. This good uniformity, despite the randomness of the reflow process, was attributed to the large affinity differential between P3HT–gold and P3HT–SiO<sub>2</sub>/OTS, which ensured that the bulk of the P3HT film retreated to the large gold contact pads, where it could be easily removed. It should be noted that the mobility values observed for the reflowed devices may have been underestimated due to the high contact resistance [13,14]; however, the deviation should have been small, as devices with a different gate length/width ratio showed identical mobility values (see Supplementary Materials).

Some interesting phenomena arose when the reflowed and non-reflowed (unsaturated-vapor-annealed) OTFTs were observed after various times of being stored in air: In terms of the mobility, the reflowed devices degraded much more rapidly than that of non-reflowed devices, while the opposite was observed in terms of the off current, as shown in Fig. 6. P3HT OTFTs are susceptible to degradations induced by O<sub>2</sub> and H<sub>2</sub>O via two main mechanisms: photo-oxidation and *p*-type doping, the former of which disrupts the conjugation of P3HT to impede charge

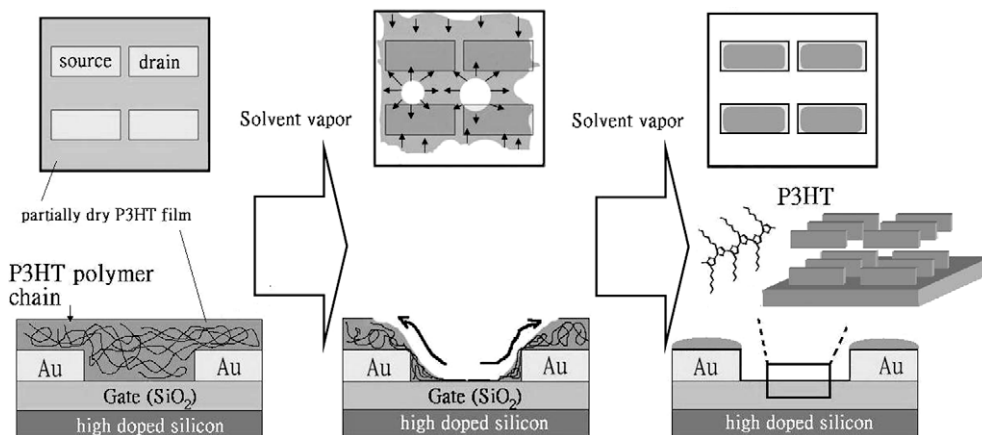


**Fig. 4.** Schematic drawing of the reflow process during saturated vapor annealing: Top row: top views; bottom row: side views.

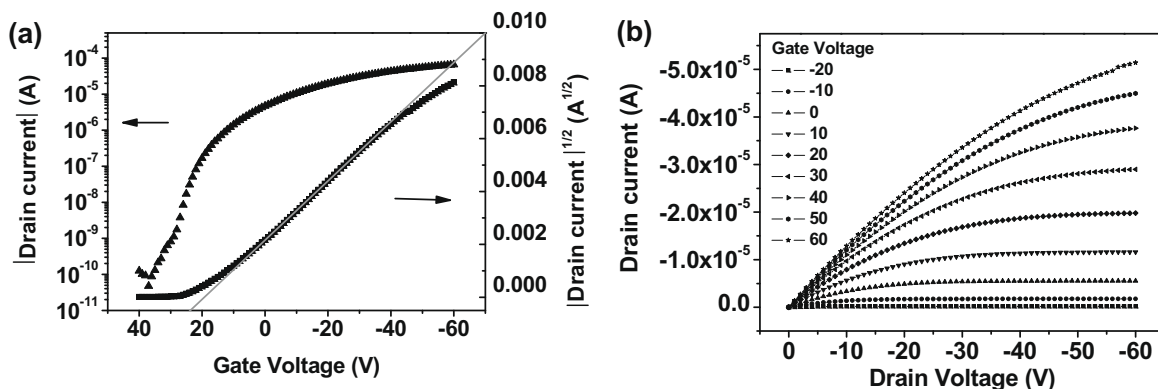


**Fig. 5.** (a) Transfer and (b) output characteristics of the P3HT OTFTs annealed in saturated solvent vapor (reflowed). The transfer characteristics were measured at a source–drain bias of 60 V.

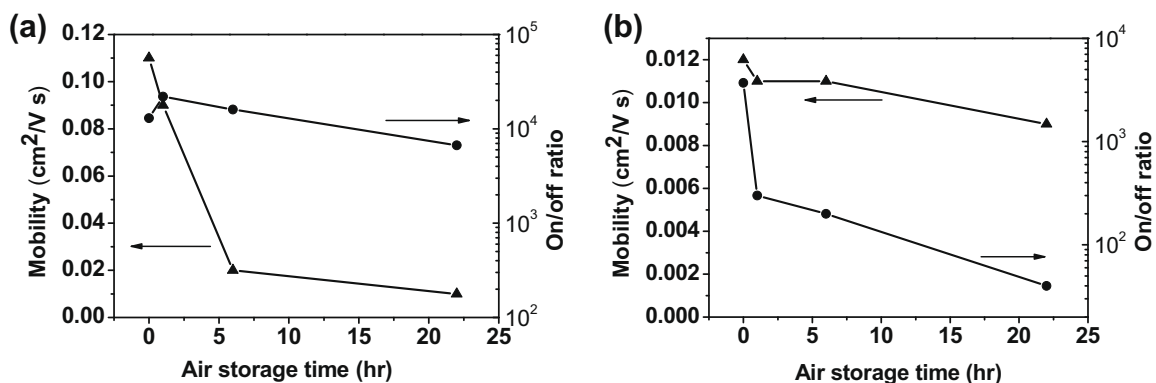


**Fig. 6.** Mobility and on/off ratio of unencapsulated P3HT OTFTs as a function of storage time in air: (a) reflowed (saturated-vapor-annealed) devices, (b) non-reflowed (unsaturated-vapor-annealed) devices.

transport and the latter of which introduces charge carriers that contribute to high off current [15–17]. The different stability in air of the two types of P3HT OTFTs can be

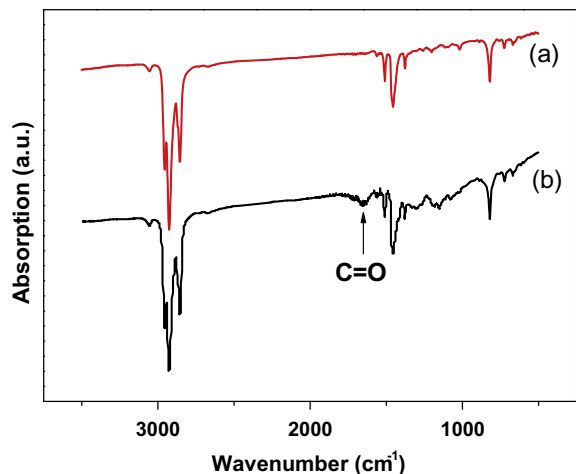


**Fig. 7.** FTIR spectra of unsaturated-vapor-annealed P3HT layer (a) before and (b) after being stored in air for 24 h under sunlight.

accounted for by considering the effects of their drastically different thickness on the two degradation mechanisms described above. In photo-oxidation, the reflowed P3HT film's ultra thinness (~2 nm) allowed the whole of itself to be quickly photo-oxidized, thereby showing rapid decline in the mobility; the non-reflowed P3HT film, on the other hand, was of regular thickness (25 nm) and therefore required more time for photo-oxidation to propagate through the film. Evidence of photo-oxidation was observed in the FTIR spectra of the non-reflowed film (Fig. 7), where a carbonyl stretching peak at 1650 cm<sup>-1</sup> appeared after air exposure; the reflowed film was too thin to have measurable IR signal. As to doping by O<sub>2</sub> and H<sub>2</sub>O, the reflowed film had far smaller capacity to absorb the dopants than the non-reflowed film, and therefore its doping-induced off current was of a much smaller magnitude.

The air-induced degradation of the reflowed P3HT OTFTs was greatly reduced by encapsulating them with either an adhesive-sealed glass plate or with a bilayer polymer film composed of a poly(methyl methacrylate) (PMMA) and a poly(vinylidene chloride-co-acrylonitrile) (PVDC-co-PAN) layer, as can be seen by comparing Fig. 6 with Fig. 8, which shows that the mobility and on/off ratio of the encapsulated devices degrade slowly (with PMMA/

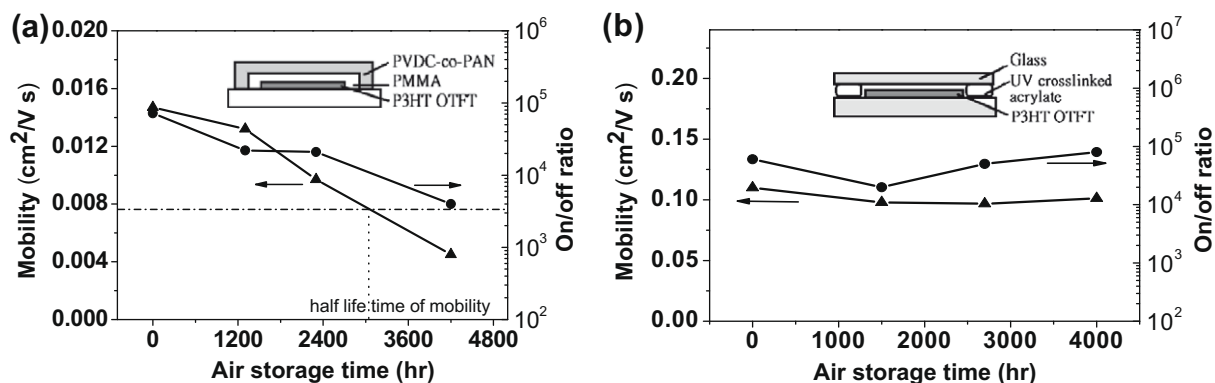


**Fig. 8.** Mobility and on/off ratio of reflowed P3HT OTFTs as a function of storage time in air: (a) encapsulated with PMMA/PVDC-co-PAN, (b) encapsulated with adhesive-sealed glass lid.

PVDC-co-PAN) or remain stable (with glass/adhesive) with time. The lifetime of the reflowed P3HT OTFTs, which is the time required to reduce the mobility by one-half of the pristine mobility, increased from 3 h without encapsulation to ~3000 h with PMMA/PVDC-co-PAN encapsulation; moreover, the devices encapsulated with adhesive-sealed glass showed only slight degradation upon 4000 h of storage in air. However, the PMMA/PVDC-co-PAN encapsulation caused pronounced upon-encapsulation decline in the mobility to the reflowed devices, from 0.11 down to 0.014 cm<sup>2</sup>/V s. This degradation was attributed to the direct contact of the P3HT layer with the PMMA film, which may interfere with charge transport in P3HT through intermixing or stress, and because the reflowed P3HT layer contained only 2–3 monolayers, the effects of the PMMA film were magnified. The encapsulation-induced degradation of the reflowed devices was avoided by the glass encapsulation, where the P3HT layer was not contacted by the encapsulation materials. The above results indicate that, although the reflowed P3HT films offer high mobility, their encapsulation or passivation requires special attention to prevent encapsulation- or passivation-induced degradations.

#### 4. Conclusion

Room-temperature solvent-vapor annealing of spin-coated P3HT films improved the field-effect mobility of the resultant OTFT devices in two distinct manners. With unsaturated solvent vapor annealing, the mobility increased moderately, from 0.0013 to 0.012 cm<sup>2</sup>/V s, because the solvent vapor enhanced crystallization of P3HT. With saturated solvent vapor annealing, the P3HT films liquefied and reflowed, leaving an ultra-thin film of 2–3 monolayers in the device area, where the P3HT chains were extended by the reflowing motion so that the mobility was greatly increased, to 0.11 cm<sup>2</sup>/V s. Upon exposure to air, the reflowed P3HT films showed more quickly declined mobility yet more slowly increased off current due to their ultra-thin thickness, as the small thickness allowed rapid and thorough photo-oxidization but low air-doping uptake. The reflowed P3HT OTFTs' lifetime were extended to more than 3000 h when they were encapsulated with either a bilayer polymer film or with an adhesive-sealed glass plate; and upon-encapsulation degradation was avoided by keeping the encapsulant from direct contact with the P3HT films, which were susceptible to intermixing with

or stress exerted by a directly contacting encapsulant due to their small thickness.

#### Acknowledgements

This work was supported by Industrial Technology Research Institute (ITRI) of Taiwan (Project No. 8351AA5130), National Science Council (Grant No. NSC 96-2221-E-002-143-MY3), and Ministry of Economics Affairs (Grant No.: 97-EC-17-A-08-S1-015). The authors thank Drs. Tarng-Shiang Hu, Chia-Hung Chou, and Hua-Chi Cheng of ITRI for their advices on the analysis of experimental results.

#### Appendix A. Supplementary data

Supplementary data associated with this article can be found, in the online version, at doi:10.1016/j.orgel.2009.04.015.

#### References

- [1] Z. Bao, A. Dodabalapur, A.J. Lovinger, *Appl. Phys. Lett.* 69 (1996) 4108.
- [2] H.E. Katz, Z. Bao, *J. Phys. Chem. B* 104 (2000) 671–678.
- [3] M. Kobashi, H. Takeuchi, *Macromolecules* 31 (1998) 7273–7278.
- [4] S. Cho, K. Lee, J. Yuen, G. Wang, D. Moses, A.J. Heeger, M. Surin, R. Lazzaroni, *J. Appl. Phys.* 100 (2006) 114503.
- [5] G. Wang, J. Swensen, D. Moses, A.J. Heeger, *J. Appl. Phys.* 93 (2003) 6137.
- [6] J.-F. Chang, B. Sun, D.W. Breiby, M.M. Nielsen, T.I. Solling, M. Giles, I.M. Culloch, H. Sirringhaus, *Chem. Mater.* 16 (2004) 4772.
- [7] H. Yang, T.J. Shin, L. Yang, K. Cho, C.Y. Ryu, Z. Bao, *Adv. Funct. Mater.* 15 (2005) 671.
- [8] D.H. Kim, Y.D. Park, Y. Jang, S. Kim, K. Cho, *Macromol. Rapid Commun.* 26 (2005) 834–839.
- [9] L.A. Majewski, J.W. Kingsley, C. Balocco, A.M. Song, *Appl. Phys. Lett.* 88 (2006) 222108.
- [10] S.C. Lim, S.H. Kim, J.H. Lee, M.K. Kim, D.J. Kim, T. Zyung, *Synth. Metals* 148 (2005) 75.
- [11] D.H. Kim, Y.D. Park, Y. Jang, H. Yang, Y.H. Kim, J.I. Han, D.G. Moon, S. Park, T. Chang, C. Chang, M. Joo, C.Y. Ryu, K. Cho, *Adv. Funct. Mater.* 15 (2005) 77.
- [12] G. Li, V. Shrotriya, J.S. Huang, Y. Yao, T. Moriarty, K. Emery, Y. Yang, *Nat. Mater.* 4 (2005) 864.
- [13] C. Reese, Z. Bao, *J. Appl. Phys.* 105 (2009) 024506.
- [14] B.H. Hamadani, D.A. Corley, J.W. Ciszek, J.M. Tour, D. Natelson, *Nano Lett.* 6 (6) (2006) 1304.
- [15] S. Hoshino, M. Yoshida, S. Uemura, T. Kodzasa, N. Takada, T. Kamata, K. Yase, *J. Appl. Phys.* 95 (2004) 5088.
- [16] S.-C. Wang, J.-C. Lou, B.-L. Liou, R.-X. Lin, C.-F. Yeh, *J. Electrochem. Soc.* 152 (1) (2005) G50–G56.
- [17] D. Li, E.-J. Borkent, R. Nortrup, H. Moon, H. Katz, Z. Bao, *Appl. Phys. Lett.* 86 (2005) 042105.

only observed at low temperatures and high current levels in a conventional Alq<sub>3</sub>-based device. This leads us to suggest that temperature and driving current would play important roles in the magnetic field effects (MFEs) on EL as mentioned above.

In this letter, we presented detailed studies on the influence of temperature and driving current upon the magnetic-field modulated EL to further investigate the MFEs in Alq<sub>3</sub>-based OLEDs with the structure of ITO/copper phthalocyanine (CuPc)/N,N'-di(naphthalene-1-yl)-N,N'-diphenyl-benzidine (NPB)/Alq<sub>3</sub>/lithium fluoride (LiF)/Al. We found that the EL intensity increases at low fields and reaches its maximum at about 35 mT. With further increasing the field, the EL intensity either saturates or decreases, depending on the temperature and driving current. The low-field-increase, which exists in all the temperature and driving current measurement range, was mainly attributed to the magnetic-field dependent singlet-to-triplet conversion of electron-hole pairs. The high-field-decrease, evidently observed at low temperatures and high current levels, was demonstrated to be in fair agreement with the magnetic-field mediated TTA process.

## 2. Experimental

The OLEDs with the structure of ITO (100 nm)/CuPc (15 nm)/NPB (60 nm)/Alq<sub>3</sub> (80 nm) LiF (1 nm)/Al (100 nm) were fabricated, where CuPc is buffer layer, NPB is the hole transport layer, and Alq<sub>3</sub> is the electron transport/emission layer, respectively. LiF was used to improve the electron injection into Alq<sub>3</sub>. All the organic materials were used as received without additional purification and deposited by thermal evaporation under high vacuum ( $\sim 10^{-6}$  Pa). The evaporation rate and thickness of the deposited layers were detected by a calibrated quartz crystal monitor. Hundred nanometer Al cathode was thermally evaporated on the LiF film through a shadow mask (active areas:  $2 \times 3$  mm<sup>2</sup>). After preparation, the samples were mounted on the cold finger of the close-cycle cryostat (Janis CCS-350s) with variable temperature that was located between the pole pieces of an electromagnet (Lakeshore EM647). The magnetic field with the maximum strength of 0.5 T was applied parallel to the device surface and measured by Hall probe GaussMeter (Lakeshore 421) which was placed close to the sample. The devices were driven by a Keithley 2400 SourceMeter and the EL intensity was measured by using a silicon photodetector and a Keithley 2000 apparatus. The photodetector was tested to make sure there was no field dependence on its output.

## 3. Results and discussion

Fig. 1a shows the magnetic field effects on EL and voltage for the device driven with constant current of 400  $\mu$ A at 15 K. It is seen that a sharp increase in EL at low magnetic fields followed by a significant decrease at high fields larger than about 35 mT. While the behavior of voltage shows a saturation at high fields after its sharp decrease at low fields. Similar MFEs in EL at constant voltage (the

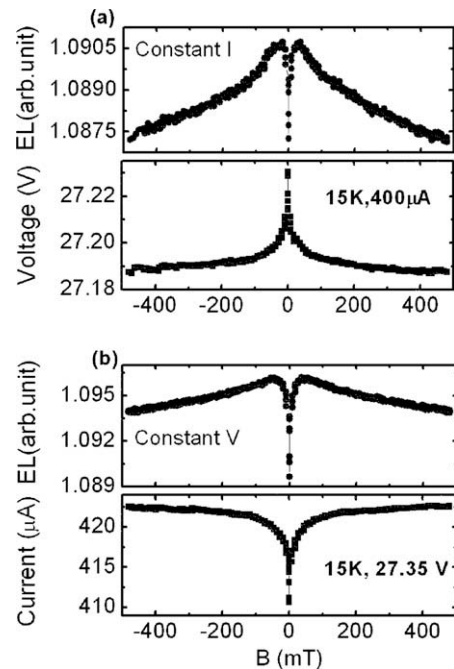
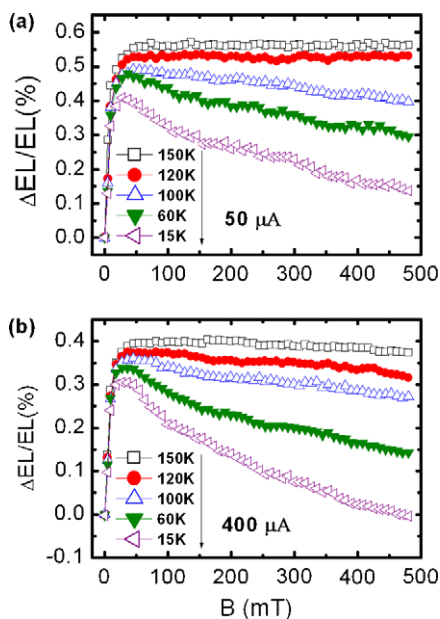


Fig. 1. (a) The magnetic field effects on EL and voltage for the device driven by 400  $\mu$ A at 15 K, (b) the magnetic field effects on EL and current for the device driven by constant voltage (27.35 V) at 15 K.

voltage bias of 27.35 V gives an injection current of  $\sim 400$   $\mu$ A) at 15 K is shown in Fig. 1b. The low-field increase in EL (low field effect, LFE) and high-field decrease in EL (high field effect, HFE) is the common feature of the studied devices at low temperatures. The MFEs on current at constant voltage bias is also shown in Fig. 1b. The current increases rapidly at low fields but then tends to saturate at high fields. The two distinct behaviors of EL at low fields and high fields suggest that the LFE and HFE should be caused by different mechanisms. This is also indicated by the different field dependences between the EL and current at high fields mentioned above.

According to the qualitative formula  $EL \propto \eta I$  [8], where  $\eta$  is the quantum efficiency of EL and  $I$  is the current, one can deduce a simple relationship as:  $\Delta EL/EL = \Delta \eta/\eta + \Delta I/I$ . It means that the variation of the EL reflects the combination of the field induced variations of both current and quantum efficiency [18]. For simplicity, in this work we focused on the constant-current driving experiment, i.e.  $\Delta I = 0$ , to exclude the extra effects caused by the field-enhanced current on EL. Fig. 2 shows the evolution of MFEs on EL over a temperature range from 15 to 150 K. The relative change of EL is described by  $\Delta EL/EL = [EL(B) - EL(0)]/EL(0)$ , where  $EL(B)$  and  $EL(0)$  are the EL in the presence and absence of a magnetic field  $B$ . As shown in Fig. 2, for the current level at both 50 and 400  $\mu$ A the LFE exists at all the temperature range and the lower the temperature is, the weaker LFE is observed. However, the HFE shows more remarkable temperature dependence. As the temperature is increased, the HFE becomes weaker and finally disappears at 150 K at current level of 50  $\mu$ A. The MFEs with different driving currents at 15 and 150 K are demonstrated



**Fig. 2.** Relative change of EL as a function of applied magnetic field at different temperatures between 15 and 150 K, (a) the driving current is 50  $\mu\text{A}$ , (b) the driving current is 400  $\mu\text{A}$ .

in Fig. 3a and 3b, respectively. All the curves show both LFE and HFE at 15 K. It's discernible that large driving current results to weak LFE and strong HFE. Furthermore, at 150 K the HFE becomes weaker compared to that at 15 K and completely vanishes at driving currents less than 200  $\mu\text{A}$  while the LFE still survives. The different temperature and driving current dependences between the LFE and

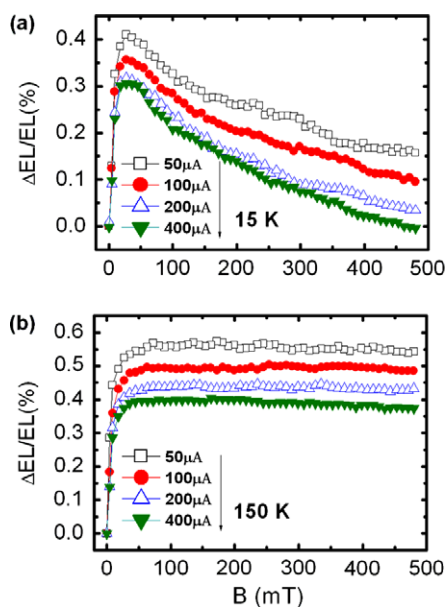


**Fig. 3.** Relative change of EL as a function of applied magnetic field in the driving current range from 50 to 400  $\mu\text{A}$ . (a) The working temperature is 15 K, (b) the working temperature is 150 K.

HFE confirm the conclusion drawn from Fig. 1 that LFE and HFE are controlled by different mechanisms.

In our case the LFEs displayed in Figs. 1–3 are somewhat similar to those observed by Kalinowski et al. [8]. In their work sharp increases in EL and also in current were observed within a small field range and these effects were attributed to the magnetic-field affected hyperfine mixing of electron-hole pairs. According to Kalinowski's pioneer interpretation, singlet intermolecular electron-hole pairs can evolve into triplet pairs via the hyperfine interaction. The spin conversion between the singlet and triplet states would be efficient between the degenerate states [19]. In the absence of a magnetic field, the singlet and triplet pairs nearly degenerate because of the negligible exchange interaction due to the large distances between the holes and electrons. So the spin conversion from the singlet to triplet pair states is efficient. When an external magnetic field greater than the hyperfine coupling strength is applied, the Zeeman splitting of triplet states removes the degeneracy between  $T_+$ ,  $T_-$  and  $S$  states, leading to a decrease in singlet-to-triplet conversion and an increase in singlet electron-hole pairs. On one hand, some of the net singlet pairs would evolve into singlet excitons and then enhance the EL intensity due to their radiative decay [8]. On the other hand, the current would also be enhanced when the other net pairs dissociate into free carriers [15]. These positive MFEs on EL and current are expected to saturate at high fields when the energy splitting between  $T_0$  and  $T_{\pm}$  states becomes much greater than the hyperfine coupling energy. This is consistent with our observed behaviors of EL at current level of 50  $\mu\text{A}$  at 120 and 150 K as shown in Fig. 2a. However, at low temperature of 15 K, the EL intensity decreases significantly at high fields larger than about 35 mT as shown in Fig. 3a. This high-field decrease of EL is not expected by Kalinowski's model, and it might originate from other reason.

Triplet-charge annihilation (TQA) has also been proposed to explain the MFEs [5]. This mechanism was well illustrated by Ern and Merrifield [6]. The TQA process may increase with decreasing temperature and rising driving current due to an increase in triplet excitons and carrier density in the device. However, in our experiment the TQA process could be neglected because of the following reasons: TQA process increases the free-to-trapped charge concentration ratio and leads to the enlargement of the current; a magnetic field-induced monotonous decrease in TQA rate constant would result in a decrease in the current [6] which is at variance with our experiment results. Fig. 1b clearly shows that the current increases with increasing magnetic field strength. It is also reported that the interaction of the triplet exciton with a deep-trapped carrier would produce phosphorescence in Alq<sub>3</sub> at low temperature [20], while this phosphorescence was found to be not dependent on magnetic field [10]. Moreover, the TQA process should be minimized for balanced charge injection [2,4]. Considering the hole mobility in NPB is higher than the electron mobility in Alq<sub>3</sub>, we insert 15 nm CuPc between ITO and NPB as buffer layer to reduce the holes injection from anode and balance it with the electrons injection from cathode [21]. So we believe that the TQA process is unimportant in the MFEs in our devices.



Another possible mechanism of MFEs on EL is based on TTA process which has been widely reported in molecular crystals [16,17], polymer-based OLEDs [22] and also Alq<sub>3</sub>-based OLEDs [3,23]. According to Merrifield's theory [24], TTA process can be modulated by a magnetic field and produce a small rise of EL at low fields and a subsequent fall at high fields. These results are similar to our observed phenomena at 15 K in which the EL contains a low-field increase and a high-field decrease (as shown in Fig. 3a). However, we fail to observe consistent behavior of EL when the temperature and driving current are varied. With elevating the temperature and lowering the driving current the HFE becomes weaker and the LFE gets larger. Interestingly, as the temperature is increased to 150 K and the driving current is decreased to 50  $\mu$ A, the HFE disappears completely while the LFE still survives and even gets larger as shown in Fig. 2a. This suggests that the low-field increase in EL, that is, LFE in our devices can not be well explained by magnetic-field mediated TTA process.

Since no single mechanism can explain all the observed MFEs on EL, a composite model is proposed here, containing both the magnetic-field dependent singlet-to-triplet conversion (Kalinowski's effect) and magnetic-field mediated TTA process. In principle, the Kalinowski's effect leads to a saturation of EL at high fields while the field mediated TTA process induces a significant decrease. Thus the decrease of EL at high fields confirms that the field mediated TTA process is dominant in the HFEs in our devices. Both the Kalinowski's effect and field mediated TTA process can cause an increase in EL at low fields but the former effect is believed to be most important. This is supported by the fact that LFE survives and even gets larger while the HFE disappears (suggesting that TTA process is suspended) at higher temperature and lower driving current, as shown in Fig. 3b. Moreover, the  $\Delta EL/EL$  curves at low current level of 50  $\mu$ A and high temperature of 120 and 150 K all sharply increase at low fields and then tend to saturate at high fields as shown in Fig. 2a, suggesting that the  $\Delta EL/EL$  caused by Kalinowski's effect approximately have the same magnetic-field dependence under these conditions. So the  $\Delta EL/EL$  curves should show a sharp low-field-increase and a high-field-saturation at low temperature if the TTA process does not occur. The  $\Delta EL/EL$  trace measured at 150 K with 50  $\mu$ A driving current is selected to characterize how the LFE would change with increasing field. Because the delayed EL caused by TTA process was observed to fall below its zero-field level at about 125 mT in OLEDs with amorphous Alq<sub>3</sub> films [10], we therefore regard the  $\Delta EL/EL$  value at 125 mT of the experiment curve as the saturated magnitude of Kalinowski's effect in our Alq<sub>3</sub>-based devices. By subtracting the MFE's component due to Kalinowski's effect from the measured  $\Delta EL/EL$  data, the contribution from the field mediated TTA process is obtained (as shown in Fig. 4a). The component due to field mediated TTA process reaches its maximum at  $B_0 = 17$  mT which corresponds to energy of about 1.7  $\mu$ eV ( $E_B = g\mu_B B_0$ ), which is very close to the zero-field splitting parameter in Alq<sub>3</sub> measured to be 1.4  $\mu$ eV by Cölle et al. [3]. The great similarities between our results with those field modulated delayed EL due to TTA observed in anthracene crystal [17]

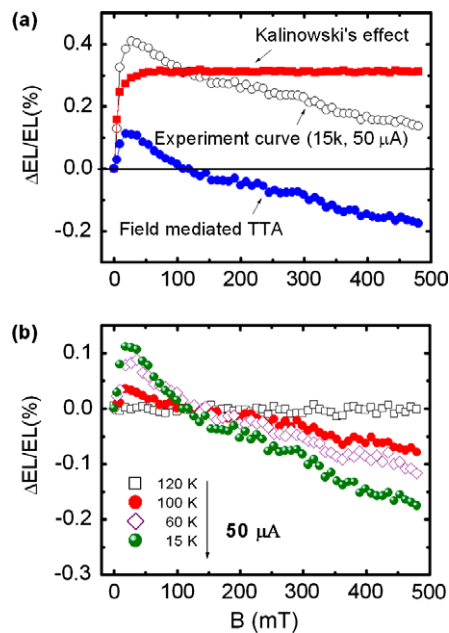


**Fig. 4.** (a) Composite model for the MFEs on EL. The Kalinowski's effect component (solid squares) dominates the low-field increase, while the field mediated TTA process part (solid circles) causes the high-field decrease; (b) effects of the pure field mediated TTA process at 50  $\mu$ A at temperature range from 15 to 120 K.

and Alq<sub>3</sub>-based OLEDs [10] strongly support our TTA interpretation for high-field decrease of  $\Delta EL/EL$ .

Interestingly, Davis and Bussman observed anthracene crystal-like MFEs in some special OLEDs and suggested that magnetic-field modulated TTA process would be operative in the MFEs [2]. But in later publication [25], enhancements of EL exceeding 14% at low magnetic field ( $\sim 80$  mT) were found at low drive levels (the drive levels so low that TTA process is unimportant). Thus, they excluded TTA mechanism for MFEs and attributed the low fields increase to a field-induced preference for charge-pair (electron-hole pair) state to form singlet exciton. Their results also confirm the conclusion that the field dependent singlet-to-triplet conversion, that is, Kalinowski's effect is dominant in the LFE. Fig. 4b shows the evolution of  $\Delta EL/EL$  caused by field mediated TTA process at 50  $\mu$ A over a temperature range from 15 to 120 K. The anthracene crystal-like MFEs become more remarkable as temperature is decreased, suggesting that stronger TTA process exhibits at low temperature. This is consistent with the experiment results observed by Cölle et al [3] that the intensity of the delayed luminescence caused by TTA shows an increase with the decreasing temperature.

It's generally believed that in OLEDs triplet excitons have much longer lifetime than singlet excitons and therefore are able to diffuse larger distance. The dissociation of the triplet excitons at the interface between Alq<sub>3</sub> and cathode can enhance the charge injection. Such an effect is called excitonic injection [8]. A magnetic field reduction in TTA rate constant reduces the number of quenched triplets, their flux towards the cathode increases the current

tending to saturation as shown in Fig. 1b. Although the triplet excitons can be increased by applying a magnetic field to decrease the interaction rate constant of TQA process, it is not a dominant process in our device because TQA has been minimized by balanced charge injection as previously discussed.

Further investigation of the temperature and driving current dependences of the HFE and LFE was demonstrated in Fig. 5. The value of the HFE is defined as  $HFE = [EL(450 \text{ mT}) - EL(35 \text{ mT})]/EL(35 \text{ mT})$ , while the magnitude of LFE is defined as  $LFE = [EL(35 \text{ mT}) - EL(0 \text{ mT})]/EL(0 \text{ mT})$ . As shown in Fig. 5a, the magnitude of the HFE becomes smaller with the increasing temperature and completely disappears at 150 K. Another feature of the HFE is that higher current level leads to larger HFE at a certain temperature. The magnitude of the LFE decreases by a factor of  $\sim 1.7$  at 15 K when increasing the current from 20 to 400  $\mu\text{A}$  (as shown in Fig. 5b). Similar driving current dependence of the LFE can also be seen at other temperatures. As mentioned above, the magnetic-field mediated TTA process is responsible for the HFE in our devices. The probability of TTA process is expected to be proportional to the square of the triplets density considering its bimolecular process [3]. And the density of triplets is proportional to the current. Therefore, it is reasonable to conclude that TTA process should be much stronger at larger driving current, leading to a more significant decrease in EL at high fields. With further decreasing the temperature, the lifetime of the triplets increases due to a reduced phonon-assisted decay [3], thus increasing the triplet density and also the total annihilation rate  $\gamma_{\text{tot}}$ , as proposed by Merrifield [24]. This is why one can observe large HFE at low temperature and

large current levels. The driving current dependence of the LFE as shown in Fig. 5b is in agreement with Kalinowski's equation [8]  $\Delta EL/EL = [\kappa_{\text{ST}}(0) - \kappa_{\text{ST}}(B)]/[\kappa_{-1} + \kappa_{\text{C}} + \kappa_{\text{ST}}(B)]$ , where  $\kappa_{-1}$  is the dissociation rate of singlet electron-hole pair,  $\kappa_{\text{C}}$  is the condensation rate from singlet pairs to singlet excitons,  $\kappa_{\text{ST}}(B)$  and  $\kappa_{\text{ST}}(0)$  are the intersystem crossing rate between singlet and triplet states with and without external magnetic field  $B$ , respectively. According to the assignment of Kalinowski et al. [8],  $\kappa_{\text{C}}$ ,  $\kappa_{\text{ST}}(B)$ , and  $\kappa_{\text{ST}}(0)$  are assumed to be constant while  $\kappa_{-1}$  is varying with applied voltage. At a low applied voltage,  $\kappa_{-1}$  is small thus almost no contribution to  $\Delta EL/EL$ . However, at a high applied voltage the  $\kappa_{-1}$  increases and contributes markedly to the denominator of the equation, leading to a decreasing in  $\Delta EL/EL$ . Given the fact that large applied voltage corresponds to high current level in the OLEDs, it is reasonable that the decrease in  $\Delta EL/EL$ , that is, the lower LFE would occur at larger driving current.

#### 4. Conclusions

In summary, we have presented detailed studies on the MFEs on EL in  $\text{Alq}_3$ -based OLEDs driving by different current levels and over a broad range of temperature (15–150 K). We found that at low temperature the MFEs consist of a sharp increase in EL at low fields and a significant decrease at high fields. The HFE becomes weaker and even disappears at higher temperatures and lower driving currents while LFE always survives, suggesting that the LFE and HFE would be caused by different mechanisms. We propose a composite model to explain the observed MFEs and attribute the HFE mostly to the magnetic-field mediated TTA process while the LFE mainly to the magnetic-field dependent singlet-to-triplet electron-hole pairs conversion.

#### Acknowledgements

This work was supported in part by the Chinese Ministry of Education under the Program for New Century Excellent Talents in Universities (Grant No. NCET-05-0772), by the National Natural Science Foundation of China (Grant No. 10504027), by Ying Tong Education Foundation (Grant No. 101006), by the Scientific Research Foundation of Chinese Ministry of Education for Returned Oversea Scholars (Grant No. (2007) 1108), and by the Science & Technology Activity of Oversea Studying Personnel.

#### References

- [1] J. Kalinowski, *Organic Light Emitting Diodes: Principles Characteristics and Processes*, Marcel Dekker, New York, 2005.
- [2] A.H. Davis, K. Bussmann, *J. Vac. Sci. Technol. A* 22 (2004) 1885.
- [3] M. Cölle, C. Gärditz, M. Braun, *J. Appl. Phys.* 96 (2004) 6133.
- [4] C. Ganzorig, M. Fujihira, *Appl. Phys. Lett.* 81 (2002) 3137.
- [5] P. Desai, P. Shakya, T. Kreuzis, W.P. Gillin, *J. Appl. Phys.* 102 (2007) 073710.
- [6] V. Ern, R.E. Merrifield, *Phys. Rev. Lett.* 21 (1968) 609.
- [7] J. Kalinowski, J. Godlewski, *Chem. Phys. Lett.* 36 (1975) 345.
- [8] J. Kalinowski, M. Cocchi, D. Virgili, P. Di Marco, V. Fattori, *Chem. Phys. Lett.* 380 (2003) 710.
- [9] J. Kalinowski, M. Cocchi, D. Virgili, V. Fattori, P. Di Marco, *Phys. Rev. B* 70 (2004) 205303.

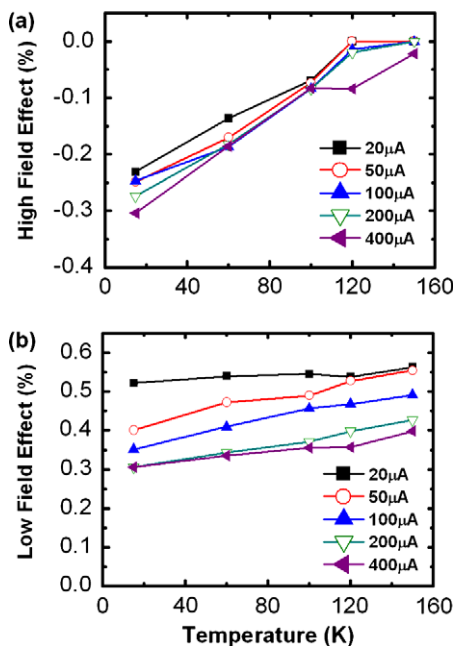


Fig. 5. The dependence of (a) high field effect and (b) low field effect on temperature in the OLED (ITO/CuPc/NPB/Alq<sub>3</sub>/LiF/Al) at different driving currents between 50 to 400  $\mu\text{A}$ .

- [10] C. Gärditz, A. Mückl, M. Cölle, *J. Appl. Phys.* 98 (2005) 104507.
- [11] Ö. Mermer, G. Veeraraghavan, T.L. Francis, M. Wohlgenannt, *Solid State Commun.* 134 (2005) 631.
- [12] T.L. Francis, Ö. Mermer, G. Veeraraghavan, M. Wohlgenannt, *New J. Phys.* 6 (2004) 185.
- [13] H. Odaka, Y. Okimoto, T. Yamada, H. Okamoto, M. Kawasaki, Y. Tokura, *Appl. Phys. Lett.* 88 (2006) 123501.
- [14] Z. Wang, Z.H. He, X.W. Tan, M.L. Tao, G.Q. Li, Z.H. Xiong, *Acta Phys. Sin.* 56 (2007) 2979.
- [15] B. Hu, Y. Wu, *Nat. Mater.* 6 (2007) 985.
- [16] R.C. Johnson, R.E. Merrifield, *Phys. Rev. B* 1 (1970) 896.
- [17] R. Belaid, T. Barhoumi, H. Bouchriha, *Synth. Met.* 131 (2002) 23.
- [18] Y. Zhang, R. Liu, Y.L. Lei, Z.H. Xiong, *Appl. Phys. Lett.* 94 (2009) 083307.
- [19] F. Ito, T. Ikoma, K. Akiyama, A. Watanabe, S. Tero-Kubota, *J. Phys. Chem. B* 109 (2005) 8707.
- [20] I. Bergenti, V. Dediu, T. Mertelj, M. Murgia, A. Riminucci, G. Ruani, C. Taliani, *Org. Electron.* 8 (2007) 256.
- [21] L.S. Hung, C.W. Tang, M.G. Mason, *Appl. Phys. Lett.* 70 (1997) 152.
- [22] S. Sinha, A.P. Monkman, *Appl. Phys. Lett.* 82 (2003) 4651.
- [23] Z.D. Popovic, H. Aziz, *J. Appl. Phys.* 98 (2005) 013510.
- [24] R.E. Merrifield, *J. Chem. Phys.* 48 (1968) 4318.
- [25] J. Wilkinson, A.H. Davis, K. Bussmann, J.P. Long, *Appl. Phys. Lett.* 86 (2005) 111109.

have shown high field-effect mobilities in thin-film states. For example, pentacene-based transistors show a hole mobility on the order of ca.  $1.0 \text{ cm}^2/\text{Vs}$  that corresponds to a performance close to that of hydrogenated amorphous silicon-based transistors. Nevertheless, in comparison to a variety of *p*-type devices, there have only been a few *n*-type OTFTs reported to date [12–18]. This dearth in study is ascribed to the fact that most *n*-type organic compounds are sensitive to environmental contaminants such as moisture and oxygen that can penetrate into the active channel region. Therefore, the transistor characteristics of most *n*-type OTFTs have been obtained either under inert atmosphere or under vacuum. Since power-efficient logic elements use complementary circuits that require both *p*- and *n*-type transistors, it is desirable to improve performance of the *n*-type devices to match that of the *p*-type devices in fabricating all organic-based electronics. Among the *n*-type materials such as  $C_n$  ( $n = 60, 70$ ), metallophthalocyanines and perylene derivatives, a series of perylene compounds have attracted particular attention given their good transport and high electron affinities. Recently, Tatemichi et al. reported the characteristics of transistors based upon *N,N'*-ditridecylperylene-3,4,9,10-tetracarboxylic diimide (P13) which is an extended  $\pi$ -conjugated molecule with a strong electron affinity (3.4 eV) [12]. The P13 transistors whose active layers were thermally annealed at  $140^\circ\text{C}$  displayed a high electron mobility of  $2.1 \text{ cm}^2/\text{Vs}$  under vacuum. Typical electron mobilities of other perylene derivatives-based transistors have been reported ranging between  $2.5 \times 10^{-3}$  and  $1.7 \times 10^{-2} \text{ cm}^2/\text{Vs}$  [14,17,18].

In this article, we report our first application of the NCBD method to prepare P13-based, *n*-type OTFTs with a top-contact structure (Fig. 1). A systematic analysis was carried out to examine the influence of surface modification and thermal post-treatment on device characteristics and operational stability. The structure-device performance relationship is also discussed. In addition, we present the comparative characteristics of transport mechanisms responsible for the conduction of electron carriers as a function of temperature from 300 down to 10 K for various devices. To the best of our knowledge, no mechanistic study of the transport phenomena of the P13-based OTFTs has been reported thus far.

## 2. Experiment

Fig. 1 shows the molecular structures of the P13 and HMDS, and a schematic diagram of a transistor along with the bias condition. The substrates consisted of a highly doped, *n*-type Si wafer coated with an aluminum layer as the gate electrode and thermally grown 2500 Å-thick  $\text{SiO}_2$  layers as the gate dielectric. A rigorous procedure for cleaning the substrates was adopted. The substrates were first cleaned by a series of sequential ultrasonic treatments in acetone, hot trichloroethylene, acetone,  $\text{HNO}_3$ , methanol, and deionized water, and then blown dry with dry  $\text{N}_2$  [19]. The substrates were finally exposed to UV (254 nm) for 15 min [20]. Such a cleaning procedure turned out to be very efficient in significantly increasing device performance. For surface modification, the cleaned

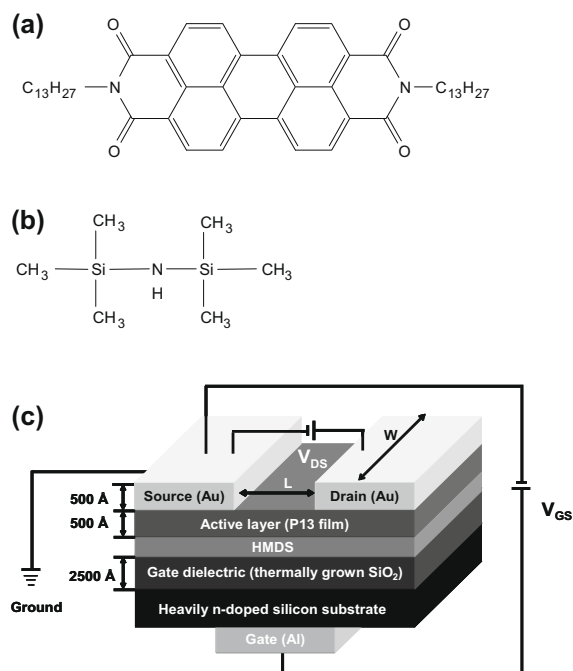


Fig. 1. Molecular structures of (a) P13 and (b) HMDS and (c) a schematic diagram of a transistor under bias conditions.

substrates were immersed in HMDS for 10 h at room temperature.

The P13 active layers were prepared by a homemade NCBD system [1]. The apparatus consisted of an evaporation crucible, a drift region, and the substrate. The as-received P13 sample was placed inside the enclosed cylindrical crucible cell (with a 1.0-mm diameter, a 1.0 mm-long nozzle) and sublimated by resistive heating between 550 and 580 K. At a working pressure of approximately  $4.5 \times 10^{-6}$  Torr, the P13 vapor underwent adiabatic supersonic expansion into the high-vacuum drift region. Highly directional, weakly bound P13 neutral cluster beams were formed at the throat of the nozzle and directly deposited onto the substrates with an average thickness of ca. 500 Å, at a rate of 0.5–0.8 Å/s. For thermal post-treatments, the active layers were heated to  $100^\circ\text{C}$  in a vacuum oven for 1 h and then slowly cooled down to room temperature. Thickness, contact angle, surface morphology, and structural properties of the P13 active layers were characterized using an alpha-step surface profile monitor, a contact-angle goniometer, atomic force microscopy (AFM), and X-ray diffractometry (XRD).

To produce the transistors with a channel width ( $W$ ) of 500  $\mu\text{m}$  and a channel length ( $L$ ) of 200  $\mu\text{m}$  in a top-contact configuration, electron-beam evaporation using a rectangular-shaped shadow mask was utilized to produce a 500 Å-thick Au source and drain electrodes. The optimized thickness and deposition rate of Au were 500 Å and 6–8 Å/s, respectively. The current–voltage ( $I$ – $V$ ) characteristics of the transistors and their temperature-dependence were measured by an optical probe station connected to a HP4140B pA meter-dc voltage source unit and a 10 K-closed cycle refrigerator, over the temperature range of 10–300 K

and at a base pressure of  $1 \times 10^{-2}$  Torr. Various parameters were derived from the fits of the  $I$ – $V$  characteristics.

### 3. Results and discussion

Characterization of the surface morphology for various NCBD-based P13 films prepared at room temperature was performed using an AFM apparatus in the non-contact mode. The 2-dimensional AFM micrographs at a nominal thickness of 500 Å are shown in Fig. 2. These P13 films exhibited complete substrate coverage with grain crystallites with the thermal post-treatment increasing grain crystallite size in both hexamethyldisilazane (HMDS)-untreated and -pretreated films. The four root-mean-square roughness ( $R_{\text{rms}}$ ) average-values for the P13 films deposited on the untreated, thermally post-pretreated, HMDS-pretreated, and HMDS-pretreated/thermally post-treated  $\text{SiO}_2$  substrates were measured  $71 \pm 8$ ,  $20 \pm 4$ ,  $41 \pm 2$ , and  $23 \pm 2$  Å, respectively. The low surface  $R_{\text{rms}}$  observed in this study clearly exhibited that the weakly bound P13 cluster beams undergo efficient fragmentation into energetic individual molecules, leading to uniform, highly packed thin films. The entire HMDS-pretreated films showed lower roughness and high packing densities, suggesting that the amphiphilic HMDS molecules provided favorable deposition conditions at the early stages of grain growth. In addition, in the case of thermally post-treated films, substantial improvement in the surface roughness due to thermal annealing has been observed. The annealing process appears to favor formation of larger grain crystallites. The effect of thermal post-treatment is more clearly displayed in the XRD measurements below.

Fig. 2 also shows the whole XRD diffractograms for four different kinds of 500 Å-thick P13 thin films. According to the previous crystallographic investigations, P13 crystals are known to have a triclinic structure. All thin films in Fig. 2 show a highly ordered structure. The strong and sharp first- and second-order peaks, as well as distinctive higher-order multiple peaks, can be fitted to a series of (0 0 1) reflection lines with multiple  $d$  spacing. In the case of as-deposited, untreated thin films, the four reflection peaks located at  $2\theta = 3.3^\circ$ ,  $6.7^\circ$ ,  $10.0^\circ$ , and  $13.3^\circ$  were assigned to (0 0 1), (0 0 2), (0 0 3), and (0 0 4). Based on the crystallographic parameters of P13, the corresponding  $d$ -spacings were determined to be 26.4, 13.2, 8.8, and 6.6 Å, respectively, which were in good agreement with the XRD measurements conducted by Tatemichi et al. [12]. For the thermally and/or surfactant-treated films in Fig. 2, a higher signal-to-noise in the XRD patterns was observed together with larger (0 0 3) and (0 0 4) reflection peaks, suggesting that the treatments significantly enhanced long-range crystallinity. It should be noted in the diffractograms that the thermal annealing effect was more pronounced in comparison to the surfactant-pretreatment effect. The high-temperature annealing seems to clearly promote the formation of larger grains with better crystallinity through a favorable self-assembling process. The XRD results are also consistent with the aforementioned AFM measurements, in which the larger grain crystallites showed more distinct, sharper reflection peaks.

The organic P13 active layers behaved as  $n$ -type semiconductors. OTFT performance was examined in the accumulation mode: as the gate electrode is positively biased with respect to the grounded source electrode, an accumulation of electrons near the  $\text{SiO}_2$  dielectric–P13 interface is induced. Typical plots of drain-source current ( $I_{\text{DS}}$ ) as a function of the drain-source voltage ( $V_{\text{DS}}$ ) for various gate-source voltages ( $V_{\text{GS}}$ ) are displayed in Fig. 3. Overall OTFT characteristics were adequately described by the standard field-effect transistor equations working in the accumulation mode. At a fixed  $V_{\text{GS}}$ ,  $I_{\text{DS}}$  increases linearly with  $V_{\text{DS}}$  in the low  $V_{\text{DS}}$  regime while  $I_{\text{DS}}$  tends to be saturated in the large  $V_{\text{DS}}$  regime due to the pinch off in the accumulation layer. In the saturation regime,  $I_{\text{DS}}$  is given by Eq. (1):

$$I_{\text{DS}} = \frac{WC_i\mu}{2L}(V_{\text{GS}} - V_{\text{T}})^2 \quad (1)$$

where  $W$  is the channel width of 500  $\mu\text{m}$ ,  $L$  is the channel length of 200  $\mu\text{m}$ ,  $\mu_{\text{eff}}$  is the field-effect mobility, and  $V_{\text{T}}$  is the threshold voltage. The value  $C_i$  is the capacitance per unit area, which is 13.8 nF/cm<sup>2</sup> for the thermally-grown, 2500 Å-thick,  $\text{SiO}_2$  gate dielectric. From the analysis of the observed  $I$ – $V$  characteristics, several device parameters can be derived and are listed in Table 1. The maximum mobilities ( $\mu_{\text{eff}}$ ) are listed with the average mobilities ( $\mu_{\text{eff}}^{\text{avg}}$ ) with the standard deviation ( $\sigma$ ). Here, it should be noted that before characterizing the performance of the devices kept in air and  $\text{N}_2$ , the operational stability was first checked under ambient conditions as a function of time. Since the P13-based devices were sensitive to moisture and oxygen, device parameters such as mobilities deteriorated with time as shown in Fig. 4a. To minimize these environmental effects, the whole parameters in Table 1 were derived as fast as possible within a duration of 2 h just after device production, as marked with the brackets in Fig. 4a.

Several characteristic features can be found in Table 1. Firstly, compared to the typical mobilities reported in the range between  $1.7 \times 10^{-2}$  and  $2.5 \times 10^{-3}$  cm<sup>2</sup>/Vs [14,17,18], all NCBD-based OTFTs showed higher room-temperature mobilities: 0.16, 0.58, 0.34, and 0.32 cm<sup>2</sup>/Vs for the untreated, thermally post-treated, HMDS-pretreated, and HMDS-pretreated/thermally post-treated thin-film transistors, respectively. A  $\mu_{\text{eff}}$  of 0.34 cm<sup>2</sup>/Vs for the HMDS-pretreated transistors was found to be comparable to the value of  $\mu_{\text{eff}} = 0.29$  cm<sup>2</sup>/Vs, measured by Hosoi and Furukawa [14]. Here, it should be noted that unlike the mobilities derived from the devices not working at all when exposed to the atmosphere [12], the whole field-effect mobilities for all NCBD-based OTFTs in this study were measured under ambient conditions. In Table 1, the surface passivation and thermal post-treatment clearly improved device performance, including mobilities, current on/off ratio ( $I_{\text{on}}/I_{\text{off}}$ ), threshold voltage ( $V_{\text{T}}$ ), and especially sub-threshold slope (SS). In particular, the drastic reduction of the subthreshold slope, generally governed by material properties, indicated that the treatment significantly improved the quality of the NCBD-based P13 active layers. It can be concluded that after thermal post-treatment and/or surfactant pre-treatment, favorable formation of

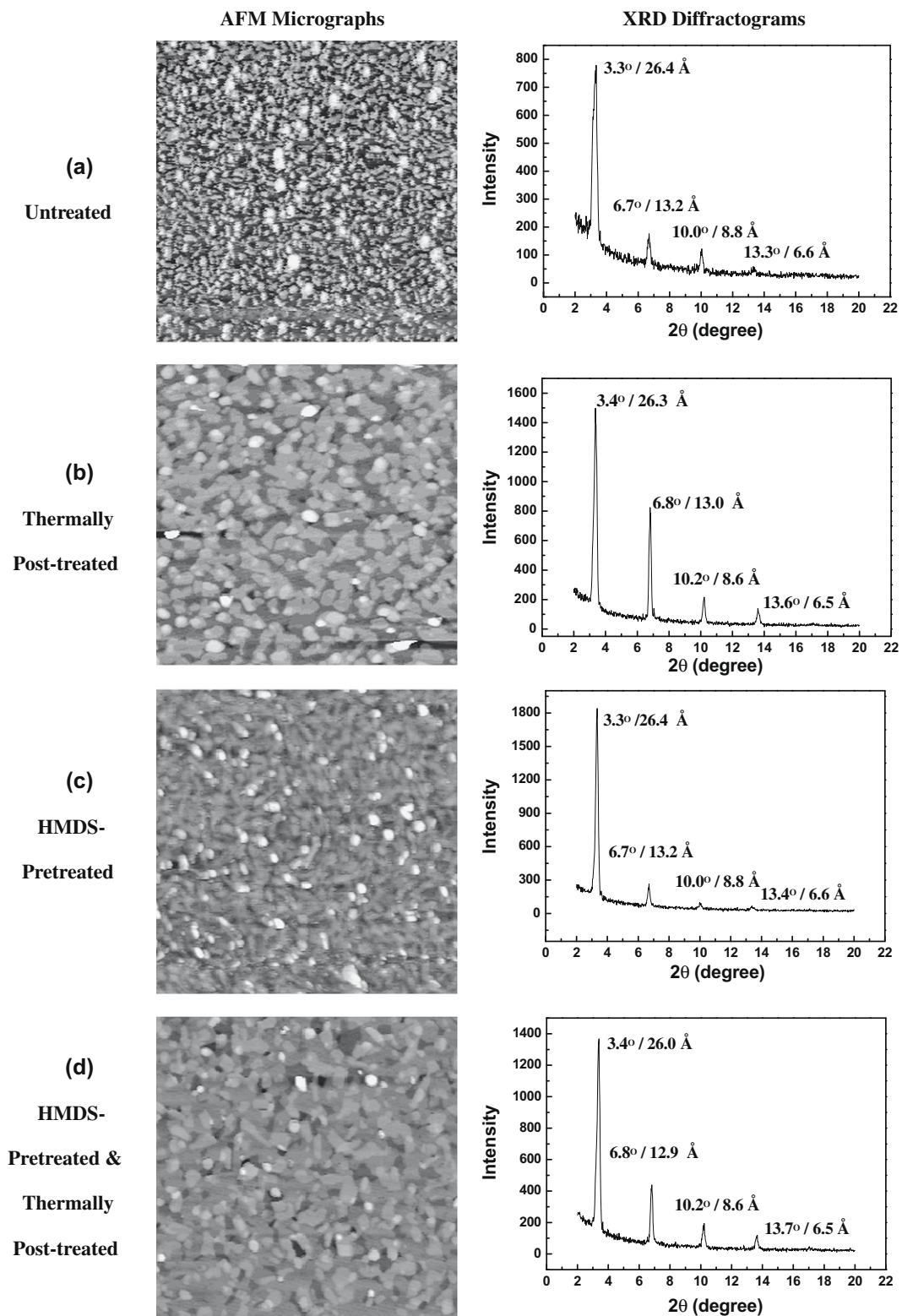


**Fig. 2.** Comparison of 2-dimensional AFM micrographs and XRD diffractograms for the four 500 Å-thick P13 thin films prepared on: (a) untreated; (b) thermally post-treated; (c) HMDS-pretreated; and (d) HMDS-pretreated/thermally post-treated SiO<sub>2</sub> substrates, using the NCBD method. The micrographs were taken over an area of 5 × 5 μm<sup>2</sup> and the diffractograms were obtained using Cu Kα radiation in a symmetric reflection, coupled θ–2θ scanning mode.

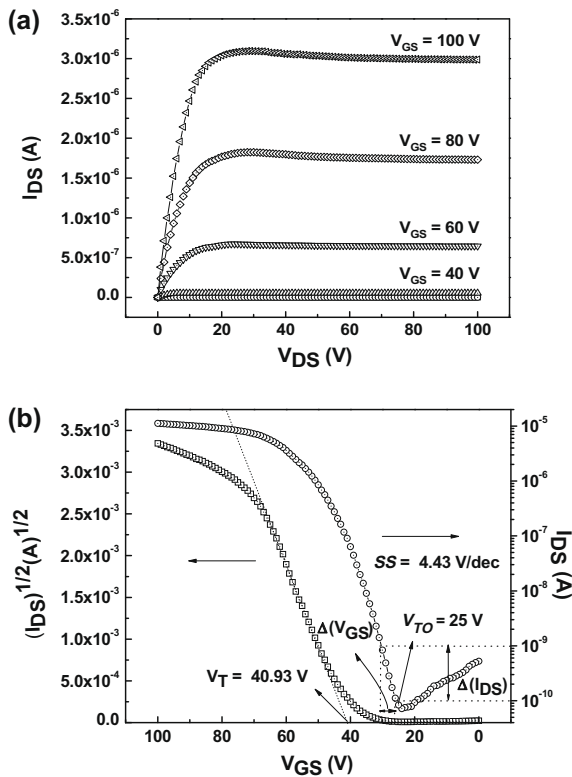


**Fig. 3.** (a) Current–voltage characteristics at various gate voltages for the thermally post-treated transistors. (b) Variation of  $I_{DS}^{1/2}$  (left axis) and  $\log(I_{DS})$  (right axis) vs.  $V_{GS}$  at a constant  $V_{DS} = 100$  V.

the P13 active layers with higher structural organization and better film connectivity induced more efficient charge-carrier transport via face-to-face intermolecular interactions between the  $\pi$ - $\pi$  stacks. The observed performance is also consistent with the results revealed in the AFM and XRD micrographs.

Secondly, total trap density ( $N_{\text{trap}}$ ) strongly correlated with device performance. The  $N_{\text{trap}}$  value can be obtained by the relationship (2):

$$N_{\text{trap}} = \frac{C_i |V_T - V_{\text{TO}}|}{e} \quad (2)$$

where  $V_{\text{TO}}$  is the turn-on voltage and  $e$  the elementary charge [21]. The four trap densities for the untreated, thermally post-treated, HMDS-pretreated, and HMDS-pre-

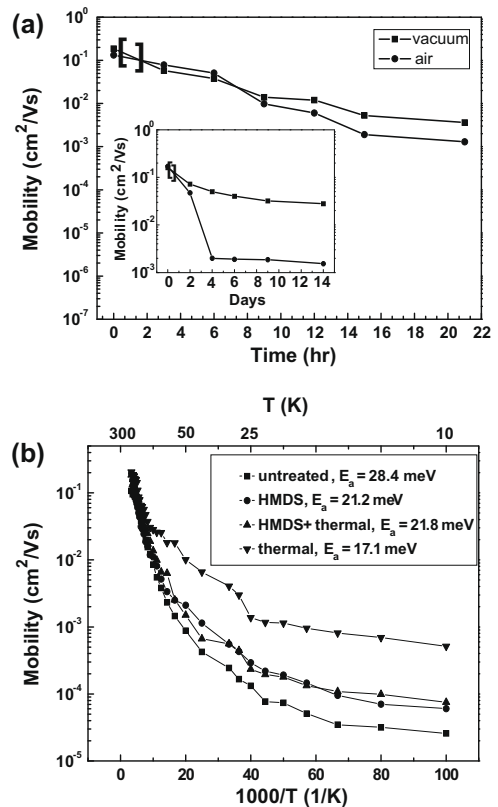


**Fig. 4.** (a) Stability of P13-based devices as a function of time (hours). Inset shows a long-term stability as a function of time (days). The brackets represent the period of measured time, during which whole device parameters were derived to minimize environmental effects. (b) Comparison of temperature-dependence of the electron mobilities for the untreated, thermally post-treated, HMDS-pretreated, and HMDS-pretreated/thermally post-treated OTFTs.

treated/thermally post-treated devices were estimated to be  $2.70 \times 10^{12}$ ,  $1.37 \times 10^{12}$ ,  $1.86 \times 10^{12}$ , and  $1.57 \times 10^{12}$  /  $\text{cm}^2$ , respectively. The traps can be identified as structural disorders and/or defects. The observed lower trap densities of the whole treated thin films can be ascribed to the characteristic growth of well-connected, polycrystalline thin films produced by the NCBD method, which were directly reflected in the efficient carrier conduction with high mobilities especially in the thermally post-treated P13-based transistors.

**Table 1**

Device parameters deduced from the OTFT characteristics.

Surface pretreatment	$\mu_{\text{eff}}$ ( $\text{cm}^2/\text{Vs}$ )	$\mu_{\text{eff}}^{\text{avg}} \pm \sigma$ ( $\text{cm}^2/\text{Vs}$ ) <sup>a</sup>	$I_{\text{on}}/I_{\text{off}}$	$V_T$ (V)	$V_{\text{TO}}$ (V)	SS (V/decade)	$N_{\text{trap}}$ ( $10^{12}/\text{cm}^2$ )	$E_a$ (meV)
Untreated	0.16	$0.11 \pm 0.03$	$10^4$	46.32	15	10.18	2.70	28.4
Thermally post-treated	0.58	$0.42 \pm 0.10$	$10^5$	40.93	25	4.43	1.37	17.1
HMDS-pretreated	0.34	$0.28 \pm 0.04$	$10^5$	37.50	16	4.29	1.86	21.2
HMDS-pretreated/thermally post-treated	0.32	$0.28 \pm 0.04$	$10^5$	36.25	18	4.00	1.57	21.8

<sup>a</sup> The mobility data ( $\mu_{\text{eff}}$ ) in the text represents the best values. Considering the distributions of the OTFT characteristics, the  $\mu_{\text{eff}}$  values lie within  $\mu_{\text{eff}}^{\text{avg}} \pm 2\sigma$  (standard deviation).

Thirdly, the temperature-dependence behavior of  $\mu_{\text{eff}}$  in the P13 films was measured for the first time to characterize the transport mechanism responsible for the conduction of mobile electron carriers. Fig. 4b shows that the typical logarithmic plots of  $\mu_{\text{eff}}$  for the untreated P13 films in the temperature range of 10–300 K. Two different mechanisms were found to exist to account for observed regions I and II. The temperature-independent region I, below 40 K, was ascribed to the quantum tunneling mechanism. Conversely, the conduction mechanism for region II (40 K < T < 300 K) corresponded to a thermally activated transport, where the electron carriers should overcome the shallow traps present in the P13 active layer through thermal excitation. The behavior in region II is well described by the Arrhenius relationship:  $\mu_{\text{eff}} \propto \exp(-E_a/kT)$ , where  $E_a$  and  $k$  are the activation energy and Boltzmann constant, respectively. From the slope analysis of the logarithmic plots, the four activation energies were estimated to be 28.4, 17.1, 21.2, and 21.8 meV for the untreated, thermally post-treated, HMDS-pretreated, and HMDS-pretreated/thermally post-treated devices, respectively. Direct comparison cannot be made due to the absence of a mechanistic study of the transport phenomena for the P13-based OTFTs. Instead, Chesterfield et al. reported the activation energies ranging between 39 and 85 meV for *N*-alkyl perylene diimide-based OTFTs [15]. The significantly lower  $E_a$  and  $N_{\text{trap}}$  values observed in this study strongly suggest that the high quality of the P13 films ultimately lead to a more efficient carrier transport in the well-connected grains, as well as the excellent mobilities in the NCBD-based OTFTs.

#### 4. Summary

Our first application of the NCBD method to prepare P13-based, *n*-type OTFTs with a top-contact structure is presented. The effects of surface passivation and thermal post-treatment on surface morphology, crystallinity, and device performance were systematically investigated, with the operational stability as a function of time. A high room-temperature field-effect mobility of 0.58 cm<sup>2</sup>/Vs for the thermally post-treated devices was obtained under ambient conditions. A comparative study of transport mechanisms in-between 10–300 K indicated that surface modification and thermal post-treatment decreased the to-

tal trap density and activation energy for carrier transport by reducing structural disorder. The fabrication of several P13-based devices, including unipolar and ambipolar light-emitting OTFTs through the NCBD method, is underway. We hope these investigations to provide further insights into the organic-based optoelectronic devices at the molecular level.

#### Acknowledgments

This work was supported by a Korea University grant and a Korea Science and Engineering Foundation (KOSEF) grant funded by the Korea government (MEST) (No. M10500000023-06J0000-02310).

#### References

- [1] J.-Y. Kim, E.-S. Kim, J.-H. Choi, *J. Appl. Phys.* 91 (2002) 1944.
- [2] H.-S. Seo, Y.-S. Jang, Y. Zhang, P.S. Abthagir, J.-H. Choi, *Org. Electron.* 9 (2008) 432.
- [3] H.-S. Seo, Y. Zhang, Y.-S. Jang, J.-H. Choi, *Appl. Phys. Lett.* 92 (2008) 223310.
- [4] H. Lim, J.-H. Choi, *J. Chem. Phys.* 124 (2006) 014710.
- [5] P.S. Abthagir, Y.-G. Ha, E.-A. You, S.-H. Jeong, H.-S. Seo, J.-H. Choi, *J. Phys. Chem. B* 109 (2005) 23918.
- [6] Y.-G. Ha, E.-A. You, B.-J. Kim, J.-H. Choi, *Synth. Met.* 153 (2005) 205.
- [7] E.-A. You, Y.-G. Ha, Y.-S. Choi, J.-H. Choi, *Synth. Met.* 153 (2005) 209.
- [8] A.M. Taurino, S. Capone, A. Boschetti, T. Toccoli, R. Verucchi, A. Pallaoro, P. Siciliano, S. Iannotta, *Sens. Actuators B* 100 (2004) 177.
- [9] Y. Wu, T. Toccoli, N. Koch, E. Iacob, A. Pallaoro, P. Rudolf, S. Iannotta, *Phys. Rev. Lett.* 98 (2007) 076601.
- [10] C.D. Dimitrakopoulos, P.R.L. Malenfant, *Adv. Mater. (Weinheim, Ger)* 14 (2002) 99.
- [11] S.R. Forrest, *Nature (London)* 428 (2004) 911.
- [12] S. Tatemichi, M. Ichikawa, T. Koyama, Y. Taniguchi, *Appl. Phys. Lett.* 89 (2006) 112108.
- [13] D.J. Gundlach, K.P. Pernstich, G. Wilckens, M. Gruter, S. Haas, B. Batlogg, *J. Appl. Phys.* 98 (2005) 064502.
- [14] Y. Hosoi, Y. Furukawa, *Mol. Cryst. Liq. Cryst.* 462 (2007) 37.
- [15] R.J. Chesterfield, J.C. McKeen, C.R. Newman, P.C. Ewbank, D.A. Da, S. Filho, J.-L. Bredas, L.L. Miller, K.R. Mann, C.D. Frisbie, *J. Phys. Chem. B* 108 (2004) 19281.
- [16] P.R.L. Malenfant, C.D. Dimitrakopoulos, J.D. Gelorme, L.L. Kosbar, T.O. Graham, *Appl. Phys. Lett.* 80 (2002) 2517.
- [17] K.N.N. Unni, A.K. Pandey, J.-M. Nunzi, *Chem. Phys. Lett.* 407 (2005) 95.
- [18] S.H. Han, K.J. Lee, S.H. Lee, J. Jang, *J. Non-Cryst. Solids* 354 (2008) 2870.
- [19] S.J. Kang, M. Noh, D.S. Park, H.J. Kim, C.N. Whang, C.H. Chang, *J. Appl. Phys.* 95 (2004) 2293.
- [20] D. Guo, S. Entani, S. Ikeda, K. Saiki, *Chem. Phys. Lett.* 429 (2006) 124.
- [21] K.P. Pernstich, S. Haas, D. Oberhoff, C. Goldmann, D.J. Gundlach, B. Batlogg, A.N. Rashid, G. Schitter, *J. Appl. Phys.* 96 (2004) 6431.



moieties are formed either from the defects already presented in the polymer (when monoalkylated fluorenes are present as impurities and incorporated into the polymer during polymerization) or later by thermal-oxidative, photo-, or electro-oxidative degradation processes of PFs [28,29]. Therefore, any method which aims to decrease the defects or enhance the anti-oxidation capability of the polyfluorene should help to suppress the green emission and to improve the stability of the blue emission [30]. Much efforts had been done through the functionalization at C-9 position of fluorene. Holmes and co-workers [31] synthesized defect-free 9,9-dioctyl-9H-fluorene via an alkylative cyclization route, which exhibited minimal green emission owing to fluorenone formation. Huang and co-workers [32] introduced spiro-fluorene into polyfluorene backbone resulting in narrower emission with a smaller tail at longer wavelength. Müllen et al. [33] introduced triphenylamine-substituted fluorene at C-9 position and developed fully arylated poly(ladder-type-pentaphenylene), which suppressed the long wavelength emission. Alkoxyphenyl substitution fluorene at C-9 position is an effective way to suppress the long wavelength emission. Lee and Hwang [34] prepared a homo-poly (9,9-bis(4'-n-octyloxyphenyl) fluorene-2,7-di-yl) (PBOPF), showing a stable blue emission with the CIE coordinates of (0.136, 0.162). It is believed that the oxidation probability of fluorene can be decreased by reducing the electron density on the reactive site through proper substitution [35]. Li et al. [36] developed novel fluorene- and phenylene-based blue light-emitting polymers with sulphonate side group. The improved spectral stability was attributed to the electron-deficient sulphonate group substituted on the phenylene backbone. Dibenzothiophene (FS) unit has excellent hole-injection/transportation character and the dibenzothiophene-fluorene copolymer is a potential blue emitter [37,38]. Unlike dibenzothiophene, dibenzothiophene-*S,S*-dioxide (FSO) possesses strong electron-withdraw ability and can significantly improve the electron affinity [39,40]. Perepichka et al. [41] introduced (3,7-diyl)dibenzothiophene-*S,S*-dioxide unit into the oligo-fluorenes, in which there were no green emission observed in the PL spectra after thermal annealing. Further studies on solvatochromic effect for fluorene-dibenzothiophene-*S,S*-dioxide oligomers in polar solvents [42] and the singlet excited-state dynamics in poly((9,9-dioctylfluorene)-*co*-(dibenzothiophene-*S,S*-dioxide)) copolymers were investigated by steady-state and time-resolved fluorescence spectroscopies. The studies revealed that the excited state of F-*S* co-oligomers/polymers have both excitonic (denoted as local exciton, LE) and charge transfer (CT) character depending on the local environment [43]. Our group also reported the copolymer based on dibenzothiophene-*S,S*-dioxide with alkoxyphenyl-substituted fluorene. Devices fabricated from these copolymers showed high efficiency and spectral stability. The excellent performances were owed to the combined results from both alkoxyphenyl substitution at C-9 position of fluorene unit which suppressed the side chain degradation and electron-deficient dibenzothiophene-*S,S*-dioxide unit [44]. Very recently, King et al. show their results of incorporating FSO at a relatively high content up to 30% into

polyfluorene which lead to broad emission due to the dual LE/CT fluorescence character [45]. In order to achieve stable and efficient blue light emission while simultaneously avoid the probable emission broadened by the CT interaction of FSO unit in high content (up to 20–30 mol%), we herein incorporated a small amount of dibenzothiophene-*S,S*-dioxide isomers (1–10 mol%) into the backbone of poly(9,9-dioctylfluorene). The influence of FSO unit on the photo- and electroluminescent properties of the copolymers were further investigated.

## 2. Experimental section

### 2.1. Materials

Reagents were distilled from appropriate drying agents prior to use. Commercially available reagents were used without further purification. 2,7-bis(4,4,5,5-tetramethyl-1,3,2-dioxaborolan-2-yl)-9,9-dioctylfluorene (**1**), 2,7-dibromo-9,9-dihexyl-fluorene (**2**), 2,8-dibenzothiophene-*S,S*-dioxide (**3**) and 3,7-dibenzothiophene-*S,S*-dioxide (**4**) were prepared according to literatures. [39–41,44].

#### 2.1.1. General procedures of Suzuki polycondensation taking PF-3,7FSO1 as an example

To a mixture of monomer **1** (321 mg, 0.50 mmol), monomer **2** (219 mg, 0.40 mmol), monomer **4** (37.4 mg, 0.1 mmol), Pd(acetate)<sub>2</sub> (2.5 mg) and tricyclohexylphosphine (5.7 mg) were dissolved in a mixture of toluene (5 ml) and THF (2 ml) under an argon atmosphere. The mixture was heated to 70 °C and stirred, then (Et)<sub>4</sub>NOH (2 ml) and deionized water (1 ml) were added into the mixture. The solution was kept in the region of 90–100 °C with vigorous stirring under argon for 48 h. At the end of polymerization, polymers were sequentially end-capped with monomer **1** and bromobenzene to remove bromine and boronic ester end groups in order to avoid a possible quenching effect or excimer formation by boronic and bromine end groups in LEDs. The whole mixture was then poured into methanol. The crude polymer was filtrated through silica gel chromatography with toluene as eluent to remove catalyst residue. The toluene solution of polymer was concentrated and reprecipitated into methanol for three times. The pure copolymer was obtained after drying under vacuum at 50 °C overnight. Yield: 222 mg, 60%. <sup>1</sup>H NMR (300 MHz, CDCl<sub>3</sub>, δ): 8.12 (s, Ar-H), 7.88 (br, 2H), 7.68 (br, 4H), 2.14 (br, 4H), 1.16–1.01 (m, 24H), 0.78 (br, 6H). Element Anal. Found: C 87.66%, H 9.51%, S 0.73%.

PF-3,7FSO1: Monomer **1** (321 mg, 0.5 mmol), monomer **2** (268.5 mg, 0.49 mmol), and monomer **4** (3.7 mg, 0.01 mmol). Yield: 224 mg, 58%. <sup>1</sup>H NMR (300 MHz, CDCl<sub>3</sub>) δ (ppm): 7.85 (br, 2H), 7.80 (br s, 2H), 7.70 (br, 2H), 2.10 (m, 4H), 1.21–0.97 (m, 24H), 0.82 (br, 6H). Anal. calcd. for PF-3,7FSO1, found: C 88.06%, H 10.17%, S 0.25%.

PF-2,8FSO1: Monomer **1** (321 mg, 0.5 mmol), monomer **2** (268.5 mg, 0.49 mmol), and monomer **3** (3.7 mg, 0.01 mmol). Yield: 228 mg, 60%. <sup>1</sup>H NMR (300 MHz, CDCl<sub>3</sub>) δ (ppm): 7.85 (br, 2H), 7.78 (br s, 2H), 7.72 (br, 2H), 2.08 (m, 4H), 1.21–0.95 (m, 24H), 0.86 (br, 6H). Anal. calcd. for PF-2,8FSO1, found: C 88.61%, H 9.74%, S 0.27%.

**PF-3,7FSO3:** Monomer **1** (321 mg, 0.5 mmol), monomer **2** (257.6 mg, 0.47 mmol), and monomer **4** (11.2 mg, 0.03 mmol). Yield: 202 mg, 53%.  $^1\text{H NMR}$  (300 MHz,  $\text{CDCl}_3$ )  $\delta$  (ppm): 7.84 (br, 2H), 7.72 (br s, 2H), 7.68 (br, 2H), 2.06 (m, 4H), 1.24–0.97 (m, 24H), 0.83 (br, 6H). Anal. calcd. for PF-3,7FSO3, found: C 87.17%, H 9.65%, S 0.47%.

**PF-2,8FSO3:** Monomer **1** (321 mg, 0.5 mmol), monomer **2** (257.6 mg, 0.47 mmol), and monomer **3** (11.2 mg, 0.03 mmol). Yield: 213 mg, 56%.  $^1\text{H NMR}$  (300 MHz,  $\text{CDCl}_3$ )  $\delta$  (ppm): 7.86 (br, 2H), 7.71 (br, 2H), 7.29 (s, 2H), 2.13 (br, 4H), 1.16 (br, 24H), 0.86–0.74 (m, 6H). Anal. calcd. for PF-2,8FSO3, found: C 89.16%, H 10.26%, S 0.29%.

**PF-3,7FSO5:** Monomer **1** (321 mg, 0.5 mmol), monomer **2** (246.6 mg, 0.45 mmol), and monomer **4** (18.7 mg, 0.05 mmol). Yield: 242 mg, 64%.  $^1\text{H NMR}$  (300 MHz,  $\text{CDCl}_3$ ,  $\delta$ ): 7.87 (br, 2H), 7.73 (br, 4H), 2.09 (s, 4H), 1.18–1.02 (br, 24H), 0.88–0.76 (m, 6H). Element Anal. Found: C 88.89%, H 9.79%, S, 0.47%.

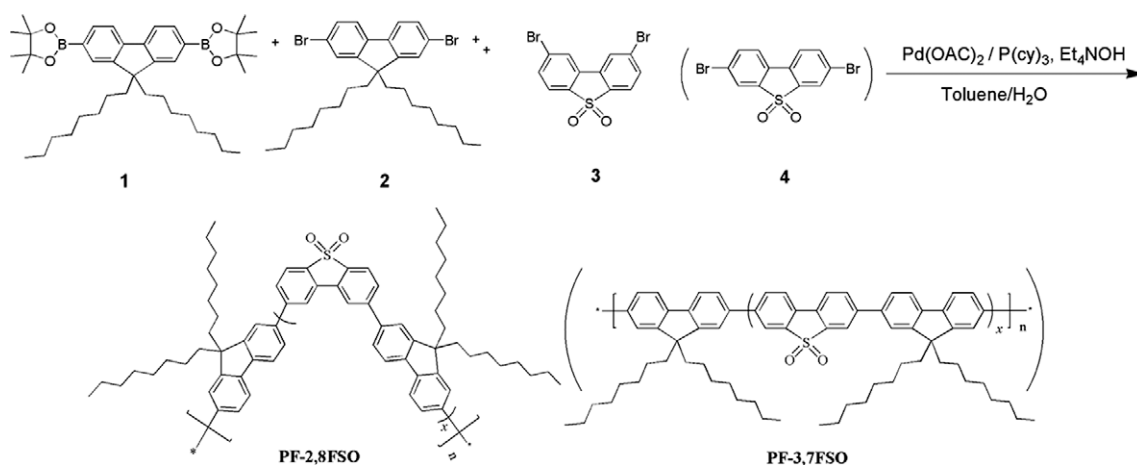
**PF-2,8FSO5:** Monomer **1** (321 mg, 0.5 mmol), monomer **2** (246.6 mg, 0.45 mmol), and monomer **3** (18.7 mg, 0.05 mmol). Yield: 196 mg, 52%.  $^1\text{H NMR}$  (300 MHz,  $\text{CDCl}_3$ ,  $\delta$ ): 7.86 (br, 2H), 7.59 (br, 4H), 2.13 (s, 4H), 1.16–0.99 (br, 24H), 0.84–0.79 (m, 6H). Element Anal. Found: C 89.37%, H 10.22%, S 0.37%.

**PF-2,8FSO10:** Monomer **1** (321.0 mg, 0.5 mmol), monomer **2** (219.2 mg, 0.40 mmol), and monomer **3** (37.4 mg, 0.10 mmol). Yield: 196 mg, 53%.  $^1\text{H NMR}$  (300 MHz,  $\text{CDCl}_3$ ,

$\delta$ ): 8.17 (s, Ar-H), 7.84 (br, 2H), 7.52 (br, 4H), 7.34 (s, Ar-H), 2.11 (s, 4H), 1.13–0.83 (br, 30H). Element Anal. Found: C 88.48%, H 9.97%, S 0.88%.

## 2.2. Measurements

$^1\text{H NMR}$  spectra were recorded on a Bruker DRX 300 spectrometer operating, respectively, at 300 MHz, in deuterated chloroform solution with tetramethylsilane as a reference. The molecular weights of the polymers were determined by a Waters GPC 2410 with tetrahydrofuran (THF) as eluent and a calibration curve with standard polystyrene as a reference. Cyclic voltammetry (CV) data were measured on a CHI660B electrochemical workstation using  $\text{Bu}_4\text{NPF}_6$  (0.1 M) in acetonitrile as electrolyte at a scan rate of 50 mV/s at room temperature under the protection of argon. A platinum electrode coated with a thin polymer film was used as the working electrode. A Pt wire was used as the counter electrode, and a calomel electrode was used as the reference electrode. Elemental analyses were performed on a Vario EL elemental analysis instrument (Elementar Co.). Thermogravimetric analyses (TGA) were performed on a Netzsch TG 209 at a heating rate of 20 °C/min. Differential scan calorimetry (DSC) measurements were performed on a Netzsch DSC 204 under  $\text{N}_2$  flow at heating and cooling rates of 20 °C/min. UV–Vis absorption spectra were recorded on a HP 8453 spectrophotometer.



**Scheme 1.** Synthetic route of the copolymers.

**Table 1**  
Structural characteristics and thermal properties of the copolymers.

Polymer	FSO content [mol%] in		$M_n$ ( $\times 10^3$ )	PDI	$T_g$ (°C)	$T_d$ (°C)
	Feed ratio	Polymer				
PF-2,8FSO1	1	–	57	1.7	72	405
PF-2,8FSO3	3	3.2	31	1.6	88	406
PF-2,8FSO5	5	4.4	17	1.7	81	405
PF-2,8FSO10	10	9.2	15	2.2	103	400
PF-3,7FSO1	1	–	17	2.3	74	396
PF-3,7FSO3	3	3.0	17	1.5	89	400
PF-3,7FSO5	5	5.5	11	1.7	110	407
PF-3,7FSO10	10	8.5	17	1.9	–	397

The PL quantum yields were measured using an Integrating Sphere IS080 (LabSphere) to collect the emitted light in all directions under the excitation of 325 nm HeCd laser (Melles Griot). The luminance ( $L$ )-current density ( $J$ )-luminance efficiency ( $LE$ ) characteristics were collected by using a Keithley 236 source measurement unit and a calibrated silicon photodiode. The luminance was calibrated by a PR-705 SpectraScan spectrophotometer (Photo Research), with simultaneous acquisition of the EL spectra and CIE coordinates, driven by Keithley model 2400 voltage-current source. The device fabrication process was described previously by the literatures [45–47]. After the samples and devices were annealed atop of a hotplate at high temperature (80–120 °C) for 1–4 h, spectral stability of PL and EL upon thermal annealing were performed in atmosphere by a PR-705 SpectraScan spectrophotometer soon after cooling down to room temperature. The stability of the blue emitting PLEDs was studied in atmosphere by applying a constant current stress with an initial luminance of 150 cd/m<sup>2</sup>. Before annealing in atmosphere and stress test, the PLEDs were encapsulated with a UV-cured epoxy resin.

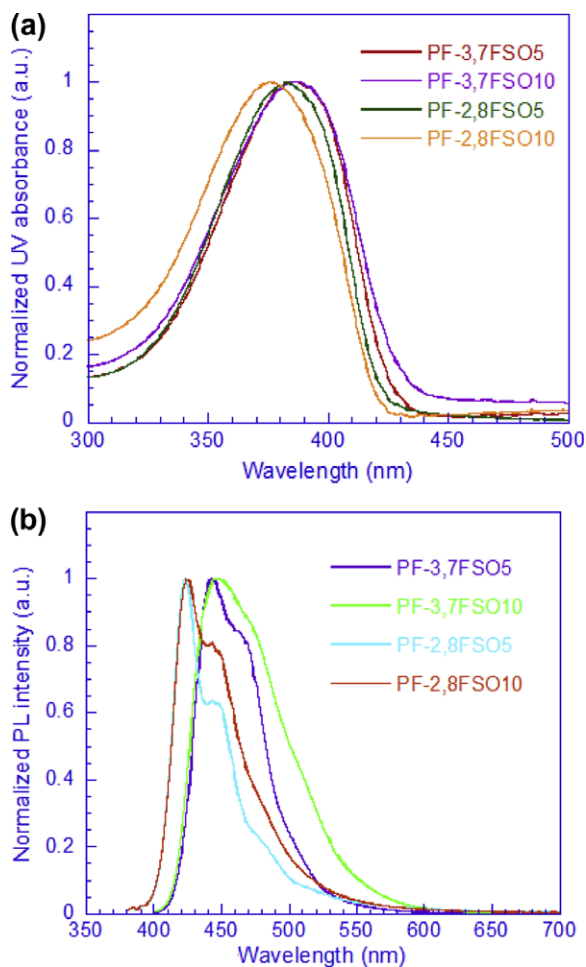


**Fig. 1.** UV-Vis absorption (a) and photoluminescence spectra (b) of the copolymers.

### 2.3. Theoretical section

Density functional theory (DFT) calculation was carried out using the Gaussian 03 series of programs. The ground state optimization were performed by DFT at B3LYP/6-31g\* level [48–50]. The sketch map of HOMO and LUMO orbital were generated by GaussView software.

## 3. Results and discussion

### 3.1. Synthesis and characterization

The synthesis route is shown in Scheme 1. Monomers 1, 2, 3 or 4 were polymerized via Suzuki polycondensation. The monomer feed molar ratios of F/2,8FSO as well as F/3,7FSO are 99:1, 97:3, 95:5, 90:10 and the corresponding polymers were referred to PF-2,8FSO1, PF-2,8FSO3, PF-2,8FSO5, PF-2,8FSO10 and PF-3,7FSO1, PF-3,7FSO3, PF-3,7FSO5, PF-3,7FSO10, respectively. The calculated values of FSO unit in copolymers were resulted from elemental analysis and listed in Table 1. The copolymers are soluble in common organic solvents, such as THF,

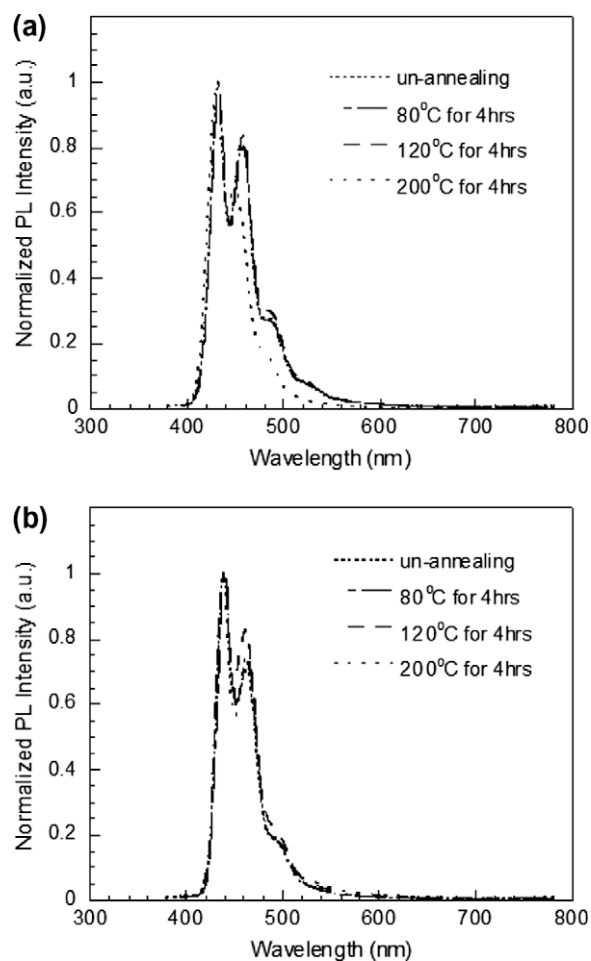


**Fig. 2.** PL spectra of PF-2,8FSO5 (a) and PF-3,7FSO1 (b) under thermal annealing in air at varied temperatures.

chloroform, and toluene at room temperature. The number-average molecular weights ( $M_n$ ) of these polymers, using THF as an eluent and polystyrene standards for calibration are between 10,000 and 50,000 g/mol with a polydispersity index (PDI) in the range of 1.5–2.3. The thermal properties of the polymers were determined by differential

scanning calorimetry (DSC) and thermal gravimetric analysis (TGA) measurements. The decomposition temperatures ( $T_d$ , corresponding to 5 wt% loss) are over 395 °C. The glass transition temperatures ( $T_g$ ) of PF-FSO copolymers, ranging from 72 to 110 °C, are higher than PFO homopolymer (70 °C). The relatively high  $T_g$  of these

**Table 2**  
Photo-physical and electrochemical properties of the copolymers.

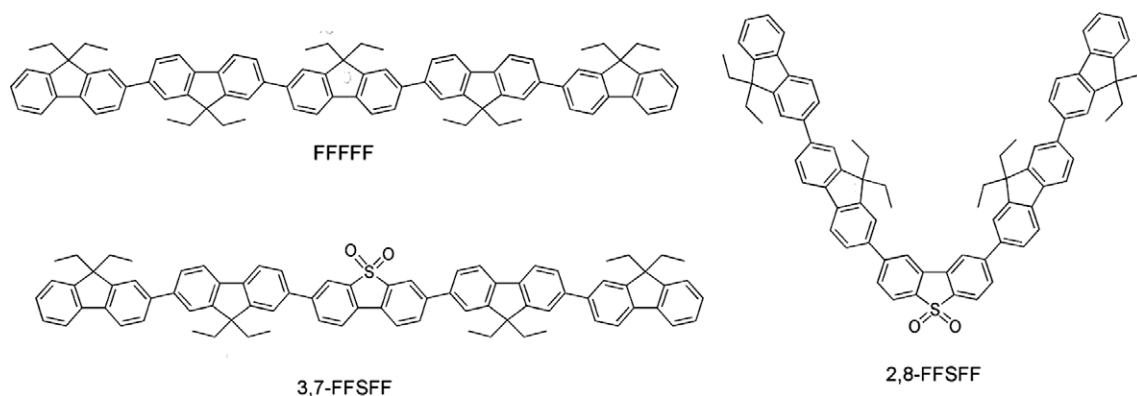
Polymer	$E_{ox}$ (V)	$E_{red}$ (V)	HOMO (eV)	LUMO (eV)	$E_g^b$ (eV)	$\lambda_{max}^{abs}$ [nm]	$\lambda_{max}^{PL}$ (nm)	QE <sub>PL</sub> <sup>c</sup> (%)
PFO <sup>a</sup>	1.36	−2.24	−5.76	−2.16	2.90	388	420	80
PF-2,8FSO1	1.44	−1.61	−5.84	−2.79	2.90	388	421	85
PF-2,8FSO3	1.39	−1.63	−5.79	−2.77	2.90	388	422	72
PF-2,8FSO5	1.40	−1.54	−5.80	−2.86	2.91	378	423	72
PF-2,8FSO10	1.43	−1.38	−5.83	−3.02	2.94	374	424	70
PF-3,7FSO1	1.41	—	−5.81	—	2.89	388	439	68
PF-3,7FSO3	1.44	−1.64	−5.84	−2.76	2.89	388	440	73
PF-3,7FSO5	1.43	−1.58	−5.83	−2.82	2.86	388	443	81
PF-3,7FSO10	1.48	−1.45	−5.88	−2.95	2.80	388	447	74

$E_{HOMO} = -(E_{ox} + 4.40)$  eV;  $E_{LUMO} = -(E_{red} + 4.4)$  eV.

<sup>a</sup> From Ref. [37].

<sup>b</sup> Onset of the absorption spectra.

<sup>c</sup> Measured in solid states.



**Scheme 2.** Modeling pentamer molecules for theoretical calculation: FFFFF (a); 3,7-FFSFF (b) and 2,8-FFSFF (c).

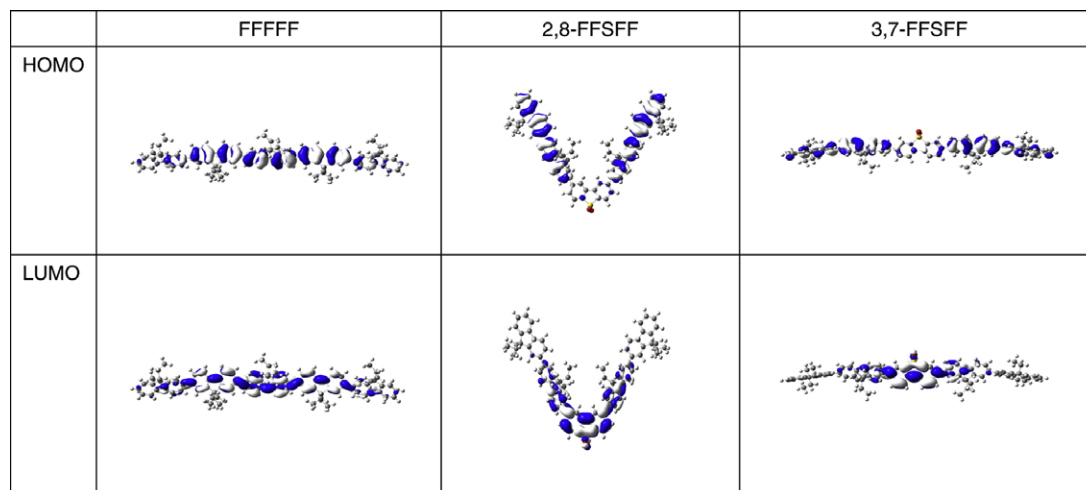


**Fig. 3.** Contour plots of the frontier molecular orbitals of the pentamers.

copolymers are important and desirable for many opto-electronic applications.

### 3.2. Photo-physical and electrochemical characteristics

The absorption spectra of PF-3,7FSO and PF-2,8FSO copolymers in film are displayed in Fig. 1a. The absorption spectra of PF-3,7FSO copolymers slightly red-shift while that of PF-2,8FSO copolymers blue-shift with increasing the FSO content (deducing from absorption edge). The PL spectra of both PF-3,7FSO and PF-2,8FSO copolymers are red-shifted with increasing the content of FSO (Fig. 1b). The absorption and emission spectra shift in different solvents, suggesting an ICT character of PF-FSO copolymers. (See supporting information)

The PL spectral stability of the copolymers PF-FSO was studied by annealing the films in air at 80, 120 and 200 °C for 4 h and then measuring the fluorescent spectra after cooling down to room temperature. Fig. 2 shows the PL spectra of the polymers PF-2,8FSO5 and PF-3,7FSO1 before and after annealing. It can be seen that the PL spectra of

copolymers remain nearly identical after annealing, indicating a highly stable spectra upon thermal annealing.

The electrochemical behaviors copolymers are examined by cyclic voltammetry (CV). The onset of oxidation potentials ( $E_{ox}$ ) of copolymers are recorded with respect to the saturated calomel electrodes (SCE) as the reference electrode [51]. The highest occupied molecular orbit (HOMO) and the lowest unoccupied molecular orbit (LUMO) energy levels of the copolymers are calculated according to the empirical formula  $E_{HOMO} = -e(E_{ox} + 4.40)$  eV and  $E_{LUMO} = -e(E_{red} + 4.40)$  eV, respectively. The estimated HOMO and LUMO energy levels lies in the range of  $-5.80$  to  $-5.90$  eV and  $-2.77$  to  $-2.95$  eV, respectively. The detailed CV data of copolymers were summarized in Table 2.

### 3.3. Theoretical computation

To understand the frontier molecular orbitals and spectral properties of the copolymers, density functional theory (DFT) were carried out to calculate the following pentamers: fluorene (FFFFF), fluorene/2,8-FSO (2,8-FFSFF) and

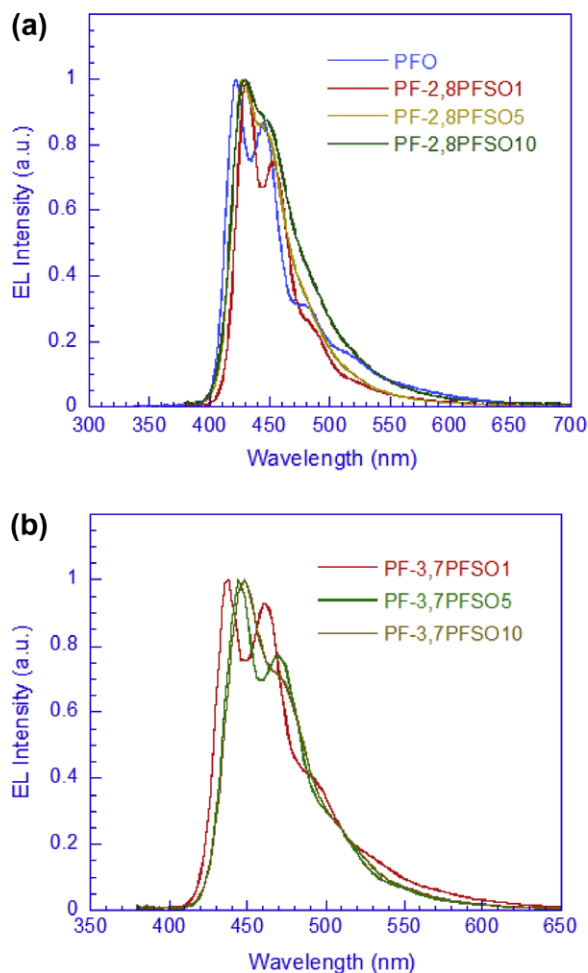


Fig. 4. EL spectra of the copolymers.

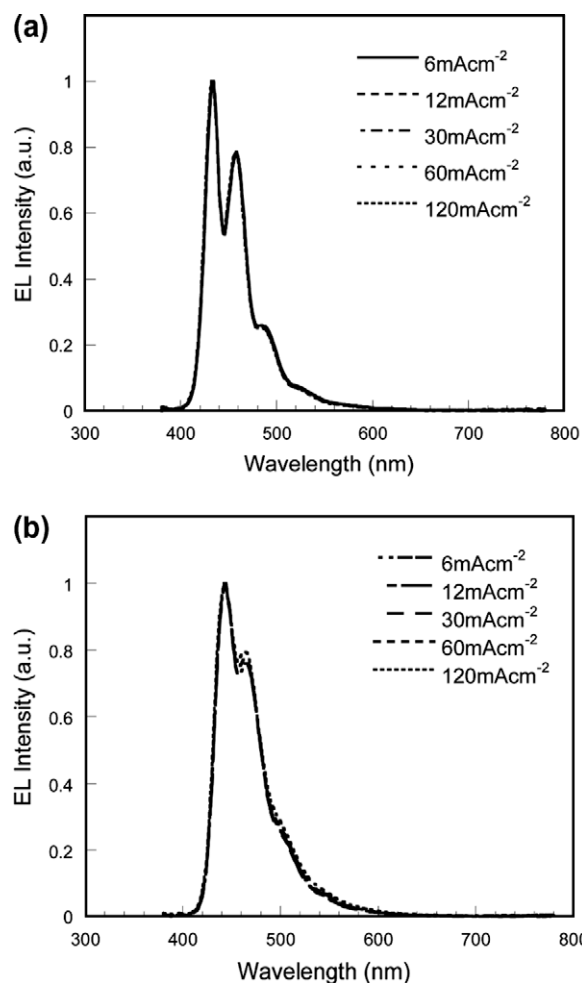


Fig. 5. EL spectra of PF-2,8FSO1 (a) and PF-3,7FSO5 (b) under different applied current densities.

fluorene/3,7-FSO (3,7-FFSFF) as shown in Scheme 2. Through computation, the energy band of dibenzothio-*S,S*-dioxide (4.85 eV) is lower than that of fluorene (5.04 eV). The HOMO–LUMO energy gaps for three pentamers decrease in the order: FFFFF (3.59 eV) > 2,8-FFSFF (3.57 eV) > 3,7-FFSFF (3.36 eV). The HOMO and LUMO orbitals of fluorene pentamers are plotted in Fig. 3. The LUMO orbital characters of the pentamers with and without FSO unit show significant differences. The HOMOs of pentamers are delocalized all over the backbone while the LUMOs of the 2,8-FFSFF and 3,7-FFSFF pentamers are strongly confined to the FSO unit. The emission transition from LUMO to HOMO in fluorene pentamer FFFFF is mainly from the fluorene to fluorene units, while the LUMO → HOMO transitions of 3,7-FFSFF and 2,8-FFSFF basically arise from FSO unit, and thus reduce the possibility of the distribution of fluorene in excitation.

### 3.4. Electroluminescent properties

The devices with the configuration of ITO/PEDOT:PSS(40 nm) /polymer(80 nm)/Ba(4 nm)/Al(120 nm) were fabricated. Fig. 4 shows the EL spectra of the copolymers. The EL spectra of PF-3,7FSO10 peaked around 450 nm is 12 nm red-shifted compared with PF-2,8FSO10. The similar trend can be observed in other PF-3,7FSO and PF-2,8FSO polymers with same amounts of FSO units. In order to testify the spectral stability, the experiments concerning on the dependence of EL spectra on current densities and annealing temperatures were carried out. The EL spectra of PF-2,8FSO1 and PF-3,7FSO5 copolymers remain nearly identical with variation of current densities from 6 to 120 mAcm<sup>-2</sup> (Fig. 5) or after annealing at 80 and 120 °C for 1 h (Fig. 6), respectively. No long wavelength emission as usually observed in fluorene-based polymers appears. In addition, the evolution of spectral stability under continuous stress has been carried out for the device with an initial luminance of 150 cd m<sup>-2</sup>. It is revealed by the online spectrophotometer, after 45 h continuous stress despite the luminance reduced by 50%, no obvious change was observed in the EL spectra of the device based on PF-3,7FSO5 (Fig. 7). Therefore, it is safe to conclude that the EL spectra of the PLEDs based on the copolymer are highly stable with a lifetime of at least 45 h. It is important to note that, longer lifetime can be expected if the initial luminance was set as a typical luminance of 100 cd m<sup>-2</sup> and a more reliable encapsulation technology was used.

Table 3 shows the device performances of PF-2,8FSO and PF-3,7FSO copolymers. All of the devices exhibit high efficiencies, especially, the device based on PF-3,7FSO5 exhibits the best overall performances, in terms of low turn on voltage of 4.4 V, a maximal luminous efficiency(LE) of 4.6 cd A<sup>-1</sup> (corresponding to an EQE of 3.8%) with the CIE coordinate of (0.15, 0.12). The devices based on PF-2,8FSO copolymers show even bluer emission with the CIE coordinates of (0.16, 0.07–0.08). For the device based on PF-2,8FSO1, a moderate turn on voltage of 5.4 V, and maximum LE of 3.7 cd A<sup>-1</sup> (EQE = 3.6%) with the CIE coordinate of (0.16, 0.07) are realized. The typical CIE coordinates of the devices for PF-2,8FSO and PF-3,7FSO copolymers are in the range of (0.16, 0.07–0.08) and

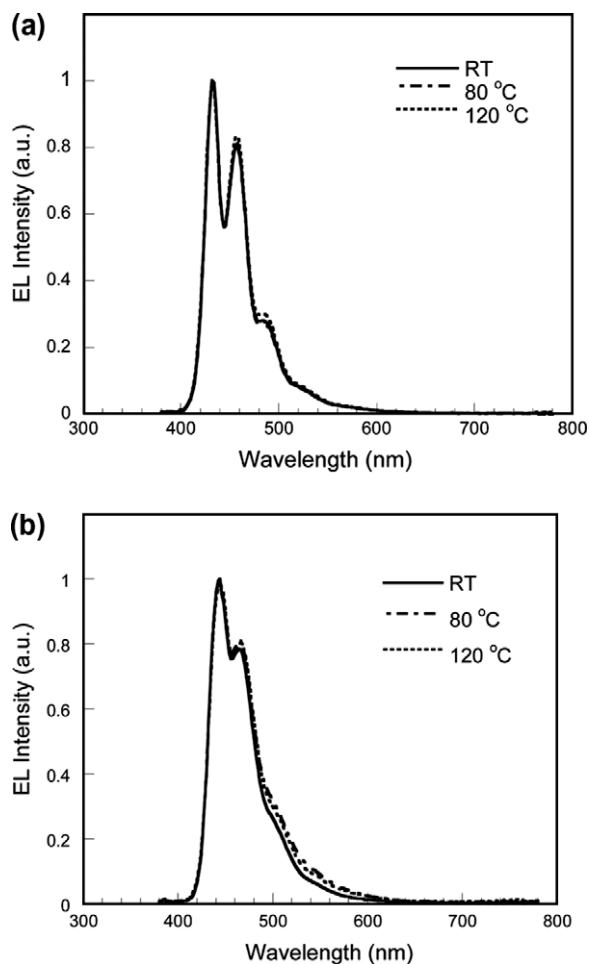


Fig. 6. EL spectra of PF-2,8FSO1 (a) and PF-3,7FSO5 (b) under varied thermal annealing temperatures for 1 h.

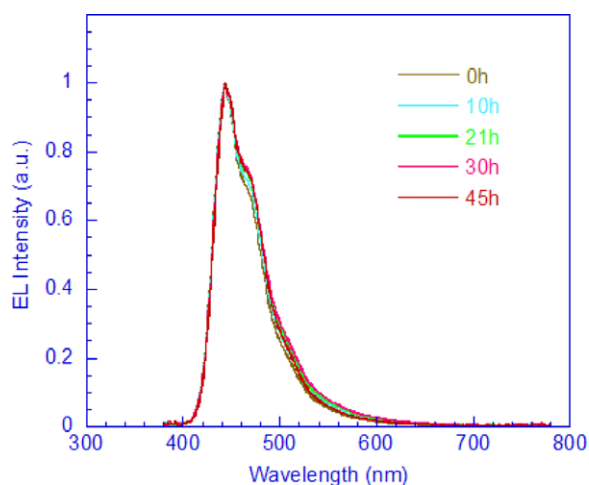


Fig. 7. Evolution of EL spectral stability of PF-3,7FSO5 during continuous luminance.

(0.15, 0.10–0.13), respectively, very close to the National Television System Committee (NTSC) standard (0.14,

**Table 3**

Device performances of copolymers.

Polymer	$V_{th}$ (V)	$L_{max}$ ( $cdm^{-2}$ )	$LE_{max}^a$ ( $cdA^{-1}$ )	$QE_{max}^a$ (%)	$J = 100 \text{ mAcm}^{-2}$				$CIE^b$	
					V (V)	L ( $cdm^{-2}$ )	LE ( $cdA^{-1}$ )	QE (%)	x	y
PF-2,8FSO1	5.4	6631	3.72	3.64	10.5	2782	2.64	2.59	0.16	0.07
PF-2,8FSO3	5.7	4947	2.80	2.61	9.4	2555	2.33	2.16	0.16	0.08
PF-2,8FSO5	5.7	5678	2.40	2.23	11.2	1523	1.64	1.52	0.16	0.08
PF-2,8FSO10	4.3	2070	1.03	0.90	5.9	886	0.91	0.79	0.16	0.08
PF-3,7FSO1	4.2	1390	1.73	1.38	15.4	894	0.99	0.80	0.16	0.13
PF-3,7FSO3	6.0	1292	1.34	0.93	10.4	531	0.51	0.35	0.15	0.10
PF-3,7FSO5	4.4	4561	4.63	3.84	10.5	2198	2.13	1.76	0.15	0.12
PF-3,7FSO10	3.5	3754	3.28	2.80	6.8	1649	1.65	1.41	0.15	0.12

$V_{th}$ , The turn on voltage, calculated with a luminance of  $1 \text{ cd/m}^2$ ;  $L_{max}$ , the maximum luminance;  $LE_{max}$ , the maximum luminance efficiency;  $QE_{max}$ , the maximum quantum efficiency.

<sup>a</sup> Collected at low current density ( $<5 \text{ mA/cm}^2$ ).

<sup>b</sup> Measured at  $12 \text{ mA/cm}^2$ .

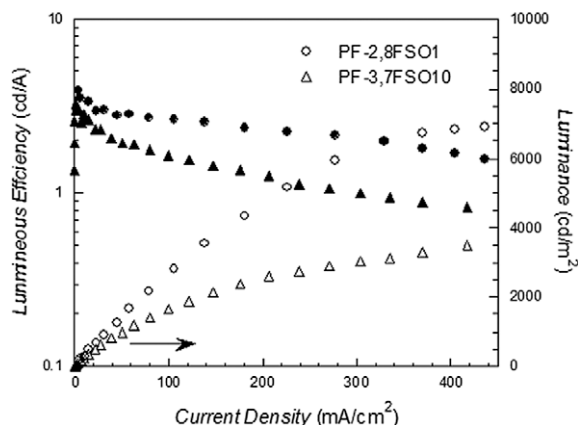


**Fig. 8.**  $L$ - $J$ - $LE$  characteristics of the device based on the copolymers.

0.08). The turn-on voltages of the devices decline with increasing the content of FSO unit in the polymers, indicating that the FSO unit may improve the carrier injection and transportation. Compared with the homo-polyfluorene PFO, there are reductions of 0.14 and 0.17 eV in LUMO levels of PF-2,8FSO10 and PF-3,7FSO10, respectively, which lowers the injection barrier of electron, and therefore improves the device performances. Moreover, the devices are able to maintain considerably high efficiencies at high current density ( $100 \text{ mAcm}^{-2}$ ), mostly of which drop less than 40% of the maximum quantum efficiencies. (As shown in Table 2) Fig. 8 shows the luminance-current density-luminous efficiency ( $L$ - $J$ - $LE$ ) characteristics of PF-2,8FSO1 and PF-3,7FSO10 copolymers. The device efficiencies of PF-2,8FSO1 and PF-3,7FSO10 remain as high as 2.0 and  $0.8 \text{ cd A}^{-1}$  at an even higher current density of  $500 \text{ mA cm}^{-2}$  with the luminance over 6800 and  $3000 \text{ cd m}^{-2}$ , respectively. The luminous efficiencies decline slightly with increasing the current density, also indicating that the materials and devices have a good stability.

#### 4. Conclusion

Fluorene-co-dibenzothiophene-*S,S*-dioxide copolymers with spectral stability and high efficiency were prepared.

The electron-withdraw FSO unit enhances the intramolecular charge transfer in polyfluorene backbone, which benefits the spectral stability by decreasing the possibility of the formation of exciton on fluorene units. Moreover, the FSO unit lowers the LUMO energy level, balances the injection and transportation both electron and hole in the polymers, and therefore improves the device efficiencies.

#### Acknowledgements

This work is financially supported by the Ministry of Science and Technology of China (Nos. 2009CB623601 and 2009CB930604) and the National Natural Science Foundation of China (No. U0634003).

#### Appendix A. Supplementary data

Supplementary data associated with this article can be found, in the online version, at doi:10.1016/j.orgel.2009.04.021.

#### References

- [1] C.W. Tang, S.A. VanSlyke, *Appl. Phys. Lett.* 51 (1987) 913.
- [2] J.H. Burroughes, D.D.C. Bradley, A.R. Broun, R.N. Marks, K. Mackay, R.H. Friend, P.L. Burn, A.B. Holms, *Nature* 347 (1990) 539.
- [3] K. Müllen, U. Scherf, *Organic Light Emitting Devices Synthesis, Properties and Applications*, Wiley-VCH, 2005.
- [4] R.J. Holmes, B.W. D'Andrade, S.R. Forrest, X. Ren, J. Li, M.E. Thompson, *Appl. Phys. Lett.* 83 (2003) 3818.
- [5] H. Yan, P. Lee, N.R. Armstrong, A. Graham, G.A. Evmenenko, P. Dutta, T.J. Marks, *J. Am. Chem. Soc.* 127 (2005) 3172.
- [6] R.D. Scurlock, B. Wang, P.R. Ogilby, J.R. Sheats, R.J. Gotitua, *J. Am. Chem. Soc.* 117 (1995) 10194.
- [7] D. Sainova, T. Miteva, H.G. Nothofer, U. Scherf, I. Glowacki, J. Ulanski, H. Fujikawa, D. Neher, *Appl. Phys. Lett.* 76 (2000) 1810.
- [8] J.R. Sheats, H. Antoniadis, M. Hueschen, W. Leonard, J. Miller, R. Moon, D. Roitman, A. Stocking, *Science* 273 (1996) 884.
- [9] U. Scherf, *E.J.W. List, Adv. Mater.* 14 (2002) 477.
- [10] D. Sainova, T. Miteva, H.G. Nothofer, U. Scherf, I. Glowacki, J. Ulanski, H. Fujikawa, D. Neher, *Appl. Phys. Lett.* 76 (2002) 1810.
- [11] A.R. Buckley, M.D. Rahn, J. Hill, J. Cabanillas-Gonzalez, A.M. Fox, D.D.C. Bradley, *Chem. Phys. Lett.* 393 (2001) 331.
- [12] M. Leelerc, *J. Polym. Sci. Part A: Polym. Chem.* 39 (2001) 2869.
- [13] X. Gong, P.K. Iyer, G.C. Bazan, D. Moses, A.J. Heeger, S.S. Xiao, *Adv. Funct. Matter.* 13 (2003) 325.
- [14] V.N. Bliznyuk, S.A. Carter, J.C. Scott, G. Klärner, R.D. Miller, D.C. Miller, *Macromolecules* 32 (1999) 361.
- [15] E. Conwell, *Trends Polym. Sci.* 5 (1997) 218.

- [16] K.H. Weinfurner, H. Fujikawa, S. Tokito, Y. Taga, *Appl. Phys. Lett.* 76 (2000) 2502.
- [17] F. Uckert, Y.H. Tak, K. Müllen, H. Bässler, *Adv. Mater.* 12 (2000) 905.
- [18] A.W. Grice, D.D.C. Bradley, M.T. Bemis, M. Inbasekaran, W.W. Wu, E.P. Woo, *Appl. Phys. Lett.* 73 (1998) 629.
- [19] G. Zeng, W.L. Yu, S.J. Chua, W. Huang, *Macromolecules* 35 (2002) 6907.
- [20] I. Prieto, J. Teetsov, M.A. Fox, D.A. Van den Bout, A.J. Bard, *J. Phys. Chem. A* 105 (2001) 520.
- [21] E. Zojer, A. Pogantsch, E. Hennebicq, D. Beljonne, J.-L. Brédas, P. Scandiucci de Freitas, U. Scherf, *E.J.W. List, J. Chem. Phys.* 117 (2002) 6794.
- [22] J.M. Lupton, M.R. Craig, E.W. Meijer, *Appl. Phys. Lett.* 80 (2002) 4489.
- [23] M. Gaal, E.J.W. List, U. Scherf, *Macromolecules* 36 (2003) 4236.
- [24] L. Romaner, A. Pogantsch, P. Scandiucci de Freitas, U. Scherf, *Adv. Funct. Mater.* 13 (2003) 597.
- [25] F. Montiilla, R. Mallavia, *Adv. Funct. Mater.* 17 (2007) 71.
- [26] E.J.W. List, R. Guentner, P.S. de Freitas, U. Scherf, *Adv. Mater.* 14 (2002) 374.
- [27] J. Jacob, J.Y. Zhang, A.C. Grimsdale, K. Müllen, M. Gaal, E.J.W. List, *Macromolecules* 36 (2003) 8240.
- [28] E.J.W. List, M. Gaal, R. Guentner, P.S. de Freitas, U. Scherf, *Synth. Met.* 139 (2003) 759.
- [29] S. Kappaun, C. Slugovc, E.J.W. List, *Adv. Polym. Sci.* 212 (2008) 273.
- [30] Y.Y. Noh, D.Y. Kim, Y. Yoshida, K. Yase, B.J. Jung, E. Lim, H.K. Shim, R. Azumi, *J. Appl. Phys.* 97 (2005) 1.
- [31] S.Y. Cho, A.B. Grimsdale, D.J. Jones, S.E. Watkins, A.B. Holmes, *J. Am. Chem. Soc.* 129 (2007) 11910.
- [32] W. Yu, J. Pei, W. Huang, A.J. Heeger, *Adv. Mater.* 12 (2000) 828.
- [33] (a) C. Ego, A.C. Grimsdale, F. Uckert, G. Yu, G. Srdanov, K. Müllen, *Adv. Mater.* 14 (2002) 809;  
(b) J. Jacob, S. Sax, M. Gaal, E.J.W. List, A.C. Grimsdale, K. Müllen, *Macromolecules* 38 (2005) 9933.
- [34] J. Lee, D. Hwang, *Chem. Commun.* 22 (2003) 2836.
- [35] X. Gong, P.K. Iyer, D. Moses, G.C. Bazan, A.J. Heeger, S.S. Xiao, *Adv. Funct. Mater.* 13 (2003) 325.
- [36] J. Li, A. Ziegler, G. Wegner, *Chem. Eur. J.* 11 (2005) 4450.
- [37] W. Yang, Q. Hou, C.Z. Liu, Y.H. Niu, J. Huang, R.Q. Yang, Y. Cao, *J. Mater. Chem.* 13 (2003) 1351.
- [38] W. Yang, Y.H. Niu, C.Z. Liu, Q. Hou, J. Huang, R.Q. Yang, X. Zeng, Y. Cao, *Synth. Met.* 135 (2003) 181.
- [39] T.H. Huang, W.T. Whang, J.Y. Shen, Y.S. Wen, J.T. Lin, T.H. Ke, L.Y. Chen, C.C. Wu, *Adv. Funct. Mater.* 16 (2006) 1449.
- [40] T.H. Huang, J.T. Lin, L.Y. Chen, Y.T. Lin, C.C. Wu, *Adv. Mater.* 18 (2006) 602.
- [41] I.I. Perepichka, I.F. Perepichka, M.R. Bryce, I.-O. Pålsson, *Chem. Commun.* 27 (2005) 3397.
- [42] F.B. Dias, S. Pollock, G. Hedley, L.O. Pålsson, A. Monkman, I.I. Perepichka, I.F. Perepichka, M. Tavasli, M.R. Bryce, *J. Phys. Chem. B* 110 (2006) 19329.
- [43] F.B. Dias, S. King, A.P. Monkman, I.I. Perepichka, M.A. Kryuchkov, I.F. Perepichka, M.R. Bryce, *J. Phys. Chem. B* 112 (2008) 6557.
- [44] J. Liu, J.H. Zou, H.B. Wu, W. Yang, C. Li, B. Zhang, Y.Y. Li, J.B. Peng, Y. Cao, *Chem. Mater.* 20 (2008) 4499.
- [45] S.M. King, I.I. Perepichka, I.F. Perepichka, F.B. Dias, M.R. Bryce, A.P. Monkman, *Adv. Funct. Mater.* 19 (2009) 586.
- [46] J. Luo, X. Li, Q. Hou, J. Peng, W. Yang, Y. Cao, *Adv. Mater.* 19 (2007) 1113.
- [47] E.G. Wang, C. Li, Y.Q. Mo, Y. Zhang, G. Ma, W. Shi, J.B. Peng, W. Yang, Y. Cao, *J. Mater. Chem.* 16 (2006) 4133.
- [48] W. Kohn, L. Sham, *J. Phys. Rev.* 140 (1965) 1133.
- [49] C. Lee, W. Yang, R.G. Parr, *Phys. Rev. B* 37 (1988) 785.
- [50] R. Ditchfield, W.J. Hehre, J.A. Pople, *J. Chem. Phys.* 54 (1971) 724.
- [51] J.L. Bredas, R. Silbey, D.S. Boudreaux, R.R. Chance, *J. Am. Chem. Soc.* 105 (1983) 6555.



grain boundaries in thin films and lead to higher device performance. They are beneficial to the studies of the intrinsic transport property and the integration of organic single crystals to micro- and nanoelectronic devices. The micro- and nanometer-sized single crystals are grown by either vapor or solution processes. The solution process is easier to carry out and potentially offers a cost-effective method for fabricating large-area electronic components from organic materials. Therefore, there is a growing need to explore organic single crystals with micro- and nanostructures for the solution-processable materials. The solubility and the high performance of thiophene-based hybrid materials make them good candidates for the studies of solution-processed single-crystal transistors.

So far, the intrinsic charge-transport properties of thiophene-based hybrid materials have seldom been studied. In this paper, we study the optical and the single-crystal FET properties of three new thiophene-based hybrid materials: 5-(9-butyl-3-carbazolyl)terthiophene (**BCTT**), 2,5-bis(9-butyl-3-carbazolyl)thiophene (**BBCT**) and 2-(9-butyl-3-carbazolyl)-5-(2-dibenzothiophenyl)thiophene (**BCDT**). Compared with **BCTT**, the molecular rigidity in **BBCT** and **BCDT** is enhanced by introducing fused-rings in the one side of thiophene, which is intended to maximize the interchain interaction by reducing the freedom of rotation in the oligomer. This variation causes significant differences in interchain aggregation, morphology and electronic properties. Beyond our expectation, **BCTT** shows the highest carrier mobility in both thin-film and single-crystal FET devices. The enhanced rigidity in the molecules of **BBCT** and **BCDT** is not in favor of the carrier transport.

## 2. Experimental

### 2.1. Chemicals and instruments

All chemicals were purchased from Aldrich and Acros and used as received without further purification. 9-Butyl-3-bromocarbazole, 9-butyl-3-carbazolylboronic acid and 2-bromodibenzothiophene were prepared according to the published procedures [26,27]. Solvents were purified and dried according to the standard procedures.

$^1\text{H}$  NMR and  $^{13}\text{C}$  NMR spectra were recorded on a Bruker Avance 400 spectrometer. Elemental analyses were performed using a German Vario EL III elemental analyzer. Absorption measurements were carried out on a TU-1800 spectrophotometer. Photoluminescence (PL) measurements were recorded on a Hitachi F-4500 fluorescence spectrophotometer with a 150 W Xe lamp. Thermogravimetric analyses (TGA) were measured on a SDT Q600 V8.0 calorimeter, under nitrogen atmosphere with a heating rate of 10–600 °C/min. The atomic force microscopy (AFM) images were obtained by using a Digital Instruments (DI) Dimension 3100 operating in tapping mode. Scanning electron microscope (SEM) measurements were performed on a Hitachi S-4800 field emission scanning electron microscope. The X-ray diffraction (XRD) investigations were carried out on a Bruker D8 advanced diffractometer equipped with Cu K $\alpha$  radiation ( $\lambda = 1.5406 \text{ \AA}$ ). The data were collected using a Ni-filtered Cu-target tube

at room temperature in the  $2\theta$  range from 2° to 40°. Single-crystal X-ray diffraction measurements were conducted on a Bruker Smart APEX2 CCD area-detector diffractometer with graphite-monochromated Mo K $\alpha$  radiation ( $\lambda = 0.71069 \text{ \AA}$ ). Processing of the intensity data were carried out using the Bruker SMART routine, and the structure was solved by direct methods and refined by a full-matrix least-squares technique on  $F^2$  using SHELXL-97 programs [28]. CCDC reference number 691,496. For crystallographic data in CIF or other electronic format, see <http://www.ccdc.cam.ac.uk>.

Organic thin-film transistors were fabricated in the top contact configuration. Organic semiconductors were deposited at a rate of  $0.1 \text{ \AA s}^{-1}$  under a pressure of about  $5.0 \times 10^{-4} \text{ Pa}$ . Gold electrodes were deposited using shadow masks with width-to-length ratio ( $W/L$ ) of ca. 60/1.

The single-crystal transistors were fabricated as follows: A minimum volume of chlorobenzene solution of sample (1 mg/mL) was injected on the octyltrichlorosilane (OTS)-pretreated  $\text{SiO}_2/\text{Si}$  substrate in a closed chamber. After the slow evaporation of the solvent, the microribbons were obtained. Then Au electrodes were thermally evaporated by laying a copper grid on the microstructures as the mask. OFET characteristics were obtained at room temperature in air on Keithley 4200 SCS.

### 2.2. Synthesis

**5-tributylstannylterthiophene.** n-BuLi (2.5 M in hexane, 1.6 mL, 4.0 mmol) was added dropwise into a solution of terthiophene (1.10 g, 4.44 mmol) in THF (20 mL) at  $-78 \text{ }^\circ\text{C}$  under nitrogen. After stirring at  $-78 \text{ }^\circ\text{C}$  for 1 h, tributyltin chloride (1.1 mL, 4.05 mmol) was added dropwise. The reaction mixture was slowly warmed up to room temperature and stirred for another 1 h. Then the mixture was partitioned between  $\text{Et}_2\text{O}$  (100 mL) and brine (150 mL) and the organic layer was dried over anhydrous  $\text{Na}_2\text{SO}_4$ . The solvent was removed under reduced pressure to give a blue viscous liquid. The product was used instantly for the next step without further characterization or purification.

**5-(9-butyl-3-carbazolyl)terthiophene (BCTT).** 5-Tributylstannylterthiophene was dissolved in dry toluene (25 mL). 9-Butyl-3-bromocarbazole (1.2 g, 3.97 mmol) and  $\text{Pd}(\text{PPh}_3)_4$  (20 mg) were added under nitrogen. Then the mixture was refluxed for 24 h. After cooling to room temperature, the mixture was poured into  $\text{H}_2\text{O}$  (40 mL) and extracted with  $\text{HCCl}_3$ . The organic phase was combined and dried over  $\text{MgSO}_4$ . Evaporation of the solvent, the product was chromatographed on silica gel (petroleum ether/THF = 14:1) to afford the yellow solid (1.33 g, 2.84 mmol, 71.5% yield).  $^1\text{H}$  NMR ( $\text{CDCl}_3$ , 400 MHz)  $\delta$ : 0.96 (t,  $J = 7.3 \text{ Hz}$ , 3H), 1.41 (m, 2H), 1.88 (m, 2H), 4.32 (t,  $J = 7.1 \text{ Hz}$ , 2H), 7.04 (dd,  $J = 3.6, 5.1 \text{ Hz}$ , 1H), 7.11–7.12 (m, 2H), 7.18–7.20 (m, 2H), 7.22–7.28 (m, 3H), 7.40 (d,  $J = 5.1 \text{ Hz}$ , 1H), 7.41 (d,  $J = 4.7 \text{ Hz}$ , 1H), 7.47–7.51 (m, 1H), 7.72 (dd,  $J = 1.7, 8.5 \text{ Hz}$ , 1H), 8.14 (d,  $J = 7.7 \text{ Hz}$ , 1H), 8.31 (d,  $J = 1.5 \text{ Hz}$ , 1H).  $^{13}\text{C}$  NMR ( $\text{CDCl}_3$ , 100.62 MHz)  $\delta$ : 13.86, 20.55, 31.17, 43.00, 108.94, 109.05, 117.62, 119.13, 120.53, 122.63, 122.77, 123.34, 123.60, 123.77, 123.93, 124.37, 124.40, 124.65, 125.21, 126.03, 127.87, 135.09, 135.79, 136.68, 137.29, 140.16, 140.98, 144.96. Anal. Calcd

for  $C_{28}H_{23}NS_3$ : C, 71.60; H, 4.94; N, 2.98; S, 20.48. Found: C, 72.05; H, 5.01; N, 2.86; S, 20.63.

**2,5-bis(9-butyl-3-carbazolyl)thiophene (BBCT).** To a mixture of 2,5-dibromothiophene (0.32 mL, 2.78 mmol), 9-butyl-3-carbazolylboronic acid (1.8 g, 6.8 mmol), sodium carbonate (6.0 g, 56.6 mmol) and palladium  $Pd(PPh_3)_4$  (20 mg) were added a degassed mixture of THF and water (3:1 in volume, 75 mL). The mixture was stirred at 80 °C for 30 h. After the mixture was cooled to room temperature, the organic layer was separated, dried over sodium sulfate and evaporated to dryness. The crude product was chromatographed on silica gel (petroleum ether) to afford the pale yellow solid (0.46 g, 0.875 mmol, 31.5% yield).  $^1H$  NMR ( $CDCl_3$ , 400 MHz)  $\delta$ : 0.97 (t,  $J = 7.3$  Hz, 6H), 1.42 (m, 4H), 1.87 (m, 4H), 4.33 (b, 4H), 7.24–7.28 (m, 2H), 7.34 (b, 2H), 7.42 (d,  $J = 7.9$  Hz, 4H), 7.49 (t,  $J = 7.2$  Hz, 2H), 7.78 (b, 2H), 8.16 (d,  $J = 7.7$  Hz, 2H), 8.37 (b, 2H).  $^{13}C$  NMR ( $CDCl_3$ , 100.62 MHz)  $\delta$ : 13.87, 20.57, 31.17, 43.00, 108.88, 108.98, 117.48, 119.01, 120.54, 122.87, 123.32, 123.93, 125.90, 139.97, 140.97, 143.88. Anal. Calcd for  $C_{36}H_{34}N_2S$ : C, 82.09; H, 6.51; N, 5.32; S, 6.09. Found: C, 82.61; H, 7.05; N, 5.305; S, 6.52.

**2-Thienyldibenzothiophene.** From 2-bromothiophene (2.86 g, 17.55 mmol) and Mg turnings (0.64 g, 26.7 mmol) in  $Et_2O$  (30 mL), the corresponding Grignard reagent was prepared and coupled with 2-bromodibenzothiophene (3.35 g, 12.74 mmol) and  $Ni(dppp)Cl_2$  (0.36 g, 0.67 mmol) in THF (30 mL). The reaction mixture was refluxed for 6 h. After cooling to room temperature, the solution was poured into water and extracted several times with  $Et_2O$ . The organic phase was combined and dried over  $MgSO_4$ . Evaporation of the solvent, the product was chromatographed on silica gel (petroleum ether) to afford the solid (1.7 g, 6.4 mmol 50.3% yield).  $^1H$  NMR ( $CDCl_3$ , 400 MHz)  $\delta$ : 7.14 (dd,  $J = 3.6, 5.1$  Hz, 1H), 7.33 (dd,  $J = 1.1, 5.1$  Hz, 1H), 7.42 (dd,  $J = 1.1, 3.6$  Hz, 1H), 7.47–7.50 (m, 2H), 7.72 (dd,  $J = 1.8, 8.3$  Hz, 1H), 7.84–7.87 (m, 2H), 8.21–8.23 (m,

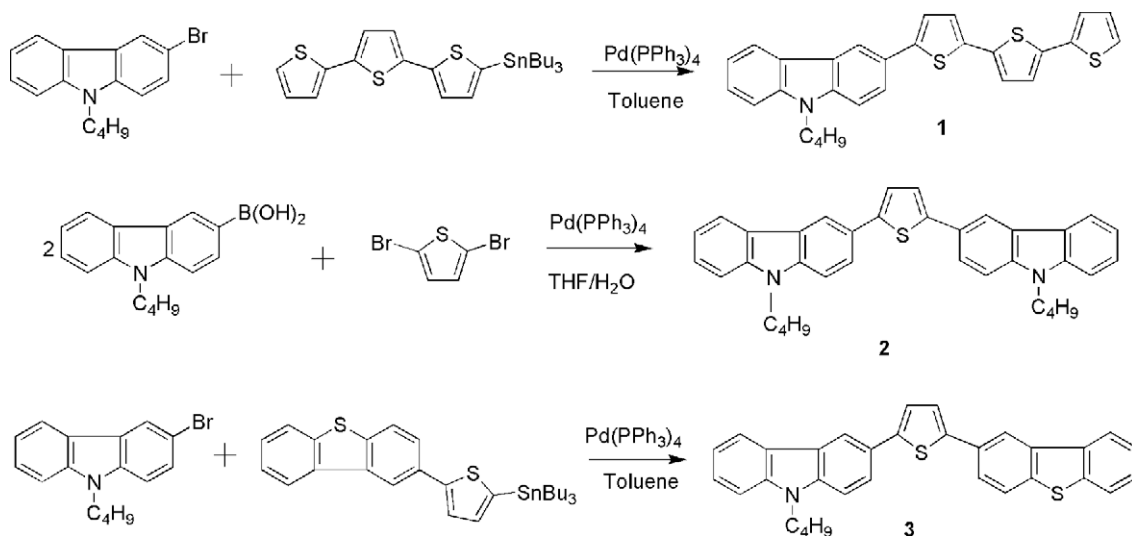
1H), 8.36 (d,  $J = 1.8$  Hz, 1H).  $^{13}C$  NMR ( $CDCl_3$ , 100.62 MHz)  $\delta$ : 118.28, 121.25, 122.45, 122.64, 122.76, 124.02, 124.31, 124.55, 126.53, 127.67, 130.62, 134.84, 135.64, 138.08, 139.48, 143.97. Anal. Calcd for  $C_{16}H_{10}S_2$ : C, 72.14; H, 3.78; S, 24.07. Found: C, 72.54; H, 3.59; S, 24.19.

**2-(9-butyl-3-carbazolyl)-5-(2-dibenzothieryl)thiophene (BCDT).** BCDT was prepared according to the same procedure as that for BCTT from 2-thienyldibenzothiophene (0.26 g, 0.98 mmol) and 9-butyl-3-bromocarbazole (0.3 g, 0.99 mmol). The product was chromatographed on silica gel (petroleum ether) to afford the pale yellow solid (0.25 g, 0.51 mmol, 52.4% yield).  $^1H$  NMR ( $CDCl_3$ , 400 MHz)  $\delta$ : 0.97 (t,  $J = 7.3$  Hz, 3H), 1.43 (m, 2H), 1.89 (m, 2H), 4.33 (t,  $J = 7.1$  Hz, 2H), 7.25–7.27 (m, 1H), 7.37 (d,  $J = 3.6$  Hz, 1H), 7.42–7.44 (m, 3H), 7.48–7.51 (m, 3H), 7.77–7.80 (m, 2H), 7.86–7.88 (m, 2H), 8.16 (d,  $J = 7.7$  Hz, 1H), 8.24–8.26 (m, 1H), 8.38 (d,  $J = 1.5$  Hz, 1H), 8.42 (d,  $J = 1.4$  Hz, 1H).  $^{13}C$  NMR ( $CDCl_3$ , 100.62 MHz)  $\delta$ : 13.40, 20.08, 30.68, 42.52, 108.45, 108.56, 117.14, 117.79, 118.61, 120.05, 121.26, 122.33, 122.45, 122.47, 122.62, 122.86, 123.47, 123.65, 124.01, 124.12, 125.05, 125.52, 126.49, 130.85, 134.91, 135.69, 137.79, 139.52, 139.63, 140.50, 141.79, 144.72. Anal. Calcd for  $C_{32}H_{25}NS_2$ : C, 78.81; H, 5.17; N, 2.87; S, 13.15. Found: C, 78.52; H, 4.87; N, 2.76; S, 13.10.

### 3. Result and discussion

#### 3.1. Synthesis and characterization

Scheme 1 illustrates the synthesis routes for the hybrid materials BCTT, BBCT and BCDT. BBCT was prepared by the Suzuki coupling. Both BCTT and BCDT were obtained by the Stille coupling. In comparison with BCTT, the ended bithienyl is replaced by a carbazolyl in BBCT and a dibenzothieryl in BCDT. These hybrid materials are readily



Scheme 1. Synthetic routes to BCTT, BBCT and BCDT.

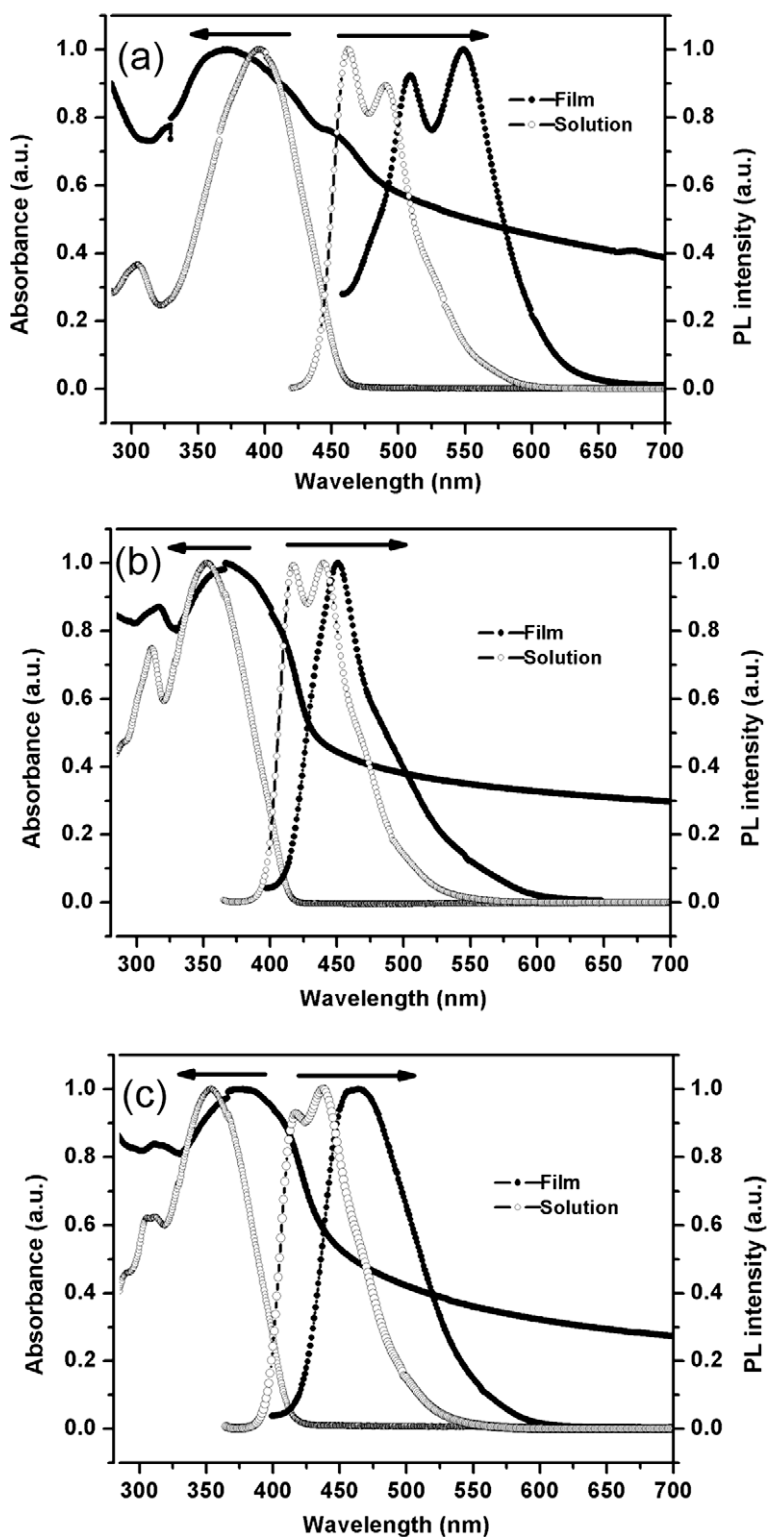


**Fig. 1.** Normalized optical absorption (UV/vis) and emission (PL) spectra in toluene solution and as thin-film of **BCIT** (a), **BBCT** (b) and **BCDT** (c). The PL spectra were obtained by exciting at 400 nm for **BCIT**, 353 nm for **BBCT** and **BCDT**.

soluble in common solvents such as THF, dichloromethane and chloroform, allowing them to be easily purified by column chromatography. The intermediate precursors and

the final products were characterized by elemental analysis,  $^1\text{H}$  and  $^{13}\text{C}$  NMR spectra. The results are consistent with the predicted chemical structures. All three compounds are

stable under 300 °C as revealed by thermogravimetric analysis (TGA) measurements.

### 3.2. Photophysical properties

Optical absorption and fluorescence emission spectra of compounds **BCTT**, **BBCT** and **BCDT** were measured both in toluene solution (concentration  $1 \times 10^{-5} \text{ mol L}^{-1}$ ) and as thin films (see Fig. 1). The absorption maxima of **BCTT**, **BBCT** and **BCDT** in solution state are located at 396, 353 and 353 nm, respectively. **BCTT** exhibits the highest  $\lambda_{\text{max}}$  due to its long effective intramolecular conjugation length. Comparison of the absorption spectra between the solution and the corresponding films reveals two drastically different behaviors. The film absorption spectrum of **BCTT** displays blue shift as compared with that in solution suggesting H aggregation. In the type of H aggregation, two interacting molecules have their long axes parallel to each other. The coupling between the transition dipoles leads to Davydov splitting of the excited level into two exciton bands, in which the low-energy transitions are forbidden. The major absorption band in the solid state corresponds to the allowed high-energy transitions of interacting molecules [10,29]. In contrast, the film spectra of **BBCT** and **BCDT** show bathochromic shift, indicating J aggregation with adjacent molecules presenting head-to-tail alignment. For this type of aggregation, the low-energy transition is allowed, which leads to a red shift of the absorption spectrum. The aggregation mode of **BBCT** and **BCDT** was further proved by powder XRD. The interlayer spacing of **BBCT** and **BCDT** is about 16 Å from the diffraction peak at the low angle. Based on the similarity of three compounds in molecule structure and the crystal structure of **BCTT**, the molecular length of **BBCT** and **BCDT** is estimated to be 21 Å. Thus, the tilt angle between the dipole direction and the line of molecule centers is about 49.6°, which is lower than 54.7°. According to the molecular exciton coupling model of Kasha et al. [30], the molecules form J-like aggregates in the solid state of **BBCT** and **BCDT**. This result is in accordance with bathochromic shift in the absorption spectra. Therefore, the change of substitution at the one end of thiophene leads to totally different aggregation modes in the solid state. The HOMO–LUMO gaps obtained from the end-absorption are 2.7 eV for **BCTT**, 3.0 eV for **BBCT** and **BCDT**, respectively. All films showed red shift of the emission maxima compared with those of the diluted solutions. The fine structure appearing in the fluorescence spectra is possibly due to vibronic coupling that is typical for oligothiophenes [31].

### 3.3. Crystal structure

The single crystal of **BCTT** was obtained by slow evaporation from chloromethane solution. Unfortunately, we were unable to obtain millimeter-sized single crystals of **BBCT** and **BCDT** despite numerous attempts. The crystal data and intensity collection parameters of **BCTT** are summarized in Table 1. Fig. 2 shows the molecular structure and packing diagram of **BCTT**. Compound **BCTT** crystallizes in the  $P2_1/n$  space group and has four inequivalent molecules per unit cell. The molecules adopt a typical herring-

bone packing motif and the two long axes of interacting molecules are aligned with each other, which leads to the blue shift of the major band in the absorption spectrum of the film in comparison with the solution. The torsion angle between the carbazole ring and the adjacent thiophene ring is 20.6°, which is larger than that of the two external thiophene rings (13.6°). There exist C–H... $\pi$  and C...S interactions between the carbazole portion and the outer thiophene ring of two closely packed molecules. These results indicate that the molecules of **BCTT** in the crystal

**Table 1**  
Crystal data, diffraction data, and refinement data of **BCTT**.

Empirical formula	C <sub>28</sub> H <sub>23</sub> NS <sub>3</sub>
Formula weight	469.65
Crystal system	Monoclinic
Space group	$P2_1/n$
<i>b</i> (Å)	9.0422(2)
$\alpha$ (°)	90
$\beta$ (°)	92.4110(10)
$\gamma$ (°)	90
Crystal size	0.34 × 0.27 × 0.11 mm
Volume (Å <sup>3</sup> )	2324.72(8)
<i>Z</i>	4
<i>D<sub>c</sub></i> (g cm <sup>-3</sup> )	1.342
<i>F</i> (0 0 0)	984
<i>T</i> (K)	293(2) K
Radiation $\lambda$ (Å)	Mo K $\alpha$ , 0.71073
Absorption coefficient (mm <sup>-1</sup> )	0.336
$2\theta_{\text{max}}$ (°) (completeness)	54.46 (99.6 %)
Reflections collected/unique	17374/5185 [ <i>R</i> (int) = 0.0326]
Data/restraints/parameters	5185/0/291
<i>R</i> <sub>1</sub> , <i>wR</i> <sub>2</sub> [ <i>I</i> > 2 $\sigma$ ( <i>I</i> )]	0.0677, 0.1915
<i>R</i> <sub>1</sub> , <i>wR</i> <sub>2</sub> (all data)	0.1005, 0.2140
Goodness of fit, <i>F</i> <sup>2</sup>	1.275
Largest diff. peak/hole (e Å <sup>-3</sup> )	0.706/−0.524
Transmission ratio	0.9640/0.8944

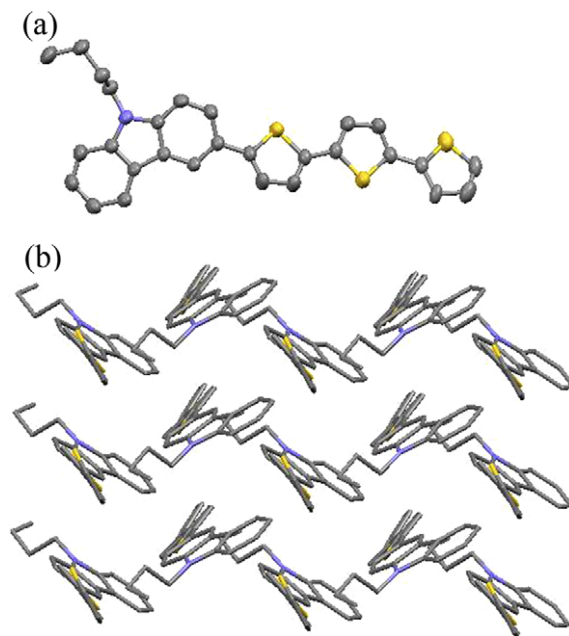


**Fig. 2.** (a) Molecular structure of **BCTT** with thermal ellipsoids constructed at the 50% probability level. (b) The crystal packing diagram along the long axis of molecules. Hydrogen atoms are omitted for clarity.

have high packing property with a large overlap of intermolecular  $\pi$ -orbitals, which is beneficial to carrier transport.

### 3.4. Investigations on the morphology

Fig. 3 illustrates the SEM images of **BCTT**, **BBCT** and **BCDT** directly precipitated on the  $\text{SiO}_2/\text{Si}$  substrate from 1 mg/mL chlorobenzene solution. The **BCTT** molecules easily assembled into 1D microribbons, which indicate that the growth of **BCTT** from solution is mainly governed by the intermolecular interactions between the  $\pi$ -conjugated molecules. Compared with **BCTT**, the microstructures of **BBCT** and **BCDT** show high flexibility. The precipitations of **BBCT** and **BCDT** from solution formed flexible microribbons. They can even bend themselves into cycles. The difference in the flexibility is closely related to the variation in the intermolecular aggregation. The weak intermolecular interaction in the J aggregation of **BBCT** and **BCDT** may result into the highly flexible microstructures.

The OFET performance is considered to have a close relationship with the film morphology. Fig. 4 shows the AFM images of the vacuum-deposited film. The film of **BCTT** reveals highly crystalline microstructure with plate-like grains in good connectivity. However, the images of **BBCT** and **BCDT** show amorphous characteristics. The morphology difference of these films would have great influence on the OFET performance.

The orientation of the vacuum-deposited films was also investigated by XRD. Fig. 5 shows the XRD patterns of **BCTT**, **BBCT** and **BCDT**, deposited on  $\text{SiO}_2/\text{Si}$  at 50 °C. In the case of **BCTT**, the sharp and strong peaks, assignable to multiple (00*l*) reflections, indicate a high degree of lamellar ordering and crystallinity. The *d*-spacing obtained from the first reflection ( $2\theta = 4.04^\circ$ ) is 21.9 Å, which is nearly one-half the distance of the unit cell *c*-axis from the single-crystal structure. This result suggests that the molecules of **BCTT** potentially adopt an edge-on orientation on the substrate, which is an ideal molecular arrangement for carrier transport. On the other hand, the films of **BBCT** and **BCDT** show no discernible reflection peak, suggesting a disorder orientation on the  $\text{Si}/\text{SiO}_2$  substrate.

### 3.5. OFET properties

Organic thin-film transistors of **BCTT**, **BBCT** and **BCDT** were fabricated using top-contact geometry. Among the three materials, both **BBCT** and **BCDT** display no transistor activities. Only **BCTT** shows moderate hole transport properties and the results are shown in Table 2. The differences in OFET performance of these hybrid materials are mainly due to the great differences in film morphology as shown by the XRD patterns and AFM micrographs. The carrier mobility strongly depends on the strength of the electronic coupling between the HOMO levels of adjacent molecules for the hole transport. The stronger intermolecular interac-

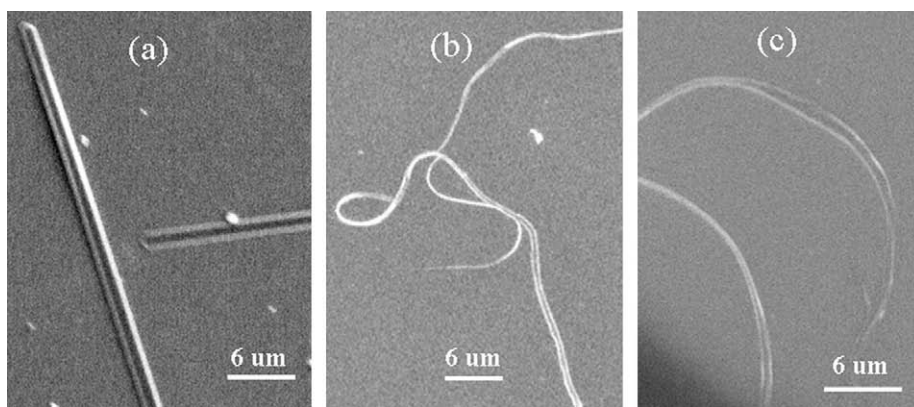


Fig. 3. SEM images of **BCTT** (a), **BBCT** (b) and **BCDT** (c). The microribbons were obtained by drop-casting 1 mg/mL chlorobenzene solution on the  $\text{SiO}_2/\text{Si}$  substrate.

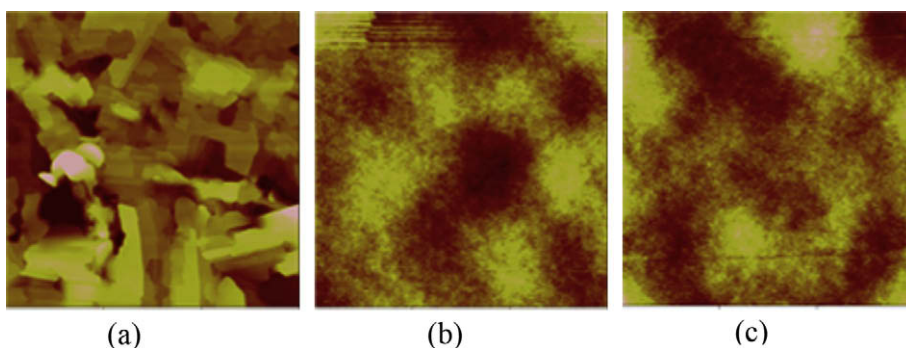
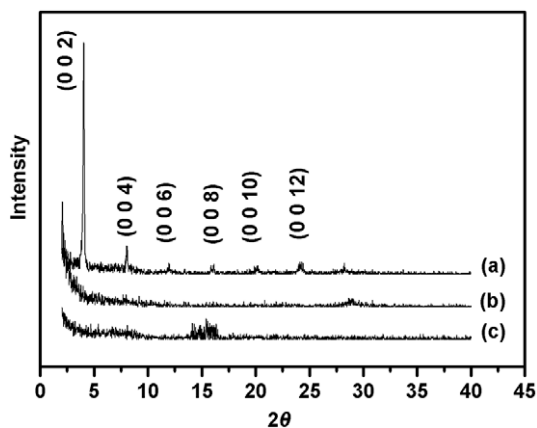


Fig. 4. AFM images of films deposited on bare  $\text{SiO}_2$  at 50 °C ( $3\ \mu\text{m} \times 3\ \mu\text{m}$ ): (a) **BCTT**; (b) **BBCT**; (c) **BCDT**.



**Fig. 5.** XRD patterns of films deposited on bare SiO<sub>2</sub> at 50 °C: (a) BCTT; (b) BBCT; (c) BCDT.

tion in organic crystalline films is more helpful for carrier transport [9].

The 1D microtransistors of BCTT, BBCT and BCDT were also fabricated and studied. A minimum volume of chlorobenzene solution of sample was injected on the OTS-pre-treated SiO<sub>2</sub>/Si substrate in a closed chamber. After the

**Table 2**

The performance of FETs based on the single-crystal and thin-film of BCTT, BBCT and BCDT.

Compound	Transistor	T <sub>sub</sub> (°C)	SiO <sub>2</sub>	Mobility (cm <sup>2</sup> V <sup>-1</sup> s <sup>-1</sup> )	I <sub>on</sub> /I <sub>off</sub> ratio
BCTT	Thin-film	50	bare	6.5 × 10 <sup>-4</sup>	10 <sup>3</sup>
		50	OTS	3.8 × 10 <sup>-3</sup>	10 <sup>5</sup>
		90	bare	2.3 × 10 <sup>-3</sup>	10 <sup>3</sup>
		90	OTS	5.8 × 10 <sup>-3</sup>	10 <sup>5</sup>
BCTT	Single-crystal	–	OTS	5.9 × 10 <sup>-2</sup>	10 <sup>4</sup> –10 <sup>5</sup>
BBCT	Single-crystal	–	OTS	4.1 × 10 <sup>-3</sup>	10 <sup>2</sup> –10 <sup>3</sup>
BCDT	Single-crystal	–	OTS	3.3 × 10 <sup>-4</sup>	10–10 <sup>2</sup>

slow evaporation of the solvent, the 1D microribbons were obtained by the self-assembly of molecules along the π–π stacking direction. The powder XRD peaks and the polarized optical microscopic images (POM) showed clearly that all these 1D microstructures were ordered crystal [32,33]. Then Au electrodes were thermally evaporated by laying a copper grid on the microribbons as the mask [25]. Fig. 6A shows the schematic of a typical structure of an FET based on a single microribbon. Fig. 6B is a representa-

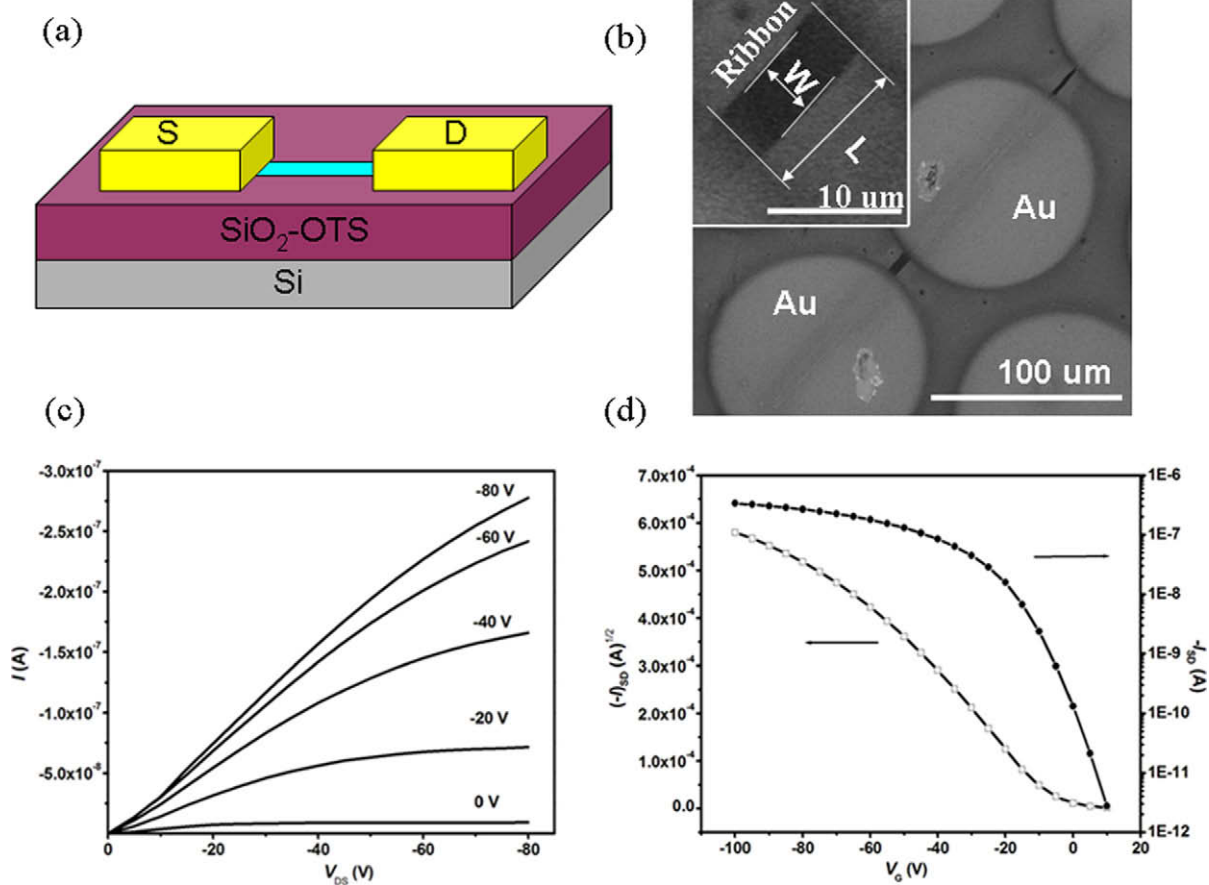


**Fig. 6.** (a) Schematic diagram of a microtransistor based on an individual microribbon. (b) SEM image of an individual BCTT microribbon and electrodes formed by copper grid mask. Inset: The magnification image of the microribbon near the electrode. (c) Output and (d) transfer characteristics of the transistor based on the individual BCTT microribbon.

tive SEM image of a top-contact device constructed from a single microribbon of **BCTT**. The channel length and width of the FET device are estimated according to the length of the **BCTT** single-crystal ribbon between the Au electrodes and the width of the ribbon, respectively. As shown in Table 2, the carrier mobilities of the single-crystal **BCTT** microtransistors are much higher than those of the thin-film transistors because of the elimination of disorder and grain boundaries, which always exist in the thin films. Fig. 6C and D show the transfer and output characteristics of the single-crystal FET. The average field-effect mobility is  $0.059 \text{ cm}^2 \text{ V}^{-1} \text{ s}^{-1}$  with an on/off current ratio of  $10^4$ – $10^5$ . The highest mobility was found to be  $0.094 \text{ cm}^2 \text{ V}^{-1} \text{ s}^{-1}$  with a very low threshold voltage of 1.1 V. The carrier mobility of **BCTT** is much higher than those of **BBCT** and **BCDT**. The main reason for this improvement is probably the stronger interchain interaction in the **BCTT** crystal with H aggregation than those in the **BBCT** and **BCDT** crystals with J aggregation. Furthermore, the devices made from single-crystal **BCTT** show good environmental stability. The carrier mobility and on/off ratio were still on the same order of magnitude as those of the freshly prepared devices after the microtransistors were exposed to ambient environment for 45 days. The good device stability is possibly due to the stability of crystals under ambient conditions and the good contact at the interface between the semiconductor and the dielectric.

#### 4. Conclusion

Three new hybrid materials based on fused-ring and thiophene were synthesized and characterized. The slight change of substituent at the one end of thiophene leads to the dramatic differences in morphology, optical and electronic properties. Molecules of **BCTT** adopt H aggregation. Whereas, both **BBCT** and **BCDT** exhibit the formation of J aggregation. The microstructures of **BBCT** and **BCDT** display high flexibility. The microtransistors of these materials were easily fabricated by direct solution process. The carrier-transport properties of **BCTT** are much higher than those of **BBCT** and **BCDT**, probably due to the stronger interchain interaction in the solid. These results would be beneficial to understanding the structure-property relationships and related studies on the intrinsic transport properties of hybrid materials.

#### Acknowledgements

We thank the State National Natural Science Foundation of China (Grant Nos. 50721002, 50590403, 90401028, 50673003) and 973 program of PR China (Grant Nos. 2004CB619002) for financial support.

#### References

- [1] C.D. Dimitrakopoulos, P.R.L. Malenfant, *Adv. Mater.* 14 (2002) 99.
- [2] A.R. Murphy, J.M.J. Fréchet, *Chem. Rev.* 107 (2007) 1066.
- [3] M.L. Tang, A.D. Reichardt, N. Miyaki, R.M. Stoltenberg, Z. Bao, *J. Am. Chem. Soc.* 130 (2008) 6064.
- [4] M. Mas-Torrent, S. Masirek, P. Hadley, N. Crivillers, N.S. Oxtoby, P. Reuter, J. Veciana, C. Rovira, A. Tracz, *Org. Electron.* 9 (2008) 143.
- [5] G.H. Gelinck, H.E.A. Huitema, E. van Veenendaal, E. Cantatore, L. Schrijnemakers, J.B.P.H. van der Putten, T.C.T. Geuns, M. Beenhakkers, J.B. Giesbers, B.-H. Huisman, E.J. Meijer, E.M. Benito, F.J. Touwslager, A.W. Marsman, B.J.E. van Rens, D.M. de Leeuw, *Nat. Mater.* 3 (2004) 106.
- [6] B.K. Crone, A. Dodabalapur, R. Sarpeshkar, R.W. Filas, Y.-Y. Lin, Z. Bao, J.H. O'Neill, W. Li, H.E. Katz, *J. Appl. Phys.* 89 (2001) 5125.
- [7] C.D. Sheraw, L. Zhou, J.R. Huang, D.J. Gundlach, T.N. Jackson, M.G. Kane, I.G. Hill, M.S. Hammond, J. Campi, B.K. Greening, J. Francl, J. West, *Appl. Phys. Lett.* 80 (2002) 1088.
- [8] B. Crone, A. Dodabalapur, A. Gelperin, L. Torsi, H.E. Katz, A.J. Lovinger, Z. Bao, *Appl. Phys. Lett.* 78 (2001) 2229.
- [9] Y. Shirota, H. Kageyama, *Chem. Rev.* 107 (2007) 953.
- [10] J. Cornil, D. Beljonne, J.-P. Calbert, J.-L. Brédas, *Adv. Mater.* 13 (2001) 1053.
- [11] X. Yang, L. Wang, C. Wang, W. Long, Z. Shuai, *Chem. Mater.* 20 (2008) 3205.
- [12] M.S.A. Abdou, F.P. Orfino, Y. Son, S. Holdcroft, *J. Am. Chem. Soc.* 119 (1997) 4518.
- [13] Y. Qiu, Y. Hu, G. Dong, L. Wang, J. Xie, Y. Ma, *Appl. Phys. Lett.* 83 (2003) 1644.
- [14] C. Pannemann, T. Diekmann, U. Hilleringmann, *J. Mater. Res.* 19 (2004) 1999.
- [15] H. Meng, Z. Bao, A.J. Lovinger, B.-C. Wang, A.M. Muzsca, *J. Am. Chem. Soc.* 123 (2001) 9214.
- [16] H. Meng, J. Zheng, A.J. Lovinger, B.-C. Wang, P.G. Van Patten, Z. Bao, *Chem. Mater.* 15 (2003) 1778.
- [17] J.A. Merlo, C.R. Newman, C.P. Gerlach, T.W. Kelley, D.V. Muires, S.E. Fritz, M.F. Toney, C.D. Frisbie, *J. Am. Chem. Soc.* 127 (2005) 3997.
- [18] K. Takimiya, Y. Kunugi, Y. Toyoshima, T. Otsubo, *J. Am. Chem. Soc.* 127 (2005) 3605.
- [19] J. Gao, L. Li, Q. Meng, R. Li, H. Jiang, H. Li, W. Hu, *J. Mater. Chem.* 17 (2007) 1421.
- [20] H. Meng, F. Sun, M.B. Goldfinger, G.D. Jaycox, Z. Li, W.J. Marshall, G.S. Blackman, *J. Am. Chem. Soc.* 127 (2005) 2406.
- [21] Q. Tang, L. Jiang, Y. Tong, H. Li, Y. Liu, Z. Wang, W. Hu, Y. Liu, D. Zhu, *Adv. Mater.* 20 (2008) 2947.
- [22] C. Reese, Z. Bao, *J. Mater. Chem.* 16 (2006) 329.
- [23] V.C. Sundar, J. Zaumseil, V. Podzorov, E. Menard, R.L. Willett, T. Someya, M.E. Gershenson, J.A. Rogers, *Science* 303 (2004) 1644.
- [24] Y. Guo, H. Zhao, G. Yu, C. Di, W. Liu, S. Jiang, S. Yan, C. Wang, H. Zhang, X. Sun, X. Tao, Y. Liu, *Adv. Mater.* 20 (2008) 4835.
- [25] S. Xiao, J. Tang, T. Beetz, X. Guo, N. Tremblay, T. Siegrist, Y. Zhu, M. Steigerwald, C. Nuckolls, *J. Am. Chem. Soc.* 128 (2006) 10700.
- [26] Z. Li, Z. Li, C. Di, Z. Zhu, Q. Li, Q. Zeng, C. Zhang, Y. Liu, C. Ye, J. Qin, *Macromolecules* 39 (2006) 6951.
- [27] O. Shimomura, T. Sato, I. Tomita, M. Suzuki, T. Endo, *J. Polym. Sci.: Part A: Polym. Chem.* 35 (1997) 2813.
- [28] G.M. Sheldrick, *SHELXL-97*, University of Gottingen, Gottingen, Germany, 1997.
- [29] A. Yassar, G. Horowitz, P. Valat, V. Wintgens, M. Hmyene, F. Deloffre, P. Srivastava, P. Lang, F. Gamier, *J. Phys. Chem.* 99 (1995) 9155.
- [30] M. Kasha, H.R. Rawls, M.A. El-Bayoumi, *Pure Appl. Chem.* 11 (1965) 371.
- [31] A. Facchetti, M.-H. Yoon, C.L. Stern, G.R. Hutchison, M.A. Ratner, T.J. Marks, *J. Am. Chem. Soc.* 126 (2004) 13480.
- [32] Y. Zhou, W. Liu, Y. Ma, H. Wang, Li Qi, Y. Cao, J. Wang, J. Pei, *J. Am. Chem. Soc.* 129 (2007) 12386.
- [33] D.H. Kim, J.T. Han, Y.D. Park, Y. Jang, J.H. Cho, M. Hwang, K. Cho, *Adv. Mater.* 18 (2006) 719.

Liq molecules in excited state would recombine with ground Liq molecules to form excimers in LEL, and also with hole transporting molecules to form exciplexes at interface between LEL and hole-transporting layer (HTL), which would induce red-shifted of electroluminescence (EL) spectra, blue-green light emitting, lowered current efficiency, and shortened lifetime of OLED [11,12].

To solve above problems, a novel Liq-derived blue-light OEM, bis[(8-hydroxyquinolin)lithium-8-hydroxyquinolin] sodium ( $[\text{Liq-q}^-]_2\cdot 2\text{Na}^+$ ), was synthesized and characterized as the blue-light OEM with better properties than Liq.

## 2. Experimental section

### 2.1. Synthesis

All chemicals and reagents were used and received from commercial sources without further purification. All reactions were carried out under a nitrogen atmosphere using standard Schlenk techniques. Liq was synthesized according to the literature route [13]. 8-Hydroxyquinoline acetone solution ( $0.5 \text{ mol L}^{-1}$ , 50 ml) and lithium hydroxide (LiOH) water solution ( $1 \text{ mol L}^{-1}$ , 12.5 ml) were poured into a two-necked flask under nitrogen. The mixture was heated ( $t = 50 \text{ }^\circ\text{C}$ ) and stirred for nearly 1 h. Then, sodium hydroxide (NaOH) water solution ( $1 \text{ mol L}^{-1}$ , 12.5 ml) was dropped into the flask, the mixture was kept on stirring for about 6 h. After reaction, the reaction mixture was filtered, and solid residue was gained. The solid residue was washed with acetone several times and further purified by acetone recrystallization. The final residue was dried in oven and purified by vacuum sublimation. Finally,  $[\text{Liq-q}^-]_2\cdot 2\text{Na}^+$  was gained as light gray-green powder in 84% yield.  $^1\text{H NMR}$  (300 MHz, DMSO,  $\delta$ ): 6.52, 6.61, 7.20, 7.29, 8.07, 8.44. IR (KBr):  $\nu = 1570, 1497, 1466, 1385, 1321, 1105, 824, 521, 445 \text{ cm}^{-1}$ . Anal. calcd for  $\text{C}_{36}\text{H}_{24}\text{O}_4\text{N}_4\text{Li}_2\text{Na}_2$ : C 67.92, N 8.81, H 3.77; found: C 66.82, N 8.68, H 3.79.

### 2.2. Properties characterization

Fluorescence spectra were recorded on LS-50B fluorescence spectrometer, and test solutions were  $[\text{Liq-q}^-]_2\cdot 2\text{Na}^+$  methanol solution ( $10^{-5} \text{ mol L}^{-1}$ ) and Liq methanol solution ( $10^{-5} \text{ mol L}^{-1}$ ). Fluorescence quantum yield was calculated according to method introduced in literature [14–16], standard sample was tris(8-hydroxyquinoline)aluminum chloroform solution ( $10^{-5} \text{ mol L}^{-1}$ ,  $\Phi_{\text{fs}} = 0.116$ ). The voltammetric curve was recorded on Autolab/PG STAT302 electrochemical system at room temperature in a solution of tetrabutylammonium perchlorate ( $n\text{-Bu}_4\text{NClO}_4$ ,  $0.1 \text{ mol L}^{-1}$ ) in dimethyl formamide (DMF) at a scan rate of  $50 \text{ mV s}^{-1}$ , the voltage increased from 0 to 1.5 V. Two platinum chips and a calomel electrode were used as working electrode, counter electrode and reference electrode, respectively, and test solutions were  $[\text{Liq-q}^-]_2\cdot 2\text{Na}^+$  methanol solution and Liq methanol solution. Fluorescence lifetime was recorded on Edinburgh Analytical Instruments F900 single-electron counting fluorescence lifetime testing instrument. Thermogravimetric (TG) and differential ther-

mal analysis (DTA) were recorded on NETZSCH STA409C thermal analyzer, protection gas and purge gas were argon at gas flow-rate between 10 and  $30 \text{ ml min}^{-1}$ , respectively, and heating rate was  $10 \text{ }^\circ\text{C min}^{-1}$ . The atomic force microscope (AFM) image of  $[\text{Liq-q}^-]_2\cdot 2\text{Na}^+$  film was recorded on SPA-300HV AFM. The X-ray photoelectron spectra (XPS) of  $[\text{Liq-q}^-]_2\cdot 2\text{Na}^+$  film was recorded on ESCALAB250 X-ray electron spectrometer.

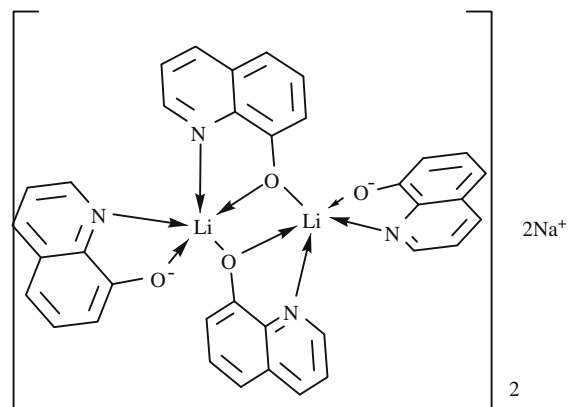


Fig. 1. The molecular structure of  $[\text{Liq-q}^-]_2\cdot 2\text{Na}^+$ .

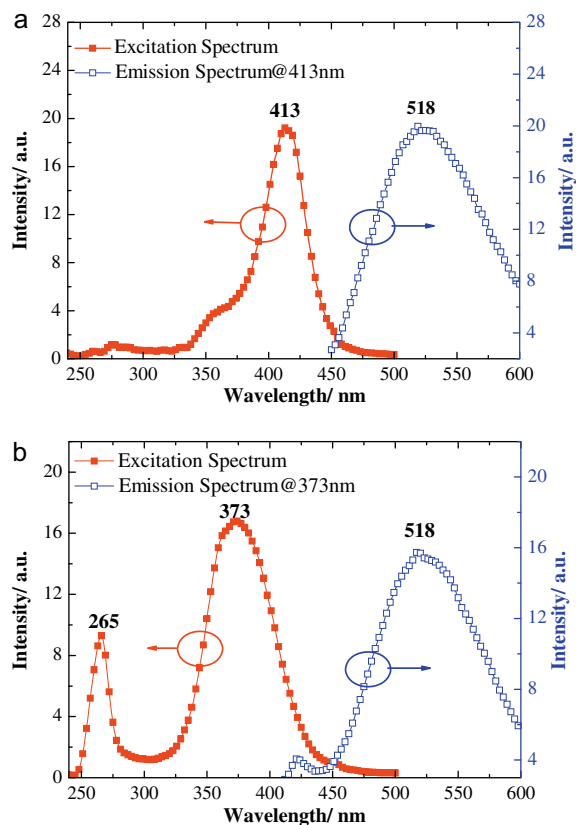


Fig. 2. The fluorescence spectra. (a)  $[\text{Liq-q}^-]_2\cdot 2\text{Na}^+$  in methanol solution; (b) Liq in methanol solution.



**Table 1**

Test data of fluorescence lifetime.

	A	B <sub>1</sub>	τ <sub>1</sub> (ns)	B <sub>2</sub>	τ <sub>2</sub> (ns)	τ (ns)
[Liq·q <sup>-</sup> ] <sub>2</sub> ·2Na <sup>+</sup>	0.6730	2.117 × 10 <sup>3</sup>	13.00	3.009 × 10 <sup>3</sup>	26.97	23.43
Liq	0.4960	2.266 × 10 <sup>3</sup>	20.66	2.710 × 10 <sup>3</sup>	8.486	16.64

### 2.3. OLED fabrication and measurements

Prepatterned indium tin oxide (ITO) substrates with an area of 4 mm × 5 mm were cleaned with deionized water, anhydrous alcohol, and anhydrous acetone in turn, and dried by nitrogen gas flow. In OLEDs, copper phthalocyanine (CuPc), N,N'-Di-[(1-naphthalenyl)-N,N'-diphenyl]-(1,1'-biphenyl)-4,4'-diamine (NPB) and aluminum (Al) were used as hole-injection layer, HTL and cathode, respectively. OLEDs were fabricated by vacuum deposition of 5 nm of CuPc, 30 nm of NPB film, 30 nm of [Liq·q<sup>-</sup>]<sub>2</sub>·2Na<sup>+</sup> or Liq and 30 nm of Al on ITO in turn. The luminance–current density–voltage–current efficiency (*L*–*J*–*U*–*η<sub>c</sub>*) characteristic of OLED was recorded on a Keithley 2400 source meter equipped with ST-900PM optical meter and integrating sphere. Electroluminescence spectra were recorded on SPR-920D fluorescence spectrometer.

## 3. Results and discussion

According to reported literature, it is suggested that the molecular structure of [Liq·q<sup>-</sup>]<sub>2</sub>·2Na<sup>+</sup> is nearly identical with that of [(Clq)(ClqH)Na]<sub>2</sub> [17]. The Li<sup>+</sup> can also conjunct with 8-hydroxyquinoline and form a similar structure of [(Clq)(ClqH)Na]<sub>2</sub>, owing to its bigger electronegativity ( $\chi = 1.0$ ) than that of Na<sup>+</sup> ( $\chi = 0.9$ ) and smaller ionic radius ( $r = 0.68 \text{ \AA}$ ) than that of Na<sup>+</sup> ( $r = 0.95 \text{ \AA}$ ). In addition, it had been reported that the actual molecular specie of Liq is [Liq<sub>2</sub>]<sup>+</sup>[Li]<sup>+</sup> [8]. During synthesis of [Liq·q<sup>-</sup>]<sub>2</sub>·2Na<sup>+</sup>, Li<sup>+</sup> conjuncts with 8-hydroxyquinoline to form [(Liq)Hq]<sub>2</sub> initially since the molecular ratio of LiOH to 8-hydroxyquinoline is 1:2. Then, [(Liq)Hq]<sub>2</sub> reacts with NaOH under heating and stirring, the H<sup>+</sup> ions of [(Liq)Hq]<sub>2</sub> are neutralized by OH<sup>-</sup> ions, the Na<sup>+</sup> ions adhere around [Liq·q<sup>-</sup>]<sub>2</sub> owing to existence of big steric hindrance in the center of [Liq·q<sup>-</sup>]<sub>2</sub>, and [Liq·q<sup>-</sup>]<sub>2</sub>·2Na<sup>+</sup> formed eventually. Hence, the molecular structure of [Liq·q<sup>-</sup>]<sub>2</sub>·2Na<sup>+</sup> is present in Fig. 1.

As shown in Fig. 1, it can be seen that [Liq·q<sup>-</sup>]<sub>2</sub>·2Na<sup>+</sup> is of stereo structure, which is distinguished from planar

**Table 2**

Test data of electrochemical property.

	E <sub>0</sub> <sup>ox</sup> (V)	E <sub>HOMO</sub> (eV) <sup>a</sup>	E <sub>LUMO</sub> (eV) <sup>c</sup>	E <sub>g</sub> (eV) <sup>b</sup>
[Liq·q <sup>-</sup> ] <sub>2</sub> ·2Na <sup>+</sup>	0.92	-5.66	-2.81	2.85
Liq	0.84	-5.58	-2.60	2.98

<sup>a</sup> The HOMO level was calculated according to the equation: E<sub>HOMO</sub> (eV) = -4.74 eV - e E<sub>0</sub><sup>ox</sup>.

<sup>b</sup> The band gap (E<sub>g</sub>) was evaluated by the energy value of crossover point of linear excitation band energy and energy axis in (hν)<sup>2</sup> vs hν curve.

<sup>c</sup> The LUMO level was calculated according to the equation: E<sub>LUMO</sub> (eV) = E<sub>HOMO</sub> + E<sub>g</sub>.

structure of Liq. Therefore, [Liq·q<sup>-</sup>]<sub>2</sub>·2Na<sup>+</sup> molecules possess large steric hindrance and long intermolecular distance between adjacent molecules.

### 3.1. Photophysical property

The fluorescence spectra of [Liq·q<sup>-</sup>]<sub>2</sub>·2Na<sup>+</sup> are shown in Fig. 2. In excitation spectrum, the peak at 413 nm (Fig. 2a) attributes to transition absorption between the Highest Occupied Molecular Orbital (HOMO) located in phenol ring and the Lowest Unoccupied Molecular Orbital (LUMO) located in pyridine ring of 8-hydroxyquinoline, and so does the peak at 373 nm for Liq (Fig. 2b) [10]. It is indicated that

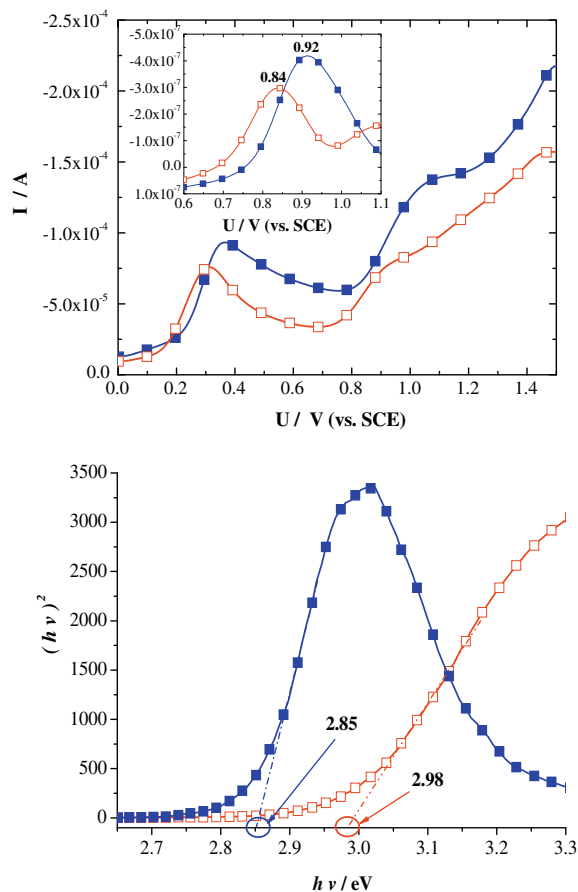


**Fig. 3.** The electrochemical property. (a) The oxidation curves: [Liq·q<sup>-</sup>]<sub>2</sub>·2Na<sup>+</sup> (—■—), Liq (—□—); the differential oxidation curves (inset): [Liq·q<sup>-</sup>]<sub>2</sub>·2Na<sup>+</sup> (—■—), Liq (—□—); (b) The (hν)<sup>2</sup> vs hν curves: [Liq·q<sup>-</sup>]<sub>2</sub>·2Na<sup>+</sup> (—■—), Liq (—□—). The (hν)<sup>2</sup> vs hν curve is determined by fluorescence excitation spectra with relationship: hνa = B(h - E<sub>g</sub>)<sup>n</sup>, where a is intensity, h is Planck's constant, ν is light wave frequency, E<sub>g</sub> is band gap, n is usually 0.5 and B is a coefficient relevant to material.

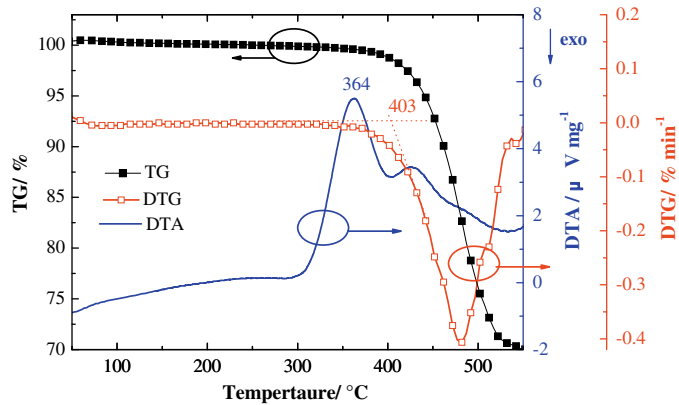


Fig. 4. The TG/DTA/DTG curves of  $[\text{Liq-q}^-]_2 \cdot 2\text{Na}^+$ .

$[\text{Liq-q}^-]_2 \cdot 2\text{Na}^+$  present a 40 nm red-shift relative to Liq in long wavelength range.

It is interesting that Liq also shows an absorption peak at 265 nm which attributes to  $\pi \rightarrow \pi^*$  transition absorption located in benzene ring [8], while this peak nearly disappears for  $[\text{Liq-q}^-]_2 \cdot 2\text{Na}^+$ . In Jablonski energy level diagram of Liq, the peaks between 265 and 373 nm attribute to  $S_0 \rightarrow S_2$  and  $S_0 \rightarrow S_1$  transition, respectively [18]. Similar to the case for inorganic semiconductor,  $\text{Na}^+$  ions in  $[\text{Liq-q}^-]_2 \cdot 2\text{Na}^+$  are reasonably regarded as  $n$ -dopant that can generate a donor level ( $E_D$ ). When  $[\text{Liq-q}^-]_2 \cdot 2\text{Na}^+$  is excited, the excited electrons from  $S_0$  level are nearly all bounded by  $E_D$  level at first and transfer to  $S_1$  level immediately, with few transfer from  $S_0$  level to  $S_2$  level [19]. Therefore, the peak at 265 nm attributing to  $S_0 \rightarrow S_2$  transition is very weak in excitation spectrum of  $[\text{Liq-q}^-]_2 \cdot 2\text{Na}^+$ . It is suggested that  $\text{Na}^+$  ions in  $[\text{Liq-q}^-]_2 \cdot 2\text{Na}^+$  ensures that most of excitation energy is consumed in HOMO  $\rightarrow$  LUMO transition to increase fluorescence quantum yield ( $\Phi_f$ ) eventually. Meanwhile, the maximum emission peak at

518 nm in fluorescence emission spectrum of  $[\text{Liq-q}^-]_2 \cdot 2\text{Na}^+$  which is similar to Liq, indicates that introduction of  $\text{Na}^+$  ions into Liq molecules had little influence on fluorescence emission.

The  $\Phi_f$  value of  $[\text{Liq-q}^-]_2 \cdot 2\text{Na}^+$  and Liq were calculated as 0.25 and 0.14, respectively, by the method introduced in literature [14–16]. Owing to stereo structure,  $[\text{Liq-q}^-]_2 \cdot 2\text{Na}^+$  molecules in solution exhibit small molecular degree of freedom, low probability of molecular collision and thus low energy loss for radiationless transition. Moreover,  $\text{Na}^+$  ions in  $[\text{Liq-q}^-]_2 \cdot 2\text{Na}^+$  can also increase  $\Phi_f$ . Therefore,  $\Phi_f$  of  $[\text{Liq-q}^-]_2 \cdot 2\text{Na}^+$  is higher than that of Liq.

The fluorescence decay curves of  $[\text{Liq-q}^-]_2 \cdot 2\text{Na}^+$  and Liq were recorded consulting Time-Related Single-Photo Counting (TCSPC) testing method and were fitted by Eq. (1). The fluorescence lifetime ( $\tau$ ) was given by Eq. (2) [20].

$$N_c(t_k) = A + B_1 \exp(-t_k/\tau_1) + B_2 \exp(-t_k/\tau_2) \quad (1)$$

$$\tau = \frac{B_1 \tau_1^2 + B_2 \tau_2^2}{B_1 \tau_1 + B_2 \tau_2} \quad (2)$$

Table 1 lists the corresponding test data. For planar structure and small intermolecular distance, excimers, which are mainly fluorescence quenching centers, are

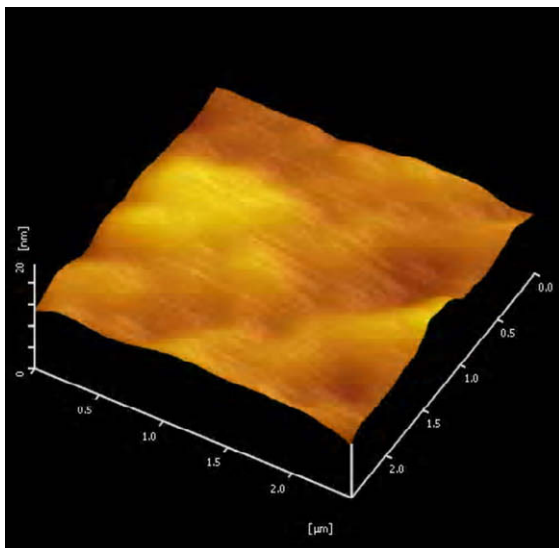


Fig. 5. The AFM image of  $[\text{Liq-q}^-]_2 \cdot 2\text{Na}^+$  film.

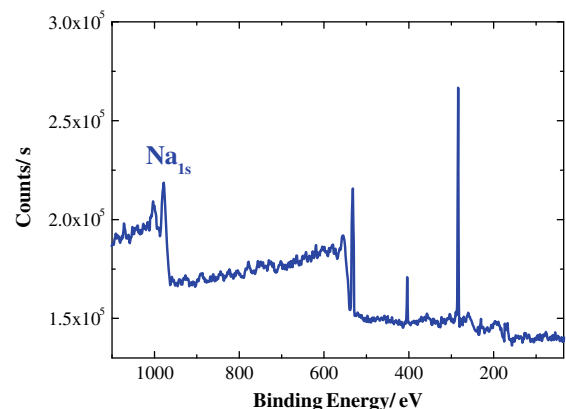


Fig. 6. The XPS spectrum of  $[\text{Liq-q}^-]_2 \cdot 2\text{Na}^+$  film.

generated when Liq is excited. However, stereo structure and big intermolecular distance of  $[\text{Liq-q}^-]_2\cdot 2\text{Na}^+$  hinder generation of excimers and prolong  $\tau$  eventually [21]. Hence, it can be seen that  $\tau$  of  $[\text{Liq-q}^-]_2\cdot 2\text{Na}^+$  (23.4 ns) is longer than that of Liq (16.64 ns).

### 3.2. Electrochemical property

The electrochemical property of  $[\text{Liq-q}^-]_2\cdot 2\text{Na}^+$  was studied according to method introduced in literature, the test results were summarized in Table 2 and Fig. 3 [22–24]. Compared with Liq,  $[\text{Liq-q}^-]_2\cdot 2\text{Na}^+$  shows smaller band gap (2.85 eV) than that of Liq (2.98 eV), which results in red-shift in fluorescence excitation spectrum, in good agreement with the conclusion gained from fluorescence spectra analysis. Wherein, the LUMO level of  $[\text{Liq-q}^-]_2\cdot 2\text{Na}^+$  (−2.81 eV) is 0.21 eV lower than that of Liq (−2.60 eV) and the HOMO level of  $[\text{Liq-q}^-]_2\cdot 2\text{Na}^+$  (−5.66 eV) is only 0.08 eV lower than that of Liq (−5.58 eV), indicating that the electron cloud density around pyridine ring of  $[\text{Liq-q}^-]_2\cdot 2\text{Na}^+$  is much lower than that of Liq, but the electron cloud density around phenol ring of  $[\text{Liq-q}^-]_2\cdot 2\text{Na}^+$  is a little smaller than that of Liq [25]. Therefore, it is presumed that  $\text{Na}^+$  ions in  $[\text{Liq-q}^-]_2\cdot 2\text{Na}^+$  molecules locate in the area between adjacent molecules and near pyridine ring.

### 3.3. Thermal property and film property

Thermal property of  $[\text{Liq-q}^-]_2\cdot 2\text{Na}^+$  was investigated by TG and DTA (Fig. 4).  $[\text{Liq-q}^-]_2\cdot 2\text{Na}^+$  presents a melting temperature ( $T_m$ ) of 364 °C in DTA curve and an onset sublimation temperature ( $T_s$ ) of 403 °C in TG curve. At the temperature lower than  $T_s$ ,  $[\text{Liq-q}^-]_2\cdot 2\text{Na}^+$  is stable and has no weight loss process, which ensures the probability that  $[\text{Liq-q}^-]_2\cdot 2\text{Na}^+$  forms amorphous film by vacuum deposition.

Additionally, the much higher molecular weight of  $[\text{Liq-q}^-]_2\cdot 2\text{Na}^+$  than Liq, may also play a role in raising its glass transition temperatures ( $T_g$ ) [26]. It is presumed that the thermal stability of  $[\text{Liq-q}^-]_2\cdot 2\text{Na}^+$  film is much better than that of Liq film, which would reduce film crystallization by Joule heat and prolong device lifetime when  $[\text{Liq-q}^-]_2\cdot 2\text{Na}^+$  is used as LEL in OLED.

By observation of AFM image, the film formability of  $[\text{Liq-q}^-]_2\cdot 2\text{Na}^+$  was characterized.  $[\text{Liq-q}^-]_2\cdot 2\text{Na}^+$  film is very compact and homogeneous (Fig. 5). Because of the connection between adjacent molecules by  $\text{Na}^+$  ions,  $[\text{Liq-q}^-]_2\cdot 2\text{Na}^+$  molecules overlap each other adhesively and deposit onto substrate uniformly during film formation by vacuum deposition. Consequently,  $[\text{Liq-q}^-]_2\cdot 2\text{Na}^+$  possesses excellent film formability.

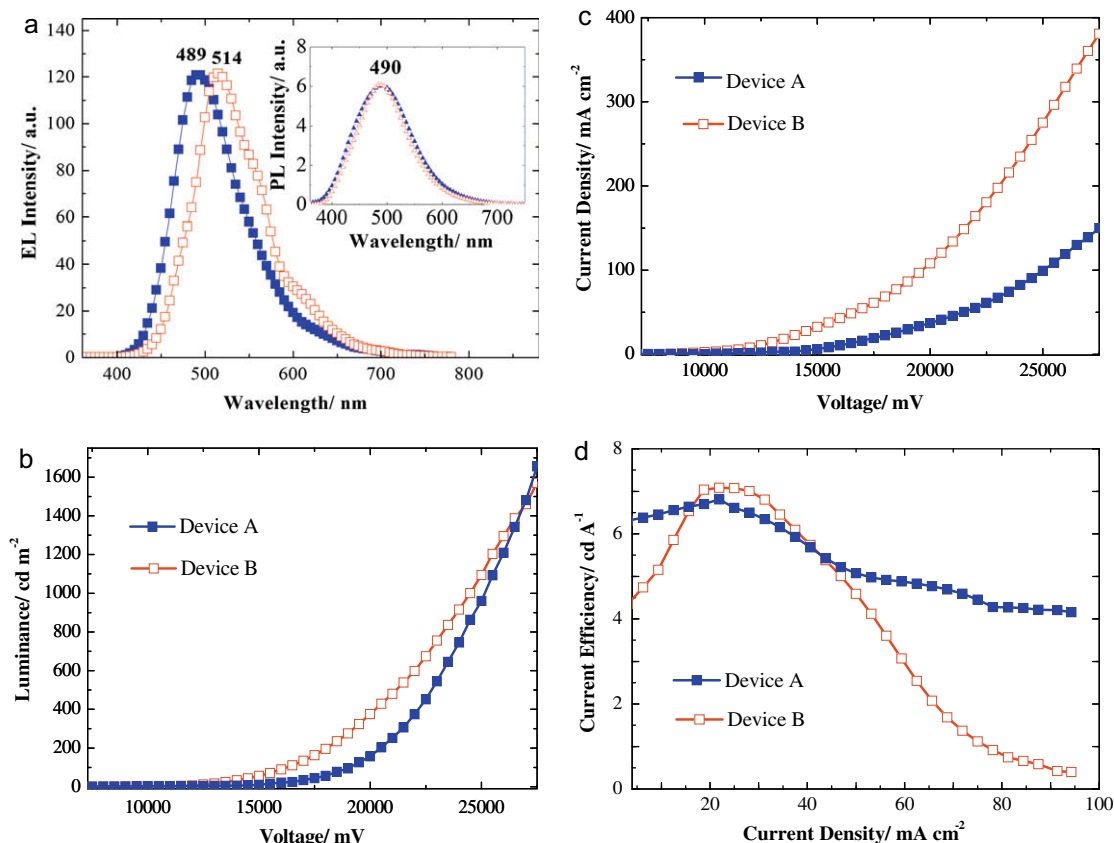


**Fig. 7.** The electroluminescence property. (a) The EL spectra of Device A (—■—) and Device B (—□—); the PL spectra (inset) of  $[\text{Liq-q}^-]_2\cdot 2\text{Na}^+$  film (—■—) and Liq film (—△—); (b) luminance ( $L$ ) versus voltage ( $U$ ) curves: Device A (—■—), Device B (—□—); (c) current density ( $J$ ) versus voltage ( $U$ ) curves: Device A (—■—), Device B (—□—); (d) current efficiency ( $\eta_c$ ) versus current density ( $J$ ) curves: Device A (—■—), Device B (—□—).

In order to identify the presence of Na<sup>+</sup> ions in [Liq-q<sup>-</sup>]<sub>2</sub>·2Na<sup>+</sup> film, the XPS of [Liq-q<sup>-</sup>]<sub>2</sub>·2Na<sup>+</sup> film was measured, as presented in Fig. 6. The peak at 1071.06 eV is attributed to Na<sub>1s</sub> binding energy, suggesting the existence of Na<sup>+</sup> ions in [Liq-q<sup>-</sup>]<sub>2</sub>·2Na<sup>+</sup> film.

### 3.4. Electroluminescence property

To illustrate electroluminescence property of [Liq-q<sup>-</sup>]<sub>2</sub>·2Na<sup>+</sup>, two OLEDs with [Liq-q<sup>-</sup>]<sub>2</sub>·2Na<sup>+</sup> and Liq as LEL separately were fabricated. The device structures were: ITO/CuPc (5 nm)/NPB (30 nm)/[Liq-q<sup>-</sup>]<sub>2</sub>·2Na<sup>+</sup> (30 nm)/Al (30 nm) (Device A) and ITO/CuPc (5 nm)/NPB (30 nm)/Liq (30 nm)/Al (30 nm) (Device B).

Owing to large steric hindrance and long intermolecular distance, it is difficult to generate excimers and exciplexes with [Liq-q<sup>-</sup>]<sub>2</sub>·2Na<sup>+</sup> as LEL in OLED. The maximum emission wavelength ( $\lambda_{\text{max}}$ ) in EL spectrum of Device A (Fig. 7a) is 489 nm, which exhibits a 25 nm blue-shift relative to Device B ( $\lambda_{\text{max}} = 514$  nm). It is indicated that [Liq-q<sup>-</sup>]<sub>2</sub>·2Na<sup>+</sup> can emit bluer light than Liq when used as LEL in OLED [8,9]. Meanwhile, it can also be seen in Fig. 7a that the EL spectrum of Device B exhibits a 24 nm red-shift relative to photoluminescence (PL) spectrum of Liq film, which is due to the presence of excimers and exciplexes in Device B. However, the EL spectrum of Device A is nearly identical with PL spectrum of [Liq-q<sup>-</sup>]<sub>2</sub>·2Na<sup>+</sup> film, verifying the fact that it is difficult to generate excimers and exciplexes when [Liq-q<sup>-</sup>]<sub>2</sub>·2Na<sup>+</sup> is used as LEL in OLED.

It has been identified by XPS that [Liq-q<sup>-</sup>]<sub>2</sub>·2Na<sup>+</sup> film contains Na<sup>+</sup> ions. In Device A, Na<sup>+</sup> ions act as electron traps. Electrons injected from cathode are captured by Na<sup>+</sup> ions at first, and recombine with holes injected from HTL to realize blue-light emission after neutralization of Na<sup>+</sup> ions [27]. Hence, it can be seen in Fig. 7b that the turn-on voltage ( $U_{\text{th}}$ ) of Device A (8.5 V) is about 1 V higher than that of Device B (7.5 V) and the luminance of Device A is a little lower than that of Device B. In OLED, excimers and exciplexes also act as fluorescence quenching centers. With increasing voltage, more excimers and exciplexes are generated in Device B, and correspondingly the luminance increment of OLED Device B is reduced. The luminance of Device A (1654 cd m<sup>-2</sup>) becomes higher than that of Device B (1570 cd m<sup>-2</sup>) when voltage increases to 27 V.

Compared with Liq, [Liq-q<sup>-</sup>]<sub>2</sub>·2Na<sup>+</sup> exhibits lower electron mobility owing to its large steric hindrance and long intermolecular distance. Hence, the current density ( $J$ ) of Device A is much smaller than that of Device B (Fig. 7c). The lower electron mobility of [Liq-q<sup>-</sup>]<sub>2</sub>·2Na<sup>+</sup> would benefit effective recombination of electrons and holes in LEL, and result in high inter quantum efficiency and current efficiency ( $\eta_{\text{C}}$ ) of OLED [28,29]. Moreover, it is more difficult in generating of excimers and exciplexes in Device A than in Device B with increasing  $J$ . As a result of the above two reasons,  $\eta_{\text{C}}$  stability of Device A is better than Device B, that is to say, the drop in  $\eta_{\text{C}}$  of Device A is much slower than that of Device B with increasing  $J$ . As presented in Fig. 7d, with increasing  $J$ , the  $\eta_{\text{C}}$  of Device A drops from 6.80 cd A<sup>-1</sup> to above 4 cd A<sup>-1</sup>, however, that of Device B drops remarkably from 7.08 cd A<sup>-1</sup> to below 1 cd A<sup>-1</sup>.

## 4. Conclusions

In summary, [Liq-q<sup>-</sup>]<sub>2</sub>·2Na<sup>+</sup> was synthesized by a simple route and its properties were characterized. Different from planar structure of Liq, stereo structure of [Liq-q<sup>-</sup>]<sub>2</sub>·2Na<sup>+</sup> results in higher  $\Phi_{\text{r}}$  and longer lifetime. Taking Liq as reference, the presence of Na<sup>+</sup> ions between adjacent [Liq-q<sup>-</sup>]<sub>2</sub>·2Na<sup>+</sup> molecules induces 40 nm red-shift in fluorescence excitation spectrum, 0.21 and 0.08 eV lowering of LUMO and HOMO, respectively. [Liq-q<sup>-</sup>]<sub>2</sub>·2Na<sup>+</sup> exhibits excellent thermal stability and film formability. When [Liq-q<sup>-</sup>]<sub>2</sub>·2Na<sup>+</sup> is used as LEL in OLED, its  $\lambda_{\text{max}}$  in EL spectrum is 489 nm and exhibits a 25 nm blue-shift relative to Liq, its luminance is higher than Liq above voltage of 27 V, and its  $\eta_{\text{C}}$  stability is better than that of Liq. In one word, [Liq-q<sup>-</sup>]<sub>2</sub>·2Na<sup>+</sup> is a novel blue-light OEM with excellent properties. In addition, [Liq-q<sup>-</sup>]<sub>2</sub>·2Na<sup>+</sup> also exhibits excellent electron injection property since [Liq-q<sup>-</sup>]<sub>2</sub>·2Na<sup>+</sup> molecules contain Na<sup>+</sup> ions. It is prospected that [Liq-q<sup>-</sup>]<sub>2</sub>·2Na<sup>+</sup> can be used as EIL in OLED to improve device performance as Liq does. This work will be published in future report.

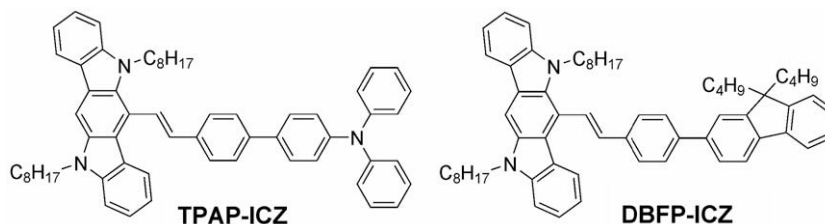
## Acknowledgments

The authors are deeply grateful to National Natural Scientific Foundation of China (20671068), Natural Science Foundation of Shanxi Province (2008011008), Shanxi Scientific Research Foundation for Returned Scholars (200523) and Scientific and Technical Key Project of Shanxi (2006031121) for financial support.

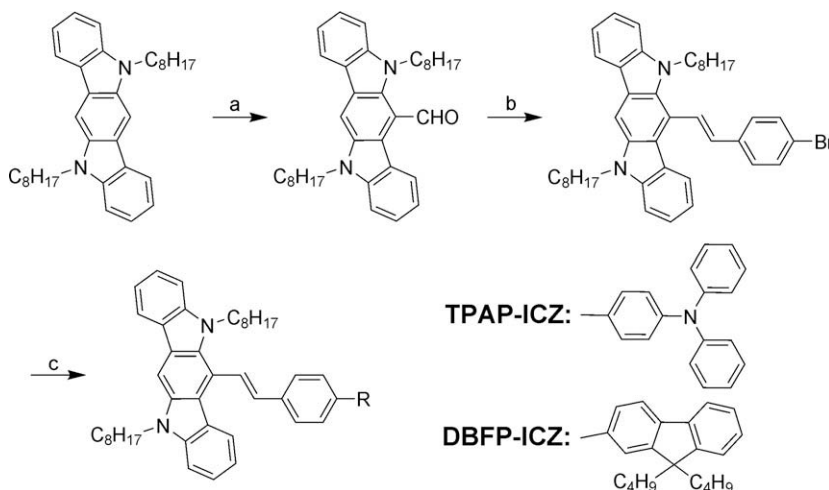
## References

- [1] J.H. Burroughes, Nature 347 (1990) 539.
- [2] W.L. Yu, J. Pei, W. Huang, A.J. Heeger, Adv. Mater. 12 (2000) 828.
- [3] H. Kageyama, K. Itano, W. Ishikawa, Y. Shirota, J. Mater. Chem. 6 (1996) 675.
- [4] Y. Kuwabara, H. Ogawa, H. Inada, N. Noma, Y. Shirota, Adv. Mater. 6 (1994) 677.
- [5] B.S. Xu, Y.Y. Hao, X.H. Fang, H. Wang, X.G. Liu, Appl. Phys. Lett. 90 (2007) 053903-1.
- [6] B.S. Xu, L.Q. Chen, X.G. Liu, H.F. Zhou, H.X. Xu, X.H. Fang, Appl. Phys. Lett. 92 (2008) 103305-1.
- [7] J. Kido, T. Matsumoto, Appl. Phys. Lett. 73 (1998) 2866.
- [8] C. Schmitz, H.W. Schmidt, M. Thelakkat, Chem. Mater. 12 (2000) 3012.
- [9] X.Y. Zheng, Y.Z. Wu, R.G. Sun, W.Q. Zhu, X.Y. Jiang, Z.L. Zhang, S.H. Xu, Thin Solid Films 478 (2005) 252.
- [10] X.H. Fang, B.S. Xu, P.D. Han, M. Chi, Y.Y. Hao, X.G. Liu, J. Mol. Struct.: THEOCHEM 848 (2008) 82.
- [11] D. Rehm, A. Weller, J. Phys. Chem. 69 (1970) 83.
- [12] F. Dechryver, Adv. Photochem. 10 (1977) 359.
- [13] B.S. Xu, Y.Y. Hao, H. Wang, H.T. Hao, H.F. Zhou, X.G. Liu, J. Li, Chinese Patent ZL031456774, 2003.
- [14] S.S. Linda, A. Padmaperuma, N. Washton, F. Endrino, G.T. Schmett, J. Marshall, D. Fogarty, P.E. Burrows, S.R. Forrest, J. Am. Chem. Soc. 123 (2001) 6300.
- [15] C.V. Bindhu, S.S. Harilal, K.V. Geetha, J. Phys. D: Appl. Phys. 29 (1996) 1074.
- [16] J.K. Yu, Y.H. Hu, Y.M. Cheng, Chem. Eur. J. 10 (2004) 6255.
- [17] A.J. Middleton, W.J. Marshall, N.S. Radu, J. Am. Chem. Soc. 125 (2003) 880.
- [18] Y.Y. Hao, H. Wang, H.T. Hao, H.F. Zhou, X.G. Liu, B.S. Xu, Chin. J. Lumin. 25 (2004) 419.
- [19] S.M. Sze, K.K. Ng, Physics of Semiconductors, third ed., Wiley and Sons, New Jersey, US, 2007.

- [20] J.R. Lakowicz, *Principles of Fluorescence Spectroscopy*, second ed., Academic/Plenum Press, New York, US, 1999.
- [21] M. Kasha, *Molecular Excitons in Small Aggregates In: Spectroscopy of the Excited States*, Plenum Press, New York, US, 1976.
- [22] J.A. Osaheni, S.A. Jenekhe, *Chem. Mater.* 7 (1995) 672.
- [23] J.L. Bredas, R. Silbey, D.S. Boudreaux, R.R. Chance, *J. Am. Chem. Soc.* 105 (1983) 6555.
- [24] (a) B.S. Xu, H.X. Xu, X.H. Fang, L.Q. Chen, H. Wang, X.G. Liu, *Org. Electron.* 9 (2008) 906;
- (b) Y.Y. Hao, B.S. Xu, Z.X. Gao, H. Wang, H.F. Zhou, X.G. Liu, *J. Mater. Sci. Technol.* 22 (2006) 1.
- [25] C.H. Chen, J.M. Shi, *Coord. Chem. Rev.* 171 (1998) 161.
- [26] P.I. Shih, C.L. Chiang, A.K. Dixit, C.K. Chen, M.C. Yuan, R.Y. Lee, C.T. Chen, E.W.G. Diau, C.F. Shu, *Org. Lett.* 8 (2006) 2799.
- [27] T.W. Lee, O.O. Park, *Adv. Mater.* 13 (2001) 1274.
- [28] T. Tsutsui, K. Yamamoto, *Jpn. J. Appl. Phys.* 38 (1999) 2799.
- [29] K. Okumoto, H. Kanno, Y. Hamaa, H. Takahashi, K. Shibata, *Appl. Phys. Lett.* 89 (2006) 063504.



**Scheme 1.** Chemical structures of luminescent compounds based on indolo[3,2-*b*]carbazole: TPAP-ICZ and DBFP-ICZ.



**Scheme 2.** Synthetic route of indolo[3,2-*b*]carbazole luminescent compounds. Reagents and conditions: (a) DMF/ $\text{POCl}_3$ , 1,2-dichloroethane; (b) *t*-BuOK, 4-bromobenzyl(triphenyl)-phosphonium, dichloromethane; (c)  $\text{Pd}(\text{PPh}_3)_4$ , THF, 2 M  $\text{Na}_2\text{CO}_3$ , 4-(diphenylamino)-phenylboronic acid or 9,9'-di-*n*-butylfluorenyl-2-boronic acid.

(as shown in Scheme 1). Electroluminescent devices using the two luminescent materials as the emitting layer were fabricated and the devices performances were reported.

## 2. Results and discussion

As shown in Scheme 2, three types of reactions, including Vilsmeier reaction, Wittig reaction, and Suzuki coupling reaction, were performed to the synthesis of luminescent materials based on indolo[3,2-*b*]carbazole. Firstly, aldehyde group was readily introduced to 6-position of indolo[3,2-*b*]carbazole through Vilsmeier reaction performed on compound **1**. And the structure of the obtained aldehyde, compound **2**, was further confirmed by X-ray single crystal analysis. Secondly, compound **3** was facily synthesized with very high yield through Wittig reaction in dry dichloromethane solutions at room temperature under ambient atmosphere. Finally, two new luminescent compounds, TPAP-ICZ and DBFP-ICZ, were obtained through Suzuki coupling reaction of compound **3** with the corresponding boronic acid. All the intermediate precursors and the final products were fully characterized by  $^1\text{H}$  NMR,  $^{13}\text{C}$  NMR, MS, and elemental analysis, and the results were well consistent with the predicted structures. The thermal properties of TPAP-ICZ and DBFP-ICZ were investigated by thermogravimetric analysis (TGA). TGA results shown the decomposition temperatures ( $T_d$ , which is corresponding

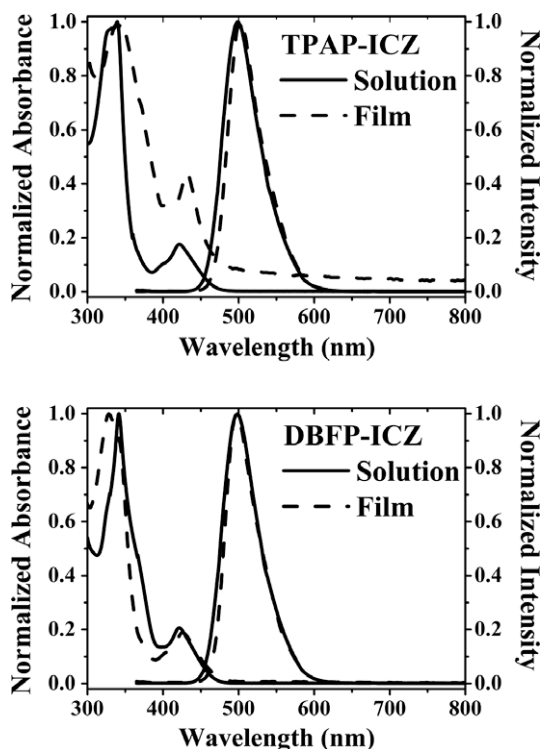
to a 5% weight loss) all above 400 °C, indicating the compounds have good thermal stabilities. However, no obvious glass transition phenomena were observed for both the two compounds according to the DSC results.

The optical properties of TPAP-ICZ and DBFP-ICZ were measured in toluene solutions ( $1 \times 10^{-5}$  M) and in the thin films deposited on quartz substrates. All the results are listed in Table 1. TPAP-ICZ and DBFP-ICZ exhibited maximum absorptions at 342 and 340 nm, respectively, in toluene solutions, which were very similar to the to the absorption maximum of 5,11-dioctylindolo[3,2-*b*]carbazole [17]. According to the literature [19], the UV absorption maximum of conjugated molecule is closely associated with its conjugation length. The very similar absorption maximum of TPAP-ICZ and DBFP-ICZ may indicate that the introduction of functional groups on 6-position of indolo[3,2-*b*]carbazole almost have no effect on the conjugation length of the whole molecule even though the functional groups were linked on 6-position of indolo[3,2-*b*]carbazole through double bond. Therefore, the absorption characteristics of TPAP-ICZ and DBFP-ICZ should be mainly accounted to the indolo[3,2-*b*]carbazole core. The absorption maximum of TPAP-ICZ and DBFP-ICZ is assigned to the second electronic excitation, while the weak absorption around ~420 nm is correspond to the  $S_0$ - $S_1$  electronic transition [20]. The optical bandgaps ( $E_g$ ) of TPAP-ICZ and DBFP-ICZ were 2.62 and 2.63 eV,

**Table 1**

Optical properties, energy band gaps and thermal stability of TPAP-ICZ and DBFP-ICZ.

Compounds	$\lambda_{ab}^{max}$ (nm)		$\lambda_{cm}^{max}$ (nm)		$E_g^{opt}$ (eV) <sup>b</sup>	$E_{ox}^{onset}$ (V)	HOMO (eV) <sup>c</sup>	LUMO (eV)	$T_d$ (°C) <sup>d</sup>
	Solution <sup>a</sup>	Film	Solution <sup>a</sup>	Film					
TPAP-ICZ	342	346	499	498	2.62	0.95	-5.10	-2.48	420
DBFP-ICZ	340	330	499	503	2.63	0.94	-5.10	-2.47	408

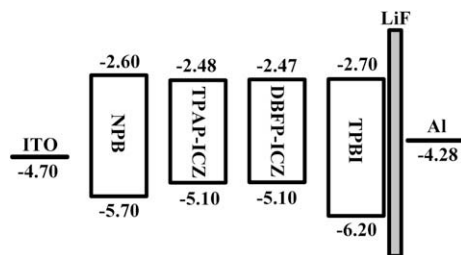
<sup>a</sup> In dilute toluene solution ( $1 \times 10^{-5}$  M).<sup>b</sup>  $E_g^{opt}$  values were determined from UV-vis absorption spectra in solution with toluene.<sup>c</sup> The HOMO levels of the compounds were determined by using the onset positions of the oxidation.<sup>d</sup> Decomposition temperature observed from TGA correspond to a 5% weight loss at  $10^\circ\text{C min}^{-1}$  under nitrogen.**Fig. 1.** Photoluminescent and UV-vis absorption spectra of TPAP-ICZ and DBFP-ICZ both in solutions and in thin films.

respectively, which were estimated from the long-wavelength absorption edge. The photoluminescent (PL) spectra of TPAP-ICZ and DBFP-ICZ are shown in Fig. 1. The two compounds were highly fluorescent both in solution and in the solid state. The fluorescent quantum yields of TPAP-ICZ and DBFP-ICZ were 0.40 and 0.45, respectively, in solution with 9,10-diphenylanthracene ( $\phi_F = 1.0$ ) as the reference. According to the PL spectra, they all exhibit narrow emission peaks located at 499 nm in toluene solution. Maybe we can presume that the emission and absorption wavelengths are controlled mostly by the indolo[3,2-*b*]carbazole unit according to their very similar optical properties. Moreover, the two compounds exhibited similar  $\lambda_{max}$  of emission both in solution and in the thin films, which indicated that there were minimal intermolecular interactions in the ground state in the films [21]. Furthermore, the two compounds showed narrow FWHM (full width at half maximum) in the thin films (which are 55 nm for TPAP-

ICZ and 57 nm for DBFP-ICZ, respectively.), thus had good color purity.

The electrochemical properties of TPAP-ICZ and DBFP-ICZ were studied by cyclic voltammetry (CV) in dichloromethane solutions with Ag/AgCl as reference electrode. All the two compounds are electrochemically reversible (as shown in Figs. S1 and S2). We also measured the CV properties of 5,11-dioctylindolo[3,2-*b*]carbazole (Fig. S3). According to the CV of 5,11-dioctylindolo[3,2-*b*]carbazole, the first and third pair of reversible peaks of TPAP-ICZ and the first and second pair of reversible peaks of DBFP-ICZ should be accounted to 5,11-dioctylindolo[3,2-*b*]carbazole, the second pair of reversible peak of TPAP-ICZ should be assigned to the triphenylamine group. The onset oxidation potentials ( $E_{ox}^{onset}$ ) of TPAP-ICZ and DBFP-ICZ were both 0.70 V. Accordingly, the highest occupied molecular orbital (HOMO) energy levels of TPAP-ICZ and DBFP-ICZ were estimated to be both 5.10 eV ( $\text{HOMO} = E_{ox}^{onset} + 4.4$  eV). The lowest unoccupied molecular orbital (LUMO) energy levels of TPAP-ICZ and DBFP-ICZ were estimated to be -2.48 and -2.47 eV, respectively, which were calculated from the HOMO energy level and energy bandgap ( $E_g$ ) determined from the threshold of the optical absorption ( $\text{LUMO} = \text{HOMO} + E_g$  eV).

To evaluate the utility of the two indolo[3,2-*b*]carbazole derivatives as the emitting layer (EML) in the EL devices, we fabricated EL devices with the configuration of indium tin oxide (ITO)/4,4'-bis[*N*-(1-naphthyl)-*N*-phenylamino]biphenyl (NPB) (30 nm)/EML (40 nm)/1,3,5-*tris*(*N*-phenylbenzimidazol-2-yl)benzene (TPBI) (40 nm)/LiF (1 nm)/Al (80 nm). NPB (HOMO = -5.70 eV, LUMO = -2.60 eV) [22] was used as the hole-transporting layer (HTL); the indolo[3,2-*b*]carbazole derivatives were used as the emitting layer (EML); TPBI (HOMO = -6.20 eV, LUMO = -2.70 eV) [23] was used as the electron-transporting layer, and LiF

**Fig. 2.** The band diagram of the ITO/NPB/TPAP-ICZ or DBFP-ICZ/TPBI/LiF/Al EL devices.

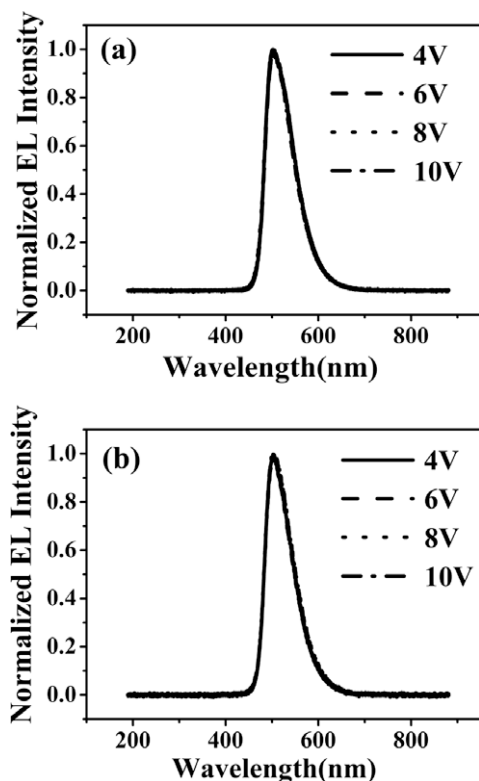


Fig. 3. The EL spectra of (a) TPAP-ICZ and (b) DBFP-ICZ.

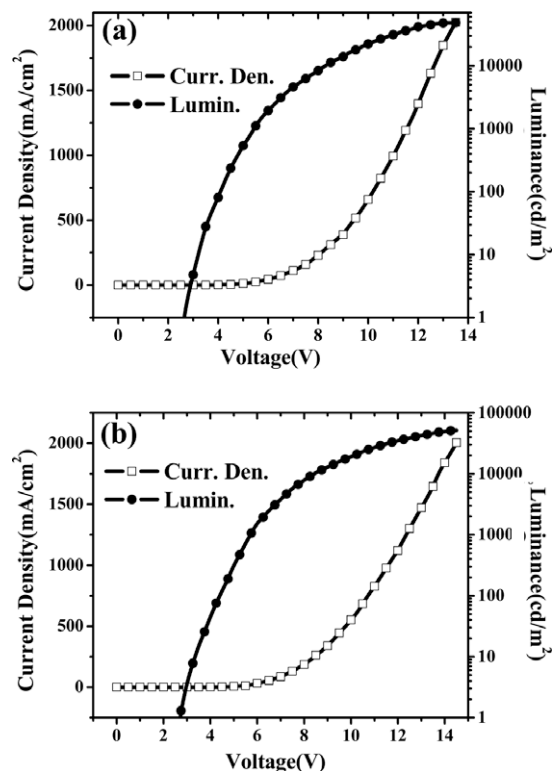


Fig. 4. The current density–voltage–luminescence ( $J$ – $V$ – $L$ ) characteristics of the EL devices: (a) TPAP-ICZ; (b) DBFP-ICZ.

was the electron-injection layer. The hypothetical band diagrams of the EL devices were depicted in Fig. 2. According to the band diagrams, there were hole transport barriers about 0.60 eV both at the NPB/TPAP-ICZ and NPB/DBFP-ICZ interfaces. In contrast, the barrier at the TPAP-ICZ/TPBI and DBFP-ICZ/TPBI interfaces for the electron transport were  $-0.22$  and  $-0.23$  eV, respectively. Therefore, for both TPAP-ICZ and DBFP-ICZ, the electrons could be more easily injected to the emitting layer than the holes. This is beneficial to the improvement of the balance of charge carrier injection and transport, and thus the hole-electron recombination becomes more efficient in emitting layer.

The EL spectra from the device are illustrated in Fig. 3. No changes are observed in the EL spectra upon being operated at various driving voltages. Notably, all the EL devices show similar peaks with that in PL spectra of the thin films. The EL maximum emission was 502 nm with narrow FWHM of 67 nm for TPAP-ICZ, while 503 nm and 70 nm for DBFP-ICZ, respectively. This indicates that both PL and EL originate from the same radiative-decay process of the single excitons [24–26].

The current density–voltage–luminescence ( $J$ – $V$ – $L$ ) characteristics of the EL devices are illustrated in Fig. 4. The EL devices exhibited excellent EL performances and all the results are summarized in Table 2. The EL devices exhibit very low turn-on voltages (brightness =  $1 \text{ cd m}^{-2}$ ) with 2.90 V for TPAP-ICZ and 2.65 V for DBFP-ICZ, respectively. The maximum luminance efficiency and maximum brightness of the EL device using TPAP-ICZ as the emitter

Table 2

Summary of EL devices performances.

Compounds	TPAP-ICZ	DBFP-ICZ
Turn-on voltage (V) <sup>a</sup>	2.9	2.65
Maximal brightness ( $\text{cd m}^{-2}$ )	65739 <sup>b</sup>	68729 <sup>c</sup>
Maximal luminance efficiency ( $\text{lm W}^{-1}$ )	6.74	7.92
Maximal current efficiency ( $\text{cd A}^{-1}$ )	6.90	7.06
Maximal external quantum efficiency (%)	2.39	2.79
EL $\lambda_{\text{max}}$ (nm) <sup>d</sup>	502	503
CIE <sup>d</sup> (x, y)	(0.224, 0.562)	(0.214, 0.568)
fwhm (nm)	70	67

<sup>a</sup> Recorded at  $1 \text{ cd m}^{-2}$ .

<sup>b</sup> Recorded at 13.5 V.

<sup>c</sup> Recorded at 13 V.

<sup>d</sup> Recorded at 8.

are  $6.90 \text{ cd A}^{-1}$  and  $65739 \text{ cd m}^{-2}$  (at 13.5 V), respectively, with the external quantum efficiency of 2.39% and the Commission Internationale de L'Eclairage (CIE) color coordinates located at (0.224, 0.562), while those of the EL device using DBFP-ICZ as the emitter were  $7.06 \text{ cd A}^{-1}$  and  $68729 \text{ cd m}^{-2}$  (at 13 V), respectively, with the external quantum efficiency of 2.79% and the CIE color coordinates of (0.214, 0.568). Given that the entire device fabrication and characterization were carried out in air without encapsulation, the unoptimized EL efficiency values reported here were remarkably high. Further improvements would



likely be obtained through the optimization of the device architectures and layer thickness. Therefore, we concluded that indolo[3,2-*b*]carbazole is a very promising block for highly efficient electroluminescent materials.

### 3. Conclusions

In summary, new efficient luminescent materials have been designed and synthesized through peripheral substitutions at 6-position of indolo[3,2-*b*]carbazole. They are highly luminescent both in solutions and in films. Electroluminescent devices with indolo[3,2-*b*]carbazole luminescent materials as the emitting layer were fabricated and exhibited excellent EL performance with low turn-on voltage, high brightness, and high efficiency. Our results demonstrated that indolo[3,2-*b*]carbazole is a very promising building block for the design of new efficient electroluminescent materials.

## 4. Experimental

### 4.1. Materials and characterization

5,11-di-*n*-octylindolo[3,2-*b*]carbazole (**1**) [17], 4-(Diphenylamino)phenylboronic acid [27], and 9,9'-di-*n*-butylfluorenyl-2-boronic acid [28] were synthesized according to the literature. The  $^1\text{H}$  NMR and  $^{13}\text{C}$  NMR spectra were obtained on a Bruker AV400 spectrometer. Elemental analyses were performed with a PE2400 elemental analyzer. UV-vis spectra were measured on a TU-1800SPC spectrophotometer. The fluorescence spectra measurements were performed with a Hitachi 4500 FL spectrophotometer. Thermal gravimetric analysis (TGA) and differential scanning calorimetry (DSC) measurements were carried out under a nitrogen atmosphere at a heating rate of  $10\text{ }^\circ\text{C min}^{-1}$  with a Perkin-Elmer Diamond thermogravimetric analyzer and a Perkin-Elmer Diamond DSC thermal analysis system, respectively. Electrochemical experiment were performed by using an EG&G model 283 electrochemical system. A platinum-disk working electrode, a platinum-wire auxiliary electrode, and an Ag/AgCl reference electrode were used in a three electrode configuration. The concentration of the samples in dichloromethane was 1.0 mM and  $\text{Bu}_4\text{NClO}_4$  (0.1 M in dichloromethane) was used as supporting electrolyte with 50 mV/s scan speed.

### 4.2. Synthesis of 5,11-di-*n*-octyl-6-formyl-indolo[3,2-*b*]carbazole (**2**)

$\text{POCl}_3$  (0.22 mL, 2.4 mmol) was slowly dropped into a dry 100 mL flask, which contained DMF (0.19 mL, 2.4 mmol) and has been cooled with ice water bath in advance. The mixture was stirring while  $\text{POCl}_3$  was dropping. A whole white solid bulk appeared in the flask soon end of dropping. 5,11-Di-*n*-octylindolo[3,2-*b*]carbazole (**1**) (962 mg, 2.0 mmol) dissolved in 30 mL 1, 2-dichloroethane was added to the flask, then ice water bath was removed. After the white solid bulk disappeared under room temperature, the reaction mixture was stirred and refluxed for about 24 h. The 1, 2-dichloromethane was evaporated out after completion of

the reaction. The remains were poured into 100 mL ice water. Sodium carbonate aqueous solution was added to modify the pH under vigorously stirring. After the pH at 8, continuously stirring was kept for about 1 h. The suspension was extracted with dichloromethane and washed with water and brine. The organic extracts were dried over anhydrous sodium sulfate. After removing the solvents under reduced pressure, the residue was purified by flash chromatography with light petroleum/dichloromethane (4:1) as eluent, and gave compound **2** (Yield: 477 mg, 40.8%) as orange solid.  $^1\text{H}$  NMR ( $\text{CDCl}_3$ , 400 MHz, ppm)  $\delta$ : 0.83–0.86 (m, 6H), 1.23–1.46 (m, 20H), 1.79–1.83 (m, 2H), 1.90–1.95 (m, 2H), 4.42–4.46 (t,  $J = 7.29$  Hz, 2H), 4.55–4.59 (t,  $J = 7.80$  Hz, 2H), 7.28–7.32 (m, 2H), 7.45–7.56 (m, 4H), 8.19 (d,  $J = 7.66$  Hz, 1H), 8.27 (s, 1H), 8.61 (d,  $J = 8.14$  Hz, 1H), 11.35 (s, 1H).  $^{13}\text{C}$  NMR ( $\text{CDCl}_3$ , 100.61 MHz, ppm)  $\delta$ : 13.65, 22.11, 26.32, 26.88, 28.20, 28.44, 28.70, 28.83, 28.92, 31.27, 31.32, 42.68, 46.79, 104.82, 108.27, 109.33, 115.54, 118.34, 119.04, 119.35, 121.25, 121.83, 122.20, 124.41, 124.90, 126.13, 135.19, 135.48, 141.65, 142.92, 189.81. Anal. Calcd for  $\text{C}_{35}\text{H}_{44}\text{N}_2\text{O}$ : C, 82.63; H, 8.72; N, 5.51. Found: C, 82.61; H, 8.69; N, 5.50. Crystal structure of compound **2**:  $\text{C}_{35}\text{H}_{44}\text{N}_2\text{O}$ ,  $M = 508.72$ , monoclinic, space group  $P2_1/c$ ,  $a = 15.566(5)\text{ \AA}$ ,  $b = 5.434(5)\text{ \AA}$ ,  $c = 18.950(5)\text{ \AA}$ ,  $\beta = 102.089(5)^\circ$ ,  $V = 1567.4(16)\text{ \AA}^3$ ,  $Z = 2$ ,  $T = 293(2)\text{ K}$ ,  $D_c = 1.078\text{ g/cm}^3$ . Unique 3592 reflections were measured by Bruker APEX2 CCD area-detector diffractometer using graphite monochromated Mo- $K\alpha$  radiations ( $\lambda = 0.71069\text{ \AA}$ ,  $2\theta < 55^\circ$ ). The structure was solved by a direct method and refined by full-matrix least-squares calculations against  $F^2$  with absorption corrections (SAD-ABS) using a program package SHELXL-97 (Sheldrick, 1997). Non-hydrogen atoms were refined anisotropically. Hydrogen atoms were placed in geometrically idealized positions and constrained to ride on their parent atoms with C–H distance in the range 0.93–0.97  $\text{\AA}$ . The final  $R_1(F) = 0.0779$  and  $wR(F^2) = 0.2117$ , for 1156 ( $I > 2\sigma(I)$ ) and independent 3592 reflections, respectively. Parameters were 182 and  $S = 0.919$ . Max shift/esd = 0.000. CCDC Reference Number 626638.

### 4.3. Synthesis of 5,11-di-*n*-octyl-6-(4-bromophenylethylenyl)indolo[3,2-*b*]carbazole (**3**)

Compound **2** (1.275 g, 2.5 mmol) and 4-bromobenzyl(triphenyl)phosphonium bromide (1.926 g, 3.75 mmol) was added to a dry 250 mL flask, and then added 100 mL dried dichloromethane. The mixture was stirred at room temperature and *t*-BuOK (2.526 g, 22.55 mmol) was slowly added to the mixture. The reaction mixture was stirred at room temperature for about 24 h. Then the suspension was extracted with dichloromethane and washed with water and brine. The organic extracts were dried over anhydrous sodium sulfate. After removing the solvents, The crude product was chromatographed on silica gel using petroleum/dichloromethane (4:1) as eluent, and gave compound **3** (Yield: 1.431 g, 86.3%) as yellow solid.  $^1\text{H}$  NMR ( $\text{CDCl}_3$ , 400 MHz, ppm)  $\delta$ : 0.84–0.88 (m, 6H), 1.14–1.31 (m, 16H), 1.38–1.39 (m, 2H), 1.45–1.47 (m, 2H), 1.73–1.76 (m, 2H), 1.93–1.97 (m, 2H), 4.38–4.41 (t,

$J = 7.32$  Hz,  $J = 7.23$  Hz, 2H), 4.45–4.39 (t,  $J = 8.02$  Hz,  $J = 7.88$  Hz, 2H), 6.93–6.97 (m, 1H), 7.04–7.08 (m, 1H), 7.21–7.25 (m, 1H), 7.37–7.47 (m, 4H), 7.49–7.61 (m, 4H), 7.97–8.02 (m, 2H), 8.18–8.25 (dd,  $J = 7.65$  Hz,  $J = 7.94$  Hz, 2H).  $^{13}\text{C}$  NMR ( $\text{CDCl}_3$ , 100.61 MHz, ppm)  $\delta$ : 14.06, 22.61, 27.07, 27.42, 28.76, 29.22, 29.25, 29.46, 31.74, 31.84, 43.19, 45.08, 97.88, 108.21, 108.77, 115.76, 117.84, 118.30, 119.97, 120.98, 121.94, 122.86, 123.21, 123.79, 125.26, 125.39, 125.88, 127.95, 132.14, 133.30, 134.85, 135.96, 136.01, 141.80, 142.65. MALDI-TOF,  $m/z$ : cal: 660.31, found: 660.2. Anal. Calcd for  $\text{C}_{42}\text{H}_{49}\text{BrN}_2$ : C, 76.23; H, 7.46; N, 4.23. Found: C, 76.60; H, 7.56; N, 4.12.

#### 4.4. Synthesis of 5,11-di-*n*-octyl-6-[4-(triphenylamino)-phenylethynyl]indolo[3,2-*b*]-carbazole (TPAP-ICZ)

Compound **3** (500 mg, 0.76 mmol), 4-(Diphenylamino)-phenylboronic acid (289 mg, 1 mmol), tetrakis(triphenylphosphine)palladium (0.116 g, 0.1 mmol), 20 mL THF and 10 mL (2 M) sodium carbonate aqueous solution under nitrogen, were added to a three-necked flask equipped with a magnetic stirrer, a reflux condenser, and a nitrogen input tube. The reaction mixture was refluxed in an oil bath under nitrogen. A yellow product was obtained after heating and stirring for about 24 h. The mixture was cooled to room temperature, extracted with 100 mL dichloromethane, washed with water and dried over anhydrous sodium sulfate. After removing the solvent under reduced pressure, the crude product was chromatographed on silica gel using petroleum/dichloromethane (4:1) as eluent, and gave TPAP-ICZ (Yield: 588 mg, 93.6%) as a yellow solid.  $^1\text{H}$  NMR ( $\text{CDCl}_3$ , 400 MHz, ppm)  $\delta$ : 0.78–0.81 (m, 3H), 0.84–0.88 (m, 3H), 1.12–1.35 (m, 16H), 1.37–1.45 (m, 2H), 1.47–1.51 (m, 2H), 1.75–1.77 (m, 2H), 1.93–1.96 (m, 2H), 4.37–4.41 (t,  $J = 7.11$  Hz,  $J = 7.12$  Hz, 2H), 4.49–4.53 (t,  $J = 7.70$  Hz,  $J = 7.76$  Hz, 2H), 7.01–7.08 (m, 4H), 7.14–7.18 (m, 7H), 7.26–7.30 (m, 4H), 7.37–7.47 (m, 4H), 7.54–7.56 (m, 2H), 7.66–7.71 (m, 4H), 7.96–8.03 (m, 2H), 8.19 (d,  $J = 7.65$  Hz, 1H), 8.34 (d,  $J = 7.93$  Hz, 1H).  $^{13}\text{C}$  NMR ( $\text{CDCl}_3$ , 100.61 MHz, ppm)  $\delta$ : 14.05, 14.07, 22.61, 22.63, 27.09, 27.44, 28.77, 29.23, 29.28, 29.32, 29.48, 29.49, 31.75, 31.86, 43.18, 45.10, 97.67, 108.11, 108.76, 116.33, 117.84, 118.21, 119.95, 121.10, 122.92, 123.03, 123.07, 123.35, 123.72, 123.83, 124.21, 124.52, 125.19, 125.80, 126.95, 127.05, 127.59, 129.31, 133.40, 134.44, 135.58, 135.65, 136.05, 140.28, 141.80, 142.65, 147.37, 147.66. MALDI-TOF,  $m/z$ : cal: 825.5, found: 825.5. Anal. Calcd for  $\text{C}_{60}\text{H}_{63}\text{N}_3$ : C, 87.23; H, 7.69; N, 5.09. Found: C, 87.62; H, 7.75; N, 5.01.

#### 4.5. Synthesis of 5,11-di-*n*-octyl-6-[4-(9,9'-di-*n*-butylfluorenyl)phenylethynyl]-indolo[3,2-*b*]carbazole (DBFP-ICZ)

DBFP-ICZ was obtained by a similar procedure as for TPAP-ICZ. Yield: 567 mg, 86.8%.  $^1\text{H}$  NMR ( $\text{CDCl}_3$ , 400 MHz, ppm)  $\delta$ : 0.63–0.72 (m, 8H), 0.79–0.82 (m, 3H), 0.85–0.88 (m, 3H), 1.06–1.16 (m, 5H), 1.19–1.34 (m, 16H), 1.36–1.44 (m, 2H), 1.46–1.50 (m, 2H), 1.53 (s, 1H), 1.76–1.80 (m, 2H), 1.92–2.00 (m, 2H), 2.04–2.06 (m, 4H), 4.41–4.54 (m, 4H), 7.06–7.10 (m, 2H), 7.30–7.50 (m, 8H),

7.64–7.67 (m, 2H), 7.74–7.81 (m, 6H), 7.98–8.09 (m, 2H), 8.21 (d,  $J = 7.70$  Hz, 1H), 8.36 (d,  $J = 7.95$  Hz, 1H).  $^{13}\text{C}$  NMR ( $\text{CDCl}_3$ , 100.61 MHz, ppm)  $\delta$ : 13.82, 13.85, 14.06, 14.08, 22.59, 22.61, 22.63, 33.10, 26.02, 27.11, 27.45, 28.81, 29.24, 29.50, 31.73, 31.86, 40.29, 43.17, 45.06, 55.12, 108.16, 108.80, 117.87, 118.27, 119.77, 120.01, 121.22, 122.91, 123.05, 123.36, 124.40, 125.19, 125.81, 126.83, 126.98, 127.11, 127.63, 135.69, 135.91, 139.42, 140.66, 140.75, 141.31, 151.00, 151.47. MALDI-TOF,  $m/z$ : cal: 858.59, found: 858.6. Anal. Calcd for  $\text{C}_{63}\text{H}_{74}\text{N}_2$ : C, 88.06; H, 8.68; N, 3.26. Found: C, 88.44; H, 8.77; N, 3.17.

#### 4.6. Device fabrication and characterization

Triple-layer devices were fabricated with a configuration of indium tin oxide (ITO)/NPB (30 nm)/EML (40 nm)/TPBI (40 nm)/LiF (1 nm)/Al (80 nm). The ITO glass was cleaned in ultrasonic baths of detergent, deionized water and acetone in sequence, and followed oxygen plasma cleaning. The organic films and metal electrode were sequentially deposited on the substrate by thermal evaporation under a vacuum of  $10^{-6}$  Torr. The deposition rates were 2–3 Å/s for the organic materials and 5–7 Å/s for the cathode metals. The emitting area of the device was 4 mm<sup>2</sup>. The thickness of films was measured by a Dektak surface profilometer. The EL spectra and current–voltage–luminance ( $J$ – $L$ – $V$ ) characteristics were measured with a Spectrascan PR650 photometer and a computer-controlled DC power supply. All the measurements of the devices were carried out under ambient conditions.

#### Acknowledgements

This work was supported by the National Natural Science Foundation (50721002, 90401028, 90401028) and 973 program (2004CB619002) of China. The authors are very grateful to Prof. Wenping Hu (Institute of Chemistry, Chinese Academy of Sciences) for helpful suggestions and discussions.

#### Appendix A. Supplementary data

Supplementary data associated with this article can be found, in the online version, at doi:10.1016/j.orgel.2009.04.019.

#### References

- [1] C.W. Tang, S.A. Van Slyke, Appl. Phys. Lett. 51 (1987) 913.
- [2] J.H. Burroughes, D.D.C. Bradley, A.R. Brown, R.N. Marks, K. Mackay, R.H. Friend, P.L. Burn, A.B. Holmes, Nature 347 (1990) 539.
- [3] S.A. Van Slyke, C.H. Chen, C.W. Tang, Appl. Phys. Lett. 69 (1996) 2160.
- [4] A.H. Tullo, Chem. Eng. News 78 (2000) 20.
- [5] A.H. Tullo, Chem. Eng. News 79 (2001) 49.
- [6] L.S. Hung, C.W. Tang, M.G. Masson, Appl. Phys. Lett. 70 (1997) 152.
- [7] T. Tsutsui, Mater. Res. Bull. 22 (1997) 39.
- [8] C.-C. Wu, Y.T. Lin, K.-T. Wong, R.T. Chen, Y.-Y. Chien, Adv. Mater. 16 (2006) 1582.
- [9] X.-T. Tao, Y.-D. Zhang, T. Wada, H. Sasade, H. Suzuki, T. Watanabe, S. Miyata, Adv. Mater. 10 (1998) 226.
- [10] K. Brunner, A. van Dijken, H. Börner, J.J.A. Bastiaansen, N.M.M. Kiggen, B.M.W. Langeveld, J. Am. Chem. Soc. 126 (2004) 6035.
- [11] J. Li, D. Liu, C.-S. Lee, H.L. Kwong, S. Lee, Chem. Mater. 17 (2005) 1208.

- [12] N. Drolet, J.-F. Morin, N. Leclerc, S. Wakim, Y. Tao, M. Leclerc, *Adv. Funct. Mater.* 15 (2005) 1671.
- [13] M. Sonntag, K. Kreger, D. Hanft, P. Strohrriegel, S. Setayesh, D. De Leeuw, *Chem. Mater.* 17 (2005) 3031.
- [14] N.-X. Hu, S. Xie, Z. Popovic, B. Ong, A.-M. Hor, *J. Am. Chem. Soc.* 121 (1999) 5097.
- [15] H.P. Zhao, X.T. Tao, F.Z. Wang, Y. Ren, X.Q. Sun, J.X. Yang, Y.X. Yan, D.C. Zou, X. Zhao, M.H. Jiang, *Chem. Phys. Lett.* 439 (2007) 132.
- [16] H.P. Zhao, X.T. Tao, P. Wang, Y. Ren, J.X. Yang, Y.X. Yan, C.X. Yuan, H.J. Liu, D.C. Zou, M.H. Jiang, *Org. Electron.* 8 (2007) 673.
- [17] Y. Wu, Y. Li, S. Gardner, B.S. Ong, *J. Am. Chem. Soc.* 127 (2005) 614.
- [18] Y. Li, Y. Wu, S. Gardner, B.S. Ong, *Adv. Mater.* 17 (2005) 849.
- [19] P.-L.T. Boudreault, S. Wakim, N. Blouin, M. Simard, C. Tessier, Y. Tao, M. Leclerc, *J. Am. Chem. Soc.* 129 (2007) 9125.
- [20] M. Belletête, N. Blouin, P.-L.T. Boudreault, M. Leclerc, G. Durocher, *J. Phys. Chem. A* 110 (2006) 13696.
- [21] Y.H. Kim, H.C. Jeong, S.H. Kim, K. Yang, S.K. Kwon, *Adv. Funct. Mater.* 15 (2005) 1799.
- [22] D.F. O'Brien, P.E. Burrows, S.R. Forrest, B.E. Koene, D.E. Loy, M.E. Thompson, *Adv. Mater.* 10 (1998) 1108.
- [23] Z. Gao, C.S. Lee, I. Bello, S.T. Lee, R.M. Chen, T.Y. Luh, J. Shi, C.W. Tang, *Appl. Phys. Lett.* 74 (1999) 865.
- [24] S. Wakim, J. Bouchard, M. Simard, N. Drolet, Y. Tao, M. Leclerc, *Chem. Mater.* 16 (2004) 4386.
- [25] P.I. Shih, Y.H. Tseng, F.I. Wu, A.K. Dixit, C.F. Shu, *Adv. Funct. Mater.* 16 (2006) 1582.
- [26] Z. Zhao, J.H. Li, P. Lu, Y. Yang, *Adv. Funct. Mater.* 17 (2007) 2203.
- [27] M.-Y. Chou, M.-K. Leung, Y.O. Su, C.L. Chiang, C.-C. Lin, J.-H. Liu, C.-K. Kuo, C.-Y. Mou, *Chem. Mater.* 16 (2004) 654.
- [28] D. Katsis, Y.H. Geng, J.J. Ou, S.W. Culligan, A. Trajkovska, S.H. Chen, L.J. Rothberg, *Chem. Mater.* 14 (2002) 1332.

It is advantageous, or may even be essential, to certain applications to employ materials with large band gap as transport or host materials. For instance, *N,N'*-bis(1-naphthyl)-*N,N'*-diphenyl-1,1'-biphenyl-4,4'-diamine ( $\alpha$ -NPD), 4,4'-Bis(*N*-carbazolyl)-1,1'-biphenyl (CBP) and other aromatic diamine or carbazole derivatives are commonly used as hole transport materials and/or as ambipolar wide band gap hosts for phosphorescent dopants in organic light emitting diodes (OLEDs) [13]. P-type doping of these materials with F<sub>4</sub>-TCNQ has been demonstrated, but is not as efficient as in the phthalocyanines. For  $\alpha$ -NPD, the HOMO energy is 280 meV lower than the LUMO energy of F<sub>4</sub>-TCNQ, resulting in a 40% lower doping efficiency when compared to F<sub>4</sub>-TCNQ doping of ZnPc [8]. Only little effect on the electrical conductivity is expected when doping CBP and other carbazole-derivatives with ionization energies (IE) significantly larger ( $\sim 1$  eV) than the electron affinity (EA) of F<sub>4</sub>-TCNQ, as was demonstrated for 4,4',4''-tris(*N*-carbazolyl)-triphenylamine (TCTA) [14].

Transition metal oxides have been the subject of recent studies on charge transport and injection in organic electronic devices, and have been found to have a significant impact on their performance. Tokito et al. used thin sputtered metal oxide as anode interlayer for OLEDs and observed a significant decrease in driving voltage [15]. Their results were subsequently confirmed and attributed to a reduction in charge injection barrier [16–21]. Other applications of these high-work function materials have included electrodes for organic thin-film transistors [22] and charge injection layers for admittance spectroscopy [23]. Thin layers of MoO<sub>3</sub> or WO<sub>3</sub> have also been used as interconnecting units in tandem OLEDs [24,25] and organic photovoltaic (OPV) cells [26], demonstrating the high relevance of transition metal oxides for organic device applications. However, despite numerous papers related to the application of transition metal oxides in organic electronic devices, the underlying physical mechanisms pertaining to their electronic structure remain somewhat undefined.

We present in this paper a comprehensive study of p-type doping of  $\alpha$ -NPD and CBP via co-evaporation with MoO<sub>3</sub>. Doping of these materials is confirmed by charge carrier transport measurements and ultraviolet and inverse photoelectron spectroscopy (UPS/IPES) on MoO<sub>3</sub> and MoO<sub>3</sub>-doped  $\alpha$ -NPD and CBP thin films deposited on various substrates. The latter two techniques provide a conclusive explanation for the observed doping.

## 2. Experimental

Doping was performed by co-evaporation of organic molecules and MoO<sub>3</sub>. MoO<sub>3</sub> (99.99% purity) and  $\alpha$ -NPD were purchased from Sigma–Aldrich. Sublimed-grade CBP was obtained from Universal Display Cooperation. For thermal evaporation of MoO<sub>3</sub>, we used a shielded high temperature evaporation source (CreaTec HTC) to minimize radiative heating of the sample. The organic materials were evaporated from resistively heated quartz crucibles. Deposition rates were measured by a quartz crystal microbalance (QCM) and controlled by the applied temperature. The deposition rate for the organic materials was  $\sim 0.1$  nm/

s and for MoO<sub>3</sub> set according to the targeted doping concentration. Characteristic film thicknesses were 50 nm for the *I*-*V* measurements and 10 nm for UPS and IPES experiments.

Device preparation for the *I*-*V* measurements and Kelvin Probe (KP) characterization was carried out at the TU Braunschweig in a multi-chamber vacuum system, with separate chambers for organic molecular beam deposition (OMBD,  $p < 10^{-8}$  Torr) and metal electrode deposition ( $p < 10^{-6}$  Torr). In-vacuo KP measurements were accomplished using a KP 6500 from McAllister Technical Services. *I*-*V* characteristics were recorded by a computer-controlled Keithley 2400 source-measure unit.

UPS and IPES spectra were taken at Princeton University using an ultra-high vacuum UPS/XPS/IPES analysis system ( $p < 5 \times 10^{-10}$  Torr), which was connected to a growth chamber ( $p < 5 \times 10^{-9}$  Torr) for the thermal evaporation of MoO<sub>3</sub> and the organic materials.

We used the He I ( $h\nu = 21.22$  eV) and He II ( $h\nu = 40.81$  eV) lines of a He discharge lamp to measure the occupied electronic states. The experimental resolution for UPS was 0.15 eV, determined from the width of a Au Fermi step. The intensity of the He lamp photon line and the sample exposure time were kept to a minimum in order to reduce photo-induced damage. Unoccupied states were measured via IPES with a resolution of 0.5 eV [42]. The Fermi level reference for UPS and IPES measurements was determined for both techniques on a Au surface. The vacuum level was obtained from the secondary-electron cutoff as seen in the low kinetic-energy regime of the He I UPS spectra. EA and IP were approximated by the intersection of a linear extrapolation of the LUMO and HOMO edges, respectively, and the background signal.

## 3. Results and discussion

Single-carrier (“hole-only”) devices were fabricated, consisting of an intrinsic or doped molecular film of CBP or  $\alpha$ -NPD sandwiched between a hole-injecting electrode, i.e. indium tin oxide (ITO) covered with a 5 nm thin MoO<sub>3</sub> layer, and aluminum, i.e. a blocking contact. Another

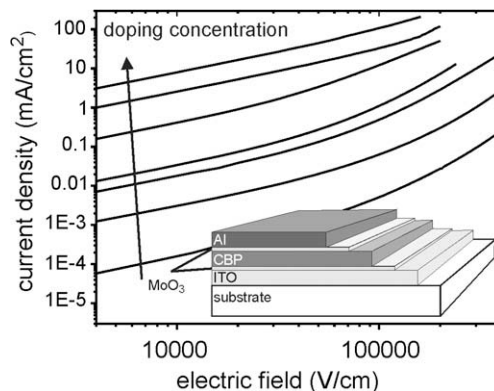


**Fig. 1.** *I*-*V* characteristics of hole-only CBP devices as a function of MoO<sub>3</sub> concentration. Doping concentration from bottom to top: 0/0.5/0.8/1.4/2.6/13.6/22.1 (mol%).

5 nm thin MoO<sub>3</sub> layer is introduced between Al and the organic semiconductor. Fig. 1 displays the current density vs. electric field (*J–E*) characteristics of CBP devices as a function of doping concentration (0–22.1 mol%). The device structure is given in the inset. Positive bias was applied to the bottom ITO contact, from which holes are injected into the device. Electron injection from the cathode can be neglected, due to the large electron injection barrier, which is even increased by inserting a MoO<sub>3</sub> interlayer. Thus, charge transport in this device is limited to holes. The current density for a given voltage increases with doping concentration, up to five orders of magnitude at the highest doping concentration investigated here. A comparable increase in current density is observed for doped  $\alpha$ -NPD devices (not shown here).

As it has been reported before that the formation of a conducting path through transport via the dopant does not occur [14], the observed increase in current density can have two different origins: (1) a reduction in barrier height for hole injection, as already observed for MoO<sub>3</sub>-doped  $\alpha$ -NPD intermediate injection layers designed to facilitate hole injection into intrinsic  $\alpha$ -NPD thin films [16], (2) a doping-induced increase in bulk conductivity. It was previously reported [3] that both effects must be taken into account when discussing transport characteristics of doped organic thin films. As the devices presented in Fig. 1 already include thin MoO<sub>3</sub>-interlayers to facilitate charge injection [18,20,21], most of the observed increase in current density can be attributed to higher bulk conductivity in the doped samples.

The doping mechanism is investigated by comparing the electronic structure of MoO<sub>3</sub>,  $\alpha$ -NPD and CBP via UPS and IPES. The filled (valence) and empty state spectra of a 30 nm thick MoO<sub>3</sub> film on Au are shown at the bottom of Fig. 2a. Both spectra are referenced to the vacuum level. The density of filled states (valence band) of MoO<sub>3</sub> was recorded with the He II line because of a significant parasitic background due to the He I\* line (23.09 eV) in the He I spectrum. The shape and position of the valence band, which are dominated by O 2sp electrons, are in agreement

with published results [27–29]. In oxygen-deficient MoO<sub>3–x</sub>, photoemission from Mo 4d orbitals would appear within the gap. The absence of gap-states suggests that the MoO<sub>3</sub> film is fully oxidized. In addition, the binding energy of the Mo 3d<sub>5/2</sub> core level (232.1 eV) determined via X-ray photoemission spectroscopy (XPS, data not shown here) is found to be in good agreement with that of the Mo<sup>6+</sup> species characteristic of stoichiometric MoO<sub>3</sub> [29,30]. The top of the valence band of the MoO<sub>3</sub> film, determined by linear extrapolation of the leading edge of the valence spectrum, is at  $9.68 \pm .1$  eV below vacuum level.

In the context of p-doping, the energy of the unoccupied states of the acceptor dopant, are of major interest. The IPES data from the MoO<sub>3</sub> film, plotted at the bottom of Fig. 2a, show the conduction band (CB) edge at 6.7 eV below vacuum level (the relevance to the doping process of measurements on a MoO<sub>3</sub> film is discussed below). Combined with the UPS results, these IPES data define a band gap of 2.98 eV, in very good agreement with the band gap determined by optical measurements [31]. The position of the Fermi level appears to be pinned slightly below the CB edge, giving a work function  $\Phi$  of 6.86 eV. The electronic structure reported here (IE = 9.68 eV and EA = 6.7 eV) is significantly different from that commonly cited in the literature (IE = 5.3 eV and EA = 2.3 eV) [20,22]. While these latter numbers do not result from direct experimental evidence, our results are confirmed by two independent, direct measurements, techniques (UPS and KP), which yield very similar work functions for MoO<sub>3</sub>. Furthermore, different preparation and analytical conditions can severely affect the experimental result, as any contamination on a high-work function surface is likely to decrease the work function.

The UPS spectra of intrinsic CBP and  $\alpha$ -NPD thin films are also included in Fig. 2a. The low binding energy edges of the HOMO features give ionization energies (IE) of 5.47 eV and 6.23 eV for  $\alpha$ -NPD and CBP, respectively. The dashed area within the plots indicates the overlap between the unoccupied states of MoO<sub>3</sub> and the occupied states of  $\alpha$ -NPD or CBP. The corresponding energy level diagrams

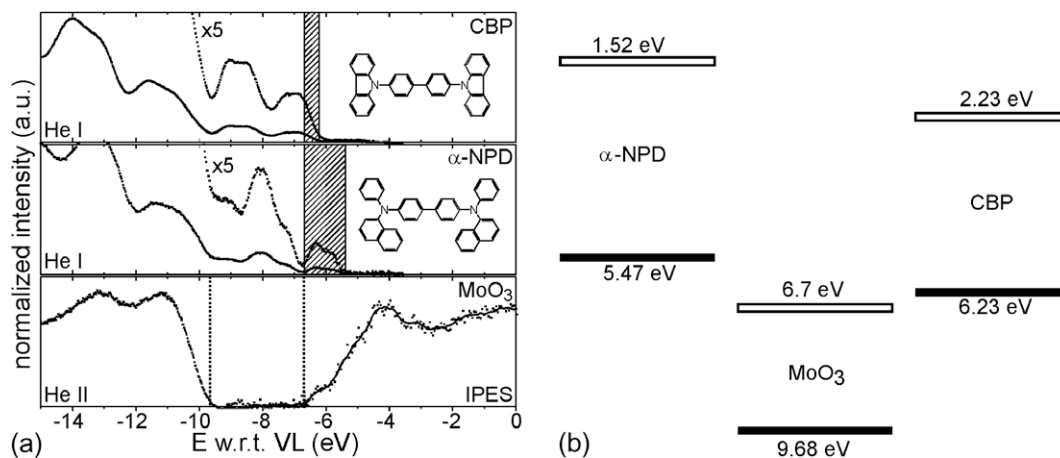
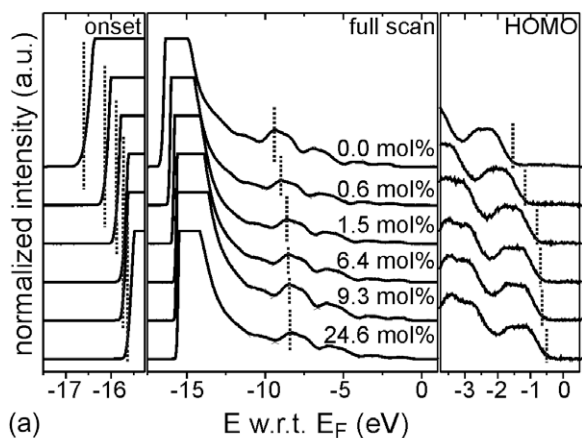


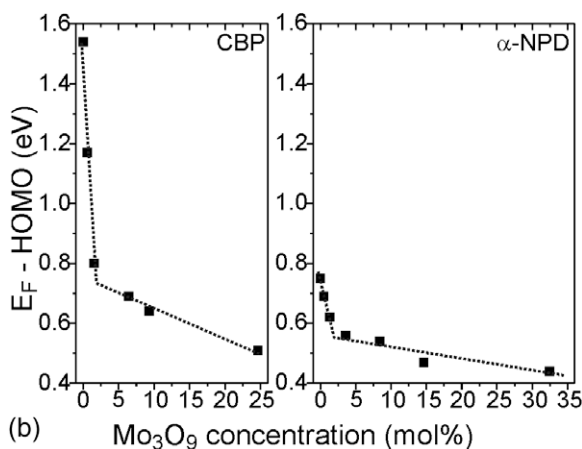
**Fig. 2.** (a) UPS and IPES spectra of a MoO<sub>3</sub> film (bottom), and UPS spectra of CBP (top) and  $\alpha$ -NPD (middle) films, referenced to vacuum level, (b) Energy level alignment derived from UPS and IPES measurements, unfilled bars represent the empty states, filled bars represent the occupied states.

(Fig. 2b and [32]) indicate that electron transfer from the HOMO of CBP or  $\alpha$ -NPD to the unoccupied states of  $\text{MoO}_3$  is energetically favorable, with likely p-doping of these organic materials. The amount of  $\text{MoO}_3$  incorporated into the organic thin film, the nature of the incorporated oxide species, and their impact on the electronic structure of the film, must be investigated. The analysis of  $\text{MoO}_3$  sublimation from a Knudsen cell via mass spectroscopy has shown a predominance of polymeric species, i.e.  $(\text{MoO}_3)_n$ ,  $n > 2$ , with a major fraction of the vapor consisting of  $\text{Mo}_3\text{O}_9$  clusters [33]. In this work, we therefore assume that mainly  $\text{Mo}_3\text{O}_9$  clusters are embedded into the organic matrix, an assumption that is largely validated below, and we refer to doping concentrations as the molar concentration of  $\text{Mo}_3\text{O}_9$  clusters. In that context, one should consider that the electronic structure of  $\text{Mo}_3\text{O}_9$  clusters may differ from that of the  $\text{MoO}_3$  thin film discussed in Fig. 2, thus putting in question the energy diagram of Fig. 2b. However, theoretical calculations on transition metal oxide clusters based on density functional theory (DFT) have been published by several groups and have been used to predict the geometry and electronic structure of these clusters [34–36]. In particular, bulk-like properties have been predicted for  $\text{W}_4\text{O}_{12}$  and larger clusters, with a band gap of 3.5 eV [36]. These results were confirmed by UPS experiments on single  $\text{Mo}_3\text{O}_9^-$  anions and ionized tungsten oxide clusters in a mass spectroscopy setup. In the neutral cluster, O 2p derived states make up the HOMO, while the LUMO is derived from Mo 4d orbitals. Furthermore, for the  $\text{Mo}_3\text{O}_9^-$  anion, a gap of 3.2 eV was measured between the singly occupied Mo 4d derived states and the doubly occupied O 2p derived states [35]. Although the neutral cluster undergoes a change in geometry upon ionization, [34] a change which may also cause a difference in energy gap, the reported gap of 3.2 eV for the anion cluster should give a fairly good estimate of the band gap of the neutral  $\text{Mo}_3\text{O}_9$  cluster. Hence, the energy gap of  $\text{Mo}_3\text{O}_9$  clusters ( $\sim 3.2$  eV) is only slightly larger than the gap we measure on  $\text{MoO}_3$  thin films ( $\sim 3.0$  eV). Therefore we suggest that the energy level alignment given in Fig. 2b gives a reasonable approximation of the electronic structure of the system, and justifies the electron transfer from the organic molecules to the  $\text{Mo}_3\text{O}_9$  clusters.

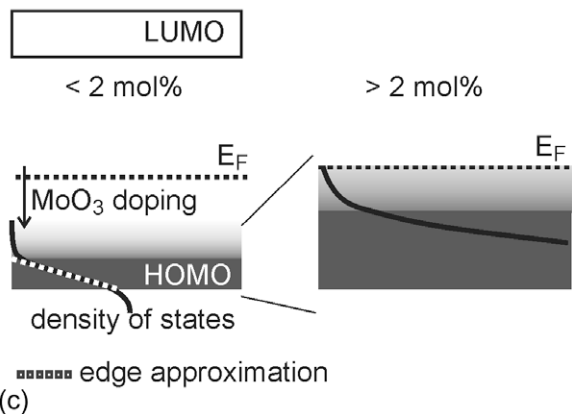
The UPS spectra of 10 nm CBP films with various  $\text{Mo}_3\text{O}_9$  doping concentrations are shown in Fig. 3a. The center plot represents the full valence spectrum recorded under He I excitation. Zoom-in plots of the secondary-electron cutoff and HOMO region are displayed on the left and right side, respectively. Vertical dotted lines mark the onset of photoemission, one of the valence features and the HOMO edge as a function of doping concentrations. A rigid shift of all these features towards lower binding energy occurs as the doping concentration increases, indicating a corresponding shift of the Fermi level within the gap towards the HOMO edge. Similar UPS measurements (not shown here) were conducted on  $\text{MoO}_3$ -doped  $\alpha$ -NPD thin films, and produced very similar results. A summary of these UPS experiments on p-doped CBP and  $\alpha$ -NPD thin films is given in Fig. 3b, where the position of the Fermi level with respect to the HOMO edge is plotted against the doping concentration. Two different regimes can be identified.



(a)



(b)



(c)

**Fig. 3.** (a) UPS spectra of  $\text{MoO}_3$ -doped CBP thin films for various  $\text{Mo}_3\text{O}_9$  doping concentrations, (b) Energy difference between Fermi level and HOMO edge vs.  $\text{Mo}_3\text{O}_9$  doping concentration in CBP (left) and  $\alpha$ -NPD (right) films on ITO substrate, (c) Fermi level position in the gap of the organic semiconductor for an intrinsic/low doped film (left) and in the Fermi level pinning regime (right).

For low doping concentrations ( $< 2$  mol%), the Fermi level rapidly shifts towards the HOMO edge. This regime corresponds to a very large (relative) increase in carrier concentration, as the organic film changes from nearly intrinsic to fairly highly doped. In the second regime, further increase

of the doping concentration (>2 mol%) results in a comparably small Fermi level shift, as the Fermi level approaches regions of large density of states and is finally pinned at about 0.5 and 0.4 eV above the CBP and  $\alpha$ -NPD HOMO edge, respectively. Similar results were previously obtained for the p-doping for  $\alpha$ -NPD with F<sub>4</sub>-TCNQ [8]. In that system, the difference between  $E_F$  pinning position and HOMO edge was explained by (i) the doping barrier for the  $\alpha$ -NPD:F<sub>4</sub>-TCNQ pair and (ii) the structural reorganization of ionized  $\alpha$ -NPD molecules, which causes energetic relaxation of the molecular state above the HOMO. In the two present cases, the doping barrier should not be an issue, the EA of MoO<sub>3</sub> being larger than the IE of the two organic materials. A likely explanation for the observed Fermi level pinning involves therefore structural and energetic disorder of thermally evaporated molecular thin films, as depicted in Fig. 3c. Charge carriers in amorphous organic solids are relatively strongly localized to single molecules and polarization significantly affects the electronic structure of these solids [37]. Structural disorder will cause energetic disorder due to differences in the polarization energy for individual molecules. Energetic disorder in organic solids is often considered by assuming a Gaussian distribution of HOMO states, as indicated in Fig. 3c. In contrast, the HOMO edge is approximated by a linear extrapolation of the experimental data (Fig. 3c: dotted line). Depending on the distribution of the density of states close to the gap, there may be a significant density of tail states above the so-called HOMO edge. For low doping concentrations (here: < 2 mol%), the Fermi level rapidly shifts towards the HOMO edge. As the Fermi level approaches the HOMO edge (>2 mol%), a small shift is sufficient to induce a large change in the population of the tail states.

The difference in the magnitude of Fermi level shift between CBP and  $\alpha$ -NPD (Fig. 3b) can be traced to the initial

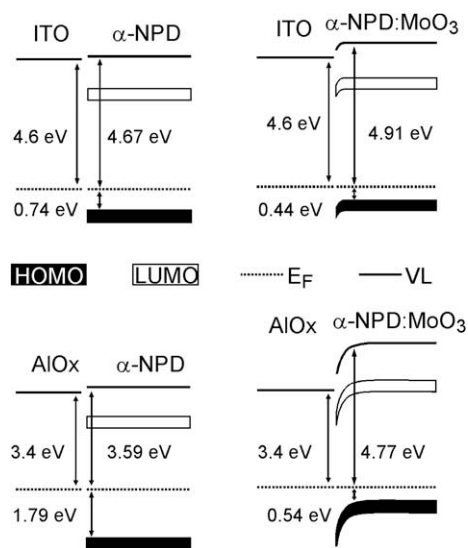


Fig. 4. Energy level diagrams of interfaces between various substrates and intrinsic or MoO<sub>3</sub>-doped  $\alpha$ -NPD thin films, as derived from UPS and KP.

position of the Fermi level in the gap of the material (Fig. 4), which in turns depends on the energy level alignment, i.e. the interface HOMO and LUMO positions, for the specific substrate. In the cases presented here, the Fermi level position in the gap is mainly determined by the work function of the underlying substrate and the IE and EA of the organic semiconductor, as only a small dipole is observed at the interface. Upon doping, the position of the Fermi level is pinned less than 0.5 eV above the HOMO edge of the organic film, and nearly independent of the substrate work function. Since the Fermi level is deeper in the gap of undoped CBP (larger IE), the shift upon doping is expected to be larger, as indeed observed.

The effect of doping on the electronic structure and the conductivity of the molecular films can, in part, be derived from the  $I$ - $V$  measurements presented in Fig. 1. The “hole-only” devices consisted of a single layer of either intrinsic or MoO<sub>3</sub>-doped CBP, sandwiched between two inorganic electrodes. Using thin interlayers of neat MoO<sub>3</sub> greatly reduces the hole injection barrier at the ITO electrode, and increases the electron injection barrier at the Al electrode, insuring unipolar transport [21]. Although injection on the ITO/MoO<sub>3</sub> side may still limit the device characteristics to a certain extent, we assume ohmic charge injection. The slope of the current density vs. electric field (log-log plot) is nearly equal to unity in the low-field regime, indicating ohmic conduction. A linear fit of the ohmic regime can then be used to evaluate the conductivity. The essence of these  $I$ - $V$  measurements is displayed in Fig. 5a, which shows the conductivity plotted against Mo<sub>3</sub>O<sub>9</sub> concentration, along with the change in surface work function  $\Phi$  measured by UPS and KP. As noted before, the Fermi level rapidly shifts towards the HOMO for low dopant concentrations (<2 mol%), inducing a rapid increase in work function. Higher doping levels lead to Fermi level pinning, which is reflected in a slower increase in  $\Phi$ . A very similar relation is found for the electrical conductivity  $\sigma$ . For low doping concentrations,  $\sigma$  drastically increases upon doping. High doping concentrations still lead to an increase in conductivity but the slope of this increase is significantly reduced. The transition between the two regimes is around 2 mol%, in excellent agreement with the transition towards Fermi level pinning observed in UPS and KP measurements.

To understand this point, we model the DOS with a Gaussian distribution

$$g_{\text{HOMO}}(E) = \frac{N_{\text{HOMO}}}{w\sqrt{2\pi}} e^{-\left(\frac{E}{w}\right)^2}, \quad (1)$$

where  $N_{\text{HOMO}}$  is the density of HOMO states and  $w$  is the Gaussian standard deviation. The energy  $E$  is referenced to the HOMO peak position, which was measured at 6.8 eV below the vacuum level.  $N_{\text{HOMO}}$  can be estimated at  $3.8 \times 10^{21} \text{ cm}^{-3}$  by assuming a film density of  $1.5 \text{ g/cm}^3$  and taking two HOMO states per molecule into account. The conductivity can be expressed as a function of Fermi energy following

$$\sigma(E_F) = e\mu_h n_h(E_F) \quad (2)$$

with  $e$  as the elementary charge,  $\mu_h$  the hole mobility and  $n_h$  the hole carrier density. Applying expression (1) and Fermi statistics, Eq. (2) can be written as

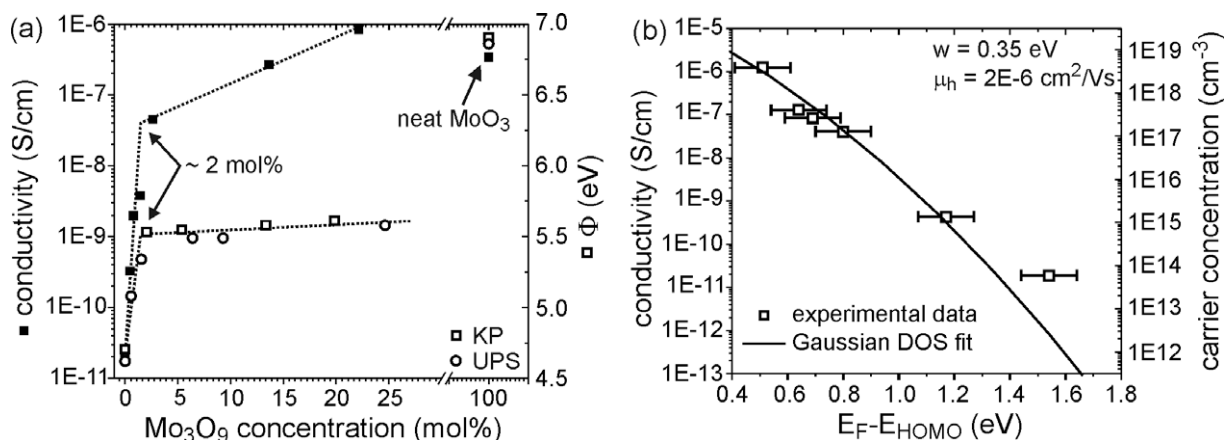


Fig. 5. (a) Evolution of conductivity and WF vs. MoO<sub>3</sub> doping concentration in CBP thin films, (b) Conductivity vs. Fermi level position for the same samples.

$$\sigma(E_F) = e\mu_h \frac{N_{\text{HOMO}}}{w\sqrt{2\pi}} \int_{-\infty}^{\infty} \frac{e^{-\left(\frac{E}{2w}\right)^2}}{1 + e^{\frac{E-E_F}{k_B T}}} dE \quad (3)$$

We assume here a constant hole mobility  $\mu_h$  to simplify the expression. Knowing that the carrier mobility in organic semiconductors may well depend, among other parameters, on the carrier concentration, [38] we expect a certain error within our calculations. The significance and impact of this error will be discussed later. In Fig. 5b we compare the experimental results for the conductivity to a calculation corresponding to Eq. (3). The experimental data was extracted from Figs. 3b and 5a by correlating the measured Fermi level position for a given doping concentration with the interpolated conductivity (see dotted line in Fig. 5a) at the same doping concentration. A close match between Eq. (3) and experiment can be established using the Gaussian standard deviation and the carrier mobility as fitting parameters. Only the intrinsic sample conductivity is much higher than predicted, which will be discussed later. The fit shown in Fig. 5b corresponds to  $w = 0.35$  eV and  $\mu_h = 2 \times 10^{-6}$  cm<sup>2</sup>/Vs. The standard deviation  $w$  is slightly larger than the corresponding value for similar calculations on n-doped pentacene (0.3 eV) [6]. Considering the lower degree of disorder in polycrystalline pentacene, both values appear very reasonable.

The discrepancy between the above CBP hole mobility and the higher mobilities determined by time-of-flight (TOF) measurements [39,40] or admittance spectroscopy (AS) [23] merits further discussion. The TOF and AS numbers were obtained for intrinsic CBP films, except for the work of Matsusue et al. [39] which included a study of electron transport in Ir-phosphor doped CBP. For these measurements, a doping concentration of a less than one percent leads to a dramatic mobility decrease to less than  $10^{-6}$  cm<sup>2</sup>/Vs. Although the interaction between matrix and dopant is clearly different for phosphor-doping (neutral dopant) than for electrochemical doping (ionized dopant), the effect of doping on charge transport should in both cases be modeled by a dopant-induced change in the DOS. Theory predicts that in disordered electronic systems, the interaction between dopant and matrix mole-

cules leads to additional broadening of tail states [41]. Furthermore, Coulomb-trapping of excess carriers at ionized dopant sites affects the carrier mobility. Depending on the initial width of the density of states distribution, a decrease in mobility of several orders of magnitude was calculated for high doping levels. Compared to the reference, our model calculations overestimate the initial width of the DOS by a factor of three or less, since broadening of the DOS due to p-doping is not been considered for reasons of simplicity. Still the mobility obtained from a model involving a Gaussian DOS is well within range of what can be expected when Coulomb trapping is considered.

Our calculations yield a carrier concentration which is equivalent to a dopant activation of about 0.5% or even less. Estimating the carrier concentration from the width of the depletion layer at the electrode interface (data not shown here) confirms a dopant activation of  $\sim 0.4\%$ . Yet, a much larger dopant activation could be expected from the energy level alignment depicted in Fig. 2b. This discrepancy may just be a result from the strong interaction, which is implied by the energy levels. The exchange of charge between the acceptor and the matrix molecules presumably leads to a strongly bound charge-transfer (CT) state, and only a small fraction of the exchanged charges participates in the current transport. As previously reported, the increase in near-infrared absorption in WO<sub>3</sub>-doped TCTA may be an indicator for such a CT state [14].

There are two reasons for the calculated fit not to agree with the data obtained for the undoped CBP sample. As already mentioned, the carrier mobility should be a function of doping concentration, and is expected to be about three orders of magnitude higher for the undoped sample. Given the fact that a constant mobility is used in our calculation, the fit is likely to underestimate the real conductivity of intrinsic thin films. Furthermore, we showed that the position of the Fermi level in undoped thin films is not an intrinsic property of the film itself, but is strongly affected by the underlying substrate. Consequently, the position of the data point for the intrinsic sample becomes arbitrary with respect to the energy scale.



#### 4. Conclusions

In conclusion, p-doping of organic large band gap materials using MoO<sub>3</sub> has been demonstrated and further investigated by photoemission spectroscopy. Very high EA (6.7 eV) and work function (6.86 eV) were measured on MoO<sub>3</sub> thin films. These values are assumed to give a good approximation of the electronic structure of Mo<sub>3</sub>O<sub>9</sub> clusters, leading to a prediction of energetically favorable electron transfer from the HOMO of many hole transport materials to the deep-lying acceptor state of embedded Mo<sub>3</sub>O<sub>9</sub> clusters. At low doping concentration (<2 mol%) in CBP and  $\alpha$ -NPD, a rapid shift of the Fermi level towards the HOMO states and a steep increase in conductivity are observed. Further increase of the doping concentration leads to Fermi level pinning several 100 meV above the HOMO edge. The experimental results were modeled using a Gaussian distribution of the DOS, which yields a reasonable explanation for the observed phenomena. Due to a similar electronic structure, our results may possibly be valid for other transition metal oxides (e.g. WO<sub>3</sub>), either being used as thin interlayer to enhance charge injection or as p-dopants for large IE host materials. Further, the observation of an extremely high-work function of MoO<sub>3</sub> may have a severe impact on other applications in related fields, for instance hybrid organic–inorganic photovoltaics.

#### Acknowledgements

Work at Princeton University was supported by the National Science Foundation (DMR-0705920). S.H., J.M., T.R. and W.K. gratefully acknowledge financial support by the German Federal Ministry for Education and Research BMBF (contract 13N8166A) and the Deutsche Forschungsgemeinschaft (DFG) through the Gottfried Wilhelm Leibniz award. M.K. acknowledges the German Academic Exchange Service (DAAD) for generous support within the post-doctoral fellowship program.

#### References

- [1] K. Walzer, B. Maennig, M. Pfeiffer, K. Leo, *Chem. Rev.* 107 (2007) 1233.
- [2] J. Kido, T. Matsumoto, *Appl. Phys. Lett.* 73 (1998) 2866.
- [3] C.K. Chan, W. Zhao, S. Barlow, S. Marder, A. Kahn, *Org. Electron.* 9 (2008) 575.
- [4] F.H. Li, M. Pfeiffer, A. Werner, K. Harada, K. Leo, N. Hayashi, K. Seki, X.J. Liu, X.D. Dang, *J. Appl. Phys.* 100 (2006).
- [5] F.H. Li, A. Werner, M. Pfeiffer, K. Leo, X.J. Liu, *J. Phys. Chem. B* 108 (2004) 17076.
- [6] C.K. Chan, A. Kahn, *Appl. Phys. A: Mater. Sci. Process.* 95 (2009) 7.
- [7] C.K. Chan, F. Amy, Q. Zhang, S. Barlow, S. Marder, A. Kahn, *Chem. Phys. Lett.* 431 (2006) 67.
- [8] W.Y. Gao, A. Kahn, *J. Appl. Phys.* 94 (2003) 359.
- [9] W.Y. Gao, A. Kahn, *Org. Electron.* 3 (2002) 53.
- [10] M. Pfeiffer, A. Beyer, T. Fritz, K. Leo, *Appl. Phys. Lett.* 73 (1998) 3202.
- [11] J. Blochwitz, M. Pfeiffer, T. Fritz, K. Leo, *Appl. Phys. Lett.* 73 (1998) 729.
- [12] J.S. Huang, M. Pfeiffer, A. Werner, J. Blochwitz, K. Leo, S.Y. Liu, *Appl. Phys. Lett.* 80 (2002) 139.
- [13] M.A. Baldo, S. Lamansky, P.E. Burrows, M.E. Thompson, S.R. Forrest, *Appl. Phys. Lett.* 75 (1999) 4.
- [14] J. Meyer, S. Hamwi, S. Schmale, T. Winkler, H.-H. Johannes, T. Riedl, W. Kowalsky, *J. Mater. Chem.* 19 (2009) 702.
- [15] S. Tokito, K. Noda, Y. Taga, *J. Phys. D: Appl. Phys.* 29 (1996) 2750.
- [16] F.X. Wang, X.F. Qiao, T. Xiong, D.G. Ma, *Org. Electron.* 9 (2008) 985.
- [17] J. Meyer, S. Hamwi, T. Bulow, H.H. Johannes, T. Riedl, W. Kowalsky, *Appl. Phys. Lett.* 91 (2007) 113506.
- [18] H. Lee, S.W. Cho, K. Han, P.E. Jeon, C.N. Whang, K. Jeong, K. Cho, Y. Yi, *Appl. Phys. Lett.* 93 (2008) 043308.
- [19] X.L. Zhu, J.X. Sun, X.M. Yu, M. Wong, H.S. Kwok, *Jpn. J. Appl. Phys.* 46 (2007) 1033.
- [20] H. You, Y.F. Dai, Z.Q. Zhang, D.G. Ma, *J. Appl. Phys.* 101 (2007) 026105.
- [21] T. Matsushima, Y. Kinoshita, H. Murata, *Appl. Phys. Lett.* 91 (2007) 253504.
- [22] C.W. Chu, S.H. Li, C.W. Chen, V. Shrotriya, Y. Yang, *Appl. Phys. Lett.* 87 (2005) 193508.
- [23] M. Hoping, C. Schildknecht, H. Gargouri, T. Riedl, M. Tilgner, H.H. Johannes, W. Kowalsky, *Appl. Phys. Lett.* 92 (2008) 213306.
- [24] H. Kanno, R.J. Holmes, Y. Sun, S. Kena-Cohen, S.R. Forrest, *Adv. Mater. (Weinheim, Germany)* 18 (2006) 339.
- [25] C.C. Chang, J.F. Chen, S.W. Hwang, C.H. Chen, *Appl. Phys. Lett.* 87 (2005) 253501.
- [26] A.G.F. Janssen, T. Riedl, S. Hamwi, H.H. Johannes, W. Kowalsky, *Appl. Phys. Lett.* 91 (2007) 073519.
- [27] R. Tokarz-Sobieraj, K. Hermann, M. Witko, A. Blume, G. Mestl, R. Schlogl, *Surf. Sci.* 489 (2001) 107.
- [28] M. Heber, W. Grunert, *Materialwiss. Werkstofftech.* 31 (2000) 864.
- [29] F. Werfel, E. Minni, *J. Phys. C: Solid State Phys.* 16 (1983) 6091.
- [30] J.G. Choi, L.T. Thompson, *Appl. Surf. Sci.* 93 (1996) 143.
- [31] T.S. Sian, G.B. Reddy, *Sol. Energy Mater. Sol. Cells* 82 (2004) 375.
- [32] W.Y. Gao, A. Kahn, *Appl. Phys. Lett.* 82 (2003) 4815.
- [33] J. Berkowitz, M.G. Inghram, W.A. Chupka, *J. Chem. Phys.* 26 (1957) 842.
- [34] S. Li, D.A. Dixon, *J. Phys. Chem. A* 111 (2007) 11093.
- [35] X. Huang, H.J. Zhai, B. Kiran, L.S. Wang, *Angew. Chem., Int. Ed.* 44 (2005) 7251.
- [36] Q. Sun, B.K. Rao, P. Jena, D. Stolcic, Y.D. Kim, G. Gantefor, A.W. Castleman, *J. Chem. Phys.* 121 (2004) 9417.
- [37] I.G. Hill, A. Kahn, Z.G. Soos, R.A. Pascal, *Chem. Phys. Lett.* 327 (2000) 181.
- [38] L. Li, G. Meller, H. Kosina, *Synth. Met.* 157 (2007) 243.
- [39] N. Matsusue, Y. Suzuki, H. Naito, *Jpn. J. Appl. Phys.* 45 (2006) 5966.
- [40] H. Matsushima, S. Naka, H. Okada, H. Onnagawa, *Curr. Appl. Phys.* 5 (2005) 305.
- [41] M.C.J.M. Vissenberg, M. Matters, *Phys. Rev. B* 57 (1998) 12964.
- [42] C.I. Wu, Y. Hirose, H. Sirringhaus, A. Kahn, *Chem. Phys. Lett.* 272 (1997) 43.

performance in EL devices with related terbium complexes. DPPOC is synthesized by modification of the chemically active C3 and C6 positions on carbazole. Phenyl substitution at the 9-position of carbazole also has little effect on the photophysical characteristics of its derivatives [17,18]. We chose diphenylphosphine oxide moieties as building blocks to synthesize TPPO derivatives for both their coordinating abilities and carrier transport properties. Thermal stability was improved by 4-tert-butylphenyl substitution at the 9-position on carbazole. The complex Tb(PMIP)<sub>3</sub>DPPOC was also synthesized and characterized. The high molecular weight of the complex precludes direct thermal evaporation so the terbium complex film was formed by co-deposition of complex **B** and DPPOC in vacuum for the OLED application. This technique was similar to previously reported work [19]. Stable pure green electroluminescence with high efficiency based on the multi-layer emission structure of terbium complexes is thus demonstrated.

## 2. Experimental

### 2.1. General information

AIQ was synthesized according to literature procedures [20] and sublimed twice prior to use. NPB and BCP were purchased from Aldrich and used after a single sublimation. Tb(PMIP)<sub>3</sub>(H<sub>2</sub>O)<sub>2</sub> and Tb(PMIP)<sub>3</sub>(TPPO)<sub>2</sub> were synthesized as in our previous report [13]. Chromatographic separation was carried out on silica gel (200–300 mesh). The <sup>1</sup>H NMR spectra were recorded on a Varian 400 MHz instrument using Me<sub>4</sub>Si as an internal reference. Mass spectra were recorded on a ZAB-HS and BIFLEX III. Elemental analyses were performed on a VARIO EL analyzer. Thermogravimetric and differential thermal analyses were carried out on Q600SDT and Q100DSC instruments at an elevation temperature rate of 10 °C/min under 100 ml min<sup>-1</sup> nitrogen. The IR spectra were recorded with a Magna-IR 750. PL spectra and phosphorescence decay lifetimes were recorded with an Edinburgh Analytical Instruments FLS920 spectrometer after removing oxygen in the solution by a vacuum technique (3 or 4 freeze-pump-thaw cycles). Absorption spectra were measured on a Shimadzu UV-3100 UV-visible spectrometer. Cyclic voltammetry was performed with a computer controlled EG&G potentiostat/galvanostat model 283. All measurements were carried out at room temperature with a conventional three electrode configuration consisting of a one compartment electrolysis cell with a platinum button, a platinum wire, a Ag/AgCl working electrode, counter electrode and reference electrode. Cyclic voltammograms were obtained at a scan rate of 50 mV s<sup>-1</sup> in HPLC-grade dichloromethane. The concentration of the complexes was 1.0 mM and each solution contained 0.1 M tetrabutylammonium hexafluorophosphate (TBAP) as an electrolyte. The highest occupied molecular orbital (HOMO) and the lowest unoccupied molecular orbital (LUMO) energy levels were calculated by reference to the ferrocene/ferrocenium energy level of -4.8 eV. Fluorescence microscopy images were taken on an OLYMPUS BX51.

### 2.2. OLED fabrication and measurement

EL devices were fabricated by sequentially depositing organic layers using thermal evaporation in one run under high vacuum ( $<8 \times 10^{-5}$  Pa) onto a cleaned indium tin oxide (ITO) glass substrate with a sheet resistance of 7 Ω/sq. The active device area was 3 × 3 mm. The cathode was made of a 200 nm thick layer of Mg<sub>0.9</sub>Ag<sub>0.1</sub> alloy with an 80 nm thick Ag cap. The thickness of the deposited layer and the evaporation speed of the individual materials were monitored in a vacuum with quartz crystal monitors. Deposition rates were maintained at 0.05–0.2 nm s<sup>-1</sup> for organic materials and 0.2–0.3 nm s<sup>-1</sup> for the Mg<sub>0.9</sub>Ag<sub>0.1</sub> alloy. All electrical testing and optical measurements were performed under ambient conditions. The EL spectra were measured with a Spectra Scan PR650. The current-voltage (*I*-*V*) and luminance-voltage (*L*-*V*) characteristics were measured with a computer controlled Keithley 2400 Sourcemeter unit with a calibrated silicon diode.

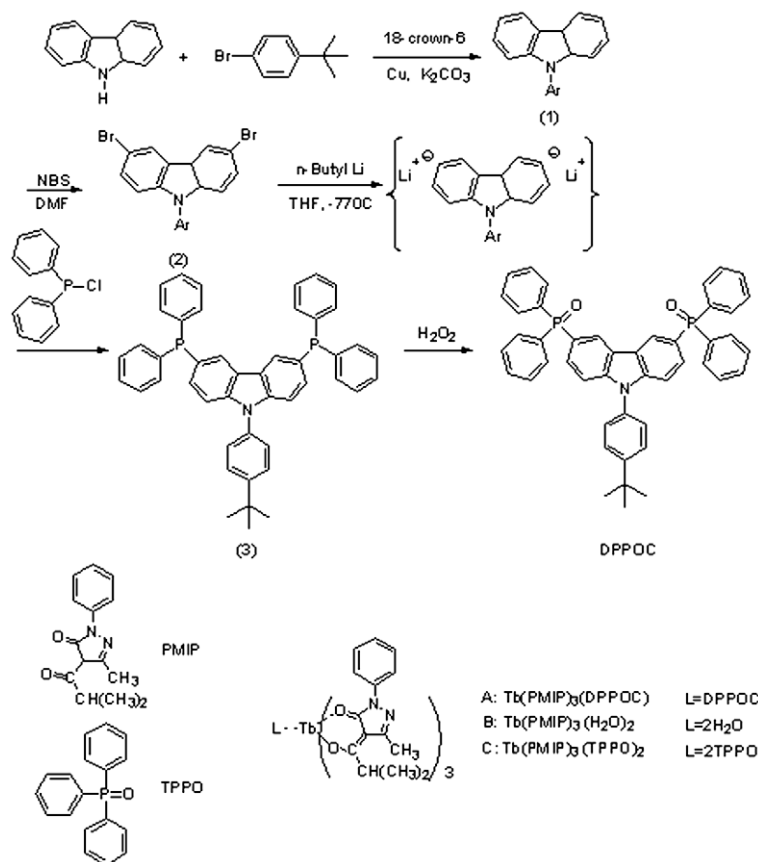
### 2.3. Materials

The synthetic route leading to DPPOC is presented in Scheme 1.

*9-(4-tert-butylphenyl)carbazole (1)*: A suspension of carbazole (1.67 g, 10 mmol), 1-bromo-4-tert-butylbenzene (2.13 g, 10 mmol), copper (2.56 g, 40 mmol), K<sub>2</sub>CO<sub>3</sub> (11.04 g, 80 mmol) and 18-crown-6 (0.53 g, 2 mmol) in 1,2-dichlorobenzene (100 ml) was stirred at 190 °C in an oil bath for 36 h under nitrogen. The solvent was evaporated and the solid residue was extracted with benzene. The combined organic extracts were evaporated and the crude product was purified via column chromatography on silica gel using a mixture of dichloromethane/petroleum ether (1/2) as eluent. The compound was further purified by recrystallization from a mixture of benzene-ether to give a white powder (2.09 g, yield 70%). <sup>1</sup>H NMR (400 MHz, CDCl<sub>3</sub>, δ): 8.14 (d, *J* = 4 Hz, 2H), 7.60 (d, *J* = 4 Hz, 2H), 7.48 (d, *J* = 4 Hz, 2H), 7.37–7.43 (m, 4H), 7.27 (d, *J* = 8 Hz, 2H), 1.43 (s, 9H). EIMS (*m/z* (%)): 299 (100) [*M*<sup>+</sup>].

*9-(4-tert-butylphenyl)-3,6-dibromocarbazole (2)*: Compound **2** was synthesized according to the literature procedure [21] in a yield of 82%. EIMS (*m/z* (%)): 457 (100) [*M*<sup>+</sup>]. <sup>1</sup>H NMR (400 MHz, CDCl<sub>3</sub>, δ): 8.18 (d, *J* = 2 Hz, 2H), 7.61 (d, *J* = 4 Hz, 2H), 7.47–7.50 (m, 2H), 7.41 (d, *J* = 6 Hz, 2H), 7.26 (d, *J* = 4 Hz, 2H), 1.42 (s, 9H).

*9-(4-tert-butylphenyl)-3,6-bis(diphenylphosphino)carbazole (3)*: Compound **2** (2.0 g, 4.37 mmol) was dissolved in tetrahydrofuran (THF, 150 ml) under a nitrogen atmosphere. The reaction vessel was immersed in a dry ice/acetone bath until the temperature was about -78 °C. To this solution 8.17 ml (13.1 mmol) of 1.6 M *n*-BuLi solution in hexane was added dropwise and stirred for 1 h. Chlorodiphenylphosphine (2.39 ml, 13.1 mmol) was then added to the solution and stirred for 3 h in a dry ice/acetone bath. The mixture was allowed to gradually warm to room temperature overnight and then quenched with water. The desired product was extracted with dichloromethane and purified by column chromatography on silica gel with dichloromethane/petroleum ether = 1/4 as eluent produc-



**Scheme 1.** Synthetic route of DPPOC and chemical structures of the terbium complexes.

ing a white solid product (1.46 g, yield 51%). EIMS ( $m/z$  (%)): 667 (100) [ $M^+$ ].  $^1\text{H NMR}$  (400 MHz,  $\text{CDCl}_3$ ,  $\delta$ ): 8.06 (d, 2 Hz, 2H), 7.57 (d,  $J = 6$  Hz, 2H), 7.44 (d,  $J = 4$  Hz, 2H), 7.37–7.40 (m, 4H), 7.33 (d, 20H), 1.40 (s, 9H).

**9-(4-*tert*-butylphenyl)-3,6-bis(diphenylphosphineoxide)-carbazole (DPPOC):** Compound **3** (1.33 g, 2 mmol) was dissolved in dichloromethane (50 ml) and excess 30%  $\text{H}_2\text{O}_2/\text{H}_2\text{O}$  (10 ml) was added with stirring to the ice bath for 1 h. The mixture was extracted with dichloromethane and dried with  $\text{MgSO}_4$ . The solution was concentrated by rotary evaporation and the crude product was purified by high vacuum thermal gradient sublimation to get the final product as a white solid (1.26 g, yield 90%). EIMS ( $m/z$  (%)): 699 (100) [ $M^+$ ].  $^1\text{H NMR}$  (400 MHz,  $\text{CDCl}_3$ ,  $\delta$ ): 8.43 (d, 6 Hz, 2H), 7.66–7.74 (m, 10H), 7.61 (d, 4 Hz, 2H), 7.52–7.54 (m, 4H), 7.42–7.48 (m, 12H), 1.41 (s, 9H). IR ( $[\text{cm}^{-1}]$ , KBr): 3042 (s,  $\nu(\text{C-H})$ ); 1622, 1592 (benzene ring); 1436  $\delta(\text{p-C}_6\text{H}_5)$ ; 1198  $\nu(\text{P=O})$ ; 1365, 1394, 1465 (t,  $\delta(\text{C-H})$ ).

**Tb(PMIP)<sub>3</sub>DPPOC:** To a 1.0 mmol solution of Tb(PMIP)<sub>3</sub>(H<sub>2</sub>O)<sub>2</sub> in 20 ml ethanol was added (dropwise) 1.0 mmol DPPOC in 50 ml ethanol while stirring and the mixture was heated to reflux for 4 h. The product was purified by recrystallization from ethanol with a yield of 80%. Anal. calcd for  $\text{C}_{90}\text{H}_{90}\text{N}_7\text{O}_9\text{P}_2\text{Tb}$ : C 66.54, H 5.33, N 6.17; Found: C 66.44, H 5.41, N 6.04. MALDI-TOF MS ( $m/z$ ): 1344 (Tb(PMIP)<sub>2</sub>(DPPOC)<sup>+</sup>, 100%), 1289 (45%). IR ( $[\text{cm}^{-1}]$ , KBr):

$\text{cm}^{-1}$ : 3057 (s,  $\nu(\text{C-H})$ ); 1614, 1593 (benzene ring); 1439  $\delta(\text{p-C}_6\text{H}_5)$ ; 1172  $\nu(\text{P=O})$ .

### 3. Results and discussion

#### 3.1. Absorption, fluorescence and phosphorescence

Fig. 1 shows the room temperature absorption ( $\text{CH}_2\text{Cl}_2$ ,  $10^{-5}$  M), fluorescence ( $\text{CH}_2\text{Cl}_2$ ,  $10^{-5}$  M) and phosphorescence (ethanol,  $10^{-5}$  M) of TPPO, DPPOC and related terbium complexes. The distinct absorption of DPPOC at shorter wavelengths of 254 and 278 nm with  $\epsilon$  around  $5 \times 10^4 \text{ dm}^3 \text{ mol}^{-1} \text{ cm}^{-1}$  may be assigned to the localized benzene  $\pi \rightarrow \pi^*$  transition and the broad absorption bands at 325–350 nm are attributed to the carbazole-based lowest  $\pi \rightarrow \pi^*$  transitions which resemble the absorption of the carbazole monomer [18]. Complex A with absorption peaks at around 253 and 277 nm has similar UV-visible characteristics to DPPOC but a much higher  $\epsilon$  of about  $1.2 \times 10^5 \text{ dm}^3 \text{ mol}^{-1} \text{ cm}^{-1}$ . This indicates that the absorption is due to both the anionic ligand PMIP and the neutral ligand DPPOC.

The PL spectra of the complexes showed strong terbium ion emission at  $\lambda = 488 \text{ nm}$  ( $^5\text{D}_4 \rightarrow ^7\text{F}_6$ ), 548 nm ( $^5\text{D}_4 \rightarrow ^7\text{F}_5$ ), 582 nm ( $^5\text{D}_4 \rightarrow ^7\text{F}_4$ ) and 617 nm ( $^5\text{D}_4 \rightarrow ^7\text{F}_3$ ). The fluorescence spectrum of DPPOC with peaks at 353

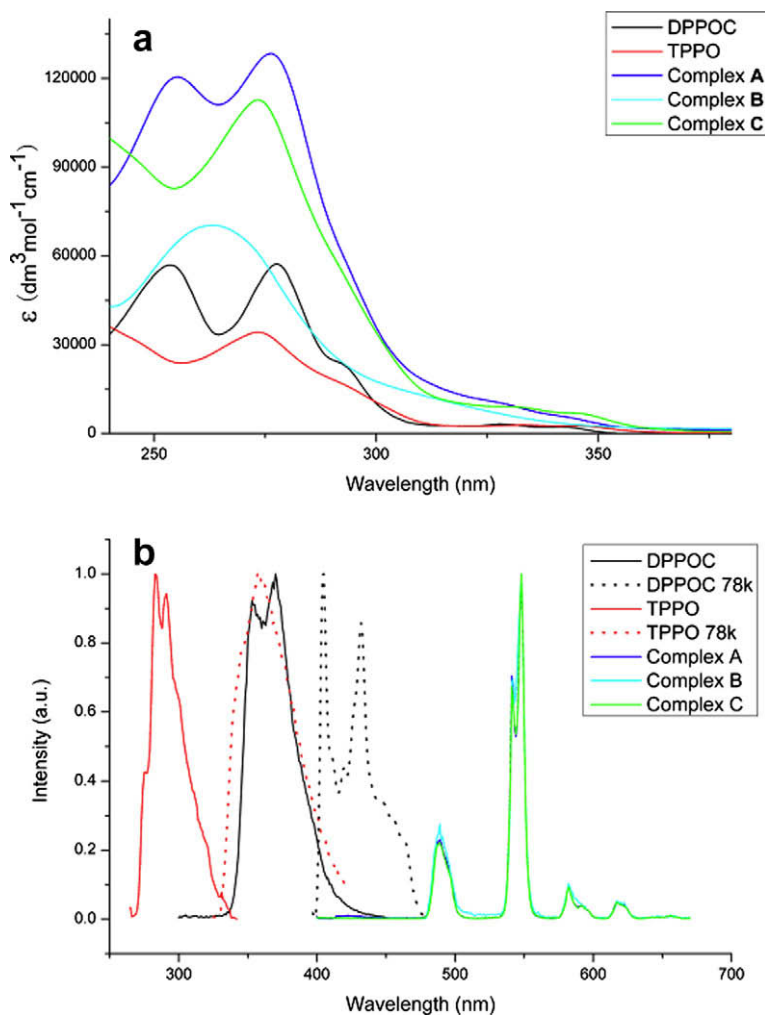


**Fig. 1.** Absorption spectra of TPPO, DPPOC and related complexes ( $10^{-5}$  M in  $\text{CH}_2\text{Cl}_2$ ) at room temperature (a), fluorescence (solid line,  $10^{-5}$  M in  $\text{CH}_2\text{Cl}_2$ ) and phosphorescence spectra (dotted line,  $10^{-5}$  M in ethanol) of neutral ligands and related terbium complexes (b).

and 370 nm as well as its gadolinium complex's phosphorescence spectrum (at 78 K) with a peak at 405 nm (see Fig. 1) are similar to those of the unsubstituted carbazole monomer. These peaks may be attributed to the lowest  $\pi-\pi^*$  transitions of the central carbazole chromophore in DPPOC [17]. The phosphorescence spectrum reveals the lowest triplet energy level of DPPOC which is estimated to be  $24,691 \text{ cm}^{-1}$  (3.04 eV). The  $4300 \text{ cm}^{-1}$  energy difference allows energy transfer between DPPOC and the  $^5\text{D}_4$  level ( $20,400 \text{ cm}^{-1}$ ) of Tb(III). The lowest triplet energy level of TPPO is at  $27,933 \text{ cm}^{-1}$  (3.46 eV). The overall luminescent quantum yields of the three terbium complexes are 10.4%, 14.6% and 16.7% for  $\text{Tb}(\text{PMIP})_3(\text{H}_2\text{O})_2$ ,  $\text{Tb}(\text{PMIP})_3(\text{TPPO})_2$  and  $\text{Tb}(\text{PMIP})_3\text{DPPOC}$ , respectively (see Table 1). DPPOC thus performs better than TPPO as a neutral ligand because of its better suited triplet energy level [22].

The deposited DPPOC film exhibits a different emission spectrum compared with its  $\text{CH}_2\text{Cl}_2$  solution and a new broad peak at 424 nm is observed (Fig. 2). There is little

overlap between the absorption spectrum of the  $\text{Tb}(\text{PMIP})_3$  film made by vacuum deposition of complex B [13] and the emission spectrum of the DPPOC film. When a vacuum co-deposited film of complex B and DPPOC (molar ratio = 1:1) was made, the fluorescence of DPPOC film at 424 nm is quenched as the emission is mainly observed from the  $^5\text{D}_4 \rightarrow ^7\text{F}_j$  ( $j = 3-6$ ) transitions of the terbium ion. The data thus confirms that the energy absorbed by DPPOC is transferred to a terbium ion and thus sensitizes it efficiently upon coordination. The emission is very weak with a peak at 420 nm which is due to unchelated DPPOC in the co-deposited film as reported previously [19].

### 3.2. IR spectra

To confirm chelation the IR spectra of the co-deposited  $\text{Tb}(\text{PMIP})_3$  and DPPOC film and the deposited DPPOC film (both 800 nm thick) were measured and compared to solid powder samples of  $\text{Tb}(\text{PMIP})_3\text{DPPOC}$  and DPPOC which were synthesized as described in the experimental section.

**Table 1**  
Photophysical data for TPPO, DPPOC and the terbium complexes.

Compounds	$\lambda_{\max}$ (abs) [nm] ( $\epsilon$ [ $\text{dm}^3 \text{mol}^{-1} \text{cm}^{-1}$ ])	$\lambda_{\text{em}}$ [nm] ( $\tau$ [ $\mu\text{s}$ ])			$\Phi^d$ (%)	
		298 K <sup>a</sup>	78 K <sup>b</sup>			
DPPOC	254 (56,810)	353 (5.6 ns)	405 (12.2)	424		
	278 (57,100)	370 (5.7 ns)	432 (11.3)			
TPPO	273 (34,200)	283 (1.5 ns)	357 (11.1)			
Complex A	254 (120,420) 276 (128,320)	488, 548 (223.2), 582, 617			488, 542 581, 618	16.7
Complex B	263 (70,280)	489, 547 (36.4), 582, 617			491, 543 584, 619	10.4
Complex C	273 (112,623)	488, 548 (204.7), 582, 617			490, 543 583, 619	14.6

<sup>a</sup> Measured in  $\text{CH}_2\text{Cl}_2$  solution at 298 K.

<sup>b</sup> Measured in ethanol solution at 78 K.

<sup>c</sup> Deposited (complexes B and C) or co-deposited film (complex A) of 100 nm.

<sup>d</sup> 298 K in  $\text{CH}_2\text{Cl}_2$  measured by using  $\text{Ru}(\text{bpy})_3\text{Cl}_2$  as Ref. [21].

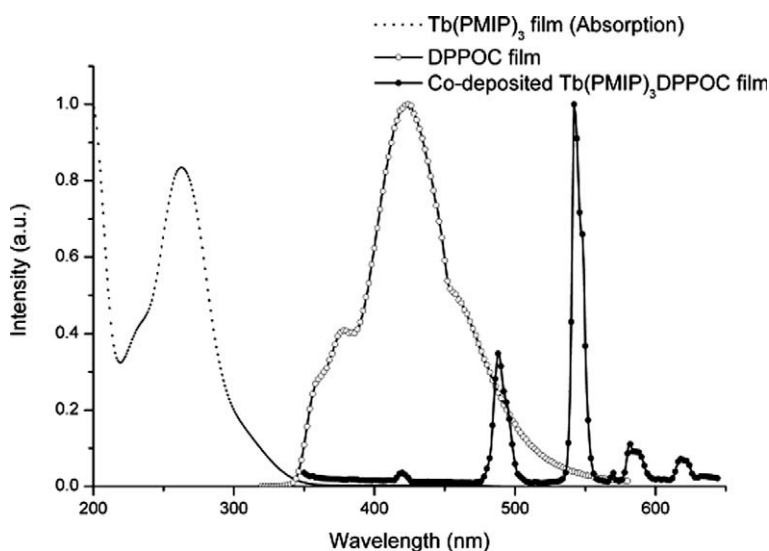


**Fig. 2.** Absorption (dotted line) spectrum of the  $\text{Tb}(\text{PMIP})_3$  film and PL spectra (solid lines) of the vacuum deposited DPPOC film and the co-deposited  $\text{Tb}(\text{PMIP})_3$  and DPPOC film.

The characteristic P=O stretching vibration of DPPOC powder is found at  $1198 \text{ cm}^{-1}$ . There are two P=O stretching vibration bands of  $\text{Tb}(\text{PMIP})_3\text{DPPOC}$  powder at  $1195 \text{ cm}^{-1}$  (similar to free DPPOC) and at  $1172 \text{ cm}^{-1}$  which is  $25 \text{ cm}^{-1}$  red shifted and shows that chelation between P=O and the terbium ion occurred. This data is similar to that for TPPO and related terbium complexes as previously reported [23]. The two different  $\nu(\text{P}=\text{O})$  absorption bands indicate that both the P=O donors in DPPOC did not chelate simultaneously. The absorption bands of  $\nu(\text{P}=\text{O})$  in the deposited DPPOC film was found at  $1194 \text{ cm}^{-1}$  and is similar to the DPPOC powder. In the co-deposited  $\text{Tb}(\text{PMIP})_3$  and DPPOC film two peaks at 1168 and  $1195 \text{ cm}^{-1}$  were observed which agrees with the  $\text{Tb}(\text{PMIP})_3\text{DPPOC}$  powder data. The chelation of DPPOC and complex B thus occurs when they are co-deposited on the substrate and the emitting material produced after co-deposition may be a mixture of polymeric materials that are linked by DPPOC bridges. This vacuum co-deposition technique is favorable for EL device fabrication.

### 3.3. Cyclic voltammetric studies

Cyclic voltammetry (CV) was conducted to investigate electrochemical properties of the compounds. The highest occupied molecular orbital (HOMO) and lowest unoccupied molecular orbital (LUMO) energy levels of the materials were estimated by CV and UV-visible. Only oxidation potentials of the terbium complexes were measured as  $\text{CH}_2\text{Cl}_2$  can not be used to determine reduction potentials from  $-2.7$  to  $-3.5 \text{ V}$  [24]. The three complexes have the same first oxidation potential and the same lowest energy absorption edge as shown in their UV-visible absorption spectra (Fig. 1). This indicates that they have similar HOMO and LUMO energy levels of 5.4 and 1.9 eV, respectively.

### 3.4. Thermal properties and morphological stabilities

Thermal properties were determined by thermogravimetric analysis (TGA) and differential scanning calorimetry (DSC). The melting point ( $T_m$ ) of DPPOC is about  $301 \text{ }^\circ\text{C}$  and

the thermal decomposition temperature ( $T_d$ ) is 440 °C with a  $T_g$  of 137 °C, which shows that DPPOC exhibits better thermal stability than TPPO ( $T_m$  156 °C,  $T_d$  228 °C and no  $T_g$  observed). The complex  $Tb(PMIP)_3DPPOC$  also shows higher thermal stability ( $T_d$  440 °C) than  $Tb(PMIP)_3(TPPO)_2$  ( $T_d$  350 °C) and  $Tb(PMIP)_3(H_2O)_2$  ( $T_d$  253 °C). The morphological stability of the material was confirmed by fluorescence micrographs and these are shown in Fig. 3. The co-deposited  $Tb(PMIP)_3DPPOC$  film (image A) was stable and showed no apparent crystallization or aggregation at 120 h after fabrication. The  $Tb(PMIP)_3(TPPO)_2$  film (image B) showed obvious dewetting after 24 h, and serious crystallization (bright spots in B3 and B4) after 48 h. These morphological changes of the amorphous films are caused by poor thermal stability of the unchelated TPPO. In accordance with our molecular design we substituted DPPOC for TPPO which produced a morphologically stable amorphous film and would thus significantly improve OLED's stability.

### 3.5. Electroluminescence properties

By introducing NPB and AIQ as hole and electron transporting materials respectively and BCP as a hole blocking material devices A1–A4 were fabricated. The structures were ITO/NPB (30 nm)/co-deposited  $Tb(PMIP)_3DPPOC$  (A1: 20 nm, A2: 30 nm, A3: 40 nm, A4: 60 nm)/BCP (10 nm)/AIQ (30 nm)/ $Mg_{0.9}Ag_{0.1}$ . Different thicknesses of co-deposited  $Tb(PMIP)_3DPPOC$  were used as the emitting layer (Fig. 4). All of the devices showed the characteristic green emission from  $Tb^{3+}$  at low voltage. At practical brightness an emission from NPB was observed and device A1 only showed a small amount of emission from the terbium complex (Fig. 5). This indicates that DPPOC has fairly good electron transport properties and that the small energy gap between the LUMO of the terbium complex and of NPB allows electron transport into the NPB layer. By increasing the thickness of the complex layer from 20 to

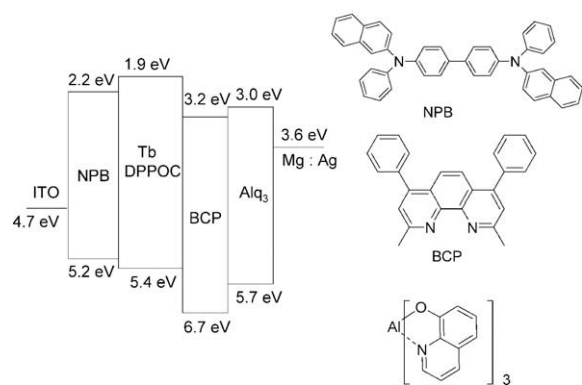


Fig. 4. The EL device structure and chemical structures of the materials employed.

60 nm the emissive area changed from NPB layer to the terbium complex layer at high voltage. The power efficiencies increased from  $2.6 \text{ lm W}^{-1}$  (6.0 V) for device A1 to  $5.2 \text{ lm W}^{-1}$  (7.0 V) for device A4 (Fig. 6). Because DPPOC has both electron and hole transporting groups, the carriers mainly recombined in the co-deposited  $Tb(PMIP)_3DPPOC$  layer when its thickness was increased. The higher PL quantum yield of the lanthanide complexes led to higher EL efficiencies. The greater thickness of the EML (emission layer), however, resulted in lower current density which limited the luminance of the devices. Device A2 had the highest luminance of  $1331 \text{ cd m}^{-2}$  at 19 V. A small improvement in efficiency at high voltage was observed but the current density and the luminance decreased significantly when the EML thickness was increased beyond 30 nm.

Devices B1–B3 with configurations of ITO/NPB (10 nm)/ $Tb(PMIP)_3$  (B1: 10 nm; B2: 15 nm, B3: 20 nm)/co-deposited  $Tb(PMIP)_3DPPOC$  (30 nm)/BCP (10 nm)/AIQ (20 nm)/

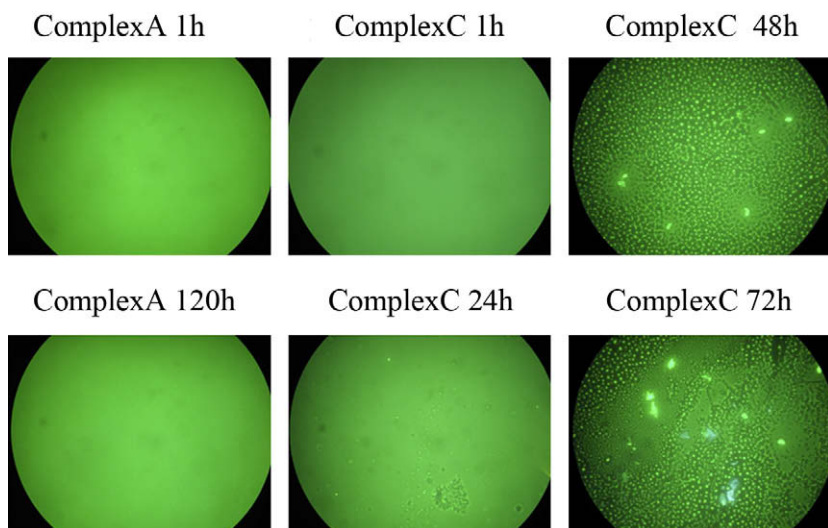


Fig. 3. Fluorescence microscopy images of vacuum co-deposited complex A ( $Tb(PMIP)_3DPPOC$ ) and complex C ( $Tb(PMIP)_3(TPPO)_2$ ) films on glass at different times after fabrication at room temperature.

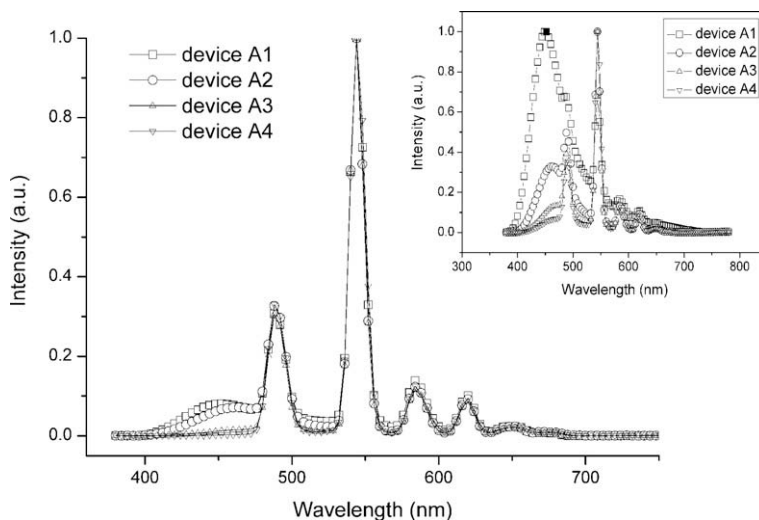


Fig. 5. Intensity normalized EL spectra of devices A1–A4 at  $100 \text{ cd m}^{-2}$  (inset: intensity normalized EL spectra at highest brightness).

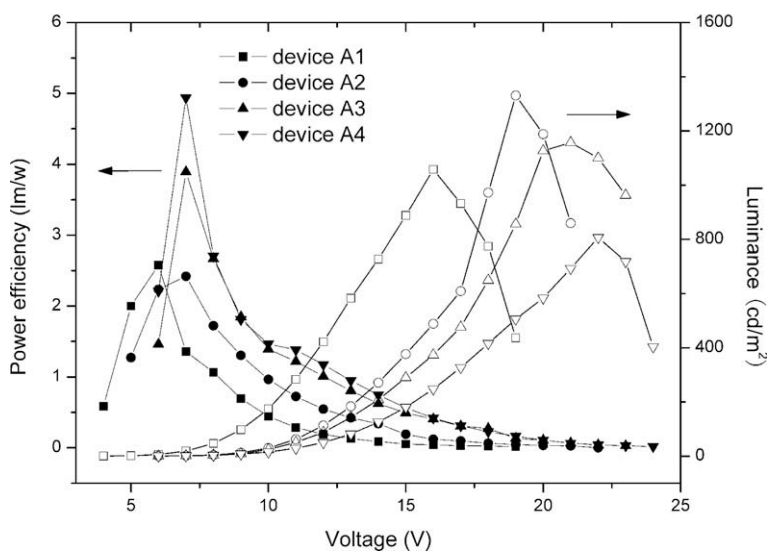


Fig. 6. Power efficiency (solid symbols) and luminance (open symbols) versus voltage of devices A1–A4.

$\text{Mg}_{0.9}\text{Ag}_{0.1}$  were fabricated to confine carriers in the emitting layer for better EL performance. Co-deposited  $\text{Tb}(\text{PMIP})_3\text{DPPPOC}$  layer was kept at 30 nm and  $\text{Tb}(\text{PMIP})_3$  complemented as hole-transporting material. With a  $\text{Tb}(\text{PMIP})_3$  layer thickness increased from 10 to 20 nm the carriers were confined within the layers of the complexes and thus more excitons contributed to the lanthanide luminescence process. Compared to device A4, from which the emission of NPB was observed at practical luminance (Fig. 5), device B3 showed pure emission that originated from the terbium complex even at the highest applied voltage (Fig. 7). The maximum brightness improved from  $1020 \text{ cd m}^{-2}$  (16 V) for A4 to  $2256 \text{ cd m}^{-2}$  (16 V) for B3 and the power efficiency from  $5.2 \text{ lm W}^{-1}$  (7 V) to  $16.1 \text{ lm W}^{-1}$  (5 V), respectively. This also confirmed that

the carrier recombination zone was confined well within the complex layers so the maximum brightness and highest efficiency were both achieved in device B3. At a practical brightness of  $119 \text{ cd m}^{-2}$  (11 V) the efficiency remained above  $4.5 \text{ lm W}^{-1}$ ,  $15.7 \text{ cd A}^{-1}$  (Fig. 8). The EML with a multilayer structure for the lanthanide ions is quite different from that of other phosphor materials such as iridium complexes. Multilayer structures with EMLs usually emit hybrid light which are used in white emitting OLEDs [25]. For lanthanide complexes extremely pure light is achievable because their emission is due to electronic transitions of the central ions and this emission is different to the MLCT emission of iridium complexes. Lanthanide complexes are advantageous as their sharp emission bands are maintained while ligands are modified to improve PL

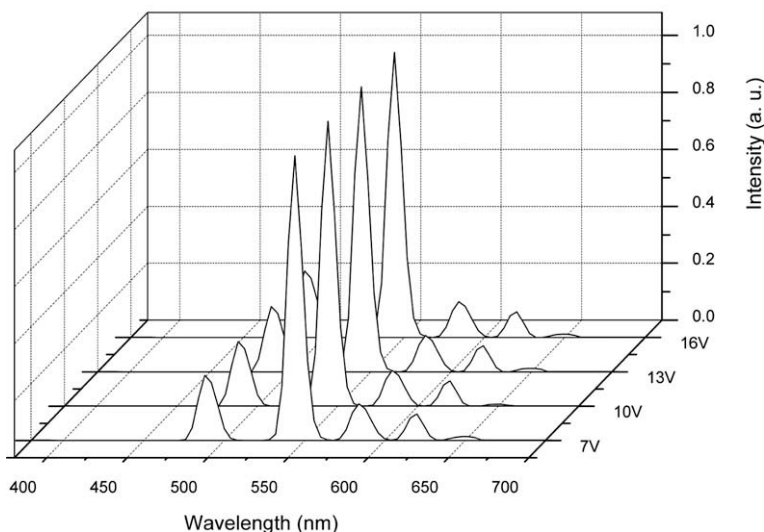


Fig. 7. EL spectra of device B3 at different applied voltages.

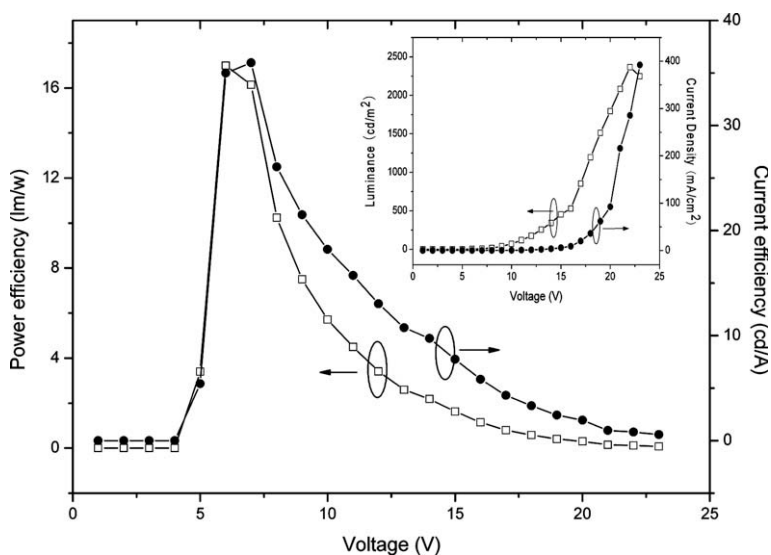


Fig. 8. Power efficiency (open squares), current efficiency (solid circles) and voltage characteristics of device B3 (inset: luminance, current density and voltage characteristics of device B3).

efficiencies. Based on this multilayer EMLs devices, recombination zone was limited and pure emission from lanthanide ions was achieved with a high efficiency.

#### 4. Conclusions

We have synthesized new diphenylphosphine oxide substituted carbazole derivative (DPPOC) that retains suitable triplet energy level while exhibiting enhanced morphological stability with a high glass transition temperature. By the vacuum co-deposition technique a terbium complex ( $\text{Tb}(\text{PMIP})_3\text{DPPOC}$ ) film was formed and OLED devices were fabricated. Electroluminescent perfor-

mance revealed that the multilayered emission structure helped to capture all the injected charges to form excitons in a confined zone. Highly pure  $\text{Tb}^{3+}$  ion emission was achieved even at the highest applied voltage and high efficiency was obtained. The modification for suitable ligands and multilayered EML structures may improve lanthanide EL properties for future use in devices.

#### Acknowledgement

This work was supported by The National Basic Research Program (2006CB601103), NNSFC (50772003, 20671006, 20821091).



## References

- [1] J. Kido, K. Nagai, Y. Ohashi, *Chem. Lett.* (1990) 657.
- [2] J. Kido, H. Hayase, K. Hongawa, K. Nagai, K. Okuyama, *Appl. Phys. Lett.* 65 (1994) 2124.
- [3] A. Edwards, C. Claude, I. Sokolik, T.Y. Chu, Y. Okamoto, R. Dorsinville, *J. Appl. Phys.* 82 (1997) 1841.
- [4] J. Kido, Y. Okamoto, *Chem. Rev.* 102 (2002) 2357.
- [5] J. Kalinowski, *Opt. Mater.* 30 (2008) 792.
- [6] J. Kalinowski, W. Stampor, M. Cocchi, D. Virgili, V. Fattori, *Appl. Phys. Lett.* (2005) 86.
- [7] J.F. Wang, R.Y. Wang, J. Yang, Z.P. Zheng, M.D. Carducci, T. Cayou, N. Peyghambarian, G.E. Jabbour, *J. Am. Chem. Soc.* 123 (2001) 6179.
- [8] Y.X. Zheng, J. Lin, Y.J. Liang, Q. Lin, Y.N. Yu, Q.G. Meng, Y.H. Zhou, S.B. Wang, H.Y. Wang, H.J. Zhang, *J. Mater. Chem.* 11 (2001) 2615.
- [9] P.P. Sun, J.P. Duan, J.J. Lih, C.H. Cheng, *Adv. Funct. Mater.* 13 (2003) 683.
- [10] H. Xin, M. Shi, X.C. Gao, Y.Y. Huang, Z.L. Gong, D.B. Nie, H. Cao, Z.Q. Bian, F.Y. Li, C.H. Huang, *J. Phys. Chem. B* 108 (2004) 10796.
- [11] J.F. Fang, D.G. Ma, *Appl. Phys. Lett.* 83 (2003) 4041.
- [12] F.S. Liang, Q.G. Zhou, Y.X. Cheng, L.X. Wang, D.G. Ma, X.B. Jing, F.S. Wang, *Chem. Mater.* 15 (2003) 1935.
- [13] X. Hao, S. Mei, M.Z. Xiao, Y.L. Fu, Q.B. Zu, K. Ibrahim, Q.L. Feng, H.H. Chun, *Chem. Mater.* 15 (2003) 3728.
- [14] H. Xin, F.Y. Li, M. Shi, Z.Q.A. Bian, C.H. Huang, *J. Am. Chem. Soc.* 125 (2003) 7166.
- [15] J.R.G. Thorne, J.M. Rey, R.G. Denning, S.E. Watkins, M. Etchells, M. Green, V. Christou, *J. Phys. Chem. A* 106 (2002) 4014.
- [16] H. Yesin, *Highly Efficient OLEDs with Phosphorescent Materials*, Wiley-VCH, 2008.
- [17] M.H. Tsai, H.W. Lin, H.C. Su, T.H. Ke, C.C. Wu, F.C. Fang, Y.L. Liao, K.T. Wong, C.I. Wu, *Adv. Mater.* 18 (2006) 1216.
- [18] K. Brunner, A. van Dijken, H. Börner, J.J.A.M. Bastiaansen, N.M.M. Kikken, B.M.W. Langeveld, *J. Am. Chem. Soc.* 126 (2004) 6035.
- [19] T. Oyamada, Y. Kawamura, T. Koyama, H. Sasabe, C. Adachi, *Adv. Mater.* 16 (2004) 1082.
- [20] T.A. Hopkins, K. Meerholz, S. Shaheen, M.L. Anderson, A. Schmidt, B. Kippelen, A.B. Padias, H.K. Hall, N. Peyghambarian, N.R. Armstrong, *Chem. Mater.* 8 (1996) 344.
- [21] K.T. Wong, Y.M. Chen, Y.T. Lin, H.C. Su, C.C. Wu, *Org. Lett.* 7 (2005) 5361.
- [22] M. Latva, H. Takalo, V.M. Mikkala, C. Matachescu, J.C. Rodriguez-Ubis, J. Kankare, *J. Lumin.* 75 (1997) 149.
- [23] S. Eliseeva, O. Kotova, O. Mirzov, K. Anikin, L. Lepnev, E. Perevedentseva, A. Vitukhnovsky, N. Kuzmina, *Synth. Met.* 141 (2004) 225.
- [24] S.G. Jung, Y.J. Kang, H.S. Kim, Y.H. Kim, C.L. Lee, J.J. Kim, S.K. Lee, S.K. Kwon, *Eur. J. Inorg. Chem.* (2004) 3415.
- [25] B.W. D'Andrade, M.E. Thompson, S.R. Forrest, *Adv. Mater.* 14 (2002) 147.

devices with different gate metals were studied by the repetitive gate voltage sweep of OTFTs, and capacitance–voltage ( $C-V$ ) and trap loss–voltage ( $G_p/\omega-V$ ) measurements of metal–insulator–semiconductor (MIS) devices. It showed that the hysteresis in OTFTs was associated with electron injection from gate electrode to insulator. The application of gate metal with high work function increased the injection barrier between gate and insulator. As a result, low hysteresis OTFTs were obtained.

## 2. Experimental

### 2.1. Materials

The Corning 7059 alkali-free glass substrates were purchased from Chengdu Guangming Optoelectronic Co. (China). The glass substrates were cleaned in two sequential steps with chromic acid lotion and deionized water in ultrasonic bath. BCBO derivatives (Fig. 1a) were synthesized according to Ref. [18]. BCBO derivatives were dissolved in tetrahydrofuran, and the solution was filtered three times through a 0.22  $\mu\text{m}$  glass syringe filter. The vanadyl-phthalocyanine (VOPc) was purchased from Aldrich Company (USA). The *para*-sexiphenyl (*p*-6P) sample was synthesized according to a described method [19]. Both of the samples were purified twice by thermal gradient sublimation prior to deposition.

### 2.2. Fabrication of vanadyl-phthalocyanine (VOPc) TFTs and MIS diodes

Fig. 1b shows the schematic structure of VOPc thin-film transistors. Before the deposition of the metals, 140 nm

BCBO films were spin-coated onto glass substrates to smooth the rough glass surfaces. Thermal-evaporated Al and Au films about 100 nm and magnetron-sputtered Cr film about 200 nm were deposited on the glass substrates respectively, and were used as gate electrodes. The room-temperature (rms) roughness of Al, Cr and Au are 1.3 nm, 1.2 nm and 1.3 nm measured by atomic force microscopy (AFM). The 200 nm  $\text{Ta}_2\text{O}_5$  films were deposited by magnetron-sputter on the gate electrodes. The rms roughness of  $\text{Ta}_2\text{O}_5$  on Al, Cr and Au is 2.7 nm, 2.5 nm and 2.6 nm, respectively. These surfaces are too rough for the growth of organic semiconductors [20]. One percent benzocyclobutenone (BCBO) thin layer was spin-coated onto the  $\text{Ta}_2\text{O}_5$  film to obtain preferable interface. Then, the BCBO film about 140 nm was cross-linked by ultraviolet exposure and formed double-layer insulator. As shown in Fig. 2, the double-layer insulator exhibits very smooth surfaces with rms roughness about 6 Å. The reduction of rms roughness for double-layer insulator is caused by the viscous BCBO solution which fills up the valley regions of the rough metal/ $\text{Ta}_2\text{O}_5$  substrate [21]. The rms of Al and Al/ $\text{Ta}_2\text{O}_5$  are also given in Fig. 2. Three nanometers *p*-6P and a 30 nm VOPc were successively deposited on the double-layer insulator by vacuum thermal deposition at a substrate temperature of 180 C under the pressure of  $10^{-4}$  Pa. We selected VOPc as the active layer because it is a kind of organic semiconductor with good physics and chemistry stability [22,23]. During the analysis of hysteresis, the influence from active layer can be excluded. VOPc showed weak epitaxy growth (WEG) behavior on the ordered *p*-6P layer [22]. The growth mode of VOPc film is changed to be layer-by-layer growth behavior rather than the island

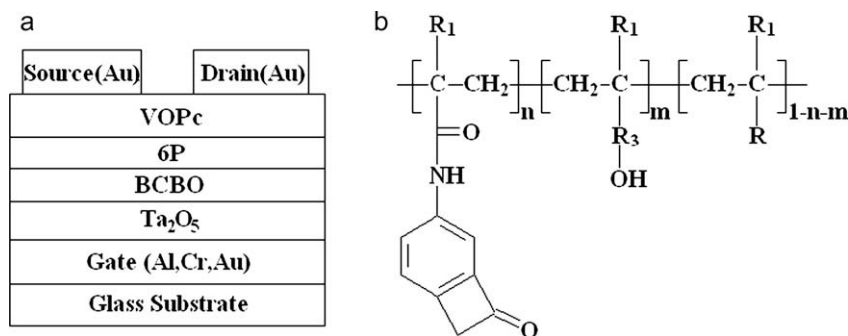


Fig. 1. (a) The structure of VOPc organic thin-film transistors with  $\text{Ta}_2\text{O}_5$ /BCBO double-layer gate insulators, and (b) the chemical structure of BCBO.

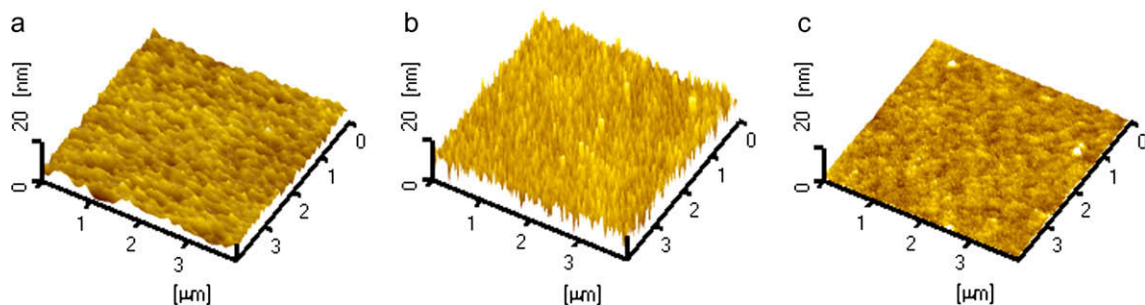
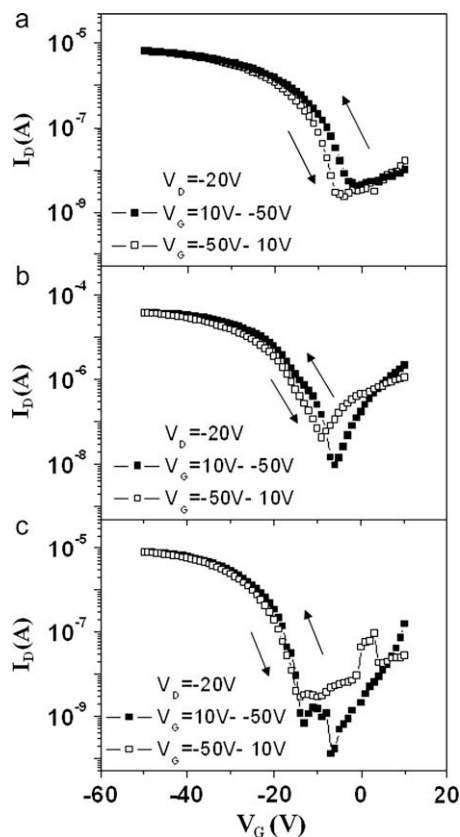
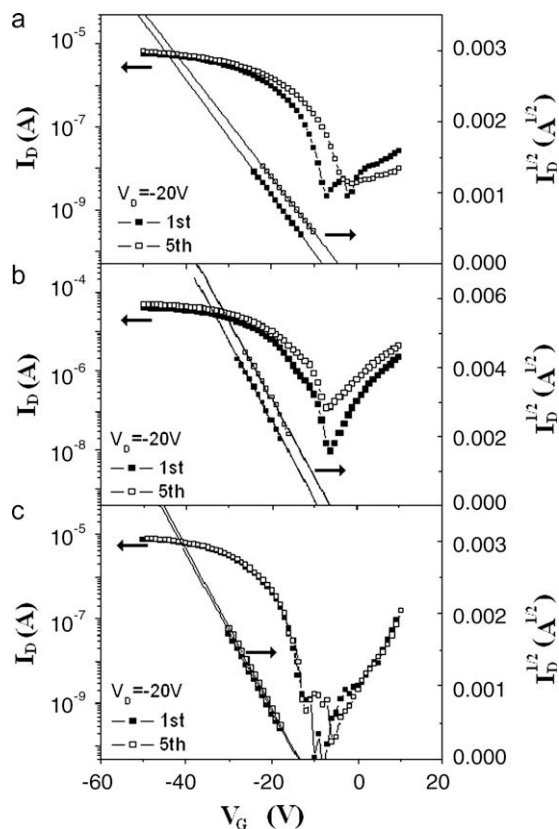


Fig. 2. The AFM images of (a) glass/Al, (b) glass/Al/ $\text{Ta}_2\text{O}_5$ , (c) glass/Al/ $\text{Ta}_2\text{O}_5$ /BCBO.



**Fig. 3.** Transfer characteristics of VOPc OTFTs (drain voltage,  $V_D = -20$  V) using the  $Ta_2O_5/BCBO$  double-layer insulators with different metals as gate electrodes: (a) Al, and (b) Cr, and (c) Au. The gate voltage swept in both directions.

growth. The weak epitaxy growth (WEG) of VOPc molecules on the  $p$ -6P layer lead to their high in-plane orientation. In addition, the VOPc films are consisted of lamellar crystals, which are intimately connected with each other. Therefore, the traps at grain boundaries and interface are quite less. Finally, 40 nm Au source/drain electrodes were thermally evaporated onto the VOPc films by a shadow mask. The defined channel width ( $W$ ) and length ( $L$ ) were 1000 and 150  $\mu\text{m}$ , respectively. The current–voltage measurements were carried out by two Keithley 236 source measurement units at room temperature. Circular dots of metal films with 2 mm diameter were also deposited onto VOPc films by the shadow mask to fabricate the MIS de-



**Fig. 4.** The transfer characteristics obtained with repetitive gate voltage sweep (drain voltage,  $V_D = -20$  V) from VOPc OTFTs with different metals as gate electrodes: (a) Al, and (b) Cr, and (c) Au.

vices. The Electrical characterization of the MIS devices was performed with an Agilent E4980A LCR meter at room temperature in a dark electromagnetic shielding box.

### 3. Results and discussion

Fig. 3 shows the transfer characteristics of VOPc TFTs with different metals Al, Cr and Au as gate electrodes at the drain voltage  $V_{DS}$  of  $-20$  V. All of the involved data are listed in Table 1. The leakage current of all TFTs is at the  $10^{-9}$  A level. This low leakage current is owing to the excellent insulation of  $Ta_2O_5/BCBO$  double-layer. Therefore, the analysis below is not affected by the leakage current. Devices with low work function metals Al and Cr as

**Table 1**

The work functions of metals, other involved device parameters.

Gate electrode	Work function <sup>a</sup> (eV)	Barrier heights <sup>b</sup> (eV)	Threshold voltage shift <sup>c</sup> (V)	Threshold voltage (V)		
				1st	5th	$\Delta V_T$
Al	4.3	0.9	2.6	-7.9	-4.0	3.9
Cr	4.5	-	2.5	-9.2	-6.2	3.0
Au	5.1	1.34	0.7	-15.1	-15.0	0.1

<sup>a</sup> The values of metal work function are obtained from Ref. [36].

<sup>b</sup> The values of barrier heights are obtained from Ref. [34].

<sup>c</sup> The threshold voltage shift of hysteresis of  $I$ - $V$ .

gate electrodes exhibited large hysteresis when the gate bias swept from 10 V to  $-50$  V and back from  $-50$  V to 10 V. The average threshold voltage shift was 2.6 V for Al as gate electrode and 2.5 V for Cr as gate electrode, respectively. But the devices using high work function metal Au as gate electrode showed a lower hysteresis under the completely same range of voltage scans. Fig. 3c shows the representative current–voltage ( $I$ – $V$ ) curves of OTFTs with Au as gate electrode. The average threshold voltage shift of several devices was 0.7 V. So, the lower hysteresis OTFTs have been realized by using Au as gate electrode instead of Al or Cr as gate electrodes.

There are several arguments as to the origin of the hysteresis of OTFTs: (1) charge injection, movement, and storage in the dielectrics [11,24–28], (2) channel/dielectric interface trap [23,29–31], (3) slow polarization of gate dielectric [24,32,33]. Slow polarization and channel/dielectric interface trap are not the dominant mechanism of the hysteresis in this case, because these devices have the same insulator materials and channel/dielectric interface. Therefore, electron injection is likely to be the dominant mechanism of hysteresis.

Repetitive gate voltage sweep of VOPc TFTs was used to analyze the reason for the variation of hysteresis, as shown in Fig. 4. Fig. 4a and b shows the transfer characteristics of the devices using Al and Cr as gate electrodes. Threshold voltage moved to more positive side until the gate voltage sweep was repeated up to five times, from  $-7.9$  V to  $-4.0$  V for Al as gate electrode and from  $-9.2$  V to  $-6.2$  V for Cr as gate electrode. It is presumed that electrons have been injected to the insulator from Cr and Al gate electrodes under the applied electric fields during the repeated voltage

sweep [25]. However, for the transistor in which Au was used as gate electrode, the fifth transfer curve almost coincided with the first transfer curve (Fig. 4c). The negligible threshold voltage shift demonstrates that electron injection decreases in a great extent compared with devices using Al and Cr as gate electrode. Robertson and coworkers have calculated the electron schottky barrier height of various metals including Al and Au on  $\text{Ta}_2\text{O}_5$ , which are 0.9 eV for Al and 1.34 eV for Au on  $\text{Ta}_2\text{O}_5$  [34]. The work function of Cr (about 4.5 eV) is slightly higher than the work function of Al (about 4.3 eV), and is lower than the work function of Au (about 5.1 eV). From the results of  $I$ – $V$  and the work function value of the three metals, the barrier height of Cr on  $\text{Ta}_2\text{O}_5$  should be slightly higher than the value of Al on  $\text{Ta}_2\text{O}_5$  and is lower than the value of Au on  $\text{Ta}_2\text{O}_5$ . In other words, the electron barrier heights of Al and Cr on  $\text{Ta}_2\text{O}_5$  are lower than the electron barrier height of Au on  $\text{Ta}_2\text{O}_5$ . Therefore, Al and Cr give electrons to  $\text{Ta}_2\text{O}_5$  insulator more easily compared with Au. In this case, it exhibited more threshold voltage shift using Al and Cr as gate electrodes. Based on the comprehensive analysis of the hysteresis characteristics, the electron injection from gate electrode to insulator may be the reason of hysteresis in these devices.

Capacitance–voltage ( $C$ – $V$ ) measurement is another effective approach to analyze the hysteresis characteristics of devices. In order to verify the place where hysteresis took place, another kind of MIS devices consisting of Cr/BCBO/6P/VOPc/Au were fabricated. Fig. 5a–d show the  $C$ – $V$  curves of MIS diodes, in which the gate bias sweep is from 20 V to  $-20$  V and back from  $-20$  V to 20 V. As shown in Fig. 5a and b, the hysteresis is negligible for Cr/BCBO/6P/

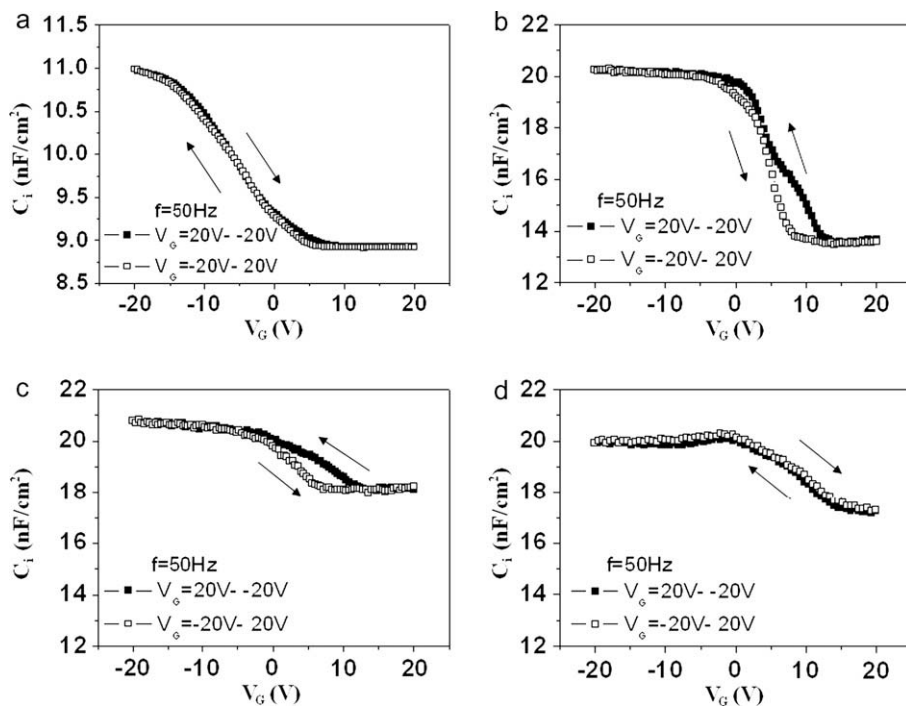


**Fig. 5.** Capacitance–voltage characteristics of VOPc MIS devices with different metals as gate electrodes and different insulators: (a) Cr–BCBO, and (b) Cr– $\text{Ta}_2\text{O}_5$ /BCBO, and (c) Al– $\text{Ta}_2\text{O}_5$ /BCBO, and (d) Au– $\text{Ta}_2\text{O}_5$ /BCBO. The gate voltage swept in both directions.

VOPc structure while it is obvious in Cr/Ta<sub>2</sub>O<sub>5</sub>/BCBO/6P/VOPc structure. This indicates that the hysteresis comes from the Ta<sub>2</sub>O<sub>5</sub> layer rather than the interface between BCBO and active layer. So, the use of BCBO as second-layer insulator eliminated the effect of the interface charges and interface traps of Ta<sub>2</sub>O<sub>5</sub> on hysteresis [15–17]. As shown in Fig. 5b–d, the hysteresis decreases with increasing work function of gate electrodes, which is consistent with the *I*–*V* characteristic of OTFTs. For the closed loop of *C*–*V* curves, the integral corresponds to the stored charge after a sweep cycle. For the Cr and Al as gate electrodes, the integral of closed loop of *C*–*V* curves are not equal to zero. Obviously, from Fig. 4b and c we can see the charge is negative. According to the reasoning above, this negative charge is owing to the electron injection from Cr and Al electrodes to Ta<sub>2</sub>O<sub>5</sub>.

Fig. 6 shows the *C*–*V* curves of MIS diodes using Ta<sub>2</sub>O<sub>5</sub>/BCBO double-layer insulator with Al, Cr and Au as gate electrodes, the gate bias is repeatedly swept from 20 V to –20 V. The *C*–*V* curves moved to more positive voltage when Al or Cr was used as gate electrode, which also indicated that electrons had been injected to Ta<sub>2</sub>O<sub>5</sub> insulator [35]. However, the *C*–*V* curve almost didn't move for devices with Au as gate electrode. It indicates electrons injected to Ta<sub>2</sub>O<sub>5</sub> insulator were decreased. Fig. 7 shows the  $G_p/\omega$ –*V* curves of MIS diodes with different metals as gate electrodes at the constant frequency of 50 Hz. At neg-

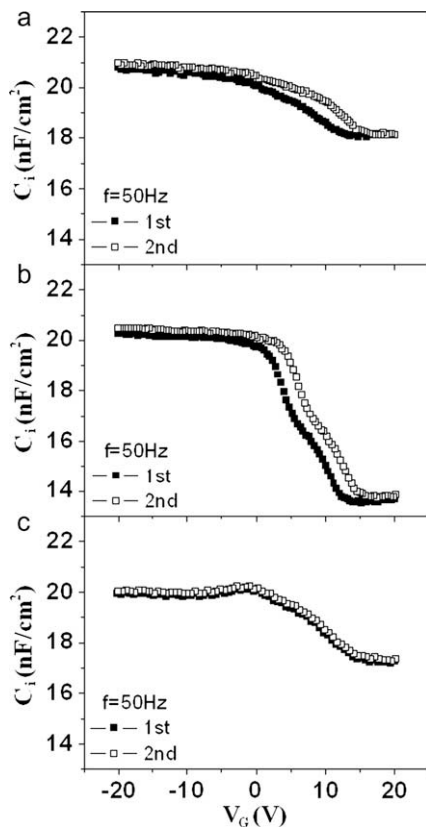


Fig. 6. Capacitance–voltage characteristics obtained with repetitive gate voltage sweep from VOPc MIS devices with different metals as gate electrodes: (a) Al, and (b) Cr, and (c) Au.

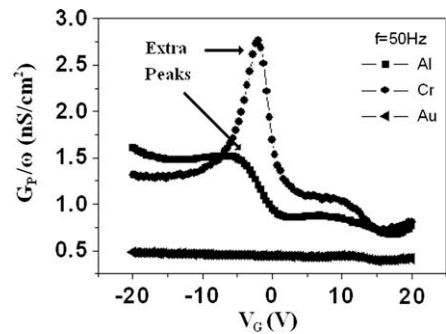


Fig. 7. The trap loss  $G_p/\omega$  of VOPc MIS diodes with Al, Cr and Au as gate electrode versus gate voltage at the constant frequency of 50 Hz.

ative voltage, extra energy loss peaks were observed when Cr or Al was used as gate electrodes compared with Au as gate electrode. Combined with experiment of repetitive gate bias sweep of *C*–*V* for devices with different metals as gate electrodes, we can conclude the generation of energy loss peaks originated from the electron injection from gate metal to Ta<sub>2</sub>O<sub>5</sub> [35]. When Au was used as gate electrode, the electron barrier between gate electrode and Ta<sub>2</sub>O<sub>5</sub> was enhanced. The higher electron barrier reduced the amount of electron injection from Au to Ta<sub>2</sub>O<sub>5</sub>. Therefore, there were no peaks in  $G_p/\omega$ –*V* curves at negative voltage region. These experiments about MIS structure also proved that the hysteresis originated from the electron injection from gate metal to Ta<sub>2</sub>O<sub>5</sub>. Therefore, choosing high work function metal as gate electrode is an effective method to fabricate low hysteresis devices.

#### 4. Conclusion

In conclusion, we have demonstrated the influence of work function of gate electrode on the hysteresis characteristics of VOPc devices with Ta<sub>2</sub>O<sub>5</sub>/BCBO as double-layer gate insulator. Hysteresis was caused mainly by electrons injection from gate electrodes to Ta<sub>2</sub>O<sub>5</sub> insulator when low work function metals, such as Cr and Al, were used as gate electrodes. Using high work function Au as gate electrode could enhance the barrier and weaken the electron injection between gate electrode and Ta<sub>2</sub>O<sub>5</sub> insulator. Thus low hysteresis organic thin-film transistors were obtained. It is a simple and effective way to decrease hysteresis.

#### Acknowledgment

This work was supported by the National Natural Science Foundation of China (50773079, 50803063) and the Special Funds for Major State Basic Research Projects (2009CB939702).

#### References

- [1] G. Horowitz, Adv. Mater. 10 (1998) 365.
- [2] C.D. Dimitrakopoulos, P.R.L. Malenfant, Adv. Mater. 14 (2002) 99.
- [3] B. Crone, A. Dodabalapur, Y.Y. Lin, R.W. Filas, Z. Bao, A. LaDuca, R. Sarapeshkar, H.E. Katz, W. Li, Nature 403 (2000) 521.

- [4] D. Knipp, R.A. Street, A. Volkel, J. Ho, *J. Appl. Phys.* 93 (2003) 347.
- [5] C.D. Dimitrakopoulos, S. Purushothaman, J. Kymissis, A. Callegari, J.M. Shaw, *Science* 283 (1999) 822.
- [6] J. Tate, J.A. Rogers, C.D.W. Jones, B. Vyas, D.W. Murphy, W.J. Li, Z.A. Bao, R.E. Slusher, A. Dodabalapur, H.E. Katz, *Langmuir* 16 (2000) 6054.
- [7] C. Bartic, H. Jansen, A. Campitelli, S. Borghs, *Org. Electron.* 3 (2002) 65.
- [8] Y. Iino, Y. Inoue, Y. Fujisaki, H. Fujikake, H. Sato, M. Kawakita, S. Tokito, H. Kikuchi, *Jpn. J. Appl. Phys., Part 1* 42 (2003) 299.
- [9] J.F. Yuan, J. Zhang, J. Wang, X.J. Yan, D.H. Yan, W. Xu, *Appl. Phys. Lett.* 82 (2003) 3967.
- [10] J. Wang, X.J. Yan, Y.X. Xu, J. Zhang, D.H. Yan, *Appl. Phys. Lett.* 85 (2004) 5424.
- [11] J.F. Yuan, J.D. Zhang, J. Wang, D.H. Yan, W. Xu, *Thin Solid Films* 450 (2004) 316.
- [12] K. Miyairi, E. Itoh, *Thin Solid Films* 499 (2006) 95.
- [13] J.G. Zhou, K.X. Yang, J.L. Zhou, Y.R. Liu, J.B. Peng, Y. Cao, *Jpn. J. Appl. Phys.* 46 (2007) 913.
- [14] Y. Zhao, G.F. Dong, L.D. Wang, Y. Qiu, *Appl. Phys. Lett.* 90 (2007) 252110.
- [15] P.C. Jjiang, J.S. Chen, *J. Electrochem. Soc.* 151 (2004) G751.
- [16] D. Briand, G. Mondin, S. Jenny, P.D. van der Wal, S. Jeanneret, N.F. de Rooij, O. Banakh, H. Keppner, *Thin Solid Films* 493 (2005) 6.
- [17] L. Pereira, P. Barquinha, E. Fortunato, R. Martins, D. Kang, C.J. Kim, H. Lim, I. Song, Y. Park, *Thin Solid Films* 516 (2008) 1544.
- [18] L.K.Z.Y. Wang, J.P. Gao, *US* (2003) 6534250 B1.
- [19] F. Garnier, G. Horowitz, X.Z. Peng, D. Fichou, *Synth. Met.* 45 (1991) 163.
- [20] .D. Knipp, R.A. Street, A. Volkel, J. Ho, *J. Appl. Phys.* 93 (2003) 347.
- [21] C.S. Kim, S.J. Jo, J.B. Kim, S.Y. Ryu, J.H. Noh, H.K. Baik, S.J. Lee, K.M. Song, *Semicond. Sci. Technol.* 22 (2007) 691.
- [22] H.B. Wang, D. Song, J.L. Yang, B. Yu, Y.H. Geng, D.H. Yan, *Appl. Phys. Lett.* 90 (2007) 253510.
- [23] L.J. Wang, G.J. Liu, H.B. Wang, D. Song, B. Yu, D.H. Yan, *Appl. Phys. Lett.* 91 (2007) 153508.
- [24] H.E. Katz, X.M. Hong, A. Dodabalapur, R. Sarpeshkar, *J. Appl. Phys.* 91 (2002) 1572.
- [25] D.K. Hwang, J.H. Park, J. Lee, J.M. Choi, J.H. Kim, E. Kim, S. Im, *J. Electrochem. Soc.* 153 (2006) G23.
- [26] C.A. Lee, D.W. Park, S.H. Jin, I.H. Park, J.D. Lee, B.G. Park, *Appl. Phys. Lett.* 88 (2006) 252102.
- [27] C.A. Lee, D.W. Park, K.D. Jung, B.J. Kim, Y.C. Kim, J.D. Lee, B.G. Park, *Appl. Phys. Lett.* 89 (2006) 262120.
- [28] D.W. Park, C.A. Lee, K.D. Jung, B.G. Park, H. Shin, J.D. Lee, *Appl. Phys. Lett.* 89 (2006) 263507.
- [29] G. Gu, M.G. Kane, J.E. Doty, A.H. Firester, *Appl. Phys. Lett.* 87 (2005) 243512.
- [30] D.K. Hwang, K. Lee, J.H. Kim, S. Im, J.H. Park, E. Kim, *Appl. Phys. Lett.* 89 (2006) 093507.
- [31] S.H. Kim, H. Yang, S.Y. Yang, K. Hong, D. Choi, C. Yang, D.S. Chung, C.E. Park, *Org. Electron.* 9 (2008) 673.
- [32] T. Jung, A. Dodabalapur, R. Wenz, S. Mohapatra, *Appl. Phys. Lett.* 87 (2005) 182109.
- [33] D.K. Hwang, M.S. Oh, J.M. Hwang, J.H. Kim, S. Im, *Appl. Phys. Lett.* 92 (2008) 013304.
- [34] J. Robertson, C.W. Chen, *Appl. Phys. Lett.* 74 (1999) 1168.
- [35] E.H. Nicollian, J.R. Brew, *MOS Physics and Technology*, Wiley, 1982, pp. 533–534 (Chapter 11).
- [36] H.B. Michaelson, *J. Appl. Phys.* 48 (1977) 4729.

thyl-containing molecule which was used as light emitting material in OLED with a turn-on voltage of 2.2 V, a maximum luminance of 8315 cd m<sup>-2</sup>, and a maximum luminescence efficiency of 1.95 cd A<sup>-1</sup>.

One of the significant properties of the electroluminescence (EL) devices is the durability. The degradation mechanisms in the OLEDs are not yet fully understood, but several studies indicate that one reason of the degradation is the morphological changes of the organic layers [20,21], such as dimerization and crystallization which seem to be caused by joule heating during device operation [22]. The organic materials tend to dimerize or crystallize when they are allowed to stand at ambient temperature or heated above their glass-transition temperature ( $T_g$ ) [23]. Thus organic materials with high  $T_g$  is propitious to realize high stability OLEDs [23–27]. In addition, it was found that the lower the energy barrier of hole injection at the interface of the ITO/hole-transporting layer (HTL), the lower joule heat produced at the interface [6,28]. For this reason, the energy barrier between the ITO/HTL interface should be as small as possible in order to implement high stable OLEDs, which means the HTM should have a proper the highest unoccupied molecular orbital (HOMO) energy level for hole injection [6]. Therefore, the ideal HTM should have excellent solubility, good film forming property from solution, high thermal stability, proper HOMO energy level for efficient hole injection and high mobility.

Along this respect, in this paper, we reported two solution-processable and thermal-stable hole-transporting triphenylamine-based dendrimers whose structures are shown in Scheme 1 [29]. As compared to those of reported cases, the dendrimers showed high thermal stability with high  $T_g$  of 115 °C for Tr-TPA3 and 140 °C for Tr-TPA9 and the Tr-TPA9-based device exhibited the turn-on voltage of 2.5 V, the maximum luminance of about 11,058 cd m<sup>-2</sup> and the maximum current efficiency of 4.01 cd A<sup>-1</sup>. The dendrimers also exhibited excellent solubility, good film

forming property, and proper HOMO energy level for hole injection.

## 2. Experimental

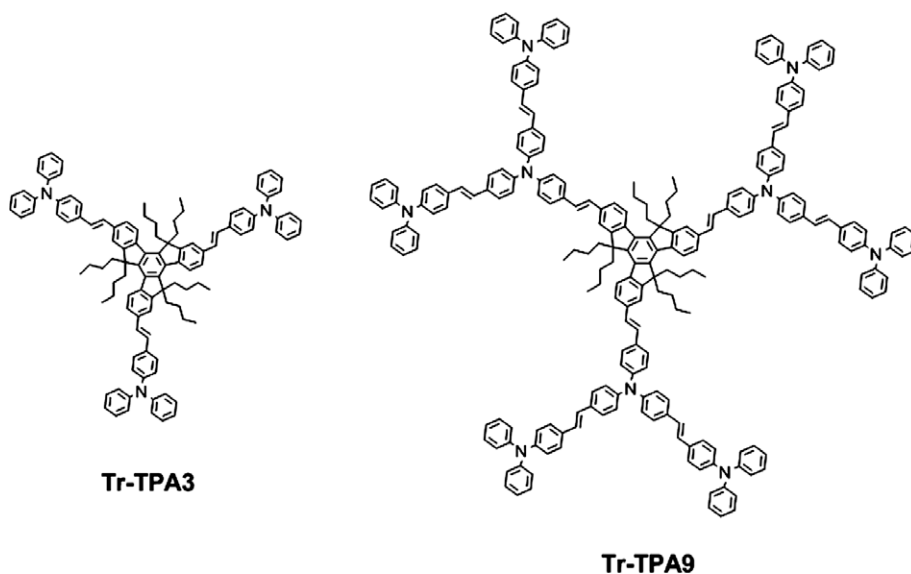
### 2.1. Materials and measurements

The synthesis of two truxene-centered dendric triphenylamine derivatives Tr-TPA3 and Tr-TPA9 have been described in our previously work [29]. Poly-(3,4-ethylene-dioxy-thiophene):poly-(styrenesulphonic acid) PEDOT:PSS was purchased from Bayer AG. Alq<sub>3</sub> and NPB were synthesized in our laboratory and purified by train sublimation.

Differential scanning calorimetry (DSC) measurements and thermogravimetric analysis (TGA) were performed on a NETZSCH (DSC-204) and a Perkin Elmer Pyris 1 analyzer under N<sub>2</sub> atmosphere, respectively. Photoluminescence (PL) and absorption spectra were recorded by a Shimadzu RF-5301PC fluorescence spectrophotometer and a Shimadzu UV-3100 spectrophotometer, respectively. Electrochemical measurements of these derivatives were performed with a Bioanalytical Systems BAS 100 B/W electrochemical workstation.

### 2.2. OLED fabrication and measurement

A double-layer devices with a configuration of ITO/dendrimers (70 nm)/Alq<sub>3</sub> (60 nm)/LiF (0.6 nm)/Al were fabricated, in which dendrimers were used as HTL and Alq<sub>3</sub> was used as the electron-transporting layer (ETL) and emitting layer. The indium-tin oxide ITO-coated (20Ω/□) glass substrates were cleaned by ultrasonic treatment in detergent solutions, rinsed with acetone, boiled in isopropyl alcohol, rinsed with methanol, and then with de-ionized water. The dendrimers was spin-coated on the pre-cleaned ITO glass at the speed of 2000 cycles/min for 30 s from the 10 mg/ml chloroform solution. The thickness of



**Scheme 1.** Chemical structures of the dendrimers.

the dendrimer layer was  $\sim 70$  nm, measured by the Ambios Technology XP-2. A 60 nm-thick  $\text{Alq}_3$  was deposited onto the hole-transporting layer (HTL) at a rate of 0.1–0.3 nm/s as the ETL and emitting layer through a mask at a pressure of  $3 \times 10^{-4}$  Pa. The devices were completed by evaporating a 0.6 nm LiF layer protected by 100 nm of Al at a base pressure of  $5 \times 10^{-4}$  Pa. A device with similar configuration but using NPB evaporation film as HTL was also prepared under the identical conditions. The hole-only devices with a general structure of ITO/PEDOT:PSS/dendrimers (70 nm)/Au (60 nm) were fabricated in the same way for hole mobility measurement by space-charge-limited current (SCLC) method. The EL spectra and current-voltage-luminescence characteristics were measured with a Spectrascan PR 650 photometer and a computer-controlled direct-current (DC) power supply. All the measurements were performed under ambient atmosphere at room temperature.

### 3. Results and discussion

#### 3.1. Thermal properties

The thermal stabilities of dendrimers were examined by DSC and TGA analysis. From the DSC thermograms of dendrimers measured at a scanning rate of  $10^\circ\text{C}/\text{min}$  in nitrogen, the dendrimers exhibited glass-transition at  $115^\circ\text{C}$  for Tr-TPA3 and  $140^\circ\text{C}$  for Tr-TPA9, respectively. The  $T_g$  of the dendrimers enhanced with the increase of the generation because the multibranched molecules with higher generation tend to hinder translational, rotational, and vibrational motions of the molecule. The  $T_g$  of dendrimers is higher by  $19^\circ\text{C}$  for Tr-TPA3 and  $44^\circ\text{C}$  for Tr-TPA9, respectively, than that of the widely used HTM NPB ( $96^\circ\text{C}$ ), suggesting better morphological stability of the dendrimers. In addition, the dendrimers shows excellent decomposition temperature by TGA measurement ( $T_d$ , which corresponded to a 5% weight loss) at  $409^\circ\text{C}$  for Tr-TPA3 and  $426^\circ\text{C}$  for Tr-TPA9, respectively. To investigate the dendrimers morphology, we prepared thin films of the dendrimers through spin-coating from chloroform solution onto ITO substrates and imaged them using atomic force microscopy (AFM, Supplementary Fig. S3). The surface topographies clearly revealed that the spin-coated films exhibited fairly smooth morphologies with a root-mean-square (RMS) surface roughness of 0.58 nm for Tr-TPA3 and 1.06 nm for Tr-TPA9. The films had smooth surfaces with no obvious crystallized aggregation or cracks which demonstrate that Tr-TPA3 and Tr-TPA9 are capable of forming amorphous films through solution processing.

#### 3.2. Photophysical properties

The absorption of dendrimers in dilute chloroform solutions and solid films are presented in Fig. 1. For the UV-vis absorption spectra in chloroform solution, Tr-TPA3 displays two absorption peaks at 311 and 392 nm, respectively. The first absorption peak in the short wavelength region at 311 nm was attributed to the triphenylamine moiety. The second absorption peak at 392 nm was as-

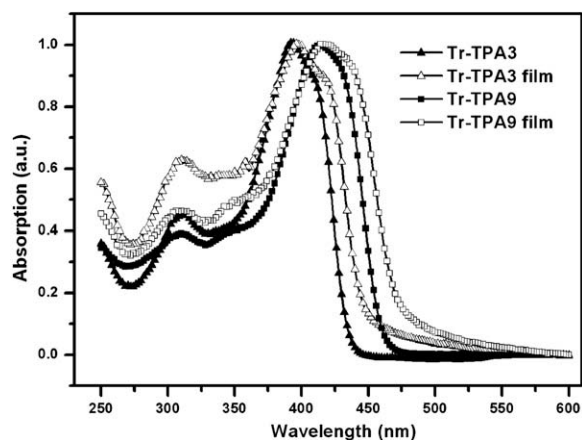


Fig. 1. Normalized absorption spectra of Tr-TPA3 and Tr-TPA9 in dilute chloroform solution ( $1 \times 10^{-6}$  M) and solid films.

cribed to the TPA-vinylene modified truxene unit [30,31]. A red-shift in the absorption maximum of Tr-TPA3 was observed in comparison with the triphenylbenzene core dendrimer (TPB-TPA3,  $\lambda_{\text{max}} = 384$  nm) [30] and truxene linked with vinylene (TM3,  $\lambda_{\text{max}} = 311$  nm) [31], which was indicative of enhanced effective conjugation length. While Tr-TPA9 displays two absorption peaks at 310 and 413 nm, which exhibit similar behavior to Tr-TPA3. These results also demonstrate that the effective conjugation length improves with the increasing generation of the dendrimers. The absorption behaviors of Tr-TPA3 and Tr-TPA9 in the solid films are quite similar to those in solution. The absorption maxima of Tr-TPA3 and Tr-TPA9 in the films are red-shifted 4 and 1 nm, which demonstrates that the higher of the generation, the smaller the red-shift in the absorption. The absorption of the dendrimers indicates that there is no aggregation in the dendrimers because of the large size of the molecules with six butyl substituents in truxene and lots of noncoplanar triphenylamines dendrons. There is no significant ordering of the dendrimers either from aggregation or crystallization, and hence the dendrimers films are in good amorphous states [32], which are very important for the application of materials in optical and electronic devices such as OLEDs.

Fig. 2 illustrates the PL spectra of dendrimers in dilute chloroform solutions and solid films. For the emission spectra in dilute chloroform solutions, Tr-TPA3 and Tr-TPA9 display similar behaviors. The emission peaks of Tr-TPA3 and Tr-TPA9 locate at 445 and 476 nm, respectively. The red-shifted of 31 nm of the emission peak of Tr-TPA9 from that of Tr-TPA3 shows that there is obvious  $\pi-\pi^*$  delocalization and the significant increase of the effective conjugation length with the increase of the generation of dendrimers [33]. The two peaks in PL of Tr-TPA3 film can be ascribed to the S1–S0 0–0 transition at about 440 nm (about  $22,750\text{ cm}^{-1}$ ) and the vibronic satellites with an appr.  $1200\text{ cm}^{-1}$  vibration, respectively. In solution the vibronic splitting is less obvious because the individual components are broadened. Tr-TPA9 displays similar behaviors to Tr-TPA3. Actually, the principal character of the PL spectra is the same for film and solution.



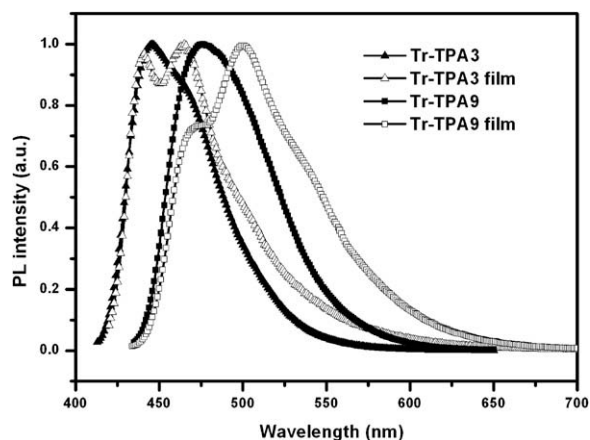


Fig. 2. Normalized fluorescence spectra of Tr-TPA3 and Tr-TPA9 in dilute chloroform solution ( $1 \times 10^{-6}$  M) and solid films.

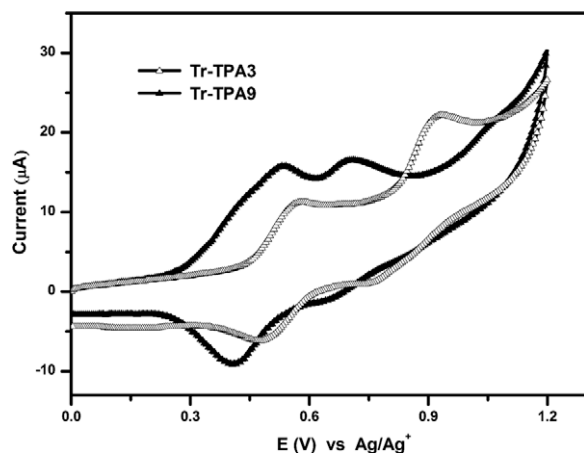


Fig. 3. Cyclic voltammograms of Tr-TPA3 and Tr-TPA9 in 0.1 M Bu<sub>4</sub>NPF<sub>6</sub>/CH<sub>2</sub>Cl<sub>2</sub>, scan rate 100 mV s<sup>-1</sup>.

### 3.3. Electrochemical properties

The electrochemical behaviors of Tr-TPA3 and Tr-TPA9 were examined by cyclic voltammetry measurement. As shown in Fig. 3, two reversible oxidation potentials for Tr-TPA3 and Tr-TPA9 were observed. The first oxidation potentials of Tr-TPA3 and Tr-TPA9 are 0.57 and 0.53 V, and the second oxidation potentials are 0.94 and 0.71 V, suggesting a successive formation of the cation radical and then dication species [10]. All of the oxidations should be attributed

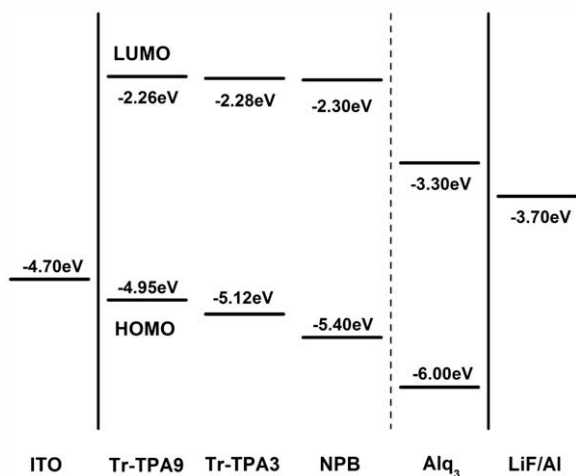


Fig. 4. Energy levels of the dendrimers, NPB and Alq<sub>3</sub>.

to the removal of electrons from the triphenylamine groups. The lower oxidation potential of Tr-TPA9 is likely to be related to the extended  $\pi$ -conjugation length [10].

On the basis of the roughly evaluated onset oxidation potentials ( $E_{\text{Red}}^{\text{onset}}$ ), the HOMO energy levels of Tr-TPA3 and Tr-TPA9 are estimated as  $-5.12$  and  $-4.95$  eV, respectively ( $\text{HOMO} = -e(E_{\text{ox}}^{\text{onset}} + 4.66)$ ) [34–36]. The LUMO energy levels of Tr-TPA3 and Tr-TPA9 are  $-2.28$  and  $-2.26$  eV, respectively, calculated from the HOMO energy level and energy bandgap ( $E_g$ ) determined from the UV–vis absorption threshold ( $\text{LUMO} = \text{HOMO} - E_g$ ). The electrochemical properties as well as the energy level parameters of the dendrimers are listed in Table 1. From Table 1 it can be seen that the electron donating ability of the dendrimers increased with the increase of the number of triphenylamine units and resulted in the enhancement of the HOMO energy level. Fig. 4 shows the energy levels of the dendrimers and that of NPB and Alq<sub>3</sub>. It can be seen that the HOMO energy level of Tr-TPA3 and Tr-TPA9 are higher than that of NPB [37], which means that the energy barrier at the interface of ITO and dendrimers is smaller than that of ITO and NPB resulting in the better hole injection from ITO to dendrimers than to NPB and lower joule heat produced at the interface during device operation.

### 3.4. EL properties

To investigate the hole-transport ability of triphenylamine-based dendrimers, double-layer OLEDs with the

Table 1  
Electrochemical properties of the dendrimers.

Compound	$E_g^a$ (eV)	$E_{\text{onset}}^{\text{ox}b}$ (V)	$E_{p1}^{\text{ox}c}$ (V)	$E_{p2}^{\text{ox}c}$ (V)	HOMO/LUMO <sup>d</sup> (eV)
Tr-TPA <sub>3</sub>	2.84	0.46	0.57	0.94	$-5.12/-2.28$
Tr-TPA <sub>9</sub>	2.69	0.29	0.53	0.71	$-4.95/-2.26$

<sup>a</sup> Determined from UV–vis absorption spectra.

<sup>b</sup>  $E_{\text{onset}}^{\text{ox}}$ : onset oxidation potential; potentials versus Ag/Ag<sup>+</sup>, working electrode glassy carbon, 0.1 M Bu<sub>4</sub>NPF<sub>6</sub>/CH<sub>2</sub>Cl<sub>2</sub>, scan rate 100 mV s<sup>-1</sup>.

<sup>c</sup>  $E_{p1}^{\text{ox}}$ : potential of first oxidation peak;  $E_{p2}^{\text{ox}}$ : potential of second oxidation peak.

<sup>d</sup>  $\text{HOMO} (\text{eV}) = -e(E_{\text{ox}}^{\text{onset}} + 4.66)$ ;  $\text{LUMO} (\text{eV}) = \text{HOMO} - E_g$ .

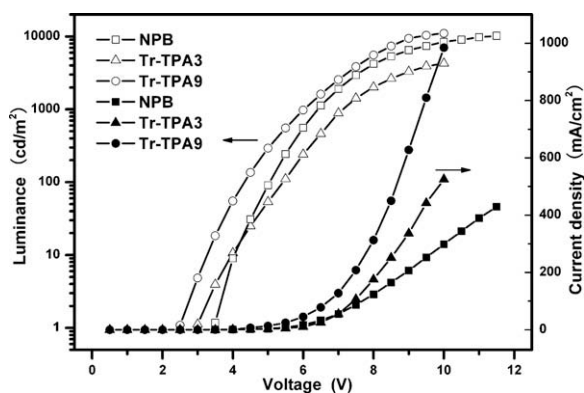


**Fig. 5.** The current density–luminance–voltage curves of the ITO/Tr-TPA3 or Tr-TPA9/Alq<sub>3</sub>/LiF/Al device and the ITO/NPB/Alq<sub>3</sub>/LiF/Al standard device.

configuration of ITO/dendrimers (70 nm)/Alq<sub>3</sub> (60 nm)/LiF/Al were fabricated, where dendrimers as HTL and Alq<sub>3</sub> as emitting layer and ETL. As comparison, a standard device with the similar structure but using NPB as the HTL was also prepared. The devices based on dendrimers showed green emission from Alq<sub>3</sub> with a peak at 528 nm, suggesting that the charge recombination is localized in the Alq<sub>3</sub> layer and dendrimers act primarily as HTM without causing exciplex formation at the interface with Alq<sub>3</sub>. The density–voltage ( $J$ – $V$ ) and luminance–voltage ( $L$ – $V$ ) characteristics of the devices are shown in Fig. 5. The Tr-TPA3-based device turns on at a voltage of 3 V, and the brightness of the device is 4265 cd m<sup>-2</sup> at 10 V. The Tr-TPA9-based device turns on at a voltage of 2.5 V, and the brightness of the device reach 11,058 cd m<sup>-2</sup> at 10 V. It is clear that the brightness of the Tr-TPA9-based device is comparable with the NPB standard device. The low turn-on voltage of the Tr-TPA3 and Tr-TPA9 devices is attribute to the lower hole injection barrier from ITO to dendrimers than that from ITO to NPB.

Fig. 6 shows the current efficiency–current density characteristics of the dendrimers devices. The Tr-TPA9-based device gives a maximum current efficiency of 4.01 cd A<sup>-1</sup>, which is substantively higher than that (3.24 cd A<sup>-1</sup>) of the Tr-TPA3-based device. The current efficiency for the Tr-TPA3-based device decreases more rapidly with increasing current density above 25 mA cm<sup>-2</sup>. While the current efficiency for the Tr-TPA9-based device remains almost constant with current density up to 150 mA cm<sup>-2</sup> and shows only a small decline even when the current density increases to 620 mA cm<sup>-2</sup>. The EL properties of the devices are summarized in Table 2. Significantly, even at the present stage when the device has not

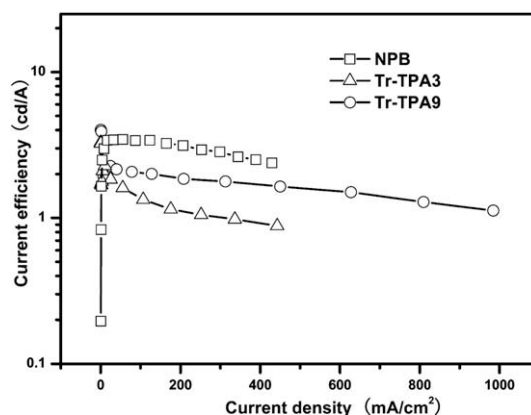


**Fig. 6.** The current efficiency–current density characteristic of the ITO/Tr-TPA3 or Tr-TPA9/Alq<sub>3</sub>/LiF/Al device and the ITO/NPB/Alq<sub>3</sub>/LiF/Al standard device.

yet to be optimized, the EL performances of the Tr-TPA9-based device are already comparable to those of the NPB/Alq<sub>3</sub> device, which suggests that Tr-TPA9 is at least as good as NPB when used as a HTM in EL devices, apart from its high  $T_g$ , good solubility and film forming property from solution.

We also evaluate the hole mobilities of the dendrimers by analyzing space-charge-limited current (SCLC) from the hole-only device with the configuration of ITO/PEDOT:PSS/dendrimers/Au [38–41], where  $L$  varied between 50 and 100 nm. The hole mobilities of the dendrimers were calculated according to the following equations [42]:

$$J_{\text{SCLC}} = \frac{9}{8} \epsilon_0 \epsilon_r \mu_0 \frac{(V_{\text{appl}} - V_{\text{bi}})^2}{L^3} \exp \left[ 0.891 \gamma \sqrt{\frac{V_{\text{appl}} - V_{\text{bi}}}{L}} \right]$$

$$\ln \left[ \frac{JL^3}{(V_{\text{appl}} - V_{\text{bi}})^2} \right] = \ln \frac{9}{8} \epsilon_0 \epsilon_r + \ln \mu_0 + 0.891 \gamma \sqrt{\frac{V_{\text{appl}} - V_{\text{bi}}}{L}}$$

The results are plotted as  $\ln(JL^3/V^2)$  versus  $(V/L)^{0.5}$ , as shown in Fig. 7. The hole mobilities of Tr-TPA3 and Tr-TPA9, calculated from the intercepts of the corresponding lines, are about 10<sup>-5</sup> cm<sup>2</sup>/Vs and 10<sup>-4</sup> cm<sup>2</sup>/Vs, respectively. The hole mobilities of dendrimers are comparable to those of well-known triphenylamine derivatives [11]. The spatial geometry of the dendrimers could be beneficial for intra- and intermolecular hole transportation and the excellent hole mobility observed in Tr-TPA9 than Tr-TPA3 is likely to be related to the extended  $\pi$ -conjugation length which may enhance the capability of the effective interchromophore interaction between the neighboring molecules [38,43].

**Table 2**

Summary of device performances.

HTL	EL (nm)	$V_{\text{on}}$ (V)	$L_{\text{max}}$ (cd m <sup>-2</sup> )	Maximum current efficiency (cd A <sup>-1</sup> )	Maximum power efficiency (lm W <sup>-1</sup> )
NPB	528	3.5	10,220	3.45	1.78
Tr-TPA <sub>3</sub>	528	3	4265	3.24	2.91
Tr-TPA <sub>9</sub>	528	2.5	11,058	4.01	3.60

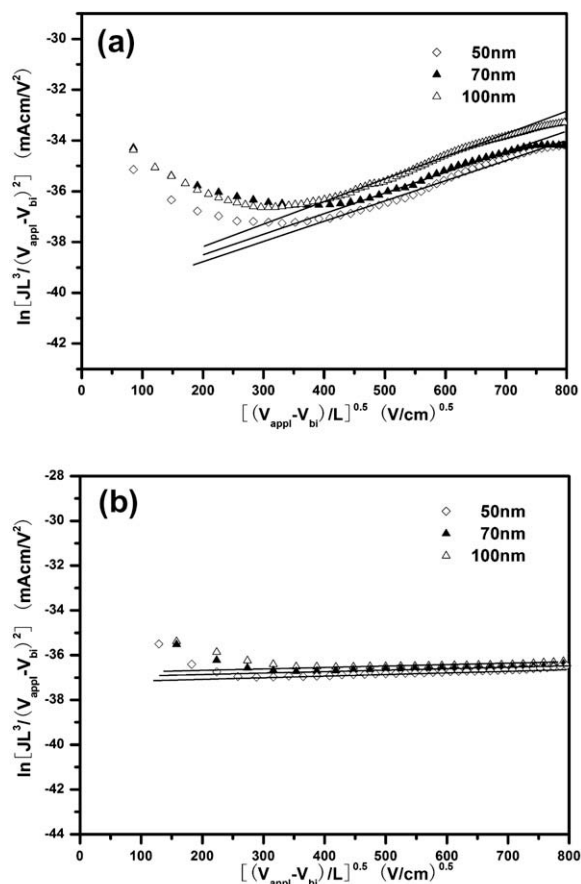


**Fig. 7.** Current–voltage data from the device of ITO/PEDOT:PSS/Tr-TPA3 or Tr-TPA9/Au, plotted in the format  $\ln[JL^3/(V^2)]$  versus  $(V/L)^{0.5}$ , where  $J$  is the current density,  $L$  is the thickness of Tr-TPA3 or Tr-TPA9 layer. The lines are the fit to the respective experimental data points. (a) Tr-TPA3 and (b) Tr-TPA9.

#### 4. Conclusions

To summarize, two novel solution-processable dendrimers, Tr-TPA3 and Tr-TPA9, were used as HTM in OLEDs. The photophysical properties of dendrimers demonstrate that the films of dendrimers are in good amorphous states. The dendrimers possess excellent solubility and good film forming property. The  $T_g$  of dendrimers is higher than that NPB, suggesting better thermal stability of the dendrimers. The Tr-TPA9-based double-layer device exhibited similar EL brightness, slightly higher maximum current efficiency and lower turn-on voltage comparing with the NPB-based device. Therefore, the triphenylamine-based dendrimers with truxene as cores can be good candidates for HTM in OLEDs.

#### Acknowledgements

This work was supported by 973 program (2009CB623605), NSFC (Grant No. 50673035), Program for New Century Excellent Talents in Universities of China Ministry of Education, the 111 Project (Grant No. B06009).

#### Appendix A. Supplementary data

Supplementary data associated with this article can be found, in the online version, at doi:10.1016/j.orgel.2009.04.024.

#### References

- [1] S.A. Jenekhe, *Adv. Mater.* 7 (1995) 309.
- [2] Y. Xu, J. Peng, J. Jiang, W. Xu, W. Yang, Y. Cao, *Appl. Phys. Lett.* 87 (2005) 193502.
- [3] F. Hide, M.A. Diaz-Garcia, B.J. Schartz, A.J. Heeger, *Acc. Chem. Res.* 30 (1997) 430.
- [4] Y. Xiong, W. Xu, C. Li, B. Liang, L. Zhao, J.B. Peng, Y. Cao, J. Wang, *Org. Electron.* 9 (2008) 533.
- [5] C.W. Tang, S.A. VanSlyke, *Appl. Phys. Lett.* 51 (1987) 913.
- [6] C. Adachi, K. Nagai, N. Tamoto, *Appl. Phys. Lett.* 66 (1995) 2679.
- [7] Y. Shiota, *J. Mater. Chem.* 10 (2000) 1.
- [8] Y. Shiota, *J. Mater. Chem.* 15 (2005) 75.
- [9] Y. Shiota, H. Kageyama, *Chem. Rev.* 107 (2007) 953.
- [10] M. Thelakkat, *Macromol. Mater. Eng.* 287 (2002) 442.
- [11] P. Stroehriegel, J.V. Grazulevicius, *Adv. Mater.* 14 (2002) 1439.
- [12] E.M. Han, L.M. Do, N. Yamamoto, M. Fujihira, *Mol. Cryst. Liq. Cryst.* 267 (1995) 411.
- [13] L. Wang, B. Liang, F. Huang, J. Peng, Y. Cao, *Appl. Phys. Lett.* 89 (2006) 151115.
- [14] J.P. Lu, P.F. Xia, P.K. Lo, Y. Tao, M.S. Wong, *Chem. Mater.* 18 (2006) 6194.
- [15] G. Zhou, W.Y. Wong, B. Yao, Z. Xie, L. Wang, *Angew. Chem.* 119 (2007) 1167.
- [16] X. Gong, H. Benmansour, G.C. Bazan, A.J. Heeger, *J. Phys. Chem. B* 110 (2006) 7344.
- [17] M.C. Gather, A. Köhnen, A. Falcou, H. Becker, K. Meerholz, *Adv. Funct. Mater.* 17 (2007) 191.
- [18] V. Promarak, M. Ichikawa, T. Sudyoasuk, S. Saengsuwan, T. Keawin, *Opt. Mater.* 30 (2007) 364.
- [19] Y. Zhou, Q.G. He, Y. Yang, H.Z. Zhong, C. He, G.Y. Sang, W. Liu, C.H. Yang, F.L. Bai, Y.F. Li, *Adv. Funct. Mater.* 18 (2008) 3299.
- [20] C. Adachi, T. Tsutsui, S. Saito, *Appl. Phys. Lett.* 56 (1990) 799.
- [21] S. Tokito, Y. Taga, *Appl. Phys. Lett.* 66 (1995) 673.
- [22] Y. Kuwabara, H. Ogawa, H. Inada, N. Nona, Y. Shiota, *Adv. Mater.* 6 (1994) 667.
- [23] K. Katsuma, Y. Shiota, *Adv. Mater.* 10 (1998) 223.
- [24] Y. Shiota, T. Kobata, N. Noma, *Chem. Lett.* (1989) 1145.
- [25] A. Higuchi, H. Inada, T. Kobata, Y. Shiota, *Adv. Mater.* 3 (1991) 549.
- [26] H. Inada, Y. Shiota, *J. Mater. Chem.* 3 (1993) 319.
- [27] Z.H. Li, M.S. Wong, H. Fukutani, Y. Tao, *Org. Lett.* 8 (2006) 4271.
- [28] M. Thelakkat, H.W. Schmitz, *Adv. Mater.* 10 (1998) 219.
- [29] H.J. Xia, J.T. He, B. Xu, S.P. Wen, Y.W. Li, W.J. Tian, *Tetrahedron* 64 (2008) 7837.
- [30] H.J. Xia, J.T. He, P. Peng, Y.H. Zhou, Y.W. Li, W.J. Tian, *Tetrahedron Lett.* 48 (2007) 5877.
- [31] X.Y. Cao, W. Zhang, H. Zi, J. Pei, *Org. Lett.* 6 (2004) 4845.
- [32] G.K. Paul, J. Mwaura, A.A. Argun, P. Taraneekar, J.R. Reynolds, *Macromolecules* 39 (2006) 7789.
- [33] Y. Jiang, J. Wang, Y. Ma, Y. Cui, Q. Zhou, J. Pei, *Org. Lett.* 8 (2006) 4287.
- [34] J. Pommerehne, H. Vestweber, W. Guss, R.F. Mahrt, H. Bässler, M. Porsch, J. Daub, *Adv. Mater.* 7 (1995) 551.
- [35] Y.H. Zhou, P. Peng, L. Han, W.J. Tian, *Synth. Met.* 157 (2007) 502.
- [36] Y.W. Li, L.L. Xue, H.J. Xia, B. Xu, S.P. Wen, W.J. Tian, *J. Polym. Sci. Part A: Polym. Chem.* 46 (2008) 3970.
- [37] Q.L. Huang, J.F. Li, G.A. Evmenenko, P. Dutta, T.J. Marks, *Chem. Mater.* 18 (2006) 2431.
- [38] C. He, Q.G. He, Y.P. Yi, G.L. Wu, F.L. Bai, Z.G. Shuai, Y.F. Li, *J. Mater. Chem.* 18 (2008) 4085.
- [39] D. Chirvase, Z. Chiguvar, M. Knipper, J. Parisi, V. Dyakonov, J.C. Hummelen, *Phys. Rev. B* 70 (2004) 235207.
- [40] G.G. Malliaras, J.R. Salem, P.J. Brock, C. Scott, *Phys. Rev. B* 58 (1998) 13411.
- [41] H.C.F. Martens, H.B. Brom, P.W.M. Blom, *Phys. Rev. B* 60 (1999) 8489.
- [42] O.J. Weiss, R.K. Krause, A. Hunze, *J. Appl. Phys.* 103 (2008) 043709.
- [43] Y.L. Liao, W.Y. Hung, T.H. Hou, C.Y. Lin, K.T. Wong, *Chem. Mater.* 19 (2007) 6350.

time scale. In order to determine the rate-limiting process, transient or ac response of a rectifier may be studied. Rectifiers in the radio-frequency range are also required for applications as radio-frequency identification tags (RFID).

Operation of organic rectifiers under ac voltage has recently been reported [13–16]. In this article, we present results from an assembly between a donor and an acceptor molecule (donor/acceptor assembly) under ac voltage. Here, we have varied frequency of ac voltage and studied the characteristics of the rectifier. From the frequency-response of rectification, we comment on the process that limits molecular rectification.

## 2. Experimental

The donor/acceptor system for the present study consists of a phthalocyanine derivative and a xanthenone molecule as a donor and an acceptor, respectively. Fig. 1 shows the energy diagram and structural formulae of the components of the diode. Molecular orbitals of such assemblies favor electron flow in the A to D direction. Briefly, the donor/acceptor (D/A) assemblies were formed by electrostatic adsorption of tetrasodium salt of copper phthalocyanine (CuPc), an inert polycation, and (sodium salt of) fluorescein in sequence. As the polycation, we have used poly(allylamine hydrochloride) (PAH,  $M_w = 70,000$ ). Due to anionic nature of CuPc derivative and fluorescein in water solution, the CuPc/PAH/fluorescein assemblies could be formed via LbL method. Adsorption of the molecules has been confirmed from the electronic absorption spectra of the LbL films on quartz substrates. In practice, a highly doped single crystalline Si wafer (1 1 1) with a resistivity of 3 m $\Omega$ .cm was first dipped in a CuPc bath. After a thorough rinse in three water baths to wash-off extra molecules that were not bound electrostatically, the substrate was dipped in a PAH bath followed by the same rinsing procedure. To complete a D/A assembly, a layer of fluorescein was deposited by dipping the slide in a fluorescein bath followed by the same rinsing protocol. The mechanism of LbL adsorption process, that is, surface charge reversal during every layer adsorption, assured that only

one monolayer was deposited during each dipping event. All the dipping baths were water-based with a dye or polycation concentration of 10 mM. The deionized water for the solution and washing baths, obtained from Milli-Q Academic, had a resistivity of 18.2 M $\Omega$ .cm.

The D/A assemblies were annealed in vacuum at 120 °C for 1 h. Electrical characteristics of the assemblies were recorded with mercury as the other electrode. The assemblies were placed in a bell-jar under vacuum ( $10^{-3}$  Torr) with the film facing downwards. Mercury blob in a metal syringe was pushed from outside the chamber to touch the film. Current–voltage ( $I$ – $V$ ) characteristics were recorded by applying a bias to the mercury electrode with respect to the doped Si substrate. As control experiments to rule out any role of interfaces, monolayers of the components, namely CuPc and fluorescein, were characterized. In addition, and more importantly, a reverse junction, that is, a junction based on monolayers of fluorescein and CuPc in sequence, was formed and characterized under the same experimental conditions. Characteristics from Si/CuPc/fluorescein/Hg and Si/fluorescein/CuPc/Hg were compared to eliminate any effect of the interfaces. For both the assemblies and their components,  $I$ – $V$  characteristics were recorded at different points on the films to check the reproducibility of the results. While absolute value of current depended on the size of mercury blobs, rectification ratio calculated from different measurements remained unaltered.

For dc measurements, a Yokogawa model 7651 programmable source provided the voltage. A Keithley model 486 picoammeter measured the dc current. Real time response of current under ac voltage and the voltage itself were recorded with a Hewlett–Packard model 5600B double-channel digital oscilloscope. A Hewlett–Packard model 3245A universal source provided sinusoidal voltages. Frequency of the ac voltage was varied between 50 Hz and 1 MHz (2 points per decade). To record time response of current through the junctions, voltage drop against a known resistor was recorded with the oscilloscope.

## 3. Results and discussion

$I$ – $V$  characteristics under dc voltage of a D/A junction with CuPc and fluorescein monolayer in sequence are shown in Fig. 2a. Characteristics from a reverse junction (A/D) are also shown in the same figure. In both the cases, doped-Si and Hg were the electrodes. Both the characteristics show rectifying behavior; direction of rectification in one case is opposite to that in the other. Opposing nature of rectification in D/A and A/D junctions first of all rules out any effect of interfaces in the observed characteristics. The results show that electron flow was always favorable from A to D moiety and hence clearly bring out rectifying nature of a D/A assembly. Further control experiments with the components of the junctions, that is, a CuPc monolayer and a fluorescein monolayer separately, returned mostly symmetric  $I$ – $V$  characteristics. The results are presented in Figs. 2b and 2c, respectively. The little variation from the symmetric nature that may be present in the characteristics can be due to different work functions of the electrodes.

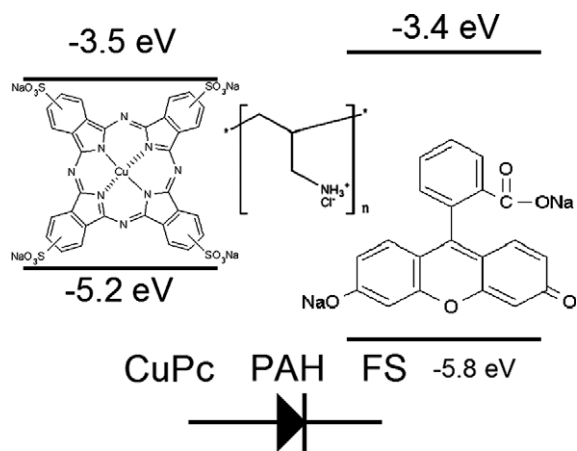
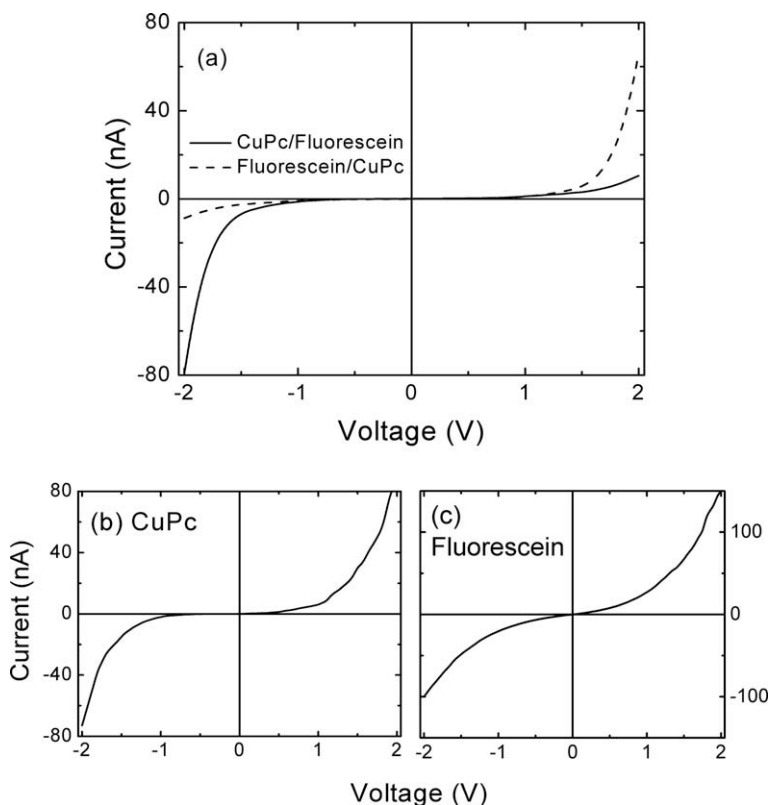


Fig. 1. Energy diagram and structural formulae of the components of a CuPc/fluorescein diode.

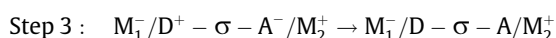
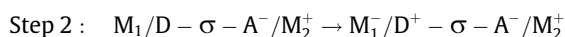


**Fig. 2.** Current–voltage characteristics of (a) D/A and A/D assemblies with the same set of electrodes (doped-Si and Hg). Characteristics from the components are shown in (b) and (c). Legends specify the monolayer that has been characterized.

We studied the rectifying assemblies under ac voltage. Frequency of sinusoidal voltage was varied between 50 Hz and 1 MHz. Typical examples for D/A assemblies under 100 Hz and 100 kHz are shown in Fig. 3a and b, respectively. Current response, along with the ac voltage, is shown in each of the figures. The assemblies act mostly as half-wave rectifiers. Current in the forward bias segment of ac voltage is much higher than that in the reverse bias segment. It should be noted here that considering the biasing arrangement, application of a negative voltage to Hg contact of Si/D/A/Hg structure meant a forward-biased D/A rectifier. We also have characterized the A/D assemblies under ac bias of different frequencies. Again, results from A/D assemblies under two typical frequencies (100 Hz and 100 kHz) are shown in Fig. 4a and b, respectively. The A/D assemblies also behaved as half-wave rectifiers. Here, current under positive-segment of sinusoidal ac voltage (forward-bias) is much higher than that in the negative-voltage segment (reverse-bias). The results hence show that the donor/acceptor assemblies based on a junction between a monolayer of donor molecules and a monolayer of acceptor molecules act as a rectifier under ac voltage or a half-wave rectifier. The components of the assemblies, namely a monolayer of CuPc or a monolayer of fluorescein expectedly did not behave as a rectifier under ac voltage (figure not shown).

It is important to know the phase-lag between the ac voltage and current. When current response is compared with the sinusoidal voltage, there is little or no phase lag

in the low frequency region. At higher frequencies, the current lagged the voltage. The phase-lag rose to  $40^\circ$  at the highest frequency of measurement (Fig. 5). Capacitive component of the D/A assembly, which can be represented as a parallel combination of a resistor and a capacitor ( $C_p-R_p$ ), may also give rise to a phase lag. Such a phase-lag between the real and imaginary components of complex impedance as a function of ac test-frequency saturated within 1 kHz. The phase-lag of current with respect to sinusoidal voltage, on the other hand, increased monotonically with the frequency of the voltage (Fig. 5). This shows that one of the steps/processes of electron flow through the donor/acceptor composite is slower than the time-scale of a half-wave of the sinusoidal voltage. It may be recalled that in the forward bias the three steps of electron movement from an electrode to the other are (1) addition of an electron from an electrode to the LUMO of acceptor moiety, (2) withdrawal of an electron from the HOMO of donor moiety to the other electrode, and (3) electron transfer from the anionic-acceptor to the cationic donor moiety of D/A complexes. The Fig. 6 shows that band-diagram of a donor/acceptor assembly under forward bias with the following steps:



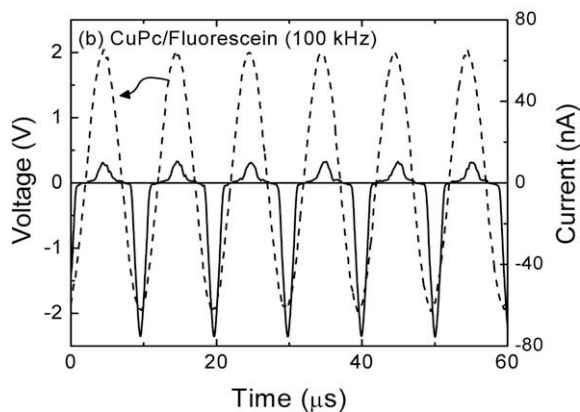
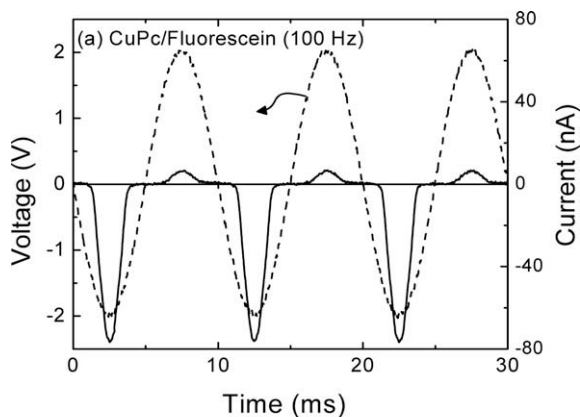


**Fig. 3.** Current and sinusoidal voltage as a function of time for D/A assemblies at two different frequencies as mentioned in the legends.

In the reverse-bias, neither addition of an electron to the donor moiety nor withdrawal of an electron from the acceptor is favorable; current in the reverse-bias is hence small. Since the former two steps may occur simultaneously, it could be interesting to know if the latter process (step 3) or the former ones (steps 1 and 2) limits the rectifier at high frequencies.

In order to find the rate-limiting process, we have plotted amplitude of forward and reverse current as a function of frequency (Fig. 7). Frequency response of rectification ratio has also been plotted in the same figure. The ratio in the D/A assembly is as such low since the ultrathin film could not withstand much bias voltage due to possibility of a breakdown under a high electric-field. The plot shows that the rectification ratio starts to decrease at higher frequencies. The decrease in the ratio is in fact due to increase in current under reverse-bias section of the voltage; the current in the forward bias remained invariant with the increase in frequency in the range of our measurement. Increase in the reverse-bias current with frequency implies that there must have been a residual effect at high-frequencies. That is, in a Si/CuPc/fluorescein/Hg rectifier at high-frequencies and under forward-bias (mercury electrode being negative), electron transfer from all the anionic-acceptors to the cationic-donors may not have become complete; upon reversal of bias at this stage, elec-

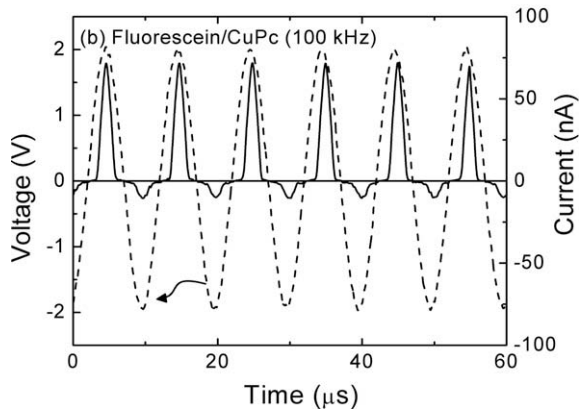
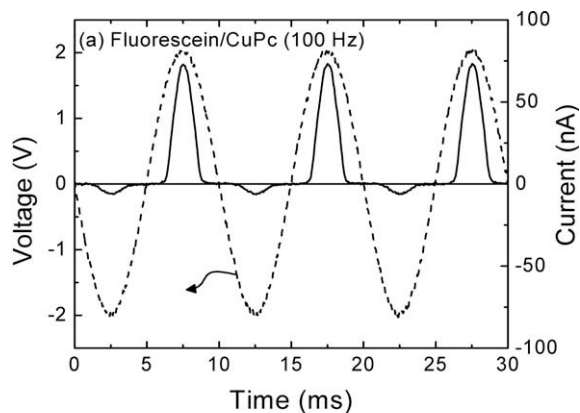


**Fig. 4.** Current and sinusoidal voltage as a function of time for A/D assemblies at two different frequencies as mentioned in the legends.

trons may have back-flowed from fluorescein-anion to Hg electrode (oxidation of reduced fluorescein). Similarly, electrons from the Si-electrode may have neutralized the

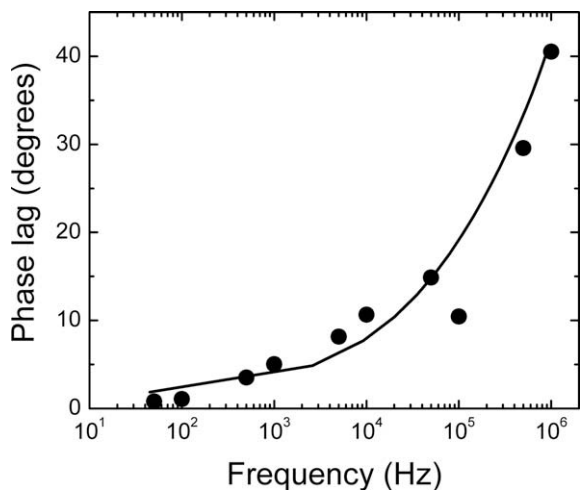


**Fig. 5.** Phase-lag of current with respect to sinusoidal voltage of a D/A assembly as a function of frequency of sinusoidal voltage. The line is to guide the eye.

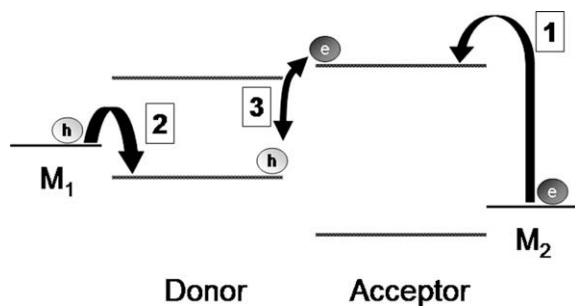


**Fig. 6.** Band diagram of a donor/acceptor assembly with doped-Si and Hg electrodes under forward bias showing the three steps (as mentioned in boxes).

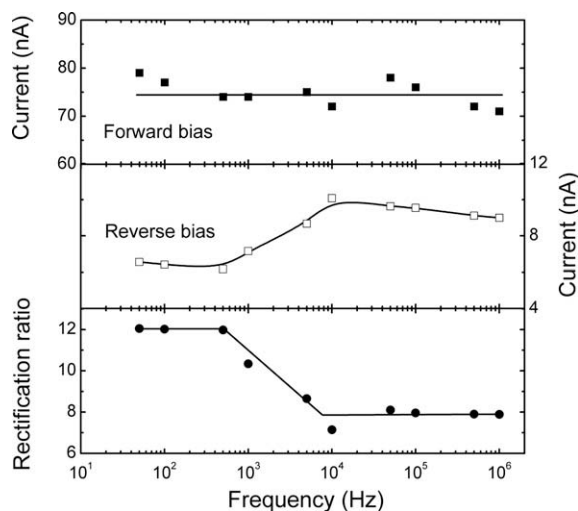


**Fig. 7.** Current under forward- and reverse-bias at 2.0 V and –2.0 V, respectively, of a D/A assembly as a function of frequency of sinusoidal voltage. Rectification ratio of the assembly at 2.0 V is shown in the lower panel of the figure. Lines are to guide the eye.

CuPc cations. These electron-movements would seem like a current flow in the external circuit. This extra current due to residual carriers along with current due to injection of carriers (electron-injection to the donor and hole-injection to the acceptor moieties) yield an increase in current in the reverse-bias at higher frequencies. The step (3) of molecular rectification, namely the charge-transfer between  $A^-$  and  $D^+$ , meant oxidation of reduced fluorescein; this process, which involves conformational-change of fluorescein molecules, might be a slow one leading to residual or left-over  $A^-$  and  $D^+$  species for the next half-cycle. These species have yielded a higher reverse-bias current in high-frequencies.

#### 4. Conclusions

In conclusion, we have shown that a donor/acceptor assembly between a molecular layer of donor molecules and another molecular layer of acceptor molecules, when sandwiched between two electrodes, acts as a half-wave rectifier under ac voltage. In a reverse junction, that is, in an acceptor/donor assembly with the same set of electrodes, the direction of rectification also reversed ruling out any effect of interfaces in the observed rectification. At higher frequencies, the current lagged the applied sinusoidal voltage. From the frequency dependence of rectification, we have commented on the time response of the three steps that are responsible for a molecular rectification. We show that the charge-transfer between an anionic-acceptor and a cationic-donor may be a slow process since a change in its conformation is involved during oxidation of the reduced-acceptors. The results show that high-frequency half-wave (molecular) rectifiers can be fabricated and characterized from an assembly of a donor and an acceptor molecule.

#### Acknowledgements

KM acknowledges CSIR Junior Research Fellowship No. 9/80(491)/2005-EMR-I, Roll No. 509342. The Department of Science and Technology, Government of India financially supported the work through Ramanna Fellowship SR/S2/RFCMP-02/2005.

#### References

- [1] A. Aviram, M.A. Ratner, *Chem. Phys. Lett.* 29 (1974) 277.
- [2] R.M. Metzger, C.A. Panetta, *New J. Chem.* 15 (1991) 209.
- [3] A.S. Martin, J.R. Sambles, G.J. Ashwell, *Phys. Rev. Lett.* 70 (1993) 218.
- [4] R.M. Metzger, B. Chen, U. Hopfner, M.V. Lakshminantham, D. Vuillaume, T. Kawai, X.L. Wu, H. Tachibana, T.V. Hughes, H. Sakurai, J.W. Baldwin, C. Hosch, M.P. Cava, L. Brehmer, G.J. Ashwell, *J. Am. Chem. Soc.* 119 (1997) 10455.
- [5] A. Jaiswal, R.R. Amaresh, M.V. Lakshminantham, A. Honciuc, M.P. Cava, R.M. Metzger, *Langmuir* 19 (2003) 9043.
- [6] K. Kitagawa, T. Morita, S. Kimura, *J. Phys. Chem. B* 109 (2005) 13906.
- [7] G.J. Ashwell, D.S. Gandolfo, *J. Mater. Chem.* 11 (2001) 246.
- [8] M.L. Chabiny, X.X. Chen, R.E. Holmlin, H. Jacobs, H. Skulason, C.D. Frisbie, V. Mujica, M.A. Ratner, M.A. Rampi, G.M. Whitesides, *J. Am. Chem. Soc.* 124 (2002) 11730.
- [9] M. Galperin, A. Nitzan, S. Sek, M. Majda, *J. Electroanal. Chem.* 550 (2003) 337.
- [10] G.J. Ashwell, W.D. Tyrrell, A.J. Whittam, *J. Am. Chem. Soc.* 126 (2004) 7102.
- [11] S.K. Pollack, J. Naciri, J. Mastrangelo, C.H. Patterson, J. Torres, M. Moore, R. Shashidhar, J.G. Kushmerick, *Langmuir* 20 (2004) 1838.
- [12] B. Mukherjee, K. Mohanta, A.J. Pal, *Chem. Mater.* 18 (2006) 3302.
- [13] S. Steudel, K. Myny, V. Arkhipov, C. Deibel, S. De Vusser, J. Genoe, P. Heremans, *Nat. Mater.* 4 (2005) 597.
- [14] K. Myny, S. Steudel, P. Vicca, J. Genoe, P. Heremans, *Appl. Phys. Lett.* 93 (2008) 093305.
- [15] S. Acharya, H. Song, J. Lee, P.S. Kwon, J.P. Lee, G. Yogendranath, Y.H. Kim, Y.H. Jang, T. Lee, S. Samal, J.S. Lee, *Org. Electron.* 10 (2009) 85.
- [16] J. Sun, B.N. Pal, B.J. Jung, H.E. Katz, *Org. Electron.* 10 (2009) 1.

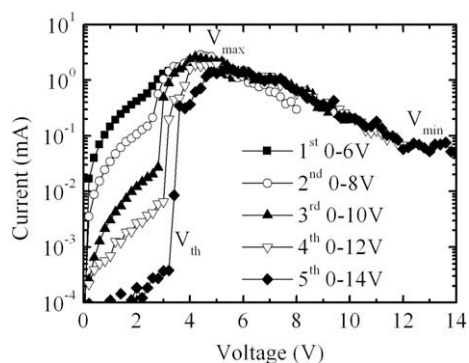


**Fig. 1.** Typical current–voltage ( $I$ – $V$ ) curves for organic bistable device with the structure ITO/Al (5 nm)/Alq<sub>3</sub> (120 nm)/Al<sub>2</sub>O<sub>3</sub> (5 nm)/Al (100 nm).

The switching from OFF to ON state could be realized in milliseconds by applying a voltage between  $V_{th}$  and  $V_{max}$ , while the switching from ON to OFF state could be achieved in microseconds by applying a voltage close to  $V_{min}$ , as is described in our recent work [23]. In previous reports, most research efforts focused on the voltage  $V$  within the switching range,  $V_{th} < V < V_{min}$ , while less attention was paid to the electrical properties beyond this range, i.e., in the voltage regions of  $V < V_{th}$  and  $V > V_{min}$ . Recently, we have found that when biased at voltages below the threshold voltage  $V_{th}$ , i.e.,  $V < V_{th}$ , the OBDs can automatically switch from OFF state to ON state after a certain period of time. Such “switch time” scales from a few seconds to about  $10^4$  s, depending on the biased voltage [23]. However, there have been no report so far to investigate the electrical properties of OBDs in the voltage range of  $V > V_{min}$  to show the effect of such higher voltage on OBDs.

In the present work, we systematically investigate the effect of higher voltage  $V > V_{min}$  on OBDs. It is found that when the scan termination voltage  $V_T$  exceeds  $V_{min}$ , the bistable effect of OBDs gets worse and worse with the increasing  $V_T$  in the following scan. When the voltage reaches a very high value of about  $2V_{min}$ , the device completely loses its bistability. However, it is found that the lost bistability can be recovered by applying a voltage pulse close to  $V_{min}$  for milliseconds or longer. The possible underlying mechanism of the OBDs studied is suggested based on the existence of micro-conducting channels in the organic layer.

## 2. Experimental

We fabricated OBDs with structure of indium tin oxide (ITO)/Al (5 nm)/tris (8-hydroxyquinoline) aluminum (Alq<sub>3</sub>) (120 nm)/Al<sub>2</sub>O<sub>3</sub> (5 nm)/Al (120 nm). The 5 nm Al layer on the ITO electrode acts as the anode to form symmetrical OBDs. Alq<sub>3</sub> used in the present study is one of the most important organic electron-transporting materials in organic light-emitting diodes. Experiments showed that insertion of 5 nm Al<sub>2</sub>O<sub>3</sub> between the organic layer and Al electrode improved the electrical stability of the devices, which means the device can endure more bistability loss

and recovery cycles before being damaged. The devices were fabricated on pre-cleaned glass substrates coated with transparent conducting ITO of sheet resistance about  $17 \Omega/\text{square}$ . The substrate was heated to  $150^\circ\text{C}$  in air after solvent cleaning and then loaded into a high vacuum chamber ( $\sim 5 \times 10^{-6}$  Pa). A 5 nm-thick aluminum (Al) layer was first deposited onto the ITO substrate with a deposition rate of  $0.3 \text{ \AA}/\text{s}$ , followed by deposition of Alq<sub>3</sub> layer of about 120 nm with deposition rate of  $1.0 \text{ \AA}/\text{s}$ , which is the optimized thickness to make the device show good NDR effect, ON/OFF ratio (the conductance comparison) and electrical stability. Then a 5 nm-thick Al layer was deposited on the Alq<sub>3</sub> layer without breaking the vacuum. Subsequently, the sample was transferred into another chamber to get the thin Al layer oxidized. Finally the sample was sent back into the vacuum chamber and a top Al electrode of 120 nm was deposited with a deposition rate of  $1 \text{ \AA}/\text{s}$ . The area of the organic bistable device was  $9 \text{ mm}^2$ , defined by 3 mm-wide ITO stripes over-crossed by 3 mm-wide top Al stripes. The current–voltage ( $I$ – $V$ ) characteristics of the devices were measured by Keithley 236. The scan step was 0.2 V and each step lasted for about 500 ms. All the measurements of bistability and switching characteristics of the devices were carried out at room temperature in a glove box ( $\text{O}_2 < 1 \text{ ppm}$ ,  $\text{H}_2\text{O} < 1 \text{ ppm}$ ). The micrograph of the devices was observed with an optical microscope.

## 3. Results and discussion

Fig. 1 shows the typical  $I$ – $V$  characteristics of a bistable device with the structure of ITO/Al (5 nm)/Alq<sub>3</sub> (120 nm)/Al<sub>2</sub>O<sub>3</sub> (5 nm)/Al (120 nm). The device was initially set to the ON state and then the applied voltage was scanned, first from 0 to 6 V, next from 0 to 8 V and so on, finally from 0 to 14 V, i.e., the termination voltage  $V_T$  increased stepwise. As shown in Fig. 1, NDR effect exists in the region between  $V_{max}$  (the voltage corresponding to the local current maximum) and  $V_{min}$  (the voltage corresponding to the local current minimum). Intermediate states, i.e., those between the ON and OFF resistance values, are obtained in the region  $V < V_{th}$  ( $V_{th}$  is the threshold voltage, at which the current increases abruptly). The larger the  $V_T$  ( $V_{max} < V_T < V_{min}$ ) is, the lower the conductance of the device in the region of  $V < V_{th}$  in the next scan will be. With the increase of termination voltage  $V_T$ , the current peak value and the corresponding voltage  $V_{max}$  show little change. The typical  $I$ – $V$  characteristics are essentially the same as those reported before by us [23] and other groups [3,4,21,22]. However, how the  $I$ – $V$  characteristics and bistable effect of the OBDs will change when  $V_T$  exceeds  $V_{min}$  has not been addressed.

Fig. 2 shows the  $I$ – $V$  characteristics of another device with the same structure but different  $V_T$  exceeding  $V_{min}$ . For this device, when the device shows complete bistability,  $V_{th}$ ,  $V_{max}$  and  $V_{min}$  are 2, 5 and 14 V, respectively. In order to investigate the effect of high voltage exceeding  $V_{min}$  on the OBDs, the device was first set to the OFF state and then the applied voltage was scanned, first from 0 to 14 V, next from 0 to 16 V and so on, finally from 0 to 28 V. Here the curve of solid squares shows the result of



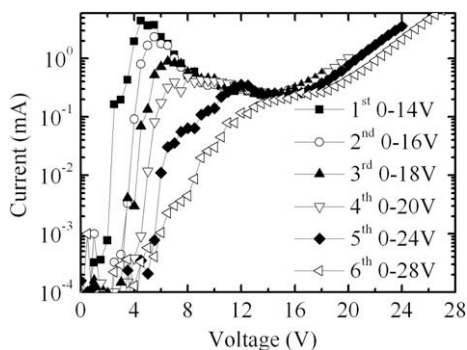


**Fig. 2.**  $I$ - $V$  characteristics of device ITO/Al (5 nm)/Alq<sub>3</sub> (120 nm)/Al<sub>2</sub>O<sub>3</sub> (5 nm)/Al (120 nm) with  $V_T$  exceeding  $V_{min}$ . The device was first set to the OFF state and then the applied voltage was scanned, first from 0 to 14 V, next from 0 to 16 V and so on, finally from 0 to 28 V.

scan from 0–14 V, with a current maximum of 4.5 mA at  $V_{max} \sim 5$  V. During the subsequent scanning from 0 to 16 V, shown by the hollow circle curve, the peak current deduced to 2.4 mA, while the corresponding voltage  $V_{max}$  increased to 5.5 V. With the  $V_T$  increasing from  $V_{min} \sim 14$  V to  $2V_{min} \sim 28$  V, the peak current decreased from 4.5 to 0.31 mA, while  $V_{max}$  increased from 4.5 to 14.5 V and the ON/OFF ratio of bistable effect got worse. In the last scan of 0–28 V, shown by the hollow left-triangle curve, the current increased with voltage monotonously, i.e., the NDR effect almost disappeared. Meanwhile, when the device was tested by applying voltage pulse with an amplitude exceeding  $V_{min}$  instead of a voltage scan  $0 \sim V_T$ , similar results were obtained, i.e., the device showed the same  $I$ - $V$  characteristics. That means the termination voltage  $V_T$  of the scanning process determined the  $I$ - $V$  characteristics of the device in the next scan.

In order to test whether the device could switch from OFF state to ON state after experiencing a high voltage of 28 V, a write voltage of 5 V was applied to the device for about 20 min. Under the write voltage of 5 V, the current was very small, of the order of  $10^{-4}$  mA, and showed little change with time. The device did not switch from the OFF state to the ON state in 20 min. This means the device lost bistability completely. Therefore, for such kind of OBDs, after applying high voltage (about  $2V_{min}$ ), the device can not realize the function of writing and hence loses bistability completely.

Further investigation shows that the bistability destroyed by high voltage can be recovered by certain method, rather than lost forever. In our experiment, it is demonstrated that for the device which has lost bistability by high voltage (28 V), a voltage pulse of  $V_{min} \sim 14$  V applied for milliseconds or longer can recover its bistability, i.e., the device can then be switched from OFF state to ON state by applying voltage pulse in the region of  $V_{th} < V < V_{max}$  (2–5 V). Therefore, it is concluded that the bistability-lost devices can recover their bistability upon the application of a voltage pulse of  $V_{min}$ . Indeed, in our experiments, it is shown that the first scan from 0–14 V on a bistability-lost device does not show NDR effect and bistability, while the next scan of 0–14 V shows NDR effect

and bistability again, shown in Fig. 3. If the scan changes from  $V$  ( $V \geq V_{min}$ ) to 0 V, for instance, from 28 to 0 V, even in the first scan, NDR effect reappears, showing the bistability recovered. This is because in such a scan process, the device experienced a voltage pulse of 14 V, resulting in immediate recovery of the bistability. Meanwhile, a series of voltage pulses with amplitude of  $V_{min}$  and shorter duration applied on the device can also recover the device bistability, although gradually. The sum of pulse durations approximately equals to the longer voltage pulse of similar amplitude with the same effect of bistability recovery. That means the effect of applied voltage pulse is accumulative over time.

In addition, applied voltage in the region of  $V_{max}$  (the maximum voltage for the device showing complete bistability, shown in Fig. 1, which does not change with the increasing termination voltage)  $\sim V_{min}$  can partly recover the bistability. Fig. 4 shows the  $I$ - $V$  characteristics of another bistability-lost device which had experienced a certain voltage between  $V_{max}$  ( $5 \text{ V} < V < V_{min}$  (12 V)). First voltage of  $2V_{min}$  (24 V) was applied on the device to destroy its bistability, then different voltage 7, 8, 10, or 12 V was applied for about 5 s on the device, and voltage was then scanned over 0–12 V. The solid square curve shows 0–12 V scan of the device after applying a constant voltage of 7 V on the device. The device did not show any NDR effect or any electrical transition (an abrupt current increase) in the region of 2–5 V either. However, constant voltage 8 V can partly recover the lost bistability – the  $I$ - $V$  curve shows weak NDR effect, as shown by the hollow circle curve in Fig. 4, with very low ON/OFF ratio (the conductance comparison). Similarly, constant voltage 10 V made the NDR effect much more obvious and better recovery of the bistability. Meanwhile, constant voltage as high as 12 V applied on the device resulted in complete recovery of the bistability, shown by the most obvious NDR effect with the highest current peak value.

We have previously suggested a phenomenological mechanism involving localized conducting micro-channels to account for the bistability [23]. These micro-channels are, in principle, similar to those existing in inorganic metal–insulator–metal structures [13], formed by incorporation of metallic nanoparticles into the organic layer during deposition of the top electrode [3,4]. The ON and

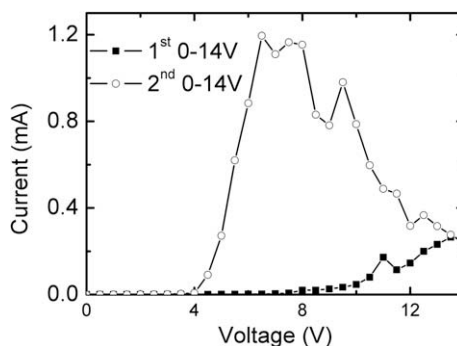


**Fig. 3.**  $I$ - $V$  characteristics of a bistability-lost device by applying a voltage of 28 V. Two 0–14 V scans were sequentially applied.

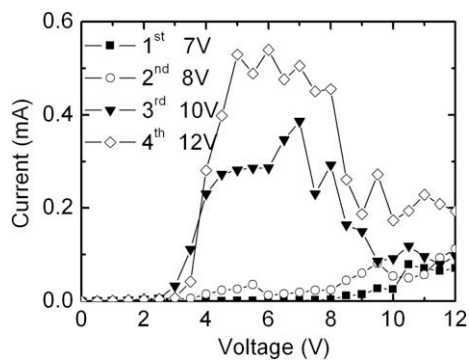


**Fig. 4.**  $I$ - $V$  characteristics of a bistability-lost device after being applied a constant voltage  $V$  between  $V_{\max}$  and  $V_{\min}$ . The device was initially set to lose its bistability by an applied voltage of 24 V, then different voltages 7, 8, 10, or 12 V were applied for about 5 s each, and then 0–12 V was scanned.

OFF states of the device are respectively related to open and close of the channels, and  $V_{\text{th}}$  mentioned above is the threshold voltage needed for the channels to be opened.

The existence of the conducting micro-channels is confirmed by the fact that the protection by the oxygen-free glove box is necessary for the measurements of the bistability and switching characterization. It is found that the appearance and the amplitude of the NDR are dependent on the oxygen content. Once a device is removed from vacuum to ambient condition, the current in the NDR region and bistability region may drop by 3–4 orders of magnitude and the device may not show any behavior of the bistability at all. Block of the conducting micro-channels due to oxidation is likely the reason for that.

Further evidence for the existence of the conducting micro-channels is from the examination of the localized pathways in  $\text{Alq}_3$  thin films deposited on ITO substrate by means of conducting atomic force microscopy (CAFM). During measurements of the current distribution in the  $\text{Alq}_3$  thin film, some localized current peaks exist in some locations of the sample while other locations have very low current. When measuring the  $I$ - $V$  characteristics (scanning from  $-10$  to  $10$  V) at the places where current peaks exist, NDR effect was observed, as shown in Fig. 5.

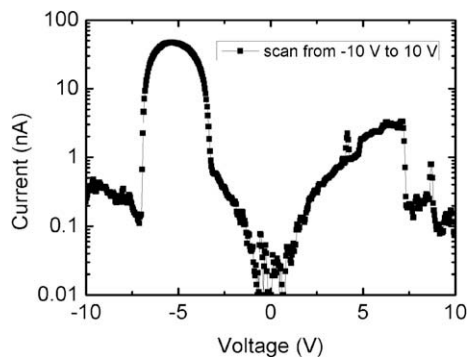


**Fig. 5.**  $I$ - $V$  curves measured by CAFM at the location where current peaks exist in the current distribution map of  $\text{Alq}_3$  thin films. The scan is from  $-10$  to  $10$  V.

No NDR effect was observed at other locations. In this case, asperities on the bottom ITO electrode rather than nanoparticle from the top electrode should be the origin of the localized conducting micro-channels.

Given the existence of the localized conducting micro-channels, the switching ON/OFF behavior of the devices can be properly explained. Overloading the micro-channels by applying a voltage higher than  $V_{\min}$  may partly disable them for conduction. The higher the voltage  $V > V_{\min}$  is applied, the more the channels are disabled. The disabled micro-channels will not contribute to the switch-on effect in the next scan, leading to the appearance of a lowered value of peak current. When the voltage reaches  $2V_{\min}$ , almost all the micro-channels are disabled, corresponding to the bistability-lost effect. On the other hand, with voltage pulse of amplitude close to  $V_{\min}$ , the switching characteristics of the micro-channels can be recovered, thus recalling the bistability. By examining the surface morphology of the device with an optical microscope, it is found that after the electrical stress of 28 V applied on the ITO/ $\text{Alq}_3$ / $\text{Al}_2\text{O}_3$ / $\text{Al}$  device local damages and bubbles appeared. In addition, it is found that after many cycles of losing and recovery of bistability by repeatedly applying high voltage and  $V_{\min}$ , the device's bistability could not be recovered any more even with voltage pulse of  $V_{\min}$  applied. The  $I$ - $V$  characteristics show normal P-N heterojunction characteristics. The micro-channels might be disabled or destroyed completely and could not recover any more.

Moreover, typical organic light-emitting diodes (OLEDs) with structure of ITO/NPB (50 nm)/ $\text{Alq}_3$  (70 nm)/LiF (1 nm)/Al were fabricated. The devices also showed typical bistability in the voltage range of 0–4 V. In the ON state, the current in the voltage range of 0–4 V was comparable with the current in the range of 6–10 V, but the devices showed no electroluminescence in the voltage region of 0–4 V while good electroluminescence was detected in the voltage region of 6–10 V. This means the high current in the region of 0–4 V in the ON state does not contribute to electroluminescence. It might flow through some localized conducting micro-channels rather than through the entire organic thin film homogeneously. In contrast, the current in the region of 6–10 V mostly consists of current flowing through the entire organic thin film homogeneously rather than through local micro-channels, and hence results in electroluminescence.

#### 4. Conclusions

In conclusion, the effect of high voltage stress exceeding  $V_{\min}$  on OBDs has been investigated. It is found that bistability can be completely destroyed under voltage of about  $2V_{\min}$  and can be recovered by applying voltage pulse of amplitude close to  $V_{\min}$  for milliseconds or longer. The existence of localized conducting micro-channels in the devices might be the origin of bistability.

#### Acknowledgements

This work is supported by CNKBRF and the National Natural Science Foundation of China.

**References**

- [1] L.P. Ma, J. Liu, Y. Yang, *Appl. Phys. Lett.* 80 (2002) 2997.
- [2] L.P. Ma, S. Pyo, J. Ouyang, Q.F. Xu, Y. Yang, *Appl. Phys. Lett.* 82 (2003) 1419.
- [3] L.D. Bozano, B.W. Kean, V.R. Deline, J.R. Salem, J.C. Scott, *Appl. Phys. Lett.* 84 (2004) 607.
- [4] L.D. Bozano, B.W. Kean, M. Beinhoff, K.R. Carter, P.M. Rice, J.C. Scott, *Adv. Funct. Mater.* 15 (2005) 1933.
- [5] D. Tondelier, K. Lmimouni, D. Vuillaume, *Appl. Phys. Lett.* 85 (2004) 5763.
- [6] J.S. Chen, D. Ma, *Appl. Phys. Lett.* 87 (2005) 23505.
- [7] A.K. Mahapatro, R. Agrawal, S. Ghosh, *J. Appl. Phys.* 96 (2004) 3583.
- [8] Y. Yang, J. Ouyang, L.P. Ma, R.J.H. Tseng, C.W. Chu, *Adv. Funct. Mater.* 16 (2006) 1001.
- [9] L.P. Ma, Q.F. Xu, Y. Yang, *Appl. Phys. Lett.* 84 (2004) 4908.
- [10] Q.X. Lai, Z.H. Zhu, Y. Chen, S. Patil, F. Wudl, *Appl. Phys. Lett.* 88 (2006) 133515.
- [11] M. Lauters, B. McCarthy, D. Sarid, G.E. Jabbour, *Appl. Phys. Lett.* 87 (2005) 231105.
- [12] R.J. Tseng, J.Y. Ouyang, C.W. Chu, J.S. Huang, Yang Yang, *Appl. Phys. Lett.* 88 (2006) 123506.
- [13] G. Dearnaley, D.V. Morgan, A.M. Stoneham, *J. Non-Cryst. Solids* 4 (1970) 593.
- [14] R.E. Thurstans, D.P. Oxley, *J. Phys. D: Appl. Phys.* 35 (2002) 802.
- [15] J. Ouyang, C.W. Chu, C.R. Szmanda, L.P. Ma, Y. Yang, *Nat. Mater.* 3 (2004) 918.
- [16] H.J. Gao, K. Sohlberg, Z.Q. Xue, H.Y. Chen, S.M. Hou, L.P. Ma, X.W. Fang, S.J. Pang, S.J. Pennycook, *Phys. Rev. Lett.* 84 (2000) 1780.
- [17] W. Tang, H.Z. Shi, G. Xu, B.S. Ong, X.D. Popovic, J.C. Deng, J. Zhao, G.H. Rao, *Adv. Mater.* 17 (2005) 2307.
- [18] J.G. Simmons, R.R. Verderber, *Proc. R. Soc. London, Ser. A* 301 (1967) 77.
- [19] T. Oyamada, H. Tanaka, K. Matsushige, H. Sasabe, C. Adachi, *Appl. Phys. Lett.* 83 (2003) 1252.
- [20] M.J. Rozenberg, I.H. Inoue, M.J. Sánchez, *Phys. Rev. Lett.* 92 (2004) 178302.
- [21] M. Terai, K. Fujita, T. Tsutsui, *Jpn. J. Appl. Phys.* 45 (2006) 3754.
- [22] M. Terai, K. Fujita, T. Tsutsui, *Mater. Res. Soc. Symp. Proc.* 965 (2007) S10-10.
- [23] M.L. Wang, J. Zhou, X.D. Gao, B.F. Ding, Z. Shi, X.Y. Sun, X.M. Ding, X.Y. Hou, *Appl. Phys. Lett.* 91 (2007) 143511.

vice. Based on these advantages, SS was studied as a gate electrode as well as a substrate in this research. Both 304 SS and 430 SS were used and the effect of the surface roughness was studied using chemical mechanical polishing (CMP) process. Aluminum oxide ( $\text{Al}_2\text{O}_3$ ) insulating layer was deposited using ALD process and was used as a gate insulator. Metal/insulator/metal (MIM, Au/ $\text{Al}_2\text{O}_3$ /304 SS, 430 SS and N++Si) structures were fabricated and characteristics such as dielectric constant and leakage current of  $\text{Al}_2\text{O}_3$  layer were measured. Pentacene TFTs with 304 SS, 430 SS and N++Si (heavily doped *n* type silicon) as a substrate were fabricated and performance of them were compared. Additionally, pentacene TFT with polished 304 SS was characterized in a bent state to check the bending on the device performance.

## 2. Experimental

304 SS and 430 SS substrate were supplied by POSCO and were polished with CMP process (KEMET P25FRS-A3) with alumina slurry of 0.05  $\mu\text{m}$  diameter for 10, 20, 30

and 40 min, respectively. Then, they were washed with distilled water and acetone. N++Si substrate (Silicon Material Inc.) was cleaned in piranha solution ( $\text{H}_2\text{SO}_4$ :  $\text{H}_2\text{O}_2 = 7:4$  vol%) for 1 h at 100 °C and washed with distilled water.  $\text{Al}_2\text{O}_3$  films of various thicknesses (50, 100, 200 and 500 nm) were deposited in a hot-wall ALD reactor on 304 SS, 430 SS and N++ Si substrate. Trimethyl aluminum and distilled water were employed as a precursor and an oxidizing reaction gas. The line from the precursor bottle to the reactor was maintained at 60 °C and the pressure and temperature of the reactor were fixed at 1 Torr and 150 °C, respectively.  $\text{N}_2$  (99.999%) gas was employed as a carrier and purge gas. Flow rate of  $\text{N}_2$  gas for purging and for carrying vaporized water was fixed at 100 sccm and 10 sccm, respectively. The ALD cycle of  $\text{Al}_2\text{O}_3$  film was precursor injection (1 s)–purge (5 s)–water vapor injection (1 s)–purge (10 s).

Pentacene (purchased from Aldrich Chemical Co.) films of 50 nm were deposited at R.T. with a deposition rate of 0.2–0.3 Å/sec in an organic molecular beam deposition (OMBD) system at a pressure of  $2 \times 10^{-6}$  Torr. Au elec-

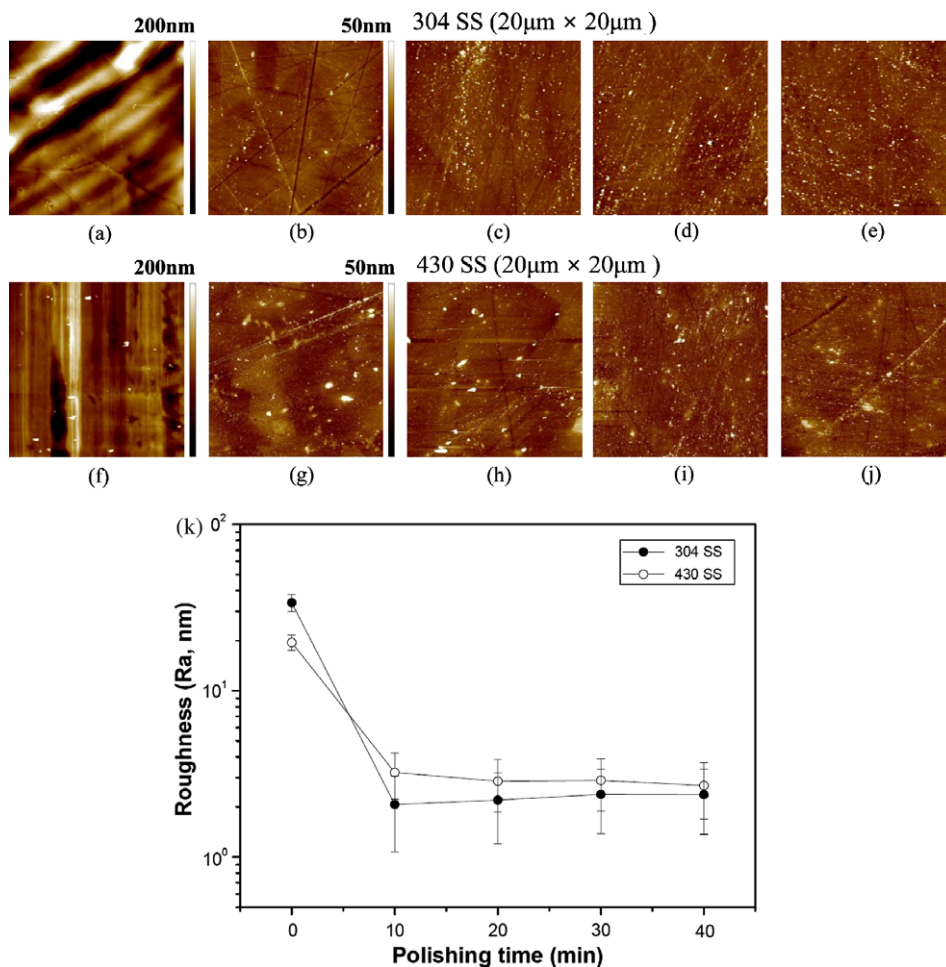


**Fig. 1.** Surface morphologies of 304 SS and 430 SS polished with an alumina slurry of 0.05  $\mu\text{m}$  diameter for various durations: (a) without polishing, (b) 10 min, (c) 20 min, (d) 30 min, (e) 40 min polishing for 304 SS, (f) without polishing, (g) 10 min, (h) 20 min, (i) 30 min, (j) 40 min polishing for 430 SS and (k) roughness of SS versus the polishing time.

trodes (50 nm) for MIM structure and pentacene TFT were formed through a shadow mask using a thermal evaporator. The channel length and width were 150 and 1500  $\mu\text{m}$ , respectively.

The morphology and surface roughness of SS and pentacene were investigated with atomic force microscope (AFM). The crystallinity of pentacene on SS was examined by X-ray diffraction (XRD) with 3C2 beam line at the Pohang Accelerator Laboratory. The dielectric constant ( $C_i$ ) at 1 MHz and leakage current of  $\text{Al}_2\text{O}_3$  film were measured using HP 5270A. The current–voltage ( $I$ – $V$ ) characteristics of pentacene TFTs were obtained using HP 4284A.

### 3. Results and discussion

Fig. 1a–j show AFM images of 304 SS and 430 SS which were polished using CMP process for various times (10, 20, 30 and 40 min) and Fig. 1k shows the change of surface roughness as a function of the polishing time. Prior to the CMP process, surface roughness of 304 SS was about 33.8 nm and that of 430 SS was about 19.5 nm. Both were smoothed down to the level of  $\sim 2.5$  nm after a CMP process of above 10 min.

Fig. 2a shows the MIM structure and Fig. 2b–d show the leakage current when the voltage of 0–40 V was applied to the top electrode on  $\text{Al}_2\text{O}_3$  of different thickness (50, 100, 200 and 500 nm) on N++Si substrate, 304 SS and 430 SS.  $\text{Al}_2\text{O}_3$  films thicker than 200 nm on each substrate showed a leakage current level as low as  $10^{-11}$  A. But the breakdown voltage was observed in the MIM structure with 100 nm  $\text{Al}_2\text{O}_3$  on 304 SS at  $\sim 5$  V and on 430 SS at  $\sim 30$  V.  $\text{Al}_2\text{O}_3$  film of 50 nm on N++Si substrate maintained insulating properties up to 20 V. The N++Si substrate has a low roughness of 0.2 nm so that  $\text{Al}_2\text{O}_3$  films on N++Si substrate shows better insulating characteristic than that on bare 304 SS or 430 SS at the same thickness. The insulating properties of  $\text{Al}_2\text{O}_3$  film on SS can be improved with reducing surface roughness using CMP process and actually, breakdown voltage was not observed in MIM structures with  $\text{Al}_2\text{O}_3$  film of 100 nm on polished 304 SS and 430 SS. On the other hand,  $C_i$  values of  $\text{Al}_2\text{O}_3$  films (100 nm) on each substrate show almost the same value of  $\sim 65$  nF/ $\text{cm}^2$  regardless of the substrate type.

Fig. 3a shows the structure of the top-contact pentacene TFT which was characterized to compare the performance of the pentacene TFTs on each substrate. Transfer charac-

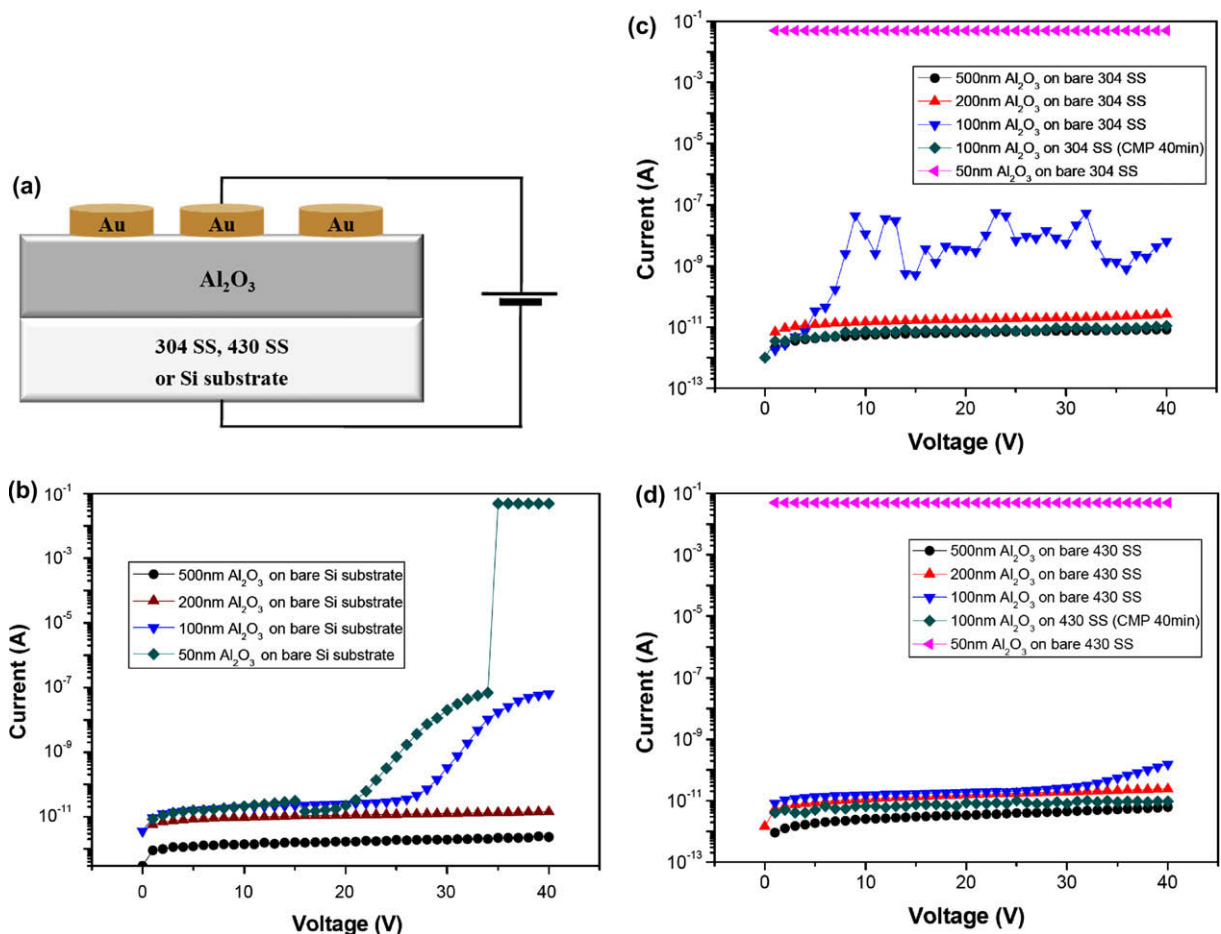
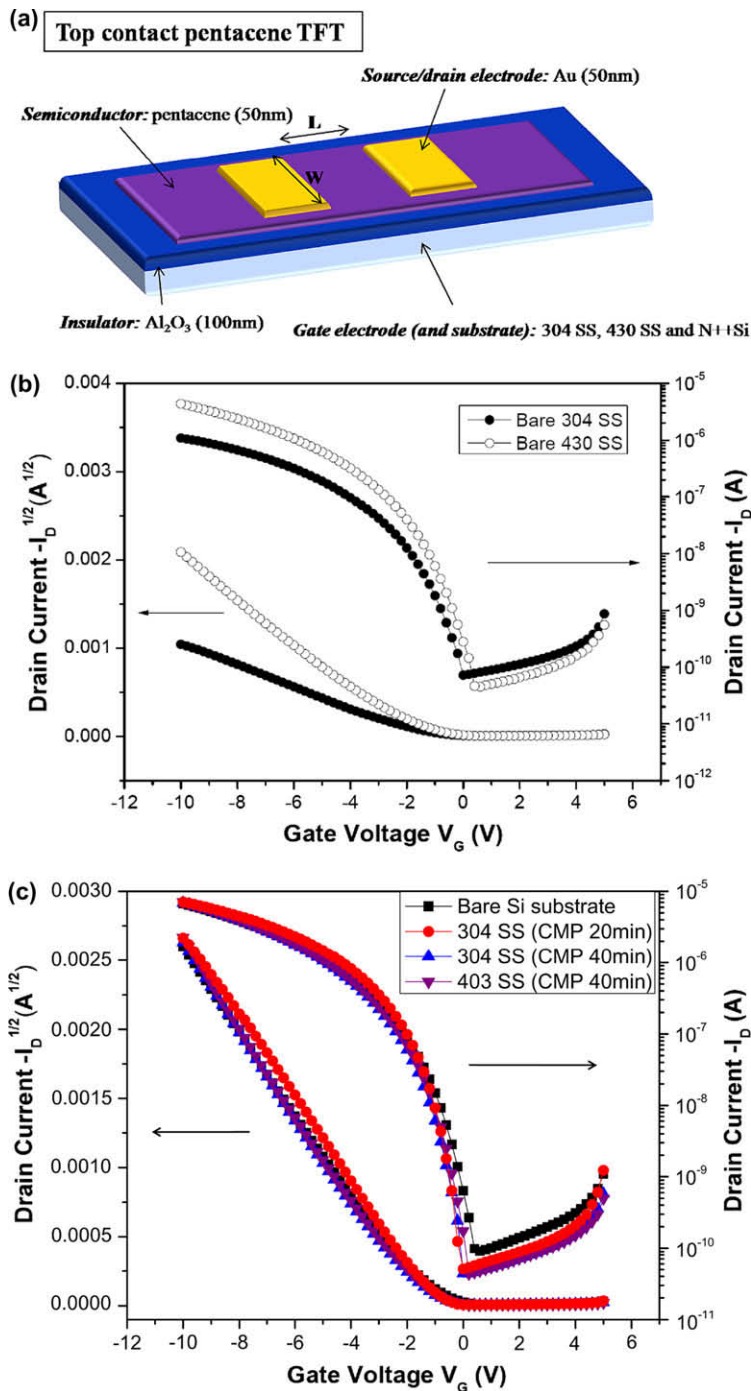


Fig. 2. (a) Metal–insulator–metal (MIM) structure of Au/ $\text{Al}_2\text{O}_3$ /304 SS, 430 SS and Si substrate and current–voltage characteristics of Au/ $\text{Al}_2\text{O}_3$ /, (b) Si substrate, (c) 304 SS and (d) 430 SS.



**Fig. 3.** (a) Schematic structure of the top-contact pentacene thin-film transistor, (b) comparative transfer characteristics of the pentacene TFT on bare 304 SS and bare 430 SS and (c) comparative transfer characteristics of pentacene TFT on Si, bare 304 SS, 20 min polished 304 SS, 40 min polished 304 SS and 40 min polished 430 SS:  $\log_{10}|I_D|$  versus  $V_G$  and  $|I_D|^{1/2}$  versus  $V_G$  at  $-10$  V.

teristics of the pentacene TFTs with bare 304 SS and 430 SS are shown in Fig. 3b and transfer characteristics of the pentacene TFTs with N++Si and polished SS are compared in Fig. 3c. All pentacene TFTs fabricated with SS showed p-type transistor-characteristics, even though their device

performance was different. Most pentacene TFTs on bare 430 SS showed higher saturation currents at each  $V_G$  than those pentacene TFTs on 304 SS, as shown in Fig. 3b, but current levels were lower than the pentacene TFTs on N++Si substrate. The saturation currents and transfer char-

**Table 1**

Summary of the pentacene OTFT characteristics fabricated on the various substrates.

Substrate	Field-effect Mobility (cm <sup>2</sup> /Vs)	On/off Current ratio	Threshold Voltage (V <sub>th</sub> )	Substrate	Field-effect Mobility (cm <sup>2</sup> /Vs)	On/off Current ratio	Threshold Voltage (V <sub>th</sub> )
N++Si	0.17–0.34	~10 <sup>5</sup>	~-1.5	OTS treated Al <sub>2</sub> O <sub>3</sub> /N++Si	0.63–0.90	~10 <sup>6</sup>	~-1
Bare 304 SS	0.005–0.17	10 <sup>3</sup> –10 <sup>4</sup>	-0.5 to -1.5	OTS treated Al <sub>2</sub> O <sub>3</sub> /430 SS	0.45–0.85	~10 <sup>6</sup>	~-1
Bare 430 SS	0.11–0.36	~10 <sup>5</sup>	-1.0 to -2.0	OTS treated Al <sub>2</sub> O <sub>3</sub> /304 SS	0.40–0.70	~10 <sup>6</sup>	~-1
304 SS (CMP 10 min)	0.23–0.40	~10 <sup>5</sup>	~-1.5	-	-	-	-
304 SS (CMP 20 min)	0.23–0.41	~10 <sup>5</sup>	~-1.5	-	-	-	-
304 SS (CMP 40 min)	0.24–0.38	~10 <sup>5</sup>	~-1.5	-	-	-	-
430 SS (CMP 40 min)	0.27–0.42	~10 <sup>5</sup>	~-1.5	-	-	-	-

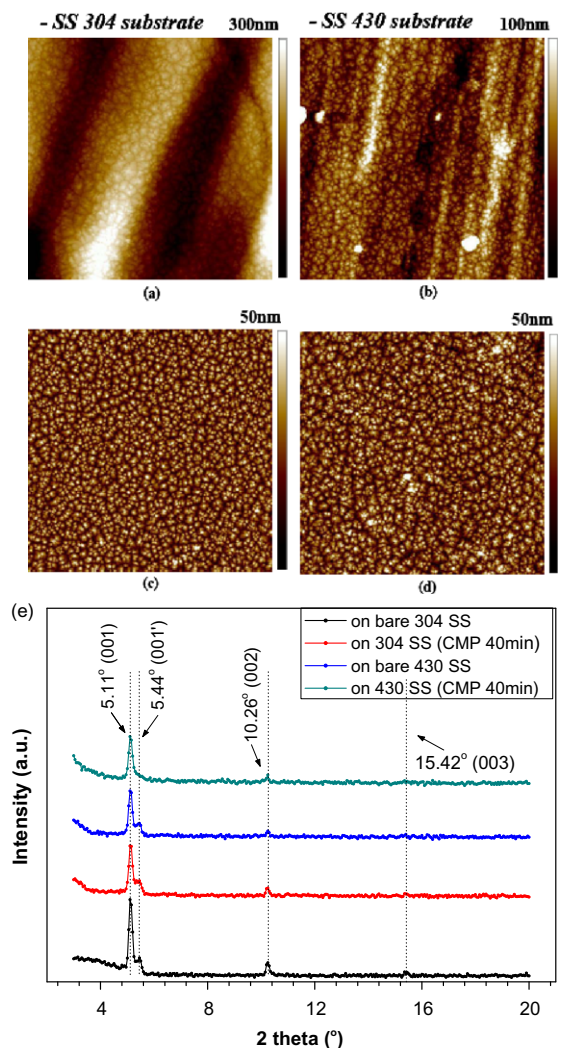
acteristics of pentacene TFTs on SS were improved with CMP process close to the pentacene TFT on N++Si substrate as shown in Fig. 3c. The field-effect mobility in the saturated regime ( $V_D = -10$  V) was calculated using the formula given below:

$$I_{DS} = \frac{WC_i}{2L} (V_G - V_T)^2 \mu \quad (1)$$

where  $I_{DS}$  is the drain current at specific gate voltage ( $V_G$ ),  $W$  is the channel width,  $L$  is the channel length,  $V_T$  is the threshold voltage,  $\mu$  is the carrier field-effect mobility and  $C_i$  is the capacitance per unit area of the gate insulator ( $C_i$  of 100 nm thick Al<sub>2</sub>O<sub>3</sub> was measured to be 65 nF/cm<sup>2</sup>). The field-effect mobility ( $\mu$ ), on/off ratio and threshold voltage ( $V_G$ ) of pentacene TFTs on various substrates are summarized in Table 1.  $\mu$  and on/off ratio of pentacene TFTs on bare 304 SS are in a wide range of 0.005–0.17 cm<sup>2</sup>/Vs and on/off ratio of 10<sup>3</sup>–10<sup>4</sup> depending on the location of the substrate.  $\mu$  and on/off ratio of pentacene TFTs on bare 430 SS are in a range of 0.11–0.36 cm<sup>2</sup>/Vs and on/off ratio of ~10<sup>5</sup>. Bare 304 SS has a roughness of 33.8 nm and that of 430 SS was about 19.5 nm and so the variation of the OTFT characteristics was significant for 304 SS but less significant for 430 SS.

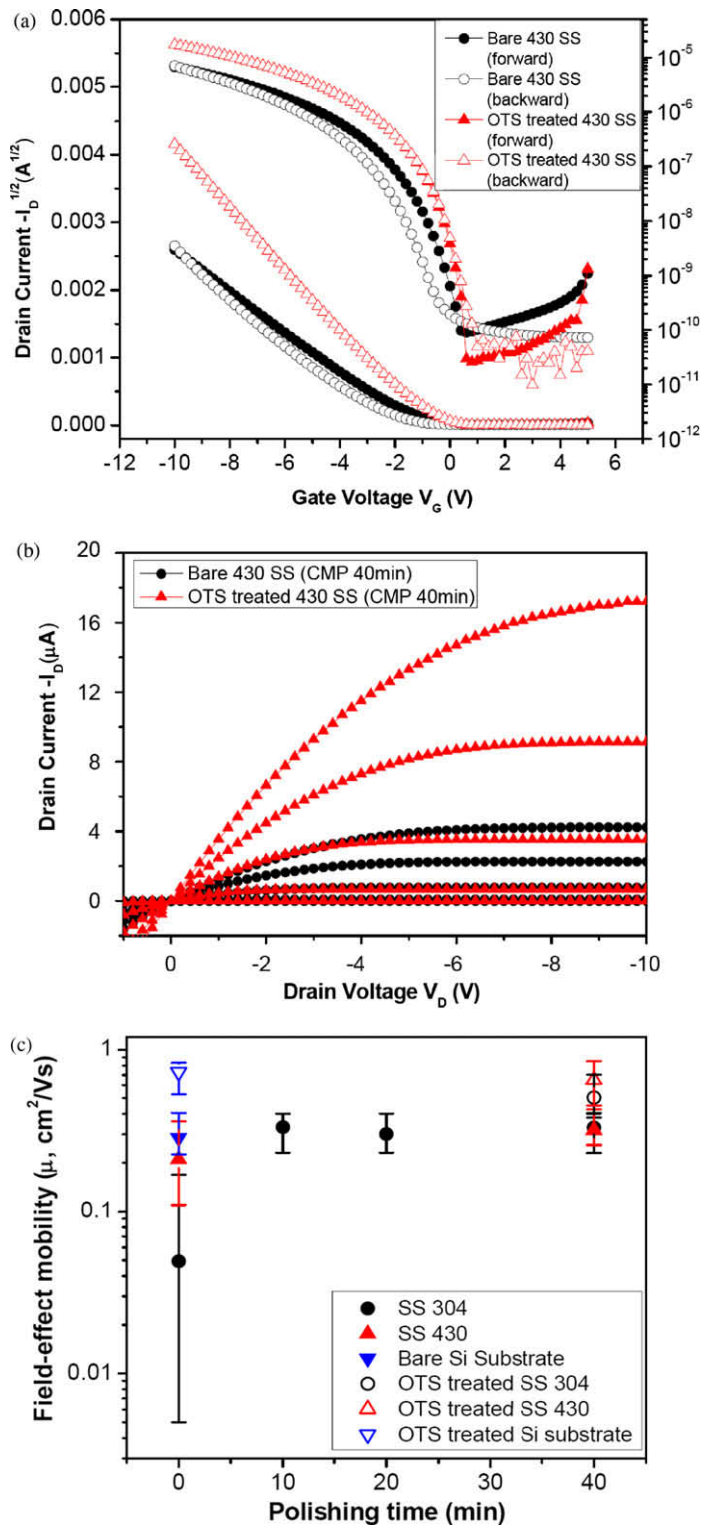
Pentacene TFTs on 304 SS and 430 SS polished using CMP process showed a high mobility of 0.25–0.40 cm<sup>2</sup>/Vs and on/off ratios of ~10<sup>5</sup> which is slightly better than pentacene TFTs on Al<sub>2</sub>O<sub>3</sub>/N++Si substrate ( $\mu$ : 0.17–0.34 cm<sup>2</sup>/Vs, on/off ratio: ~10<sup>5</sup>). The local variation was not significant for polished substrate.

Fig. 4a and b show the morphology of the pentacene film grown on Al<sub>2</sub>O<sub>3</sub> (100 nm) deposited on bare 304 SS and 430 SS and Fig. 4c and d show the morphology of the pentacene film grown on Al<sub>2</sub>O<sub>3</sub> (100 nm) deposited on polished 304 SS and 430 SS. Even though the roughness of the bare SS are much higher than the polished SS, grain shape and grain size of the pentacene film on bare SS are nearly the same as on polished SS. Crystallinity of the pentacene film on Al<sub>2</sub>O<sub>3</sub> (100 nm) deposited on bare SS and polished SS is shown in Fig. 4e and the peaks show that the crystallinity is almost the same for all the pentacene films. XRD patterns contain the series of (0 0  $k$ ), indicating the thin film phase of material and (0 0  $k'$ ), indicating the crystalline bulk phase of the material [11,12]. Both the thin film and the bulk phase mean highly ordered and crystallized states. Thin film phases of (0 0  $k$ ) were mainly observed at both pentacene films grown on Al<sub>2</sub>O<sub>3</sub>(100 nm) deposited on bare SS and polished SS, and there is no significant change in intensity of (0 0  $k$ ) between pentacene films



**Fig. 4.** AFM images of pentacene (50 nm) grown on Al<sub>2</sub>O<sub>3</sub> (100 nm). (a) Bare 304 SS, (b) bare 430 SS, (c) 40 min polished 304 SS and (d) 40 min polished 430 SS and XRD spectrum of pentacene (50 nm) grown on Al<sub>2</sub>O<sub>3</sub> (100 nm)/bare SS and polished SS.

grown on Al<sub>2</sub>O<sub>3</sub> (100 nm) deposited on bare SS and polished SS. Based on above results, it was confirmed that properties including crystallinity and morphology of pentacene film grown on Al<sub>2</sub>O<sub>3</sub> (100 nm) deposited on bare SS are almost similar to that grown on Al<sub>2</sub>O<sub>3</sub> (100 nm)



**Fig. 5.** (a) Comparative transfer characteristics:  $\log_{10}|I_D|$  versus  $V_G$  and  $|I_D|^{1/2}$  versus  $V_G$  at  $-10$  V, (b) output characteristics: drain current ( $I_D$ ) versus drain voltage ( $V_D$ ) of pentacene TFT with and without OTS treatment on  $Al_2O_3$  (100 nm)/40 min polished 430 SS and (c) field-effect mobility versus polishing time of SS.



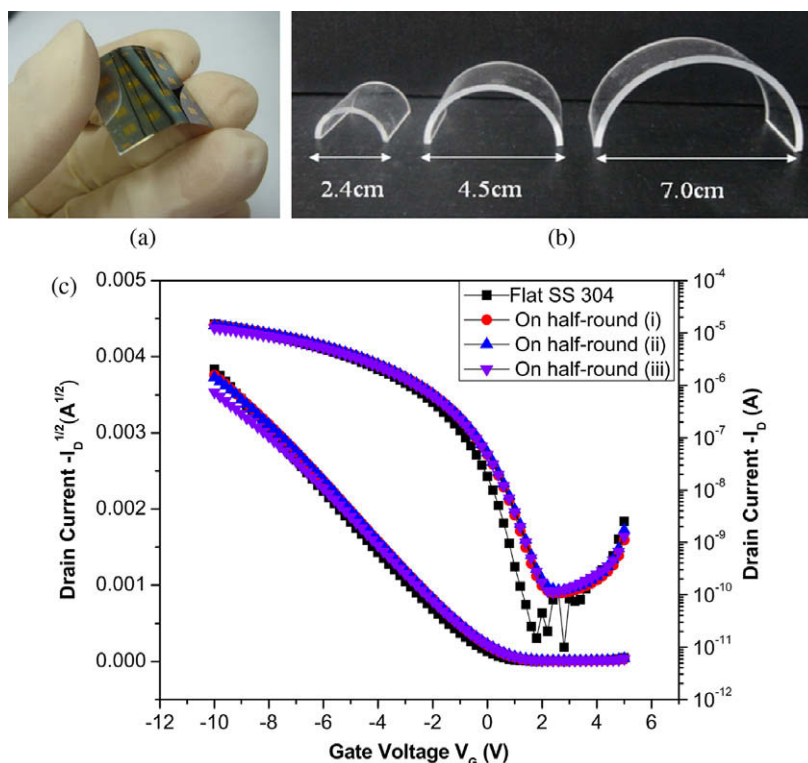


**Fig. 6.** (a) Optical image of fabricated pentacene TFT in bent state, (b) half-round glass tubes with different diameters ( $D =$  (i) 70, (ii) 45 and (iii) 24 mm) and (c) comparative transfer characteristics of pentacene TFT with OTS treated  $\text{Al}_2\text{O}_3(100 \text{ nm})/40 \text{ min}$  polished 304 SS in bent state:  $\log_{10}|I_D|$  versus  $V_G$  and  $|I_D|^{1/2}$  versus  $V_G$  at  $-10 \text{ V}$ .

deposited on polished SS. Good pentacene TFTs on bare SS show mobility of  $\sim 0.3 \text{ cm}^2/\text{Vs}$  and on/off ratio of  $\sim 10^5$ , which is nearly at the same level of pentacene TFTs on polished SS.

OTS monolayer has been widely employed as a buffer layer to improve the crystallinity of organic semiconductor grown on it [12–14]. OTS treatment was performed on  $\text{Al}_2\text{O}_3$  layer to improve the performance of the pentacene TFTs. In Fig. 5a and b, transfer and output characteristics of pentacene TFT with OTS treated  $\text{Al}_2\text{O}_3/430 \text{ SS}$  are compared to the pentacene TFTs with bare  $\text{Al}_2\text{O}_3/430 \text{ SS}$ . With OTS treatment, the saturation currents at the same  $V_G$  were increased and the hysteresis between forward and backward transfer curve was removed. As shown in Table 1, the  $\mu$  and on/off ratio of pentacene TFTs on SS were improved with OTS treatment up to  $0.40\text{--}0.85 \text{ cm}^2/\text{Vs}$  and  $\sim 10^6$ , respectively. These values are comparable to the performance of the pentacene TFTs with OTS treated  $\text{Al}_2\text{O}_3/\text{N++Si}$  substrate ( $0.63\text{--}0.90 \text{ cm}^2/\text{Vs}$  and  $\sim 10^6$ ). The mobility of pentacene TFTs on various substrates are shown all together in Fig. 5c, and this graph confirms that high performance pentacene TFT can be fabricated with polished SS as with N++Si substrate.

Not like N++Si substrate, SS is bendable and  $I\text{--}V$  characteristics of the pentacene TFT with OTS treated  $\text{Al}_2\text{O}_3/304 \text{ SS}$  were measured in bent state as well as in flat state. Pentacene TFTs were bent over a half-round glass tube with bending diameter ( $D$ ) of 24, 45 or 70 mm during the

$I\text{--}V$  measurement. The pentacene TFT in bent state is shown in Fig. 6a and half-round glass tubes with different diameters were shown in Fig. 6b.  $\mu$  and  $V_{\text{th}}$  of pentacene TFTs without bending strain is  $0.50 \text{ cm}^2/\text{Vs}$  and  $-0.49 \text{ V}$ .  $\mu$  is decreased by 14% when OTFT was placed on the curved surface with  $D = 70 \text{ mm}$ , by 16% with  $D = 45 \text{ mm}$  and by 24% with  $D = 24 \text{ mm}$ , and  $V_{\text{th}}$  is slightly shifted to the positive direction. Nevertheless, the device performed well showing the standard transistor characteristics including the linear regime and the saturation regime and on/off ratio was also maintained at  $\sim 10^6$  steadily in bent state, as shown in Fig. 6c. It was already pointed out that tensile strain in the FET device induced an increase in the inter-grain boundaries and the interdomain structural mismatch leading to the decrease in the mobility of OTFT devices [7]. Also it was pointed out that tensile strain caused a larger spacing between molecules resulting in a decrease in the mobility [8].

#### 4. Conclusion

In summary, we fabricated pentacene OTFT with aluminum oxide as a gate dielectric on a rough SS substrate and on a polished SS using CMP process. MIM structures and pentacene TFTs on a rough and polished SS were fabricated and characterized. Pentacene TFTs on a rough SS showed a wide range of device characteristics depending on the location at the substrate surface and mostly poorer perfor-

mance was obtained compared to the device on a flat N++Si substrate. With polishing using CMP process, performance of the pentacene TFTs on SS was improved up to the same level of pentacene TFT on the N++Si substrate. Leakage current through Al<sub>2</sub>O<sub>3</sub> layer on SS was also reduced with polishing. Additionally, mobility and on/off ratio of pentacene TFT on SS was increased with OTS treatment. Characteristics of the pentacene TFTs on SS in bent state were also measured and it was confirmed that the mobility was reduced with the tensile strain.

### Acknowledgments

This research was supported by the Korea Science and Engineering Foundation (KOSEF) through the National Research Laboratory Project, the POSCO Steel Science Research Program and by Grant No. RTI04-01-04 from the Regional Technology Innovation Program of the Ministry of Knowledge & Economy (MKE), and the Pohang Accelerator Laboratory for providing the synchrotron radiation source at the 3C2 beamlines used in this study. The author

D.J. Yun is grateful to Hyunjin Park, Researcher at NCNT for supporting the AFM analysis.

### References

- [1] B.C. Shekar, J. Lee, S.W. Rhee, *Korean J. Chem. Eng.* 21 (2004) 267.
- [2] S.W. Rhee, D.J. Yun, *J. Mater. Chem.* 18 (2008) 5437.
- [3] D. Braga, G. Horowitz, *Adv. Mater.* 21 (2009) 1.
- [4] D.J. Yun, S.W. Rhee, *J. Electrochem. Soc.* 155 (2008) H899.
- [5] K. Hong, J.W. Lee, S.Y. Yang, K. Shin, H. Jeon, S.H. Kim, C. Yang, C.E. Park, *Org. Electron.* 9 (2008) 21.
- [6] P.V. Necliudov, M.S. Shur, D.J. Gundlach, T.N. Jackson, *Solid-State Electron.* 47 (2003) 259.
- [7] C. Yang, J. Yoon, S.H. Kim, K. Hong, D.S. Chung, K. Heo, C.E. Park, M. Ree, *Appl. Phys. Lett.* 92 (2008) 243305.
- [8] T. Sekitani, Y. Kato, S. Iba, H. Shinaoka, T. Someya, T. Sakurai, S. Takagi, *Appl. Phys. Lett.* 86 (2005) 073511.
- [9] A. Sari, K. Kaygusuz, *Renew. Energy* 28 (2003) 939.
- [10] M.G. Kang, N.G. Park, K.S. Ryu, S.H. Chang, K.J. Kim, *Sol. Energy Mater. Sol. Cells* 90 (2006) 574.
- [11] D.J. Yun, S.W. Rhee, *J. Electrochem. Soc.* 155 (2008) H357.
- [12] H.S. Lee, D.H. Kim, J.H. Cho, M. Hwang, Y. Jang, K. Cho, *J. Am. Chem. Soc.* 130 (2008) 10556.
- [13] I. Kymissis, C.D. Dimitrakopoulos, S. Purushothanman, *IEEE Trans. Electron Dev.* 48 (2001) 1060.
- [14] K.P. Pernstich, S. Haas, D. Oberhoff, C. Goldmann, D.J. Gundlach, B. Batlogg, A.N. Rashid, G. Schitter, *J. Appl. Phys.* 96 (2004) 6431.

of the emitting layers by the stamp transfer printing method and an efficiency improvement by the double layer emitting structure was demonstrated.

## 2. Experimental

A device structure of indium tin oxide (ITO, 150 nm)/polyethylene-3,4-dioxythiophene:polystyrenesulfonate (PEDOT:PSS, 60 nm)/poly(9,9'-dioctylfluorene-co-bis-N,N'-(4-ethoxycarbonylphenyl)-bis-N,N'-phenyl-benzidine (PFO-co-NEPB, 30 nm)/4,4',4''-tris(N-carbazolyl)triphenylamine (TCTA):tris(2-phenylpyridine)iridium ( $\text{Ir}(\text{ppy})_3$ ) (20 nm, 5% doping)/3-(biphenyl-4-yl)-4-phenyl-5-(4-tert-butylphenyl)-1,2,4-triazole (TAZ): $\text{Ir}(\text{ppy})_3$  (20 nm, 5% doping)/2,9-dimethyl-4,7-diphenyl-1,10-phenanthroline (BCP, 5 nm)/tris(8-hydroxyquinoline)aluminium ( $\text{Alq}_3$ , 20 nm)/LiF (1 nm)/Al (200 nm) was used to prepare the double emitting layer device. Single emitting layer devices with TCTA: $\text{Ir}(\text{ppy})_3$  or TAZ: $\text{Ir}(\text{ppy})_3$  were also fabricated to compare the device performances of the double emitting layer PHOLED. Fig. 1 shows the device structures of the soluble PHOLEDs used in this work. The TCTA: $\text{Ir}(\text{ppy})_3$  and the TAZ: $\text{Ir}(\text{ppy})_3$  layers were coated from a 1.0 wt% toluene solution. The wt% was a concentration of the host material. The coated emitting layer was baked at 110 °C for 30 min to remove residual solvent. The stamp transfer printing of the TAZ: $\text{Ir}(\text{ppy})_3$  layer using polymethylsiloxane (PDMS) stamp was carried out according to the procedure reported earlier [12]. Detailed process for the stamp transfer printing is described in Fig. 2. Current density–voltage–luminance characteristics of the devices were obtained by Keithley 2400 source measurement unit and a CS 1000 spectroradiometer.

## 3. Results and discussion

A double layer emitting structure was reported in a vacuum deposited PHOLEDs and the quantum efficiency was significantly improved compared with common single layer PHOLEDs [9–11]. However, the double layer emitting structure could not be realized in soluble PHOLEDs because of intermixing of the two emitting layers during spin-coating. The problem can be avoided by using a dry patterning method which utilizes a transfer process for the film for-

mation [12,13]. In this work, a stamp transfer printing process was used to fabricate the double emitting layer green PHOLEDs and device performances were investigated. The transfer process was reproducible and the yield of the device was over 90%.

Fig. 3 shows the current density–voltage–luminance curves of the single and double layer green PHOLEDs. The current density was high in the PHOLED with the double layer emitting structures, while it was low in the PHOLEDs with single layer emitting structure. The current density was greatly enhanced in the green PHOLED with the double layer emitting structure. The increased current density in the double emitting layer device can be explained by the efficient hole and electron injection from the charge transport layers. Hole injection from the PFO-co-NEPB to the TCTA: $\text{Ir}(\text{ppy})_3$  emitting layer and the electron injection from the BCP to the TAZ: $\text{Ir}(\text{ppy})_3$  layer are efficient because there is little energy barrier for the charge injection as can be seen in the energy level diagram (Fig. 4). Compared with the double emitting layer device, the hole injection is limited in the TAZ: $\text{Ir}(\text{ppy})_3$  device and the electron injection is hindered in the TCTA: $\text{Ir}(\text{ppy})_3$  device, resulting in low current density. The luminance–voltage curves were similar to the current density–voltage curves even though the luminance of the TAZ: $\text{Ir}(\text{ppy})_3$  device was low. The low luminance of the TAZ: $\text{Ir}(\text{ppy})_3$  device is due to electron leakage from the emitting layer to the hole transport layer as seen in the EL spectra of the device (Fig. 6).

The quantum efficiency and power efficiency of the green PHOLEDs are shown in Fig. 5. The efficiency of the double emitting layer device was much higher than that of the single layer device. The high efficiency of the double emitting layer device is due to charge confinement and charge balance in the emitting layer. Both holes and electrons are effectively injected from the hole and electron transport layers and charge balance is improved in the double emitting layer structure. In the case of the TCTA: $\text{Ir}(\text{ppy})_3$  device, the charge balance is degraded because of poor electron injection. Poor hole injection in the TAZ: $\text{Ir}(\text{ppy})_3$  device disrupts the charge balance, decreasing the quantum efficiency of the TAZ: $\text{Ir}(\text{ppy})_3$  device. Therefore, the stacking of the two emitting layers by the stamp transfer printing method was effective to enhance the quantum efficiency of the soluble green PHOLEDs. The quantum efficiency of the green PHOLEDs was quadrupled by the stacking of the

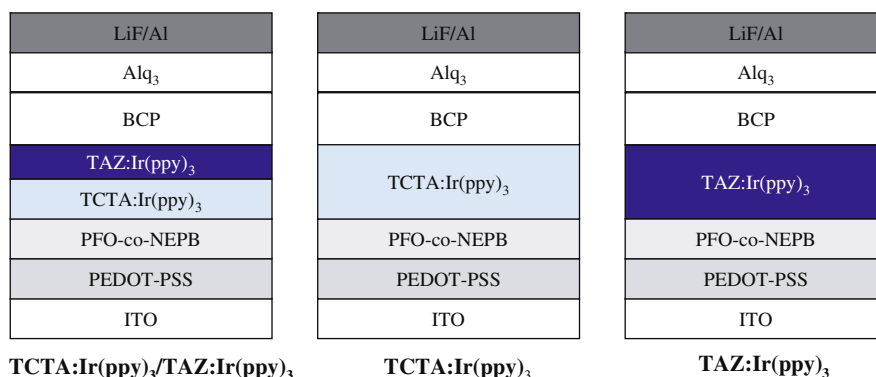


Fig. 1. Device structures of the double emitting layer device and single emitting layer devices.

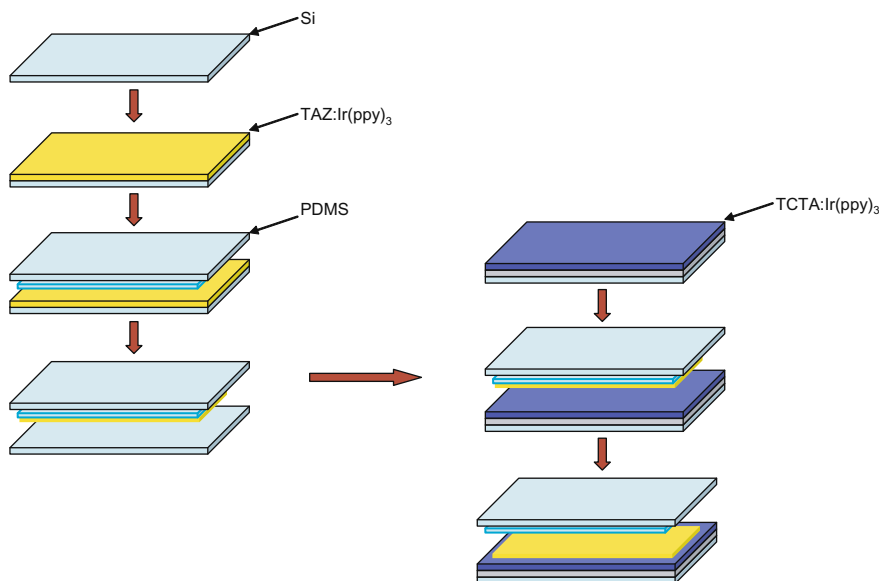


Fig. 2. Stamp transfer printing process for the fabrication of the stacked emitting layers.

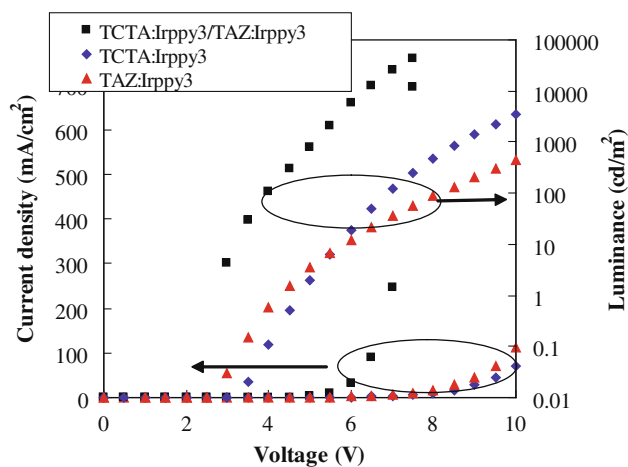


Fig. 3. Current density–voltage–luminance curves of the TCTA:Ir(ppy)<sub>3</sub>, TAZ:Ir(ppy)<sub>3</sub>, and TCTA:Ir(ppy)<sub>3</sub>/TAZ:Ir(ppy)<sub>3</sub> devices.

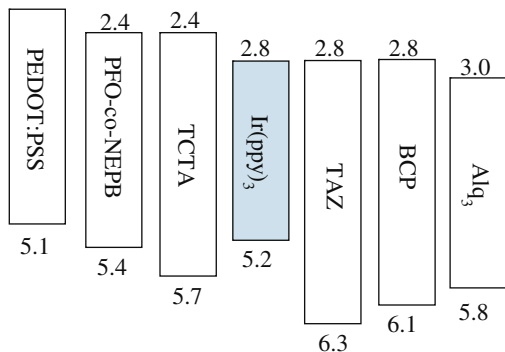


Fig. 4. Energy level diagram of the materials used in this work.

two emitting layers. In addition, the power efficiency was also greatly improved due to the high quantum efficiency and high current density.

The EL spectra of the soluble green PHOLEDs fabricated in this work are shown in Fig. 6. The EL spectra were measured at 1000 cd/m<sup>2</sup>. The double emitting layer device showed a typical EL emission of Ir(ppy)<sub>3</sub> based green PHOLEDs. Peak maximum of the EL spectra was observed at 515 nm and no peak except for the Ir(ppy)<sub>3</sub> was detected in the device. The TCTA:Ir(ppy)<sub>3</sub> device exhibited a similar EL spectrum. However, the EL spectrum of the TAZ:Ir(ppy)<sub>3</sub> device was different from those of the TAZ:Ir(ppy)<sub>3</sub> and double emitting layer devices. In addition to the Ir(ppy)<sub>3</sub> emission, a broad peak was observed in the blue emission region. The broad blue emission peak is originated from

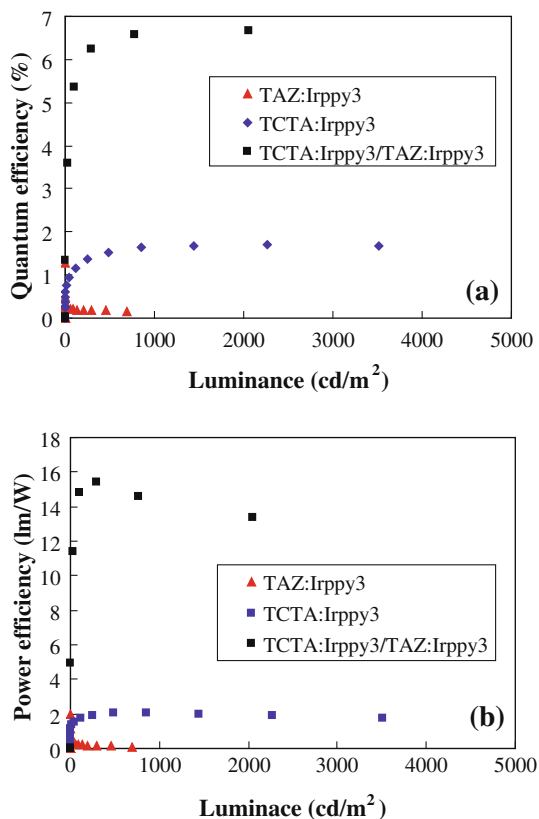


Fig. 5. Quantum efficiency–luminance (a) and power efficiency–luminance (b) curves of the TCTA:Ir(pp<sub>y</sub>)<sub>3</sub>, TAZ:Ir(pp<sub>y</sub>)<sub>3</sub>, and TCTA:Ir(pp<sub>y</sub>)<sub>3</sub>/TAZ:Ir(pp<sub>y</sub>)<sub>3</sub> devices.

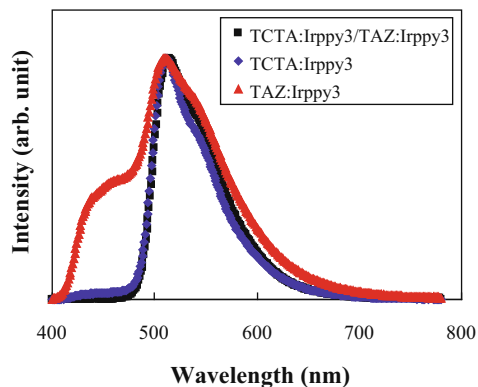


Fig. 6. Electroluminescence spectra of the TCTA:Ir(pp<sub>y</sub>)<sub>3</sub>, TAZ:Ir(pp<sub>y</sub>)<sub>3</sub>, and TCTA:Ir(pp<sub>y</sub>)<sub>3</sub>/TAZ:Ir(pp<sub>y</sub>)<sub>3</sub> devices.

the emission of the PFO-co-NEPB hole transport material. There is an energy barrier of 0.9 eV between the PFO-co-NEPB and TAZ, limiting the hole injection from the PFO-co-NEPB to TAZ emitting layer and hole accumulation at the interface between the PFO-co-NEPB and TAZ. In addition to the hole accumulation, TAZ has a strong electron transport character and electrons can be transported to the interface between the PFO-co-NEPB and TAZ emitting layer. The hole accumulation and high electron density near PFO-co-NEPB induces electron leakage from the TAZ layer to the PFO-co-NEPB layer in spite of 0.4 eV energy barrier, leading to hole–electron recombination at the interface between PFO-co-NEPB and TAZ. Hole blocking properties of the TAZ due to the highest occupied molecular orbital of 6.3 eV contribute to the charge accumulation and PFO-co-NEPB emission. The PFO-co-NEPB emission is responsible for the low current efficiency of the TAZ:Ir(pp<sub>y</sub>)<sub>3</sub> device.

#### 4. Conclusions

In summary, high efficiency soluble green PHOLEDs could be developed by using the double layer emitting structure fabricated by the stamp transfer printing method. Two emitting layers could be effectively stacked by the stamp transfer printing process and the current efficiency of the green PHOLEDs could be improved by more than four times.

#### References

- [1] M.A. Baldo, D.F.O. Brian, Y. You, A. Shoustikov, S. Sibley, M.E. Thompson, S.R. Forrest, *Nature* 395 (1998) 151.
- [2] C. Adachi, M.A. Baldo, Mark E. Thompson, Stephen R. Forrest, *J. Appl. Phys.* 90 (2001) 5048.
- [3] H. Kim, Y. Byun, R.R. Das, B.K. Choi, P.S. Ahn, *Appl. Phys. Lett.* 91 (2007) 093512.
- [4] J.J. Park, T.J. Park, W.S. Jeon, R. Pode, J. Jang, J.H. Kwon, E.S. Yu, M.Y. Chae, *Org. Electron.* 10 (2009) 181.
- [5] X. Yang, D.C. Muller, D. Neher, K. Meerholtz, *Adv. Mater.* 18 (2006) 948.
- [6] R. Bauer, W.J. Finkenzeller, U. Bogner, M.E. Thompson, H. Yersin, *Org. Electron.* 9 (2008) 641.
- [7] S. Lamansky, R.C. Kwong, M. Nugent, P.I. Djurovich, M.E. Thompson, *Org. Electron.* 2 (2001) 53.
- [8] S. Tokito, M. Suzuki, F. Sato, M. Kamachi, K. Shirane, *Org. Electron.* 4 (2003) 105.
- [9] K.S. Yook, S.O. Jeon, C.W. Joo, J.Y. Lee, *Appl. Phys. Lett.* 93 (2008) 113301.
- [10] X. Zhou, D.S. Qin, M. Pfeiffer, J. Blochwitz-Nimoth, A. Werner, J. Drechsel, B. Maennig, K. Leo, M. Bold, P. Erk, H. Hartmann, *Appl. Phys. Lett.* 81 (2002) 4070.
- [11] G. He, M. Pfeiffer, K. Leo, M. Hofmann, J. Birnstock, R. Pudzich, J. Salbeck, *Appl. Phys. Lett.* 85 (2004) 3912.
- [12] C.W. Joo, S.O. Jeon, K.S. Yook, J.Y. Lee, *Org. Electron.* 10 (2009) 372.
- [13] J.Y. Lee, S.T. Lee, *Adv. Mater.* 16 (2004) 51.

**Table 1**

Physical and electrical characteristics of the hybrid dielectrics.

Dielectric type	Thickness (nm)	Dielectric constant	Surface roughness (nm)	Capacitance (nF/cm <sup>2</sup> )	Dielectric strength (MV/cm)
15 mol% Zr(OPr <sup>i</sup> ) <sub>4</sub> hybrid dielectrics (YHD15)	140	5.3	0.242	33	2.3
30 mol% Zr(OPr <sup>i</sup> ) <sub>4</sub> hybrid dielectrics (YHD30)	105	6.3	0.263	53	2.1

materials were potential candidates for gate dielectrics in OTFTs [11]. Choi and Bae also studied methacryloxypropyl trimethoxysilane and diphenylsilanediol based hybrid materials for application as gate dielectrics [12]. In our previous work, we selected 3-methacryloxypropyltrimethoxysilane and Zr alkoxide as precursors to design a dielectric with a high dielectric constant and low leakage current. The resulting photopatternable hybrid dielectric exhibited excellent surface morphology, a high dielectric constant (5.5), and reasonable dielectric strength (1.5–2.0 MV/cm) [10]. In this letter, we focus on an in-depth investigation of the microstructural features of hybrid dielectrics as a function of Zr alkoxide content in an attempt to understand its influence on TFT performance.

## 2. Experimental

The organic–inorganic hybrid gate dielectric solution was synthesized by sol–gel reactions between 3-methacryloxypropyltrimethoxysilane (MEMO, Sigma–Aldrich), zirconium isopropoxide (Zr(OPr<sup>i</sup>)<sub>4</sub>, 70% in 1-propanol, Sigma–Aldrich), and methacrylic acid (MAA, 97%, Sigma–Aldrich). In the first step, MEMO solution was mixed with 0.2 M HCl as a catalyst, followed by vigorous stirring for 30 min. A mixture of Zr(OPr<sup>i</sup>)<sub>4</sub>, MAA, and 1-propanol was also prepared at a 1:1:1 molar ratio. The Zr(OPr<sup>i</sup>)<sub>4</sub> to MEMO solution ratio was varied to control the dielectric constant of the resulting gate dielectric. Two different molar ratios of MEMO:Zr(OPr<sup>i</sup>)<sub>4</sub> = 8.5:1.5 (denoted YHD15) and 7:3 (denoted YHD30) were selected. When Zr(OPr<sup>i</sup>)<sub>4</sub> was mixed with MEMO, the alkoxy groups present in both precursors were partially hydrolyzed. DI-water was then added to facilitate the hydrolysis and condensation reac-

tions. After further stirring for 24 h in air, the synthesized sol–gel solution was diluted with 1-propanol to control viscosity.

Hybrid dielectric films were obtained by spin coating the precursor solution at 4000 rpm for 30 s on an n-type heavily doped silicon wafer substrate. After spin coating, the films were immediately prebaked at 110 °C on a hot plate in air for 30 min to evaporate the solvent and improve adhesion to the substrate. A final thermal treatment was carried out at 170 °C for 3 h. For comparison with the hybrid dielectric, a PVP dielectric was also prepared from poly(4-vinylphenol) and poly(melamine-co-formaldehyde) as a cross-linking agent, in propylene glycol monomethyl ether acetate (PGMEA). These materials were mixed in the weight ratio 10:5:85. The PVP dielectric films were obtained by spin coating the precursor solution at 4000 rpm for 30 s on an n-type heavily doped silicon wafer substrate and cross-linking at 175 °C for 30 min in air.

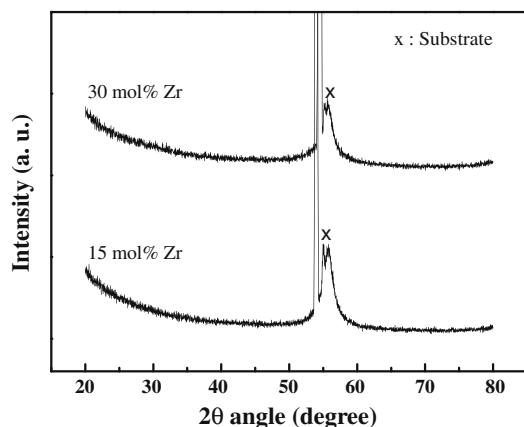


**Fig. 1.** XRD patterns of 15 mol% Zr(OPr<sup>i</sup>)<sub>4</sub> and 30 mol% Zr(OPr<sup>i</sup>) hybrid dielectrics.

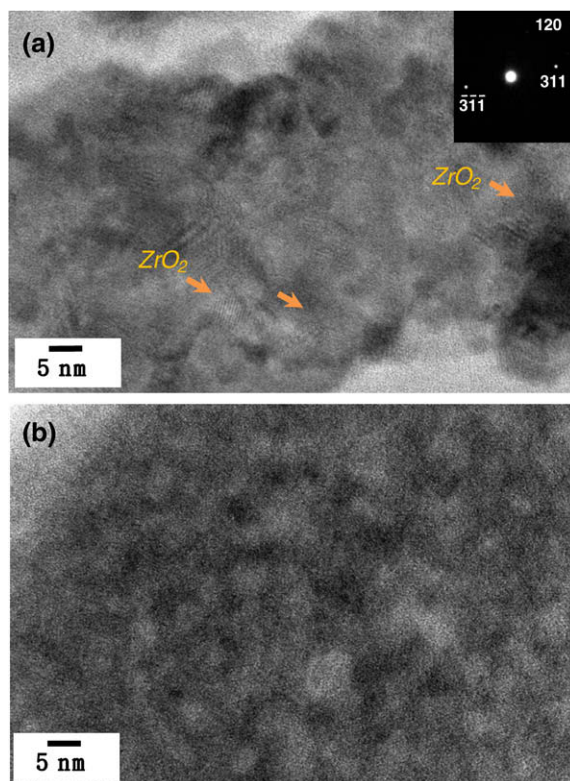


**Fig. 2.** HRTEM images of: (a) 15 mol% Zr(OPr<sup>i</sup>)<sub>4</sub> and (b) 30 mol% Zr(OPr<sup>i</sup>) hybrid dielectrics. The inset shows the diffraction pattern of a selected area. Arrows indicate the selected particulate crystalline ZrO<sub>2</sub> phase among many nanocrystals.

To study the electrical performance of gate dielectrics, capacitance–voltage ( $C-V$ ) at 1 MHz and leakage current–voltage ( $I-V$ ) characteristics were measured using an Agilent 4284A precision LCR meter and an Agilent 5263A source-measure unit, respectively. Solution-processed OTFTs based on either the hybrid sol-gel dielectric or PVP were also fabricated. To fabricate co-planar transistors, Au/Cr electrodes were deposited through a shadow mask on either the hybrid dielectric or PVP film. The channel electrodes had the dimension of the width  $\sim 3$  mm and the length  $\sim 50$   $\mu\text{m}$ . Bis(triisopropylsilylethynyl) pentacenes (TIPS-PEN) were then drop-cast as an organic semiconductor between the source and drain electrodes, and the samples were annealed at 100 °C in a vacuum oven for 20 min. The transistor on–off ratio, mobility, and threshold voltage were measured in air.

The microstructure and chemical composition of the hybrid films were observed by X-ray diffraction (XRD, X'Pert-PRO MRD, Phillips), high-resolution transmission electron microscopy (HRTEM, JEM-4010, JEOL), and X-ray photoelectron spectroscopy (XPS, Escalab 220-XL). XPS spectra were recorded in the constant energy mode at 50 eV. The C 1s lines were taken as internal references with a binding energy (BE) of 285 eV. The crystal structures and film morphologies of TIPS-PENs deposited on different dielectrics were compared by optical mode of confocal

laser scanning microscopy (LEXT OLS3000, Olympus) and XRD analysis.

### 3. Results and discussion

An organic–inorganic hybrid precursor solution was synthesized using a mixture of MEMO and  $\text{Zr}(\text{OPr}^i)_4$ . MEMO is a silicon-based alkoxide with a three alkoxy groups and one methacryl group, which can be cross-linked by either photo- or thermal-energy.  $\text{Zr}(\text{OPr}^i)_4$  is a typical zirconium-based alkoxide with four alkoxy groups. We synthesized hybrid solution containing either 15 or 30 mol%  $\text{Zr}(\text{OPr}^i)_4$  to control the dielectric properties. The two different compositions showed slightly different characteristics. The dielectric film properties are summarized in Table 1. The surface roughness in a  $2 \times 2$   $\mu\text{m}$  scan area was similar and the average RMS values for YHD15 and YHD30 were 0.242 and 0.263 nm, respectively. The YHD30 dielectric film was slightly thinner than the YHD15 film even though the two films were coated under identical processing conditions. The leakage current of the two films was also nearly identical. The dielectric strength, defined as the electric field at a current density of  $10^{-6}$  A/cm<sup>2</sup>, changed slightly from 2.1 to 2.3 MV/cm with increasing zirconium alkoxide. By contrast, the dielectric constant,

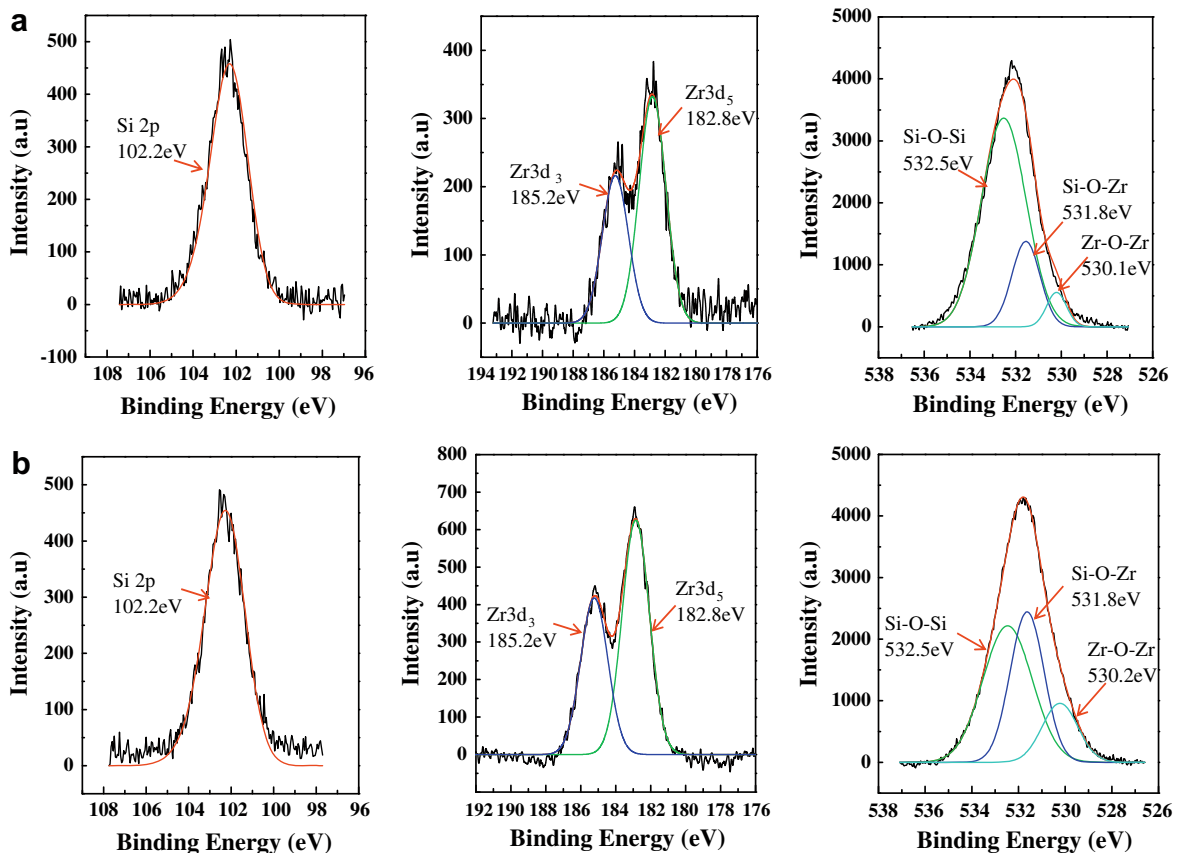


Fig. 3. XPS spectra of hybrid dielectrics showing Si 2p, Zr 3d, and O 1s spectra: (a) 15 mol%  $\text{Zr}(\text{OPr}^i)_4$  and (b) 30 mol%  $\text{Zr}(\text{OPr}^i)_4$ .

which is influenced by the Zr concentration, increased from 5.3 at 15 mol%  $\text{Zr}(\text{OPr}^i)_4$  to 6.3 at 30 mol%  $\text{Zr}(\text{OPr}^i)_4$ .

XRD patterns of both hybrid dielectric films are shown in Fig 1. Sharp diffraction patterns observed at  $2\theta = 53.8^\circ$  and  $55.6^\circ$  originate from the Si wafer substrate. There are no other diffraction peaks that can correspond to  $\text{ZrO}_2$  or relevant crystalline phases, indicating that the hybrid material is amorphous regardless of the Zr precursor content. Further microstructural investigation of the hybrid dielectrics was performed by HRTEM. As shown in Fig. 2a,  $\sim 5$  nm crystallites are distributed in the amorphous-like matrix in the YHD15 dielectric film. More crystallites of similar sizes are observed in the YHD30 dielectric film. Because the  $\text{ZrO}_2$  nuclei are surrounded by a rigidly grafted siloxane backbone, their growth is limited to a few nanometer-sized clusters regardless of the difference in Zr precursor concentration. Selected area diffraction (SAD) patterns obtained from both samples show the presence of crystalline  $\text{ZrO}_2$  as shown in Fig 2a (inset). Monoclinic  $\text{ZrO}_2$  is thermodynamically stable, but ortho-

rhombic  $\text{ZrO}_2$  exists in a metastable phase due to the surface energy effect. No other diffraction patterns except for  $\text{ZrO}_2$  appear. HRTEM analysis confirmed that the hybrid dielectrics comprised  $\text{ZrO}_2$  crystallites embedded in an amorphous organosiloxane matrix; these crystals were too small to detect using X-ray analysis [13]. Fig. 2b shows the presence of an increased number of nanocrystallites in the YHD30 dielectric film.

The chemical composition and bonding nature of the constituents were studied by XPS. Wide scan spectra of both YHD15 and YHD30 films contain Zr 3d, O 1s, C 1s and Si 2p peaks. Nearly identical Si spectra were detected for both films as shown in Fig. 3. The Si peak could be fitted to Si 2p with a 102.2 eV BE, which was shifted by 1.2 eV compared to the Si 2p BE for  $\text{SiO}_2$ . A similar Si 2p BE shift was observed by Guittet et al. in which the zirconium silicate (zircon,  $\text{ZrSiO}_4$ ) Si 2p BE is smaller than  $\text{SiO}_2$  by a factor of 1.35 eV [14]. This chemical shift depends on the number of second nearest neighboring Zr atoms, indicative of the presence of zirconium silicate in our hybrid films [15,16].

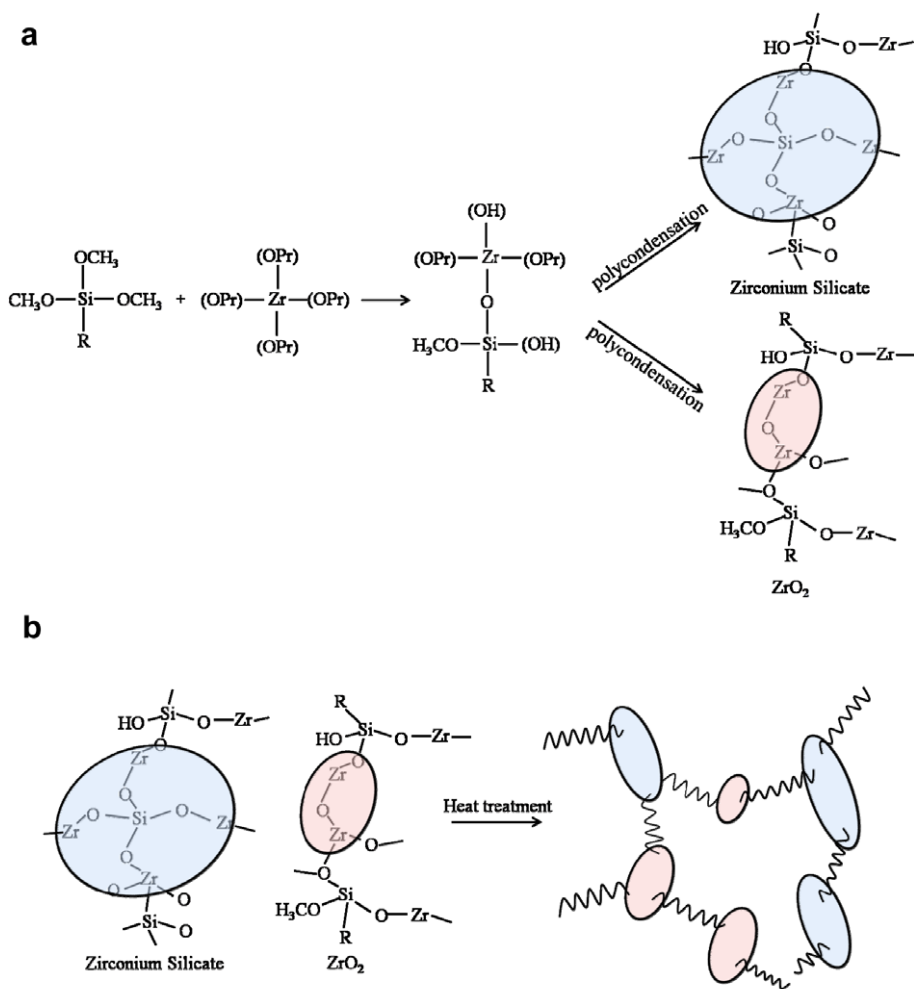


**Fig. 4.** Schematics showing the formation mechanism of the nanoparticle-dispersed hybrid dielectrics via sol-gel reaction: (a) hydrolysis and condensation reactions between MEMO and  $\text{Zr}(\text{OPr}^i)_4$  precursors, leading to  $\text{ZrO}_2$  and  $\text{ZrSiO}_4$  particles and (b) the overall microstructure after crosslinking. The spring represents the organosiloxane matrix.



The Zr 3d spectrum consists of doublet peaks in which Zr 3d3 and Zr 3d5 spin-orbital splitting are characterized by 185.2 and 182.8 eV BEs, respectively. The Zr 3d BEs were slightly shifted toward a higher value compared to  $ZrO_2$ . These data are consistent with a previous report in which Zr 3d BEs of  $ZrSiO_4$  were 0.5 eV larger than  $ZrO_2$  [14,16,17]. An increased Zr 3d BEs also indicates the formation of zirconium silicate. The Si 2p and Zr 3d BE shifts can be explained by the principle of electronegativity equalization. Electrons are more withdrawn from Zr in zirconium silicate than  $ZrO_2$ , because the Si and O electronegativities are larger than Zr [17]. In addition, the Zr doublet intensity increases about two-fold as the Zr precursor concentration increases from 15 to 30 mol%, indicating increased  $ZrO_2$  and zirconium silicate concentrations (Fig. 3). The O 1s spectrum can be resolved into three peaks as shown in Fig. 3. The peak at a 532.5 eV BE is assigned to oxygen in the Si–O–Si species, whereas the 530.1 eV is peak considered oxygen in the Zr–O–Zr species. An additional peak at a 531.8 eV BE located between the Si–O–Si and Zr–O–Zr oxygen peaks can be attributed to O in a Zr–O–Si bonding configuration, considering that the peak is shifted 1.6 eV toward a higher energy from  $ZrO_2$  [16,17].

The oxygen atoms are commonly involved in three major phases in the hybrid dielectric: organosiloxane,  $ZrO_2$ , and  $ZrSiO_4$ . Thus, quantitative analysis of the O 1s three peaks can provide the relative composition of each phase. The relative concentration of Si–O–Si, Si–O–Zr, and Zr–O–Zr species in the YHD15 film was 75.2%, 18.3%, and 6.5%, respectively, and 59.4%, 26.6% and 14% in YHD30. This result clearly supports the idea that increased zirconium silicate and  $ZrO_2$  form with increased Zr(OPr<sup>i</sup>). The  $ZrO_2$  content in YHD15 is approximately two times that in YHD30.

XPS analysis confirmed that the hybrid dielectrics are composed of organosiloxane,  $ZrO_2$ , and  $ZrSiO_4$ . It is believed that amorphous  $ZrSiO_4$  and  $ZrO_2$  crystallites are present in the amorphous organosiloxane matrix. These small particulates are uniformly distributed, so that there is no difference in the film surface roughness, as described in Table 1, even though the number of particles differs. In contrast, the dielectric constant ( $\epsilon$ ) increases with increasing Zr precursor concentration. Both  $ZrSiO_4$  ( $\epsilon = 12.6$ ) and  $ZrO_2$  ( $\epsilon = 25$ ) have high dielectric constants and are considered promising alternatives to conventional  $SiO_2$  gate dielectrics [17,18]. Therefore, increased  $ZrSiO_4$  and  $ZrO_2$  phases would increase the dielectric constant of an organosiloxane matrix. A hybrid dielectric composed of three phases can be estimated using the following generalized rule of mixture [19]:

$$\epsilon_{\text{eff}} = f_1 \epsilon_1 + f_2 \epsilon_2 + f_3 \epsilon_3 + \dots = \sum_i f_i \epsilon_i,$$

where  $\epsilon_{\text{eff}}$  is the dielectric constant of a composite material,  $f_i$  is the volume fraction and  $\epsilon_i$  is the dielectric constant of constituent phase  $i$ . Using the volume fraction for each phase obtained from the O 1s spectra analysis, the calculated dielectric constants are 5.04 for YHD15 and 6.38 for YHD30, which agree relatively well with the experimentally measured values in Table 1.

The formation mechanism for sol-gel derived  $ZrO_2/ZrSiO_4$  particle-dispersed hybrid material is schematically depicted in Fig. 4. First, MEMO is partially hydrolyzed in a pre-mixing step. The resulting silanol group (Si–OH) is relatively stable under acidic conditions and not subject to self-condensation. When mixed with Zr isopropoxide,

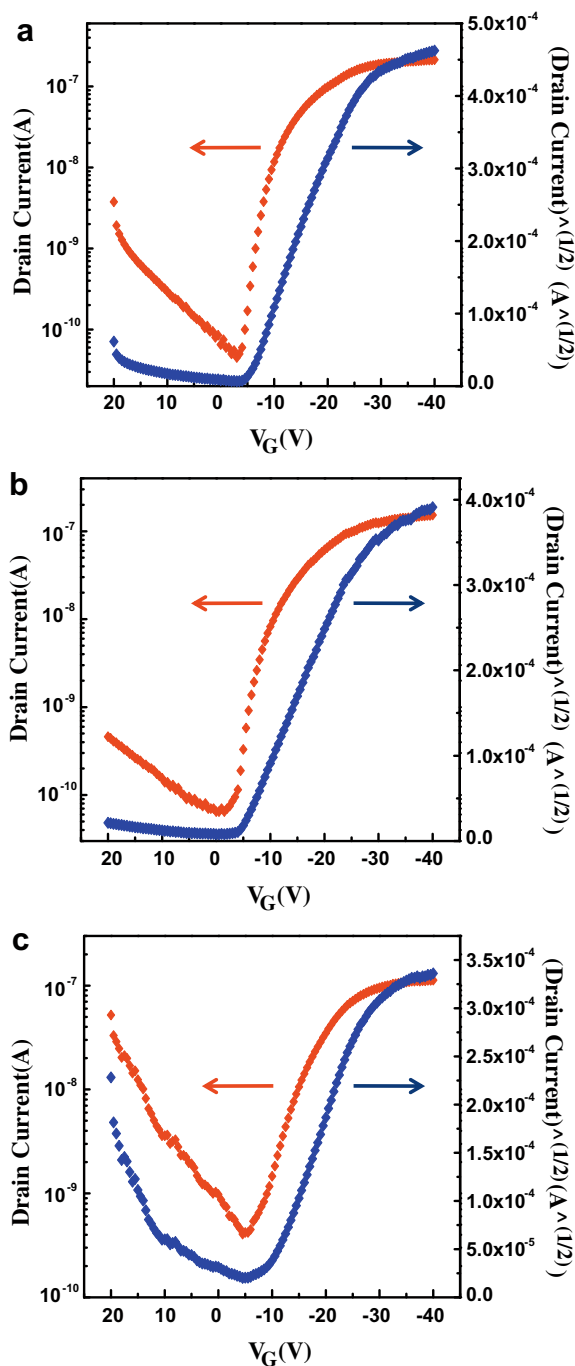


Fig. 5. Transfer characteristics of organic thin-film transistors fabricated using: (a) 15 mol%  $Zr(OPr^i)_4$ , (b) 30 mol%  $Zr(OPr^i)$  hybrid dielectrics and (c) PVP. Drain voltage was set to  $-20$  V.

the Si–OH group joins with a Zr precursor via hydrolysis-condensation, producing –Si–O–Zr– networks as an intermediate product. Further re-hydrolysis and polycondensation of –Si–O–Zr– upon introducing additional water results in ZrSiO<sub>4</sub> formation within the organosiloxane matrix. It is believed that not all Zr precursors undergo polycondensation with MEMO. In our synthetic conditions, variable reactivity toward hydrolysis and condensation of the two precursors prevent a continuous silica–zirconia network from forming. Methacrylic acid coordinated with Zr alkoxide sterically hinders immediate re-hydrolysis and polycondensation with MEMO. Rather, slow polycondensation occurs between the remaining Zr precursor at a later stage, leading to ZrO<sub>2</sub> particles nucleated within the organosiloxane matrix. As a result, ZrO<sub>2</sub> particles and zirconium silicate coexist in the amorphous matrix as confirmed by XPS analysis.

Fig. 5 shows the electrical characteristics of TIPS–PEN TFTs based on the YHD15 and YHD30 dielectrics. The devices work in the accumulation mode with a well-defined linear regime at  $V_D < V_G$  followed by a saturation regime at  $V_D > V_G$  for a given gate voltage  $V_G$ . Furthermore, the amplification mode of  $I_D$  is observed when  $V_G$  increases. A negative  $I_D$  under a negative  $V_D$  and  $V_G$  indicates the transport of

holes in these devices, therefore, the organic layer behaves as a p-type semiconductor. The threshold voltage  $V_T$  and field-effect mobility  $\mu$  in the saturation region were determined by plotting the square root of the drain current versus gate voltage and fitting the data to the following equation [20]:

$$I_D = \frac{WC}{2L} \mu (V_G - V_T)^2$$

where  $C$  is the capacitance of the dielectric,  $W$  is the channel width, and  $L$  is the channel length. The OTFT based on the YHD15 hybrid dielectric has an off-current of  $4.5 \times 10^{-11}$  A, an on/off-current ratio of  $4.5 \times 10^3$ , a carrier mobility of  $1.3 \times 10^{-2}$  cm<sup>2</sup> V<sup>-1</sup> s<sup>-1</sup>, and a threshold voltage of  $-5$  V. The OTFT based on the YHD30 hybrid dielectric has an off-current of  $6.5 \times 10^{-11}$  A, an on/off-current ratio of  $2 \times 10^3$ , a carrier mobility of  $1.1 \times 10^{-2}$  cm<sup>2</sup> V<sup>-1</sup> s<sup>-1</sup>, and a threshold voltage of  $-1$  V. The characteristic electric parameters of these devices are summarized in Table 2.

All electrical parameters except for  $V_T$  are similar for both devices. It was clear that using hybrid dielectrics with a high dielectric constant significantly reduces the threshold voltage from  $-5$  to  $-1$  V. We fabricated OTFT based on

**Table 2**

Electrical performance parameters, off-current ( $I_{OFF}$ ), on-current ( $I_{ON}$ ), threshold voltage ( $V_T$ ), and field-effect carrier mobility ( $\mu_{FET}$ ) of OTFTs fabricated using hybrid dielectrics.

Dielectric type	$I_{ON}$ (A)	$I_{OFF}$ (A)	$V_T$ (V)	$\mu_{FET}$ (cm <sup>2</sup> V <sup>-1</sup> s <sup>-1</sup> )
15 mol% Zr(OPr <sup>i</sup> ) <sub>4</sub> hybrid dielectrics	$2.1 \times 10^{-7}$	$4.5 \times 10^{-11}$	$-5$	$1.3 \times 10^{-2}$
30 mol% Zr(OPr <sup>i</sup> ) <sub>4</sub> hybrid dielectrics	$1.5 \times 10^{-7}$	$6.5 \times 10^{-11}$	$-1$	$1.1 \times 10^{-2}$
PVP dielectrics	$1.1 \times 10^{-7}$	$4.2 \times 10^{-10}$	$-6$	$1.2 \times 10^{-2}$

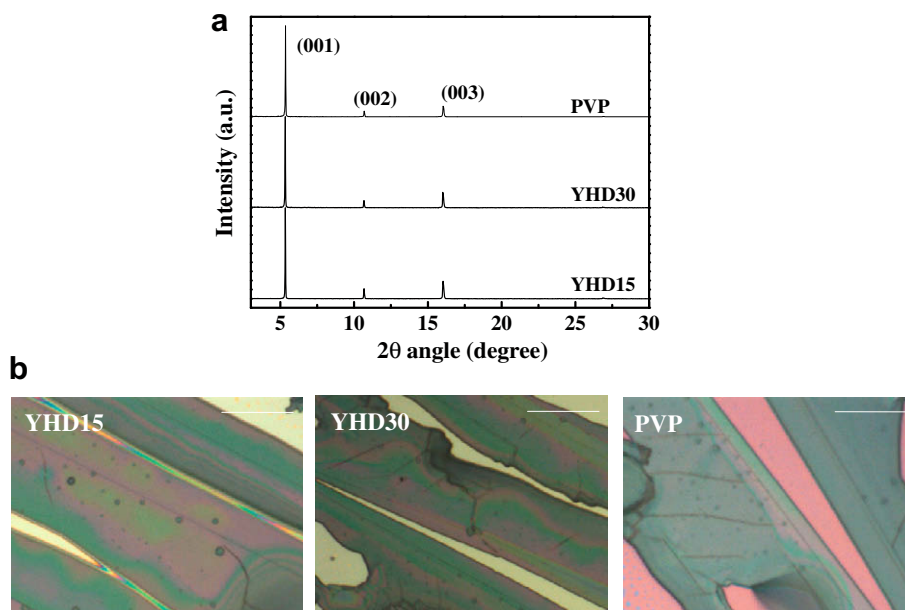


**Fig. 6.** (a) X-ray diffraction patterns and (b) film morphologies of TIPS–PENs deposited onto YHD15, YHD30, and PVP dielectric layer. The inserted scale is 30 μm.

PVP dielectric, a widely investigated organic material, for comparison. The PVP-based transistor has an off-current of  $4.2 \times 10^{-10}$  A, an on/off-current ratio of  $2.6 \times 10^2$ , a carrier mobility of  $1.2 \times 10^{-2}$  cm<sup>2</sup> V<sup>-1</sup> s<sup>-1</sup>, and a threshold voltage of  $-6$  V. Higher off-current in TFT with PVP dielectric layer is attributed to the hydroxyl group in the PVP dielectric, which acts as trap-sites for charge carriers and in turn contributes to a high leakage current through a dielectric layer. In TIPS–PEN TFTs, other electric parameters, such as on-current, mobility, and threshold voltage, are directly related to the structures of TIPS–PEN [21]. We investigated the crystal structures and film morphologies of TIPS–PENs deposited onto the dielectric layers. As shown in Fig. 6, All TIPS–PENs are well-crystallized and exhibit long lamellar structures regardless of the dielectric material types. This is in agreement with the fact that all TFTs show similar field-effect mobility values and on-currents. However, it is noted that  $V_T$  of each TFT is quite different, depending on the dielectric layer.

The threshold voltage depends on various factors such as the capacitance of the gate dielectric, the flat-band voltage caused by the work function difference between the gate electrode and the semiconductor, and the density of trap states residing in semiconductor channel [22]. It can be assumed that the flat-band voltage and the amount of trap states in the semiconductor are identical for all transistors tested here, as these parameters are related to the intrinsic properties of the electrode and the semiconductor, irrelevant to the dielectrics. Therefore, it can be suggested that the capacitance difference primarily influences the threshold voltage shift. Additionally,  $V_T$  of TFT with PVP dielectric is also affected by water molecules absorbed from air. The interaction between hydroxyl groups in PVP dielectric and water molecules leads to dissociation of hydroxyl groups and the generation of mobile ions [23]. The corresponding mobile ions are drifted by an applied gate voltage, which induces more charge carriers at semiconductor/dielectric interface and in turn shifts a threshold voltage toward a zero bias. In contrast, the hydroxyl group in YHD dielectrics is nearly eliminated by a proper thermal treatment. Thus, it is considered that the threshold voltage of TFT based on YHD is not influenced by water molecules in air. We observed that when TFT is fabricated using YHD dielectric whose capacitance is similar to that of a 200 nm-thick thermally-grown SiO<sub>2</sub>,  $V_T$  of TFT based on YHD is almost identical to that of TFT based on a 200 nm-thick thermally-grown SiO<sub>2</sub> [10]. A thermally-grown SiO<sub>2</sub> is well-known for a stable dielectric under air atmosphere.

Taken the consideration of the interaction effect of the dielectric with water that can shift the threshold voltage toward a zero voltage,  $V_T$  of TFT based on PVP dielectric is still  $-6$  V, whereas TFT based on YHD30 dielectric exhibit  $-1$  V. This observation supports that the influence of higher capacitance is predominant over a water-induced  $V_T$  shift and enables the TFT based on YHD dielectric with smaller threshold voltage (the capacitance of PVP, YHD15, and YHD30 is 10, 33, and 53 nF/cm<sup>2</sup>, respectively). Both the presence of fewer hydroxyl groups and the incorporation of high- $k$  ZrO<sub>2</sub> phase make YHD-based dielectrics

better to PVP-based dielectrics, in terms of lower off-current, higher on/off current ratio, and threshold voltage closer to a zero bias.

#### 4. Conclusions

We performed microstructural and chemical investigations on sol–gel derived organic–inorganic hybrid dielectrics. HRTEM revealed that ZrO<sub>2</sub> crystallites of approximately 5 nm are uniformly distributed in the amorphous organosiloxane matrix, although these could not be detected by X-ray. XPS analysis confirmed that another phase, ZrSiO<sub>4</sub>, coexists as an amorphous phase in the matrix. The relative ZrO<sub>2</sub>, ZrSiO<sub>4</sub>, and organosiloxane compositions can be estimated by deconvoluting the O 1s spectrum. The effective dielectric constant of the hybrid dielectric was calculated using a general rule of mixture. The calculated values match the experimentally-measured dielectric constants, indicating that the hybrid dielectric is composed of three phases. OTFTs based on hybrid dielectrics exhibited better electrical performance to those based on PVP. Using a dielectric with a higher dielectric constant and fewer hydroxyl groups allowed us to fabricate a transistor with a lower off-current, higher on/off current ratio, and lower threshold voltage.

#### Acknowledgement

This work was supported by the Korea Science and Engineering Foundation (KOSEF) through the National Research Lab. Program funded by the Ministry of Education, Science and Technology (No. R0A-2005-000-10011-0).

#### References

- [1] C.D. Dimitrakopoulos, D.J. Mascaro, *J. Res. Dev.* 45 (2001) 11.
- [2] H. Edzer, A. Huitema, G.H. Gelinck, J. Bas, P.H. Van der Putten, K.E. Kuijk, K.M. Hart, E. Cantatore, D.M. De Leeuw, *Adv. Mater.* 14 (2002) 1201.
- [3] B.K. Crone, A. Dodabalapur, Y.Y. Lin, R.W. Filas, A. Laduca, R. Sarpeshkar, H.E. Karz, W. Li, *Nature* 403 (2000) 521.
- [4] B.K. Crone, A. Dodabalapur, R. Sarpeshkar, A. Gelperin, H.E. Katz, Z.N. Bao, *J. Appl. Phys.* 91 (2002) 10140.
- [5] J.A. Rogers, A. Bao, A. Dodabalapur, A. Makhija, *IEEE Electron. Dev. Lett.* 21 (2000) 3.
- [6] C.D. Sheraw, L. Zhou, J.R. Huang, D.J. Gundlach, T.N. Jackson, M.G. Kane, I.G. Hill, M.S. Hammond, J. Campi, B.K. Greening, J. Francl, J. West, *Appl. Phys. Lett.* 80 (2002) 1088.
- [7] S.Y. Park, M. Park, H.H. Lee, *Appl. Phys. Lett.* 85 (2004) 2283.
- [8] L. Chua, H. Sirringhaus, R.H. Friend, *Appl. Phys. Lett.* 84 (2004) 3400.
- [9] R. Parashkov, E. Becker, G. Ginev, T. Riedl, H.H. Johannes, W. Kowalsky, *J. Appl. Phys.* 95 (2004) 1594.
- [10] S. Jeong, S. Lee, D. Kim, H. Shin, J. Moon, *J. Phys. Chem. C* 111 (2007) 16083.
- [11] Z. Bao, V. Kuck, J.A. Rogers, M.A. Paczkowski, *Adv. Func. Mater.* 12 (2002) 526.
- [12] C.G. Choi, B. Bae, *Org. Electron.* 8 (2007) 743.
- [13] L. Armelao, H. Bertagnolli, D. Bleiner, M. Groenewolt, S. Gross, V. Krishnan, C. Sada, U. Schubert, E. Tondello, A. Zattin, *Adv. Func. Mater.* 17 (2007) 1671.
- [14] M.J. Guittet, J.P. Crocombette, M. Gautier-Soyer, *Phys. Rev. B* 65 (2001) 125117.
- [15] F. Giustino, A. Bongiorno, A. Pasquarello, *Appl. Phys. Lett.* 81 (2002) 4233.
- [16] K. Seo, P.C. McIntyre, H. Kim, K.C. Saraswat, *Appl. Phys. Lett.* 86 (2005) 82904.
- [17] V. Bansal, A. Syed, S.K. Bhargava, A. Ahmad, M. Sastry, *Langmuir* 23 (2007) 4993.

- [18] W.B. Blumenthal, *The Chemical Behavior of Zirconium*, Van Nostrand, Princeton, NJ, 1958.
- [19] S.O. Kasap, *Principles of Electronic Materials and Devices*, McGraw Hill, 2002.
- [20] D.H. Kim, D.Y. Lee, H.S. Lee, W.H. Lee, Y.H. Kim, J.I. Han, K. Cho, *Adv. Mater.* 19 (2007) 678.
- [21] J. Chen, C.K. Tee, M. Shtein, J. Anthony, C.D. Martin, *J. Appl. Phys.* 103 (2008) 114513.
- [22] C.R. Kagan, P. Andry, *Thin-Film Transistors*, Marcel Dekker, New York, 2003.
- [23] T.G. Bäcklund, R. Österbacka, H. Stubb, J. Bobacka, A. Ivaska, *J. Appl. Phys.* 98 (2005) 074504.

with low  $\Phi_m$  metal are needed to understand clearly how the interaction between the metal and the organic layer affects the energy-level alignment at organic/metal interfaces. In this paper, we present the systematic study of the VL shifts at Cu-phthalocyanine (CuPc)/metal interfaces over a wide range of  $\Phi_m$  ( $\approx 2.5$ – $5.3$  eV) using the Kelvin probe (KP) method. We observed the transition of the energy-level alignment from  $\Phi_m$  dependence to  $\Phi_m$  independence by decreasing  $\Phi_m$ . Our results show that the injection barrier cannot be shorter than a threshold value. This transition can be explained by considering that the ID layer on the metal surface plays two major roles in the energy-level alignment: the formation of the ID and the passivation of the metal surface. Considering the roles of the ID layer, we propose a model of the energy-level alignment at organic/electrode interfaces that includes clean and passivated metal substrates.

## 2. Experimental

CuPc with a quoted purity of 99% and sublimation grade was purchased from Sigma–Aldrich. We used Au, Ag, Mg, Ca, and Sm films deposited by vacuum evaporation on silicon wafers as metal substrates. The CuPc films were vacuum deposited onto these substrates in ultra-high vacuum (UHV) ( $\sim 1 \times 10^{-6}$  Pa). The thickness and the rate of deposition ( $\sim 0.1$  nm/min) of the CuPc film were monitored with a quartz crystal microbalance. The deposition was performed in a stepwise manner with the KP measurements at each step. The KP measurements were also performed in UHV ( $\sim 8 \times 10^{-8}$  Pa) using an apparatus described elsewhere [12].

## 3. Results and discussion

Fig. 1 shows the VL energy of the CuPc film ( $\epsilon_{\text{vac}}^F$ ) relative to the substrate Fermi level ( $E_F$ ) deposited on metal

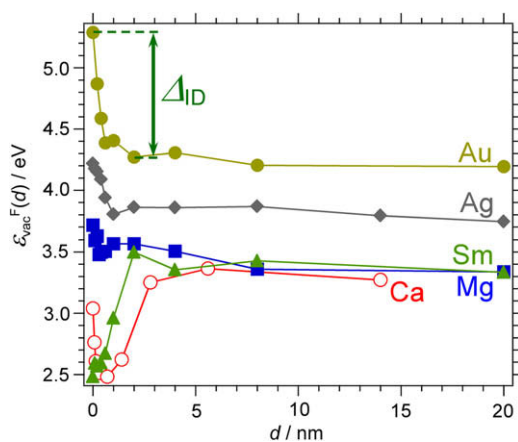


**Fig. 1.** Variation in the  $\epsilon_{\text{vac}}^F$  on Au, Ag, Mg, Ca, and Sm substrates as a function of the CuPc thickness  $d$ . The  $\epsilon_{\text{vac}}^F$  sharply shifts right at the interfaces when the thickness is less than 1 nm. In the thicker region than 1 nm, the  $\epsilon_{\text{vac}}^F$  were almost independent of the thickness on Au and Ag substrates. The little VL shifts observed on these substrates within 1–2 nm may be induced by the changing of the molecular orientation [13,14]. These shifts are caused by the ID formation; the  $\Delta_{\text{ID}}$  for the CuPc film on Au substrate is shown.

substrates as a function of the film thickness ( $d$ ) using the KP method. The large shifts of  $\epsilon_{\text{vac}}^F$  observed at the interface ( $d < 5$  nm) of all the substrates were indicated by the charge redistribution at the interface. The  $\epsilon_{\text{vac}}^F$  sharply shifted right at the interfaces when the thickness was less than 1 nm. In the thicker region than 1 nm, the  $\epsilon_{\text{vac}}^F$  were almost independent of the thickness on Au and Ag substrates. The little VL shifts observed on these substrates within 1–2 nm may be induced by the changing of the molecular orientation [13,14]. It should be noted that such VL shifts are not caused by the final-state screening because the KP measurement does not use the photoionization process [12]. These shifts were caused by the ID formation [1]. The  $\epsilon_{\text{vac}}^F(\text{ID})$  was defined as

$$\epsilon_{\text{vac}}^F(\text{ID}) = \Phi_m + \Delta_{\text{ID}} \quad (1)$$

where the  $\Delta_{\text{ID}}$  is the VL shift caused by the ID layer. On the other hand, gentle downward shifts on the Mg substrate and sharp upward shifts on Ca and Sm substrates were observed when the thickness increased up to 5 nm. It should be stressed that such energy-level shifts at the interface were responsible for the energy-level alignment at the thick film region because little VL shifts occurred in the thicker region than 5 nm on all the substrates.

Fig. 2 shows the  $\epsilon_{\text{vac}}^F(\text{bulk})$ , which was defined as the  $\epsilon_{\text{vac}}^F$  of the thick films ( $d = 14$  nm for Ca and  $d = 20$  nm for others) against  $\Phi_m$  of the various metal substrates based on the results in Fig. 1. Open circles identify results in this work. Closed circles represent the results taken from Refs. [14–16]. The  $\epsilon_{\text{vac}}^F(\text{bulk})$  depended on  $\Phi_m$  at the higher  $\Phi_m$  above Mg with  $S = 0.5 \pm 0.1$  ( $S = d\epsilon_{\text{vac}}^F(\text{bulk})/d\Phi_m$ ). On the other hand, the  $\epsilon_{\text{vac}}^F(\text{bulk})$  no longer depended on  $\Phi_m$  at the lower  $\Phi_m$  below Mg with  $S = 0.0 \pm 0.1$ . The Mg substrate is supposed to remain around the critical value of  $\Phi_m$ . In this paper, we refer to the regions with  $S = 0$  and

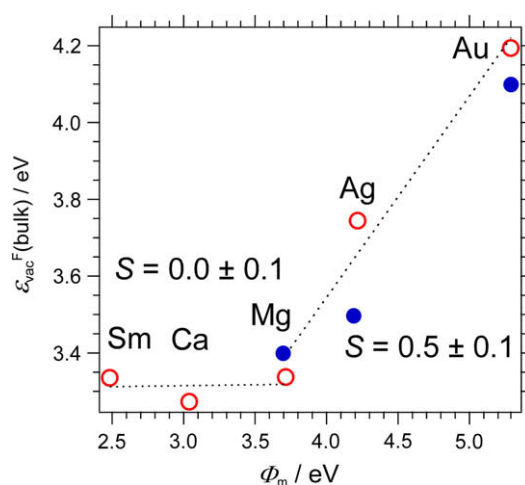


**Fig. 2.** The  $\epsilon_{\text{vac}}^F(\text{bulk})$  are plotted as a function of  $\Phi_m$ ; the  $\epsilon_{\text{vac}}^F(\text{bulk})$  stands for the  $\epsilon_{\text{vac}}^F$  at 20 nm (Au, Ag, Mg, and Sm) and 14 nm (Ca). Open circles identify results in this work. Closed circles represent the results taken from Refs. [14–16]. The dotted lines show the results of fitting analysis by the least squares method with linear function  $S$ . The estimated  $S$  parameters are given in the figure.

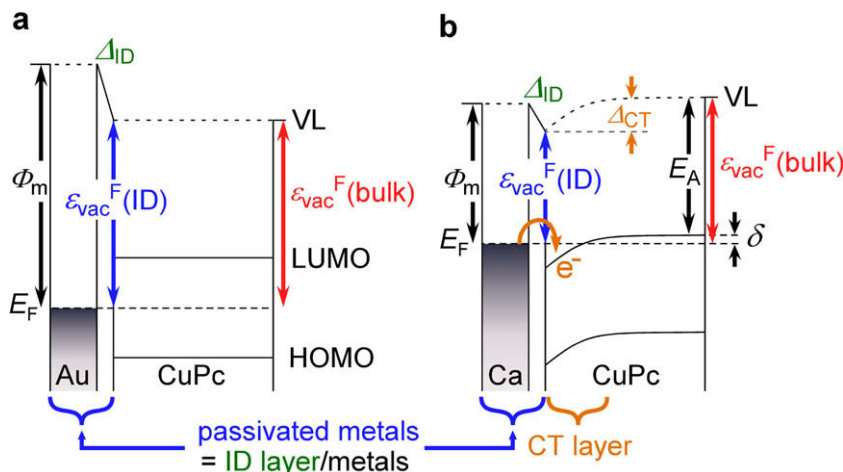


**Fig. 3.** The schematics of the energy-level diagrams in: (a) the noninteger  $S$  regime and (b) the  $E_F$  pinning regime. The  $\Delta_{ID}$  is caused by the ID formation. The  $\varepsilon_{vac}^F(ID)$  can be regarded as the work function of the passivated metal substrates. In (a) the noninteger  $S$  regime, little VL shift occurred in the thicker region than the ID layer. Therefore the energy-level alignment is mainly determined by the  $\Delta_{ID}$ , and the  $\varepsilon_{vac}^F(bulk)$  satisfies Eq. (2). In (b) the  $E_F$  pinning regime, the spontaneous CT from the metal to the CuPc film (CT layer) should occur via tunneling through the ID layer until Eq. (4) is satisfied. The  $\delta$  is the maxima barrier height for the occurrence of the spontaneous CT.

$S = 0.5$  as the “ $E_F$  pinning regime” and the “noninteger  $S$  regime,” respectively. The energy-level alignment models for organic/metal interfaces such as the IDIS model, electronegativity model, and MIGS model cannot explain the separated  $S$  regimes and the VL shift in the case of the CuPc/Ca interface.

The energy-level alignment at CuPc/metal interfaces is discussed with the simple model depicted in Fig. 3. Fig. 3a and b represents the energy-level alignments at the CuPc/Au interface as an example of the noninteger  $S$  regime and the CuPc/Ca interface as an example of the  $E_F$  pinning regime, respectively. When the CuPc molecule adsorbs on a metal surface, the ID layer is formed at the interface. It is still difficult to predict the estimation of the  $\Delta_{ID}$  quantitatively, because the ID layer should be formed from multiple origins, as shown in Ref. [1]. In this discussion, we consider the ID layer as a role of passivating the metal surface. Such passivation of the metal surface by the ID layer prevents the molecular orbital of the CuPc layer from overlapping the metal wave functions. It means that the ID layer/metals are the passivated metal substrates, and the  $\varepsilon_{vac}^F(ID)$  is the work function of the passivated substrates. Consequently, the energy-level alignment at the thicker film region than the ID layer/metal interfaces can be described as the system at organic/passivated substrate interfaces [8–11].

In the noninteger  $S$  regime with high  $\Phi_m$ , little VL shift occurred in the thicker region than the ID layer as shown in Fig. 1. Therefore the energy-level alignment is mainly determined by the  $\Delta_{ID}$ , and the  $\varepsilon_{vac}^F(bulk)$  satisfies the equation:

$$\varepsilon_{vac}^F(bulk) \sim \varepsilon_{vac}^F(ID) = \Phi_m + \Delta_{ID} \quad (2)$$

On the other hand, in the  $E_F$  pinning regime, the lowest unoccupied molecular orbital (LUMO) level of the CuPc layer on the passivated metal substrate stayed below the substrate  $E_F$ ; for instance, in the case of the CuPc/Ca interface, the LUMO level of the CuPc ( $d > 1$  nm) layer should be

located below the  $E_F$  by 0.66 eV because  $\varepsilon_{vac}^F(ID)$  and the electron affinity ( $E_A$ ) of CuPc are 2.5 and 3.16 eV [17], respectively; and the spontaneous charge transfer (CT) from the metal to the CuPc ( $d > 1$  nm) layer occurred via tunneling through the ID layer to establish the thermodynamic equilibrium. The spontaneous CT will take place if the following condition is found:

$$\varepsilon_{vac}^F(ID) < E_A + \delta \quad (3)$$

where the  $\delta$  is the relaxation energy which is the maxima barrier height for the occurrence of the spontaneous CT. It means that the spontaneous CT will occur until the LUMO level of the CuPc layer is located above the  $E_F$  by the  $\delta$ . From the results of the inverse photoemission spectroscopy at CuPc/Mg, Ca, and Sm interfaces (not presented here), the  $\delta$  was estimated to be about 0.4 eV [18]. According to the ICT model, it is supposed to be existed the ICT states just below the LUMO level of molecules. Although the origin of the ICT states in small molecules such as the CuPc molecule is still unclear, energy differences between LUMO levels of molecules (or polymers) and ICT states are good agreement with the  $\delta$  at CuPc/metals interfaces [8,9]. The complicated behaviors of the VL shifts at low  $\Phi_m$  substrates such as Mg, Ca, and Sm, as observed in Fig. 1, must be caused by the charge redistribution with the spontaneous CT from the passivated metal substrates into CuPc layers, and this induced the VL shifts ( $\Delta_{CT}$ ) from a 1 nm to 5 nm thickness, i.e.,  $\Delta_{CT} = 0.9$  eV and 0.5 eV for Ca and Sm, respectively. The spontaneous CT no longer occurs and the VL shift is not observed if the following condition is satisfied:

$$\varepsilon_{vac}^F(ID) + \Delta_{CT} = E_A + \delta \quad (4)$$

here, the “ $\varepsilon_{vac}^F(ID) + \Delta_{CT}$ ” corresponded to the  $\varepsilon_{vac}^F(bulk)$ , and we can rewrite Eq. (4) as a simpler equation:

$$\varepsilon_{vac}^F(bulk) = E_A + \delta \quad (5)$$

The  $\varepsilon_{\text{vac}}^{\text{F}}$ (bulk) is mainly determined by the  $E_{\text{A}}$  of organic molecule. We suppose that little VL shifts in the thicker region than 5 nm at CuPc/Mg, Ca, and Sm interfaces are observed, and the spontaneous CT no longer occurs because Eq. (5) is satisfied.

#### 4. Conclusion

In conclusion, we investigated the energy-level alignment at CuPc/metal interfaces. It was found that there are separated  $S$  regimes with the noninteger  $S$  regime and the  $E_{\text{F}}$  pinning regime. The organic layer on a metal surface plays two important roles in the energy-level alignment: the ID formation and the passivation of the metal surface. In the noninteger  $S$  regime, the energy-level alignment is mainly determined by the  $\Delta_{\text{ID}}$  because little VL shifts occurred in the thicker region than the ID layer. This shows that the organic layer on the ID layer is little influenced by the passivated metal substrate. On the other hand, in the  $E_{\text{F}}$  pinning regime, the energy-level alignment is determined not only by the  $\Delta_{\text{ID}}$  but also by the spontaneous CT between the organic film and the passivated metal substrate. In this regime, while the  $\Delta_{\text{ID}}$  scattered in various metal substrates, the same energy-level alignments were realized for the thick film region. In the case of 3,4,9,10-perylene tetracarboxylic dianhydride (PTCDA)/metal interfaces, a similar trend has been reported [19]. Although the obvious differences in interface states depending on the metals were observed, the same energy-level alignments for the thick film region were also realized. The model we suggested can also explain the energy-level alignments at PTCDA/metal interfaces and other reported results [20,21].

Finally, this model, which deals with the energy-level alignment between the thicker region than the ID layer and the passivated metal substrate, provides a new perspective on the energy-level alignment at organic/electrode interfaces that include clean and passivated metal substrates.

#### Acknowledgments

This work was supported by the Grant-in-Aid for Scientific Research (S) (Grant No. 19105005), the Research Fellowship for Young Scientists, and Grant for Basic Science Research Projects (No. 060816). We thank the Japan Society for the Promotion of Science and the Sumitomo Foundation. This paper is dedicated to the late Prof. K. Seki.

#### References

- [1] H. Ishii, K. Sugiyama, E. Ito, K. Seki, *Adv. Mater.* 11 (1999) 605.
- [2] S.M. Sze, *Physics of Semiconductor Devices*, second ed., Wiley, New York, 1981.
- [3] H. Vázquez, R. Oszwaldowski, P. Pou, J. Ortega, R. Pérez, F. Flores, A. Kahn, *Europhys. Lett.* 65 (2004) 802.
- [4] H. Vázquez, W. Gao, F. Flores, A. Kahn, *Phys. Rev. B* 71 (2005) 041306.
- [5] J.X. Tang, C.S. Lee, S.T. Lee, *Appl. Phys. Lett.* 87 (2005) 252110.
- [6] Y.C. Zhou, J.X. Tang, Z.T. Liu, C.S. Lee, S.T. Lee, *Appl. Phys. Lett.* 93 (2008) 093502.
- [7] W. Mönch, *Appl. Phys. Lett.* 88 (2006) 112116.
- [8] C. Tengstedt, W. Osikowicz, W.R. Salaneck, I.D. Parker, C.-H. Hsu, M. Fahlman, *Appl. Phys. Lett.* 88 (2006) 053502.
- [9] M. Fahlman, A. Crispin, X. Crispin, S.K.M. Henze, M.P. de Jong, W. Osikowicz, C. Tengstedt, W.R. Salaneck, *J. Phys.: Condens. Matter.* 19 (2007) 183202.
- [10] H. Fukagawa, S. Kera, T. Kataoka, S. Hosoumi, Y. Watanabe, K. Kudo, N. Ueno, *Adv. Mater.* 19 (2007) 665.
- [11] N. Koch, A. Vollmer, *Appl. Phys. Lett.* 89 (2006) 162107.
- [12] N. Hayashi, H. Ishii, Y. Ouchi, K. Seki, *J. Appl. Phys.* 92 (2002) 3784.
- [13] H. Yamane, Y. Yabuuchi, H. Fukagawa, S. Kera, K.K. Okudaira, N. Ueno, *J. Appl. Phys.* 99 (2006) 093705.
- [14] H. Peisert, M. Knupfer, T. Schwieger, J.M. Auerhammer, M.S. Golden, J. Fink, *J. Appl. Phys.* 91 (2002) 15.
- [15] J.X. Tang, C.S. Lee, S.T. Lee, *Appl. Surf. Sci.* 252 (2006) 3948.
- [16] F. Song, H. Huang, W. Dou, H. Zhang, Y. Hu, H. Qian, H. Li, P. He, S. Bao, Q. Chen, W. Zhou, *J. Phys.: Condens. Matter* 19 (2007) 136002.
- [17] R. Murdey, N. Sato, M. Bouvet, *Mol. Cryst. Liq. Cryst.* 455 (2006) 211.
- [18] Y. Tanaka, K. Kanai, Y. Ouchi, K. Seki, *Mater. Res. Soc. Symp. Proc.*, submitted to publication.
- [19] S. Duhm, A. Gerlach, I. Salzmann, B. Bröker, R.L. Johnson, F. Schreiber, N. Koch, *Org. Electron.* 9 (2008) 111.
- [20] J.X. Tang, C.S. Lee, S.T. Lee, Y.B. Xu, *Chem. Phys. Lett.* 396 (2004) 92.
- [21] S. Toyoshima, K. Kuwabara, T. Sakurai, T. Taima, K. Sato, H. Kato, K. Akimoto, *J. Appl. Phys.* 46 (2007) 2692.

We find  $W = 0.5 \mu\text{m}$ , which translates into  $\beta = 10^{-2}$ , in good agreement with recent theoretical predictions [1].

Before turning to the results obtained on OFETs, we need to discuss the methodology that enabled us to directly compare experimental surface potentials to theoretical model predictions.

SKPM offers the unique possibility to look inside operational electronic devices on truly nanoscopic length scales [9]. A drawback of SKPM is that the obtained potential traces do not reflect the real surface potential  $V(x)$  but rather a convolution of  $V(x)$  with a usually unknown instrument response function [10–14]. The physical reason for this is that not only the tip apex contributes to the signal but the entire metalized tip, consisting of apex, cone and lever, interacts with the sample due to the relatively long range of the electrostatic force [15]. As a result, the obtained surface potentials are distorted in both shape and magnitude; the error in the latter may exceed 40%, even at nominally zero lift height [15]. To surmount these intrinsic SKPM limitations, two fundamentally different approaches are possible, i.e. prediction and reconstruction.

Prediction methods aim to convolute a ‘real’ surface potential, which e.g. follows from theoretical considerations, with a theoretically or experimentally known tip response. So far, all reported prediction methods are based on a theoretical tip response [10,11,15]. Reconstruction methods aim to deconvolute the experimental surface potential with a theoretically or experimentally known response function in order to extract the real surface potential [12,13].

For our present purposes, we developed a flexible and convenient method for both predicting and reconstructing SKPM surface potentials. In contrast to previous works, the entire instrument response is contained in an *experimentally* determined transfer function. Hence, there is no need to explicitly evaluate the electrostatic interactions using either (approximate) analytical expressions [10–12,16] or brute force numerics [15]. The method is equally valid for SKPM based on electrostatic force detection, as employed here, as for SKPM based on force gradient detection [16].

The hypothesis underlying the (re)construction of SKPM measurements is that the measured surface potential  $y$  is a convolution of the real surface potential  $x$  with a transfer function  $h$ , i.e.  $y = h \otimes x$ . For brevity and to stress the general nature of the methodology, in the following discussion signals are denoted as  $x$  and  $y$ , rather than as  $V$ 's. In general,  $h$  will depend on the measurement system, in this case the tip geometry, its orientation with respect to the sample and the vertical distance from the sample. Since all electrostatic forces are implicitly contained in the transfer function  $h$  there is no need to quantify any electrostatic forces. From the convolution theorem we then have [17]

$$F(y) = F(h)F(x) \quad (2)$$

where  $F()$  indicates the Fourier transform. The transfer function  $h$  is experimentally determined from a reference measurement. This is most conveniently done on a step edge, for which case the mathematical link between  $x_{\text{step}}$ ,  $y_{\text{step}}$  and  $h$  is simply

$$F(h) = F(y'_{\text{step}}) \quad (3)$$

where the prime denotes the spatial derivative. Eq. (3) follows by applying (2) to the step edge,  $F(y_{\text{step}}) = F(h)F(x_{\text{step}})$ . Using the property  $F(y') = i\omega F(y)$  and taking the spatial derivative of both  $x_{\text{step}}$  and  $y_{\text{step}}$ , one obtains  $F(y'_{\text{step}}) = F(h)F(x'_{\text{step}})$ . This reduces to (3) by using  $x'_{\text{step}} = \delta$  with  $\delta$  the Dirac delta function and  $F(\delta) = 1$ . Once the transfer function  $h$  of a particular configuration is determined, any experimental surface potential can be inverted to obtain the ‘real’ surface potential  $x$  using  $x = F^{-1}(F(y)/F(h))$  and similarly for prediction from a known  $x$ . Here,  $F^{-1}$  denotes the inverse Fourier transform. Numerical implementation of these equations is relatively straightforward [18].

In order to be applicable to thin film OFETs, the transfer function  $h$  should formally be determined on a step buried under a dielectric layer. However, electrostatic finite element calculations (not shown) indicate that the effect of a  $\sim 100$  nm thick polymer layer with  $\epsilon_r \approx 3$  on the surface potential is negligible as compared to the experimental uncertainty.

In order to experimentally determine the step edge response, we made a step edge of a few monolayers of Ti on Au, see top inset of Fig. 1. These reference samples were manufactured using standard UV photolithography. Starting from chemically cleaned silicon wafers with 200 nm of thermal  $\text{SiO}_2$  on top, 5 nm of Ti as adhesion layer and 25 nm of Au were subsequently deposited by electron beam evaporation under high vacuum conditions. A classical lift-off procedure was employed to pattern a second Ti layer on top of the Au. The SKPM-AFM was a Veeco/Dimension 3100/extended Nanoscope IIIa working in lift mode under ambient conditions. We used Pt-coated Si tips (Olympus OMCL-AC240TM-B2,  $f_0 \approx 70$  kHz,  $k \approx 2$  N/m,  $R_{\text{apex}} < 25$  nm).

The main panel of Fig. 1 shows typical SKPM measurements on the Ti:Au step edge for different lift heights  $z_{\text{lift}}$ . The relatively small difference in work functions observed between Ti and Au is due to the ambient conditions during the experiments, but the actual step height does not affect the procedure. The right inset is the transfer function  $h$  for increasing lift height. The increasing width with increasing lift height reflects the obvious loss in spatial resolution. Moreover, the asymmetric shape of  $h$  is due to the asymmetric measurement configuration in which the cantilever is oriented perpendicular to the step edge. An orientation parallel to the edge yields a symmetric  $h$  [15]. In principle, additional broadening of  $h$  also results from fabrication imperfections, like the step edge not being perfectly straight and infinitely steep, while uncertainty in  $h$  may also arise due to inter-tip variations. We estimate the total resulting effect to be around 50 nm, which is small compared to the broadening by the non-local electrostatic coupling which we are interested in, and aim to correct for.

We now return to the problem of measuring the actual recombination profile in an ambipolar OFET. The methodology described above was applied to surface potentials measured by SKPM on ambipolar OFETs that have been extensively described before [8,19]. In short, these devices consist of a thin nickel dithiolene (NiDT) layer on a  $\text{Si/SiO}_2$



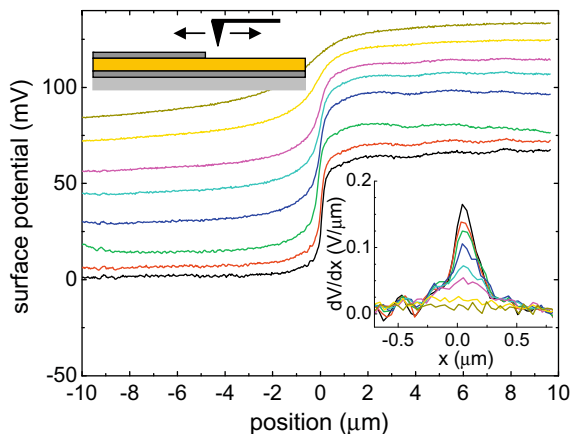


**Fig. 1.** Main panel: SKPM step edge response with the tip orthogonal to the channel for different lift heights, lines are the measured surface potential over the step edge at (bottom to top)  $z_{\text{lift}} = 0, 25, 50, 100, 150, 200, 500, 1000$  nm. Top inset: layout of Ti (dark gray) step edge on Au (yellow) sample deposited on  $\text{SiO}_2$  (light gray), scanned by an SKPM probe (black). Right inset: transfer function  $h$  for different  $z_{\text{lift}}$  (For interpretation of the references to colour in this figure legend, the reader is referred to the web version of this article.).

(200 nm) substrate with Ti/Au bottom contacts in a circular transistor configuration with a channel width and length of 2500 and  $10 \mu\text{m}$ , respectively, see inset to Fig. 2. By choosing proper bias conditions electron and hole accumulation regions, separated by a recombination zone, are simultaneously present. Electron and hole mobilities that are used in the numerical drift–diffusion calculations discussed below are obtained from transport characteristics and equal  $1 \times 10^{-11}$  and  $2 \times 10^{-12} \text{ m}^2/\text{Vs}$  for holes and electrons, respectively.

In Fig. 2 two different prediction methods are applied to a representative surface potential as measured by SKPM on the NiDT ambipolar transistor. The required input signal,  $x$  in (2), is calculated from the variable range hopping model discussed in Ref. [19] using  $V_g - V_{\text{th}} = 5.3 \text{ V}$  and  $V_{\text{sd}} = 9 \text{ V}$  and is shown as blue line. It is important to point out that this model assumes  $W = 0$ , i.e.  $\beta = \infty$ . From that, the black line is calculated using (2) with a transfer function  $h$  obtained from (3) as discussed above. Clearly, the predicted curve follows the experimental one closely. For comparison we also used a computationally much more demanding 3D finite element model to predict the SKPM response of  $x$  [15]. The result is shown as red line, and is in close agreement with the much easier obtained result of (2). From this we conclude that the transfer function method provides a convenient way to transform a known surface potential into an actual SKPM response. However, a close inspection of both curves in the recombination zone reveals a maximum field that is significantly higher than observed experimentally. Below, this will be related to the nonzero value of  $W$ .

In Fig. 3, the experimental response and its reconstructed surface potential are compared to the theoretical surface potential for again  $V_g - V_{\text{th}} = 5.3 \text{ V}$  and  $V_{\text{sd}} = 9 \text{ V}$ . Both the magnitude reduction of the experimental curve and most of its asymmetric distortion due to the asymmet-

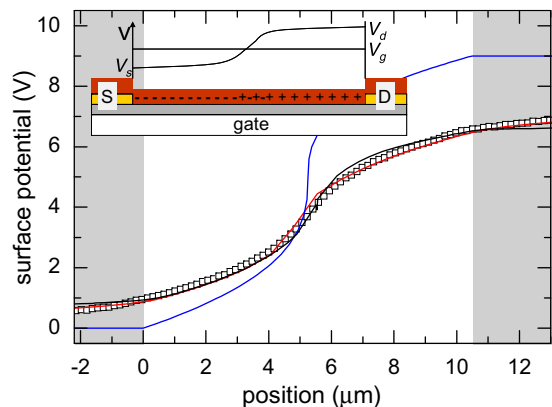


**Fig. 2.** Comparison of surface potential prediction methods applied to an ambipolar OFET. Symbols: experiment taken for  $V_{\text{sd}} = 9 \text{ V}$  and  $V_g - V_{\text{th}} = 5.3 \text{ V}$  at  $z_{\text{lift}} = 100 \text{ nm}$ ; lines: transfer function method (black), 3D numerical (red) and theoretical potential used as input (blue). Inset: schematic layout of the ambipolar OFET. When  $0 < V_g - V_{\text{th}} < V_{\text{sd}}$  with  $V_g, V_{\text{th}}$  and  $V_{\text{sd}}$  the gate, threshold and source-drain voltage, respectively, electron and hole accumulation layers form on the left and right of a recombination zone, respectively. The source is grounded (For interpretation of the references to colour in this figure legend, the reader is referred to the web version of this article.).

ric tip-channel orientation are removed by the transfer function procedure outlined above. However, the infinite field at the point where n- and p-type accumulation regions meet, as implicitly assumed in the model of Ref [19], is not observed. At this point, it is tempting to take the width of the derivative profile of the reconstructed surface potential, shown as thin black line in the insets of Fig. 3, as a measure of the actual recombination zone width  $W$ . However, despite the fact that the analytical model underlying (1) correctly predicts the recombination profile,

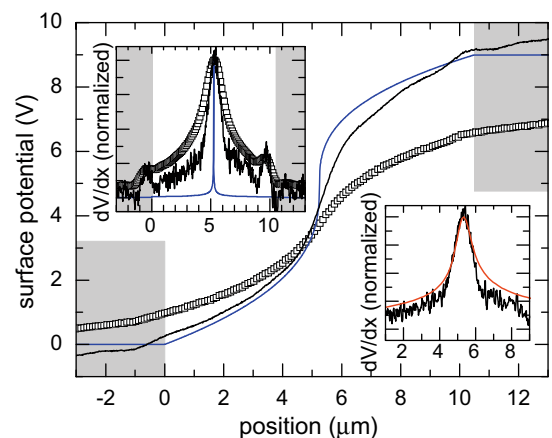


**Fig. 3.** Reconstruction of the surface potential of an ambipolar OFET. Symbols: experiment taken for  $V_{\text{sd}} = 9 \text{ V}$  and  $V_g - V_{\text{th}} = 5.3 \text{ V}$  at  $z_{\text{lift}} = 100 \text{ nm}$ ; lines: transfer function method (black) and theoretical potential as calculated according to Ref. [19] (blue). Upper inset: normalized first derivative of the curves in the main panel. Lower inset: zoom-in on reconstructed first derivative profile (black) and calculated profile for a recombination zone width of  $0.5 \mu\text{m}$  (red) (For interpretation of the references to colour in this figure legend, the reader is referred to the web version of this article.).

it makes no predictions of the corresponding potential profile, and the widths of the two profiles are usually not equal [8]. Since an analytical calculation of the potential profile in an ambipolar transistor is only possible under assumption of a zero recombination zone width [19], we performed a numerical drift-diffusion analysis as outlined in Ref. [8]. The (spatial derivative of the) resulting potential profile is compared to the reconstructed experimental profile in the lower inset of Fig. 3. We find optimal agreement between the two derivative profiles when parameters that give rise to a recombination zone width of 0.5  $\mu\text{m}$  are used. With  $d = 200$  nm and estimating  $\delta = 3$  nm, it follows from (1) that  $\beta \approx 10^{-2}$ , which is also used in the numerical calculations. This implies that the bimolecular recombination rate is two orders of magnitude below the value predicted by the Langevin expression. This finding is in good agreement with the results from Monte Carlo simulations by Groves and Greenham [1] who find values for  $\beta$  between  $10^{-1}$  and  $10^{-2}$  for similar parameters as in the present experiment.

Summarizing, we presented a practical method for prediction and reconstruction of surface potentials measured by SKPM. The method is based on (de)convolution with a transfer function containing the whole electrostatic tip-sample coupling. The transfer function is experimentally calibrated on an 'ideal' step edge. Using this method we determined a recombination zone width of 0.5  $\mu\text{m}$  for a NiDT ambipolar OFET, indicating a bimolecular recombination rate that is two orders of magnitude below the Langevin value.

### Acknowledgments

The work of D.S.H.C. is made possible by a NanoNed Grant (NanoNed is the Dutch nanotechnology initiative by the Ministry of Economic Affairs). We gratefully acknowledge Reinder Coehoorn and Dago de Leeuw for stimulating discussions.

### References

- [1] See e.g. C. Groves, N.C. Greenham, *Phys. Rev. B* 78 (2008) 155205. and references therein.
- [2] For a recent review see e.g. J. Zaumseil, H. Sirringhaus, *Chem. Rev.* 107 (2007) 1296.
- [3] T. Takenobu, S.Z. Bisri, T. Takahashi, M. Yahiro, C. Adachi, Y. Iwasa, *Phys. Rev. Lett.* 100 (2008) 066601.
- [4] For a recent review see e.g. I.D.W. Samuel, G.A. Turnbull, *Chem. Rev.* 107 (2007) 1272.
- [5] R.C.G. Naber, M. Bird, H. Sirringhaus, *Appl. Phys. Lett.* 93 (2008) 023301.
- [6] E.B. Namdas, M. Tong, P. Ledochowitsch, S.R. Mednick, J.D. Yuen, D. Moses, A.J. Heeger, *Adv. Funct. Mater.* 21 (2009) 799.
- [7] S. Verlaak, D. Cheyns, M. Debucquoy, V. Arkhipov, P. Heremans, *Appl. Phys. Lett.* 85 (2004) 2405.
- [8] M. Kemerink, D.S.H. Charrier, E.C.P. Smits, S.G.J. Mathijssen, D.M. de Leeuw, R.A.J. Janssen, *Appl. Phys. Lett.* 93 (2008) 033312.
- [9] M. Nonnenmacher, M.P. O'Boyle, H.K. Wickramasinghe, *Appl. Phys. Lett.* 58 (1991) 2921.
- [10] Y. Shen, D.M. Barnett, P.M. Pinsky, *Rev. Sci. Instrum.* 79 (2008) 023711.
- [11] A. Liscio, V. Palermo, P. Samori, *Adv. Funct. Mater.* 18 (2008) 907.
- [12] E. Strassburg, A. Boag, Y. Rosenwaks, *Rev. Sci. Instrum.* 76 (2005) 083705.
- [13] A. Schwartzman, E. Grunbaum, E. Strassburg, E. Lepkifker, A. Boag, Y. Rosenwaks, T. Glatzel, Z. Barkay, M. Mazzer, K. Barnham, *J. Appl. Phys.* 98 (2005) 084310.
- [14] H.O. Jacobs, P. Leuchtmann, O.J. Homan, A. Stemmer, *J. Appl. Phys.* 84 (1998) 1168.
- [15] D.S.H. Charrier, M. Kemerink, B.E. Smalbrugge, T. de Vries, R.A.J. Janssen, *ACS Nano* 2 (2008) 622.
- [16] A. Gil, J. Colchero, J. Gómez-Herrero, A.M. Baró, *Nanotechnology* 14 (2003) 332.
- [17] E.O. Brigham, *The Fast Fourier Transform and its Applications*, Prentice-Hall, Englewood Cliffs, 1988.
- [18] Numerical noise and spurious peaks in FFT signals could greatly be reduced by making all discrete signals  $X_N = (x_1, \dots, x_N)$  periodic by extending them to  $X_{2N} = (x_1, \dots, x_N, \dots, x_1)$ . To avoid extrapolation to low frequencies in Fourier space, the size of the reference scan was at least the size of the to-be-converted measurement or calculation. In the inversion procedure, a high frequency cutoff was used to avoid division-by-zero errors at frequencies where  $F(h)$  is close to zero.
- [19] E.C.P. Smits, S.G.J. Mathijssen, M. Cölle, A.J.G. Mank, P.A. Bobbert, P.W.M. Blom, B. de Boer, D.M. de Leeuw, *Phys. Rev. B* 76 (2007) 125202.

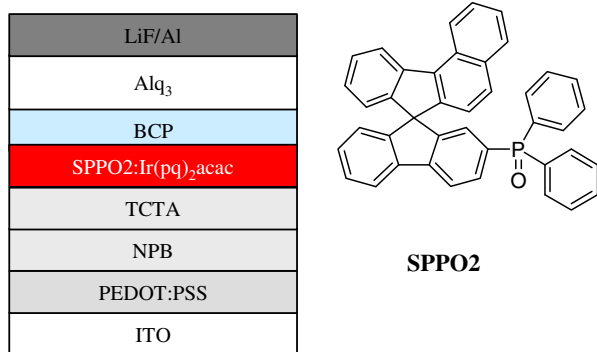


**Fig. 1.** Chemical structure of SPPO2 and device structures of red PHOLEDs used in this work.

(Alq<sub>3</sub>, 20 nm)/LiF(1 nm)/Al(200 nm). The doping concentrations of Ir(pq)<sub>2</sub>acac were 10%, 15% and 20%. A mixed host device with TCTA:PH1 host instead of the SPPO2 was also fabricated as a standard device [12]. The SPPO2 host material was synthesized by coupling of diphenylphosphine with spirofluorene unit and detailed synthesis will be reported in other work. Chemical structure of SPPO2 and device structure are shown in Fig. 1. Current density–voltage–luminance and electroluminescence characteristics of the red PHOLEDs were measured with Keithley 2400 source measurement unit and CS 1000 spectroradiometer.

The SPPO2 host material has a glass transition temperature of 119 °C and it forms an amorphous film with a surface roughness less than 1 nm due to a twisted structure of the rigid spirobenzofluorene unit. The highest occupied molecular orbital (HOMO) and the lowest unoccupied molecular orbital (LUMO) of the SPPO2 were 6.0 and 2.4 eV, respectively. The HOMO level of SPPO2 is suitable for hole injection and the electron transporting property of the phosphine oxide and the spirobenzofluorene unit is appropriate for balancing holes and electrons in the emitting layer. The electron transport property of the SPPO2 was confirmed by the electron only devices and the SPPO2 electron only device showed higher current density than the common Alq<sub>3</sub> electron only device. In addition, the triplet energy bandgap of the SPPO2 measured from low temperature photoluminescence is 2.4 eV which is suitable for triplet energy transfer from the SPPO2 to red emitting Ir(pq)<sub>2</sub>acac with a triplet bandgap of 2.2 eV. Therefore, the SPPO2 can be used as a host material for red PHOLEDs.

Fig. 2 shows the current density–voltage–luminance curves of the red PHOLEDs with different doping concentration. The current density of the red PHOLEDs was increased according to the increase of doping concentration and the luminance showed a similar tendency. The high current density in the highly doped devices can be explained by the charge trapping effect of the red dopant. The LUMO level of the Ir(pq)<sub>2</sub>acac is 3.0 eV compared with 2.4 eV of the SPPO2. Therefore, electrons are trapped by the Ir(pq)<sub>2</sub>acac and electron transport in the Ir(pq)<sub>2</sub>acac doped emitting layer is retarded due to the electron trapping effect [13]. Energy level diagram of the SPPO2 device is

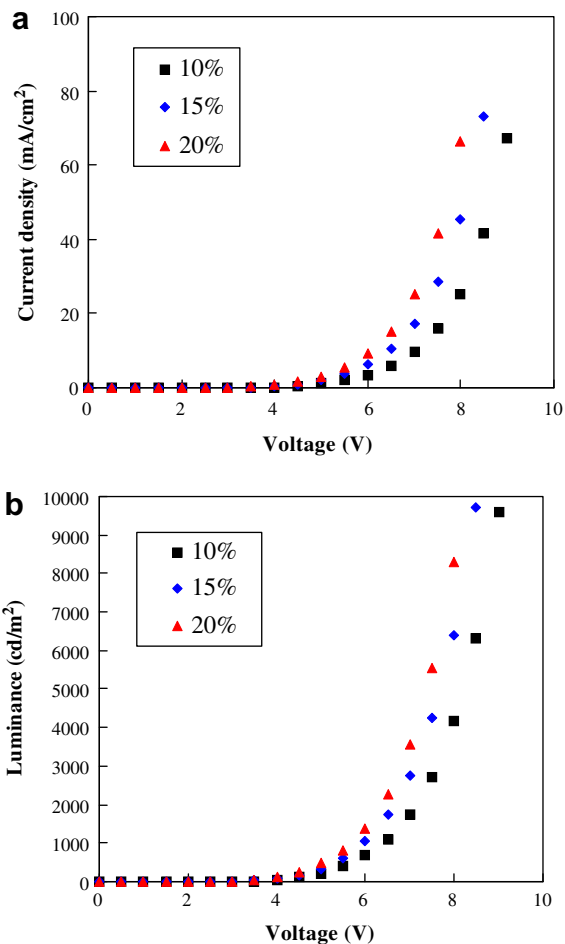


**Fig. 2.** Current density–voltage–luminance characteristics of red PHOLEDs with SPPO2 as a host according to doping concentration. (a) Current density–voltage and (b) luminance–voltage.

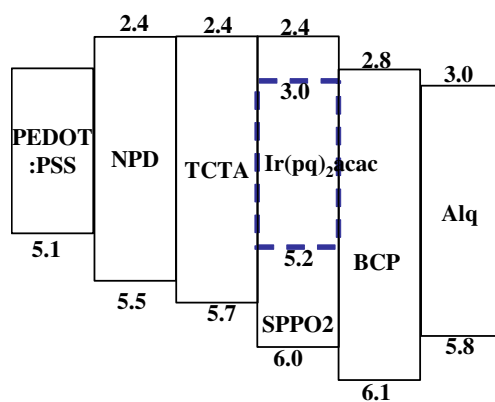


**Fig. 3.** Energy level diagram of the SPPO2 device.

shown in Fig. 3. At low doping concentration, the long hopping distance between dopant materials limits the electron hopping between the red dopant materials. As the doping concentration is increased, the hopping distance between

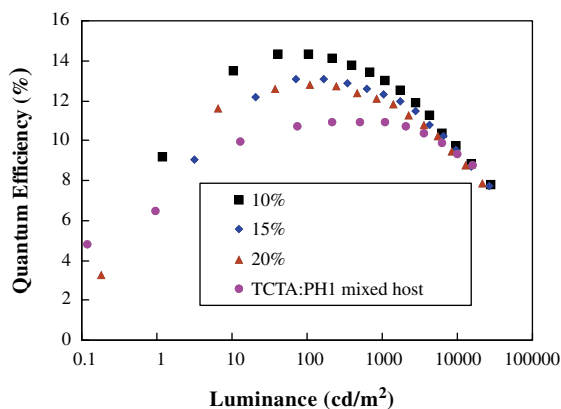


**Fig. 4.** Quantum efficiency of red PHOLEDs with SPPO2 as a host according to doping concentration. The efficiency was compared with that of the TCTA:PH1 host reported in previous work [12].

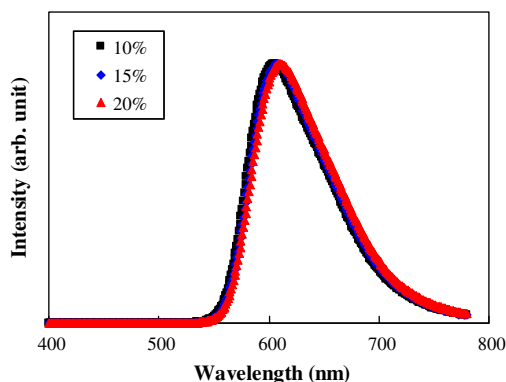


**Fig. 5.** Electroluminescence spectra of red PHOLEDs with SPPO2 as a host according to doping concentration.

the red dopants is decreased, resulting in enhanced electron transport. Therefore, high current density was obtained in the highly doped red PHOLEDs.

Quantum efficiency of the red PHOLEDs is shown in Fig. 4. The quantum efficiency was decreased at high doping concentration due to concentration quenching effect and a maximum quantum efficiency was obtained in the red PHOLED with 10% doping concentration. The quantum efficiency of the 10% Ir(pq)<sub>2</sub>acac doped red PHOLED was 14.3% at 100 cd/m<sup>2</sup> with a current efficiency of 20.4 cd/A. The high efficiency of the SPPO2 red devices can be explained by the charge balance in the emitting layer. Even though SPPO2 has an electron transport character, efficient hole injection from the TCTA to the SPPO2 balances holes and electrons in the SPPO2 emitting layer. The low quan-

tum efficiency of the highly doped device is due to concentration quenching effect [7].

The quantum efficiency of the SPPO2 device was compared with that of the mixed host device which can balance holes and electrons in the light-emitting layer. TCTA:PH1 mixed host structure which was reported in our previous work was used [13]. Even though an efficiency roll-off was observed in the SPPO2 device, the SPPO2 device showed better quantum efficiency than the mixed host device over all luminance range investigated. This indicates that the SPPO2 host is better than the TCTA:PH1 mixed host in terms of charge balance in the emitting layer.

The EL spectra of SPPO2 red devices are shown in Fig. 5. The SPPO2 devices showed typical EL spectra of Ir(pq)<sub>2</sub>acac. The peak maximum of the EL spectra was 607 nm and the spectra were red-shifted at high doping concentration. There was little charge leakage out of the emitting layer and only emission from the dopant material was observed. Therefore, it can be concluded that charge confinement and charge balance in the SPPO2 light-emitting layer are responsible for the improved quantum efficiency in the SPPO2 red devices.

In summary, a phosphine oxide derivative with a spiro-benzofluorene backbone structure, SPPO2, was effective as a red phosphorescent host. A high quantum efficiency of 14.3% and a current efficiency of 20.4 cd/A were obtained due to a triplet bandgap of 2.4 eV for efficient energy transfer and a charge balance in the light-emitting layer. The SPPO2 also showed a smooth surface morphology with an average surface roughness less than 1 nm and a high glass transition temperature of 119 °C. Therefore, the SPPO2 is promising as a host in red and deep red phosphorescent devices.

## References

- [1] M.A. Baldo, D.F. O'Brien, Y. You, A. Shoustikov, S. Sibley, M.E. Thompson, S.R. Forrest, *Nature* 395 (1998) 151.
- [2] J.Y. Lee, J.H. Kwon, H.K. Chung, *Org. Electron.* 4 (2003) 143.
- [3] D.F. O'Brien, M.A. Baldo, M.E. Thompson, S.R. Forrest, *Appl. Phys. Lett.* 74 (1999) 442.
- [4] C. Adachi, M.A. Baldo, S.R. Forrest, S. Lamansky, M.E. Thompson, R.C. Kwong, *Appl. Phys. Lett.* 78 (2001) 1622.
- [5] Y. Kawamura, S. Yanagida, S.R. Forrest, *J. Appl. Phys.* 92 (2002) 87.
- [6] A. Tsuboyama, H. Iwawaki, M. Furugori, T. Mukaide, J. Kamatani, S. Igawa, T. Moriyama, S. Miura, T. Takiguchi, S. Okada, M. Hoshino, K. Ueno, *J. Am. Chem. Soc.* 125 (2003) 12971.
- [7] M.A. Baldo, M.E. Thompson, S.R. Forrest, *Pure Appl. Chem.* 71 (1999) 2095.
- [8] J.Y. Lee, *Appl. Phys. Lett.* 89 (2006) 223517.
- [9] T. Tsuji, S. Kawami, S. Miyaguchi, T. Naijo, T. Yuki, S. Matsuo, H. Miyazaki, *SID Int. Symp. Digest Tech. Papers* 35 (2004) 900.
- [10] Hiroshi Kanno, Kaori Ishikawa, Yoshitaka Nishio, Ayataka Endo, Chihaya Adachi, Kenichi Shibata, *Appl. Phys. Lett.* 90 (2007) 123509.
- [11] S.H. Kim, J. Jang, J.Y. Lee, *Synth. Met.* 157 (2007) 228.
- [12] S.H. Kim, J. Jang, J.Y. Lee, *J. Lumin.* 128 (2008) 2035.
- [13] J.Y. Lee, *Appl. Phys. Lett.* 89 (2006) 153503.

electrode of the O-CMOS devices. These wafers were cleaned with acetone, ethanol, and de-ionized water. Then, in order to remove involuntary organic residue, the surface of the 300-nm-thick SiO<sub>2</sub> gate dielectric, which grew by plasma enhanced chemical vapor deposition on the substrate at a temperature of 250 °C previously, was cleaned by use of oxygen (O<sub>2</sub>) plasma. A polyimide (PI, Nissan RN-1349) layer of 100 nm was spun onto the SiO<sub>2</sub> layer. The PI layer was soft-baked and hard-baked for 5 min at 80 °C and 60 min at 220 °C, respectively. Although the processing temperature is slight higher than most of plastic substrates, it still has an opportunity to apply on polymer substrate with high glass temperature, e.g. polycarbonate (PC) which  $T_g$  is above 250 °C. Nevertheless, further lowering of the processed temperature is still required to meet the requirements of most flexible plastics substrate and in progress. Both the SiO<sub>2</sub> and PI layers were acted as the main gate dielectric with capacitance of  $\sim 4.0$  nF/cm<sup>2</sup> measured at 10 kHz for the O-CMOS devices. The active layers of *p*-channel and *n*-channel are 70-nm-thick pentacene film and *N,N'*-dioctyl-3,4,9,10-perylene tetracarboxylic diimide (PTCDI-C<sub>8</sub>H<sub>17</sub>) film, respectively, in which the deposition rate are all 0.5 Å/s on the PI layer at sublimation pressure of  $1 \times 10^{-5}$  torr. The pentacene was purchased from Aldrich Chem. Co. and the PTCDI-C<sub>8</sub>H<sub>17</sub> was synthesized by us. Finally, the 80-nm-thick silver film was deposited to form source/drain electrodes upon the surface of the pentacene and PTCDI-C<sub>8</sub>H<sub>17</sub> films through a shadow mask in order to complete the O-CMOS device under vacuum of  $4 \times 10^{-6}$  torr. The channel length ( $L$ ) of O-CMOS is 100 μm, but the width ( $W$ ) of *p*-type and *n*-type transistors are 500 and 2000 μm, respectively, for matching performances of these two transistors as shown in Fig. 1. For comparison, the O-CMOS without the PI modification layer were fabricated simultaneously with the same processes. The current–voltage ( $I$ - $V$ ), transfer, and alternating current signals of devices were measured by use of a semiconductor parameter analyzer (Keithley 4200-SCS). To minimize

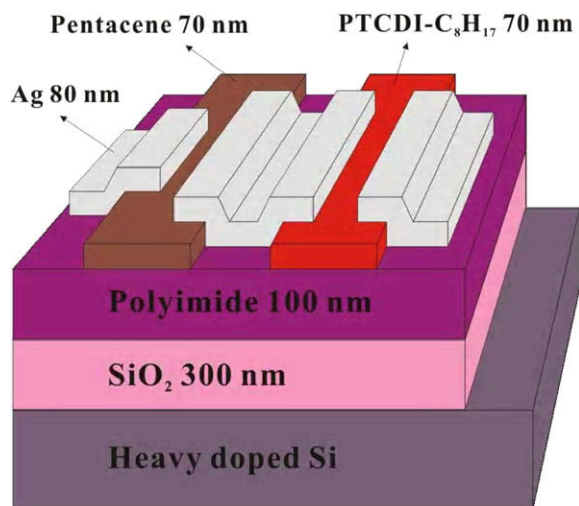
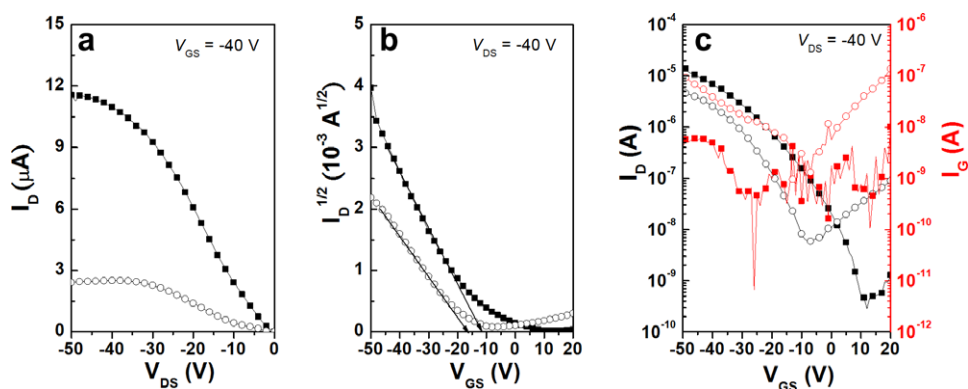


**Fig. 1.** The structure of an O-CMOS inverter with PI modification layers composed of *p*-type and *n*-type transistors.

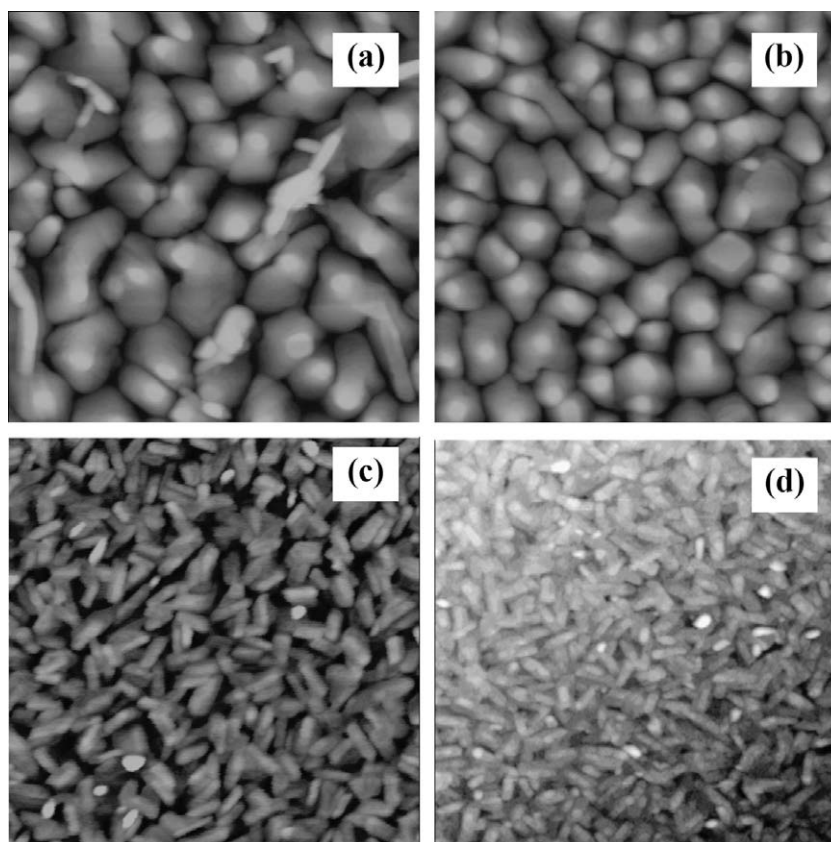
the influence of H<sub>2</sub>O from the ambient air on the electrical properties of devices, the electrical characteristics of O-CMOS were measured in a dry nitrogen-atmosphere glove box under dark conditions.

Fig. 2 shows the *p*-type electrical characteristics of the pentacene-based transistors with and without the PI as modification layers. The drain current of transistor with PI is higher than that without PI, as shown in Fig. 2a, when the gate voltage ( $V_{GS}$ ) was fixed at  $-40$  V and source-drain voltage ( $V_{DS}$ ) was scanned from 0 to  $-50$  V. The current–voltage characteristics ( $\sqrt{I_D} - V_{GS}$ ) of the device with the PI layer reveal that the threshold voltage ( $V_{tp}$ ) is about  $-12.90$  V when the source-drain voltage ( $V_{DS}$ ) was fixed at  $-40$  V and gate-source voltage ( $V_{GS}$ ) varied from 20 to  $-50$  V; however, the  $V_{tp}$  of the device without PI layer shifts to  $-16.79$  V, as shown in Fig. 2b. The trap states of pentacene film near the surface of the PI layer were smaller than that near SiO<sub>2</sub> layer due to the non-polar surface of the PI layer which was appropriate for the growth of the pentacene film. The grain size for pentacene grown on PI surface is larger than that grown directly on SiO<sub>2</sub> surface, as shown in Fig. 3a and b. Besides, the pentacene film on PI has good homogeneity associated with superior molecular microstructures and larger intermolecular couplings as compared to that on SiO<sub>2</sub> [17]. Low trap states resulted in low threshold voltage for OTFTs [7]. Therefore, the device with the PI layer has higher field-effect mobility ( $\mu = 0.921$  cm<sup>2</sup> V<sup>-1</sup> s<sup>-1</sup>) and lower subthreshold slope ( $ss = 4.71$  V/decade) than that without PI layer whose  $\mu$  and  $ss$  are  $0.221$  cm<sup>2</sup> V<sup>-1</sup> s<sup>-1</sup> and  $10.79$  V/decade, respectively. The PI layer has an additional advantage to suppress the leakage current of OTFT so that the on/off ratio increases and gate-leakage-current decreases about one order for the device with the PI layer when compared with the device lacking the PI layer, as shown in Fig. 2c.

Next, the *n*-type PTCDI-C<sub>8</sub>H<sub>17</sub>-based transistors with and without PI as modification layers were measured by the semiconductor analyzer in order to investigate the electrical properties. From the output curves in Fig. 4a, the drain current of the device with the PI is better than that without PI when the  $V_{GS}$  was fixed at 40 V and  $V_{DS}$  was varied from 0 to 50 V. The superior  $V_{tn}$  of 5.87 V and  $\mu$  of  $0.341$  cm<sup>2</sup> V<sup>-1</sup> s<sup>-1</sup> were obtained from transfer curve in Fig. 4b for the device with the PI layer; however, the device without the PI layer had negative  $V_{tn}$  and poor  $\mu$  ( $0.01$  cm<sup>2</sup> V<sup>-1</sup> s<sup>-1</sup>). The performance enhancements of the device when inserting the PI layer were due to the surface energy match for PI (38 mJ/m<sup>2</sup>) and PTCDI-C<sub>8</sub>H<sub>17</sub> (32 mJ/m<sup>2</sup>) films obtained from contact angle measurements of H<sub>2</sub>O and CH<sub>2</sub>I<sub>2</sub>. Furthermore, the PTCDI-C<sub>8</sub>H<sub>17</sub> on PI surface displays the larger grain texture than that on SiO<sub>2</sub> surface (surface energy of 60 mJ/m<sup>2</sup>). Negative shift  $V_{tn}$  for *p*-transistor and normally-on *n*-type transistor with the PI modification layer were attributed to richly negative center on the SiO<sub>2</sub> surface. The improved on/off ratio and  $ss$  and suppression of leakage current for the *n*-type transistor with the PI layer when compared to the device without the PI layer are similar to *p*-type transistors as shown in Fig. 4c. Moreover, both the pentacene and the PTCDI TFTs have fairly large gate leakage currents, about 10 nA, due to the SiO<sub>2</sub> gate-dielectric grown at low temperature.



**Fig. 2.** The electrical characteristics of the pentacene-based OTFT. (a) Output curves, (b) curves of the field-effect mobilities and threshold voltage ( $I_{DS}^{1/2} - V_{GS}$ ), and (c) curves of the on/off ratio, subthreshold swing ( $\log(I_{DS}) - V_{GS}$ ), and leakage currents ( $\log(I_G) - V_{GS}$ ). Symbols: the devices (■) with and (○) without PI modification layers.



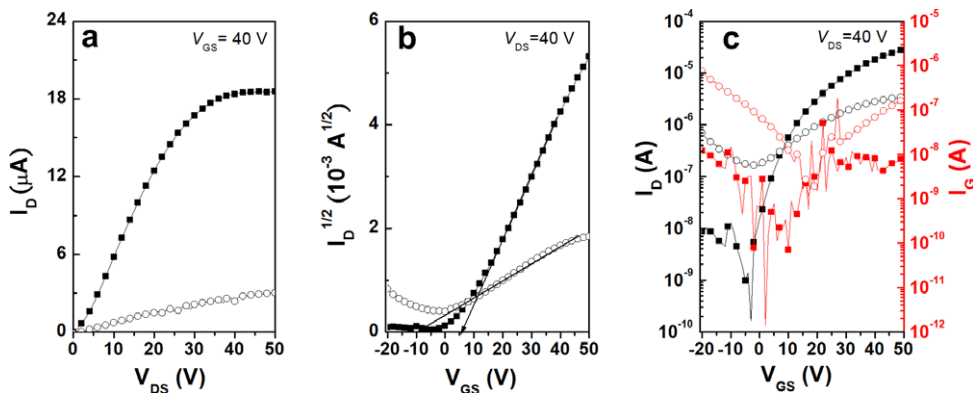
**Fig. 3.** Atomic force microscope images of pentacene films deposited on (a) PSPI and (b) SiO<sub>2</sub> dielectrics. PTCDI-C<sub>8</sub>H<sub>17</sub> films deposited on (c) PSPI and (d) SiO<sub>2</sub> dielectrics. All images are 2 μm × 2 μm in size.

Fig. 5 shows the voltage transfer characteristics and gains of O-CMOS inverters composed of the above-mentioned *p*-transistor and *n*-transistor. The input voltage ( $V_I$ ) was varied from 0 to 50 V at  $V_{DD}$  of 30, 40, and 50 V. The O-CMOS inverters demonstrate the switch from high to low states which correspond to the basic logic bit from “1” to “0”. Compared with the O-CMOS inverter without the PI modification layer, the device with the PI layer has symmetric voltage transfer curves in which the verti-

cal segment occurs at  $V_I = V_{DD}/2$  and is bounded by  $V_o(A) = V_{DD}/2 - V_{tp}$ ,  $V_o(B) = V_{DD}/2 - V_{tn}$ . The performance of switching an O-CMOS inverter can be generally determined by noise margins at high and low logic levels. The noise margins for high ( $NM_H$ ) and low ( $NM_L$ ) are defined as [18]

$$NM_H = V_{OH}(E) - V_{IH}(D) \quad (1)$$

$$NM_L = V_{IL}(C) - V_{OL}(F) \quad (2)$$



**Fig. 4.** The electrical characteristics of the PTCDI-C<sub>8</sub>H<sub>17</sub>-based OTFT. (a) Output curves, (b) curves of the field-effect mobilities and threshold voltage ( $I_D^{1/2} - V_{GS}$ ), and (c) curves of the on/off ratio, subthreshold swing ( $\log(I_D) - V_{GS}$ ), and leakage currents ( $\log(I_G) - V_{GS}$ ). Symbols: the devices with (■) and without (○) the PI modification layers.

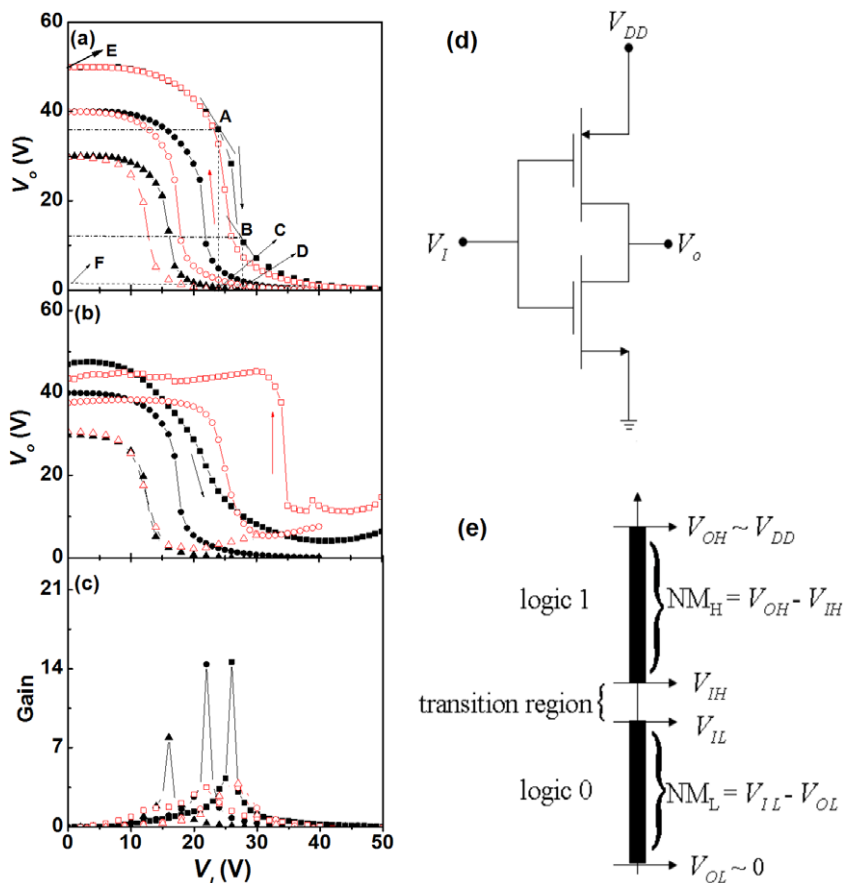


**Fig. 5.** Hysteresis transfer curves of O-CMOS inverters in both forward (closed symbol) and reverse (open symbol) processed. (a) The device with the PI layer; (b) the device without the PI layer. (c) The corresponding signal gains. Symbols: the devices with (closed symbol) and without (open symbol) the PI modification layers. (d) The circuit of O-CMOS. (e) The logic-level diagram of O-CMOS. The applied  $V_{DS}$ : (▲) triangle 30 V, (●) circle 40 V, and (■) square 50 V.

where  $V_{OH}$ (E) and  $V_{OL}$ (F) are maximum and minimum output voltages, respectively;  $V_{IH}$ (D) and  $V_{IL}$ (C) are input voltages at  $\partial V_o / \partial V_i = -1$  as shown in Fig. 5a. The  $NM_H$  and  $NM_L$  are estimate to be 45% and 47.4% of  $V_{DD} = 50$  V, respec-

tively. Especially, the noise margin at high level matches that at low level. The voltage of transition region between  $V_{IH}$  and  $V_{IL}$  is below 10% of the  $V_{DD}$  as shown in Fig. 5e. However, the noise margins of organic complementary

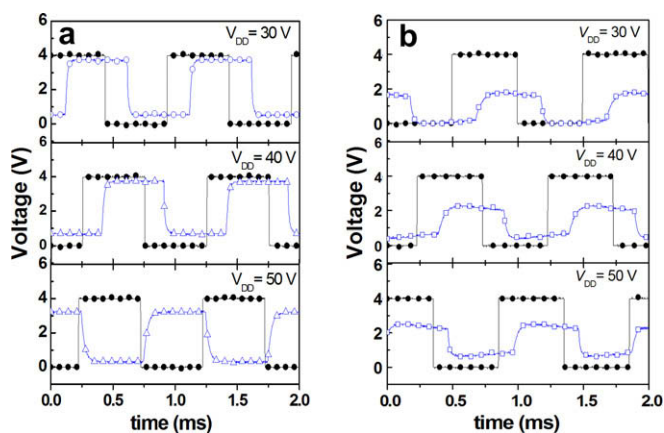


**Fig. 6.** The dynamic characteristics operation of O-CMOS inverters employing (a) the PI, (b) without the PI at 1 kHz and various  $V_{DD}$ . The close symbol represents the input signal ( $V_i$ ) and open symbol represents the output ( $V_o$ ).

inverters exceed 50% in literature reports, in which the difference of  $NM_H$  and  $NM_L$  is greater than 10% for some reports [12,19,20]. Therefore, the characteristics of the device with the PI modification layer have the potential for applications in organic inverter circuit designs. Moreover, the small hysteresis phenomenon was observed in the device with the PI layer because of the good matches of drain-currents in both transistors. For obtaining the drain-currents match, the  $W/L$  of  $p$ - and  $n$ -transistors were adjusted to optimize the voltage transfer curve and noise margin of O-CMOS as shown in Fig. 5a and b. The gain of CMOS device was defined as the slope  $\partial V_o/\partial V_i$  of the transfer curve. When the O-CMOS was fabricated on a  $\text{SiO}_2$  surface, it showed a very low gain as shown in Fig. 5c. The gain was improved by above five times of magnitude when the O-CMOS was fabricated on the PI surface.

The generally studied CMOS demonstrates an important application of MOSFET, namely, its use as a voltage-controlled switch. The characteristics for dynamically operating the O-CMOS inverters are shown in Fig. 6. When the amplitude of alternating input  $V_i$  (1 kHz) was fixed at 4 V and  $V_{DD}$  varied from 30 to 50 V at step of 10 V, the amplitude of the alternating output  $V_o$  for the O-CMOS with the PI layer is almost the same as the input. However, the amplitude of the alternating  $V_o$  for the O-CMOS without the PI layer is half of the input because of the mismatch of the drain current and field-effect mobility between  $n$ -type and  $p$ -type transistors. The propagation delay time ( $t_p$ ) decreases with the increase of  $V_{DD}$  ( $t_p$  inversely proportional to  $\mu$  and  $V_{DD}$ ) for all O-CMOS inverters, in which the definition of delay time is the same as inorganic CMOS inverter [18]. The propagation delay time of 52  $\mu\text{s}$  was obtained for the O-CMOS inverter at  $V_{DD} = 50$  V among all devices; furthermore, it behaved as an ideal CMOS inverter.

In summary, organic semiconductors pentacene and PTCDI- $\text{C}_8\text{H}_{17}$  were used to fabricate O-CMOS inverters integrated with the PI as surface modification layer on dielectric. The performances of the devices were dramatically improved by introducing PI films. An ideal O-CMOS inverter has been achieved and the  $n$ -type organic semiconductors with various alkyl groups are in progress.

## Acknowledgements

This work was supported by the National Science Council, Taiwan, through Grant NSC 96-2112-M-006-015-MY3 and NSC 96-2221-E-006-287.

## References

- [1] C.J. Drury, C.M.J. Mutsaers, C.M. Hart, M. Matters, D.M. de Leeuw, *Appl. Phys. Lett.* 73 (1998) 108.
- [2] B. Crone, A. Dodabalapur, Y.-Y. Lin, R.W. Filas, Z. Bao, A. LaDuca, R. Sarpeshkar, H.E. Katz, W. Li, *Nature (London)* 403 (2000) 521.
- [3] G.H. Gelinck, H.E.A. Huijtema, E. Van Veenendaal, E. Cantatore, L. Schrijnemakers, J.B.P.H. Van der Putten, T.C.T. Geuns, M. Beenhakkers, J.B. Giesbers, B.-H. Huisman, E.J. Meijer, E.M. Benito, F.J. Touwslager, A.W. Marsman, B.J.E. Van Rens, D.M. de Leeuw, *Nat. Mater.* 3 (2004) 106.
- [4] H. Klauk, M. Halik, U. Zschieschang, F. Eder, D. Rohde, G. Schmid, C. Dehm, *IEEE Trans. Electron Devices* 52 (2005) 618.
- [5] M. Shtein, J. Mapel, J.B. Benziger, S.R. Forrest, *Appl. Phys. Lett.* 81 (2002) 268.
- [6] H. Klauk, M. Halik, U. Zschieschang, G. Schmid, W. Radlik, *J. Appl. Phys.* 92 (2002) 5259.
- [7] W.Y. Chou, C.W. Kuo, H.L. Cheng, Y.R. Chen, F.Y. Yang, D.Y. Shu, C.C. Liao, F.C. Tang, *J. Appl. Phys.* 45 (2006) 7922.
- [8] S. Ando, R. Murakami, J. Nishida, H. Tada, Y. Inoue, S. Tokito, Y. Yamashita, *J. Am. Chem. Soc.* 127 (2005) 14996.
- [9] S. Tatemichi, M. Ichikawa, T. Koyama, Y. Taniguchi, *Appl. Phys. Lett.* 89 (2006) 112108.
- [10] T.D. Anthopoulos, B. Singh, N. Marjanovic, N.S. Sariciftci, A.M. Ramil, H. Sitter, M. Cölle, D.M. de Leeuw, *Appl. Phys. Lett.* 89 (2006) 213504.
- [11] D.J. Gundlach, K.P. Pernstich, G. Wilckens, M. Gräter, S. Haas, B. Batlogg, *J. Appl. Phys.* 98 (2005) 064502.
- [12] S. Tatemichi, M. Ichikawa, S. Kato, T. Koyama, Y. Taniguchi, *Phys. Stat. Sol. (RRL)* 2 (2) (2008) 47–49.
- [13] K.H. Lee, Jeong-M. Choi, S. Im, B.H. Lee, K.K. Im, M.M. Sung, *Appl. Phys. Lett.* 91 (2007) 23502.
- [14] M.S. Oh, D.K. Hwang, K. Lee, W.J. Choi, J.H. Kim, S. Im, *J. Appl. Phys.* 102 (2007) 076104.
- [15] H. Klauk, U. Zschieschang, J. Pflaum, Marcus Halik, *Nature Mater.* 445 (2007) 745–748.
- [16] M.S. Oh, W. Choi, K. Lee, D.K. Hwang, S. Im, *Appl. Phys. Lett.* 93 (2008) 033501.
- [17] W.Y. Chou, C.W. Kuo, H.L. Cheng, Y.R. Chen, F.C. Tang, F.Y. Yang, D.Y. Shu, C.C. Liao, *Appl. Phys. Lett.* 89 (2006) 112126.
- [18] K.C. Smith, A.S. Sedra, in: *Microelectronic Circuit*, 4th ed., Oxford, New York, 1998, p. 428.
- [19] M. Kitamura, Y. Arakawa, *Appl. Phys. Lett.* 91 (2007) 053505.
- [20] S.D. Vusser, S. Steudel, K. Myny, J. Genoe, P. Heremans, *Appl. Phys. Lett.* 88 (2006) 162116.



donor/acceptor combination using pentacene/PTCDI- $C_8$  thus can harvest light efficiently throughout the visible solar spectrum. PTCDI- $C_8$  thin film also shows high electron mobility ( $0.6 \text{ cm}^2 \text{ V}^{-1} \text{ s}^{-1}$ ) [18], which ensures balanced field-effect mobilities for n- and p-channels within the device.

In this letter, we report on the photovoltaic properties of an efficient donor/acceptor combined pentacene/PTCDI- $C_8$  heterojunction. Solar cell parameters precisely estimated using the model recently reported by Ishibashi et al. [19] are reported.

The photovoltaic devices were fabricated on patterned indium tin oxide (ITO) coated glass substrates. The sheet resistance of the ITO anode was  $10 \Omega/\square$ . All organic materials were purchased from Sigma–Aldrich. Prior to organic layer deposition, ITO substrates were cleaned thoroughly

in acetone, isopropyl alcohol and de-ionized water in sequence using an ultrasonic cleaner followed by drying with nitrogen gas. Cleaned ITO anodes were treated with microwave oxygen plasma for 30 s. A 40 nm thick poly(3,4-ethylenedioxythiophene)–poly(styrenesulfonate) (PEDOT:PSS) layer was spin coated on ITO anodes from a 2.8 wt% water solution. Spin coated PEDOT:PSS substrates were annealed at around  $110^\circ\text{C}$  for 1 h to remove the solvent completely. A 50 nm thick pentacene (99.9%) layer was thermally evaporated with a deposition rate of  $\sim 0.5 \text{ \AA/s}$  followed by the deposition of a 40 nm thick PTCDI- $C_8$  (98%) layer. A 10 nm thick electron transporting layer (ETL) of Tris-(8-hydroxyquinolato) aluminum ( $\text{AlQ}_3$ ) was then deposited on the top of the PTCDI- $C_8$  layer to prevent it from being damaged during metal deposition and to enhance the

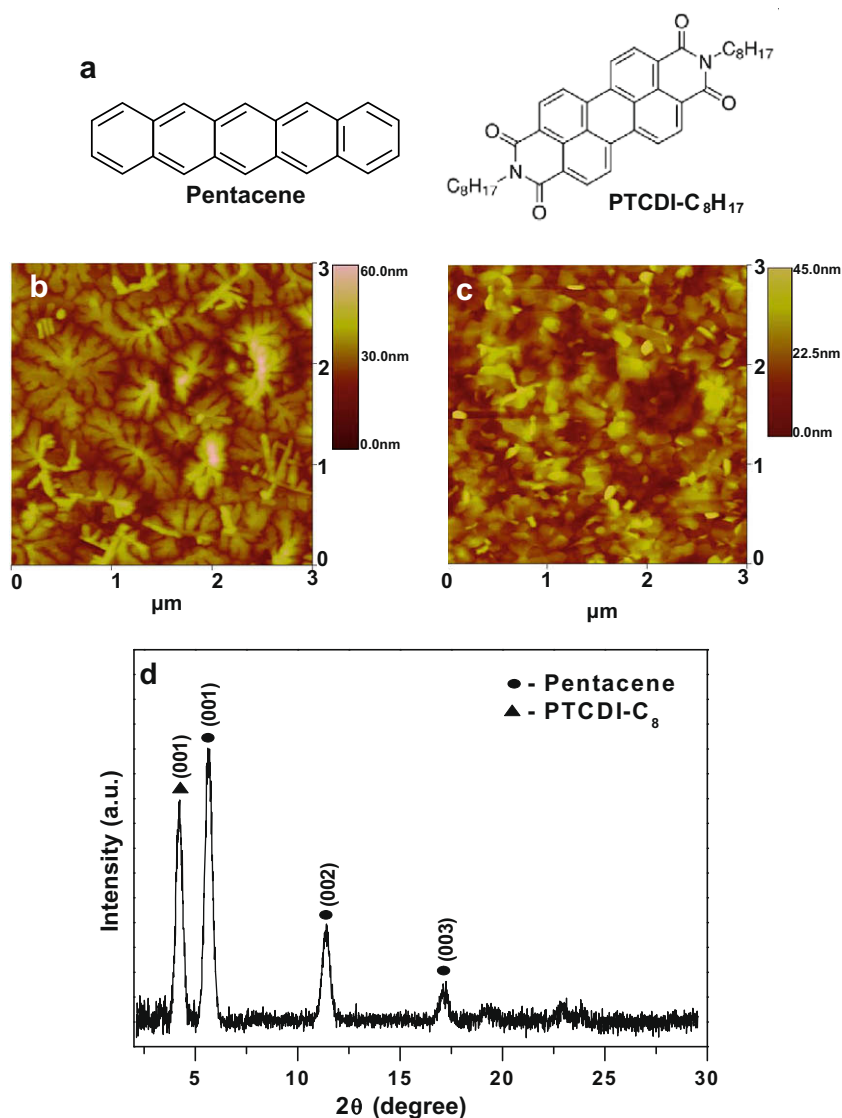


**Fig. 1.** (a) The chemical structure of pentacene and PTCDI- $C_8$ , (b) AFM micrograph of the 50 nm thick pentacene film deposited on ITO/PEDOT:PSS substrates, (c) AFM micrograph of the 40 nm thick PTCDI- $C_8$  film deposited on ITO/PEDOT:PSS/pentacene substrates, (d) X-ray diffraction pattern of pentacene/PTCDI- $C_8$  heterojunctions deposited on ITO/PEDOT:PSS substrates.

electron collection efficiency from the PTCDI-C<sub>8</sub> layer to the Al cathode [20]. Finally, an 80 nm thick aluminum top electrode strip was deposited by thermal evaporation through a shadow mask to define a square shaped active area of 4 mm<sup>2</sup>. Base pressure during the thermal evaporation was  $5 \times 10^{-6}$  mbar. The thickness of different layers was monitored by quartz crystal monitor and was verified by stylus profilometer (Veeco Dektak3). Atomic force microscopy (AFM) (Veeco Nanoscope-IV) in tapping mode was used to study the surface morphology of different layers of the device. The crystallinity of the pentacene/PTCDI-C<sub>8</sub> bilayer was studied using a Philips X-Pert PRO MRD X-ray diffractometer with CuK $\alpha$  radiation ( $\lambda = 0.15418$  nm). The absorption spectra of the pentacene/PTCDI-C<sub>8</sub> heterojunctions were investigated in the wavelength range 300–1100 nm using a UV–VIS–NIR spectrophotometer (Perkin–Elmer Lambda 45). Current density–voltage (*J–V*) characteristics of the devices were measured using a Keithley 4200–SCS measurement unit in dark and under AM 1.5 illumination (Newport 67005 solar simulator) with a power density of 100 mW/cm<sup>2</sup>. The photocurrent action spectrum was measured under short circuit condition at a chopping frequency of 180 Hz with a lock-in amplifier (Stanford research system-SR830 DSP) during illumination with the monochromatic light from a broadband source. All the device characterizations have been carried out under ambient condition.

The performance of the organic photovoltaic devices depends significantly on the morphology of the active layers. Active layers with small and disordered grains may limit the cell performance due to the large number of defect states and recombination losses. Several factors including deposition rate, substrate temperature and the nature of the substrate can influence the film morphology and crystallinity [21,22]. Here pentacene films were deposited at a slow evaporation rate of  $\sim 0.5$  Å/s to realize larger crystalline domains [21]. For investigating the morphology of the different layers of the device, tapping mode AFM was performed on both pentacene and PTCDI-C<sub>8</sub> layers. Fig. 1a shows the morphology of pentacene film deposited on ITO/PEDOT:PSS substrates. The film contains crystalline grains of 800–1100 nm sizes with layered structures. Fig. 1b shows the morphology of PTCDI-C<sub>8</sub> layer deposited on ITO/PEDOT:PSS/pentacene substrates, with uniform and densely packed structures. For further analysis, X-ray diffraction (XRD) experiments were performed on pentacene/PTCDI-C<sub>8</sub> heterojunctions deposited on ITO/PEDOT:PSS substrates under conventional ( $\theta$ – $2\theta$ ) configuration. Fig. 1c shows the corresponding XRD patterns. PTCDI-C<sub>8</sub> film shows strong diffraction peak at 4.2° with a d-spacing of 2.10 nm corresponding to the (0 0 1) plane [23] whereas pentacene exhibits a predominant thin film phase with a d-spacing of 1.56 nm at 5.6°, 11.3° and 17.2° corresponding to the (0 0 1), (0 0 2) and (0 0 3) planes, respectively [22,24–26]. Prominent diffraction peaks of pentacene and PTCDI-C<sub>8</sub> layers ensure the higher degree of crystallinity of both the p- and n-channels, resulting in low recombination losses and reduced microscopic shorts within the device.

To compare the spectral response of heterojunction device, we have investigated the independent absorption

spectra of a 50 nm thick pentacene film, 40 nm thick PTCDI-C<sub>8</sub> film and the combined pentacene/PTCDI-C<sub>8</sub> heterojunctions in 300–1100 nm wavelength range using a UV–VIS–NIR spectrophotometer. Fig. 2a represents the corresponding absorption spectra of different layers. PTCDI-C<sub>8</sub> shows significant absorption in the wavelength range 400–600 nm with peaks at 488, 523 and 567 nm. On the other hand pentacene has strong absorption properties in the range of 500–700 nm with peaks at 583 and 667 nm and visible kinks at 501, 543 and 629 nm. Altogether, the pentacene/PTCDI-C<sub>8</sub> heterojunctions show strong absorption throughout the visible solar spectrum. Fig. 2b shows the photocurrent action spectrum of the device. It closely follows the absorption profile of pentacene/PTCDI-C<sub>8</sub> heterojunctions with maximum external quantum efficiency (EQE) of  $\sim 60\%$  at 493 nm, which is one of the highest, reported so far for organic photovoltaic devices. External quantum efficiency (EQE) was measured using the relation:

$$\text{EQE}(\%) = \left( \frac{100 \times 1240 \times J_{sc}}{\lambda P_0} \right), \quad (1)$$

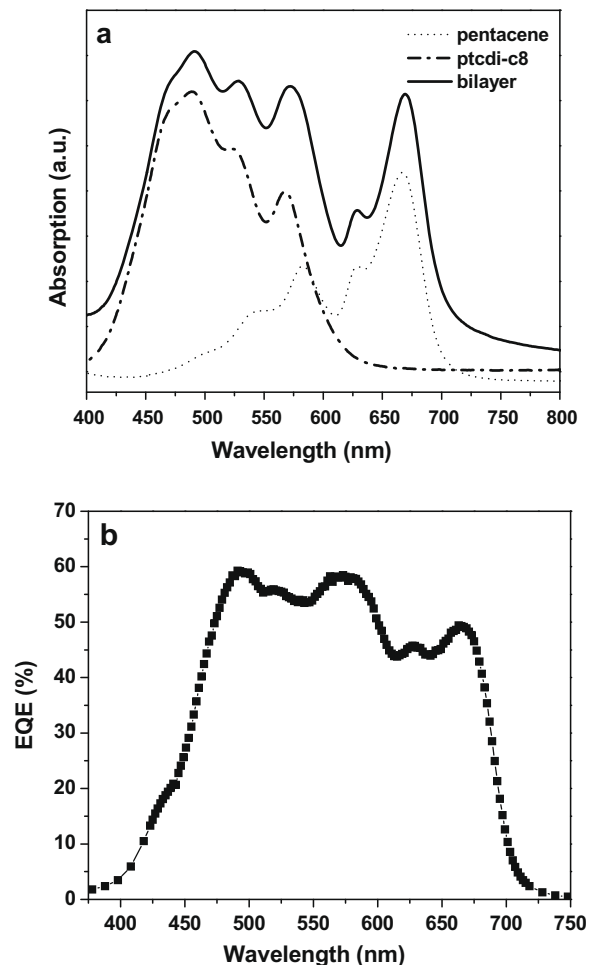


Fig. 2. (a) Absorption spectrum of a 50 nm thick pentacene film, 40 nm thick PTCDI-C<sub>8</sub> film and the pentacene (50 nm)/PTCDI-C<sub>8</sub> (40 nm) heterojunctions deposited on glass substrates, (b) photocurrent action spectra of the device; EQE reaches  $\sim 60\%$  at the PTCDI-C<sub>8</sub> peak absorption.

where  $P_0$  is the incident light intensity of the source ( $\text{mW}/\text{cm}^2$ ),  $J_{SC}$  is the short-circuit current density ( $\text{mA}/\text{cm}^2$ ), and  $\lambda$  is the wavelength (nm) of incident radiation. It is quite interesting to note that the highest peak of the photocurrent action spectrum corresponds to the maximum absorption peak of the PTCDI- $C_8$  films. This reveals the significant contribution of PTCDI- $C_8$  layer to the device performance in terms of strong light absorption and efficient exciton dissociation at the pentacene/PTCDI- $C_8$  interface.

Fig. 3a shows the  $J$ - $V$  characteristics of ITO/PEDOT:PSS/pentacene (50 nm)/PTCDI- $C_8$  (40 nm)/AlQ<sub>3</sub> (10 nm)/Al devices under dark and 100  $\text{mW}/\text{cm}^2$  AM 1.5 simulated solar irradiation conditions. The device exhibits a short-circuit current density ( $J_{SC}$ ) of  $3.0 \text{ mA}/\text{cm}^2$ , an open-circuit voltage ( $V_{OC}$ ) of 0.60 V, and a high fill factor (FF) of 65%. These device parameters lead to power conversion efficiency ( $\eta$ ) of 1.2%. Similar results have been found using PTCDI- $C_{13}$ , another derivative of PTCDI, as acceptor materials by Pandey et al. [27]. The high fill factor indicates reduced recombination loss and high shunt resistance ( $R_{SH}$ ) of the device [28].

These may be due to the excellent morphology and high charge carrier mobilities of both the p- and n-channel of the devices. For further clarification, the precise measurement of all solar cell parameters have been made by analysing the  $J$ - $V$  curve, shown in Fig. 3a under AM 1.5 illumination, using the model given by Ishibashi et al. [19]. Shunt resistance ( $R_{SH}$ ) has been independently derived from the slope of the  $J$ - $V$  curve at  $J = J_{SC}$  ( $V = 0$ ). Fig. 3b shows the experimental data together with the calculated  $R_{SH}$  of the device. Other parameters have been estimated from the  $y$ -intercept and the slope of the plot of  $(-dV/dI)$  as a function of  $\{I_{SC} - I - [V - R_s(I_{SC} - I) - nk_B T/q]/R_{SH}\}^{-1}$ , as shown in Fig. 3c, where  $I_{SC}$ ,  $R_s$ ,  $R_{SH}$ ,  $q$ ,  $n$ ,  $k_B$  and  $T$  are the short-circuit current, series resistance, shunt resistance, electron charge, the ideality factor, the Boltzmann constant and the temperature, respectively. The plot of  $(-dV/dI)$  exhibits a good linearity in agreement with the model [19]. The device shows a series resistance ( $R_s$ ) of  $18 \Omega \text{ cm}^2$ , a shunt resistance ( $R_{SH}$ ) of  $2.5 \text{ k}\Omega \text{ cm}^2$  with an ideality factor ( $n$ ) of 1.6. Low ideality factor

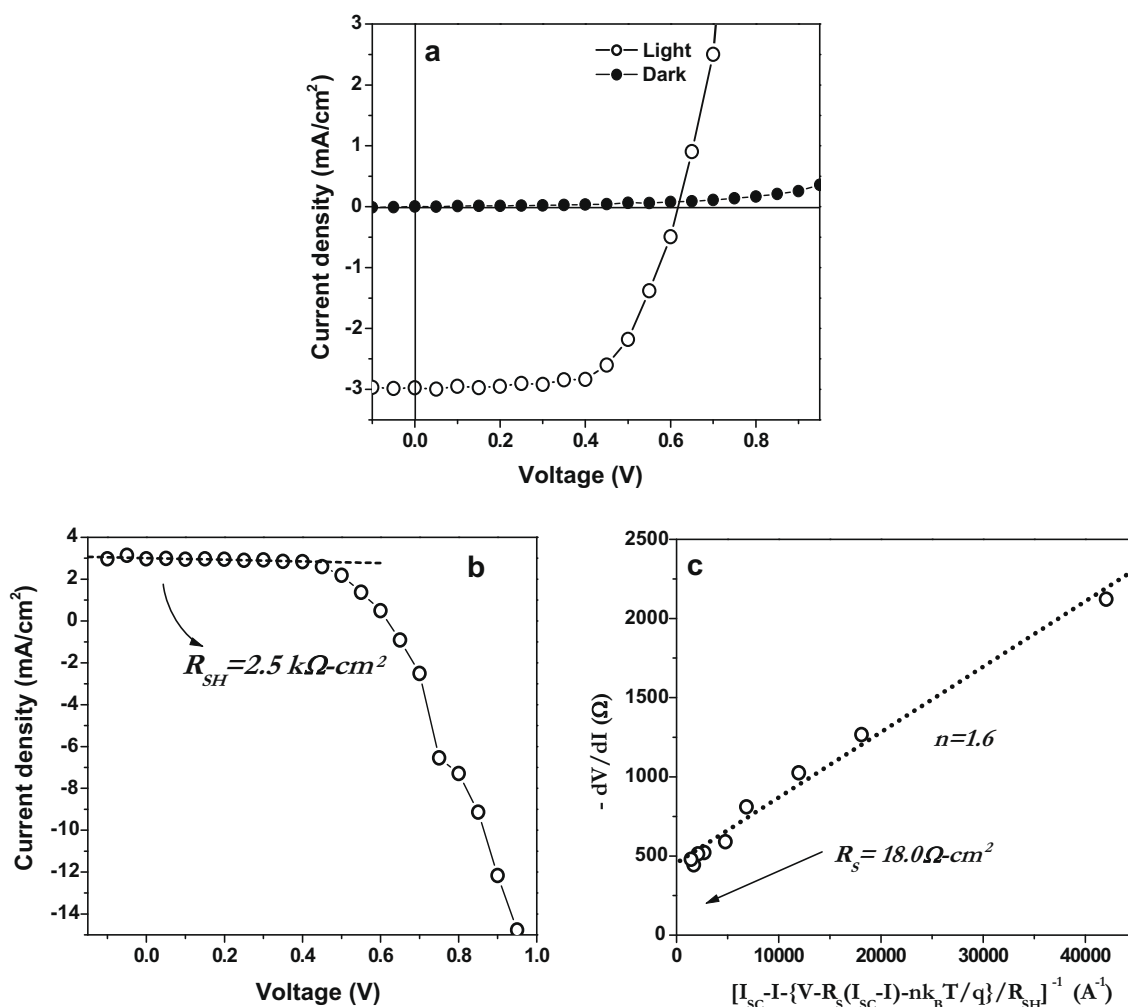


Fig. 3. (a)  $J$ - $V$  characteristics of ITO/PEDOT:PSS/pentacene (50 nm)/PTCDI- $C_8$  (40 nm)/AlQ<sub>3</sub> (10 nm)/Al devices under dark and 100  $\text{mW}/\text{cm}^2$  AM 1.5 simulated solar irradiation conditions, (b) the analysis of the  $J$ - $V$  curve under illumination for the calculation of the device shunt resistance ( $R_{SH}$ ), (c) the plot of  $(-dV/dI)$  as a function of  $\{I_{SC} - I - [V - R_s(I_{SC} - I) - nk_B T/q]/R_{SH}\}^{-1}$  for the estimation of device series resistance ( $R_s$ ) and ideality factor ( $n$ ).

(<2.0) confirms reduced recombination losses within the device. The saturation current ( $I_0$ ) and photocurrent ( $I_{ph}$ ) of the cell have been estimated to be 53.8 pA and 118.3  $\mu$ A, respectively.

To conclude, we have demonstrated the operation of an efficient solar cell based on pentacene/PTCDI-C<sub>8</sub> discrete heterojunctions. The absorption spectrum and the photocurrent action spectrum of the device confirm that PTCDI-C<sub>8</sub> can be a more suitable choice as an acceptor material than C<sub>60</sub> for photovoltaic applications. The most promising point with this donor/acceptor combination is that the device exhibits efficient light harvesting throughout the visible region of the solar spectrum. Further improvement of the device performance may be achieved by post- or pre-fabrication annealing treatments and by optimizing the active layers thickness.

### Acknowledgement

One of the authors (S. Karak) acknowledges CSIR, Govt. of India for awarding Junior Research Fellowship.

### References

- [1] C.W. Tang, Appl. Phys. Lett. 48 (1986) 183.
- [2] P. Peumans, A. Yakimov, S.R. Forrest, J. Appl. Phys. 93 (2003) 3693.
- [3] J.J.M. Halls, C.A. Walsh, N.C. Greenham, E.A. Marseglia, R.H. Friend, S.C. Moratti, A.B. Holmes, Nature (London) 376 (1995) 498.
- [4] P. Peumans, V. Bulovic, S.R. Forrest, Appl. Phys. Lett. 76 (2000) 2650.
- [5] S.E. Shaheen, C.J. Brabec, N.S. Sariciftci, F. Padinger, T. Fromherz, J.C. Hummelen, Appl. Phys. Lett. 78 (2001) 841.
- [6] P. Peumans, S.R. Forrest, Appl. Phys. Lett. 79 (2001) 126.
- [7] J.G. Xue, S. Uchida, B.P. Rand, S.R. Forrest, Appl. Phys. Lett. 85 (2004) 5757.
- [8] G. Li, V. Shrotriya, J.S. Huang, Y. Yao, T. Moriarty, K. Emery, Y. Yang, Nat. Mater. 4 (2005) 864.
- [9] Y. Terao, H. Sasabe, C. Adachi, Appl. Phys. Lett. 90 (2007) 103515.
- [10] S. Yoo, B. Domercq, B. Kippelen, Appl. Phys. Lett. 85 (2004) 5427.
- [11] A.K. Pandey, J.M. Nunzi, Appl. Phys. Lett. 89 (2006) 213506.
- [12] S.F. Nelson, Y.-Y. Lin, D.J. Gundlach, T.N. Jackson, Appl. Phys. Lett. 72 (1998) 1854.
- [13] O.D. Jurchescu, J. Baas, T.T.M. Palstra, Appl. Phys. Lett. 84 (2004) 3061.
- [14] Y.Y. Lin, D.J. Gundlach, S.F. Nelson, T.N. Jackson, IEEE Electron Dev. Lett. 18 (1997) 606.
- [15] A.C. Mayer, M.T. Lloyd, D.J. Herman, T.G. Kasen, G.G. Malliaras, Appl. Phys. Lett. 85 (2004) 6272.
- [16] D.M. Nanditha, M. Dissanayake, Ross A. Hatton, Richard J. Curry, S.R.P. Silva, Appl. Phys. Lett. 90 (2007) 113505.
- [17] I. Salzmann, S. Duhm, R. Opitz, Robert L. Johnson, Jürgen P. Rabe, Norbert Koch, J. Appl. Phys. 104 (2008) 114518.
- [18] P.R.L. Malenfant, C.D. Dimitrakopoulos, J.D. Gelorme, L.L. Kosbar, T.O. Graham, A. Curioni, W. Andreoni, Appl. Phys. Lett. 80 (2002) 2517.
- [19] K. Ishibashi, Y. Kimura, M. Niwano, J. Appl. Phys. 103 (2008) 094507.
- [20] Z.R. Hong, Z.H. Huang, X.T. Zeng, Chem. Phys. Lett. 425 (2006) 62.
- [21] J. Yang, T.-Q. Nguyen, Org. Electron. 8 (2007) 566.
- [22] C.D. Dimitrakopoulos, A.R. Brown, A. Pomp, J. Appl. Phys. 80 (1996) 2501.
- [23] T.N. Krauss, E. Barrena, Xue N. Zhang, Dimas G. de Oteyza, J. Major, V. Dehm, F. Wurthner, Leide P. Cavalcanti, H. Dosch, Langmuir 24 (2008) 12742.
- [24] S. Schiefer, M. Huth, A. Dobrinevski, B. Nickel, J. Am. Chem. Soc. 129 (2007) 10316.
- [25] D. Nabok, P. Puschnig, C. Ambrosch-Draxl, O. Werzer, R. Resel, Detlef-M. Smilgies, Phys. Rev. B 76 (2007) 235322.
- [26] D. Knipp, R.A. Street, A. Volkel, J. Ho, J. Appl. Phys. 93 (2003) 347.
- [27] A.K. Pandey, S.D. Seignon, J.M. Nunzi, Appl. Phys. Lett. 89 (2006) 113506.
- [28] A. Moliton, J.M. Nunzi, Polym. Int. 55 (2006) 583.

of the load capacitance are very strict. Also, the supply voltage needed to drive an organic circuit has to be considered. It has been estimated that a rectifier based on an organic diode would need to deliver a supply voltage of 10 V and a current of 100  $\mu$ A from an incoming RF signal at 13.56 MHz [9].

In order to exploit the opportunities associated with organic electronics, rectifier diodes based on organic semiconductors should be manufactured with technologies that offer high throughput and reliable processing. So far most of the work has concentrated on evaporated semiconductors and evaporated or sputtered metal electrodes patterned by shadow masking [8,9]. Photolithographic patterning has also been used to define the metal structures [10]. In some studies, spin casting has been used either to deposit the organic semiconductor layer or to deposit an intermediate layer, such as PEDOT:PSS (poly(3,4-ethylenedioxythiophene) poly(styrenesulfonate)), on top of one of the electrodes [7–9]. Spin casting, though it is based on solution processing, cannot be considered a high throughput process. High throughput processes, such as coating and printing technologies, need to be demonstrated to manufacture organic rectifier diodes on a scale that can be of industrial interest.

In this letter we report an organic diode rectifier that delivers excellent DC output at AC input frequencies approaching the RFID HF standard and was made using only mass printing based patterning methods. No shadow mask, ink jet, photolithography or other fine patterning processes were used. The semiconductor layer was sandwiched between copper and silver electrodes and diodes with different semiconductor thicknesses were characterized with respect to their  $J$ - $V$  and rectifying properties. Contrary to most of the previous studies where the devices have been fabricated either in vacuum or inert atmosphere, the processing and characterization was performed in ambient laboratory conditions. This was enabled by using PTAA (poly(triarylamine)) as the semiconducting layer. PTAA is a well-known amorphous conjugated polymer whose electrical properties have been shown not to degrade in air [12,13].

The diodes were fabricated on metallized polyester (poly(ethylene terephthalate), PET) film, Melinex ST506 from Dupont Teijin Films, using printing processes that are compatible with roll-to-roll fabrication. A 100 nm copper layer was sputtered onto the PET film. The copper was subsequently patterned using a wet etching process in which the etch resist, UV-curable XV1000-2 from Sun Chemical, was printed using rotary screen printing. After etching, the samples were cleaned by rinsing with de-ionized water and 2-propanol. The diodes were fabricated in a dust-free environment (non-certified but close to ISO 14644-1 class 5) at room temperature and RH of 40–50.

The patterned semiconductor layer, poly(triarylamine) PTAA, was single printed with a laboratory-scale automatic gravure printing press, Labrater Automatic from Norbert Schläfli Maschinen, and cured at 115 °C for 5 min. Although the press is sheet-fed, it imitates roll-to-roll printing closely. The anode material, silver ink PM460A from Acheson Industries Ltd., was also deposited with the gravure press and cured at 115 °C for 5 min. Orthogonal

solvents were chosen to avoid interfacial dissolving or mixing of the layers. The resistance of the printed silver lines was measured to be 0.3  $\Omega/\square$ . Diodes with three different PTAA thicknesses were fabricated. Film thicknesses were measured with a Veeco diCaliber Scanning Probe Microscope in the non-contact mode.

The DC  $J$ - $V$  characteristics of the diodes were measured using a Keithley 236. The DC output signals were measured for AC supply signals of zero-to-peak amplitude of 10 V. The diode capacitance was measured with HP4192A, and rectification properties with an SRS DS345 30 MHz function generator and Tektronix TDS 3014B oscilloscope. A 47 nF discrete capacitor was used as the load capacitor. The oscilloscope had a 1 M $\Omega$  || 16 pF input impedance. The internal load of the oscilloscope was used as the load resistor. The circuit performance was confirmed by testing a few different capacitor and resistor values. All measurements were made in laboratory conditions in dark.

Thicknesses measured by AFM for the PTAA layers were 400 nm, 600 nm and 1100 nm. These values were confirmed by capacitance–frequency measurements. As the frequency is increased, the initially high capacitance decreases. At low frequencies, the interface states follow the alternating current signal while at high frequencies they cannot follow the signal. At this region, the capacitance is constant indicating that the semiconductor is fully depleted and the capacitance is the bulk capacitance of the semiconductor. Using the relative permittivity of the semiconductor ( $\epsilon_r = 3$ ) and the active area 4 mm<sup>2</sup>, the capacitance values of 90, 160 and 220 pF translate into thicknesses of 1200 nm, 700 nm and 500 nm, respectively. Although the capacitance measurements gave systematically slightly higher values for the film thicknesses compared to the AFM measurements, the thickness values are in the same range. The difference can be attributed to a thickness variation between the edge of the PTAA (measured thickness by AFM) and the centre (diode area). Also the relative permittivity value is only an estimate for PTAA semiconductors.

In the Schottky diodes reported here, a printed silver layer acted as the anode and a patterned copper layer as the cathode. The forward current in the diodes depends on the quality of the ohmic contact, and thus the energy barrier between the silver and the highest occupied molecular orbital (HOMO) of the semiconductor. The reverse current depends on the Schottky barrier height between the copper and the highest occupied molecular orbital of the semiconductor. The current in the devices is carried almost exclusively by holes.

In a vertical rectifier diode structure, the semiconductor thickness needs to be thick enough to sustain the voltage applied across the diode but thin enough for charge carriers to move in the semiconducting material at high frequencies. The printing process and the surface properties of the substrate pose restrictions on how thin a layer can be printed. In gravure printing, the resulting film thickness is determined by the printing cylinder cup depth and line density. The rheology of the ink, surface energies of the ink and the substrate, printing pressure and speed also affect the ink transfer from the cup to the substrate. In the diodes reported here, the yield of working devices was im-

proved when the semiconductor layer was double printed with shallow printing cups compared to single printed with deep cups. However, by optimizing the substrate smoothness and ink properties the semiconductor does not need to be double printed.

The log  $J$ - $V$  characteristics are depicted in Fig. 1. At 5 V, the samples showed a current density of  $2000 \mu\text{A}/\text{cm}^2$ ,  $800 \mu\text{A}/\text{cm}^2$  and  $280 \mu\text{A}/\text{cm}^2$  for semiconductor thicknesses of 500 nm, 700 nm and 1200 nm, respectively. In the reverse bias regime, the currents slowly increased for the two diodes with thinner semiconductors, with the current density values at  $-5 \text{ V}$  of  $60 \text{ nA}/\text{cm}^2$  and  $30 \text{ nA}/\text{cm}^2$ . In the thickest diode, the current density at  $-5 \text{ V}$  is  $1\text{--}3 \text{ nA}$  or lower; this is close to the detection limit of the measurement unit. The rectification ratio for all diodes was over 10,000. The diode characteristics showed no significant degradation when the performance was followed for 4 weeks after fabrication. During this period, the diodes were stored and characterized in ambient laboratory conditions.

Rectified output voltages at frequencies up to 10 MHz for diodes with three different PTAA thicknesses are shown in Fig. 2. In these measurements, the input AC zero-to-peak signal was 10 V. The output voltages were constant at approximately 7.4 V, 6.6 V and 5.4 V for PTAA thicknesses of 500 nm, 700 nm and 1200 nm, respectively, for frequencies up to 10,000 Hz and decayed slowly at higher frequencies. At 1 MHz, the output voltage for the thinnest diode was approximately 5.4 V and at 10 MHz approximately 2.7 V. When the AC zero-to-peak signal was increased to 25 V, the thinnest diode gave a DC voltage of 18 V at 1 MHz. This yields a maximum field over the diode of  $0.87 \text{ MV}/\text{cm}$ . At AC voltages larger than 25 V, the diode started to degrade and the output DC voltage decreased. At frequencies over 1 MHz the impedance mismatch of the circuit and the available measurement instruments caused a decrease in the effective input voltage, which lead to a lowering of the rectifier output voltage in Fig. 2; in other words, optimized input circuitry would be expected to yield better rectification performance.

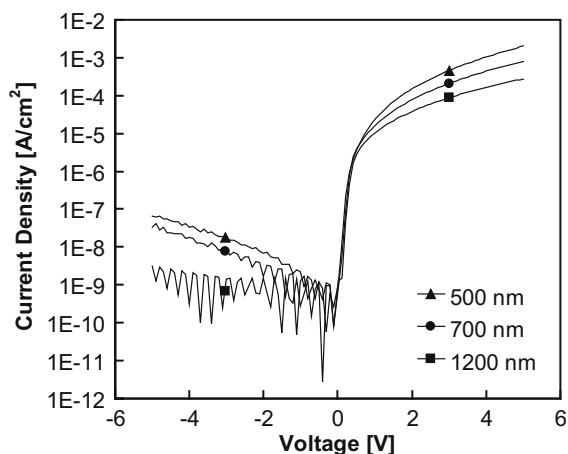


Fig. 1.  $J$ - $V$  characteristics of printed diodes with different PTAA thicknesses.

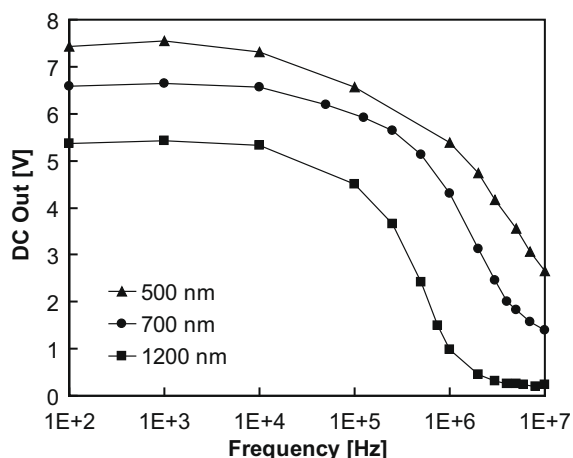


Fig. 2. DC output voltage for 10 V AC input signal as a function of frequency in printed PTAA diodes.

The measured AC response for a printed PTAA diode in a configuration where the diode was connected to a load capacitor ( $47 \text{ nF}$ ) and load resistor ( $1 \text{ M}\Omega$ ) is shown in Fig. 3. The input signal was provided by a function generator. At 1 MHz, the diode was able to rectify an input signal with 10 V zero-to-peak amplitude into a 5.4 V stable DC current. To power an organic circuit, the rectified DC voltage should be as high as possible and the voltage drop across the diode should be as small as possible. Since the organic layer is already relatively thin (500 nm) for a mass printed layer on an inherently non-flat substrate, the challenges in forming thinner films and thus achieving higher frequency rectification are considerable. However, the result achieved here shows the potential of completely printed diodes at MHz frequencies.

To operate as high efficiency DC converters at frequencies required for HF RFID tags, the diode characteristics still need to be improved. This can be done by reducing the diode area, improving the ohmic contact of the diode or

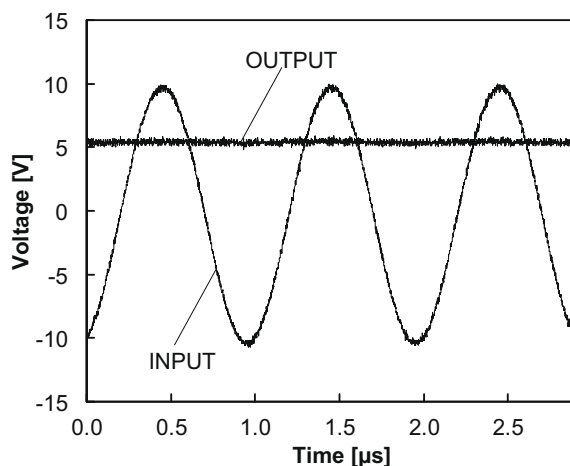


Fig. 3. Rectifying DC output signal at 1 MHz with an input AC signal of 10 V for a diode with PTAA thickness of 500 nm.

modifying the mobility and thickness of the semiconductor [14]. The active diode area, 4 mm<sup>2</sup>, is rather large, which resulted in a high capacitance over the diode. Secondly, the contact between silver and PTAA is most probably not completely ohmic, resulting in injection limited rather than space charge limited current. The contact could be improved by choosing an anode with a lower Schottky barrier with the HOMO level of PTAA. Such a gravure printable anode could be for example modified PEDOT–PSS. However, there are concerns related to the stability and high acidity of PEDOT–PSS which can affect the diode performance [15]. The third option to improve the rectification properties of the diode is to improve the mobility of the semiconductor or reduce the printed thickness. Although materials with higher mobilities are being developed, for printable semiconductors it is also of importance that the materials can be formulated to an ink that has the right properties for mass printing. This poses some limitations in terms of suitable solvents and the rheological properties of the ink. Additionally, the printing process will most likely introduce inhomogeneities in the organic film thickness. Here, the surface roughness of the underlying patterned metal (and also the polyester substrate) will also have an effect.

With regard to the semiconductor thickness, rectifying properties at high frequency will improve if the thickness is reduced, as shown in equation [8]:

$$f_{\max} = \frac{\mu(V_{AC} - V_{DC})}{L^2} \quad (1)$$

where  $V_{AC}$  = supply AC voltage amplitude,  $V_{DC}$  = output DC voltage,  $\mu$  = carrier mobility, and  $L$  = film thickness, yields the maximum operating frequency ( $f_{\max}$ ) of the diode. The frequency is inversely proportional to the square of the semiconductor thickness. Extrapolating from Fig. 2 that a diode with a semiconductor thickness of 400 nm gives an initial output DC voltage of 8 V, a diode with this thickness would operate at a frequency in the range of 13.56 MHz with an output DC voltage of 4.5 V. This is the frequency needed for RFID applications. Here, it has to be pointed out that when the thickness is reduced also the reverse current of the device will increase, as depicted in Fig. 1. This will worsen the rectification ratio. However, the increase in reverse current may be relatively small when the diode is operated at high frequencies.

In conclusion, a roll-to-roll compatible mass printing process was demonstrated for the fabrication of organic diodes for use in a high frequency rectifier. A PTAA diode, manufactured and measured in air, showed rectification up to 10 MHz with an active layer thickness of 500 nm. By optimizing the device geometry, electrodes, printing parameters and semiconductor properties, the diodes presented here can be improved to rectify at frequencies required for HF RFID applications. The diodes also showed a stable  $J$ – $V$  performance under ambient room conditions. This study thus shows the possibility of RF-compatible organic rectifier diodes that can be manufactured with roll-to-roll printing processes.

## Acknowledgements

We would like to express our gratitude to Juhani Virtanen from UPM Raflatac as well as Prof. Ronald Österbacka and Dr. Himadri Majumdar from Åbo Akademi University for AFM measurements and fruitful discussions.

## References

- [1] S.R. Forrest, *Nature* 428 (2004) 911.
- [2] T. Mäkelä, S. Jussila, H. Kosonen, T.G. Bäcklund, H.G.O. Sandberg, H. Stubb, *Synth. Met.* 153 (2005) 285.
- [3] A. Maaninen, M. Tuomikoski, L. Kivimäki, T. Kololuoma, M. Välimäki, M. Leinonen, M. Känsäkoski, *Proc. SPIE* 5956 (2005) 595604.
- [4] D. Zielke, A.C. Hübler, U. Hahn, N. Brandt, M. Bartzsch, U. Fügmann, T. Fischer, J. Veres, S. Ogier, *Appl. Phys. Lett.* 87 (2005) 123508.
- [5] A.C. Hübler, F. Doetz, H. Kempa, H.E. Katz, M. Bartzsch, N. Brandt, I. Hennig, U. Fügmann, S. Vaidyanathan, J. Granstrom, S. Liu, A. Sydorenko, T. Zillger, G. Schmidt, K. Preissler, E. Reichmanis, P. Eckerle, F. Richter, T. Fischer, U. Hahn, *Org. Electron.* 8 (2007) 480.
- [6] S.M. Sze, K.K. Ng, *Physics of Semiconductor Devices*, third ed., John Wiley and Sons, New Jersey, 2007.
- [7] L.S. Roman, M. Berggren, O. Inganäs, *Appl. Phys. Lett.* 75 (1999) 3557.
- [8] S. Steudel, K. Myny, V. Arkhipov, C. Deibel, S. de Vusser, J. Genoe, P. Heremans, *Nat. Mater.* 4 (2005) 597.
- [9] S. Steudel, S.D. Vusser, K. Myny, M. Lenes, J. Genoe, P. Heremans, *J. Appl. Phys.* 99 (2006) 114519.
- [10] Y. Ai, S. Gowrisanker, H. Jia, I. Trachtenberg, E. Vogel, R.M. Wallace, B.E. Gnade, R. Barnett, H. Stiegler, H. Edwards, *Appl. Phys. Lett.* 90 (2007) 262105.
- [11] K. Myny, S. Steudel, P. Vicca, J. Genoe, P. Heremans, *Appl. Phys. Lett.* 93 (2008) 093305.
- [12] J. Veres, S. Ogier, S. Leeming, B. Brown, D. Cupertino, *Mater. Res. Soc. Symp. Proc.* 708 (2002) BB8.7.1.
- [13] X.F. Lu, L.A. Majewski, A.M. Song, *Org. Electr.* 9 (2008) 473.
- [14] C.-Y. Huang, S.-Y. Lin, S.-S. Cheng, S.-T. Chou, C.-Y. Yang, T.-M. Ou, M.-C. Wu, I.-M. Chan, Y.-J. Chan, *J. Vac. Sci. Technol.*, B 25 (2007) 43.
- [15] K. Kawano, R. Pacios, D. Poplavskyy, J. Nelson, D.D.C. Bradley, J.R. Durrant, *Sol. Energy Mater. Sol. Cells* 90 (2006) 3520.

Organic photovoltaic devices utilizing phosphorescent materials have previously been demonstrated, either by employing directly a phosphorescent small molecular or polymer layer [11–14], or by inducing phosphorescence in a fluorescent host via a proximity effect of a heavy-metal-atom containing phosphor dopant [15]. However, because phosphorescent organic semiconductors are typically characterized by low mobilities and absorption that do not overlap well with the solar spectrum [13], their use as active, absorbing layers may be difficult to realize. One notable exception [2] is the acceptor  $C_{60}$ , which has a high charge carrier mobility of  $5 \times 10^{-2} \text{ cm}^2/\text{Vs}$ , and  $L_D \approx 40 \text{ nm}$  owing to its near unity ISC efficiency [16], albeit with an absorption spectrum still focused in the blue wavelength range.

Here, we demonstrate enhanced photocurrent from a fluorescent material via the process of sensitized phosphorescence. We employ a host:guest system where a fluorescent host material continues to be used for light absorption as well as for charge and exciton transport. The guest serves only to convert initially generated host singlet excitons into triplet excitons, as its low concentration prevents efficient transport and absorption. An advantage of this approach to create triplet excitons on a fluorescent host stems from the fact that due to the lack of an efficient triplet decay pathway, triplet states in fluorescent materials [17,18] generally possess significantly longer lifetimes compared with phosphors containing heavy-metal atoms [19] (e.g. ms compared to  $\mu\text{s}$ ). To allow for the above processes to occur, the host:guest system needs to obey the following criteria: First, that the lowest excited singlet state of the dopant is lower than that of the host material ( $S_{1,\text{dopant}} < S_{1,\text{host}}$ ), and there is sufficient overlap between the emission of the host and absorption of the guest to allow for efficient singlet energy transfer (SET). Second, that the triplet energy of the dopant molecule is greater than that of the host ( $T_{1,\text{dopant}} > T_{1,\text{host}}$ ) for efficient triplet energy transfer (TET) to occur. In addition, care should be taken to allow for efficient charge transport of photogenerated carriers through the host material. Therefore, an additional criterion for a donor material is that the highest occupied molecular orbital (HOMO) of the dopant is greater than that of the host to prevent holes from being trapped on the guest material which would ultimately reduce photocurrent. In the case of an acceptor material, care should be taken that the lowest unoccupied molecular orbital of the dopant is lower than that of the host material to prevent electron trapping.

To demonstrate that the process of sensitized phosphorescence can be used to increase the photocurrent of an absorbing layer, we use as an example the phenyl-substituted poly(*p*-phenylene vinylene) (PPV) donor polymer Super Yellow (SY) doped with the phosphorescent molecule platinum octaethylporphyrin (PtOEP). Furthermore, we investigate the effect of doping with the Pt-free analogue octaethylporphyrin (OEP) to demonstrate the opposite effect: a dopant that allows SET but not TET is expected to actually reduce the photocurrent. Fig. 1a shows the absorption (Shimadzu UV-1601PC) and emission (Shimadzu RF-5301PC) of a pure SY film as well as films doped with PtOEP, whereas Fig. 1b shows SY films

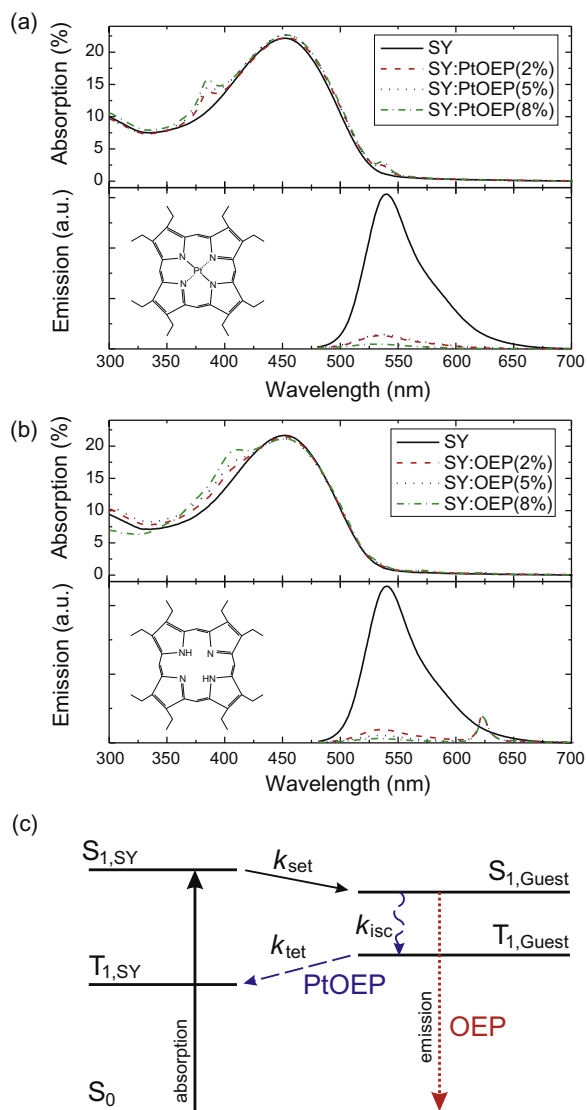


**Fig. 1.** (a) Absorption (top panel) and photoluminescence (PL) (bottom panel) of 15 nm thick SY and SY:PtOEP thin films with various compositions. The molecular structure of PtOEP is shown as an inset to the bottom panel. (b) Absorption (top panel) and PL (bottom panel) of 15 nm thick SY and SY:OEP thin films with various compositions. The molecular structure of OEP is shown as an inset to the bottom panel. (c) The formation pathways of excitons generated in doped SY. Following absorption in SY to excite a molecule from the ground state ( $S_0$ ) to the first excited singlet state ( $S_{1,\text{SY}}$ ) there is singlet energy transfer to the guest at a rate  $k_{\text{set}}$ . For the guest PtOEP (blue dashed arrows), intersystem crossing converts singlet excitons to triplet excitons from  $S_{1,\text{Guest}}$  to  $T_{1,\text{Guest}}$  at a rate  $k_{\text{isc}}$ . Finally, the lower triplet energy of SY ( $T_{1,\text{SY}}$ ) quenches the PtOEP triplets with a rate  $k_{\text{tet}}$ . In the case of an OEP guest (red dotted arrow), the lack of an efficient ISC pathway results in singlet emission.

doped with OEP. The absorption shoulders of PtOEP and OEP are present in the doped films, at wavelengths of  $\lambda = 385$  and  $535 \text{ nm}$  for PtOEP and at  $\lambda = 410 \text{ nm}$  for OEP, and the intensity of these peaks increases with doping concentration. The SY emission (excitation at  $\lambda = 385 \text{ nm}$ ), with its peak at  $\lambda = 540 \text{ nm}$ , is quenched rapidly as a result of the introduction of either dopant. Significantly, PtOEP



phosphorescence [20] at  $\lambda = 650$  nm is not present, whereas OEP fluorescence at  $\lambda = 625$  nm is observed. This suggests the excitonic pathways illustrated schematically in Fig. 1c, where for the case of PtOEP there is efficient SET from SY to PtOEP molecules, followed by ISC, and finally TET back to SY owing to the lower triplet energy of SY ( $\approx 1.6$  eV) compared to that of PtOEP ( $\approx 1.9$  eV), a phenomenon which has been shown previously for PtOEP in PPV hosts [21]. In the case of OEP, SET onto the OEP dopant occurs, but since OEP is a fluorescent molecule, ISC efficiency is very low and singlet OEP emission is observed.

For the demonstration of sensitized phosphorescence in a solar cell, we use the following device structure: indium–tin–oxide (ITO)/poly(3,4-ethylenedioxythiophene):poly(styrene sulfonate) (PEDOT) (30 nm)/SY (15 nm)/C<sub>60</sub> (30 nm)/bathocuproine (BCP) (8 nm)/Al (80 nm). Here, ITO/PEDOT serves as the anode, SY as the donor layer, C<sub>60</sub> as the acceptor layer, BCP as an exciton blocking layer, and Al as the cathode. The reason for employing only a 15 nm thick SY layer is because the use of thicker layers led to a rapidly increasing series resistance for the device, reducing the fill factor (FF) as well as, and even more significantly, the short circuit current density  $J_{SC}$ . The ITO coated glass substrates were solvent cleaned followed by UV/O<sub>3</sub> treatment for 10 min. The PEDOT (H.C. Starck, Baytron P VPAI4083) solution was spincoated at 3000 rpm for 60 s, followed by baking at 120 °C. The SY was dissolved in toluene at a concentration of 1.7 mg/ml, with doping of PtOEP or OEP by weight, followed by spincoating at 2000 rpm for 60 s. The C<sub>60</sub>, BCP, and Al layers were then deposited in an ultrahigh vacuum chamber (base pressure  $< 5 \times 10^{-9}$  Torr). The device area was measured with an optical microscope, with an average area of 3.3 mm<sup>2</sup>. The current density vs. voltage ( $J$ - $V$ ) characteristics were measured using an Agilent 4156C parameter analyzer with illumination from a LOT-Oriel 1000 W Xe arc lamp fitted with

AM 1.5D filters. Calibration was performed by a KG3 band pass filter and a calibrated Si detector.

The schematic energy diagram of this device is shown in the inset to Fig. 2, where we also show the  $J$ - $V$  characteristics of devices with undoped SY, SY:PtOEP(5%) and SY:OEP(5%) donor layers in the dark and under 100 mW/cm<sup>2</sup> AM1.5D simulated solar illumination. The undoped SY-based device has  $J_{SC} = 3.2$  mA/cm<sup>2</sup>, open circuit voltage  $V_{OC} = 0.86$  V, FF = 0.54, and power conversion efficiency  $\eta_p = 1.5\%$ . The doped devices have the same value of  $V_{OC}$ , which indicates that the host SY acts as the charge conducting material, a property which is expected for films containing a low concentration of dopant ( $< 10\%$ ) and also owing to the shallower HOMO of SY (5.2 eV) with respect to that of either PtOEP (5.3 eV) or OEP (5.5 eV). The PtOEP-doped device has a dark current almost identical to that of the undoped device, and  $J_{SC} = 3.5$  mA/cm<sup>2</sup>, FF = 0.52, and  $\eta_p = 1.6\%$  under illumination. In this case, the photocurrent is increased by almost 10%, whereas the FF is slightly decreased, which could indicate that the presence of the PtOEP dopant molecule interrupts charge carrier transport in the SY matrix, making the collection of photogenerated charges more difficult. For the case of 5% OEP doping,  $J_{SC} = 2.8$  mA/cm<sup>2</sup>, FF = 0.41, and  $\eta_p = 1\%$ . Here, the OEP dopant increases the series resistance of the cell, as reflected in the lower dark current at  $V \geq 0.7$  V as compared to the other devices. This has the effect of reducing the FF, but does not significantly impact  $J_{SC}$ , as an equally reduced photocurrent can be observed even for negative voltages, where photogenerated carriers are efficiently extracted by the applied field.

To understand better the influence of the dopant and whether sensitized phosphorescence plays a role in the device operation, we show in Fig. 3 the dependence of  $J_{SC}$  on dopant concentration for either PtOEP or OEP doping. It should be noted that the roughness and therefore interfacial area of the donor–acceptor heterojunction does not increase with doping concentration, as measurements by

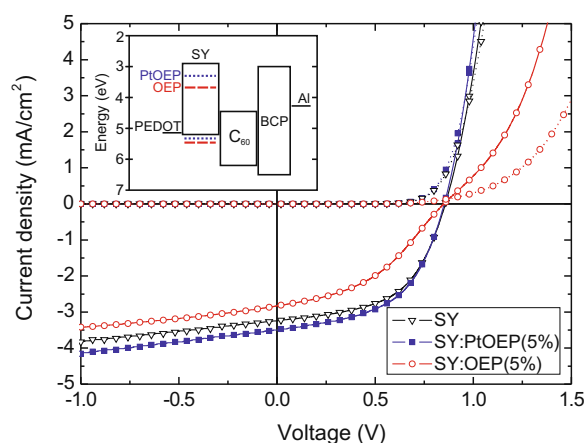


**Fig. 2.** Current density vs. voltage characteristics in the dark (dotted lines) and under 100 mW/cm<sup>2</sup> AM1.5D solar illumination (solid lines) with the following device structure: ITO/PEDOT (30 nm)/donor layer (15 nm)/C<sub>60</sub> (30 nm)/BCP (8 nm)/Al (80 nm). The donor layer is either pure SY (open black triangles), SY:PtOEP(5%) (filled blue squares), or SY:OEP(5%) (open red circles). Inset: schematic energy diagram of the device structure.

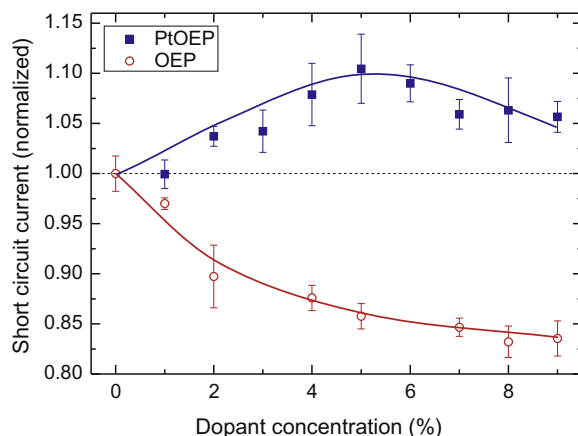


**Fig. 3.** The normalized short circuit current density vs. dopant concentration for the device structure of Fig. 2 with either PtOEP (filled squares) or OEP (open circles) as the dopant. The data points are representative of the average value of six devices while the error bar indicates the standard deviation. The lines serve as guides to the eye.

atomic force microscopy of doped (8%) and undoped SY films have smooth surface morphologies with root mean square roughnesses of 0.6 nm (data not shown). With an increase in PtOEP concentration,  $J_{SC}$  increases by approximately 10%, peaking at a dopant concentration of 5%, beyond which the increase in  $J_{SC}$  is reduced. In contrast, the addition of OEP to the SY matrix always results in a decrease of  $J_{SC}$ , which appears to saturate at a reduction of approximately 15–18%. This can be understood by considering again the results of Fig. 1, where SY singlets are immediately quenched by the addition of small amounts of the dopant. Once a sufficient doping level has been reached in order to quench a large percentage of the SY excitons, increasing the dopant concentration only suppresses further the transport of charges and/or triplet excitons in the SY layer, resulting in a decreased performance and therefore the presence of an optimal PtOEP concentration. Indeed, the fact that both dopants efficiently quench SY excitons but only PtOEP doping leads to an enhancement of  $J_{SC}$  provides significant evidence that excitons are returned to SY in that case, whereas with OEP doping they are lost.

As further evidence of the sensitized phosphorescence mechanism, we consider the external quantum efficiency ( $\eta_{EQE}$ ) spectra of doped and undoped devices, as shown in Fig. 4a. To highlight the relative contributions from SY and  $C_{60}$ , we also show the calculated absorption efficiency ( $\eta_A$ ) spectra for SY and  $C_{60}$  (using a transfer-matrix based calculation). The SY contribution is centered at  $\lambda = 455$  nm, whereas  $C_{60}$  is responsible for the shoulder at  $\lambda = 435$  nm and the tail extending to  $\lambda = 650$  nm. The reduction of  $\eta_{EQE}$  at  $\lambda \leq 375$  nm is due to reflection and absorption from the glass/ITO substrate, resulting in a “false peak” in the measured  $\eta_{EQE}$  at  $\lambda = 375$  nm. The  $\eta_{EQE}$  spectrum of the cell with a pure SY donor layer shows distinct features of both SY and  $C_{60}$ . From  $\eta_A$ , it is clear that there is a larger contribution to the photocurrent originating from the  $C_{60}$  acceptor layer compared to that of SY,

which contributes approximately 15% of the total current, and which is consistent with the fact that OEP doping results in a reduction of  $J_{SC}$  by approximately the same amount (cf. Fig. 3). The calculated  $\eta_{EQE}$  spectrum for the undoped device closely fits that of the measured data, and yields an estimate of  $L_D = 4 \pm 1$  nm, in excellent agreement to that of other PPV derivatives [22]. For the device with a SY:OEP(5%) donor layer, the contribution from SY is barely visible, functioning instead almost completely on  $C_{60}$ . Indeed, spectral fitting for this device requires  $L_D \approx 1$  nm, indicating that only SY excitons formed at the interface with  $C_{60}$  are able to contribute. This is consistent with the fact that OEP quenches most SY excitons and confines them to the OEP dopant (where emission is observed, cf. Fig. 1b), eliminating the opportunity to dissociate at the donor-acceptor interface.

The  $\eta_{EQE}$  spectrum of the SY:PtOEP(5%) shows instead an enhancement of the SY signal, peaking at  $\lambda = 450$  nm to  $\eta_{EQE} = 45\%$ . Here, SY contributes approximately 21% of the total current, an increase of about 40% compared to the undoped SY donor layer. In this case,  $L_D$  of SY triplet excitons is longer than that of singlet excitons, and therefore a larger percentage of photons absorbed in the SY layer are able to contribute to photocurrent. We are again able to obtain an excellent spectral fit, and this provides an estimate of  $L_D = 9 \pm 1$  nm, significantly greater than that of the pure SY film. Indeed, the reported fluorescence lifetime of SY is 400 ps [23], whereas the triplet lifetime has been estimated from delayed fluorescence to be 5.6 ms [17], and therefore an increase in  $L_D$  could be expected. If we take the difference between  $\eta_{EQE}$  of doped and undoped devices, we obtain the curves as shown in Fig. 4b. Here the difference between the PtOEP-doped and pure SY devices is a result of increased signal from SY, as well as small contributions from PtOEP at  $\lambda = 385$  and 535 nm. These contributions from PtOEP provide further evidence of the triplet transfer process, as direct absorption of PtOEP generates triplet excitons which

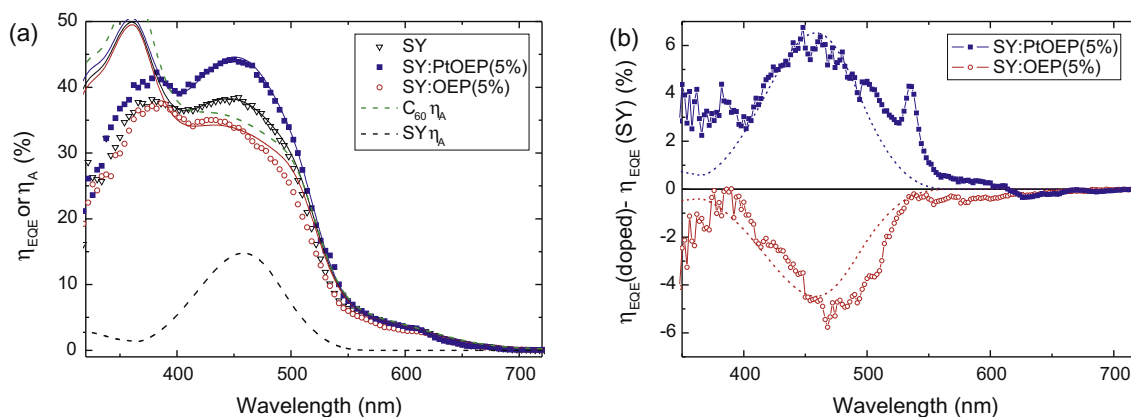


**Fig. 4.** (a) Measured external quantum efficiency ( $\eta_{EQE}$ ) spectra for the device structures of Fig. 2 with donor layers of pure SY (open black triangles), SY:PtOEP(5%) (filled blue squares), or SY:OEP(5%) (open red circles). The solid lines show the calculated  $\eta_{EQE}$  spectra, with colors corresponding to that of the data points. The dashed lines show the calculated absorption efficiencies ( $\eta_A$ ) of the SY (black) and  $C_{60}$  (green) layers within the device structure. (b) The difference in  $\eta_{EQE}$  between devices with doped and pure SY donor layers. The blue line with solid squares shows the device with PtOEP doping, and the red line with open circles shows the device with OEP as a dopant. The dotted lines represent the differences in the fits shown in (a). (For interpretation of the references to color in this figure legend, the reader is referred to the web version of this article.)

transfer to SY and are transported to the donor–acceptor interface, contributing to photocurrent. By contrast, the difference between the OEP-doped device and pure SY is negative and corresponds to a loss in the SY spectral response. Also in this spectrum, no additional contribution from the OEP dopant is observed, as would be expected for these immobile singlet excitons.

In conclusion, we have experimentally demonstrated an organic solar cell with a donor layer enhanced by the process of sensitized phosphorescence. By converting optically excited singlet excitons to triplet excitons efficiently,  $L_D$  was more than doubled, from  $4 \pm 1$  to  $9 \pm 1$  nm, which in turn increased the signal from this layer by 40%. In contrast, a similar dopant which lacks the ability to convert host singlet excitons to triplet excitons was shown to reduce the photocurrent from the host material. The ability to increase  $L_D$ , ideally toward distances equal to the absorption length in organic materials will allow simplified bilayer architectures to possess efficiencies approaching that of BHJ devices, or will at least relax the restrictions placed on the phase separation of blends. The design rules and methodology demonstrated here should lead to the development of new materials with suitable mobility and absorption spectra in order to optimize sensitized phosphorescent organic solar cells.

#### Acknowledgements

The authors would like to thank A. Hadipour and A. Kadashchuk for helpful discussions. One of the authors (S.S.) would like to acknowledge the FWO-Vlaanderen for financial support.

#### References

- [1] G. Li, V. Shrotriya, J.S. Huang, Y. Yao, T. Moriarty, K. Emery, Y. Yang, *Nat. Mater.* 4 (2005) 864.
- [2] B.P. Rand, J. Genoe, P. Heremans, J. Poortmans, *Prog. Photovolt.* 15 (2007) 659.
- [3] J.Y. Kim, K. Lee, N.E. Coates, D. Moses, T.-Q. Nguyen, M. Dante, A.J. Heeger, *Science* 317 (2007) 222.
- [4] J. Peet, J.Y. Kim, N.E. Coates, W.L. Ma, D. Moses, A.J. Heeger, G.C. Bazan, *Nat. Mater.* 6 (2007) 497.
- [5] B.C. Thompson, J.M.J. Fréchet, *Angew. Chem., Int. Ed.* 47 (2008) 58.
- [6] A. Hadipour, B. de Boer, P.W.M. Blom, *Adv. Funct. Mater.* 18 (2008) 169.
- [7] P. Peumans, A. Yakimov, S.R. Forrest, *J. Appl. Phys.* 93 (2003) 3693.
- [8] J.J.M. Halls, C.A. Walsh, N.C. Greenham, E.A. Marseglia, R.H. Friend, S.C. Moratti, A.B. Holmes, *Nature* 376 (1995) 498.
- [9] G. Yu, J. Gao, J.C. Hummelen, F. Wudl, A.J. Heeger, *Science* 270 (1995) 1789.
- [10] B.P. Rand, D.P. Burk, S.R. Forrest, *Phys. Rev. B* 75 (2007) 115327.
- [11] F.Q. Guo, Y.G. Kim, J.R. Reynolds, K.S. Schanze, *Chem. Commun.* 17 (2006) 1887.
- [12] A. Kohler, H.F. Wittmann, R.H. Friend, M.S. Khan, J. Lewis, *Synth. Metal* 77 (1996) 147.
- [13] Y. Shao, Y. Yang, *Adv. Mater.* 17 (2005) 2841.
- [14] M. Arif, K. Yang, L. Li, P. Yu, S. Guha, S. Gangopadhyay, M. Förster, U. Scherf, *Appl. Phys. Lett.* 94 (2009) 063307.
- [15] Z.H. Xu, B. Hu, J. Howe, *J. Appl. Phys.* 103 (2008) 043909.
- [16] M. Terazima, N. Hirota, H. Shinohara, Y. Saito, *J. Phys. Chem.* 95 (1991) 9080.
- [17] A. Gerhard, H. Bässler, *J. Chem. Phys.* 117 (2002) 7350.
- [18] D. Hertel, S. Setayesh, H. Nothofer, U. Scherf, K. Müllen, H. Bässler, *Adv. Mater.* 13 (2001) 65.
- [19] M. Thompson, *MRS Bull.* 32 (2007) 694.
- [20] M.A. Baldo, D.F. O'Brien, Y. You, A. Shoustikov, S. Sibley, M.E. Thompson, S.R. Forrest, *Nature* 395 (1998) 151.
- [21] F. Laquai, C. Im, A. Kadashchuk, H. Bässler, *Chem. Phys. Lett.* 375 (2003) 286.
- [22] D.E. Markov, E. Amsterdam, P.W.M. Blom, A.B. Sieval, J.C. Hummelen, *J. Phys. Chem. A* 109 (2005) 5266.
- [23] C. Im, J.M. Lupton, P. Schouwink, S. Heun, H. Becker, H. Bässler, *J. Chem. Phys.* 117 (2002) 1395.

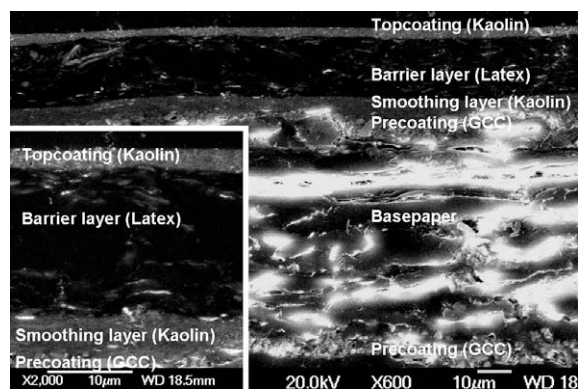


**Fig. 1.** Cross-section scanning electron microscope (SEM) image showing the layer structure of the substrate. The insert shows a higher magnification.

published by several companies and research groups. The most common carrier surface is still plastic film, but paper-based substrates are gaining increasing attention. E-Ink Corp. has demonstrated an electrophoretic display with an ink-on-paper-like appearance and contrast [8]. However, the display was constructed on metal foil, instead of on paper. Linköping University and Acreo AB have presented a fully functional all-polymer electrochromic display on polyethylene-coated fine paper [9]. While RFID tags on paper are already available on the market, the tags are produced by laminating an aluminum foil on paper instead of by printing [10]. The recyclability of such laminated or extrusion coated substrates is poor. The substrate presented in the current work is recyclable, which could be one of the main advantages when developing paper-based printed electronics.

We have developed a multilayer-coated paper-based substrate that is suitable for printed electronics and functionality. The multilayer structure consists of the following layers: precoating, smoothing layer, barrier coating and a top coating (Figs. 1 and 2) [11]. Each of the layers has its specific function that allows a printed device to operate

successfully. The precoated basepaper (90 g/m<sup>2</sup>) was first blade-coated with a 7 g/m<sup>2</sup> kaolin layer to decrease the root mean square (RMS) surface roughness from ca. 600 to 300 nm (Fig. 2). On this smoothing layer a barrier layer was coated, consisting of acrylic or styrene acrylic copolymer latex either as 100% latex or blended with mineral pigments (coat weight 0.5–20 g/m<sup>2</sup>). The surface was made polar by blending mineral pigments (PCC) with the barrier latex, which makes it possible to coat an aqueous top coat on the barrier layer. The total surface energy of the barrier layer was 33.0 mN/m (apolar component 27.4 mN/m and polar component 5.6 mN/m). If improved barrier properties are aimed for, then high aspect ratio platy pigments are preferred. The top layer is thin and smooth (coat weight 0.7–5 g/m<sup>2</sup>, layer thickness 0.8–6 µm and RMS surface roughness 55–75 nm) consisting of mineral pigments blended with 7–12 pph of styrene-butadiene latex as binder. PCC and Kaolin were studied for use in this layer in order to provide as different absorption properties as possible; PCC giving high and Kaolin low porosity. However, a whole range of other pigments such as fine GCC and Talc or blends of them could also be considered for use in this layer [12,13]. The sorption properties can be adjusted through controlled thickness and porosity enabling optimized printability of given functional materials. The materials in the coating structure were chosen in order to retain the recyclability and sustainability of the substrate.

The RMS surface roughness was measured as an average of three 100 × 100 µm<sup>2</sup> images for every layer and compared with a 50 µm thick Mylar<sup>®</sup> A substrate, which is known to be a fairly rough plastic surface on which working organic transistors have been printed [14,15]. After calendaring, multilayer-coated paper samples with RMS roughness as low as 55 nm were obtained. Respectively, the roughness of Mylar<sup>®</sup> A was ca. 30 nm. Roughness levels around 100 nm can in the paper industry be considered relatively smooth [16,17].

The barrier layer both controls the absorption of the inks and enables the functioning of the printed device. An example of a sorption test for a semiconductor ink,

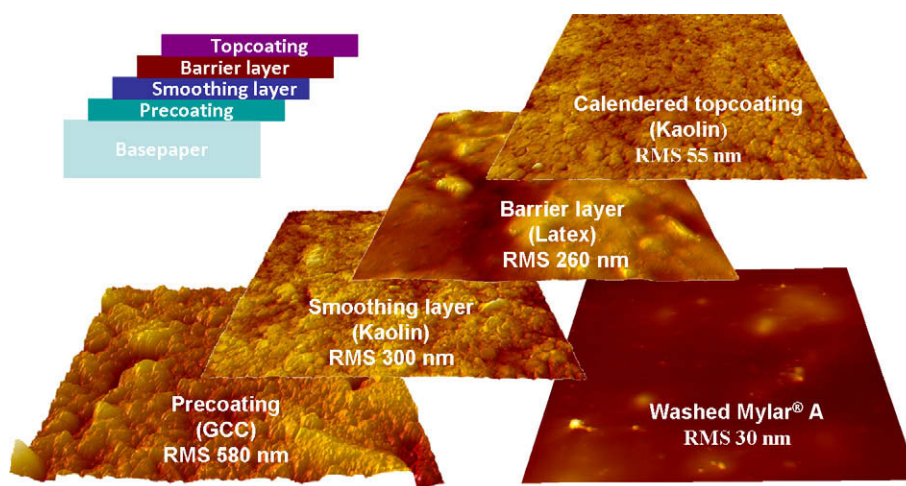


**Fig. 2.** Atomic force microscope (AFM) images (20 × 20 µm<sup>2</sup>) of each layer showing the changes in surface roughness. The RMS roughness was measured from 100 × 100 µm<sup>2</sup> images.

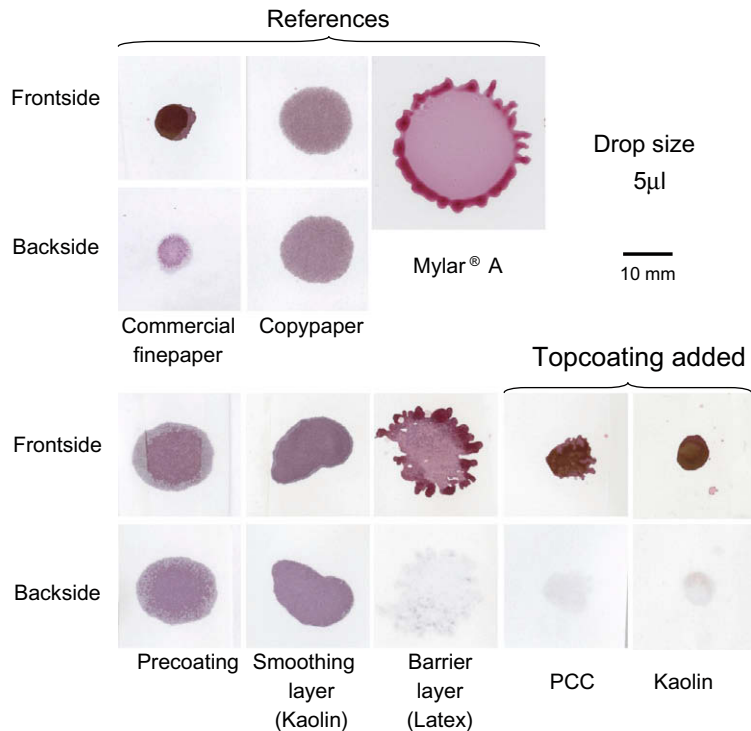


**Fig. 3.** Drop tests with the organic semiconductor P3HT in DCB. The visible spots on the backside indicate that the active material has penetrated through the paper substrate.

regioregular poly(3-hexylthiophene) P3HT dissolved in ortho-dichlorobenzene (DCB), is shown in Fig. 3. Compared with commercial paper substrates, the multilayer-coated paper shows superior barrier properties. Additionally, the printability (ink spreading) of the P3HT solution was much better controlled than e.g., on Mylar® A. The amount of ink applied was the same for each sample (5 µl), and the

scanned areas were  $25 \times 25 \text{ mm}^2$  except for the Mylar® A where an area of  $35 \times 35 \text{ mm}^2$  was needed because of the excessive droplet spreading. Note also the clearly visible undesired coffee stain effect of P3HT on Mylar® A. The barrier layer withstands solvents such as water, alcohols, ethanediol, DCB, chlorobenzene, xylene, toluene and ethyl acetate.

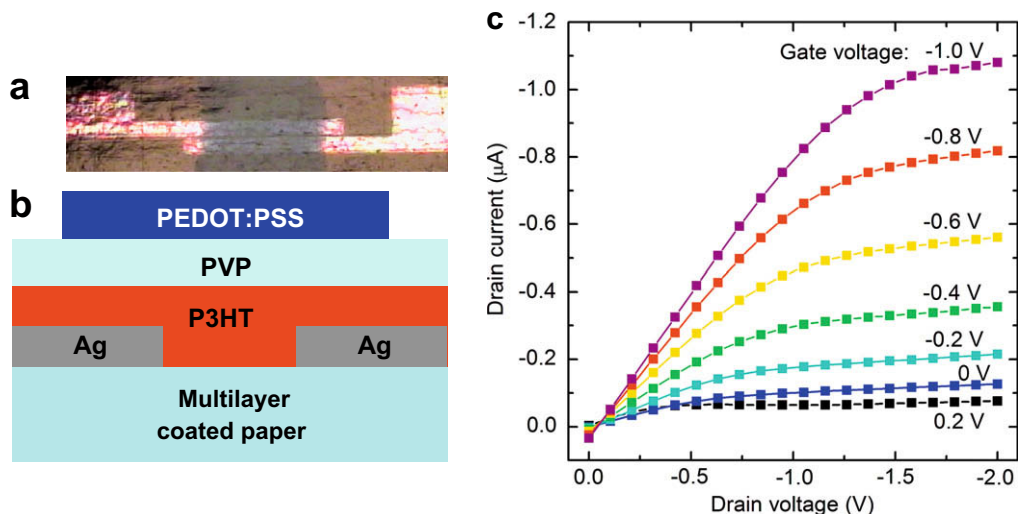


**Fig. 4.** Optical (a) and schematic (b) images of the HIFET. Current–voltage characteristics for the transistor on paper measured in room atmosphere at a relative humidity of 19% (c).

If printing with silver-based inks, sintering with sufficient thermal energy is required. During sintering the insulating organic stabilizing agents are decomposed from the surface of the nanoparticles, ensuring high conductivity. If low-cost plastic films, such as Mylar® A are used as substrate, sintering can be carried out in an oven (e.g., 60 min at 120 °C). A more efficient way to sinter is to use infrared radiation (IR) (e.g., 10 s at 180 °C). An advantage of IR is that it rapidly increases the temperature in the sintering layer, and also makes roll-to-roll processing possible. IR could not be used for Mylar® A, because it immediately deformed when exposed to the required amount of IR radiation. In the current study, IR sintering did not have any effect on the barrier properties of the paper substrate.

A hygroscopic insulator field effect transistor (HIFET) [14,15,18] was chosen as the printed device as a proof of concept of the substrate (Fig. 4). The transistor consists of inkjet printed (drop spacing 25 µm) silver (Ag) source and drain electrodes/contacts, P3HT as semiconductor, poly(4-vinylphenol) (PVP) as insulator and poly(3,4-ethylenedioxythiophene):poly(styrenesulfonate) (PEDOT:PSS) as gate electrode. The semiconductor and insulator layers were spin-coated and the gate was drop-cast. The paper substrate consisted of precoating (GCC), smoothing layer (Kaolin), barrier layer (styrene-acrylate) and a 2.1 µm thick top coating (Kaolin blended with styrene-butadiene binder, Tg 8 °C and particle size 140 nm, RMS roughness 74 nm). Fig. 4 demonstrates a working transistor with output curves showing current modulation at low voltages and is similar to the characteristics of a corresponding transistor on a PET substrate [15]. The measurement was done at a rather low relative humidity (19%) and the HIFET has earlier been shown to work at a relative humidity around 20–60% showing faster response at higher humidity levels [19]. Hygroscopic properties of the top coating can be adjusted by use of hydrophilic dispersants, such as commonly used Na-salts of polyacrylic acids [20]. The paper substrate can also be used for printed chemoresistors, such as biosensors or chemical sensors [21]. In principle, the functionalised material itself can be a conductive ink, an organic conductor, semiconductor or insulator, dissolved in a suitable solvent.

In summary, we have demonstrated a recyclable paper-based substrate where good barrier properties have been combined with controlled printability, as well as smooth-

ness necessary for printed functionality. The multilayer-coated papers were produced in laboratory scale using blade, rod and reverse gravure coating in three steps. For large scale manufacturing, curtain coating could be considered as a potential manufacturing method. As long as the base substrate is a standard paper or board, the developed paper substrate is easily recyclable along with other waste paper.

## Acknowledgements

Academy of Finland under Grant 118650 (A.M.) is acknowledged for financial support. The authors would like to thank Dr. Tapio Mäkelä for advice in printing experiments.

## References

- [1] T.J. Kimpimäki, Dispersion coating and product applications, Fapet Oy (2000).
- [2] T.J. Kimpimäki, TAPPI 1997 Coating Conference, vol. 259, TAPPI Press, Atlanta, 1997.
- [3] W.K. Asbeck, J. Coat. Technol. 64 (1992) 47.
- [4] J.J. Mefford, in: First International Polymer Dispersion Coating Conference, 1997.
- [5] K. Santamäki, First International Polymer Dispersion Coating Conference, 1997.
- [6] T. Schuman, M. Wikström, M. Rigdahl, Prog. Org. Coat. 51 (3) (2004) 228.
- [7] T. Schuman, A. Karlsson, J. Larsson, M. Wikström, M. Rigdahl, Prog. Org. Coat. 54 (4) (2005) 360.
- [8] Y. Chen, J. Au, P. Kazlas, A. Ritenour, H. Gates, J. Goodman, Tech. Dig. – Int. Electron Dev. Meet. (2002) 389.
- [9] P. Andersson, D. Nilsson, P.O. Svensson, M. Chen, A. Malmström, T. Remonen, T. Kugler, M. Berggren, Adv. Mater. 14 (2002) 1460.
- [10] R. Oberle, Patent WO(2008063785).
- [11] R. Bollström, A. Määttänen, P. Ihalainen, M. Toivakka, J. Peltonen, Patent application FI(20095089).
- [12] P.A.C. Gane, G.P. Matthews, J. Schoelkopf, C.J. Ridgway, D.C. Spielmann, TAPPI Adv. Coat. Fund. Symp. Proc. 213 (1999).
- [13] C. Nutbeem, J.C. Husband, J.S. Preston, PITA Coat. Conf. Proc. (2005).
- [14] D. Tobjörk, N. Kaihovirta, T. Mäkelä, F.S. Pettersson, R. Österbacka, Org. Electron. 9 (2008) 931.
- [15] N. Kaihovirta, D. Tobjörk, T. Mäkelä, R. Österbacka, Appl. Phys. Lett. 93 (2008) 053302.
- [16] P. Oittinen, H. Saarelma, Printing, Fapet Oy (1998).
- [17] G. Ström, M. Karathanasis, Nord. Pulp Paper Res. J. 23 (2) (2008) 156.
- [18] H.G.O. Sandberg, T.G. Bäcklund, R. Österbacka, H. Stubb, Adv. Mater. 16 (2004) 1112.
- [19] T.G. Bäcklund, R. Österbacka, H. Stubb, J. Bobacka, A. Ivaska, Appl. Phys. 98 (2005) 074504.
- [20] P.A.C. Gane, C.J. Ridgway, Adv. TAPPI Fund. Symp. (2008).
- [21] U. Lange, N.V. Roznyatovskaya, V.M. Mirsky, Anal. Chim. Acta 614 (2008) 1.

## 2. Experiment

Bottom contact pentacene TFTs with parylene as the gate dielectric were photo-lithographically fabricated and evaluated. The process steps involved in the fabrication of our pentacene TFTs have been discussed in detail previously [16,17]. The resulting TFTs used for this study showed mobilities of  $0.2 \pm 0.02 \text{ cm}^2/\text{V-s}$  with very stable threshold voltages of  $-2.5 \pm 0.2 \text{ V}$  and on/off ratio of  $5 \times 10^4 \pm 1 \times 10^4$  [17]. Drive current was  $0.12 \mu\text{A}/\mu\text{m}$  at  $-20 \text{ V}$  gate bias. For the CVS studies, we used the metal-insulator-metal (MIM) capacitor structure shown in Fig. 1 to evaluate the time dependent breakdown characteristics of the devices described above. The MIM capacitors were fabricated on Si wafers coated with  $\text{Si}_3\text{N}_4$  followed by 50 nm thick chromium films deposited by e-beam evaporation to form the bottom metal electrode. The parylene C used in our work was deposited using a Specialty Coating Systems PDS Model 2010 Labcoater 2. Parylene C was deposited by chemical vapor deposition (CVD) at room temperature by passing parylene through a vaporizing zone ( $175 \text{ }^\circ\text{C}$ ), a pyrolysis zone ( $690 \text{ }^\circ\text{C}$ ) and

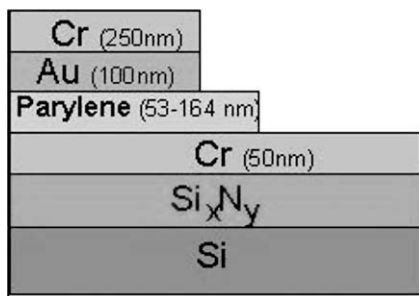


Fig. 1. MIM capacitor schematic cross-section used in the evaluation of TDDB characteristics of parylene.

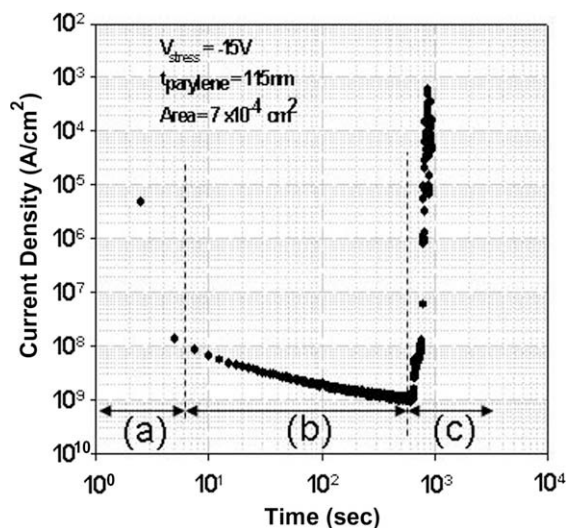


Fig. 2. Current–time response of parylene capacitor (115 nm) showing three different regimes of operation.

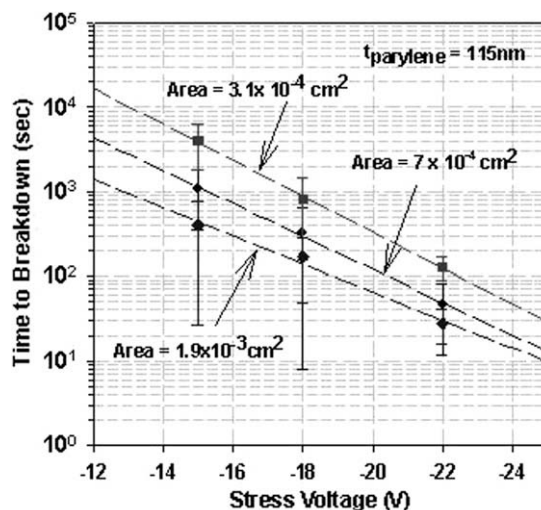


Fig. 3. Time-to-breakdown vs. applied voltage for a 115 nm thick parylene device for different device areas.

into the chamber where parylene polymerizes on the substrate which is held at room temperature. The base pressure of the system was 5 mTorr and the deposition pressure was 15–22 mTorr. Three different parylene thicknesses were evaluated in this work: 53 nm, 115 nm and 164 nm. Parylene thicknesses were determined by ellipsometry and profilometry. Top metal contacts were formed using a shadow mask process by evaporating 100 nm of Au followed by 250 nm of Cr.

## 3. Results and discussion

Time dependent dielectric breakdown (TDDB) characteristics [18] of the parylene capacitors were obtained by monitoring the current–time response using an HP

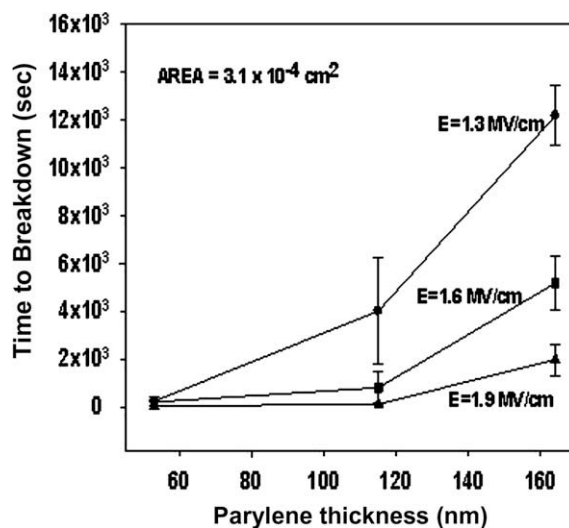
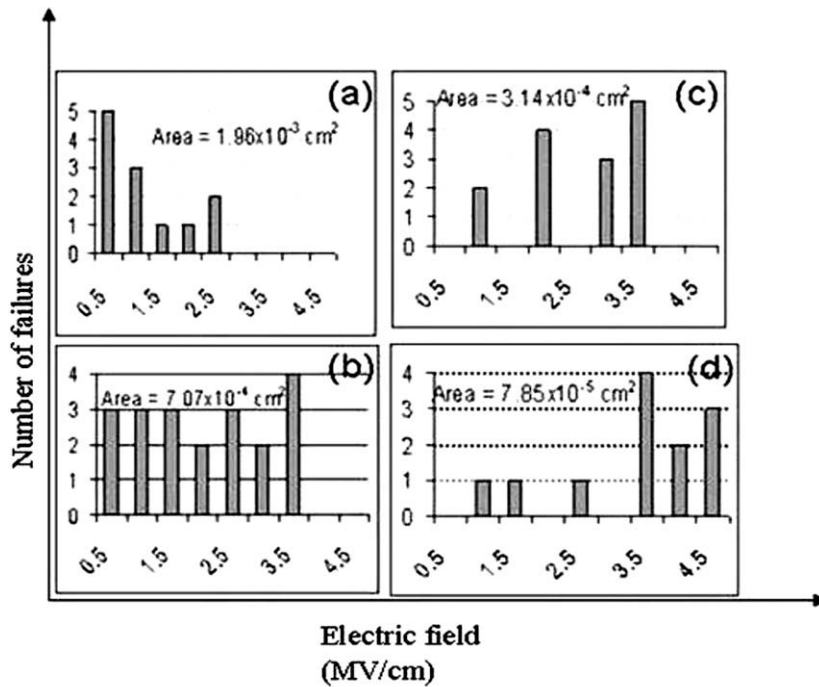


Fig. 4. Time-to-breakdown vs. parylene film thickness obtained at different electric fields.



**Fig. 5.** (a–d) Distribution of number of failures as a function of applied electric field for capacitor areas  $1.96 \times 10^{-3}$ ,  $7.07 \times 10^{-4}$ ,  $3.14 \times 10^{-4}$  and  $7.85 \times 10^{-5}$  cm<sup>2</sup>, respectively, indicating a shift towards intrinsic breakdown at higher electric fields.

4155A Semiconductor Parameter Analyzer controlled with a Labview data acquisition system. For these measurements, the bottom electrode was negatively biased with respect to the top electrode. A typical current–time response curve of a parylene capacitor is shown in Fig. 2. These data show that the parylene capacitor response for –15 V applied voltage can be divided into three regimes: (a) regime where the current density decreases from an initially high value due to the displacement current from charging the capacitor, (b) a steady state region where current density is almost constant over a period of time, and (c) a breakdown region where the current rapidly increases several orders of magnitude. In this study we define time-to-breakdown ( $t_b$ ) of the capacitor as the time needed for the current density to increase  $10\times$  from the minimum current density value [18].

Fig. 3 shows the mean time-to-breakdown for a 115 nm thick parylene film. Three areas ( $3.1$ ,  $7$  and  $19 \times 10^{-4}$  cm<sup>2</sup>) and three stress voltages (–15 V, –18 V and –22 V) were used to fully characterize the time-to-breakdown. As expected, for a given area the time-to-breakdown decreases as applied voltage increases, whereas for a given applied voltage the time-to-breakdown increases as the area of the capacitor decreases. This indicates that the breakdown mechanism is defect dominated. Fig. 3 also indicates a power law dependence of  $t_b$  with applied voltage, given by Eq. (1) [18]

$$t_b \propto V^{-n} \quad (1)$$

where  $V$  is the applied voltage and  $n$  is a positive integer with a value in the range of 5–9. Similar power law dependence is observed for 53 nm and 164 nm thick parylene

films. In Fig. 4 we compare  $t_b$  as a function of film thickness at different electric fields and a given device area. For thinner parylene films,  $t_b$  is less dependent on applied electric field than for thicker films. In other words,  $t_b$  for thinner films is predominantly determined by the number of defects in the dielectric, rather than the applied electric field.  $t_b$  shows a power law dependence of capacitor area. Given the fact that  $t_b$  shows a power law dependence for both applied voltage and device area we estimated (by extrapolation of curves) the lifetime of pentacene-based TFTs with respect to gate dielectric reliability for a parylene thickness of 115 nm. For this estimate we used a W/L ratio and fixed gate bias of  $1000 \mu\text{m}/6 \mu\text{m}$  and –10 V, respectively. Results show a lifetime of  $\sim 945$  h operating continuously under these conditions. We note that, besides the impact of gate dielectric in device lifetime, some other factors such as drain-source voltage induced stress and pentacene degradation due to moisture and oxygen could also result in reduced operating lifetime.

Defect density in the parylene thin film (164 nm) was experimentally determined using the time-zero-breakdown technique [19]. In this technique several parylene capacitors with different areas are stressed by varying the applied voltage until dielectric breakdown is observed. The defect density is then calculated by dividing the total number of failures by the total area of the capacitors tested. Using this technique, we evaluated a 164 nm thick parylene film and calculated a defect density of approximately  $1.2 \times 10^3$  defects/cm<sup>2</sup>. Fig. 5a–d shows the distribution of the number of failures at different applied electric fields for different device areas. It is observed that as device area decreases, the number of devices failing at the higher elec-



tric fields increases. As device area decreases there are fewer defects in that area and the capacitor breaks down at higher fields. This indicates a shift from extrinsic breakdown towards intrinsic breakdown [19]. Using the defect density above we estimate the number of defects in the dielectric to be 0.075 for a transistor size of 1000  $\mu\text{m}/6 \mu\text{m}$ .

#### 4. Conclusion

In summary, the time dependent breakdown characteristics of parylene used as a gate dielectric in pentacene-based TFTs was evaluated. The time-to-breakdown is determined to have a power law distribution over the applied voltage and device area and is shown to be driven by the number of defects in the dielectric. Defect density in our parylene thin films was calculated to be  $1.2 \times 10^3$  defects/cm<sup>2</sup>. The impact of parylene reliability on pentacene-based TFT lifetime is estimated based on the power law dependence and is found to be 945 h. It is shown that the use of parylene C (as gate dielectric) does not limit the pentacene TFT device lifetime as pentacene degradation due to moisture and oxygen is more likely to have a larger effect on TFT device lifetime than parylene degradation [4].

#### References

- [1] D.J. Gundlach, Y.Y. Lin, T.N. Jackson, S.F. Nelson, D.G. Schlom, *IEEE Electron Device Lett.* 18 (1997) 87.
- [2] G. Horowitz, *Adv. Mater.* 10 (1998) 365.
- [3] D.J. Gundlach, L. Zhou, J.A. Nicholas, T.N. Jackson, P.V. Necliudov, M.S. Shur, *J. Appl. Phys.* 100 (2006) 024509.
- [4] T. Sekitani, S. Iba, Y. Kato, Y. Noguchi, T. Someya, *Appl. Phys. Lett.* 87 (2005) 073505.
- [5] Y. Wang, H. Cheng, Y. Wang, T. Hu, J. Ho, C. Lee, T. Lei, C. Yeh, *Thin Solid Films* 467 (2004) 215.
- [6] J. Lee, J.H. Kim, S. Im, *J. Appl. Phys.* 95 (2004) 7.
- [7] H. Klauk, M. Halik, U. Zschieschang, F. Eder, G. Schmid, C. Dehm, *Appl. Phys. Lett.* 82 (2003) 23.
- [8] C. Jung, A. Maliakal, A. Sidorenko, T. Siegrist, *Appl. Phys. Lett.* 90 (2007) 062111.
- [9] J.B. Koo, S.J. Yun, J.W. Lim, S.H. Kim, C.H. Ku, S.C. Lim, J.H. Lee, T. Zyung, *Appl. Phys. Lett.* 89 (2006) 033511.
- [10] Y. Choi, I. Kim, Harry L. Tuller, A.I. Akinwande, *IEEE Trans. Electron Devices* 52 (2005) 12.
- [11] Z.-T. Zhu, J.T. Mason, R. Dieckmann, G.G. Malliaras, *Appl. Phys. Lett.* 81 (2002) 4643.
- [12] Y. Vertsimakha, A. Verbitsky, *Syn. Met.* 109 (2001) 291.
- [13] A.B. Brown, C.P. Jarrett, D.M. de Leeuw, M. Matters, *Syn. Met.* 88 (1997) 37.
- [14] S. Verlaak, V. Arkhipov, P. Heremans, *Appl. Phys. Lett.* 82 (2003) 745.
- [15] P.V. Necliudov, M. Shur, D.J. Gundlach, T.N. Jackson, *Mater. Res. Soc. Symp. Proc.* 660 (2001) JJ7.10.1.
- [16] S. Gowrisanker, Y. Ai, H. Jia, M.A. Quevedo-Lopez, H.N. Alshareef, E. Vogel, B. Gnade, *Appl. Phys. Lett.* 92 (2008) 153305.
- [17] A gate dielectric last approach to integrate organic based devices on plastic substrates, in: S. Gowrisanker, Y. Ai, M.A. Quevedo-Lopez, H.N. Alshareef, B. Gnade (Eds.), *Flexible Electronics and Displays Conference and Exhibition*, 2008.
- [18] H.N. Al-Shareef, Duane Dimos, *J. Am. Ceram. Soc.* 80 (1997) 3127.
- [19] T. Hori, *Gate dielectrics and MOS ULSI: principles, technologies and applications*, Springer Series in Electronics and Photonics 34, Springer, 1997, p. 172.

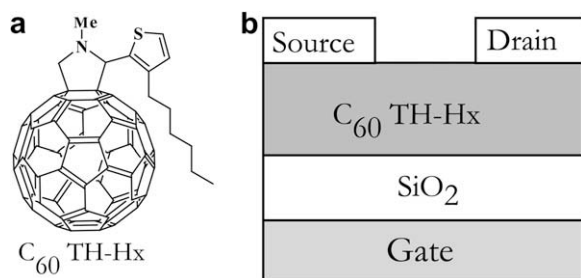


**Fig. 1.** (a) The chemical structure of  $C_{60}$ TH-Hx and (b) schematic structure of a top-contact OTFT device ink-jet-printed with  $C_{60}$ TH-Hx.

dielectric layer, as well as metal electrodes, exhibited mobilities of up to  $0.1 \text{ cm}^2 \text{ V}^{-1} \text{ s}^{-1}$  [11].

Here we report a new  $C_{60}$  derivative, which contains an alkylated thiophene unit, for solution-processable OTFTs. More importantly, we have fabricated high-performance n-type OTFT devices by means of the ink-jet-printing method. The fabrication process was carefully optimized in order to achieve a uniform morphology and the desired molecular orientation. The chemical structure of  $C_{60}$ -fused *N*-methyl-2-(3-hexylthiophen-2-yl)pyrrolidine ( $C_{60}$ TH-Hx) is shown in Fig. 1a.  $C_{60}$ TH-Hx was newly synthesized in our laboratory via a Prato reaction between  $C_{60}$  and 3-hexylthiophene-2-carboxaldehyde with *N*-methylglycine. The material dissolves well in a variety of organic solvents and is hence suitable for solution-processable OTFT devices.

The redox behavior of  $C_{60}$ TH-Hx was studied by means of cyclic voltammetry experiments performed at a scan rate of 50 mV/s in a three-electrode cell using a platinum-plate working electrode, a platinum-wire counter electrode, and an  $\text{Ag}/\text{Ag}^+$  (0.1 mol/L) reference electrode. Tetrabutylammonium tetrafluoroborate ( $\text{Bu}_4\text{NBF}_4$ , 0.1 mol/L) in *o*-dichlorobenzene was used as the supporting electrolyte. The potentials are quoted relative to the ferricenium/ferrocene couple. By combining the optical data obtained from UV/vis spectroscopy studies with the electrochemical measurements, the values of the lowest unoccupied molecular orbital (LUMO) and the highest occupied molecular orbital (HOMO) levels were estimated to be 3.8 and 5.3 eV, respectively. Thus, the calculated HOMO–LUMO energy band gap is 1.36 eV. The reported LUMO and HOMO values for  $C_{60}$  derivatives including PCBM are in the range of 3.5–3.8 eV and 5.7–6.1 eV, respectively [12,13]. It was noticed that upon introducing a thiophene unit, the HOMO energy level increased whereas the LUMO energy level remained relatively constant due to its highly localized state around  $C_{60}$ .

Top-contact transistors shown in Fig. 1b were fabricated on a common gate of heavily doped n-type silicon wafers covered with a 3000 Å-thick silicon dioxide ( $\text{SiO}_2$ ) dielectric layer. The substrates were treated with hexamethyldisilazane (HMDS) or octadecyltrichlorosilane (OTS) to produce hydrophobic dielectric surfaces. Amounts of 0.5 and 1.0 wt% of  $C_{60}$ TH-Hx were dissolved in chlorobenzene for spin-coating and ink-jet printing, respectively. A film thickness of 30 nm was obtained at a spin rate of 2000 rpm for 60 s. For the ink-jet method, the printer consisted of a single-nozzle drop-on-demand piezoelectric print head and a two-axis motorized positioning system with a CCD camera for visualization of the droplet ejection. Uniform droplet ejection was achieved by applying a 25  $\mu\text{s}$ -long 35 V pulse at a frequency of 600 Hz. At this time, the ejecting solution volume was controlled to 15–20 picoliters from the nozzle, which has a diameter 30  $\mu\text{m}$ . The vertical separation between the nozzle and the substrate was typically 0.5 mm. Bilayer top-contact electrodes consisting of Mg/Al (10 nm/120 nm) were evaporated under high vacuum ( $10^{-6}$  mbar) through a shadow mask. The channel length ( $L$ ) and width ( $W$ ) of the transistors were 50  $\mu\text{m}$  and 3 mm, respectively.

All the OTFT devices were encapsulated by a glass can and getters in an inert argon environment inside a glove box system. Electrical measurements were performed at room temperature under Ar atmosphere using an HP4156C semiconductor parameter analyzer. Parameters such as mobility,  $I_{\text{on}}/I_{\text{off}}$  ratio, and threshold voltage were calculated based on standard semiconductor FET equations in the saturation-current regime [14], see Table 1. All OTFTs showed very well-defined linear and saturation-regime output characteristics. As an example, the current-voltage characteristics of a  $C_{60}$ TH-Hx OTFT obtained by ink-jet printing on a Si/SiO<sub>2</sub> substrate treated with HMDS are shown in Fig. 2a. Fig. 2b shows the transfer characteristics of ink-jet-printed  $C_{60}$ TH-Hx. For comparison, the characteristics of spin-coated  $C_{60}$ TH-Hx are also shown. The ink-jet-printed  $C_{60}$ TH-Hx devices exhibited an excellent n-channel performance with a highest mobility of  $2.8 \times 10^{-2} \text{ cm}^2 \text{ V}^{-1} \text{ s}^{-1}$ , an  $I_{\text{on}}/I_{\text{off}}$  ratio of about  $1 \times 10^6$ , and a threshold voltage of 7 V. In the case of the spin-coated  $C_{60}$ TH-Hx devices, a maximum mobility of  $1.8 \times 10^{-2} \text{ cm}^2 \text{ V}^{-1} \text{ s}^{-1}$  was achieved on the HMDS-treated substrates.

On the contrary, the PCBM devices showed a maximum mobility of  $5.8 \times 10^{-3} \text{ cm}^2 \text{ V}^{-1} \text{ s}^{-1}$ , also on HMDS-treated substrates. These results indicate that the newly synthesized  $C_{60}$ TH-Hx material has better properties than PCBM, with high electron mobility, for n-type OTFTs. In addition,

**Table 1**

Performance of PCBM- and  $C_{60}$ TH-Hx-based OTFTs fabricated by means of spin-coating and ink-jet printing after different surface treatments of the Si/SiO<sub>2</sub> substrates.

Sample	Processing method	Top electrodes	Surface treatment	Mobility ( $\text{cm}^2 \text{ V}^{-1} \text{ s}^{-1}$ )	$I_{\text{on}}/I_{\text{off}}$ ratio	Threshold voltage (V)
PCBM	Spin-coating	Mg/Al	HMDS	$5.8 \times 10^{-3}$	$\approx 1 \times 10^4$	18
			OTS	$3.3 \times 10^{-3}$	$\approx 1 \times 10^5$	7
$C_{60}$ TH-Hx	Spin-coating	Mg/Al	HMDS	$1.8 \times 10^{-2}$	$\approx 1 \times 10^5$	14
			OTS	$1.4 \times 10^{-2}$	$\approx 1 \times 10^5$	29
$C_{60}$ TH-Hx	Ink-jet printing	Mg/Al	HMDS	$2.8 \times 10^{-2}$	$\approx 1 \times 10^6$	7

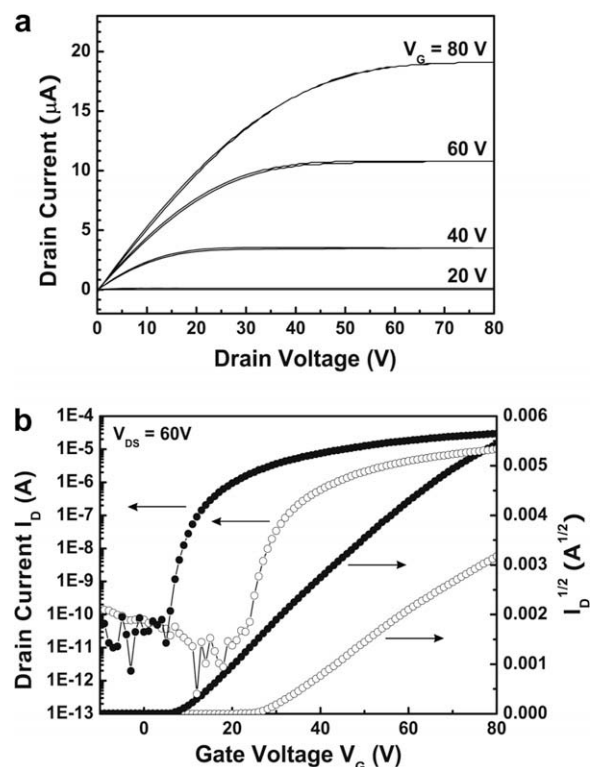


**Fig. 2.** (a)  $I_D$ - $V_D$  characteristics of a  $C_{60}$ TH-Hx OTFT processed by ink-jet printing. (b)  $I_D$ - $V_G$  and  $I_D^{1/2}$ - $V_G$  plots of ink-jet-printed (closed circles) and spin-coated (open circles)  $C_{60}$ TH-Hx.

the performance of OTFT devices was found to depend on the type of top electrode. When a high work-function electrode such as a gold is employed in spin-coated  $C_{60}$ TH-Hx devices, the electron mobility decreases to  $3.1 \times 10^{-3} \text{ cm}^2 \text{ V}^{-1} \text{ s}^{-1}$  while the  $I_{\text{On}}/I_{\text{Off}}$  ratio increases to about  $1 \times 10^6$ . Since the energy level of the LUMO of  $C_{60}$ TH-Hx is 3.8 eV, the electron-injection current can be limited to high work-function Au ( $\approx 5.1 \text{ eV}$ ) by the contacts. Similar effects have also been reported for other systems based on different materials [15,16]. All the results reported herein are highly reproducible; further optimization of the device performance by using different annealing conditions, as well as an assessment of the long-term stability of the devices, is underway. Interestingly, the performance of ink-jet-printed  $C_{60}$ TH-Hx devices is superior to those of spin-coated and PCBM-based devices, with the ink-jet-printed  $C_{60}$ TH-Hx devices showing increased mobility and on/off current ratio as well as a reduced threshold voltage. This result indicates that the processing conditions significantly affect the OTFT device performance due to the different evaporation behaviors of the solvents during the drying process, which plays a key role in controlling the film morphology and crystalline structure.

Fig. 3 shows AFM images of spin-coated and ink-jet-printed  $C_{60}$ TH-Hx films on HMDS-treated  $\text{SiO}_2/\text{Si}$  substrates. Rough surface and inhomogeneous grain sizes with a diameter of about 200–600 nm are observed in the spin-

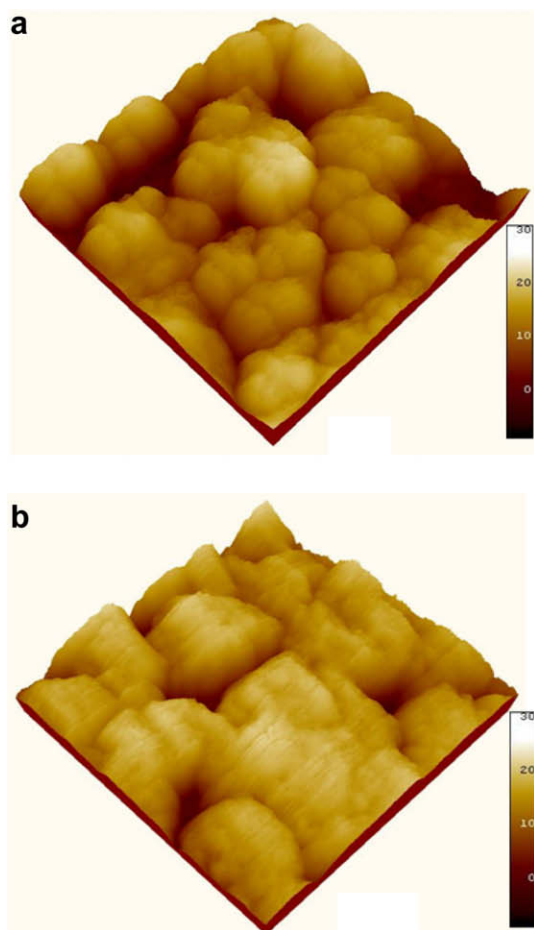


**Fig. 3.**  $3 \times 3 \mu\text{m}^2$  AFM images of (a) spin-coated and (b) ink-jet-printed  $C_{60}$ TH-Hx films on an HMDS-treated  $\text{SiO}_2/\text{Si}$  substrate. The images were taken in the contact mode.

coated film. However a smoother surface and less grain boundaries are observed for the ink-jet-printed  $C_{60}$ TH-Hx films compared to the spin-coated ones. To obtain a well-ordered crystalline structure and a uniform surface, sufficient time must be available for evaporation of the solvent at the contact line so that nucleation can occur. Cho et al. demonstrated the influence of an evaporation-induced flow within a droplet on the crystalline microstructure of an ink-jet-printed pentacene derivative, namely, 6,13-bis(triisopropylsilylethynyl)pentacene, by varying the composition of the solvent [17]. The choice of an appropriate solvent provided a uniform morphology as well as the desired molecular orientation required to improve the effective field-effect mobility. Therefore, we believe that ink-jet-printed  $C_{60}$ TH-Hx devices used with a chlorobenzene solvent can provide more time for the molecules to assemble into large crystalline domains during solvent drying. The resulting highly crystalline  $C_{60}$ TH-Hx devices with smooth surfaces exhibit excellent electron mobilities.

In summary, we have demonstrated high-performance n-type OTFTs based on a newly developed material,  $C_{60}$ TH-Hx. The devices were fabricated using the ink-jet-

printing method, and a better film quality was obtained in this case as compared to devices fabricated by spin-coating; this has led to improved OTFT performance. The best performance achieved with the ink-jet-printed devices was characterized by an electron mobility of  $2.8 \times 10^{-2} \text{ cm}^2 \text{ V}^{-1} \text{ s}^{-1}$ , an  $I_{\text{on}}/I_{\text{off}}$  ratio of about  $1 \times 10^6$ , and a threshold voltage of 7 V. These results support the use of C<sub>60</sub>TH-Hx in future organic electronic applications.

### Acknowledgements

This study was supported by a grant from the Fundamental R&D Program for Core Technology of Materials funded by the Ministry of Knowledge Economy, Republic of Korea (M2007010004). K.-S. Lee thanks the Asian Office of Aerospace Research and Development (AOARD-08-4086), Air Force Office of Scientific Research, USA, for their support. T.-D. Kim acknowledges supports from University Research Program in Hannam University (2009).

### References

- [1] M. Halik, H. Klauk, U. Zschieschang, G. Schmid, W. Radlik, W. Weber, *Adv. Mater.* 14 (2002) 1717.
- [2] H. Sirringhaus, *Adv. Mater.* 17 (2005) 2411.
- [3] A.R. Murphy, J.M.J. Fréchet, *Chem. Rev.* 107 (2007) 1066.
- [4] H. Sirringhaus, P.J. Brown, R.H. Friend, M.M. Nielsen, K. Bechgaard, B.M.W. Langeveld-Voss, A.J.H. Spiering, R.A.J. Janssen, E.W. Meijer, P. Herwig, D.M. de Leeuw, *Nature* 401 (1999) 685.
- [5] B.S. Ong, Y. Wu, P. Liu, S. Gardner, *J. Am. Chem. Soc.* 126 (2004) 3378.
- [6] M. Chikamatsu, S. Nagamatsu, Y. Yoshida, K. Saito, K. Yase, K. Kikuchi, *Appl. Phys. Lett.* 87 (2005) 203504.
- [7] X. Zhan, Z. Tan, B. Domercq, Z. An, X. Zhang, S. Barlow, Y. Li, D. Zhu, B. Kippelen, S.R. Marder, *J. Am. Chem. Soc.* 129 (2007) 7246.
- [8] R.C. Haddon, A.S. Perel, R.C. Morris, T.T.M. Palstra, A.F. Hebard, R.M. Fleming, *Appl. Phys. Lett.* 67 (1995) 121.
- [9] N. Stingelin-Stutzmann, E. Smits, H. Wondergem, C. Tanase, P. Blom, P. Smith, D. de Leeuw, *Nat. Mater.* 4 (2005) 601.
- [10] T.B. Singh, N. Marjanović, P. Stadler, M. Auinger, G.J. Matt, S. Günes, N.S. Sariciftci, R. Schwödiauer, S. Bauer, *J. Appl. Phys.* 97 (2005) 083714.
- [11] T.-W. Lee, Y. Byun, B.-W. Koo, I.-N. Kang, Y.-Y. Lyu, C.H. Lee, L. Pu, S.Y. Lee, *Adv. Mater.* 17 (2005) 2180.
- [12] E.J. Meijer, D.M. de Leeuw, S. Setayesh, E. van Veenendaal, B.-H. Huisman, P.W.M. Blom, J.C. Hummelen, U. Scherf, T.M. Klapwijk, *Nat. Mater.* 2 (2003) 678.
- [13] T.D. Anthopoulos, F.B. Kooistra, H.J. Wondergem, D. Kronholm, J.C. Hummelen, D.M. de Leeuw, *Adv. Mater.* 18 (2006) 1679.
- [14] G. Horowitz, M.E. Hajlaoui, R. Hajlaoui, *J. Appl. Phys.* 87 (2000) 4456.
- [15] D.J. Gundlach, L. Zhou, J.A. Nichols, T.N. Jackson, P.V. Necliudov, M.S. Shur, *J. Appl. Phys.* 100 (2006) 024509.
- [16] P.H. Wobkenberg, D.D.C. Bradley, D. Kronholm, J.C. Hummelen, D.M. de Leeuw, M. Colle, T.D. Anthopoulos, *Synth. Met.* 158 (2008) 468.
- [17] J.A. Lim, W.H. Lee, H.S. Lee, J.H. Lee, Y.D. Park, K. Cho, *Adv. Funct. Mater.* 18 (2008) 229.

equilibrium conditions, and so, in contrast to previous studies, precise thin film growth is possible at a monolayer level [9–14]. As a result, *p*–*n* junctions can be formed on a single molecular scale and charge transfer between adjacent molecules can be expected.

Molecular superlattices were fabricated on Si substrates with thermally oxidized surface layers (SiO<sub>2</sub>) in a high vacuum ( $\sim 10^{-6}$  Pa). The deposition rates were less than 0.03 molecular layers (MLs) per min. Atomic force microscopy (AFM) images (SII SPI-4000, dynamic force mode) and X-ray reflection (XRR) spectra (Bruker AXS, D8 Discover, Cu K $\alpha$ ;  $\lambda = 0.154$  nm) [15,16] were obtained from various films grown at different substrate temperatures with a view to optimizing the growth conditions and examining the morphology, thickness and molecular orientation. By using XRR fitting, the layer densities were estimated to be in the 1.3–1.5 g/cm<sup>3</sup> range, which is comparable to the values reported in previous studies [17,18].

First, we verified the growth of the first PTCDI-C<sub>8</sub> monolayer on the SiO<sub>2</sub> surface. The molecular structure is shown in Fig. 1a. Fig. 1b shows the XRR spectrum of the PTCDI-C<sub>8</sub> monolayer grown at an optimized substrate temperature of 140 °C [8]. The measurement was carried out immediately after the deposition. The thickness was estimated to be 2.7 nm ( $\pm 0.1$  nm) from the fitting curve, indicating that the long axis of the molecule (2.97 nm) was oriented vertically to the surface normal with a small tilting angle [8,17,18]. A schematic illustration is shown in the inset of Fig. 1b. Fig. 1c is an AFM image of PTCDI-C<sub>8</sub> (0.6 ML), which clearly shows two-dimensional growth with flat terraces. The surface profile of the AFM images (a typical profile is shown in the inset) revealed that the terraces had an average height of 2.2 nm, which is smaller than that estimated with XRR, and involved a certain fluctuation of about  $\pm 0.2$  nm. We found that the thickness (height) had a tendency to decrease with time. For example, the reduction in thickness to approximately 1.8 nm ( $\pm 0.2$  nm) was confirmed by XRR and AFM 2 months after the deposition (not shown here). These results imply that the PTCDI-C<sub>8</sub> monolayer on the SiO<sub>2</sub> is unstable and the molecular orientation inclines gradually.

Next, we examined the surface morphologies, thickness and molecular orientation of quaterrylene/PTCDI-C<sub>8</sub> double layers (see Fig. 2a). The AFM images in Fig. 2b–d shows the surface morphologies of the quaterrylene layers deposited on the underlying PTCDI-C<sub>8</sub> monolayer. A clear dependence on the substrate temperature was observed. Quaterrylene layers tended to grow in a three-dimensional manner below 150 °C. Meanwhile, the substrate temperature at 160 °C produced 2D layers at the monolayer level. As a result, a well-defined quaterrylene/PTCDI-C<sub>8</sub> bilayer was formed. The surface profile shown in the inset proves that the quaterrylene molecules have an upright orientation, i.e., the long axis of the molecule (1.8 nm) is perpendicular to the SiO<sub>2</sub> surface normal.

To examine the total thickness of the quaterrylene/PTCDI-C<sub>8</sub> bilayer, the XRR spectrum was measured as shown in Fig. 3a. It should be noted that the total thickness estimated with the XRR measurement was only 3.0 nm, which was less than the sum for the two molecules (2.8 + 1.8 nm). We speculate that the reduction in the total thickness can be attributed to the instability of the PTCDI-C<sub>8</sub> layer as already mentioned. The orientation of the PTCDI-C<sub>8</sub> layer changed during the quaterrylene deposition presumably as a result of heating the substrate. To confirm this presumption, we investigated the effect of temperature on the PTCDI-C<sub>8</sub> orientation by thermally treating a PTCDI-C<sub>8</sub> single layer on SiO<sub>2</sub> at 160 °C for 3 h after the deposition. The XRR spectrum in Fig. 3b reveals that the thickness was reduced to 1.2 nm. This result means that the thermal treatment caused the molecules to lie flat as shown in the inset. Based on these analyses, we concluded that the quaterrylene/PTCDI-C<sub>8</sub> bilayer consisted of a vertically orientated quaterrylene layer (1.8 nm) on a prostrate PTCDI-C<sub>8</sub> layer (1.2 nm), which yielded a total thickness of 3.0 nm.

Subsequent layers were deposited and the molecular orientations of each layer were examined. The substrate temperatures were optimized to 160 °C for all the upper layers (2nd–4th layers), in a similar way to that shown in Fig. 2. AFM images were obtained to confirm the surface flatness as shown on the right in Fig. 4a. The XRR spectra

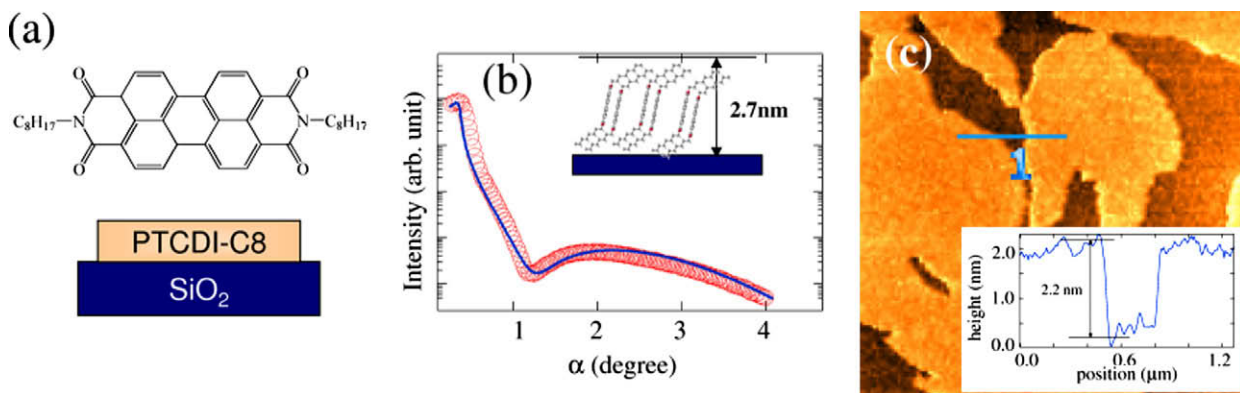


**Fig. 1.** (a) Chemical structure of PTCDI-C<sub>8</sub> molecule. (b) XRR spectrum of PTCDI-C<sub>8</sub> monolayer. The experimental result (red circles) and fitted line (blue line) revealed a layer thickness of 2.8 nm. The molecular orientation is shown in the inset. (c)  $5 \times 5 \mu\text{m}^2$  AFM image of 0.6 ML PTCDI-C<sub>8</sub>. The surface profile shows the PTCDI-C<sub>8</sub> layer is 2.2 nm thick, suggesting the layer undergoes a gradual change in orientation. (For interpretation of the references to color in this figure legend, the reader is referred to the web version of this article.)

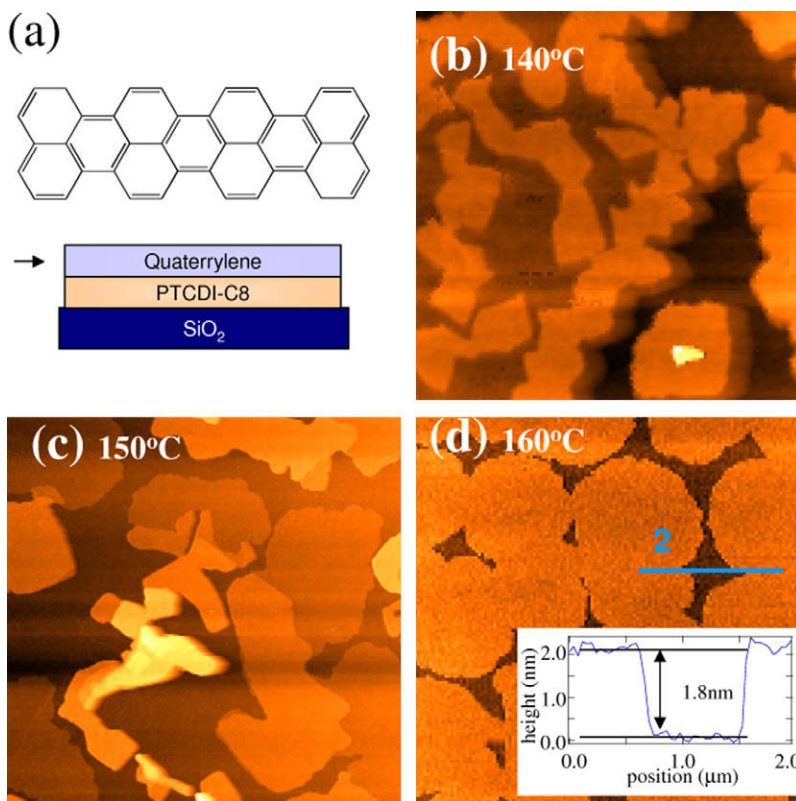


**Fig. 2.** (a) Chemical structure of quaterrylene molecule. (b–d)  $5 \times 5 \mu\text{m}^2$  AFM images of quaterrylene layers grown on the PTCDI-C<sub>8</sub> monolayer at various substrate temperatures. The optimum substrate temperature for growing a 2D layer was 160 °C.

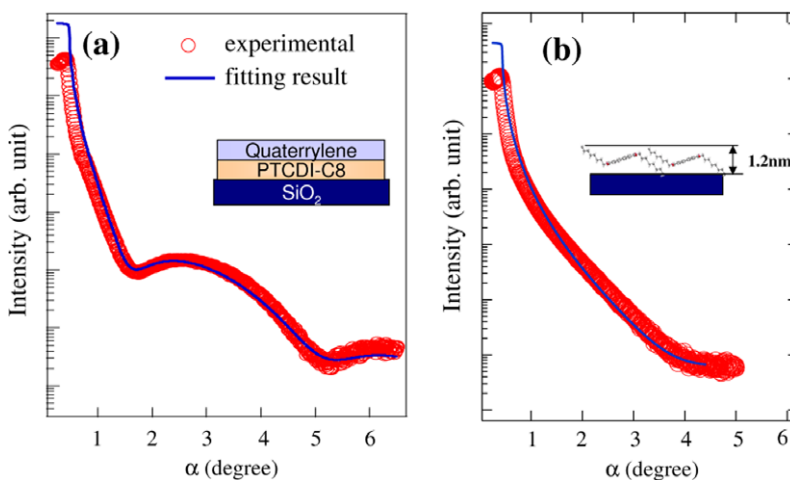


**Fig. 3.** (a) XRR spectrum of a PTCDI-C<sub>8</sub>/quaterrylene double layer. The experimental result (red circles) and fitted line (blue line) revealed a total thickness of 3.0 nm. (b) XRR spectrum of the PTCDI-C<sub>8</sub> monolayer after thermal treatment, which indicates a change in molecular orientation (see Fig. 1b). (For interpretation of the references to color in this figure legend, the reader is referred to the web version of this article.)

in Fig. 4b were measured from thus prepared PTCDI-C<sub>8</sub>/quaterrylene multiple layers. The fitted pattern revealed the thicknesses of the respective layers as shown in Fig. 4b. The quaterrylene layers (2nd and 4th layers) were very stable with a constant thickness of 1.7 nm, which is almost the same as that of the upright orientation. On

the other hand, the thickness of the PTCDI-C<sub>8</sub> layer (3rd layer) sandwiched between quaterrylenes exhibited a certain variation: 2.3 nm for as-deposited and 1.8 nm after the 4th layer deposition. This variation in thickness resulted from the instability of the PTCDI-C<sub>8</sub> layer and the thermal effect that occurred during the deposition of the other layers

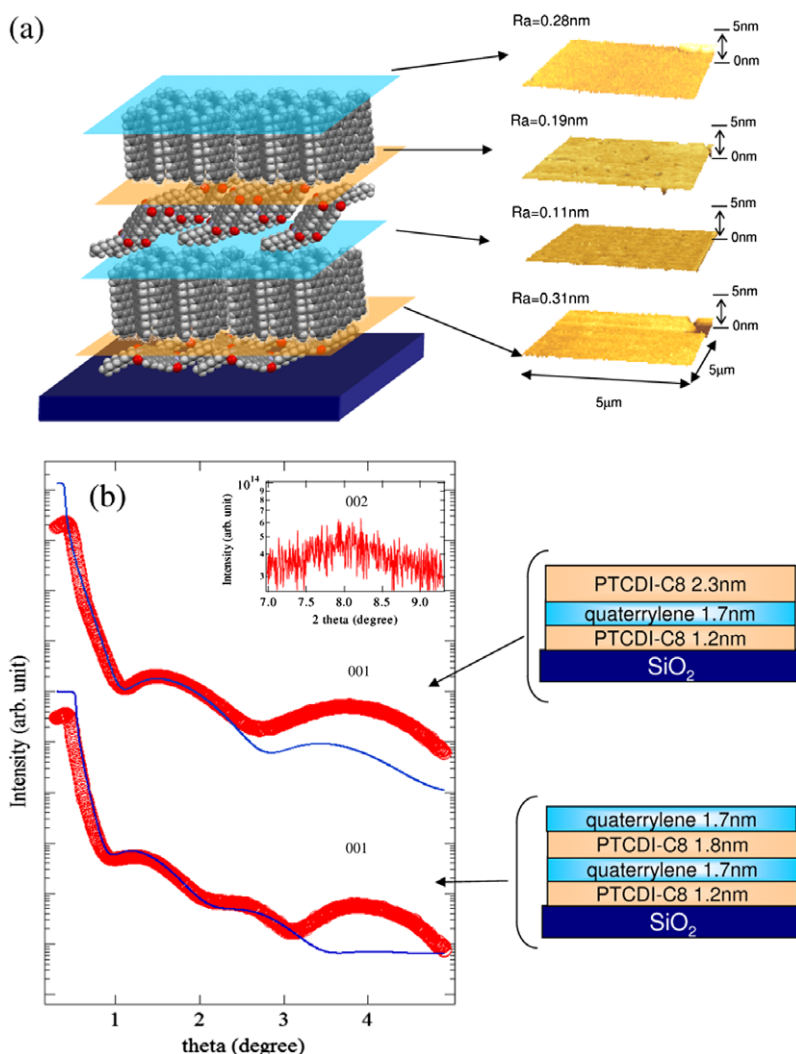


**Fig. 4.** (a) Illustration of PTCDI-C<sub>8</sub>/quaterrylene superlattice and AFM images of respective layers. The flat surfaces of each layer confirm well-defined 2D growth. (b) XRR spectra of PTCDI-C<sub>8</sub>/quaterrylene superlattice. The film constitution and the thicknesses of each layer are shown in the illustration. The disagreement between the experimental results (red circles) and fitted lines (blue lines) around 4 degrees is attributed to the diffraction peak from the (0 0 1) lattice plane. The peak from the (0 0 2) plane observed around 8 degrees is shown in the inset as a reference. (For interpretation of the references to color in this figure legend, the reader is referred to the web version of this article.)

as discussed for the first PTCDI-C<sub>8</sub> layer. In the XRR spectra, we observed a disagreement between the experimental data and the fitted patterns of around 4 degrees. This is accounted for by the fact that the diffraction peak from the (0 0 1) lattice plane of PTCDI-C<sub>8</sub> and quaterrylene layers overlapped the reflection patterns. To illustrate this effect, the diffraction peak from the (0 0 2) plane observed around 8 degrees is shown in the inset.

In summary, we produced a molecular superlattice of quaterrylene/PTCDI-C<sub>8</sub> using a fine process, where we precisely optimized the deposition conditions for 2D layer growth. The morphologies and molecular orientations in each layer were clarified by AFM and XRR. As a result, the molecular superlattice was found to consist of inclined PTCDI-C<sub>8</sub> and upright quaterrylene layers. The molecules in this study function as *n*- and *p*-type semiconductors,

respectively [19,20]. Therefore, this successful layer by layer growth of a molecular superlattice, which has offsets at the HOMO–LUMO energy levels, opens up the possibility of carrier transfer and carrier confinement in a similar manner to that observed with conventional inorganic semiconductors.

## References

- [1] M. Ichimura, S.H. Noh, T. Ishibashi, N. Ueda, S. Tamura, SPIE Proc. 5937 (2005) 593703.
- [2] M. Ohishi, M. Shiraishi, R. Nouchi, T. Nozaki, T. Shinjo, Y. Suzuki, Jpn. J. Appl. Phys. 46 (2007) L605.
- [3] S. Sakai, K. Yakushiji, S. Mitani, K. Takanashi, H. Naramoto, P.V. Avramov, K. Narumi, V. Lavrentiev, Y. Maeda, Appl. Phys. Lett. 89 (2006) 113118.
- [4] F. Sawano, I. Terasaki, H. Mori, T. Mori, M. Watanabe, N. Ikeda, Y. Nogami, Y. Noda, Nature 437 (2005) 522.

- [5] N. Toyota, M. Lang, J. Müller, *Low-Dimensional Molecular Metals*, Springer Series in Solid-State Sciences, vol. 154, Springer-Verlag, Berlin Heidelberg, 2007.
- [6] H. Sasaki, Y. Wakayama, T. Chikyow, E. Barrena, H. Dosch, K. Kobayashi, *Appl. Phys. Lett.* 88 (2006) 081907.
- [7] R. Hayakawa, M. Petit, Y. Wakayama, T. Chikyow, *Org. Electron.* 8 (2007) 631.
- [8] M. Petit, R. Hayakawa, Y. Wakayama, T. Chikyow, *J. Phys. Chem. C* 111 (2007) 12747.
- [9] F.F. So, S.R. Forrest, Y.Q. Shi, W.H. Steier, *Appl. Phys. Lett.* 56 (1990) 674.
- [10] A. Ishitani, T. Nonaka, *Surf. Interface Anal.* 21 (1994) 356.
- [11] E. Kuwahara, H. Kusai, T. Nagano, T. Takayanagi, Y. Kubozono, *Chem. Phys. Lett.* 413 (2005) 379.
- [12] T. Schmitz-Hübsch, F. Sellam, R. Staub, M. Törker, T. Fritz, C.h. Kübel, K. Müllen, K. Leo, *Surf. Sci.* 445 (2000) 358.
- [13] F. Sellam, T. Schmitz-Hübsch, M. Toerker, S. Mannsfeld, H. Proehl, T. Fritz, K. Leo, C. Simpson, K. Müllen, *Surf. Sci.* 478 (2001) 113.
- [14] T. Diemel, C. Loppacher, S.C.B. Mannsfeld, R. Forker, T. Fritz, *Adv. Mater.* 20 (2008) 959.
- [15] V. Holy, J. Kubena, I. Ohlidal, K. Lischka, W. Plotz, *Phys. Rev. B* 47 (1993) 15896.
- [16] XRR simulations and fitting were calculated by using DIFFRAC<sup>plus</sup> LEPTOS software (Bruker AXS).
- [17] A.L. Briseno, S.C.B. Mannsfeld, C. Reese, J.M. Hancock, Y. Xiong, S.A. Jenekhe, Z. Bao, Y. Xia, *Nano Lett.* 7 (2007) 2847.
- [18] T.N. Krauss, E. Barrena, X.N. Zhang, D.G. de Oteyza, J. Major, V. Dehm, F. Würthner, L.P. Cavalcanti, H. Dosch, *Langmuir* 24 (2008) 12742.
- [19] Reid J. Chesterfield, John C. McKeen, Christopher R. Newman, Paul C. Ewbank, Demtrio A. da Silva Filho, Jean-Luc Brdas, Larry L. Miller, Kent R. Mann, C. Daniel Frisbie, *J. Phys. Chem. B* 108 (2004) 19281.
- [20] Ryoma Hayakawa, Matthieu Petit, Yutaka Wakayama, Toyohiro Chikyow, *J. Phys. Chem. C* 111 (2007) 18703.



$$\sigma = \sigma_0 \exp(-s_c) \quad (3)$$

where  $\sigma_0$  is a prefactor and  $s_c$  is the exponent of the critical percolation conductance  $G_c = G_0 e^{-s_c}$  [6]. The onset of percolation is determined by calculating the critical average number of bonds  $B_c$  per site:

$$B_c = \frac{N_b(s_c, E_F)}{N_s(s_c, E_F)} \quad (4)$$

where  $B_c = 2.8$  for a 3-D amorphous system,  $N_b$  and  $N_s$  are the density of bonds and the density of sites in a percolation system, respectively. The total density of bonds could be calculated by integrating in energy, over the distance  $r_{ij}$ , the product of all available sites (at energy  $E_i$ ) and all the available target states (at energy  $E_j$ ) that satisfy the percolation criterion:

$$\begin{aligned} N_b &= \int_{\mathbb{R}^3} g(E_i)g(E_j)\theta(s_c - s_{ij})dE_j dE_i dx_{ij} dy_{ij} dz_{ij} \\ &= 4\pi \int_{\mathbb{R}^+} r_{ij}^2 \int_{\mathbb{R}^2} g(E_i)g(E_j)\theta(s_c - s_{ij})dE_j dE_i dr_{ij} \end{aligned} \quad (5)$$

where  $r_{ij} = \sqrt{x_{ij}^2 + y_{ij}^2 + z_{ij}^2}$ ,  $g(E)$  is the density of states and  $\theta$  is the step function that represents the percolation criterion. The density of localized sites  $N_s$  can be calculated by excluding all sites that do not satisfy the percolation criterion:

$$N_s = \int_{\mathbb{R}} g(E)\theta(s_c K_B T - |E - E_F|)dE \quad (6)$$

Finally, exploiting the carriers concentration equation, the Fermi level  $E_F$  is straightforwardly calculated:

$$p = \int_{-\infty}^{+\infty} g(E)(1 - f(E, E_F))dE \quad (7)$$

where  $f(E, E_F)$  is the Fermi–Dirac distribution:

$$f(E, E_F) = \frac{1}{1 + \exp\left(\frac{E - E_F}{K_B T}\right)} \quad (8)$$

Combining Eqs. (4)–(6) along with Eqs. (7) and (8) to calculate the Fermi energy level, the implicit integral Eq. (4) may be numerically solved and the exponent  $s_c$  of the critical percolation conductance is calculated:

$$\frac{N_b(s_c, E_F)}{N_s(s_c, E_F)} - 2.8 = 0 \Rightarrow s_c \quad (9)$$

This approach was first used by Vissenberg and Matters [6] to derive an approximate analytical expression of the mobility in an organic thin-film transistor by assuming an exponential DOS:

$$g_E(E) = \frac{N_t}{K_B T_0} \exp\left(\frac{E}{K_B T_0}\right)\theta(-E) \quad (10)$$

where  $N_t$  is the total number of states per unit volume and  $T_0$  is the characteristic temperature. Thanks to the mathematical properties of the exponential function, they were able to derive a closed analytical expression of the carriers concentration, of  $s_c$ , and of the conductivity as well. The expression of the mobility as a function of the holes concentration  $p$  and of the temperature  $T$  reads:

$$\mu(p, T) = \frac{\sigma_0}{e} \left( \frac{\left(\frac{T_0}{T}\right)^4 \sin\left(\frac{\pi T}{T_0}\right)}{(2\alpha)^3 B_c} \right)^{\frac{T_0}{T}} p^{\frac{T_0}{T}-1} \quad (11)$$

where  $e$  is the electron charge. This is a very good approximation of the real mobility at large concentrations as, for instance, in the channel of organic thin film transistors (OTFTs) [7]. On the other hand, this expression does not correctly account for the mobility at low carriers concentrations, experimentally observed in organic light emitting diodes (OLEDs), that is almost constant. The field and temperature dependencies of the mobility of OLEDs is well described by a 3-D transport model based on hopping in a correlated Gaussian disordered system [8–10]:

$$\mu = \mu_\infty \exp \left\{ - \left( \frac{3\sigma_{DOS}}{5K_B T} \right)^2 + 0.078 \left[ \left( \frac{\sigma_{DOS}}{K_B T} \right)^{\frac{3}{2}} - 2 \right] \sqrt{\frac{eaE}{\sigma_{DOS}}} \right\} \quad (12)$$

where  $\mu_\infty$  is the zero-field mobility when  $T \rightarrow \infty$ ,  $a \approx 1/N^{1/3}$  is the intersite spacing and  $\sigma_{DOS}$  is the width of the gaussian density of states defined as:

$$g_G(E) = \frac{N_t}{\sqrt{2\pi}\sigma_{DOS}} \exp \left[ - \left( \frac{E}{\sqrt{2}\sigma_{DOS}} \right)^2 \right] \quad (13)$$

As reported in [11,12], the hole mobility measured on OLEDs shows large differences compared to the hole mobility measured on OTFTs. The large mobility differences, up to three orders of magnitude, measured on the two types of devices originates from the strong dependence of the mobility on the charge carrier concentration and in turn on the density of states. As a matter of fact, based on OLEDs and OTFTs device measurements, Tanase et al. [11] suggested that the mobility increase could be explained by means of a single gaussian DOS.

The parameters of Eqs. (11) and (12) are reported in Table 1. They are calculated by fitting the experimental mobility at high (OTFTs) and low (OLEDs) concentrations,  $a = 1.4$  nm is taken from the literature [13]. Since the extracted exponential DOS is well approximated by the gaussian DOS at large carrier concentrations, they concluded that the hole mobility in disordered conjugated polymers could be unified in one single charge transport model.

In this paper, by calculating the exact numerical solution of the VRH Eq. (9) on a generic DOS we show that the gaussian function is a very good approximation of the real DOS at low concentrations only ( $<10^{15}$  carrier/cm<sup>3</sup>). Furthermore, we show that a single gaussian function is a good approximation of the real DOS only for some spe-

**Table 1**

Total number of states per unit volume  $N_t$ , width of the exponential distribution of localized states  $T_0$ , pre-exponential factor  $\sigma_0$ , overlap parameter  $\alpha^{-1}$  and width of the gaussian DOS  $\sigma_{DOS}$  for both P3HT and OC<sub>1</sub>C<sub>10</sub> – PPV [11].

Material	$N_t$ (cm <sup>-3</sup> )	$T_0$ (K)	$\sigma_0$ (S/cm)	$\alpha^{-1}$ (Å)	$\sigma_{DOS}$ (meV)
P3HT	$3 \times 10^{20}$	425	$1.6 \times 10^4$	1.6	98
OC <sub>1</sub> C <sub>10</sub>	$3 \times 10^{20}$	540	$3.1 \times 10^5$	1.4	112

cific disordered organic materials, as for instance P3HT (poly(3-hexyl thiophene)), but generally, it is not able to correctly account for the mobility in the whole range of carrier concentration of other materials. It is worth adding that the numerical solution of VRH is in perfect agreement with the analytical expression of Vissenberg and Matters [6]. Finally, exploiting the numerical approach, we were able to calculate the exact numerical DOS that reproduces the mobility in the whole range of carriers concentration for several organic semiconductors as for instance P3HT and  $OC_1C_{10}$  (poly(2-methoxy-5-(3',7'-dimethyloctyloxy)-p-phenylene vinylene)). Basing on the numerical DOS, we were able to investigate the accuracy of several analytical approximations of the DOS and to understand the physical mechanism that influences the mobility behavior. In Fig. 1, the mobility of P3HT and  $OC_1C_{10}$  calculated by numerically solving Eq. (9) is shown versus carriers concentration. The numerical solution is compared with experimental results both for the gaussian and for the exponential DOS (parameters are reported in Table 1). The numerical mobility at high carriers concentration calculated with the exponential DOS accurately describes the mobility for both PPV materials (the analytical approximation Eq. (11) is overlapped to the numerical one and it is not shown in the figure). The numerical mobility of P3HT calculated by means of a single gaussian DOS accurately describes the experimental data both at low concentrations (OLEDs regime) and at high concentrations (OTFTs regime). At very high concentrations ( $>2 \times 10^{19}$  carriers/cm<sup>3</sup>) it is slightly larger than the experimental one.

On the other hand, the mobility of  $OC_1C_{10}$  – PPV calculated following the same approach is accurate at low concentrations only and fails at high concentration values. The  $OC_1C_{10}$  – PPV mobility abruptly raise when the carriers concentration exceeds  $10^{16}$  cm<sup>-3</sup> and the kink of the characteristic, corresponding to the transition from the low to high concentration regime, could not be explained by means of a single gaussian function. Furthermore, at high concentrations, the slope of the numerical mobility is close to the experimental one while its absolute value is about one order of magnitude lower. In the VRH framework,

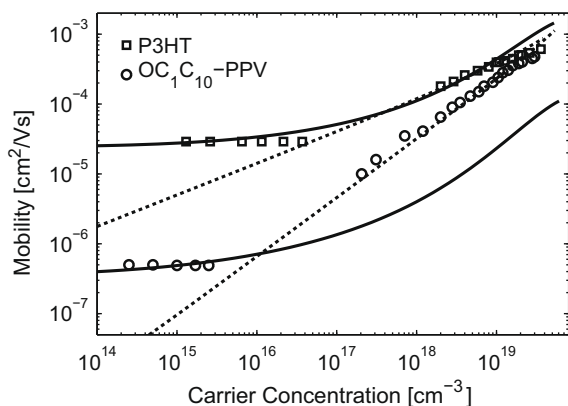


**Fig. 1.** Experimental (symbols) and calculated (lines) mobility as a function of carrier concentration for two different conjugated polymers P3HT and  $OC_1C_{10}$  – PPV (solid line gaussian DOS, dashed line exponential DOS).

the mobility behavior can be roughly explained by remembering that the mobility is energetically activated; hence, the mean carriers energy in the single gaussian DOS is lower than the real one. To further investigate this issue, we have numerically solved Eq. (9) within an optimization framework in order to calculate the exact numerical DOS that fits the  $OC_1C_{10}$  – PPV experimental mobility at room temperature. The optimized numerical DOS is shown in Fig. 2 along with its analytical approximation. The real DOS is very well approximated by:

$$g_N(E) = \min \left\{ N_t^{NE} \exp \left( \frac{E}{K_B T_0^{NE}} \right) \theta(-E), \frac{N_t^{NG}}{\sqrt{2\pi}\sigma_{NG}} \times \exp \left[ - \left( \frac{E}{\sqrt{2}\sigma_{NG}} \right)^2 \right] \right\} \quad (14)$$

where  $N_t^{NE} = 3 \times 10^{20}$  cm<sup>-3</sup>,  $T_0^{NE} = 540$  K,  $N_t^{NG} = 10^{26}$  cm<sup>-3</sup> and  $\sigma_{NG} = 80 \times 10^{-3}$  eV. It is worth noting that the parameters of the exponential DOS at low carrier density are the same of Table 1. Furthermore, the analytical DOS could be easily expressed by combining the functions following the Matissen rule:  $1/g_N(E) = 1/g_{Nexp}(E) + 1/g_{NGauss}(E)$ . In Fig. 3, the mobility of  $OC_1C_{10}$  – PPV numerically calculated with the analytical DOS of (Eq. (14)) is plotted versus the carrier density at different temperatures. A very good agreement results in the whole set of experimental data at different concentrations and temperatures. Same considerations hold for the mobility of several other disordered organic materials. Therefore, it is reasonable to assert that the mobility of disordered organic materials can be explained by the VRH theory both at low and at high carrier concentrations, while the DOS depending on the material could be approximated by a single gaussian function, an exponential function, or by a combination of them. At high holes concentration the DOS is exponential, at low holes concentration is gaussian and for some materials, as for instance P3HT, a single gaussian function can account for the high concentration regime as well. To further check our approach, in Fig. 4 the mobility calculated by means of the analytical DOS of Eq. 14 is compared with the mobility calculated basing on the experimental DOS reported in

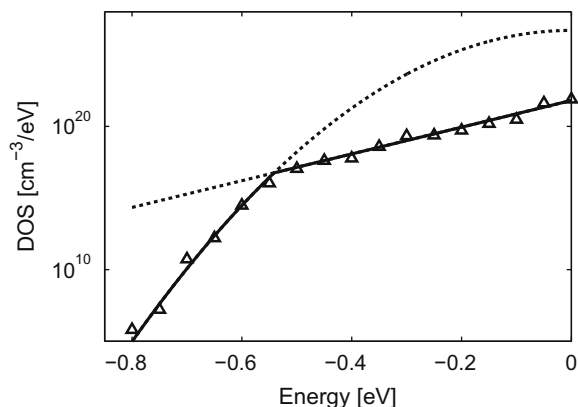


**Fig. 2.** Numerical (symbols) and analytical (solid line) DOS extracted by fitting Eq. (9) on experimental mobility. Dashed lines are the extensions of the exponential and gaussian fitting curves.

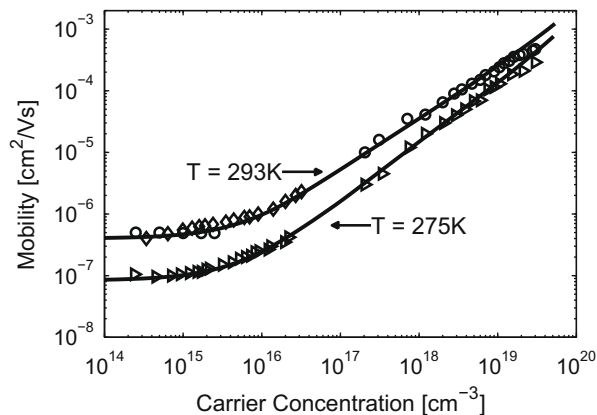


**Fig. 3.** Experimental (symbols) and calculated (solid lines)  $OC_1C_{10}$  – PPV mobility as a function of charge carrier concentration at two different temperatures ( $\circ$  experimental mobility at  $T = 293$  K [11],  $\diamond$  experimental mobility at  $T = 293$  K [14],  $\triangleright$  experimental mobility at  $T = 275$  K [14]).

[10] and with the experimental one of [11]. One can see a very good agreement at high energy while the apparent remarkable difference at low energy is exactly the same reported by the authors [10] (Fig. 4b). They attribute this discrepancy to the presence of anions that tends to localize the mobile holes. In the light of our analysis, it is clear that the presence of anions that localize the mobile holes strongly influence the DOS at low carrier concentration and this affects the mobility as well. Finally, in order to investigate the dependence of the mobility on the carrier density at low concentrations, in Fig. 5 the charge carrier as a function of the Fermi level of  $OC_1C_{10}$  – PPV is shown: the numeric DOS is compared with the exponential one (Table 1). In the concentration range corresponding to OLEDs measurements ( $10^{14}$ – $10^{16}$  carriers/cm<sup>3</sup>), the charge density calculated with the exponential DOS is larger than the numeric one which is roughly gaussian. Since the Fermi level is a measure of the carriers mean energy, the average carriers energy calculated with the numeric DOS turns out to be lar-

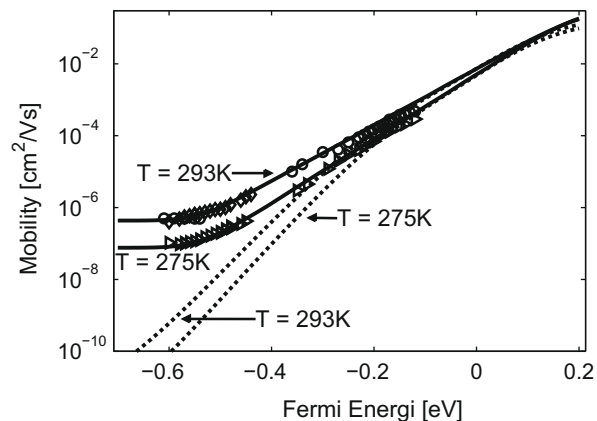


**Fig. 4.** Experimental (symbols) and calculated (lines)  $OC_1C_{10}$  – PPV mobility as a function of the Fermi energy level at two different temperatures ( $\circ$  experimental mobility at  $T = 293$  K [11],  $\diamond$  experimental mobility at  $T = 293$  K [14],  $\triangleright$  experimental mobility at  $T = 275$  K [14]). Solid line, analytical DOS of (Eq. 14), dashed lines, experimental DOS of [10].

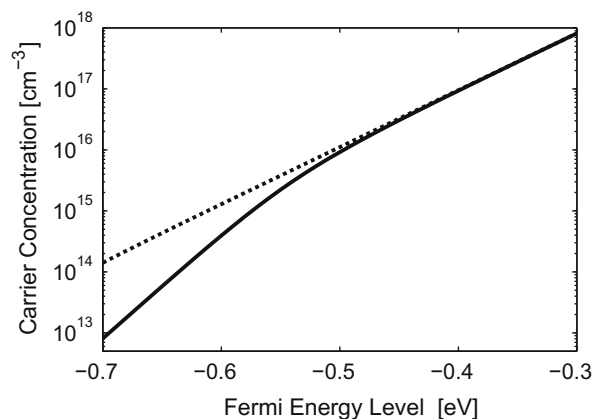


**Fig. 5.** Carrier concentration as a function of Fermi energy level. (dashed line: exponential DOS, solid line: extracted gaussian-like DOS).

ger. In a VRH framework, the mobility based on energy-activated hopping is larger as well. Furthermore, in a gaussian DOS thanks to the quadratic exponential dependence of the density of states on Fermi energy level is larger and almost pinned and the hopping is easier (Eq. (1)). Hence the mobility is larger and large variations of the charge density correspond to small changes of the carriers mean energy and of the mobility as well.

Concluding, the hole mobility of disordered organic semiconductors was calculated by numerically solving the VRH equations. Our calculations show that the hole mobility can be explained by means of the VRH also in the low concentration regime and that the strong dependence on the charge carrier density is strictly correlated to the shape of the DOS. Furthermore, we have numerically calculated the exact DOS of P3HT and  $OC_1C_{10}$  – PPV showing that in general a single gaussian function is not sufficient to explain the mobility behavior in the whole range of concentrations (OLED, OTFT); depending on the material, it can be approximated by a single gaussian, an exponential, or by a combination of them.

## References

- [1] V. Ambegaokar, B.I. Haperin, J.S. Langer, Phys. Rev. B 4 (1971) 2612.
- [2] S.D. Baranovskii, I.P. Zvyagin, H. Cordes, S. Yamasaki, P. Thomas, J. Non-Cryst. Solids 299 (2002) 416.
- [3] I.I. Fishchuk, V.I. Arkhipov, A. Kadashchuk, P. Heremans, H. Bassler, Phys. Rev. B 76 (2007) 045210.
- [4] A. Miller, E. Abraham, Phys. Rev. 120 (1960) 745.
- [5] S. Kirkpatrick, Rev. Mod. Phys. 45 (1973) 574.
- [6] M.C.J.M. Vissenberg, M. Matters, Phys. Rev. B 57 (1998) 12964.
- [7] F. Torricelli, Zs. M. Kovács Vajna, L. Colalongo, Appl. Phys. Lett. 92 (2008) 113306.
- [8] H. Bassler, Phys. Status Solidi B 175 (1993) 15.
- [9] S.V. Novikov, D.H. Dunlap, V.M. Kenkre, P.E. Parris, A.V. Vannikov, Phys. Rev. Lett. 81 (1998) 4472.
- [10] I.N. Hulea, H.B. Brom, A.J. Houtepen, D. Vanmaekelbergh, J.J. Kelly, E.A. Meulenlamp, Phys. Rev. Lett. 93 (2004) 166601.
- [11] C. Tanase, E.J. Meijer, P.W.M. Blom, D.M. de Leeuw, Phys. Rev. Lett. 91 (2003) 216601.
- [12] C. Tanase, P.W.M. Blom, D.M. de Leeuw, E.J. Meijer, Phys. Status Solidi A 201 (2004) 1236.
- [13] H.C.F. Martens, P.W.M. Blom, H.F.M. Schoo, Phys. Rev. B 61 (2000) 7489.
- [14] C. Tanase, P.W.M. Blom, D.M. de Leeuw, Phys. Rev. B 70 (2004) 193202.

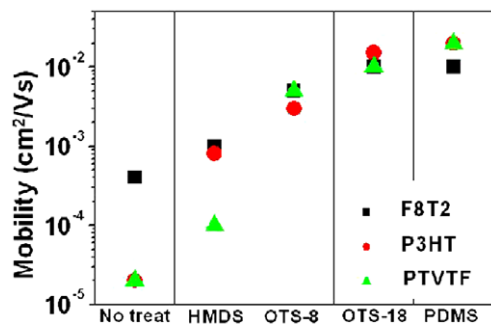


**Fig. 1.** Correlation between the surface treatment of the SiO<sub>2</sub> dielectric layer and the field-effect mobility. Hydrophobicity of the dielectric surface increases from left to right.

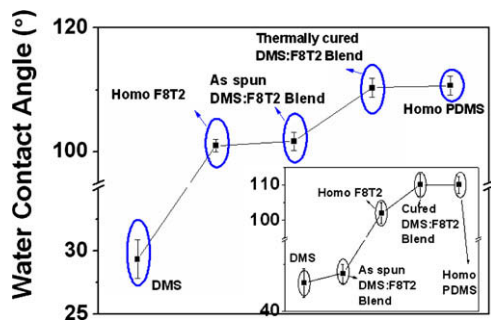


**Fig. 2.** Water contact angles on the top surfaces of various films. Inset: measured at the bottom surface. (Because DMS can be cured even at room temperature, the water contact angle of the bottom surface for the DMS film is a little larger than that of top surface.)

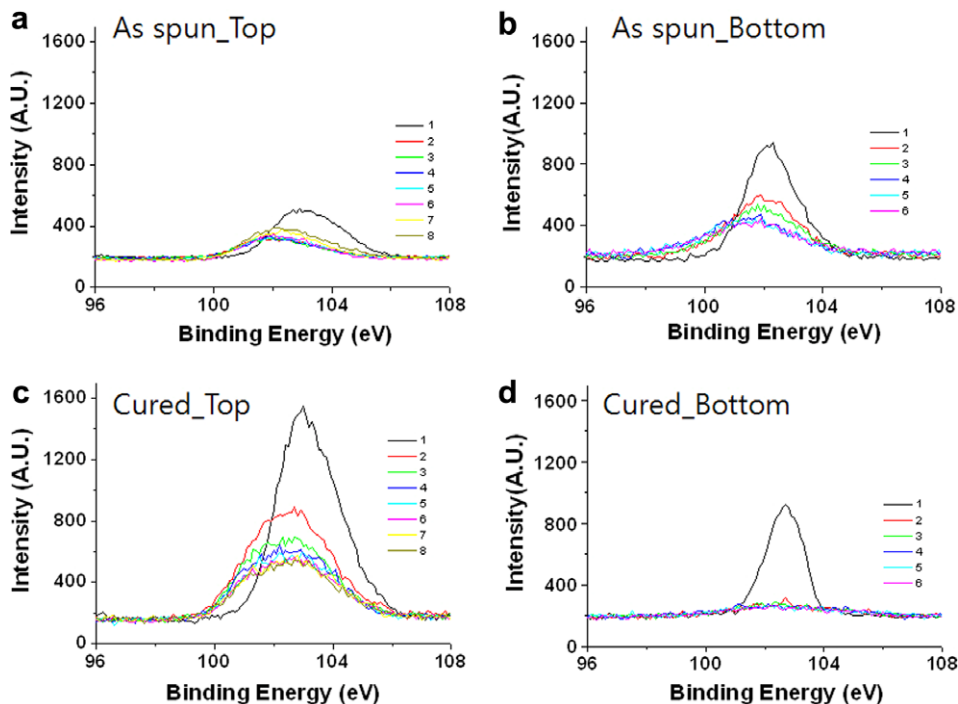


**Fig. 3.** Silicon content measured with X-ray photoelectron spectroscopy (XPS) as a function of the Ar sputtering time for the top surface of the as-spun film (a), the bottom surface of the as-spun film (b), the top surface of the cured film, (c) and the bottom surface of the cured film (d).

ilazene (HMDS) [10], octadecyltrichlorosilane (OTS) [11,12], and other silanes [13]. Recent studies have established that among the silanes examined to date, the most hydrophobic molecule, OTS, is the best surface modifier for SiO<sub>2</sub> dielectric layers, in that its use results in more edge-on structures and better electrical characteristics of the over-deposited polymeric semiconductor layer [5,6,14]. Another approach to modifying the dielectric surface to enhance conjugated polymer deposition is the phase separation method. Cho and coworkers have fabricated a hydrophobic semiconductor-top and hydrophilic poly(methylmethacrylate) (PMMA)-bottom structure with high mobility [15]. Such dielectric surface treatment via simple phase separation is of great interest from the viewpoint of OFET commercialization, given the time-consuming nature of the SAM treatment procedure.

Polymeric semiconductors exhibit optimized transistor characteristics when deposited on hydrophobic surfaces, so it is expected to be useful to fabricate a hydrophobic semiconductor-top and a more hydrophobic polymer-bottom structure via phase separation, as arises for a semiconductor on a hydrophobic SAM layer. In the present study, therefore, a hydrophobic PDMS-bottom and F8T2-top structure was fabricated by spin coating a dimethylsiloxane (DMS)/poly(9,9-dioctylfluorene-alt-bithiophene) (F8T2) blend with a curing agent onto a silicon oxide substrate, and then subjecting the resulting layer to thermal treatment. After thermal treatment, the DMS-bottom layer was cured to polydimethylsiloxane (PDMS) and became thinner as a result of the upward motion of the hydrophobic PDMS molecules, as confirmed using XPS, contact angle

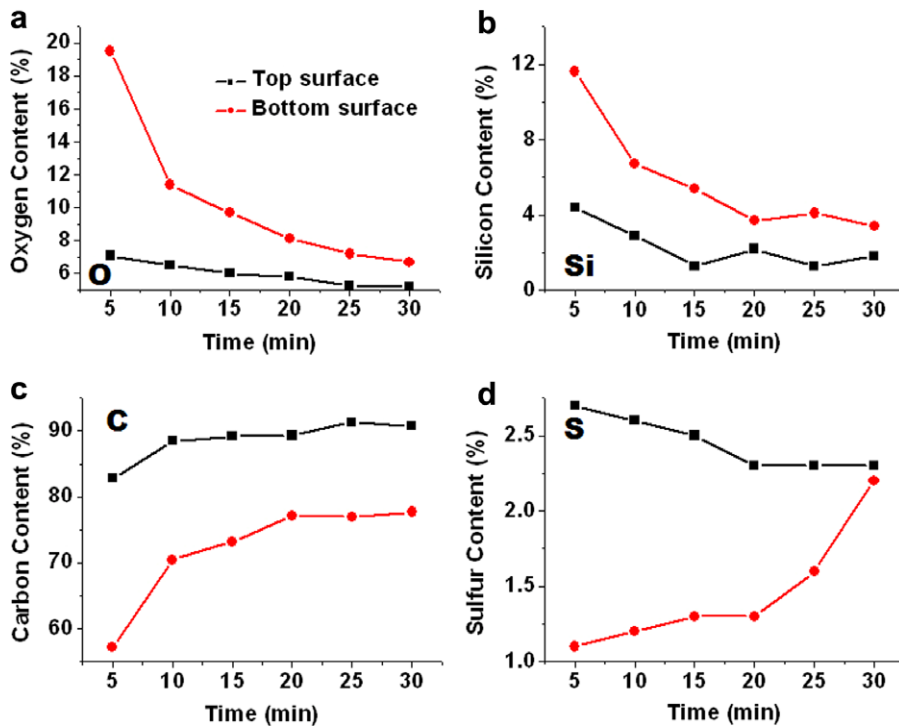


Fig. 4. (a) Oxygen, (b) silicon, (c) carbon, and (d) sulfur contents of the top and bottom surfaces of as-spun films, as measured using X-ray photoelectron spectroscopy (XPS) with Ar sputtering.

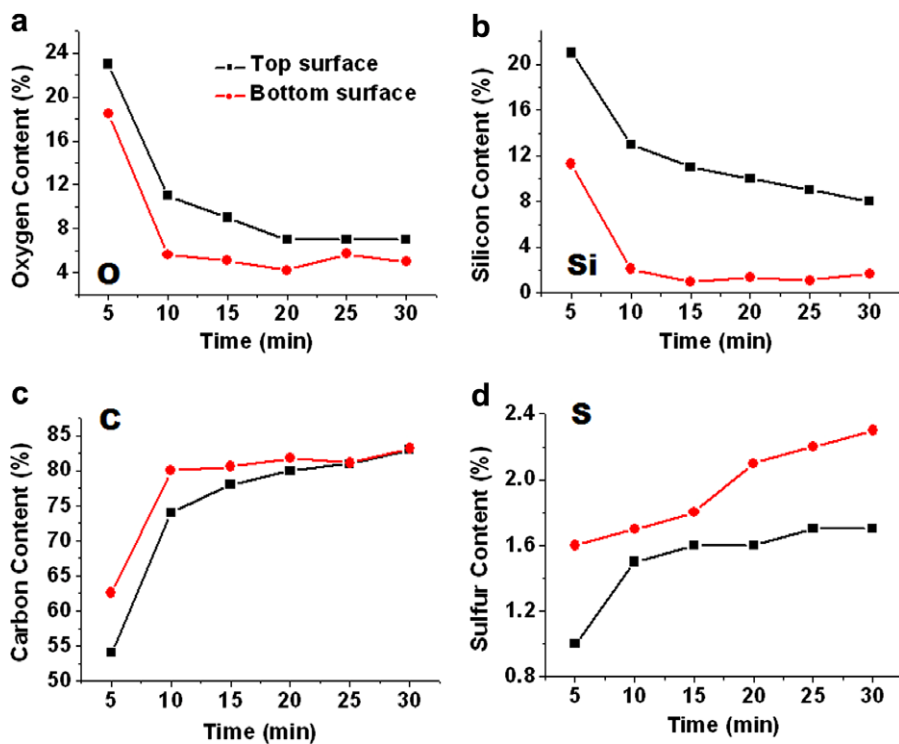


Fig. 5. (a) Oxygen, (b) silicon, (c) carbon, and (d) sulfur contents of the top and bottom surfaces of thermally cured films, as measured using X-ray photoelectron spectroscopy (XPS) with Ar sputtering.

measurements, and AFM analysis. An OFET device fabricated from a DMS:F8T2 blend on an untreated SiO<sub>2</sub> dielectric layer was found to exhibit a high FET mobility of 0.01 cm<sup>2</sup>/Vs, which is similar to that obtained with an OTS-treated SiO<sub>2</sub> dielectric layer.

## 2. Experimental

F8T2 ( $M_n = 20,668$  g/mol,  $M_w = 43,137$  g/mol) was purchased from Aldrich Chemical Co. Sylgard 184 Silicone Elastomer containing dimethylsiloxane and a curing agent (10:1 [w/w]) was purchased from Dow Corning Co. and used without further purification.

Bottom gate–top contact OFETs were fabricated on a common gate of highly *n*-doped silicon with a 300 nm thick thermally grown SiO<sub>2</sub> dielectric layer. Films of DMS:F8T2 with various DMS contents (3–30 wt%) were spin coated at 2000 rpm from 0.7 wt% chloroform solution. DMS:F8T2 blend films were cured for 1 h at 120 °C in a convection oven. Gold source and drain electrodes (100 nm) were evaporated on top of the semiconductor. In all measure-

ments, we used a channel length ( $L$ ) of 150 μm and a channel width ( $W$ ) of 1500 μm. The electrical characteristics of the FETs were measured in air using Keithley 236 and 2400 source/measure units. AFM (Multimode IIIa, Digital Instruments) operating in tapping mode was used to examine the surface morphologies of the semiconductors. The carrier mobility was calculated in the saturation regime from the slope of a plot of the square root of the drain current versus gate voltage ( $V_G$ ) by fitting the data to the following equation:  $I_{DS} = (WC_i/2L)\mu(V_G - V_{th})^2$ , where  $I_{DS}$  is the drain current,  $\mu$  is the carrier mobility, and  $V_{th}$  is the threshold voltage. XPS analyses were performed using an ESCA equipped with a Mg Ka X-ray source, 1253.6 eV.

## 3. Results and discussion

First, we investigated the suitability of a PDMS layer as a dielectric surface modifier. Three polymeric semiconductors known to exhibit high mobilities ( $>10^{-2}$  cm<sup>2</sup>/Vs), specifically F8T2, P3HT, and poly[(1,2-bis-(2'-thienyl)vinyl-5',5''-diyl)-alt-(9,9-dioctyldecylfluorene-2,7-diyl)] (PTVTF) [14], were used as the active layers of thin film transistors

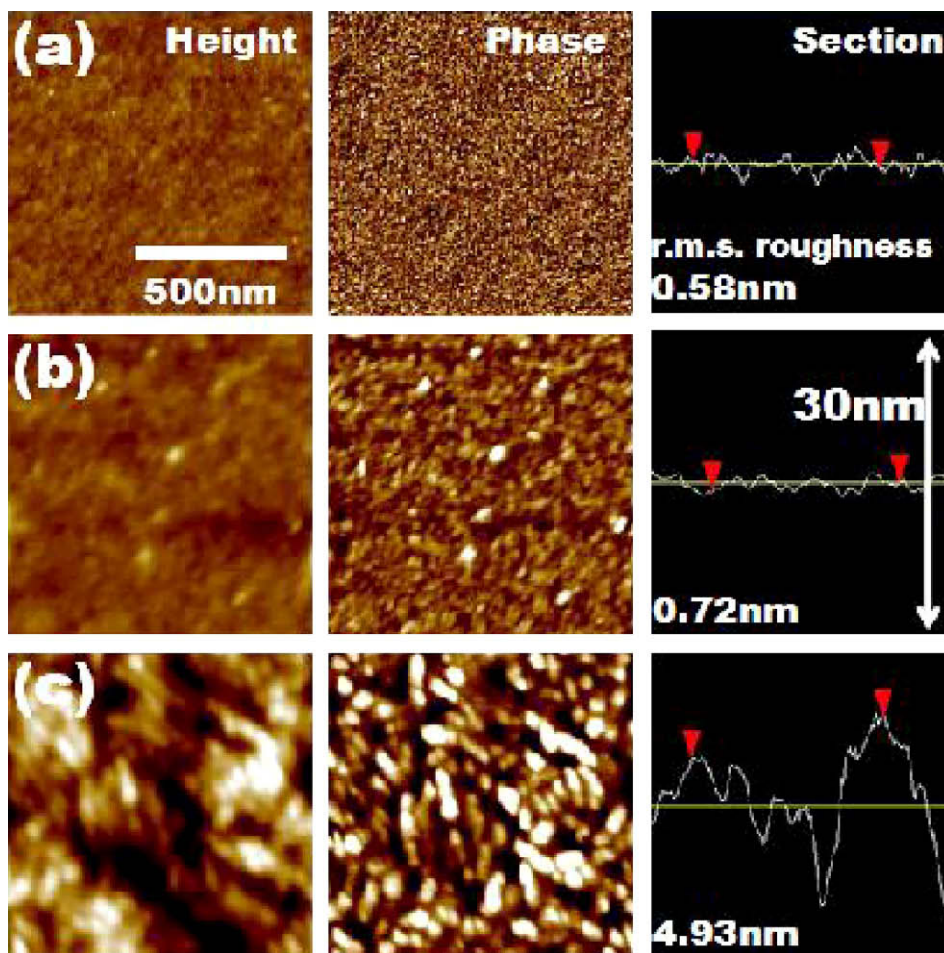


**Fig. 6.** Atomic force microscopy (AFM) images of (a) homo F8T2, (b) as-spun DMS:F8T2 blend, and (c) thermally cured DMS:F8T2 blend. In (a–c), the image on the left shows the height, the middle image shows the phase, and the image on the right shows a section with the r.m.s. roughness.

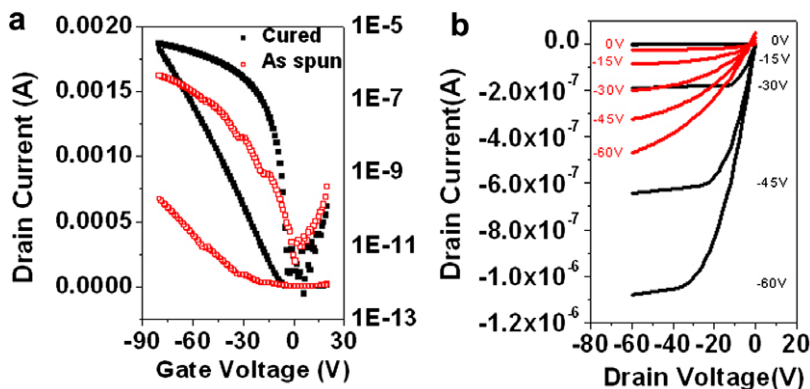


Fig. 7. (a) Transfer characteristics of as-spun and thermally cured DMS:F8T2 blend OTFTs measured under ambient air, and (b) the output characteristics for various gate voltages.

with a bottom gate–top contact geometry. In each case, the SiO<sub>2</sub> dielectric surface was modified with HMDS, OTS-8, OTS-18, or PDMS. The SAM treatments were carried out as described elsewhere. For the spin-coated PDMS layer, we used Sylgard 184 Silicone Elastomer containing dimethylsiloxane and a curing agent (10:1 [w/w]) in toluene. The water contact angle of the untreated dielectric was  $25 \pm 2^\circ$ , while those of the surface-treated dielectrics were  $68 \pm 2^\circ$  (HMDS),  $99 \pm 2^\circ$  (OTS),  $108 \pm 1^\circ$  (ODTS), and  $110 \pm 1^\circ$  (PDMS). The FET mobilities obtained for these transistors are summarized in Fig. 1. We found that regardless of the type of semiconductor, the FET mobility increased as the SiO<sub>2</sub> dielectric surface became more hydrophobic. The most hydrophobic modifier examined, PDMS, was found to be a good dielectric surface modifier.

Fig. 2 shows the water contact angles of the various films tested in this study. Based on the huge difference between the contact angles of as-spun DMS ( $29 \pm 2^\circ$ ) and thermally cured PDMS ( $110 \pm 1^\circ$ ), it is expected that when DMS and the curing agent are blended with the polymeric semiconductor ( $103 \pm 1^\circ$ ) and spin coated, the hydrophilic DMS will preferentially bind to the hydrophilic SiO<sub>2</sub> substrate to generate a bottom layer. This outcome appears likely because the water contact angles at top surface of homo F8T2 and the as-spun DMS:F8T2 blend are almost the same. Also, at the bottom surface, water contact angle of as-spun DMS and DMS:F8T2 blend are similar. To investigate the distributions of the chemical species in the layers, XPS analysis was performed for both the bottom and top surfaces of the film by carrying out Ar sputtering with an average etching rate of 0.6 nm/min. The bottom surface of the as-spun film was separated from the SiO<sub>2</sub> dielectric by immersion in liquid nitrogen, which induces separation due to the difference in thermal expansion coefficient between the organic and inorganic layers. Fig. 3 shows the Si 2p XPS spectra of the top (a) and bottom surfaces (b) of the as-spun film, and the top (c) and bottom (d) surfaces of the thermally cured film. In addition, the O, C and S contents were determined for the as-spun and thermally cured films (Figs. 4 and 5, respectively). In the as-spun film, the silicon and oxygen contents of the top surface are much lower than those of the bottom surface (Fig. 4a and b). On the other hand, the carbon and sulfur contents, which

are mainly due to F8T2, dominate in the top surface (Fig. 4c and d). These findings indicate that the spun film of the DMS:F8T2 blend with curing agent is phase separated, with hydrophilic DMS forming the bottom layer. Comparison of the data in Figs. 4 and 5 reveals another interesting phenomenon associated with thermal curing. Specifically, thermal curing induces a decrease in the oxygen and silicon contents of the bottom surface, indicating that the thickness of the PDMS layer decreases as a result of the thermal curing. At the same time, thermal curing induces dramatic increases in the oxygen and silicon contents of the top surface. These trends indicate that the hydrophobic PDMS molecules move up through the film; PDMS has a very low  $T_g$  ( $-127^\circ\text{C}$ ) and a low  $T_m$  ( $-54^\circ\text{C}$ ). The hypothesis that PDMS molecules move up through the film is supported by the observation that the water contact angle of the cured film of the DMS:F8T2 blend is very similar to that of the PDMS homopolymer. Given that the presence of too much surface modifier in the channel region can hinder charge transport, the thinning of the PDMS layer during thermal curing may improve the transistor performance. Furthermore, because the thermally cured film is covered with PDMS due to the upward motion of PDMS, the cured DMS:F8T2 blends are resistant to solvents such as chloroform, chlorobenzene, and toluene, which is important for solution-processed passivation. This

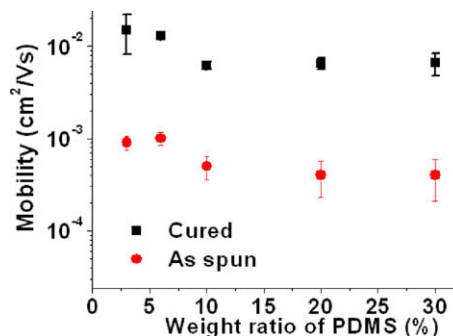


Fig. 8. Dependence of the FET mobility on the weight ratio of the DMS:F8T2 blend.

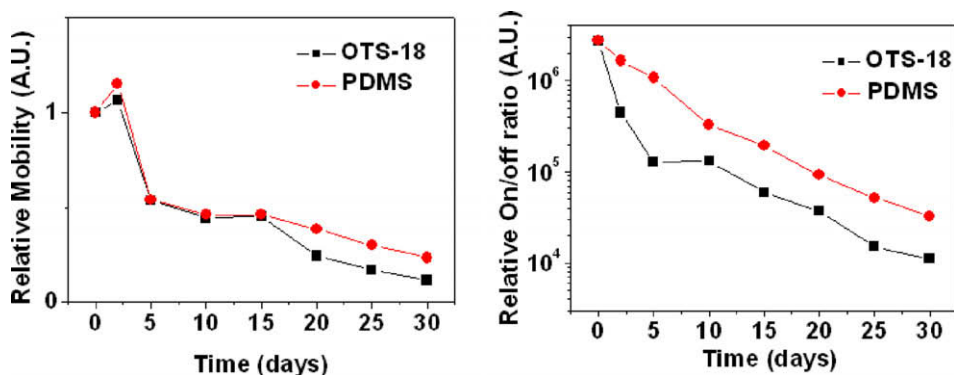


Fig. 9. Time dependence of the FET mobility and the on/off ratio for F8T2 on an OTS-18 treated SiO<sub>2</sub> dielectric and for a DMS:F8T2 blend on a SiO<sub>2</sub> dielectric.

resistance to organic solvents is another advantage of DMS:polymeric semiconductor blends.

The AFM analysis results are shown in Fig. 6. The AFM image of the surface of the as-spun DMS:F8T2 blend shows a homogeneous surface morphology with some nanorod-like crystalline domains, similar to the surface of the F8T2 homopolymer. After thermal curing, the surface has a very rough morphology with an r.m.s. roughness of 4.9 nm (Fig. 6d). In particular, the phase image of the cured film reveals the co-existence of quite different phases. Since there is an increase in the PDMS content of the top surface after thermal curing, the features in this image are thought to result from co-existing crystalline F8T2 and amorphous PDMS phases.

F8T2 FET devices with PDMS-treated dielectric layers were fabricated with a bottom gate–top contact geometry. For the spin-coating of the DMS:F8T2 blend with the curing agent, toluene, chloroform, and chlorobenzene were used as solvents. The performance of the resulting devices was independent of the solvent used. Representative transfer and output curves of the as-spun and thermally cured DMS:F8T2 blend FET devices are shown in Fig. 7. The average FET mobility of the thermally cured devices was found to be 0.013 cm<sup>2</sup>/Vs, with an average on/off ratio of 2 × 10<sup>6</sup>. The corresponding values for the as-spun devices, however, were much lower (average mobility 9 × 10<sup>−4</sup> cm<sup>2</sup>/Vs and on/off ratio 3 × 10<sup>4</sup>). To examine the relationship between the weight ratio of PDMS (DMS + curing agent) and FET performance, devices were fabricated using various weight ratios of PDMS (3, 6, 10, 20 and 30 wt%); the FET mobilities are summarized in Fig. 8. When the weight ratio of PDMS was 3 or 6 wt%, the FETs exhibited optimum performance with mobilities over 10<sup>−2</sup> cm<sup>2</sup>/Vs. For PDMS contents of 10 wt% or more, however, the mobility decreased to less than 10<sup>−2</sup> cm<sup>2</sup>/Vs. This result indicates that the presence of too much PDMS disturbs charge transport in the channel region. In addition, we also tested a P3HT:DMS blend and obtained a similar mobility (above 10<sup>−2</sup> cm<sup>2</sup>/Vs), which shows that the phase separation of DMS:polymer blends can be applied to other polymeric semiconductors.

Finally, to investigate the air-stability of the DMS:F8T2 blend devices, the shelf lifetime of a DMS:F8T2 device was compared with the lifetimes of OFET devices based

on F8T2 homopolymer with an OTS-treated SiO<sub>2</sub> dielectric layer over a 30-day period (Fig. 9). The thermally cured DMS:F8T2 blend was found to exhibit slightly better air stability, especially in terms of the on/off ratio. Since the top surface is not fully covered by the PDMS layer, it is not clear whether a clear passivation effect has been demonstrated. However, we are currently investigating ways to dramatically enhance the air stability of this blend system by increasing the thickness of the top PDMS layer and by treating the top PDMS layer with oxygen plasma.

#### 4. Conclusions

By spin coating a DMS:F8T2 blend onto a SiO<sub>2</sub> substrate and then subjecting the resulting layer to thermal curing, we fabricated a hydrophobic PDMS-bottom and semiconductor F8T2-top structure with a mobility of 1 × 10<sup>−2</sup> cm<sup>2</sup>/Vs, as confirmed with XPS, AFM, and contact angle measurements. Using this DMS:F8T2 blend, hydrophobic dielectric surface treatment and passivation can be achieved simultaneously by simply coating the blend onto the SiO<sub>2</sub> dielectric.

#### Acknowledgement

This research was supported by a Grant (F0004011-2008-31) from the Information Display R&D Center, a 21st Century Frontier R&D Program funded by the Ministry of Knowledge Economy of Korea.

#### References

- (a) R.A. Street, W.S. Wong, S.E. Ready, I.L. Chabiny, A.C. Arias, S. Limb, A. Salleo, R. Lujan, *Mater. Today* 9 (2006) 32; (b) B.S. Ong, Y. Wu, Y. Li, P. Liu, H. Pan, *Chem. Eur. J.* 14 (2008) 4766.
- (a) Z. Bao, Y. Feng, A. Dodabalapur, *Chem. Mater.* 9 (1997) 1299; (b) H. Sirringhaus, T. Kaxase, R.H. Friend, T. Shimoda, M. Inbasekaran, W. Wu, E.P. Woo, *Science* 290 (2000) 2123; (c) I. Osaka, G. Sauv , R. Zhang, T. Kowalewski, R.D. McCullough, *Adv. Mater.* 19 (2007) 4160.
- G.H. Gelinck, H.E.A. Huitema, E. Van Veenendaal, E. Cantatore, L. Schrijnemakers, J.B.P.H. Van Der Putten, T.C.T. Geuns, M. Beenhakkers, J.B. Giesbers, B. Huisman, E.J. Meijer, E.M. Benito, F.J. Touwslager, A.W. Marsman, B.J.E. van Rens, D.M. de Leeuw, *Nat. Mater.* 3 (2004) 106.



- [4] H. Sirringhaus, P.J. Brown, R.H. Friend, M.M. Nielsen, K. Bechgaard, B.M.W. Langeveld-Voss, A.J.H. Spiering, R.A.J. Janssen, E.W. Meijer, P. Herwig, D.M. de Leeuw, *Nature* 401 (1999) 685.
- [5] B.S. Ong, Y. Wu, P. Liu, S. Gardner, *J. Am. Chem. Soc.* 126 (2004) 3378.
- [6] I. McCulloch, M. Heeney, C. Bailey, K. Genevicius, I. MacDonald, M. Shkunov, D. Sparrowe, S. Tierney, R. Wagner, W. Zhang, M.L. Chabinyc, R.J. Kline, M.D. McGehee, M.F. Toney, *Nat. Mater.* 5 (2006) 328.
- [7] T. Umeda, S. Tokito, D. Kumaki, *J. Appl. Phys.* 101 (2007) 054517.
- [8] R.J. Kline, M.D. McGehee, E.N. Kadnikova, J. Liu, J.M.J. Frechet, *Adv. Mater.* 15 (2003) 1519.
- [9] M.L. Chabinyc, M.F. Toney, R.J. Kline, I. McCulloch, M. Heeney, *J. Am. Chem. Soc.* 129 (2007) 3226.
- [10] H. Sirringhaus, N. Tessler, R.H. Friend, *Science* 280 (1998) 1741.
- [11] Y.Y. Lin, D.J. Gundlach, S. Nelson, T.N. Jackson, *IEEE Electron Device Lett.* 18 (1997) 606.
- [12] J. Collet, O. Tharaud, C. Legrand, A. Chapoton, D. Vuillaume, *Mater. Res. Soc., Symp. Proc.* 488 (1998) 407.
- [13] A. Salleo, M.L. Chabinyc, M.S. Yang, R.A. Street, *Appl. Phys. Lett.* 81 (2002) 4383.
- [14] D.S. Chung, S.J. Lee, J.W. Park, D.B. Choi, D.H. Lee, J.W. Park, S.C. Shin, Y.H. Kim, S.-K. Kwon, C.E. Park, *Chem. Mater.* 20 (2008) 3450.
- [15] L. Qiu, J.A. Lim, X. Wang, W.H. Lee, M. Hwang, K. Cho, *Adv. Mater.* 20 (2008) 1141.

statistical methods to investigate the filament based memory system. The devices were based on a metal/polymer/metal structure, similar to the crosslinkable devices we reported earlier. Polyfluorene (PFO) with dimethyl-benzyl end capping group was chosen as the polymer active layer. Since it contains no known donor and acceptor pairs and only carbon and hydrogen in its chemical formula, the possibility of occurrence of other reported switching mechanisms [4,17–19] is negligible. Batch to batch variation is also lower in the commercially available polymer. We studied the variations between devices with the same processes and the variations between switching cycles within the same device. We proposed a model to explain the results.

## 2. Experimental

PFO was purchased from American Dye Source and used without further purification. The polymer was dissolved in chlorobenzene (1 wt% of the solvent), and filtered with a 0.45  $\mu\text{m}$  syringe filter. The polymer solution was spin coated onto the glass substrates with pre-patterned indium tin oxide (ITO). Finally, a 50 nm thick aluminum layer was thermally evaporated on top of the polymer film, at a rate of 0.1 nm per second. The device structure is shown in the inset of Fig. 1. The active area of the device was defined by the overlapped region of the top and bottom electrodes, which is about 0.2  $\text{mm}^2$ .

The current–voltage (*IV*) characteristics were measured in a vacuum probe station with an Agilent 4155C semiconductor parameter analyzer. The capacitance was measured using an HP 4284A LCR meter. Cross-section scanning electron microscope (xSEM) images were taken by a FEI Nova 600 Nanolab Dualbeam™ SEM/Focused ion beam (FIB).

## 3. Results and discussion

A typical *IV* curve, as shown in Fig. 1, had similar shape as previously studied crosslinkable polymer memory devices [9]. Starting from the low conductivity state (OFF state), when the voltage increased to between 3 and 4 V,

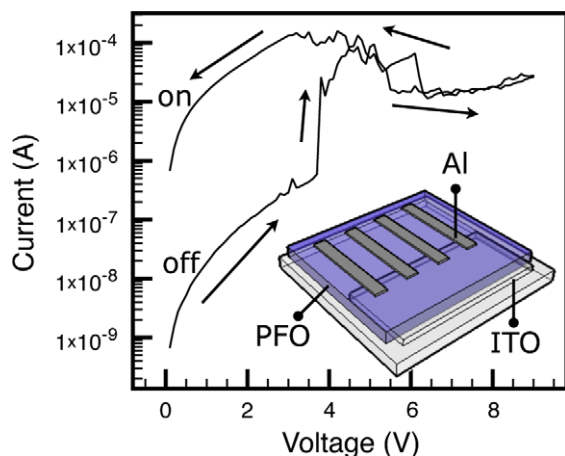


Fig. 1. Basic *IV* of the polymer memory device. The inset shows the device structure. The ITO bottom electrode is connected as the ground.

the device switched abruptly to a high conductivity state (ON state). A negative differential resistance (NDR) region followed and the current reached a minimum at about 6 V. During the reverse sweep, the device stayed at the ON state even when the voltage dropped below 4 V. The device could also be written to the ON state by a voltage pulse of 4 V, and erased to the OFF state by a pulse between 8 and 10 V. The device was read at 1 V, without disturbing its state.

No noticeable differences in the shape of the *IV* curves were observed when the switching behavior was tested through a temperature range of  $-20$ – $85$   $^{\circ}\text{C}$ . The conductivities of both ON and OFF devices were also stable for more than 20 h at  $85$   $^{\circ}\text{C}$ . The capacitances of the device at both states were the same, and depended only on the thickness of the polymer film.

It was noticeable that some of the devices, especially the ones with thicker polymer layers, required an initial forming process [20] before the observation of the memory phenomena. These devices were formed by applying a voltage bias higher than the 4 V writing voltage, ranging from 5 to above 20 V, with a 10  $\mu\text{A}$  current compliance (note: during the erasing process, the current compliance was set at 10 mA). The forming process could also be considered as an abnormal writing process which used a higher voltage since the current compliance would keep the device in the ON state. After the forming process, the device could be switched ON by a writing voltage as low as that of the devices which did not require forming, i.e. 4 V.

### 3.1. Device to device variation

Since the required forming voltage, or the initial writing voltage, varies from device to device, we first analyzed the distribution of the voltages. We define the switching probability as the percentage of devices which can be successfully written to ON state and erased to OFF state at least one time. The ON state is defined as the state with a current above 100 nA at 1 V, and OFF state is below 10 nA at 1 V. All the writing (forming) pulses were limited with a 10  $\mu\text{A}$  compliance. For every device, the initial writing voltage was 4 V, and if it was not successful, the writing (forming) voltage was increased by 1 V until the device was successfully written.

Fig. 2a shows the switching probability as a function of forming voltage for devices with different values of polymer layer thickness. Generally, the switching probability increased with higher forming voltage. The figure also shows that devices with thinner polymer layers were more likely to be switched successfully. Devices with thicker films which did not work at first might work after using a higher forming voltage. However, as shown in Fig. 2b, the probability was not determined by the electric field based on the average thickness of the film. For example, devices with 400 nm thick polymer layers did not have the same switching probability as those with 40 nm thick polymer layers even if 40 V was used. This is consistent with our previous understanding that the switching processes happen at some non-uniform regions within the devices [10].

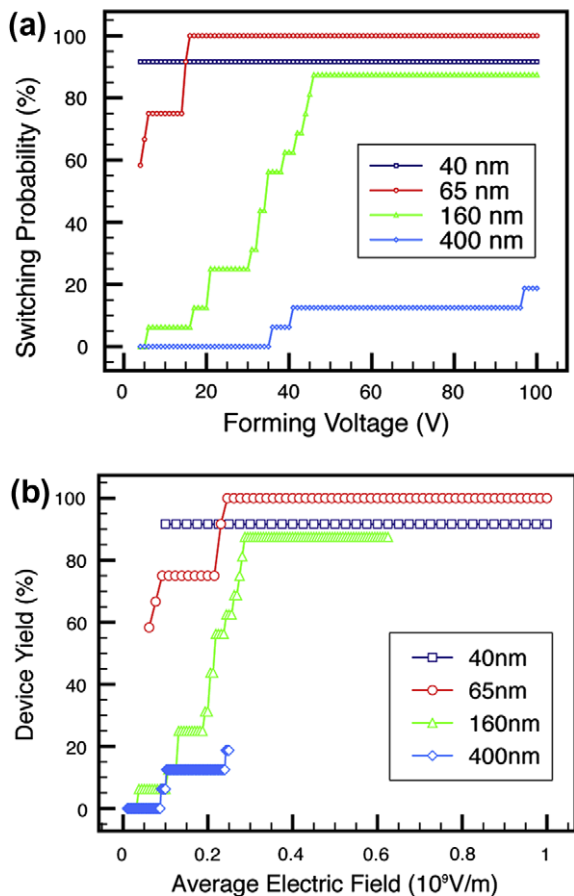


**Fig. 2.** Switching probability for devices with different polymer layer thickness, as a function of (a) forming voltage, (b) average electric field calculated from dividing the forming voltage by the average polymer film thickness.

Next, we studied the non-uniformities of our device using cross-section scanning electron microscope (xSEM). Cross-section slices of the device were prepared using focused ion beam (FIB). In most regions of the device, the polymer film thickness was uniform at 50 nm, as shown in Fig. 3a. However, at a few spots, we observed a much narrower gap between the electrodes (Fig. 3b). Localized electric field at these spots could be much greater than at other regions. Therefore we believe that these spots are crucial for the switching phenomenon, and their existence determines the device switching probability.

According to this observation, we attribute the switching behavior to the formation and rupture of filamentary conductive paths [10,21–23] at localized spots [8] such as the one shown in Fig. 3b, similarly to the switching mechanism proposed for oxide based resistive memories [12]. During the forming and writing processes, a conductive link can build between the electrodes possibly as a result of the ionization and injection of metallic materials into the film under high electric field [22]. The erasing process at 10 V results in a very high current flowing through the conductive link, causing the rupture of the link [10,22,24,25].

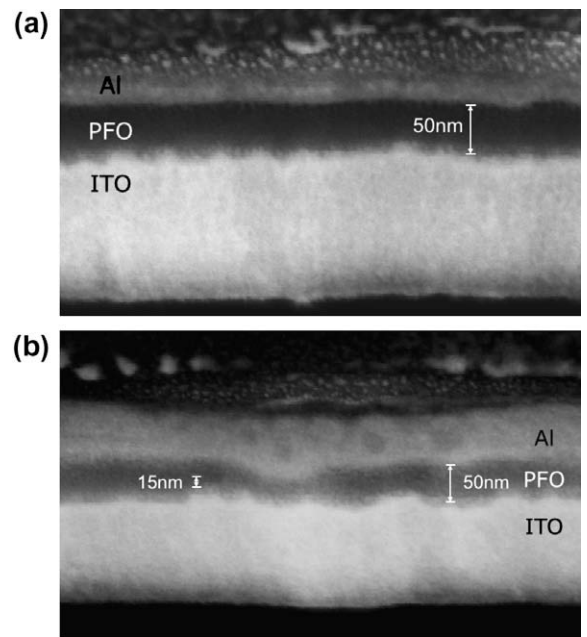


**Fig. 3.** Cross-section SEM images of the device at different spots. (a) In uniform regions. (b) In non-uniform regions.

The distribution of electric field near the protrusion from the electrode was studied by solving the Poisson equation using the 3D finite element method. The geometries used in our model were based on the xSEM image. The metallic and polymeric films were simplified as parallel plates. The protrusion from the metal was modeled as a hemisphere with 30 nm radius. Using the capacitance data and geometry of our device, we estimated that the dielectric constant of our polymer film to be around 4.

Fig. 4a shows the distribution of electric field for a 40 nm device under a normal writing voltage of 4 V. The maximum local field strength at the tip of the protrusion can reach  $4.86 \times 10^8$  V/m, which is more than four times that of the uniform regions. The calculated electric field at localized spots during the writing process is consistent with the data from Cu/P3HT/Al memory system previously reported by Joo et al. [22], which is above  $10^8$  V/m.

Fig. 4b shows the simulated electric field distribution for devices with different thickness. The voltages used are determined by the minimum voltage required for the maximum switching probability (Fig. 2a), which are 4 V for 40 nm devices, 16 V for 65 nm devices, 50 V for 160 nm devices, and 100 V for 400 nm devices. In all cases the protrusion is assumed to have a radius of 30 nm. The electric field along the vertical line crossing the protrusion tip has been plotted as a function of vertical position  $z$ . For 40, 65 and 160 nm devices, the minimum values of the electric field inside the polymer film are about the same, which are above  $3.0 \times 10^8$  V/m. Correspondingly in Fig. 2, the three types all gave high switching probability (>80%) with necessary writing voltages. For the 400 nm device, even at 100 V, the electric field in the polymer film is comparatively lower (below  $2.5 \times 10^8$  V/m), and this can be correlated with its low switching probability (<20%).

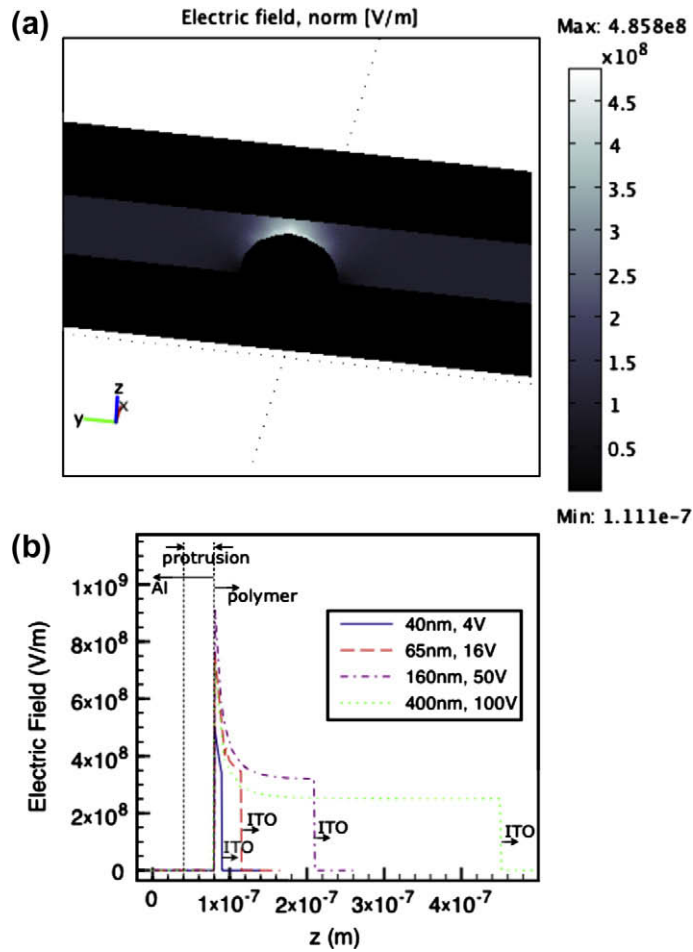


Fig. 4. Electric field distribution at a localized switching spot in our model. (a) In a 40 nm device. (b) Along the vertical line crossing the protrusion tip.

Therefore we suggest that the switching probability may be related to the localized electric field near the protrusions from the electrode. The role of the high electric field might include: (1) producing a high current and localized heating which dissociate the metal ions from the electrode surface, and (2) driving the metal ions to the other electrode to form a conductive link.

### 3.2. Cycle to cycle variation

For the same device, the switching capability also varied as write-erase cycles were performed on the device. Typically, after several hundreds of write-erase cycles, the devices could not be written to the ON state with a 4 V pulse. When this happened, using the same forming process as mentioned earlier can turn the device back to the ON state. On the other hand, though at relatively lower probability, there were also cases where the devices became more difficult to be erased. In such situations, using a higher erasing voltage, eg. 12 V, could turn the device to the OFF state.

With this in mind, we designed a different cycling test approach which dynamically adjusts both the writing and

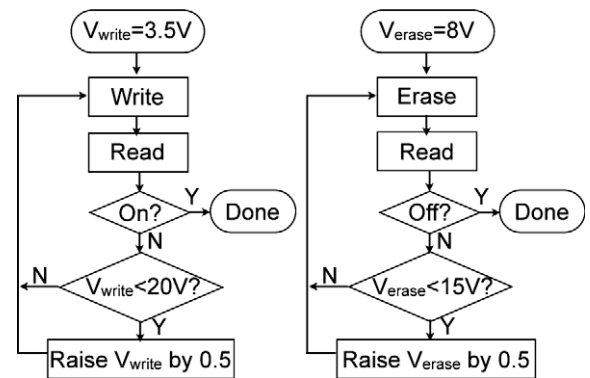
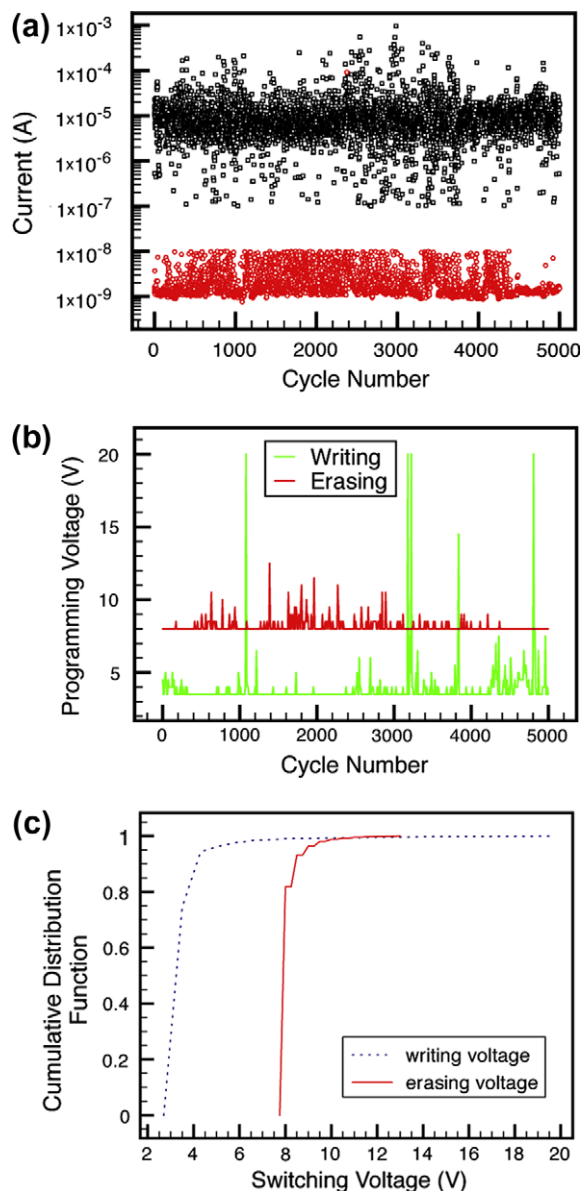


Fig. 5. Flow chart for the writing and erasing procedures in the dynamic voltage cycling test.

erasing voltages. Instead of using single values for writing and erasing voltages, we set a range for writing and erasing voltages. In each cycle, the writing process began with the minimum writing voltage in the specified range. We determined the status of the device right after the writing pulse

by measuring the current at 1 V. If the writing process failed, it was repeated with a voltage raised by 0.5 V, until the voltage reaches the upper limit of the range. The erasing process was almost the same, except that the voltage range was different from the one used for writing. A current compliance of 10  $\mu\text{A}$  was set during the writing processes. The flow chart for the writing and erasing procedures are shown in Fig. 5.

This cycling test was applied on devices with 100 nm thick polymer film. The writing voltage ranged from 3.5 to 20 V with 10  $\mu\text{A}$  current compliance, while the erasing voltage was set between 8 and 15 V. Fig. 6a shows that



**Fig. 6.** Cycling test results. (a) The ON state and OFF state currents read at each cycle. The black squares represent the ON state current, and the red circles represent the OFF state current. (b) The actual writing and erasing voltages used at each cycle. (c) The distribution of switching voltages.

the device worked persistently through 5000 cycles. Fig. 6b reveals the actual voltages used for writing and erasing in each cycle. It was found that the device normally switched at the minimum writing (3.5 V) and erasing (8 V) voltages. However, at certain cycles, higher writing or erasing voltages were needed to ensure a successful switching. These gave rise to the peaks in the recorded voltage values. Fig. 6c shows the distribution of writing and erasing voltages.

We further develop our model in order to explain the dynamic process during repeated switching cycles. After the disconnecting process during erasing, a new gap distance might be established. In normal cases, the new gap should be close enough so that the next writing within 4 V could be successful, as seen in Fig. 6b. However, due to any kind of variations, at certain probability, the gap could be widened and/or the tip could be smoothed, so that in the next cycle, much higher writing voltage would be required, corresponding to the peaks in the writing voltage curve in Fig. 6b. It is also shown in Fig. 6b that there are certain peaks in the erasing voltage curve, which means that at certain cycles, the device could not be erased with 8 V pulse. This could be explained by the variation in the filament thickness formed during each cycle.

#### 4. Conclusion

We have statistically characterized the polyfluorene based memory cells. The switching probability of the devices was linked to the required switching voltage. Based on the variation of required switching voltages among different devices as well as switching cycles, we developed a model which suggests that protrusions from the electrodes are dominating the switching phenomenon, and their varying geometries contribute to the variations in the reproducibility of the memory effect.

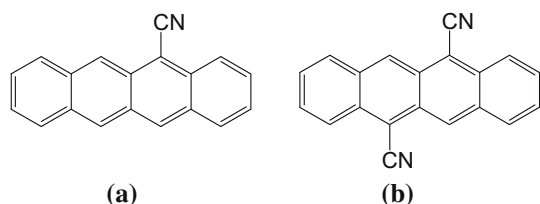
The switching sites introduced by the nonuniform geometries have to be better controlled in order to overcome the inconsistency and make the polymer memory devices reproducible and reliable enough for commercialization. In low cost applications where switching speed is less critical and device driving circuit can be more flexibly designed, applying a device programming scheme which dynamically adjusts the switching voltages would be a practical solution. For high end applications, the device structure should be fundamentally improved to minimize the changes of the switching sites. Our future work will include both the memory driving circuit design and device structural optimization to achieve a highly reliable polymer memory system.

#### Acknowledgements

The authors would like to thank Mr. Noah Bodzin from UCLA for helping SEM imaging, Mr. Ke Sun, Mr. Guanwen Yang and Dr. Rui Dong, Ms. Teresa Chen and Ms. Kitty Cha from UCLA for valuable technical discussions, and the Focus Center Research Program's (FCRP) Functional Engineered Nano Architectonics (FENA) for funding and support.

## References

- [1] J.C. Scott, L.D. Bozano, *Advanced Materials* 19 (11) (2007) 1452–1463.
- [2] Yang Yang, Jianyong Ouyang, Liping Ma, Ricky Jia-Hung Tseng, Chih-Wei Chu, *Advanced Functional Material* 16 (2006) 1001–1014.
- [3] L.P. Ma, J. Liu, Y. Yang, *Applied Physics Letters* 80 (2002) 2997–2999.
- [4] Ricky J. Tseng, Jiaying Huang, Jianyong Ouyang, Richard B. Kaner, Yang Yang, Ricky Jia-Hung Tseng, Jiaying Huang, Jianyong Ouyang, Richard B. Kaner, Yang Yang, *Nano Letters* 5 (6) (2005) 1077–1080.
- [5] Jianyong Ouyang, Chih-Wei Chu, Charles R. Szmada, Liping Ma, Yang Yang, *Nature Materials* 3 (2004) 918–922.
- [6] F. Verbakel, S.C.J. Meskers, R.A.J. Janssen, H.L. Gomes, A.J.M. van den Biggelaar, D.M. de Leeuw, *Organic Electronics* 9 (2008) 829–833.
- [7] Tae-Wook Kim, Hyejung Choi, Seong-Hwan Oh, Minseok Jo, Gunuk Wang, Byungjin Cho, Dong-Yu Kim, Hyunsang Hwang, Takhee Lee, *Nanotechnology* 20 (2009) 025201.
- [8] Michael Cölle, Michael Büchel, Dago M. de Leeuw, *Organic Electronics* 7 (2006) 305–312.
- [9] W.L. Kwan, R.J. Tseng, W. Wu, Q. Pei, Y. Yang, *IEDM Technical Digest* (2007) 237–240.
- [10] W.L. Kwan, R.J. Tseng, Y. Yang, *Philosophical Transactions A* 367 (1905) (in press).
- [11] W.L. Kwan, B. Lei, Y. Shao, S. Prihodko, N. Bodzin, Y. Yang, *Journal of Applied Physics* 105 (12) (2009), in press.
- [12] G. Dearnaley, D.V. Morgan, A.M. Stoneham, *Journal of Non-Crystalline Solids* 4 (1970) 593–612.
- [13] Seung Chul Chae, Jae Sung Lee, Sejin Kim, Shin Buhm Lee, Seo Hyoung Chang, Chunli Liu, Byungnam Kahng, Hyunjung Shin, Dong-Wook Kim, Chang Uk Jung, Sunae Seo, Myoung-Jae Lee, Tae Won Noh, *Advanced Materials* 20 (2008) 1154–1159.
- [14] M.L. Wang, J. Zhou, X.D. Gao, B.F. Ding, Z. Shi, X.Y. Sun, X.M. Ding, X.Y. Hou, *Applied Physics Letters* 91 (2007) 143511.
- [15] U. Russo, D. Ielmini, C. Cagli, A.L. Lacaita, *IEEE Transaction on Electron Devices* 56 (2) (2009) 193–200.
- [16] An. Chen, *Non-Volatile Memory Technology Symposium* 9 (2008) 1–5.
- [17] Chih Wei Chu, Jianyong Ouyang, Jia-Hung Tseng, *Advanced Materials* 17 (2005) 1440–1443.
- [18] Liang Li, Qi-Dan Ling, Siew-Lay Lim, Yoke-Ping Tan, Chunxiang Zhu, Daniel Siu Hhung Chan, En-Tang Kang, Koon-Gee Neoh, *Organic Electronics* 8 (2007) 401–406.
- [19] Arup K. Rath, Amlan J. Pal, *Organic Electronics* 9 (4) (2008) 495–500.
- [20] F. Verbakel, S.C.J. Meskers, R.A.J. Janssen, *Applied Physics Letters* 91 (2007) 192103.
- [21] W.-J. Joo, T.-L. Choi, J. Lee, S.K. Lee, M.-S. Jung, N. Kim, J.M. Kim, *Journal of Physical Chemistry B* 110 (2006) 23812.
- [22] W.-J. Joo, T.-L. Choi, K.-H. Lee, Y. Chung, *Journal of Physical Chemistry B* 111 (2007) 7756–7760.
- [23] W.-J. Joo, T.-L. Choi, K.-H. Lee, *Thin Solid Films* 516 (2008) 3133–3137.
- [24] Y.-S. Lai, C.-H. Tu, D.-L. Kwong, J.S. Chen, *Applied Physics Letters* 87 (2005) 122101.
- [25] M. Kim, S. Choi, M. Ree, O. Kim, *IEEE Electron Device Letters* 28 (11) (2007) 967–969.



**Scheme 1.** Chemical structures of (a) 5-cyanotetracene (1CT) and (b) 5,11-dicyanotetracene (2CT).

hand, Chao [14] proposed that cyanated pentacene could have small reorganization energies based on theoretical calculations.

Here we first report the synthesis of two novel organic molecules, 5-cyanotetracene (1CT) and 5,11-dicyanotetracene (2CT), as shown in Scheme 1. Our quantum mechanical (QM) calculations predicted that the reorganization energies of 1CT and 2CT are 0.1017 and 0.0881 eV, respectively. Especially, the reorganization energy of 2CT is the smallest among those of all existing organic compounds to the best of our knowledge. We predict that the hole mobilities of 1CT and 2CT are  $2.9$  and  $2.2 \text{ cm}^2 \text{ V}^{-1} \text{ S}^{-1}$ , respectively, which are comparable to the predicted hole mobility of rubrene,  $3.6 \text{ cm}^2 \text{ V}^{-1} \text{ S}^{-1}$ . Moreover, the synthesized cyanated tetracenes are very stable under air condition.

## 2. Results and discussion

We performed the quantum mechanics (QM) calculations at hybrid density functional theory (DFT) with UB3LYP/6-311g(d,p) level to calculate reorganization energy [15]. The geometries were fully optimized. For the tetracene framework, our calculations showed that the 5-, 11-terminal substitution positions are superior for reducing reorganization energy. As shown in Table 1, the

calculated reorganization energy of 1CT and 2CT are 0.1017 and 0.0881 eV, respectively. We make the comparisons of reorganization energies for those tetracene and pentacene derivatives. The tetracene derivatives 5,11-dichlorotetracene and rubrene have the calculated reorganization energies of 0.1472 and 0.1521 eV [16], respectively. Moreover, the pentacene derivatives Hexathiapentacene [17] and 6,13-bis(Methylthio)-pentacene [18] have the calculated reorganization energies of 0.1428 and 0.1172 eV [16], respectively. To the best of our knowledge, the 2CT has the lowest reorganization energy among the existing compounds. This result agrees with Marks et al.'s conclusion that the -CN polar functional group results in the decrease of the reorganization energy [9].

The ionization potentials (IP) of 1CT and 2CT are 6.964 and 7.281 eV, respectively. They are close to IP of 5,11-dichlorotetracene, 6.740 eV. Since 5,11-dichlorotetracene functions as p-type semiconductor [13], we expect that 1CT and 2CT would function as p-type semiconductors as well at similar conditions.

Based on the calculation results, we decided that both 1CT and 2CT are valuable p-type organic semiconductors to synthesize. Thus we addressed synthetic routes of these designed compounds as shown in Scheme 2. Since the Friedel-Crafts reaction has been proved to be a useful method for the synthesis of monocyno-derivatives of reactive aromatic hydrocarbons [19], we synthesized 1CT by direct cyanation of tetracene with cyanogen bromide employing aluminium chloride as catalyst. In the case of 2CT, the targeted compound could be obtained in two steps: (1) 5,11-dichlorotetracene (DCT) was synthesized by chlorination of tetracene with solid copper (II) chloride in chlorobenzene at  $110^\circ\text{C}$  for 5 h; then using Pd (II)/ligand as the catalyst system, 2CT was synthesized by cyanation of DCT with potassium hexacyanoferrate(II) in 1-methyl-2-pyrrolidone solution. Both 1CT and 2CT were isolated by column chromatography and subsequently re-crystallized from chloroform solutions.

**Table 1**

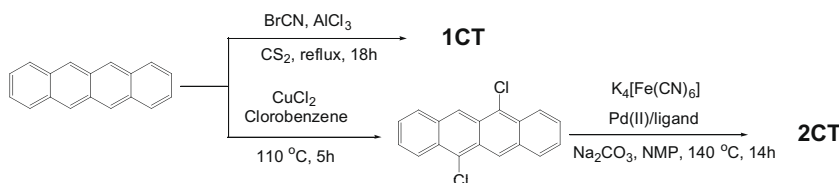
Calculated self-organization energy ( $\lambda$ ), HOMO, LUMO levels and HOMO–LUMO gaps ( $\Delta E$ )<sup>a</sup>.

	$\lambda$ (eV)	HOMO(eV)	LUMO(eV)	$\Delta E$ (eV)
1CT	0.1017	-5.52 (5.19 <sup>b</sup> )	-2.88 (2.96 <sup>b</sup> )	2.64 (2.23 <sup>b</sup> , 2.29 <sup>c</sup> )
2CT	0.0881	-5.93 (5.42 <sup>b</sup> )	-3.40 (3.34 <sup>b</sup> )	2.53 (2.08 <sup>b</sup> , 2.19 <sup>c</sup> )
Tetracene	0.1157	-4.87	-2.09	2.78
Pentacene	0.0976	-4.84	-2.64	2.20
Rubrene	0.1521	-4.93	-2.31	2.62

<sup>a</sup> Calculated at the UB3LYP/6-311g(d,p) level.

<sup>b</sup> This work, results evaluated from cyclic voltammetry (CV).

<sup>c</sup> This work, results evaluated from UV-vis.



**Scheme 2.** Synthesis of 1CT and 2CT.

The synthesized 1CT and 2CT were very stable both in solution and crystal form. As shown in Fig. 1, 2CT in chloroform solution remained unchanged under ambient laboratory conditions for several months. As a comparison, the rubrene in chloroform solution lost its color after three days. The oxidized rubrene compound is a mixture with the NMR spectrum provided in Supporting Information (SI). Since the impurities in organic semiconductors dramatically decrease the hole mobility, we expect that our synthesized air-stable 1CT and 2CT promise more friendly device fabrication and packaging environments.

To investigate the electrical properties of 1CT and 2CT, we carried out cyclic voltammetry (CV) (Fig. 2) and UV-vis absorbance measurements (Fig. 3). Based on the oxidation onsets of CV, we estimated that the HOMOs of 1CT and 2CT are 5.19 and 5.42 eV, respectively. The difference between oxidation and reduction onsets of CV gives that band gaps of 1CT and 2CT are roughly 2.23 and 2.08 eV, respectively. The absorption edge of the maximum UV-

vis spectrum is corresponding to the HOMO-LUMO energy gap. 1CT chloroform solution has an adsorption edge at 543 nm, which suggests that the band gap is roughly 2.29 eV. Similar analysis suggests the band gap of 2CT in chloroform is 2.19 eV. The band gaps estimated from CV and UV-vis are in good agreement each other. In addition, these values are fairly consistent with the calculated band gaps which were shown in Table 1.

Single crystals grown from chloroform solution were used for the structural analysis (the crystallographic data of 1CT and 2CT were presented in SI). As shown in Fig. 4a and c, the X-ray crystallographic analysis has revealed that the molecular packing of 1CT is packed in a herringbone-type pattern, while 2CT showing face-to-face slipped stacking with an intermolecular distance of 3.403 Å between neighboring molecules along the *a*-axis. In the 1CT crystal, there are four face-to-edge *T* type dimers and one face-to-face *P* type dimer. In the 2CT crystal, there are two face-to-edge *T* type dimers and one face-to-face *P* type dimer.



**Fig. 1.** The comparison of oxygen resistances for 2CT and rubrene in chloroform solution. (from left to right, the first and the third samples are initial 2CT and rubrene solution; the second is 2CT solution after three months and the fourth is rubrene solution after three days, respectively).

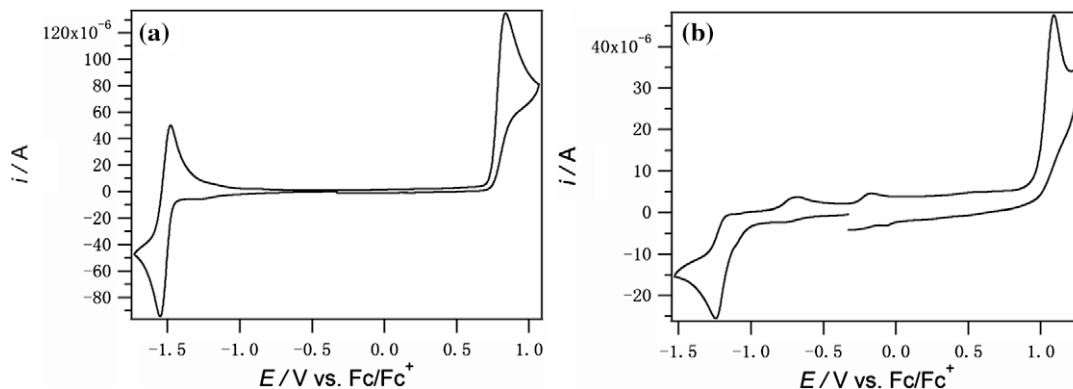


**Fig. 2.** Cyclic voltammogram of (a) 1CT and (b) 2CT.



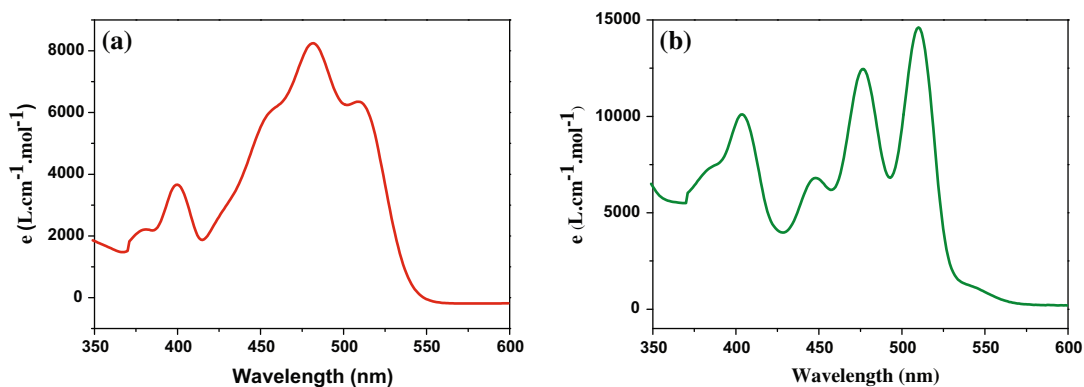


Fig. 3. UV-vis spectra of (a) 1CT and (b) 2CT.

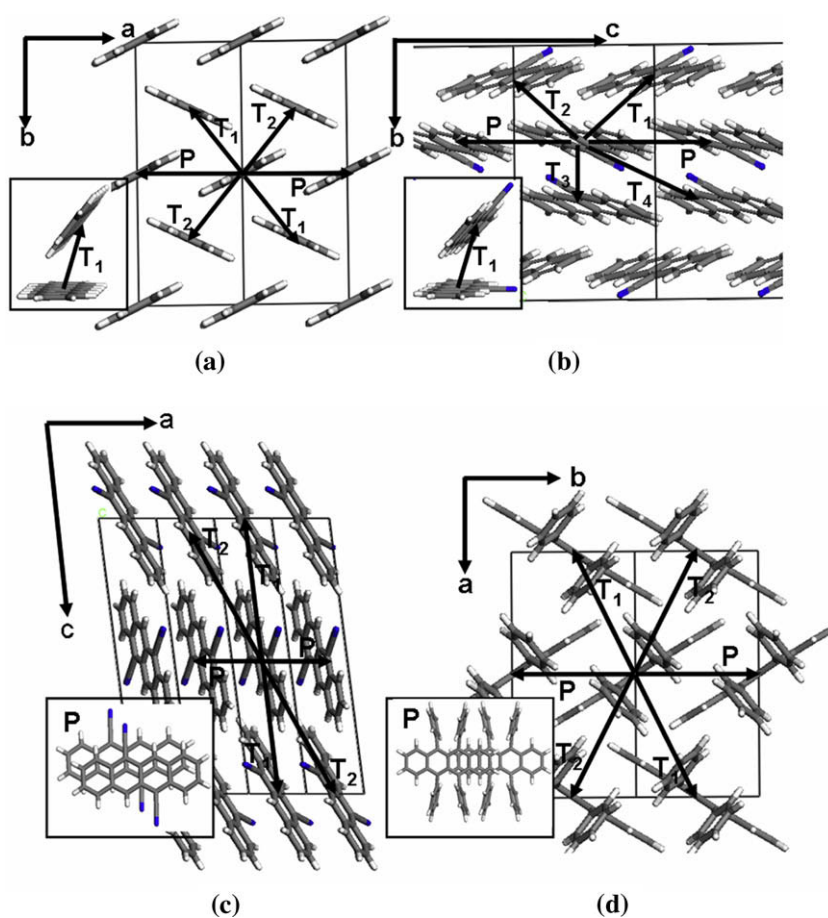


Fig. 4. Comparison of crystal structures of (a) 1CT (herringbone-type structure), (b) pentacene, (c) 2CT (face-to-face  $\pi$ -stacks) and (d) rubrene.

Based on the crystal structures, we carried out DFT calculations at PW91/TZ2P level to calculate intermolecular couplings between neighbor molecules in crystals. As for comparison, we also calculated the intermolecular couplings in rubrene and pentacene, which are two benchmark organic materials with the highest hole mobilities [8]. In the pentacene crystal, the tilt angles of face-to-edge

dimers  $T_1$  and  $T_2$  dimer are both  $51.3^\circ$  and the separating distances are about  $5 \text{ \AA}$ . In the 1CT crystal, the geometries of  $T_1$  and  $T_2$  dimers with the tilt angles of  $47.8^\circ$  and the separating distance of  $5.5 \text{ \AA}$  are similar to the herringbone face-to-edge dimers in the pentacene crystal. The  $T_1$  and  $T_2$  dimers in the 1CT crystal have the electronic couplings about  $0.078 \text{ eV}$  close to the couplings of face-to-edge

**Table 2**

Predicted hole mobility in *a*–*b* plane and calculated intermolecular couplings in crystal structures of pentacene, rubrene, 1CT and 2CT.

	Predicted $\mu(\text{cm}^2 \text{V}^{-1} \text{s}^{-1})$	$V(\text{eV})$	$\lambda(\text{eV})$
Pentacene	2.6	$V_{T1} = 0.085$ $V_{T2} = 0.048$ $V_p = 0.032$	0.0976
Rubrene	3.6	$V_{T1} = 0.019$ $V_{T2} = 0.019$ $V_p = 0.089$	0.1521
1CT	2.9	$V_{T1} = 0.078$ $V_{T2} = 0.078$ $V_{T3} = 0.032$ $V_{T4} = 0.012$ $V_p = 0.027$	0.1017
2CT	2.2	$V_{T1} = 0.006$ $V_{T2} = 0.005$ $V_p = 0.084$	0.0881

dimers in pentacene (0.085 eV). As shown in Fig. 2c, the pitch and roll angles of *P* dimers in the 2CT crystal are 27.56° and 17.19°, respectively, which are similar to that of *P* dimers in the rubrene crystal (30.89° and 0°) [8]. These results suggest that the intermolecular couplings in 2CT may look like that in rubrene. On the other hand, 2CT shows more dense packing than rubrene. The intermolecular distance between neighboring molecules in 2CT is 3.663 Å [8]. The close  $\pi$ -stacking of 2CT should be advantageous for charge transport since both molecular modeling [7,20] and experimental evidence [4,21] suggested that a high mobility is expected for an organic semiconductor with a dense packing structure. The calculated intermolecular coupling of *P* dimer in 2CT is 0.084 eV, which is comparable to that of *P* dimer in rubrene, 0.089 eV. We did not discuss the *L* dimers (out of transport layer plane) since the charge transport in crystals is two dimensional transport while charge transport between layers is less efficient.

Obtaining the crystal structures of cyanated tetracene derivatives, we carried out the calculation of hole mobilities based on the theoretical model we previously developed [7] and the results are shown in Table 2. The calculated hole mobilities of our air-stable cyanated tetracene derivatives in *a*–*b* plane are  $2.9 \text{ cm}^2 \text{V}^{-1} \text{s}^{-1}$  for 1CT and  $2.2 \text{ cm}^2 \text{V}^{-1} \text{s}^{-1}$  for 2CT, respectively. They are close to the calculated hole mobility of rubrene,  $3.6 \text{ cm}^2 \text{V}^{-1} \text{s}^{-1}$ . Since our synthesized compounds are air-stable, it makes them attractive to real applications.

### 3. Conclusion

We synthesized two novel cyanated tetracene derivatives, 1CT and 2CT. The X-ray crystallographic analysis has revealed the molecular packing of 1CT is packed in a herringbone-type pattern, while 2CT showing a face-to-face packing with a relative short intermolecular distance of 3.403 Å between neighboring molecules along the *a*-axis. Compared with the well-known semiconductor, e.g. rubrene, the synthesized 2CT show more stability which is confirmed by NMR. The reorganization energy of 2CT predicted by UB3LYP/6-311g(d,p) is 0.0881 eV, which is the lowest among known compounds. The calculated hole

mobilities of these air-stable cyanated tetracene derivatives in *a*–*b* plane are  $2.9 \text{ cm}^2 \text{V}^{-1} \text{s}^{-1}$  for 1CT and  $2.2 \text{ cm}^2 \text{V}^{-1} \text{s}^{-1}$  for 2CT, respectively. These oxygen-resisted organics may offer potential to fabricate the flexible electronics under air conditions. Efforts have been undertaken to determine the semiconducting properties of these new compounds in organic field effect transistors.

## 4. Experimental section

### 4.1. Synthesis of 1CT

Tetracene (1.01 g, 4.43 mmol) and anhydrous  $\text{AlCl}_3$  (1.18 g, 8.87 mmol) were placed in a flask containing  $\text{CS}_2$  (20 ml) under argon and the mixture was stirred at room temperature for 15 min. Cyanogen bromide (0.94 g, 8.87 mmol) in more  $\text{CS}_2$  (15 ml) was then slowly added with stirring. The mixture was then stirred and boiled under reflux for 18 h, then cooled, and poured into crushed ice/conc. HCl. The combined  $\text{CHCl}_3$  extracts were washed with water, dried with  $\text{MgSO}_4$  and the solvents were removed by rotary evaporation. The solid residue was chromatographed ( $\text{SiO}_2$ , ethyl acetate/hexane) and then recrystallized from  $\text{CHCl}_3$  to afford product (0.21 g, 18.8%).  $^1\text{H NMR}$   $\delta$  7.47–7.54 (*m*, 3H), 7.63–7.67 (*m*, 1H), 8.01–8.08 (*m*, 3H), 8.38 (*d*, 1H,  $J = 8.8$ ), 8.70 (*s*, 1H), 8.87 (*s*, 1H), 8.99 (*s*, 1H). Elemental anal. Found: C, 89.41; H, 4.79; N, 5.52. Calcd for  $\text{C}_{19}\text{H}_{11}\text{N}$ : C, 90.09; H, 4.38; N, 5.53. HRMS (EI): calcd for  $\text{C}_{19}\text{H}_{11}\text{N} [\text{M}^+]$ : 253.0886; found (*m/z*): 253.0883.

### 4.2. Synthesis of 2CT

5,11-dichlorotetracene was synthesized according to literature [13]. Potassium hexacyanoferrate(II) (0.736 g, 2 mmol), which is yielded by grinding  $\text{K}_4[\text{Fe}(\text{CN})_6] \cdot 3\text{H}_2\text{O}$  to a fine powder and drying in vacuum at 80 °C overnight, 5,11-dichlorotetracene (1.667 g, 5.61 mmol),  $\text{Na}_2\text{CO}_3$  (0.212 g, 2 mmol),  $\text{Pd}(\text{OAc})_2$  (0.127 g, 0.56 mmol), Tri-*tert*-butylphosphonium tetrafluoroborate (0.325 g, 1.12 mmol) and 20 ml NMP were mixed in a Schlenk flask under argon. The reaction mixture was then heated to 140 °C slowly and held at that temperature for 14 h. The reaction mixture was then cooled to room temperature, diluted with chloroform and filtered through Celite. The product was isolated by column chromatography ( $\text{SiO}_2$ , ethyl acetate/hexane) after washing the filtrate with water, drying over sodium sulfate and distilling the solvents. (0.406 g, 26%).  $^1\text{H NMR}$   $\delta$  7.65–7.69 (*m*, 2H), 7.76–7.80 (*m*, 2H), 8.20 (*d*, 2H,  $J = 8.72$ ), 8.45 (*d*, 2H,  $J = 8.64$ ), 9.32 (*s*, 2H). Elemental anal. Found: C, 86.36; H, 3.75; N, 10.47. Calcd for  $\text{C}_{20}\text{H}_{10}\text{N}_2$ : C, 86.31; H, 3.62; N, 10.07. HRMS (EI): calcd for  $\text{C}_{20}\text{H}_{10}\text{N}_2 [\text{M}^+]$ : 278.0838; found (*m/z*): 278.0832.

### 4.3. Computational method

The reorganization energies ( $\lambda$ ) in Eq. (1) were calculated directly from the adiabatic potential energy surfaces, shown as Eq. (2) [7]:

$$\lambda = \lambda_0 + \lambda_+ = (E_0^* - E_0 + E_+^* - E_+) \quad (2)$$

where  $E_0$  and  $E_+$  represent the energies of the neutral and cation species in their lowest energy geometries, respectively;  $E_0^*$  and  $E_+^*$  are the energies of the neutral and cation states with the geometries of the cation and neutral species, respectively. This description holds as long as the potential energy surfaces are harmonic, and the  $\lambda_0$  and  $\lambda_+$  terms are close in energy. We used UB3LYP/6-311g(d,p) level calculation implemented in the Jaguar program [15] to calculate the reorganization energy.

Geometries for dimer calculations were obtained from the observed x-ray crystal structure. The intermolecular couplings ( $V$ ) [22] in Eq. (1) can be calculated directly from the spatial overlap ( $S_{RP}$ ), charge transfer integral ( $J_{RP}$ ), and site energies ( $H_{RR}$ ,  $H_{PP}$ ). The intermolecular coupling,  $V$ , is given by:

$$V = \left| \frac{J_{RP} - S_{RP}(H_{RR} + H_{PP})/2}{1 - S_{RP}^2} \right| \quad (3)$$

We employed the Amsterdam density functional (ADF) [23] program to calculate all couplings. The TZ2P basis set in ADF was used and the local density functional VWN was employed in the conjunction with the PW91 gradient corrections.

After obtained reorganization energy and intermolecular coupling in Eq. (1), we can write the diffusion coefficient of organic semiconductor as [7]:

$$D = \frac{1}{2n} \sum_i r_i^2 W_i P_i \quad (4)$$

where  $n$  is the spatial dimensionality;  $i$  represents a specific hopping pathway with hopping distance  $r_i$  (the intermolecular center-to-center distances of different dimer types).  $P$  is the hopping probability which is calculated as by:

$$P_i = \frac{W_i}{\sum_i W_i} \quad (5)$$

The hole mobility  $\mu$  from charge hopping is then evaluated from the Einstein relation:

$$\mu = \frac{e}{k_B T} D \quad (6)$$

## Acknowledgement

The authors thank Prof. W.A. Goddard III for the theoretical suggestions and thank Prof. R.D. Webster, and

Ms. Y.-L. Hui for the useful discussions. This research was supported by the Ministry of Education in Singapore (ARC24/07, no. T206B1218RS) and Nanyang Technological University (RG54/07 and SUG41/06).

## Appendix A. Supplementary data

Supplementary data associated with this article can be found, in the online version, at doi:10.1016/j.orgel.2009.05.016.

## References

- [1] J.A. Rogers, Z. Bao, K. Baldwin, A. Dodabalapur, B. Crone, V.R. Raju, V. Kuck, H. Katz, K. Amundson, J. Ewing, P. Drzaic, Proc. Natl. Acad. Sci. USA 98 (2001) 4835–4840.
- [2] A.L. Briseno, S.C.B. Mannsfeld, M.M. Ling, S. Liu, R.J. Tseng, C. Reese, M.E. Roberts, Y. Yang, F. Wud, Z. Bao, Nature 444 (2007) 913–917.
- [3] K. Takimiya, H. Ebata, K. Sakamoto, T. Izawa, T. Otsubo, Y. Kunugi, J. Am. Chem. Soc. 128 (2006) 12604–12605.
- [4] L. Li, Q. Tang, H. Li, X. Yang, W. Hu, Y. Song, Z. Shuai, W. Xu, Y. Liu, D. Zhu, Adv. Mater. 19 (2007) 2613–2617.
- [5] H. Sirringhaus, R.J. Wilson, R.H. Friend, Science 280 (1998) 1741–1744.
- [6] V.C. Sundar, J. Zaumseil, V. Podzorov, E. Menard, R.L. Willett, T. Someya, M.E. Gershenson, J.A. Rogers, Science 303 (2004) 1644–1646.
- [7] W.-Q. Deng, W.A. Goddard III, J. Phys. Chem. B 108 (2004) 8614–8621.
- [8] V. Coropceanu, J. Cornil, D.A. da Silva Filho, Y. Olivier, R. Silbey, J.-L. Brédas, Chem. Rev. 107 (2007) 926–952.
- [9] G.R. Hutchison, M.A. Ratner, T.J. Marks, J. Am. Chem. Soc. 127 (2005) 2339–2350.
- [10] G. Yu, S.W. Yin, Y.Q. Liu, Z.G. Shuai, D.B. Zhu, J. Am. Chem. Soc. 125 (2003) 14816–14824.
- [11] R.A. Marcus, J. Chem. Phys. 24 (1956) 966–978.
- [12] N.S. Hush, J. Chem. Phys. 28 (1958) 962–972.
- [13] H. Moon, R. Zeis, E.-J. Borkent, C. Besnard, A.J. Lovinger, T. Siegrist, C. Kloc, Z. Bao, J. Am. Chem. Soc. 126 (2004) 15322–15323.
- [14] M. Kuo, H. Chen, I. Chao, Chem. Eur. J. 13 (2007) 4750–4758.
- [15] Jaguar 6.6, Schrodinger Inc., Portland, Oregon, 2006.
- [16] S.H. Wen, A. Li, J.L. Song, K.L. Han, W.A. Goddard, W.Q. Deng, J. Phys. Chem. B, in press.
- [17] A.L. Briseno, Q. Miao, M.M. Ling, C. Reese, H. Meng, Z.N. Bao, F.J. Wudl, J. Am. Chem. Soc. 128 (2006) 15576–15577.
- [18] K. Kobayashi, R. Shimaoka, M. Kawahata, M. Yamanaka, M.K. Yamaguchi, Org. Lett. 8 (2006) 2385–2388.
- [19] P.H. Gore, F.S. Kamounah, A.Y. Miri, Tetrahedron 35 (1979) 2927–2929.
- [20] J. Cornil, D. Beljonne, J.P. Calbert, J.-L. Brédas, Adv. Mater. 13 (2001) 1053–1067.
- [21] M.D. Curtis, J. Cao, J.W. Kampf, J. Am. Chem. Soc. 126 (2004) 4318–4328.
- [22] K. Senthilkumar, F.C. Grozema, F.M. Bickelhaupt, L.D.A. Siebbeles, J. Chem. Phys. 119 (2003) 9809–9817.
- [23] G.T. Velde, F.M. Bickelhaupt, E.J. Baerends, C.F. Guerra, S.J.A. Van Gisbergen, J.G. Snijders, T.J. Ziegler, J. Comput. Chem. 22 (2001) 931–967.

oxide as the anode interlayer for improving the PSC performance has seldom been reported.

The aim of this work is to realize a low-cost and high-efficiency inverted PSC hybridized with ZnO nanorod arrays by introduction of a solution-processed vanadium oxide ( $V_2O_5$ ) as the anode interlayer. Our investigation shows that the photovoltaic device performance is improved by the introduction of the  $V_2O_5$  interlayer due to the efficient suppression of the leakage currents at the organic/metal interface. Compared to the conventional BHJ structure (indium tin oxide (ITO)/PEDOT:PSS/active layer/Al), the use of the inverted structure overcomes some obstacles such as the facile oxidation of Al [15] and the electrical inhomogeneities of PEDOT:PSS as well as its corrosion to ITO [16]. The inverted PSCs utilize an air-stable high work-function electrode as the back contact to collect holes and metal-oxide nanostructures at the ITO to collect electrons [17–19]. Furthermore, it has been reported that the ZnO nanorods have beneficial effects of collecting and transporting electrons in the inverted PSCs hybridized with the ZnO nanorods [20]. Our works combine these advantages of  $V_2O_5$  interlayer and ZnO nanorods, which thereby suppress the leakage currents and improve the collection and transportation of the charge carriers, resulting in enhancements of PCE, open-circuit voltage ( $V_{OC}$ ), and fill factor (FF) of the devices. In addition, the  $V_2O_5$  interlayer can serve as an optical spacer to increase light absorption, leading to an increased short-circuit density ( $J_{SC}$ ). Moreover, the  $V_2O_5$  interlayer and ZnO nanorod arrays both are fabricated from simple solution-based processes, which are well-suited for use in high-throughput roll-to-roll manufacturing.

## 2. Experimental

The structure and the energy level diagram of the inverted PSCs of ITO/ZnO/P3HT:PCBM/ $V_2O_5$ /Ag are schematically presented in Fig. 1. Devices were fabricated on cleaned ITO-coated glass substrates ( $\sim 7 \Omega/\text{sq.}$ ). ZnO seed layer ( $\sim 50 \text{ nm}$ ) was spin-coated from a 0.5-mol solution of zinc acetate dihydrate in 2-methoxyethanol followed by annealing at  $200^\circ\text{C}$  for an hour in air. Hydrothermal

growth of the ZnO nanorod arrays ( $\sim 100 \text{ nm}$  in length and  $\sim 50 \text{ nm}$  in diameter) was achieved by suspending the ZnO seed-coated substrates in an aqueous solution of 50-mM zinc nitrate at  $90^\circ\text{C}$  in an oven. Subsequently, a solution containing 20-mg P3HT and 20-mg PCBM in 1-ml *o*-dichlorobenzene (*o*-DCB) was spin-coated on top of the ZnO nanorods and dried slowly over the course of 40 min in air, forming the photoactive layer with a thickness of  $\sim 300 \text{ nm}$ .  $V_2O_5$  powder (Riedel-de Haën, 99%) was homogeneously dispersed and suspended in isopropanol at different concentrations by using ultrasonic agitation. During the process of the ultrasonic agitation, it was observed that the  $V_2O_5$  powder was pulverized to smaller particles. After the ultrasonic agitation, the color of the  $V_2O_5$  colloidal solution is uniformly orange. Then the  $V_2O_5$  colloidal solution was spin-casted in air on top of the photoactive layer. Finally, silver film ( $\sim 200 \text{ nm}$ ) was deposited on top in a vacuum of  $2 \times 10^{-6}$  torr.

Devices were unencapsulated, stored in air, and illuminated at  $100 \text{ mW}/\text{cm}^2$  from a ThermoOriel 150 W solar simulator with AM 1.5G filters. The solar simulator was calibrated using a reference Si solar cell. All electrical measurements were carried out in air at room temperature. The active area of the device irradiated by the light was defined as  $10 \text{ mm}^2$  by using a photomask, so no extra current outside of the defined area was collected. Current density–voltage ( $J$ – $V$ ) curves were measured with a Keithley 2400 source measurement unit. The surface morphologies of the photoactive layers were measured by atomic force microscopy (AFM). The reflectance spectra of the devices were obtained using a Perkin–Elmer Lambda 35 UV–vis spectrophotometer. The transmission spectrum of the  $V_2O_5$  layer was measured using the same UV–vis spectrophotometer. The crystallinity of  $V_2O_5$  was analyzed at room temperature by X-ray diffraction (XRD) using Cu  $K\alpha$  radiation.

## 3. Results and discussion

In order to avoid mixing or damaging the photoactive layer during the coating of  $V_2O_5$ , the selection of solvent

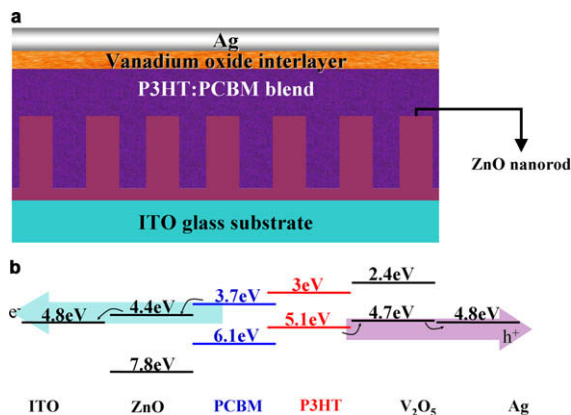


Fig. 1. (a) Device structure of the photovoltaic cells. (b) Energy band diagram for the photovoltaic cells in this study. The work function value of Ag is referred to the Ref. [28].

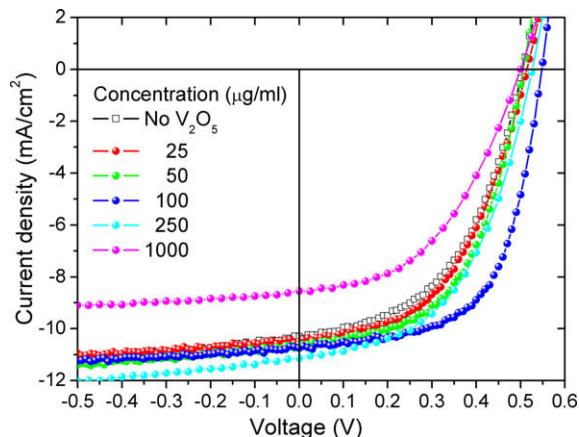


Fig. 2. The  $J$ – $V$  curves of the photovoltaic devices with the  $V_2O_5$  interlayer from various concentrations under  $100 \text{ mW}/\text{cm}^2$  AM 1.5G irradiation.

**Table 1**

Photovoltaic parameters and efficiencies of inverted PSCs with the V<sub>2</sub>O<sub>5</sub> interlayer from various concentrations (solvent:isopropanol).

Concentration (μg/ml)	$J_{sc}$ (mA/cm <sup>2</sup> )	$V_{oc}$ (V)	FF (%)	PCE (%)	$R_s$ (Ω cm <sup>2</sup> )	$R_{sh}$ (Ω cm <sup>2</sup> )
No. V <sub>2</sub> O <sub>5</sub>	10.21	0.50	49.36	2.52	2.24	394
25	10.49	0.51	49.91	2.67	2.12	570
50	10.61	0.51	53.96	2.92	2.10	579
100	10.75	0.55	60.21	3.56	1.35	620
250	11.16	0.52	51.35	2.98	3.4	431
1000	8.55	0.50	46.78	2	6.3	250

for V<sub>2</sub>O<sub>5</sub> is an important issue. That is, the solvent for V<sub>2</sub>O<sub>5</sub> must be orthogonal to *o*-DCB. Several solvents including toluene, chlorobenzene, 2-methoxyethanol, dichlorometh-

ane, and isopropanol have been experimented for the V<sub>2</sub>O<sub>5</sub>. However, only the use of isopropanol as the solvent has negligible influences on the previously deposited photoactive layer due to the polar characteristics of these solvents. In general, the polarity of a solvent is related to its dielectric constant [21]. The relative dielectric constant ( $\epsilon_r$ ) of isopropanol is  $\sim 20$ , which is much larger than that of the P3HT/PCBM film ( $\epsilon_r \sim 3.5$ ) [22]. It is believed that the large dielectric constant qualifies isopropanol as an orthogonal solvent in this work.

Fig. 2a shows the *J*-*V* characteristics of the devices with various concentrations of V<sub>2</sub>O<sub>5</sub>. The device without the V<sub>2</sub>O<sub>5</sub> interlayer exhibits a  $J_{sc}$  of 10.21 mA/cm<sup>2</sup>, a  $V_{oc}$  of 0.5 V, and a FF of 49.36%, resulting in a PCE of 2.52%. The performance is similar to other reports on the same struc-

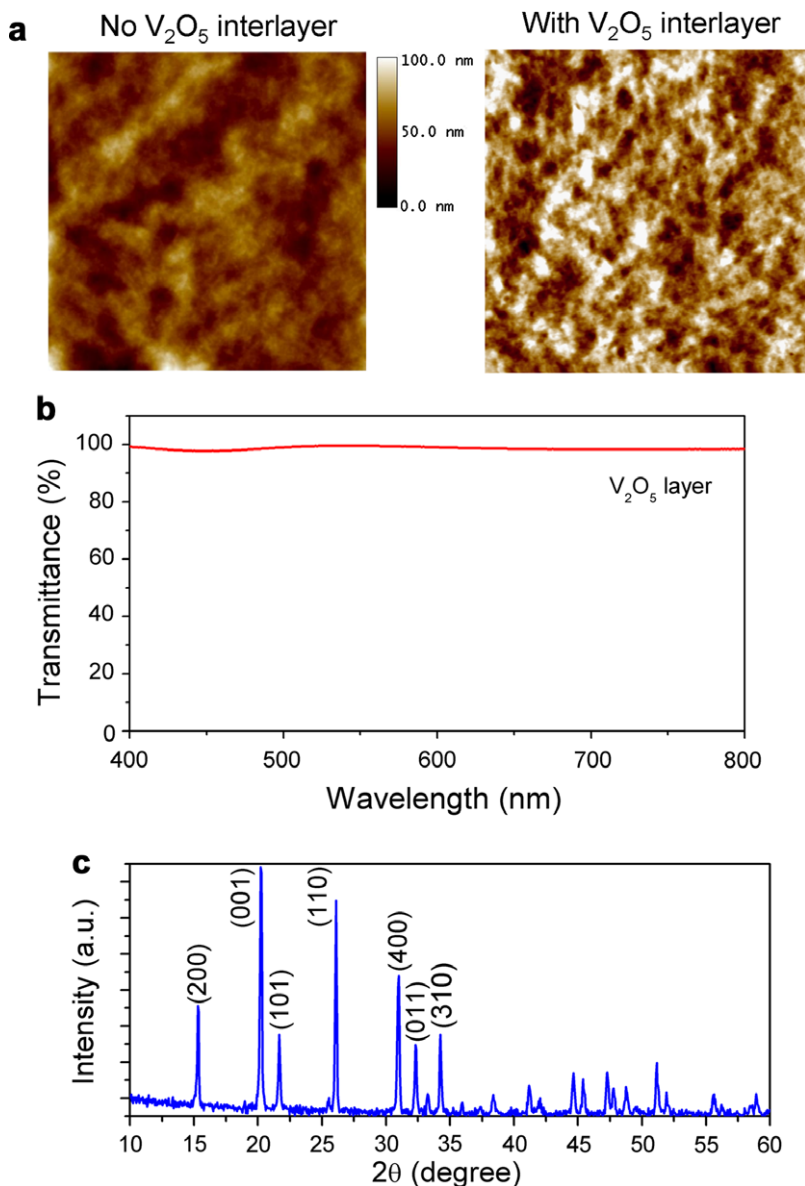


**Fig. 3.** (a) AFM images of the photoactive layers covered with and without the optimum V<sub>2</sub>O<sub>5</sub> interlayer. AFM image scans are 5 × 5 μm. (b) Transmission spectrum of the V<sub>2</sub>O<sub>5</sub> layer (from the 100 μg/ml V<sub>2</sub>O<sub>5</sub> colloidal solution) on a glass substrate. (c) XRD spectrum of V<sub>2</sub>O<sub>5</sub>.

ture without the  $V_2O_5$  interlayer [16,19]. Introducing a 25- $\mu\text{g/ml}$   $V_2O_5$  interlayer, PCE is slightly improved to 2.67% with  $J_{SC}$  of 10.49  $\text{mA/cm}^2$ ,  $V_{OC}$  of 0.51 V, and FF of 49.91%. When the concentration of  $V_2O_5$  further increases to 100  $\mu\text{g/ml}$ , the device has a significant improvement with  $J_{SC}$  of 10.75  $\text{mA/cm}^2$ ,  $V_{OC}$  of 0.55 V, and FF of 60.21%. This results in a considerable improvement of PCE up to 3.56%, a 41% improvement. These results show that the  $V_2O_5$  can act as a functional interlayer to enhance the photovoltaic performance.

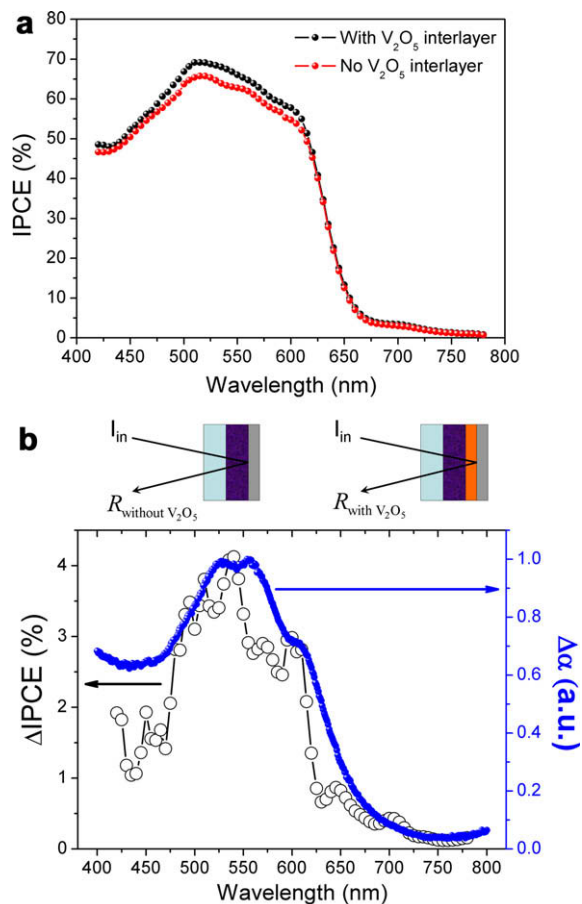
A series of  $V_2O_5$  concentrations (25, 50, 100, 250, and 1000  $\mu\text{g/ml}$ ) is further investigated and summarized in Table 1. The  $J_{SC}$ ,  $V_{OC}$ , and FF increase with the  $V_2O_5$  concentration from 25 to 100  $\mu\text{g/ml}$ . The highest PCE of 3.56% is achieved at the concentration of 100  $\mu\text{g/ml}$ , showing that the optimum  $V_2O_5$  interlayer is obtained. As a low-concentration  $V_2O_5$  interlayer is introduced (50  $\mu\text{g/ml}$  or less), the improvement of device performance is not obvious. It is suspected that the concentration is too low to cover the photoactive layer completely. As a result, the leakage current will not be efficiently reduced. However, as the concentration of  $V_2O_5$  increases to 1000  $\mu\text{g/ml}$ , most  $V_2O_5$  particles cluster together ( $\sim 2 \mu\text{m}$  in average), resulting in the increased contact resistance and thus leading to a low photocurrent ( $J_{SC} \sim 8.55 \text{ mA/cm}^2$ ).

Fig. 3a shows the AFM images of the photoactive layer covered with and without the optimum  $V_2O_5$  interlayer. The  $V_2O_5$  particles can be clearly observed. The root-mean-square roughness ( $\sigma_{RMS}$ ) of the photoactive layer with the optimum  $V_2O_5$  interlayer is  $\sim 18.4 \text{ nm}$ , which is about the 2 times of that without  $V_2O_5$  ( $\sigma_{RMS} \sim 10.6 \text{ nm}$ ). The AFM images clearly indicate that at the concentration of 100  $\mu\text{g/ml}$  the photoactive layer is almost fully covered with  $V_2O_5$ . Fig. 3b shows the transmission spectrum of the  $V_2O_5$  layer deposited from the 100  $\mu\text{g/ml}$   $V_2O_5$  colloidal solution on a glass substrate. It shows that the  $V_2O_5$  layer is almost transparent in the visible region (transmittance  $> 97\%$ ). Fig. 3c shows the XRD spectrum of  $V_2O_5$ . The diffraction peaks appears in the  $2\theta$  range from  $10^\circ$  to  $35^\circ$  characterizing the orthorhombic crystalline structure of  $V_2O_5$ .

Note that the performance of the device without the  $V_2O_5$  interlayer in our experiments has similar performance to other reports [20,23]. By introducing the optimum  $V_2O_5$  interlayer, the device has significant improvements in FF (from 0.49 to 0.6) and  $V_{OC}$  (from 0.5 to 0.55 V). This indicates that  $V_2O_5$  efficiently suppresses the leakage currents at the organic/Ag interface. Considering the device without  $V_2O_5$ , both P3HT and PCBM are in direct contact with Ag. It is possible for electrons to transfer from PCBM to Ag, thereby increasing the leakage currents. However, incorporating a  $V_2O_5$  interlayer introduces two additional interfaces, organic/ $V_2O_5$  and  $V_2O_5$ /Ag. As shown in Fig. 1b, the conduction band of  $V_2O_5$  ( $-2.4 \text{ eV}$ ) (Ref. [8]) is higher than the lowest unoccupied molecular orbital level of PCBM ( $-3.7 \text{ eV}$ ), showing that  $V_2O_5$  can block the reverse electron flow from PCBM to Ag. Thereby,  $V_2O_5$  can effectively prevent the leakage current at the organic/Ag interface. In addition, the valence band of  $V_2O_5$  ( $-4.7 \text{ eV}$ ) (Ref. [8]) is close to the highest occupied molecular orbital level of P3HT ( $-5.1 \text{ eV}$ ), revealing that  $V_2O_5$  will help collecting holes.

Moreover, the series resistance ( $R_S$ , defined from the  $J$ - $V$  curves near 1.5 V under light illumination) is 1.35  $\Omega \text{ cm}^2$  and 3.09  $\Omega \text{ cm}^2$  for the device with and without the optimum  $V_2O_5$  interlayer, respectively. The shunt resistance ( $R_{SH}$ , defined from the  $J$ - $V$  curves near 0 V under light illumination) is 610  $\Omega \text{ cm}^2$  and 376  $\Omega \text{ cm}^2$  for the device with and without the optimum  $V_2O_5$  interlayer, respectively. It is known that the high  $R_{SH}$  indicates less leakage current across the cell and contributes to the improved FF and  $V_{OC}$  [24]. Another evidence for less leakage current is the rectification ratio (RR, defined as the current ratio at  $\pm 1.5 \text{ V}$  from the  $J$ - $V$  curves measured in the dark). The RR of the device without  $V_2O_5$  is  $4.37 \times 10^2$ , while that of the device with the optimum  $V_2O_5$  interlayer increases to  $1.77 \times 10^4$ . The high RR and elevated  $R_{SH}$  both are strong evidences showing that the  $V_2O_5$  interlayer can serve as an electron-blocking layer to effectively prevent the leakage currents, resulting in the dramatic improvement in PCE.

Fig. 4a compares the incident photon-to-current conversion efficiency (IPCE) spectrum of the devices with and without the optimum  $V_2O_5$  interlayer. The IPCE is defined as the number of photogenerated charge carriers



**Fig. 4.** (a) IPCE spectra for the devices with and without the optimum  $V_2O_5$  interlayer. (b) The change in absorption spectrum [ $\Delta\alpha(\lambda)$ ] and the difference in IPCE spectrum [ $\Delta IPCE(\lambda)$ ] resulting from the insertion of the optimum  $V_2O_5$  interlayer. The inset is a schematic of the optical beam path in the both samples. The variables are defined in the text.

contributing to the current per incident photon. The device with  $V_2O_5$  interlayer shows the typical spectral response of P3HT:PCBM blend with a maximum IPCE of  $\sim 69\%$  at 515 nm, while for the device without  $V_2O_5$  interlayer, the peak reaches  $\sim 65\%$  only. The IPCE spectra are consistent with the measured  $J_{SC}$  in the devices. The insertion of  $V_2O_5$  demonstrates a substantial enhancement of  $\sim 6\%$  at 515 nm in the IPCE. This enhancement agrees with the increase in  $J_{SC}$  ( $\sim 5\%$  increase in the device with  $V_2O_5$ ). It indicates that the  $V_2O_5$  interlayer also contributes to the increase in photocurrent.

To further clarify the role of the  $V_2O_5$  interlayer, we measured the reflectance ( $R$ ) spectra of the devices with and without the optimum  $V_2O_5$  interlayer. Since the two devices are identical except the addition of the  $V_2O_5$  layer, comparison of the reflectance yields information on the additional absorption,  $\Delta\alpha(\lambda)$ , in the photoactive layer as a result of the spatial redistribution of the light intensity by the  $V_2O_5$  interlayer (Fig. 4b). The  $\Delta\alpha(\lambda)$  is given by [25]

$$\Delta\alpha(\lambda) \approx -\frac{1}{2\sqrt{2}d} \ln \left( \frac{R_{\text{with } V_2O_5}(\lambda)}{R_{\text{without } V_2O_5}(\lambda)} \right)$$

where  $R_{\text{with } V_2O_5}(\lambda)$  is the reflection from a device with the  $V_2O_5$  interlayer,  $R_{\text{without } V_2O_5}(\lambda)$  is the reflection from an identical device without the  $V_2O_5$  interlayer, and  $d$  is the thickness of the photoactive layer ( $d$  is  $\sim 300$  nm in both). The result shows a clear increase in absorption over the spectral region of the interband transitions. Since the spectral features of the P3HT absorption are evident in the  $\Delta\alpha$  spectrum, the increased absorption arises from a better match of the spatial distribution of the light intensity to the position of the photoactive layer. Fig. 4b also shows the difference in IPCE spectrum,  $\Delta IPCE(\lambda)$ , between the devices with and without the optimum  $V_2O_5$  interlayer. This spectrum reveals three peaks at 510, 540, and 600 nm, respectively. It implies that the contribution of the  $V_2O_5$  interlayer in photocurrent is mainly at the three peaks which are vibronic features from the P3HT molecules [26]. Moreover, the feature of the  $\Delta IPCE$  spectrum is analogous with  $\Delta\alpha$  spectrum, showing that the increased optical absorption is nearly transferred to the photocurrent. Evidently, the  $V_2O_5$  interlayer functions as an optical spacer to increase the optical absorption by spatially redistributed the light intensity and thereby increase the photocurrent.

Although PEDOT:PSS layer can be solution processed, its hygroscopic nature is likely to form insulating patches due to the water adsorption, thus degrading the devices [27]. In contrast,  $V_2O_5$  is relatively insensitive to water and stable in air. The solution-processed  $V_2O_5$  interlayer can serve as a barrier preventing oxygen or water from entering and degrading the photoactive layer. In addition, this approach does not need annealing treatment like PEDOT:PSS nor vacuum equipments, so it is simple, expeditious, and effective. This is very important for commercial realization of low-cost and large-area printed solar cells.

#### 4. Conclusion

In conclusion, we have demonstrated the use of the solution-processed  $V_2O_5$  as the anode interlayer in in-

verted PSCs hybridized with ZnO nanorods. The optimum  $V_2O_5$  interlayer is obtained at the concentration of 100  $\mu\text{g/ml}$ , because the photoactive layer is almost completely covered with  $V_2O_5$  at this condition. The highest PCE of 3.56% is achieved for the device with the optimum  $V_2O_5$  interlayer, which is comparable to that of the devices with a vacuum-deposited  $V_2O_5$  interlayer [28]. Our investigations show that the  $V_2O_5$  interlayer can effectively prevent the leakage currents at the organic/Ag interface leading to improvements in  $V_{OC}$ , FF,  $R_S$ , and  $R_{SH}$ . The optical absorption and IPCE are also improved by the optical spacer effect of the  $V_2O_5$  interlayer, thus leading to the increased photocurrent. Compared to the vacuum-deposited techniques, this approach is simple, expeditious, and effective. It is also advantageous for potential applications to mass production of various large-area printed electronics with a very low cost.

#### Acknowledgement

This work was supported by the National Science Council, Taiwan, Republic of China, with Grant Nos. NSC96-2221-E-002-277-MY3, NSC97-2218-E-002-013, and NSC97-2221-E-002-039-MY3.

#### References

- [1] F.C. Krebs, Polymer solar cell modules prepared using roll-to-roll methods: knife-over-edge coating, slot-die coating and screen printing, *Sol. Energy Mater. Sol. Cells* 93 (2009) 465–475.
- [2] F.C. Krebs, Fabrication and processing of polymer solar cells: a review of printing and coating techniques, *Sol. Energy Mater. Sol. Cells* 93 (2009) 394–412.
- [3] F.C. Krebs, M. Jørgensen, K. Norrman, O. Hagemann, J. Alstrup, T.D. Nielsen, J. Fyenbo, K. Larsen, J. Kristensen, A complete process for production of flexible large area polymer solar cells entirely using screen printing – first public demonstration, *Sol. Energy Mater. Sol. Cells* 93 (2009) 422–441.
- [4] C.J. Brabec, J.R. Durrant, Solution-processed organic solar cells, *MRS Bull.* 33 (2008) 670–675.
- [5] C.J. Brabec, J.A. Hauch, P. Schilinsky, C. Waldauf, Production aspects of organic photovoltaics and their impact on the commercialization of devices, *MRS Bull.* 30 (2005) 50–52.
- [6] C.J. Brabec, N.S. Sariciftci, J.C. Hummelen, Plastic solar cells, *Adv. Funct. Mater.* 11 (2001) 15–26.
- [7] G. Li, V. Shrotriya, J.S. Huang, Y. Yao, T. Moriarty, K. Emery, Y. Yang, High-efficiency solution processable polymer photovoltaic cells by self-organization of polymer blends, *Nat. Mater.* 4 (2005) 864–868.
- [8] A.J. Moule, K. Meerholz, Controlling morphology in polymer-fullerene mixtures, *Adv. Mater.* 20 (2008) 240–245.
- [9] B.C. Thompson, J.M.J. Fréchet, Organic photovoltaics – polymer-fullerene composite solar cells, *Angew. Chem. Int. Ed.* 47 (2008) 58–77.
- [10] S. Günes, H. Neugebauer, N.S. Sariciftci, Conjugated polymer-based organic solar cells, *Chem. Rev.* 107 (2007) 1324–1338.
- [11] V. Shrotriya, G. Li, Y. Yao, C.W. Chu, Y. Yang, Transition metal oxides as the buffer layer for polymer photovoltaic cells, *Appl. Phys. Lett.* 88 (2006) 073508.
- [12] M.D. Irwin, B. Buchholz, A.W. Hains, R.P.H. Chang, T.J. Marks, P-type semiconducting nickel oxide as an efficiency-enhancing anode interfacial layer in polymer bulk-heterojunction solar cells, *Proc. Nat. Acad. Sci. USA* 105 (2008) 2783–2787.
- [13] C. Tao, S. Ruan, X. Zhang, G. Xie, L. Shen, X. Kong, W. Dong, C. Liu, W. Chen, Performance improvement of inverted polymer solar cells with different top electrodes by introducing a  $\text{MoO}_3$  buffer layer, *Appl. Phys. Lett.* 93 (2008) 193307.
- [14] C. Tao, S.P. Ruan, G.H. Xie, X.Z. Kong, L. Shen, F.X. Meng, C.X. Liu, X.D. Zhang, W. Dong, W.Y. Chen, Role of tungsten oxide in inverted polymer solar cells, *Appl. Phys. Lett.* 94 (2009) 043311.
- [15] M. Jørgensen, K. Norrman, F.C. Krebs, Stability/degradation of polymer solar cells, *Sol. Energy Mater. Sol. Cells* 92 (2008) 686–714.

- [16] M.P. de Jong, L.J. van Ijzendoorn, M.J.A. de Voigt, Stability of the interface between indium-tin-oxide and poly(3,4-ethylenedioxythiophene)/poly(styrenesulfonate) in polymer light-emitting diodes, *Appl. Phys. Lett.* 77 (2000) 2255–2257.
- [17] M.S. White, D.C. Olson, S.E. Shaheen, N. Kopidakis, D.S. Ginley, Inverted bulk-heterojunction organic photovoltaic device using a solution-derived ZnO underlayer, *Appl. Phys. Lett.* 89 (2006) 143517.
- [18] F.C. Krebs, Air stable polymer photovoltaics based on a process free from vacuum steps and fullerenes, *Sol. Energy Mater. Sol. Cells* 92 (2008) 715–726.
- [19] F.C. Krebs, Y. Thomann, R. Thomann, J.W. Andreasen, A simple nanostructured polymer/ZnO hybrid solar cell-preparation and operation in air, *Nanotechnology* 19 (2008) 424013.
- [20] K. Takanezawa, K. Hirota, Q.S. Wei, K. Tajima, K. Hashimoto, Efficient charge collection with ZnO nanorod array in hybrid photovoltaic devices, *J. Phys. Chem. C* 111 (2007) 7218–7223.
- [21] T.H. Lowery, K.S. Richardson, *Mechanism and Theory in Organic Chemistry*, third ed., Harper Collins Publishers, New York, 1987.
- [22] L.J.A. Koster, V.D. Mihailetschi, P.W.M. Blom, Ultimate efficiency of polymer/fullerene bulk heterojunction solar cells, *Appl. Phys. Lett.* 88 (2006) 093511.
- [23] D.C. Olson, J. Piris, R.T. Collins, S.E. Shaheen, D.S. Ginley, Hybrid photovoltaic devices of polymer and ZnO nanofiber composites, *Thin Solid Films* 496 (2006) 26–29.
- [24] A. Moliton, J.M. Nunzi, How to model the behaviour of organic photovoltaic cells, *Polym. Int.* 55 (2006) 583–600.
- [25] J.K. Lee, N.E. Coates, S. Cho, N.S. Cho, D. Moses, G.C. Bazan, K. Lee, A.J. Heeger, Efficacy of TiO<sub>x</sub> optical spacer in bulk-heterojunction solar cells processed with 1,8-octanedithiol, *Appl. Phys. Lett.* 92 (2008) 243308.
- [26] Y. Kim, S. Cook, S.M. Tuladhar, S.A. Choulis, J. Nelson, J.R. Durrant, D.D.C. Bradley, M. Giles, I. McCulloch, C.S. Ha, M. Ree, A strong regioregularity effect in self-organizing conjugated polymer films and high-efficiency polythiophene: fullerene solar cells, *Nat. Mater.* 5 (2006) 197–203.
- [27] K. Kawano, R. Pacios, D. Poplavskyy, J. Nelson, D.D.C. Bradley, J.R. Durrant, Degradation of organic solar cells due to air exposure, *Sol. Energy Mater. Sol. Cells* 90 (2006) 3520–3530.
- [28] K. Takanezawa, K. Tajima, K. Hashimoto, Efficiency enhancement of polymer photovoltaic devices hybridized with ZnO nanorod arrays by the introduction of a vanadium oxide buffer layer, *Appl. Phys. Lett.* 93 (2008) 063308.



at high temperature so far. Therefore, it is important that the materials used in OLEDs fabrication have high thermal stability as well as ease of sublimation. In particular, molecules of high vapor pressure are needed for mass production, since a large number of samples need to be loaded on a tray at once.

The solution process in OLEDs has recently attracted much attention due to its low cost and ease of device fabrication. Molecules showing good solubility in common organic solvents are suitable for this process. If the molecules have poor solubility, the performance of a solution-processed OLEDs is significantly lowered due to aggregation [13]. Consequently, in order to be suitable molecules for both processes, the molecules need to have high thermal stability, good solubility and an ease of sublimation originated from high vapor-pressure.

Triarylsilyl moieties are known for high chemical stability as well as improved solubility, and thus give improved efficiency compared to alkyl substituents in OLEDs [14]. However, triarylsilyl possess some drawbacks such as lower yield, complexities in synthesis, a delicate purification process and low vapor pressure. On the contrary, trimethylsilyl moieties are introduced easily into the ligand backbone and their derivatives are synthesized in high yields. In addition, trimethylsilyl functional groups confer to molecules such attributes as higher vapor pressure, thermal stability (high  $T_g$ ), good solubility and steric bulk via higher volume. Such properties of the silyl moiety effectively hinder the aggregation and excimer formation of ppy-based Ir(III) complexes [15]. Therefore, the combination of ppy and bulky trimethylsilyl moieties would be expected to be the best way to achieve an efficient phosphorescent emitter. Herein, we describe the results of our investigation into the preparation, thermal and optical properties and electroluminescent characteristics of a new Ir(ppy)<sub>3</sub> derivative containing trimethylsilyl moieties.

## 2. Experiments

All experiments were performed under dry N<sub>2</sub> atmosphere using standard Schlenk technique. All solvents were freshly distilled over appropriate drying reagents prior to use. All starting materials were purchased from either Aldrich or Strem and used without further purification. <sup>1</sup>H NMR and mass spectra were recorded on a Bruker DRX 500 MHz spectrometer and JEOL-JMS 700 instrument, respectively. UV/vis and photoluminescent spectra for all samples with concentrations in the range of 10–50 μM were obtained from UV/vis spectrometer Lambda 900 and a Perkin Elmer Luminescence spectrometer LS 50B, respectively. All solutions for photophysical experiments were degassed with more than three repeated freeze-pump-thaw cycles in a vacuum line. Melting points were determined on an Electrothermal 9100 apparatus. Emission lifetimes were measured with the fourth harmonic of a Q-switched Nd-YAG laser using the upper excite state energy transfer with a pulse duration of 6 ns and a repetition rate of 10 Hz. The laser beam had a diameter of 5 mm and an optical power of ~ 50 mJ. The emission from the film was recorded by a gated intensified diode array detector through a monochromator. The system allows for an

integration time (gate width) of detection from 100 ns to 10 ms and a variable delay after excitation. Ultraviolet photoemission spectroscopy (UPS) was conducted according to previous report [16]. Absolute emission quantum yield ( $\eta_{\text{PL}}$ ) and its dependence for doping concentration were measured by an integrating sphere [17]. Cyclic voltammetry was performed with an Autolab potentiostat by Echochemie under nitrogen atmosphere in a one-compartment electrolysis cell consisting of a platinum wire working electrode, a platinum wire counter electrode, and a quasi Ag/AgCl reference electrode. Cyclic voltammograms were monitored at scan rates of either 100 mV s<sup>-1</sup> or 50 mV s<sup>-1</sup> and recorded in distilled dichloromethane. The concentration of the complex was maintained at 0.5 mM or less and each solution contained 0.1 M of tetrabutylammoniumhexafluorophosphate (TBAP) as the electrolyte. The ferrocenium/ferrocene couple was used as the internal standard.

### 2.1. 1-Bromo-3-(trimethylsilyl)benzene

To a stirring solution of 1,3-dibromobenzene (25 g, 0.11 mol) in diethyl ether (250 mL) was cooled to -78 °C. Addition of n-BuLi (29.4 g, 0.11 mol, 2.5 M in hexane) over 20 min resulted in a pale yellow solution. After stirring for 1 h at this temperature and then quenched with TMSCl (12.7 g, 0.12 mol). The solution was allowed to warm to room temperature overnight. Water (40 mL) was added to the above solution. The organic layer was separated and washed with brine, dried (MgSO<sub>4</sub>), and concentrated under reduced pressure. The crude material was purified by vacuum distillation. The fraction boiling at 79–80 °C (1.5 mmHg) was collected as a clear oil (20 g, 85%) <sup>1</sup>H NMR (CDCl<sub>3</sub>)  $\delta$  7.54 (s, 1H), 7.39 (d, 1H), 7.34 (d, 1H), 7.14 (t, 1H), 0.19 (s, 9H).

### 2.2. 3-(Trimethylsilyl)phenylboronic acid

To a stirring solution of 1-bromo-3-(trimethylsilyl)benzene (10 g, 43.6 mmol) in diethyl ether (100 mL) was cooled to -78 °C. Addition of n-BuLi (13.3 g, 48 mmol, 2.5 M in hexane) over 20 min resulted in a yellow solution. After stirring for 30 min at this temperature and then quenched with (C<sub>2</sub>H<sub>5</sub>O)<sub>3</sub>B (19.1 g, 130.9 mmol). The solution was allowed to warm to room temperature overnight. The mixture was then cooled to 0 °C and acidified with 1 N HCl. A white precipitate formed. The mixture was stirred for 1 h and then the layers were separated, and the aqueous was extracted with ethylacetate (2 × 100 mL). The organic layers were combined, washed with 1 N HCl, dried (MgSO<sub>4</sub>), and concentrated under reduced pressure. Further drying under vacuum afforded 5.4 g (64%) of a white solid. The compound was generally used in the following step without further purification: mp 138–140 °C; <sup>1</sup>H NMR (CDCl<sub>3</sub>)  $\delta$  8.46 (s, 1H), 8.25 (d, 1H), 7.8 (d, 1H), 7.54 (t, 1H), 0.39 (s, 9H).

### 2.3. 2-Bromo-5-trimethylsilylpyridine

To a stirring solution of 2,5-dibromopyridine (10 g, 42.2 mmol) in diethyl ether (100 mL) was cooled to

–78 °C. Addition of n-BuLi (11.7 g, 42.2 mmol, 2.5 M in hexane) over 20 min resulted in a dark brown solution. After stirring for 1 h at this temperature and then quenched with TMSCl (5.50 g, 50.6 mmol). The solution was allowed to warm to room temperature overnight. Water (100 mL) was added to the above solution. The organic layer was separated and the aqueous layer was extracted with diethyl ether (2 × 80 mL). The organic layers were combined, dried (MgSO<sub>4</sub>), and concentrated under reduced pressure. The crude material was purified by vacuum distillation. The fraction boiling at 86–87 °C (1.5 mmHg) was collected as a clear oil (20 g, 85%) <sup>1</sup>H NMR (CDCl<sub>3</sub>) δ 7.54 (s, 1H), 7.39 (d, 1H), 7.34 (d, 1H), 7.14 (t, 1H), 0.19 (s, 9H).

#### 2.4. Ligand dsippy

2-Bromo-5-trimethylsilylpyridine (5.0 g, 21.7 mmol), 3-(trimethylsilyl)phenylboronic acid (5.06 g, 26.1 mmol), and Pd(PPh<sub>3</sub>)<sub>4</sub> (0.75 g, 0.65 mmol), were dissolved in THF (45 mL). A solution of 2 M K<sub>2</sub>CO<sub>3</sub> (15 mL) was added, and the mixture was refluxed with stirring for 18 h in an atmosphere of nitrogen. After being cooled, the mixture was poured into aqueous EDTA and extracted with ether. The organic layer was dried over MgSO<sub>4</sub>. The solvent was removed under reduced pressure to give a yellow oil. The crude product was purified by chromatography on silica gel (EtOAc/hexane, 1/5, v/v) to obtain a colorless oil (5.92 g, 91%); IR (KBr) 3042, 2950, 1591, 1480, 1437, 1250 cm<sup>-1</sup>; <sup>1</sup>H NMR (CD<sub>2</sub>Cl<sub>2</sub>) δ 8.97 (dd, 1H), 8.41 (dd, 1H), 8.16 (m, 1H), 8.01 (dd, 1H), 7.88 (dd, 1H), 7.75 (sex, 1H), 7.60 (sex, 1H), 0.50 (s, 9H), 0.49 (s, 9H). <sup>13</sup>C-NMR(CD<sub>2</sub>Cl<sub>2</sub>): δ 157.69, 153.99, 141.97, 140.99, 138.70, 134.13, 133.18, 131.94, 128.18, 127.55, 119.93, –1.14, –1.35. Anal. Calcd for C<sub>17</sub>H<sub>25</sub>NSi<sub>2</sub> (299.15): C, 68.16; H, 8.41; N, 4.68. Found: C, 68.21; H, 8.39; N, 4.67.

#### 2.5. Complex Ir(dsippy)<sub>3</sub>

Ligand dsippy (3 g, 10.0 mmol) and Ir(acac)<sub>3</sub> (1.22 g, 2.50 mmol) were dissolved in ethylene glycol (50 mL), and the mixture was heated to reflux under nitrogen for 25 h. The reaction mixture was then cooled to room temperature, 1 N HCl was added, and the mixture was filtered to give a crude product, and then flash chromatographed on silica column using dichloromethane to yield 1.1 g (42%). The compound was then further purified by sublimation. IR (KBr) 3040, 2949, 1581, 1476, 1435, 1248 cm<sup>-1</sup>; <sup>1</sup>H-NMR (CD<sub>2</sub>Cl<sub>2</sub>): δ 7.98 (d, 3H), 7.86 (s, 3H), 7.80 (d, 3H), 7.52 (s, 3H), 7.04 (d, 3H), 6.94 (d, 3H), 0.29 (s, 27H), 0.12 (s, 27H); <sup>13</sup>C-NMR(CD<sub>2</sub>Cl<sub>2</sub>): δ 166.70, 161.47, 150.34, 144.01, 141.14, 136.96, 133.23, 129.83, 124.23, 119.73, 118.27, –1.87, –1.93; MS (FAB): *m/z* = 1087[M<sup>+</sup>]. Anal. Calcd for C<sub>51</sub>H<sub>72</sub>N<sub>3</sub>Si<sub>6</sub>Ir (1087.40): C, 56.31; H, 6.67; N, 3.86. Found: C, 56.35; H, 6.59; N, 3.82.

The glass substrate pre-coated with indium-tin-oxide (ITO) was cleaned by an ultrasonic bath of acetone, followed by 2-propanol. Surface treatment was carried out by exposing ITO to a UV-ozone plasma. OLEDs using CBP as host material is fabricated as follows. The hole-injecting layer, a 10 nm thick film of copper phthalocyanine (CuPc)

was deposited on ITO surface by high vacuum thermal evaporation and a 40 nm thickness 4,4-bis[N-(naphthyl)-N-phenyl-amino]biphenyl (α-NPD) as hole-transporting layer was deposited onto the CuPc. Ir(dsippy)<sub>3</sub> (dsippy = ditrimethylsilyl-substituted ppy) doped host CBP layer were thermally co-evaporated on the α-NPD layer. Ir(dsippy)<sub>3</sub> doping concentrations was 8% in CBP. A 10 nm thick BCP (2,9-dimethyl-4,7-diphenyl-1,10-phenanthroline) layer was then deposited as the exciton-blocking and followed by a 40 nm Alq<sub>3</sub> (*tris*-(8-hydroxyquinoline) aluminum(III)) as an electron transporting layer. Finally LiF (1 nm) and Al (100 nm) were deposited on top of the organic layers by thermal evaporation. The fabricated multilayer organic light-emitting devices have the structure of ITO/CuPc (10 nm)/α-NPD (40 nm)/CBP-Ir(dsippy)<sub>3</sub> (20 nm)/BCP (10 nm)/Alq<sub>3</sub> (40 nm)/LiF (1 nm)/Al (100 nm).

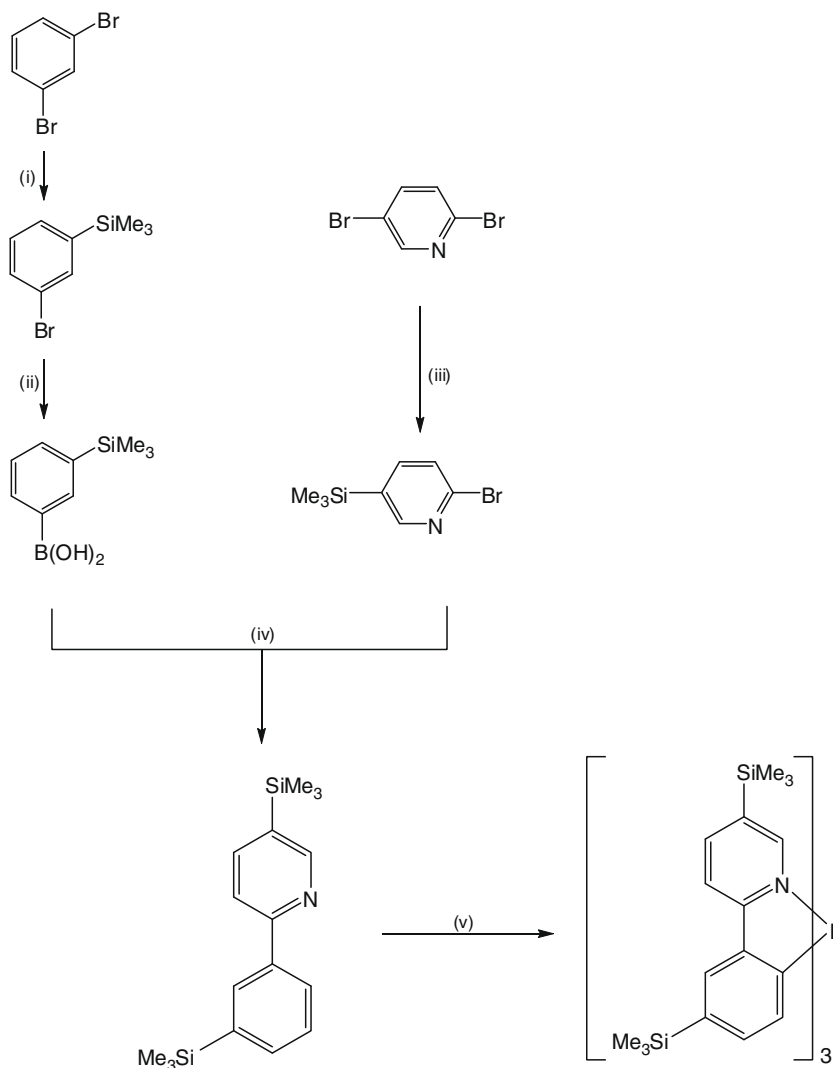
### 3. Results and discussion

The ligand 2-phenylpyridine, containing trimethylsilyl moieties, was synthesized by Suzuki coupling [18], through the reaction of 2-bromo-5-trimethylsilylpyridine with the corresponding 3-trimethylsilyl phenylboronic acid in the presence of K<sub>2</sub>CO<sub>3</sub> and Pd(PPh<sub>3</sub>)<sub>4</sub> catalyst as shown in Scheme 1. This ligand was obtained in good yields (91%).

The titled complex, Ir(dsippy)<sub>3</sub>, was synthesized by slight modification of the previous synthetic methodology reported by Watts and co-workers [19]. Through the reaction of Ir(acac)<sub>3</sub> with the trimethylsilyl-substituted ppy ligands under high temperature (>200 °C), the complex was obtained in moderate yields (42%). Both the ligand and the iridium complex were characterized by NMR, mass spectrometry and elemental analyses. In the <sup>1</sup>H-NMR spectra, the complex exhibits six well-resolved peaks in the phenyl region due to the ppy rings, indicating that it has a *facial* geometry around the Ir metal center. Ir(dsippy)<sub>3</sub> is highly soluble in common organic solvent and slightly soluble even in hexane. It may be due to introduced bulky trimethylsilyl groups. This complex is very stable up to approximately 290 °C without degradation under N<sub>2</sub> atmosphere. The decomposition temperature, which is defined as 5% weight loss, is 295 °C. The glass transition (*T*<sub>g</sub>) in DSC experiment appears at 184 °C (Fig. 1).

Moreover, Ir(dsippy)<sub>3</sub> displayed a consistent and reproducible DSC diagram during two cycles of heating and cooling, proving that this complex is thermally stable up to its melting transition. The *T*<sub>g</sub> value observed for the complex is considerably higher than that of Ir(ppy)<sub>3</sub>. This suggests that the introduction of silyl moieties in the ppy ring leads to a dramatic increase in thermal stability.

The UV-vis spectra of the complex in solution exhibit strong absorption bands from 250 to 320 nm ( $\epsilon > 10^4$  mol<sup>-1</sup> dm<sup>3</sup> cm<sup>-1</sup>), indicating that the electronic transitions are mostly ligand-centered (LC)  $\pi$ - $\pi^*$  (Fig. 2). As compared to the absorption of Ir(ppy)<sub>3</sub>, the absorption patterns of Ir(dsippy)<sub>3</sub> are similar in the 250–550 nm spectral region [20]. Intraligand (IL)  $\pi$ - $\pi^*$  transitions and metal-to-ligand charge transfer (<sup>1</sup>MLCT,  $d\pi(\text{Ir})$ - $\pi(\text{ppy})$ ) transitions are observed in the region of 350–440 nm. In



**Scheme 1.** Synthetic routes of Ir(disppy)<sub>3</sub>. Reagents and conditions: (i) n-BuLi (−78 °C), TMSCl, RT, overnight; (ii) n-BuLi (−78 °C), B(OEt)<sub>3</sub>, RT, overnight; (iii) n-BuLi (−78 °C), TMSCl, RT, overnight; (iv) Pd(PPh)<sub>3</sub>, 2 M-K<sub>2</sub>CO<sub>3</sub>, reflux, 18 h, THF; (v) Ir(acac)<sub>3</sub>, ethylene glycol, reflux, 25 h.

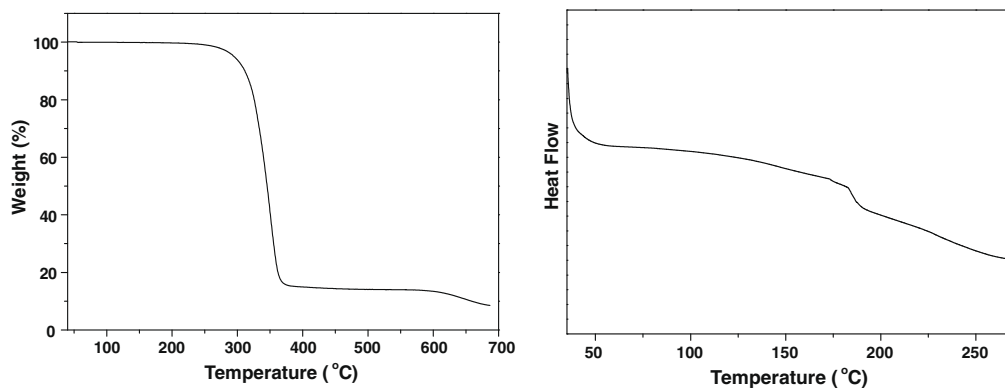


**Fig. 1.** TGA (left) and DSC data (right) of Ir(disppy)<sub>3</sub> under N<sub>2</sub> atmosphere.

addition, weaker absorption tails at 450–480 nm, which can be assigned as triplet metal-to-ligand charge transfer

(<sup>3</sup>MLCT), are also observed. Despite the fact that the Ir(disppy)<sub>3</sub> complex shows similar patterns to that of Ir(ppy)<sub>3</sub> in

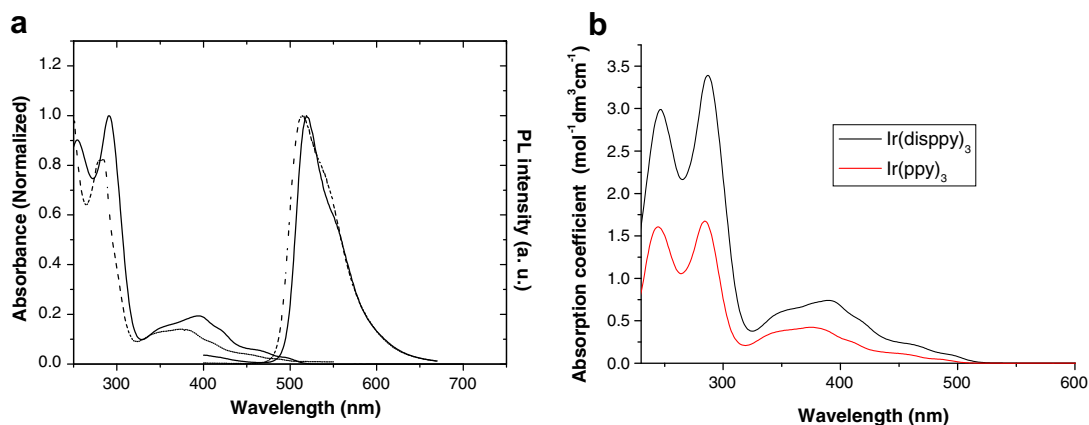


**Fig. 2.** (a) The absorption and emission spectra of Ir(disppy)<sub>3</sub>. Solid line (diluted solution), dashed line (neat thin film). Wavelength/nm (log  $\epsilon$ ): 291(5.01), 394(4.32), 419(4.15), 460(3.61). (b) Absorption spectra of Ir(disppy)<sub>3</sub> and Ir(ppy)<sub>3</sub> at the same concentration. ( $[M] = 1.0 \times 10^{-5}$ , solvent: 1,2-dichloroethane).

absorption spectrum, it should be noted that a strikingly higher extinction coefficient was observed for Ir(disppy)<sub>3</sub> in the charge transfer region (Fig. 2b). The larger molar extinction coefficient observed for <sup>1</sup>MLCT and <sup>3</sup>MLCT relative to that of Ir(ppy)<sub>3</sub> indicates that the substituted silyl groups play a key role in the enhancement of the spin-orbit coupling.

The emission spectra of complex in solution and in film at room temperature are dominated by phosphorescence in the region of 500–600 nm with maximum values of 519 and 513 nm, respectively.

In addition, the emission spectrum of 8%-Ir(disppy)<sub>3</sub> doped CBP film is almost the same spectrum of neat film. There are no characteristic emission peaks from CBP, indicating that the emission primarily originates from Ir(disppy)<sub>3</sub>. Furthermore, no shift of the emission peak was observed, even at a higher doping concentration (30% or 50%). These results apparently support the conclusion that effective energy transfer from the host (CBP) to the dopant the (Ir complex) occurs in the emissive layer.

Interestingly, the emission spectrum of Ir(disppy)<sub>3</sub> in the solid state is blue-shifted in comparison to the diluted solution ( $10^{-5}$ – $10^{-6}$  M) and the emission spectrum in solution shows a narrow band with a small full-width at half-maximum (solution: 50 nm, thin film: 60 nm). In general, the maximum emission band in the solid state appears at lower energies as compared to that in solution due to the difference in dielectric constant of the environment [21,22]. This observation may indicate that bulky trimethylsilyl groups hamper intermolecular interactions even in the solid state. However, on the one hand, virtually identical shapes of the spectra of Ir(disppy)<sub>3</sub> and Ir(ppy)<sub>3</sub> were observed, thus indicating that the same excited and/or ground states were involved in the phosphorescent transitions. On the other hand, the part of the trimethylsilyl groups seems to have a negligible effect on the shift of emission maxima, which was demonstrated further by the electrochemical determination of HOMO and LUMO levels.

To investigate electronic effects on the ppy rings caused by trimethylsilyl groups, cyclic voltammetry experiments

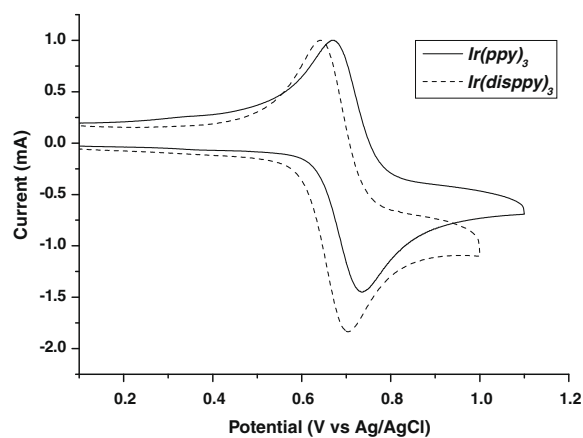


**Fig. 3.** Cyclic voltammograms of Ir(ppy)<sub>3</sub> (solid line) and Ir(disppy)<sub>3</sub> (dashed line) measured in CH<sub>2</sub>Cl<sub>2</sub>:CH<sub>3</sub>CN [1:1(v/v)] at a scan rate of 100 mV/s.

(Ag/AgCl with a ferrocene/ferrocenium, Fc/Fc<sup>+</sup>, internal standard) for the complex including Ir(ppy)<sub>3</sub> were carried out under the same experimental conditions. Due to the limited range available in dichloromethane and the inability of our instrument to measure reliable reduction potential below  $-2.0$  V, we have obtained only the reliable oxidation potentials.

Ir(disppy)<sub>3</sub> shows a single reversible oxidation at 0.67 V (*E*<sub>pa</sub>), while the reversible oxidation of Ir(ppy)<sub>3</sub> appears at 0.70 V (*E*<sub>pa</sub>). Ir(ppy)<sub>3</sub> shows a slightly higher reversible oxidation, as shown in Fig. 3. The HOMO level for Ir(disppy)<sub>3</sub> was estimated on the basis of an oxidation potential of  $-4.8$  eV (below vacuum level) for Fc/Fc<sup>+</sup> [23]. The onset potential of oxidation for Ir(disppy)<sub>3</sub> was determined to be 0.60 V (vs Ag/AgCl), corresponding to 0.50 V (vs Fc/Fc<sup>+</sup>), hence, the HOMO level for Ir(disppy)<sub>3</sub> is estimated to be  $-5.30$  eV. This value is slightly higher than that of Ir(ppy)<sub>3</sub>, showing that the trimethylsilyl substituent introduced to the ppy ring has no significant effect on the HOMO energy level. To obtain HOMO energy more

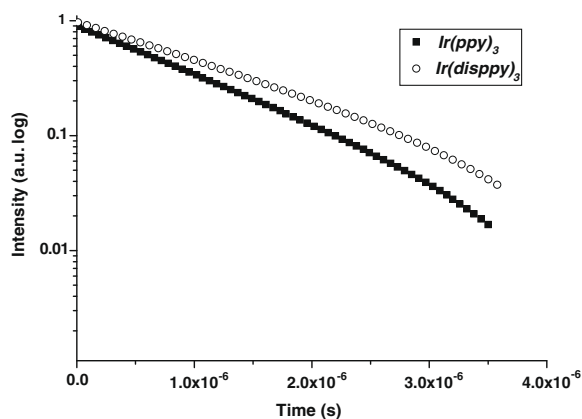


Fig. 4. PL decay of Ir(ppy)<sub>3</sub> and Ir(disppy)<sub>3</sub> in thin film at room temperature.

accurately, ultraviolet photoemission spectroscopy (UPS) was measured and its result was presented in supporting information. Based on UPS data, HOMO energy of Ir(disppy)<sub>3</sub> appears at  $-5.2$  eV, which is similar to that of electrochemical data.

In order to determine the LUMO of the complex, the optical band gap was used. The optical band gap of the complex was determined by its absorption threshold in thin film. The estimated value is  $2.59$  eV, thus, the LUMO level of <sup>3</sup>MLCT is estimated to be  $-2.71$  eV.

The absolute PL efficiencies ( $\eta_{\text{PL}}$ ) of 8 wt%-Ir(disppy)<sub>3</sub>:CBP and 8 wt%-Ir(ppy)<sub>3</sub>:CBP film are  $52 \pm 2\%$  and  $84 \pm 2\%$ , respectively. To gain a deeper insight into the factors influencing photoluminescence quantum yields, measured the life time in the excited states for both Ir(disppy)<sub>3</sub> and Ir(ppy)<sub>3</sub> as shown in Fig. 4. The observed lifetime ( $\tau_{\text{obs}}$ ) for Ir(disppy)<sub>3</sub> at room temperature is  $1.45$   $\mu\text{s}$ , which is longer than that of Ir(ppy)<sub>3</sub> ( $1.0$   $\mu\text{s}$ ), as shown in Fig. 4. Using the following two equations (Eqs. (1) and (2)), the values for the radiative ( $kr$ ) and non radiative ( $knr$ ) decay rates were determined [22].

$$\text{QE(PL)} = kr / (kr + knr) \quad (1)$$

$$1/\tau = kr + knr \quad (2)$$

The calculated values of the radiative ( $kr$ ) and non radiative ( $knr$ ) decay rates for Ir(disppy)<sub>3</sub> are  $3.6 \times 10^5 \text{ s}^{-1}$  and  $3.3 \times 10^5 \text{ s}^{-1}$ , respectively. While the radiative ( $kr$ ) and non radiative ( $knr$ ) decay rates for Ir(ppy)<sub>3</sub> are  $8.4 \times 10^5 \text{ s}^{-1}$  and  $1.6 \times 10^5 \text{ s}^{-1}$ , respectively. This result indicates that the higher quantum yield of Ir(ppy)<sub>3</sub> than that of Ir(disppy)<sub>3</sub> in 8 wt% doping level is most likely due to its faster radiative decay rate [24].

To compare concentration quenching between Ir(ppy)<sub>3</sub> and Ir(disppy)<sub>3</sub> at varied doping concentration, we have conducted PL efficiency ( $\eta_{\text{PL}}$ ) measurement [25–27]. The  $\eta_{\text{PL}}$  of the films was measured using an integrating sphere under nitrogen atmosphere. The Ir(ppy)<sub>3</sub>:CBP film showed an  $\eta_{\text{PL}}$  of 84% at 8 wt%, 42% at 30 wt% and 24% at 50 wt%, respectively, while the Ir(disppy)<sub>3</sub>:CBP film showed 52.0%, 52.4% and 43.97% at each doping levels (wt%) (see Fig. 5). This result further support that the self-quenching in Ir(ppy)<sub>3</sub>:CBP film is more effective than observed results in Ir(disppy)<sub>3</sub>:CBP film. This increased emission quantum yield as compared to Ir(ppy)<sub>3</sub> in high doping level may be supposed to the lack of thermal vibrations and various intermolecular excited-state interactions caused by the introduction of bulky trimethylsilyl groups into ppy ring. Henceforth, the bulky silyl group on ppy ring seems to play a key role in preventing self-quenching.

To compare the electroluminescence (EL) characteristics of Ir(disppy)<sub>3</sub>, we also fabricated EL devices using Ir(ppy)<sub>3</sub>. These contained a similar structure under the same experimental conditions. Devices with the Ir phosphor doped into the emissive layer were fabricated. EL device performance was conducted by using Ir(disppy)<sub>3</sub> and Ir(ppy)<sub>3</sub> as dopant, and CBP, (4,4'-N,N'-dicarbazole-biphenyl) as a host in all cases. The device structure used in this work contained a typical multi-layer structure, employing the following components: ITO as the anode, CuPc (10 nm) as the hole injection material, 1,4-bis[(1-naphthylphenyl)amino]biphenyl (NPD: 40 nm) as the hole transport material, Ir(disppy)<sub>3</sub> and Ir(ppy)<sub>3</sub> (weight 8%) as the dopant material, CBP as the host material (20 nm), 2,9-dimethyl-4,7-diphenyl-1,10-phenanthroline (BCP:10 nm) as the hole blocking material, tris(8-hydroxy-quinoline)aluminum

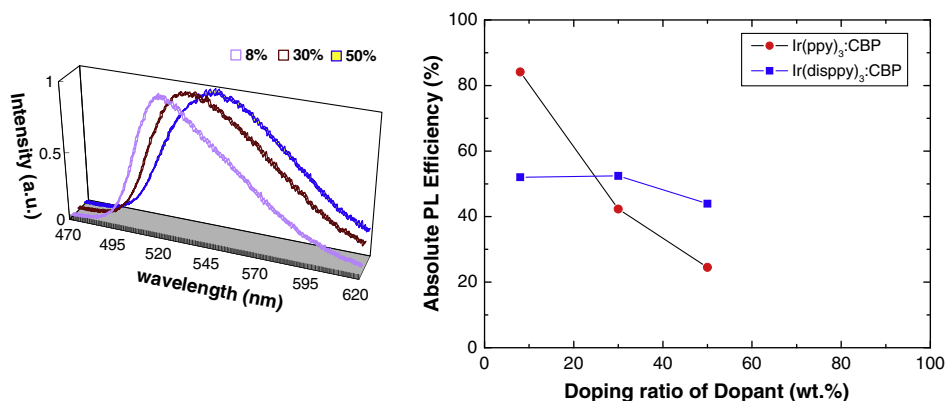


Fig. 5. Left: PL spectra of Ir(disppy)<sub>3</sub>:CBP film measured at each dopant concentration. Right: PL quantum efficiency vs dopant concentration in Ir(disppy)<sub>3</sub>:CBP film.

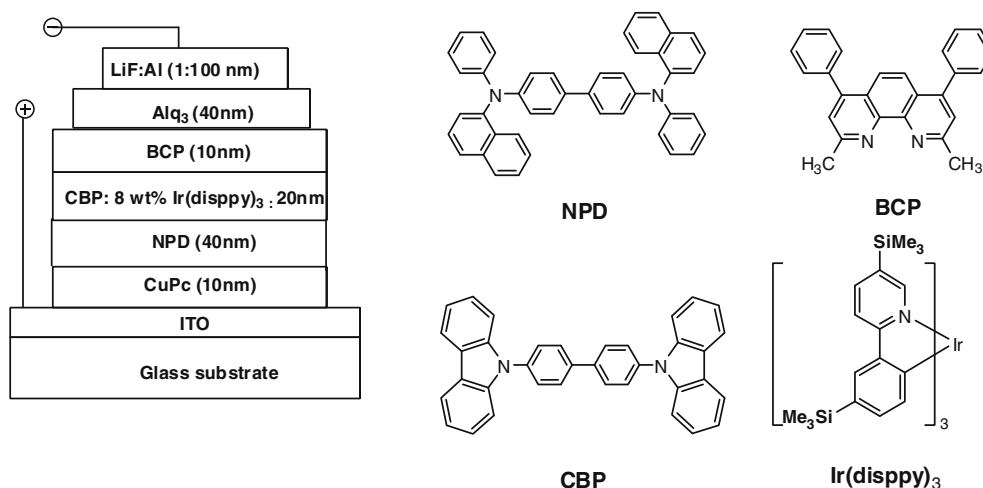


Fig. 6. Device structures and molecular structures used in this study.

Table 1

Electroluminescent data of Ir(ppy)<sub>3</sub> (reference) and Ir(disppy)<sub>3</sub> 8 wt%-doped OLEDs.

	EL ( $\lambda_{\max}$ ) (nm)	Operating voltage (V) <sup>a</sup>	Luminous efficiency (cd/A) <sup>a</sup>	Power efficiency (lm/W) <sup>a</sup>
Ir(ppy) <sub>3</sub>	516	8.7	32.5	11.7
Ir(disppy) <sub>3</sub>	524	7.4	39.2	17.3

<sup>a</sup> At 10 mA/cm<sup>2</sup>.

(AlQ<sub>3</sub>: 40 nm) as the electron transport material, LiF as the electron injection layer, (1 nm) and Al (100 nm) as the cathode, as shown in Fig. 6.

Both complexes display strong green emission in the range of 510–530 nm in the EL spectra, which are well matched to those of the PL spectra in dilute solution. More detailed EL characteristics are shown in Table 1. Turn-on voltages (defined as 10 mA/cm<sup>2</sup>) of Ir(ppy)<sub>3</sub> and Ir(disppy)<sub>3</sub> are 8.7 V and 7.1 V, respectively (Fig. 7).

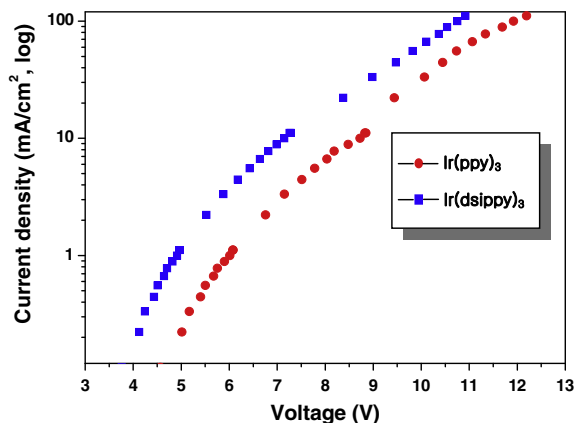


Fig. 7. Voltage vs current density characteristics of Ir(ppy)<sub>3</sub> and Ir(dsippy)<sub>3</sub>: 8 wt%-doped devices.

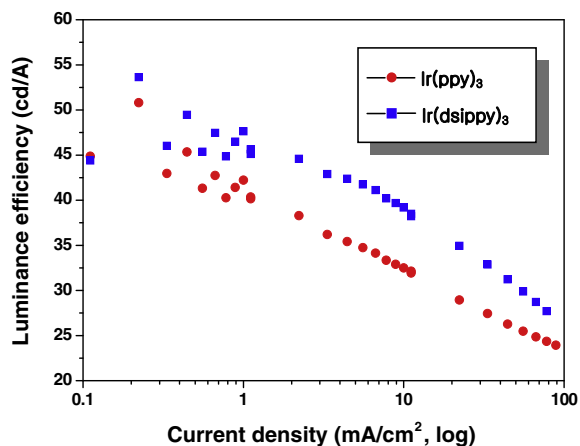


Fig. 8. Luminance efficiency vs current density characteristics of Ir(ppy)<sub>3</sub> and Ir(dsippy)<sub>3</sub>: 8 wt%-doped devices.

The intermolecular interactions (e.g.,  $\pi$ - $\pi$  stacks in molecular crystals) in the solid state and the ability to trap charges in the emissive layer are considered the most important factors in determining the operating voltage.

Effective charge trapping by the dopants increases driving voltages in OLEDs [28]. If the dopant material functions as a hole trap, the HOMO level of dopant could rise above that of the host material. In other words, materials having lower oxidation potential can function effectively in hole trapping in OLEDs. Therefore, the observed lower operating voltages for Ir(dsippy)<sub>3</sub>, relative to Ir(ppy)<sub>3</sub>, are predominantly caused by the lack of effective hole trapping. These results are consistent with the electrochemical behaviors of Ir(dsippy)<sub>3</sub> and Ir(ppy)<sub>3</sub>. As expected, the device fabricated using Ir(dsippy)<sub>3</sub> exhibited higher brightness and power efficiency, as well as stronger EL intensity than in Ir(ppy)<sub>3</sub> (see Figs. 8 and 9). The efficiency of the devices at 10 mA/cm<sup>2</sup> are 32.5 cd/A and 39.2 cd/A, for Ir(ppy)<sub>3</sub> and Ir(dsippy)<sub>3</sub> respectively. Details of electroluminescent data are presented in Table 1.

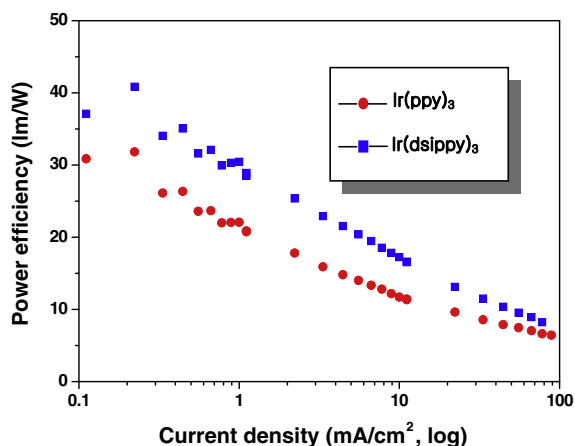


Fig. 9. Power efficiency vs current density characteristics of Ir(ppy)<sub>3</sub> and Ir(dsippy)<sub>3</sub>: 8 wt%-doped devices.

#### 4. Conclusions

A novel *fac-tris*{2-(3'-trimethylsilylphenyl)-5-trimethylsilylpyridinato}iridium, Ir(dsippy)<sub>3</sub>, has been synthesized and its photo-electroluminescent and electrochemical properties have been characterized. This material shows high thermal stability and strong green phosphorescence emission in thin film. This complex demonstrates very high thermal stability, and good solubility in common organic solvent, as well as ease of sublimation due to its high vapor pressure which makes it suitable for mass production. A diminution of turn-on voltage of Ir(dsippy)<sub>3</sub> was observed when this was used as an emitter in the EL performance test. In addition, a significant improvement of the power efficiency (17.3%), which is nearly 200% higher than that of Ir(ppy)<sub>3</sub>, was observed under the same conditions.

#### Acknowledgements

This study was supported by a grant from the Fundamental R&D Program for Core Technology of Materials funded by the Ministry of Knowledge Economy of Korea, and partially supported by the Strategic Technology Development Program (10030814). Dr. S.O. Jung, J.-W. Park, and S.O. Kim acknowledge for the financial support of Human Resource Training Project for Strategic Technology.

#### Appendix. Supplementary data

Supplementary data associated with this article can be found, in the online version, at doi:10.1016/j.orgel.2009.05.018.

#### References

- [1] M.A. Baldo, D.F. O'Brien, Y. You, A. Shoustikov, S. Sibley, M.E. Thompson, S.R. Forrest, *Nature* 393 (1998) 151.
- [2] M.A. Baldo, M.E. Thompson, S.R. Forrest, *Nature* 403 (2000) 750.
- [3] M.A. Baldo, S. Lamansky, P.E. Burrows, M.E. Thompson, S.R. Forrest, *Appl. Phys. Lett.* 75 (1999) 4.
- [4] S. Watanabe, N. Ide, J. Kido, *Jpn. J. Appl. Phys.* 46 (2007) 1186 (reference cited therein).
- [5] S. Lamansky, P. Djurovich, D. Murphy, F. Abdel-Razzaq, R. Kwong, I. Tsyba, M. Bortz, B. Mui, R. Bau, M.E. Thompson, *Inorg. Chem.* 40 (2001) 1704.
- [6] H.J. Bolink, E. Coronado, S.G. Santamaria, M. Sessolo, N. Evans, C. Klein, E. Baranoff, K. Kalyanasundaram, M. Graetzel, M.K. Nazeeruddin, *Chem. Commun.* (2007) 3276.
- [7] V.V. Grushin, N. Herron, D.D. LeCloux, W.J. Marshall, V.A. Petrov, Y. Wang, *Chem. Commun.* (2001) 1494.
- [8] S. Jung, Y. Kang, H.-S. Kim, Y.-H. Kim, C.-L. Lee, J.-J. Kim, S.-K. Lee, S.-K. Kwon, *Eur. J. Inorg. Chem.* 16 (2004) 3415.
- [9] S. Lee, K.-M. Park, K. Yang, Y. Kang, *Inorg. Chem.* 48 (2009) 1030.
- [10] M.A. Baldo, D.F. O'Brien, M.E. Thompson, S.R. Forrest, *Phys. Rev. B.* 60 (1999) 14422.
- [11] M. Klessinger, J. Michl, *Excited States and Photochemistry of Organic Molecules*, VCH, Weinheim, 1995.
- [12] H.Z. Xie, M.W. Liu, O.Y. Wang, X.H. Zhang, C.S. Lee, L.S. Hung, S.T. Lee, P.F. Teng, H.L. Kwong, H. Zheng, C.M. Che, *Adv. Mater.* 13 (2001) 1245.
- [13] J. Qiao, L.D. Wang, J.F. Xie, G.T. Lei, G.S. Wu, Y. Qiu, *Chem. Commun.* (2005) 4560.
- [14] Y. You, C.-G. An, D.-S. Lee, J.-J. Kim, S.Y. Park, *J. Mater. Chem.* 16 (2006) 4706.
- [15] X.-M. Liu, J. Xu, X. Lu, C. He, *Org. Lett.* 7 (2005) 2829.
- [16] K.H. Jong, W.L. Sang, Y. Yang, K. Shin, H. Jeon, S.H. Kim, C. Yang, C.E. Park, *Org. Electron.* 9 (2008) 21.
- [17] Y. Kawamura, H. Sasabe, C. Adachi, *Jpn. J. Appl. Phys. Part 1* 43 (2004) 7729.
- [18] A. Suzuki, *J. Organomet. Chem.* 576 (1999) 147.
- [19] K. Dedeian, P.I. Djurovich, F.O. Garces, G. Carlson, R.J. Watts, *Inorg. Chem.* 30 (1991) 1685.
- [20] K.A. King, P.J. Spellane, R.J. Watts, *J. Am. Chem. Soc.* 107 (1985) 1431.
- [21] J. Salbeck, N. Yu, J. Bauer, F. Weissortel, H. Estgen, *Synth. Met.* 91 (1997) 209.
- [22] S.H. Lee, B.-B. Jang, T. Tsutsui, *Macromolecules* 35 (2002) 1356.
- [23] S.-C. Lo, C.P. Shipley, R.N. Bera, R.R. Harding, A.R. Cowley, P.L. Burn, D.W. Samuel, *Chem. Mater.* 18 (2006) 5119.
- [24] C.-H. Yang, Y.-M. Cheng, Y. Chi, C.-J. Hsu, F.-C. Fang, K.-T. Wong, P.-T. Chou, C.-H. Chang, M.-H. Tsai, C.-C. Wu, *Angew. Chem. Int. Ed.* 46 (2007) 2418.
- [25] A. Endo, K. Suzuki, T. Yoshihara, S. Tobita, M. Yahiro, C. Adachi, *Chem. Phys. Lett.* 460 (2008) 155.
- [26] Y. Kawamura, K. Goushi, J. Brooks, J.J. Brown, H. Sasabe, C. Adachi, *Appl. Phys. Lett.* 86 (2005) 07110.
- [27] W. Holzer, A. Penzkofer, T. Tsuboi, *Chem. Phys.* 308 (2005) 93.
- [28] X. Gong, J.C. Ostrowski, D. Moses, G.C. Bazan, A.J. Heeger, *Adv. Funct. Mater.* 13 (2003) 439.

range, the contact resistance  $R_C$  plays a key role on OTFT downscaling and can limit speed performance of logic circuits. Understanding the architecture and process parameters that govern the contact resistance  $R_C$  is key to properly afford the miniaturization process of organic electronic circuits.

The contact resistance  $R_C$  of an OTFT is affected by the OTFT architecture. Staggered OTFTs are transistors where the metal electrodes and the gate dielectric lay on opposite sides with respect to the OSC thin film. In these architectures the contact resistances  $R_C$  can be hundred times lower than in the coplanar case, where the metal electrodes and the gate dielectric lay on the same side with respect to the semiconducting organic layer [16]. Typically, organic thin film transistors with top-gate/bottom-contact configuration fall in the class of staggered OTFTs, while bottom-gate/bottom-contact one fall in the coplanar case. Following the analysis by T. J. Richards and H. Sirringhaus in Ref. [17], the contact resistance of a staggered OTFT is not too much influenced by the height of the energy barrier occurring at the metal/OSC interface [18–20]. Indeed, the contacts have an ohmic behavior in staggered OTFTs and are conversely non-ohmic in coplanar OTFTs [21,22]. In staggered OTFTs the voltage drop due to the contacts is mainly localized between the metal/OSC interface and the accumulation layer [23,24]. Conversely, in a coplanar configuration the main contribution to the voltage drop is localized at the injecting contact area i.e. at the metal/organic-semiconductor interface. Moreover, it has been observed, in p-type OTFTs and especially in the staggered geometry, that the contact resistance  $R_C$  has a distinctive decrease as the gate voltage  $V_G$  decreases [25–27].

In spite of the role that the contact resistance has in determining the performances of a staggered OTFT, so far, the dependence of the contact resistance on the gate voltage is not well understood. In particular, its link with the material properties of the OSC thin film and the influence of the accumulation layer has not been considered. In this work, we focused on this task: a compact analytical model of the dependence of the contact resistance  $R_C$  on the gate voltage  $V_G$  has been developed, for the case of staggered OTFTs having a polycrystalline OSC thin film as the active channel.

The paper is organized as follows. In Section 2 previous efforts to model the dependence of the contact resistance on the gate bias in staggered OTFTs are shortly reviewed, and their shortcomings explained. In Section 3, it is introduced the charge trapping occurring at the grain boundaries of a polycrystalline OSC thin film, as a fundamental process influencing the contact resistance. In Sections 4 we report a new model of contact resistance, as a function of the gate bias  $V_G$ , based on the two contributions given by: (a) the charge trapping occurring at the grain boundaries and (b) the electric field generated by the accumulation layer. The resulting model is then employed, in Section 4.3, to pave the way for downscaling the device geometry and related technological parameters. Finally, in Section 5 the key results obtained are summarized, together with conclusion remarks.

## 2. Models of contact resistance in staggered OTFTs

According to the literature, two empirical models consider explicitly the dependence of the contact resistance on the gate bias, in staggered OTFTs.

The first empirical model extends to organic TFTs the model proposed by Luan and Neudeck [28] for amorphous silicon TFTs. According to Luan and Neudeck's model, the contact resistance  $R_C$  of a staggered OTFT can be conceived as a minimum effective contact resistance  $R_{Cint}$ , determined by the metal/OSC interface, which is in series with a bulk contact resistance  $R_{Cbulk}$  ( $R_C = R_{Cint} + R_{Cbulk}$ , see Fig. 1). The latter contribution  $R_{Cbulk}$  is determined by the OSC thin film that injected carriers have to cross in order to reach the accumulation layer.  $R_{Cbulk}$  can be expressed as an effective sheet resistance which depends on the gate bias  $V_G$  and in this model, the width-normalized contact resistance can be written as:

$$R_C \times W = \frac{|I_0|}{\mu C_i (V_G - V_{th})} + R_{Cint} \times W, \quad (1)$$

where  $|I_0|$  and  $R_{Cint} \times W$  are the coordinates of the common intersection point of the best-fit lines obtained from a Transfer Line Method (TLM) [25,29],  $\mu$  is an effective electrical mobility of the organic semiconductor,  $C_i$  is the gate capacitance per unit area, and  $V_{th}$  a threshold voltage of the OTFT.

The second model, recently proposed by Richards and Sirringhaus [17], considers that two contributions can lower the bulk contact resistance  $R_{Cbulk}$  with the gate voltage  $V_G$ : (1) the increase of the injecting contact area which occurs as the channel resistance scales down, explained by the current crowding model [30], (2) the increase of the carriers density in the OSC thin film accumulation layer induced by the gate voltage  $V_G$ .

In panel 1 (a), we have schematically reported the source contact region of a staggered p-OTFT. In the picture, the bulk, interface contact resistances and the distribution of holes in the OSC thin film, considered in reference [17], are evidenced.

In spite of the agreement of these two models with experiments, both of them neglect that charge carriers injected through the metal electrodes into the accumulation layer can be trapped by trap states localized within the thickness of the OSC thin film.

On the other hand, the effect of trapping on the contact resistance  $R_C$  can be modeled empirically by recurring to the Meyer–Neldel rule (MNR) [31], which describes the multiple trapping and release (MTR) process of carriers occurring through trap states that are distributed within the gap of the OSC.

In the MNR trap states have an exponential energy distribution characterized by the average energy  $E_B$  (measured with respect to the valence band  $E_V$ ) and the width  $E_{MN}$ , named the Meyer–Neldel energy [32].

The elements that characterize the MNR model have been sketched in Fig. 1. In particular, panel 1(b), reports the position of the energy trap  $E_B$  with respect to the energy injecting barrier  $\phi_b$  of the metal/OSC interface and the Fermi level  $E_F$  of the metal. In panel 1(c) we have sketched the band diagram of an OSC thin film as seen in



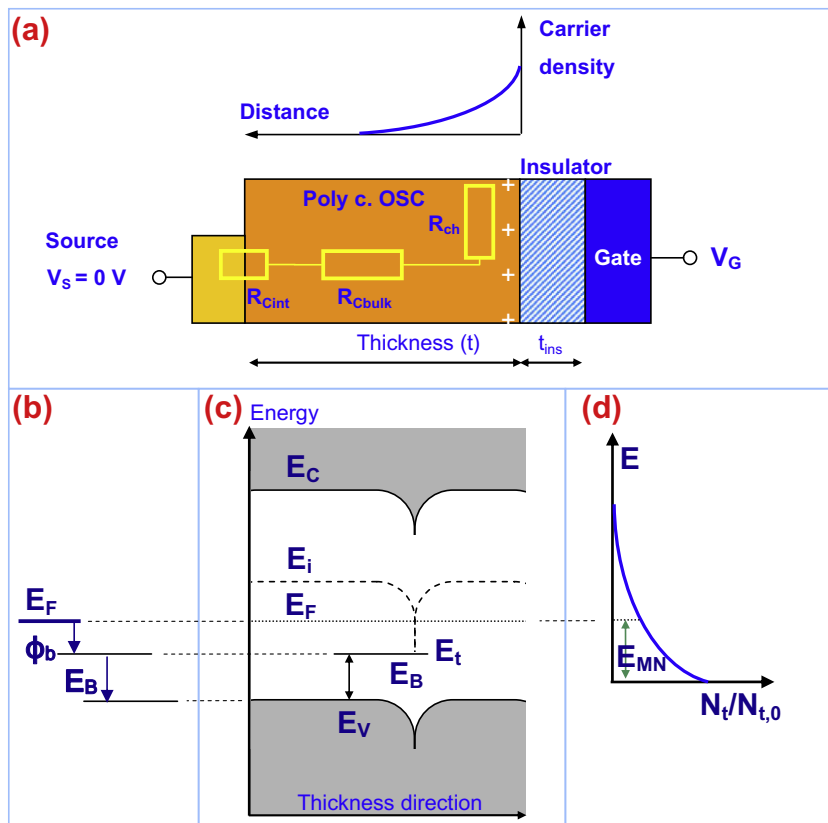


**Fig. 1.** Panel (a) reports a sketch of the source contact area in a staggered OTFT. The OTFT is characterized by the thickness  $t$  of the polycrystalline organic semiconductor (Poly c. OSC) and the thickness of the insulator  $t_{ins}$ . The carrier density as a function of the distance with respect to the active layer has an exponential trend. The contributions to the contact resistance  $R_C$  are the interface  $R_{Cint}$  and the bulk contact resistance  $R_{Cbulk}$ . In the empirical model of Luan and Neudeck [28] both contributions are considered in series  $R_C = R_{Cint} + R_{Cbulk}$ . Panel (b) shows two distinct energy barriers  $\phi_b$  and  $E_B$  contributing to the interface and bulk contact resistance, respectively. Holes injected at the Fermi level  $E_F$  thermally activated have to overcome the total energy barrier  $\phi_b + E_B$ . Panel (c) sketches the band diagram of a polycrystalline OSC thin film.  $E_v$  and  $E_c$  are the valence and conduction band edge, respectively,  $E_i$  is the intrinsic Fermi level,  $E_F$  the Fermi level. A trap is located at an energy  $E_t$  with respect to  $E_i$ , along the thickness  $t$  of the OSC thin film. A trapped carrier has to overcome in the average an energy barrier  $E_B$  to reach the valence band. According to the grain boundary trapping model, the trapping process is attributed to the presence of traps at the grain boundaries. Panel (d), according to the (Meyer–Neldel rule) MNR model traps are distributed exponentially as a function of the energy  $E$  separating the trap from the valence band.  $E_{MN}$  marks the width of the distribution;  $E_B$  is the average energy of the traps.

the transversal (or charge injection) direction and reported the energy  $E_B$  of the trap state. Panel 1(d) depicts the exponential energy distribution of traps characterized by the Meyer–Neldel energy  $E_{MN}$ . Incidentally, we may observe as in the case of a self assembled monolayer, the energy gap which localizes the trap states can be larger in the transverse direction with respect to the OSC energy gap in the longitudinal direction because of the  $\pi$ -stacking. In such case, the formation of traps is favored along the transverse direction.

In the MNR model, the contact resistance can be expressed as:

$$R_C \propto \exp\left(\frac{E_B}{kT} - \frac{E_B}{E_{MN}}\right), \quad (2)$$

where  $E_B$  is the average energy of the traps,  $E_{MN}$  the Meyer–Neldel energy,  $k$  the Boltzmann constant and  $T$  the operating temperature.

Although trapping is a fundamental process in a staggered OTFT, the MNR cannot be employed directly to mod-

el the dependence of the contact resistance on the gate bias. This is because we need to specify the nature of the trapping process which determines the energy trap  $E_B$ . Although this cannot be done in general, it can be pursued if we consider how the trapping process occurs in a polycrystalline OSC thin film of a staggered OTFT.

### 3. Trapping processes in polycrystalline semiconductor thin films

In a polycrystalline OTFT, charge trapping processes occur at the grains boundaries (GBs) and can be described by the grain boundary trapping model (GBTM) [33].

Such a model has been previously considered in the literature to model the mobility in polycrystalline organic semiconductor thin film [34]. However, very recently it has been reported that the grains size of polycrystalline OSCs has an influence on the contact resistance [25,26] of staggered OTFTs.

In particular, Jin et al. [25] by recurring to a Levinson's plot [35], correlate the number of traps  $N_t$  per unit surface with the average grain size and show that the grain size influences the trend of the contact resistance. In a similar way, Wang et al. [26] argue that traps at the grain boundary can be at the origin of the bulk contact resistance.

Although both works agree on the origin of the contact resistance in staggered OTFT by considering the influence of trapping processes at the grain boundaries, none of them fully develop a grain boundary trapping model for the bulk contact resistance. Indeed, Jin et al. model the contact resistance in the frame of the MNR rule without specifying the origin of the energy trap  $E_B$  or its connection with the GB traps.

Because of such evidences it is worth to investigate the connection between the contact resistance and trapping processes occurring at the grain boundaries. In fact, according to the GBTM model an energy barrier  $E_B$  determines the hopping of trapped charge carriers between two grains. Indeed, in a polycrystalline OSC thin film grain boundaries contact also metal electrodes. As a consequence charges trapped at the grain boundary can determine a barrier to the carrier injection and hence influence the bulk contact resistance. For this reason we have investigate if an energy barrier  $E_B$  determined by the grain boundaries charge trapping can influence the bulk contact resistance as well as its dependence on the gate voltage  $V_G$ . On the other hand, thermoionic emission is at the base of the conduction process necessary to overcome the energy barrier at the contact level as well as among grains. Moreover, the grain boundary trapping model shares some common features with the MNR empirical modeling approach. Namely, an exponential energy tail determined by the thermal promoted phenomenon and a trapping process determined by traps of energy  $E_B$  which are localized at the GBs. Within the frame of the GBTM the same band diagram depicted in Fig. 1c can be adopted, once the energy trap  $E_B$  is attributed to traps at the grain boundaries.

In conclusion, although experimental evidences indicate that the bulk contact resistance in staggered OTFT is connected with trapping processes at the grain boundaries, it lacks today an empirical model which gives an indication of the influence of traps localized at GBs. On the other hand, this model can be formulated if the magnitude of the energy  $E_B$  of the trap can be controlled by the gate bias  $V_G$ .

## 4. Results and discussion

In the following, the dependence of the energy barriers contributing to the bulk and interface contact resistance on the gate bias  $V_G$  is obtained and merged into a new model of contact resistance, valid for staggered OTFTs. Finally, the model of contact resistance is extended by investigating the effects of device geometrical and technological parameters towards a downscaling approach.

### 4.1. Bulk contact resistance

Within the framework of the GBTM model the energy barrier at the grain boundary is:

$$E_B = \frac{q^2 N_t^2}{8\epsilon N_D}, \quad (3)$$

where  $N_D$  is the concentration of shallow donors and  $\epsilon$  is the dielectric constant of the OSC bulk material. Such a formulation of the energy barrier  $E_B$  can take into account the gate bias  $V_G$  dependence of the contact resistance. In fact, at low drain voltage  $V_{SD}$ , a bias  $V_G$  applied to the gate induces a charge density  $-N_C$  at the OSC/insulator interface which equals  $-N_C = -C_i V_G/q$ , where  $C_i = \epsilon_{ins}/t_{ins}$  is the gate capacitance per unit area of the dielectric, with  $\epsilon_{ins}$  the dielectric constant of the gate insulator,  $t_{ins}$  the thickness of the gate insulator and  $q$  the electron unit charge. On the other hand, when a charge density  $-N_C$  is induced at the OSC/insulator interface, the energy barrier  $E_B$  lowers by  $\Delta E_B$  because the concentration of donors modifies from  $N_D$  to  $N_D - N_C/t$ , where  $t$  is the thickness of the OSC thin film. As a consequence the contact resistance modifies accordingly into the expression:

$$R_C = R_{C0} \exp\left(\frac{E_B + \Delta E_B}{kT}\right), \quad (4)$$

where

$$\Delta E_B = E_B \frac{N_G}{N_D t - N_G}, \quad (5)$$

and  $(k\tilde{T})^{-1} = (kT)^{-1} - (E_{MN})^{-1}$  is determined by the contribution of the Meyer–Neldel energy  $E_{MN}$ .

By substituting Eq. (5) into Eq. (4), with the hypothesis that  $N_D < 0$  the energy barrier resulting from the trapping process at grain boundaries under the control of the gate bias  $V_G$ , becomes:

$$\begin{aligned} E_B + \Delta E_B &= E_B \frac{N_D t}{N_D t - N_G} = \frac{q^2 N_t^2}{8\epsilon} \frac{t}{N_D t - N_G} \\ &= \frac{q^2 N_t^2 t}{8\epsilon} \frac{1}{|N_G| - |N_D|t} = \frac{q^3 N_t^2 t}{8\epsilon C_i} \frac{1}{|V_G| - \frac{q|N_D|t}{C_i}}. \end{aligned} \quad (6)$$

Hence, the contribution of this kind of trapping process to the specific contact resistance  $R_C \times W$  can be expressed by means of the MNR rule exponential law as:

$$(R_C \times W) = (R_C \times W)_0 \exp\left(\frac{q^3 N_t^2 t}{8\epsilon C_i k\tilde{T}} \frac{1}{|V_G| - V_{th}}\right), \quad (7)$$

where  $V_{th} = q|N_D|t/C_i$  is a threshold bias.

We have tested Eq. (7) with the experimental data reported by Jin et al. in Ref. [25] for the dependence of the contact resistance with the gate bias. In the work of Jin et al. [25], a pentacene 50 nm thin film is deposited on a silicon thermal oxide substrate under two different temperatures of the substrate and completed in an OTFT. According to their experimental results the two different temperatures of deposition of the pentacene allow a control on the trap density  $N_t$  per unit area and determine a set of two values which are  $N_t = 5.6 \times 10^{11} \text{ cm}^{-2}$  and  $N_t = 1.2 \times 10^{12} \text{ cm}^{-2}$ , respectively. From their data, for a thermal oxide of 35 nm and a permittivity of the thermal oxide of 3.9, a value of  $9.86 \times 10^{-4} \text{ F/m}^2$  for the gate capacitance  $C_i$  per unit area can be deduced. In Fig. 2 we have reported in dotted lines the fit of the specific contact resistance data  $R_C \times W$  of Jin et al. by employing Eq. (7) with  $V_{th}$  and  $(R_C \times W)_0$  as best-fit parameters, for the two

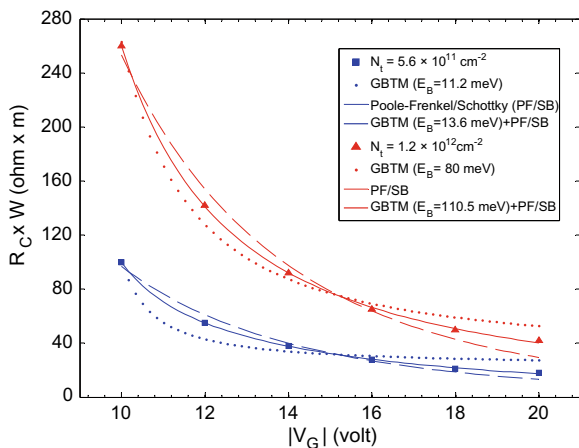


**Fig. 2.** Best-fit of the specific contact resistance  $R_C \times W$  data extracted from ref [25] as a function of the absolute value of the gate voltage  $|V_G|$ . ■ data refer to the case of a trap density  $N_t = 5.6 \times 10^{11} \text{ cm}^{-2}$ , ▲ data refer to a trap density  $N_t = 1.2 \times 10^{12} \text{ cm}^{-2}$ . The thickness  $t$  of the OSC is  $t = 50 \text{ nm}$  and  $\epsilon = 6$  is the relative dielectric constant of the OSC. The thickness of the gate insulator  $t_{\text{ins}} = 35 \text{ nm}$  and its relative dielectric constant is  $\epsilon_{\text{ins}} = 3.9$ , the gate capacitance per unit area is  $C_i = 9.86 \times 10^{-4} \text{ F/m}^2$ . The best-fit in dotted curves (...) has been obtained by employing the grain boundary trapping model (GBTM) expressed by Eq. (7) with  $(R_C \times W)_0$  and  $V_{\text{th}}$  as parameters; the dashed curves (---) regard the Poole-Frenkel/Schottky lowering model of Eq. (10) with  $(R_C \times W)_0$  and  $\alpha$  as parameters; the solid line curves (—) are the combination of the two models (GBTM and Poole-Frenkel/Schottky) as given by Eq. (11), with  $(R_C \times W)_0$ ,  $V_{\text{th}}$  and  $\alpha$  as parameters. According to the best-fit of Eq. (7) the GBTM model provides a threshold voltage of  $V_{\text{th}} = 8.5 \text{ V}$  and a contribution to the energy barrier  $E_B = 11.2 \text{ meV}$  in the  $N_t = 5.6 \times 10^{11} \text{ cm}^{-2}$  case, and  $V_{\text{th}} = 5.56 \text{ V}$  and a contribution to the energy barrier  $E_B = 80 \text{ meV}$  for  $N_t = 1.2 \times 10^{12} \text{ cm}^{-2}$ . According to the best fit of Eq. (11), a threshold voltage of  $V_{\text{th}} = 7.2 \text{ V}$  and a contribution to the energy barrier  $E_B = 13.6 \text{ meV}$  in the  $N_t = 5.6 \times 10^{11} \text{ cm}^{-2}$  case, and  $V_{\text{th}} = 4.0 \text{ V}$  with a contribution to the energy barrier  $E_B = 110.5 \text{ meV}$  for  $N_t = 1.2 \times 10^{12} \text{ cm}^{-2}$ , has been obtained.

case of the density of traps  $N_t$ . In the fit a Meyer–Neldel energy  $E_{MN} = 64 \text{ meV}$  reported in Ref. [27] and a dielectric constant for pentacene of 6 has been assumed. An evaluation of the energy barrier  $E_B$  can be obtained from Eq. (3) by considering the ratio between the quantity  $q^3 N_t^2 t / (8 \epsilon C_i k T)$  and the fitted value of the threshold bias  $V_{\text{th}}$ .

According to the fit we obtained a value of  $E_B = 11.2 \text{ meV}$  for  $N_t = 5.6 \times 10^{11} \text{ cm}^{-2}$  and  $E_B = 80 \text{ meV}$  for  $N_t = 1.2 \times 10^{12} \text{ cm}^{-2}$ , respectively. Both values are consistent, being lower than the corresponding activation energies values which have been experimentally measured and reported in Ref. [25].

Although the fit reproduces the trend of the contact resistance with the gate voltage, it shows systematic deviations from the experimental values. Namely, the fitted dotted curves obtained from Eq. (7) are systematically below the experimental data for values of  $|V_G|$  below  $\sim 15 \text{ V}$ , and systematically above the experimental data values for higher values of  $|V_G|$ .

#### 4.2. Interface contact resistance

The systematic deviations of the GBTM model reported in previous section suggest that this model alone cannot

fully describe the decrease of the contact resistance with the gate voltage increase in staggered OTFTs. As a fact, in the hypothesis of a very low density of traps  $N_t$  we should expect a negligible energy barrier  $E_B$  determining the bulk contact resistance. However, until now we have not examined whether the contact resistance that emerges at the interfaces of the drain and source regions can contribute to the decrease of the contact resistance with the gate bias.

From a heuristic point of view, an evaluation of the interface contact resistance can be achieved from the value of the energy barrier height  $\phi_h$  which emerges at the metal electrode/OSC interface. In fact, if charge carriers are thermally injected into the OSC accumulation layer after overcoming the metal/OSC interface, the contact resistance  $R_C$  can be expressed as:

$$R_C = R_{C0} \exp(\phi_h/kT), \quad (8)$$

with  $R_{C0}$  having the dimension of a resistance.

On the other hand, within the frame of the canonical theory of metal/semiconductor Schottky barrier, we can express  $R_{C0}$  as:

$$R_{C0} = \frac{h^3}{4\pi e^2 m^* k T} \frac{1}{Wt}, \quad (9)$$

where  $m^*$  is the carrier effective mass,  $e$  the electron charge,  $h$  the Planck constant,  $k$  the Boltzmann constant,  $T$  is the temperature and  $W$  the electrode width. In the case of an Au/pentacene interface, with an energy barrier height of  $\phi_h = 0.85 \text{ eV}$  [18], an OSC layer thickness of  $50 \text{ nm}$  and an effective mass equal to the electron mass, a value of  $11.3 \text{ M}\Omega \text{ cm}$  can be estimated for the width normalized contact resistance  $R_C \times W$  at room temperature ( $T = 298 \text{ K}$ ). Such a value is four orders of magnitude larger than the average value of  $50 \text{ k}\Omega \text{ cm}$  reported for staggered OTFTs in references [25–27]. If we still consider valid a formulation of the contact resistance based on the occurrence of a Boltzmann factor, a value of  $50 \text{ k}\Omega \text{ cm}$  for the width-normalized contact resistance can be obtained, with a lower energy barrier height of  $\phi_b = 0.6 \text{ eV}$ .

On the other hand, it is well known that, at the OSC/source electrode, holes have to overcome a lower interface energy barrier  $\phi_b$  [23], because of the Schottky mechanism. This effect is determined by an image potential at the source electrode generated by the electric field which emerges in the OSC thin film.

What is the origin of such electric field? In a staggered OTFT, the OSC/electrode interfaces at the source and at the drain are opposite an accumulation layer switched on by the gate voltage  $V_G$ . Such accumulation layer generates an electric field whose intensity can be linked to the charge density  $-C_i V_G$  of the accumulation layer. An evaluation of the intensity of the electric field according to the equation  $E_{\text{field}} = C_i |V_G| / \epsilon$ , with data reported in Section 4.1 for pentacene, provides a value of  $\sim 10^8 \text{ V/m}$ .

On one hand, the electric field generated by the accumulation layer is known to lower the source electrode energy barrier because of the Schottky mechanism while, on the other hand, such value of the electric field is high enough to possibly influence the drain contact region. However, the influence to the drain contact region cannot be

attributed to a Schottky mechanism: indeed, in this region, holes move from the accumulation layer to the drain electrode. Therefore another mechanism must be considered.

It is known that carriers extraction in an insulator can occur based on a Poole-Frenkel mechanism [36]: if high voltage is applied to electrodes on opposite sides of an insulating film, a high electric field is generated, which results in a lowering of the energy barrier of trapped carriers, and corresponds to an abrupt increase of the electric current flowing through the film.

The case of a staggered OTFT differs from the pure insulator case considered by the Poole-Frenkel. In an OTFT, the total drain current is controlled by the bias applied to the drain, for a given  $V_G$ , and in the linear regime a low current flows in the OTFT. Nevertheless, a high electric field occurs at the OSC/dielectric interface of the drain, so that locally, in the drain contact region, the electric field generated by the accumulation layer can also determine a lowering of the energy barrier of trapped carriers, in a similar way to a Poole-Frenkel mechanism. Therefore, we have modeled the lowering of the interface energy barrier at the source electrode and drain interface region determined by a Schottky and a Poole-Frenkel mechanism, respectively.

In Fig. 3 we have reported the schematization of a staggered p-type OTFT, where the effects of the electric field generated by the accumulation layer on the source electrode and on the drain electrode, respectively, have been highlighted.

We quantify all the above discussed phenomena in the following way. In a Poole-Frenkel mechanism as well as in a Schottky mechanism the energy barrier is lowered by a quantity which is  $(q^3 E_{\text{field}} / (4\pi\epsilon))^2$ . By considering the expression of the electric field determined by the accumulation layer, we have that the lowering of the energy barrier is proportional to  $(q^3 C_i |V_G| / (4\pi\epsilon^2))^{1/2}$ . In order to

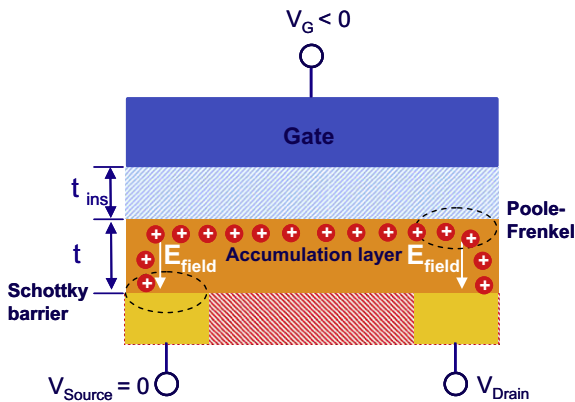


**Fig. 3.** Schematic of the contact regions in a staggered p-type organic film transistor. Holes form the accumulation layer as the gate voltage switches on, for negative gate voltages. The accumulation layer generates an electric field that has a different action on the source and on the drain of the OTFT. On the source it generates a Schottky effect that lowers the energy barrier that holes injected at the source electrode have to overcome; at the drain the electric field of the accumulation layer act because of a Poole-Frenkel effect that extracts holes from the accumulation layers towards the drain. The action of the drain bias is to unbalance the accumulation layer surface density and generate a current.

take into account the Poole-Frenkel effect, occurring at the drain and of the Schottky barrier lowering occurring at the source, we fitted the data from Jin et al. by means of the following equation:

$$(R_C \times W) = (R_C \times W)_0 \times \exp\left(-\alpha \frac{q^{3/2} (C_i / 4\pi)^{1/2}}{\epsilon k \tilde{T}} \sqrt{|V_G|}\right), \quad (10)$$

with  $\alpha$  and  $(R_C \times W)_0$  as parameters. The dashed lines of the graph of Fig. 2 report the results of such a fit. Also in this case the trend of the dependence of the contact resistance on the gate voltage is reproduced. However slight deviations occur in an opposite fashion with respect to the case of the GBTM model, suggesting that possibly both the phenomena underneath the two models, a trapping process for the bulk contact resistance and a Poole-Frenkel/Schottky mechanism for the interface contact resistance, can act in the lowering of the contact resistance with the gate voltage.

In order to investigate this hypothesis we fitted again the data from Jin et al. by employing the combination of the two energy barriers:

$$(R_C \times W) = (R_C \times W)_0 \times \exp\left(\frac{q^3 N_t^2 t}{8\epsilon C_i k \tilde{T}} \frac{1}{|V_G| - V_{th}} - \alpha \frac{q^{3/2} (C_i / 4\pi)^{1/2}}{\epsilon k \tilde{T}} \sqrt{|V_G|}\right). \quad (11)$$

The solid lines of the graph of Fig. 2 report the fit we obtained from Eq. (11) for the two cases of  $N_t = 5.6 \times 10^{11} \text{ cm}^{-2}$  and  $N_t = 1.2 \times 10^{12} \text{ cm}^{-2}$ , respectively. We may observe a fair agreement of the fitted curves with the experimental data and, based on the computed values of the threshold voltages  $V_{th}$ , the following values of the energy barrier of  $E_B = 13.6 \text{ meV}$  for  $N_t = 5.6 \times 10^{11} \text{ cm}^{-2}$  and  $E_B = 110.5 \text{ meV}$  for  $N_t = 1.2 \times 10^{12} \text{ cm}^{-2}$ , have been obtained. These values are consistent with the experimental values of the activation energies reported in Ref. [25].

As a main conclusion from the fitting we can consider that the trapping process at the grain boundary can raise the energy barrier that holes have to overcome, whereas the energy barrier at the contacts interface is mainly lowered by a Poole-Frenkel/Schottky mechanism determined by the accumulation layer.

In the condition of a very low effect of the trapping process, the Poole-Frenkel/Schottky mechanism has the main influence on the contact resistance. By employing the experimental data reported by Minari et al. [27] we fitted, according to Eq. (10), the specific contact resistance measured as a function of the gate bias and found also a good agreement with their results.

The Poole-Frenkel/Schottky mechanism that lowers the energy barrier in Eq. (10), depends on the gate capacitance  $C_i$  by means of the electric field generated by the accumulation layer. Analogously, in developing the GBTM in Section 4.1 we observed as the gate capacitance has also an

influence on the energy barrier determined by the grain boundary.

The dependence of the contact resistance on the gate voltage and its connection to the gate capacitance suggests that in a staggered configuration in order to decrease the contact resistance it is necessary to increase the overlap area of the gate with the contact electrodes. However, this has as a consequence an increase of the gate overlap capacitance which can affect high speed performances of the OTFT.

#### 4.3. Co-scaling of bulk and interface contact resistance

The contact resistance  $R_C$  marks a lower limit to the total resistance of an OTFT. As the channel length  $L$  of the OTFT downscales, aiming at improving the speed performances and density of organic electronic integrated circuits, the channel resistance decreases and the contact effects become the predominant term in the total resistance. As a consequence, in order to increase the performances of a staggered OTFT, it is necessary to modify opportunely the contact resistance.

In Section 4.1 and 4.2, we have discussed the influence of trapping processes at the grain boundaries and interface effects on the contact resistance and formulated an equation model (Eq. (11)) where geometrical and physical quantities that can affect the contact resistance have been discussed. Assuming valid our model, we have investigated how the specific contact resistance changes from the two cases we have considered, as we vary the thickness  $t$  of the semiconductor OSC and the gate capacitance  $C_i$ , by keeping constant all the other parameters.

The results of such an investigation have been plotted in Fig. 4a–c. Fig. 4a reports a 3D plot of the specific contact resistance  $R_C \times W$  obtained from Eq. (11) reported as a function of the thickness  $t$  and the gate capacitance  $C_i$  of the gate dielectric. The upper surface refers to the case of a trap density of  $N_t = 1.2 \times 10^{12} \text{ cm}^{-2}$ , the lower surface refers to the case of  $N_t = 5.6 \times 10^{11} \text{ cm}^{-2}$ . We have supposed that the same threshold voltage  $V_{th}$  of 4 V and 7.2 V is valid for different values of  $t$  and  $C_i$ , for the upper and lower surfaces respectively. Whereas all the calculations refer to a value for the gate voltage of  $V_G = -14 \text{ V}$  and at room temperature.

Fig. 4b and c are cross-sections of the 3D plot of Fig. 4a. In Fig. 4b, we investigate the specific contact resistance as a function of the thickness  $t$  of the OSC for the two cases  $N_t = 5.6 \times 10^{11} \text{ cm}^{-2}$  and  $N_t = 1.2 \times 10^{12} \text{ cm}^{-2}$ , respectively. In doing such a calculation we have considered that the same threshold bias holds as we vary the thickness ( $V_{th} = 7.2 \text{ V}$  for the case of  $N_t = 5.6 \times 10^{11} \text{ cm}^{-2}$ ,  $V_{th} = 4 \text{ V}$  for the case of  $N_t = 1.2 \times 10^{12} \text{ cm}^{-2}$ ) and a gate capacitance of  $C_i = 9.86 \times 10^{-4} \text{ F/m}^2$ . As a general fact, because the trapping process is most likely to occur as the thickness of the OSC increases, the specific contact resistance increases with the OSC thickness. Moreover, the specific contact resistance as a function of the OSC thickness depends on the density of traps  $N_t$  and increases with the density of traps  $N_t$ .

Analogously, we can infer as the specific contact resistance  $R_C \times W$  varies because of changes of the gate capac-

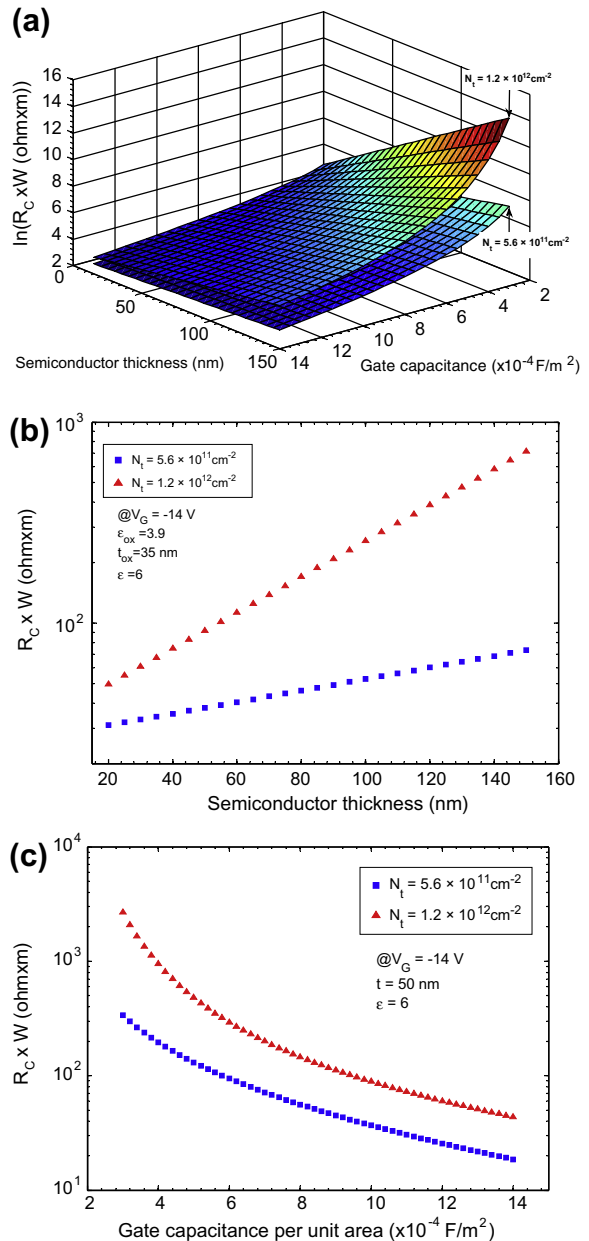


**Fig. 4.** (a) 3D plot of the specific contact resistance  $R_C \times W$  (ln plot) interpolated as a function of the semiconductor thickness  $t$  and gate capacitance  $C_i$ . The upper surface refers to the case of a trap density of  $N_t = 1.2 \times 10^{12} \text{ cm}^{-2}$  with a  $V_{th} = 7.2 \text{ V}$  and constant for all cases, the lower surface to  $N_t = 5.6 \times 10^{11} \text{ cm}^{-2}$  and  $V_{th} = 4.0 \text{ V}$ . All calculations are considered at room temperature and at a gate bias of  $-14 \text{ V}$ . (b) Cross section of the 3D plot at  $C_i = 9.86 \times 10^{-4} \text{ F/m}^2$  reporting the increase of the specific contact resistance  $R_C \times W$  (in log scale), with the increase of the organic semiconductor thickness in the range of 15–150 nm. The two data set refer to a density of traps of  $N_t = 5.6 \times 10^{11} \text{ cm}^{-2}$  and  $N_t = 1.2 \times 10^{12} \text{ cm}^{-2}$ , respectively. (c) Cross section of 3D plot at the OSC thickness of  $t = 50 \text{ nm}$  reporting the decrease of the specific contact resistance  $R_C \times W$  (in log scale) with the increase of the gate capacitance per unit area  $C_i$  in the range  $3 \times 10^{-4} \text{ F/m}^2$  to  $1.4 \times 10^{-3} \text{ F/m}^2$ . The two data set refer to the density of traps of  $N_t = 5.6 \times 10^{11} \text{ cm}^{-2}$  and  $N_t = 1.2 \times 10^{12} \text{ cm}^{-2}$ , respectively.

itance per unit area  $C_i$ . In Fig. 4c we report the decrease of the specific contact resistance  $R_C \times W$  (in log scale) with

the increase of the gate capacitance per unit area  $C_i$  in the range  $3 \times 10^{-4}$  to  $1.4 \times 10^{-3}$  F/m<sup>2</sup>. We interpolated the values by considering valid the same threshold voltages  $V_{th}$  of 7.2 V and 4 V for the cases  $N_t = 5.6 \times 10^{11}$  cm<sup>-2</sup> and  $N_t = 1.2 \times 10^{12}$  cm<sup>-2</sup>, respectively. The gate bias of  $V_G = -14$  V and the room temperature has also been assumed, whereas the thickness of the organic semiconductor was 50 nm for this case. As a general trend the specific contact resistance decreases as we increase the gate capacitance per unit area. Moreover the specific contact resistance is lower as the trap density  $N_t$  decreases.

## 5. Conclusion

In conclusion, we have modeled the dependence of the bulk contact resistance  $R_{Cbulk}$  on the gate bias  $V_G$ , within the frame of the grain boundary trapping model (GBTM) and the MNR rule. By following such an approach, we provided an analytical expression of the dependence of the specific contact resistance  $R_C \times W$  on  $V_G$ . The GBTM model determines a contribution  $E_B$  to the energy barrier that injected holes have to overcome. This contribution caused by the trapping process occurring in the bulk OSC layer interposed between the electrodes and accumulation layer of the OTFT, is indicated as a principal contribution. However, from a best-fit of the experimental data gained from the literature [25], we have observed slight deviations that can be attributed to other mechanisms. In this paper we have shown that the electric field generated by the accumulation layer opposite the source and drain electrode can give also a dependence of the interface contact resistance on the gate bias. In particular, the accumulation layer in a staggered OTFT determines a Schottky lowering of the interface energy barrier  $\phi_b$  at the source electrode. On the other hand, the high value of the electric field determines a Poole-Frenkel mechanism consisting in the extraction of holes from the accumulation layer at the drain contact region.

We have shown that the combination of the contributions to the specific contact resistance determined by the GBTM model and the Poole-Frenkel/Schottky model can provide a model of the dependence of the contact resistance on the gate bias  $V_G$ . Because of the link of the gate bias  $V_G$  to the gate capacitance  $C_i$  the contact resistance is strictly related to the charge induced by the gate electrode in the accumulation layer as well as on the overlap area of the gate electrode with the electrodes contacts. As a consequence the contact resistance is strictly related to the gate capacitance of the OTFT. Given the validity of our model, we inferred on the possibility to scale-down the contact resistance by implementing the parameters which are involved in the model.

## Acknowledgments

The authors acknowledge Dr. Sun Hun Jin for kindly allowing the use of the contact resistance data reported

in Ref. [25]; Eng. Elena Umana for helping us in the graph editing process. The work is partially funded by the EC FP7 under grant agreement n° 212311 of the ONE-P project.

## References

- [1] D.R. Gamota, P. Brazis, K. Kalyanasundaram, J. Zhang (Eds.), Printed Organic and Molecular Electronics, Kluwer Academic Publishers, 2003, ISBN: 1-4020-7707-6.
- [2] C.D. Dimitrakopoulos, P.R.L. Malenfant, Adv. Mater. 14 (2) (2002) 99.
- [3] E. Cantatore, T.C.T. Geuns, G.H. Gelinck, E. van Veenendaal, A.F.A. Grijthuijzen, L. Schrijnemakers, S. Drews, D.M. de Leeuw, IEEE J Solid-State Circuits 42 (1) (2007) 84.
- [4] K. Myny, M.J. Beenhakkers, N.A.J.M. van Aerle, G.H. Gelinck, J. Genoe, W. Dehaene, P. Heremans, "A 128b Organic RFID Transponder Chip, Including Manchester Encoding and ALOHA Anti-Collision Protocol, Operating with a Data Rate of 1529b/s", IEEE Int. Solid-State Circuits Conf. (ISSCC 2009), Session 11.6, 2009, p. 206.
- [5] H. Pang, H.-C. Yuan, M.G. Lagally, G.K. Celler, Z. Ma, in: Proceedings Device Research Conference, 65th Annual, 2007.
- [6] S.D. Brotherton, C. Glasse, C. Glaister, P. Green, F. Rohlfing, J.R. Ayres, Appl. Phys. Lett. 82 (N2) (2004) 293.
- [7] Y.-Y. Noh, N. Zhao, M. Caironi, H. Sirringhaus, Nat. Nanotechnol. 2 (2007) 784.
- [8] R. Matsubara, N. Ohashi, M. Sakai, K. Kudo, M. Nakamura, Appl. Phys. Lett. 92 (2008) 242108.
- [9] D. Knipp, R.A. Street, A. Volkel, J. Ho, J. Appl. Phys. 93 (2003) 347.
- [10] T. Minari, T. Memoto, S. Isoda, J. Appl. Phys. 99 (2006) 034506.
- [11] O.D. Jurchescu, J. Baas, T.T.M. Palstra, Appl. Phys. Lett. 84 (2004) 3061.
- [12] V. Podzorov, E. Menard, A. Borissov, V. Kiryukhin, J.A. Rogers, M.E. Gershenson, Phys. Rev. Lett. 93 (2004) 086602.
- [13] S.K. Park, T.N. Jackson, J.E. Anthony, D.A. Mourey, Appl. Phys. Lett. 91 (6) (2007) 063514.
- [14] Y.-H. Kim, Y.U. Lee, J.-I. Han, S.-M. Han, M.-K. Han, J. Electrochem. Soc. 154 (12) (2007) 995.
- [15] T. Miyadera, T. Minari, K. Tsukagoshi, H. Ito, Y. Aoyagi, Appl. Phys. Lett. 91 (2007) 013512.
- [16] I.G. Hill, Appl. Phys. Lett. 87 (2005) 163505.
- [17] T.J. Richards, H. Sirringhaus, J. Appl. Phys. 102 (2007) 094510.
- [18] N. Kocha, A. Kahn, J. Ghijsen, J.-J. Pireaux, J. Schwartz, R.L. Johnson, A. Elschner, Appl. Phys. Lett. 82 (1) (2003) 70.
- [19] K. Hong, J.W. Lee, S.Y. Yang, K. Shin, H. Jeon, S.H. Kim, C. Yang, C.E. Park, Org. Electron. 9 (2008) 21.
- [20] D.J. Gundlach, L. Zhou, J.A. Nichols, T.N. Jackson, P.V. Necliudov, M.S. Shur, J. Appl. Phys. 100 (2006) 024509.
- [21] P.V. Necliudov, M.S. Shur, D.J. Gundlach, T.N. Jackson, J. Appl. Phys. 88 (2000) 6594.
- [22] R.A. Street, A. Salleo, Appl. Phys. Lett. 81 (15) (2002) 2887.
- [23] T. Li, J.W. Balk, P.P. Ruden, I.H. Campbell, D.L. Smith, J. Appl. Phys. 91 (2002) 4312.
- [24] T. Li, P.P. Ruden, I.H. Campbell, D.L. Smith, J. Appl. Phys. 93 (2003) 4017.
- [25] S.H. Jin, K.D. Jung, H. Shin, B.-G. Park, J.D. Lee, Synth. Met. 156 (2006) 196.
- [26] S.D. Wang, T. Miyadera, T. Minari, Y. Aoyagi, K. Tsukagoshi, Appl. Phys. Lett. 93 (2008) 043311.
- [27] T. Minari, T. Miyadera, K. Tsukagoshi, Y. Aoyagi, H. Ito, Appl. Phys. Lett. 91 (2007) 053508.
- [28] S. Luan, G.W. Neudeck, J. Appl. Phys. 72 (2) (1992) 766.
- [29] G. Horowitz, J. Mater. Res. 19 (7) (2004) 1946.
- [30] C.S. Chiang, S. Martin, J. Kanicki, Y. Ugai, T. Yukawa, S. Takeuchi, Jpn. J. Appl. Phys., Part 1 37 (1998) 5914.
- [31] W. Meyer, H. Neldel, Z. Tech. Phys. Leipzig 18 (1937) 588.
- [32] The density of traps as a function of energy is equivalent to an exponential density of states (DOS).
- [33] G. Baccarani, B. Riccò, G. Spadini, J. Appl. Phys. 49 (11) (1978) 5565.
- [34] S. Verlaak, V. Arkhipov, P. Heremans, Appl. Phys. Lett. 82 (5) (2003) 745.
- [35] J. Levinson, F.R. Shepherd, P.J. Scanlon, W.D. Westwood, G. Este, M. Rider, J. Appl. Phys. 53 (2) (1982) 1193.
- [36] J. Frenkel, On pre-breakdown phenomena in insulators and electronic semi-conductors, Phys. Rev. 54 (8) (1938) 647.

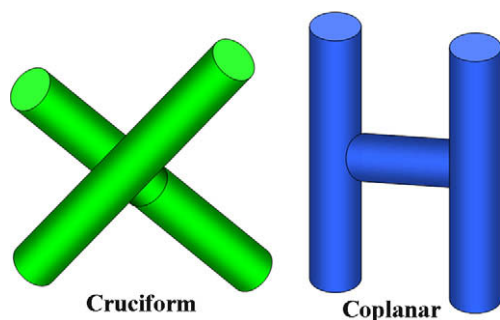
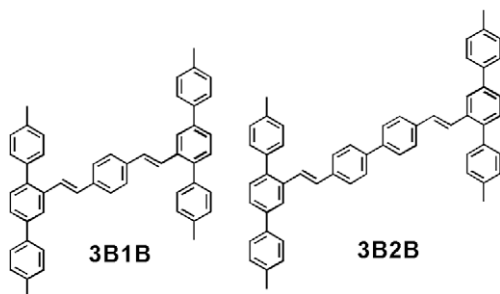


**Fig. 1.** Schematic diagram of cruciform and coplanar molecular structures.

fluorescence is strongly quenched [6]. In order to obtain high solid-state fluorescence efficiency OPV derivatives, much work has been done to prevent the aggregation of DSB derivatives. Involving the stereo-linkages into the phenylenevinylene chromophores was mostly considered [4]. Remarkable practices should be referred here are the cruciform oligo(phenylenevinylene)s constructed by Ma's group [5,14b]. Through the cruciform chemical structure, (see Fig. 1) the morphology of the materials can be adjusted to facilitate the fluorescence radiation.

It is undoubted that, compounds with large  $\pi$ -conjugate scale and rigid coplanar configurations usually have high fluorescence quantum yield in dilute solutions. It is the intermolecular interactions, but not the coplanar conjugated molecules themselves that depress their solid-state fluorescence.

Till now, nearly all the reported hyper-branched molecules were supposed to be non-coplanar [2,7–9]. In this study, we reported that multi-branched conjugated compound with a coplanar configuration that inclined to form amorphous film, and the aggregation-induced fluorescence quenching effect was weakened due to the steric hindrance of the multi-branched structure. The topology of the chemical structure, with four arm-branches attached to a linear bone, looks like the letter "H" (As shown in Scheme 1).



**Scheme 1.** Chemical structure of the H-shaped molecules.

With facile synthesis routes, the purpose of establishing coplanar and rigid conjugate conformation while with less aggregated stacking mode is realized.

## 2. Experimental

### 2.1. Chemicals and instruments

All reagents and starting materials in the synthetic procedures are commercial available and used as received. The TG and DSC were measured on a Diamond Differential Scanning Calorimeter under nitrogen atmosphere.  $^1\text{H}$  NMR and  $^{13}\text{C}$  NMR spectra were recorded at 25 °C using Bruker Avance 400 spectrometer. Microanalyses (C, H, N) were performed using a German Vario EL III elemental analyzer. Electro-spray mass spectrum (ES-MS) was recorded on a Finnigan LCQ mass spectrograph, and the concentration of the samples was about 1.0 mmol/mL. Absorption measurements were carried out on a TU-1800 spectrophotometer. Photoluminescence (PL) measurements were recorded using a Hitachi F-4500 fluorescence spectrophotometer with a 150 W Xe lamp. The fluorescence lifetime measurement was performed on the Edinburgh FLS920 spectrofluorometer with hydrogen flash lamp (pulse duration 1 ns) as the excitation source on the same spectrofluorometer. XRD investigations were carried out on a Bruker D8 advanced diffractometer equipped with Cu K $\alpha$  radiation ( $\lambda = 1.5405 \text{ \AA}$ ). The data were collected using a Ni-filtered Cu-target tube at room temperature. Single-crystal structural analysis was performed on a Bruker APEX [2] CCD area-detector diffractometer. By SHELXL-97 program, the structures were resolved with direct method and refined by Full-matrix least-squares method on F2. The AFM images were obtained by using a Digital Instruments (DI) Dimension 3100 AFM operating in contact mode. PL efficiencies were determined using a solution of quinine sulfate as a standard (ca.  $1 \times 10^{-6} \text{ M}$  in 0.1 M  $\text{H}_2\text{SO}_4$ , having a quantum yield of 55%). Solvents were purified and dried according to standard procedures.

The thermal properties of the two H-shaped compounds were investigated by using differential scanning calorimetry (DSC) and thermogravimetric analysis (TGA). Both of them exhibit high TG and high thermal stability with the decomposition temperatures upto  $\sim 400 \text{ }^\circ\text{C}$ . (Details are shown in Table 1).

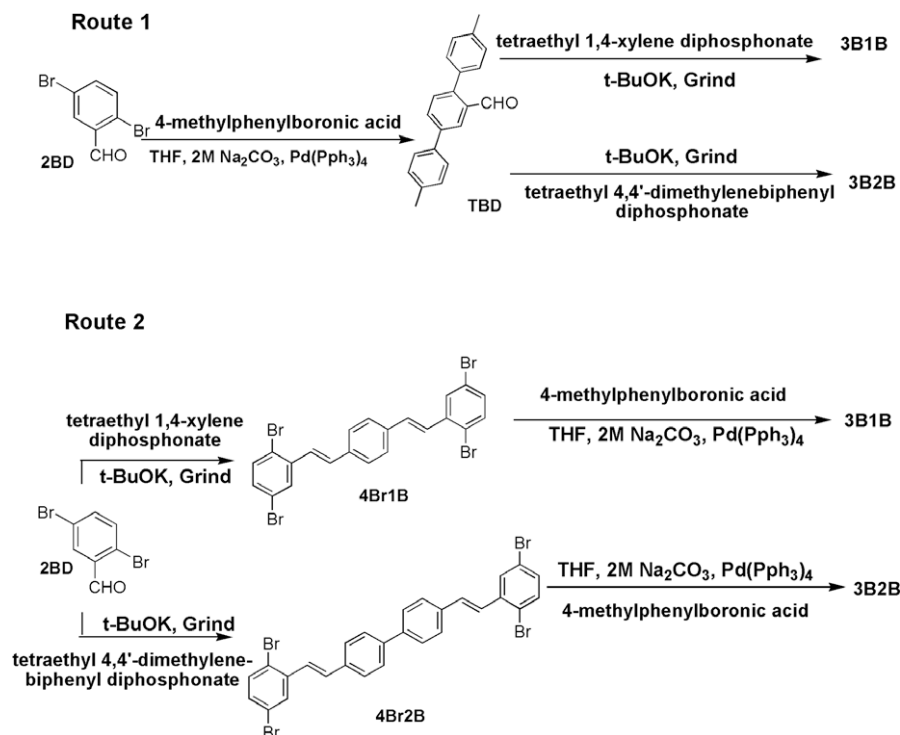
### 2.2. Synthesis

The synthetic route to the two H-shaped molecules is shown in Scheme 2.

**TBD.** This compound was synthesized by the Suzuki coupling method. Under argon atmosphere, to a stirred mixture of 1.32 g (5 mmol) of 2,5-dibromobenzaldehyde and 2.72 g (20 mmol) of 4-methylphenylboronic acid in

**Table 1**  
Optical and thermal properties of H-shaped molecules.

Compound	$\lambda_{\text{max}}^{\text{abs}}$ (nm)	$\lambda_{\text{max}}^{\text{PL}}$ (nm)	$\Phi_{\text{f}}$	$T_{\text{g}}$ ( $^\circ\text{C}$ )	$T_{\text{m}}$ ( $^\circ\text{C}$ )	$T_{\text{d}}$ ( $^\circ\text{C}$ )
3B1B	299 (363)	409	0.72	177	298	411
3B2B	358 (299)	411	0.78	165	290	450



Scheme 2. The synthetic route of the H-shaped molecules.

10 ml THF and 5 ml 2 M  $\text{Na}_2\text{CO}_3$ , 0.05 g of  $\text{Pd}(\text{PPh}_3)_4$  was added. The mixture was heated to 85 °C for 10 h. After cooling, the mixture was poured into water and then extracted with  $\text{CH}_2\text{Cl}_2$  for three times, washed with water and dried with  $\text{Na}_2\text{SO}_4$ , filtrated and evaporated the solvent. The residue was purified by column chromatography (silica gel, petrol ether/ethyl acetate = 5:1) to give white solids of 1.32 g (Yield 92%).  $^1\text{H}$  NMR (400 MHz,  $\text{CDCl}_3$ , ppm)  $\delta$ : 2.432 (d, 6H), 7.258 (s, 1H), 7.307 (m, 5H), 7.511 (d, 1H,  $J = 8.0$ ), 7.582 (dd, 2H,  $J = 6.6$ ,  $J = 1.6$ ), 7.857 (dd, 1H,  $J = 8$ ,  $J = 2.1$ ), 8.241 (d, 1H,  $J = 2.0$ ), 10.048 (s, 1H).  $^{13}\text{C}$  NMR ( $\text{CDCl}_3$ , 100.57 MHz, ppm)  $\delta$ : 20.699, 20.764, 125.188, 126.444, 128.760, 129.240, 129.577, 130.847, 131.356, 133.479, 134.067, 136.177, 137.352, 137.630, 139.905, 144.073, 192.235.

**4Br1B.** This compound was synthesized by the solventless Wittig–Horner method. About 1.32 g (5 mmol) of 2,5-dibromobenzaldehyde, 0.537 g (1.67 mmol) of tetraethyl 1,4-xylene diphosphonate and 2.8 g (25 mmol) fresh t-BuOK were placed in a dry mortar. The mixture was milled vigorously for about 15 min. Then the mixture was dispersed in 80 mL methanol, filtrated and the solids were washed with methanol for two times. The product was light yellow powders, 0.75 g (Yield 75%).  $^1\text{H}$  NMR (400 MHz,  $\text{CDCl}_3$ , ppm)  $\delta$ : 7.045 (d, 2H,  $J = 16$ ), 7.237 (dd, 2H,  $J_1 = 8.6$ ,  $J_2 = 2$ ), 7.400 (d, 2H,  $J = 16$ ), 7.450 (d, 2H,  $J = 8.4$ ), 7.566 (s, 4H), 7.800 (d, 2H,  $J = 2$ ).  $^{13}\text{C}$  NMR ( $\text{CDCl}_3$ , 100.57 MHz, ppm)  $\delta$ : 121.057, 122.135, 126.040, 126.937, 128.969, 131.121, 131.598, 133.900, 136.258, 138.493.

**4Br2B.** 4Br2B was synthesized according to the same procedure of 4Br1B using 1.32 g (5 mmol) of 2,5-dibromobenzaldehyde, 0.757 g (1.67 mmol) of tetraethyl

4,4'-dimethylenebiphenyl diphosphonate and 2.8 g (25 mmol) fresh t-BuOK. The product was light yellow powders, 0.92 g (Yield 82%).  $^1\text{H}$  NMR (400 MHz,  $\text{CDCl}_3$ , ppm)  $\delta$ : 7.083 (d, 2H,  $J = 16$ ), 7.243 (dd, 2H,  $J_1 = 8.8$ ,  $J_2 = 2.4$ ), 7.417 (d, 2H,  $J = 16$ ), 7.454 (d, 2H,  $J = 8.4$ ), 7.649 (m, 8H), 7.815 (d, 2H,  $J = 2.4$ ).  $^{13}\text{C}$  NMR ( $\text{CDCl}_3$ , 100.57 MHz, ppm)  $\delta$ : 121.065, 122.131, 125.816, 126.792, 127.046, 128.953, 131.092, 131.642, 133.915, 135.335, 138.522, 139.938.

**3B1B.** (Route 1) The synthesis of 3B1B was by a solventless Wittig–Horner method. 0.573 g (2 mmol) of TBD, 0.214 g (0.664 mmol) of tetraethyl 1,4-xylene diphosphonate and 1 g (9 mmol) fresh t-BuOK were placed in a dry mortar. The mixture was milled vigorously for about 15 min. Then the mixture was dispersed in 80 mL methanol, filtrated and the solids were washed with methanol for two times. The pure product was obtained by recrystallization from  $\text{CH}_2\text{Cl}_2$ –ethanol (10–1), 0.31 g (Yield 73%). (Route 2) The synthesis of 3B1B in route 2 was by a Suzuki coupling method. Under argon atmosphere, to a stirred mixture of 0.299 g (0.5 mmol) of 4Br1B and 0.544 g (4 mmol) of 4-methylphenylboronic acid in 12 ml THF and 5 ml 2 M  $\text{Na}_2\text{CO}_3$ , 0.05 g of  $\text{Pd}(\text{PPh}_3)_4$  was added. The mixture was heated to 85 °C for 30 h. After cooling, the organic solvent was evaporated; the residue was filtrated and washed by water, and then dissolved in  $\text{CH}_2\text{Cl}_2$ , filtrated through a silica gel funnel to remove the Pd (0) catalyst residue. The pure product was obtained by recrystallization from  $\text{CH}_2\text{Cl}_2$ –ethanol (10–1), as light yellow crystallites, 0.18 g (Yield 57%).  $^1\text{H}$  NMR (400 MHz,  $\text{CDCl}_3$ , ppm)  $\delta$ : 2.431 (d, 6H), 7.138 (m, 6H), 7.295 (m, 20H), 7.394 (d, 2H,  $J = 7.9$ ), 7.541 (dd, 2H,  $J = 7.9$ ,  $J = 1.8$ ),



7.590 (d, 4H,  $J = 8.1$ ), 7.929 (d, 2H,  $J = 1.7$ ).  $^{13}\text{C}$  NMR ( $\text{CDCl}_3$ , 100.57 MHz, ppm)  $\delta$ : 20.675, 20.754, 123.901, 125.760, 126.397, 126.541, 127.493, 128.435, 128.613, 129.070, 129.312, 130.273, 135.226, 136.386, 136.434, 136.739, 137.106, 137.546, 139.377, 139.791. Anal. Cal. For  $\text{C}_{50}\text{H}_{42}$ : C, 93.41; H, 6.59. Found: C, 93.09; H, 6.37. Crystal data for 3B1B ( $\text{C}_{50}\text{H}_{42}$ ):  $M_r = 642.87$ , Triclinic, space group  $P\bar{1}$ ,  $a = 10.0165(2)$  Å,  $\alpha = 74.649(2)^\circ$ ,  $b = 12.2636(3)$  Å,  $\beta = 75.141(2)^\circ$ ,  $c = 17.0433(4)$  Å,  $\gamma = 68.5490(10)^\circ$ ,  $V = 1849.07(7)$  Å $^3$ ,  $Z = 2$ ,  $\rho_{\text{calcd}} = 1.155$  Mg/m $^3$ ,  $T = 293(2)$  K, Crystal size  $0.43 \times 0.13 \times 0.03$  mm,  $R_1 = 0.0579$ ,  $wR_2 = 0.1221$ , [ $I > 2\sigma(I)$ ].

**3B2B.** (Route 1) The synthesis of 3B2B in route 1 was according to the same procedure of 3B1B (Route 1) using 0.573 g (2 mmol) of TBD, 0.302 g (0.664 mmol) of tetraethyl 4,4'-dimethylenebiphenyl diphosphonate and 1 g (9 mmol) fresh *t*-BuOK. The product was bright yellow crystallites, 0.37 g (Yield 77%). (Route 2) The synthesis of 3B2B in route 2 was according to the same procedure of 3B1B (Route 2) using 0.337 g (0.5 mmol) of 4Br2B and 0.544 g (4 mmol) of 4-methylphenylboronic acid in 14 ml THF and 6 ml 2 M  $\text{Na}_2\text{CO}_3$ , 0.05 g of  $\text{Pd}(\text{PPh}_3)_4$ , the product was 0.237 g (Yield 66%).  $^1\text{H}$  NMR (400 MHz,  $\text{CDCl}_3$ , ppm)  $\delta$ : 2.438 (d, 6H), 7.195 (m, 6H), 7.314 (m, 16H), 7.412 (d, 2H,  $J = 7.9$ ), 7.476 (d, 4H,  $J = 8.3$ ), 7.580 (m, 10H), 7.955 (d, 2H,  $J = 1.6$ ).  $^{13}\text{C}$  NMR ( $\text{CDCl}_3$ , 100.57 MHz, ppm)  $\delta$ : 20.690, 20.772, 123.989, 125.815, 126.556, 126.582, 127.717, 128.459, 128.528, 129.085, 129.334, 130.297, 135.230, 136.260, 136.417, 136.761, 137.105, 137.538, 139.151, 139.375, 139.807. Anal. Cal. For  $\text{C}_{56}\text{H}_{46}$ : C, 93.55; H, 6.45. Found: C, 93.29; H, 6.29. Crystal data for 3B2B ( $\text{C}_{56}\text{H}_{46}$ ):  $M_r = 718.93$ , Triclinic, space group  $P\bar{1}$ ,  $a = 6.332(5)$  Å,  $\alpha = 92.416(5)^\circ$ ,  $b = 13.359(5)$  Å,  $\beta = 96.844(5)^\circ$ ,  $c = 24.105(5)$  Å,  $\gamma = 102.027(5)^\circ$ ,  $V = 1975.3$  (18) Å $^3$ ,  $Z = 2$ ,  $\rho_{\text{calcd}} = 1.209$  Mg/m $^3$ ,  $T = 293(2)$  K, Crystal size  $0.37 \times 0.11 \times 0.05$  mm,  $R_1 = 0.0701$ ,  $wR_2 = 0.1733$ , [ $I > 2\sigma(I)$ ].

### 2.3. Device fabrication and characterization

OLED devices were fabricated by thermal vacuum-deposition under  $1.33 \times 10^{-4}$  Pa. Patterned indium tin oxide (ITO) were cleaned with detergent, de-ionized water,

acetone and then de-ionized water in an ultrasonic bath (30 min each cycle), and finally treated in an ultraviolet-ozone chamber. Deposition rates were monitored with a quartz oscillation crystal and controlled at about 0.1 nm/s for organic layers and about 0.5 nm/s for metal layers. The active area of the device was about 4 mm $^2$ . The thickness of films was measured by a Dektak surface profilometer. The EL spectra and current-voltage-luminance ( $J$ - $L$ - $V$ ) characteristics were measured with a Spectrascan PR 650 photometer and a computer-controlled DC power supply. All the measurements of the devices were carried out under ambient conditions.

## 3. Results and discussion

### 3.1. Synthesis and characterization

Scheme 2 shows the synthesis of the two H-shaped molecules. Two synthetic routes are employed. Two kinds of classic organic reactions are adopted, Suzuki and Wittig–Horner [10]. In route 1, 2BD reacted with the boronic acid through the Suzuki coupling reactions to give an aldehyde-containing intermediates TBD with the yield of 92%. Then, the two H-shaped molecules were obtained by solid-state Wittig–Horner reactions between the intermediate and two diphosphonate compounds (yields 73% and 77%, respectively). Route 2 is, actually, a reversed procedure of route 1. 2BD firstly took a solid-state Wittig–Horner reaction with the two diphosphonates to form another two mediate products 4Br1B and 4Br2B (yields 75% and 82%, respectively). Then the Suzuki reactions between 4Br1B, 4Br2B and the boronic acid produced the two H-shaped products with the yields of 57% and 75%, respectively. The structure of the molecules were verified by  $^1\text{H}$  NMR,  $^{13}\text{C}$  NMR and elemental analysis and confirmed by X-ray crystallographic analysis.

### 3.2. Crystal structure analysis: coplanar configuration of the H-shaped molecules

For organic semiconductors, many physical properties (e.g., optoelectronics and charge transport) are highly

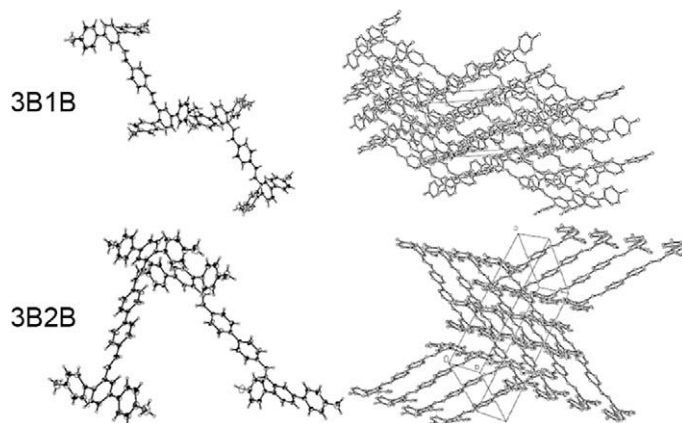
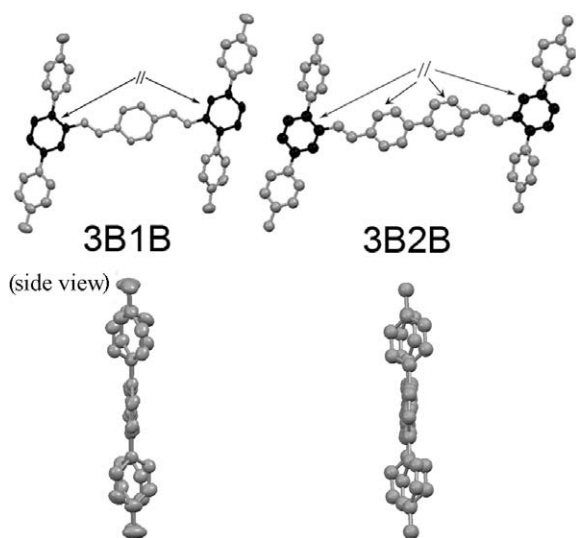


Fig. 2. The X-ray structures and crystal packings of 3B1B and 3B2B, two crystallographically independent conformations appear in both of them.

dependent on their molecular configuration and the stacking mode. Thus, information of the crystal structures plays an important role in the exploration of structure–property relationship. Nevertheless, crystal structures of hyper-branched molecules are difficult to obtain due to their large molecular size and the multi-branched structures. Here, after many experimental attempts, single crystals of the two H-shaped molecules have been obtained by a very slow growing process, and their crystallographic structures were determined by X-ray diffraction. (See Fig. 2) In the crystals of the two H-shaped compounds, each molecule shows a quasi-coplanar “H” shape; the supposed twisted configurations through the central phenylenevinylene chain do not appear. The two phenyl rings as the crunodes on the two sides of “H” are parallel exactly to each other, even for the biphenyl linked 3B2B, and the two phenyl rings of the central biphenyl in 3B2B are coplanarized exactly, too (See Fig. 3). There are moderate twist angles between the single bonds linked phenyl rings along each side of the terphenyl dipoles. Anyhow, just as what we can see from the side view of these H-shaped molecules, the two side dipoles of “H” are parallel to each other, and the whole molecule is located in a plane just with little deviations. So, we call them quasi-coplanar molecules. This special factor can ensure the unbroken conjugation of the whole H-shaped molecule. And they should be totally different from those twisted or cruciform ones in terms of morphology (aggregation mode) and aggregated optical properties. To gain insight as to why these molecules adopt coplanar configurations, the quantum chemical calculation using a DFT/B3 LYP/6-31G (d) method [3a,5a] was performed on 3B2B, the result showed a non-coplanar H-shape, with a twist angle of  $\sim 40^\circ$  between the two sides terphenyl dipoles of the molecule. It shows that, the theoretical calculations may not always reflect the information of the actual situation. We consider that, maybe it is the comparative long distance between the side



**Fig. 3.** Molecular configuration of the H-shaped molecules. In each molecule, the blackened phenyl rings on each side of “H” are parallel to each other. Blow: side view of the two molecules.

dipoles and the intrinsic property of the central phenylenevinylene chain, cooperatively make this H-shaped topology a coplanar one. Although the topology of H-shape is not a new concept [11], the construction we proposed here bears an exact non-twisted “H” shape. This coplanar configuration can endow molecules with an integrative two-dimensional conjugations, thus, the enlarged delocalized  $\pi$  electrons would enhance their fluorescence yield. And intriguingly, there are two crystallographically independent conformations in both of the two H-shaped molecules, they make alternate stackings, which may enhance their solid-state fluorescence [12]. Now, we have seen the novel coplanar configuration of the H-shaped molecules, in the following researches, by testing their optical properties in solutions, thin films and crystallites, and their EL performances, the effects of different morphologies are shown.

### 3.3. Morphology and optical properties of the H-shaped molecules

For the photophysics properties of the H-shaped molecules, firstly, the UV–vis absorption and photoluminescence spectra of the two compounds in several solutions were recorded. They exhibit very weak solvent polarity dependence due to the absence of any electron donor or acceptor groups. Fig. 4 shows the spectra in THF ( $1 \mu\text{M}$ ) (Detailed data are tabulated in Table 1). Due to the two-dimensional conjugations of the H-shaped molecules, their absorption profiles show two-peaks spectra. The short wavelength absorption band (299 nm) may be related to the side terphenyl dipoles; while the long wavelength absorption band ( $\sim 360$  nm) may be related to the central DSB or distyrylbiphenyl portion. Their PL emissions present shoulder peaks for each compound. Thanks to the large  $\pi$ -conjugate scale and rigid planar configurations, both of the H-shaped molecules are with quite high fluorescence quantum yields, bright blue light can even be observed under solar irradiation.

In order to understand well how the two-dimensional conjugation affects the electronic structure, the shapes of HOMO-1, HOMO, LUMO, LUMO+1 of 3B2B are shown in Fig. 5. As shown in Fig. 5, the majority of the electron

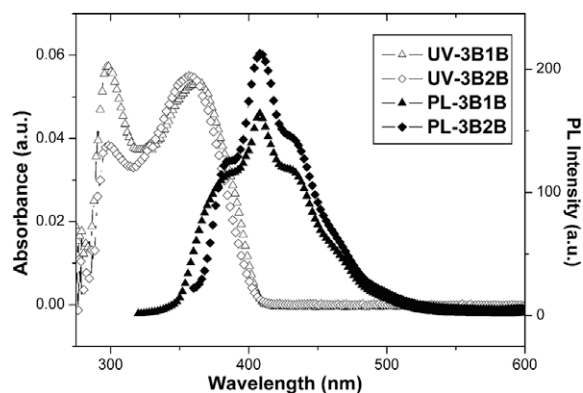


**Fig. 4.** UV–vis absorption and PL spectra of the H-shaped molecules in THF.

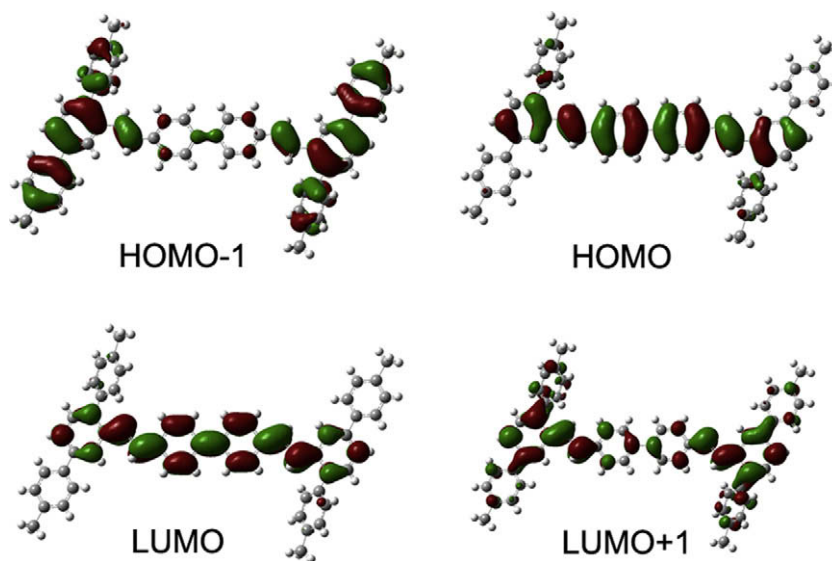


Fig. 5. Frontier HOMOs and LUMOs of 3B2B. (Calculations were based on DFT/B3LYP/6-31G (d).)

distribution of the HOMO and LUMO were found to be located over the distyrylbiphenyl entity, while the electron distribution of the HOMO-1 and LUMO+1 were found to be located mainly over the two side terphenyl dipoles. The energy levels of the orbitals from HOMO-1 to LUMO+1 are  $-5.53$ ,  $-5.14$ ,  $-1.47$  and  $-0.93$  eV, respectively.

The most that we want to show here are the solid-state optical properties of these coplanar H-shaped molecules, and their dependence on different morphologies. When the compounds are vacuum sublimated on substrate to form films, what is easy to imagine is, considering the short deposition time for several tens of nanometers' organic compounds, it is hard for the multi-branched molecules to adopt close packing in just a few minutes, even though they bear coplanar structures. Amorphous films should be formed.

To verify this speculation, X-ray diffraction (XRD) analysis was taken on 3B2B powders and film. As shown in Fig. 6, for the powders of 3B2B, there are sharp diffraction peaks in the XRD patterns, indicating that they are apparently crystalline. While for the sublimated films, only inconspicuous broad peak appears on their XRD patterns, meaning that they are determinately amorphous. The XRD measurement of the same film sample after storage for two months under ambient conditions shows no trend of crystallization, indicating that this amorphous film of coplanar hyper-branched molecules is morphological stable. The morphology of the thin film is a key factor related to the performance of thin film devices of organic materials. As shown in Fig. 7, the atomic force microscopy (AFM) topography of the sublimated films demonstrate that the 3B2B film is continuous, neat and smooth.

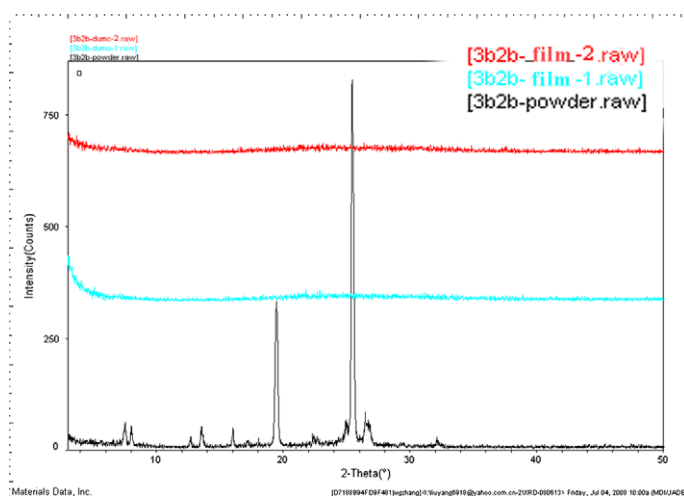


Fig. 6. Comparison of XRD patterns of 3B2B powders (black), thin film-1 (as prepared, blue) and thin film-2 (after two months, red). (For interpretation of the references to colour in this figure legend, the reader is referred to the web version of this article.)

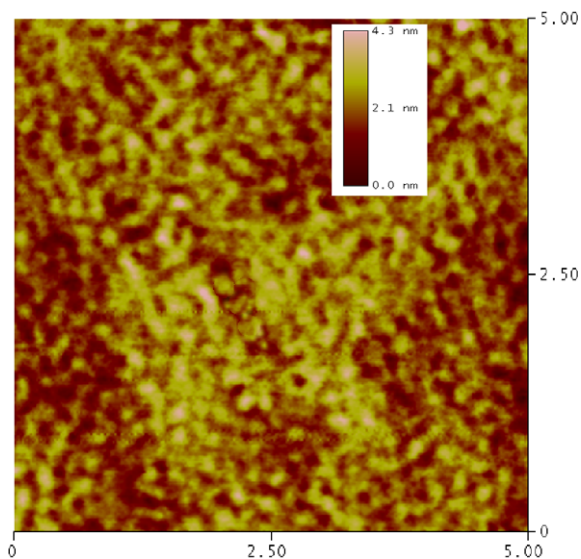


Fig. 7. AFM topography images of 3B2B films deposited on ITO coated glass at room temperature.

The essence of the difference is proposed in Fig. 8. The coplanar H-shaped molecules adopt a close packing mode in crystallites, they stack layer by layer, and the  $\pi$ - $\pi$  distance between two adjacent molecular planes is about 3.64 Å. While in the amorphous films, thanks to the molecules' intrinsic characteristics of multi-branches, they can not stay close to each other owing to the intermolecular steric hindrance, just like two hedgehogs can not keep close to each other. In the sublimation process, they would make random, disorder and unconsolidated packing (As shown in Fig. 8, left). Thus, the  $\pi$ - $\pi$  interactions should be very weak in such environment. Different morphology results in different optical properties. As shown in Fig. 9, in solution (THF), 3B2B shows blue–purple light; in the sublimated films, it has a blue fluorescence; while in crystalline powders, it luminescent obviously green (The details see the spectrum in Fig. 10 and data in Table 2).

Taken the morphology (aggregation mode) and the fluorescence property of the coplanar hyper-branched molecules together, we can see that they are consistent with each other. In the amorphous thin films, they make a disorder and unconsolidated packing, there are less intermolecular  $\pi$ - $\pi$  actions, the circumstance of the interactions is some what like that in solutions. Thus, the spectra of the film shows relative small red-shift to that of in the solutions (blue emitting); while in crystallites, the layer

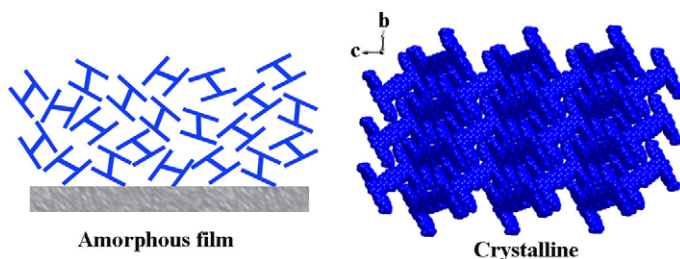


Fig. 8. Molecular packings of coplanar H-shaped molecules (3B2B) in amorphous films (proposed) and in crystallites.

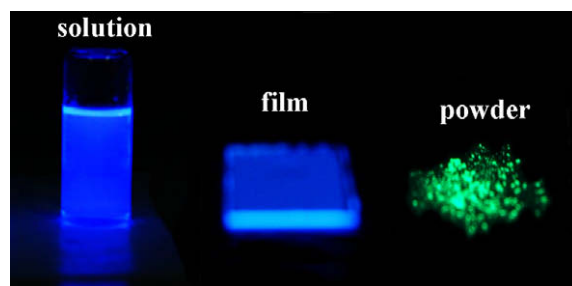


Fig. 9. Photos of the fluorescence emissions of 3B2B in solution (THF), thin film and powders under UV light (365 nm).

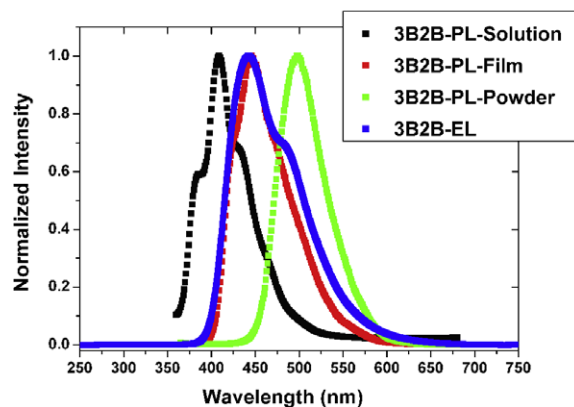


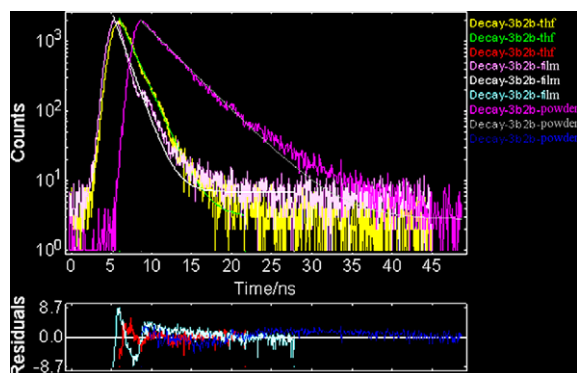
Fig. 10. PL spectra of 3B2B in solution, thin film and powders and the EL spectrum of device based on 3B2B.

Table 2

Fluorescence properties of 3B2B in different morphologies.

3B2B	$\lambda_{\text{max}}^{\text{em}}$ (nm)	$\tau$ (ns)
In THF	411	1.65
Thin film	445	1.37
Powder (crystalline)	500	3.86
EL device	443	–

by layer close packing of the coplanar molecules leads to the intensive intermolecular  $\pi$ - $\pi$  interactions, and subsequently result in largely red-shift (green emitting). These arguments can also be verified by the time-resolved photoluminescence spectra of the solution, film and crystallites of 3B2B. The time-resolved fluorescence can provide valuable information about the interaction of molecule in the excited state with its environment [13]. Just as illustrated



**Fig. 11.** PL lifetime spectra of 3B2B in solution (yellow), thin film (pink) and powders (deep pink). (For interpretation of the references to colour in this figure legend, the reader is referred to the web version of this article.)

by the emission decay lifetime spectra in Fig. 11 and the lifetime data in Table 2, the fluorescence decay curves of 3B2B in solution and in the thin film nearly resemble to each other; while that of in the crystallites is much more longer than the two formers. The lifetime in crystallites is 2–3 times longer than that of in solution and in the thin film. The thin film and powders, although both of them are in solid state, with different morphology and different aggregation mode, there are intrinsic changes in the molecules' environment, and have distinct optical behaviors.

### 3.4. Electroluminescence properties of the H-shaped molecules

Considering the effective inhibition of intermolecular  $\pi$ - $\pi$  interactions in the thin films of the two coplanar

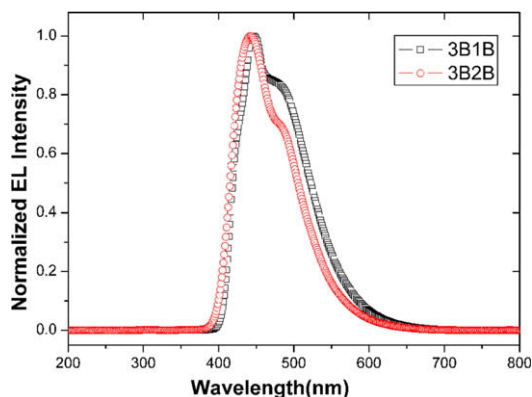


**Fig. 12.** EL spectra of the devices based on the two H-shaped molecules (configuration A).

**Table 3**

EL properties of H-shaped molecules based devices.

Device <sup>a</sup>	$V_{\text{onset}}$ (V)	$L_{\text{max}}$ (cd cm <sup>-2</sup> )	$\eta_{\text{Imax}}$ (cd A <sup>-2</sup> )	$\eta_{\text{Lmax}}$ (lm W <sup>-1</sup> )	CIE (x, y)	$\lambda_{\text{max}}^{\text{EL}}$ (nm)
3B1B/A	3.6	18623	2.4	1.6	(0.17, 0.18)	446
3B1B/B	3.7	18667	2.6	2.2	(0.16, 0.18)	446
3B2B/A	3.3	18964	2.3	2.2	(0.16, 0.14)	443
3B2B/B	3.7	20490	2.8	2.6	(0.16, 0.14)	443

<sup>a</sup> Configuration A: ITO/NPB (40 nm)/H-shaped molecules(30 nm)/AIQ (30 nm)/LiF (1 nm)/Al (80 nm); Configuration B: ITO/NPB (40 nm)/H-shaped molecules(30 nm)/BCP (10 nm)/AIQ (30 nm)/LiF (1 nm)/Al (80 nm).

conjugated molecules, enhanced electroluminescence performances can be expected. Employing the two H-shaped molecules as emitting materials, typical OLEDs were fabricated. The device configuration was: ITO/NPB (40 nm)/H-shaped (40 nm)/AIQ (30 nm)/LiF (1 nm)/Al (80 nm) (NPB = 4,4'-bis(1-naphthyl-N-phenylamino)-biphenyl, acted as hole transport layer; AIQ = tris(8-hydroxyquinoline)aluminum, acted as electron-transport layer). Both of the devices had rather low turn on voltages of 3.6 and 3.3 V. The devices exhibited bright blue light, with the Commission Internationale de l'Eclairage (CIE) coordinates of (0.17, 0.19) (3B1B) and (0.16, 0.14) (3B2B), and showed hardly no variations with the change of applied voltage. The naked devices were found to be with good stability during the measuring process, just as their nice morphological stability of the sublimated films. Fig. 12 gives their EL spectra. The device luminance efficiencies ( $\eta_c$ ) are 2.4 (3B1B) and 2.3 (3B2B) cd A<sup>-1</sup>, and their power efficiencies ( $\eta_p$ ) are 1.6 (3B1B) and 2.2 (3B2B) lm W<sup>-1</sup> (All details are summarized in Table 3). At an operating voltage of 10 V, the brightness of these coplanar H-shaped molecules based devices approached or even exceeded 10000 cd m<sup>-2</sup> (See Fig. 13). It should be noted that the values are quite high, there is no evidence indicating that the aggregation-induced fluorescence quenching. And as shown in Fig. 10, the EL spectrum of 3B2B nearly overlaps with its PL spectrum in thin film, indicating that the blue emission comes from just the 3B2B layer. Maybe thanks to the larger  $\pi$ -conjugation and a more planar configuration of 3B2B than that of 3B1B, the PL and EL performances of 3B2B are better than those of 3B1B. To

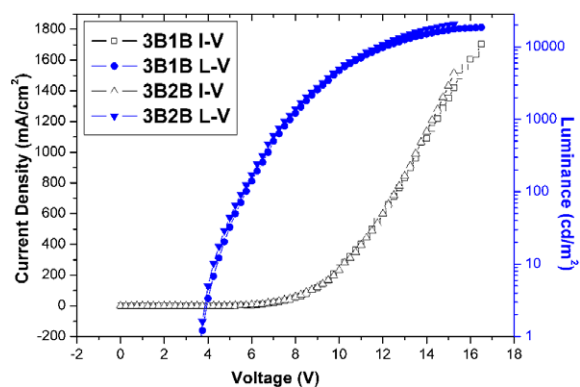


**Fig. 13.** Current density ( $I$ )-voltage ( $V$ ) and luminance ( $L$ )-voltage ( $V$ ) characteristics of devices based on the two H-shaped molecules. (Configuration B.)

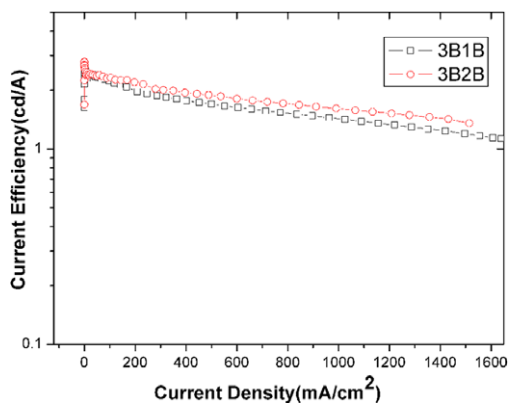


Fig. 14. Current efficiency vs. current density characteristics of devices based on the two H-shaped molecules. (Configuration B.)

optimize the device efficiency, BCP (2,9-dimethyl-4,7-diphenyl-1,10-phenanthroline) was chosen as a hole-blocking layer (10 nm) to insert between the H-shaped emitters and the electron-transport layer AlQ. As shown in Fig. 13 and Fig. 14, the resultant devices were found to be promoted in terms of both efficiency and brightness, the turn on voltages were slightly elevated to 3.7 V for a higher charge injection barrier. Their luminance efficiencies reached 2.6 and 2.8  $\text{cd A}^{-1}$ , and the power efficiencies reached 2.2 and 2.6  $\text{lm W}^{-1}$ , respectively. For the 3B2B based devices, an  $L_{\text{max}}$  of 20490  $\text{cd m}^{-2}$  was obtained. In summary, these results are comparable with those of the non-coplanar or spiro-configurations compounds [4,5a,6,10], and are higher than the performances of the tetrahedral OPVs or the cruciform dimeric OPVs with cross arrangement dipoles which have similar constructing blocks to our H-shaped molecules and with the same EL device configuration [5a,14]. This demonstrate that, if we choose an appropriate topology of chemical structure, such as this H-shaped multi-branched construction, the conjugated compounds based on coplanar configurations likewise can be with reduced aggregation-induced fluorescence quenching effect, and show high EL performances as the non-coplanar ones.

#### 4. Conclusion

In conclusion, with facile synthesis routes, a new series of H-shaped molecules have been synthesized. X-ray crystal structures of them showed that every molecule possesses a coplanar “H” shape, without twist between the two side dipoles. The sublimated thin films with amorphous morphologies show significant blue-shifted and enhanced photoluminescence than those of the crystalline powders. Employing these coplanar H-shaped molecules as non-doped emitters, high brightness blue OLEDs were fabricated. The devices showed a maximum luminance of 20490  $\text{cd m}^{-2}$  and a luminance efficiency of 2.8  $\text{cd A}^{-1}$  (2.6  $\text{lm W}^{-1}$ ) with the CIE coordinate of (0.16, 0.14). These results are comparable with or even better than those of the devices based on the non-coplanar or spiro-configuration compounds. The results indicate that the multi-branched conjugated molecules with coplanar

configurations are appropriate for high performance EL applications. Works to explore new coplanar multi-branched conjugated compounds may be a new way for high efficient OLEDs. Moreover, the chemical structure of the H-shaped molecules can be easily rendered variously, which will attract more attentions in other electronic and optical related fields, such as TPA (two-photon absorption) and fluorescent sensors.

#### Acknowledgments

We are grateful for financial support from the National Natural Science Foundation of China (Grant No. 50721002, 50673003, 50603011) and 973 program of PR China (2004CB619002, 90401028).

#### References

- [1] (a) C.W. Tang, S.A. VanSlyke, *Appl. Phys. Lett.* 51 (1987) 913; (b) K. Mullen, U. Scherf, *Organic Light-Emitting Devices. Synthesis, Properties and Applications*, Wiley, Weinheim, Germany, 2006.
- [2] J. Roncali, P. Leriche, A. Cravino, *Adv. Mater.* 19 (2007) 2045.
- [3] (a) Y.H. Kim, D.C. Shin, S.H. Kim, C.H. Ko, H.S. Yu, Y.S. Chae, S.K. Kwon, *Adv. Mater.* 13 (2001) 1690; (b) C.C. Wu, Y.T. Lin, K.T. Wong, R.T. Chen, Y.Y. Chien, *Adv. Mater.* 16 (2004) 61; (c) S.L. Tao, Z.K. Peng, X.H. Zhang, P.F. Wang, C.S. Lee, S.T. Lee, *Adv. Funct. Mater.* 15 (2005) 1716; (d) Y. Wei, C.T. Chen, J. Am. Chem. Soc. 129 (2007) 7478; (e) F. Huang, Y. Zhang, M.S. Liu, Y.-J. Cheng, A.K.-Y. Jen, *Adv. Funct. Mater.* 17 (2007) 3808.
- [4] (a) S. Wang, W.J. Oldham, R.A. Hudack, G.C. Bazan, *J. Am. Chem. Soc.* 122 (2000) 5695; (b) T. Gu, G. Accorsi, N. Armaroli, D. Guillon, J.F. Nierengarten, *Tetrahedron Lett.* 42 (2001) 2309; (c) G. Yu, S. Yin, Y. Liu, J. Chen, X. Xu, X. Sun, D. Ma, X. Zhan, Q. Peng, Z. Shuai, B. Tang, D. Zhu, W. Fang, Y. Luo, *J. Am. Chem. Soc.* 127 (2005) 6335.
- [5] (a) F. He, H. Xu, B. Yang, Y. Duan, L.L. Tian, K.K. Huang, Y.G. Ma, S.Y. Liu, S.H. Feng, J.C. Shen, *Adv. Mater.* 17 (2005) 2710; (b) F. He, L.L. Tian, X.Y. Tian, H. Xu, Y.H. Wang, W.J. Xie, M. Hanif, J.L. Xia, F.Z. Shen, B. Yang, F. Li, Y.G. Ma, Y.Q. Yang, J.C. Shen, *Adv. Funct. Mater.* 17 (2007) 1551.
- [6] P.M. Ruiz, B. Behnisch, K.H. Schweikart, M. Hanack, L. Ler, D. Oelkrug, *Chem. Eur. J.* 6 (2000) 1294.
- [7] X.T. Tao, Y.D. Zhang, T. Wada, H. Sasabe, H. Suzuki, T. Watanabe, S. Miyata, *Adv. Mater.* 10 (1998) 226.
- [8] S.H. Lo, P.L. Burn, *Chem. Rev.* 107 (2007) 1097.
- [9] P.L. Burn, S.-C. Lo, I.D.W. Samuel, *Adv. Mater.* 19 (2007) 1675.
- [10] (a) N. Miyaura, A. Suzuki, *Chem. Rev.* 95 (1995) 2457; (b) J.X. Yang, X.T. Tao, C.X. Yuan, Y.X. Yan, L. Wang, Z. Liu, Y. Ren, M.H. Jiang, *J. Am. Chem. Soc.* 127 (2005) 3278; (c) Y. Liu, X.T. Tao, F.Z. Wang, X.G. Dang, D.C. Zou, Yan. Ren, M.H. Jiang, *Org. Electron.* 9 (2008) 609.
- [11] (a) N. Zhou, L. Wang, D.W. Thompson, Y. Zhao, *Org. Lett.* 10 (2008) 3001; (b) Q. Kong, D. Zhu, Y. Quan, Q. Chen, J. Ding, J. Lu, Y. Tao, *Chem. Mater.* 19 (2007) 3309; (c) L. Xie, X. Hou, C. Tang, Y. Hua, R. Wang, R. Chen, Q. Fan, L. Wang, W. Wei, B. Peng, W. Huang, *Org. Lett.* 8 (2006) 1363.
- [12] (a) Z. Xie, B. Yang, F. Li, G. Cheng, L. Liu, G. Yang, H. Xu, L. Ye, M. Hannif, S. Liu, D. Ma, Y. Ma, *J. Am. Chem. Soc.* 127 (2005) 14152; (b) J. Cornil, D. Beljonne, J.-P. Calbert, J.-L. Brédas, *Adv. Mater.* 13 (2001) 1053.
- [13] (a) J.R. Lakowicz, *In Principles of Fluorescence Spectroscopy*, second ed., Kluwer Academic/Plenum Publishers, New York, 1999; (b) J. Slavic, *Fluorescence Microscopy and Fluorescent Probes*, Plenum Press, New York, 1996.
- [14] (a) M.R. Robinson, S. Wang, G.C. Bazan, Y. Cao, *Adv. Mater.* 12 (2000) 1701; (b) F. He, G. Cheng, H. Zhang, Y. Zheng, Z. Xie, B. Yang, Y. Ma, S. Liu, J. Shen, *Chem. Commun.* (2003) 2206.

blend on transparent indium tin oxide (ITO) glass. Such a polymer–organic blend system can be easily applied by simple spin coating or printing techniques. In order to achieve the maximum power conversion efficiency for a given material system, organic photovoltaic devices require low series resistance and high shunt resistance. It is also required to have two ohmic contacts in order that bulk series resistance is minimized; first is that between the positive electrode and the active layer, and second is that between the active layer and the metallic electrode. Sandwiching the active layer made of poly(3-hexylthiophene)/[6,6]-phenyl-C61-butyric acid methyl ester (P3HT/PCBM) blend is the hole extraction layer (poly(3,4-ethylenedioxythiophene):poly(4-styrene sulfonate) [PEDOT:PSS] coated ITO) and a negative electrode, metallic conductor such as

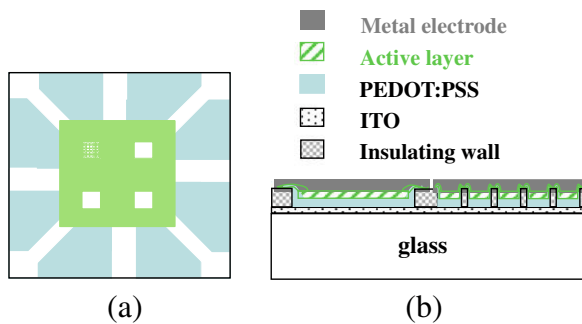


**Fig. 1.** (a) Schematics and actual picture of insulation layer coating on etched ITO and (b) cross-sectional schematics of fully processed device.

Al. Because of a relatively low conversion efficiency of single OPV devices, they need to be fabricated with large scale connectivity. On the other hand, resistivity at large area hole extraction and active layer will induce an increase of series resistance which results in a reduction of current flow, thus affecting the conversion efficiency. A close relationship between the device area and the conversion efficiency is now well established [6].

In this study, we focus on our efforts to partition the hole extraction layer into smaller areas by means of the insulating walls so as to minimize the lateral contribution on the series resistance, thus to prevent lowering of the efficiency by increasing the overall active area. We demonstrate that this method is universally applicable to all organic materials used in OPV. Also, our method will provide a distinct advantage of implementing by simple printing such as inkjet, gravure, offset and screen, lithography, and soft contact transfer. We should note here that our method differs from the conventional module fabrication technique that inserts low resistance metal lines between active areas.

## 2. Material and methods

### 2.1. Fabrication of devices

PEDOT:PSS (poly(3,4-ethylene dioxythiophene):poly(styrene sulfonate)) aqueous dispersions (Baytron<sup>®</sup> AI4083, P and PH-500) were used as the hole extraction layer, spin coated on top of 300–400 nm thick ITO coated

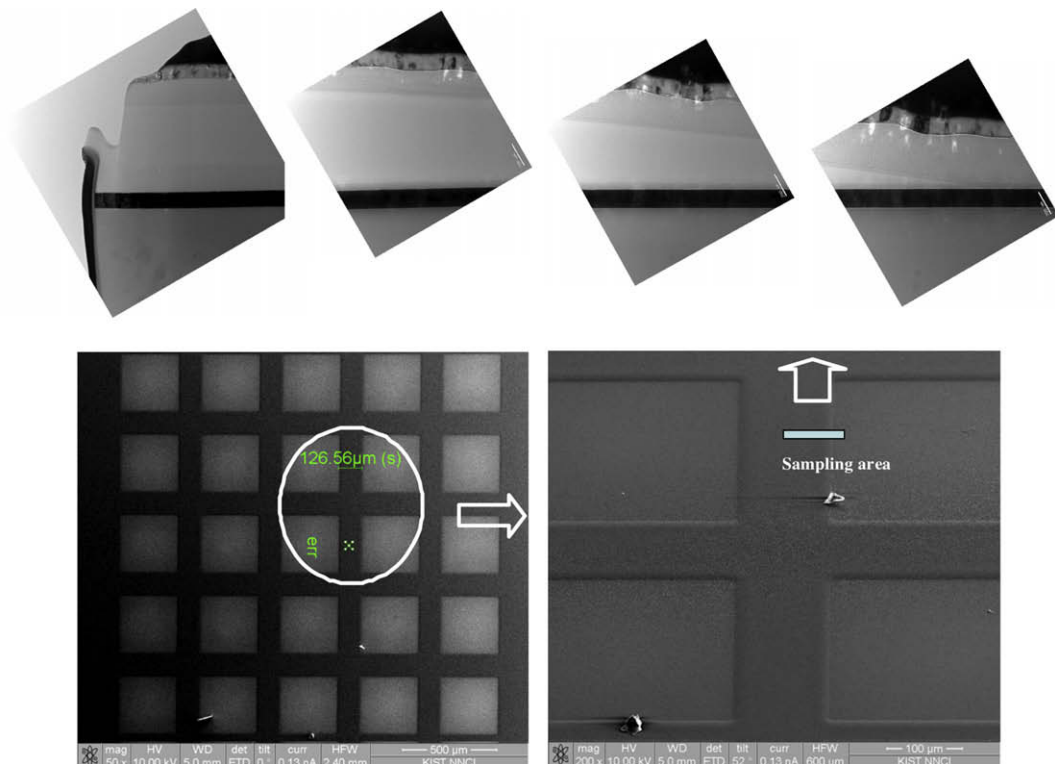


**Fig. 2.** FIB-TEM images; bottom left: partitioned cell, top images: cross-sectional images from insulating wall edge to center of wall.

glass. In the case of DMSO blended PH-500, the ratios of PH-500: methanol: DMSO were 1: 2: 5%, respectively. The PEDOT:PSS stock solution was spin coated at 2000 rpm for 40 seconds to form about 35 nm thick film, then was baked at 200 °C for 10 min in a high purity nitrogen environment glove box. ITO glass was cleaned by boiling in chloroform, isopropyl alcohol and acetone for 30 min in each solvent, sonification for 15 min in 50:50 isopropyl alcohol and acetone solution, and finally rinsed with deionized water. A typical example of the next step of sample preparation is as follows: 2.4 wt% of P3HT and PCBM blend with 1:0.6 ratio by weight was dissolved in anhydrous chlorobenzene and was spin coated on prepared PEDOT:PSS coated ITO glass at 2500 rpm for 40 s. The thickness of resulting active layer was 220 nm and pre-annealed at 150 °C for 10 min. 0.8 nm thick LiF, which served as a buffer layer, was deposited on top of the active layer and 150 nm thick aluminum was evaporated by thermal vapor deposition at  $10^{-6}$ – $10^{-7}$  Torr, and prepared device was post annealed at 120 °C for 10 min. All of the processing was performed in the glove box with high purity nitrogen envi-

ronment. Photocrosslinkable positive photoresist resin of acrylate derivates (Nippon Zeon Corp.) was used to form partitioning wall of height of 500  $\mu\text{m}$ . Standard partitioned subcell area was  $300 \times 300 \mu\text{m}$ , and the partitioning wall was 200  $\mu\text{m}$  in width and 500  $\mu\text{m}$  in height. After finishing the series of the preparation processes, the device was encapsulated with glass plate using an UV curable resin in a high purity nitrogen environment glove box.

## 2.2. Characterization

For cross-sectional transmission electron microscope (TEM) (FEI TECNAI F20) observation of device, a thin flake in situ lift-out sample was prepared using focused ion-beam (FIB) machine (FEI Nova600) with a Ga ion focused beam. Thickness of coated film was measured with surface profiler (TENCOR<sup>®</sup>, P-10  $\alpha$ -step). Oriel Class A type solar simulator (IEC 904) with Oriel Reference Cell (calibrated data taken by NREL) was used as a light source and all measurement was performed under 1 sun condition (100 mW/cm<sup>2</sup>). The measurements were not corrected for reflection

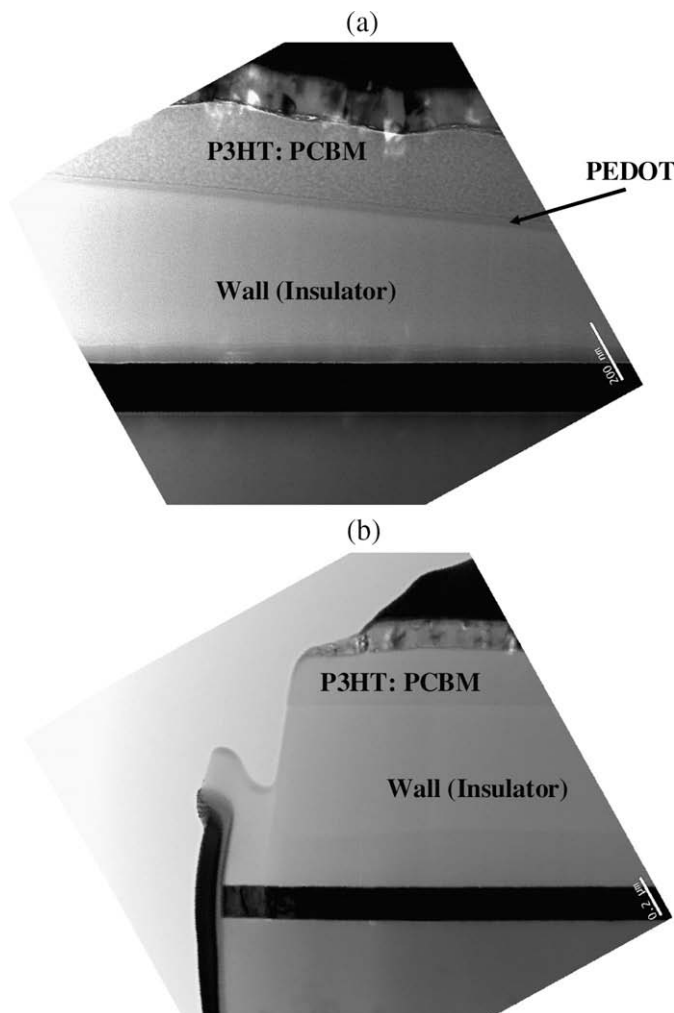


**Fig. 3.** FIB-TEM images; (a) interface area of partitioning wall and (b) center position of partitioning wall.



losses and light absorption in the ITO electrode. Current–voltage characteristics were determined with Keithley 2400 source–measure unit.

### 3. Results and discussion

In Fig. 1 is displayed our fabrication design of photovoltaic cells consisting of smaller sized subcells to the conventional cell size, i.e.  $0.04 \text{ cm}^2$ . Eventually we have increased the total cell size to  $1 \text{ cm}^2$ , to which we will return at the end. Parenthetically, the size of  $1 \text{ cm}^2$  is quite a large cell for OPV. Our test coupon is made of three single cells of  $0.04 \text{ cm}^2$ , one partitioned cell with actual active area of  $0.027 \text{ cm}^2$  which consisting of 25 subcells of the same size ( $300 \mu\text{m} \times 300 \mu\text{m}$ ), and  $200 \mu\text{m}$  space between them. These are so formed by an insulator on top of one inch by one inch ITO coated glass as shown in Fig. 1. The partitioned subcells form a single cell upon covering its top with an Al electrode.

It is quite simple to build the insulating walls to disconnect the hole extraction layer by means of a curable resin via a lithographic method. With TEM micrographs in Fig. 2 and Fig. 3, we show that the hole extraction layer (PEDOT:PSS) is discontinued at few tens of micrometer away from the edge of insulating walls so that the series resistance is reduced through a smaller active area. Each divided active area acts like an isolated small cell so that the series resistance is reduced. In order to elucidate the effect of partitioning the active areas, a cell without partitioning wall is used as the reference.

Fig. 4 shows the profiles of current density vs. bias voltage ( $J$ – $V$ ) between single and partition cells for three different formulations of hole extraction layer. The results are

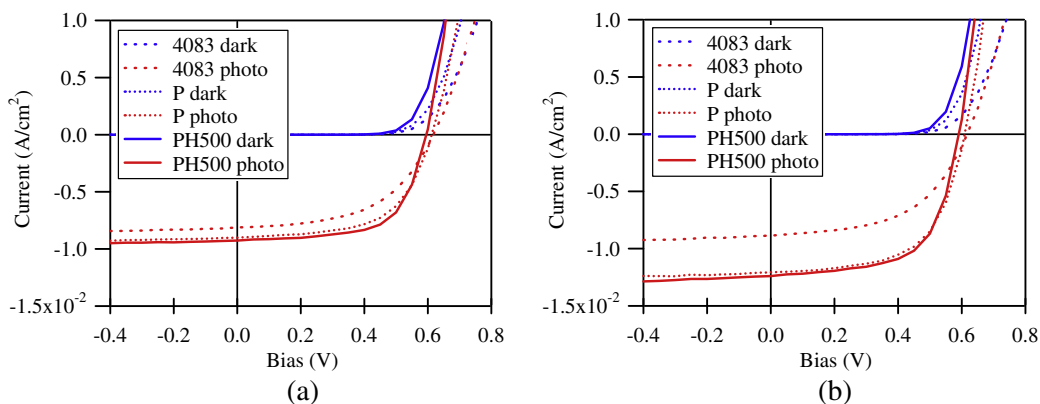


Fig. 4.  $J$ – $V$  characteristics for three different hole extraction layers; (a) single cell and (b) partition cells.

Table 1

Influence of conductivity of hole extraction layer on performance of OPV device (s: single area cell; p: partitioned cell).

Conductive layer	Area	Open circuit voltage (V)	Current density ( $\text{mA}/\text{cm}^2$ )	Fill factor	Series resistance ( $\Omega \text{ cm}^2$ )	Efficiency
Baytron Al 4083 (10–3 S/cm)	s	0.617	8.12	0.526	7.47	2.64
	p	0.616	8.86	0.527	7.40	2.88
Baytron P (1 S/cm)	s	0.615	8.72	0.609	3.33	3.27
	p	0.609	12.06	0.602	2.43	4.42
Baytron PH-500 (100 S/cm)	s	0.596	9.27	0.641	2.22	3.54
	p	0.591	12.39	0.626	1.81	4.58

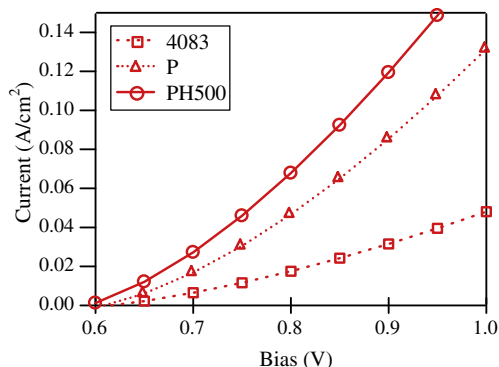


Fig. 5. Transmittance of ITO and insulating walls, and absorption characteristics of P3HT/PCBM blend.

summarized in Table 1. When Baytron 4083 is used as the hole extraction layer having a low conductivity ( $\sim 10$ – $3 \text{ S/cm}$ ), there was no detectable difference between the single and partitioned cells. However, when the conductivities were higher (Baytron P:  $\sim 1 \text{ S/cm}$  and Baytron PH-500 blended with dimethyl sulfoxide:  $\sim 100 \text{ S/cm}$ ), there were significant differences in the efficiency between the two, and the degree of this difference was in the order of conductivity of the hole extraction layer formulations. Henceforth, we refer Baytron PH-500 blended with dimethyl sulfoxide (DMSO) as simply PH-500. Clearly, the observed enhancements of the current density and efficiency are closely correlated to the conductivity of the hole extraction layer. Thus, we infer that there exist lateral contributions of the series resistance from the rest of active area to a subcell for the bulk resistance. As is shown in

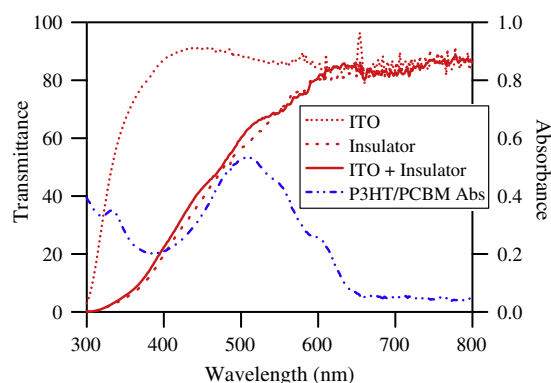
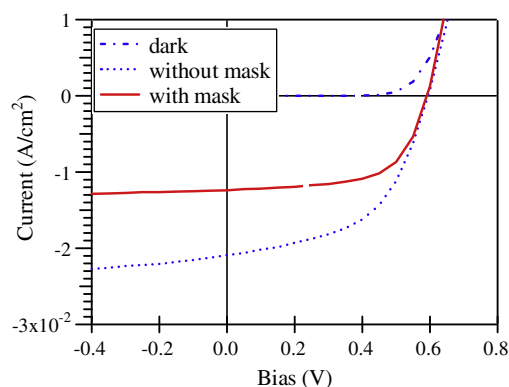
**Table 2**Influence of wall to active area ratio (active area was  $300 \mu\text{m} \times 300 \mu\text{m}$ ).

Conductive layer	Wall width ( $\mu\text{m}$ )	Open circuit voltage (V)	Current density ( $\text{mA}/\text{cm}^2$ )	Fill factor	Series resistance ( $\Omega \text{cm}^2$ )	Efficiency
Baytron Al 4083 ( $10^{-3} \text{ S}/\text{cm}$ )	None	0.590	8.53	0.460	22.68	2.35
	20	0.595	8.23	0.460	25.62	2.27
	50	0.593	8.27	0.480	23.25	2.39
	100	0.595	8.47	0.490	15.49	2.46
	200	0.595	8.27	0.500	10.78	2.49
Baytron PH-500 ( $100 \text{ S}/\text{cm}$ )	None	0.596	8.09	0.570	8.09	2.75
	20	0.602	7.75	0.564	8.51	2.63
	50	0.592	9.23	0.586	6.21	3.20
	100	0.586	10.26	0.517	6.27	3.11
	200	0.596	12.93	0.561	4.63	4.32

Fig. 5, the lowering of series resistance can be observed clearly by the increasing slope of the current density vs. bias voltage profile above the open circuit voltage; the inverse of slope in the figure represents the bulk series resistance. Despite the enhanced conductivity of the hole extraction layer, it still has a relatively high resistance compared to that of the electrode. Such a high resistance of the hole extraction layer is attributed to the contributions from far away areas, whereas such is not the case with a low conductive hole extraction layer. In short, for highly conductive hole extraction layers, the deleterious effect of the lateral contributions of the series resistance from the rest of active areas to the bulk resistance is rather significant. Therefore, the enhancement of the efficiency will be substantial over that of a cell made with low conductivity formulations if the hole extraction layer is disconnected from each other by partitioning into smaller area subcells.

We have also investigated the influence of wall to active area ratio using different partitioned cells and the results are summarized in Table 2. The power conversion efficiency was increased with increasing partitioning wall width. When Baytron Al 4083 was used as the hole extraction layer, there was no detectable difference in the power conversion efficiency among the different wall widths. However, when Baytron PH-500 was used, there were significant differences in the efficiency and the series resistance among wall widths, and the degree of this difference was in the order of wall widths. This result is quite reasonable since lateral contributions of the series resistance from the rest of active area to the subcell should be decreased with increasing wall width.

We now turn to the uncertainty with respect to the estimate of active cell area. As was shown in Fig. 2 with the cross-sectional TEM micrographs by focused ion-beam (FIB), we estimate that the boundary of PEDOT:PSS coating is about  $30 \mu\text{m}$  from the edge of insulating wall. Since PEDOT:PSS has to be coated over rather tall insulating walls, having a height of  $500 \mu\text{m}$  at the center position, our cell coating process is different from the coating on flat ITO surface. Unlike the reported edge effect (effective areas are  $300\text{--}400 \mu\text{m}$  from the edge) [7] when PEDOT:PSS is coated on a flat surface, the actual active area in our device starts about  $30 \mu\text{m}$  away from the edge since the PEDOT:PSS does not extend flush to the edge. This issue is being raised because the size of active area is critical to the efficiency, particularly when the active area is small

**Fig. 6.** Transmittance of ITO and insulating walls, and absorption characteristics of P3HT/PCBM blend.**Fig. 7.**  $J$ - $V$  characteristics of a partitioned device with and without mask.

[7]. In addition, the insulating wall materials with the  $500 \mu\text{m}$  height at the center, as referred to in the above, absorb visible light and the transmittance at the P3HT/PCBM blend absorption region is less than 50% as shown in Fig. 6. Therefore, the actual exciton formation in the area between the insulating wall to the PEDOT:PSS coating edge may be small but still needs to be accounted for in the estimate of the efficiency. Thus, the actual active area in the partitioned cell is subject to a certain range of uncertainty. Nevertheless, we emphasize that the trend of increasing current extraction with a high conductivity of the hole extraction layer by partitioning is firmly established.

**Table 3**  
Characteristics of large area cell.

Conductive layer	Area	Open circuit voltage (V)	Current density (mA/cm <sup>2</sup> )	Fill factor	Series resistance ( $\Omega$ cm <sup>2</sup> )	Efficiency
Baytron Al 4083 (10 <sup>-3</sup> S/cm)	s	0.590	8.53	0.460	22.68	2.35
	p	0.595	8.27	0.500	10.78	2.49
Baytron PH-500 (100 S/cm)	s	0.596	8.09	0.570	8.09	2.75
	p	0.596	12.93	0.561	4.63	4.32

It is well known that artifacts caused by the edge effect are to be taken into account with care [7,8]. In fact, it is a point of a recent controversy with the solar cell efficiency [9]. According to the report by Cravino et al. [7] a small area cell like ours is significantly affected by the edge effect as expected. We thus examine the edge effect by masking the device area. Fig. 7 shows *J*-*V* characteristics of the partitioned device with and without mask. When the entire fabricated device was exposed to incident light without masking, the power conversion efficiency was about 6.5; the current density was  $\sim 20.9$  mA/cm<sup>2</sup> and the fill factor was 0.523. On the other hand, when the mask was placed so as to expose only active area to the incident light, the power conversion efficiency was reduced to 4.6; the current density was  $\sim 12.4$  mA/cm<sup>2</sup> and the fill factor was 0.626. Thus, we conclude that the edge effect is indeed significant relative to the actual power conversion efficiency. It can be readily understood that the current density decrease and fill factor increase are caused by the charges formed only in the active area.

Finally, we come to the issue of a large area size cell of 1 cm<sup>2</sup>. Despite difficulty in quantifying the power conversion efficiency arising from the uncertainty of actual active area within the partitioned walls, the key point of this study is clear: One can fabricate a large area OPV device without sacrificing the power conversion efficiency, if not enhancing, when hole extraction layer is partitioned into smaller subcells. A large area cell ( $\sim 1$  cm<sup>2</sup>) was prepared by the same manner as described in the above. To elucidate the partitioning effect, a single area cell with the comparable active area was also prepared. The results are summarized in Table 3. As was seen in Table 3, the partitioned cell performance with Baytron Al 4083 showed no distinct difference from that of single cell (efficiency change from 2.35 to 2.49). On the other hand, the partitioned cell performance with Baytron PH-500 showed about 40% improvement in the efficiency over that of single cell (efficiency change from 2.75 to 4.32). Notwithstanding any uncertainty relative to the absolute estimate of the power conversion efficiency arising from the active area uncertainty, the results in Table 3 make it compelling that the partitioning works when compare to a device with the same overall active area.

Major factor causing this difference is the series resistance, noted by the slope of *J*-*V* curve beyond open circuit voltage (Fig. 5). As discussed previously, the partitioning of hole extraction layer caused the series resistance decrease. This is entirely consistent with a report by Yoo et al. [10] that the series resistance increased with the number of cells upon connecting them in series. Since the areas of these two cells were same, it was clear that a partitioned

cell with a high conductivity hole extraction layer would have a lower series resistance resulting in enhanced current extraction leading to improved power conversion efficiency.

#### 4. Conclusion

We conclude with these results that the partitioning of the active area into smaller areas can improve the power conversion efficiency of organic photovoltaic devices. The lateral serial contributions to the series bulk resistance of the hole extraction layer with a high conductivity profoundly affect the power conversion efficiency. Our method reported here is to be differentiated from the conventional metal line insertion for the purposes of increasing the current output as used in photovoltaic industry.

#### Acknowledgments

This work was supported by the KIST R&D program and the Korea Science and Engineering Foundation (KOSEF) the Basic Research Program grant fund (No. R01-2006-000-10087-0).

#### References

- [1] J.J.M. Halls, C.A. Walsh, N.C. Greenham, E.A. Marseglia, R.H. Friend, S.C. Moratti, A.B. Holmes, Efficient photodiodes from interpenetrating polymer networks, *Nature* 376 (1995) 498–500.
- [2] J.Y. Kim, K. Lee, N.E. Coates, D. Moses, T.-Q. Nguyen, M. Dante, A.J. Heeger, Efficient tandem polymer solar cells fabricated by all-solution processing, *Science* 317 (2007) 222–225.
- [3] M. Hiramoto, H. Fujiwara, M. Yokoyama, Three-layered organic solar cell with a photoactive interlayer of codeposited pigments, *Appl. Phys. Lett.* 58 (1991) 1062–1064.
- [4] A. Dhanabalan, J.K.J. van Duren, P.A. van Hal, J.L.J. van Dongen, R.A.J. Janssen, Synthesis and characterization of a low bandgap conjugated polymer for bulk heterojunction photovoltaic cells, *Adv. Funct. Mater.* 11 (2001) 255–262.
- [5] L.J.A. Koster, V.D. Mihailetchi, P.W. Blom, Ultimate efficiency of polymer/fullerene bulk heterojunction solar cells, *Appl. Phys. Lett.* 88 (2006) 093511.
- [6] A.K. Pandey, J.M. Nunzi, B. Ratier, A. Moliton, Size effect on organic optoelectronics devices: example of photovoltaic cell efficiency, *Phys. Lett. A* 372 (2008) 1333–1336.
- [7] A. Cravino, P. Schilinsky, C.J. Brabec, Characterization of organic solar cells: the importance of device layout, *Adv. Funct. Mater.* 17 (2007) 3906–3910.
- [8] M.-S. Kim, M.-G. Kang, L. Jay Guo, J. Kim, Choice of electrode geometry for accurate measurement of organic photovoltaic cell performance, *Appl. Phys. Lett.* 92 (2008) 133301.
- [9] P. Fairley, Solar cell squabble: organic photovoltaics could be dirt cheap, but their efficiency is in dispute, *IEEE Spectrum* 45 (2008) 36–40.
- [10] S. Yoo, W.J. Potscavage, B. Domercq, J. Kim, J. Holt, B. Kippelen, Integrated organic photovoltaic modules with a scalable voltage output, *Appl. Phys. Lett.* 89 (2006) 233516.

applications. The main reason is attributed to random-oriented behavior of phthalocyanine crystals. Many grain boundary and deflections were found in films that bring lots of charge traps that degrade the efficiency of charge transportation. More recently, Yan's group proposed an effective method to improve the mobility of phthalocyanine by weak epitaxy growth technology [11]. They

prepared phthalocyanine films on the top of rod-like molecules (para-sexiphenyl and 2, 2'; 7', 2''-terphenanthrenyl) and realized high field-effect mobilities [11–13].

In this paper, two typical phthalocyanine compounds, titanyl-phthalocyanine (TiOPc) and CuPc, were selected as material pair to realize high-performance OFET. Both of them possess excellent chemical and thermal tolerances,

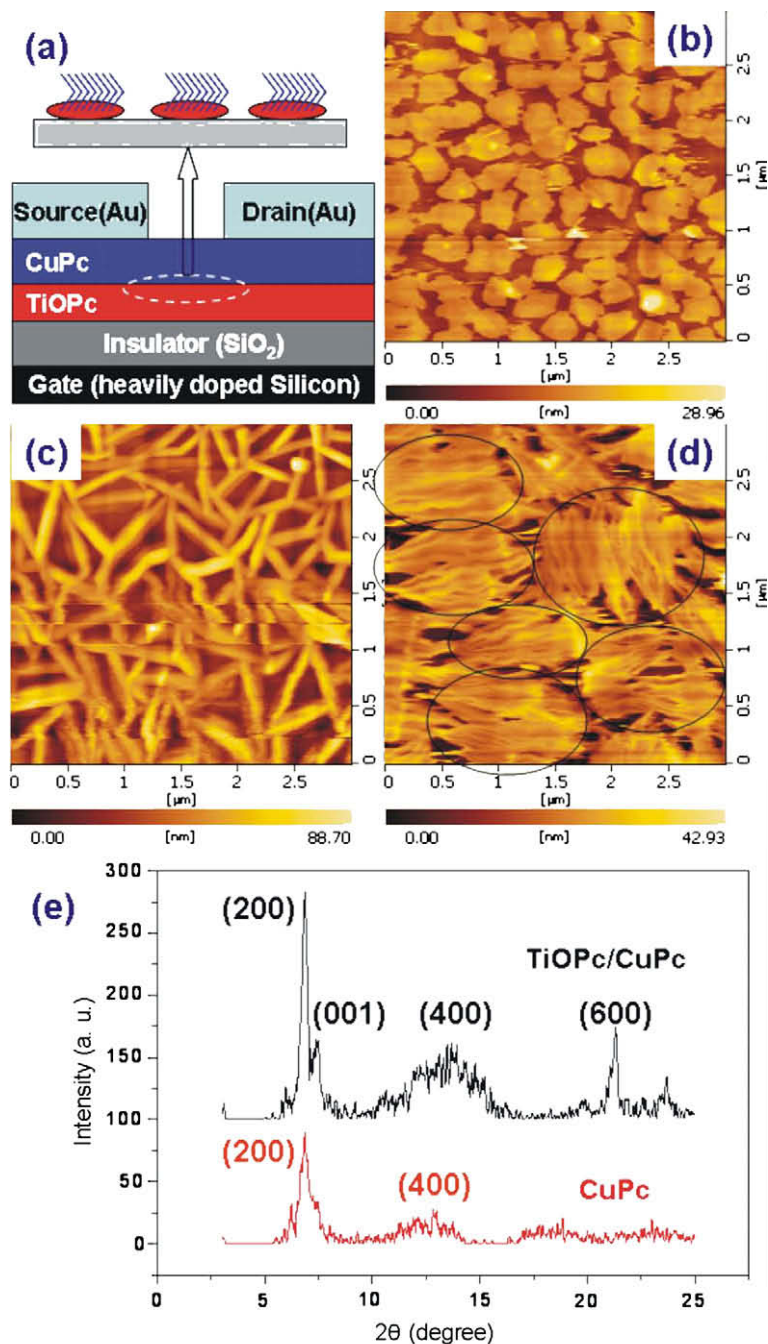


**Fig. 1.** (a) Schematics of OFET with top contact based on CuPc/TiOPc as the active layers. The growth model of CuPc on TiOPc template was shown on the top of device. (b) AFM image of 5 nm TiOPc on OTS/SiO<sub>2</sub>. (c) AFM image of 20 nm CuPc on OTS/SiO<sub>2</sub>. (d) AFM image of 20 nm CuPc on 5 nm TiOPc. (e) X-ray diffraction pattern of CuPc (20 nm) grown on TiOPc template (5 nm) and CuPc (20 nm) grown on OTS/SiO<sub>2</sub>.

especially attractive low-cost. In air phthalocyanines undergo no noticeable degradation up to 400–500 °C, and even strong acids and bases cannot affect them [14]. TiOPc is a nonplanar molecule with significant molecular overlaps and short intermolecular distances [15]. It often exhibits quasi-intrinsic semiconductor state, p-type in air doping by oxygen and n-type in high vacuum conditions [16]. Comparing with another family member, metal phthalocyanine such as CuPc, TiOPc has lower mobility possibly due to poor film quality [15]. However, it exhibits disk-like crystal shape that is clearly distinguished from CuPc with needle-like shape at high-temperature substrate [17]. This unique characteristic makes it to be an excellent template molecule to prepare high-quality CuPc film. In this study, CuPc grown on the top of TiOPc exhibited domain-oriented, closely stacked film morphology. The corresponding OFET revealed a high field-effect mobility of 0.12 cm<sup>2</sup>/V s, and 10<sup>5</sup> on/off current ratio.

## 2. Experiment

OFET devices with top contact (Fig. 1a) were fabricated according to the following procedure. Heavily doped n-type silicon wafers (0.01–0.15 Ω cm) were acted as gate electrode and substrate. A layer of oxide (SiO<sub>2</sub>) with unit capacitance of 8 nF/cm<sup>2</sup> covered on the substrate was served as gate insulator by thermal growth. The wafers were ultrasonically cleaned with acetone, isopropyl alcohol, and ultra purified water, respectively. Then these wafers were inserted to octadecyltrichlorosilane (OTS) solution (chloroform as solvent, 2 mM) for 24 h to form a self-assembly monolayer in order to optimize the surface properties of SiO<sub>2</sub> [15]. TiOPc and CuPc with various thicknesses were deposited in succession at a base pressure of (4–5) × 10<sup>-4</sup> Pa at a rate of 1 Å/s, while the substrates were held at 200 °C. The thickness values were recorded by quartz crystal. Subsequently to prepare the source/drain electrodes, gold film with 30 nm was evaporated through shadow mask defining channel width of 3800 μm and length of 180 μm, respectively. For comparison, OFETs based on TiOPc or CuPc single-layer with 25 nm were fabricated and held with the same condition described above. All organic source samples were purchased from Sigma–Aldrich without further purification. Electrical characteristics of OFETs were performed in ambient by a semiconductor parameter analyzer (Agilent technology 4155C). The atomic force microscopy (AFM) images were performed by SPI 4000 with tapping mode. X-ray diffraction (XRD) was measured in D/Max-2550 with Cu Kα source (λ = 1.541 Å).

## 3. Results and discussion

Fig. 1b displays the morphology of the TiOPc thin-film with 5 nm covered on the substrate of OTS/SiO<sub>2</sub> recorded by AFM images. It exhibited typical discontinuous island crystals with disk-like shape consisting of several monodomains analogous to conventional phenyl-derives that were distinguished from CuPc film with needle-like shape

(Fig. 1c). This result is due to the titanyl atom perpendicular to phthalocyanine ring and then forming out-plane structure that resulted in layer-by-layer growth manner with “edge-on” molecular orientation, similar report may be found elsewhere [18]. Moreover, the domain height is ~10 nm, which is attributed to strong diffusion behavior of TiOPc molecules at a high substrate temperature. The mean domain size of TiOPc is ~250 nm and ratio of grain area is 68% by SPI 4000 analysis. Thus a molecular template was ready for the growth of CuPc. Fig. 1d shows the morphologies of 20 nm CuPc film based on 5 nm TiOPc template. It can be found that CuPc firstly grown on the top of TiOPc monodomain and then connected with each other. In each domain area, CuPc grains oriented along a constant direction and formed well-ordered arrangement marked by dark circles in Fig. 1d. AFM analysis showed that a root mean square roughness of CuPc/TiOPc is 6.8 nm which is lower than that of CuPc/OTS/SiO<sub>2</sub> with 9.1 nm. In contrast to CuPc on OTS/SiO<sub>2</sub> (Fig. 1b), a morphological transform from random orientation to domain-order orientation may be clearly observed by utilizing TiOPc template at a high substrate temperature by comparing Fig. 1c and d. XRD results (Fig. 1e) indicated that the CuPc film on TiOPc exhibited high crystallization and typical β crystal phase, in which 6.8° and 7.0° correspond to (2 0 0) and (0 0 1)

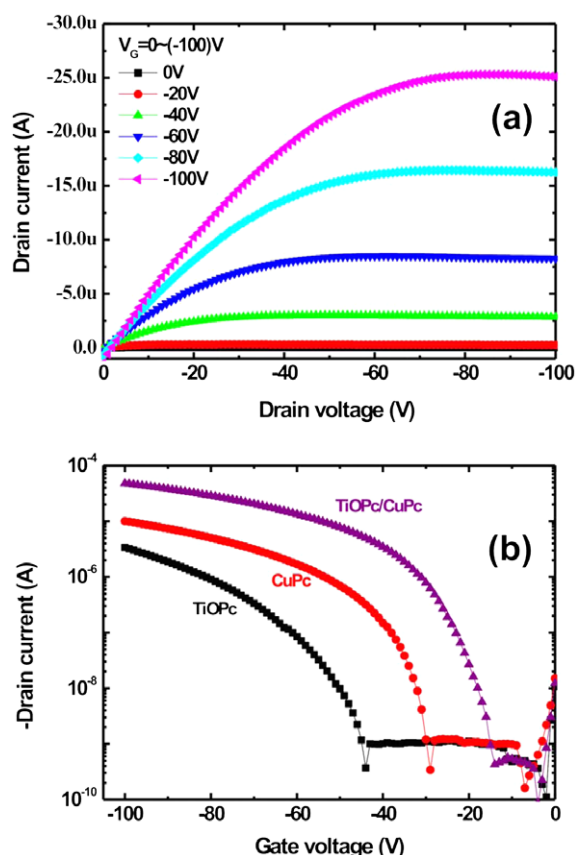
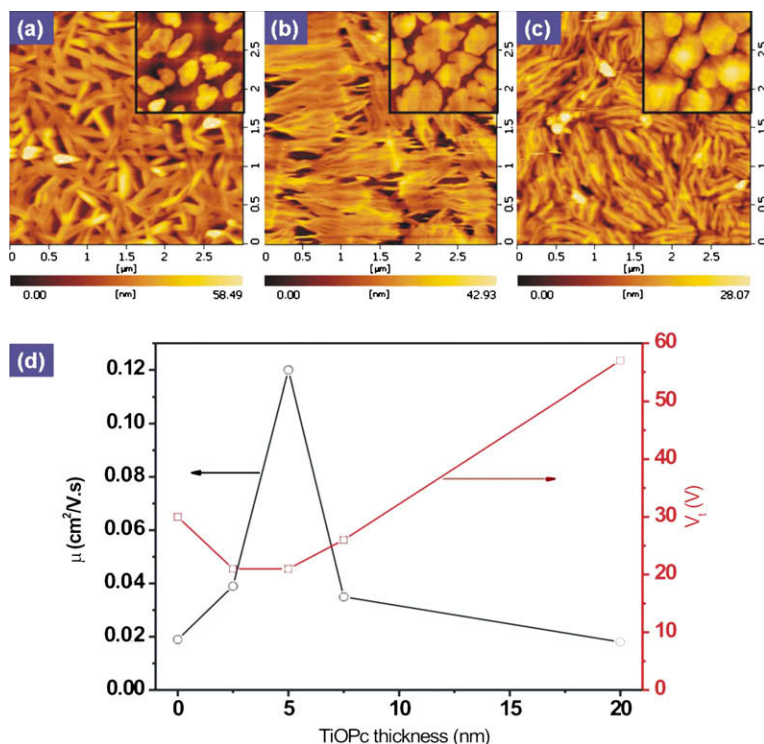


Fig. 2. (a) The output characteristics of CuPc (20 nm)-based OFET utilizing TiOPc (5 nm) molecular template. (b) Three transfer characteristics for TiOPc/OTS/SiO<sub>2</sub>, CuPc/OTS/SiO<sub>2</sub>, and CuPc/TiOPc/OTS/SiO<sub>2</sub> OFETs. All active layers of devices were controlled at 25 nm.

planes of the  $\beta$  form, respectively [18]. This result implied that CuPc molecules grown adopting a herringbone structure that stand up on TiOPc stacking along  $b$ -axis are in the P21/a space group [18]. The growth mode of CuPc on TiOPc template is illustrated in Fig. 1. For comparison, the XRD patterns of CuPc growth on OTS/SiO<sub>2</sub> were also presented. A single sharp diffraction peak was found at  $2\alpha$  of ca.  $6.8^\circ$  ( $7.0^\circ$  is not exhibited that distinguished the CuPc on TiOPc template), which corresponds to the (2 0 0) lattice planes. It revealed that the crystalline structure is parallel to substrate defined as a metastable herringbone-like  $\alpha$  phase [19]. The appearance of new diffraction peak in CuPc/TiOPc implied a new crystal phase and improved film order.

The electrical characteristics of OFET devices with 20 nm CuPc on 5 nm TiOPc are presented in Fig. 2a and b, which displayed typical hole-accumulation mode under various gate and drain biases. Field-effect mobility and on/off current ratio extracted from saturation region were  $0.12 \text{ cm}^2/\text{V s}$  and beyond  $10^5$ , respectively. Threshold voltage of  $-19 \text{ V}$  was obtained from transfer curves. Here it should be figured out that high threshold voltage must come from low capacitance of gate insulator ( $8 \text{ nF}/\text{cm}^2$ ). However, it does not obstruct us to obtain clear results in this work. For comparison, the transfer characteristics of single-layer CuPc and TiOPc devices are also shown in Fig. 2b, from which a mobility of  $0.018 \text{ cm}^2/\text{V s}$  for TiOPc and that of  $0.019 \text{ cm}^2/\text{V s}$  for CuPc have been obtained which indicated that an improvement has been achieved ( $0.12 \text{ cm}^2/\text{V s}$  for TiOPc/CuPc devices). The domain-oriented

film and closely stacked between domains resulted in low trap concentration and reduced hopping distance of carriers, which may be responsible for the improvements. The threshold voltages of these devices were extracted,  $-58 \text{ V}$  for TiOPc and  $-32 \text{ V}$  for CuPc, which revealed that threshold voltage was simultaneously reduced by applying TiOPc template ( $-19 \text{ V}$ ). TiOPc is a typical quasi-intrinsic semiconductor. It operates in n-type operation mode in inert ambient, and the majority carriers are electrons in film possibly originating from residual impurities working as n-type dopants [20]. In our devices, holes are induced by these electrons in TiOPc and pre-accumulated at the side of CuPc due to the difference of Fermi energy level when put them together. This provides an enhanced hole-accumulation effect under given gate bias that results in the decrease of threshold voltage. The amount of threshold voltage shift may be described by  $\Delta V_{\text{th}} = \Delta Q_{\text{deep}}/C_i$  [21], where  $\Delta V_{\text{th}}$  is the shift of threshold voltage,  $\Delta Q_{\text{deep}}$  is the trap charges that could be filled by the gate voltage, and  $C_i$  is the unit capacitance of gate insulator. So  $\Delta Q_{\text{deep}}$  may be established to be  $1.04 \times 10^{11} \text{ cm}^{-2}$  that represented the difference of trap charge concentration between conventional CuPc-based devices and herein CuPc/TiOPc-based devices. Furthermore, we note that the off-state current of CuPc/TiOPc OFET has a slight decrease that is different from those heterojunction devices in the previous reports [12,13]. It is possibly attributed to the energy level of CuPc and TiOPc that are similar which induces the amount of accumulated charges at the interface decrease and then result in a low bulk conductivity [22]. As a result, the whole device performances were



**Fig. 3.** AFM images (a) 20 nm CuPc on 2.5 nm TiOPc. (b) 20 nm CuPc on 5 nm TiOPc. (d) 20 nm CuPc on 7.5 nm TiOPc. The insets are TiOPc films (2.5, 5, and 7.5 nm) grown on OTS/SiO<sub>2</sub> substrate. (c) The TiOPc thickness dependence on device performances of OFETs. The thickness of CuPc was kept at 20 nm.

improved due to the optimization of film properties by templating effects, as well as heterojunction functions.

For further clarifying the TiOPc template effects, the thickness dependence of device performances was investigated. The 20 nm CuPc film morphologies growth on TiOPc with different thicknesses have been shown in Fig. 3. The insets in Fig. 3a–c are the AFM images of TiOPc with different thicknesses (2.5, 5, and 7.5 nm), in which the film continuity was gradually improved with the increase of thickness that resulted. According to 2.5 nm TiOPc substrate, CuPc grains are similar with CuPc/OTS due to many vacancy areas of TiOPc film (see inset Fig. 3a). However, the grains exhibited domain-oriented arrangement when the TiOPc thickness is 5 nm. Further increasing the thickness to 7.5 nm, CuPc grains formed closer contact and domain orientation seemed to be slightly lowered that is attributed to the improvement of TiOPc continuity. As a result, the TiOPc thickness played a crucial role for the growth of CuPc. 5 nm is a critical thickness for the form of high-ordered, domain-oriented CuPc film. Fig. 3d shows mobility and threshold voltage as a function of TiOPc thickness. It can be found that the highest mobility and the lowest threshold voltage were obtained from the devices with 5 nm TiOPc template. The decrease of TiOPc thickness induces the reduction of the domain-oriented area of CuPc, which results in the drop of device performances. On the other hand, when further increasing TiOPc thickness (7.5 nm) to form continuity film, it probably exhibits TiOPc charge transportation behavior that leads to low mobility. In this case, the electrical characteristics of OFET are comparable with those of single-layer TiOPc device when the TiOPc thickness is successively increased to 20 nm. Thereby, a peak value of device performance appears with the change of TiOPc thicknesses.

Both the morphology of organic heterojunction films and its corresponding electrical structure have strong influences on OFET performances, simultaneously, they have an intimate correlation. Generally, this system is very complicated, involving many factors such as energy level, polycrystalline film morphology, and interface properties of two components. According to this topic, relative studies are just beginning. TiOPc/CuPc pair will provide a distinguished example to detect some unique characteristics that occurred in organic semiconductors, which are expected to push the study of new organic electrical devices.

#### 4. Conclusion

In summary, CuPc film with domain-oriented crystal structure has been prepared by employing titanil-phthalocyanine (TiOPc) as molecular template deposited at a high substrate temperature. CuPc molecules stand up on the top of TiOPc domains, at the same time closely stacking among domains and high-order arrangement were observed. The

corresponding OFETs devices were fabricated that exhibited an improved device performance, a  $0.12 \text{ cm}^2/\text{V s}$  of mobility and a  $10^5$  of on/off ratio. Threshold voltage also revealed a decrease of 13 V compared with that of conventional devices. All results were attributed to the controlling of film morphology and heterojunction functions realized by the TiOPc template. These indicated that molecular template is an effective method for the preparation of high-quality thin-film applied in organic optoelectronics.

#### Acknowledgements

This research was supported by the National Natural Science Foundation of China (60806007) and Shanghai Rising-Star Program (07QA14023), and Science and Technology Commission of Shanghai Municipality Program (08DZ1140702).

#### References

- [1] T.D. Anthopoulos, D.M. de Leeuw, E. Cantatore, S. Setayesh, E.J. Meijer, C. Tanase, J.C. Hummelen, P.W.M. Blom, *Appl. Phys. Lett.* 85 (2004) 4205.
- [2] J. Zaumseil, R.H. Friend, H. Sirringhaus, *Nature Mat.* 5 (2006) 69.
- [3] B. Crone, A. Dodabalapur, Y.Y. Lin, R.W. Filas, Z. Bao, A. Laduca, R. Sarpeshkar, N.E. Katz, W. Li, *Nature (London)* 403 (2000) 521.
- [4] T. Someya, T. Sekitani, S. Iba, Y. Kato, H. Kawaguchi, T. Sakurai, *Proc. Natl. Acad. Sci. USA* 101 (2004) 9966.
- [5] K. Takimiya, Y. Kunugi, Y. Kouda, H. Ebata, Y. Toyoshima, T. Otsubo, *J. Am. Chem. Soc.* 128 (2006) 3044.
- [6] K. Yamada, J. Takeya, K. Shigeto, K. Tsukagoshi, Y. Aoyagi, Y. Iwasa, *Appl. Phys. Lett.* 88 (2006) 122110.
- [7] Z. Bao, A.J. Lovinger, A. Dodabalapur, *Appl. Phys. Lett.* 69 (1996) 3066.
- [8] T.W. Kelly, D.V. Muires, P.F. Baude, T.P. Smith, T.D. Jones, *Mat. Res. Soc. Symp. Proc.* 771 (2003) L6.5.1.
- [9] J. Zhang, J. Wang, H. Wang, D. Yan, *Appl. Phys. Lett.* 84 (2004) 142.
- [10] R. Zeis, T. Siegrist, C. Kloc, *Appl. Phys. Lett.* 86 (2005) 022103.
- [11] H.B. Wang, F. Zhu, J.L. Yang, Y.H. Geng, D.H. Yan, *Adv. Mater.* 19 (2008) 2168.
- [12] H.B. Wang, X.J. Wang, H.C. Huang, D.H. Yan, *Appl. Phys. Lett.* 93 (2008) 103307.
- [13] H.B. Wang, X.J. Wang, B. Yu, Y.H. Geng, D.H. Yan, *Appl. Phys. Lett.* 93 (2008) 113303.
- [14] J. Simon, J.J. Andre, *Molecular Semiconductors: Photoelectrical Properties and Solar Cells*, Springer-Verlag, Berlin, Heidelberg, 1985.
- [15] L.Q. Li, Q.X. Tang, H.X. Li, X.D. Yang, W.P. Hu, Y.B. Song, Z.G. Shuai, W. Xu, Y.Q. Liu, D.B. Zhu, *Adv. Mater.* 19 (2007) 2613.
- [16] H. Tada, H. Touda, M. Takada, K. Matsushige, *Appl. Phys. Lett.* 76 (2000) 873.
- [17] H.B. Wang, D. Song, J.L. Yang, B. Yu, Y.H. Geng, D.H. Yan, *Appl. Lett. Phys.* 90 (2007) 253510.
- [18] S.M. Bayliss, S. Heutz, R. Cloots, R.L. Middleton, G. Rumbles, T.S. Jones, *Adv. Mater.* 12 (2000) 203.
- [19] Z.N. Bao, A.J. Lovinger, A. Dodabalapur, *Adv. Mater.* 9 (1997) 42.
- [20] T. Nishi, K. Kanai, Y. Ouchi, M.R. Willis, K. Seki, *Chem. Phys.* 325 (2006) 121.
- [21] H. Kawaguchi, M. Taniguchi, T. Kawai, *Appl. Phys. Lett.* 94 (2009) 093305.
- [22] M. Brumbach, D. Placencia, R. Armstrong, *J. Phys. Chem. C* 112 (2008) 3142.

removal. Additionally, most of the recent researches typically have used organic/polymer substance for the depositing materials [16].

In this report, we demonstrate high-resolution patterned inorganic Ag nanoparticulate electrodes and organic semiconductors using non-relief-lithography patterning technology for all printed organic thin film transistors (OTFTs). Using surface patterning of self-assembled monolayer (SAM) by direct deep-ultraviolet (DUV) light exposure, photoresist processing can be avoided and barrier-like structure for defining electrodes were fabricated from non-relief-lithography process [8]. Additionally, for fast and cost effective processing, dip-casting process was carried out by controlling withdrawal speed of the surface-patterned substrates. In particular, our emphasis is on identifying the physical conditions that ensure ideal processes for all printed OTFTs and electronics using the novel surface patterning process and dip-casting.

## 2. Experimental

Fig. 1 shows the experimental procedure which was used to obtain Ag nanoparticulate electrodes and all printed TFTs. A hydrophobic octadecyltrichlorosilane (OTS) SAM was formed by immersing the substrate into a 30 mM solution of OTS in hexane. Subsequently, ultrasonication process was performed and another OTS formation process was carried out for building dense and stable SAM. Spatial patterning of OTS covered substrates was achieved using DUV exposure through a quartz mask [17,18]. The DUV radiation was obtained from a low pressure mercury lamp with primary output wavelengths of 254 nm (90%) and 185 nm (10%). The 185 nm exposure results in rapid removal of the OTS SAM layer. Our preliminary measurement of contact angles from water droplet has shown 100° and 20° before and after OTS removal, respectively on SiO<sub>2</sub> surface. Deep ultraviolet light exposure was conducted by UV ozone cleaner (UV253H, Filgen, Japan).

Ag nanoparticulate solution including an average nanoparticle diameter of 10–20 nm was purchased from InkTec ([www.inktec.com](http://www.inktec.com)) Company. For controlling Ag ink viscosity, ethanol was added into the original solution and stirred at the temperature 60 °C for 2 h. The ink viscosity was measured by SV-10 (Sine-Wave vibro viscometer, A&D Company, Japan). Dip-casting process was performed to fabricate Ag electrodes using home-made dip-casting system with a stepping motor in air ambient at room temperature. Surface patterned substrates (patterned hydrophilic area on SiO<sub>2</sub>/Si) were fully immersed into the Ag nanoparticulate solution and withdrawn with a controlled speed. After waiting for 30 min, the patterned Ag electrodes were annealed with a temperature of 180 °C for 30 min on a hot plate in air ambient. The resistivity of Ag electrodes were averaged by measuring at least four point in a sample.

The bottom gate and bottom contact *all printed* OTFTs were fabricated on heavily doped p-type Si wafers with a 200 nm thermally grown SiO<sub>2</sub> layer. The Si wafer was used as both substrate and common gate electrode, while the SiO<sub>2</sub> layer acted as a gate dielectric layer. Using the non-relief patterned surface patterning, source/drain Ag electrodes for TFTs were fabricated on thermally oxidized silicon wafer by controlling various dip-casting parameters. For the organic and inorganic active layer deposition, two deposition methods such as an ink-jetting and a dip-casting were used, respectively. The solution-processed organic semiconductors, 6,13-bis(triisopropyl-silylethynyl) pentacene (TIPS-pentacene) [19], was prepared from 2 wt% chlorobenzene solution. After second surface patterning process on the pre-patterned Ag electrodes, active organic semiconductor layer deposition was performed by using piezoelectric ink-jet printing system (Unijet UJ2100). The piezoelectric ink-jet nozzle had a diameter of 50 μm (orifice size of 50 μm). The frequency of the jetting was 150 Hz and the diameter of the ink drop was approximately 30–50 μm. All the electrical measurements were performed using Keithley 4200-SCS in a dark and air ambient at room temperature.

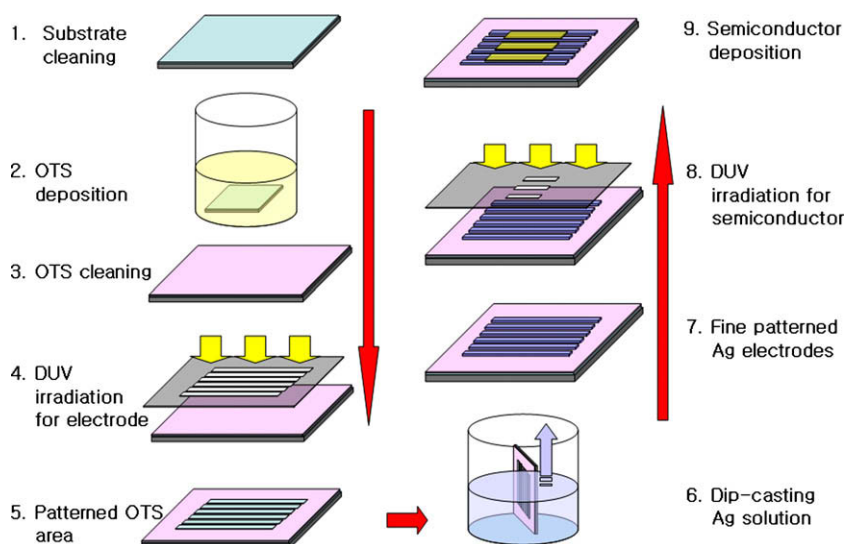


Fig. 1. Process flow of non-relief-lithography process for patterning solution-processed organic semiconductors.



### 3. Results and discussion

#### 3.1. Non-relief lithographic patterning of nanoparticulate Ag electrodes

To fabricate the barrier-like structure, a functional SAM (see experimental section) was patterned onto the substrate using deep ultra-violet (DUV) light exposure. The deposited nanoparticulate Ag solution can be steered into the desired hydrophilic areas by low surface energy SAMs and the barrier-like structure. Because this approach does not require photoresist coating, development, and removal processes, the non-relief patterning of a SAM can easily result in a fine-patterned barrier-like structure, making it cost effective. Direct DUV exposure of a SAM also offers great flexibility for two dimensional patterning. Patterning is not limited to surface energy effects and chemical reactivity or other surface properties can be used to meet the needs of specific applications [18]. DUV irradiation of silane SAMs typically induces a photochemical reaction which involves cleavage of Si–O or O–C bonds to form a reactive oxygen radical, which can react with atmospheric oxygen and moisture to form silanol or hydroxyl groups and produce a hydrophilic surface [20]. Thus, for a hydrophobic SAM, DUV irradiation can result in a hydrophobic to hydrophilic transformation.

Firstly, we investigated the influence of withdrawal speed of substrates which may be effective to control ink volume deposited on hydrophilic area. In dip-casting process, a patterned OTS substrate is immersed into Ag nanoparticulate solution for a certain time (around 1 min), and then withdrawn at a well-defined speed under controlled temperature and atmospheric conditions. Ethanol was mixed into original nanoparticulate Ag solution with a var-

ious volume ratio to control the ink viscosity. Fig. 2a shows optical micrographs of patterned Ag nanoparticulate electrode arrays from various withdrawal speeds. As shown in Fig. 2b, thinner thickness (thus smaller amount of ink in a hydrophilic area) was obtained from slower withdrawal speed because of stronger liquid–liquid interaction than liquid–solid (substrate) interaction [7,21]. The electrodes from lower withdrawal speed from 1–10 mm/min. typically have shown some aggregation of Ag nanoparticulates with no fine-patterning structures (less than 40  $\mu\text{m}$ ), which is possibly due to fast solidification of Ag nanoparticulates from small amount of solvent in thinner film. Additionally, a significant aggregation of the ink was also observed at faster withdrawal speed (Fig. 2a). Typically smaller volume of ink has led to thinner film and thus higher convective and Marangoni flow enhanced by the increased surface tension may induce faster evaporation of solvents in the films [22]. In our experiments, the thinner films from withdrawal speed from 1–10 mm/min. result in fast solvent evaporation before the splitting of ink, inducing incomplete dewetting or splitting. Fig. 2c indicates the averaged line width and pitch as a function of withdrawal speed from 10 times repeated experiments. The thicker films from the faster withdrawal speed are also problematic for fine-patterning process.

The influence of Ag ink viscosity was also studied while maintaining withdrawal speed of 50 mm/min. Ink viscosity was controlled by the addition of ethanol into original nanoparticulate Ag solution. High ink viscosity (>2 mPa s) typically has led to too thick film which is beyond the critical thickness  $H_c$  for fine-pattern splitting. In contrast, lower viscosity ink induced too thin film and thus fast evaporation of solvent occurred before the splitting of ink, resulting in incomplete dewetting. Similar to the

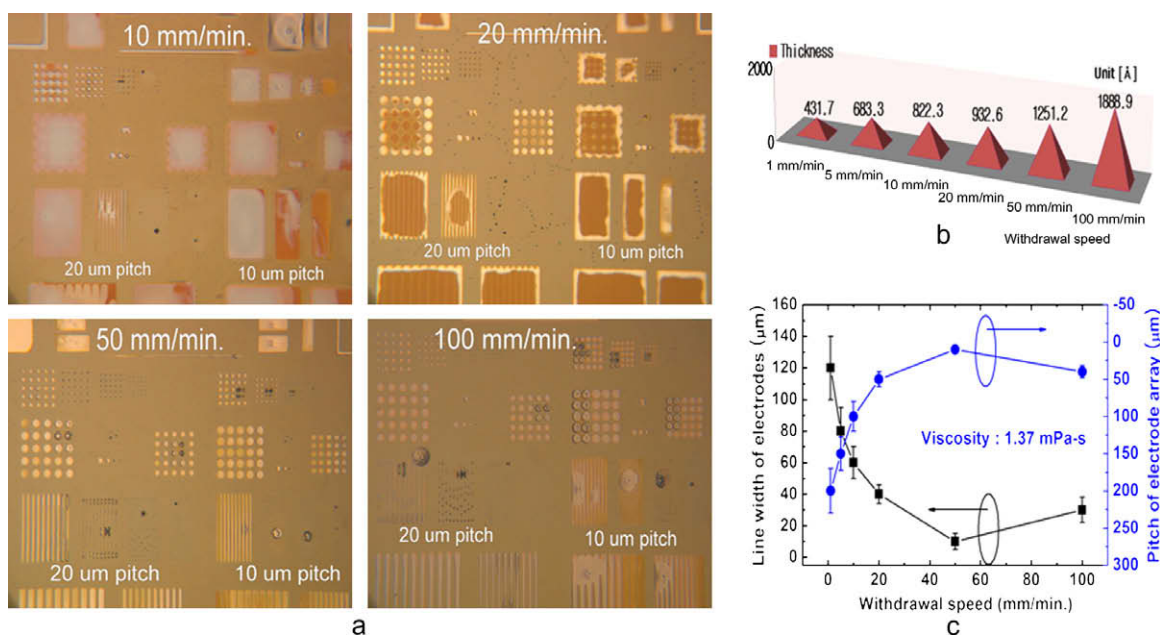


**Fig. 2.** (a) Optical micrographs of patterned Ag nanoparticulate electrodes from surface patterning and dip-casting process, (b) an averaged thickness of patterned electrodes as a function of withdrawal speed, and (c) an averaged line width and pitch of electrodes as a function of withdrawal speed.

influence of withdrawal speed, ink viscosity also appears to be closely related to the ink volume or liquid thickness on the pre-patterned area [23,24]. Fig. 3a and b demonstrates the optical and confocal micrographs which show relatively uniform distribution of dip-cast Ag electrode from the surface patterning and dip-casting process. These images may provide additional information regarding thickness uniformity of the self-formed Ag electrodes. The dip-casted Ag dots or line arrays from optimal conditions typically have shown an average thickness 120 nm with  $\pm 15$  nm variations and more than 80% uniformity. Fig. 3c shows an average limit of electrode resolution and pitch as a function of ink viscosity. Fig. 3d shows the resistivity of Ag electrodes as a function of electrode thickness and viscosity. For the application of printed electronics, the conductivity of electrodes is also critical for large area electronics and device performance. Typically, the direct printed Ag electrodes including thickness  $>50$  nm shows resistivity of low  $10^{-5} \Omega \text{ cm}$  ranges through annealing at  $180^\circ\text{C}$  for 30 min, which is a little bit higher or similar to that of vacuum deposited metal thin films.

From our experiments, the differential wettability from solution process seems to be mainly defined by contact angles and geometry of surface. Incomplete splitting of ink was typically observed in samples which had too fast/slow withdrawal speed and higher ink viscosity which are likely to related with volume of the ink solution on hydrophilic area. According fluid-dynamic model [25], in a homogeneous solid substrate, the contact angle  $\theta$  satisfies the Young equation [26].

$$\cos(\theta) = (\sigma_{VS} - \sigma_{LS})/\sigma_{LV}$$

where  $\sigma_{VS}$ ,  $\sigma_{LS}$ , and  $\sigma_{LV}$  are the vapor–solid, liquid–solid, and liquid–vapor interfacial tensions, respectively. In our preliminary experiments, the contact angles of  $100^\circ$  ( $\theta_8$ :

contact angle on hydrophobic area) and  $20^\circ$  ( $\theta_7$ : contact angle on hydrophobic area) were measured on hydrophobic area (OTS SAM) and patterned hydrophilic area, respectively. During the dip-casting process, the hydrophilic stripes are completely covered by Ag ink, and the contact lines of this channel are located at the surface domain boundaries. As more Ag ink adds onto the hydrophilic stripes, the thickness of ink increases but they still have the shape of cylindrical or spherical caps and their contact lines are still pinned at the domain boundaries, resulting in increased contact angles, which no longer satisfies the Young equation. With appropriate ink volume (from withdrawal speed/ink viscosity), the contact angle of Ag ink at the boundaries are well consistent with differential wettability condition [27] such as

$$\theta_8 < \theta < \delta_\gamma$$

If the ink volume on the hydrophilic stripes is more than a critical value (or thickness  $H_c$ ), the contact angle exceeds  $\theta_8$ , developing a bulge as soon as the contact angle  $\theta > \theta_8$ . If the two neighboring bulges are enough close to merge or bridge, the patterned Ag electrodes typically have shown instable patterning properties. This is well consistent with our observation which indicates narrow process-window in fine-pitch electrode arrays as well as instable Ag ink patterns from too fast withdrawal speed and high ink viscosity.

As well as the effect of contact angle change, the patterning resolution during dip-casting process seems to be also affected by polarity and vapor pressure of solvents. Typically, a polar solvent is affected more by a hydrophobic surface, resulting in higher resolution patterning possible [14]. The flowing speed of the Ag nanoparticulate solution on the heterogeneous surface should be faster than that of solvent evaporation speed, which can steer the liquid into

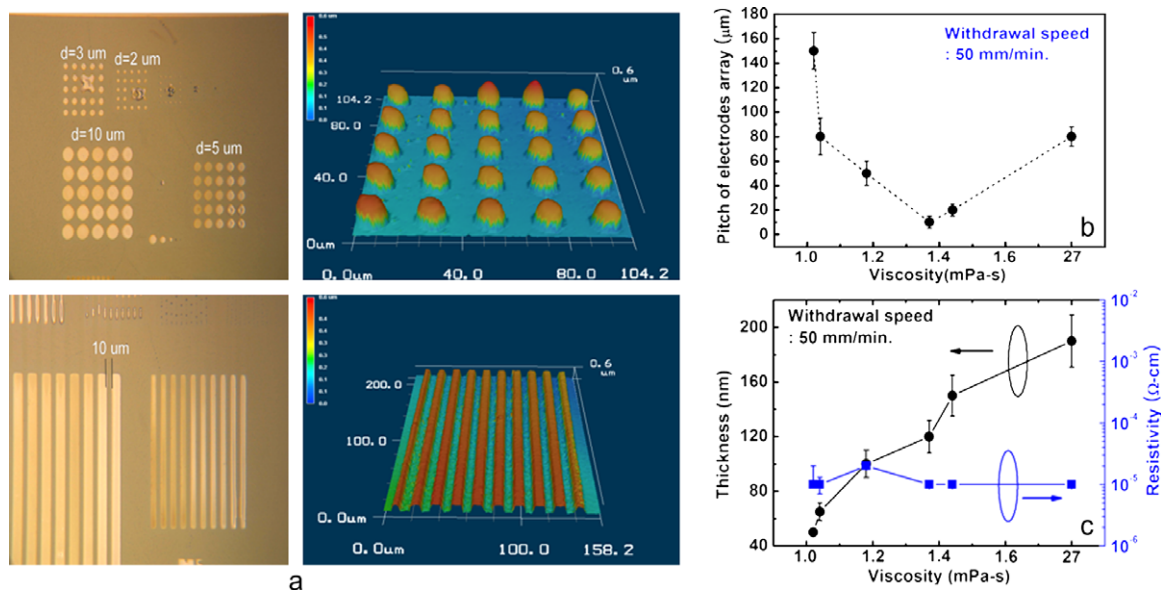


Fig. 3. (a) Optical micrographs (left) and confocal 3D micrographs (right) of patterned Ag nanoparticulate electrodes, (b) an averaged pitch of patterned electrodes as a function of ink viscosity, and (c) an averaged thickness and resistivity of patterned electrode as a function of ink viscosity.

desired area before solidification of the ink solution on hydrophobic area. In our experiments, ethanol is continuously evaporated during the dip-cast process, inducing change of interface/surface energy of the liquid on the hydrophilic stripes. Therefore, if the solidification exceeds a critical value before splitting occurred, the interaction energy for repelling between the liquid and hydrophobic solid is critically diminished, resulting in poor dewetting properties. Therefore, solvents including lower vapor pressure may limit the resolution of electrode arrays due to their faster evaporation speed. For the results described here, it is likely that patterning geometry, withdrawal speed, ink viscosity, solvent polarity, and vapor pressure are some of the key factors for the simple and high-resolution Ag nanoparticulate patterning process.

Fig. 4 shows simple comparison between direct printed Ag nanoparticulate electrodes by well-controlled ink-jet printing including ink drop size of around  $35\ \mu\text{m}$  on non-surface treated substrate and dip-cast Ag nanoparticulate electrodes on differentially patterned substrate using the non-relief-lithography patterning technology. As shown in this figure, while it may be difficult to obtain high resolution and fine-pitch electrodes on untreated surface even using a well-controlled direct ink-jet printing due to the larger ink-droplet and the difficulty of controlling ink spread, the dip-cast electrodes with non-relief patterned lithography patterning have shown high-resolution and fine-pitch, implying simple and high-resolution patterning possible.

### 3.2. All printed organic thin film transistors

The bottom gate and bottom contact *all printed OTFTs* were fabricated on heavily doped p-type Si wafers with a 200 nm thermally grown  $\text{SiO}_2$  layer. The Si wafer used as both substrate and common gate electrode, while the  $\text{SiO}_2$  layer acted as a gate dielectric layer. Using the non-relief patterned surface patterning, source/drain Ag electrodes for TFTs were built on thermally oxidized silicon wafer. Fig. 5a shows the optical micrograph of fabricated source and drain electrodes on  $\text{SiO}_2$  layer. The channel length of 5–10  $\mu\text{m}$  were easily achieved using the non-relief-patterned surface patterning and dip-casting process. To achieve fine patterning of organic and inorganic semiconductors, *second* non-relief-patterned surface patterning

was performed with the identical process of first surface patterning, resulting in a new barrier structure for confining semiconductor solutions.

Firstly, TIPS-pentacene from 2 wt% chlorobenzene solution was ink-jetted over the pre-patterned barrier-like structure. The schematic diagram of fabricated bottom contact and bottom gate TIPS-pentacene OTFTs was demonstrated (bottom of Fig. 5b). As shown in Fig. 5b, dropped TIPS-pentacene ink was automatically confined within the patterned OTS area. The diameter of dropped ink was around  $30\ \mu\text{m}$  with a volume of 30 pl. Fig. 5c shows  $\sqrt{I_D}$  and  $\log(I_D)$  versus  $V_{GS}$  characteristics for  $V_{DS} = -40\ \text{V}$ , and  $I_D$  versus  $V_{DS}$  characteristics for the TIPS-pentacene OTFT with a surface energy patterned source–drain electrode and active layer deposited from a 2 wt% chlorobenzene solution. All electrical measurements were performed in an air ambient at room temperature. The device had a gate length of  $10\ \mu\text{m}$ , a gate width of  $100\ \mu\text{m}$ , and a 200 nm-thick silicon dioxide gate dielectric. The electrical characteristics such as field-effect mobility of about  $0.03\text{--}0.06\ \text{cm}^2/\text{V s}$ , on/off current ratios  $> 106$ , and subthreshold slope  $< 0.7\ \text{V/decade}$  were obtained from more than 20 devices measurements. The typical performance of all printed OTFTs fabricated from the surface patterning and dip-casting process was similar to that of same configuration OTFTs ( $0.02\text{--}0.06\ \text{cm}^2/\text{V s}$ ) from ink-jet printed semiconductors and photolithographically patterned bottom contact electrodes [14,28,29].

Although we demonstrate non-relief-lithography-patterned Ag nanoparticulate source/drain electrodes based OTFTs, adopting the novel patterning technology to polymer substrate or organic dielectric is still problematic due to the difficulty of chemical reaction between OTS and polymer substance. Recently, a successful non-relief-lithography patterning of organic semiconductors on polymer gate dielectric materials was reported using a composite silane SAM layers [30]. The composite SAM layer was used as a base layer to promote dense and uniform formation of phenyl groups, which cannot be achieved by direct reaction between the SAMs and the polymer surface. The composite layer also contains alkyl groups which lead a hydrophobic state. Additionally, in our recent experiments, differential surface states were successfully obtained on polymer substrates and dielectric materials using the same non-relief-lithography patterning

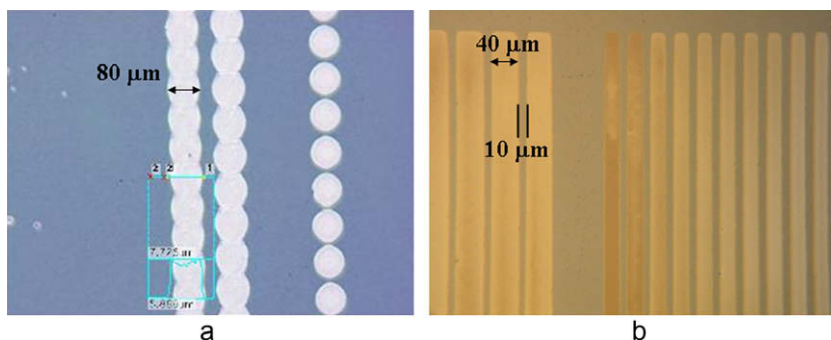
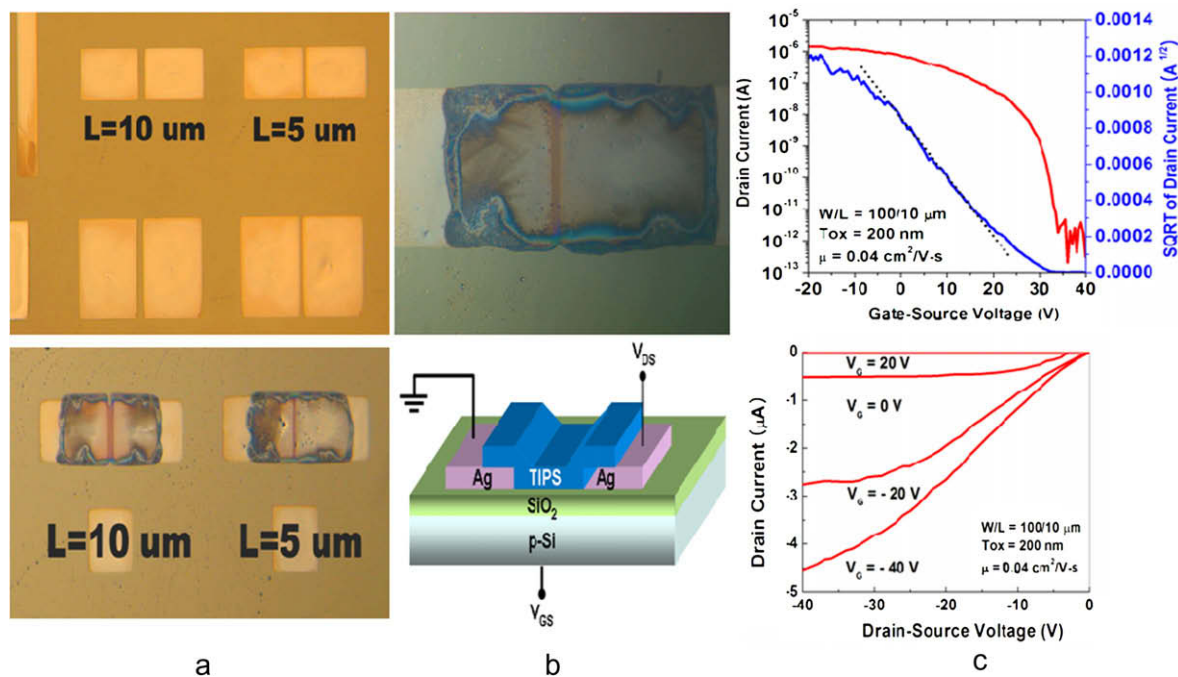


Fig. 4. Optical micrographs of (a) direct ink-jet printed Ag nanoparticulate electrodes on untreated surface and (b) patterned Ag nanoparticulate electrodes using the non-relief patterned lithography patterning and dip-casting.



**Fig. 5.** (a) Optical micrograph of patterned Ag nanoparticulate source/drain electrodes for unit TFT and simple circuit from surface patterning and dip-casting process, (b) optical micrographs of ink-jet printed TIPS-pentacene on the patterned electrodes, and (c) electrical characteristics of all printed TIPS-pentacene OTFT ( $\sqrt{I_{DS}} - V_{GS}$  and  $\log(I_{DS}) - V_{GS}$  ( $V_{DS} = -40 \text{ V}$ ),  $I_{DS} - V_{DS}$ ) from surface patterning and dip-casting.

process and a specially developed surface surfactant. Based on the recently developed technologies and materials, we believe that forming multi-stacking layers will be possible from the non-relief patterning technology and dip-casting for all printed high-resolution flexible OTFTs and electronics.

#### 4. Conclusions

In summary, using a surface patterning, photoresist-free process and simple dip-casting, we have fabricated reproducible all solution-processed transistors with patterned active layers and source/drain electrodes. The influences of ink viscosity, deposition speed, solvent polarity, and boiling point were systematically investigated to obtain high-resolution and fine-pitch printed Ag nanoparticulate electrodes. Based on the patterned electrodes, we have demonstrated all printed high-resolution and short channel OTFTs. This simple patterning technology for solution-processed inorganic and organic materials can provide not only high resolution but also reproducible and high performance flexible printed electronics. This work demonstrates that surface energy patterning technology may provide a path to low-cost and high performance all printed electronics.

#### Acknowledgements

The authors gratefully acknowledge financial support by a grant (F0004024-2008-31) from Information Display

R&D Center, one of the 21st Century Frontier R&D Program funded by the Ministry of Knowledge Economy of Korean government.

#### References

- [1] T.-W. Lee, Y. Byun, B. Koo, I.-N. Kang, Y.-Y. Lyu, C.H. Lee, L. Pu, S.Y. Lee, *Adv. Mater.* 17 (2005) 2180.
- [2] D. Collings, Patel, *Handbook of Liquid Crystal Research*, Oxford University Press, New York, 1997.
- [3] Y.G.H. Gelinck, T.C.T. Geuns, D.M. de Leeuw, *Appl. Phys. Lett.* 77 (2000) 1487.
- [4] S. Subramanian, S.K. Park, S.R. Parkin, V. Podzorov, T.N. Jackson, J.E. Anthony, *J. Am. Chem. Soc.* 130 (2007) 2706.
- [5] W.U. Huynh, J.J. Dittmer, A.P. Alivisatos, *Science* 295 (2002) 2425.
- [6] S.A. McDonald, G. Konstantatos, S. Zhang, P.W. Cyr, E.J.D. Klem, L. Levina, E.H. Sargent, *Nat. Mater.* 4 (2005) 138.
- [7] J.Z. Wang, Z.H. Zheng, H.W. Li, W.T.S. Huck, H. Sirringhaus, *Nat. Mater.* 3 (2004) 171.
- [8] S.K. Park, D.A. Mourey, S. Subramanian, J.E. Anthony, T.N. Jackson, *Adv. Mater.* 20 (2008) 4145.
- [9] D.J. Gundlach, J.E. Royerl, S.K. Park, S. Subramanian, L.C. Teague, B.H. Hamadani, O.D. Jurchescu, A.J. Moad, O. Kirillov, C.A. Richter, J.G. Kushmerick, L.J. Richter, T.N. Jackson, J.E. Anthony, *Nat. Mater.* 7 (2008) 216.
- [10] K.J. Lee, M.J. Motala, M.A. Meitl, W.R. Childs, E. Menard, A.K. Shim, J.A. Rogers, R.G. Nuzzo, *Adv. Mater.* 17 (2005) 2332.
- [11] J.A. Wigenius, M. Hamedi, O. Ingansa, *Adv. Funct. Mater.* 18 (2008) 1.
- [12] S.C.B. Mannsfeld, A. Sharei, S. Liu, M.E. Roberts, I. McCulloch, M. Heeney, Z. Bao, *Adv. Mater.* 20 (2008) 4044.
- [13] J.Z. Wang, J. Gu, F. Zenhausern, H. Sirringhaus, *Appl. Phys. Lett.* 88 (2006) 133502.
- [14] C.R. Kagan, T.L. Breen, L.L. Kosbar, *Appl. Phys. Lett.* 79 (2001) 3536.
- [15] J.A. Rogers, Z. Bao, K. Baldwin, A. Dodabalapur, V.R. Raju, H. Katz, K. Amundson, J. Ewing, P. Drzaic, *Proc. Natl. Acad. Sci.* 98 (2001) 4835.
- [16] E. Menard, J. Park, S. Jeon, D. Shir, Y. Nam, M. Meitl, J.A. Rogers, *Chem. Rev.* 107 (2007) 1117.

- [17] A. Kyveris, E. Maruscak, M. Senchyna, *Nuclei Acids Res.* 24 (1996) 3040.
- [18] A. Brechling, M. Pohl, U. Kleineberg, U. Heinzmann, J. Biotechnol. 112 (2004) 115.
- [19] S.K. Park, D.A. Mourey, J.E. Anthony, T.N. Jackson, *Appl. Phys. Lett.* 91 (2007) 063514.
- [20] C.S. Dulcey, J.H. Georger, V. Krauthamer, D.A. Stenger, T.L. Fare, J.M. Calvert, *Science* 252 (1991) 551.
- [21] M. Brinkmann, R. Lipowsky, *J. Appl. Phys.* 92 (2002) 4296.
- [22] R.D. Deegan, O. Bakajin, T.F. Dupont, G. Huber, S.R. Nagel, T.A. Witten, *Nature* 389 (1997) 827.
- [23] K. Kargupta, A. Sharma, *J. Chem. Phys.* 116 (2002) 3042.
- [24] J. Silver, Z.H. Mi, K. Takamoto, P. Bungay, J. Brown, A. Powell, *J. Colloid, Interface Sci.* 219 (1999) 81.
- [25] H. Gau, S. Herminghaus, P. Lenz, R. Lipowsky, *Science* 283 (1999) 46.
- [26] J.S. Rowlinson, B. Widom, *Molecular Theory of Capillarity*, Clarendon, Oxford, 1982.
- [27] P. Lenz, R. Lipowsky, *Phys. Rev. Lett.* 90 (1998) 1920.
- [28] H. Siringhaus, T. Kawase, R.H. Friend, T. Shimoda, M. Inbasekaran, W. Wu, E.P. Woo, *Science* 290 (2000) 2133.
- [29] Y.H. Kim, S.K. Park, S.G. Park, M.K. Han, J.I. Han, *ECS Trans.* 16 (2008) 267.
- [30] T. Minari, M. Kano, T. Miyadera, S. Wang, Y. Aoyagi, K. Tsukagoshi, *Appl. Phys. Lett.* 94 (2009) 093307.

Until now, PCE up to 5% has been achieved from the BHJ of poly(3-hexylthiophene) (P3HT) blended with PCBM [1]. Although the transport properties have been dramatically improved by vertical phase separation of both donor and acceptor due to the self-organization effect [2–5], they still lack the absorption in the red and infrared regions. Therefore, great deal efforts have been undertaken to enhance the  $J_{SC}$  of solar cells by enhancing the absorption spectra of active layers. Recently, much work has been focused on synthesis the conjugated polymers [6–13]. Among several types of organics materials, polymer with electron donor–acceptor architectures is one of the most efficient ways to synthesize the narrow bandgap polymers. The effect of intramolecular charge transfer between the electron donor and acceptor units has been found in the polymers with donor–acceptor architectures leading to a narrow bandgap [14–21].

Recently, much BHJ polymer solar cells using polyfluorene based alternating copolymers as donor have been reported due to their high charge carrier mobility [22,17]. However, polyfluorene copolymers in general have high bandgaps giving blue-shift optical absorption and hence have limited the photocurrent generation. For example, poly[9,9'-dioctyl-fluorene-co-bithiophene] (F8T2) only absorbs light at wavelengths less than 500 nm [23]. Even though F8T2 exhibits excellent thermo tropic liquid crystallinity allowing better chain packing via self-assembly [24], the poor absorption still depresses the extraction of photocurrent dramatically. In this article, the BHJ device performance of a low-bandgap polyfluorene copolymer which comprises the phenothiazine units is reported. The copolymer used for here is referred to as PF-PThCVPTZ. With the incorporation of phenothiazine units into PF,

the absorption can be stretched due to the donor–acceptor structure.

## 2. Experimental

### 2.1. Synthetic procedures

#### 2.1.1. Synthesis

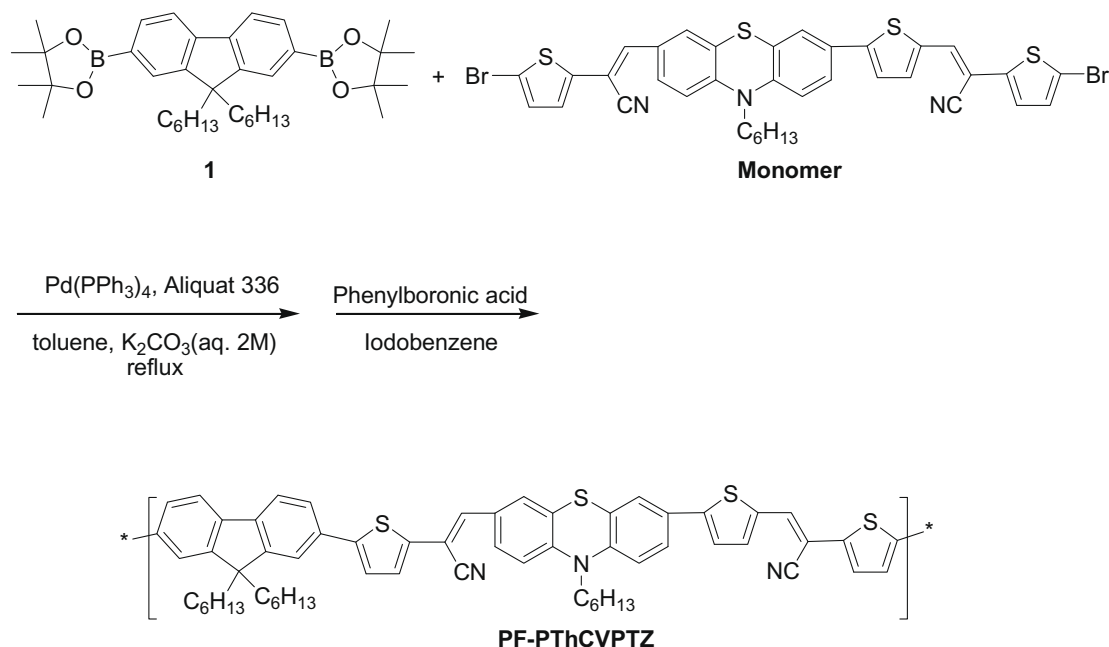
Monomer was synthesized according to a reported procedure [25], and the characterization is described as follows. The copolymer PF-PThCVPTZ is shown in Scheme 1, and this synthetic procedure is described as follows.

#### 2.1.2. Monomer

Yield: 53%.  $^1\text{H}$  NMR ( $\text{CDCl}_3$ , ppm),  $\delta$ : 7.72 (dd,  $J = 8.7$ , 1.8 Hz, 1H), 7.45–7.36 (m, 3H), 7.29–7.18 (m, 3H), 7.07–7.01 (m, 5H), 6.79 (d,  $J = 8.7$  Hz, 2H), 3.80 (t,  $J = 7.2$  Hz, 2H), 1.80 (m, 2H), 1.45–1.14 (m, 6H), 0.89 (m, 3H).  $^{13}\text{C}$  NMR ( $\text{CDCl}_3$ , ppm),  $\delta$ : 148.11, 146.00, 143.66, 140.67, 140.14, 138.08, 135.80, 134.54, 132.05, 131.00, 130.89, 130.67, 128.54, 128.11, 127.49, 126.56, 125.31, 124.32, 123.88, 123.53, 122.87, 116.56, 116.49, 115.43, 114.99, 112.64, 112.62, 102.51, 100.94, 48.00, 31.35, 29.67, 26.49, 22.59, 13.98. MS (EI):  $m/z$  [ $M^+$ ] 788.94, calcd  $m/z$  [ $M^+$ ] 789.0. Anal. Calcd for  $\text{C}_{36}\text{H}_{27}\text{Br}_2\text{N}_3\text{S}_4$ : C, 54.75; H, 3.45; N, 5.32. Found: C, 55.19; H, 3.90; N, 4.82.

#### 2.1.3. General procedure for the synthesis of PF-PThCVPTZ

The synthetic route of polymers is shown in Scheme 1. The polymerizations was carried out through the palladium(0)-catalyzed Suzuki coupling reactions. Into 50 mL of two-neck flask, 1 equiv of monomer and 1 equiv of 2,7-bis-(4,4,5,5-tetramethyl-1,3,2-dioxaborolan-2-yl)-9,9-



Scheme 1. Synthetic routes of PF-PThCVPTZ.

dihexylfluorene (1) were added in 10 mL of anhydrous toluene. The Pd(0) complex, Pd{P(*p*-tolyl)}<sub>3</sub> (1 mol%), was transferred into the mixture in a dry environment. Then, 2 M aqueous potassium carbonate and the phase transfer catalyst, i.e., aliquat 336 (several drops), were subsequently transferred via cannula into the previous mixture under nitrogen. The reaction mixture was stirred at 90 °C for 2 days, and then the excess amount of iodobenzene and phenylboronic acid, the end-capper, dissolved in 1 mL of anhydrous toluene was added and stirring for 4 h, respectively. The reaction mixture was cooled to 50 °C and added slowly into a vigorously stirred mixture of 300 mL of methanol. The polymers were collected by filtration and reprecipitation from methanol. The crude polymers were further purified by washing with acetone for 3 days in a Soxhlet apparatus to remove oligomers and catalyst residues. The resulting polymers were soluble in common organic solvents.

## 2.2. Fabrication of photovoltaic devices

The PV devices in this study consists of a layer of PF-PThCVPTZ:PCBM blend thin film sandwiched between transparent anode indium tin oxide (ITO) and metal cathode. Before device fabrication, the ITO glasses (1.5 × 1.5 cm<sup>2</sup>) were ultrasonically cleaned in detergent, de-ionized water, acetone and isopropyl alcohol before the deposition. After routine solvent cleaning, the substrates were treated with UV ozone for 15 min. Then, a modified ITO surface was obtained by spin-coating a layer of poly(ethylene dioxythiophene): polystyrenesulfonate (PEDOT:PSS) (~30 nm). After baking at 130 °C for 1 h, the substrates were then transferred into a nitrogen-filled glove box. The polymer PV devices were fabricated by spin-coating blend of PF-PThCVPTZ:PCBM on the PEDOT:PSS modified ITO surface. Subsequently, a 30 and 100 nm thick of calcium and aluminum was thermally evaporated under vacuum at a pressure below 6 × 10<sup>-6</sup> Torr through a shadow mask. The active area of the device was 0.12 cm<sup>2</sup>. In the hole-only devices, the MoO<sub>3</sub> was used to replace Ca with higher work function ( $\Phi = 5.3$  eV), which is a good hole injection contact for PF-PThCVPTZ:PCBM [26]. The MoO<sub>3</sub> was thermally evaporated with a thickness of 20 nm and then capped with 50 nm of Al. For the electron-only devices, PEDOT:PSS layer was replaced with CsCO<sub>3</sub> ( $\Phi = 2.9$  eV) which has been used as an efficient electron injection layer [27]. The Cs<sub>2</sub>CO<sub>3</sub> was thermally evaporated with a thickness of 2 nm. The active layers were annealed at 130 °C for 20 min before the hole and electron-only devices were fabricated.

## 2.3. Characterization of polymer films and PV devices

Cyclic voltammetry (CV) studies were performed with a three-electrode cell with 0.1 M LiClO<sub>4</sub>/ACN using ITO as the working electrode, a platinum sheet as the counter electrode, and nonaqueous Ag/Ag<sup>+</sup> (containing 0.01 M AgNO<sub>3</sub> and 0.1 M TBAClO<sub>4</sub> in ACN) as the reference electrode. For measuring absorption and photoluminescence (PL) emission properties of polymer films, samples were fabricated on a glass substrate. The UV–visible absorption spec-

tra were measured using a Jasco-V-670 UV–visible spectrophotometer. PL spectra were obtained using a Hitachi F-4500 photoluminescence. Surface morphologies were observed by an atomic force microscopy (AFM, Digital instrument NS 3a controller with D3100 stage). The thickness of all polymer films was measured using a surface profiler (Alpha-step IQ, KLA Tencor). Current–voltage (*J*–*V*) characteristics were measured in the glove box under nitrogen atmosphere with simulated AM 1.5 G irradiation at 100 mW/cm<sup>2</sup> using a xenon lamp based solar simulator (Thermal Oriel 1000 W). The light intensity was calibrated by a mono-silicon photodiode with KG-5 color filter (Hamamatsu, Inc.). The external quantum efficiency (EQE) action spectrum was obtained at short-circuit condition. The light source was a 450 W Xe lamp (Oriel Instrument, model 6266) equipped with a water-based IR filter (Oriel Instrument, model 6123NS). The light output from the monochromator (Oriel Instrument, model 74100) was focused onto the photovoltaic cell under test.

## 3. Results and discussion

The CV was performed to investigate the electronic state of the PF-PThCVPTZ. As shown in Fig. 1a, the CV of PF-PThCVPTZ presents an oxidation process ( $E_{\text{ox}}^{1/2} = 0.89$  V vs. Ag/Ag<sup>+</sup>) and a reduction process ( $E_{\text{red}}^{1/2} = -1.08$  V). Furthermore, the  $E_{\text{ox}}^{\text{onset}}$  and  $E_{\text{red}}^{\text{onset}}$  are 0.78 and -0.81 V, respectively, which allows us to calculate the highest molecular orbital (HOMO) and lowest molecular orbital (LUMO) according to following equation [28]:  $E_{\text{HOMO/LUMO}} = [-(E_{\text{onset}} - 0.45) - 4.8]$  eV. The factor of 0.45 and 4.8 are derived from the formal potential for ferrocene vs. Ag/Ag<sup>+</sup> and the energy level of ferrocene below the vacuum. On the basis of these electrochemical data, the HOMO and LUMO levels can be defined as -5.13 and -3.54 eV. Therefore, the bandgap offset between the LUMOs of PF-PThCVPTZ and PCBM is enough for electrons to be driven forward. Moreover, the polymer also reveals a multiply

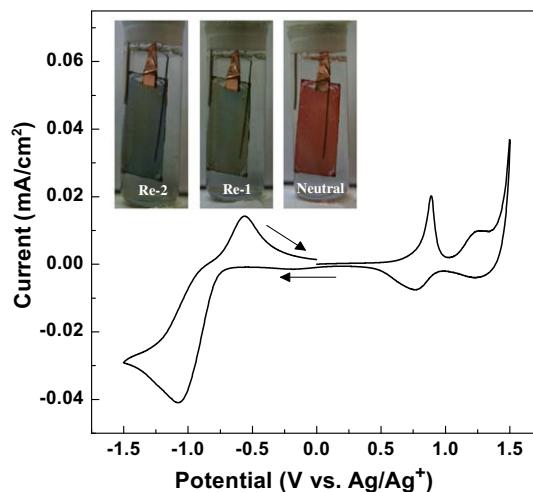


Fig. 1. Cyclic voltammogram of PF-PThCVPTZ film cast on a platinum wire in 0.1 M LiClO<sub>4</sub>/acetonitrile at 50 mV/s. (Inset: picture of the polymer film on the ITO electrode at different coloration states.)

colored electrochromic property. Fig. 1a shows the photographs of PF-PThCVPTZ films in uncharged (neutral, red), half (Re-1, green) and full (Re-2, blue) reduction states. The film colors are homogeneously distributed across the electrode surface and the color changes are easily detected by the naked eye.

The normalized optical absorption spectra of the PF-PThCVPTZ in solution and solid film and PL emission spectra of pristine polymer and their blend films with PCBM are depicted in Fig. 2. The solid film shows similar absorption pattern compared with the one of solution. However, slight red-shift still can be observed due to the interchain association and aggregation in the solid state. The PF-PThCVPTZ

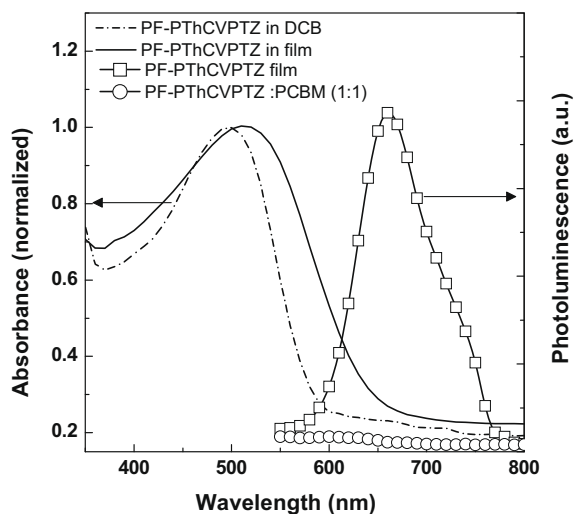


Fig. 2. UV-vis spectrum in DCB (dash line) and in the solid state (solid line), photoluminescence in solid state ( $\square$ ) and photoluminescence quenching for PF-PThCVPTZ:PCBM (1:1) ( $\circ$ ).

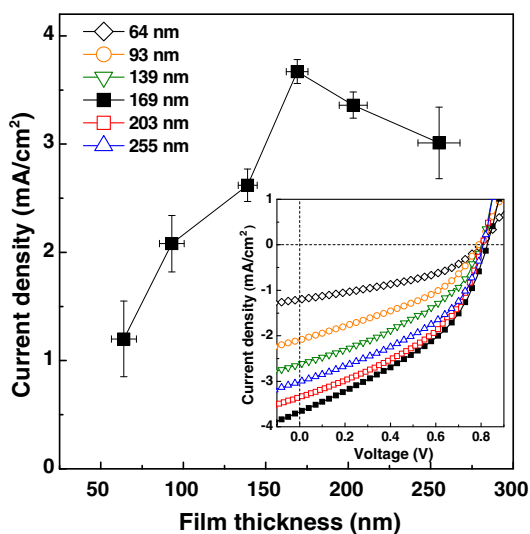


Fig. 3.  $J_{sc}$  plotted as a function of the thickness of active layer for the PF-PThCVPTZ:PCBM solar cells. (Inset: corresponding  $J$ - $V$  characteristics.)

film reveals a spectral absorption with a peak at 510 nm and an absorption onset at 645 nm. Furthermore, the corresponding PL emission maxima  $\lambda_{em}$  of PF-PThCVPTZ is centered at 660 nm. The PL emission is significantly quenched by the addition of 50 wt% PCBM. This highly efficient photoluminescence quenching is the consequence of ultrafast photoinduced charge transfer from the polymer to PCBM. Based on these characterizations, the copolymer is an excellent candidate to fabricate the photovoltaic devices.

The current density for the devices with varying active layer thickness are plotted in Fig. 3. The devices were fabricated by spin coating a solution of PF-PThCVPTZ/PCBM (1:1 in weight, 4 mg/mL) dissolved in 1,2-dichlorobenzene (DCB). The  $V_{oc}$  remains unchanged at about 0.8 V on changing the active layer thickness as shown in the inset. However, the  $J_{sc}$  and the PCE of the devices vary significantly with thickness. The  $J_{sc}$  varies from as low as 1.20 mA/cm<sup>2</sup> (for the device with active layer thickness,

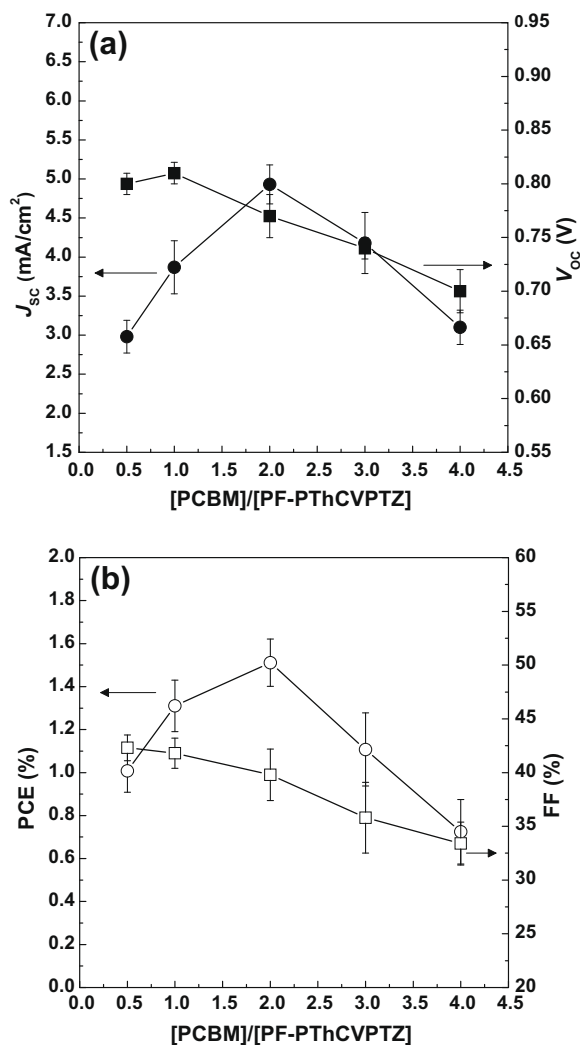


Fig. 4.  $J_{sc}$ ,  $V_{oc}$ , FF and PCE plotted as a function of the composition for the PF-PThCVPTZ:PCBM solar cells.



$t = 64$  nm) to as high as  $3.67$  mA/cm<sup>2</sup> ( $t = 170$  nm) and back to  $3.0$  mA/cm<sup>2</sup> ( $t = 255$  nm). The increased  $J_{SC}$  is contributed from the larger absorbance with thicker active layer. However, the  $J_{SC}$  decreases with a thickness larger than  $169$  nm due to the large series resistance and poor charge transport leading to a serious recombination [29]. An efficiency of  $1.23\%$  is achieved for the device with  $t = 170$  nm.

Fig. 4 shows the performance parameters of the measured devices, namely  $J_{SC}$ ,  $V_{OC}$ , FF and PCE as a function of PCBM weight ratios. First, the  $J_{SC}$  increases from  $2.98$  for the device with containing  $33$  wt% PCBM to  $3.87$ , and  $4.93$  mA/cm<sup>2</sup> for those containing  $50$  and  $66$  wt% PCBM. However, the  $J_{SC}$  decreases with a larger PCBM weight ratio as shown in Fig. 3a which means that a higher PCBM weight ratio leads to an imbalanced mobility between donor and acceptor, thus impeding the charge transport. Second, the  $V_{OC}$  and the FF strongly decrease with PCBM loading, resulting in a doubling of the calculated PCE when increasing the PCBM concentration from  $33$  to  $80$  wt%. According to our previous work [30], we have found that the values for  $V_{OC}$  and FF based on polyfluorene copolymer

decrease monotonically with increasing fullerene content in the BHJ films. This can be rationalized by the incomplete charge generation and transport resulted from the aggregation of the large amount of fullerenes [31]. The best cell has an active layer thickness of about  $180$  nm, containing  $66$  wt% of PCBM with a  $J_{SC}$  of  $4.93$  mA/cm<sup>2</sup>, a  $V_{OC}$  of  $0.77$  V, a FF of  $40\%$ , and a PCE of  $1.51\%$ .

In order to control the morphology of the blending films, we investigated the effect of solvents with different boiling points. Fig. 5 compares the morphology of the films cast from chloroform (CF), chlorobenzene (CB), DCB and 1,2,4-trichlorobenzene (TCB) with the boiling points of  $60$ ,  $132$ ,  $180$  and  $218$  °C, respectively. The images are obtained in tapping mode for a  $2 \times 2$  μm<sup>2</sup> surface area. It can be found the films spin-cast from CB, DCB and TCB show a coarse chainlike feature stretching across the surfaces. With higher boiling point, the chainlike feature is more obvious and the root mean square (RMS) also increases from  $4.3$  (for the film cast from CB) to  $7.8$  (TCB). These chainlike features are originated from the strong  $\pi$ - $\pi$  stacking of the polymer chains which is believed to enhance the charge transport [32,33]. This feature

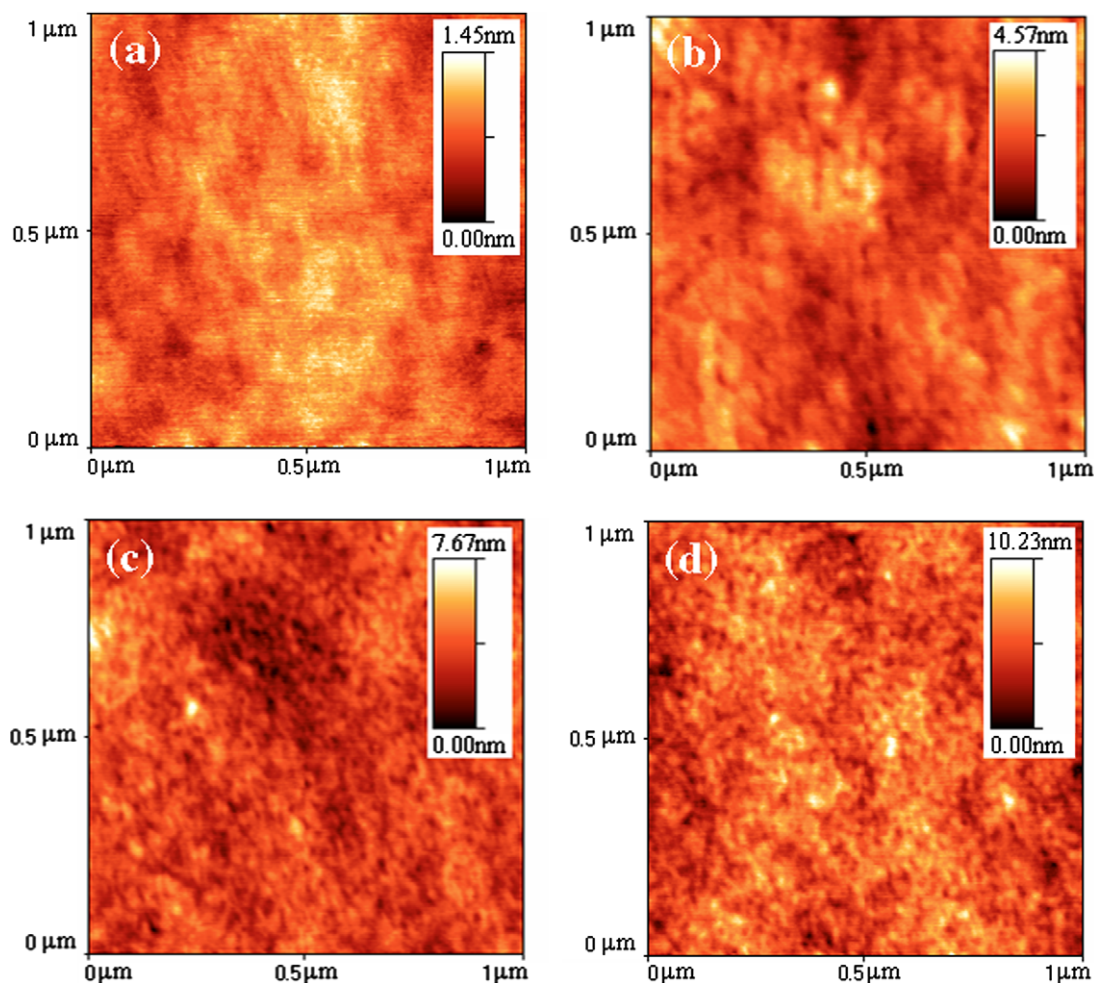


Fig. 5. AFM images of the blended films cast from (a) CF, (b) CB, (c) DCB and (d) TCB.

is well known and easily reproducible for the P3HT:PCBM blends using slow growth with high boiling point solvent such as TCB or DCB. In contrast, the film prepared from CF solution appears a very smooth surface without apparent nanostructure. Although CF is a good solvent for PF-PThCVPTZ, however, its low boiling point and rapid evaporation limit the time for crystallization during the spin-coating process.

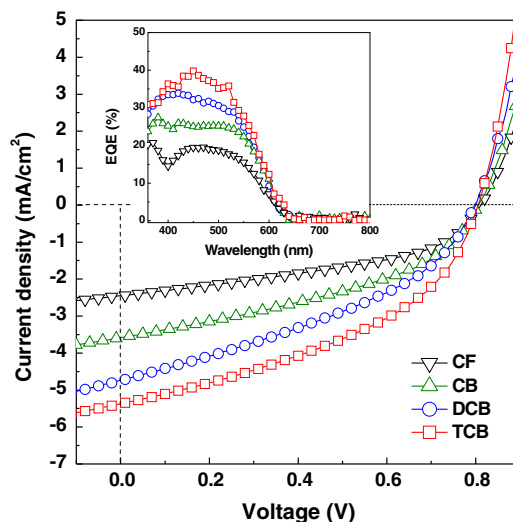
To further understand the dependence of charge transfer properties on morphologies that were introduced by varying the solvents, we have performed dark current measurements on hole-only and electron-only devices based on the blend films. The charge mobilities were calculated by space-charge limited current (SCLC) [34]. The dark current is given by  $J = 9\epsilon_0\epsilon_r\mu V^2/8L^3$ , where  $\epsilon_0\epsilon_r$  is the permittivity of the polymer,  $\mu$  is the carrier mobility, and  $L$  is the device thickness. The hole and electron mobilities of the blend films prepared from different solvents are summarized in Table 1. For the device made by CF have the lowest hole and electron mobility. Overall, the largest mobility can be found in the devices fabricated from TCB. The hole and electron mobility up to  $1.93 \times 10^{-8}$  and  $2.41 \times 10^{-8} \text{ m}^2 \text{ V}^{-1} \text{ s}^{-1}$  is observed. Furthermore, we observed more balanced charge mobility ( $\mu_h/\mu_e = 0.8$ ) in the film cast from TCB which can enhance the photocurrent.[35,36] For both DCB and TCB (which has a higher boiling point) it takes 10–15 min for the film to dry, while films cast from CF would dry within a few seconds of spinning. Therefore, the molecules in TCB can self-organization over a long time to form a thermodynamically favored structure leading to higher charge mobility [37,38].

Fig. 6 shows the  $J$ - $V$  curves and EQE of the PV devices fabricated from various solvents. The  $J_{SC}$  values of the devices fabricated from CF, CB, DCB and TCB are 2.45, 3.58, 4.73 and  $5.37 \text{ mA/cm}^2$ , and the FF values are 45.4, 41.4, 38.3 and 43.0%, respectively. The  $V_{OC}$  values of all cases are almost the same (0.80 V). As a result, the PCE of 1.84% is the highest among these devices which is obtained from TCB. The highest  $J_{SC}$  of device fabricated from TCB can be realized by the slow growth effect which provides a charge transport channel formed from self-organization leading to a higher photocurrent. This is supported by EQE characterization. After measuring the  $J$ - $V$  curves, the devices were encapsulated in a nitrogen-filled glove box, and the EQE of the devices were measured in air. As shown in the inset, the devices exhibit a photoresponse covering from 350 to 650 nm. It can be seen that the EQE values increase by using solvents with higher boiling points. These results are in good agreement with the values of  $J_{SC}$ . The EQE for the device fabricated from CF shows a maximum

**Table 1**

A summary of the charge mobility for the PF-PThCVPTZ:PCBM films cast from different solvents.

Solvent	Boiling point (°C)	Thickness (nm)	$\mu_h$ ( $\text{m}^2 \text{ V}^{-1} \text{ s}^{-1}$ )	$\mu_e$ ( $\text{m}^2 \text{ V}^{-1} \text{ s}^{-1}$ )	$\mu_h/\mu_e$
CF	60	178 ± 2	$8.07 \times 10^{-9}$	$1.39 \times 10^{-8}$	0.58
CB	132	172 ± 3	$1.18 \times 10^{-8}$	$1.91 \times 10^{-8}$	0.62
DCB	180	168 ± 2	$1.74 \times 10^{-8}$	$2.24 \times 10^{-8}$	0.78
TCB	218	171 ± 1	$1.93 \times 10^{-8}$	$2.41 \times 10^{-8}$	0.80



**Fig. 6.**  $J$ - $V$  curves of the PF-PThCVPTZ:PCBM solar cells fabricated from different solvents. (Inset: corresponding EQE characteristics.)

of 20.7% at a wavelength of 370 nm. On the other hand, for the device fabricated from TCB, the EQE maximum increases to 39.8 at 450 nm leading to a larger  $J_{SC}$ .

#### 4. Conclusion

An alternating PF copolymer, PF-PThCVPTZ, containing a low-bandgap donor-acceptor segment has been designed and synthesized for use in PV devices. A broad absorption spectrum in PF-PThCVPTZ film covers the visible solar spectrum, resulting in an extended photocurrent response. Under AM 1.5 G  $100 \text{ mA/cm}^2$  illumination, the devices fabricated from TCB with 67 wt% PCBM reveal a PCE of 1.84%. Based on these findings, PF-PThCVPTZ is a potential candidate for application in polymer solar cells.

#### Acknowledgements

The authors are also grateful to the National Science Council (NSC), Taiwan, (NSC 96-2221-E-001-017-MY2 and NSC 96-2628-E-007-030-MY2) and Academia Sinica, Taiwan for financial support.

#### References

- [1] J.Y. Kim, S.H. Kim, H.H. Lee, K. Lee, W. Ma, X. Gong, A.J. Heeger, *Adv. Mater.* 18 (2006) 572.
- [2] G. Li, V. Shrotriya, J. Huang, Y. Yao, T. Moriarty, K. Emery, Y. Yang, *Nat. Mater.* 4 (2005) 864.
- [3] M. Campoy-Quiles, T. Ferenczi, T. Agostinelli, P.G. Etchegoin, Y. Kim, T.D. Anthopoulos, P.N. Stavrinou, D.D.C. Bradley, J. Nelson, *Nat. Mater.* 7 (2008) 158.
- [4] G. Li, Y. Yao, H. Yang, V. Shrotriya, G. Yang, Y. Yang, *Adv. Funct. Mater.* 17 (2007) 1636.
- [5] S.S. van Bavel, E. Sourry, G. de With, J. Loos, *Nano Lett* 9 (2009) 507.
- [6] A. Gadisa, W. Mammo, L.M. Andersson, S. Admassia, F. Zhang, M.R. Andersson, O. Inganäs, *Adv. Funct. Mater.* 17 (2007) 3836.
- [7] P.T. Boudreault, A. Michaud, M. Leclerc, *Macromol. Rapid Commun.* 28 (2007) 2176.
- [8] N. Blouin, A. Michaud, D. Gendron, S. Wakim, E. Blair, R.N. Plesu, M. Belletête, G. Durocher, Y. Tao, M. Leclerc, *J. Am. Chem. Soc.* 130 (2008) 732.
- [9] Y. Li, Y. Zou, *Adv. Mater.* 20 (2008) 2952.

- [10] Y. Liang, Y. Wu, D. Feng, S.T. Tsai, H.J. Son, G. Li, L. Yu, *J. Am. Chem. Soc.* 131 (2009) 56.
- [11] J. Hou, H.Y. Chen, S. Zhang, G. Li, Y. Yang, *J. Am. Chem. Soc.* 130 (2008) 16144.
- [12] W.Y. Wong, X.Z. Wang, Z. He, K.K. Chan, A.B. Djurišić, K.Y. Cheung, C.T. Yip, A.M.C. Ng, Y.Y. Xi, C.S.K. Mak, W.K. Chan, *J. Am. Chem. Soc.* 129 (2007) 14372.
- [13] J. Hou, T.L. Chen, S. Zhang, H.Y. Chen, Y. Yang, *J. Phys. Chem. C* 113 (2009) 1601.
- [14] A.B. Tamayo, B. Walker, T.Q. Nguyen, *J. Phys. Chem. C* 112 (2008) 11545.
- [15] F. Zhang, J. Bijleveld, E. Perzon, K. Tvingstedt, S. Barrau, O. Inganäs, M.R. Andersson, *J. Mater. Chem.* 18 (2008) 5468.
- [16] H.A. Becerril, N. Miyaki, M.L. Tang, R. Mondal, Y.S. Sun, A.C. Mayer, J.E. Parmer, M.D. McGehee, Z. Bao, *J. Mater. Chem.* 19 (2009) 591.
- [17] W. Mammo, S. Admassie, A. Gadisa, F. Zhang, O. Inganäs, M.R. Andersson, *Sol. Energy Mater. Sol. Cells* 91 (2007) 1010.
- [18] M. Sun, L. Wang, X. Zhu, B. Du, R. Liu, W. Yang, Y. Cao, *Sol. Energy Mater. Sol. Cells* 91 (2007) 1681.
- [19] J. Peet, J.Y. Kim, N.E. Coates, W.L. Ma, D. Moses, A.J. Heeger, G.C. Bazan, *Nat. Mater.* 6 (2007) 497.
- [20] D. Mühlbacher, M. Scharber, M. Morana, Z. Zhu, D. Waller, R. Gaudiana, C. Brabec, *Adv. Mater.* 18 (2006) 2884.
- [21] Z. Zhu, D. Waller, R. Gaudiana, M. Morana, D. Mühlbacher, M. Scharber, C. Brabec, *Macromolecules* 40 (2007) 1981.
- [22] H. Sirringhaus, T. Kawase, R.H. Friend, T. Shimoda, M. Inbasekaran, W. Wu, E.P. Woo, *Science* 290 (2000) 2123.
- [23] J. Jo, D. Vak, Y.Y. Noh, S.S. Kim, B. Lim, D.Y. Kim, *J. Mater. Chem.* 18 (2008) 654.
- [24] S. Rait, S. Kashyap, P.K. Bhatnagar, P.C. Mathur, S.K. Sengupta, J. Kumar, *Sol. Energy Mater. Sol. Cells* 91 (2007) 757.
- [25] K.C. Li, Y.C. Hsu, J.T. Lin, C.C. Yang, K.H. Wei, H.C. Lin, *J. Polym. Sci. Part A: Polym. Chem.* 13 (2008) 4285.
- [26] V. Shrotriya, G. Li, Y. Yao, C.W. Chu, Y. Yang, *Appl. Phys. Lett.* 88 (2006) 073508.
- [27] V. Shrotriya, Y. Yao, G. Li, Y. Yang, *Appl. Phys. Lett.* 89 (2006) 063505.
- [28] S. Janietz, D.D.C. Bradley, M. Grell, C. Giebeler, M. Inbasekaran, E.P. Woo, *Appl. Phys. Lett.* 73 (1998) 2453.
- [29] J.H. Huang, Z.Y. Ho, D. Kekuda, C.W. Chu, K.C. Ho, *J. Phys. Chem. C* 112 (2008) 19125.
- [30] J.H. Huang, C.P. Lee, Z.Y. Ho, D. Kekuda, C.W. Chu, K.C. Ho, *Sol. Energy Mater. Sol. Cells* (2009). doi:10.1016/j.solmat.2009.02.019.
- [31] J.H. Huang, C.Y. Yang, Z.Y. Ho, D. Kekuda, M.C. Wu, F.C. Chien, P. Chen, C.W. Chu, K.C. Ho, *Org. Electron.* 10 (2009) 27.
- [32] J.F. Chang, B. Sun, D.W. Breiby, M.M. Nielsen, T.I. Sölling, M. Giles, I. McCulloch, H. Sirringhaus, *Chem. Mater.* 16 (2004) 4772.
- [33] J.H. Huang, Z.Y. Ho, D. Kekuda, Y. Chang, C.W. Chu, K.C. Ho, *Nanotechnology* 20 (2009) 025202.
- [34] W.D. Gill, *J. Appl. Phys.* 43 (1972) 5033.
- [35] H.Y. Chen, H. Yang, G. Yang, S. Sista, R. Zadoyan, G. Li, Y. Yang, *J. Phys. Chem. C* 113 (2009) 7946.
- [36] J.H. Huang, D. Kekuda, C.W. Chu, K.C. Ho, *J. Mater. Chem.* 19 (2009) 3704.
- [37] C.M. Björström, A. Bernasik, J. Rysz, A. Budkowski, S. Nilsson, M. Svensson, M.R. Andersson, K.O. Magnusson, E. Moons, *J. Phys.: Condens. Matter.* 17 (2005) L529.
- [38] S.Y. Heriot, R.A.L. Jones, *Nat. Mater.* 4 (2005) 782.

In this article, we study how the electric polarization or dipole moment of a ferroelectric polymer can induce NDR effect in organic devices. As a ferroelectric polymer, we have chosen poly(vinylidene fluoride) (PVDF), which is particularly important as non-volatile memory elements with high stability and excellent solubility. We show how the electric polarization of PVDF induces NDR in an organic molecule that otherwise does not exhibit any NDR effect.

## 2. Experimental

The molecule of interest in this work is fluorescein, which is a molecule in the xanthene class known for organic memories [9]. Fluorescein has exhibited electrical bistability through carrier-transporting channels [24]. Molecular structure of fluorescein is shown in the inset of Fig. 1. It can be mixed well with PVDF in a common solvent to form spun-cast films. Powder form of PVDF ( $M_w = 534,000$ ), obtained from Aldrich Chemical Company, was sonicated to dissolve in THF. In this work, we have varied the concentration of fluorescein in PVDF matrix between 5% and 50%. Apart from PVDF:fluorescein films, thin-films were obtained from only PVDF and fluorescein. All the films were spun from 20 mg/ml solution in tetrahydrofuran (THF) to keep the thickness the same (around 150 nm). The films were annealed at 60 °C for 4 h. Indium tin oxide (ITO) coated glass substrates acted as the base electrode; aluminum (Al), thermally evaporated under  $10^{-6}$  Torr, was the top electrode. PVDF thin-films had an electroactive  $\beta$ -phase due to residual stresses between the films and the substrates. Formation of  $\beta$ -phase of PVDF films was also supported by X-ray diffraction (XRD) spec-

trum that has showed a peak at 21°; the spectrum has matched well with the reported result [25].

To record  $I$ - $V$  characteristics, bias was applied to the ITO electrode with respect to the Al one. Capacitance-voltage ( $C$ - $V$ ) plots were recorded in a parallel mode by a Solartron 1260 Impedance Analyzer. While the test voltage was 100 mV rms, frequency of test signal was kept at a fixed value (50, 500, 1k and 10k Hz). Open- and short-circuit compensations were performed with standard normalization procedure in order to minimize the effect of any stray and wire capacitances. The instruments were controlled with a personal computer via a general-purpose interface bus (GPIB). The measurements were carried out with SMART software.

## 3. Results and discussion

We have recorded  $I$ - $V$  characteristics of different devices with varied concentration of fluorescein in PVDF. Films, which are initially unpolarized, have been characterized; after application of a suitable voltage, the ferroelectric polymer becomes polarized; then the films were again characterized for many times. To record the effect of polarization, we scanned voltage from zero to a negative value (or a positive value) in succession. Results from a typical device, with 20% fluorescein in PVDF, in the negative bias region are shown in Fig. 1a. The unpolarized film shows non-ohmic current-voltage characteristics. Once the films are poled by the application of a bias ( $V_{Max}$ , the value up to which voltage was scanned),  $I$ - $V$  of the devices becomes NDR in nature. The NDR effect repeated in subsequent sweeps and cycles without any decrease in the ef-

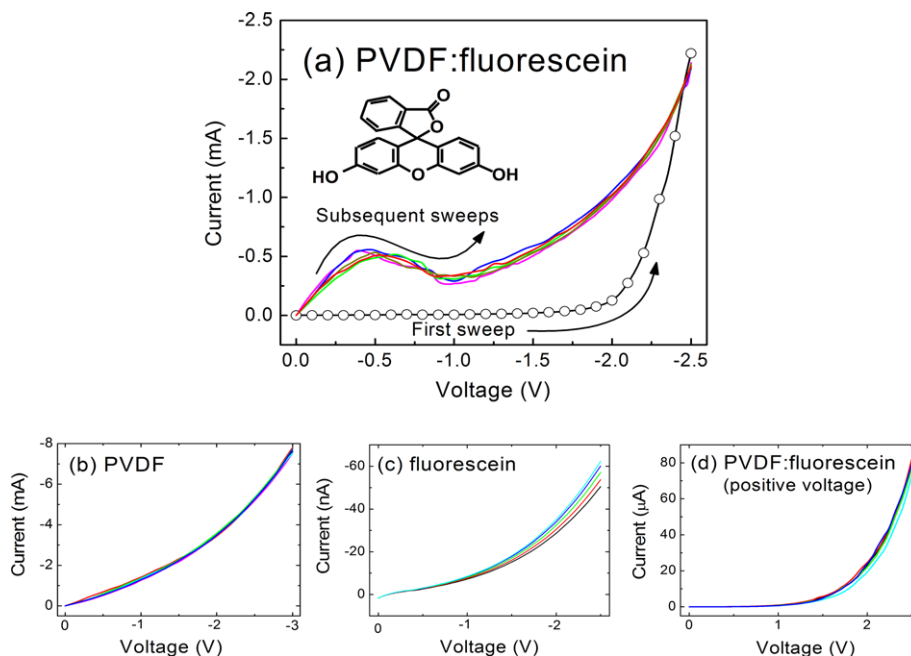


**Fig. 1.** Current-voltage characteristics of (a) PVDF:fluorescein (20 wt.%) (b) PVDF, and (c) fluorescein under multiple voltage sweeps to a negative bias. Characteristics for the PVDF:fluorescein system under multiple voltage sweeps to a positive bias is shown in (d). Different sweeps are shown by lines of different colors except in (a), where the first sweep is represented by open symbols. Molecular structure of fluorescein is shown in the inset of (a).

fect. There was no role of scan-speed in the 20–200 mV/s range on the observation. The NDR effect can only be erased by an application of an opposite voltage (positive voltage, in this case).

The role of a ferroelectric polymer in the observed NDR has been tested by several control experiments. The NDR effect could not be observed in devices based only on PVDF or fluorescein. Both the devices returned non-ohmic  $I$ - $V$  characteristics, which have not changed in successive voltage-scans. The plots are shown in Fig. 1b and c, respectively. Similar sweeps towards a positive voltage did not yield any NDR in PVDF:fluorescein films or its components. Absence of NDR in PVDF:fluorescein films under successive scans to a positive voltage is shown in Fig. 1d. In the positive voltage direction, NDR did not appear even during sweeps to a higher value. The results in Fig. 1a, in conjunction with that in Fig. 1b–d show that the ferroelectric polymer induces NDR in fluorescein in the negative voltage region. This could be due to the induced polarization in PVDF; fluorescein in an inert polymer, such as poly (methyl methacrylate) does not exhibit any NDR.

Upon application of a suitable negative bias at the ITO electrode (with Al being the ground) nearing the coercive voltage during the first voltage sweep, polarization occurs in the ferroelectric film. The electric polarization of PVDF now leads to band-bending with the ITO electrode at the interface [21]. The band-bending expectedly facilitates electron-injection in the device. Fluorescein, being electron-transporting in nature, now receives more electrons (from ITO electrode) than the pre-polarization situation and becomes reduced. The reduced fluorescein molecules have a higher conductivity than the neutral one as evidenced by energy minimization calculation on xanthene molecules [26]. In the second and subsequent voltage sweeps towards the same direction, the (magnitude) current at a particular voltage hence become higher than that in the first voltage sweep. Now, with an increase in the (the magnitude of) voltage with more electron-injection, the molecules undergo a second reduction; the doubly reduced molecules have a lower conductivity than the singly reduced ones. The (magnitude of) current hence decreases with an increase in (magnitude of) voltage in the  $I$ - $V$  characteristics. With further increase in voltage, the current shows usual increase due to non-ohmic contact with the electrodes. The  $I$ - $V$  characteristics hence become NDR in nature.

When bias was swept towards a positive voltage in a PVDF:fluorescein device, polarization of the ferroelectric polymer occurs in the opposite direction. Due to band-bending, hole injection from the ITO electrode becomes possible. Carrier injection from the Al electrode is hindered possibly due to an oxide layer formed during thermal evaporation of the top electrode. Since fluorescein is electron-acceptor in nature, the injected holes cannot reduce the molecules to a higher-conducting state. The injected holes may further tend to decrease the conductivity of fluorescein, as shown by lower current in Fig. 1d as compared to that in Fig. 1a. Since there was no possibility of reduction or double-reduction of the molecules, NDR effect was hence not observed in the positive bias direction of the  $I$ - $V$  characteristics.

To substantiate polarization-assisted double-reduction in fluorescein molecules, we have recorded  $I$ - $V$  characteristics after application of voltage pulse of different amplitudes (Fig. 2). With an increase in the amplitude of voltage pulse that induces polarization in the ferroelectric polymer, the degree of electric polarization is expected to increase till saturation is reached. The Fig. 2 however shows that the NDR effect did not increase with an increase in the degree of polarization. With an increase in the amplitude of voltage pulse, the NDR occurred at a lower bias in voltage-scans with the NDR peak shifting to a lower (amplitude of) voltage. The higher degree of polarization might have speeded up the second reduction of fluorescein molecules shifting the appearance of NDR to a lower (amplitude of) voltage. When the amplitude of preceding voltage pulse decreased below a threshold value (2.5 V), there was no polarization of the ferroelectric polymer; neither first nor second reduction was possible and consequently no NDR effect was observed.

Role of the ferroelectric polymer in inducing NDR effect in fluorescein can best be understood by varying the concentration of the organic molecule in PVDF matrix. Concentration of fluorescein in the thin-films has been varied between 5 and 50 wt.%. Thickness of the active layer of all the devices were however the same. We have compared the NDR effect in these devices after application of a voltage pulse. All the devices show NDR effect; the effect was however small in the extreme systems. The peak-to-valley ratio is a measure of NDR effect; a plot of the ratio versus fluorescein concentration goes through a peak (Fig. 3). The results are in consistent with Fig. 1b and c evidencing absence of NDR in PVDF- and fluorescein-based devices, respectively. The systems in the extreme cases are not favorable to observe NDR. When concentration of fluorescein is low, the molecules do not form many percolative channels between the two electrodes resulting in low device current. As the other extreme, at a higher fluorescein concentration, the PVDF matrix is nearly discontinuous to polarize and hence to build a density of charge carriers. The fluorescein molecules, due to its high-bandgap and correspondingly fewer electron-injection, could not be electroreduced to exhibit NDR effect. At an intermediate

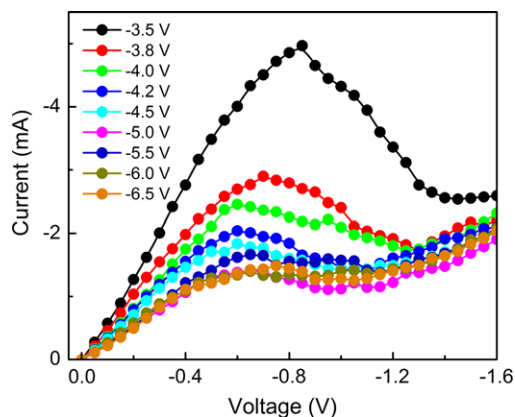
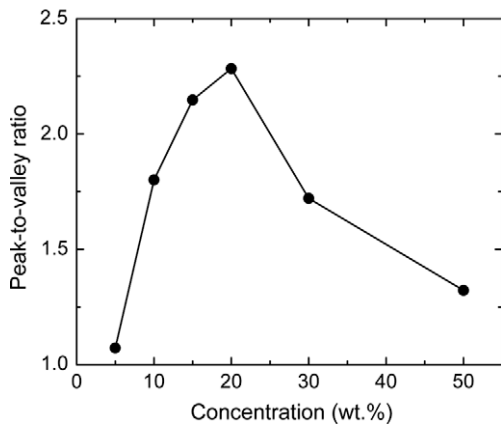


Fig. 2. Current–voltage characteristics of a PVDF:fluorescein (20 wt.%) film after application of voltage pulse (width = 5 s) of different amplitude (as shown in the legend).



**Fig. 3.** Peak-to-valley ratio of negative differential resistance for PVDF:fluorescein films with different concentration of fluorescein. The line is to guide the eye.

fluorescein concentration in PVDF, the molecules form percolative networks between the two electrodes in the device. Also, the ferroelectric polymer could become polarized and subsequently facilitate electroreduction in a large number of fluorescein molecules. Under application of external voltage, the reduced molecules may then undergo a second reduction to yield a large NDR in the devices.

To substantiate electric polarization of the polymer, we have measured capacitance of the devices. Measurements were carried out at fixed (test) frequencies under a dc voltage sweep. Results from a PVDF:fluorescein (20%) device at 10 kHz are shown in Fig. 4. Capacitance values for five consecutive sweeps (from 0 to  $-3.2$  V) are shown in the figure. In the first sweep when the ferroelectric polymer was yet to be polarized, capacitance was initially high. With polarization of the polymer followed by first electroreduction of fluorescein molecules, conductance of the device increases. The capacitance of the device hence decreased. During the subsequent sweeps, a dip in the  $C$ - $V$  plots might point to the sign change in differential resistance (peak in the  $I$ - $V$

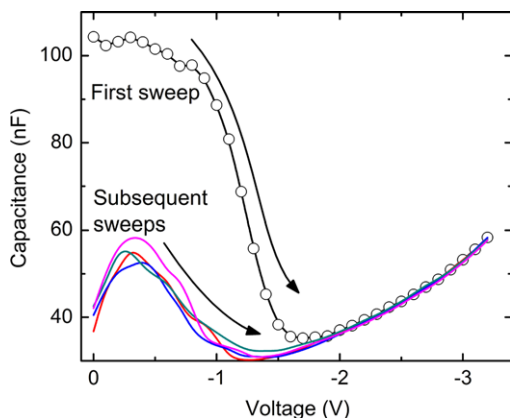


**Fig. 4.** Capacitance-voltage plots of a PVDF:fluorescein (20 wt.%) film under multiple voltage sweeps to a negative bias. While the first sweep is represented by open symbols, results for other sweeps are shown by lines of different colors. Frequency of test ac signal was 10 kHz.

characteristics) in the devices. Measurements carried out at different test frequencies yielded similar nature in the  $C$ - $V$  characteristics; magnitude of capacitance however decreased with an increase in ac test frequency.

#### 4. Conclusions

In summary, we have shown that NDR in fluorescein could be induced by the use of PVDF polymer. While neither the fluorescein nor the ferroelectric polymer exhibit NDR, devices based on fluorescein in PVDF matrix yield reproducible NDR effect. We have inferred that electric polarization of the ferroelectric polymer enhances carrier injection followed by reduction and then a double-reduction of fluorescein molecules in the device to result NDR nature in the  $I$ - $V$  characteristics. We have substantiated our findings by varying the concentration of fluorescein in PVDF matrix and by varying the degree of polarization (by applying voltage pulse of different amplitudes).

#### Acknowledgements

AKR acknowledges CSIR Junior Research Fellowship No. 09/080(0505)/2006-EMR-I (Roll No. 503974). The authors also acknowledge financial supports through projects SR/S2/RFCMP-02/2005 and 2007/37/2/BRNS.

#### References

- [1] J. Chen, M.A. Reed, A.M. Rawlett, J.M. Tour, *Science* 286 (1999) 1550.
- [2] N.P. Guisinger, M.E. Greene, R. Basu, A.S. Baluch, M.C. Hersam, *NanoLetters* 4 (2004) 55.
- [3] W. Tang, H.Z. Shi, G. Xu, B.S. Ong, Z.D. Popovic, J.C. Deng, J. Zhao, G.H. Rao, *Adv. Mater.* 17 (2005) 2307.
- [4] H.S. Majumdar, J.K. Baral, A. Laiho, J. Ruokolainen, O. Ikkala, R. Osterbacka, *Adv. Mater.* 18 (2006) 2805.
- [5] S.Y. Quek, J.B. Neaton, M.S. Hybertsen, E. Kaxiras, S.G. Louie, *Phys. Rev. Lett.* 98 (2007) 066807.
- [6] A. Bandyopadhyay, Y. Wakayama, *Appl. Phys. Lett.* 90 (2007) 023512.
- [7] J.S. Chen, L.L. Xu, J. Lin, Y.H. Geng, L.X. Wang, D.G. Ma, *Semicond. Sci. Technol.* 21 (2006) 1121.
- [8] J. Lin, D.G. Ma, *J. Appl. Phys.* 103 (2008) 124505.
- [9] A. Bandhopadhyay, A.J. Pal, *J. Phys. Chem. B* 107 (2003) 2531.
- [10] B. Mukherjee, A.J. Pal, *Appl. Phys. Lett.* 85 (2004) 2116.
- [11] H.S. Majumdar, A. Bolognesi, A.J. Pal, *Synth. Met.* 140 (2004) 203.
- [12] Y. Yang, L.P. Ma, J.H. Wu, *MRS Bull.* 29 (2004) 833.
- [13] Y.S. Lai, C.H. Tu, D.L. Kwong, J.S. Chen, *Appl. Phys. Lett.* 87 (2005) 122101.
- [14] R. Muller, S. De Jonge, K. Myny, D.J. Wouters, J. Genoe, P. Heremans, *Appl. Phys. Lett.* 89 (2006) 223201.
- [15] M. Terai, K. Fujita, T. Tsutsui, *Jpn. J. Appl. Phys. Part 1 - Regul. Pap. Brief Commun. Rev. Pap.* 45 (2006) 3754.
- [16] M. Colle, M. Buchel, D.M. de Leeuw, *Org. Electron.* 7 (2006) 305.
- [17] F. Verbakel, S.C.J. Meskers, R.A.J. Janssen, H.L. Gomes, A.J.M. Van den Biggelaar, D.M. de Leeuw, *Org. Electron.* 9 (2008) 829.
- [18] S. Paul, *IEEE Trans. Nanotechnol.* 6 (2007) 191.
- [19] T.J. Reece, S. Ducharme, A.V. Sorokin, M. Poulsen, *Appl. Phys. Lett.* 82 (2003) 142.
- [20] Y. Yonekuta, K. Susuki, K.C. Oyaizu, K.J. Honda, H. Nishide, *J. Am. Chem. Soc.* 129 (2007) 14128.
- [21] K. Asadi, D.M. De Leeuw, B. De Boer, P.W.M. Blom, *Nat. Mater.* 7 (2008) 547.
- [22] Z.J. Hu, M.W. Tian, B. Nysten, A.M. Jonas, *Nat. Mater.* 8 (2009) 62.
- [23] H. Kliehm, R. Tadros-Morgane, *J. Phys. D Appl. Phys.* 38 (2005) 1860.
- [24] A.K. Rath, A.J. Pal, *Langmuir* 23 (2007) 9831.
- [25] S. Ramasundaram, S. Yoon, K.J. Kim, C. Park, *J. Polym. Sci. Pol. Phys.* 46 (2008) 2173.
- [26] A. Bandyopadhyay, A.J. Pal, *Appl. Phys. Lett.* 84 (2004) 999.

lead to a substantial progress in the field, with the best power conversion efficiencies achieved in the laboratory currently being in the 5–6% range [1–3].

For a given material system, the control of the blend structure at the nanoscale is, in fact, one of the most effective ways to significantly enhance the organic solar cell efficiency. In the case of the most extensively studied material systems (e.g. poly(3-hexylthiophene) (P3HT) and soluble fullerene derivative PCBM), 10-fold increases in the power conversion efficiency have been reported when comparing devices based on as-spun active layers, and active layers with a controlled structure [4]. Typical protocols include slow drying of the active layer, thermal and vapor annealing, as well as appropriate solvent (or solvent mixture) choices [4–8]. A comprehensive review on the effect that morphology has on bulk heterojunction solar cells has been recently published by Yang and Loos [9]. Interestingly, it has been found that for the case of P3HT:PCBM blends, all of these fabrication protocols result in a similar optimized morphology (see Ref. [8] and references therein). This consists of a bicontinuous blend of the electron donor (the polymer chains) and electron acceptor (the fullerene molecules), with crystalline domains on the nanometer-length scale, and a composition gradient normal to the device electrodes. The optimum size of the nanodomains represents a compromise between good charge transport (large interconnected domains that form percolating pathways) and efficient charge generation (i.e. large exciton dissociation rate, which requires domains around twice as big as the exciton diffusion length,  $\sim 10$  nm) [8,9]. The composition gradient improves the contact selectivity thus reducing the leakage current.

Moreover, the post-deposition treatments, and in particular thermal annealing, have also an additional positive effect: they – in principle – increase the OPV stability by means of the concomitant stabilization of the active layer blend compared to the frozen non-equilibrium morphology of the as cast films [9]. This is particularly important if one takes into account that the relatively low glass transition temperatures that most soluble conjugated polymers exhibit may cause a morphology change as the temperature significantly rises during device operation [9]. In the process of stabilizing the morphology, thermal annealing does, however, also yield large-scale phase separation [8,10–12]. For instance, annealing at 140 °C for one hour a 1:1 (in wt.%) regio regular P3HT:PCBM blend film leads to micron-sized PCBM clusters (see Fig. 1a) that are not beneficial to OPV performance. The fabrication of OPVs with appropriate control over the nanostructure is, therefore, a key challenge for which currently only a few general rules – regarding optimum composition – have been found [11].

In this paper we investigate the possibility of using ternary mixing in order to control the blend morphology. The rationale is that small amounts of an amorphous polymer may form a dilute matrix which would allow the formation of small crystallites but prevent the large-scale phase separation of the components. For devices based on blending PCBM with P3HT of two different molecular weights [13], it was observed that the advantages of both low molecular weight (efficient charge generation) and high molecular

weight (enhanced transport) could be combined and thus this type of ternary mixing resulted in enhanced device performance. Here we have chosen ternary blends of PCBM with regio regular (RR-) P3HT and regio random (RRa-) P3HT. We will show that besides a very efficient control of the blend morphology, regio random P3HT also adds several other functionalities, such as energy transfer to the more crystalline RR-P3HT, enhanced charge generation and improved open circuit voltage, all with minimum cost in terms of charge carrier mobility. The final ternary-based devices, even without optimization procedure, are about 20% more efficient than the conventional annealed blends when excited with low intensity monochromatic light.

## 2. Experimental section

### 2.1. Materials and thin film fabrication

Regio regular (Aldrich #669067, regioregularity >95% head-to-tail regioregular (HNMR), Mn = 17,500) and regio random poly(3-hexylthiophene) P3HT (Aldrich #510823, regioregularity = 1:1 (head-to-head):(head-to-tail) linkages of regioisomers, no data available of Mn) were purchased from Aldrich and used as received. Herein, regio regular and regio random materials are denoted RR-P3HT and RRa-P3HT, respectively. [6,6]-Phenyl C<sub>61</sub>-butyric acid methyl ester (PCBM) was obtained from Luminescence Technology and was also used as received.

Binary blends consisting of RR-P3HT and RRa-P3HT were prepared from different solution concentrations (from 15 to 50 g/l) in high grade chlorobenzene, and spin coated at varying spin speeds (2000–4000 rpm) so to produce different thicknesses. The relative concentration of regular and random (RR-P3HT:RRa-P3HT) polymers was varied in 0.25 steps: (1:0), (0.75:0.25), (0.5:0.5), (0.25:0.75) and (0:1). The mobility on binary systems was measured in devices containing around 150-nm-thick films deposited from a total 50 mg/ml solution.

For ternary blends, total 60 mg/ml solutions in chlorobenzene were prepared, from which 30 mg was PCBM, and the other 30 mg split between RR-P3HT and RRa-P3HT, so to finally produce constant (1:1) fullerene:(polymer) concentrations. The relative content of regular P3HT and random P3HT was varied leading to the following PCBM:RR-P3HT:RRa-P3HT concentrations (1:1:0), (1:0.9:0.1), (1:0.75:0.25), (1:0.5:0.5), (1:0.25:0.75) and (1:0:1). Herein, we denote conventional blend the films comprising the (1:1:0) ratio, i.e. (1:1) PCBM:RR-P3HT, and it will be used as reference. Moreover, a different set of devices was fabricated from solutions made by adding RRa-P3HT to a 1:1 PCBM:RR-P3HT (60 mg/ml) solutions, ending up in the following relative concentrations: (1:1:0.1) and (1:1:0.25). For the devices, a two-step process was identified during spin speed optimization: 1000 rpm for 3 s in order to produce a homogeneous distribution of the solution throughout the substrate, followed by 90 s at 2000 rpm. This protocol typically resulted in active layers with thickness in the 85–105 nm range.

The solutions were spin coated on cleaned quartz substrates or on ITO-covered glass (150-nm-thick ITO layer

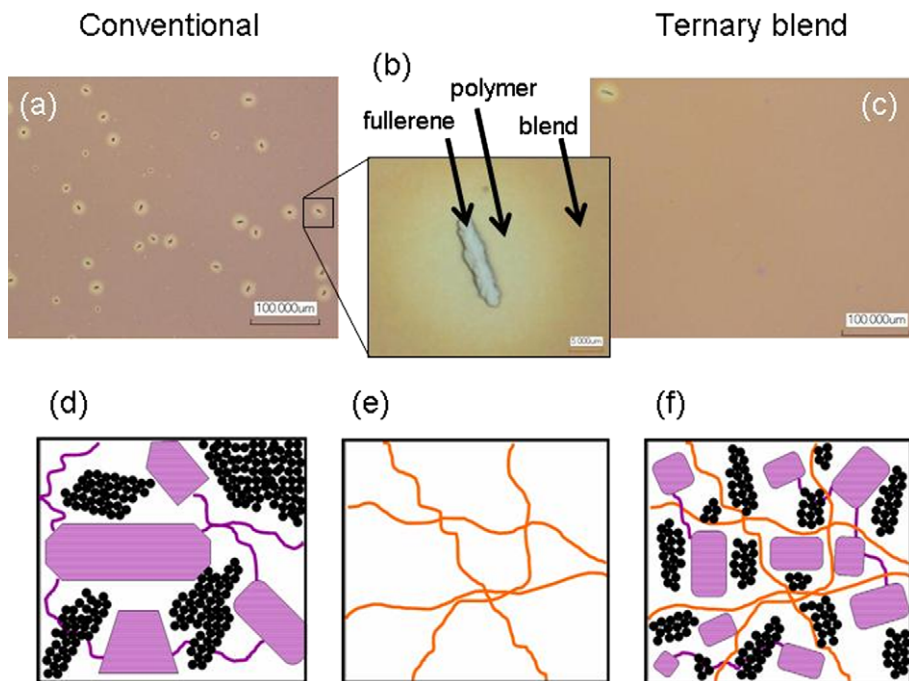


**Fig. 1.** Comparison of the microscale morphology of the conventional blend and the ternary systems. (a–c) UV laser microscope images of annealed ternaries with PCBM:regular P3HT:random P3HT concentrations of (a) 1:1:0; (b) 1:1:0 (zoom-in detail); and (c) 4:3:1; (d–f) schematics of (d) a conventional PCBM:regular P3HT blend; (e) dilute random matrix; and (f) ternary system comprising a dilute random P3HT matrix filled with crystallites of PCBM and regular P3HT.

with a sheet resistance of  $10 \Omega/\text{sq}$ , SLR grade, Sanyo Vacuum Industries Co. Ltd). For the solar cells, PEDOT:PSS (Baytron P VP Al 4083 (H.C. Starck)) was spin coated (3000 rpm for 90 s) onto the ITO-coated glass and annealed at  $200^\circ\text{C}$  for 20 min. The ternary systems were thermally annealed at  $140^\circ\text{C}$  for 1 h inside a nitrogen-filled Glovebox ( $\text{O}_2$  and  $\text{H}_2\text{O}$  levels less than 2 ppm).

## 2.2. Thin film characterization

Film thicknesses were measured using a Dektak 3030 profilometer (and double checked with the thicknesses deduced from the absorption data using the optical constants from Ref. [8]). Scanning laser microscopy images were taken using a Keyence VK-9700 microscope. At least 10 images were employed for each sample in order to obtain average values of the density of large-scale (micron size) aggregates of PCBM. Atomic Force Microscopy (AFM) was carried out with an SPA 400 system by Seiko Instruments, Inc. Typically, at least three AFM images were taken for each sample and their surface roughness was analyzed using the Spisiel 32 piece of software. X-ray diffraction (XRD) experiments were conducted using a Material Analysis and Characterization SRA system, model M18XHF, which employs a  $\text{Cu K}\alpha 2$  source (40 kV, 60 mA) with wavelength  $0.1544390 \text{ nm}$ . Upon background removal, the data were fitted with a Gaussian function in order to obtain the peak intensity, width and angular position at the maximum. These data were then used to deduce the average interplane distance within the crystallites (from Bragg's law), estimate crystallite size (from Scherrer's relationship)

and overall degree of crystallinity (integrating the area underneath the XRD peak).

The thin film absorption spectra were measured using a Perkin-Elmer Lambda750 UV/Vis spectrometer from 300 to 800 nm. Photoluminescence (PL) data were collected using a Perkin-Elmer LS55 Fluorescence Spectrometer. Unless otherwise stated, the PL excitation wavelength was set to 450 nm (around the absorption maximum for RR-P3HT).

Pristine polymer films deposited onto pre-cleaned ITO/glass substrates were used to measure the HOMO levels of the polymers by means of a Riken Keiki AC-2 ultraviolet photoelectron spectrometer. The experimental set-up is similar to that of conventional UPS but it does not require vacuum. On the other hand, the precision of our apparatus is smaller than that of a conventional UPS in vacuum, with uncertainty values  $\sim 0.03 \text{ eV}$ . Using ultraviolet photoelectron spectroscopy we obtained a HOMO value of  $4.61 \pm 0.03 \text{ eV}$  for regio regular P3HT, while that of regio random P3HT was found to be  $4.73 \pm 0.03 \text{ eV}$ . The slightly smaller values obtained here for RR-P3HT (often around 5 eV) might be related to possible effects of the ITO surface on the measurement. We note that two samples with different thicknesses were measured for each polymer, and each sample was measured twice. The deviation between measurements and samples is smaller than the  $0.03 \text{ eV}$  uncertainty values.

## 2.3. Device fabrication and characterization

Single carrier devices were fabricated and the dark current–voltage characteristics measured and analyzed in the



space charge limited (SCL) regime following the references [4] and [14]. Hole only devices consisted of the active material (binary or ternary system) spin coated onto glass/ITO substrates, and capped with a 5-nm evaporated MoO<sub>3</sub> layer followed by a 100-nm-thick Al contact. The evaporation mask defined 4 pixels in each sample with a 4-mm<sup>2</sup> area for each pixel. For the electron only devices, the structure was glass/ITO/Al/blend/Ba/Al, where both Ba and Al were evaporated. High-purity MoO<sub>3</sub> (6 N grade, Mitsuwa Chemicals Co., Ltd), Ba (Aldrich), and Al (AL-011480, Nilaco Co.) source materials were employed as delivered. The standard deviation of the fit to the SCL equations for the electron only devices was slightly higher than that for the hole only devices, indicating a larger error on the extracted electron mobilities. The reported mobility data are average values over the four pixels of each sample at a given film composition.

For the solar cells, the active blend was spin coated on top of PEDOT:PSS coated glass/ITO substrates in a clean room, and then transferred into an interconnected Glovebox where the Al electrode was thermally evaporated. Thermal annealing of the devices was done inside the Glovebox before the deposition of the contacts. All of the devices were encapsulated with a glass cap using an ultraviolet curing epoxy resin. The 15-min exposure to the UV radiation was performed from the Al metal side to avoid photodegradation of the organic layers across the active region.

The current–voltage characteristics of the encapsulated devices were measured outside the Glovebox, using a semiconductor characterization system (SCS4200, Keithley Instruments Inc.) at room temperature. For light *J–V* and EQE measurements, the above instrument was coupled to a JASCO CT-25C grating monochromator which selects the wavelength coming from a USHIO Optical Modulex light source. The intensity of the monochromatic light was fixed at 20 μW after calibration against a standard Coherent Fieldmaster photodiode with circular detecting area of 8 mm in diameter (resulting in an illumination density of 400 mW/m<sup>2</sup>). In order to explore the light intensity dependence of the solar cell parameters, the light intensity was varied using optical density filters between 0.3 and 45 μW. The encapsulated devices were kept in air and darkness for 10 months, when some of them were measured again to check the variation in performance with time.

### 3. Results and discussion

#### 3.1. Characterization of binary and ternary systems

Fig. 1a shows a representative laser microscopy image of a conventional PCBM:RR-P3HT (1:1) blend film annealed at 140 °C for 1 h. To start with, annealing leads to the appearance of large size aggregates as clearly seen in the image. These aggregates, which are not present in the as-spun films, are rich in PCBM molecules [8,11] and are surrounded by a polymer-rich region, seen here as a halo-like structure. It has been shown that PCBM nucleates into these aggregates upon annealing [8], or, in other words,

once they are large enough to be seen using a microscope, they grow bigger in size, but their number remains constant. The average diameter of the region containing one PCBM aggregate and the associated P3HT halo is around 13 μm (see Fig. 1b), in good agreement with previous reports [8].

Such a large phase separation is, in principle, detrimental for solar cell performance since it is several orders of magnitude larger than the exciton diffusion length (~tenths of nm's), and thus charge generation is strongly inhibited on these regions. By averaging over 10 microscope images across the sample, we estimate the density of PCBM micron-sized domains to be around 700 aggregates per square mm. If we consider the average size of the aggregates, this means that around 9% of the area is covered with these structures, and thus, 9% of the film is not acting positively as light-to-electricity converter. The introduction of the regio random polymer into the blend has a marked effect on the structure of the film. Substituting 25% of RR-P3HT by RRa-P3HT (1:0.75:0.25 sample Fig. 1c) already decreases in more than two orders of magnitude the density of these large aggregates, down to just 3 aggregates/mm<sup>2</sup>. This represents less than 0.04% of the total film area. The density is further reduced for larger amounts of the RRa-P3HT polymer in the ternary system. The samples with compositions 1:0.5:0.5 and 1:0.25:0.75 have 1 aggregate/mm<sup>2</sup> and 0.15 aggregates/mm<sup>2</sup>, respectively (not shown). It is clear that this approach is extremely efficient at controlling the microscopic morphology of the blend films.

An important question that needs to be answered is whether the introduction of the RRa-P3HT chains yields an overall amorphous structure, not only at the micron level, but also down to the nanoscale. If the resulting morphology is totally amorphous, the mobility would likely fall and the absorption would be blue shifted, and as a consequence, the overall solar cell performance would be poor. As we will see below, the RR-P3HT chains can still crystallize in the ternary blends and, in addition, the extent of the phase separation is now greatly controlled with microscopic scale phase separation being almost totally suppressed. We will come back to this point below. The eventual appearance of micron-sized aggregates also in ternary systems containing RRa-P3HT (<3 aggregates/mm<sup>2</sup>) is, in most cases, associated with film defects, such as edges of the substrate, in which inhomogeneities in film composition might be present. An optimization of the film fabrication conditions may, therefore, lead to an even smaller number of large size aggregates in films based on ternary blends.

The advantages of controlling the large-scale phase separation by using RRa-P3HT rather than other amorphous conventional polymers, such as polystyrene or polymethylmethacrylate, is twofold. First, we expect high chemical affinity amongst the blended materials due to the common backbone between RRa- and RR-P3HT polymers. Other glassy polymers could promote an even larger phase separation if the interaction between chains overcomes the entropy increase granted by mixing (following Flory's theory of mixing). Optical and atomic force microscopy images show no evidence of large-scale phase separation in

RR-P3HT:RRa-P3HT binaries or in ternary blends (see details below). Second, perhaps even more importantly, RRa-P3HT can act as an active matrix, helping the proper functioning of the devices and even adding functionality. In the following, we demonstrate several examples of this added functionality of the multicomponent system.

Fig. 2 shows the normalized absorption (solid lines) and photoluminescence emission (dashed lines) of RRa-P3HT (blue) and RR-P3HT (red). The red shift spectra of the regular polymer compared to that of the random polymer is associated to different molecular packing morphologies. Regioregularity enables a better ordering of chains into lamella crystallites where the polymer adopts a planar conformation with longer conjugation lengths and fewer defects, such as twists and radicals on the chains [15,16]. Regio random chains form, on the other hand, glassy films whose optoelectronic properties are governed by individual chain processes [15,16]. The crystallization of P3HT results in the appearance of pronounced structures in the absorption and PL spectra – phonon replica – not present in the data for RRa-P3HT films. Interestingly, the long wavelength shoulder observed in the absorption of RR-P3HT has been assigned to two-dimensional excitations [17,18], and hence is a direct consequence of the good interchain interactions within the crystallites. The intensity of this shoulder has, in fact, been found to be directly proportional to the X-ray deduced overall degree of P3HT crystallinity in P3HT:PCBM blend films subjected to various annealing treatments [19]. Another indication of the degree of chain interaction is given by the PL quantum efficiency ( $\eta$ ). Jiang et al. showed that RRa-P3HT has a much larger  $\eta$  (~8%) than RR-P3HT (~0.5%) [15] due to the isolation of chains in the random case. Here, we also found that RRa-films exhibit more than one order of magnitude higher PL than RR-P3HT films with comparable thicknesses (see Fig. 3b). It is thus apparent that regioregularity strongly determines the degree of interchain interaction [16].

From the electronic point of view, one important effect of the aforementioned interactions is that the band gap of RR-P3HT is about 0.3 eV smaller than that of RRa-P3HT, as estimated by extrapolating the absorption edge. This implies that RR-P3HT will be more appropriate for harvesting

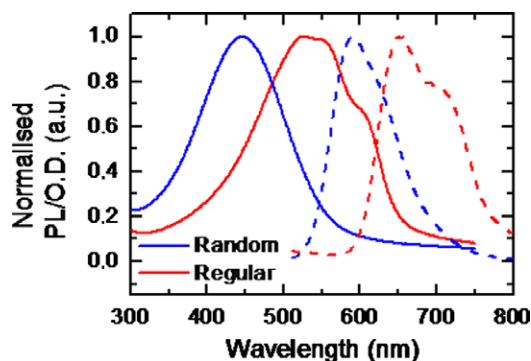


Fig. 2. Optical properties of the pristine polymer. Normalized absorption (solid line) and emission (dashed line) for regio random P3HT (blue) and regio regular P3HT (red). (For interpretation of the references to colour in this figure legend, the reader is referred to the web version of this article.)

light in the red and infrared parts of the sun's spectrum. Charge mobility will also depend on the interaction between neighboring chains [17] and, in fact, hole mobility in RRa- is several orders of magnitude lower than for RR-P3HT (we will come back to this point below). Therefore, in order to ensure good charge generation (and short circuit current) in OPVs based on ternary systems, the amount of RRa-P3HT should, in principle, be small compared to that of RR-P3HT.

Enhancing the interchain interactions typically leads to the splitting of the HOMO and LUMO levels (e.g. by means of Davydov splitting). Quantum chemical calculations have shown that bringing polymer chains closer together decreases (in absolute terms) the HOMO level [20]. The glassy morphology of the RRa-P3HT films can be associated to an effective isolation of the polymer chains, and thus, one may expect a larger (again in absolute terms) HOMO level [15,20]. Using air ultraviolet photoelectron spectroscopy we found a 0.12 eV shift comparing the two polymers, with higher HOMO for RRa-P3HT, as expected from the argument above. On the other hand, the open circuit voltage ( $V_{oc}$ ) in OPVs is proportional to the difference between the HOMO of the electron donor (polymer) and the LUMO of the electron acceptor (fullerene) [21], and thus one may expect an enhancement in the  $V_{oc}$  values for OPVs based on ternary systems. This is, in fact, what is experimentally observed, as we will show.

Fig. 3a and b shows the absorption and emission spectra, respectively, of binaries consisting of a varying concentration of RR-P3HT:RRa-P3HT, as well as the pristine materials for reference. The spin coating conditions were controlled in order to have films with comparable thicknesses (~80 nm). The dotted lines in Fig. 3a correspond to a linear addition of the absorption of the pristine materials weighted by the composition fraction of each material. For instance, the absorption of the 0.75:0.25 binary is simulated (with no fitting parameters) by adding the absorption of RR-P3HT multiplied by 0.75 and the absorption of RRa-P3HT multiplied by 0.25. The surprisingly good agreement between the measured and simulated data suggests that, on the one hand, there is not strong interaction between the two polymers in terms of absorption (no new steady state species are created), and on the other side, the crystallization of RR-P3HT is not inhibited by the presence of the random chains. The latter is very important, especially after Chirvase and co-workers pointed out that PCBM molecules prevent the crystallization of RR-P3HT, which is only restored upon thermal annealing [10]. We note that the data shown in Fig. 3 correspond to non-annealed binary films.

The PL spectra for binaries cannot, however, be modeled using a linear combination of the PL spectra of the pristine materials. The addition of a small amount of RR-P3HT (25%) reduces the PL yield by sixfold, almost down to the level of RR-P3HT (see Fig. 3b). Given the good spectral overlap between the emission of RRa-P3HT films and the absorption of RR-P3HT (see Fig. 2), energy transfer from the random to the regular chains seems a plausible explanation for this. Comparison between the PL recorded using two different excitation wavelengths (450 nm and 550 nm, the latter being the maximum absorption for RR-P3HT, not

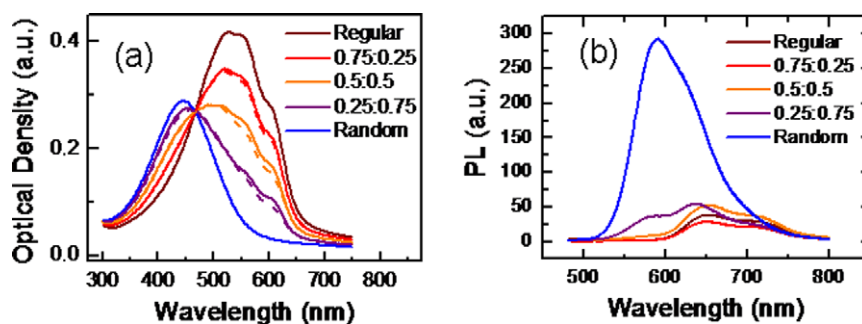


Fig. 3. Optical properties of binary systems. (a) Absorption and (b) emission of Regular:Random P3HT binary films.

shown) also points towards this explanation. Whether a real (re-absorption) or a virtual (energy transfer properly speaking) process of transferring the absorbed photon energy from regio random to regio regular, or even a combination of both, is not clear at this stage. In any case, the PL spectra strongly indicate that the transfer is actually happening and thus the absorption of light in the regio random chains is followed by a transfer of a substantial part of that energy to regio regular material where electrons are excited and through which the transport of carriers can be greatly facilitated. A detailed time-resolved study on the PL dynamics could bring useful information in this respect.

The efficient charge transfer (exciton dissociation) between the polymer chains and fullerene molecules, necessary step for charge generation, is often seen experimentally as a strong reduction in the PL quantum yield upon blending the polymer with the fullerene molecules. PCBM is an extremely efficient PL quencher in both cases RR- and RRa-P3HT (contrast for instance Figs. 3b and 4b). Comparing the PL exhibited by films containing the same amount of polymer with and without PCBM, it is possible to estimate the degree of PL quenching. It turns out that the PL quenching is much more pronounced (~50 times more) in RRa-P3HT than in RR-P3HT. The most likely reason for this is the finer intermixing between components achieved in PCBM:RRa-P3HT films compared to the conventional blend, resulting from the glassy morphology of the random polymer with very little – or even none – tendency to crystallize. It has been shown that the crystallization of P3HT is, in fact, one of the main factors driving the

diffusion of PCBM molecules into phase-separated regions [8] and thus, a non-crystallizing polymer (such as RRa-P3HT) may accommodate more easily the fullerene molecules within polymer chain voids. This view is supported by the lack of micron-sized PCBM aggregates in the ternary systems: fullerene molecules are somehow anchored in the voids left by the dilute random matrix. AFM images of PCBM:RRa-P3HT films show no evidence of phase separation and the corresponding surface roughness remains extremely small (<0.6 nm) after mixing the random polymer with the fullerene molecules. Therefore, random P3HT might, interestingly, lead to an efficient charge generation due to the resulting morphologies of their films. Ternary systems show a gradual decrease in the PL intensity with increasing RRa-P3HT concentration, as shown in Fig. 4b, which suggests an increased capability for PL quenching, or exciton splitting with adding RRa-P3HT.

As for the case of the conventional PCBM:RR-P3HT blends, the incorporation of the fullerene molecules precludes the formation of P3HT crystallites in the as-spun films also in the ternary systems. Similarly, thermal annealing (at 140 °C for 1 h) enhances the crystallization also in the ternaries. Fig. 4a shows the absorption spectra for annealed ternary blends. Judging by the ratio of the intensities of the maximum and the shoulder centered at around 650 nm, one may risk to say that ternary blends are equally, or even slightly more, crystalline (in relative terms) than the conventional binary [22].

Surface roughness, as obtained from AFM images, has often revealed the degree of crystallinity in the films

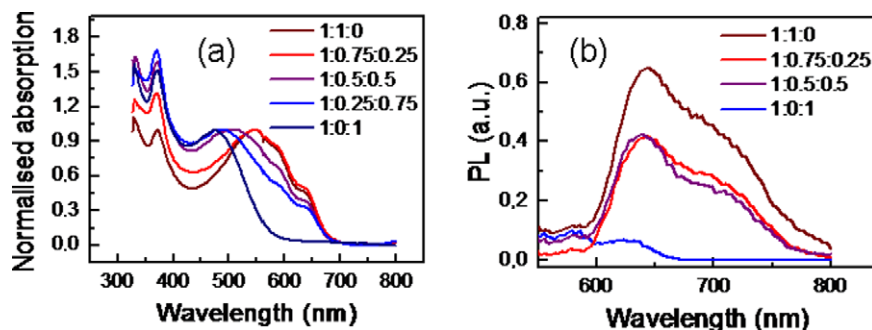


Fig. 4. Optical properties of ternary systems. (a) Absorption and (b) emission of ternary films with constant solution concentration (60 mg/ml), and constant PCBM:polymer concentration (1:1), with varying relative concentrations of regular and random P3HT.

underneath (see e.g. Ref. [23]). We have taken AFM images of the ternary systems and confirm the increase in roughness (crystallinity) upon annealing suggested by the absorption spectra. Fig. 5a and b compare the morphology of a film based on the conventional blend before and after thermal annealing, respectively. The Ra surface roughness increases from 0.6 to 0.7 nm upon annealing. All of the as-spun ternary films are smoother than the conventional blend, but, interestingly, the surface roughness for the ternaries increase to larger values than that of the PCBM:RR-P3HT blend with annealing (see e.g. Fig. 4c and d and Table 1). This may again suggest that the degree of crystallization is larger in ternary systems than in the conventional blend. However, another possible explanation could be that the three components are phase separating and thus produce a rougher surface. For comparison, it might be noted that the Ra roughness of the pristine RR- and RRa-P3HT films is 6.6 nm and 0.3 nm, respectively. The AFM deduced roughness values for the ternary films are summarized in Table 1.

In order to get a better understanding of the aforementioned phenomena suggested by the absorption and AFM data, we have performed X-ray diffraction (XRD) measurements on annealed ternary films. The data for these exper-

iments are shown in Fig. 5e, including those of the pristine RR-P3HT film used here as reference. The material parameters deduced from the analysis of the results are summarized in Table 1. We note that the sample containing only regio random P3HT does not show any diffraction peak, in accordance to the expected lack of crystallinity. Our deduced 1.72 nm interplane distance (following Bragg's law) agrees well with previous data for P3HT [19]. Moreover, it seems to slightly increase from 1.72 nm to 1.76 nm with increasing RRa-P3HT concentration from 0% to 75% in the total polymer content. Although we do not have a full explanation for this, it might be due to the fact that the regio regular crystallites are immersed in a soft matrix of the random material, which may shrink in order to accommodate the expanding (through annealing) regio regular crystallites; while in the case of the conventional blend, the crystallites cannot expand because they might be in contact with other, equally hard, crystallites. If this was the case, it might be interesting to see the effect that a semi-crystallizing matrix that formed harder crystallites would have on the interplane distance (and even hole mobility) of P3HT:PCBM blends. Some support for this very initial hypothesis may come from the fact that when the effect of a rigid substrate interface is made apparent (by decreasing film thickness), P3HT chains pack into different type of crystallites [24].

The RR-P3HT crystallite size was estimated using Scherrer's relationship and the average sizes we find are larger than those reported by Zhokhavets et al. [19], as one could expect given the fact that our annealing times are much longer (1 h in our case, and 5 min in theirs). Importantly, as the content of regio random is increased, the crystallite size is greatly reduced from around 16 nm for the PCBM:RR-P3HT:RRaP3HT (1:1:0) film to ca. 10 nm for the (1:0.25:0.75) sample. This suggests that there might be an increase in polymer chain entanglement with increasing random concentration which prevents the formation of large crystallites. We note that we have employed only the optimum annealing temperature for the conventional blend, and thus there is room for optimizing the thermal annealing procedure for the ternary systems which may require longer annealing times, or higher annealing temperatures to create crystallites of the same size as the conventional blend.

By integrating the area of the XRD peak, one may obtain a measure of the degree of crystallinity of the film [19]. Interestingly, this evaluation again indicates that ternary systems are more crystalline than the conventional blend (see Table 1), in agreement with the absorption and AFM data, and thus rules out the hypothesis of the large-scale phase separation of the three materials as the main explanation of the increased roughness in annealed ternary films compared to the conventional binary.

Therefore, all of the evidences suggest that the structure of ternary films consists of crystallites of regular P3HT – of smaller size than those found in the conventional blend – embedded into a random polymer matrix, and where PCBM can only form small aggregates and not the micron-sized structures often observed in the conventional case. Fig. 1d and f schematically depict the nanomorphology of the conventional binary and the proposed ternary

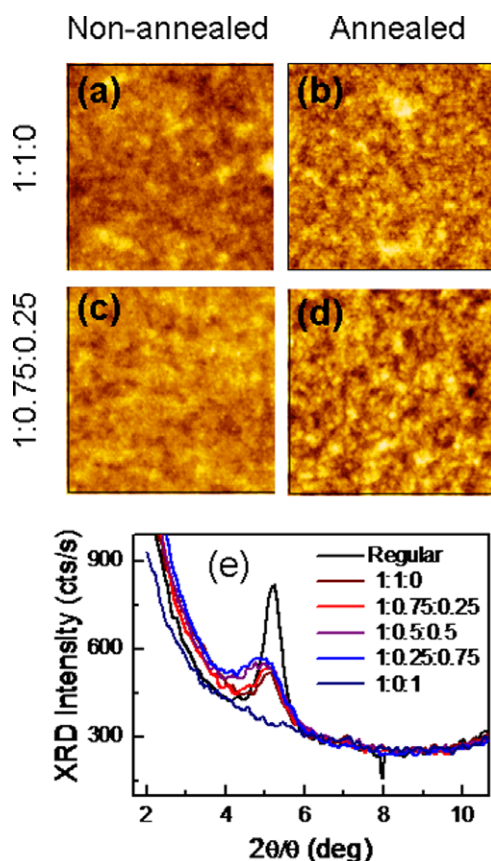


**Fig. 5.** Investigation on the crystallinity of ternary systems.  $3 \times 3 \mu\text{m}$  AFM images for 1:(1:0) (a) non-annealed and (b) annealed; and for 4:(3:1) (c) non-annealed and (d) annealed. (e) XRD intensity for ternary systems and reference pristine regular P3HT.

**Table 1**

Summary of morphologic, photophysical and device parameters for ternary systems.

	1:1:0	1:0.75:0.25	1:0.5:0.5	1:0.25:0.75	1:0:1
Interplane distance (nm)	1.72	1.73	1.75	1.76	NA
Crystallite size (nm)	16.2	13.7	10.1	9.8	0
Crystallinity (arb. units)	657	755	774	728	0
Absorption (550 nm)	0.418	0.346	0.275	0.198	0.123
lambda max Abs (nm)	546	548	512	479	473
Ra roughness (nm)	0.7	1	1.2	0.9	1
RMS roughness (nm)	0.9	1.3	2	1.3	0.6
Hole mobility ( $\text{m}^2/\text{V s}$ )	2.20E-08	9.12E-09	2.76E-09	3.48E-09	–
Electron mobility ( $\text{m}^2/\text{V s}$ )	2.38E-09	8.41E-10	3.35E-10	1.77E-10	–
$J_{sc}$ ( $\text{mA}/\text{cm}^2$ ) (550 nm)	0.0119	0.0090	0.0064	0.0020	0.0001
$J_{sc}/\text{Abs}$ (550 nm)	0.0285	0.0259	0.0233	0.0102	0.0007
$100^*J_{max}^*V_{max}/\text{Abs}$ (550 nm)	0.534	0.577	0.518	0.204	0.003
$V_{oc}$ (mV) (550 nm)	331	384	390	391	147

systems, respectively. The study of the ternary system phase diagram would also be interesting to gain further insight into the phase separation capabilities of the materials as well as optimum temperatures and compositions [11].

Summarizing the main results up to now, from a structural point of view, the random P3HT chains define a dilute matrix, or soft scaffolding, within which crystallites of the regular P3HT chains and aggregates of PCBM molecules can be formed in a controlled fashion (using the available but limited free volume), preventing large-scale phase separation of the components.

### 3.2. Charge carrier mobilities

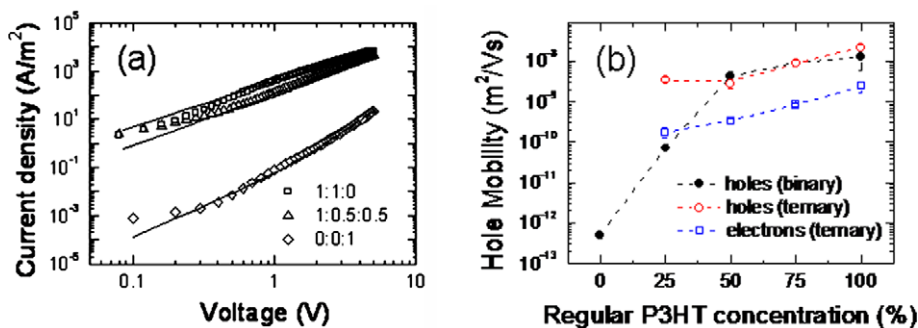
In order to understand the effect of ternary mixing in the carrier mobilities, devices have been fabricated in which the active blend film was sandwiched between two contacts that were selected in a way so to obtain hole only or electron only devices (see Section 2). By varying the film thickness we identified the range of thicknesses in which the current–voltage characteristics are governed by the space charge limited (SCL) regime. We then deduced the zero field hole and electron mobilities by fitting the current–voltage curves following Refs. [4] and [14]. Fig. 6a shows three representative cases. The experimental points (symbols) are very well fitted with the SCL equation for over three to four orders of magnitude in the values of the current density.

Fig. 6b shows the SCL deduced hole (circles) and electron (squares) mobilities for binary (solid symbols) and annealed ternary (open symbols) systems. Each data point is the average of the mobility values extracted from four devices. The hole mobility values obtained for the conventional blends agree well with those reported in the literature for annealed samples [4] ( $\sim 1.2 \cdot 10^{-8} \text{ m}^2 \text{ V}^{-1} \text{ s}^{-1}$ ). As for the electron mobility, our values are slightly smaller than those reported, perhaps due to a possible small partial oxidation of the evaporated Al electrode before the spin coating of the active blend, or to a small underestimation of the electron mobility values resulting from higher fitting standard deviations. Regio random P3HT shows a hole mobility of almost five orders of magnitude lower than that of regio regular P3HT. Interestingly, this value ( $\sim 5 \cdot 10^{-13} \text{ m}^2 \text{ V}^{-1} \text{ s}^{-1}$ ) is not very far from the hole

mobility values of  $\sim 3 \cdot 10^{-12} \text{ m}^2 \text{ V}^{-1} \text{ s}^{-1}$  exhibited by non-annealed (or low temperature annealed) regular P3HT blended with PCBM [4]. It seems clear, therefore, that the low mobility of RRa-P3HT is the result of lack of crystallinity and the associated weak interchain interactions (c.f. RR-P3HT).

Perhaps the most important result in this section is the finding that the carrier mobilities are only slightly affected by the introduction of this – very low mobility – polymer. Amazingly, substituting 75% of the regio regular chains by regio random chains in the ternary system only decreases the hole mobility from  $\sim 1.2 \cdot 10^{-8} \text{ m}^2 \text{ V}^{-1} \text{ s}^{-1}$  to  $\sim 3.5 \cdot 10^{-9} \text{ m}^2 \text{ V}^{-1} \text{ s}^{-1}$ , i.e. less than one order of magnitude. For comparison, it is worth noting that thermal annealing has a much stronger effect on charge transport: the as-spun conventional blend has almost four orders of magnitude lower hole mobility than the thermally annealed (at 130–150 °C) case [4]. However, this interesting result may not be unexpected on the light of the morphology investigations reported above: absorption, photoluminescence, AFM and XRD data all indicate that the ternary systems are also highly crystalline. Goffri et al. have also found a similar behavior for the field effect transistor hole mobility of P3HT blended with semicrystalline commodity polymers [25], so perhaps this is a relatively general trait of semiconducting polymers independent of whether mobility is measured across the film thickness or in the perpendicular direction, and even at totally different carrier density values. There are two possible readings for this phenomenon. First, the material percolation threshold requires very little amount of the crystallizing component (less than 25% in our case), probably due to the extended length of the polymeric macromolecule. A second interpretation could be, however, that most of the film is, in practice, not contributing (at least positively) to the transport of charges. The second possibility opens one important question: how could one process a film so to employ 100% of the material to actively participate in the charge transport? This key question has, to our knowledge, not been answered yet.

The slight mobility decrease might be related to smaller crystallite sizes. We find a linear relationship between charge mobility and crystallite size, with the holes having a stronger dependence (in terms of the slope of the fitted



**Fig. 6.** Study of the carrier mobility in binary and ternary systems. (a) Typical current density versus voltage curves for a conventional blend (open squares), a ternary blend with composition 1:0.5:0.5 (open triangles) and regio random P3HT (open diamonds). The solid lines are the fits to the SCL equations; (b) Hole (circles) and electron (squares) mobilities deduced for single carrier devices based on regular:random binaries (solid symbols) and ternary (open symbols) systems.

straight line). On the other hand, the mobility values do not seem to be so clearly related to the overall degree of P3HT crystallinity, i.e. when plotted together, the experimental points scatter through the graph with no distinguishable trend. This apparent contradiction was also observed in pristine P3HT films with different molecular weights: lower molecular weight P3HT is much more crystalline but, nonetheless, its mobility is lower than that of higher molecular weight P3HT [26,27]. This can be explained in terms of poorer connectivity and more insulating grain boundaries for the more crystalline polymer [26]. This explanation could be perfectly applied here, since smaller crystallites (even at a constant total crystallinity) would exhibit many more grain boundaries than larger crystallites. It is important to emphasize that, compared to the almost four orders of magnitude changes in field effect mobility [26] (or 15 times in the SCL mobilities [27]) observed when increasing the number average molecular weight from 3.2 to ca. 40 kDa, in our case the effect is very mild, with a decrease in zero field mobility of less than one order of magnitude when substituting 75% of RR-P3HT by RRa-P3HT.

It is important to note that binary and ternary systems have very similar hole mobilities for RRa-P3HT concentrations smaller than 50% with respect to the concentration of RR-P3HT. However, it seems that the percolation threshold for the binary happens at higher random concentration than in the ternary system. The thermal annealing (only applied here to the ternaries) may help to enhance hole mobility in the ternary systems containing 75% of regio random, when compared to the values for non-annealed binary RR-P3HT:RRa-P3HT blends with also 75% or RRa-P3HT, even when the crystallinity of the binaries is expected to be high according to their absorption spectra (Fig. 3a). Alternatively, this difference between binary and ternary blends may support the report by Tuladhar and co-workers [28], who were able to demonstrate that PCBM not only helps to enhance the hole mobility of the polymer by a possible modification of the polymer chain packing, but they also found that the hole and electron mobilities deduced using the time of flight technique for a system consisting of PCBM embedded into an insulating polystyrene matrix have a similar value, independently of

the film thickness. This strongly indicates that PCBM actively contributes to the hole mobility (polystyrene is an insulator). In other words, comparison between the mobility values deduced for regular:random binaries and the ternary systems may indicate that PCBM is also actively enhancing the hole mobility in our case.

### 3.3. Solar cells based on ternary systems

Fig. 7 shows the performance of solar cells based on ternary blend films with different RR- to RRa-composition ratios, and keeping the overall polymer to fullerene weight ratio constant (1:(X:Y)) with  $X + Y = 1$ . The current density vs. voltage curves measured at monochromatic light (550 nm, 20  $\mu$ W) show two clear trends with increasing regio random composition in the ternary: (i) decrease in the  $J_{sc}$ ; and (ii) increase in the  $V_{oc}$ . Table 1 summarizes these values.

The case of the  $V_{oc}$  can be understood in terms of the increase in the relative importance of the regio random chains in the charge generation. As we discussed above, the non-interacting chains of RRa-P3HT yield a higher HOMO than the crystalline P3HT [15,20]. Since the  $V_{oc}$  is proportional to the difference between the energy levels of the donor HOMO and acceptor LUMO [21], an increase in the polymer HOMO may be responsible for the observed increase in  $V_{oc}$ . This conclusion is supported by a recent study made with polythiophenes with different alkyl chain lengths (P3AT). It was found that the  $V_{oc}$  of annealed devices made with different P3ATs increases from 500 to 600 mV with increasing alkyl length – and thus reducing interchain interactions – from butyl to dodecyl [29]. A very recent report [30] on solar cells based on the addition of higher-HOMO level MDMO-PPV chains to the conventional PCBM:P3HT blends also shows improved  $V_{oc}$ , and thus again supports our hypothesis.

It is important to note that the increase in  $V_{oc}$  is not linearly proportional to the amount of RRa-P3HT, but, instead, it has a strong effect already for low random concentrations and then saturates at about 50%. This can be understood in terms of the resulting ternary blend morphology, since the PCBM molecules might accommodate themselves more easily in the polymer voids left by the amorphous

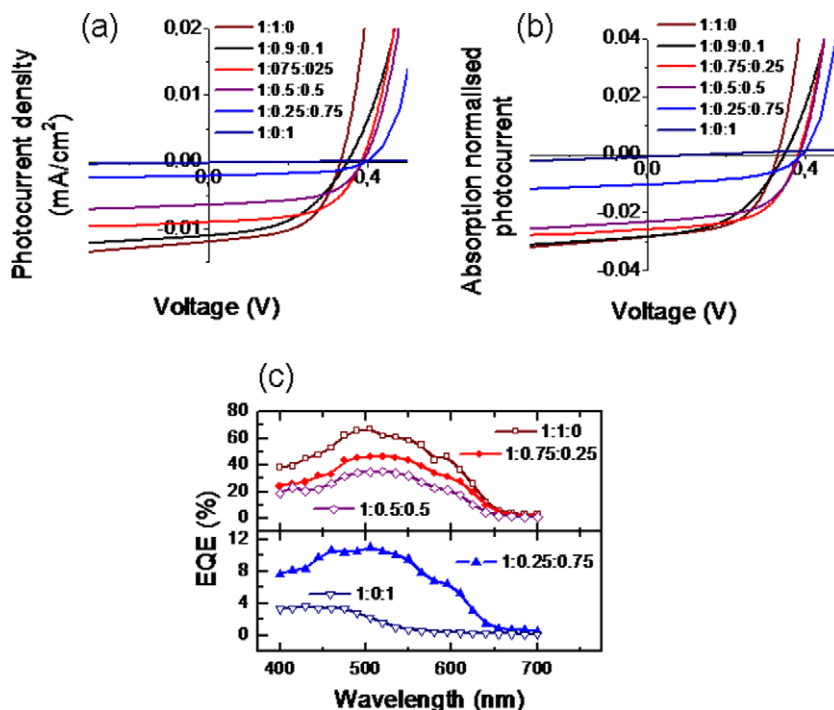


**Fig. 7.** Solar cell characteristics for devices based on the ternary systems.  $J$ - $V$  curves (a),  $J$ - $V$  curves normalized by the absorption at 550 nm (b) and EQE (c) for devices based on ternaries with constant solution concentration (60 mg/ml), and constant PCBM:polymer concentration (1:1), with varying relative concentrations of regular and random P3HT.

RRa-P3HT matrix than to be embedded into the RR-P3HT crystallites. This interpretation is supported by the PL quenching data shown in Fig. 4b. The measured superlinear behavior in the enhancement of  $V_{oc}$  with increasing RRa-P3HT content relaxes the apparent compromise between the observed opposite trends of  $J_{sc}$  and  $V_{oc}$ .

With respect to the decrease in the  $J_{sc}$ , it may be associated to the combination of two main factors: (1) a decrease in the absorption of the ternary active layer at 550 nm; and (2) a decrease in carrier mobility with increasing RRa-content. To evaluate the relative importance of these two factors, we have plotted in Fig. 7b the  $J$ - $V$  characteristics normalized by the absorption of the films at 550 nm. From this graph, it seems that there are two distinct regimes: up to concentrations containing 50% of RRa-, the effect of reduced mobility is only small; however, for larger amounts of the regio random polymer the polymer percolation threshold for good device operation is overpass and then the  $J_{sc}$  drastically falls.

We have recently demonstrated a similar compromise between  $J_{sc}$  and  $V_{oc}$  in organic solar cells using another approach but with a similar argument in terms of the energy levels of the active materials [31]. By inserting an ultrathin metal-phthalocyanine layer (CuPc or ZnPc, HOMO - 5.1 eV) at the bilayer interface between pentacene (HOMO  $\sim$  5.0 eV) and fullerene, a higher  $V_{oc}$  was observed. The  $V_{oc}$  increased with increasing CuPc or ZnPc layer thickness as a result of the higher-HOMO level; however, the  $J_{sc}$  decreased due to the lower mobility of the phthalocyanine than that of pentacene [31]. A compromise in phthalocyanine thickness was found between enhanced  $V_{oc}$  and

reduced  $J_{sc}$  so to finally obtain higher device efficiencies. Similarly, in the ternary blends case, increasing in excess the concentration of the low mobility random chains can lead to surpassing the threshold composition for percolation of the highly conductive regio regular P3HT chains and thus the photocurrent drops. However, the compromise between device parameters in the ternary blends is much more relaxed, as we will show below.

It is worth noticing that there could be an alternative explanation for the observed trends in photocurrent and open circuit voltage. This interpretation is based on the idea that the addition of the random chains may result in a different recombination constant. Assuming that the theory of Langevin recombination is valid in the ternary systems, a reduction in the mobility could cause a reduction of the recombination constant and therefore a lower photocurrent and a higher open circuit voltage, as it is sometimes observed in OPV systems based on polymers with low charge carrier mobilities [32]. As we will see, the fact that we can decouple the effect in  $J_{sc}$  and  $V_{oc}$  for low RRa-P3HT concentrations may suggest that this effect is significant only for large RRa-P3HT relative concentrations.

The different absorption spectra for varying compositions (Fig. 3 (a)) are also reflected in the external quantum efficiency (EQE), as shown in Fig. 7c. It is even possible to distinguish the RRa-P3HT absorption peak centered at around 450 nm in the EQE of the devices based on the 1:0.25:0.75 composition (top curve in bottom panel). This further indicates the active role that the random P3HT plays in the solar cell. We note that the relatively large inhomogeneity of the light intensity through the beam

spot leads to EQE uncertainties of the order of 5% in the deduced EQE values reported here.

Our results suggest that if the lower absorption is compensated for, small concentrations of RRa-P3HT could lead to overall better device performance by increasing  $V_{oc}$  while keeping  $J_{sc}$  constant. A straightforward way of doing this without the need for systematic optimization is to fabricate solar cells based on blends which keep the PCBM:RR-P3HT ratio (1:1) constant, and then adding small amounts of the RRa-P3HT into the solution. Fig. 8 shows the  $J$ - $V$  characteristics under the same illumination conditions as above for devices based on ternary films with PCBM:RR-P3HT:RRa-P3HT compositions 1:1:0.1 and 1:1:0.25, as well as the 1:1:0 conventional blend for reference. As we have predicted, once the absorption of light at 550 nm is kept constant, the  $J_{sc}$  shows an almost constant value within the experimental uncertainty. In fact, the EQE spectra at 0 V for these three devices are almost identical (not shown). On the other hand, the  $V_{oc}$  for solar cells based on ternary systems is clearly enhanced by more than 100 mV with respect to the reference conventional blend, as shown in Fig. 8. This is fully consistent with the 0.12 eV increase in HOMO level for RRa-P3HT compared to RR-P3HT, as deduced here using ultraviolet photoelectron spectroscopy. Moreover, the fill factor also slightly improves by ternary mixing. Overall, there is a 20% increase in the maximum power obtained at 550 nm,  $V_{max}J_{max}$  comparing the reference (1:1:0) and the sample with 25% added random polymer chains (1:1:0.25), which may indicate a 20% enhancement in efficiency in the current illumination conditions.

In order to check the evolution of device performance and morphology with time, these three samples (with four devices per sample) were measured again after a period of 10 months, through which they were kept in air and in darkness. These solar cells still work perfectly fine after this time span, which suggests that the glass encapsulation and darkness ambient conditions have prevented chemical oxidation of the active layers and interfaces. Nonetheless, there are some changes in the current/voltage curves after this time, which we preliminarily assign to morphologic relaxation of the films over time. These changes over time are much larger than the pin to pin differences amongst

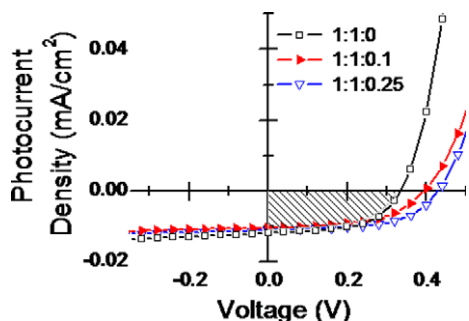


**Fig. 8.** Solar cell characteristics for devices based on the ternary systems with equivalent short circuit current.  $J$ - $V$  curves for devices based on ternaries with constant PCBM:regular P3HT concentration (1:1), with added regio random P3HT 1:1:0 (open squares), 1:1:0.1 (filled triangles) and 1:1:0.25 (open down triangles).

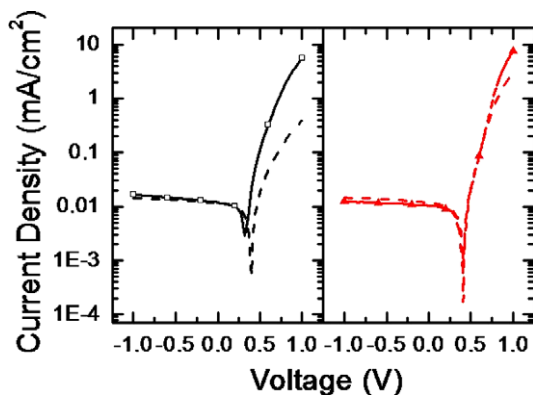


**Fig. 9.**  $J$ - $V$  curves in logarithmic scale for PCBM:Regular P3HT concentration (1:1:0), (open squares, left panel) and with added Regio Random P3HT 1:1:0.1 (filled triangles, right panel) as prepared (solid lines) and after 10 months (dashed lines).

the four pins in a given sample. The percentage change of the  $J$ - $V$  curves (see Fig. 9) when comparing the samples as fabricated and after 10 months is much more pronounced (~75% more) for the conventional binary than for the ternary-based samples. These data suggest that the natural entanglement of the glassy amorphous RRa-P3HT chains helps to stabilize the film morphology and thus, positively contributes to increase the effective lifetime of the cells. These preliminary results are currently being systematically investigated in order to further test the hypothesis of improved morphological stability.

The OPV performance under varying light intensities shows that the  $V_{oc}$  of the conventional binary-based cells increases with light intensity towards the  $V_{oc}$  of the ternary system cells (see Fig. 10). This may suggest that the regular chains that do not form part of the crystallites, and thus are found in a more amorphous state, begin to participate on the photovoltaic action for higher light intensities, perhaps after the expected charge traps are filled. Our proposed ternary system-based devices exhibit a less strong intensity dependence of performance (and always higher  $V_{oc}$  regardless of the light intensity), as deduced from the slopes of

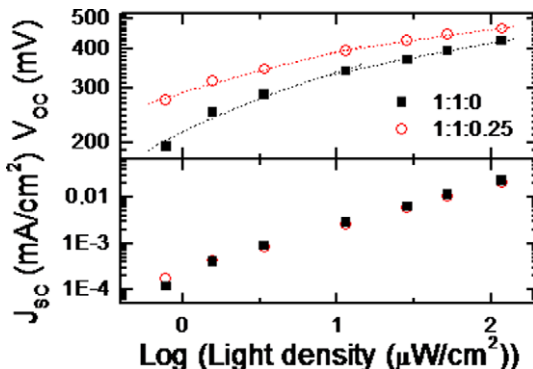


**Fig. 10.** Solar cell characteristics as a function of the incident light intensity. Light intensity dependence of the open circuit voltage (top panel) and short circuit current (bottom panel) for a conventional blend (squares) and a 1:1:0.25 ternary blend (circles).



the linear fits in Fig. 10. This may be originated, as we have mentioned, by a reduced recombination constant arising from slightly lower mobilities in the ternary systems than the conventional blend [32]. This weaker dependence in light intensity could mean a significant advantage when this type of device is used in low light intensity applications such as highly sensitive photodiodes and solar cells placed indoors or at particular outdoor conditions (e.g. cloudy days or early and late hours of the day).

Although there are clearly a large number of parameters that could be further optimized, such as polymer molecular weights [26,27], ternary composition [11,25], thermal annealing treatment [4,33] and film thickness [34,35], it is patent that the presented strategy results in a more controlled blend structure and enhanced solar cell performance. The device optimization might be facilitated by the measurement of the phase diagram of the ternary system, which will aid to predict the optimum composition ratio and thermal annealing treatment [11]. Moreover, the natural entanglement of the glassy chains may also help to provide long-term morphological stability, as suggested by our preliminary results, which would help to keep a constant performance of the devices under operation at elevated temperatures. Some of these investigations are currently being carried out and will be published elsewhere.

Finally, we believe that the ternary mixing approach is very general, and could be used to control the morphology at the micro- and nano-scales for a large variety of semi-crystalline polymers with poor capability for quality film formation when blended with fullerenes and otherwise good optoelectronic properties. Examples of this include polythiophenes with different alkyl side chains, such as poly(3-butylthiophene) (P3BT) [29,36], Selene-substituted regio regular poly(3-hexyl)selenophene (P3HS) [37], and very low band gap regular poly(3-decyloxythiophene-2,5-diyl) (P3DOT) [38], to name but a few. Furthermore, other dilute polymer matrices might be used to add different functionalities, such as simultaneous optimization of charge generation and transport [13,30] or chemical and mechanical stability [25], which could permit an overall more efficient and stable organic solar cell and thus bring closer the market uptake turn point of this technology.

#### 4. Conclusions

To summarize, in this contribution we have investigated ternary systems consisting in adding regio random P3HT into the conventional regular P3HT:PCBM blends. The rationale for this was to be able control the formation of microscale phase separation through the natural entanglement of random polymer chains, while allowing the formation of crystallites at the nanoscale in the voids left by the diluted polymer matrix. We successfully demonstrate that ternary mixing helps to control the morphology by reducing the area covered with unwanted micron-sized aggregates from 9% in the conventional blend, down to less than 0.04% for the ternaries. Moreover, the addition of random polymer chains does not prevent the crystallization of their regular counterparts and we found, in fact, that the overall degree of film crystallization is enhanced in the ter-

nary blends, at the expenses of smaller crystallite sizes. This results in the fact that concentrations of up to 50% of the random polymer in the total polymer content have a very small effect on charge carrier mobilities, compared, for instance, to the effects due to thermal annealing or molecular weight. Finally, we fabricated solar cells based on ternary systems and show that they exhibit a similar short circuit current but ca. 100 mV positively shifted open circuit voltage which results in enhanced device efficiency. The origin of this shift is associated to a higher polymer HOMO arising from the isolated – non-interacting – nature of the random chains.

#### Acknowledgments

M.C.Q. would like to thank the Japan Society for Promotion of Science for granting a postdoctoral fellowship under which most of this research was carried out and also acknowledges the Japan Advanced Institute of Science and Technology (JAIST) for their great hospitality. The authors are very grateful to Mr. T. Nakayama (of JAIST) for the photoelectron spectroscopy measurements.

#### References

- [1] C.J. Brabec, J.R. Durrant, *MRS Bull.* 33 (2008) 670.
- [2] J.Y. Kim, K. Lee, N.E. Coates, D. Moses, T.-Q. Nguyen, M. Dante, A.J. Heeger, *Science* 317 (2007) 222.
- [3] M.A. Green, K. Emery, Y. Hishikawa, W. Warta, *Prog. Photovolt: Res. Appl.* 17 (2009) 85.
- [4] V.D. Mihailetschi, H. Xie, B. de Boer, L.J.A. Koster, P.W.M. Blom, *Adv. Funct. Mater.* 16 (2006) 699.
- [5] S.E. Shaheen, C.J. Brabec, N.S. Sariciftci, F. Padinger, T. Fromherz, J.C. Hummelen, *Appl. Phys. Lett.* 78 (2001) 841.
- [6] W. Ma, C. Yang, X. Gong, K. Lee, A.J. Heeger, *Adv. Funct. Mater.* 15 (2005) 1617.
- [7] G. Li, V. Shrotriya, J. Huang, Y. Yao, T. Moriarty, K. Emery, Y. Yang, *Nat. Mater.* 4 (2005) 864.
- [8] M. Campoy-Quiles, T. Ferenczi, T. Agostinelli, P.G. Etchegoin, Y. Kim, T.D. Anthopoulos, P.N. Stavrinou, D.D.C. Bradley, J. Nelson, *Nat. Mater.* 7 (2008) 158.
- [9] X. Yang, J. Loos, *Macromolecules* 40 (2007) 1353.
- [10] D. Chirvase, J. Parisi, J.C. Hummelen, V. Dyakonov, *Nanotechnology* 15 (2004) 1317.
- [11] C. Müller, T.A.M. Ferenczi, M. Campoy-Quiles, J.M. Frost, D.D.C. Bradley, P. Smith, N. Stingelin-Stutzmann, J. Nelson, *Adv. Mater.* 20 (2008) 3510.
- [12] E. Klimov, W. Li, X. Yang, G.G. Hoffmann, J. Loos, *Macromolecules* 39 (2006) 4493.
- [13] W. Ma, J.Y. Kim, K. Lee and Alan J. Heeger, *Macromol. Rapid Commun.* 28 (2007) 1776.
- [14] T. Matsushima, Y. Kinoshita, H. Murata, *Appl. Phys. Lett.* 91 (2007) 253504.
- [15] X. M. Jiang, R. Österbacka, O. J. Korovyanko, C. P. An, B. Horovitz, R. A. J. Janssen and Z. V. Vardeny, *Adv. Funct. Mater.* 12(2002) 587.
- [16] Tian-An Chen, Xiaoming Wu, and Reuben D. Rieke, *J. Am. Chem. Soc.* 117 (1995) 233.
- [17] H. Sirringhaus, N. Tessler, R.H. Friend, *Science* 280 (1998) 1741.
- [18] M. Campoy-Quiles, J. Nelson, D.D.C. Bradley, P.G. Etchegoin, *Phys. Rev. B* 76 (2007) 235206.
- [19] U. Zhokhavets, T. Erb, G. Gobsch, M. Al-Ibrahim, O. Ambacher, *Chem. Phys. Lett.* 418 (2006) 347.
- [20] D. Beljonne, J. Cornil, H. Sirringhaus, P.J. Brown, M. Shkunov, R.H. Friend, J.-L. Brédas, *Adv. Funct. Mater.* 11 (2001) 229.
- [21] M.C. Scharber, D. Mühlbacher, M. Koppe, P. Denk, C. Waldauf, A.J. Heeger, C.J. Brabec, *Adv. Mater.* 18 (2006) 789.
- [22] This argument is based on the proportionality between the crystallinity of the film and the intensity of the 650 nm shoulder found by Zhokhavets et al. in Ref. [19].
- [23] Y. Kim, S. Cook, S.M. Tuladhar, S.A. Choulis, J. Nelson, J.R. Durrant, D.D.C. Bradley, M. Giles, I. McCulloch, C.-S. Ha, M. Ree, *Nat. Mater.* 5 (2006) 197.

- [24] D.M. DeLongchamp, B.M. Vogel, Y. Jung, M.C. Gurau, C.A. Richter, A. Kirillov, J. Obrzut, D.A. Fischer, S. Sambasivan, L.J. Richter, E.K. Lin, *Chem. Mater.* 17 (2005) 5610.
- [25] S. Goffri, C. Müller, N. Stingelin-Stutzmann, D.W. Breiby, C.P. Radano, J.W. Andreasen, R. Thompson, R.A.J. Janssen, M.M. Nielsen, P. Smith and H. Sirringhaus, *Nat. Mater.* 5 (2006) 950.
- [26] R.J. Kline, M.D. McGehee, *J. Macromol. Sci. C: Pol. Rev.* 46 (2006) 27.
- [27] C. Goh, R.J. Kline, M.D. McGehee, et al., *Appl. Phys. Lett.* 86 (2005) 122110.
- [28] S.M. Tuladhar, D. Poplavskyy, S.A. Choulis, J.R. Durrant, D.D.C. Bradley, J. Nelson, *Adv. Funct. Mater.* 15 (2005) 1171.
- [29] L.H. Nguyen, H. Hoppe, T. Erb, S. Günes, G. Gobsch, N.S. Sariciftci, *Adv. Funct. Mater.* 17 (2007) 1071.
- [30] Y. Kim, M. Shin, H. Kim, Y. Ha, C.-S. Ha, *J. Phys. D: Appl. Phys.* 41 (2008) 225101.
- [31] Y. Kinoshita, T. Hasobe, H. Murata, *Appl. Phys. Lett.* 91 (2007) 083518.
- [32] L.J.A. Koster, V.D. Mihailetchi, R. Ramaker, P.W.M. Blom, *Appl. Phys. Lett.* 86 (2005) 123509.
- [33] H. Kim, M. Shin, Y. Kim, *J. Phys. Chem. C* 113 (2009) 1620.
- [34] G. Li, V. Shrotriya, Y. Yao, Y. Yang, *J. Appl. Phys.* 98 (2005) 043704.
- [35] K.O. Sylvester-Hvid, T. Ziegler, M.K. Riede, N. Keegan, M. Niggemann, A. Gombert, *J. Appl. Phys.* 102 (2007) 054502.
- [36] H. Xin, F.S. Kim, S.A. Jenekhe, *J. Am. Chem. Soc.* 130 (2008) 5424.
- [37] A.M. Ballantyne, L. Chen, J. Nelson, D.D.C. Bradley, Y. Astuti, A. Maurano, C.G. Shuttle, J.R. Durrant, M. Heeney, W. Duffy, I. McCulloch, *Adv. Mater.* 19 (2007) 4544.
- [38] C. Shi, Y. Yao, Y. Yang, Q. Pei, *J. Am. Chem. Soc.* 128 (2006) 8980.

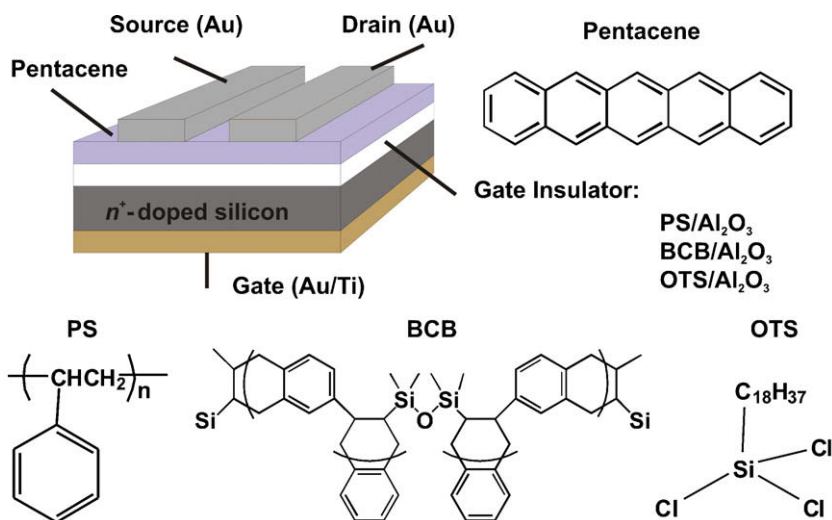


Fig. 1. Schematics of a pentacene OFET along with the chemical structures of the materials used in the study.

Crosslinkable BCB can provide a high-quality hydroxyl-free interface [10] to organic semiconductors with a high dielectric breakdown strength exceeding 3 MV/cm [11]. With poly ( $\alpha$ -methylstyrene) (PMS) as a surface modification layer on gate dielectrics, a record mobility of 7 cm<sup>2</sup>/V s in a thin-film pentacene transistor has been reported [12]. Here, polystyrene (PS) instead of PMS was used due to its lack of dipole moment (such as CH<sub>3</sub><sup>-</sup> in PMS). Both BCB and PS have already been demonstrated as stable gate dielectrics for *n*-channel C<sub>60</sub> OFETs by our group [13].

## 2. Experimental details

Pentacene transistors were fabricated on heavily *n*-doped silicon substrates (*n*<sup>++</sup>-Si, as the gate electrode) with a 100 nm-thick Al<sub>2</sub>O<sub>3</sub> layer deposited by atomic layer deposition (ALD) as a gate dielectric insulator. The process details and dielectric characterization of Al<sub>2</sub>O<sub>3</sub> by ALD are described elsewhere [14]. A top-contact OFET device geometry was used as shown in Fig. 1. To better control the interfacial properties at the dielectric and the pentacene layer, as well as enhance the device operation stability and reproducibility, the Al<sub>2</sub>O<sub>3</sub> dielectric surface was passivated with different hydroxyl-free polymers (PS and BCB in this work) as thin buffer layers. The thin polymeric layers were formed and processed as follows. The BCB thin films from diluted Cyclotene™ 3022 were crosslinked at 250 °C on a hot plate for 1 h in a N<sub>2</sub>-filled glovebox. PS

films were spin-coated from a 4 mg/ml solution in toluene and annealed at 130 °C on a hot plate for 1 h. The Al<sub>2</sub>O<sub>3</sub> surface was also modified with a self-assembled monolayer (SAM) with octadecyl-trichlorosilane (OTS) molecules. OTS has been widely known as a good tunneling barrier to hydroxyl groups on oxide surfaces due to its long alkyl chain, and a good surface layer for controlling structural order of pentacene films. OTS layer was formed by soaking the substrates in a 5 mM toluene solution of OTS for 15 h in a dry N<sub>2</sub>-filled glovebox. The capacitance density *C*<sub>OX</sub> (nF/cm<sup>2</sup>) was measured from parallel-plate capacitors with 12 varying contact areas. The added buffer layer on Al<sub>2</sub>O<sub>3</sub> reduced the capacitance density *C*<sub>OX</sub> from 66.4 nF/cm<sup>2</sup> to 64.1 nF/cm<sup>2</sup> with OTS, to 46.8 nF/cm<sup>2</sup> with BCB, and to 42.7 nF/cm<sup>2</sup> with PS. The results on *C*<sub>OX</sub> are listed in Table 1 and were used to calculate the OFET electrical parameters.

Pentacene (Aldrich), purified using gradient zone sublimation, was deposited at a rate of 1 Å/s to a thickness of 50 nm. 60 nm-thick Au as S/D electrodes were deposited at a rate 1 Å/s on top of pentacene through a shadow mask in the same chamber without breaking the vacuum. The substrates were held unheated during the deposition and the chamber vacuum was about 5 × 10<sup>-8</sup> Torr. The samples were transferred in a vacuum tight vessel without being exposed to atmospheric conditions into a N<sub>2</sub>-filled glovebox (O<sub>2</sub>, H<sub>2</sub>O < 1 ppm) for electrical testing. The electrical measurements were performed using an Agilent E5272A source/monitor unit in the dark.

Table 1

Summary of the electrical parameters for pentacene OFETs with different dielectric surfaces. *rms*, root-mean-square surface roughness;  $\theta$ , water contact angle on the dielectric surface;  $\mu$ , field-effect mobility; *V*<sub>TO</sub>, turn-on voltage; *V*<sub>T</sub>, threshold voltage; *S*, subthreshold slope; *I*<sub>on/off</sub>, on/off current ratio;  $\tau$ , characteristic trapping time;  $\beta$ , dispersion parameters.

Pentacene OFETs with	<i>rms</i> (Å)	$\theta$ (°)	<i>C</i> <sub>OX</sub> (nF/cm <sup>2</sup> )	$\mu$ (cm <sup>2</sup> /Vs)	<i>V</i> <sub>TO</sub> (volts)	<i>V</i> <sub>T</sub> (volts)	<i>S</i> (V/dec)	<i>I</i> <sub>on/off</sub> × 10 <sup>5</sup>	$\tau$ (s)	$\beta$
PS/Al <sub>2</sub> O <sub>3</sub>	2.3	84	42.7	0.64	-1.6	-3.39	0.20	7.2	1.5 × 10 <sup>8</sup>	0.41
BCB/Al <sub>2</sub> O <sub>3</sub>	2.4	86	46.8	0.47	-1.6	-3.62	0.26	3.8	2.4 × 10 <sup>5</sup>	0.41
OTS/Al <sub>2</sub> O <sub>3</sub>	4.1	98	64.1	0.36	0.2	-0.86	0.30	1.7	2.1 × 10 <sup>6</sup>	0.42

The chemical and physical surface properties of the dielectrics, including surface wetting properties, surface roughness, and surface defect density are important parameters that affect the electrical performance of OFETs, through the morphology/structural ordering of organic semiconductor films and the charge transport at the dielectric/semiconductor interface. To characterize the surface properties, the surface morphology of  $\text{Al}_2\text{O}_3$  with different surface modification layers was investigated by AFM (Digital Instruments NanoScope™ Scanning Probe Microscopes). The root-mean-square (*rms*) surface roughness of the dielectric surfaces with different surface treatment was estimated to be below 5 Å when measured over an area of  $1\ \mu\text{m} \times 1\ \mu\text{m}$ , as listed in Table 1. With polymeric surfaces, the dielectric surface roughness of 100 nm-thick  $\text{Al}_2\text{O}_3$  was further decreased to below 3 Å after spin coating. The effect of surface roughness on the charge transport at the interface can be negligible for a *rms* value smaller than 5 Å [15,16]. The surface energy of the dielectric surface with different buffering layers was studied by contact angle measurement using DI water, with the results listed in Table 1. All the surfaces became highly hydrophobic with aqueous contact angles around  $90^\circ$ , indicating low surface energy with BCB, PS or OTS as passivation layers on the dielectric surface.

The morphology of pentacene films can be affected by the deposition conditions (substrate temperature, deposition rate and thickness) as well as the dielectric surface

properties (surface roughness, surface energy, and etc). Here, the deposition conditions of pentacene were kept constant. AFM and X-ray diffraction (XRD) were used to characterize the film morphology and the structural ordering of pentacene molecules, as illustrated in Fig. 2. Pentacene films on all dielectric surfaces exhibited high structural order and displayed island formation. However, the grain size varied significantly for the substrates with different surface energy and surface roughness. The morphology of pentacene shows small grains on OTS-treated  $\text{Al}_2\text{O}_3$ , probably caused by the large surface roughness of the dielectrics. The pentacene growth on the smoother dielectric surfaces (PS and BCB in this case), on the other hand, was less disturbed and prone to form large grains and good connectivity. The slight difference on the grain size with PS and BCB can be attributed to the different surface energy. The diffraction spectrum of island films consisted of crystalline peaks with a first diffraction peak at  $2\theta = 5.74^\circ$ , corresponding to “thin film” spacing of 15.4 Å, and the presence of higher order peaks was observed. The lattice spacing corresponds to a tilt of the molecules of  $17.1^\circ$  to the surface normal, assuming a triclinic single crystal structure. The presence of a “bulk” phase of pentacene with a spacing of 14.4 Å was not observed since the substrate temperature was held at room temperature during deposition. The XRD peak intensity mirrored the grain size of the crystalline structure observed in the AFM images; films with larger grains showed higher intensity.

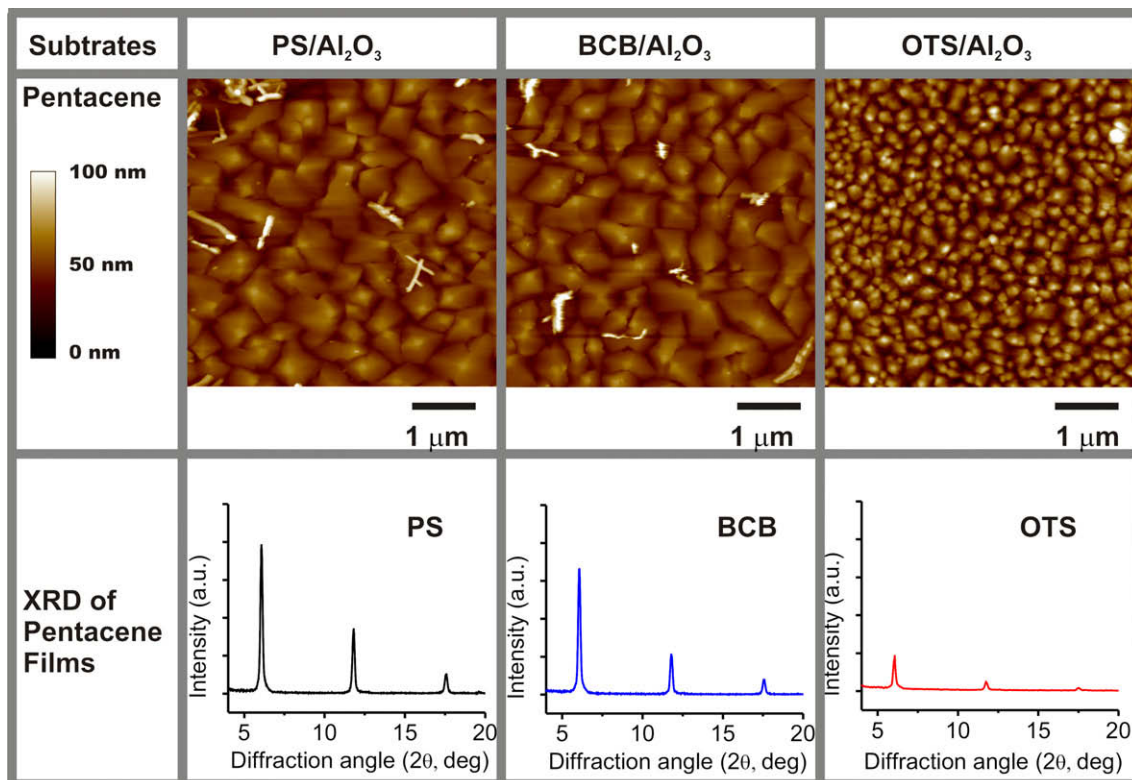


Fig. 2. AFM images and XRD patterns of pentacene films on the different dielectric surfaces.

### 3. Operational stability and electrical characterization

In order to accurately characterize the device performance, the devices need to be stable during measurement. Testing procedures like hysteresis scans and duty-cycle-like tests were used to test the stability and reproducibility of the devices. The fabrication and testing were carried-out in a  $N_2$ -filled glove box in the dark so that the device instabilities induced by light, water, and oxygen were avoided. The electrical instability/degradation is attributed to both trapping by shallow and deep states. For deeper trapping sites, longer trapping time/relaxation time is required. The trapping at the shallow sites is usually reversible sometimes even at room temperature. The ratio and distribution of shallow and deep traps are dependent on the materials, fabrication, and device operation. Electrical instability induced by the trapping on different time scales can manifest itself as a hysteresis, a current decay, or a threshold voltage shift. The devices showing hysteresis are less stable, and this property is highly undesirable when the devices are not used as memory devices.

The hysteretic transfer characteristics were measured with a resolution of 20 ms and duration of several seconds in the saturation regime with  $V_{DS} = -10$  V. The representative transfer curves and normalized output curves ( $I_{DS}$  was normalized by the capacitance density  $C_{OX}$ ) are compared in Fig. 3 for the devices with the same geometry (channel length  $L$  of 100  $\mu\text{m}$  and channel width  $W$  of 1000  $\mu\text{m}$ ) and different dielectric surface treatments. On the time

scale of this measurement, negligible hysteresis and threshold voltage shift were found in transistors with polymeric dielectric surfaces as well as OTS-treated dielectric surfaces. Next, all devices were repeatedly stressed by measuring transfer characteristics in the saturation regime 100 times with a 2 s waiting time between cycles. The superimposed measured transfer curves from the first 10 cycles and the last 10 cycles are shown in Fig. 4. Here again, no significant performance degradation could be observed in any of the transistors under investigation. The shape of the successive transfer curves remained unchanged during hysteresis scans and during 100 duty-cycle scans, indicating there exists no shallow states from structure defects within the semiconductor or the gate dielectric caused by the applied gate field [17]. In these two types of measurements, the rest time between successive stressing was varied between 20 ms to several seconds and no changes could be observed. We can speculate that either no fast trapping had occurred or that the trapped charges were de-trapped/released during the rest time. Negligible threshold voltage shift occurred on this time scale, indicating a good electrical stability and reproducibility for devices under normal operation using  $Al_2O_3$  gate dielectrics with PS, BCB, and OTS passivation layers. This can be attributed to the low concentration of shallows traps at the dielectric surfaces. Trapping species expected at  $Al_2O_3$  surfaces, such as highly polar  $Al(OH)_3$ , absorbed water molecules, or other impurities, are screened by the hydroxyl-free polymers used to passivate the surface.

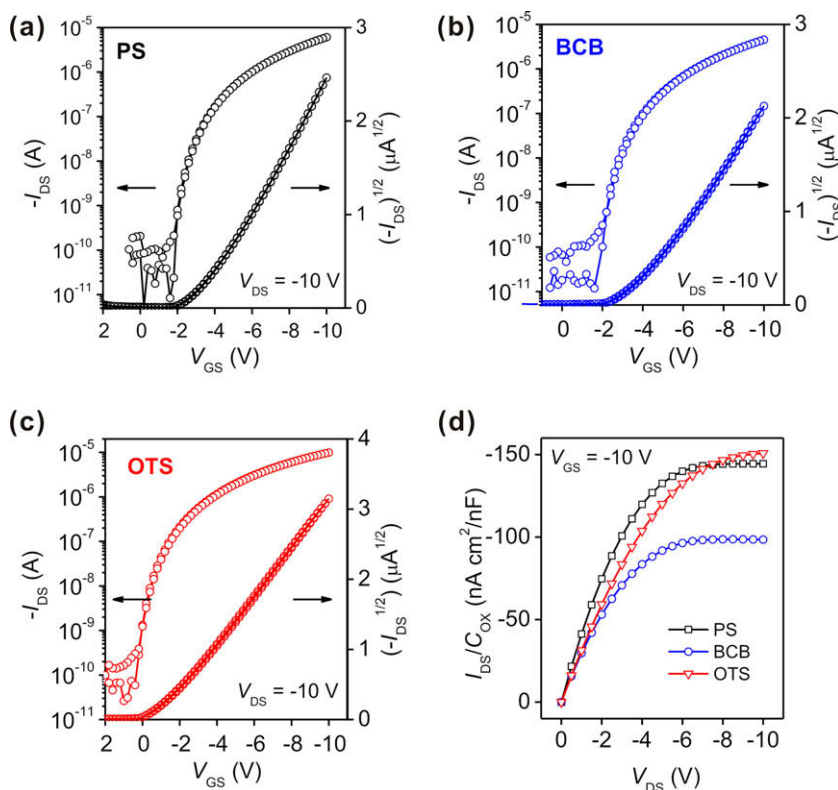
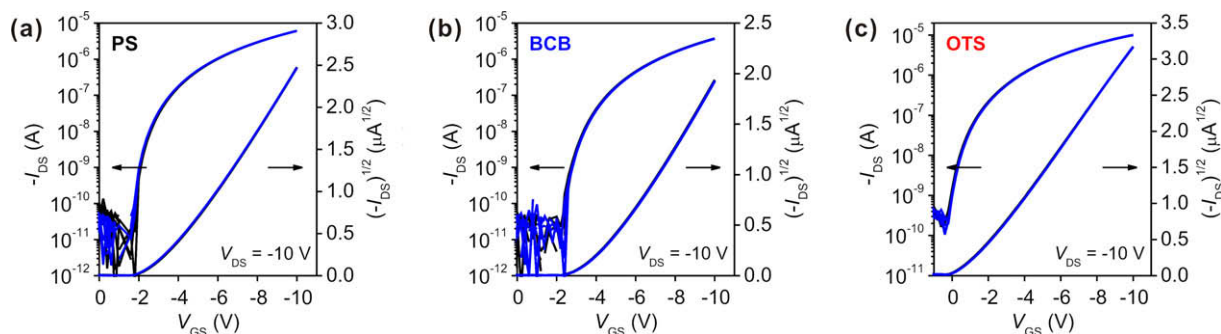


Fig. 3. (a)–(c) Hysteretic transfer characteristics with  $V_{DS} = -10$  V. (d) Comparison of output characteristics with  $V_{GS} = -10$  V.



**Fig. 4.** Superimposed transfer curves from the first 10 scans (black) and the last scans (blue) during a duty-cycle-like test with 100 scans and 2 s rest time between cycles. (For interpretation of the references to colour in this figure legend, the reader is referred to the web version of this article.)

With good stability under normal operating conditions, the device performance parameters can be extracted reliably from a forward gate bias scan as seen in Fig. 3. Field-effect mobilities  $\mu$  and threshold voltages  $V_T$  were calculated in the saturation regime defined by standard MOSFET models by fitting the  $\sqrt{I_{DS}}$  vs.  $V_{GS}$  data to the square law. Also extracted from the transfer characteristics are the turn-on voltage ( $V_{TO}$ ) and the on/off current ratio ( $I_{on/off}$ ). The extracted electrical parameters ( $\mu$ ,  $V_{TO}$ ,  $V_T$ ,  $S$ , and  $I_{on/off}$ ) are summarized and compared in Table 1 along with  $rms$  and  $C_{OX}$  previously measured.

Devices with PS and BCB dielectric surfaces show similar electrical performance with high mobility, low sub-threshold voltage, and high on/off current ratios. The higher mobility from pentacene transistors on PS can be correlated to the structural ordering of pentacene films: larger grains, higher XRD intensity and less trapping. Since OTS might not fully passivate the  $Al(OH)_3$  groups on the surface, these electron-trapping residuals could give rise to an earlier turn-on voltage and lower threshold voltages in pentacene OFETs with OTS.

To investigate the dependence of mobility on the channel length  $L$ , field-effect mobilities of devices are statistically plotted over the inverse of channel length ( $L^{-1}$ ) with a channel width  $W = 1000 \mu m$  in Fig. 5a. All the devices with different dielectric surfaces show a similar trend: the mobility remains nearly independent of channel

length larger than  $25 \mu m$ . However, the device mobility with short channels of  $25 \mu m$  increases instead of decreasing like in many organic transistors where the channel current is contact-limited due to the large Schottky barrier at the metal/organic interface. The higher mobilities at short-channel devices could be explained through the presence of fewer traps in the grain boundaries existing within a shorter length. It also implies a very low contact resistance and good ohmic contact between Au S/D electrode and pentacene films.

To gain a better understanding of the effect of the contacts on the mobility, the contact resistance of pentacene transistors with PS as a surface treatment layer was extracted using the transmission line method (TLM) based on the dependence of current–voltage characteristics on channel length. In the linear regime, the overall device resistance  $R_{on}$  can be considered as the sum of the channel resistance  $R_{ch}$  and a total contact resistance  $R_C$  according to Rolland [18]. A set of devices with channel lengths ranging from  $L = 50$  to  $200 \mu m$  and a fixed channel width of  $W = 1000 \mu m$  was used to calculate the contact resistance at a low drain-source voltage ( $V_{DS}$ ) of  $-0.1 V$  for  $V_{GS}$  values ranging from  $-3$  to  $-10 V$ . The width-normalized contact resistance ( $R_C W$ ) was estimated using the y intercept of the least squares when extrapolating  $R_{on} W$  to  $L = 0 \mu m$ , as plotted in Fig. 5b. The contact resistance drops drastically with  $V_{GS}$  since the resistance of pentacene film was

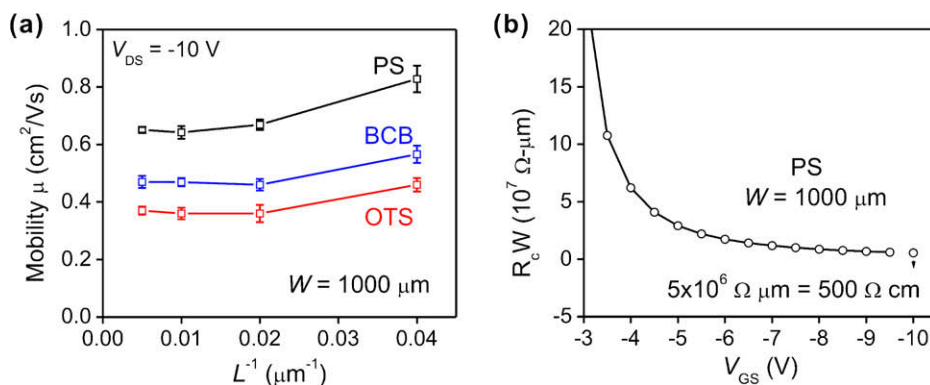


**Fig. 5.** (a) The dependence of mobility on the inverse of channel length. (b) The width-normalized contact resistance obtained from pentacene OFETs with PS dielectric interface.

reduced by the increasingly induced charge density in the accumulation regime with  $V_{GS}$ . A low  $R_C W$  of  $500 \Omega \text{ cm}$  was achieved at  $V_{GS} = -10 \text{ V}$ . This value is even lower than the best result reported by Klauk et al. [19]. Since the contact resistance between the Au S/D electrodes and pentacene films is quite low and the values are similar for the devices with different dielectric surfaces, its change during the operation can be negligible compared to that of the channel resistance with a long channel length such as  $L = 100 \mu\text{m}$ . Therefore, the effect of contact resistance on the electrical stability can be ignored in this study.

#### 4. Bias stress effect

To further explore the effect of different dielectric interfaces on the stability of pentacene transistors, the time-dependent decay of  $I_{DS}$  was tested under dc bias stress with  $V_{GS} = V_{DS} = -10 \text{ V}$  for 1 h, as plotted in Fig. 6a. The current decay in this experiment exhibited typical features of bias stress instability showing an exponential decay function. The trapping rate slows down with stressing time since the density of the vacant trapping sites decreases as more holes are trapped with time. Then, trapped charges screen the electrical field and in turn cause the negative shift of the threshold voltage.

The bias stress instability can be described by a stretched-exponential function based on threshold voltage shift ( $\Delta V_T$ ) or drain-source channel current decay. A stretched-exponential equation was proposed by Libsch and Kanicki based on  $\Delta V_T$  [20]:

$$|\Delta V_T(t)| = |V_{GS} - V_{TO}| \left\{ 1 - \exp \left[ - \left( \frac{t}{\tau} \right)^\beta \right] \right\}. \quad (1)$$

$V_{GS} - V_{TO}$  is the effective voltage drop across the gate insulator and  $V_{TO}$  is the initial threshold voltage at  $t = 0 \text{ s}$ . The dispersion parameter  $\beta$  is the stretched-exponential factor, reflecting the width of the involved trap distribution. The constant  $\tau$  represents the characteristic trapping time of the carriers. The trapping/detrapping process is assumed thermally activated.

The above model can be extended with the measurement of drain-source channel on-current decay with time

under dc bias stress [21]. Using on-current degradation instead of threshold voltage shift to estimate stability can avoid the error and inaccuracy caused by the measurement and extraction of threshold voltages. The derivation of stretched-exponential function based on on-current degradation was carried-out as follows.

The current–voltage characteristics in the saturation regime can be described as:

$$I_{DS} = \frac{1}{2} \mu C_{OX} \frac{W}{L} (V_{GS} - V_{TO})^2 = K(V_{GS} - V_{TO})^2. \quad (2)$$

When the device has been operated for a long period of time  $t$  that resulted in a threshold voltage shift  $\Delta V_T$ , the current–voltage characteristics after an elapsed time  $t$  can be expressed as:

$$I_{DS}(t) = K[V_{GS} - (V_{TO} + \Delta V_T(t))]^2. \quad (3)$$

Then, the current decay with time  $\Delta I_{DS}(t)$  can be described as:

$$\Delta I_{DS}(t) = \frac{I_{DS}(t)}{I_{DS0}} = \frac{[V_{GS} - (V_{TO} + \Delta V_T(t))]^2}{(V_{GS} - V_{TO})^2}. \quad (4)$$

Combining a stretched-exponential function for  $\Delta V_T$  from Eq. (1), a stretched-exponential function for  $\Delta I_{DS}(t)$  can be reduced to:

$$\Delta I_{DS}(t) = \frac{I_{DS}(t)}{I_{DS0}} = \exp \left[ -1 \left( \frac{t}{\tau} \right)^\beta \right] \quad (5)$$

As shown in Fig. 6a, the solid points are the experimental data and the line is a fit according to Eq. (5). The simulated results indicate that the experimental data can be fitted with Eq. (5) where the on current in the channel was obtained in the saturation regime.

The threshold voltage shift under the same condition can be calculated from Eq. (1) using the fitting parameters listed in Table 1, as shown in Fig. 6b. The dispersion parameter  $\beta$ , reflecting the width of the involved trap distribution, is similar (0.41–0.42) in the devices with polymeric interfaces and SAM. The values are similar to the value obtained by Mathijssen [3,22] using hexamethyldisilazane (HMDS) SAM to passivate the dielectric surface. The  $\beta$  value was found to be lower with higher HMDS coverage

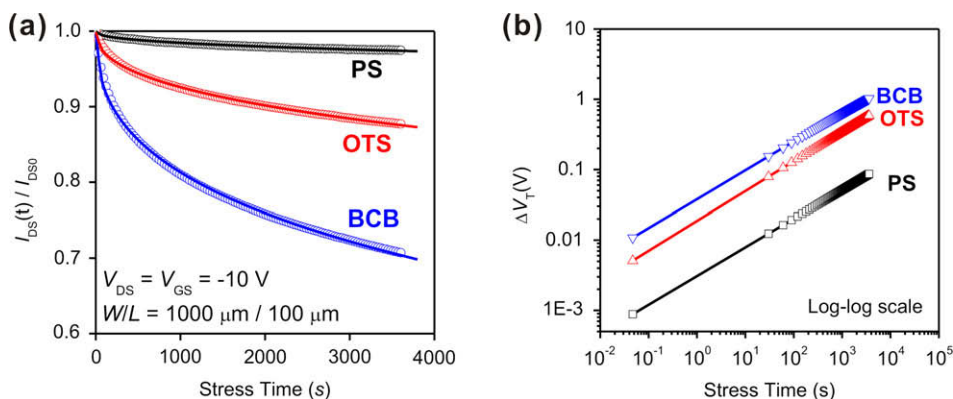


**Fig. 6.** (a) Drain-source current decay when stressed with  $V_{GS} = V_{DS} = -10 \text{ V}$  for 1 h with a resolution of 20 ms. The points are experimental data and the dash lines are the fitting curves using Eq. (5). (b) Threshold voltage shift ( $\Delta V_T$ ) was simulated with the fitting parameters obtained from Fig. 6a.

[3]. The stability during dc bias stress can be quantitatively compared with the trapping time  $\tau$  at room temperature. Longer times  $\tau$  are desirable because they lead to transistors with smaller threshold voltage shifts and increased stability. Since polar Al(OH)<sub>3</sub> groups can act as traps, the presence of a spatial barrier between the mobile charge carriers and the traps results in a much longer time scale for the threshold voltage shift dynamics. Therefore, the stability of the devices with treated dielectric surfaces (PS, BCB or OTS SAM) was improved with values for  $\tau$  in the range of  $10^5$ – $10^8$  s, with small  $\Delta V_T$  below 1 V. Among them, pentacene OFETs with a PS-treated gate dielectric surface show the highest stability with the trapping time even longer than that of amorphous Si thin film transistors (TFTs) [23]. Pentacene transistors passivated with PS exhibit an outstanding stability with estimated  $\Delta V_T$  of 0.2 V after 3600 s stressed under dc bias with  $V_{GS} = V_{DS} = -10$  V based on the values of  $\beta$  and  $\tau$  extracted by fitting the current decay. Devices with OTS-treated surfaces also show good stability with time constants in the range of  $10^6$ – $10^7$  s, which agrees well with the results reported by Miyadera using  $\beta$ -phenethyltrichlorosilane SAM [24].

We notice that the stability with BCB-treated gate dielectrics in pentacene OFETs is poorer than that of devices with PS or OTS SAM. This observation is in contrast with the results obtained in *n*-channel C<sub>60</sub> OFETs where devices with BCB-treated gate dielectrics were found to be most stable [13]. Hence, there is a fundamental difference in the trapping mechanisms giving rise to the degradation of the electrical performance of C<sub>60</sub> and pentacene-based OFETs with BCB-treated gate dielectrics. The non-polar nature of BCB seems to rule out a dipolar origin to the trapping mechanisms occurring in pentacene OFETs, therefore further investigation is required to explore the origin of this slow trapping mechanism. It is worth pointing out that in C<sub>60</sub> OFETs, passivation of the gate dielectric with PS acted almost as effectively as BCB to stabilize the electrical performance. Therefore, the results presented in this paper also indicate that PS offers a good compromise to achieve stable operation both in C<sub>60</sub> and pentacene OFETs. Indeed, with PS as the gate dielectric passivation layer, organic complementary inverters with high noise margins and dc gains have been demonstrated recently [25].

The characteristic trapping time  $\tau$  ( $10^5$ – $10^8$ ) is several orders of magnitude longer than the time duration for hysteresis and repeatability ( $10^{-3}$ – $10$  s) testing. In other words, when the devices experienced short-time stress, no bias stress effect was introduced. To further investigate the trap distribution and the activation energy of traps, the measurement of current decay at various thermal temperatures is required.

This model is able to predict the threshold shift behavior for any time duration. However, this model only addresses the electrical stress with dc bias. In AMLCD, a-Si:H TFTs are subjected to pulsed gate bias addressing with a typical frequency of 60 Hz [26]. The magnitude of threshold voltage shift caused by ac stress or pulsed gate bias is significantly lower. A logical explanation is that the trapped charges at the shallow states will be released if the rest time between the testing is longer than the trapping time.

## 5. Conclusion

We studied the device performance and operational stability of pentacene OFETs in which the gate dielectric was passivated by PS and BCB polymers or by OTS. The device performance was found to correlate with the structural ordering of pentacene films and the surface properties of gate dielectrics. Both PS and BCB passivation can yield devices with high charge mobility due to the formation of pentacene films with large grain size on the smooth surface with low surface energy. However, when measured under prolonged dc gate bias, the electrical performance of devices with BCB deteriorated. The stability of devices with OTS was found superior but the best overall performance was obtained in devices passivated with PS.

## Acknowledgements

This material is based upon work supported in part by the STC Program of the National Science Foundation under Agreement No. DMR-0120967 and by the Office of Naval Research. This work was performed in part at the Microelectronics Research Center at Georgia Institute of Technology, a member of the National Nanotechnology Infrastructure Network, which is supported by NSF (Grant No. ECS-03-35765). We also would like to thank Dr. Soo Young Kim from Prof. Seth R. Marder's research group for the XRD measurement of the pentacene films.

## References

- [1] H.L. Cheng, W.Y. Chou, C.W. Kuo, Y.W. Wang, Y.S. Mai, F.C. Tang, S.W. Chu, *Adv. Funct. Mater.* 18 (2008) 285.
- [2] T.N. Ng, J.H. Daniel, S. Sambandan, A.C. Arias, M.L. Chabiny, R.A. Street, *J. Appl. Phys.* 103 (2008) 044506.
- [3] S.G.J. Mathijssen, M. Kemerink, A. Sharma, M. Coelle, P.A. Bobbert, R.A.J. Janssen, D.M. de Leeuw, *Adv. Mater.* 20 (2008) 975.
- [4] S.D. Wang, T. Minari, T. Miyadera, Y. Aoyagi, K. Tsukagoshi, *Appl. Phys. Lett.* 92 (2008) 063305.
- [5] T. Richards, H. Sirringhaus, *Appl. Phys. Lett.* 92 (2008) 023512.
- [6] D. Kumaki, T. Umeda, S. Tokito, *Appl. Phys. Lett.* 92 (2008) 093309.
- [7] C. Kim, A. Facchetti, T.J. Marks, *Adv. Mater.* 19 (2007) 2561.
- [8] M.-H. Yoon, C. Kim, A. Facchetti, T.J. Marks, *J. Am. Chem. Soc.* 128 (2006) 12851.
- [9] S.Y. Yang, K. Shin, C.E. Park, *Adv. Funct. Mater.* 15 (2005) 1806.
- [10] L.-L. Chua, J. Zaumseil, J.-F. Chang, E.C.W. Ou, P.K.H. Ho, H. Sirringhaus, R.H. Friend, *Nature* 434 (2005) 194.
- [11] L.-L. Chua, P.K.H. Ho, H. Sirringhaus, R.H. Friend, *Appl. Phys. Lett.* 84 (2004) 3400.
- [12] T.W. Kelley, D.V. Muyres, F.P. Baude, T.P. Smith, T.D. Jones, *Materials Research Society, San Francisco, CA, United States*, 2003 (p. 169).
- [13] X.-H. Zhang, B. Domercq, B. Kippelen, *Appl. Phys. Lett.* 91 (2007) 092114.
- [14] X.-H. Zhang, B. Domercq, X. Wang, S. Yoo, T. Kondo, Z.L. Wang, B. Kippelen, *Org. Electron.* 8 (2007) 718.
- [15] S. Steudel, S. De Vusser, S. De Jonge, D. Janssen, S. Verlaak, J. Genoe, P. Heremans, *Appl. Phys. Lett.* 85 (2004) 4400.
- [16] S.E. Fritz, T.W. Kelley, C.D. Frisbie, *J. Phys. Chem. B* 109 (2005) 10574.
- [17] A. Salleo, F. Endicott, R.A. Street, *Appl. Phys. Lett.* 86 (2005) 263505.
- [18] A. Rolland, J. Richard, J.P. Kleider, D. Mencaraglia, *Jpn. J. Appl. Phys. Part 1* 35 (1996) 4257.
- [19] H. Klauk, U. Zschieschang, M. Halik, *J. Appl. Phys.* 102 (2007) 074514/1.
- [20] F.R. Libsch, J. Kanicki, *Appl. Phys. Lett.* 62 (1993) 1286.
- [21] C.C. Shih, Y.S. Lee, K.L. Fang, C.H. Chen, F.Y. Gan, *IEEE Trans. Device Mater. Reliab.* 7 (2007) 347.
- [22] S.G.J. Mathijssen, M. Colle, H. Gomes, E.C.P. Smits, B. de Boer, I. McCulloch, P.A. Bobbert, D.M. de Leeuw, *Adv. Mater.* 19 (2007) 2785.



- [23] S.C. Deane, R.B. Wehrspohn, M.J. Powell, *Phys. Rev. B* 58 (1998) 12625.
- [24] T. Miyadera, S.D. Wang, T. Minari, K. Tsukagoshi, Y. Aoyagi, *Appl. Phys. Lett.* 93 (2008) 033304.
- [25] X.-H. Zhang, J. William, J. Potscavage, S. Choi, B. Kippelen, *Appl. Phys. Lett.* 94 (2009) 043312.
- [26] C.R. Kagan, P. Andry, *Thin-Film Transistors*, CRC Press, Boca Raton, FL, USA, 2003.

the Ag anode. P3HT was known to be a hole-transport material and has been frequently applied in the devices of organic field-effect transistor [12,13] and photovoltaic [14–16]. The hole-transport property of P3HT is supposed to be advantageous to the hole-injection from an Ag anode. Furthermore, it had been shown that P3HT molecules bond chemically to Ag or Cu substrates through the linkage of S atom in the thiophene ring [17]. Therefore, it is possible to prepare a P3HT thin layer on Ag surface using a facile self-assembly process. This strategy was first examined in this work.

In a previous research [18], it was found that a SAM containing a terminal group of high electronegativity (e.g. fluorine) triggers a high work function of the modified surface. Based on this result, an electron-withdrawing function group, 1-fluoro-2-nitro-4-azidobenzene (FNAB), was introduced into the terminal tail ( $-C_6H_{13}$ ) of the P3HT thin layer. This modified anode, Ag/P3HT/FNAB, was proved to have a higher work function and is more efficient to enhance the hole-injection. The importance of P3HT in the present strategy was confirmed by comparing the result with another device using 3-methylthiophene ( $CH_3TP$ )-modified Ag anode.

## 2. Experimental

Two T-PLEDs (ITO/Ag/HY-PPV/Ca/Ag and ITO/modified Ag/HY-PPV/Ca/Ag) were prepared in this study. Ag film of 150 nm thickness is deposited on the cleaned ITO glass substrate by thermal evaporation under a base pressure  $10^{-6}$  torr and a deposited rate of 0.1 Å/s. After formation of Ag film, Ag anode was immersed in a chloroform solution containing 0.1 wt% P3HT for 30 min. After rinsing with chloroform and dried in a nitrogen steam, the P3HT modified anode, Ag/P3HT, was prepared. For the Ag/P3HT/FNAB anode, appropriate amount of FNAB solution was spread on Ag/P3HT substrate and air-dried in dark. FNAB was prepared by diazotization reaction of 4-fluoro-3-nitroaniline (FNA) as the procedure reported in the literature [19–21]. The FNAB-covered substrate was then exposed to a UV lamp (365 nm) for 20 min to carry out the nitrene reaction between azide ( $N_3$ ) group of FNAB and methyl group ( $-CH_3$ ) of P3HT. The substrate was then washed in succession by chloroform, and acetone, and dried in a nitrogen steam. The substrate was delivered to a vacuum chamber at  $10^{-2}$  torr for 1 h and then transferred to the nitrogen-filled glove-box. The proposed structures for the prepared

P3HT and P3HT/FNAB thin layers were schematically shown in Fig. 1. “High-yellow” phenyl-substituted poly(*para*-phenylenevinylene) copolymer (HY-PPV) was used as the light-emissive layer and was spin-coated onto the Ag anodes. Finally, a semi-transparent top cathode, Ca (12 nm)/Ag (17 nm), was vapor deposited under  $10^{-6}$  torr. The active pixel area of the device was 6 mm<sup>2</sup>. The current–voltage ( $I$ – $V$ ) and brightness–voltage ( $L$ – $V$ ) characteristics were measured using a current/voltage source measurement unit (Keithley 2400) and a calibrated silicon photodiode driven by a Keithley source. The EL spectra are measured by a CCD array spectrum meter (Ocean optics USB2000). All the measurements are performed in a nitrogen-filled glove-box. XPS spectra were measured by JEOL, JAMP-9500F auger electron spectroscopy with a Mg  $K\alpha$  source (1253.6 eV). The work function of the anode electrodes were measured by a Riken Keiki AC-2 photoelectron spectroscopy in air.

## 3. Results and discussion

Table 1 shows the contact angle of water on base and modified Ag substrates. The contact angle of water on base Ag surface is 77.0°, ascribed to the absorption of hydrocarbon and carbonaceous impurities to the atmosphere [22]. After modification by P3HT, the contact angle increases slightly to about 107.1°, a value consistent to the contact angle measured for alkyl-chain terminated surfaces (90–110°) [23,24]. Therefore, the hydrophobic property of the P3HT modified Ag surface is attributed to the exposing of alkyl chains ( $-C_6H_{13}$ ) contained in P3HT molecules.

After incorporation of FNAB by nitrene reaction, the contact angle of water on the Ag/P3HT/FNAB substrate was measured to be 92.6°. The effect of UV light illumination (required for nitrene reaction) on the P3HT properties was also examined by exposing the Ag/P3HT under UV lamp (365 nm) for 20 min. The contact angle measured for the UV-treated Ag/P3HT substrate was 106.5°, which is nearly identical to the result of non-UV-treated Ag/P3HT. This result suggests that the UV light illumination does not make significant change to the surface wettability of Ag/P3HT and, therefore, after the nitrene reaction, any variation in the contact angle should be resorted to the incorporation of FNAB [20]. For the ideal molecular model proposed in Fig. 1, the terminated ( $-CH_3$ ) group was replaced by a less hydrophobic group FNAB. Therefore, it is

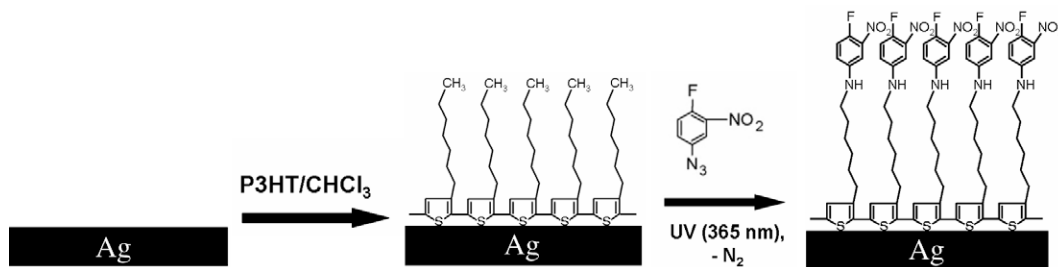
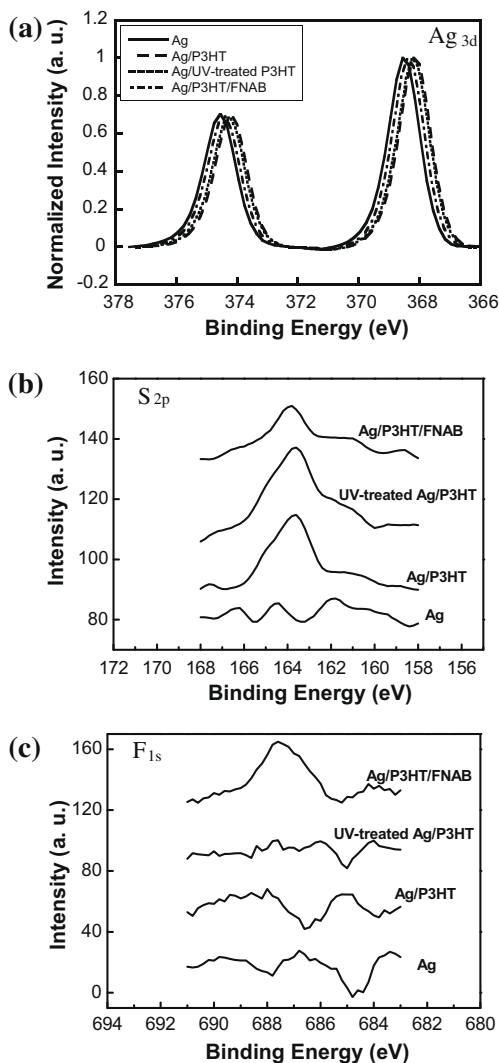


Fig. 1. The process for the deposition of P3HT and FNAB.

**Table 1**

Contact angle of water on base and modified substrates.

Substrates	Contact angle of water (°)
Ag	77.0
Ag/P3HT	107.1
Ag/UV-treated P3HT	106.5
Ag/P3HT/FNAB	92.6

**Fig. 2.** High resolution XPS scans of  $\text{Ag}_{3d}$  (a),  $\text{S}_{2p}$  (b), and  $\text{F}_{1s}$  (c) regions for the base and modified Ag anodes.

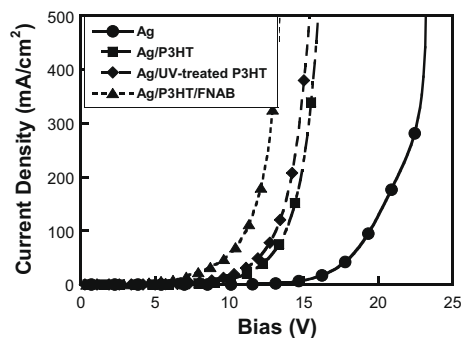
reasonable that the contact angle will become smaller after the nitrene reaction.

The surface compositions of the substrates were measured by XPS. Fig. 2 shows the high resolution XPS spectra scanning over the binding energy range of  $\text{Ag}_{3d}$ ,  $\text{S}_{2p}$ , and  $\text{F}_{1s}$ . In Fig. 2a, peaks corresponding to  $\text{Ag}_{3d_{3/2}}$  and  $\text{Ag}_{3d_{5/2}}$  were observed on all the substrates, including the modified and unmodified ones. In comparison with the base Ag substrate, the binding energy of  $\text{Ag}_{3d}$  decreases slightly after

the modification of P3HT or P3HT/FNAB, attributable to the chemical bonding of silver to the sulfur atom in P3HT [26]. For the  $\text{S}_{2p}$  peaks shown in Fig. 2b, the peaks appear only on Ag/P3HT, Ag/UV-treated P3HT, and Ag/P3HT/FNAB anodes, demonstrating the presence of P3HT molecules on the modified Ag surfaces. The feature peaks of  $\text{S}_{2p}$  exhibit a doublet structure at 162.1/163.6 eV, corresponding to  $\text{S}_{2p_{3/2}}$  and  $\text{S}_{2p_{1/2}}$  peaks of silver-thiolate sulfur species ( $\text{Ag-S-R}$ ) [25]. This result gives further evidence to the chemical linkage of sulfur to the silver substrate. In Fig. 2c, the peak at 687.6 eV observed on Ag/P3HT/FNAB surface is consistent with the binding energy of a fluorine atom bonded to an aromatic ring. It is reasonable that  $\text{F}_{1s}$  peak does not appear on the other Ag anodes.

The effect of the P3HT and P3HT/FNAB modification on the hole-injection was studied first by using hole-dominated devices which using aluminum as cathodes. The  $J$ - $V$  characteristics of these devices are shown in Fig. 3. It was found that the threshold voltage of charge injection decreases significantly due to the modification of Ag anode. Furthermore, the Ag/P3HT/FNAB anode demonstrates a superior effect, than Ag/P3HT, in enhancing the hole-injection.

The enhancement effect of these modified layers was studied by measuring the work function of the related anodes using AC2 and the result were shown in Table 2. It appears that the work functions of these anodes increase in the order: Ag (4.35 eV) < Ag/P3HT (4.42 eV) < Ag/UV-treated P3HT (4.47 eV) < Ag/P3HT/FNAB (4.65 eV). It is noteworthy that the highest occupied molecular orbital (HOMO) of P3HT measured by AC2 is 4.68 eV [26]. The work function measured for Ag/P3HT, 4.42 eV, indicates that the P3HT assembled on the Ag surface is not in a bulk state, but as an ultrathin-film. The HOMO level of HY-PPV was reported to be 5.2 eV [27]. Therefore, the barrier height for the hole-injection decreases with increasing work function of these electrodes. The deposition of P3HT layer on an Ag surface causes only a slightly increase of work function (0.07 eV), which is similar to the increment of work function (0.05 eV) caused by the following UV-treatment. Comparing between Ag/P3HT and Ag/UV-treated P3HT anode, the slightly decrease of threshold voltage of the Ag/UV-treated P3HT anode is attributed to the small increase of the work function after the UV-treatment.

**Fig. 3.**  $J$ - $V$  characteristics for ITO/Ag/HY-PPV/Al and ITO/modified Ag/HY-PPV/Al devices.

**Table 2**

Work function measured by AC2 for the base and modified Ag anodes.

Substrates	Work function (eV)
Ag	4.35
Ag/P3HT	4.42
Ag/UV-treated P3HT	4.47
Ag/P3HT/FNAB	4.65

However, in comparison with the base Ag anode, the threshold voltage of Ag/P3HT anodes decreases significantly due to the presence of P3HT thin layer, which cannot be attributed completely to the small increment of work function. Therefore, the intrinsic property of the P3HT thin layer should play a role to enhance the hole-injection from the Ag anode to HY-PPV layer, probably associated with the hole-transport characteristic of P3HT.

For the Ag/P3HT/FNAB anode which has the best performance in hole-injection, the work function greatly increases from 4.42 to 4.65 eV due to the incorporation of FNAB, attributed to the presence of the fluorine and NO<sub>2</sub> group at the terminated group of the thin layer. The high electronegativity of fluorine atoms and NO<sub>2</sub> group triggers a polarization of electrons toward the end groups, inducing a dipole moment on the surface, shifting the vacuum energy to a higher level, and therefore, leading to a higher work function of the Ag/P3HT/FNAB anode [4]. The large increment of work function due to the incorporation of FNAB is reasonably responsible for significant decrease of threshold voltage of the Ag/P3HT/FNAB anode.

In order to identify the intrinsic property effect of P3HT on the hole-injection, 3-methylthiophene (CH<sub>3</sub>TP), a molecule with similar structure as the repeated unit of P3HT, was also used to modify the Ag anode. The CH<sub>3</sub>TP-modified Ag anode (Ag/CH<sub>3</sub>TP), as well as the anode further modified by FNAB (Ag/CH<sub>3</sub>TP/FNAB), was used to fabricate hole-dominated devices. The *J*-*V* curves measured for these devices were shown in Fig. 4. The result shows that the threshold voltage measured for the Ag/CH<sub>3</sub>TP device is much higher than that for the bare Ag anode. That is, introduction of the CH<sub>3</sub>TP layer triggers an additional resistance to the hole-injection, a result contrary to the effect of P3HT. However, for the following UV-treatment and FNAB modification, their enhancement effects are similar to that ob-

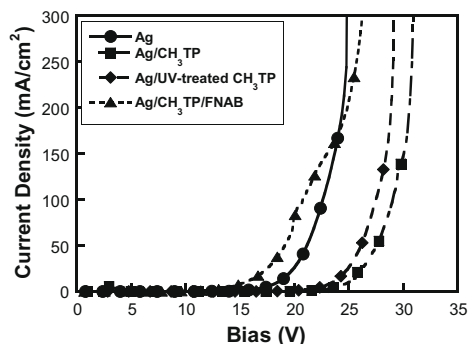


**Fig. 4.** *J*-*V* characteristics for ITO/Ag/HY-PPV/Al and ITO/modified Ag/HY-PPV/Al devices.

served for P3HT. Since CH<sub>3</sub>TP is not a semi-conducting material as P3HT, the presence of a CH<sub>3</sub>TP layer forms a passivation layer on Ag surface which obstructs the transport of charges. On the other hand, insertion a thin layer with p-type semi-conducting characteristic (e.g. P3HT) between Ag anode and emitting layer is advantageous to the hole-injection. It is inferred that the presence of an ultra-thin hole-conducting layer triggers an easier injection of holes from Ag to HY-PPV layer. However, the real mechanism is presently not understood completely.

After confirming the effect of modified layers on the hole-injection, these modified anodes were applied to fabricate top-emitting devices. Fig. 5 shows the *J*-*V* and *L*-*V* characteristics of the top-emitting devices with the structures of ITO/Ag(150 nm)/HY-PPV/Ca(12 nm)/Ag(17 nm), ITO/Ag(150 nm)/P3HT/HY-PPV/Ca(12 nm)/Ag(17 nm), and ITO/Ag/P3HT/FNAB/HY-PPV/Ca(12 nm)/Ag(17 nm). The results show that the effects of P3HT and P3HT/FNAB layers on the threshold voltages of *J*-*V* (Fig. 5a) and *L*-*V* (Fig. 5b)

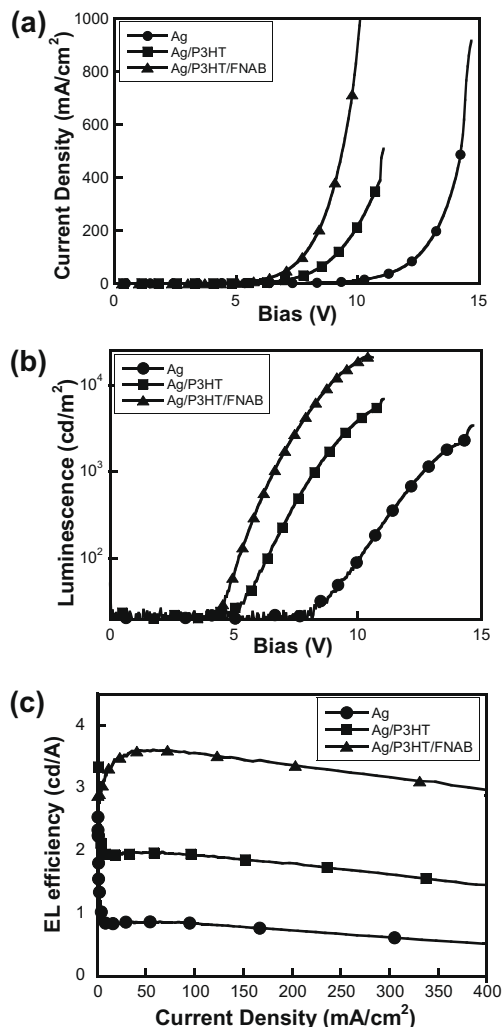


**Fig. 5.** *J*-*V* characteristics for ITO/Ag/HY-PPV/Ca/Ag and ITO/modified Ag/HY-PPV/Ca/Ag devices.

curves are similar to those on the hole-dominated devices shown in Fig. 3. The maximum brightness obtained from the base Ag, Ag/P3HT, and Ag/P3HT/FNAB anodes are 3432 cd/m<sup>2</sup> (at 14.67 V), 6960 cd/m<sup>2</sup> (at 11.06 V), and 21339 cd/m<sup>2</sup> (at 10.46 V), respectively. The luminous efficiencies (*LE*) shown in Fig. 5c demonstrate that the Ag/P3HT/FNAB anode has the highest efficiency, which is about four times higher than the efficiency of a base device. At a light intensity of 1000 cd/m<sup>2</sup>, the *LE* of the base Ag, Ag/P3HT, and Ag/P3HT/FNAB device are 0.82, 1.97, and 3.51 cd/A, respectively. The highest performance of Ag/P3HT/FNAB anode is attributed both to the hole-transport characteristic of P3HT and the increase of work function induced by the incorporation of FNAB.

#### 4. Conclusion

P3HT thin layer was proved to be an efficient modified layer of an Ag anode for enhancing the hole-injection of a T-PLED. The introduction of the P3HT causes little increase in the work function and, therefore, the enhancement effect of the P3HT thin layer is ascribed to its hole-conducting characteristic. By using a nitrene reaction, FNAB can be incorporated into the terminal group of the P3HT thin layer, which leads to a significant increase of work function and a further improvement in the hole-injection and device performance. By using the present strategy, the luminous efficiency of a T-PLED can be increased to a value four times higher than that of a base device.

#### References

- [1] H.-W. Choi, S.-Y. Kim, K.-B. Kim, Y.-H. Tak, J.-L. Lee, *Appl. Phys. Lett.* 86 (2005) 012104.
- [2] C.-W. Chen, P.-Y. Hsieh, H.-H. Chiang, C.-L. Lin, H.-M. Wu, C.-C. Wu, *Appl. Phys. Lett.* 83 (2003) 5127.
- [3] S. Khodabakhsh, D. Poplavskyy, S. Heutz, J. Nelson, D.D.C. Bradley, H. Murata, T.S. Jones, *Adv. Funct. Mater.* 14 (2004) 1205.
- [4] B. de Boer, A. Hadipour, M.M. Mandoc, T. van Woudenberg, P.W.M. Blom, *Adv. Mater.* 17 (2005) 621.
- [5] M.-C. Hung, K.-Y. Wu, Y.-T. Tao, H.-W. Huang, *Appl. Phys. Lett.* 89 (2006) 203106.
- [6] J. Chu, Q. Huang, J.G.C. Veinot, H. Yan, T.J. Mark, *Adv. Mater.* 14 (2002) 565.
- [7] J. Chu, Q. Huang, J.G.C. Veinot, H. Yan, Q. Wang, G.R. Hutchison, A.G. Richter, G. Evmenenko, P. Dutta, T.J. Mark, *Langmuir* 18 (2002) 9958.
- [8] J.E. Malinsky, G.E. Jabbour, S.E. Shaheen, J.D. Anderson, A.G. Richter, T.J. Marks, N.R. Armstrong, B. Kippelen, P. Dutta, N. Peyghambarian, *Adv. Mater.* 11 (1999) 227.
- [9] C.-C. Hsiao, C.-H. Chang, M.-C. Hung, N.-J. Yang, S.-A. Chen, *Appl. Phys. Lett.* 86 (2005) 223505.
- [10] Y. Koide, Q. Wang, J. Chu, D.D. Benson, T.J. Marks, *J. Am. Chem. Soc.* 122 (2000) 11266.
- [11] B. Choi, J. Rhee, H.H. Lee, *Appl. Phys. Lett.* 79 (2001) 2109.
- [12] L. Bürgi, H. Sirringhaus, R.H. Friend, *Appl. Phys. Lett.* 80 (2002) 2913.
- [13] Z. Bao, A. Dodabalapur, A.J. Lovinger, *Appl. Phys. Lett.* 69 (1996) 4108.
- [14] O. Douhéret, L. Lutsen, A. Swinnen, M. Bresselge, K. Vandewal, L. Goris, J. Manca, *Appl. Phys. Lett.* 89 (2006) 032107.
- [15] D.J.D. Moet, L.J.A. Koster, B. de Boer, P.W.M. Blom, *Chem. Mater.* 19 (2007) 5856.
- [16] L. Shen, G. Zhu, W. Guo, C. Tao, X. Zhang, C. Liu, W. Chen, S. Ruan, Z. Zhong, *Appl. Phys. Lett.* 92 (2008) 073307.
- [17] A. Lachkar, A. Selmani, E. Sacher, M. Leclerc, R. Mokhliss, *Synth. Met.* 66 (1994) 209.
- [18] L.-W. Chong, Y.-L. Lee, T.-C. Wen, T.-F. Guo, *Appl. Phys. Lett.* 89 (2006) 233513.
- [19] A. Naqvi, P. Nahar, *Anal. Biochem.* 327 (2004) 68.
- [20] S.K. Arya, P.R. Solanki, R.P. Singh, M.K. Pandey, M. Datta, B.D. Malhotra, *Talanta* 69 (2006) 918.
- [21] G.W.J. Fleet, R.R. Porter, J.R.K. Knowles, *Nature* 224 (1969) 511.
- [22] C.E. Taylor, S.D. Garvey, J.E. Pemberton, *Anal. Chem.* 68 (1996) 2401.
- [23] Y.-L. Lee, H.-Y. Wu, C.-H. Chang, Y.-M. Yang, *Thin Solid Film* 423 (2003) 169.
- [24] T.L. Metroke, J.S. Gandhi, A. Applett, *Prog. Org. Coat.* 50 (2004) 231.
- [25] S. He, J. Yao, S. Xie, H. Gao, S. Pang, *J. Phys. D: Appl. Phys.* 34 (2001) 3425.
- [26] W.-Y. Chou, S.-T. Lin, H.-L. Cheng, F.-C. Tang, Y.-J. Lin, C.-F. You, Y.-W. Wang, *Appl. Phys. Lett.* 90 (2007) 222103.
- [27] X. Gong, D. Moses, A.J. Heeger, S. Liu, A.K.-Y. Jen, *Appl. Phys. Lett.* 83 (2003) 183.

In this paper, we report efficient red, green, and blue (RGB) single layer phosphorescent OLEDs with a configuration of ITO/dopant:TPBi/LiF/Al, in which TPBi is 1,3,5-tris(*N*-phenylbenzimidazole-2-yl)benzene for electron transport, while the dopant was varied among tris(1-phenylisoquinoline)iridium [Ir(piq)<sub>3</sub>], tris(2-phenylpyridine)iridium [Ir(ppy)<sub>3</sub>] and bis(3,5-difluoro-2-(2-pyridyl)phenyl-(2-carboxypyridyl)iridium [Flrpic] to realize different emission colors. Subsequently, the device structure was optimized by inserting a pure dopant buffer layer to ITO/dopant/dopant:host/LiF/Al for efficiency and stability improvement, as well as maintaining the simple material selection and fabrication. It was found that efficient simplified RGB phosphorescent OLEDs could be realized by utilizing the triplet dopant's charge transport properties to directly accept and transport holes from ITO anode to the emission zone.

## 2. Experimental

Ir(piq)<sub>3</sub>, Ir(ppy)<sub>3</sub>, and TPBi were purchased from Lum-Tec, used as received. Flrpic was synthesized according to the literature [20], sublimated prior to use. To construct an appropriate device configuration for RGB devices, we first used green dopant Ir(ppy)<sub>3</sub> to optimize the overall device thickness, doping concentration, thickness of the buffer layer and so forth. We then applied these parameters to fabricate red and blue OLEDs. All devices were fabricated in a Kurt J. Lesker LUMINOS<sup>®</sup> cluster tool, using a method described previously [21]. Briefly, the commercially patterned anode with a sheet resistance of 15 Ohms/sq was ultrasonically cleaned with a standard regiment of Alconox<sup>®</sup>, acetone, and methanol followed by ultraviolet (UV) ozone treatment prior to loading into a deposition chamber. Iridium complexes, TPBi and LiF were deposited in a dedicated organic ultrahigh vacuum chamber with a base pressure of  $\sim 10^{-8}$  Torr. The Al cathode lines (2 mm wide) were deposited orthogonally to the ITO anode lines (1 mm wide) in a separate metallization chamber with a base pressure of  $\sim 10^{-7}$  Torr. A total of four different device structures were fabricated on a single substrate to elimi-

nate possible run-to-run variability caused by potential variations in process conditions. The luminance–current density–voltage (*L–I–V*) was measured using HP4140B picoammeter and Minolta LS-110 luminance meter. The electroluminescent (EL) spectra were recorded using an USB2000-UV-vis Miniature Fiber Optic Spectrometer. The constant current density during lifetime testing was provided by a Keithley 2400 source. All measurements were carried out in ambient atmosphere and at room temperature.

## 3. Results and discussion

Fig. 1 shows a schematic device structure, chemical structure and energy level diagram of the molecules used in this work. The work function of ITO and HOMOs for Ir(piq)<sub>3</sub>, Ir(ppy)<sub>3</sub>, Flrpic and TPBi are  $\sim 5.0$  [10], 5.1 [22], 5.4 [23], 5.8 [16] and 6.3 [24] eV, respectively. Based on the energy level alignment, the hole injection barrier from ITO to TPBi ( $\sim 1.3$  eV) is extremely high, while hole injection into Ir(piq)<sub>3</sub>, Ir(ppy)<sub>3</sub>, and Flrpic are energetically favorable with barriers of only  $\sim 0.1$ , 0.4, and 0.8 eV, respectively. This suggests that single layer phosphorescent OLEDs might be made possible by injecting holes directly into the iridium complex dopant rather than into the TPBi host.

It is known that the recombination zone in bilayer structure OLEDs is easily defined at the HTL and ETL interface [1,25]. However, for the single layer device, there is no heterointerface, the holes and electrons have to be recombined during transport or they will contribute to dark current. Furthermore, the hole–electron pair should be formed in a region away from both the anode and cathode; otherwise exciton quenching will occur and be responsible for lowering the device performance [26,27]. Hence the overall thickness of the single layer device has to be optimized in order to create an efficient zone for the recombination. We maintained the doping concentration at  $\sim 10$  wt% (the typical doping concentration for phosphorescent OLEDs in literature) in the devices ITO/Ir(ppy)<sub>3</sub>:TPBi ( $\sim 10$  wt%)/LiF (1 nm)/Al (100 nm), and varied the thickness between 60, 80, 100, and 120 nm. The characteristics of the four

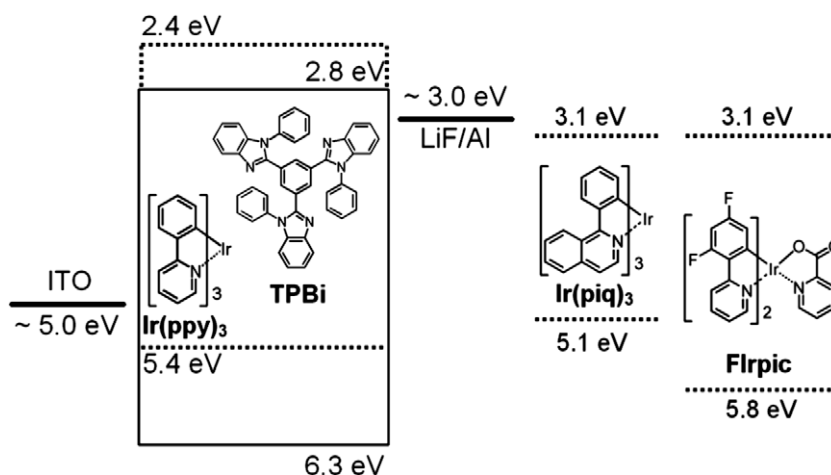


Fig. 1. Chemical structure and energy level diagram of the investigated molecules.

devices are summarized in Fig. 2. Similar to previously reported single layer devices [17], the device has higher driving voltage when the thickness is increased. The turn-on voltage for the device with a 60 nm thickness is only 2.9 V, while this was increased gradually to 3.8 V as the overall thickness increased to 120 nm. However, the device has higher efficiencies as the thickness increased, for example, the maximum current efficiency increased from 4.2 to 14.8 cd/A, and the power efficiency increased from 2.5 to 6.8 lm/W when the overall thickness is increased from 60 to 120 nm. Based on the performances of both driving voltage and efficiency of the four devices, we choose 100 nm as the device thickness in the following experiments.

We noticed that the above four devices have maximum current efficiency at high luminance (over 1000 cd/m<sup>2</sup>), which may be attributed to an inefficient hole injection from anode to dopant since there should be no problem for electron injection into and transport in TPBi. Considering that increasing the doping concentration may lead to enhanced injection and increased transporting channels, another three devices using the configuration of ITO/Ir(ppy)<sub>3</sub>:TPBi (100 nm)/LiF/Al were fabricated with doping concentrations of 14, 18 and 37 wt%, respectively. Fig. 3 shows their performance, as well as that of the reference device with a doping concentration of 10 wt%. The driving voltage decreased remarkably as the doping concentration

increased from 10 to 14 wt% and 18 wt%. However, the difference between the devices with a doping concentration of 37 and 18 wt% is small. This indicates that 18 wt% of Ir(ppy)<sub>3</sub> doped TPBi is sufficient for hole injection and transport. With an optimized doping concentration, the device performed the best, the device yields 34.5 cd/A current and 44.1 lm/W power efficiencies at 1 cd/m<sup>2</sup>, and 23.4 cd/A and 15.5 lm/W even when the luminance was increased to 1000 cd/m<sup>2</sup> under an applied voltage of 4.7 V. Moreover, the maximum efficiency obtained here is as high as, or even higher than, that of some multilayer phosphorescent OLEDs [28].

For the single layer device, though the holes can be injected into and transported on the Ir(ppy)<sub>3</sub> dopant, the recombination zone is expected to be close to the anode because TPBi is a good electron transporting molecule. Therefore, the efficiency could be further improved by inserting a buffer layer between the anode and the emission layer. To maintain the simple fabrication process, we used Ir(ppy)<sub>3</sub> as the buffer layer and fabricated another three devices with a configuration of ITO/Ir(ppy)<sub>3</sub>/Ir(ppy)<sub>3</sub>:TPBi (18 wt%, 100 nm)/LiF/Al, where the thickness of the Ir(ppy)<sub>3</sub> buffer layer is 1, 5, and 10 nm, respectively. Fig. 4 shows the EL spectra comparison of the devices with and without the Ir(ppy)<sub>3</sub> buffer layer. Both devices emitted a pure green light with an emission peaking around 520 nm, and international commission on illumination (CIE) chromaticity coordinate of (0.31, 0.63), which originates

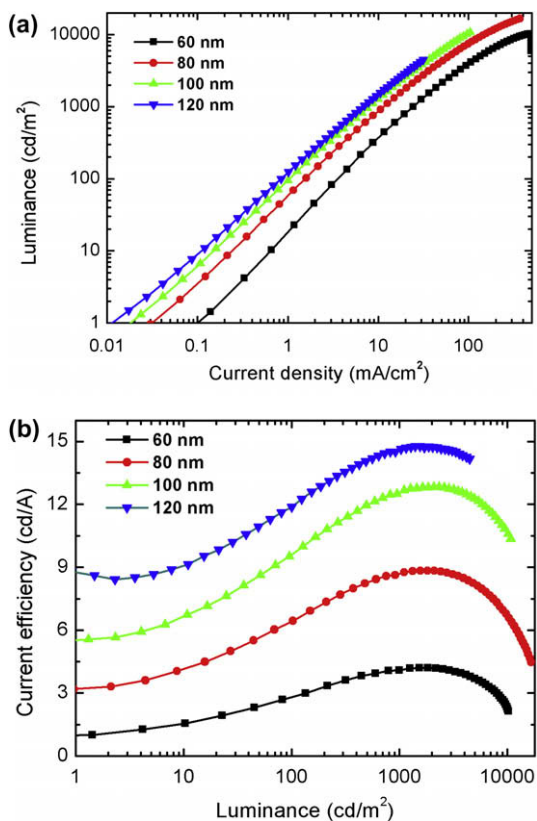


Fig. 2. (a) Luminance–current density and (b) current efficiency–luminance characteristics of devices ITO/Ir(ppy)<sub>3</sub>:TPBi (~10 wt%)/LiF/Al as a function of device thickness.

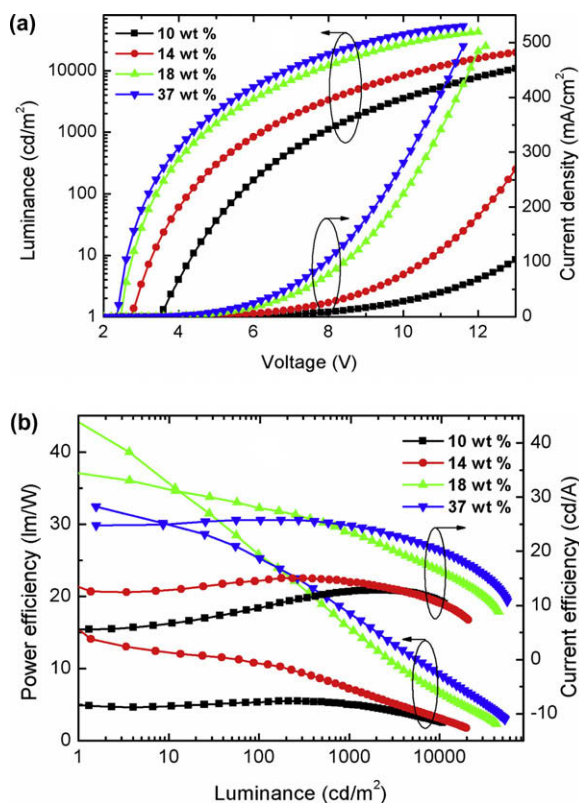


Fig. 3. (a)  $L$ – $I$ – $V$  and (b) current- and power efficiency–luminance characteristics of devices ITO/Ir(ppy)<sub>3</sub>:TPBi (100 nm)/LiF/Al as a function of doping concentration.

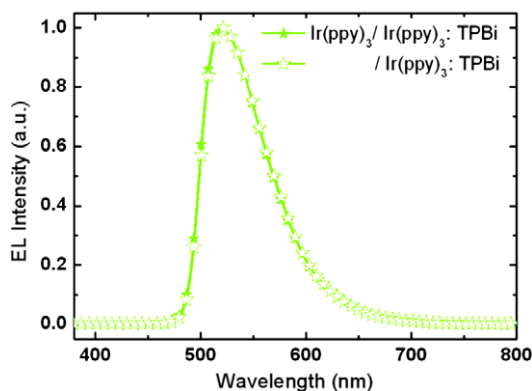


Fig. 4. EL spectra comparison between the green devices with and without the Ir(ppy)<sub>3</sub> buffer layer.

from the Ir(ppy)<sub>3</sub> dopant. Moreover, the device with a Ir(ppy)<sub>3</sub> buffer layer has an identical EL spectrum to that of the device without the buffer layer, indicating that holes and electrons are recombined in the Ir(ppy)<sub>3</sub>:TPBi layer rather than Ir(ppy)<sub>3</sub> layer, otherwise there will be a red-shifted emission because of heavy triplet-triplet quenching in pure Ir(ppy)<sub>3</sub> layer.

Fig. 5 shows the  $L$ - $I$ - $V$  and efficiency-luminance characteristics of the three devices, as well as that of the reference device without a Ir(ppy)<sub>3</sub> buffer layer. With the insertion of a 1 nm thick Ir(ppy)<sub>3</sub> buffer layer, the device performs with a much lower driving voltage and higher efficiency. In addition, further decreasing driving voltage and increasing efficiency are observed by increasing the Ir(ppy)<sub>3</sub> buffer layer thickness from 1 to 10 nm. As a result, the best performance was achieved in the device with an Ir(ppy)<sub>3</sub> thickness of 10 nm. The maximum current and power efficiencies were 43.3 cd/A and 56.2 lm/W at 1 cd/m<sup>2</sup>, respectively, and the efficiencies remain as high as 34.6 cd/A and 25.2 lm/W even when the luminance was increased to 1000 cd/m<sup>2</sup> at a low applied voltage of only 4.3 V.

It should be noted that the Ir(ppy)<sub>3</sub> buffer layer only improves device performance at low doping concentrations. Table 1 summarizes the characteristics comparison between devices with a configuration of ITO/Ir(ppy)<sub>3</sub>/Ir(ppy)<sub>3</sub>:TPBi (37 wt%, 100 nm)/LiF/Al, in which the thickness of Ir(ppy)<sub>3</sub> varied between 0 and 1 nm. As can be seen from the table, the devices with and without a Ir(ppy)<sub>3</sub> buffer layer have identical performance. This can be easily understood since holes are easily injected into and transported on the Ir(ppy)<sub>3</sub> dopant at higher doping levels, leading to a recombination zone at sufficient distance away from the anode.

The Ir(ppy)<sub>3</sub> buffer layer not only improves driving voltage and efficiency, but also improves the device stability. Fig. 6 shows the accelerated lifetime trend of the two simplified devices with and without a Ir(ppy)<sub>3</sub> layer, as well as that of a three layer reference device ITO/ $\alpha$ -NPD (40 nm)/Ir(ppy)<sub>3</sub>:CBP (20 nm)/TPBi (60 nm)/LiF (1 nm)/Al (100 nm), where  $\alpha$ -NPD and CBP are 4,4'-bis[*N*-(1-naphthyl)-*N*-phenyl-amino] biphenyl and 4,4'-*N,N'*-dicarbazole-biphenyl, respectively. Since lifetime was measured

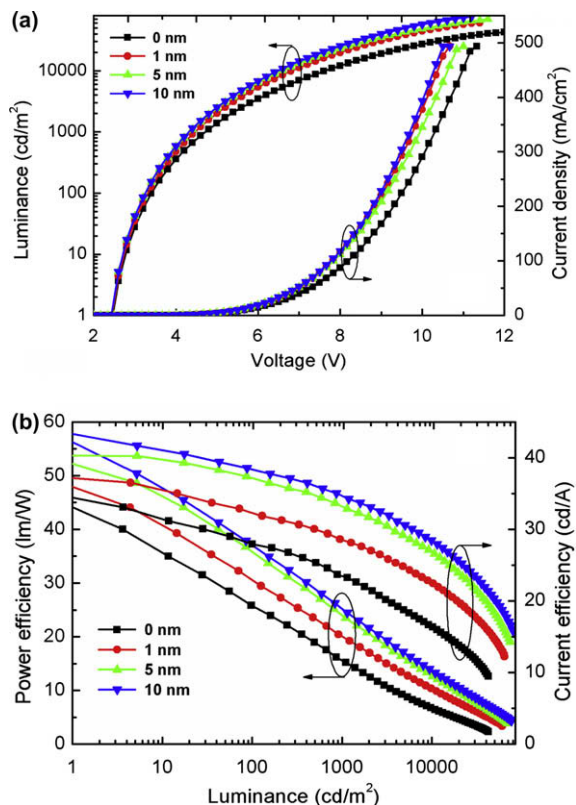


Fig. 5. (a)  $L$ - $I$ - $V$  and (b) efficiency-luminance characteristics of devices ITO/Ir(ppy)<sub>3</sub> (0, 1, 5, 10 nm)/Ir(ppy)<sub>3</sub>:TPBi (18 wt%, 100 nm)/LiF/Al.

Table 1

Characteristics comparison of the simplified green devices with and without the Ir(ppy)<sub>3</sub> buffer layer at a high doping concentration of 37%.

Thickness <sup>a</sup> [nm]	$V_{on}$ <sup>b</sup> [V]	$\eta_c^c$ at 10 cd m <sup>-2</sup> (V), 1000 cd m <sup>-2</sup> (V) [cd A <sup>-1</sup> ]	$\eta_p^c$ at 10 cd m <sup>-2</sup> (V), 1000 cd m <sup>-2</sup> (V) [lm W <sup>-1</sup> ]
1	2.35	25.25 (2.64), 24.79 (4.32)	29.67 (2.64), 17.80 (4.32)
0	2.36	25.07 (2.66), 24.72 (4.34)	29.64 (2.66), 17.73 (4.34)

<sup>a</sup> The thickness of the buffer layer Ir(ppy)<sub>3</sub>.

<sup>b</sup>  $V_{on}$  is taken as a reference point at which the luminance is 1 cd/m<sup>2</sup>.

<sup>c</sup> The data for current efficiency ( $\eta_c$ ) and power efficiency ( $\eta_p$ ) applied bias at exactly given luminance were deduced by luminance-voltage-efficiency curves.

in air, the exact values are meaningless. Here, the lifetime trends of the three devices are compared for their relative stability. As can be seen from the figure, the device without an Ir(ppy)<sub>3</sub> buffer layer between the ITO and emission layer has a very short lifetime, which could be attributed to multiple factors such as ion diffusion from the anode into the emission layer. The device with an Ir(ppy)<sub>3</sub> buffer layer has a much improved stability, even better than that of a typical three layer OLED.

Encouraged by the results of the simplified green devices, we also test the concept "direct hole injection into and transport on triplet dopant" in red and blue OLEDs. With a similar device configuration deduced above, two



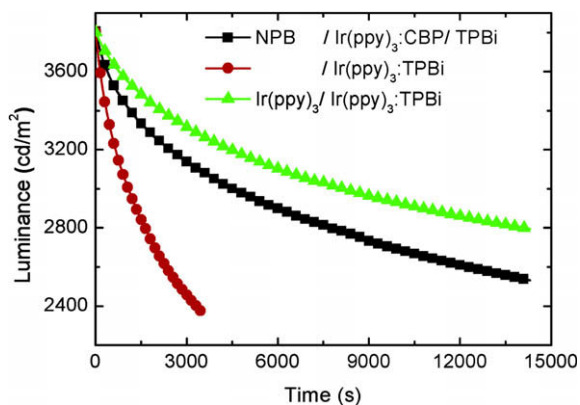


**Fig. 6.** Lifetime trends of two simplified devices with and without a 10 nm Ir(ppy)<sub>3</sub> layer, as well as that of a three layer device with a configuration of ITO/NPB (40 nm)/Ir(ppy)<sub>3</sub>:CBP (20 nm)/TPBi (60 nm)/LiF/Al.

red-emitting devices with configurations of ITO/Ir(piq)<sub>3</sub> (0 or 10 nm)/Ir(piq)<sub>3</sub>:TPBi (21 wt%, 100 nm)/LiF/Al and two blue-emitting devices with configurations of ITO/Flrpic (0 or 10 nm)/Flrpic:TPBi (18 wt%, 100 nm)/LiF/Al were fabricated. It should be noted that the red and blue device configuration fabricated here has not been optimized. The parameters optimized in the green device, including device thickness, doping concentration, and thickness of the buffer layer, may not be the best for red and blue devices because each dopant has different hole injection barrier and carrier mobility. Their EL spectra, as well as  $L$ - $I$ - $V$  and efficiency-luminance characteristics are shown in Figs. 7 and 8, respectively.

The red-emitting devices, either with or without a 10 nm thick Ir(piq)<sub>3</sub> buffer layer, had an identical emission with a maximum wavelength around 628 nm, CIE chromaticity coordinate of (0.69, 0.33), which is the same as those reported for other Ir(piq)<sub>3</sub> based devices [29]. The device without a Ir(piq)<sub>3</sub> buffer layer had current and power efficiencies around 3.7 cd/A and 3.2 lm/W at 1 cd/m<sup>2</sup>, and 2.7 cd/A and 0.8 lm/W at 1000 cd/m<sup>2</sup> under 11.0 V applied bias, respectively. The performance was improved somewhat by inserting a 10 nm thick Ir(piq)<sub>3</sub> buffer layer, hav-

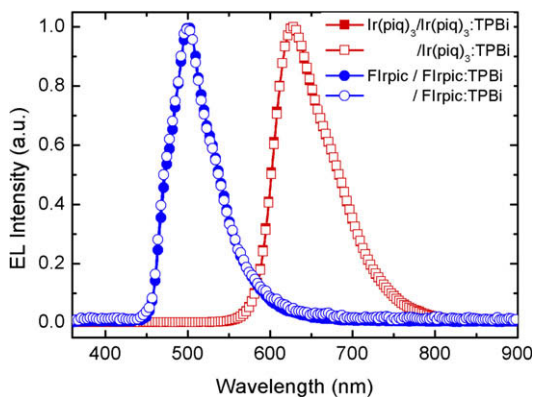


**Fig. 7.** EL spectra of devices ITO/Ir(piq)<sub>3</sub> (0 or 10 nm)/Ir(piq)<sub>3</sub>:TPBi (21 wt%, 100 nm)/LiF/Al and ITO/Flrpic (0 or 10 nm)/Flrpic:TPBi (18 wt%, 100 nm)/LiF/Al.

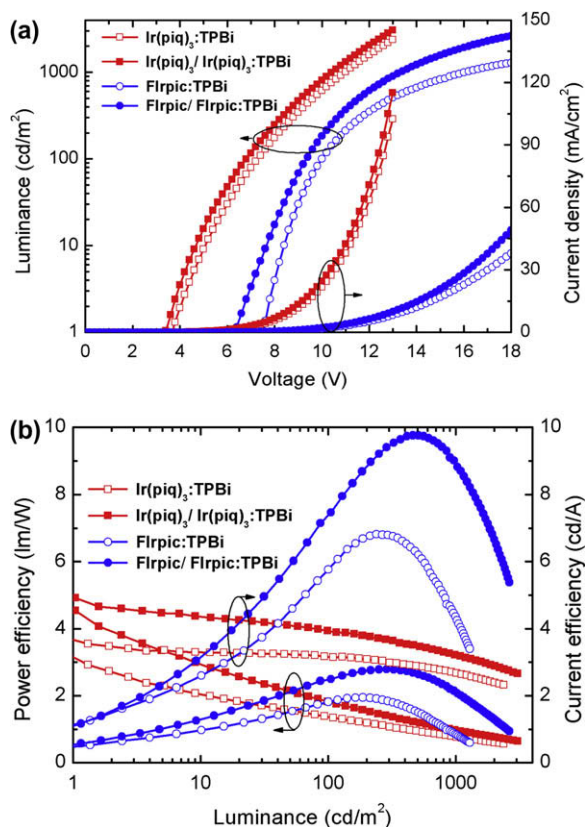


**Fig. 8.** (a)  $L$ - $I$ - $V$ , and (b) efficiency-luminance characteristics of ITO/Ir(piq)<sub>3</sub> (0 or 10 nm)/Ir(piq)<sub>3</sub>:TPBi (21 wt%, 100 nm)/LiF/Al and ITO/Flrpic (0 or 10 nm)/Flrpic:TPBi (18 wt%, 100 nm)/LiF/Al.

ing current and power efficiencies around 4.9 cd/A and 4.6 lm/W at 1 cd/m<sup>2</sup>, and 3.2 cd/A and 1.0 lm/W at 1000 cd/m<sup>2</sup> under 10.4 V applied bias, respectively.

As for the blue-emitting devices, the devices with and without a 10 nm thick Flrpic buffer layer also have identical emission band around 500 nm with CIE chromaticity coordinate of (0.20, 0.49). The emission spectra observed here are different to those reported for Flrpic-based devices, having an emission peak around 470 nm with a sub-peak around 500 nm [30]. It is known that there are two emission bands associated with two different triplet states in Flrpic. Here the dominate 500 nm emission band may be explained by the fact that the triplet energy level of TPBi is low (2.67 eV, [31]) and consequently results in a favored energy transfer to the lower triplet state of Flrpic [32].

Similarly, the insertion of 10 nm thick Flrpic buffer layer improves device performance, having lower driving voltage and higher efficiencies. For example, the device without the Flrpic buffer layer has a turn-on voltage of 7.6 V, maximum current and power efficiencies around 6.8 cd/A (239 cd/m<sup>2</sup>, 11.2 V) and 1.9 lm/W (187.6 cd/m<sup>2</sup>, 10.8 V). The turn-on voltage decreased to 6.4 V, and the efficiencies increased to 9.8 cd/A (460.4 cd/m<sup>2</sup>, 11.4 V) and 2.8 lm/W (287 cd/m<sup>2</sup>, 10.6 V), respectively, by inserting a 10 nm Flrpic layer. Still, the blue-emitting devices have much higher

**Table 2**  
Characteristics of the simplified RGB OLEDs.

Device structure <sup>a</sup>	V <sub>on</sub> [V]	η <sub>c</sub> at 1 cd m <sup>-2</sup> (V), 1000 cd m <sup>-2</sup> (V) [cd A <sup>-1</sup> ]	η <sub>p</sub> at 1 cd m <sup>-2</sup> , 1000 cd m <sup>-2</sup> [lm W <sup>-1</sup> ]	λ <sub>EL</sub> <sup>b</sup> [nm]
Ir(ppy) <sub>3</sub> /Ir(ppy) <sub>3</sub> :TPBi	2.4	43.3 (2.4), 34.6 (4.3)	56.2, 25.2	520
/Ir(ppy) <sub>3</sub> :TPBi	2.4	34.5 (2.4), 23.4 (4.7)	44.1, 15.5	521
Ir(piq) <sub>3</sub> /Ir(piq) <sub>3</sub> :TPBi	3.4	4.9 (3.4), 3.2 (10.4)	4.6, 1.0	627
/Ir(piq) <sub>3</sub> :TPBi	3.7	3.7 (3.7), 2.7 (11.0)	3.2, 0.8	628
Flrpic/Flrpic:TPBi	6.3	1.1 (6.3), 8.9 (13.3)	0.5, 2.1	500
/Flrpic:TPBi	7.5	1.1 (7.5), 4.4 (16.0)	0.5, 0.8	501

<sup>a</sup> The anode and cathode are ITO and LiF (1 nm)/Al (100 nm), respectively. The thickness of the iridium complex buffer layer and doped emission layer are 10 and 100 nm, respectively. The doping concentration for green, red, and blue OLEDs are 18, 21, and 18 wt%, respectively.

<sup>b</sup> EL spectra were taken at a luminance higher than 1000 cd/m<sup>2</sup>.

driving voltage than that of the red- and green-emitting devices, which is not surprising since the hole injection barrier from ITO to Flrpic is ~0.8 eV; this is much higher than that to Ir(piq)<sub>3</sub> (0.1 eV) and Ir(ppy)<sub>3</sub> (0.4 eV). The efficiency for the blue-emitting device was obtained at high applied voltage, which is also indicative of inefficient hole injection. This might be improved by employing new anode materials with higher work function [33].

#### 4. Conclusion

In summary, we have demonstrated single layer phosphorescent OLEDs with a configuration of ITO/dopant:TPBi/LiF/Al and ITO/dopant/dopant:TPBi/LiF/Al (Table 2). These simplified structures are applicable to red, green, and blue OLEDs with common phosphorescent dopants Ir(piq)<sub>3</sub>, Ir(ppy)<sub>3</sub>, and Flrpic, respectively. Efficient performance of the simplified single layer devices is attributed to direct hole injection into, and transport on the triplet dopants. This concept indicates a new way to fabricate simplified OLEDs with competitive performance by utilizing charge injection and transport properties of the dopants. Moreover, the concept also shows a possible new direction for developing future OLEDs is to synthesize phosphorescent dopants with better carrier injection and transporting ability.

#### Acknowledgments

We wish to acknowledge Ontario Centres of Excellence and Natural Sciences and Engineering Research Council (STPGP-351047-07) of Canada for financial support.

#### References

- [1] C.W. Tang, S.A. Vanslyke, Appl. Phys. Lett. 51 (1987) 913.
- [2] J. Greener, K.C. Ng, K.M. Vaeth, T.M. Smith, J. Appl. Polym. Sci. 106 (2007) 3534.
- [3] L.S. Zhou, A. Wanga, S.C. Wu, J. Sun, S. Park, T.N. Jackson, Appl. Phys. Lett. 88 (2006) 083502.
- [4] F. So, J. Kido, P. Burrows, MRS Bull. 33 (2008) 663.
- [5] A.R. Duagal, C.M. Heller, J.J. Shiang, J. Liu, L.N. Lewis, J. Display Technol. 3 (2007) 184.
- [6] C. Adachi, M.A. Baldo, M.E. Thompson, S.R. Forrest, J. Appl. Phys. 90 (2001) 5048.
- [7] M.A. Baldo, D.F. O'Brien, Y. You, A. Shoustikov, S. Sibley, M.E. Thompson, S.R. Forrest, Nature 395 (1998) 151.
- [8] C. Adachi, M.A. Baldo, S.R. Forrest, S. Lamansky, M.E. Thompson, R.C. Kwong, Appl. Phys. Lett. 78 (2001) 1622.
- [9] C. Adachi, R.C. Kwong, P. Djurovich, V. Adamovich, M.A. Baldo, M.E. Thompson, S.R. Forrest, Appl. Phys. Lett. 79 (2001) 2082.
- [10] C. Adachi, M.A. Baldo, S.R. Forrest, M.E. Thompson, Appl. Phys. Lett. 77 (2000) 904.
- [11] M.A. Baldo, S. Lamansky, P.E. Burrows, M.E. Thompson, S.R. Forrest, Appl. Phys. Lett. 75 (1999) 4.
- [12] D.F. O'Brien, M.A. Baldo, M.E. Thompson, S.R. Forrest, Appl. Phys. Lett. 74 (1999) 442.
- [13] Z.Q. Gao, M. Luo, X.H. Sun, H.L. Tam, M.S. Wong, B.X. Mi, P.F. Xia, K.W. Cheah, C.H. Chen, Adv. Mater. 21 (2009) 688.
- [14] M.T. Lee, J.S. Lin, M.T. Chu, M.R. Tseng, Appl. Phys. Lett. 94 (2009) 083506.
- [15] M.E. Kondakova, T.D. Pawlik, R.H. Young, D.J. Giesen, D.Y. Kondakov, C.T. Brown, J.C. Deaton, J.R. Lenhard, K.P. Klubek, J. Appl. Phys. 104 (2008) 094501.
- [16] L.D. Hou, L. Duan, J. Qiao, W. Li, D.Q. Zhang, Y. Qiu, Appl. Phys. Lett. 92 (2008) 263301.
- [17] P.A. Lane, G.P. Kushto, Z.H. Kafafi, Appl. Phys. Lett. 90 (2007) 023511.
- [18] X.H. Yang, D. Neher, D. Hertel, T.K. Daubler, Adv. Mater. 16 (2004) 161.
- [19] Z. Ge, T. Hayakawa, S. Ando, M. Ueda, T. Akiike, H. Miyamoto, T. Kajita, M.A. Kakimoto, Chem. Mater. 20 (2008) 2532.
- [20] S. Lamansky, P. Djurovich, D. Murphy, F. Abdel-Razzaq, H.E. Lee, C. Adachi, P.E. Burrows, S.R. Forrest, M.E. Thompson, J. Am. Chem. Soc. 123 (2001) 4304.
- [21] M.G. Helander, Z.B. Wang, Z.H. Lu, Appl. Phys. Lett. 93 (2008) 083311.
- [22] T.J. Park, W.S. Jeon, J.J. Park, S.Y. Kim, Y.K. Lee, J. Jang, J.H. Kwon, R. Podes, Appl. Phys. Lett. 92 (2008) 113308.
- [23] D. Kolosov, V. Adamovich, P. Djurovich, M.E. Thompson, C. Adachi, J. Am. Chem. Soc. 124 (2002) 9945.
- [24] J. Meyer, S. Hamwi, T. Bulow, H.H. Johannes, T. Riedl, W. Kowalsky, Appl. Phys. Lett. 91 (2007) 113506.
- [25] C.W. Tang, S.A. Vanslyke, C.H. Chen, J. Appl. Phys. 65 (1989) 3610.
- [26] A.L. Burin, M.A. Ratner, J. Phys. Chem. A 104 (2000) 4704.
- [27] S.C. Tse, K.K. Tsung, S.K. So, Appl. Phys. Lett. 90 (2007) 213502.
- [28] To understand the reliability of our results, we fabricated a standard phosphorescent device with a configuration of ITO/α-NPD (40 nm)/Ir(ppy)<sub>3</sub>:CBP (~9 wt%, 20 nm)/BCP (6 nm)/AlQ (20 nm)/LiF/Al, where BCP and AlQ are 2,9-dimethyl-4,7-diphenyl-phenanthroline and tris-(8-hydroxy-quinoline)aluminum, respectively. The power efficiency at 100 cd/m<sup>2</sup> of the standard device was 23 lm/W, which was comparable to the value of 19 lm/W reported by Forrest et al. with an Mg:Ag cathode.
- [29] D.S. Qin, Y. Tao, J. Appl. Phys. 97 (2005) 044505.
- [30] S.J. Yeh, M.F. Wu, C.T. Chen, Y.H. Song, Y. Chi, M.H. Ho, S.F. Hsu, C.H. Chen, Adv. Mater. 17 (2005) 285.
- [31] S. Takizawa, V.A. Montes, P. Anzenbacher Jr., Chem. Mater. (2009), doi:10.1021/cm9004954.
- [32] J.J. Lin, W.S. Liao, H.J. Huang, F.I. Wu, C.H. Cheng, Adv. Funct. Mater. 18 (2008) 485.
- [33] I.M. Chan, F.C. Hong, Thin Solid Films 450 (2004) 304.

fluorescence detection system for a disposable lab-on-a-chip device.

For many OPD applications, spectral selectivity is critical. An OPD used for biological imaging must discriminate between strong excitation and weak fluorescent emission signals that have narrow spectral separation (and often must furthermore distinguish the emission of multiple fluorescent dyes). To this end, Pais et al. [6] incorporated two cross-aligned polarizer films to separate the fluorescence signal from the excitation light source. Addressing spectral selectivity requirements for colorimetry applications, Antognazza et al. [11] used three distinct organic materials in the active layers of their OPDs, demonstrating photoresponse curves that mirrored the standard color matching function. Seo et al. [12] demonstrated a color sensor by vertically stacking three photodetectors that were individually sensitive to only blue, green, or red light. However, the color separation characteristics in the stacked sensor were sub-optimal, primarily due to the broad absorption spectra of the active organic layers. Achieving wavelength selectivity by simply using organic dyes with different absorption spectra often presents additional practical challenges, particularly in optimizing the electrical characteristics of the detector.

Optical microcavity effects provide an alternative approach to tune the wavelength selectivity of a photodetector. These effects arise due to the interference of electromagnetic waves in dielectric cavities sandwiched by reflective layers, in which the optical path length is on the order of a wavelength. As with a Fabry–Perot interferometer, the microcavity structure exhibits spectral selectivity due to resonant optical modes in the cavity. Lupton et al. [13] utilized this effect in an OPD by replacing the cavity layer with photoactive materials, fabricating a Bragg reflector below the indium tin oxide (ITO) substrate and depositing a semi-transparent silver top electrode to form the top mirror. The spectral selectivity of the device was shown to depend on the bilayer cavity thickness, although the sensitivity and spectral selectivity remained relatively low due to a relatively low cavity quality (Q) factor caused by parasitic absorption in the thick photoactive layers. Furthermore, the maxima of the standing wave of the resonant field were positioned far from the donor–acceptor interface where exciton dissociation takes place, lowering the quantum efficiency of the detector.

In this work, we demonstrate a microcavity organic photodetector that incorporates a conductive, transparent optical spacer inside the cavity and places the organic heterojunction near a peak intensity of the resonant field. This results in a stronger optical microcavity (an enhanced Q factor) and hence increases the sharpness of the spectral response. Detector sensitivity is enhanced by two orders of magnitude over prior work [13], and the peak wavelength can be tuned across a much wider range. We also study the effects of metal mirror roughness on the external quantum efficiency (EQE) spectrum, accounting for roughness explicitly in our optical model and demonstrating excellent agreement between predicted and measured EQE when topographical data obtained via atomic force microscopy (AFM) is incorporated. Finally, we study the angular dependence and frequency response of our devices.

Appropriate optical spacer materials should exhibit low electrical and optical losses, as well as a properly matched work function to reduce contact resistance. Optical spacers such as  $\text{TiO}_x$  [14], bathocuproine (BCP), and  $\text{C}_{60}$  [1] have previously been used in organic solar cells. Archetypal organic solar cells, however, are weak microcavities since they are most often deposited onto ITO electrodes, resulting in a low cavity Q factor. Instead, we use thin metal films for both anode and cathode [15], and employ a considerably thicker optical spacer to substantially increase the strength of the electric field near the organic heterojunction, thereby enhancing the narrow-band quantum efficiency of the device. We use vacuum-deposited molybdenum trioxide ( $\text{MoO}_3$ ) as the optical spacer, facilitating the fabrication of the photodetector by conventional vacuum thermal evaporation. As shown in Fig. 1,  $\text{MoO}_3$  has good transparency over a broad range of the visible spectrum (where the EQE peaks of our OPDs are located). Current–voltage measurements of a 40 nm Ag/140 nm  $\text{MoO}_3$ /50 nm Al structure yielded Ohmic characteristics with a resistivity of  $5 \times 10^5 \Omega \text{ cm}$ , which is several orders of magnitude lower than that of most organic materials. The work function of  $\text{MoO}_3$  is known to be 5.8 eV [16], enabling efficient hole collection.

To precisely identify OPD structures with desired external quantum efficiency (EQE) spectra, we employed optical models based on the transfer matrix approach, which predicts the optical field distribution within the multilayer structure. These models were coupled to exciton transport equations that account for exciton generation, extinction, and diffusion [1,17,18]. We assumed literature values for exciton diffusion length (100 Å for CuPc and 300 Å for  $\text{C}_{60}$ ) [1], and assumed 100% charge dissociation and extraction efficiency. The simulated device layer structure has a 50 nm Al anode, variable thickness  $\text{MoO}_3$  spacer, 20 nm copper phthalocyanine (CuPc) donor, 40 nm  $\text{C}_{60}$  acceptor, 7 nm BCP exciton blocking layer, and 40 nm semi-transparent silver cathode. Wavelength-dependent optical constants for these layers were taken from literature [18–21]. A cross-sectional diagram of the photodetector structure is illustrated in the inset of Fig. 1. Calculated electric field profiles within the device for the visible range of incident wavelengths are shown in Fig. 2a, assuming a 150 nm thick

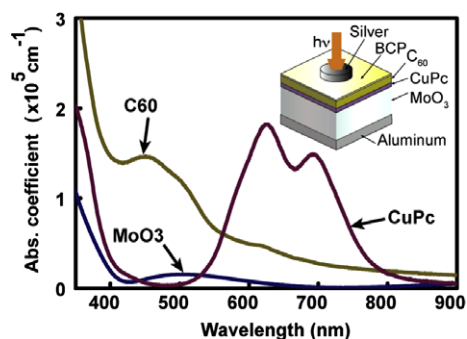
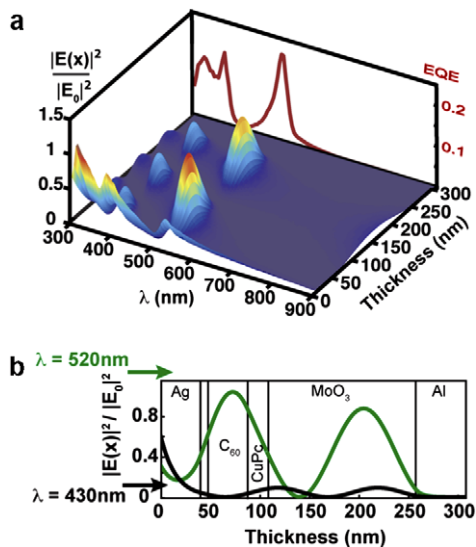


Fig. 1. A comparison of the absorption coefficients of  $\text{MoO}_3$ , CuPc, and  $\text{C}_{60}$ , indicating that a  $\text{MoO}_3$  film remains transparent across the visible spectrum. (inset) A cross-sectional illustration of the photodetector structure.



**Fig. 2.** (a) Calculated electric field intensity  $|E|^2$  distribution throughout the photodetector for a range of incident wavelengths. The thickness axis denotes the distance from the air–cathode interface, on which light is incident. The external quantum efficiency (EQE) is plotted also along the back plane of the graph to represent the strong correlation between  $|E|^2$  and EQE. (b) A plot comparing  $|E|^2$  profiles inside the OPD for 430 nm and 520 nm incident light. A strong second mode can be seen for 520 nm illumination. The device structure used in the simulation for both (a) and (b) is: 50 nm Al / 150 nm MoO<sub>3</sub> / 20 nm CuPc / 40 nm C<sub>60</sub> / 7 nm BCP / 40 nm Ag.

MoO<sub>3</sub> optical spacer. The engineered spectral responsivity is apparent in Fig. 2b, which compares the electric field profile for the 430 nm non-resonant wavelength to that of the 520 nm wavelength, which is near the second resonant mode of the microcavity. The left peak for the resonant mode is very close to the organic heterojunction, leading to increased optical absorption in this region and hence larger photocurrent. Even though the light couples in through a 40 nm thick semi-transparent silver film, the peak light intensity near the donor–acceptor junction is comparable to that of a conventional ITO based solar cell [17,18]. Below the wavelength of the second resonant mode, there exist third and fourth resonant modes in the electric field contour, indicating possible absorption in the ultra-violet range. Thicker spacers make the peaks narrower, and push the higher resonant mode into the visible range, similar to the Fabry–Perot interferometer. The calculated EQE spectrum, plotted in Fig. 2a, shows a strong correlation with the resonant electric field. Note that the EQE spectrum of a microcavity device can be largely decoupled from the absorption spectra of the active photosensitive materials (Fig. 1), a consequence of the strong resonant effects.

Following our optical analysis, we fabricated device structures having layer sequences and thicknesses identical to those modeled (within experimental error), deposited onto 1 mm thick glass substrates using vacuum thermal evaporation (VTE) at  $10^{-6}$  Torr and 1–2 Å/s evaporation rate. The nominal layer sequence was as follows: thick aluminum that serves as the bottom mirror and an-

ode, MoO<sub>3</sub> optical spacer varied from 110 nm to 220 nm thick, CuPc electron donor, C<sub>60</sub> electron acceptor, BCP hole and exciton blocking layer, and semi-transparent silver serving as the top mirror and cathode. Cathodes were defined by depositing through a shadow-mask, which was mounted in atmosphere immediately after depositing the C<sub>60</sub> layer. Device photocurrent was measured in atmosphere using a transimpedance amplifier at zero bias, with the photodetector illuminated by monochromated light from a halogen lamp; a lock-in amplifier (at 89 Hz chopping frequency) was used to enhance the signal-to-noise ratio in determining the EQE. Incident light power was measured using a calibrated silicon photodetector (Newport 818-SL).

For a device having a target resonant mode at 520 nm, our calculation suggested a 150 nm thick optical spacer. This resonant peak was confirmed by EQE measurements on a fabricated device with 150 nm optical spacer thickness, as shown in Fig. 3e. Despite the accuracy of the pre-

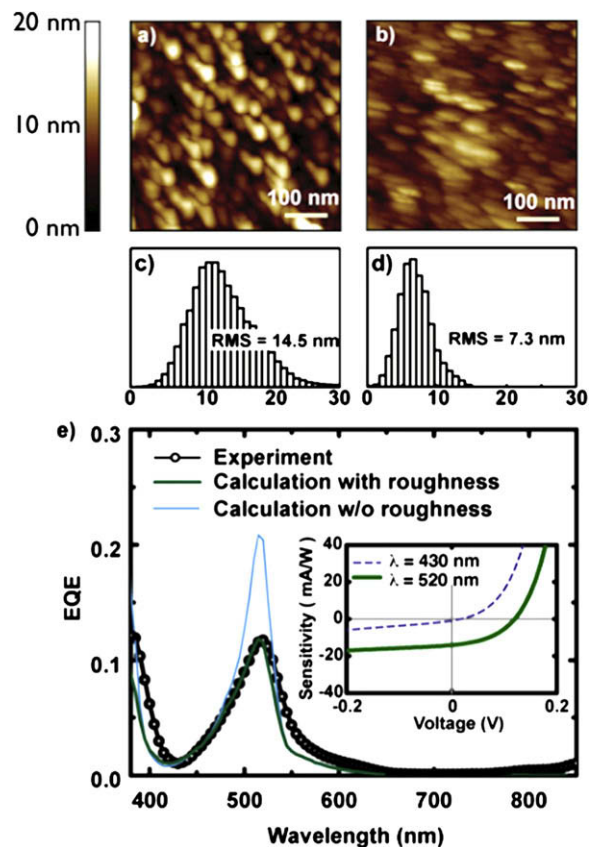


**Fig. 3.** Atomic force microscopy (AFM) scans of (a) aluminum thin films deposited onto glass substrates, and (b) silver thin films deposited onto the organic layers of BCP, C<sub>60</sub> and CuPc on the aluminum, along with histograms (c–d) of the measured surface height values, which exhibit a Gaussian distribution. The root-mean-square (RMS) roughness measures 14.5 nm for aluminum and 7.3 nm for silver. (e) A plot superimposing the measured and calculated external quantum efficiency spectra. Two calculated spectra are shown – one that does not take electrode roughness into account, and one that does. (inset) A plot of photodetector sensitivity for illumination wavelengths of 430 nm and 520 nm, showing clear spectral selectivity.

dicted peak position, there is a mismatch in the peak height. This is due to a lowering of the cavity Q factor, most likely a result of the roughness of the evaporated metal mirrors. To include the scattering caused by mirror roughness in our optical model, we used Filinski's theory [22] of modified reflection coefficients, which accounts for phase variations resulting from small height differences by a Gaussian distribution characterized by the root-mean-square (RMS) of the film topography. Atomic force micros-

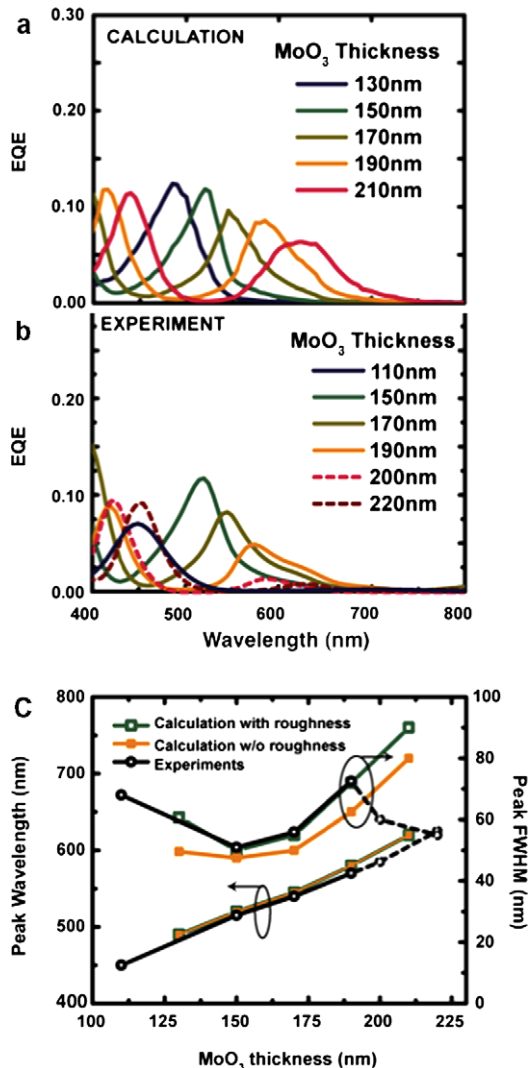


**Fig. 4.** (a) Calculated and (b) measured external quantum efficiency spectra versus incident wavelength for optical spacer layers of different thickness. The calculated response predicts that the resonance peak can be shifted from 490 nm to 620 nm (corresponding to optical spacer thicknesses of 130–210 nm). The observed peak in the response shifts from 450 nm to 630 nm for spacer thickness ranging from 110 nm to 220 nm, while other elements of the OPD structure remain unchanged. (c) A further comparison between theory and experiment, plotting the peak position versus spacer layer thickness; two sets of calculated peaks are shown for calculations that either do or do not account for electrode roughness. Note that the dotted lines in (b) and the last two experimental data points in (c) were obtained from heterostructures that use  $\alpha$ -NPD instead of CuPc for the electron donor layer, to demonstrate control of the width of the spectrum via absorber layer composition.

copy (AFM) was used to quantify the roughness of the aluminum and silver films, as shown in Figs. 3a–d. We found RMS roughness values of 14.5 nm for aluminum deposited onto glass substrates, and 7.3 nm for silver films deposited onto the organic layers. Incorporating Filinski's correction into our optical model and using these RMS values explicitly resulted in excellent agreement with experiment, as shown in Fig. 3e. In the inset of Fig. 3e we compare the sensitivity of the detector to monochromatic light at wavelengths of 430 nm and 520 nm, corresponding respectively to the valley and peak of the EQE spectrum of the heterostructure. The sensitivity ratio for these two wavelengths was 15 at zero applied bias. Further measurements of the EQE spectra under a reverse bias of 2 V showed no changes in the wavelength peak or spectral width, although the magnitude of the peak increased slightly, as the sensitivity curve (inset of Fig. 3e) indicates.

To further demonstrate the spectral selectivity of the microcavity-based organic photodetector, we calculated (again accounting for roughness) the position of the resonance peak for a range of spacer thicknesses between 130 nm and 210 nm, predicting that the resonance peak would span wavelength ranges from 490 nm to 620 nm (Fig. 4a). These predictions were confirmed experimentally, as shown in Fig. 4b. By varying only the optical spacer thickness in the fabricated device structures, we are able to span a 450 nm to 630 nm range with the EQE spectrum. Some discrepancy between simulation and experiment is present for longer wavelengths, attributable to two effects. Firstly, the extinction coefficients used in our model for this wavelength range are based on literature values [20]; however, these coefficients can vary in practice for deposited films due to differences in film morphology. We separately performed optical absorption measurements on Ag thin films deposited in our thermal evaporation system and found that they had a slightly higher extinction coefficient for longer wavelengths than predicted in [20]. Secondly, we note that the two experimental

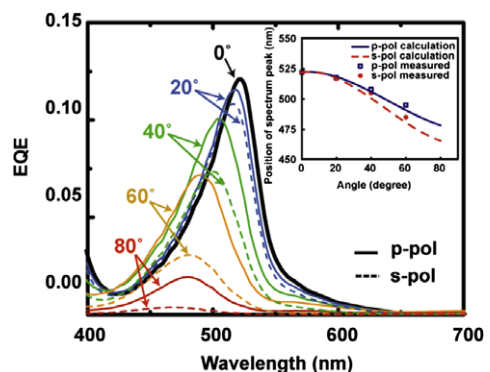


**Fig. 5.** A plot of the EQE spectra for several incident angles ( $0^\circ$  = normal incidence), including both p- and s-polarized light, calculated for a microcavity photodetector employing a 150 nm thick optical spacer. The peak blue-shifts with increasing angle, while the absolute magnitude of the EQE reduces at shallower incidence, regardless of polarization, due to a combination of increased reflectivity and increased absorption of light in the top silver mirror. The inset shows similar changes in peak wavelength measured experimentally.

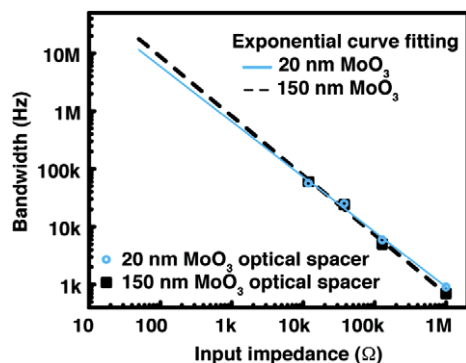


**Fig. 6.** A plot of the  $-3$  dB bandwidths of OPDs employing a thick MoO<sub>3</sub> spacer layer (50 nm Al / 150 nm MoO<sub>3</sub> / 20 nm CuPc / 40 nm C<sub>60</sub> / 7 nm BCP / 40 nm Ag) and thin MoO<sub>3</sub> spacer (50 nm Al / 20 nm MoO<sub>3</sub> / 20 nm CuPc / 40 nm C<sub>60</sub> / 7 nm BCP / 40 nm Ag) as measured at several input impedances by a 300 MHz bandwidth oscilloscope. A green LED ( $\lambda = 530$  nm) with intensity of 1.3 mW/cm<sup>2</sup> was modulated in a square wave pattern, illuminating a circular device 1 mm in diameter through a focusing objective. The bandwidth extrapolated at 50  $\Omega$  input impedance is  $\sim 15$  MHz, and decreases only negligibly upon the addition of the MoO<sub>3</sub> optical spacer, indicating that the small resistance of the optical spacer contributes very little to the RC time constant.

EQE spectra for photodetectors with optical spacer thicknesses of 200 nm and 220 nm (dashed lines in Fig. 4b) were obtained from a heterostructure that used N,N'-di-[(1-naphthalenyl)-N,N'-diphenyl]-(1,1'-biphenyl)-4,4'-diamine ( $\alpha$ -NPD) instead of CuPc for the donor layer. While substituting a different absorber demonstrates the ability to further control the spectral response, it also leads to reduced detector sensitivity, in this case due to the low intrinsic optical absorption of C<sub>60</sub> and  $\alpha$ -NPD near the second resonant peak of the microcavity mode (590 nm and 620 nm for the two dashed spectra). Fig. 4c plots the peak position versus spacer layer thickness as a more direct comparison between theory and experiment. The two experimental data points with the largest spacer thicknesses correspond to the C<sub>60</sub>/ $\alpha$ -NPD heterostructure and demonstrate the ability to significantly reduce the photodetector response peak width with proper choice of absorber. The agreement observed between model and experiment suggest that our model can serve as a viable design tool.

Optical microcavities tend to be sensitive to the angle and polarization of incident light. We calculated EQE spectra at several incident angles for a microcavity photodetector employing a 150 nm thick optical spacer. The inclined incident (and polarized) light ( $0^\circ =$  normal incidence) blue-shifted the peak wavelength of the photodetector, as shown in Fig. 5, attributable to the decreased optical phase difference of reflection at higher angles, as predicted by Fabry–Perot theory. Similar peak wavelength changes were measured experimentally, as shown in the inset of Fig. 5. The absolute magnitude of the EQE was progressively smaller at oblique incidence, regardless of polarization, attributed to a combination of increased reflectivity and increased attenuation of light in the top silver electrode. As a result, variation of the EQE spectrum with incident angle is minimal. We note that, while small, this manifestation of microcavity effects at varying incidence

angles could constrain some applications. It also potentially could be used as a means to actively tune the spectral response of a given OPD.

The frequency response of a photodetector is another important design consideration; one might suspect that inserting additional transport layers in a heterostructure could significantly reduce the response time. However, we find that the insertion of MoO<sub>3</sub> introduces negligible delays in the response time of the detector. We measured the bandwidth of two device structures with different MoO<sub>3</sub> thicknesses: 50 nm Al / 150 nm MoO<sub>3</sub> / 20 nm CuPc / 40 nm C<sub>60</sub> / 7 nm BCP / 40 nm Ag and 50 nm Al / 20 nm MoO<sub>3</sub> / 20 nm CuPc / 40 nm C<sub>60</sub> / 7 nm BCP / 40 nm Ag. These OPDs were defined by 1 mm diameter circular cathodes and were illuminated by a green LED ( $\lambda = 530$  nm) with 1.3 mW/cm<sup>2</sup> intensity that was modulated by a function generator (Agilent 33120A). The transient OPD response for a range of load resistances was measured using a 300 MHz bandwidth oscilloscope (Tektronix TDS 3032B) as shown in Fig. 6. The bandwidth extrapolated at 50  $\Omega$  input impedance is approximately 15 MHz. This bandwidth is significantly lower than that measured in [1] for certain devices (430 MHz), most likely due to the fact that the devices in [1] were thinner, contained multiple junctions, and were measured in reverse bias and at higher illumination intensity. Importantly, the bandwidth of our device was measured to decrease only negligibly upon the addition of the MoO<sub>3</sub> optical spacer (see Fig. 6), indicating that the small resistance of the optical spacer contributes very little to the RC time constant.

In summary, we developed a means for tuning the spectral response of an organic photodetector across the visible spectrum by engineering its optical microcavity through the insertion of an electrically conducting and optically transparent spacer layer. We tested this concept using a spacer layer of thermally evaporated MoO<sub>3</sub>, which exhibits good transparency and hole transport properties that do not limit the OPD's spectral or temporal response. Our calculations of the detector's photoresponse match well with experiments, particularly when the measured roughness of the electrodes (mirrors) is taken into account explicitly. We anticipate applications of this type of tunable organic photodetector design in colorimetry, fluorescence detection, and large-area flexible imagers, and photovoltaic cells.

## Acknowledgements

The authors would like to thank the National Science Foundation (Grant Nos. ECS-0523986 and ECS-0507301) and the Air Force Office of Scientific Research (Grant No. FA9550-06-1-0399) for their financial support.

## References

- [1] P. Peumans, A. Yakimov, S. Forrest, *J. Appl. Phys.* 93 (2003) 3693.
- [2] M. Ramuz, L. Buerki, C. Winnemisser, P. Seitz, *Org. Electron.* 9 (2008) 369.
- [3] T.N. Ng, W.S. Wong, M.L. Chabiny, S. Sambandan, R.A. Street, *Appl. Phys. Lett.* 92 (2008) 213303.
- [4] Xu Xin, Davanco Marcelo, Qi Xiangfei, F.R. Stephen, *Org. Electron.* 9 (2008) 1122.

- [5] O. Hofmann, X.H. Wang, J. Demello, D. Bradley, A. Demello, *Lab Chip* 5 (2005) 863.
- [6] A. Pais, A. Banerjee, D. Klotzkin, I. Papautsky, *Lab Chip* 8 (2008) 794.
- [7] T. Morimune, H. Kam, Y. Ohmori, *Jpn. J. Appl. Phys. Part 1* 45 (2006) 546.
- [8] P. Peumans, V. Bulovic, S. Forrest, *Appl. Phys. Lett.* 76 (2000) 3855.
- [9] F.B. Myers, L.P. Lee, *Lab Chip* 8 (2008) 2015.
- [10] B. Yao, G. Luo, L. Wang, Y.D. Gao, G.T. Lei, K. Ren, L. Chen, Y. Wang, Y. Hu, Y. Qiu, *Lab Chip* 5 (2005) 1041.
- [11] M. Antognazza, U. Scherf, P. Monti, G. Lanzani, *Appl. Phys. Lett.* 90 (2007) 163509.
- [12] H. Seo, S. Aihara, T. Watabe, H. Ohtake, M. Kubota, N. Egami, *Jpn. J. Appl. Phys. Part 2* 46 (2007) L1240.
- [13] J.M. Lupton, R. Koeppel, J.G. Muller, J. Feldmann, U. Scherf, U. Lemmer, *Adv. Mater.* 15 (2003) 1471.
- [14] J.Y. Kim, K. Lee, N.E. Coates, D. Moses, T.-Q. Nguyen, M. Dante, A.J. Heeger, *Science* 317 (2007) 222.
- [15] B. O'connor, C. Haughn, K.H. An, K. Pipe, M. Shtein, *Appl. Phys. Lett.* 93 (2008) 223304.
- [16] T. Oyamada, Y. Sugawara, Y. Terao, H. Sasabe, C. Adachi, *Jpn. J. Appl. Phys. Part 1* 46 (2007) 1734.
- [17] B. O'connor, K.H. An, K.P. Pipe, Y. Zhao, M. Shtein, *Appl. Phys. Lett.* 89 (2006) 233502.
- [18] L. Pettersson, L. Roman, O. Inganäs, *J. Appl. Phys.* 86 (1999) 487.
- [19] V. Nirupama, P. Reddy, O. Hussain, S. Uthanna, *Ionics* 13 (2007) 451.
- [20] D. Palik, G. Ghosh, *Handbook of Optical Constants of Solids*, Academic Press, 1985.
- [21] E.F. Schubert, *Refractive index and extinction coefficient of materials*, <<http://www.rpi.edu/%7eschubert/>>.
- [22] I. Filinski, *Phys. Status Solidi B* 49 (1972) 577.

driving voltage of  $\sim 5$  V can be achieved by using diphosphine oxide derivatives as host [17–19]. The low driving voltage can be rationalized by the following two reasons. One is the *intrinsic* good electron-transporting ability of diphosphine oxide derivatives, which can be helpful to the transport of electrons in the bulky organic layer. The other contribution comes from the reduction of the energy barrier between diphosphine oxide derivatives and LiF/Al cathode since these materials have a low LUMO level of 2.9 eV. However, the diphosphine oxide derivatives have a low-lying HOMO level of 6.6 eV, which causes a large energy barrier for the transport of holes from nearby HTL into the host. Consequently, the quantum efficiency of blue PHOLEDs based on diphosphine dioxide derivatives as host was significantly below 100%.

To summarize the development of host material in the previous studies, an appropriate blue phosphorescent host material should not only have a high triplet excited state as well as bipolar transport property, but also a minimum energy barrier between the host and adjacent carrier-transporting material. Unfortunately, up to now, it is not an easy task to find a host material that will satisfy all the above-mentioned requirements. In this paper, we will introduce a composite emitter incorporating a carrier-transporting material into the emitter composed of diphosphine oxide derivatives host and organometallic iridium dopant. The problematic transport of holes from the HTL into diphosphine oxide derivatives host can be alleviated through the adoption of carrier-transporting material, thus the probability of carrier recombination can be increased and the driving voltage can be decreased. Consequently, a blue PHOLED with a power efficiency of 20 lm/W and low driving voltage of 4.2 V at practical brightness of 1000 cd/m<sup>2</sup> is achieved.

## 2. Experimental

The composite emitter comprises a wide-band-gap host, 2,8-bis(diphenylphosphoryl)dibenzothiophen (PPT) [18], which has a triplet excited state of 3.0 eV, a blue phosphorescent dopant, iridium(III)bis((4,6-difluorophenyl)-pyridinate-N,C<sup>2'</sup>)picolinate (Flrpic), which possessed a triplet excited state of 2.62 eV [2], and a carrier-transporting material, 4,4',4''-tri(*N*-carbazolyl)triphenylamine (TCTA), which possessed a triplet excited state of 2.76 eV [2] as well as a good hole-transporting ability ( $1.6 \times 10^{-4}$  cm<sup>2</sup>/Vs at  $10^5$  V/cm) [The data was measured by time-of-flight method, the detailed results will be reported in elsewhere]. In addition, an electron-blocking layer (EBL), bis[4-(*p,p'*-ditolylamino)phenyl]diphenylsilane (DTASi) [20], with high triplet excited state of 2.95 eV and a high-lying LUMO level of 2.2 eV was used to confine all generated exciton in emitter. A high electron mobility material ( $10^{-4}$  cm<sup>2</sup>/Vs at  $10^5$  V/cm), 4,7-diphenyl-1,10-phenanthroline (Bphen) [21], and 20% (vol%) cesium carbonation (Cs<sub>2</sub>CO<sub>3</sub>) doped with Bphen [22] were used as ETL and *n*-ETL, respectively, to achieve low driving voltage. The device architecture used is ITO (150 nm)/NPB (45 nm)/DTASi (15 nm)/composite emitter (15 nm)/Bphen (25 nm)/*n*-ETL (20 nm)/Al (100 nm), where 4,4'-bis[*N*-(1-naphthyl)-*N*-phenyl-amino]biphenyl (NPB) is HTL. In order to investigate the effect of doping carrier-transporting material in Flrpic/PPT emitter, the doping concentration of blue dopant was fixed at 15% and the doping concentration of 0%, 10%, and 20% for the carrier-transporting material were tested.

Fig. 1 shows the detailed molecular structures of materials and architecture of device used in this study. All the materials were deposited by thermal evaporation in an UL-

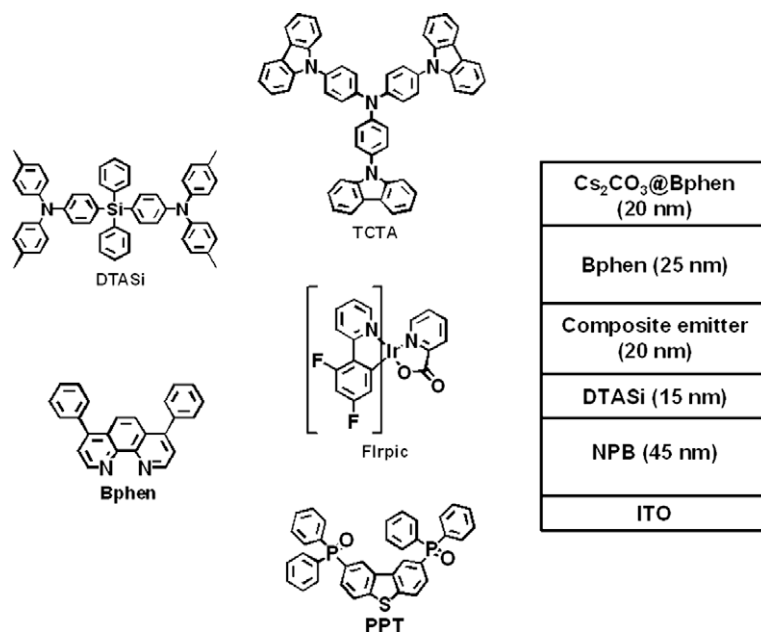


Fig. 1. Molecular structures and device architecture used in the experiment.



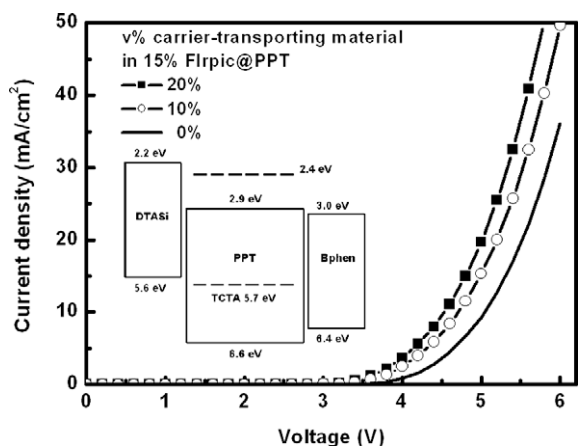


Fig. 2. Current density–voltage ( $J$ – $V$ ) characteristics of blue PHOLEDs as well as the device energy diagram (inset).

VAC Solciet OLED coater at a base vacuum of  $10^{-7}$  Torr. The device performance of luminance yield and EL spectra,  $CIE_{x,y}$  color coordinates were measured by a Minolta luminance meter and a Photo Research PR-650 spectrophotometer driven by a programmable dc source, respectively.

### 3. Results and discussion

Fig. 2 shows the dependence of current density–voltage ( $J$ – $V$ ) characteristics of the blue PHOLEDs on the doping concentration of carrier-transporting material in emitter. Lower driving voltage was observed in the device with doping carrier-transporting material in emitter as compared with that of undoped device. For instance, the driving voltage at current density of  $20 \text{ mA/cm}^2$  is  $5.0 \text{ V}$  for doping 20% carrier-transporting material in the emitter and  $5.6 \text{ V}$  for the undoped device. The decreased driving voltage can be attributed to the transport of holes from EBL (DTASi) into host (PPT) which was promoted through doping carrier-transporting material (TCTA) in emitter, since TCTA possesses a good hole-transporting ability and

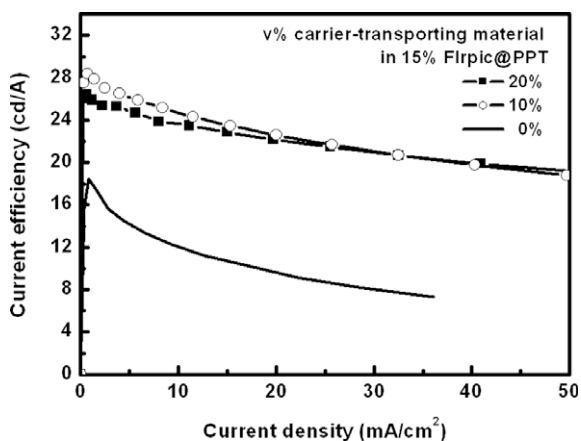


Fig. 3. Current efficiency–current density ( $cd/A$ – $J$ ) characteristics of blue PHOLEDs.

a HOMO level ( $5.7 \text{ eV}$ ) lying between that of DTASi ( $5.6 \text{ eV}$ ) and PPT ( $6.6 \text{ eV}$ ). The device energy diagram is shown in the inset of Fig. 2.

Fig. 3 shows the dependence of current efficiency–current density ( $cd/A$ – $J$ ) characteristics of the blue PHOLEDs on the doping concentration of carrier-transporting material in the emitter. When doping 10% carrier-transporting material in the emitter, the device exhibited a current efficiency of  $26.8 \text{ cd/A}$  with low driving voltage of  $4.2 \text{ V}$  ( $J \sim 4 \text{ mA/cm}^2$ ), which is 2 times higher than that of the undoped device with  $12.3 \text{ cd/A}$  and  $5.0 \text{ V}$  ( $J \sim 8.2 \text{ mA/cm}^2$ ) at a practical brightness of  $1000 \text{ cd/m}^2$ . The current efficiency sustains as high as  $25 \text{ cd/A}$  when the doping concentration of carrier-transporting material is increased to 20% in the emitter. We believe the dramatic enhancement in current efficiency when doping carrier-transporting material in the emitter is resulted from the “hole-facilitating” character of carrier-transporting material, which can increase the concentration of holes in the emitter as opposed to that of undoped device. Therefore, the probability of carrier recombination can be increased.

In addition, at current density of  $20 \text{ mA/cm}^2$ , the device with 10% carrier-transporting material doped in emitter exhibited a current efficiency of  $22.6 \text{ cd/A}$ , which is 2.5 times higher than that of undoped device with only  $9.2 \text{ cd/A}$ . This result demonstrates that the problematic efficiency roll-off in blue PHOLEDs can also be suppressed by doping carrier-transporting material in the emitter. For instance, the efficiency roll-off from low ( $1 \text{ mA/cm}^2$ ) to high current density ( $40 \text{ mA/cm}^2$ ) is 29% and 23% for 10% and 20% carrier-transporting material in the emitter, respectively, while it is nearly 60% for the undoped device. The suppression of efficiency roll-off in blue PHOLEDs when doping carrier-transporting material in the emitter can be attributed to the “hole-facilitating” character of carrier-transporting material, which can reduce the accumulated holes at the EBL (DTASi) and Flrpic/PPT emitter interface to inhibit triplet-polaron quenching. Triplet-polaron quenching has been reported to be one of the major reasons for efficiency roll-off in PHOLEDs [23]. The detailed device performances of these blue PHOLEDs are summarized in Tables 1 and 2.

In order to prove that the transport of holes from EBL (DTASi) into Flrpic/PPT emitter was promoted by doping carrier-transporting material, two additional device architectures were fabricated; one has a pure PPT layer inserted in-between the EBL and emitter while the other has a TCTA:PPT (10:90) composite layer. The detailed device architectures and energy diagram are depicted in Fig. 4. When inserted a pure PPT layer in-between the EBL and Flrpic/PPT emitter, the device exhibited a very low current efficiency ( $<1 \text{ cd/A}$ ) and its EL spectrum displayed three dominant peak emissions at  $420$ ,  $472$ , and  $580 \text{ nm}$  as shown in Fig. 5, which were originated from NPB, Flrpic, and the exciplex emission of DTASi/PPT, respectively. This phenomenon can be rationalized by the following mechanism. Firstly, according to the energy diagram, the holes and electrons were accumulated at the EBL/pure PPT interface. Secondly, a portion of the carriers recombined and the others formed the DTASi/PPT exciplex. Thirdly, the excitons diffused to either anode or cathode side across the

**Table 1**

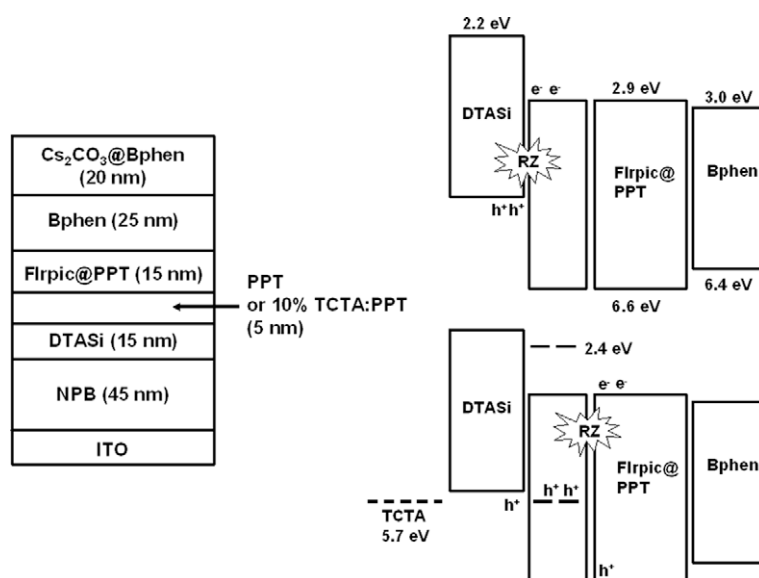
Device performances of blue PHOLEDs.

Emitter			Voltage (V) At 1000 cd/m <sup>2</sup> , (at 20 mA/cm <sup>2</sup> )	Current efficiency (cd/A)	Power efficiency (lm/W)	EQE (%)	CIE <sub>x,y</sub>	Efficiency roll-off (%) From 1 to 40 mA/cm <sup>2</sup>
Host	v (%) TCTA	v (%) Flrpic						
PPT	0	15	5.0 (5.6)	12.3 (9.2)	7.7	5.5	0.18, 0.38	60
	10		4.2 (5.2)	26.8 (22.6)	20	12.1	0.17, 0.36	29
	20		4.2 (5.0)	25 (22.2)	18.7	11.4	0.17, 0.36	23

**Table 2**

Summary of the characteristics of devices using Flrpic as the blue phosphorescent dopant.

Emitter (Dopant: Flrpic)		Voltage (V) At 1000 cd/m <sup>2</sup>	Current efficiency (cd/A)	Power efficiency (lm/W)	EQE (%)	Reference
Host	Carrier-transporting material					
PPT	TCTA	4.2	26.8	20	12.1	This work
TCZ1	–	6.8	23	10.5	10.2	[13]
CzSi	–	5.0 <sup>a</sup>	24 <sup>a</sup>	16 <sup>a</sup>	12 <sup>a</sup>	[14]
SimCP	–	–	–	11.9 <sup>b</sup>	14.4 <sup>b</sup>	[15]
mCP	–	–	–	8.9 <sup>b</sup>	7.5 <sup>b</sup>	[16]
MPO12	–	4.8 <sup>c</sup>	–	–	9.1 <sup>c</sup>	[17]
PO15	–	5.2 <sup>c</sup>	–	–	9.8 <sup>c</sup>	[18]
DBF	–	5.4 <sup>c</sup>	21.2 <sup>c</sup>	12.5 <sup>c</sup>	8.0 <sup>c</sup>	[19]

<sup>a</sup> Reported at 100 cd/m<sup>2</sup>.<sup>b</sup> Reported at maximal value.<sup>c</sup> Reported at 800 cd/m<sup>2</sup>.**Fig. 4.** Device architectures and energy diagram with a pure PPT or TCTA:PPT layer inserted in-between EBL and Flrpic/PPT emitter.

interfacial barriers of DTASi and PPT both of which have high excited state. Finally, the low excited energy of NPB and Flrpic captured the excitons to give the light emission.

On the contrary, when inserted a TCTA:PPT (10:90) composite layer in-between the EBL and Flrpic/PPT emitter, the device with a current efficiency of 11.5 cd/A at a brightness of 1000 cd/m<sup>2</sup> was closed to that of device with whole Flrpic/PPT emitter shown in Fig. 3. And also, the EL spectrum displayed only one dominant peak emission at 472 nm without detecting the emission from the exciplex of DTASi/PPT. This phenomenon further supports the spec-

ulation that the transport of holes from the EBL into PPT is promoted by doping carrier-transporting material. Therefore, the holes and electrons can no longer accumulate at EBL/PPT interface and the recombination zone is shifted toward the Flrpic/PPT emitter.

#### 4. Summary

For solid-state lighting application, the low efficiency and the problematic efficiency roll-off are critical issues to be overcome in blue PHOLEDs. Here, we have proposed

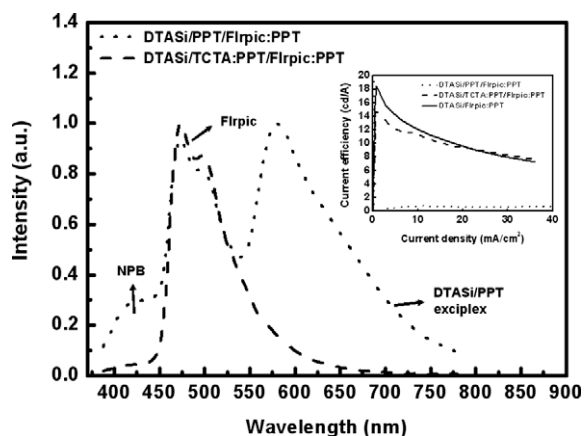


Fig. 5. EL spectra of device with a pure PPT or TCTA:PPT layer inserted in-between EBL and Flrpic/PPT emitter as well as current efficiency–current density ( $cd/A$ – $J$ ) characteristics (inset).

a composite emitter concept and shown that doping a carrier-transporting material in the conventional blue phosphorescent emitter composed of wide-band-gap host and dopant can efficiently facilitate the transport of carriers into the emitter, as well as increase the carrier recombination and reduce carrier accumulation at interface. We showed that this composite blue phosphorescent emitter not only can decrease the driving voltage of device, but also increase the current efficiency as well as suppress the efficiency roll-off problem often encountered at high current density.

### Acknowledgment

This work was supported by National Science and Technology Development Fund (Grant No. 8354DL1000) of the National Science Council of Taiwan.

### References

- [1] B.W. D'Andrade, J. Esler, C. Lin, V. Adamovich, S. Xia, M.S. Weaver, R. Kwong, J.J. Brown, in: Proceedings of the International Display Workshops, Nigata, 2008, p. 143.
- [2] S.J. Su, E. Gnmori, H. Sasabe, J. Kido, *Adv. Mater.* 20 (2008) 4194.
- [3] M.T. Lee, J.S. Lin, M.T. Chu, M.R. Tseng, *Appl. Phys. Lett.* 93 (2008) 13306.
- [4] S.H. Eom, Y. Zheng, E. Wrzesniewski, J. Lee, N. Chopra, F. So, J. Xue, *Appl. Phys. Lett.* 94 (2009) 153303.
- [5] T. Nakayama, K. Hiyama, K. Furukawa, H. Ohtani, in: Proceedings of Society for Information Display, Long Beach, CA, 2007, p. 1018.
- [6] Y. Sun, S.R. Forrest, *Appl. Phys. Lett.* 91 (2007) 263503.
- [7] G. Schwartz, M. Pfeiffer, S. Reineke, K. Walzer, K. Leo, *Adv. Mater.* 19 (2007) 3672.
- [8] Y. Sun, N.C. Giebink, H. Kanno, B. Ma, M.E. Thompson, S.R. Forrest, *Nature* 440 (2006) 908.
- [9] B.W. D'Andrade, R.J. Holmes, S.R. Forrest, *Adv. Mater.* 16 (2004) 624.
- [10] M.A. Baldo, D.F. O'Brien, Y. You, A. Shoustikov, M.E. Thompson, S.R. Forrest, *Nature* 395 (1998) 151.
- [11] C. Adachi, M.A. Baldo, M.E. Thompson, S.R. Forrest, *J. Appl. Phys.* 90 (2001) 5048.
- [12] S. Tokito, T. Iijima, Y. Suzuri, H. Kita, T. Tsuzuki, F. Sato, *Appl. Phys. Lett.* 83 (2003) 569.
- [13] M.H. Tsai, Y.H. Hong, C.H. Chang, H.C. Su, C.C. Wu, A. Matoliukstyte, J. Simokaitiene, S. Grigalevicius, J.V. Grazulevicius, C.P. Hsu, *Adv. Mater.* 19 (2007) 862.
- [14] M.H. Tsai, H.W. Lin, H.C. Su, T.H. Ke, C.C. Wu, F.C. Fang, Y.L. Liao, K.T. Wong, C.I. Wu, *Adv. Mater.* 18 (2006) 1216.
- [15] S.J. Yeh, W.C. Wu, C.T. Chen, Y.H. Hong, Y. Chi, M.H. Ho, S.F. Hsu, C.H. Chen, *Adv. Mater.* 17 (2005) 285.
- [16] R.J. Homes, S.R. Forrest, Y.J. Tung, R.C. Kwong, J.J. Brown, S. Garon, M.E. Thompson, *Appl. Phys. Lett.* 82 (2003) 2422.
- [17] X. Cai, A.B. Padmaperuma, L.S. Sapochak, P.A. Vecchi, P.E. Burrows, *Appl. Phys. Lett.* 92 (2008) 083308.
- [18] L.S. Sapochak, A.B. Padmaperuma, P.A. Vecchi, X. Cai, P.E. Burrows, *Proc. SPIE* 6655 (2007) 665506-1.
- [19] P.A. Vecchi, A.B. Padmaperuma, H. Qiao, L.S. Sapochak, P.E. Burrows, *Org. Lett.* 8 (2006) 4211.
- [20] N. Ide, T. Komoda, J. Kido, *Proc. SPIE* 6333 (2006) 63330M-1.
- [21] S. Naka, H. Okada, H. Onnagawa, T. Tsutsui, *Appl. Phys. Lett.* 76 (2000) 197.
- [22] T. Hasegawa, S. Miura, T. Moriyama, T. Kimura, I. Takaya, Y. Osata, H. Mizutai, in: Proceedings of the Society for Information Display, Seattle, WA, 2004, p.154.
- [23] M.A. Baldo, C. Adachi, S.R. Forrest, *Phys. Rev. B* 62 (2000) 10967.

transparency using an interference effect [7]. DMD-transparent electrodes based on ZnS/Ag/ZnS (ZAZ) and WO<sub>3</sub>/Ag/WO<sub>3</sub> (WAW) had previously been studied as anodes and cathodes, respectively, for OLEDs [7,8]. Transmission larger than 80% and sheet resistance smaller than 10–20 Ω/sq. were reported in those systems. However, OLED devices based on those electrodes turned out inefficient mainly due to poor hole (electron) injection properties of Ag/ZnS (Ag/WO<sub>3</sub>) systems. Moreover, all those devices were fabricated on conventional glass substrates, and thus the potential of DMD electrodes for flexible OLEDs was not known. In this work, we introduce the optimal ZnS/Ag/WO<sub>3</sub> (ZAW) electrode structure that leads to OLED devices that not only exhibit a performance and operational stability comparable to or better than ITO-based devices but also show the flexibility far superior to that of ITO-based devices. Mechanical flexibility of ZAW electrodes and OLEDs based on them is carefully evaluated as a function of radius of curvature for bending and as a function of the number of bending cycles. Mechanisms/interfaces limiting the flexibility of OLED devices are also discussed.

## 2. Experimental

Before deposition of electrode materials, polyethylene terephthalate (PET) substrates (PANAC co., 250 μm) were cleaned using soapy water, deionized (DI) water, acetone, and isopropyl alcohol (IPA) successively in an ultrasonic bath, and were treated by air plasma (PDC-32G, Harrick plasma) for 5 min. Right after the plasma treatment, PET films were spun-coated with transparent photoresist (SU-8, Kayaku Microchem) at 3000 rpm (30 s) for planarization of their surfaces. Those planarized PET films were dried in the oven at 120 °C for 1 h and then loaded into a deposition chamber in which ZnS (Alfa Aesar, 99.99%), Ag (Alfa Aesar, 99.999%) and WO<sub>3</sub> (Alfa Aesar, 99.99%) were deposited sequentially on the PET film by vacuum thermal evaporation. Sample holders and evaporation source were approximately 0.6 m apart, and no damage or deformation was observed in PET substrates without active cooling for substrates.

OLED devices under study were based on N,N'-Bis(naphthalen-1-yl)-N,N'-bis(phenyl)-benzidine (NPB) as a HTL, tris(8-hydroxy-quinolato) aluminium (Alq<sub>3</sub>) as an emitting and electron transporting layer [9], and LiF/Al as a cathode with transparent DMD anodes in a structure of ZnS/Ag/WO<sub>3</sub> as shown in Fig. 1a. (Also refer to Fig. 1b for energy-level diagram. The highest occupied molecular orbital (HOMO) of WO<sub>3</sub> is given as the range of values considering the values reported in the literature [10,11].) Control samples on conventional ITO on polyethylene naphthalate (PEN) substrates (Pecell Technology Inc., 250 μm) were also fabricated in the same batch for comparison.

All the measurement was carried out in an N<sub>2</sub>-filled glove box that is directly connected to the deposition chamber. Current density–voltage (*J*–*V*) and luminance–voltage (*L*–*V*) characteristics were recorded using a source-measure unit (Model 2400, Keithley), a photodiode (FDS100-CAL, Thorlab) with the calibrated spectral re-

sponse, and a pre-calibrated fiber-optic spectrometer (EPP-2000-UV-VIS-NIR, StellarNet). For a bending cycle test, we used a custom-made bending tester which can modulate both the number of bending cycles and the radius of curvature.

## 3. Results and discussion

### 3.1. The properties of ZAW multilayer electrodes

In DMD electrodes, both outer and inner dielectric layers, or *D*<sub>o</sub> and *D*<sub>i</sub> layers as shown in Fig. 1a, respectively, are used to enhance the optical transparency. It is known that a dielectric layer with a higher refractive index *n* has an advantage in that it can fulfill the optimum 'zero-reflection' condition with a thicker metal film, making it easier to realize a low sheet resistance without sacrificing the transmission [12]. A good example illustrating the advantage of using high-*n* dielectric layers is presented in Fig. 2 which clearly shows the calculated maximum achievable transmission *T* in both *D*<sub>i</sub>MD<sub>o</sub>/glass geometry (air-to-air *T*) and organic layers/*D*<sub>i</sub>MD<sub>o</sub>/glass geometry (organic-to-air *T*) increases monotonically as *n* of *D*<sub>o</sub> layer increases. (Calculation is based on the transfer-matrix formalism of multilayer thin films [12,13].) In such respect, ZnS (*n* = 2.35 ± 0.05 at λ = 550 nm) [7] has been chosen as *D*<sub>o</sub> layer rather than WO<sub>3</sub> (*n* = 1.95 ± 0.05 at λ = 550 nm) [14]. For *D*<sub>i</sub> layer, however, we chose WO<sub>3</sub> because it is known to have a good hole injecting property to common organic HTLs [10]. ZnS was previously tried by Pang et al. for *D*<sub>i</sub> layer in OLED devices based on ZAZ anodes, but there was a significant increase in turn-on voltage with respect to ITO-based devices [7], indicating that the hole injection of ZAZ electrodes is fairly limited when compared to that of ITO electrodes. In our own trial, devices based on ZAZ electrode indeed showed the turn-on voltage as large as 10.7 V, which is approximately four times larger than that of typical ITO-based NPB/Alq<sub>3</sub> devices.

In addition to the selection of dielectric layers and optimization of their optical structure, our study indicates that one of the key factors in achieving both high transmission and low sheet resistance in these DMD electrodes is in fact to obtain uniform and continuous metal thin films, as their thickness is typically in the range of 5–20 nm. Making the metal films thicker could ease the continuity issue but would result in a rapid decrease in optical transmission. Fig. 3 shows the two distinctive cases for scanning electron microscopy (SEM) images of Ag films with a nominal thickness of 10 nm that were deposited at the same batch. The Ag films grown on a bare microscope slide glass (Fig. 3a) exhibited a morphology characterized with numerous small clusters of silvers that are essentially separated from one another, resulting in the sheet resistance *R*<sub>SH</sub> that is too high to be measured. On the other hand, the Ag films grown on a microscope slide glass planarized by SU-8 films (Fig. 3b) exhibited continuous and uniform film morphologies. In such case, *R*<sub>SH</sub> values of Ag films having the thickness of 12 and 20 nm were 14.5 and 6.0 Ω/sq., respectively, which are comparable to the results reported by O'Connor et al. [15].

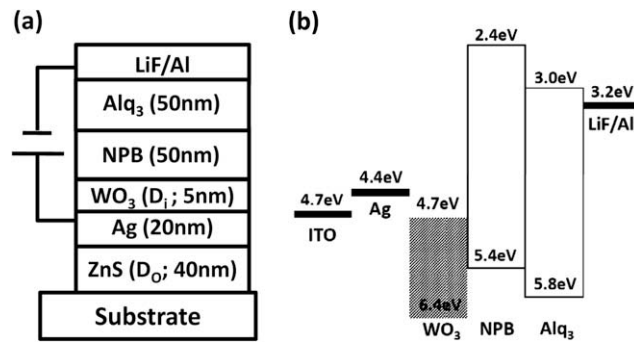


**Fig. 1.** (a) Schematic device structure of the OLED device with ZnS/Ag/WO<sub>3</sub> (ZAW) anodes under study and (b) its energy-level diagram.  $D_1$  layer refers to the inner dielectric layer which interfaces with organic semiconductors and  $D_0$  layer refers to the outer dielectric layer which is closer to a substrate. The HOMO of WO<sub>3</sub> layer is given as a range of values considering the values reported in the literature.

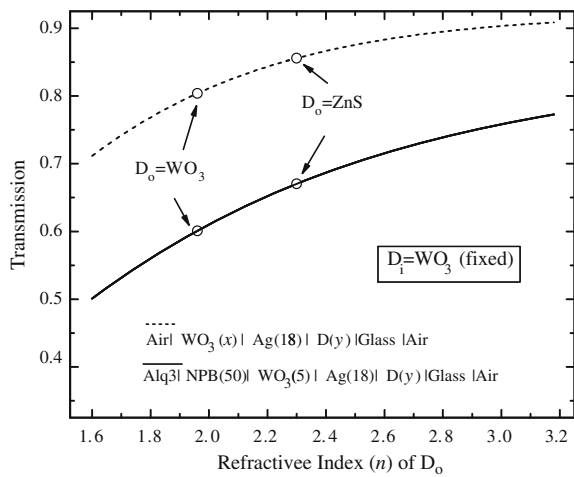


**Fig. 2.** Maximum achievable transmission ( $T$ ) at  $\lambda = 550$  nm in both  $D_1(\text{WO}_3, x \text{ nm})/\text{M}(\text{Ag}, 18 \text{ nm})/D_0(y \text{ nm})/\text{glass}$  geometry (air-to-air  $T$ ; dashed line) and  $\text{Alq}_3(50 \text{ nm})/\text{NPB}(50 \text{ nm})/D_1(\text{WO}_3, 5 \text{ nm})/\text{M}(\text{Ag}, 18 \text{ nm})/D_0(y \text{ nm})/\text{glass}$  geometry (Alq<sub>3</sub>-to-air  $T$ ; solid line) as a function of refractive index ( $n$ ) of  $D_0$  layer.  $x$  and  $y$  refer to the thickness of a dielectric layer that is allowed to vary to find optimum condition. Calculation is based on the transfer-matrix formalism of multilayer thin films [12,13].

In a DMD electrode prepared on a glass substrate, ZnS layer with a thickness of a few tens of nanometer was able to provide a smoothing effect by itself, and therefore, high quality Ag films could be achieved on its top without an additional planarization layer. However, in case of PET substrates, successful DMD electrodes could not be realized without the planarization layer. This is regarded due to the typical high roughness of their surfaces and accidental occurrence of peaks even higher than 50–100 nm [16]. Fig. 4a compares  $R_{\text{SH}}$  of ITO on PEN substrates with ZnS (40 nm)/Ag ( $x$  nm,  $x = 10, 15, 20$ ) layers deposited on PET substrates planarized by the SU-8 layer as a function of the radius of curvature  $r_c$  after repeated bending. The experiment was done by bending a substrate 50 times against a cylindrical object with the substrate-side facing the object, resulting in a tensile stress on electrode layers (see the inset of Fig. 4a). First of all, one can note that the  $R_{\text{SH}}$  values of ZnS/Ag electrodes on PET substrates are comparable to the values observed in glass-based samples, indicating the effectiveness of SU8-based planarization in achieving low  $R_{\text{SH}}$  values on plastic substrates. Moreover, the observed tendency of  $R_{\text{SH}}$  with respect to  $r_c$  demonstrates the superiority of these multilayer electrodes in terms of mechanical flexibility over conventional ITO electrodes on PEN substrates. As one can easily note in the atomic force microscopy (AFM) images presented in Fig. 4b, formation of deep cracks was observed in the ITO films on PEN substrates after the repeated bending at  $r_c$

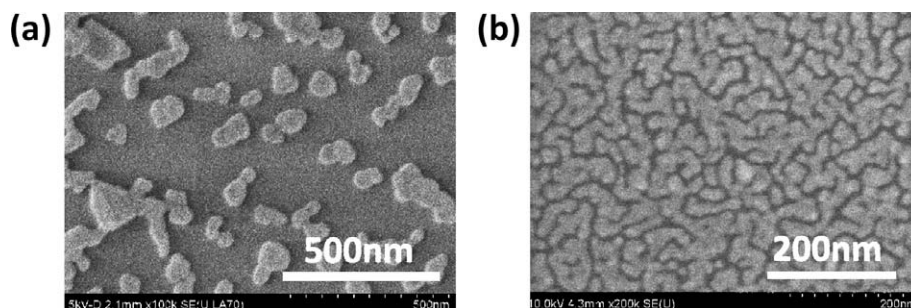


**Fig. 3.** Scanning electron microscopy (SEM) images of Ag films with a nominal thickness of 10 nm grown on (a) a bare glass substrate, and (b) a glass substrate planarized by SU-8 polymer films.

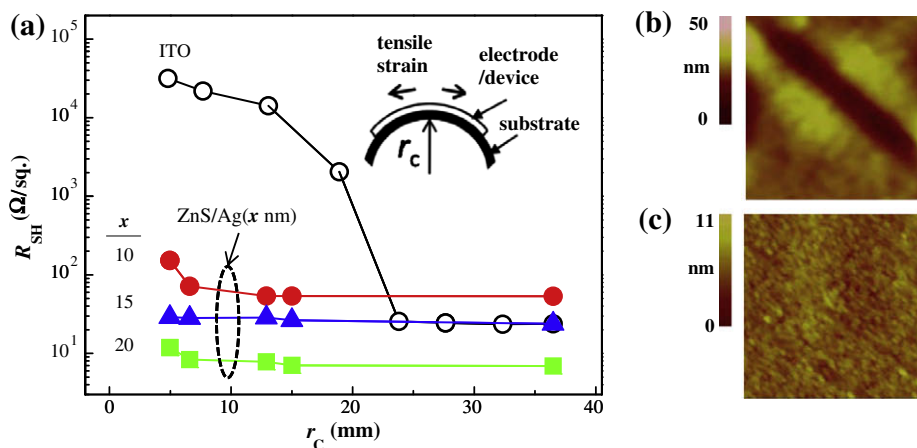


**Fig. 4.** (a) Sheet resistance ( $R_{SH}$ ) of ITO on PEN substrates (open circles) and ZnS(40 nm)/Ag ( $x$  nm,  $x = 10, 15, 20$ ) layers grown on PET substrates (closed shapes) planarized by an SU-8 layer, as a function of a radius of curvature ( $r_c$ ) after being bent 50 times against cylindrical objects with the radius of  $r_c$ . Atomic force microscopy (AFM) images for surface morphology of (b) ITO (top,  $3 \times 3 \mu\text{m}^2$ ) on PEN and (c) ZnS (40 nm)/Ag on planarized PET (Ag on top) (bottom,  $1 \times 1 \mu\text{m}^2$ ) after the bending test at  $r_c$  of 5 mm. Inset in (a): schematic diagram showing the bending test geometry.

of 5 mm [4]. On the other hand, the ZnS/Ag multilayer films exhibited only the hint of slight bending-induced line defects after the same bending experiment (see Fig. 4c), accounting for the fact that its  $R_{SH}$  value remained almost unchanged down to  $r_c$  of  $\sim 5$  mm. Such low level of degradation in  $R_{SH}$  under the harsh bending condition is considered to result from the fact that sheet conduction in these multilayer electrodes occurs mostly within the metal films, which inherently have a good ductility [17].

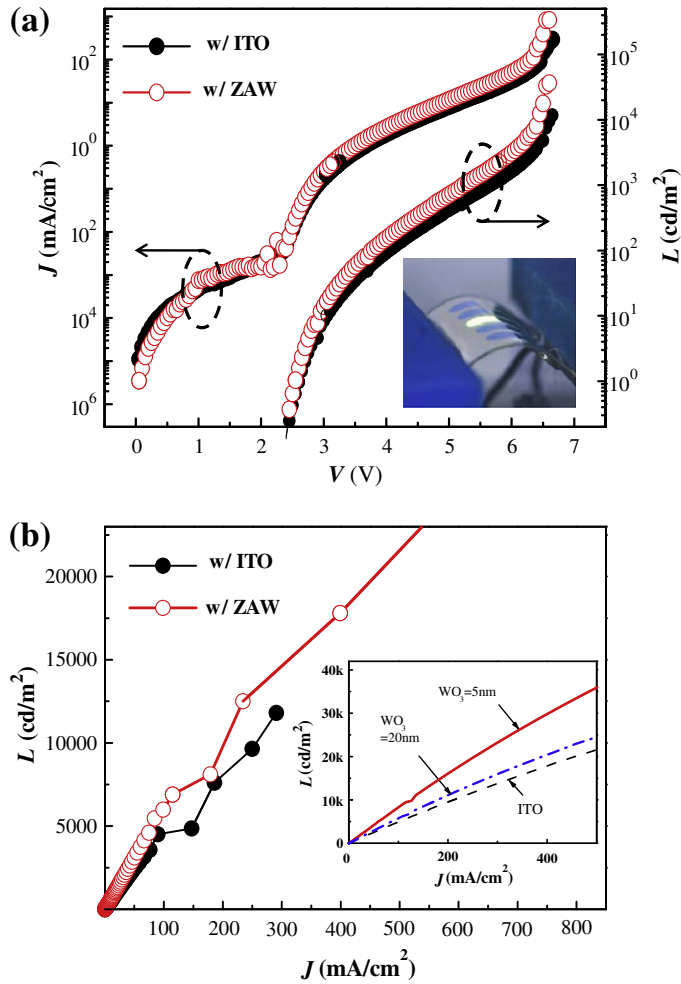
### 3.2. The device performance and flexibility of OLEDs with ZAW anodes

Fig. 5a and b compare the performance of the OLED devices based on the proposed ZAW structure on PET substrates with the ITO-based control devices. The ZAW-based devices exhibit desirable OLED characteristics such as a turn-on voltage ( $V_{TO}$ ) as small as 2.4 V and a luminous efficacy ( $\eta_L$ ) of 6.2 cd/A at 1000  $\text{cd}/\text{m}^2$  with the maximum external quantum efficiency (EQE) of 2.0%. (See also the inset of Fig. 5a for the ZAW-based device under operation while it is bent.) This level of performance is well compared with those of ITO-based control samples which exhibited  $V_{TO}$  of 2.4 V,  $\eta_L$  of 5.0 cd/A at 1000  $\text{cd}/\text{m}^2$ , and the maximum EQE of 1.7%. Also in the independent study using glass substrates (see the inset of Fig. 5b), devices based on the same ZAW structure was shown to exhibit a better performance than devices based on ITO electrodes, and moreover, they outperformed devices based on ZAW electrodes with a thicker  $\text{WO}_3$  layer, although the current geometry had a lower air-to-air transparency ( $\sim 60\%$  at  $\lambda = 550$  nm) than those with a thicker  $\text{WO}_3$  layer [8]. It is not necessarily unusual because optimization of any OLED structure should carefully consider both optical and electrical aspects, and moreover, because optical optimization should consider a situation pertaining to the whole OLED configuration rather than simple air-to-air transmission of electrodes. Detailed description for optimization of

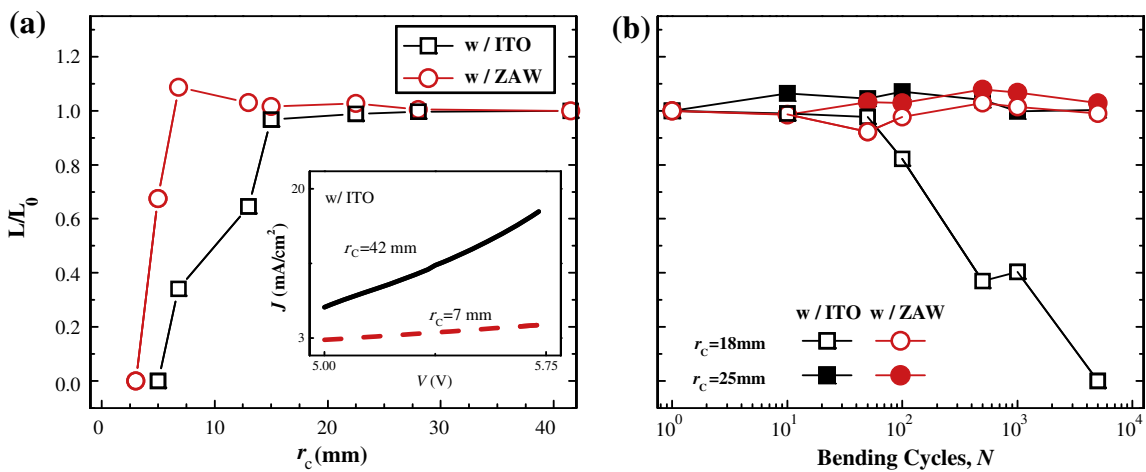
ZAW-based OLED device structure will be reported elsewhere [18].

Fig. 6a presents the luminance ( $L$ ) of the flexible OLEDs as a function of  $r_c$  under the same bending test (=50-time bending; tensile stress as shown in the inset of Fig. 4a) used for the results in Fig. 4. Test was done by monitoring  $L$  at the bias  $V$  of 5.25 and 4.85 V for ITO-based and ZAW-based devices, respectively, which initially resulted in  $L$  of  $510 \pm 10 \text{ cd}/\text{m}^2$ . One can easily note that ITO-based devices started to exhibit a rapid bending-induced degradation as  $r_c$  became smaller than 15 mm, and then lost all the luminescent output at  $r_c$  of 5 mm. Comparison between  $J$ - $V$  characteristics (the inset of Fig. 6a) for  $r_c$  of 42 and 7 mm shows a significant change in their forward slopes, indicating that the degradation comes partly from the increase in  $R_{SH}$  of ITO electrodes. On the other hand, the ZAW-based devices exhibited no degradation down to  $r_c$  of 7 mm and started to lose about 30% of the initial  $L$  at  $r_c$  of 5 mm. Below  $r_c$  of 5 mm, however, the ZAW-based devices also lost all the luminescent output.

As can be seen in Fig. 6b, ZAW-based devices exhibited a significantly better performance than ITO-based devices also in a dynamic test in which their  $L$  values are recorded as a function of bending cycles  $N$  after bending the devices  $N$  times (tensile stress) at  $r_c$  of 18 and 25 mm, respectively. Both types of devices maintained the initial luminance ( $500 \pm 10 \text{ cd}/\text{m}^2$ ) up to  $N$  of  $5 \times 10^3$  at  $r_c$  of 25 mm. However, the ITO-based devices showed a rapid degradation after  $N$  of  $10^2$  and eventually became non-operable after  $N$  of approximately  $10^3$  at  $r_c$  of 18 mm, although  $r_c$  of 18 mm was the radius of curvature at which the ITO-based devices began to show only a glimpse of degradation at the 50-time-bending quick test described in Fig. 6a. On the other hand, the ZAW-based devices maintained the proper OLED characteristics without any degradation up to the maximum  $N$  we tried ( $=5 \times 10^3$ ) at both  $r_c$  values, demonstrating their excellent reliability under repeated tensile stress.



**Fig. 5.** (a) Current density–voltage ( $J$ - $V$ ), luminance–voltage ( $L$ - $V$ ), and (b)  $L$ - $J$  characteristics of OLED devices with ITO (closed circles) or with ZAW (open circles). Inset in (a): a photograph of an OLED with ZAW electrodes under operation while it is bent (compressive stress applied in this picture). Inset in (b):  $L$ - $J$  characteristics of rigid OLED devices with ITO on a glass or with ZAW on a glass with the thickness of  $WO_3$  being 5 or 20 nm.



**Fig. 6.** (a) Change in  $L$  of the ITO-based (squares) and ZAW-based (circles) OLED devices as a function of  $r_c$  after the same bending test used in Fig. 4. [Tensile stress applied, as shown in Fig. 4a.] Inset in (a):  $J$ - $V$  characteristics of ITO-based devices near observation point for  $r_c$  of 42 mm (solid) and 7 mm (dashed). (b) Change in  $L$  as a function of bending cycles ( $N$ ) measured at  $r_c$  of 18 and 25 mm.  $L$  values are normalized to the respective initial values  $L_0$  in (a) and (b).

Fig. 7 presents the optical microscope images of OLED device active layers taken after the bending test corresponding to Fig. 6a at  $r_c$  of 15, 7, and 5 mm. In case of ITO-based devices (Fig. 7a), rather macroscopic line defects were observed in a direction parallel to the bending axis for small  $r_c$  values. The image of the ITO-based devices taken after deposition of Al over the whole sample area on the device side (the inset of Fig. 7a) shows that such line defects extend into the non-active area having ITO or ITO/organic layers only, indicating that the degradation observed in that range of  $r_c$  is mainly due to the formation of the cracks within the ITO layer that were observed also in Fig. 4b.

On the other hand, ZAW-based devices virtually show no change down to  $r_c$  of 7 mm and start to exhibit multiple of short line defects in the active area at  $r_c$  of  $\sim 5$  mm (see Fig. 7b). These line defects were only visible when those samples were seen from the emission side through the substrate, suggesting that bending-induced strain resulted in local defects *internally* within the device active layers. In order to pinpoint the interfaces or layers that originate defects in these devices, thin Al layer was deposited on the device side of the whole samples as in the ITO case. Images taken after the blanket deposition of Al (the inset of Fig. 7b) reveal that those line defects observed in ZAW devices exist only in the location where cathode metal and organic layer both exist, indicating that either of the cathode metal or organic layers, or interface between them is the one most subject to creation of defects upon severe bending-induced tensile strain. Considering that both metal and organic layers typically have a good ductility and that areas only with anode and organic layers do not show defects, one can conclude that it is mainly the delamination occurring at the cathode metal–organic interface that induced the short line defects in the ZAW-based devices. This reminds us that one has to carefully consider the effect of bending-induced strain on some critical interfaces [19] while continuing to develop highly flexible electrodes, in

order to realize ultra-flexible OLED devices or similar systems.

In addition to the device performance and mechanical flexibility, the operational stability cannot be overemphasized for any electrode technology to be practically meaningful. Fig. 8 shows the change in luminance  $L$  and voltage  $V$  of ZAW-based and ITO-based flexible OLEDs as a function of time under a supply of constant current  $I_0$  of 1 mA. In this condition, the initial luminance values  $L_0$  were 1600 and 610  $\text{cd/m}^2$  for the ZAW-based and the ITO-based devices, respectively. Both devices maintain the initial luminance quite well throughout the testing time-span of 60,000 s ( $\approx 16.7$  h), as shown in Fig. 8a. The voltage required to support the current of 1 mA for the ITO-based device exhibited a gradual increase as time passed. Overall  $\sim 10\%$  increase in the voltage was observed after operation for 60,000 s in the ITO-based device. Such behavior can be attributed to appearance of localized inactive areas which effectively decrease the device area and thus increase current density for a given current. Different from the case of ITO-based devices, the voltage for the ZAW-based devices remained almost constant except for a small fluctuation at an early stage. It is not yet clear whether ITO-based flexible devices are inherently poor in operational stability or it is rather specific to the batch of devices we tested. Nevertheless, the above results clearly demonstrate the competence of ZAW electrodes for flexible OLEDs with a high operational stability.

Another important aspect to consider for device stability particularly in flexible OLEDs is to protect a device from permeation of water vapor and oxygen, because most plastic substrates do not provide a sufficient protection by themselves due to their porous nature [20]. It is known that some dielectrics and metal layers can improve the barrier properties of plastic substrates [20]. DMD electrodes may then play an additional role as a gas barrier to some degree, as  $\text{TiO}_x$  buffer layers used in organic solar cells were shown to work also as a barrier layer that reduced the air-sensitiv-

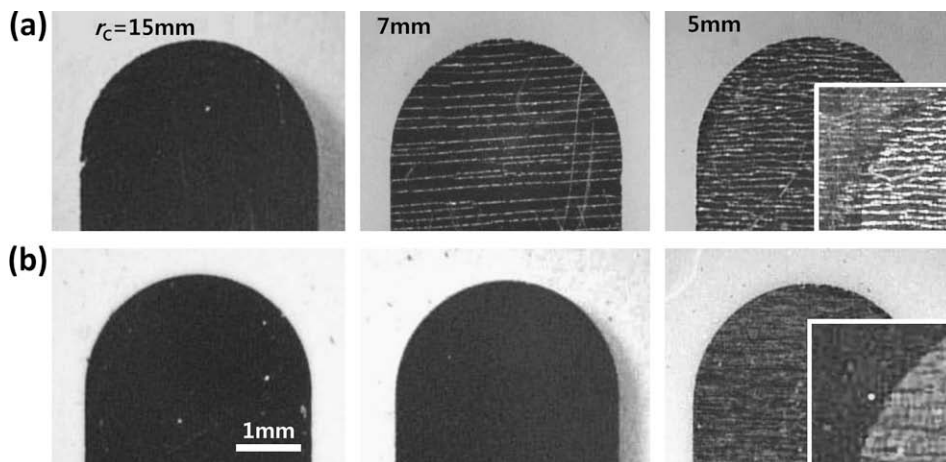


**Fig. 7.** Images of the device active area (appears as dark finger-like shapes) for (a) ITO-based devices and (b) ZAW-based devices taken from the emission side through substrates after 50-time-bending test in Fig. 6a at  $r_c = 15, 7,$  and  $5$  mm. Inset: images taken after deposition of Al layer over the whole sample area to tell whether cracks exist also in non-active area. Note that the ITO-based devices have cracks also in non-active layers, indicating the major portion of cracks comes from ITO itself.



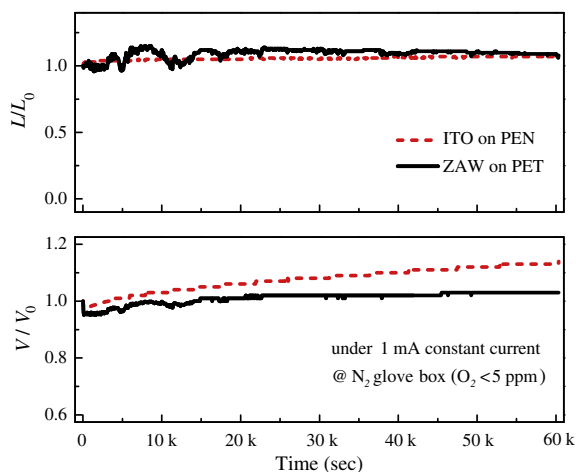


**Fig. 8.** Luminance  $L$  and voltage  $V$  of ZAW-based (—) and ITO-based (---) flexible OLEDs monitored as a function of time under a supply of constant current of 1 mA. Values are normalized to their respective initial values  $L_0$  and  $V_0$ .

ity of the cells [21]. A further study is needed to analyze the operational and environmental stability of these flexible OLEDs under various conditions and to develop a proper barrier structure that considers both optical and flexible properties of the overall device structure.

#### 4. Conclusions

In summary, we have successfully demonstrated highly flexible OLEDs by replacing ITO electrodes with ZnS/Ag/WO<sub>3</sub> (ZAW) multilayer transparent electrodes showing an ideal balance among sufficiently low sheet resistance, mechanical flexibility, and carrier-injection compatibility with OLEDs. Performance as well as operational stability of the OLED devices with the proposed electrode geometry was shown to be comparable to or even better than that of ITO-based control devices. Readers are cautioned that ZAW electrodes presented in this work may not be the only DMD electrodes suitable for flexible organic devices. Because all DMD electrodes rely on ultrathin metals for efficient conduction, one may in general expect that they can potentially be used as highly flexible transparent electrodes in many demanding applications, with the following guidelines met: (i) outer dielectrics to have a high refractive index and a low (possibly zero) extinction coefficient at visible wavelength; (ii) metal to have a high conductivity with a low extinction coefficient at visible wavelength, and to have a tendency to form a uniform, continuous thin film; and (iii) inner dielectric to have a relevant carrier-injection (collection) property to (from) adjacent semiconductors to be used in OLEDs and transparent thin-film transistors (organic solar cells).

Flexibility of the current OLED devices was only limited by the rather abrupt formation of delamination that occurred at interfaces between cathode metals and adjacent organic layers at a radius of curvature of  $\sim 5$  mm. This limit may be further reduced by the careful engineering of a multilayer structure so that device layers may be located

near neutral mechanical plane [22]. Since the minimum radius of curvature allowing for a consistent operation of flexible devices is highly important in making roll-type devices more compact and reliable, the work reported here is likely to bring the promise of OLEDs and other similar organic devices for future ultraportable displays and electronic appliances much closer.

#### Acknowledgement

This work was supported by the Brain Korea 21 project, School of Information Technology, KAIST, 2009, by the ERC program of the Korea Science and Engineering Foundation (KOSEF) grant funded by the Korea Ministry of Education, Science and Technology (MEST) (No. R11-2007-045-01001-0), and by the Human Resource Training Project for Strategic Technology by the Korea Industrial Technology Foundation (KOTEF). Authors are grateful to S. Han and J.-M. Choi for taking AFM and optical microscope images of samples.

#### References

- [1] S.R. Forrest, *Nature* 428 (2004) 911.
- [2] D.U. Jin, J.K. Jeong, H.S. Shin, M.K. Kim, T.K. Ahn, S.Y. Kwon, J.H. Kwack, T.W. Kim, Y.G. Mo, H.K. Chung, in: *Digest of Technical Papers – SID International Symposium*, vol. 37, 2006, p. 1830.
- [3] A. Yoshida, S. Fujimura, T. Miyake, T. Yoshizawa, H. Ochi, A. Sugimoto, H. Kubota, T. Miyadera, S. Ishizuka, M. Tsuchida, H. Nakada, in: *Digest of Technical Papers – SID International Symposium*, vol. 34, 2003, p. 856.
- [4] G.F. Wang, X.M. Tao, R.X. Wang, *Nanotechnology* 19 (2008) 145201.
- [5] X. Crispin, F.L.E. Jakobsson, A. Crispin, P.C.M. Grim, P. Andersson, A. Volodin, C. Van Haesendonck, M. Van Der Auweraer, W.R. Salaneck, M. Berggren, *Chem. Mater.* 18 (2006) 4354.
- [6] J. Li, L. Hu, L. Wang, Y. Zhou, G. Grüner, T.J. Marks, *Nano Lett.* 6 (2006) 2472.
- [7] (a) H. Pang, Y. Yuan, Y. Zhou, J. Lian, L. Cao, J. Zhang, X. Zhou, *J. of Luminescence* 122–123 (2007) 587; (b) X. Liu, X. Cai, J. Qiao, J. Mao, N. Jiang, *Thin Sol. Films* 441 (2003) 200.
- [8] S.Y. Ryu, J.H. Noh, B.H. Hwang, C.S. Kim, S.J. Jo, J.T. Kim, H.S. Jeong, C.H. Lee, S.Y. Song, S.H. Choi, S.Y. Park, *Appl. Phys. Lett.* 92 (2008) 023306.
- [9] S.A. Van Slyke, C.H. Chen, C.W. Tang, *Appl. Phys. Lett.* 69 (1996) 2160.
- [10] J. Meyer, S. Hamwi, T. Bülow, H.-H. Johannes, T. Riedl, W. Kowalsky, *Appl. Phys. Lett.* 91 (2007) 113506.
- [11] C. Tao, S. Ruan, G. Xie, X. Kong, L. Shen, F. Meng, C. Liu, X. Zhang, W. Dong, W. Chen, *Appl. Phys. Lett.* 94 (2009) 043311.
- [12] H.A. Macleod, *Thin-Film Optical Filters*, second ed., Macmillan Publisher Company, NY, 1986, pp. 499–501.
- [13] L.A.A. Pettersson, L.S. Roman, O. Inganäs, *J. Appl. Phys.* 86 (1999) 487.
- [14] S.M.A. Durrani, E.E. Khawaja, M.A. Salim, M.F. Al-Kuhaili, A.M. Al-Shukri, *Sol. Energy Mater. Sol. Cells* 71 (2002) 313.
- [15] B. O'Connor, C. Haughn, K.-H. An, K.P. Pipe, M. Shtein, *Appl. Phys. Lett.* 93 (2008) 223304.
- [16] B.A. MacDonald, K. Rollins, D. MacKerron, K. Rakos, R. Eveson, K. Hashimoto, B. Rustin, *Engineered films for display technologies*, in: G.P. Crawford (Ed.), *Flexible Flat Panel Displays*, Wiley, UK, 2005, pp. 20–22.
- [17] J.F. Shackelford, *Introduction to Materials Science for Engineers*, sixth ed., Prentice Hall, NJ, 2005, pp. 186–250.
- [18] C. Yun, H. Cho, S. Yoo, in preparation.
- [19] O. van der Sluis, R.A.B. Engelen, P.H.M. Timmermans, G.Q. Zhang, in: *Ninth Int. Conf. on Thermal, Mechanical and Multiphysics Simulation and Experiments in Micro-Electronics and Micro-Systems*, EuroSimE 2008, 2008, Art. No. 452506.
- [20] J.S. Lewis, M.S. Weaver, *IEEE J. Sel. Top. Quantum Electron.* 10 (2004) 45.
- [21] K. Lee, J.Y. Kim, S.H. Park, S.H. Kim, S. Cho, A.J. Heeger, *Adv. Mater.* 19 (2007) 2445.
- [22] Z. Suo, E.Y. Ma, H. Gleskova, S. Wagner, *Appl. Phys. Lett.* 74 (1999) 1177.

To create such a detector clearly requires the use of an inherently flexible electronic device that can be fabricated over a large area and that is sensitive to the passage of X-rays. This combination of properties can be achieved by using an inorganic phosphor that is placed in contact with an organic photovoltaic device (OPV), with the OPV detecting luminescence emitted by the phosphor following the passage of the X-rays. Here, the use of an OPV is particularly beneficial as such devices can in principle be fabricated over relatively large areas onto a fully-flexible plastic substrate [11]. Indeed, an organic-semiconductor based system has recently been used to detect 70 kV X-rays used in medical imaging applications, with the device having sufficient level of radiation stability [12] and low dark-current [13] to make it suitable for practical imaging applications. Other recent reports on the sensitivity of organic materials such as polyfluorenes and poly(triarylamines) [14] and pentacene [15] to X-rays having an energy of 10's of kV also suggest such materials are often characterised by very promising levels radiation hardness, suggesting applications as electronic materials suitable for use in space-environments [15].

In this work, we focus on the detection of X-rays having higher energy (6 MV) using an OPV-based detector. Such X-rays are more highly penetrating (less well stopped) than those used in imaging (e.g. the total mass attenuation coefficient of 70 kV X-rays in  $\text{SiO}_2$  is around 10 times greater than that of 6 MV X-rays [16]). Furthermore, the MV X-rays used in radiotherapy are typically delivered at dose-rates that are much larger than that used in imaging applications ( $\sim 100 \text{ mGy s}^{-1}$  compared to  $< 1 \text{ mGy s}^{-1}$  [17]). A practical detector for such MV X-rays must therefore have a linear response over a wide exposure range, and be able to withstand the passage of a significant radiation flux through its active layer without its functionality being compromised by radiation-induced damage. Concerns arise however as to the ability of organic-semiconductors to withstand the passage of a significant dose of MV X-rays without the generation of charge traps resulting from local ionisation. Whilst kV X-rays have been shown to generate a sufficient quantity of luminescence within a thin scintillator film that is detectable by an OPV [12,13], it is not clear whether significantly more penetrating X-rays of interest here would generate a detectable optical signal. As we report however, the devices that we have created have a sensitivity that is an order of magnitude better than that of a conventional (small-area) silicon p–n junction based device. Furthermore, we show that the organic X-ray detector prototyped is remarkably radiation tolerant, with only a small loss (2%) in sensitivity measured over the course of a relatively large (360 Gy) radiation exposure.

## 2. Experimental

The OPVs that we have used are based on a thin-film blend of the conjugated polymer poly(3-hexylthiophene) [P3HT] and the fullerene derivative PCBM. This material system currently represents the state of the art for organic photovoltaic devices, with the highest external quantum efficiencies (EQE) recorded being around 80% at 500 nm

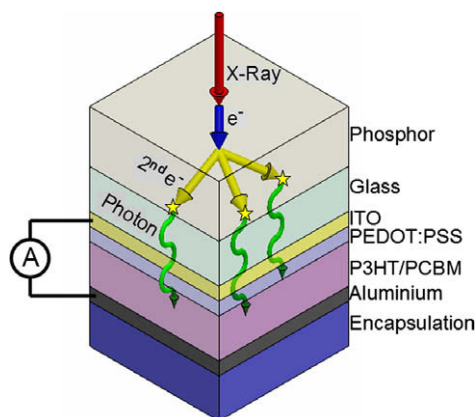


**Fig. 1.** Schematic of the detector operation. The incident X-rays (red) produce a forward-scattered primary electron (blue) which then produces secondary ionisation electrons (yellow). This secondary ionisation excites the phosphor, whose luminescence (green) is detected by the organic photovoltaic device. (For interpretation of the references to colour in this figure legend, the reader is referred to the web version of this article.)

[18,19]. A schematic of the devices is shown in Fig. 1. Briefly, devices are fabricated by spin-casting a layer of PEDOT:PSS onto an ITO anode which is then baked in  $\text{N}_2$  for 10 min at  $100^\circ\text{C}$  to remove adsorbed water. The substrates are then transferred to an overpressure nitrogen glovebox, where an 1:0.8 (by mass) blend solution of P3HT:PCBM in chlorobenzene is spin-cast onto the ITO/PEDOT:PSS anode. A cathode consisting 100 nm of aluminium is then evaporated onto the organic thin-film at a base pressure of  $< 10^{-6}$  mBar. The devices are encapsulated by bonding a 0.5 mm glass sheet onto their surface using a UV curable glue. Finally, the devices are annealed at  $150^\circ\text{C}$  for 60 min. Measurements using a calibrated solar-simulator operating at  $100 \text{ mW cm}^{-2}$  (Oriel Instruments AM1.5 solar-simulator calibrated with an NREL  $4 \text{ cm}^2$  silicon reference cell) indicate that the devices have a typical power conversion efficiency (PCE) of 3.7% immediately following fabrication. However, since OPVs undergo a period of degradation when initially illuminated, the devices were aged for 30 min under 1 sun (AM 1.5) illumination to improve their stability. This process resulted in devices with a typical PCE of 3%. The measured EQE of the OPV devices is shown in Fig. 1. Here, it can be seen that our devices have a peak EQE of 57% at 504 nm (post aging). Each device has an active area of  $4.5 \text{ mm}^2$ , which is defined by the overlap of the anode and cathode strips.

As a phosphor we have used the material  $\text{Gd}_2\text{O}_2\text{S:Tb}$ . This was purchased from Applied Scintillation Technologies in the form of a flexible substrate that was coated with the phosphor at an area density of  $279 \text{ mg/cm}^2$ . In the experiments described, the substrate was placed in contact with the OPV such that luminescence emitted was directly incident upon the transparent anode. To evaluate the efficiency of the composite detector, we have used the linear accelerator facility at St. James's University Hospital in Leeds. The machine forms part of a dedicated research facility, however the linac is typical of machines used to

deliver megavoltage radiotherapy treatments around the world. This machine provides 6 MV X-rays up to a maximum dose rate of  $\sim 100 \text{ mGy s}^{-1}$  (approximately equivalent to  $10^{14} \text{ photons s}^{-1} \text{ m}^2$ ).

### 3. Results and discussion

The MV X-rays studied here can interact with matter in one of two ways; by Compton scattering and via pair-production. In both processes, a high-energy electron (or positron) is forward-scattered (by a distance of  $\sim 1.5 \text{ cm}$  in water), producing a shower of secondary ionisation. In radiation therapy these low-energy ( $< 100 \text{ keV}$ ) secondary electrons are used to deliver the energy that destroys malignant tissue. In our detector, the secondary electrons created excite the  $\text{Gd}^{3+}$  (which is contained within a ceramic host-matrix) that then transfers its energy to the rare-earth  $\text{Tb}^{3+}$  dopant [20,21]. The luminescence from the  $\text{Tb}^{3+}$  is then detected by the OPV. The emission spectra of the phosphor recorded under X-ray illumination is shown in Fig. 2. It can be seen that the peak emission wavelength (540 nm) coincides well with the peak sensitivity of the OPV (504 nm), ensuring efficient detection. Indeed, from the overlap integral of the two spectra, we calculate that in an idealised device (i.e. having no optical loss), the luminescent photons should be detected with an efficiency of 44%.

Fig. 3a plots the photocurrent from the device as a function of X-ray dose rate. We find that the X-rays are detected with a sensitivity of  $0.086 \text{ C m}^{-2} \text{ Gy}^{-1}$  over the entire range of dose-rates explored, confirming the applicability of the device as a dosimeter. Control experiments in which no phosphor layer was used show that X-rays can be detected directly by the OPV itself but that the sensitivity is over two orders of magnitude lower. This relative insensitivity of the OPV to direct exposure to X-rays results from the fact that the active semiconductor is relatively thin ( $\sim 150 \text{ nm}$  in total), and thus the rate of charge generation within the OPV semiconductor layers is very low. We can also estimate the quantum efficiency ( $\eta$ ) of the device (photoelectrons per X-ray absorbed in the phosphor) using  $\eta = k/\gamma$  where  $k$  is the rate at which electrons are produced at the terminals (calculated directly from the current) and  $\gamma$  is the rate at which X-rays are absorbed. The rate at which X-rays are absorbed is calculated using  $\gamma = \rho DA/E$

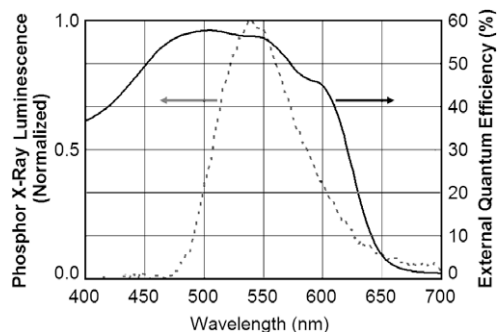


Fig. 2. The external quantum efficiency of the organic photovoltaic device shown together with X-ray excited luminescence spectra of the phosphor.

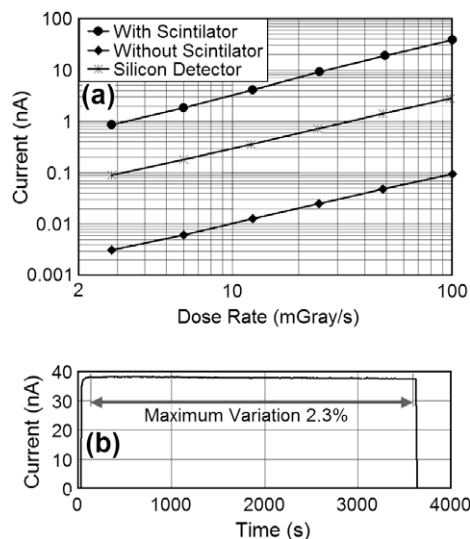


Fig. 3. Part (a) shows a log-log plot of output current versus X-ray dose rate for the OPV both with and without the phosphor present as well as for the reference silicon detector. Part (b) shows the current recorded from the device as a function of time whilst exposed to a constant X-ray dose rate of  $\sim 100 \text{ mGy s}^{-1}$ .

where  $\rho$  is the sheet density of the phosphor,  $D$  is the dose rate,  $A$  is the pixel area and  $E$  is the average energy of an X-ray (which is a third of the acceleration voltage). This leads to an overall efficiency of  $\sim 62,000$  electrons per absorbed X-ray photon. By dividing this figure by the OPV luminescent photon detection efficiency and assuming an optical loss of a half, we estimate the phosphor yield to be 47,000 photons per MeV. This value compares favourably with similar scintillators in the literature [22].

For comparison, we have also recorded the current generated by a commercial (Scanditronix EDP-10) silicon p-n junction based X-ray detector under identical conditions to that described above. This device is based on a silicon detector that is encapsulated within a stainless-steel/epoxy block (6.5 mm thick  $\times$  12 mm diameter), and works by directly collecting the ionised charge produced within the detector (rather than via the detection of luminescence). Encouragingly, we find that the photocurrent produced by the OPV/phosphor detector was  $\sim 14$  times larger than that recorded from the silicon-based devices when exposed to the same radiation flux. We note that a similar combination of OPV and an  $\text{Gd}_2\text{O}_2\text{S:Pr}$  phosphor have been used [12] to detect 70 kV X-rays. In such previous work, the lower energy X-rays were detected with a sensitivity of  $1.28 \text{ C m}^{-2} \text{ Gy}^{-1}$  (when the OPV was run in short-circuit mode); a factor of  $\sim 15$  times higher than that demonstrated here. We believe that the 10 times higher penetration depth of the 6 MV X-rays used here most likely accounts for this difference in sensitivity.

It is clear that our device works as a radiation detector, however it is important to assess its relative stability under continuous exposure to X-rays. Devices were therefore subjected to prolonged operation (with phosphor present) and the output current monitored. This is plotted in Fig. 3b in which it can be seen that over the course of the exposure

(which lasts a period of 60 min and corresponds to a total radiation dose of 360 Gy) (the detected photocurrent drops) by around 2%. Measurements of the OPV PCE after such exposure failed to identify any significant degradation in device efficiency, demonstrating a relatively promising level of stability. Indeed, the typical dose received by a device during an individual radiation therapy treatment would be  $\sim 2$  Gy, indicating that our un-optimized detector could survive many individual radiation exposures. We believe the relative radiation stability of an OPV results from the fact that the organic-semiconductor layer used in the OPV is very thin (conjugated polymers are direct-gap semiconductors and thus have very high extinction coefficients). For this application, this relative thinness is a distinct advantage as the rate of damage that occurs to the organic-semiconductor via direct interaction with the highly penetrating (and thus weakly interacting) MV X-rays is low. This observation is commensurate with the fact that the directly-generated photocurrent within the OPV is also low.

Finally, transparency is an important feature of any thin-film device that is to be used in real-time dosimetry during radiation therapy. We have therefore used the commercial silicon detector described above to determine the attenuation in X-ray flux passing through either the OPV, or the phosphor, or the stacked OPV and phosphor. We find that the intensity X-ray beam is attenuated by a 1.3% when passing through the phosphor, by 1.7% when passing through the OPV and thus by 3% when passing through the entire stacked device. This is a relatively low rate of attenuation, and would not compromise the efficacy of a typical radiation treatment.

#### 4. Conclusions

We have prototyped a MV X-ray detector consisting of a flexible phosphor layer in contact with an organic photovoltaic fabricated from P3HT:PCBM. X-rays incident on the phosphor generate luminescence that is then detected by the organic photovoltaic. In order to increase the stability of the detectors, the organic photovoltaics were aged for 30 min under AM 1.5 simulated sunlight in order to remove any initial degradation in performance, however, even after this process the external quantum efficiency was greater than 55% at the peak wavelength emitted by the phosphor. This well matched spectral response between the phosphor and the organic photovoltaic resulted in a device having a sensitivity higher than a commercial silicon detector. The system also had excellent radiation hardness with less than 2% variance in output recorded

over 360 Grays of radiation dose. Our measurements therefore suggest that organic detectors may find application as real-time, patient-specific dosimeters used in the imaging of X-rays for radiotherapy treatment.

#### Acknowledgements

We thank the UK EPSRC for funding this work via grants EP/F016433 (Optimising polymer photovoltaic devices through control of phase-separation) and EP/F056370 (High-efficiency block copolymer solar cells – a scaleable prototype for low cost energy generation). We also thank John McMillan (University of Sheffield) for useful and enlightening discussions.

#### References

- [1] R.R. da Silva, D. Mery, *Insight* 49 (2007) 603–609.
- [2] P. Suortti, W. Thomlinson, *Phys. Med. Biol.* 48 (2003) R1–R35.
- [3] A. Olivo, D. Chana, R. Speller, *J. Phys. D: Appl. Phys.* 41 (2008) 225503.
- [4] J.T. Parsons, B.D. Greene, T.W. Speer, S.A. Kirkpatrick, D.B. Barhorst, T. Yanckowitz, *Int. J. Radiat. Oncol. Biol. Phys.* 50 (2001) 953–959.
- [5] D. Followill, P. Geis, A. Boyer, *Int. J. Radiat. Oncol. Biol. Phys.* 38 (1997) 667–672.
- [6] M.K. Bucci, A. Bevan, M. Roach CA Cancer, *J. Clin.* 55 (2005) 117–134.
- [7] T. Kron, L. Duggan, T. Smith, *Phys. Med. Biol.* 43 (1998) 3235–3259.
- [8] M.J. Butson, T. Cheung, P.K.N. Yua, *Appl. Radiat. Isotopes* 62 (2005) 631–634.
- [9] M. Essers, B.J. Mijneer, *Int. J. Radiat. Oncol. Biol. Phys.* 43 (1999) 245–259.
- [10] E.B. Podgorsak, M.B. Podgorsak, *IAEA Radiation Oncology Physics: A Handbook for Teachers and Students* 534–536, in: E.B. Podgorsak (Ed.), International Atomic Energy Agency, Vienna, 2005.
- [11] S.-I. Na, S.-S. Kim, J. Jo, D.-Y. Kim, *Adv. Mater.* 20 (2008) 4061–4067.
- [12] R.E. Keivanidis, N.C. Greenham, H. Sirringhaus, R.H. Friend, J.C. Blakesley, R. Speller, M. Campoy-Quiles, T. Agostinelli, D.D.C. Bradley, J. Nelson, *Appl. Phys. Lett.* 92 (2008) 023304.
- [13] T. Agostinelli, M. Campoy-Quiles, J.C. Blakesley, R. Speller, D.D.C. Bradley, *Appl. Phys. Lett.* 93 (2008) 203305.
- [14] C.R. Newman, H. Sirringhaus, J.C. Blakesley, R. Speller, *Appl. Phys. Lett.* 91 (2007) 142105.
- [15] R.A.B. Devine, M.-M. Ling, A.B. Mallik, M. Roberts, Z. Bao, *Appl. Phys. Lett.* 88 (2006) 151907.
- [16] R.G. Jaeger, E.P. Blizzard, A.B. Chilton, M. Grotenhuis, A. Hönl, Th.A. Jaeger, H.M. Eisenlohr (Eds.), *Engineering Compendium on Radiation Shielding*, vol. 2, Springer-Verlag, Berlin/Heidelberg, 1975 (p. 183).
- [17] K.C. Young, M.L. Ramsdale, A. Rust, J. Cooke, *Br. J. Radiol.* 70 (1997) 1036–1042.
- [18] S.-H. Jin, B.V.K. Naidu, H.-S. Jeon, S.-M. Park, J.-S. Park, S.C. Kim, J.W. Lee, Y.-S. Gal, *Sol. Energy Mater. Sol. Cells* 91 (2007) 1187–1193.
- [19] M. Lenes, G.-J.A.H. Wetzelaer, F.B. Kooistra, S.C. Veenstra, J.C. Hummelen, P.W.M. Blom, *Adv. Mater.* 20 (2008) 2116–2119.
- [20] S.W. Allison, M.R. Cates, G.T. Gillies, *Rev. Sci. Instr.* 73 (2002) 1832–1834.
- [21] E.I. Gorokhova, V.A. Demidenko, S.B. Rodnyi, C.W.E. van Eijk, *IEEE Trans. Nucl. Sci.* 52 (2005) 3129–3132.
- [22] P. Leecoq, A. Annenkov, A. Gektin, M. Korzhik, C. Pedrini, *Inorganic Scintillators for Detector Systems: Physical Principles and Crystal Engineering*, Springer, New York, 2006 (p. 25).

[14–16]. In these tandem cells, the subcells were connected by external circuits to realize parallel connection. In this letter, we demonstrate a tandem polymer PV cell with the two stacked subcells having complementary absorption in parallel connection without using external circuit connection. A semitransparent metal layer combined with inorganic semiconductor compounds is utilized as the intermediate electrode of the two subcells to create the required built-in potential for collecting photo-generated charges. The advantage of this kind of tandem polymer solar cells is that each subcell can be optimized individually to achieve a highest  $J_{SC}$  since the overall  $J_{SC}$  of the stacked cell is the sum of the two subcells.

## 2. Experimental details

Fig. 1a shows the structure of the tandem polymer PV cells and the chemical structures of the active materials used in this study. The conjugated polymers of poly[2,6-(4,4-bis-(2-ethylhexyl)-4H-cyclopenta[2,1-b;3,4-b']dithiophene)-alt-4,7-(2,1,3-benzothiadiazole)] (PCPDTBT) and poly(3-hexylthiophene) (P3HT) are synthesized by our group with the number-average molecular weight ( $M_n$ ) of 21,000 g/mol and a polydispersity index (PDI) of 3.15 for PCPDTBT, and a  $M_n$  of 24,000 g/mol, a PDI of 1.59 and a regioregularity higher than 97% for P3HT, respectively. The P3HT and PCPDTBT with different band-gaps are used as electron donors, which are blended with electron acceptor of [6,6]-phenyl C61-butyric acid methyl ester (PCBM) (purchased from Solenne Co. with a purity higher than 99%, used as received) to serve as the active layers in different subcells, respectively. As shown in Fig. 1a, the device was fabricated on a patterned indium tin oxide (ITO)-coated glass substrate with  $10 \Omega/\text{square}$  sheet resistance. An electron transport layer of titanium oxide ( $\text{TiO}_x$ ) was prepared by means of sol-gel chemistry. Tetrabutyl titanate ( $\text{Ti}(\text{OC}_4\text{H}_9)_4$ , 10 mL) was as a precursor and mixed with ethanol (100 mL) and de-ionized water (2 mL) together. The mixture solution was heated to  $80^\circ\text{C}$  and stirred for 2 h to form a  $\text{TiO}_x$  precursor sol-gel solution. The precursor sol-gel solution was diluted in ethanol and spin-coated onto the ITO glass substrate in air with a  $0.45 \mu\text{m}$  filter at 3000 r.p.m. for 60 s. The film is subjected to hydrolysis to form a 10-nm-thick  $\text{TiO}_x$  layer (the ratio of Ti to O is 1:1.74). Then the substrate was transferred into a nitro-

gen-filled glove box and annealed at  $150^\circ\text{C}$  for 10 min on a hot plate. A PCPDTBT:PCBM (1:3 in weight ratio) layer was spin-coated from chlorobenzene solution with a  $0.45 \mu\text{m}$  filter on the  $\text{TiO}_x$  layer at 900 r.p.m. for 60 s to serve as the active layer of the front subcell. The connecting layers of molybdenum oxide ( $\text{MoO}_3$ , purchased from Alfa Aesar with a purity higher than 99.99%) (10 nm)/Al (2 nm)/Ag (15 nm)/ $\text{MoO}_3$  (10 nm) were deposited successively via thermal evaporation in vacuo at a base pressure of about  $4 \times 10^{-4}$  Pa. The evaporation rates for all layers were 0.2 nm/s. Then the P3HT:PCBM (1:0.8 in weight ratio) active layer of the back subcell was spin-coated from chlorobenzene solution with a  $0.45 \mu\text{m}$  filter at 700 r.p.m. for 60 s. Finally, a 100-nm-thick Al was deposited to serve as the top cathode. The finished PV cells were thermally annealed at  $110^\circ\text{C}$  for 5 min on a hot plate inside the glove box and encapsulated for measurement. The active area of the tandem polymer PV cells is ca.  $0.14 \text{cm}^2$ .

In order to measure in situ the device performance of the subcells and tandem cell, respectively, the ITO and top Al electrodes of the tandem polymer PV cells were patterned as shown in Fig. 1b that gives the top view of the patterned device configuration. It can be seen that there are four tandem PV cells on one substrate. From this kind of patterned device configuration, the device performance of the front and back subcells can be measured from right top and right bottom devices, respectively. The device performance of the tandem PV cell can be measured from the left two devices.

Current density–voltage ( $J$ – $V$ ) characteristics of the PV cells were measured using a computer-controlled Keithley 236 source meter in the dark and under AM1.5G illumination from a calibrated solar simulator with irradiation intensity of  $100 \text{mW}/\text{cm}^2$ . The incident photon-to-current collection efficiency (IPCE) was measured with a lock-in amplifier at a chopping frequency of 280 Hz during illumination with the monochromatic light from a Xenon lamp. The absorption and transmittance spectra were measured using Shimadzu UV-3600 spectrophotometer.

## 3. Results and discussion

Fig. 2 shows the energy level diagram of the tandem polymer PV cells. Since the two subcells are stacked in parallel connection, the front subcell is designed with an in-

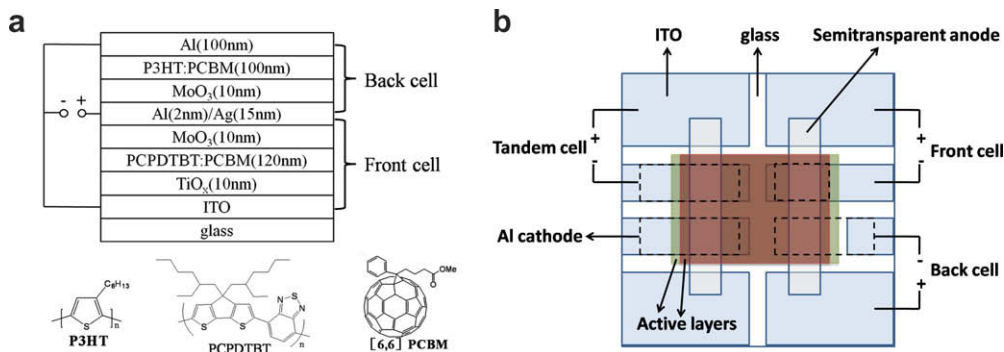


Fig. 1. (a) The device configuration of the tandem polymer PV cell and the chemical structures of the used materials. (b) The top view of the patterned device configuration in which the subcells' performance can be measured in situ.

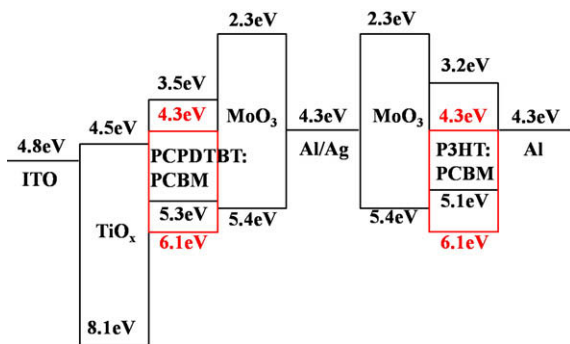


Fig. 2. Energy level diagram of the tandem polymer PV cell.

verted configuration. In the front subcell,  $\text{TiO}_x$  is used as an electron transport layer between the ITO electrode and the active layer. The lowest unoccupied molecular orbital (LUMO) level of  $\text{TiO}_x$  (4.5 eV) provides an ohmic contact with the LUMO level of PCBM (4.3 eV) for the electrons generated in the front cell [10,17]. The  $\text{TiO}_x$  layer also acts as a hole-blocking layer since its highest occupied molecular orbital (HOMO) level is ca. 8.1 eV [10,17,18]. A thin  $\text{MoO}_3$  layer with a HOMO level of 5.4 eV is inserted between the semitransparent metal anode and the active layer to serve as the hole transport layer [19–23]. Therefore, the insertion of the  $\text{TiO}_x$  and  $\text{MoO}_3$  layers makes the front subcell to form an inverted structure. In the back subcell, a thin layer of  $\text{MoO}_3$  is also introduced between the semitransparent metal anode and the active layer to extract holes. The top Al cathode provides ohmic contacts with the LUMO level of PCBM to realize efficient electron extraction. The energy level alignment of the materials involved in the tandem polymer PV cell shows that the two subcells are in parallel connection.

Fig. 3 shows the absorption spectra of PCPDTBT:PCBM (1:3) and P3HT:PCBM (1:0.8) composite films used as the active layers in the tandem polymer PV cells. The absorption of the PCPDTBT:PCBM (1:3) composite film covers from 400 to 900 nm with strong absorption located at the range of 650–800 nm. The absorption of the

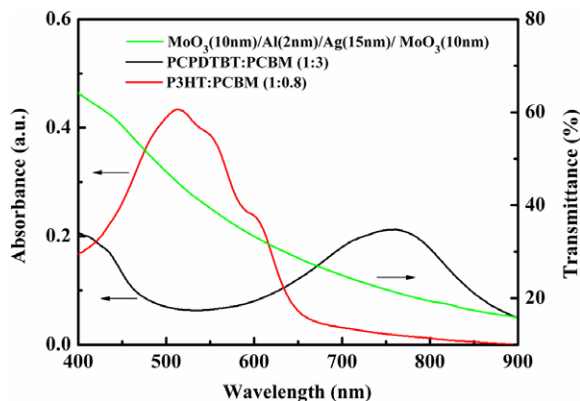


Fig. 3. Absorption spectra of the PCPDTBT:PCBM (1:3) and P3HT:PCBM (1:0.8) bulk heterojunction composite films and transmittance of the middle connecting unit of  $\text{MoO}_3$  (10 nm)/Al (2 nm)/Ag (15 nm)/ $\text{MoO}_3$  (10 nm).

P3HT:PCBM film covers the visible spectral range from 400 to 650 nm, just falling in the valley of the PCPDTBT:PCBM absorption spectrum. The complementary absorption of the PCPDTBT:PCBM (1:3) and P3HT:PCBM (1:0.8) composites in the tandem polymer cells may effectively enhance the solar light harvesting. Transmittance of the multilayer structure of the  $\text{MoO}_3$  (10 nm)/Al (2 nm)/Ag (15 nm)/ $\text{MoO}_3$  (10 nm) connecting the two active layers is also shown in Fig. 3. It can be seen that the transmittance of the middle connecting layers decreases with the wavelength increasing. The transmittance is higher than 40% below 550 nm. When the wavelength is above 600 nm, the transmittance is less than 30%. In order to ensure more photons passing through the middle connecting layers and efficient light absorption in the back subcell, the P3HT:PCBM composite film is used as the active layer of the back subcell.

$J$ - $V$  characteristics of the tandem polymer PV cell together with the front and back subcells under AM1.5G illumination with an intensity of  $100 \text{ mW/cm}^2$  are shown in Fig. 4 and the detailed parameters of these PV cells are summarized in Table 1. The  $J$ - $V$  characteristics of the two subcells are measured in the stacked structure, and the  $J$ - $V$  characteristic of the tandem polymer PV cell is measured with the ITO and top Al cathode being connected as shown in Fig. 1b. The front PCPDTBT:PCBM PV cell has a  $V_{OC}$  of 0.65 V, a  $J_{SC}$  of  $6.49 \text{ mA/cm}^2$  and a calculated FF of 0.34. Therefore, the overall PCE for this cell is ca. 1.45%. For the back P3HT:PCBM PV subcell, the  $V_{OC}$ ,  $J_{SC}$  and FF is 0.60 V,  $4.25 \text{ mA/cm}^2$  and 0.49, respectively, leading to a PCE of 1.24%. The  $V_{OC}$  of the tandem polymer PV cell is 0.65 V, similar to each of the two subcells and the FF is 0.42. The  $J_{SC}$  of the tandem cell reaches  $11.32 \text{ mA/cm}^2$ , close to the sum of the  $J_{SC}$ 's of the two subcells indicating that the two subcells are in parallel connection. The overall efficiency of the tandem polymer PV cell is ca. 3.10%. Interestingly, this value is even higher than the sum of those of the two subcells. This may be attributed to the reduced overall series resistance ( $R_s$ ) when the two subcells are stacked in parallel connection. The  $R_s$  of the front subcell, back subcell and the tandem cell are 35, 15 and  $11 \Omega \text{ cm}^2$ , respectively, deduced from the illuminated  $J$ - $V$

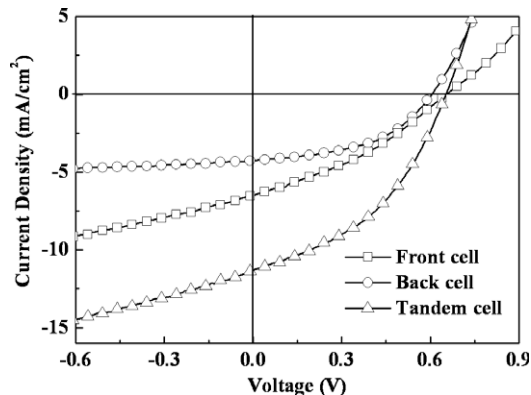
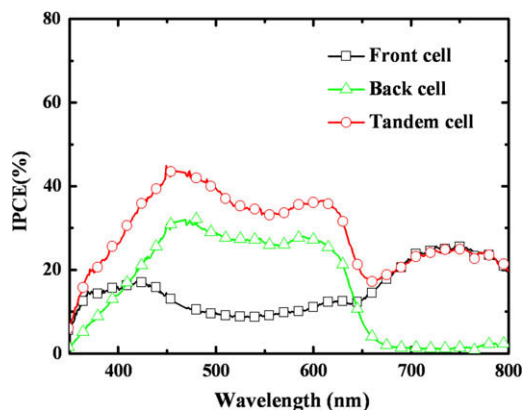


Fig. 4. The  $J$ - $V$  characteristics of the front PCPDTBT:PCBM PV cell, the back P3HT:PCBM PV cell and the tandem polymer solar cell under  $100 \text{ mW/cm}^2$  simulated AM1.5G illumination.

**Table 1**  
Photovoltaic parameters for the front cell, back cell and tandem cell.

Device	$V_{oc}$ (V)	$J_{sc}$ (mA/cm <sup>2</sup> )	FF	PCE (%)	$R_s$ ( $\Omega$ cm <sup>2</sup> )
Front cell	0.65	6.49	0.34	1.45	35
Back cell	0.60	4.25	0.49	1.24	15
Tandem cell	0.65	11.32	0.42	3.10	11



**Fig. 5.** IPCE spectra of the front PCPDTBT:PCBM PV cell, the back P3HT:PCBM PV cell and the tandem polymer solar cell.

curves of these PV cells at a voltage above 1 V. The low  $R_s$  of the tandem polymer PV cell leads to improved  $J_{sc}$  and PCE.

Fig. 5 shows the IPCE spectra of the two subcells and the tandem PV cell. It can be seen that each subcell shows the known spectral response of its bulk heterojunction composite, which is in good agreement with the absorption spectra of the two composites as shown in Fig. 3. The front PCPDTBT:PCBM cell covers from 350 to 800 nm showing two dominant IPCE peaks with ca.17% at 430 nm and 26% at 750 nm. The back P3HT:PCBM cell exhibits a IPCE of 30% at a range of 450–620 nm. The tandem PV cell shows an improved IPCE which is sum of the two subcells.

#### 4. Conclusion

In summary, we fabricated a parallel-connected tandem polymer solar cell with two different conjugated polymer/fullerene derivative blends as the active layers in the two subcells to improve the spectral coverage. The required built-in potential in the subcells is created by using inorganic semiconductor compounds as the charge transport layers and parallel-connected tandem PV cell is realized. Although the achieved efficiency of ca. 3.10% is not very

high, the proposed structure of the stacked polymer solar cell possesses great potential to realize high PCE if the two subcells are well optimized and the middle connecting semitransparent metal layer is replaced by highly transparent ITO.

#### Acknowledgements

The authors acknowledge the financial support by the National Natural Science Foundation of China (Nos. 50873100, 20834005 and 20621401) and the Chinese Academy of Sciences (KJXC2-YW-M11).

#### References

- [1] G. Yu, J. Gao, J.C. Hummelen, F. Wudl, A.J. Heeger, *Science* 270 (1995) 1789.
- [2] C.J. Brabec, N.S. Sariciftci, J.C. Hummelen, *Adv. Funct. Mater.* 11 (2001) 15.
- [3] K.M. Coakley, M.D. McGehee, *Chem. Mater.* 16 (2004) 4533.
- [4] J. Peet, J.Y. Kim, N.E. Coates, W.L. Ma, D. Moses, A.J. Heeger, G.C. Bazan, *Nat. Mater.* 6 (2007) 497.
- [5] W.L. Ma, C.Y. Yang, X. Gong, K. Lee, A.J. Heeger, *Adv. Funct. Mater.* 15 (2005) 1617.
- [6] J.Y. Kim, S.H. Kim, H.-Ho. Lee, K. Lee, W. Ma, X. Gong, A.J. Heeger, *Adv. Mater.* 18 (2006) 572.
- [7] M.D. Irwin, D.B. Buchholz, A.W. Hains, R.P.H. Chang, T.J. Marks, *PNAS* 105 (2008) 2783.
- [8] M.M. Wienk, M.G.R. Turbiez, M.P. Struijk, M. Fonrodona, R.A.J. Janssen, *Appl. Phys. Lett.* 88 (2006) 153511.
- [9] X. Wang, E. Perzon, W. Mammo, F. Oswald, S. Admassie, N.-K. Persson, F. Langa, M.R. Andersson, O. Inganäs, *Thin Solid Films* 511–512 (2006) 576.
- [10] J.Y. Kim, K. Lee, N.E. Coates, D. Moses, T.Q. Nguyen, M. Dante, A.J. Heeger, *Science* 317 (2007) 222.
- [11] G. Dennler, H.J. Prall, R. Koeppel, M. Egginger, R. Autengruber, N.S. Sariciftci, *Appl. Phys. Lett.* 89 (2006) 073502.
- [12] A. Hadipour, B. de Boer, J. Wildeman, F.B. Kooistra, J.C. Hummelen, M.G.R. Turbiez, M.M. Wienk, R.A.J. Janssen, P.W.M. Blom, *Adv. Funct. Mater.* 16 (2006) 1897.
- [13] M. Lenes, L.J.A. Koster, V.D. Mihailetchi, P.W.M. Blom, *Appl. Phys. Lett.* 88 (2006) 243502.
- [14] V. Shrotriya, E.H. Wu, G. Li, Y. Yao, Y. Yang, *Appl. Phys. Lett.* 88 (2006) 064104.
- [15] A. Hadipour, B. de Boer, P.W.M. Blom, *J. Appl. Phys.* 102 (2007) 074506.
- [16] S. Tanaka, K. Mielczarek, R. Ovalle-Robles, B. Wang, D. Hsu, A.A. Zakhidov, *Appl. Phys. Lett.* 94 (2009) 113506.
- [17] C. Waldauf, M. Morana, P. Denk, P. Schilinsky, K. Coakley, S.A. Choulis, C.J. Brabec, *Appl. Phys. Lett.* 89 (2006) 233517.
- [18] A. Hayakawa, O. Yoshikawa, T. Fujieda, K. Uehara, S. Yoshikawa, *Appl. Phys. Lett.* 90 (2007) 163517.
- [19] H.C. Im, D.C. Choo, T.W. Kim, J.H. Kim, J.H. Seo, Y.K. Kim, *Thin Solid Films* 515 (2007) 5099.
- [20] C.C. Chang, J.F. Chen, S.W. Hwang, C.H. Chen, *Appl. Phys. Lett.* 87 (2005) 253501.
- [21] S. Tokito, K. Noda, Y. Taga, *J. Phys. D* 29 (1996) 2750.
- [22] V. Shrotriya, G. Li, Y. Yao, C.W. Chu, Y. Yang, *Appl. Phys. Lett.* 88 (2006) 073508.
- [23] M.Y. Chan, C.S. Lee, S.L. Lai, M.K. Fung, F.L. Wong, H.Y. Sun, K.M. Lau, S.T. Lee, *J. Appl. Phys.* 100 (2006) 094506.

The double heterostructure OPV cells were fabricated on pre-cleaned glass substrates pre-coated with an ITO anode. ITO glass is pre-cleaned following an oxygen plasma treatment for 3 min prior to use for device fabrication. Films were grown at room temperature with a base pressure of  $2 \times 10^{-5}$  Torr in the following sequence: thermal evaporation of PTFE layer varied between 0.3, 0.5 and 1.0 nm; 20 nm thick film of the donor-like copper phthalocyanine(CuPc); followed by a 40 nm thick film of the acceptor-like buckyball  $C_{60}$ . A 12 nm thick large band-gap material, bathocuproine(BCP) was deposited as an exciton-blocking layer(EBL) because a previous report has found that BCP can be used to transport electrons to the cathode from the adjoining acceptor layer through the cathode-induced defect states in EBL energy gap, at the same time as effectively blocking excitons in the lower-energy-gap acceptor layer from recombining at the cathode [4]. Subsequently, an 100 nm thick Al cathode was deposited by thermal evaporation through a shadow mask. A Honle UV America Inc. UV light source SOL 500 I was used, with a stabilization period of at least 10 min prior to UV exposure on PTFE films. The work function of ITO/PTFE layers before and after UV exposure were determined by examining the contact potential difference(CDP) of the sample using a Kelvin probe arrangement (SKP5050, KP Technologies). All the current–voltage ( $I$ - $V$ ) measurements were made with a Keithley 2400 source meter in air ambient, in dark and under  $82 \text{ mW/cm}^2$  solar irradiance (Oriel light source). The active area for all the devices was in excess of  $0.1 \text{ cm}^2$  for this study. The consistency of the device performance was obtained by measuring a minimum of 5 samples for each individual devices structure.

In Fig. 1, the  $J_{sc}$  of the devices are plotted as a function of the PTFE thicknesses. It is clear that the device with 0.5 nm of PTFE as the buffer layer has better performances in term of  $J_{sc}$ ,  $V_{oc}$  and FF compare to reference device with and without PEDOT:PSS. By inserting a 0.3 nm of PTFE, the  $J_{sc}$  increase 75% from 1.6 to 2.8  $\text{mA/cm}^2$ , while the  $V_{oc}$  remained constant at 0.41 V (Table 1). The  $V_{oc}$  are significantly increased from 0.41 to 0.49 V when the PTFE layer thickness increased to 1.0 nm. However, the  $J_{sc}$  is de-

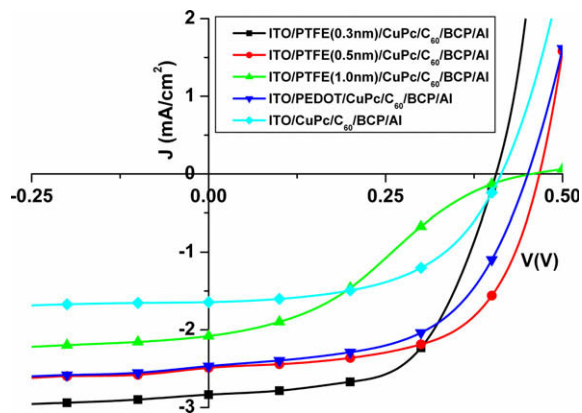


Fig. 1.  $I$ - $V$  characteristics of OPV devices with and without PEDOT:PSS and with the different PTFE thicknesses.

Table 1

List of device performance of OPV devices without PTFE, with PTFE and with UV treated PTFE.

Device structure	Teflon thickness (nm)	$J_{sc}$ ( $\text{mA/cm}^2$ )	$V_{oc}$ (V)	FF (%)	$\eta$ (%)
ITO/CuPc/ $C_{60}$ /BCP/Al	–	1.6	0.41	54.9	0.44
ITO/PEDOT:PSS/CuPc/ $C_{60}$ /BCP/Al	–	2.5	0.44	52.4	0.70
ITO/PTFE/CuPc/ $C_{60}$ /BCP/Al	0.3	2.8	0.4	60.9	0.83
	0.5	2.5	0.45	59.1	0.81
	1.0	2.1	0.47	27.9	0.34
After ultraviolet-illuminated fluoropolymer ITO buffer layers					
ITO/PTFE/CuPc/ $C_{60}$ /BCP/Al	0.3	3.1	0.41	58.5	0.91
	0.5	4.8	0.48	56.3	1.58
	1.0	4.3	0.49	42.5	1.09

creased when the PTFE thickness increase. Since PTFE is an insulating material, with an extremely high resistivity of  $10^{18} \Omega/\text{cm}$  for its bulk properties, and a large value for its ionization potential of 9.8 eV [11], it is reasonable to expect that the short-circuit current densities of OPVs decrease with increasing thickness of the PTFE layer.

To study the effect UV treatment on the ITO/PTFE layers, Kelvin probe measurements were conducted on ITO, ITO/PTFE(0.5 nm) and ITO/PTFE(0.5 nm) with different UV exposure times with the resultant the work functions listed in Table 2. The work function of the anode was shown increase to from 4.83 eV (bare ITO) to 5.00 eV after a 0.5 nm PTFE layer was deposited on the ITO. For the UV-illuminated ITO/PTFE samples, the work function increased approximately to  $\sim 5.17$  eV after 5 min of UV-illumination. However, further increase of the UV exposure time decreased the work function of ITO/UV-illuminated PTFE layer as shown in Table 2.

A similar treatment on the ITO buffer layer was used to make organic photovoltaic devices. The  $I$ - $V$  characteristics of these OPV devices under solar simulator illumination are shown in Fig. 3. The  $J_{sc}$  and  $V_{oc}$  of the devices improved in parallel with the increased UV-illumination time for the initial 5 min. However, further increase of the UV-illumination time beyond 5 min saw a decrease in the  $J_{sc}$  and the  $V_{oc}$ . This observation is in agreement with the results from work function measurements where the work function increased for the first 5 min, with further increase in the illumination time reducing the work function of the ITO/PTFE anode.

Table 2

Work function of ITO, ITO/PTFE and ITO/PTFE with different UV exposure time measured by Kelvin probe.

Sample	UV exposure time	Work function eV ( $\pm 0.01$ )
Oxygen plasma cleaned ITO	–	4.84
ITO/PTFE(0.5 nm)	–	5.00
	1 min	5.13
	4 min	5.15
	5 min	5.17
	7 min	5.17
	10 min	5.02



The high  $J_{sc}$  in OPV devices with PTFE layer are mainly due to the reduction in the barrier height between ITO and organic matrix [11] and subsequently improved hole extraction processes. The improvement in current extraction from CuPc layer to anode is mainly due to the smaller barrier of charge extraction and, hence, an increased photo-generated current under forward bias was observed with the increment in  $J_{sc}$ . As shown in Fig. 1, the  $V_{oc}$  of the devices are strongly dependent on the PTFE thicknesses. For the reference devices, with the structure of ITO/CuPc/C<sub>60</sub>/BCP/Al and ITO/PEDOT:PSS/CuPc/C<sub>60</sub>/BCP/Al, the typical  $V_{oc}$  were found to be 0.41 V and 0.44 V, respectively (Table 1). However, the  $V_{oc}$  is found to be improved up to 0.55 V for the device with 1 nm of UV treated PTFE buffer layer (Fig. 2). The work function of the ITO surface typically varies from 3.90 to 4.80 eV depending on the surface treatment [12,13]. After inserting the untreated PTFE layer and the UV treated PTFE layer, the  $V_{oc}$  is improved from 0.41 to 0.49 V, because of the strong dipole layer created by the negatively charged fluorine rich untreated PTFE layer and UV treated PTFE layer that has modified the surface and further increased the effective work function of the ITO. As show in Table 1, the devices with UV treated PTFE buffer

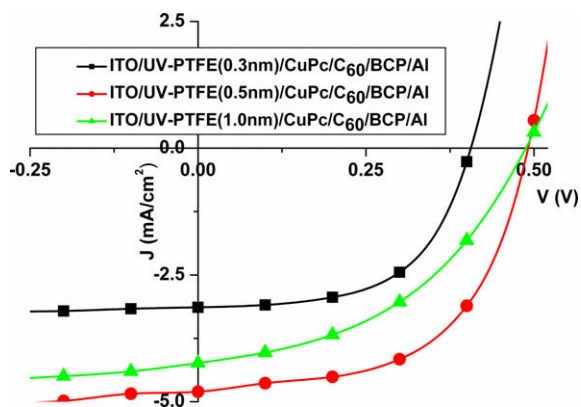


Fig. 2.  $I$ - $V$  characteristic of OPV devices consist of ITO/PTFE with different thicknesses exposed to 5 min UV treatment.

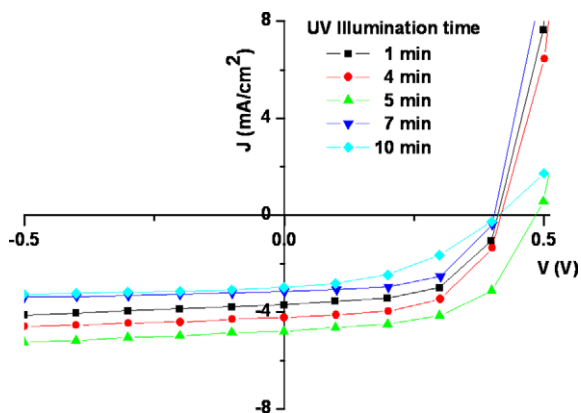


Fig. 3. The  $I$ - $V$  characteristics of OPV devices consisting of PTFE (0.5 nm) as a buffer layer on ITO, which is exposed to different UV exposure times.

layer exhibited at least a factor of 2 increases in term of power conversion efficiency, compared to the devices with untreated PTFE buffer layer. Among the device with PTFE, a device with a 0.5 nm UV treated PTFE buffer layer exhibited the best performance with the PCE of 1.58%, which is attributed to the good coverage of 0.5 nm UV treated PTFE on the ITO to modify the ITO surface without increase in the surface resistance of ITO/UV treated PTFE anode. It can be seen from Fig. 2 that  $J_{sc}$  of the structure ITO/UV treated PTFE(0.5 nm)/CuPc/C<sub>60</sub>/BCP/Al is the highest because of the smallest hole extraction barrier. Interestingly, UV treatment of PTFE buffer layer can significantly change the contact properties [11]. Our results show that while the pristine PTFE layer is useful for reducing the contact barrier, its effect is considerably enhanced by UV-illumination.

Modification of polymers by exposure to UV irradiation has been reported previously [14,15]. Radiation energy can be absorbed via ionization, phonon excitation and atomic displacement. This causes bond breaking, followed by scissoring and subsequent release of volatile fragments, which may result in the cross-linking through C-C bonding. In our case, clusters of  $sp^2$  bonding may also be formed, leading to an increased in conductivity [8]. At present, there is no clear explanation with regard to the interaction of UV light with PTFE properties and PTFE is found to be highly resistant to UV exposure [16]. However, UV-illumination on a few atomic layers of PTFE may have a very different interactions compared to UV radiation and impact on bulk properties of PTFE. In 2004, Tong and his co-workers have shown that UV-illumination on fluorocarbon coatings  $CF_x$  (the basic structure of PTFE), created the graphitic regions identified by X-ray photoelectron spectroscopy results. This leads to the higher conductivity of the  $CF_x$  layer and further improved OLED performance [8]. The same explanation may apply to the UV-illuminated PTFE layer where the  $J_{sc}$  of the OPV is improved due to the relatively higher conductivity of PTFE after UV-illumination.

In summary, insertion of UV treated PTFE buffer layer at the anode of ITO/organic interface can significantly improve the  $J_{sc}$ ,  $V_{oc}$  and PCE of bulk-heterojunction OPV. The improved performance in the UV treated PTFE-coated ITO contact are consistent with its small hole extraction barrier. This fluoro-material also offers a significant advantage in that the film can be simply prepared by thermal evaporation.

## Acknowledgement

The authors gratefully acknowledge the financial support received from EPSRC in the form of a Portfolio Partnership Award and China Scholarship Council to partially fund this research.

## References

- [1] W.U. Huynh, J.J. Dittmer, A.P. Alivisatos, Science 295 (2002) 2425.
- [2] W. Ma, C. Yang, X. Gong, K. Lee, A.J. Heeger, Adv. Funct. Mater. 15 (2005) 1617.
- [3] G. Li, V. Shrotriya, J. Huang, Y. Yao, T. Moriarty, K. Emery, Y. Yang, Nat. Mater. 4 (2005) 864.
- [4] P. Peumans, S.R. Forrest, Appl. Phys. Lett. 79 (2001) 126.

- [5] P. Peumans, S. Uchida, S.R. Forrest, *Nature* 425 (2003) 58.
- [6] S. Uchida, J. Xue, B.P. Rand, S.R. Forrest, *Appl. Phys. Lett.* 84 (2001) 4218.
- [7] P. Peumans, A. Yakimov, S.R. Forrest, *J. Appl. Phys.* 93 (2003) 3693.
- [8] S.W. Tong, C.S. Lee, Y. Lifshitz, D.Q. Gao, S.T. Lee, *Appl. Phys. Lett.* 84 (2004) 4032.
- [9] Y.D. Gao, L.D. Wang, D.Q. Zhang, L. Duan, G.F. Dong, *Appl. Phys. Lett.* 82 (2003) 155.
- [10] B. Kang, L.W. Tan, S.R.P. Silva, *Appl. Phys. Lett.* 93 (2008) 133302.
- [11] S.W. Tong, K.M. Lau, M.K. Fung, C.S. Lee, Y. Lifshitz, S.T. Lee, *Appl. Surf. Sci.* 252 (2006) 3806.
- [12] F. Nüesch, L.J. Rothberg, E.W. Forsythe, Q.T. Le, G. Yongli, *Appl. Phys. Lett.* 74 (1999) 880.
- [13] J.S. Kim, M. Granström, R.H. Friend, N. Johansson, W.R. Salaneck, R. Daik, W.J. Feast, F. Cacialli, *J. Appl. Phys.* 84 (1998) 6859.
- [14] J. Heitz, V. Svorcik, L. Bacakova, K. Rockova, E. Ratajova, T. Gumpenberger, D. Bauerle, B. Dvorankova, H. Kahr, I. Graz, C. Romanin, *J. Biomed. Mater. Res. Part A* 67A (2003) 130.
- [15] V. Svorcik, K. Rockova, E. Ratajova, J. Heitz, N. Huber, D. Bauerle, L. Bacakova, B. Dvorankova, V. Hnatowicz, *Nucl. Inst. Meth. Phys. Res. Sec. B-Beam Inter. Mater. Atoms* 217 (2004) 307.
- [16] K. Gotoh, Y. Nakata, M. Tagawa, M. Tagawa, *Colloids Surf. A-Physico-Chem. Eng. Aspects* 224 (2003) 165.

behavior within a bulk HJ polymer cell, but have not considered the potential differences in alternative device structures [15].

The OPV cells studied in this work were based on copper phthalocyanine (CuPc) donor molecules and C<sub>60</sub> acceptor molecules. Devices with three different HJ structures were fabricated: planar (or bilayer) [16,17], mixed [18–20], and planar-mixed [21,22]. The photoactive region in the planar devices consisted of 20 nm thick CuPc followed by 40 nm thick C<sub>60</sub>; the photoactive region in the mixed HJ devices was a CuPc:C<sub>60</sub> mixed layer with varying thickness and mixing ratio. The planar-mixed HJ structure consisted of a 20 nm thick CuPc:C<sub>60</sub> mixed layer (with a 1:2 weight ratio) sandwiched between a 10 nm thick CuPc layer and a 30 nm thick C<sub>60</sub> layer. These structures were chosen specifically to provide different situations for carrier generation and transport, thereby influencing the behaviors of the drift and diffusion photocurrents. For example, the diffusion current in a mixed HJ device is expected to be minimal as charges are generated across the entire active layer and there are no obvious potential barriers for charge transport in either direction; in a planar HJ device the diffusion current should be significant as charges are only generated at the HJ interface and the energy level offsets at the donor–acceptor interface (~1 eV) [16,23] prevent electrons and holes from diffusing into the donor and acceptor layer, respectively, giving rise to a concentration gradient.

The OPV cells were fabricated on glass substrates pre-coated with patterned indium–tin oxide (ITO) (~15 Ω/□ sheet resistance) anode stripes using a high vacuum thermal evaporator with a base pressure of approximately 10<sup>-7</sup> Torr. Prior to use, the glass substrates were successively sonicated in a solution of Liquinox (by Alconox), deionized water, acetone, and isopropanol, and were exposed to a UV–ozone environment for 15 min immediately prior to loading into the deposition chamber. During deposition, quartz crystal microbalances were used to monitor the mixing ratio and total film thickness. An 8 nm thick exciton blocking layer [13] of bathocuproine (BCP) was deposited on the organic active region prior to the deposition of a 100 nm thick aluminum cathode. CuPc (Sigma–Aldrich) was purified by gradient zone sublimation [24] prior to use; high purity C<sub>60</sub> (MER Corp.) and BCP (Lumtech) were used as purchased.

The photocurrent voltage and wavelength dependencies of the OPV cells were measured using a Stanford Research Systems 830DSP lock-in amplifier and Keithley 428 current amplifier. White light from a Xe-arc lamp was shined through an Oriel monochromator to provide a monochromatic light; this light was chopped at 800 Hz using a mechanical chopper prior to incidence on the devices. The monochromatic light intensity, P<sub>0</sub>, was measured using a calibrated Newport Si detector and was on the order of 1–10 μW/cm<sup>2</sup>. A white light bias from a halogen lamp with an intensity of approximately one sun (or 100 mW/cm<sup>2</sup>) was also used to illuminate the devices to set up the electric field and charge carrier distribution within the device as specified by the ASTM E1021 standard [25]. In this configuration, the total current of the device consists of the dark current, the photocurrent due to the

constant white light bias, and the photocurrent due to the periodically varying monochromatic light; the results obtained by the lock-in amplifier only correspond to the last component.

Based on the measured photocurrent density, J<sub>ph</sub>, the external quantum efficiency η<sub>EQE</sub> is determined as  $\eta_{EQE}(V, \lambda) = \frac{hc}{q\lambda} \frac{J_{ph}(V, \lambda)}{P_0(\lambda)}$ , where V is the applied voltage bias, λ is the incident monochromatic wavelength, and h, c, and q are Planck's constant, the speed of light, and the elementary charge, respectively. Under forward bias, the ITO anode and Al cathode were connected to positive and negative potentials, respectively. The current (both dark and photo) is defined as positive when it flows from anode to cathode. Fig. 1 shows the dependencies of η<sub>EQE</sub> at λ = 650 nm for the three different CuPc:C<sub>60</sub> HJ structures. For both the planar and planar-mixed devices, η<sub>EQE</sub> monotonically decreases with the increase of the applied voltage, V, from η<sub>EQE</sub> > 10% at the short-circuit (V = 0 V) to < 0.05% at V = 1 V. Data at V > 1 V were unreliable due to overloading in the current amplifier. The voltage-dependence of the photocurrent for each of these two devices does not show significant changes as the wavelength of the incident monochromatic light is varied.

For the mixed HJ device, which has a 90 nm thick 1:1 (by weight) CuPc:C<sub>60</sub> active layer, η<sub>EQE</sub> reaches a minimum value at V ≈ 0.55 V and is restored to ~10% at V ≈ 0.70 V. For comparison, the open-circuit voltage under one sun illumination is approximately V<sub>OC</sub> ≈ 0.5 V for these devices [22]. Shown in the inset is the phase change of the photocurrent recorded from the lock-in amplifier. While the phase does not change significantly in either the planar or planar-mixed devices, it is shifted by 180° for the mixed HJ devices at the same voltage where the minimum of η<sub>EQE</sub> is observed. This suggests that in the planar and planar-mixed devices, the photocurrent remains negative, i.e. flowing from cathode to anode, at any voltage. However, in the mixed HJ device, the photocurrent exhibits a reversal of direction as the voltage is increased from 0 to 1 V, with η<sub>EQE</sub> = 0 occurring at V<sub>0</sub> ≈ 0.55 V (V<sub>0</sub> defined as the voltage

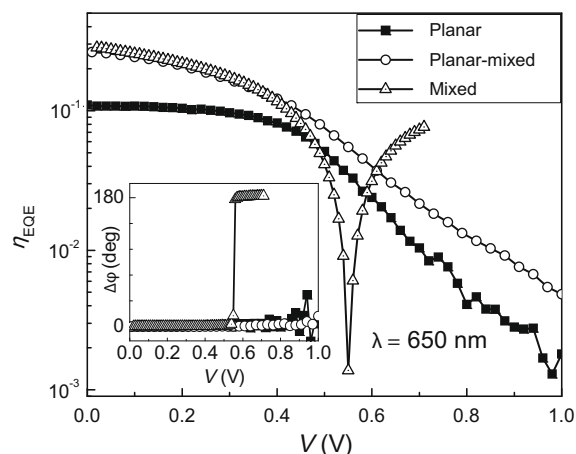


**Fig. 1.** External quantum efficiency, η<sub>EQE</sub>, at λ = 650 nm of three different organic photovoltaic heterojunction structures as a function of the applied bias, V. Inset shows the phase change for the photocurrent, Δφ, as obtained from the lock-in amplifier.

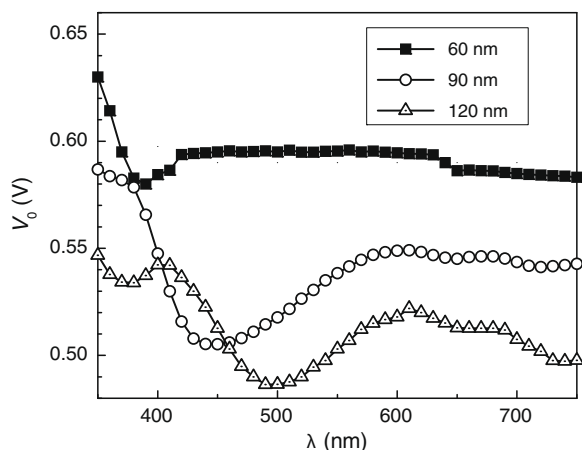


**Fig. 2.** Dependence of the zero-photocurrent bias  $V_0$  on the wavelength of the incident monochromatic light,  $\lambda$ , for mixed HJ photovoltaic cells with 60, 90, or 120 nm thick CuPc:C<sub>60</sub> (1:1) mixed active layers.

at which the photocurrent vanishes). At  $V > V_0$ , the photocurrent is positive, i.e. flowing from anode to cathode.

The zero-photocurrent bias,  $V_0$ , of the mixed HJ devices is shown to be dependent on the wavelength of the incident monochromatic light and the mixed layer thickness, exhibited in Fig. 2. For a device with a 90 nm (1:1) CuPc:C<sub>60</sub> mixed layer,  $V_0$  has a maximum of 0.58 V at  $\lambda \leq 380$  nm and reaches a minimum of 0.51 V at  $\lambda \approx 440$  nm. When  $\lambda > 600$  nm,  $V_0$  is relatively independent of  $\lambda$ , with  $V_0 \approx 0.55$  V. When the mixed layer thickness is reduced to 60 nm, the  $V_0$  minimum wavelength is blue-shifted, to  $\lambda \approx 390$  nm. Conversely, by increasing the mixed layer thickness to 120 nm, the global minimum for  $V_0$  is red-shifted to  $\lambda \approx 500$  nm, with a local minimum emerging at  $\lambda \approx 380$  nm.

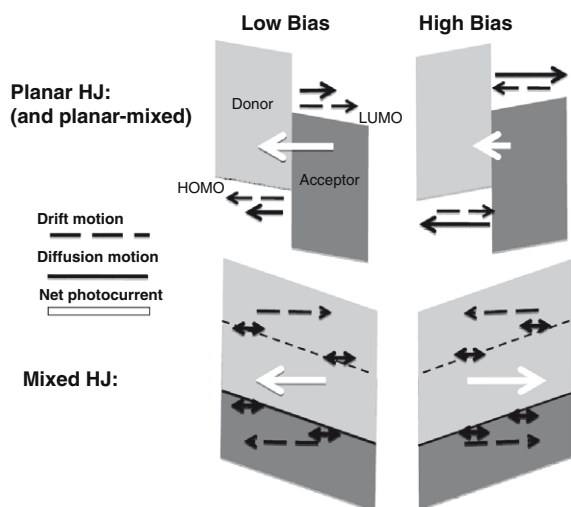


**Fig. 3.** Schematic energy level diagrams of the donor–acceptor heterojunctions illustrating the behaviors of the drift and diffusion photocarrier motions at high and low positive biases. The net photocurrent direction is also indicated. Here, HOMO and LUMO stand for the highest occupied and lowest unoccupied molecular orbitals, respectively.

To explain the different observed photocurrent behaviors in each HJ device structure, we have considered the drift and diffusion motions of the photocarriers. As shown in Fig. 3, in planar HJ devices excitons dissociate at a distinct interface between the two planar layers, giving rise to a strong carrier concentration gradient within the device. The energy level offsets at the interface,  $\sim 1$  eV for the CuPc/C<sub>60</sub> interface [16,23], will also confine holes within the donor layer and electrons in the acceptor layer. The internal electric field points from the cathode to the anode when the applied bias  $V$  is low (or negative). As a result, both the drift and diffusion motions drive carriers away from the HJ interface, with holes moving toward the anode, and electrons the cathode. However, at sufficiently high applied biases, so that the internal electric field points from the anode to the cathode, the drift current tends to move carriers towards the HJ interface, resulting in an increased carrier concentration gradient that in turn increases the driving force for diffusion. Hence, as the applied bias is increased the negative diffusion current increases accordingly. As we did not observe a change in the overall photocurrent direction in the planar and planar-mixed HJ devices, this suggests that at high applied biases, the negative diffusion current is more than enough to overcome the positive drift current. The steady decrease in the photocurrent with bias at  $V > 0.5$  V can be understood by considering the heterojunction interface as a “leaky capacitor”. With holes confined in the donor side and electrons in the acceptor side, the interface is effectively a capacitor. Hence, when the photocarriers corresponding to the monochromatic light are generated at the two sides of the capacitor, it is understandable that an overall negative photocurrent will be produced with the discharging of the capacitor through the external circuit. There are, however, two main carrier leakage mechanisms within the capacitor, which become increasingly significant with the increase of the applied bias. As the bias is increased and more charge carriers accumulate at the interface, interface recombination of electrons and holes becomes more significant. In addition, the charge carriers will increasingly be able to overcome the potential barrier height at the interface by thermally assisted tunneling with an increased positive electric field. Both mechanisms lead to a reduced magnitude of the negative photocurrent at high biases.

In mixed HJ devices, charge carrier generation is distributed throughout the active layer, leading to no significant contiguous concentration gradient. In addition, there are no potential barriers within the active region to limit the transport of charge carriers in either direction. Diffusion is therefore a minor component compared to the drift current, except when the applied bias is such that the drift current vanishes as the internal electric field approaches zero. Note that CuPc and C<sub>60</sub> molecules are homogeneously mixed at the ratios considered here [26]; hence we do not expect any significant variation in the local electric field distribution. Consequently, with the reversal of the electric field direction at sufficiently high biases, the direction of the drift current is reversed as well, leading to the total photocurrent changing from negative to positive.

The above explanation suggests that  $V_0$  must occur at a bias when the internal electric field is negligible in mixed

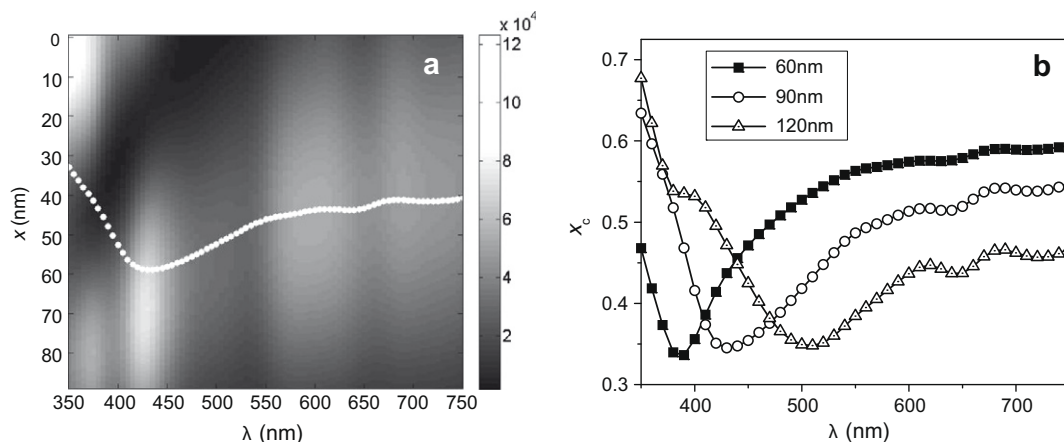


**Fig. 4.** (a) Calculated carrier generation field within a 90 nm thick CuPc:C<sub>60</sub> (1:1) mixed layer as a function of the distance from the anode/organic interface,  $x$ , and the wavelength of incident light,  $\lambda$ . Indicated in white dots are the weighted average centers of charge generation at each wavelength,  $x_c$ . (b) Calculated wavelength dependence of  $x_c$  in CuPc:C<sub>60</sub> mixed HJ devices with a 60, 90, or 120 nm thick active layer.

HJ devices. To explain the wavelength dependence of  $V_0$  in these devices, one has to consider the details of carrier generation within the mixed layers. Fig. 4a shows the calculated carrier generation field  $G(x, \lambda)$  within a 90 nm thick CuPc:C<sub>60</sub> (1:1) active layer. Also indicated on the plot in white dots are the weighted average centers of charge generation at each wavelength, denoted as  $x_c$ . Here,  $G(x, \lambda) = \alpha(\lambda) \cdot I(x, \lambda)$ , where  $x$  is the distance from the anode/organic interface,  $\alpha(\lambda)$  is the absorption coefficient of CuPc:C<sub>60</sub> (1:1), and  $I(x, \lambda)$  is the optical intensity field, which is calculated using a transfer-matrix method [13]. The interference of the incident light and the portion of light reflected off the metal cathode leads to a standing optical wave whose peak intensity is located approximately at a distance of  $(2m + 1)\lambda/4n$  away from the metal cathode, where  $n$  is the refraction index of the organic materials and  $m = 0, 1, 2, \dots$  is an integer indicating the order of interference. Hence, at  $\lambda \geq 450$  nm, with the increase of  $\lambda$ , the peak optical intensity position shifts away from the cathode, causing a similar shift in  $x_c$ . However, at  $\lambda \leq 400$  nm, the emergence of the second-order ( $m = 1$ ) intensity peak draws  $x_c$  much closer to the anode. At  $\lambda \approx 430$  to 440 nm,  $x_c$  is closest to the cathode. Fig. 4b shows a comparison of the wavelength dependence of the average center of charge generation in mixed HJ devices with different CuPc:C<sub>60</sub> active layer thicknesses. Compared with the experimental  $V_0$  data shown in Fig. 2, we see a strong resemblance between the wavelength dependencies of  $V_0$  and  $x_c$ , especially in the wavelengths of  $V_0$  minima.

While a comprehensive device model may be needed to fully explain the correlation between  $V_0$  and  $x_c$ , we hypothesize that it is related to the details of the diffusion current. In a CuPc:C<sub>60</sub> (1:1) mixture, the hole mobility is approximately three orders of magnitude lower than the electron mobility,  $\sim 10^{-5}$  cm<sup>2</sup>/V s vs.  $\sim 10^{-2}$  cm<sup>2</sup>/V s [26]. Logically, the charge extraction from the active region is limited by hole transport. When most holes are generated closer to the cathode, the corresponding hole diffusion current becomes lower due to the longer distance holes need to travel

to reach the anode. Thus, it requires a smaller positive drift current to cancel the negative diffusion current, and therefore a lower forward bias, leading to a lower  $V_0$ .

To summarize, we have found that the molecular heterojunction structure has significant effects on the photocarrier behavior in organic photovoltaic cells. The interplay between carrier diffusion and drift leads to an always negative photocurrent in planar and planar-mixed HJ cells where distinct interfaces for charge generation and barrier heights preventing charge transport in certain directions exist. The drift current generally dominates in a mixed HJ cell, leading to a reversal of photocurrent direction at high biases compared to that at the short-circuit condition; however, when the internal electric field is negligible the diffusion current becomes dominant and the detailed distribution of charge carriers throughout the mixed layer results in a wavelength dependence of the diffusion current and, consequently, a varying zero-photocurrent voltage.

## Acknowledgement

The authors gratefully acknowledge financial support from the National Science Foundation CAREER Program (ECCS-0644690) for this work.

## References

- [1] S.R. Forrest, Nature 428 (2004) 911.
- [2] S.E. Shaheen, D.S. Ginley, G.E. Jabbour, MRS Bull. 30 (2005) 10.
- [3] M. Kim, J. Kim, J.C. Cho, M. Shtein, L.J. Guo, J. Kim, Appl. Phys. Lett. 90 (2007) 123113.
- [4] G.P. Kushto, W. Kim, Z.H. Kafafi, Appl. Phys. Lett. 86 (2005) 093502.
- [5] H. Spanggaard, F.C. Krebs, Sol. Energy Mater. Sol. Cells 83 (2004) 125.
- [6] C.J. Brabec, Sol. Energy Mater. Sol. Cells 83 (2004) 273.
- [7] C.W. Tang, Appl. Phys. Lett. 48 (1986) 183.
- [8] G. Yu, J. Gao, J.C. Hummelen, F. Wudl, A.J. Heeger, Science 270 (1995) 1789.
- [9] J.J.M. Halls, C.A. Walsh, N.C. Greenham, E.A. Marseglia, R.H. Friend, S.C. Moratti, A.B. Holmes, Nature 376 (1995) 498.
- [10] J. Xue, S. Uchida, B.P. Rand, S.R. Forrest, Appl. Phys. Lett. 85 (2004) 5757.
- [11] W. Ma, C. Yang, X. Gong, K. Lee, A. Heeger, Adv. Funct. Mater. 15 (2005) 1617.

- [12] X. Yang, J. Loos, S.C. Veenstra, W.J.H. Verhees, M.M. Wienk, J.M. Kroon, M.A.J. Michels, R.A.J. Janssen, *Nano Lett.* 5 (2005) 579.
- [13] P. Peumans, A. Yakimov, S.R. Forrest, *J. Appl. Phys.* 93 (2003) 3693.
- [14] B. Gregg, *J. Phys. Chem. B* 107 (2003) 4688.
- [15] A. Moliton, J. Nunzi, *Polym. Int.* 55 (2006) 583.
- [16] P. Peumans, S.R. Forrest, *Appl. Phys. Lett.* 79 (2001) 126.
- [17] J. Xue, S. Uchida, B.P. Rand, S.R. Forrest, *Appl. Phys. Lett.* 84 (2004) 3013.
- [18] S. Uchida, J. Xue, B.P. Rand, S.R. Forrest, *Appl. Phys. Lett.* 84 (2004) 4218.
- [19] P. Sullivan, S. Heutz, S.M. Schultes, T.S. Jones, *Appl. Phys. Lett.* 84 (2004) 1210.
- [20] T. Tsuzuki, Y. Shirota, J. Rostalski, D. Meissner, *Sol. Energy Mater. Sol. Cells* 61 (2000) 1.
- [21] J. Xue, B.P. Rand, S. Uchida, S. Forrest, *Adv. Mater.* 17 (2005) 66.
- [22] J. Xue, B.P. Rand, S. Uchida, S.R. Forrest, *J. Appl. Phys.* 98 (2005) 124903.
- [23] B.P. Rand, D.P. Burk, S.R. Forrest, *Phys. Rev. B* 75 (2007) 115327.
- [24] S.R. Forrest, *Chem. Rev.* 97 (1997) 1793.
- [25] V. Shrotriya, G. Li, Y. Yao, T. Moriarty, K. Emery, Y. Yang, *Adv. Funct. Mater.* 16 (2006) 2016.
- [26] B.P. Rand, J. Xue, S. Uchida, S.R. Forrest, *J. Appl. Phys.* 98 (2005) 124902.

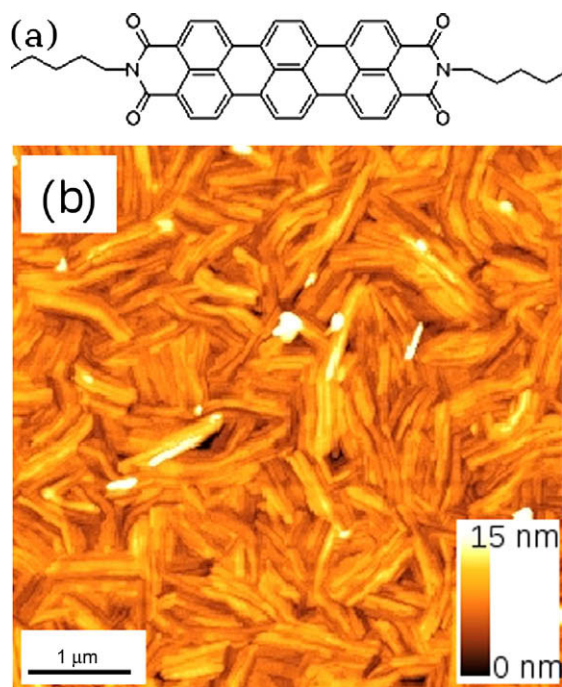


**Fig. 1.** (a) Chemical structure of the TTCDI-5C molecule. (b) AFM image of the TTCDI-5C thin film.

affinity [9]. In the present study, we investigate the behaviour of the charge carrier mobility of OTFTs constructed using *N,N'*-Bis(*n*-pentyl)terrylene-3,4:11,12-tetracarboxylic diimide (TTCDI-5C, cf. Fig. 1a) with different metal electrodes to assess carrier transport in these OTFTs.

## 2. Experiments

TTCDI-5 thin films were deposited on SiO<sub>2</sub>/Si substrate in vacuum with a base pressure below  $5 \times 10^{-9}$  Torr. A deposition rate of about 0.06 ml min<sup>-1</sup> was used for all films prepared in this work. The thin films thickness is 15 nm. A detailed description of experimental procedure was given in previous work [9]. Fig. 1b presents an AFM image of a TTCDI film deposited at an optimized substrate temperature of 140 °C. Film morphology consists of compact rectangular grains with an average area of 0.06 μm<sup>2</sup>/grain. Roughness of the surface is 2 nm. From XRD spectra (not shown here), we found the molecules were highly ordered and oriented with the (0 0 1) axis normal to the surface substrate.

For the thin film transistors (OTFT), all experiments including molecular deposition, electrode contact as well as electrical measurement were carried out in vacuum. First, the TTDCI films were deposited on thermally grown SiO<sub>2</sub> (200 nm)/p-Si (0 0 1) substrates. Metals of electrodes

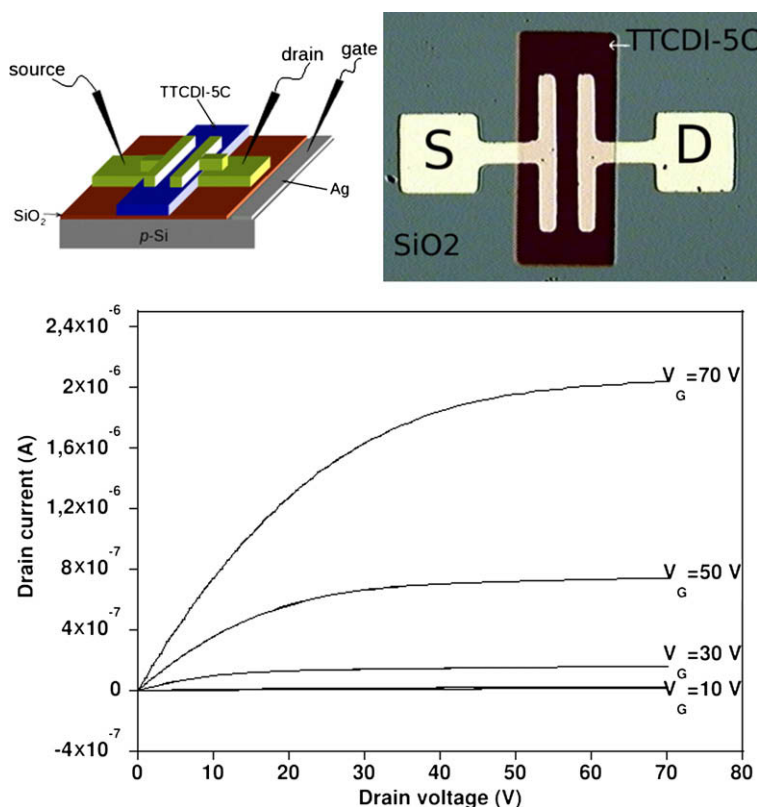


**Fig. 2.** Scheme and optical microscope image of the top-contact TTCDI-5C OTFT (top), typical drain current–drain voltage curves of TTCDI-5C OFET (bottom).

with a thickness of 50 nm were deposited using an e-beam evaporator for aluminium and a heated crucible for gold. The channel length was 50  $\mu\text{m}$  and the width 400  $\mu\text{m}$ . An illustration and photograph of the top-contact OTFT structure are shown in Fig. 2 (top). OTFTs thus prepared were transferred into the electrical measurement chamber for transistor analysis by means of a vacuum transfer system to avoid exposure to air. Electrical measurements were performed in vacuum of  $10^{-5}$  Torr at a variable temperature from 50 to 310 K.

### 3. Results and discussion

#### 3.1. Thermal behaviour of carriers mobilities

Fig. 2 (bottom) presents typical  $I_D$ - $V_D$  curves of the TTCDI-5C transistors at room temperature (gold electrode). A clear difference in the threshold voltages ( $V_t$ ) was observed depending on electrode metals. The  $V_t$  for Au and Al electrodes were 20 and 16 V, respectively. The main reason for the lower  $V_t$  in the Al electrode device originate from its lower work function (4.3 eV for Al and 5.1 eV for Au).

We calculated the mobilities of the TTCDI-5C OTFTs in the temperature range from 50 to 310 K in both devices prepared using gold or aluminium electrodes using the following equation [10,11]:

$$I_{D,\text{sat}} = \frac{W}{2L} C_{\text{ox}} \mu_{\text{sat}} (V_G - V_T)^2$$

where  $C_{\text{ox}}$ ,  $\mu_{\text{sat}}$  and  $V_T$  are the gate dielectric capacitance per unit area, field effect mobility at saturation regime and the threshold voltage, respectively. Then we prepared the Arrhenius plots of the carrier mobilities of the OTFTs which are shown in Fig. 3. These plots can be divided into two ranges: less temperature dependent range from 50 to 150 K and thermal activation temperature range from 150 to 310 K. Below 150 K, it can be regarded that the carriers are trapped at the defects and temperature is not high enough to activate these trapped carriers to conduction. This is a property of the TTCDI film and is not related to the metal used to prepare the electrodes.

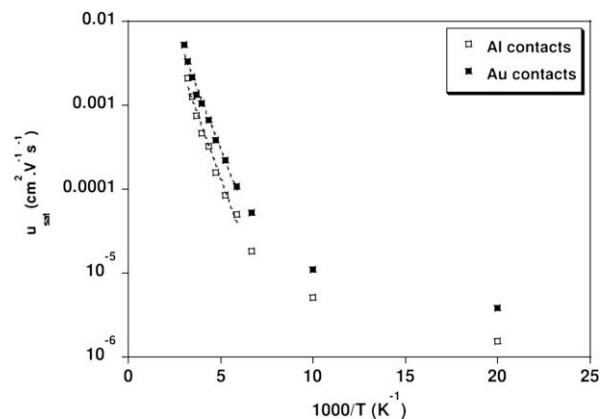


Fig. 3. Arrhenius plot of the carrier mobilities of the TTCDI-5C OFETs with gold and aluminium contacts.

A clear difference depending on the electrode material was observed in the temperature range above 170 K. To interpret this observation, we referred to the multiple trapping and release model (MTR). It supposes that charge transport in the semiconductor is ruled by charges trapping into localized states in the forbidden gap followed by thermal release [8,12]. Thus we fitted the Arrhenius plots using next equation:

$$\mu = \mu_0 \exp\left(\frac{-E_a}{k_B T}\right)$$

where  $\mu$ ,  $k_B$  and  $E_a$  are carrier mobility, the Boltzmann constant and the activation energy, respectively. The activation energies were determined to be 130 and 85 meV for Au and Al contacts, respectively.

#### 3.2. Discussion

Two distinct factors –trapping at the interface and energy mismatch between work function and LUMO– are probably contributing to the difference in the activation energy. In the following sections, we discuss respective factors.

##### 3.2.1. Trapped carriers

To explain the difference between the values of the activation energies, we first evaluated carrier traps. In Fig. 4, both OTFTs exhibited positive threshold voltage shifts with decreasing temperature. Indeed at lower temperature there is less thermal energy available to activate trapped carriers into delocalized states. Thus more carriers remain trapped and screen the gate field. Therefore, OTFTs required a greater gate voltage to enable conduction [7,13]. The shifts in the threshold voltage  $\Delta V$  were 23 V for the Au contacts and 15 V for the Al contacts. The number of trapped carriers can be estimated using the following equation with the elementary charge  $e$  [7,13]:

$$N_t = \frac{\Delta V C_{\text{ox}}}{e}$$

In the case of gold electrodes,  $N_t$  is about  $2.4 \times 10^{12}$  carriers/cm<sup>2</sup> while the corresponding value for the aluminium electrodes is  $1.9 \times 10^{12}$  carriers/cm<sup>2</sup>. These values seem to

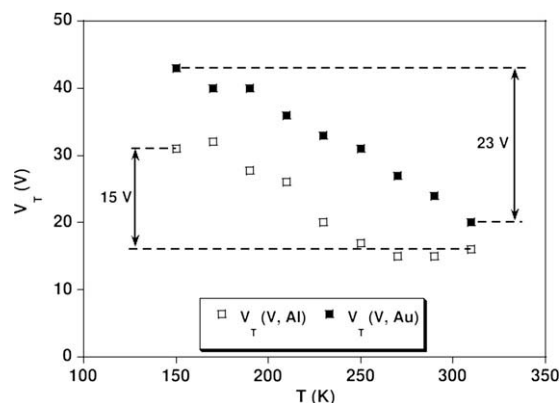
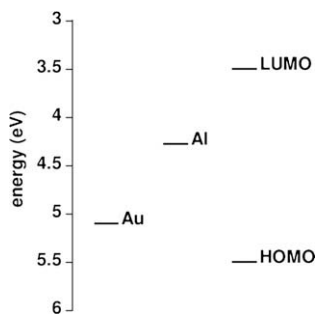


Fig. 4. Evolution of the threshold voltage versus the temperature.





**Fig. 5.** Energy diagram of HOMO/LUMO levels of TTCDI-5C molecules and work function of gold and aluminium.

be quite high when compared with the molecular density of TTCDI thin films which is typically in the range of  $10^{14}$  molecules/cm<sup>2</sup>. However  $N_t$  is a total summation of carriers including those trapped at the insulator/organic and the metal/organic interfaces, as well as those fixed in the insulator and organic films. Among these trapped carriers, the observed difference in  $N_t$  for the respective electrode metals can be ascribed to the carriers trapped at the metal/organic interfaces. This means that the activation energies should be determined by taking into account the carrier transfer at the metal/TTCDI interface. Here we note that the threshold voltage of the OTFT with Al electrodes remained lower than that with gold electrodes. This gap is linked to the defects at the metal/organic layer interface in addition to the relative work function of the metals. Regarding the defects, it should be mentioned that Al was deposited using a cooled e-beam evaporator while gold was deposited using a heated crucible so that the substrate temperature for the case during gold deposition was slightly higher possibly generating defects and increasing the numbers of trapped carriers at the Au/TTCDI interface.

### 3.2.2. HOMO/LUMO levels and metals work functions

With respect to the work functions of the electrode metals, we examined the energy-level diagram involving HOMO/LUMO levels and work functions of the electrode metals as shown in Fig. 5. In passing from gold to aluminium, the difference in energy between work function and the LUMO level of TTCDI-5C molecules is reduced. Consequently injection of electrons into the LUMO, as well as into the defects states, becomes easier causing a decrease in the energy for activating the charges into the organic layer. This explains the difference between the activation energies ( $E_a$ ) of the different metal electrodes. Also, the mismatch between the Al work function and the LUMO is still around 0.78 eV according to our diagram so that this

barrier should affect the charges injection. This point has been raised previously and it has been proposed that the presence of an interfacial electric dipole layer lowers the barrier to electron injection and the apparent metal work function can vary by up to 1 eV [14–16].

## 4. Conclusion

In summary we have designed OTFTs based on TTCDI-5C which operated as n-channel transistors. Two kinds of transistors were prepared containing gold or aluminium electrodes. Dependences of the carriers mobility and threshold voltage on temperature were investigated. Two different behaviours were observed for carrier transport: a temperature independent behaviour below 170 K and a thermally activated one at higher temperature. Activation energies were calculated from the temperature dependence of the carrier mobility. Those were 85 meV for aluminium contacts and 130 meV for gold contacts. The difference in activation energies can be explained by the energy matching mainly between work function of electrodes metals and the LUMO level of the TTCDI-5C molecules. Additionally, defects and dipoles produced at the metal/molecule interface also influence carrier transport. These experimental results emphasize the importance of optimizing the energy levels of molecules with work functions of the metal electrodes, as well as the interface formation techniques.

## References

- [1] C.D. Dimitrakopoulos, P.R.L. Malenfant, *Adv. Mater.* 14 (2002) 99.
- [2] G. Horowitz, *J. Mater. Res.* 19 (2004) 1946.
- [3] T.W. Kelley, P.F. Baude, C. Gerlach, D.E. Ender, D. Muires, M.A. Haase, D.E. Voge, S.D. Theiss, *Chem. Mater.* 16 (2004) 4413.
- [4] V. Podzorov, S.E. Sysoev, E. Loginova, V.M. Pudalov, M.E. Gershenson, *Appl. Phys. Lett.* 83 (2003) 3504.
- [5] H. Sirringhaus, R.H. Friend, X.C. Li, S.C. Moratti, A.B. Holmes, N. Feeder, *Appl. Phys. Lett.* 71 (1997) 3871.
- [6] D. Knipp, R.A. Street, B. Krusor, R. Apte, J. Ho, J. Non-Cryst. Solids 299 (2002) 1042.
- [7] R.J. Chesterfield, J.C. McKeen, C.R. Newman, P.C. Ewbank, D.A. da Silva Filho, J.-L. Bredas, L.L. Miller, K.R. Mann, C.D. Frisbie, *J. Phys. Chem. B* 108 (2004) 19281.
- [8] R.J. Chesterfield, J.C. McKeen, C.R. Newman, C.D. Frisbie, P.C. Ewbank, K.R. Mann, L.L. Miller, *J. Appl. Phys.* 95 (2004) 6396.
- [9] M. Petit, R. Hayakawa, Y. Shirai, Y. Wakayama, J.P. Hill, K. Ariga, T. Chikyow, *Appl. Phys. Lett.* 92 (2008) 163301.
- [10] C.R. Newman, C.D. Frisbie, D.A. da Silva Filho, J.-L. Bredas, P.C. Ewbank, K.R. Mann, *Chem. Mater.* 16 (2004) 4436.
- [11] G. Horowitz, *Adv. Mater.* 10 (1998) 365.
- [12] G. Horowitz, M.E. Hajlaoui, R. Hajlaoui, *J. Appl. Phys.* 87 (2000) 4458.
- [13] G. Horowitz, P. Delannoy, *J. Appl. Phys.* 70 (1991) 469.
- [14] I.H. Campbell, J.D. Kress, R.L. Martin, D.L. Smith, N.N. Barashkov, J.P. Ferraris, *Appl. Phys. Lett.* 71 (1997) 3528.
- [15] I.G. Hill, A. Rajagopal, A. Kahn, Y. Hu, *Appl. Phys. Lett.* 73 (1998) 662.
- [16] L.-L. Chua, J. Zaumseil, J.-F. Chang, E.C.-W. Ou, P.K.-H. Ho, H. Sirringhaus, R.H. Friend, *Nature* 434 (2005) 194.

Au memory device. The nonpolar switching is different from the previous reported WORM characteristics [12,13] and the bipolar switching characteristics [16,17]. Au electrodes are used in order to avoid oxidation [18] and the disputation about the use of Al electrode. It is found that no “forming” process is required to induce the resistive switching. The device area dependence, reproducibility, data retention, and nondestructive readout properties are also investigated.

## 2. Experiment

Fig. 1a and b show the schematic structure of PEDOT: PSS, which serves as an active layer in our memory devices. It has a tunable high electrical conductivity and high stability in air. The memory devices are fabricated using the following procedures. After a standard clean using sulfuric acid, hydrofluoric acid, and acetone sequentially, 10 nm Cr and 50 nm Au are deposited successively by an electron beam evaporator on a silicon substrate as the bottom electrode. Then a layer of PEDOT: PSS (1.3 wt% dispersion in H<sub>2</sub>O) is spun on the bottom electrode initially at 500 rpm for 6 s, then at 3000 rpm for 60 s. After spin coating, the film is baked on a hot plate at 95 °C for 5 min in air. The film thickness is about 90 nm measured by a Veeco Dektak150. The top electrode is 80 nm Au deposited directly on the top of the PEDOT: PSS film with a shadow mask by the same electron beam evaporator. Then the sample is etched in oxygen plasma for 5 minutes to remove excess PEDOT: PSS using the gold electrode as an etching mask. Fig. 1c shows the schematic diagram of the memory device with a Au/PEDOT: PSS/Au sandwiched structure. All electrical measurements are performed at room temperature in darkness. The current–voltage characteristics are measured by a Keithley 4200 semiconductor characterization system.

## 3. Results and discussion

Fig. 2 shows the typical *I*–*V* characteristics of the Au/PEDOT: PSS/Au memory devices, in which the bias polarity is defined with reference to the bottom Au electrode. Different from the previous results on ITO/PEDOT: PSS/Al

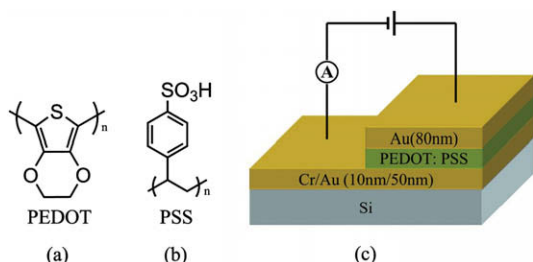


**Fig. 1.** The structure of (a) PEDOT which has the properties of tunable high electrical conductivity and high stability in air, (b) PSS which is used as aqueous polyelectrolyte in the polymerization of 3,4-ethylene-dioxythiophene to form a dark blue, aqueous PEDOT/PSS dispersion, and (c) the schematic diagram of the device with Au/PEDOT: PSS/Au structure.

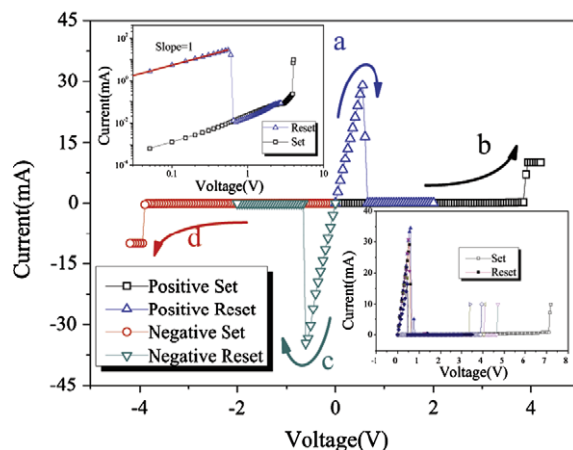


**Fig. 2.** Typical nonpolar *I*–*V* switching characteristics of Au/PEDOT: PSS/Au memory devices, the sweep sequence and direction are indicated by the alphabets and arrows, respectively. The upper inset is the *I*–*V* fitting of ON-state in log–log scale, demonstrating a linear correlation, and the bottom inset is the reproducibility of the resistive switching characteristics under dc sweeping mode.

[16], no “forming” process is required to induce the resistive switching in our devices. The fresh devices are usually in the ON-state with a resistance of hundred ohms. When the bias voltage is increased to about 1 V in either polarity, the device enters the OFF-state (curve a or c). This bias voltage is referred to as the reset voltage ( $V_{\text{reset}}$ ). In order to turn the device back to the ON-state, a current-limited set voltage ( $V_{\text{set}}$ ) in either polarity should be added to the device (curve b or d). This limited current is called the compliance current. The typical resistances of the ON- and OFF-state at 100 mV are on the order of  $10^2 \Omega$  ( $R_{\text{on}}$ ) and  $10^5 \Omega$  ( $R_{\text{off}}$ ), respectively. From the top inset of Fig. 2, the ratio between the ON- and OFF-state is determined to be about  $10^3$ . It is found that the devices exhibit a nonpolar switching behavior, i.e., the back and forth switching between the ON- and OFF-state could be realized in either positive bias or negative bias. There are other two kinds of resistance switching memory devices: unipolar and bipolar switching. In a unipolar resistance switching memory device, the operation is restricted to a special bias polarity; in a bipolar device, write and erase must be performed in the opposite bias polarity. Although the nonpolar switching behavior is widely reported in inorganic memory devices, such as V-doped SrZrO<sub>3</sub> [19], Cu doped SiO<sub>2</sub> [20] and Cu doped ZrO<sub>2</sub> [21], it is seldom reported in organic memory devices. The nonpolar device can be write, erase, and read in only one bias, while the bi-polar device must be write and erase in different polarity of bias. This operating bias flexibility makes it easy to achieve memory application for the nonpolar switching characteristic compared to the bipolar one.

The bottom inset of Fig. 2 shows the reproducibility of the resistive switching characteristics under a dc sweeping mode. Although  $V_{\text{set}}$  and  $V_{\text{reset}}$  show some variations,  $V_{\text{set}}$  is always higher than  $V_{\text{reset}}$ . No overlap between them is observed. Beginning from either resistance state (ON or OFF), the Au/PEDOT: PSS/Au memory devices can be switched to

the other one by choosing a proper voltage value irrespective of bias polarity.

The compliance current ( $I_{\text{comp}}$ ) during set process is necessary to prevent a permanent breakdown in memory devices. Shown in Fig. 3a is the change of reset current ( $I_{\text{reset}}$ , defined as the peak current during the reset process) and ON-state resistance ( $R_{\text{on}}$ ) when  $I_{\text{comp}}$  varies from 100  $\mu\text{A}$  to 10 mA. The  $I_{\text{reset}}$  increases and  $R_{\text{on}}$  decreases with the increasing of compliance current.

To further evaluate the performance of PEDOT: PSS memory devices, the scalability and resistance uniformity are studied on devices with different areas. The active area dependence of both ON and OFF resistance is shown in Fig. 3b. Each point represents an average value of ten different devices. Although the OFF-state resistance exhibits a clear dependence on the device area, the ON-state resistance shows a little dependence on device area. The resistance of the OFF-state increases about  $4 \times 10^3$  times when the area of the devices shrinks  $4 \times 10^3$  times, while the resistance of ON-state increases only 30 times at the same device area decreasing. This result also shows the ratio of  $R_{\text{on}}$  and  $R_{\text{off}}$  increases with device area decreasing, and provides promising scaling down prospect of Au/PEDOT: PSS/Au devices. As shown in Fig. 3b, the error bars indicate standard deviation, according to which the resistance uniformity of each size devices is concentrated enough to distinguish the ON- and OFF-state.

Besides scalability and resistance uniformity, the retention time is also an important parameter for memory devices. Fig. 4 shows the retention ability at room temperature in darkness. By applying a continuous readout voltage (@ 100 mV), the device resistance is sampled every 60 s. The resistances of both ON- and OFF-state are stable and show no significant degradation over  $10^4$  s continuous stress test. This could provide low misreading rate, indicate nonvolatile nature and nondestructive readout property of the devices. The nonpolar nonvolatile characteristics of the devices can be observed after the retention testing.

To understand the mechanism of nonpolar switching behavior of PEDOT: PSS based devices, the  $I$ - $V$  curve of

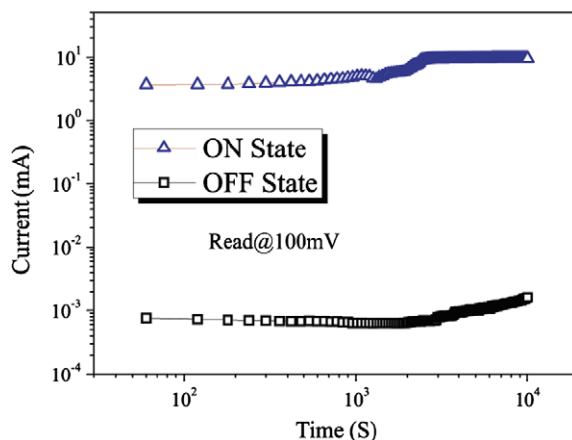


Fig. 4. Retention test upon continuous readout voltage (@ 100 mV). The devices are tested at room temperature in darkness.

ON-state is fitted with linear fitting in log-log scale. As shown in the upper inset of Fig. 2, the ON-state fitting curve demonstrates that the  $I$ - $V$  characteristics follows a linear ohmic conduction (slope is close to 1). One of the probable models for the linear conducting behavior is the forming of conductive paths in insulating film. The conductive path mechanism is further confirmed by the dependence of the ON- and OFF-state resistance on the device area. The high conductive current in the ON-state is determined by a set of conductive paths [15], whose total effective cross-section area is much smaller than the device area and not sensitive to device area. In contrast, the low conductive current in the OFF-state is decided by the leakage current of the PEDOT: PSS film, which is proportional to the area of the device in principle.

Based on the analysis above, it is concluded that the forming and rupture of conductive paths is probably related with the oxidation and reduction of the PEDOT: PSS film. As shown in Fig. 5, hole hopping transport through PEDOT involves extraction and injection at each PEDOT site, which corresponds to transient reduction-oxidation cycles [22]. Initially, the device stays at the ON-state and the current transmits through the PEDOT<sup>+</sup> conductive paths, which exist in the oxide state of PEDOT: PSS film. As a reset voltage adds to the device, the holes, referred to  $h^+$ , are extracted from the PEDOT<sup>+</sup> and transported to the cathode where the holes are neutralized. The PEDOT<sup>+</sup> conductive paths change to low conductive PEDOT chains and the device changes to OFF-state. When a much higher current-limited voltage is added to the device at OFF-state, the holes are injected into the PEDOT again at the strong electric field and presence of Au. The low conductive PEDOT chains return to PEDOT<sup>+</sup> conductive paths and the device is set back to ON-state correspondingly. However, it is not sure that the oxidation and reduction of PEDOT: PSS is the only mechanism. Au atoms penetrating into the film during metal deposition and other defects may also influence the formation of conductive paths. Further studies are required to understand the detailed process of conductive paths formation.

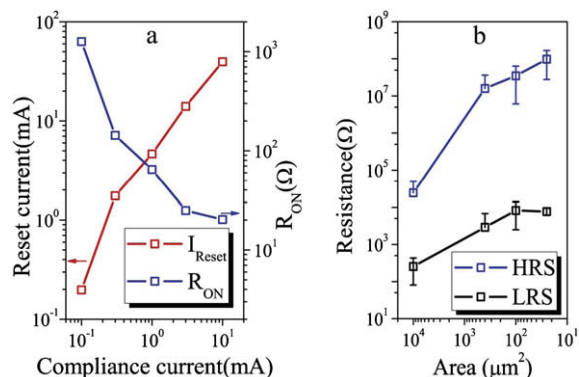
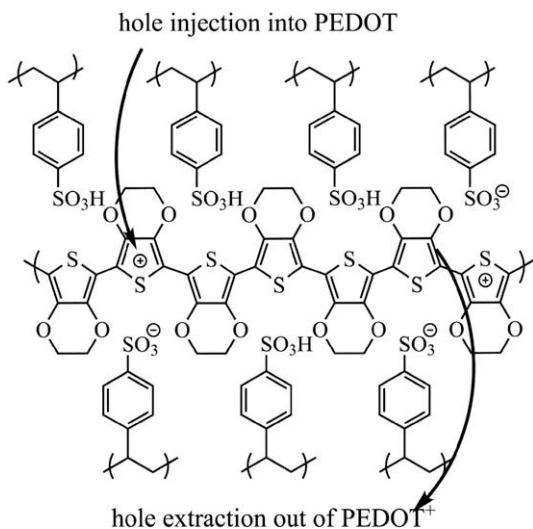


Fig. 3. (a) Dependence of ON-state resistance ( $R_{\text{on}}$ ) and reset current ( $I_{\text{reset}}$ ) on the set compliance current ( $I_{\text{comp}}$ ), and (b) the device area dependence of ON- and OFF-state resistance. Each point of the plots represents averaged values of ten different devices, and the error bars indicate the standard deviations of the devices.



**Fig. 5.** Schematic diagram of the holes ( $h^+$ ) injection and extraction process in PEDOT, which correspond to the forming and rupture of conductive paths.

#### 4. Conclusion

The Au/PEDOT: PSS/Au sandwiched structure is fabricated and investigated for nonvolatile memory applications. It shows a nonpolar resistance switching characteristics, which is different from both the WORM characteristics and the bipolar switching characteristics reported before. No “forming” process is required to induce the resistive switching of the devices. This memory device shows reproducible resistive switching, a large ratio ( $>10^3$ ) of  $R_{\text{off}}$  and  $R_{\text{on}}$ , a long retention time ( $10^4$  s), and nondestructive readout. The area dependence of ON- and OFF-state guarantees the sufficient sensing margin when the device is scaling down. According to the experiment results, the nonpolar switching behavior is due to the forming and rupture of the conductive paths in the PEDOT: PSS film. The oxidation and reduction of the PEDOT is considered to be the probable mechanism to explain the forming and rupture of conductive paths in Au/PEDOT: PSS/Au devices.

#### Acknowledgements

This work is supported in part by the National Basic Research Program of China (973 Program) under Grant 2006CB806204, 2009CB939703 and in part by the National Natural Science Foundation of China under Grants 90607022, 60676001, 60676008, and 60825403, and Synchrotron Radiation Fund of Innovation Project of Ministry of Education under Grant 20070156S.

#### References

- [1] A. Dodabalapur, L. Torsi, H.E. Katz, *Science* 268 (1995) 270.
- [2] Y. Sun, Y. Liu, D. Zhu, *J. Mater. Chem.* 15 (2005) 53.
- [3] J.H. Burroughes, D.D.C. Bradley, A.R. Brown, R.N. Marks, K. Mackay, R.H. Friend, P.L. Burn, A.B. Holmes, *Nature (London)* 347 (1990) 539.
- [4] M. Cavallini, F. Biscarini, S. Leon, F. Zerbetto, G. Bottari, D.A. Leigh, *Science* 299 (2003) 531.
- [5] V.S. Reddy, S. Karak, S.K. Ray, A. Dhar, *Org. Electr.* 10 (2009) 138.
- [6] B. Cho, T.W. Kim, M. Choe, G. Wang, S. Song, T. Lee, *Org. Electr.* 10 (2009) 473.
- [7] W. Ma, C. Yang, X. Gong, K. Lee, A.J. Heeger, *Adv. Funct. Mater.* 15 (2005) 1617.
- [8] R.A. Street, M. Mulato, R. Lau, J. Ho, J. Graham, Z. Popovic, J. Hor, *Appl. Phys. Lett.* 78 (2001) 4193.
- [9] V. Sholin, S.A. Carter, R.A. Street, A.C. Arias, *Appl. Phys. Lett.* 92 (2008) 063307.
- [10] L. Groenendaal, F. Jonas, D. Freitag, H. Pielartzik, J.R. Reynolds, *Adv. Mater. (Weinheim, Ger.)* 12 (2000) 481.
- [11] P. Ravirajan, D.D.C. Bradley, J. Nelson, S.A. Haque, J.R. Durrant, H.J.P. Smit, J.M. Kroon, *Appl. Phys. Lett.* 86 (2005) 143101.
- [12] S. Möller, C. Perlov, W. Jackson, C. Taussig, S.R. Forrest, *Nature (London)* 426 (2003) 166.
- [13] S. Möller, S.R. Forrest, C. Perlov, W. Jackson, C. Taussig, *J. Appl. Phys.* 94 (2003) 7811.
- [14] X. Xu, R.A. Register, S.R. Forrest, *Appl. Phys. Lett.* 89 (2006) 142109.
- [15] P.J. Chia, Y.C. Yeo, J.H. Burroughes, R.H. Friend, P.K.H. Ho, *Appl. Phys. Lett.* 93 (2008) 033314.
- [16] Z. Liu, F. Xue, Y. Su, K. Varahramyan, *Mater. Res. Soc. Symp. Proc.* 19 (2005) 35. 1.
- [17] H. Ha, O. Kim, *Appl. Phys. Lett.* 93 (2008) 033309.
- [18] M. Colle, M. Buchel, D.M. de Leeuw, *Org. Electr.* 7 (2006) 305.
- [19] C.C. Lin, C.Y. Lin, M.H. Lin, C.H. Lin, T.Y. Tseng, *IEEE Trans. Electron. Devices* 54 (2007) 3146.
- [20] C. Schindler, S.C.P. Thermadam, R. Waser, M.N. Kozicki, *IEEE Trans. Electron. Devices* 54 (2007) 2762.
- [21] W. Guan, S. Long, Q. Liu, M. Liu, W. Wang, *IEEE Electron. Device Lett.* 29 (2008) 434.
- [22] P.J. Chia, L.L. Chua, S. Sivaramakrishnan, J.M. Zhuo, L.H. Zhao, W.S. Sim, Y.C. Yeo, P.K.H. Ho, *Adv. Mater.* 19 (2007) 4202.

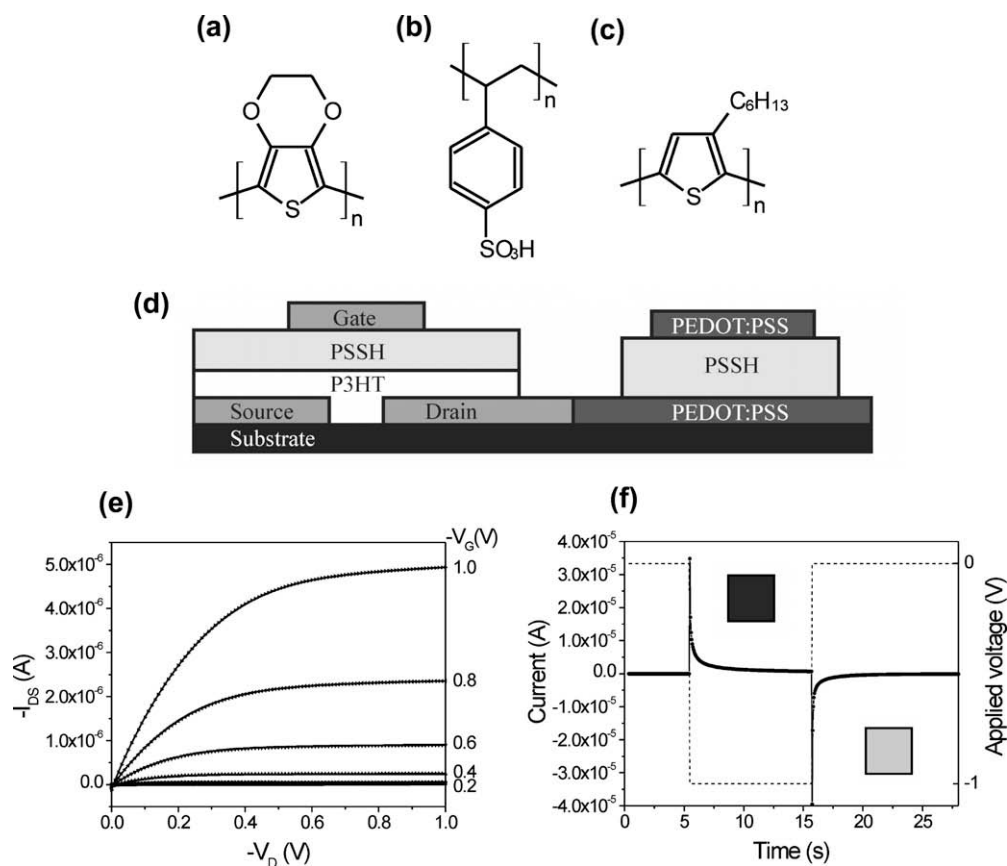


**Fig. 1.** The chemical structures of: (a) PEDOT, (b) PSSH and (c) P3HT. (d) The schematic cross section shows the monolithic integration of an electrolyte-gated OFET and an organic electrochromic pixel device. The graphs report the electrical characteristics of the isolated components: (e) The output characteristics of an EDLC-OFET with a channel width-to-length ratio ( $W/L$ ) equal to 2000/7. (f) The charging/discharging current (solid line) versus time when a voltage (dashed line) is applied between the two PEDOT:PSS electrodes in the electrochromic pixel.

conventional dielectrics typically operate at low voltages (<2 V) only for ultra-thin gate insulating layers (<50 nm); hence making printing impossible. Recent reports indicate that electrolytes constitute a promising electronic insulating layer to separate the gate electrode and the semiconductor [13–20]. This class of OFETs has a unique feature suitable for reel-to-reel manufacturing: the operating potential, of few volts, does not strictly depend on the electrolyte thickness [15]. One class of electrolytes used is proton conducting polyanionic membranes [15,19], such as polystyrenesulfonic acid (PSSH) [19] (Fig. 1b). The formation of the electric double layer capacitors (EDLCs) at the semiconductor/electrolyte and electrolyte/gate interfaces occurs at low voltages. The high capacitance and the quick response of the EDLC enable fast enhancement mode switching ( $\sim 50 \mu\text{s}$ ) and low-voltage operation (<1 V) of the EDLC-OFETs.

In this letter, we demonstrate the monolithic integration of an EDLC-OFET, including regio-regular poly(3-hexylthiophene) (P3HT) (Fig. 1c) as the semiconductor, and a PEDOT:PSS-based electrochromic display cell. The compatibility of the two devices is ensured by the common patterned PSSH layer acting both as the gate insulator in the OFET structure and as the proton transporting layer in the electrochromic display (Fig. 1d).

In this work, no attempts were made to achieve a fully printed OFET, rather our major goal was to demonstrate operational compatibility between the electrolyte-gated OFET and the electrochemical (EC) display device. To construct the OFET sketched in Fig. 1d, gold electrodes are patterned on a silicon wafer with thermally grown oxide by using photolithography and wet-etching. First, a 20 nm thick layer of P3HT is spin-coated from chloroform and then covered with a thin layer (85 nm) of PSSH. A titanium top gate contact is vacuum deposited through a shadow mask to complete the transistor. The output characteristics of this EDLC-OFET, with a channel length and width of 7 and 2000  $\mu\text{m}$ , respectively, shows current modulation already below 1 V (Fig. 1e) and a maximum current throughput of around 5  $\mu\text{A}$ . Upon negative gate bias, mobile protons migrate towards the gate electrode and the immobile polyanionic chains  $\text{PSS}^-$  remain at the vicinity of the P3HT layer, which allows for the formation of a positively charged conducting channel between the source and the drain electrodes (p-channel). It should be noted that polyanions are immobile and, hence, cannot penetrate the organic semiconductor. Thus, electrochemical doping of the semiconductor bulk is entirely prevented, in contrast to EC transistors where current modulation is governed by bulk electrochemistry. The calculated carrier mobility for

the EDLC–OFET at saturation is in order of  $3.67 \cdot 10^{-3} \text{ cm}^2 \text{ V}^{-1} \text{ s}^{-1}$ .

The electrochromic display cell consists of a PSSH (AGFA PSSH 5% in water) layer sandwiched between two PEDOT:PSS (AGFA ICP-1010) electrodes, see Fig. 1b. The top polymer electrode serves as the electrochromic display element, while the counter electrode is hidden below the PSSH electrolyte. A white titanium dioxide nanopowder is added to the electrolyte to increase the color contrast. In its pristine transparent state, PEDOT:PSS is composed of positively doped PEDOT chains neutralized by sulfonate anions attached to the polystyrene chains (PSS). When a potential difference is applied between the two electrodes, the PEDOT of the negatively biased top electrode is reduced (undoped) and turns blue. During this electro-reduction, protons migrate from the PSSH electrolyte into the top PEDOT:PSS electrode to neutralize the sulfonate anions (previously the doping counter-charge for PEDOT). The oxidation takes place at the bottom electrode. This electrochemical reaction is characterized by a current peak of around  $33 \mu\text{A}$  (for  $1 \text{ mm}^2$  sized display cell) during the first second (Fig. 1f). At 16 s, the potential is then set to zero and the top PEDOT:PSS electrode is re-oxidized to its transparent state. This electrochemical process is reversible such as that the display cell can be repeatedly cycled many times. Beside its low operating voltage, the electrochromic display pixel shows a high degree of bi-stability; i.e. the pixel electrode remains reduced while the electrodes are disconnected. Many combined factors are dictating the switch time of an electrochromic pixel, such as the ionic resistance of the PSS layer which depends on geometrical parameters and water content (proton mobility and concentration). For low ionic resistance, the reaction can be limited by the electron transport rates, which depends on the applied voltage.

The EDLC–OFET and the electrochromic display pixel are assembled into a smart pixel circuit by coating partially the gold drain electrode of the transistor with the PEDOT:PSS bottom electrode of the pixel. The characteristics of the individual components and the smart pixels are measured using a Keithley 4200-SCS Semiconductor Characterization System in ambient atmosphere (40% relative humidity, room temperature). The smart pixel is updated in four steps: (i)  $V_G = 0 \text{ V}$ ,  $V_P = -1.2 \text{ V}$ ; (ii)  $V_G = -1.2 \text{ V}$ ,  $V_P = -1.2 \text{ V}$ ; (iii)  $V_G = 0 \text{ V}$ ,  $V_P = 0 \text{ V}$ ; (iv)  $V_G = -1.2 \text{ V}$ ,  $V_P = 0 \text{ V}$ . During the entire updating cascade, the current is monitored (Fig. 2a) and the direction of the electron, the hole and the proton currents are illustrated in Fig. 2b. The potential drop ( $V_{\text{drop}}$ ) across the transistor channel is continuously measured during the entire updating scheme in Fig. 2c. Firstly, despite the applied voltage across the display cell ( $V_P = -1.2 \text{ V}$ ), the pixel remains in its off-state (PEDOT:PSS transparent) as indicated by the negligible current (curve (i) in Fig. 2a) that passes through the smart pixel. The transistor suppress updating of the display cell since it is in its high impedance state ( $V_G = 0 \text{ V}$ ) as indicated by the large potential drop across the transistor (step (i) in Fig. 2c). Secondly, as  $V_G$  is set to  $-1.2 \text{ V}$ , the transistor channel opened and the potential across the OFET drops (step (ii) in Fig. 2c). Since  $V_P$  equals  $-1.2 \text{ V}$ , the major part of the potential drop is across the display pixel. Holes flow

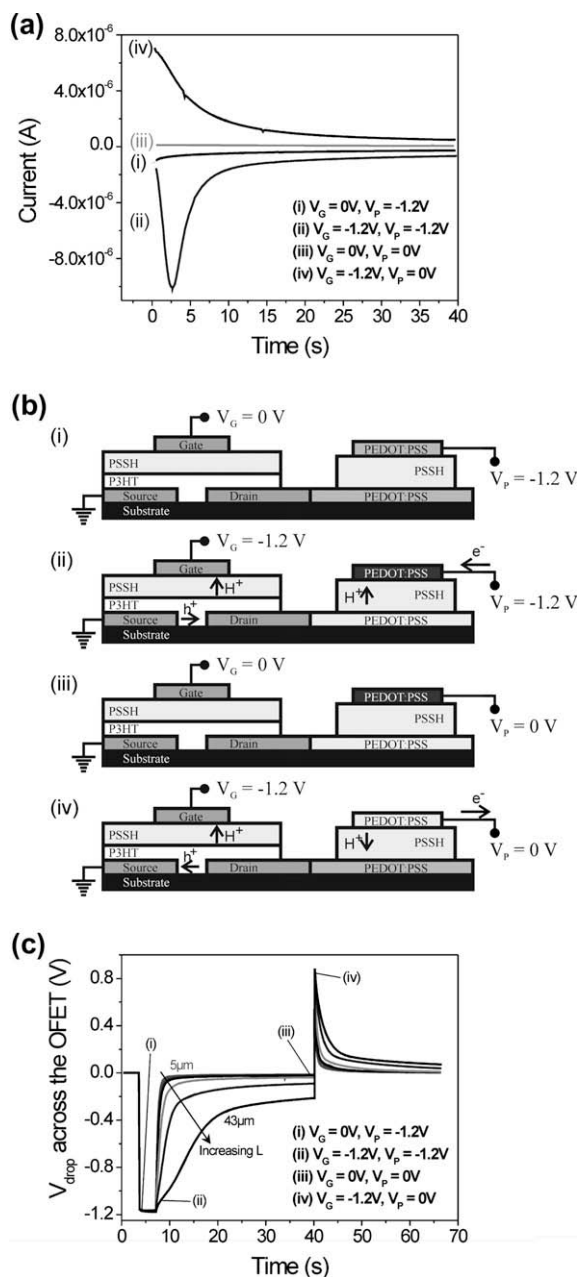


**Fig. 2.** The updating scheme of the smart pixel is realized in four combinations of electrical biases: (i)  $V_G = 0 \text{ V}$ ,  $V_P = -1.2 \text{ V}$ ; (ii)  $V_G = -1.2 \text{ V}$ ,  $V_P = -1.2 \text{ V}$ , (iii)  $V_G = 0 \text{ V}$ ,  $V_P = 0 \text{ V}$ , (iv)  $V_G = -1.2 \text{ V}$ ,  $V_P = 0 \text{ V}$ . (a) Time evolution of the current crossing the smart pixel after each of the four steps. The two devices are integrated on a silicon substrate and the OFET has  $W/L = 154$ . (b) The sketch of the smart pixel illustrates the direction of charge carriers (electron, hole and proton) involved in the four steps. (c) Evolution of the potential drop across the transistors for various channel lengths (5, 7, 9, 13, 23 and  $43 \mu\text{m}$ ) during the updating scheme (i) to step (iv).

through the OFET (curve (ii) in Fig. 2a), which leads to oxidation of the bottom PEDOT:PSS electrode while PEDOT of the top electrode is reduced and turns blue. Thirdly, for  $V_G = 0 \text{ V}$  and  $V_P = 0 \text{ V}$ , charges cannot leak through the OFET (curve (iii) in Fig. 2a) and the pixel remains blue. In step

(iii) in Fig. 2c the pixel acts as a loaded battery such that the potential across the OFET is opposite as compared to the first updating step shown in step (ii) in Fig. 2c. Finally, the pixel is discharged to its transparent off-state by opening the transistor channel ( $V_G = -1.2$  V) and keeping  $V_P$  at 0 V (curve (iv) in Fig. 2a). The efficiency of the smart pixel relates to the amount of charges that can be stored over long period of times. After a full cycle, we found a charge mismatch of about 9% between charging and discharging steps, which we attribute to the spontaneous re-doping of the reduced PEDOT by dioxygen. Note that this side reaction does not damage the electroactivity of the conducting polymer or the reversibility of the process.

The dynamic switch characteristics of the display pixels can be quantified with the time evolution of the charging/discharging current (Fig. 3a and b) and the associated color changes (Fig. 3c and d). The electrochromism is followed by irradiating a pixel of 1 mm<sup>2</sup> with a red laser (peaking at 650 nm to match the absorptions peak for a neutral blue-colored PEDOT:PSS) at an incident angle of 45° and detecting the diffused light with a Si-photodiode placed in the normal direction vs. the pixel surface (inset in Fig. 3c). A low photocurrent corresponds to a high degree of absorption of the red light, i.e. the PEDOT of the display cell is reduced and is deep blue. The response of the smart pixel is recorded for different OFET dimension;  $W = 2000$  μm and  $L$  equals 43, 23, 13, 9, 7 and 5 μm. The response time of the display pixel depends significantly

on the channel length; which indicates that the rate of the PEDOT:PSS electrochemical reaction of the display pixel is not the limiting updating mechanism for the specific PSS thickness and  $V_P$  chosen. The response time of the electrochromic display pixel is correlated to the current delivered by the OFET; which is proportional to  $W/L$ . Shorter channel lengths result in a larger current levels (Fig. 3b) and a pixel that correspondingly switches on and off relatively faster (<1 s) (Fig. 3d). The reduction process of the pristinely doped top electrode is not limiting the updating rate because of its high electrical conductivity (~10 S/cm). Interestingly, the off-switching is fast and only weakly dependent on the transistor channel length. In this case, the limiting factor for updating is not the current through the OFET but instead the high impedance of the reduced (colored) PEDOT of the top display electrode. The bottom PEDOT:PSS electrode is not limiting since in its highly doped state. Noteworthy, for long transistor channels (>15 μm), the electrochromic display pixel is unable to reach its fully reduced blue-colored state within the chosen time scale. Because the full reduction of the top PEDOT electrode cannot be reached for long transistor channels, there are fewer charges stored in the display pixel and the resistance of the pixel top electrode remains low. These two factors contribute together to fast discharging of the cell for long channels. The maximum charging current varies between 34 μA for  $L = 5$  μm and 5 μA for  $L = 43$  μm (Fig. 3b). This corresponds to a switch-

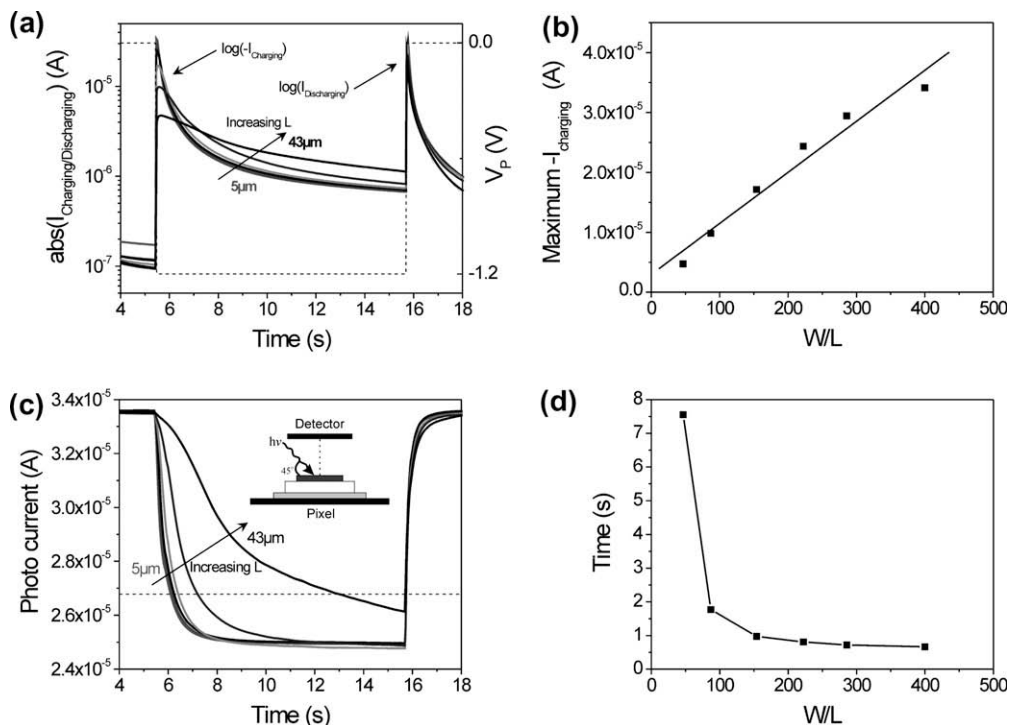


**Fig. 3.** (a) Charging/discharging currents (solid line) vs. time supplied by transistors with different channel lengths ( $L = 5, 7, 9, 13, 23$  and  $43$  μm, and width  $W = 2000$  μm) at  $V_G = -1.2$  V and  $V_P = -1.2$  V or 0 V (dashed line). (b) Maximum charging current vs.  $W/L$  (filled squares), recorded as the top of the charging current in (a). The solid line is the linear fit of the measured maximum charging currents. (c) Photo-currents reflect the kinetic of the color change in the pixel for various transistor channel lengths. The setup of this measurement is shown as an inset. (d) Time of the 20% of the maximum photo-currents (dashed line in c) vs.  $W/L$ .

ing time of 0.66 and 7.6 s for channel lengths of 5 and 43  $\mu\text{m}$  (Fig. 3d).

In summary, we have presented a monolithic integration of an EDLC-OFET and an organic electrochromic pixel, i.e. a combination of a solid state device operating in a field-effect mode and a display cell operating in an electrochemical mode. Electrolyte gated-OFETs are more compatible with electrochemical displays than OFETs with traditional dielectrics for the following reasons: (i) low operating voltage (<1 V) independent of the electrolyte thicknesses, (ii) the large current throughput (5  $\mu\text{A}$  for  $W/L = 285$ ) because of the large capacitance of the EDLCs (20  $\mu\text{F}/\text{cm}^2$ ); and (iii) acceptance to humid environments. Even though this type of transistor delivers less charge as compared to the electrochemical transistor equivalence, it is still capable of switching 1  $\text{mm}^2$ -sized display cells. Such electrolyte-gated smart pixels possess relatively faster updating speeds, lower power consumption (thanks to the enhancement mode operation of the OFET) and no parasitic propagation of a reduction front, as compared to smart pixels built with EC transistors. The versatility of electrolyte-gating provided by the PSS layer, as it serves as both the gate insulator in the transistor and as the electrolyte in the display pixel, implies manufacturing with less materials and processing steps. This, in turn, promises for easy manufacturing of low-voltage operating and matrix-addressed displays using standard printing techniques.

### Acknowledgements

The authors gratefully acknowledge the Swedish Foundation for Strategic Research (OPEN project), VINNOVA (Centerprise project), the Royal Swedish Academy of Sciences (KVA), the Swedish Research Council and Linköping University for financial support of this project. In addition,

the authors wish to thank AGFA Gevaert N.V. for providing the PEDOT:PSS and the PSSH material.

### References

- [1] A. Dodabalapur, Z. Bao, A. Makhija, J.G. Laquindanum, V.R. Raju, Y. Feng, H.E. Katz, J. Rogers, *Appl. Phys. Lett.* 73 (1998) 142.
- [2] G.H. Gelinck, H.E.A. Huitema, E. van Veenendaal, E. Cantatore, L. Schrijnemakers, J.B.P.H. van der Putten, T.C.T. Geuns, M. Beenhakkers, J.B. Giesbers, B.-H. Huisman, E.J. Meijer, E.M. Benito, F.J. Touwslager, A.W. Marsman, B.J.E. van Rens, D.M. de Leeuw, *Nat. Mater.* 3 (2004) 106.
- [3] E. Huitema, G. Gelinck, B. Van Der Putten, E. Cantatore, K. Kuijk, K. Hart, D. De Leeuw, *J. Soc. Info. Displ.* 10 (2002) 195.
- [4] H.E.A. Huitema, G.H. Gelinck, J.B.P.H. Van Der Putten, K.E. Kuijk, C.M. Hart, E. Cantatore, P.T. Herwig, A.J.J.M. Van Breemen, D.M. De Leeuw, *Nature* 414 (2001) 599.
- [5] J.A. Rogers, Z. Bao, *J. Poly. Sci. Part A: Polym. Chem.* 40 (2002) 3327.
- [6] K.L. Tzeng, H.F. Meng, M.F. Tzeng, Y.S. Chen, C.H. Liu, S.F. Horng, Y.Z. Yang, S.M. Chang, C.S. Hsu, C.C. Chi, *Appl. Phys. Lett.* 84 (2004) 619.
- [7] L. Zhou, A. Wanga, S.-C. Wu, J. Sun, S. Park, T.N. Jackson, *Appl. Phys. Lett.* 88 (2006) 083502.
- [8] T. Zyung, S.H. Kim, H.Y. Chu, J.H. Lee, S.C. Lim, J.I.K. Lee, O.H. Jiyong, *Proc. IEEE* 93 (2005) 1265.
- [9] P. Andersson, R. Forchheimer, P. Tehrani, M. Berggren, *Adv. Funct. Mater.* 17 (2007) 3074.
- [10] P. Andersson, D. Nilsson, P.O. Svensson, M. Chen, A. Malmström, T. Remonen, T. Kugler, M. Berggren, *Adv. Mater.* 14 (2002) 1460.
- [11] P. Andersson, D. Nilsson, P.O. Svensson, M. Chen, A. Malmström, T. Remonen, T. Kugler, M. Berggren, *Mater. Res. Soc. Symp. Proc.* 736 (2003) D6.6.
- [12] T. Johansson, N.K. Persson, O. Inganäs, *J. Electrochem. Soc.* 151 (2004).
- [13] S. Chao, M.S. Wrighton, *J. Am. Chem. Soc.* 109 (1987) 6627.
- [14] A.S. Dhoot, J.D. Yuen, M. Heeney, I. McCulloch, D. Moses, A.J. Heeger, *PNAS* 103 (2006) 11834.
- [15] L. Herlogsson, X. Crispin, N.D. Robinson, M. Sandberg, O.J. Hagel, G. Gustafsson, M. Berggren, *Adv. Mater.* 19 (2007) 97.
- [16] D. Nilsson, M. Chen, T. Kugler, T. Remonen, M. Armgarth, M. Berggren, *Adv. Mater.* 14 (2002) 51.
- [17] M.J. Panzer, C.D. Frisbie, *J. Am. Chem. Soc.* 127 (2005) 6960.
- [18] M.J. Panzer, C.D. Frisbie, *J. Am. Chem. Soc.* 129 (2007) 6599.
- [19] E. Said, X. Crispin, L. Herlogsson, S. Elhag, N.D. Robinson, M. Berggren, *Appl. Phys. Lett.* 89 (2006) 143507.
- [20] M. Taniguchi, T. Kawai, *Appl. Phys. Lett.* 85 (2004) 3298.



dopant has resulted in improved efficiency, retaining the color co-ordinates [12].

External quantum efficiency (EQE) of OLED depends heavily on the efficiency of carrier injection and recombination as well as on the electron–hole balancing. Therefore, in order to achieve the maximal efficiency, a balanced carrier recombination in the emissive layer (EML) is a must for the device. Especially in the blue OLED, the recombination region should be confined within the EML closer to the anode side to avoid the recombination at the EML/electron transport layer (ETL) interface to ensure color purity [13]. However, the commonly used configuration of OLEDs does not provide the required conditions for a balanced carrier injection/transport that leads to efficient recombination. One of the reasons is that the injected hole is more mobile than the injected electron under the same applied electric field. Therefore, establishing an electron–hole balance by reducing the number of holes or increasing the number of electrons reaching the EML is considered one of the most direct and viable solutions to improve device efficiency. Hole Blocking Layers (HBLs) are generally used for this purpose but they in turn increase the operating voltages [14–16]. These HBLs most commonly are placed after EML, closer to cathode. Another approach has been to place HBL between HTL and EML. Divayana et al. [15] incorporated a HBL between Hole Injection Layer (HIL) and HTL, with a view that it would cause minimal increase in operating voltage, but this would clearly depend more on the choice of materials.

Another alternative is to use graded layers as in green OLED obtained from graded HTL and ETL [17]. But arguably the most effective approach providing a balance between loss of process ease and increased efficiency would be to use multiple quantum wells (MQW) structures [18–20] which are of two types. In one, the energy levels of the material having wider energy gap sandwich the energy levels of the material with the narrow energy gap, thus confining both electrons and holes in the latter. In the other, both highest occupied molecular orbital (HOMO) and lowest unoccupied molecular orbital (LUMO) levels of both the materials involved in the quantum well structure are offset in the same direction.

Among the MQW structures, Divayana and Sun [9] fabricated blue OLED by sequentially incorporating multiple layers of host and dopant for better control of process compared to co-evaporated host and dopant. Qiu et al. [18], in a green OLED, incorporated multiple layers of NPB (N,N'-diphenyl-N,N'-bis (1,1'-biphenyl)-4,4'-diamine)/rubrene adjacent to anode such that electrons and holes can be trapped in the rubrene layer. Therefore, as more and more multiples of these layers are incorporated, the emission changes from green to that of rubrene, allowing color tuning. While more common are MQWs with HOMO and LUMO levels in one well material offset with respect to the adjacent material in opposite direction, Wang et al. [20] demonstrated increased efficiency of a blue OLED by employing NPB/TMADN (2,3,6,7-tetramethyl-9,10-dinaphthyl-anthracene) MQW with staggered energy levels. This has resulted in improved performance of blue OLEDs marked by an increase in current efficiency to 4.1 cd/A

for the MQW device from 3.4 cd/A for the standard hetero-junction structure.

In this paper, we describe a facile method of fabricating a blue OLED with improved efficiency by stepwise insertion of HTL into EML thereby achieving multiple HTL/EML interfaces in the EML and the performance of such a modified device is compared with that of a conventional one with the same materials. The experimental observations are qualitatively explained by simulation.

## 2. Experimental

Device area of 16 mm<sup>2</sup> was photolithographically defined on Indium Tin Oxide (ITO) (sheet resistance <10 Ω/□) coated glass, which was used as substrate. Prior to organic layer evaporation, the substrates were thoroughly cleaned with the routine cleaning procedure and subjected to oxygen plasma treatment. Evaporation of organic materials and metal was carried out under high vacuum (~10<sup>-7</sup> Torr). The structure of the conventional device and the corresponding energy level diagram are shown in Fig. 1. A HIL (DS205 from Doosan Electromaterials) of thickness 100 nm was deposited first. Then sequentially multiple steps of NPB (as HTL) and EML (consisting of a blue host, BH2 from Kodak, with 1% blue dopant BD3 from Kodak, deposited by co-evaporation from two crucibles placed symmetrically below the substrate) were deposited keeping the total thickness of HTL to be 20 nm and that of EML 30 nm. A 25 nm thick layer of Alq<sub>3</sub> (Tris-(8-hydroxyquinoline) aluminum) was deposited as the ETL. Finally a

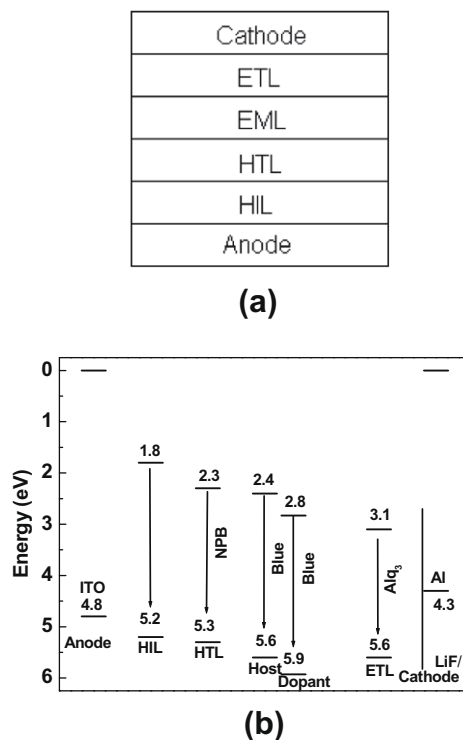


Fig. 1. (a) The conventional device structure and (b) the energy level diagram of the device depicted in (a).

1 nm thick LiF layer and 150 nm thick Al layer were deposited as the cathode. All devices were encapsulated with UV-curable resin and glass cover under inert conditions. The electro-optical characteristics of the fabricated devices were measured using a CS-1000 Minolta spectroradiometer and a Keithley 2400 SMU. All measurements were carried out on encapsulated devices.

### 3. Results and discussion

For comparing the performance of multiple HTL/EML layers based devices, the standard devices were made consisting of ITO(150 nm) /HIL(100 nm) /HTL(20 or 30 nm) /EML(30 nm) /ETL(25 nm) /LiF(1 nm) /Al(150 nm). These devices are labeled Device 1 and Device 2 based on thickness of HTL as 20 or 30 nm, respectively. While a significant effort in this work is on investigating multiple HTL layers in a device, these two devices are used to examine if thickness of HTL itself has a dominant effect in the device performance.

Fig. 1b shows the energy level diagram of these standard devices. There is an energy offset of 0.3 eV between the HOMO of the EML host and HOMO of the HTL. This creates a barrier for hole injection from HTL to EML. Hence holes could pile up at this interface and their probability of radiative recombination with the electrons reaching this interface is high. But it is commonly believed that holes have much higher mobility in HIL and HTL than electrons in ETL and, in addition, electrons suffer from injection difficulty at the cathode. This leads to charge imbalance, leading to many holes escaping to cathode without recombining. Accordingly, a poor current efficiency of such devices is explained.

In the standard device, as Fig. 1b indicates, we note an energy barrier to hole transport between HTL and EML, but no barrier for electrons. Conventional methods incorporate a separate hole blocking layer to increase luminance. But, since the HTL/EML interface naturally offers a barrier to hole transport, in the present work, it is possible to divide up the total HTL and EML thicknesses in many parts and include them as repeated structures forcing holes to encounter this barrier as many times; this arrangement, in turn, could increase the efficiency of blue OLED by slowing down the holes. Dividing the HTL thickness of Device 1 in two parts, in our improved Device 3, we have inserted two repeating structures of HTL and EML, keeping their total thickness the same as in Device 1. Accordingly, the device structure is ITO(150 nm) /HIL(100 nm) /HTL(10 nm) /EML(15 nm) /HTL(10 nm) /EML(15 nm) /ETL(25 nm) /LiF(1 nm) /Al(150 nm). Similarly, in Device 4, the HTL/EML units are repeated three times according to the scheme ITO(150 nm) /HIL(100 nm) /HTL(10 nm) /EML(10 nm) /HTL(6 nm) /EML(10 nm) /HTL(4 nm) /EML(10 nm) /ETL(25 nm) /LiF(1 nm) /Al(150 nm). Here we have selected the thickness of different HTL segments such that its thickness decreases towards the cathode, because of an expectation that concentration of holes will reduce further away from anode. The materials are so selected that the LUMO levels of HTL and EML host are similar, implying little energy barrier to electron transport.

Thus, while additional barrier is provided to hole transport by repeating the HTL/EML unit, electron transport remains unaffected.

#### 3.1. Current–voltage–luminance characteristics

Fig. 2 shows the current density versus voltage ( $J$ - $V$ ) characteristics of all the devices (symbols only). Typical data from 16 identical devices is plotted for each stack. Devices 1 and 2, which differ only in the HTL thickness, have similar  $J$ - $V$  characteristics, indicating hole mobility in HTL does not limit the carrier transport. But, the current density in the standard devices is much higher than those with the multiple layers (Devices 3 and 4), consistent with the additional hole barriers introduced at HTL/EML interface. Among these two also, the Device 4 with three such interfaces has lower currents than Device 3 with two interfaces.

A small increase in voltage for same current, in principle, is acceptable as long as luminance also increases, resulting in increased current and power efficiency. These situations will imply lower non-radiative recombination of holes in the device or at cathode, the very reason for which multiple HTL/EML interfaces were introduced. Clearly, as demonstrated in Fig. 3, for a current density, luminance in Device 3 is greater than that in the standard devices. In principle, the luminance should increase with further increase in number of such interfaces. However, the luminance in Device 4 remains the same, possibly because either most electrons are already recombining within two units of HTL/EML, or increasing the number of interfaces (for same total thickness) forces thinner layers, which may result in poor control on film deposition. Additional consequences of increased number of interfaces and thinner films may be adverse effect of interface states, diffusion of excitons out of EML and emission quenching by NPB cation. All these are discussed in a greater detail later.

Two important figures of merit that define the performance of a device are the current and power efficiency, apart from reliability issues, such as life-time. The current efficiency of our devices with multiple HTL/EML interfaces is compared in Fig. 4, in which a current efficiency of

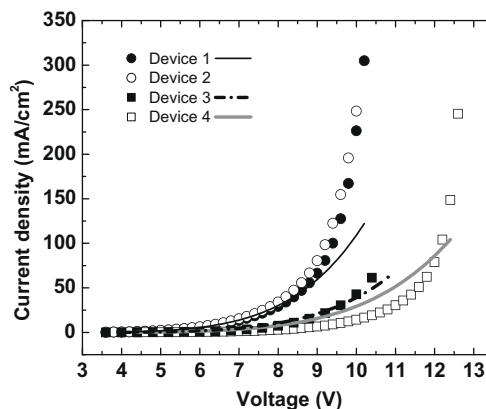


Fig. 2. Current density–voltage characteristics of the devices. Dots are experimental data and solid lines are simulated curves for devices 1, 3 and 4.

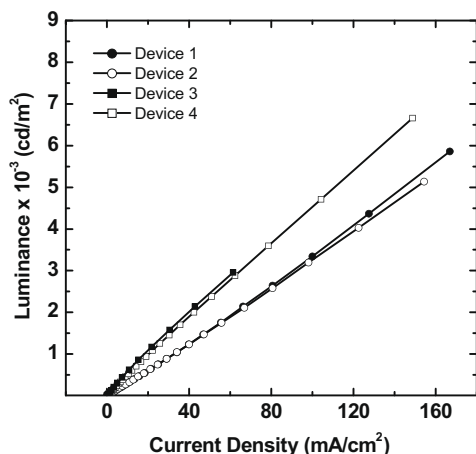


Fig. 3. Current density–luminance characteristics of the devices studied.

approximately 3 cd/A is shown for both the standard Devices 1 and 2. The Device 3 with two HTL/EML interfaces exhibits the maximum current efficiency of 5.8 cd/A, and the Device 4 with three HTL/EML interfaces 5 cd/A, at a current density of 10 mA/cm<sup>2</sup>. This indicates that the multilayer HTL/EML structure significantly improves the device efficiency, approximately 1.9 times at low current densities and 1.5 times at its higher values. The luminance at any current density from Device 3 and 4 appear similar (see Fig. 3). But at low current densities, slightly higher luminance in device 3 tends to amplify the current efficiency; note that this result is repeatable. But at higher current densities, this difference seems to reduce, with current efficiencies both for Device 3 and 4 becoming similar. It may also be noted that the HTL thickness (compare Device 1 and 2) variation does not impact luminance, just like the current density, and hence current efficiency.

The second figure of merit is power efficiency, which is compared in Table 1. Using voltage required for 1 cd/m<sup>2</sup> emission as the basis, the luminance threshold voltage increases from 3.6 V in standard devices to 4–5 V in multilayer structure. But, correspondingly, the current

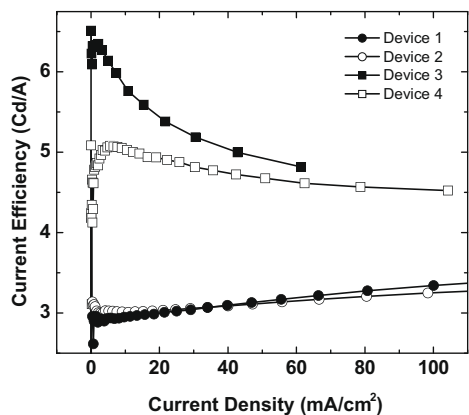


Fig. 4. Current density–current efficiency characteristics of the four devices.

efficiencies increase from 3 cd/A to between 5 and 6 cd/A. However, although the voltage of operation would increase by including the multi-layers, the power efficiency still increases to 2.2 lm/W for Device 3 and, in Device 4, remains similar (1.5 lm/W) to those of standard devices (1.4 lm/W). Therefore, the gain in current efficiency combined with either an increase or similar power efficiency by including multilayer structure can possibly justify the increased voltage of operation.

### 3.1.1. The CIE color co-ordinates

A typical electroluminescence (EL) spectrum of emission from these devices is depicted in Fig. 5a. Along with it, also shown are the photoluminescence (PL) spectra of 500 nm thick blue host and dopant films (excitation at 370 nm). The PL of host with 1% dopant is also included in the same figure. The PL of host with dopant closely follows the dopant emissions, indicating substantial energy transfer to it. Further, the electroluminescent (EL) emission is in accordance with the corresponding PL for host with 1% dopant, except an additional peak beyond 500 nm (see the encircled portion). Since this peak is entirely missing in the PL spectrum and is reasonably broad and located where we expect Alq<sub>3</sub> to emit, this additional peak in EL is from the ETL. The color co-ordinates of device emission are, therefore, negatively affected by this emission.

Full color displays would require blue emission which is as saturated as possible. Typically, more important is the CIE *y*-co-ordinate, which should be closer to 0.15. The CIE (*x*, *y*) co-ordinates for all four devices are shown in Fig. 5b. The CIE *x*-co-ordinate remains relatively unchanged from device to device, although the devices with multiple HTL/EML interface yield a better color co-ordinate, especially at higher voltages. The CIE *y*-co-ordinate, however, shows much more significant improvement towards deeper blue in multiple interface devices. The improved emission by including multiple interfaces would accompany lower recombination in ETL (Alq<sub>3</sub>), which also therefore shifts the emission to deeper blue in comparison to the standard devices.

Furthermore, in the practical voltage range, above 6 V, the color co-ordinates in Device 3 and 4 do not change with voltage. Thus, these devices may be suitable for display applications.

### 3.2. Device simulation

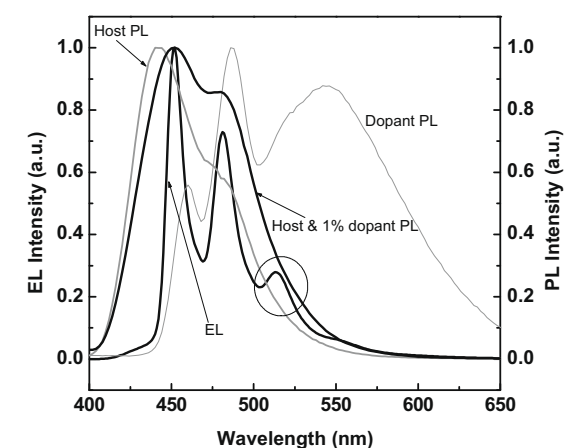
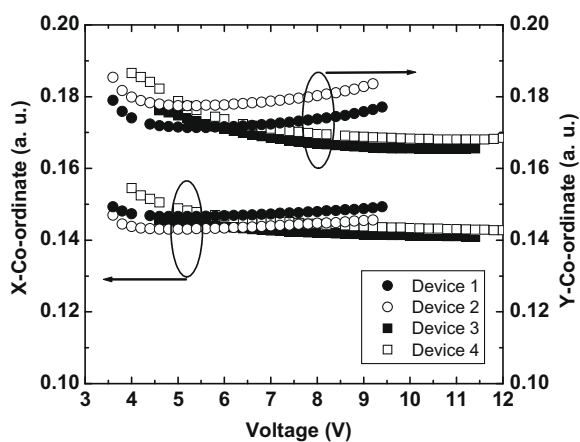
In order to gain insight into the role of multilayer structures in modifying charge transport and recombination zone, we developed a simulator. A set of partial differential equations governing underlying physics of the device is based on drift-diffusion approximation [21,22]. The injection/extraction of carriers is modeled with thermionic emission along with the field dependent barrier lowering and its time reversed back flowing process according to the approach of Malliaras and Scott [23,24]. The organic-organic interface discontinuity has been modeled according to the approach of Crone et al. [25], assuming no dipoles/sheet charges at the interface, but distributed pile-up of charges being allowed. The recombination in the device is bimolecular with Langevin coefficient. The density

**Table 1**

Electroluminescent characteristics of the devices studied. The distribution of the HTL thickness of each device is also given. Threshold voltages are for a luminance of 1 cd/m<sup>2</sup>. Current efficiency and power efficiency are measured at 10 mA/cm<sup>2</sup>.

	Threshold voltage (V)	Current efficiency (cd/A)	Power efficiency (lm/W)
Device 1 HTL:EML (20 nm:30 nm)	3.6	2.9	1.4
Device 2 HTL:EML(30 nm:30 nm)	3.6	3.0	1.4
Device 3 HTL:EML(10 nm:10 nm/10 nm:10 nm)	4.0	5.8	2.2
Device 4 HTL:EML(10 nm:10 nm/6 nm:10 nm/4 nm:10 nm)	4.8	5.0	1.5

of states in organic materials in the simulator is fixed to its molecular density and dielectric constant of all layers is taken as 3. Finally, before using the simulator here, it has been validated with previously published simulation results of other groups [24–26].

**(a)****(b)**

**Fig. 5.** (a) Typical photoluminescence (PL) spectra of host, dopant and host with 1% dopant and electroluminescence (EL) spectrum of the standard device. The peak encircled in the EL spectrum is the green emission due to the recombination in the ETL, Alq<sub>3</sub> (b) CIE color coordinates of the devices.

The simulated  $J$ - $V$  characteristics are compared with the experimental data in Fig. 2 (solid lines) for Devices 1, 3 and 4. The mobility of both electrons and holes are assumed to be of the type,  $\mu = \mu_0 e^{\sqrt{E/E_0}}$  where  $E$  is the electric field. Accordingly, the other mobility parameters ( $\mu_0$  and  $E_0$ ) listed in Table 2 are so selected that best match of  $J$ - $V$  characteristics are obtained for all three devices for the same set of mobility parameters. The simulation suffers from limitations that it does not include exciton diffusion or trap distribution in the organic materials and the only transport levels are discrete LUMO and HOMO levels. As a result, the match of  $J$ - $V$  characteristics with experimental data is not perfect, but a similar trend allows us to approximately probe the differences between Devices 1, 3 and 4.

In order to evaluate the effect of introducing multiple HTL/EML layers, based on Fig. 2, we select two current levels, 15 mA/cm<sup>2</sup> (low) and 80 mA/cm<sup>2</sup> (high), to examine the spatial distribution of electron and hole currents and recombination. In both cases, as shown in Fig. 6, holes injected from anode in Device 1 encounter the first barrier at HTL/EML interface (at 120 nm) causing a pile-up of holes ( $p$ , thin solid line); correspondingly, there is little or no voltage drop in HIL and HTL. Also, a large number of holes are seen to reach cathode. On the other hand, in Device 1, the electrons ( $n$ , thin solid line) injected at cathode also pile-up at ETL/EML (at 150 nm) interface. Beyond that, the electron concentration drops rapidly, with few electrons reaching the anode. As a consequence, the electron current ( $J_n$ ) in ETL is large, dropping off to nearly zero beyond ETL towards the anode. Nonetheless, significant hole current ( $J_p$ ) is seen reaching the cathode. Furthermore, since ETL has significant population of both electrons and holes, a large amount of recombination ( $R$ ), defined as rate of holes or electrons recombining per unit volume, takes place in ETL. The radiative part of this recombination leads to Alq<sub>3</sub> green emission, which is to be avoided. That, our devices are primarily blue, and such large recombination in ETL is suggested by simulations indicates either vicinity of ETL to the cathode leads to substantial non-radiative recombination or this large recombination in ETL may be a consequence of our selection of simulation parameters (carrier mobilities and transport levels). However, in the latter case also, qualitative differences arising from different device structures (Devices 1, 3 and 4) can still be meaningfully predicted.

Apart from the recombination in EML, primary recombination leading to blue emission occurs at HTL/EML inter-

**Table 2**  
Simulation parameters.

	HIL	HTL	EML	ETL
$\mu_0$ for holes (zero field hole mobility) ( $\text{m}^2/\text{Vs}$ )	$6 \times 10^{-8}^*$	$6.1 \times 10^{-9}^*$	$1.8 \times 10^{-9}$	$1.8 \times 10^{-12}$
$\mu_0$ for electrons (zero field electron mobility) ( $\text{m}^2/\text{Vs}$ )	$6 \times 10^{-10}^*$	$6.1 \times 10^{-11}^*$	$1.8 \times 10^{-8}^*$	$1.8 \times 10^{-11}$
$E_0$ for holes (V/m)	$2 \times 10^6$	$4.44 \times 10^7$	$1.11 \times 10^7$	$1.04 \times 10^7$
$E_0$ for electrons (V/m)	$2 \times 10^6$	$4.44 \times 10^7$	$1.11 \times 10^7$	$1.04 \times 10^7$

\* These mobility values even if increased by 10 times make only a minor difference in calculations.

face (120 nm for Device 1) where the holes pile-up, as do electrons due to a small barrier. This small barrier for electrons leads to only a small increase in electron concentration compared to that of holes. The corresponding recombination is also shown in Fig. 6 for both current densities. We estimate the recombination current that leads to blue emission by integrating the recombination rate between 1 nm on either side of HTL/EML interface (119–121 nm for Device 1) and multiplying it by electron charge. Accordingly, for Device 1, this current is estimated as 0.06 and 0.56  $\text{mA}/\text{cm}^2$  at a total current density of 15 and 80  $\text{mA}/\text{cm}^2$ , respectively.

Upon introducing the multiple junctions of HTL and EML, such as in Device 3, the electrons and holes now

pile-up wherever the same interfaces as in Device 1 are available. Accordingly, the hole current reaching cathode decreases with a corresponding increase in electron current at the same location (see Fig. 6). As a consequence, the green recombination in ETL reduces (compare Device 1 with Device 3; due to log scale in Fig. 6, the change appears small), consistent with color co-ordinate improvement observed experimentally.

In Device 3, multiple HTL/EML interfaces which block holes lead to added blue emission at each of these interfaces. The recombination current near HTL/EML interface is estimated as 0.95  $\text{mA}/\text{m}^2$  (from Fig. 6a) and 2.10  $\text{mA}/\text{m}^2$  (from Fig. 6b). Thus, in this device the recombination current at low total current density increases to 0.95  $\text{mA}/$

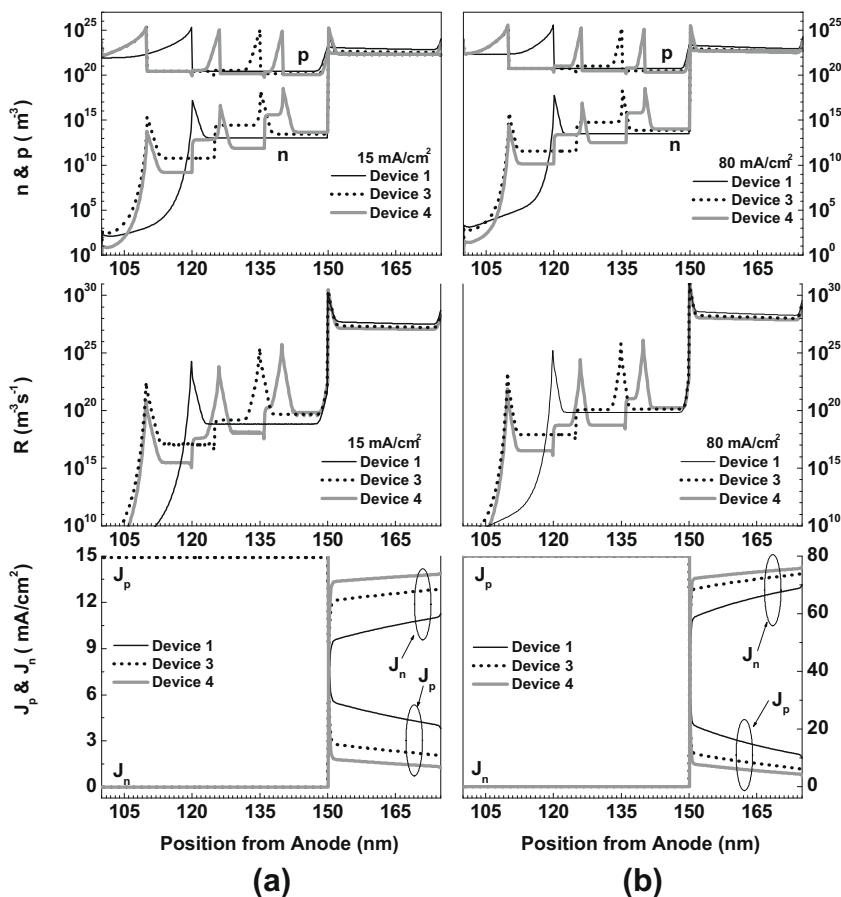


**Fig. 6.** (a) Spatial distribution of electron density ( $n$ ) and current ( $J_n$ ), hole density ( $p$ ) and current ( $J_p$ ) and electron and hole recombination rates ( $R$ ) at 15  $\text{mA}/\text{cm}^2$  total current density and (b) the same at 80  $\text{mA}/\text{cm}^2$ .

$\text{m}^2$  from  $0.06 \text{ mA/m}^2$  in Device 1, which experimentally is observed as an increase in current efficiency. At a higher total current density, this increase in calculated recombination current is from  $0.56 \text{ mA/m}^2$  in Device 1 to  $2.10 \text{ mA/m}^2$  in Device 3, representing a smaller increase than that at lower total current density. The same has been observed experimentally, where the improvement in current efficiency at lower current density is much more significant than that at higher current density (see Fig. 4)

Since there is still a substantial number of holes recombining at cathode, adding one more HTL/EML interface in Device 4 leads to predicting still higher electron current and lower hole current at cathode, lower recombination in ETL and increased recombination current to 2.15 (from Fig. 6a  $4.21 \text{ mA/m}^2$  (from Fig. 6b) at HTL/EML interface. Experimentally, however, we observe lower current efficiency in Device 4 in comparison to Device 3.

This observation is similar to the result of inserting multiple layers of rubrene confined between NPB, where four layers resulted in maximum current efficiency [18]. The same group also reports a  $\text{Alq}_3$  OLED with multiple layers of NPB and CuPc together constituting the HTL [27]. In this device, four such layers yield best efficiency, presumably, according to the authors, due to poor film quality of thinner layers and negative impact of surface states. In another MQW structure with phosphorescent materials, the cause of decline in EL efficiency beyond a number of multiple layers is ascribed to exciton diffusing out of the emissive region [28]. Therefore, in case of Device 4, a fall in current efficiency could be due to poor control in depositing thinner films, increased impact of interface states or exciton diffusion away from EML into HTL which has lower efficiency of radiative recombination; none of these effects are included in the simulation models.

Apart from these reasons, more recently, Young et al. [29] reported absorption spectrum of NPB cation to be at similar energies as a blue OLED emission. With this spectral overlap and a large Förster radius in a blue OLED, they ascribed quenching of emission at the HTL (NPB)/EML interface. Our simulation of the devices also indicates accumulation of holes (and thus NPB cation) at this interface. Hence, blue emission from the OLED in which the number of HTL/EML interfaces is increased is a balance of two opposing phenomena, the increased emission due to reasons as simulated here and its decrease due to quenching by NPB cation. This clearly explains why the EL efficiency decreases in Device 4, after an increase in Device 3.

#### 4. Conclusions

In conclusion, we have fabricated a standard blue OLED (Devices 1 and 2), in which we have an energy barrier to hole transport between HTL and EML, but no barrier for electrons. Therefore, instead of a conventional method in which a separate hole blocking layer is introduced to increase luminance, we have exploited this hole blocking feature in a standard device by inserting multiple layers of HTL and EML of a blue OLED and achieved excellent improvement in device current and power efficiency. This

can be attributed to the increased recombination probability at the HTL/EML interfaces with only a marginal increase in operating voltage. Selecting materials that exhibit HOMO level offset between HTL and EML, but not in the LUMO levels, helps develop an increased carrier concentration and consequent recombination rate near the interface. The same HOMO level mismatch between HTL and EML reduces the hole current in the device. Together these factors lead to an improved current efficiency. These observations were then explained using device simulation. The simulated results qualitatively agree with the experimental observations and corroborate the assumption that multiple HTL/EML interfaces increase the recombination rate if the HOMO level mismatch can help pile up holes at such interfaces and this leads to improved efficiency. In the present case the color co-ordinates are also improved upon introducing more than one HTL/EML interfaces because this reduces chances of radiative recombination at the ETL. It appears that this technique could be applied to red and green emitters as well.

#### Acknowledgments

This work was financially supported by Department of Science and Technology, Government of India, New Delhi and Samtel Color Ltd, New Delhi.

#### References

- [1] A.R. Duggal, J.J. Shiang, C.M. Heller, D.F. Foust, *Appl. Phys. Lett.* 80 (2002) 3470.
- [2] H. Kanno, Y. Hamada, H. Takahashi, *IEEE J. Sel. Top. Quant.* 10 (2004) 30.
- [3] J. Kido, M. Kimura, K. Nagai, *Science* 267 (1995) 1332.
- [4] S.-W. Wen, M.-T. Lee, C.H. Chen, *IEEE/OSA J. Disp. Technol.* 1 (2005) 90.
- [5] S. Tokito, T. Iijima, Y. Suzuri, H. Kita, *Appl. Phys. Lett.* 83 (2003) 569.
- [6] T. Nakayama, K. Hiyama, K. Furukawa, H. Ohtani, *J. SID* 16 (2008) 231.
- [7] P. Wellmann, M. Hofmann, O. Zeika, A. Werner, J. Birnstock, R. Meerheim, G. He, K. Walzer, M. Pfeiffer, K. Leo, *J. SID* 13 (2005) 393.
- [8] Y. Divayana, X.W. Sun, B.J. Chen, G.Q. Lo, C.Y. Jiang, K.R. Sarma, *Appl. Phys. Lett.* 89 (2006) 173511.
- [9] Y. Divayana, X.W. Sun, *Org. Electron.* 9 (2008) 136.
- [10] C.-H. Liao, M.-T. Lee, C.-H. Tsai, C.H. Chen, *Appl. Phys. Lett.* 86 (2005) 203507.
- [11] F. Wei, X. Zhang, J. Cao, M.A. Khan, W. Zhu, X. Jiang, Z. Zhang, *Displays* 28 (2007) 186.
- [12] X.R. Wang, J.S. Chen, H. You, D.G. Ma, R.G. Sun, *Jpn. J. Appl. Phys.* 44 (2005) 8480.
- [13] S.W. Culligan, A.C.-A. Chen, J.U. Wallace, K.P. Klubek, C.W. Tang, S.H. Chen, *Adv. Funct. Mater.* 16 (2006) 1481.
- [14] K. Walzer, B. Maennig, M. Pfeiffer, K. Leo, *Chem. Rev.* 107 (2007) 1233.
- [15] Y. Divayana, B.J. Chen, X.W. Sun, K.S. Sarma, *Appl. Phys. Lett.* 88 (2006) 083508.
- [16] Y. Kijima, N. Asai, S.I. Tamura, *Jpn. J. Appl. Phys.* 1 38 (1999) 5274.
- [17] D. Ma, C.S. Lee, S.T. Lee, L.S. Hung, *Appl. Phys. Lett.* 80 (2002) 3641.
- [18] Y. Qiu, Y. Gao, L. Wang, P. Wei, L. Duan, D. Shang, G. Dong, *Appl. Phys. Lett.* 81 (2002) 3540.
- [19] J. Takada, H. Awaji, M. Koshioka, A. Nakajima, W.A. Nevin, *Appl. Phys. Lett.* 61 (1992) 2184.
- [20] L. Wang, Y. Gao, Y. Kan, Z. Shu, Y. Qiu, *Jpn. J. Appl. Phys.* 43 (2004) L63.
- [21] B. Ruhstaller, T. Beierlein, H. Riel, S. Karg, J.C. Scott, W. Riess, *IEEE J. Sel. Top. Quant. Electron* 9 (2003) 723.
- [22] B. Ruhstaller, S.A. Carter, S. Barth, H. Riel, W. Riess, J.C. Scott, *J. Appl. Phys.* 89 (2001) 4575.
- [23] J.C. Scott, G.G. Malliaras, *Chem. Phys. Lett.* 299 (1999) 115.
- [24] G.G. Malliaras, J.C. Scott, *J. Appl. Phys.* 85 (1999) 7426.

- [25] B.K. Crone, P.S. Davids, I.H. Campbell, D.L. Smith, *J. Appl. Phys.* 87 (2000) 1974.
- [26] P.S. Davids, I.H. Campbell, D.L. Smith, *J. Appl. Phys.* 82 (1997) 6319.
- [27] Y. Qiu, Y. Gao, P. Wei, L. Wang, *Appl. Phys. Lett.* 80 (2002) 2628.
- [28] G. Cheng, S. Qiu, F. Li, J. Feng, Y. Ma, S. Liu, *Jpn. Soc. of Appl. Phys.* 2 4A (2003) 376.
- [29] R.H. Young, J.R. Lenhard, D.Y. Kondakov, T.K. Hatwar, *SID. Int. Symp. Dig.* 705 (2008).

its excellent electrical characteristics. However, it has been reported that the processing condition of C-PVP requires very high temperature (higher than 175 °C) rendering C-PVP unsuitable to fabricate electronic devices on various flexible substrate [22–31]. It has been reported that cross-linking reaction between PVP and cross-linker (CLA) occurs at high temperature and it enhances the mechanical, thermal and electrical properties of C-PVP. However, we believe there is high possibility that the processing temperature of C-PVP can be reduced much below 100 °C.

In this paper, we report low-temperature processability of poly(4-vinylphenol) based gate dielectric by investigating the effect of composition and processing temperature on the thermal, mechanical and electrical characteristics of the gate dielectric. We also report the fabrication of flexible OTFT and complementary inverter with the low-temperature processable C-PVP. In order to investigate the effect of composition and processing conditions on mechanical, thermal and electrical properties of gate dielectrics, we have prepared six gate dielectrics based on PVP (G1–G6). The results and discussion section begins with the preparation of the gate dielectrics and their physical properties according to the composition and processing condition using pencil hardness test, thermogravimetry analysis, contact angle measurement and electrical analysis. It is followed by a discussion for the fabrication and performance of OTFTs with the six gate dielectrics and complementary inverter on a flexible substrate.

## 2. Experimental

### 2.1. Materials

Pentacene and Copper hexafluorophthalocyanine (F16CuPc) for the active layer formation were purchased from Aldrich Company and used without further purification. G1 and G2 Gate dielectric solutions were prepared from 10 wt.% poly(4-vinylphenol) (PVP) ( $M_w = 20,000$  g/mol) in *n*-butanol and *n*-propanol, respectively, and followed by curing at 60 °C/10 min and 125 °C/60 min for G1 and at 40 °C/10 min and 70 °C/60 min under vacuum ( $10^{-2}$  Torr) for G2. G3, G4 and G5 gate dielectric solutions was prepared from 10 wt.% PVP and 5 wt.% cross-linking

agent (CLA), poly(melamine-co-formaldehyde) methylated ( $M_n = 511$  g/mol) in PGMEA, *n*-butanol and *n*-propanol, respectively. The spin-coated films were cured at 80 °C/10 min and 175 °C/60 min under vacuum ( $10^{-2}$  Torr) for G3, at 60 °C/10 min and 125 °C/60 min under vacuum ( $10^{-2}$  Torr) for G4 and at 40 °C/10 min and 70 °C/60 min under vacuum ( $10^{-2}$  Torr) for G5. G6 gate dielectric solution was prepared from 6 wt.% PVP and 3 wt.% CLA in *n*-propanol and cured at 40 °C/10 min and 70 °C/60 min under vacuum ( $10^{-2}$  Torr).

### 2.2. Device fabrication

Top-contact pentacene OTFTs were fabricated on a glass substrate on which a 200 nm indium tin oxide (ITO) layer was patterned as the gate electrode by a conventional photolithographic method. The ITO/glass substrate was cleaned using the general cleaning process for electronic application: sonication in detergent, deionized water, acetone, and isopropanol in that order for 15 min at room temperature. The gate dielectrics solution was spin-coated on top of the ITO gate electrode as a gate insulator and then cured under the preparation conditions summarized in Table 1. A 50 nm thick pentacene layer was deposited on top of the gate dielectric through a shadow mask by a thermal evaporation at a pressure of  $5 \times 10^{-6}$  Torr. The evaporation rate of pentacene and substrate temperature were 0.3 Å/s and 90 °C, respectively. OTFTs were then completed by thermally evaporating a 50 nm thick source and drain gold electrode on top of the pentacene layer through a shadow mask (channel length ( $L$ ) = 50 μm and width ( $W$ ) = 1000 μm). Metal–insulator–metal (MIM) device were prepared for capacitance and leakage current measurements of the gate dielectrics. The MIM devices were completed by evaporating the top gold electrode. The final thickness of gate dielectric films were controlled to 500 nm. The active area of MIM device was 1.75 mm<sup>2</sup>. Flexible complementary inverters were fabricated on an ITO coated polyethersulfone (PES) substrate. The gate dielectrics solution was spin-coated on top of the ITO gate electrode and then cured under the preparation conditions summarized in Table 1. Then, a 50 nm thick pentacene and copper hexafluorophthalocyanine (F16CuPc) were deposited by a vacuum thermal evaporation for a p-type and n-type active layer, respectively. The deposition rate and substrate temperature were 0.3 Å/s and 90 °C, respec-

**Table 1**  
Solution composition, curing condition and physical and electrical properties of the gate dielectrics.

	Composition (PVP wt%/CLA wt%)	Curing temp/ time (°C/min) <sup>a</sup>		Thickness (nm)	Solvent (bp/°C)	Contact angle (°)	Capacitance (pF/mm <sup>2</sup> )
G1	10/0	60/10	125/60	350	<i>n</i> -Butanol (117.2)	79	70–75
G2	10/0	40/10	70/60	700	<i>n</i> -Propanol (97)	71	35–40
G3	10/5	80/10	175/60	600	PGMEA <sup>b</sup> (146)	80	40–45
G4	10/5	60/10	125/60	400	<i>n</i> -Butanol	80	70–75
G5	10/5	40/10	70/60	700	<i>n</i> -Propanol	72	35–40
G6	6/3	40/10	70/60	300	<i>n</i> -Propanol	71	75–80

<sup>a</sup> All gate dielectrics were cured under vacuum ( $10^{-2}$  Torr). First and second column corresponds pre-baking and post curing temperature and time, respectively.

<sup>b</sup> Propylene glycol monomethyl ether acetate.



tively. The complementary inverter was completed by forming a 50 nm thick gold electrode on top of the active semiconductor layer. The channel length and width for p-type OTFT were 250 and 200  $\mu\text{m}$ , respectively. The channel length and width for n-type OTFT were 50 and 4000  $\mu\text{m}$ , respectively.

### 2.3. Characterizations

The thickness of gate dielectrics was determined using an AMBIOS XP-100 surface profiler. All atomic force microscopy (AFM) images (512 pixels wide) of the surface of gate dielectrics were taken with a Digital Instrument Nanoscope IV operating in tapping mode in air using a low-force imaging technique (a small tip-sample contact area), which is beneficial for high-resolution imaging of polymers. Water contact angle on the gate dielectrics was measured using DSA100 drop shape analyzer. The electrical characterization of OTFT and complementary inverter were carried out using a HP4145B semiconductor parameter analyzer controlled by LabView program. Capacitance of the gate dielectrics was measured with a HP 4294A LCR meter. All electrical measurements of the devices were carried out in air without any encapsulation. Thermogravimetry analysis was carried out using PERKIN ELMER thermogravimetry analyzer TGA 7. Pencil hardness test of gate dielectrics was measured with WA-008 pencil hardness tester.

## 3. Results and discussion

Fig. 1 shows the chemical structure of PVP and C-PVP gate dielectric along with the chemical structure of CLA used for the fabrication of OTFT and complementary inverter. For this study six gate dielectrics (labeled as from G1 to G6) were prepared by spin coating the gate dielectric solutions in organic solvents with a different boiling temperature. The spin-coated films were further cured under different processing conditions for the preparation of the gate dielectrics. Organic solvents used for the preparation of the gate dielectrics were PGMEA (b.p. 146 °C), *n*-butanol (b.p. 117 °C) and *n*-propanol (b.p. 97 °C).

G1 and G2 gate dielectrics were prepared by spin coating a solution composed of only PVP ( $M_w = 20,000$  g/mol) in *n*-butanol (G1) and *n*-propanol (G2), followed by curing

at 125 °C (G1) and 70 °C (G2). Other gate dielectrics (G3–G6) were prepared by spin coating a solution composed of PVP and cross-linking agent, poly(melamine-co-formaldehyde) methylated ( $M_n = 511$  g/mol, CLA) in different organic solvents, followed by curing at different temperature; G3: PGMEA and 175 °C, G4: *n*-butanol and 125 °C, G5: *n*-propanol and 70 °C and G6: *n*-propanol and 70 °C. G5 and G6 were prepared under the same process condition except that the concentration of the two solutions is different for the thickness control. The composition of the gate dielectrics, processing condition, thickness and physical and electrical properties of G1~G6 were summarized in Table 1.

It is well-known that cross-linked polymer thin-film usually shows stronger mechanical properties than non-cross-linked one due to the network structure formation between polymer chains by a cross-linking reaction. We expect that G3–G6 with CLA have the network structure and thus their mechanical and thermal properties are stronger than G1 and G2. In order to investigate mechanical properties of the gate dielectrics, we carried out pencil hardness test for G1, G3, G4 and G5 gate dielectric deposited on ITO/glass substrate and the results were shown in Fig. 2a. Gate dielectric G1 (PVP only) was completely removed by 4H pencil. Gate dielectric G3, which was prepared by the method reported previously by other groups (cured at higher than at 175 °C) [22–31], showed improved mechanical properties, little scratch by 4H pencil. This is because the linear structured main chain of PVP was changed to network structured one through a cross-linking process by the CLA at that high temperature. Gate dielectric G4 and G5 cured at 125 °C and 70 °C, respectively, showed comparable mechanical properties to that of G3 and much better than G1. From the pencil hardness test results, it can be inferred that the cross-linking reaction can be occurred at as low as 70 °C so that the curing temperature of gate dielectrics based on PVP can be reduced to 70 °C by simply changing the solvent from PGMEA to *n*-propanol with a lower boiling temperature.

In order to further support the possibility of cross-linking reaction at that low-temperature, we carried out thermogravimetry analysis (TGA) for the G1, G3, G4 and G5 gate dielectrics as shown in Fig. 2b. For the TGA measurement all the gate dielectric solutions were spin-cast on a glass substrate and pre-cured according to the preparation

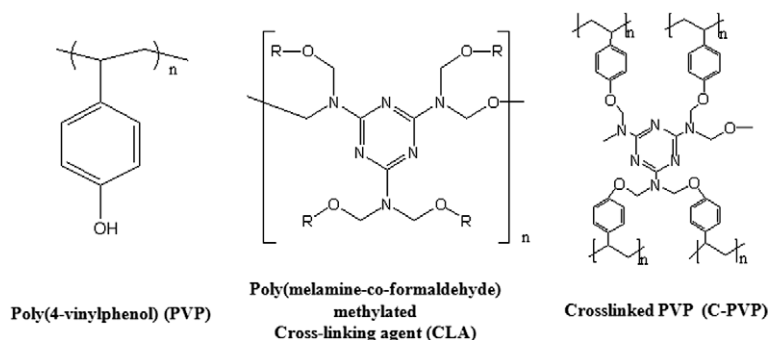
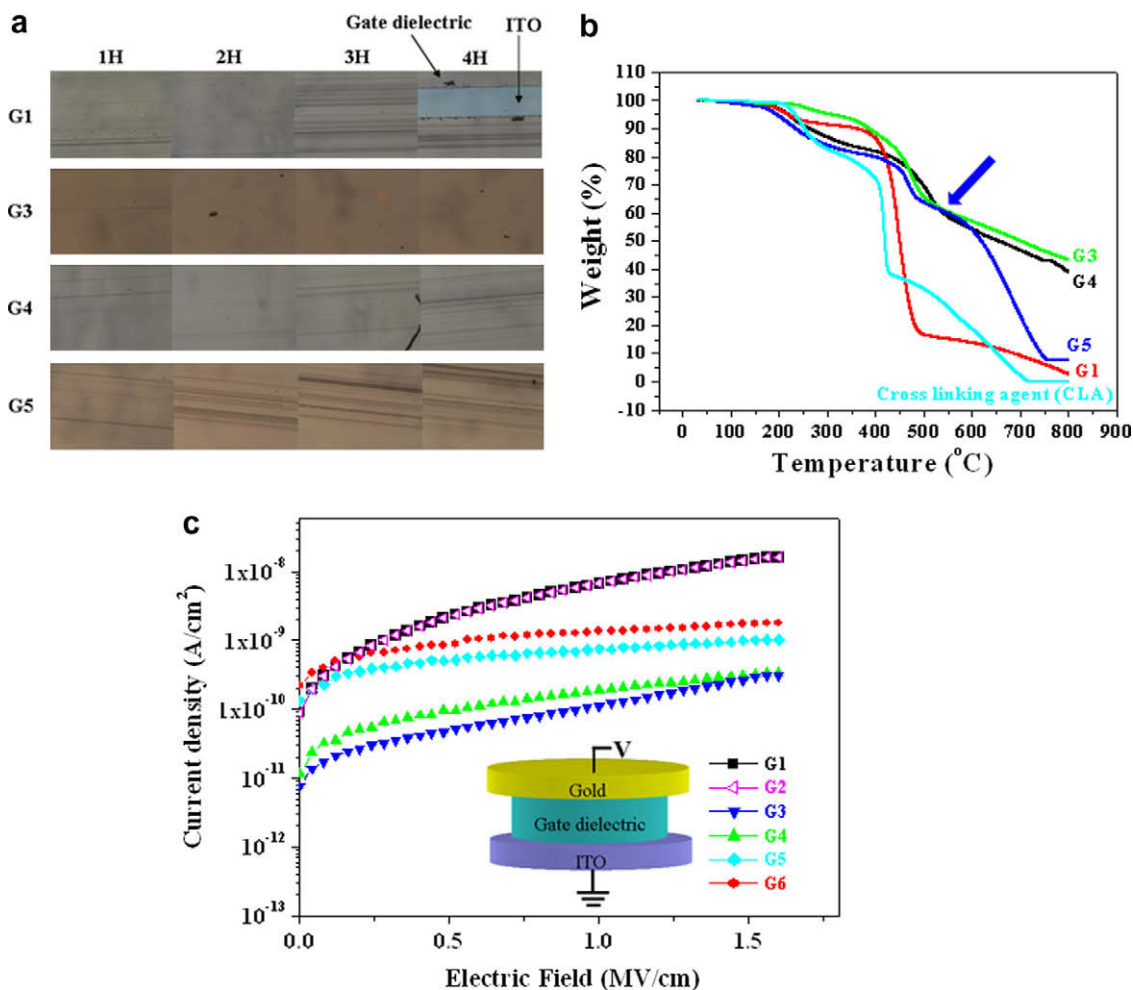


Fig. 1. Chemical structure of poly(4-vinylphenol) (PVP), poly(melamine-co-formaldehyde) methylated (cross-linking agent, CLA) and cross-linked PVP (C-PVP).



**Fig. 2.** (a) Pencil hardness test, (b) thermogravimetry analysis (TGA) thermograms for the G1, G3, G4 and G5 gate dielectrics and CLA and (c) leakage current density as a function of applied electric field ( $J$ - $E$ ) for all gate dielectrics.

method for each gate dielectric. Then the films were peeled out from the substrate and used for the TGA measurement. An abrupt weight loss was observed at  $410^{\circ}\text{C}$  for G1 and the residual weight around  $600^{\circ}\text{C}$  is almost zero. It indicates that the linear structured main chain of G1 is thermally weak and starts to decompose around  $410^{\circ}\text{C}$  and decomposed almost completely around  $600^{\circ}\text{C}$ .

On the other hand, for G3 prepared from PVP and CLA solution in PGMEA, no abrupt weight loss was observed in the entire range of temperature and residual weight was about 45% even at  $800^{\circ}\text{C}$  indicating that linear structured main chain of PVP was changed to network structured one through a cross-linking reaction by the CLA at  $175^{\circ}\text{C}$ . For G4 prepared from PVP/CLA solution in *n*-butanol by a curing at  $125^{\circ}\text{C}$ , it showed almost identical thermal behavior to G3 indicating that the cross-linking reaction has been fully occurred even at  $125^{\circ}\text{C}$ . G5 prepared from PVP/CLA solution in *n*-propanol by a curing at  $70^{\circ}\text{C}$  showed similar thermal behavior to G3 and G4 up to  $600^{\circ}\text{C}$  (indicated by an arrow), but when further heated, weight loss was observed. Please note that the first weight

loss was observed in the temperature range of  $200$ – $300^{\circ}\text{C}$ . The different behavior is caused by the different pre-curing condition for TGA samples (See Table 1). In order to make sure that the different thermal behavior of G3, G4 and G5 from that of G1 and G2 is not caused by CLA itself, we recorded TGA thermogram of CLA. The thermogram of CLA shows very different thermal behavior from the gate dielectrics. That is, the CLA starts to decompose before PVP does and is thermally very weak. It indicates that the better thermal behavior of G3, G4 and G5 than G1 is caused not by the added CLA but by a cross-linking reaction. In separate experiments we measured FT-IR spectra of G3 and G5. It was found that the two spectra were almost identical with each other. It gives us another indirect evidence for the cross-linking reaction between PVP and CLA at the low temperature.

The leakage current of gate dielectrics is one of the important concerns regarding high performance OTFTs. To determine the leakage current of the gate dielectrics, we prepared metal-insulator-metal (MIM) devices on the pre-cleaned ITO/glass substrates by sandwiching the gate

dielectric between bottom ITO and top gold electrode as shown in the inset of Fig. 2c. The active area was  $1.75 \text{ mm}^2$ . The plots of current density and an applied electric field ( $J$ - $E$ ) for the gate dielectrics are shown in Fig. 2c. It showed non-linear  $J$ - $E$  behavior, which is typical for MIM devices based on polymeric gate dielectric. Although the leakage current ( $1.0 \times 10^{-9} \text{ A/cm}^2$  at  $1.5 \text{ MV/cm}$ ) of G5 and G6 is higher than that ( $1.0 \times 10^{-10} \text{ A/cm}^2$  at  $1.5 \text{ MV/cm}$ ) of G3 and G4 cured at  $175^\circ\text{C}$  and  $125^\circ\text{C}$ , respectively, it is much lower than that ( $2.0 \times 10^{-8} \text{ A/cm}^2$  at  $1.5 \text{ MV/cm}$ ) of G1 and G2, which is PVP only gate dielectric cured at  $125^\circ\text{C}$  and  $70^\circ\text{C}$ , respectively. The breakdown voltage of the gate dielectrics was more than  $1.5 \text{ MV/cm}$ . Capacitance of the gate dielectrics was measured using the same MIM devices and the values was summarized in Table 1.

From the results of pencil hardness, TGA analysis and leakage current density measurement, it can be inferred again that the curing temperature of PVP based gate dielectrics can be reduced up to  $70^\circ\text{C}$  by choosing an appropriate solvent without any significant change in electrical, thermal and mechanical properties of the gate dielectrics.

The water contact angle on the gate dielectrics were measured and found to be in the range of  $71$ – $80^\circ$  (see Table 1) indicating that the composition and processing condition does not significantly influence surface properties of the gate dielectric. Fig. 3 shows the AFM images of pentacene deposited on gate dielectrics (G3, G4 and G6). Although the composition and curing conditions of the gate dielectrics are different from each other, the AFM images of pentacene are almost identical with each other having  $2$ – $3 \mu\text{m}$

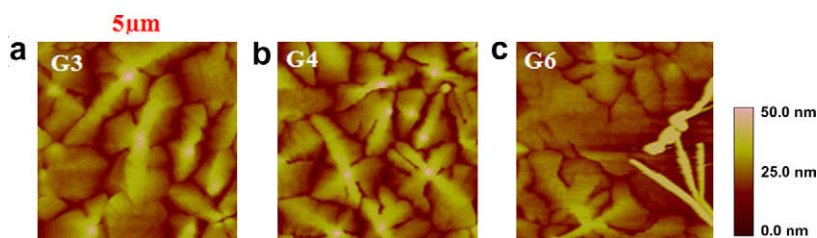


Fig. 3. AFM image of  $50 \text{ nm}$  thick pentacene film on (a) gate dielectrics G3, (b) gate dielectrics G4 and (c) gate dielectrics G6.

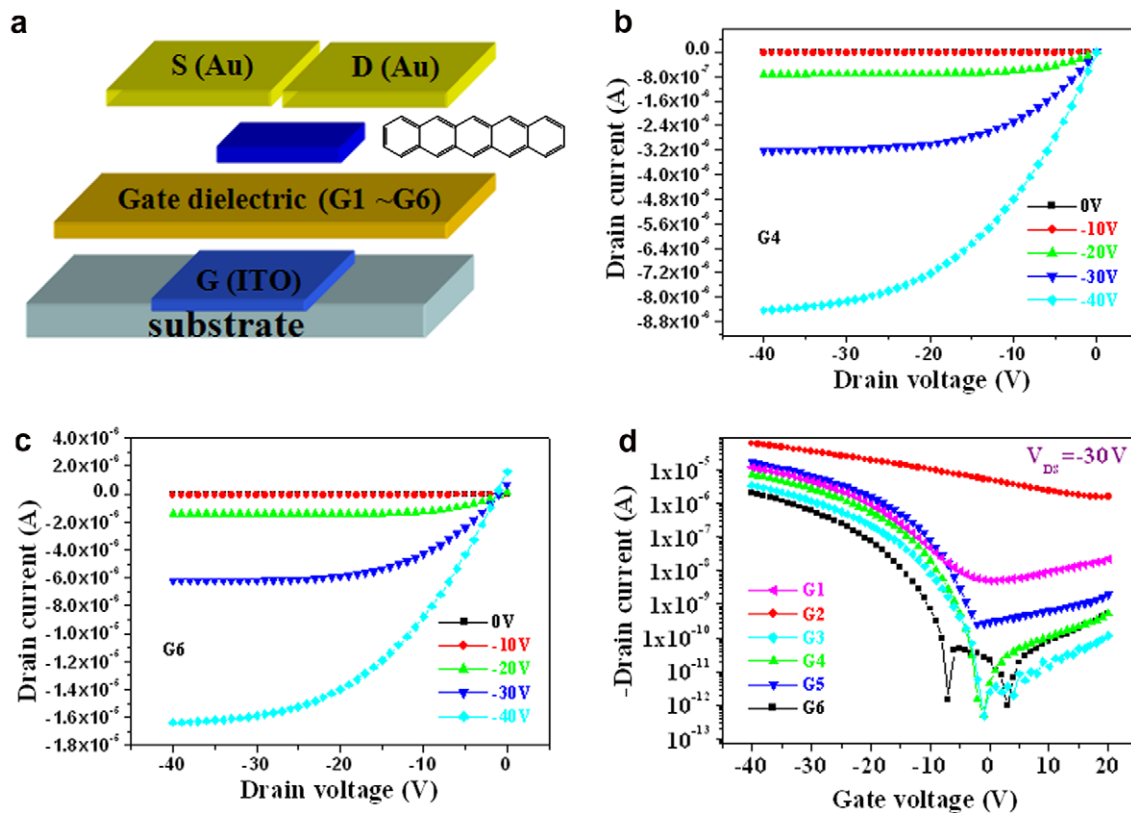


Fig. 4. (a) Schematic diagram of pentacene OTFTs. Output characteristic curves at various  $V_{gs}$  (from  $0 \text{ V}$  to  $-40 \text{ V}$  with a step of  $-10 \text{ V}$ ) for pentacene OTFTs with G4 (b) and G6 (c). Transfer characteristic curves (d) for pentacene OTFTs with all gate dielectrics (G1–G6). While  $V_{ds}$  was swept from  $+20$  to  $-40 \text{ V}$  and  $V_{ds}$  was set at  $-30 \text{ V}$ . The OTFT has a channel length of  $50 \mu\text{m}$  and a channel width of  $1000 \mu\text{m}$ .

**Table 2**

Performance parameters of pentacene OTFTs with the gate dielectrics. All parameters were extracted in the saturation region.

	$V_{th}$ (V)	$I_{on}/I_{off}$	$\mu$ (cm <sup>2</sup> /V s)	$ss$ (V/dec)
G1	−6 to −14	$7 \times 10^2$ – $2 \times 10^3$	0.13–0.25	7–11
G2	–	30	–	–
G3	−15 to −17	$7 \times 10^5$ – $2 \times 10^6$	0.1–0.13	0.7–0.9
G4	−13 to −15	$8 \times 10^5$ – $2 \times 10^6$	0.08–0.12	0.7–0.9
G5	−15 to −21	$1 \times 10^4$ – $1 \times 10^5$	0.07–0.11	0.8–2.8
G6	−8 to −13	$1 \times 10^4$ – $5 \times 10^4$	0.2–0.5	2.5–3.0

big leaf-like crystals. It tells us again that the composition and processing condition does not affect the surface property of gate dielectrics and growth of pentacene on them.

Based on the finding for low-temperature processability of PVP based gate dielectrics, we have fabricated OTFTs and

flexible complementary inverter. A top-contact geometry was used for analyzing the electrical characteristics of pentacene OTFTs. The device fabrication procedures are depicted in Fig. 4a. The output (drain current vs. drain voltage,  $I_{ds}$  vs.  $V_{ds}$ ) and transfer (drain current vs. gate voltage,  $I_{ds}$  vs.  $V_{gs}$ ) characteristic curves of the pentacene OTFTs with G1–G6 gate dielectrics are measured and are shown in Fig. 4b–d. The output curves of the OTFTs with G4 and G6 cured at 125 °C and 70 °C, respectively, at various  $V_{gs}$  (from 0 V to −40 V with a step of −10 V) are shown in Fig. 4b and c. It showed typical p-type characteristics with a clear transition from linear to saturation behavior. At a given  $V_{gs}$ ,  $I_{ds}$  initially increased linearly with small negative  $V_{ds}$  and then saturates at high voltage. Fig. 4d shows transfer characteristic curves of OTFTs with G1–G6, where  $V_{ds}$

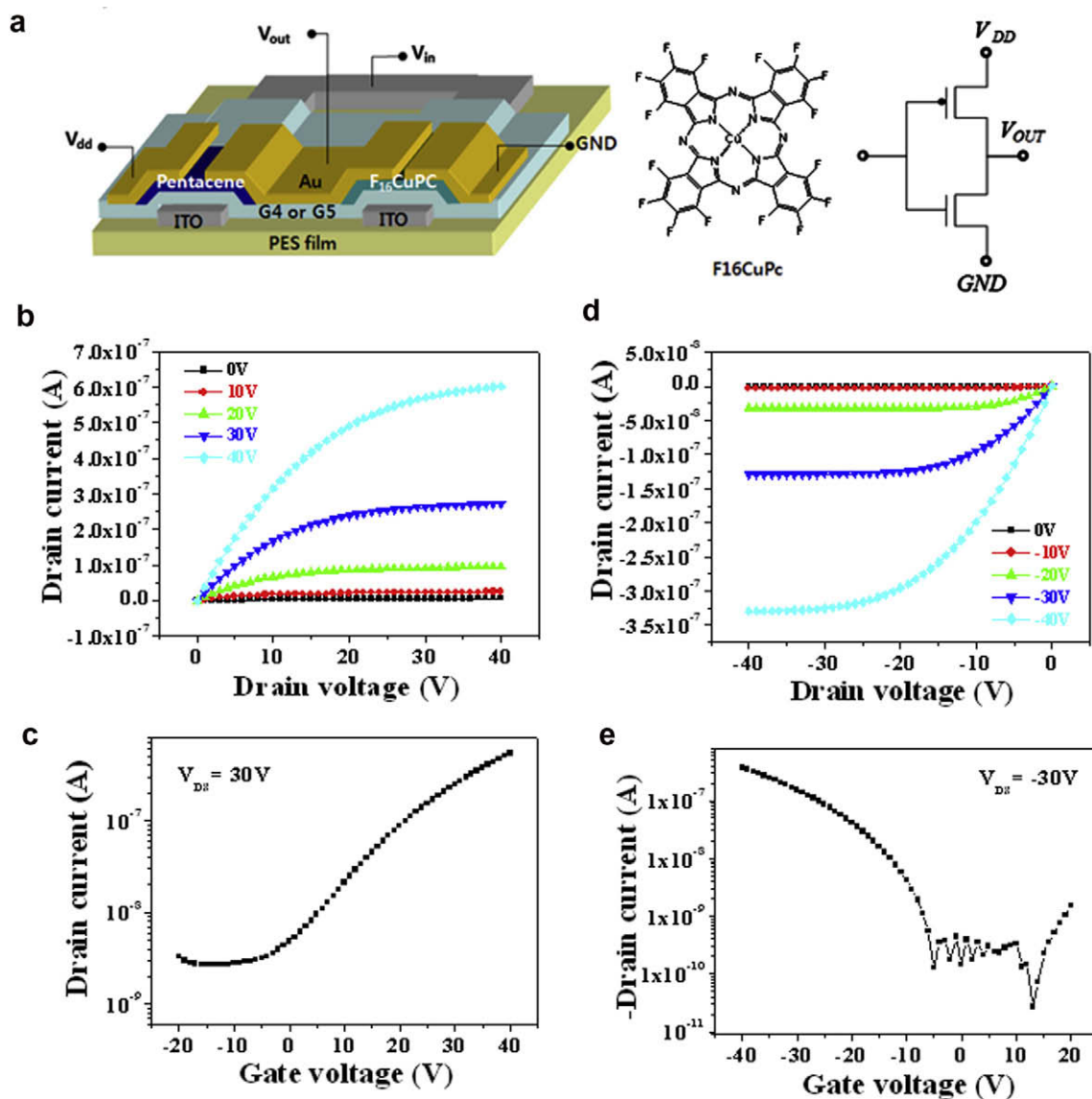


**Fig. 5.** (a) Schematic structure of the complementary inverter along with the chemical structure of F16CuPc as a n-type semiconductor, output (b) and transfer (c) characteristic curves of n-type OTFT ( $L = 50 \mu\text{m}$ ,  $W = 4000 \mu\text{m}$ ), and output (d) and transfer (e) characteristic curves of p-type OTFT ( $L = 250 \mu\text{m}$ ,  $W = 200 \mu\text{m}$ ) built in complementary inverter with G5 gate dielectric (cured at 70 °C) on a PES substrate.

was swept from +20 to –40 V and  $V_{ds}$  was set at –30 V. The field-effect mobility ( $\mu$ ) was extracted from the plot of  $\sqrt{I_{ds}}$  vs.  $V_{gs}$  in a saturation regime based on the following equation:

$$I_{ds} = \frac{WC_i}{2L} \mu (V_{gs} - V_{Th})^2 \quad (1)$$

where  $W$ ,  $L$ ,  $V_{Th}$  and  $C_i$  are channel width, channel length, threshold voltage and capacitance per unit area, respectively.  $V_{Th}$  was determined from the plot of the square root of the  $I_{ds}$  and  $V_{gs}$  by extrapolating the measured data to  $I_{ds} = 0$ . The inverse subthreshold swing ( $ss$ ), which is a measure of how sharply the device transits from the OFF to the ON state, is given by

$$ss = \left[ \frac{d \log(I_{ds})}{dV_{gs}} \right]^{-1}$$

The performance parameters of the OTFTs with G1–G6 were summarized in Table 2.

The OTFTs with G1 and G2, which are PVP only gate dielectric cured at 125 °C and 70 °C, respectively, showed high leakage current caused by poor electrical characteristics of G1 and G2 (see Fig. 2c). The performance of OTFTs with G4 (cured at 125 °C) is almost identical to that of reference OTFT with G3 prepared by the curing condition reported previously (175 °C/1 h). Furthermore, the OTFTs with G5 and G6 (cured at 70 °C) showed much better performance than OTFTs with G1 and G2, and it showed comparable performance to the reference OTFT with G3 except for a little decrease of  $I_{ON}/I_{OFF}$  and increase of  $ss$ . This indicates that C-PVP can be prepared by curing at 70 °C using *n*-propanol with a lower boiling temperature instead of PGMEA and act as a good gate dielectric.

Based on the results of OTFTs, we prepared the flexible complementary inverter by integrating p- and n-type OTFTs on a single PES substrate through a thermal vacuum evaporation and spin coating process. Fig. 5a shows the schematic structure of the complementary inverter along with the chemical structure of F16CuPc. Pentacene and F16CuPc were used as p- and n-type semiconductor,

respectively, and G4 and G5 were used as a gate dielectric. The electrical characteristics of each p- and n-type OTFTs of the complementary inverter with G4 (cured at 125 °C) were measured right after fabrication. The calculated  $\mu$ ,  $V_{Th}$ ,  $I_{ON}/I_{OFF}$  and  $ss$  of the F16CuPc OTFT with a channel length and width of 50  $\mu\text{m}$  and 4000  $\mu\text{m}$  were  $0.24 \times 10^{-2} \text{ cm}^2/\text{Vs}$ , 14 V,  $3 \times 10^2$  and 10 V/dec, respectively. These device performance parameters are all similar to those of F16CuPc with silicon dioxide and polyimide gate dielectric indicating that the G4 is also suitable for a gate dielectric of n-type OTFT [32]. The calculated  $\mu$ ,  $V_{Th}$ ,  $I_{ON}/I_{OFF}$  and  $ss$  of the pentacene OTFT with a channel length and width of 250  $\mu\text{m}$  and 200  $\mu\text{m}$  were  $0.12 \text{ cm}^2/\text{Vs}$ , –12 V,  $3 \times 10^4$  and 1.8 V/dec, respectively.

Compared with the performance parameters of single pentacene OTFT with G4 (see Fig. 4), the pentacene OTFT of the complementary inverter shows a little worse performance. This may be due to the additional processes to fabricate the n-type OTFT and/or the longer channel length to match the  $I_{ds}$  of p- and n-type OTFTs for symmetric noise margin of the organic complementary inverter. We also have fabricated flexible complementary inverter with G5 gate dielectric, which is cured at 70 °C on a PES substrate. Fig. 5b and c show the output and transfer characteristic curves of the F16CuPc OTFT, respectively, and Fig. 5d and e shows the output and transfer characteristic curves of the pentacene OTFT, respectively. The calculated  $\mu$ ,  $V_{Th}$ ,  $I_{ON}/I_{OFF}$  and  $ss$  of the F16CuPc OTFT were  $0.3 \times 10^{-2} \text{ cm}^2/\text{Vs}$ , 7 V,  $1 \times 10^2$  and 20 V/dec, respectively. The calculated  $\mu$ ,  $V_{Th}$ ,  $I_{ON}/I_{OFF}$  and  $ss$  of the pentacene OTFT were  $0.18 \text{ cm}^2/\text{Vs}$ , –12 V,  $3 \times 10^3$  and 2.6 V/dec, respectively.

The performance of the inverter is almost similar to that of inverter with G4. Fig. 6 shows the voltage transfer ( $V_{out} - V_{in}$ ) characteristic curve of the complementary inverter with G4 and G5. The supply voltage ( $V_{DD}$ ) is 40 V. The swing range of  $V_{out}$  for both inverters is the same as  $V_{DD}$ , which ensures “zero” static power consumption in digital circuits. Fig. 6 also shows almost symmetric noise margin as intended. For the inverter with G4, the noise margins for low and high voltage are 17 V and 14 V,

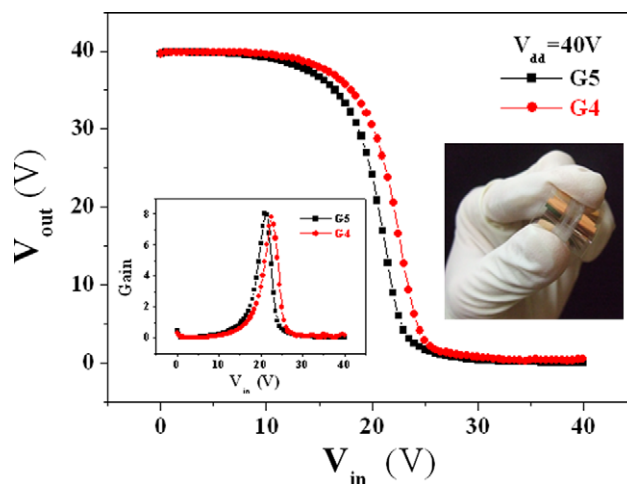


Fig. 6. The voltage transfer ( $V_{out} - V_{in}$ ) characteristic curve of the complementary inverter based on F16CuPc (n-type) and pentacene (p-type) OTFTs. Inset: the signal gain and the photograph of the inverter.

respectively. The logic threshold, i.e.  $V_{in}$  where  $V_{in}$  is equal to  $V_{out}$ , is 22.5 V and the maximum voltage gain ( $\partial V_{out}/\partial V_{in}$ ) of 7.8 is obtained at  $V_{in} = 22.5$  V. The inverter with G5 showed almost identical characteristics to that of the inverter with G4 as shown in Fig. 6. The logic threshold is 21 V and the maximum voltage gain ( $\partial V_{out}/\partial V_{in}$ ) of 8.1 is obtained at  $V_{in} = 21.0$  V. The photograph of the flexible complementary inverter is shown in the inset of Fig. 6.

#### 4. Conclusions

We have investigated the effect of composition and processing conditions on the thermal, mechanical and electrical properties of the PVP based gate dielectric using pencil hardness test, thermogravimetry analysis and electrical analysis. Unlike the reports telling that high processing temperature is required to prepare C-PVP gate dielectric, we found that the processing temperature can be reduced to up to 70 °C which allows most polymeric materials to be suitable to flexible substrate. Using the prepared low-temperature processable C-PVP gate dielectric we have successfully fabricated high performance pentacene and F16CuPc OTFTs, and flexible complementary inverter on a plastic substrate.

#### Acknowledgement

This study was supported by KOSEF through EPB Center (R11-2008-052-03003).

#### References

- [1] T.W. Kelley, P.F. Baude, C. Gerlach, D.E. Ender, D. Muires, M.A. Haase, D.E. Vogel, S.D. Thesis, Chem. Mater. 16 (2004) 4413.
- [2] C. Wang, P.J. Bos, Dispalys 25 (2004) 187.
- [3] P. Mach, S.J. Rodriguez, R. Nortrup, P. Wiltzius, J.A. Rogers, Appl. Phys. Lett. 78 (2001) 3592.
- [4] C.D. Sheraw, L. Zhou, J.R. Huang, D.J. Gundlach, T.N. Jackson, M.G. Kane, I.G. Hill, M.S. Hammond, J. Campi, B.K. Greening, J. Francl, J. West, Appl. Phys. Lett. 80 (2002) 1088.
- [5] C.D. Dimitrakopoulos, P.R.L. Malenfant, Adv. Mater. (Weinheim, Ger.) 14 (2002) 99.
- [6] H. Yan, Z. Chen, Y. Zheng, C. Newman, J.R. Quinn, F. Dotz, M. Kastler, A. Facchetti, Nature 457 (2009) 679.
- [7] Y.G. Seol, N.-E. Lee, S.H. Park, J.Y. Bae, Org. Electron. 9 (2008) 413.
- [8] A.L. Briseno, S.C.B. Mannsfeld, M.M. Ling, S. Liu, R.J. Tseng, C. Reese, M.E. Roberts, Y. Yang, F. Wudl, Z. Bao, Nature 444 (2006) 913.
- [9] Alejandro L. Briseno, Ricky J. Tseng, M.M. Ling, Eduardo H. L. Falcao, Y. Yang, F. Wudl, Z. Bao, Adv. Mater. 18 (2006) 2320.
- [10] Y.G. Seol, H.Y. Noh, S.S. Lee, J.H. Ahn, N.-E. Lee, Appl. Phys. Lett. 93 (2008) 013305.
- [11] H. Klauk, M. Halik, U. Zschieschang, G. Schmid, W. Radik, J. Appl. Phys. 92 (2002) 5259.
- [12] S.H. Jin, J.W. Yu, C.A. Lee, B.G. Park, J.D. Lee, J.H. Lee, Society for Information Display International Symposium 34 (2003) 1088.
- [13] Y. Yun, C. Pearson, M.C. Petty, J. Appl. Phys. 105 (2009) 034508.
- [14] S. Pyo, Y.J. Lee, J.Y. Jeon, M.H. Yi, S.K. Kwon, J. Appl. Phys. 99 (2006) 073711.
- [15] J. Shim, L. Jung, S. Pyo, Y.K. Kim, Thin Solid Films 441 (2003) 284.
- [16] T. Inenaga, J. Matsushita, M. Yamada, H. Fukai, Y. Nishioka, Mol. Cryst. Liq. Cryst. 471 (2007) 195.
- [17] X. Zhang, W.J. Potscavage Jr., S. Choi, B. Kippelen, Appl. Phys. Lett. 94 (2009) 043312.
- [18] Dhananjay, C. Chu, C. Ou, M. Wu, Z. Ho, K. Ho, S. Lee, Appl. Phys. Lett. 92 (2008) 232103.
- [19] S. Tatemichi, M. Ichikawa, S. Kato, T. Koyama, Y. Taniguchi, Phys. Stat. Sol. 2 (2008) 47.
- [20] J. Wang, B. Wei, J. Zhang, Semicond. Sci. Technol. 23 (2008) 055003.
- [21] M.S. Oh, K. Lee, K.H. Lee, S.H. Cha, J.M. Choi, B.H. Lee, M.M. Sung, S. Im, Adv. Funct. Mater. 19 (2009) 726.
- [22] D.K. Hwang, K. Lee, J.H. Kim, S. Im, J.H. Park, E. Kim, Appl. Phys. Lett. 89 (2006) 93507.
- [23] F.C. Chen, C.W. Chu, J. He, Y. Yang, J. Lin, Appl. Phys. Lett. 85 (2004) 15.
- [24] C.W. Chu, C.F. Sung, Y.Z. Lee, K. Cheng, Org. Electron. 9 (2008) 262–266.
- [25] H.S. Byun, Y. Xu, C.K. Song, Thin Solid Films 493 (2005) 278.
- [26] D.K. Hwang, C.S. Kim, J.M. Choi, K. Lee, J.H. Park, E. Kim, H.K. Baik, J.H. Kim, S. Im, Adv. Mater. 18 (2006) 2299.
- [27] D.K. Hwang, K. Lee, J.H. Kim, S. Im, J.H. Park, E. Kim, Appl. Phys. Lett. 89 (2006) 093507.
- [28] H. Klauk, M. Halik, U. Zschieschang, G. Schmid, W. Radlik, J. Appl. Phys. 92 (2002) 9.
- [29] M. Halik, H. Klauk, U. Zschieschang, G. Schmid, S. Ponomarenko, S. Kirchmeyer, W. Weber, Adv. Mater. 15 (2003) 11.
- [30] M. Halik, H. Klauk, U. Zschieschang, T. Kriem, G. Schmid, W. Radlik, Appl. Phys. Lett. 81 (2002) 289.
- [31] D.K. Hwang, K. Lee, J.H. Kim, S. Im, J.H. Park, E. Kim, C.S. Kim, H.K. Baik, Appl. Phys. Lett. 88 (2006) 243513.
- [32] Y. Oh, S. Pyo, M. Yi, S. Kwon, Org. Electron. 7 (2006) 77.

amorphous Si (a-Si:H) TFTs [11–15]. Low temperature a-Si:H thin-film transistors are generally n-channel [11,12,16] while organic semiconductors such as pentacene are generally p-channel [9,17,18]. Recently, pentacene-based thin-film transistors have had significant improvement, and are now comparable to a-Si:H TFTs [7,9,19]. Also, organic semiconductors showing n-type behavior with mobilities in the order of those of a-Si:H have been achieved; although this has been achieved in relatively simple devices [20,21].

In this work we demonstrate a novel CMOS integration approach that incorporates inorganic a-Si:H as the n-channel element and pentacene as the p-channel element using photolithography-based processing. Furthermore, the devices are fabricated on flexible substrates (PEN) and the maximum processing temperature is kept below the glass transition temperature of the substrate (<180 °C). Although CMOS devices have recently been demonstrated [5,7,9,20,22–24], our integration approach demonstrates an all-photolithography-based integration to fabricate several logic components integrated in the same substrate and compatible with current backplane manufacturing technology.

## 2. Results and discussion

The integration of a-Si:H and pentacene has been demonstrated in rigid substrates and by interconnecting the discrete devices [5,7]. As opposite to those initial reports, the CMOS integration scheme presented in this work involves fabricating the CMOS devices in a flexible substrate and using standard interconnection technology. The process starts by fabricating the a-Si:H nMOS devices first, followed by the pentacene pMOS devices. The resulting CMOS circuits are then encapsulated using parylene as passivation and vias are opened for further testing. A schematic cross-section and optical photograph of the CMOS devices on PEN are shown in Fig. 1a and b, respectively.

The detailed process is as follows. After planarization of the flexible substrate (PEN) the nMOS TFTs (a-Si:H) are fabricated using an inverted staggered architecture with

the gate underneath and the semiconductor and source/drain on top (Fig. 1a). The components of the a-Si:H TFTs are: molybdenum as gate metal, Si<sub>3</sub>N<sub>4</sub> gate dielectric, and aluminum as the source-drain metallization. Data lines and contacts are formed by deposition and patterning the n<sup>+</sup> doped a-Si:H via PECVD and Al metal by DC sputtering. The maximum process temperature for nMOS fabrication was 180 °C. This process is completed at the Flexible Display Center at Arizona State University.

Typical current voltage characteristics for the resulting n-channel a-Si:H TFTs are shown in Fig. 2. From Fig. 2a we extracted a saturation mobility of 0.75 cm<sup>2</sup>/V s with an  $I_{on}/I_{off}$  current ratio >10<sup>8</sup>. Subthreshold slope is approximately 0.35 V/decade and threshold voltage of ~1.14 V. Fig. 2b shows a typical  $I_{DS}-V_{DS}$  family of curves for the n-channel a-Si:H process described above. Well behaved transistors characteristics are observed.

After nMOS fabrication, pentacene-based pMOS TFTs are fabricated at UT-Dallas. pMOS TFTs are fabricated using a bottom gate approach. In our process, the gate insulator (parylene) is deposited after the inter-level dielectric (ILD) [12,25,26]. This fabrication process includes aluminum as gate metal, parylene as ILD (500 nm), parylene (100 nm) as gate dielectric and gold as source-drain contacts and interconnect metallization. The pMOS fabrication process starts with the ILD (0.5 μm of parylene) deposition over Al gate metal formed during nMOS fabrication. The ILD is deposited at room temperature and patterned to define the metal gate vias and channel region (Fig. 1a). Next, gold (100 nm) is deposited by e-beam evaporation and patterned to form source-drain contacts and interconnects. Pentacene (150 nm) is then deposited at room temperature to create the active channel [27]. Finally, the devices are capped using a parylene encapsulation process and vias are opened for device testing. As we reported, this approach provides a pristine and hydrophobic surface, which provides a favorable surface for pentacene growth [25,26]. If the gate dielectric layer is patterned before patterning the ILD layer the gate dielectric surface becomes hydrophilic due to exposure to the RIE oxygen resulting in degraded pentacene performance [25].

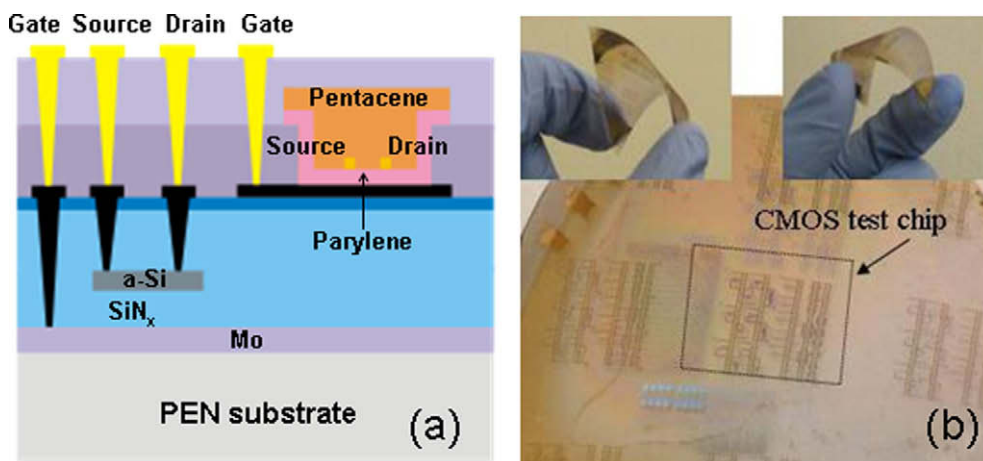


Fig. 1. (a) Cross-section of the integrated flexible CMOS. (b) Photograph of flexible CMOS fabricated on PEN.

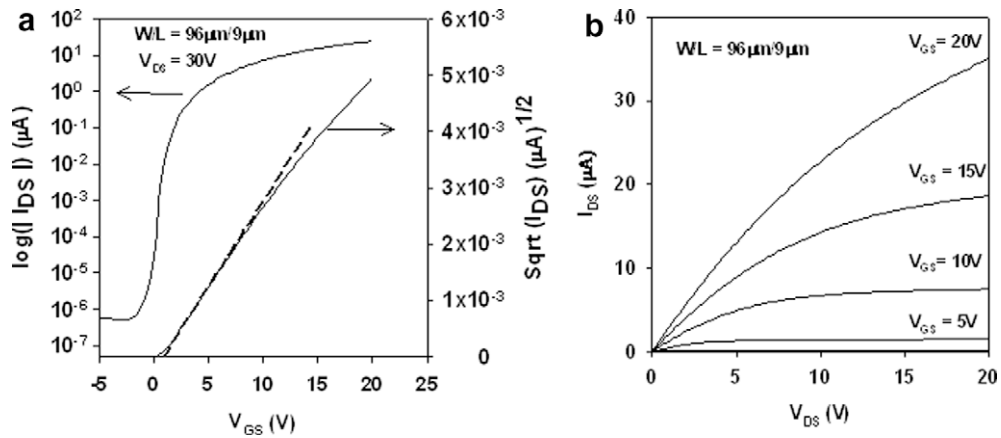


Fig. 2. (a)  $I_{DS}$ – $V_{GS}$  for a-Si:H nMOS TFTs. (b)  $I_{DS}$ – $V_{DS}$  for a-Si:H nMOS TFTs.

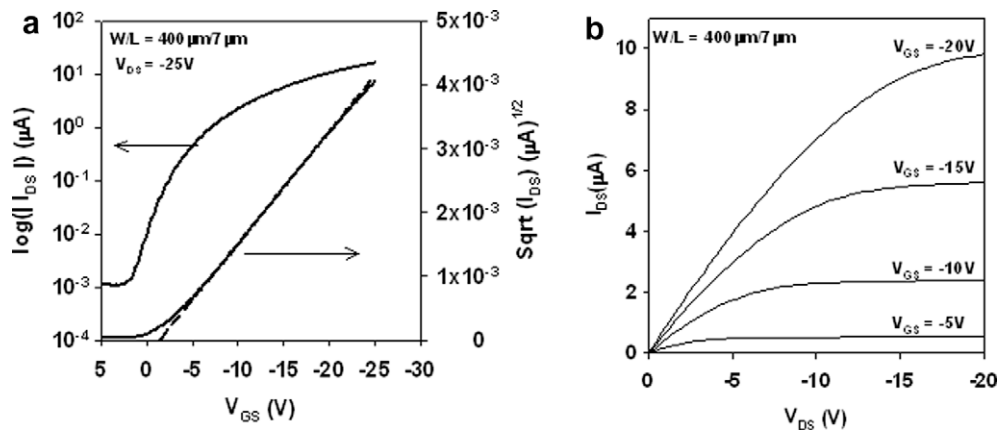


Fig. 3. (a)  $I_{DS}$ – $V_{GS}$  for pentacene pMOS TFTs. (b)  $I_{DS}$ – $V_{DS}$  for pentacene pMOS TFTs. Excellent transistor behavior is observed.

Fig. 3b shows typical  $I_{DS}$ – $V_{DS}$  for the pMOS transistors obtained using the process described above. From these results we extracted a hole mobility of  $(0.05 \text{ cm}^2/\text{V s})$  and threshold voltage of  $-1.4 \text{ V}$ . Fig. 3b shows the  $I_{DS}$ – $V_{DS}$  curve-family, where drain-source voltage ( $V_{DS}$ ) is swept from  $0 \text{ V}$  to  $-25 \text{ V}$  for different gate voltages ( $V_{GS}$ ). Excellent transistor characteristics are observed. The resulting circuits fabricated with the integration approach described above are discussed next.

Fig. 4a shows an optical image of a CMOS inverter, fabricated with the process described above. A typical voltage transfer curve for inverters is shown in Fig. 4b. The CMOS inverter has  $W/L$  for pMOS and nMOS of  $500/5$  and  $100/11 \mu\text{m}$ , respectively. The inverter transition point is at  $V_{DD}/2$ , as expected from our circuit simulations, and shows a maximum DC gain of  $\sim 16$ . Figs. 5a and b show optical images and input–output characteristics for 2-input NAND and NOR gates, respectively. In both cases, for input A, a square wave with a  $20 \text{ ms}$  period and  $50\%$  duty cycle is used; for input B, a square wave with a  $40 \text{ ms}$  period and  $50\%$  duty cycle is used. As expected for a NAND gate, the output stays high except when both A and B are logic high.

On the other hand, for NOR gates the output stays low except when both A and B are logic low, as expected. These results demonstrate that with our integration approach we can achieve working CMOS devices on flexible substrates.

It is well known that many types of TFTs are electrically unstable, and their performance degrades with electrical usage and/or ambient conditions [28]. We have performed initial electrical stress testing of the integrated devices and the results are shown in Fig. 6. Fig. 6a (top) shows an optical image of a pMOS device from an inverter before stress; no noticeable defects observed. However, after stress, defects in the dielectric appear and are likely due to weak spots present in the parylene dielectric. Recently, we reported detailed time dependent dielectric breakdown (TDDB) studies of parylene [29]. We demonstrated that TDDB has a power law distribution and that the parylene breakdown is mainly driven by defects in the dielectric. This is likely the cause of the parylene gate dielectric breakdown observed in the pMOS devices used to fabricate our CMOS circuits (Fig. 6b). Nevertheless, the devices functioned for approximately  $8 \text{ h}$  before failure ( $50\%$  duty cycle).



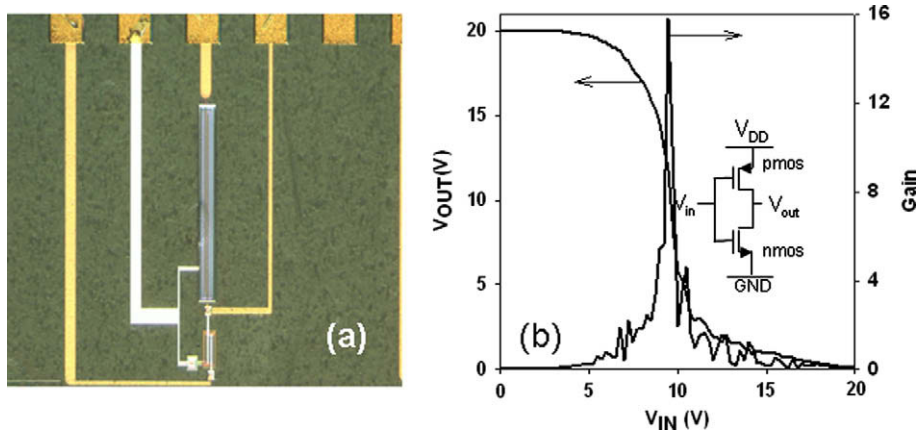


Fig. 4. (a) Optical image of the resulting CMOS inverter. (b) Voltage transfer curve and gain of the hybrid CMOS inverter.

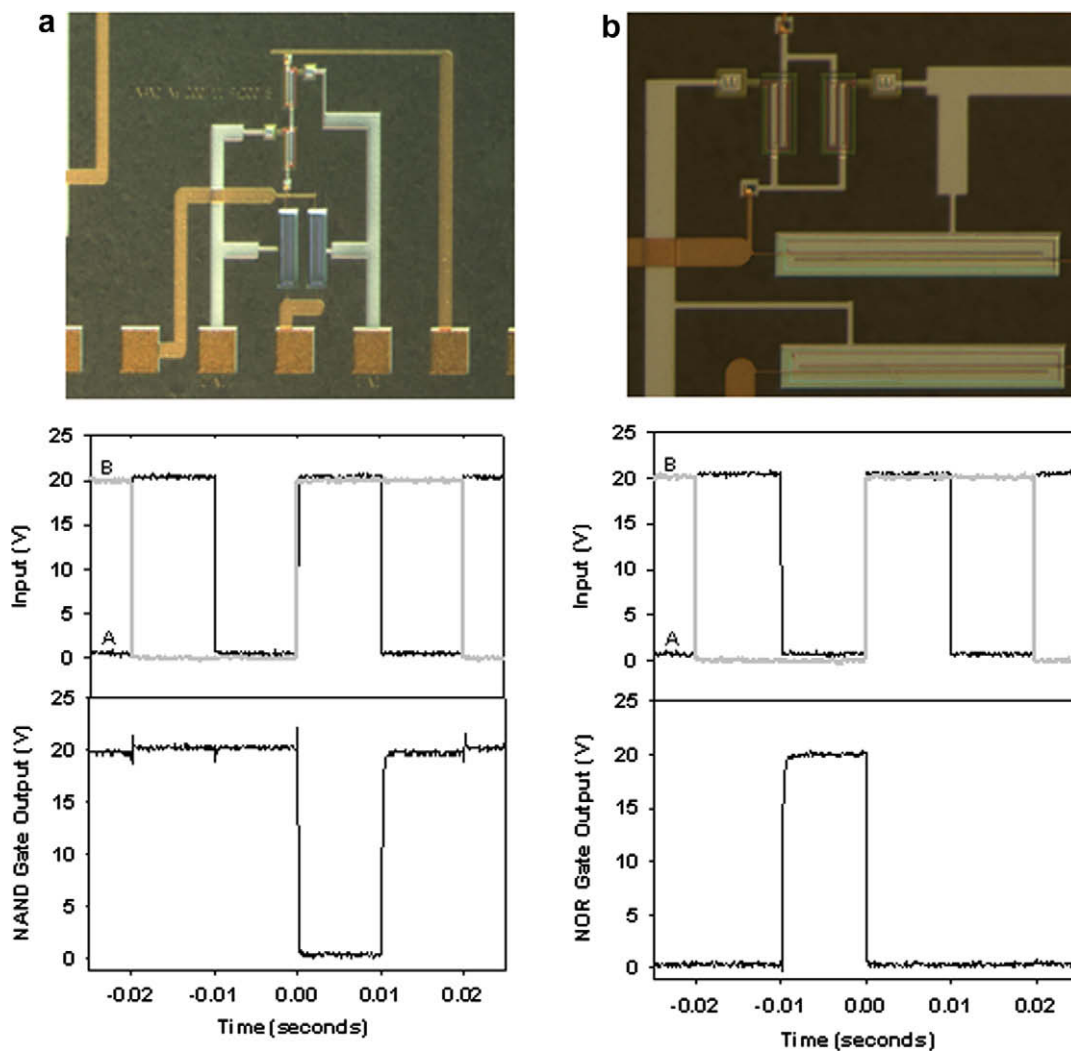
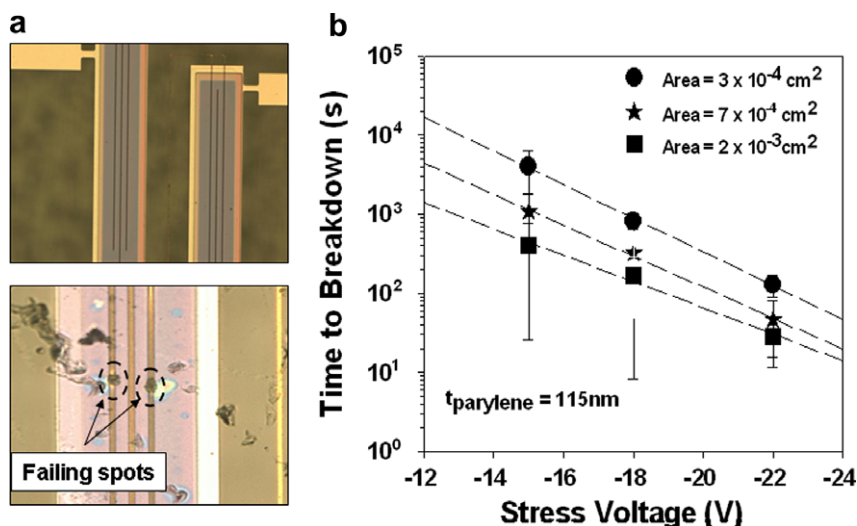


Fig. 5. (a) Optical image of the resulting NAND (top) and logic verification (bottom). (b) Optical image of the resulting NOR (top) and logic verification (bottom).



**Fig. 6.** (a) Optical image showing as fabricated (top) and stressed devices (bottom). (b) Area and voltage dependence for parylene TDDB. For a given stress voltage the larger the area the lower the time to breakdown. This indicates the presence of defects in the parylene dielectric.

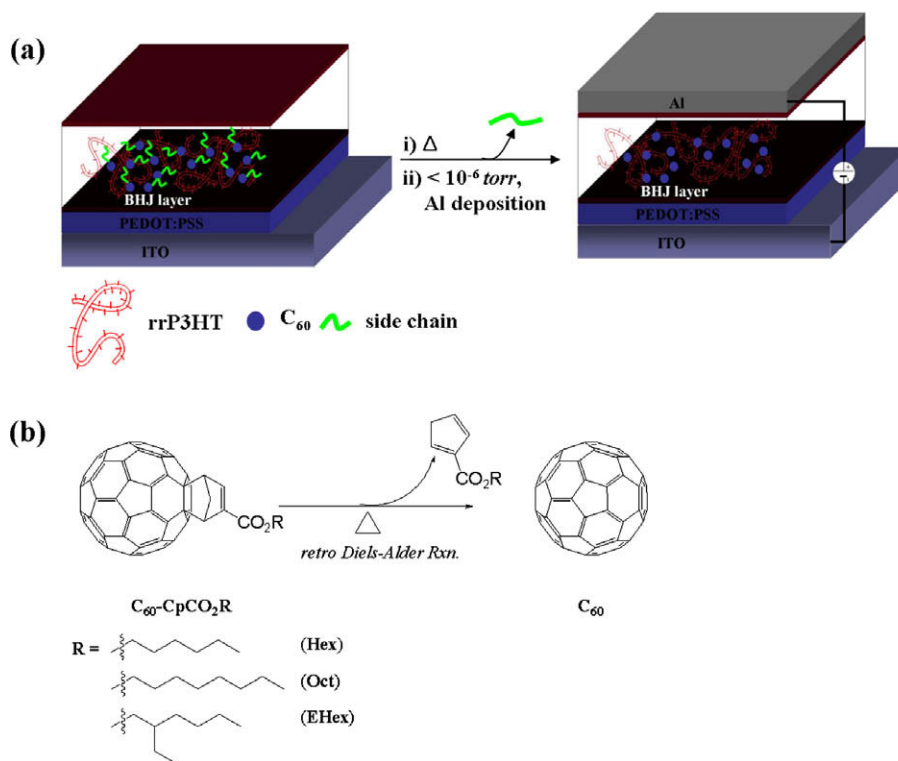
### 3. Conclusions

We have demonstrated a novel integration approach for pentacene pMOS and a-Si:H nMOS. These TFTs were integrated on a flexible PEN substrate to fabricate CMOS circuits including inverters, NAND and NOR gates. The maximum processing temperatures are 180 °C for nMOS and 120 °C for the pMOS. Inverters with a gain of 16 were demonstrated and 2-input NAND and NOR gates with excellent logic behavior were demonstrated. Initial reliability of these devices indicates that the parylene gate dielectric in the pMOS limits device lifetime due to electrical stress. We are currently evaluating alternate gate dielectrics to improve CMOS device reliability.

### References

- [1] T. Aoyama, K. Ogawa, Y. Mochizuki, N. Konishi, Inverse staggered poly-Si and amorphous Si double structure TFT's for LCD panels with peripheral driver circuits integration, *IEEE Transactions on Electron Devices* 43 (1996) 701–705.
- [2] M. Yamano, H. Takesada, M. Yamasaki, Y. Okita, H. Hada, The 5-inch size full color liquid-crystal television addressed by amorphous-silicon thin-film transistors, *IEEE Transactions on Consumer Electronics* 31 (1985) 39–46.
- [3] M.C. LeMieux, Z.N. Bao, Flexible electronics stretching our imagination, *Nature Nanotechnology* 3 (2008) 585–586.
- [4] M. Hamedi, R. Forchheimer, O. Inganäs, Towards woven logic from organic electronic fibres, *Nature Materials* 6 (2007) 357–362.
- [5] A. Dodabalapur, J. Baumbach, K. Baldwin, H.E. Katz, Hybrid organic/inorganic complementary circuits, *Applied Physics Letters* 68 (1996) 2246–2248.
- [6] L. Han, P. Mandlik, K.H. Cherenack, S. Wagner, Amorphous silicon thin-film transistors with field-effect mobilities of  $2 \text{ cm}^2/\text{V s}$  for electrons and  $0.1 \text{ cm}^2/\text{V s}$  for holes, *Applied Physics Letters* 94 (2009) 162105.
- [7] M. Bonse, D.B. Thomasson, H. Klauk, D.J. Gundlach, T.N. Jackson, Integrated a-Si:H/pentacene inorganic/organic complementary circuits, Presented at International Electron Device Meeting, 1998.
- [8] H. Iechi, Y. Watanabe, H. Yamauchi, K. Kudo, Characterization of zinc oxide and pentacene thin film transistors for CMOS inverters, *IEICE Transactions on Electronics* E91C (2008) 1843–1847.
- [9] J.H. Na, M. Kitamura, Y. Arakawa, Complementary two-input NAND gates with low-voltage-operating organic transistors on plastic substrates, *Applied Physics Express* (2008) 1021803.
- [10] M.S. Oh, D.K. Hwang, K. Lee, W.J. Choi, J.H. Kim, S. Im, S. Lee, Pentacene and ZnO hybrid channels for complementary thin-film transistor inverters operating at 2 V, *Journal of Applied Physics* 102 (2007) 076104.
- [11] S.M. Venugopal, D.R. Allee, Integrated a-Si:H source drivers for 4 QVGA electrophoretic display on flexible stainless steel substrate, *Journal of Display Technology* 3 (2007) 57–63.
- [12] G.B. Raupp, S.M. O'Rourke, C. Moyer, B.P. O'Brien, S.K. Ageno, D.E. Loy, E.J. Bawolek, D.R. Allee, S.M. Venugopal, J. Kaminski, D. Bottesch, J. Dailey, K. Long, M. Marrs, N.R. Munizza, H. Haverinen, N. Colaneri, Low-temperature amorphous-silicon backplane technology development for flexible displays in a manufacturing pilot-line environment, *Journal of the Society for Information Display* 15 (2007) 445–454.
- [13] S.M. Venugopal, D.B. Allee, Z. Li, L.T. Clark, Threshold-voltage recovery of a-S:H digital circuits, *Journal of the Society for Information Display* 14 (2006) 1053–1057.
- [14] A. Nathan, B.R. Chalamala, Flexible electronics technology, part II: materials and devices, *Proceedings of the IEEE* 93 (2005) 1391–1393.
- [15] A. Nathan, B.R. Chalamala, Special issue on flexible electronics technology, part 1: systems and applications, *Proceedings of the IEEE* 93 (2005) 1235–1238.
- [16] A. Sazonov, D. Striakhilev, C.H. Lee, A. Nathan, Low-temperature materials and thin film transistors for flexible electronics, *Proceedings of the IEEE* 93 (2005) 1420–1428.
- [17] G. Horowitz, R. Hajlaoui, R. Bourguiga, M. Hajlaoui, Theory of the organic field-effect transistor, *Synthetic Metals* 101 (1999) 401–404.
- [18] G. Horowitz, Organic field-effect transistors, *Advanced Materials* 10 (1998) 365–377.
- [19] Y.Y. Lin, D.J. Gundlach, S.F. Nelson, T.N. Jackson, Pentacene-based organic thin-film transistors, *IEEE Transactions on Electron Devices* 44 (1997) 1325–1331.
- [20] H. Yan, Y. Zheng, R. Blache, C. Newman, S. Lu, J. Woerle, A. Facchetti, Solution processed top-gate n-channel transistors and complementary circuits on plastics operating in ambient conditions, *Advanced Materials* 20 (2008) 3393–3398.
- [21] R. Schmidt, J.H. Oh, Y.S. Sun, M. Deppisch, A.M. Krause, K. Radacki, H. Braunschweig, M. Konemann, P. Erk, Z. Bao, F. Wurthner, High-performance air-stable n-channel organic thin film transistors based on halogenated perylene bisimide semiconductors, *Journal of the American Chemical Society* 131 (2009) 6215–6228.
- [22] J.H. Na, M. Kitamura, Y. Arakawa, Low-voltage-operating organic complementary circuits based on pentacene and C60 transistors, *Thin Solid Films* 517 (2009) 2079–2082.
- [23] M.S. Oh, W. Choi, K. Lee, D.K. Hwang, S. Ima, Flexible high gain complementary inverter using n-ZnO and p-pentacene channels on polyethersulfone substrate, *Applied Physics Letters* 93 (2008) 033510.

- [24] X.H. Zhang, W. Potscavage, S. Choi, B. Kippelena, Low-voltage flexible organic complementary inverters with high noise margin and high dc gain, *Applied Physics Letters* 94 (2009) 043312.
- [25] S. Gowrisanker, Y. Ai, H. Jia, M.A. Quevedo-Lopez, H.N. Alshareef, I. Trachtenberg, H. Stiegler, H. Edwards, R. Barnett, B.E. Gnade, Organic thin-film transistors with low threshold voltage variation on low-temperature substrates, *Electrochemical and Solid State Letters* 12 (2009) H50–H53.
- [26] S. Gowrisanker, A. Yuming, M.A. Quevedo-Lopez, H. Jia, E. Vogel, B. E. Gnade, A gate dielectric last approach to integrate organic based devices on plastic substrates, in: *Proceedings of the Flexible Electronics and Displays Conference and Exhibition, 2008*, pp. 1–3.
- [27] S. Gowrisanker, Y. Ai, M.A. Quevedo-Lopez, H. Jia, H.N. Alshareef, E. Vogel, B. Gnade, Impact of semiconductor/contact metal thickness ratio on organic thin-film transistor performance, *Applied Physics Letters* 92 (2008) 153305.
- [28] R. Shringarpure, S. Venugopal, Z. Li, L.T. Clark, D.R. Allee, E. Bawolek, D. Toy, Circuit simulation of threshold-voltage degradation in a-Si:H TFTs fabricated at 175 °C, *IEEE Transactions on Electron Devices* 54 (2007) 1781–1783.
- [29] S. Gowrisanker, M.A. Quevedo-Lopez, H.N. Alshareef, B. Gnade, TDDB of parylene gate dielectrics, *Organic Electronics* 10 (5) (2009) 1024–1027.



**Scheme 1.** (a) Schematic depiction of P3HT/C<sub>60</sub> BHJ solar cell using novel approach with retro Diels–Alder reaction, (b) structure of soluble fullerene derivatives.

solubilizing group [13]. But more dramatically, polyacetylene was processed from a soluble precursor and converted to insoluble polyacetylene via a retro Diels–Alder reaction by Feast et al. [14] and a phthalocyanine was generated *in situ* via a retro Diels–Alder reaction by Aramaki et al. [15].

We thus have attempted a novel approach for high-efficiency BHJ solar cells utilizing a BHJ active layer consisting of poly(3-hexylthiophene) (P3HT) as a donor and buckminsterfullerene, C<sub>60</sub> as an acceptor. Recently, we synthesized the modified fullerene derivatives [16], hexyl 5,6-C<sub>60</sub>-bicyclo[2.2.1]hept-2-ene-2-carboxylate (C<sub>60</sub>-CpCO<sub>2</sub>Hex), octyl 5,6-C<sub>60</sub>-bicyclo[2.2.1]hept-2-ene-2-carboxylate (C<sub>60</sub>-CpCO<sub>2</sub>Oct), and 2-ethylhexyl 5,6-C<sub>60</sub>-bicyclo[2.2.1]hept-2-ene-2-carboxylate (C<sub>60</sub>-CpCO<sub>2</sub>EHex) to provide better solubility in organic solvents. Interestingly, the addends with their solubilizing side chain, in these derivatives, are easily dissociated into pure C<sub>60</sub> and side chain by retro Diels–Alder (DA) reaction over 100 °C. A BHJ film of P3HT and one of the above mentioned modified fullerene derivatives spun-cast from solution converts efficiently into one consisting of P3HT and pure C<sub>60</sub> after heat-treatment above 100 °C (Scheme 1).

## 2. Results and discussion

The soluble fullerene derivatives, C<sub>60</sub>-CpCO<sub>2</sub>Hex, C<sub>60</sub>-CpCO<sub>2</sub>Oct, and C<sub>60</sub>-CpCO<sub>2</sub>EHex used in this study were synthesized from Diels–Alder reaction of C<sub>60</sub> and Thiele's esters that are made by DCC coupling reaction of Thiele's

acid (dicyclopentadiene dicarboxylic acid) and hexanol, octanol, and 2-ethylhexanol, respectively. The retro DA reaction of these derivatives occurs by simple annealing above 100 °C, and the dissociated side chains are evaporated below 200 °C, as shown by thermogravimetric analysis (TGA).

All C<sub>60</sub>-CpCO<sub>2</sub>Hex, C<sub>60</sub>-CpCO<sub>2</sub>Oct, and C<sub>60</sub>-CpCO<sub>2</sub>EHex films by solution processing reveal typical behavior of ideal n-type OFETs as shown in Fig. 1. A non-negligible big difference between C<sub>60</sub>-CpCO<sub>2</sub>Hex, C<sub>60</sub>-CpCO<sub>2</sub>Oct, and C<sub>60</sub>-CpCO<sub>2</sub>EHex in the  $I_{ds}$  vs.  $V_{gs}$  is not clearly observed. The linear plot of  $I_{ds}^{1/2}$  vs.  $V_{gs}$  derived from the measurements of  $I_{ds}$  vs.  $V_{gs}$  yields electron mobilities of  $\mu_1 = 1.4 \times 10^{-3}$  cm<sup>2</sup>/V s,  $\mu_2 = 1.5 \times 10^{-3}$  cm<sup>2</sup>/V s, and  $\mu_3 = 3.1 \times 10^{-3}$  cm<sup>2</sup>/V s for C<sub>60</sub>-CpCO<sub>2</sub>Hex ( $\mu_1$ ), C<sub>60</sub>-CpCO<sub>2</sub>Oct ( $\mu_2$ ), and C<sub>60</sub>-CpCO<sub>2</sub>EHex ( $\mu_3$ ), respectively.

BHJ films were prepared under optimized conditions according to the following procedure reported previously [7]. In the course of studying the characteristics of over 500 solar cells, we have determined the optimum component ratio for the BHJ consisting of P3HT/C<sub>60</sub>-CpCO<sub>2</sub>R. The characteristics of device performance were compared with a P3HT/C<sub>60</sub> BHJ solar cell as reference device. To clarify the new approach for P3HT/C<sub>60</sub> BHJ solar cells, we investigated the change of infrared (IR) absorption for P3HT/C<sub>60</sub>-CpCO<sub>2</sub>Hex BHJ films. Fig. 2 shows the FTIR spectra of as-prepared P3HT/C<sub>60</sub>-CpCO<sub>2</sub>Hex BHJ film (red line),<sup>1</sup> after annealing at

<sup>1</sup> (For interpretation of the references to colour in Fig. 2, the reader is referred to the web version of this article.)

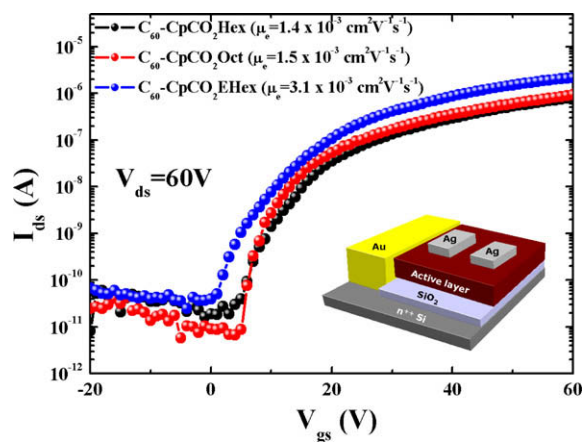


Fig. 1. FET device performance of  $C_{60}$ -CpCO<sub>2</sub>Hex (black line),  $C_{60}$ -CpCO<sub>2</sub>Oct (red line), and  $C_{60}$ -CpCO<sub>2</sub>EHex (blue line) films by solution processing. (For interpretation of the references to colour in this figure legend, the reader is referred to the web version of this article.)

120 °C (black line), followed by vacuum drying (blue line). The carbonyl stretching peak of at 1700  $cm^{-1}$  from  $C_{60}$ -CpCO<sub>2</sub>Hex ester group appears clearly in the as-prepared film and decreases in intensity after annealing at 120 °C,

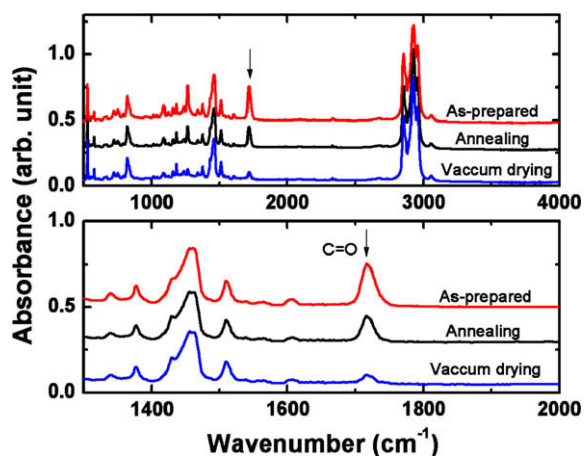


Fig. 2. Infrared (IR) spectra of as-prepared P3HT/ $C_{60}$ -CpCO<sub>2</sub>Hex BHJ film (red line) after annealing at 120 °C (black line) followed by vacuum drying (blue line). (For interpretation of the references to colour in this figure legend, the reader is referred to the web version of this article.)

indicating the dissociation into pure  $C_{60}$  and volatile side chain. The peak almost disappeared after vacuum drying below  $<10^{-6}$  torr of the annealed P3HT/ $C_{60}$ -CpCO<sub>2</sub>Hex

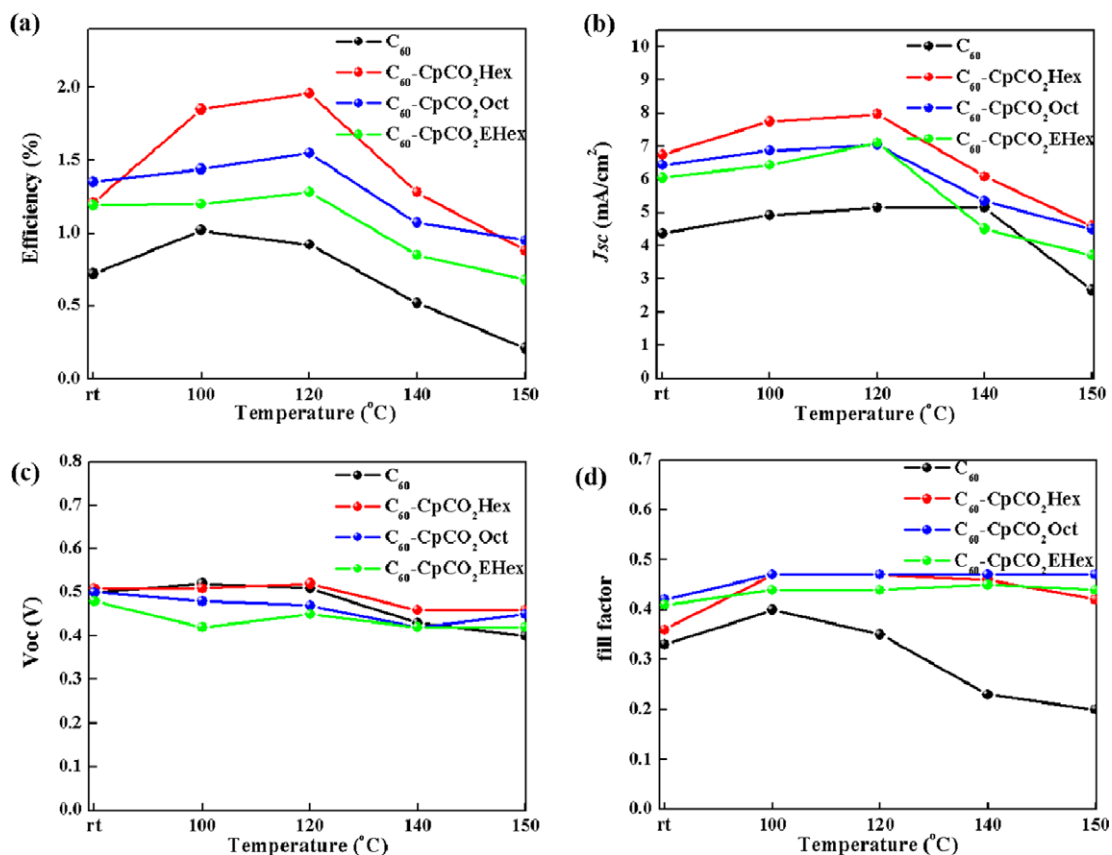


Fig. 3. Photovoltaic device characteristics (efficiency (a),  $J_{sc}$  (b),  $V_{oc}$  (c), and  $FF$  (d)) of ref. P3HT/ $C_{60}$  (black) and P3HT/ $C_{60}$  induced from P3HT/ $C_{60}$ -CpCO<sub>2</sub>R ( $R = \text{Hex}$  (red),  $\text{Oct}$  (blue), and  $\text{EHex}$  (green)) film. (For interpretation of the references to colour in this figure legend, the reader is referred to the web version of this article.)

BHJ film at 120 °C. Similar results were also observed with the other addends,  $C_{60}$ -CpCO<sub>2</sub>Oct and  $C_{60}$ -CpCO<sub>2</sub>EHex. From these results, it is clear that the retro DA reaction approach applied to P3HT/ $C_{60}$ -CpCO<sub>2</sub>R (R = Hex, Oct, and EHex) BHJ films, produces a P3HT/ $C_{60}$  BHJ film and the dissociated side chain could be removed under the high vacuum conditions required for the aluminum electrode deposition.

Fig. 3 shows the photovoltaic device characteristics (e.g.  $J_{sc}$ ,  $V_{oc}$ , FF, and power-conversion efficiency) of refs. P3HT/ $C_{60}$  and P3HT/ $C_{60}$  resulting from P3HT/ $C_{60}$ -CpCO<sub>2</sub>R (R = Hex, Oct, and EHex) films. The P3HT/ $C_{60}$  BHJ film from P3HT/ $C_{60}$ -CpCO<sub>2</sub>R exhibits better performance than the ref. P3HT/ $C_{60}$ . The optimum efficiencies of these thermally generated P3HT/ $C_{60}$  BHJ devices, from all P3HT/ $C_{60}$ -CpCO<sub>2</sub>R, are observed after post-annealing at 120 °C and that are significantly degraded beyond this temperature

The ref. P3HT/ $C_{60}$  BHJ device exhibits a decreased efficiency above 100 °C. As shown in Fig. 2, the  $C_{60}$ -CpCO<sub>2</sub>Hex yields the highest performance among these  $C_{60}$ -CpCO<sub>2</sub>R (R = Hex, Oct, and EHex) fullerene derivatives. The efficiency is two times higher than that obtained with  $C_{60}$ , likely derived from high  $J_{sc}$  and fill factor. The values obtained from all devices are similar. Besides, interestingly, the decrease in efficiency of P3HT/ $C_{60}$  BHJ devices derived from P3HT/ $C_{60}$ -CpCO<sub>2</sub>R by annealing above 120 °C are mainly governed by the decrease in their  $J_{sc}$  but the decrease in efficiency of ref. P3HT/ $C_{60}$  BHJ device above 100 °C is caused by the decrease in their fill factor. These results indicate that the morphology of P3HT/ $C_{60}$  BHJ film based on P3HT/ $C_{60}$ -CpCO<sub>2</sub>R BHJ film could be better than as-prepared P3HT/ $C_{60}$  BHJ film and the use of  $C_{60}$ -CpCO<sub>2</sub>-Hex gives the best P3HT/ $C_{60}$  BHJ film, compared to the others.

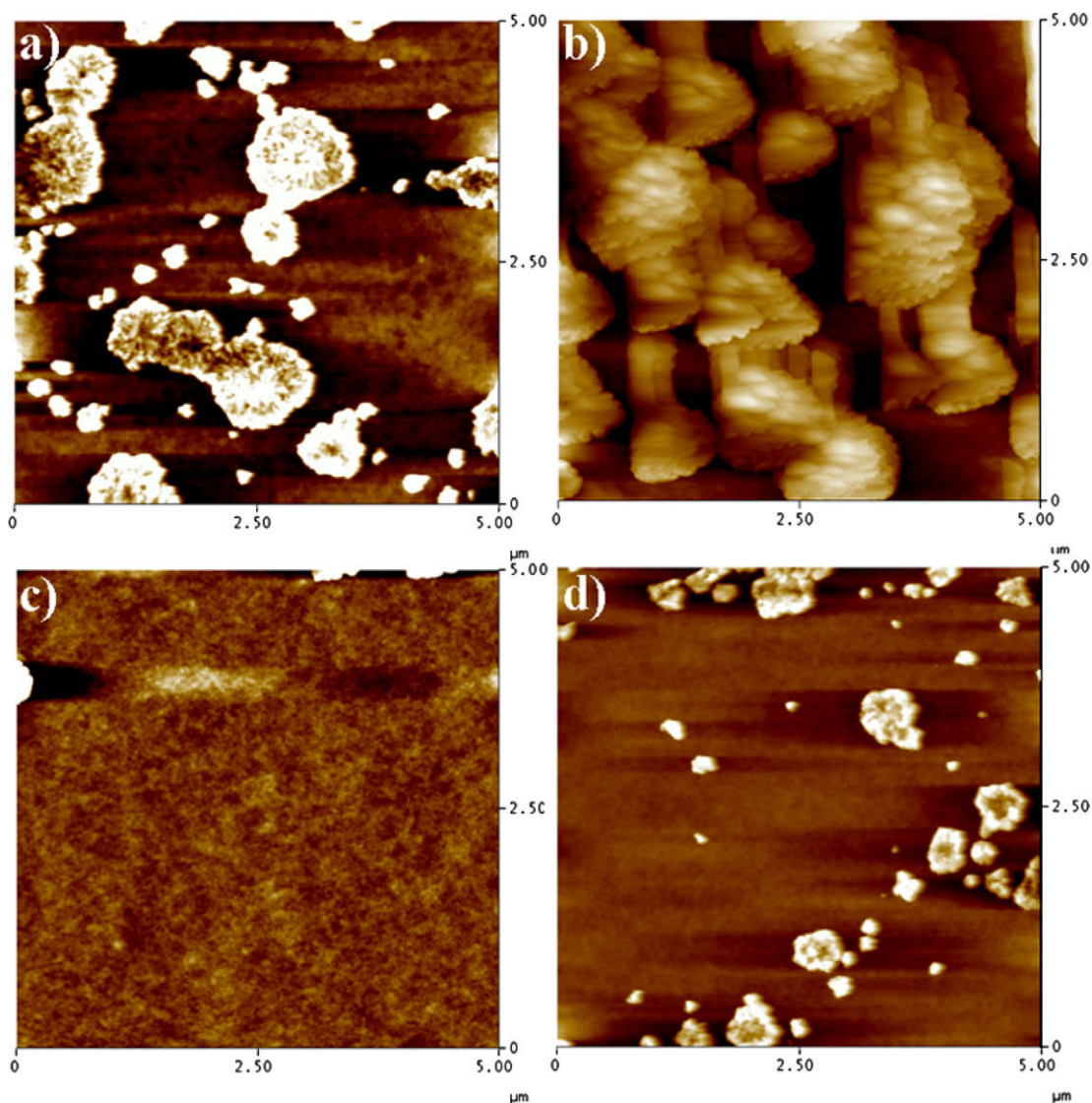


Fig. 4. Tapping mode AFM images of ref. P3HT/ $C_{60}$  BHJ film after annealing at 120 °C (a) and 140 °C (b) and P3HT/ $C_{60}$  BHJ film induced from P3HT/ $C_{60}$ -CpCO<sub>2</sub>Hex BHJ film after annealing at 120 °C (c) and 140 °C.

Fig. 4 shows the tapping mode AFM images of ref. P3HT/C<sub>60</sub> BHJ film after annealing at 120 °C (a) and 140 °C (b) and the images of P3HT/C<sub>60</sub> BHJ film produced from the P3HT/C<sub>60</sub>-CpCO<sub>2</sub>Hex BHJ film after annealing at 120 °C (c) and 140 °C (d). As shown in Fig. 3, the ref. P3HT/C<sub>60</sub> BHJ film at 120 °C exhibits large aggregated domains of C<sub>60</sub> due to its strong Van der Waals interaction but even though the P3HT/C<sub>60</sub>-CpCO<sub>2</sub>Hex BHJ film at 120 °C, had converted into a P3HT/C<sub>60</sub> BHJ film, it exhibited much better morphology compared with the reference P3HT/C<sub>60</sub> BHJ film. Although more and larger aggregate domains of C<sub>60</sub> are observed in the reference film at 140 °C, the film based on P3HT/C<sub>60</sub>-CpCO<sub>2</sub>Hex BHJ at 140 °C shows relatively less aggregated morphology. These results indicate that the P3HT/C<sub>60</sub> BHJ film converted from well-defined P3HT/C<sub>60</sub>-CpCO<sub>2</sub>Hex BHJ film by retro DA reaction produces better morphology than that of the ref. P3HT/C<sub>60</sub>. Note that the polymer in a well-blended former film can slow down the aggregation of C<sub>60</sub> with increasing temperature, resulting in a better bicontinuous network.

### 3. Conclusions

In conclusion, we have demonstrated a new approach for high-efficiency BHJ solar cells utilizing a BHJ active layer consisting of P3HT as a donor and buckminsterfullerene, C<sub>60</sub> as acceptor. P3HT/C<sub>60</sub> BHJ films generated by facile separation of C<sub>60</sub> from its soluble adduct, C<sub>60</sub>-CpCO<sub>2</sub>R (R = Hex, Oct, and EHex) by retro Diels–Alder reaction above 100 °C exhibit enhanced performances and showing better morphologies, compared to an as-prepared P3HT/C<sub>60</sub> BHJ film. In addition, the polymer in the former film reduces the aggregation of C<sub>60</sub> with increasing temperature, an effect that is absent in the latter films with concomitant decrease in efficiency of P3HT/C<sub>60</sub> BHJ solar cells.

### 4. Experimental

Poly(3,4-ethylene-dioxythiophene):poly(styrenesulfonate) PEDOT:PSS (Baytron PH) was spun-cast on an indium tin oxide (ITO)-coated glass substrate from aqueous solution to form a film of thickness around 40 nm. The substrate was dried for 10 min at 140 °C in air, then transferred into a glove-box to spin-cast the active layer. A solution containing a mixture of P3HT/C<sub>60</sub>-CpCO<sub>2</sub>R (R = Hex, Oct, and EHex) (1:0.7) in chlorobenzene was then spun-cast on top of the PEDOT:PSS layer. Subsequently, after the film was dried at 80 °C for 10 min, followed by

retro DA reaction at 120 °C in N<sub>2</sub> atmosphere, the device was pumped down in vacuum (<10<sup>-6</sup> torr; 1 torr = 133 Pa), and a ~100 nm thick Al electrode was deposited on top. For calibration of the solar simulator, we first carefully minimized the mismatch of the spectrum (the simulating spectrum) obtained from the Xenon lamp (300 W Oriel) and the solar spectrum using an AM1.5G filter. We then calibrated the light intensity using calibrated standard silicon solar cells with a proactive window made from KG5 filter glass traced to the National Renewable Energy Laboratory (NREL). Measurements were done with the solar cells inside the glove-box using an optical fiber to guide the light from the solar simulator outside the glove-box. Current density–voltage curves were measured with a Keithley 236 source measurement unit. The AFM images were obtained with a Dimension 3100 atomic force microscope.

### Acknowledgement

The research was supported by the Institute for Collaborative Biotechnology at UCSB and MC-CAM.

### References

- [1] N.S. Sariciftci, L. Smilowitz, A.J. Heeger, F. Wudl, *Science* 258 (1992) 1474.
- [2] G. Yu, J. Gao, J.C. Hummelen, F. Wudl, A.J. Heeger, *Science* 270 (1995) 1789.
- [3] C.J. Brabec, N.S. Sariciftci, J.C. Hummelen, *Adv. Funct. Mater.* 11 (2001) 15.
- [4] S. Gunes, H. Neugebauer, N.S. Sariciftci, *Chem. Rev.* 107 (2007) 1324.
- [5] W. Ma, C. Yang, X. Gong, K. Lee, A.J. Heeger, *Adv. Funct. Mater.* 15 (2005) 1617.
- [6] H. Hoppe, N.S. Sariciftci, *J. Mater. Chem.* 16 (2006) 45.
- [7] J. Peet, J.Y. Kim, N.E. Coates, W.L. Ma, D. Moses, A.J. Heeger, G.C. Bazan, *Nature Mater.* 6 (2007) 497.
- [8] J.K. Lee, W. Ma, C.J. Brabec, J. Yuen, J.S. Moon, J.Y. Kim, K. Lee, G.C. Bazan, A.J. Heeger, *J. Am. Chem. Soc.* 130 (2008) 3619.
- [9] (a) J. Hou, H.Y. Chen, S. Zhang, G. Li, Y. Yang, *J. Am. Chem. Soc.* 130 (2008) 16144; (b) N. Blouin, M. Leclerc, *Acc. Chem. Res.* 41 (2008) 1110.
- [10] C. Yang, J.Y. Kim, S. Cho, J.K. Lee, A.J. Heeger, F. Wudl, *J. Am. Chem. Soc.* 130 (2008) 6444.
- [11] J.J.M. Halls, K. Piechler, R.H. Friend, S.C. Moratti, A.B. Holmes, *Appl. Phys. Lett.* 68 (1996) 3120.
- [12] A. Ltaief, J. Davenas, A. Bouazizia, R. Ben Chaabanea, P. Alcouffeb, H. Ben Ouada, *Mater. Sci. Eng. C* 25 (2005) 67.
- [13] C. Edder, P.B. Armstrong, K.B. Prado, J.M.J. Fréchet, *Chem. Commun.* (2006) 1965.
- [14] J.E. Edwards, W.J. Feast, D.C. Bot, *Polymer* 25 (1984) 98.
- [15] A. Hirao, T. Akiyama, T. Okujima, H. Yamada, H. Uno, Y. Sakai, S. Aramaki, N. Ono, *Chem. Commun.* (2008) 4714.
- [16] Y. Wang, F. Wudl, unpublished.

of molecules due to their ability to self-assemble into microscopic elongated crystalline aggregates, or ‘nanofibers’ [6]. In addition to their polarized and highly anisotropic photoluminescence output [7] and their wave guiding [8] and lasing [9] properties, chemical functionalization of these molecular building blocks opens the way for the specific tailoring of nanofiber properties at the molecular level [10]. Electrical interfacing to individual nanofibers allows the electrical properties to be studied [11] and could enable the fabrication of nanoscale LEDs (as electroluminescence has been observed from oligophenylene thin films [12]) with configurable properties.

We have previously conducted experimental investigations of charge transport in a large number of individual nanofibers made from *para*-hexaphenylene (p6P) molecules and have found their hole mobility to be above  $0.3 \text{ cm}^2 \text{ V}^{-1} \text{ s}^{-1}$  [13]. In this work, we present a similar investigation of two other types of nanofibers made from 5,5'-di-4-biphenyl-2,2'-bithiophene (PPTTPP) [14,15] and 4-4'-di-2,2'-dithienyl-biphenyl (TTPPTT) [15], respectively, and compare the results here with those from the p6P nanofibers. The molecular structures, crystal lattice geometries, and fluorescence microscopy images of all three materials are shown in Fig. 1.

To complement the experimental studies, we have also used quantum-mechanical calculations to study the charge transport properties. There are two main regimes of charge transport in organic molecular crystals, the band-like regime, similar to ‘conventional’ charge trans-

port in inorganic single crystals, or the hopping regime, where the carrier is localized on one molecule through the formation of a self-trapped state (a polaron) and transport occurs through a thermally activated hopping mechanism [19]. The band-like regime is generally observed only at low temperatures in highly ordered samples [20], so that the hopping mechanism is usually in effect at temperatures relevant for practical technological applications. In the hopping regime, the carrier mobility is proportional to the intersite electron transfer rate  $k_{ij}$ , which, in the semi-classical approximation, can be evaluated by the Marcus equation [19,21],

$$k_{ij} = t_{ij}^2 \sqrt{\frac{\pi}{\hbar^2 k_B T \lambda_{ij}}} \exp\left(-\frac{(\Delta E_{ij} - \lambda_{ij})^2}{4\lambda_{ij} k_B T}\right), \quad (1)$$

where  $t_{ij}$  is the transfer integral,  $\lambda_{ij}$  is the reorganization energy,  $\Delta E_{ij}$  is the energy difference between the initial and final states,  $T$  is the temperature, and  $k_B$  and  $\hbar$  are the Boltzmann and Planck constants, respectively. Since the energy difference between initial and final states in a crystal is often vanishingly small [22], the two parameters governing the transfer rate at a particular temperature are the reorganization energy and transfer integral. Here, we have used density functional theory (DFT) to evaluate differences in reorganization energies and transfer integrals of the three types of molecular crystals and have related these calculated charge transfer parameters to experimentally determined charge carrier mobilities.

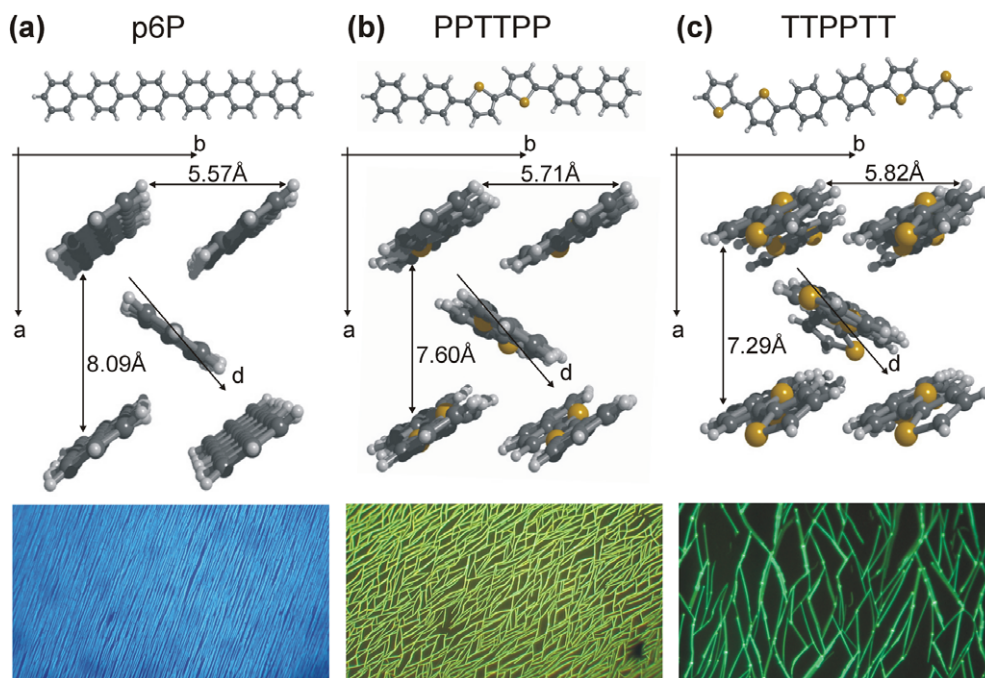


**Fig. 1.** Molecular and crystal structures of (a) p6P, (b) PPTTPP, and (c) TTPPTT. The geometric data of the crystal structures are from Refs. [16–18], respectively. The arrows indicate the crystal lattice directions used in the density functional theory calculations. The bottom part shows fluorescence microscopy images of nanofibers made from the above molecules (p6P nanofibers,  $112 \mu\text{m} \times 63 \mu\text{m}$ ; PPTTPP nanofibers,  $223 \mu\text{m} \times 125 \mu\text{m}$ ; TTPPTT,  $130 \mu\text{m} \times 74 \mu\text{m}$ ).



## 2. Methods

### 2.1. Experimental details

The nanofibers are fabricated by physical vapor deposition of the molecules from a Knudsen cell onto a heated muscovite mica substrate under high vacuum conditions [6]. Through interaction with the electrical surface dipoles of the mica substrate, the molecules align and self-assemble into nanofiber aggregates with typical cross-sectional dimensions of a few hundred nanometers (width) by tens of nanometers (height) and a length of tens of micrometers. The fluorescence micrographs in Fig. 1 show the three types of as-grown nanofibers on mica substrates. Upon growth, a few nanofibers are transferred from the mica substrate to a prefabricated device substrate consisting of an elevated silicon dioxide platform on a silicon chip. The nanofiber transfer is accomplished by gently pressing the mica substrate against the device substrate under conditions of high humidity, which releases the nanofibers from the mica substrate. By inspection with a fluorescence microscope, a suitable nanofiber is identified and a set of electrodes is made using a silicon nanowire as a local shadow mask during metal deposition to form the two gold top contacts on the nanofiber [11]. Gold has a relatively high work function and, consequently, the use of gold contacts leads to hole conduction [13]. After metal deposition, the nanowire shadow mask is removed by mechanical manipulation, and the sample is wire bonded for electrical characterization. The electrical measurements are carried out using a home built setup consisting of a Labview-controlled NI PCI-6229 DAQ device and Stanford Research SR570 current pre-amplifier. The transport properties are studied by two-point measurements in which current is measured as the applied voltage is increased from 0 V. The sample dimensions, in particular the uncoated length of the nanofiber (distance between electrodes) and its cross-sectional dimensions, have been determined from SEM and AFM (tapping mode) measurements.

### 2.2. Theoretical details

To determine the charge transfer rate,  $k_{ij}$ , using Eq. (1), the transfer integral and the reorganization energy must be calculated. The transfer integral is determined mainly by the intermolecular overlap of the frontier molecular orbitals of the involved molecules – HOMO (highest occupied molecular orbital) for hole transfer and LUMO (lowest unoccupied molecular orbital) for electron transfer. Therefore, its value depends on molecular packing structure. Recently, Valeev et al. [22] described a transfer integral calculation method that includes the influence from site energy differences that can arise from geometric differences and polarization effects between inequivalent molecules in the crystal unit cell. By defining one-electron dimer states from localized monomer orbitals ( $\psi_i$ ) and assuming that the dimer HOMO and HOMO–1 (LUMO+1 and LUMO) originate only from the interaction of the monomer HOMOs (LUMOs), the site energies  $e_i$  and transfer integrals  $t_{ij}$  are obtained from

$$e_i = \langle \psi_i | \hat{H} | \psi_i \rangle \quad (2)$$

$$t_{ij} = \langle \psi_i | \hat{H} | \psi_j \rangle, \quad (3)$$

where  $\hat{H}$  is the Hamiltonian. Since Eq. (1) assumes an orthogonal basis and the monomer orbitals are, in fact, not strictly orthogonal, the transfer integral as determined by Eq. (3) cannot be applied directly. First, an orthonormal basis set is required and is obtained using Löwdin's symmetric transformation [22] to give

$$t_{12}^{eff} = \frac{t_{12} - \frac{1}{2}(e_1 - e_2)S_{12}}{1 - S_{12}^2}, \quad (4)$$

where  $S_{12}$  is the overlap integral. Here, density functional theory (DFT) is used together with Eqs. (2)–(4) for calculation of transfer integrals.

The reorganization energy comprises both inter- and intramolecular contributions [1]. The intermolecular part is due to the polarization and relaxation of the surrounding medium. The intramolecular part is due to the changes in equilibrium geometries of both the donor and acceptor molecules upon charge transfer and, therefore, consists of two terms related to each of the molecules involved: (1) the relaxation of the donor molecule upon going from the charged-state geometry to the neutral-state geometry ( $\lambda_0$ ) and (2) the relaxation of the acceptor molecule upon going from the neutral-state geometry to the charged-state geometry ( $\lambda_1$ ), respectively. The intramolecular reorganization energy is determined from the adiabatic potential surfaces as

$$\lambda_0 = E_{0/1} - E_{0/0} \quad (5)$$

$$\lambda_1 = E_{1/0} - E_{1/1}, \quad (6)$$

where  $E_{0/0}$  and  $E_{1/1}$  are the ground state energies of the neutral and charged molecule, respectively,  $E_{1/0}$  is the energy of the charged state at the optimal geometry of the neutral state, and  $E_{0/1}$  is the energy of the neutral state at the geometry of the charged molecule. The intramolecular reorganization energy is determined by calculating the energies at the various optimized geometries of a single molecule in the gas phase. In the gas phase, all three molecules considered here will exhibit significant inter-ring torsional angles that are not observed in the solid-state geometry where the molecules exhibit more coplanar geometries. To be consistent with the geometries observed in the crystal structure, intramolecular reorganization energies have been obtained by constraining the molecules to planar geometries during the optimization process.

The transfer integral calculations have been performed using the Amsterdam Density Functional [23] and Gaussian 98 [24] software packages, while the calculation of the intramolecular reorganization energies was done using Gaussian 98 [24]. For the transfer integral calculations, the PW91 functional was used with a DZP basis set. This functional was found by Huang and Kertesz to provide results in closest agreement with experimental values [25]. In the calculation of reorganization energies, hybrid functionals that include a fraction of Hartree–Fock exchange provide higher estimates of reorganization energies than pure DFT methods. By comparison with experimental re-

sults from photoelectron spectroscopy studies on oligoacenes [26] and oligothiophenes [27], recent reports found the B3LYP functional to yield values closest to experiments. Therefore, the B3LYP functional is used in the calculations of intramolecular reorganization energies.

### 3. Results and discussion

#### 3.1. Experiment

Fig. 2a shows a typical current–voltage data set from an individual nanofiber (a TTPPTT oligomer type) contacted

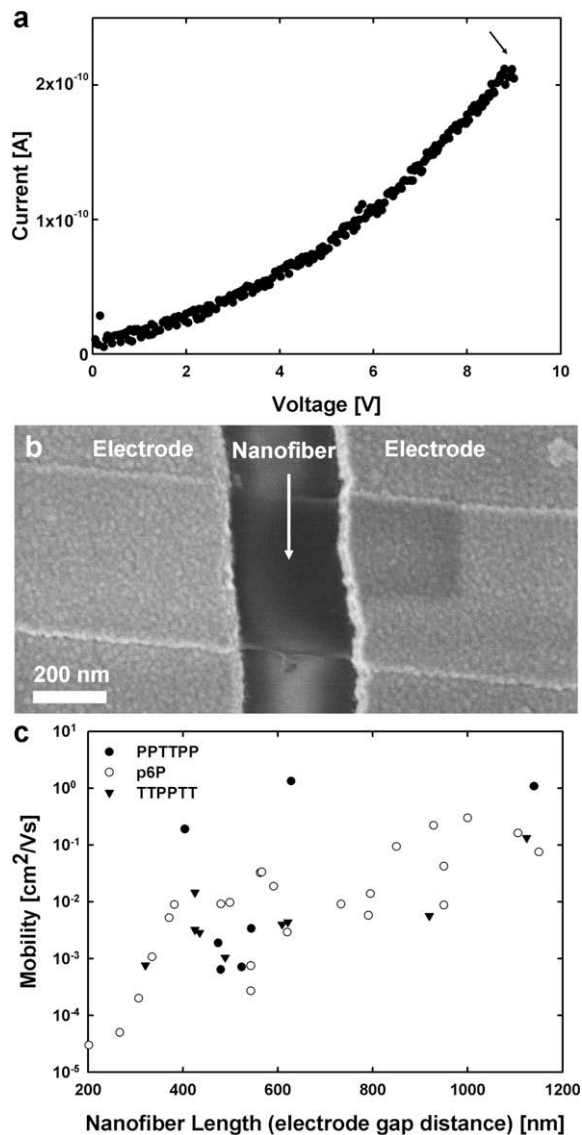


**Fig. 2.** (a) Typical result of a current versus voltage measurement on a single nanofiber (here made from TTPPTT molecules) contacted with two gold electrodes. The point indicates the point used in the calculation of the mobility as described in the text. (b) Scanning electron microscopy image of a nanofiber supported on silicon dioxide and contacted with two gold electrodes. (c) Charge carrier mobility estimates from individual p6P, PPTTPP and TTPPTT nanofibers based on the Mott–Gurney formalism as described in the text.

with gold electrodes. We use the Mott–Gurney formalism to analyze the data, as has been done in previous studies [13]. This allows the charge carrier mobility  $\mu$  to be estimated from

$$\mu_{\min} = \frac{8IL^3}{9\epsilon_r\epsilon_0AV^2}, \quad (7)$$

where  $I$  is the current,  $L$  is the device length,  $\epsilon_r\epsilon_0$  is the dielectric permittivity,  $A$  is the cross-sectional area, and  $V$  is the applied voltage. The use of Eq. (7) implicitly assumes charge transport in the space-charge limited (SCL) regime and does not account for additional current-limiting factors such as interface barriers or charge traps. These factors effectively reduce the current from its theoretical maximum. The resulting mobility estimated from Eq. (7) should, therefore, be interpreted as a lower bound to the accurate value of the mobility.

A TTPPTT nanofiber with gold electrodes is seen in the SEM image in Fig. 2b, from which the uncoated length (321 nm) and width (428 nm) are obtained. The height (35 nm) is determined from AFM data (not shown), and  $A$  is found as the product of the width and height. We estimate the uncertainty on the length and width data to be  $\pm 5\%$  and on the height data to be  $\pm 10\%$ . The uncertainty on the mobility is considered to be affected primarily by the uncertainty on the SEM and AFM data. This leads to a worst-case uncertainty on  $\mu_{\min}$  of  $+35\%/ -26\%$ . Ten samples were prepared for each of the PPTTPP and TTPPTT nanofibers. From those samples, seven PPTTPP and nine TTPPTT samples exhibited current–voltage characteristics that indicate current flow through the nanofibers. The remaining samples displayed much lower resistances, which upon closer inspection were found to originate from short circuits caused by metal residues from the contacting process. Fig. 2c shows these 16 mobility values versus nanofiber length together with the data from 24 p6P nanofiber samples from Ref. [13].

Since charge carrier mobility is an intrinsic material parameter, no length dependence is expected. The mobility data presented in Fig. 2c seems to indicate that the longer the nanofiber, the higher the estimated mobility. This implies that for the shorter nanofibers, the estimate provided by Eq. (7) is significantly below the true mobility, most likely due to contact effects that reduce the current. This is not unexpected, as contact effects are more severe for short samples where the bulk nanofiber resistance is comparably small. For longer nanofibers, however, the contribution from the nanofiber bulk to the resistance is higher, and Eq. (7) is expected to provide a better estimate. Therefore, we expect that the long nanofibers provide the best estimate of the true mobility. The largest estimated carrier mobility is found for PPTTPP and is  $1 \text{ cm}^2 \text{ V}^{-1} \text{ s}^{-1}$ . Both p6P and TTPPTT exhibit carrier mobilities approximately an order of magnitude below that.

#### 3.2. Theory

The transport properties and hence charge mobility in molecular crystals exhibit a directional anisotropy. By selecting different combinations of molecules, the effective

transfer integrals along various crystal directions indicated in Fig. 1 can be found and are listed in Table 1. Pentacene is often regarded as a benchmark for evaluating electronic coupling strengths and hole mobilities, with typical mobility values of more than  $1 \text{ cm}^2 \text{ V}^{-1} \text{ s}^{-1}$  at room temperature [28] and with values up to  $35 \text{ cm}^2 \text{ V}^{-1} \text{ s}^{-1}$  having been reported [29]. For comparison, the transfer integrals for pentacene are larger than those calculated for the systems that are investigated here. In pentacene, the effective hole transfer integral (along the d1 diagonal direction) is 85 meV [30]. The intramolecular reorganization energies relevant for both hole and electron transfer in p6P, PPTTPP, and TTPPTT molecules were calculated and are listed in Table 2. Reorganization energies for pentacene and hexathiophene ( $\alpha$ -6T) are provided for comparison.

In order to obtain an estimate of the charge transfer rate, the charge transfer parameters we have calculated can be injected into Eq. (1). The contribution of the intermolecular part to the total reorganization energy is usually assumed to be smaller than or of same order of magnitude as the intramolecular contribution [1,32]; exact values are difficult to estimate since they require to take account of the lattice phonons. Here, since we are mainly interested in trends, we have chosen to take into account the potential contributions of the intermolecular reorganization energy to the entire reorganization energy in an effective way: we have simply calculated the hole and electron transfer rates along the diagonal direction in the p6P crystal for different amounts of external reorganization energy, shown in Fig. 3. If an intermolecular reorganization energy of 0.1 eV is used, transfer rates of  $3 \times 10^{12} \text{ s}^{-1}$  and  $3 \times 10^{10} \text{ s}^{-1}$  for electron and hole transfer are obtained, respectively. Fig. 3 illustrates that when similar values for the external reorganization energies are used for both electron and hole transfer, the hopping rate for electrons is  $\sim 10^2$  larger than for holes in this crystal direction.

The intermolecular contribution to the reorganization energy is generally less dependent on the chemical structure than the intramolecular part [1]. Thus, as a first step, we assumed that the external contributions were similar in all the systems considered here and evaluated the charge carrier transfer rates relative to that in pentacene. Due to its superior transport properties, the latter can be considered as a benchmark system and its transfer rate has been found by inserting the previously quoted transfer integral and reorganization energy into Eq. (1). The charge transport parameters for oligophenylene and oligophenylene-thiophene crystals have been calculated to describe charge transport in nanofiber structures. In order to make

**Table 2**

B3LYP/6-31G(d) intramolecular reorganization energies ( $\lambda$ ) for p6P, PPTTPP, and TTPPTT, in comparison to the hexathiophene and pentacene values.

	$\lambda_{\text{hole}}$ (meV)	$\lambda_{\text{electron}}$ (meV)
p6P	162	192
PPTTPP	225	236
TTPPTT	195	185
$\alpha$ -6T <sup>a</sup>	255	
Pentacene <sup>b</sup>	97	132

<sup>a</sup> Ref. [27].

<sup>b</sup> Ref. [31].

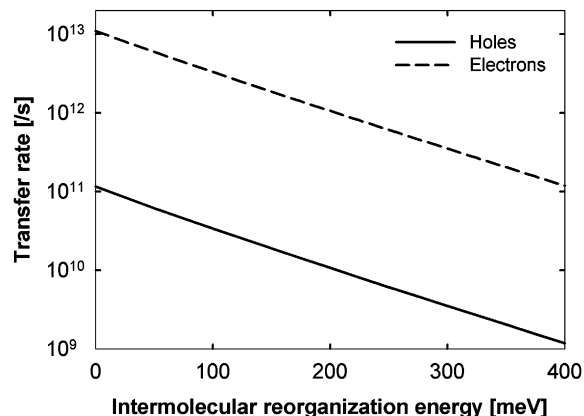


**Fig. 3.** Hole and electron transfer rates in the d direction of the p6P crystal as a function of varying the amount of intermolecular reorganization energy.

this correlation, we consider the transfer integrals corresponding to charge transfer along the long direction of the nanofiber, which approximately corresponds to the direction of the applied electric field in the experimental geometry shown in Fig. 2. For p6P, this would correspond to the charge transfer occurring in the d direction of the crystal (see Fig. 1). Since the contact face between the growth substrate and the PPTTPP or TTPPTT crystals is currently not known experimentally, the direction of the applied electric field relative to the crystal structure is also unknown. Therefore, a charge hopping direction similar to that observed in p6P is assumed, i.e. along the diagonal. For hole transfer, we find that the transfer rates in p6P and PPTTPP are similar and approximately three orders of magnitude smaller than in pentacene. The large hole transfer integral along the d direction in TTPPTT (see Table 1) re-

**Table 1**

Absolute values of the effective transfer integrals ( $t_{\text{eff}}$ ) along different crystal directions in p6P, PPTTPP, and TTPPTT.

	$t_{\text{eff},a}$ (meV)	$t_{\text{eff},b}$ (meV)	$t_{\text{eff},d}$ (meV)	$t_{\text{eff},\text{cofacial}}^a$ (meV)
p6P hole (HOMO)	0	16	4	247
p6P electron (LUMO)	1	71	44	297
PPTTPP hole (HOMO)	0	7	5	252
PPTTPP electron (LUMO)	1	77	37	308
TTPPTT hole (HOMO)	0	8	24	255
TTPPTT electron (LUMO)	1	62	56	308

<sup>a</sup> Cofacial dimer configuration with a separation distance of 3.6 Å.

sults in a hopping rate (using a planar geometry to calculate the intramolecular reorganization energy)  $\sim 10^{-2}$  times that of pentacene.

### 3.3. Discussion

The experimentally found carrier mobilities are up to  $1 \text{ cm}^2 \text{ V}^{-1} \text{ s}^{-1}$  for PPTTPP and roughly an order of magnitude smaller for both p6P and TTPPTT. The value of  $1 \text{ cm}^2 \text{ V}^{-1} \text{ s}^{-1}$  for PPTTPP is one of the largest observed mobilities for such nanoscale organic crystals. These results can be compared with the mobility found in pentacene of up to  $35 \text{ cm}^2 \text{ V}^{-1} \text{ s}^{-1}$ . However, it should be noted that pentacene molecules cannot to our knowledge self-assemble into nanofibers and are, therefore, less suited for applications that require structuring at the nanoscale. Based on the transfer rate calculations, crude estimates of the mobility can be made from the Einstein relation  $\mu = eD/k_B T$ , in which  $e$  is the electronic charge and  $D$  the diffusion coefficient [33].  $D$  can be estimated from  $D = L^2 k_{ij}/2$ , where  $L$  is the effective length of charge transfer that can be approximated by the center of mass distance [33]. By neglecting the intermolecular reorganization energy, this leads to mobility estimates of  $10^{-2} \text{ cm}^2 \text{ V}^{-1} \text{ s}^{-1}$  for p6P and PPTTPP, while TTPPTT is predicted to have a mobility of  $10^{-1} \text{ cm}^2 \text{ V}^{-1} \text{ s}^{-1}$ . For comparison, this type of calculation provides an estimate of the mobility in pentacene of  $10^1 \text{ cm}^2 \text{ V}^{-1} \text{ s}^{-1}$ . We again emphasize that the approximations made here render these mobility estimates rather crude.

The theoretical evaluations of the transfer rates (and thus mobilities) for all three systems considered here result in values that are two to three orders of magnitude lower than that found in pentacene, in reasonable agreement with the experimental findings. However, while PPTTPP is found experimentally to exhibit the highest mobility, theory estimates TTPPTT to be the better conductor. The likely explanation resides in the assumption we made of equal intermolecular contributions to the reorganization energy of all systems; we come back to this point below.

In general, the LUMO transfer integral is larger than the corresponding HOMO transfer integral. The magnitude of the transfer integrals along different directions can be rationalized by considering the molecular structures in Fig. 1. The distance between molecules in a pair has a strong influence on the degree of electronic interaction [19]. As seen in Table 1, the electronic coupling strength is large in the cofacial geometry. Since the dimers taken out of the crystal structure in the *a* and *b* directions are essentially displaced cofacial dimers, and since the molecules oriented along the *b* direction are significantly closer to one another than the molecules along the *a* direction, the transfer integrals are found to be larger along the *b* direction.

The reorganization energies in the oligophenylene and oligophenylene–thiophene molecules are larger than the corresponding values determined for pentacene. This is consistent with the observed lower charge mobilities. The molecular backbone of these structures is less rigid than in pentacene, which has very low reorganization en-

ergy on the order of 0.1 eV [34]. The reorganization energy for hexathiophene is also included in Table 2, since hexathiophene would be the next molecular structure in the sequence of p6P, PPTTPP, and TTPPTT. An increase in reorganization energy is observed upon the presence of thiophene rings with TTPPTT having a lower reorganization energy than PPTTPP. We recall that the reorganization energies have been calculated while constraining the molecules to planar geometries, which is reasonable in the case of p6P and PPTTPP for which on average approximately coplanar geometries are observed in the crystal structure [17,35]. In contrast, TTPPTT exhibits a wavy oscillation in the geometry along the long axis of the molecule [18] (seen clearly looking down the long axis of the molecule shown in Fig. 1). We speculate that the wavy structure in the crystal phase could give rise to more significant intermolecular contributions to the reorganization energy; this might be the origin of the discrepancy in the trends between the calculated transfer rates and the measured carrier mobilities in our series of compounds.

## 4. Conclusions and outlook

The charge transport properties for three molecular systems: p6P, PPTTPP, and TTPPTT, all of which can self-assemble into nanofiber structures, have been investigated both experimentally and theoretically. The experimental study was made by electrical two-point measurements on individual nanofibers. The analysis of the electrical measurements is based on the Mott–Gurney formalism, which describes charge transport in the space-charge limited régime. Therefore, it provides estimates of the lower bound of the carrier mobility. Experimentally, all three types of nanofibers were found to exhibit carrier mobility ranging from 0.1 to  $1 \text{ cm}^2 \text{ V}^{-1} \text{ s}^{-1}$  with PPTTPP nanofibers having the highest mobility.

In such molecular crystals, charge transport occurs via incoherent hopping between neighboring molecules. We analyzed the transport parameters on the basis of the semi-classical Marcus theory, which relates the rate of charge transfer to the transfer integral between the two molecules involved in the transfer process and to the reorganization energies accompanying the charge relocation. The transfer integrals in various crystal directions and the intramolecular reorganization energies were estimated for the three systems by density functional theory calculations. In the crystal direction corresponding to the charge transport direction in the experimentally realized geometry, the theoretical estimates of the magnitude of the carrier mobilities in p6P, PPTTPP, and TTPPTT with respect to that for pentacene were found to be in good agreement with experiment.

Further experimental effort is now focused on investigating the charge transport properties in a field-effect transistor configuration to enable the determination of the field-effect mobility. Furthermore, other types of nanofibers can be formed from other phenylene-based molecules, which could exhibit improved electrical characteristics. The next step will be to include theoretical

modeling of these systems to determine the most promising candidates for experiments.

### Acknowledgements

We thank Dr. Manuela Schiek for providing the nanofiber samples incl. the synthesis of the PPTTPP and TTPPTT molecules. The VILLUM KANN RAMUSSEN FONDEN and the Danish research councils FTP and FNU are acknowledged for financial support. This work has been partly supported by the MRSEC Program of the National Science Foundation under Award DMR-0212302.

### References

- [1] J.-L. Brédas, D. Beljonne, V. Coropceanu, J. Cornil, *Chem. Rev.* 104 (2004) 4971.
- [2] R.H. Friend, R.W. Gymer, A.B. Holmes, J.H. Burroughes, R.N. Marks, C. Taliani, D.D.C. Bradley, D.A. Dos Santos, J.L. Brédas, M. Logdlund, W.R. Salaneck, *Nature* 397 (1999) 121.
- [3] C.J. Brabec, N.S. Sariciftci, J.C. Hummelen, *Adv. Funct. Mater.* 11 (2001) 15.
- [4] G. Horowitz, *Adv. Mater.* 10 (1998) 365.
- [5] C.D. Dimitrakopoulos, D.J. Mascaró, *IBM J. Res. and Dev.* 45 (2001) 11.
- [6] F. Balzer, H.G. Rubahn, *Appl. Phys. Lett.* 79 (2001) 3860.
- [7] J. Brewer, C. Maibohm, L. Jozefowski, L. Bagatolli, H.G. Rubahn, *Nanotechnology* 16 (2005) 2396.
- [8] F. Balzer, V.G. Bordo, A.C. Simonsen, H.G. Rubahn, *Phys. Rev. B* 67 (2003) 115408/1.
- [9] F. Quochi, F. Cordella, A. Mura, G. Bongiovanni, F. Balzer, H.G. Rubahn, *Appl. Phys. Lett.* 88 (2006) 041106/1.
- [10] M. Schiek, F. Balzer, K. Al-Shamery, J.R. Brewer, A. Lützen, H.G. Rubahn, *Small* 4 (2008) 176.
- [11] J. Kjelstrup-Hansen, H.H. Henrichsen, P. Bøggild, H.-G. Rubahn, *Thin Solid Films* 515 (2006) 827.
- [12] M. Klemenc, F. Meghdadi, S. Voss, G. Leising, *Synth. Met.* 85 (1997) 1243.
- [13] H.H. Henrichsen, J. Kjelstrup-Hansen, D. Engstrøm, C.H. Clausen, P. Bøggild, H.-G. Rubahn, *Org. Electron.* 8 (2007) 540.
- [14] F. Balzer, M. Schiek, H.-G. Rubahn, K. Al-Shamery, A. Lützen, *J. Vac. Sci. Technol. B* 26 (2008) 1619.
- [15] F. Balzer, M. Schiek, A. Lützen, K. Al-Shamery, H.-G. Rubahn, *Proc. SPIE* 6470 (2007) 647006/1.
- [16] K.N. Baker, A.V. Fratini, T. Resch, H.C. Knachel, W.W. Adams, E.P. Socci, B.L. Farmer, *Polymer* 34 (1993) 1571.
- [17] S. Hotta, M. Goto, R. Azumi, M. Inoue, M. Ichikawa, Y. Taniguchi, *Chem. Mater.* 16 (2004) 237.
- [18] M.-H. Yoon, A. Facchetti, C.E. Stern, T.J. Marks, *J. Am. Chem. Soc.* 128 (2006) 5792.
- [19] J.L. Brédas, J.P. Calbert, D.A. Da Silva Filho, J. Cornil, *Proc. Natl. Acad. Sci. U.S.A.* 99 (2002) 5804.
- [20] W. Warta, N. Karl, *Phys. Rev. B* 32 (1985) 1172.
- [21] R.A. Marcus, *Rev. Mod. Phys.* 65 (1993) 599.
- [22] E.F. Valeev, V. Coropceanu, D.A. Da Silva Filho, S. Salman, J.-L. Brédas, *J. Am. Chem. Soc.* 128 (2006) 9882.
- [23] G. Te Velde, F.M. Bickelhaupt, E.J. Baerends, C. Fonseca Guerra, S.J.A. Van Gisbergen, J.G. Snijders, T. Ziegler, *J. Comput. Chem.* 22 (2001) 931.
- [24] M.J. Frisch, G.W. Trucks, H.B. Schlegel, G.E. Scuseria, M.A. Robb, J.R. Cheeseman, J. Montgomery, J.A., T. Vreven, K.N. Kudin, J.C. Burant, J.M. Millam, S.S. Iyengar, J. Tomasi, V. Barone, B. Mennucci, M. Cossi, G. Scalmani, N. Rega, G.A. Petersson, H. Nakatsuji, M. Hada, M. Ehara, K. Toyota, R. Fukuda, J. Hasegawa, M. Ishida, T. Nakajima, Y. Honda, O. Kitao, H. Nakai, M. Klene, X. Li, J.E. Knox, H.P. Hratchian, J.B. Cross, C. Adamo, J. Jaramillo, R. Gomperts, R.E. Stratmann, O. Yazyev, A.J. Austin, R. Cammi, C. Pomelli, J.W. Ochterski, P.Y. Ayala, K. Morokuma, G.A. Voth, P. Salvador, J.J. Dannenberg, V.G. Zakrzewski, S. Dapprich, A.D. Daniels, M.C. Strain, O. Farkas, D.K. Malick, A.D. Rabuck, K. Raghavachari, J.B. Foresman, J.V. Ortiz, Q. Cui, A.G. Baboul, S. Clifford, J. Cioslowski, B.B. Stefanov, G. Liu, A. Liashenko, P. Piskorz, I. Komaromi, R.L. Martin, D.J. Fox, T. Keith, M.A. Al-Laham, C.Y. Peng, A. Nanayakkara, M. Challacombe, P.M.W. Gill, B. Johnson, W. Chen, M.W. Wong, C. Gonzalez, J.A. Pople, Gaussian 03, Revision B.05, Gaussian, Inc., Wallingford CT, 2004.
- [25] J. Huang, M. Kertesz, *J. Chem. Phys.* 122 (2005) 234707/1.
- [26] R.S. Sánchez-Carrera, V. Coropceanu, D.A. da Silva Filho, R. Friedlein, W. Osikowicz, R. Murdey, C. Suess, W.R. Salaneck, J.-L. Brédas, *J. Phys. Chem. B* 110 (2006) 18904; J.C. Sancho-García, *Chem. Phys.* 331 (2007) 321.
- [27] D.A. da Silva Filho, V. Coropceanu, D. Fichou, N.E. Gruhn, T.G. Bill, J. Gierschner, J. Cornil, J.-L. Brédas, *Phil. Trans. R. Soc. A* 365 (2007) 1435.
- [28] S.F. Nelson, Y.Y. Lin, D.J. Gundlach, T.N. Jackson, *Appl. Phys. Lett.* 72 (1998) 1854.
- [29] O.D. Jurchescu, J. Baas, T.M. Palstra, *Appl. Phys. Lett.* 84 (2004) 3061.
- [30] V. Coropceanu, J. Cornil, D.A. Da Silva Filho, Y. Olivier, R. Silbey, J.-L. Brédas, *Chem. Rev.* 107 (2007) 926.
- [31] V. Coropceanu, M. Malagoli, D.A. da Silva Filho, N.E. Gruhn, T.G. Bill, J.L. Brédas, *Phys. Rev. Lett.* 89 (2002) 275503/1.
- [32] G.R. Hutchison, M.A. Ratner, T.J. Marks, *J. Am. Chem. Soc.* 127 (2005) 2339.
- [33] M.-Y. Kuo, H.-Y. Chen, I. Chao, *Chem. Eur. J.* 13 (2007) 4750.
- [34] N.E. Gruhn, D.A. da Silva Filho, T.G. Bill, M. Malagoli, V. Coropceanu, A. Kahn, J.-L. Brédas, *J. Am. Chem. Soc.* 124 (2002) 7918.
- [35] R. Resel, *Thin Solid Films* 433 (2003) 1.

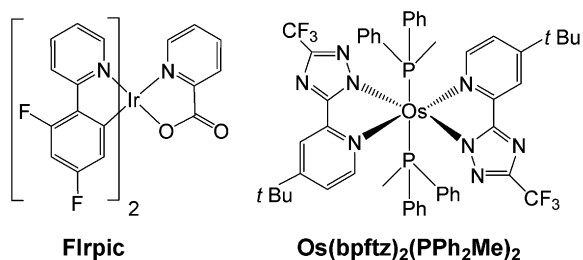


**Fig. 1.** The molecular structures of blue phosphorescent iridium complex Flrpic and the orange phosphorescent osmium complex Os(bpftz)<sub>2</sub>(PPh<sub>2</sub>Me)<sub>2</sub>.

represents a monodentate phosphine ligand] (as shown in Fig. 1) were employed in the preparation and studies of WOLEDs. The widely used blue phosphorescent emitter, Flrpic, exhibits very high photoluminescence (PL) quantum efficiency (>90%) in wide-gap hosts [6–8]. On the other hand, the Os complex Os(bpftz)<sub>2</sub>(PPh<sub>2</sub>Me)<sub>2</sub> with high steric hindrance shows orange–red emission around 603 nm, short excited-state lifetime (0.97 μs) and high PL quantum yield of ~90% in solution [9–11]. The present and related Os complexes had been used to fabricate highly efficient orange to red phosphorescent OLEDs with external quantum efficiencies approaching 20% [9–11]. Thus both iridium and osmium triplet emitters are intrinsically very efficient.

Selected spectral data of Os(bpftz)<sub>2</sub>(PPh<sub>2</sub>Me)<sub>2</sub>: MS (FAB, <sup>192</sup>Os): *m/z* 1130 (M<sup>+</sup>), 930 (M<sup>+</sup>–PPh<sub>2</sub>Me), 730 (M<sup>+</sup>–2PPh<sub>2</sub>Me). <sup>1</sup>H NMR (400 MHz, d<sub>6</sub>-acetone): δ 10.04 (d, 2H, *J*<sub>HH</sub> = 6.8 Hz), 7.26–7.24 (m, 4H), 7.15–7.09 (m, 4H), 7.00 (t, 4H, *J*<sub>HH</sub> = 7.6 Hz), 6.93–6.86 (m, 8H), 6.65–6.60 (m, 4H), 1.29 (s, 18H, <sup>1</sup>Bu), 1.22 (d, 6H, *J*<sub>HP</sub> = 3.2 Hz, Me). UV/Vis λ<sub>max</sub> (CH<sub>2</sub>Cl<sub>2</sub>): 401 (16,000), 448 (2500), 520 (1400) nm (ε, M<sup>-1</sup>cm<sup>-1</sup>); EL λ<sub>max</sub> (degassed CH<sub>2</sub>Cl<sub>2</sub>, RT): 603 nm; φ = 0.91; τ<sub>obs</sub> = 972 ns. EL λ<sub>max</sub> (as thin film): 613 nm; τ<sub>obs</sub> = 136 ns. Anal. Calcd. for C<sub>50</sub>H<sub>50</sub>F<sub>6</sub>N<sub>8</sub>OsP<sub>2</sub>: C, 53.18; N, 9.92; H, 4.46. Found: C, 53.30; N, 10.06; H, 4.62.

## 2.2. OLED fabrication

All compounds used were subject to temperature-gradient sublimation under high vacuum before use. OLEDs were fabricated on the ITO-coated glass substrates with

multiple organic layers sandwiched between the transparent bottom indium–tin-oxide (ITO) anode and the top metal cathode. The organic and metal layers were deposited by vacuum evaporation in a vacuum chamber with a base pressure of <10<sup>-6</sup> torr. The deposition system permits the fabrication of the complete device structure in a single vacuum pump-down without breaking vacuum. The deposition rate of organic layers was kept at ~0.2 nm/s. The active area of the device is 2 × 2 mm<sup>2</sup>, as defined by the shadow mask for cathode deposition.

## 2.3. Device characterizations

Current–voltage–luminance (*I–V–L*) characterization of the devices was measured using an Agilent 4155B semiconductor parameter analyzer and a Si photodiode calibrated with Photo Research PR650. EL spectra of devices were collected by a calibrated CCD spectrograph. Total photon output from the device (either from the viewing direction or from all surfaces of the device) was measured in an integrating sphere containing a calibrated photodetector.

## 3. Results and discussion

The first type of WOLEDs using these two complexes (i.e. Device A in Fig. 2) involved co-doping both emitters into the wide-gap host 1,3-bis(9-carbazolyl)benzene (mCP) as the emitting layer (EML) [12,13]. The structure of Device A was: ITO/α-NPD (30 nm)/TCTA (30 nm)/mCP: Firpic 8 wt.%; Os(bpftz)<sub>2</sub>(PPh<sub>2</sub>Me)<sub>2</sub> 0.5 wt.% (15 nm)/TAZ (50 nm)/LiF (0.5 nm)/Al (150 nm), where 4,4'-bis[N-(1-naphthyl)-N-phenyl-amino] biphenyl (α-NPD) and 4,4'-tris(carbazol-9-yl)-triphenylamine (TCTA) were used as the hole-transport layers (HTLs) [14,15], 3-(4-biphenyl)-4-phenyl-5-(tert-butylphenyl)-1,2,4-triazole (TAZ) as the electron-transport layer (ETL) [16], and LiF as the electron-injection layer [17].

Fig. 3a shows the electroluminescence (EL) spectra of Device A (normalized at the emission peak of the Os complex) at different brightness levels, and Fig. 3b shows the corresponding 1931 CIE coordinates. The EL shows contributions from both blue emission of Firpic and red emission of the Os complex, giving a white emission. The efficiency characteristics and the current–voltage–luminance (*I–V–L*)

LiF/Al	LiF/Al	LiF/Al	LiF/Al	LiF/Al	50 nm
TAZ	TAZ	TAZ	TAZ	TAZ	15 nm
mCP: Firpic: Os	mCP: Firpic	mCP: Firpic	mCP: Firpic	mCP: Firpic: Os	5 nm
TCTA	TCTA	TCTA	mCP	TCTA	25 nm
α-NPD	α-NPD	α-NPD	TCTA: Os	TCTA: Os	30 nm
ITO	ITO	ITO	α-NPD	α-NPD	
Glass	Glass	Glass	ITO	ITO	
			Glass	Glass	
<b>Device A</b>	<b>Device B</b>	<b>Device C</b>	<b>Device C1</b>	<b>Device D</b>	

**Fig. 2.** Schematic structures of various devices.

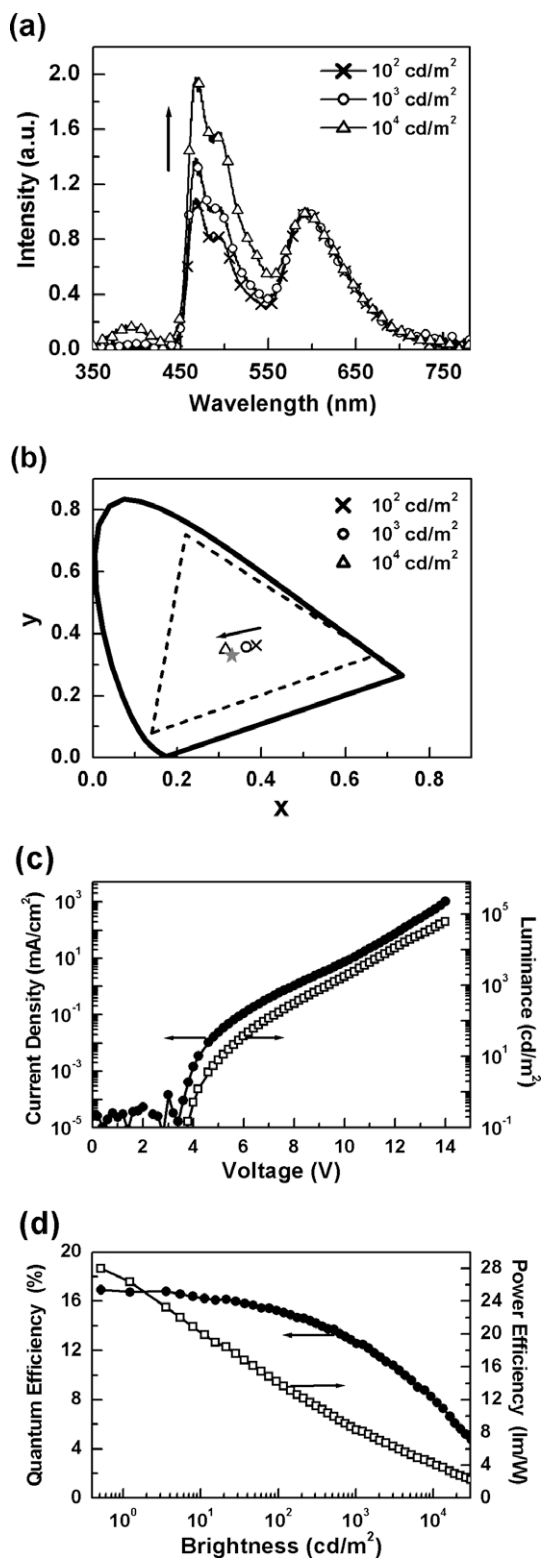


**Fig. 3.** (a) The normalized EL spectra of Device A at different brightness levels; (b) CIE coordinates of different brightness levels. (c) Current-voltage-luminescence ( $I$ - $V$ - $L$ ) characteristics. (d) External quantum efficiency/power efficiency (in the forward viewing direction) versus brightness.

characteristics of Device A are shown in Fig. 3c and d, respectively, and are summarized in Table 1. Impressively, with a simple single-emitting-layer configuration, the Device A shows rather high peak efficiencies of 17% photon/electron, 35.6 cd/A, and 28 lm/W for the forward viewing directions. Such high quantum efficiency implies a high internal quantum efficiency of nearly 85% in the device (assuming  $\sim 20\%$  optical out-coupling efficiency from the device). At the practical brightness of  $100$  cd/m<sup>2</sup>, the forward viewing efficiencies remained high at around 15.1%, 30.4 cd/A, and 13.6 lm/W. For lighting applications, the light emitted from all surfaces of the substrate can in principle be redirected to the forward direction by some lighting fixtures; hence the total efficiencies of the device were also characterized using an integrating sphere setup [18,19]. The total quantum and power efficiencies measured in the sphere were about 1.7 times larger than the forward viewing efficiencies, consistent with previous reports [2]. As such, Device A gave a peak total external quantum efficiency and a total power efficiency of 28.8% and 47.5 lm/W, respectively.

The high quantum efficiencies of the WOLED A were indeed surprising, since the control blue-emitting device with a structure similar to A exhibited substantially lower efficiencies. This control blue-emitting OLED (Device B, Fig. 2) had the structure of: ITO/ $\alpha$ -NPD (30 nm)/TCTA (30 nm)/mCP: Firpic 8 wt.%/TAZ (50 nm)/LiF (0.5 nm)/Al (150 nm), which was nearly the same as that of Device A except for no Os complex co-doped into the mCP host. Such a blue-emitting device gave a substantially lower peak external quantum efficiency of  $\sim 4.8\%$  (in the forward viewing directions, Fig. 4c and Table 1). With co-doping a smaller amount of the Os complex in the emitting layer (i.e. Device A), the quantum efficiency of the whole system was more than tripled, indicating that the Os complex had additional and critical functionalities other than just serving as an energy acceptor for the blue emitter Firpic.

To investigate the role of the Os complex, a third testing device structure (Device C, Fig. 2) with the Os complex doped into a portion (25 nm) of the hole-transport layer, TCTA, was then fabricated and characterized. This device had the structure of: ITO/ $\alpha$ -NPD (30 nm)/TCTA: Os(bpftz)<sub>2</sub>(PPh<sub>2</sub>Me)<sub>2</sub> 3.0 wt.% (25 nm)/TCTA (5 nm)/mCP: Firpic 8 wt.% (15 nm)/TAZ (50 nm)/LiF (0.5 nm)/Al (150 nm). The EL spectra and corresponding CIE coordinates of Devices B and C are shown in Fig. 4a and b, respectively. The external quantum efficiency versus luminance of Devices B and C are shown in Fig. 4c. As shown in Fig. 4a, EL from Device C shows dominant blue emission of Firpic, yet the peak quantum efficiency is now largely raised to 11.7% (25.7 cd/A) as compared to 4.8% observed for Device B (Fig. 4c and Table 1). It is also worth mentioning that by replacing the 5-nm non-doped TCTA buffer in Device C with the higher-energy-gap mCP (Device C1, Fig. 2), the efficiency of the blue OLED can be further increased to 14% due to better confinement of high-energy triplet excitons (Table 1).

Comparing device results of Devices A, B, and C clearly suggests that doping the Os complex into either the hole-transport layer TCTA or the mCP host layer had improved the balance between hole and electron injection/transport

**Table 1**

Summary of devices characteristics.

Device	Efficiency (max.) [% cd/A, lm/W]	Efficiency (at $10^2$ cd/m <sup>2</sup> ) [% cd/A, lm/W]	Total efficiency [% lm/W]	CIE coordinates (at $10^2$ , $10^4$ cd/m <sup>2</sup> )
A	17.0, 35.6, 28.0	15.1, 30.4, 13.6	28.8, 47.5	(0.388, 0.363), (0.315, 0.348)
B	4.8, 10.2, 6.1	4.4, 9.3, 4.9	–	(0.170, 0.356), (0.172, 0.355)
C	11.7, 25.7, 12.6	11.7, 25.6, 11.8	–	(0.178, 0.359), (0.208, 0.366)
C1	14.0, 28.7, 16.8	13.6, 27.9, 12.2	–	(0.205, 0.344), (0.220, 0.344)
D	14.9, 29.3, 17.8	13.1, 25.9, 8.9	25.4, 35.3	(0.334, 0.362), (0.311, 0.356)

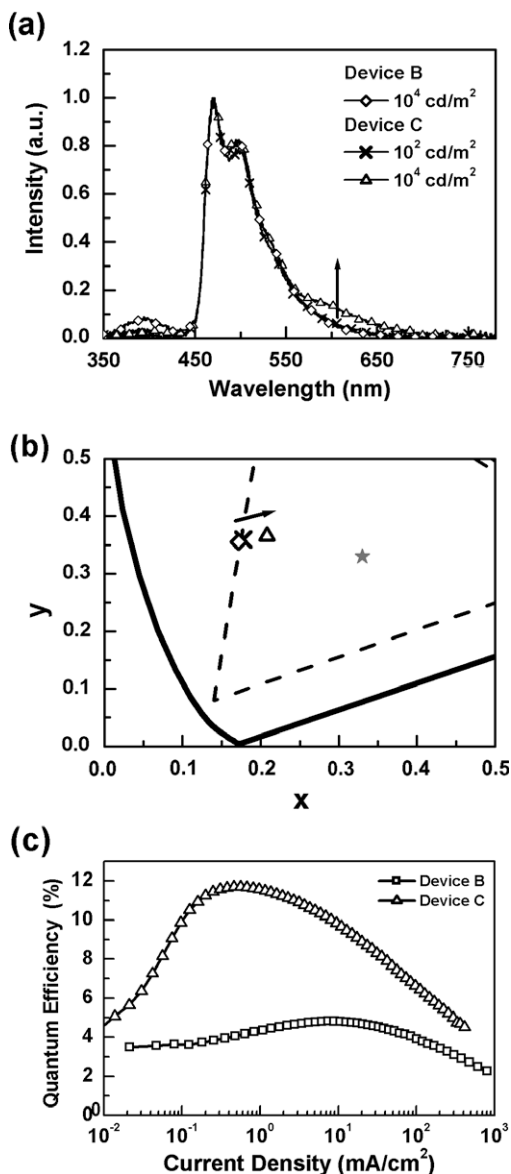


**Fig. 4.** (a) The EL spectra of Device B and C at different brightness levels; (b) CIE coordinates of Device B and C at different brightness levels; (c) external quantum efficiency (in the forward viewing direction) versus current density for Device B and C.

into the emitting layer mCP:Flrpic, thus greatly enhanced the EL efficiency. Electrochemical characterizations of related Os complexes show that they in general possessed low oxidation potentials (and thus low ionization poten-

tial). The ionization potential of the present Os complex estimated from the oxidation potential is about 4.8 eV [9], which is substantially lower than those of TCTA, mCP and Flrpic (all of 5.5–6.0 eV) [6,12–15]. In view of such an energy-level relationship, it is well expected that the Os complex functioned as an effective hole traps in both Devices A and C, retarding hole-transport and reducing excessive hole-injection into the emitting region [20–23]. Indeed, the lower voltage of Device B compared to those of Devices A and C (as compared in Fig. 5) clearly supports this hole-trapping picture. This hole trapping also reduces excessive hole-injection into the electron-transport layer since the UV emission from the electron-transport layer TAZ was generally reduced by doping the Os complex [24]. The accumulation of trapped holes might also help establish a stronger electric field for enhancing electron injection into the emitting layer. Overall, all these factors contributed to better balance of the carrier transport for both carriers and the efficiency enhancement.

The efficiencies of Device A are impressive, yet one notices that it showed a significant color shift when the bias/brightness was increased (Fig. 3a and b). Blue emission from Flrpic grows relatively to Os(bpftz)<sub>2</sub>(PPh<sub>2</sub>Me)<sub>2</sub> emission at higher current densities, causing the 1931 CIE coordinates to blue-shift from (0.388, 0.363) to (0.315, 0.348) at the brightness of  $10^2$ – $10^4$  cd/m<sup>2</sup>. Color variation with increased bias is commonly seen in WOLEDs [25–27]. This issue may be mitigated by creating another channel in the device for the high-energy excitons to remain appropriately relaxed or be transferred to the lower-energy excited states of Os complexes even at high excitation densities. The bias- and brightness-dependent EL spectra of Device C (Fig. 4a and b) indeed provided a good hint to the design of such a device. In Device C, the contribution of the Os emission (although smaller) increased with the brightness, contrary

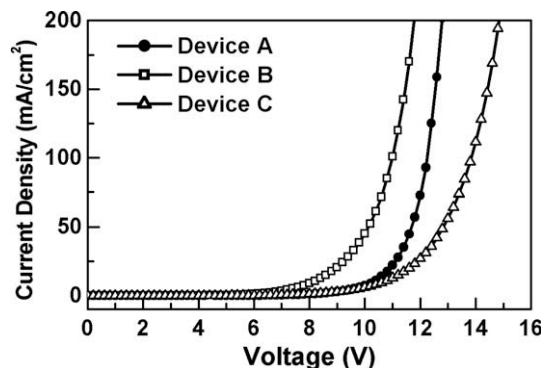


**Fig. 5.** Current–voltage (*I*–*V*) characteristics of Devices A, B, and C.



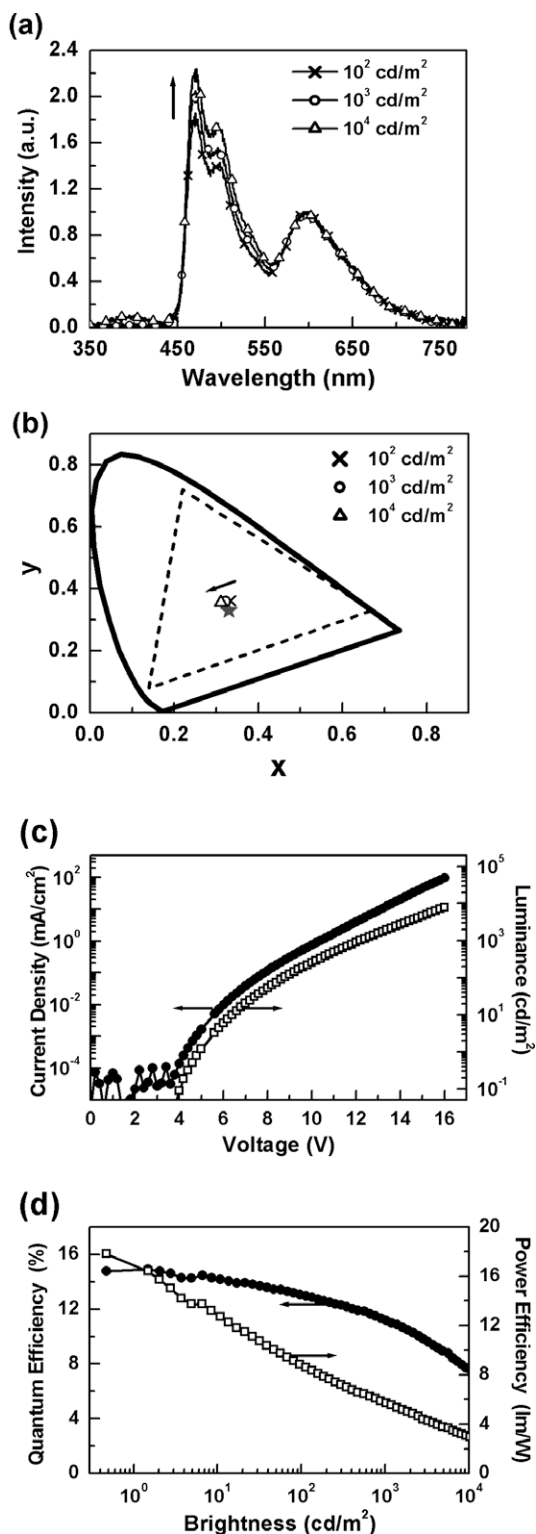


**Fig. 6.** (a) The normalized EL spectra of Device D at different brightness levels; (b) CIE coordinates of Device D at different brightness levels; (c) Current–voltage–luminescence ( $I$ – $V$ – $L$ ) characteristics. (d) External quantum efficiency/power efficiency versus brightness.

to the case of Device A. Such characteristic suggests that in Device C, at higher bias/brightness, either the carrier recombination zone shifted closer to the TCTA:Os(bpftz)<sub>2</sub>(PPh<sub>2</sub>Me)<sub>2</sub> layer or a portion of the high-energy excitons in the mCP:Flrpic layer migrated to the TCTA:Os(bpftz)<sub>2</sub>(PPh<sub>2</sub>Me)<sub>2</sub> layer (which is possible because the triplet energy of the 5-nm buffer TCTA was lower than that of Flrpic), increasing the emission from the Os complex.

Making use of such phenomena, the second type of WOLEDs in this work, Device D (Fig. 2), was fabricated using the structure of: ITO/ $\alpha$ -NPD (30 nm)/TCTA:Os(bpftz)<sub>2</sub>(PPh<sub>2</sub>Me)<sub>2</sub> 3.0 wt.% (25 nm)/TCTA (5 nm)/mCP:Flrpic 8 wt.%: Os(bpftz)<sub>2</sub>(PPh<sub>2</sub>Me)<sub>2</sub> 0.3 wt.% (15 nm)/TAZ (50 nm)/LiF (0.5 nm)/Al (150 nm). Device D simultaneously incorporated a red EML and a white EML. On one hand, the concentration of the Os complex in the white EML was decreased to suppress the red emission from the white EML and to achieve a more balanced white at lower biases. On the other hand, the Os complex in the TCTA layer enhanced the red emission at higher biases. The resulting EL spectra and CIE coordinates of Device D at different brightnesses are shown in Fig. 6a and b. Compared to Device A, the variation of EL spectra with biases in Device D was greatly reduced, substantially improving the color stability. As shown in Fig. 6b, for the brightness of  $10^2$ – $10^4$   $\text{cd/m}^2$ , only a small shift of CIE coordinates from (0.334, 0.362) to (0.311, 0.356) was observed, giving ( $\Delta x = -0.023$ ,  $\Delta y = -0.006$ ). Fig. 6c and d show the  $I$ – $V$ – $L$  characteristics and efficiency of Device D. Device D gives peak efficiencies of 14.9%, 29.3  $\text{cd/A}$ , and 17.8  $\text{lm/W}$  in the forward viewing direction, corresponding to total peak efficiencies of 25.4% and 30.3  $\text{lm/W}$  measured by the integrating sphere. At the practical brightness of 100  $\text{cd/m}^2$ , this device exhibits efficiencies of 8.9  $\text{lm/W}$ , 13.1%, and 25.9  $\text{cd/A}$  in the forward viewing direction. The EL characteristics of devices are summarized in Table 1.

#### 4. Conclusions

In summary, we have shown that the unique multifunctional capabilities of the orange–red phosphorescent Os complex are highly useful for achieving excellent internal and external efficiencies of WOLEDs. This is not only due to the high emission efficiency of the Os complex, but also due to its effective hole trapping capability, which is beneficial and useful for balancing hole/electron transport when doped at appropriate locations of the device. Furthermore, by placing an emitting/trapping layer incorporating the Os complex in the proximity of a white-emitting layer also incorporating the Os complex, we also report an efficient phosphorescent WOLED structure that would provide improved color stability versus biases/brightnesses. Overall, we conclude that the multi-functionality of the phosphorescent Os complex may be of use for designs of highly efficient white phosphorescent OLEDs.

#### Acknowledgements

The authors gratefully acknowledge the financial support from National Science Council and Ministry of Economic Affairs of Taiwan.

## References

- [1] J. Kido, M. Kimura, K. Nagai, *Science* 267 (1994) 1332–1334.
- [2] S. Tokito, T. Iijima, T. Tsuzuki, F. Sato, *Appl. Phys. Lett.* 83 (2003) 2459–2461.
- [3] B.W. D'Andrade, R.J. Holmes, S.R. Forrest, *Adv. Mater.* 16 (2004) 624–628.
- [4] B.W. D'Andrade, S.R. Forrest, *Adv. Mater.* 16 (2004) 1585–1595.
- [5] Y. Sun, N.C. Giebink, H. Kanno, B. Ma, M.E. Thompson, S.R. Forrest, *Nature* 440 (2006) 908–912.
- [6] Y. Kawamura, K. Goushi, J. Brooks, J.J. Brown, H. Sasabe, C. Adachi, *Appl. Phys. Lett.* 86 (2005) 071104.
- [7] M.-H. Tsai, H.-W. Lin, H.-C. Su, T.-H. Ke, C.-C. Wu, F.-C. Fang, Y.-L. Liao, K.-T. Wong, C.-I. Wu, *Adv. Mater.* 18 (2006) 1216–1220.
- [8] N. Chopra, J. Lee, Y. Zheng, S.-H. Eom, J. Xue, F. So, *Appl. Phys. Lett.* 93 (2008) 143307.
- [9] P.-I. Shih, C.-F. Shu, Y.-L. Tung, Y. Chi, *Appl. Phys. Lett.* 88 (2006) 251110.
- [10] Y.-L. Tung, S.-W. Lee, Y. Chi, Y.-T. Tao, C.-H. Chien, Y.-M. Cheng, P.-T. Chou, S.-M. Peng, C.-S. Liu, *J. Mater. Chem.* 15 (2005) 460–464.
- [11] F. Huang, P.-I. Shih, C.-F. Shu, Y. Chi, A.K.-Y. Jen, *Adv. Mater.* 21 (2009) 361–365.
- [12] R.J. Holmes, S.R. Forrest, Y.-J. Tung, R.C. Kwong, J.J. Brown, S. Garon, M.E. Thompson, *Appl. Phys. Lett.* 82 (2003) 2422–2424.
- [13] S.-H. Eom, Y. Zheng, N. Chopra, J. Lee, F. So, J. Xue, *Appl. Phys. Lett.* 93 (2008) 133309.
- [14] C.-C. Wu, Y.-T. Lin, K.-T. Wong, R.-T. Chen, Y.-Y. Chien, *Adv. Mater.* 16 (2004) 61–65.
- [15] T.-C. Chao, T.-T. Lin, C.-Y. Yang, T.-S. Hung, H.-C. Chou, C.-C. Wu, K.-T. Wang, *Adv. Mater.* 17 (2005) 992–996.
- [16] J. Kido, C. Ohtaki, K. Hongawa, K. Okuyama, K. Nagai, *Jpn. J. Appl. Phys.* 32 (Pt. 2) (1993) L917–L920.
- [17] L.S. Hung, C.W. Tang, M.G. Mason, *Appl. Phys. Lett.* 70 (1997) 152–154.
- [18] S.R. Forrest, D.D.C. Bradley, M.E. Thompson, *Adv. Mater.* 15 (2003) 1043–1048.
- [19] Y. Sun, S.R. Forrest, *Nat. Photonics* 2 (2008) 483–487.
- [20] S.A. Van Slyke, C.H. Chen, C.W. Tang, *Appl. Phys. Lett.* 69 (1996) 2160–2162.
- [21] N. von Malm, J. Steiger, R. Schmechel, H. von Seggern, *J. Appl. Phys.* 89 (2001) 5559–5563.
- [22] H. Aziz, Z.D. Popovic, *Appl. Phys. Lett.* 80 (2002) 2180–2182.
- [23] V.V. Jarikov, *Appl. Phys. Lett.* 92 (2008) 244103.
- [24] C.-H. Chang, Y.-J. Lu, C.-C. Liu, Y.-H. Yeh, C.-C. Wu, *J. Disp. Technol.* 3 (2007) 193–199.
- [25] X.-M. Yu, H.-S. Kwok, W.-Y. Wong, G.-J. Zhou, *Chem. Mater.* 18 (2006) 5097–5103.
- [26] G. Schwartz, M. Pfeiffer, S. Reineke, K. Walzer, K. Leo, *Adv. Mater.* 19 (2007) 3672–3676.
- [27] K.S. Yook, J.Y. Lee, *Appl. Phys. Lett.* 92 (2008) 193308.

OFETs using the “macroscopic-sized” semiconductor single crystals. Here the macroscopic-sized crystals are roughly a 0.1-mm-square (or more) in size and the semiconductor devices can readily be made on them. Such crystals were hard to make by conventional vacuum deposition methods [8,9,15–17] including hot wall epitaxy (HWE) [18–23].

Our method resembles the physical vapor transport (PVT) [2–4,7,24–26] in that the crystal growth is carried out at an ordinary pressure. However, our method is more suitable for making the thin crystals directly onto the substrate; the PVT methods are mostly used for the fabrication of free-standing single crystals. Moreover, we need only a small size apparatus. The apparatus can be accommodated in a ~10-cm cube (excluding a space of an inert atmosphere).

To achieve highest possible performance the crystals must have the smallest possible number of defects. Although in our initial attempt the crystals involved many cracks as in the case of the previous paper [13], we have been successful in removing them by inserting self-assembled monolayers (SAMs) between the semiconductor crystal and the device substrate. At the same time, the SAMs play a role in constructing a uniform interface between the organic semiconductor layer and the gate insulator [27].

Fig. 1a shows a schematic geometry of the apparatus. It is characterized by a couple of plates (one of which acts as the FET device substrate) put in close proximity such that their distance is kept less than 1 mm (typically 0.7 mm) by spacers placed at either side. Two heaters are vertically set in close contact with these plates. The source organic material is placed to be sublimed on the lower plate. The temperatures of the two heaters are regulated so that the bottom heater temperature can be held by 5–10 °C higher than that of the upper heater, allowing the crystals to grow directly on the upper substrate. In virtue of the narrow space surrounded with the two plates the crystal growth proceeds nearly at the thermodynamic equilibrium. This

enables us to produce high-quality single crystals with macroscopic size. The resulting crystals are well-defined polygons with individual sides clearly appearing. Moreover, these crystals are of the thickness of a hundred to several hundreds of nanometers and perfectly suited to forming the devices.

## 2. Experimental

### 2.1. Substrate preparation

We used for the substrates quarried Si wafers (~1 cm × 1 cm) with a thermally grown SiO<sub>2</sub> layer (300 nm in thickness). The substrates were cleansed in a hot aqueous solution of sulfuric acid and hydrogen peroxide for 1 h and subsequently rinsed with distilled water in an ultrasonic cleaner for 10 min. These substrates were treated with three different species of SAMs. For the **1,1,1,3,3,3**-hexamethyldisilazane (HMDS) treatment, the substrates were exposed to HMDS vapor at 80–85 °C for 2 h and further immersed with toluene, acetone and isopropyl alcohol in the ultrasonic cleaner for 3–5 min each to remove the excess HMDS. In the case of phenyltrichlorosilane (PTS) the substrates were immersed into its 0.86 M toluene solution for 6 h and subsequently rinsed with toluene, acetone, and isopropyl alcohol in the ultrasonic cleaner for 10 min each. With the octadecyltrichlorosilane (OTS) treatment the substrates were immersed for 16 h in its 12.5 mM solution of a hexane/toluene mixture (hexane:toluene = 2:8) and rinsed similarly. All these substrates were further cleansed with ethanol vapor before use.

### 2.2. Crystal growth

Of the organic semiconductors, we chose from among thiophene/phenylene co-oligomers (TPCOs) 1,4-bis(5-phenylthiophen-2-yl)benzene (AC5) [28] and 5,5'-diphenyl-2,2':5',2'':5'',2''':5''',2''''-quinquethiophene (P5T) [29]. Their structural formulae are depicted in Fig. 1b (AC5) and c (P5T). Their synthesis and purification methods are described in the literature [28,29].

The source organic material placed on the lower plate faced the oxide layer of the quarried Si wafer substrate attached to the upper heater (Fig. 1a). The bottom heater (to sublime the source material) is 5, 3 and 10 cm in width, height and length, respectively. The corresponding sizes of the upper heater (for the substrate) are 5, 3 and 5 cm. These are composed of a copper block equipped with a sheath heater. This configuration permits us to grow the crystal in firm contact with the oxide layer of the Si substrate and subsequently to shape the device. The crystal growth is routinely performed in a nitrogen atmosphere with the gas flow rate of 40 ml/min to prevent the organic material from degrading. In the case of the AC5 (P5T) growth the temperature of the upper heater was kept steadily at 223 °C (265 °C) for 5.5 h (8.5 h). The temperature of the bottom heater was kept at 230 °C (270 °C) for the first 1 h and then lowered monotonically to 223 °C (265 °C) taking another 4.5 h (7.5 h) in the case of the AC5 (P5T) growth.

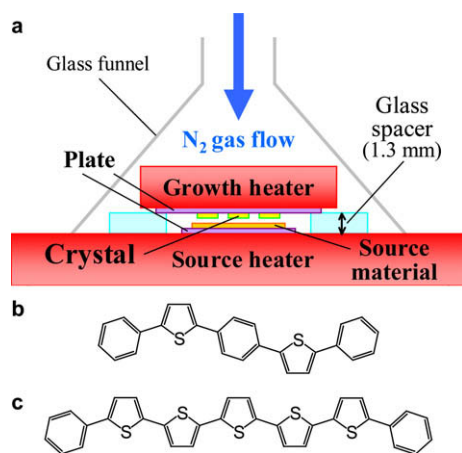


**Fig. 1.** (a) Schematic diagram of the crystal growth apparatus. The distance of a couple of plates (the upper one of which acts as a substrate) is kept less than 1 mm (typically 0.7 mm) by glass spacers placed at either side. Two heaters are vertically set in close contact with these plates. (b and c) Structural formulae of the organic semiconductor materials. (b) AC5 and (c) P5T.

### 2.3. Structural characterization and electrical measurements

The nonpolarizing and polarizing micrographs of the grown crystals and fabricated devices were taken with a NIKON ELIPSE LV100POL microscope equipped with an Hg lamp. The X-ray diffraction of the AC5 crystals (placed on the substrates) was measured on a Rigaku RINT 2500 X-ray diffractometer with Cu K $\alpha$  radiation. The thickness of the crystals was measured with an ULVAC DEKTAK-3ST surface profiler. The surface feature of the AC5 crystal grown on the HMDS-treated substrate was precisely observed using a Veeco Instruments Di Multimode IIIa atomic force microscope (AFM) operated in a tapping mode. The electrical measurements were carried out for the crystal devices using an Advantest R6245 two-channel voltage current source/monitor under an ambient environment and under vacuum ( $\sim 10^{-3}$  Pa).

## 3. Results and discussion

### 3.1. Crystal growth and characterization

Fig. 2 shows a micrograph of an AC5 crystal (grown on the SiO<sub>2</sub>/Si substrate without surface treatment). The crystal is a hexagon with each side ranging from 172 to 251  $\mu\text{m}$ . Many cracks were present on its surface. These cracks were likely to be generated during the crystal growth process because of the difference in thermal expansion coefficients between the AC5 crystal and the substrate. The orientation of the cracks is parallel to the crystal axes. Fig. 3 shows polarizing micrographs of a crystal grown on the substrate treated with HMDS. The micrographs were taken under the diagonal position (Fig. 3a) and the extinction position (Fig. 3b) of the crossed Nicols. The hexagon crystal is free from the cracks. The size of the crystal sides ranged from 199 to 222  $\mu\text{m}$ . An entirely vanishing view of the crystal at the extinction position (Fig. 3b) demonstrates the formation of a single crystal.

Fig. 3c shows the X-ray diffraction pattern of AC5 crystals grown on the HMDS-treated substrate. Only the first-

and higher-order peaks (up to 14th at 59.9 $^\circ$ ) of the same diffraction plane are observed. The plane distance is evaluated from these peaks to be  $d = 21.74$   $\text{\AA}$ , in good agreement with the half distance of the  $ab$ -plane (21.63  $\text{\AA}$ ) [30]. We determined the crystal axes as in Fig. 3a by comparing the characteristic angles of the crystal with the crystallographic data [30]. Fig. 3d shows the surface profile of the AC5 crystal scanned along the crystal  $b$ -axis. The crystal has a uniform thickness of 820 nm within an error of  $\sim 3$  nm. Fig. 3e shows the three-dimensional AFM picture of the AC5 crystal scanned over an area of  $2 \mu\text{m} \times 2 \mu\text{m}$ . Fig. 3f shows its depth profile as a function of the position. The observed step height is estimated to be  $\sim 0.27$  nm, indicating that the surface of the AC5 crystal is exceedingly flat with its roughness of at most the molecular length.

With a PVT method Liu et al. [13] fabricated micrometer-sized patterns of organic semiconductor single crystals with controlled sizes and shapes. Recently, we have demonstrated in the solution process that the crystals are selectively grown on the friction-transferred poly(tetrafluoroethylene) with the crystal axes preferentially oriented parallel to the drawing direction [31]. Our present method can consistently be combined on demand with such an epitaxial method to produce the micrometer-sized patterns.

### 3.2. Field-effect transistors made of the grown crystals

The crystals obtained by our method can immediately be applied to the OFET devices. Fig. 4a shows a micrograph of the device made of an AC5 crystal grown on the HMDS-treated substrate (top-contact configuration). The thickness of this particular crystal was 624 nm. Fig. 4b schematically shows the device structure. For the device to perform the normal action, it will be indispensable to secure the ohmic contact between the semiconductor layer and (source and drain) electrodes. This is done with the AC5 device by improving the deposition of metal; the substrate surface was tilted  $\sim 30^\circ$  to the deposition source to completely cover the crystal edges with gold (see the inset of Fig. 4b) [32]. The gold electrodes (70 nm in thickness) were formed in vacuum (less than  $3 \times 10^{-3}$  Pa) so as to be the drain and source contacts. The resulting parallel electrodes define the channel length as 20.4  $\mu\text{m}$  and the width as 131.0  $\mu\text{m}$ . The silicon wafer and the silicon dioxide layer were used as a gate contact and a gate insulator, respectively. Fig. 4c represents the output characteristics of the AC5 device in air. The device shows the typical p-type performance. Compared to our previous top-contact AC5 crystal devices [14,33], the convex-downward behavior of the drain current near the origin is drastically suppressed. The estimated mobility and threshold voltage at the saturation region were 0.040  $\text{cm}^2/\text{Vs}$  and  $-0.72$  V, respectively. Those measured in vacuum were 0.037  $\text{cm}^2/\text{Vs}$  and  $-2.0$  V. The mobility is significantly larger than those of our previous studies [14,33,34].

P5T crystal devices exhibit even better device performances. Fig. 5a shows a micrograph of the device made of a P5T crystal on the HMDS-treated substrate. The thickness of this particular crystal was 100 nm. Deposited gold electrodes define the channel length as 10.4  $\mu\text{m}$  and the

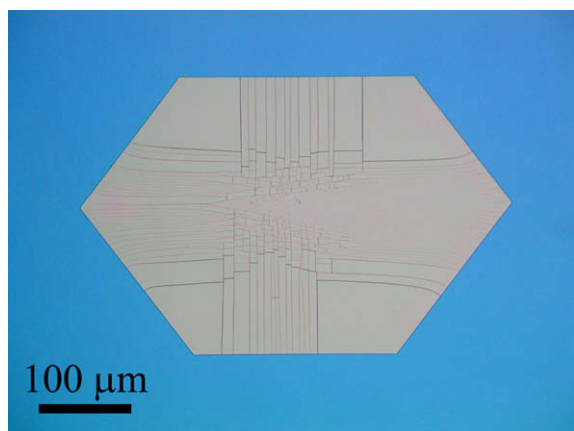
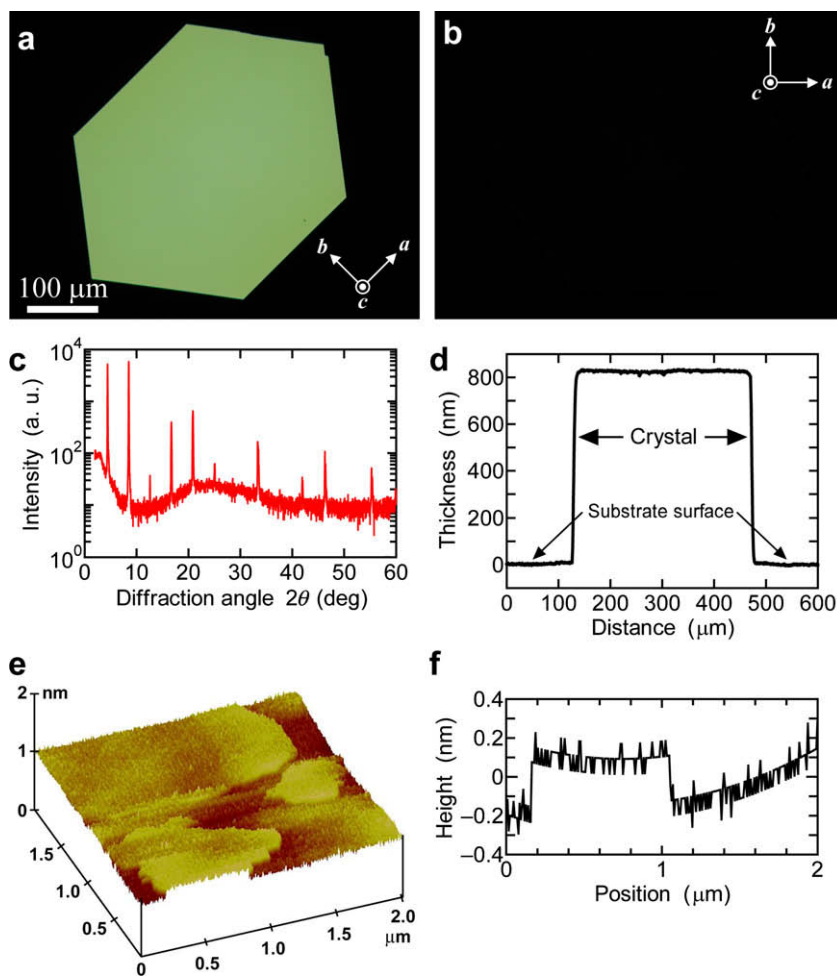


Fig. 2. Micrograph of an AC5 crystal on the SiO<sub>2</sub>/Si substrate without surface treatment.



**Fig. 3.** (a and b) Polarizing micrographs of an AC5 crystal on the SiO<sub>2</sub>/Si substrate treated with HMDS before the crystal growth. These were taken under (a) the diagonal position and (b) the extinction position (i.e. rotated by 45° relative to the diagonal position) of the crossed Nicols. An entirely vanishing view of the crystal at the extinction position demonstrates the formation of a single crystal. (c) X-ray diffraction pattern of AC5 crystals on the HMDS-treated substrate. (d) Surface profile of the AC5 crystal. (e) Three-dimensional AFM picture of the AC5 crystal and (f) its depth profile.

channel width as 46.3 μm. The width was the average of  $w_1$  and  $w_2$  (Fig. 5a). The P5T device exhibits an excellent performance and sustains it both in air and in vacuum. To demonstrate this, we have repeatedly carried out the electrical measurements both in air and in vacuum (total 15 measurements in air and 10 measurements in vacuum) during fifteen days after the device fabrication. The device was stored in a vacuum desiccator after the measurements. Fig. 5b represents the output characteristics of the said P5T device measured in air at the last day. The p-type FET performance is characterized as follows: (i) the saturation in the drain current is clearly noted at higher drain-source voltages. (ii) the drain currents increase linearly with drain-source voltage around the origin (see Fig. 5c as the enlarged diagram); even a hint of a convex-downward behavior is unnoticeable.

The device sustains the aforementioned characteristics throughout the whole courses of data acquisition both in air and in vacuum. During these courses the device steadily keeps the mobility and threshold voltage. Taking into

account all these data (obtained both in air and vacuum), the mobilities ranged 0.09–0.13 cm<sup>2</sup>/V s and the threshold voltages ranged –11.6 to –0.27 V. Notice that the varying range of the threshold voltages (~11 V) is by far smaller than the corresponding number ~100 V which was observed by Kumaki et al. [35] for the pentacene-based OFET in air. They attributed this shift to the deprotonation of SiOH on the gate insulator surface caused by the adsorption of H<sub>2</sub>O and O<sub>2</sub> [35]. This contrast is due probably to that in the present studies the crystals are in close contact with the gate insulator assisted by the SAMs. This prevents air and moisture from infiltrating into that interface and, hence, ensures the steady device performance.

Similar device performances were attained in the P5T crystal devices fabricated on the substrates treated with the other SAMs. Fig. 6a shows the output characteristics of the P5T crystal device on the PTS-treated substrate. The characteristics of the OTS-treated device are indicated in Fig. 6b. The channel length and width of the PTS device

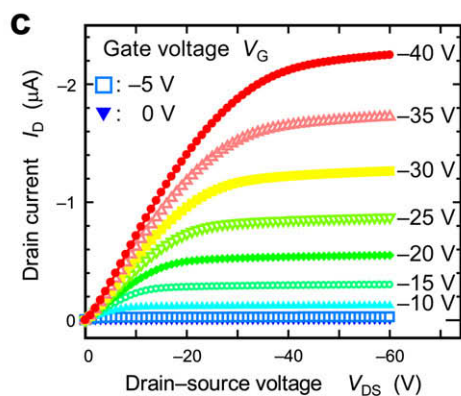
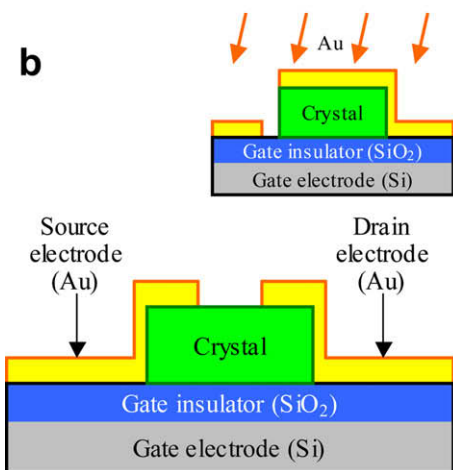
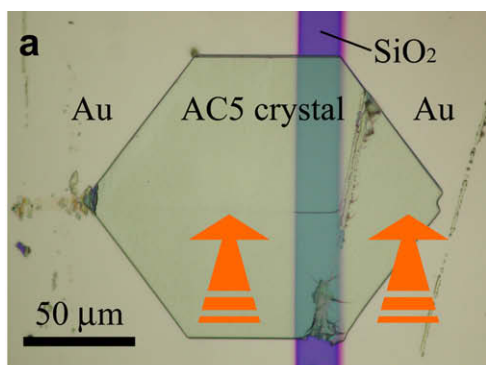


**Fig. 4.** (a) Micrograph of the device using an AC5 crystal on the HMDS-treated substrate (top-contact configuration). The gold electrodes were deposited on the substrate obliquely from the bottom shown as the thick arrows. (b) Schematic structure of the AC5 crystal OFET. The inset shows the side view of the device with the arrows representing the gold deposition. (c) The output characteristics of the AC5 device measured in air.

are 9.7  $\mu\text{m}$  and 20.7  $\mu\text{m}$ , respectively. Those of the OTS device are 10.0  $\mu\text{m}$  and 70.8  $\mu\text{m}$ . These SAM-treated devices exhibited the steady device performances as well. We examined the device performance during eleven (a hundred) days after the PTS (OTS) device fabrication. For the PTS device, the mobility and threshold voltage measured in air (in vacuum) at the last day were 0.13  $\text{cm}^2/\text{V s}$

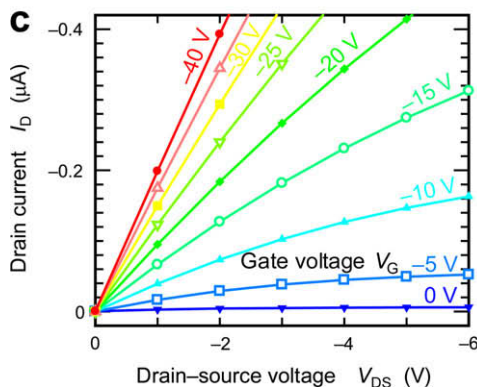
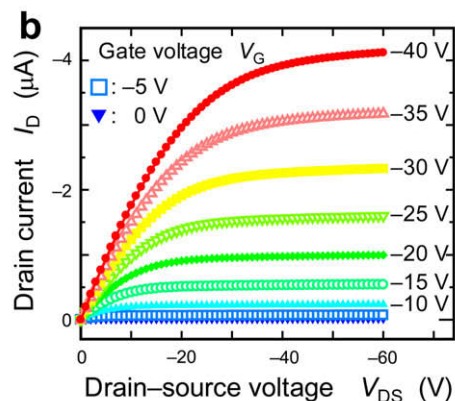
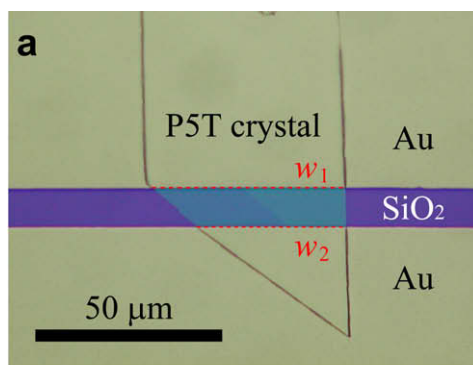


**Fig. 5.** (a) Micrograph of the top-contact OFET device made of a P5T thin crystal. The substrate was treated with HMDS. (b) The output characteristics of the P5T device. The measurements were repeatedly carried out both in air and in vacuum during fifteen days after the device fabrication. The particular characteristics were obtained in air at the last day. The carrier mobility and threshold voltage were estimated to be 0.10  $\text{cm}^2/\text{V s}$  and  $-0.27\text{ V}$  in the saturation region, respectively. (c) Enlarged characteristics of (b) around the origin.

(0.13  $\text{cm}^2/\text{V s}$ ) and  $-5.4\text{ V}$  ( $-9.4\text{ V}$ ) in the saturation region, respectively; those for the OTS device were 0.051  $\text{cm}^2/\text{V s}$  (0.056  $\text{cm}^2/\text{V s}$ ) and 3.2 V ( $-2.2\text{ V}$ ). For this device the mobility tended to increase with time during the course of the storage; the threshold voltage varied  $\sim 20\text{ V}$  across the 0 V.

The mobilities we have recorded for the AC5 devices are two times as high as those obtained previously [14,33,34]. The highest mobility achieved in the present studies was

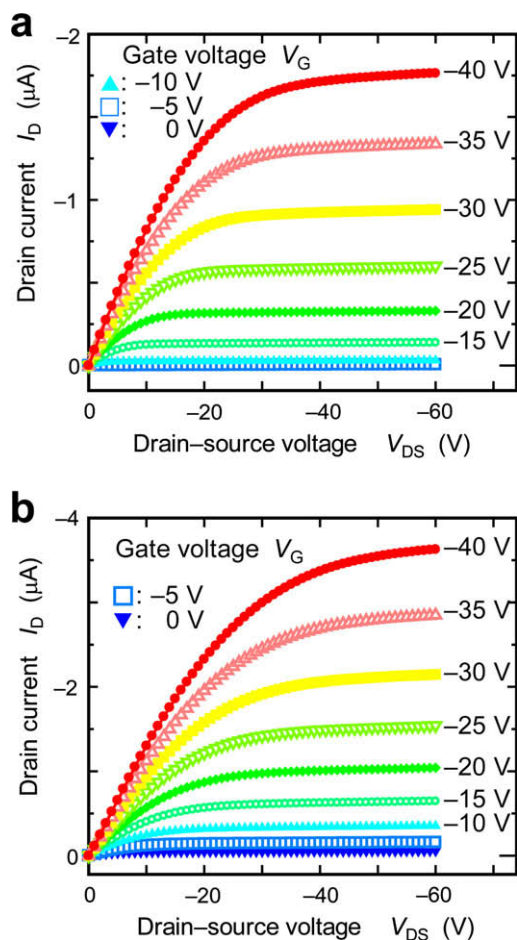


**Fig. 6.** Output characteristics of the P5T crystal OFET devices on the substrate treated with (a) PTS and (b) OTS. The PTS-treated device was measured both in air and in vacuum during eleven days. OTS-treated one was similarly measured during a hundred days. Both the characteristics were obtained in air at the last day.

0.13 cm<sup>2</sup>/V s for the P5T device, comparable to that of a related TPCO material, 5,5'-bis(4-biphenyl)-2,2':5,2''-terthiophene (BP3T) [14]. Nonetheless, the mobility level was two orders of magnitude lower than that of e.g. a rubrene-based device [7]. Two major issues are present in the OFET studies. One is related to the electrical contact between the organic layer and the electrodes and the other is pertinent to the choice of the gate insulator materials. The former issue was improved appreciably (see Figs. 5 and 6 for the complete suppression of the convex-downward behavior). With the other issue, however, we were not able to fully optimize the gate insulator materials. Recently Bisri et al. [36] recorded a mobility 1.6 cm<sup>2</sup>/V s for the BP3T-based device, an order of magnitude higher than that obtained for the same material [14]. The point was that Bisri et al. [36] used poly(methyl methacrylate) for the gate insulator, whereas Yamao et al. [14] used SiO<sub>2</sub> for it. On the basis of this illustration the gate insulator materials will have to be further explored including the SAM species [7,37,38].

#### 4. Conclusions

We have developed the method of making the high-quality thin single crystals directly onto the SiO<sub>2</sub>/Si substrates in a vapor phase. The growth apparatus requires only a small space (~10-cm cube). The crystal growth is carried out within the narrow space surrounded with the two plates that are in close contact with heaters. In virtue of this configuration, the crystal growth proceeds nearly at the thermodynamic equilibrium, producing well-defined thin single polygon TPCO crystals of several hundreds of micrometers in size. In particular, we have succeeded in growing the exceedingly flat crack-free single crystals on the substrates treated with HMDS, PTS, and OTS as SAMs.

We have fabricated the top-contact OFETs using the TPCO crystals. The devices show the excellent performance and keep it steadily both in air and in vacuum more than ten days (maximum a hundred days). The pivotal points are summarized as follows: (i) the ohmic contact is fully secured between the organic semiconductor layer and the (source and drain) electrodes. (ii) The firm and uniform interface is formed between the organic layer and the gate insulator. The good ohmic contact is achieved by using the thin crystals (the P5T devices) or by the oblique metal deposition on the crystal (the AC5 device). The SAM is inserted as a part of the gate insulator between the semiconductor crystal and the device substrate to produce the ideal organic layer/gate insulator interface. The present method of the crystal growth can thus be suitably applied to other optical and electronic devices as well as the OFETs.

#### Acknowledgements

This work was supported by Grant-in-Aid for Science Research in a Priority Area "Super-Hierarchical Structures" (Grant No. 17067009) and by Grant-in-Aid for Exploratory Research (Grant No. 20655041) from the Ministry of Education, Culture, Sports, Science and Technology, Japan.

#### References

- [1] M. Mas-Torrent, M. Durkut, P. Hadley, X. Ribas, C. Rovira, J. Am. Chem. Soc. 126 (2004) 984–985.
- [2] A.L. Briseno, R.J. Tseng, M.-M. Ling, E.H.L. Falcao, Y. Yang, F. Wudl, Z. Bao, Adv. Mater. 18 (2006) 2320–2324.
- [3] V.C. Sundar, J. Zaumseil, V. Podzorov, E. Menard, R.L. Willett, T. Someya, M.E. Gershenson, J.A. Rogers, Science 303 (2004) 1644–1646.
- [4] R. Zeis, T. Siegrist, Ch. Kloc, Appl. Phys. Lett. 86 (2005) 022103.
- [5] K. Nakamura, M. Ichikawa, R. Fushiki, T. Kamikawa, M. Inoue, T. Koyama, Y. Taniguchi, Jpn. J. Appl. Phys. 44 (2005) L1367–L1369.
- [6] M. Ichikawa, H. Yanagi, Y. Shimizu, S. Hotta, N. Suganuma, T. Koyama, Y. Taniguchi, Adv. Mater. 14 (2002) 1272–1275.
- [7] J. Takeya, M. Yamagishi, Y. Tominari, R. Hirahara, Y. Nakazawa, T. Nishikawa, T. Kawase, T. Shimoda, S. Ogawa, Appl. Phys. Lett. 90 (2007) 102120.
- [8] Y. Yamada, H. Yanagi, Appl. Phys. Lett. 76 (2000) 3406–3408.
- [9] H. Yanagi, T. Morikawa, S. Hotta, K. Yase, Adv. Mater. 13 (2001) 313–317.
- [10] M. Ichikawa, R. Hibino, M. Inoue, T. Haritani, S. Hotta, K. Araki, T. Koyama, Y. Taniguchi, Adv. Mater. 17 (2005) 2073–2077.
- [11] F. Sasaki, S. Kobayashi, S. Haraichi, S. Fujiwara, K. Bando, Y. Masumoto, S. Hotta, Adv. Mater. 19 (2007) 3653–3655.
- [12] T. Yamao, K. Yamamoto, Y. Taniguchi, T. Miki, S. Hotta, J. Appl. Phys. 103 (2008) 093115.
- [13] S. Liu, S.C.B. Mannsfeld, W.M. Wang, Y.-S. Sun, R.M. Stoltenberg, Z. Bao, Chem. Mater. 21 (2009) 15–17.

- [14] T. Yamao, T. Miki, H. Akagami, Y. Nishimoto, S. Ota, S. Hotta, *Chem. Mater.* 19 (2007) 3748–3753.
- [15] D.K. Hwang, K. Kim, J.H. Kim, S. Im, D.-Y. Jung, E. Kim, *Appl. Phys. Lett.* 85 (2004) 5568–5570.
- [16] J. Wang, H. Wang, X. Yan, H. Huang, D. Jin, J. Shi, Y. Tang, D. Yan, *Adv. Funct. Mater.* 16 (2006) 824–830.
- [17] F. Yang, M. Shtein, S.R. Forrest, *J. Appl. Phys.* 98 (2005) 014906.
- [18] A. Lopez-Otero, *Thin Solid Films* 49 (1978) 3–57.
- [19] Y. Inoue, T. Hoshino, S. Takeda, K. Ishino, A. Ishida, H. Fujiyasu, H. Kominami, H. Mimura, Y. Nakanishi, S. Sakakibara, *Appl. Phys. Lett.* 85 (2004) 2340–2342.
- [20] H. Yanagi, T. Ohara, T. Morikawa, *Adv. Mater.* 13 (2001) 1452–1455.
- [21] H. Plank, R. Resel, S. Purger, J. Keckes, A. Thierry, B. Lotz, A. Andreev, N.S. Sariciftci, H. Sitter, *Phys. Rev. B* 64 (2001) 235423.
- [22] F. Quochi, F. Cordella, R. Orrù, J.E. Communal, P. Verzeroli, A. Mura, G. Bongiovanni, A. Andreev, H. Sitter, N.S. Sariciftci, *Appl. Phys. Lett.* 84 (2004) 4454–4456.
- [23] Y. Chen, I. Shih, *Appl. Phys. Lett.* 94 (2009) 083304.
- [24] Ch. Kloc, R.A. Laudise, *J. Cryst. Growth* 193 (1998) 563–571.
- [25] Ch. Kloc, P.G. Simpkins, T. Siegrist, R.A. Laudise, *J. Cryst. Growth* 182 (1997) 416–427.
- [26] R.A. Laudise, Ch. Kloc, P.G. Simpkins, T. Siegrist, *J. Cryst. Growth* 187 (1998) 449–454.
- [27] J. Veres, S. Ogier, G. Lloyd, D. de Leeuw, *Chem. Mater.* 16 (2004) 4543–4555.
- [28] S. Hotta, H. Kimura, S.A. Lee, T. Tamaki, *J. Heterocyclic Chem.* 37 (2000) 281–286.
- [29] S. Hotta, S.A. Lee, T. Tamaki, *J. Heterocyclic Chem.* 37 (2000) 25–29.
- [30] T. Yamao, Y. Taniguchi, K. Yamamoto, T. Miki, S. Ota, S. Hotta, M. Goto, R. Azumi, *Jpn. J. Appl. Phys.* 46 (2007) 7478–7482.
- [31] T. Yamao, H. Akagami, Y. Nishimoto, S. Hotta, Y. Yoshida, *J. Nanosci. Nanotechnol.*, in press.
- [32] S.Z. Bisri, T. Takenobu, Y. Yomogida, T. Yamao, M. Yahiro, S. Hotta, C. Adachi, Y. Iwasa, *Proc. SPIE* 6999 (2008) 69990Z.
- [33] T. Yamao, S. Ota, T. Miki, S. Hotta, R. Azumi, *Thin Solid Films* 516 (2008) 2527–2531.
- [34] T. Yamao, H. Kuriki, T. Miki, S. Hotta, *J. Nanosci. Nanotechnol.* 9 (2009) 165–168.
- [35] D. Kumaki, T. Umeda, S. Tokito, *Appl. Phys. Lett.* 92 (2008) 093309.
- [36] S.Z. Bisri, T. Takenobu, Y. Yomogida, H. Shimotani, T. Yamao, S. Hotta, Y. Iwasa, *Adv. Funct. Mater.* 19 (2009) 1728–1735.
- [37] L.-L. Chua, J. Zaumseil, J.-F. Chang, E.C.-W. Ou, P.K.-H. Ho, H. Sirringhaus, R.H. Friend, *Nature* 434 (2005) 194–199.
- [38] T.G. Bäcklund, R. Österbacka, H. Stubb, J. Bobacka, A. Ivaska, *J. Appl. Phys.* 98 (2005) 074504.



[9,10]. In this paper we can rule out this influence. Also fiber isolation is not needed and the use of solvent mixtures is avoided, which may allow for easier recycling of processing solvent. We found an optimal efficiency at a 42% fiber content of the casting solution and show that it can be linked to the morphology of the active layer.

## 2. Experimental

### 2.1. Preparation of P3HT fibers

P3HT was prepared via the Rieke method [11]. The regioregularity was determined at >94.5% and it had a  $M_n$  of  $23.7 \text{ kg mol}^{-1}$  (polydispersity index of 1.80) as determined by Analytical Size Exclusion Chromatography (SEC). The SEC was performed using a Spectra series P100 (Spectra Physics) pump equipped with two mixed-B columns (10  $\mu\text{m}$ ,  $2 \times 30 \text{ cm}$ , Polymer Labs) and a Refractive Index detector (Shodex) at 60 °C. Chlorobenzene was used as the eluent at a flow rate of 1.0 mL/min. Molecular weight distributions are given relative to polystyrene standards. P3HT fibers were prepared by slow cooling of an orange coloured 0.7 wt% P3HT solution in *p*-xylene, as described elsewhere [11].

### 2.2. Solar cell fabrication

After the preparation of the P3HT fibers in the *p*-xylene solution, PCBM ([6-6]-phenyl  $\text{C}_{61}$ -butyric acid methyl ester (Solenne)) was added to the solution in a 1:1 weight ratio with P3HT to act as acceptor material. The casting solution was stirred for  $\sim 48 \text{ h}$  at room temperature. The solar cells were prepared starting from indium tin oxide (ITO, 100 nm) coated glass plates that were successively cleaned in a soap solution, demineralised water and acetone, each for 10 min in an ultrasonic bath. This was followed by cleaning in boiling isopropanol for 10 min. A 25 nm thick poly(3,4-ethylenedioxythiophene-polystyrenesulfonate (PEDOT-PSS (Bayer))) layer was spin-coated on the clean glass/ITO substrates. The substrates were dried for 20 min on a hot plate at 120 °C. The active layer (P3HT:PCBM 1:1), was spin-coated at 750 rpm on top of the PEDOT-PSS layer. The solution from which the active layer was spin-coated, was heated gradually to several temperatures (between 37 and 50 °C). At each temperature used for the experiment, the solution was left to stabilize for at least 30 min before the active layer was spin-coated on top of the PEDOT-PSS layer. After deposition of the active layer, the devices were left in vacuum ( $10^{-6} \text{ mbar}$ ) to get rid of the remaining solvent. Finally, a calcium layer ( $\sim 25 \text{ nm}$ ) and an aluminium layer ( $\sim 70 \text{ nm}$ ) were evaporated to form the top contact of the solar cell. Each photovoltaic device had an active area of  $25 \text{ mm}^2$ . The *I*-*V*-characteristics were measured with an Oriel solar simulator equipped with a Xenon Short Arc lamp with a power of 150 W.

### 2.3. Morphology of the active layer studied with TEM

For each solution temperature, the morphology of the active layer was studied. A thin film, identical to the active

layer of the solar cell, was deposited on a cleaned glass substrate, using the same procedure as for preparing the complete solar cell. This film was isolated by etching with 40% hydrofluoric acid (HF) to remove the glass substrate and then put on a copper TEM-grid. TEM-measurements were performed with a Philips CM12-STEM. The SAED patterns, recorded through TEM, originally suffered from a large background that resembled inelastic scattering. To improve the signal-to-noise ratio, integration across the complete diffraction ring was done, from which a fitted background due to inelastic scattering was subtracted (under the assumption that the blend in between the fibers is quasi-amorphous [12]).

### 2.4. Determination of the fiber content in the solution

At each solution temperature used for preparing a photovoltaic device, a small amount ( $< 50 \mu\text{L}$ ) of the casting solution was isolated just after spin-coating and diluted in  $\sim 3 \text{ mL}$  of *p*-xylene of the same temperature. UV-Vis measurements (with a Varian Cary 500 Scan UV-Vis-NIR spectrophotometer) were performed on this highly diluted solution after cooling to room temperature. The obtained UV-Vis spectra were fitted as a sum of previously recorded spectra of PCBM, well-dissolved P3HT and fully fibrillar P3HT, all in *p*-xylene. The known relation between the latter two spectra allowed for the determination of the fiber content [11].

## 3. Results and discussion

Fig. 1 shows the photovoltaic (PV) parameters of solar cells with a nanofiber-P3HT:PCBM 1:1 active layer as a function of casting solution temperature together with the fiber content of the solution at each temperature. The graph shows that the fiber content of the solution is very sensitive to temperature. When raising the temperature from 37 to 50 °C, the fiber content of the solution decreases from 60% to 14%. The solar cell efficiency displays a quadratic dependence on temperature. An optimal efficiency of  $\sim 3.2\%$  is found for a solution temperature of 45 °C. At this temperature, the fiber content was 42%. When comparing the different PV-parameters, it seems that the behavior of the efficiency is strongly related to the behavior of the short circuit current  $J_{sc}$ . The open circuit voltage  $V_{oc}$  of the solar cells has an increasing trend. The fill factor follows a rather rough course.

The origin of the dependence of the photovoltaic performance on the temperature of the casting solution can be found in the active layer morphology. Fig. 2 shows Bright Field Transmission Electron Microscopy (BFTEM) images of the active layers. The active layer spin-coated from a solution at a relatively low temperature (37 °C) shows large (up to 50  $\mu\text{m}$ ) needles (Fig. 2(a, left)). Spots in the Selected Area Electron Diffraction (SAED) patterns of the needles confirm that they are groups of PCBM single crystals [13]. In between the needles, fibers of P3HT are visible (Fig. 2(a, right)). They appear dark against a light background. SAED also gives information about this part of the active layer. In Fig. 3, the residual intensities of the

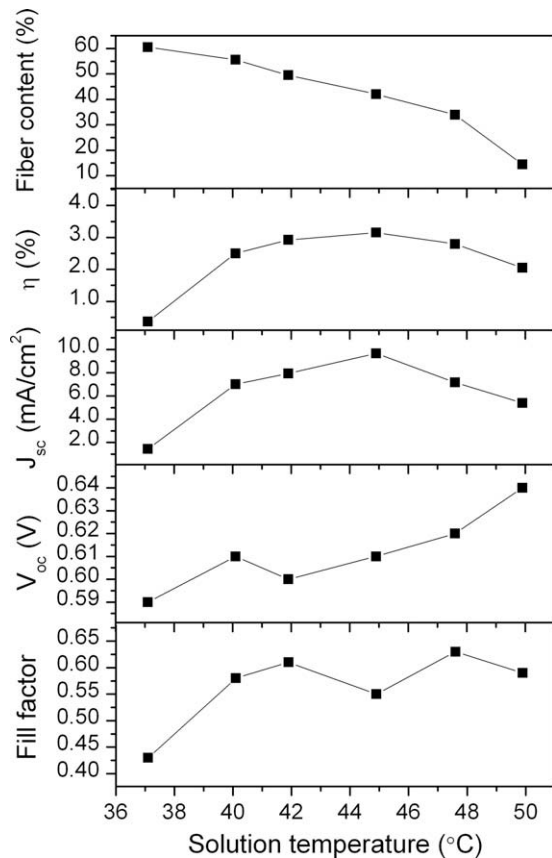


**Fig. 1.** Fiber content of the casting solution, efficiency  $\eta$ , short circuit current  $J_{sc}$ , open circuit voltage  $V_{oc}$ , and fill factor of nanofiber-P3HT:PCBM (1:1) solar cells as a function of solution temperature.

SAED patterns of the homogeneous areas of the active layers are shown (the area in between the PCBM crystals). These curves were obtained after integration across the diffraction ring followed by subtraction of a fitted background due to inelastic scattering (*cf.* Experimental). For the film spin-coated at 37 °C, the residual intensity SAED pattern shows a clear peak at 0.38 nm (Fig. 3). This peak can be attributed to the superposition of the (0 0 2) and (0 2 0) reflections from the crystal planes of semi-crystalline P3HT [14]. The remainder of the SAED pattern appears featureless and no peaks corresponding to PCBM can be distinguished. This indicates that the major part of PCBM is assembled in the needles. By slightly increasing the solution temperature to ~40 °C, a change in morphology is immediately observed. The PCBM needles have grown larger (Fig. 2b). We believe that the PCBM needles were formed in the casting solution during the long (>48 h) stirring at room temperature and elevated temperatures and not during spin-coating of the active layer. The spin-coating takes <120 s, which does not leave much time for the formation of such large needles. The long time available during stirring together with the perfect crystal shape and dependence of the crystal size on the temperature of the casting solution, all indicate that the crystals were formed during stirring of the casting solution by an Ost-

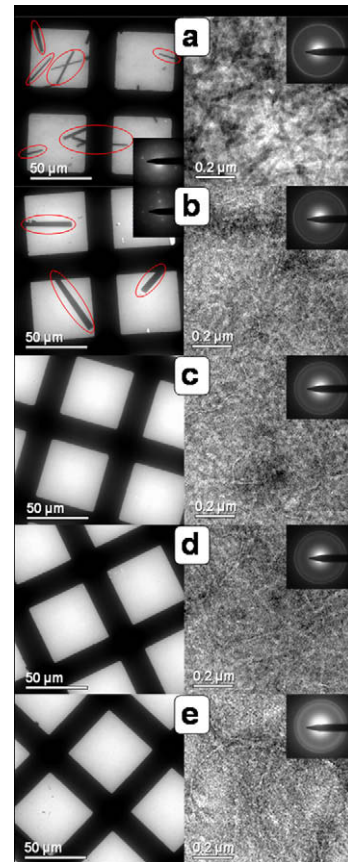


**Fig. 2.** Bright Field TEM images of P3HT:PCBM 1:1 spin-coated from a solution at 37.1 °C (a), 40.5 °C (b), 41.9 °C (c), 44.9 °C (d) and 49.9 °C (e), at low temperatures PCBM assembles in needle-like structures, P3HT fibers appear as dark or light areas depending on the presence of PCBM within the polymer matrix. The insets show the SAED patterns of either the PCBM needles (left) or the homogeneous P3HT:PCBM regions (right).

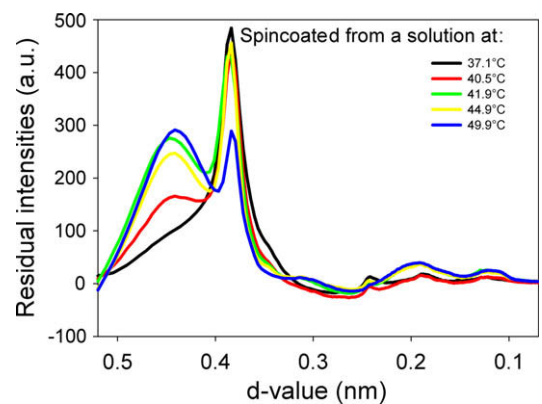


**Fig. 3.** Residual intensities of the SAED patterns of the polymer:PCBM matrix for several solution temperatures.

wald ripening process [15]. Higher temperatures accelerate the Ostwald ripening; therefore less but larger PCBM needles are visible at the solution temperature of ~40 °C. These needles have grown at the expense of the needles

that were present in solution at  $\sim 37$  °C. For the solution temperature of  $\sim 40$  °C, a small increase in the diffraction intensity at 0.46 nm can be seen in the SAED pattern of the area in between the needles (Fig. 3). This small peak indicates that some amount of nano-crystalline PCBM [16] is now present in between the fibers. Apparently a small part of the PCBM has dissolved in the *p*-xylene at this temperature; the PCBM is no longer completely grouped in the needles. This gives a higher yield of exciton dissociation at the polymer:PCBM interface and thus a higher  $J_{sc}$  and better solar cell performance (cf. Fig. 1). As opposed to the film made from a solution at 37 °C, the P3HT fibers are now visible as light areas in the BFTEM image (Fig. 2). This is caused by the presence of PCBM with a higher density in between the polymer matrix [2]. A further increase of the solution temperature leads to the disappearance of the PCBM needles (Fig. 2). For solution temperatures of  $\sim 42$  °C,  $\sim 45$  °C (Fig. 3) and  $\sim 48$  °C (not shown) strong peaks corresponding to both P3HT (at 0.38 nm) and PCBM (at 0.2, 0.31 and 0.46 nm [16]) are present. These temperatures also correspond to the best photovoltaic performances (Fig. 1). Good charge transport due to crystalline P3HT, in combination with a large interfacial area between polymer and PCBM render good solar cells. At a solution temperature of  $\sim 50$  °C, there is a slight drop in solar cell efficiency. At this point the fiber content has decreased strongly, which will likely result in less efficient hole transport.

#### 4. Conclusion

We have demonstrated that the fiber content of the P3HT-fiber:PCBM casting solution can be easily controlled by temperature. Meanwhile, the dissolution of PCBM varies with temperature. The combined effect can be used to control the active layer morphology in photovoltaic devices and thus also their performance. An optimal solar cell efficiency was found at a solution temperature of  $\sim 45$  °C when the fiber content was 42%. BFTEM images of the active layer morphology combined with SAED patterns revealed that this optimal photovoltaic efficiency occurred when the PCBM was dissolved completely at the highest possible fiber content. The initial increase in efficiency with temperature of the casting solution could be attributed to an increased solubility of PCBM in the casting solu-

tion. At temperatures lower than 41 °C, PCBM formed large ( $>50$   $\mu\text{m}$ ) needles in the casting solution by Ostwald ripening, resulting in poorly mixed active layers and low solar cell efficiencies. At temperatures of 45 °C and higher, the PCBM was dissolved well and, after reaching its maximum, the solar cell efficiency started to decrease again with decreasing fiber content (due to the increasing solution temperature).

#### Acknowledgements

The research was carried out in the framework of the SBO-project 030220 "PolySpec", the FWO-project R-1226 and the interregional project OLED+. The work, as part of the project "SOHYDs" within the European Science Foundation EUROCORES Programme was also supported from funds by the FWO (G.0685.06) and the EC Sixth Framework Programme, under Contract No. ERAS-CT-2003-980409. Sabine Bertho is research assistant of the Fund for Scientific Research, Flanders (Belgium) (FWO).

#### References

- [1] F. Padinger, R.S. Rittberger, N.S. Sariciftci, *Adv. Funct. Mater.* 13 (2003) 85.
- [2] X. Yang, J. Loos, S.C. Veenstra, W.J.H. Verhees, M.M. Wien, J.M. Kroon, M.A.J. Michels, R.A.J. Janssen, *Nano Lett.* 5 (2005) 579.
- [3] Y. Kim, S.A. Choulis, J. Nelson, D.D.C. Bradley, *Appl. Phys. Lett.* 86 (2005) 063502.
- [4] X. Yang, G. Lu, L. Li, E. Zhou, *Small* 3 (2007) 611.
- [5] W. Ma, C. Yang, X. Gong, K. Lee, A.J. Heeger, *Adv. Funct. Mater.* 15 (2005) 1617.
- [6] S. Berson, R. De Bettignies, S. Bailly, S. Guillerez, *Adv. Funct. Mater.* 17 (2007) 1377.
- [7] L. Li, G. Lu, X. Yang, *J. Mater. Chem.* 18 (2008) 1984.
- [8] A.J. Moulé, K. Meerholz, *Adv. Mater.* 20 (2008) 240.
- [9] W. Ma, J.Y. Kim, K. Lee, A.J. Heeger, *Macromol. Rapid Commun.* 28 (2007) 1776.
- [10] P. Schilinsky, U. Asawapirom, U. Scherf, M. Biele, C.J. Brabec, *Chem. Mater.* 17 (2005) 2175.
- [11] W.D. Oosterbaan, V. Vrindts, S. Berson, S. Guillerez, O. Douhéret, B. Ruttens, J. D'Haen, P. Adriaensens, J. Manca, L. Lutsen, D. Vanderzande, *J. Mater. Chem.*, in press. doi:10.1039/b900670b.
- [12] L. Reimer, *Transmission Electron Microscopy*, Springer-Verlag, Berlin, 1989.
- [13] M.T. Rispens, A. Meetsma, R. Rittberger, C.J. Brabec, N.S. Sariciftci, J.C. Hummelen, *Chem. Commun.* (2003) 2116.
- [14] S. Hugger, R. Thomann, T. Heinzel, T. Thurn-Albrecht, *Colloid Polym. Sci.* 282 (2004) 932.
- [15] R. Boistelle, J.P. Astier, *J. Cryst. Growth* 90 (1988) 14.
- [16] X. Yang, J.K.J. van Duren, M.T. Rispens, J.C. Hummelen, R.A.J. Janssen, M.A.J. Michels, J. Loos, *Adv. Mater.* 16 (2004) 802.

in combination with its technological compatibility in terms of materials (e.g. dielectrics including SiO<sub>2</sub> and polymers) and device architecture with standard bottom-contact transistors used in circuits.

In this work, we study the injection of electrons and holes in bilayer gate dielectric memory transistors, and demonstrate a reprogrammable ambipolar memory transistor in which trapping of electrons and holes from the transistor channel into the gate dielectric allows to program and erase the memory device at low voltages. The ambipolar nature of carrier injection in our device is illustrated by comparing the behavior of the ambipolar memory transistor with that of a unipolar p-type (a pentacene device measured in air) and a unipolar n-type device (based on a perylene derivative).

## 2. Experimental

### 2.1. Organic memory transistor fabrication

The transistors in this study have a bottom gate structure with top source and drain contacts as depicted in Fig. 1. All devices were fabricated on a highly n-doped Si wafer, which serves as the gate electrode, with 20 nm of thermally grown SiO<sub>2</sub> on top. On this substrate, a thin layer of poly(α-methyl styrene) (PαMS) was deposited by spin-coating a 0.1 wt.% PαMS (Fluka, Mw ~700,000) solution in toluene at 4000 rpm, followed by drying at 120 °C for 1 min on a hot plate. The thickness of the PαMS layer was measured by ellipsometry to be 3–5 nm. The SiO<sub>2</sub> and the PαMS layers form together the gate dielectric of the memory transistor. Subsequently, a 40-nm thick layer of pentacene or *N,N'*-dithidecyl-3,4,9,10-perylenetetracarboxylic diimide (PTCDI-C<sub>13</sub>H<sub>27</sub>) was deposited by thermal vacuum evaporation ( $p \sim 10^{-8}$  Torr). The deposition rate and the substrate temperature during pentacene deposition were 0.25 Å/s and 68 °C, respectively. PTCDI-C<sub>13</sub>H<sub>27</sub>

was evaporated at room temperature at a rate of 0.40 Å/s. Finally, Au (on the pentacene devices) or LiF/Al (on the PTCDI-C<sub>13</sub>H<sub>27</sub> devices) source and drain contacts were evaporated through a shadow mask.

The transistors had channel lengths,  $L$ , ranging from 50 μm to 210 μm. The channel width,  $W$ , was 2000 μm. For the pentacene devices, the initial hole mobility, extracted from the linear regime,  $\mu_{h,init}$  and the initial threshold voltage  $V_{T,init}$  were typically  $\sim 0.8$  cm<sup>2</sup>/(V s) and  $\sim -1$  V. For the devices with PTCDI-C<sub>13</sub>H<sub>27</sub> the initial electron mobility  $\mu_{e,init}$  was  $\sim 0.1$  cm<sup>2</sup>/(V s) and  $V_{T,init} \sim 1$  V.

### 2.2. Measurement method

Electrical data was obtained using two computer controlled Keithley 2602 units in a darkened nitrogen glovebox. Samples were not subjected to air, unless differently stated.

The typical measurement protocol was as follows. First, the initial characteristics were measured. The initial turn-on voltage of the device was determined. We defined the turn-on voltage,  $V_{on}$ , as the gate-source voltage  $V_{GS}$  at which the drain current  $I_D$  reaches 100 pA. Then, the device is subjected to a series of programming pulses, with intermediate gate voltage sweeps. The drain-source voltage during programming  $V_{DS,prog}$  is always kept at 0 V.

The exact measurement procedure is illustrated in Fig. 2. We apply two subsequent pulses with the same duration,  $t_{prog}$ , and equal but opposite gate voltage,  $V_{GS,prog}$ . The pulse with negative  $V_{GS,prog}$  shifts the transfer characteristics towards negative  $V_{GS}$ , while the positive  $V_{GS,prog}$  shifts them towards positive  $V_{GS}$ . This is done twice to have a stable result. After each of the last two pulses, a small part of the transfer characteristics is measured to determine the  $V_{on}$ .  $V_{on-}$  denotes the turn-on voltage after the negative pulse, and  $V_{on+}$  denotes the value after the positive pulse.  $\Delta V_{on}$  is defined as the difference between  $V_{on+}$  and  $V_{on-}$ . This last value is the memory window between the two different memory states. These measurement steps can then be repeated for different  $t_{prog}$  or  $|V_{GS,prog}|$ .

## 3. Results and discussion

### 3.1. Charge carrier trapping as a function of programming voltage

In Fig. 3a, we plotted the transfer characteristics of pentacene transistors, obtained with the measurement procedure described above and with a series of programming pulses of  $\pm 17$  V and  $\pm 20$  V. In this case,  $t_{prog}$  was kept constant at 1.5 ms. A shift of the turn-on voltage with the same polarity as the gate voltage is observed. This is attributed to the trapping of electronic charges in the vicinity of the semiconductor/insulator interface [6]. When pentacene is deposited directly on SiO<sub>2</sub>, the change in turn-on voltage was less than 1 V (data not shown). This indicates that the presence of the PαMS is key to achieve the desired charge trapping and that these charge carriers are probably trapped in the polymer dielectric and/or at the interface between the polymer dielectric and SiO<sub>2</sub>.

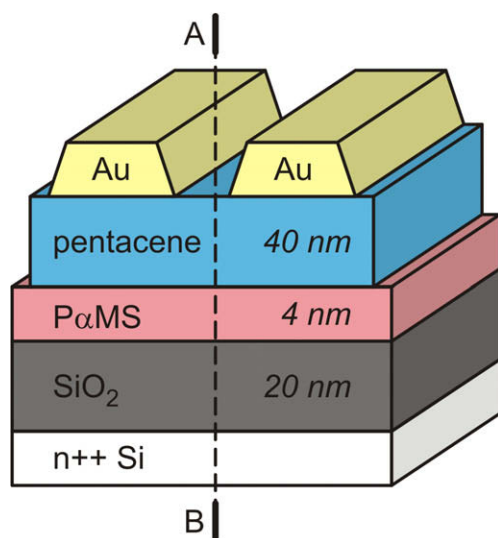


Fig. 1. Schematic view of a pentacene memory transistor. The band diagrams in Fig. 11 are taken along the line AB.

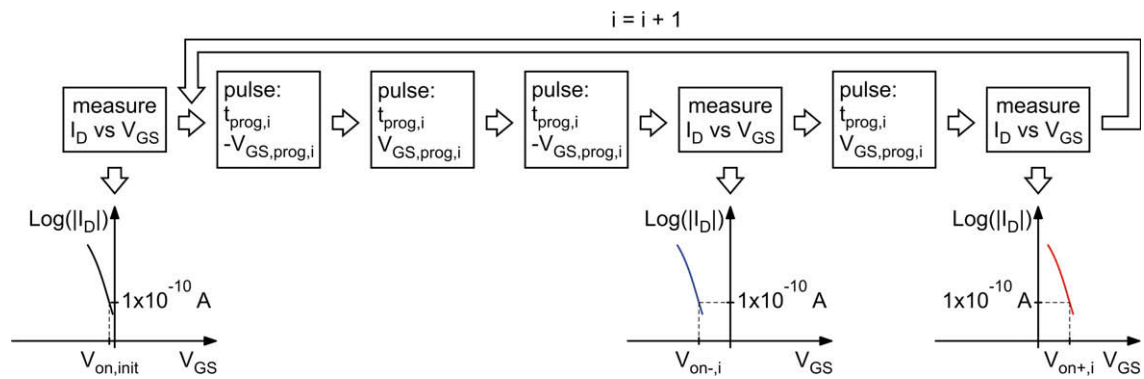


Fig. 2. Measurement flow diagram used to measure  $V_{on-}$  and  $V_{on+}$  in function of  $t_{prog}$  and  $|V_{GS,prog}|$ .

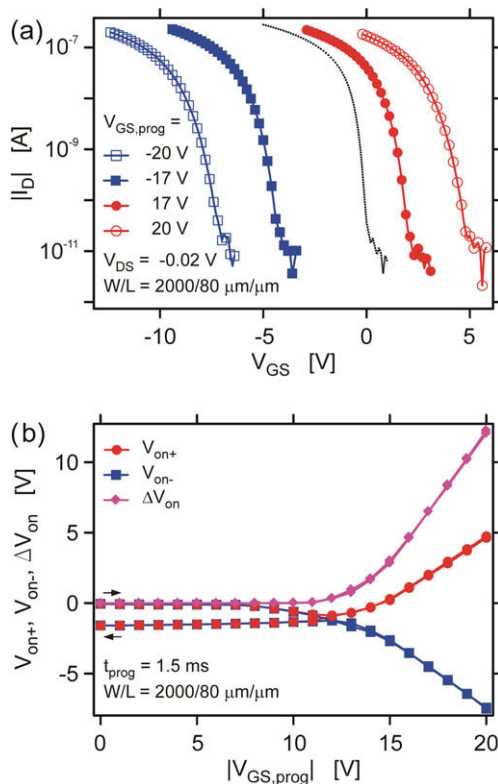


Fig. 3. For a pentacene device: (a)  $I_D$  vs.  $V_{GS}$  in the initial state (dotted line) and after programming pulses with  $t_{prog} = 1.5$  ms and  $V_{GS,prog} = -17$  V (filled squares)/17 V (filled circles)/-20 V (open squares)/20 V (open circles). (b)  $V_{on-}$ ,  $V_{on+}$  and  $\Delta V_{on}$  as a function of  $|V_{GS,prog}|$  for  $t_{prog} = 1.5$  ms. The measured device is the same as in (a).

In Fig. 3b,  $V_{on-}$ ,  $V_{on+}$  and  $\Delta V_{on}$  are shown in function of  $|V_{GS,prog}|$ . For small values of  $|V_{GS,prog}|$ , the transfer characteristics are hardly changed.  $\Delta V_{on}$  is much smaller than 1 V. However, when  $|V_{GS,prog}|$  increases, the effect becomes significant above a critical value of  $|V_{GS,prog}| \sim 10$  V.  $\Delta V_{on}$  reaches a maximum value of 12 V for the highest value of  $|V_{GS,prog}|$  being 20 V. When the device is subsequently subjected to a series of decreasing programming pulses,  $\Delta V_{on}$  as obtained in the backward series is identical to the values

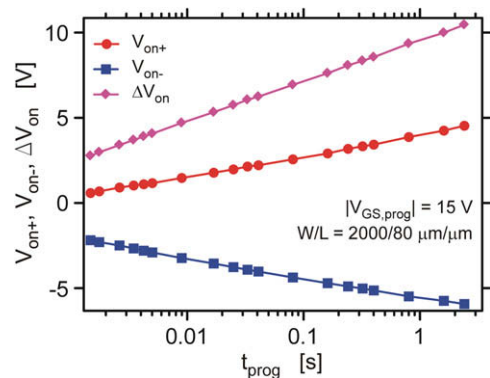


Fig. 4. For a pentacene device:  $V_{on-}$ ,  $V_{on+}$  and  $\Delta V_{on}$  as a function of  $t_{prog}$  for  $|V_{GS,prog}| = 15$  V.

obtained in the forward series (i.e. with increasing  $|V_{GS,prog}|$ ). When the final  $V_{on-}$  and  $V_{on+}$  are compared to  $V_{on-,init}$ , a small, overall shift is observed.

The data in Fig. 3 illustrates a number of important attributes that makes this effect promising to utilize as memory cells. Most notably is the negligible threshold voltage shifts at low programming voltages which allows non-destructive read-out. Furthermore, the large value of  $\Delta V_{on}$  allows easy read-out as this is translated into a large difference in source-drain current for the different programmed states. Finally, this large memory window can be reached at low voltages thanks to the thin gate dielectric (both  $\text{SiO}_2$  and  $\text{P}\alpha\text{MS}$  layers). Interestingly,  $V_{on}$  can be shifted towards both positive and negative voltages by a sufficiently large respectively positive and negative pulse to the gate. This indicates that both electrons and holes are trapped in the gate dielectric.

### 3.2. Charge trapping as a function of programming time

The trapping mechanism of the charge carriers is further characterized by investigating the dependence of  $V_{on-}$ ,  $V_{on+}$  and  $\Delta V_{on}$  on  $t_{prog}$ . To do so, the measurement procedure described above is repeated with an increasing  $t_{prog}$  while  $|V_{GS,prog}|$  is kept constant. In Fig. 4 can be seen that both  $V_{on-}$  and  $V_{on+}$  increase logarithmically with  $t_{prog}$ . The logarithmic time dependence of the amount of trapped

charge on the programming time is well-known in charge trapping devices:  $Q_{tr}(t) = r_d \log(1 + t/t_0)$  with  $Q_{tr}$  the amount of trapped charges. This relation can be predicted for charge injection where the injection current depends exponentially on the density of the previously injected charge and points to tunneling from the semiconductor into the dielectric as the trapping mechanism [12,13].

### 3.3. Retention

In Fig. 5, the retention of the trapped charge after a programming pulse of  $-20$  and  $20$  V is shown. In between the different measurement points, the sample was kept in the dark in the glovebox, without applying any voltages. Each data point is the average of a measurement on four different devices.  $V_{on+}$  decreases to  $0$  V within 3 h. This indicates that the electrons are trapped in shallow traps and that the positive part of the memory window cannot be used for practical applications.  $V_{on-}$  on the other hand, is only reduced to  $-3$  V after 3 months. The holes are deeply trapped in a more complex distribution, making it possible to use the negative part of the memory window. In Ref. [11], the positive part of the memory window is used (program and erase electrons). In those devices, the thicker polymer dielectric blocks the electrons from tunneling back to the channel, improving the retention but also increasing the programming voltage. In our device we combine low programming voltages with a large retention for the negative part of the memory window (program and erase holes).

### 3.4. Supply of charge carriers in the channel

A condition for the tunneling of the charge carriers into the gate dielectric is the presence of these charge carriers in the channel. Fig. 6 illustrates that both holes and electrons can be accumulated in our pentacene device. The initial transfer characteristics, measured from  $-3$  V to  $14.5$  V show both a hole current and an electron current with mobilities ( $\mu_h \sim 0.8$  cm<sup>2</sup>/(V s),  $\mu_e \sim 0.01$  cm<sup>2</sup>/(V s)) of the same order of magnitude as the values reported in literature [14]. This proves that our memory device is ambipolar. A second transfer sweep, measured from  $14.5$  V to

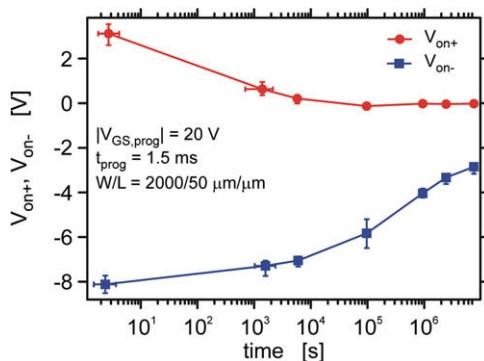


**Fig. 5.** Retention measurement for a pentacene device. The first point of the  $V_{on-}$  curve is reached after a pulse with  $|V_{GS,prog}| = 20$  V and  $t_{prog} = 1.5$  ms. The first point of the  $V_{on+}$  curve is reached after a pulse with  $|V_{GS,prog}| = 20$  V and  $t_{prog} = 1.5$  ms.

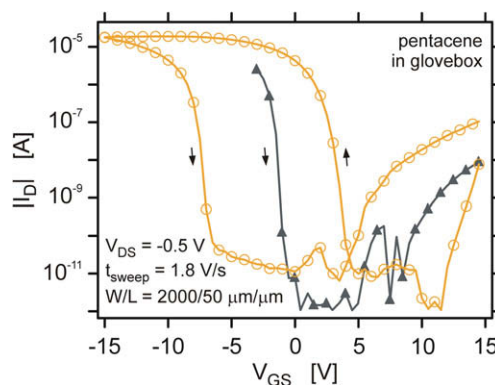


**Fig. 6.** The initial transfer characteristics of a pentacene device measured from  $-3$  V to  $14.5$  V (filled triangles), followed by a sweep from  $14.5$  V to  $-15$  V and back (open circles).

$-15$  V and back to  $14.5$  V shows how the memory transistor is programmed during the sweep: the  $V_{on}$  of the first part of this sweep is shifted towards a more positive  $V_{GS}$  with respect to  $V_{on,init}$ , by the accumulation of electrons in the transistor channel and subsequent tunneling in the gate dielectric, around  $14.5$  V. In the second part of the sweep,  $V_{on}$  is shifted to a  $V_{GS}$  more negative than  $V_{on,init}$  by the accumulation and the tunneling of holes, around  $-15$  V. Although  $t_{prog}$  and  $V_{GS,prog}$  are not accurately defined during this kind of sweeps, such measurement confirms that  $V_{on,init}$  can be moved both towards more positive and more negative biases by the accumulation and the tunneling of electrons and holes, respectively.

Fig. 7 shows the temperature dependence of  $V_{on-}$  and  $V_{on+}$ .  $V_{on-}$  is the result of the accumulation and tunneling of holes and shows to be temperature-independent.  $V_{on+}$ , on the other hand, decreases at lower temperatures. As the tunneling process itself is temperature-independent, the temperature dependence of  $V_{on+}$  might result from the temperature dependent supply of electrons in the channel [15,16]. In Fig. 8 we plot the electron mobility and  $V_{on+}$  on an Arrhenius plot. The fact that both can be fitted with the same activation energy  $E_{A,e} = 53$  meV, indicates that the supply of electrons is indeed limiting the tunneling of the electrons [15,16]. For the holes, with a

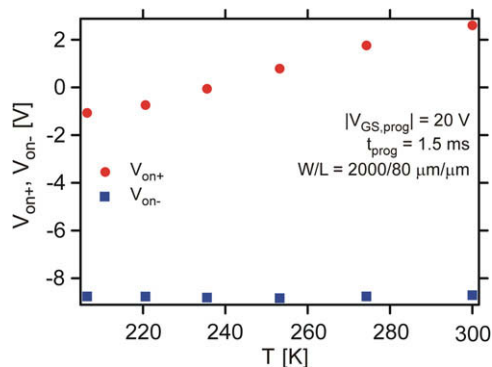


**Fig. 7.** For a pentacene device:  $V_{on-}$  and  $V_{on+}$  as a function of the temperature for  $t_{prog} = 1.5$  ms and  $|V_{GS,prog}| = 20$  V.

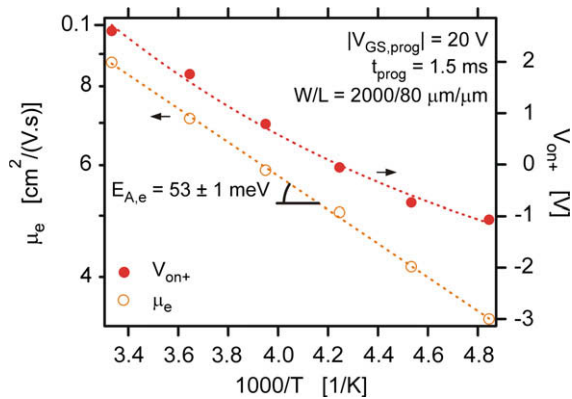


**Fig. 8.** The electron mobility (open circles) and  $V_{on+}$  (filled circles) of a pentacene device, in function of  $1000/T$ .  $V_{on+}$  was measured with  $t_{prog} = 1.5$  ms and  $V_{GS,prog} = 20$  V. The symbols are measurement points, the dotted lines fits with an Arrhenius equation (activation energy = 53 meV).

mobility of almost two orders of magnitude higher, the supply in the channel is not the limiting factor and  $V_{on-}$  is temperature-independent. The activation energy for the hole mobility,  $E_{A,h}$  is 22 meV, which is similar to values reported in literature for pentacene on OTS-treated  $\text{SiO}_2$  [17].

The finding that a lack of electrons reduces the memory window in this type of memory transistors should be kept in mind during the interpretation of results reported in literature. In the study of Baeg et al. [18], the memory window was shown to be smaller for a polar polymer dielectric like PVP (poly(4-vinyl phenol)) or PVA (poly vinyl alcohol) than for P $\alpha$ MS. Such polar dielectrics contain OH-groups which are known to decrease the electron mobility [19]. According to our findings, the smaller memory window in these devices could be partly explained by the poorer electron supply. Similarly, Katz et al., showed that hydrophobic dielectrics lead to larger shifts in  $V_T$  than hydrophilic ones [6], which we can directly relate to the corresponding electron mobilities expected to be larger on hydrophobic dielectrics compared to on hydrophilic dielectrics. Furthermore, illuminating the devices during programming improves the trapping of electrons but not that of holes [20]. We suggest that the effect of illumination is to supply extra electrons which can be trapped, analogous to how illumination accelerates bias stress [21]. Supplying more holes by illumination has no effect, as holes are already omnipresent in the channel.

### 3.5. Hole trapping only

Exposure of pentacene transistors to humid air leads to electron traps in the pentacene [22,23], which hampers the accumulation of electrons [24], leading to near-zero electron mobility. In Fig. 9a, we show the characteristics of a pentacene device which was left in air for 1 day and then measured in air: no electron current can be measured in the initial sweep from  $-3$  V to 14.5 V. Consequently,  $V_{on}$  cannot be shifted towards more positive  $V_{GS}$  during the next sweep from 14.5 V to  $-15$  V and back. On the other

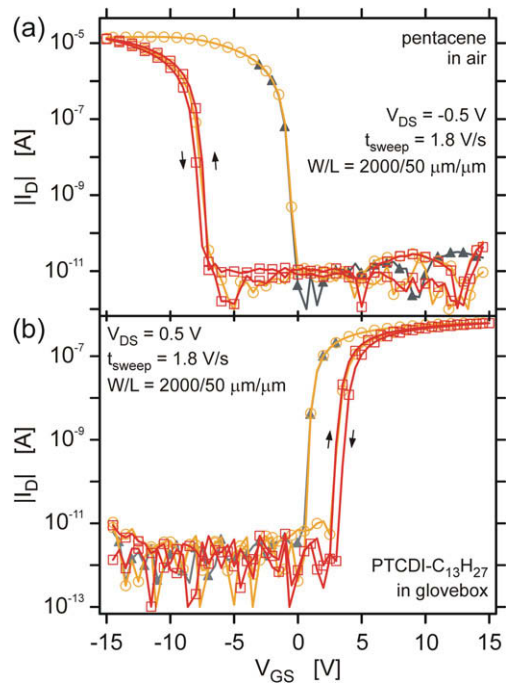


**Fig. 9.** (a) The initial transfer characteristics for a pentacene device, brought in air for 1 day and measured in air from  $-3$  V to 14.5 V (filled triangles), followed by a first sweep from 14.5 V to  $-15$  V and back (open circles) and a second sweep from 14.5 V to  $-15$  V and back (open squares). (b) The initial transfer characteristics for a PTCDI- $\text{C}_{13}\text{H}_{27}$  device measured in the glovebox from 3 V to  $-14.5$  V (filled triangles), followed by a first sweep from  $-14.5$  V to 15 V and back (open circles) and a second sweep from  $-14.5$  V to 15 V and back (open squares).

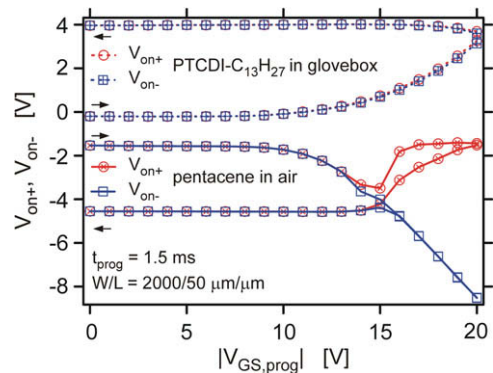


**Fig. 10.**  $V_{on-}$  and  $V_{on+}$  as a function of  $|V_{GS,prog}|$  for  $t_{prog} = 1.5$  ms for a pentacene device, brought in air for 1 day and measured in air (open symbols and full line) and for a PTCDI- $\text{C}_{13}\text{H}_{27}$  device measured in the glovebox (open symbols and dotted line).

hand, holes can still be accumulated and  $V_{on}$  can still shift towards more negative  $V_{GS}$ . We note that the mobility of the holes decreased somewhat, to  $\mu_h \sim 0.6$   $\text{cm}^2/(\text{V s})$ , by the exposure to air, probably caused by moisture-related traps [25]. Remarkably, if the sweep from 14.5 V to  $-15$  V and back is measured a second time, no difference in  $V_{on}$  for the first and the second part of the sweep can

be noticed. This means that even at 14.5 V trapped holes cannot be removed from the dielectric and as a result the memory window is actually decreased to zero. When Fig. 9a is compared with Fig. 6, it becomes clear that the electrons are needed to overwrite the tunneled holes which can otherwise not be removed from the dielectric at these gate fields. A similar observation can be made in Fig. 10 for the same pentacene sample measured in air. At  $|V_{GS,prog}| = 15$  V, holes can be trapped but not be removed, while in Fig. 3b, for a pentacene sample in the glovebox, the holes could be trapped and removed at  $|V_{GS,prog}| = 15$  V. If in Fig. 10,  $|V_{GS,prog}|$  is increased to 20 V, the trapped holes can be removed from the dielectric, but still no electrons can be trapped. We draw from this experiment the important conclusion that in this type of memory devices ambipolarity in the transistor channel, i.e. the possibility to accumulate both types of charge carriers in the device channel, is a requirement for achieving reprogrammability at low gate fields.

### 3.6. Electron trapping only

To verify the more general validity of the statement that ambipolarity is required for erasing a programmed memory state at relatively low gate fields, we carried out experiments using the perylene derivative PTCDI-C<sub>13</sub>H<sub>27</sub> as the organic semiconductor. PTCDI-C<sub>13</sub>H<sub>27</sub> is a good electron conductor; hole conduction has not been reported for this material. In Fig. 9b, a PTCDI-C<sub>13</sub>H<sub>27</sub> device measured in the glovebox only shows electron current and no hole current. In a memory device with bilayer oxide/P $\alpha$ MS dielectric,  $V_{on}$  can only be shifted towards more positive  $V_{GS}$  by tunneling of abundantly present electrons, but not towards more negative  $V_{GS}$ . When scanning to 15 V, the memory can be programmed only once, and trapped electrons cannot be removed from the dielectric. Similar results in Fig. 10 for the same PTCDI-C<sub>13</sub>H<sub>27</sub> sample: electrons can be trapped from  $|V_{GS,prog}| = 10$  V on, but cannot be removed. Even if  $|V_{GS,prog}|$  is increased to 20 V, the electrons stay trapped in

the dielectric. This is the pendant case of the pentacene device in air, and corroborates the statement that in order to erase trapped charges at relatively low gate fields, it is required to overwrite them with charges of the opposite sign, rather than to remove them by detrapping.

### 3.7. Model

From the figures in 3.4–3.6, it is obvious that to maximize the memory window of organic charge carrier trapping memory transistors, the accumulation of both holes and electrons needs to be possible. In this case, both charge carriers can be supplied in the channel, and one type of charge carrier can be used to overwrite the other, trapped, one.

A possible explanation for this behavior is schematically drawn in the band diagram in Fig. 11, taken along a vertical line in Fig. 1. In Fig. 11a, a charge carrier, a hole in this case, is accumulated in the channel and subsequently tunnels into the dielectric upon the application of an appropriate  $V_{GS}$ . The vertical electric field drops mainly over the two gate insulators and the driving force to tunnel into the dielectric is large. In a first approximation:

$$E_{P\alpha MS} = V_{GS} \frac{\epsilon_{SiO_2}}{t_{P\alpha MS} \epsilon_{SiO_2} + \epsilon_{P\alpha MS} t_{SiO_2}} \quad (1)$$

In our device for  $V_{GS,prog} = 15$  V,  $E_{P\alpha MS} = 9$  MV/cm. We assume that the trap in the gate dielectric that stores the injected charge carrier is deep. In Fig. 11b, in an ambipolar device, electrons can be accumulated in the channel and tunnel into the dielectric. The positively charged hole traps are likely to attract such electrons, such that injected electrons can erase the initially positively trapped charge, before a net negative charge of trapped electrons is stored in the gate dielectric. Also for electron injection, the electric field drops mainly over the two insulators. In Fig. 11c, we sketch the situation when an equal gate voltage is applied in a unipolar device, pentacene measured in air for example. No electrons are accumulated, such that

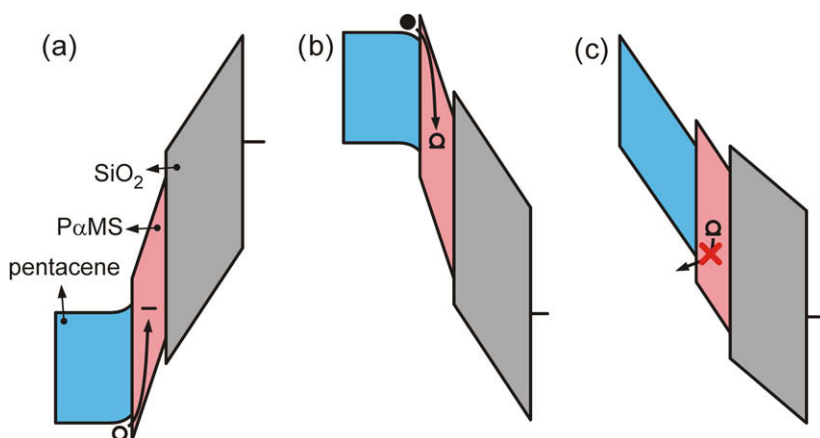


**Fig. 11.** Schematic band diagram of a pentacene memory transistor during programming, taken along the line AB in Fig. 1. (a) A hole can tunnel from the channel into the dielectric upon the application of a negative  $V_{GS}$  (–15 V for example). (b) Measured in the glovebox: an electron can tunnel from the channel into the dielectric and overwrite the trapped hole upon the application of a low positive  $V_{GS}$  (15 V for example). (c) Measured in air: a trapped hole cannot be pushed back to the channel upon the application of a low positive  $V_{GS}$  (15 V for example).



part of the electric field drops over the organic semiconductor, reducing the electric field over the gate insulators. The remaining field, to first approximation:

$$E_{P2MS} = V_{GS} \frac{\epsilon_{SiO_2} \epsilon_{pentacene}}{\epsilon_{P2MS} \epsilon_{SiO_2} \epsilon_{pentacene} + \epsilon_{P2MS} \epsilon_{SiO_2} \epsilon_{pentacene} + \epsilon_{P2MS} \epsilon_{SiO_2} \epsilon_{pentacene}} \quad (2)$$

is insufficient to detrapp the trapped hole from its deep hole trap ( $E_{P2MS}$  is only 3 MV/cm for  $V_{GS,prog} = 15$  V).

#### 4. Conclusions

We fabricated an ambipolar bilayer organic transistor device, in which both holes and electrons can be accumulated in the channel and subsequently trapped into the gate dielectric. As both charge carriers can be trapped, a large memory window, extending on both sides of the initial turn-on voltage can be realized. Only the negative part of this memory window can be used (trapped holes) as the retention of the positive part (trapped electrons) is too low. The trapping mechanism for both charge carriers showed to be tunneling from the channel into the dielectric.

Our measurements indicate that the supply of the charge carriers in the channel can be a limiting factor for the memory behavior. This is for example the case for the low mobility electrons in the pentacene devices: further lowering their mobility results in a decreased memory window. This has its consequences for the chosen polymer insulator as this material will not only be part of the charge storage medium but also needs to be carefully chosen to not hinder the electron transport in the organic semiconductor.

Finally, we also show that the optimal method to erase a trapped charge carrier from the dielectric is overwriting it with a charge carrier of opposite polarity. Although the retention of the electrons is low, these electrons are necessary to lower the voltage to erase the trapped holes.

#### Acknowledgments

The authors would like to thank K. Maturova from the Department of Applied Physics at the Technische Universiteit Eindhoven for fruitful discussions. M. Debucquoy

acknowledges the Institute for the Promotion of Innovation through Science and Technology in Flanders (IWT-Vlaanderen) for financial support. This work was performed in collaboration between IMEC and TNO in the frame of the Holst Centre.

#### References

- [1] E. Cantatore, T.C.T. Geuns, G.H. Gelinck, E. van Veenendaal, A.F.A. Gruijthuijsen, L. Schrijnemakers, S. Drews, D.M. de Leeuw, IEEE J. Solid-State Circuits 42 (2007) 84.
- [2] K. Myny, M. Beenhakkers, N. van Aerle, G.H. Gelinck, J. Genoe, W. Dehaene, P. Heremans, Int. Sol. St. Circ. Conf. Dig. Tech. Papers 2009 (2009) 206.
- [3] R.C.G. Naber, C. Tanase, P.W.M. Blom, G.H. Gelinck, A.W. Marsman, F.J. Touwslager, S. Setayesh, D.M. De Leeuw, Nat. Mater. 4 (2005) 243.
- [4] R. Schroeder, L.A. Majewski, M. Grell, Adv. Mater. 16 (2004) 633.
- [5] F.A. Yildirim, C. Ucurum, R.R. Schlieve, W. Bauhofer, R.M. Meixner, H. Goebel, W. Krautschneider, Appl. Phys. Lett. 90 (2007) 083501.
- [6] H.E. Katz, X.M. Hong, A. Dodabalapur, R. Sarpeshkar, J. Appl. Phys. 91 (2002) 1572.
- [7] T.B. Singh, N. Marjanovic, G.J. Matt, N.S. Sariciftci, R. Schwödlauer, S. Bauer, Appl. Phys. Lett. 85 (2004) 5409.
- [8] L. Zhen, W. Guan, L. Shang, M. Liu, G. Liu, J. Phys. D: Appl. Phys. 41 (2008) 135111.
- [9] W.L. Leong, P.S. Lee, A. Lohani, Y.M. Lam, T. Chen, S. Zhang, A. Dodabalapur, S.G. Mhaisalkar, Adv. Mater. 20 (2008) 2325.
- [10] W. Wu, H. Zhang, Y. Wang, S. Ye, Y. Guo, C. Di, G. Yu, D. Zhu, Y. Liu, Adv. Funct. Mater. 18 (2008) 2593.
- [11] K.J. Baeg, Y.Y. Noh, J. Ghim, S.J. Kang, H. Lee, D.Y. Kim, Adv. Mater. 18 (2006) 3179.
- [12] A.V. Ferris-Prabhu, IEEE Trans. Electron Dev. ED-24 (1977) 524.
- [13] M.J. Powell, C. van Berkel, J.R. Hughes, Appl. Phys. Lett. 54 (1989) 1323.
- [14] T.B. Singh, F. Meghdadi, S. Günes, N. Marjanovic, G. Horowitz, P. Lang, S. Bauer, N.S. Sariciftci, Adv. Mater. 17 (2005) 2315.
- [15] S.W. Wright, J.C. Anderson, Thin Solid Films 62 (1979) 89.
- [16] W.A. Schoonveld, J.B. Oostinga, J. Vrijmoeth, T.M. Klapwijk, Synth. Met. 101 (1999) 608.
- [17] H.-S. Seo, Y.-S. Jang, Y. Zhang, P. Syed Abthagir, J.-H. Choi, Org. Electron. 9 (2008) 432.
- [18] K.J. Baeg, Y.Y. Noh, J. Ghim, B. Lim, D.Y. Kim, Adv. Funct. Mater. 18 (2008) 3678.
- [19] L.L. Chua, J. Zaumseil, J.F. Chang, E.C.W. Ou, P.K.H. Ho, H. Sirringhaus, R.H. Friend, Nature 434 (2005) 194.
- [20] Y. Guo, C.-A. Di, S. Ye, X. Sun, J. Zhenf, Y. Wen, W. Wu, G. Yu, Y. Liu, Adv. Mater. 21 (2009) 1954.
- [21] M. Debucquoy, S. Verlaak, S. Steudel, K. Myny, J. Genoe, P. Heremans, Appl. Phys. Lett. 91 (2007) 103508.
- [22] G. Gu, M.G. Kane, Appl. Phys. Lett. 92 (2008) 053305.
- [23] F. De Angelis, G. Das, E. Di Fabrizio, Chem. Phys. Lett. 462 (2008) 234.
- [24] T. Hallam, C.M. Dutty, T. Minakata, M. Ando, H. Sirringhaus, Nanotechnology 20 (2009) 025203.
- [25] D. Knipp, A. Benor, V. Wagner, T. Muck, J. Appl. Phys. 101 (2007) 044504.

The combination of  $H_{16}CuPc$  and  $F_{16}CuPc$  was used before in bilayered field-effect transistors (FET) [11–13] to obtain ambipolar transport. For both materials a threshold voltage shift was observed if the respective other material is deposited on top of the transport material in the FET. For thicker layers the second deposited material opens an additional channel for the opposite charge carrier type to give ambipolar transport. The threshold voltage shift was related to a charge transfer with holes accumulating in  $H_{16}CuPc$  and electrons in  $F_{16}CuPc$ . Therefore the bilayer structure can be used to engineer the threshold voltage in FETs.

Mixed crystals of strong DA systems like TTF-TCNQ are well-known since the 1970s [14]. However, the growth of crystalline thin films of two organic semiconductors by vacuum deposition is a relatively new aspect for organic electronics. It has been demonstrated that charge transfer salts, such as TTF-TCNQ and its many derivatives, can be deposited as crystalline films by thermal evaporation of the bulk material [15]. The formation of mixed crystalline films by co-evaporation of molecules has only recently been observed for rod-like molecules [16], such as sexithiophene (6T), sexiphenyl (6P) and dihexylsexithiophene (DH6T). Thereby the structure of the films is predominantly determined by the size of the conjugated system. It was also shown that pentacene and perfluoro-pentacene can be grown as intercalated mixed crystalline layers on top of  $SiO_2$ ; thereby the ionization energy can be continuously varied by the layer composition [17].

Here we present a study of blends using hydrogenated copper-phthalocyanine  $H_{16}CuPc$  in combination with its per-fluorinated version  $F_{16}CuPc$ . In addition to studying the fundamental structural, optical, and electrical properties centering around the question of the formation of mixed crystals we investigate the usability of these materials for photovoltaic cells as planar and bulk-heterojunction devices.

## 2. Experimental

The materials used in this study were purchased from Sigma Aldrich as sublimation grade and additionally purified by temperature gradient sublimation; for  $F_{16}CuPc$  the

sublimation procedure was repeated once. The structural formulae are given in Fig. 1. The organic semiconductor films were deposited by thermal evaporation from two independent low-temperature effusion cells in a vacuum better than  $10^{-7}$  mbar. The thickness of the films was controlled via deposition monitors using quartz microbalances. For mixed films two independent monitors were used. The layer sequence for the bilayer structure consists of  $H_{16}CuPc$  deposited on the hole injecting layer followed by  $F_{16}CuPc$ . The deposition rates were  $0.35 \text{ \AA/s}$  for neat films and up to  $1.4 \text{ \AA/s}$  for the material with the higher volume fraction in the mixtures. As substrates glass slides covered with 130 nm of indium-tin oxide (ITO) and 30 nm of the conducting polymer polyethylenedioxythiophene-polystyrenesulfonate (PEDOT:PSS, purchased from H.C. Starck as BAYTRON P) were used. For the optical absorption measurements the films were deposited on quartz glass slides. During the deposition of the phthalocyanine molecules the substrate was held either at room temperature (about 300 K) or at an elevated temperature (about 375 K).

The charge transport properties were analyzed in both unipolar and ambipolar diodes. For hole-only diodes the active organic layer was deposited on an ITO/PEDOT:PSS anode and a 100 nm thick Au film with a thin interlayer of 2,3,5,6-tetrafluoro-7,7,8,8-tetracyano-quinodimethane ( $F_4TCNQ$ ) was used as hole injecting layer [18]. The electron-only diodes contained a 100 nm thick Al bottom electrode and a 100 nm thick Al electrode on the top of the organic film with a 0.5 nm thick interface doping layer of LiF for the latter one. Using an ITO/PEDOT:PSS bottom contact together with a LiF/Al top electrode ambipolar injection and charge transport were obtained. The active organic layer in all investigated devices consisted of an 80 nm thick film of neat or blended materials (volume mixing ratio of 1:1). The active area was about  $2 \times 2 \text{ mm}^2$ . Electrical characterization was performed without air-exposure under vacuum or in a nitrogen filled glove box.

To analyze the current–voltage characteristics the measured curves were fitted by the model of trap-free space charge limited currents (SCLC, Eq. (1)) [19] combined with a Poole–Frenkel type field-dependent mobility [20], which gives the current density as

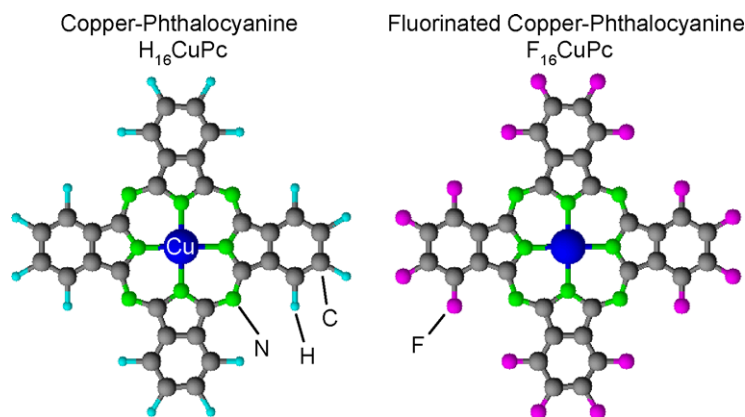


Fig. 1. Structural formulae of hydrogen-terminated copper phthalocyanine  $H_{16}CuPc$  and fluorine-terminated copper phthalocyanine  $F_{16}CuPc$ .

$$j_{\text{SCLC}} = \frac{9}{8} \cdot \mu_0 \cdot \epsilon_0 \epsilon_r \frac{V_{\text{eff}}^2}{d^3} \exp \left[ \gamma \sqrt{\frac{V_{\text{eff}}}{d}} \right]. \quad (1)$$

This equation contains a zero-field mobility  $\mu_0$  and a field activation parameter  $\gamma$ .  $d$  is the film thickness and  $V_{\text{eff}}$  the effective applied voltage  $V - V_{\text{Bi}}$ , with  $V_{\text{Bi}}$  being the built-in voltage, i.e. the difference of the work functions at both electrodes. The parameters  $\mu_0$ ,  $\gamma$  and  $V_{\text{Bi}}$  are determined by fitting the measured data in the higher voltage range above  $V_{\text{Bi}}$ .

Devices showing ambipolar injection and transport, i.e. devices comprising ITO/PEDOT:PSS and LiF/Al electrodes were additionally investigated as solar cells. In this case the active organic film consisted either of an 80 nm thick 1:1 blend or two neat layers with 40 nm thickness for each material. Current–voltage characteristics of the solar cells were measured in darkness and under illumination. The intensity of the solar simulator (AM1.5 filters) was varied up to 100 mW/cm<sup>2</sup>, i.e. one sun.

In addition to the electrical measurements, the neat and blended organic films were analyzed by scanning force microscopy (SFM) and specular X-ray reflectometry. The SFM measurements were performed using a Thermo Microscopes Autoprobe CP-Research in non-contact mode. The X-ray scattering measurements were conducted on a GE/Seifert X-ray diffractometer (Cu  $K\alpha 1$  radiation, multi-layer mirror, and double bounce compressor monochromator). The optical absorption spectra were recorded for films deposited on quartz glass substrates using a Perkin Elmer Lambda 950 with a spectral range from 0.5 to 5.0 eV. X-ray scattering, SFM, and optical absorption measurements were performed under ambient conditions.

### 3. Results and discussion

#### 3.1. Structural properties

The morphology of phthalocyanine films deposited on PEDOT:PSS/ITO was determined by non-contact scanning force microscopy. The results are shown in Fig. 2. Neat films evaporated at room temperature have a granular structure with a typical grain size of about 50 nm. Phthalocyanine films deposited at elevated temperature display a needle-like structure with a typical length of about 300 nm. The higher temperature during evaporation allows a faster diffusion of the molecules and thereby a better ordering resulting in these needle-like crystals. Blended phthalocyanine films show a similar morphology and roughness as the neat films at the same deposition conditions. This similarity in morphology is a first indication for the formation of mixed crystalline films. To confirm this, the films were further analyzed by X-ray scattering.

Fig. 3 shows the out-of-plane first order diffraction peak for the neat films as well as for the 1:1 blend deposited at room temperature. Importantly, the blended H<sub>16</sub>CuPc/F<sub>16</sub>CuPc film shows only one diffraction peak located between the diffraction peaks of the neat materials. The peak width is similar to that of the neat films and the lattice spacing lies between those of the neat materials, consistent with a truly mixed crystalline film, which was

already observed for 1:1 mixtures of different hydrogen terminated planar phthalocyanines [21]. The dependence of the lattice spacing on the concentration is summarized in Fig. 3(right). Additional blend ratios are included (3:1 and 1:3) which were not presented in Fig. 3(left) for clarity reasons. The lattice parameter for the mixed crystal system H<sub>16</sub>CuPc/F<sub>16</sub>CuPc changes linearly with the concentration between the lattice parameters of the neat materials. This linear change is related to the gradual change of the content of the two planar molecular species with different diameter in the blends. The more crystalline films deposited at higher substrate temperature show basically the same lattice spacing with a slightly reduced peak width related to larger crystallites with coherent diffraction in agreement with the SFM analysis.

At this point it is useful to compare the results with other structural data. Identified by the Bragg-reflection at  $q_z = 0.48 \text{ \AA}^{-1}$ , neat thin films of H<sub>16</sub>CuPc on PEDOT:PSS crystallize in the  $\alpha$ -phase, which is common for H<sub>16</sub>CuPc thin film growth [22]. This structure was earlier determined to be isostructural with other phthalocyanine  $\alpha$ -phases, which show a herringbone structure with two molecules per unit cell [23]. However a later reexamination has shown that the H<sub>16</sub>CuPc  $\alpha$ -phase has a triclinic structure with only one molecule per unit cell [24]. According to this structural data the peak at  $q_z = 0.48 \text{ \AA}^{-1}$  corresponds to the (100) reflection, which means that the H<sub>16</sub>CuPc molecules are standing nearly upright and stack in the direction parallel to the substrate. For growth on SiO<sub>2</sub> F<sub>16</sub>CuPc thin films exhibit two polymorphs coined  $\beta$ -phase and  $\beta_{\text{bilayer}}$ -phase [25,26]. The two polymorphs exhibit different in-plane-stacking behaviour, in particular the  $\beta$ -phase has a herringbone arrangement, where as the  $\beta_{\text{bilayer}}$ -phase has a single molecule per unit cell and forms stacks parallel to the substrate similar to the H<sub>16</sub>CuPc  $\alpha$ -phase. Since both F<sub>16</sub>CuPc polymorphs have an identical out-of-plane spacing, it cannot be determined by the data of Fig. 3 whether a herringbone arrangement is present in the neat film or not.

Due to the different size of the terminating atoms the size of the molecule varies and thereby also the lattice spacing  $a$  perpendicular to the substrate (see Fig. 4) [24,26]. The values are about 1.24 nm for the  $\alpha$ -phase of H<sub>16</sub>CuPc and about 1.43 nm for F<sub>16</sub>CuPc films, respectively. Several other molecular arrangements have been observed. E.g. H<sub>16</sub>CuPc crystallizes in a  $\beta$ -phase when heated higher than 480 K [27]. For the present study the key point is not the subtle differences between different polymorphs, but rather the fact that the ordering motifs for both compounds are similar, thus facilitating the formation of mixed crystalline films. Fig. 4 shows schematic film structures for the neat phthalocyanines and a 1:1 mixture. A gradual change of the layer spacing can be rationalized by a varying content of the two molecular species with different size and a change of the tilt angle.

We note that the observation of a single diffraction peak in the blends does not automatically imply the formation of an ordered mixed crystalline film with an in-plane superstructure (as Fig. 4 would suggest). It merely indicates that both constituents are homogeneously mixed on a molecular length scale without detectable phase separation or precipitation.

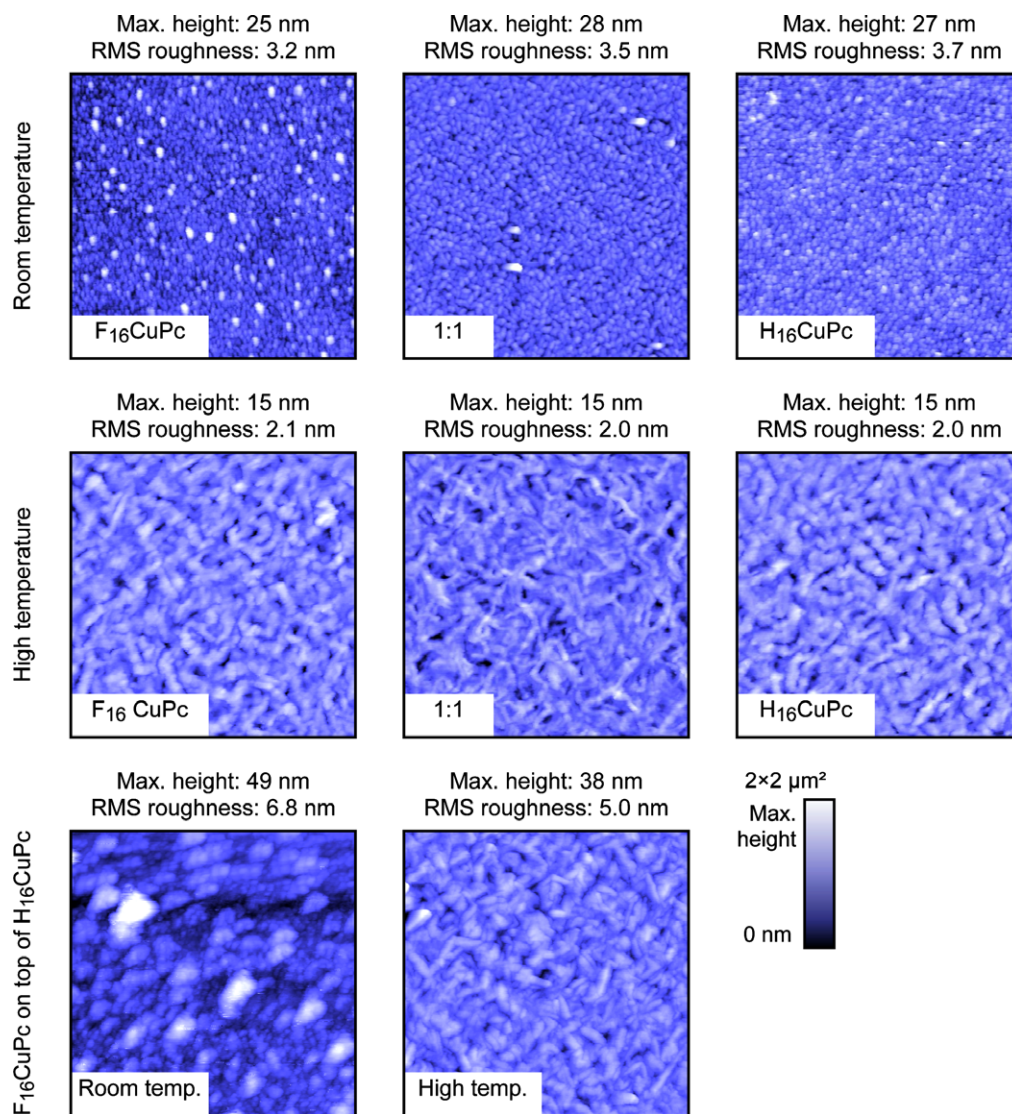


**Fig. 2.** Scanning force microscopy images taken in non-contact mode for neat F<sub>16</sub>CuPc and H<sub>16</sub>CuPc films as well as for a 1:1 blended film grown at 300 K (upper row) and 375 K (middle row) on PEDOT:PSS films. In the lower row the surface morphology of F<sub>16</sub>CuPc films deposited on top of a H<sub>16</sub>CuPc film is shown for deposition at room and high temperature, respectively. The total image size is  $2 \times 2 \mu\text{m}^2$ . The max height is given as the difference between the lowest value (dark blue) and the highest value (white) in each of the images. (For interpretation of the references to colour in this figure legend, the reader is referred to the web version of this article.)

The bilayer system containing a neat H<sub>16</sub>CuPc and a neat F<sub>16</sub>CuPc film was analyzed, too. The SFM images are shown in Fig. 2 (third row). The F<sub>16</sub>CuPc film on top of the H<sub>16</sub>CuPc film evaporated at room temperature is full of fissures. When the evaporation is performed at elevated temperature the film is closed and displays needle-like crystals. The room temperature grown film already shows XRD peaks (see Fig. 3), but only films evaporated at elevated temperatures have closed layers and can be used for bilayer devices.

### 3.2. Optical properties

Fig. 5 shows the optical absorption under normal incidence for neat phthalocyanine films as well as a blended

and a bilayer film. Both materials are almost transparent in the range of 2.5 eV to 3.0 eV. The absorption of H<sub>16</sub>CuPc films between 1.4 and 2.3 eV is related to the Q-band and the absorption in the UV-range (between 3.1 and 4.0 eV) to the B-band [28]. The Q-band absorption of H<sub>16</sub>CuPc shows one strong peak at about 1.81 eV in solution and displays two strong peaks in the solid state (peaks at 1.80 eV and 1.97 eV). As mentioned before F<sub>16</sub>CuPc films crystallize in two different crystal structures [25,26] with different absorption behaviour. In the visible range one structure is related to the peaks at 1.89 eV and 1.77 eV and the other structure has a large crystal shift resulting in a peak around 1.56 eV [29].

The measured spectrum of the blend (Fig. 5, left) shows one strong peak at 1.97 eV and a shoulder at about 1.80 eV.

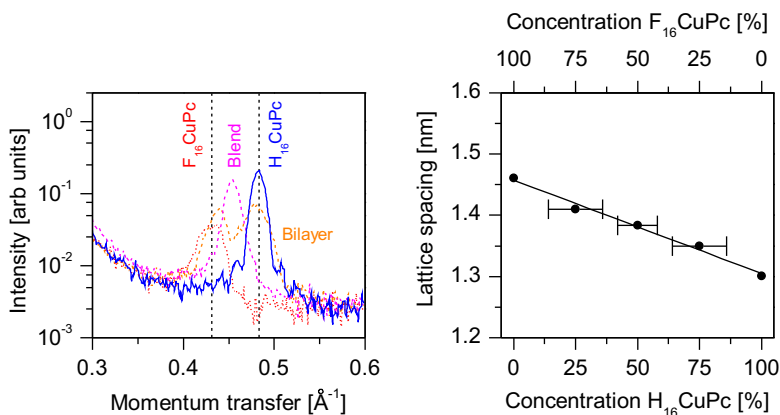


**Fig. 3.** (left) X-ray diffraction spectra of neat films, a 1:1 blend and a bilayer structure evaporated onto PEDOT:PSS at room temperature. (right) Analysis of the lattice spacing determined from X-ray scattering spectra of films with different mixing ratios. The straight line is the linear fit of the measurement points.

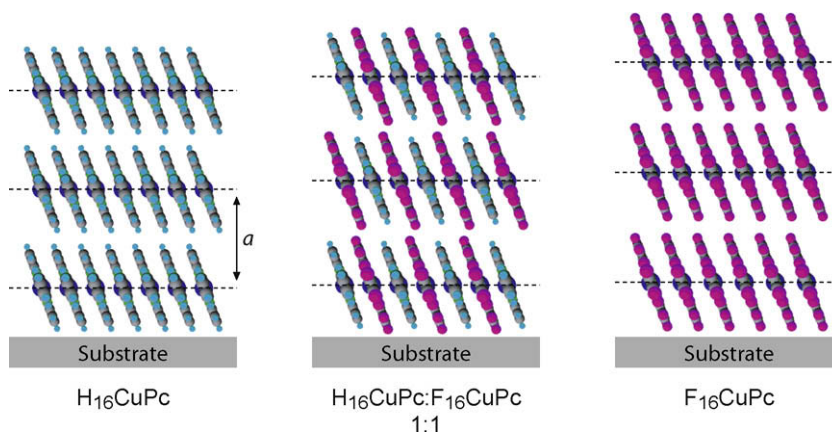


**Fig. 4.** Schematic molecular arrangement for neat and mixed phthalocyanine films. The interlayer spacing changes gradually from H<sub>16</sub>CuPc to the blend and further to F<sub>16</sub>CuPc. For easier visualization an ordered structure of the blend is assumed. The lattice parameter  $a$  is about 1.3 nm related to the  $\alpha$ -phase in H<sub>16</sub>CuPc and about 1.45 nm for F<sub>16</sub>CuPc [24,26].

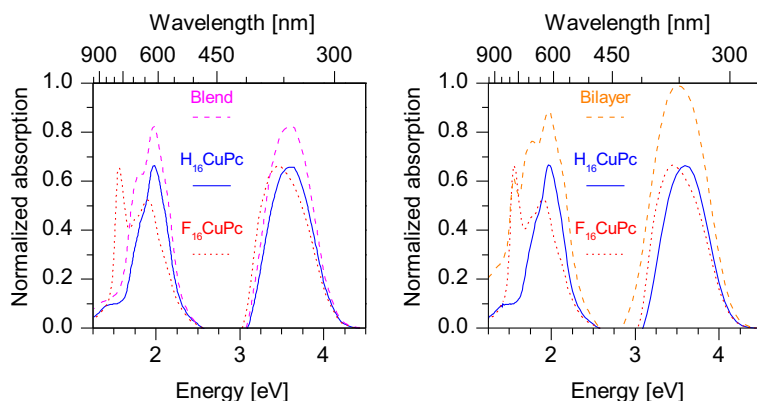


**Fig. 5.** Absorption spectra of neat as well as blended (left) and bilayered (right) films using H<sub>16</sub>CuPc and F<sub>16</sub>CuPc deposited on quartz glass substrates at room temperature. The bilayer structure consists of an H<sub>16</sub>CuPc film on top of an F<sub>16</sub>CuPc film which shows the similar behaviour as the opposite film sequence. Additionally a higher on-set at the low energy side of the spectrum is observed for the bilayer structure as for the other samples which is related to differences in the interference effect due to the larger film thickness.

These features are located in the spectral range where both molecules show absorption. In addition, the far red-shifted peak at 1.56 eV in F<sub>16</sub>CuPc disappears indicating that the related packing motif is no longer present in the blend. This is another demonstration of the formation of mixed crystalline films by co-evaporation of the two different phthalocyanine molecules.

The absorption of a bilayered film (F<sub>16</sub>CuPc on top of a H<sub>16</sub>CuPc film) is shown in Fig. 5(right). There all peaks of the neat films are present and scale with the doubled film thickness in the bilayered system (40 nm H<sub>16</sub>CuPc + 40 nm F<sub>16</sub>CuPc) as compared to the neat films (40 nm).

### 3.3. Electrical properties

The current–voltage characteristics were measured using various electrodes to realize hole-only, electron-only and ambipolar transport [30] and are shown in Fig. 6. In all samples unipolar electron currents are higher than unipolar hole currents. For the ambipolar transport, however, there is a huge difference between neat materials and the 1:1 blend. While for the former the ambipolar current is close to the current in the electron-only devices, indicating that the current is carried mostly by electrons, the latter system shows a reduction of the current by about four orders of magnitude in comparison to the ambipolar currents of the neat films and both unipolar currents in the blend. The resulting mobilities using the before described SCLC model are also shown in Fig. 6.

The unipolar mobilities of the blend are located between the unipolar mobilities of the neat materials. This alignment of the unipolar mobilities shows similar  $\pi$ - $\pi$ -overlap in the mixed crystalline films as in the neat films. However, the ambipolar mobility in the blended film is orders of magnitude lower than both unipolar mobilities and the ambipolar mobilities of the neat materials. The same trend is observed for films grown on room temperature substrates, though, the reduction of the ambipolar mobility is more pronounced in the heated films. As the unipolar mobilities in the 1:1 mixture are just in between the values for neat films, the ambipolar transport cannot be limited by the absence of percolation pathways. The strongly reduced ambipolar mobility should rather be related to the simultaneous presence of both charge carrier types in the mixture. A possible explanation is the formation of charge transfer (CT) excitons by the injected charge carriers. These CT states will then limit the transport by blocking the occupied molecules for further injected charge carriers; they would be self-trapped. The idea of generation of charge transfer excitons is supported by the high EA of F<sub>16</sub>CuPc. As mentioned in the introduction, the IP is 5.0 eV for H<sub>16</sub>CuPc and 6.1 eV for F<sub>16</sub>CuPc, respectively. Taking identical transport gaps of 2.3 eV for both materials [31], results in a LUMO level of F<sub>16</sub>CuPc being only 1.2 eV above the HOMO of H<sub>16</sub>CuPc. Thus, an intermolecular low-lying CT state could be possible in H<sub>16</sub>CuPc/F<sub>16</sub>CuPc blends. However, as we do not see a signature in the optical absorption measured down to 0.6 eV (not shown here),

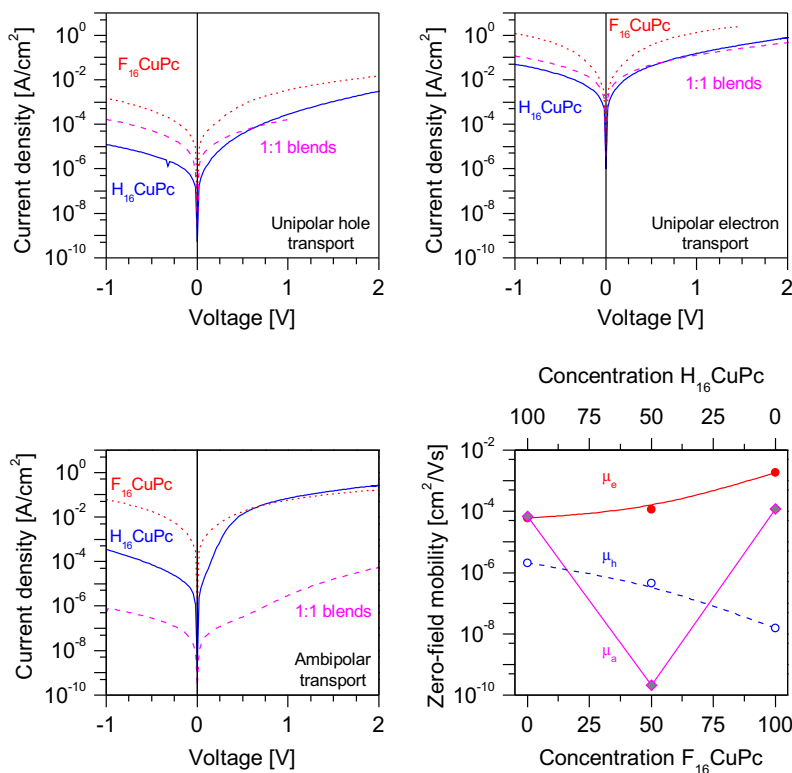


**Fig. 6.** Current–voltage characteristics of electron-only, hole-only and ambipolar diodes with neat H<sub>16</sub>CuPc and F<sub>16</sub>CuPc as well as a 1:1 blend as active layer. All films were deposited using high substrate temperatures. The lower right diagram shows the zero-field mobilities determined using an SCLC model for all nine diodes.

a direct electronic transition into and from this CT state seems to be not allowed, thus stabilizing the charge separated state. Consistently, due to the ambipolar nature of CT excitons the unipolar mobilities would not be affected.

The possibility of self-trapped CT excitons was suggested before for molecular crystals consisting of stacked alternating donor–acceptor molecules, such as anthracene-PMDA [32]. Materials of this type are insulating and CT excitons created by optical excitation are not mobile. We suggest that this could also happen in the system presented here for simultaneous injection of electrons and holes into a 1:1 blend.

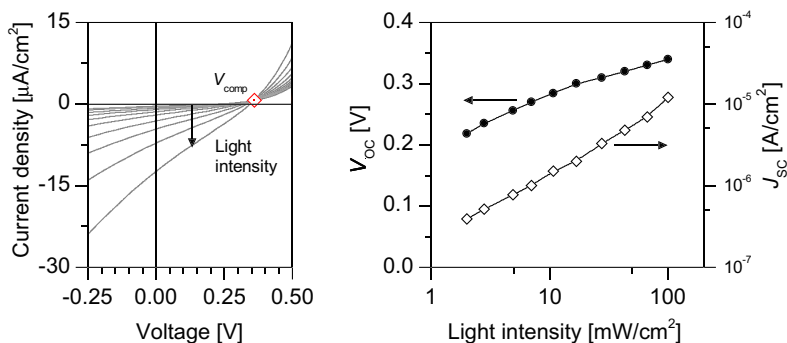
We note that, strictly speaking, differences between electron-only and ambipolar devices could also be caused by different film growth modes, because in the former case Al is used as substrate whereas the latter films are grown on PEDOT:PSS. However, as there is also a large difference of the mobility in the blend between unipolar hole-only and ambipolar devices, which have the same PEDOT:PSS layer as anode, we do not consider the substrate as the decisive parameter for the significant drop of the ambipolar mobility in the 1:1 blend.

### 3.4. Photovoltaic cells

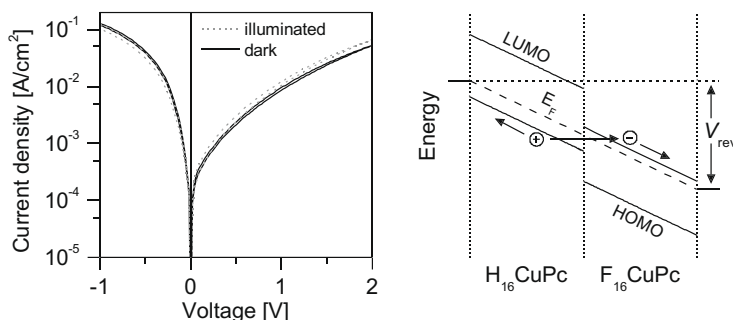
Organic donor and acceptor materials are promising candidates for photovoltaic cells [34]. In these cells the generated excitons dissociate into free charge carriers at the donor/acceptor interface by an ultra-fast photo-induced charge transfer [35,36]. To create this donor/acceptor interface bilayered (planar heterojunction) [4] and blended (bulk-heterojunction) [5,37] photovoltaic cells are employed. In bilayered systems the dissociation is localized at the interface between the two layers, while in bulk-heterojunction cells it occurs within the whole volume of the blended film. Due to this mixture of donor and acceptor materials the photon-to-current conversion efficiency and the power conversion efficiency were found to increase [5,37,38]. An obvious choice for donor–acceptor blends are organic semiconducting materials in their hydrogenated and fluorinated form, since they combine potentially suitable electronic properties with potential structural compatibility of the two constituents.

Fig. 7 shows the  $I$ – $V$  characteristics for a solar cell containing a blended  $H_{16}CuPc/F_{16}CuPc$  film as active layer deposited at elevated temperature. The measurement includes the dark current and the current under various illumination intensities up to one sun. The compensation voltage is about 0.36 eV [33] and slightly higher than the open circuit voltage at the highest intensity. The short circuit currents are orders of magnitude lower than comparable cells made from  $CuPc/C_{60}$  blends [39,40]. Regarding the low ambipolar mobility in the  $H_{16}CuPc/F_{16}CuPc$  blends the very low photocurrents are probably related to the above mentioned self-trapping process. However, the charge transfer excitons are not formed by a direct optical transition but rather by a photo-induced charge transfer after light absorption by one of the two molecular species. The fill factor of about 25% and a power conversion efficiency of only 0.002% shows the ill performance and the limited usability of this system in photovoltaic cells. Comparable solar cells deposited at room temperature show an even smaller open circuit voltage and similar short circuit currents as the heated ones. The power conversion efficiency is reduced to 0.001%.

Fig. 8 (left) shows the  $I$ – $V$  characteristics of the planar  $H_{16}CuPc/F_{16}CuPc$  heterojunction in the dark and under white light illumination at one sun. Comparing to Fig. 6 one immediately notices a remarkable difference: the dark current at 2 V is about 6 orders of magnitude higher than in the blend, however, there is almost no effect of illumination. Even more remarkable is the fact that the reverse current at  $-1$  V is about one order of magnitude higher than the forward current at  $+1$  V. Forward biasing allows for the injection of electrons into  $F_{16}CuPc$  and holes into  $H_{16}CuPc$ . Both carrier species are transported to the interface between both materials where they recombine. The formation of CT excitons is not an issue in this case due to the applied electric field across the interface. Under reverse bias conditions the injection of charge carriers should be blocked by large energy barriers at the electrodes. However, if the energy offset between the HOMO of  $H_{16}CuPc$  and the LUMO of  $F_{16}CuPc$  is small enough, tunneling of electrons from the further into the latter should be possible as shown in Fig. 8(right). This effect of creating an electron-hole pair under reverse bias conditions at an interface between a



**Fig. 7.** (left) Current–voltage characteristics for the blended  $H_{16}CuPc/F_{16}CuPc$  solar cell with an active layer deposited at high temperature. The curves are shown for different white light intensities (simulated AM1.5 illumination). The compensation voltage  $V_{comp}$  is determined as the crossing point of all curves [33]. (right) Open circuit voltage ( $V_{oc}$ ) and short circuit current density ( $J_{sc}$ ) determined from the left diagram as function of the light intensity.



**Fig. 8.** (left) Current–voltage characteristic for an ambipolar  $H_{16}CuPc/F_{16}CuPc$  bilayer diode in the dark and under one sun illumination. (right) Energy level diagram for an  $H_{16}CuPc/F_{16}CuPc$  bilayer diode to explain the charge generation layer under reverse bias conditions. The energy levels for  $H_{16}CuPc$  are taken from our own measurements and the energy levels for  $F_{16}CuPc$  from the literature [41].

p- and an n-type material is known as charge generation layer and has been employed in multilayer stacked organic LEDs and tandem solar cells [42,43]. We also investigated the influence of light for the planar heterojunction. As visible in Fig. 8 the forward current is only weakly increased by photo-generated charge carriers. In backward direction, however, this photo-induced change is obscured by the higher current due to the charge generation layer. Due to the absence of an open circuit voltage and the weak influence of light, this planar heterojunction can not be used as photoactive interface in organic photovoltaic cells.

#### 4. Summary

In conclusion, we have shown that molecularly mixed crystalline films can be grown by co-evaporation of  $H_{16}CuPc$  and  $F_{16}CuPc$  on device-relevant ITO/PEDOT:PSS substrates. These blends show the usual X-ray spectrum and needle-like film morphology known from neat films of phthalocyanines. Due to different size of the molecules, a continuous change of the lattice spacing is observed by changing the mixing ratio. Optical absorption measurements confirm this scenario: they are not just a superposition of the spectra of neat materials, as would be expected for phase-separated blends, but show distinct new features. In particular the disappearance of the characteristic band at 1.56 eV in  $F_{16}CuPc$  is a clear indication of molecular mixing of both species.

A CT exciton could serve as an explanation for the unexpectedly low charge carrier mobility in ambipolar blends, which is found to be orders of magnitude lower than the ambipolar mobility in neat materials and the electron and hole mobilities in unipolar devices. The reduced mobility is also the origin of the poor performance of photovoltaic cells containing  $H_{16}CuPc/F_{16}CuPc$  blends. The charge collection efficiency is drastically reduced by the suggested formation of bound CT excitons. In contrast, a bilayered  $H_{16}CuPc/F_{16}CuPc$  device works as a charge generation layer which could be of interest in tandem solar cells.

#### Acknowledgement

This work was supported by the Deutsche Forschungsgemeinschaft under Priority Programme 1355 “Elementary Processes of Organic Photovoltaics”.

#### References

- [1] C.C. Lenzoff, A.B.P. Lever (Eds.), Phthalocyanines, VCH, New York, 1996.
- [2] J. Simon, J.-J. André, Molecular Semiconductors, Springer, Berlin, 1984.
- [3] S.A. van Slyke, C.H. Chen, C.W. Tang, Organic electroluminescent devices with improved stability, *Appl. Phys. Lett.* 69 (1996) 2160–2162.
- [4] C.W. Tang, Two-layer organic photovoltaic cell, *Appl. Phys. Lett.* 48 (1986) 183–185.
- [5] J. Rostalski, D. Meissner, Monochromatic versus solar efficiencies of organic solar cells, *Sol. Energy Mater. Sol. C* 61 (2000) 87–95.
- [6] T. Stübinger, W. Brütting, Exciton diffusion and optical interference in organic donor–acceptor photovoltaic cells, *J. Appl. Phys.* 90 (2001) 3632–3641.
- [7] P. Peumans, A. Yakimov, S.R. Forrest, Small molecular weight organic thin-film photodetectors and solar cells, *J. Appl. Phys.* 93 (2003) 3693–3723.
- [8] M. Riede, T. Mueller, W. Tress, R. Schueppel, K. Leo, Small-molecule solar cells – status and perspectives, *Nanotechnology* 19 (2008) 424001.
- [9] H. Brinkmann, C. Kelting, S. Makarov, O. Tsaryova, G. Schnurpfeil, D. Wöhrlé, D. Schlettwein, Fluorinated phthalocyanines as molecular semiconductor thin films, *Phys. Stat. Sol. (a)* 205 (2008) 409–420.
- [10] M. Knupfer, H. Peisert, Electronic properties of interfaces between model organic semiconductors and metals, *Phys. Stat. Sol. (a)* 201 (2004) 1055–1074.
- [11] J. Wang, H.B. Wang, X.J. Yan, H.C. Huang, D.H. Yan, Organic heterojunction and its application for double channel field-effect transistors, *Appl. Phys. Lett.* 87 (2005) 093507.
- [12] H. Wang, J. Wang, H. Huang, X. Yan, D. Yan, Organic heterojunction with reverse rectifying characteristics and its application in field-effect transistors, *Org. Electron.* 7 (2006) 369–374.
- [13] R. Ye, M. Baba, K. Suzuki, K. Mori, Dependence of ambipolar transport on first active layer thickness in organic homostructure transistors, *Jpn. J. Appl. Phys.* 46 (2007) 2878–2881.
- [14] D. Jérôme, H. Schulz, Organic conductors and superconductors, *Adv. Phys.* 31 (1982) 299–490.
- [15] Y. Takahashi, T. Hasegawa, Y. Abe, Y. Tokura, G. Saito, Organic metal electrodes for controlled p- and n-type carrier injections in organic field-effect transistors, *Appl. Phys. Lett.* 88 (2006) 073504.
- [16] J.-O. Vogel, I. Salzmann, R. Opitz, S. Duhm, B. Nickel, J.P. Rabe, N. Koch, Sub-nanometer control of the interlayer spacing in thin films of intercalated rodlike conjugated molecules, *J. Phys. Chem. B* 111 (2007) 14097–14101.
- [17] I. Salzmann, S. Duhm, G. Heimel, M. Oehzelt, R. Kniprath, R.L. Johnson, J.P. Rabe, N. Koch, Tuning the ionization energy of organic semiconductor films: the role of intramolecular polar bonds, *J. Am. Chem. Soc.* 130 (2008) 12870–12871.
- [18] A. Opitz, M. Kraus, M. Bronner, J. Wagner, W. Brütting, Bipolar transport in organic field-effect transistors: organic semiconductor blends versus contact modification, *New. J. Phys.* 10 (2008) 065006.
- [19] N. Mott, R. Gurney, Electronic Processes in Ionic Crystals, Clarendon Press, Oxford, 1940.
- [20] P. Murgatroyd, Theory of space-charge limited current enhanced by Frenkel effect, *J. Phys. D: Appl. Phys.* 3 (1970) 151–156.



- [21] E.A. Lucia, F.D. Verderame, Spectra of polycrystalline phthalocyanines in the visible region, *J. Chem. Phys.* 48 (1968) 2674–2681.
- [22] O. Berger, W.-J. Fischer, B. Adolph, S. Tierbach, V. Melev, J. Schreiber, Studies on phase transformations of Cu-phthalocyanine thin films, *J. Mater. Sci.* 11 (2000) 331–346.
- [23] M. Ashida, N. Uyeda, E. Suito, Unit cell metastable-form constants of various phthalocyanines, *B. Chem. Soc. Jpn.* 39 (1966) 2616–2624.
- [24] A. Hoshino, Y. Takenaka, H. Miyaji, Redetermination of the crystal structure of alpha-copper phthalocyanine grown on KCl, *Acta Crystallogr. B* 59 (2003) 393–403.
- [25] J.O. Ossó, F. Schreiber, V. Kruppa, H. Dosch, M. Garriga, M.I. Alonso, F. Cerdeira, Controlled molecular alignment in phthalocyanine thin films on stepped sapphire surfaces, *Adv. Func. Mater.* 12 (2002) 455–460.
- [26] D.G. de Oteyza, E. Barrena, J.O. Ossó, S. Sellner, H. Dosch, Thickness-dependent structural transitions in fluorinated copper-phthalocyanine (F<sub>16</sub>CuPc) films, *J. Am. Chem. Soc.* 128 (2006) 15052–15053.
- [27] J.Y. E, S. Kim, E.J. Lim, K.J. Lee, D.J. Cha, B. Friedman, Effects of substrate temperature on copper(II) phthalocyanine thin films, *Appl. Surf. Sci.* 205 (2003) 274–279.
- [28] D. Datta, V. Tripathi, P. Gogoi, S. Banerjee, S. Kumar, Ellipsometric studies on thin film CuPc:C60 blends for solar cell applications, *Thin Solid Films* 516 (2008) 7237–7240.
- [29] M.I. Alonso, M. Garriga, J.O. Ossó, F. Schreiber, E. Barrena, H. Dosch, Strong optical anisotropies of F<sub>16</sub>CuPc thin films studied by spectroscopic ellipsometry, *J. Chem. Phys.* 119 (2003) 6335–6340.
- [30] W. Brütting (Ed.), *Physics of Organic Semiconductors*, Wiley-VCH, Weinheim, 2005.
- [31] I. Hill, A. Kahn, Z. Soos, R. Pascal, Charge-separation energy in films of  $\pi$ -conjugated organic molecules, *Chem. Phys. Lett.* 327 (2000) 181–188.
- [32] M. Pope, C.E. Swenberg, *Electronic Processes in Organic Crystals and Polymers*, Oxford University Press, New York, 1999.
- [33] V.D. Mihailetschi, L.J.A. Koster, J.C. Hummelen, P.W.M. Blom, Photocurrent generation in polymer-fullerene bulk heterojunctions, *Phys. Rev. Lett.* 93 (2004) 216601.
- [34] C.J. Brabec, V. Dyakonov, U. Scherf, *Organic Photovoltaics*, Wiley-VCH, Weinheim, 2008.
- [35] N.S. Sariciftci, L. Smilowitz, A.J. Heeger, F. Wudl, Photoinduced electron-transfer from a conducting polymer to buckminsterfullerene, *Science* 258 (1992) 1474–1476.
- [36] B. Kraebel, D. McBranch, N.S. Sariciftci, D. Moses, A.J. Heeger, Ultrafast spectroscopic studies of photoinduced electron-transfer from semiconducting polymers to C<sub>60</sub>, *Phys. Rev. B* 50 (1994) 18543–18552.
- [37] G. Yu, J. Gao, J.C. Hummelen, F. Wudl, A.J. Heeger, Polymer photovoltaic cells – enhanced efficiencies via a network of internal donor-acceptor heterojunctions, *Science* 270 (1995) 1789–1791.
- [38] T. Stübinger, W. Brütting, Photocurrent spectra of bilayers and blends of the organic donor-acceptor system CuPc/C<sub>60</sub>, *SPIE Proc.* 4465 (2002) 102–112.
- [39] J.G. Xue, B.P. Rand, S. Uchida, S.R. Forrest, Mixed donor-acceptor molecular heterojunctions for photovoltaic applications. II. Device performance, *J. Appl. Phys.* 98 (2005) 124903.
- [40] A. Opitz, M. Bronner, J. Wagner, M. Götzenbrunner, W. Brütting, Ambipolar organic semiconductor blends for photovoltaic cells, *SPIE Proc.* 7002 (2008) 70020J.
- [41] K. Lau, J. Tang, H. Sun, C. Lee, S. Lee, D. Yan, Interfacial electronic structure of copper phthalocyanine and copper hexadecafluorophthalocyanine studied by photoemission, *Appl. Phys. Lett.* 88 (2006) 173513.
- [42] M. Kröger, S. Hamwi, J. Meyer, T. Dobbertin, T. Riedl, W. Kowalsky, H.-H. Johannes, Temperature-independent field-induced charge separation at doped organic/organic interfaces: experimental modeling of electrical properties, *Phys. Rev. B* 75 (2007) 235321.
- [43] B. Yu, F. Zhu, H. Wang, G. Li, D. Yan, All-organic tunnel junctions as connecting units in tandem organic solar cell, *J. Appl. Phys.* 104 (2008) 114503.

(BL), can an adequate solution to both issues at the same time be achieved?

## 2. Theory

To understand the mechanism of bending a device comprising more than one layer, one can imagine a 175  $\mu\text{m}$  thick polyethylene terephthalate (PET) substrate covered with a 100 nm ITO thin-film to have a structure somewhat analogous to a leaf spring, with 1750 soft leaves and one hard leaf, each 100 nm thick and connected in parallel. In contrast to the leaf spring, however, here the adjacent surfaces of neighbouring leaves are firmly bound to one another. When the structure is bent so that the uppermost surface of the thin layer is concave, it is reasonable to assume that there will be one “leaf” out of the 1751, which maintains its original length, and all others laid above it are stretched whilst those below it are compressed. The one with its original length is called the neutral layer (NL). The position of this layer is crucial because the strain in any of these springs is proportional to the distance from itself to the neutral layer. This will be deduced later.

To determine the position of NL in a multi-layer structure, others such as Kim and co-workers [7] and Hsueh [8] have put forward analytical solutions. In these studies, both the position of the NL and the stress in the layers are considered to be unknown parameters, and are solved with equations of equilibrium of static force and torque in the cross section. In the work presented here, the method introduced enables us to consider the multi-layer bending situation, visually. It is not a new concept since engineers have used routinely it to deal with the stress problems that arise when building with multi-material composite beams [9]. However, it is equally applicable to the realm of plastic electronics, where the nanoarchitectures involved comprise multiple thin layers on a much thicker flexible support, a particular example of which would be a flexible OLED device.

For the longitudinal stress in a plain film being bent, the stress is given by:

$$\begin{aligned}\sigma &= E' \varepsilon \\ E' &= \frac{E}{1-\nu^2}\end{aligned}\quad (1)$$

where the Young's modulus of the film material is  $E$ ,  $\nu$  is the Poisson's ratio,  $E'$  is the reduced elastic modulus and the strain of the film is  $\varepsilon$ . This strain is defined by:

$$\varepsilon = \frac{\Delta l}{l}\quad (2)$$

where  $l$  is the original unbent length, and  $\Delta l$  is the change of length after bending. Although these thin-films are not real springs, the strain caused by bending is only about 0.01 even when the radius is 10 mm. This means the higher order terms are negligible and Hooke's Law is still valid. When an arbitrary segment of a homogeneous film with a symmetric cross section is analysed, the NL should be right at the centre of the film. Assume the layer denoted by  $\overline{ab}$  in Fig. 1a is the NL, and by definition its length remains unchanged on bending to an extent where  $R$  defines the radius of curvature experienced by the NL. Set the

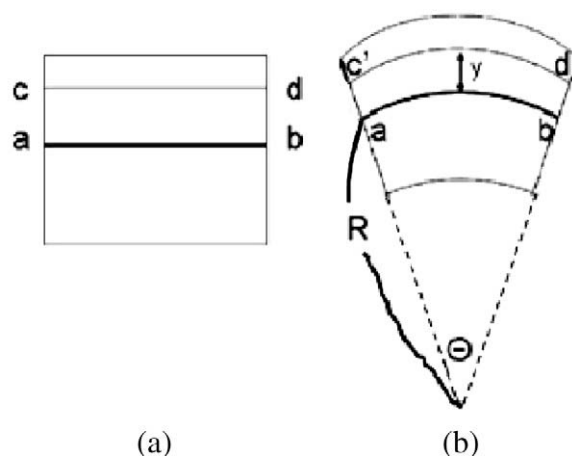


Fig. 1. One segment of a single-material beam before (a) and after (b) bending. Layer  $ab$  is the Neutral Layer; Layer  $cd$ ,  $c'd'$  is the same layer before and after bending with radius  $R$ .

length of  $\overline{ab}$  to be  $l$ . Now consider the strain of another layer in the film,  $\overline{cd}$ , say, when the radius of curvature at the NL ( $\overline{ab}$ ) is  $R$ . Before bending (Fig. 1a):

$$\overline{cd} = \overline{ab} = l\quad (3)$$

whilst after bending (Fig. 1b) the new length of  $\overline{cd}$  becomes  $\overline{c'd'}$ , so that

$$\overline{ab} = l = R\theta\quad (4)$$

$$\overline{c'd'} = l + \Delta l = (R + y) \cdot \theta\quad (5)$$

where  $y$  is the distance from the layer to NL. The strain in the  $cd$  element at this distance from the NL thus becomes:

$$\varepsilon(y) = \Delta l/l = y/R\quad (6)$$

Therefore, the stress in any layer in a film with its distance from the NL being  $y$  is

$$\sigma(y) = \frac{E'y}{R}\quad (7)$$

The total bending moment  $M$  at one end of the segment is

$$M = \int_{-C}^{h-C} \sigma wy dy = \frac{E'}{R} \int_{-C}^{h-C} wy^2 dy = \frac{E'}{R} I_x\quad (8)$$

where  $h$  is the thickness of the film,  $C$  is the displacement from the bottom of the film to the NL,  $w$  is the width of the cross section and  $I_x$  is the second moment of area of the cross section. So we have the following equation to describe the stress developed in the layer as a result of bending completely:

$$\frac{\sigma}{y} = \frac{E'}{R} = \frac{M}{I_x}\quad (9)$$

From the above, the most critical property is the position of the NL. In a single-material, the position of NL is easy to determine. It is just at the centroidal axis of the cross section, so the distance from the layer of interest to the NL,  $y$ , will be known. When the architecture comprises two or more layers of different materials, for example ITO on a PET substrate, slightly more effort is required.

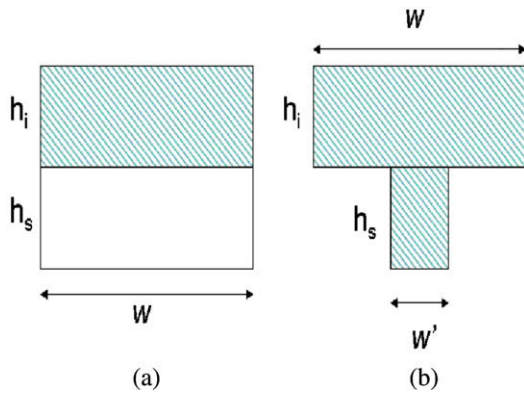


**Fig. 2.** Cross-section (a) and effective cross-section according to the top layer (b) of a two-material composite beam. The thickness of each layers are  $h_i$  and  $h_s$ .

Fig. 2a shows the cross section of the typical ITO coated PET substrate where  $h_s$  is the thickness of the substrate, and  $h_i$  is the thickness of ITO. Assume both layers are with the same width  $w$  and different Young's modulus:  $E_s$  and  $E_i$ . The total bending moment is

$$M = \int \sigma w y dy = \frac{E'_s}{R} \int_{-C}^{h_s-C} w y^2 dy + \frac{E'_i}{R} \int_{h_s-C}^{h_s-C+h_i} w y^2 dy$$

$$= \frac{E'_s}{R} I_x^s + \frac{E'_i}{R} I_x^i = \frac{E'_i}{R} \left( \frac{E'_s}{E'_i} I_x^s + I_x^i \right) \equiv \frac{E'_i}{R} I_x^{\text{effective}} \quad (10)$$

$C$  is the position of NL from the bottom of substrate. The position of  $C$  is chosen at the  $y = 0$  axis in the integration to determine the second moment of area instead of the conventional choice of the centroidal axis of the individual cross section. Formally, it is determined by equating the net force acting on the cross section under bending, to zero as follows:

$$0 = \frac{E'_s}{R} \int_{-C}^{h_s-C} w y dy + \frac{E'_i}{R} \int_{h_s-C}^{h_s-C+h_i} w y dy \quad (11)$$

Eq. (10) shows that the total bending moment  $M$  of an ITO/PET composite film is the same as the pure ITO film with the effective cross section  $I_x^{\text{effective}}$ . Compared with Eq. (8), it can be seen that the effective cross section is really the original cross section of ITO plus the cross section of PET with the new width  $w'$  given by:

$$w' = \frac{E'_s}{E'_i} w \quad (12)$$

Therefore, in the case of longitudinal stress, an ITO/PET composite film (as shown in Fig. 2a) is identical to the pure ITO film (as shown in Fig. 2b). This greatly reduces the effort of solving the position of NL from Eq. (11) to simply determining the centroidal axis of the effective cross section as if it were made from a single-material. When dealing with structures of more than two layers, with each layer having a different Young's modulus, the task of determining the position of NL using the Eq. (11) becomes even more complicated. However, the method we used here requires only the calculation of the effective cross section by

determining  $w'$  of each layer, using the reduced elastic modulus of the layer of interest as the denominator in Eq. (12). Once the equivalent cross section is determined, with the assumption that all the layers are now made from an identical material to the layer of interest, the NL is targeted at the position of centroidal axis of this effective cross section, and the stress in the layer of interest is just a factor times its distance from the NL in the effective cross section: the calculation has transformed the multi-material composite film into a single-material film made solely from the layer under investigation.

### 3. Results and discussion

Due to the poor performance of plastic substrates with respect to permeation of water and oxygen, mentioned earlier, one or more extra barrier layers would usually be inserted between the ITO layer and the PET substrate. The question is: is it possible that a single additional layer could both reduce the stress in the ITO to give it an extra relief when bending and provide an adequate oxygen/water barrier at the same time?

Glass, for example, has a permeation rate of oxygen and water vapour lower than the detection limit [10] and is therefore a good candidate for the protecting layer. Typically, an oxygen permeation rate for soda lime float glass is given as  $<10^{-15} \text{ (cm}^3 \text{ STP) cm}^{-2} \text{ mm}^{-1} \text{ s}^{-1} \text{ (mm Hg)}^{-1}$ . Applying the conventional assumption that permeability is inversely proportional to the layer thickness, and proportional to pressure difference across the layer, the permeability for a 1 mil (25  $\mu\text{m}$ ) film thickness, and a 1 atm pressure difference, is estimated to be  $<2.6 \times 10^{-2} \text{ cm}^3 \text{ m}^{-2} \text{ day}^{-1}$ , in the conventionally adopted units for discussing OLED device performance. By comparison, both oxygen and water permeation rates in 25  $\mu\text{m}$  thick films of  $\text{SiO}_x$  produced by plasma-enhanced chemical vapour deposition (PECVD) have been measured, and are  $8 \times 10^{-2} \text{ cm}^3 \text{ m}^{-2} \text{ day}^{-1}$  at 1 atm pressure difference and  $0.5 \text{ g m}^{-2} \text{ day}^{-1}$  at  $>90\%$  relative humidity, respectively [11]. The upper limits for adequate OLED device performance are currently thought to be on the order of  $10^{-3} \text{ cm}^3 \text{ m}^{-2} \text{ day}^{-1}$  (oxygen) and  $10^{-5} \text{ g m}^{-2} \text{ day}^{-1}$  (water), where material composition, layer thickness, and pressure difference are variables to achieve these values.

The reduced elastic modulus of ITO, glass, and PET film are assumed to be 120 GPa [12], 74 GPa, and 5 GPa, respectively, as in Table 2. If the total thickness of glass plus PET composite substrate is kept constant at 175  $\mu\text{m}$ , with a typical ITO thickness of 100 nm, and the whole composite subjected to a bend radius of 10 cm, then from Eq. (7) the thicknesses of glass and PET optimized by simulation are 35  $\mu\text{m}$  and 140  $\mu\text{m}$ , respectively, as shown in Fig. 3. This structure would reduce the stress in ITO from the plain PET substrate – and, indeed, also a plain glass substrate – by a factor of 2.5.

To further understand how the overlaid OLED and cathode layers would affect the ITO stress, a knowledge of the Young's modulus of these organic layers is required. The lack of such information is partly because the PET substrate is softer than the organic layer which leads to the

**Table 1**

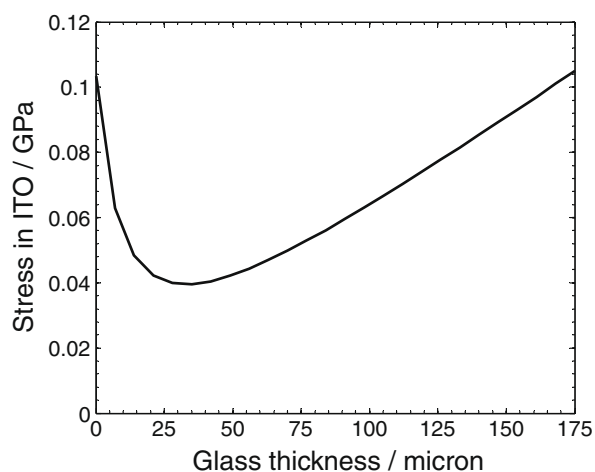
The list of samples tested by nano-indentation technology.

	Substrate material	Substrate thickness (mm)	Coating material	Coating thickness (nm)
Sample 1	PET	0.1	Alq <sub>3</sub>	100
Sample 2	PET	0.1	Alq <sub>3</sub>	200
Sample 3	PET	0.1	NPD	200

**Table 2**

The value of Young's modulus and reduced elastic modulus used in the simulation.

	Young's modulus (GPa)	Reduced elastic modulus (GPa)
Al	70	78
OLED	N/A	12
ITO	120	120
BL	N/A	6–70
PET	4	5
Glass	70	74

**Fig. 3.** The stress in ITO against the thickness of glass buffer layer with the fixed "glass/PET" composite substrate thickness. The bending radius is 100 mm.

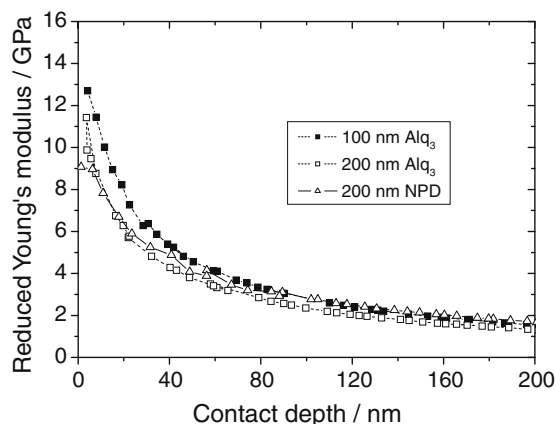
difficulty for the elasticity measurement. However, with the aid of triboindenter technology, the surface of the sample can be probed on the scale of several nanometers, thus allowing the effect of the soft base to be filtered out. Three samples are prepared, as listed in Table 1, in order to gauge the elastic property of *N,N'*-bis(naphthalen-1-yl)-*N,N'*-bis(phenyl)benzidine (NPD) and tris-(8-hydroxyquinoline)aluminum (Alq<sub>3</sub>). The PET substrate was cleaned first with acetone, and then with isopropanol in an ultrasonic bath for 5 min each. Three separate samples were prepared by evaporating 100 nm of Alq<sub>3</sub>, 200 nm of Alq<sub>3</sub> and 200 nm of NPD, respectively, on the PET substrate separately using the Kurt J. Lesker thermal evaporator under the vacuum of  $5 \times 10^{-7}$  mbar.

The Young's moduli of the samples were measured by standard nano-indentation techniques. For each material nano-indentation tests were performed under displace-

ment control with maximum displacements from 10 nm to 1000 nm using a Hysitron Triboindenter fitted with a sharp Berkovich diamond indenter (tip end radius  $\sim 50$  nm). The diamond tip shape was carefully calibrated with a fused silica test sample (using the standard Oliver and Pharr method [13]) before and after testing with no change in shape recorded.

The indenter displacement is made up of two components, the plastic depth of the indent (contact depth) and the elastic deflection of the surface at the edge of the contact. The contact depth is typically  $<0.67$  of the maximum displacement. Nano-indentation load–displacement curves were recorded for each indent and only those where evidence of plastic deformation was observed (i.e. the loading and unloading curves are different) were used in the analysis of Young's modulus by the Oliver and Pharr method [13]. In this approach, the initial slope of the unloading curve can be used to determine the contact depth and the elastic modulus of the sample (effectively from the recovery of the elastic deflection of the surface) based upon the Sneddon flat punch solution. This requires the contact area to be calculated from the contact depth based upon an accurate knowledge of the tip end shape and defines the need for careful tip calibration as mentioned previously.

The result is shown in Fig. 4. The reduced elastic modulus in the *y*-axis direction only differs from the real Young's modulus by a factor of  $(1 - \nu^2)^{-1}$ . Because the thickness of the organic layers are 100 nm and 200 nm, the readings of the reduced elastic modulus at the contact depth deeper than a third of the coating thickness are greatly dominated

**Fig. 4.** Reduced elastic modulus of 100 nm Alq<sub>3</sub> (solid square), 200 nm Alq<sub>3</sub> (open square), and 200 nm NPD (open triangle) against the probing depth in the triboindenter measuring. All samples are deposited on 100 nm thick PET films.

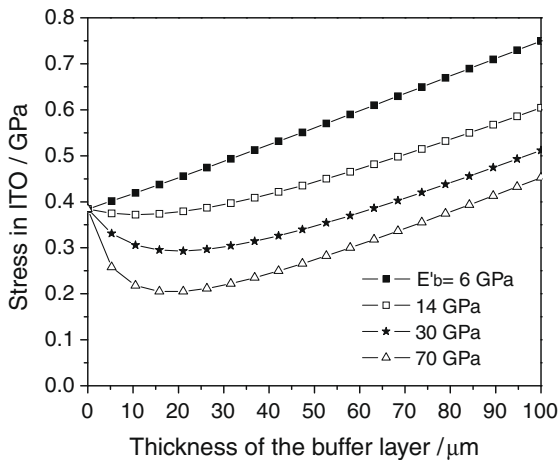


**Fig. 5.** The stress in ITO against the thickness of buffer layer with different buffer layer Young's modulus in the five-layers structure: PET(100  $\mu\text{m}$ )/Buffer(0–100  $\mu\text{m}$ )/ITO(100 nm)/OLED(100 nm)/Aluminium (100 nm). The bending radius is 15 mm.

by the PET substrate. The Young's modulus commonly used for PET film is 4 GPa, and the Poisson's ratio lies between 0 and 0.5. However, the reduced elastic modulus in this regime is measured to be lower than 4 GPa, rather than larger values in the range 4–5 GPa as the common values above suggest. We believe this might be due to the thin planarization layer (smoothing layer) coated by the supplier (DuPont Teijin Films), which could be softer than PET.

When the contact depth is within a third of the coating thickness, the measured reduced elastic modulus contains an increasing contribution from the thin coating itself. So the value of the reduced modulus when the contact depth is extrapolated to zero can approximate the Young's modulus of the coating layer deposited. From Fig. 4, all the three samples have about same value of 12 GPa when the

contact depth approaches zero regardless of the difference in their thickness. For such a thin coating on a compliant substrate it is difficult to completely filter out the effect of the substrate and there may be considerable scatter in the extrapolated modulus due to the quality of the data available for extrapolation. Fracture in the coating can lead to discontinuities in observed behaviour and, at low indenter penetrations where most data is needed for accurate extrapolation, plastic deformation is limited. Thus, although this extrapolation process has been adopted in ISO 14577-4 (2007) for the assessment of the reduced modulus of thin coatings there remain some questions about its validity; for instance for a substrate harder or softer than the coated layer, the modulus determined by nano-indentation can be different [14]. The way the small molecules grow on different materials could alter the elastic response of the coating as well, therefore, we measured the samples on a PET substrate in order to keep everything the same as a working FOLED device. A full study of the Young's modulus of Alq<sub>3</sub> and NPD on different substrates to assess the reliability of the data is the subject of further work.

For OLED operation in a flexible regime, the value of 12 GPa suggests that the materials in small molecule based OLEDs are not remarkably different in their elastic moduli relative to either the long chain polymer materials in PLEDs (typ. 2–6 GPa) or, say, a PET support (4 GPa). Only the ITO (120 GPa) and metal cathode layers such as aluminium (70 GPa) require more careful attention.

The five-layers structure: PET (100  $\mu\text{m}$ )/Buffer ( $x$ )/ITO (100 nm)/OLED (100 nm)/Aluminium (100 nm) is simulated with different values of reduced elastic modulus of the buffer layer (BL) and different thicknesses,  $x$ . The extension to accommodate the multiple thin layers in this case is particularly straightforward. The combined thickness of the thin layer stack is nearly three orders of magnitude less than that of the support, so the position of the neutral layer is determined almost exclusively by the composition of the thicker support. The stress in each of the

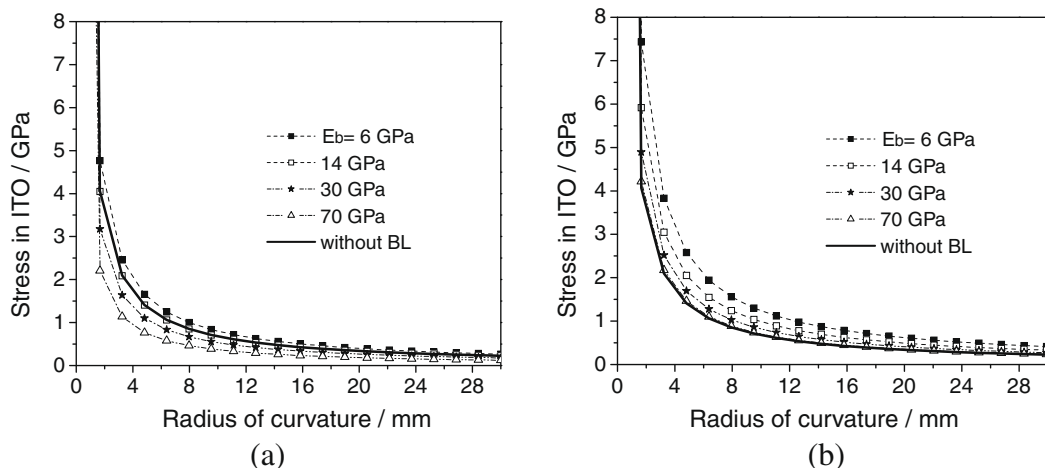


**Fig. 6.** The stress in ITO against the device bending radius with different buffer layer Young's modulus in the five-layers structure: (a) PET(100  $\mu\text{m}$ )/Buffer(20  $\mu\text{m}$ )/ITO(100 nm)/OLED(100 nm)/Aluminium(100 nm). (b) PET(100  $\mu\text{m}$ )/Buffer(100  $\mu\text{m}$ )/ITO(100 nm)/OLED(100 nm)/Aluminium(100 nm).

thin layers is then determined by the reduced elastic modulus of the thin layer, the distance from the neutral plane to the surface on which the thin layer is coated and the bend radius, just as for the single thin layer case. The reduced elastic modulus of the PET substrate is set to be 5 GPa. Assuming the bending radius is 15 mm, the stress in ITO against the thickness of BL is shown in Fig. 5. This shows a series of different buffer layer moduli, in the whole device structure. In contrast to Fig. 4, the PET layer now has a constant thickness and the buffer thickness is increased from zero. As the buffer material modulus increases, values in the range 14–70 GPa exhibit minima in ITO stress at a thicknesses of 15–20% of the PET layer. When the reduced elastic modulus of BL is smaller than 14 GPa, the ITO stress is increased. For a BL modulus of 70 GPa, the stress has the maximum reduction – about 50% – for a thickness of 20  $\mu\text{m}$ . However, a larger stress occurs when it is thicker than 70  $\mu\text{m}$ . This is the result of the competition between the changing of the NL position and the distance of ITO layer from NL as mentioned before. The stress in ITO against the bending radius with BL thickness of 20  $\mu\text{m}$  and 100  $\mu\text{m}$  is shown in Fig. 6a and b. This simulation presents a very interesting result. For the former thickness, it seems that the larger the Young's modulus, the better. But the effect will saturate eventually. However, the latter suggests that when BL is as thick as the PET layer (100  $\mu\text{m}$ ), the stress in ITO will never be reduced no matter what material is chosen. The value of Young's modulus and reduced elastic modulus used in the simulation is in Table 2.

#### 4. Conclusion

An alternative approach to calculate the stress developed in a thin-film multi-layer has been adopted. With this method, the position of the NL can be determined and a concept of visualising changes in stress as the structural architecture is fine-tuned has emerged. A plastic/glass composite substrate with the thickness of 140  $\mu\text{m}$  and 35  $\mu\text{m}$  respectively, acting to provide a flexible barrier to oxygen and water vapour, has been predicted to reduce the stress in ITO deposited on the glass surface by a factor of 2.5, compared with 175  $\mu\text{m}$  of either glass or PET on its own. The yield strength of ITO (the limit beyond which material deformation is irreversible) corresponding to a failure strain of ca. 1%, is 1.2 GPa [15]. The support composition above can be shown to adequately protect a thin ITO layer to bend radii significantly less than 1 cm; indeed, the stress in the ITO layer is predicted to reach its yield strength value at a bend radius as low as 3.3 mm. This prediction is particularly interesting, since currently, flexible glass as thin as 50  $\mu\text{m}$  has been achieved, and the prospect of 30  $\mu\text{m}$  is reported to be within reach [16]. The discussion of break stress in the flexible glass itself is beyond the scope of this report, and will be disclosed in the forthcoming patent literature [17]. As a guide, flexible glass with a thickness in the region of 30  $\mu\text{m}$  exhibits a break stress of ca. 0.15 GPa. It is estimated that a composite glass/PET support of 175  $\mu\text{m}$  total thickness could with-

stand a bend radius of 1.2 cm for a range of 10–40  $\mu\text{m}$  glass thickness without breakage.

Finally, a practical five-layer OLED device structure has been simulated using the reduced elastic modulus values for NPD and Alq<sub>3</sub> measured here. It shows that the choice of the BL material's modulus, and its thickness relative to that of the underlying PET, are crucial in reducing the stress in ITO. For BL thicknesses equal to that of the PET, the BL is unable to decrease the ITO stress, regardless of its modulus. One has to bear in mind that all the materials in this simulation are assumed to be elastic. The mechanism of creep (changing of strain under fixed applied stress) and stress relaxation (changing of stress under fixed applied strain) is omitted. The mechanism of cracking is also not considered. There would be some cracks generated initially on each film during their fabrication, and the initial pattern of these cracks would not be expected to be the same for every sample. Nevertheless, reducing the stress in the most brittle layer should still slow down or prevent cracks from migrating further, thereby extending the device lifetime.

Practically, for commercial FOLED devices, it is generally necessary to cover the device with an extra encapsulation layer. With a careful choice of the thickness and elastic property of this encapsulating layer, it is possible to further reduce the distance between NL and the brittle anode layer thus diminish the stress even to zero. However, the problem of deformation or delamination between layers, either due to thermal stress or bending, may become the dominant concern in the FOLED device degradation.

#### Acknowledgements

Chien-Jung Chiang gratefully acknowledges the support of a PhD studentship from Durham University, UK and the Kodak European Research Laboratory, Cambridge.

#### References

- [1] M. Hack, V. Adamovich, in: 7th International Conference on Electroluminescence of Molecular Materials and Related Phenomena, 2008.
- [2] S. Forrest, in: 7th International Conference on Electroluminescence of Molecular Materials and Related Phenomena, 2008.
- [3] M. Stolka (Ed.), Organic Light Emitting Diodes for General Illumination, OIDA, 2002, p. 52.
- [4] H. Aziz, G. Xu, Synthetic Metals 80 (1996) 7.
- [5] S. Gardonio, L. Gregoratti, P. Melpignano, L. Aballe, V. Biondo, R. Zamboni, M. Murgia, S. Caria, M. Kiskinova, Organic Electronics 8 (2007) 37.
- [6] D.G. Howells, B.M. Henry, Y. Leterrier, J.-A.E. Manson, J. Madocks, H.E. Assender, Surface and Coatings Technology 202 (2008) 3529.
- [7] S.K. Park, Jeong I. Han, D.G. Moon, W.K. Kim, Japan Journal of Applied Physics 42 (2003) 623.
- [8] C. Hsueh, Journal of Applied Physics 91 (2002) 9652.
- [9] J. Case, A.H. Chilver, Strength of Materials and Structures – An Introduction to the Mechanics of Solids and Structures, second ed., Edward Arnold, 1971, pp. 189–201.
- [10] A. Plichta, A. Weber, A. Habeck, Flexible Electronics – Materials and Device Technology 769 (2003) 273.
- [11] G.L. Graff, P.E. Burrows, R.E. Williford, R.F. Praino, Barrier layer technology for flexible displays, in: G.P. Crawford (Ed.), Flexible Flat Panel Displays, John Wiley, Chichester, 2005, pp. 57–77 (Chapter 4).
- [12] Y. Leterrier, L. Médico, F. Demarco, J.-A.E. Manson, U. Betz, F. Escolá, M. Kharrazi Olsson, F. Atamny, Thin Solid Films 460 (2004) 156.
- [13] W.C. Oliver, G.M. Pharr, Journal of Materials Research 7 (6) (1992) 1564.

- [14] A.A. Pelegri, X. Huang, *Composites Science and Technology* 68 (2008) 147.
- [15] P.C.P. Bouten, P.J. Sikkeveer, Y. Leterrier, Mechanics of ITO on plastic substrates for flexible displays, in: G.P. Crawford (Ed.), *Flexible Flat Panel Displays*, John Wiley, Chichester, 2005, pp. 99–120 (Chapter 6).
- [16] Methods for the production of flexible glass are disclosed in the following patents: WO 2005/110741 and WO 2008/093153.
- [17] C.J. Winscom, Method and composition to minimise mechanical stress in thin multilayer devices on flexible supports, Eastman Kodak Co.(US/US), (Patent submitted for publication), 2008.

open-circuit voltages of around 1 V. Moreover, in contrast to many other conjugated polymers, the lowest unoccupied molecular orbital (LUMO) energy level at 3.4 eV is close in energy to that of PCBM. Therefore, less voltage is lost during electron transfer at the D–A interface [7]. However, the photovoltaic performance of PF10TBT cells is strongly dependent on the molecular weight (MW) of the polymer [8]. Low MW devices show significantly lower short-circuit currents and fill factors, resulting in a reduction of the maximum output power by a factor of 2 compared to the best high MW devices.

For the further design of new donor polymers understanding of the dependence of solar cell performance on their chemical and structural properties is crucial. Low fill factors are commonly attributed to unbalanced charge carrier transport in the polymer and fullerene phase [9]. Molecular weight dependent hole mobilities have been observed in regioregular poly(3-hexylthiophene) (P3HT), using field-effect transistor measurements [10–12], space-charge limited currents [13] and the time-of-flight technique [14]. Most studies revealed an increase of the hole mobility with increasing molecular weight. Suggested causes include differences in chain packing, interconnectivity of the polymer network, backbone conformation and interchain hopping. It has been pointed out by Goodman and Rose that in a solar cell with a significant difference in the hole- and electron mean free path, accumulation of the slowest charge carriers will lead to a nonuniform electric field in the device [15]. When the slowest carrier has a very low mobility the photocurrent can even reach a maximum electrostatically allowed limit at high light intensity [9]. This space-charge limited (SCL) photocurrent has a three quarter power dependence on light intensity and a square root dependence on voltage, which limits the fill factor to 0.42.

A different cause of a low fill factor was recently identified in solar cells from a narrow band gap polymer and PCBM [16]. The low fill factor again results from a square root dependence of the photocurrent on voltage, albeit for entirely different physical reasons than in the space-charge limited case. Here, the photocurrent is limited by a small product of mobility and lifetime of free charge carriers due to recombination or trapping and is described by [15]:

$$J_{\text{ph}} = qG(\mu_{h(e)}\tau_{h(e)})^{1/2}V^{1/2} \quad (1)$$

where  $G$  is the generation rate of free charge carriers and  $\mu_{h(e)}$  and  $\tau_{h(e)}$  are the mobility and lifetime of free holes (electrons), respectively. Experimentally, this recombination limited photocurrent can be discriminated from the SCL case since it depends linearly on light intensity. Furthermore, the saturation voltage  $V_{\text{sat}}$ , at which the photocurrent loses its half power dependence on voltage, is independent of light intensity for the recombination limited case, whereas for the SCL photocurrent it scales with the square root of light intensity. In this study we investigate the origin of the low fill factor and photocurrent in low molecular weight PF10TBT:PCBM solar cells. A half power dependence of the photocurrent on voltage is observed and its origin is revealed by a combination of optical and electrical measurements and device simulations.

## 2. Experimental

PF10TBT was synthesized at the Netherlands Organisation for Applied Scientific Research (TNO) and used as received. In this study two batches were used, which will be identified by their weight average molecular weight ( $M_w$ ) in the remainder of this paper. The low MW polymer had  $M_w \sim 5.1 \times 10^3$  g/mol and polydispersity index PDI  $\sim 1.7$ , the high MW batch had  $M_w \sim 1.9 \times 10^5$  g/mol and PDI  $\sim 3.5$ . The electron acceptor, PCBM, was obtained from Solenne. Polymer and fullerene were mixed in a 1:4 weight ratio and dissolved in chlorobenzene. Since the solubility of high MW PF10TBT in chlorobenzene at room temperature is low, solutions were stirred and processed at 90 °C. ITO-patterned glass substrates were cleaned, treated in a UV-ozone reactor and coated with a 40–60 nm thin hole-transporting buffer layer of PEDOT:PSS (H.C. Starck GmbH). The photoactive layer was spin coated in air with typically 80–100 nm thickness. Solar cells were finalized with evaporation of a 1 nm LiF/100 nm Al cathode to ensure an ohmic electron contact with the PCBM phase. To study hole transport properties of the blend, an electron-blocking 20 nm Pd/80 nm Au top contact was applied instead of the LiF/Al cathode.

Current-voltage characteristics were recorded using a Keithley 2400 SourceMeter. Measurements were performed in the dark and under illumination from an uncalibrated Steuernagel SolarConstant 1200 metal halide lamp with an estimated intensity equivalent to ca. 1.3 suns, as determined by comparison of measured and calculated short-circuit current densities (see below).

Spectral responsivity (SR) measurements were carried out with a lock-in amplifier, a transimpedance amplifier and a focused, chopped monochromatic beam from a quartz tungsten halogen lamp and several narrow band pass filters. An estimation of the short-circuit current density ( $J_{\text{sc}}$ ) under standard test conditions was calculated by convolving the SR spectrum with the AM1.5G reference spectrum, using the verified premise of a linear dependence of  $J_{\text{sc}}$  on light intensity. The estimated illumination intensity for the material under study was taken as the ratio of the measured and calculated  $J_{\text{sc}}$ .

The refractive index  $n$  and extinction coefficient  $k$  of thin films of PF10TBT:PCBM were determined with variable-angle spectroscopic ellipsometry (VASE), using a VASE ellipsometer from J.A. Woollam Co., Inc. The VASE measurements were combined with transmission and reflection measurements to enable accurate fits of the experimental ellipsometric data in the employed wavelength range from 300 to 1500 nm. The optical constants of glass, ITO, quartz, silicon and PEDOT:PSS were determined first. For ITO and PEDOT:PSS, anisotropic optical constants were found. Since illumination during current-voltage measurements takes place at normal incidence, the components in the direction perpendicular to the plane of the substrate were used in the transfer-matrix calculations. The optical properties of LiF and aluminum were taken from literature. Next, the  $n$  and  $k$  of composite layers of PF10TBT and PCBM on various substrates were determined by fitting the data with several Gaussian oscillators. No



indications of anisotropy in the active layers were found and the data were interpreted with a uniform dielectric function throughout the layer.

### 3. Results and discussion

Fig. 1 shows the photovoltaic performance of equally thick PF10TBT:PCBM solar cells that were made using low (squares) and high (circles) molecular weight PF10TBT. The differences in fill factor and short-circuit current density are striking. Although both cells are 95 nm thick, the high MW cell produces a 30% higher  $J_{sc}$  compared to its low MW counterpart. The fill factor increases significantly with molecular weight as well: it improves from 0.45 to 0.63. In the remainder of this article, we will systematically address the importance of the various effects of a change in molecular weight on device performance.

First, considering the marked difference in  $J_{sc}$ , one might anticipate a change in absorption due to variations in, for example, interchain interactions [12,17]. Usually low MW polymers exhibit a blue-shift in solid-state absorption. In a photovoltaic cell this may alter the number of photogenerated excitons and therefore the magnitude of the photocurrent, depending on the overlap of the absorption profile with the irradiance spectrum. When the absorption maximum changes in magnitude as well, the effect of changing MW on  $J_{sc}$  may be intensified. Fig. 2 shows the refractive index  $n$  and extinction coefficient  $k$  of composite layers of PF10TBT and PCBM, as determined with variable-angle spectroscopic ellipsometry. In the region where PF10TBT contributes most to the absorption of the blend layer, i.e., between 450 and 650 nm, the extinction coefficient of the low MW sample (black solid line) is indeed blue-shifted. In addition, the magnitude of  $k$  in this region is much lower. Due to optical interference effects, which play an important role in thin films capped with a highly reflective aluminum cathode [18], it is expected that the extent to which a change in optical constants influences the absorption in the active layer varies with the thickness of

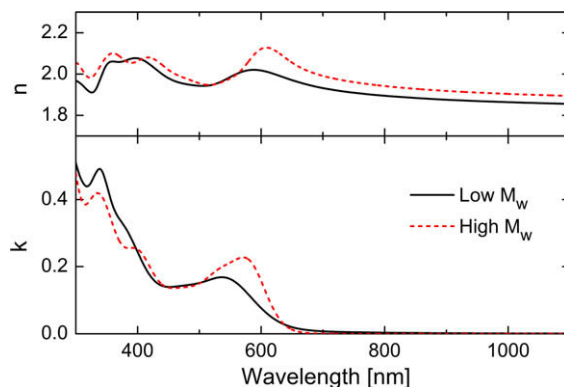


Fig. 2. Index of refraction  $n$  and extinction coefficient  $k$  of PF10TBT:PCBM layers on glass. The heterojunction from the low MW polymer (solid line) shows reduced absorption compared to the one containing high MW PF10TBT (dotted line). (For interpretation of the references to colour in this figure legend, the reader is referred to the web version of this article.)

the layer. The consequences of reduced absorption in low MW solar cells can be quantified by modeling of the optical electric field inside the device [18–20]. Using the transfer-matrix approach described by Pettersson et al. in Ref. [18], provided with the optical constants of Fig. 2 and the AM1.5G solar irradiance spectrum, we calculated the amount of photons that are absorbed each second in the bulk of the active layer as a function of position in the device, for both MW cases. The results are shown in Fig. 3. The active layer in the low MW device clearly absorbs less photons due to its lower extinction coefficient, yet the difference between the profiles is not as large as one might expect from consideration of the optical constants. Integration of the photon absorption rates over the position gives total photon absorption rates of  $4.8 \times 10^{20} \text{ m}^{-2} \text{ s}^{-1}$  and  $5.1 \times 10^{20} \text{ m}^{-2} \text{ s}^{-1}$  for low and high MW, respectively. Since these cells show a linear dependence of  $J_{sc}$  on light intensity, the observed difference of 30% in short-circuit current density cannot be explained by this increase of

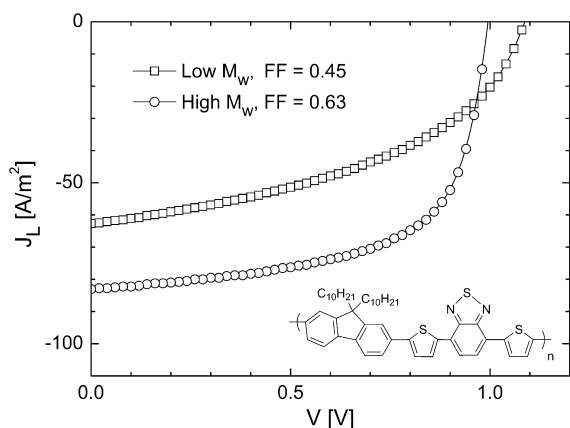


Fig. 1. Current density under illumination ( $J_L$ ) versus voltage characteristics of PF10TBT:PCBM solar cells made from low (squares) and high (circles) molecular weight PF10TBT. Both active layers were approximately 95 nm thick. The inset shows the chemical structure of PF10TBT.

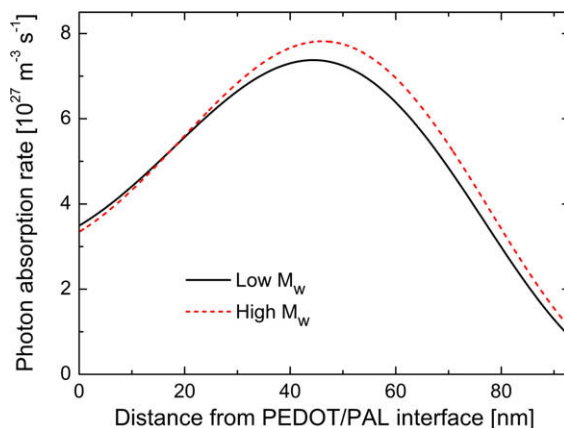


Fig. 3. Photon absorption profiles calculated for the devices of Fig. 1, using the optical constants presented in Fig. 2. (For interpretation of the references to colour in this figure legend, the reader is referred to the web version of this article.)

6% in absorption only. Furthermore, no significant influence on the fill factor would be expected. We therefore conclude that optics only account for a minor part of the variation in photovoltaic performance.

Other than optical effects, a change of molecular weight might cause electronic differences. As stated in the introduction, space-charge effects can limit the fill factor of an organic solar cell to 0.42. Such a limitation can only occur if charge transport in the solar cell is strongly unbalanced. A significant effect of polymer molecular weight on the electron mobility in the PCBM phase is highly unlikely, since the acceptor constitutes the largest part (80 wt.%) of the active layer. The electron mobility  $\mu_e$  can be probed by consideration of the current through the solar cells in the dark. In fullerene-based solar cells, the dark current under forward bias is usually dominated by electrons due to their high mobility in the PCBM phase. As shown in Fig. 4, the dark current of the PF10TBT:PCBM solar cells under study is well described by the single carrier space-charge limited current (SCLC) [21],

$$J = \frac{9}{8} \epsilon_0 \epsilon_r \mu_e \frac{V^2}{L^3} \quad (2)$$

with  $L$  the layer thickness,  $\mu_e = 8 \times 10^{-8} \text{ m}^2/\text{Vs}$  for low MW PF10TBT and  $\mu_e = 1 \times 10^{-7} \text{ m}^2/\text{Vs}$  for the high MW case. The applied voltage was corrected for the built-in voltage ( $V_{\text{bi}}$ ) and resistive losses in the ITO/PEDOT anode ( $V_{\text{RS}}$ ). The relative dielectric constant  $\epsilon_r$  was taken as the spatial average of PF10TBT and PCBM. As expected, the electron mobility is hardly affected by the molecular weight of the polymer and its value is close to what has been found previously for PCBM in fullerene-based solar cells [22–24]. Limitations to the photocurrent, if any, should therefore be caused by a low hole mobility in the low MW polymer. To elucidate the influence of molecular weight on hole transport in PF10TBT based solar cells, we prepared hole-only

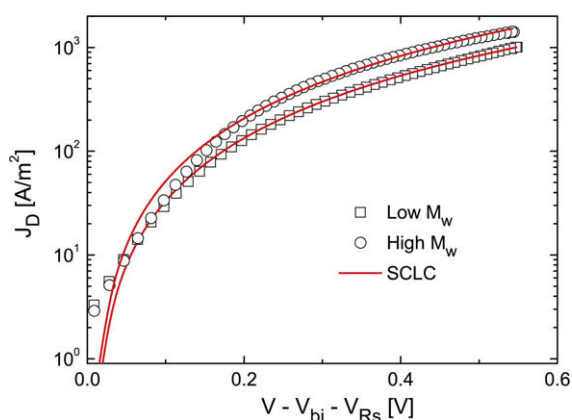


**Fig. 4.** Determination of the electron mobility from the dark current of PF10TBT:PCBM solar cells (symbols) using the single carrier SCLC (solid lines). The fits reveal an electron mobility in PCBM of  $\mu_e = 8 \times 10^{-8} \text{ m}^2/\text{Vs}$  for low MW PF10TBT and  $\mu_e = 1 \times 10^{-7} \text{ m}^2/\text{Vs}$  for the high MW case. The applied voltage was corrected for the built-in voltage ( $V_{\text{bi}}$ ) and the voltage loss over the ITO/PEDOT anode ( $V_{\text{RS}}$ ). (For interpretation of the references to colour in this figure legend, the reader is referred to the web version of this article.)

diodes from PF10TBT:PCBM bulk heterojunctions in a 1:4 weight ratio. The current density versus effective voltage characteristics presented in Fig. 5 were measured at room temperature for two such devices using low MW (squares) and high MW (circles) PF10TBT. The single carrier space-charge limited currents were modeled using exactly the same low-field hole mobility of  $6 \times 10^{-9} \text{ m}^2/\text{Vs}$  (solid lines). Hence, no effect of molecular weight on the mobility in the PF10TBT phase was found. Measurements on pristine polymer layers revealed similar mobility values in both MW cases, showing that the hole transport in the PF10TBT:PCBM blend is also not affected by PCBM loading. This behavior contrasts to the case of MDMO-PPV:PCBM heterojunctions [23,25] and to what has been reported for a similar polyfluorene copolymer [26]. From temperature-dependent measurements, the thermal activation energy of hole transport in the blend was found to be 0.33 eV in both cases. This exactly equals the theoretically predicted value, obtained from the relation between the universal mobility prefactor  $\mu_0 = 3 \times 10^{-3} \text{ m}^2/\text{Vs}$  and the above-mentioned low-field mobility at room temperature [27]. Since the hole mobility in the blend is constant with molecular weight, and differs only an order of magnitude with the electron mobility in PCBM, a space-charge limitation of the photocurrent in these relatively thin solar cells is highly unlikely [28].

Fig. 6 presents a comparison of the photocurrent of two cells based on low (squares) and high (circles) molecular weight PF10TBT, plotted versus effective voltage. Here, the experimental photocurrent is defined as the difference between the current density under illumination  $J_L$  and in the dark  $J_D$ , thus  $J_{\text{ph}} = J_L - J_D$ . Since the photocurrent is zero at  $V = V_0$ , the horizontal axis represents the effective voltage available for charge extraction from the device. In both cases the photocurrent nicely saturates at high effective voltage, indicating that at sufficiently large reverse bias all photogenerated bound pairs are dissociated and

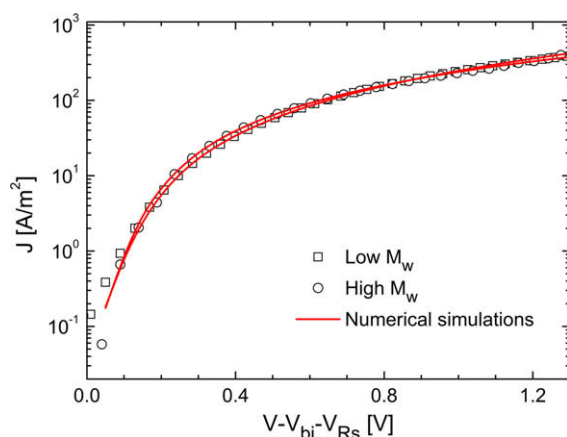


**Fig. 5.** Current–voltage data of hole-only diodes of bulk heterojunctions containing low (squares) and high (circles) MW PF10TBT. The solid lines represent numerical simulations, both using a low-field hole mobility of  $\mu_h = 6 \times 10^{-9} \text{ m}^2/\text{Vs}$ . The applied voltage was corrected for the built-in voltage ( $V_{\text{bi}}$ ) and the voltage loss over the ITO/PEDOT anode ( $V_{\text{RS}}$ ). (For interpretation of the references to colour in this figure legend, the reader is referred to the web version of this article.)

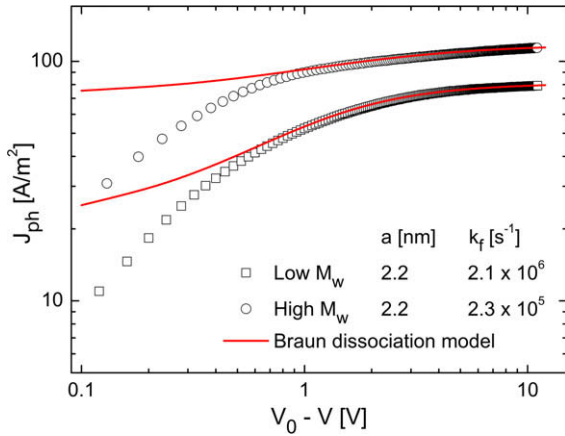


**Fig. 6.** Experimental photocurrents in solar cells from low (squares) and high (circles) molecular weight PF10TBT. The lines denote calculations of  $J_{ph} = qGL$ , using a field and temperature-dependent generation rate  $G(T, E) = G_{max}P(T, E)$  as given by Braun's model of dissociation of charge transfer states [30]. (For interpretation of the references to colour in this figure legend, the reader is referred to the web version of this article.)

extracted from the device. The occurrence of saturation was verified with temperature-dependent measurements (not shown). At lower voltages, however, the photocurrent of the low MW cell clearly depends stronger on the electric field as compared to the high MW cell. In this voltage regime, a square root dependence is observed. This is indicated by the tilted dotted lines with slope  $\frac{1}{2}$  in Fig. 7, which shows intensity dependence measurements of the photocurrent in the low MW solar cell. The experimental photocurrent depends linearly on light intensity and the saturation voltage  $V_{sat}$  is intensity independent. This combination of voltage and intensity dependence of the photocurrent is a clear fingerprint of a recombination limited photocurrent.

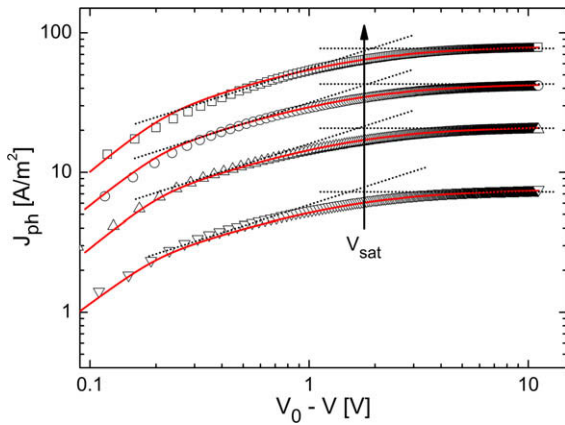


**Fig. 7.** Intensity dependent photocurrent of the same low MW device as shown in Fig. 6. The tilted dotted lines denote slope  $\frac{1}{2}$ , indicating  $J_{ph} \propto V^{0.5}$ , whereas the horizontal dotted lines mark the saturated photocurrent at each intensity. The solid lines represent numerical device simulations. (For interpretation of the references to colour in this figure legend, the reader is referred to the web version of this article.)

Application of Eq. (1) in the square root regime reveals a free carrier lifetime of approximately 0.5  $\mu$ s. However, as was mentioned before, illumination of organic solar cells does not directly result in free charge carriers: instead, after charge transfer a bound electron–hole pair is created. Due to the high Coulomb binding energy in organic solar cells, only a certain fraction of all photogenerated bound electron–hole pairs  $G_{max}$  is dissociated into free charge carriers, depending on field and temperature, and therefore contributes to the photocurrent  $J_{ph} = qGL$ . Consequently, the generation rate  $G$  of free charge carriers can be described by:

$$G(T, E) = G_{max}P(T, E) \quad (3)$$

where  $P(T, E)$  is the probability for charge separation at the donor/acceptor interface. The photogeneration of free charge carriers in low-mobility materials can be explained by the geminate recombination theory of Onsager [29]. An important addition to the theory has been made by Braun [30], who stressed the importance of the fact that the bound electron–hole pair (or charge transfer state) has a finite lifetime. In Braun's model, the probability that a bound polaron pair dissociates into free charge carriers at a given electric field  $E$  and temperature  $T$  is given by:

$$P(T, E) = \frac{k_{diss}(E)}{k_{diss}(E) + k_f} \quad (4)$$

with  $k_f$  the rate constant with which the bound electron–hole pair decays to its ground state, and  $k_{diss}(E)$  the rate constant for separation into free carriers, which is given by [30]:

$$k_{diss}(E) = \frac{3k_R}{4\pi a^3} e^{-E_B/k_B T} \left[ 1 + b + \frac{b^2}{3} + \frac{b^3}{18} + \frac{b^4}{180} + \dots \right] \quad (5)$$

with  $a$  the initial separation distance of the bound electron–hole pair at the interface,  $b = e^3 E / 8\pi \epsilon_0 \epsilon_r k_B^2 T^2$ , and  $E_B$  the binding energy of the electron–hole pair.

Once separated, the charge carriers can again form a bound pair with rate constant  $k_R$ . The dissociation model uses Onsager theory for field-dependent dissociation rate constants for weak electrolytes [29] for  $k_{diss}(E)$ , Langevin recombination of free electrons and holes [31] and a Gaussian distribution of donor–acceptor distances. Then, the generation rate of free electrons and holes depends on the charge carrier mobilities  $\mu_e$  and  $\mu_h$  of the electrons and holes respectively, the relative dielectric constant  $\epsilon_r$ , the initial separation of e–h pairs  $a$ , and the ground state recombination rate  $k_f$ .

As expressed in Eq. (4), the relative magnitudes of dissociation and decay rates determine a field and temperature-dependent dissociation probability of bound pairs  $P(T, E)$ . Consequently, when the photocurrent of an organic solar cell is interpreted using Eq. (1), the obtained lifetime is in fact an *effective* lifetime, equal to  $P(T, E)\tau$ , where  $\tau$  is now the true lifetime of free charge carriers [16]. Using device modeling, we can determine whether a low effective lifetime originates from short lifetimes of bound pairs (low  $P$ ) or free carriers (low  $\tau$ ).

We continue the investigation of the molecular weight dependent photocurrents in Fig. 6 by modeling the field-

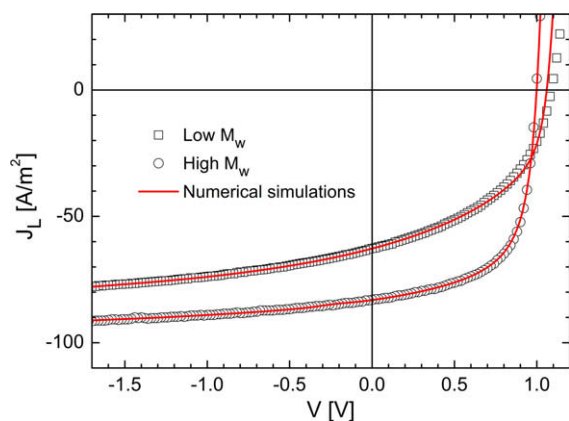


**Fig. 8.** Experimental (symbols) and simulated (lines) current–voltage characteristics of the solar cells of Fig. 1 under illumination. The lines show numerical fits that only differ in the used values of  $G_{\max}$  (representing enhanced absorption in high MW PF10TBT) and  $k_f$  (obtained from Fig. 6). (For interpretation of the references to colour in this figure legend, the reader is referred to the web version of this article.)

dependent generation. The solid lines represent calculations of the photocurrent according to  $J_{\text{ph}} = qGL$ , using a field and temperature-dependent generation rate of free carriers as given by Braun's model [30,32]. The dissociation probability  $P(T,E)$  is parameterized by the initial separation distance of the bound electron–hole pair  $a$  and the decay rate  $k_f$ , which are now the only fit parameters since  $L$  is measured separately and  $G_{\max}$  can be calculated directly from  $J_{\text{ph}} = qG_{\max}L$  in the saturation regime. The fits reveal a value of  $a = 2.2$  nm, irrespective of molecular weight. However, the decay rate  $k_f$  in the low MW cell is at  $2.1 \times 10^6 \text{ s}^{-1}$  an order of magnitude higher than  $k_f$  of the high MW cell. This value of  $k_f$  is in very good agreement with the effective lifetime of free carriers as determined from Eq. (1), since  $(0.5 \mu\text{s})^{-1} = 2 \times 10^6 \text{ s}^{-1}$ .

To model the photocurrent over the entire effective voltage range, we utilized our numerical device model [33]. Since diffusion of charge carriers is now also taken into account, the photocurrent can be simulated at low effective voltage as well. In the simulations, shown in Fig. 7, the experimentally determined values of the charge carrier mobilities, layer thickness, dissociation parameters  $a$  and  $k_f$ , and generation rate of bound pairs  $G_{\max}$  were used. The calculations excellently fit the measured data at various light intensities. This clearly shows that the photocurrent of low molecular weight PF10TBT:PCBM cells is limited by recombination of short-lived bound electron–hole pairs. We speculate that the limitation arises from insufficient phase separation, resulting in localization of bound pairs in isolated donor–acceptor regions, which prohibits efficient dissociation. Indeed, transmission electron microscopy (TEM) measurements on blends of varying molecular weight have revealed little contrast in blends of low MW PF10TBT with PCBM, whereas pronounced PCBM and polymer rich regions were observed in high MW films [8].

Fig. 8 presents a direct comparison of the simulated current–voltage characteristics under illumination of the cells

**Table 1**

Parameters used to fit the current–voltage characteristics presented in Fig. 8.

Parameter	Symbol	Value	
		Low MW	High MW
Band gap	$E_{\text{gap}}$	1.47 eV	1.38 eV
Electron mobility	$\mu_e$	$8 \times 10^{-8} \text{ m}^2/\text{Vs}$	$1 \times 10^{-7} \text{ m}^2/\text{Vs}$
Hole mobility	$\mu_h$	$6 \times 10^{-9} \text{ m}^2/\text{Vs}$	$6 \times 10^{-9} \text{ m}^2/\text{Vs}$
Eff. density of states	$N_c$	$2.5 \times 10^{25} \text{ m}^{-3}$	$2.5 \times 10^{25} \text{ m}^{-3}$
Generation rate	$G_{\max}$	$6.0 \times 10^{27} \text{ m}^{-3} \text{ s}^{-1}$	$6.6 \times 10^{27} \text{ m}^{-3} \text{ s}^{-1}$
Rel. dielectric constant	$\epsilon_r$	3.6	3.6
Initial e/h pair distance	$a$	2.2 nm	2.2 nm
e/h Pair decay rate	$k_f$	$2.1 \times 10^6 \text{ s}^{-1}$	$2.3 \times 10^5 \text{ s}^{-1}$

of Fig. 1. The model parameters that were used to fit the current–voltage curves are summarized in Table 1. Compared with the simulation of the curve of the low MW cell, only three input parameters were changed to fit that of the high MW cell: the slightly higher, experimentally determined electron mobility was used,  $G_{\max}$  was increased by 10% and the previously determined lower decay rate  $k_f = 2.3 \times 10^5 \text{ s}^{-1}$  was used. The increase in  $G_{\max}$  closely agrees with the small (6%) enhancement in the calculated absorption for high MW cells as presented in Fig. 3. For these relatively thin active layers, using a constant generation rate  $G_{\max}$  throughout the active layer does not change the simulation results compared to the use of the calculated optical profile as input [34]. The slightly higher  $V_{\text{oc}}$  of the low MW cell originates from the inversely proportional relationship between the polymer band gap and the average number of repeating units in each chain [35]. At short-circuit conditions, the average dissociation probability of bound electron–hole pairs in the high MW cell is 19% higher (relative) than in the low MW device, due to the reduction in  $k_f$ . Thus, the concomitant effects of enhanced absorption (10%) and more efficient dissociation (19%) add up to the observed increase of short-circuit current (30%) and fill factor.

#### 4. Conclusions

Using optical and electronic device modeling, we have unraveled the molecular weight dependence of the short-circuit current density and fill factor of PF10TBT:PCBM solar cells. The use of high molecular weight PF10TBT causes an enhancement of the extinction coefficient of the blend layer, resulting in a slight increase in the amount of photons that are absorbed. Charge transport in both phases was found to be virtually unaffected by a change in molecular weight. The electron mobility in the blend is only slightly higher for high MW PF10TBT and a reasonably high, molecular weight independent hole mobility was measured in blend layers as well as pristine polymer layers, which renders the influence of space-charge on the photocurrent insignificant. Intensity dependence measurements confirmed that the photocurrent of low molecular weight cells is recombination limited. From numerical device simulations, we conclude that a low dissociation prob-

ability of short-lived bound electron–hole pairs is the main cause of the poor performance. The limitation is most likely caused by insufficient phase separation, which leads to localization of charges on isolated parts of the donor and acceptor phases.

## Acknowledgements

This work was funded by SenterNovem via the EOS Long Term program ZOMER (EOS LT 03026). This work was partly supported by the Dutch Polymer Institute (DPI), Project DPI No. 524.

## References

- [1] G. Yu, J. Gao, J.C. Hummelen, F. Wudl, A.J. Heeger, *Science* 270 (1995) 1789.
- [2] M.A. Green, K. Emery, Y. Hishikawa, W. Warta, *Prog. Photovoltaics Res. Appl.* 17 (2009) 85.
- [3] M. Svensson, F. Zhang, S.C. Veenstra, W.J.H. Verhees, J.C. Hummelen, J.M. Kroon, O. Inganäs, M.R. Andersson, *Adv. Mater.* 15 (2003) 988.
- [4] O. Inganäs, M. Svensson, F. Zhang, A. Gadisa, N.K. Persson, X. Wang, M.R. Andersson, *Appl. Phys. A* 79 (2004) 31.
- [5] T. Yohannes, F. Zhang, M. Svensson, J.C. Hummelen, M.R. Andersson, O. Inganäs, *Thin Solid Films* 449 (2004) 152.
- [6] L.H. Slooff, S.C. Veenstra, J.M. Kroon, D.J.D. Moet, J. Sweelssen, M.M. Koetse, *Appl. Phys. Lett.* 90 (2007) 143506.
- [7] D.J.D. Moet, L.H. Slooff, J.M. Kroon, S.S. Chevtchenko, J. Loos, M.M. Koetse, J. Sweelssen, S.C. Veenstra, in: *Proceedings of the MRS Fall Meeting, Warrendale, PA, Boston, 2007*, pp. CC03–CC09.
- [8] S.C. Veenstra, D.J.D. Moet, J. Sweelssen, S.S. van Bavel, E. Voroshazi, M.M. Koetse, J. Loos, B. de Boer, P.W.M. Blom, J.M. Kroon, *Polyfluorene:[C60]PCBM Based Solar Cells; A Correlation Between the Molecular Weight of the Polymer and the Photovoltaic Performance*, Presented at the E-MRS 2009 Spring Meeting, Strasbourg, France, 2009.
- [9] V.D. Mihailetschi, J. Wildeman, P.W.M. Blom, *Phys. Rev. Lett.* 94 (2005) 126602.
- [10] R.J. Kline, M.D. McGehee, E.N. Kadnikova, J. Liu, J.M.J. Fréchet, *Adv. Mater.* 15 (2003) 1519.
- [11] R.J. Kline, M.D. McGehee, E.N. Kadnikova, J. Liu, J.M.J. Fréchet, M.F. Toney, *Macromolecules* 38 (2005) 3312.
- [12] A. Zen, J. Pflaum, S. Hirschmann, W. Zhuang, F. Jaiser, U. Asawapirom, J.P. Rabe, U. Scherf, D. Neher, *Adv. Funct. Mater.* 14 (2004) 757.
- [13] C. Goh, R.J. Kline, M.D. McGehee, E.N. Kadnikova, J.M.J. Fréchet, *Appl. Phys. Lett.* 86 (2005) 122110.
- [14] A.M. Ballantyne, L. Chen, J. Dane, T. Hammant, F.M. Braun, M. Heeney, W. Duffy, I. McCulloch, D.D.C. Bradley, J. Nelson, *Adv. Funct. Mater.* 18 (2008) 2373.
- [15] A.M. Goodman, A. Rose, *J. Appl. Phys.* 42 (1971) 2823.
- [16] M. Lenes, M. Morana, C.J. Brabec, P.W.M. Blom, *Adv. Funct. Mater.* 19 (2009) 1106.
- [17] J.-F. Chang, J. Clark, N. Zhao, H. Sirringhaus, D.W. Breiby, J.W. Andreasen, M.M. Nielsen, M. Giles, M. Heeney, I. McCulloch, *Phys. Rev. B* 74 (2006) 115318.
- [18] L.A.A. Pettersson, L.S. Roman, O. Inganäs, *J. Appl. Phys.* 86 (1999) 487.
- [19] Z. Knittel, *Optics of Thin Films*, John Wiley and Sons, 1976.
- [20] H. Hoppe, N. Arnold, N.S. Sariciftci, D. Meissner, *Sol. Energy Mater. Sol. Cells* 80 (2003) 105.
- [21] M.A. Lampert, P. Mark, *Current Injection in Solids*, Academic Press, New York, 1970.
- [22] V.D. Mihailetschi, J.K.J. van Duren, P.W.M. Blom, J.C. Hummelen, R.A.J. Janssen, J.M. Kroon, M.T. Rispen, W.J.H. Verhees, M.M. Wienk, *Adv. Funct. Mater.* 13 (2003) 43.
- [23] V.D. Mihailetschi, L.J.A. Koster, P.W.M. Blom, C. Melzer, B. de Boer, J.K.J. van Duren, R.A.J. Janssen, *Adv. Funct. Mater.* 15 (2005) 795.
- [24] V.D. Mihailetschi, H.X. Xie, B. de Boer, L.J.A. Koster, P.W.M. Blom, *Adv. Funct. Mater.* 16 (2006) 699.
- [25] C. Melzer, E.J. Koop, V.D. Mihailetschi, P.W.M. Blom, *Adv. Funct. Mater.* 14 (2004) 865.
- [26] K.G. Jespersen, F. Zhang, A. Gadisa, V. Sundström, A. Yartsev, O. Inganäs, *Org. Electron.* 7 (2006) 235.
- [27] N.I. Craciun, J. Wildeman, P.W.M. Blom, *Phys. Rev. Lett.* 100 (2008) 056601.
- [28] M. Lenes, L.J.A. Koster, V.D. Mihailetschi, P.W.M. Blom, *Appl. Phys. Lett.* 88 (2006) 243502.
- [29] L. Onsager, *J. Chem. Phys.* 2 (1934) 599.
- [30] C.L. Braun, *J. Chem. Phys.* 80 (1984) 4157.
- [31] L.J.A. Koster, V.D. Mihailetschi, P.W.M. Blom, *Appl. Phys. Lett.* 88 (2006) 052104.
- [32] V.D. Mihailetschi, L.J.A. Koster, J.C. Hummelen, P.W.M. Blom, *Phys. Rev. Lett.* 93 (2004) 216601.
- [33] L.J.A. Koster, E.C.P. Smits, V.D. Mihailetschi, P.W.M. Blom, *Phys. Rev. B* 72 (2005) 085205.
- [34] J.D. Kotlarski, P.W.M. Blom, L.J.A. Koster, M. Lenes, L.H. Slooff, *J. Appl. Phys.* 103 (2008) 084502.
- [35] R. Hoffmann, C. Janiak, C. Kollmar, *Macromolecules* 24 (1991) 3725.

planarity, high symmetry, electron delocalization property and high conductivity and have been studied widely for a long time [10,11]. The highest mobility reported so far in Pc based OFET was a single crystal CuPc-FET, where the mobility reaches as high as  $1.0 \text{ cm}^2 \text{ V}^{-1} \text{ s}^{-1}$  [12]. The solution-processed OFETs fabricated from amphiphilic tris(phthalocyaninato) rare earth triple-decker complexes have been revealed to display excellent FET performance with the carrier mobility as high as  $0.60 \text{ cm}^2 \text{ V}^{-1} \text{ s}^{-1}$  and current modulation of  $10^5$  [13].

The present work explores the potential of a nonperipherally octahexyl substituted lead phthalocyanine (PbPc), the chemical structure of which is shown in Fig. 1a, as an active material for OFET devices. The compound was chosen because of its low band gap (1.2 eV) energy [14] and for its solubility in common organic solvents, enabling its ready formulation as thin films by the conventional spin-coating technique and capability of demonstrating nonvolatile memory phenomena [15]. The synthesis of the material was reported earlier by Burnham et al. [16]. As yet only one report in the literature has addressed the potentiality of PbPc as an active material for OFET [14], but memory functionality of the material was not investigated. In this study, we have shown that OFET based on PbPc can efficiently be used as a nonvolatile organic memory device with continuous write-read-erase-read switching performance.

## 2. Experimental section

The OFETs were fabricated on patterned indium tin oxide (ITO) coated glass substrate which acted as a gate electrode. Before using, ITO substrates were cleaned successively with detergent, de-ionized water, acetone and isopropyl alcohol in ultrasonic bath. Polyvinyl alcohol (PVA, Mol. Weight: 100,000), purchased from Fluka Chemicals, was dissolved in distilled water (15 wt%) and after filtering with  $0.2 \mu\text{m}$  syringe filters, was spin coated on ITO substrate at 2000 rpm. The thickness of the dielectric layer was measured by a Dektak (3030) surface profilometer to be around 450 nm. After drying the film at  $110^\circ\text{C}$  for 1 h in vacuum, a solution of PbPc in tetrahydrofuran, with a

concentration of  $4 \text{ mg ml}^{-1}$ , was spun on top of PVA film rotating at 2000 rpm. The deposited films (60 nm) were then dried in a vacuum oven ( $10^{-3}$  Torr) at  $90^\circ\text{C}$  for 3 h to allow complete evaporation of solvent and surface moisture. On top of the PbPc layer, gold (Au) was vacuum evaporated (below  $10^{-5}$  Torr) at  $0.3 \text{ \AA/s}$  through a patterned interdigitated shadow mask to make source/drain (50 nm) contact. The channel length and width of the OFETs were  $60 \mu\text{m}$  and  $6.4 \text{ mm}$ , respectively. The schematic diagram of the OFET device is shown in Fig. 1c. The electrical characteristics of the OFETs were obtained at room temperature under ambient condition using Hewlett-Packard (HP) 4140B semiconductor parameter analyzer. We have characterized as many as 10 devices, out of which eight devices worked excellently and two devices did not show any FET properties.

## 3. Results and discussions

Fig. 2 presents the tapping mode atomic force microscope (AFM) images of the PVA surface on ITO substrate (Fig. 2a) and the annealed PbPc film on top of the dielectric layer (Fig. 2b). The images in both the cases show almost smooth surfaces with very low roughness (less than 2 nm). The surface analysis of the dielectric layer indicate that there is lack of pinholes throughout the film with an rms surface roughness of 0.75 nm enabling effective carrier transport throughout the film.

The output characteristics of PbPc FETs with gold drain-source electrodes are shown in Fig. 3; displaying the drain-source current  $I_{DS}$  versus the applied drain-source voltage  $V_{DS}$  for different gate voltages  $V_G$  applied to the ITO substrate, which acted as a gate. The device exhibits a field effect with operation in a p-type accumulation mode. The linear and saturation regions can be observed clearly with the increase of drain voltage ( $V_{DS}$ ). The matching of HOMO energy level of PbPc (5.2 eV) with the work function of gold (5.1 eV) can ensure efficient hole injection into the semiconductor channel which further ensured high device performance in OFETs based on PbPc.

We observed a difference in  $V_{GS}-I_{DS}$  plots when different biases are applied to the gate electrode. Fig. 4 shows the evolution of the hysteresis in the transfer characteristics of PbPc FET, displaying memory windows of the devices as swept to the various gate voltage ranges. Three different gate voltages ( $V_G = 30, 40$  and  $50 \text{ V}$ ) have been plotted in the figure. The gate bias was swept in a loop, i.e., from 0 to  $+V_{Max}$ ,  $+V_{Max}$  to  $-V_{Max}$ , and finally from  $-V_{Max}$  to  $+V_{Max}$ , keeping the source-drain voltage as constant ( $V_{DS} = -50 \text{ V}$ ). The clockwise hysteresis direction indicates that when a negative gate bias is applied, holes are injected into the PbPc channel, corresponding to the programming (writing) process, and when a positive gate bias is applied, holes are injected from the PbPc channel, corresponding to the erasing process. The injection or ejection of holes in the gate dielectric will lead to a threshold voltage ( $V_t$ ) shift, which is the so called memory window. When the gate voltage cycling range is enlarged, the shift of the threshold voltage ( $\Delta V_t$ ) of the forward and backward sweeps becomes wider. This memory window forms the basis for

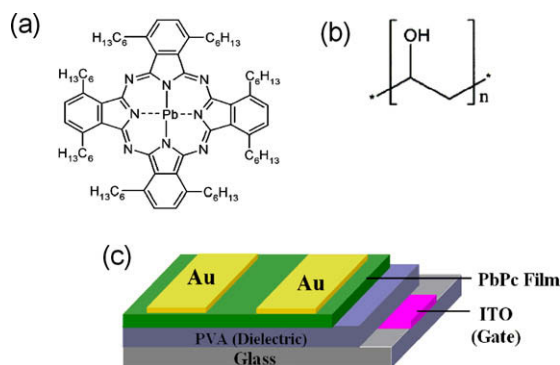
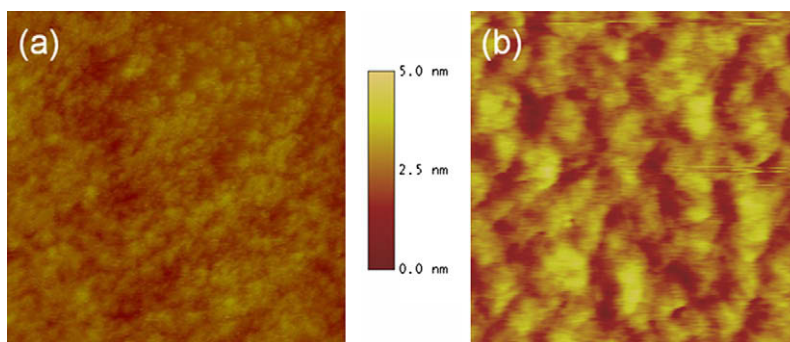
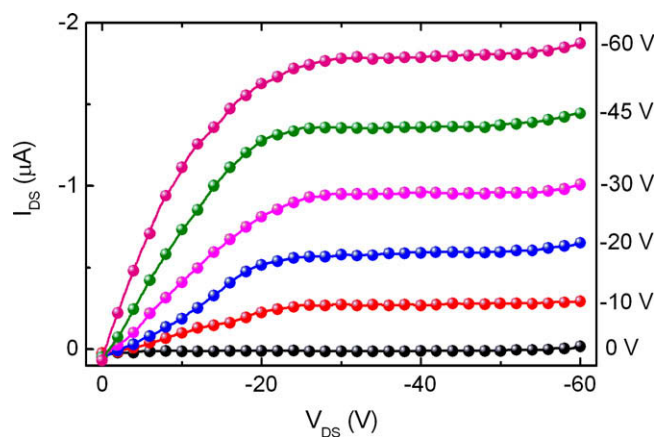


Fig. 1. Chemical structure of (a) nonperipherally substituted octahexyl lead phthalocyanine compound (PbPc) and (b) polyvinyl alcohol (PVA). (c) Schematic presentation of the OFET device.



**Fig. 2.** Tapping mode AFM images of (a) PVA (dielectric) surface on ITO substrate and (b) spun cast PbPc film on top of the PVA surface. Area of the image scanned is  $1 \times 1 \mu\text{m}^2$  with a height scale of 5 nm.



**Fig. 3.** Output characteristics of the OFET based on PbPc channel and PVA gate dielectric. Channel length and width of the OFET are  $60 \mu\text{m}$  and  $6.4 \text{ nm}$ , respectively. Different gate voltages ( $V_G$ ) applied on the device are indicated in the figure.

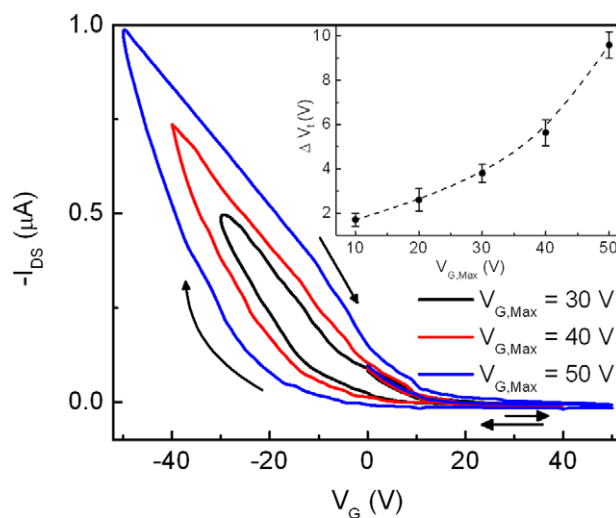


**Fig. 4.** Transfer characteristics of the OFET demonstrating the nonvolatile memory for different gate voltages ( $V_G$ ) and fixed  $V_{DS} = -50 \text{ V}$ . Arrows show the direction of voltage sweep of  $V_G$ . Inset shows the dependence of the threshold voltage shift ( $\Delta V_t$ ) with the amplitude of the maximum applied gate voltage ( $V_{G,Max}$ ) for eight (8) measured devices. The variation in  $\Delta V_t$  from device to device has been indicated by error bars.

PbPc FETs working as memory devices. The shifts in  $V_t$  by 5.63 and 9.59 V are observed when the gate voltages are scanned, respectively, to  $V_{Max} = 40$  and  $V_{Max} = 50$  V with respect to the initial cycle of  $V_{Max} = 10$  V, where the memory window of only 1.7 V can be observed (not shown). Different gate voltages have been applied to the device for the evolution of the hysteresis. The dependence of the memory window, i.e., the shift in threshold voltage ( $\Delta V_t$ ) with the maximum gate voltage applied ( $V_{G,Max}$ ) is shown in the inset of Fig. 4. We have measured eight different devices and the results are summarized in the figure. The figure shows that with increase in amplitude of gate voltage ( $V_{G,Max}$ ), the memory window increases nonlinearly. This means that higher the value of  $V_{G,Max}$ , larger is the rate of increment of  $\Delta V_t$ . In other words, the increase in  $\Delta V_t$  is more pronounced at higher  $V_G$ . The similar trends have been observed from all the devices with a slight fluctuation in the value of  $\Delta V_t$  (indicated by error bars).

The hysteresis and memory behaviors in OFETs are normally proposed to be due to the charge storage [17], slow polarization of the gate dielectric [7] and electron trapping in the semiconductor [18]. The observation of hysteresis in the present OFET device is proposed to be due to locally trapped charges that induce shifts in  $V_t$  [9]. When a large negative gate bias is applied, the injected holes are trapped in the interface, leading to the built in electric field along the direction opposite to the applied field. This built in electric field screens the external field, resulting in more negative gate bias needed to turn the transistors on, and thus a negative directional  $V_t$  shift occurs (Fig. 4). Once the charges are trapped in the interface, they remain trapped leading to on state of the device, until at large positive bias the charges become detrapped and the device goes to the off state. The charging and discharging of PVA films has been known for quite a long time and was also reported by other groups [19,20]. We also have measured the gate leakage current ( $I_G$ ) of the OFET as  $V_G$  is scanned in a loop with fixed

drain–source voltage ( $V_{DS} = -50$  V). It can be seen from Fig. 5 that the maximum leakage current of the device is as low as 40 nA which is 25-folds lower than the corresponding drain current. With regard to the large threshold voltage shifts in the “forward” and “reverse” sweeps of the gate voltage, we applied different drain voltages,  $V_{DS}$ , to observe sizable differences in  $I_{DS}$  values. The memory effect is pronounced even at low  $V_{DS}$  (e.g.,  $V_{DS} = -30$  V) as shown in Fig. 5. The drain current and memory window, however, decrease with decrease in magnitude of drain voltage.

Fig. 6 presents a representative result of write–read–erase–read (WRER) cycle tests conducted on the devices for hours. Only a section of the results is depicted in the figure. In the write–read–erase–read cycle, the “write” (i.e., on state) is made by applying a negative voltage pulse ( $-40$  V) and the “erase” (off state) is achieved through erasing the on state by applying a positive voltage pulse with an amplitude of 40 V. A small probe voltage ( $-20$  V) pulse is employed to read the on state (write) and off state (erase) of the device. The drain voltage, during the measurement, was kept constant at  $V_{DS} = -30$  V. The probe current in the on state is clearly higher than that in the off state. The ratio between the read currents in the on and off states (on/off ratio) of the PbPc FET was maintained to be more than five. The device has been operated under more than 60 WRER cycles and no current degradation is observed for either of the states. Also, during the test, it produces good rewritable characteristics.

One of the important parameters of any storage device is its memory retention time, which is defined as the time for which the memory can be read out unequivocally to be in the on or in the off state. We investigated the charge retention properties of the PbPc FET, i.e., the relaxation dynamics of trapped charge carriers after writing or erasing of the device, the results of which are summarized in Fig. 7. A voltage pulse of  $\pm 40$  V was chosen to write (on)

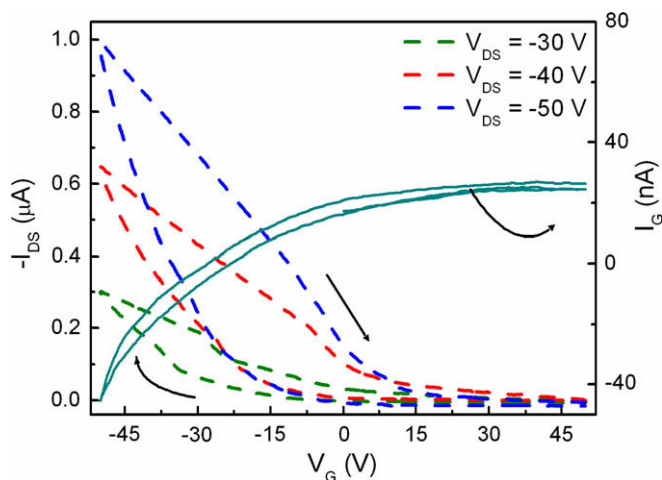
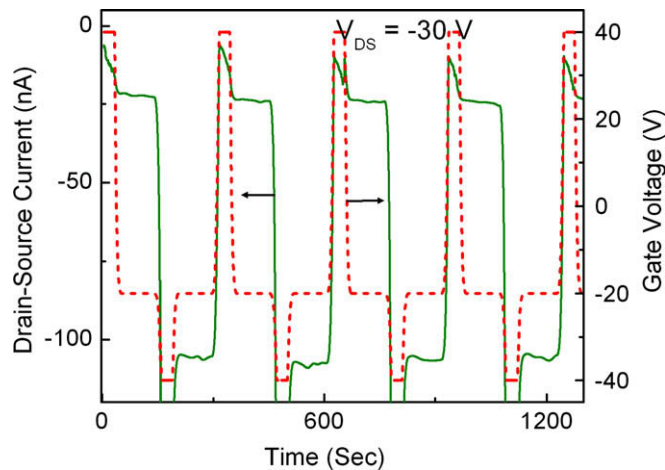


Fig. 5. Transfer characteristics of the OFET for different drain ( $V_{DS}$ ) voltages. Gate leakage current ( $I_G$ ) is plotted on the right axis. Arrows indicate the sweep directions of  $V_G$ .





**Fig. 6.** Memory operation (write-read-erase-read) cycle with writing at  $V_G = -40$  V, erasing at  $V_G = 40$  V, and reading at  $V_G = -20$  V.  $V_{DS}$  was kept at  $-30$  V throughout the measurement.

or erase (off) the states of the device, followed by a read out of the states of the device by a  $-20$  V read pulse (width = 2 s). The drain voltage was kept constant at  $V_{DS} = -30$  V throughout the measurement. Fig. 7 shows current as a function of time for each of the two cases. To reduce the additive effect of the “probe” or “read” voltage on the existing state, we applied the “read” voltage in a pulse mode with a duty cycle of only 12%. It can be found from the figure that the device remains stable for more than 5 h in either of the states with no noticeable degradation. However, after 5.5 h, the device degraded a little with slight decrease in current. Here, we have calculated the time dependence of on/off ratio for different devices from their retention time measurements. The results are depicted in the inset of Fig. 7. Though there is a little variation in on/off ratio from device to device (as indicated by error bars), an average value of seven is maintained for all the devices for prolonged period of time.

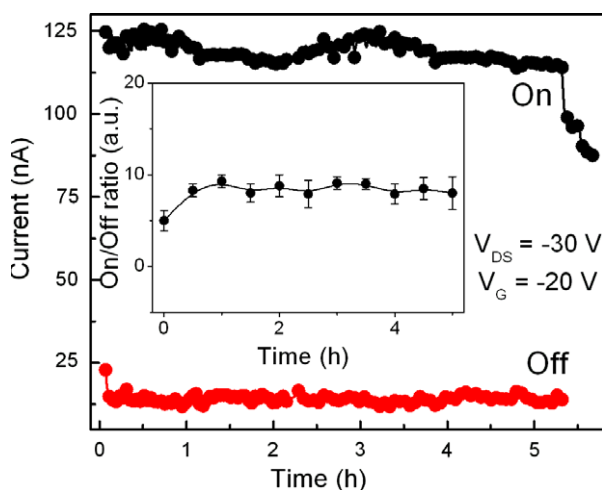


**Fig. 7.** Data retention measurement of the On- (write) and off state (Erase) drain current ( $I_{DS}$ ) of the OFET device measured at  $V_G = -20$  V.  $V_{DS}$  was kept at  $-30$  V throughout the experiment. Inset shows the plot of on/off ratio with time for different devices.

#### 4. Conclusions

In summary, a programmable field-effect transistor with organic electret (PVA) as the gate insulator and lead phthalocyanine as the active semiconductor has been fabricated through solution processing. The device exhibited hysteresis and memory upon sweeping of the gate bias in the forward and reverse scan. Trapping and detrapping of charge carriers in the dielectric/semiconductor interface is proposed to be the mechanism behind the memory phenomena. The memory window increased with increase in magnitude of gate voltage or source–drain voltage. The device showed reproducible write–read–erase–read switching cycles and data retention of more than 5 h. The device fabrication by cheap solution processing makes it suitable for large area and low cost electronics. The memory performance of the device, though very promising, can further be improved by optimizing the device geometry, fabrication method and operating conditions.

#### References

- [1] C.W. Tang, S.A. VanSlyke, *Appl. Phys. Lett.* 51 (1987) 913.
- [2] J.H. Burroughes, D.D.C. Bradley, A.R. Brown, R.N. Marks, K. Mackay, R.H. Friend, P.L. Burns, A.B. Holmes, *Nature (London)* 347 (1990) 539.
- [3] G. Horowitz, *Adv. Mater. (Weinheim, Ger.)* 10 (1998) 365.
- [4] G.H. Gelinck, H.E. Huitema, E. van Veenendaal, E. Cantatore, L. Schrijnemakers, J.B.P.H. van der Putten, T.C.T. Geuns, M. Beenhakkers, J.B. Giesbers, B.-H. Huisman, E.J. Meijer, E. Mena Benito, F.J. Touwslager, A.W. Marsman, B.J.E. van Rens, D.M. de Leeuw, *Nat. Mater.* 3 (2004) 106.
- [5] S.W. Liu, J.H. Lee, C.C. Lee, C.T. Chen, J.K. Wang, *Appl. Phys. Lett.* 91 (2007) 142106.
- [6] K.N.N. Unni, R. de Bettignies, S. Dabos-Seignon, J.M. Nunzi, *Appl. Phys. Lett.* 85 (2004) 1823.
- [7] R.C.G. Naber, B. De Boer, P.W.M. Blom, D.M. de Leeuw, *Appl. Phys. Lett.* 87 (2005) 203509.
- [8] G.H. Gelinck, A.W. Marsman, F.J. Touwslager, S. Setayesh, D.M. de Leeuw, R.C.G. Naber, P.W.M. Blom, *Appl. Phys. Lett.* 87 (2005) 092903.
- [9] Th.B. Singh, N. Marjanović, G.J. Matt, N.S. Sariciftci, R. Schwödau, S. Bauer, *Appl. Phys. Lett.* 85 (2004) 5409.
- [10] A.W. Snow, W.R. Barger, in: C.C. Lezoff, A.B.P. Lever (Eds.), *Phthalocyanines Properties and Applications*, vol. 1, VCH, New York, 1989.
- [11] Z. Bao, A.J. Lovinger, A. Dodabalapur, *Appl. Phys. Lett.* 69 (1996) 3066.

- [12] R. Zeis, T. Siegrist, Ch. Kloc, *Appl. Phys. Lett.* 86 (2005) 022103.
- [13] Y. Chen, W. Su, M. Bai, J. Jiang, X. Li, Y. Liu, L. Wang, S. Wang, *J. Am. Chem. Soc.* 127 (2005) 15700.
- [14] T. Yasuda, T. Tsutsui, *Jpn. J. Appl. Phys.* 45 (2006) L595.
- [15] B. Mukherjee, A.K. Ray, A.K. Sharma, M.J. Cook, I. Chambrier, *J. Appl. Phys.* 103 (2008) 074507.
- [16] P.M. Burnham, I. Chambrier, D.L. Hughes, B. Isare, R.J. Poynter, A.K. Powell, M.J. Cook, *J. Porphyr. Phthalocyanines* 10 (2006) 1202.
- [17] K.J. Baeg, Y.Y. Noh, J. Ghim, S.J. Kang, H. Lee, D.Y. Kim, *Adv. Mater.* 18 (2006) 3179.
- [18] A.R. Vökel, R.A. Street, D. Knipp, *Phys. Rev. B* 66 (2002) 195336.
- [19] K. Lakshminarayana, Y. Dasaradhu, V.V.R.N. Rao, *Mater. Lett.* 21 (1994) 425.
- [20] P. Frübing, M. Wegener, R.G. Mulhaupt, A. Buchsteiner, W. Neumann, L. Brehmer, *Polymer* 40 (1999) 3413.

photocurrent of  $\sim 9\%$  at the maximum power voltage of 0.35 V and at  $B = 100$  mT. They explained the enhancement of photocurrent as the result of an increase in the concentration of T excitons due to the enlarged intersystem crossing (ISC) rate of excitons from S state to T state. The different explanations on the above various MFEs observed in similar systems show that the mechanism of the MC effect in organic semiconductors remains obscure and more investigation is required.

In this work, we studied the MC of P3HT:PCBM based bulk heterojunction solar cells (BHJSCs) in dark and under illumination. The dark current always decreases with the applied magnetic field ( $-MC$ ). However, when light illumination is turned on, the photocurrent is enhanced by the applied magnetic field ( $+MC$ ). Because the photocurrent is in the opposite direction of the injection current, the MC trace of current under illumination exhibits a sign change around the open circuit voltage  $V_{oc}$ . We suggest that the  $+MC$  in photocurrent is due to the field-suppressed ISC of  $e-h$  pairs from S state to T state and  $-MC$  under illumination is mainly contributed by the dominating  $-MC$  in dark current because  $I_{photo} \approx I_{dark}$  at those voltages. While the  $-MC$  in dark current is associated with the space charge limited current (SCLC). Other possible mechanisms for  $\pm MC$  effects are also discussed.

## 2. Experimental

Our BHJSCs consist of a blended P3HT:PCBM (1:1 in weight) thin film sandwiched between poly(3,4-ethylenedioxythiophene)/poly(styrenesulfonate) (PEDOT:PSS) coated indium tin oxide (ITO) and a modified metallic cathode. After the traditional cleaning process and UV/O<sub>3</sub> treatment, a PEDOT:PSS layer of  $\sim 50$  nm thick was spin coated onto the ITO covered glass substrate and then annealed for an hour at 100 °C in vacuum. Then  $\sim 100$  nm thick P3HT:PCBM photovoltaic layer (solved in dichlorobenzene) was spin coated onto the PEDOT:PSS layer and dried in vacuum at 90 °C for an hour. A 1 nm thick lithium fluoride (LiF) and a 100 nm thick aluminum cathode were thermally evaporated onto the organic layers through a shadow mask (active areas:  $1 \times 3$  mm<sup>2</sup>) in high vacuum ( $\sim 10^{-5}$  Pa). During the measurement process, the samples were mounted on the cold finger of a close-cycle cryostat (Janis CCS-350s) which was located between the pole pieces of an electromagnet (Lakeshore EM647). The magnetic field with the maximum strength of 200 mT was applied parallel to the device surface and measured by Hall probe GaussMeter (Lakeshore 421) placed close to the sample. The  $J-V$  characteristics in dark or under illumination were measured by a Keithley 2400 SourceMeter and a halogen lamp with light intensity  $\sim 50$  mW/cm<sup>2</sup> was used as the light source.

## 3. Results and discussion

Fig. 1 shows the MCs at two typical biases in the dark and under illumination as a function of the applied magnetic field. The open circuit voltage  $V_{oc}$  is 0.55 V in this device. The MC is defined as  $[I(B) - I(0)]/I(0)$ , where  $I(B)$  and

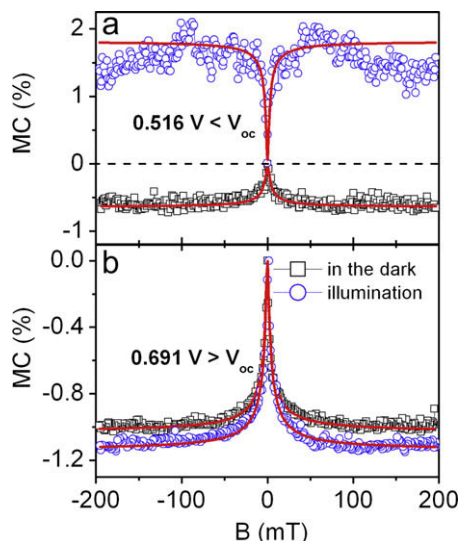


**Fig. 1.** (a) MC vs. magnetic field in the P3HT:PCBM based BHJ solar cell device in dark and under illumination at the bias voltages of (a) 0.516 V, below the  $V_{oc}$  of the studied device; (b) 0.691 V, above the  $V_{oc}$ . The red solid lines are guides to the eyes. (For interpretation of the references to colour in this figure legend, the reader is referred to the web version of this article.)

$I(0)$  are the currents in the presence and absence of a magnetic field  $B$ . As shown in Fig. 1a,  $-MC$  in dark current with value of  $\sim 0.7\%$  is observed at 0.516 V below  $V_{oc}$ . When light illumination is turned on, the MC response shows a sign change and produces positive trace in photocurrent as shown in Fig. 1a. The same phenomenon is observed at other bias below  $V_{oc}$ . The red lines in this figure are added just as guides to the eyes. However, both the MCs in the dark and under illumination are negative at bias above  $V_{oc}$ . Typical traces at 0.691 V are selected and displayed in Fig. 1b.

Fig. 2 illustrates the current variation  $\Delta I = I(B) - I(0)$  under an external magnetic field ( $\sim 50$  mT) as a function of

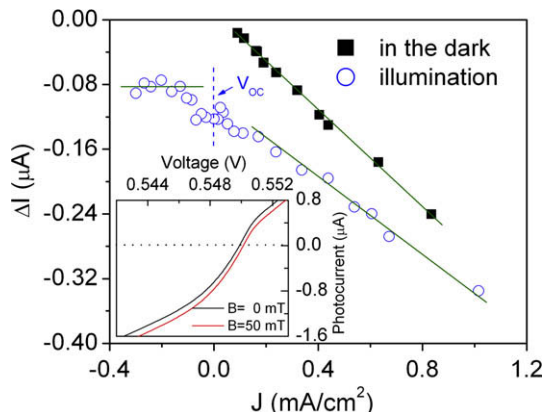


**Fig. 2.** Current variations  $\Delta I = I(B) - I(0)$  under magnetic field of 50 mT as a function of  $J$  for the device in the dark and under illumination. The inset is the photocurrent under field (50 mT) and with no field as a function of the applied voltage. The olive solid lines are guides to the eyes.

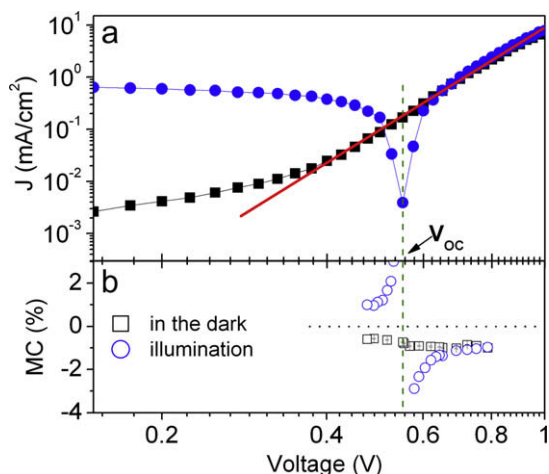


**Fig. 3.** (a) Dark  $J$ - $V$  characteristics (black solid square) and illuminated  $J$ - $V$  characteristics (blue solid circle) of the device. The red solid line represents a power law fit to the  $\log(J)$  vs.  $\log(V)$  in the bias region (0.4–1.0 V). (b) MC of current in the dark (black open square) and under illumination (blue open circle) vs.  $\log(V)$ . (For interpretation of the references to colour in this figure legend, the reader is referred to the web version of this article.)

the current density  $J$  in the dark as well as under illumination. The photocurrents in the presence and absence of a  $B$  field  $\sim 50$  mT are compared in the inset (only show the currents around  $V_{oc}$ ). Nearly constant enhancement of photocurrent is observed for all bias below  $V_{oc}$  due to the action of the magnetic field. When increasing the voltage, the photocurrent become positive and its variations are linear with  $J$ . Similar linear change is also observed in dark current. The observed phenomena suggest that the distinct  $J$  dependences of  $\Delta I$  in negative and positive  $J$  region must be related with two different mechanisms of MC.

To investigate the correlations between the MC effect and the current character in our devices, we measured  $J$ - $V$  characteristics in a small voltage range (0.15–1.0 V) in dark and under illumination, respectively. As shown in Fig. 3a, at low voltages the  $J$ - $V$  characteristics in dark are linear. At higher voltages (0.4–1.0 V), power law behavior of  $J \propto V^m$  with  $m \sim 6$  (red solid line)<sup>1</sup> are observed. The  $J$ - $V$  characteristics under illumination also contain two different regimes: (i) when  $V < V_{oc}$ , the current is dominated by the diffusion of photo-generated charges under the built-in electric field, (ii) when  $V > V_{oc}$ , the current under illumination is slightly larger than the dark current, i.e.  $I_{photo} \approx I_{dark}$ . The MC-voltage curves are displayed in Fig. 3b. In dark condition, the MC response is always negative and shows a weak dependence on the applied voltages. However, under illumination, +MC at bias below  $V_{oc}$  and -MC at bias above  $V_{oc}$  are observed. The inversion and large values of MC occur at voltages close to  $V_{oc}$ . In fact, this feature of MC response in current under light is not intriguing and has been reported by Desai et al. [18]. It can be easily understood that though the applied magnetic field only slightly enhances the negative photocurrent, a

drastic MC response is yielded at bias voltages around  $V_{oc}$  due to the denominator  $I(0)$  is nearly zero when the bias voltage approaches  $V_{oc}$ .

At the voltages below  $V_{oc}$ , the measured augment of photocurrent with an applied  $B$  field is very similar with the result reported by Shakya et al. [17]. Instead of thinking that the external magnetic field can increase the ISC rate of excitons from S state to T state, we consider the magnetic field affected hyperfine modulation on the conversion of e-h pairs from S to T. Kalinowski et al. [1,2] suggested that the hyperfine interactions of electrons or holes with surrounding nuclei could partially convert the S e-h pairs into T pairs with a rate constant  $K_{ST}$ . In the absence of an external magnetic field, the S and T ( $T_0$  and  $T_{\pm}$ ) pair states nearly degenerate because of the negligible exchange interactions, resulting in an effective S  $\rightarrow$  T conversion due to the hyperfine mixing. When a magnetic field is applied, the triplet degeneracy is removed and the hyperfine mixing can only occur between S and the  $T_0$  state, leading to a decrease in  $K_{ST}$  and an increase in the concentration of S pairs. Under light illumination, the S excitons are generated in the blend by absorbing the photons. They can diffuse to the P3HT/PCBM interface and form the correlated S e-h pairs through a charge transfer process. Because the S e-h pairs have a stronger ionic character than T pairs, they have higher probability for dissociation or charge separation [1,19]. Under the light illumination with constant density, the applied  $B$  field boosts the population of S e-h pairs and therefore enlarges the photocurrent. In addition, a slight high field ( $B > 50$  mT) decrease can be identified in the MC response of photocurrent when  $V < V_{oc}$ . Similar phenomenon has also been observed by Kalinowski et al. in the photoconductance of Alq<sub>3</sub> film [1]. Their pioneer interpretation based on the electronic Zeeman effect attributed this MFE to a non-negligible exchange interaction between S and T e-h pairs. Increasing the magnetic field pushes the  $T_+$  state toward S state, and a sudden increase in the ISC rate from S to  $T_+$  pair states and a minimum in the concentration of the S pairs can be expected at a level crossing field. A weak decreasing trend in the MFE on the photocurrent or photoconductance can be expected if considering a Gaussian distribution of the e-h pairs' distance instead of a constant charge separation distance for all e-h pairs.

In addition to the dissociation of S e-h pairs and S excitons, the reactions between the electrode and T excitons constitute another channel for the generation of photocurrent. T excitons can diffuse to the electrode interface owing to their long diffusion lengths for charge reaction, T + electrode  $\rightarrow$  e + h, giving the so-called excitonic injection contribution to the total current [1,2,20]. But such a process in the blends should be much weaker than in the polymer films because the phase separation of donor and acceptor can greatly facilitate the interfacial dissociation of excitons and consequently increase the exciton dissociation efficiency. It was estimated that almost all the T excitons are highly probable to reach the donor/acceptor interface and dissociate into free charge carriers [17]. Hence we do not suggest that the T excitons induced excitonic injection of current is an important channel in the magnetic field effect on the photocurrent.

<sup>1</sup> For interpretation of color in Fig. 3, the reader is referred to the web version of this article.

According to the above discussed mechanism of MFE on photocurrent, the nearly constant  $\Delta I$  in photocurrent at bias below  $V_{oc}$  as shown in Fig. 2 is due to the constant density of light illumination. When the applied voltage is larger than  $V_{oc}$ , the variations of current under illumination are linear with  $J$  and show a small difference in slope with the variations of dark current. This small difference could be caused by the photo-generated charges which fill the traps or drift in the blend.

As frequently been observed, the bulk transport in organic semiconductors is often dominated by the space charge limited current with an exponential traps distribution which leads to the relationship between  $J$  and  $V$  as  $J \propto V^m$ . Referring to Fig. 3a, the  $J$ - $V$  characteristics of our BHJSC device exhibit similar behavior as  $J \propto V^6$  (red solid line), which is likely a signature of trap filling [21]. Therefore we suggest that the  $-MC$  effect in dark current might be associated with the case of SCLC. This can be also confirmed by the case of current under illumination. At bias larger than  $\sim 0.6$  V, the current under illumination is also governed by the SCLC. The MC effects at this current regime under illumination are negative and have only a small difference in their values compared to the  $-MC$  effect of dark current. Similar effect has also been found in OLED by Bloom et al. who measured the magnetoresistance (MR) effect of the devices (device was current biased and the voltage drop was measured) [12,13]. Their findings show that when the  $I(V)$  exhibits power law behavior ( $I \propto V^6$ ), the MR is positive ( $-MC$  effect), and with the deviation from the power law the MR starts to decrease and even becomes negative ( $+MC$  effect). Currently the microscopic origin of the correlation between the SCLC and  $-MC$  is still unclear. More dedicated experiments are required to solve this issue and further development of theoretical model will also be a great challenge. At large bias, the current under illumination of our device is actually dominated by the dark current, for instant, at  $V = 0.691$  V,  $I_{photo} \approx I_{dark}$ . Therefore in this voltage regime, the MC response is mainly due to the MFE on dark current. We ascribe the small difference between the  $-MC_{photo}$  and  $-MC_{dark}$  to the influence of the MFE on the photo-generated charge carriers which would decrease the injection current.

Recently, several groups have used bipolaron model to explain the MR effect of the organic devices [4,5,12–14]. This model relies on the spin dependent formation of doubly occupied sites during the hopping transport of charge carriers through the organic film [22]. As indicated in  $J$ - $V$ , the SCLC with an exponential traps distribution would probably favor the formation of bipolarons. Since the donor and acceptor phases are separated in P3HT:PCBM blend, positive polaron pairs ( $P^+P^+$ ) and negative polaron pairs ( $P^-P^-$ ) should be formed in the P3HT polymer phase and fullerene phase, respectively. However, as seen in Fig. 3b, the  $-MC$  response in dark current seems to be voltage independent. Such a phenomenon is inconsistent with the bipolaron mechanism because the large concentration of bipolarons should be able to result in the increase of the magnitude of MC. Within the bias range of 0.5–0.8 V, the current density increases nearly two orders as shown in Fig. 3a. A stronger MC response should be anticipated but

it is not observed in the experiment. Therefore the bipolaron model is not suitable to explain our observations.

#### 4. Conclusion

We have investigated the MC effects in P3HT:PCBM based BHJSCs in the dark and under illumination. We observed a sign change in MC response under illumination occurred at the bias close to  $V_{oc}$ . At bias below  $V_{oc}$ , the  $+MC$  in photocurrent can be explained by the field dependent hyperfine mixing between the S and T e-h pairs, leading to an enhancement in S pair dominated charge dissociation and photocurrent. At bias larger than  $V_{oc}$ , both current under light and in the dark show similar  $-MC$  effect. Because the current under illumination at bias above  $V_{oc}$  is mainly due to the injection current (dark current), the  $-MC$  can be attributed to the MFE on dark current which displays the clear character of space charge limited current with an exponential traps distribution. Our study leads to the insight into the fundamental magnetic field dependent properties of the excitonic states formed in organic optoelectronic devices.

#### Acknowledgements

This work was supported in part by Ying Tong Education Foundation (Grant No.101006), by the National Natural Science Foundation of China (Grant No. 10504027), by the State Education Ministry under the NCET Program (Grant No. NCET-05-0772), by the Scientific Research Foundation of State Education Ministry for Returned Oversea Scholars (Grant No. (2007) 1108), and by the state Personnel Ministry under the STA Program for the Science & Technology Activity of Oversea Studying Personnel.

#### References

- [1] J. Kalinowski, J. Szmytkowski, W. Stampor, Chem. Phys. Lett. 378 (2003) 380.
- [2] J. Kalinowski, M. Cocchi, D. Virgili, P. Di Marco, V. Fattori, Chem. Phys. Lett. 380 (2003) 710.
- [3] J. Kalinowski, M. Cocchi, D. Virgili, V. Fattori, P. Di Marco, Phys. Rev. B 70 (2004) 205303.
- [4] Ö. Mermer, G. Veeraraghavan, T.L. Francis, Y. Sheng, T.D. Nguyen, M. Wohlgenannt, A. Köhler, M.K. Al-Suti, M.S. Khan, Phys. Rev. B 72 (2005) 205202.
- [5] T.D. Nguyen, Y. Sheng, J. Rybicki, M. Wohlgenannt, Phys. Rev. B 77 (2008) 235209.
- [6] Y. Zhang, R. Liu, Y.L. Lei, Z.H. Xiong, Appl. Phys. Lett. 94 (2009) 083307.
- [7] Y.L. Lei, Y. Zhang, R. Liu, P. Chen, Q.L. Song, Z.H. Xiong, Org. Electron. 10 (2009) 889.
- [8] Y. Wu, Z. Xu, B. Hu, J. Howe, Phys. Rev. B 75 (2007) 035214.
- [9] B. Hu, Y. Wu, Nat. Mater. 6 (2007) 985.
- [10] P. Desai, P. Shakya, T. Kreuzis, W.P. Gillin, J. Appl. Phys. 102 (2007) 073710.
- [11] V. Prigodin, J.D. Bergeson, D. Lincoln, A. Epstein, Phys. Rev. Lett. 100 (2008) 067201.
- [12] F.L. Bloom, W. Wagemans, M. Kemerink, B. Koopmans, Phys. Rev. Lett. 99 (2007) 257201.
- [13] F.L. Bloom, W. Wagemans, M. Kemerink, B. Koopmans, Appl. Phys. Lett. 93 (2008) 263302.
- [14] F.L. Bloom, W. Wagemans, B. Koopmans, J. Appl. Phys. 103 (2008) 07F320.
- [15] T.H. Lee, T.F. Guo, J.C.A. Huang, T.C. Wen, Appl. Phys. Lett. 92 (2008) 153303.
- [16] F.J. Wang, H. Bässler, Z.V. Vardeny, Phys. Rev. Lett. 101 (2008) 236805.

- [17] P. Shakya, P. Desai, T. Kreouzis, W.P. Gillin, S.M. Tuladhar, A.M. Ballantyne, J. Nelson, J. Phys.: Condens. Matter 20 (2008) 452203.
- [18] P. Desai, P. Shakya, T. Kreouzis, W.P. Gillin, Phys. Rev. B 76 (2007) 235202.
- [19] M. Wohlgenannt, Z.V. Vardeny, J. Phys.: Condens. Matter 15 (2003) R83.
- [20] R. Signerski, J. Kalinowski, I. Koropeczy, S. Nešpuorek, Thin Solid Films 121 (1984) 175.
- [21] A.J. Campbell, D.D.C. Bradley, D.G. Lidzey, J. Appl. Phys. 82 (1997) 6326.
- [22] P.A. Bobbert, T.D. Nguyen, F.W.A. van Oost, B. Koopmans, M. Wohlgenannt, Phys. Rev. Lett. 99 (2007) 216801.

channel through ambipolar transport. In fabricating efficient ambipolar OLEFETs, balanced carrier conduction and controlled positioning of the recombination region are crucial. So far, either utilizing single ambipolar materials or combining two unipolar materials through co-evaporated or bilayered structures have been applied to realize ambipolar carrier conduction [15–23]. In most cases of single component- and co-evaporated blend-based OLEFETs, however, efficient light emission has not been observed due to the difficulties in achieving a balanced injection and carrier transport. While there is a physical separation between hole and electron transports, bilayer heterojunction-based OLEFETs have demonstrated well-balanced ambipolarity with high carrier mobilities and have consequently improved luminescence by tuning the gate voltage.

Another critical factor in fabricating high-performance OLEFETs is the preparation of good thin films. Unlike traditional vapor deposition and/or solution-processing methods, the neutral cluster beam deposition (NCBD) method employed in this study is a less popular, but promising deposition approach [24]. Neutral cluster beams of weakly bound organic molecules are generated at the throat of the nozzle when the vapor-phase molecules evaporated by resistive heating undergo adiabatic supersonic expansion in a high-vacuum. The unique characteristics of a neutral

cluster beam are its high translational kinetic energy and directionality. The collision of such directional, energetic neutral clusters with a substrate of interest induces their facile decomposition into individual molecules, where their subsequent migration leads to the formation of smooth, uniform thin films. The novel scheme allows for significant improvement in surface morphology, crystallinity, packing density, and room temperature substrate deposition, whose unique advantages cannot be easily achieved through traditional vapor deposition techniques. In recent years a series of optoelectronic devices have been successfully prepared and characterized utilizing the NCBD method [25–33].

In this article, we describe our application of the NCBD method to fabricate bilayer heterojunction-based OLEFETs by successively superimposing two layers of  $\alpha,\omega$ -dihexylsexithiophene (DH6T) and  $N,N'$ -ditridecylperylene-3,4,9,10-tetracarboxylic diimide (P13). DH6T and P13 are hole- and electron-transporting materials with high mobilities and the relative positions of their highest occupied and lowest unoccupied molecular orbitals (HOMOs and LUMOs) are well-matched to form singlet excitons for high luminescence; the (HOMO, LUMO) levels of DH6T and P13 are estimated to be (–5.2 and –2.9 eV) and (–5.4 and –3.4 eV), respectively (Fig. 1). For the first time, our air-stable, heterojunction-based OLEFETs successfully

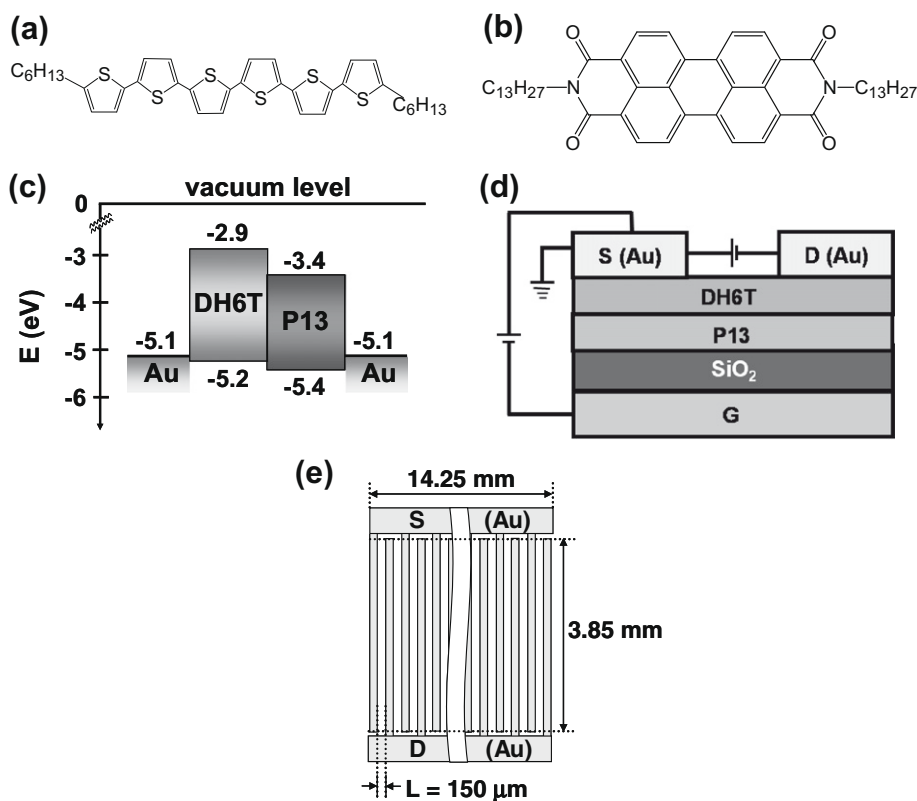


**Fig. 1.** Molecular structures of (a) DH6T and (b) P13. (c) Energy level diagram (units in eV) for the Au source electrode/P13 (bottom)/DH6T (top)/Au drain electrode device. (d) Schematic cross-sectional view of the top-contact transistor with its bias condition. (e) Electrode configuration of the OLEFET device with a multi-digitated, long channel-width geometry.

demonstrated good field-effect characteristics, stress-free operational stability, and electroluminescence based on well-balanced ambipolarity under ambient conditions.

## 2. Experiment

A homemade NCBD apparatus was employed to prepare the P13 and DH6T active layers [24]. The apparatus consisted of a pair of evaporation crucibles, a drift region, and the substrate. The as-received samples were placed inside the enclosed cylindrical crucibles (1.0 mm diameter, a 1.0 mm-long nozzle) and sequentially sublimated by separate resistive heating between 530 and 570 K for P13 and

480 and 510 K for DH6T. Each sample vapor then underwent adiabatic supersonic expansion into the high-vacuum drift region at a working pressure of approximately  $6 \times 10^{-6}$  Torr. Highly directional, weakly bound neutral cluster beams were formed at the throat of the nozzle and directly deposited onto the substrates. The optimum thickness and deposition rate were 300 Å at 1.0–2.0 Å/s for P13 and 150 Å at 0.5–1.0 Å/s for DH6T, respectively.

The OLEFET devices with a multi-digitated, long channel-width geometry were fabricated in the top-contact configuration as shown in Fig. 1. The substrates consisted of a highly doped, *n*-type Si wafer coated with an Al layer as the gate electrode and thermally grown 2000 Å-thick

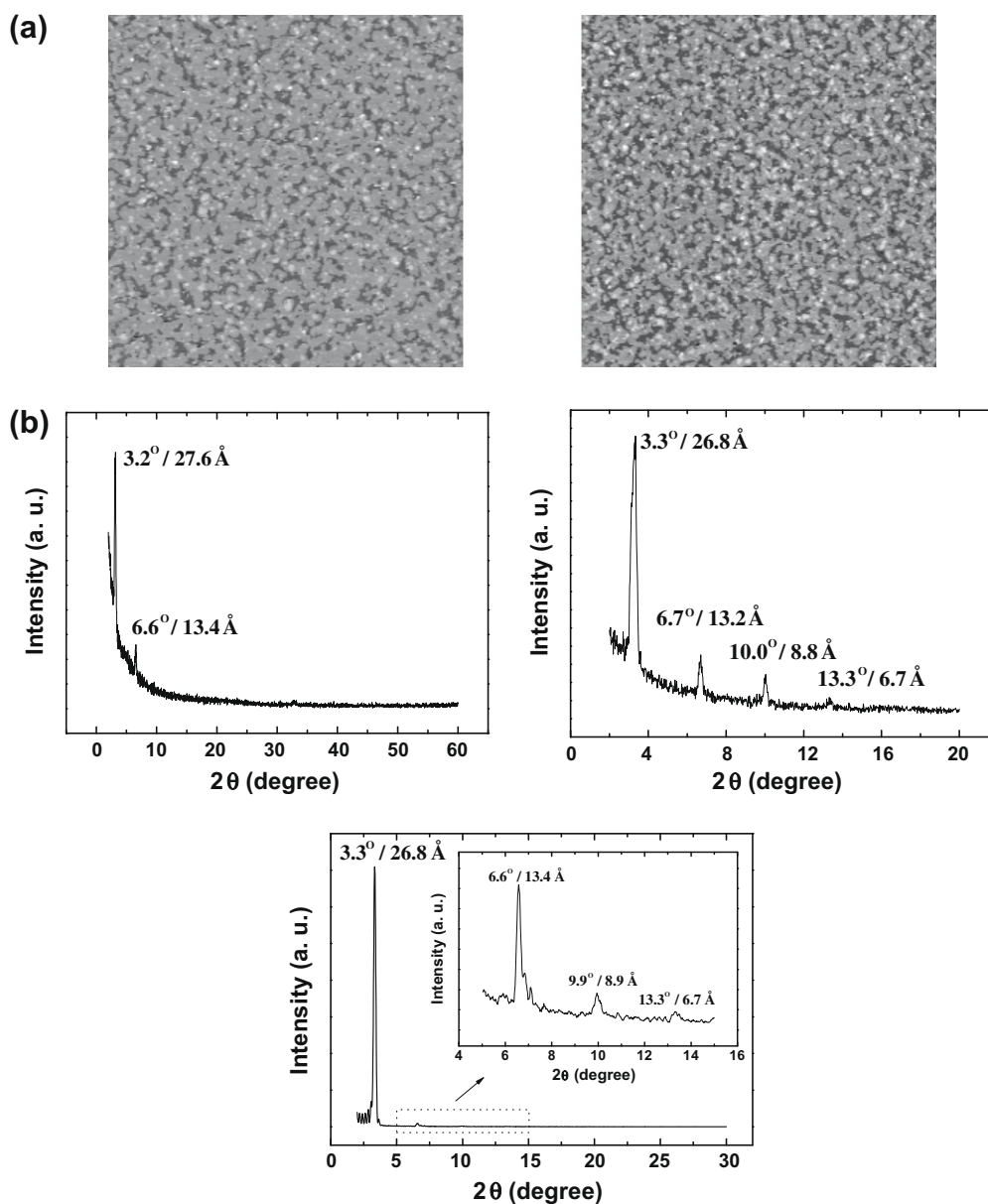


Fig. 2. (a) Comparison of two-dimensional AFM micrographs ( $10 \times 10 \mu\text{m}^2$  area) for the DH6T and P13/DH6T thin films. (b) Comparison of X-ray diffractograms for the DH6T, P13, and P13/DH6T thin films deposited on the  $\text{SiO}_2$  substrates at room temperature.



SiO<sub>2</sub> layers as the gate dielectric. A rigorous cleaning procedure and UV treatment were necessary to improve OLEFET performance, involving a series of sequential ultrasonic treatments in acetone, hot trichloroethylene, acetone, HNO<sub>3</sub>, methanol, deionized water, and blown dry with dry N<sub>2</sub>. The substrates were finally exposed to UV (254 nm) for 15 min [34,35]. The multi-digitated transistors had a significantly longer channel-width ( $W$ ) of 180.95 mm at a channel length ( $L$ ) of 150  $\mu\text{m}$ . Electron-beam evaporation using a properly shaped shadow mask was utilized to produce 500  $\text{\AA}$ -thick Au source and drain electrodes at a deposition rate of 6–8  $\text{\AA}/\text{s}$ . The current–voltage characteristics of OLEFETs and their light emission intensities were measured simultaneously in air, using an optical probe attached to an HP4140B pA meter–dc voltage source unit and an 818-UV Si photodiode with an 1830-C power meter (Newport Co.).

### 3. Results and discussion

Surface analysis using an AFM apparatus was carried out to perform the comparative characterization of surface morphologies for the DH6T and P13/DH6T films deposited on SiO<sub>2</sub> substrates at room temperatures. The root-mean-square ( $R_{\text{rms}}$ ) values for the DH6T and P13/DH6T films were also measured as about 11 and 12  $\text{\AA}$ , respectively. Both films exhibited complete coverage with the highly packed grain crystallites, suggesting that the P13 bottom layer did not disturb the deposition conditions at the early stages and subsequent grain growth. The effect of the P13 bottom layer on the sequential deposition of DH6T active layer was also examined by the X-ray diffraction measurements using Cu  $K\alpha$  radiation in a symmetric reflection, coupled  $\theta$ – $2\theta$  scanning mode. Fig. 2b shows the XRD diffractograms for three different kinds of DH6T (300  $\text{\AA}$ ), P13 (500  $\text{\AA}$ ), and P13 (300  $\text{\AA}$ )/DH6T (150  $\text{\AA}$ ) films. All thin films show a highly ordered structure. The sharp first-order peaks, as well as distinctive higher-order multiple peaks can be fitted to a series of (0 0 1) reflection lines with multiple  $d$  spacing. The XRD peaks of DH6T films located at  $2\theta = 3.2^\circ$  and  $6.6^\circ$  correspond to  $d$ -spacings of 27.6 and 13.4  $\text{\AA}$ . The four reflection peaks of P13 films located at  $2\theta = 3.3^\circ$ ,  $6.7^\circ$ ,  $10.0^\circ$ , and  $13.3^\circ$  were assigned to be the  $d$ -spacings of 26.8, 13.2, 8.8, and 6.7  $\text{\AA}$ , respectively. In the case of the P13/DH6T bilayer films, strong and narrow first-order peaks were observed. Although the higher-order multiple peaks were much weaker compared to those in the DH6T films, the reflection peaks clearly showed the feature of the DH6T layer, indicating that the P13 layer placed at the bottom supports the crystalline growth of the DH6T top layer without causing the structural mismatch at the interface.

Fig. 3 displays the typical output characteristics of P13 (bottom)/DH6T (top)-based OLEFETs obtained under ambient conditions. The plot clearly exhibits the characteristic  $I_{\text{DS}} = I_{\text{DS}}(V_{\text{DS}}, V_{\text{DS}})$  dependence expected for ambipolar devices, where  $I_{\text{DS}}$  is the drain-source current,  $V_{\text{DS}}$  the drain-source voltage, and  $V_{\text{GS}}$  the gate-source voltage. In the case of the reverse drain mode ( $V_{\text{DS}} < 0$ ), there is a crossover point from electron-dominated current to hole-

dominated current. At low  $V_{\text{GS}} = 0$  to  $-20$  V, the drain current due to electron injection at the drain electrode decreases quadratically with decreasing  $V_{\text{DS}}$  (increasing  $|V_{\text{DS}}|$ ). In the region of  $V_{\text{GS}} \leq -30$  V, the drain current induced by hole injection from the grounded source electrode appeared to contribute substantially and showed a typical  $p$ -type transistor working in the accumulation mode. At a fixed  $-V_{\text{GS}}$ ,  $I_{\text{DS}}$  initially decreased linearly with decreasing  $V_{\text{DS}}$  with  $I_{\text{DS}}$  tending to saturate due to a pinch

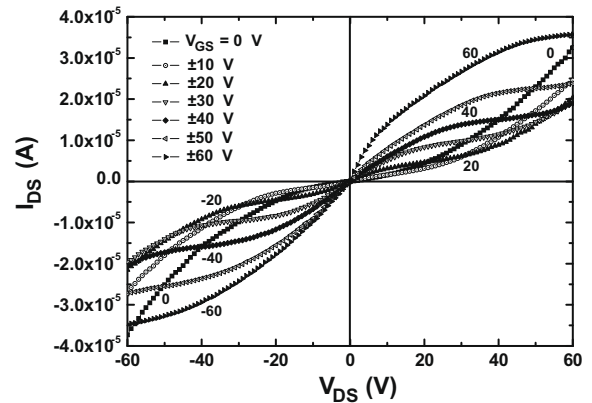


Fig. 3. Typical output characteristics of P13/DH6T-based OLEFETs obtained under ambient conditions.

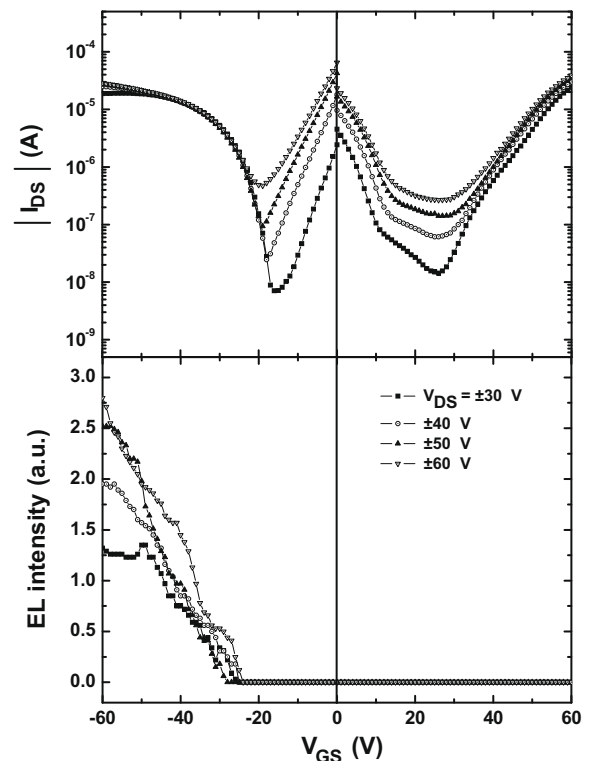


Fig. 4. Typical transfer curves of P13/DH6T-based OLEFETs in the saturation regime together with the gate-dependence of the electroluminescence characteristics. Each transfer scan was run at a constant  $V_{\text{DS}}$ .

off in the accumulation layer. On the contrary, in the forward drain mode ( $V_{DS} > 0$ ), a totally inverse phenomenon occurs. There is a crossover from the hole-dominated current to the electron-dominated current. At  $V_{GS} = 0$ – $20$  V, the drain current due to the hole injection at the drain electrode increased quadratically with increasing  $V_{DS}$ . In the region of  $V_{GS} \geq 30$  V, the drain current induced by electron injection from the grounded source electrode appeared to contribute substantially and showed a typical  $n$ -type transistor working in the accumulation mode.

The extent of transport balance between the hole and electron carriers can be directly examined in the transfer characteristics. Fig. 4 shows the typical transfer curves in the saturation regime. Each transfer scan was run with a constant  $V_{DS}$ . In principle, for well-balanced ambipolar transistors, a symmetric form of the transfer curve centered near the  $I_{DS}$  minimum is expected. A good balance, especially in the positive  $V_{GS}$  region, is demonstrated in Fig. 4. Using standard FET analysis, quantitative carrier mobilities ( $\mu_{eff}$ ) can be calculated in the saturation regime by the following relationship:

$$I_{DS} = \frac{WC_i\mu_{eff}}{2L}(V_{GS} - V_T)^2$$

where  $C_i$  is the capacitance per unit area of the  $\text{SiO}_2$  gate dielectric and  $V_T$  is the threshold voltage. For thermally grown, 2000 Å-thick  $\text{SiO}_2$ , the value for  $C_i$  is known to be  $17.25 \text{ nF cm}^{-2}$ . A hole mobility ( $\mu_{eff}^h$ ) of  $2.22 \times 10^{-2} \text{ cm}^2/\text{Vs}$  at  $V_{DS} = -60$  V is estimated to be nearly equal to an electron mobility ( $\mu_{eff}^n$ ) of  $2.78 \times 10^{-2} \text{ cm}^2/\text{Vs}$  at  $V_{DS} = 60$  V, implying that a well-balanced ambipolar carrier transport is clearly achieved in our OLEFETs. Several other device parameters can be also derived from the fits of the observed  $I$ - $V$  characteristics for more than 10 OLEFETs and are listed in Table 1. The maximum hole and electron mobilities are also listed with the corresponding average mobilities ( $\mu_{eff}^{avg}$ ) with the standard deviation ( $\sigma$ ). The  $\mu_{eff}$  values at room temperature are comparable to or somewhat less than those obtained from the NCBD-based single-layer OFET devices, which are among the best to date for polycrystalline DH6T- and P13-based transistors using  $\text{SiO}_2$  dielectric layers without any thermal post-treatment.

Herein, it should be noted that our measurements were carried out under ambient conditions, unlike most of the previous OLEFET investigations conducted either under inert atmosphere or vacuum conditions. In addition, due to

environmental effects, the deposition sequence of two active layers has been found to be critical in the fabrication process of stable bilayer heterojunction-based OLEFETs. In this study, by inverting the deposition sequence, the transistors with the bilayered structure of P13 superimposed on top of DH6T were also fabricated and characterized. However, since most  $n$ -type organic-based devices, including P13 devices, are sensitive to environmental contaminants such as moisture and oxygen that penetrate the channel region, device parameters such as mobilities deteriorate with time and therefore the OLEFETs do not

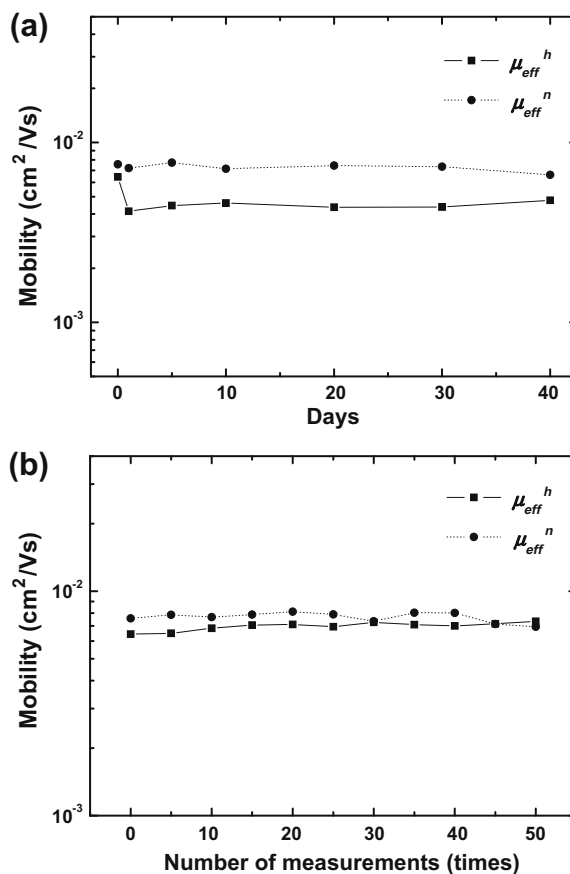


Fig. 5. Hole and electron mobilities of P13/DH6T-based OLEFETs monitored as a function of (a) time (days) and (b) number of measurements.

Table 1

Device parameters deduced from the characteristics of single-layer OFETs and bilayer heterojunction-based OLEFETs.

Classification (thickness)	$\mu_{eff}^n$ ( $\text{cm}^2/\text{Vs}$ )	$\mu_{eff}^{n,avg} \pm \sigma^a$ ( $\text{cm}^2/\text{Vs}$ )	$V_T^n$ (V)	$\mu_{eff}^h$ ( $\text{cm}^2/\text{Vs}$ )	$\mu_{eff}^{h,avg} \pm \sigma^a$ ( $\text{cm}^2/\text{Vs}$ )	$V_T^h$ (V)	$V_{DS}$ (V)
DH6T <sup>b</sup> (300 Å)	–	–	–	$4.5 \times 10^{-2}$	$0.025 \pm 0.016$	–9.3	–60
P13 <sup>c</sup> (500 Å)	0.16	$0.11 \pm 0.03$	46.3	–	–	–	100
P13/DH6T (300 Å/150 Å)	$2.44 \times 10^{-2}$	$1.27 \times 10^{-2} \pm 1.00 \times 10^{-2}$	34.7	$1.83 \times 10^{-2}$	$1.23 \times 10^{-2} \pm 1.02 \times 10^{-2}$	–12.7	$\pm 30$
	$2.56 \times 10^{-2}$	$1.21 \times 10^{-2} \pm 9.28 \times 10^{-3}$	33.9	$1.99 \times 10^{-2}$	$1.36 \times 10^{-2} \pm 1.14 \times 10^{-2}$	–11.5	$\pm 40$
	$2.63 \times 10^{-2}$	$1.21 \times 10^{-2} \pm 8.51 \times 10^{-3}$	32.4	$2.15 \times 10^{-2}$	$1.37 \times 10^{-2} \pm 1.15 \times 10^{-2}$	–10.0	$\pm 50$
	$2.78 \times 10^{-2}$	$1.21 \times 10^{-2} \pm 9.34 \times 10^{-3}$	28.9	$2.22 \times 10^{-2}$	$1.31 \times 10^{-2} \pm 1.14 \times 10^{-2}$	–8.5	$\pm 60$

<sup>a</sup> The mobility data in the text represents the best values. Considering the distributions of the OFET and OLEFET characteristics, the all  $\mu_{eff}$  values lie within  $\mu_{eff}^{avg} \pm 2\sigma$  (standard deviation).

<sup>b</sup> Ref. [26].

<sup>c</sup> Ref. [27].

show reproducible device characteristics and operational stability. Similar deterioration phenomena were also reported in the P13-based organic devices [19,36]. On the other hand, as described in the previous section, when DH6T was deposited on top of the P13 layer, the DH6T layer appeared to act as a protective passivation layer and significantly improved operational stability. As displayed in Fig. 5a, the hole and electron mobilities monitored as a function of time did not change substantially, *even after 40 days*. Furthermore, the alleged stress phenomenon in our OLEFETs was not observed. The degradation process is known to occur when the devices are repeatedly operated. Fig. 5b shows the hole and electron mobilities as a function of the number of measurements. Transistor characteristics were consistently reproducible during repetitive operations up to 50, clearly manifesting that the operational stabilities of our OLEFETs were well maintained without degradation. Therefore, the bilayer structure with an air-stable organic compound deposited atop

as a protective passivation layer presented a reliable scheme in producing air-stable, stress-free ambipolar OLEFETs.

The gate-dependence of the electroluminescence characteristics corresponding to the transfer curves is also shown in Fig. 4. The light emission was observed in the region of  $V_{GS} \leq -25$  V. In cases of single-layer OLEFETs, the maximum emission is generally expected to occur at  $V_{GS} = 0.5 V_{DS}$ , where an equal voltage drop for hole and electron carriers exists. To the contrary, emission in bilayer heterojunction-based OLEFETs are not required to satisfy the relationship. Instead, as revealed in Fig. 3, the position of the emission maximum shifts slightly with decreasing  $V_{GS}$  (increasing  $|V_{GS}|$ ) and the intensity increases with decreasing  $V_{DS}$  (increasing  $|V_{DS}|$ ). On the basis of the energy level diagram and the device structure in Figs. 1 and 6a, the operating mechanism to account for the observed light emission can be described as follows. When the gate electrode is negatively biased, the large electric field causes the

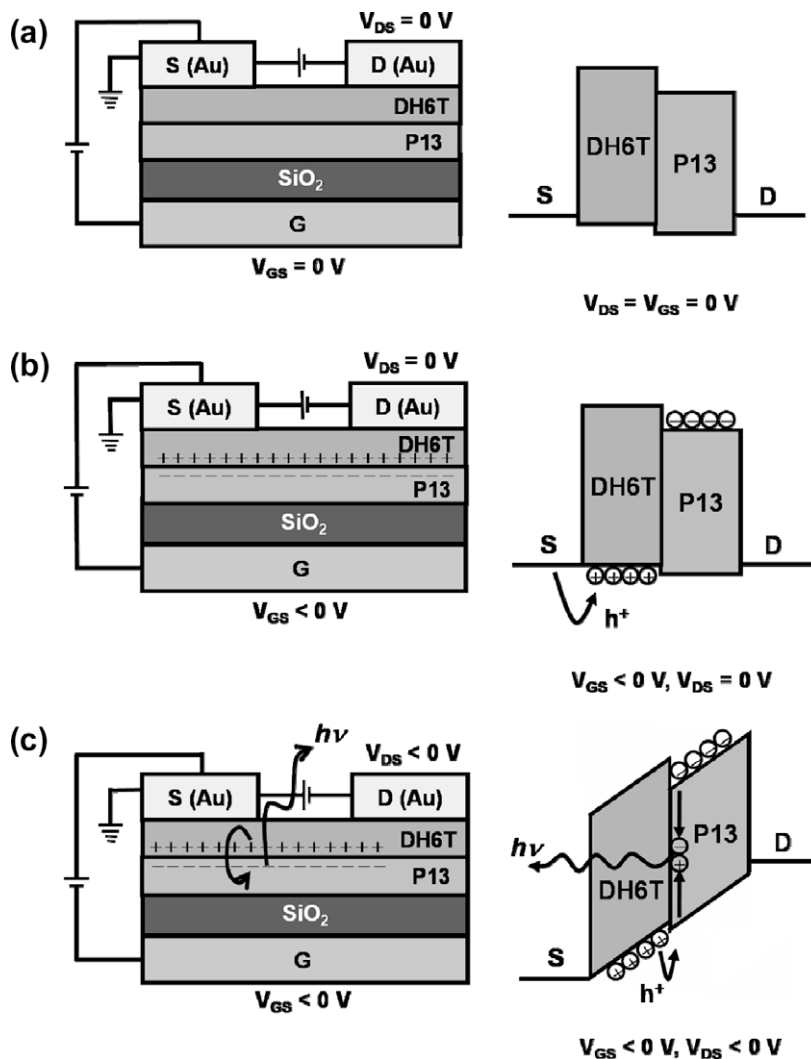


**Fig. 6.** Device operation and energy level diagram. (a)  $V_{GS} = V_{DS} = 0$  V. (b)  $V_{GS} < 0$  V,  $V_{DS} = 0$  V. When the gate is negatively biased, the HOMO and LUMO levels shift up with respect to the Fermi levels of the Au metal electrodes and formation of the P13/DH6T dipole layer occurs. (c)  $V_{GS} < 0$  V,  $V_{DS} < 0$  V. At the proper negative  $V_{DS}$ , some carrier recombination takes place in the P13 layer to form the exciton leading to the electroluminescence.

HOMO and LUMO levels in both semiconductors to shift up with respect to the Fermi levels of the Au electrodes, inducing formation of a positively charged accumulation layer in the bottom of the DH6T layer (Fig. 6b); the holes injected from the Au electrodes are transferred into the DH6T layer with high hole mobility (Table 1) to form the active channel placed near the organic interface. Since P13 is an electron-transporting material with negligible hole mobility, the formation of such an active channel does not take place in the P13 layer. Instead, due to the positive charges placed at the interface, the favorable electrostatic interaction induces the attraction of the negative charges in the P13 layer with high electron mobility, leading to formation of the DH6T/P13 dipole layer. Afterwards, upon application of the proper negative drain voltage, the mobile holes can flow into the P13 layer and some carrier recombination takes place to form the exciton leading to the observed electroluminescence (Fig. 6c). Here, since P13 has a smaller energy gap and the higher energy barrier for hole transport from DH6T to P13 exists compared to that for the electron transport from P13 to DH6T, most light emission is highly likely to occur in the P13 layer. Our observation of the luminescence process stands in contrast with the measurements for the  $\alpha,\omega$ -dihexylquaterthiophene (DH4T)/P13-based ambipolar OLEFETs conducted under vacuum conditions by Dinelli et al. [19]. While the  $V_{GS}$  dependence of the emission intensity examined under vacuum conditions was similar to that in this study, the light emission due to the balanced transport was reported to occur only when the DH4T layer was placed at the bottom, in direct contact with the dielectric, irrespective of the deposition sequence of the two layers. Further experimental and theoretical investigations related to the conduction mechanisms of bilayer heterojunction-based OLEFETs are required.

#### 4. Summary

The air-stable, heterojunction-based OLEFETs with well-balanced ambipolarity were fabricated for the first time, and good field-effect characteristics, stress-free operational stability, and electroluminescence were demonstrated under ambient conditions. Fabrication and characterization of several OLEFETs using various  $\pi$ -conjugated molecules through the NCBD method are underway. We hope these studies to provide further insights into the operating mechanisms and the structure-performance relationships at the molecular level.

#### Acknowledgments

This work was supported by a Korea University grant and a Korea Science and Engineering Foundation (KOSEF)

grant funded by the Korea government (MEST) (No. M1050000023-06J0000-02310).

#### References

- [1] G. Horowitz, D. Fichou, X. Peng, Z. Xu, F. Garnier, *Solid State Commun.* 72 (1989) 381.
- [2] H. Sirringhaus, N. Tessler, R.H. Friend, *Science* 280 (1998) 1741.
- [3] R.H. Friend, R.W. Gymer, A.B. Holmes, J.H. Burroughes, R.N. Marks, C. Taliani, D.D.C. Bradley, D.A. Dos Santos, J.L. Bredas, M. Logdlund, W.R. Salaneck, *Nature (London)* 397 (1999) 121.
- [4] C.W. Tang, S.A. VanSlyke, *Appl. Phys. Lett.* 51 (1987) 913.
- [5] T.N. Jackson, Y.Y. Lin, D.J. Gundlach, H. Klauk, *IEEE J. Sel. Top. Quantum Electron.* 4 (1998) 100.
- [6] A. Hepp, H. Heil, W. Weise, M. Ahles, R. Schmechel, H.V. Seggern, *Phys. Rev. Lett.* 91 (2003) 157406.
- [7] C. Santato, R. Capelli, M.A. Loi, M. Murgia, F. Cicoira, V.A.L. Roy, P. Stallinga, R. Zamboni, C. Rost, S.F. Karg, M. Muccini, *Synth. Met.* 146 (2004) 329.
- [8] C. Santato, I. Manunza, A. Bonfiglio, F. Cicoira, P. Cosseddu, R. Zamboni, M. Muccini, *Appl. Phys. Lett.* 86 (2004) 141106.
- [9] J. Reynaert, D. Cheyns, D. Janssen, R. Muller, V.I. Arkhipov, J. Genoe, G. Borghs, P. Heremans, *J. Appl. Phys.* 97 (2005) 114501.
- [10] C. Santato, F. Cicoira, P. Cosseddu, A. Bonfiglio, P. Bellutti, M. Muccini, R. Zamboni, F. Rosei, A. Mantoux, P. Doppelt, *Appl. Phys. Lett.* 88 (2006) 163511.
- [11] T. Takahashi, T. Takenobu, J. Takeya, Y. Iwasa, *Adv. Funct. Mater.* 17 (2007) 1623.
- [12] T. Takenobu, S.Z. Bisri, T. Takahashi, M. Yahiro, C. Adachi, Y. Iwasa, *Phys. Rev. Lett.* 100 (2008) 066601.
- [13] M. Muccini, *Nat. Mater.* 5 (2006) 605.
- [14] F. Cicoira, C. Santato, *Adv. Funct. Mater.* 17 (2007) 3421.
- [15] C. Rost, S. Karg, W. Riess, M.A. Loi, M. Murgia, M. Muccini, *Appl. Phys. Lett.* 85 (2004) 1613.
- [16] C. Rost, S. Karg, W. Riess, M.A. Loi, M. Murgia, M. Muccini, *Synth. Met.* 146 (2004) 237.
- [17] J. Zaumseil, R.H. Friend, H. Sirringhaus, *Nat. Mater.* 5 (2006) 69.
- [18] M.A. Loi, C. Rost-Bietsch, M. Murgia, S. Karg, W. Riess, M. Muccini, *Adv. Funct. Mater.* 16 (2006) 41.
- [19] F. Dinelli, R. Capelli, M.A. Loi, M. Muccini, A. Facchetti, T.J. Marks, *Adv. Mater.* 18 (2006) 1416.
- [20] J. Zaumseil, C.L. Donley, J.-S. Kim, R.H. Friend, H. Sirringhaus, *Adv. Mater.* 18 (2006) 2708.
- [21] R. Capelli, F. Dinelli, M.A. Loi, M. Murgia, R. Zamboni, M. Muccini, *J. Phys.: Condens. Matter* 18 (2006) S2127.
- [22] C. Di, G. Yu, Y. Liu, X. Xu, D. Wei, Y. Song, Y. Sun, Y. Wang, D. Zhu, *Adv. Funct. Mater.* 17 (2007) 1567.
- [23] J. Zaumseil, C.R. McNeill, M. Bird, D.L. Smith, P.P. Ruden, M. Roberts, M.J. McKiernan, R.H. Friend, H. Sirringhaus, *J. Appl. Phys.* 103 (2008) 064517.
- [24] J.-Y. Kim, E.-S. Kim, J.-H. Choi, *J. Appl. Phys.* 91 (2002) 1944.
- [25] H.-S. Seo, Y.-S. Jang, Y. Zhang, P.S. Abthagir, J.-H. Choi, *Org. Electron.* 9 (2008) 432.
- [26] H.-S. Seo, Y. Zhang, Y.-S. Jang, J.-H. Choi, *Appl. Phys. Lett.* 92 (2008) 223310.
- [27] Y. Zhang, H.-S. Seo, M.-J. An, J.-H. Choi, *Org. Electron.* 10 (2009) 895.
- [28] H. Lim, J.-H. Choi, *J. Chem. Phys.* 124 (2006) 014710.
- [29] P.S. Abthagir, Y.-G. Ha, E.-A. You, S.-H. Jeong, H.-S. Seo, J.-H. Choi, *J. Phys. Chem. B* 109 (2005) 23918.
- [30] Y.-G. Ha, E.-A. You, B.-J. Kim, J.-H. Choi, *Synth. Met.* 153 (2005) 205.
- [31] E.-A. You, Y.-G. Ha, Y.-S. Choi, J.-H. Choi, *Synth. Met.* 153 (2005) 209.
- [32] M. Kim, B.-H. Jeon, J.-Y. Kim, J.-H. Choi, *Synth. Met.* 135–136C (2003) 743.
- [33] H. Lim, B.-J. Kim, J.-H. Choi, *Synth. Met.* 135–136C (2003) 81.
- [34] S.J. Kang, M. Noh, D.S. Park, H.J. Kim, C.N. Whang, C.H. Chang, *J. Appl. Phys.* 95 (2004) 2293.
- [35] D. Guo, S. Entani, S. Ikeda, K. Saiki, *Chem. Phys. Lett.* 429 (2006) 124.
- [36] S. Tatemichi, M. Ichikawa, T. Koyama, Y. Taniguchi, *Appl. Phys. Lett.* 89 (2006) 112108.

promising technique for eliminating the need for alternating organic/inorganic stacks in the encapsulation of organic electronics, because of its unique capability of forming defect-free inorganic films at low temperatures [20–22]. Thin-film encapsulation of organic light-emitting diodes and small-molecule organic PVs using a single-layer ALD  $\text{Al}_2\text{O}_3$  film, either with or without an organic capping layer, has been attempted with promising results [23–25], but has not been reported for polymer bulk-heterojunction PVs.

In this study, ALD was employed to deposit inorganic metal oxide thin films to encapsulate polymer bulk-heterojunction PVs, where blended poly-3-hexothiothiophene (P3HT) and [6,6]-phenyl C61 butyric acid methylester (PCBM) comprised the active layer. The objectives were: (1) eliminating  $\text{O}_2/\text{H}_2\text{O}$ -caused degradations to the PVs' characteristics and (2) achieving high efficiency in the encapsulated PVs. The effects of the temperature and duration of the ALD process on the efficiency of the encapsulated PVs were determined to select the optimal settings. The intrinsic degradation rate of the PVs, i.e., the degradation rate under  $\text{O}_2/\text{H}_2\text{O}$ -free environment, was determined as a baseline, against which the encapsulated PVs were evaluated. Two types of ALD films,  $\text{Al}_2\text{O}_3$  and an  $\text{Al}_2\text{O}_3/\text{HfO}_2$  nanolaminate, were tested, and their gas permeation rate and microstructure were determined to improve their effectiveness as encapsulating films.

## 2. Experimental

### 2.1. Device fabrication and characterization

The cross-sectional structure of the PV devices used in this study from anode to cathode was: indium tin oxide (ITO)/poly(3,4-ethylenedioxythiophene):poly(styrenesulfonate) (PEDOT:PSS)/P3HT:PCBM/Al/encapsulation, as illustrated in Fig. 1a. The PEDOT:PSS layer (thickness = 50 nm) was spin-coated from Baytron PH500 (Bayer AG) followed by baking at 180 °C for 60 min in a glove box. The P3HT:PCBM layer (thickness = 110 nm) was spin-coated from a mixed solution of 1 wt.% P3HT ( $\text{Mn} = 50000 \text{ g mol}^{-1}$ , regioregularity = 98.5%, purchased from Rieke Metals and used as received) and 0.8 wt.% PCBM (purchased from Nano-C and used as received) in anhy-

drous chlorobenzene. The Al layer (thickness = 250 nm) was formed by thermal evaporation through a shadow mask under high vacuum ( $10^{-6}$  torr). The control devices were annealed at 140 °C for 60 min in the glove box followed by encapsulation with a glass lid sealed with UV-curable epoxy resin (A1438, Addison Clear Wave; used after degassing under vacuum for 2 h). The current density–voltage ( $J$ - $V$ ) characteristics of the devices were measured with a Keithley 2400 source meter under simulated AM1.5G illumination (ThermoOriel and ScienceTech solar simulators with integrated intensity =  $100 \text{ mW cm}^{-2}$ ), which was calibrated with a Hamamatsu silicon photodiode with KG-5 filter against an NREL-calibrated solar simulator. The lifetime of the devices, defined as the time required for the power conversion efficiency (PCE) to drop to 50% of the initial value, was measured by monitoring the change in their IV characteristics with the storage time either in air or in the glove box. All air storage tests reported in this work were conducted in ambient light at 28 °C and 60% relative humidity unless noted otherwise.

### 2.2. Atomic layer deposition

Savannah 100 ALD system by Cambridge Nanotech Inc. was used to deposit ALD  $\text{Al}_2\text{O}_3$  and  $\text{HfO}_2$  films. The  $\text{Al}_2\text{O}_3/\text{HfO}_2$  nanolaminated films were composed of 52 pairs of alternating 2 Å  $\text{Al}_2\text{O}_3$  and 3 Å  $\text{HfO}_2$  layers. The precursors used for  $\text{Al}_2\text{O}_3$  and  $\text{HfO}_2$  were trimethylaluminum (TMA)/ $\text{H}_2\text{O}$  and tetrakis(dimethylamido)hafnium (TDMAHF)/ $\text{H}_2\text{O}$ , respectively. The deposition temperature was 140 or 150 °C and the chamber pressure was 0.1 Torr. High-purity  $\text{N}_2$  (flow rate = 20 sccm) was used as carrier gas for the precursors. The ALD cycle for  $\text{Al}_2\text{O}_3$  consisted of the following steps: a 0.03 s pulse of TMA, a 5 s purge with  $\text{N}_2$ , a 0.02 s pulse of  $\text{H}_2\text{O}$ , and a 5 s purge with  $\text{N}_2$ ; the ALD cycle for  $\text{HfO}_2$  was the same except for the first step, which was a 0.1 s pulse of TDMAHF. It should be noted that the TMA and TDMAHF pulses were placed before the  $\text{H}_2\text{O}$  pulse to prevent incursion of  $\text{H}_2\text{O}$  into the devices, as the adsorbed TMA or TDMAHF molecules would rapidly consume the incoming  $\text{H}_2\text{O}$  molecules before they could enter the devices [22]. A cycle produced 1 Å and 1.2 Å for  $\text{Al}_2\text{O}_3$  and  $\text{HfO}_2$ , respectively, as determined by ellipsometry (EP3, Nanofilm Tech.). For the ALD process with a soak period for each of the precursors (during which the reactor contained a precursor without being pumped or purged), the steps in the cycle were a 0.1 s pulse of TMA, a 25 s soak, a 25 s purge with  $\text{N}_2$ , a 0.1 s pulse of  $\text{H}_2\text{O}$ , a 25 s soak, and a 25 s purge with  $\text{N}_2$ .

### 2.3. Surface characterization

Scanning electron microscopy (SEM) and energy-dispersive X-ray spectroscopy (EDX) analyses were conducted with a field-emission SEM (JSM-6700F, JEOL) operated at an accelerating voltage 10 kV, and the samples were coated a thin layer of platinum (~3 nm) before analysis. Water contact angles were measured using a Ramé-Hart contact angle goniometer (Model 100), where the sessile drop of 2–3  $\mu\text{l}$  in volume was dispensed with a microsyringe and the contact angle was measured within 30 s after its formation.

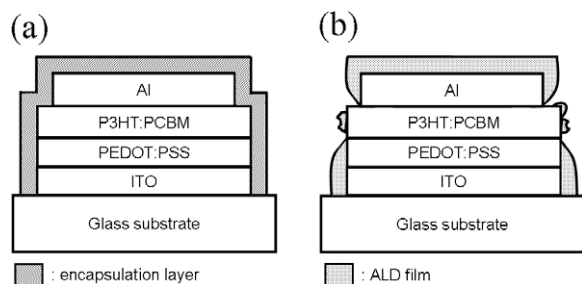


**Fig. 1.** Schematics of the cross-section of the PV devices: (a) encapsulated by a barrier film with complete coverage over all device surface and (b) encapsulated by a barrier film that has poor surface coverage over the P3HT/PCBM layer.

#### 2.4. Helium permeation measurement

The helium transmission rate (HeTR) of the ALD films was measured at room temperature with ALD films deposited on polyimide substrates (thickness = 50  $\mu\text{m}$ ; area = 5  $\text{cm}^2$ ). The samples were sealed with a rubber gasket between two isolated volumes, one of which contained He at constant 0.5 atm and the other of which was connected to a helium leak detector (ASM142, Alcatel). He molar flow rates through the samples were recorded with the leak detector, which divided by the sample area followed by subtracting the substrate contribution were the HeTR values. Detailed measurement setup and procedures can be found elsewhere [26].

### 3. Results and discussion

As the ALD encapsulation process was operated at elevated temperatures, it inevitably annealed the active layer and changed its morphology. Given that the performance of bulk-heterojunction polymer photovoltaics is crucially dependent upon the morphology of the active layer [27], it was important to determine the temperature and total time of the ALD process that would produce the optimal morphology. The effects of ALD time on the PCE of encapsulated cells are shown in Fig. 2 for two ALD temperatures, 140  $^{\circ}\text{C}$  and 150  $^{\circ}\text{C}$ . With both of the ALD temperatures, the PCE increased initially with increasing time, but the trend reversed after the PCE reaching an maximum at 30 and 60 min for 150 and 140  $^{\circ}\text{C}$ , respectively. This is similar to the effects of thermal annealing reported elsewhere [28,29]. Thermal annealing increases the PCE by inducing aggregation of the P3HT and the PCBM domains, which facilitates transport of charge carriers through the domains, but prolonged thermal annealing reduces the PCE by causing over-aggregation of the domains, which excessively reduces the bulk-heterojunction area that is critical for charge generation. We verified that the heating action of the ALD process was the sole cause of the observed encapsulation-induced changes in the PCE, as devices that

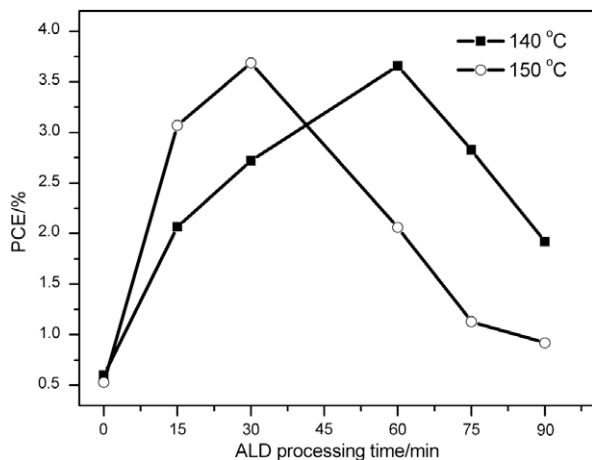


Fig. 2. PCE of the ALD-encapsulated devices versus the ALD processing time at 140  $^{\circ}\text{C}$  or 150  $^{\circ}\text{C}$ .

were thermally annealed (without the ALD process) under the same temperature/time condition as those of the ALD process showed almost identical after-annealing characteristics to those of the ALD-encapsulated devices (Fig. 3 and Table 1). This also indicates that the ALD precursors, although highly reactive, did not cause damage to the devices during the encapsulation process. Of the two ALD temperatures tested, 140  $^{\circ}\text{C}$  was used in the rest of this study because its optimal time in terms of the PCE of encapsulated devices, 60 min, allowed greater flexibility in fine-tuning the conditions of the ALD process.

To accurately evaluate the effectiveness of our encapsulation methods, i.e., their capability of blocking  $\text{O}_2$  and  $\text{H}_2\text{O}$  from air, we first determined the degradation profile of control devices in an  $\text{O}_2$ - and  $\text{H}_2\text{O}$ -free environment, as shown in Fig. 4, against which we compared the degradation profiles of encapsulated devices stored in air. The control devices (annealed at 140  $^{\circ}\text{C}$  for 60 min without undergoing ALD) were encapsulated with adhesive-sealed glass plates and then stored in a glove box with below 0.5 ppm  $\text{O}_2$  and  $\text{H}_2\text{O}$  concentrations to minimize any possible  $\text{O}_2$  or  $\text{H}_2\text{O}$  incursion. As can be seen in Fig. 4, the control devices degraded slowly but significantly even in the nominally  $\text{O}_2/\text{H}_2\text{O}$ -free environment. This degradation behavior agrees with those reported elsewhere for P3HT/PCBM bulk-heterojunction PVs whose morphology were optimized with thermal annealing or controlled drying and whose initial PCE were >2.4% [30]. We attribute the inherent instability of the cells to two known mechanisms: (1) reaction of the aluminum cathode with P3HT/PCBM under sun light [30,31], and (2) gradual shift in the P3HT/PCBM morphology from the optimum that was initially achieved by thermal annealing [32]. It should be noted that the PCE stabilized after reaching  $\sim 1.6\%$  (45% of initial PCE) and remained above 1.4% (40% of initial PCE) for over 3000 h, which was consistent with the reported stability of P3HT/PCBM bulk-heterojunction PVs whose initial PCE was low (<1%) [33]. The degradation profile of the glass-encapsulated control devices stored in air was also determined

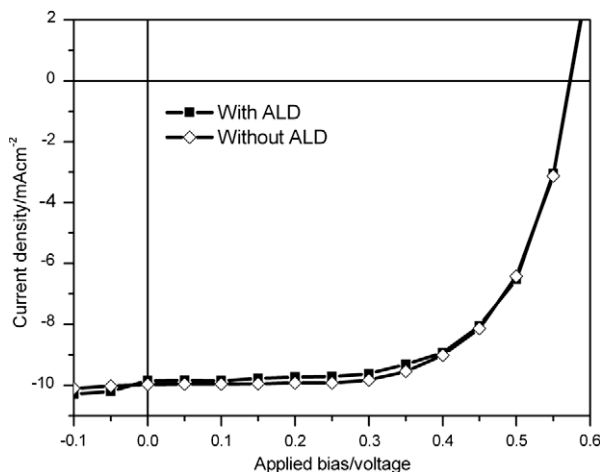


Fig. 3.  $J$ - $V$  characteristics of a device encapsulated with the ALD  $\text{Al}_2\text{O}_3$  process at 140  $^{\circ}\text{C}$  for 60 min and another device annealed at 140  $^{\circ}\text{C}$  for 60 min without undergoing ALD.

**Table 1**  
Characteristics of the devices plotted in Fig. 3.

Condition	$V_{oc}$ (volt)	$J_{sc}$ (mA/cm <sup>2</sup> )	FF (%)	PCE (%)
With ALD encapsulation	0.58	9.85	63.4	3.62
With annealing, but without ALD	0.58	9.98	63.2	3.66

$V_{oc}$ : open-circuit voltage.

$J_{sc}$ : short-circuit current density.

FF: fill factor.

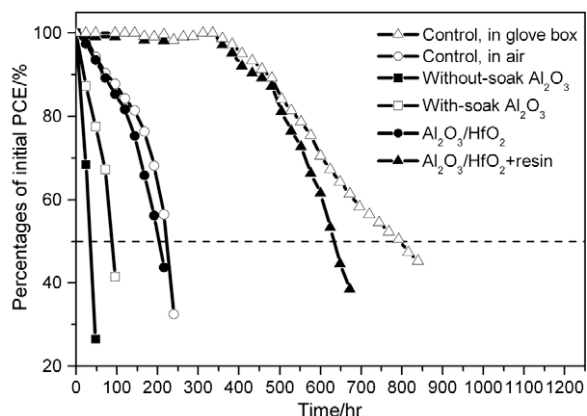


**Fig. 4.** Degradation profiles of the devices with various encapsulations. All profiles except for that of the control were measured over storage in air at 28 °C with 60% relative humidity. The initial PCE of the devices ranged from 3.1% to 3.7%. The  $\text{Al}_2\text{O}_3/\text{HfO}_2$  nanolaminated films were made with the with-soak process.

(also shown in Fig. 4): They degraded much more quickly than stored in the glove box, indicating that degradation caused by  $\text{O}_2$  and  $\text{H}_2\text{O}$  permeating through the adhesive at the device perimeter was significant. It was this  $\text{O}_2$ - and  $\text{H}_2\text{O}$ -caused degradation that this study aimed to eliminate, and the issue of inherent instability is the topic of our ongoing work and will not be discussed here.

In encapsulating the PVs with ALD films, we observed three issues: (1) poor nucleation of ALD films on the surface of the P3HT/PCBM active layer that was exposed at the edges of the devices, which led to incomplete coverage of the ALD films (and therefore incomplete encapsulation) at the device edges (see Fig. 1b for a schematic illustration); (2) rapid hydrolysis of the ALD films in air, which caused the encapsulating films to disintegrate as the devices aged; (3) susceptibility of the ALD films to mechanical damages during device characterization and handling. As can be seen in Fig. 1, the device surfaces to be encapsulated by the ALD film included the Al cathode, the PCBM/P3HT active layer, the PEDOT:PSS layer and the ITO anode. Among the surfaces, the PCBM/P3HT layer was hydrophobic and therefore difficult for the ALD film to nucleate [34], while the other layers contained hydroxyl groups at their surfaces as chemisorption sites for facile ALD nucleation [35] and were therefore well-nucleated (see Supplementary materials). The poor nucleation of ALD films on P3HT/PCBM was observable with SEM and EDS. The surface of a P3HT/PCBM film coated with a 5 nm ALD  $\text{Al}_2\text{O}_3$  layer appeared highly inhomogeneous under SEM (Fig. 5a), and EDS analyses (Fig. 5c and d) confirmed that the surface contained both  $\text{Al}_2\text{O}_3$ -coated (bright patches in SEM) and uncoated or little-coated areas (dark patches); on the other

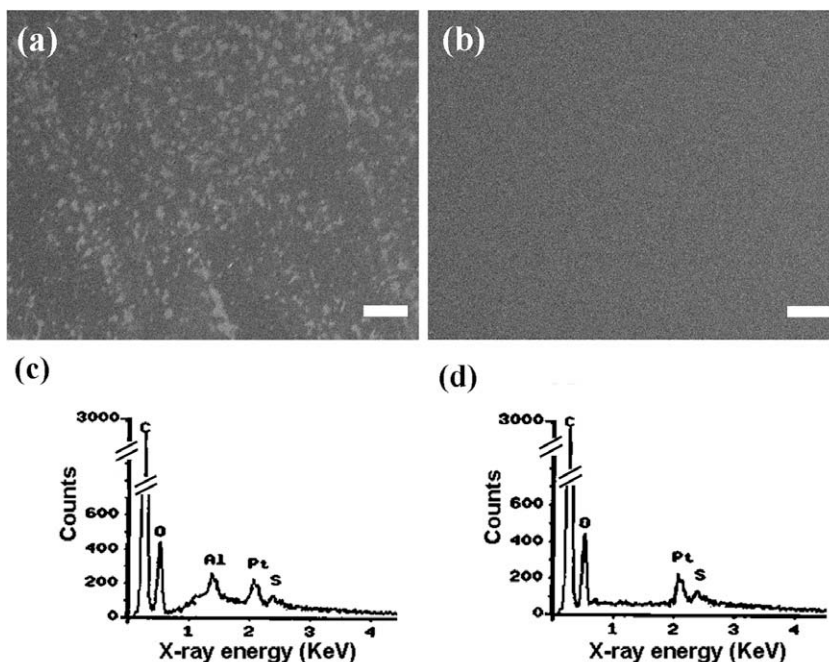


**Fig. 5.** SEM images of the ALD  $\text{Al}_2\text{O}_3$  films deposited on a P3HT/PCBM film (a) without-soak, and (b) with-soak. The scale bars are 1  $\mu\text{m}$ . (c) EDS spectrum taken at the bright patches in (a); (d) EDS spectrum taken at the dark patches in (a).

hand, the ALD-coated Al, ITO and PEDOT:PSS surfaces were homogeneous (featureless) under SEM and were not shown. The poor nucleation was due to the lack of chemisorption sites (e.g.  $-OH$  groups) on the P3HT/PCBM surface. Nucleation of the ALD films was improved by employing a 25 s soak period for each of the ALD precursors in the first 5 cycles of the ALD process. The soak periods improved nucleation by allowing more precursor molecules to adhere to the P3HT/PCBM surface through physisorption/absorption, thereby improving surface coverage and uniformity of the ALD films. The improvement can be seen in the SEM image in Fig. 5b, where the P3HT/PCBM surface was free of heterogeneous features after being coated with the with-soak ALD process. In terms of the degradation rate of encapsulated devices, the with-soak ALD process also showed significant improvement over the without-soak process, as shown in Fig. 4: with a 26 nm ALD  $Al_2O_3$  film as encapsulation, the devices encapsulated using the with-soak process had  $\sim 2.5$ -fold longer in-air lifetime than the devices encapsulated using the without-soak process. However, even with the nucleation issue addressed, the ALD-encapsulated devices still showed significant air-induced degradation, as determined by comparing the degradation profile with that of the control. This was attributed

to hydrolysis of the  $Al_2O_3$  films upon exposure to humidity in air, which created defects in the  $Al_2O_3$  films.

The degradation of the ALD  $Al_2O_3$  films during storage in air was evident under SEM (Fig. 6b), which shows severe delamination of a  $Al_2O_3$  film from the device surface after 200 h. Meanwhile, the water contact angle of the film's surface (insets of Fig. 6b) also greatly reduced, from  $68^\circ$  to  $23^\circ$ . Conversely, films stored in lower humidity (30% relative humidity instead of 60%) were able to withstand longer storage before delaminating. In terms of barrier performance, the helium transmission rate (HeTR) through the  $Al_2O_3$  films increased by a factor of  $\sim 7$  after 50 h of storage in air, which was due to defects created by the delamination. The fact that degradation was faster at higher humidity and that the  $Al_2O_3$  surface became more hydrophilic upon air exposure indicated that hydrolysis was the cause of the degradation, given the strong tendency of  $Al_2O_3$  to hydrolyze into  $Al(OH)_x$  [36]. Because of the low thickness of the ALD films, the effects of hydrolysis, including volume expansion and micro-structural changes, can occur not only at the surface but also throughout the bulk of the films, and therefore the degradation was much more pronounced than with thicker films. The resistance to hydrolysis was greatly increased in the  $Al_2O_3/HfO_2$

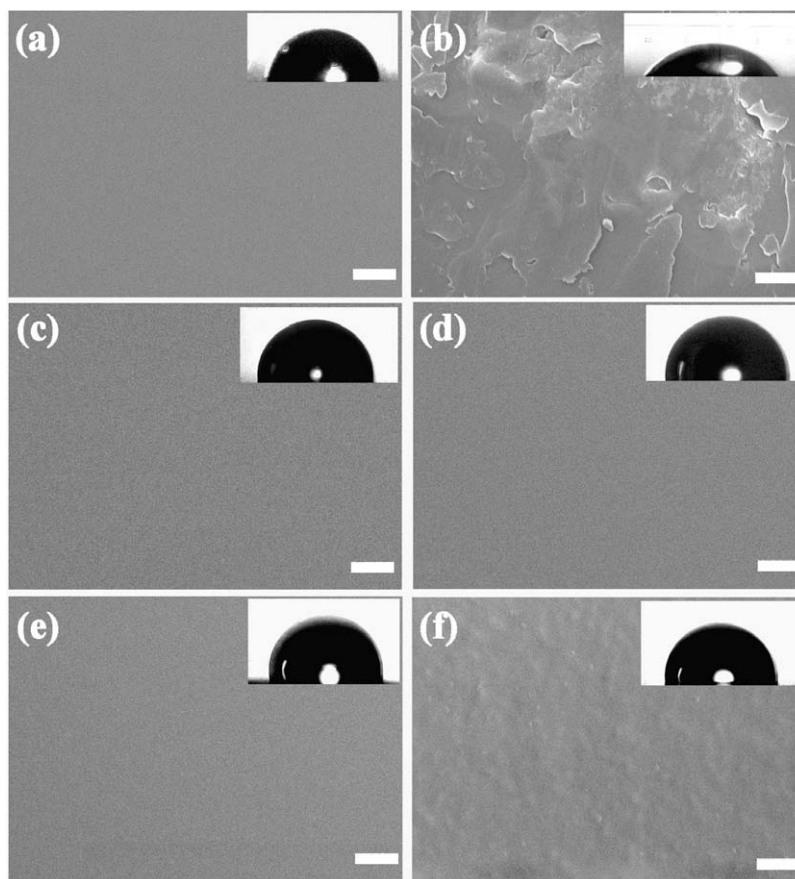


**Fig. 6.** SEM images and water contact angles (inset) of ALD films deposited on the solar cells, before and after storage in air at  $28^\circ C$  with 60% relative humidity: (a) as-deposited  $Al_2O_3$ , (b)  $Al_2O_3$  after storage, (c) as-deposited  $Al_2O_3/HfO_2$  nanolaminate, (d)  $Al_2O_3/HfO_2$  nanolaminate after storage, (e) as-deposited two-layer  $Al_2O_3/HfO_2$  and (f) two-layer  $Al_2O_3/HfO_2$  after storage. The scale bars in the SEM images are  $1\ \mu m$ .



nanolaminated films, where the  $\text{HfO}_2$  layers, being more hydrophobic than  $\text{Al}_2\text{O}_3$  (water contact angle =  $89^\circ$  for  $\text{HfO}_2$  versus  $68^\circ$  for  $\text{Al}_2\text{O}_3$ , see insets of Fig. 6), served as moisture barriers that prevented humidity from building up in the  $\text{Al}_2\text{O}_3$  layers. The increased resistance to humidity can be seen in the SEM images and water contact angle measurements shown in Fig. 6c and d. Upon being stored for 200 h in air, the surface of the  $\text{Al}_2\text{O}_3/\text{HfO}_2$  nanolaminated films remained free of defects under SEM; moreover, the water contact angle remained constant at  $89^\circ$ , which is the characteristic value of  $\text{HfO}_2$  surface [37]. The absence of hydrolysis-induced damage in the nanolaminates was also confirmed by their constant HeTR over >400 h of storage in air, as shown in Fig. 7. With good hydrolysis-resistance, the  $\text{Al}_2\text{O}_3/\text{HfO}_2$  nanolaminated films were significantly more effective encapsulation for the devices than  $\text{Al}_2\text{O}_3$ , slowing the degradation rate by  $\sim 2$  folds (Fig. 4). It should be noted that a two-layer  $\text{Al}_2\text{O}_3/\text{HfO}_2$  laminate (a 12 nm  $\text{Al}_2\text{O}_3$  layer capped with a 14 nm  $\text{HfO}_2$  layer) was also tested and found less effective than the multilayer nanolaminate, as shown in Fig. 6e and f, where the two-layer laminate still showed hydrolysis-induced delamination. This may be due to the crystalline nature of ALD  $\text{HfO}_2$  films, which yields ample grain boundaries as rapid gas-diffusion pathways and therefore were not effective  $\text{H}_2\text{O}$  barriers for the underlying  $\text{Al}_2\text{O}_3$  layer [38,39]. The hydrolysis-resistance of the multilayer nanolaminate, on the other hand, is attributed to the interspersed  $\text{Al}_2\text{O}_3$  layers, which amended defects in the underlying  $\text{HfO}_2$  layers and enhanced nucleation of the overcoated  $\text{HfO}_2$  layers.

The  $\text{Al}_2\text{O}_3/\text{HfO}_2$ -encapsulated devices, however, required a UV-curable epoxy resin film as a capping layer to approach the degradation profile of the control, as shown in Fig. 4. The requirement of the capping layer may be attributed to following two reasons. Firstly, the  $\text{Al}_2\text{O}_3/\text{HfO}_2$  film was susceptible to accidental damages during device characterization and handling due to its small thickness, and the resin layer provided mechanical protection. Notably, the role of the resin layer as an additional permeation barrier was minimal because of its much

higher permeability than the oxide layer (by several orders of magnitude [18]). Secondly, the hydrophobicity of the PCBM/P3HT surface may still have caused small defects in the ALD film even with the with-soak process employed. This would suggest that the PCBM/P3HT surface may be more difficult for ALD nucleation than the C60/pentacene surface studied elsewhere, where a 200 nm ALD  $\text{Al}_2\text{O}_3$  film was found adequate as an encapsulating film for C60/pentacene bulk-heterojunction solar cells [25]. It should be noted that in addition to the 26 nm ALD encapsulating films, we also tested thicker films (100–200 nm) and found that they yielded poorer results (see Supplementary materials). This may be accounted for with the two following mechanisms: (1) the barrier performance of ALD films plateaus in the 10–30 nm thickness range, above which little improvement is gained [20,21]; (2) the processing time for depositing the thicker films was longer than what was optimal (60 min at  $140^\circ\text{C}$ ) in terms of the annealing effect, and therefore the resulted devices were over-annealed and more prone to degradation.

#### 4. Conclusion

A two-layer thin-film encapsulation structure, which consisted of an 26 nm ALD  $\text{Al}_2\text{O}_3/\text{HfO}_2$  nanolaminated film and a UV-curable epoxy resin film, effectively protected P3HT/PCBM bulk-heterojunction photovoltaic cells from degradations caused by ambient gases, allowing the cells to show in-air degradation profile that was nearly identical to that of the control devices stored in a nominally  $\text{O}_2/\text{H}_2\text{O}$ -free environment. The ALD process also served as a thermal annealing step, which upon optimization in terms of temperature and processing time resulted in a 3.66% initial PCE. The surface coverage of the ALD films over the P3HT/PCBM surface was improved by employing a precursor soaking step, which enhanced nucleation. The nanolaminated structure prevented the  $\text{Al}_2\text{O}_3$  layers from hydrolysis-induced disintegration in the presence of humidity, as the  $\text{HfO}_2$  layers served as hydrophobic barriers against moisture while the  $\text{Al}_2\text{O}_3$  layers amending

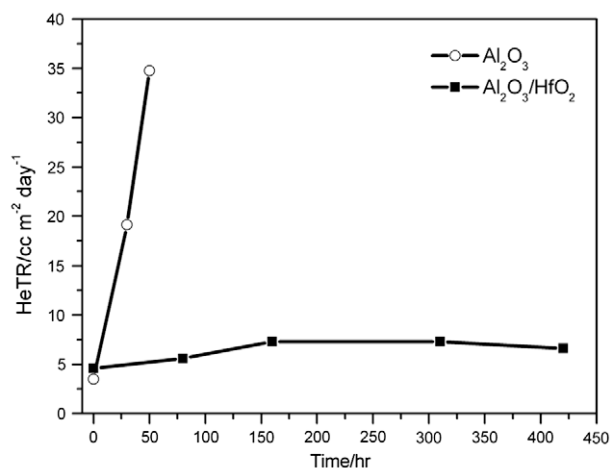


Fig. 7. HeTR of the ALD  $\text{Al}_2\text{O}_3$  film and  $\text{Al}_2\text{O}_3/\text{HfO}_2$  nanolaminate versus storage time in air at  $28^\circ\text{C}$  with 60% relative humidity.

defects in and enhancing nucleation of the HfO<sub>2</sub> layers, thereby enabling the nanolaminated films to maintain constant barrier performance over time in air. The significant inherent degradation of the devices, i.e., degradation unrelated to ambient gases, were attributed to reaction of the cathode with the active layer and change in the morphology of the active layer, and it will be addressed through non-encapsulation means that is the subject of our ongoing work.

### Acknowledgements

This work was supported by Ministry of Economics Affairs (Grant No.: 97-EC-17-A-08-S1-015), National Science Council (Grants No. NSC 96-2221-E-002-143-MY3, 98-ET-E-002-007-ET, and 97-2218-E-002-012-), and Chung-Shan Institute of Science and Technology. The authors thank Profs. Wen-Chang Chen and Kuo-Huang Hsieh for providing device characterization equipments and inputs on the analysis of experimental results.

### Appendix A. Supplementary data

Supplementary data associated with this article can be found, in the online version, at doi:10.1016/j.orgel.2009.07.008.

### References

- [1] J.Y. Kim, K. Lee, N.E. Coates, D. Moses, T.-Q. Nguyen, M. Dante, A.J. Heeger, *Science* 317 (2007) 222.
- [2] S. Gunes, H. Neugebauer, N.S. Sariciftci, *Chem. Rev.* 107 (2007) 1324.
- [3] B.C. Thompson, J.M.J. Fréchet, *Angew. Chem. Int. Ed.* 47 (2008) 58.
- [4] K.M. Coakley, M.D. McGehee, *Chem. Mater.* 16 (2004) 4533.
- [5] M. Jorgensen, K. Norrman, F.C. Krebs, *Sol. Energy Mater. Sol. Cells* 92 (2008) 686.
- [6] K. Kawano, R. Pacios, D. Poplavskyy, J. Nelson, D.D.C. Bradley, J.R. Durrant, *Sol. Energy Mater. Sol. Cells* 90 (2006) 3520.
- [7] D. Gupta, M. Bag, K.S. Narayana, *Appl. Phys. Lett.* 92 (2008) 093301.
- [8] B. Paci, A. Generosi, V.R. Albertini, P. Perfetti, R. de Bettignies, M. Firon, J. Leroy, C. Sentein, *Appl. Phys. Lett.* 87 (2005) 194110.
- [9] B. Paci, A. Generosi, V.R. Albertini, P. Perfetti, R. de Bettignies, J. Leroy, M. Firon, C. Sentein, *Appl. Phys. Lett.* 89 (2006) 043507.
- [10] K. Norrman, N.B. Larsen, F.C. Krebs, *Sol. Energy Mater. Sol. Cells* 90 (2006) 2793.
- [11] M. Drees, H. Hoppe, C. Winder, H. Neugebauer, N.S. Sariciftci, W. Schwinger, F. Schaeffler, C. Topf, M.C. Scharber, Z. Zhu, R. Gaudiana, *J. Mater. Chem.* 15 (2005) 5158.
- [12] C.H. Woo, B.C. Thompson, B.J. Kim, M.F. Toney, J.M.J. Fréchet, *J. Am. Chem. Soc.* 130 (2008) 16324.
- [13] S. Bertho, G. Janssen, T.J. Cleij, B. Conings, W. Moons, A. Gadisa, J. D'Haen, E. Goovaerts, L. Lutsen, J. Manca, D. Vanderzande, *Sol. Energy Mater. Sol. Cells* 92 (2008) 753.
- [14] G. Dennler, C. Lungenschmied, H. Neugebauer, H.S. Sariciftci, M. Latreche, G. Czeremuszkin, M.R. Wertheimer, *Thin Solid Films* 511 (2006) 349.
- [15] C. Lungenschmied, G. Dennler, H. Neugebauer, S.N. Sariciftci, M. Glatthaar, T. Meyer, A. Meyer, *Sol. Energy Mater. Sol. Cells* 91 (2007) 379.
- [16] M.S. Weaver, L.A. Michalski, K. Rajan, M.A. Rothman, J.A. Silvernail, J.J. Brown, P.E. Burrows, G.L. Graff, M.E. Gross, P.M. Martin, M. Hall, E. Mast, C. Bonham, W. Bennett, M. Zumhoff, *Appl. Phys. Lett.* 81 (2002) 2929.
- [17] J.S. Lewis, M. Weaver, *IEEE J. Sel. Top. Quantum Electron.* 10 (2004) 45.
- [18] G.L. Graff, R.E. Williford, P.E. Burrows, *J. Appl. Phys.* 96 (2004) 1840.
- [19] J. Granstrom, J.S. Swensen, J.S. Moon, G. Rowell, J. Yuen, A.J. Heeger, *Appl. Phys. Lett.* 93 (2008) 193304.
- [20] M.D. Groner, S.M. George, R.S. McLean, P.F. Carcia, *Appl. Phys. Lett.* 88 (2006) 051907.
- [21] E. Langereis, M. Creatore, S.B.S. Heil, M.C.M. van de Sanden, W.M.M. Kessels, *Appl. Phys. Lett.* 89 (2006) 081915.
- [22] C.-Y. Chang, F.-Y. Tsai, S.-J. Jhuo, M.-J. Chen, *Org. Electron.* 9 (2008) 667.
- [23] A.P. Ghosh, L.J. Gerenser, C.M. Jarman, J.E. Fornalik, *Appl. Phys. Lett.* 86 (2005) 223503.
- [24] S.-H.K. Park, J. Oh, C.-S. Hwang, J.-I. Lee, Y.S. Yang, H.Y. Chu, *Electrochem. Solid-State Lett.* 8 (2005) H21.
- [25] W.J. Potscavage, S. Yoo, B. Domercq, B. Kippelen, *Appl. Phys. Lett.* 90 (2007) 253511.
- [26] F.-Y. Tsai, E.L. Alfonso, D.R. Harding, S.H. Chen, *J. Phys. D: Appl. Phys.* 34 (2001) 3011.
- [27] W. Ma, C. Yang, X. Gong, K. Lee, A.J. Heeger, *Adv. Funct. Mater.* 15 (2005) 1617.
- [28] M. Reyes-Reyes, K. Kim, D.L. Carroll, *Appl. Phys. Lett.* 87 (2005) 083506.
- [29] K. Inoue, R. Ulbricht, P.C. Madakasira, W.M. Sampson, S. Lee, J. Gutierrez, J.P. Ferraris, A.A. Zakhidov, *Synth. Met.* 154 (2005) 41.
- [30] B. Paci, A. Generosi, V.R. Albertini, R. Generosi, P. Perfetti, R. de Bettignies, C. Sentein, *J. Phys. Chem. C* 112 (2008) 9931.
- [31] B. Paci, A. Generosi, V.R. Albertini, P. Perfetti, R. de Bettignies, C. Sentein, *Sol. Energy Mater. Sol. Cells* 92 (2008) 799.
- [32] M.O. Reese, A.J. Morfa, M.S. White, N. Kopidakis, S.E. Shaheen, G. Rumbles, D.S. Ginley, *Sol. Energy Mater. Sol. Cells* 92 (2008) 746.
- [33] F.C. Krebs, *Sol. Energy Mater. Sol. Cells* 90 (2006) 3633.
- [34] C.A. Wilson, R.K. Grubbs, S.M. George, *Chem. Mater.* 17 (2005) 5625.
- [35] B.C. Bunker, G.C. Nelson, K.R. Zavadil, J.C. Barbour, F.D. Wall, J.P. Sullivan, C.F. Windisch Jr., M.H. Engelhardt, D.R. Baer, *J. Phys. Chem. B* 106 (2002) 4705.
- [36] J.R. Scott, G.S. Groenewold, A.K. Gianotto, M.T. Benson, *J. Phys. Chem. A* 104 (2000) 7079.
- [37] T. Nishide, S. Honda, M. Matsuda, M. Ide, *Thin Solid Films* 371 (2000) 61.
- [38] S.J. Ding, D.W. Zhang, L.-K. Wang, *J. Phys. D: Appl. Phys.* 40 (2007) 1072.
- [39] M.S. Joo, B.J. Cho, C.C. Yeo, D.S. Chan, S.J. Whoang, S. Mathew, L.K. Bera, N. Balasubramanian, D.L. Kwong, *IEEE Trans. Electron Dev.* 50 (2003) 2088.

molecular systems. For example, charge separation by internal photoemission and exciton dissociation were distinguished by surface photovoltage spectroscopy in porphyrin layers deposited on gold [11].

A possible strategy to engineer surface work functions is related to the deposition of oriented molecules with donor–acceptor pairs (D–A), in which the A and D units are strong electron-withdrawing and electron-donating moieties, respectively. The appropriate choices of the molecular geometry and the A and D units characteristics allows the control of the dipole direction and magnitude. Furthermore, it is possible to tune the metal work function using molecular structures that hold D–A moieties with the capacity to form electropolymerized films over the metal surface. The electrochemical polymerization permits fine control over thickness and polymer properties; allowing to obtain stable and reproducible organic films over metal electrode. In this way, Shi et al. recently showed the capability of electrochemically deposited poly(3,4-ethylenedioxythiophene) (PEDOT) derivatives in the tuning of gold and ITO work functions [12].

In this work, we report the changes on gold surface work function by electropolymeric spirobifluorene-based bipolar films obtained from the monomers shown in Fig. 1. Recently, has been reported the electro-optical properties of polymer thin films on conducting substrate obtained by electropolymerization of pendant electroactive triphenylamine (TPA) units in spirofluorene derivatives [13–18]. Also, endcapping polyfluorenes with hole-transporting moieties showed the improvement of the performance of OLEDs [19–22]. The spiro linkage improves the morphological stability of the materials while retaining their electrical properties [23]. Moreover, the perpendicular arrangement of the two molecular halves leads to a high steric demand of the resulting rigid structure, efficiently suppressing molecular interactions between the  $\pi$ -systems [23]. In the present case, the spiro configuration

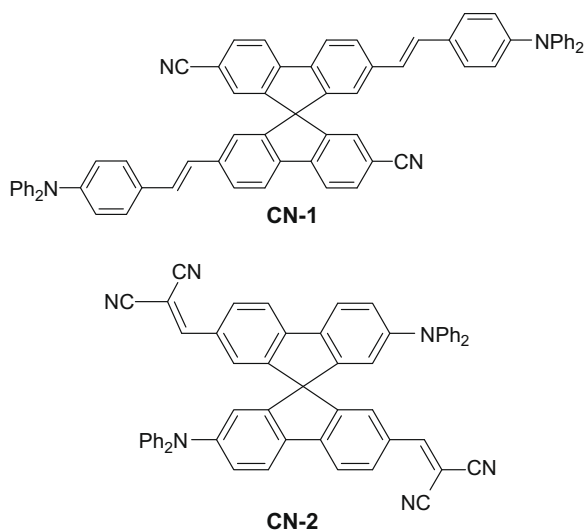


**Fig. 1.** Molecular structures of the spirobifluorene donor–acceptor bipolar systems.

that bonds perpendicularly the two D–A moieties with a tetrahedral carbon impedes the  $\pi$ -orbital interaction between the different D–A substituents in the two molecular branches (Fig. 1). The electron-donating (D) moieties are TPA groups and the electron-withdrawing (A) are the cyano ones. In particular, **CN1** molecules showed the capability to form stable electrogenerated polymeric films. Meanwhile **CN2** is structurally related to **CN1**, but with higher electron acceptor capacity due to the presence of four cyano acceptor groups, and **CN2** does not form an electropolymer due to the stability of its radical cation [18]. Here, the electrodeposited layers of **CN1** were coated with **CN2** by dipping in solution to investigate the role of the presence of an acceptor surface layer on the polymeric film. Changes of the surface work function and charge separation were studied by measurements of the contact potential difference (CPD) and surface photovoltage spectra (SPV) [24] in Kelvin-probe arrangement [25,26] in order to distinguish charge separation mechanisms for different electronic transitions. It will be shown that spirobifluorene compounds with donor–acceptor pairs are suitable for engineering of the surface work function and open new opportunities in design and study of molecular architectures with applications in organic electronics.

## 2. Experimental

### 2.1. General

All the chemicals used were provided by Sigma–Aldrich in spectroscopic or electrochemical grade and used without purification. The synthesis and characterization of **CN1** and **CN2** molecules have been described elsewhere [18,27]. The **CN1** polymer was obtained both, as film by electropolymerization over Au electrode, and in solution by chemical oxidation reaction [28].

### 2.2. Sample preparation

Layers of **CN1** molecules were electro deposited on Au electrodes from 0.55 mM in acetonitrile (MeCN) solution containing 0.1 M tetra *n*-butylammonium perchlorate (TBAP) as supporting electrolyte [18]. The Au electrodes were evaporated on glass coated with Cr as adhesion layer. The electro deposition was performed by cyclic voltammetry (CV) at the scan rate of 0.1 V/s. A platinum coil was used as counter electrode and a silver wire as a pseudo-reference electrode. Ferrocene was added to the cell as an internal standard. Fig. 2a shows 32 voltammograms of successive electro deposition of **CN1** on a gold electrode. Upon oxidation, the TPA undergoes radical cation dimerization to produce tetraphenylbenzidine (TPB). The two TPA substituents act independently, in the two molecular branches, rendering the electropolymerization processes feasible [17,18]. The successive increase of the current indicates the formation of an electroactive film over the gold surface.

After rinsing in MeCN and exchanging the electrolyte to 0.1 M TBAP in MeCN, the electrodeposited layers of **CN1** show the typical redox responses whereas the current density increases with the number of electro deposition cycles

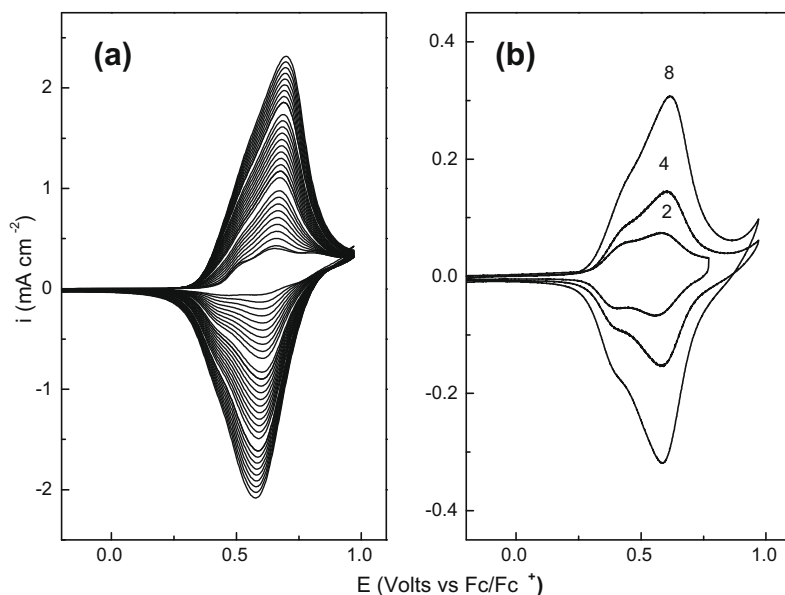


**Fig. 2.** (a) Successive cyclic voltammograms of **CN1** electro deposition on Au electrode (0.55 mM in MeCN, 0.1 M TBAP). (b) Cyclic voltammograms of electrodeposited **CN1** grown at different potential cycle numbers (MeCN, 0.1 M TBAP).

(Fig. 2b). This behavior demonstrated the formation of stable layers of **CN1** with different thickness. Each polymer sample was investigated before and after dipping in **CN2** solution, in order to investigate the role of a surface layer with preferentially acceptor like character.

### 2.3. Kelvin-probe and surface photovoltage spectroscopy

The contact potential difference was measured with a Kelvin-probe (Delta Phi Besocke) in a home-made vacuum chamber (pressure  $2 \times 10^{-5}$  mbar). The same Kelvin-probe was used for investigations with surface photovoltage spectroscopy. The sample was illuminated through the vibrating gold mesh. A quartz prism monochromator (SPM2) with a halogen lamp was used for illumination in the photon energy range from 0.6 to 4 eV. The samples were stabilized in the dark before starting the surface photovoltage measurements. The scan rate of the surface photovoltage measurements was identical for all measurements. The accuracy of the absolute CPD signal is unknown due to the presence of uncontrolled adsorbates. We assumed that the relative influence of the adsorbates is the same for all samples. The measurement accuracies of the CPD and SPV signals were less than 1 mV. Transition energies were obtained with accuracies of the order of 10 meV.

## 3. Results and discussion

### 3.1. Analysis of the contact potential difference

Fig. 3 shows the dependence of the contact potential difference of Au electrodes coated with **CN1** film on the number of electrochemical deposition cycles. The behavior of the contact potential difference describes the change of

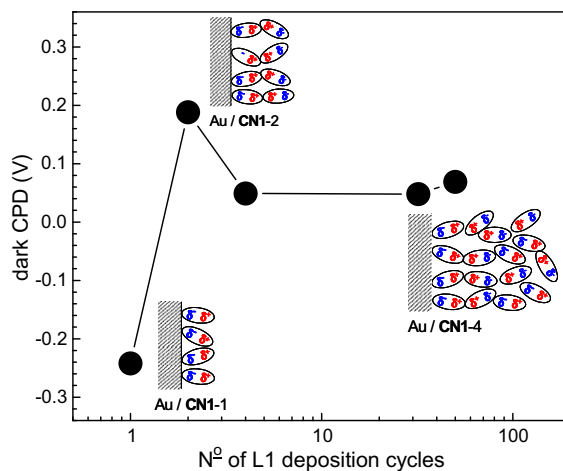


**Fig. 3.** Dependence of the contact potential difference of Au electrodes coated with **CN1** film on the number of electrochemical deposition cycles.

the surface work function after layer deposition, i.e. the change of the surface dipole. The contact potential difference (CPD) of gold was set to 0 V. The measurements of the CPD were performed in the dark after relaxation of the signal to a constant value. The CPD was about  $-0.24$  V after one electrochemical deposition cycle of **CN1** molecules (**CN1-1**, Fig. 3). The value of CPD increased to about 0.2 V after two electrochemical deposition cycles (**CN1-2**) and remained nearly constant for more deposition cycles. The insets in Fig. 3 depict the idealized scheme of the orientation of **CN1** molecules after one, two and more cycles of electro deposition. The lowest CPD was measured after one cycle which can be interpreted as a preferential orientation of  $-\text{CN}$  groups towards the gold surface. It is

know the strong surface binding ability of the cyano nitrogen. Surface-enhanced Raman spectroscopy of a series of nitrile compounds [29–31] adsorbed on gold indicated the formation of  $\sigma$ -bonding of the nitrile nitrogen to the metal surface. Thus, it is not unlikely that **CN1** monomer acquire a preferential orientation over electrode surface in the electropolymerization mechanism. We suggest that the cyano groups pick up electrons and link to the gold surface. On the other hand, the CPD jumped to its maximum after two deposition cycles of **CN1**. This can be explained in terms of preferential orientation of  $-\text{CN}$  groups towards the external surface. In this case, the  $-\text{NPh}_2$  groups of the first and second layer would bond each other during electropolymerization [18], so that the surface dipole changes the sign. For thick layers, CPD decreases to an average value. Obviously preferential orientation of surface dipoles is lost.

However, a layer of **CN2** (which does not have electropolymerization capability) over naked gold surface obtained by dipping procedure shows small positive  $\Delta\text{CPD}$  effect (Fig. 4). The observed behaviors could be due to different molecular structural organization in the deposited layers. In the case of **CN1** films, the polymerized structure can holds a preferential dipole orientation over gold surface, which is not present in the case of **CN2** layer over naked gold. This shows the importance of electropolymerization procedure in the control of electrode work function. On the other hand, the value of CPD did not change after depositing **CN2** molecules on the Au/**CN1-1** sample (see Fig. 4). Therefore, the deposition of **CN2** molecules on **CN1** film by dipping does not change the preferential surface dipole orientation.

### 3.2. Analysis of the surface photovoltage spectra

The contact potential difference changed under illumination due to separation of photo-generated charge carriers. Contact potential difference spectra are shown in

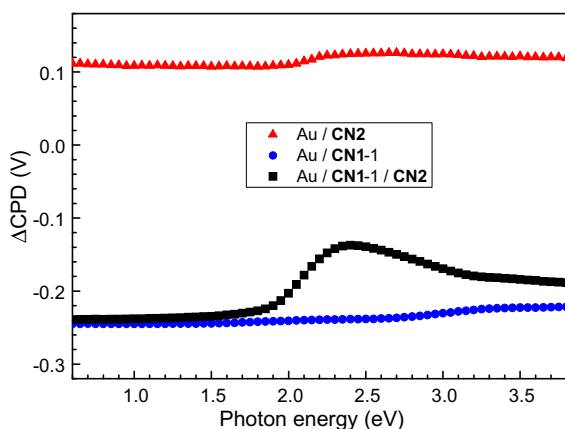


**Fig. 4.** Contact potential difference spectra under illumination of an Au electrode dipped in **CN2** molecule solution (Au/**CN2**, red triangles), an Au electrode with electrodeposited **CN1** film after one electrochemical deposition cycle (Au/**CN1-1**, blue circles) and dipped in **CN2** molecule solution (Au/**CN1-1/CN2**, black squares). (For interpretation of the references to colour in this figure legend, the reader is referred to the web version of this article.)

Fig. 4 for the Au/**CN2**, Au/**CN1-1**, and Au/**CN1-1/CN2** samples. A photoinduced increase of the contact potential difference means a preferential separation of photo-generated electrons (holes) towards the external (internal) surface whereas a photoinduced decrease of the contact potential difference means a preferential separation of photo-generated holes (electrons) towards the external (internal) surface. For the Au/**CN2** and Au/**CN1-1** samples the contact potential difference increases under illumination, i.e. electrons are separated preferentially towards the external surface. It should be noted, as is shown in Fig. 4, that the light induced change of the contact potential difference was quite small after electro deposition of layers of **CN1** only, and clearly increased after dipping in **CN2** solution. Remarkably **CN2** over the naked gold surface shows only a small SPV effect.

Fig. 5 shows the (negative) surface photovoltage spectra of the Au/**CN2**, Au/**CN1-1**, and Au/**CN1-1/CN2** samples together with the shapes of the optical density spectra of the **CN1** polymer and **CN2** molecules in diluted solution. For the Au/**CN2** sample the SPV signal sets on at photon energy of 1.95 eV (onset of the T1 transition). For comparison, the electronic transition sets on at a photon energy of 2.23 eV for the optical density spectrum. Therefore, the electronic transitions of the SPV spectrum are red-shifted

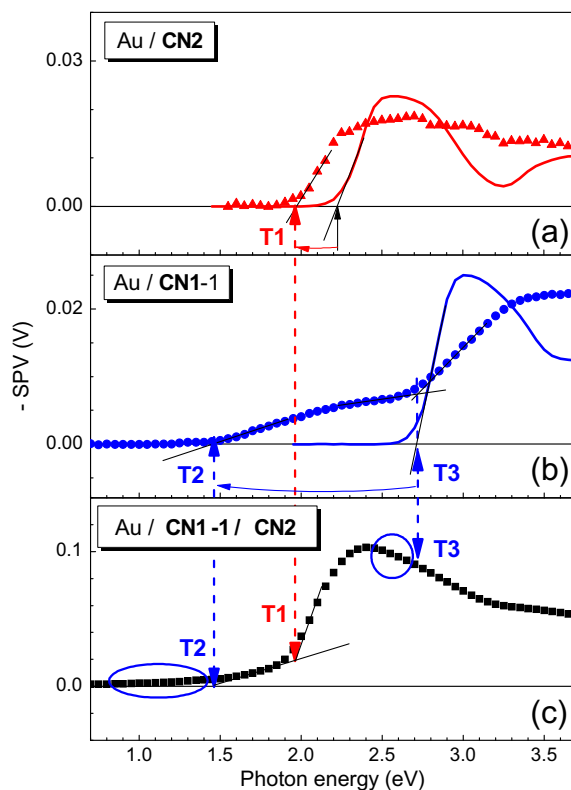


**Fig. 5.** Negative surface photovoltage spectra of Au/**CN2** (a), Au/**CN1-1** (b) and Au / **CN1-1 / CN2** (c). The red and blue solid lines in (a) and (b) show the shapes of the optical density spectra of **CN2** (a) and **CN1** (b) molecules in solution. T1, T2 and T3 denote the onset of optical transitions. (For interpretation of the references to colour in this figure legend, the reader is referred to the web version of this article.)

by 0.28 eV in comparison to the optical density spectrum. The SPV signal remains nearly constant at photon energies higher than about 2.4 eV.

For the Au/CN1-1 sample two transitions (T2 and T3) can be distinguished in the SPV spectrum. The T2 and T3 transitions set on at a photon energies of 1.45 and 2.71 eV, respectively. For comparison, the electronic transition sets on at 2.71 eV in the optical density spectrum. Therefore, the T3 and T2 transitions of the SPV spectrum correspond to the un-shifted and red-shifted by 1.26 eV electronic transition of the optical density spectrum, respectively. The separations of photo-generated charge carriers lead always to the increase of the contact potential difference of the Au/CN1-1 sample.

All three transitions appear also in the SPV spectrum of the Au/CN1-1/CN2 sample as demonstrated in Fig. 4c. The SPV signals related to the T1 and T2 transitions have the same sign as for the Au/CN1-1 and Au/CN2 samples. At photon energies larger than 2.45 eV the separation of photo-generated charge carriers lead to a decrease of the contact potential difference of the Au/CN1-1/CN2 sample. The reason for this decrease is a change of the direction of separation of photo-generated charge carriers for the T3 transition.

The analysis of the SPV spectrum of the Au/CN1-1/CN2 sample shows that the T2 and T3 transitions are “broadened” towards lower photon energies, i.e. charge separation begins even at photon energies less than the onsets of the T2 and T3 transitions taken from the SPV spectrum of the Au/CN1-1 sample.

### 3.3. Dependence of the T1, T2 and T3 transitions on the CN1 layer thickness

The SPV spectra did not change qualitatively if the thickness of the CN1 layer was increased by increasing the number of electrochemical deposition cycles. The detailed deconvolution of the SPV spectra is rather complicated since the spectra contain integrated and non-integrated components. For the discussion of the charge separation mechanisms a qualitative analysis will be sufficient. Therefore, here we describe the general tendencies of the thickness dependent SPV signals for the T1, T2 and T3 transitions.

For the Au/CN1 samples the thickness dependencies of the SPV signals related to the T2 and T3 transitions can be distinguished if comparing the values of the SPV signals at 2.4 and 3.4 eV (Fig. 5a). The (negative) SPV signal related to the T2 transition (value at 2.4 eV) increases with increasing number of electrodeposition cycles from 7 mV (Au/CN1-1) to 17 (Au/CN1-2) and 33 (Au/CN1-4) mV. For very large numbers of electrodeposition cycles the SPV signal related to the T2 transition decreases to 20 (Au/CN1-32) and 3 (Au/CN1-50) mV.

Contributions of the different transitions to the SPV signal can be estimated if considering differences of the SPV at characteristic energies where one or two transitions dominated the SPV spectrum. For the analysis we assume that the SPV signals of the various transitions are independent of each other and that the SPV signal related to the T2 transition tends to saturation at higher photon energies.

The (negative) SPV signal related to the T3 transition of the Au/CN1 samples can be described as the difference between the SPV signal obtained at 2.4 and 3.4 eV (see also Fig. 6a). The SPV signals related to the T3 transition are 15, 16, 21 mV for the Au/CN1-1, Au/CN1-2 and Au/CN1-4 samples, respectively what is nearly constant if comparing with the T2 transition. The SPV signal of the T3 transition decreases very strongly to 3 and 1 mV for the Au/CN1-32 and Au/CN1-50 samples, respectively.

The (negative) SPV signal of the T1 transition can be estimated from the SPV spectra of the Au/CN1/CN2 samples in comparison to the Au/CN1 samples if assuming a linear superposition. Fig. 6b shows the values of the SPV signals measured at 2.4 eV for the Au/CN1/CN2 samples together with the difference between these values and those values measured at 2.4 eV for the Au/CN1 samples. It can be seen that the SPV signal related to the T1 transition decreases continuously with increasing number of electrodeposition cycles from 96 (Au/CN1-1/CN2), 64 (Au/CN1-2/CN2), 54 (Au/CN1-4/CN2), 35 (Au/CN1-32/CN2), 23 (Au/CN1-50/CN2) mV.

### 3.4. (d) Mechanisms of charge separation

The T1 and T2 transitions should be related to internal photoemission of photo-generated electrons from Au into

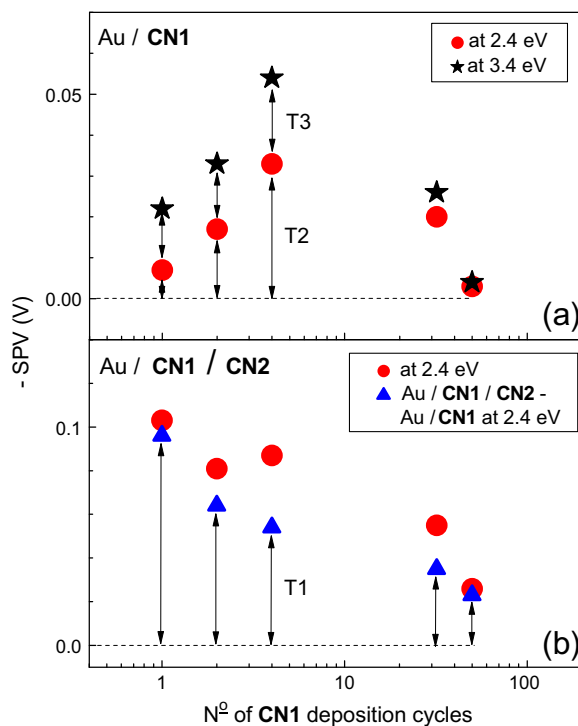


**Fig. 6.** Dependence of the negative values of the surface photovoltage on the number of electrochemical deposition cycles of CN1 molecules for Au/CN1 samples: (a) at 2.4 (red circles) and 3.4 (black stars) eV and of Au/CN1/CN2 samples (b) at 2.4 eV (red circles) and of the difference of the surface photovoltages of the Au/CN1/CN2 and Au/CN1 samples at 2.4 eV. (For interpretation of the references to colour in this figure legend, the reader is referred to the web version of this article.)

the LUMO levels of the molecules (Fig. 7). In such case the red-shifted onsets of the transitions spectra in comparison to the optical density spectra correspond to the difference between the Fermi-level of the Au and the energy of the HOMO level of the respective molecule.

The SPV signal of the T1 transition decreased with increasing number of **CN1** electrodeposition cycles. This can be understood with respect to Eq. (1).

$$\text{SPV} = \frac{\Delta d}{\varepsilon \cdot \varepsilon_0} \cdot \Delta Q \quad (1)$$

A surface photovoltage signal contains information about the amount of charge separated in space ( $\Delta Q$ ) and about the distance over which the centres of positive and negative charges are separated ( $\Delta d$ , charge separation length) where  $\varepsilon_0 = 8.85 \times 10^{-12} \text{ As/(Vm)}$  and  $\varepsilon$  is the relative dielectric constant. Both parameters  $\Delta Q$  and  $\Delta d$  can be varied by changing the thickness of ultra-thin layers in charge selective layer systems. Thus, the charge separation length increases linearly with increasing number of **CN1** electrodeposition cycles. However, the probability of internal photoemission of electrons from Au into the **CN2** layer decreases exponentially with increasing distance. Therefore the overall SPV signal of the T1 transition decreases with increasing number of **CN1** electrodeposition cycles (Fig. 6b).

Regarding to an exponential decrease of the charge transfer rate for internal photoemission with increasing distance, it is really surprising that the SPV signal of the T1 transition remains relatively large even for Au/**CN1**-32/**CN2** and Au/**CN1**-50/**CN2** samples. We believe that prolonged electrodeposition of **CN1** leads to the formation of porous or dendrite like structures giving space for quite inhomogeneous penetration of **CN2** molecules during dipping. In order to investigate the film permeability, we performed CV with a model redox couple in solution (ferrocene), both over bare Au and Au/**CN1** films. The ferrocene redox potential lies within the potential window where the **CN1** film does not show an electrochemical response and, therefore, behaves solely as a blocking layer

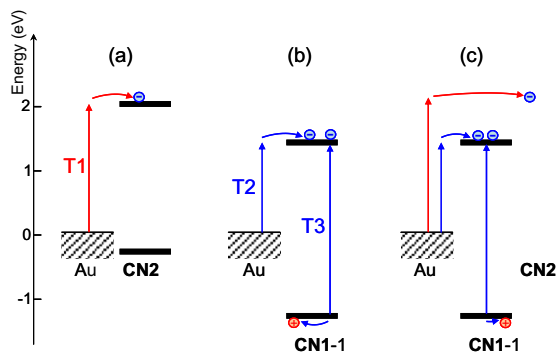


**Fig. 7.** Energy diagram of the T1, T2 and T3 transitions in Au/**CN2** (a), Au/**CN1**-1 (b) and Au/**CN1**-1/**CN2** (c) samples. The transitions T1 and T2 are related to internal photoemission of electrons from the Au electrode into LUMO levels of the **CN1** and **CN2** molecules, the transitions T3 is related to light absorption in the **CN1**-1 film.

on the Au electrode. If the polymer film forms an ideal compact layer, without defects or pinholes, not Faradaic current should be observed in the CV. However, in our case we obtained typical s-shape ultramicroelectrode voltammogram in the ferrocene oxidation over Au/**CN1** film. As it is known, this kind of behavior is evidence of a high coverage of the Au bare electrode by a film with pores spaced far apart in relation to the radius of the pores [32]. This fact supports our assumption about **CN2** molecules penetration during dipping process.

On the other hand, the SPV signal of the T2 transition increased with increasing number of **CN1** electrodeposition cycles for **CN1**-1 to **CN1**-4 (Fig. 6a). This is not surprising since the amount of electrons emitted from Au to longer distances in the **CN1** film increases with increasing number of **CN1** electrodeposition cycles. However, the SPV signal of the T2 transition decreased for **CN1**-32 and **CN1**-50 layers. The origin of this effect is unclear, but could be due to morphological changes in the film with thickness increasing.

The SPV signal of the T3 transition has to be related to light absorption in the **CN1** film. The (negative) SPV signal of the T3 transition of the Au/**CN1** samples is practically constant for **CN1**-1, **CN1**-2 and **CN1**-4 since the charge separation length and the amount of photons absorbed in the first monolayer of **CN1** molecules are practically unchanged. It means also that the ordering of the first **CN1** monolayer at the Au surface is preserved during the following polymerization process. For **CN1**-32 and **CN1**-50 the amount of **CN1** molecules in front of the first **CN1** monolayer acts as an optical filter limiting strongly photon absorption in the **CN1** monolayer at the Au surface leading to a strong decrease of the SPV signal. The (positive) SPV signal of the T3 transition in Au/**CN1**/**CN2** samples at energies values higher than 2.35 eV is probably due to hole injection from **CN1** excited state into **CN2** molecules.

#### 4. Conclusions

It has been shown that the work function of conducting surfaces can be engineered by electrodeposition of spirobifluorene compounds with donor–acceptor pairs. It should be mentioned that a modification of the work function of organic polymers is also possible due to electrochemically driven oxidation/reduction (for example, in PEDOT:PSS [33]). Related effects may disturb changes of the work function and charge separation caused by changes of preferential orientation of electrodeposited molecules. Some advantages of the used spirobifluorene derivatives are their synthetic versatility, stability and charge transport capability. The results showed that the formation of electrosynthetic films is a versatile tool for surface work function tuning. Surface dipole of a gold layer can be changed over more than 0.4 V by electrodeposition of **CN1** molecules, and the surface dipole can be modified by internal photoemission. The highest SPV was reached after the combination of **CN1** electrodeposited film and coated with **CN2** molecule layer. This might become interesting for molecular electronics.

## Acknowledgements

The work has been supported by the DAAD-MINCYT grant number DA0601. We also thank to Consejo Nacional de Investigaciones Científicas y Técnicas (CONICET-Argentina), Agencia Nacional de Promoción Científica y Tecnológica (ANPCYT-Argentina), Secretaría de Ciencia y Técnica de la Universidad Nacional de Río Cuarto (SECYT-UNRC).

## References

- [1] X. Crispin, V. Geskin, A. Crispin, J. Cornil, R. Lazzaroni, W.R. Salaneck, J.-L. Brédas, *J. Am. Chem. Soc.* 124 (2002) 8131.
- [2] T. Nakamura, E. Koyama, Y. Shimoi, S. Abe, T. Ishida, K. Tsukagoshi, W. Mizutani, H. Tokuhisa, M. Kanesato, I. Nakai, H. Kondoh, T. Ohta, *J. Phys. Chem. B* 110 (2006) 9195.
- [3] M.P. Nikiforov, U. Zerweck, P. Milde, Ch. Loppacher, T.-H. Park, H.T. Uyeda, M.J. Therien, L. Eng, D. Bonnell, *Nano Lett.* 8 (2008) 110.
- [4] R. Rosseau, V. De Renzi, R. Mazarello, D. Marchetto, R. Biagi, S. Scandolo, U. Del Pennino, *J. Phys. Chem. B* 110 (2006) 10862.
- [5] N. Gozlan, U. Tisch, H. Haick, *J. Phys. Chem. C* 112 (2008) 12988.
- [6] K. Homg, L.W. Lee, S.Y. Yang, K. Shin, H. Jeon, S.H. Kim, C. Yang, C.E. Park, *Org. Electron.* 9 (2008) 21.
- [7] B.H. Hamadani, D.A. Corley, J.W. Ciszek, J.M. Tour, D. Nateson, *Nano Lett.* 6 (2006) 1303.
- [8] C.-C. Hsiao, C.-H. Chang, H.-H. Lu, S.-A. Chen, *Org. Electron.* 8 (2007) 343.
- [9] C.-P. Cho, Y.-T. Tao, *Langmuir* 23 (2007) 7090.
- [10] N.S. Sariciftci, L. Smilowitz, A.J. Heeger, F. Wudl, *Science* 258 (1992) 1474.
- [11] Y. Zidon, Y. Shapira, Th. Dittrich, L. Otero, *Phys. Rev. B* 75 (2007) 195327.
- [12] Y. Shi, S.-C. Luo, W. Fang, K. Zhang, E.M. Ali, F.Y.C. Boey, J.Y. Ying, J. Wang, H.-H. Yu, L.-J. Li, *Org. Electron.* 9 (2008) 859.
- [13] K.-T. Wong, Y.-H. Lin, H.-H. Wu, F. Fungo, *Org. Lett.* 9 (2007) 4531.
- [14] S. Lu, T. Liu, L. Ke, D.G. Ma, S.-J. Chua, W. Huang, *Macromolecules* 38 (2005) 8494.
- [15] T. Oyamada, C.-H. Chang, T.-C. Chao, F.-C. Fang, C.-C. Wu, K.-T. Wong, H. Sasabe, C. Adachi, *J. Phys. Chem. C* 111 (2007) 111.
- [16] C.-C. Wu, W.-G. Liu, W.-Y. Hung, T.-L. Liu, Y.-T. Lin, H.-W. Lin, K.-T. Wong, Y.-Y. Chien, R.-T. Chen, T.-H. Hung, T.-C. Chao, Y.-M. Chen, *Appl. Phys. Lett.* 87 (2004) 052103.
- [17] J. Naterá, L. Otero, L. Sereno, F. Fungo, N.-S. Wang, Y.-M. Tsai, T.-Y. Hwu, K.-T. Wong, *Macromolecules* 40 (2007) 4456.
- [18] L. Otero, L. Sereno, F. Fungo, Y.-L. Liao, C.-Y. Lin, K.-T. Wong, *Chem. Mater.* 18 (2006) 3495.
- [19] J.P.J. Markham, E.B. Namdas, T.D. Anthopoulos, I.D.W. Samuel, G.J. Richards, P.L. Burn, *Appl. Phys. Lett.* 85 (2004) 1463.
- [20] W.-Y. Lai, R. Zhu, Q.-L. Fan, L.-T. Hou, Y. Cao, W. Huang, *Macromolecules* 39 (2006) 3707.
- [21] P.A. Levermore, R. Xia, W. Lai, X.H. Wang, W. Huang, D.D.C. Bradley, *J. Phys. D: Appl. Phys.* 40 (2007) 1896.
- [22] Z. Li, C. Di, Z. Zhu, G. Yu, Z. Li, Q. Zeng, Q. Li, Y. Liu, J. Qin, *Polymer* 47 (2006) 7889.
- [23] T.P.I. Saragi, T. Spehr, A. Siebert, Th. Fuhrmann-Lieker, J. Salbeck, *Chem. Rev.* 107 (2007) 1011.
- [24] I. Mora-Seró, Th. Dittrich, G. García-Belmonte, J. Bisquert, *J. Appl. Phys.* 100 (2006) 103705.
- [25] L. Kronik, Y. Shapira, *Surf. Sci. Rep.* 37 (1999) 1.
- [26] Th. Dittrich, S. Bönisch, P. Zabel, S. Dube, *Rev. Sci. Instrum.* 79 (2008) 113903.
- [27] C.-L. Chiang, C.-F. Shu, C.-T. Chen, *Org. Lett.* 7 (2005) 3717.
- [28] Chemical polymerization synthesis and characterization will be published elsewhere.
- [29] P. Gao, M.J. Weaver, *J. Phys. Chem.* 89 (1985) 5040.
- [30] D.S. Corrigan, P. Gao, L.-W.H. Leung, M.J. Weaver, *Langmuir* 2 (1986) 744.
- [31] I.C.N. Diógenes, I.M.M. De Carvalho, E. Longhotti, L.G.F. Lopes, L.M.A. Temperini, G.F.S. Andrade, I.S. Moreira, *J. Electroanal. Chem.* 605 (2007) 1.
- [32] A.J. Bard, in: *Integrated Chemical Systems*, Wiley, New York, 1994, p. 196 (Chapter 5).
- [33] See, for example A. Petr, F. Zhang, H. Peisert, M. Knupfer, L. Dunsch, *Chem. Phys. Lett.* 385 (2004) 140.



it is commonly observed that the more the absorption of an organic compound is shifted towards low energies, the less the compound is able to stand long term exposition to ambient atmosphere [12], especially for a device under operating conditions (applied bias, illumination, temperature). To overcome this issue it is often necessary to develop encapsulation techniques for the efficient isolation of the device active layer from oxygen and moisture [13], thus increasing complexity and costs, and reducing the mentioned advantages of the organic technology.

Employing squaraine dyes, thanks to their good absorption properties in the red-NIR region, as the active absorbing material in bulk-heterojunction configuration with Phenyl-C61-Butyric-Acid-Methyl-Ester (PCBM), we explored the possibility to develop fast and efficient NIR detectors capable of operating in air without need for an encapsulation.

Since the charge transport properties are crucial in determining the optoelectronic behavior of devices, we realized detectors in parallel with transistors, from which we could easily extract charge carrier mobilities. In order to provide a fair comparison of the two devices, we developed photodetectors with a planar architecture, so to have the same current flow with respect to the substrate as in transistors [14].

## 2. Experimental

### 2.1. Synthesis and characterization of the materials employed

Squaraines AlkSQ and GlySQ were prepared according to the literature procedure [15,16].

PCBM was purchased from Aldrich Chemicals and used without further purification.

HOMO and LUMO energies were estimated by Cyclic Voltammetry (CV) considering the redox peak and the optical band gap [17].

### 2.2. Devices preparation

Both the pristine and the bulk-heterojunction devices were obtained by a two steps spin-coating (60s at 100 rpm followed by 60s at 1000 rpm) of a 10 mg ml<sup>-1</sup> chloroform solution. For bulk-heterojunction films, the 1:1 and 1:3 by weight blend solutions of squaraine and PCBM were stirred overnight prior deposition, in order to promote the mixing of the two components.

UV-vis absorption spectra (transmission mode) of films were measured on 500 μm thick fused silica substrates with a Fourier Transform Infrared Spectrometer Nicolet MAGNA 560.

Photodetectors were obtained by depositing the active material on a 500 μm thick fused silica substrate, patterned by lithography with 40 nm thick interdigitated gold contacts with channel length of 6 μm and width of 15 mm or 5 mm. The photodetectors, biased with a voltage of 60 V, were irradiated by means of a set of light emitting diodes (LEDs) providing 500 μs long light pulses. The resulting photocurrent was read by connecting the device to a low-noise transimpedance amplifier. The external quan-

tum efficiency (EQE) was calculated as the ratio of the number of collected charges, determined by integrating the transient output photocurrent during the radiation pulse, and the number of incident photons, obtained by calibrating the LEDs (giving a light intensity of about 30 mW cm<sup>-2</sup>) by means of a silicon photodetector. Electrical cross-talk between the detector circuit and the driving LEDs has been avoided by carefully aluminum shielding each component of the set-up with the only exception of the coupling window between the emitting LED and the photodetector active area, and by suitably choosing the detector-LED distance (about 13 mm). Trains of light pulses were recorded at the output of a band-pass filter connected to the transimpedance amplifier in order to improve the signal to noise ratio.

Transistors were realized with the same deposition technique onto a 500 μm thick p<sup>+</sup>-doped silicon wafer acting as the gate and provided with a 130 nm thick SiO<sub>2</sub> dielectric. Gold source and drain contacts were defined by lithography directly onto the oxide in a bottom contact configuration, yielding devices with 15 mm channel width and 6 μm channel length. Field-effect mobility was extracted from the transfer characteristic curves in the saturation region ( $|V_{DS}| = 30$  V and  $|V_{GS}|$  ranging from 0 V to 30 V). Contact resistances were extracted in the linear regime ( $|V_{DS}| = 1$  V and  $|V_{GS}|$  ranging from 0 V to 30 V), according to the procedure outlined in Ref. [18].

All the electrical characterizations were performed both in vacuum (at 10<sup>-6</sup> mbar) and in air.

AFM analyses were performed in non-contact mode through a Nanosurf EasyScan 2 system.

## 3. Results and discussion

Squaraines are the condensation product of electron rich molecules, usually activated arenes, π-excessive heterocycles, and heteroaromatic anhydrobases, with squaric acid [19]. Thanks to their peculiar sharp and intense absorption mainly localized in the red-NIR region [20], along with remarkable stability and wide molecular structure diversity, squaraines have been exploited in a number of technologically relevant applications including photoconductivity [19,21], data storage [22], light emitting field-effect transistors [23], solar cells [24,15], nonlinear optics [25], highly stable fluorescent NIR dyes [26] and fluorescence patterning [27].

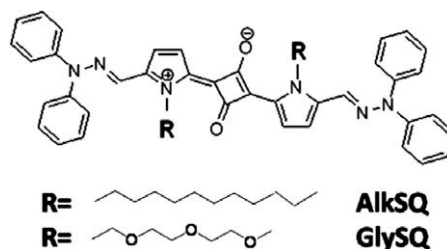


**Fig. 1.** Chemical structure of **AlkSQ** and **GlySQ**, differing one from the other by the presence of either alkyl side chains (**AlkSQ**) or glycolic side chains (**GlySQ**).

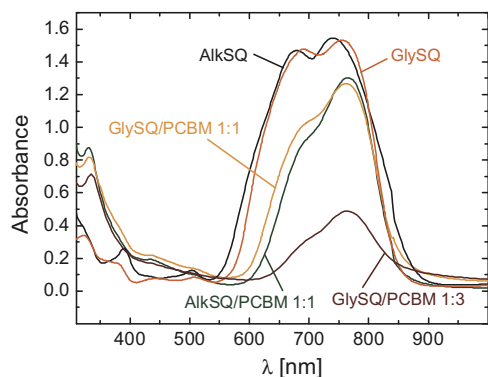


**Fig. 2.** Solid state absorption spectra of films based on pristine and blended squaraines **AlkSQ** and **GlySQ**. In the passage from a pristine squaraine film to a bulk-heterojunction film, the absorbance tail in the UV region is enhanced due to the presence of PCBM.

Among the various possible substitution patterns around the squarylium core that have been described in the literature [28], we exploited hydrazone end-capped symmetric squaraines in order to achieve at the same time an efficient absorption in the red and NIR regions (Figs. 1 and 2) and a reversible redox behavior. As non-functionalized squaraines are known to be particularly insoluble and high-melting point derivatives, on the pyrrolic nitrogen we introduced a long functionalization chain in order to provide solubility in chlorinated solvents, where the PCBM is also particularly soluble.

### 3.1. Alkyl functionalized squaraine

We started with a pristine squaraine functionalized with an *alkyl* chain, named in the following **AlkSQ** (see Fig. 1): this functionalization enabled us to prepare films by spin-coating of a 10 mM chloroform solution of the dye. The obtained films were rough (25 nm rms) and

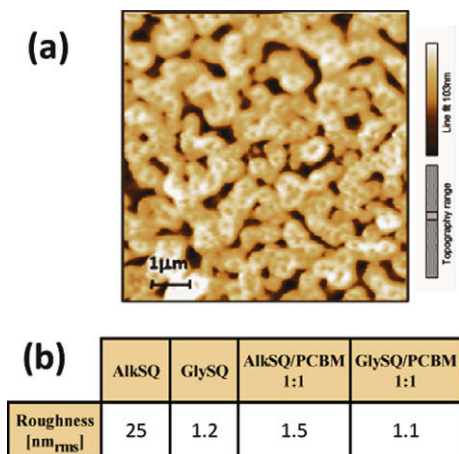


**Fig. 3.** (a) AFM image of the pristine **AlkSQ** spin-coated film showing the presence of micron sized structures – (b) Rms value of the film roughness for devices based on the pristine squaraines and the bulk-heterojunctions, extracted by the AFM analysis.

showed the formation of globular, micron sized structures clearly distinguishable in the AFM height images (Fig. 3). We attributed this behavior to a natural tendency of **AlkSQ** towards self-assembling, possibly enhanced by its hydrophobic character leading to a repulsive interaction with the polar substrate (silica).

When characterized in vacuum, the resulting device showed an External Quantum Efficiency (EQE) under pulsed illumination of 4.9% in the NIR, with the peak of the EQE located at 670 nm, as shown in Fig. 4 (see Section 2 for details on EQE measurement). Despite this interesting efficiency, the device was unsuitable for signal detection since its response time was unsatisfactory: the transient response to 500 μs long light pulses showed a 90–10% decay time as long as 3 ms (see Figs. 5 and 6). To better investigate this aspect, we performed the electrical characterization of the corresponding thin-film transistor, extracting a hole mobility  $\mu_h$  of  $6 \times 10^{-5} \text{ cm}^2 \text{ V}^{-1} \text{ s}^{-1}$  whereas no electron mobility  $\mu_n$  was detected (see Fig. 6). If holes were dominating the transients, the hole transit time (calculated as  $L^2/\mu_h V$ , with  $L$  interelectrode spacing and  $V$  applied bias voltage) should be an estimate

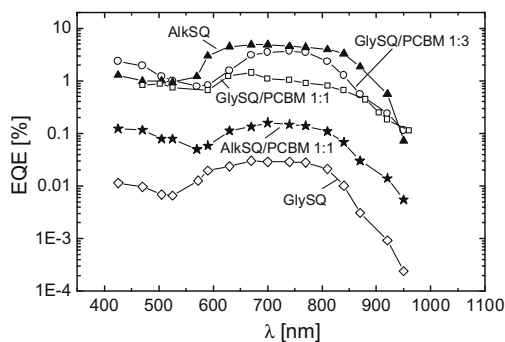


**Fig. 4.** External Quantum Efficiency of planar photodetectors based on pristine **AlkSQ** (–▲–), **AlkSQ/PCBM** blend with 1:1 by weight ratio (–★–), pristine **GlySQ** (–◇–), **GlySQ/PCBM** blend with 1:1 by weight ratio (–□–) and **GlySQ/PCBM** blend with 1:3 by weight ratio (–○–) upon light irradiation with 500 μs long light pulses. Lines are only a guide to the eye.

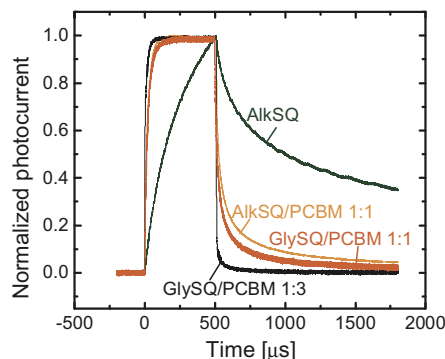


**Fig. 5.** Transient response of the detectors based on pristine **AlkSQ** (green), **AlkSQ/PCBM** 1:1 blend (orange), **GlySQ/PCBM** 1:1 blend (red) and **GlySQ/PCBM** 1:3 blend (black) to a 500 μs long light pulse at a wavelength of 670 nm. (For interpretation of the references to colour in this figure legend, the reader is referred to the web version of this article.)

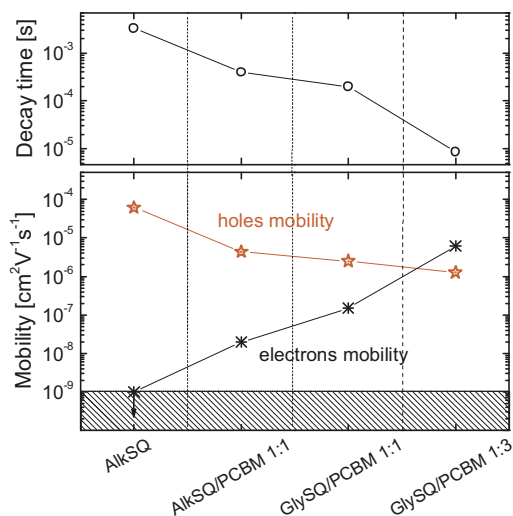


**Fig. 6.** Trend of the decay time and of the mobility for both holes and electrons in devices based on pristine and blended squaraines. In devices based on the bulk-heterojunction of **GlySQ** and PCBM in 1:3 ratio, electrons mobility and response speed are improved at the same time with respect to the other samples. In such detectors, the optimal balance between holes mobility and electrons mobility is achieved.

by excess of transients themselves. In our case the hole transit time turned out to be in the range of 400  $\mu\text{s}$ , which was about an order of magnitude lower than the 90–10% photodetector decay time. As a consequence, transients were dominated by electrons, slowly drifting and, likely, trapped at the grain boundaries [29–31]. To address this point, the EQE was measured under CW illumination. In this case, the measured EQE was as high as 200% in the NIR (the difference with 4.9% under pulsed light arising because the steady state was not reached within the pulse duration). This means that pristine **AlkSQ**-based devices were affected by a photoconductive gain [32], due to easy injection and circulation of holes while photogenerated electrons were trapped [33].

In addition, the device could not be operated in ambient air because the dark currents, which were in the range of tens of nA in vacuum, reached the value of tens of  $\mu\text{A}$  in air and were characterized by an erratic and noisy behavior. This was due to p-doping of the dye: in fact **AlkSQ**-based transistors showed an on/off ratio as high as  $10^4$  in vacuum, but as low as few units in air. It is likely that doping was highly facilitated by the surface roughness, leading to deep penetration of oxygen/moisture into the film [34,35].

Given the morphology as the source of the ambient instability, and the unbalanced mobilities hampering the response speed, we turned to the deposition of a blend of **AlkSQ** with a suitable molecule. We chose PCBM, because: (i) it belongs to the same solubility class of **AlkSQ**, therefore it is expected to favorably and effectively mix with **AlkSQ** acting as a disturbing agent against the **AlkSQ** self-aggregation; (ii) it is electronically active being a very good electron conductor; (iii) it has a LUMO level which is located at about 4.0 eV below the vacuum level, 0.2 eV lower than the LUMO of **AlkSQ** (3.8 eV), thus it is poten-

tially able to act as electron acceptor material in the bulk-heterojunction [36].

The obtained 1:1 by weight ratio blend films indeed possessed a roughness of about 1 nm, in contrast to the 25 nm rms of the pristine film (Fig. 3), and were essentially featureless. Air stability was also achieved as no difference could be observed in the dark currents (about 100 pA) and in the EQE measured in vacuum or in ambient conditions. In addition the response time decreased by one order of magnitude, reaching a 90–10% decay time of 400  $\mu\text{s}$  (Figs. 5 and 6), thanks to PCBM which hampered **AlkSQ** crystallization, suppressed the electron trapping process and created percolation paths for electrons. In fact, from transistor measurements we extracted an electron mobility of  $2 \times 10^{-8} \text{ cm}^2 \text{ V}^{-1} \text{ s}^{-1}$  (see Fig. 6).

Despite this goods, the pulsed EQE of the detector strongly reduced from 4.9% to 0.2%, as shown in Fig. 4: this means that no photoconductive gain mechanism was occurring, even though a relatively large (100 fold) mobility unbalance was still present (given  $\mu_h = 4.4 \times 10^{-6} \text{ cm}^2 \text{ V}^{-1} \text{ s}^{-1}$ ). Since photoconductive gain requires, in addition to unbalanced mobilities, an ohmic contact for the injection of the more mobile carrier, we conclude that PCBM blending also had an impact on the contacts injecting properties. To investigate this, we extracted the contact resistances from transistor measurements [18]: from pristine to blended **AlkSQ**, contact resistances for holes grew larger by a factor of 10 (from 12  $\text{M}\Omega/\text{cm}$  to 106  $\text{M}\Omega/\text{cm}$ ). This can be explained by considering that the hole mobility diminished by a factor of about 10 from pristine to blended **AlkSQ**, likely due to the less ordered nature of the latter film, and recalling that semiconductor charge transport properties are known to strongly affect current injection in organic semiconductors [37]. In addition, a lower ionization potential due to aggregation and hence a more facile injection cannot be excluded in pristine **AlkSQ**. This worsening of hole injecting properties from pristine to blended **AlkSQ** is confirmed by the drop of the dark currents of a factor  $10^2$  (from about 30 nA to 100 pA at 60 V), which is not merely justifiable as the consequence of a ten-times smaller hole mobility and suggests ohmic injection in the pristine **AlkSQ** and injection limited conduction regime in the blend. In conclusion, hole injection efficiency is high (ohmic) in pristine **AlkSQ** whereas is poor in the blend, thus preventing the gain mechanism to occur despite the unbalanced mobilities.

Since holes were not effectively injected to maintain electrical neutrality, space charge build-up was expected, limiting the EQE to the unsatisfactory value of 0.2%<sup>2</sup> [38,39] by collapsing the active device area to a small region close to the contact biased to collect the slow carrier (electrons). The ultimate cause of the bad transport properties of the device can be traced back to the fact that, belonging to the same solubility class, PCBM and **AlkSQ** can probably mix even too efficiently, affording almost no phase segregation and yielding poor percolation pathways for electrons [40–42].

<sup>2</sup> In addition, effects on the exciton binding energy due to the expected different molecular packing from pristine **AlkSQ** to blended **AlkSQ** cannot be excluded.

### 3.2. Glycolic functionalized squaraine

To solve this problem, we chemically tailored the squaraine exploiting a glycolic functionalization pattern (named **GlySQ**, see Fig. 1) instead of the alkyl one. The glycol functionalization provided the dye with a higher hydrophilic character, thus reducing its mixing capabilities with PCBM, while preserving the favorable dye solution processability.

Firstly, we discuss pristine **GlySQ** and compare it to pristine **AlkSQ**, because the comparison strengthens our previous observations. In fact, at the molecular level the two **GlySQ** and **AlkSQ** do not differ in their optoelectronic properties (as the kind of functionalization on the pyrrolic nitrogen does not affect in a relevant way the squaraine spectroelectrochemical properties – Fig. 2), therefore any differences in devices performances can be traced back to differences at the film level, in terms of degree of order, molecular packing and morphology. We found that, thanks to the good wetting capabilities towards polar surfaces provided by the glycol chain, pristine **GlySQ** yielded smooth films (the rms roughness was 1.2 nm – Fig. 3), and the related devices<sup>3</sup> turned out to be air stable: this confirms the key role of morphology in yielding air stable devices. On the other hand, the hole mobility was relatively low ( $5 \times 10^{-6} \text{ cm}^2 \text{ V}^{-1} \text{ s}^{-1}$ ), due to the amorphous nature of the film. In addition, pristine **GlySQ** photodetectors showed an EQE of only 0.11% when measured under CW illumination, ruling out gain mechanisms. The lack of gain, despite a probable large mobility unbalance (the electron mobility was undetected), suggests non-ohmic contacts: this is in agreement with contact resistances being as large as 150 M $\Omega$ /cm in this case, which is the same order of magnitude classified to yield poor injecting contacts in case of **AlkSQ**/PCBM. This comparison confirms the role of aggregation and hence of mobility in determining the degree of charge injection from the contacts and, ultimately, the occurrence of photoconductive gain.

Turning now to the **GlySQ**/PCBM 1:1 blend, we measured in transistors a practically unchanged mobility for holes ( $\mu_h = 2.5 \times 10^{-6} \text{ cm}^2 \text{ V}^{-1} \text{ s}^{-1}$ ) compared to **AlkSQ**/PCBM, but a mobility for electrons of  $1.5 \times 10^{-7} \text{ cm}^2 \text{ V}^{-1} \text{ s}^{-1}$  (Fig. 6), which was one order of magnitude higher. This is the evidence that by tailoring the squaraine solubility class it is possible to control the degree of phase separation. As a consequence of the improved electron transport, the device optoelectronic properties were enhanced: the EQE reached the value of 1.3% (at 670 nm), while the 90–10% decay time in response to a 500  $\mu\text{s}$  light pulse turned out to be of about 200  $\mu\text{s}$  (see Figs. 4–6). The AFM image showed a featureless and smooth morphology (similar to **AlkSQ**/PCBM blends – see Supporting information) which conferred air stability to the device. In addition, the device had a striking shelf-life: measurements carried out in air on a device stored for 1 year under ambient atmosphere with no precaution whatsoever regarding oxygen and moisture contamination, demonstrated an

overall decrease in the EQE lower than 25% (see Supporting information), and no detectable aging related degradation was observed in the response time.

Finally, with the aim of further enhancing the device performance, we started an optimization study of the **GlySQ**:PCBM blend. Since in the 1:1 blend electrons still had a mobility one order of magnitude lower than holes, we increased the PCBM content obtaining a **GlySQ**:PCBM 1:3 by weight ratio blend, in order to get better efficiency [39] and transit time. Transistor measurements showed that this latter blend succeeded into balancing the mobility of the charge carriers giving  $\mu_h = 1.27 \times 10^{-6} \text{ cm}^2 \text{ V}^{-1} \text{ s}^{-1}$  and  $\mu_n = 6.25 \times 10^{-6} \text{ cm}^2 \text{ V}^{-1} \text{ s}^{-1}$  (Fig. 6). As a consequence, EQE in the NIR improved, reaching the remarkable value of about 3.5%, and the 90–10% fall time (upon 500  $\mu\text{s}$  light pulse) diminished by one order of magnitude reaching a value below 10  $\mu\text{s}$  (Fig. 5). Detector speed was further investigated by testing with light pulses as short as 100 ns (at 670 nm), obtaining a 90–10% fall time of about 240 ns, as shown in Fig. 7a. The dependence of the fall time on the pulse duration is currently not understood and will be the subject of further investigation, but nevertheless this suggests that detection of fast light pulses is indeed feasible with this technology. In fact, by suitably amplifying the device photocurrent (see Section 2), we were able to detect a

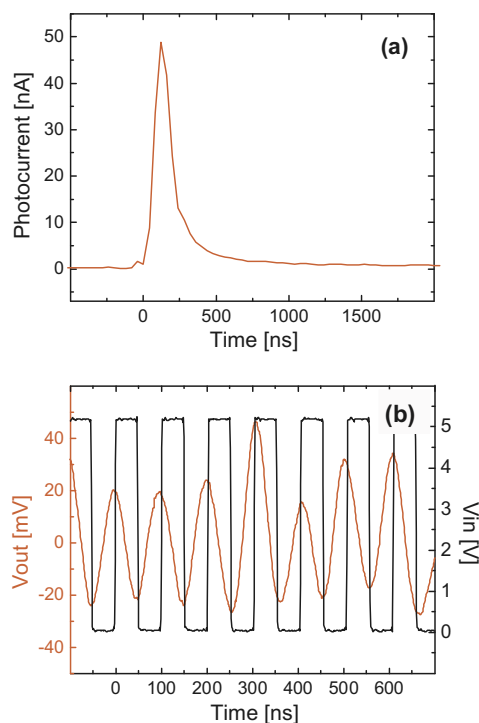


**Fig. 7.** (a) Photocurrent response of the photodetector based on **GlySQ**/PCBM 1:3 blend to a 100 ns light pulse stimulation at a wavelength of 670 nm. (b) Time response of the same detector to a train of light pulses at a wavelength of 670 nm and with a 10 MHz repetition frequency. The photo-response of the device is recorded at the output of a band-pass filter connected to the transimpedance amplifier (see Section 2), which introduces a group delay that is responsible for the occurrence of the peaks of the output voltage in a shifted position (delayed) with respect to the corresponding light pulse.

<sup>3</sup>  $I_{\text{on}}/I_{\text{off}}$  ratio in FETs in the order of  $10^3$  both in vacuum and under air exposure.

train of light pulses with a repetition frequency as high as 10 MHz, as the single shot acquisition of Fig. 7b shows. In addition, the ratio between the photogenerated and the dark current (with the device biased at 60 V), which is particularly important for applications [43,44], exceeded  $10^4$ , with dark currents values settling around 10 pA. All these characteristics, thanks to a smooth morphology, were maintained even in ambient air operation.

#### 4. Conclusions

We have studied planar photodetectors operating in the red-NIR range of the spectrum and based on the bulk-heterojunction of squaraine dyes and PCBM as active materials. Guided by the comparison of pulsed and CW illumination tests on the photodetectors, as well as by the transport properties extracted from FET structures, we have addressed the efficiency, speed, and stability issues working both at the chemical level, by tailoring the squaraine substitution pattern, and at the device level, by tuning the blend composition, thus achieving: (i) a smooth morphology, which enables long term air stability with no need for encapsulation (over one year lifetime in the 1:1) (ii) a good balance between holes and electrons mobility, which leads to high EQE (3.5% at 670 nm in 3:1 blend) and fast response speed in the range of few hundreds of nanoseconds.

#### Acknowledgments

The authors are grateful to the Italian MIUR for support through the FIRB project RBNE033KMA. We would like also to thank Carlo Tarantini, Alessandro Ghilardi and Antonio Iacchetti for their precious contribution in the experimental activity.

#### Appendix A. Supplementary material

Supplementary data associated with this article can be found, in the online version, at doi:10.1016/j.orgel.2009.07.011.

#### References

- [1] J.C. Blakesley, P.E. Keivanidis, M. Campoy-Quiles, C.R. Newman, Y. Jin, R. Speller, H. Sirringhaus, N.C. Greenham, J. Nelson, P. Stavrinou, *Nuclear Instrum. Meth. Phys. Res. A* 580 (2007) 774–777.
- [2] X. Xu, M. Davanco, X. Qi, S.R. Forrest, *Org. Electron.* 9 (2008) 1122–1127.
- [3] M.R. Antognazza, U. Scherf, P. Monti, G. Lanzani, *Appl. Phys. Lett.* 90 (2007) 163509.
- [4] A. Pais, A. Banerjee, D. Klotzkin, I. Papautsky, *Lab Chip* 8 (2008) 794–800.
- [5] K.H. An, B. O'Connor, K.P. Pipe, Y. Zhao, M. Shtein, *Appl. Phys. Lett.* 93 (2008) 033311.
- [6] A.C. Niemeyer, I.H. Campbell, F. So, *Appl. Phys. Lett.* 91 (2007) 103504.
- [7] Y. Yao, Y. Liang, V. Shrotriya, S. Xiao, L. Yu, Y. Yang, *Adv. Mater.* 19 (2007) 3979–3983.
- [8] T. Morimune, H. Kajii, Y. Ohmori, *IEEE Photon. Technol. Lett.* 18 (24) (2006).
- [9] P. Polishuk, *IEEE Commun. Mag.* 44 (9) (2006) 140–148.

- [10] T. Agostinelli, M. Caironi, D. Natali, M. Sampietro, G. Dassa, E.V. Canesi, C. Bertarelli, G. Zerbi, J. Cabanillas-Gonzalez, S. De Silvestri, G. Lanzani, *J. Appl. Phys.* 104 (2008) 114508.
- [11] M. Sampietro, G. Ferrari, D. Natali, Italian Pat. No. MI2002A000231.
- [12] For a recent review on low optical gap polymers see J. Roncali, *Macromol. Rapid Commun.* 28 (2007) 1761–1775. and ref. therein.
- [13] S. Na, S. Kim, J. Jo, K. Lee, S. Park, D. Kim, *J. Photochem. Photobiol. A: Chem.* 194 (2008) 161–166.
- [14] I. Nausieda, K. Ryu, I. Kymissis, A. Akinwande, V. Bulović, C.G. Sodini, *IEEE Trans. Electron Dev.* 55 (2) (2008) 527–532.
- [15] F. Silvestri, M.D. Irwin, L. Beverina, A. Facchetti, G.A. Pagani, T.J. Marks, *J. Am. Chem. Soc.* 130 (2008) 17640–17641.
- [16] L. Beverina, A. Abbotto, M. Landenna, M. Cerminara, R. Tubino, F. Meinardi, S. Bradamante, G.A. Pagani, *Org. Lett.* 7 (2005) 4257.
- [17] C.-C. Wu, J.C. Sturm, R.A. Register, J. Tian, E.P. Dana, M.E. Thompson, *IEEE Trans. Electron Dev.* 44 (1997) 1269.
- [18] D. Natali, L. Fumagalli, M. Sampietro, *J. Appl. Phys.* 101 (2007) 014501.
- [19] A.H. Schmidt, in: R. West (Ed.), *Oxocarbons*, Academic Press, New York, 1980, p. 185.
- [20] (a) K.Y. Law, *J. Phys. Chem.* 91 (1987) 5184; (b) K.Y. Law, *Chem. Rev.* 93 (1993) 449.
- [21] K.Y. Law, F.C. Bailey, *J. Org. Chem.* 57 (1992) 3278.
- [22] (a) M. Emmelius, G. Pawlowski, H.W. Vollmann, *Angew. Chem.* 101 (1989) 1475; (b) M. Emmelius, G. Pawlowski, H.W. Vollmann, *Angew. Chem., Int. Ed. Engl.* 28 (1989) 1445.
- [23] E.C.P. Smits, S. Setayesh, T.D. Anthopoulos, M. Buechel, W. Nijssen, R. Coehoorn, P.W.M. Blom, B. de Boer, D.M. de Leeuw, *Adv. Mater.* 19 (2007) 734.
- [24] (a) A. Burke, L. Schmidt-Mende, S. Ito, M. Graetzel, *Chem. Commun.* 3 (2007) 234; (b) J.-H. Yum, P. Walter, S. Huber, D. Rentsch, T. Geiger, F. Nuesch, F. De Angelis, M. Grätzel, M.K. Nazeeruddin, *J. Am. Chem. Soc.* 129 (2007) 10320.
- [25] (a) C.-T. Chen, S.R. Marder, L.T. Cheng, *Chem. Commun.* 259 (1994); (b) C.-T. Chen, S.R. Marder, L.T. Cheng, *J. Am. Chem. Soc.* 116 (1994) 3117.
- [26] J.R. Johnson, N. Fu, E. Arunkumar, W.M. Leevy, S.T. Gammon, D. Piwnica-Worms, B.D. Smith, *Angew. Chem., Int. Ed.* 46 (2007) 5528.
- [27] L.-H. Liu, K. Nakatani, R. Pansu, J.-J. Vachon, P. Tauc, E. Ishow, *Adv. Mater.* 19 (2007) 433.
- [28] For a comprehensive paper on squaraine design opportunities see D. Keil, H. Hartmann, *Dyes Pigments* 49 (2001) 161–179 (and references therein).
- [29] L. Lepnev, A. Vaschenko, A. Vitukhnovskiy, S. Eliseeva, O. Kotova, S. Torgova, N. Kuzmina, *Synth. Met.* 156 (2006) 624–632.
- [30] G. Blatter, F. Greuter, *Phys. Rev.* 33 (1986) 6.
- [31] M. Hiramoto, T. Imahigashi, M. Yokoyama, *Appl. Phys. Lett.* 64 (1994) 2.
- [32] E.H. Sargent, *Adv. Mater.* 20 (2008) 3958–3964.
- [33] G. Matsunobu, Y. Oishi, M. Yokoyama, M. Hiramoto, *Appl. Phys. Lett.* 81 (7) (2002) 1321–1322.
- [34] L.A. Majewski, J.W. Kingsley, C. Balocco, A.M. Song, *Appl. Phys. Lett.* 88 (2006) 222108.
- [35] Y. Wen, Y. Liu, C. Di, Y. Wang, X. Sun, Y. Guo, J. Zheng, W. Wu, S. Ye, G. Yu, *Adv. Mater.* 21 (2009) 1–5.
- [36] G. Yu, J. Gao, J.C. Hummelen, F. Wudl, A.J. Heeger, *Science* 270 (1995) 1789.
- [37] Y. Shen, M.W. Klein, D.B. Jacobs, J.C. Scott, G.G. Malliaras, *Phys. Rev. Lett.* 86 (2001) 3867–3870.
- [38] T. Agostinelli, M. Caironi, D. Natali, M. Sampietro, P. Biagioni, M. Finazzi, L. Duò, *J. Appl. Phys.* 101 (2007) 114504.
- [39] M. Caironi, T. Agostinelli, D. Natali, M. Sampietro, R. Cugola, M. Catellani, S. Luzzati, *J. Appl. Phys.* 102 (2007) 024503.
- [40] J. Davenas, P. Alcouffe, A. Ltaief, A. Bouazizi, *Macromol. Symp.* 233 (2006) 203–209.
- [41] L.H. Nguyen, H. Hoppe, T. Erb, S. Günes, G. Gobsch, N. Serdar Sariciftci, *Adv. Funct. Mater.* 17 (2007) 1071–1078.
- [42] M. Campoy-Quiles, T. Ferenczi, T. Agostinelli, P.G. Etchegoin, Y. Kim, T.D. Anthopoulos, P.N. Stavrinou, D.D.C. Bradley, J. Nelson, *Nat. Mater.* 7 (2008) 158–164.
- [43] T. Agostinelli, M. Campoy-Quiles, J.C. Blakesley, R. Speller, D.D.C. Bradley, J. Nelson, *Appl. Phys. Lett.* 93 (2008) 203305.
- [44] S. Uemura, R. Sakaida, T. Kawai, T. Kamata, *Synth. Met.* 153 (2005) 277–280.

donor/acceptor couple is limited to ~5% due to the incomplete match with the solar spectrum and the large offset of the LUMO energy levels of the donor and acceptor [3,12,13].

The maximum photon flux of the solar spectrum (at 1.6–1.8 eV) lies slightly beyond the reach of most organic conjugated polymers, which have band gaps >1.8 eV. Despite of significant progress in the synthesis and processing of low band gap polymers, which are capable of absorbing a broad range of solar photons, only a few polymeric systems have achieved power conversion efficiency comparable with P3HT [14,15]. A possible route to overcome the low performance often observed with low band gap polymer might be the use of low band gap small molecule as donor.

Solution processable small molecules have attractive features such as low band gap and high charge carrier mobility than conjugated polymers. These small molecule donors can be more easily synthesized in many variant and purify (e.g. of trace metal catalysis employed in the synthesis) are intrinsically more mono-dispersive, and are often environmentally more stable [16–18]. There are several families of solution processable small molecules that have been used as donor materials in BHJ solar cells [19–22].

Triphenylamine (TPA) seems to be a promising candidate as the electron-rich moieties and polymers containing TPA unit have presented high photoluminescence efficiency, good hole-transporting ability, outstanding photoconductivity, three-dimensional steric, and good light-harvesting properties. Due to the non-coplanarity of the three phenyl ring, TPA and related derivatives can be viewed as 3D systems and the amorphous character of these materials offers possibilities to develop active materials for optoelectronic devices with optical and charge-transport properties. Moreover their amorphous behavior, electronic and redox properties are also important and might be influenced by the type of structures. Dendritic or hyperbranched structures with TPA derivatives, which show interesting properties like energy transfer, and light-harvesting antenna, have received significant attentions. The three-dimensional structure of a branched polymer or monomer might improve carrier transport to offer favourable electrical properties. Certain BHJ solar cells based on materials containing TPA have been reported very recently [23,24].

Benzothiadiazole (BTD) is a commonly used electron acceptor, which can conjugatively link with an electron-rich molecule to form low band gap functional polymers or small molecules, and materials prepared in this manner showed usefulness in light emitting diodes, solar cells, light-harvesting and other optical or electronic functional devices [25,26].

Cyano groups could be used as the electron-withdrawing units. Materials with high electron affinities played a crucial role in the development of high-performance conjugated polymer optoelectronic devices [27]. The introduction of cyano groups onto a poly(*p*-phenylenevinylene) backbone has been proved an effective way of lowering the LUMO level of the polymer [28]. Furthermore, the electrochemical stability of the polymers could be enhanced by

introducing cyano groups [29], which is also desirable for optoelectronic devices.

In this investigation we report the synthesis and characterization of two new vinylene compounds, **TPA-TNP** and **BTD-TNP**, which contain triphenylamine and benzothiadiazole segments, respectively. The first compound is a star-shaped molecule, while the second is a linear molecule. Their chromophore was extended by incorporating thiophene and then vinylene moieties to the central TPA and BTD unit. Moreover, a cyano and a nitro substituent were inserted into the vinylene bond and the terminal phenyls, respectively. The chemical structure of the compounds was designed so as to broadening their absorption. The thermal, photophysical, electrochemical and photovoltaic properties of these compounds were systematically investigated.

## 2. Experimental

### 2.1. Characterization methods

IR spectra were recorded on a Perkin-Elmer 16PC FT-IR spectrometer with KBr pellets. <sup>1</sup>H NMR (400 MHz) spectra were obtained using a Bruker spectrometer. Chemical shifts ( $\delta$  values) are given in parts per million with tetramethylsilane as an internal standard. UV–vis spectra were recorded on a Beckman DU-640 spectrometer with spectrograde THF. The PL spectra were obtained with a Perkin Elmer LS45 luminescence spectrometer. The PL spectra were recorded with the corresponding excitation maximum as the excitation wavelength. TGA was performed on a DuPont 990 thermal analyzer system. Ground samples of about 10 mg each were examined by TGA and the weight loss comparisons were made between comparable specimens. Dynamic TGA measurements were made at a heating rate of 20 °C/min in atmospheres of N<sub>2</sub> at a flow rate of 60 cm<sup>3</sup>/min. Thermomechanical analysis (TMA) was recorded on a DuPont 943 TMA using a loaded penetration probe at a scan rate of 20 °C/min in N<sub>2</sub> with a flow rate of 60 cm<sup>3</sup>/min. The TMA experiments were conducted at least in duplicate to ensure the accuracy of the results. The TMA specimens were pellets of 10 mm diameter and ~1 mm thickness prepared by pressing powder of sample for 3 min under 8 kp/cm<sup>2</sup> at ambient temperature. The *T<sub>g</sub>* is assigned by the first inflection point in the TMA curve and it was obtained from the onset temperature of this transition during the second heating. Elemental analyses were carried out with a Carlo Erba model EA1108 analyzer.

### 2.2. Reagents and solvents

Tributyl-2-thienyl-stannane was prepared from the reaction of thiophene with *n*-BuLi in hexane and subsequently with tributylchlorostannane according to the literature [30]. 4-Nitrobenzyl cyanide was synthesized from the nitration of benzyl cyanide with concentrated nitric and sulfuric acid [31]. *N,N*-Dimethylformamide (DMF) and tetrahydrofuran (THF) were dried by distillation over CaH<sub>2</sub>. Toluene was dried by distillation over sodium. All

other reagents and solvents were commercially purchased and were used as supplied.

### 2.3. Preparation of compound TPA-TNP

A flask was charged with a solution of **3** (0.48 g, 0.83 mmol) and 4-nitrobenzyl cyanide (0.41 g, 2.52 mmol) in anhydrous ethanol (20 mL). Sodium hydroxide (0.33 g, 8.25 mmol) dissolved in anhydrous ethanol (10 mL) was added portion-wise to the stirred solution. The mixture was stirred for 1 h at room temperature under N<sub>2</sub> and then was concentrated under reduced pressure. Compound **TPA-TNP** precipitated as a dark green solid by cooling into a refrigerator. It was filtered off, washed thoroughly with water and dried (0.44 g, 53%).

FT-IR (KBr, cm<sup>-1</sup>) (Fig. 1a): 3044, 2924, 2158, 1654, 1584, 1522, 1490, 1440, 1346, 1320, 1290, 1186, 1108, 1014, 854.

<sup>1</sup>H NMR (CDCl<sub>3</sub>, ppm) (Fig. 1b): 8.19 (m, 6H, phenylene "f"); 7.67 (broad, 3H, vinylene "d"); 7.48 (m, 6H, phenylene "e"); 7.32–7.31 (m, 6H, thiophene "c"); 7.23 (m, 6H, phenylene "b"); 7.09 (m, 6H, phenylene "a").

Anal. Calc. for C<sub>57</sub>H<sub>33</sub>N<sub>7</sub>O<sub>6</sub>S<sub>3</sub>: C, 67.91; H, 3.30; N, 9.72. Found: C, 67.23; H, 3.36; N, 9.68%.

### 2.4. Preparation of compound BTD-TNP

A flask was charged with a solution of **7** (0.14 g, 0.39 mmol) and 4-nitrobenzyl cyanide (0.13 g, 0.80 mmol)

in anhydrous ethanol (15 mL). Sodium hydroxide (0.10 g, 2.50 mmol) dissolved in anhydrous ethanol (8 mL) was added portion-wise to the stirred solution. The mixture was stirred for 1 h at room temperature under N<sub>2</sub> and then was concentrated under reduced pressure. Compound **BTD-TNP** precipitated as a dark green solid by cooling into a refrigerator. It was filtered off, washed thoroughly with water and dried (0.16 g, 64%).

FT-IR (KBr, cm<sup>-1</sup>): 3078, 3044, 2952, 2922, 2150, 1654, 1586, 1522, 1476, 1344, 1292, 1184, 1108, 1016, 936, 876, 830.

<sup>1</sup>H NMR (CDCl<sub>3</sub>, ppm): 8.13 (m, 4H, phenylene ortho to nitro); 7.83 (m, 2H, benzothiadiazole); 7.69 (s, 2H, vinylene); 7.47 (m, 4H, phenylene meta to nitro); 7.21 (m, 4H, thiophene).

Anal. Calc. for C<sub>32</sub>H<sub>16</sub>N<sub>6</sub>O<sub>4</sub>S<sub>3</sub>: C, 59.62; H, 2.50; N, 13.04. Found: C, 59.37; H, 2.43; N, 12.95%.

### 2.5. Fabrication of photovoltaic cells

The photovoltaic performance of the devices was performed with the structures ITO/**TPA-TNP**:PCBM/Al (device A) and ITO/**BTD-TNP**:PCBM/Al (device B). The small molecules **TPA-TNP** and **BTD-TNP** were used as donor and PCBM as acceptor, which were defined as devices A and B. Both the devices were prepared in air, on the pre-cleaned indium tin oxide coated glass substrates. The active layer of blend was prepared by spin coating on ITO glass using a solution of **TPA-TNP**:PCBM or **BTD-TNP**:PCBM (1:1 ratio by wt) in

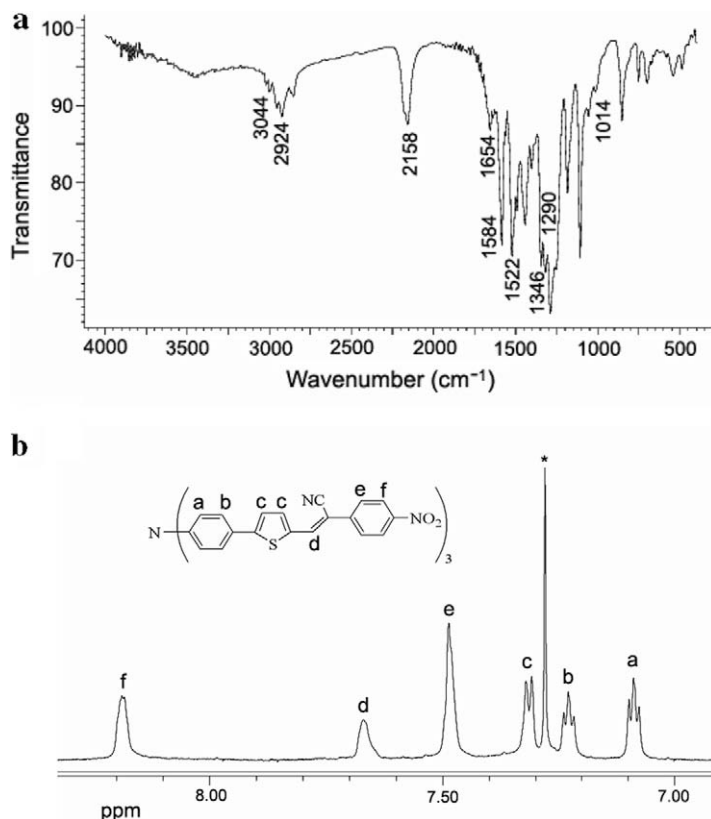


Fig. 1. FT-IR spectrum (a) and <sup>1</sup>H NMR spectrum in CDCl<sub>3</sub> solution (b) of compound **TPA-TNP**.

1,2-dichlorobenzene. The thermal annealing was carried out at 100 °C for 10 min in a glove box. The thickness of the active layer in all devices is around  $100 \pm 5$  nm. Finally, to complete the devices, the Al electrode was deposited onto the blend film by thermal evaporation at the vacuum around  $10^{-5}$  Torr. The effective area of all devices is about 25 mm<sup>2</sup>. All of the current–voltage characteristics of the devices were measured in air using a Keithley electrometer having built in power supply. A 100 W tungsten–halogen lamp was used as light source. For the photovoltaic measurements, the devices were illuminated through the ITO side with an illumination intensity of 100 mW/cm<sup>2</sup>.

### 3. Results and discussion

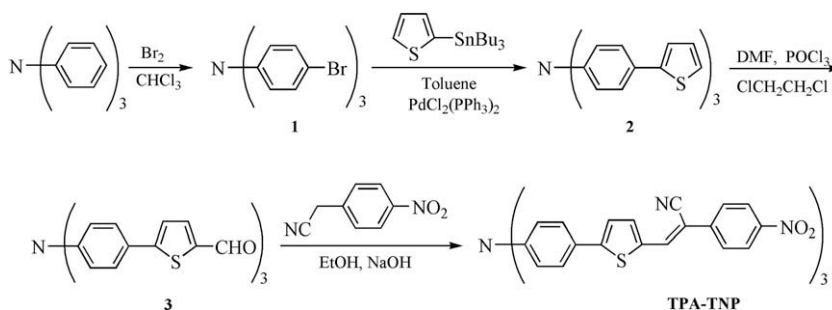
#### 3.1. Synthesis and characterization

Schemes 1 and 2 outline the synthesis of the target compounds **TPA-TNP** and **BTD-TNP** which are derivatives of the triphenylamine and benzothiadiazole, respectively. The intermediate compounds **1** [32], **2** [33], **3** [33], **4**, [34], **5** [34], **6** [6a] and **7** [33,35] were synthesized according to the literature. Compounds **TPA-TNP** and **BTD-TNP** were prepared by reacting 4-nitrobenzyl cyanide with **3** and **7**, respectively, in anhydrous ethanol in the presence of NaOH. This reaction could be catalyzed with *tert*-BuOK instead of NaOH. **TPA-TNP** and **BTD-TNP** were soluble in common organic solvents such as THF, chloroform and dichloromethane even though they lacked of aliphatic chains. **TPA-TNP** displayed higher solubility in these sol-

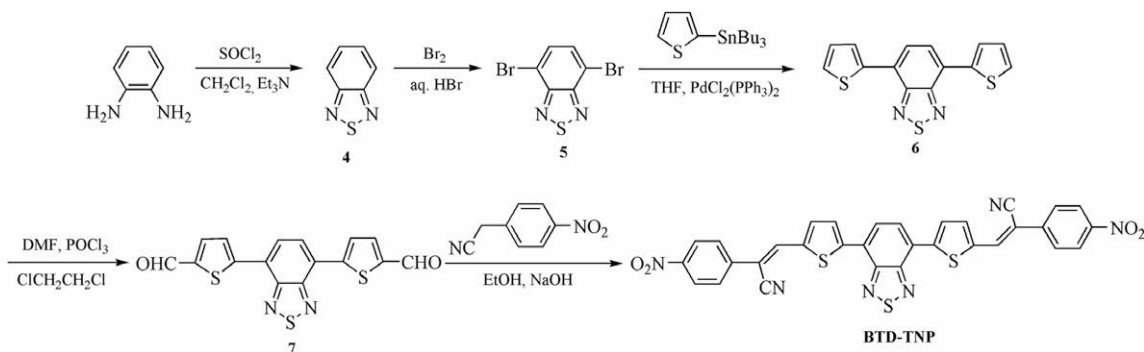
vents than **BTD-TNP** due to the dendronized nature of the former and the non-coplanar conformation of the triphenylamine core.

The chemical structures of the compounds were confirmed by FT-IR and <sup>1</sup>H NMR spectroscopy. Fig. 1 depicts the IR and <sup>1</sup>H NMR spectra of compound **TPA-TNP**. The IR spectrum (Fig. 1a) showed characteristic absorption bands at 3044 (aromatic C–H stretching); 1584, 1490, 1440 (C=C aromatic ring stretching band); 2158 (cyano group); 1654 (C=C olefinic stretching vibration); 1522, 1346 (nitro group) and 1014 cm<sup>-1</sup> (trans olefinic bond). Furthermore, **TPA-TNP** displayed characteristic absorption at 2924, 1320 and 1290 cm<sup>-1</sup> assigned to the triphenylamine. Finally, compound **BTD-TNP** displayed absorptions at 2952, 2922, 1476, 1292, 1108, 876 and 830 cm<sup>-1</sup> associated with the benzothiadiazole unit.

The <sup>1</sup>H NMR spectrum of **TPA-TNP** (Fig. 1b) exhibited an upfield peak at 8.19 ppm assigned to the phenylene protons labeled “f” which was deshielded by the electron-withdrawing nitro group. The vinylic proton “d” resonated at a relatively higher shift (7.67 ppm) than that of the usual vinylic protons owing to the cyano substituent on the vinylic bond. The aromatic protons “e”, “c”, “b” and “a” gave signals at 7.48, 7.32–7.31, 7.23 and 7.09 ppm, respectively. Likewise, the <sup>1</sup>H NMR spectrum of **BTD-TNP** showed upfield resonances at 8.13 (phenylene ortho to nitro) and 7.83 ppm (benzothiadiazole). Finally, the vinylic protons, the aromatic protons meta to nitro and the thiophene gave peaks at 7.69, 7.47 and 7.21 ppm, respectively.



Scheme 1. Synthesis of compound **TPA-TNP**.



Scheme 2. Synthesis of compound **BTD-TNP**.



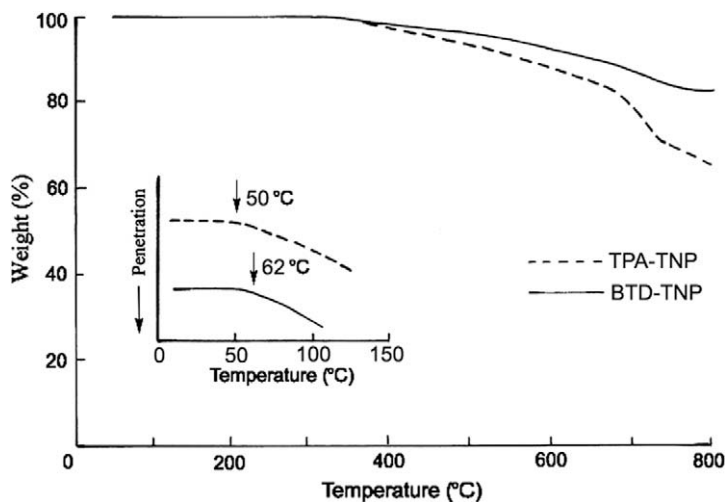


**Fig. 2.** TGA thermograms of compounds **TPA-TNP** and **BTD-TNP** in  $N_2$ . The inset shows the TMA traces of these compounds. Conditions:  $N_2$  flow,  $60\text{ cm}^3/\text{min}$ ; heating rate,  $20\text{ }^\circ\text{C}/\text{min}$ .

**Table 1**  
Thermal and optical properties of compounds **TPA-TNP** and **BTD-TNP**.

Compound	TPA-TNP	BTD-TNP
$T_d^a$ ( $^\circ\text{C}$ )	456	521
$Y_c^b$ (%)	65	82
$T_g^c$	50	62
$\lambda_{a,max}^d$ in solution (nm)	357, 469, 638	348, 469, 650
$\lambda_{a,max}^d$ in thin film (nm)	359, 473, 640	359, 452, 640
$E_g^{opte}$	1.67 eV (744 nm) <sup>f</sup>	1.65 eV (751 nm) <sup>f</sup>

Numbers in italic indicate the long wavelength absorption maximum.

<sup>a</sup> Decomposition temperature corresponding to 5% weight loss in  $N_2$  determined by TGA.

<sup>b</sup> Char yield at  $800\text{ }^\circ\text{C}$  in  $N_2$  determined by TGA.

<sup>c</sup> Glass transition temperature determined by TMA.

<sup>d</sup>  $\lambda_{a,max}$ : the absorption maxima from the UV–vis spectra in THF solution or in thin film.

<sup>e</sup>  $E_g$ : The optical band gap calculated from the onset of the thin film absorption.

<sup>f</sup> Numbers in parentheses indicate the onset of the thin film absorption.

Thermal characterization of compounds was accomplished by TGA and TMA (Fig. 2). The decomposition temperature ( $T_d$ ), the char yield ( $Y_c$ ) at  $800\text{ }^\circ\text{C}$  in  $N_2$  by TGA as well as the glass transition temperature ( $T_g$ ) by TMA are listed in Table 1. Both compounds displayed good thermal stability since were stable up to  $\sim 350\text{ }^\circ\text{C}$ , decomposed above  $450\text{ }^\circ\text{C}$  and afforded  $Y_c$  of 65–82%. This feature is attributable to the absence of aliphatic chains in the molecules. **BTD-TNP** was more thermally stable than **TPA-TNP** and exhibited higher  $T_d$  and  $Y_c$  values. However, the  $T_g$ 's were relatively low ( $50\text{--}62\text{ }^\circ\text{C}$ ) due to the monomeric character of the compounds.

### 3.2. Photophysical properties

Fig. 3 depicts the UV–vis absorption spectra in both THF solution ( $10^{-5}\text{ M}$ ) and thin film of the compounds. All the spectroscopic features are summarized in Table 1.

The absorption spectra (Fig. 3) of the compounds had the same pattern in both solution and thin film with three maxima ( $\lambda_{a,max}$ ) around 360, 460 and 650 nm. It should be emphasized that the absorption spectra of the compounds were broad and covered a wide range of the UV–vis and near-infrared spectrum up to about 800 nm. This feature is desirable for the photovoltaic properties of the compounds. The presence of the nitro groups at the terminal phenyls of the molecules contributed to the broadening of their absorption as has been well established in the literature [36]. Even though the long wavelength  $\lambda_{a,max}$  in thin film was identical for both compounds (650 nm), **BTD-TNP** showed an absorption onset at slightly higher wavelength and consequently lower optical band gap ( $E_g^{opt}$ ) than **TPA-TNP**. Specifically, the thin film absorption onset was located at 744 and 751 nm which correspond to  $E_g^{opt}$  of 1.65 and 1.67 eV for **TPA-TNP** and **BTD-TNP**, respectively (Table 1). These  $E_g^{opt}$  values are significantly lower as compared to related materials. Particularly, a series of related triphenylamine–thienylenevinylene star-shaped molecules<sup>57</sup> have shown  $E_g^{opt}$  of 2.38–1.78 eV. In addition,  $E_g^{opt}$  of 2.14 eV has been reported for star-shaped molecule with triphenylamine as core and benzo[1,2,5]thiadiazole vinylene as arms [37]. Finally, a conjugated copolymer [38] based on 4,7-dithien-2-yl-2,1,3-benzothiadiazole and 2,7-dibenzosilole had  $E_g^{opt}$  of 1.90 eV.

For the photoinduced efficient charge transfer in bulk heterojunction photovoltaic devices, the relative position of the lowest unoccupied molecular orbital (LUMO) of the donor (D) and acceptor (A) components used in photoactive layer is crucial. For the initiation of photoinduced charge transfer process, the difference between the LUMO level of D and A should be larger than the binding energy of excitons [39,40]. The magnitude of exciton binding energy in most of the organic semiconductor is about 0.5 eV [41]. The highest occupied molecular orbital (HOMO) and the LUMO energy levels of the compounds estimated from cyclic voltammetry measurement are  $-4.9$  and  $-3.2$  eV for

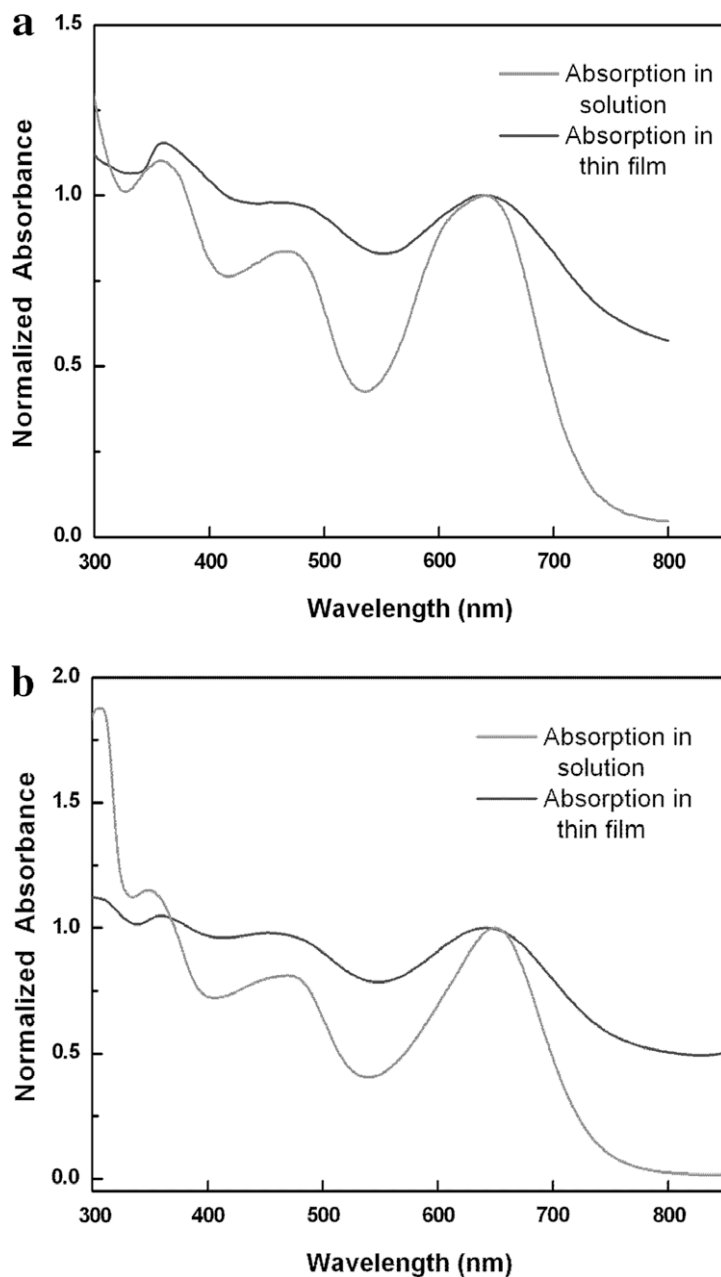


Fig. 3. Normalized UV-vis absorption spectra in THF solution and thin film of compounds **TPA-TNP** (a) and **BTD-TNP** (b).

**TPA-TNP**,  $-4.9$  and  $-3.25$  eV for **BTD-TNP** and  $-4.1$  and  $-6.6$  eV for PCBM. The difference between the LUMO levels of these small molecules and PCBM is comparatively larger than the binding energy of the exciton. Therefore, the relevant energy level positions and the absorption in long wavelength region suggest that these new small molecules should be effective donors in BHJ with PCBM as acceptor in photovoltaic devices.

### 3.3. Electrical properties of **BTD-TNP** and **TPA-TNP** films

The  $J$ - $V$  characteristics of the ITO/**BTD-TNP**/Al and ITO/**TPA-TNP**/Al devices in the dark are shown in Fig. 4. The  $J$ - $V$

characteristics of the devices show asymmetrical and exhibit rectification. This behavior can be explained by the small work function of the Al electrode and the p-type semi-conductivity of both organic layers. The rectification effect observed in this device is due to the formation of a Schottky barrier at the Al-organic layer and Ohmic contact with the ITO electrode. In the present device, the Fermi level of the ITO ( $-4.7$  eV) matches closely to the HOMO level of both compounds **BTD-TNP** and **TPA-TNP** and indicates the formation of Ohmic contact for hole injection from ITO electrode, whereas the Al forms the Schottky barrier with both organic compounds, which is responsible for the rectification effect.

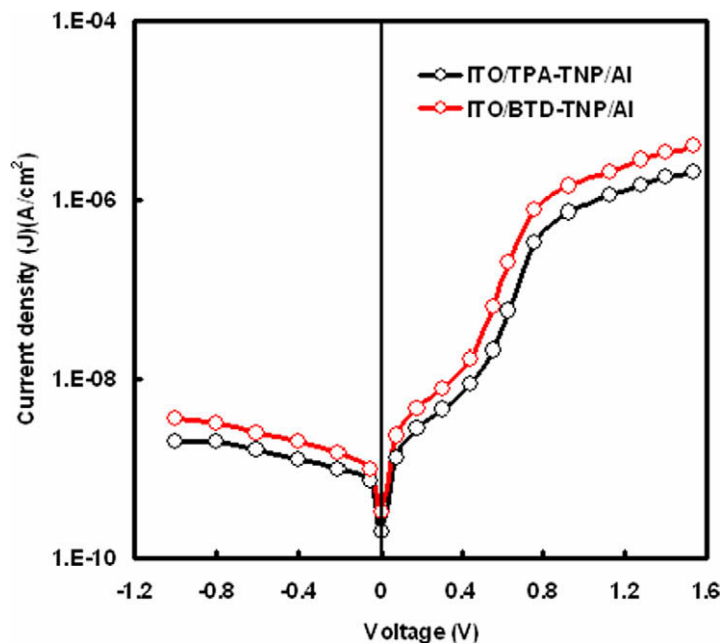


Fig. 4. Current–voltage characteristics of the devices based on TPA-TNP and BTD-TNP in the dark.

In order to get information about the position of Fermi level and charge carrier mobility for the present organic compounds, we have measured the current–voltage characteristics of the devices in the dark at different temperatures ranging from 300 to 380 K. It was found that the  $J$ – $V$  characteristics in low voltage region (0–0.3 V), the slope of  $\log(J)$ – $\log(V)$  curves at different temperature range is about unity, indicating the Ohmic conduction in this region as observed for phthalocyanines [42] and other small molecules [43]. The  $J$ – $V$  characteristics in this region are described by the following expression

$$J = N_v q \mu (V/d) \exp[-E_F/kT] \quad (1)$$

where  $N_v$  is the density of the state in HOMO level taken as  $10^{27} \text{ m}^{-3}$ ,  $q$  is the electronic charge,  $E_F$  is the position of Fermi level above the HOMO level,  $V$  is the applied voltage,  $d$  is the thickness of organic film,  $k$  is the Boltzmann's constant and  $T$  is the temperature. By plotting the  $\log(J)$  against  $1000/T$  at voltage of 0.2 V (as shown in Fig. 5), and fitting the data in accordance to Eq. (1), the values of  $E_F$  and  $\mu$  are being estimated as 0.45 eV and  $2.2 \times 10^{-5} \text{ cm}^2/\text{V s}$ , respectively for TPA-TNP. Similarly, the values of  $E_F$  and  $\mu$  for BTD-TNP are 0.41 eV and  $4.4 \times 10^{-5} \text{ cm}^2/\text{V s}$ , respectively.

In order to get information about the formation of Schottky barrier, we measured the incident photon to the current efficiency (IPCE) of the devices. The values of IPCE have been estimated using the following expression:

$$\text{IPCE} = 1240 J_{sc} / \lambda P_{in} \quad (2)$$

where  $J_{sc}$  ( $\text{mA}/\text{cm}^2$ ) is the short circuit photocurrent density for monochromatic irradiation and  $\lambda$  (nm) and  $P_{in}$  ( $\text{W}/\text{m}^2$ ) are the wavelength and the intensity of the monochromatic light, respectively. The IPCE spectra of the ITO/BTD-TNP/Al

device, illuminating through the ITO and Al side are shown in Fig. 6. Similar results were also obtained for the device based on TPA-TNP. It can be seen from Fig. 6 that the IPCE spectra of the device, illuminating through the Al side follow the absorption spectra of BTD-TNP (see Fig. 3). Since the binding energy of the exciton in the organic semiconductor is about 0.3 eV, the photocurrent in devices based on these materials is only due to the dissociation of excitons into free carriers at the Schottky barrier or p–n junction present in the devices. When the device is illuminated through the Al side, photons corresponding to the absorption peak of BTD-TNP are absorbed near the Al/BTD-TNP interfaces, generate excitons in this region and subsequently dissociate into free carrier, resulting higher photocurrent. However, the photons corresponding to the low and long wavelength regions (low absorption), penetrate more into the bulk of organic layer and are absorbed far from the Al/BTD-TNP interface and generate the excitons there. Only few excitons are able to reach the Al/BTD-TNP interface resulting low photocurrent because of short exciton diffusion length (10–15 nm) in organic semiconductors. The IPCE spectra of the device illuminating through ITO do not follow the absorption spectra of BTD-TNP. When the device is illuminated through the ITO side, the incident light penetrate more into the Al/BTD-TNP interface, at the wavelengths, where the absorption is low and generate excitons near this interface and subsequently dissociated into free carriers, resulting high photocurrent. However, when the absorption coefficient of organic layer is high, the excitons are generated near the ITO/BTD-TNP interface and only few excitons reach the Al/BTD-TNP interface resulting low photocurrent.

From the above results, we conclude that these materials behave as p-type organic semiconductors with average

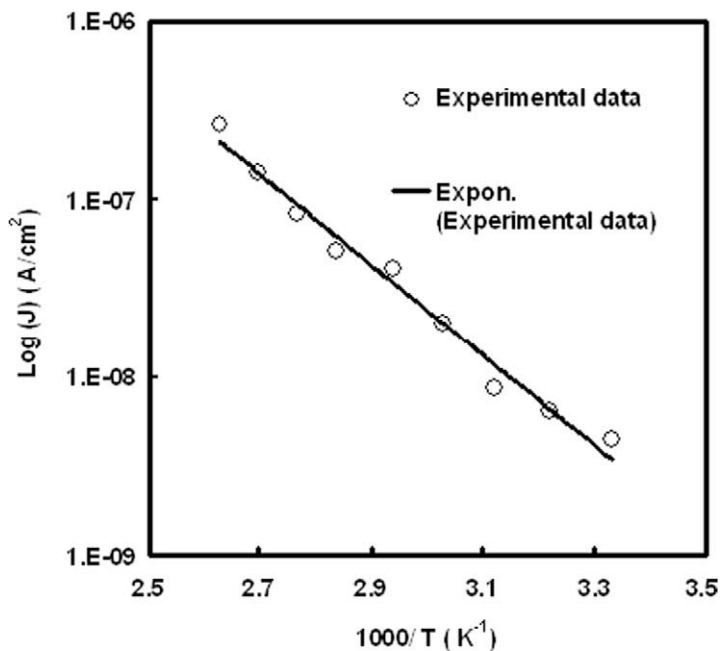


Fig. 5. Variation of  $\log(j)$  with  $1000/T$  in Ohmic region for ITO/BTD-TNP/Al device.

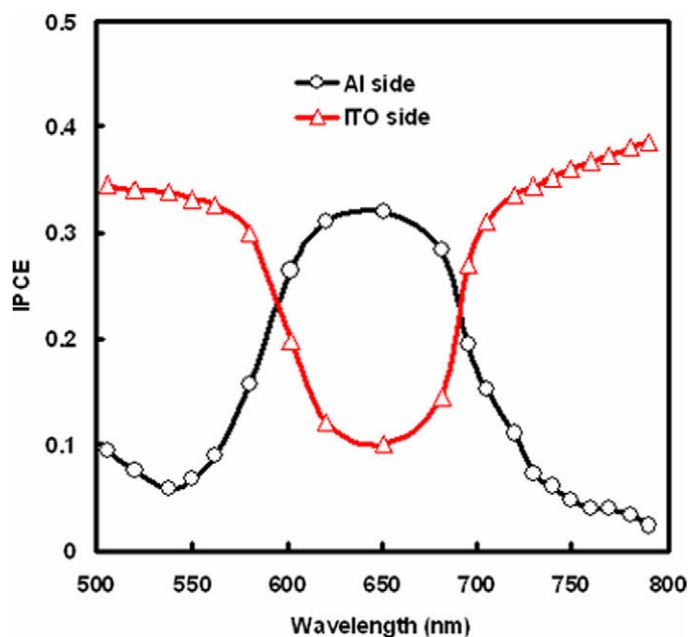


Fig. 6. IPCE spectra of the ITO/BTD-TNP/Al device illuminating through ITO and Al side.

hole mobility of the order of  $10^{-5}$   $\text{cm}^2/\text{V s}$  which form an Ohmic contact and Schottky barrier with high work function ITO electrode and low work function Al electrode, respectively. The generation of photocarrier in this device is due to the dissociation of excitons into free charge carriers due to the built in field at the Al–organic layer interface. These materials can be used as electron donors for bulk heterojunction photoactive devices.

#### 3.4. Photovoltaic properties of blend TPA-TNP and BTD-TNP with PCBM

The IPCE spectra of the devices based on TPA-TNP:PCBM and BTD-TNP:PCBM having same structure, illuminating through the ITO side, are shown in the Fig. 7. It seems from this figure that the IPCE spectra of the device match closely to the absorption spectra of the

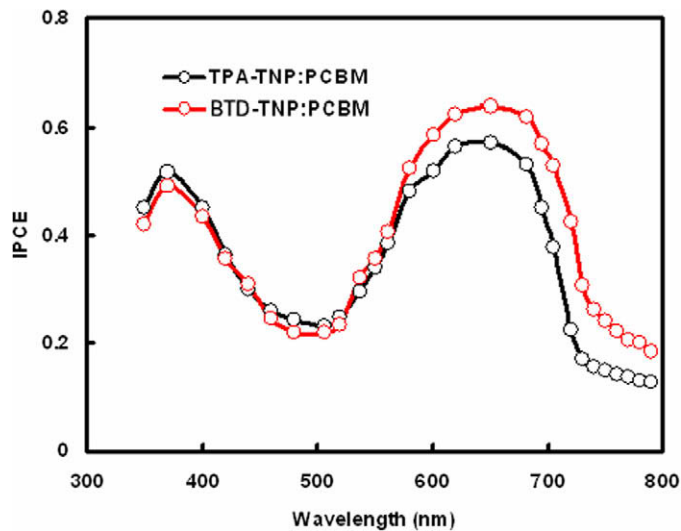


Fig. 7. IPCE spectra of the devices using **BTD-TNP:PCBM** and **TPA-TNP:PCBM** layers, illuminating through the ITO side.

active layer. This suggests the formation of donor and acceptor interfaces throughout the bulk of the active layer. The peak around 370 nm corresponds to the absorption of the PCBM. The IPCE value for these devices which corresponds to the absorption peak of donor (**TPA-TNP** or **BTD-TNP**) is higher than that for the device using only **TPA-TNP** or **BTD-TNP** due to the formation of large D–A interfacial area, resulting effective dissociation of exciton into free charge carriers.

The current–voltage characteristics ( $J$ – $V$ ) of the photovoltaic devices based on **TPA-TNP:PCBM** and **BTD-TNP:PCBM** blends were measured using an illumination

intensity of  $100 \text{ mW/cm}^2$ , and are shown in Figs. 8a and 8b, respectively, along with the  $J$ – $V$  characteristics for the devices using only **TPA-TNP** or **BTD-TNP**. Under illumination, the device based on **TPA-TNP** and **BTD-TNP** gives a power conversion efficiency ( $\eta$ ) of 0.08%, and 0.09%, respectively, while the device with **TPA-TNP:PCBM** and **BTD-TNP:PCBM** gives  $\eta$  of about 1.13% and 1.32%, respectively. The overall photovoltaic performance of the devices using the blend active layers is much higher than that of **TPA-TNP** or **BTD-TNP**. The improvement in the overall photovoltaic performance can be attributed to the formation of bulk D/A heterojunction through the volume of

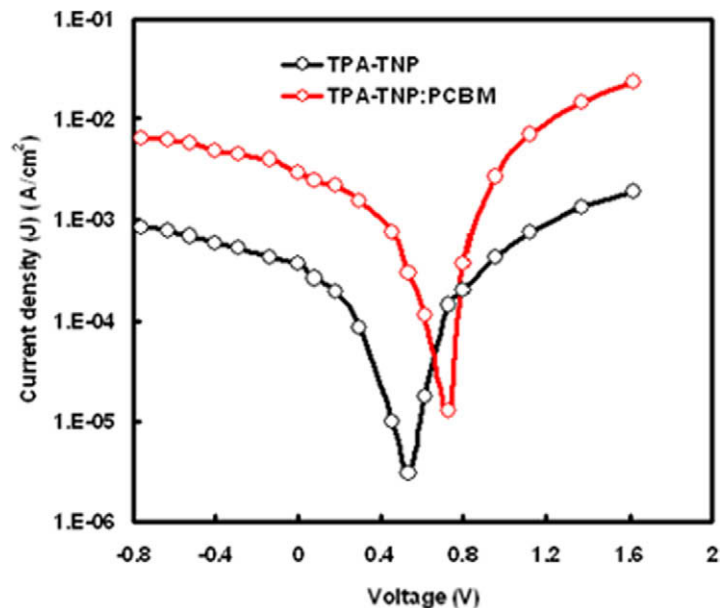


Fig. 8a. Current–voltage characteristics of the devices based on **TPA-TNP** and **TPA-TNP:PCBM** under illumination of  $100 \text{ mW/cm}^2$ .

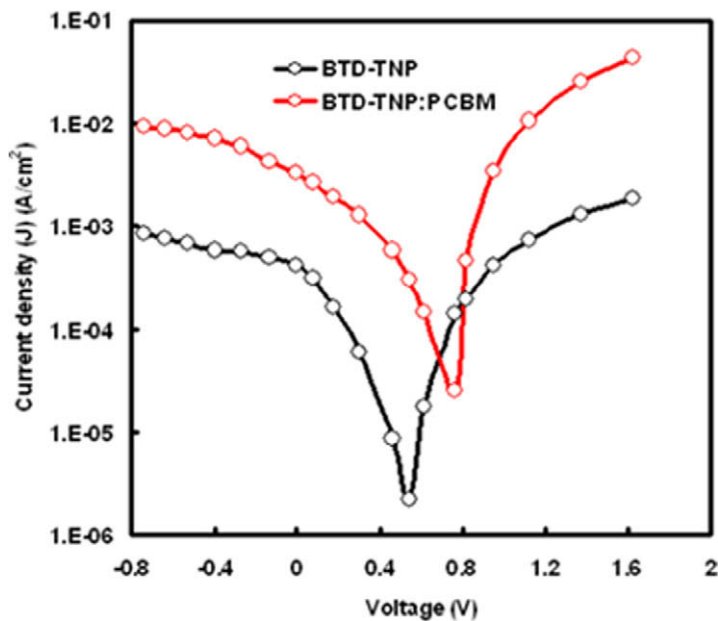


Fig. 8b. Current–voltage characteristics of the devices based on **BTD-TNP** and **BTD-TNP:PCBM** under illumination intensity of  $100 \text{ mW/cm}^2$ .

active layer that leads to an efficient dissociation of photo-generated exciton into free charge carriers and subsequent charge transfer from donor to acceptor. The slightly higher power conversion efficiency for the device with **BTD:PCBM** than device with **TPA-TNP** has been attributed to the more efficient photoinduced charge transfer in former device.

We have investigated the effect of thermal annealing on the photovoltaic properties of the **BTD-TNP:PCBM** (1:1 ratio) based device (Fig. 9) and the photovoltaic parameters are listed in Table 2. It can be seen from this table that significant improvement in the photovoltaic performance was

achieved upon thermal annealing (the power conversion efficiency increases from 1.32% to 2.42%). The open circuit voltage is slightly lower than that for the un-annealed one. The short circuit photocurrent increases by almost one order of magnitude and the fill factor also increases. Therefore, it is concluded that the annealing process plays an important role in the improvement of the device performance.

Different models have been proposed for the origin of  $V_{oc}$  [44,45]. In a single layered organic photovoltaic device, in which the active layer is composed of one type organic

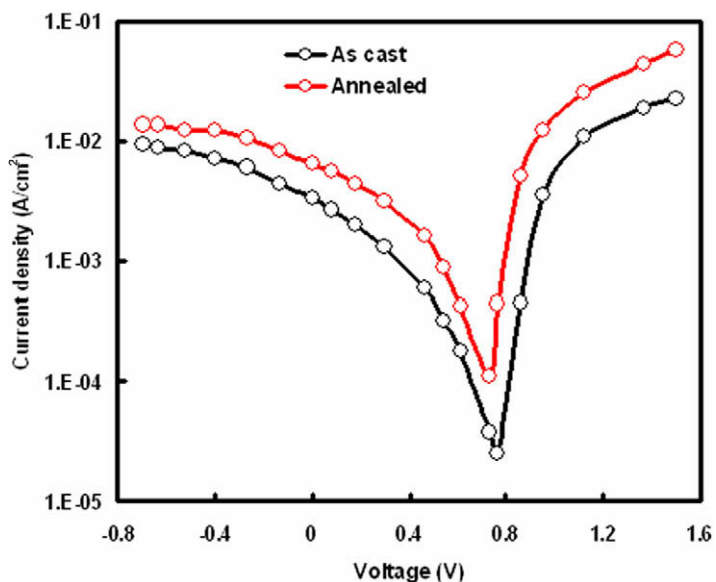


Fig. 9. Current–voltage characteristics of the devices based on as cast and thermally annealed **BTD-TNP:PCBM** blends under illumination intensity of  $100 \text{ mW/cm}^2$ .

**Table 2**

Photovoltaic parameters of the devices.

Device	Short circuit current ( $J_{sc}$ ) (mA/cm <sup>2</sup> )	Open circuit voltage ( $V_{oc}$ ) (V)	Fill factor	Power conversion efficiency ( $\eta$ ) (%)
ITO/ <b>TPA-TNP</b> /Al	0.36	0.54	0.42	0.08
ITO/ <b>BTD-TNP</b> /Al	0.42	0.53	0.44	0.09
ITO/ <b>TPA-TNP</b> :PCBM/Al	2.9	0.76	0.49	1.13
ITO/ <b>BTD-TNP</b> :PCBM/Al	3.37	0.78	0.50	1.32
ITO/ <b>BTD-TNP</b> :PCBM (annealed)/Al	6.42	0.70	0.54	2.42

semiconductor, donor or acceptor, the open circuit voltage,  $V_{oc}$  is principally determined by the difference in the work functions between the two metal electrodes: the metal-insulator-metal (MIM) model [45]. In this model the organic layer is assumed to have a negligible amount of intrinsic charge carriers and can therefore be considered as an insulator. Hence, the upper limit of the  $V_{oc}$  can be calculated from the estimation of the difference between the work function of the two electrodes. The  $V_{oc}$  of the ITO/**TPA-TNP**/Al device is 0.54 V, which closely matches the work function difference (0.6 eV) between the ITO (4.8 eV) and the cathode Al (4.2 eV). However, the MIM model cannot be applied to solar cells with a BHJ structure. It has been found that the  $V_{oc}$  is highly dependent on the LUMO level of the acceptors, suggesting that a Fermi level pinning between the negative electrode and acceptor could be the origin of the Ohmic like behavior of the acceptor-negative electrode contact [44].

The large values for  $J_{sc}$  and FF, upon thermal annealing imply lower series resistance and higher carrier mobility. Thus, the increased efficiency upon thermal annealing results from higher nanoscale crystallinity due to the demixing between the two components in the bulk heterojunction film after thermal annealing.

Fig. 10 shows the experimental  $J_{ph}$  of the devices using as cast and annealed **BTD-TNP**:PCBM blends in a double

logarithmic plot as a function of the effective voltage ( $V_o - V$ ). As can be seen in this figure, the photocurrent shows a strong enhancement, when the thermally annealed blend is used as active layer for the device. The short circuit current ( $J_{sc}$ ) increases by a factor of 1.9, the FF increases by a factor of 1.08 and the overall enhancement of  $\eta$  by about a factor of 1.82, when compared to the device with the cast blend. The effect of the thermal annealing on the solar cells performance in terms of physical parameters such as charge carrier mobility and photocurrent generation efficiency in these devices will be discussed in a following section of the paper.

In present device, after the photoinduced electron transfer at the donor/acceptor interfaces present in bulk photoactive layer and subsequent dissociation, the electrons are localized in the PCBM phases, whereas the holes remain in the **BTD-TNP**. Subsequently, the free electrons and holes must be transported via PCBM and **BTD-TNP** pathways towards the electrodes to produce the photocurrent. Therefore, the electron transport in PCBM and hole transport in **BTD-TNP** are crucial for understanding the photocurrent generation in the **BTD-TNP**:PCBM blend film. For pure PCBM the electron mobility was about  $2.0 \times 10^{-3}$  cm<sup>2</sup>/V s [46], which is about 100 times higher than the hole mobility in pure **BTD-TNP** as discussed earlier. An important question is whether these mobilities

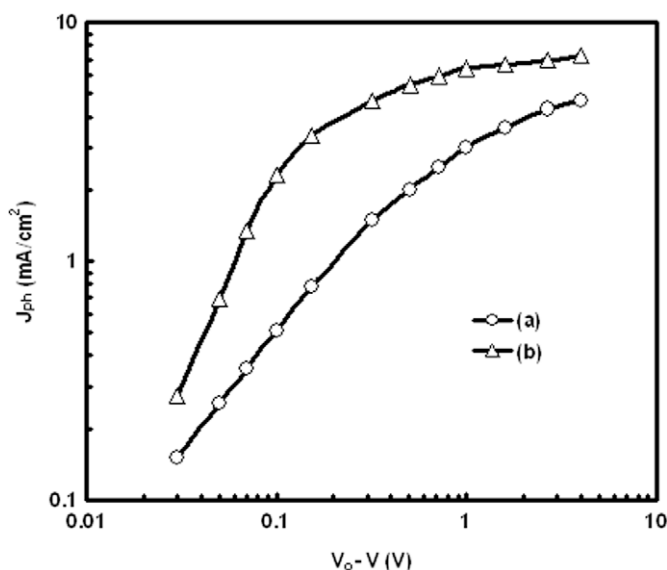


**Fig. 10.** Variation of photocurrent ( $J_{ph}$ ) with effective applied voltage ( $V_o - V$ ) of ITO/**BTD-TNP**:PCBM/Al device employing (a) as cast and (b) annealed photoactive layers.

are modified or not, when the materials are blended as in the active layer of the photovoltaic device. We have measured the hole and electron mobility in the blend using the space charge limited current (SCLC) method.

In order to measure the SCLC for only one type of charge carrier in the blend, the other charge carrier must be suppressed by a large injection barrier, resulting in an electron or hole only device. This approach has been successfully used to measure the hole and electron mobility in the conjugated polymer:PCBM blend [47,48], polymer:polymer blend [46], conjugated polymer: inorganic metal oxide nanoparticles blends [49,50] and CuPc:C<sub>60</sub> blend [51]. Since the HOMO and LUMO offsets between the compound **BTD-TNP** and PCBM are approximately 1.7 and 0.8 eV, respectively (HOMO and LUMO levels have been estimated from cyclic voltammetry measurements as discussed earlier), the transport of charge carriers in the mixed blend layer should occur along the paths consisting of only a single molecular species, i.e. compound **BTD-TNP** for holes and PCBM for electrons. Therefore, we model the  $J$ - $V$  characteristics for electron and hole only devices using the SCLC theory [52].

$$J = \frac{9}{8} \varepsilon \varepsilon_0 \mu(E) \theta \frac{V^2}{d^3} \quad (3)$$

where  $\varepsilon = 3.2$  is the relative dielectric constant of the organic film,  $\varepsilon_0$  is the vacuum dielectric constant,  $\theta \leq 1$  is the shallow trapping factor (where  $\theta = 1$  in the trap free limit),  $d$  is the film thickness and  $\mu(E)$  is the electric field ( $E$ ) dependent charge carrier mobility, given by Poole Frenkel law [53]

$$\mu(E) = \mu_0 \exp[\gamma(E)^{1/2}] \quad (4)$$

where  $\mu_0$  is the mobility at  $E = 0$  and  $\gamma$  denotes the field activation parameter. The field dependence arises from the interaction between the charge carriers and randomly oriented permanent dipoles in a molecular film, where charge carriers are transported by thermally assisted hopping [53].

Fig. 11a shows the  $J$ - $V$  characteristics of the **BTD-TNP**:PCBM blend film (as cast and annealed) sandwiched between ITO and Au electrodes (hole only device). In this configuration, holes are injected from ITO (work function of  $\phi_{\text{ITO}} = 4.8$  eV) into HOMO of compound **BTD-TNP**, whereas electron injection from Au into LUMO of PCBM is suppressed due to its high work function of 5.1 eV. The experimental curves are fitted to the above equations and the zero field hole mobility in the blend (as cast) is about  $6.5 \times 10^{-5}$  cm<sup>2</sup>/V s, which is lower than the value for **BTD-TNP**. However, when the annealed blend film is used in the device, the zero field mobility is increased by one order of magnitude (from  $6.5 \times 10^{-5}$  to  $3.4 \times 10^{-4}$  cm<sup>2</sup>/V s).

The  $J$ - $V$  characteristics of the **BTD-TNP**:PCBM blend (as cast and annealed film) sandwiched between two Al electrodes, to allow the efficient injection of electron from Al into the LUMO of PCBM are shown in Fig. 11b. In this device, the high injection barrier between Al and HOMO of **BTD-TNP** suppress the injection of holes and the device behaves as electron only device. The electron mobilities which were estimated using these curves are about  $1.86 \times 10^{-3}$  and  $3.4 \times 10^{-3}$  cm<sup>2</sup>/V s, for the as cast and annealed film, respectively. From these results, we conclude that the electron and hole mobilities are more balanced for the device in which the annealed blend is used, resulting efficient charge transportation and collection that enhance the power conversion efficiency.

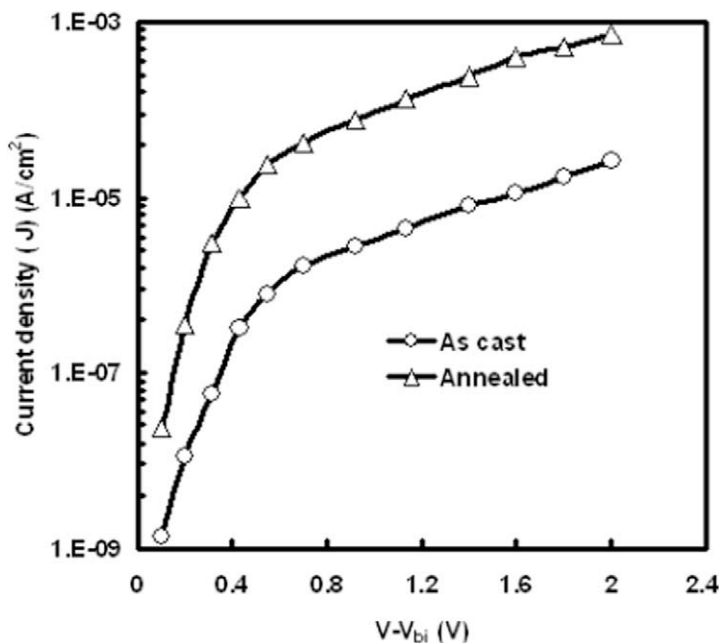


Fig. 11a. Current density–voltage characteristics in the dark for hole only device using **BTD-TNP**:PCBM films.



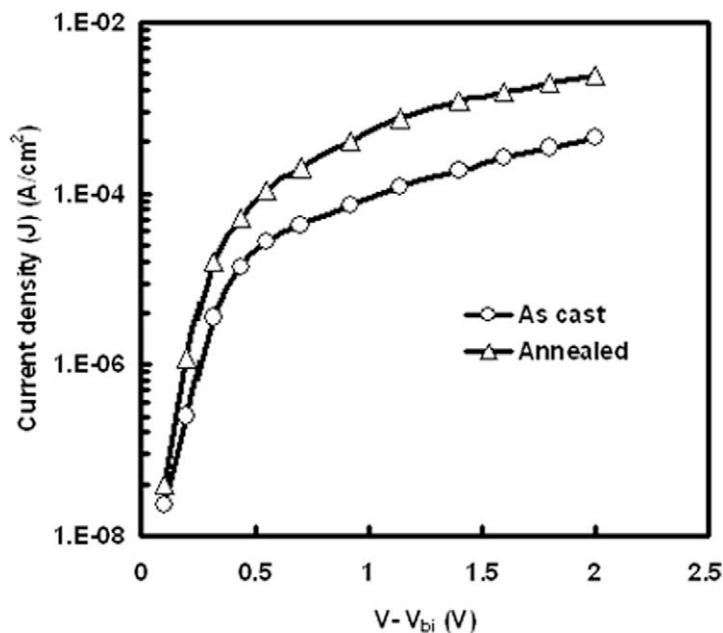


Fig. 11b. Current density–voltage characteristics in the dark for electron only device using BTD-TNP:PCBM films.

The LUMO level of compound **BTD-TNP** is at considerably higher energy level than that of PCBM and provides the sufficient energy to the excitons to dissociate into the free holes and electrons. The holes and electrons are collected at the respective electrodes by their transportation through the percolating paths of **BTD-TNP** and PCBM, respectively. The large difference between the electron and hole mobilities in the device with as cast film, results unbalanced charge transport due to the accumulation of space charge near the electrode. In this case the space charge limits the photocurrent. However, when the annealed film is used for the device, the difference between the electron and hole mobilities is reduced and the space charge no longer limits the charge transportation due to the more balanced charge transportation in device based on the annealed film.

#### 4. Conclusions

Starting from triphenylamine and benzothiadiazole two new vinylene compounds **TPA-TNP** and **BTD-TNP** were synthesized. These compounds were soluble in common organic solvents like THF, chloroform and dichloromethane. They showed relatively low glass transition temperature and high thermal stability. Both compounds displayed broad absorption with longer wavelength absorption maximum at 638–650 nm and optical band gap of 1.65–1.67 eV. The photovoltaic properties of the bulk heterojunction devices based on **TPA-TNP** and **BTD-TNP** as electron donor and PCBM as electron acceptor were investigated through analyzing their current–voltage characteristics. The power conversion efficiency of the device **BTD-TNP**:PCBM (annealed) blend is about 2.42%, which is attributed to the balanced charge transport in the device.

#### References

- [1] Y.F. Li, Y.P. Zou, *Adv. Mater.* 20 (2008) 2952–2958.
- [2] M. Svensson, F. Zhang, S.C. Veenstra, W.J.H. Verhees, J.C. Hummelen, J.M. Kroon, O. Inganäs, M.R. Andersson, *Adv. Mater.* 15 (2003) 988–991.
- [3] M.C. Scharber, D. Mühlbacher, M. Koppe, P. Denk, C. Waldauf, A.J. Heeger, C.J. Brabec, *Adv. Mater.* 18 (2006) 789–794.
- [4] M.X. Chen, E. Perzon, N. Ronissson, S.K.M. Jönsson, M.R. Andersson, M. Fahlman, M. Berggren, *Synth. Met.* 146 (2004) 233–236.
- [5] C.J. Brabec, C. Winder, N.S. Sariciftci, J.C. Hummelen, A. Dhanabalan, P.A. van Hal, R.A.J. Janssen, *Adv. Funct. Mater.* 12 (2002) 709–712.
- [6] (a) C. Kitamura, S. Tanaka, Y. Yamashita, *Chem. Mater.* 8 (1996) 570–578;  
(b) E.E. Havinga, W. Hoefeten, H. Wynberg, *Synth. Met.* 199 (1993) 55–70.
- [7] S. Mazumdar, S. Dallakyan, M. Chandross, *Synth. Met.* 139 (2003) 769–772.
- [8] F. Zhang, E. Perzon, X. Wang, W. Mammo, M.R. Andersson, O. Inganäs, *Adv. Funct. Mater.* 15 (2005) 745–750.
- [9] X. Wang, E. Perzon, F. Oswald, F. Langa, S. Admassie, M.R. Andersson, O. Inganäs, *Adv. Funct. Mater.* 15 (2005) 1665–1670.
- [10] L.M. Campos, A. Tontcheva, S. Günes, G. Sonmez, H. Neugebauer, N.S. Sariciftci, F. Wudl, *Chem. Mater.* 17 (2005) 4031–4033.
- [11] M.M. Wienk, M.G.R. Turbiez, M.P. Struijk, M. Fonrodona, R.A.J. Janssen, *Appl. Phys. Lett.* 88 (2006) 153511/1–153511/3.
- [12] H. Hoppe, N.S. Sariciftci, *J. Mater. Chem.* 16 (2006) 45–61.
- [13] W. Ma, C. Yang, X. Gong, K. Lee, A.J. Heeger, *Adv. Funct. Mater.* 15 (2005) 1617–1622.
- [14] J. Peet, J.Y. Kim, N.E. Coates, W.L. Ma, D. Moses, A.J. Heeger, G.C. Bazan, *Nat. Mater.* 6 (2007) 497–500.
- [15] M.M. Wienk, M. Turbiez, J. Gilot, R.A. Janssen, *Adv. Mater.* 20 (2008) 2556–2560.
- [16] M. Brumbach, D. Placencia, N.R. Armstrong, *J. Phys. Chem. C* 112 (2008) 3142–3151.
- [17] B.P. Rand, J. Genoe, P. Heremans, J. Poortmans, *Prog. Photovolt: Res. Appl.* 15 (2007) 659–676.
- [18] S. Yoo, W.J. Potscavage, B. Domercq, S.H. Han, T.D. Li, S.C. Jones, R. Szoszkiewicz, D. Levi, E. Riedo, S.R. Marder, B. Kippelen, *Solid-State Electron.* 51 (2007) 1367–1375.
- [19] S. Roquet, A. Cravino, P. Leriche, O. Aleveque, P. Frere, J. Roncali, *J. Am. Chem. Soc.* 128 (2006) 3459–3466.
- [20] A.B. Tamayo, B. Walker, T.Q. Nguyen, *J. Phys. Chem. C* 112 (2008) 11545–11551.

- [21] M.T. Lloyd, A.C. Mayer, S. Subramanian, D.A. Mournay, D.J. Herman, A. Bapat, J.E. Anthony, G.G. Malliaras, *J. Am. Chem. Soc.* 129 (2007) 9144–9149.
- [22] L. Valentini, D. Bagnis, A. Marrocchi, M. Seri, A. Taticche, J.M. Kenny, *Chem. Mater.* 20 (2008) 32–34.
- [23] Y. Zhang, H.-L. Yip, O. Acton, S.K. Hau, F. Huang, A.K.-Y. Jen, *Chem. Mater.* 21 (2009) 2598–2600.
- [24] C. He, Q. He, Y. Yi, G. Wu, F. Bai, Z. Shuai, Y. Li, *J. Mater. Chem.* 18 (2008) 4085–4090.
- [25] P.F. Xia, J. Lu, C.H. Kwok, H. Fukutani, M.S. Wong, Y. Tao, *J. Polym. Sci., Part A: Polym. Chem.* 47 (2008) 137–148.
- [26] Y. Yang, Y. Zhou, Q. He, C. He, C. Yang, F. Bai, Y. Li, *J. Phys. Chem. B* 113 (2009) 7745–7752.
- [27] F. Hide, Y. Greenwald, F. Wudl, A.J. Heeger, *Synth. Met.* 85 (1997) 1255–1256.
- [28] J.J.M. Halls, C.A. Walsh, N.C. Greenham, E.A. Marseglla, R.H. Friend, S.C. Moratti, A.B. Holmes, *Nature* 376 (1995) 498–500.
- [29] M.S. Liu, X.Z. Jiang, S. Liu, P. Herguth, A.K.-Y. Jen, *Macromolecules* 35 (2002) 3532–3538.
- [30] Y. Xia, J. Luo, X. Deng, X. Li, D. Li, X. Zhu, W. Yang, Y. Cao, *Macromol. Chem. Phys.* 207 (2006) 511–520.
- [31] G.R. Robertson, *Org. Synth. II* (1922) 57–58.
- [32] J. Cremer, P. Baeuerle, *J. Mater. Chem.* 16 (2006) 874–884.
- [33] S. Roquet, A. Cravino, P. Leriche, O. Alévêque, P. Frère, J. Roncali, *J. Am. Chem. Soc.* 128 (2006) 3459–3466.
- [34] F.S. Mancilha, B.A. DaSilveira Neto, A.S. Lopes, P.F. Moreira Jr., F.H. Quina, R.S. Gonçalves, J. Dupont, *Eur. J. Org. Chem.* 21 (2006) 4924–4933.
- [35] X. Zhang, R. Yamaguchi, K. Moriyama, M. Kadowaki, T. Kobayashi, T. Ishi-i, T. Thiemanna, S.J. Mataka, *Mater. Chem.* 16 (2006) 736–740.
- [36] Y. He, X. Wang, J. Zhang, Y. Li, *Macromol. Rapid Commun.* 30 (2009) 45–51.
- [37] G. Wu, G. Zhao, C. He, J. Zhang, Q. He, X. Chen, Y. Li, *Sol. Energy Mater. Sol. Cells* 93 (2009) 108–113.
- [38] P.-L.T. Boudreault, A. Michaud, M. Leclerc, *Macromol. Rapid Commun.* 28 (2007) 2176–2179.
- [39] G. Yu, J. Gao, J.C. Hummelen, F. Wudl, A.J. Heeger, *Science* 270 (1995) 1789–1791.
- [40] H.J. Snaith, A.C. Arias, A.C. Morteani, C. Silva, R.H. Friend, *Nano Lett.* 2 (2003) 1353–1357.
- [41] S. Barth, H. Bassler, *Phys. Rev. Lett.* 79 (1997) 4445–4449.
- [42] G.D. Sharma, V.S. Choudhary, J. Janu, M.S. Roy, *Mater. Sci.: Poland* 25 (2007) 1173–1191.
- [43] M.S. Roy Manmeeta, P. Jaiswal, G.D. Sharma, *J. Appl. Phys.* 94 (2003) 7692–7701.
- [44] C.J. Brabec, A. Cravino, D. Meissner, N.S. Sariciftci, T. Fromherz, M.T. Rispens, L. Sanchez, J.C. Hummelen, *Adv. Funct. Mater.* 11 (2001) 374–380.
- [45] V.D. Mihailetschi, J.K.J. van Duren, P.W.M. Blom, J.C. Hummelen, R.A.J. Janssen, J.M. Kroon, M.T. Rispens, W.J.H. Verhees, M.M. Wienk, *Adv. Funct. Mater.* 13 (2003) 43–46.
- [46] M.M. Mandoc, W. Verman, L.J.A. Koster, M.M. Koetse, J.J. Sweelssen, B. de Boer, P.W.M. Blom, *J. Appl. Phys.* 101 (2007) 104512/1–104512/5.
- [47] V.D. Mihailetschi, L.J.A. Koster, P.W.M. Blom, C. Melzer, B. de Boer, J.K.J. van Duren, R.A.J. Janssen, *Adv. Funct. Mater.* 15 (2005) 795–801.
- [48] P.W.M. Blom, V.D. Mihailetschi, L.J.A. Koster, D.E. Markov, *Adv. Mater.* 19 (2007) 1551–1566.
- [49] L.J.A. Koster, W.J. van Strien, W.J.E. Beek, P.W.M. Blom, *Adv. Funct. Mater.* 17 (2007) 1297–1302.
- [50] G.D. Sharma, P. Suresh, P. Balraju, S.K. Sharma, M.S. Roy, *Sol. Energy Mater. Sol. Cells* 92 (2008) 900–908.
- [51] B.P. Rand, J. Xue, S. Uchida, S.R. Forrest, *J. Appl. Phys.* 98 (2005) 124902/1–124902/7.
- [52] M. Pope, C.E. Swenberg, *Electron Processes in Organic Crystals and Polymers*, second ed., Oxford University Press, New York, 1999. p. 1376.
- [53] D.H. Dunlap, P.E. Parris, V.M. Kenkre, *Phys. Rev. Lett.* 77 (1996) 542–545.

performance [19], more research has been done to better control morphology via this facile solvent or solvent mixture method [17,20–24]. By far, it has been developed into one of the most powerful approaches to modify the morphology of photoactive layer and thus improve device performance. Peet et al. have demonstrated that longer charge carrier life time can be achieved by adding alkanethiol to the P3HT:PCBM composites in toluene due to an improved morphology with the formation of ordered structure in the untreated film [25]. Also by using this solvent additive method, Peet et al. have obtained the highest efficiency device to date in low-band gap polymers [26,27]. Though the solvents used and systems or materials investigated are different, one of the key tasks for all these works is to substantially improve the crystallinity of components in the composite film while maintaining large interfacial area.

Generally, for any semi-crystalline polymers, besides the molecular configuration, their crystallinity is frequently influenced by the crystallization conditions which could be classified into thermodynamic and kinetic determinations. Traditional polymer physics has revealed that crystallization temperature, time and the environments, e.g. external force, spatial confinement, surface and so on, play significant role in determining the crystallization behaviors of semi-crystalline polymers. Previously, most efforts have been diverted to the investigations on how to directly increase the crystallinity or tune the morphology of component itself in the composite. However, less attention has been paid to study how the crystallization behaviors of a specific component are affected by the other components involved in the composite, which has been shown that it plays a key role in determining the morphology of the thin composite film served as the photoactive layer of bulk-heterojunction polymer solar cells [28].

C60, as the first discovered fullerene molecule, is much cheaper than the widely used PCBM or other novel fullerene derivatives in organic Photovoltaic (PV) devices [29–33]. Therefore, C60 is a worthy candidate for lower production cost devices. Whereas, the performance of device based on P3HT:C60 composite film is usually lower than that based on P3HT:PCBM composite at present. To reveal the hindrances towards efficient polymer PV devices based on the low cost C60, we carry out comparative studies by choosing two composites consisting of the same electron donor material P3HT but different acceptors C60 and PCBM. In this work, we show that though the difference between C60 and PCBM is small in terms of molecular structure, the crystallization of P3HT is severely affected by C60 when compared with PCBM, resulting in distinct crystallinity variation of P3HT in untreated P3HT:C60 and P3HT:PCBM composite films spin coated from solution in the widely used ODCB solvent. The reason for the extremely low crystallinity of P3HT in P3HT:C60 composite has been analyzed and the solution to solve this problem has been proposed.

## 2. Experimental details

### 2.1. Materials

P3HT with  $M_w = 100,000$  g/mol, regioregularity greater than 98.5%, was purchased from Rieke Metals Inc. C60,

PCBM and ODCB (anhydrous, 99%) were purchased from Sigma–Aldrich Co. Ltd. Chlorobenzene (CB), 1,2,4-trichlorobenzene (TCB), tetralin, 1-Methylnaphthalene (M-naph) and 1-Chloronaphthalene (Cl-naph) were purchased from Beijing Chemical Reagent Co. Ltd., China. All these materials were used as received without further treatment.

### 2.2. Sample preparation

For C60 and PCBM solubility measurements, first, certain amount of C60 or PCBM was added into 1 ml solvent under intensive stirring for more than 24 h at room temperature. Second, the solutions were placed in quiet condition for at least 12 h to check if there was solid precipitating from the solution. Third, if no solid or precipitate was found, more C60 or PCBM was added to further dissolve in the solution until very little amount saturating crystallites are observed by optical microscopy. And for the solubility of P3HT, the solution was heated to 50 °C to completely dissolve P3HT by stirring for overnight and then cooled down to room temperature. Thus obtained solution was placed in quiet condition for 2 days to achieve thermodynamic equilibrium state. It is well known that if P3HT forms ordered aggregates, an absorption peak centered at ca. 610 nm will appear in its UV–vis absorption spectrum [34–36]. Therefore, UV–vis absorption measurements were performed on the solution. The approximate solubility of P3HT could be obtained by determining the concentration at which the peak at around 610 nm (see Fig. 1) just appears.

With respect to the preparation of composites, given amount of C60 or PCBM was firstly dissolved in solvents or solvent mixtures by intensive stirring. Afterwards, the designated amount of P3HT was added into the solution to get a mixture with P3HT:C60 = 5:4 or P3HT:PCBM = 1:1 by weight. These mixtures were continuously stirred in the dark for more than 12 h so that solutions with a concentration of 8.0 mg/ml for P3HT were obtained.

The thin films were obtained via spin coating (Laurell Spin Processor WS-400B 6NPP Lite) the as prepared solutions onto pre-cleaned glass cover slides. The spin coating speed of 500–1500 rpm was selected so as to eventually achieve homogeneous thin films having dimensions in order of one square centimeter and thickness of ca. 80 nm.

PV cells were fabricated according to standard device fabrication procedures. i.e. the photoactive layer was first fabricated by depositing the prepared solution on well-cleaned glass substrates covered with 100 nm thick layers of indium tin oxide (ITO) and a spin coated layer of poly(3,4-ethylenedioxythiophene):poly(styrene sulfonate) (PEDOT:PSS). The thickness of the photoactive layer is around 80 nm for all the devices. The devices were completed by evaporation of 1 nm LiF layer and subsequently 100 nm Al layer as cathode.

### 2.3. Characterization: transmission electron microscopy (TEM)

The spin coated films were floated on distilled water, then transferred to 400-mesh copper grids and dried in

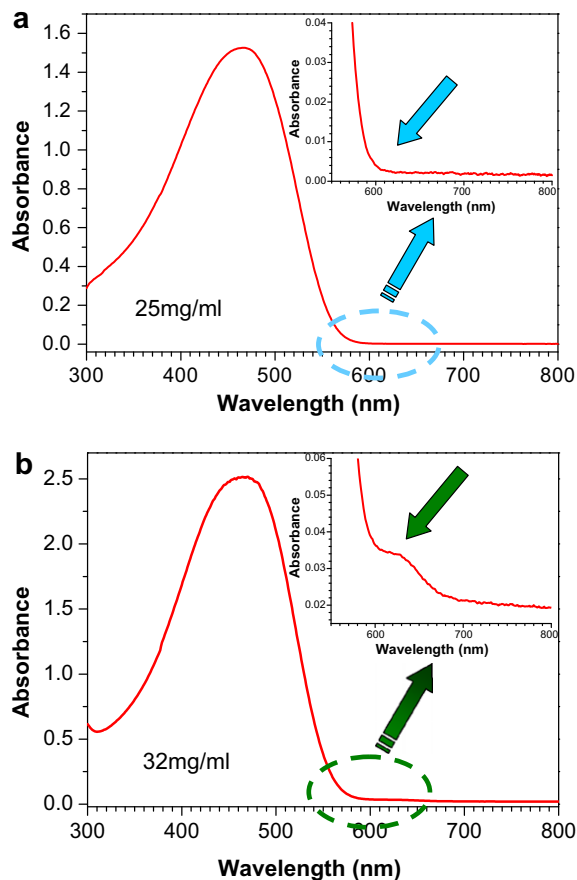


**Fig. 1.** UV-vis absorbance spectra of P3HT with a concentration of (a) 25 mg/ml (b) 32 mg/ml in ODCB solution.

vacuum overnight. TEM was performed on a JEOL JEM-1011 transmission electron microscope operated at an acceleration voltage of 100 kV. To quantitatively relate the diffraction intensity in selected area electron diffraction (SAED) patterns to the crystallinity of the specimen investigated, all these SAED patterns were performed by using a standard recording mode. i.e. fixed magnification, filed-limiting aperture of 100  $\mu\text{m}$ , current density of 0.6  $\text{pA cm}^{-2}$  and exposure time of 11.0 s for SAED acquisition. Identical settings were used for film development and digitalization.

#### 2.4. Film thickness measurements

Film thickness measurements were performed with a Veeco DekTak 6 M stylus profiler via measuring the height step between sample surface and the scrape.

#### 2.5. Wide angle X-ray diffraction (WAXD)

WAXD profiles were obtained by using a Bruker D8 Discover Reflector with fixed X-ray wavelength of 1.542  $\text{\AA}$ . The diffraction was recorded at  $\theta$ - $2\theta$  symmetry scanning mode with scan angle from  $2\theta$   $3^\circ$ – $18^\circ$ .

#### 2.6. Atomic force microscope

Surface topography was observed by atomic force microscopy (AFM) operating in tapping mode on Agilent 5500 at room temperature.

#### 2.7. UV-vis absorption spectroscopy

The obtained mixed solutions and films were directly used in UV-vis absorption spectroscopy investigations. The UV-vis absorption spectra were acquired on a Lambda 750 spectrometer (Perkin-Elmer, Wellesley, MA).

#### 2.8. Infrared spectroscopy

Infrared spectra were obtained using a Bruker Vertex 70 FTIR spectrometer. Samples were prepared by drop casting solution onto potassium bromide substrates and placed in dark ambient condition for solvent evaporation. Afterwards, the obtained films on potassium bromide substrates were dried in vacuum to exclude the remaining solvents. Thermal annealing was performed directly on potassium bromide substrates in inert atmosphere at 180  $^\circ\text{C}$  for 20 min.

#### 2.9. Device characterization

Spectral response data were determined in air with a Keithley-2400 source meter, using monochromatic light from a xenon lamp in combination with a monochromator. A calibrated Si cell was used as reference. The performance characterization for the PV cells was also carried out with a Keithley-2400 source meter. The cells are illuminated by a tungsten-halogen lamp (filtered by a Schott KG1 and GG385 filter resulting in a spectral range of 400–900 nm with a maximum at 650 nm) at an intensity of 100  $\text{mW/cm}^2$ .

### 3. Results and discussion

#### 3.1. The substantial crystallization suppression of P3HT in its composite with C60

Both the untreated thin films of P3HT:C60 and P3HT:PCBM composites basically give similar morphology, as shown by bright-field TEM images in Fig. 2, however, there are quite a few short and bright rods observed in the P3HT:PCBM composite. These nanorods are attributed to the P3HT crystals as dispersed in smooth thin film with relatively high density of the matrix. However, SAED patterns (The inset in each figure) which are in situ obtained disclose obviously different crystalline order in between the two composite films. For P3HT:C60 composite film, except for one diffused diffraction ring can be well resolved from the SAED pattern (Inset of Fig. 2a), which is associated to the diffraction from C60 nanocrystallites [7,37], only an indistinct diffraction ring (indicated by the arrow in Fig. 2a) with  $d$ -spacing of 0.39 nm is observed outside. However, the SAED pattern for the untreated P3HT:PCBM composite film gives much clearer diffraction ring (indi-

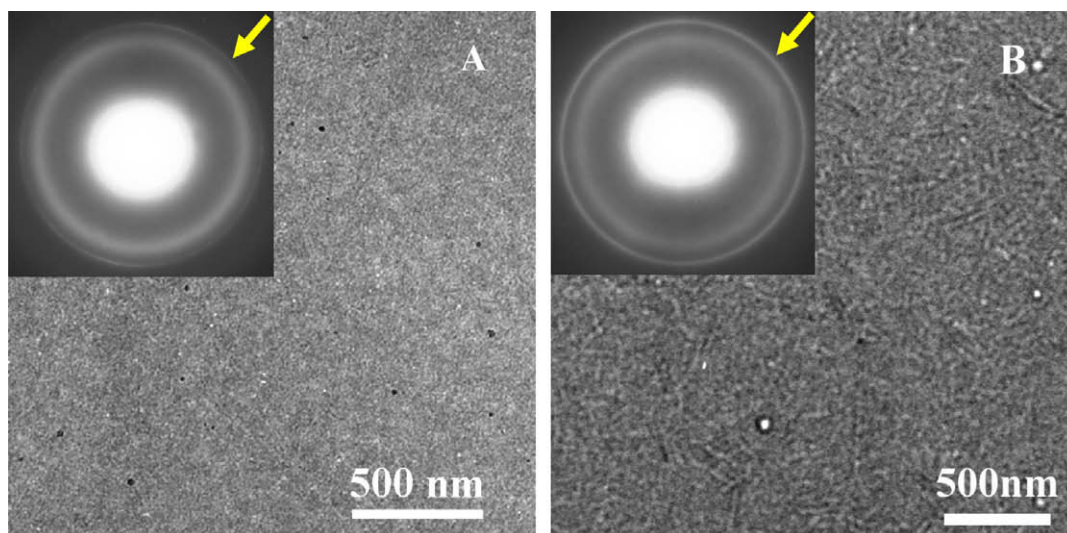


**Fig. 2.** BF-TEM images and corresponding SAED patterns (up-left inset) of the untreated composite films spin coated from ODCB solution. (A) P3HT:C60 (5:4, w/w), (B) P3HT:PCBM (1:1, w/w).

cated by the arrow in Fig. 2b) with  $d$ -spacing of 0.39 nm outside the broad diffractions which is ascribed to PCBM nanocrystallites [38,39]. As is known, the diffraction ring with  $d$ -spacing of 0.39 nm is associated to the reflections from crystallographic (0 2 0) planes of typical whisker-like P3HT crystals [40]. Since SAED pattern has been well established for semi-quantitative crystallinity analysis and proven to be a feasible and powerful tool in this field [7,8,28], we are able to draw a preliminary conclusion that the crystallization of P3HT in the composite with C60 has been substantially suppressed compared to that in P3HT:PCBM composite, as proven by the low electron diffraction intensity of crystallographic (0 2 0) planes of P3HT in the inset of Fig. 2a.

The crystallinity variation in these two untreated composites was further verified by WAXD measurements. As shown in Fig. 3a, the diffraction profile associated to untreated P3HT:C60 composite shows a broad and hardly to be resolved diffraction peak at  $2\theta = 5^\circ$ , which is assigned to the reflections of crystallographic (1 0 0) planes of P3HT crystals [41,42]. The very low diffraction intensity in combination with its broad peak reveals very low crystallinity and quite small crystalline aggregates of P3HT in this specimen. In contrast, for the P3HT:PCBM composite a well resolved diffraction peak is observed at the same position. Particularly, the diffraction intensity of this peak is even comparable with that of thermally annealed P3HT:C60 composite film at  $150^\circ\text{C}$  for 20 min. It should be noted that the position and the width of the crystallographic (1 0 0) peaks in P3HT:C60 annealed film and untreated P3HT:PCBM film are slightly different. The relatively small  $d$ -spacing of P3HT crystallographic (1 0 0) planes in untreated P3HT:PCBM film is mainly resulted from the side-chain interdigitation which is usually observed in untreated films prepared by solution deposition method. Though the P3HT crystallite size calculated by using the Scherrer equation is smaller in the untreated

P3HT:PCBM film when compared to that in thermally annealed P3HT:C60 film, the WAXD results clearly indicate

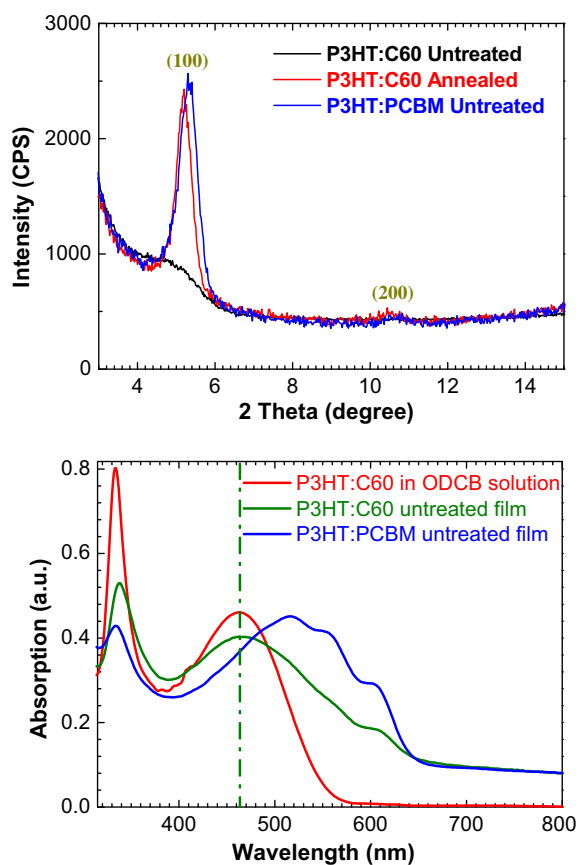


**Fig. 3.** WAXD profiles (a) and UV-vis absorption spectra (b) of P3HT composites.

that the crystallinity of P3HT in untreated P3HT:C60 film is much lower than that in untreated P3HT:PCBM film.

For crystallizable conjugated polymers, the crystallinity in solid film can also be qualitatively determined by UV–vis absorption at specific wavelengths. The UV–vis absorption spectra of thin films of P3HT composites with C60 or PCBM are shown in Fig. 3b. The spectrum of P3HT:C60 mixture in ODCB is also included for comparison. Two peaks at 334 and 461 nm, respectively, are observed for P3HT:C60 composites in ODCB solution. This spectrum is actually the simple superposition of individual absorption from C60 molecules and the intra-chain  $\pi$ – $\pi^*$  transition of P3HT single chain in the solution. For the P3HT:C60 solid composite film spin coated from above mentioned ODCB solution, a weak absorption peak additionally appeared at ca. 607 nm, which is associated to the inter-chain  $\pi$ – $\pi^*$  transition of P3HT, and the intensity of this peak is correlated to the degree of inter-chain packing order [35,43,44]. Therefore, the weak intensity at 607 nm again confirms low crystallinity of P3HT in its untreated composite film with C60. However, with respect to the untreated P3HT:PCBM composite film, three peaks associated to the optical absorption of P3HT can be well resolved in Fig. 3b. Besides, the absorbance peak related to  $\pi$ – $\pi$  ordered inter-chain packing at ca. 607 nm becomes more prominent and its intensity is increased when compared to that in untreated P3HT:C60 composite film, revealing the crystallinity of P3HT in P3HT:PCBM composite film is much higher than that in P3HT:C60 composite.

Based on the above observations, we have shown that the crystallization of P3HT in untreated P3HT:C60 composite has been substantially suppressed and its crystallinity is much lower than that in untreated P3HT:PCBM composite. Generally, decreased crystallinity of a crystallizable polymer in the composite compared to its pure bulk sample is usually ascribed to the result of “dilution effect” [45–47], which hinders the ordered packing of adjacent polymer chains by mechanical or spatial separation of other components in the composite. However, both composites (P3HT:C60 and P3HT:PCBM) employed in this study are prepared with identical conditions, i.e. the identical molar ratio between the two components, the same solvent, concentration and conditions used for solution preparation and thin film deposition. The only difference is the one component used in the composites, in which PCBM is decorated with a substitute on C60 cage. However, the crystallization of P3HT in the untreated P3HT:PCBM composite film is not extremely suppressed. Thereby, the low crystallinity of P3HT in the untreated P3HT:C60 composite could not be explained by the conventional “dilution effect”. Recently, McGehee et al. [48] have shown that some fullerene derivatives will intercalate between the side chains of conjugated polymers to form bimolecular crystals and thus influence the phase separation and photovoltaic performance of the composite films. However, they found that PCBM could not form such bimolecular crystals with P3HT due to the reason that there is insufficient room between hexyl-side chains for intercalation to occur. Based on their experimental results and simulation [48], the molecules with diameter smaller than 0.6 nm can intercalate between the adjacent hexyl-side chains of P3HT whose dis-

tance is 0.78 nm [49,50]. However, the diameter of C60 molecule is 0.71 nm which is much larger than 0.6 nm and comparable to the distance between adjacent hexyl-side chains, thus there is not enough free volume between the hexyl-side chains to accommodate the C60 molecules. Therefore, the different crystallization behaviors of P3HT in between the composite of P3HT:C60 and P3HT:PCBM can not be interpreted by the bimolecular crystals yet.

### 3.2. The mechanism for substantially suppressed crystallization of P3HT in P3HT:C60 composites

As shown in Fig. 3b, the obvious red shift of main absorption of P3HT in the untreated P3HT:PCBM composite film compared to that of P3HT in the solution reveals that longer effective conjugation length could be obtained in solid state even when “diluted” by PCBM. However, the main absorption peak of P3HT in untreated P3HT:C60 composite film nearly maintains the same as that in ODCB solution. Based on the origin of the UV–vis absorption at this position for P3HT, we can conclude that the effective conjugation length of P3HT in the untreated P3HT:C60 composite film is hardly increased upon solidification from ODCB solution.

To get deeper insight into the conformation of P3HT chains, we resort to FT-IR spectroscopy investigations. As shown in Fig. 4a, only one main absorption peak at  $821\text{ cm}^{-1}$ , which is assigned to the absorption of out of plane CH deformation of the thiophene ring [51], is observed in pure P3HT film. For pure C60 film, all the absorption peaks locate in the region with wave number less than  $800\text{ cm}^{-1}$  for the range of  $500$ – $1000\text{ cm}^{-1}$ . However, the intensity of the peak at  $821\text{ cm}^{-1}$  decreases and a new absorption additionally appears at ca.  $836\text{ cm}^{-1}$  for P3HT in the untreated P3HT:C60 composite, resulting in a very broad absorption within the region in between the wave number of  $821$  and  $836\text{ cm}^{-1}$ . Whereas upon thermal annealing at  $180\text{ }^\circ\text{C}$  for 20 min, the broadened absorption at  $821$ – $836\text{ cm}^{-1}$  will restore to the same shape and intensity as that observed in pure P3HT, with disappearance of the newly emerged peak at  $836\text{ cm}^{-1}$ . As a reference, we have also performed FT-IR measurements on the MDMO-PPV system. However, untreated MDMO-PPV:C60 composite shows the simple superposed spectrum of C60 and MDMO-PPV (Fig. 4c) in the whole region. Therefore, the peak at  $836\text{ cm}^{-1}$  is ascribed to the split of  $821\text{ cm}^{-1}$ . Both the decreased absorption at the band of  $821\text{ cm}^{-1}$  and the appearance of the split peak at  $836\text{ cm}^{-1}$  suggest that the chain conformations of P3HT in pure P3HT and P3HT:C60 composite are different. It has been reported that C60 is “wrapped” by the alkyl-side chain of P3HT in the untreated film of P3HT:C60 [52]. However, as is proven, fullerenes will form homogenous nanoscale crystallites instead of molecularly distributing in solid film when spin coated from solution [38]. Therefore, the hexyl-side chains of P3HT will actually wrap the C60 nanoaggregates. The inclusion of C60 nanocrystallites onto P3HT chains will greatly influence on their conformations. It is known that the peak at  $821\text{ cm}^{-1}$  is assigned to out of plane CH deformation of 3-alkylthiophene on the backbone, the appearance of split at  $836\text{ cm}^{-1}$  indicates that the backbone has

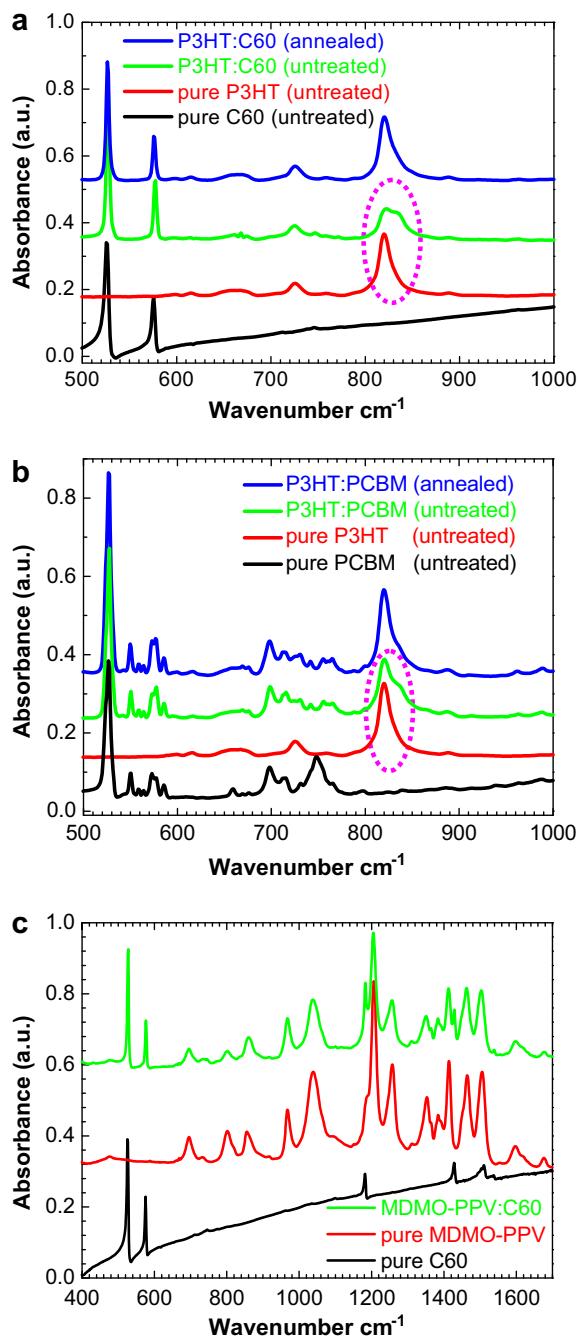


**Fig. 4.** FT-IR spectra of (a) pure P3HT and C60, respectively, and both their untreated and thermally annealed composite films; (b) pure P3HT and PCBM, respectively, and both their untreated and thermally annealed composite films; (c) pure MDMO-PPV and C60, respectively, and their untreated composite film. Some curves have been shifted along Y-axis for clarity.

been influenced by the trapped C60 nanoscale crystallites, which makes the thiophene-thiophene plane distort to each other. Subsequently, the crystallization of P3HT during spin coating process may be severely hindered by the inclusion of C60 nanoscale crystallites onto its chains.

Due to the high similarity between C60 and PCBM, comparable phenomenon could also be observed in P3HT:PCBM composite, as shown in Fig. 3b. However, for P3HT in the untreated P3HT:PCBM composite, the intensity of the original absorption at  $821\text{ cm}^{-1}$  does not drop down that much compared to pure P3HT, and the newly emerged absorption at  $836\text{ cm}^{-1}$  appears like a shoulder peak due to its low intensity. This behavior is obviously different from that of P3HT in the P3HT:C60 composite, which reveals that the distortion of P3HT between thiophene rings in P3HT:PCBM untreated film is much weaker than that in P3HT:C60 untreated film.

As a derivative of C60, PCBM has higher solubility in the most organic solvents upon chemical decoration on its C60 cage, while its physical properties are expected to be preserved. Upon a series of solubility determinations on fullerenes and P3HT in ODCB, we find that C60 shows comparable solubility to P3HT (see Table 1), whereas, PCBM has much higher solubility than P3HT. Based on these results, we can conclude that when using ODCB as solvent, C60 and P3HT will nearly simultaneously crystallize from the solution during spin coating. However, due to high symmetry of C60 molecules, they will form large number of nanoscale crystallites in the concentrated and viscous solution in a very short time. Since the crystallization of P3HT is a relatively slow process, the presented large number of nanoscale crystallites in the viscous solution will severely hinder the ordered packing of crystallizable P3HT chains, which results in severe crystallization suppression of P3HT. Therefore, the P3HT chains in the untreated P3HT:C60 film spin coated from ODCB solution will nearly maintain their original chain conformation in the solution, in contrast to the observation in most cases that the effective conjugation length in a solid film is longer than that in the solution. This difference is in consistency with the results of FT-IR and UV-vis measurements (Figs. 4a and 3b). However, in the P3HT:PCBM composite, P3HT becomes saturated first and it will crystallize from the ODCB solution before PCBM starts to form tiny crystallites. In this case, the crystallization of P3HT is less influenced by the “dilution effect”, leading to higher crystallinity which conforms to the observations by TEM, XRD, UV-vis and FT-IR as shown in Figs. 2, 3a and 4b, respectively. Therefore, we propose that the tremendous difference of P3HT crystallinity in between C60:P3HT and PCBM:P3HT untreated composite films spin coated from ODCB solution

**Table 1**

The solubility of P3HT and fullerenes in different solvents at room temperature (The temperature in the lab varies in between 18 and 22 °C).

Solvent	b.p. (°C)	C <sub>60</sub> (mg/ml)	P3HT (mg/ml)	PCBM (mg/ml)
ODCB	180	28	30	>50
TCB	214	8	30	>50
CB	130	7	30	>50
Tetralin	207	16	0.5	>50
M-Naph	244	35	20	>50
Cl-Naph	259	56	12	>50
Tetralin/CB (1:1, v/v)		8	17	>50
M-Naph/CB (1:20, v/v)		8	18	>50
Cl-Naph/CB (1:33, v/v)		9	18	>50

may correlate to the different solubility of the components in ODCB.

To verify this assumption, we first choose TCB as solvent for thin film deposition due to its comparable boiling point with ODCB but lower solubility of C60 (Table 1). Upon choosing a speed as high as 3000 rpm for TCB solution but only 600 rpm for ODCB solution, a comparable drying time during spin coating process could be achieved for both solutions. However, the crystallinity of P3HT in the P3HT:C60 untreated film from TCB is higher than that from ODCB as proven by red shift and three obvious electron vibration bands in the UV–vis absorbance spectrum (Fig. 5a). Second, if CB is used to prepare the film, C60 will also crystallize from the solution before P3HT due to rather low solubility of C60 in it. As is shown in Fig. 5a, although the volatility of CB is higher than ODCB, we are still able to observe that P3HT shows longer conjugation length in the P3HT:C60 film as is indicated by ca.10 nm red shift in the UV–vis absorbance spectrum when compared to the film prepared from ODCB solution. This result is more obvious in the films prepared by drop casting (inset in Fig. 5a), with the appearance of prominent absorption at 607 nm associated to increased crystallinity of P3HT. Finally, we use mixed solvent CB/tetralin (1:1, v/v) to further check our assumption. Tetralin is a very poor solvent for P3HT but

shows modest solubility for C60. It is anticipated that C60 will precipitate from the solution later than P3HT due to the lower volatility of tetralin comparing with CB. As is shown in Fig. 5b, the addition of tetralin into the CB solution does not cause any ordered precursors of P3HT in the solution [17], but the optical absorption spectrum of the untreated P3HT:C60 film shows obvious red shift and very prominent three electronic vibration bands, indicating that the crystallinity of P3HT in such composite is substantially increased. Similar results can also be obtained by replacing tetralin with less amount of M-naph or Cl-naph which show even higher solubility of C60 than tetralin. It should be noted that both M-naph and Cl-naph are low volatile solvents due to their high boiling points, thus longer crystallization time is obtained when P3HT is spin coated from M-naph or Cl-naph comparing with CB, and higher crystalline P3HT is anticipated. However, only little amount of M-naph or Cl-naph is added into the CB solvent (M-naph/CB, 1:20; Cl-naph/CB, 1:33, by volume), the increased crystallinity of P3HT contributed by the high boiling point is negligible. Moreover, we find that in the case that C60 forming crystallites before P3HT, the crystallinity of P3HT is not as high as in that C60 forming crystallites from the solution after P3HT, as is confirmed by the UV–vis absorbance measurements (Fig. 5). This finding is different from the results obtained by Yao et al. in P3HT/PCBM system [23], in which the formation of PCBM “clusters” benefit the crystallization of P3HT and improvement of morphology. Such difference could be originated from the different crystallization ability between C60 and PCBM. As is known, lower symmetry of PCBM makes it more difficult to nucleate, which eventually results in less in quantity but larger in size for PCBM “clusters” during crystallization from the solution. In the cases of C60 forming crystallites before P3HT, the higher crystallizability of C60 results in larger number of C60 nanocrystallites, as confirmed by the homogeneously distributed C60 nanocrystallites obtained in P3HT:C60 composite [7], in contrast to only a few PCBM crystals observed in P3HT:PCBM system. With the presence of these homogeneously dispersed crystallites in the concentrated and viscous solution, the subsequent crystallization of P3HT will be hindered, leading to low crystallinity. Whereas, in the cases that low volatile solvent with high solubility of C60 such as tetralin, M-naph or Cl-naph is added into the main solvent CB, some part of C60 molecules will preferentially dissolve in it. Therefore, during spin coating, the C60 molecules dissolved in the low volatile solvent is still molecularly dispersed, while P3HT starts to crystallize from its good solvent CB which is relatively volatile. Therefore, during spin coating, less C60 nanocrystallites appear in the concentrated solution, which facilitates the formation of more highly crystalline P3HT fibers in the final composite film. It should be pointed out that other factors such as interaction parameters, surface energy, and interfacial tension may also contribute to the formation of crystalline P3HT to some extent [53]. However, the solubility may play an important role in determining the crystallinity of P3HT because only by using the low volatile solvent with higher solubility of fullerene, higher crystallinity of P3HT or larger ordered aggregates of conjugated polymers can

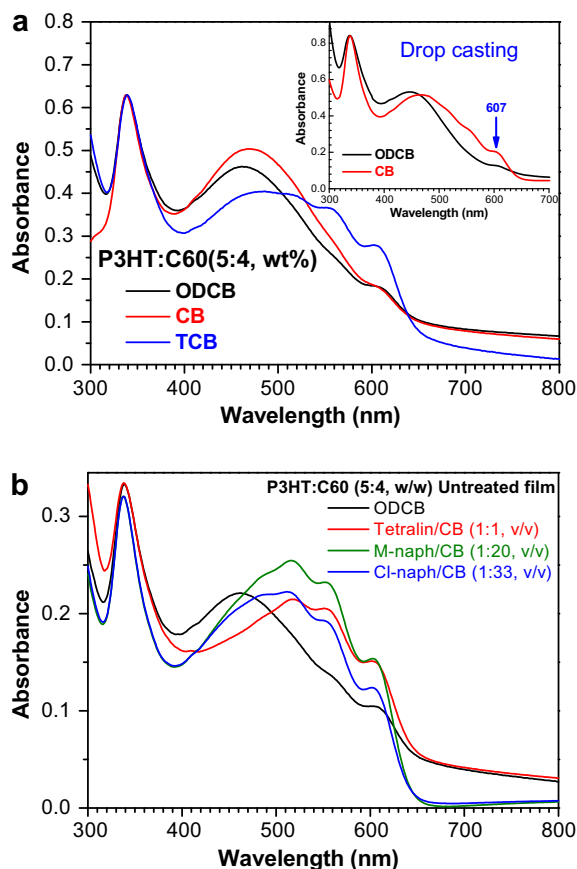


Fig. 5. UV–vis absorbance spectra of the P3HT:C60 untreated films prepared from different solvents and solvent mixtures via spin coating.



be obtained as is shown above and reported by Lee et al. [26], respectively. Therefore, our observations have proven that the comparable solubility of C60 and P3HT in ODCB is mainly responsible for the extremely low crystallinity of P3HT in P3HT:C60 untreated film prepared from ODCB solution, thus the low performance of device. Recently, Troshin et al. have shown that the solubility of PCBM in organic solvents will also severely influence the phase separation scale via forming different sizes of PCBM domains in the composite film with P3HT and thus it plays an important role in determining the final device performance [33]. Therefore, the influence of component solubility on the final device performance is universal and it should be taken into account while designing new materials for more efficient photovoltaic devices.

### 3.3. Solutions for constructing high performance P3HT:C60 polymer solar cells

With only two short substitute side groups on the fullerene cage, the difference between PCBM and C60 should be very small in terms of optoelectronic physics, however, up to now the solar cells based on P3HT:C60 composite usually show lower power conversion efficiency than its counterpart system P3HT:PCBM composite. As shown in Fig. 6a, current density–voltage ( $J$ – $V$ ) curves reveal significantly different performance of the untreated devices by using these two composites. Except for the slight difference in open-circuit voltage ( $V_{oc}$ ), quite low  $J_{sc} = 1.74 \text{ mA/cm}^2$  and  $FF = 0.34$  are obtained in devices based on P3HT:C60 composite, in contrast to the device based on P3HT:PCBM composite which shows  $J_{sc} = 5.20 \text{ mA/cm}^2$  and  $FF = 0.40$ , respectively, as illuminated by a halogen lamp with an intensity of  $100 \text{ mW/cm}^2$ . In Fig. 6b, for both untreated devices, the device based on P3HT:C60 composite shows a very narrow photocurrent spectral response and quite low  $IPCE$  values compared to that of the untreated P3HT:PCBM device. These differences eventually result in more than triple folds variation in power conversion efficiency of 0.34% for P3HT:C60 and 1.23% for P3HT:PCBM composite, respectively. The unsatisfactory performance of the devices based on untreated P3HT:C60 composite is mainly attributed to the very low crystallinity of P3HT within the photoactive layer, which results in two negative influences on the device performance. On one hand, low crystallinity will cause mismatch between the optical absorption of photoactive layer and solar spectrum. On the other hand, it will lead to low hole mobility, which results in inefficient hole transport to the anode. Consequently, the probability of charge recombination increases. Thereby, higher crystallinity is required for P3HT:C60 solar cells to further improve device performance.

The above mentioned mixed solvent method has shown its feasibility to increase the crystallinity of P3HT in P3HT:C60 composite, therefore it has shown the potential application in constructing more efficient photovoltaic devices. As we known, besides the crystallinity of P3HT, the morphology of photoactive layer also plays an important role in determining the device performance. In Fig. 7a, for the P3HT:C60 composite film spin coated from ODCB, the phase separation scale is very small and the whole surface

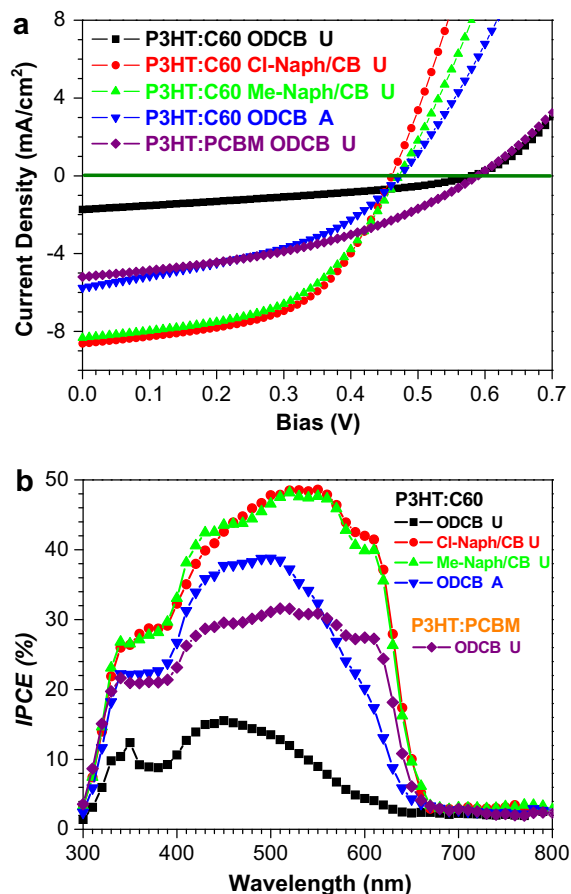
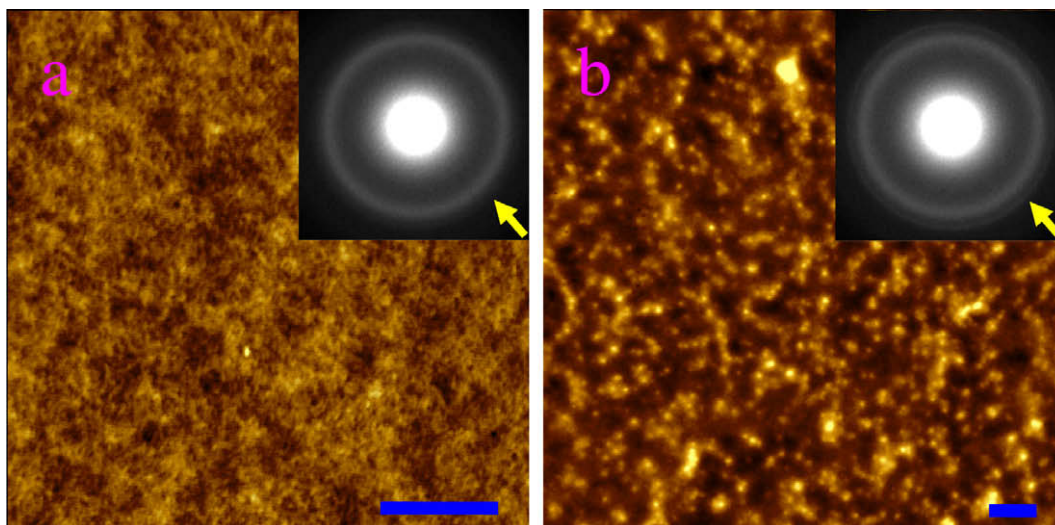


Fig. 6. Current density–voltage characteristics of P3HT:C60 (5:4 by weight) and P3HT:PCBM(1:1 by weight) polymer solar cells and their corresponding  $IPCE$  properties. (U: untreated; A: annealed).

is quite smooth, indicating that P3HT is nearly molecularly mixing with C60 nanocrystallites without constructing interpenetrating networks. However, for the P3HT:C60 untreated film prepared from Cl-naph/CB (Fig. 7b), homogeneously distributed aggregates ascribing to C60 crystallites are observed over the film. The average domain size increases greatly and the surface roughness is an order of magnitude higher than that observed in Fig. 7a, implying that the phase separation scale between C60 and P3HT has been increased. The formation of larger C60 crystallites is mainly contributed by the longer drying time obtained for “selectively extracted” C60 molecules to crystallize when low volatile solvent with higher solubility of C60 is added into the main solvent CB. Moreover, from the inset SAED patterns we can find that the diffraction intensity of P3HT crystallographic (0 2 0) plane as is indicated by the arrow in Fig. 7b is higher than that in Fig. 7a, implying that the crystallinity of P3HT in P3HT:C60 film prepared by using Cl-naph/CB solvent mixture has really been enhanced when compared with that prepared by using ODCB. The formation of larger C60 crystallites in combination with long P3HT fibers contributes to an improved morphology in which not only large interface area for exciton dissociation is preserved but also bi-continuous pathways



**Fig. 7.** AFM images showing the topography of the P3HT:C60 untreated films prepared from (a) ODCB and (b) Cl-naph/CB (1:33, v/v) via spin coating. Inset in each figure is its corresponding SAED. Scale bar: 500 nm. RMS in (a) and (b) is 1.0 nm and 11.2 nm, respectively.

are constructed for more efficient charge transport through the film. Therefore, better device performance can be anticipated. As shown in Fig. 6a, current density–voltage ( $J$ – $V$ ) measurements reveal that, for the untreated device based on a thin P3HT:C60 composite film spin coated from M-naph/CB solution, short circuit current density ( $J_{sc}$ ) has been increased from 1.74 to 8.33 mA/cm<sup>2</sup>, and also an increased filling factor ( $FF$ ) from 0.34 to 0.52 has been achieved in contrast to the untreated device prepared from pure ODCB solution. Generally, a large serial resistance and too small parallel resistance (shunt) tend to result in reduced  $FF$  [1]. Therefore, quite large serial resistance exists in the untreated P3HT:C60 photoactive layer prepared from pure ODCB while substantially decreased serial resistance is achieved in the photoactive layer prepared by using the M-naph/CB mixed solvents. Besides, a somewhat decreased open-circuit voltage ( $V_{oc}$ ) from 0.58 to 0.47 V is observed, which is most probably attributed to the enhanced electric conductivity of the composite film contributed from substantially increased crystallinity of P3HT included [17,20]. However, these parameters eventually could result in power conversion efficiency (PCE) up to 2.04%, which is higher than that via thermal annealing in our investigations. Furthermore, the device with comparable efficiency of 2.1% is obtained by using Cl-naph/CB (1:33, v/v) mixture (Fig. 6a), which is the highest efficiency to date for bulk-heterojunction devices achieved in untreated P3HT:C60 composite. This remarkably increased device performance by using Cl-naph is mainly attributed to the substantially increased crystallinity of P3HT and thus improved morphology in the composite, and the contribution from its inherent high boiling point is very limited [54].

The increased device performance is further proven by  $IPCE$  measurements. In Fig. 6b, comparing with the untreated device prepared from pure ODCB, the device prepared from M-naph/CB and Cl-naph/CB solution show not only much broader response range but also higher  $IPCE$

values covering from 350 nm to 650 nm, with a maximum ~48% at ca.550 nm. We find that there is ~13% variation between the  $J_{sc}$  calculated from  $IPCE$  and that observed in  $J$ – $V$  measurements for the untreated device prepared from M-naph/CB and Cl-naph/CB. This might be attributed to degradation of photoactive layer caused by the diffusion of humidity and oxygen for performing  $IPCE$  measurements on devices in air without encapsulation. As a reference, the device prepared from ODCB solution shows modest increase of  $IPCE$  after thermal annealing, which is consistent with the device performances obtained above.

Therefore, the crystallinity of P3HT in the untreated P3HT:C60 composite film could be substantially enhanced by choosing an appropriate low volatile solvent to form solvent mixtures with the main solvent, which should satisfy these two criterions. Firstly, both P3HT and C60 could be dissolved in this solvent mixture to achieve a solution with required concentration. Second, C60 should have much higher solubility than P3HT in the low volatile solvent. In such a case, P3HT will on one hand saturate from the solution before C60, achieving both longer effective conjugation length and higher crystallinity in the untreated composite film. On the other hand, the preferentially dissolved C60 molecules have more time to form larger crystallites, which ensures more continuous pathways for electron transport. It should be noted that the efficiency of the PV device fabricated from the solvents mixture in which C60 has higher solubility than that of P3HT is comparable to those devices prepared via post-treatment (thermal annealing or solvent vapor treatment), although the compositions still need to be further optimized to realize more efficient PV devices [55]. However, the short circuit current has already reached a considerable high value and it is comparable to those obtained in P3HT:PCBM devices upon post-treatments, implying an improved morphology has been achieved in the composite film (Fig. 7b). The improved morphology not only increases the optical absorption of the photoactive layer in red re-

gion due to the enhanced crystallinity of P3HT, but also provides continuous pathways for faster charge carrier transportation towards anode. Therefore, we have identified the influence of specific component solubility on the crystallization of other components involved in the composite, and also successfully demonstrated an approach to achieve more efficient devices based on P3HT:C60 composite. Furthermore, our results provide additional rules for designing new materials for optoelectronic application, i.e. not only the importance of its optoelectronic property, but also its other properties, e.g. solubility in the solvent and its influence on the crystallization and morphology of counterpart component involved in the composite should be taken into account.

#### 4. Conclusion

We have demonstrated substantial crystallization suppression of P3HT in the untreated P3HT:C60 composite film prepared from ODCB solution and its hardly increased conjugation length compared to that in solution. This has been confirmed to be mainly associated to the comparable solubility of C60 and P3HT in ODCB, which leads to formation of numerous C60 nano-crystallites in the solution and suppresses the subsequent crystallization of P3HT. Based on this finding, we propose the solutions to improve both the crystallinity and effective conjugation length of P3HT in the untreated P3HT:C60 composite via adding small amount of low volatile solvent with much higher solubility of C60 than P3HT into the main solvent. In such a case, C60 will become saturated in the solution later than P3HT, which lessens the dilution effect of C60 aggregates on the crystallization of P3HT. As a consequence, both crystallinity and effective conjugation length of P3HT could be increased in the composite, contributing to an improved morphology for the photoactive layer and thus better device performance. These results not only demonstrate the feasibility of constructing high performance photovoltaic devices based on the composites of P3HT and low cost C60, but also provide additional rules for designing new materials for polymer optoelectronic devices.

#### Acknowledgement

This work was financially supported by National Natural Science Foundation of China (Grant No. 20604029, 20874100). X.N.Y. thanks the supports from the Fund for Creative Research Groups (Grant No. 50621302).

#### References

- [1] C.J. Brabec, N.S. Sariciftci, J.C. Hummelen, F. Padinger, T. Fromherz, J.C. Hummelen, *Adv. Funct. Mater.* 11 (2001) 15.
- [2] H. Hoppe, N.S. Sariciftci, *J. Mater. Res.* 19 (2004) 1924.
- [3] K.M. Coakley, M.D. McGehee, *Chem. Mater.* 16 (2004) 4533.
- [4] N.S. Sariciftci, L. Smilowitz, A.J. Heeger, F. Wudl, *Science* 258 (1992) 1474.
- [5] G. Yu, J. Gao, J.C. Hummelen, F. Wudl, A.J. Heeger, *Science* 270 (1995) 1789.
- [6] J.Y. Kim, K. Lee, N.E. Coates, D. Moses, T.-Q. Nguyen, M. Dante, A.J. Heeger, *Science* 317 (2007) 222.
- [7] X.N. Yang, G.H. Lu, L.G. Li, E.L. Zhou, *Small* 3 (2007) 611.
- [8] X.N. Yang, J. Loos, S.C. Veenstra, W.J.H. Verhees, M.M. Wienk, J.M. Kroon, M.A.J. Michels, R.A.J. Janssen, *Nano Lett.* 5 (2005) 579.
- [9] L.H. Nguyen, H. Hoppe, T. Erb, S. Günes, G. Gobsch, N.S. Sariciftci, *Adv. Funct. Mater.* 17 (2007) 1071.
- [10] W.L. Ma, C.Y. Yang, X. Gong, K. Lee, A.J. Heeger, *Adv. Funct. Mater.* 15 (2005) 1617.
- [11] G. Li, V. Shrotriya, J. Huang, Y. Yao, T. Moriarty, K. Emery, Y. Yang, *Nat. Mater.* 4 (2005) 864.
- [12] M. Reyes-Reyes, K. Kim, J. Dewald, R. López-Sandoval, A. Avadhanula, S. Curran, D.L. Carroll, *Org. Lett.* 7 (2005) 5749.
- [13] K. Kim, J. Liu, M.A.G. Nambhoorthy, D.L. Carroll, *Appl. Phys. Lett.* 90 (2007) 163511.
- [14] F. Padinger, R.S. Rittberger, N.S. Sariciftci, *Adv. Funct. Mater.* 13 (2003) 85.
- [15] G. Li, Y. Yao, H. Yang, V. Shrotriya, G. Yang, Y. Yang, *Adv. Funct. Mater.* 17 (2007) 1636.
- [16] G.H. Lu, L.G. Li, X.N. Yang, *Small* 4 (2008) 601.
- [17] L.G. Li, G.H. Lu, X.N. Yang, *J. Mater. Chem.* 18 (2008) 1984.
- [18] S. Berson, R.D. Bettignies, S. Bailly, S. Guillerez, *Adv. Funct. Mater.* 17 (2007) 1377.
- [19] F. Zhang, K.G. Jespersen, C. Björström, M. Svensson, M.R. Andersson, V. Sundström, K. Magnusson, E. Moons, A. Yartsev, O. Inganäs, *Adv. Funct. Mater.* 16 (2006) 667.
- [20] A.J. Moulé, K. Meerholz, *Adv. Mater.* 20 (2008) 240.
- [21] A.R. Campbell, J.M. Hodgkiss, S. Westenhoff, I.A. Howard, R.A. Marsh, C.R. McNeill, R.H. Friend, N.C. Greenham, *Nano Lett.* 8 (2008) 3942.
- [22] C.N. Hoth, P. Schilinsky, S.A. Choulis, C.J. Brabec, *Nano Lett.* 8 (2008) 2806.
- [23] Y. Yao, J. Hou, Z. Xu, G. Li, Y. Yang, *Adv. Funct. Mater.* 18 (2008) 1783.
- [24] J. Jaczewska, A. Budkowski, A. Bernasik, E. Moons, J. Rysz, *Macromolecules* 41 (2008) 4802.
- [25] J. Peet, C. Soci, R.C. Coffin, T.Q. Nguyen, A. Mikhailovsky, D. Moses, G.C. Bazan, *Appl. Phys. Lett.* 89 (2006) 252105.
- [26] J.K. Lee, W.L. Ma, C.J. Brabec, J. Yuen, J.S. Moon, J.Y. Kim, K. Lee, G.C. Bazan, A.J. Heeger, *J. Am. Chem. Soc.* 130 (2008) 3619.
- [27] J. Peet, J.Y. Kim, N.E. Coates, W.L. Ma, D. Moses, A.J. Heeger, G.C. Bazan, *Nat. Mater.* 6 (2007) 497.
- [28] J.X. Geng, T.Y. Zeng, *J. Am. Chem. Soc.* 128 (2006) 16827.
- [29] S.A. Backer, K. Sivula, D.F. Kavulak, J.M.J. Fréchet, *Chem. Mater.* 19 (2007) 2927.
- [30] F.B. Kooistra, J. Knol, F. Kastenberg, L.M. Popescu, W.J.H. Verhees, J.M. Kroon, J.C. Hummelen, *Org. Lett.* 9 (2007) 551.
- [31] M. Lenes, G.-J.A.H. Wetzelaer, F.B. Kooistra, S.C. Veenstra, K.J. Hummelen, P.W.M. Blom, *Adv. Mater.* 20 (2008) 2116.
- [32] R.B. Ross, C.M. Cardona, D.M. Guldi, S.G. Sankaranarayanan, M.O. Reese, N. Kopidakis, J. Peet, B. Walker, G.C. Bazan, E.V. Keuren, B.C. Holloway, M. Drees, *Nat. Mater.* 8 (2009) 208.
- [33] P.A. Troshin, H. Hoppe, J. Renz, M. Egginger, J.Y. Mayorova, A.E. Goryachev, A.S. Peregudov, R.N. Lyubovskaya, G. Gobsch, N.S. Sariciftci, V.F. Razumov, *Adv. Funct. Mater.* 19 (2009) 779.
- [34] T. Yamamoto, D. Komarudin, M. Arai, B.-L. Lee, H. Sugauma, N. Asakawa, Y. Inoue, K. Kubota, Shintaro Sasaki, T. Fukuda, H. Matsuda, *J. Am. Chem. Soc.* 120 (1998) 2047.
- [35] P.J. Brown, D.S. Thomas, A. Köhler, J.S. Wilson, J.-S. Kim, C.M. Ramsdale, H. Sirringhaus, R.H. Friend, *Phys. Rev. B* 67 (2003) 064203.
- [36] N. Kiri, E. Jähne, H.-J. Adler, M. Schneider, A. Kiri, G. Gorodyska, S. Minko, D. Jehnichen, P. Simon, A.A. Fokin, M. Stamm, *Nano Lett.* 3 (2003) 707.
- [37] C.Y. Yang, A.J. Heeger, *Synth. Met.* 83 (1996) 85.
- [38] X.N. Yang, J.K.J. van Duren, M.T. Rispens, J.C. Hummelen, R.A.J. Janssen, M.A.J. Michels, J. Loos, *Adv. Mater.* 16 (2004) 802.
- [39] X.N. Yang, J.K.J. van Duren, R.A.J. Janssen, M.A.J. Michels, J. Loos, *Macromolecules* 37 (2004) 2151.
- [40] K. Tashiro, M. Kobayashi, T. Kawai, K. Yoshino, *Polymer* 38 (1997) 2867.
- [41] H. Sirringhaus, P.J. Brown, R.H. Friend, M.M. Nielsen, K. Bechgaard, B.M.W. Langeveld-Voss, A.J.H. Spiering, R.A.J. Janssen, E.W. Meijer, P. Herwig, D.M. de Leeuw, *Nature* 401 (1999) 685.
- [42] T.J. Prosa, M.J. Winokur, J. Moulton, P. Smith, A.J. Heeger, *Macromolecules* 25 (1992) 4364.
- [43] M.C. Gurau, D.M. Delongchamp, B.M. Vogel, E.K. Lin, D.A. Fischer, S. Sambasivan, L.J. Richter, *Langmuir* 23 (2007) 834.
- [44] U. Zhokhavets, T. Erb, G. Gobsch, M. Al-Ibrahim, O. Ambacher, *Chem. Phys. Lett.* 418 (2006) 347.
- [45] W. Li, X. Kong, E. Zhou, D. Ma, *Polymer* 46 (2005) 11655.
- [46] B. Nandan, L.D. Kandpal, G.N. Mathur, *J. Appl. Polym. Sci.* 90 (2003) 2906.

- [47] W.-B. Liao, A.S. Liu, W.-Y. Chiu, *Macromol. Chem. Phys.* 203 (2002) 294.
- [48] A.C. Mayer, M.F. Toney, S.R. Scully, J. Rivnay, C.J. Brabec, M. Scharber, M. Koppe, M. Heeney, I. McCulloch, M.D. McGehee, *Adv. Funct. Mater.* 19 (2009) 1173.
- [49] K.J. Ihn, J. Moulton, P. Smith, *J. Polym. Sci. Part B: Polym. Phys.* 31 (1993) 735.
- [50] D.H. Kim, J.T. Han, Y.D. Park, Y. Jang, J.H. Cho, M. Hwang, A.K. Cho, *Adv. Mater.* 18 (2006) 719.
- [51] G. Louarn, M. Trznadel, J.P. Buisson, J. Laska, A. Pron, M. Lapkowski, S. Lefrant, *J. Phys. Chem.* 100 (1996) 12532.
- [52] C. Yang, J.G. Hu, A.J. Heeger, *J. Am. Chem. Soc.* 128 (2006) 12007.
- [53] S. Nilsson, A. Bernasik, A. Budkowski, E. Moons, *Macromolecules* 40 (2007) 8291.
- [54] F.-C. Chen, H.-C. Tseng, C.-J. Ko, *Appl. Phys. Lett.* 92 (2008) 103316.
- [55] C. Müller, T.A.M. Ferenczi, M. Campoy-Quiles, J.M. Frost, D.D.C. Bradley, P. Smith, N. Stingelin-Stutzmann, J. Nelson, *Adv. Mater.* 20 (2008) 3510.

few differences between the organic salt-doped devices and the frozen-junction LECs. The differences include the fact that the forward- and reverse-biased current–voltage ( $I$ – $V$ ) and luminance–voltage ( $L$ – $V$ ) curves of the typical LECs are almost symmetric in contrast to the diode-like behavior of the organic salt-doped devices even at an elevated temperature. The fact that the organic salt-doped devices strongly depend on the thickness of active layer in contrast to the LECs is another claimed difference. Unlike the dynamic-junction LECs, however, the frozen-junction LECs show the unipolar light emission which means the light emission can only be detected if the applied voltage polarity is the same as during the precharging process, i.e., positive [14,15]. Since the ions are rendered immobile in the frozen-junction LECs, the  $I$ – $V$  and  $L$ – $V$  characteristics should be asymmetric and similar to those of the conventional organic LEDs. Moreover, in that the frozen-junction LECs retains all the advantages of LECs operating in the dynamic-junction LECs including the insensitiveness of cathode material and balanced carrier injection [2,15], the frozen-junction LECs have clear advantages. Nevertheless, since the state of ions present in the organic salt-doped devices has not yet been known clearly as such that the few previous reports [11–13] had claimed that the ions should exist as being separated with the active organics near electrodes, we think that it should be clarified by examining the operating characteristics of the organic salt-doped devices. In this study, we show that the organic salt-doped devices behave similarly with the frozen-junction LECs in that the devices exhibit much improved carrier balance, which is one of the characteristics of LECs.

## 2. Experimental details

We used poly(*N*-vinyl carbazole) (PVK;  $M_w = 1,100,000$ ) as a host polymer for the devices, which was supplied from Aldrich and used without further purification. For a single emissive layer, a hole transporting *N,N'*-diphenyl-*N,N'*-bis(3-methylphenyl)-[1,1'-biphenyl]-4,4'-diamine (TPD, Aldrich), an electron transporting 2-(4-biphenyl)-5-(4-*tert*-butylphenyl)-1,3,4-oxadiazole (PBD, American Dye Source), and a phosphorescent green emitter *fac*-tris(2-phenylpyridine)iridium ( $\text{Ir}(\text{ppy})_3$ , Gracel) were added in the PVK host polymer with an appropriate composition. A mixture of the active organics was dissolved in a mixed solvent of dichloroethane ( $\text{C}_2\text{H}_4\text{Cl}_2$ ) and chloroform ( $\text{CHCl}_3$ ). As an organic salt, an appropriate amount of tetra-*n*-butylammonium tetrafluoroborate ( $\text{Bu}_4\text{NBF}_4$ , Aldrich) was added in the solution mixture for the single emissive layer. A hole injection material, poly(3,4-ethylenedioxythiophene) doped with poly(styrene sulfonate) (PEDOT:PSS) (Baytron P, Al 4083), was used for the devices.

For this study, PLEDs with ITO/PEDOT:PSS/PVK + TPD + PBD +  $\text{Ir}(\text{ppy})_3$  +  $\text{Bu}_4\text{NBF}_4$ /Al structure were fabricated. For the devices, a hole injecting PEDOT:PSS was first spin coated on pre-cleaned ITO substrates for 30 s at 1500 rpm to have the thickness of 40 nm and then baked at 110 °C for 5 min. For all the devices, the weight ratio of active organic materials used was set to PVK:PBD:TPD: $\text{Ir}(\text{ppy})_3 = 0.61:0.24:0.09:0.06$ . These materials were dissolved in a

mixed solvent of dichloroethane and chloroform with a ratio of 3:1. The active layer was spin coated for 30 s at 1000 rpm to have the thickness of 70 nm and then baked for 30 s at 80 °C. In order to investigate the effect of organic salt on the device performance, the devices was doped with the organic salt  $\text{Bu}_4\text{NBF}_4$  at a concentration of 0.6 wt.%. For some samples, 1 nm thick LiF layer was thermally evaporated on top of the active layer at a pressure of  $5 \times 10^{-7}$  torr. An Al cathode layer (120 nm) was formed on top of the devices via thermal deposition at a pressure of  $5 \times 10^{-7}$  torr. After the devices were fabricated, they were treated thermally and electrically for the activation of organic salt. For the activation, the devices were brought on the surface of hot plate maintained at an elevated temperature of 65 °C, and then a preset voltage was applied to the devices for a period of time.

All electrical measurements were performed under ambient condition. The current–voltage–luminance ( $I$ – $V$ – $L$ ) characteristics were measured using a source measure unit (Keithley 2400) and using a luminance meter (Minolta CS100). The electroluminescence (EL) spectra and device efficiencies of the devices were recorded by using Minolta CS1000.

## 3. Results and discussion

When PVK-based single emissive layer has been doped with the organic salt  $\text{Bu}_4\text{NBF}_4$ , the anions  $\text{NBF}_4^-$  and cations  $\text{Bu}_4\text{N}^+$  should be separated and forced to move toward the corresponding electrodes under an applied bias. For this purpose the fabricated devices were subject to the simultaneous thermal and electrical annealing, which we call this process with the activation of organic salt. Due to the rigid and non-electrolytic nature of PVK host polymer, the layer has been heated to an elevated temperature in order to help the ions to move through the polymer more easily. In this study the layer was heated to 65 °C for increasing the mobility of ions. The temperature was selected well below the glass transition temperature ( $T_g$ ) of PVK which is known to range from 162 to 225 °C depending on its molecular weight. An external voltage was applied for a certain time period while the temperature of the layer was maintained (at 65 °C). Even though the higher voltage is quite beneficial in increasing the velocity of the ion movement, there is also the disadvantage that the devices could be degraded by intense light emission and current flow at the high voltage during the process. In this study, an applied voltage of 13 V was selected and the activation time was varied for the salt activation.

In case of the salt-doped but un-activated devices (without LiF layer), the  $L$ – $V$  curve exhibited the abrupt increase in luminance up to 30,000  $\text{cd/m}^2$  around 27 V as shown in Fig. 1a. Normally, polymer LED devices without the electron-injecting LiF layer are known to show the gradual increase in luminance with a high turn-on voltage. This unique feature in the light emission from the salt-doped un-activated devices has been reported in the literature [10]. The activation for a short 10 s at 13 V affected little the  $L$ – $V$  curve. The longer the time for the activation

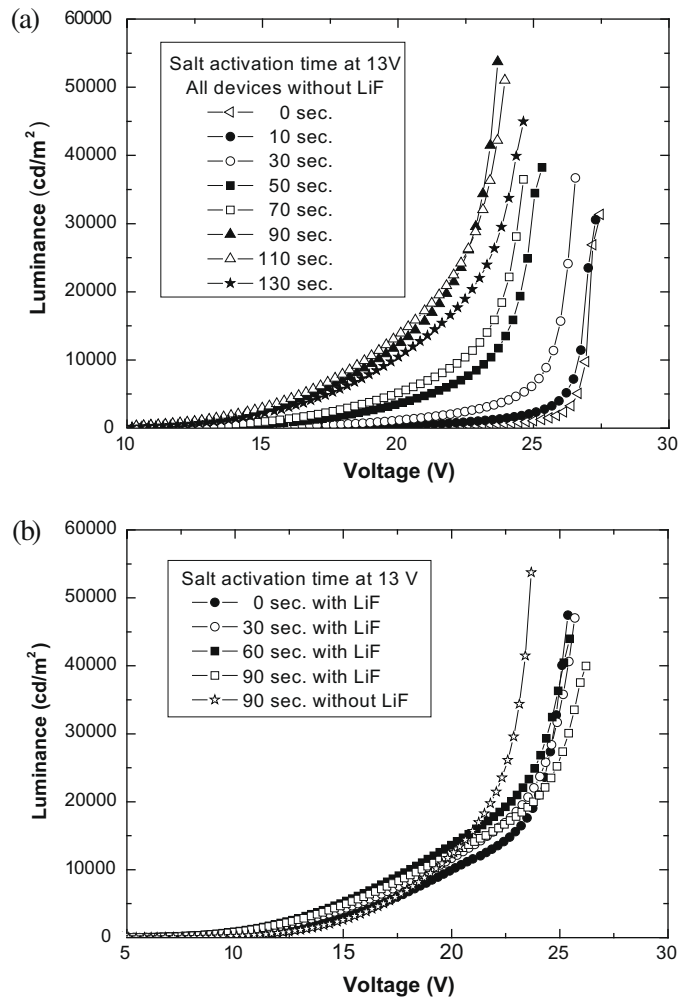


**Fig. 1.** (a) The luminance–voltage curves for the salt-doped devices (without LiF layer) measured after the salt activation at 13 V and 65 °C for various time durations. (b) The comparison between the luminance–voltage curves for the salt-doped devices with and without LiF layer after the salt activation at 13 V and 65 °C.

process was, the lower the turn-on voltage became and the higher the maximum luminance reached. Beyond a certain time of activation, the process started not to affect the  $L$ – $V$  curve advantageously. The highest luminance was obtained with the devices activated for around 90–110 s at the temperature and applied voltage of 65 °C and 13 V, respectively. It is obvious from the figure that the salt doping helps to inject carriers more efficiently to result in lower turn-on voltage and enhanced luminance after an appropriate salt activation.

As shown in Fig. 1b, the  $L$ – $V$  curves of the salt-doped devices with conventional LiF layer were found to show different behavior. First thing to note is that the salt activation process does not affect appreciably the  $L$ – $V$  curve of the devices with LiF layer. We think that it is because the electron injection occurs dominantly with the help of the LiF layer rather than the doped organic salt. Also due to the LiF layer, the devices are turned on at lower operating voltages compared with those without LiF layer. At voltages from 15 to 23 V, however, the increase in luminance with increasing

voltage tends to slow down before the luminance rises sharply around 25 V. On the contrary, the luminance of the salt-activated devices (90 s.) without LiF layer increases steadily with increasing voltage and finally reaches a higher luminance at a lower applied voltage. We consider that it is responsible for the fact that the salt doping helps to have the holes and electrons balanced in the devices while the LiF layer helps the injection of electrons only.

Even though we do not know how the organic salt exists in the devices at this stage of research, it is obvious that the incorporated ions provide the positive effect on the device performance from Fig. 1. In order to correlate the increase in luminance with the electrical current flowed through the devices, we showed the  $I$ – $V$  and  $L$ – $V$  curves together for two devices (without LiF layer) after the activation for 10 and 110 s in Fig. 2. In the figures the scales in luminance and current density were adjusted so as for the maximum point of luminance and current density to be overlapped. In this way, the relative behavior in luminance and current density with respect to the

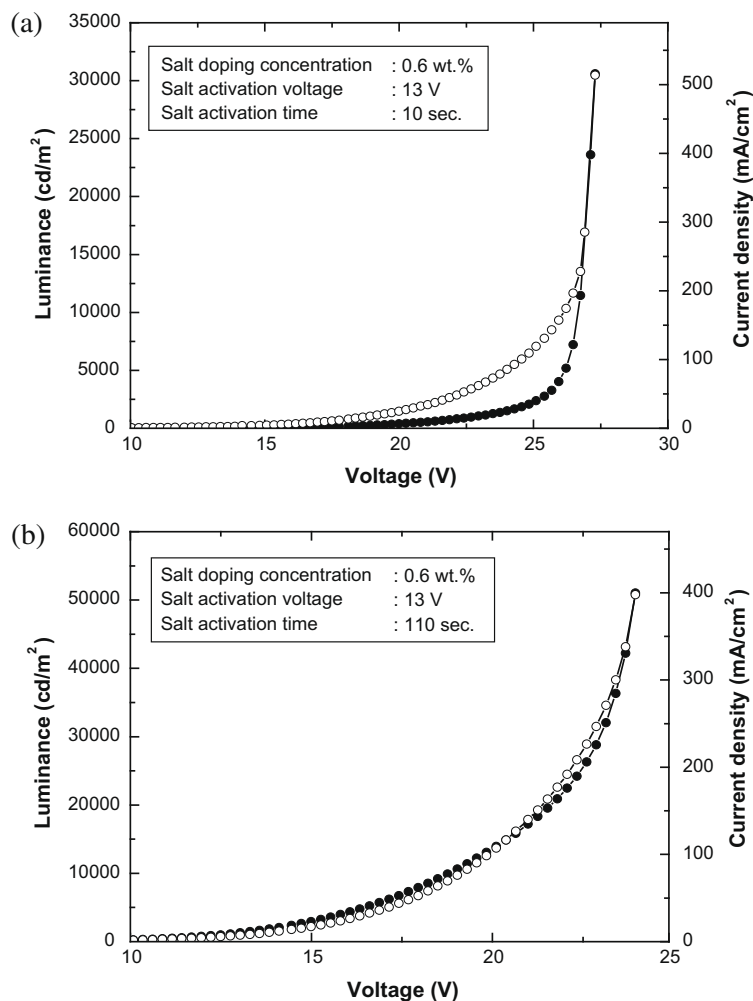


**Fig. 2.** The current density–voltage (open symbol) and luminance–voltage (solid symbols) curves for the salt-doped devices after the activation for (a) 10 s and (b) 110 s. The scales of luminance and current density were adjusted so as to have the maxima of luminance and current density coincide in the graph.

applied voltage can be easily investigated. For the device activated for 10 s, it was observed that the luminance was measured relatively low throughout the operating voltage while the current flowed in a considerable amount through the device. The discrepancy between luminance and current density curves was reduced as the activation time increases (not shown here). Finally, when the salt activation is completed after the simultaneous thermal and electrical annealing (salt activation) for 110 s, the  $L$ – $V$  and  $I$ – $V$  curves became closely matched up to the highest luminance above  $50,000 \text{ cd/m}^2$ . From this observation, we can deduce a couple of view-points for the operational characteristic of the devices. The first thing to note is the fact that the current should have been consumed somewhere, not being utilized for the emission during the activation when the activation of organic salt is not enough. We think that the current could have been consumed for the electrochemical doping processes near electrodes. Even though it is not clear yet at this moment, it is likely that the n-doping occurs in electron transporting PBD with  $\text{Bu}_4\text{N}^+$  while the p-doping oc-

curs in hole transporting PVK [9,10,16,18] or TPD [17,19] with  $\text{BF}_4^-$ . Another important thing to note from Fig. 2b is that in whole luminance level the electrons and holes are balanced to form excitons for the light emission. Since the balance of electrons and holes is a characteristic of LECs, we think that the organic salt-doped devices in this study are similar to the frozen LECs formed by the electrochemical doping of the organic salt into the functional organics in the active layer. Even though the organic salt-doped devices behave similarly to the frozen LECs, however, there is also a distinct difference between the two kinds of devices, in that the  $I$ – $V$  characteristics of the salt-doped devices were influenced by the addition of LiF layer as shown in Fig. 1 while those of the frozen LECs should be insensitive to the electrode structures.

For comparison, we showed the similar  $L$ – $V$  and  $I$ – $V$  curves for the un-doped and salt-doped devices with an electron-injecting LiF layer in Fig. 3. In the figure, we have arbitrarily scaled the  $L$ – $V$  and  $I$ – $V$  curves so as for the curves to fit as close as possible each other. As can be seen

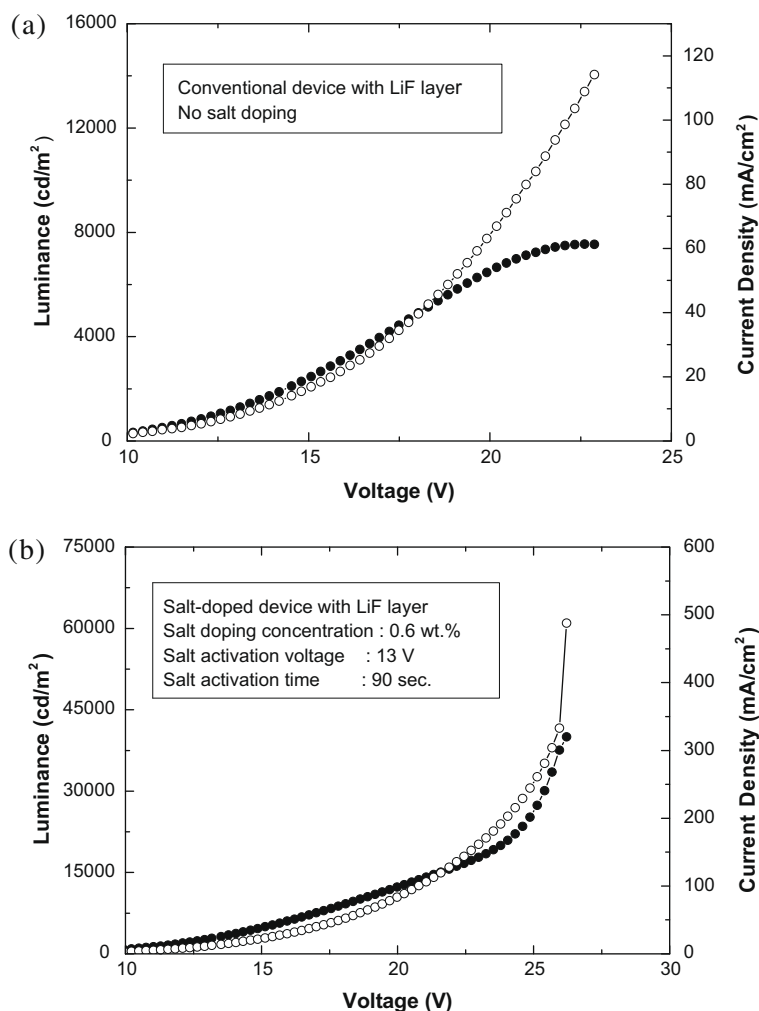


**Fig. 3.** The current density–voltage (open symbol) and luminance–voltage (solid symbols) curves for the (a) un-doped device with LiF layer and (b) salt-doped devices with LiF layer after the activation for 90 s. The scales of luminance and current density were adjusted so as to have the curves fit as close as possible.

in the figure, the  $L$ – $V$  and  $I$ – $V$  curves were found to be quite different unlike the curves for the previous salt-doped devices without LiF layer. The addition of LiF layer facilitates the injection of electrons at the cathode via the reduction of energy barrier independently with the hole injection. In the case of conventional un-doped devices with LiF layer, the current density keeps increasing while the increase in brightness tends to slow down at high applied voltages. This tendency is significantly reduced when the conventional devices with LiF layer are simply doped with the organic salt as shown in Fig. 3b. We think that the organic salt doping greatly improves the carrier balance in the devices such as the case of frozen-junction LECs. But still the carrier balance cannot be achieved if the LiF layer is used in the devices.

In order to investigate the relations between the  $L$ – $V$  and  $I$ – $V$  curves further, we show the luminance–current density ( $L$ – $I$ ) curves for the devices (without LiF layer) after the salt activation for different times in Fig. 4. When the

salt activation is incomplete (salt activation time less than 90 s), the concave  $L$ – $I$  curves are observed in low current density region which means that the current flows through the devices much more compared with the light emission in the region. After the salt activation is complete (salt activation time longer than 90 s), the  $L$ – $I$  curves become almost linear showing that the electrons and holes are balanced for the emission throughout the whole region of current density. In the whole region, the luminous efficiency was found close to 15 cd/A. We show an enlarged graph of the lower left box of Fig. 4a in Fig. 4b. The maximum luminous efficiency was found close to 20 cd/A and always higher than 13 cd/A with the luminance level from 0 to 10,000 cd/m<sup>2</sup>.

The maximum luminance of the conventional un-doped devices with the LiF layer was found 14,000 cd/m<sup>2</sup> as shown in Fig. 5, while that of salt-doped devices (with the LiF layer) after the activation leached higher than 40,000 cd/m<sup>2</sup>. The maximum luminance of the salt-doped



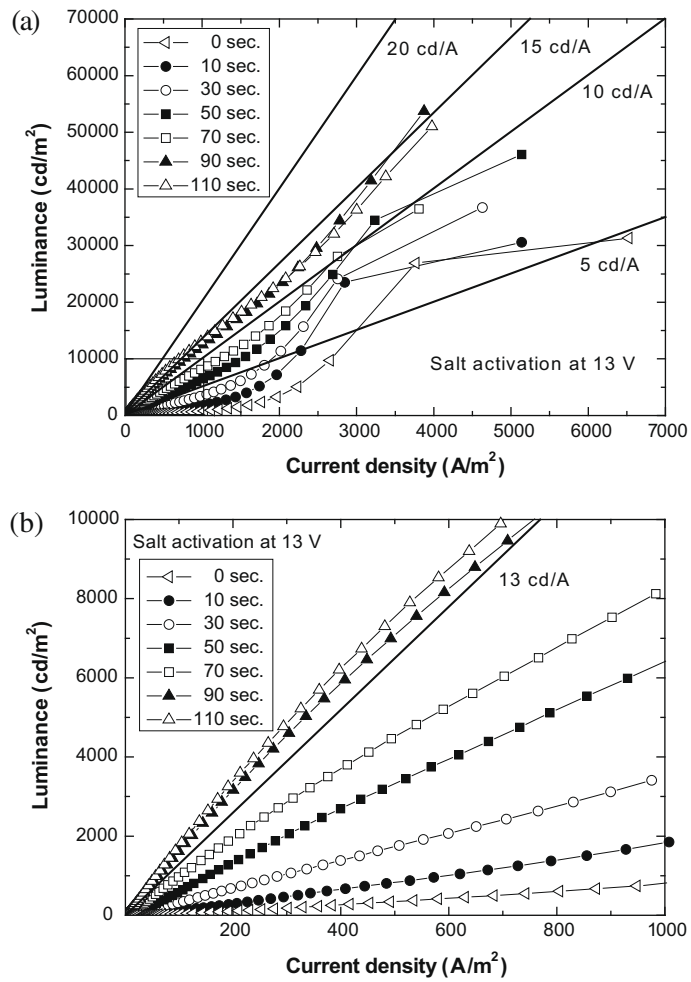


**Fig. 4.** (a) The luminance–current density curves for the salt-doped devices without LiF layer after the activation for various time durations. (b) The enlarged graph of the box at bottom-left corner of (a).

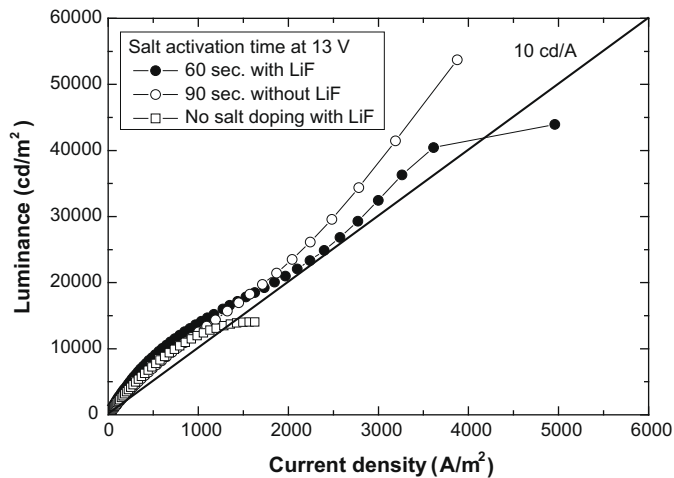


**Fig. 5.** The comparison between the luminance–current density curves for the salt-doped and un-doped devices.

device without the LiF layer was found even higher with a linear  $L$ - $I$  characteristic. An important thing to note from the figure is that the salt doping makes the devices possible to handle much higher current density. We think that it is due to the enhanced balance of electrons and holes provided by the salt doping. Up to the luminance of 55,000 cd/m<sup>2</sup>, the luminous efficiency was found steadily over 10 cd/A, even showing the higher efficiency with the higher current density. It should be mentioned here that the organic salt-doped devices showed high luminous efficiency even up to high current density, which means that the salt doping did not help only for the carrier injection but also for the carrier mobility. As can be seen in Fig. 5, the luminance tends to saturate above the current density of 1000 A/m<sup>2</sup> for the conventional devices with LiF layer. Even though the PBD acting as an electron transporting material in our PVK-based electro-phosphorescent LEDs, main host material in the PLEDs with ITO/PEDOT:PSS/PVK + TPD + PBD + Ir(ppy)<sub>3</sub> + Bu<sub>4</sub>NBF<sub>4</sub>/Al structure is PVK. The hole mobility is known to be generally much greater than the electron mobility in PVK-based LEDs, because PVK is one of the famous hole transporting materials [20]. As increasing driving voltage, the energy barriers for hole and electron injection might be decreased resulting increase of hole and electron population in the emitting layer. Therefore, the injected holes will accumulate at the interface between the emitting layer and Al cathode because of the difference of charge carrier mobility. Presumably, the saturation in luminance might be due to the exciton quenching which may be caused by the hole accumulation at cathode interface [21,22]. From the experimental results shown in Fig. 5, however, the doping of organic salt in the devices seems to prevent the saturation in luminance regardless of the existence of LiF injection layer. Therefore, the doping of organic salt seems to increase the carrier mobility, more importantly the electron mobility in the emissive layer in that the high luminous efficiency is sustained even up to high current density of 4000 A/m<sup>2</sup>. Since the electrical conductivity is directly proportional to the carrier mobility at a fixed doping concentration, the sustainment of high luminous efficiency at high current density evidences the increased carrier mobility upon the doping of organic salt.

#### 4. Conclusions

We have showed that the doping of organic salt into a polymer emissive layer and the appropriate activation could greatly enhance the balance of electrons and holes in the devices. By enhancing the carrier balance, the salt-doped devices have exhibited much higher luminance compared with un-doped counterparts. The salt-doped devices showed the maximum luminance of 55,000 cd/m<sup>2</sup> after the salt activation. Due to the enhanced carrier balance, the luminous efficiency of about 15 cd/A was maintained throughout the whole luminance range up to the maximum luminance.

#### Acknowledgement

This work was supported by a grant from Gyeonggi Province through the GRRC (Gyeonggi Regional Research Center) program in Sungkyunkwan University.

#### References

- [1] Q. Pei, G. Yu, C. Zhang, Y. Yang, A.J. Heeger, Polymer light-emitting electrochemical cells, *Science* 269 (1995) 1086–1088.
- [2] G. Yu, Y. Cao, M. Andersson, J. Gao, A.J. Heeger, Polymer light-emitting electrochemical cells with frozen p-i-n junction at room temperature, *Adv. Mater.* 10 (1998) 385–388.
- [3] J.A. Manzanares, H. Reiss, A.J. Heeger, Polymer light-emitting electrochemical cells: a theoretical study of junction formation under steady-state conditions, *J. Phys. Chem. B* 102 (1998) 4327–4336.
- [4] J. Gao, Y. Li, G. Yu, A.J. Heeger, Polymer light-emitting electrochemical cells with frozen junctions, *J. Appl. Phys.* 86 (1999) 4594–4599.
- [5] F.-C. Chen, Y. Yang, Q. Pei, Phosphorescent light-emitting electrochemical cell, *Appl. Phys. Lett.* 81 (2002) 4278–4280.
- [6] J. Gao, J. Dane, Planar polymer light-emitting electrochemical cells with extremely large interelectrode spacing, *Appl. Phys. Lett.* 83 (2003) 3027–3029.
- [7] Y. Shao, G.C. Bazan, A.J. Heeger, Long-lifetime polymer light-emitting electrochemical cells, *Adv. Mater.* 19 (2007) 365–370.
- [8] Q. Sun, Y. Li, Q. Pei, Polymer light-emitting electrochemical cells for high-efficiency, low-voltage electroluminescent devices, *J. Disp. Technol.* 3 (2007) 211–224.
- [9] Y. Sakuratani, M. Asai, M. Tokita, S. Miyata, Enhanced electron injection and electroluminescence in poly(*N*-vinyl carbazole) film doped with ammonium salt, *Synth. Met.* 123 (2001) 207–210.
- [10] Y. Sakuratani, M. Asai, H. Yamamoto, M. Tokita, T. Watanabe, S. Miyata, Transition phenomenon in salt-doped organic electroluminescent devices at high bias voltage, *Mol. Cryst. Liq. Cryst.* 378 (2002) 157–166.
- [11] E. Itoh, T. Yamashita, K. Miyairi, Effective ionic charge polarization using typical supporting electrolyte and charge injection phenomena in molecularly doped polymer light-emitting diodes, *J. Appl. Phys.* 92 (2002) 5971–5976.
- [12] S.S. Oh, J.H. Park, S.W. Kim, B. Park, Enhanced light emission from phosphorescent single-layered organic light-emitting devices doped with ionic salt by simultaneous thermal and electrical annealing, *J. Appl. Phys.* 102 (2007) 074503.
- [13] B. Park, M.Y. Han, S.S. Oh, Solution processable ionic p-i-n phosphorescent organic light-emitting diodes, *Appl. Phys. Lett.* 93 (2008) 093302.
- [14] J. Gao, G. Yu, A.J. Heeger, Polymer light-emitting electrochemical cells with frozen p-i-n junction, *Appl. Phys. Lett.* 71 (1997) 1293.
- [15] J.-H. Shin, S. Xiao, A. Fransson, L. Edman, Polymer light-emitting electrochemical cells: frozen-junction operation of an “ionic liquid” device, *Appl. Phys. Lett.* 87 (2005) 043506.
- [16] T.-W. Lee, H.-C. Lee, O.O. Park, High-efficiency polymer light-emitting devices using organic salts: a multilayer structure to improve light-emitting electrochemical cells, *Appl. Phys. Lett.* 81 (2002) 214–216.
- [17] S. Janietz, B. Schulz, M. Torronen, G. Sundholm, Electrochemical investigations on poly(phenylene-1,3,4-oxadiazoles), *Eur. Polym. J.* 29 (1993) 545–549.
- [18] M. Ikeda, Formation of ion pairs and carrier transport in undoped and dye-doped poly(*N*-vinylcarbazole) films, *J. Phys. Soc. Jpn.* 60 (1991) 2031–2039.
- [19] Y.Q. Liu, H. Ma, A.K.-Y. Jen, Synthesis and characterization of a novel bipolar polymer for light-emitting diodes, *Chem. Commun.* (1998) 2747–2748.
- [20] P. D’Angelo, M. Barra, A. Cassinese, M.G. Maglione, P. Vacca, C. Minarini, A. Rubino, *Solid-State Electron.* 51 (2007) 123–129.
- [21] A.L. Burin, M.A. Ratner, *J. Phys. Chem. A* 104 (2000) 4704–4710.
- [22] C. Hochfilzer, G. Leising, Y. Gao, E. Forsythe, C.W. Tang, *Appl. Phys. Lett.* 73 (1998) 2254–2256.

the performance of TEOLEDs encapsulated with each of these polyurea/ $\text{Al}_2\text{O}_3$  pairs were tested to find optimal thin-film encapsulation design in regard to efficiency and lifetime of TEOLEDs.

In this study, we fabricated TEOLEDs by using Ag(100 nm)/ITO(10 nm) as a reflective anode, LiF(1 nm)/Mg:Ag(10:1 mass ratio, 18 nm) as a semitransparent cathode [11], and tris(8-hydroxyquinolino)aluminum ( $\text{Alq}_3$ ) doped with 2-wt% 2,3,6,7-tetrahydro-1H, 5H, 11H-10-(2-benzothiazolyl)quinolizino-[9,9a,1gh] Coumarin (C-545T) as an emitting layer (EML).  $N,N'$ -Bis(1-naphthyl)- $N,N'$ -diphenyl-1,1'-biphenyl-4,4'-diamine (NPB) and  $\text{Alq}_3$  were used as a hole transport layer (HTL) and an electron transport layer (ETL), respectively. Thickness of HTL, EML, and ETL were selected to optimize microcavity effect, so that the structure of TEOLEDs was Ag(100 nm)/ITO(10 nm)/NPB(190 nm)/ $\text{Alq}_3$ (33 nm) + C-545T(2 wt%)/ $\text{Alq}_3$ (30 nm)/LiF(1 nm)/Mg:Ag(18 nm)/NPB(60 nm). The 60-nm NPB capping layer was added for refractive-index matching to maximize light extraction [12]. Prior to deposit organic layers, reflective anode Ag/ITO was treated with 60-watt oxygen plasma for 90 s. All the organic layers and the Mg:Ag semitransparent cathode were deposited via thermal evaporation in vacuum better than  $1.33 \times 10^{-4}$  Pa.

We tested 6 different encapsulation schemes for identical TEOLEDs. The first TEOLED, Device A, was encapsulated

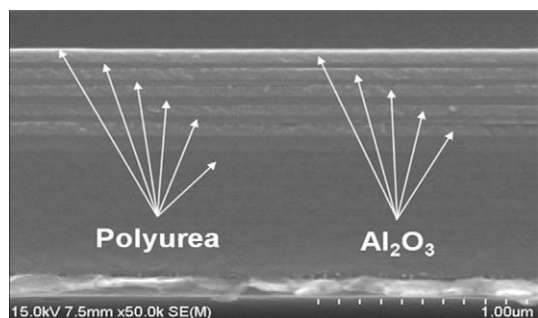


**Fig. 1.** Cross-sectional SEM image of 5 pairs of  $\text{Al}_2\text{O}_3$ /polyurea layers on top of a 0.8- $\mu\text{m}$ -thick polyurea layer. Polyurea and  $\text{Al}_2\text{O}_3$  layers were deposited by alternating sputtering and VDP processes, respectively.

with glass under nitrogen atmosphere while placing getter on one side not to block the light path. The other 5 TEOLEDs were encapsulated with alternating layers of  $\text{Al}_2\text{O}_3$  and polyurea, and labeled according to the number of  $\text{Al}_2\text{O}_3$ /polyurea layer pairs: Device B-1, B-2, B-3, B-4, and B-5. Inorganic  $\text{Al}_2\text{O}_3$  layers were deposited by RF magnetron sputtering under the condition of 42-sccm argon flow, 0.29-Pa working pressure, and 300-W RF power. Organic polyurea layers were deposited at room-temperature from isocyanate monomer and diamine precursor via vapor deposition polymerization (VDP) at the working pressure of 0.49 Pa, and the deposition rate was 1 nm/s. For thin-film encapsulation, we first transferred a TEOLED to the VDP chamber to deposit 0.8- $\mu\text{m}$  thick polyurea that was necessary to minimize damage to TEOLED during  $\text{Al}_2\text{O}_3$  sputtering. Next, the TEOLED was transferred back and forth between the sputtering and VDP chambers to deposit 50-nm  $\text{Al}_2\text{O}_3$  and 20-nm polyurea layers in sequence. The structure of encapsulation layer for Device B-1 was polyurea(0.8  $\mu\text{m}$ )/ $\text{Al}_2\text{O}_3$ (50 nm)/polyurea(20 nm), and those for other devices were similar except the number of  $\text{Al}_2\text{O}_3$ (50 nm)/polyurea(20 nm) pairs on top of the 0.8- $\mu\text{m}$  thick polyurea layer. The active area of all the TEOLEDs were  $2 \times 2 \text{ mm}^2$ . Keithley238 and PR650 were used as a source-measurement unit and a luminance meter, respectively, in measuring  $I$ - $V$ - $L$ (current-voltage-luminance) characteristics.

**Fig. 1** shows a cross-sectional scanning electron microscopy (SEM) image of 5 pairs of  $\text{Al}_2\text{O}_3$ (50 nm)/polyurea(20 nm) layers on top of the 0.8- $\mu\text{m}$  thick polyurea layer, which is equivalent to the thin-film encapsulation for Device B-5. Polyurea and  $\text{Al}_2\text{O}_3$  layers appear darker and less dark in the SEM image, respectively. This SEM picture confirms the formation of a good quality stack of  $\text{Al}_2\text{O}_3$  and polyurea layers by alternating sputtering and VDP processes.

In **Fig. 2a**, we compare operation characteristics of Device B-5 (thin-film-encapsulated TEOLED) and Device A (glass-encapsulated TEOLED). It is interesting to note that current density variation with respect to driving voltage is almost identical between Device A and Device B-5. This observation indicates that our thin-film encapsulation pro-

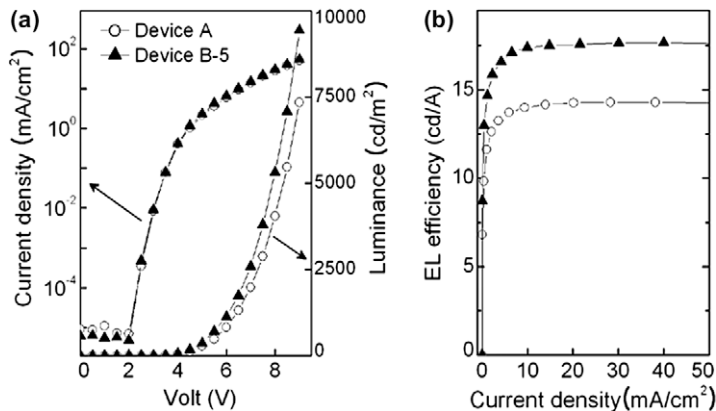


**Fig. 2.** Comparison of the operating characteristics of Device B-5 (thin-film-encapsulated TEOLED) with those of Device A (glass-encapsulated TEOLED): (a) current density and luminance versus applied voltage, and (b) luminance yield (EL efficiency) versus current density.

cess did not induce any damage to the TEOLEDs. However, there is a noticeable increase in luminance of Device B-5 compared to that of Device A at identical bias voltages. We attribute the luminance increase of Device B-5 to the optical effects of the thin-film stack. The luminance increase results in improvement of electroluminescence (EL) efficiency as shown in Fig. 2b. At the current density of 10 mA/cm<sup>2</sup>, the EL efficiency of Device B-5 is 17.4 cd/A that corresponds to 23.4% improvement from 14.1 cd/A of Device A.

Table 1 shows the position and width of EL peaks, from which CIE color coordinates are deduced, and the EL efficiency of the aforementioned six TEOLEDs at the current density of 10 mA/cm<sup>2</sup>. It is obvious that there is a periodic dependence of TEOLED performance on the number of Al<sub>2</sub>O<sub>3</sub>/polyurea pairs for the thin-film encapsulation devices. In particular, when even number of Al<sub>2</sub>O<sub>3</sub>/polyurea pairs was used, the EL efficiency was improved only 11% (Device B-2) and 15% (Device B-4) compared to that of Device A with glass encapsulation. However, there were respectively 30%, 25%, and 23% improvement in the EL efficiency when one (Device B-1), three (Device B-3), and five (Device B-5) pairs of Al<sub>2</sub>O<sub>3</sub>/polyurea layers were used for encapsulation. It is apparent that the optics of multi-layer stacks resulted in the observed periodic variation of the EL efficiency, and the position and width of EL peaks.

We simulated the experimentally observed EL peaks through the combination of the photoluminescence (PL) spectrum of the Coumarin-doped Alq<sub>3</sub>, which we used to represent the original emission from the EML, with the rigorous modeling of multi-layer optical effects that stem from the structure of each device. It was surprising to find that slight thickness adjustment of two NPB layers and a thick polyurea layer was sufficient to simulate the EL spectra of all five thin-film-encapsulated TEOLEDs. The thickness values of these layers, which we used to produce the simulated EL spectra in Fig. 3a, are listed in Table 1. To manifest the origin of the periodic variation of the EL efficiency, we compared the simulated transmittance of the five encapsulating thin films at the wavelengths corresponding to EL peaks. As shown in Fig. 3b, the transmittance varies periodically with respect to the increase of number of Al<sub>2</sub>O<sub>3</sub>-polyurea pairs, and higher transmittance is available from odd number of Al<sub>2</sub>O<sub>3</sub>-polyurea pairs. It is worth emphasizing that the EL efficiency of each of the five thin-film-encapsulated TEOLEDs is better than that of Device A. In the case of glass-encapsulated TEOLEDs, wave-guide-mode loss is inevitable because the light emitted from the EML has to enter an encapsulating glass, having

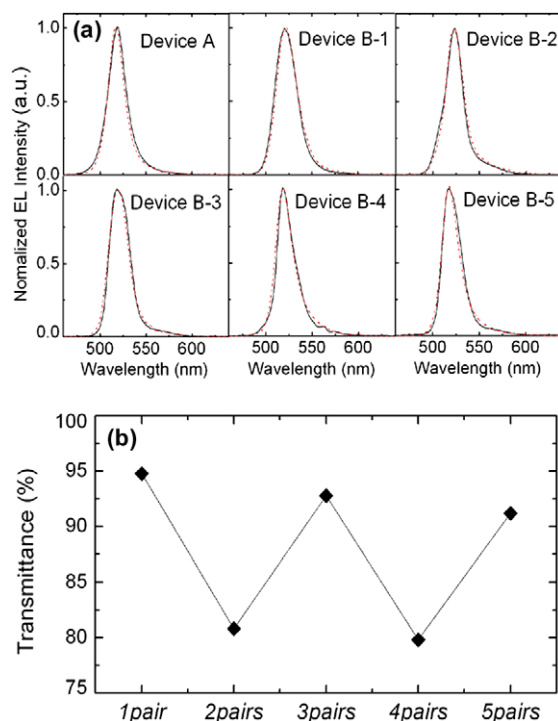


Fig. 3. (a) Comparison of EL spectra (dash lines) simulated based on the structural parameters in Table 1 with measured EL spectra (solid lines); (b) systematic variation of simulated transmittance of the five encapsulating thin films at the wavelengths corresponding to EL peaks.

refractive-index of 1.53, through the air gap. However, similar refractive-indexes of Al<sub>2</sub>O<sub>3</sub> and polyurea, 1.66 for Al<sub>2</sub>O<sub>3</sub> and 1.52 for polyurea, makes thin-film-encapsulated devices free from wave-guide loss.

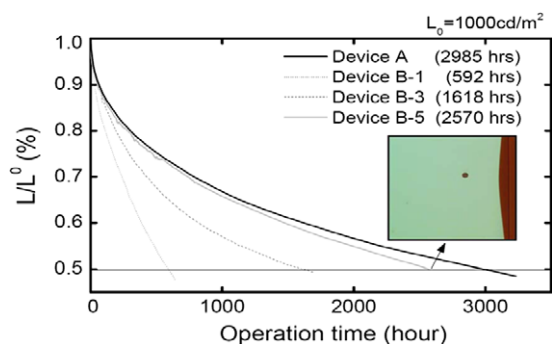
Fig. 4 shows the decrease of luminance, starting from the initial value of 1000 cd/m<sup>2</sup>, with respect to operation time for Device A, and Device B-1, B-3, and B-5. We find that the half-decay lifetime of Device B-1 was only 592 hours, whereas that of Device A was 2985 h. It seems that 1- $\mu$ m thick polyurea and one pair of Al<sub>2</sub>O<sub>3</sub>/polyurea layers were not sufficient enough to block permeation of water vapor and oxygen. However, as we increased the number of Al<sub>2</sub>O<sub>3</sub>/polyurea pairs to three (Device B-3) and five (Device B-5), the half-decay lifetime improved to 1618 and 2570 h, respectively. It is worth emphasizing that the half-decay lifetime of Device B-5 (2570 h) is about 86% of that of Device A (2985 h). The variation of lifetime indicates that protection against the permeation of water va-

Table 1

Details of EL performance for a series of top-emission OLEDs at the current densities of 10 mA/cm<sup>2</sup>.

Device	Structure (nm)										EL performance			
	Ag/ITO	NPB	EML	Alq <sub>3</sub>	LiF	Mg:Ag	NPB	Polyurea	Al <sub>2</sub> O <sub>3</sub> /polyurea	EL effi. (cd/A)	EL peak (nm)	FWHM (nm)	CIE (CIE <sub>x</sub> , CIE <sub>y</sub> )	
A (Glass Encap)	100/10	189	33	30	1	18	62	–	–	14.1	520	23	(0.148, 0.763)	
B-1		188					62	800	1 pair	18.3	520	28	(0.143, 0.768)	
B-2		190					62	806	2 pairs	15.6	524	22	(0.156, 0.758)	
B-3		188					62	795	3 pairs	17.6	520	25	(0.144, 0.766)	
B-4		189					61	790	4 pairs	16.2	524	22	(0.152, 0.759)	
B-5		189					61	810	5 pairs	17.4	520	23	(0.146, 0.763)	

Basic unit for thin-film encapsulation is Al<sub>2</sub>O<sub>3</sub>(50 nm) and polyurea(20 nm).



**Fig. 4.** Comparison of half-decay lifetime of the TEOLEDs encapsulated with 1, 3, and 5 pairs of  $\text{Al}_2\text{O}_3$  and polyurea layers (Device B-1, B-3, and B-5, respectively) to that of the glass-encapsulated TEOLED (Device A). Initial luminance  $L_0$  was  $1000 \text{ cd/m}^2$ . Inset shows a photograph of the device with 5 pairs of  $\text{Al}_2\text{O}_3$  and polyurea layers (Device B-5) after the lifetime test.

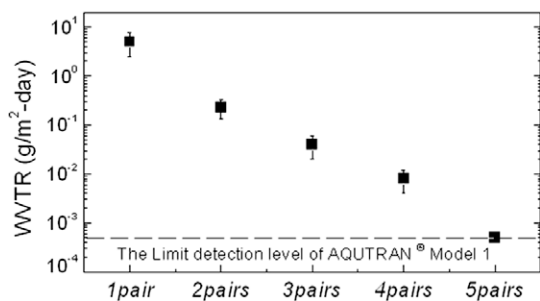


**Fig. 5.** The result of WVTR measurement at  $37.8^\circ\text{C}$  and 100% RH for a set of  $\text{Al}_2\text{O}_3(50 \text{ nm})/\text{polyurea}(20 \text{ nm})$  layers on a PET film. Each data point represents the average of three-sample measurements. The WVTR of one, two, three, four, and 5 pairs of  $\text{Al}_2\text{O}_3(50 \text{ nm})/\text{polyurea}(20 \text{ nm})$  layers on a PET film were measured as 5, 0.23, 0.04, 0.008, and  $0.0005 \text{ g/m}^2 \text{ day}$ , respectively, whereas the WVTR of a bare PET film was  $8.2 \text{ g/m}^2 \text{ day}$ .

por and ambient oxygen improves in accordance with the increase of the number of  $\text{Al}_2\text{O}_3/\text{polyurea}$  pairs. Nevertheless, the EL peak positions of Device B-1, B-3, and B-5 are identical, and the widths of EL peaks of these TEOLEDs are similar, so that their  $\text{CIE}_{x,y}$  color coordinates are only slightly different, because thin-film encapsulation is designed in such a way to minimize the change in color coordinates from those of the original glass-encapsulated TEOLED, Device A.

Inset in Fig. 4 is a photograph of the device with 5 pairs of  $\text{Al}_2\text{O}_3$  and polyurea layers (Device B-5) after the lifetime test, which shows that the degradation of the  $\text{Al}_2\text{O}_3/\text{polyurea}$ -encapsulated OLEDs occurred typically from the edge due to the permeation of water vapor and ambient oxygen through the polyurea layers. Fig. 5 shows the result of independent measurement of water vapor transition rate (WVTR) for a set of  $\text{Al}_2\text{O}_3(50 \text{ nm})/\text{polyurea}(20 \text{ nm})$  layers on PET films. This WVTR measurement was carried out at  $37.8^\circ\text{C}$  and 100% RH by using the AQUTRAN Model-1 (MOCON Co. Ltd.) with the detection range from  $5 \times 10^{-4}$  to  $60 \text{ g/m}^2 \text{ day}$ . The average of three-sample measurements for each number of  $\text{Al}_2\text{O}_3(50 \text{ nm})/\text{polyurea}(20 \text{ nm})$  pairs showed that the WVTR of one, two, three, four, and 5 pairs

of  $\text{Al}_2\text{O}_3(50 \text{ nm})/\text{polyurea}(20 \text{ nm})$  layers on a PET film are 5, 0.23, 0.04, 0.008, and  $0.0005 \text{ g/m}^2 \text{ day}$ , respectively. It should be noted that the WVTR of the four pairs of  $\text{Al}_2\text{O}_3/\text{polyurea}$  layers on a PET film is about three orders of magnitude smaller than that of a bare PET film, which is  $8.2 \text{ g/m}^2 \text{ day}$ , and that the WVTR of the 5 pairs of  $\text{Al}_2\text{O}_3/\text{polyurea}$  layers on a PET film is close to the detection limit of the apparatus we used.

In summary we developed a room-temperature process for thin-film encapsulation of TEOLEDs via alternating stacking of organic polyurea and inorganic  $\text{Al}_2\text{O}_3$  layers. Initial deposition of a  $0.8\text{-}\mu\text{m}$ -thick polyurea layer on top of TEOLEDs turned out to be effective to prevent TEOLEDs from experiencing noticeable damage during sputtering processes. We were able to prove that 5 pairs of  $\text{Al}_2\text{O}_3/\text{polyurea}$  layers were sufficient for significant improvement of half-decay lifetime of the TEOLED, to the 86% of the lifetime of the glass-encapsulated TEOLED. Moreover, we achieved 23% improvement in EL efficiency without noticeable change in color coordinates because the thickness of the  $\text{Al}_2\text{O}_3/\text{polyurea}$  pairs, the thick polyurea buffer layer, the transparent Mg:Ag layer, and the two NPB layers were selected to maximize light extraction without color distortion. Independent measurement of WVTR for a set of  $\text{Al}_2\text{O}_3/\text{polyurea}$  layers on PET films showed that the barrier property against water vapor can be so good that the WVTR can be as low as  $5 \times 10^{-4} \text{ g/m}^2 \text{ day}$  with 5 pairs of  $\text{Al}_2\text{O}_3/\text{polyurea}$  layers, which indicates that the hybrid thin-film encapsulation based on  $\text{Al}_2\text{O}_3/\text{polyurea}$  layers has the application potential in developing flexible top-emitting OLEDs.

## Acknowledgements

S.L. acknowledges the financial support by the Ministry of Science and Technology through the Nanoscopia Center of Excellence at Ajou University and by the Korea Research Foundation (Grant No. KRF-2007-412-J04003).

## References

- [1] Sung Mook Chung, Chi-Sun Hwang, Jeong-Ik Lee, Sang Hee Ko Park, Yong Suk Yang, Lee-Mi Do, Hye Yong Chu, Synth. Met. 158 (2008) 561.
- [2] Anna B. Chwang, Mark A. Rothman, Sokhanno Y. Mao, Richard H. Hewitt, Michael S. Weaver, Jeff A. Silvernail, Kamala Rajan, Michael Hack, Julie J. Brown, Xi Chu, Lorenza Moro, Todd Krajewski, Nicole Rutherford, Appl. Phys. Lett. 83 (2003) 413.
- [3] S.-N. Lee, S.-W. Hwang, C.H. Chen, Jpn. J. Appl. Phys. 46 (2007) 7432.
- [4] F.L. Wong, M.K. Fung, S.L. Tao, S.L. Lai, W.M. Tsang, K.H. Kong, W.M. Choy, C.S. Lee, S.T. Lee, J. Appl. Phys. 104 (2008) 014509.
- [5] J. Granstrom, J.S. Swensen, J.S. Moon, G. Rowell, J. Yuen, A.J. Heeger, Appl. Phys. Lett. 93 (2008) 193304.
- [6] H.-K. Kim, M.S. Kim, J.-W. Kang, J.-J. Kim, M.-S. Yi, Appl. Phys. Lett. 90 (2007) 13502.
- [7] A.P. Ghosh, L.J. Gerenser, C.M. Jarman, J.E. Fornalik, Appl. Phys. Lett. 86 (2005) 223503.
- [8] H. Lifka, H.A. van Esch, J.J.W.M. Rosink, SID 04 Digest, pp. 1384–1387.
- [9] L. Moro, T.A. Krajewski, N.M. Rutherford, O. Philips, R.J. Visser, M. Gross, W.D. Bennett, G. Graff, SPIE 5214 (2004) 83.
- [10] M. Hemerik, R. van Erven, R. Vangheluwe, J. Yang, T. van Rijswijk, R. Winter, B. van Rens, SID 06 DIGEST, pp. 1571–1574.
- [11] B.J. Chen, X.W. Sun, K.S. Wong, X. Hu, Opt. Exp. 13 (2005) 2631.
- [12] L.S. Hung, C.W. Tang, M.G. Mason, P. Raychaudhuri, J. Madathil, Appl. Phys. Lett. 78 (2001) 544.

or hole-transport material [8]. Thus the circuit is complete and the system regenerative.

To date the most efficient dye sensitizers have been based on heteroleptic ruthenium complexes such as the 'gold standard' [*cis*-di(thiocyanato)-bis(4,4'-dicarboxylate-2,2'-bipyridyl)]ruthenium(II) **1** (N3) [9]. The development of the ruthenium dyes has focused on the following key properties: improving light absorption both in terms of wavelength range and molar extinction coefficient – the lowest energy transition is believed to exhibit 'metal-to-ligand charge transfer' (MLCT) character which leads to intramolecular spatial charge separation in the excited state; strong adsorption and binding to the support photoanode; and rapid (*fs*) and efficient injection of the excited electron into the TiO<sub>2</sub>. This combination of properties yields peak internal quantum efficiencies of near 100%.

The power conversion efficiency ( $\eta$ ) of a DSSC is strongly related to the light harvesting efficiency (LHE) of

the dye sensitizers. The LHE has been estimated using Eq. (1) [10]:

$$LHE(\lambda) = 1 - 10^{-\varepsilon(\lambda) \cdot I} \quad (1)$$

where,  $\varepsilon$  is molar extinction coefficient at wavelength  $\lambda$  and  $I$  is the adsorption capacity onto the TiO<sub>2</sub> photoanode (the dye uptake). From Eq. (1) it is clear that the molar extinction coefficient must be maximized over the solar wavelength range. This imperative has motivated numerous studies to fine tune the absorption properties of the ruthenium complexes by introducing conjugated moieties to one of the bipyridyl ligands of the basic structure of **1** [11–14]. This approach has given rise to ruthenium complexes with enhanced  $\varepsilon$  and absorptions at longer wavelengths compared to **1**. However, the enhanced spectral properties of such ruthenium complexes have not always led to the expected improvements in overall device effi-

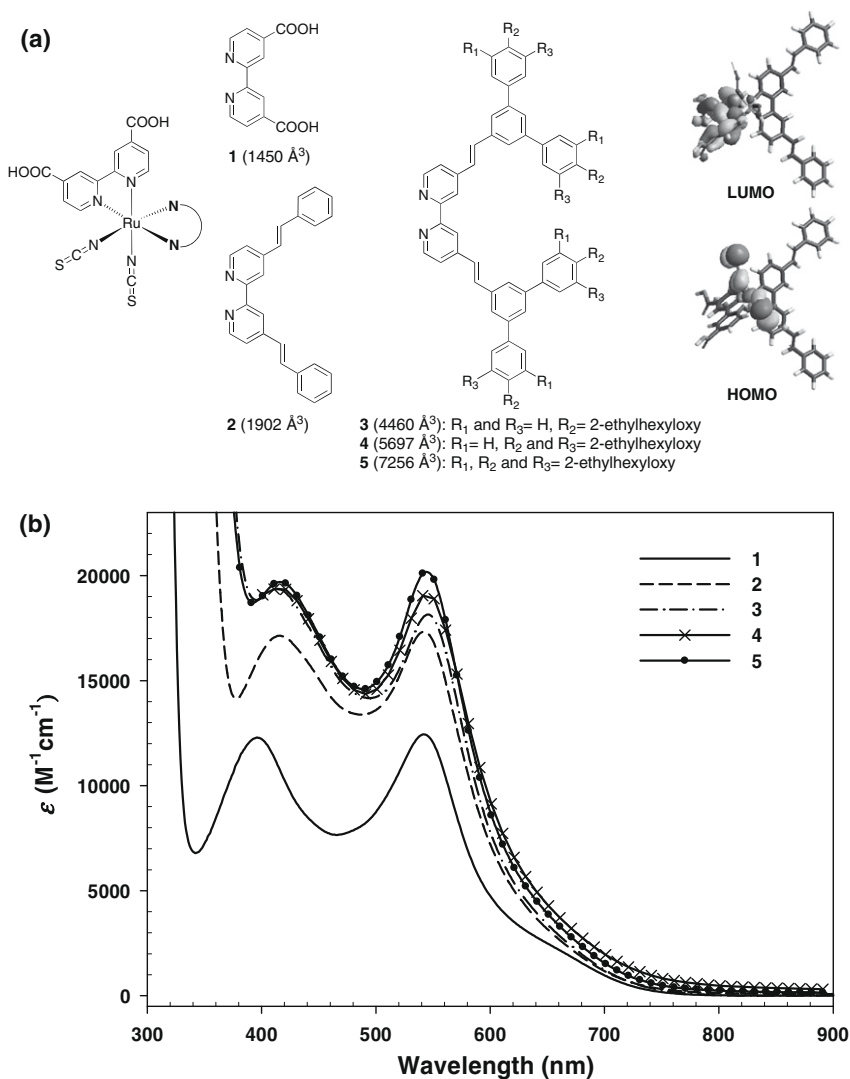


**Fig. 1.** (a) The chemical structures of the materials and graphical representation of the frontier orbitals of **2** calculated by the ZINDO-1 parameter method (HyperChem 7.0). Note, the distributions of the frontier orbitals in all compounds were similar to that shown for **2**. (b) The UV/visible absorption spectra of the materials (5 × 10<sup>-5</sup> mol L<sup>-1</sup>) in *N,N*-dimethylformamide.

ciency ( $\eta$ ) [15–17] with some apparently contradictory results in dye comparison studies [11,15].

In this manuscript we use ruthenium complex-cored dendrimers where  $\Gamma$  (the adsorption capacity or dye uptake) from Eq. (1) can be tuned to understand why improvements in device performance have not always followed increased light absorption and to explain the aforementioned conflicting device performance. In most reports on DSSCs the role of adsorption has been largely ignored, or if commented on not studied in any detail [12]. The dendrimers are similar to N3 (Fig. 1: **1**) but with the carboxylic acid moieties on one bipyridyl ligand replaced with first generation biphenyl dendrons connected to the ligand via vinyl units (Fig. 1: **3**, **4**, and **5**) [18]. The dendronised complexes have the same chromophores and only differ in the number of surface groups. The use of the same chromophore means that the absorption properties will be essentially the same enabling the direct investigation of the effect of molecular volume through Eq. (1). We also compare the properties of the non-dendronised complex **2** (Fig. 1), which has the same extended conjugated bipyridyl ligand but without the branched dendrons and surface groups for comparison.

## 2. Results and discussion

The first step in understanding the role of adsorption in device performance was the determination of the molecular volumes of the dendrimers. The propensity of N3 to aggregate in solution [18] and the polar carboxylic acid groups meant that gradient diffusion NMR and gel permeation chromatography were not useful, and hence the molecular volumes of the materials in this study were determined by semi-empirical quantum chemical calculations (see Section 4). The molecular volumes are shown in Fig. 1a along with a model showing the HOMO (highest occupied molecular orbital) and LUMO (lowest unoccupied molecular orbital) states of **2**. An interesting observation from these calculations is that for all the materials the

HOMO resides mainly on the ruthenium and isothiocyanate moieties and the LUMO on the 4,4'-dicarboxy-2,2'-bipyridyl unit meaning that the lowest energy transitions, and hence optoelectronic properties of all the studied materials should be similar.

Most studies on ruthenium sensitizers focus on the improvement of the long wavelength absorption. Fig. 1b shows a comparison of the absorption spectra of our materials and N3 **1** at a concentration of  $5 \times 10^{-5} \text{ mol L}^{-1}$  in *N,N*-dimethylformamide. The  $\lambda_{\text{max}}$  and  $\epsilon$  of the longer wavelength band for **2** [ $\lambda_{\text{max}}$ : 543 nm, ( $\epsilon [\text{M}^{-1} \text{cm}^{-1}] = 17,300$ )] are slightly red-shifted and increased, respectively relative to **1** [ $\lambda_{\text{max}}$ : 541 nm, ( $\epsilon [\text{M}^{-1} \text{cm}^{-1}] = 12,400$ )]. Introducing the (2-ethylhexyloxy) surface group containing phenyl moieties to form the first generation dendronised ligands of **3**, **4**, and **5** also causes a slight shift of the  $\lambda_{\text{max}}$  and an increase in the molar absorption coefficients [ $\lambda_{\text{max}}$ : 546 nm, ( $\epsilon [\text{M}^{-1} \text{cm}^{-1}] = 18,100$ ); [ $\lambda_{\text{max}}$ : 547 nm, ( $\epsilon [\text{M}^{-1} \text{cm}^{-1}] = 19,200$ ); and [ $\lambda_{\text{max}}$ : 548 nm, ( $\epsilon [\text{M}^{-1} \text{cm}^{-1}] = 20,200$ )], respectively]. However, it is important to note that in addition to the absorption increase in the longer wavelength band, the molar extinction coefficients of the new compounds are higher over all wavelengths indicating that they should be better light harvesters than **1**. Based only on the absorption characteristics of the materials the efficiency of the DSSCs made with the new dyes should be expected to increase in the order  $\mathbf{1} < \mathbf{2} < \mathbf{3} < \mathbf{4} < \mathbf{5}$ .

However, as stated earlier the performance of a DSSC is not only based on the absorption of the harvesting (macro) molecule but also on the total amount of dye present. The dye uptake was determined by immersing the  $\text{TiO}_2$  photoanodes ( $0.88 \text{ cm}^2$  surface area) into a cuvette of dye solution ( $1 \times 10^{-4} \text{ mol L}^{-1}$ ), and the change in the absorbance of the dye solution at  $\lambda_{\text{max}}$  of the longest wavelength band was measured *in situ* as a function of time (see Section 4). The dye uptake amount ( $\Gamma$ ) was then determined by comparison with standard solutions of known dye concentration. Fig. 2 shows the dye uptake profiles as a function of time for the materials of Fig. 1. In all cases the

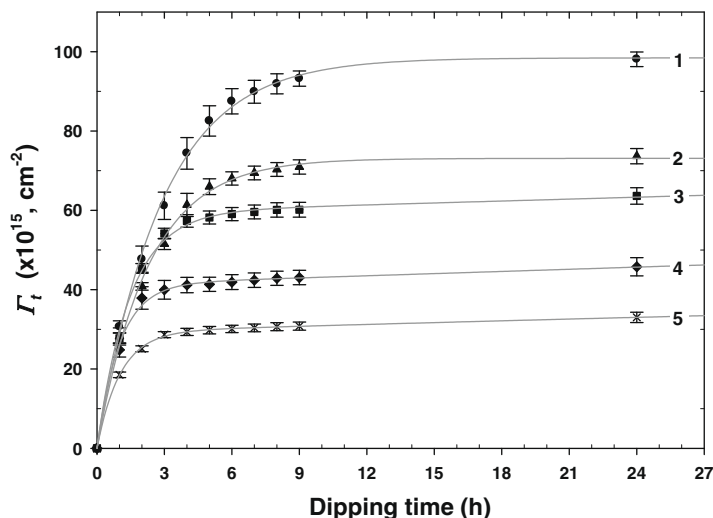


Fig. 2. The adsorption data for the Ru complexes onto  $\text{TiO}_2$  films measured over a period of 24 h (solid line represents the numerical regression fit).

rate of dye adsorption is initially rapid and eventually reaches a plateau. The plateau represents the equilibrium value associated with maximum dye uptake. These profiles are typical for organic adsorbates into nano-porous inorganic matrices [19,20]. The chemisorption of all the materials onto the surface of the  $\text{TiO}_2$  was confirmed by infrared spectroscopy, which showed absorptions corresponding to bidentate- or bridging-mode bonding of two carboxylate units [ $1610\text{ cm}^{-1}$ :  $\nu_{\text{as}}(-\text{CO}_2^-)$  and  $1380\text{ cm}^{-1}$ :  $\nu_{\text{s}}(-\text{CO}_2^-)$ ] [18] in a similar manner to that reported for other ruthenium complexes [21,22] independent of the molecular volume. The fact that all the materials bind in the same way to the  $\text{TiO}_2$  and their long wavelength optical transitions are similar means that the electronic communication between

the dyes and the  $\text{TiO}_2$  will be essentially the same. Hence differences observed in performance can be directly related to the effect of molecular volume and how much dye is adsorbed. It can clearly be seen in Fig. 2 that the molecular volume affects dye uptake with the smallest dye **1** ( $98.1 \times 10^{15}/\text{cm}^2$ ) having the greatest amount of dye-adsorbed, and then decreasing in the order **2** ( $73.7 \times 10^{15}/\text{cm}^2$ ) > **3** ( $63.6 \times 10^{15}/\text{cm}^2$ ) > **4** ( $45.8 \times 10^{15}/\text{cm}^2$ ) > **5** ( $33.0 \times 10^{15}/\text{cm}^2$ ). The exact mechanism(s) by which molecular volume affects dye uptake are reported in detail elsewhere [18,23]. In summary, the kinetic studies of the adsorption show that at equilibrium the amount of dye uptake is controlled by the dye occupancy area (steric hindrance). Furthermore, chemisorption (rather than bulk

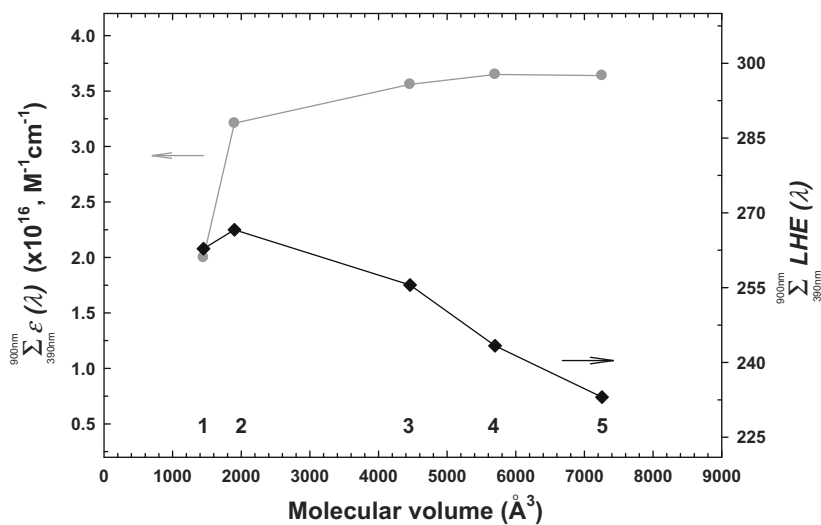


Fig. 3. Plot of the integrated absorption coefficient (grey circle) and light harvesting efficiency (black diamond) from 390 nm to 900 nm versus the molecular volume of the Ru complexes.

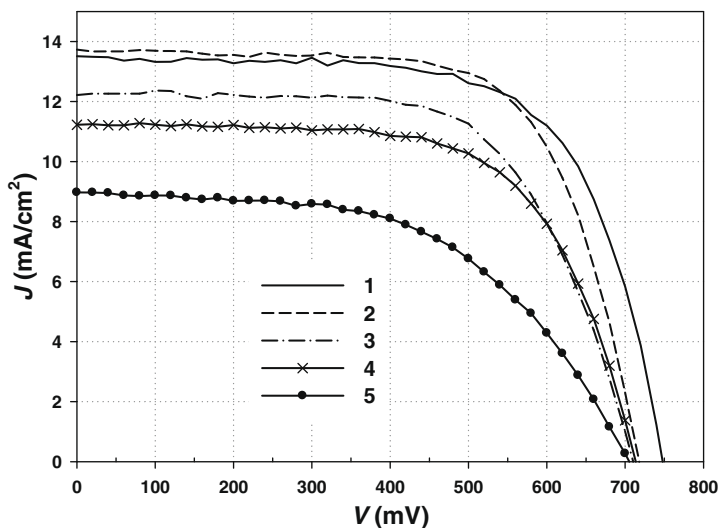


Fig. 4.  $J$ - $V$  curves for devices constructed from compounds 1–5. Note the results shown are representative of multiple devices for each dye and do not represent the highest efficiencies obtained.



diffusion) is the rate-limiting step in the uptake process and kinetic hindrance also controls the initial rate. Hence, for a photoanode substrate of specific binding site density and mesoscopic porosity, the dye uptake is directly related to molecular volume.

To summarize thus far, the light absorption data shows that the new dyes absorb more strongly than **1**. In contrast, **1** is adsorbed to a greater extent than the new ruthenium complexes. To see how these two parameters affect the

overall LHE of the ruthenium complex based materials we calculated the LHE by two different methods. In the first case we only took into account the light absorption and integrated  $\varepsilon$  (from Fig. 1b) from 390 to 900 nm, thus avoiding the contribution of the TiO<sub>2</sub> nanoparticle absorption [ $E_g = \text{ca. } 3.2 \text{ eV}$  (390 nm) for anatase] [24]. Fig. 3 shows that the integrated  $\varepsilon$  values for **2**, **3**, **4** and **5** are higher than that of **1**. However, when the adsorption is taken into account in the calculation of the LHE, the order reverses apart

**Table 1**

Parameters calculated using  $J$ - $V$  sweeps for multiple devices (at least five in each case) using the measured illumination intensity ( $\sim 100 \text{ mW/cm}^2$ ).

Compound	Cell area ( $\text{cm}^2$ )	$J_{sc}$ ( $\text{mA cm}^{-2}$ )	$V_{oc}$ (V)	$FF$	$\eta$ (%)
1	$0.19 \pm 0.02$	$13.58 \pm 0.20$	$0.75 \pm 0.01$	$0.68 \pm 0.02$	$6.94 \pm 0.12$
2	$0.20 \pm 0.02$	$14.45 \pm 0.50$	$0.74 \pm 0.01$	$0.68 \pm 0.01$	$7.19 \pm 0.11$
3	$0.21 \pm 0.01$	$13.24 \pm 0.60$	$0.72 \pm 0.01$	$0.66 \pm 0.02$	$6.32 \pm 0.13$
4	$0.19 \pm 0.02$	$11.21 \pm 0.38$	$0.71 \pm 0.01$	$0.66 \pm 0.01$	$5.26 \pm 0.08$
5	$0.19 \pm 0.01$	$8.49 \pm 0.23$	$0.71 \pm 0.01$	$0.62 \pm 0.04$	$3.69 \pm 0.19$

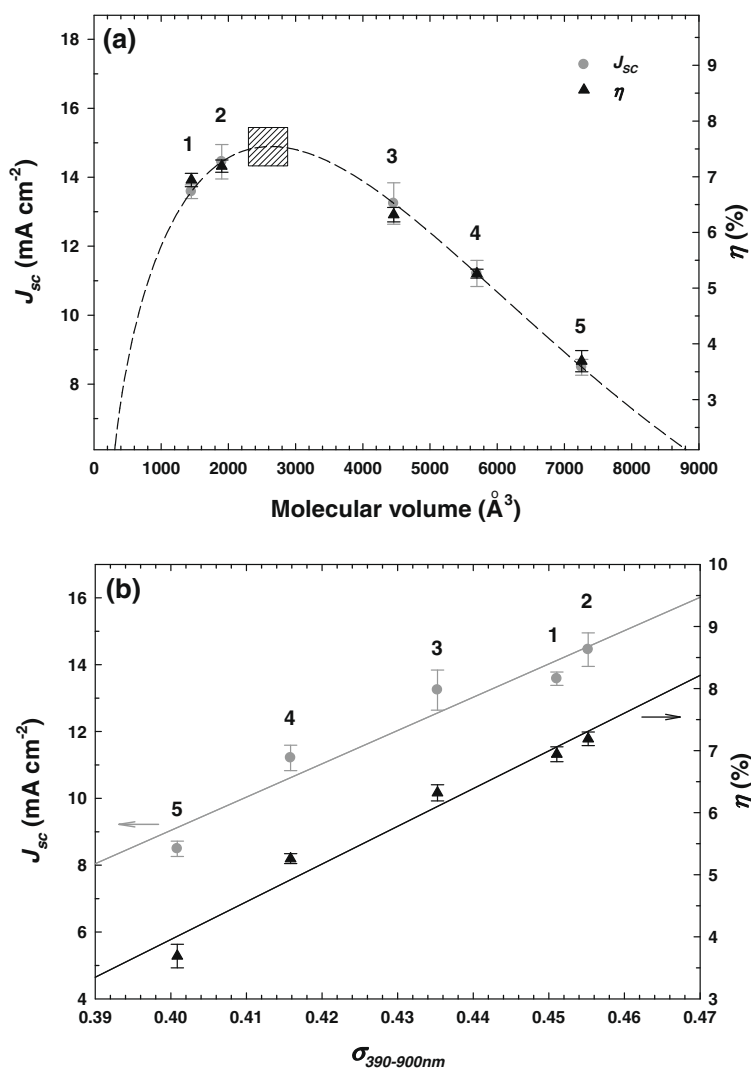


**Fig. 5.** (a, b) Plot of short-circuit photocurrent density (grey circle) and power conversion efficiency (black triangle) versus the molecular volume of the Ru complexes (a) and the  $\sigma$  index calculated from modified light harvesting efficiency equation (b) under AM 1.5G illumination ( $100 \text{ mW cm}^{-2}$ ).

from **2**, which has a higher overall light harvesting efficiency than **1**. These results show strongly that molecular volume will play a first order role in the light harvesting efficiency.

In order to understand the effect of molecular volume and test whether the calculated LHE correlates with device efficiency, batches of devices were constructed from the dyes (see Section 4). It is important to note that in each case, dye uptake was optimized according to the kinetics and solvent systems used to obtain the data in Fig. 2. It is also important to note that short-circuit current densities ( $J_{sc}$ ) and conversion efficiencies ( $\eta$ ) were measured on multiple devices to obviate cell-to-cell fabrication differences and that measurements were validated at two external laboratories for cross-calibration purposes (results in agreement to within 5% of the measured values). Current–voltage curves for typical devices containing each material are shown in Fig. 4 and the average measured diode parameters for each dye batch ( $J_{sc}$ ,  $V_{oc}$ , Fill Factor ( $FF$ ) and  $\eta$ ) along with statistics under standard AM1.5G conditions are summarized in the Table 1.

Fig. 5a illustrates how  $J_{sc}$  and  $\eta$  vary with molecular volume. The striking correlation between the molecular volume and device performance is immediately clear. Although **4** and **5** have higher  $\epsilon$ , we do not see enhancement of  $\eta$  due to their high molecular volumes and reduced uptake per unit  $\text{TiO}_2$  area. **2** Appears close to the optimum in this trade-off, but the form of the dependence suggests that there is (as yet) unexplored opportunity to maximize device efficiency in these ruthenium complexes. Scaling our best **1** results with the highest so far obtained ( $\sim 11\%$ ) would suggest that this molecular volume tuning approach could yield overall conversion efficiencies of  $>13\%$  with ruthenium dyes (square box in Fig. 5a).

Finally, we have determined the relationship between the LHE and the device performance. In the first analysis we determined the LHE from Eq. (1), which takes into account the molar extinction coefficient and the adsorption. However, to more accurately determine the LHE it is necessary to include a weighting due to the response of the dye to the AM1.5 spectrum. When the AM1.5 spectrum is taken into account it is possible to determine a normalized light harvesting efficiency ( $\sigma_{390-900\text{ nm}}$ ) according to Eq. (2):

$$\sigma_{390-900\text{ nm}} = \frac{\int_{390\text{ nm}}^{900\text{ nm}} \Phi_p(\lambda)(1 - 10^{-\epsilon(\lambda)\Gamma})d\lambda}{\int_{390\text{ nm}}^{900\text{ nm}} \Phi_p(\lambda)d(\lambda)} \quad (2)$$

where  $\Phi_p(\lambda)$  is the AM1.5 hemispherical irradiance incident on a  $37^\circ$  tilted plane measured in  $\text{Wm}^{-2}\text{ nm}^{-1}$  as enunciated by (for example) ISO 9854-1 [25], and Eq. (2) represents a weighted ordinate normalization for the solar spectrum, and  $\epsilon$  and  $\Gamma$  are as determined previously. Fig. 5b shows this normalized light harvesting efficiency ( $\sigma_{390-900\text{ nm}}$ ) plotted against the measured  $J_{sc}$  and  $\eta$  from the devices based on each dye. In both cases there is a systematic linear relationship confirming that, all else being equal, both  $\epsilon$  and  $\Gamma$  are first order parameters in device efficiency. Furthermore, this correlation suggests that the simple solution measurements of absorption and adsorption can be used to predict the light harvesting efficiency

of potential new ruthenium dye systems without recourse to device construction.

### 3. Conclusion

In summary, we have demonstrated that dendronized light harvesting ruthenium complexes can be used for DSSCs. We have used this dendritic architectural approach to tune the dye molecular volume while leaving the optoelectronic characteristics the same, allowing a systematic investigation of the effect of the molecular volume on the light harvesting efficiency for the first time. We have demonstrated that molecular volume and molar extinction coefficient are both first order parameters in achieving high conversion efficiencies. Enhanced solar absorption does not necessarily lead to enhanced light harvesting efficiency because of the associated increase in molecular volume. Our analysis provides a strategy for molecular engineering new ruthenium complex based dyes whereby tuning the molecular volume in conjunction with the extinction coefficient could ultimately yield higher efficiency dye systems. Dendronisation also has the potential to improve other device properties including: reducing dye desorption, leading to longer device lifetimes; tuning solubility and compatibility with electrolyte systems (particularly in all-solid-state structures); and controlling parasitic reaction rates.

### 4. Experimental

#### 4.1. Materials

The compounds **2**, **3**, **4**, and **5** were prepared according to the previous reference [18]. All organic solvents used for UV/vis absorption and dye adsorption measurements were of spectroscopic quality from Aldrich, and *N,N*-dimethylformamide (DMF) was distilled before use.  $\text{TiO}_2$  electrodes were purchased from Dyesol Pty. Ltd. (Queanbeyan, NSW Australia) and consisted of a 11–12  $\mu\text{m}$  thick film of 20 nm anatase particles randomly interspersed with 400 nm scattering centers (10% by weight) with a specific surface area of approximately 70–80  $\text{m}^2/\text{g}$  deposited onto 15  $\Omega^2$  fluorine doped tin-oxide (FTO) coated glass. The platinum catalyst electrodes were purchased from Dyesol and consisted of 12  $\times$  9  $\text{mm}^2$  area of platinum screen printed onto a glass substrate coated 15  $\Omega^2$  FTO. The molecular volumes (represented by the overlapping van der Waals atomic spheres model) of the ruthenium complexes were calculated by the quantitative structure–activity relationship (QSAR) property [26,27] module in the HyperChem 7.0 package after geometry optimization using a ZINDO-1 parameter [28,29]. This methodology has been used extensively to yield realistic molecular volumes at a relatively low computational cost [26,27].

#### 4.2. Dye adsorption measurements

The optimized solvent compositions for adsorption of **1** [*t*-butanol:acetonitrile (1:1)], **2** [DMF:acetonitrile (1:1)], **3** [DMF:acetonitrile (9:1)], **4** [DMF:acetonitrile (9:1)] and **5**

[DMF:acetonitrile (1:1)] were used in the study. The absorption spectra of the initial dye solution ( $1 \times 10^{-4} \text{ mol L}^{-1}$ ) were measured by a Cary 5000 UV–VIS–NIR spectrophotometer. The prepared  $\text{TiO}_2$  substrates (ca.  $0.88 \text{ cm}^2$  of active area) which were baked at  $450 \text{ }^\circ\text{C}$  for 30 min and kept at  $80 \text{ }^\circ\text{C}$  before immersion into the dye solution in a UV cuvette ( $1 \text{ cm} \times 1 \text{ cm}$ ). The absorbance changes were monitored hourly for 9 h and then at 24 h. The chemisorption of all Ru complexes onto  $\text{TiO}_2$  films were characterized by ATR-FT-IR spectrometer (Spectrum 100, Perkin Elmer).

#### 4.3. Solar cell fabrication and characterization

Prior to dye sensitization, the  $\text{TiO}_2$  films (active area: ca.  $0.20 \text{ cm}^2$  measured by using the ImageJ software package) were treated with a solution of titanium tetrachloride solution and heated to  $\sim 450 \text{ }^\circ\text{C}$  for 30 min before being allowed to cool to  $\sim 80 \text{ }^\circ\text{C}$ . The  $\text{TiO}_2$  films were immersed in the dye solution ( $3 \times 10^{-4} \text{ mol L}^{-1}$ ) at room temperature for 24 h to adsorb dye onto the  $\text{TiO}_2$  surfaces. Excess dye was removed by rinsing with DMF and acetonitrile. Platinum (Pt) counter electrodes on FTO glass was also preheated to  $\sim 450 \text{ }^\circ\text{C}$  for 10 min and a single hole (ca.  $0.5 \text{ mm}$  diameter) was drilled in the Pt electrode to allow for electrolyte filling. The dye-adsorbed  $\text{TiO}_2$  electrode and Pt counter electrodes were assembled into a sealed sandwich-type cell by heating a hot-melt ionomer film (Surlyn 1702,  $25 \text{ }\mu\text{m}$  thickness, Solaronix) as a spacer between the electrodes. An electrolyte solution (electrolyte of  $0.6 \text{ M}$  1-*n*-butyl-3-methylimidazole iodide,  $0.03 \text{ M}$  iodide,  $0.1 \text{ M}$  guanidinium thiocyanate, and  $0.5 \text{ M}$  tert-butylpyridine in 15/85 (v/v) mixture of valeronitrile and acetonitrile) was injected by a vacuum backfilling method. Finally, the hole was sealed by using Bynel (Dyesol) and a glass cover slide ( $0.1 \text{ mm}$  thickness).

Device efficiencies were measured with a Thermo Oriel 150 W Xenon arc lamp which was designed to give  $\sim 100 \text{ mW/cm}^2$  using AM1.5D and AM0 filters. Prior to each measurement, the solar simulator illumination intensity was measured using a Hamamatsu reference silicon photodiode (S1133) with white light filter (spectral mismatch  $< 5\%$  with respect to an N3 DSSC response). The exact white light illumination intensity was used in each case for the power conversion calculations. The  $J$ – $V$  characteristics were measured using a Keithley Source Meter Unit (SMU) and an appropriate photomask to illuminate only the cell area. The  $J$ – $V$  scan and acquisition were driven by purpose-written LabView software. The cell data for each dye were averaged using at least 5 devices for consistency and the statistics calculated on that basis. Incident photon to electron conversion efficiencies (IPCE) were also measured for representative devices from each batch using the same Thermo Oriel lamp and a Princeton Instruments Acton SpectraPro 2300i monochromator equipped with the PI SpectraHub data acquisition system and a Newport 818-UV silicon photodiode. The reference diode and multiple devices were also cross-calibrated (IPCE and  $J$ – $V$ ) with two separate laboratories (CSIRO Melbourne and Monash University, Melbourne, Australia) and the results found to be in agreement to within 5%.

#### Acknowledgements

This work was funded by the Australian Research Council (PLB Federation Fellowship), the Queensland State Government (PM Smart State Senior Fellowship), the Australian Department of Science, Education and Training (International Science Linkage scheme – International Consortium for Organic Solar Cells), the University of Queensland (Strategic Initiative – Centre for Organic Photonics and Electronics) and the Korea Research Foundation Grant funded by the Korean Government (MOEHRD) (KRF-2005-214-D00268). The authors acknowledge the prior contribution of Michael Deceglie (now at Caltech) and Dr David Blake in establishing the photovoltaic testing equipment and Mr Karsten Kruger in standard cell calibration. Finally, the authors also wish to acknowledge partners of the DEST ISL program in particular Dr Scott Watkins (CSIRO Melbourne) and Dr Udo Bach (Monash University, Melbourne).

#### References

- [1] B. O'Regan, M. Grätzel, *Nature* 353 (1991) 737.
- [2] P. Xie, F. Guo, *Curr. Org. Chem.* 11 (2007) 1272.
- [3] W.R. Duncan, O.V. Prezhdo, *Annu. Rev. Phys. Chem.* 58 (2007) 143.
- [4] M. Grätzel, *Nature* 414 (2001) 338.
- [5] M.A. Green, K. Emery, Y. Hishikawa, W. Warta, *Prog. Photovolt: Res. Appl.* 16 (2008) 61.
- [6] M.K. Nazeeruddin, P. Pechy, T. Renouard, S.M. Zakeeruddin, R. Humphry-Baker, P. Comte, P. Liska, L. Cevey, E. Costa, V. Shklover, L. Spiccia, G.B. Deacon, C.A. Bignozzi, M. Grätzel, *J. Am. Chem. Soc.* 123 (2001) 1613.
- [7] S.R. Scully, M.T. Lloyd, R. Herrera, E.P. Giannelis, G.G. Malliaras, *Synth. Met.* 144 (2004) 291.
- [8] U. Bach, D. Lupo, P. Comte, J.E. Moser, F. Weissortel, J. Salbeck, H. Spreitzer, M. Grätzel, *Nature* 395 (1998) 583.
- [9] M.K. Nazeeruddin, A. Kay, I. Rodicio, R. Humphry-Baker, E. Mueller, P. Liska, N. Vlachopoulos, M. Grätzel, *J. Am. Chem. Soc.* 115 (1993) 6382.
- [10] M. Grätzel, *Platinum Metals Rev.* 38 (1994) 151.
- [11] P. Wang, C. Klein, R. Humphry-Baker, S.M. Zakeeruddin, M. Grätzel, *J. Am. Chem. Soc.* 127 (2005) 808.
- [12] C.-Y. Chen, S.-J. Wu, C.-G. Wu, J.-G. Chen, K.-C. Ho, *Angew. Chem. Int. Ed.* 45 (2006) 5822.
- [13] D. Kuang, S. Ito, B. Wenger, C. Klein, J.-E. Moser, R. Humphry-Baker, S.M. Zakeeruddin, M. Grätzel, *J. Am. Chem. Soc.* 128 (2006) 4146.
- [14] F. Gao, Y. Wang, J. Zhang, D. Shi, M. Wang, R. Humphry-Baker, P. Wang, S.M. Zakeeruddin, M. Grätzel, *Chem. Commun.* (2008) 2635.
- [15] M.K. Nazeeruddin, T. Bessho, L. Cevey, S. Ito, C. Klein, F. De Angelis, S. Fantacci, P. Comte, P. Liska, H. Imai, M. Grätzel, *J. Photochem. Photobiol. Chem.* 185 (2007) 331.
- [16] C.-Y. Chen, S.-J. Wu, J.-Y. Li, C.-G. Wu, J.-G. Chen, K.-C. Ho, *Adv. Mater.* 19 (2007) 3888.
- [17] K.-J. Jiang, J.-B. Xia, N. Masaki, S. Noda, S. Yanagida, *Inorg. Chim. Acta* 361 (2008) 783.
- [18] B.-K. An, P.L. Burn, P. Meredith, *Chem. Mater.* 21 (2009) 3315.
- [19] M. Özacar, İ.A. Şengil, *Colloid Surf. A: Physicochem. Eng. Aspects* 242 (2004) 105.
- [20] Z. Yaneva, B. Koumanova, *J. Colloid Interface Sci.* 293 (2006) 303.
- [21] K.S. Finnie, J.R. Bartlett, J.L. Woolfrey, *Langmuir* 14 (1998) 2744.
- [22] K. Hara, H. Sugihara, Y. Tachibana, A. Islam, M. Yanagida, K. Sayama, H. Arakawa, G. Fujihashi, T. Horiguchi, T. Kinoshita, *Langmuir* 17 (2001) 5992.
- [23] B.-K. An, B. Langley, P.L. Burn, P. Meredith, in: *Proc. SPIE Optics and Photonics, San Diego*, 2009.
- [24] A. Bendavid, P.J. Martin, A. Jamting, H. Takikawa, *Thin Solid Films* 355–356 (1999) 6.
- [25] ASTM Standard G173, Standard Tables for Reference Solar Spectral Irradiances: Direct Normal and Hemispherical on 37 Tilted ASTM Standard G173, Standard Tables for Reference Solar Spectral Irradiances: Direct Normal and Hemispherical on 37 Tilted Surface, ASTM International, West Conshohocken, PA: <http://www.astm.org>.

- [26] J.T. Edward, *Can. J. Chem.* 76 (1998) 1294.
- [27] A.R. Katritzky, U. Maran, V.S. Lobanov, M. Karelson, *J. Chem. Inf. Comput. Sci.* 40 (2000) 1.
- [28] A.A.C. Pinheiro, R.S. Borges, L.S. Santos, C.N. Alves, *J. Mol. Struct. Theochem.* 672 (2004) 215.
- [29] X. Chen, *J. Mol. Struct. Theochem.* 763 (2006) 83.

On the other hand, high-performance true-blue phosphorescent dopants are also under intensive development [8–12]. Some reported Ir complexes have been proven highly efficient; however, the emission spectra are still not the desired true-blue color [8–10]. Previously, we reported that a parent heteroleptic Ir<sup>III</sup> complex (**Ir1** [Ir(dfppy)(fppz)<sub>2</sub>], Fig. 1) possessing one cyclometalated 4,6-difluorophenyl-2-pyridyl chelate (dfppy) and two 3-(trifluoromethyl)-5-pyridyl pyrazolate ligands (fppz) can produce true-blue phosphorescence with CIE<sub>y</sub> of ~0.2 [12]. Yet, the EL quantum efficiency achieved is till below 10% photon/electron. In this work, by placing tertiary butyl or methyl substituents at different locations of chelates, we are able to synthesize three additional derivatives **Ir2** [Ir(dfppy)(fbppz)<sub>2</sub>], **Ir3** [Ir(dfmppy)(fbppz)<sub>2</sub>], and **Ir4** [Ir(dfbppy)(fbppz)<sub>2</sub>] (Fig. 1), aiming at further raising the EL efficiencies of true-blue phosphorescent OLEDs based on such materials. Subsequent results show that the EL efficiency of true-blue OLEDs based on these new emitters can raise up to 13.7% photon/electron, 20.4 cd/A and showing true-blue color chromaticity with CIE<sub>x,y</sub> coordinates (0.157, 0.189).

## 2. Experimental

### 2.1. Material synthesis and characterization

The preparation of the iridium complexes were best executed by heating of a 1:1 mixture of 4,6-difluorophenyl

pyridine (dfppy), 4-methyl-2-(2,4-difluorophenyl)pyridine (dfmppy) or 4-*tert*-butyl-2-(2,4-difluorophenyl)pyridine (dfbppy) and IrCl<sub>3</sub>·3H<sub>2</sub>O in methoxyethanol (140 °C, 4 h), followed by addition of 2.1 equiv. of 3-trifluoromethyl-5-(2-pyridyl) pyrazole (fppz) or 3-(trifluoromethyl)-5-(4-*tert*-butylpyridyl) pyrazolate (fbppz) in presence of Na<sub>2</sub>CO<sub>3</sub> (140 °C, 12 h). The products are then separated by column chromatography on silica gel eluting with a mixture of ethyl acetate and hexane (1:1) or with pure CH<sub>2</sub>Cl<sub>2</sub>. The synthetic logic relies on the prior generation of an intermediate with formula [(dfppy)IrCl<sub>2</sub>]<sub>x</sub> or [(dfmppy)IrCl<sub>2</sub>]<sub>x</sub> or [(dfbppy)IrCl<sub>2</sub>]<sub>x</sub> [13], which would react with the two equiv of fppz or fbppz anions in the subsequent reaction. **Ir1** [Ir(dfppy)(fppz)<sub>2</sub>], **Ir2** [Ir(dfppy)(fbppz)<sub>2</sub>], **Ir3** [Ir(dfmppy)(fbppz)<sub>2</sub>], and **Ir4** [Ir(dfbppy)(fbppz)<sub>2</sub>] were obtained from these one-pot reactions in moderate yields. Spectroscopic examinations were also performed to confirm their structural identity and sample purity.

### 2.2. OLED fabrication and characterization

All as-synthesized compounds were subject to temperature-gradient sublimation under high vacuum before use. OLEDs were fabricated on the ITO-coated glass substrates with multiple organic layers sandwiched between the transparent bottom indium-tin-oxide (ITO) anode and the top metal cathode. The organic and metal layers were deposited by thermal evaporation in a vacuum chamber with a base pressure of <10<sup>-6</sup> torr. The deposition rate of

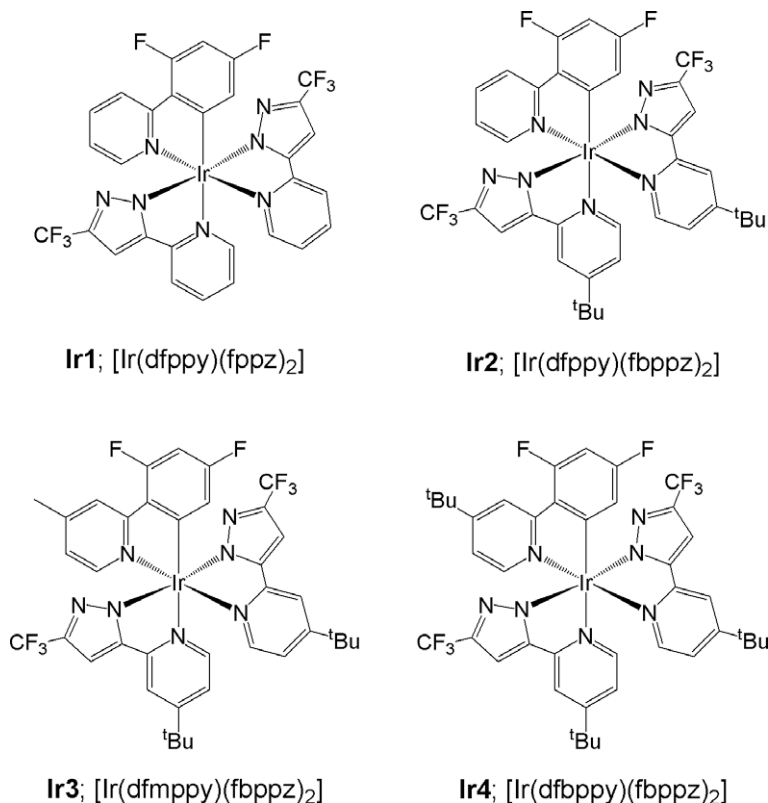


Fig. 1. Structural drawings of iridium complexes **Ir1–Ir4**.

organic layers was kept at  $\sim 0.2$  nm/s. The deposition system permitted the fabrication of the complete device structure in a single pump-down without breaking vacuum. The active area of the device was  $2 \times 2$  mm<sup>2</sup>, as defined by the shadow mask for cathode deposition.

Current–voltage–luminance ( $I$ – $V$ – $L$ ) characterization of the devices was measured using a source–measurement unit (SMU) and a Si photodiode calibrated with Photo Research PR650. EL spectra of devices were collected by a calibrated CCD spectrograph. UV/Vis spectra were measured using a Shimadzu UV-1650PC spectrophotometer.

### 3. Results and discussions

#### 3.1. Emission properties of Ir complexes

Photoluminescence (PL) of Ir complexes was measured using a Charge-Coupled Device (CCD) spectrograph and the 325 nm line of the He–Cd laser as the excitation source. For determining PL quantum yields, the samples (either solutions or thin films) were mounted in a calibrated integrating sphere coupled with the CCD spectrograph. By comparing the spectral intensities of the excitation laser and the PL emission, quantum yields (PLQY) were determined [14]. All four Ir(III) complexes show similar PL spectral profiles and quantum yields of nearly 50–80% (either in solutions or as dopants in wide-gap host films), as summarized in Fig. 2 and Table 1.

#### 3.2. Testing of device structures

For achieving true-blue OLEDs with these large-triplet-energy phosphorescent Ir complexes (i.e.  $E_T \geq 2.7$  eV), host materials with wide-triplet-gap are essential to prevent reverse energy transfer from guest molecule back to the host matrix [15]. Furthermore, the device structures must be carefully designed to achieve more balanced carrier injection/transport and appropriate confinement of carriers and excitons. We therefore used the parent complex **Ir1** to test the suitability of host materials and device configurations (Figs. 3 and 4).

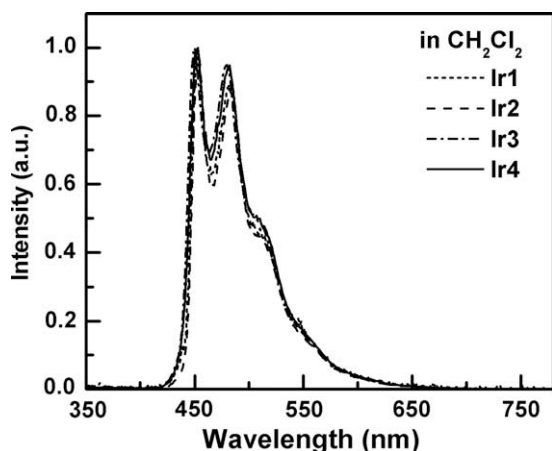


Fig. 2. PL spectra of **Ir1**–**Ir4** recorded in degassed CH<sub>2</sub>Cl<sub>2</sub> solution.

**Table 1**

The emission properties of iridium complexes **Ir1**–**Ir4**.

	$E_m$ $\lambda_{max}/nm^a$	Q.Y.
<b>Ir1</b>	450, 479, 511 (sh), 554 (sh)	0.51 <sup>a</sup> , 0.45 <sup>b</sup>
<b>Ir2</b>	451, 480, 511 (sh), 546 (sh)	0.80 <sup>a</sup> , 0.74 <sup>b</sup>
<b>Ir3</b>	447, 475, 502 (sh), 546 (sh)	0.58 <sup>a</sup> , 0.52 <sup>b</sup>
<b>Ir4</b>	449, 479, 507 (sh), 546 (sh)	0.68 <sup>a</sup> , 0.60 <sup>b</sup>

<sup>a</sup> Data obtained in degassed CH<sub>2</sub>Cl<sub>2</sub> solution at RT with the concentration of  $10^{-5}$  M.

<sup>b</sup> Obtained from in 8 wt.%-doped thin films using CzSi as the host material.

Devices A was first constructed employing CzSi as the host material (Fig. 3). Complex **Ir1** exhibits similar PLQY in both dilute solutions and as doped thin film of the wide-gap host CzSi, which had been reported to possess a large triplet energy of 3.02 eV [16]. Therefore, CzSi is appropriate for **Ir1** in terms of confinement of triplet excitons on dopants. The device structure was: ITO/ $\alpha$ -NPD (30 nm)/TCTA (30 nm)/CzSi doped with 15 wt.% of **Ir1** (25 nm)/TAZ (50 nm)/LiF (0.5 nm)/Al (150 nm), where 4,4'-bis[N-(1-naphthyl)-N-phenyl-amino] biphenyl ( $\alpha$ -NPD) and 4,4',4'-tris(carbazol-9-yl)-triphenylamine (TCTA) were used as the hole-transport layers (HTLs) [17], 3-(4-biphenyl)-4-phenyl-5-(*tert*-butylphenyl)-1,2,4-triazole (TAZ) as the electron-transport layer (ETL) [18], LiF as the electron-injection layer [19], and aluminum as the cathode. The structural drawing of materials and device architecture used for our investigation are shown in Figs. 3 and 4, respectively.

The recorded EL characteristics of device A are depicted in Fig. 5 and Table 2. This device showed EL predominantly from **Ir1**, but with only a modest external quantum efficiency of about 3.3% photon/electron, which was substantially lower than its PLQY recorded in solution. In addition, EL spectra of the device showed a notable emission in near-UV region, which implied carrier recombination in the charge-transport layers (TCTA and/or TAZ, both are known to exhibit near-UV emission at  $\sim 400$  nm) [20].

To achieve better confinement of triplet excitons and/or carriers in the emitting layer, two additional device architectures B and C were constructed and tested (Fig. 4). In device B, a thin layer of non-doped CzSi (3 nm) and UGH2 [*p*-bis(triphenylsilyl)benzene, 3 nm] were inserted between the emission and hole-transport layers and between the emission and electron-transport layers, respectively [21,22]. The hole-transporting CzSi possesses high triplet energy [16] and, thus, is capable to block the high-energy triplet excitations (on the dopant) from migrating to TCTA (with a lower triplet energy than the dopant) [17]. On the other hand, the electron-transporting UGH2 with high triplet energy (3.18 eV) [23,24] is expected to retard the high-energy triplet excitations (on the dopant) from migrating to TAZ (with a lower triplet energy than the dopant) [18]. In device C, double emission layers [25–27] (25-nm hole-transporting CzSi and 3-nm electron-transporting UGH2 doped with 15 wt.% **Ir1**) were used to achieve better balance between hole and electron injection/transport and thus to move the exciton formation zone away from the interfaces between the carrier-transport layers, taking

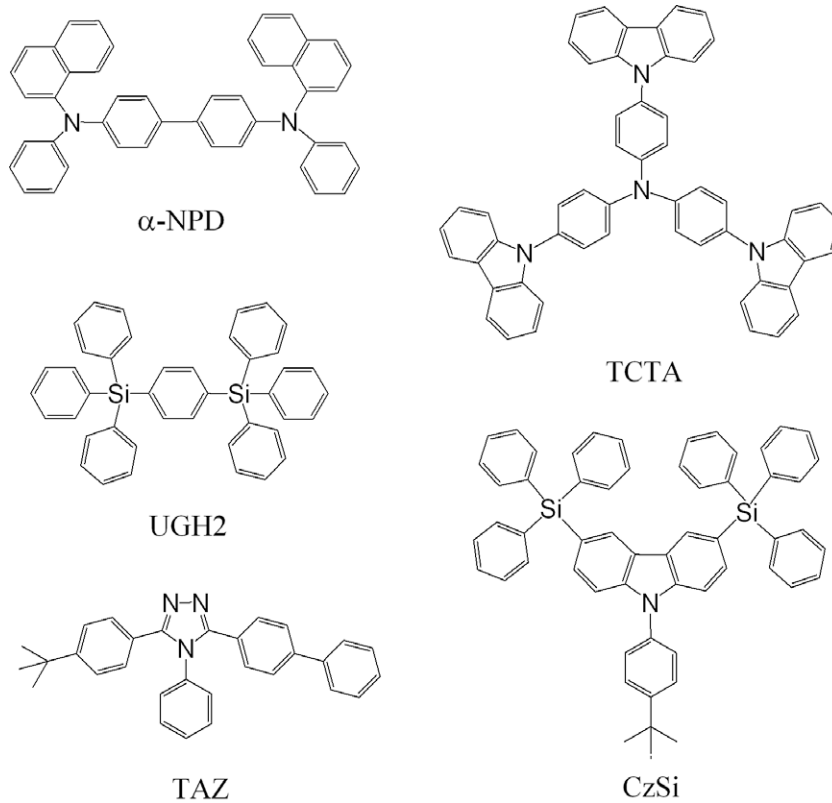


Fig. 3. Structural drawings of functional materials used in OLEDs.

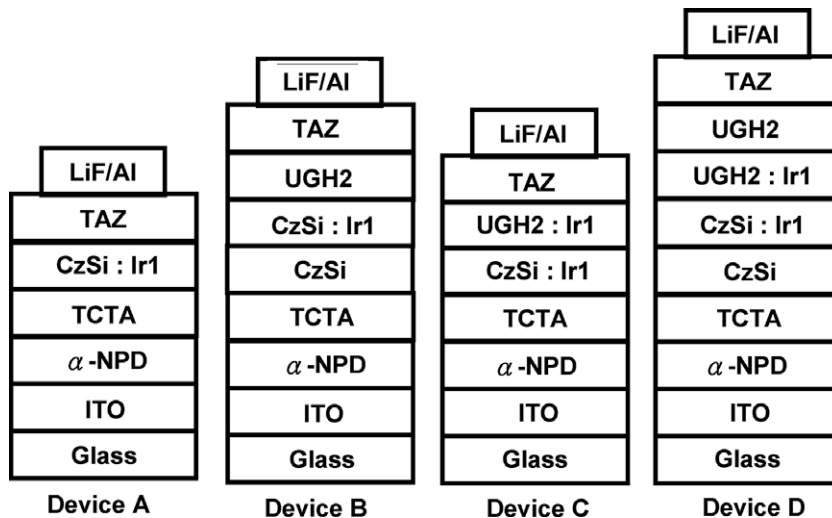
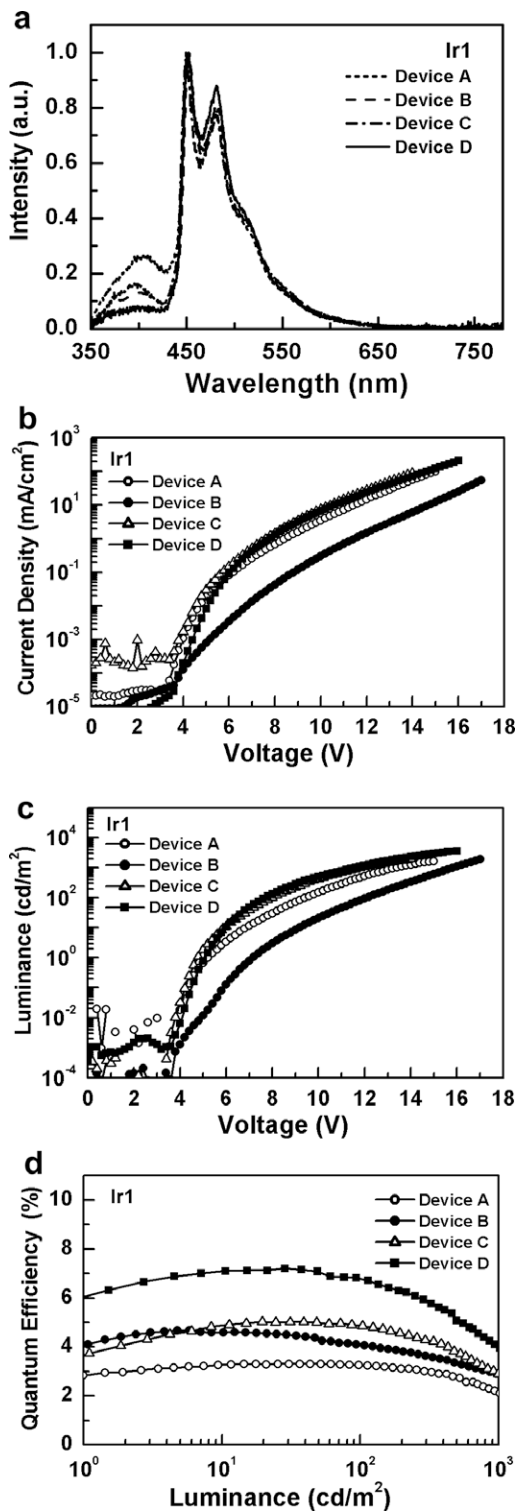


Fig. 4. Schematic device structures employed in this study.

advantage of the inherent physical nature of both CzSi and UGH2.

Again, EL characteristics of device B and C are shown in Fig. 5 and Table 2. In comparison to those of device A, peak quantum efficiencies of devices B and C (4.7%

and 5.0%) are substantially enhanced, indicating the effectiveness of the added electron and hole buffer layers. We thus decided to combine the fabrication concept of devices B and C, giving the device D, which had the device structure of: ITO/ $\alpha$ -NPD (30 nm)/TCTA (30 nm)/CzSi



**Fig. 5.** (a) EL spectra, (b) current–voltage characteristics, (c) luminance versus voltage, (d) external quantum efficiency versus luminance for devices A, B, C, and D.

(3 nm)/CzSi doped with 15 wt.% of **Ir1** (25 nm)/UGH2 doped with 15 wt.% of **Ir1** (3 nm)/UGH2 (2 nm)/TAZ (50 nm)/LiF (0.5 nm)/Al (150 nm). By simultaneously

adopting the double emission layers and the high-triplet-energy buffer layers on two opposite sides of the emitting layers for better confinement of triplet excitons and carriers, device D further raised the peak quantum efficiency up to 7.2% (11.7 cd/A, 6.4 lm/W) (Fig. 5 and Table 2).

### 3.3. Optimization of dopant concentrations

After establishing the effective device structure for the phosphorescent emitter (**Ir1**), we then varied the dopant concentration in the emission layers to further optimize device performances. Upon fixing the architecture of device D, the concentration of **Ir1** was next varied from 6 wt.% to 20 wt.%. The EL characteristics of devices for these devices are shown in Fig. 6 and Table 3. The highest EL quantum efficiency was obtained around a dopant concentration of ~6 wt.% (similarly for the other three Ir complexes, as will be seen later in Table 4). At this concentration, the device gave peak efficiencies of up to 8.6%, (13.1 cd/A, and 8.2 lm/W), which is possibly attributed to the reduced concentration quenching and triplet–triplet annihilation.

### 3.4. Comparing EL characteristics of various Ir complexes

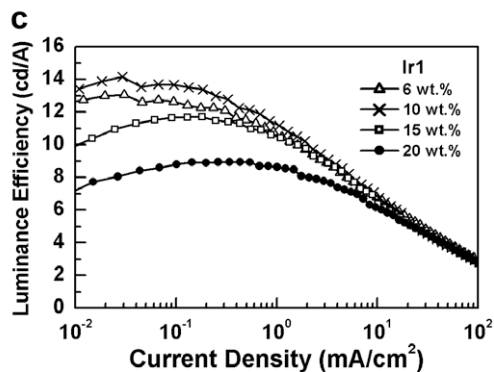
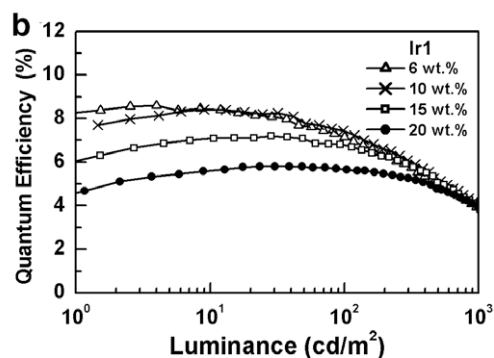
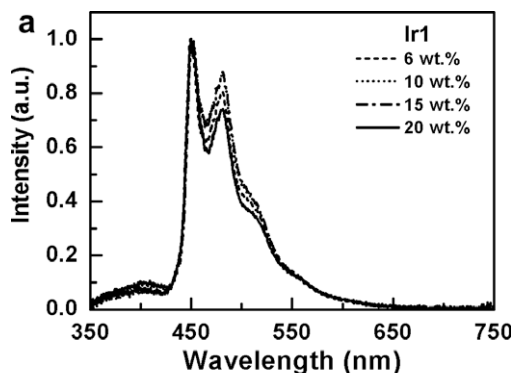
It seems to us that the optimized EL efficiencies of **Ir1** are somewhat equivalent to the PLQY of the dopant, suggesting that other modified blue-emitting phosphors, such as **Ir2–Ir4**, are equally applicable in fabrication of OLEDs employing similar device structure and adequate dopant concentration. In Table 4, EL characteristics of type-D devices incorporating all four iridium-based blue emitters (**Ir1**, **Ir2**, **Ir3**, and **Ir4**), with varied dopant concentrations from 6 wt.%, 8 wt.%, to 10 wt.%, are summarized. All Ir complexes show the highest EL efficiency around the dopant concentration of 6 wt.%. To verify that it is indeed an optimized concentration, in particular, we also examined **Ir4** devices with an even more extended concentration range of 2–10 wt.% (Table 4). Lower EL efficiencies were observed at concentrations lower than 6 wt.%, perhaps due to the incomplete energy transfer from hosts to guests.

Fig. 7 compares EL characteristics of type-D devices using these Ir(III) complexes at the optimized dopant concentration of 6 wt.%. All devices exhibited turn-on voltages of slightly smaller than 4 V. The peak efficiencies were (8.6%, 13.1 cd/A, 8.2 lm/W) for **Ir1**, (11.0%, 18 cd/A, 12.8 lm/W) for **Ir2**, (13.0%, 20 cd/A, 14.1 lm/W) for **Ir3**, and (13.7%, 20.4 cd/A, 14.0 lm/W) for **Ir4**, respectively. Except for the more significant deviation in the EL efficiency of **Ir2** (maybe associated with the detailed energy levels of each compound), these peak EL quantum efficiencies are somewhat close to the ideal values one would expect from PLQY's of these Ir complexes (in doped thin films, Table 1), assuming similar internal quantum efficiencies in both PL/EL and assuming a ~20% optical out-coupling efficiency. Such results suggest the effectiveness of the present device architecture for true-blue phosphors. The devices retained rather high efficiencies at the practical brightness of 100 cd/m<sup>2</sup>. Among all these Ir complexes, **Ir3** and **Ir4** gave highest EL efficiencies. In particular, **Ir4** gave the highest



**Table 2**  
Device structures and EL characteristics of devices A, B, C, and D.

Device	Device structure							External quantum efficiency [%] (max.)	Luminance efficiency [cd/A <sup>-1</sup> ] (max.)	Power efficiency [lm/W <sup>-1</sup> ] (max.)
	$\alpha$ -NPD [nm]	TCTA [nm]	CzSi [nm]	CzSi: dopant 15 wt.% [nm]	UGH2: dopant 15 wt.% [nm]	UGH2 [nm]	TAZ [nm]			
A	30	30	0	25	0	0	50	3.3	4.6	2.4
B	30	30	3	25	0	3	50	4.7	7.2	2.8
C	30	30	0	25	3	0	50	5.0	7.6	3.8
D	30	30	3	25	3	2	50	7.2	11.7	6.4



**Fig. 6.** EL characteristics of type-D devices with varied Ir1 concentrations.

peak efficiencies of (13.7%, 20.4 cd/A, 14.0 lm/W) and the high brightness of up to 14,460 cd/m<sup>2</sup> at 18 V. The superior performances of both Ir3 and Ir4 over those of Ir1 and Ir2

**Table 3**  
EL characteristics of type-D devices with varied Ir1 concentrations.

Concentration of Ir1		External quantum efficiency [%] (max.)	Luminance efficiency [cd/A <sup>-1</sup> ] (max.)	Power efficiency [lm/W <sup>-1</sup> ] (max.)
6 wt.%	Peak	8.6	13.1	8.2
	100 cd/m <sup>2</sup>	7.1	10.8	4.3
10 wt.%	Peak	8.4	14.2	8.4
	100 cd/m <sup>2</sup>	7.4	11.5	4.7
15 wt.%	Peak	7.2	11.7	6.4
	100 cd/m <sup>2</sup>	6.8	10.6	4.4
20 wt.%	Peak	5.8	8.9	4.6
	100 cd/m <sup>2</sup>	5.7	8.6	3.3

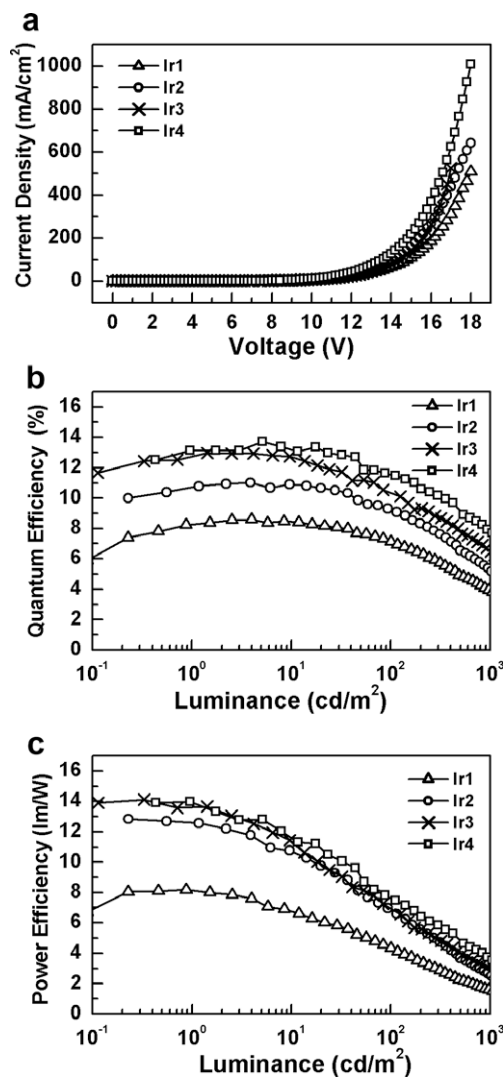
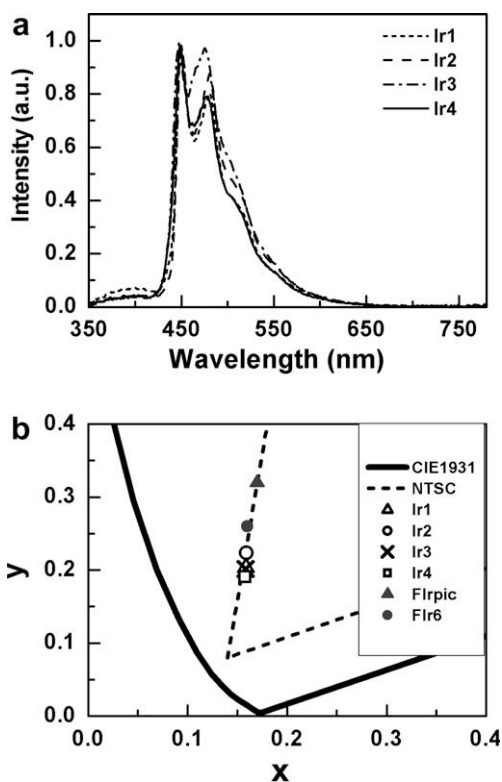
are considered to arise from (i) the improved dispersion between the host and dopant upon incorporating either methyl or *tert*-butyl groups on the dopant phosphors and (ii) the reduced back energy transfer from dopant to host due to their increased spatial separation. This observation is consistent with a recent report that bulky *tert*-butyl group on pyridyl ring of green-emitting analogues of [Ir(*p*-py)<sub>3</sub>] reduces the need for development of hosts with a high triplet level for electrophosphorescent devices [28]. Again, the related iridium phosphors with *tert*-butyl substituted benzothiazolate and benzoimidazolate chromophores were also used for fabrication of red-emitting polymer LEDs [29]. Apparently, the steric influences would reduce aggregation and phase separation in polymer LEDs, which seems to dominate how to give high efficiencies under lower current density.

Moreover, these devices all showed the anticipated blue phosphorescence deriving from the Ir(III) dopants, for which the respective EL spectra and CIE coordinates are shown in Fig. 8a and b. It is notable that all these blue-emitting devices exhibited color chromaticity with the CIE<sub>y</sub> value being smaller or around 0.2. In particular, the Ir4 device had the most blue-shifted emission with CIE<sub>x,y</sub> coordinates of (0.157, 0.189), which is much superior than those obtained from the blue phosphorescent complexes such as bis(4',6'-difluorophenylpyridinato)iridium(III) picolinate (Flrpic) and bis(4',6'-difluorophenylpyridinato)iridium(III) tetra(1-pyrazolyl)borate (Flr6), their CIE<sub>x,y</sub> coordinates are also marked in Fig. 8b as reference [8–10]. Thus these new iridium dopants Ir1–Ir4 are promising for blue phosphorescent OLEDs with high EL efficiencies and adequate color chromaticity, both are extremely important for display and lighting applications.

**Table 4**

EL characteristics of type-D devices with the Ir(III) dopants at selected concentrations.

Emissive dopant	Concentration (wt.%)	External quantum efficiency [%] (max.)	Luminance efficiency [ $\text{cd}/\text{A}^{-1}$ ] (max.)	Power efficiency [ $\text{lm}/\text{W}^{-1}$ ] (max.)	Maximum luminance [ $\text{cd}/\text{m}^{-2}$ ]	CIE coordinate (x,y)
Ir1	6	8.6	13.1	8.2	4700	(0.159, 0.203)
	10	8.4	14.2	8.4	4060	
Ir2	6	10.9	18.0	12.8	5830	(0.159, 0.224)
	8	10.9	18.4	13.2	5240	
	10	9.5	16.6	11.0	4750	
Ir3	6	13.0	20.0	14.1	7990	(0.158, 0.202)
	8	12.6	20.1	14.3	7720	
	10	12.0	19.5	13.1	7040	
Ir4	2	11.0	16.7	12.1	6140	(0.157, 0.189)
	4	11.9	18.2	12.3	7190	
	6	13.7	20.4	14.0	14460	
	8	13.2	19.7	13.1	14140	
	10	11.2	17.1	11.1	12740	

**Fig. 7.** EL characteristics of type-D devices using Ir1–Ir4 with doping concentration of 6 wt.%.**Fig. 8.** (a) EL spectra, (b) CIE coordinates of type-D devices using 6 wt.% of iridium complexes Ir1–Ir4.

#### 4. Conclusions

A series of new device architectures were evaluated for construction of true-blue phosphorescent OLEDs. It involves a double emission layers (one hole-transport, one electron-transport) and double buffer (confinement) layers for enhancing the performance characteristics. In addition, we also added methyl and bulky *tert*-butyl substituents to the parent true-blue emitting iridium phosphor Ir1, and

obtained an improved performance characteristic for OLEDs fabricated under identical conditions. Thus, combination of these new phosphors and the double emission and buffer layers architectures afforded the true-blue electrophosphorescence with high efficiencies up to (13.7% photon/electron, 20.4 cd/A) and with CIE<sub>x,y</sub> color coordinates of (0.157, 0.189). Consequently, high-efficiency OLEDs in the blue/deep-blue region were successfully prepared. We thus believe that our device integration, plus the new design of Ir(III) phosphors presented in this study should convince the readers of its perspective en route to the true-blue phosphorescent OLEDs.

## Acknowledgements

The authors gratefully acknowledge the financial support from National Science Council and Ministry of Economic Affairs of Taiwan.

## References

- [1] Y. Kawamura, K. Goushi, J. Brooks, J.J. Brown, H. Sasabe, C. Adachi, *Appl. Phys. Lett.* 86 (2005) 071104.
- [2] R.J. Holmes, S.R. Forrest, T. Sajoto, A. Tamayo, P.I. Djurovich, M.E. Thompson, J. Brooks, Y.-J. Tung, B.W. D'Andrade, M.S. Weaver, R.C. Kwong, J.J. Brown, *Appl. Phys. Lett.* 87 (2005) 243507.
- [3] S.-C. Lo, C.P. Shipley, R.N. Bera, R.E. Harding, A.R. Cowley, P.L. Burn, I.D.W. Samuel, *Chem. Mater.* 18 (2006) 5119–5129.
- [4] T. Sajoto, P.I. Djurovich, A. Tamayo, M. Yousufuddin, R. Bau, M.E. Thompson, R.J. Holmes, S.R. Forrest, *Inorg. Chem.* 44 (2005) 7992–8003.
- [5] C.-F. Chang, Y.-M. Cheng, Y. Chi, Y.-C. Chiu, C.-C. Lin, G.-H. Lee, P.-T. Chou, C.-C. Chen, C.-H. Chang, C.-C. Wu, *Angew. Chem. Int. Ed.* 47 (2008) 4542–4545.
- [6] Y.-C. Chiu, J.-Y. Hung, Y. Chi, C.-C. Chen, C.-H. Chang, C.-C. Wu, Y.-M. Cheng, Y.-C. Yu, G.-H. Lee, P.-T. Chou, *Adv. Mater.* 21 (2009) 2221–2225.
- [7] Y.-C. Chiu, Y. Chi, J.-Y. Hung, Y.-M. Cheng, Y.-C. Yu, M.-W. Chung, G.-H. Lee, P.-T. Chou, C.-C. Chen, C.-C. Wu, H.-Y. Hsieh, *ACS Appl. Mater. Int.* 1 (2009) 433–442.
- [8] J.-J. Lin, W.-S. Liao, H.-J. Huang, F.-I. Wu, C.-H. Cheng, *Adv. Funct. Mater.* 18 (2008) 485–491.
- [9] N. Chopra, J. Lee, Y. Zheng, S.-H. Eom, J. Xue, F. So, *Appl. Phys. Lett.* 93 (2008) 143307.
- [10] S.-H. Eom, Y. Zheng, N. Chopra, J. Lee, F. So, J. Xue, *Appl. Phys. Lett.* 93 (2008) 133309.
- [11] S.-J. Yeh, M.-F. Wu, C.-T. Chen, Y.-H. Song, Y. Chi, M.-H. Ho, S.-F. Hsu, C.-H. Chen, *Adv. Mater.* 17 (2005) 285–289.
- [12] C.-H. Yang, Y.-M. Cheng, Y. Chi, C.-J. Hsu, F.-C. Fang, K.-T. Wong, P.-T. Chou, C.-H. Chang, M.-H. Tsai, C.-C. Wu, *Angew. Chem. Int. Ed.* 46 (2007) 2418–2421.
- [13] T.-C. Lee, C.-F. Chang, Y.-C. Chiu, Y. Chi, T.-Y. Chan, Y.-M. Cheng, C.-H. Lai, P.-T. Chou, G.-H. Lee, C.-H. Chien, C.-F. Shu, J. Leonhardt, *Chem. Asian J.* 4 (2009) 742–753.
- [14] J.C. de Mello, H.F. Wittmann, R.H. Friend, *Adv. Mater.* 9 (1997) 230–232.
- [15] R.J. Holmes, S.R. Forrest, Y.-J. Tung, R.C. Kwong, J.J. Brown, S. Garon, M.E. Thompson, *Appl. Phys. Lett.* 82 (2003) 2422–2424.
- [16] M.-H. Tsai, H.-W. Lin, H.-C. Su, T.-H. Ke, C.-C. Wu, F.-C. Fang, Y.-L. Liao, K.-T. Wong, C.-I. Wu, *Adv. Mater.* 18 (2006) 1216–1220.
- [17] C.-C. Wu, Y.-T. Lin, K.-T. Wong, R.-T. Chen, Y.-Y. Chien, *Adv. Mater.* 16 (2004) 61–65.
- [18] J. Kido, C. Ohtaki, K. Hongawa, K. Okuyama, K. Nagai, *Jpn. Appl. Phys.* 32 (1993) L917–L920 (Pt. 2).
- [19] L.S. Hung, C.W. Tang, M.G. Mason, *Appl. Phys. Lett.* 70 (1997) 152–154.
- [20] C.-H. Chang, Y.-J. Lu, C.-C. Liu, Y.-H. Yeh, C.-C. Wu, *J. Disp. Technol.* 3 (2007) 193–199.
- [21] V.I. Adamovich, S.R. Cordero, P.I. Djurovich, A. Tamayo, M.E. Thompson, B.W. D'Andrade, S.R. Forrest, *Org. Electron.* 4 (2003) 77–87.
- [22] M. Ikai, S. Tokito, Y. Sakamoto, T. Suzuki, Y. Taga, *Appl. Phys. Lett.* 79 (2001) 156–158.
- [23] R.J. Holmes, B.W. D'Andrade, S.R. Forrest, X. Ren, J. Li, M.E. Thompson, *Appl. Phys. Lett.* 83 (2003) 3818–3820.
- [24] X. Ren, J. Li, R.J. Holmes, P.I. Djurovich, S.R. Forrest, M.E. Thompson, *Chem. Mater.* 16 (2004) 4743–4747.
- [25] X. Zhou, D.S. Qin, M. Pfeiffer, J. Blochwitz-Nimoth, A. Werner, J. Drechsel, B. Maennig, K. Leo, M. Bold, P. Erk, H. Hartmann, *Appl. Phys. Lett.* 81 (2002) 4070–4072.
- [26] G. He, M. Pfeiffer, K. Leo, M. Hofmann, J. Birnstock, R. Pudzich, J. Salbeck, *Appl. Phys. Lett.* 85 (2004) 3911–3913.
- [27] D. Qin, Y. Tao, *J. Appl. Phys.* 97 (2005) 044505.
- [28] S.M. King, H.A. Al-Attar, R.J. Evans, A. Congreve, A. Beeby, A.P. Monkman, *Adv. Funct. Mater.* 16 (2006) 1043–1050.
- [29] X. Wei, J. Peng, J. Cheng, M. Xie, Z. Lu, C. Li, Y. Cao, *Adv. Funct. Mater.* 17 (2007) 3319–3325.

tionally its  $T_1$  energy is 2.56 eV (corresponding to 483 nm, which is estimated from the  $T_1$  emission [3]). It does not have sufficient high triplet state energy for blue phosphorescent dopants such as iridium bis(4,6-difluorophenylpyridinato) picolate (Flrpic) with 2.66 eV  $T_1$  energy and iridium bis(4,6-difluorophenylpyridinato-N, C $^{2'}$ ) [5-(2-pyridyl)tetrazolate] (FlrN4) with 2.71 eV  $T_1$  energy [4].

Recently three fluorescent materials were investigated to check their suitability as host for blue OLEDs. They are 1,3-bis(9-carbazolyl)benzene (mCP), 3,5-bis(9-carbazolyl)tetraphenylsilane (SimCP), and bis(3,5-di(9H-carbazol-9-yl) phenyl)diphenylsilane (SimCP2). The molecular structures are shown in Fig. 1. Two 3,5-di(9H-carbazol-9-yl) phenyl groups are attached to Si in SimCP2, which is different from SimCP with only one 3,5-di(9H-carbazol-9-yl) phenyl group.

Of the three materials, we found that SimCP2 host gives external quantum efficiency  $\eta_{\text{ext}}$  of 17.7% and power efficiency of 24.2 lm/W at 100 cd/m $^2$  for Flrpic blue emitter from OLED device with structure of ITO/PEDOT:PSS(35 nm)/14 wt% Flrpic:host(35 nm)/TPBi(28 nm)/LiF/Al [5]. This power efficiency is much higher than 10.4 and 5.9 lm/W in the cases of SimCP and mCP hosts, respectively [5]. Here TPBi means 1,3,5-tris(N-phenyl-benzimidazol-2-yl)benzene, which is used as electron transport layer.

Several papers have reported the EL efficiency of Flrpic doped in CBP, mCP, and SimCP hosts. For example, 8.9 lm/W ( $\eta_{\text{ext}} = 7.5\%$ ) and 7.7 lm/W ( $\eta_{\text{ext}} = 6.1\%$ ) were obtained from devices of ITO/CuPc/ $\alpha$ -NPD/6%Flrpic:host/BAlq/LiF/Al with mCP and CBP hosts, respectively [6], 9.3 lm/W ( $\eta_{\text{ext}} = 12.3\%$ ) and 12.9 lm/W ( $\eta_{\text{ext}} = 14.4\%$ ) from devices of ITO/ $\alpha$ -NPD/7%Flrpic:host/TPBi/LiF/Al with mCP and SimCP hosts [7], and 13.3 lm/W ( $\eta_{\text{ext}} = 10.4\%$ ) from device of ITO/TNATA/ $\alpha$ -NPD/7%Flrpic:mCP/13%Flrpic:mCP/Bphen/LiF/Al [8]. To our knowledge, there have been no previous reports of EL efficiency higher than 24.2 lm/W and 17.7% which were obtained using Flrpic doped in SimCP2 host. Very high external quantum efficiency of 43.3% was recently reported using Flrpic doped in mCP [9]. However, its device structure is quite different from previous ones, e.g., tandem white OLED structure which has two EL units connected with a charge generation layer and two emitting layers. Green-red emitting (fbi) $_2$ Ir(acac) (0.75 wt%) is codoped with Flrpic (6.5 wt%) in mCP host

to obtain white emission from the emitting layer. Therefore we cannot compare this case with the case of blue emission from Flrpic doped in SimCP2.

The present paper attempts to clarify the reason why the SimCP2 is a novel host material for blue emitter. We report not only thermal and electrical properties but also spectroscopic property of SimCP2, because the optical property of SimCP2 is unknown. Comparison with mCP and SimCP is also presented.

## 2. Experimental method

SimCP2 was synthesized as follows. Bis(4-(3,5-dibromophenyl) diphenylsilane) (4.17 g and 6.4 mmol) [10] and carbazole (5.34 g and 30.7 mmol) were dissolved in dry xylenes (40 mL) containing potassium carbonate (12.72 g and 92.0 mmol) and palladium acetate (0.057 g and 0.25 mmol). After the injection of tri-tert-butylphosphine (0.20 mL and 0.8 mmol), the resulting mixture was stirred for 16 h at refluxing temperature under the protection of nitrogen atmosphere. After cooling to ambient temperature, the reaction was quenched with excess water (100 mL). The mixture was extracted with dichloromethane. The organic phase was washed with water and dried by magnesium sulfate. After the removal of magnesium sulfate, the mixture was evaporated to dryness and the residual was subjected for flash column chromatography (silica gel, dichloromethane/hexanes, 2/8). The product was isolated as a white powder and became a faint yellow glassy solid after sublimation.

The glass transition temperature was measured with a differential scanning calorimetry (Perkin-Elmer DSC-6) method. The highest occupied molecular orbital (HOMO) energy was measured with a Riken Keiki AC-2 photoelectron emission spectrometer. The carrier mobility was measured with the time of flight (TOF) method that has been described before [11].

For optical study, thin films of neat SimCP2 were prepared by thermal vacuum deposition. The deposition was performed using a high-vacuum thermal evaporator (ULVAC) at a chamber pressure of  $10^{-6}$  Torr. Film thickness of neat SimCP2 was determined by quartz thickness monitor (ULVAC CRTM-6000) and it was 30 nm. Thin films of polystyrene (PS) doped with 3, 5, 10, 15, and 20 wt% Sim-

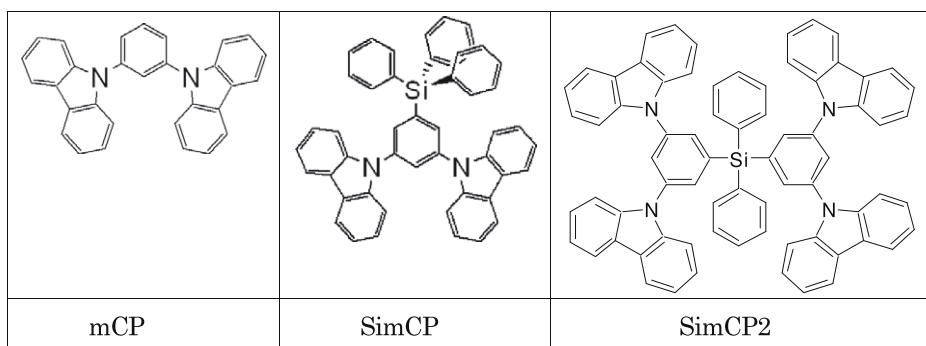


Fig. 1. Molecular structures of mCP, SimCP, and SimCP2.

CP2 were prepared by spin-coating a dichloromethane solution onto quartz substrates at ambient temperature.

Optical absorption spectra were measured with a Shimadzu UV-3100PC spectrophotometer. The photoluminescence (PL) and photoluminescence excitation (PLE) spectra were measured at various temperatures between 10 and 300 K with a Spex Fluorolog-3 fluorophotometer. The excitation source was a 450 W Xe-lamp. Filters were used to avoid the half and second harmonics of the excitation light.

### 3. Experimental results and discussion

#### 3.1. Glass morphology, HOMO energy, and carrier mobility

Fig. 2 shows the DSC thermogram of neat SimCP2 film. The glass transition temperature ( $T_g$ ) was estimated to be 148 °C. It is higher than  $T_g$  of mCP and SimCP, which are 55 and 101 °C, respectively [11]. The heat exchange energy related to this phase transition increases on going from mCP to SimCP to SimCP2, i.e., from 0.9 to 1.1 to 1.9 kJ/mol. Although it was not detected for SimCP2 by DSC, the heat exchange energy at the melting temperature also increases on going from mCP to SimCP, i.e., from 33.9 to 82.6 kJ/mol, which are all significantly larger than the heat exchange for the glass phase transition. We have put the sample (SimCP2) under the microscope and heated the sample up to 180 °C. We saw no phase transition (solid to liquid) happened to the sample. From these results, it is concluded that the endothermic signal around 148 °C is due to glass transition and not due to phase transition of melting.

Fig. 3 shows the photoelectron spectra of the neat SimCP2 film. The HOMO energy is estimated as 6.12 eV, which are close to the 6.15 and 6.10 eV HOMO energies of mCP and SimCP, respectively [4]. The photoelectron spectra were also measured at room temperature after the neat film was heated at 70 °C, 120 °C, and 150 °C (Fig. 3), but no change was observed among them.

The neat film, which was kept in open air at room temperature after annealing at 150 °C, shows morphological stability, i.e., neither aggregation nor crystallization was

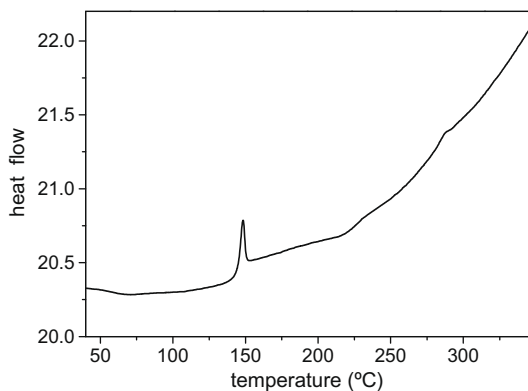


Fig. 2. DSC (differential scanning calorimetry) thermogram of SimCP2 which was obtained during heating of the neat SimCP2 film from 40 °C to 350 °C.

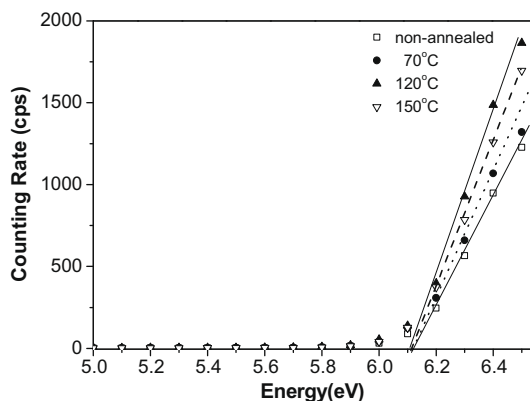
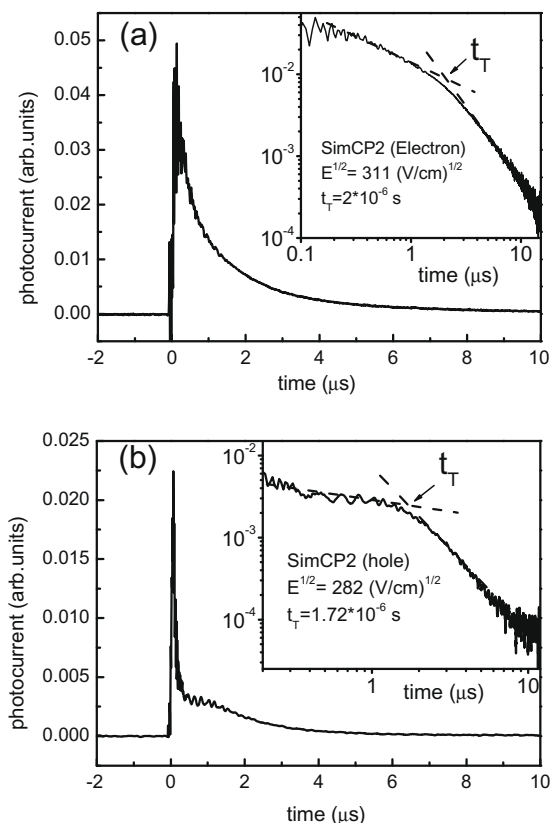


Fig. 3. The HOMO energy of SimCP2 obtained from the photoelectron emission spectroscopy for neat non-annealed SimCP2 film and neat SimCP2 films annealed at 70 °C, 120 °C and 150 °C.

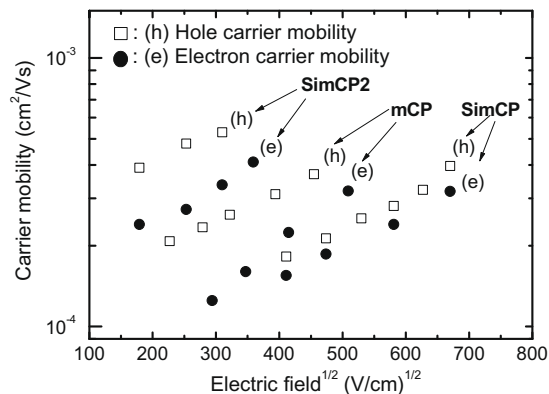
observed after 60 days when we look the film by eyes. In cases of neat mCP and SimCP films, quick morphology degradation was found after annealing at 70 °C [11]. This indicates that the SimCP2 film is morphologically more stable and more robust to water and oxygen molecules than mCP and SimCP. This is consistent with Fig. 3 which shows that no change occurs in the HOMO energy value between the SimCP2 films unheated and heated at 150 °C. From this result we confirm that high glass transition point is necessary to obtain morphologically stable and uniform amorphous thin films.

Fig. 4 shows example of the TOF curve for electron and hole carriers of neat SimCP2 film with thickness of 220 nm, respectively. The carrier mobility  $\mu$  is estimated using equation  $\mu E = L/t_T$ , where  $E$  is electric field,  $L$  is film thickness, and  $t_T$  is transit time which is determined from the log–log plotted curve as shown in inset of Fig. 4. Carrier mobility of electron and hole is plotted against electric field in Fig. 5, and compared with those of mCP and SimCP. Like the cases of various organic semiconductors [12,13], the electron and hole mobility of SimCP2, mCP and SimCP follows the linear relationship with applied electric field (Poole–Frenkel model) when the mobility is log plotted against square root of electric field. The hole and electron mobility in SimCP2 is found to be  $4.8 \times 10^{-4}$  and  $2.7 \times 10^{-4} \text{ cm}^2 \text{ V}^{-1} \text{ s}^{-1}$ , respectively, at electric field of  $9 \times 10^4 \text{ V cm}^{-1}$ . This indicates that SimCP2 has a balanced bipolarity although the hole mobility is a little higher than the electron mobility. The mobility is higher for SimCP2 than for mCP and much higher than for SimCP. High charge carrier mobility of the material is one of the factors that can reduce the driving voltage of OLED and hence increase the power efficiency (lm/W) of the device.

Based on the Poole–Frenkel model, the mobility at zero-field (called zero-field mobility) is obtained by extraction. Table 1 summarizes the zero-field electron and hole mobility for SimCP2, mCP, and SimCP. For comparison, the mobility is also shown for neat films of CBP [14,15] and N, N'-bis(1-naphthyl)-N, N'-diphenyl-1,1'-biphenyl-4,4'-diamine ( $\alpha$ -NPD) [16] in Table 1. The zero-field mobility of SimCP2 is lower than those of CBP, while it is higher than those of NPB and Alq<sub>3</sub>.



**Fig. 4.** Example of transient time of flight curves for electrons (a) and holes (b) of SimCP2 measured at electric fields 311 and 282 V/cm, respectively. Inset shows the log–log plotted curve.



**Fig. 5.** Plot of electron and hole mobilities of SimCP2 against the electric field, compared with those of mCP and SimCP.

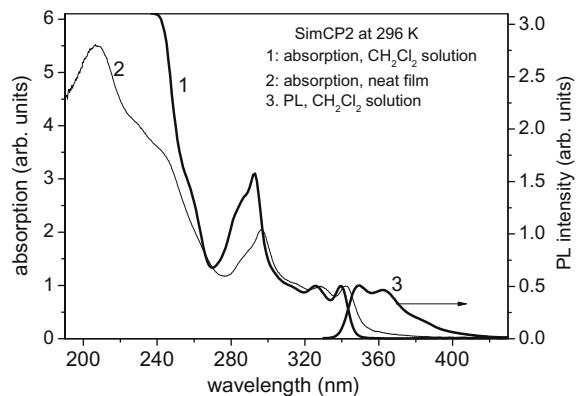
### 3.2. Spectroscopic properties

Fig. 6 shows absorption and emission spectra of SimCP2 diluted in dichloromethane ( $\text{CH}_2\text{Cl}_2$ ) solution and absorption spectrum of neat SimCP2 film. Similar absorption spectrum was also obtained from SimCP2 diluted in chloroform ( $\text{CHCl}_3$ ) solution. Absorption peaks due to SimCP2 molecule are observed at 339, 325,

**Table 1**

Zero-field mobilities,  $\mu_{\text{oh}}$  and  $\mu_{\text{oe}}$  for holes and electrons, respectively, in neat SimCP2, mCP, SimCP, CBP, and  $\alpha$ -NPD films.

	$\mu_{\text{oh}}$ ( $\text{cm}^2 \text{V}^{-1} \text{s}^{-1}$ )	$\mu_{\text{oe}}$ ( $\text{cm}^2 \text{V}^{-1} \text{s}^{-1}$ )
SimCP2	$2.4 \times 10^{-4}$	$1.3 \times 10^{-4}$
mCP	$1.2 \times 10^{-4}$	$3.4 \times 10^{-5}$
SimCP	$5.8 \times 10^{-5}$	$5.0 \times 10^{-5}$
CBP	$3.8 \times 10^{-4}$ [14,15]	$4.4 \times 10^{-4}$ [14,15]
$\alpha$ -NPD	$1.8 \times 10^{-4}$ [16]	$1.0 \times 10^{-5}$ [16]



**Fig. 6.** Absorption and PL spectra of SimCP2 in  $\text{CH}_2\text{Cl}_2$  and absorption spectrum of neat SimCP2 film. Absorption spectrum is cut at  $\lambda < 240$  nm for the case of solution because of strong absorption by the solvent.

311, 292, 285, and about 255 nm for the solution. On the other hand, absorption peaks are observed at 342, 328, 313, 296, 290, 240, 227, and 207 nm in the neat film. Two absorption spectral line shapes are quite similar to each other. The emission spectrum consists of three vibronic peaks at 349, 363 and 378 nm where their intensities decrease with decreasing photon energy. This emission is attributed to the  $S_1$  emission, i.e., emission due to electronic transition from the lowest singlet state  $S_1$  to the ground state  $S_0$ .

Fig. 7 shows the absorption spectra of SimCP2 in PS films doped with 5 and 15 wt% SimCP2 and in neat SimCP2 film. The three spectra are quite similar to each other. This

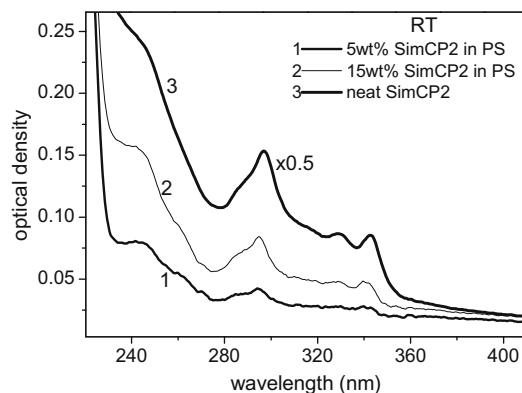


**Fig. 7.** Absorption spectra of SimCP2 which are measured using PS films with 5 and 15 wt% SimCP2 and using neat SimCP2 film at 296 K.

indicates that no aggregation is formed with increasing concentration of the dopant. We observe the absorption edge (i.e., onset) at about 348 nm (3.56 eV). The lowest unoccupied molecular orbital (LUMO) energy is approximated by the difference of the HOMO energy and the absorption edge of the UV absorption spectra [17–19]. Therefore, from the HOMO energy of 6.12 eV, the LUMO energy of SimCP2 is determined to be 2.56 eV.

Fig. 8 shows the PL and PLE spectra for PS films doped with 3, 15, and 20 wt% SimCP2 at 10 K. The PLE spectra for 370 nm  $S_1$  emission (curves 4 and 5) consist of peaks at 338.1, 324.1, 311.0, and 293.0 nm, which are quite similar to the absorption spectra of Figs. 6 and 7. The PLE bands at 338.2, 325.1, and 311 nm are attributable to the  $S_1$  state.

Intense emission peaks are observed at 343.8, 360.1, and 378 nm for the 3 wt% film, and weak PL bands are observed at 412.2, 433, and 441.8 nm. Like the case of mCP and SimCP [4,11], the latter bands are attributed to the  $T_1$  emission. Although the  $T_1$  emission is enhanced with decreasing temperature, it is too weak to observe clearly for the 20 wt% doped film even at 10 K. It is noted that the  $T_1$  emission intensity decreases with increasing concentration and not observed in neat film (see Fig. 9).

Comparison of the PL spectra among SimCP2, mCP, and SimCP is presented in Fig. 10, where the spectra are normalized at the most intense peak height of the zero-phonon band of the  $S_1$  emission. The spectrum of SimCP2 is quite similar to those of mCP and SimCP. Taking into account that SimCP and SimCP2 consist of one and two mCP molecules, respectively, this indicates that the  $S_1$  and  $T_1$  electronic states of mCP, SimCP, and SimCP2 are determined predominantly by mCP molecule. Difference, however, is found among the three materials, e.g., the vibronic structure in the  $S_1$  emission. The intensity ratio of the one-phonon vibronic band to the most intense zero-phonon band is 0.53, 0.76, and 0.90 for SimCP2, mCP, and SimCP, respectively. The Huang–Rhys parameter (or called Huang–Rhys factor)  $S$  is approximately estimated from this intensity ratio [20,21], i.e.,  $S = 0.53$  for SimCP2.

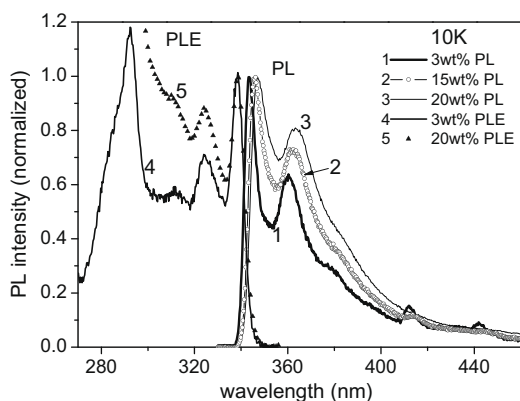


Fig. 8. PL spectra of SimCP2 which are measured using PS films with 3, 15, and 20 wt% SimCP2 excited at 305 nm at 10 K, and PLE spectra of SimCP2 for 370 nm emission which are measured using PS films with 3 and 20 wt% SimCP2 at 10 K.

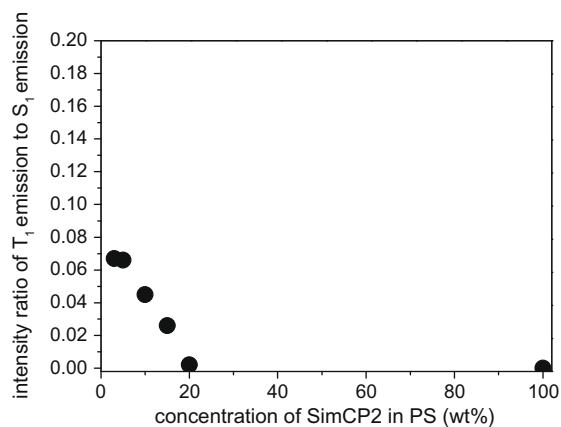


Fig. 9. Intensity ratio of the 412 nm  $T_1$  emission to the 344 nm  $S_1$  emission at 12 K plotted against concentration of SimCP2 doped in polystyrene.

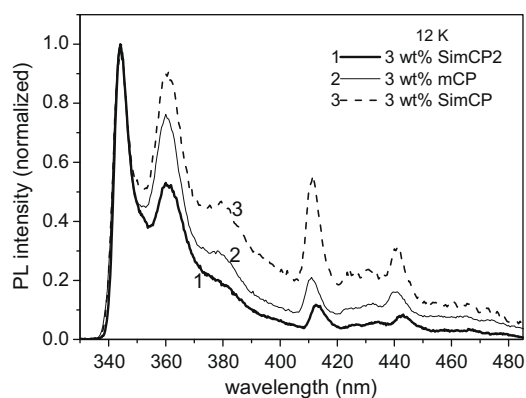


Fig. 10. PL spectra of mCP, SimCP and SimCP2 at 12 K, which were obtained from the PS films doped with 3 wt% mCP, SimCP and SimCP2, respectively.

The Huang–Rhys factor becomes large with increasing the distance between the equilibrium position  $Q(S_1)_0$  of the  $S_1$  electronic excited state and the equilibrium position  $Q(S_0)_0$  of the  $S_0$  ground state. The distance becomes large when the electron–phonon coupling in the excited state becomes largely different from the coupling in the ground state [21]. Therefore Fig. 10 suggests that the electron–phonon coupling difference between the  $S_1$  and  $S_0$  states is smaller in SimCP2 than in mCP and SimCP.

Another difference of the PL spectra among SimCP2, mCP, and SimCP is the intensity ratio of the  $T_1$  emission to the  $S_1$  emission. The ratio is approximately estimated from the ratio of intense zero-phonon band intensity of the  $T_1$  emission to that of the  $S_1$  emission, which is 0.08, 0.12, and 0.35 for SimCP2, mCP, and SimCP, respectively. The ratio reflects strength of spin–orbit coupling. Therefore Fig. 10 indicates that the spin–orbit coupling is weaker for SimCP2 than for mCP and SimCP. The weak spin–orbit coupling reduces the rate of intersystem crossing (ISC) from the  $S_1$  state to the triplet states. In the case of FIrpic doped in hosts with high gap energy such as SimCP2, mCP, and

SimCP, the Förster energy transfer (ET) occurs from the excited singlet state of the host to the singlet state of Flrpic dopant. If the ISC rate is low, we expect high energy transfer to the dopant from competition between two relaxation processes of ISC and ET. Therefore it is suggested that SimCP2 host with lower ISC rate gives higher energy transfer rate to the dopant than mCP and SimCP hosts, resulting in higher external quantum efficiency and higher power efficiency for SimCP2 than for mCP and SimCP. This is consistent with the results obtained from Flrpic-based OLED devices that are mentioned in Section 1.

#### 4. Summary

SimCP2. presents the most intense zero-phonon  $S_1$  emission band at 344 nm and the  $T_1$  emission band at 412 nm, which gives 3.01 eV as the  $T_1$  energy. The HOMO and LUMO energies are determined to be 6.12 and 2.56 eV, respectively. High gap energy is also observed for mCP and SimCP. SimCP2, however, is morphologically more stable than mCP and SimCP because of  $T_g$  of 148 °C which is much higher than mCP and SimCP, and additionally SimCP2 has higher mobility for both electron and hole ( $4.8 \times 10^{-4}$  and  $2.7 \times 10^{-4}$   $\text{cm}^2 \text{V}^{-1} \text{s}^{-1}$ , respectively, at electric field of  $9 \times 10^4$   $\text{V cm}^{-1}$ ) than mCP and SimCP. The zero-field mobility is also higher for SimCP2 than for mCP and SimCP. The intersystem crossing rate is smaller for SimCP2 than for mCP and SimCP, leading to higher rate of energy transfer to Flrpic dopant from SimCP2 host than from mCP and SimCP hosts. From these thermal, electrical, and optical properties, we understand that SimCP2 is superior to mCP and SimCP as the host material for blue phosphorescence emitter in OLEDs. The PL and absorption spectra of SimCP2 are not so different from those of mCP and SimCP because they are determined predominantly by the common mCP moiety. However, the glass transition point and morphological stability are quite different. Unlike the case of SimCP, two mCP moieties locate around Si symmetrically in SimCP2. It is suggested that such a molecular structure gives rise to very stable morphology for SimCP2 because molecule with asymmetric structure such as SimCP leads to form aggregation at lower temperature.

#### Acknowledgements

This work was partly supported by the Grant-in-Aid for the Scientific Research from the Japan Society for Science Promotion (Project No. 19560018) and the City Area Program 2008 (Mutsu-Ogawara-Hachinohe Area) from the Ministry of Education, Culture, Sports, Science and Technology in Japan. This work was also supported by Academia Sinica and the National Science Council of Taiwan.

#### References

- [1] Y.T. Tao, Q. Wang, Y. Shang, C.L. Yang, L. Ao, J.G. Qin, D.G. Ma, G. Shuai, *Chem. Commun.* 2009 (2009) 77.
- [2] M.H. Ho, B. Balaganesan, T.Y. Chu, T.M. Chen, C.H. Chen, *Thin Solid Films* 517 (2008) 943.
- [3] T. Tsuboi, H. Murayama, S.-J. Yeh, C.-T. Chen, *Opt. Mater.* 29 (2007) 1299.
- [4] T. Tsuboi, H. Murayama, S.-J. Yeh, M.-F. Wu, C.-T. Chen, *Opt. Mater.* 31 (2008) 366.
- [5] J.H. Jou, W.B. Wang, C.T. Chen, S.Z. Chen, M.F. Hsu, C.J. Wang, M.F. Wu, S.W. Liu, S.M. Shen, C.C. Chen, C.P. Liu, in: *Proceedings of the IDW'08*, 2008, p. 107.
- [6] R.J. Holmes, S.R. Forrest, Y.-J. Tung, R.C. Kwong, J.J. Brown, S. Garon, M.E. Thompson, *Appl. Phys. Lett.* 82 (2003) 2422.
- [7] S.-J. Yeh, W.-C. Wu, C.-T. Chen, Y.-H. Song, Y. Chi, M.-H. Ho, S.-F. Hsu, C.H. Chen, *Adv. Mater.* 17 (2005) 285.
- [8] J. Lee, J.-I. Lee, K.-I. Song, S.J. Lee, H.Y. Chu, *Appl. Phys. Lett.* 92 (2008) 133304.
- [9] Q. Wang, J.Q. Ding, Z.Q. Zhang, D.G. Ma, Y.X. Cheng, L.X. Wang, F.S. Wang, *J. Appl. Phys.* 105 (2009) 076101.
- [10] L.-H. Chan, R.-H. Lee, C.-F. Hsieh, H.-C. Yeh, C.-T. Chen, *J. Am. Chem. Soc.* 124 (2002) 6469.
- [11] M.-F. Wu, S.-J. Yeh, C.-T. Chen, H. Murayama, T. Tsuboi, W.-S. Li, I. Chao, S.-W. Liu, J.-K. Wang, *Adv. Funct. Mater.* 17 (2008) 1887.
- [12] P.M.W. Blom, M.J.M. de Jong, M.G. van Munster, *Phys. Rev. B* 55 (1997) R656.
- [13] B.H. Hamadani, D. Natelson, *J. Appl. Phys.* 95 (2004) 1227.
- [14] J.C. Bolinger, L. Fradkin, K.J. Lee, R.E. Palacios, P.F. Barbara, *Proc. Nat. Acad. Sci.* 106 (2009) 1342.
- [15] N. Matsusue, Y. Suzuki, H. Naito, *Jpn. J. Appl. Phys.* 44 (2005) 3691.
- [16] C.C. Lee, Y.D. Jong, P.T. Huang, Y.C. Chen, P.J. Hu, Y. Chang, *Jpn. J. Appl. Phys.* 44 (2005) 8147.
- [17] X.-Q. Wang, C.Z. Wang, B.L. Zhang, K.M. Ho, *Phys. Rev. Lett.* 69 (1992) 69.
- [18] H.S. Cho, T.K. Ahn, S.I. Yang, D.H. Kim, H.D. Kim, *Chem. Phys. Lett.* 375 (2003) 292.
- [19] M. Baldo, Ph.D. Thesis, Princeton University, USA, 2001.
- [20] M. Pope, C.E. Swenberg, *Electronic Processes in Organic Crystals*, Clarendon Press, Oxford, 1982 (Chapter II.F).
- [21] B. Henderson, G.F. Imbusch, *Optical Spectroscopy of Inorganic Solids* Oxford Sci. Publ., Oxford, 1989 (Chapter 5).



## 2. Experimental

The following configuration was used for device fabrication: indium tin oxide (ITO, 150 nm)/N,N'-diphenyl-N,N'-bis-[4-(phenyl-m-tolyl-amino)-phenyl]-biphenyl-4,4'-diamine (DNTPD, 60 nm)/N,N'-di(1-naphthyl)-N,N'-diphenylbenzidine (NPB, 20 nm)/4,4',4''-tris(N-carbazolyl)triphenylamine(TCTA)/TCTA:PH1:iridium(III) tris(2-phenylpyridine)(Ir(ppy)<sub>3</sub>):iridium(III) bis(2-phenylquinoline) acetylacetonate(Ir(pq)<sub>2</sub>acac)(x nm)/TCTA:PH1 (5 nm)/2-methyl-9,10-di(2-naphthyl) anthracene (MADN):DAF (30-x nm, 7%)/2,9-dimethyl-4,7-diphenyl-1,10-phenanthroline (BCP, 5 nm)/tris(8-hydroxyquinoline) aluminum (Alq<sub>3</sub>, 20 nm)/LiF (1 nm)/Al (200 nm). The doping concentrations of Ir(ppy)<sub>3</sub> and Ir(pq)<sub>2</sub>acac were 10% and 0.7%, respectively. The relative composition of TCTA:PH1 in the red/green layer was fixed at 3:1 and the thickness of the red and green emitting layer was 5 and 10 nm, respectively. An interlayer which separates the fluorescent blue emitting layer from the red/green emitting layer was inserted between the two emitting layers and the TCTA:PH1 interlayer compositions were 9:1 and 3:1. The PH1 was supplied from Merck Co. and it had a spirobifluorene backbone structure with good electron transport properties. The highest occupied molecular orbital of the PH1 was 5.9 eV, while the lowest unoccupied molecular orbital was 2.8 eV. A blue device with MADN as the host in the blue fluorescent emitting layer was also fabricated to evaluate the performance of the DAF dopant. The device structure for the evaluation of the DAF dopant in the blue device was ITO (150 nm)/DNTPD (60 nm)/NPB (30 nm)/MADN:DAF (30 nm, x%)/Alq<sub>3</sub> (20 nm)/LiF (1 nm)/Al (200 nm). The doping concentrations of the DAF dopant were 3%, 5% and 7%. Fig. 1 shows a schematic diagram of the device structures of the white device and chemical structure of the dopant materials used in this work. The energy levels of the materials were measured by cyclic voltammetry.

The current density–voltage–luminance characteristics and electroluminescence (EL) spectra of the WOLEDs were measured in the normal direction without any outcoupling enhancements using a Keithley 2400 source measurement unit and a CS 1000 spectroradiometer. Lambertian distribution of the light emission was assumed for the measurement of the luminance.

## 3. Results and discussion

The DAF dopant used in this study had a diphenylaminofluorene emitting core unit combined with a styryl group, and high efficiency could be realized through an extended conjugation structure. In addition, a deep blue color could be obtained due to the wide bandgap of the fluorene group in the backbone structure and the t-butyl blocking group. The device performances of the DAF blue dopant were optimized by controlling the doping concentration of the DAF. Fig. 2 shows the quantum efficiency–luminance curves of the DAF-doped blue fluorescent device. The quantum efficiency of the blue fluorescent device was optimized at a doping concentration of 7%, and a high quantum efficiency of 7.1% at 1000 cd/m<sup>2</sup> was obtained. The quantum efficiency of the DAF device was superior to other blue fluorescent devices reported earlier [10,11], and the use of DAF in WOLEDs can increase their quantum efficiency.

The EL spectra of the blue fluorescent devices with the DAF dopant are shown in Fig. 3. The DAF-doped blue device showed a maximum peak at 459 nm with vibration peaks at high wavelength. Pure deep blue emission was observed from the DAF-doped device and the color coordinate of the blue device was (0.15, 0.18).

The doping concentration of DAF in the WOLEDs was fixed at 7% and a mixed host emitting structure codoped with red and green phosphorescent emitting materials was used. The mixed host emitting structure is advantageous because the charge balance can be controlled easily

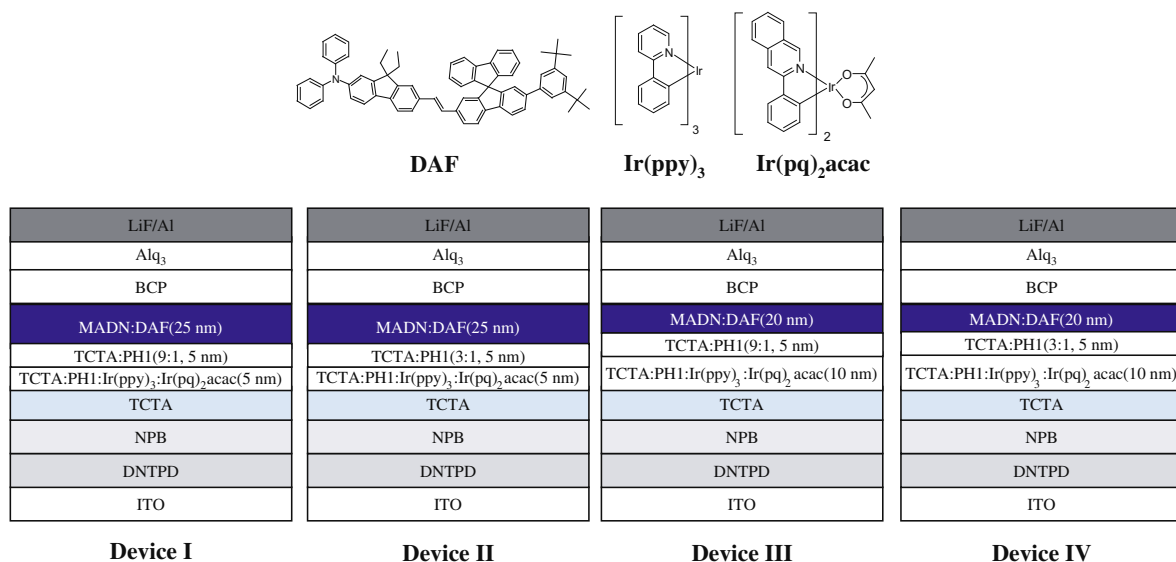


Fig. 1. Chemical structure of the DAF dopant and device structure of the white organic light-emitting diodes.

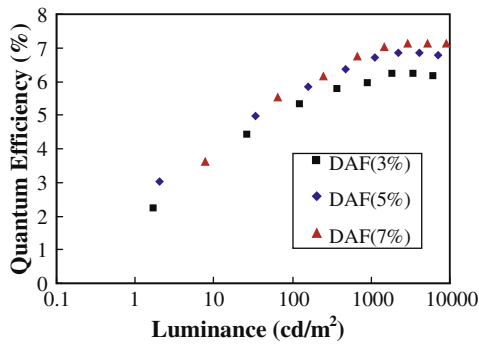


Fig. 2. Quantum efficiency–luminance curves of the blue fluorescent devices with the DAF blue dopant.

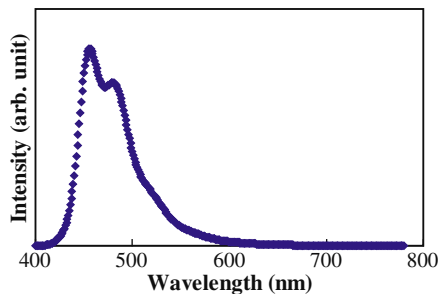


Fig. 3. Electroluminescence spectra of the blue fluorescent device doped with DAF at a doping concentration of 7%.

by just changing the host composition and charge injection from the charge transport layer [12]. In this study, a mixed host of TCTA and PH1 was used as the host material in the red/green emitting layer. The PH1 host was reported in previous work and has good electron transport properties [12]. The TCTA to PH1 ratio in the red/green emitting layer was optimized to TCTA:PH1 (3:1) as the quantum efficiency of the red/green doped TCTA:PH1 mixed host devices was maximized in the TCTA:PH1 (3:1) device. The doping concentrations of  $\text{Ir}(\text{ppy})_3$  and  $\text{Ir}(\text{pq})_2\text{acac}$  were 10% and 0.7%, respectively, in order to balance the intensity of red and green emission. The total thickness of the emitting layer was 30 nm and the thickness of the red and green emitting layers were 5 nm and 10 nm, respectively. A mixed layer of TCTA and PH1 was used to control the emission spectra of the WOLEDs, and the interlayer structure was managed to match the color index of the WOLEDs.

Fig. 4 shows the current density–voltage and luminance–voltage curves of the WOLEDs with different interlayer and emitting layer structures. The current density was not affected greatly by the interlayer structure and a similar current density was obtained in the WOLEDs fabricated in this study. The current density is determined mainly by charge injection from the charge transport layers to the emitting layer and the thickness of the organic layers. All devices had the same interface structure between the emitting layer and charge transport layers, and the thickness of the total emitting layer was the same in all devices, resulting in a similar current density. The lumi-

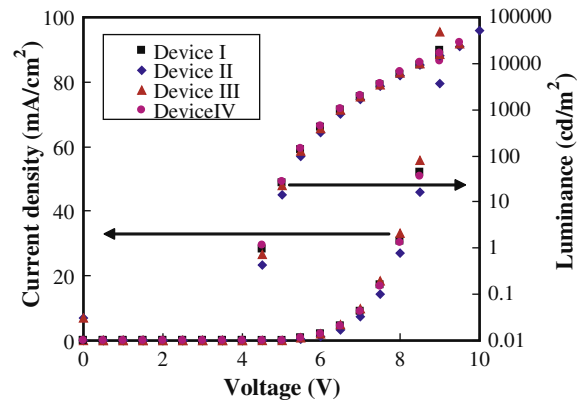


Fig. 4. Current density–voltage–luminance curves of the white organic light-emitting diodes with different interlayer and emitting layer structures.

nance of the WOLEDs followed the same trend as the current density.

Fig. 5 presents the quantum efficiency–luminance and power efficiency–luminance curves of the WOLEDs. The quantum efficiency was dependent on the interlayer structure, and devices I and III with the TCTA:PH1 (9:1) interlayer showed a lower efficiency than devices II and IV with the TCTA:PH1 (3:1) interlayer. The effect of the emitting layer thickness on the quantum efficiency was not significant. The high quantum efficiency of devices II and IV can be explained by the high quantum efficiency of the

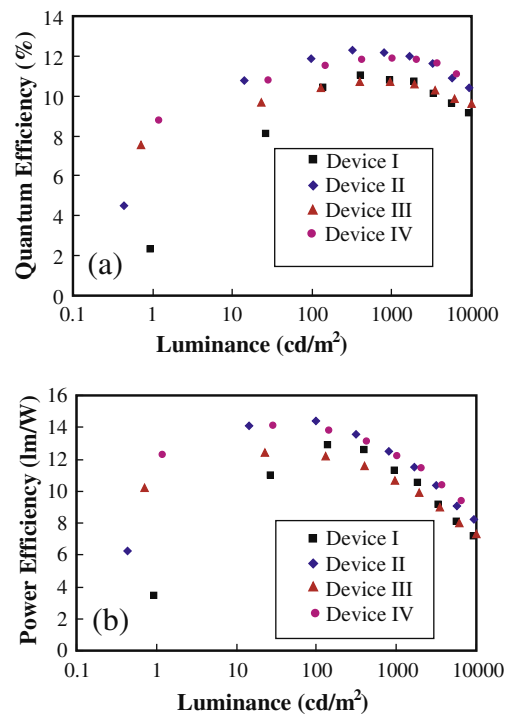


Fig. 5. Quantum efficiency–luminance (a) and power efficiency–luminance (b) curves of the white organic light-emitting diodes with different interlayer and emitting layer structures.

red/green phosphorescent emitting layer. The DAF-doped blue device showed a quantum efficiency of 7.1%, while the red/green device had a quantum efficiency of 13.1%. Therefore, more red/green emission rather than blue emission might improve the quantum efficiency of WOLEDs. The TCTA:PH1 (9:1) interlayer has a strong hole transporting character and shifts the emission zone of the emitting layer from red/green to the blue emitting layer, as shown in Fig. 6. Therefore, high quantum efficiency was obtained in devices II and IV. The quantum efficiency of the devices II and IV were 12.3% and 11.9% respectively.

The power efficiency of the WOLEDs is also shown in Fig. 5. The power efficiency of the device II and IV was higher than that of the device I and III due to the high quantum efficiency of the device II and IV. The power efficiency at 1000 cd/m<sup>2</sup> was 12.2 lm/W, which is higher than that of other pure color WOLEDs for display applications [7–9]. Although any p-doped or n-doped charge transport layer was not applied in this work, a fairly high power efficiency was achieved and the power efficiency can be improved over 20 lm/W if high mobility charge transport layer or p/n-doped charge transport layer is used.

The normalized EL spectra of the WOLEDs (Fig. 6) clearly show red, green and blue peaks. The interlayer and thickness of each emitting layer was found to affect the EL spectra of the WOLEDs. The blue emission was intensified in the WOLED with a TCTA:PH1 (9:1) interlayer and a thick blue emitting layer. More holes were injected from the red/green layer to the blue layer using the TCTA:PH1 (9:1) interlayer instead of TCTA:PH1 (3:1) due to the hole transport properties of TCTA, resulting in strong blue emission. The strong blue emission of the device with a thick blue emitting layer was attributed to the high probability of exciton formation in the thick emitting layer. The color coordinates of device I with the TCTA:PH1 (9:1) interlayer and the 25 nm thick blue emitting layer was (0.34, 0.36), which is suitable for display applications. There was a red shift in the color coordinates of the other devices and device IV showed color coordinates of (0.38, 0.38).

The change in the EL spectra of device IV was monitored according to the luminance to determine the color stability of the WOLEDs. Fig. 7 shows the EL spectra of device IV from 150 to 6500 cd/m<sup>2</sup>. There was little change in the

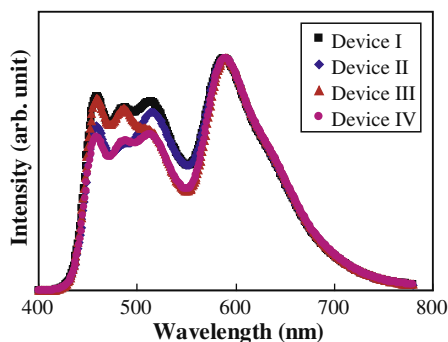


Fig. 6. Electroluminescence spectra of the white organic light-emitting diodes with different interlayer and emitting layer structures.

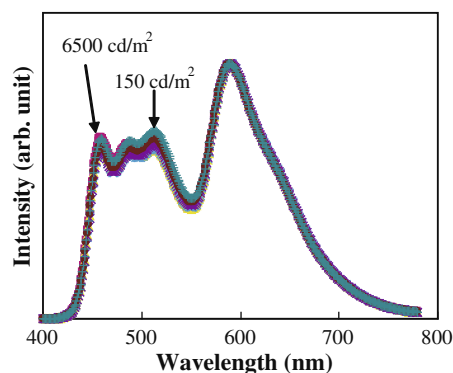


Fig. 7. Electroluminescence spectra of the device IV according to luminance.

spectra according to luminance from 150 to 6500 cd/m<sup>2</sup>, even though the blue emission was slightly higher at high luminance. The good color stability of device II originated from the balanced emission zone shift due to the mixed interlayer and mixed host structure in the emitting layer.

#### 4. Conclusions

High efficiency pure color WOLEDs were fabricated for display applications using a high efficiency DAF blue fluorescent dopant. A high quantum efficiency of 12.3% was obtained from the WOLED with the DAF dopant. The WOLED showed pure white color coordinates between (0.34, 0.36) and (0.38, 0.38), which were stable up to a luminance of 6500 cd/m<sup>2</sup>.

#### Acknowledgement

This work was partially supported by the GRRC program of Gyeonggi province [GRRC Dankook 2009-B01, Materials development for high efficiency organic solid state lighting], Grant No. RTI04-01-02 from the Regional Technology Innovation Program of the Ministry of Knowledge Economy (MKE) and MKE/ITEP [10028439-2008-21].

#### References

- [1] G. Schwartz, M. Pfeiffer, S. Reineke, K. Walzer, K. Leo, *Adv. Mater.* 19 (2007) 3672.
- [2] G. Schwartz, S. Reineke, K. Walzer, K. Leo, *Appl. Phys. Lett.* 92 (2008) 053311.
- [3] S.H. Kim, J. Jang, J.Y. Lee, *Appl. Phys. Lett.* 91 (2007) 123509.
- [4] Y. Wang, Y. Hua, X. Wu, L. Zhang, Q. Hou, S. Yin, M.C. Petty, *Appl. Phys. Lett.* 92 (2008) 123504.
- [5] C. Ho, M. Lin, W. Wong, W. Wong, C.H. Chen, *Appl. Phys. Lett.* 92 (2008) 083301.
- [6] K.S. Yook, S.O. Jeon, C.W. Joo, J.Y. Lee, *Appl. Phys. Lett.* 93 (2008) 073302.
- [7] K.S. Yook, S.O. Jeon, C.W. Joo, J.Y. Lee, M.S. Kim, H.S. Choi, S.J. Lee, C.W. Han, Y.H. Tak, *Org. Electron.* 10 (2009) 681.
- [8] G. Cheng, Y. Zhao, Y. Zhang, S. Liu, F. He, H. Zhang, Y. Ma, *Appl. Phys. Lett.* 84 (2004) 4457.
- [9] D. Qina, Y. Tao, *Appl. Phys. Lett.* 86 (2005) 113507.
- [10] M.-H. Ho, Y.-S. Wu, S.-W. Wen, T.-M. Chen, C.H. Chen, *Appl. Phys. Lett.* 91 (2007) 083515.
- [11] S.J. Lee, J.S. Park, K.-J. Yoon, Y.-I. Kim, S.-H. Jin, S.K. Kang, Y.-S. Gal, S. Kang, J.Y. Lee, J.-W. Kang, S.-H. Lee, H.-D. Park, J.-J. Kim, *Adv. Funct. Mater.* 18 (2008) 3922.
- [12] S.H. Kim, J. Jang, J.Y. Lee, *Appl. Phys. Lett.* 91 (2007) 083511.

phthalocyanine CuPc, although they proceed quite high hole mobility values [15,16]. The aim of this study is to compare the obtained results with those reported previously for the interfaces formed between Au and ITO substrates and thin films of other MePcs as well as different organic molecules.

## 2. Experimental

The experiments were carried out in an ultra high vacuum system, described previously [17]. ITO films on glass substrates with a sheet resistance of  $\sim 10 \Omega/\text{cm}^2$  were ultrasonically cleaned ex situ with ethanol followed by thorough rinsing in deionised water. After this chemical cleaning, in situ Ar ion sputtering (argon pressure of  $5 \times 10^{-6}$  mbar, accelerating voltage of 1 KeV and an incidence angle of  $45^\circ$ ) was used in order to remove carbon contamination from the ITO surface. ITO surface was characterized by XPS and UPS. Commercial NiPc and CoPc powders (Alfa Aesar) were thermally evaporated in the preparation chamber, from a home-made deposition source kept at  $425^\circ\text{C}$  and  $385^\circ\text{C}$ , respectively and thin films with total thickness of  $\sim 10.0$  nm were deposited on ITO surface at a vacuum about  $5 \times 10^{-8}$  mbar and room temperature. Each deposition step was followed by XPS (non-monochromatic AlK $\alpha$  source at 1486.6 eV) and UPS (HeI at 21.22 eV) measurements. The spectrometer was calibrated by the Au4f $_{7/2}$  core level peak ( $84.10 \pm 0.05$  eV) for clean Au foil. The XPS resolution measured by the full width at half maximum (FWHM) of the Au4f $_{7/2}$  was 1.7 eV for a constant pass energy of 97.0 eV. All XP spectra were fitted with mixed Gaussian and Lorentzian functions after the subtraction of a Shirley-type background. The thickness of the organic film was estimated from the intensity ratio of the substrate XPS In3d $_{5/2}$  and the overlayer C1s peak, assuming a layered-like growth mode for the initial deposition steps. During the UPS measurements, a negative bias of 12.28 V was applied to the sample to separate secondary electrons originating from sample and spectrometer and to estimate the absolute work function value from the Ultra-Violet Photoemission spectra. The overall analyser resolution is determined from the width of the Au Fermi edge (0.16 eV). Therefore, work function and HOMO cut-off positions determined from the high binding energy cut-offs and HOMO onsets of UP spectra were corrected for the analyser broadening by adding 0.08 eV.

## 3. Results and discussion

Carbon and oxygen species, in the form of OH groups, were the only contaminants detected at the surface of ITO after the ex situ chemical cleaning. The XPS and UPS results showed that both ITO surfaces are identical after the in situ cleaning procedure. After argon ion sputtering the carbon peak was eliminated, while a small amount of hydroxides remained at the surface. For perfectly stoichiometric ITO surface the value of  $[\text{O}]/(1.5[\text{In}] + 2[\text{Sn}])$ , where  $[X]$  is the concentration of species  $X$  as determined from the XPS measurement, would equal to one [18]. In the present study, this ratio for the sputtered ITO was

found to be  $\sim 0.6$  and this deviation from unity expresses a deficiency of oxygen atoms at the surface. Furthermore, the total cation content ( $[\text{Sn}]/[\text{In}]$ ) was decreased from 0.13 to 0.06 after the sputtering procedure. Sn cations are responsible for the conductivity of ITO.

According to the UPS results the work function of the sputtered-clean ITO surface was determined equal to be  $4.2 \pm 0.1$  eV, in good agreement to reported values for similar treated surfaces [19]. The valence band maximum (VBM) was found to be at  $1.0 \pm 0.1$  eV in good agreement with references [20] and considering an energy gap equal to 3.6 eV according to literature [21,22], the position of the Fermi level is closer to the valence band.

Upon the deposition of the organic materials on ITO, the XPS ITO core level peaks (In3d, Sn3d, O1s) attenuate as new XPS peaks (C1s, N1s, Ni2p and Co2p) related to the organic materials (NiPc and CoPc) appear at the X-ray photoelectron wide scan spectrum of the surface (not shown) and their intensity increases as the organic film becomes thicker. In both interfaces, the characteristic peaks of the substrate remain stable in shape and binding energy position until they completely disappear from the spectra after the deposition of a thick organic layer. The core levels (C1s, N1s, Ni2p $_{3/2}$ , Co2p $_{3/2}$ ) of the organic molecules (NiPc and CoPc) are shifted towards lower binding energies as the organic film grows thicker. Fig. 1 shows the change in the binding energy of the XPS C1s peak in both cases (NiPc/ITO and CoPc/ITO), as a function of the organic film coverage. For comparison, the corresponding change of the C1s peak during the formation of the NiPc/Au interface, studied previously, is also traced [23]. According to Fig. 1, the C1s peak in the NiPc/ITO interface exhibits a slight ( $\sim 0.1$  eV) shift towards lower binding energies for NiPc coverage up to less than 1.0 nm. Similar behaviour is observed at the CoPc/ITO interface, where the C1s peak exhibits a larger downward shift of  $\sim 0.5$  eV. For thicker organic films the C1s peak remains stable in both interfaces, which indicates the absence of band bending at the organic energy levels. All the XPS MePc related peaks (N1s, Ni2p $_{3/2}$ , Co2p $_{3/2}$ ) exhibit similar behaviour to the C1s peak.

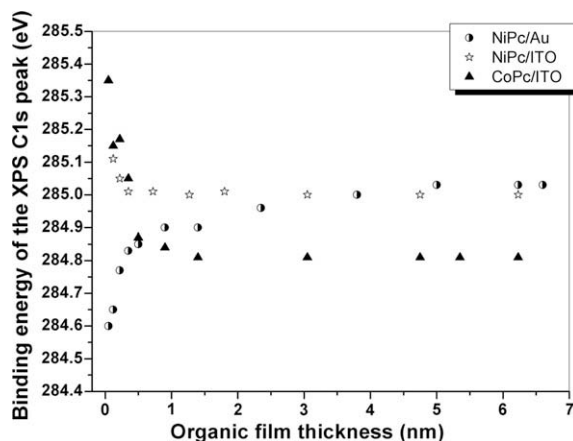


Fig. 1. Energetic shifts of the XPS C1s peak during the formation of the NiPc/Au, NiPc/ITO and CoPc/ITO interfaces.

For the NiPc/ITO interface, the XPS C1s peak for a 5.0 nm thick organic film is located at  $284.95 \pm 0.05$  eV of binding energy and can be resolved into three components according to the different chemical bonds of C atoms in the MePcs molecule. The main peak centered at 284.80 eV is due to the benzene-C atoms. A lower intensity peak at 286.20 eV of binding energy is attributed to the pyrrole-C atoms, while a small contribution from the benzene-C shake up feature which has been suggested to appear at similar binding energy cannot be excluded, although it cannot be resolved experimentally [24,25]. Finally, a shake up feature of the pyrrole-C atoms is found at a binding energy of about 2 eV higher from the main contribution of C–N bonds to the overall C1s peak. Similar results were obtained by the analysis of the XPS C1s peak for a thick ( $\sim 5.0$  nm) CoPc film.

The XPS N1s peak of the organic film has lower intensity than that of C1s peak because of the atomic ratio N/C ( $=8/32$ ) in the MePc's molecule. The N1s peak of the NiPc overlayer consists of a broad peak at  $399.30 \pm 0.05$  eV and a weaker feature at higher binding energies. The main peak can be ascribed to the two chemically nonequivalent nitrogen atoms of the organic molecule, separated by about 0.30 eV, but not resolved experimentally, while the weaker peak is attributed to the satellites of the main peak [26]. The Ni $2p_{3/2}$  peak is a unique peak due to C–N–Ni bonds and appears at  $855.90 \pm 0.05$  eV of binding energy [27]. In the case of CoPc/ITO interface the Co $2p_{3/2}$  peak appears at  $780.80 \pm 0.05$  eV of binding energy and is attributed to the bonding between the Cobalt atom and the four central nitrogen atoms in the Pc's molecule [27].

Any covalent chemical interaction between ITO and MePcs is expected to result in the appearance of additional peaks at different binding energies than those observed at the XPS spectra of the bulk materials (ITO, NiPc and CoPc). In the absence of new features in the measured core line spectra and a broadening of the XPS peaks at thinner films compared to the thicker organic layers, we conclude that there is no significant chemical reaction between the oxide substrate and the organic semiconductors.

The observed XPS core level shifts towards lower binding energies occurred at small coverage could be explained by increasing efficiency of intra-layer screening, going from individually adsorbed molecules to a complete layer as the chemical reaction was excluded. The screening of the photohole generated in the organic film at lower coverage occurs mostly by the neighbour organic molecules and less by the weakly metallic substrate, thereby enhancing the screening and thus reducing the binding energy. However, the dielectric constant of the organic molecules is similar to that of ITO indicating that no final state effects are expected [28]. Consequently, the XPS shifts at the MePc/ITO interfaces can be explained only in the context of a possible formation of a dipole layer across the interface at the very first steps of deposition. Comparing the behaviour of the core levels at the above studied interfaces with that observed at the NiPc/Au interface [23], an opposite dependence of the binding energies as a function of the coverage is found, as presented in Fig. 2. The NiPc/Au interface was found to be non-reactive and the initial binding energy shift is attrib-

uted exclusively to the decreasing effect of metal screening by the substrate. The photohole which is generated in the organic molecule is screened more effectively near a metal surface at submonolayer coverage, where the screening induced by the other organic molecules is still quite weak, than away from the metal. The further small shift observed at thicker organic films, is attributed to band bending at the organic energy levels. A possible gradual structural rearrangement of the NiPc molecules deposited on Au at thicker coverage, can be ruled out according to recent studies, where core level shifts point towards lower binding energies, which is not the case in the present study [29]. Similar variations of the energetic position of the core levels are also present at the CuPc/ITO and CuPc/Au interfaces for organic film thickness up to 1.5 nm [10,11]. In the case of Au substrate, the final state screening effects significantly affect the binding energy of the core levels which are shifted at  $\sim 0.5$  eV towards higher binding energies, while at the CuPc/ITO interface an opposite binding energy shift of  $\sim 0.4$  eV is observed and it is attributed to charge transfer from the organic molecules to ITO. This is also confirmed by the broadening of the C1s peak at submonolayer coverage compared to thick layer [10,11,28], which cannot be resolved experimentally in the present study.

By the UPS data, presented in Fig. 2 we can draw additional useful information in order to explain the observed XPS shifts. Fig. 2a and b present the changes of the UP spectra of the NiPc/ITO and CoPc/ITO interfaces respectively, after every deposition step up to  $\sim 10.0$  nm of organic film thickness. The full spectra are shown in the centre part of each figure. The bottom spectrum represents the clean ITO substrate where the upper part of the filled valence band including the broad structures at 5.0 eV and 10.4 eV mainly consist of O2p derived levels [30,31]. After the deposition of  $\sim 0.3$  nm ( $\sim 1$  ML) of organic material on the sputtered-clean ITO surface, new features appear at the valence band spectra and upon incremental deposition of the molecular film those of O2p gradually attenuate. The valence band structure of NiPc and CoPc is fully developed at  $\sim 2.0$  nm of coverage and exhibits four distinct features at binding energies 1.50 eV, 3.80 eV, 6.60 eV and 8.85 eV in the case of the NiPc overlayer and five main features at 1.25 eV, 2.10 eV, 3.55 eV, 6.15 eV and 8.60 eV of binding energy in the case of CoPc, in agreement with theoretical calculations [32]. No other features in the energy range of the UP spectra are observed, which would point to a chemical reaction between ITO and the organic molecules, confirming also the XPS results.

The HOMO (highest occupied molecular orbital) feature of the MePcs is firstly observed at about monolayer coverage as shown in the right part of Fig. 2a and b. As the coverage increases, beyond 1 ML, the HOMO peak is shifted towards higher binding energies for about 0.2 eV in both interfaces, while it appears to be slightly broader with a decreasing organic film thickness. The HOMO<sub>cut-off</sub> position for the thick NiPc and CoPc layers was found to be at 1.00 eV and 0.80 eV of binding energy, respectively. The thickness dependence of the HOMO peak can be explained by increasing efficiency of intra-layer screening as the coverage increases, since the possibility of an interaction

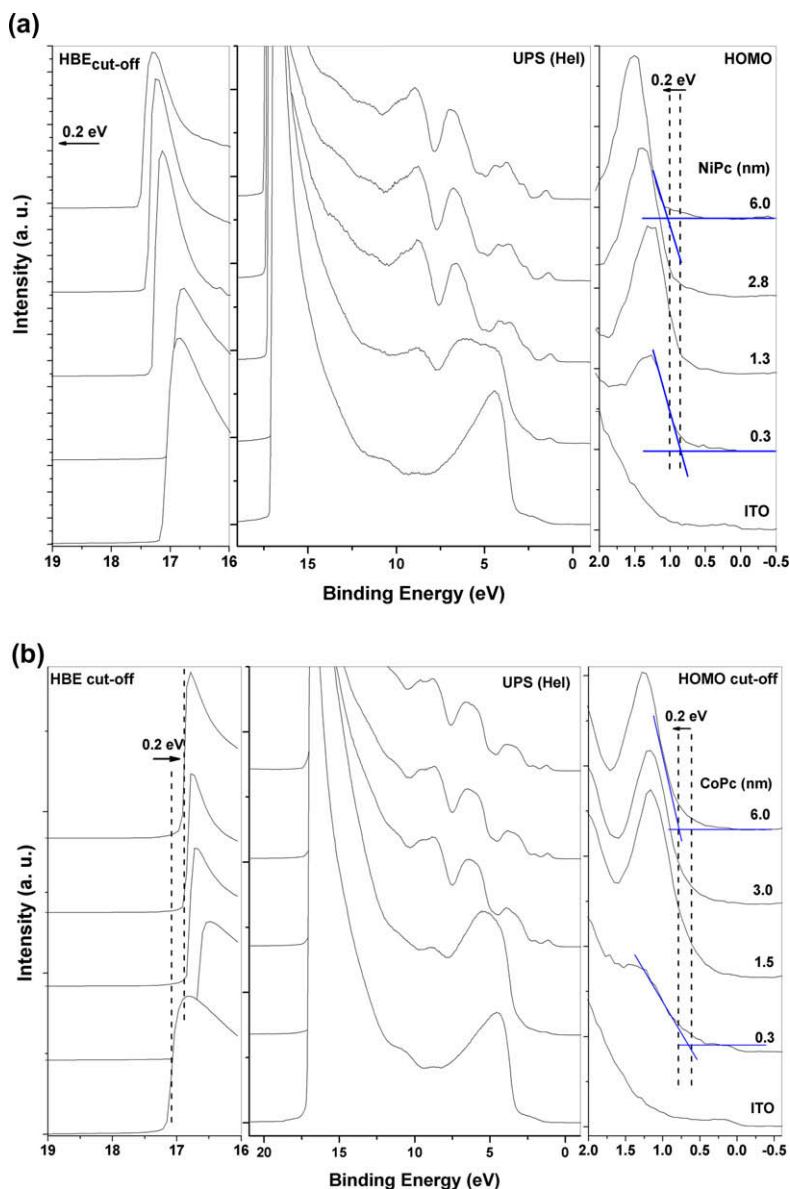


**Fig. 2.** Hel UPS spectra of the (a) NiPc/ITO and (b) CoPc/ITO interfaces. The full spectra are shown in the center part. On the right part, the development of the HOMO peak and on the left, the high binding energy cut-off regions are shown magnified for clarity.

through charge transfer was excluded by the XPS results [33].

Fig. 2a and b displays the evolution of the UPS during the formation of both interfaces (NiPc and CoPc on ITO). In the case of ITO surface, the work function can be measured by subtracting the total width of the UP spectra from the HeI (21.22 eV) radiation. The width of the spectra is determined by the position of the high binding energy cut-off (HBE), shown at the left part of Fig. 2a and b, in respect to the Fermi level of the analyser. According to these figures, during the deposition of the first few atomic organic monolayers, the  $HBE_{cut-off}$  at the NiPc/ITO interface is shifted to higher binding energies corresponding to the lowering of the vacuum level ( $E_{vac}^F$ ) at the sample surface, while in the case of CoPc/ITO the observed shift

is towards lower binding energies, yielding an increase of the  $E_{vac}^F$ . The changes of the vacuum level after every deposition step are shown in Fig. 3. In the same graph, the energetic shift of C1s peak during the formation of the NiPc/ITO interface is also traced for comparison. According to Fig. 3, at the early stages of deposition and up to the completion of one organic monolayer the  $E_{vac}^F$  in both interfaces (NiPc/ITO and CoPc/ITO) shows a tendency towards higher values, while for thicker films it changes until it reaches a plateau. At the NiPc/ITO interface there is a total decrease of the  $E_{vac}^F$  of 0.2 eV, while in the case of CoPc/ITO interface, the total absolute value for the  $E_{vac}^F$  increase is 0.2 eV.

According to Fig. 3, the fact that both the core level shifts and the main change of the HBE cut-off occur up to same organic

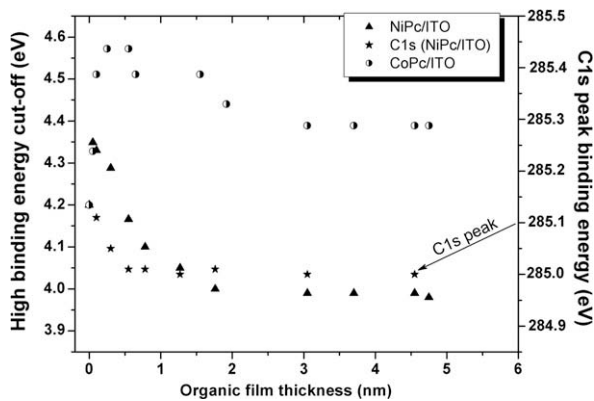


**Fig. 3.** Variation of the high binding energy cut-off region for the NiPc/ITO and CoPc/ITO interfaces as the organic layer increases. In the same graph the energetic shifts of the XPS C1s peak during the formation of the NiPc/ITO interface are also displayed.

coverage, suggests that these shifts should be considered in the context of the formation of a dipole layer across the interface. In addition, we note that the shift in HOMO energy level matches the shift in vacuum cut-off energies, which shows that the spectral energy shifts are purely a result of different interfacial dipoles [34].

Several research groups have studied the formation of organic/metals and organic/semiconductor interfaces by surface science techniques and have reached to similar conclusions about the physical phenomena that occur at the interfaces. The Fermi level alignment at organic/metal interfaces can be explained through the formation of an interface dipole (eD) and a possible band bending at the organic energy levels. The formed dipole can be attributed to several reasons such as: (i) charge transfer due to the different values for the work function ( $\Phi$ ), the electron affinity ( $E_A$ ) and the ionization potential ( $I$ ) of the organic material, (ii) to the formation of gap states due to chemical interaction yielding the change of the Fermi level position in the gap of the organic semiconductor and, (iii) the modification of the substrate surface dipole due to the presence of the organic molecules [35,36]. Smaller values for the interface dipole are expected at the organic/semiconductor and organic/organic interfaces, where the charge transfer mechanism will be less pronounced or absent, since there are no free electrons or effective density of states, nor surface dipole due to the tailing of the electron cloud towards the vacuum as in the case of metal surfaces [37,38].

In the case of organic/metal interfaces, the surface dipole of a metal is modified by the presence of the conjugated organic molecules. The repulsion between the molecule electrons and the metal surface electrons compresses the electron tail resulting in the decrease of the metal work function. This process leads also to an increase in the distance between the Fermi level and the organic HOMO position which is the barrier for the injection of holes [23,36]. That is the reason why at the organic/metal interfaces we expect higher interface dipoles as well as barriers for hole injection compared to the organic/ITO interfaces.

In the present study, in the absence of chemical interaction between MePcs and ITO as well as the formation of

additional gap states, the observed vacuum level shift should be attributed to the formation of an interfacial dipole layer possibly due to the reduction of the substrate surface dipole. At the NiPc/ITO interface, the total  $E_{vac}^F$  change ( $-0.2 \pm 0.1$  eV) leads to a dipole of  $-0.2$  eV, while in the case of the CoPc/ITO interface the formatted dipole is  $+0.2$  eV due to a total  $0.2 \pm 0.1$  eV increase of  $E_{vac}^F$ . The formation of the eD could be explained as a result of a net charge exchange between the MePcs and ITO. In particular, at the NiPc/ITO interface the observed outward pointing dipole (“+” away from the surface) indicates a net charge transfer from the NiPc molecules to the ITO, while in the case of the CoPc/ITO interface, the downward pointing electric dipole points at a charge transfer from ITO surface to the organic layer. The dipoles found at the MePc/ITO interfaces (0.2 eV) are considerable smaller than these measured at the NiPc/Au interface (1.0 eV) and this is due to the different chemical character of the substrates, as ITO has significantly less density of states close to the Fermi level compared to a metal like Au and also lower work function value (the work function for the clean polycrystalline Au foil was found to be 5.20 eV). Respectively, at the CuPc/Au interface the interface dipole was found to be (1.2 eV) significantly higher than that in the case of ITO substrate (0.3 eV) due to the pillow effect which affect the metal surface dipole.

The direction of the dipole formed at the interface is related to the electronic properties of the organic semiconductor. The ionization potential for the NiPc layer was found equal to  $5.0 \pm 0.1$  eV and  $5.2 \pm 0.1$  eV for the

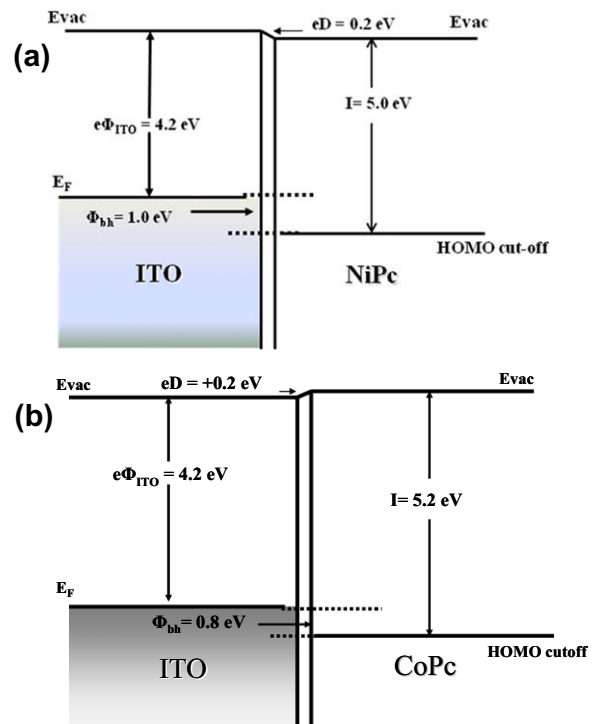


**Fig. 4.** Schematic energy level diagram deduced from the photoemission measurements for the (a) NiPc/ITO and (b) CoPc/ITO interfaces, considering Fermi level alignment.

CoPc, respectively. The different value of the ionization potential for the two above MePcs, points at different electronic properties between the two organic materials and results in the formation of dipoles with different direction in both studied interfaces.

The hole injection barrier ( $\Phi_{bh}$ ) was also determined at the organic semiconductor/ITO interfaces. In the case of NiPc/ITO interface it is found equal to  $1.0 \pm 0.1$  eV, while at the CoPc/ITO interface  $0.8 \pm 0.1$  eV.

Finally, Fig. 4 summarizes the energy level line-up at the interfaces that NiPc and CoPc form with the ITO-coated glass substrate, as derived by the photoemission results. The determined values for the interface dipole, ionization potential and barrier for hole injection have been added in the diagrams for better comparison between Cobalt and Nickel phthalocyanines. The  $\Phi_{bh}$  at the NiPc/ITO interface is found 0.2 eV higher than in the case of CoPc. Comparing NiPc/ITO and CuPc/ITO interfaces the  $\Phi_{bh}$  is found similar ( $\sim 1.0$  eV). Furthermore, if we consider the interfaces that ITO forms with several other organic molecules (Ooct-OPV5, Alq<sub>3</sub>, TPD et al.) the  $\Phi_{bh}$  is found to be significantly lower at the MePc/ITO interfaces, indicating that metal phthalocyanines, can improve the hole injection process when applied as active layer in electronic devices.

#### 4. Summary

The combination of the photoemission results for the study of the interfaces between two metal phthalocyanines and ITO showed that a chemical interaction, as well as a modification of the surface dipole of ITO by the presence of the organic molecules, is excluded. Formation of a dipole layer across the interfaces occurs and the formed dipoles point to different directions as a result of the higher ionization potential determined for the CoPc overlayer compared to the NiPc. The barrier for the injection of holes was found to be lower at the CoPc/ITO interface revealing the beneficial applications of this material compared to other metal phthalocyanines.

#### References

- [1] Zhong Zhi You, Jiang Ya Dong, Appl. Surf. Sci. 249 (2005) 271.
- [2] J. Cui, A. Wang, N.L. Edleman, J. Ni, P. Lee, N.R. Armstrong, T.J. Marks, Adv. Mater. 13 (19) (2001) 1476.

- [3] A.S. Wan, A.J. Makinen, P.A. Lane, G.P. Kushto, Chem. Phys. Lett. 446 (2004) 317.
- [4] H. Peisert, T. Schwieger, M. Knupfer, M.S. Golden, J. Fink, J. Appl. Phys. 88 (3) (2000) 1535.
- [5] Th. Kugler, W.R. Salaneck, H. Rost, A.B. Holmes, Chem. Phys. Lett. 310 (1999) 391.
- [6] K. Book, H. Bassler, A. Elschner, S. Kirchmeyer, Org. Electron. 4 (2003) 227.
- [7] A. Siokou, V. Papaefthimiou, S. Kennou, Surf. Sci. 482–485 (2001) 1186.
- [8] I.G. Hill, A. Kahn, J. Appl. Phys. 86 (4) (1999) 2116.
- [9] J. Blochwitz, T. Fritz, M. Pfeiffer, K. Leo, D.M. Alloway, P.A. Lee, N.R. Armstrong, Org. Electron. 2 (2001) 97.
- [10] H. Peisert, M. Knupfer, T. Schwieger, J. Fink, Appl. Phys. Lett. 80 (16) (2002) 2916.
- [11] H. Peisert, M. Knupfer, T. Schwieger, J.M. Auerhammer, M.S. Golden, J. Fink, J. Appl. Phys. 91 (8) (2002) 4872.
- [12] S. Riad, Thin Solid Films 370 (2003) 253.
- [13] M. Thelakkat, C. Schmitz, H.-W. Schmidt, Adv. Mater. 14 (2002) 577.
- [14] M. Trometer, R. Even, J. Simon, A. Dupon, et al., Sens. Actuators B 8 (1992) 129.
- [15] T.S. Shafai, T.D. Anthopoulos, Thin Solid Films 398–399 (2001) 361.
- [16] M. Ofuji, K. Ishikawa, H. Takezoe, et al., Appl. Phys. Lett. 86 (2005) 062114.
- [17] F. Petraki, S. Kennou, S. Nespurek, J. Appl. Phys. 103 (033710) (2008) 1.
- [18] V. Papaefthimiou, S. Kennou, Surf. Sci. 566–568 (1) (2004) 497.
- [19] D.J. Milliron, I.G. Hill, C. Shen, A. Kahn, J. Schwartz, J. Appl. Phys. 87 (2000) 572.
- [20] L. Chkoda, C. Heske, M. Sokolowski, E. Umbach, F. Steuber, J. Staudigel, M. Stobel, J. Simmerer, Synth. Met. 111–112 (2000) 315.
- [21] A. Klein, Appl. Phys. Lett. 77 (13) (2000) 2009.
- [22] Y. Gassenbauer, A. Klein, Solid State Ionics 173 (2004) 141.
- [23] F. Petraki, V. Papaefthimiou, S. Kennou, Org. Electron. 8 (2007) 522.
- [24] B. Brena, Y. Luo, M. Nyberg, S. Carniato, et al., Phys. Rev. B 70 (195214) (2004) 1.
- [25] A. Ruocco, F. Evangelista, R. Gotter, A. Attili, G. Stefani, J. Phys. Chem. C 112 (6) (2008) 2016.
- [26] J. Ahlund, K. Nilson, J. Schiessling, et al., J. Chem. Phys. 125 (034709) (2006) 1.
- [27] R.J. Ewen, C.L. Honeybourne, J. Phys.: Condens. Matter 3 (1991) S303.
- [28] M. Knupfer, H. Peisert, Phys. State Solid (a) 201 (6) (2004) 1055.
- [29] S. Dhhm, G. Heimel, I. Salzmann, H. Glowatzki, et al., Nat. Mater. 7 (2008) 326.
- [30] H. Ofner, J. Kraft, R. Hofmann, S.L. Surnev, F.P. Netzer, J.J. Paggel, K. Horn, Surf. Sci. 316 (1994) 112.
- [31] C.S. Fang, F.M. Pan, W.S. Tse, S.R. Horng, Surf. Sci. 211/212 (1989) 279.
- [32] B. Bialek, I.G. Kim, J.I. Lee, Synth. Met. 129 (2002) 151.
- [33] T.S. Ellis, M.D. Ulrich, S.L. Hulbert, J.E. Rowe, J. Appl. Phys. 100 (2006) 093515-9.
- [34] M. Andreasson, M. Tengelin-Nilsson, T.G. Andersson, L. Ilver, J. Kanski, Org. Electron. 6 (2005) 175.
- [35] H. Ishii, K. Sugiyama, E. Ito, K. Seki, Adv. Mater. 11 (8) (1999) 605.
- [36] A. Kahn, N. Koch, W. Gao, J. Polym. Sci. B 41 (2003) 2529.
- [37] N. Koch, ChemPhysChem 8 (2007) 1438.
- [38] M. Fahlman, A. Crispin, X. Crispin, S.K.M. Henze, et al., J. Phys.: Condens. Matter 19 (2007) 183202-1.



insulator interface can be altered by its surface modification for performance improvement of OTFTs [10–12].

Pentacene is a promising organic semiconducting material for OTFTs due to its high mobility and good semiconducting properties. A thermal evaporation-deposited pentacene film on SiO<sub>2</sub> surface consists of a substrate-induced “thin film” phase and a “triclinic bulk” phase that can be detected only when its thickness is large enough. The triclinic structure of the pentacene single crystal composes two molecules in a unit cell with lattice parameters of  $a = 0.628$  nm,  $b = 0.771$  nm,  $c = 1.444$  nm,  $\alpha = 76.75^\circ$ ,  $\beta = 88.01^\circ$ , and  $\gamma = 84.52^\circ$  [13], and the pentacene molecules are packed into a layered structure to form a herringbone pattern. Thickness-driven phase transformation from orthorhombic to “triclinic bulk” phase is believed to take place in the thin films [14,15]. However, the modified-layer-driven microstructure transformation of a pentacene polymorphic film at a fixed thickness has not yet been reported. Further, pentacene films on various modified gate insulator surfaces could reveal their polycrystalline structure and morphologies as well. Since the structural change of an organic semiconductor layer in the channel is critical to the OTFTs performance, there is a great need to investigate the growth dynamics and microstructure transformation of a pentacene film caused by modified-layers on the dielectric surface for fundamental insights, leading to further improvement of OTFT performance.

In this work, we fabricated a series of pentacene OTFTs with various interface modified-layers on thermally grown SiO<sub>2</sub> gate insulator by using phenyltrimethoxysilane C<sub>6</sub>H<sub>5</sub>Si(OCH<sub>3</sub>)<sub>3</sub> (PhTMS) for performance improvement, while investigating the structural phase transformations induced by various modified-layer such as octadecyltrichlorosilane (OTS) and PhTMS on SiO<sub>2</sub> gate insulator. For the first time, we experimentally studied effects of the modified-layer on the molecular vibrational modes and structure change of the organic semiconductor. These microstructure transformations might imply the carrier transport improvement in pentacene OTFT devices.

## 2. Experimental

Top-contact (TC) pentacene OTFTs were fabricated with heavily doped silicon substrates by thermally growing 310 nm SiO<sub>2</sub> (SiO<sub>2</sub>, dielectric constant  $k = 3.35$ ) dielectric layer as the gate electrodes (Fig. 1a). The SiO<sub>2</sub>/Si substrates were diced followed sequentially by cleaning in sulfuric acid/hydrogen peroxide (7:5 v/v) at room temperature for 45 min, rinsing thoroughly with de-ionized (DI) water, ultra-sonicating for 30 min in acetone and DI water, rinsing and drying under nitrogen. The cleaned substrates were immediately coated with PhTMS or OTS modified-layer via spin coating at a rate of 3000 rps for 30 s. The coating solutions containing 2.3% PhTMS and 2.3% OTS in toluene (v/v) were used, respectively for spin-coated modifications [16]. The molecular structures of PhTMS and OTS and chemical process between modified-layer and surface of SiO<sub>2</sub>/Si substrate are shown in Fig. 1b–d, respectively. A 60 nm-pentacene thin film was subsequently deposited under a vacuum of  $\sim 10^{-6}$  Pa at a deposition rate of 0.03 nm/s and room temperature for the substrate. Finally, Au source and drain electrodes (60 nm thickness) were deposited by thermal evaporation through a shadow mask. All devices were fabricated to have an identical channel width and length ratio of  $W/L = 570 \mu\text{m}/57 \mu\text{m}$ . All electrical characterizations were carried out under ambient conditions using Agilent Semiconductor Analyzer (E5270B) + Cascade probe station.

## 3. Results and discussions

The output characteristics of the fabricated devices in Fig. 2 show saturation behaviors at high  $V_{DS}$  for all devices. Interestingly, the saturation currents are increased remarkably with modified-layers, especially with PhTMS. As shown in Fig. 2c, the output characteristics of the PhTMS-treated OTFT device  $t$  display a pronounced curvature at low  $V_{DS}$ , indicating the existence of contact resistance ( $R_C$ ), possibly due to the energy barrier for

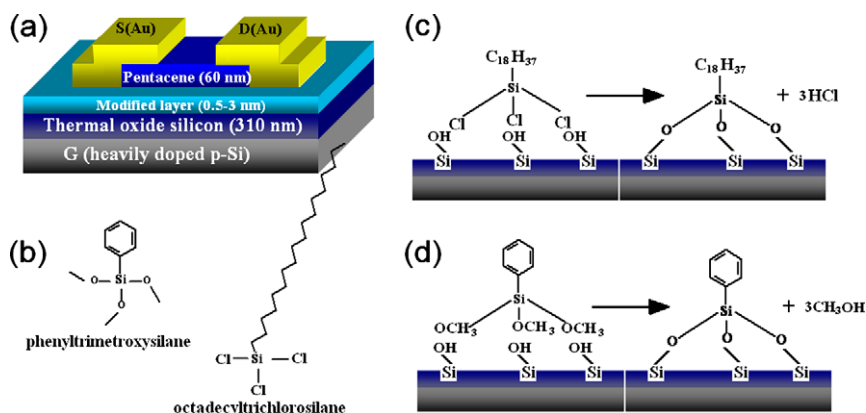


**Fig. 1.** (a) Schematic view of top-contact OTFT using different silane modified-layer/SiO<sub>2</sub> gate insulators; (b) structure of phenyltrimethoxysilane and OTS; (c) chemical process between OTS and surface of SiO<sub>2</sub>/Si substrate; and (d) chemical process between phenyltrimethoxysilane and surface of SiO<sub>2</sub>/Si substrate.

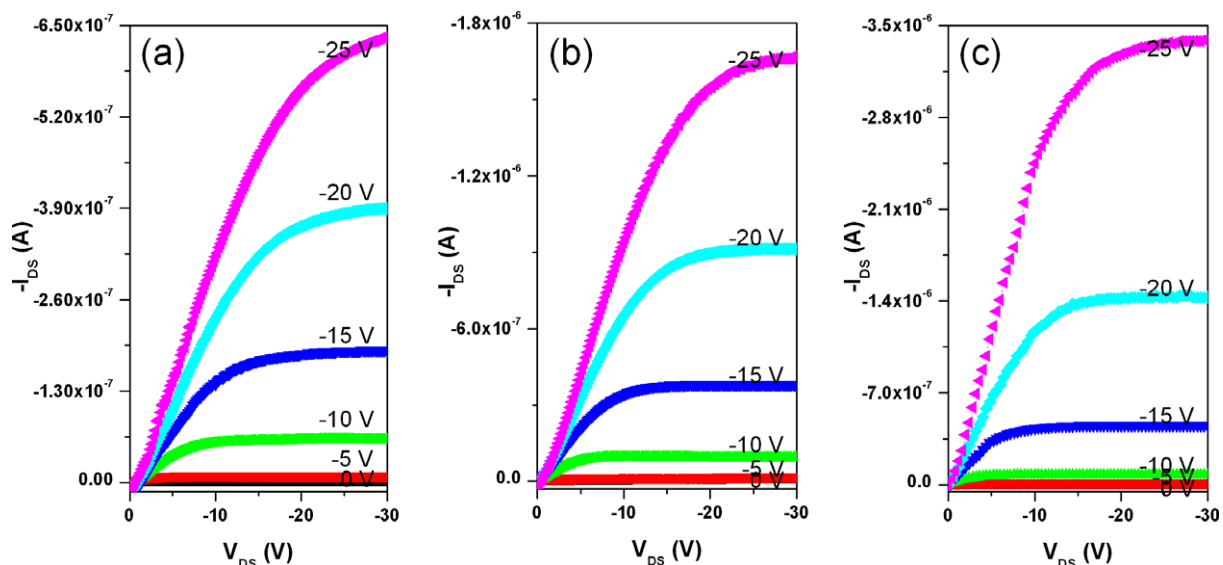


**Fig. 2.** Output current  $I_{DS}$  vs drain  $V_{DS}$  as a function of  $V_{GS}$  for top-contact pentacene OTFTs with (a) bare  $\text{SiO}_2$ , (b) OTS and (c) PhTMS-treated  $\text{SiO}_2$  gate insulator.

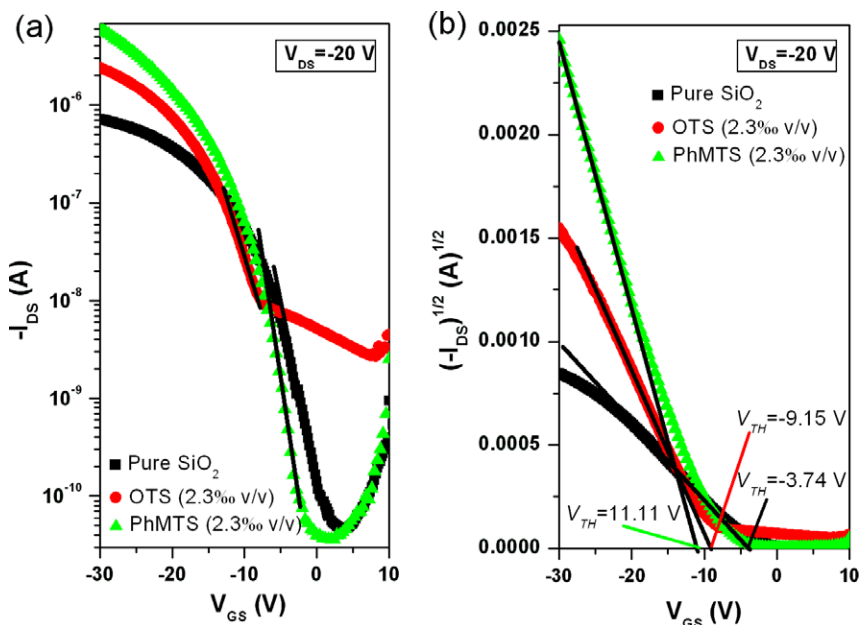


**Fig. 3.** (a) Corresponding transfer characteristics and (b) the curve of square root of drain current vs. gate voltage for OTFTs devices with various modified-layers at  $V_{DS} = -20$  V. The channel length and width are  $57 \mu\text{m}$  and  $570 \mu\text{m}$ , respectively.

**Table 1**

The electrical performance for OTFTs devices with various buffer layer at interface between pentacene and  $\text{SiO}_2$  insulators, OTFTs devices with channel width/length ratio of 10 at  $V_{DS}$  of  $-20$  V.

Sample on $\text{SiO}_2/\text{Si}$ substrate	Capacitance per unit area $C_i$ ( $\text{nF}/\text{cm}^2$ )	Field-effect mobility ( $\text{cm}^2/\text{Vs}$ )	Threshold voltage (V)	Sub-threshold slope (V/decade)	On/off current ratio
PhTMS	10.57	0.32	$-11.11$	0.42	$1.58 \times 10^5$
OTS	10.47	0.12	$-9.15$	1.53	$1.36 \times 10^3$
Bare- $\text{SiO}_2$	10.82	0.03	$-3.76$	4.11	$1.48 \times 10^4$

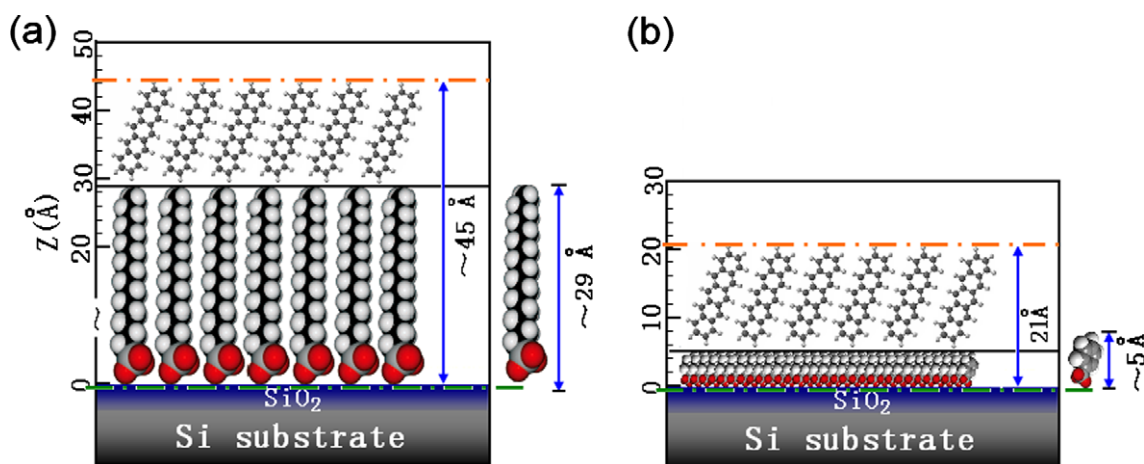


Fig. 4. Schematic view of interface between pentacene and SiO<sub>2</sub> gate insulator, (a) OTS-treated SiO<sub>2</sub> and (b) PhTMS-treated SiO<sub>2</sub> gate insulator.

carrier injection [17,18]. Fig. 3 illustrates the transfer characteristics of the OTFTs with  $V_{GS}$  swept from 10 to  $-30$  V at constant  $V_{DS}$  of  $-20$  V. The field-effect mobilities of the OTFTs were calculated in the saturation regime, as shown in Fig. 3b, using the relationship given by [19]

$$\mu_{EF} = \frac{2L}{WC_i} \left( \frac{\partial \sqrt{I_{DS}}}{\partial V_{GS}} \right)^2 \quad (1)$$

where  $I_{DS}$  and  $C_i$  are the drain current and the capacitance per unit area of the gate layer, respectively; while  $W$  and  $L$

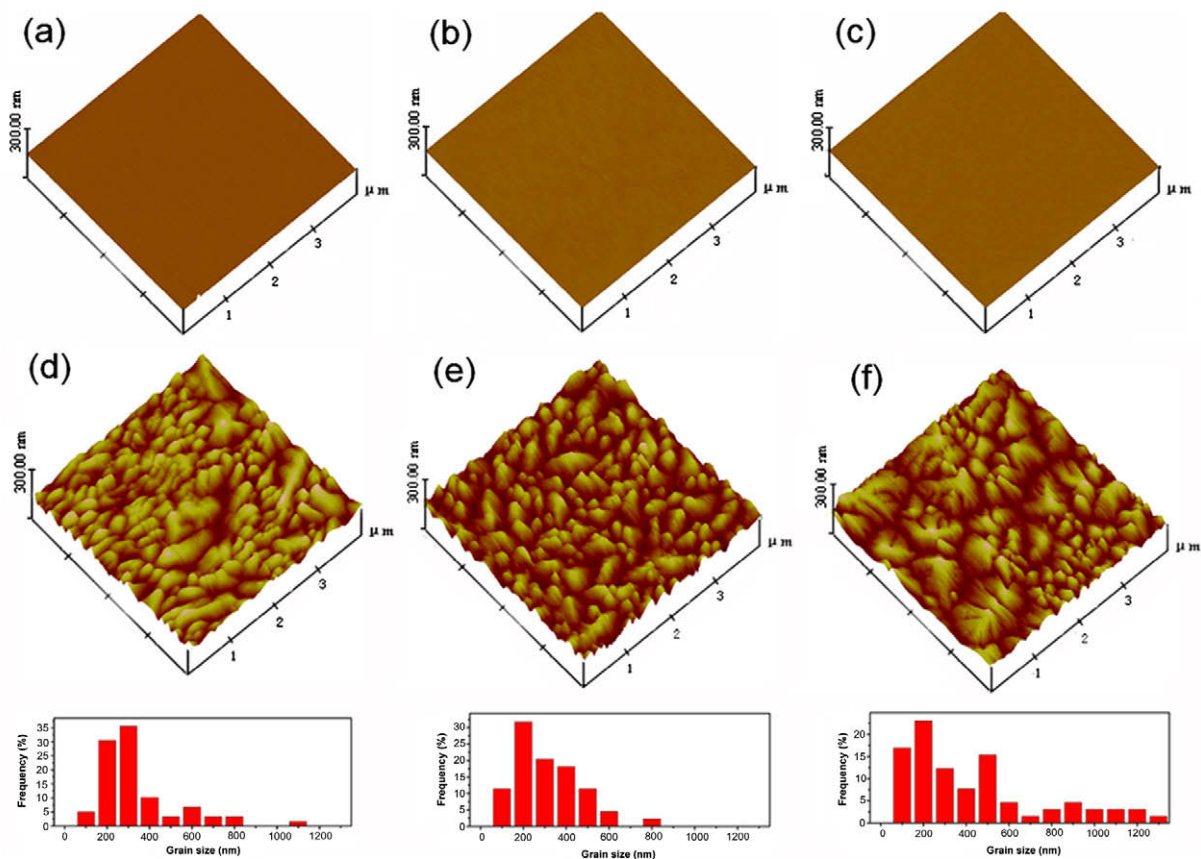


Fig. 5. Three-dimensional AFM images of different gate insulators: (a) bare SiO<sub>2</sub>/Si substrate, (b) OTS/SiO<sub>2</sub>/Si insulator, (c) PhTMS/SiO<sub>2</sub>/Si insulator; (d–f) are AFM images of pentacene film deposited on corresponding substrate and their grain size distributions. Pentacene film has an average thickness of 60 nm. The scale bar represents 4 μm × 4 μm.

are device channel width (570  $\mu\text{m}$ ) and length (57  $\mu\text{m}$ ), respectively.

From Fig. 3a and b electrical parameters of OTFTs including on/off ratio, threshold voltage and sub-threshold swing were extracted and summarized in Table 1. Fig. 3a shows the measured drain current at an applied positive gate voltage from +5 to +10 V. An *n*-type behavior of pentacene OTFTs is expected, but am-bipolar behavior is not observed because of the large electron-injection barrier from the gold electrode to the pentacene layer. For am-bipolar characteristics of a pentacene device, *n*-channel operation is only observed in a vacuum [20–22]. Therefore, the measured drain current at a positive gate voltage might come from leaks through gate insulators when the gate and drain current are considered together in Fig. 3a.

After PhTMS treatment, the carrier mobility is 0.32  $\text{cm}^2/\text{Vs}$  at  $V_{\text{DS}} = -20$  V, which is about eleven and three times higher than that without any treatment and with OTS treatment, respectively. This clearly indicates that the dielectric modification could significantly improve the carrier mobility. The sub-threshold slope is also improved to 0.42 V/decade for PhTMS-treated OFETs. Such a mobility improvement is very likely contributed from the matched surface energy and chemical functionality at the pentacene/insulator interface [23]. Static water contact angles were measured to determine the surface energy. The results show that the bare  $\text{SiO}_2$  typically has a contact angle between 20° and 25°, while OTS- and PhTMS-treated  $\text{SiO}_2$  have contact angles between 75° and 80° and between 55° and 60°, respectively, indicating that the surface en-

ergy of the PhTMS-treated  $\text{SiO}_2$  is lower than that of bare  $\text{SiO}_2$  (59.27  $\text{mJ}/\text{m}^2$ ), but higher than that of OTS-treated  $\text{SiO}_2$  (28.12  $\text{mJ}/\text{m}^2$ ), and is very close to that of pentacene films (43  $\text{mJ}/\text{m}^2$ ) [24,21]. Thus during preparation, covalent bonds can form through reactions between surface  $[-\text{OH}]$  groups on the  $\text{SiO}_2/\text{Si}$  surface and  $[-\text{Cl}, -\text{OCH}_3]$  groups of OTS and PhTMS. Fig. 4 shows the bonding structure between the molecule and the substrate surface, in which the molecular length is calculated through chemical bond length. After formation of a pre-stretched configuration with the substrate, it is possible to modify the interface by tuning the surface terminal group ( $-\text{C}_{18}\text{H}_{37}$ ,  $-\text{C}_6\text{H}_5$ ) of the modified-layer. The matched surface energy and surface terminal group could improve the crystallization of pentacene thin films, thereby, enhancing the device performance [25].

Roughness of the gate insulator surface is reported to affect the carrier mobility greatly [21]. AFM was used to investigate the effect of the dielectric surface roughness on the morphology of the grown pentacene film and the device performance. The measured three-dimensional AFM images of  $\text{SiO}_2$  gate dielectric surface with different modified-layers shown in Fig. 5a-c illustrate identical smooth surfaces with the root-mean-square (RMS) roughness ( $R_q$ ) in the range of 0.3–0.6 nm, which is very comparable to the thermal  $\text{SiO}_2$  surface ( $R_q \approx 0.4$  nm). Hence, the possibility of effects of the surface roughness of gate insulators on the morphology of the pentacene thin film and OTFT performance can be excluded for the performance improvement.

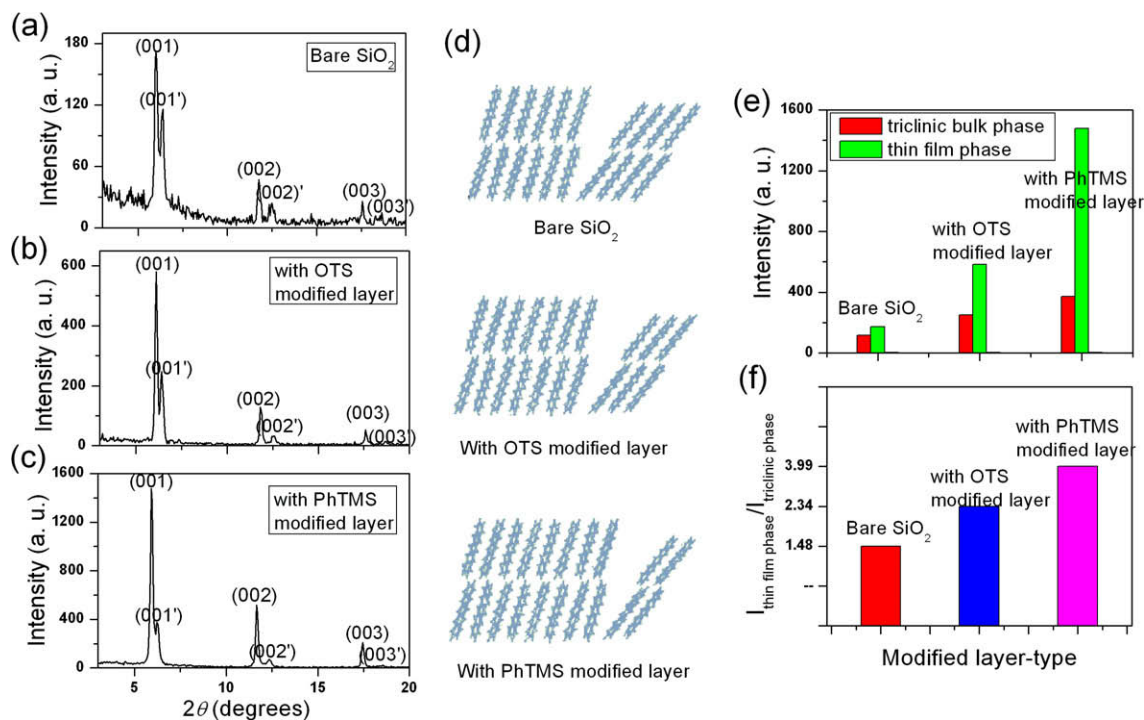


**Fig. 6.** XRD patterns of pentacene on treated- $\text{SiO}_2/\text{Si}$  substrates with various modified-layers, (a) bare  $\text{SiO}_2/\text{Si}$ ; (b) with OTS; (c) with PhTMS; (d) corresponding growth model of pentacene thin films; (e) diffraction peak intensities of “thin film” and “triclinic bulk” phase and (f) the ratio of diffraction peak intensities between  $I_{\text{thin film}}$  and  $I_{\text{triclinic bulk}}$  of pentacene films on corresponding substrates.

However, the AFM morphologies of the pentacene thin films deposited onto these physically identical gate insulator surface (Fig. 5d–f) exhibit distinct features. On PhTMS/SiO<sub>2</sub>/Si gate insulator, pentacene grains have a dendritic structure with significantly larger grains than others while having a broad size distribution range from 100 nm to 1.3 μm and each grain displays a layered structure (a series of terraces are shown in Fig. 5f). However, a dramatic morphological change with an observed large number of small grains with the size distribution from 100 nm to 600 nm appears in the pentacene film on OTS/SiO<sub>2</sub> gate insulator, as shown in Fig. 5e. Normally, the OTFT performances, particularly the carrier mobility, can be considerably improved when the grain size of the semiconductor increases, while significantly decreased with small grain size because of more grain boundaries as trap sites of charge in polycrystalline and small-molecule organic semiconductor [26,27]. This may explain why the mobility is greatly enhanced particularly by PhTMS modified-SiO<sub>2</sub>/Si

gate insulator (Fig. 5f). For more deep scientific insight, the effect of the dielectric layer modification possibly indicates that the surface modified molecules enhance the favorable crystal packing and the texture with all grains oriented into the [0 0 1] direction, approximately perpendicular to the substrate for a high degree of intermolecular  $\pi$ -orbital overlap in the plane of the film, thus boosting the carrier mobility [28].

#### 4. Growth model and structure phase transformation of pentacene films

To form the solid phase (for example “thin film” or “triclinic bulk” phase) in pentacene films [29–32], pentacene molecules are arranged in a herringbone pattern with the molecule's center at (0, 0, 0) and (1/2, 1/2, 0) (see Figs. 5 and 7e [15]). The intermolecular bonding in pentacene is a result of the dipole–dipole interactions and weak van der Waals interactions. Consequently, it can be reasonably

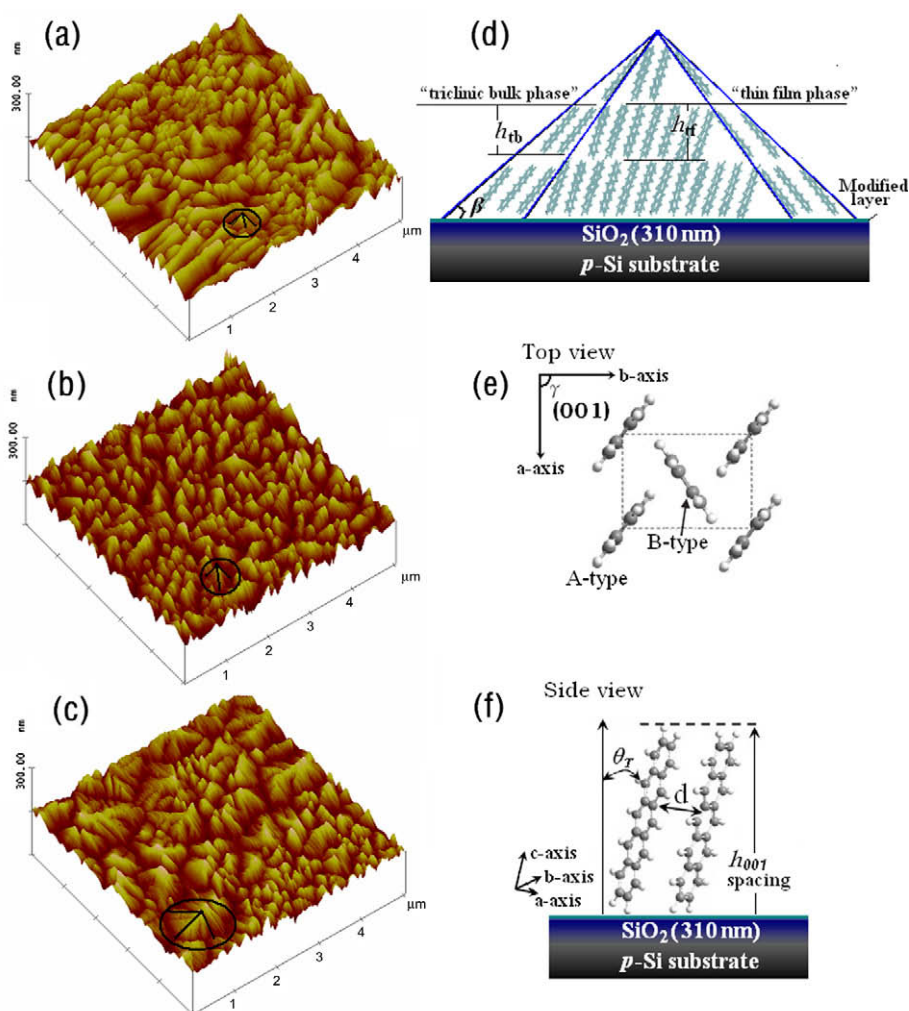


**Fig. 7.** Three-dimensional AFM images of pentacene film deposited on different gate insulators: (a) bare SiO<sub>2</sub>/Si, (b) OTS/SiO<sub>2</sub>/Si, (c) PhTMS/SiO<sub>2</sub>/Si insulator (d) the growth model of pentacene on various substrates, (e) Normal top view of the a–b planes of thin-films pentacene and (f) the side view. On SiO<sub>2</sub> substrate, grains are oriented with the a–b plane parallel to the substrate.

assumed that  $d$  varies with various modified-layers between pentacene and gate insulators. The  $d$  value could be derived from the in-plane lattice parameters ( $a, b, \gamma$ ) and the tilt angle ( $\theta_T$ ) of pentacene molecule using [33]

$$d^2 = \frac{1}{4} (\cos \theta_T)^2 [(a \sin \gamma)^2 + (b - a \cos \gamma)^2] \quad (2)$$

The in-plane lattice parameters of pentacene in its “thin film” phase ( $h_{001} = 15.4 \text{ \AA}$ ) were reported as  $a = 5.77 \text{ \AA}$ ,  $b = 7.49 \text{ \AA}$ , and  $\gamma = 91.2^\circ$ . Based on the  $h_{001}$ -spacing and the length of the pentacene molecule (ca.  $16.2 \text{ \AA}$ ), the  $\theta_T$  could be derived (see also Fig. 7) [34].

The pentacene molecules grown on the  $\text{SiO}_2$  surface are packed into a layer structure with a herringbone pattern as shown in Fig. 5d, which is further confirmed by XRD measurements (Fig. 6a) that the films consist of a dominant phase with a first-order diffraction peak of  $5.91^\circ$  corresponding to an  $h_{001}$ -spacing of  $15.4 \text{ \AA}$ , attributed to the “thin film” phase, and also a secondary phase with a second-order diffraction peak of  $6.32^\circ$  corresponding to an  $h_{001}$ -spacing of  $14.5 \text{ \AA}$ , ascribed to the “triclinic bulk” phase. The intensity of XRD spectrum for bare  $\text{SiO}_2$  seems low ( $<200$  counts). It is possibly due to larger mismatch of surface energy between pentacene and  $\text{SiO}_2$  gate insulator [32].

As shown in Fig. 7f, after OTS and PhTMS modified-layer treatment, the tilt angle ( $\theta_T$ ) of pentacene molecule from  $c$ -axis toward  $a$ -axis in lattice unit cell is decreased, resulting in the gradual transition from the “triclinic bulk” to the “thin film” phase (see Fig. 6b–d). The diffraction peak intensities of the “thin film” and “triclinic bulk” phase and their ratio for different substrates are shown in Fig. 6e and f. It is known that the “thin film” phase of pentacene is high mobility phase. Therefore, the performance improvements of OTFTs with the various modified-layer treated- $\text{SiO}_2$  insulators are mainly due to the modified-layer-driven microstructure transformation of pentacene polymorphic films and the separation distance between adjacent pentacene molecules is reduced. It is necessary to maximize the value of  $l$  ( $l$ , reflecting the strength of intermolecular electronic interactions between adjacent molecular) while the reorganization energy ( $E_i$ ) has to be low and to ensure efficient carrier transport in pentacene films [35], which already was proved by Sancho-Garcia and Olivier et al. [36,37].

Based on the experimental results and analysis above, a growth model of pentacene on various substrates is proposed as shown in Fig. 7d. At the early stage of growth, the pentacene tends to assemble vertically on the substrate to form the orthorhombic phase [37]. With formation of the grains, the grain boundaries are gradually produced along with the grain steep hillsides. Then, the pentacene grows on the inclined plane, leading to a increased  $\theta_T$  as shown in Fig. 7f. The “thin film” and “triclinic bulk” phase of pentacene films could form at a higher thickness level [38,8], and the unit cell of the crystal contains two pentacene molecules (see Fig. 7e).

## 5. Conclusions

In a brief, PhTMS was used to modify  $\text{SiO}_2$  insulator and significantly enhanced the pentacene based OTFTs. The experimental results show a decreased tilt angle ( $\theta_T$ ) of

pentacene molecules from  $c$ -axis toward  $a$ -axis after the modification of  $\text{SiO}_2$  insulator, indicating that polymorphs transformation from the “triclinic bulk” phase to the “thin film” phase and orthorhombic phase occurs. The results provide strong evidence that the performance improvement of OTFT after PhTMS modification is related to the microstructure transformation of the semiconductor. It suggests that the modified-layer may alter the molecular geometry and further induce structural phase transitions in the pentacene films for the performance improvement.

## Acknowledgements

This work was supported by the Singapore A\* STAR under Grant No: 052117 0031, the NSFC Grant No: (10774013, 10804006), 863 program Grant No: 2006AA03Z0412 and the EDSTIFBJTU Grant No: 48024.

## References

- [1] L. Herlogsson, Y.Y. Noh, N. Zhao, X. Crispin, H. Sirringhaus, M. Berggren, *Adv. Mater.* 20 (2008) 4708.
- [2] C.N. Hoth, P. Schilinsky, S.A. Choulis, C.J. Brabec, *Nano Lett.* 8 (2008) 2806.
- [3] J.A. Bardecker, H. Ma, T. Kim, F. Huang, M.S. Liu, Y.J. Cheng, G. Ting, A.K.Y. Jen, *Adv. Funct. Mater.* 18 (2008) 3964.
- [4] W.Y. Lai, R. Xia, Q.Y. He, P.A. Levermore, W. Huang, D.D.C. Bradley, *Adv. Mater.* 21 (2009) 355.
- [5] L. Torsi, G.M. Farinola, F. Marinelli, M.C. Tanese, *Nat. Mater.* 7 (2008) 412.
- [6] C.D. Sheraw, L. Zhou, J.R. Huang, D.J. Gundlach, T.N. Jackson, M.G. Kane, I.G. Hill, M.S. Hammond, J. Campi, B.K. Greening, J. Francl, J. West, *Appl. Phys. Lett.* 80 (2002) 1088.
- [7] H. Alves, A.S. Molinari, H.X. Xie, A.F. Morpurgo, *Nat. Mater.* 7 (2008) 574.
- [8] A.C. Mayer, A. Kazimirov, G.G. Malliaras, *Phys. Rev. Lett.* 97 (2006) 105503.
- [9] M.C.J.M. Vissenberg, M. Matters, *Phys. Rev. B* 57 (1998) 12964.
- [10] H. Klauk, M. Halik, U. Zschieschang, G. Schmid, W. Radlik, *J. Appl. Phys.* 92 (2002) 5259.
- [11] M. Halik, H. Klauk, U. Zschieschang, G. Schmid, C. Dehm, M. Schutz, S. Maisch, F. Effenberger, M. Brunnbauer, F. Stellacci, *Nature* 431 (2004) 963.
- [12] G.S. Tulevski, Q. Miao, A. Afzali, T.O. Graham, C.R. Kagan, C. Nuckolls, *J. Am. Chem. Soc.* 128 (2006) 1788.
- [13] D. Holmes, S. Kumaraswamy, A.J. Matzger, K.P.C. Vollhardt, *Chem. Eur. J.* 5 (1999) 3399.
- [14] I.N. Hulea, S. Fratini, H. Xie, C.L. Mulder, N.N. Iossad, G. Rastelli, S. Ciuchi, A.F. Morpurgo, *Nat. Mater.* 5 (2006) 982.
- [15] C.D. Dimitrakopoulos, A.R. Brown, A. Pomp, *J. Appl. Phys.* 80 (1996) 2501.
- [16] G.C. Yuan, Z. Xu, C. Gong, Q.J. Cai, Z.S. Lu, J.S. Shi, F.J. Zhang, S.L. Zhao, N. Xu, C.M. Li, *Appl. Phys. Lett.* 94 (2009) 153308.
- [17] M. McDowell, I.G. Hill, *Appl. Phys. Lett.* 88 (2006) 073505.
- [18] C. Boula, J.V. Davidovits, F. Rondelez, D. Vuillaume, *Phys. Rev. Lett.* 76 (1996) 4797.
- [19] G.C. Yuan, Z. Xu, S.L. Zhao, F.J. Zhang, J.Z. Huang, J.Y. Huang, X.Y. Tian, X.R. Xu, *Chin. Phys. B* 17 (2008) 3822.
- [20] E.J. Meijer, D.M. De Leeuw, S. Setayesh, E. Van Veenendaal, B.-H. Huisman, P.W.M. Blom, J.C. Hummelen, U. Scherf, T.M. Klapwijk, *Nat. Mater.* 2 (2003) 678.
- [21] S.Y. Yang, K. Shin, C.E. Park, *Adv. Funct. Mater.* 15 (2005) 1806.
- [22] J.G. Laquindanum, H.E. Katz, A. Dodabalapur, A.J. Lovinger, *J. Am. Chem. Soc.* 118 (1996) 11331.
- [23] D.H. Kim, J.A. Rogers, *Adv. Mater.* 20 (2008) 4887.
- [24] S.C. Lim, S.H. Kim, J.H. Lee, M.K. Kim, D.J. Kim, T. Zyung, *Synth. Met.* 148 (2005) 75.
- [25] M. Mezger, H. Reichert, S. Schoder, J. Okasinski, H. Schroder, H. Dosch, D. Palms, J. Ralston, V. Honkimaki, *Proc. Natl. Acad. Sci. USA* 103 (2006) 18401.
- [26] K. Yamaguchi, S. Takamiya, M. Minami, Y. Doge, Y. Nishide, H. Osuga, K. Uno, I. Tanka, *Appl. Phys. Lett.* 93 (2008) 043302.

- [27] O. Acton, G. Ting, H. Ma, J.W. Ka, H.L. Yip, N.M. Tucker, A.K.Y. Jen, *Adv. Mater.* 20 (2008) 3697.
- [28] J. Cornil, J.P. Calbert, J.L. Bredas, *J. Am. Chem. Soc.* 123 (2001) 1250.
- [29] C.C. Mattheus, G.A. de Wijs, R.A. de Groot, T.T.M. Palstra, *J. Am. Chem. Soc.* 125 (2003) 6323.
- [30] H.L. Cheng, W.Y. Chou, C.W. Kuo, Y.W. Wang, Y.S. Mai, F.C. Tang, S.W. Chu, *Adv. Funct. Mater.* 18 (2008) 285.
- [31] T. Minakata, H. Imai, M. Ozaki, K. Saco, *J. Appl. Phys.* 72 (1992) 5220.
- [32] H.L. Cheng, Y.S. Mai, W.Y. Chou, L.R. Chang, X.W. Liang, *Adv. Funct. Mater.* 17 (2007) 3639.
- [33] C.E. Bonner, C.C. Chess, C. Meegoda, S. Stefanos, G.B. Loutts, *Opt. Mater.* 26 (2004) 17.
- [34] L.F. Drummy, D.C. Martin, *Adv. Mater.* 17 (2005) 903.
- [35] Y. Olivier, V. Lemaire, J.L. Bredas, J. Cornil, *J. Phys. Chem. A* 110 (2006) 6356.
- [36] J.C. Sancho-Garcia, G. Horowitz, J.L. Bredas, J. Cornil, *J. Chem. Phys.* 119 (2003) 12563.
- [37] S.E. Fritz, S.M. Martin, C.D. Frisbie, M.D. Ward, M.F. Toney, *J. Am. Chem. Soc.* 126 (2004) 4084.
- [38] F. Dinelli, M. Murgia, P. Levy, M. Cavallini, F. Biscarini, D.M.D. Leeuw, *Phys. Rev. Lett.* 92 (2004) 116802.

Inverse photoemission spectroscopy (IPES) is one of the frequently used techniques to determine directly the electron affinity in solids [3]. This gives electron transport level, namely, the LUMO (lowest unoccupied molecular orbital level) level occupied by one electron and the HOMO is filled. Exciton level, namely, LUMO level occupied by an electron which is bound to the hole in the HOMO level is the optical transition energy determined by absorption/emission spectroscopy. However concern has been raised on the large exciton binding energies in organic solids which makes the transport level and exciton level to be different [4]. It is of interest to compute all the energy levels for organic solids by a method of calculation uniformly applied to a wide variety of molecules and compare with experimental values. In a recent report electron affinity of isolated molecule was computed theoretically and compared with the value in solid state with an assumption that 'solid state effect' is same for all molecules [4]. This assumption may not hold well for a wide range of molecules that are used in organic electronics. For example, polarization energy of organic molecules in solid state

can vary from 0.9 eV to 3.0 eV [5,6]. Thus, a realistic modeling of solid state effect in theoretical calculations is required. The calculation must take into consideration distribution of charge in the molecule and 'solvation' of the molecule in solid by molecules of its own type. In this context, polarizable continuum model (PCM) is shown to be successful in recent studies [7–9].

In a recent paper [9], we reported calculation of ionization potential (HOMO level) in solid state using (density functional theory) DFT and PCM. In continuation of the previous work, a method is now described to determine the electron affinity of organic molecules in solid state using DFT and PCM. We show that the computationally determined EA for 13 organic molecular solids agree well with the experimental values, validating the proposed method. In addition to the determination of EA, we also discuss calculation of the optical band gap, transport gap ( $E_t$ ) and exciton binding ( $E_b$ ) energies of the molecules. An important feature of our method is that no experimental data for the molecule, other than the molecular structure, is required to determine the EA value in solid state.

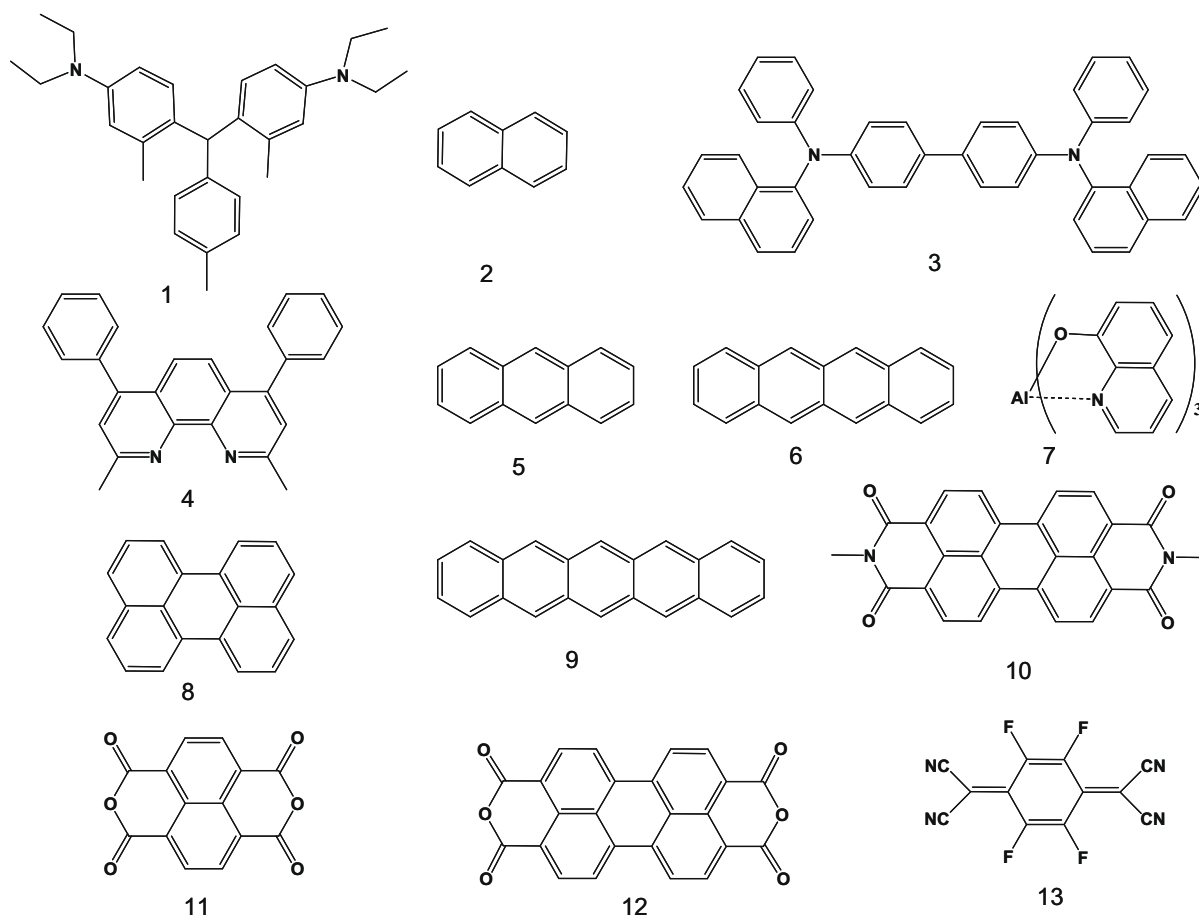


**Fig. 1.** (1) Bis[4-(*N,N*-diethylamino)-2-methylphenyl](4-methylphenyl)methane (MPMP) (2) Naphthalene (3) *N,N'*-bis-(1-naphthyl)-*N,N'*-diphenyl-[1,1'-biphenyl]-4,4'-diamine (NPD) (4) 4,7-diphenyl-1,10-phenanthroline (BCP) (5) Anthracene (6) Tetracene (7) *Tris*(8-hydroxyquinolate)aluminium(III)  $AlQ_3$  (8) Perylene (9) Pentacene (10) *N*-methyl Perylene tetracarboxylic diimide (mPTCDI) (11) Naphthalene tetracarboxylic dianhydride (NTCDA) (12) Perylene tetracarboxylic dianhydride (PTCDA) (13) 2,3,5,6-tetrafluoro-7,7,8,8-tetracyano-*p*-quinodimethane (F4TCNQ).



## 2. Methods of computation

Thirteen organic molecules, for which experimental values of electron affinity of solid films are known, were chosen for this study. Density functional theory (DFT) was used in all the calculations using Gaussian03 [10]. The DFT method used here is based on the hybrid B3LYP functional [11]. The geometries of all the molecules were optimized at 6-31G (d) basis functions. Molecular cavity for polarizable continuum model (PCM) was built by following the new definition using united atom model [12], i.e., by putting a sphere around each atom except hydrogen. Hydrogen atoms are enclosed in the sphere of the atom to which they are bonded.

The molecule in solid was considered as solvated by molecules of its own type. The solvent in the PCM calculation is defined by the dielectric constant, the number of solvent molecules in unit volume and radius of the molecule. Following methods were used to obtain these values. The dielectric constant,  $\epsilon$  was obtained by Clausius–Mossotti equation

$$\frac{\epsilon - 1}{\epsilon + 2} = \frac{4\pi}{3} \frac{\rho}{M} N_A \alpha,$$

where  $\rho$ ,  $M$ ,  $N_A$  and  $\alpha$  are the density of material, molecular mass, Avogadro number and the electronic polarizability, respectively.  $\rho N_A/M$  is reciprocal of the molecular volume. Molecular volume was obtained at 6-31G (d) level (tight option was taken in all the calculation for better accuracy). Isotropic polarizability (at zero frequency) of molecules was calculated for the optimized geometry of the molecules at 6-31G (d) level. Radius of the molecule is defined as the radius of a sphere which has equivalent volume of the concerned molecule.

Single point energy of the molecule was calculated at 6-311++G(d,p) level with PCM, The single negative state with

the same molecular geometry of the molecule was also calculated using same basis set and PCM. The difference in energies gave the vertical electron affinity in the solid state. Single point calculation of the molecule is also done without PCM, which gives the gas phase electron affinity. Ionization potentials in the solid state were also determined using the method reported earlier [9]. Singlet optical transition energy was calculated using time-dependent density functional theory (TD-DFT) at 6-311++G(d,p) level and PCM. Singlet optical transition energy for isolated molecule was also determined using TD-DFT at the same basis set level.

## 3. Results and discussion

Fig. 1 shows the molecular structures for 13 organic molecules, which are commonly used in organic electronics for different purposes. In organic solids, molecules are solvated by the molecules of its own type. The solvent is modeled as an isotropic, continuous dielectric that surrounds a solute cavity. This simple model is appropriate for amorphous and glassy solid films. Though experimental values of dielectric constant and density for some molecules in solid state are known, we used consistently the calculated values for dielectric constant and molecular volume, so that calculation can be done for any new molecule without reference to the experimental value.

Table 1 shows the calculated values of dielectric constant, number of molecules in  $1000 \text{ \AA}^3$ , radius of the molecule, EA in gas phase and solid state. Experimental values of EA reported for these molecules in solid state are also given. Fig. 2 shows a plot between calculated and experimental value of electron affinity in solid state. The plot shows an excellent linear correlation. The slope of the fitted line is  $1.05 \pm 0.05$ , the intercept value is  $0.05 \pm 0.13$  and the correlation coefficient  $r^2 = 0.988$ . This correlation

**Table 1**

Calculated values for dielectric constant, number of molecules in  $1000 \text{ \AA}^3$ , radius of the molecule, calculated values of EA in gas phase and EA in solid using PCM and experimental EA values of solid films using IPES.

Compound	Dielectric constant ( $\epsilon$ )	Molecules in $1000 \text{ \AA}^3$	Radius of molecule ( $\text{\AA}$ )	EA in gas phase calculation (eV)	EA in solid calculation (eV)	EA by IPES (eV)	Reference for EA by IPES
(1) MPMP	2.61	1.61	5.290	-0.29	0.22	0.05	[16]
(2) Napthalene	2.43	5.27	3.564	-0.30 <sup>a</sup>	0.8	1.11	[6]
(3) NPd	4.21	1.60	5.350	0.62	1.41	1.52	[17]
(4) BCP	2.91	2.05	4.883	0.41	1.34	1.56	[18]
(5) Anthracene	2.95	4.10	3.873	0.51 <sup>b</sup>	1.62	1.7	[6]
(6) Tetracene	3.69	3.44	4.107	1.07 <sup>c</sup>	2.2	1.8	[6]
(7) Alq <sub>3</sub>	2.69	1.78	5.118	0.91	1.66	1.96	[17]
(8) Perylene	3.45	3.24	4.193	0.94 <sup>d</sup>	2.05	2.5	[6]
(9) Pentacene	4.82	3.02	4.291	1.49 <sup>e</sup>	2.63	2.75	[19]
(10) m PTCDI	3.52	2.00	4.920	2.64	3.5	3.95	[20]
(11) NTCDA	2.89	3.86	3.952	2.90	3.75	4.02	[18]
(12) PTCDA	4.63	2.75	4.429	3.07	3.86	4.10	[20]
(13) F4TCNQ	3.75	3.59	4.051	4.16	5.03	5.24	[21]

Reported values of EA, theoretical Ref. [13] and experimental in Ref. [14].

<sup>a</sup> -0.26, -0.19 eV.

<sup>b</sup> 0.53, 0.57 eV.

<sup>c</sup> 1.08, 1.04 eV.

<sup>d</sup> NA, 0.96 eV.

<sup>e</sup> 1.479, 1.35 eV.

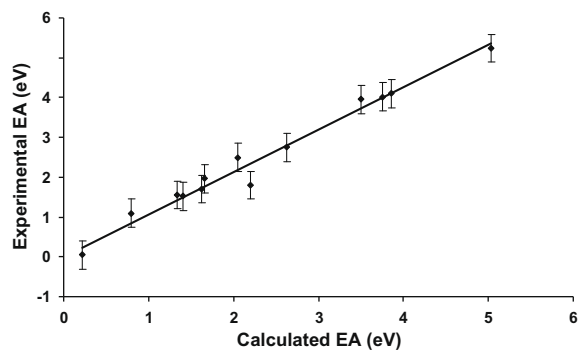


Fig. 2. Plot of calculated electron affinity using DFT and PCM with experimental values for 13 organic molecules in solid state (see Table 1).

shows that it is possible to determine the electron affinity of organic molecules in solid state within  $\pm 0.35$  eV, which is the typical error associated with the experimental values.

For the sake of comparison, EA values were calculated for isolated molecules in gas phase, which are also shown in Table 1. It is gratifying to note that the calculated values of EA in gas phase for some of the molecules match well (see Table 1) with the calculated values of adiabatic EA using DFT, reported earlier [13]. These values are also close to the experimental values in gas phase compared therein [13,14]. The large difference between EA value of molecules in isolated condition and solid state shows that the 'solvation' effect on the value of EA is quite substantial.

Ionization potential for the 13 molecules in solid state were determined by a similar method, reported earlier [9]. The difference in EA and IP is the transport gap ( $E_t$ ) in organic solid (Table 2), which is the energy difference between free electron and free hole levels in organic solid. Fig. 3 shows a linear correlation with near unity slope between experimentally obtained transport gap and computationally determined transport gap. This result shows that calculated IP values are independently in good agreement with experimental values. Transport gap in molecular solids is an important parameter as it gives the minimum

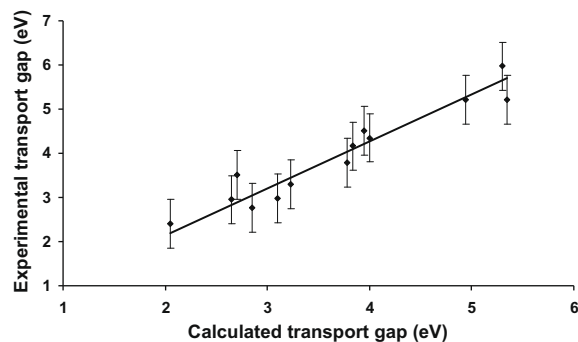


Fig. 3. Plot of calculated transport gap with experimental values (UPS and IPES) for 13 organic molecules in solid state (see Table 2).

energy required for the formation of a free electron and hole pair.

Time dependent DFT (TD-DFT), together with PCM was shown to be a successful method to compute optical transitions in aqueous and non-aqueous solutions [15]. Thus, lowest energy singlet optical transitions for the 13 organic molecules in solid state were calculated using TD-DFT and PCM as the 'solvation' model. Table 2 shows the lowest optical transition energy ( $E_{opt}$ ) in solid state as well as the value in gas phase for isolated molecule. The difference in energy between optical transition of isolated molecule and 'solvated' molecule is small (0–0.15 eV). In solids, the optical transition is associated with electronic transition. For the rest of the paper, the lowest energy optical transition is referred to as the optical band gap or exciton level in solids. For all the molecules, calculated optical band gap ( $E_{opt}$ ) in solid state is less than the calculated transport gap ( $E_t$ ) and the difference is the exciton binding energy. It may be noted that the exciton binding energy mainly depends on the dielectric constant of the material, molecular size and charge distribution on the molecule. Because of the molecular nature of organic solids and low dielectric constant the binding energy is high for the 13 molecules (0.5–1.7 eV).

Pentacene (planar molecule) and Alq<sub>3</sub> (non-planar molecule) are studied extensively for which physical and opti-

Table 2

Calculated values of IP in solid using PCM, experimental IP values of solid films using UPS, transport gap ( $E_t$ ), optical transition ( $E_{opt}$ ) in gas and solid phase, and exciton binding energy ( $E_b$ ).

Compound	IP calculation (eV)	IP UPS (eV)	Reference for IP by UPS	$E_t$ UPS and IPES	$E_t$ calculation (eV)	$E_{opt}$ gas phase calculation (eV)	$E_{opt}$ with PCM calculation (eV)	$E_b$ (eV)
(1) MPMP	5.44	5.4	[16]	5.35	5.22	4.11	4.01	1.21
(2) Naphthalene	6.77	6.4	[5]	5.29	5.97	4.34	4.31	1.66
(3) NPD	5.20	5.3	[22]	3.78	3.79	2.97	2.97	0.82
(4) BCP	6.56	6.5	[23]	4.94	5.22	3.75	3.75	1.47
(5) Anthracene	5.97	5.7	[5]	4.0	4.35	3.19	3.16	1.19
(6) Tetracene	5.40	5.1	[5]	3.3	3.20	2.43	2.40	0.80
(7) Alq <sub>3</sub>	5.82	5.8	[23]	3.84	4.16	2.71	2.83	1.33
(8) Perylene	5.56	5.2	[5]	2.7	3.51	2.77	2.69	0.82
(9) Pentacene	5.03	4.85	[5]	2.1	2.4	1.89	1.85	0.55
(10) m PTCDI	6.44	6.6	[20]	2.65	2.94	2.36	2.26	0.68
(11) NTCDA	8.26	7.97	[18]	3.95	4.51	3.38 <sup>a</sup>	3.29 <sup>a</sup>	1.22
(12) PTCDA	6.62	6.62	[20]	2.52	2.76	2.39	2.28	0.48
(13) F4TCNQ	8.01	8.34	[21]	3.1	2.98	2.62 <sup>a</sup>	2.48 <sup>a</sup>	0.50

<sup>a</sup> Very low oscillator strength.

cal data are reported. A comparison of calculated and experimental values are as follows. Calculated vs experimental, Pentacene. Dielectric constant: 4.82 vs. 4 [24]; number of molecules per  $1000 \text{ \AA}^3$ : 3.02 vs. 2.87 [25], (based on density  $1.33 \text{ g/cm}^3$ ); IP: 5.03 vs. 4.85 eV [5]; EA: 2.63 vs. 2.75 eV [19];  $E_{\text{opt}}$ : 1.85 vs. 1.9 eV [26].  $\text{Alq}_3$ : dielectric constant: 2.69 and  $3.0 \pm 0.3$  [27]; number of molecules per  $1000 \text{ \AA}^3$ : 1.78 vs. 1.68 [28], (based on density  $1.282 \text{ g/cm}^3$ ); IP: 5.82 vs. 5.80 eV [23]; EA: 1.66 vs. 1.96 eV [17];  $E_{\text{opt}}$ : 2.83 vs.  $2.7 \pm 0.1$  eV [29]. These molecules are known to be polymorphic crystalline materials. Considering that the experimental values are for crystalline solid and the calculated values are appropriate for amorphous/glassy solid the agreement is reasonable within  $\pm 15\%$  for the energy level parameters.

The above results and discussions establish that energy level parameters of organic molecular solids which are important for organic electronics can be calculated with reasonable accuracy using molecular structure as the only input in the calculation. However, precise calculation of energy levels, especially for anion radicals, will require special attention to specific wavefunction associated with the odd electron [30,31].

#### 4. Conclusions

A method is described for theoretical calculation of realistic electron affinity, ionization potential, transport gap, optical band gap (exciton energy) and exciton binding energy of organic molecules in solid state using the DFT, TD-DFT method and polarizable continuum model. This method gives a good estimate of all the energy levels in organic solids. The method requires the molecular structure as the only input and therefore a very useful method to design molecules for organic electronics.

#### Acknowledgements

The authors wish to thank Prof. K.L. Narasimhan for useful discussion and suggestions.

#### References

- [1] J. Shinar, *Organic Light-Emitting Devices*, Springer-Verlag, New York, 2003.
- [2] K. Walzer, B. Maennig, M. Pfeiffer, K. Leo, *Chem. Rev.* 107 (2007) 1233.
- [3] I.G. Hill, A. Kahn, Z.G. Soos, R.A. Pascal Jr., *Chem. Phys. Lett.* 327 (2000) 181.
- [4] P.I. Djurovich, E.I. Mayo, S.R. Forrest, M.E. Thompson, *Org. Electron.* 10 (2009) 515.
- [5] N. Sato, K. Seki, H. Inokuchi, *J. Chem. Soc., Faraday Trans.* 77 (1981) 1621.
- [6] K.H. Frank, P. Yannoulis, R. Dudde, E. Koch, *J. Chem. Phys.* 89 (1988) 7569.
- [7] J. Tomasi, B. Mennucci, R. Cammi, *Chem. Rev.* 105 (2005) 2999.
- [8] S. Miertus, E. Scrocco, J. Tomasi, *Chem. Phys.* 55 (1981) 117.
- [9] P.K. Nayak, N. Periasamy, *Org. Electron.* 10 (2009) 532.
- [10] M.J. Frisch et al., *Gaussian 03, Revision C.02*, Gaussian Inc., Wallingford, CT, 2004.
- [11] C.J. Cramer, *Essentials of Computational Chemistry*, Wiley, England, 2003.
- [12] V. Barone, M. Cossi, J. Tomasi, *J. Chem. Phys.* 107 (1997) 3210.
- [13] A. Modelli, L. Mussoni, D. Fabbri, *J. Phys. Chem. B* 110 (2006) 6482.
- [14] L. Crocker, T. Wang, P. Kebarle, *J. Am. Chem. Soc.* 115 (1993) 7818.
- [15] L.Y. Wang, Q.W. Chen, G.H. Zhai, Z.Y. Wen, Z.X. Zhang, *J. Mol. Struct.: THEOCHEM* 778 (2006) 15.
- [16] Y. Wang, W. Gao, S. Braun, W.R. Salaneck, F. Amy, C. Chan, A. Kahn, *Appl. Phys. Lett.* 87 (2005) 193501.
- [17] I.G. Hill, A. Kahn, J. Cornil, D.A. dos Santos, J.L. Bredas, *Chem. Phys. Lett.* 317 (2000) 444.
- [18] C.K. Chan, E.G. Kim, J.L. Bredas, A. Kahn, *Adv. Funct. Mater.* 16 (2006) 831.
- [19] C.D. Lindstrom, M. Muntwiler, X.Y. Zhu, *J. Phys. Chem. B* 111 (2007) 6913.
- [20] D.R.T. Zahn, G.N. Gavrila, M. Gorgoi, *Chem. Phys.* 325 (2006) 99.
- [21] W.Y. Gao, A. Kahn, *Org. Electron.* 3 (2002) 53.
- [22] B.W.D. Andrade, S. Datta, S.R. Forrest, P. Djurovich, E. Polikarpov, M.E. Thompson, *Org. Electron.* 6 (2005) 11.
- [23] I.G. Hill, A. Kahn, *J. Appl. Phys.* 86 (1999) 4515.
- [24] T. Li, J.W. Balk, P.P. Ruden, I.H. Campbell, D.L. Smith, *J. Appl. Phys.* 91 (2002) 4312.
- [25] R.B. Campbell, J.M. Robertson, *Acta Crystallogr.* 15 (1962) 289.
- [26] M. Knupfer, H. Berger, *Chem. Phys.* 325 (2006) 92.
- [27] R.L. Martin, J.D. Kress, I.H. Campbell, D.L. Smith, *Phys. Rev. B: Condens. Matter* 61 (2000) 15804.
- [28] M.W. Shina, H.C. Lee, K.S. Kim, S. Lee, J. Kim, *Thin Solid Films* 363 (2000) 244.
- [29] S.Y. Kim, S.Y. Ryu, J.M. Choia, S.J. Kanga, S.P. Parka, S. Ima, C.N. Whanga, D.S. Choi, *Thin Solid Films* 398–399 (2001) 78.
- [30] M. Guerra, *J. Phys. Chem. A* 103 (1999) 5983.
- [31] M. Guerra, *J. Phys. Chem. A* 101 (1997) 7874.

but has been found to improve by two to three orders (300–600 S/cm) by adding high boiling point polar compounds or solvents (diethylene glycol, ethylene glycol, dimethylsulfoxide, sorbitol, mannitol, glycerol) into the solution mixture. The exact reason for the improvement is still unclear, but has been suggested to be linked to changes in the PEDOT morphology and chain interaction [16].

There have been many demonstrations of utilizing PEDOT:PSS as a replacement to ITO as the transparent anode electrode in the conventional device architecture, however, these electrodes show a much lower conversion efficiency compared to ITO due to the lower conductivity of the PEDOT:PSS [17–19]. Recently, it was demonstrated by improving the PEDOT:PSS conductivity through processing with a high boiling point solvent, these organic polymer electrodes could reach efficiencies as high as 3% [3]. The top cathode electrode in these devices is still deposited by high vacuum which makes the processing less ideal for low-cost solar cells. To avoid using high vacuum to deposit the top electrode, an inverted architecture can be used which uses a high work function metal anode (Ag, Au) to collect holes and an metal oxide (TiO<sub>2</sub>, ZnO) as an electron selective layer at the ITO interface to collect electrons. Previously, we have demonstrated that this type of unencapsulated inverted architecture solar cell using an evaporated Ag electrode stored 40 days in ambient retains over 80% of its conversion efficiency [20]. Furthermore, we demonstrated the possibility to utilize non-vacuum solution processible Ag nanoparticles as the top electrode in inverted solar cells by spraycoating leading to efficiencies as high as 3% [21]. It has already recently been demonstrated that PEDOT:PSS can also be used as the replacement anode electrode (energy level of  $-5.1$  eV) in inverted solar cells by spraycoating the polymer. However, due to the thick films formed from spraycoating, the electrodes are non-transparent and require high vacuum to remove excess moisture to improve the performance [22]. There have been currently no studies on utilizing PEDOT:PSS as a replacement cathode electrode to replace ITO as the transparent charge collecting contact in inverted solar cells.

This letter reports on the replacement of the ITO transparent conducting oxide electrode with a solution processible PEDOT:PSS electrode as the electron collecting cathode in inverted solar cells. The thickness of the PEDOT:PSS electrode was varied showing that the thickness can affect both the transparency and sheet resistance of the electrode

and therefore the final performance of the solar cell. These electrodes were also applied to flexible polymer substrates showing similar performance to glass substrates. These inverted flexible substrate PEDOT:PSS electrode devices show  $\sim 20\%$  lower in conversion efficiency compared to ITO based flexible substrate inverted devices. Cyclic bending tests were performed on these flexible substrates showing slight performance degradation from the PEDOT:PSS based electrodes while the ITO based electrodes show significant degradation after 300 bend cycles. PEDOT:PSS was also used to replace the anode Ag electrode in ITO based inverted solar cells demonstrating a semi-transparent solar cell. The semi-transparency of these cells allows for new potential power generating applications such as solar windows or other applications that require semi-transparency. Additionally, both the top anode and bottom cathode electrodes were replaced with PEDOT:PSS demonstrating a completely solution processed semi-transparent inverted solar cell.

The inverted device architectures that were used in this study are shown in Fig. 1. To fabricate the ITO electrode based inverted solar cells, ITO-coated glass substrates ( $15 \Omega/\square$ ) and ITO-coated plastic substrates ( $60 \Omega/\square$ ) (Bay-view Optics) were cleaned with detergent, de-ionized water, acetone, and isopropyl alcohol. A thin layer of ZnO nanoparticles (ZnO-NPs) ( $\sim 50$  nm), synthesized using the method described by Beek et al. [23], was spin-coated onto ITO-coated glass. A monolayer of C<sub>60</sub>-SAM was then deposited as previously reported to improve the contact properties between the metal oxide and the active layer. [24,25]. Afterward, a chlorobenzene solution of poly(3-hexylthiophene) (P3HT) (Rieke Metals) and [6,6]-phenyl C<sub>61</sub>-butyric acid methyl ester (PCBM) (American Dye Source) (60 mg/ml) with a weight ratio of (1:0.6) was spin-coated on the ZnO modified layer to achieve a thickness of ( $\sim 210$  nm) and annealed at 160 °C for 10 min in an Ar filled glovebox. After annealing, PEDOT:PSS (CLEVIOS™ P VP Al 4083) was spin-coated onto the active layer to achieve a thickness of  $\sim 50$  nm and annealed for 10 min at 120 °C. The silver electrode was vacuum deposited (100 nm) at a pressure of  $1 \times 10^{-6}$  torr to complete the device. For PEDOT:PSS electrode based inverted solar cells, glass and plastic substrates were cleaned with detergent, de-ionized water, acetone, and isopropyl alcohol. The substrates were treated by O<sub>2</sub> plasma for 2 min to improve wettability of the PEDOT:PSS solution. A solution of PEDOT:PSS (CLEVIOS™ PH500) with the addition of 5% DMSO was sonicated

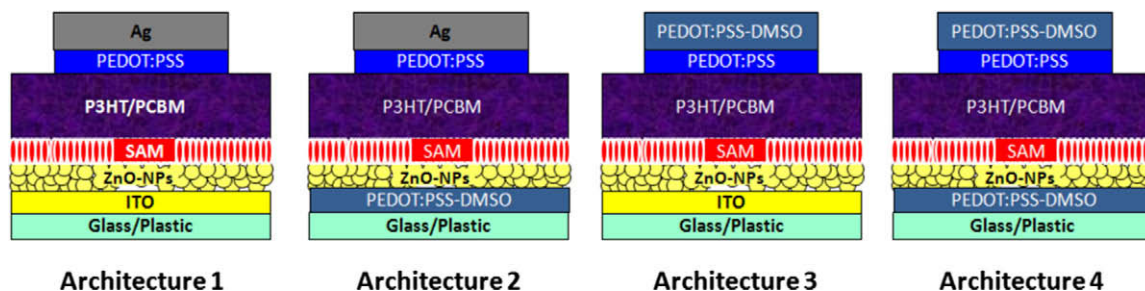
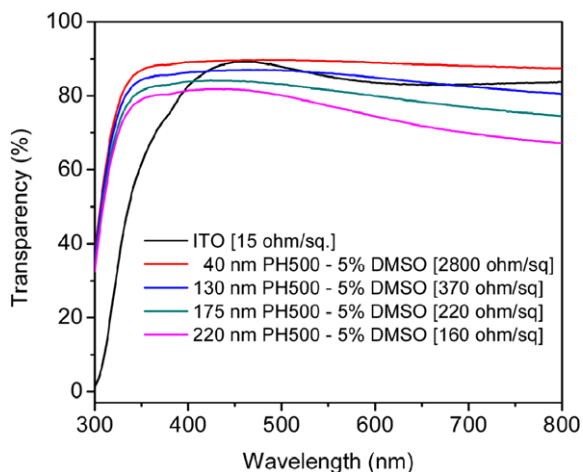
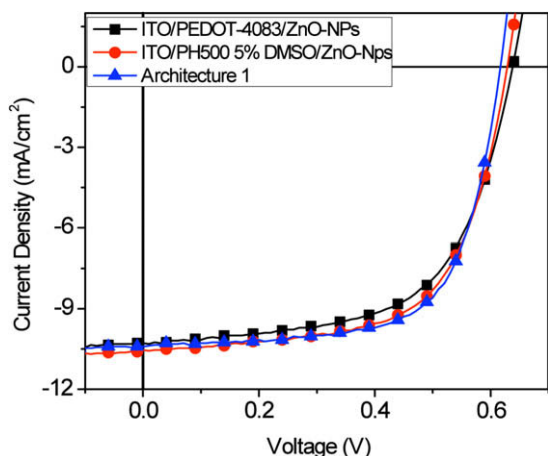


Fig. 1. Device architectures of the inverted solar cells using various cathode and anode electrodes.



**Fig. 2.** Transparency vs. wavelength of varying thicknesses of PEDOT:PSS - 5% DMSO electrodes on glass as compared to transparency of ITO on glass as referenced against air. Legend also indicates corresponding sheet resistances obtained as measured by 4-point probe.



**Fig. 3.** Illuminated  $J$ - $V$  characteristics of functioning inverted devices fabricated on ITO substrates with an  $\sim 80$  nm PEDOT:PSS CLEVIOS™ P VP Al 4083 or CLEVIOS™ PH500 with 5% DMSO inserted between the ITO and ZnO-NPs as compared to inverted devices with only ITO and ZnO-NPs.

for 5 min prior to use. For the first layer ( $\sim 40$  nm), the PEDOT:PSS solution was spin-coated onto the  $O_2$  plasma treated substrates at 7 krpm for 30 s and annealed at  $120^\circ\text{C}$  for a 2 min. Subsequent PEDOT:PSS layers were spin-coated at 2 krpm for 20 s and annealed at  $120^\circ\text{C}$  for a 2 min to achieve the desired thickness ( $\sim 130$  nm,  $\sim 175$  nm,  $\sim 220$  nm). The final PEDOT:PSS layers were annealed for 10 min at  $120^\circ\text{C}$  prior to depositing the rest of the layers as described in the ITO-based devices to complete the device. To deposit the top PEDOT:PSS anode electrodes for the semi-transparent devices, a patterned PDMS stamp was pressed onto the substrates of the top buffer PEDOT:PSS (CLEVIOS™ P VP Al 4083) and heated at  $120^\circ\text{C}$  for 30 s. After which, the sample was removed from the hotplate and the PDMS stamp was peeled off removing only the PEDOT:PSS from the active layer in contact with the stamp leaving behind a patterned PEDOT:PSS layer. Solutions of the PEDOT:PSS and DMSO were spin-coated at 3–5 krpm which coats only the area with the patterned PEDOT:PSS. Multiple PEDOT:PSS layers were built up by annealing the layers at  $120^\circ\text{C}$  for 2 min prior to spincoating the next layer. The unencapsulated solar cells were tested under ambient conditions using a Keithley 2400 SMU and an Oriel Xenon lamp (450 W) with an AM1.5 filter. A mask was used to define the device illumination area of  $0.0314\text{ cm}^2$  to minimize photocurrent generation from the edge of the electrodes [26,27]. The light intensity was calibrated to  $100\text{ mW/cm}^2$  using a calibrated silicon solar cell with a KG5 filter which has been previously standardized at the National Renewable Energy Laboratory.

To evaluate the possibility for using PEDOT:PSS as a transparent electrode to replace ITO, both the transparency and sheet resistance of different thicknesses of PEDOT:PSS processed with DMSO were measured. Fig. 2 shows the transparency as measured by UV-Vis spectroscopy of various thicknesses of PEDOT:PSS on glass substrates referenced against air which were compared to ITO-coated glass substrates. A PEDOT:PSS layer that is  $\sim 130$  nm thick has comparable transparency to the ITO-coated glass substrate. However, the sheet resistance of the PEDOT:PSS layer as measured by four point probe is  $\sim 25$  times higher than that of ITO ( $15\ \Omega/\square$ ). Thicker PEDOT:PSS layers show a reduction in sheet resistance to as low as  $160\ \Omega/\square$  with a

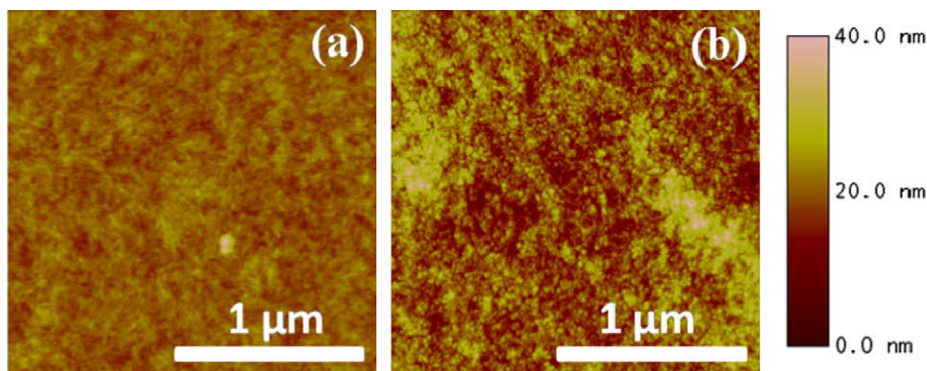


**Fig. 4.** (a) AFM image of  $\sim 130$  nm PEDOT:PSS - 5% DMSO layer coated onto glass. (b) AFM image of ZnO-NPs spin-coated on top of the PEDOT:PSS - 5% DMSO electrode.

~220 nm thick film, but also show a decrease in transparency due to the absorbance from the PEDOT:PSS film.

Replacement of ITO electrode with PEDOT:PSS as the anode has already been demonstrated in conventional architecture devices, but there has not been any study utilizing it as a cathode to collect electrons. To assess the feasibility of using PEDOT:PSS as a cathode, inverted solar cells were fabricated by spincoating a thick ~80 nm PEDOT:PSS layer from CLEVIOS™ P VP Al 4083 or CLEVIOS™ PH500 with 5% DMSO onto ITO-coated glass substrates prior to spincoating the ZnO-NPs electron selective layer followed by the rest of the device layers as described in the experimental section. Interestingly, the inverted solar cells with the PEDOT:PSS inserted between the ITO and ZnO-NPs layers behaved similarly to devices without the PEDOT:PSS layer as can be seen by Fig. 3. It has already been shown in literature that the interface contact between the heavily p-doped PEDOT:PSS and the unintentionally heavily n-doped ZnO in solar cells can be ohmic leading to minimal energy losses and minimal degradation of the voltage in the cell [28]. From this result and finding, “ITO-free” inverted solar cells using PEDOT:PSS as the cathode and ZnO-NPs as the electron selective layer were investigated. An atomic force microscopy image of a ~130 nm PEDOT:PSS film on glass in Fig. 4a shows a relatively smooth topography having a surface roughness of 1.7 nm RMS. Fig. 4b shows a much rougher surface topography (4.1 nm RMS) and different morphology after spincoating the ZnO-NPs on top of the PEDOT:PSS layer signifying that the ZnO-NPs layer is coated on top.

The illuminated  $J$ - $V$  characteristics of the inverted solar cell devices fabricated with different electrode PEDOT:PSS thicknesses as compared to ITO-based devices are shown in Fig. 5a and Table 1 summarizes these device performance parameters. Devices fabricated using a ~40 nm thick PEDOT:PSS as the electrode had a short circuit current ( $J_{sc}$ ), fill factor (FF), and power conversion efficiency (PCE) of 9.59 mA/cm<sup>2</sup>, 39.4%, and 2.32% respectively. Increasing the PEDOT:PSS electrode thickness to ~130 nm lead to an improvement in the overall PCE reaching ~3.08%, however a lowering of the  $J_{sc}$  to 9.41 mA/cm<sup>2</sup> while an increase in FF to 53.3% is observed. Electrodes using a ~175 nm PEDOT:PSS film show further decrease in  $J_{sc}$  to 8.57 mA/cm<sup>2</sup> while further increasing of FF to 57.2% leading to efficiencies of 2.99%. Increasing the PEDOT:PSS electrode thickness to ~220 nm again shows further lowering of  $J_{sc}$  (8.15 mA/cm<sup>2</sup>) and improved FF (60.0%) which gives a PCE of 2.98%. This trend of lower photocurrent and increasing fill factor as a function of increasing PEDOT:PSS electrode thickness can be correlated to the lower transparency and reduced sheet resistance with increasing layer thickness. The transparency and sheet resistance of the electrodes are important to consider as they can affect both the photocurrent and fill factor device parameters. The lower transparency leads to a reduction of the potential photons that are able to be absorbed by the active layer therefore leads to lower photocurrent densities. The reduction in sheet resistance minimizes the resistance losses in the solar cells and improves fill factor. With higher sheet resistance, the energy

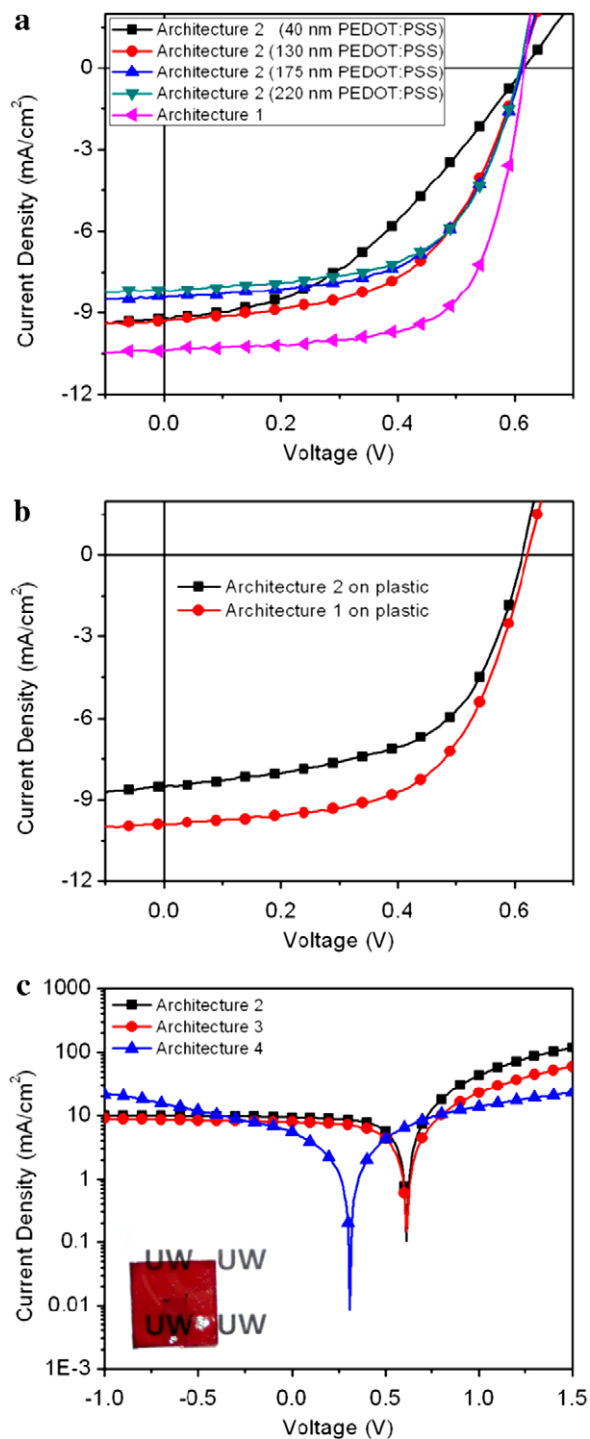


Fig. 5. (a) Illuminated  $J$ - $V$  characteristics of inverted devices fabricated from various thicknesses of PEDOT:PSS – 5% DMSO as cathode electrodes on glass as compared to ITO-based cathode electrodes. (b) Illuminated  $J$ - $V$  characteristics of inverted devices fabricated from PEDOT:PSS – 5% DMSO cathode electrodes on plastic substrates and ITO-based cathode electrodes on plastic substrates. (c) Illuminated log  $J$ - $V$  characteristics of inverted devices with architecture 2–4. Inset: semi-transparent solar cell using ITO cathode and PEDOT:PSS – 5% DMSO anode electrodes (architecture 3).

**Table 1**

Average device performance of inverted ZnO-NP/C<sub>60</sub>-SAM/P3HT:PCBM bulk-heterojunction solar cells fabricated using glass/PEDOT:PSS, plastic/PEDOT:PSS, glass/ITO and plastic/ITO as the cathode electrode and vacuum deposited Ag as the anode electrode. Average device performance of semi-transparent inverted solar cells using PEDOT:PSS as the anode electrode on glass/ITO and glass/PEDOT:PSS cathode electrodes. Average was obtained from multiple device tests.

Electrode (cathode)	Electrode (anode)	V <sub>oc</sub> (V)	J <sub>sc</sub> (mA/cm <sup>2</sup> )	FF (%)	PCE (%)
ITO/glass	Ag	0.62	10.25	66.6	4.20
PEDOT:PSS (~40 nm)/glass	Ag	0.61	9.59	39.4	2.32
PEDOT:PSS (~130 nm)/glass	Ag	0.61	9.41	53.3	3.08
PEDOT:PSS (~175 nm)/glass	Ag	0.61	8.57	57.2	2.99
PEDOT:PSS (~220 nm)/glass	Ag	0.61	8.15	60.0	2.98
ITO/plastic	Ag	0.61	9.86	61.2	3.73
PEDOT:PSS (~175 nm)/plastic	Ag	0.62	8.42	57.7	2.99
ITO/glass	PEDOT:PSS	0.61	7.86	52.0	2.51
PEDOT:PSS (~130 nm)/glass	PEDOT:PSS	0.31	5.49	27.7	0.47

lost from the lateral charge collection through the PEDOT:PSS electrode become much more apparent. This can be observed in PEDOT:PSS devices with ~40 nm and ~220 nm films showing an improved fill factor from 39.4% to 60.0% when the sheet resistance was decreased from 2800 Ω/□ to 160 Ω/□. Due to the competing effects of the photocurrent and fill factor, the PCE efficiency of the devices saturates to ~3% as the thickness of the PEDOT:PSS electrode is increased. Solar cells fabricated from ITO-coated glass substrates had an average PCE of ~4.20%, J<sub>sc</sub> = 10.25

mA/cm<sup>2</sup>, FF = 66.6% and V<sub>oc</sub> = 0.62 V which are over 1% higher than the PEDOT:PSS based electrodes. This is due to the higher transparency (~10% higher) and lower sheet resistance (~10 times less) as compared to the ~220 nm thick PEDOT:PSS electrode.

To demonstrate that this PEDOT:PSS electrode can be applied onto flexible substrates, solar cells using a ~175 nm PEDOT:PSS electrode were fabricated onto plastic substrates. The devices fabricated from the PEDOT:PSS electrode show similar performance (PCE ~3%) to that of solar cells fabricated onto glass substrates as shown in Fig. 5b. These cells are still however ~20% lower in efficiency compared to ITO based plastic substrates which have an average PCE of ~3.7%. Another important consideration for the practicality of flexible electronics which is often ignored is the mechanical stability. The mechanical stability of these flexible solar cell devices was evaluated by subjecting them to a cyclic bending (bend radius ~7.4 mm) test. Fig. 6a shows the illuminated J–V characteristics of a flexible ITO based electrode device subjected to multiple bending cycles. As the number of bend cycles is increased, a decrease in J<sub>sc</sub> and fill factor can be observed and eventually even a lowering of V<sub>oc</sub>. This was compared to devices fabricated from the PEDOT:PSS electrodes which show negligible degradation in J<sub>sc</sub> and V<sub>oc</sub>, but some slight

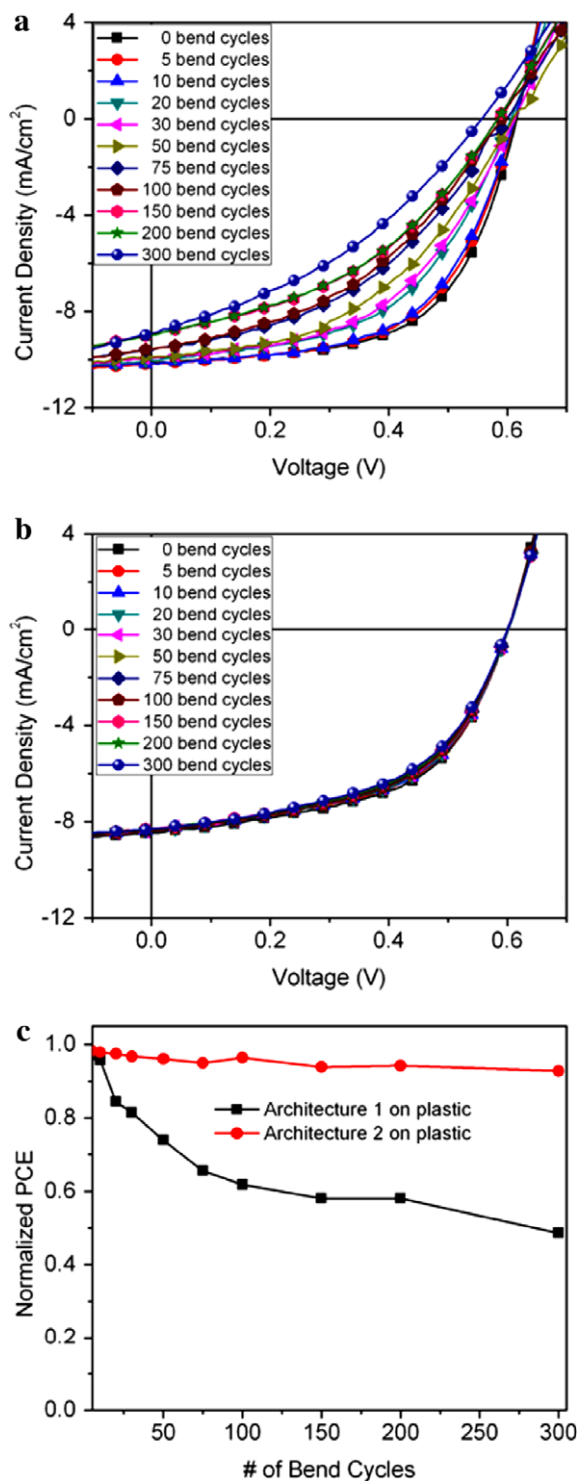


**Fig. 6.** (a) Plot of illuminated  $J$ - $V$  characteristics of inverted devices fabricated from flexible ITO electrode substrates under multiple bending cycles. (b) Plot of illuminated  $J$ - $V$  characteristics of inverted devices fabricated from flexible PEDOT:PSS - 5% DMSO electrode substrates under multiple bending cycles. (c) Comparison of the normalized power conversion efficiency of devices fabricated from flexible ITO and flexible PEDOT:PSS electrodes as a function of bending cycles.

degradation in fill factor after multiple bend cycles (Fig. 6b). The normalized device efficiency of these electrodes were compared as a function of bending cycles showing a retention of  $\sim 92\%$  in the PEDOT:PSS electrodes while only  $\sim 50\%$  in the ITO electrodes after 300 bend cycles (Fig. 6c). The improved mechanical stability from the PEDOT:PSS electrodes as compared to ITO electrodes is an important step to the eventual realization of flexible electronic devices.

Recently, there has been a successful demonstration of spraycoating PEDOT:PSS as an anode electrode in inverted solar cells achieving efficiencies of  $\sim 2\%$ , however, this electrode is thick and non-transparent [22]. We have developed a technique to selectively remove the PEDOT:PSS buffer layer in our inverted solar cell by using a patterned PDMS stamp (Fig. 7). By heating the substrates at an elevated temperature ( $\sim 120^\circ\text{C}$  for 30 s) with the PDMS stamp, the stamp can be removed to selectively lift-off regions of PEDOT:PSS leaving behind the hydrophobic polymer/PCBM active layer. By spincoating solutions of the highly conductive PEDOT:PSS which only wets the PEDOT:PSS buffer layer, a patterned top semi-transparent an-

ode electrode can be formed. From this, semi-transparent inverted devices using ITO-coated glass substrates as the cathode and PEDOT:PSS as the top anode were fabricated. Fig. 5c shows the log  $J$ - $V$  characteristics of these semi-transparent solar cells. These solar cells had an average PCE of 2.51%, a  $V_{oc} = 0.61\text{ V}$ ,  $J_{sc} = 7.86\text{ mA/cm}^2$ , and  $FF = 52.0\%$ . The lower performance especially in photocurrent is most likely due to the non-reflective electrode which unlike Ag does not reflect any unabsorbed light back into the active layer for further absorbance. In addition, the higher sheet resistance of the electrodes (ITO  $15\ \Omega/\square$ , PEDOT:PSS  $\sim 370\ \Omega/\square$ ) can also contribute to losses in device performance. Furthermore, an all solution processed semi-transparent inverted solar cell is demonstrated by replacing the bottom ITO electrode with a PEDOT:PSS electrode. These PEDOT:PSS top anode and PEDOT:PSS bottom cathode solar cells show a PCE of 0.47%,  $V_{oc} = 0.31\text{ V}$ ,  $J_{sc} = 5.49\text{ mA/cm}^2$  and  $FF = 27.7\%$ . The relatively low efficiency is attributed to the much higher sheet resistance of the two electrode contacts ( $>400\ \Omega/\square$ ) which leads a significant deterioration in all the solar cell performance parameters due to the high resistance from the lateral

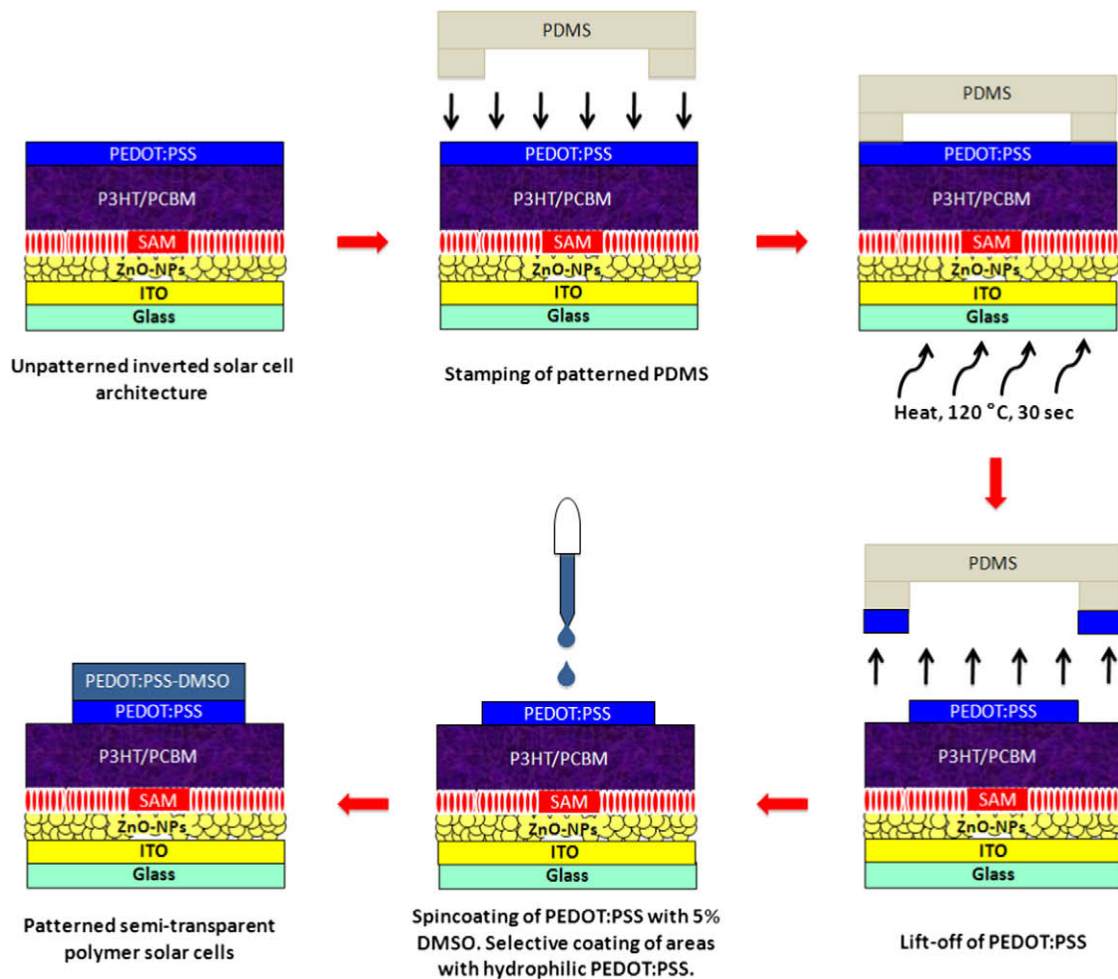


**Fig. 7.** Schematic of patterning PEDOT:PSS by PDMS removal of PEDOT:PSS. Selective removal of the hydrophilic PEDOT:PSS leaves behind the hydrophobic P3HT:PCBM film where spincoating of the conducting PEDOT:PSS–DMSO wets only the region with the PEDOT:PSS pattern leading to semi-transparent solar cells.



charge transport through the PEDOT:PSS electrodes. In addition, the significant drop in  $V_{oc}$  is likely attributed to the reduced built-in field of the device due to the symmetric PEDOT:PSS electrodes used for both contacts. Because of the high sheet resistance, the active device area is limited to a small area in order to minimize the lateral current losses through the electrodes. The sheet resistance of two electrode contacts can potentially be improved by using metalized grids. Using very dense metalized grids should limit the lateral current flow losses and lead to lower sheet resistances. This approach will become important when considering the scaling of the size of the solar cell device to larger active areas.

In conclusion, the replacement of ITO with PEDOT:PSS as the cathode electrode in inverted solar cells has been demonstrated. As the thickness of the PEDOT:PSS electrode was systematically increased, both the transparency and sheet resistance decreased which affected the photocurrent and fill factor of the solar cells. As the transparency of the electrode decreased, the available photons to be absorbed by the active layer were reduced leading to a lower photocurrent density. However, this lowering of photocurrent was offset by an increase in fill factor due to the lower sheet resistance which led to saturation in PCE of  $\sim 3\%$  as the electrode thickness was increased. These PEDOT:PSS electrodes were applied onto flexible plastic substrates showing similar device efficiencies to devices fabricated on glass. The flexible PEDOT:PSS electrodes has better mechanical stability than the flexible ITO based electrodes showing a conversion efficiency retention of  $\sim 92\%$  as compared to  $\sim 50\%$  under 300 cyclic bends, respectively. Semi-transparent inverted solar cells using ITO as the cathode and PEDOT:PSS as the top anode showed PCE of 2.51%. A completely solution processed semi-transparent inverted solar cell was demonstrated by replacing the ITO cathode with a PEDOT:PSS cathode and a PEDOT:PSS top anode showing efficiencies of 0.47%. The semi-transparency of these devices can potentially lead to window based solar applications or other application where semi-transparency is required. More importantly, the replacement of ITO as a transparent electrode with a cheaper transparent electrode will be needed to realizing low-cost flexible polymer solar cells.

### Acknowledgements

This work was supported by the National Science Foundation's NSF-STC program under Project No. DMR-0120967

and the DOE "Future Generation Photovoltaic Devices and Process" program under Project No. DE-FC36-08GO18024/A000. A. K. Y. J. thanks the Boeing-Johnson Foundation for financial support. S. K. H. and H. L. Y. thank the Intel Foundation PhD Fellowship.

### References

- [1] G. Li, V. Shrotryiya, J.S. Huang, Y. Yao, T. Moriarty, K. Emery, Y. Yang, *Nat. Mater.* 4 (2005) 864.
- [2] J. Peet, J.Y. Kim, N.E. Coates, W.L. Ma, D. Moses, A.J. Heeger, G.C. Bazan, *Nat. Mater.* 6 (2007) 497.
- [3] S.I. Na, S.S. Kim, J. Jo, D.Y. Kim, *Adv. Mater.* 20 (2008) 1.
- [4] J. van de Lagemaat, T.M. Barnes, G. Rumbles, S.E. Shaheen, T.J. Coutts, C. Weeks, I. Levitsky, J. Peltola, P. Glatkowski, *Appl. Phys. Lett.* 88 (2006) 233503.
- [5] M.W. Rowell, M.A. Topinka, M.D. McGehee, H.J. Prall, G. Dennler, N.S. Sariciftci, L. Hu, G. Gruner, *Appl. Phys. Lett.* 88 (2006) 233506.
- [6] R.C. Tenent, T.M. Barnes, J.D. Bergenson, A.J. Ferguson, B. To, L.M. Gedvilas, M.J. Heben, J.L. Blackburn, *Adv. Mater.* 21 (2009) 1.
- [7] J. Wu, H.A. Becerril, Z. Bao, Z. Liu, Y. Chen, P. Peumans, *Appl. Phys. Lett.* 92 (2008) 263302.
- [8] V.C. Tung, L.-M. Chen, M.J. Allen, J.K. Wassei, K. Nelson, R.B. Kaner, Y. Yang, *Nano Lett.* 9 (2009) 1949.
- [9] K. Tvingstedt, O. Inganas, *Adv. Mater.* 19 (2007) 2893.
- [10] M.G. Kang, M.S. Kim, J. Kim, L.J. Guo, *Adv. Mater.* 20 (2008) 1.
- [11] J.Y. Lee, S.T. Connor, Y. Cui, P. Peumans, *Nano Lett.* 8 (2008) 689.
- [12] J. Owen, M.S. Son, K.H. Yoo, *Appl. Phys. Lett.* 90 (2007) 033512.
- [13] J. Hanisch, E. Ahlswede, M. Powalla, *Euro. Phys. J. Appl. Phys.* 37 (2007) 261.
- [14] Y. Zhou, F. Zhang, K. Tvingstedt, S. Barrau, F. Li, W. Tian, O. Inganas, *Appl. Phys. Lett.* 92 (2008) 233308.
- [15] E. Ahlswede, W. Muhleisen, M. Wahinuddin bin Moh Wahi, J. Hanisch, M. Powalla, *Appl. Phys. Lett.* 92 (2008) 143307.
- [16] J. Ouyang, Q. Xu, C.-W. Chu, Y. Yang, G. Li, J. Shinar, *Polymer* 45 (2004) 8443.
- [17] F. Zhang, M. Johansson, M.R. Andersson, J.C. Hummelen, O. Inganas, *Adv. Mater.* 14 (2002) 662.
- [18] S. Admassie, F. Zhang, A.G. Manoj, M. Svensson, M.R. Andersson, O. Inganas, *Solar Energy Mater. Solar Cells* 90 (2006) 133.
- [19] J. Huang, X. Wang, Y. Kim, A.J. deMello, D.D.C. Bradley, J.C. deMello, *Phys. Chem. Chem. Phys.* 8 (2006) 3904.
- [20] S.K. Hau, H.L. Yip, N.S. Baek, J. Zou, K. O'Malley, A.K.Y. Jen, *Appl. Phys. Lett.* 92 (2008) 253301.
- [21] S.K. Hau, H.L. Yip, K. Leong, A.K.Y. Jen, *Org. Electron.* 10 (2009) 719.
- [22] Y.F. Lim, S. Lee, D.J. Herman, M.T. Lloyd, J.E. Anthony, G.G. Malliaras, *Appl. Phys. Lett.* 93 (2008) 193301.
- [23] W.J.E. Beek, M.M. Wienk, M. Kemerink, X. Yang, R.A.J. Janssen, *J. Phys. Chem. B* 109 (2005) 9505.
- [24] S.K. Hau, H.L. Yip, H. Ma, A.K.Y. Jen, *Appl. Phys. Lett.* 93 (2008) 233304.
- [25] S.K. Hau, H.-L. Yip, O. Acton, N.S. Baek, H. Ma, A.K.-Y. Jen, *J. Mater. Chem.* 18 (2008) 5113.
- [26] A. Cravino, P. Schilinsky, C.J. Brabec, *Adv. Funct. Mater.* 17 (2007) 3906.
- [27] M.-S. Kim, M.-G. Kang, L.J. Guo, J. Kim, *Appl. Phys. Lett.* 92 (2008) 133301.
- [28] J. Gilot, M.M. Wienk, R.A.J. Janssen, *Appl. Phys. Lett.* 90 (2007) 143512.

long excited triplet lifetime of 1.29  $\mu\text{s}$ . Therefore it could be conjectured that the interaction between CuPc and Ir(piq)<sub>2</sub>acac phosphors would occur by codoping the two phosphors into the same host in EL device. In terms of above arguments it is speculated that the interaction should be an energy transfer from the red emitting Ir-complex to CuPc phosphor. In this letter, we fabricate CuPc and Ir(piq)<sub>2</sub>acac codoped device with CBP as host to enhance the NIR emission of CuPc. By optimizing the device structure the NIR emission intensity of CuPc was enhanced by factors of about fifteen compared with the reference device without the Ir-complex codopant.

All the chemicals were commercially available. Organic films and Al cathode were deposited on indium tin oxide (ITO) glass substrate with a sheet resistance of 25  $\Omega/\square$  by thermal evaporation in a vacuum chamber with a base pressure  $<3.0 \times 10^{-4}$  Pa. Various OLEDs with an active area of  $2 \times 3 \text{ mm}^2$  were fabricated and encapsulated under drying  $\text{N}_2$  atmosphere for device analysis. The NIR EL signals were focused into a monochromator and detected with a liquid-nitrogen-cooled Ge detector, using standard lock-in techniques, and the NIR photoluminescence (PL) signals were detected by spectrophotometer with a InGaAs photodiode with a boxcar averager. The transient decays of Ir(piq)<sub>2</sub>acac were measured by a spectrophotometer with a Spex 1403 photomultiplier with a boxcar averager, under excitation by Nd:YAG laser at a wavelength of 355 nm with 10 ns pulse width. The absorption spectrum of neat CuPc film were recorded at a UV-Vis-NIR scanning spectrophotometer UV3101 (SHIMADZU), and the PL spectrum of Ir(piq)<sub>2</sub>acac film determined by Hitachi F-4500 spectrophotometer equipped with a continuous 150 W Xe-arc lamp. The electrode work functions, the data of the highest occupied molecular orbital (HOMO) and the lowest unoccupied molecular orbital (LUMO) levels of m-MTDATA, TPD, CBP, Ir(piq)<sub>2</sub>acac, and TPBI were cited from literatures [14,15].

Firstly, we investigated the PL of CuPc film and Ir(piq)<sub>2</sub>acac:CuPc blend film. Under an illumination of 355 nm Nd:YAG laser with energy density 30  $\text{mW}/\text{cm}^2$ , no emission was observed from a 40 nm CuPc film. But in the 40 nm blend film Ir(piq)<sub>2</sub>acac:CuPc, we observed the

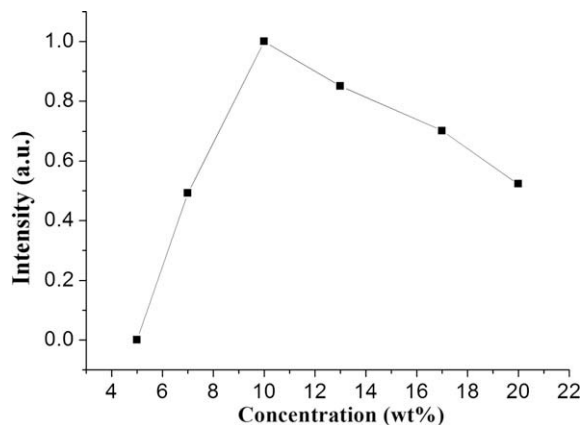


Fig. 1. CuPc EL intensity in 1.1  $\mu\text{m}$  as a function of concentration of Ir(piq)<sub>2</sub>acac dopant.

1120 nm emission of CuPc. By modifying the weight ratio of the two components, the Ir(piq)<sub>2</sub>acac:CuPc blend film with 1:1 weight ratio emits the most intensive NIR emission from CuPc, and the intensity can be compared with that of  $\text{Yb}^{3+}$  in (dibenzoylmethanato)<sub>3</sub>-(bathophenanthroline)-ytterbium which under an illumination of 532 nm Nd:YAG laser with energy density 50  $\text{mW}/\text{cm}^2$ .

Based on the results of PL, we fabricated OLED devices with structures of ITO/m-MTDATA (20 nm)/TPD (20 nm)/CBP: CuPc:Ir(piq)<sub>2</sub>acac ( $x, y$  wt%, 30 nm)/TPBI (40 nm)/LiF(1 nm)/Al (150 nm), here,  $x$  and  $y$  express the concentrations of Ir(piq)<sub>2</sub>acac and CuPc. m-MTDATA, TPD and TPBI denote 4,4',4''-tris[3-methyl-phenyl(phenyl)-amino] triphenylamine, N,N'-diphenyl-N,N'-bis(3-methylphenyl)-1,1'-biphenyl-4,4'-diamine, and 2,2',2''-(1,3,5-benzenetriyl)tris-[1-phenyl-1H-benzimidazole], respectively.

Fig. 1 shows CuPc EL intensity as a function of concentration of Ir(piq)<sub>2</sub>acac dopant, and the optimal concentrations of Ir(piq)<sub>2</sub>acac and CuPc locates 10 and 12 wt%, respectively. The device with the optimal concentration called optimal device, and the 12 wt% CuPc monodoped device will be called reference device. Because we adopted m-MTDATA as hole injection layer, LiF as cathode buffer layer, and TPD, a low efficient PL and EL material, as hole transport layer, the NIR emission intensity of the reference device was enhanced by about two times comparing with the reported CuPc device [12] under the same measurement condition.

Fig. 2 shows the EL spectra at the NIR spectral zone for the optimal and reference devices, respectively. It can be seen that the CuPc EL intensity was enhanced by about 15 times compared with reference device. Furthermore, in optimal device, the red emission of Ir(piq)<sub>2</sub>acac was too weak to be detected, although the maximal current efficiency and luminance of the Ir(piq)<sub>2</sub>acac monodoped device can offer 10.17 cd/A and 11 000  $\text{cd}/\text{m}^2$ , respectively. Inset denotes the chemical structures of CuPc and Ir(piq)<sub>2</sub>acac. In order to understand the enhanced mechanism

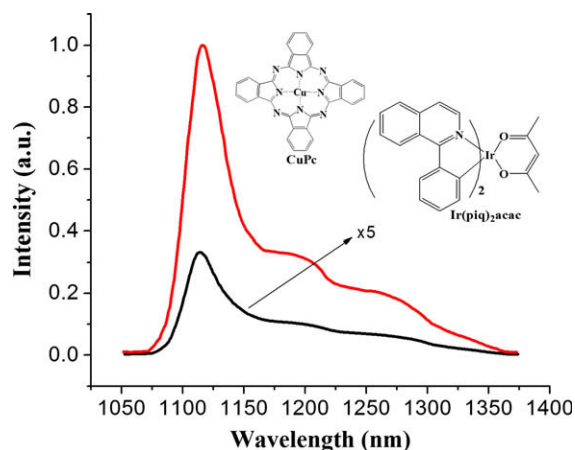


Fig. 2. The NIR EL spectra of CuPc in the optimized device (red) and reference device (black). (The absolute emission intensity is not referred to in this work purely because of the difficulty for our testing system.). (For interpretation of the references to colour in this figure legend, the reader is referred to the web version of this article.)

of the NIR emission of CuPc, we determined the absorption spectrum of CuPc film and emission spectrum of Ir(piq)<sub>2</sub>acac film. It is found that there is a markedly overlapping between the two spectral bands, as indicated in Fig. 3, which implies that the energy transfer from the Ir-complex to CuPc in device would occur. Besides we also measured the photoluminescence transient decays in the 50 nm thick CBP: Ir(piq)<sub>2</sub>acac (10 wt%), and CBP: Ir(piq)<sub>2</sub>acac: CuPc (10, 12 wt%) mixing film, respectively. It is found that the excited triplet lifetime of Ir(piq)<sub>2</sub>acac in the CBP: Ir(piq)<sub>2</sub>acac mixing film is 1.29 μs, while in the codoped films it was shortened to 0.82 μs. Basing on the above-mentioned spectral overlapping and the shortened excited triplet lifetime of Ir(piq)<sub>2</sub>acac phosphor, we can deduce that the improvement in NIR EL intensity is mainly attributed to the primarily energy transfer to CuPc from the red emitting Ir-complex.

To further prove the energy transfer from the red Ir-complex to CuPc in the codoped devices, we also fabricated other two series of OLED devices. Series A: ITO/m-MTDATA (20 nm)/TPD (20 nm)/CBP: CuPc (*x* wt% 30 nm)/CBP: Ir(piq)<sub>2</sub>acac (*y* wt% 30 nm)/TPBI (40 nm)/LiF(1 nm)/Al (150 nm); Series B: ITO/m-MTDATA (20 nm)/TPD (20 nm)/CBP: Ir(piq)<sub>2</sub>acac (*y* wt% 30 nm)/CBP: CuPc (*x* wt% 30 nm)/TPBI (40 nm)/LiF(1 nm)/Al (150 nm). We have taken any values of *x* and *y* in the two series devices, but the NIR emission enhancement was not as much as the optimal device. The reasons could be understood as follow. In CuPc and Ir(piq)<sub>2</sub>acac codoped device the intermolecular contact between two dopants are more close and behaves more favorite for Dexter energy transfer. For the other two series devices, the two dopants distribute in two layers separately, so the probable energy transfer process is only the Förster mechanism, which leads to lower efficiency process comparing with the codoping system. Therefore we conclude that the two phosphors codoped device provides more favorite surroundings for the sensitization of CuPc emission by the red Ir-complex than other device system.

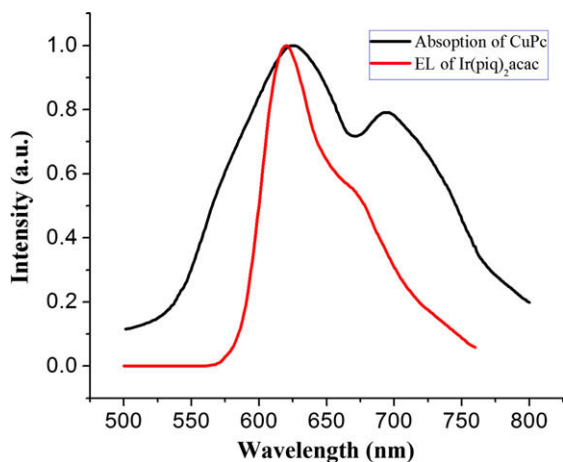


Fig. 3. The absorption spectrum of neat CuPc film and PL spectrum of Ir(piq)<sub>2</sub>acac. (For interpretation of the references to colour in this figure legend, the reader is referred to the web version of this article.)

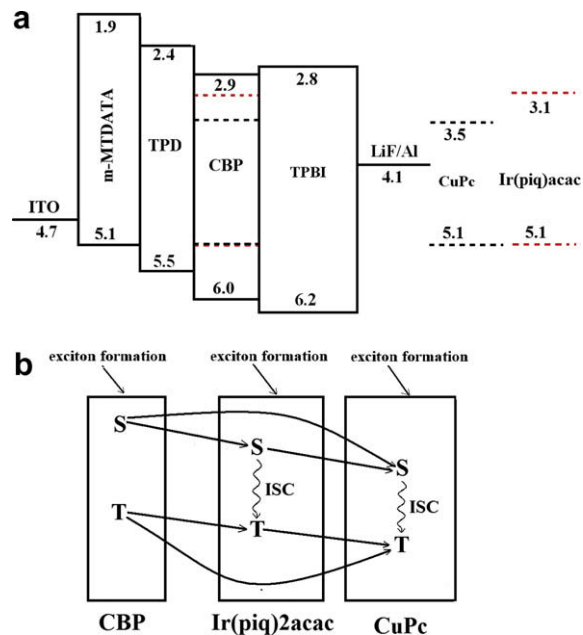


Fig. 4. The schematic energy diagram of the codoped device (a) and the energy transfer processes in the codoped system (b). (For interpretation of the references to colour in this figure legend, the reader is referred to the web version of this article.)

In term of the codoped device structure, here we show the schematic energy diagram, as in Fig. 4. Under the energy diagram, the improvement of NIR emission of CuPc was also understood as follows. Under excitation of the electrical field, the excitons are firstly formed on CBP molecules with the singlet-to-triplet ratio of 1/3. On the other hand, triplet excitons can be formed directly on the phosphor centers by trapping both the injected holes and electrons. The singlet energy of CBP can be directly transferred to that of both Ir(piq)<sub>2</sub>acac and CuPc via Förster process, while the triplet of CBP can be directly transferred to the triplet states of Ir(piq)<sub>2</sub>acac and CuPc by Dexter process. The singlet energy of the two phosphors may rapid converted to their triplet states by intersystem crossing (ISC) due to strong spin orbit coupling. Due to the efficient ISC of Ir(piq)<sub>2</sub>acac, energy transfer from the singlet of Ir(piq)<sub>2</sub>acac to CuPc is less and hence can be ignored. Because the triplet energy level of Ir(piq)<sub>2</sub>acac is about 0.6 eV lower than that of CBP, which restricts the back energy transfer from Ir(piq)<sub>2</sub>acac to CBP, thus, there are two probable pathways to relaxation of Ir(piq)<sub>2</sub>acac triplet, i.e., one is radiating to its ground states and another is transferring to CuPc triplet. Weak emission of Ir(piq)<sub>2</sub>acac in the two phosphors codoped EL device indicates that the fraction of the radiation of Ir(piq)<sub>2</sub>acac should be small. The shorter excited lifetime of CuPc (<50 ns) [16] comparing with Ir(piq)<sub>2</sub>acac (1.29 μs) is another essential conditions for the energy transfer from Ir(piq)<sub>2</sub>acac to CuPc. Thus, nearly all the exciton energies could be transferred to the CuPc triplet, as a result the NIR emission of CuPc increased.

Curry and Gillin have reported the NIR EL emission from erbium (III) tris(8-hydroxyquinolate) (ErQ) based de-

vice with structure of Si/NPB (40 nm)/ErQ (50 nm)/Al (200 nm), and a internal quantum efficiency of  $\sim 0.01\%$  was obtained [17]. We have fabricated the similar EL device using ITO rather than Si as the anode substrate. By comparing the heights of EL emission peaks which origin from  $\text{Er}^{3+}$  in ErQ device and CuPc in our sensitized device under the same determining condition, the internal quantum efficiency of the sensitized emission of CuPc was estimated roughly. Basing on the estimation, our sensitized CuPc device with the red Ir-phosphor offers an internal quantum efficiency of about 0.1%, which is little higher than that of CuPc reported by Rosenow et al. [18].

In summary, the NIR emission of CuPc was enhanced by Ir(piq)<sub>2</sub>acac in codoped device system. The improvement was attributed to the intermolecular energy transfer from Ir(piq)<sub>2</sub>acac to CuPc in the same host (CBP). The observation of the enhanced NIR emission of the CuPc would inspire us to design and develop other new type of sensitized phosphorescent OLEDs by intermolecular energy transfer processes. The concept can also be used for the application in efficient organic photovoltaic cells with new triplet materials.

#### Acknowledgements

This work was supported by the National Natural Science Foundation of China (Grant Nos. 10604054 and 60877027), Pillar Project in Bureau of science and technology of Changchun city (No. 08KZ24), and Knowledge Inno-

vation Project of The Chinese Academy of Sciences (No. KJCX2-YW-M11).

#### References

- [1] C.W. Tang, S.A. VanSlyke, *Appl. Phys. Lett.* 51 (1987) 913.
- [2] B.W. D'Andrade, J. Brooks, M.E. Thompson, S.R. Forrest, *Adv. Mater.* 14 (2002) 147.
- [3] Y.R. Sun, N.C. Giebink, H. Kanno, B. Ma, M.E. Thompson, S.R. Forrest, *Nature* 440 (2006) 908.
- [4] H. Kajii, T. Taneda, Y. Ohmori, *Thin Solid Films* 438 (2003) 334.
- [5] E.L. Williams, J. Li, G.E. Jabbour, *Appl. Phys. Lett.* 89 (2006) 083506.
- [6] F. Meinardi, N. Colombi, S. Destri, W. Porzio, S. Blumstengel, M. Cerminara, R. Tubino, *Synth. Met.* 137 (2003) 959.
- [7] Z.R. Hong, C.J. Liang, R. Li, F.X. Zang, D. Fan, W.L. Li, *Appl. Phys. Lett.* 79 (2001) 1942.
- [8] F.X. Zang, W.L. Li, Z.R. Hong, H.Z. Wei, M.T. Li, X.Y. Sun, *Appl. Phys. Lett.* 84 (2004) 5115.
- [9] R.J. Curry, W.P. Gillin, A.P. Knights, R. Gwilliam, *Appl. Phys. Lett.* 77 (2000) 2271.
- [10] C.J. Yang, C. Yi, M. Xu, J.H. Wang, Y.Z. Liu, X.C. Gao, *Appl. Phys. Lett.* 89 (2006) 233506.
- [11] C. Borek, K. Hanson, P.I. Djurovich, M.E. Thompson, K. Aznavour, R. Bau, Y.R. Sun, S.R. Forrest, J. Brooks, L. Michalski, J. Brown, *Angew. Chem.* 119 (2007) 1127.
- [12] C.H. Cheng, Z.Q. Fan, S.K. Yu, W.H. Jiang, X. Wang, G.T. Du, Y.C. Chang, C.Y. Ma, *Appl. Phys. Lett.* 88 (2006) 213505.
- [13] C.H. Yang, C.C. Tai, I.W. Sun, *J. Mater. Chem.* 14 (2004) 947.
- [14] Y. Shirota, Y. Kuwabara, H. Inada, T. Wakimoto, H. Nakada, Y. Yonemoto, S. Kawami, K. Imai, *Appl. Phys. Lett.* 65 (1994) 807.
- [15] H.A. Bronstein, C.E. Finlayson, K.R. Kirov, R.H. Friend, C.K. Williams, *Organometallics* 27 (2008) 2980.
- [16] P.S. Vincett, E.M. Voigt, K.E. Rieckhoff, *J. Chem. Phys.* 55 (1971) 4131.
- [17] R.J. Curry, W.P. Gillin, *Appl. Phys. Lett.* 77 (2000) 2271.
- [18] T.C. Rosenow, K. Walzer, K. Leo, *J. Appl. Phys.* 103 (2008) 043105.

are commonly used in PhOLEDs. Since the electron mobility of PVK is poor, most PVK-based PhOLEDs have an electron transporting component added to the emitting layer. One substance commonly used for this purpose is 1,3-bis[5-(4-*tert*-butylphenyl)-1,3,4-oxadiazole-2-yl]benzene (OXD-7), which has a lowest unoccupied molecular orbital (LUMO) at  $-2.7$  eV and a highest occupied molecular orbital (HOMO) lower than  $-6.5$  eV [11].

In a recent investigation aimed at developing high efficiency OLEDs, we have found that solution-processed, red emissive PhOLEDs can be fabricated by adding (Et-Cvz-PhQ)<sub>2</sub>Ir(pic) or (EO-Cvz-PhQ)<sub>2</sub>Ir(pic) as phosphorescent dopants to a host polymer matrix comprised of PVK blended with the hole transport material N,N'-diphenyl-N,N'-(bis(3-methylphenyl)-[1,1-biphenyl]-4,4'-diamine (TPD) and the electron transport material OXD-7. TPD was employed as a co-dopant in the emitting layer for two reasons. First, the utilization of PEDOT:PSS leaves a ca. 0.6 eV barrier for hole injection to PVK. Thus, it is expected that addition of a sufficiently large concentration of TPD would cause a reduction in the barrier for hole injection. Second, TPD, when used in high loadings and doped into PVK, has been shown to function as a hole transporting layer [12]. As a result, addition of TPD should allow holes to penetrate more deeply into the emitting layer.

In this investigation, the red emissive Ir complexes, (Et-Cvz-PhQ)<sub>2</sub>Ir(pic) and (EO-Cvz-PhQ)<sub>2</sub>Ir(pic), were synthesized by using procedures developed in our previous work [13]. The 2-(2-methoxyethoxy)ethyl unit instead of an ethyl unit are introduced into the carbazole moiety in these substances in order to enhance their solubilities. PVK, OXD-7 and TPD were purchased from Sigma-Aldrich and Lum. Tec. Co. The devices fabricated in the current study had the configuration ITO/PEDOT:PSS/PVK:OXD-7:TPD:Ir complex/cathode. The molecular structures of (Et-Cvz-PhQ)<sub>2</sub>Ir(pic) and (EO-Cvz-PhQ)<sub>2</sub>Ir(pic) along with the PhOLED configuration and the HOMO and LUMO energy levels of the materials are shown in Fig. 1.

The cathode consisted of Ba/Al with a 20 nm thick layer of OXD-7 between the emitting and electron injection layers. The anode, consisting of ITO/glass substrates pre-coated with PEDOT:PSS (H.C.Stack, 4083), was used as a buffer layer. Prior to spin coating with PEDOT:PSS, the ITO was pre-cleaned and UV-ozone treated for 15 min. Then, a 40 nm thick layer of PEDOT:PSS was spin coated onto the ITO and baked at 150 °C for 20 min. Individual solutions of PVK, OXD-7, TPD and (Et-Cvz-PhQ)<sub>2</sub>Ir(pic) or (EO-Cvz-PhQ)<sub>2</sub>Ir(pic) in chlorobenzene were mixed to give various weight percentages. The solutions, filtered by using a 0.45 μm PTFE (hydrophobic) syringe filter, were spin coated onto the PEDOT:PSS layer in order to obtain emitting layer thicknesses of 70–80 nm. In all cases, the concentrations of the dopants, (Et-Cvz-PhQ)<sub>2</sub>Ir(pic) or (EO-Cvz-PhQ)<sub>2</sub>Ir(pic), were 6 wt.%.

The emitting layer was then annealed at 80 °C for 30 min. A typical cathode, consisting of OXD-7/Ba/Al (20 nm OXD-7, 3 nm Ba, and 100 nm Al), was deposited with effective area of 4 mm<sup>2</sup> at a pressure of  $5 \times 10^{-6}$  Torr. The cathode thickness was measured by using a  $\alpha$ -Step IQ surface profiler (KLA Tencor, San Jose, CA). In order to evaluate the performances of the PhOLEDs, current density–voltage–luminance ( $J$ – $V$ – $L$ ) values were determined by using a current/voltage source meter (Keithley 236) and an optical power meter (CS-1000). All measurements were carried out at room temperature under an ambient atmosphere without encapsulation.

The HOMO and LUMO energies ( $-5.15$  and  $-2.63$  eV, respectively) of (Et-Cvz-PhQ)<sub>2</sub>Ir(pic) and (EO-Cvz-PhQ)<sub>2</sub>Ir(pic) were determined by using cyclic voltammetry. The similarities of the molecular structures of the Ir complexes give rise to similar electro-optical properties. Energy band diagrams show that the, respective HOMO and LUMO energy levels of these complexes lie above and below those of PVK. Thus, it is possible that the Ir complexes will trap both electrons and holes in the PhOLED configuration. The LUMO energy level of OXD-7 is well aligned with that

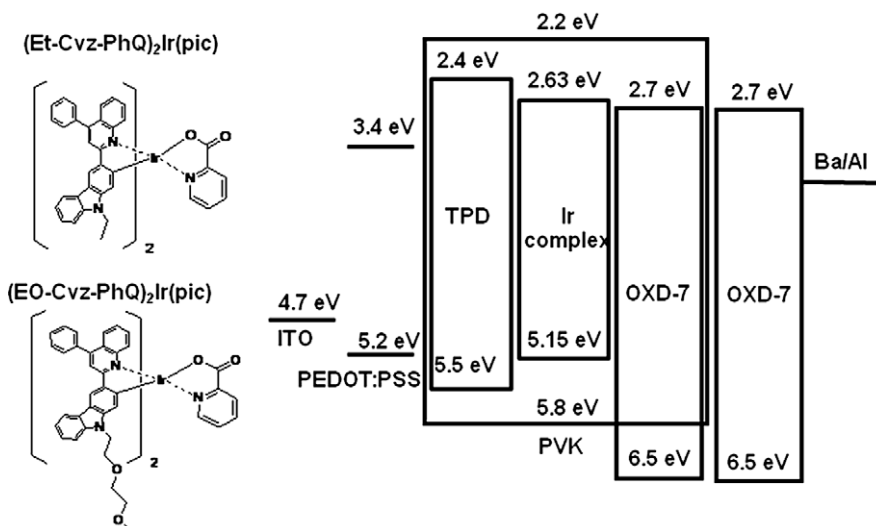
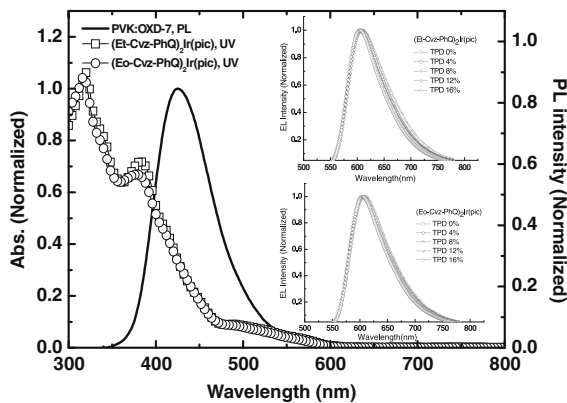


Fig. 1. Molecular structures of (Et-Cvz-PhQ)<sub>2</sub>Ir(pic) and (EO-Cvz-PhQ)<sub>2</sub>Ir(pic) and the energy band diagram of PhOLED.



**Fig. 2.** Normalized absorption spectra of  $(\text{Et-Cvz-PhQ})_2\text{Ir(pic)}$  and  $(\text{EO-Cvz-PhQ})_2\text{Ir(pic)}$  and photoluminescence spectrum of PVK doped with OXD-7 in film state. Inset: doping concentration dependence of EL spectra.

of the Ir complexes in the emitting layer, an important factor that should facilitate carrier injection into the both the transport molecules and the complexes.

The absorption spectra of Ir complexes and emission spectrum of PVK doped with OXD-7 in film state are shown in Fig. 2. As can be seen by viewing these spectra, good overlap exists between the emission band of the host and the metal-to-ligand charge transfer (MLCT) absorption

bands of the Ir complexes, an outcome which ensures efficient Förster energy transfer between hosts and guests and/or direct charge trapping of the Ir complexes.

In order to investigate the effect of TPD on performance, PhOLEDs were fabricated with variable concentrations (0%, 4%, 8%, 12% and 16%) of TPD. As shown in the inset of Fig. 2, the EL spectra of PhOLEDs, using  $(\text{Et-Cvz-PhQ})_2\text{Ir(pic)}$  and  $(\text{EO-Cvz-PhQ})_2\text{Ir(pic)}$ , display peaks corresponding to the dopant emission maximum of 608 nm, an excellent color purity at a CIE coordinate of (0.62, 0.38), and the absence of emissions from PVK, TPD and OXD-7.

Current density–voltage–luminance ( $J$ – $V$ – $L$ ) characteristics of  $(\text{Et-Cvz-PhQ})_2\text{Ir(pic)}$  and  $(\text{EO-Cvz-PhQ})_2\text{Ir(pic)}$  at several different concentrations of TPD in PVK:OXD-7 are shown in Fig. 3. The maximum brightness of the  $(\text{Et-Cvz-PhQ})_2\text{Ir(pic)}$  and  $(\text{EO-Cvz-PhQ})_2\text{Ir(pic)}$  based PhOLEDs, in the absence of TPD in emitting layer, were 1779 and 1414  $\text{cd/m}^2$ , respectively. However, the addition of increasing concentrations of TPD led to dramatic increases in the performances of PhOLEDs. Maximum brightnesses of the PhOLEDs using  $(\text{Et-Cvz-PhQ})_2\text{Ir(pic)}$  and  $(\text{EO-Cvz-PhQ})_2\text{Ir(pic)}$  (8768 and 6285  $\text{cd/m}^2$ , respectively) were obtained when the concentration of TPD was 16 wt.%. The  $J$ – $V$  characteristics of the PhOLEDs clearly demonstrate that current density is directly dependent on the TPD concentration. The results indicate that the enhancement of the current density is related to improved hole injection caused by

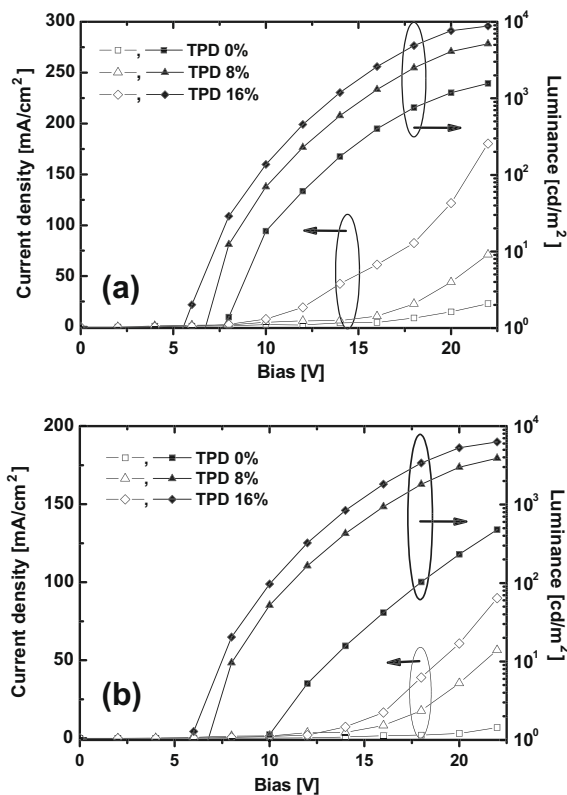


**Fig. 3.** Current density–voltage–luminance ( $J$ – $V$ – $L$ ) characteristics of (a)  $(\text{Et-Cvz-PhQ})_2\text{Ir(pic)}$  and (b)  $(\text{EO-Cvz-PhQ})_2\text{Ir(pic)}$  with different TPD concentration.

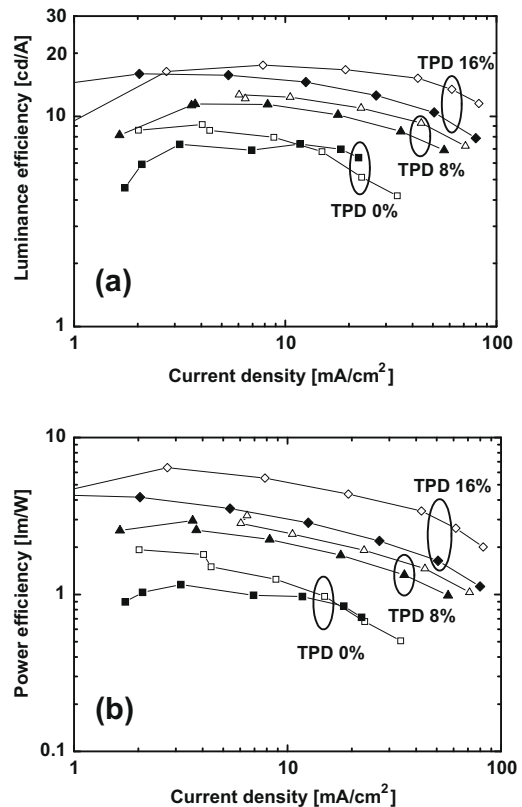


**Fig. 4.** (a) The luminescence efficiency and (b) power efficiency of OLEDs using  $(\text{Et-Cvz-PhQ})_2\text{Ir(pic)}$  [open] and  $(\text{EO-Cvz-PhQ})_2\text{Ir(pic)}$  emitter [close] with different TPD concentration as a function of current density.

**Table 1**

Performances of PVK:OXD-7 based on devices and different TPD concentrations.

EML	TPD (%)	Turn-on (V) <sup>a</sup>	$L_{\max}$ (cd/m <sup>2</sup> )	$\text{EQE}_{\max}$ (%)	$\text{LE}_{\max}$ (cd/A)	PE (lm/W)	CIE (x, y) <sup>b</sup>
(Et-Cvz-PhQ) <sub>2</sub> Ir(pic)	0	7	1779	6.21	9.15	1.93	0.621, 0.377
(Et-Cvz-PhQ) <sub>2</sub> Ir(pic)	4	6.5	4407	7.51	11.3	2.87	0.625, 0.373
(Et-Cvz-PhQ) <sub>2</sub> Ir(pic)	8	6	5148	7.89	12.67	3.18	0.616, 0.382
(Et-Cvz-PhQ) <sub>2</sub> Ir(pic)	12	5.5	5284	9.92	16.0	4.37	0.619, 0.379
(Et-Cvz-PhQ) <sub>2</sub> Ir(pic)	16	5	8768	10.6	17.54	6.42	0.618, 0.380
(Et-Cvz-PhQ) <sub>2</sub> Ir(pic)	20	5	6598	9.99	16.33	4.10	0.618, 0.379
(Et-Cvz-PhQ) <sub>2</sub> Ir(pic)	25	4.5	5849	9.01	15.23	3.98	0.619, 0.379
(Et-Cvz-PhQ) <sub>2</sub> Ir(pic)	30	4.5	5301	6.89	10.60	2.52	0.622, 0.376
(Eo-Cvz-PhQ) <sub>2</sub> Ir(pic)	0	8.5	1414	4.96	7.40	1.16	0.624, 0.375
(Eo-Cvz-PhQ) <sub>2</sub> Ir(pic)	4	7.5	3205	6.89	10.60	2.53	0.622, 0.377
(Eo-Cvz-PhQ) <sub>2</sub> Ir(pic)	8	6.5	3902	7.11	11.45	2.96	0.615, 0.382
(Eo-Cvz-PhQ) <sub>2</sub> Ir(pic)	12	6	5324	8.67	14.76	4.21	0.612, 0.385
(Eo-Cvz-PhQ) <sub>2</sub> Ir(pic)	16	5.5	6285	9.65	15.92	4.34	0.618, 0.380
(Eo-Cvz-PhQ) <sub>2</sub> Ir(pic)	20	5.5	5586	9.24	14.63	4.08	0.619, 0.377
(Eo-Cvz-PhQ) <sub>2</sub> Ir(pic)	25	5.5	4928	8.11	12.16	2.56	0.618, 0.379
(Eo-Cvz-PhQ) <sub>2</sub> Ir(pic)	30	5	4321	6.63	10.86	2.21	0.621, 0.377

<sup>a</sup> Luminance is 1 cd/m<sup>2</sup>.<sup>b</sup> Values recorded at a current density 30 mA/cm<sup>2</sup>.

the presence of TPD in the emitting layer, a phenomenon that can be explained in terms of the  $L$ - $V$  characteristics of the PhOLEDs as shown in Fig. 3.

The results of current density–luminescence efficiency measurements of the PhOLEDs (Fig. 4, Table 1) show that PhOLEDs based on Et-Cvz-PhQ)<sub>2</sub>Ir(pic) and EO-Cvz-PhQ)<sub>2</sub>Ir(pic), that do not contain TPD have respective external quantum, luminance and power efficiencies of 6.21%, 9.15 cd/A and 1.93 lm/W, and 4.96%, 7.40 cd/A and 1.16 lm/W, respectively. When the concentration of TPD in the PhOLEDs consisting of (Et-Cvz-PhQ)<sub>2</sub>Ir(pic) was 16 wt.%, the turn-on voltage was significantly reduced from 7 to 5 V and the external quantum, power and luminance efficiencies were increased to 10.56%, 6.42 lm/W and 17.5 cd/A, respectively. The performances of the PhOLED using the (EO-Cvz-PhQ)<sub>2</sub>Ir(pic) emitter have similar TPD concentration dependences as those of the device based (Et-Cvz-PhQ)<sub>2</sub>Ir(pic). Specifically, the injection barrier for the hole is reduced from 0.6 to 0.3 eV with increasing TPD concentration and it reaches an effectively optimized value at 16 wt.% concentration of TPD. As a result, the driving voltage was reduced and this led to an improved PhOLED performance.

The respective triplet energy levels ( $T_1$ ) of the (Et-Cvz-PhQ)<sub>2</sub>Ir(pic) and (EO-Cvz-PhQ)<sub>2</sub>Ir(pic) emitters were estimated to be 2.18 eV and 2.11 eV by using low temperature (77 °K) phosphorescence spectroscopy. Energy transfer from the triplet state of the Ir complexes to the triplet states of the charge-transport materials does not take place because the triplet energies of charge-transporting materials [TPD ( $T_1 \sim 2.34$  eV), OXD-7 ( $T_1 \sim 2.7$ )] [14] and host material [PVK ( $T_1 \sim 2.5$  eV)] are higher than those of the Ir complexes. This finding indicates that a triplet energy confinement on the Ir complexes emitter is sufficient to cause high quantum efficiencies of the devices.

In this investigation we explored the performance characteristics of red emissive PhOLEDs, based on (Et-Cvz-PhQ)<sub>2</sub>Ir(pic) and (EO-Cvz-PhQ)<sub>2</sub>Ir(pic) and having a

configuration of ITO/PEDOT:PSS/PVK:OXD-7:TPD:Ir complex/cathode. The effects of TPD concentration in the PhOLEDs were determined. By increasing the TPD concentration up to 16 wt.%, the performance of PhOLEDs was markedly increased. Importantly, the PhOLED consisting of (Et-Cvz-PhQ)<sub>2</sub>Ir(pic) and containing an optimum TPD concentration exhibited maximum external quantum, power and luminance efficiency values of 10.56%, 6.42 lm/W and 17.5 cd/A.

## Acknowledgments

This work was supported by the Korea Science and Engineering Foundation (KOSEF) grant funded by the Korea government (MEST) (Nos. 10600000157-06J0000-15710 and R11-2008-088-01-003-0).

## References

- [1] D.D.C. Bradley, *Curr. Opin. Solid State Mater. Sci.* 1 (1996) 789.
- [2] M.A. Baldo, D.F. O'Brien, Y. You, A. Shoustikov, S. Sibley, M.E. Thompson, S.R. Forrest, *Nature (London)* 395 (1998) 151.
- [3] S.A. Choulis, Y. Kim, J. Nelson, D.D.C. Bradley, M. Giles, M. Shkunov, I. McCulloch, *Appl. Phys. Lett.* 85 (2004) 3890.
- [4] G.E. Johnson, K.M. McGrane, M. Stolka, *Pure Appl. Chem.* 67 (1995) 175.
- [5] H. Yang, D. Neher, *Appl. Phys. Lett.* 84 (2004) 2476.
- [6] M. Suzuki, S. Tokito, F. Sato, T. Igarashi, K. Kondo, T. Koyama, T. Yamaguchi, *Appl. Phys. Lett.* 86 (2005) 103507.
- [7] B.W. D'Andrade, S.R. Forrest, *Adv. Mater. (Weinheim, Ger.)* 16 (2004) 1585.
- [8] V. Cleave, G. Yahioglu, P. Le Barny, R.H. Friend, N. Tessler, *Adv. Mater. (Weinheim Ger.)* 11 (1999) 285.
- [9] M.J. Yang, T. Tsutsui, *Jpn. J. Appl. Phys., Part 2* 39 (2000) L82.
- [10] C.L. Lee, K.B. Lee, J.J. Kim, *Appl. Phys. Lett.* 77 (2000) 2280.
- [11] X.H. Yang, F. Jaiser, S. Klinger, D. Neher, *Appl. Phys. Lett.* 88 (2006) 021107.
- [12] D.M. Pai, J.F. Yanus, M. Stolka, *J. Phys. Chem.* 88 (1984) 4714.
- [13] S.J. Lee, J.S. Park, M. Song, I.A. Shin, Y.I. Kim, J.W. Lee, J.W. Kang, Y.S. Gal, S. Kang, J.Y. Lee, S.H. Jung, H.S. Kim, M.Y. Chae, S.H. Jin, *Adv. Funct. Mater.* 14 (2009) 2198.
- [14] J. Lee, N. Chopra, S.H. Eom, Y. Zheng, J. Xue, F. So, J. Shi, *Appl. Phys. Lett.* 93 (2008) 123306.

Although encapsulation of the device can protect it from water and oxygen of the environment and many of the processes cited above have been identified and controlled, few studies have explored degradation of Alq<sub>3</sub> films by exposure to light and the related photo degradation products, responsible for quenching of luminescence. Priestley and collaborators [13] studied photo degradation of thermally evaporated Alq<sub>3</sub>. Photo oxidation was carried out under illumination with full spectrum by a 150 Watt xenon lamp while blowing air or oxygen through the cell. Transient photoluminescence and photoconductive response were measured and the sample which was photo oxidated in oxygen showed more pronounced degradation effects in comparison with that in air, which allowed them to conclude that water vapor, always present in air, does not contribute substantially to the photo oxidation. The same work reported that photo oxidation could introduce chemical modifications in Alq<sub>3</sub> through incorporation of O<sub>2</sub> molecules in its chemical structure, whose products resulted in quenching of photoluminescence. Thangaraju et al. [14] studied the decrease of photoluminescence of Alq<sub>3</sub> films upon the effects of air and white light for various time periods. They concluded that photoluminescence intensity decreases with increasing light exposure time. Infrared (IR) absorption measurements were performed in order to determine the structural changes on Alq<sub>3</sub>. The spectrum shows a band at 1697 cm<sup>-1</sup> that corresponds to vibrational band of carbonyl group, which would act as a luminescence quencher. Similar results were also reported by Kumar and collaborators [15]. Nevertheless, neither of these studies concentrated efforts in attempt to elucidate the chemical structures of the degradation products.

In this work we investigate the stability of Alq<sub>3</sub> thin films under light and air exposure, with consequent photoluminescence decrease. With this aim, thermally deposited Alq<sub>3</sub> thin films were exposed to UV radiation and analyzed through Fourier transform infrared spectroscopy (FTIR) and optical absorption in UV–Vis region. Several possible degradation products are proposed and density functional theory (DFT) calculations of vibrational frequencies and reaction Gibbs free energies are performed. Based on comparisons between experimental and theoretical data, we identify the most likely degradation products of Alq<sub>3</sub>.

## 2. Experimental details

Alq<sub>3</sub> thin films (100 nm thick) were thermally deposited in high vacuum environment onto glass, quartz and silicon substrates. The substrates were initially cleaned by ultrasonication using a detergent solution, followed by toluene degreasing, and then cleaned again by ultrasonication with pure isopropyl alcohol. The base pressure for deposition was  $6.67 \times 10^{-4}$  Pa and during the evaporation the pressure was roughly  $9.33 \times 10^{-4}$  Pa. The deposition rate was about 0.1 nm/s. The layer thickness was controlled in situ through a quartz crystal monitor and confirmed by profilometer measurements. The films were exposed for 11 h to UV radiation, using a He–Xe lamp ( $\lambda = 307$  nm). The incident power density was roughly 0.42 mW/cm<sup>2</sup> for all irradiated samples. The irradiated and non-irradiated films

were analyzed through Fourier transform infrared spectroscopy (FTIR) and optical absorption in UV–Vis region. All the measurements were carried out in ambient atmosphere.

## 3. Computational details

The modified mer-Alq<sub>3</sub> structures were first submitted to a conformational search using semiempirical methods available on the HyperChem Software [16]. The most stable structures were selected and submitted to *ab initio* density functional theory (DFT) optimization calculations and vibrational frequency calculations, carried out using Gaussian 03 package [17]. Frequency calculations were done to confirm the stability of the structure and to generate the IR spectra. The calculations were performed with TPSS (Tao, Perdew, Staroverov, and Scuseria) meta-GGA functional [18] of Kohn–Sham DFT, in combination with 6–31G(d,p) basis set [17]. TPSS is a nonempirical meta-GGA, which was submitted to several tests on molecules, solids, and solid surfaces, all showing its good performance for a diverse range of properties and systems [19].

Due to the neglect of mechanical anharmonicity, approximations in the treatment of electron correlation and basis set effects, theoretical vibrational frequencies typically overestimate experimental ones. It is a common practice to rescale the theoretical frequencies in order to match experiments, so we use a scaling factor of 0.992, chosen to match experimental and our theoretical spectra for Alq<sub>3</sub>.

## 4. Results and discussion

### 4.1. Selection of degradation products and reactions

Earlier experimental and theoretical works have shown that meridional (mer) isomer of Alq<sub>3</sub> is the predominant form, over facial (fac) form, both in solution and in sublimed films [20–24]. Therefore, structural modifications suggested here are all derived from mer-Alq<sub>3</sub>, shown in Fig. 1.

Alq<sub>3</sub> is a trischelate organic complex with a distorted octahedral symmetry. Consequently, the three quinolate ligands are not equivalent, and receive labels a, b, and c (Fig. 1), according to their different Al–O and Al–N bond lengths, as obtained from X-ray structure analysis [20]. According to Thangaraju et al. [14], only one of the three 8-hydroxyquinoline (HQ) units in the Alq<sub>3</sub> molecule suffers chemical structural modifications during light exposure, resulting, as evidenced by infrared absorption spectra, in the introduction of a carbonyl group in the chelate. The same work gives a possible explanation for the chemical modification based on redox behavior associated with Al–O bond. Then, in the present work, our first proposal for degradation products of Alq<sub>3</sub> consists in the rupture of one of the Al–O bonds and consequently rupture of the benzene ring of one HQ unit (Fig. 2a). More precisely, the c-quinolate ligand is chosen to be modified since our theoretical calculations (and also previous work [25]) shows that it has the largest Al–O bond length.



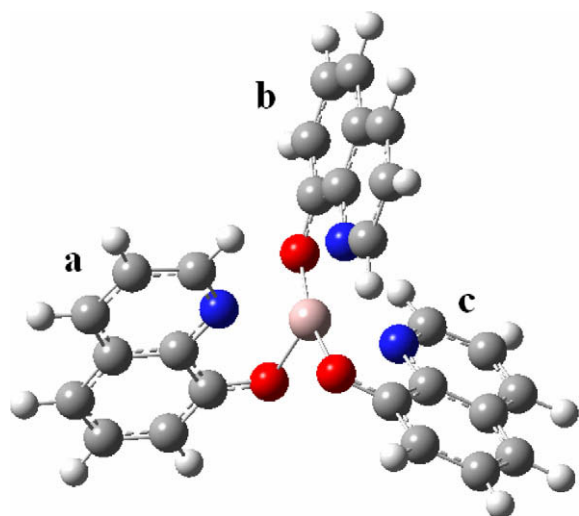


**Fig. 1.** The geometry of mer-Alq<sub>3</sub> with labels a–c indicating the three different quinolate ligands. Pink, red, blue, dark grey and light grey balls represent Al, O, N, C and H atoms, respectively. (For interpretation of the references in colour in this figure legend, the reader is referred to the web version of this article.)

Therefore, our first suggestions of degradation products are complex molecules with broken Al–O bond and modifications on *c*-quinolate oxygen by including carbonyl units in the form of aldehyde, carboxyl acid or ketone groups. All these choices produce chelates that show IR spectra which are not in good agreement with experiments. As a representative example of this class, we present in more detail the results for aldehyde substitution. (Fig. 2, product P1).

Another class of modifications in the Alq<sub>3</sub> molecule involves keeping the Al–O bond intact and breaking the phenoxide ring (Fig. 2, P2, P3, P4 and P5). These changes can result from oxidation, while the previous modifications are result from reduction. Oxidations are more plausible to occur here since measurements are carried out in the air. It is well known that UV light, as used in the present study, produce O<sub>3</sub> from air O<sub>2</sub> [26], therefore it is important to consider that degradation occurs in the presence of both O<sub>2</sub> and O<sub>3</sub> and then, oxygenations and ozonolysis reactions are considered, as shown in Table 1.

Following this analysis, we generated four structures, the products P2, P3, P4 and P5 (Fig. 2). All these products have one extra oxygen atom at one end of the broken ring, forming a carboxylate group bounded to Al, but they differ

**Table 1**

Ozonolysis and oxygenation degradation reactions and respective Gibbs free energy differences for products P2–P5.

Ozonolysis	
Alq <sub>3</sub> + O <sub>3</sub> → P2	–569 kJ/mol
Alq <sub>3</sub> + 2/3 O <sub>3</sub> → P3	–338 kJ/mol
Alq <sub>3</sub> + 5/3 O <sub>3</sub> → P4 + H <sub>2</sub> C <sub>2</sub> O <sub>2</sub>	–921 kJ/mol
Alq <sub>3</sub> + 7/3 O <sub>3</sub> → P4 + H <sub>2</sub> C <sub>2</sub> O <sub>4</sub>	–1445 kJ/mol
Alq <sub>3</sub> + 4/3 O <sub>3</sub> → P5 + H <sub>2</sub> C <sub>2</sub> O <sub>2</sub>	–687 kJ/mol
Alq <sub>3</sub> + 2 O <sub>3</sub> → P5 + H <sub>2</sub> C <sub>2</sub> O <sub>4</sub>	–1211 kJ/mol
Oxygenations	
Alq <sub>3</sub> + 3/2 O <sub>2</sub> → P2	–408 kJ/mol
Alq <sub>3</sub> + O <sub>2</sub> → P3	–231 kJ/mol
Alq <sub>3</sub> + 5/2 O <sub>2</sub> → P4 + H <sub>2</sub> C <sub>2</sub> O <sub>2</sub>	–653 kJ/mol
Alq <sub>3</sub> + 7/2 O <sub>2</sub> → P4 + H <sub>2</sub> C <sub>2</sub> O <sub>4</sub>	–1070 kJ/mol
Alq <sub>3</sub> + 2 O <sub>2</sub> → P5 + H <sub>2</sub> C <sub>2</sub> O <sub>2</sub>	–473 kJ/mol
Alq <sub>3</sub> + 3 O <sub>2</sub> → P5 + H <sub>2</sub> C <sub>2</sub> O <sub>4</sub>	–890 kJ/mol

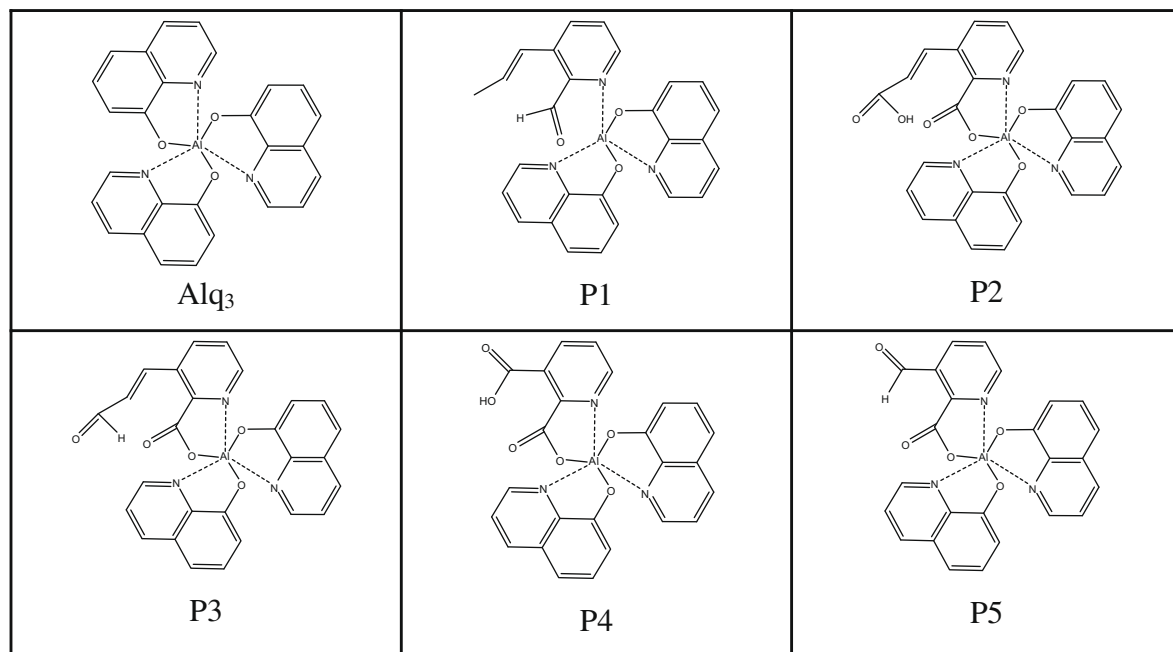


**Fig. 2.** Schematic representation of possible mechanisms for Alq<sub>3</sub> degradation: (i) Rupture of Al–O bond and consequent rupture of the ring, which leads to degradation product P1; (ii) rupture only of the ring, preserving the Al–O bond and leading to products P2–P5.

in the chemical groups at the other extremity of the ring: products P2 and P4 have carboxyl acids, and products P3 and P5 have aldehyde groups. However, in products P4 and P5 two extra C atoms are removed the phenoxide side. As shown in Table 1, for chemical reactions involving P4

and P5, removal of extra C atoms was balanced by extra products: ethanedioic acid (or oxalic acid,  $H_2C_2O_4$ ) and ethanedial (or glyoxal,  $C_2H_2O_2$ ). These reactions are based on oxidation of quinoline and ozonolysis mechanism, which can produce carboxylic acid, aldehyde, and ketone

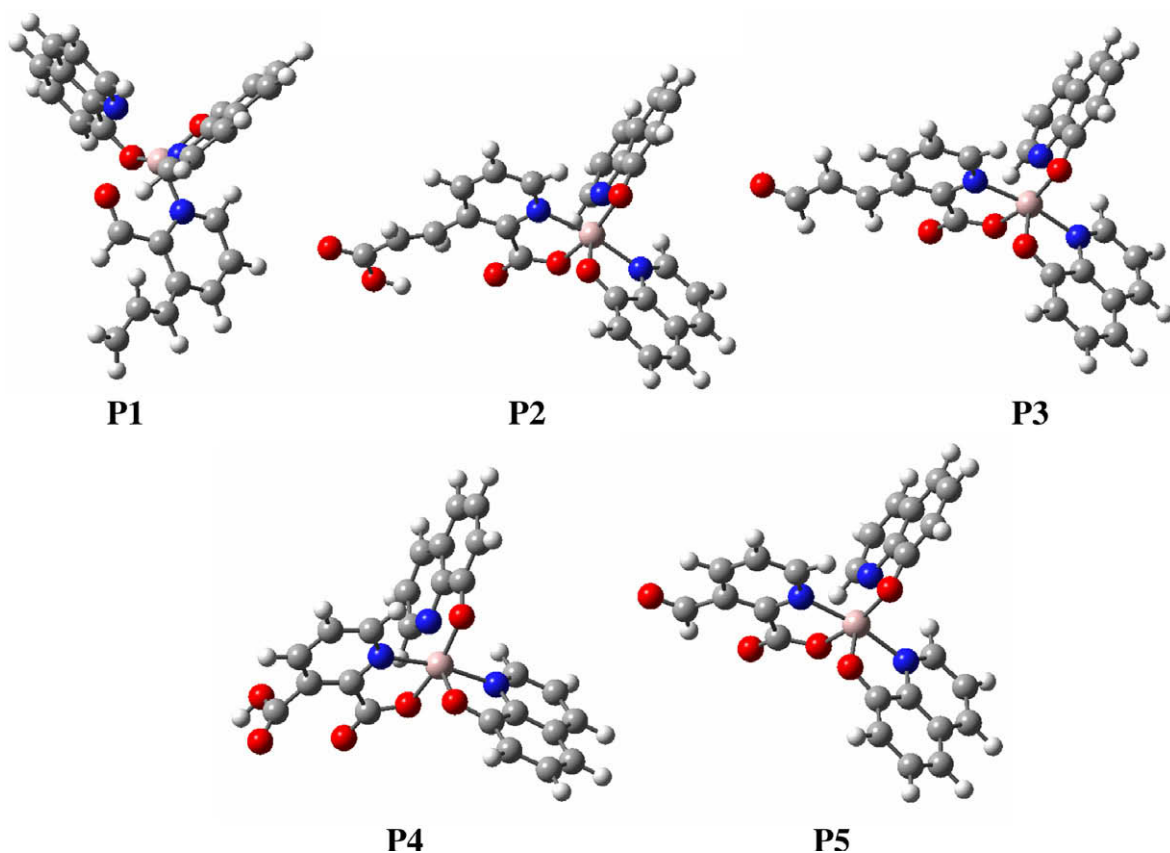


Fig. 3. Optimized structures of degradation products, P1, P2, P3, P4 and P5.

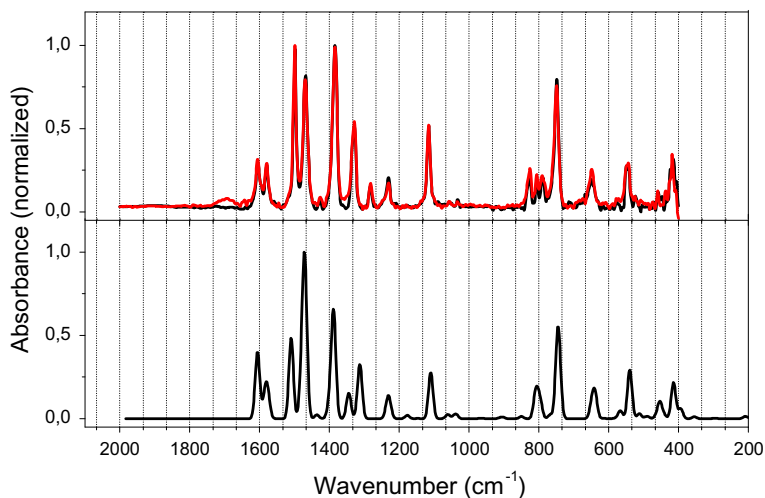


Fig. 4. Infrared spectra obtained for Alq<sub>3</sub>. The top panel shows experimental results obtained for irradiated (red) and non-irradiated (black) Alq<sub>3</sub>. The lower panel shows the theoretical IR spectrum for pristine Alq<sub>3</sub>. (For interpretation of the references in colour in this figure legend, the reader is referred to the web version of this article.)

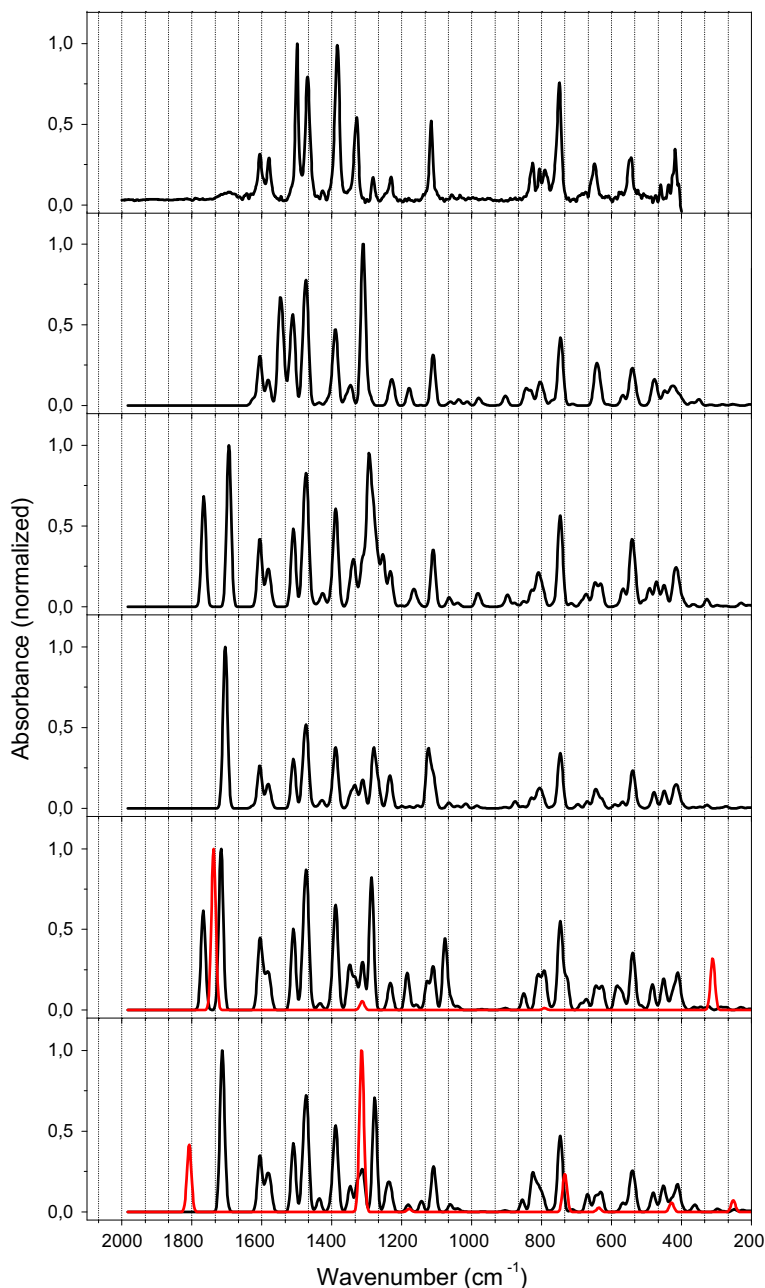
through breaking of double bonds of one of the quinolines, consistent with the spatial localization of frontier molecular orbitals. [27–29]. We only consider modifications in one of the quinoline since, according to theoretical results, the HOMO and LUMO of Alq<sub>3</sub> are localized at only one of quinolate ligands [25]. Fig. 3 shows the optimized structures of degradation products, P1–P5.

Table 1 shows the Gibbs free energy differences for all reactions. As we see, all reactions are favorable. The most favorable reaction is the ozonolysis responsible for the for-

mation of P4 and ethanedioic acid, followed by P5 and ethanedioic acid.

#### 4.2. IR theoretical versus experimental spectra

We now compare experimental IR spectra with theoretical ones. We start by testing our methodology with pristine Alq<sub>3</sub>, shown in Fig. 4. The agreement is very good, except for small discrepancies in the regions from 1340 cm<sup>-1</sup> to 1250 cm<sup>-1</sup> and from 840 cm<sup>-1</sup> to 770 cm<sup>-1</sup>.



**Fig. 5.** Experimental infrared spectrum of irradiated Alq<sub>3</sub> and theoretical spectra of products P1–P5, as well as reaction subproducts. From upper to lower panels, spectra are shown in the following order: irradiated Alq<sub>3</sub> film (experimental), P1, P2, P3, P4 (black) plus glyoxal (red) and P5 (black) plus oxalic acid (red). (For interpretation of the references in colour in this figure legend, the reader is referred to the web version of this article.)

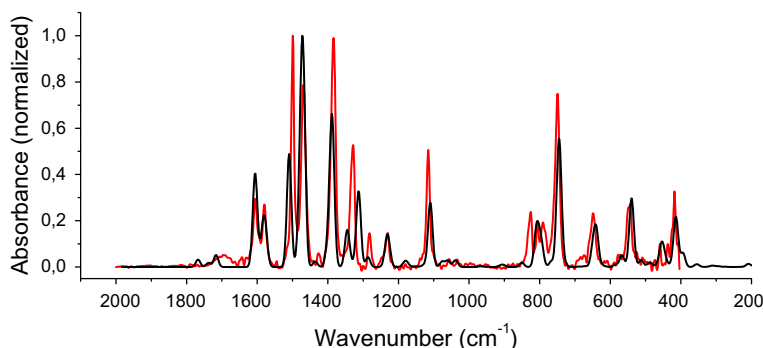


**Fig. 6.** Experimental (red) and theoretical (black) IR spectra for degraded Alq<sub>3</sub>. The theoretical spectrum is a composition between 95% pristine Alq<sub>3</sub> and 5% of products P4 and ethanedial. (For interpretation of the references in colour in this figure legend, the reader is referred to the web version of this article.)

These discrepancies could be attributed to anharmonic effects for modes involving hydrogen atoms and to the fact that calculations are performed for isolated molecules, whereas experiments are done in thin films. In fact, recent works show that calculated vibrational frequencies for aromatic rings including solvent effects show up to 21 cm<sup>-1</sup> difference between frequencies obtained in vacuum and considering the environment [30,31]. Fig. 4 also shows the IR spectrum for the irradiated sample, for comparison with the pristine case. The essential difference between them is a band around 1697 cm<sup>-1</sup>, which corresponds to a vibrational band of the carboxyl group.

In Fig. 5, we plot again the spectrum of the irradiated sample (upper panel), in order to compare it with the theoretical spectra for the P1–P5 products. For all the plots, the height of the most intense peak was normalized to 1. The products P2 and P4, which have only carboxyl acid and not aldehyde, show two extra peaks around 1766 cm<sup>-1</sup> and 1694 cm<sup>-1</sup> (for P2) and 1768 cm<sup>-1</sup> and 1716 cm<sup>-1</sup> (for P4). On the other hand, products P3 and P5, which have aldehyde groups in the structure, show only one peak at 1704 cm<sup>-1</sup> and 1714 cm<sup>-1</sup>, respectively. All these peaks are related to C=O vibrations and they occur in the same spectral region as the experimental peak at 1697 cm<sup>-1</sup>. Based on the fact that it is not possible to see a double-peak structure from experiments, we could be inclined to favor products P3 and P5. However, the experimental feature at 1697 cm<sup>-1</sup> is somewhat broad and we cannot definitely rule out that it is composed of two unresolved peaks. Fig. 5 also shows the calculated IR spectra of possible degradation subproducts ethanedial (glyoxal) and etanedioic acid (oxalic acid).

On the other hand, product P1, obtained from breaking the Al–O bond (a reduction reaction, unlikely to occur in an environment rich in O<sub>2</sub> and O<sub>3</sub>) does not show peaks in region of interest, besides showing a peak at 1548 cm<sup>-1</sup>, which does not appear in experimental spectrum. These results indicate that, contrary to previous suggestions, P1 and related compounds are unlikely degradation products of Alq<sub>3</sub>.

It is important to notice that the intensity ratio of the carbonyl peak with respect to other peaks in all the products P2–P5 is much larger theoretically than experimentally. This simply results from the fact that degradation is

not complete, i.e., only a small fraction of the molecules suffer degradation reactions. Therefore, a closer agreement between theoretical and experimental IR spectra can be achieved if one properly combines the theoretical spectra of degraded and non-degraded Alq<sub>3</sub> so as to match the experimental peak heights. Of course, this procedure should be regarded as semi-quantitative at most, since the exact composition of degradation products is unknown (products P2–P5 can be present at the same time in the degraded samples). However, just as an illustration, we show the result of such fitting procedure in Fig. 6, for the particular case of product P4 with ethanedial. In this case, the ratio between the degraded and non-degraded spectral components is approximately 5%, which gives a rough estimate of the fraction of degraded molecules in the sample.

## 5. Conclusions

In conclusion, the products of photo degradation of Alq<sub>3</sub> films under UV radiation were investigated through the comparison of experimental results and theoretical calculations. The experimental IR spectrum obtained from irradiated Alq<sub>3</sub> thin films exhibits a peak assigned to a vibrational band of carbonyl group at 1697 cm<sup>-1</sup>, exactly as obtained by Thangaraju et al. [14]. Different degradation products were proposed and the feasibility of them was analyzed by Gibbs free energy calculations and by comparing theoretical and experimental IR spectra.

Among the five suggested degradation products, P1, a product involving the breaking of Al–O bond and resultant from reduction process was considered the only unlikely option, since its theoretical IR spectrum showed poor agreement with experiments. This is not unexpected, since the experiments were performed in highly oxidizing environment. Nevertheless, it is important to point out that P1-like products were previously suggested in literature. The other suggested products, P2–P5, involve keeping the Al–O bond and breaking the phenoxide ring. To the best of our knowledge, such degradation products have not been previously considered in literature. Theoretical IR spectra for these products are all in good agreement with experimental results and Gibbs free energy calculations show that all suggested reactions leading to them are thermodynamically

favorable. The association between theory and experimental IR indicates that the degradation of Alq<sub>3</sub> forms carboxylate groups bound to Al.

## Acknowledgements

This work was supported by Brazilian agencies CNPq, FAPERJ.

## References

- [1] Z. Shen, P.B. Burrows, V. Bulovic, S.R. Forrest, M.E. Thompson, Three-color, tunable, organic light-emitting devices, *Science* 276 (1997) 2009–2011.
- [2] H. Aziz, Z.D. Popovic, N.X. Hu, A.M. Hor, G. Xu, Degradation mechanism of small molecule-based organic light-emitting devices, *Science* 283 (1999) 1900–1902.
- [3] Z.D. Popovic, H. Aziz, N.X. Hu, A.M. Hor, G. Xu, Long-term degradation mechanism of tris(8-hydroxyquinoline) aluminum-based organic light-emitting devices, *Synth. Met.* 111–112 (2000) 229–232.
- [4] Z.D. Popovic, H. Aziz, Reliability and degradation of small molecule-based organic light-emitting devices, *IEEE J. Sel. Top. Quant.* 8 (2002) 362–371.
- [5] H. Aziz, Z. Popovic, S. Xie, A. Hor, N. Hu, C.P. Tripp, G. Xu, Humidity-induced crystallization of tris-(8-hydroxyquinoline) aluminum layers in organic light-emitting devices, *Appl. Phys. Lett.* 72 (1998) 756–758.
- [6] E.M. Han, L.M. Do, N. Yamamoto, M. Fujihira, Crystallization of organic thin films for electroluminescent devices, *Thin Solid Films* 273 (1996) 202–208.
- [7] S.Y. Cheng, J.S. Wang, G. Xu, Microstructural studies of organic light-emitting devices by Monte Carlo simulation of two-dimensional triangles, *Phys. Rev. B* 62 (2000) 11405–11411.
- [8] B.H. Cumpston, K.F. Jensen, Photo-oxidation of polymers used in electroluminescent devices, *Synth. Met.* 73 (1995) 195–199.
- [9] J. McElvain, H. Antoniadis, M.R. Hueschen, J.N. Miller, D.M. Roitman, J.R. Sheats, R.L. Moon, Formation and growth of black spots in organic light-emitting diodes, *J. Appl. Phys.* 80 (1996) 6002–6007.
- [10] P.E. Burrows, V. Bulovic, S.R. Forrest, L.S. Sapochak, D.M. McCarty, M.E. Thompson, Reliability and degradation of organic light emitting devices, *Appl. Phys. Lett.* 65 (1994) 2922–2924.
- [11] H. Aziz, G. Xu, Electric-field-induced degradation of poly(*p*-phenylenevinylene) electroluminescent devices, *J. Phys. Chem. B* 101 (1997) 4009–4012.
- [12] Y. Luo, H. Aziz, Z.D. Popovic, G. Xu, Degradation mechanisms in organic light-emitting devices: metal migration model versus unstable tris-(8-hydroxyquinoline) aluminum cationic model, *J. Appl. Phys.* 101 (2007) 034510.1–034510.4.
- [13] R. Priestley, I. Sokolik, A.D. Walser, C.W. Tang, R. Dorsinville, Photooxidation effects on picosecond photoluminescence and photoconductivity in tris-(8-hydroxyquinoline) aluminum (Alq<sub>3</sub>), *Synth. Met.* 84 (1997) 915–916.
- [14] K. Thangaraju, J. Kumar, P. Amaladass, A.K. Mohanakrishnan, V. Narayanan, Study on photoluminescence from tris-(8-hydroxyquinoline) aluminum thin films and influence of light, *Appl. Phys. Lett.* 89 (2006) 082106.1–082106.3.
- [15] S. Kumar, V.K. Shukla, A. Tripathi, Ellipsometric investigations on the light induced effects on tris-(8-hydroxyquinoline) aluminum (Alq<sub>3</sub>), *Thin Solid Films* 477 (2005) 240–243.
- [16] HyperChem(TM) release 7.5, Hypercube, Inc., 1115 NW 4th Street, Gainesville, Florida 32601, USA, 2002.
- [17] M.J. Frisch et al., Gaussian, Inc., Wallingford, CT, 2004.
- [18] J. Tao, J. Perdew, V.N. Staroverov, G.E. Scuseria, Climbing the density functional ladder: nonempirical meta-generalized gradient approximation designed for molecules and solids, *Phys. Rev. Lett.* 91 (2003) 146401.1–146401-4.
- [19] J. Perdew, J. Tao, V.N. Staroverov, G.E. Scuseria, Meta-generalized gradient approximation: explanation of a realistic nonempirical density functional, *J. Chem. Phys.* 120 (2004) 6898–6911.
- [20] M. Brinkmann, G. Gadret, M. Muccini, C. Taliani, N. Masciocchi, A. Sironi, Correlation between molecular packing and optical properties in different crystalline polymorphs and amorphous thin films of mer-tris-(8-hydroxyquinoline)aluminum(III), *J. Am. Chem. Soc.* 122 (2000) 5147–5157.
- [21] G.P. Kushto, Y. Iizumi, J. Kido, Z.H. Kafafi, A matrix-isolation spectroscopic and theoretical investigation of tris-(8-hydroxyquinolinato) aluminum(III) and tris-(4-methyl-8-hydroxyquinolinato) aluminum(III), *J. Phys. Chem. A* 104 (2000) 3670–3680.
- [22] A. Curioni, M. Boero, W. Andreoni, Alq<sub>3</sub>: ab initio calculations of its structural and electronic properties in neutral and charged states, *Chem. Phys. Lett.* 294 (1998) 263–271.
- [23] A. Curioni, W. Andreoni, R. Treusch, F.J. Himpsel, E. Haskai, P. Seidler, C. Heske, S. Kakar, T. van Buuren, L.J. Terminello, Atom-resolved electronic spectra for Alq<sub>3</sub> from theory and experiment, *Appl. Phys. Lett.* 72 (1998) 1575–1577.
- [24] R.L. Martin, J.D. Kress, I.H. Campbell, D.L. Smith, Molecular and solid-state properties of tris-(8-hydroxyquinolate)-aluminum, *Phys. Rev. B* 61 (2000) 15804–15811.
- [25] J. Zhang, G. Frenking, Quantum chemical analysis of the chemical bonds in tris(8-hydroxyquinolinato) aluminum as a key emitting material for OLED, *J. Phys. Chem. A* 108 (2004) 10296–10301.
- [26] M.J. Dyer, C.G. Bressler, R.A. Copeland, Photodissociation of solid oxygen with tunable ultraviolet laser light: ozone production monitored via Fourier-transform infrared spectroscopy, *Chem. Phys. Lett.* 266 (1997) 548–553.
- [27] R. Criegee, Mechanism of ozonolysis, *Angew. Chem., Int. Ed. Engl.* 14 (1975) 745–752.
- [28] C. Geletneky, S. Berger, The mechanism of ozonolysis revisited by 17O-NMR spectroscopy, *Eur. J. Org. Chem.* (1998) 1625–1627.
- [29] P.S. Bailey, Ozonation in Organic Chemistry, *Nonolefinic Compounds*, vol. II, Academic Press, New York, 1982.
- [30] A. Yilmaz, O. Bolukbasi, M. Bakiler, An experimental and theoretical vibrational spectra of isonizide, *J. Mol. Struct.* 872 (2008) 182–189.
- [31] D.K. Singh, S.K. Srivastava, A.K. Ojha, B.P. Asthana, Vibrational study of thiophene its solvation in two polar solvents DMSO and methanol by Raman spectroscopy combined with ab initio and DFT calculations, *J. Mol. Struct.* 892 (2008) 384–391.

diffusion through or even around the top electrode into the photo-active layer, which slows down degradation processes appreciably thus making it a tedious task to understand the mechanisms of the interaction of oxygen with the active layer. The use of gas permeable electrodes together with the exclusion of water from the ambient atmosphere provides a direct and efficient tool to study oxygen induced degradation on the timescale of minutes which allows the observation of the concomitant existence of reversible and irreversible oxygen effects.

## 2. Experimental

To manufacture the semi-transparent cell, an inverted architecture was chosen, which allows the placement of the hole extraction layer on top of the cell. After cleaning the glass/ITO substrate ( $15 \Omega/\square$ ) by sonication in acetone and isopropanol, a proprietary electron extraction layer was applied, followed by the P3HT:PCBM (ratio 1:0.8) active layer, and a highly conductive PEDOT:PSS formulation ( $50 \text{ S/cm}$ ), which acts as the hole extraction layer and as the electrode. For the electron extraction layer (EEL), several different organic and inorganic materials were employed. All layers are applied out of solution by doctor blading. The devices were completed with thermal evaporation of 500 nm of Ag, either as a metal grid (fingers with a distance of 2 mm and a width of 0.15 mm), or as a solid electrode in the case of reference devices (Fig. 1). The processing of the cells is described in more detail elsewhere [14]. The PEDOT:PSS layer has a conductivity of around  $100\text{--}200 \Omega/\square$  and an optical absorption loss of ca. 20%. Before evaporation, all cells were annealed in nitrogen at  $140^\circ\text{C}$  for 5 min.

For characterization, the cells were illuminated with the AM1.5 g spectrum of a Steuernagel Solartest 1200 solar simulator at  $100 \text{ mW/cm}^2$ . All reported results are cor-

rected by the determined mismatch factor of 0.75. *JV*-characteristics (current density vs. voltage) were recorded using a Keithley 2400 SMU together with a Keithley 7001 Multiplexer system and custom software. To avoid errors in cell area, associated with the use of the highly conductive PEDOT:PSS, all measurements were performed with a shadow mask, with an area of  $72 \text{ mm}^2$ , placed directly on top of the cells [15]. During the measurements the cells were placed in a custom holder that allows illumination of the cells from both sides under controlled atmospheres. The holder was sealed on all sides, such that it could be selectively flooded with either dry nitrogen (99.9%  $\text{N}_2$ ,  $\text{H}_2\text{O} < 1 \text{ ppm}$ ) or synthetic air (80%  $\text{N}_2$ , 20%  $\text{O}_2$ ,  $\text{H}_2\text{O} < 1 \text{ ppm}$ ) during the measurements.

## 3. Results

Results of the initial *JV*-characterization in dry nitrogen are shown in Fig. 2 and the performance parameters are summarized in Table 1. The semi-transparent cells perform at the same level as the cells with the solid metal electrode, indicating that in these cells almost all light is collected in the first pass through the semiconductor. When illuminated from the grid electrode side there is a ca. 25% drop in the short circuit current ( $J_{sc}$ ), which agrees well with the measured 20% absorption loss due to the PEDOT:PSS layer in conjunction with a 7% shadowing loss due to the antenna structure. Cells with solid electrodes and grid electrodes show the same fill factors and have the same injection currents, indicating that the grid spacing of 2 mm is sufficiently small, in agreement with what is expected from literature [16,17].

To investigate the influence of oxygen, two sets of samples, each consisting of four cells with semi-transparent electrodes, were prepared. One set of samples was kept under dry nitrogen, while the second set was exposed to syn-

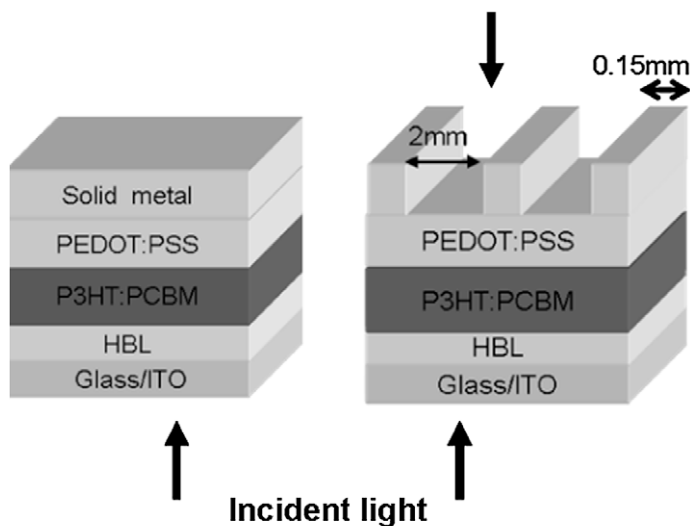


**Fig. 1.** Cell stack; solid metal electrode (diffusion dense) and grid metal electrode (diffusion open). For the experiments shown in Figs. 2 and 3, an organic HBL was used.

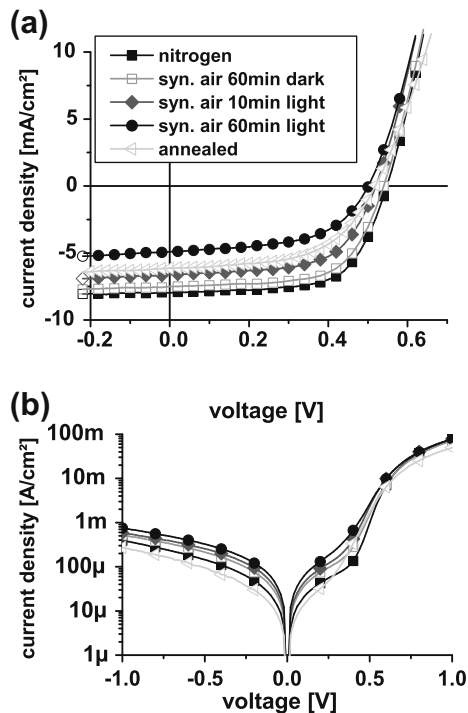


**Fig. 2.** (a) Light *JV*-characteristics of a PEDOT:PSS cell with a grid metal electrode (mesh width 2 mm) at different illumination times under dry nitrogen and synthetic air and after annealing at 140 °C for 5 min inside the GB. Devices were illuminated from the ITO side. (b) Dark *jV* curve under nitrogen and synthetic air.

thetic air. For the first 60 min all cells were stored in the dark, and only exposed to light during the *JV*-measurement (for less than 1 min per measurement) after 30 and 60 min.

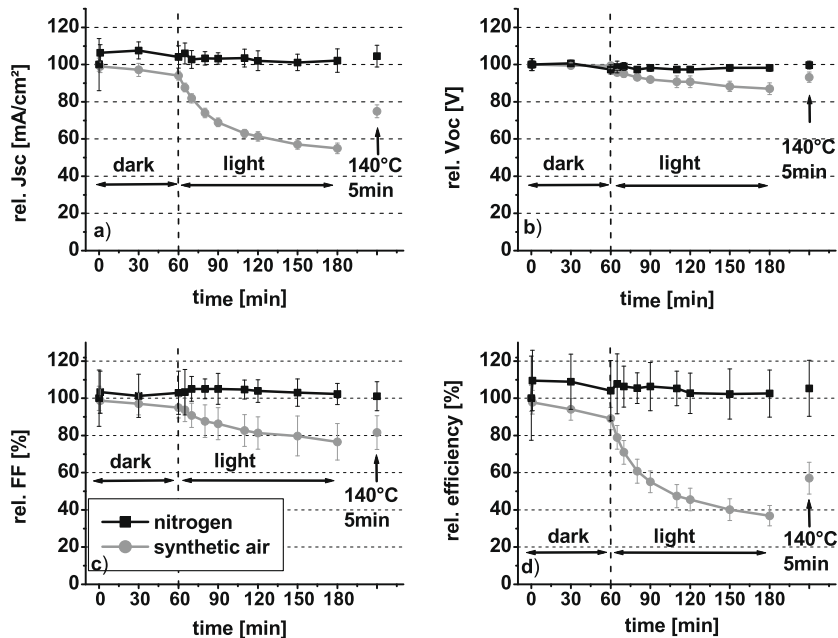


**Fig. 3.** Relative changes of the performance parameters as a function of time in the dark (first 60 min) and under illumination (from 60 to 180 min) for two sets of solar cells, stored under dry nitrogen (black) and dry synthetic air (grey), respectively. (a) Short circuit current ( $J_{sc}$ ), (b) open circuit voltage ( $V_{oc}$ ), (c) fill factor (FF), (d) efficiency. All *JV*-measurements were performed under AM1.5 illumination.

**Table 1**

Comparison of the initial performance of solar cells with solid and grid metal electrode illuminated from the ITO side.

	$J_{sc}$ [mA/cm <sup>2</sup> ]	$V_{oc}$ [V]	FF [%]	Efficiency [%]
Solid metal electrode	8.19	0.54	64	2.83
Grid metal electrode	7.97	0.54	66	2.84

Following the 60 min of storage in the dark, the cells were continuously exposed to light for 120 min, and *JV*-sweeps were performed after 5, 10, 30, 60 and 120 min.

The evolution of the performance parameters is shown in Fig. 3 for a cell comprising an organic EEL. The results for cells with inorganic EELs are qualitatively the same. In the dark, in both in nitrogen and synthetic air, the performance changes only little. When AM1.5 illumination is turned on, in the nitrogen atmosphere only small changes in performance are observed. However, when the cells are exposed to oxygen and light at the same time, a dramatic effect on cell performance is observed. The largest change is observed in  $J_{sc}$ , which decreases by more than 50% during 120 min of exposure. At the same time the fill factor (FF) drops by ca. 20%, and the open circuit Voltage ( $V_{oc}$ ) by ca. 15%, resulting in a total loss of efficiency by more than 60% within 2 h of exposure. A small increase of the dark leakage current in reverse bias indicates doping of the photo-active layer upon exposure to oxygen and light. The degrading effect caused by light and oxygen is also responsible for the small  $J_{sc}$  drop observed after the exposure to oxygen in the dark, where the samples had to be illuminated during characterization, effectively adding up to a total of ca. 3 min of light exposure during the 60 min of dark exposure.

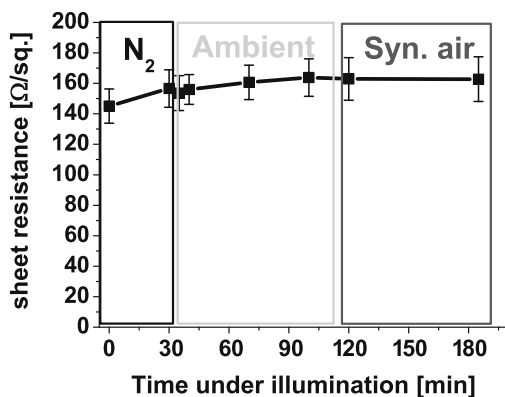


Fig. 4. Surface resistance of a PEDOT:PSS layer exposed to different atmospheres under AM 1.5 illumination as a function of time.

To investigate the reversibility of the degradation processes caused by exposure to light and oxygen, the degraded devices were heated on a hot plate at 140 °C for 5 min under nitrogen atmosphere. The heat treatment restores about 30% of the loss of performance, with most of the recovery observed for  $J_{sc}$  (Fig. 3).

In order to examine the loss of conductivity of PEDOT:PSS as a possible source for the drop of performance, we performed resistivity measurements using the transmission line method [18] on PEDOT:PSS layers which were exposed to a variety of conditions (Fig. 4). Obviously, the small changes in resistivity under oxygen and illumination obtained in these experiments cannot account for the dramatic decrease in  $J_{sc}$  which we observe in our cells.

Other possible sources for the observed degradation are oxygen induced effects on P3HT or PCBM. The stability of P3HT has been studied extensively in Organic Field Effect Transistors (OFETs). A number of studies found an increase in the off-current of OFETs which is the result of p-doping due to the formation of a charge transfer complex (CTC) between P3HT and oxygen [19–23]. CTC formation is significantly accelerated by the exposure to light [19]. Several publications note that the effects of oxygen are either partially or fully reversible through vacuum storage or by annealing the polymer near the glass transition temperature, with the degree of reversibility depending on the conditions during exposure to oxygen.

The effect of oxygen on films and single crystals of  $\text{C}_{60}$  has also been studied by several groups.  $\text{C}_{60}$  shows a decrease of both dark [24–29] and photoconductivity [30] by up to five orders of magnitude, upon exposure to oxygen which acts as a compensating dopant in the n-type semiconductor  $\text{C}_{60}$ . These doping effects can be reversed by heating the samples in vacuum [28]. Exposure of  $\text{C}_{60}$  to light in the presence of oxygen leads to the formation of deep localized traps [25,31] due to irreversible chemical reactions [32–34].

#### 4. Conclusion

In this paper we demonstrate the use of inverted semi-transparent cells with gas permeable top electrodes as a

tool to investigate environmental degradation of organic solar cells. The simultaneous exposure of these cells to oxygen and light results in a strong reduction of  $J_{sc}$ , accompanied by only small reductions in  $V_{oc}$  and FF, which hints to the deterioration of charge separation in the photo-active layer [13,35] rather than to problems with charge extraction at the interfaces. The latter are usually characterized by an increase in the serial resistance and/or the appearance of a kink in the fourth quadrant, which strongly reduces the FF. This interpretation is further confirmed by the fact that no change in the conductivity of the PEDOT:PSS layer is found. Moreover, the degradation behavior of the cells shows strong similarities to that observed in OFETs, e.g., the partial recovery of cell performance by heat treatment under nitrogen. While our measurements are not able to resolve all the details of the degradation process, they indicate that both, the reversible and the irreversible component of the observed degradation take place in the photo-active layer. At this point in time it is not possible to resolve the question whether the degradation is due to chemical changes of the P3HT, PCBM or both species. Further work is also needed to investigate the doping of the active layer.

Semi-transparent cells with gas permeable top electrodes are a useful tool for investigating degradation mechanisms in organic solar cells, allowing the observation of reversible and irreversible oxygen effects on short time scales. This method is thus a significant step forward in quantifying and analyzing the degradation of polymer solar cells.

#### Acknowledgement

We acknowledge the financial support by the German Ministry for Research (BMBF project “OPV Stability”, FKZ 03SF0334A).

#### References

- [1] C.J. Brabec, Organic photovoltaics: technology and market, *Sol. Energy Mater. Sol. Cells* 83 (2004) 273–292.
- [2] T. Aernouts, P. Vanlaeke, W. Geens, J. Poortmans, P. Heremans, S. Borghs, R. Mertens, R. Andriessen, L. Leenders, Printable anodes for flexible organic solar cell modules, *Thin Solid Films* 451–452 (2004) 22–25.
- [3] M. Glatthaar, M. Niggemann, B. Zimmermann, P. Lewer, M. Riede, A. Hinsch, J. Luther, Organic solar cells using inverted layer sequence, *Thin Solid Films* 491 (2005) 298–300.
- [4] K. Tvingstedt, O. Inganäs, Electrode grids for ITO-free organic photovoltaic devices, *Adv. Mater.* 19 (2007) 2893–2897.
- [5] J. Huang, G. Li, Y. Yang, A semi-transparent plastic solar cell fabricated by a lamination process, *Adv. Mater.* 20 (2008) 415–419.
- [6] Y. Zhou, F. Li, S. Barrau, W. Tian, O. Inganäs, F. Zhang, Inverted and transparent solar cell prepared with vacuum-free processing, *Sol. Energy Mater. Sol. Cells* 93 (2009) 497–500.
- [7] F.C. Krebs, S.A. Gevorgyan, J. Alstrup, A roll-to-roll process to flexible polymer solar cells: model studies, manufacture and operational stability studies, *J. Mater. Chem.* (2009), doi:10.1039/B823001C.
- [8] M. Jørgensen, K. Norrman, F.C. Krebs, Stability/degradation of polymer solar cells, *Sol. Energy Mater. Sol. Cells* 92 (2008) 686–714.
- [9] S.A. Gevorgyan, M. Jørgensen, F.C. Krebs, A setup for studying stability and degradation of polymer solar cells, *Sol. Energy Mater. Sol. Cells* 92 (2008) 736–745.
- [10] M.H. Petersen, S.A. Gevorgyan, F.C. Krebs, Thermocleavable low band gap polymers and solar cells therefrom with remarkable stability toward oxygen, *Macromolecules* 41 (2008) 8986–8994.



- [11] K. Norrman, F.C. Krebs, Lifetimes of organic photovoltaics: using TOF-SIMS and O<sub>2</sub> isotopic labelling to characterise chemical degradation mechanisms, *Sol. Energy Mater. Sol. Cells* 90 (2006) 213–227.
- [12] K. Norrman, S.A. Gevorgyan, F.C. Krebs, Water-induced degradation of polymer solar cells studied by H<sub>2</sub>18O labeling, *Appl. Mater. Interfaces* 1 (2009) 102–112.
- [13] M. Glatthaar, M. Riede, N. Keegan, K. Sylvester-Hvid, B. Zimmermann, M. Niggemann, A. Hinsch, A. Gombert, Efficiency limiting factors of organic bulk heterojunction solar cells identified by electrical impedance spectroscopy, *Sol. Energy Mater. Sol. Cells* 91 (2007) 390–393.
- [14] C. Waldauf, M. Morana, P. Denk, P. Schilinsky, K. Coakley, S.A. Choulis, C.J. Brabec, Highly efficient inverted organic photovoltaics using solution based titanium oxide as electron selective contact, *Appl. Phys. Lett.* 89 (2006) 233517.
- [15] A. Cravino, P. Schilinsky, C.J. Brabec, Characterization of organic solar cells: the importance of device layout, *Adv. Funct. Mater.* 17 (2007) 3906–3910.
- [16] A. Goetzberger, B. Voß, J. Knobloch, *Sonnenenergie: Photovoltaik*, second ed., Teubner Verlag, 1997.
- [17] A. Cheknane, B. Benyoucef, J.-P. Charles, R. Zerdoum, M. Trari, Minimization of the effect of the collecting grid in a solar cell based silicon, *Sol. Energy Mater. Sol. Cells* 87 (2005) 557–565.
- [18] S.S. Cohen, Contact resistance and methods for its determination, *Thin Solid Films* 104 (1983) 361–379.
- [19] H.-H. Liao, C.-M. Yang, C.-C. Liu, S.-F. Horng, H.-F. Meng, J.-T. Shy, Dynamics and reversibility of oxygen doping and de-doping for conjugated polymer, *J. Appl. Phys.* 103 (2008) 104506.
- [20] S. Hoshino, M. Yoshida, S. Uemura, T. Kodzasa, N. Takada, T. Kamata, K. Yase, Influence of moisture on device characteristics of polythiophene-based field-effect transistors, *J. Appl. Phys.* 95 (5) (2004) 5088.
- [21] M.L. Chabinyk, R.A. Street, J.E. Northrup, Effects of molecular oxygen and ozone on polythiophene-based thin-film transistors, *Appl. Phys. Lett.* 90 (2007) 123508.
- [22] H.-J. Egelhaaf, L. Lüer, D. Oelkrug, G. Winter, P. Haisch, M. Hanack, Influence of oxygen doping on the photoconductivity of pi-conjugated molecules, *Synth. Met.* 84 (1997) 897–898.
- [23] L. Lüer, H.-J. Egelhaaf, D. Oelkrug, G. Cerullo, G. Lanzani, B.-H. Huisman, D.d. Leeuw, Oxygen-induced quenching of photoexcited states in polythiophene films, *Org. Electron.* 5 (2004) 83–89.
- [24] C.H. Lee, G. Yu, B. Kraabel, D. Moses, V.I. Srdanov, Effects of oxygen on the photocarrier dynamics in a C60 film: studies of transient and steady-state photoconductivity, *Phys. Rev. B* 49 (15) (1994) 10572–10576.
- [25] H. Habuchi, S. Nitta, D. Han, S. Nonomura, Localized electronic states related to O<sub>2</sub> intercalation and photoirradiation on C60 films and C70 films, *J. Appl. Phys.* 87 (12) (2000) 8580–8588.
- [26] R. Könenkamp, G. Priebe, B. Pietzak, Carrier mobilities and influence of oxygen in C60 films, *Phys. Rev. B* 60 (16) (1999) 11804–11808.
- [27] C.P. Jarrett, K. Pichler, R. Newbould, R.H. Friend, Transport studies in CeO and C60/C70 thin films using metalinsulatorsemiconductor field-effect transistors, *Synth. Met.* 77 (1996) 35–38.
- [28] A. Tapponnier, I. Biaggio, P. Günter, Ultrapure C60 field effect transistors and the effect of oxygen exposure, *Appl. Phys. Lett.* 86 (2005) 112114.
- [29] T. Arai, Y. Murakami, H. Suematsu, K. Kikuchi, Y. Achiba, I. Ikemoto, Resistivity of single crystal C60 and effect of oxygen, *Solid State Commun.* 84 (8) (1992) 827–829.
- [30] M. Kaiser, W.K. Maser, H.J. Byrne, A. Mittelbach, S. Roth, Photoconductivity of thin films fullerenes; effect of oxygen and thermal annealing, *Solid State Commun.* 87 (4) (1993) 281–284.
- [31] E.A. Katz, D. Faiman, B. Mishori, Y. Shapira, A.I. Shames, S. Shtutina, S. Goren, Changes in the photoelectrical properties and generation of photoinduced defects under light/air exposure of C60 thin films, *J. Appl. Phys.* 84 (6) (1998) 3333–3337.
- [32] A. Hamed, Y.Y. Sun, Y.K. Tao, R.L. Meng, P.H. Hor, Effects of oxygen and illumination on the in situ conductivity of C60 films, *Phys. Rev. B* 47 (16) (1993) 10873–10880.
- [33] K.M. Creegan, J.L. Robbins, W.K. Robbins, J.M. Millar, R.D. Sherwood, P.J. Tindall, D.M. Cox, J.P. McCauley, R.T. Gallagher, Synthesis and Characterization of Cm0, the First Fullerene Epoxide, *J. Am. Chem. Soc.* 114(3) (1992) 1103–1107.
- [34] P.C. Eklund, A.M. Rao, P. Zhou, Y. Wang, J.M. Holden, Photochemical transformation of C and C<sub>60</sub> films, *Thin Solid Films* 257 (1995) 185–203.
- [35] M. Glatthaar, N. Mingirulli, B. Zimmermann, T. Ziegler, R. Kern, M. Niggemann, A. Hinsch, A. Gombert, Impedance spectroscopy on organic bulk-heterojunction solar cells, *Phys. Stat. Sol. A* 202 (11) (2005) R125–R127.

When donor and acceptor molecules are combined to prepare donor- $\sigma$ -acceptor molecules through the  $\sigma$ -bond, they are promising candidates for the construction of molecular rectifiers [12,13] or organic solar cells [14–16], either as active layers or as models for the investigation of the origin of the photoinduced energy and electron transfer.

As an electron acceptor, PDI is a well-known n-type semiconducting molecule and a photostable dye suitable for applications in organic solar cells [17,18]. Thus, PDIs have been recently linked to small molecules [[60] fullerene, pyrenes, phthalocyanines, porphyrins, or tetra-thiafulvalene], thiophene-based oligomers, and conjugated polymers, as the donor counterpart aiming toward the induction of PET [19–22].

Charge transfer complexation is often observed in the ground states of solids through strong intermolecular interactions, which are sometimes unavoidable. There are several reports explaining how two electronically opposite moieties can be isolated to form a self-organized individual/homogeneous domain with a mesoscopic scale. Bauer et al. recently reported the energy transfer and PET processes of donor- $\sigma$ -acceptor molecules in terms of absorption and photophysical properties [23]. Tetraphenylbenzidine and PDI were selected to be an electron donor and an electron acceptor, respectively. A long alkylene spacer was employed to make two semiconducting moieties separate to show their independent electronic and photophysical properties, claiming to be a good model for the study of energy- and electron-transfer processes in dual function semiconductors.

More recently, an oligo(p-phenylenevinylene)-fullerene dyad was employed for efficient photovoltaic cells. They were fabricated with a configuration of ITO/poly(3,4-ethylenedioxythiophene):poly(styrene sulfonic acid) (PEDOT:PSS)/dyad/poly-(dimethyl siloxane-b-methyl methacrylate)/Al. The PCE reached 1.28% which is the highest reported value for dyad-based photovoltaic cell [24].

X-shaped, organic soluble semiconducting molecules were reported by authors of the present study [25]. 1,2,4,5-Tetrakis((E)-2-(5'-hexyl-2,2'-bithiophen-5-yl)vinyl)-benzene (HPBT) contains bithiophene units in four peripheral arms. The molecule is highly soluble in organic solvents and is pseudo-planar and easily stacked, inducing a high degree of crystallization. The carrier mobility of organic thin film transistors fabricated with HPBT was measured to be  $3.0\text{--}5.0 \times 10^{-3} \text{ cm}^2/\text{V s}$ . The employment of HPBT-based donors in combination with PDIs can be quite useful, as HPBT with relatively high quantum yield undergoes aromatization upon oxidation, providing thermodynamically stable radical ionic species. Thus, we decided to synthesize HPBT- $n$ (PDI) ( $n = 1, 2, \text{ and } 4$ ), in which a PDI electron accepting unit has been covalently attached to an HPBT through flexible alkylene spacer(s), providing a high degree of freedom to both semiconducting moieties. It was anticipated that the incorporation of HPBT as a donor and PDI as an acceptor moiety would result in self-organized thermal crystallization by virtue of a high degree of independent aggregation.

## 2. Experiment

### 2.1. Synthesis

Compounds **1**, **4**, **7**, **8**, **13**, **21**, and **22** were synthesized by following the literature method [25–29].

**Compound 2:** A mixture of 6-amino-1-pentanol (16.0 g, 0.16 mol) and zinc acetate (0.07 g, 0.38 mmol) in *N,N*-dimethylacetamide (DMAc) (250 mL) was heated to 110 °C under a nitrogen atmosphere. Compound **1** (26.0 g, 0.041 mol) was added and the reaction mixture was stirred at 110 °C for 3 h. Then, the reaction continued at 160 °C for 15 h under a nitrogen atmosphere. The excess solvent was distilled off. The crude product was purified by silica-gel column chromatography using chloroform. The product was precipitated into methanol. The material was filtered and dried in a vacuum oven. Yield: 20.0 g (68%).  $^1\text{H NMR}$  (300 MHz,  $\text{CDCl}_3$ )  $\delta$  (ppm) 8.63–8.52 (m, 8H), 5.24–5.14 (m, 1H), 4.22 (t, 2H), 3.70 (t, 2H), 2.30–2.23 (m, 2H), 1.97–1.77 (m, 4H), 1.74–1.65 (m, 2H), 1.32–1.21 (m, 26H), 0.834 (t, 6H). Anal. calcd for  $\text{C}_{46}\text{H}_{54}\text{N}_2\text{O}_5$ : C 77.28; H 7.61; N 3.92, found: C 76.71.0; H 6.97; N 3.20. MS ( $m/z$ ): [ $\text{M}^+\text{H}$ ] calcd for  $\text{C}_{46}\text{H}_{54}\text{N}_2\text{O}_5$  714.4; found 715.6.

**Compound 3:** Compound **2** (15.0 g, 20.0 mmol), 4-dimethylaminopyridine (DMAP) (1.28 g, 10.4 mmol), and triethylamine (TEA) (3.18 g, 31.4 mmol) were dissolved in 250 mL of dichloromethane. And succinic anhydride (4.72 g, 47.2 mmol) was added and the reaction mixture was allowed to stir for 24 h under argon at room temperature. The reaction mixture was extracted by chloroform and water. The crude product was purified by silica-gel column chromatography (eluent; ethyl acetate:chloroform, 1:6, v/v). The solid product was precipitated into methanol. The product was filtered and dried in a vacuum oven. Yield: 15.0 g (88%).  $^1\text{H NMR}$  (400 MHz,  $\text{CDCl}_3$ )  $\delta$  (ppm) 8.56–8.43 (m, 8H), 5.19–5.15 (m, 1H), 4.20–4.13 (m, 4H), 2.72–2.65 (m, 4H), 2.28–2.20 (m, 2H), 1.91–1.85 (m, 2H), 1.81–1.70 (m, 4H), 1.57–1.51 (m, 2H), 1.40–1.10 (m, 24H), 0.80 (t, 6H). Anal. calcd for  $\text{C}_{50}\text{H}_{58}\text{N}_2\text{O}_8$ : C 73.68; H 7.17; N 3.44, found: C 74.0; H 6.87; N 3.20. MS ( $m/z$ ): [ $\text{M}^+\text{H}$ ] calcd for  $\text{C}_{50}\text{H}_{58}\text{N}_2\text{O}_8$  814.4; found 814.8.

**Compound 5:** Compound **4** (14.0 g, 42.5 mmol) and potassium acetate (8.34 g, 85.0 mmol) were dissolved in 300 mL of DMF. The reaction mixture was allowed to stir for 24 h under argon at 60 °C. The mixture was extracted by chloroform and water. The crude product was purified by silica-gel column chromatography (eluent; ethyl acetate:hexane = 1:10, v/v) to yield 6-(2,2'-bithiophen-5-yl)-hexyl acetate, **5**. Yield: 9.0 g (83%).  $^1\text{H NMR}$  (400 MHz,  $\text{CDCl}_3$ ):  $\delta$  (ppm) 7.13 (d,  $J = 4.0$  Hz, 1H), 7.08 (d,  $J = 4.4$  Hz, 1H), 6.97–6.70 (m, 2H), 6.65 (d,  $J = 3.52$  Hz, 1H), 4.03 (t, 2H), 2.76 (t, 2H), 2.02 (s, 3H), 1.70–1.57 (m, 4H), 1.37 (t, 4H). Anal. calcd for  $\text{C}_{16}\text{H}_{20}\text{O}_2\text{S}_2$ : C 62.30; H 6.54; S 20.79, found: C 62.46; H 6.54; S 20.63. MS ( $m/z$ ): [ $\text{M}^+\text{H}$ ] calcd for  $\text{C}_{16}\text{H}_{20}\text{O}_2\text{S}_2$  308.1; found 308.4.

**Compound 6:** DMF (14.6 g, 0.2 mmol) and 1,2-dichloroethane (300 mL) was stirred at 0 °C.  $\text{POCl}_3$  (6.33 g, 41.3 mol) was slowly added to the mixture for 30 min. Compound **5** (8.50 g, 27.5 mmol) in 1,2-dichloroethane (20 mL) was added dropwise over 20 min. The mixture

was stirred for 12 h at 60 °C. After completing the reaction, it was poured into 300 mL of ice water, and neutralized with NaHCO<sub>3</sub> aqueous solution. The aqueous solution was extracted with chloroform. The organics were then dried over Na<sub>2</sub>SO<sub>4</sub>, filtered, and the solvent was removed *in vacuo*. The resulting product was purified by silica-gel column chromatography (eluent: dichloromethane:hexane = 12:1, v/v) to yield 6-(5'-formyl-2,2'-bithiophen-5-yl)hexyl acetate, **6**. Yield: 8.20 g (89%). <sup>1</sup>H NMR (400 MHz, CDCl<sub>3</sub>): δ (ppm) 9.83 (s, 1H), 7.65 (d, *J* = 4.28 Hz, 1H), 7.18–7.16 (m, 2H), 6.74 (d, *J* = 3.52 Hz, 1H), 4.06 (t, 2H), 2.82 (t, 2H), 2.04 (s, 3H), 1.74–1.60 (m, 4H), 1.42 (t, 4H). Anal. calcd for C<sub>17</sub>H<sub>20</sub>O<sub>3</sub>S<sub>2</sub>: C 60.68; H 5.99; S 19.06, found: C 60.65; H 5.90; S 19.17. MS (*m/z*): [M<sup>+</sup>+H] calcd for C<sub>16</sub>H<sub>20</sub>O<sub>2</sub>S<sub>2</sub> 336.1; found 337.3.

**Compound 9:** Octaethyl benzene-1,2,4,5-tetrayltetrakis(methylene)tetrphosphonate, **8** (2.71 g, 3.99 mmol), compound **6** (1.1 g, 3.23 mmol), and compound **7** (2.7 g, 9.70 mmol) were dissolved in 250 mL of dried THF. And potassium *tert*-butoxide (0.94 g, 8.40 mmol) in THF was slowly added and the reaction mixture was allowed to stir for 7 h under argon. It was poured into ethanol and HCl was added to obtain solid precipitate. The resulting product was purified by silica-gel column chromatography (eluent: toluene) to yield 6-(5'-((E)-4-((E)-2-(5'-heptyl-2,2'-bithiophen-5-yl)vinyl)-2,5-bis((E)-2-(5'-hexyl-2,2'-bithiophen-5-yl)vinyl) styryl)-2,2'-bithiophen-5-yl)-hexyl acetate, **9**. Yield: 0.90 g (18%). <sup>1</sup>H NMR (300 MHz, CDCl<sub>3</sub>): δ (ppm) 7.64 (s, 2H), 7.13 (s, 8H), 7.03–6.98 (m, 12H), 6.69 (d, *J* = 3.57 Hz, 4H), 4.06 (t, 2H), 2.79 (t, 8H), 2.05 (s, 3H), 1.71–1.63 (m, 10H), 1.42–1.28 (m, 22H), 0.89 (t, 9H). Anal. calcd for C<sub>72</sub>H<sub>80</sub>O<sub>2</sub>S<sub>8</sub>: C 70.08; H 6.53; S 20.79, found: C 69.12; H 5.96; S 20.30. MS (*m/z*): [M<sup>+</sup>+H] calcd for C<sub>72</sub>H<sub>80</sub>O<sub>2</sub>S<sub>8</sub> 1232.4; found 1232.3.

**Compound 10:** Compound **9** (0.80 g, 0.648 mmol) was dissolved in 250 mL of dried THF. LiOH (0.12 g, 2.85 mmol) in H<sub>2</sub>O was added to mixture and allowed to stir for 24 h under argon. The mixture was neutralized with HCl aqueous solution. The aqueous solution was extracted with chloroform. The organics were then dried over Na<sub>2</sub>SO<sub>4</sub>, filtered, and the solvent was removed *in vacuo*. The resulting product was purified by silica-gel column chromatography (eluent: chloroform) to yield 6-(5'-((E)-4-((E)-2-(5'-heptyl-2,2'-bithiophen-5-yl)vinyl)-2,5-bis((E)-2-(5'-hexyl-2,2'-bithiophen-5-yl)vinyl)-styryl)-2,2'-bithiophen-5-yl)hexan-1-ol, **10**. Yield: 0.6 (85%). <sup>1</sup>H NMR (400 MHz, CDCl<sub>3</sub>): δ (ppm) 7.63 (s, 2H), 7.13 (d, 8H), 7.02–6.98 (m, 12H), 6.68 (d, *J* = 4.76 Hz, 4H), 3.68–3.62 (m, 2H), 2.83–2.77 (m, 8H), 1.73–1.63 (m, 10H), 1.44–1.28 (m, 22H), 0.89 (t, 9H). MS (*m/z*): [M<sup>+</sup>+H] calcd for C<sub>70</sub>H<sub>78</sub>OS<sub>8</sub> 1190.4; found 1191.0.

**Compound 12:** Compound **8** (1.44 g, 2.12 mmol) and compound **6** (3.0 g, 8.91 mmol) were dissolved in 250 mL of dried THF. And potassium *tert*-butoxide (3.0 g, 27.0 mmol) in THF was slowly added and the reaction mixture was allowed to stir for 7 h under argon. When the spot of compound **11** disappeared in the TLC, the mixture was poured into excess amount of H<sub>2</sub>O. The filtrate was concentrated and organics were then dried over Na<sub>2</sub>SO<sub>4</sub>, filtered, and the solvent was removed *in vacuo*. The resulting product was purified by silica-gel column chromatography

(eluent: chloroform) to yield 6,6',6'',6'''-(5',5'',5''',5''''-(1E,1'E,1''E,1'''E)-2,2',2'',2'''-(benzene-1,2,4,5-tetrayl)tetrakis-(ethene-2,1-diyl)tetrakis(2,2'-bithiophene-5',5'-diyl))-tetra hexan-1-ol. Yield: 0.7 g (28%). <sup>1</sup>H NMR (300 MHz, CDCl<sub>3</sub>): δ (ppm) 7.89 (s, 2H), 7.49 (d, *J* = 15.0 Hz, 4H), 7.24–7.15 (m, 16H), 6.81 (d, *J* = 3.6 Hz, 4H), 4.37 (t, 4H), 2.79 (t, 8H), 2.51 (s, 8H), 1.63–1.33 (m, 32H). Anal. calcd for C<sub>70</sub>H<sub>78</sub>O<sub>4</sub>S<sub>8</sub>: C 67.81; H 6.34; S 20.69, found: C 67.14; H 6.51; S 19.81.

**Compound 14:** Compound **7** (4.62 g, 16.6 mmol) and compound **13** (4.0 g, 8.32 mmol) were dissolved in 250 mL of freshly dried THF. Potassium *tert*-butoxide (1.86 g, 16.64 mmol) in THF was slowly added and the reaction mixture was allowed to stir for 24 h under argon. It was poured ethanol to quench potassium *tert*-butoxide. The resulting crude product was purified by silica-gel column chromatography (eluent: chloroform) to yield 5',5''-(1E,1'E)-2,2'-(2,5-dibromo-1,4-phenylene)bis(ethene-2,1-diyl)bis(5-hexyl-2,2'-bithiophene). Yield: 4.5 g (70%). <sup>1</sup>H NMR (400 MHz, CDCl<sub>3</sub>): δ (ppm) 7.81 (s, 2H), 7.17 (d, *J* = 15.6 Hz, 2H), 7.11 (d, *J* = 15.6 Hz, 2H), 7.04–7.02 (m, 6H), 6.71 (d, *J* = 3.6 Hz, 2H), 2.80 (t, 4H), 1.71–1.66 (m, 4H), 1.39–1.30 (m, 12H), 0.90 (t, 6H). MS (*m/z*): [M<sup>+</sup>+H] calcd for C<sub>38</sub>H<sub>40</sub>Br<sub>2</sub>S<sub>4</sub> 782.0, found 782.3. Anal. calcd for C<sub>38</sub>H<sub>40</sub>Br<sub>2</sub>S<sub>4</sub>: C 58.16; H 5.14; S 16.34, found: C 58.85; H 5.01; S 17.16.

**Compound 15:** Methyltriphenylphosphonium iodide (6.0 g, 14.8 mmol) and potassium-*tert*-butoxide (1.66 g, 14.8 mmol) were mixed in 200 mL THF. The mixture was turned to be a yellow suspension. The reaction was allowed to stir for 10 min at room temperature and 50 mL THF solution of compound **6** (5.0 g, 14.8 mmol) was slowly added into the mother mixture. After completion of the reaction, it was poured ethanol and hexane. The filtrate was concentrated and hexane was added to make precipitation of triphenylphosphate. The organics were then dried over Na<sub>2</sub>SO<sub>4</sub>, filtered, and the solvent was removed *in vacuo*. The resulting product was purified by silica-gel column chromatography (eluent: chloroform) to yield 6-(5'-vinyl-2,2'-bithiophen-5-yl)hexyl acetate. Yield: 1.5 g (31%). <sup>1</sup>H NMR (300 MHz, CDCl<sub>3</sub>): δ (ppm) 6.97–6.93 (m, 2H), 6.84 (d, *J* = 3.9 Hz, 1H), 6.79–6.69 (m, 1H), 6.67 (d, *J* = 3.6 Hz, 1H), 5.53 (d, *J* = 16.5 Hz, 1H), 5.13 (d, *J* = 10.8 Hz, 1H), 4.05 (t, 2H), 2.78 (t, 2H), 2.04 (s, 3H), 1.73–1.62 (m, 4H), 1.45–1.37 (m, 4H). MS (*m/z*): [M<sup>+</sup>+H] calcd for C<sub>18</sub>H<sub>22</sub>O<sub>2</sub>S<sub>2</sub> 334.1; found 334.1. Anal. calcd for C<sub>18</sub>H<sub>22</sub>O<sub>2</sub>S<sub>2</sub>: C 64.63; H 6.63; S 19.17, found: C 64.75; H 6.64; S 19.31.

**Compound 16:** Compound **14** (0.44 g, 1.8 mmol), compound **15** (1.3 g, 4.0 mmol), and tri-*o*-tolylphosphine (0.22 g, 0.72 mmol) were dissolved in 200 mL of DMF. Then, tributylamine (0.67 g, 3.6 mmol) was added into the mixture. After 10 min stirring, Pd(OAc)<sub>2</sub> (0.040 g, 0.18 mmol) was added and the mixture was stirred at 95 °C overnight. Then, water (150 mL) was added to the reaction mixture. The resultant precipitate was filtered and washed with methanol twice. The precipitate was purified by silica-gel column chromatography (eluent: chloroform:hexane = 2:1, v/v). Yield: 0.57 g (24%). <sup>1</sup>H NMR (300 MHz, CDCl<sub>3</sub>): δ (ppm) 7.60 (s, 2H), 7.12–6.97 (m, 20H), 6.67 (d, *J* = 3.0 Hz, 4H), 4.06 (t, 4H), 2.79 (t, 8H),

2.05 (s, 6H), 1.70–1.62 (m, 12H), 1.42–1.31 (m, 20H), 0.90 (t, 6H). MS (*m/z*): [*M*<sup>+</sup>+H] calcd for C<sub>74</sub>H<sub>82</sub>O<sub>4</sub>S<sub>8</sub>: 1290.4; found 1291.7. Anal. calcd for C<sub>74</sub>H<sub>82</sub>O<sub>4</sub>S<sub>8</sub>: C 68.79; H 6.40; S 19.86, found: C 67.94; H 6.35; S 20.14.

**Compound 17:** Compound **16** (1.50 g, 1.14 mmol) were dissolved in 200 mL of THF. LiOH (1.0 g, 23.8 mmol) in H<sub>2</sub>O was added to mixture and allowed to stir for 24 h under argon at 75 °C. It was poured into excess amount of H<sub>2</sub>O. The filtrate was concentrated and organics were then dried over NaSO<sub>4</sub>, filtered, and the solvent was removed *in vacuo*. The resulting product was purified by silica-gel column chromatography (eluent; 1,2-dichloroethane:THF = 10:1, v/v). Yield: 1.2 g (86%). <sup>1</sup>H NMR (400 MHz, CDCl<sub>3</sub>): δ (ppm) 7.65 (s, 2H), 7.15 (s, 8H), 7.03–6.99 (m, 12H), 6.69 (d, *J* = 3.2 Hz, 4H), 3.68–3.62 (m, 4H), 2.83–2.77 (m, 8H), 1.73–1.63 (m, 10H), 1.43–1.20 (m, 22H), 0.89 (t, 6H). MS (*m/z*): [*M*<sup>+</sup>+H] calcd for C<sub>70</sub>H<sub>78</sub>O<sub>2</sub>S<sub>8</sub>: 1206.3; found 1206.4. Anal. calcd for C<sub>70</sub>H<sub>78</sub>O<sub>2</sub>S<sub>8</sub>: C 69.60; H 6.51; S 21.24, found: C 68.76; H 6.19; S 23.63.

**HPBT-1(PDI), 18:** Compound **10** (0.59 g, 0.49 mmol), compound **3** (0.64 g, 0.79 mmol), dicyclohexylcarbodiimide (DCC) (0.17 g, 0.837 mmol), and 4-(dimethylamino)pyridium-4-toluene sulfonate (DPTS) (0.22 g, 0.74 mmol) were dissolved in 150 mL of 1,2-dichloromethane at room temperature under argon. The reaction mixture was allowed to stir for 24 h. After completion of the reaction, the solution was concentrated to the crude solid. Using chloroform, dissolution and filtration were repeated for removing white dicyclohexyl urea. The resulting mixture was poured into methanol to make the precipitate and the crude product was filtered. The resulting product was purified by silica-gel column chromatography (eluent; chloroform:ethyl acetate = 50:1, v/v) and soxhlet extraction (methanol, 24 h). Yield: 0.82 g (83%). <sup>1</sup>H NMR (400 MHz, CDCl<sub>3</sub>): δ (ppm) 8.61–8.50 (m, 8H), 7.48 (d, *J* = 5.6 Hz, 2H), 7.03–6.93 (m, 18H), 6.91 (d, *J* = 4.0 Hz, 2H), 6.69–6.66 (m, 4H), 5.18–5.10 (m, 1H), 4.12–4.08 (m, 6H), 2.80 (t, 8H), 2.62 (s, 4H), 2.23–2.14 (m, 2H), 1.91–1.82 (m, 4H), 1.70–1.67 (m, 12H), 1.52–1.19 (m, 48H), 0.90 (t, 9H), 0.81 (t, 6H). Anal. calcd for C<sub>120</sub>H<sub>137</sub>O<sub>8</sub>S<sub>8</sub>: C 72.47; H 6.79; N 1.41; S 12.90, found: C 72.73; H 6.65; N 1.20; S 12.13.

**HPBT-2(PDI), 19:** Compound **17** (0.7 g, 0.57 mmol), compound **3** (1.63 g, 2.0 mmol), DCC (0.47 g, 2.29 mmol), and DPTS (0.62 g, 2.11 mmol) were dissolved in 150 mL of 1,2-dichloromethane at room temperature under argon. The reaction mixture was allowed to stir for 36 h. After completion of the reaction, the solution was concentrated to the crude solid. Using chloroform, dissolution and filtration were repeated for removing white dicyclohexyl urea. The resulting mixture was poured into methanol to make the precipitate and the crude product was filtered. The resulting product was purified by silica-gel column chromatography (eluent: chloroform:THF = 20:1, v/v) and soxhlet extraction (methanol, 24 h). Yield: 1.1 g (68%). <sup>1</sup>H NMR (400 MHz, CDCl<sub>3</sub>): δ (ppm) 8.56–8.45 (m, 16H), 7.37 (s, 2H), 6.99 (m, 20H), 6.68 (d, *J* = 3.6 Hz, 4H), 5.18–5.12 (m, 2H), 4.12–4.08 (m, 12H), 2.82–2.77 (m, 8H), 2.62 (s, 8H), 2.23–2.17 (m, 4H), 1.89–1.84 (m, 8H), 1.72–1.63 (m, 14H), 1.52–1.19 (m, 74H), 0.90 (t, 6H), 0.81 (t, 12H). Anal. calcd for C<sub>170</sub>H<sub>190</sub>N<sub>4</sub>O<sub>16</sub>S<sub>8</sub>: C 72.87; H 6.84; N 2.00; S 9.16, found: C 72.75; H 6.64; N 1.66; S 9.72.

**HPBT-4(PDI), 20:** Compound **12** (0.5 g, 0.4 mmol), compound **3** (1.47 g, 1.8 mmol), DCC (0.39 g, 1.89 mmol), and DPTS (0.498 g, 1.69 mmol) were dissolved in 150 mL of 1,2-dichloromethane at room temperature under argon. The reaction mixture was allowed to stir for 36 h at 60 °C. After completion of the reaction, the solution was concentrated to the crude solid. Using chloroform, dissolution and filtration were repeated for removing white dicyclohexyl urea. The resulting mixture was poured into methanol to make the precipitate and the crude product was filtered. The resulting product was purified by silica-gel column chromatography (eluent: chloroform:THF = 10:1, v/v) and soxhlet extraction (methanol, 24 h). Yield: 0.5 g (28%). <sup>1</sup>H NMR (400 MHz, CDCl<sub>3</sub>): δ (ppm) 8.56–8.33 (m, 32H), 7.13 (s, 2H), 6.97 (d, *J* = 3.6 Hz, 4H), 6.93 (d, *J* = 3.6 Hz, 4H), 6.84 (d, *J* = 3.6 Hz, 4H), 6.78 (d, *J* = 15.6 Hz, 6H), 6.68–6.64 (m, 6H), 5.16–5.12 (m, 4H), 4.13–4.07 (m, 24H), 2.83–2.79 (m, 8H), 2.62 (s, 16H), 2.23–2.18 (m, 8H), 1.90–1.85 (m, 16H), 1.75–1.66 (m, 28H), 1.51–1.42 (m, 22H), 1.36–0.20 (m, 96H), 0.81 (t, 24H). Anal. calcd for C<sub>270</sub>H<sub>302</sub>N<sub>4</sub>O<sub>32</sub>S<sub>8</sub>: C 73.24; H 6.87; N 2.53; S 5.79, found: C 72.22; H 6.24; N 2.08; S 4.88.

## 2.2. Instrumental analysis

<sup>1</sup>H NMR spectra were recorded on a Varian Mercury NMR 400 Hz spectrometer using deuterated chloroform purchased from Cambridge Isotope Laboratories, Inc. Elemental analyses were performed by the Center for Organic Reactions (Sogang University, Seoul, Korea) using an EA1112 (Thermo Electron Corp.) elemental analyzer. Mass analysis was performed on a JMS-AX505WA (JEOL) mass spectrometer. Thermal properties were studied under a nitrogen atmosphere on a Mettler DSC 821<sup>e</sup> instrument. Thermal gravimetric analysis (TGA) was conducted on a Mettler TGA50 (temperature rate 10 °C/min under N<sub>2</sub>). The redox properties of HPBT-*n*(PDI) were examined using cyclic voltammetry (Model: EA161 eDAQ). Thin films were coated on a platinum plate using chloroform as a solvent. The electrolyte solution employed was 0.10 M tetrabutylammonium hexafluorophosphate (Bu<sub>4</sub>NPF<sub>6</sub>) in freshly dried methylene chloride (MC). The Ag/AgCl and Pt wire (0.5 mm in diameter) electrodes were utilized as reference and counter electrodes, respectively. The scan rate was at 50 mV/s. The X-ray diffraction (XRD) experiment (2θ = 1°–40°) was performed at varying temperatures using the synchrotron radiation (1.542 Å) of the 3C2 beam line at the Pohang Synchrotron Laboratory, Pohang, Korea. The film samples were fabricated by drop-casting on a silicon wafer, followed by drying at 80 °C under vacuum. Absorption spectra of samples in a film were obtained using a UV-vis spectrometer (HP 8453, photodiode array type) in the wavelength range of 190–1100 nm. PL spectra were recorded with a Hitachi's F-7000 FL Spectrophotometer.

## 2.3. OPV device fabrication

ITO (indium tin oxide) glass (resistance of 19.5 Ω/cm) was cleaned by a conventional cleaning method. This cleaned ITO-coated glass was treated with O<sub>2</sub> plasma with a microwave-generated plasma reactor (Plasmatic Systems

Inc., PLASMATIC-PREENII, 24 GHz) for 15 min, and a 30 nm thick PEDOT:PSS layer (Baytron P,  $1 \text{ S cm}^{-1}$ ) was deposited by spin-coating. HPBT-*n*(PDI) (thickness = 150 nm) was dissolved in anhydrous monochlorobenzene (conc. 2 wt.%), then 0.8 nm thick LiF was vacuum deposited on top of the active layer and the 150 nm thick aluminum was evaporated. The thickness of the photoactive film was measured with a surface profiler (TENCOR®, P-10  $\alpha$ -step). Current–voltage characteristics were measured with a Keithley 2400 source-measure unit. A 300 W Xe lamp was used as a light source to produce an intensity of  $100 \text{ mW cm}^{-2}$  (AM 1.5). The intensity of the incoming light power was measured with a calibrated broadband optical power meter (Spectra Physics model 404).

### 3. Results and discussion

#### 3.1. Materials synthesis and properties

First a multi-step synthesis was performed for new donor- $\sigma$ -acceptor molecules, such as **18**, **19**, and **20** (see Scheme 1 and 2). Scheme 1 illustrates the synthesis of PDI derivative, **3** and thiophene-based carbaldehyde, **6**. The synthesis of **3** was conducted using a modified literature method [17b,19a,22a].

Succinic anhydride was reacted in the presence of dimethyl aminopyridine/triethylamine to attach the carboxylic acid group to the hydroxyl group in the PDI precursor molecule, **2**. In order to synthesize 6-(5'-formyl-2,2'-bithiophen-5-yl)hexyl acetate, **6**, compound **4** was reacted with potassium acetate in DMF to yield compound **5**. Then, using Vilsmeier-Haak reaction condition, formylation was performed in a good yield (89%).

In order to prepare the X-shaped thiophene-based molecule, **10**, **6** and **7** were employed for the Horner–Emmons coupling reaction [25]. After mixing two carbonyl compounds with 1:3 ratio, Horner–Emmons coupling reaction into octaethyl benzene-1,2,4,5-tetrayltetrakis(methylene)tetraphosphonate, **8** produces 6-(5'-((E)-4-((E)-2-(5'-heptyl-2,2'-bithiophen-5-yl)vinyl)-2,5-bis((E)-2-(5'-hexyl-2,2'-bithiophen-5-yl)vinyl)styryl)-2,2'-bithiophen-5-yl)-hexyl acetate, **9**. After deprotecting an acetate group in **9** to generate hydroxyl group in the presence of lithium hydroxide, **10** was prepared successfully. Following the same coupling method for **10**, the compound **12** bearing four hydroxyl groups at the outer periphery was also pre-

pared by using **6–8** and *in situ* deprotection reaction of acetate groups in compound **11** was conducted in the presence of excess amount of potassium *tert*-butoxide (see Scheme 2).

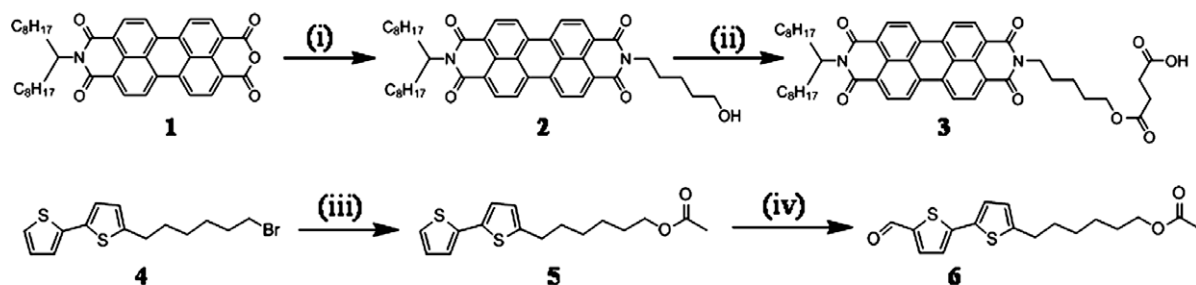
When preparing the compound **17**, we synthesized 5',5''-(1E,1'E)-2,2'-(2,5-dibromo-1,4-phenylene)bis(ethene-2,1-diyl)bis(5-hexyl-2,2'-bithiophene), **14** by reacting **7** with tetraethyl (2,5-dibromo-1,4-phenylene)bis(methylene)diphosphonate, **13**. Using 6-(5'-formyl-2,2'-bithiophen-5-yl)hexyl acetate, Wittig reaction was performed to produce 6-(5'-vinyl-2,2'-bithiophen-5-yl)hexyl acetate using methyltriphenylphosphonium iodide and potassium-*tert*-butoxide in THF.

Then, Pd-catalyzed Heck coupling reaction with tri-*o*-tolylphosphine ligand was performed to yield compound 6,6'-(5',5''-(1E,1'E)-2,2'-(2,5-bis((E)-2-(5'-hexyl-2,2'-bithiophen-5-yl)vinyl)-1,4-phenylene)bis(ethene-2,1-diyl)bis(2,2'-bithiophene-5',5'-diyl))bis(hexane-6,1-diyl) diacetate, **16**. Deprotection reaction of acetate groups yields **17** bearing two hydroxyl groups (see Scheme 3).

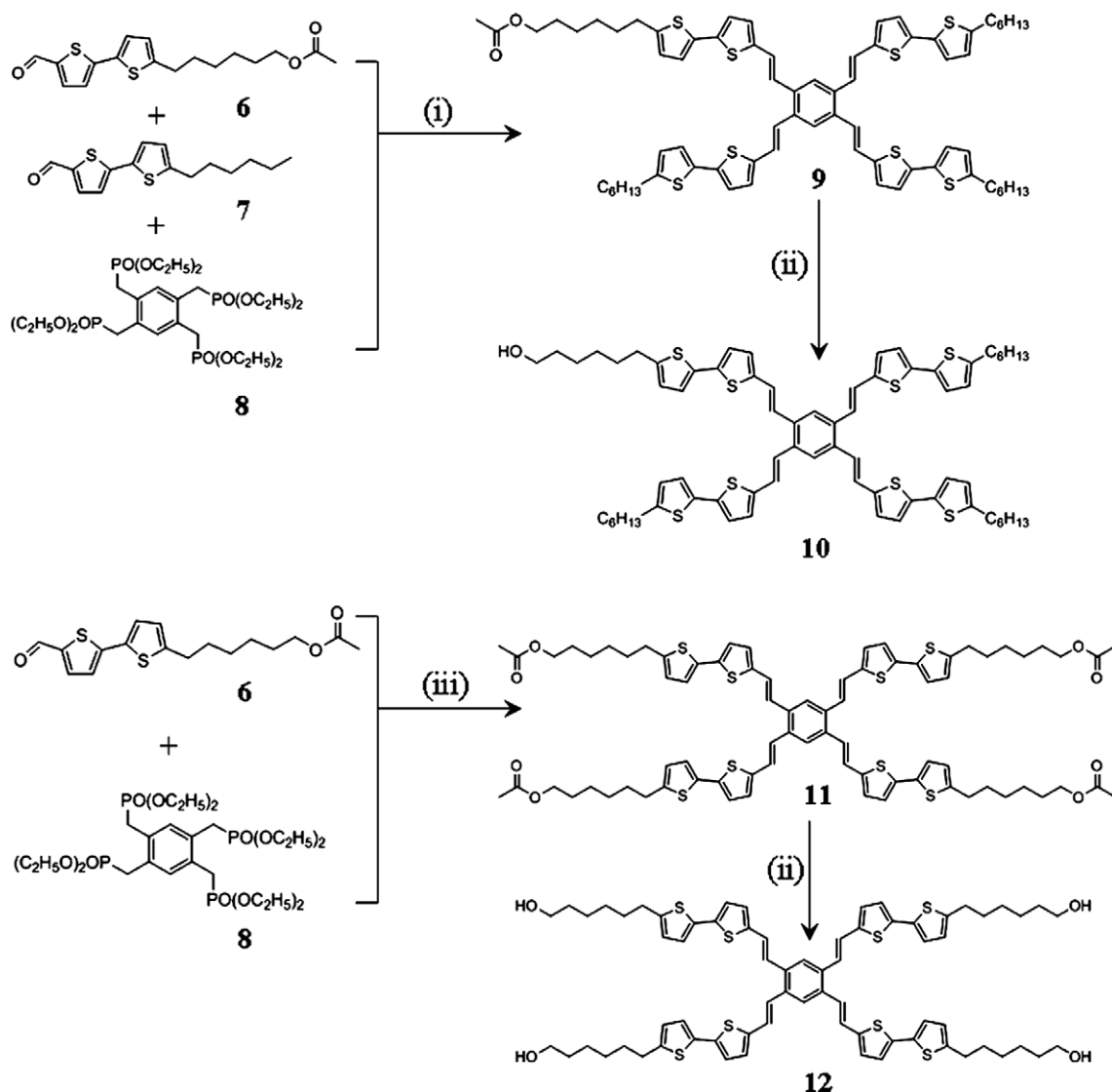
Then, individual donor molecule such as **10**, **12**, or **17**, bearing hydroxyl group(s) and **3** bearing a carboxylic acid group were combined through dicyclohexylcarbodiimide (DCC) catalyzed esterification in the presence of 4-(dimethylamino)-pyridium-4-toluene sulfonate (DPTS). Finally, three new donor- $\sigma$ -acceptor molecules: HPBT-1(PDI), **18**, HPBT-2(PDI), **19**, and HPBT-4(PDI), **20**, were successfully synthesized for the study (see Scheme 4).

We also prepared 1,2,4,5-tetrakis((E)-2-(5'-hexyl-2,2'-bithiophen-5-yl)vinyl)benzene (HPBT) having four hexyl substituted bithiophene peripheral groups, which will be denoted as **21** in this work [25]. In addition, a symmetric PDI molecule, **22** was also synthesized by following the literature method for using it as a n-type semiconducting molecule [26]. The identity and purity of the synthesized materials were confirmed by  $^1\text{H}$  NMR, mass spectrometry, and elemental analysis. They were found to have good self-film forming properties and were well-soluble in various organic solvents such as chloroform, xylene, methylene chloride (MC), monochlorobenzene, and tetrahydrofuran (THF).

The thermal properties of the donor- $\sigma$ -acceptor molecules were characterized by thermogravimetric analysis (TGA) and differential scanning calorimetry (DSC). DSC measurements were carried out at a heating (cooling) scan rate of  $10$  ( $-10$ )  $^\circ\text{C}/\text{min}$  under  $\text{N}_2$  with the highest temperature below the decomposition temperature. In DSC



**Scheme 1.** Reagents and conditions: (i) 5-aminopentan-1-ol, DMAC,  $\text{Zn}(\text{OAc})_2$ ,  $160^\circ\text{C}$ , 15 h, (ii) succinic anhydride, TEA, DMAP, 1,2-dichloroethane, r.t., 24 h, (iii) KOAc, DMF,  $60^\circ\text{C}$ , 24 h, (iv)  $\text{POCl}_3$ , DMF, 1,2-dichloroethane,  $60^\circ\text{C}$ , 12 h.



**Scheme 2.** Reagents and conditions; (i) <sup>t</sup>BuOK, THF, r.t., 7 h, (ii) LiOH, THF, r.t., 15 h.

thermograms, **18** and **19** exhibited a distinct crystalline-isotropic transition at 140 °C and 117 °C, respectively. The crystallization temperatures of **18** and **19** were also observed at 111 °C and 87 °C, during the cooling cycle. In contrast, **20** did not show a crystalline melting temperature, but it did show a glass transition temperature at 75 °C only, indicating its amorphous nature (see Table 1). TGA measurements at a heating rate of 10 °C/min under nitrogen revealed good thermal stability of the donor-σ-acceptor molecules. These molecules exhibit the onset decomposition temperatures at around 389–391 °C. The density of PDI unit did not affect the decomposition behavior.

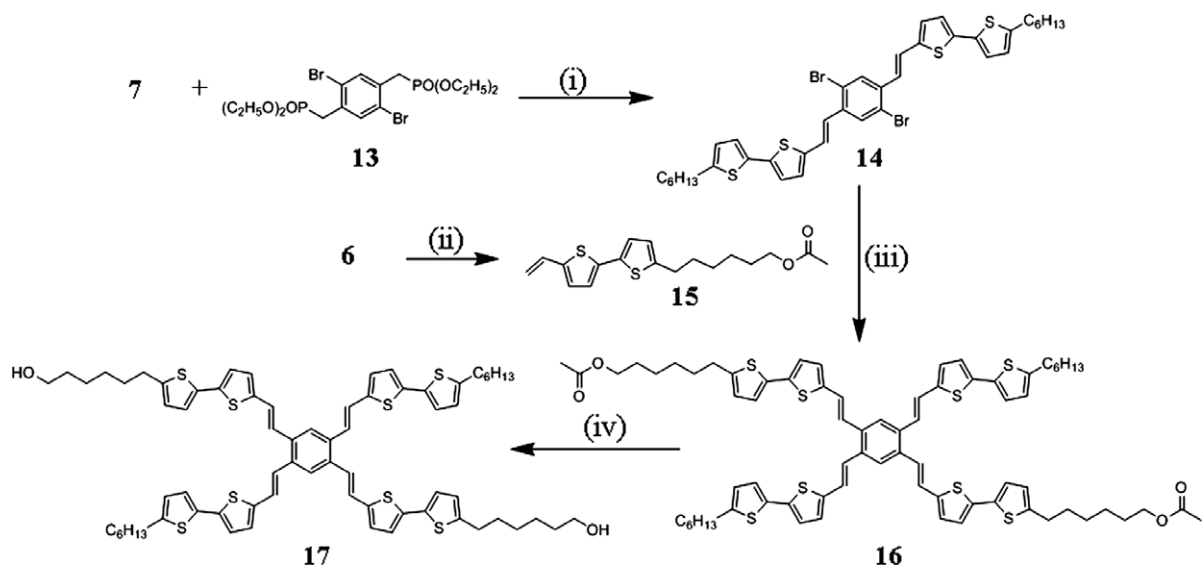
### 3.2. Absorption and photoluminescence spectroscopy

The absorption spectra of HPBT-*n*(PDI)s were recorded both in solution (conc.  $5 \times 10^{-6}$  M in CHCl<sub>3</sub>) and in film

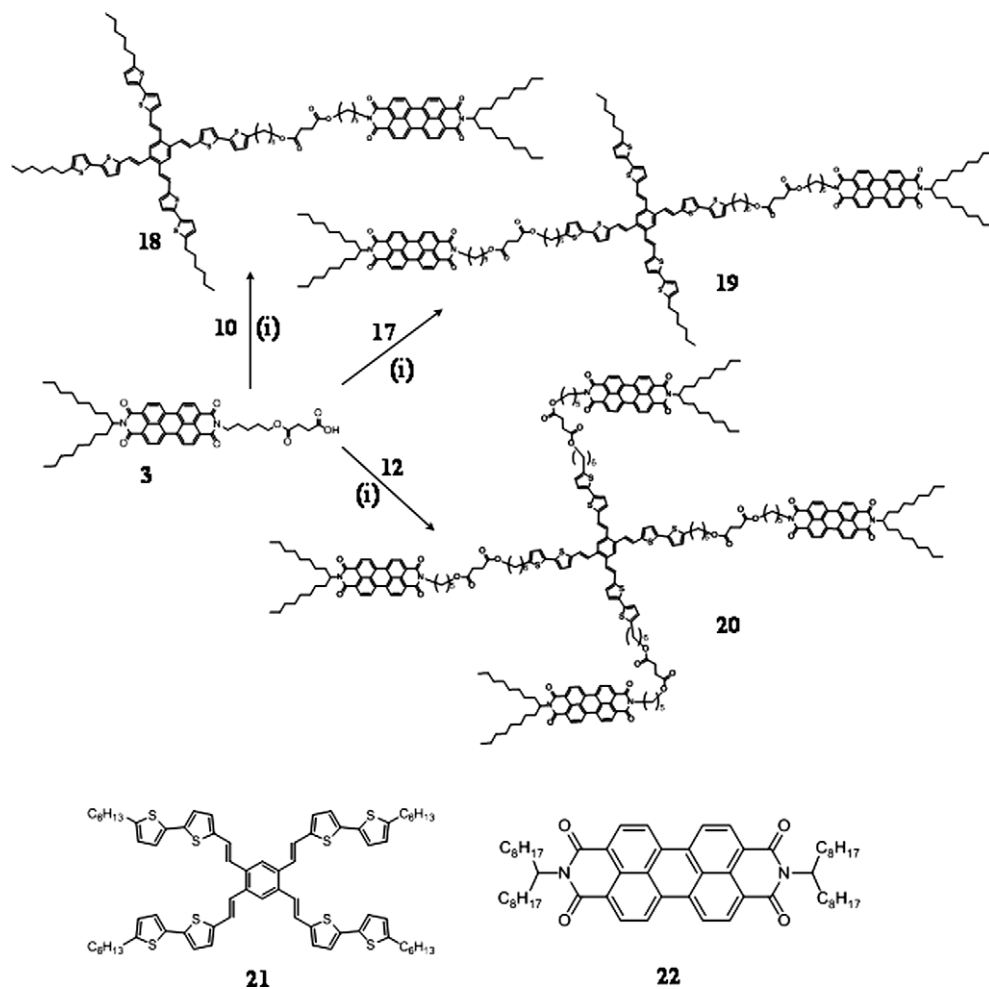
states. The solution of **22** exhibited a typical singlet transition in the range of 410–550 nm with a well-resolved vibronic structure, attributed to the vibration of the perylene structural unit.

Meanwhile, the donor, **21** showed absorption bands in the range of 300–510 nm. The spectra of HPBT-*n*(PDI)s illustrated that coupled compounds demonstrate  $\pi-\pi^*$  energy transitions in individual **21** and **22**. The absorption spectrum of **18** showed characteristic bands arising from the presence of the PDI groups, with maxima at 527, 486, and 422 nm in the solution state, the latter overlapping with the lowest energy band from HPBT ( $\lambda_{\text{max}} = 419$  nm). In the spectra of **19** and **20**, three characteristic bands at 456, 489, and 527 nm were commonly observed and their absorbance was shown to be linearly proportional to the number of PDI units in the molecule (see Fig. 1A).

Fig. 1B shows the absorption spectra of the thin films of **18**, **19**, and **20**. Compared to the solution spectra, a drastic



**Scheme 3.** Reagents and conditions: (i)  $t\text{BuOK}$ , THF, r.t., 24 h, (ii)  $\text{CH}_3\text{PPh}_3$ ,  $t\text{BuOK}$ , THF, r.t., 20 min, (iii)  $\text{Pd}(\text{OAc})_2$ , TBA,  $P(o\text{-tolyl})_3$ , DMF,  $95^\circ\text{C}$ , 24 h, (iv)  $\text{LiOH}$ , THF, r.t., 15 h.

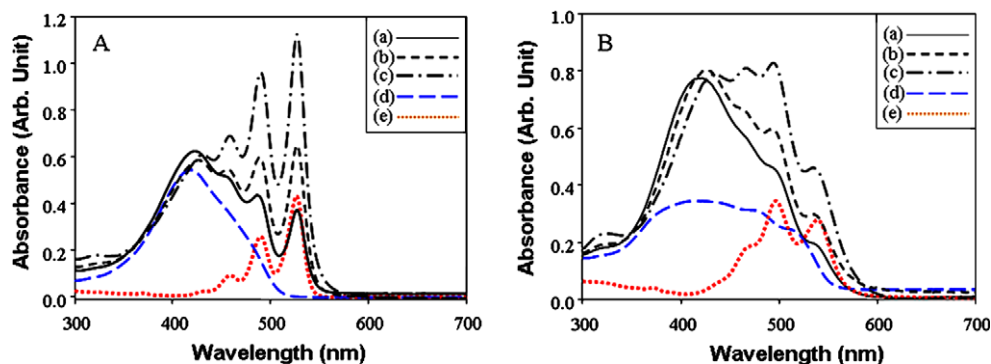


**Scheme 4.** Reagents and conditions: (i) DCC, DPTS, 1,2-dichloromethane, r.t., 36 h. Structures of HPBT, **21** and PDI, **22** molecules.

**Table 1**

Measured and calculated parameters of synthesized molecules.

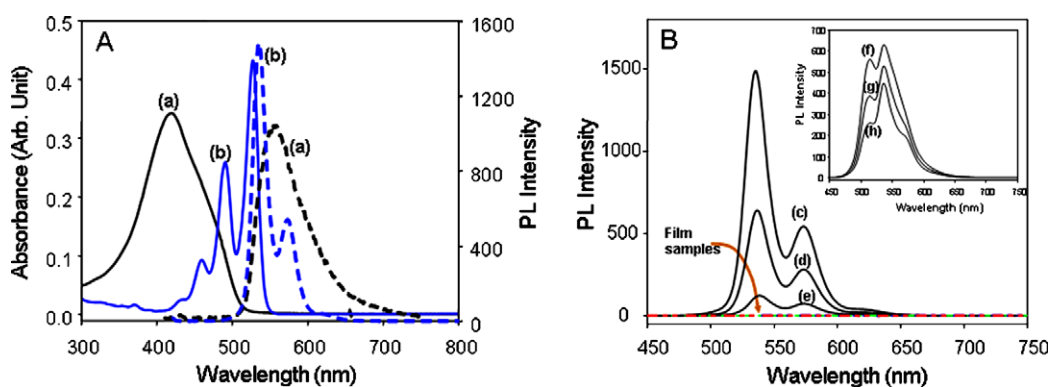
	$\lambda_{\max}$ (nm), solution: CHCl <sub>3</sub>	Optical bandgap (eV)	$E_{\text{onset}}^{\text{ox}}$ (V)	$E_{\text{onset}}^{\text{re}}$ (V)	HOMO (eV)	LUMO (eV)	$T_g$ (°C)	$T_m$ (°C)	$T_{\text{dec}}$ (°C)
21	419	2.23	0.85	–	–5.25	–3.02 <sup>a</sup>	–	171	365
22	457, 490, 527	2.18	1.75	–0.67	–6.15	–3.72	–	110	415
18	422, 486, 527	2.16	0.85	–0.68	–5.25	–3.71	–	140	389
19	427, 456, 489, 527	2.16	0.84	–0.69	–5.24	–3.71	77	117	390
20	430, 456, 489, 527	2.12	0.85	–0.67	–5.25	–3.72	75	–	391

<sup>a</sup> Optical bandgap+ $E_{\text{HOMO}}$ .**Fig. 1.** UV-vis absorption spectra of the synthesized compounds. (A) CHCl<sub>3</sub> solution state (conc;  $5 \times 10^{-6}$  M), (B) film state. (a) **18**, (b) **19**, (c) **20**, (d) **21**, (e) **22**.

spectral change in the film state was observed; possibly attributable to a high degree of intermolecular interaction [24,29,25,30]. The HPBT moieties can interact strongly to induce broadening of the spectrum. In addition, PDI molecules can also exhibit intermolecular interaction to induce spectral broadening and a bathochromic shift. A linear additive spectral feature was maintained, similar to the solution spectra of HPBT-*n*(PDI). It should be noted that the absorption spectra of HPBT-*n*(PDI) exhibit superposition of the characteristics peaks of pure HPBT and pure PDI without indications of additional spectral features in either the solution or in the solid state. This observation indicates that there is no significant interaction between the electroactive units in the ground state.

The HOMO and LUMO energy values must fulfill the energetic conditions required for the energy transfer as well as for the electron transfer. The energy is transferred from the excited donor to the acceptor, which can be interpreted as photoluminescence (PL) quenching of the donor and a simultaneous emission from the acceptor.

In Fig. 2A, absorption spectra of **21** and **22** and corresponding PL spectra were overlaid. From the figure, it is readily observed that the emission spectrum of HPBT and the absorption spectrum of PDI are favorably overlapped, which enables efficient Förster energy transfer. In a solution state, an efficient energy transfer process could occur to exhibit the unique emission of PDI only. Only the three solution samples of HPBT-*n*(PDI) showed fluorescent emission behavior ( $\lambda_{\text{excitation}} = 418$  nm) resulting from PDI moi-

**Fig. 2.** (A) Absorption and photoluminescence spectra of **21** and **22** in solution (conc;  $5 \times 10^{-6}$  M) states. Solid line: absorption spectrum, Dotted line: PL spectrum. (B) PL spectra of HPBT-*n*(PDI)s both in solution and film states. (c) **18**, (d) **19**, (e) **20**. Inset: solution PL spectra of blend samples of **21** and **22**. (f) **21:22** = 1:1, (g) **21:22** = 1:2, (h) **21:22** = 1:4 (mole ratio).



ety, indicating highly efficient energy transfer from HPBT. In the inset of Fig. 2B, the PL spectra of blend samples with **21** and **22** were displayed with the blend ratio. Three ratios were selected as the same mole ratios in HPBT-*n*(PDI)s. The emission spectrum of **21** is clearly overlapped with that of **22**. The PL intensity at 550 nm emitted from **21** was enhanced with the mole fraction of **21** in the mixture. Shortly, covalent bonding between the donor and acceptor increases the energy transfer efficiency even in the solution states.

All film samples were selectively excited at 400 nm; **3** had minimal absorbance at this wavelength. No emission behaviors were observed in three film samples (see Fig. 2B, dotted lines). The PL quenching behaviors can be explained as follows; the aggregation-induced self-quenching of the excited states of HPBT and PDI units can occur. In the other respect, it might be due to the intermolecular electron transfer from the photoexcited HPBT to PDI moieties. The photoinduced charge transfer in other conjugated molecular composites by PL quenching can be found in the literatures [31]. Besides a rapid electron transfer process, some diffusion-limited processes were also suggested [32].

### 3.3. Electrochemical analysis

To probe the electrochemical properties of HPBT-*n*(PDI) films, cyclic voltammetry was carried out in a three-electrode cell setup. All potentials reported were referenced to an Fc/Fc<sup>+</sup> standard. The results are tabulated in Table 1. Voltammograms of HPBT-*n*(PDI) in the film state showed that the lowest oxidative waves of **18**, **19**, and **20** were at +0.85, +0.84, and +0.85 V, respectively, which indicates no significant effect by the density of the electron acceptor. The oxidation potentials of the three molecules were almost identical to that of **21** ( $E_{\text{onset}}^{\text{ox}} = +0.85$  V). As shown in Table 1: **18**, **19**, and **20** have HOMO levels of -5.25, -5.24, and -5.25 eV, respectively, which indicates no significant effect by the density of the electron acceptor. The oxidation potentials and HOMO levels of the three molecules were almost identical to that of **21**. In addition, **18**, **19**, and **20** have LUMO energy levels of -3.71, -3.71, and -3.72 eV, respectively. The LUMO level is almost consistent with that ( $E_{\text{LUMO}} = 3.72$  eV) of the individual PDI molecule, **22**.

Although two opposite electroactive moieties were bound together, HOMO and LUMO levels were not significantly changed, which implies that the two moieties were isolated well enough so as not to be able to interact with each other, even in the solid state; this is also reflected in the fact that the UV-vis absorption spectrum shows no charge transfer band.

It should be noticed that HOMO levels of **21** and all donor- $\sigma$ -acceptor molecules are almost similar to that of poly(3-hexylthiophene). ( $E_{\text{HOMO}} \sim 5.20$ – $5.21$  eV) Considering the LUMO level ( $E_{\text{LUMO}} \sim 3.77$ – $3.82$  eV) of PDI unit, the combined molecules may exhibit reasonably high open circuit voltage ( $V_{\text{oc}}$ ) in the photovoltaic devices as this energy is closely related to the energy difference between the HOMO of an electron donor and the LUMO of an electron-accepting molecules. As can be seen from the energy

levels, there is an adequate energy offset for electron transfer from HPBT to the PDI unit.

Shortly, resulting from absorption spectral analysis and electrochemical analysis, the electron donor and accepting molecules do not interact intra- and intermolecularly significantly. Therefore, we can employ their isolated electronic properties for optoelectronic applications. In particular, regarding the photovoltaic devices, we can utilize their structural uniqueness, displaying the covalent binding of electron donor and electron acceptor. One of the important issues is whether their intrinsically opposite semiconducting domain can be separated in a nano-scale regime for generating the continuous electron and hole channels in one matrix.

### 3.4. Materials structures

In order to study the crystallinity and variation of crystalline conformation of HPBT-*n*(PDI), X-ray diffraction (XRD) experiments were performed at varying temperatures using the synchrotron radiation (1.542 Å) of the 3C2 beam line. The film samples ( $t \sim 50$ – $60$  nm) were fabricated by spin-coating on silicon wafer, followed by drying at 80 °C under vacuum (solvent: chloroform, concentration of the solution: 10 mg/mL). The measurements were obtained in a scanning interval of  $2\theta$  between 1° and 40°. As previously reported [21], HPBT molecules are well associated and stacked by the interaction between terminal hexyl groups, which are already known to induce long-range ordering. In the literature, well-defined XRD patterns also demonstrate facile crystallization of planar PDI molecules [30–33].

First, the diffraction scans of the film of **18** were displayed in a small angle region under a heating and cooling cycle. In the as-coated sample, two major diffraction peaks were observed, which are attributed, to some degree, to lamella ordering. When the temperature of the sample was increased to 80 °C, a very high intensity and narrow diffraction peak appeared at  $2\theta = 3.13^\circ$  ( $d = 28.24$  Å). Although a weak diffraction peak was observed at around  $5.57^\circ$  ( $d = 15.80$  Å), the main peak at  $3.13^\circ$  is clearly assigned to the edge-to-edge transverse packing of the peripheral arms in HPBT moieties, which is fairly consistent with the calculated distance ( $d = 29.0$  Å).

Upon subsequent heating to 150 °C, the peak at  $3.13^\circ$  disappears and the peak at  $5.57^\circ$  grows, accompanying the weak and broad reflection peaks at  $14.7^\circ$  ( $d = 6.02$  Å). At this high temperature, it is noted that PDI molecules begin to be ordered by independent crystallization. During the cooling cycle, the crystallinity in the PDI molecular domains is maintained or a little enhanced and it is possible to regenerate the relatively small crystalline domain with the HPBT moieties.

As a result, the HPBT moieties are self-associated to be highly crystallized at around 80–90 °C. The X-ray diffraction (XRD) result in the small angle region and the schematic diagram of the expected localized molecular conformation are depicted in Fig. 3. However, we cannot exclude the possibility for HPBT-1(PDI) to exhibit intercalation between the donor and acceptor moieties.

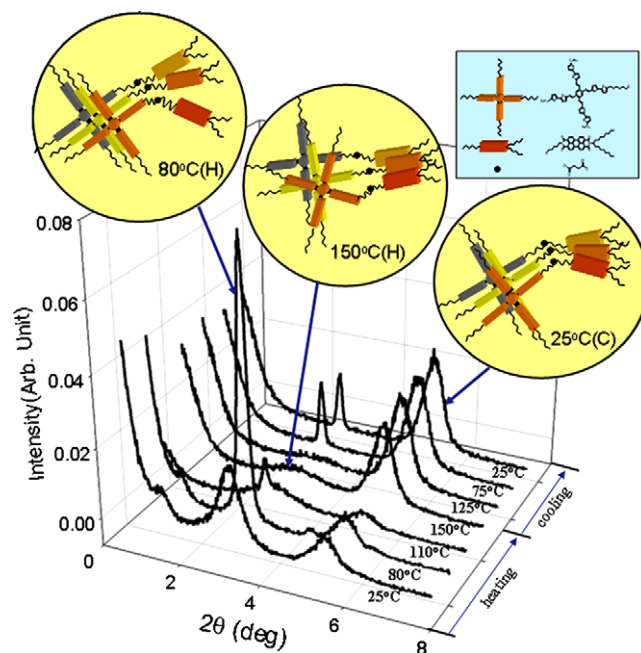


**Fig. 3.** XRD analysis of HPBT-1(PDI), **18** with the temperature. Possible molecular geometry of the HPBT and PDI unit in the solid state. (H): heating cycle, (C) cooling cycle.

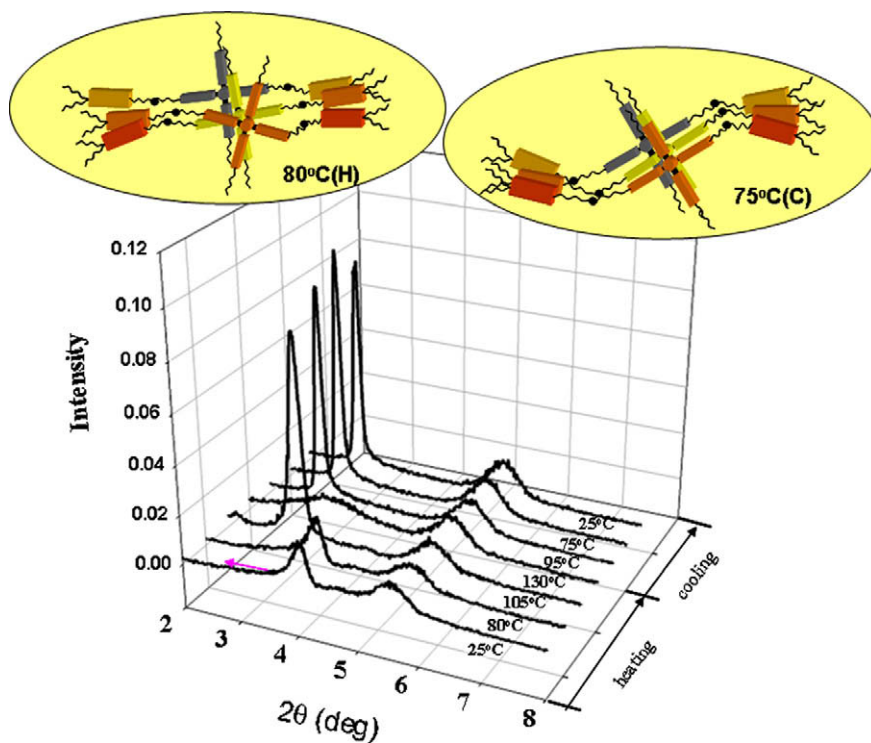


**Fig. 4.** XRD analysis of HPBT-2(PDI), **19** with the temperature. Possible molecular geometry of the HPBT and PDI unit in the solid state. (H) Heating cycle, (C) cooling cycle.

Meanwhile, the XRD results of **19** showed different X-ray diffractograms with the temperature (see Fig. 4). The diffraction scans of the film of **19** also displayed in a small

angle region under a heating and cooling cycle. At 25 and 80 °C, we could observe two small diffraction peaks at 3.33 ( $d = 26.54 \text{ \AA}$ ) and 5.56° ( $d = 15.7 \text{ \AA}$ ) from the ordering

of HPBT and PDI units to a small extent. At 105 °C, the lower angle diffraction peak shifted to 3.28° whose  $d$ -spacing is 26.95 Å, which indicates that the HPBT moieties placed in an energetically favorable ordered structure. At 130 °C, the diffraction intensity arising from HPBT ordering significantly reduced. When cooling cycle, very strong diffraction peak at 2.96° ( $d = 29.86$  Å) appeared again with smaller full width at half maximum and maintained until cooling to 25 °C.

Compared to the diffraction behaviors of **18**, the HPBT moieties exhibited relatively more uniform ordering. At this temperature range during cooling, it is noted that HPBT central moieties induce high degree of lamella ordering accompanied with PDI ordering. The HPBT moieties are highly self-associated to be crystallized until cooling from melting temperature to 25 °C. The compound **20** showed less crystalline property and amorphous nature compared to that of **18** and **19**, which is due to the steric effect of HPBT moiety.

### 3.5. Photovoltaic properties

Finally, the potential of the newly synthesized donor- $\sigma$ -acceptor molecules as photoactive materials in a PV cell is explored. In a macroscopic respect, the solid state of HPBT- $n$ (PDI) can form either an intermolecular charge transfer complex or heterogeneous domains. It is more likely to be a bulk heterojunction in which **21** and **22** are connected through covalent bonding. The electronically opposite two moieties were aggregated in individual domains that can form a uniform interpenetrating network.

The device configurations are as follows: **Device A**: ITO/PEDOT:PSS/**21:22** (1:1, mole ratio)/LiF/Al, **Device B**: ITO/PEDOT:PSS/**18**/LiF/Al, **Device C**: ITO/PEDOT:PSS/**19**/LiF/Al, **Device D**: ITO/PEDOT:PSS/**20**/LiF/Al. Fig. 5 illustrates the device configurations and the current density–voltage characteristics of the most effective as-fabricated devices in the dark and under air mass (AM) 1.5 simulated solar illumination. The PV device performances are tabulated in Table 2. The PCE of the **21:22** (1:1 mol ratio) blend device was calculated to be 0.04% ( $V_{oc} = 0.55$  V,  $J_{sc} = 0.28$  mA cm<sup>-2</sup>, fill factor = 0.28), which is significantly poor. Highly improved device performance was observed when using **18** as the photoactive layer than with the device using the blend sample.

In **Device B**, the sample was annealed at 80 °C for 20 min. The PV cell gave a relatively large PCE of 0.22% with a  $V_{oc}$  ranging from 0.62 to 0.63 V. It should be noted that the sample annealed at 120 °C only exhibited 0.038% of the PCE. As a result of the XRD study, the association of HPBT moieties were disrupted at 120 °C to randomize the p-channels for hole transport. Crystallization of HPBT moieties at 80 °C is significant to the enhancement of PV properties. The annealed **Device C** exhibited a relatively low  $J_{sc}$  value and 0.034% of the PCE. Since larger amount of PDI moiety in the photoactive layer exists, interpenetrating network cannot be formed uniformly; p-channel HPBT domain was surrounded by n-channel moieties and hole transporting channel might be disrupted. Therefore, it exhibits poor hole transport through the HPBT moieties to induce charge build-up, which results in poor PCE. As

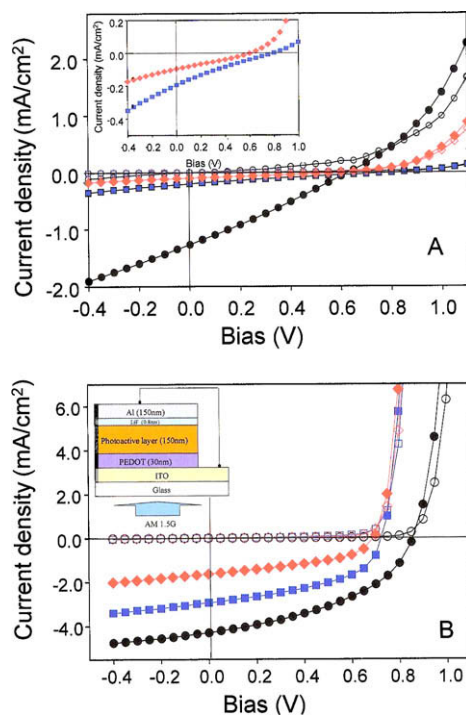


**Fig. 5.** Current density–voltage characteristics of PV devices under AM 1.5 simulated solar illumination of 100 mW cm<sup>-2</sup>. Filled symbol: photo-current density, open symbol: dark current density. (A) (circle) **18**, (square) **19**, (diamond) **20**. Inset: expanded curves of **19** and **20**-based PV devices. (B) (circle) **18**:PCBM, (square) **19**:PCBM, (diamond) **20**:PCBM based device (1:4 M ratio). Inset: PV device configuration.

**Table 2**

Summary of device performance for HPBT- $n$ (PDI) and its blend with PCBM based photovoltaic (PV) cells.

	$V_{oc}$ (V)	$J_{sc}$ (mA cm <sup>-2</sup> )	FF	PCE (%)
Device A	0.549	-0.277	0.277	0.040
Device B	0.629	-1.267	0.273	0.217
Device c	0.798	-0.195	0.218	0.034
Device D	0.607	-0.097	0.283	0.017
Device E	0.855	-4.300	0.435	1.600
Device F	0.722	-2.935	0.490	1.039
Device G	0.690	-1.636	0.455	0.513

can be expected, the amorphous **20**-based **Device D** exhibited a much lower PCE value of approximately 0.017%.

Subsequently, efforts were made to improve the PV properties by adding PCBM into the donor- $\sigma$ -acceptor molecules. Three more devices were also fabricated for characterization under an identical device configuration: **Device E**: ITO/PEDOT:PSS/**18**:PCBM/LiF/Al, **Device F**: ITO/PEDOT:PSS/**19**:PCBM/LiF/Al, **Device G**: ITO/PEDOT:PSS/**20**:PCBM/LiF/Al. When PCBM was added into the molecules (1:4 mol ratio), the film samples showed significant increment of the absorption in the visible range. Resulting from the addition of extra PCBM molecules, the device performances were significantly enhanced, as was expected. Keeping in mind the previous tendencies of the PCEs in the three devices, **B**, **C**, and **D**, **Device E** exhibited the best efficiency ( $\eta = 1.60\%$ ); the value is higher than seven times

that of **Device B**. The other two devices also showed significant enhancement of PCE compared to the devices containing no PCBM. **Devices F** and **G** exhibited almost 15–16-fold  $J_{sc}$  values, providing 30 times higher PCE, respectively, when compared to **Devices C** and **D** containing no PCBM (see Table 2). Enhancement of PCE arises from the increase of the short circuit current ( $J_{sc}$ ) which is mainly attributed to increase of absorption in the visible range.

#### 4. Conclusion

New donor- $\sigma$ -acceptor molecules bearing the cruciform p-type HPBT molecule and PDI derivatives have been demonstrated. HPBT-1(PDI), **18** and HPBT-2(PDI), **19** are typical molecules displaying mesoscopic self-organization by virtue of crystallization of HPBT moieties. PV devices were fabricated, either with PCBM or without PCBM. Additional PCBM enhance the absorption in the visible light region. Thus the power conversion efficiency and fill factor were significantly enhanced. The results in this work demonstrate the high potential of donor- $\sigma$ -acceptor molecules as photovoltaic materials. Instead of HPBT moiety, a low-bandgap donor molecule is introduced in D- $\sigma$ -A structures and characterization of their ability is now in progress.

#### Acknowledgements

This research was mainly supported by Korea Science and Engineering Foundation, (KOSEFR-0120070001128402008) Particularly, Prof. D.H. Choi thanks the financial support by the Seoul R&BD Program (2008–2009) and second stage of the Brain Korea 21 Project in 2009 (Korea Research Foundation) X-ray experiments at PLS were supported by the Ministry of Science and Technology and Pohang Steel Company.

#### References

- [1] P.A. Liddell, G. Kodis, A.L. Moore, T.A. Moore, D. Gust, *J. Am. Chem. Soc.* **124** (2002) 7668.
- [2] T. Oike, T. Kurata, K. Takimiya, T. Otsubo, Y. Aso, H. Zhang, Y. Araki, O. Ito, *J. Am. Chem. Soc.* **127** (2005) 15372.
- [3] M. Lor, J. Thielemans, L. Viaene, M. Cotlet, J. Hofkens, T. Weil, C. Hampel, K. Müllen, J.W. Verhoeven, M.V.d. Auweraer, F.C. De Schryver, *J. Am. Chem. Soc.* **124** (2002) 9918.
- [4] E. Peeters, P.A. van Hal, S.C.J. Meskers, R.A.J. Janssen, E.W. Meijer, *Chem. Eur. J.* **8** (2002) 4470.
- [5] Y. Chen, M.E. El-Khouly, X.-D. Zhuang, N. He, Y. Araki, Y. Lin, O. Ito, *Chem. Eur. J.* **13** (2007) 1709.
- [6] S. Xiao, M.E. El-Khouly, Y. Li, Z. Gan, H. Liu, L. Jiang, Y. Araki, O. Ito, D. Zhu, *J. Phys. Chem. B* **109** (2005) 3658.
- [7] S. Fukuzumi, K. Ohkubo, J. Ortiz, A.M. Gutiérrez, F. Fernández-Lázaro, A. Sastre-Santos, *J. Phys. Chem. A* **112** (2008) 10744.
- [8] (a) E.E. Neuteboom, S.C.J. Meskers, E.H.A. Beckers, S. Chopin, R.A.J. Janssen, *J. Phys. Chem. A* **110** (2006) 12363; (b) L.X. Chen, S. Xiao, L. Yu, *J. Phys. Chem. B* **110** (2006) 11730; (c) B.K. Kaletas, R. Dobrawa, A. Sautter, F. Würthner, M. Zimine, L.D. Cola, R.M. Williams, *J. Phys. Chem. A* **108** (2004) 1900.
- [9] T.B.M. Bell, A. Stefan, S. Masuo, T. Vosch, M. Lor, M. Cotlet, J. Hofkens, S. Bernhardt, K. Müllen, M.V.d. Auweraer, J.W. Verhoeven, F.C. De Schryver, *Chem. Phys. Chem.* **6** (2005) 942.
- [10] M. Cotlet, S. Masuo, M. Lor, E. Fron, M.V.d. Auweraer, K. Müllen, J. Hofkens, F.D. De Schryver, *Angew. Chem., Int. Ed.* **43** (2004) 6116.
- [11] J. Qu, N.J. Pschirer, D. Liu, A. Stefan, F.C. De Schryver, K. Müllen, *Chem. Eur. J.* **10** (2004) 528.
- [12] (a) A. Aviram, M.A. Ratner, *Chem. Phys. Lett.* **29** (1974) 277; (b) R.M. Metzger, *J. Mater. Chem.* **9** (1999) 2027.
- [13] (a) S. Zhou, Y. Liu, W. Qiu, Y. Xu, X. Huang, Y. Li, L. Jiang, D. Zhu, *Adv. Funct. Mater.* **12** (2002) 65; (b) K. Stokbro, J. Taylor, M. Brandbyge, *J. Am. Chem. Soc.* **125** (2003) 3674; (c) G. Ho, J.R. Heath, M. Kondratenko, D.F. Perepichka, K. Arseneault, M. Pézolet, M.R. Bryce, *Chem. Eur. J.* **11** (2005) 2914; (d) M.J. Ford, R.C. Hoft, A.M. McDonagh, M.B. Cortie, *J. Phys.: Condens. Matter* **20** (2008) 374106.
- [14] T. Nishizawa, K. Tajima, K. Hashimoto, *J. Mater. Chem.* **17** (2007) 2440.
- [15] B. Mi, Y. Dong, Z. Li, J.W.Y. Lam, M. Häupler, H.H.Y. Sung, H.S. Kwok, Y. Dong, I.D. Williams, Y. Liu, Y. Luo, Z. Shuai, D. Zhu, B.Z. Tang, *Chem. Commun.* (2005) 3583.
- [16] (a) T. Nishizawa, K. Tajima, K. Hashimoto, *Nanotechnology* **19** (2008) 424017; (b) H. Neugebauer, M.A. Loi, C. Winder, N.S. Sariciftci, G. Cerullo, A. Gouloumis, P. Vazquez, T. Torres, *Solar Energy Mater. Solar Cells* **83** (2004) 201; (c) G. Possamai, N. Camaioni, G. Ridolfi, L. Franco, M. Ruzzi, E. Menna, G. Casalbore-Miceli, A.M. Fichera, G. Scorrano, C. Corvaja, M. Maggini, *Synthetic Met.* **139** (2003) 585.
- [17] (a) J. Li, F. Dierschke, J. Wu, A.C. Grimsdale, K. Müllen, *J. Mater. Chem.* **16** (2006) 96; (b) W.S. Shin, H.H. Jeong, M.K. Kim, S.H. Jin, M.R. Kim, J.W. Lee, J.W. Lee, Y.S. Gal, *J. Mater. Chem.* **16** (2006) 384; (c) R. de Bettignies, Y. Nicolas, P. Blanchard, E. Levillain, J.M. Nunzi, J. Roncali, *Adv. Mater.* **15** (2003) 1939.
- [18] (a) Z. Tan, E. Zhou, X. Zhan, X. Wang, Y. Li, S. Barlow, S.R. Marder, *Appl. Phys. Lett.* **93** (2008) 073309; (b) Y. Liu, C. Yang, Y. Li, Y. Li, S. Wang, J. Zhuang, H. Liu, N. Wang, X. He, Y. Li, D. Zhu, *Macromolecules* **38** (2005) 716; (c) B. Rybtchinski, L.E. Sinks, M.R. Wasielewski, *J. Am. Chem. Soc.* **126** (2004) 12268.
- [19] (a) E.E. Neuteboom, S.C.J. Meskers, P.A. van Hal, J.K.J. van Duren, E.W. Meijer, R.A.J. Janssen, H. Dupin, G. Pourtois, J. Cornil, R. Lazzaroni, J.L. Brédas, D. Beljonne, *J. Am. Chem. Soc.* **125** (2003) 8625; (b) J. Cremer, P. Bäuerle, *Eur. J. Org. Chem.* (2005) 3715; (c) J. Baffreau, S. Leroy-Lhez, N. Van Anh, R.M. Williams, P. Hudhomme, *Chem. Eur. J.* **14** (2008) 4974; (d) Y. Shibano, T. Umeyama, Y. Matano, N.V. Tkachenko, H. Lemmetyinen, Y. Araki, O. Ito, H. Imahori, *J. Phys. Chem. C* **111** (2007) 6133.
- [20] M. Sommer, S.M. Lindner, M. Thelakktat, *Adv. Funct. Mater.* **17** (2007) 1493.
- [21] (a) S. Fukuzumi, K. Ohkubo, J. Ortiz, A.M. Gutiérrez, F. Fernández-Lázaro, A. Sastre-Santos, *Chem. Commun.* (2005) 3814; (b) J. Cremer, P. Bäuerle, *J. Mater. Chem.* **16** (2006) 874.
- [22] (a) S. Leroy-Lhez, J. Baffreau, L. Perrin, E. Levillain, M. Allain, M.-J. Blesa, P. Hudhomme, *J. Org. Chem.* **70** (2005) 6313; (b) Y. Zhang, L.-Z. Cai, C.-Y. Wang, G.-Q. Lai, Y.-J. Shen, *New J. Chem.* **32** (2008) 1968; (c) E.E. Neuteboom, P.A. van Hal, R.A.J. Janssen, *Chem. Eur. J.* **10** (2004) 3907.
- [23] P. Bauer, H. Wietasch, S.M. Lindner, M. Thelakktat, *Chem. Mater.* **19** (2007) 88.
- [24] T. Nishizawa, H.K. Lim, K. Tajima, K. Hashimoto, *Chem. Commun.* (2009) 2469.
- [25] K.H. Kim, Z. Chi, M.J. Cho, J.-I. Jin, M.Y. Cho, S.J. Kim, J.-S. Joo, D.H. Choi, *Chem. Mater.* **19** (2007) 4925.
- [26] L.D. Wescott, D.L. Mattern, *J. Org. Chem.* **68** (2003) 10058.
- [27] H. Langhals, W. Jona, *Chem. Eur. J.* **4** (1998) 2110.
- [28] H. Li, M. Parameswaran, M.H. Nurawati, Q. Xu, S. Valiyaveetil, *Macromolecules* **41** (2008) 8473.
- [29] C. Xia, J. Locklin, J.H. Youk, T. Fulghum, R.C. Advincula, *Langmuir* **18** (2002) 955.
- [30] S. Kokyunku, M. Kus, S. Demic, I. Kaya, E. Ozdemir, S. Icli, *J. Polym. Sci. Part A: Polym. Chem.* **46** (2008) 1974; (b) Q. Peng, K. Park, T. Lin, M. Durstock, L. Dai, *J. Phys. Chem. B* **112** (2008) 2801.
- [31] (a) H. Kim, J.Y. Kim, K. Lee, Y. Park, Y. Jin, H. Suh, *Curr. Appl. Phys.* **1** (2001) 139; (b) M. Theander, A. Yartsev, D. Zigmantas, V. Sundström, W. Mammo, M.R. Andersson, O. Inganäs, *J. Mater. Chem.* **44** (2009) 1283; (c) F. Meng, J. Hua, K. Chen, H. Tian, L. Zuppiroli, F. Nüesch, *J. Mater. Chem.* **15** (2005) 979;

- (d) T. Otsubo, Y. Aso, K. Takimiya, J. Mater. Chem. 12 (2002) 2565;  
(e) A.M. Ramos, M.T. Rispens, J.K.J. Van Duren, J.C. Hummelen, R.A.J. Janssen, J. Am. Chem. Soc. 123 (2001) 6714.
- [32] S. Trotzky, T. Hoyer, W. Tuszynski, C. Lienau, J. Parisi, J. Phys. D 42 (2009) 055105.
- [33] (a) M. Petit, R. Hayakawa, Y. Wakayama, T. Chikyow, J. Phys. Chem. C 111 (2007) 12747;  
(b) K. Balakrishnan, A. Datar, T. Naddo, J. Huang, R. Oiker, M. Yen, J. Zhao, L. Zang, J. Am. Chem. Soc. 126 (2006) 7390;  
(c) G. Sui, J. Orbulescu, M. Mabrouki, R.M. Leblanc, S. Liu, B.A. Gregg, Chem. Phys. Chem. 3 (2002) 1041.

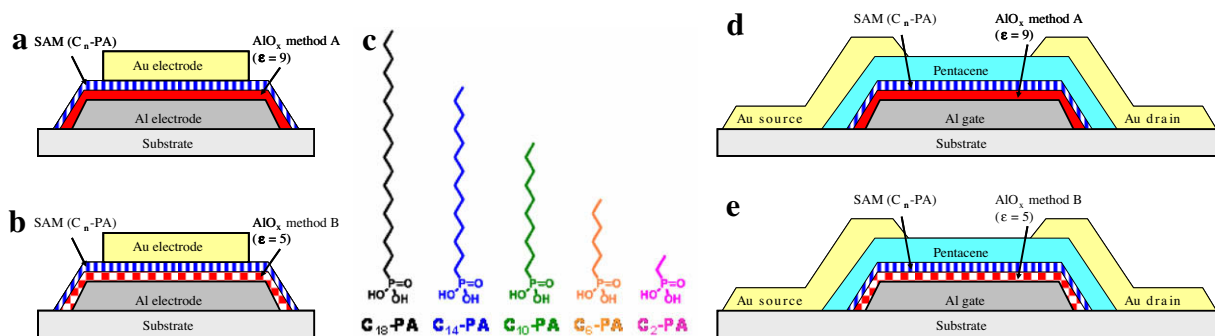


**Fig. 1.** Schematic cross sections of capacitors and thin-film transistors with thin AlO<sub>x</sub>/SAM dielectric. (a) Capacitor with AlO<sub>x</sub> grown by oxygen plasma (method A). (b) Capacitor with AlO<sub>x</sub> grown by mild-air plasma (method B). (c) Chemical structures of *n*-alkyl phosphonic acids C<sub>*n*</sub>-PA. (d) Pentacene TFT with AlO<sub>x</sub> grown by oxygen plasma (method A). (e) Pentacene TFT with AlO<sub>x</sub> grown by mild-air plasma (method B).

SAM dielectrics is comparable to or smaller than the current density through the gate dielectrics of modern silicon field-effect transistors that use high-temperature-grown inorganic gate oxides with a thickness of 2–3 nm [25,26].

In order to better understand the properties of the thin oxide/SAM double-layer dielectrics it is necessary to distinguish between the influence of the thin oxide and the influence of the molecular monolayer on the performance of the double-layer dielectric. In this work we compare the electrical characteristics of thin aluminum oxide/SAM double-layer dielectrics prepared using two different oxidation procedures and five different aliphatic phosphonic acids (Fig. 1c) on aluminum electrodes. To separate the effects of the oxide and the SAM on the insulating properties, we have performed current-voltage measurements on metal/oxide/SAM/metal capacitors and cyclic voltammetry measurements on ITO/SAM devices.

## 2. Experimental

The aluminum oxide (AlO<sub>x</sub>) layers have a thickness of about 3.6 nm and the SAMs range in thickness from 0.4 to 2.4 nm. For each combination of oxidation procedure and SAM thickness, capacitor devices (Al/AlO<sub>x</sub>/SAM/Au) and bottom-gate, top-contact pentacene organic TFTs (in which the AlO<sub>x</sub>/SAM stack serves as the gate dielectric) were fabricated and characterized.

The aluminum electrodes were prepared by thermal evaporation of 30 nm thick aluminum through a stencil mask onto glass substrates. To create a thin AlO<sub>x</sub> layer, the surface of the freshly evaporated aluminum was plasma-activated using one of two methods. Method A is an oxygen-plasma treatment performed in a turbo-pumped parallel-plate reactive ion etcher (process pressure: 0.1 mbar, plasma frequency: 13.56 MHz, plasma power: 200 W, duration: 30 s) that produces an AlO<sub>x</sub> layer with a thickness of about 3.6 nm and a permittivity of nine [2]. Method B is a mild-air plasma (2 mbar, 40 kHz, 200 W, 120 s) which creates an AlO<sub>x</sub> film with approximately the same thickness and surface roughness (rms roughness = 1.5 nm, measured by atomic force microscopy) as method A, but with smaller density and hence smaller permittivity (ε = 5). After the plasma treatment, the substrates

were immersed in a 2-propanol solution containing 5 mM of one of five different alkyl phosphonic acids (dicyl-PA [C<sub>2</sub>-PA], hexyl-PA [C<sub>6</sub>-PA], decyl-PA [C<sub>10</sub>-PA], tetradecyl-PA [C<sub>14</sub>-PA], octadecyl-PA [C<sub>18</sub>-PA]) to allow a monolayer with a thickness approximately proportional to the length of the molecule (assuming similar molecular tilt angles) to self-assemble on the hydroxyl-terminated surface of the plasma-oxidized aluminum. The solution was kept at room temperature, and substrates remained in solution for about 24 h. Substrates were then rinsed with 2-propanol, dried, and briefly baked at a temperature of 60 °C on a hotplate. Static contact angles of 105–110° were obtained for all films, except for the substrates with C<sub>2</sub>-PA on which a slight corrosion of the aluminum patterns was observed and a smaller static contact angle of 80° was measured. The capacitors were completed by evaporating 30 nm thick gold through a stencil mask on top of the SAMs, resulting in capacitors with areas of 30 × 30 μm<sup>2</sup>, 50 × 50 μm<sup>2</sup> and 100 × 100 μm<sup>2</sup> (Fig. 1a and b). Organic TFTs were completed by evaporating 30 nm thick pentacene on top of the SAM-coated aluminum gate stack through a stencil mask, followed by evaporating 30 nm thick gold through another stencil mask to create the source/drain contacts (Fig. 1d and e). The pentacene TFTs have a channel length (*L*) of 30 μm and a channel width (*W*) of 450 μm.

For cyclic voltammetry measurements, the SAMs were prepared on ITO-coated glass substrates from solution with the same process described above for the Al/AlO<sub>x</sub>/SAM/Au capacitors, but without an AlO<sub>x</sub> layer and without a metal top contact. Static contact angles after SAM formation on ITO were similar to those for SAMs on aluminum oxide (105–115°). The ITO/SAM devices have an electrode area of 288 mm<sup>2</sup>, which is much larger than the area of the Al/AlO<sub>x</sub>/SAM/Au capacitors. The cyclic voltammetry measurements were carried out in a 0.9% NaCl(aq) solution using K<sub>3</sub>[Fe(CN)<sub>6</sub>] as a redox-active indicator.

## 3. Results and discussion

### 3.1. Capacitor devices

To investigate the dielectric properties of the double-layer insulator stacks we have measured the capacitance

of each Al/AIO<sub>x</sub>/SAM/Au device at frequencies from 10 kHz to 1 MHz and the current density through each stack as a function of applied voltage up to dielectric breakdown. Each measurement was repeated on at least four capacitors. The results are independent of the capacitor cell area. The measured capacitances are summarized in Table 1 and compared with the capacitances calculated using the equation  $C_{\text{total}} = 1/(1/C_{\text{SAM}} + 1/C_{\text{AlO}_x})$  assuming a permittivity of 2.5 for the SAM [27], a permittivity of nine for the oxygen-plasma-grown AlO<sub>x</sub>, a permittivity of five for the mild-air-plasma-grown AlO<sub>x</sub>, a thickness of 3.6 nm for the AlO<sub>x</sub>, and a thickness between 0.41 and 2.44 nm for the SAM, depending on alkyl chain length. The measured capacitances are between 0.38 μF/cm<sup>2</sup> for mild-air-plasma-grown AlO<sub>x</sub>/C<sub>18</sub>-PA SAM and 1.75 μF/cm<sup>2</sup> for oxygen-plasma-grown AlO<sub>x</sub>/C<sub>2</sub>-PA SAM, and they are in good agreement with the calculated values.

Fig. 2 shows the measured current density as a function of applied voltage. For the series of capacitors with oxygen-plasma-grown AlO<sub>x</sub> ( $\epsilon = 9$ ; see Fig. 2a), the breakdown voltage is essentially the same (4.4 V) for devices without SAM and devices with short SAM (C<sub>6</sub>-PA, C<sub>2</sub>-PA). When the SAM chain length is increased to C<sub>10</sub> and beyond, a monotonic increase in breakdown voltage is observed, up to 5 V for C<sub>18</sub>-PA. With the exception of the devices with C<sub>2</sub>-PA (which appears to corrode the aluminum) the current density at low voltages ( $\sim 1$ –2 V) is similar for all devices with SAM regardless of chain length and slightly smaller than for devices without SAM ( $4 \times 10^{-7}$  A/cm<sup>2</sup> at 1 V;  $4 \times 10^{-6}$  A/cm<sup>2</sup> at 2 V). When the voltage is increased beyond 2 V, the increase in current density with increasing voltage is greater for the devices with shorter SAM chain length than for those with longer SAM chain length. At large voltage ( $\sim 4$  V), the current density through the devices with C<sub>18</sub>-PA SAM is two orders of magnitude smaller than through the devices without SAM, confirming the important role of the SAM in limiting the current density.

The devices based on mild-air-plasma-grown AlO<sub>x</sub> ( $\epsilon = 5$ ) show slightly different results (see Fig. 2b). Most significantly, the devices without SAM have a smaller breakdown voltage and a larger current density than the oxygen-plasma-grown AlO<sub>x</sub> without SAM (breakdown voltage is 4 V instead of 4.4 V; current density at 2 V is  $1 \times 10^{-1}$  A/cm<sup>2</sup> instead of  $2 \times 10^{-5}$  A/cm<sup>2</sup>). We attribute

these findings to the lower quality of the mild-air-plasma-grown AlO<sub>x</sub> compared with the oxygen-plasma-grown AlO<sub>x</sub> (lower density, larger number of leakage paths). Consequently, the devices with mild-air-plasma-grown AlO<sub>x</sub> and SAM also show larger current density than the oxygen-plasma-grown AlO<sub>x</sub>/SAM devices. In the devices with C<sub>10</sub>-PA, C<sub>14</sub>-PA and C<sub>18</sub>-PA SAM the current density at 2 V is larger by about one order of magnitude ( $\sim 3 \times 10^{-5}$  A/cm<sup>2</sup> instead of  $4 \times 10^{-6}$  A/cm<sup>2</sup>), while the devices with C<sub>6</sub>-PA SAM show a more pronounced dependence on the oxide quality and hence a current density that is more than two orders of magnitude larger ( $8 \times 10^{-4}$  A/cm<sup>2</sup> instead of  $4 \times 10^{-6}$  A/cm<sup>2</sup> at 2 V) than for the devices with oxygen-plasma-grown AlO<sub>x</sub>. This indicates that at least for the longer alkyl chains the lower quality of the mild-air-plasma-grown AlO<sub>x</sub> is compensated by the SAMs. When the voltage is increased beyond 2 V, the increase in current density with increasing voltage is essentially the same for the devices with C<sub>10</sub>-PA, C<sub>14</sub>-PA and C<sub>18</sub>-PA SAM, while the breakdown voltage shows the same trend with SAM chain length as in the series with oxygen-plasma-grown AlO<sub>x</sub>, indicating that the electrical properties at large electrical fields are dominated by the SAMs, rather than the oxide. Due to the smaller permittivity of the mild-air-plasma-grown AlO<sub>x</sub>, the capacitance measured in these devices is smaller, but follows the trend related to the contribution of the SAM chain length (see Table 1).

### 3.2. Cyclic voltammetry

To study the chain-length-dependent insulating properties of the phosphonic acid SAMs without the contribution of the insulating metal oxide (AlO<sub>x</sub>) we have also prepared monolayers of C<sub>6</sub>-PA, C<sub>10</sub>-PA and C<sub>18</sub>-PA SAMs on conducting indium tin oxide (ITO) electrodes and performed cyclic voltammetry (CV) measurements. Note that in contrast to the Al/AIO<sub>x</sub>/SAM/Au capacitors discussed in the previous section, the ITO/SAM devices for the cyclic voltammetry analysis have no AlO<sub>x</sub> layer and no Au contact. Therefore, any pinholes present in the SAM would be permeable for the electrolyte and thus result in a substantial leakage current that would be expected to be independent of the alkyl chain length. On the other hand, if the pinhole density is negligible, the currents through the SAM will be due to

**Table 1**  
Electrical parameters of capacitors and pentacene TFTs.

		C <sub>18</sub> -PA (2.44 nm) <sup>a</sup>	C <sub>14</sub> -PA (1.95 nm) <sup>a</sup>	C <sub>10</sub> -PA (1.43 nm) <sup>a</sup>	C <sub>6</sub> -PA (0.91 nm) <sup>a</sup>	C <sub>2</sub> -PA (0.41 nm) <sup>a</sup>
Capacitance (meas.)(μF/cm <sup>2</sup> )	Oxidation	0.67	0.8	0.86	1	1.75
Capacitance (calc.)(μF/cm <sup>2</sup> )	<b>Method A</b>	0.64	0.75	0.91	1.15	1.56
Mobility (cm <sup>2</sup> /Vs)	(Oxygen plasma)	0.18	0.28	0.15	0.05	–
I <sub>b</sub> /I <sub>c</sub>	AlO <sub>x</sub>	$5 \times 10^3$	$7 \times 10^3$	$2 \times 10^3$	$2 \times 10^2$	–
On/off ratio	( $\epsilon = 9$ )	$7 \times 10^5$	$2 \times 10^6$	$2 \times 10^6$	$2 \times 10^4$	–
Capacitance (meas.)(μF/cm <sup>2</sup> )	Oxidation	0.38	0.78	0.86	0.86	0.9
Capacitance (calc.)(μF/cm <sup>2</sup> )	<b>Method B</b>	0.52	0.59	0.68	0.81	1
Mobility (cm <sup>2</sup> /Vs)	(Mild-air plasma)	0.17	0.13	0.03	–	–
I <sub>b</sub> /I <sub>c</sub>	AlO <sub>x</sub>	$2 \times 10^2$	$9 \times 10^1$	7	–	–
On/off ratio	( $\epsilon = 5$ )	$2 \times 10^6$	$3 \times 10^5$	$5 \times 10^3$	–	–

<sup>a</sup> Calculated using CambridgeSoft Chem3D Pro; [www.cambridgesoft.com](http://www.cambridgesoft.com).

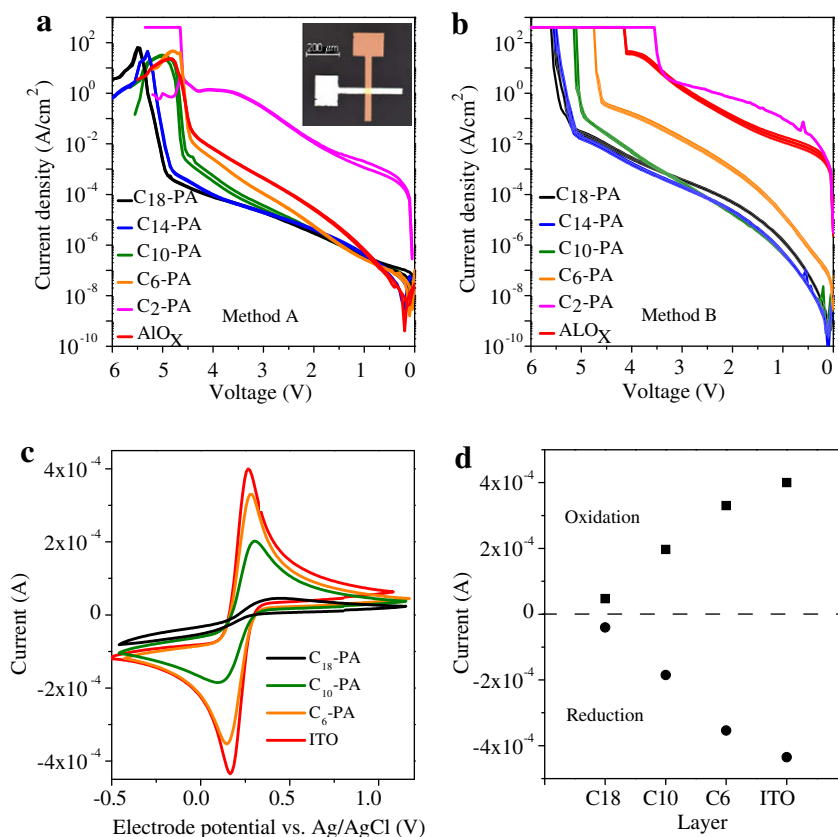


**Fig. 2.** Current density as a function of voltage of Al/AIO<sub>x</sub>/SAM/Au capacitors with an area of 50 × 50 μm. (a) AIO<sub>x</sub> grown by oxygen plasma (method A). Inset: photographic image of a capacitor. (b) Capacitor with AIO<sub>x</sub> grown by mild-air plasma (method B). (c) CV of SAM-coated ITO electrodes in 0.9% NaCl (aq.) with K<sub>3</sub>[Fe(CN)<sub>6</sub>] redox indicator (50 mV/s, Ag/AgCl and Pt counter electrode). (d) CV-current of the oxidation and reduction peaks vs. alkyl chain length of the SAM.

quantum-mechanical tunneling, with a monotonic dependence on the molecular chain length.

The experimental results are summarized in Fig. 2c and d. In all measurements, the redox behavior is reversible, without noticeable damage to the organic monolayers. The results show that the indicator response decreases monotonically with increasing molecular chain length. The CV measurements thus confirm the conclusions from the Al/AIO<sub>x</sub>/SAM/Au capacitor measurements, namely that the insulating properties of the SAMs are indeed a strong, monotonic function of the molecular chain length.

### 3.3. Organic transistors

In a field-effect transistor, the voltage-dependent current through the gate dielectric leads to an undesired gate current during device operation. Thus, for transistors the quality of the dielectric is best described by the gate current ( $I_G$ ) and by the ratio between the drain current and the gate current ( $I_D/I_G$ ) as a function of gate-source voltage ( $V_{GS}$ ).

The gate currents as a function of gate-source voltage of pentacene TFTs based on oxygen-plasma-grown AIO<sub>x</sub> ( $\epsilon = 9$ ) with four different SAMs (C<sub>6</sub>-PA, C<sub>10</sub>-PA, C<sub>14</sub>-PA and C<sub>18</sub>-PA) are shown in Fig. 3a. The drain currents as a

function of gate-source voltage of the same TFTs are shown in Fig. 3b. In general, these devices exhibit small gate currents and large  $I_D/I_G$  ratios, as observed previously for C<sub>18</sub>-PA SAMs on oxygen-plasma-grown AIO<sub>x</sub> [2]. However, a monotonic increase in gate current is observed as the SAM chain length is reduced from C<sub>18</sub>-PA to C<sub>14</sub>-PA, C<sub>10</sub>-PA and C<sub>6</sub>-PA ( $1.5 \times 10^{-10}$  A,  $3.7 \times 10^{-10}$  A,  $6.1 \times 10^{-10}$  A and  $3.2 \times 10^{-9}$  A at  $V_{GS} = -2.5$  V). In devices with C<sub>2</sub>-PA SAM the gate current exceeds the drain current, making these devices unsuitable for practical applications. For each TFT the charge carrier mobility was calculated in the saturation regime using the standard formalism for field-effect transistors:  $\mu = 2L/(W \cdot C_{die}) \cdot (\partial I_D/\partial V_{GS})^2$ , where  $C_{die}$  is the measured dielectric capacitance,  $I_D$  is the drain current, and  $V_{GS}$  is the gate-source voltage. Mobilities of 0.18 cm<sup>2</sup>/Vs for C<sub>18</sub>-PA, 0.28 cm<sup>2</sup>/Vs for C<sub>14</sub>-PA and 0.15 cm<sup>2</sup>/Vs for C<sub>10</sub>-PA were calculated for the TFTs with oxygen-plasma-grown AIO<sub>x</sub>. Devices based on C<sub>6</sub>-PA exhibit a notably smaller mobility of 0.05 cm<sup>2</sup>/Vs. In addition to the mobility and the ratio between drain current and gate current ( $I_D/I_G$ ), Table 1 also lists the ratio between the maximum and the minimum drain current (on/off ratio) of each TFT.

The TFTs with mild-air-plasma-grown AIO<sub>x</sub>/SAM gate dielectrics (permittivity of AIO<sub>x</sub> = 5) show a larger gate leakage compared to the TFTs with oxygen-plasma-grown



$\text{AlO}_x$  (see Fig. 4). To prevent the gate currents from exceeding 10 nA these TFTs were measured only up to a maximum gate-source voltage of  $-2$  V. In addition to the generally larger gate currents, the increase in gate current with reduced SAM chain length from  $\text{C}_{18}$ -PA to  $\text{C}_{14}$ -PA and  $\text{C}_{10}$ -PA is more pronounced ( $7.3 \times 10^{-10}$  A,  $3.4 \times 10^{-9}$  A and  $1.5 \times 10^{-8}$  A at  $V_{GS} = -2.0$  V). As a consequence, the  $I_D/I_G$  ratio is smaller by about one to two orders of magnitude than in TFTs with oxygen-plasma-grown  $\text{AlO}_x$  (see Table 1). As a result of this trend, the  $\text{C}_{14}$ -PA SAM is a lower limit in terms of the minimum chain length for the mild-plasma-grown oxide. In TFTs with  $\text{C}_2$ -PA SAM (aluminum corrosion) and  $\text{C}_6$ -PA SAM the gate current exceeds the drain current, in line with the trend observed for the current density in the capacitors. Using the measured capacitance values, charge carrier mobilities of  $0.17 \text{ cm}^2/\text{Vs}$  for  $\text{C}_{18}$ -PA,  $0.13 \text{ cm}^2/\text{Vs}$  for  $\text{C}_{14}$ -PA and  $0.03 \text{ cm}^2/\text{Vs}$  for  $\text{C}_{10}$ -PA have been calculated.

For both series of TFTs (oxygen-plasma-grown  $\text{AlO}_x$ , mild-air-plasma-grown  $\text{AlO}_x$ ) the mobility decreases as the alkyl chain length of the SAM is reduced from  $\text{C}_{14}$ -PA

to  $\text{C}_{10}$ -PA and to  $\text{C}_6$ -PA. This indicates that the ordering in the SAM is systematically reduced as the alkyl chain length and hence the strength of the cohesive interactions between the phosphonic acid molecules is reduced [28], since less ordering in the SAM is likely to also induce less ordering in the pentacene layer and thus lower mobility.

Hill et al. have recently reported pentacene TFTs with a 100 nm thick  $\text{SiO}_2$  gate dielectric obtained by thermal oxidation of the silicon substrate and functionalized with alkyl phosphonic acid SAMs with alkyl chain length ranging from  $\text{C}_6$ -PA to  $\text{C}_{18}$ -PA [29]. Due to the excellent insulation provided by the thick  $\text{SiO}_2$  layer, the gate current in these TFTs is insignificant. The largest mobility was obtained with a  $\text{C}_8$ -PA SAM ( $1.2 \text{ cm}^2/\text{Vs}$ ). As the chain length was increased from  $\text{C}_8$ -PA to  $\text{C}_{18}$ -PA, the mobility decreased monotonically to  $0.2 \text{ cm}^2/\text{Vs}$ . For TFTs with a  $\text{C}_6$ -PA SAM a mobility of  $0.5 \text{ cm}^2/\text{Vs}$  was reported. It appears that the trend of the mobility as a function of alkyl chain length observed by Hill et al. is quite different from the one we have observed in our TFTs. However, the results are not easily compared, since the mechanisms that con-

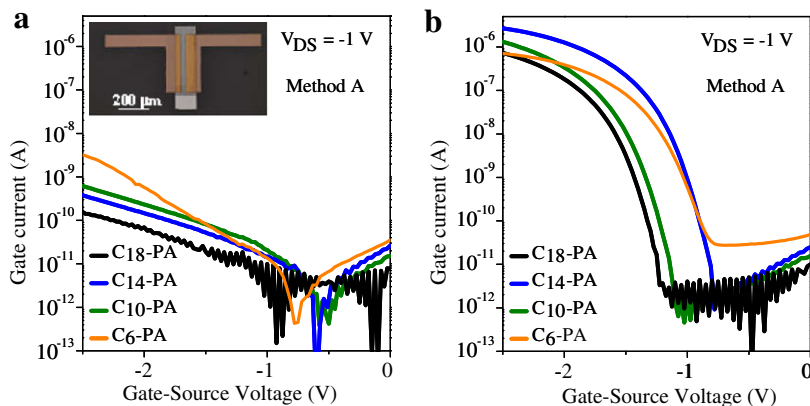


**Fig. 3.** Electrical characteristics of pentacene TFTs with oxygen-plasma-grown  $\text{AlO}_x$ /SAM gate dielectrics (method A). (a) Gate current as a function of gate-source voltage. Inset: Photograph of a TFT. (b) Drain current as a function of gate-source voltage.

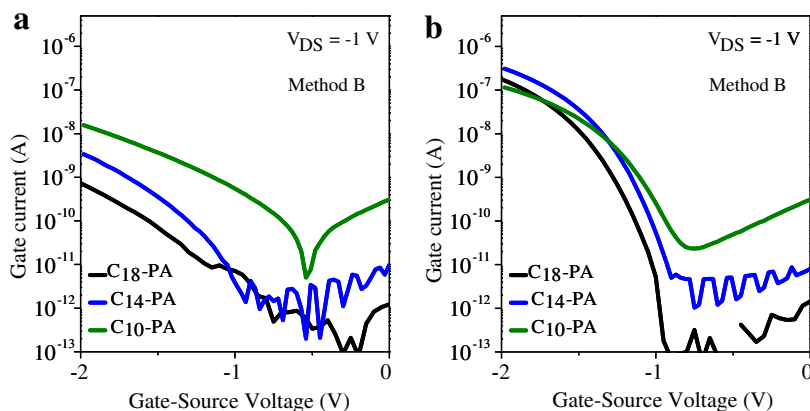


**Fig. 4.** Electrical characteristics of pentacene TFTs with mild-air-plasma-grown  $\text{AlO}_x$ /SAM gate dielectrics (method B). (a) Gate current as a function of gate-source voltage. (b) Drain current as a function of gate-source voltage.

tol adsorption, binding, and monolayer formation of alkyl phosphonic acids on aluminum oxide and on silicon dioxide are fundamentally different [30], and so the microscopic structure of the monolayers is expected to be quite different as well.

#### 4. Conclusion

We have demonstrated that varying the molecular chain length ( $n$ ) of aliphatic  $C_n$ -phosphonic acids influences the electrical characteristics of SAMs based on these molecules. In capacitors that utilize  $AlO_x$ /SAM stacks as double-layer dielectrics the breakdown voltage correlates with the chain length of the self-assembling molecules, while the current density at low fields and the increase in current density with increasing voltage are determined by the quality of the thin  $AlO_x$  layer underneath the SAM. The important role of the chain length of the organic self-assembling molecules in determining the insulating properties of the monolayers has been confirmed using cyclic voltammetry measurements on large-area ITO/SAM devices. Similar trends were found for the gate current in pentacene TFTs that utilize an  $AlO_x$ /SAM stack as the gate dielectric. Reliable low-voltage transistor operation with mobility greater than  $0.1 \text{ cm}^2/\text{Vs}$  has been observed for gate dielectrics with  $C_{18}$ -PA and  $C_{14}$ -PA SAM on  $AlO_x$  of different quality. When using a high-quality oxygen-plasma-grown  $AlO_x$ , the SAM approach can be extended to SAMs as short as  $C_{10}$ -PA. This suggests that low-cost processes for the activation of the metal gate electrodes are suitable and that alkyl chains shorter than  $C_{18}$  provide adequate insulating properties for large-area devices.

#### Acknowledgements

We thank T. Erlbacher for expert technical assistance. Partial financial support (A.J. and M.B.) was provided by the Deutsche Forschungsgemeinschaft (grant DFG-HA 2952/2). Additionally we thank to the Cluster of Excellence “Engineering of Advanced Materials”.

#### References

- [1] H.B. Akkerman, P.W.M. Blom, D.M. De Leeuw, B. De Boer, *Nature* 441 (2006) 69–71.
- [2] H. Klauk, U. Zschieschang, J. Pflaum, M. Halik, *Nature* 445 (2007) 745–748.
- [3] M. Mottaghi, P. Lang, F. Rodriguez, A. Rumyantseva, A. Yassar, G. Horowitz, S. Lenfant, D. Tondelier, D. Vuillaume, *Adv. Funct. Mater.* 17 (2007) 597–604.
- [4] D.J. Gundlach, L. Jia, T.N. Jackson, *IEEE Electr. IEEE Electr. Dev. Lett.* 22 (2001) 571–573.
- [5] S. Kobayashi, T. Nishikawa, T. Takenobu, S. Mori, T. Shimoda, T. Mitani, H. Shimotani, N. Yoshimoto, S. Ogawa, Y. Iwasa, *Nat. Mater.* 3 (2004) 317–322.
- [6] A.L. Briseno, S.C.B. Mannsfeld, M.M. Ling, S. Liu, R.J. Tseng, C. Reese, M.E. Roberts, Y. Yang, F. Wudl, Z. Bao, *Nature* 444 (2006) 913–917.
- [7] U. Zschieschang, M. Halik, H. Klauk, *Langmuir* 24 (2008) 1665–1669.
- [8] A. Ulman, *An Introduction to Ultrathin Films: From Langmuir-Blodgett to Self-Assembly*, Academic Press, Boston, 1991 (Part 3).
- [9] M.H. Yoon, A. Facchetti, T.J. Marks, *Proc. Natl. Acad. Sci. USA* 102 (2005) 4678.
- [10] K.P. Pernstich, S. Haas, D. Oberhoff, C. Goldmann, D.J. Gundlach, B. Batlogg, A.N. Rashid, G. Schitter, *J. Appl. Phys.* 96 (2004) 6431–6437.
- [11] H.B. Akkerman, R.C.G. Naber, B. Jongbloed, P.A. van Hal, P.W.M. Blom, D.M. De Leeuw, B. De Boer, *Proc. Natl. Acad. Sci. USA* 104 (2007) 11161–11166.
- [12] J.M. Buriak, *Chem. Rev.* 102 (2002) 1271–1308.
- [13] Y.-L. Loo, J.W.P. Hsu, R.L. Willett, K.W. Baldwin, K.W. West, J.A. Rogers, et al., *J. Vac. Sci. Technol. B* 20 (2002) 2853–2856.
- [14] H.B. Akkerman, A.J. Kronemeijer, P.A. van Hal, P.W.M. Blom, D.M. De Leeuw, B. De Boer, *Small* 4 (2008) 100–104.
- [15] P.A. van Hal, E.C.P. Smits, T.C.T. Geuns, H.B. Akkerman, B.C. De Brito, S. Perissinotto, G. Lanzani, A.J. Kronemeijer, V. Geskin, J. Cornil, P.W.M. Blom, B. De Boer, D.M. De Leeuw, *Nat. Nanotechnol.* 3 (2008) 749–754.
- [16] G. Robert, V. Derycke, M.F. Goffman, S. Lenfant, D. Vuillaume, J.-P. Bourgoin, *Appl. Phys. Lett.* 93 (2008) 143117.
- [17] J. Collet, D. Vuillaume, *Appl. Phys. Lett.* 73 (1998) 2681–2683.
- [18] J. Collet, O. Tharaud, A. Chapoton, D. Vuillaume, *Appl. Phys. Lett.* 76 (2000) 1941–1943.
- [19] M. Halik, H. Klauk, U. Zschieschang, G. Schmid, C. Dehm, M. Schutz, S. Malsch, F. Effenberger, M. Brunnbauer, F. Stellacci, *Nature* 431 (2004) 963–966.
- [20] Y.D. Park, D.H. Kim, Y. Jang, M. Hwang, J.A. Lim, K. Cho, *Appl. Phys. Lett.* 87 (2005) 243509.
- [21] D.H. Kim, J.T. Han, Y.D. Park, Y. Jang, J.H. Cho, M. Hwang, K. Cho, *Adv. Mater.* 18 (2006) 719–723.
- [22] K.D. Kim, C.K. Song, *Appl. Phys. Lett.* 88 (2006) 233508.
- [23] H. Ma, O. Acton, G. Ting, J.W. Ka, H.-L. Yip, N. Tucker, R. Schofield, A.K.-Y. Jen, *Appl. Phys. Lett.* 92 (2008) 113303.
- [24] P.H. Wöbkenberg, J. Ball, F.B. Kooistra, J.C. Hummelen, D.M. De Leeuw, D.D.C. Bradley, T.D. Anthopoulos, *Appl. Phys. Lett.* 93 (2008) 013303.
- [25] K. Sekine, Y. Saito, M. Hirayama, T. Ohmi, *IEEE Trans. Electr. Dev.* 48 (2001) 1550–1555.
- [26] S.-H. Lo, D.A. Buchanan, Y. Taur, W. Wang, *IEEE Electr. Dev. Lett.* 18 (1997) 209–211.
- [27] P. Fontaine, D. Goguenheim, D. Deresmes, D. Vuillaume, M. Garet, F. Rondelez, *Appl. Phys. Lett.* 62 (1993) 2256–2258.
- [28] D.M. Spori, N.V. Venkataraman, S.G.P. Tosatti, F. Durmaz, N.D. Spencer, S. Zürcher, *Langmuir* 23 (2007) 8053–8060.
- [29] I.G. Hill, C.M. Weinert, L. Kreplak, B.P. van Zyl, *Appl. Phys. A* 95 (2009) 81–87.
- [30] E.L. Hanson, J. Schwartz, B. Nickel, N. Koch, M.F. Danisman, *J. Am. Chem. Soc.* 125 (2003) 16074–16080.

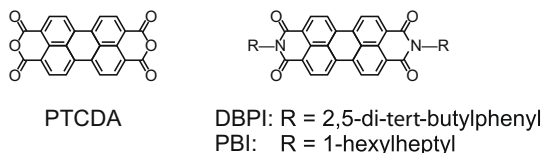


**Fig. 1.** Skeletal formulas of 3,4,9,10-perylene-tetracarboxylic dianhydride (PTCDA,  $C_{24}H_8O_6$ ), *N,N'*-bis(2,5-di-*tert*-butylphenyl)-3,4:9,10-perylene-bis(dicarboximide) (DBPI,  $C_{52}H_{50}N_2O_4$ ), and *N,N'*-bis(1-hexylheptyl)-3,4:9,10-perylenebis(dicarboximide) (PBI,  $C_{50}H_{62}N_2O_4$ ).

to the first ML, but rather extends into the second ML, at least.

## 2. Experimental

PTCDA films were grown by means of organic molecular beam epitaxy (OMBE) on substrates kept in ultrahigh vacuum (UHV) at room-temperature. The quality of the substrates and of the deposited films was monitored by Auger electron spectroscopy (AES), low-energy electron diffraction (LEED), and scanning tunneling microscopy (STM). The good quantitative agreement of the PTCDA film structures observed by us on Au(111) and Au(100) with the published ones [7–10] decisively enhances the comparability between different measurements. Briefly summarized, our epitaxial PTCDA films exhibit flat-lying molecules forming two closed MLs before island growth sets in (Stranski–Krastanov growth, cf. Refs. [7,9]). Film thicknesses were estimated using a quartz crystal microbalance and calibrated more precisely with STM.

Beside the well-accessible molecular frontier orbitals (highest occupied molecular orbital (HOMO) and lowest unoccupied molecular orbital (LUMO)) measured, e.g., with photoelectron spectroscopies [1–4], it has been challenging to determine the optical absorption behavior of ultrathin films on metal surfaces because standard setups in transmission geometry are inappropriate. However, the application of DRS [11,12] followed by a numerical algorithm with the purpose to extract the dielectric function of the molecular adsorbate [13] allows for a detailed optical characterization of such systems. In general, the relation between electronic and optical behavior tends to be intricate since the electronic transport gap  $E_{\text{transport}}$  differs from the optical gap  $E_{\text{optical}}$  by the exciton binding energy  $E_{\text{exciton}}$  which can be as large as 1 eV [14]. In addition, (de-)localization, diffusion, and dielectric screening of molecular excitons are naturally to be distinguished from those of free charge carriers. No attempt will therefore be made to directly establish energy diagrams, but some relevant *indirect* conclusions will be drawn from the optical measurements performed here aiming for an explanation of the observed behavior. Note that a thorough theoretical analysis of large aromatic molecules adsorbed on metal surfaces is still rather demanding. While density functional theory (DFT) can achieve consistency with the experimental determination of the workfunction modification and the HOMO/LUMO alignment with respect to the substrate Fermi energy [15], a reliable prediction of the optical absorption behavior of such systems is currently not feasi-

ble. Calculations of stacked PTCDA, i.e., 2 ML or more on a metal surface are not available at present.

Optical spectra were recorded during deposition, i.e., without interruption of the film growth, using a home-built DRS setup described previously [12,16]. The experimental accuracy is estimated to be  $\pm 0.02$  eV for spectral positions ( $\pm 0.04$  eV for spectral differences). It is outlined in Ref. [12], that the application of the DRS technique can routinely achieve submonolayer resolution, with very good signal-to-noise ratios even down to a surface coverage of 0.1 ML of aromatic molecules. The DRS compares the reflectance of a bare substrate  $R(E, 0)$  with the reflectance  $R(E, d)$  of the same substrate covered with an adsorbate of thickness  $d$  as follows:

$$\text{DRS}(E, d) := \frac{R(E, d) - R(E, 0)}{R(E, 0)} \quad (1)$$

We extract the complex dielectric function  $\hat{\varepsilon}(E, d) = \varepsilon'(E, d) - i\varepsilon''(E, d)$  from the DRS with the help of a *model-free* numerical algorithm fulfilling Kramers–Kronig consistency [13]. The imaginary part  $\varepsilon''$  is discussed here as a measure for the absorbance behavior of the adsorbate in dependency of the film thickness, thereby closely monitoring the interface formation. The DRS intensity is in first approximation proportional to the film thickness (cf. Ref. [11]) as manifested in Fig. 2. In contrast to the DRS, the complex dielectric function being a material property bears an *indirect* thickness-dependence only, since the observed spectral developments are caused by molecule–molecule or molecule–substrate interactions and *not* merely by the amount of material.

In the following, we will discuss the thickness-dependent  $\varepsilon''$  spectra of our PTCDA films on gold substrates. As the optical behavior of PTCDA on Au(100) resembles that on Au(111) to a large extent, the latter surface will be in focus here. The identification of the spectral features of the PTCDA films will then be substantiated by comparison with soluble perylene derivatives which are optically very

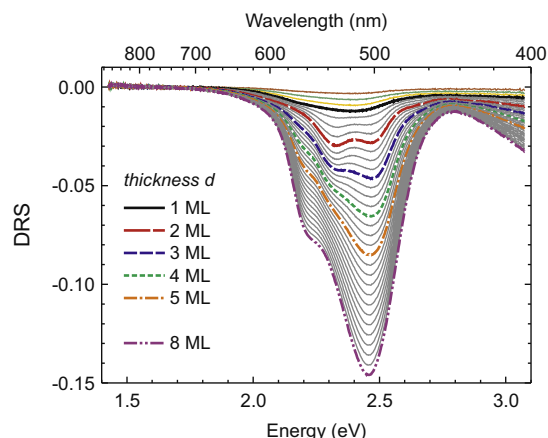


**Fig. 2.** Differential reflectance spectra (DRS, cf. Eq. (1)) of PTCDA films on Au(111). The DRS intensity is in first approximation proportional to the film thickness (cf. Ref. [11]) as manifested in this spectral series.  $\varepsilon''$  values were extracted from these spectra up to  $d \approx 1$  ML (cf. Fig. 6, lower part). Thin gray lines represent intermediate film thicknesses.

similar to PTCDA. Finally, we will propose an explanation for the assumed charge transfer effects in the context of interface dipole ( $\Delta$ ) formation.

### 3. Results and discussion

The DRS as a function of PTCDA film thickness on Au(111) is shown in Fig. 2. Motivated by the abruptly emerging sharp features in the DR spectra we expand the two components (metal/ $n$  MLs PTCDA) to a hypothetical three-phase system (metal/1st ML PTCDA/ $(n-1)$  MLs PTCDA) by setting a new baseline after completion of the 1st ML of PTCDA, such that

$$\text{DRS}^*(E, d^*) := \frac{R(E, d^*) - R(E, d_0)}{R(E, d_0)}, \quad (2)$$

where  $d^* = d - d_0$  means the reduced nominal film thickness, and  $R(E, d_0)$  is the reflectance of the metal covered with  $d_0 := 1$  ML of PTCDA. We would like to emphasize that we do not introduce any sort of model here, as Eq. (2) is in fact an approximation based on the observation that the optical response of the first ML appears to be separated from further layers grown on top, as demonstrated in the following. It is already visible in Fig. 2 that the DRS signal of up to  $d \approx 1$  ML is broad and essentially featureless. Distinct peaks suddenly appear upon growing the 2nd ML of PTCDA, as also evidenced in the  $\text{DRS}^*$  (cf. Fig. 3).

A closeup view of the  $\text{DRS}^*$  of  $d^* = 1$  ML of PTCDA on Au(111) as plotted in Fig. 3 is given in Fig. 4 on an inverted scale for convenience. Additionally, the substrate's coefficients  $A$  and  $B$  for gold, as introduced in Ref. [12], are depicted. They are derived from the substrate bulk dielectric function  $\hat{\epsilon} = \epsilon' - i\epsilon''$  [17]. It was shown in Ref. [12] that the DRS can be approximated by  $\text{DRS} \approx -(8\pi d/\lambda) \times A \times \epsilon''_{\text{film}}$  provided that the condition  $|A| \gg |B|$  is fulfilled. This so-called McIntyre approximation [11] is also valid for  $\text{DRS}^*$  and  $d^*$  with similar accuracy. It can be seen in Fig. 4 that  $|A| \gg |B|$  holds indeed for gold at low photon energies  $E \lesssim 2.3$  eV. Then, two completely independent

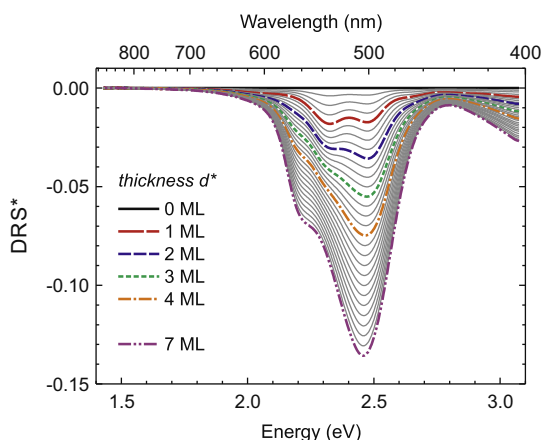


**Fig. 3.** Reduced differential reflectance spectra ( $\text{DRS}^*$ , cf. Eq. (2)) of PTCDA films on Au(111).  $\epsilon''$  values were extracted from the highlighted spectra for  $d^* > 0$  ML (cf. Fig. 6, upper part). Thin gray lines represent intermediate film thicknesses.

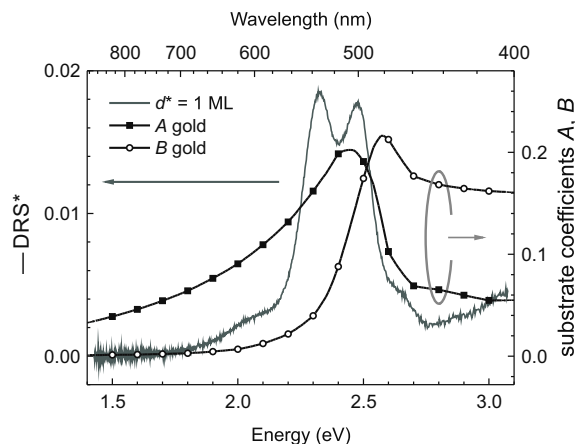


**Fig. 4.** Unfiltered reduced differential reflectance spectrum of  $d^* = 1$  ML of PTCDA on Au(111) from Fig. 3, plotted here on an inverted scale (i.e.,  $-\text{DRS}^*$ ) for convenience. In addition, the substrate's coefficients  $A$  and  $B$  for gold are plotted on a separate scale. Note that  $|A| \gg |B|$  for  $E \lesssim 2.3$  eV, see text for details.

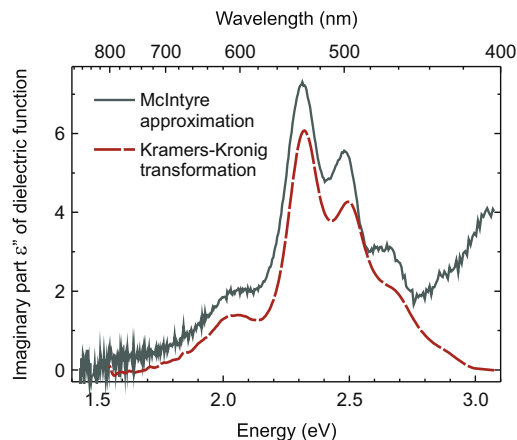


**Fig. 5.** Imaginary part  $\epsilon''_{\text{film}}$  of the dielectric function of  $d^* = 1$  ML of PTCDA on Au(111) derived from the measured  $\text{DRS}^*$  shown in Fig. 4 by two independent methods: McIntyre approximation ( $\epsilon''_{\text{film}} \approx \text{DRS}^* \times \lambda / (-8\pi d^* \times A)$  (no noise filtering) and Kramers–Kronig transformation (smoothed during application of the numerical algorithm).

analysis methods can be used to extract the imaginary part  $\epsilon''_{\text{film}}$  of the adsorbate dielectric function: (i) the McIntyre approximation given above and in Ref. [12], and (ii) the model-free numerical algorithm based on the Kramers–Kronig transformation. It is evident in Fig. 5 that both methods yield comparable results, and especially the position and the shape of the peaks are indeed very similar. Admittedly, the overall height of these two spectra is not identical, which is particularly apparent for high photon energies, where the condition  $|A| \gg |B|$  is invalid for gold, and hence the McIntyre approximation can not be applied. Still, it is very clear from Fig. 5 that a peak at 2.05 eV (see below) is observed for both analysis techniques, and no artificial features are introduced by the numerical method chosen for the evaluation of our data.

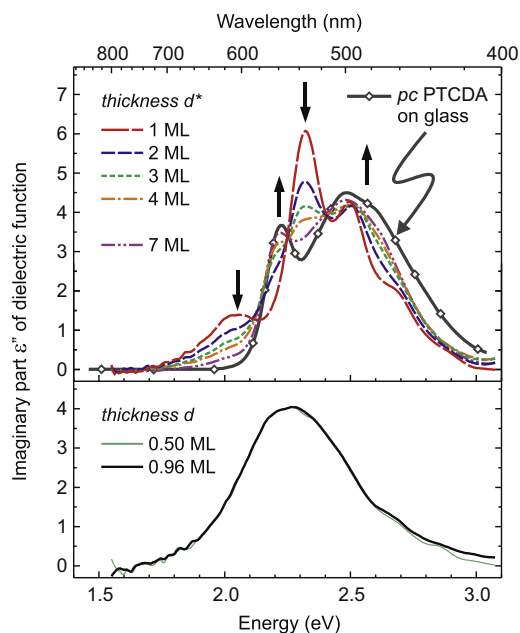


**Fig. 6.** Imaginary part  $\epsilon''$  of the dielectric function of PTCDA films on Au(111). The  $\epsilon''$  spectra for  $d \leq 1$  ML were extracted from the original DRS depicted in Fig. 2, while those for  $d \geq 1$  ML (i.e.,  $d^* > 0$  ML) are based on the DRS depicted in Fig. 3 (see text). For clarity, only selected spectra are presented. Arrows indicate the development with increasing film thickness. The independently determined  $\epsilon''$  spectrum of a comparatively thick polycrystalline (pc) PTCDA film on glass is shown in comparison (adapted from Ref. [18]).

The  $\epsilon''$  spectra extracted from the original DRS and from the reduced DRS, i.e., DRS\*, are depicted in Fig. 6. The broad character of the 1st ML of PTCDA in the DRS directly translates to broad  $\epsilon''$  spectra centered at 2.26 eV. As a matter of fact, the submonolayer spectra ( $d < 1$  ML) exhibit virtually no deviation from the  $d \approx 1$  ML spectrum and therefore only a selection is shown in Fig. 6. Because of the large intermolecular distance between nearest neighbors the in-plane dimerization should be negligible, as recently demonstrated for insulating substrates [19,20]. However, the spectrum of the 1st ML of PTCDA on Au(111) does not exhibit the monomeric shape known on inert (i.e., non-metallic) surfaces, most evidently on mica and KCl [19,20]. This behavior must be due to a comparatively strong coupling of molecular orbitals to electronic states extending perpendicularly from the metal surface. Consequently, significant broadening of the adsorbate levels, as described, e.g., by the Anderson–Newns model [21,22], is observed which may be additionally accompanied by charge transfer. This effect is also called metal–organic “hybridization” in the literature [15,23] and has been observed for the molecular energy levels by means of photoelectron spectroscopy and electron energy loss spectroscopy measurements [6,24]. The impact of this phenomenon on the optical transitions of molecular adsorbates on metal surfaces as reported here has been described previously in Ref. [25].

For PTCDA thicknesses higher than  $d > 1$  ML (i.e.,  $d^* > 0$  ML), several peaks emerge, as depicted in the upper

part of Fig. 6 and also in Fig. 5, and show almost no variation until completion of the 2nd ML (i.e.,  $d^* = 1$  ML; intermediate film thicknesses omitted for clarity). Clearly, this spectrum of  $d^* = 1$  ML can be divided into two different parts which will now be discussed separately.

In the range  $E \geq 2.2$  eV the spectral shape can be assigned to neutral monomers since the main feature at 2.32 eV with its vibronic progression of  $\Delta E \approx 0.17$  eV corresponds to the spectra recorded in solution and on insulating surfaces [19,20]. This means in turn that there can only be marginal coupling between the 2nd and the 1st ML of PTCDA providing further legitimation for the above three-phase approach. This is somehow surprising as one would intuitively expect physical dimerization between face-to-face stacked aromatic molecules. However, for  $E \geq 2.2$  eV the 2nd ML of PTCDA remarkably behaves optically like an ensemble of monomers, or, in other words, like the 1st ML on an insulating substrate. Taking into account our results for quaterylene heteroepitaxially grown on an atomically thin hexa-*peri*-hexabenzocoronene ML [25] we conclude that the energy levels of the 1st PTCDA ML on Au must also differ considerably from the levels of decoupled PTCDA in the subsequent layers, thereby inhibiting noticeable coupling.

It is intriguing to note that in the range  $E \lesssim 2.2$  eV a new peak at 2.05 eV (or 2.03 eV, respectively, for an identical PTCDA thickness on Au(100)) has emerged which does not belong to the absorbance of neutral PTCDA monomers. Considering the  $\epsilon''$  spectra of comparatively thick PTCDA films on glass [18] it is obvious that this feature can also not be explained by aggregation effects. Hence, it must be of different nature, and we attribute this peak to PTCDA radical cations (PTCDA<sup>•+</sup>). For a univocal identification of this feature it would be advisable to compare our  $\epsilon''$  values to absorbance spectra of charged PTCDA in solution. However, to our knowledge such data are not available which is probably due to PTCDA’s rather poor solubility. Still, several publications contain optical absorption spectra of soluble neutral and charged PTCDA derivatives, namely DBPI and PBI (cf. Fig. 1) with a high degree of optical equivalence of the according perylene-derived chromophores [26,27]. Although ionized with dissimilar methods, the energy difference  $\Delta E$  of the cationic main peaks with respect to the associated neutral molecules amounts to 0.29 eV and 0.28 eV, respectively (cf. Fig. 7). Here, we compare relative peak positions rather than absolute values due to the presence of different solvent shifts and dielectric backgrounds in the respective experiments. The positions of the new PTCDA peaks observed here shifted by 0.27 eV and 0.29 eV compared to the main monomeric features on Au(111) and Au(100), respectively, nicely agree with the above values. In contrast, the spectral signatures of the anionic PTCDA derivatives exhibit a multitude of pronounced features shifted by more than 0.5 eV toward lower energies compared to the absorption peaks of the corresponding neutral species [26,27]. Hence, we can exclude the presence of anionic PTCDA in the 2nd ML on Au(111) and Au(100).

The two parts of the  $d^* = 1$  ML spectrum can thus be assigned to the cationic and neutral PTCDA absorption, respectively. For an estimation of their proportionate

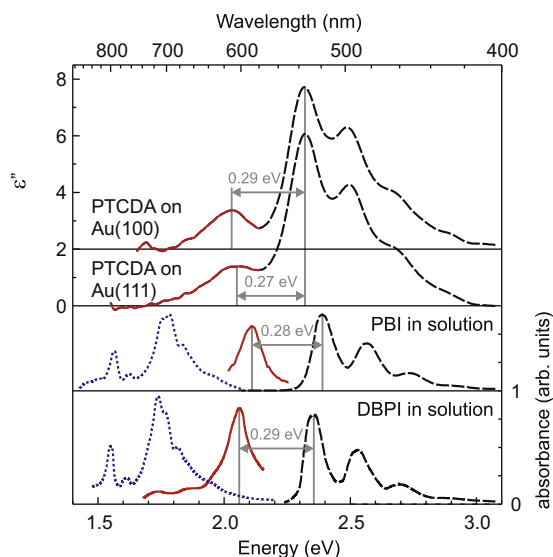


**Fig. 7.**  $\epsilon''$  spectra for  $d^* = 1$  ML of PTCDA on Au(111) and Au(100) compared to absorbance spectra of dissolved DBPI and PBI, in the neutral (dashed lines), anionic (dotted lines), and cationic (solid lines) states, not to scale (adapted from Refs. [26,27], reproduced by permission of the owner societies). The dissimilar dielectric environments cause energetic shifts of the complete spectra, yet the differences between cationic peaks and main transitions of the neutral species are almost identical. For clarity, the spectra are shifted on the vertical scale.

contributions we determine the *relative* oscillator strengths of both parts ( $OS_{\text{charged}} + OS_{\text{neutral}} = OS_{\text{total}}$ ) via

$$OS = \int_{\text{absorption band}} \epsilon''(E) E dE \quad (3)$$

(cf. Ref. [28]) by fitting the  $\epsilon''(E) \times E$  curves with several Gaussian functions (not shown here). Assuming similar *molecular* oscillator strengths (i.e., per molecule), the fraction of charged molecules with respect to the total number of molecules can be expressed as  $OS_{\text{charged}}/OS_{\text{total}}$  and amounts to about 20%, in a first order approximation.<sup>4</sup> This value remains almost constant in between  $0 \text{ ML} \leq d^* \leq 1 \text{ ML}$ .

For further increasing film thickness a characteristic development of the  $\epsilon''$  spectra sets in (Fig. 6 upper part,  $d^* > 1 \text{ ML}$ ). The monomeric features begin to disappear, and the spectral shape broadens forming a new shoulder at  $\approx 2.2 \text{ eV}$ . The peak at 2.05 eV (or 2.03 eV, respectively) assigned to cationic PTCDA vanishes suggesting that the 3rd ML and further layers bear no or just very few charges, and, accordingly, this feature diminishes with rising film thickness as the fraction of neutral PTCDA steadily increases. The development is accompanied by distinct intersections of all spectra in three isosbestic points at  $\approx 2.12 \text{ eV}$ ,  $2.25 \text{ eV}$ , and  $2.40 \text{ eV}$ . Here, we would like to place emphasis on an independently measured  $\epsilon''$  spectrum of a

<sup>4</sup> Judging from absorbance data of dissolved DBPI [26] one may conclude that the fraction of the *molecular* oscillator strengths of the cation with respect to the neutral species can be as low as  $\approx 0.6$ , which would consequently mean an even higher percentage of charged molecules in the  $d^* = 1 \text{ ML}$  spectrum reported here.

rather thick polycrystalline (*pc*) PTCDA film on a glass substrate [18] which also coincides very nicely with these intersections. Further, the fast convergence of our  $\epsilon''$  spectra toward the *pc* bulk behavior is remarkable as it indicates that the adsorbate dielectric function becomes substrate-independent at quite low film thicknesses. Isosbestic points are an expression of aggregation to higher quasi-one-dimensional PTCDA stacks, i.e., the physical monomer  $\rightarrow$  oligomer transition [19,29]. The persistence of the monomeric feature at 2.32 eV for several nominal MLs confirms the Stranski-Krastanov growth with clusters forming on top of a closed 2 ML thick film.

All of the above key statements about the optical spectra and their film-thickness-dependent development made primarily for PTCDA on Au(111) are equally valid on Au(100) as substrate, except for some very slight deviations within the experimental accuracy on the energy scale (cf. Fig. 7). Consequently, we can rule out that our observations would be a mere effect of film structure which exhibits a number of different phases and orientations due to the distinct substrate symmetries and surface reconstructions [8]. The dissimilarities between PTCDA films on Au(111) and Au(100) actually play only a minor role in the respective optical response. Hence, we will not explicitly discuss the results obtained for PTCDA on Au(100) in detail.

Although classified as a weakly interacting system [6,15], the suggested charging of PTCDA on Au can only arise from the proximity of the metal surface. However, the explanation of the charge transfer is not trivial as it should have the most intense impact on the layer of contact. It seems unlikely that only the 2nd PTCDA ML would directly transfer charge to Au. The very broad optical absorption of the 1st PTCDA ML on Au (cf. Fig. 6,  $d \approx 1 \text{ ML}$ ) does actually not permit an unambiguous identification of possible charged features but does also not contradict charging effects in the first place. However, as stated in a recent ultraviolet photoelectron spectroscopy (UPS) study “no clear signature of molecule–metal reaction-induced peaks within the energy gap region of PTCDA was observed in the spectra of PTCDA/Au(111), even at sub-monolayer coverage” [6]. Thus, it seems contradictory to optically detect a (partly) positively charged 2nd ML. To resolve this apparent discrepancy we would like to focus on the interface dipole ( $\Delta$ ) formation upon molecular adsorption. In fact, the vacuum level is decreased by 0.2 eV for 1 Å and further by roughly the same value up to 48 Å of PTCDA [6]. This means in particular that  $\Delta$  between the 1st and 2nd MLs does *not* vanish on Au(111). Although such an interface dipole may have several causes [1], it will be more often than not an expression of charge transfer whose direction is correlated to the sign of  $\Delta$ : for a decrease of the vacuum level upon deposition of a molecular layer one would expect an accumulation of positive charges on the adsorbate’s side of the interface [2–4]. This complies with our observation of molecular cations at the interface between 1st and 2nd MLs of PTCDA on Au(111) and Au(100).

#### 4. Conclusions

In summary, the optical spectra of thin PTCDA films on Au presented here suggest that there is a clear difference in

the electronic properties between the layer of contact and further layers grown on top. The behavior of the 2nd PTCDA ML is somewhat unexpected though: surprisingly, physical dimerization does not occur between the face-to-face stacked 1st and 2nd PTCDA MLs on Au(111) and Au(100). The interaction between the contact layer and the Au surface is efficient enough to shift the molecular energy levels considerably and to cause consequently a decoupling effect of further layers. Yet, the most important observation is the occurrence of charged PTCDA in these solid state optical spectra. From the optical data we deduce the formation of a (partly) positively charged 2nd ML of PTCDA films on Au(111) and Au(100). Assuming a similar molecular oscillator strength for neutral PTCDA and the cation we estimate the fraction of charged PTCDA to be  $\approx 20\%$ . We conclude that the interface dipole formation between 1st and 2nd MLs of PTCDA on Au as reported before [6] is responsible for the charging observed here. The simple correlation of the sign of the interface dipole to the direction of charge transfer as proposed in this contribution might not reflect the full picture, but it can give at least an appropriate tendency. Further experimental and theoretical work will be necessary to yield a comprehensive explanation of charge transfer effects in the proximity of metals.

## Acknowledgements

We acknowledge financial support from the Deutsche Forschungsgemeinschaft (Grant No. FR875/6,9,10). R.F. was supported by the Studienstiftung des deutschen Volkes. We thank Karl Leo, Egbert Zojer, and Karin Zojer for stimulating discussions.

## Appendix A. Supplementary data

Supplementary data associated with this article can be found, in the online version, at doi:10.1016/j.orgel.2009.08.005.

## References

- [1] H. Ishii, K. Sugiyama, E. Ito, K. Seki, Energy level alignment and interfacial electronic structures at organic/metal and organic/organic interfaces, *Adv. Mater.* 11 (1999) 605–625.
- [2] A. Kahn, N. Koch, W. Gao, Electronic structure and electrical properties of interfaces between metals and  $\pi$ -conjugated molecular films, *J. Polym. Sci. Part B: Polym. Phys.* 41 (2003) 2529–2548.
- [3] J. Hwang, A. Wan, A. Kahn, Energetics of metal–organic interfaces: new experiments and assessment of the field, *Mater. Sci. Eng., R* 64 (2009) 1–31.
- [4] S. Braun, W.R. Salaneck, M. Fahlman, Energy-level alignment at organic/metal and organic/organic interfaces, *Adv. Mater.* 21 (2009) 1450–1472.
- [5] S. Picozzi, A. Pecchia, M. Gheorghe, A. Di Carlo, P. Lugli, B. Delley, M. Elstner, Schottky barrier height at an organic/metal junction: a first-principles study of PTCDA/X (X = Al, Ag) contacts, *Phys. Rev. B* 68 (2003) 195309.
- [6] S. Duhm, A. Gerlach, I. Salzmann, B. Bröker, R.L. Johnson, F. Schreiber, N. Koch, PTCDA on Au(111), Ag(111) and Cu(111): correlation of interface charge transfer to bonding distance, *Org. Electron.* 9 (2008) 111–118.
- [7] I. Chizhov, A. Kahn, G. Scoles, Initial growth of 3,4,9,10-perylenetetracarboxylic-dianhydride (PTCDA) on Au(111): a scanning tunneling microscopy study, *J. Cryst. Growth* 208 (2000) 449–458.
- [8] S. Mannsfeld, M. Toerker, T. Schmitz-Hübsch, F. Sellam, T. Fritz, K. Leo, Combined LEED and STM study of PTCDA growth on reconstructed Au(111) and Au(100) single crystals, *Org. Electron.* 2 (2001) 121–134.
- [9] T. Wagner, A. Bannani, C. Bobisch, H. Karacuban, M. Stöhr, M. Gabriel, R. Möller, Growth of 3,4,9,10-perylenetetracarboxylic-dianhydride crystallites on noble metal surfaces, *Org. Electron.* 5 (2004) 35–43.
- [10] L. Kilian, E. Umbach, M. Sokolowski, A refined structural analysis of the PTCDA monolayer on the reconstructed Au(111) surface – “rigid or distorted carpet?”, *Surf. Sci.* 600 (2006) 2633–2643.
- [11] J.D.E. McIntyre, D.E. Aspnes, Differential reflection spectroscopy of very thin surface films, *Surf. Sci.* 24 (1971) 417–434.
- [12] R. Forker, T. Fritz, Optical differential reflectance spectroscopy of ultrathin epitaxial organic films, *Phys. Chem. Chem. Phys.* 11 (2009) 2142–2155.
- [13] R. Nitsche, T. Fritz, Determination of model-free Kramers–Kronig consistent optical constants of thin absorbing films from just one spectral measurement: application to organic semiconductors, *Phys. Rev. B* 70 (2004) 195432.
- [14] M. Knupfer, Exciton binding energies in organic semiconductors, *Appl. Phys. A* 77 (2003) 623–626.
- [15] L. Romner, D. Nabok, P. Puschnig, E. Zojer, C. Ambrosch-Draxl, Theoretical study of PTCDA adsorbed on the coinage metal surfaces, Ag(111), Au(111) and Cu(111), *New J. Phys.* 11 (2009) 053010.
- [16] H. Proehl, R. Nitsche, T. Diemel, K. Leo, T. Fritz, *In situ* differential reflectance spectroscopy of thin crystalline films of PTCDA on different substrates, *Phys. Rev. B* 71 (2005) 165207.
- [17] M.J. Weber (Ed.), *Handbook of Optical Materials*, CRC Press, Boca Raton, 2003.
- [18] A.B. Djurišić, T. Fritz, K. Leo, Modeling the optical constants of organic thin films: application to 3,4,9,10-perylenetetracarboxylic dianhydride (PTCDA), *Opt. Commun.* 183 (2000) 123–132.
- [19] H. Proehl, T. Diemel, R. Nitsche, T. Fritz, Formation of solid-state excitons in ultrathin crystalline films of PTCDA: from single molecules to molecular stacks, *Phys. Rev. Lett.* 93 (2004) 097403.
- [20] T. Diemel, C. Loppacher, S.C.B. Mannsfeld, R. Forker, T. Fritz, Growth-mode-induced narrowing of optical spectra of an organic adlayer, *Adv. Mater.* 20 (2008) 959–963.
- [21] P.W. Anderson, Localized magnetic states in metals, *Phys. Rev.* 124 (1961) 41–53.
- [22] D.M. Newns, Self-consistent model of hydrogen chemisorption, *Phys. Rev.* 178 (1969) 1123–1135.
- [23] L. Romner, G. Heimel, J.-L. Brédas, A. Gerlach, F. Schreiber, R.L. Johnson, J. Zegenhagen, S. Duhm, N. Koch, E. Zojer, Impact of bidirectional charge transfer and molecular distortions on the electronic structure of a metal–organic interface, *Phys. Rev. Lett.* 99 (2007) 256801.
- [24] F.S. Tautz, M. Eremtchenko, J.A. Schaefer, M. Sokolowski, V. Shklover, E. Umbach, Strong electron–phonon coupling at a metal/organic interface: PTCDA/Ag(111), *Phys. Rev. B* 65 (2002) 125405.
- [25] R. Forker, D. Kasemann, T. Diemel, C. Wagner, R. Franke, K. Müllen, T. Fritz, Electronic decoupling of aromatic molecules from a metal by an atomically thin organic spacer, *Adv. Mater.* 20 (2008) 4450–4454.
- [26] W.E. Ford, H. Hiratsuka, P.V. Kamat, Photochemistry of 3,4,9,10-perylenetetracarboxylic dianhydride dyes. 4. Spectroscopic and redox properties of oxidized and reduced forms of the bis(2,5-ditert-butylphenyl)imide derivative, *J. Phys. Chem.* 93 (1989) 6692–6696.
- [27] T. Kircher, H.-G. Löhmansröben, Photoinduced charge recombination reactions of a perylene dye in acetonitrile, *Phys. Chem. Chem. Phys.* 1 (1999) 3987–3992.
- [28] T. Diemel, R. Forker, K. Leo, T. Fritz, Optical differential reflectance spectroscopy of molecular thin films on a metal: evidence for strong oscillator strength increase, *J. Phys. Chem. C* 111 (2007) 14593–14596.
- [29] H. Mauser, Spectroscopy of chemical reaction kinetics. 1. Theory of isosbestic points, *Z. Naturforsch.* B23 (1968) 1021–1025.

ratio. A 30 nm-thick electron-transporting layer of Alq<sub>3</sub> (Sigma–Aldrich, 99.995%) was sublimated at  $6.66 \times 10^{-4}$  Pa pressure. Finally, a 200 nm aluminum cathode was deposited by thermal evaporation in the same vacuum to complete the device. Fig. 1 shows the energy band diagram of the overall structure.

The PVK/Alq<sub>3</sub> bi-layer yields a greenish, 50 nm-wide electroluminescence spectrum. To widen the spectrum and achieve white light emission, red-emitting quantum dots were incorporated in PVK. CdSe/ZnS core-shell quantum dots (Evident Technologies Ltd.) of 5.8 nm in diameter were dispersed in the PVK:toluene solution. The weight ratio (*R*) of CdSe/ZnS to PVK was set at 0.9:10. To add spectral components to the blue side of the electroluminescence spectrum, it is necessary to use quantum dots with a smaller diameter. However, we found that such particles only emit weakly and tend to be unstable because of their large surface/volume ratio. A different approach is to use phosphorescent molecules. To this end, we dissolved blue-light-emitting molecules Ir(III)DP into PVK to enhance the spectrum in the 450–500 nm region. The weight ratios of CdSe/ZnS to Ir(III)DP and to PVK are 0.9:10 and 8.3:10, respectively.

### 3. Results and discussion

Fig. 2 shows the normalized electroluminescence spectra of the device with and without the addition of quantum dots or Ir(III)DP. The luminescence of the reference structure (without quantum dots or molecules) peaks at 526 nm and takes a greenish appearance, whereas quantum dots produce a luminescence spectrum centered at 620 nm with a 30 nm FWHM. The color pictures in Fig. 3 show color coordinates that gradually approach that of pure white light (0.33, 0.33).

For devices without Ir(III)DP, the external quantum yield is 0.45% (at a bias of 14 V) without QDs and 0.40% (at a bias of 14 V) when QDs are included into the device at weight ratio *R* = 9%. Here, we stress that our main goal was not to optimize the device but rather to understand how the QDs affect the operating mechanisms of OLEDs. For this task the measurement of quantum yield is especially valuable.

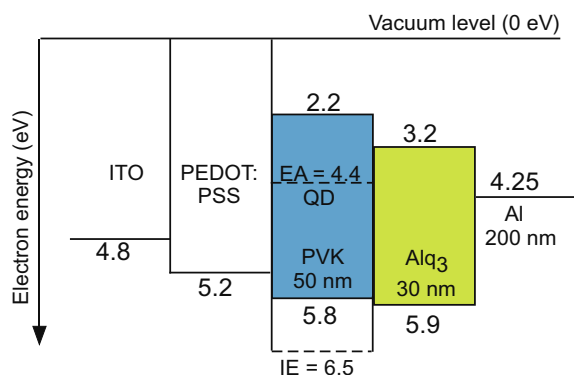


Fig. 1. Energy band diagram of the PVK/Alq<sub>3</sub> reference organic device [4,5]. Electron affinity (EA) and ionization energy (IE) values of QDs are taken from Ref. [11].

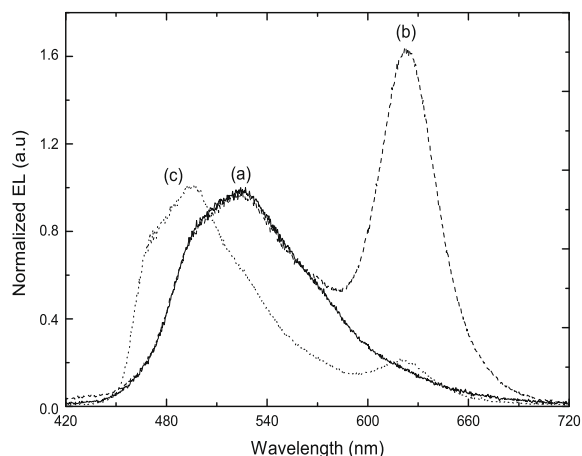


Fig. 2. Electroluminescence spectrum of (a) the reference PVK/Alq<sub>3</sub> device, (b) with red-emitting quantum dots and (c) with Ir(III)DP plus red-emitting quantum dots. Device (c), the only one with blue-emitting molecules, shows a blue shift and produces white light of better quality.

The arrangement offers a high degree of flexibility. The characteristic of the device's electroluminescence spectrum can be controlled by choosing various ratios of Ir(III)DP and quantum dot to PVK, and by using different quantum dot sizes. However, because the three types of light emitters interact in a non-trivial way, the relative emission efficiency is not a simple function of concentration or voltage. To fully exploit and tailor the device to a specific application, it is important to understand the luminescence mechanisms involved. For example, quantum dots can luminesce *via* Förster energy transfer of excitons [6–9] and/or injection of electron–hole pairs [10–13]. Having a large absorption cross section, these particles can also, in theory, be excited by absorbing photons generated inside the device with energies above the CdSe band gap (<700 nm). The rest of this paper focuses on exploring these mechanisms.

Fig. 4 shows the surface morphology of various PVK films with and without quantum dots. The microscope pictures show that the surface of pure PVK is homogeneous on a small scale. On the other hand, PVK with quantum dots (*R* = 3%, image b), shows small aggregates dispersed on the surface. At higher concentration, *R* = 9%, the surface morphology suggests aggregates, on the same scale as reported by Son et al. in Ref. [15]. In their work on PVK films with quantum dots, TEM images reveal PVK clusters enveloped with quantum dots. Aggregation, it seems, takes the form of a blend of the two materials, making the film effectively uniform on a scale above 300 nm. The fact that quantum dots would be thus embedded into the film (and not just concentrated at the surface) is an important element in explaining the operation of the OLED.

We now proceed with an analysis of the emission profiles of devices with and without quantum dots. It is significant that the EL spectrum of the reference OLED (Fig. 2a) shows no evidence of light emission by the PVK. Since excitons are mainly formed at PVK/Alq<sub>3</sub> interface, and since holes easily migrate from PVK to Alq<sub>3</sub> (the potential barrier



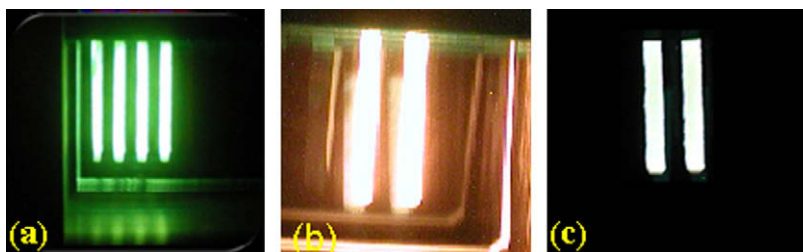


Fig. 3. Pictures of the devices (a–c) of Fig. 2. The color coordinates of (a), (b) and (c) are (0.3, 0.55), (0.43, 0.45) and (0.24, 0.415), respectively.

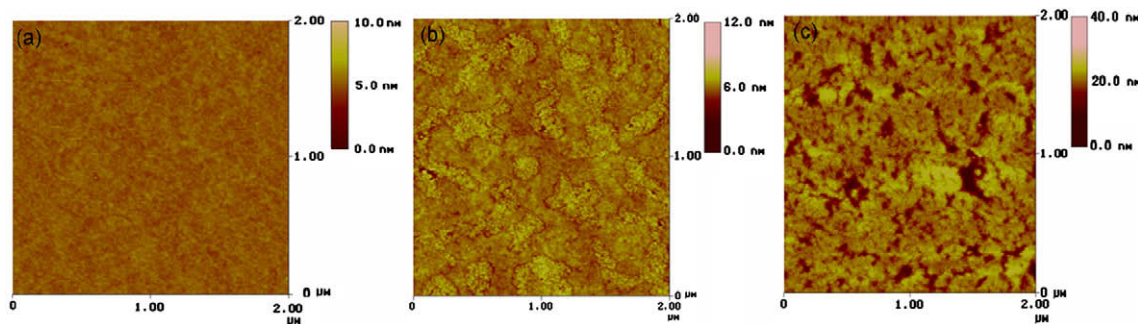


Fig. 4. Atomic force microscope images the surface morphology of various PVK: QDs layers.

is only 0.1 eV versus the 1 eV barrier for electrons going from Alq<sub>3</sub> into PVK), electron–hole recombination occurs principally in the Alq<sub>3</sub> layer, in accordance with previous works [16,17]. Fig. 5 shows the electroluminescence spectrum of the PVK/Alq<sub>3</sub> device with quantum dots. At low voltages, near the threshold voltage of 12 V, the spectrum is dominated by Alq<sub>3</sub> emission, but as the voltage increases, the contribution from quantum dots exceeds that of Alq<sub>3</sub>.

The overlap between the QD absorption profile and the photoluminescence spectrum of Alq<sub>3</sub> [9] suggests the possibility of exciton transfer from Alq<sub>3</sub> to QDs via the Förster mechanism [18]. Coe et al. [7] demonstrated that, for a tri-layer hybrid QDs/organic LED, the Förster energy transfer of excitons from organic materials to the QDs dominates the EL process rather than charge injection into QDs. As Fig. 6 illustrates, at low voltages the majority of excitons recombining in Alq<sub>3</sub> do so very close to the interface with

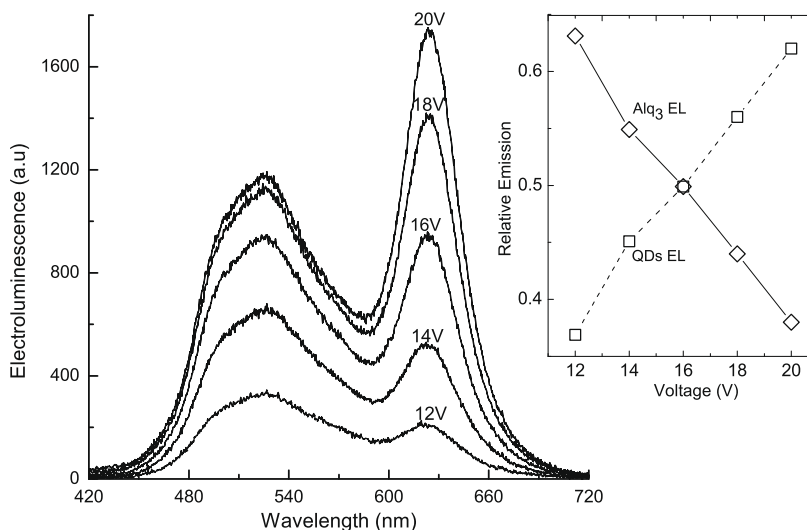
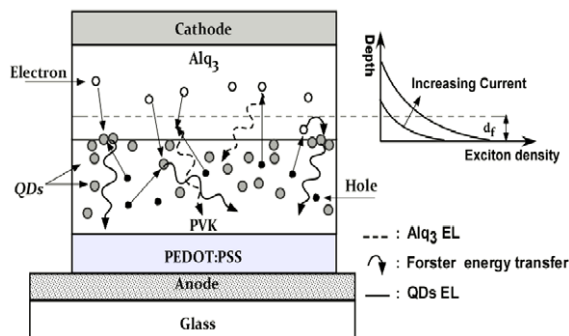


Fig. 5. Emission spectra profiles of ITO/PEDOT: PSS/PVK: QD/Alq<sub>3</sub>/Al devices with quantum dots. The relative contribution of QDs and Alq<sub>3</sub> varies with voltage, as shown in inset.



**Fig. 6.** Exciton generation and luminescence processes in a quantum dot-doped OLED.

PVK. This favours excitonic pumping of QDs, which are located in the PVK. Increasing voltage causes excitons to recombine further into Alq<sub>3</sub> and farther away from QDs, which does not favour the Förster mechanism. (Exciton energy transfer to quantum dots occurs within the Förster radius  $d_f$ ). In our devices, however, quantum dots consistently emit more efficiently at higher voltages, in spite of the fact that electroluminescence from Alq<sub>3</sub> saturates (see Fig. 5). Furthermore, QDs emit steadily even when emission from Alq<sub>3</sub> declines with time. This trend is clearly shown in Fig. 7, whereby the red emission of QDs exhibits remarkable stability for over 15 s. These data suggests that Förster energy transfer is not the dominant excitation process of QDs in our OLEDs. Instead, charge injection appears to be an important additional mechanism of electroluminescence in QDs.

Fig. 8 shows how doping PVK with QDs does not change the shape of the  $I$ - $V$  curve. In both concentrations shown, the curves are best fitted by a space-charge-limited conduction model (SCLC) with an exponential distribution of traps [20]. The current density  $J$  is well described by the equation [19]

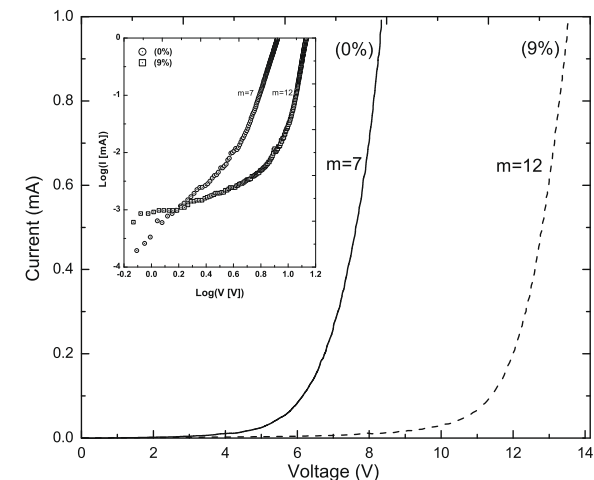


**Fig. 8.** Current–voltage curves of ITO/PEDOT:PSS/PVK:(CdSe/ZnS)/Alq<sub>3</sub>/Al devices with CdSe/ZnS mass loadings of 0% and 9%.

$$J = q^{(1-m)} \varepsilon^m \mu_{\text{ef}} \frac{N_{\text{ef}}}{N_{\text{tr}}^m} \left( \frac{m}{m+1} \right)^m \left( \frac{2m+1}{m+1} \right)^{m+1} \frac{V^{m+1}}{d^{2m+1}}$$

where  $q$  is the electron charge,  $m$  is a characteristic energy distribution parameter of traps,  $\varepsilon$  is the electrical permittivity,  $\mu_{\text{ef}}$  is the effective mobility,  $N_{\text{ef}}$  is the density of states in the transport band,  $N_{\text{tr}}$  is the total concentration of traps,  $V$  is the applied voltage and  $d$  is the sample thickness. However, doping does induce a decrease of current density and an increase of  $m$  from 7 to 12. According to SCLC theoretical framework, this variation in  $m$  indicates that traps are deeper in the doped structure. As it should be and shown in Fig. 1, the electron affinity level of the QDs is well below the PVK LUMO level. This suggests that electrons could easily be trapped by QDs. Then, doping PVK with QDs results in, (1) an increase in traps concentration and thus a decrease in current density and (2) an increase in  $m$  because QDs act as deep traps. In contrast, the PVK HOMO level is well above the QDs ionization energy level. The holes injected in the PVK/QDs layer then diffuse through the PVK molecules. Because holes can tunnel through the Zn shell into the valence band of the CdSe quantum dots (attracted by the trapped electron), the QDs can thus emit light via electron–hole pair recombination. Therefore, the charge injection into QDs appears to be an important mechanism of excitation in quantum dots which adds to the Förster energy transfer.

On the other hand, the mechanism of photoemission from Ir(III)DP also appears to be from current excitation. Indeed, photoexcitation would require absorption of light at wavelengths below 450 nm, whereas very little light is emitted by Alq<sub>3</sub> below 500 nm.

#### 4. Conclusions

In conclusion, we have demonstrated a hybrid organic device for generation of electroluminescence with adjustable properties. By using different excitation mechanisms for light emission, quantum dots add flexibility to OLED composition and can be used towards the manipulation

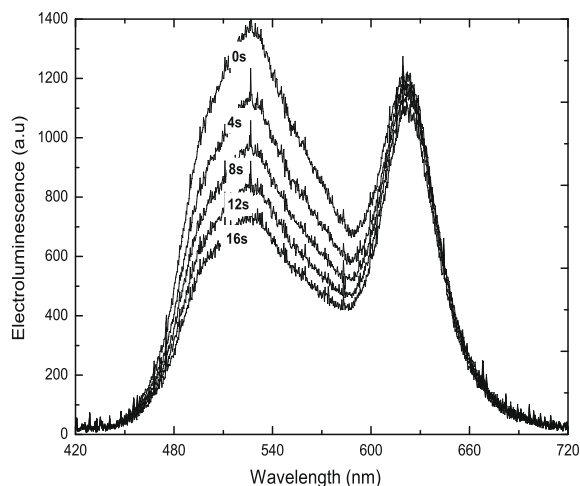


**Fig. 7.** The temporal evolution of the electroluminescence ITO/PEDOT:PSS/PVK:(CdSe/ZnS)/Alq<sub>3</sub>/Al device a constant voltage of 30 V applied.

of their spectral emission profile in order to produce, among others, white light of high quality.

### Acknowledgements

This work was supported by NSERC, the Canada Research Chair program, the New Brunswick Innovation Fund and the Atlantic Innovation Fund.

### References

- [1] J.H. Park, J.Y. Kim, B.D. Chin, Y.Ch. Kim, J.K. Kim, O.O. Park, *Nanotechnology* 15 (2004) 1217.
- [2] Y. Xuan, D. Pan, N. Zhao, X. Ji, Dongge Ma, *Nanotechnology* 17 (2006) 4966.
- [3] P.O. Anikeeva, J.E. Halpert, M.G. Bawendi, V. Bulovic, *Nano Letters* 7 (2007) 2196.
- [4] R.K. Ligman, L. Mangolini, U.R. Kortshagen, S.A. Campbella, *Applied Physics Letters* 90 (2007) 061116.
- [5] K. Seki, E. Ito, H. Ishii, *Synthetic Metals* 91 (1997) 137.
- [6] S. Coe-Sullivan, W.K. Woo, M. Bawendi, V. Bulovic, *Nature* 420 (2002) 800.
- [7] S. Coe-Sullivan, W.K. Woo, T.S. Steckel, M. Bawendi, V. Bulovic, *Organic Electronics* 4 (2003) 123.
- [8] Y. Li, A. Rizzo, M. Mazzeo, L. Carbone, L. Manna, R. Cingolani, G. Gigli, *Applied Physics* 97 (2005) 113501.
- [9] P.O. Anikeeva, C.F. Madigan, J.E. Halpert, M.G. Bawendi, V. Bulovic, *Physical Review B* 78 (2008) 085434.
- [10] H. Mattoussi, L.H. Radzilowski, B.O. Dabbousi, M.F. Rubner, *Journal of Applied Physics* 83 (1998) 7965.
- [11] R.A.M. Hikmet, D.V. Talapin, H. Weller, *Journal of Applied Physics* 93 (2003) 3509.
- [12] H. Yang, P.H. Holloway, B.B. Ratna, *Journal of Applied Physics* 93 (2003) 586.
- [13] S. Chaudhary, M. Ozkan, Warren C.W. Chan, *Applied Physics Letters* 84 (2004) 2925.
- [14] D.-I. Son, J.-H. Kim, D.-H. Park, W.K. Choi, F. Li, J.H. Ham, T.W. Kim, *Nanotechnology* 19 (2008) 055204.
- [15] C.W. Tang, S.A. VanSlyke, *Applied Physics Letters* 51 (1987) 913.
- [16] P.E. Burrows, Z. Shen, V. Bulovic, D.M. McCarty, S.R. Forrest, *Applied Physics* 79 (1997) 7991.
- [17] Th. Förster, *Annals of Physics* 437 (1948) 55.
- [18] J. Kalinowski, *Organic Light-Emitting Diodes*, CRC Press, 2005.
- [19] B. Torriß, M.Sc. thesis, Université de Moncton, Canada, 2009.

the electrode metal surface with strong electron acceptor or donor molecules prior to deposition of the active organic semiconductor [12,13]. For instance, the hole injection barrier (HIB; energy difference between the highest occupied molecular level and the metal Fermi-level) from Au into vacuum sublimed molecular layers can be reduced by up to 1.2 eV with a monolayer of the acceptor 2,3,5,6-tetrafluoro-7,7,8,8-tetracyanoquinodimethane (F4-TCNQ) [12]. The underlying mechanism has been clearly identified as a bidirectional charge transfer between the metal (e.g., Cu) and F4-TCNQ [14,15]. This introduces dipoles at the metal surface with their negative ends oriented away from the surface, which increases the metal work function ( $\Phi$ ). The energy levels of any organic material deposited on top of this modified electrode are then re-aligned relative to this modified surface potential [12].

However, to date this powerful adjustment of the HIB at metal/organic interfaces was only shown to be operative under very restrictive conditions, *i.e.*, ultrahigh vacuum (UHV), on atomically clean metal surfaces, and *in situ* vacuum sublimed acceptor layers and organic semiconductors. These conditions are quite different from those that prevail during low-cost device fabrication, *e.g.*, by spin-coating or printing techniques in inert gas or even ambient atmosphere, where the presence of (residual) oxygen, water and hydrocarbons result in ubiquitous impurities/contamination of interfaces.

Our present work explores the possibility of transferring the concept of optimizing the HIB at metal/organic interfaces with strong electron acceptors from UHV to solution-based methods in ambient conditions that are realistic for actual device fabrication. Using X-ray photoelectron spectroscopy (XPS) and photoelectron emission yield (PEY) spectroscopy we show that Cu electrode surfaces can be appropriately modified with the acceptors tetracyanoquinodimethane (TCNQ) and F4-TCNQ (for acceptors' chemical structure see Fig. 1) by simple solution casting, leading to high  $\Phi$  values – even stable in air on timescales of *ca.* one hour. Such modified Cu electrodes are proven to result in significantly improved performance in flexible polymer OFETs built on poly(ethyleneterephthalate)-foil, as revealed by higher  $I_{on}$  and lower  $V_T$  values.

## 2. Experimental

All experiments are based on Cu covered and pre-patterned poly(ethyleneterephthalate)-foil (Cu/Pet-foil) (from Fraunhofer IZM, München, Germany), that was also used as substrate for OFET fabrication. The modification process of the Cu surface with acceptor molecules comprised two key preparation steps.

- (1) Etching off the native oxide layer at the Cu surface by washing in 2 M hydrochloric acid (HCl) and subsequent rinsing in deionized water and ethanol. After this treatment in ambient atmosphere samples were brought into an inert gas glove-box for further processing.
- (2) F4-TCNQ (Fluka) and TCNQ (Fluka) were applied to Cu electrodes by drop casting from chlorobenzene solution (1 mg/ml). Subsequently samples were

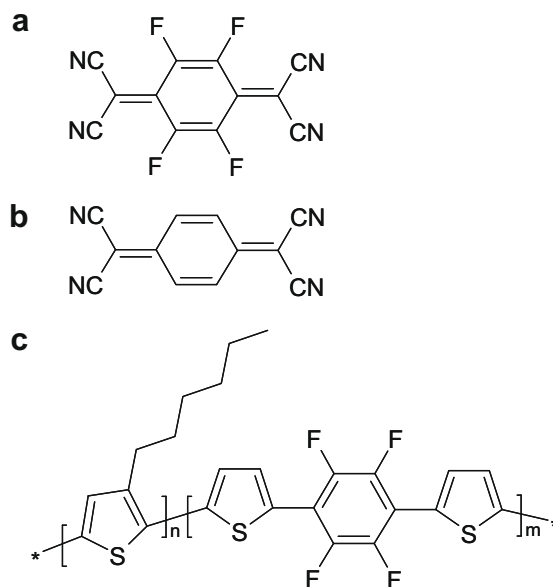


**Fig. 1.** Chemical structure of (a) TCNQ, (b) F4-TCNQ, and (c) poly(3-hexylthiophene)-dithienyltetrafluorobenzene (P3HT-TFT).

washed in copious amounts of chlorobenzene to remove excess non-chemisorbed (on Cu) acceptor molecules.

Before any treatment (pristine) and after each preparation step, the chemical composition of Cu electrodes was studied using X-ray photoelectron spectroscopy (XPS), and the surface work function was determined by photoelectron emission yield (PEY) spectroscopy.

XPS spectra were collected with a hemispherical Multi-technique Electron Spectrometer (Kratos Analytical), with monochromatized  $K\alpha$  line radiation of an aluminum anode for excitation, and an analyzer pass energy of 20 eV. The base pressure in the analysis chamber was  $2 \times 10^{-10}$  mbar. Fitting of XPS spectra was performed with the program WINSPEC (developed at the University of Namur, Belgium).

Sample  $\Phi$  was determined from PEY spectra recorded at ambient conditions with an AC-2 Photoelectron-Spectrometer (Riken Keiki Co., Ltd.). The apparatus detects photoemitted electrons per second (CPS) as a function of photon energy using a UV light source for excitation and a gas-flow Geiger counter. For the relation between CPS and photon energy Bouwman and Sachtler adopted an approximated equation [16]

$$\text{CPS} = \frac{M(h\nu - \phi)^2}{2k^2} \quad (1)$$

Here  $M$  is an emission constant,  $h\nu$  the photon energy,  $\phi$  the work function, and  $k$  the Boltzmann constant. In this method the value of  $\phi$  is determined by a linear extrapolation of  $\text{CPS}^{1/2}$  to zero yield [17]. PEY spectra were fitted using the software provided by the spectrometer supplier.

OFETs were fabricated in a top-gate and bottom-contact configuration, comprising the pre-structured Cu/PET-foil as substrate and source/drain electrodes. The pre-structuring process was done at the Fraunhofer IZM (München, Germany) using photolithography, with channel length

$L = 40 \mu\text{m}$  and channel width  $W = 40 \mu\text{m}$ . For OFET preparation with acceptor modified electrodes, the entire pre-structured Cu/PET-foil was treated as described above for Cu electrodes. As active polymer layer (channel) we used the statistical co-polymer poly(3-hexylthiophene)-dithienyltetrafluorobenzene (P3HT-TFT), which comprises poly(3-hexylthiophene) (P3HT) segments with additional 5 mol% of 1,4-dithienyl-2,3,5,6-tetrafluorobenzene (TFT) in the main-chain (for chemical structure see Fig. 1) with a molecular weight of  $M_w = 22,300 \text{ g/mol}$ . This polymer was chosen as semiconducting material because it is more stable against doping by oxygen compared to standard P3HT [18], resulting in better device stability and longer lifetime. P3HT-TFT was spin cast from chlorobenzene solution (10 mg/ml) in inert atmosphere, resulting in a film thickness of 30 nm. The organic gate dielectric layer P121 (Merck KGaA) was spin cast in inert conditions with a thickness of 1  $\mu\text{m}$ . After each spin-coating process samples were annealed at 120 °C for 30 min. The silver gate electrode was evaporated subsequently using a shadow mask. The OFET electrical characteristics were measured directly after fabrication in ambient conditions in the dark, using two Source-Measure Units 236 combined with a Trigger-Control Unit 2361 and Metrics Software (Keithley Instruments).

### 3. Results and discussion

First, we present the chemical and work function analysis of acceptor-treated Cu electrodes in comparison to

pristine Cu, in order to establish that the acceptors are indeed chemisorbed and lead to the desired increase of  $\Phi$ . Fig. 2 shows XPS wide-range survey spectra of the Cu electrodes (on the Cu/PET-foil) as received (“untreated”, Fig. 2a), after etching with HCl to remove the native surface oxide layer (“etched”, Fig. 2b), and after TCNQ and F4-TCNQ solution treatment (Fig. 2c and d). Apparently, the Cu surface is heavily oxidized in its as-received state and contaminated with carbon species (surface stoichiometry 35% Cu, 25% C, 40% O). After HCl etching the surface carbon content remains essentially unchanged, and the amount of oxygen decreases to 16%; but it does not vanish completely due to finite time in ambient air (*i.e.*, re-oxidation occurs) during transport into inert gas glove-box or XPS chamber. This is further exemplified by more detailed XPS spectra of the O1s region (Fig. 3). The O1s peaks can be adequately fitted by two peaks, where the peak at lower binding energy (BE) of *ca.* 530.5 eV represents oxygen atoms in the surface copper oxide (*i.e.*,  $\text{Cu}_2\text{O}$  and  $\text{CuO}$ ) that forms (immediately) after exposure to oxygen. The peak at higher BE (centered at *ca.* 532 eV) is due to a range of electron deficient oxygen species, *e.g.*, surface hydroxyl groups ( $-\text{OH}$ ) and oxygen bound to carbon in various configurations (“C–O”); due to a superposition of many different species a more detailed assignment is impracticable). The etching process does not change the intensity ratio of these two peaks dramatically (compare Fig. 3a and b).

The intensity ratio of the two peaks in the O1s spectrum after treatment of etched Cu electrodes with TCNQ-solution (Fig. 3c) is similar to that of just etched Cu;

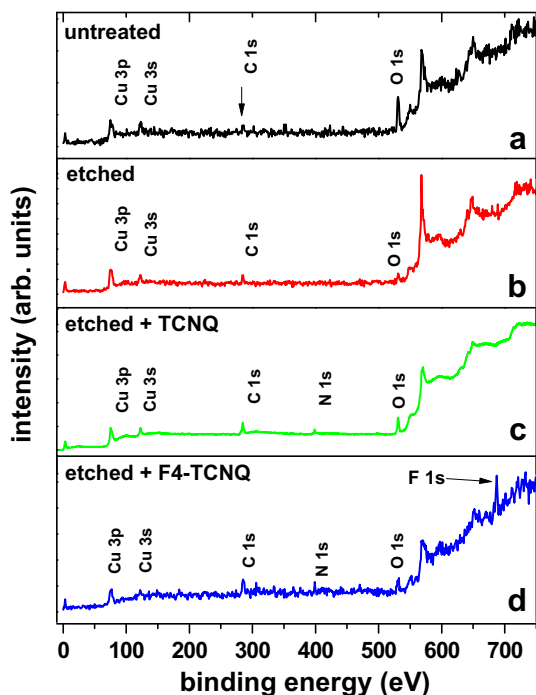


**Fig. 2.** XPS survey spectra of the Cu electrode of a Cu/PET-foil (a) untreated, (b) etched with HCl, (c) etched and treated with TCNQ solution, (d) etched and treated with F4-TCNQ solution. [The strong emission feature near 567 eV binding energy is due to Cu LMM Auger processes (kinetic energy of *ca.* 915 eV)].

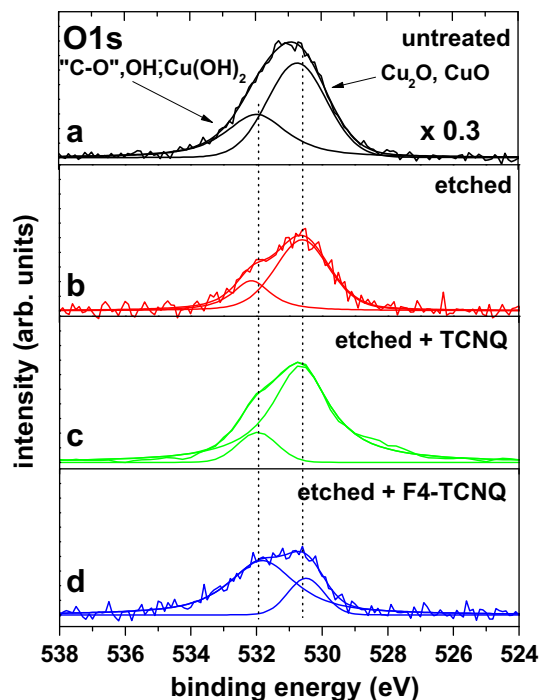


**Fig. 3.** XPS O1s spectra of the Cu electrode of a Cu/PET-foil (a) untreated, (b) etched with HCl, (c) etched and treated with TCNQ solution, (d) etched and treated with F4-TCNQ solution. The intensity of spectrum (a) was multiplied by 0.3.

noteworthy, the overall oxygen content of the TCNQ-treated surface is even slightly higher than that of etched Cu. This is most likely due to the *ca.* two times longer transport time through air of acceptor-treated samples. Furthermore, this observation indicates that TCNQ does not cover the Cu surface completely or that TCNQ cannot inhibit Cu oxidation efficiently. In contrast, F4-TCNQ solution treatment of Cu leads to a small overall decrease of the surface oxygen content, and the intensity ratio of metal oxide (low BE) and contamination (high BE) species is almost reversed compared to etched Cu (Fig. 3d). This suggests that the Cu surface coverage with F4-TCNQ is higher than achieved with TCNQ, and that this acceptor layer efficiently slows down surface metal oxidation.

Detailed XPS scans of the N1s region directly evidence the stable adsorption of both molecular acceptors on Cu (Fig. 4); note that excess acceptors were removed by washing with the solvent (*c.f.* Section 2). While no nitrogen is present on pristine and etched Cu surfaces (Fig. 4a and b), clear N1s signals are measured after TCNQ and F4-TCNQ solution treatment (Fig. 4c and d). The main contributions of the two N1s spectra (low BE component in each spectrum) are assigned to chemisorbed acceptor molecules that form charge transfer complexes with the Cu surface (TCNQ\* and F4-TCNQ\*) [12], and the high BE component in each spectrum is assigned to shake-up satellites. High photoemission intensity of such satellite peaks can occur for strongly chemisorbed molecules [19]. We cannot formally rule out the presence of residual neutral acceptor species; however, this is very unlikely due to solvent wash-

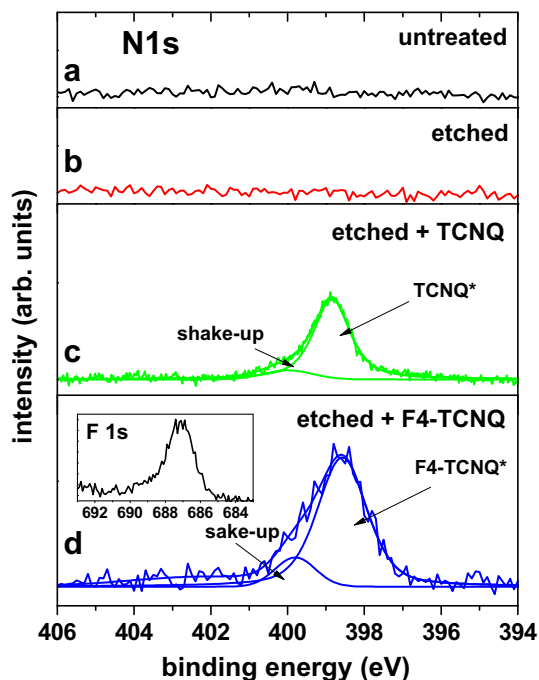


**Fig. 4.** XPS N1s spectra of the Cu electrode of a Cu/PET-foil (a) untreated, (b) etched with HCl, (c) etched and treated with TCNQ solution, (d) etched and treated with F4-TCNQ solution. The inset in (d) is the corresponding F1s spectrum.

ing. In addition, we find a clear F1s XPS signal for F4-TCNQ-treated Cu surfaces (inset in Fig. 4d), as expected. A consistent quantification of the fraction of nominal full acceptor monolayer coverage is not possible by XPS, but the N1s and F1s intensities show that coverage in the (sub-)monolayer regime is reached (higher coverage yet with F4-TCNQ than with TCNQ), which also represents the theoretical limit. Repeated acceptor solution treatment of Cu electrodes did not result in higher coverage.

After having established that both acceptors can be stably chemisorbed on the Cu electrode, we turn towards the surface work function. PEY spectra taken at ambient conditions of the differently treated Cu surfaces are shown in Fig. 5.  $\Phi$  of untreated Cu is 4.8 eV, and decreases to 4.5 eV after HCl etching. This is due to the reduction of polar surface groups and the removal of the surface oxide layer, as observed by XPS (see Figs. 2 and 3). Note that despite the higher work function of the Cu surface with the native oxide its use as electrode is inadvisable as the oxide layer will act as spacer for charge tunneling into an active organic layer, which is detrimental for achieving high current density.  $\Phi$  increases to 4.9 eV for the TCNQ solution treated electrode and to 5.1 eV for F4-TCNQ-treated Cu (Fig. 5c and d). Such an increase in  $\Phi$  is expected due to the net electron transfer from the metal to the molecules [14]. The fact that the increase in  $\Phi$  due to TCNQ is smaller than that for F4-TCNQ can be rationalized by the lower

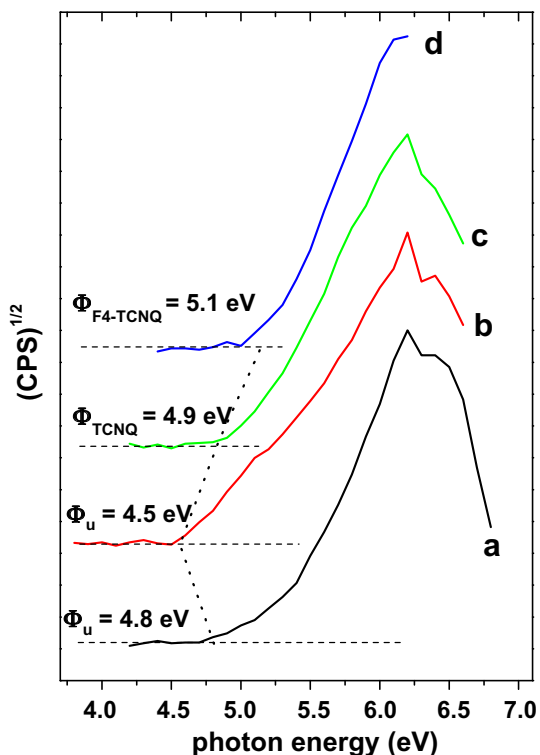


**Fig. 5.** PEY spectra (measured in air) of the Cu electrode of a Cu/PET-foil (a) untreated, (b) etched with HCl, (c) etched and treated with TCNQ solution, (d) etched and treated with F4-TCNQ solution. The extracted work function ( $\Phi$ ) values are indicated.

electron affinity of TCNQ, and the lower overall surface coverage (see XPS results). However, the achieved effect for F4-TCNQ solution treatment is smaller than that of an evaporated F4-TCNQ monolayer on a Cu(1 1 1) single crystal in UHV, for which a maximum  $\Phi$  of 5.6 eV was reported [14]. This is not surprising, as the present experimental conditions deviate significantly from UHV. The Cu surface after HCl etching is still contaminated with various hydrocarbon species and contains some oxide. This already reduces the surface area available for intimate acceptor-metal interaction (*i.e.*, charge transfer), *i.e.*, the surface dipole density that is responsible for increasing  $\Phi$ . Moreover, details of the F4-TCNQ/Cu charge transfer may be different from the UHV case due to the contaminants and oxide (*e.g.*, amount of charge transferred, molecular conformation). Nonetheless, these results demonstrate that the general method of increasing metal surface  $\Phi$  by adsorption of strong electron acceptor molecules is transferable from UHV to device fabrication relevant conditions, even using solution processing.

Finally, we show that the electrode  $\Phi$  increase can reduce  $R_c$  in a device, using OFETs as example. The influence of solution-based acceptor electrode modification in OFETs with P3HT-TFT as semiconductor was investigated in comparison to conventional OFETs with only HCl etched Cu electrodes. The output characteristics of such OFETs (Fig. 6) exhibit typical p-type performance with well defined saturation behavior.  $I_{on}$  in the saturation regime at  $-60$  V gate-source voltage ( $V_{gs}$ ) increases from  $6.1 \times 10^{-6}$  A for OFETs without acceptor modified Cu electrodes to  $9.9 \times 10^{-6}$  A for TCNQ modification, and to  $1.2 \times 10^{-5}$  A for F4-TCNQ modification. This is consistent with the increase of the electrode  $\Phi$  shown above. In the simple model of the Schottky–Mott limit, the hole injection

barrier (HIB) at electrode/organic interfaces can be estimated as the difference between the electrode  $\Phi$  and the organic material ionization energy [20]. For the present electrodes and the ionization energy of P3HT-TFT of *ca.* 5.1 eV [18] this leads to the following HIB values: 0.6 eV for etched Cu, 0.2 eV for TCNQ-treated Cu, and the HIB would even become zero for F4-TCNQ-treated Cu. A decrease of the HIB consequently leads to higher  $I_{on}$ , as holes can be accumulated more effectively in the channel.

Transfer characteristics were taken at  $-60$  V source-drain voltage ( $V_{ds}$ ) varying  $V_{gs}$  from  $+20$  V to  $-60$  V (Fig. 7a). Since the source-drain current ( $I_{ds}$ ) in the saturation part of the transfer characteristic can be described with

$$I_{ds,sat} = \frac{W}{2L} C \mu_{sat} (V_{gs} - V_T)^2 \quad (2)$$

where  $W$  is the channel width and  $L$  the channel length, the saturation mobility ( $\mu_{sat}$ ) and the threshold voltage ( $V_T$ ) can be calculated from the slope and the intercept of a line drawn through the linear part of an  $I_{ds}^{1/2}$  vs.  $V_{gs}$  plot (Fig. 7b). The values obtained in this way (together with other characteristic sample and device parameters) are summarized in Table 1. It can be seen that  $V_T$  decreases from  $-20$  V to  $-10$  V for TCNQ electrode modification and to  $-7$  V for F4-TCNQ modification. In addition, a shift in the off-state towards positive  $V_{gs}$  of more than 20 V due to the acceptor modification of the Cu electrodes is observed (Fig. 7a). Both observations indicate that even for  $V_{gs} = 0$  V (*i.e.*, no charge carrier accumulation) positive charges are available in the channel, resulting in a finite current between source and drain electrodes; *i.e.*, after electrode modification the gate has to be biased positively to turn it off. This is a consequence of the vanishing barrier for hole injection after

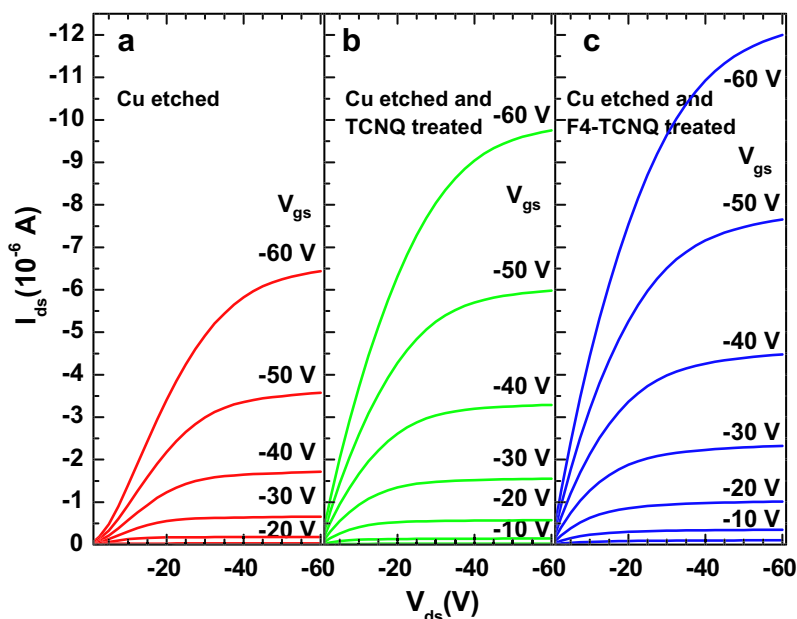


**Fig. 6.** Output characteristics of P3HT-TFT p-type OFETs with (a) unmodified, (b) TCNQ, and (c) F4-TCNQ modified Cu electrodes. Device channel length  $L = 40$   $\mu$ m, channel width  $W = 40$  mm and gate capacitance  $C_i = 1, 5$  nF  $\text{cm}^{-2}$ .

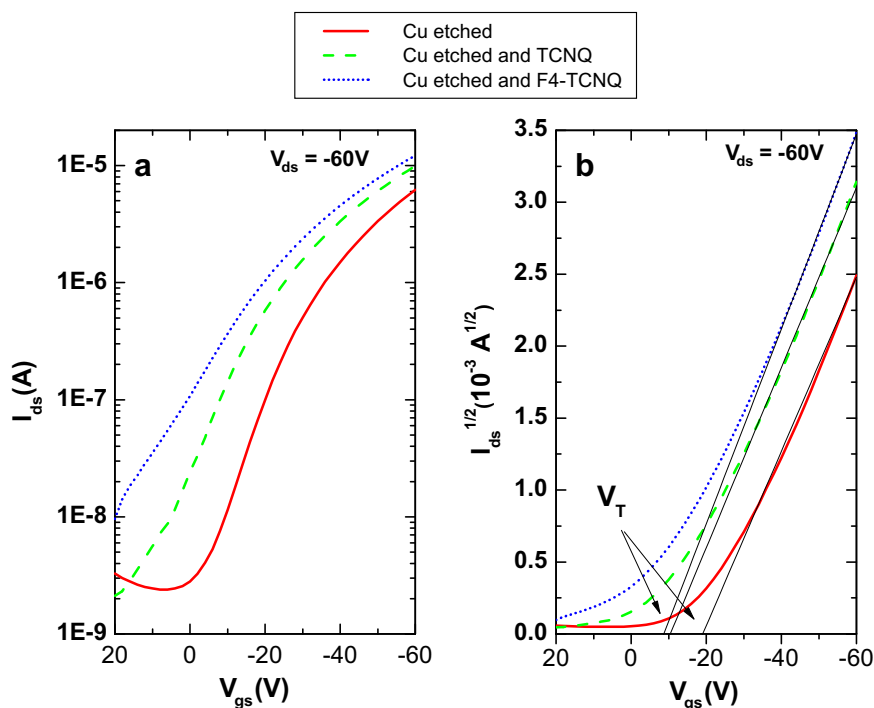


**Fig. 7.** Transfer characteristics (a) show well-defined on and off states. Square-root plots (b) show good linear behavior in the saturation regime and a decrease of the threshold voltage ( $V_{Th}$ ) for OFETs with acceptor modified Cu electrodes.

**Table 1**

Surface work function values and key OFET performance parameters with and without acceptor solution treated Cu electrodes.

Treatment of the Cu electrode surface	HCl etched	Etched and TCNQ	Etched and F4-TCNQ
Work function $\Phi$ [eV]	4.5	4.9	5.1
Mobility $\mu_{sat}$ [ $\text{cm}^2/\text{Vs}$ ]	$4.9 \times 10^{-3}$	$5.2 \times 10^{-3}$	$5.6 \times 10^{-3}$
Threshold voltage $V_T$ [V]	-20	-10	-7
On-current $I_{on}$ [A]	$6.1 \times 10^{-6}$	$9.9 \times 10^{-6}$	$1.2 \times 10^{-5}$
$(I_{on}/I_{off})_{max}$	$2.6 \times 10^3$	$4.0 \times 10^3$	$>1.3 \times 10^3$

acceptor-treatment of the electrodes, as holes can diffuse into the channel region without having to overcome (significant) energy barriers. In addition, it may be possible that some residual (not strongly Cu-bound) acceptor molecules penetrate into the organic semiconductor layer during spin-coating of the polymer, which can result in p-type doping of P3HT-TFT. We cannot formally rule out the presence of F4-TCNQ molecules on the PET substrate even after washing with copious amounts of the solvent used for spin-coating the polymer (which is also a good solvent for the acceptor). However, even if this were the case it is unlikely that these contributed to doping because they should be stationary in/on PET as they were not even removed by the solvent. This is supported by our observation that transistor performance did not depend on the number of washing cycles.

It is worth pointing out that  $\mu_{sat}$  was constant at ca.  $5 \times 10^{-3} \text{ cm}^2/\text{Vs}$  regardless of the Cu electrode modification. This is a strong indication that the solution-based TCNQ and F4-TCNQ deposition on the Cu electrode does

not influence the morphology/structure of the spin coated active polymer, as the carrier mobility depends critically on these parameters.

#### 4. Conclusions

We demonstrated the feasibility of using solution-based processing to increase the work function of metal electrodes with strong electron acceptor molecules. The work function in air for Cu electrodes was increased from 4.5 eV (pristine) to 4.9 eV (with TCNQ) and 5.1 eV (F4-TCNQ). Furthermore, it was shown that this method can be used to reduce the contact resistance at electrode/organic semiconductor interfaces. The on-current of flexible polymer OFETs was increased from  $6.4 \times 10^{-6}$  A (pristine Cu) to more than  $1.2 \times 10^{-5}$  A (with F4-TCNQ), and the threshold voltage was reduced from -20 V to -7 V. The simplicity of our solution-based process to achieve favorable electrode/organic interface energetics can readily be adapted for other electrode materials and printing



techniques to realize a wide range of different organic electronic devices, such as light emitting diodes or photovoltaic cells, without the need for impractical and rigorous UHV conditions.

### Acknowledgements

Authors thank A. Holländer and F. Pippich for assistance with XPS measurements, D. Sainova for assistance with OFET preparation, and G. Heimel for valuable discussions. This work was supported in part by the DFG (SPP1355) and the European Commission under Contract No. NMP-3-CT-2006-033197 (“ICONTROL”). NK acknowledges financial support by the Emmy Noether-Program (DFG).

### References

- [1] C. Dimitrakopoulos, P. Malenfant, *Adv. Mater.* 14 (2002) 99–117.
- [2] H. Sirringhaus, *Adv. Mater.* 17 (2005) 2411.
- [3] H. Sirringhaus, P.J. Brown, R.H. Friend, M.M. Nielsen, K. Bechgaard, B.M.W. Langeveld-Voss, A.J.H. Spiering, R.A.J. Janssen, E.W. Meijer, P. Herwig, D.M. de Leeuw, *Nature* 401 (1999) 685.
- [4] H. Yang, S.W. LeFevre, C.Y. Ryu, Z. Bao, *Appl. Phys. Lett.* 90 (2007) 172116.
- [5] A. Zen, J. Pflaum, S. Hirschmann, W. Zhuang, F. Jaiser, U. Asawapirom, J.P. Rabe, U. Scherf, D. Neher, *Adv. Funct. Mater.* 14 (2004) 757.
- [6] B. Stadlober, U. Haas, H. Gold, A. Haase, G. Jakopic, G. Leising, N. Koch, S. Rentenberger, E. Zojer, *Adv. Funct. Mater.* 17 (2007) 2687.
- [7] G.S. Tulevski, C. Nuckolls, A. Afzali, T.O. Graham, C.R. Kagan, *Appl. Phys. Lett.* 89 (2006) 183101.
- [8] P.V. Pesavento, K.P. Puntambekar, C.D. Frisbie, J.C. McKeen, P.P. Ruden, *J. Appl. Phys.* 99 (2006) 094504.
- [9] D.J. Gundlach, L.L. Jia, T.N. Jackson, *IEEE Electron. Dev. Lett.* 22 (2001) 571.
- [10] S. Khodabakhsh, D. Poplavskyy, S. Heutz, J. Nelson, D. Bradley, H. Murata, T. Jones, *Adv. Funct. Mater.* 14 (2004) 1205.
- [11] S. Rentenberger, A. Vollmer, E. Zojer, R. Schennach, N. Koch, *J. Appl. Phys.* 100 (2006) 053701.
- [12] N. Koch, S. Duhm, J.P. Rabe, A. Vollmer, R.L. Johnson, *Phys. Rev. Lett.* 95 (2005) 237601.
- [13] B. Bröker, R.P. Blum, J. Frisch, A. Vollmer, O.T. Hofmann, R. Rieger, K. Müllen, J.P. Rabe, E. Zojer, N. Koch, *Appl. Phys. Lett.* 93 (2008) 243303.
- [14] L. Romaner, G. Heimel, J.-L. Brédas, A. Gerlach, F. Schreiber, R.L. Johnson, J. Zegenhagen, S. Duhm, N. Koch, E. Zojer, *Phys. Rev. Lett.* 99 (2007) 256801.
- [15] G.M. Rangger, O.T. Hofmann, L. Romaner, G. Heimel, B. Bröker, R.P. Blum, R.L. Johnson, N. Koch, E. Zojer, *Phys. Rev. B* 79 (2009) 165306.
- [16] R. Bouwman, W.M.H. Sachtler, *J. Catal.* 19 (1970) 127.
- [17] T. Sakurai, Y. Momose, K. Nakayama, E.-J. Surf. Sci. Nanotechnol. 3 (2005) 179.
- [18] D. Sainova, S. Janietz, U. Asawapirom, L. Romaner, E. Zojer, N. Koch, A. Vollmer, *Chem. Mater.* 19 (2007) 1472.
- [19] A. Hauschild, K. Karki, B.C.C. Cowie, M. Rohlfling, F.S. Tautz, M. Sokolowski, *Phys. Rev. Lett.* 94 (2005) 036106.
- [20] A. Kahn, N. Koch, W. Gao, *J. Polym. Sci. B* 41 (2003) 2529.

spatial resolution, which to date is limited only by tool-making capabilities. Apart from its unrivalled high-resolution, NIL has several more advantages over competing patterning methods such as self-aligned ink-jet printing [7] or high-resolution ink-jet printing [8]. It allows a higher aspect ratio, a larger number of compatible materials, a shorter process times which is inherent to parallel structuring techniques and an easier implementation into a standard r2r facility [9,10].

Hot Embossing is the oldest NIL technique and has already proven to be applicable in defining sub-micrometer channel lengths of OTFTs based on rigid silicon substrates [11,26] as well as of entirely patterned OTFTs based on thin organic gate dielectrics and on polyester film substrates [13]. However, in the latter case Hot Embossing can be detrimental to the fabrication process of large circuits since it often requires a temperature surpassing the glass transition temperature of the duroplastic films, thereby generating dimensional instabilities and complicated registration. Furthermore, Hot Embossing always produces a residual layer of the thermoplastic resist which has to be removed by anisotropic etching. This etching process is particularly undesirable because it is costly, difficult to control and might be harmful for an organic layer underneath.

In an alternative approach – UV-Nanoimprint Lithography (UV-NIL) – the thermoelastic imprint resist is replaced by a UV-curable polymer, bringing about several advantages in comparison to Hot Embossing. With UV-NIL, pressure, process time and thermal stress for the substrate can be significantly reduced during imprinting. Due to the major advances in nanometre patterning along with low-cost and high throughput [14], substantial work has been put into the development of suitable UV-curable polymer materials [15–17]. Today, a large number of UV-NIL resists are commercially available such as Amonil-MMS4 by AMO GmbH or mr-UVCur06 by micro resist technology GmbH. So far, none of them enables both residue-free imprinting and a lift-off process by a sufficiently gentle solvent.

Here we report on a novel nanoimprint process for the fabrication of entirely patterned submicron OTFTs in a bottom-gate configuration. This process requires no extra temperature budget, imprints residue-free thereby rendering etching obsolete, is time saving due to short curing times, eco-friendly due to a water-based lift-off and fully r2r compatible. This method is based on UV-NIL combined with a novel imprint resist whose outstanding chemical and physical properties are responsible for the excellent results in structure transfer to both rigid and flexible substrates. It is shown that the UV-NIL technique works perfectly even when ultra-thin organic and hybrid films are used as gate dielectrics. Employing this method, functional submicron pentacene-based OTFTs are fabricated, which show good saturation of the drain currents, low switch-on voltage ( $\sim 3$  V) and a sufficient on-off ratio ( $10^3$ ) of the drain current.

## 2. Materials and methods

We have fabricated submicron coplanar OTFTs with pentacene as the active layer and a bilayer of about

100 nm of a benzocyclobutene derivative (BCB) and 30 nm of poly(vinyl cinnamate) (PVCi) as the gate dielectric. All devices have a channel width to length ratio ( $W/L$ ) of 50. The aluminum gate electrodes are fabricated on a pre-cleaned glass substrate by a combination of a photolithographic process, e-beam evaporation of a 45 nm thick metal layer and a lift-off procedure using acetone as the solvent. The BCB layer is applied onto the aluminum gate electrodes by spin coating 0.33 wt.% of XU 71918 (Dow Chemicals) dissolved in 1,3,5-trimethylbenzene (Aldrich). The layer is crosslinked at 290 °C for 60 s on a hotplate. The PVCi layer (Aldrich) is fabricated by spin coating a solution of 0.2 wt.% of PVCi in chloroform at 2000 rpm. It is prebaked for 5 min at 80 °C to remove the solvent and UV-crosslinked for 60 min at 254 nm with a Benda NU-72 KM UV-lamp in inert atmosphere.

The thickness and optical constants of the dielectric layers are determined by ellipsometry based on a variable angle spectroscopic ellipsometer (VASE, J.A. Woolam Inc). The layer thickness is determined by fitting the ellipsometry data employing a simple Cauchy-model for the refractive index to be 29–31 nm for PVCi and 97 nm for BCB [18].

The silicon imprint stamp is patterned by electron beam lithography. The resist structures are permanently transferred to the silicon stamp by reactive ion etching (SF<sub>6</sub>-Ar) resulting in a final depth of about 1 μm. After stripping, an anti-sticking layer (perfluorochloroethyl-trichlorosilane) is applied to the stamp.

The UV-NIL-resist ACMO is fabricated by a mixture of GENOCURE<sup>\*</sup> LTM and ACMO (acryloyl morpholine, both by Rahn AG) and chloroform at a mass ratio of 1:20:400, yielding a low-viscous material. Spin coating at 2000 rpm results in a homogeneous layer with a thickness of 600 nm. Curing is performed through UV exposure at 365 nm for a maximum time of 2 min. The UV-NIL structuring of the gold source-drain electrodes is done in an EVG 620 mask-aligner. A 30 nm thick gold layer is deposited by either e-beam or thermal evaporation. The lift-off is performed by dissolving the UV-resist with deionized water.

The 40 nm thick pentacene layer is thermally evaporated onto the sample in high-vacuum conditions at a rate of 0.2 nm/min for the first 5 nm and 0.8 nm/min for the remaining 35 nm.

Prior to the focused ion beam/scanning electron microscopy (FIB/SEM) investigations the specimens are covered with a 20 nm carbon layer to minimize charging of the sample. In the focused ion beam instrument Pt layers are grown by electron beam induced deposition (EBID) followed by ion beam assisted deposition (IBAD). These Pt layers protect the surface against incoming Ga ions during the cutting out and milling of the lamellas. The lamellas are transferred to a transmission electron microscopy (TEM) grid and thinned down to several tens of nanometre.

The TEM investigations are performed using a Philips CM20 (S)TEM (twin lens) with a thermionic LaB<sub>6</sub> cathode operated at 200 kV equipped with a Gatan Imaging Filter (GIF 200). For energy dispersive X-ray spectroscopy an HPCe detector (Noran/Thermo Fisher Scientific) employing Noran System Six software is used. Electron energy loss spectroscopy (EELS) and energy filtered TEM (EFTEM) are performed using a Gatan Imaging Filter (GIF) with a

1024 × 1024 CCD (YAG scintillator) attached to the microscope. Elemental maps were calculated using the three-window-technique.

### 3. Results and discussion

#### 3.1. Imprint resist

The key component of our UV-NIL process for the patterning of submicron-spaced source and drain electrodes is an imprint resist called UV-NIL-ACMO, which is based on an acryloyl morpholine monomer (ACMO). It is curable by UV-initiated radical polymerization, is soluble in water, and shows a low viscosity. The actually applied special formulation of UV-NIL-ACMO is composed of ACMO mixed with a photoinitiator blend (GENOCURE) and highly diluted in chloroform, resulting in a low viscosity.

Acryloyl morpholine (for the chemical formula see Fig. 1a) is perfectly matches our NIL processes requirements for a variety of reasons: It provides removability by a lift-off process due to the lack of functional groups that could crosslink during polymerization, thereby preventing its solubility. Furthermore, the lift-off process can be accomplished with water as a cheap and eco-friendly solvent because of similarities in the polarity of the functional side group (morpholine) and the solvent water.

#### 3.2. Residue-free UV-Nanoimprint Lithography

The principle of the UV-NIL process is illustrated in Fig. 2a. The first step (A) is to align the silicon stamp, which contains the elevated source–drain electrode pattern, with respect to the gate electrode. This is done in a mask-aligner. The aligned stamp is pressed into the low-viscous resist at low pressure, displacing the resist underneath the source–drain structures (B). A novelty here is the etch-free

process enabled by residue-free displacement of the UV-NIL-ACMO resist due to the high difference in polarity of resist and stamp. Curing is performed by UV exposure for up to 2 min, depending on the initiator concentration, during which the source–drain pattern is permanently transferred into the resist. After removing the stamp (C) the source–drain material – in the present case gold – is evaporated onto the device (D). The subsequent lift-off is performed by dissolving the resist with deionized water; the evaporated gold layer on top of the resist is removed while the imprinted areas are preserved (E). An optical microscope image of the source–drain structures after the lift-off step is shown in Fig. 2b illustrating the complete transfer of the stamp's source–drain pattern into the gold layer. The lift-off works perfectly for the complete electrode pattern and even for the large contact pads. Finally the active semiconductor material, here pentacene, is evaporated thus finalizing the transistor structure (F). In Fig. 2c an AFM phase signal of the pentacene layer on top of the contacts and the channel is displayed. The difference in morphology is distinctive: small ( $\leq 200$  nm) grains are formed on the gold layer, whereas terraced crystalline grains with a maximum size of about one micron are observed on the gate dielectric in the channel. Such a pentacene grain size is reasonable for an rms-roughness of the BCB/PVCI layer of approximately 0.4 nm [19–21].

The residue-free imprint is facilitated by the use of the aforementioned water-soluble low viscosity UV-NIL-ACMO resist in combination with an adjustment of the stamp's surface energy to maximize the contact angle. In order to minimize the polarity of the silicon stamp it was rinsed with perfluorochloroethyl-trichlorosilane.

Contact angle measurements of the UV-NIL-ACMO resist and water on the modified silicon stamp reveal that the contact angle of the imprint resist on the modified stamp is very high ( $82^\circ$ , see Fig. 1b) and approaches that

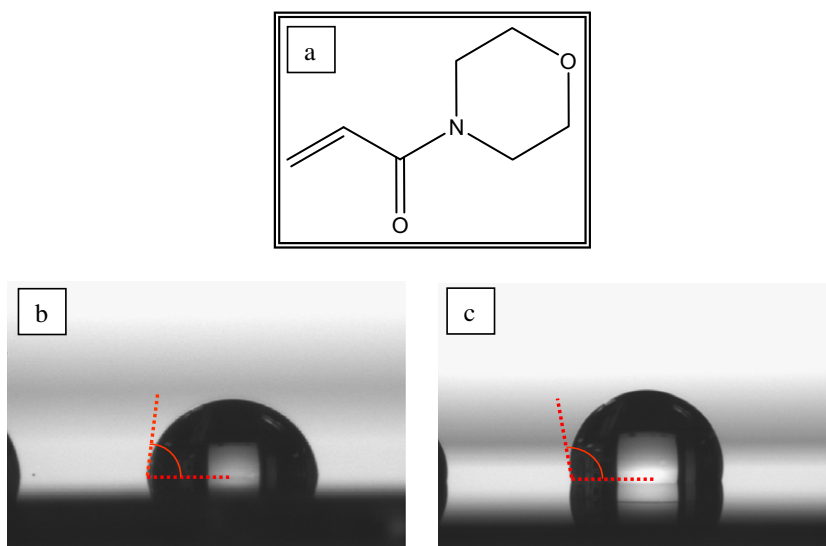


**Fig. 1.** (a) Chemical formula of acryloyl morpholine. Comparison of the contact angle of (b) the UV-imprint resist and of (c) water on the anti-sticking layer (perfluorochloroethyl-trichlorosilane) modified silicon stamp.

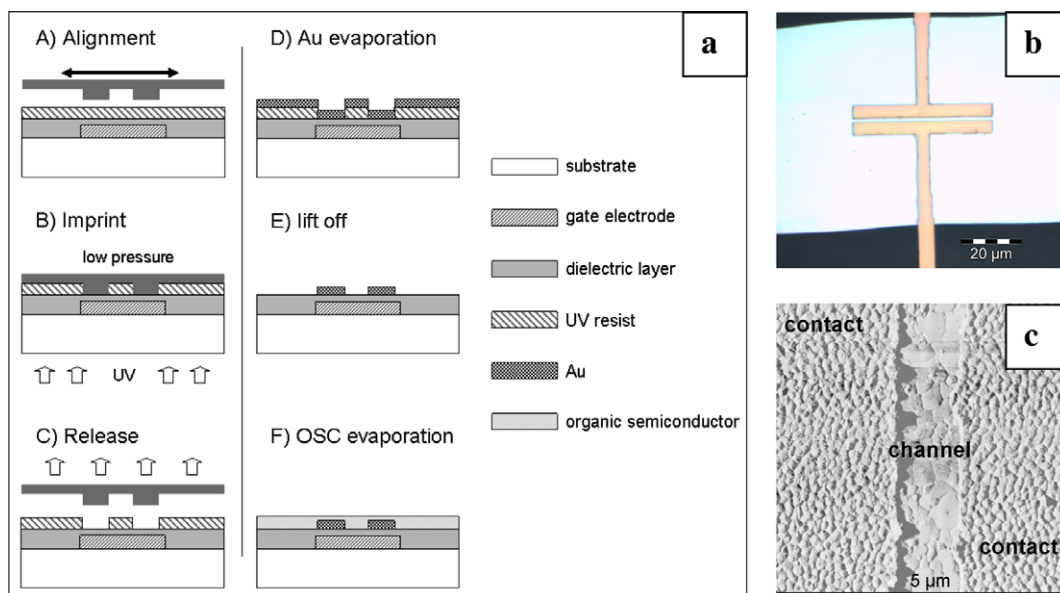


**Fig. 2.** (a) Scheme of the residue-free UV-NIL process: A silicon stamp containing the source–drain structures is aligned with respect to the gate electrodes of a resist-coated substrate (A). The stamp is pressed into the resist, thereby completely displacing the resist below the source–drain structures (B). Subsequently the resist is cured by UV exposure. After the stamp removal (C) the source–drain material is evaporated onto the substrate (D). The imprint resist is dissolved with water which leaves the metal source–drain electrodes well preserved (E). Finally the sample is covered by an organic active layer, pentacene. (b) Optical microscope image of the gold source–drain pattern of a submicron OTFT with  $L = 950$  nm after lift-off. (c) AFM phase image ( $5 \times 5 \mu\text{m}$ ) of the pentacene layer formed on top of the contacts and in the submicron channel. The gate dielectric is BCB/PVCI.

of water on the modified silicon stamp ( $100^\circ$ , see Fig. 1c). In addition to the low resist viscosity we suggest that a large difference in the polarity of the modified silicon stamp (non-polar) and the resist (polar) is an important factor for the absence of a residual layer.

In order to characterize the individual layers of the transistor devices the specimens were investigated by transmission electron microscopy (TEM). Cross section lamellas of the samples were prepared using a focused ion beam instrument (FIB, compare Fig. 3a inset) [22]. Fig. 3 shows a sample after the imprint step. SEM images of the lamella and its cutout are shown in Fig. 3a and the inset, respectively. The organic layers are clearly observed

as dark areas in-between the glass substrate and the platinum layers used for sample protection during FIB-cutting. The image gives an overview of the appearance of the imprinted troughs for the electrodes and the resist in the center as a placeholder for the channel. A more detailed view is presented in Fig. 3b, it is a TEM bright field image showing one edge of the resist in the channel. The glass substrate, the aluminum electrode and the organic layers can clearly be distinguished. The three involved polymer layers BCB, PVCI and UV-NIL-ACMO appear as a single layer. However, since their elemental composition is distinctly different, the layers can be identified by analytical methods such as electron energy loss spectroscopy.

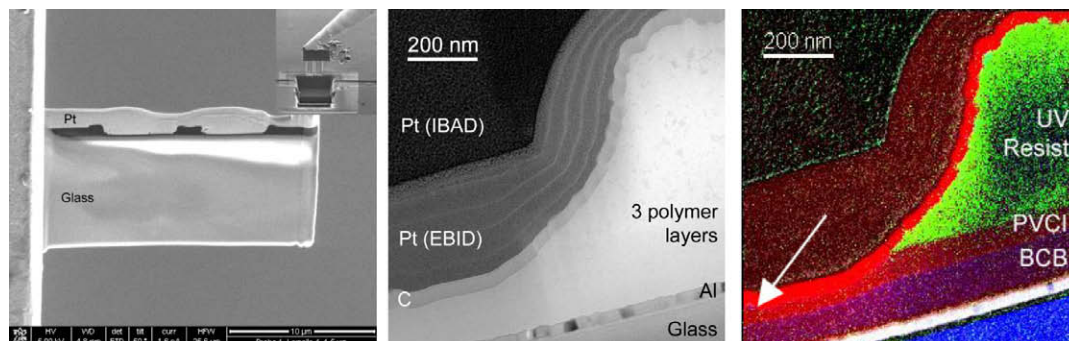


**Fig. 3.** A sample after the imprint step. (a) A cross section lamella of the sample, where the imprinted organic layer appears dark in-between the glass and protective Pt layers. The lift out of the FIB prepared lamella is seen in the inset. (b) A TEM bright field image of the edge of the channel. (c) Superposition of EELS elemental maps (N = green; Si = blue; C = red; Al = white) enables a clear distinction of the three involved polymers. The white arrow points towards a bump in the imprinted area which is identified as PVCI. A UV-resist residual can be excluded. IBAD = ion beam assisted deposition, EBID = electron beam induced deposition. (For interpretation of the references to colour in this figure legend, the reader is referred to the web version of this article.)

BCB can be identified by its silicon content and UV-NIL-ACMO by its nitrogen content. A superposition of elemental maps of different elements is shown in Fig. 3c, where the nitrogen map is green (representing UV-NIL-ACMO), the silicon map is blue (representing BCB and glass), the carbon map is red and the aluminum map is white (representing the gate electrode). Now the three polymer layers can clearly be distinguished by a color code. In this way it is shown that the UV-NIL-ACMO resist is fully displaced; no residue is observed in the imprinted areas. Even bumps in the surface, indicated by the white arrow in Fig. 3c, can be identified as PVCi, thus corroborating the residue-free imprint. Despite the perfect displacement of the resist it is worth noting that both the BCB and particularly the PVCi layer seem to be compressed due to the imprint step. The influence of the compression on the electrical performance of the dielectric layers will be topic of further investigations. Furthermore, it is observed that the appearance of the resist is wedge-shaped. This is a direct consequence of the stamp's rounded edges stemming from an isotropic etch step during the stamp fabrication. With NIL all structures of the stamp (including artifacts and defects) are strictly and precisely transferred to the resist/sample.

Since no residuals of UV-NIL-ACMO are left at imprinted areas the specimen can be covered with the source–drain electrode material without prior etching. This is particularly favorable since the dielectric layers are fairly thin and thus can easily be damaged by the etching process. The final transistor structure is shown in Fig. 4, where a scheme (Fig. 4a) and a cross section TEM image (Fig. 4b) are presented. As shown, the gold electrode is perfectly preserved in the imprinted region (right part of the image) whereas it is gone in the channel where the UV-NIL-ACMO was dissolved (left part of the image).

### 3.3. Electrical characterization of submicron OTFTs fabricated by residue-free UV-NIL

The introduced residue-free UV-NIL route obviously leads to well-defined transistor structures. Devices with channel lengths down to 700 nm were fabricated. Consequently, appropriate device characteristics are expected.

The results of the  $I(V)$ -characterization of submicron transistors based on the 130 nm thick BCB/PVCi bilayer as the gate dielectric are shown in Fig. 5. Important parameters such as the specific gate capacitance  $C_i$  and the dielectric breakdown voltage  $E_{br}$  that are intrinsic to the gate dielectric are also specified in the table. The motivation for the usage of an additional ultra-thin PVCi layer forming the direct interface to pentacene is to adjust the surface energy and roughness in such a way that the semiconductor growth is optimized.

In the output characteristics (second column in Fig. 5) no difference is observed between devices with submicron channel lengths varying from 950 to 700 nm and constant  $W/L$  ratio, which is an indication for a constant charge carrier mobility  $\mu$ . All curves show saturation of the drain current. This is due to the fact that the gate dielectric layer thickness is smaller by more than a factor 5 than the channel length, thus preventing an unbalanced increase of the lateral electric field with respect to the vertical one. As was shown previously [11–13], an adequate downscaling of channel length and dielectric layer thickness leads to short channel effects such as channel length modulation resulting in a loss of current saturation. Moreover, at small drain voltages the drain current increases perfectly linear meaning that the transport is not limited by the contact resistance. Hysteresis effects between forward and reverse drain voltage sweeps are negligible.

From the semi-logarithmic representation of the transfer characteristics  $I_D(V_G)$  in saturation (first column in Fig. 5) the subthreshold swing  $S$  and the switch-on voltage  $V_{so}$  were determined. The latter is taken as the gate voltage at which the drain current is one order of magnitude higher than the off-current  $I_{off}$ . The transfer characteristics of submicron devices for different channel lengths collapse into one curve as is expected for transistors having identical geometry ( $W/L$  ratio) and mobility. All submicron OTFTs are normally-on as is reflected by the small positive  $V_{so}$  (see Fig. 5). A shift of the onset of transistor operation to the positive voltage regime was reported to be induced by negative charges in the BCB dielectric probably caused by water [23,24].

The charge carrier mobility of the UV-NIL fabricated submicron OTFTs is in the range of  $10^{-3}$  cm<sup>2</sup>/Vs which is

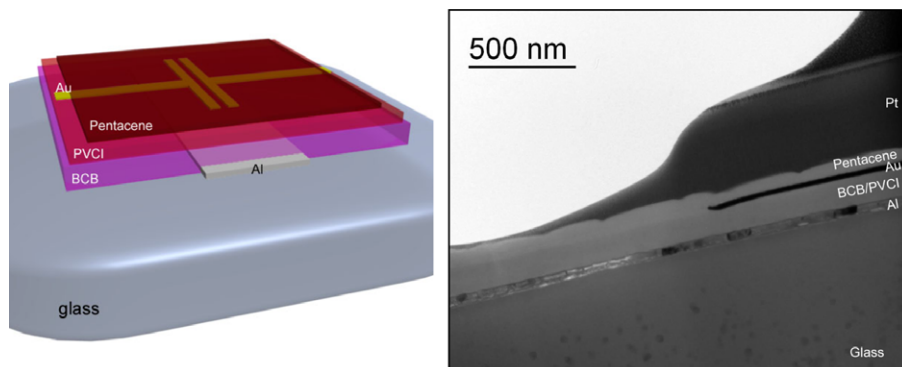


**Fig. 4.** (a) A scheme of a completed transistor structure and (b) a corresponding TEM bright field image of a cross section lamella. The gold electrode is well preserved at the imprinted areas and lifted off elsewhere.

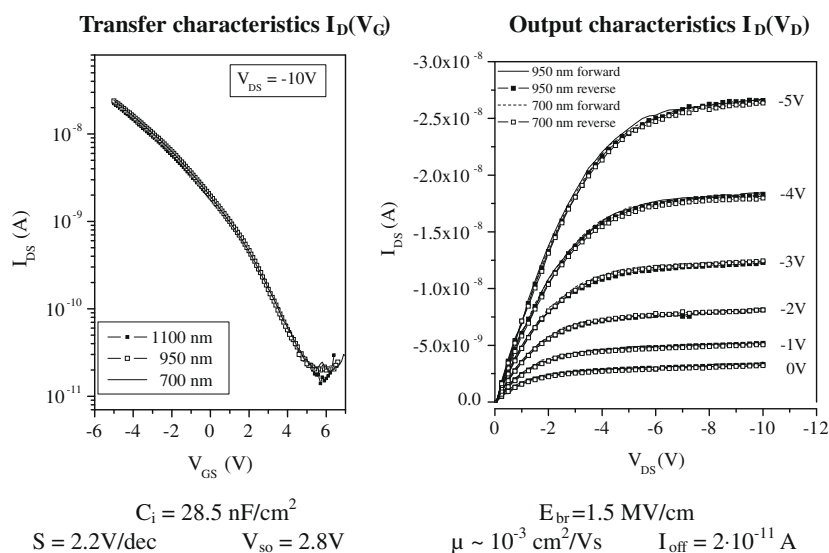


**Fig. 5.** Electrical performance of UV-NIL fabricated pentacene OTFTs based on a double layer of BCB/PVCI as the gate dielectric. In the first and the second columns the saturated transfer and output characteristics of the submicron transistors are shown. Critical parameters revealing the properties of the gate dielectric are also listed, such as the specific gate capacitance  $C_i$  and the breakdown voltage  $E_{br}$ . From the transfer characteristics important transistor parameters are extracted: the subthreshold swing  $S$ , the switch-on voltage  $V_{so}$ , the off-current  $I_{off}$  and the charge carrier mobility in saturation  $\mu$ .

rather low compared to hot embossed submicron OTFTs with  $\text{SiO}_2$  as the gate dielectric [12]. One parameter that influences the mobility and is directly related to the channel resistance is the pentacene grain size. As deduced from the AFM phase image in Fig. 2c the maximum pentacene grain size is well below  $1.5 \mu\text{m}$ , which we found to be the average threshold for grain boundary limited transport [25]. If the grain size is smaller than one micron the transport is dominated by grain boundary effects. This leads to a decreased mobility in the range of  $10^{-3} \text{ cm}^2/\text{Vs}$  as is indeed observed in the BCB/PVCI submicron transistors. Moreover, the large amount of interface trap states that is reflected by a large subthreshold swing [26] – compared to hot embossed devices [12,13], – clearly has a negative effect on the mobility because it obstructs the charge transport by scattering carriers at the pentacene-dielectric interface. With an additional UV-ozone treatment, as described in Ref. [12], the pentacene grain size could be strongly increased both in the channel and on the contacts thus resulting in charge carrier mobilities up to  $0.3 \text{ cm}^2/\text{Vs}$  for  $\text{SiO}_2$ -based submicron OTFTs.

#### 4. Conclusion

In summary, we have fabricated fully functional OTFTs with submicron channel lengths using an improved UV-NIL process. The nanoimprinted OTFTs are comprised of pentacene as active semiconductor and a thin bilayer gate dielectric composed of BCB and PVCI. With our novel UV-NIL process, devices with channel lengths down to 700 nm were fabricated, showing good drain current saturation and low switch-on voltages. This process is based on a UV-NIL resist formulation containing acryloyl morpholine, which perfectly matches the requirements of fast and precise nanoimprinting of organic electronic components. Since no heating step is involved in the process,

thermal stress can be disregarded and, more importantly, thermally unstable materials can be used as substrates and gate dielectrics. Furthermore, UV-NIL-ACMO is cured by UV-initiated radical polymerization which reduces the fabrication time considerably, thus enabling a high throughput. Remarkable is the absence of any residual layer of UV-NIL-ACMO after the imprint step, which makes etching obsolete. This is particularly convenient, since  $\text{O}_2$ -etching of organic dielectrics is known to increase the gate leakage and the number of OH-groups acting as traps at the interface. Furthermore, reactive ion etching is difficult to implement in a standard printing line. Finally, UV-NIL-ACMO allows a lift-off with deionized water, which is a substantial advantage due to its ubiquitous availability, its potential for immediate recycling and its environmental sustainability, resulting in a decrease of the production costs and an increase of process safety. Optimization is still needed with respect to the semiconductor/dielectric interface which shows an increased number of traps leading to reduced effective charge carrier mobilities after the UV-imprint step. Here, a special treatment prior to the application of the semiconductor could be beneficial and furthermore increase the pentacene grain size. In conclusion, UV-NIL has a huge potential as a high-resolution patterning process for large-area fabrication of flexible organic electronics.

#### Acknowledgement

The authors would like to thank the Austrian Nanoinitiative for funding.

#### References

- [1] For a review see Z. Bao, J. Locklin (Eds.), Organic Field Effect Transistors, CRC Press, Boca Raton, 2007.

- [2] Commercialization of Organic Electronics, *MRS Bull.* 33 (7) 2008 653–705.
- [3] E. Cantatore, T.C.T. Geuns, G.H. Gelinck, E. van Veenendaal, A.F.A. Gruijthuijzen, L. Schrijnemakers, S. Drews, D.M. De Leeuw, *IEEE J. Solid-State Circuits* 42 (2007) 84.
- [4] W. Clemens, Application of Printed RFID and Smart Objects, Paper presented at Printed Electronics USA 2007, IDTechEx, Cambridge, UK, 2007.
- [5] H. Sirringhaus, C.W. Sele, T. von Werne, C. Ramsdale, in: H. Klauk (Ed.), *Organic Electronics*, Wiley-VCH Verlag GmbH and Co. KGaA, Weinheim, 2006.
- [6] D. Zielke, A.C. Huebler, U. Hahn, N. Brandt, M. Bartzsch, U. Fügmann, T. Fischer, J. Veres, S. Ogier, *Appl. Phys. Lett.* 87 (2005) 123508.
- [7] Y.-Y. Noh, N. Zhao, M. Caironi, H. Sirringhaus, *Nat. Nanotechnol.* 2 (2007) 784.
- [8] T. Someya, Y. Noguchi, U. Zschieschang, H. Klauk, T. Someya, *PNAS* 105 (2008) 4976.
- [9] S. Ahn, L.J. Guo, *Adv. Mater.* 20 (2008) 2044.
- [10] Claus Taussig, Roll-to-Roll Manufacturing of Electronics on Flexible Substrates using Self-Aligned Imprint Lithography, Paper presented at Printed Electronics Europe Dresden 2008, IDTechEx, Cambridge, UK, 2008
- [11] M.D. Austin, S.Y. Chou, *Appl. Phys. Lett.* 81 (2002) 4431.
- [12] B. Stadlober, U. Haas, H. Gold, A. Haase, G. Jakopic, G. Leising, N. Koch, S. Rentenberger, E. Zojer, *Adv. Funct. Mater.* 17 (2007) 2687.
- [13] U. Haas, H. Gold, A. Haase, G. Jakopic, B. Stadlober, *Appl. Phys. Lett.* 92 (2007) 043511.
- [14] A. Fuchs, M. Bender, U. Plachetka, L. Kock, N. Koo, T. Wahlbrink, H. Kurz, *Curr. Appl. Phys.* 8 (2008) 669.
- [15] P. Voisin, M. Zelsmann, R. Cluzel, E. Pargon, C. Gourgon, J. Boussey, *Microelectron. Eng.* (2007), doi:10.1016/j.mee.2007.01.086.
- [16] S. Scheerlinck, D. Van Thourhout, R. Baets; Nano Imprint Lithography for Photonic Structure Patterning, in: *Proceedings Symposium IEEE/LEOS Benelux 2005*, Mons, p. 63.
- [17] G.Y. Jung, S. Ganapathiappan, A. Douglas, A. Ohlberg, A. Deirdre, L. Olynick, Y. Chen, W.M. Tong, R.S. Williams, *Nano Lett.* 4 (2004) 1225.
- [18] A. Fian, A. Haase, B. Stadlober, G. Jakopic, N.B. Matsko, W. Grogger, G. Leising, *Anal. Bioanal. Chem.* 390 (2008) 1455.
- [19] B. Stadlober, U. Haas, H. Maresch, A. Haase, *Phys. Rev. B* 74 (2006) 165302.
- [20] D. Knipp, R.A. Street, A. Vöckel, J. Ho, *J. Appl. Phys.* 93 (2003) 347.
- [21] S. Steudel, S. De Vusser, S. De Jonge, D. Janssen, S. Verlaak, J. Genoe, P. Heremans, *Appl. Phys. Lett.* 85 (2004) 4400.
- [22] L.A. Giannuzzi, F.A. Stevie, *Introduction to Focused Ion Beams*, Springer, 2004.
- [23] S.G.J. Mathijssen, M. Kemerink, A. Sharma, M. Cölle, P.A. Bobbert, R.A.J. Janssen, D.M. De Leeuw, *Adv. Mater.* 20 (2008) 975.
- [24] A. Wang, I. Kymissis, V. Bulovic, A.I. Akinwande, *Appl. Phys. Lett.* 89 (2006) 112109.
- [25] A. DiCarlo, F. Piacenza, A. Bolognesi, B. Stadlober, H. Maresch, *Appl. Phys. Lett.* 86 (2005) 263501.
- [26] M. Zirkl, A. Haase, A. Fian, H. Schön, C. Sommer, G. Jakopic, G. Leising, B. Stadlober, I. Graz, N. Gaar, R. Schwödiauer, S. Bauer-Gogonea, S. Bauer, *Adv. Mater.* 19 (2007) 2241.

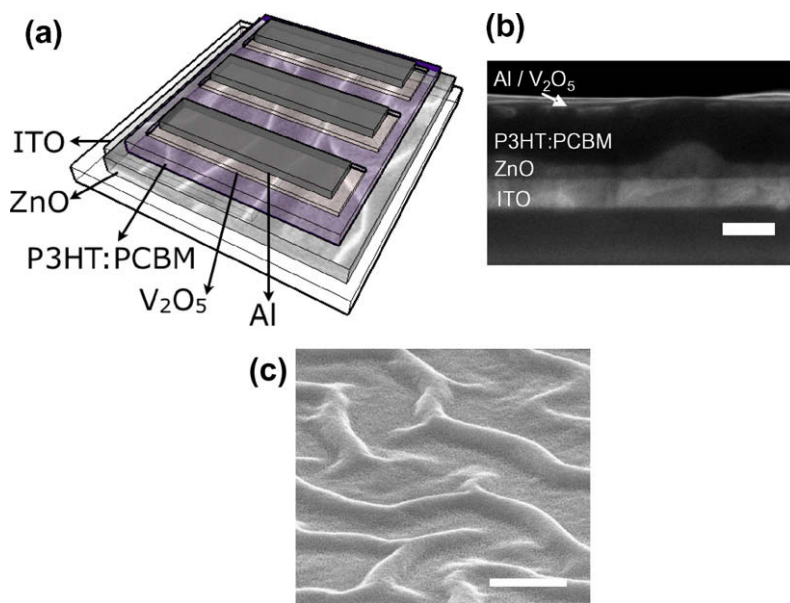


**Fig. 1.** (a) Device structure, (b) SEM cross-sectional image of the inverted polymer solar cell, scale bar: 200 nm and (c) SEM image of the ZnO nano-ridge film, scale bar: 500 nm.

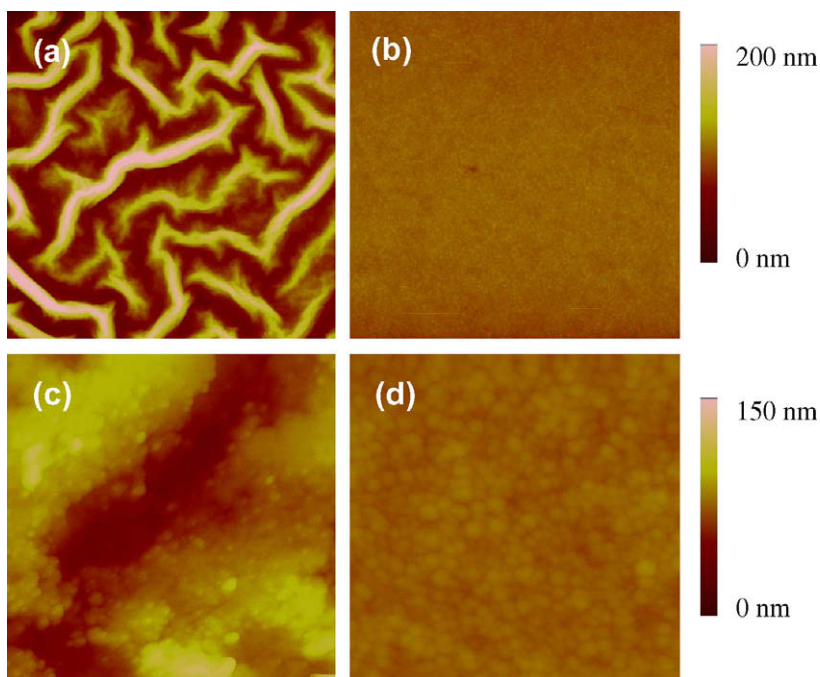


**Fig. 2.** AFM images of the (a) ZnO nano-ridge and (b) ZnO nanoparticle planar films showing a  $5 \mu\text{m} \times 5 \mu\text{m}$  surface area. Close-up AFM images of ZnO nano-ridge (c) and ZnO nanoparticle planar (d) films showing a  $500 \text{ nm} \times 500 \text{ nm}$  surface area.

## 2. Experimental

The fabrication of sol-gel processed ZnO nanoparticle films with planar and nano-ridge structures were made from spin coating the same precursor solution but annealing under different conditions. The precursor solution, con-

sisting of 0.75 M zinc acetate dihydrate and 0.75 M monoethanolamine in 2-methoxyethanol [18], was first spun-coated onto indium tin oxide (ITO) substrates at 2000 rpm for 40 s. For the ZnO planar film, the substrate was immediately placed onto a hot plate that was preheated at 275 °C and annealed for 5 min. In order to form



the ZnO nano-ridge film, the spin-coated substrate was first placed onto a hot plate that was initially at room temperature while it was still not completely dry. The temperature was then raised at a ramping rate of 50 °C/min to 275 °C and the substrates were subsequently removed from the hot plate when the final temperature was reached. We noticed an increase in sheet resistance of the ITO films when the substrates were heated at higher temperatures, so the annealing temperature the ZnO films was limited at 275 °C. Quartz substrates were used when measuring the transmittance of the ZnO films.

The resulting ZnO films were rinsed in de-ionized water, acetone, and isopropyl alcohol and then dried to remove residual organic material from the surface. All processes thus far were done in ambient air. The substrates were then transferred into a nitrogen-filled glovebox for polymer coating. Poly(3-hexylthiophene) (P3HT) and [6,6]-phenyl C<sub>61</sub> butyric acid methyl ester (PCBM) blend films were spun-coated onto the substrates from a 1:1 wt-ratio solution in 1,2-dichlorobenzene (20 mg of P3HT/ml of solvent) at 600 rpm using the slow-growth method [1], followed by annealing on a hot plate at 110 °C for 10 min. To complete the solar cell devices, a 10 nm layer of V<sub>2</sub>O<sub>5</sub> (serving as a buffer layer for hole collection [8]), following by 70 nm of Al was deposited by thermal evaporation through shadow masks. The device area, as defined by the overlap between the ITO and Al electrodes, was 0.09 cm<sup>2</sup>. The solar cells were measured under simulated illumination at AM 1.5 G, 100 mW/cm<sup>2</sup> with a Keithley 2400 source meter controlled by a computer program.

### 3. Results and discussion

The atomic force microscope (AFM) images of the nano-ridge and planar films are shown in Fig. 2a and b, respectively. Nano-ridges of ZnO nanoparticles with thickness ranging from 50 nm to 120 nm were formed and the valley to valley distance of the nano-ridges was about 500 nm. The ZnO nano-ridge structure was formed by the reorganization of gel particles during the slow drying process [19,20]. The ZnO planar film was relatively smooth with an r.m.s. roughness of about 2.6 nm. The r.m.s. roughness of the nano-ridge film was about 4.0 nm at the top of the ridge. As the morphologies are very different between the two structures, it is difficult to make a direct comparison in the r.m.s. roughness between them. Fig. 2c and d shows the close-up AFM images of the nano-ridge and planar films, respectively.

The transmittance spectra of the ZnO films and absorbance of the ZnO films coated with P3HT:PCBM are shown in Fig. 3. The ZnO nano-ridge film had a slightly lower transmittance over a broad range of wavelengths as compared to the ZnO planar film. This was due to the increase in light scattering by the nano-ridges and was consistent with the white foggy appearance of the film [21]. The polymer films with both types of ZnO morphology showed very similar absorption.

The current–voltage (*J–V*) characteristics of the solar cell devices with ZnO nano-ridge and planar films under simulated sunlight were shown in Fig. 4a. The device perfor-

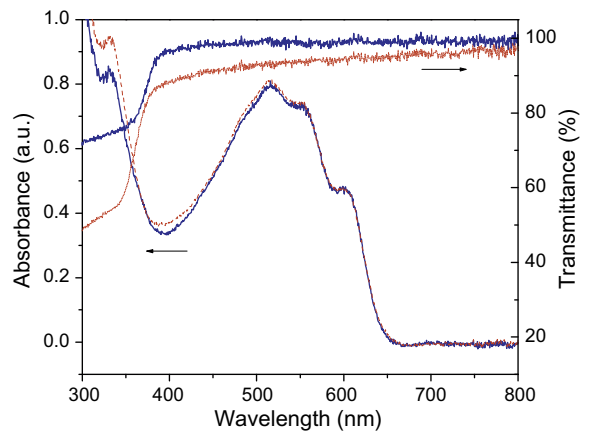


Fig. 3. The absorbance spectra for P3HT:PCBM on ZnO nano-ridge film (dotted line) and planar film of ZnO nanoparticles (bold line) and the transmittance spectra of the nano-ridge film (dotted line) and planar film (bold line).

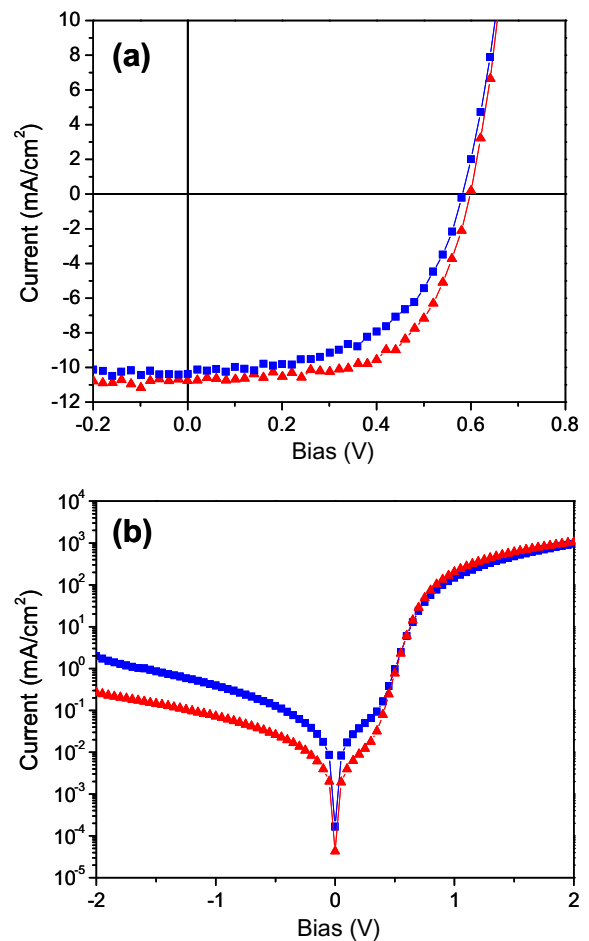


Fig. 4. (a) Current density–voltage (*J–V*) curves of the ZnO nano-ridge (triangle) and ZnO nanoparticles (square) devices under 100 mW/cm<sup>2</sup> AM 1.5 irradiation. (b) Dark *J–V* curves of the same devices.

**Table 1**

The device performance of inverted ZnO polymer solar cells. The values in parentheses are average values over 20 devices.

ZnO structure	Active polymer	$V_{oc}$ (V)	$J_{sc}$ (mA/cm <sup>2</sup> )	PCE (%)	FF (%)	$R_{shunt}/\Omega$ (cm <sup>2</sup> )	$R_{series}/\Omega$ (cm <sup>2</sup> )
NP	P3HT	0.80 (0.79)	0.19 (0.18)	0.06 (0.05)	44 (42)	4.60E4 (4.26E4)	15.0 (15.3)
NR	P3HT	0.74 (0.74)	0.37 (0.35)	0.15 (0.14)	56 (55)	1.11E5 (1.06E5)	14.3 (14.5)
NP	P3HT:PCBM	0.58 (0.58)	10.41 (10.35)	3.20 (3.06)	53 (51)	2.30E4 (1.77E4)	1.4 (1.6)
NR	P3HT:PCBM	0.60 (0.60)	10.76 (10.57)	4.00 (3.87)	62 (61)	1.42E5 (1.11E5)	1.4 (1.5)

mance is summarized in Table 1. The ZnO nano-ridge device showed a remarkable improvement over the device with the planar film. The average power conversion efficiency of 20 devices fabricated with nano-ridge films was 3.87%, while devices with planar films showed an efficiency of only 3.06%. The best device performance obtained from the nano-ridge device was 4.00%. The major improvement in device performance arises from the higher fill factor (FF) of the ZnO nano-ridge device, while the open circuit voltage ( $V_{oc}$ ) and short-circuit current density ( $J_{sc}$ ) remained almost unchanged. This is reflected in the series and shunt resistance as well. The shunt resistance showed a difference of about an order of magnitude while the series resistance was almost the same. Thus, it is unlikely that the improvement in the device performance is due to the change in carrier concentration or work function. We attributed this enhancement to lower leakage current due to the improvement in hole blocking capability and electron collection efficiency of the nano-ridge structured film.

The dark  $J$ - $V$  curve (Fig. 4b) shows a lower leakage and higher forward bias current for the ZnO nano-ridge device, indicating better charge selectivity over the ZnO planar film. This is due to the difference in the packing density of the films. As the ZnO nano-ridge film is formed by a slower heating process, there is sufficient time for the gel film to structurally relax before crystallizing, resulting in a denser film [18] than that of ZnO planar film [22]. A denser film with fewer defects would be more effective in blocking the transport of holes, leading to lower leakage current, i.e. a larger shunt resistance and higher FF.

To clarify whether the nano-ridge structure of the ZnO played a role in improving charge extraction, bilayer devices without PCBM were also fabricated. The  $J_{sc}$  for the ZnO nano-ridge bilayer device was close to two times higher than that of the device with the ZnO planar film, indicating a much larger interfacial area for charge separation. Similar to the results of ZnO nanorods [22,23], we believe that our ZnO played a comparable role, albeit a smaller one, to that of the ZnO nanorods-based solar cells. The larger surface area of electrode contact and undulate network structure minimized the distance charge carriers need to travel in the active polymer to reach the electrodes.

#### 4. Conclusion

We reported a ZnO nano-ridge structured film that can be formed by a simple ramp annealing process. The nano-

ridge structure has comparable excellent electron collection properties as that of ZnO nanorods and yet can be made with similar simple fabrication processes as the ZnO planar film. The effect of the viscosity of the solution and the solvent evaporation rate on the nano-structured pattern is to be further studied. Both inverted bulk heterojunction polymer solar cells and ZnO:P3HT hybrid solar cells showed remarkable improvements in efficiency when the ZnO nano-ridge structure was used. We attributed the improvement in FF to higher electron selectivity and more efficient charge collection, leading to a 4.00% inverted polymer solar cell.

#### Acknowledgments

The authors would like to thank Dr. Ziruo Hong, Mr. Raymond Chen and Mr. Bao Lei from UCLA for technical discussion, and financial support from Office of Naval Research (Fund No. N00014-04-1-0434). In addition, N. Sekine would also like to thank Fuji Electric Advanced Technology Co., Ltd. for granting him a sabbatical leave for conducting this research. C.H. Chou would also like to thank the National Science Council of Taiwan, Project NSC-0962917-1-009-112 for financial support.

#### References

- [1] G. Li, V. Shrotriya, J. Huang, Y. Yao, T. Moriarty, K. Emery, Y. Yang, *Nat. Mater.* 4 (2005) 864.
- [2] M.L. Ma, C.Y. Yang, X. Gong, K. Lee, A.J. Heeger, *Adv. Funct. Mater.* 15 (2005) 1617.
- [3] J. Peet, J.Y. Kim, N.E. Coates, W.L. Ma, D. Moses, A.J. Heeger, G.C. Bazan, *Nat. Mater.* 6 (2007) 497.
- [4] J. Hou, H.Y. Chen, S. Zhang, G. Li, Y. Yang, *J. Am. Chem. Soc.* 130 (2008) 16144.
- [5] S.K. Hau, H.L. Yip, N.S. Baek, J. Zou, K. O'Malley, A.K.Y. Jen, *Appl. Phys. Lett.* 92 (2008) 253301.
- [6] L.M. Chen, Z. Hong, G. Li, Yang Yang, *Adv. Mater.* 21 (2009) (published online).
- [7] Z. Xu, L.M. Chen, G.W. Yang, C.H. Huang, J. Hou, Y. Wu, G. Li, C.S. Hsu, Y. Yang, *Adv. Funct. Mater.* 19 (2009) (published online).
- [8] G. Li, C.W. Chu, V. Shrotriya, J. Huang, Y. Yang, *Appl. Phys. Lett.* 88 (2006) 253503.
- [9] H.H. Liao, L.M. Chen, Z. Xu, G. Li, Y. Yang, *Appl. Phys. Lett.* 92 (2008) 173303.
- [10] C. Waldauf, M. Morana, P. Denk, P. Schilinsky, K. Coakley, S.A. Choulis, C.J. Brabec, *Appl. Phys. Lett.* 89 (2006) 233517.
- [11] G.K. Mor, K. Shankar, M. Paulose, O.K. Varghese, C.A. Grimes, *Appl. Phys. Lett.* 91 (2007) 152111.
- [12] Mi-Hyae Park, Juo-Hao Li, Ankit Kumar, Gang Li, Yang Yang, *Adv. Mater.* 19 (2009) 1241.
- [13] M.S. White, D.C. Olson, S.E. Shaheen, N. Kopidakis, D.S. Ginley, *Appl. Phys. Lett.* 89 (2006) 143517.

- [14] A.K.K. Kyaw, X.W. Sun, C.Y. Jiang, G.Q. Lo, D.W. Zhao, D.L. Kwong, *Appl. Phys. Lett.* 93 (2008) 221107.
- [15] L. Vayssieres, *Adv. Mater.* 15 (2003) 464.
- [16] Z. Wang, X.F. Qian, J. Yin, Z.K. Zhu, *Langmuir* 20 (2004) 3441.
- [17] K. Takanezawa, K. Tajima, K. Hashimoto, *Appl. Phys. Lett.* 93 (2008) 063308.
- [18] M. Ohyama, H. Kozuka, T. Yoko, *Thin Solid Films* 306 (1997) 78.
- [19] R.D. Deegan, O. Bakajin, T.F. Dupont, G. Huber, S.R. Nagel, T.A. Witten, *Nature* 389 (1997) 827.
- [20] E. Rabani1, D.R. Reichman, P.L. Geissler, L.E. Brus, *Nature* 426 (2003) 271.
- [21] Y.S. Kim, W.P. Tai, S.J. Shu, *Thin Solid Films* 491 (2005) 153.
- [22] K. Takanezawa, K. Hirota, Q.S. Wei, K. Tajima, K. Hashimoto, *J. Phys. Chem. C* 111 (2007) 7218.
- [23] D.C. Olson, S.E. Shaheen, R.T. Collins, D.S. Ginley, *J. Phys. Chem. C* 111 (2007) 16670.



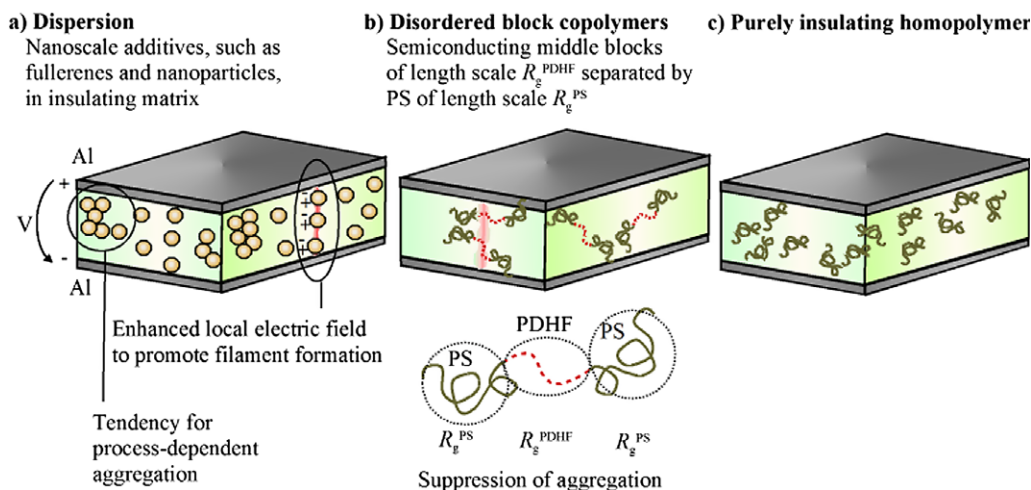


**Fig. 2.** Suggested schemes for the effect of dispersions. (a) Dispersion of fullerenes or nanoparticles in inert matrix. Local enhanced electric field in the dielectric constituents is also illustrated, which might control filament formation. (b) Semiconducting polymer chains (PDFH) forming the middle block of a block copolymer with insulating end blocks (PS). In the disordered state, the PDFH chains of average sizes  $R_g^{\text{PDHF}} \approx 2$  nm are separated by the PS chains (radius of gyration  $R_g^{\text{PS}} \approx 4$  nm). (c) Purely insulating polymer film, where the formation of the filaments is suggested to be controlled solely by the electrode surface structures and device inhomogeneities.

bottom electrode did not show a clear threshold voltage value during the first sweep and the current values were high already in the beginning of the first scan. However, the first sweep was usually noisy, i.e. NDR was achieved only after the forming sweep. The plasma treated electrodes had a threshold voltage value near 5 V, after which the high current level was achieved. After the  $I$ - $V$  measurements, the same devices were used for programming tests. The devices were written to a low conductivity state (OFF state) by applying a 100 ms voltage pulse of 9 V, and to a high conductivity state (ON state) with a 100 ms voltage pulse of 4 V. The current levels were read with 1 V after each writing step. Also all the electronic measurements were performed in a nitrogen glove box to eliminate environmental effects.

### 3. Results and discussion

#### 3.1. $I$ - $V$ measurements

At first we investigated devices with PS-*b*-PDHF-*b*-PS or PS layers between the electrodes with only a native oxide layer. The electrode overlap area was systematically varied from 4.7 to 0.38 mm<sup>2</sup>. Fig. 3 shows the  $I$ - $V$  curves for 85 nm thick polymer films in all cases, averaged from 3 to 4 devices. The presented results are collected from one polymer film containing devices of each overlap area, ensuring that the manufacturing process is exactly the same for each device. The averaged values are presented to clarify the differences. The first forming sweeps are not included in the figures. In both cases, NDR was observed, where curiously the current levels are slightly higher for PS. The figures show that the chemical nature of the polymer does not have a significant influence on the NDR effect. Also a simple insulating polymer like polystyrene shows strong NDR behaviour, enabling the mem-

ory effect, thus agreeing previous observations [4,6] and supporting the hypothesis of filamentary conduction. Interestingly, the figures also show that the shape of the  $I$ - $V$  curve smoothens when the device area increases, i.e. the smallest area produces a noisy curve. This suggests that the probability of having enough working filaments is higher when the area is large. Note also that the current values rise when the area increases, i.e. approximate scalability at large device areas is achieved. This suggests that instead of just one filament, several working filaments contribute to the device operation, which might be compared to previous results which present infrared camera pictures of devices showing only few hot spots, corresponding to a conducting filament or possibly groups thereof in the ON state [17]. Scalability enables us to tune the current levels with size, even though the minimum size is limited by the regularity of the  $I$ - $V$  curves. Thus the electrode overlap area cannot be miniaturized much below millimeter-scale for such simple devices. One can conclude, that the hypothesis of incorporating homogenous dispersion of semiconducting polymer chains due to disordered structure of block copolymers to trigger filament growth does not receive experimental support, which suggests to emphasize electrode surface engineering.

Next we studied the effect of an additional aluminium oxide layer on the bottom electrodes. Fig. 4 shows the  $I$ - $V$  curves of the 4.7 mm<sup>2</sup> devices having an 85 nm thick PS-*b*-PDHF-*b*-PS layer sandwiched between the aluminium electrodes and an oxide layer on the bottom electrode, which was either a native oxide layer or produced with an oxygen plasma treatment. The forming sweeps are again not included in the figure and the graph shows individual, consecutive sweeps of two different devices (no averaging was done). Surprisingly, the additional oxide layer seems to clearly reduce the probability of having a clear current maximum in the NDR curve, in contrast to the previous results [18]. This suggests that either the peaks of the bottom

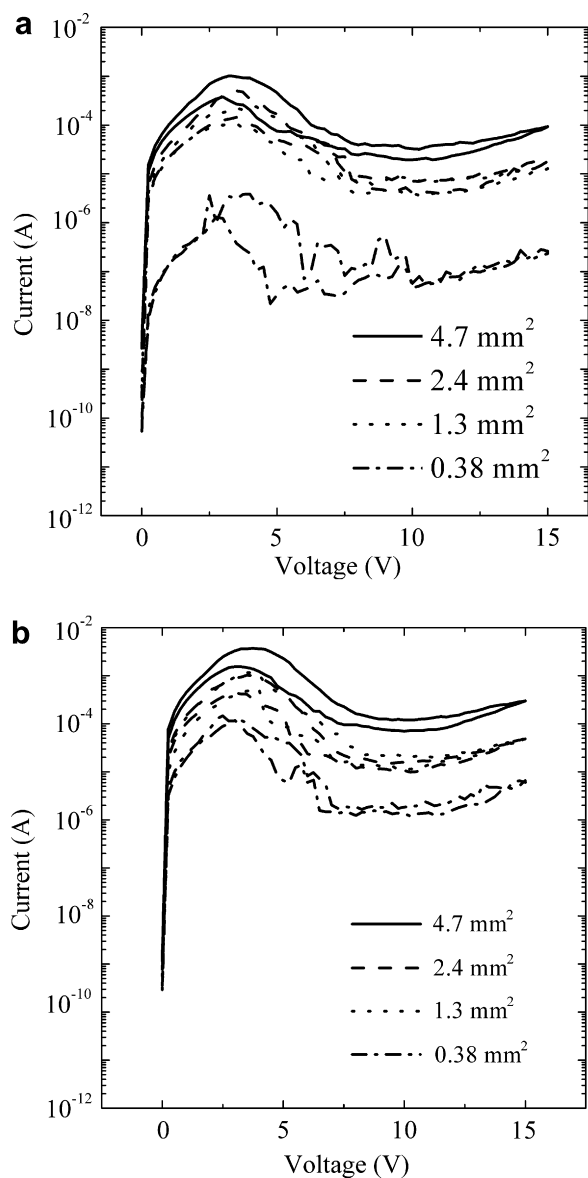


**Fig. 3.** NDR and the effect of device area on the  $I$ - $V$  characteristics for: (a) a PS- $b$ -PDHF- $b$ -PS and (b) a PS layer sandwiched between aluminium electrodes.

electrode are flattened, or the morphology of the oxide layer changes during the plasma treatment. Either way, the filaments do not have enough starting points to grow after the plasma treatment.

The surface roughness of the both oxide layers was studied with AFM on a small scale and with an optical profiler on a larger scale. The numerical surface roughness values, measured with either method, did not differ significantly when plasma-treated and native oxide layers were compared. In addition, the optical profiler studies did not reveal any existence of random higher oxide peaks, which might act as starting points for the filaments. However, the resolution of the optical profiler might not be enough to detect such peaks. It is thus not quite clear whether it is

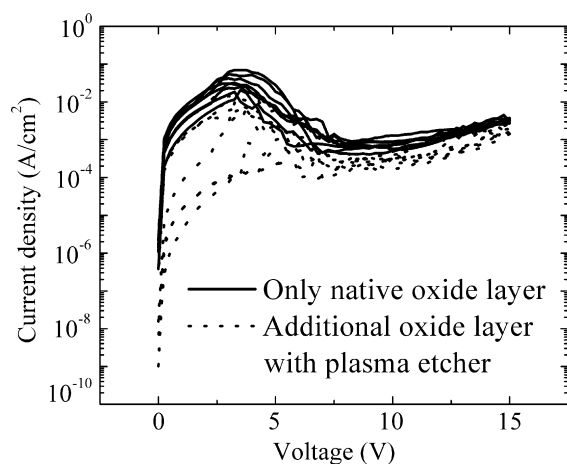


**Fig. 4.** The effect of oxygen plasma treatment of the bottom electrode on the negative differential resistance of PS- $b$ -PDHF- $b$ -PS (85 nm) memory device.

the possible smoothing of the oxide or morphological changes that degrade NDR in the plasma-treated devices. Nonetheless, it is evident that just the presence of the oxide layer does not guarantee reliable operation, as shown also by Steyrlleuthner et al. [20], but the processing method of the oxide has an effect also.

### 3.2. Programming

We tested all the described devices by applying a 4 V pulse to switch the devices to the ON state and a 9 V pulse to switch them to the OFF state, keeping the reading voltage at 1 V. Fig. 5 shows the best results for the programming cycle of the devices incorporating PS- $b$ -PDHF- $b$ -PS for the area of 4.7 mm<sup>2</sup> using the native oxide and ~85 nm film thickness. Fig. 5 illustrates that in principle the present devices could allow memory device operation.

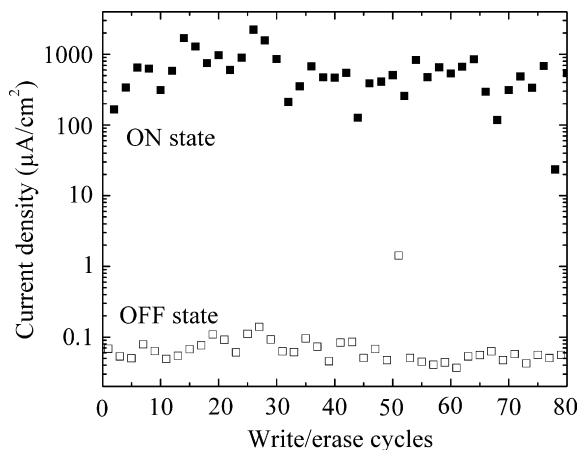


**Fig. 5.** Programming results showing consistent switching and ON-OFF current ratios greater than three orders of magnitude for PS- $b$ -PDHF- $b$ -PS (85 nm), utilizing the largest device area (4.7 mm<sup>2</sup>) and only native oxide on the bottom electrode.

But notably, the reproducibility still remains poor, even though NDR was easy to produce for a sufficiently high device area ( $>4\text{ mm}^2$ ) and a thin polymer film ( $<100\text{ nm}$ ). These results further suggest that reliable operation requires control over the surface topography to create starting points to the filaments, at least in order to keep the device area below mm scale. Since both the aluminium oxide layer and a certain amount of starting points for the growth of the filaments appear to be prerequisite for reproducible operation, the best suggestion for printable devices could be patterning of the bottom electrode or the substrate underneath. This might be possible by using surface-patterned electrodes – metallic or polymeric – and roll-to-roll atomic layer deposition [28] to provide the aluminium oxide layer on the bottom electrode.

#### 4. Conclusions

We tested whether well dispersed semiconducting polymer chains with radius of gyration of ca. 2 nm as separated by insulating polymer chains with radius of gyration of ca. 4 nm, i.e. a disordered triblock copolymer polystyrene-*block*-poly(9,9-di-*n*-hexyl-2,7-fluorene)-*block*-polystyrene, would allow control of filament formation upon electroforming, in comparison to purely insulating PS. The present work did not show major differences in the electronic properties of thin film memory devices in these two cases. Programming of the polymeric devices to distinct ON and OFF states was possible, but not reliably reproducible. The current passing through the device was area dependent, which implies that multiple filaments contribute to the memory effect, but scalability was suppressed for small areas. The larger device area ( $4.7\text{ mm}^2$ ) also improved the stability of the NDR curve, indicating that multiple defects on the bottom electrode are needed in order to guide the growth of the filaments. Also the processing method of the aluminium oxide layer on the bottom electrode had a significant effect on the NDR. In comparison to a native oxide layer, devices with oxygen plasma treated bottom electrodes showed inferior *I*-*V* characteristics, most probably due to the differences in the oxide layer morphology or smoothness. Thus the critical step in possible forthcoming work would be to study if the filament-forming process can be nucleated by a surface topography treatment.

#### Acknowledgements

We wish to thank Prof. Ronald Österbacka, Dr. Himadri Majumdar, Dr. Jayanta Baral and Fredrik Jansson for valuable discussions and Tomi Hassinen for help with studying the oxygen plasma treated Al-electrodes. TEKES FinNano program is acknowledged for funding the project.

#### References

- [1] D.R. Gamota, P. Brazis, K. Kalyanasundaram, J. Zhang, Printed Organic and Molecular Electronics, Kluwer Academic Publishers, Boston, 2004. p. 695.
- [2] J.C. Scott, L.D. Bozano, Adv. Mater. 19 (2007) 1452–1463.
- [3] Q.-D. Ling, D.-J. Liaw, C. Zhu, D.S.-H. Chan, E.-T. Kang, K.-G. Neoh, Progr. Polym. Sci. 33 (2008) 917–978.
- [4] M. Cölle, M. Büchel, D.M. de Leeuw, Org. Electron. 7 (2006) 305–312.
- [5] L.D. Bozano, B.W. Kean, V.R. Deline, J.R. Salem, J.C. Scott, Appl. Phys. Lett. 84 (2004) 607–609.
- [6] H. Pagnia, N. Sotnik, Phys. Stat. Sol. (a) 108 (1988) 11–65.
- [7] L.D. Bozano, B.W. Kean, M. Beinhoff, K.R. Carter, P.M. Rice, J.C. Scott, Adv. Funct. Mater. 15 (2005) 1933–1939.
- [8] L.P. Ma, J. Liu, Y. Yang, Appl. Phys. Lett. 80 (2002) 2997–2999.
- [9] F. Verbakel, S.C.J. Meskers, R.A.J. Janssen, Appl. Phys. Lett. 89 (2002) 102103.
- [10] A. Laiho, H.S. Majumdar, J.K. Baral, F. Jansson, R. Österbacka, O. Ikkala, Appl. Phys. Lett. 93 (2008) 203309.
- [11] C.W. Chu, J. Ouyang, J.-H. Tseng, Y. Yang, Adv. Mater. 17 (2005) 1440–1443.
- [12] Y. Yang, J. Ouyang, L. Ma, R.J.-H. Tseng, C.-W. Chu, Adv. Funct. Mater. 16 (2006) 1001–1014.
- [13] H.S. Majumdar, A. Bandyopadhyay, A. Bolognesi, A.J. Pal, J. Appl. Phys. 91 (2002) 2433–2437.
- [14] H.K. Henisch, W.R. Smith, Appl. Phys. Lett. 24 (1974) 589–591.
- [15] G. Dearnaley, D.V. Morgan, A.M. Stoneham, J. Non-Cryst. Solids 4 (1970) 593–612.
- [16] G. Dearnaley, A.M. Stoneham, D.V. Morgan, Rep. Prog. Phys. 33 (1970) 1129–1191.
- [17] F.L.E. Jakobsson, X. Crispin, M. Cölle, M. Büchel, D.M. de Leeuw, M. Berggren, Org. Electron. 8 (2007) 559–565.
- [18] F. Verbakel, S.C.J. Meskers, R.A.J. Janssen, H.L. Gomes, M. Cölle, M. Büchel, D.M. de Leeuw, Appl. Phys. Lett. 91 (2007) 192103.
- [19] W.-J. Joo, T.-L. Choi, K.-H. Lee, Thin Solid Films 516 (2008) 3133–3137.
- [20] R. Steyrleuthner, S. Bange, D. Neher, J. Appl. Phys. 105 (2009) 064509.
- [21] S. Paul, A. Kanwal, M. Chhowalla, Nanotechnology 17 (2006) 145–151.
- [22] J.G. Simmons, R.R. Verderber, Proc. R. Soc. Lond. A 301 (1967) 77–102.
- [23] R.E. Thurstans, D.P. Oxley, J. Phys. D: Appl. Phys. 35 (2002) 802–809.
- [24] I.W. Hamley, The Physics of Block Copolymers, Oxford University Press, USA, 1998.
- [25] J. Ling, N. Fomina, G. Rasul, T.E. Hogen-Esch, J. Phys. Chem. B 112 (2008) 10116–10122.
- [26] A.E.T. Kuiper, M.F. Gillies, V. Kottler, G.W. 't Hooft, J.G.M. van Berkum, C. van der Marel, Y. Tamminga, J.H.M. Snijders, J. Appl. Phys. 89 (2001) 1965–1972.
- [27] W.-T. Li, D.A.P. Bulla, R. Boswell, Surf. Coat. Technol. 201 (2007) 4979–4983.
- [28] C.M.A. Heller, A.G. Erlat, E.M. Breitung, Systems and Methods for Roll-To-Roll Atomic Layer Deposition on Continuously Fed Objects, Appl. No. PCT/US2007/066029, Patent No. WO/2008/057625, 2008.

cells can dramatically influence the air stability of the devices. Specifically, annealing the polymer photoactive layer after top electrode deposition results in air stable polymer solar cells; the average device efficiency is maintained at 90% of the highest value even after exposure to air for 10 days. On the other hand, annealing the photoactive layer prior to top electrode deposition results in devices with stability that is far inferior compared to devices whose photoactive layer was annealed after top electrode deposition. We attribute this discrepancy in the stability of devices to differences in the metal grain structure of the top electrode, which in turn is a direct manifestation of the underlying morphology of the photoactive layer.

## 2. Experimental

Inverted bulk-heterojunction polymer solar cells were fabricated on pre-patterned indium tin oxide (ITO) on glass (15  $\Omega$ /sq.; Colorado Concept Coatings). Prior to the deposition of the polymer photoactive layer, we deposited a 30 nm thick layer of titania via hydrolysis of titanium isopropoxide ( $\text{Ti}[\text{OCH}(\text{CH}_3)_2]_4$ , Aldrich, 99.999%) as the electron transport layer [10,11]. Specifically, titanium isopropoxide was dissolved in isopropyl alcohol to make a 1 wt.% solution and the solution stirred for at least 30 min. The solution was then spin coated on pre-patterned ITO/glass substrates at 4500 rpm for 30 s. Hydrolysis occurred at room temperature for 1 h before the substrates were annealed at 170  $^\circ\text{C}$  for 10 min. The polymer photoactive layer (180 nm) consisted of poly(3-hexylthiophene), P3HT (Merck Chemicals Ltd.), and a fullerene derivative of [6,6]-phenyl- $\text{C}_{61}$ -butyric acid methyl ester, or PCBM (American Dye Source, Inc.), which were first codissolved at equimass ratio in chlorobenzene to yield a 2.4 wt.% solution prior to spin coating on titania-coated substrates. Thermal annealing of the polymer photoactive layer took place at 140  $^\circ\text{C}$  for 30 min either before or after top electrode deposition. The top electrode consisted of 80 nm of silver deposited via thermal evaporation through a stencil mask resulting in devices with an active area of 0.127  $\text{cm}^2$ . The schematic of our device architecture is

shown in the inset of Fig. 1a. We have previously demonstrated inverted polymer solar cells with gold top electrodes [10,11]. Given that silver is more reflective than gold [12] and it readily oxidizes in air to form silver oxide with a work function that facilitates hole collection [13], we opted to use silver as our top electrodes in this study. All the devices examined in this study were fabricated and tested in air without any external packaging or encapsulation. The devices were stored in air and tested periodically for extended periods to gauge the air stability. Current density–voltage ( $J$ – $V$ ) characteristics of the devices were measured with a Keithley 2400 source measurement unit under AM 1.5G 100  $\text{mW}/\text{cm}^2$  illumination. Atomic force microscope (AFM) images of the polymer photoactive layer and of the silver top electrode were acquired on a Veeco multimode AFM with a nanoscope IIIa controller in tapping mode.

## 3. Results and discussion

Fig. 1 contains the  $J$ – $V$  characteristics of representative polymer solar cells acquired under illumination with exposure to air. Specifically, the  $J$ – $V$  characteristics in Fig. 1a were acquired on a polymer solar cell in which its photoactive layer was annealed before silver electrode deposition whereas the  $J$ – $V$  characteristics in Fig. 1b were acquired on an analogous polymer solar cell in which thermal annealing took place after silver electrode deposition. The individual  $J$ – $V$  curves shown in Fig. 1 were acquired after the polymer solar cells had been illuminated for ten minutes where upon the transient photovoltaic characteristics associated with the filling of shallow electron traps in titania have saturated [11]. As fabricated, the polymer solar cell in which its photoactive layer was annealed before silver electrode deposition exhibits a short-circuit current density,  $J_{\text{sc}}$ , of 3.6  $\text{mA}/\text{cm}^2$  and an open-circuit voltage,  $V_{\text{oc}}$ , of 0.32 V. We extracted a fill factor (FF) of 0.29 for the same device, amounting to a device efficiency,  $\eta$ , of 0.32%. The average device characteristics, along with relevant standard deviations of five devices tested are recorded in Table 1. On exposure to air for two days, both the  $J_{\text{sc}}$

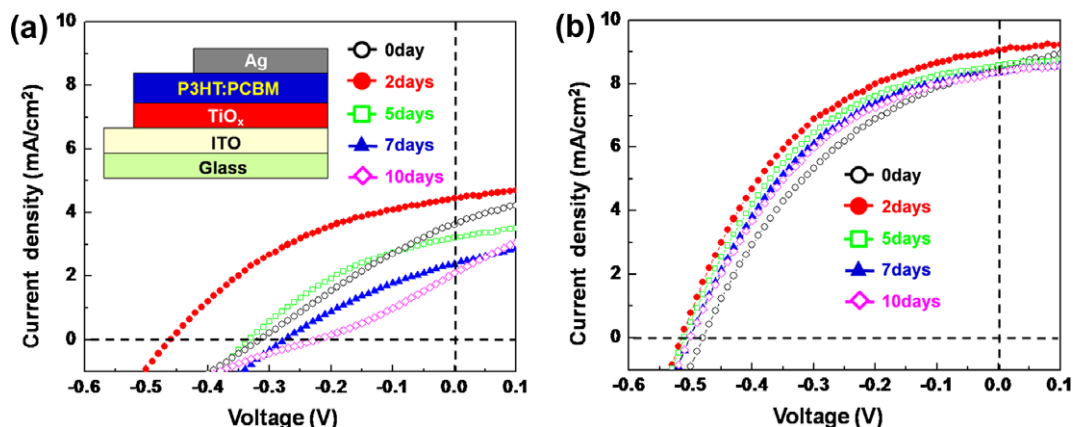


**Fig. 1.**  $J$ – $V$  characteristics under illumination (100  $\text{mW}/\text{cm}^2$ ) of inverted polymer solar cells as function of exposure time in air for devices in which the photoactive layer was annealed (a) before and (b) after top electrode deposition. The inset shows a scheme of our inverted polymer solar cell architecture with silver top electrode; no external packaging or encapsulation was used. All devices were fabricated and tested in air.



**Table 1**

Photovoltaic characteristics of polymer solar cells as function of exposure time in air for devices in which the photoactive layer was annealed before and after top electrode deposition.

	$J_{sc}$ (mA/cm <sup>2</sup> )	$V_{oc}$ (V)	Fill factor	Efficiency (%)
<i>Annealed before Ag deposition</i>				
0 day	3.63 ± 0.36	0.32 ± 0.02	0.29 ± 0.01	0.32 ± 0.08
2 days	4.44 ± 0.67	0.46 ± 0.03	0.39 ± 0.03	0.81 ± 0.11
5 days	3.22 ± 0.19	0.33 ± 0.02	0.30 ± 0.02	0.38 ± 0.05
7 days	2.38 ± 0.11	0.28 ± 0.02	0.31 ± 0.02	0.20 ± 0.02
10 days	2.09 ± 0.10	0.22 ± 0.02	0.18 ± 0.01	0.09 ± 0.01
<i>Annealed after Ag deposition</i>				
0 day	8.50 ± 0.61	0.48 ± 0.02	0.37 ± 0.02	1.88 ± 0.11
2 days	9.06 ± 0.78	0.51 ± 0.01	0.37 ± 0.01	2.09 ± 0.18
5 days	8.71 ± 0.37	0.51 ± 0.01	0.37 ± 0.02	1.96 ± 0.09
7 days	8.66 ± 0.61	0.51 ± 0.01	0.37 ± 0.01	1.85 ± 0.15
10 days	8.58 ± 0.20	0.51 ± 0.02	0.37 ± 0.01	1.80 ± 0.10

(4.4 mA/cm<sup>2</sup>) and the  $V_{oc}$  (0.46 V) of the same device improve dramatically, resulting in a concomitant increase in the FF (0.39) and  $\eta$  (0.81%). That the device improves with storage was previously observed with inverted polymer solar cells with gold top electrode; this improvement in the photovoltaic characteristics is attributed to oxygen doping of P3HT [11,14]. On extended storage in air, however, the photovoltaic characteristics of the device deteriorate significantly. After ten days in air, the  $J_{sc}$  and the  $V_{oc}$  drop to 2.1 mA/cm<sup>2</sup> and 0.22 V, respectively, resulting in

an FF of 0.18 and an  $\eta$  of 0.09%. The air stability of inverted polymer solar cells in which the photoactive layer was thermally annealed prior to silver electrode deposition appears to be not significantly better than analogous solar cells made in the conventional architecture. On the other hand, the scenario is different when we examined inverted polymer solar cells that were thermally annealed after silver electrode deposition; relevant  $J$ - $V$  characteristics of a representative device are shown in Fig. 1b for comparison. As fabricated, this inverted polymer solar cell exhibits a  $J_{sc}$  of 8.5 mA/cm<sup>2</sup>, and a  $V_{oc}$  of 0.48 V, resulting in an FF of 0.37 and an  $\eta$  of 1.9%. The difference in the photovoltaic characteristics of the as-fabricated devices is attributed to the strong temperature dependence of silver oxidation [18]. Because oxygen diffuses significantly faster at 140 °C compared to at room temperature, the silver top electrode oxidizes at a faster rate in the device that is annealed after silver deposition. And since that the rate at which the work function of silver is altered is tied to the rate of silver oxidation, this difference is manifested as discrepancies in the photovoltaic characteristics of the two devices acquired on the 0th day.

Storage in air for two days results in oxygen doping of P3HT; the device characteristics improve as a consequence. Specifically, the  $J_{sc}$  and  $V_{oc}$  increase to 9.1 mA/cm<sup>2</sup> and 0.51 V, respectively, resulting in an increase in the overall efficiency (2.1%). In sharp contrast to the device character-

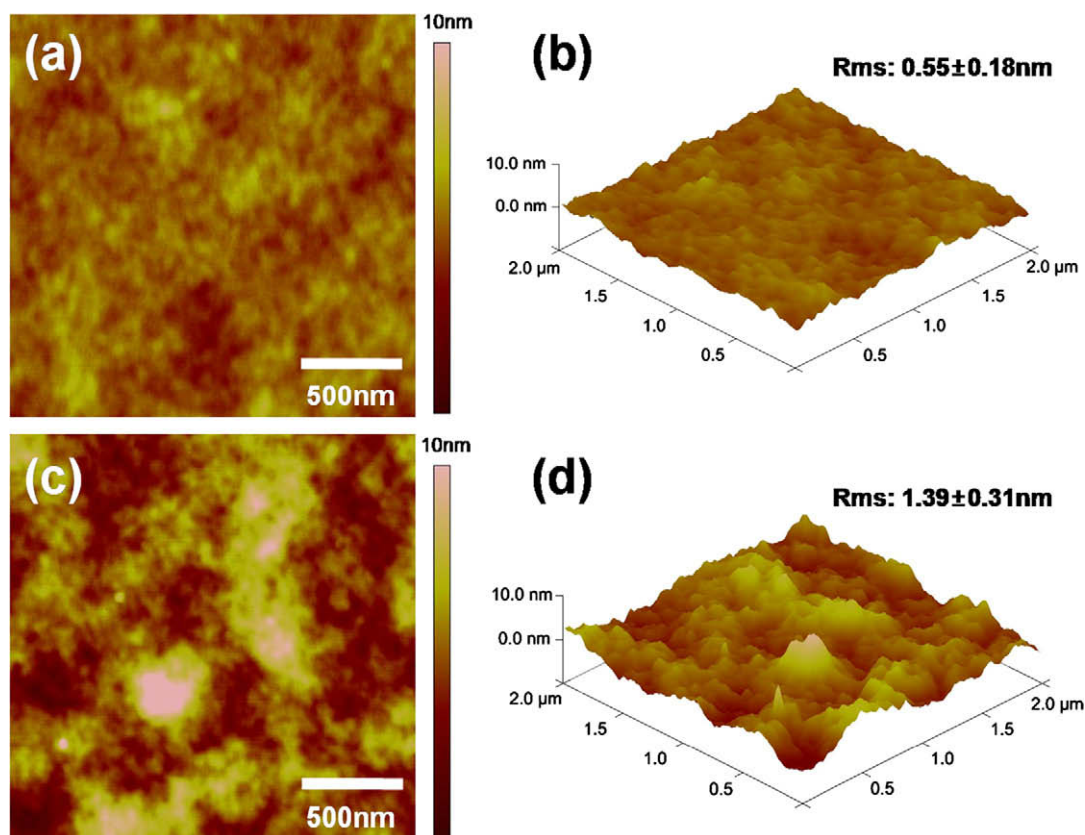


**Fig. 2.** AFM (a) height and (b) 3D renditions of as-cast P3HT:PCBM on titania and (c) height and (d) 3D renditions of P3HT:PCBM thermally annealed at 140 °C for 30 min.

istics shown in Fig. 1a, the photovoltaic characteristics of the inverted polymer solar cell that was thermally annealed after silver electrode deposition do not vary significantly on extended exposure to air. After ten days in air, the  $J_{sc}$  and  $V_{oc}$  of the same device remain at  $8.6 \text{ mA/cm}^2$  and  $0.51 \text{ V}$ , respectively. As such,  $\eta$  (1.8%) remains at 90% of its peak value over the duration of this study.

While it is generally accepted that the details of processing conditions can dramatically alter device characteristics [15–19], it is initially surprising to learn that the annealing sequence of the polymer photoactive layer can influence the stability of inverted solar cells. To examine how the annealing sequence of the polymer photoactive layer is affecting the air stability of devices, we carried out AFM studies to characterize the morphology of as-cast

and thermally annealed P3HT:PCBM films on titania. Fig. 2 contains the AFM height images of (a) as-cast and (c) thermally annealed P3HT:PCBM films. The corresponding three-dimensional renditions of the height images are shown in Figs. 2b and d, respectively. The as-cast P3HT:PCBM film is smooth; we extracted a root-mean-square (rms) roughness of  $0.55 \pm 0.18 \text{ nm}$  from this  $2 \times 2$  micrometer image. The film roughens significantly with thermal annealing; we extracted an rms roughness of  $1.39 \pm 0.31 \text{ nm}$  from Fig. 2b. This roughening of P3HT:PCBM films was previously observed and was attributed to the phase separation and crystallization of P3HT and PCBM on heating [20,21]. Given that the morphology of the polymer photoactive layer is different during the deposition of the top electrode, it necessarily influences

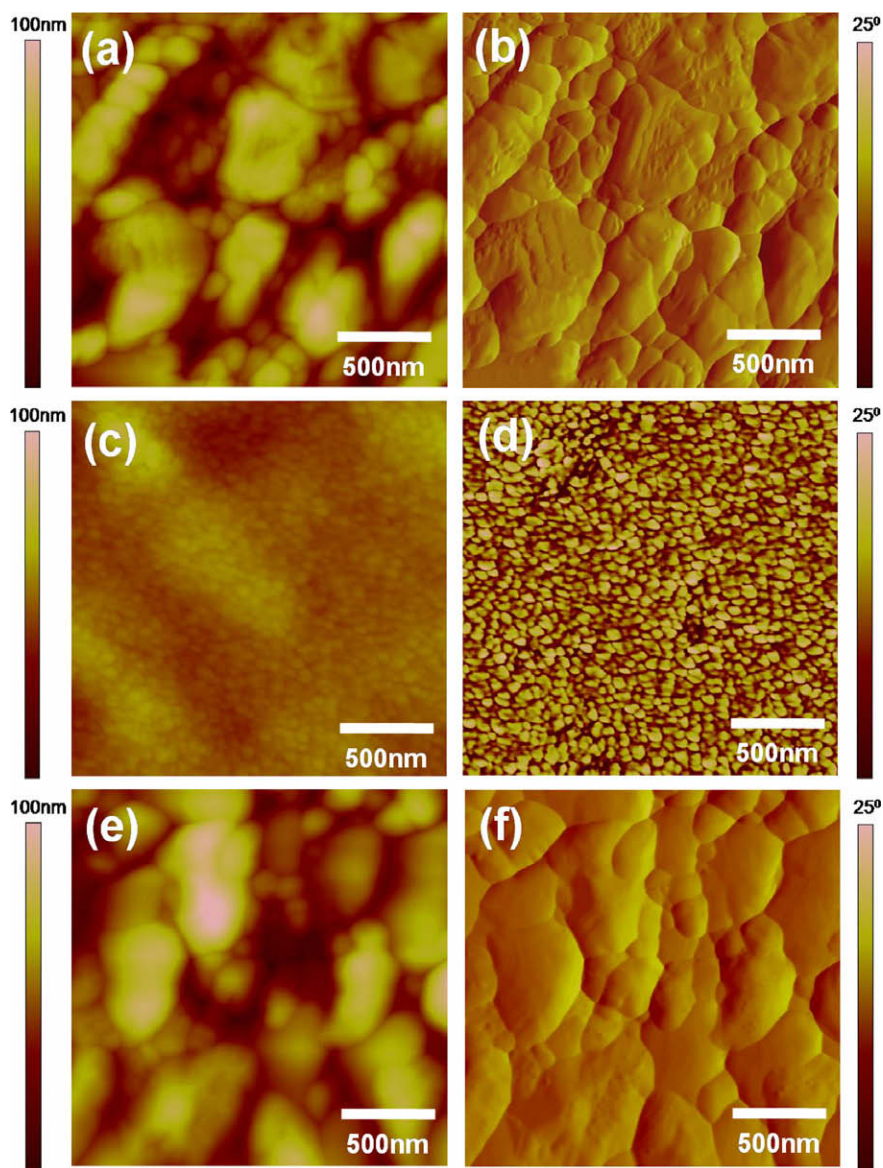


**Fig. 3.** AFM (a) height and (b) phase contrast images of the silver top electrode on as-cast P3HT:PCBM; (c) height and (d) phase contrast images of the silver top electrode on thermally annealed P3HT:PCBM; and (e) height and (f) phase contrast images of the silver top electrode on as-cast P3HT:PCBM after the bilayers have been thermally annealed at  $140 \text{ }^\circ\text{C}$  for 30 min.

the grain structure of the subsequently deposited metal. We thus conducted AFM studies to characterize the grain structure of silver that is deposited on as-cast and thermally annealed P3HT:PCBM films on titania. Figs. 3a and b contain the height and phase contrast images of 80 nm of silver that is deposited on as-cast P3HT:PCBM on titania whereas Figs. 3c and d contain the height and phase contrast images of silver that is deposited on thermally annealed P3HT:PCBM on titania. We observe drastic differences when comparing these two sets of images. Specifically, the grain size of silver that is deposited on as-cast P3HT:PCBM is large, of order several hundred nanometers, compared to silver that is deposited on thermally annealed P3HT:PCBM (of order tens of nanometers grain size). The larger grains also appear to be more interconnected in the silver film that is deposited on as-cast P3HT:PCBM. The difference in grain size and grain structure must stem from differences in the morphology of the underlying polymer photoactive layer. The as-cast P3HT:PCBM film is smooth and featureless; silver that is subsequently deposited on this polymer forms interconnected grains that are hundreds of nanometers in size. In contrast, the thermally annealed P3HT:PCBM film is significantly rougher; we observe tall spikes and deep valleys in the scan window shown in Fig. 2d. Such surface heterogeneities can in turn serve as additional nucleation sites during silver deposition [22]. It follows that silver that is deposited on such film forms smaller, less interconnected grains. As a final comparison, we conducted AFM on silver that is deposited on as-cast P3HT:PCBM after the bilayers have been thermally annealed at 140 °C for 30 min; the height and phase contrast images corresponding to this silver surface is shown in Figs. 3e and f. We observe that these images exhibit silver grain size and structure that are comparable to those in Figs. 3a and b, a strong indication that the morphology of the electrode is defined during silver deposition; thermal annealing after the deposition of silver does not further influence its morphology.

Our microscopy study implicates a strong correlation between the grain size of the silver electrode and the air stability of our inverted polymer solar cells. Devices are significantly more stable in air when the silver grains are interconnected and the average grain size large. The silver electrode with a larger grain size has a lower density of grain boundary through which moisture can diffuse. Given that extended exposures to moisture can damage the polymer photoactive layer [4,6], we speculate it is the suppression of moisture diffusion through the silver electrode that has significantly extended the air stability of our inverted polymer solar cells. When the polymer photoactive layer is thermally annealed prior to electrode deposition, the roughness of the photoactive layer provides additional nucleation opportunities for silver, resulting in films with small grains and high grain boundary densities. Such films allow significant moisture diffusion through grain boundaries, leading to decreasing device characteristics with time.

Fig. 4 compares the stability of our inverted polymer solar cells; the average efficiency of inverted polymer solar cells in which the photoactive layer was annealed before (open circles) and after (filled circles) silver electrode deposition is plotted as a function of exposure to air. For

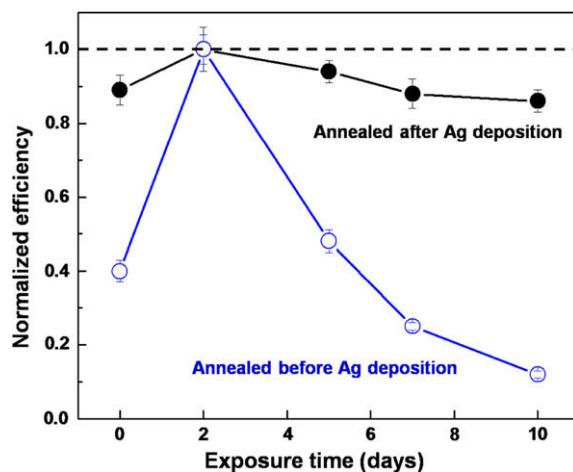


Fig. 4. Normalized average device efficiency as function of exposure time in air for devices in which the photoactive layer was annealed before (open symbols) and after (solid symbols) top electrode deposition. The error bars represent standard deviations calculated from the testing of five devices.

ease of comparison, the device efficiencies for both types of devices were normalized against the highest values. Devices in which the polymer photoactive layer was annealed before silver deposition experience a sharp increase in efficiency during initial exposure to air due to the oxygen doping of P3HT [14]. The efficiency decreases dramatically beyond the second day because moisture that diffuses through the grain boundaries in the silver electrode can react with the photoactive layer. In contrast, the average efficiency of devices that were thermally annealed after silver deposition is maintained at 90% of its highest value.

#### 4. Conclusion

Our study demonstrates that the details of processing not only affect device performance; they can dramatically influence device stability. In this particular case, the sequence with which the photoactive layer is annealed alters the grain structure of the top electrode, which in turn influences the level of moisture penetration into the photoactive layer. The elucidation of such processing-structure-function relationships should lead to the engineering of more robust, next-generation devices.

#### Acknowledgements

We gratefully acknowledge funding from the Photovoltaics Program at ONR (N000140811175) and the MRSEC Program through the NSF-sponsored Princeton Center for Complex Materials (DMR-081960). JBK and YSK acknowledge funding from KOSEF (2009-0079463).

#### References

- [1] Y.-L. Loo, I. McCulloch, MRS Bulletin 33 (2008) 653.
- [2] S.H. Park, A. Roy, S. Beaupre, S. Cho, N. Coates, J.S. Moon, D. Moses, M. Leclerc, K. Lee, A.J. Heeger, Nat. Photonics 3 (2009) 297.

- [3] S.K. Hau, H.L. Yip, N.S. Baek, J. Zou, K.O. Malley, A.K.Y. Jen, *Appl. Phys. Lett.* 92 (2008) 253301.
- [4] M. Jorgensen, K. Norrman, F.C. Krebs, *Sol. Energy Mater. Sol. Cells* 92 (2008) 686.
- [5] K. Kawano, R. Pacios, D. Poplavskyy, J. Nelson, D.D.C. Bradley, J.R. Durrant, *Sol. Energy Mater. Sol. Cells* 90 (2006) 3520.
- [6] F.C. Krebs, K. Norrman, *Prog. Photovoltaics* 15 (2007) 697.
- [7] W.J. Potscavage, S. Yoo, B. Domercq, B. Kippelen, *Appl. Phys. Lett.* 90 (2007) 253511.
- [8] N. Kim, W.J. Potscavage, B. Domercq, B. Kippelen, S. Graham, *Appl. Phys. Lett.* 94 (2009) 163308.
- [9] T. Ameri, G. Dennler, C. Waldauf, P. Denk, K. Forberich, M.C. Scharber, C.J. Brabec, K. Hingerl, *J. Appl. Phys.* 103 (2008) 084506.
- [10] C.S. Kim, L.L. Tinker, B.F. DiSalle, E.D. Gomez, S. Lee, S. Bernhard, Y.-L. Loo, *Adv. Mater.* 21 (2009) 3110.
- [11] C.S. Kim, S. Lee, E.D. Gomez, J.B. Kim, Y.-L. Loo, *Appl. Phys. Lett.* 94 (2009) 113302.
- [12] H.W. Jang, J.H. Son, J.L. Lee, *Appl. Phys. Lett.* 90 (2007) 012106.
- [13] H.W. Choi, S.Y. Kim, K.B. Kim, Y.H. Tak, J.L. Lee, *Appl. Phys. Lett.* 86 (2005) 012104.
- [14] M.S.A. Abdou, F.P. Orfino, Y. Son, S. Holdcroft, *J. Am. Chem. Soc.* 119 (1997) 4518.
- [15] H. Hoppe, N.S. Sariciftci, *J. Mater. Chem.* 16 (2006) 45.
- [16] M. Campoy-Quiles, T. Ferenczi, T. Agostinelli, P.G. Etchegoin, Y. Kim, T.D. Anthopoulos, P.N. Stavrinou, D.D.C. Bradley, J. Nelson, *Nat. Mater.* 7 (2008) 158.
- [17] L.H. Nguyen, H. Hoppe, T. Erb, S. Gunes, G. Gobsch, N.S. Sariciftci, *Adv. Funct. Mater.* 17 (2007) 1071.
- [18] J.B. Kim, C.S. Kim, Y.S. Kim, Y.-L. Loo, *Appl. Phys. Lett.*, submitted for publication.
- [19] G. Li, V. Shrotriya, Y. Yao, Y. Yang, *J. Appl. Phys.* 98 (2005) 043704.
- [20] G. Li, V. Shrotriya, J. Huang, Y. Yao, T. Moriarty, K. Emery, Y. Yang, *Nat. Mater.* 4 (2005) 864.
- [21] H. Kim, W.W. So, S.J. Moon, *Sol. Energy Mater. Sol. Cells* 91 (2007) 581.
- [22] M. Ohring, *The Materials Science of Thin Films*, Academic Press, 2001.

in an Ohno potential, Kobrak and Bittner indicated that the electroluminescence quantum yield may be as high as 59%, substantially greater than the 25% predicted by simple spin statistics [7].

Since the spin of an exciton is closely related to the spin orientations of polarons which the exciton derives from, it is expected that the manipulation of polaron spin orientation may open a way to tune the relative population of singlet/triplet excitons and consequently enhance the electroluminescence efficiency. The spin orientation of a polaron is mainly determined by (i) the magnetism of the electrode from which spin polarized electrons (or holes) are provided and (ii) spin-conserving transport in the polymer spacer. On one hand, since spin injection into  $\pi$ -conjugated polymers has been recently achieved [8,9], it is possible to employ ferromagnetic materials instead of conventional electrodes in a PLED to achieve spin controlled charge injection [10]. On the other hand, electron spin diffusion length is expected long in conjugated polymers due to the weak spin-orbital coupling and hyperfine interaction [11], which provides possible long-range spin-conserving transport and spin-conserving recombination [12]. Therefore, the spin-PLED structure with ferromagnetic electrodes can be used to control the spin orientation of polarons, improve the yield of singlet excitons, and consequently enhance the electroluminescent efficiency.

Since the basic process of photoemission in PLEDs is the formation of excitons, the dynamic intrachain collision process of oppositely charged polarons has been studied under different strength of an external electric field [13]. Especially, the intrachain spin-dependent formation of excitons in PLEDs and factors affecting the formation in PLEDs have been studied from the energy point of view [7,14]. However, much less is known about the yields of excitons in a spin PLEDs. In this paper, we will consider the formation of singlet and triplet excitons from two spin polarons in a conjugated polymer chain, where the angle between the spin orientations of the polarons is focused. By simulating the collision of the polarons using a dynamic evolution method and analyzing the product after collision, we try to find the yields of singlet and triplet excitons. The model and method are described in the following section. Results and discussion are shown in Section 3. Finally a conclusion is given in the last section.

## 2. Model and formula

Our simulations begin with two oppositely charged polarons which already form at a polymer chain, as shown in Fig. 1. Under an external electric field, two polarons will

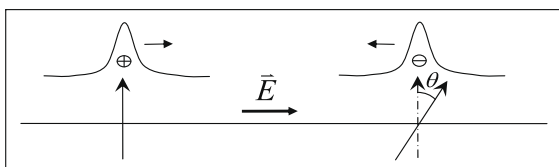


Fig. 1. The scheme of two oppositely charged polarons with spin angle  $\theta$ .

move towards each other along the chain and then a collision will take place.

We describe the system by an extended Su–Schrieffer–Heeger (SSH) + Hubbard model, and the external electric field is also involved

$$H = H_{SSH} + H_{Hub} + H_{ext}, \quad (1)$$

where the extended SSH model is [15,16]

$$H_{SSH} = - \sum_{n,s} [t_0 - \alpha(u_{n+1} - u_n) - (-1)^n t_e] (C_{n+1,s}^\dagger C_{n,s} + h.c.) + \frac{K}{2} \sum_n (u_{n+1} - u_n)^2 + \frac{M}{2} \sum_n \dot{u}_n^2. \quad (2)$$

Here  $t_0$  denotes the zero-displacement hopping integral between the  $n$ th and  $(n+1)$ th atoms,  $\alpha$  the electron–lattice coupling constant,  $u_n$  the displacement of the  $n$ th site from its equidistant position and  $t_e$  the Brazovskii–Kirova symmetry breaking term for a non-degenerate polymer [16].  $C_{n,s}^\dagger (C_{n,s})$  denotes electron creation (annihilation) operator at site  $n$  with spin  $s$ .  $K$  is the elastic constant and  $M$  the mass of a CH group.

The Hubbard model [17]

$$H_{Hub} = U \sum_n C_{n,\uparrow}^\dagger C_{n,\uparrow} C_{n,\downarrow}^\dagger C_{n,\downarrow} \quad (3)$$

is used to describe the electron–electron (e–e) interactions and is treated in a simple mean-field approximation.  $U$  is the on-site repulsion between electrons with spin-up and spin-down.

An external electric field is applied to drive the charged polarons,

$$H_{ext} = - \sum_{n,s} |e|E(na + u_n) (C_{n,s}^\dagger C_{n,s} - 0.5), \quad (4)$$

where  $E$  is the applied electric field.  $e$  and  $a$  are the electronic charge unit and the lattice constant, respectively.

The wavefunction of an electronic state consists of both spin-up and spin-down components:

$$|\Psi_\mu(t)\rangle = \sum_n \begin{pmatrix} \psi_{\mu,\uparrow}(n,t) \\ \psi_{\mu,\downarrow}(n,t) \end{pmatrix} |n\rangle. \quad (5)$$

The spin orientation of the electronic state is given in probability by  $\cos \theta_\mu = \frac{\sum_n |\psi_{\mu,\uparrow}(n,t)|^2 - \sum_n |\psi_{\mu,\downarrow}(n,t)|^2}{\sum_n (|\psi_{\mu,\uparrow}(n,t)|^2 + |\psi_{\mu,\downarrow}(n,t)|^2)}$ .  $\theta_\mu = 0^\circ$  and  $\theta_\mu = 180^\circ$  denote that the electron is in a spin-up and spin-down state, respectively.

The simulation starts from the state that the hole and the electron have been injected to the polymer. A positive and negative polarons have formed at the left and right sides, respectively. In the calculations, we assume that the spin orientation of the left positive polaron is along  $+\vec{z}$  direction, which is denoted as spin-up. And the spin orientation of the right negative polaron is described by spin angle  $\theta$ , which is the magnetization angle of the electrodes. Since the two polarons are separated far enough, they are independent of each other. The initial lattice configuration of the system without e–e interactions is a combination of two isolated polaron lattice configurations without e–e interactions, while the initial lattice configuration of the system with e–e interactions is a combination of two isolated polaron lattice configurations with e–e interactions

of the same strength. The initial wavefunctions are given by linear combinations of the wavefunctions obtained from the initial lattice configuration. The aim of linear combinations is to make sure that the two polarons are isolated. The spin orientation of a polaron is same with that of its unpaired electronic state. Therefore for the left positive and right negative polarons, the spin angles of their unpaired electronic states are set by linear combinations to be  $\theta_{\text{positive}} = 0$  and  $\theta_{\text{negative}} = \theta$ , respectively, to ensure the spin orientation of the corresponding polaron.

It should be mentioned that the spin orientation of the polaron is supposed to be determined by the wavefunction. Therefore, in the present calculations the dynamic evolution of spin polaron is given by the evolutions of its electronic states, the spin-up and spin-down parts of which are established respectively. The evolution of the electronic state is obtained by solving the time-dependent Schrödinger equation,

$$\begin{aligned} i\hbar\dot{\psi}_{\mu,s}(n,t) &= [U\rho_{n,n}^{-s}(t) - |e|E(na + u_n)]\psi_{\mu,s}(n,t) \\ &\quad - [t_0 - \alpha(u_{n+1} - u_n) - (-1)^n t_e]\psi_{\mu,s}(n+1,t) \\ &\quad - [t_0 - \alpha(u_n - u_{n-1}) - (-1)^n t_e]\psi_{\mu,s}(n-1,t). \end{aligned} \quad (6)$$

Due to the strong electron–lattice coupling in polymer, the lattice  $\{u_n\}$  will distort with the evolution of electronic state, which is determined classically by Newton equation

$$\begin{aligned} M\ddot{u}_n(t) &= K[u_{n+1}(t) + u_{n-1}(t) - 2u_n(t)] + 2\alpha[\rho_{n,n+1}^c(t) \\ &\quad - \rho_{n-1,n}^c(t)] - |e|E(t)[\rho_{n,n}^c(t) - 1]. \end{aligned} \quad (7)$$

The charge density matrix  $\rho_{n,n'}^c$  is given by

$$\begin{aligned} \rho_{n,n'}^c(t) &= \rho_{n,n'}^{\uparrow}(t) + \rho_{n,n'}^{\downarrow}(t), \\ \rho_{n,n'}^s(t) &= \sum_{\mu} \psi_{\mu,s}^*(n,t) f_{\mu} \psi_{\mu,s}(n',t). \end{aligned} \quad (8)$$

$f_{\mu}$  denotes the time-independent distribution function of electronic state  $|\Psi_{\mu}(t)\rangle$  determined by the initial occupations. The coupled differential Eqs. (6) and (7) can be solved numerically with a Runge-Kutta method of order eight with step-size control [18], which has been proved to be an effective approach to study the electronic state evolution [19,20].

The state  $|\Psi(t)\rangle$  of the whole electronic system at time  $t$  is obtained through a Slater determinant of the occupied single-electron evolutionary wavefunction  $|\Psi_{\mu}(t)\rangle$ . If we consider a collision of a pair of polarons, the product after collision usually is a mixed state, which may contain excitons and polarons. To recognize the final state, we introduce the instantaneous eigenstate  $|\Phi^K(t)\rangle$  of a system, where  $K$  denotes the state index or one kind of product after collision in the present case.  $|\Phi^K(t)\rangle$  is constructed by the instantaneous single-electron eigen wavefunctions

$$|\Phi_V(t)\rangle = \sum_n \begin{pmatrix} \phi_{v,\uparrow}(n,t) \\ \phi_{v,\downarrow}(n,t) \end{pmatrix} |n\rangle \quad (10)$$

with the occupation presenting a certain product. The component  $\phi_{v,s}$  is determined by the instantaneous eigenvalue equation

$$\begin{aligned} \varepsilon_v(t)\phi_{v,s}(n,t) &= [U\rho_{n,n}^{-s}(t) - |e|E(na + u_n)]\phi_{v,s}(n,t) \\ &\quad - [t_0 - \alpha(u_{n+1} - u_n) - (-1)^n t_e]\phi_{v,s}(n+1,t) \\ &\quad - [t_0 - \alpha(u_n - u_{n-1}) - (-1)^n t_e]\phi_{v,s}(n-1,t), \end{aligned} \quad (11)$$

where  $\varepsilon_v(t)$  is the instantaneous eigen energy level.

Yield  $I_K(t)$  of state  $|\Phi^K(t)\rangle$  in final state  $|\Psi(t)\rangle$  is given by

$$I_K(t) = |\langle\Phi^K(t)|\Psi(t)\rangle|^2 \quad (12)$$

The parameters for the polymer are those referring to *cis*-polyacetylene [21],  $t_0 = 2.5$  eV,  $\alpha = 4.1$  eV/Å,  $t_e = 0.05$  eV,  $K = 21$  eV/Å<sup>2</sup>,  $a = 1.22$  Å,  $M = 1349.14$  eV fs<sup>2</sup>/Å<sup>2</sup>. The electric field applied to the polymer is set to be  $E_0 = 5 \times 10^{-4}$  V/Å.

### 3. Results and discussion

It has been known that the collision of two oppositely charged polarons may form exciton states. There are two types of interactions that may lead to the formation of a bound excitons in organic polymer. One is the direct Coulomb attractions between two oppositely charged polarons. The other is the electron–lattice interactions. A positive and a negative polarons are confined in the same lattice defect to form a self-trapping state, which is unique in organic molecules. Let us firstly consider the situation that the e–e interactions are neglected, in which case the formation of exciton is due to the interactions between electrons and lattice. From Eqs. (6) and (7), we know that, in this approximation, spin will be a good quantum number. Therefore, evolutions of the charge distribution and the lattice configuration are independent of the spin angle  $\theta$ . Evolutions of net charge  $\rho_n(t) \equiv \rho_{n,n}^c(t) - 1$  and order parameter  $y_n(t) = (-1)^n [2u_n(t) - u_{n+1}(t) - u_{n-1}(t)]/4$  are depicted in Fig. 2, respectively. Before collision, the two polarons move towards each other along the chain and keep their shapes unchanged. After collision, from the charge distribution, it seems that there are two separate wave-packets. However, the net charge quantity included in each wave-packet becomes less, which means that the polarons may exchange some charges after collision. From the lattice configuration, there are some lattice oscillations left after collision. Such oscillations are some new phonon modes created in the collision process [22,13], which is not concerned in the present work. Except for these lattice oscillations, the lattice distortions induced by the residual charges keep moving under the driving field. Since the charge quantity included in the two wave-packets is same but the opposite sign, the total charge of the system is conserved during the collision. Therefore, we can just treat of the charge quantity included only one wave-packet when the charge property is talked about. It should be mentioned that in the present work there are no spin-flip interactions involved, so that the total spin of system is also conserved during the collision.

It has been known that the products of collision contain singlet and triplet excitons as well as positive and negative polarons. The spin of an exciton is related to the spin orientations of the two polarons or spin angle  $\theta$  between them. We use Eq. (12) with different electronic occupation to give

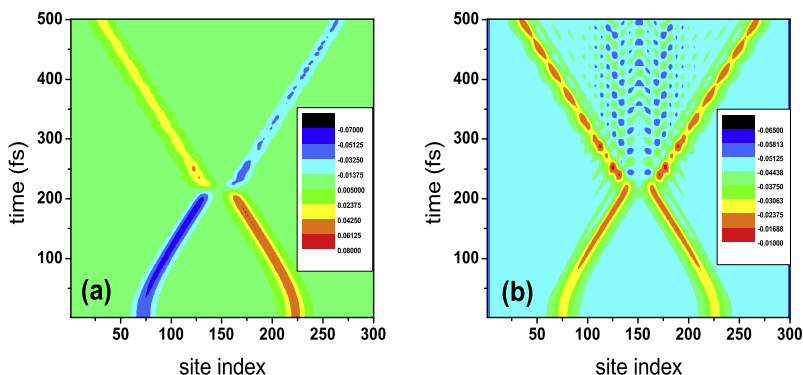


**Fig. 2.** Evolution of (a) net charge distributions  $\rho_n(t)$  and (b) staggered bound parameter  $y_n(t)$ . In (a), the blue and cyan areas represent the positive net charge, and the red and yellow ones denote negative charge distributions. In (b), the red and yellow areas indicate the center of localized wave-packets. (For interpretation of the references to colour in this figure legend, the reader is referred to the web version of this article.)

the yield of each kind of products. The yield of singlet excitons is obtained from a singlet exciton occupation on the instantaneous eigen level  $\varepsilon_v(t)$ ; similar approaches are applied to the triplet excitons and polaron pairs. The results are shown in Fig. 3. With the present parameters, the total yield of excitons is only about 33.50%, which indicates that it is not a complete annihilation. Since the e–e interactions are not included, the total yield of excitons is independent of the spin angle  $\cos\theta$ . For a collision with parallel spins ( $\theta = 0^\circ$ ) of polarons, no singlet exciton is produced, and consequently all the excitons are triplet. By increasing the spin angle  $\theta$ , some singlet excitons are produced and at the same time the yield of triplet excitons is decreased. For a collision of spin antiparallel polarons ( $\theta = 180^\circ$ ), the yield of singlet excitons reaches the maximum. In such case the yields of singlet and triplet excitons are the same, and each is about 16.75%. It is found that the yields of singlet and triplet are directly proportional to  $\cos\theta$  (insets in Fig. 3). Therefore the yield of singlet excitons can be controlled by the spin manipulation of injected polarons and consequently electroluminescent efficiency can be improved.

However, when the e–e interactions are involved, the total yield of excitons will change with spin angle  $\theta$ . Taking

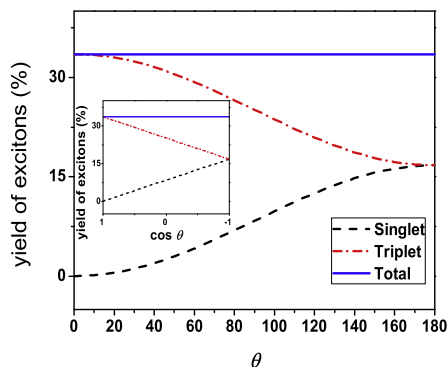


**Fig. 3.** The yield of singlet excitons, triplet excitons, and total excitons as a function of the angle  $\theta$  (or  $\cos(\theta)$  in inset) in the absence of e–e interactions.

$U = 0.3$  eV as an example, a maximum yield of about 38.09% is obtained in the case of spin-parallel polaron collision ( $\theta = 0^\circ$ ). With the increasing of the angle, it is found that the yield will decrease and reach the minimum, about 22.72%, around  $\theta = 100^\circ$ . By further increasing the angle  $\theta$ , the yield increases again and reaches about 33.50% for a spin-antiparallel collision (Fig. 4a). Therefore, the e–e interactions will adjust the yield of excitons with different spin angles of the polarons.

Then let us analyze the yield of singlet excitons included in each collision. For a spin-parallel collision, there is no singlet excitons created and the yield of singlet excitons is zero, which is independent of the e–e interactions. For a spin-antiparallel collision, the yield of singlet and the triplet excitons are equal, which is independent of the e–e interactions either. For the other cases, as showed in Fig. 4b, it is found that the yield of singlet excitons is depressed by e–e interactions. For example, for a collision of polarons with angle  $\theta = 100^\circ$ , the yield of singlet excitons decreases from 9.83% at  $U = 0$  eV to 6.14% at  $U = 0.3$  eV. As a mean-field treatment is applied in the present work, we only investigate the situation of weak e–e interactions and it is found that the stronger e–e interactions are, the more significant depression is induced on the singlet exciton formation.

In the presence of e–e interactions, the spin angular dependence of the yield of excitons can be reflected by the order of energy levels. At the beginning, two polarons are far from each other. Considering the spin freedom of electrons, each polaron has four isolated levels in the energy gap. For the positive polaron with up spin, apparently only spin-up one of two lower isolated energy levels is occupied. Consequently, the spin-up and spin-down charge distributions of the whole system are different. The on-site repulsion between spin-up and spin-down electrons represented by the Hubbard e–e interactions breaks the spin degeneracy of energy levels. Therefore, the empty spin-down one of the two lower isolated energy levels is a little higher than the spin-up one. For the two empty higher isolated energy levels, the spin-down one is also a little higher than the spin-up one. However, for the negative polaron with arbitrary  $\theta$ , the order of the two higher isolated energy levels is determined by their occupation probabilities.

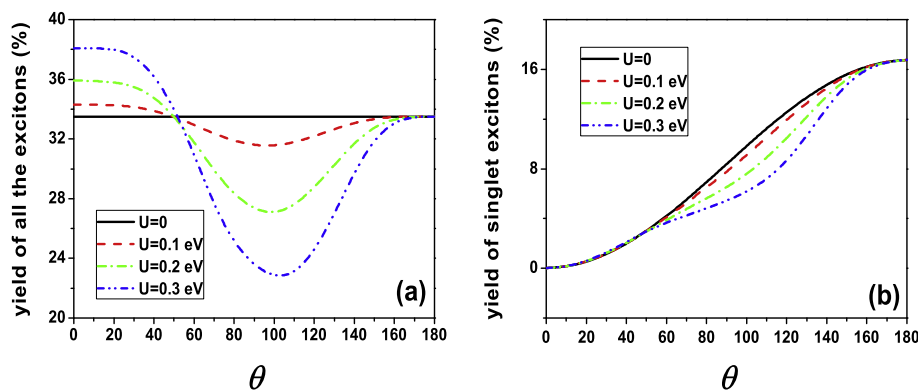


Fig. 4. The yield of (a) total excitons and (b) singlet excitons as a function of the angle  $\theta$  without or with e–e interactions.

The occupation probability on the spin-up (spin-down) one of higher isolated energy levels is  $\cos^2(\theta/2)[\sin^2(\theta/2)]$ . Due to the on-site repulsion between spin-up and spin-down electrons, the energy level with more charge occupation probability is lower than the other one. Therefore, the order of the energy levels is indirectly determined by the spin orientation of the negative polaron. In addition, the order of two occupied lower isolated energy levels is identical to the order of higher isolated energy levels. Since there is no spin-flip interaction in the present model, the spin during charge transfer is conserved. Then the charge transfer probability during the collision is determined by the order of energy levels. Therefore, the charge transfer probability during the collision is also indirectly determined by the spin orientations of the polarons or the spin angle between the polarons. Moreover, the order of the energy levels after collision is determined by the charge transfer probability during the collision. Therefore, the amount of the residual charges localized in each generated wave-packet is affected by the e–e interactions (Fig. 5). For example, the amount of residual charges is 0.546e when the e–e interactions are neglected. But when the e–e interactions are included, it is found that the amount is a non-monotonous function of the spin angle  $\theta$ . For a spin-parallel collision, the amount of residual charges will be 0.467e at  $U = 0.3$  eV. By increasing the spin angle  $\theta$ , the amount of

residual charges is increased. The maximum of the residual charges is 0.702e, which appears at about  $\theta = 100^\circ$ . However, for a spin-antiparallel collision the amount is identical to the case without e–e interactions. As an exciton is neutral, less residual charges correspond to a higher yield of excitons. As a result, the dependence of singlet exciton formation rate on spin angle is also strongly affected by e–e interactions.

#### 4. Conclusion

In this paper, we studied the dependence of exciton formation rate on the spin orientation of polarons by simulating the collision process of two polarons. It was found that neglecting e–e interactions, the yield of total excitons is independent of  $\theta$ , while the yield of singlet and triplet exciton presents a linear variation with  $\cos \theta$ , where  $\theta$  is the angle between the spin orientations of polarons. However, the on-site e–e interactions will break the spin degeneracy of energy levels. Although, the yield of singlet excitons from spin-parallel or spin-antiparallel polaron is not influenced by the e–e interactions, the presence of e–e interactions shows a depression on the yield of singlet exciton in the other cases. In the manufacture of spin PLEDs to improve the luminescent efficiency, the e–e interactions should be unfavorable factors.

#### Acknowledgments

This work was supported by the National Basic Research Program of China (Grant Nos. 2009CB929204 and 2010CB923402) and the National Natural Science Foundation of the People's Republic of China (Grant No. 10874100). The Author J. Lei would like to thank Y. Li, W. Liu, and Z. Qu for useful discussion.

#### References

- [1] J.H. Burroughes, D.D.C. Bradley, A.R. Brown, R.N. Marks, K. Mackay, R.H. Friend, P.L. Burn, A.B. Holmes, *Nature* 347 (1990) 539.
- [2] R.H. Friend, R.W. Gymer, A.B. Holmes, J.H. Burroughes, R.N. Marks, C. Taliani, D.D.C. Bradley, D.A.D. Santos, J.L. Brédas, M. Löglund, W.R. Salaneck, *Nature* 397 (1999) 121.
- [3] A. Köhler, J.S. Wilson, R.H. Friend, *Adv. Mater.* 14 (2002) 701.

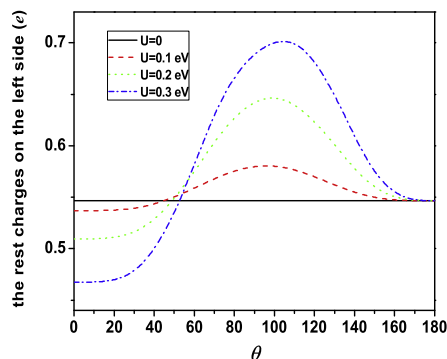


Fig. 5. Dependence of the residual charges on the spin angle between two polarons after collision.



- [4] M. Wohlgenannt, Z.V. Vardeny, *J. Phys.: Condens. Matter* 15 (2003) R83.
- [5] Y. Cao, I. Parker, G. Yu, C. Zhang, A. Heeger, *Nature* 397 (1999) 414.
- [6] A. Burin, M. Ratner, *J. Chem. Phys.* 109 (1998) 6092.
- [7] M.N. Kobrak, E.R. Bittner, *Phys. Rev. B* 62 (2000) 11473.
- [8] V. Dediu, M. Murgia, F.C. Matocotta, C. Taliani, S. Barbanera, *Solid State Commun.* 122 (2002) 181.
- [9] S. Majumdar, R. Laiho, P. Laukkanen, I.J. Vayrynen, H.S. Majumdar, R. Sterbacka, *Appl. Phys. Lett.* 89 (2006) 122114.
- [10] A. Hayer, A. Kohler, E. Arisi, I. Bergenti, A. Dediu, C. Taliani, M. Al-Suti, M.S. Kahn, *Synth. Met.* 147 (2004) 155.
- [11] V.I. Krinichnyi, *Synth. Met.* 108 (2000) 173.
- [12] M. Reufer, M.J. Walter, P.G. Lagoundakis, A.B. Hummel, J.S. Kolb, H.G. Roskos, U. Scherf, J.M. Lupton, *Nature Mater.* 4 (2005) 340.
- [13] Z. An, B. Di, H. Zhao, C.Q. Wu, *Eur. Phys. J. B* 63 (2008) 71.
- [14] S. Karabunarliev, E.R. Bittner, *Phys. Rev. Lett.* 90 (2003) 057402.
- [15] W.P. Su, J.R. Schrieffer, A.J. Heeger, *Phys. Rev. Lett.* 42 (1979) 1698.
- [16] S.A. Brazovskii, N.N. Kirova, *JETP Lett.* 33 (1981) 4.
- [17] J. Hubbard, *Proc. R. Soc. London, Ser. A* 276 (1963) 238.
- [18] R.W. Brankin, I. Gladwell, L.F. Shampine, RKSUITE: Software for ODE IVPS, <<http://www.netlib.org>>.
- [19] Y. Ono, A. Terai, *J. Phys. Soc. Jpn.* 59 (1990) 2893.
- [20] A. Johansson, S. Stafström, *Phys. Rev. Lett.* 86 (2001) 3602.
- [21] A.J. Heeger, S. Kivelson, J.R. Schrieffer, W.P. Su, *Rev. Mod. Phys.* 60 (1988) 781.
- [22] M. Kuwabara, Y. Ono, A. Terai, *J. Phys. Soc. Jpn.* 60 (1991) 1286.

printing, combines robustness, speed and proven roll-to-roll compatibility with a good accuracy [3]. Another advantage compared to gravure-off set and flexographic printing is the absence of a rubber transfer plate, which lacks sufficient resilience against the organic solvents typically used for LEP inks (e.g. toluene, anisole, xylene, etc.) to allow for a robust and stable printing process. Furthermore, gravure printing does not suffer from plate or screen wear, typically observed for off-set lithography and screen printing. Roll-to-roll inkjet printing is generally believed to be insufficiently fast and robust, despite advantages relating to non-contact fluid transfer and digital free-form flexibility.

To avoid time consuming trial-and-error experimentation, it is desirable to model the printing process in order to be able to predict optimal process conditions for printed layer formation. Since gravure printing is a complex process involving many non-linearly interrelated parameters, statistical modeling, despite its 'black-box' nature, is often preferred over physical modeling. Artificial neural networks (ANN) have proven to be useful predictive statistical models for a wide range of applications [4]. ANNs are capable of modeling any linear or non-linear relationship between sets of input and output parameters. ANNs applied in manufacturing technology are often based on a supervised learning protocol during which the network is repetitively exposed to input data with a known (e.g. measured) response. During this process a cost function is minimized by adapting the network's coefficients. Once properly trained, the network is capable of calculating the correct response to new values and combinations of the input parameters, not previously included in the training data set. In the field of the graphic arts, artificial neural networks have shown to be viable tools in process control and development. Well-known examples are color processing and proofing [5], inkjet printing [6], and off-set lithography [7]. Also in fields related to graphical printing, such as solder paste printing for printed circuit boards, the use of neural networks for process optimization has been reported [8]. Ding et al. [9] recently reported on the use of a fuzzy neural network to establish the link between process parameters and gravure printed dot features.

The gravure printing process has to some extent also been modeled physically. One should discriminate here between forward gravure printing [10–12] (image transfer, as is the case for this work), whereby the web and the gravure roll move in the same direction, and reverse gravure [13], which is essentially a coating technique, as gravure roll and web move in opposite directions. The forward gravure printing models, though elegant, generally oversimplify the real life situation as they only describe single cell withdrawal events in two dimensions. These models could, for instance, be used to predict the ratio of transferred to contained ink as a function of the separation velocity between gravure roll and substrate. However, their limited geometrical scope renders them unsuitable for the actual prediction of printed layer thickness and homogeneity in large area applications. The overall process is yet too complex to be modeled reliably in a physical manner using state of the art computing facilities.

In this paper, we show for the first time the application of ANN modeling in printed organic electronics. The net-

work models the characteristics of forward, direct roto-gravure printed layers of LEP on a non-porous, conductive poly-(ethylenedioxythiophene)/poly(styrene sulfonate)-covered poly(ethylene terephthalate) substrate (PET-PEDOT/PSS). The network is set-up and trained to predict the relation between three input parameters: (i) gravure cell engraving depth, (ii) printing speed, and (iii) LEP concentration, and three output parameters: (i) mean printed layer thickness, (ii) relative root mean square (RMS) roughness, and (iii) printed layer anisotropy. We clarify the selection of these parameters and show how fairly accurate predictions can be made once the network has been properly trained. We give a quantitative definition of printed layer anisotropy, since we believe that root mean square deviation by itself insufficiently describes printed layer homogeneity, especially for printed OLED lighting applications. Finally, we show how the trained network can be used to map the input parameter space for each output parameter in order to find optimum values and to gain qualitative insight in the behavior of the ink during the printing process.

## 2. Materials and methods

The LEP gravure printing inks were based on an in-house developed light-emitting polymer. This LEP had a weight-averaged molecular weight of 628 kDa and a polydispersity index of 2.1. The sample solutions were prepared by dissolving the LEP in a 30/70 (w/w) mixture of toluene and anisole under nitrogen (Table 2 lists the used LEP concentrations). In order to increase the optical absorptivity of the printed layers in the visible wavelength range we added Oil Blue N as a low molecular weight dye to the formulations. What's more, the addition of the dye fully quenched the polymer's fluorescence, thus ruling out possible disturbing optical factors stemming from the polymer's intrinsic emissive properties. The amount of dye (by weight) was kept twice as low as the polymer quantity. Owing to its low molecular weight and concentration, the dye was assumed to not influence the rheological properties of the inks.

Prints were made using an IGT Testing Systems F1 lab-scale printability tester running in direct forward gravure mode. Commercial Orgacon EL-350 PEDOT/PSS-coated PET foil (Agfa-Gevaert) with a total thickness of 125  $\mu\text{m}$  was used as substrate. The PEDOT/PSS layer has been applied by slot coating, which gives very homogenous layers with low amplitude undulations (typically a few %) extending over several tens of centimeters. The Orgacon foil was mounted onto the backing roller of the gravure printer and cleaned by gentle wiping with a non-scratching cloth containing 2-propanol. For making a print, typically about 0.5 mL LEP/dye ink was applied onto the gravure roll in the nip between the doctor blade and the roller, after which the ink was printed in one pass at a given speed setting and a constant gravure roll-to-substrate force setting of 250 N. The gravure roll used in this study contained patterned areas of square pyramidal cells, stylus engraved (120° stylus angle) under a screen angle of 53° at a density of 70 lines/cm. The total engraved pattern contained ten patches,

each having a surface area of about 6 cm<sup>2</sup>. Each patch corresponds to a different cell engraving depth in the range 11–48 μm, roughly corresponding to an ink containment volume of 0.2–12 mL/m<sup>2</sup>. The printed layers were left to dry under ambient conditions in a matter of seconds.

The printed LEP/dye layers were characterized using a microdensitometer (Joyce-Loebl MDM-6), fitted with a Philips halogen lamp, type 7012 (12 V, 50 W). The microdensitometer measured and recorded the integrated optical density of a sample layer as a function of X, Y-coordinate, on a scale with a cut-off value of 4096. The printed layers were scanned at a lateral resolution of 20 μm using a wavelength range of 300 < λ < 800 nm. The total measured optical density of the printed layers (i.e., the summed values for the LEP, the dye, and the PET-PEDOT/PSS substrate), was typically in the range 1800–2100, considerably below the cut-off threshold. The crude optical density data was corrected for the optical density of the 125 μm thick PET-PEDOT/PSS substrate, as recorded at the site of each printed patch. Correction occurred by subtraction of the substrate's optical density from the total measured value. The thus corrected optical density of the printed LEP/dye layers was in the range 50–200. The scanning software was adapted as to scan exclusively within the printed patches corresponding to the various cell engraving depth levels. The edges of the prints were not included in the scans to avoid artifacts related to incomplete engraving, often observed at the edges of engraved patterns on gravure rolls. When printing an OLED, one would make sure that such edge artifacts would fall outside the active (emissive) area of the device. The scanning data was filtered, normalized, and processed using MATLAB R2008a.

In order to convert the measured optical density values into actual printed layer thickness information, we recorded the optical density of reference LEP/dye layers of known thickness, spin-coated from toluene solution on glass slides. This solution contained 10 mg/mL of LEP and 5 mg/mL Oil Blue N, giving the same LEP-to-dye ratio as used for the gravure printing inks involved in the neural network study. The measured values were corrected by subtracting the optical density of the glass substrate. The absolute thickness of the reference samples was determined using a Veeco DekTAC M6 stylus profilometer.

Neural network analyses were performed using a home-built algorithm in C++. The ANN used in this study (Fig. 1) was a double layer Perceptron (MLP) neural net, using feed forward of input data and back propagation of error information [4]. The output of the hidden (V) and output units (Y) was calculated using logistic sigmoidal and linear transfer functions (Eqs. (1) and (2), respectively).

$$f(x) = \frac{a - b}{1 + \exp(-sx)} + a \quad (1)$$

$$f(x) = sx. \quad (2)$$

Here,  $x$  and  $f(x)$ , respectively, represent the neuron's input and output;  $a$  and  $b$  are the lower and upper asymptotic values of the logistic sigmoid, and  $s$  is the steepness. During training the synaptic weights ( $w_{ij}$  and  $z_{jk}$ ) and bias values ( $b$ ) were optimized in an iterative procedure, minimizing the cost function expressed by Eq. (3).

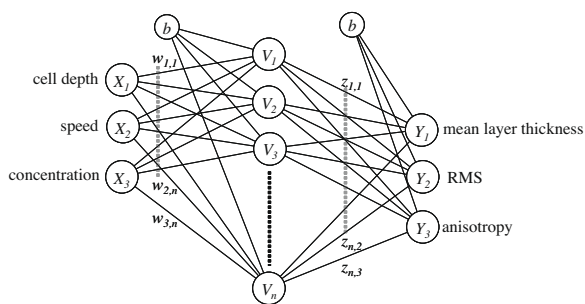


**Fig. 1.** Neural network architecture used in this study; input, hidden, and output units are denoted X, V, and Y, respectively; synaptic weights are denoted  $w_{ij}$  and  $z_{jk}$  for the first and second layer, respectively; the bias units are denoted  $b$ .

$$E = \sum_i (t_i - y_i)^2. \quad (3)$$

Here,  $t_i$  and  $y_i$  represent the target (measured) response and calculated output corresponding to a certain set of input parameters (input vector). Usually, a neural net is not allowed to reach maximum convergence to avoid over-fitting, as an over-fitted network will be better at memorizing its training data set than predicting output to new input data. To avoid over-fitting a separate testing data set was used to check the network's predictive capability during training. Prior to training all input data was normalized in a bipolar fashion:  $-1 \leq n \leq 1$ . This allowed faster training and ensured the error information terms calculated for the output parameters to be of comparable magnitude. Relating to this, we chose the asymptotic values of the sigmoid activation function of the hidden units (Eq. (1)) to be  $a = -1.2$  and  $b = 1.2$ , slightly extending beyond the largest and smallest target values [4]. For presentation the calculated data was denormalized. The steepness of both activation functions ( $s$  in Eqs. (1) and (2)) was set to 0.5.

### 3. Results and discussion

We start with defining the ANN's input and output parameters. The input parameters are settings relating to the printing process (printing parameters), whereas the output parameters are quantifiable characteristics of the printed LEP/dye layers. The printing parameters may be categorized as gravure roll-, process-, ink-, or substrate-related. Table 1 lists the most important parameters in this categorized fashion. Naturally, these parameters do not all influence the printed layer characteristics equally strongly. We selected (i) cell engraving depth ( $d$ ), (ii) printing speed ( $v$ ), and (iii) LEP concentration ( $c$ ) as a limited, but highly relevant set of input parameters for the neural network model. These input parameters represent three of the four categories defined above. Their selection is partly based on prior experience with LEP printing. We also note that several of the parameters defined in Table 1 can be expressed as functions of the selected parameters. For example, rheological parameters such as zero shear viscosity and fluid elasticity, are strongly related to the solute

**Table 1**

Summary of the gravure printing parameter space.

Gravure roll	Process	Ink	Substrate
Cell engraving depth	Pressure/force	Viscosity	Material
Cell shape	Printing speed	Elasticity	Surface energy
Screen angle		Surface tension	Roughness
Stylus angle		Volatility	Pre-treatment
Surface energy		Solvent composition	Cleaning method
Radius		Polymer concentration	
		Molecular weight	

concentration. Other parameters, such as surface tension and evaporation rate, are not included in the model, as we used the same solvent system throughout the study. In this context, we assumed the polymer (and dye) concentration not to have an appreciable effect on the surface tension and evaporation, especially in the early stages of drying during which solute transport is most likely to occur. Naturally, if one would want the neural network to also predict the solvent characteristics, a more extended model is necessary. By using the same gravure roll which is cleaned the same way prior to printing, we did not vary the parameters in the gravure roll category, except for cell engraving depth. We found a gravure roll force exceeding 150 N to be of little influence on the thickness and appearance (homogeneity) of the prints. Forces below this value did not allow full (web wide) transfer of the ink. From the substrate category no parameters were selected. The reason for this is the limited number of available possibilities to vary the nature of the rather delicate PEDOT/PSS layer. We settled down on the mild cleaning method described in the Experimental Section as a suitable non-destructive pre-treatment that still allows proper wetting of the LEP ink.

Three output parameters were defined (see Fig. 1): (i) mean printed layer thickness, (ii) roughness, and (iii) 'stripiness' or anisotropy. In order to obtain reasonable estimates of the mean printed layer thickness, optical density scans produced by the microdensitometer were converted into actual thickness matrices using the calibration curve depicted in Fig. 2. This line was constructed by recording the optical density of spin-coated LEP/Oil Blue N layers (same ratio as for the gravure printing inks) on glass substrates (the inset illustratively showing the absorption spectrum of the LEP/Oil Blue N blend). The layers were coated at different spinning velocities, giving a range of thicknesses. The absolute thickness of these reference layers was determined using profilometry. These values were then plotted as a function of the measured optical density. As the graph shows, the data suggest a linear relationship between thickness and optical density, at least within the window of the measurement. Despite this (partial) linearity, the curve does not seem to obey the Beer–Lambert law, as the suggested straight line does not pass through the origin of the graph. In stead, it would abscise the horizontal axis at an optical density of about 45. However, physically, the origin itself should lie on the curve, as a zero optical density is recorded when no material is present at all. Unfortunately, it proved difficult to obtain homogeneous layers with a thickness in the range 0–75 nm. We

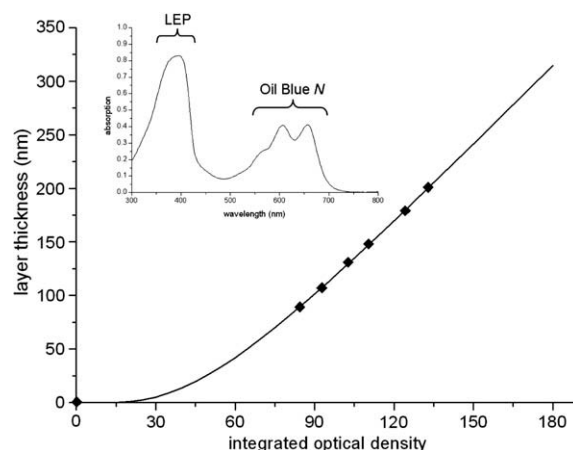


**Fig. 2.** Layer thickness as a function of integrated optical density for spin-coated reference layers of the 2:1 LEP/Oil Blue N mixture on glass slides. The line is a fit to the measured values, including the origin as an extra data point. The curve has been extrapolated into the upper range of the optical density values measured by the microdensitometer on the gravure printed layers. For illustration: the inset depicts the absorption spectrum of the LEP/dye mixture in the range  $300 < \lambda < 800$  nm.

therefore included the origin as one extra data point and, as an approximation, fitted a calibration curve using a continuous, fully differentiable mathematical function capable of passing through the origin as well as describing the linear behavior observed for higher optical densities, as suggested by the measurement. The mean printed layer thickness was obtained simply by calculating the average value of the thickness matrix. The (relative root-mean-square) roughness of the printed layers was defined as the standard deviation from the mean taken as a fraction (or percentage) from the mean value. Below we will mostly use the term 'roughness' to denote the relative RMS roughness.

The third output parameter, the printed layer anisotropy, requires a little more clarification. In general, printed layer irregularities may occur during three stages of the gravure printing process: (i) ink transfer (e.g. due to fluid film or ligament instabilities), (ii) leveling on the substrate (e.g. due to incomplete merging or leveling of deposited fluid dots from separate engraved cells), and (iii) drying (surface tension-driven flow of solute during solvent evaporation). The latter cause was assumed to be strongly suppressed by the relatively high viscosity of the LEP inks (around 30 mPa s at  $t = 0$ , as determined by separate measurements), as well as the rapid viscosity increase due to

the high volatility of the solvent mixture. This assumption was supported by the fact that the printed LEP layers did not show signs of the well-known ‘coffee stain effect’ [14] or other drying patterns that can be attributed to surface tension-induced solute transport [15]. For this, we suggest that the irregularities encountered in the gravure printed LEP layers predominantly originated from instabilities during fluid transfer or incomplete merging and leveling, or a combination of both. The appearance of the print depends on which of the two causes prevails. Fig. 3 depicts photographs of four exemplary gravure printed layers fabricated with the same LEP ink, printed at different cell engraving depths. Although this ink was based on a different LEP (a poly(*p*-phenylenevinylene) derivative) than the one used in the neural network study, the printed layer appearance as a function of gravure roll engraving depth is qualitatively similar. At a low engraving depth (22–30  $\mu\text{m}$ ) the amount of ink transferred to the substrate is

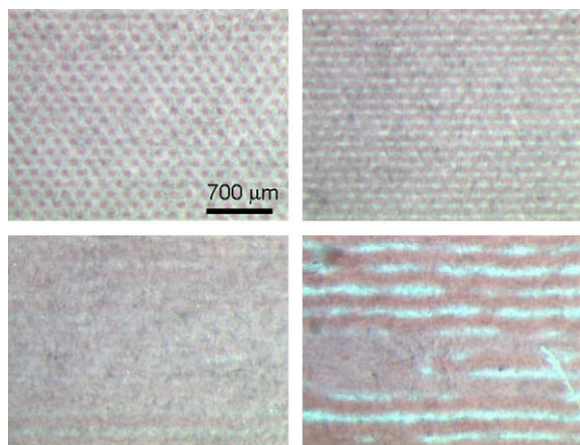


**Fig. 3.** Light emitting polymer gravure printed ( $v = 0.9$  m/s,  $c = 10$  mg/mL) onto PET-ITO foil at different cell engraving depths (stylus angle  $120^\circ$ , screen angle  $53^\circ$ , 70 lines/cm): 22  $\mu\text{m}$  (top left: separate dots of ink corresponding to engraved cells), 30  $\mu\text{m}$  (top right: dots start to merge), 34  $\mu\text{m}$  (bottom left: merging leads to an integral layer), 38  $\mu\text{m}$  (bottom right: ridges and trenches appear parallel to the printing direction). The grainy appearance of the prints is caused by the fact that they have been photographed against a white paper background.

simply too low to give integral printed layers (see Fig. 3, top left and top right). The print corresponding to a 22  $\mu\text{m}$  cell depth does not show merging of the fluid dots at all. The dots only start merging once more fluid is applied, and give an integral layer at an engraving depth of 34  $\mu\text{m}$  (Fig. 3, bottom left). At larger cell depths (e.g. 38  $\mu\text{m}$ ) too much ink is applied, which leads to the formation of ridges of polymer running parallel to the printing direction (Fig. 3, bottom right). Notably, regions adjacent to the ridges show considerable ink depletion. The formation of these ridges may be explained by a collapse of multiple fluid ligaments pulled from adjacent cells. The irregularity of these layers is anisotropic, as the ridges appear exclusively parallel to the printing direction.

It immediately becomes clear that although the roughness as defined above gives a good indication of general layer homogeneity, it does not provide any information about the appearance or anisotropy of the irregularities encountered in the printed layers. This is illustrated by Fig. 4. This figure shows optical density scans of LEP layers printed using different sets of input parameters (left:  $d = 46$   $\mu\text{m}$ ,  $v = 0.5$  m/s,  $c = 22$  mg/mL; right:  $d = 42$   $\mu\text{m}$ ,  $v = 1.5$  m/s,  $c = 22$  mg/mL). Similar roughness values were obtained (6.2% and 6.5%, respectively), despite the large difference in appearance of the prints. Fig. 4 (right) shows isotropically distributed irregularities, whereas print Fig. 4 (left) has a much more stripy appearance due to ridge formation parallel to the printing direction. For OLED production it is desirable to be able to predict printed LEP layer roughness in general terms, as well as in terms of anisotropy or directionality. This is explained as follows. Scattering renders intensity variations in the emitted light due to highly frequent, isotropically distributed layer thickness variations to be much less obvious than variations stemming from a relatively small number of ridges in an essentially smooth layer (see Fig. 5). Furthermore, as mentioned, a deficiency of printed material is encountered adjacent to the ridges, giving the risk of shorts.

The question now raises how to quantify the anisotropy. In tribology, the kurtosis ( $Ku$ ) of a distribution is often used to discriminate between a layer with an isotropic (Gaussian) distribution of many irregularities (low  $Ku$ ) and one that is essentially flat, except for a few

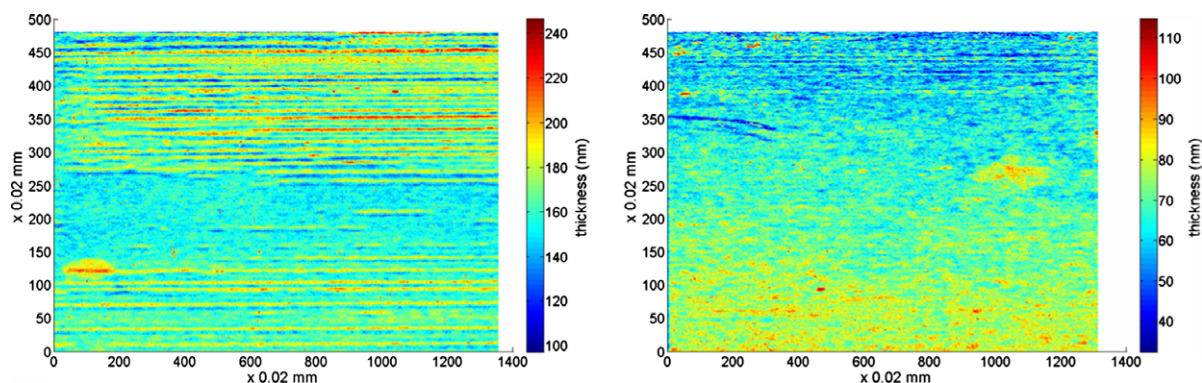


**Fig. 4.** Color-height images of gravure printed LEP layers corresponding to different input parameter sets: left,  $d = 46$   $\mu\text{m}$ ,  $v = 0.5$  m/s,  $c = 22$  mg/mL; right,  $d = 42$   $\mu\text{m}$ ,  $v = 1.5$  m/s,  $c = 22$  mg/mL. The prints have roughness and anisotropy values of 11.9% and 42.9, and 12.7% and 3.8, respectively.

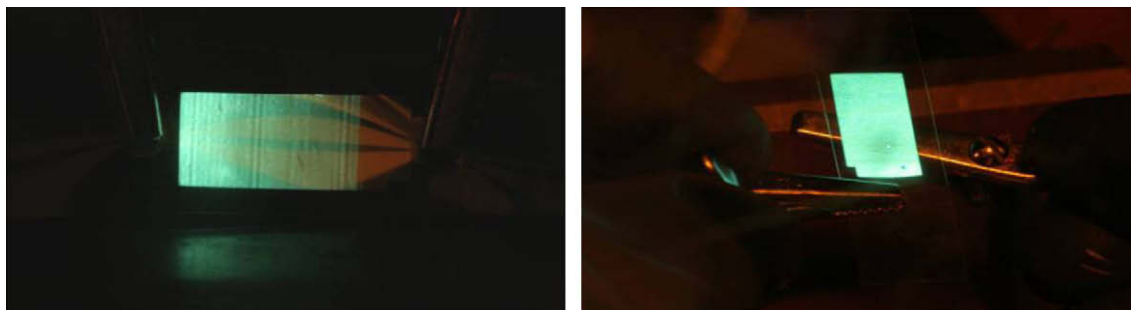


**Fig. 5.** Gravure printed flexible OLED devices ( $33 \times 15$  mm): left, printed LEP layer containing ridges of polymer in the printing direction; right, printed LEP layer containing highly frequent, isotropically distributed irregularities, apart from two dust particle-induced spots.

large deviations (high  $Ku$ ). The kurtosis is defined by Eq. (4).

$$Ku = \frac{1}{mn\sigma^4} \sum_{i=1}^m \sum_{j=1}^n Z(i,j)^4. \quad (4)$$

Here, the layer is represented by an  $m \times n$  matrix of local height values  $Z(i,j)$ , and  $\sigma$  is the standard deviation of the height distribution. Unfortunately, due to the nature of the scanning data and the high noise-sensitivity relating to the 4th power  $Z$ - and  $\sigma$ -dependency,  $Ku$  did not discriminate properly between gravure printed layers with high and low anisotropy: the prints represented by Fig. 4 have a kurtosis of 3.5 and 3.9, respectively. For this reason, we wrote an algorithm dedicated to recognize and quantify the anisotropy. This algorithm, which is essentially represented by Eq. (5), performs separate row- and column-wise summations of the elements of binary representations of the scanning data matrices. Amplification factors were implemented which magnitudes increase with the longitudinal extent of the ridges (represented by “ones”) and trenches (represented by “zeros”). Hypothetically, if comparable numbers of ridges would run both parallel and perpendicular to the printing direction, the anisotropy ( $A$ ) will be low:

$$A = \frac{\sum_{i=1}^m \sum_{j=1}^n \chi_{ij}^{\text{row}} u_{ij}^b}{\sum_{j=1}^n \sum_{i=1}^m \chi_{ij}^{\text{column}} u_{ij}^b}. \quad (5)$$

Here,  $\chi_{ij}^{\text{row}}$  and  $\chi_{ij}^{\text{column}}$  are the amplification factors for the row and column summations, respectively, and  $u_{ij}^b$  are the binarized optical density values (0 or 1). The amplification factor was increased stepwise as long as the value of a matrix element did not differ from that of the previous neighboring element in the same row or column. In case the next neighboring element did have a different value the amplification factor was reset to one, effectively indicating the end of a ridge or trench. The necessary binary representations of the scans were obtained using Eq. (6).

$$U_b(i,j) = H(Z(i,j) - \bar{Z}). \quad (6)$$

Here,  $H$  is the Heaviside step function and  $\bar{Z}$  the mean height (or optical density). Eq. (5) proved much less discriminative when applied to non-binarized data, resulting

**Table 2**

Levels of the input parameters used to build up the total data set.

Level	Cell depth ( $\mu\text{m}$ )	Printing speed (m/s)	Concentration (mg/mL)
1	30	0.5	22
2	34	0.8	27
3	38	1.0	30
4	42	1.2	–
5	44	1.5	–
6	46	–	–

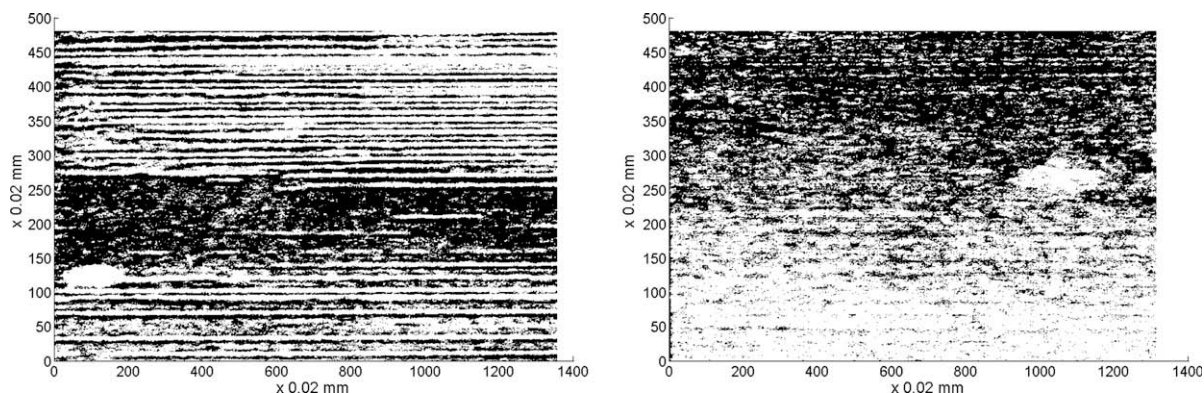


**Fig. 6.** Binarized versions of the prints presented by Fig. 4; white represents thickness values exceeding the mean, whereas black represents areas with a thickness lower than the mean.

in a loss of information on anisotropy. Fig. 6 represents binarized versions of the scans depicted in Fig. 4. We note that the print corresponding to Fig. 4 (right) and Fig. 6 (right) shows an anisotropy in a different sense in that the layer thickness is generally higher on top of the print

than at the bottom. This effect, which is observed for a minority of the prints, is explained by partial incomplete filling of the engraved cells during inking of the gravure roll. This hardly avoidable issue relates to the operational limitations of the gravure printer in combination with

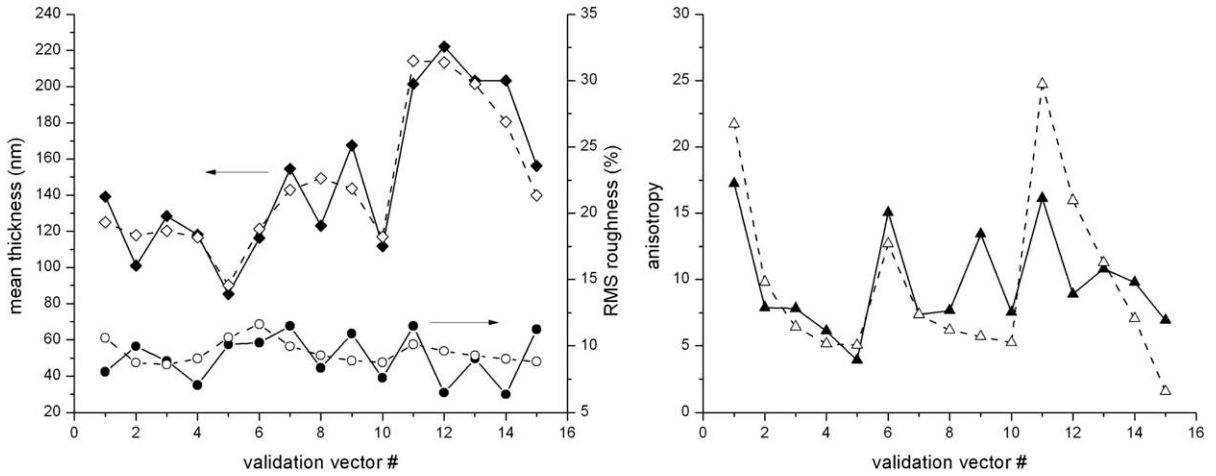


Fig. 7. Measured (closed/solid) and predicted (open/dashed) values for mean printed layer thickness (left), relative RMS roughness (left), and feature anisotropy (right) for the validation data set (prints corresponding to  $d = 44 \mu\text{m}$ ).

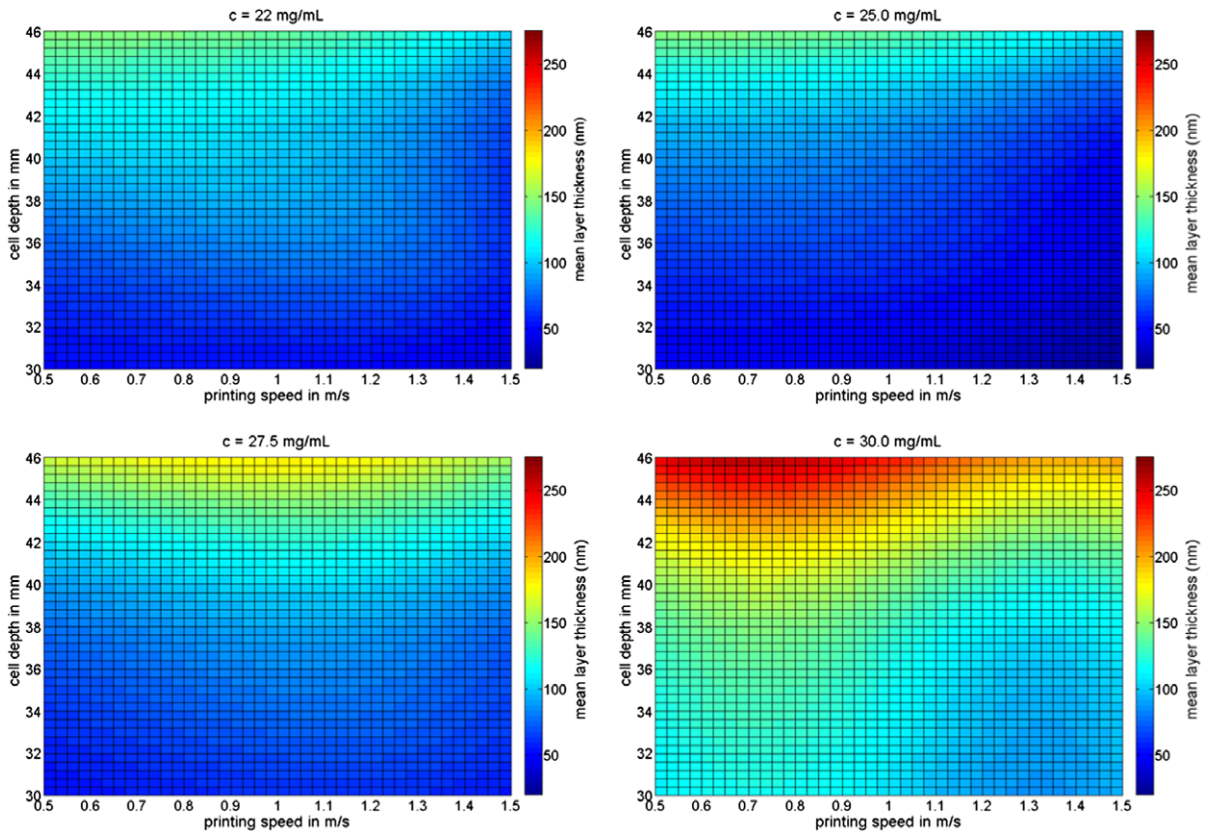


Fig. 8. Calculated mean layer thickness plotted in color grades as a function of cell depth ( $d$ ) (in  $\mu\text{m}$ ) and printing speed ( $v$ ) (in m/s) at  $c = 22.0, 25.0, 27.5,$  and  $30.0 \text{ mg/mL}$  (top left to bottom right).

the manual operation, and will be absent in an industrial gravure printing environment owing to automated inking. These fluctuations are not accounted for by the neural network and will to some extent impart uncertainty in the prediction accuracy. On the other hand, we note that the algorithm expressed by Eq. (5) is relatively insensitive to this kind of printed layer anisotropy.

Using Eqs. (5) and (6), the anisotropy of the prints represented by Fig. 4 was determined to be 42.9 and 3.8, respectively, clearly discriminating between the two prints. Unfortunately, the quality of the scanning data was not sufficient to include quantitative information about the height of the ridges as well.

To build up an input–output data set for training and validation of the neural net, we performed prints and scans varying the input parameters at preset levels (Table 2). Three LEP concentration levels were chosen in a realistic range (22, 27, and 30 mg/mL), corresponding to a suitable dry LEP layer thickness, without the viscosity becoming too high or too low for proper printing. Five levels of printing speed were selected, effectively covering the whole speed range setting of the gravure printer (0.5, 0.8, 1.0, 1.2, and 1.5 m/s). As for cell engraving depth, six levels were used in the range 30–46  $\mu\text{m}$  (i.e. 30, 34, 38, 42, 44, and 46  $\mu\text{m}$ ). By experience we know that LEP layers printed with gravure cell depths in this range typically give working OLEDs. Prints produced at lower cell depth values do not give integral layers due to incomplete merging of the depos-

ited ink dots. Cell depth values exceeding the indicated range usually give highly irregular, rather messy prints having areas containing hardly any material and areas in which material is accumulated into very thick patches. Both extremes usually lead to short circuited devices.

As the total cell depth range expressed by Table 2 has been patch-wise engraved onto the same gravure roll, we were able to acquire all cell depth information within one single print (per level of LEP concentration and speed setting). Practically, the whole study required only 15 prints (three concentration levels  $\times$  5 speed levels) and 4 scans, as the set-up allowed us to scan four printed strips of substrate in one session. Thus we collected a total data set of  $3 \times 5 \times 6 = 90$  three-element input-target vector pairs. Of this total data set all vector pairs corresponding to a 44  $\mu\text{m}$  cell depth (15 in total) were kept aside for validation of the trained network. Of the remaining 75 vector pairs ten were randomly selected to form the testing set. The 65 vector pairs left formed the actual training data set. During training, the network was iteratively exposed to the 65 training vectors, during which the synaptic weight and bias values were optimized to reduce the cost function (Eq. (3)). At set times during training the predictive power of the network was assessed by calculating the total squared error of the predicted output to the testing data set. Once this value did not further decrease, training was aborted and the optimized weight and bias values were saved.

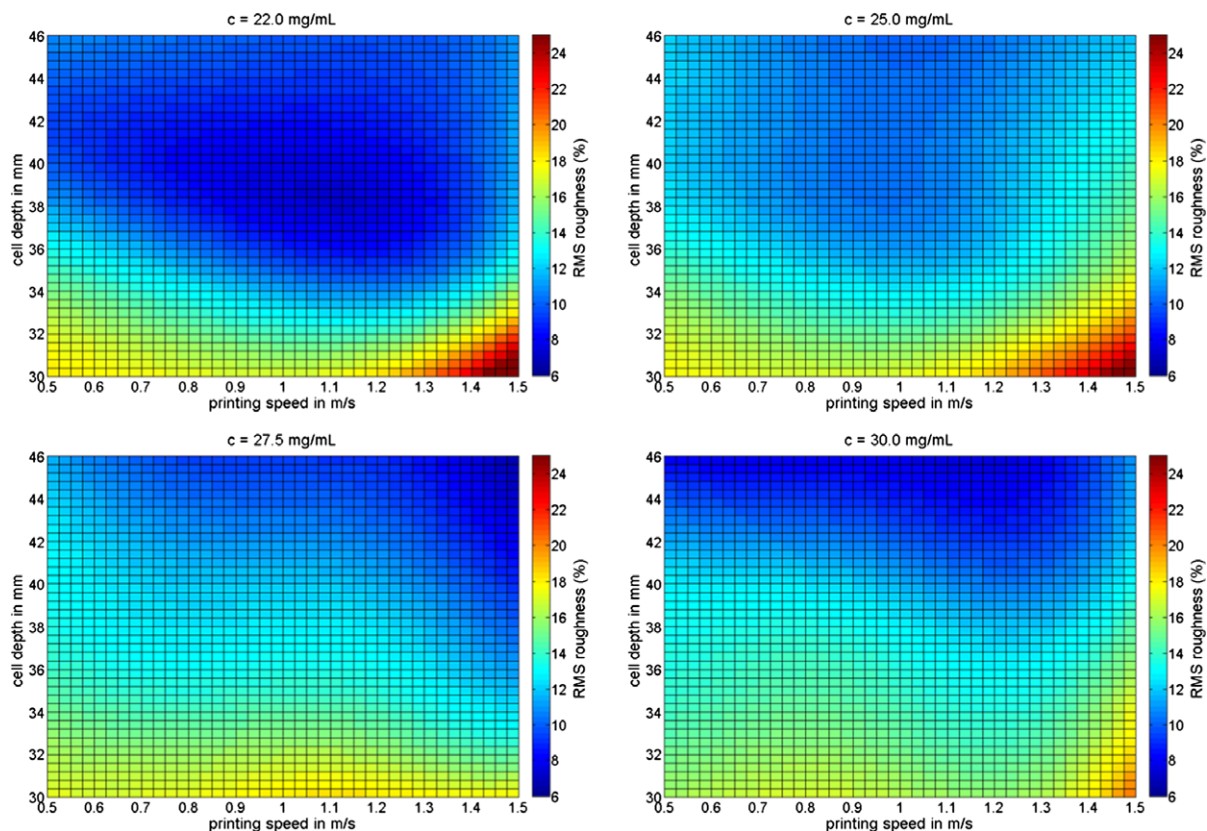


**Fig. 9.** Calculated relative RMS roughness plotted in color grades as a function of cell depth ( $d$ ) (in  $\mu\text{m}$ ) and printing speed ( $v$ ) (in m/s) at  $c = 22.0, 25.0, 27.5,$  and  $30.0$  mg/mL (top left to bottom right).



As for the hidden layer it is well known that a large number of units may lead to fast convergence of the net, which is an advantage if computational time is a limiting factor. However, many hidden units and fast convergence impart the risk of over-fitting. The optimal number of hidden units was determined to be around 12 by trial-and-error. We varied the actual contents of the training and testing sets to check whether the selection of testing vectors had a significant effect on the prediction error of the testing set. We found that this was not the case as long as the testing set was randomly chosen.

After training to optimal convergence, the validation vector set, corresponding to the 44  $\mu\text{m}$  cell engraving depth, was fed into the neural net. Fig. 7 shows that the net is indeed capable of predicting the output to this new input set with a very reasonable accuracy. The prediction error is generally around 10%, 20%, and 25% for mean layer thickness, roughness, and anisotropy, respectively. Especially for roughness and anisotropy, though, some values were predicted with an error that falls outside the range indicated by this ‘typical’ prediction error. The number of these outliers, as well as their deviation from the error distribution, somewhat depends on the distribution of the training data over the training and testing data sets. General trends in the printed layer characteristics as a function of the input parameters are very well distinguished by the neural net. Issues such as mechanical play of parts of the

printer’s engine, and experimental errors induced by fluctuations in manual operation may lead to experimental deviations that are not easily captured by any (statistical) model. We further note that all output parameters are less accurately calculated when any one of the input parameters is left out during training. One could, for instance, imagine that the mean layer thickness is predominantly determined by concentration and cell depth, the printing speed being of little or no influence. However, leaving out printing speed as an input parameter led to significantly larger prediction errors. In general, the mean printed layer thickness may seem somewhat higher than ideal for the fabrication of OLEDs, but we note that these layers contain  $\sim 30$  vol.% dye (assuming a density of  $1 \text{ g/cm}^3$  for both LEP and dye). Omitting the dye would indeed give LEP layers with a thickness in the desired range.

As mentioned above, the optimized synaptic weight and bias values were stored after training. This allowed us to systematically calculate the output of the trained net as a function of the full space determined by the three input parameters. Figs. 8–10 represent color-height plots of the mean layer thickness, roughness and anisotropy as a function of cell engraving depth and printing speed, calculated at four different polymer concentration levels. Fig. 8 clearly shows a general increasing trend of the mean layer thickness with concentration. This is to be expected, but the effect is not linear: no large changes are observed

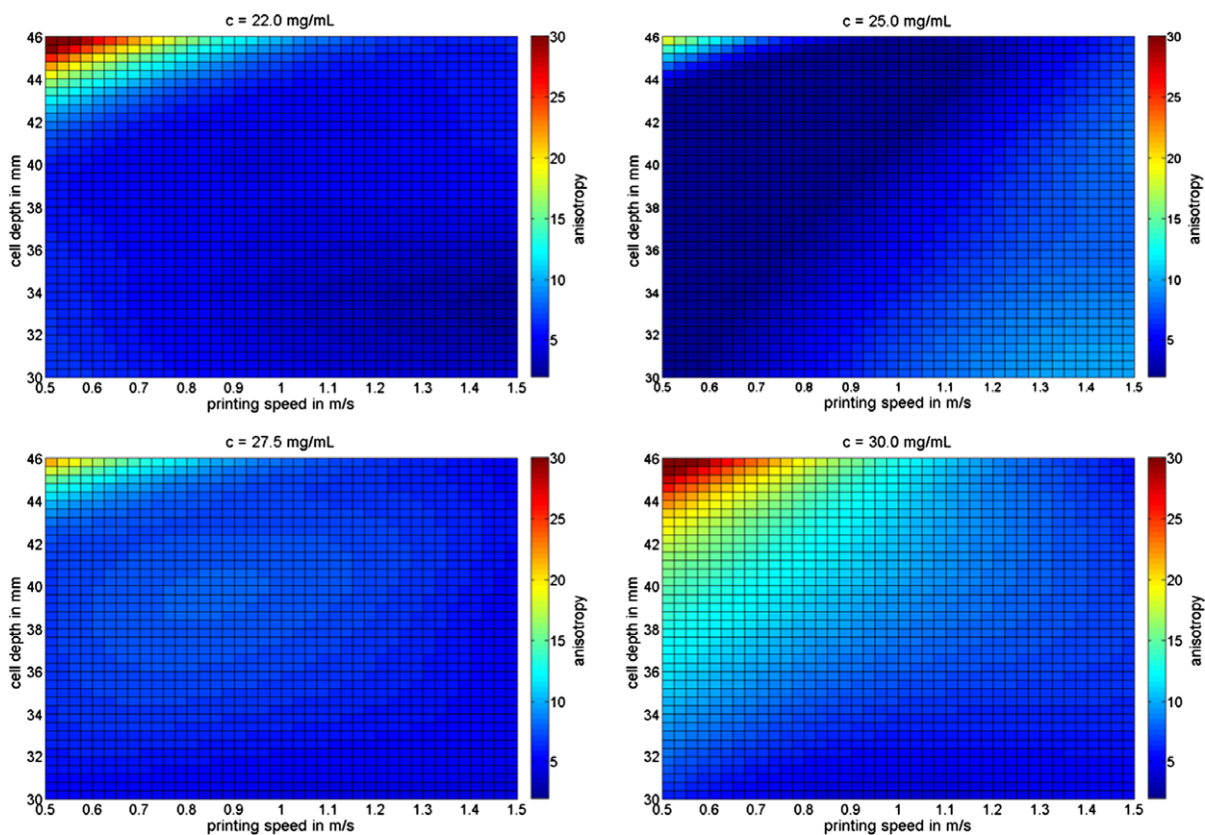


**Fig. 10.** Calculated anisotropy plotted in color grades as a function of cell depth ( $d$ ) (in  $\mu\text{m}$ ) and printing speed ( $v$ ) (in m/s) at  $c = 22.0, 25.0, 27.5,$  and  $30.0 \text{ mg/mL}$  (top left to bottom right).

for a polymer concentration in the range  $c = 22.0 - 27.0$  mg/mL, whereas a pronounced increase of the mean thickness is predicted for higher concentrations. This may be indicative of a non-linear increase in fluid elasticity due to an increasing polymer entanglement density with concentration. Separate viscosity measurements showed the overlap concentration of this LEP to be around 25 mg/mL in toluene/anisole 30/70 (w/w), which falls within the tested concentration range (see Table 2). In contrast, no strong dependency of the mean layer thickness on printing speed is observed. Expectedly, a general increase of layer thickness with cell engraving depth is predicted. The non-linearity of this increase, however, becomes more pronounced at high LEP concentrations. This is indicative of an increasingly non-Newtonian behavior with polymer concentration.

As for the roughness (Fig. 9), at low polymer concentrations ( $22.0 < c < 24.5$  mg/mL) an optimum (minimum) is predicted for intermediate speed and cell engraving depth settings (0.9–1.2 m/s and 36–40  $\mu\text{m}$ , respectively). This optimum seems to shift towards higher engraving depths for higher LEP concentrations ( $c > 26.0$  mg/mL). Besides this optimum, the roughness shows a trend-wise decrease with increasing cell engraving depth for the entire LEP concentration range. Interestingly, this relation changes from non-linear at low concentrations to more linear at high concentrations. This is indicative of a difficulty in the leveling of the printed dots at low cell engraving depths, despite the fact that integral layers are obtained. Expectedly, this effect becomes more pronounced if the viscosity increases due to a rise in LEP concentration. It is further noted that for any LEP concentration the roughness is highest when a low cell depth is used in combination with a high printing speed. This is especially the case for low LEP concentrations. Together with the low mean layer thickness obtained under these conditions, this is explained by a very low fluid transfer volume.

A high anisotropy at any concentration is obtained by combining a high cell engraving depth with a low printing speed (Fig. 10), the effect being most pronounced at high concentrations ( $\sim 30.0$  mg/mL). Gradually going down in polymer concentration, it decreases to a minimum around  $c = 26.0$  mg/mL, but increases again at lower concentrations. A minimum in anisotropy is obtained for intermediate concentrations ( $23.5 < c < 25.5$  mg/mL) in combination with intermediate to low printing speed and cell engraving depth settings (0.5–1.1 m/s and 30–42  $\mu\text{m}$ , respectively). Clearly, for the whole concentration range a much stronger speed-dependence is observed for the anisotropy than for the mean layer thickness and the roughness. This indicates that the directionality of the irregularities in a print is strongly related to the rheology of the ink.

#### 4. Conclusions

We have shown that artificial neural network modeling may be used as a viable tool to predict gravure printed light-emitting polymer layer characteristics for flexible OLED lighting applications. The gravure printed LEP layers were analyzed using microdensitometry, after which the

scanning data was converted into (local) layer thickness information and used to train a multi-layer neural network using error back propagation. Polymer concentration, printing speed and cell engraving depth were used as input parameters. Mean layer thickness, roughness, and feature anisotropy were defined as output parameters of the neural net. Despite the limited number of input parameters a reasonable to fair prediction accuracy was obtained once new input data was fed into the trained network. The prediction error for the three output parameters was of the order anisotropy > roughness > mean layer thickness. Calculating the magnitude of the output parameters as a function of the total space determined by the input parameters can be used as a way to find optimal printing conditions. The plots also express the highly non-linear dependency of the output on the input parameters.

#### References

- [1] For more information on OLED devices see: K. Müllen, U. Scherf (Eds.), *Organic Light Emitting Devices*, Wiley-VCH Verlag, Weinheim, 2006.
- [2] (a) 3rd Press Release OLLA Project, 14 May 2007;  
(b) M. Tuomikoski, R. Suhonen, M. Välimäki, T. Maaninen, A. Maaninen, M. Sauer, P. Rogin, M. Mennig, S. Heusing, J. Puetz, M.A. Aegerter, *Proc. SPIE – Int. Soc. Opt. Eng.*, 2006, p. 6192 (art. no. 619204);  
(c) M. Tuomikoski, R. Suhonen, M. Välimäki, A. Maaninen, *IEEE/LEOS Opt. MEMS 2005: Int. Conf. Opt. MEMS Appl.*, 2005, pp. 141–142 (art. no. 1540118).
- [3] E. Jewell, T.C. Claypole, G. Davies, *Proc. Tech. Assoc. Graph. Arts, TAGA (2006)* 419–429. and references cited therein.
- [4] L. Fausett, *Fundamentals of Neural Networks*, Prentice Hall, New Jersey, 1994.
- [5] (a) E. Köse, T. Şahinbaşkan, I. Güler, *Exp. Syst. Appl.* 36 (2009) 745–754;  
(b) X. Su, Y. Wang, T. Zhang, *High Tech. Lett.* 9 (2003) 39–43;  
(c) G. Wermuth, *Farbe Lack* 110 (2004) 30–37;  
(d) Rose, Oded, US Patent 5200816, 1991;  
(e) Rose, Oded, US Patent 5285297, 1992.
- [6] (a) R. Schettini, D. Bianucci, G. Mauri, S. Zuffi, *Proc. CGIV (2004)* 393–397;  
(b) S.-C. Chen, Y.-C. Yeh, W.-L. Chen, *Int. J. El.* 89 (2002) 19–34;  
(c) J.R.G. Evans, M.J. Edirisinghe, P.V. Coveney, J. Eames, *J. Eur. Ceram. Soc.* 21 (2001) 2291–2299.
- [7] (a) C. Englund, A. Verikas, *Int. J. Adv. Man. Tech.* 39 (2008) 919–930;  
(b) L. Bergman, A. Verikas, *Proc. IASTED (2004)* 173–178;  
(c) C. Englund, A. Verikas, *Eng. Appl. Art. Intell.* 18 (2005) 759–768.
- [8] (a) T. Yang, T.-N. Tsai, J. Yeh, *Eng. Appl. Art. Intell.* 18 (2005) 335–341;  
(b) N. Morad, H.K. Yii, M.S. Hitam, C.P. Lim, *Proc. IEEE Region 10 Ann. Int. Conf.* 3 (2000) III-479–III-483;  
(c) S.L. Ho, M. Xie, L.C. Tang, K. Xu, T.N. Goh, *IEEE Trans. El. Pack. Man.* 24 (2001) 323–332.
- [9] L. Ding, P.E. Bamforth, M.R. Jackson, R.M. Parkin, *Proc. Control (2004)*.
- [10] C.A. Powell, M.D. Savage, J.T. Guthrie, *Int. J. Num. Meth. Heat Fluid Flow* 12 (2002) 338–355.
- [11] X. Yin, S. Kumar, *Phys. Fluid* 17 (2005) 063101.
- [12] X. Yin, S. Kumar, *Chem. Eng. Sci.* 61 (2006) 1146–1156.
- [13] (a) R.W. Hewson, N. Kapur, P.H. Gaskell, *Chem. Eng. Sci.* 61 (2006) 5487–5499;  
(b) N. Kapur, *Chem. Eng. Sci.* 58 (2003) 2875–2882;  
(c) L.W. Schwartz, *J. Eng. Math.* 42 (2002) 243–253;  
(d) C.A. Powell, M.D. Savage, P.H. Gaskell, *Trans. IChemE* 78 (2000) 61–67;  
(e) L.W. Schwartz, P. Moussalli, P. Campbell, R.R. Eley, *Trans. IChemE* 76 (1998) 22–28;  
(f) H. Benkreira, R. Patel, *Chem. Eng. Sci.* 48 (1993) 2329–2335.
- [14] (a) R.D. Deegan, O. Bakajin, T.F. Dupont, G. Huber, S.R. Nagel, T.A. Witten, *Phys. Rev. E* 62 (2000) 756–765;  
(b) R.D. Deegan, O. Bakajin, T.F. Dupont, G. Huber, S.R. Nagel, T.A. Witten, *Nature* 389 (1997) 827–829.
- [15] R.D. Deegan, *Phys. Rev. E* 61 (2000) 475–485.

[8,9]. TEM images have shown improved phase separation by increasing the domain sizes of P3HT and PCBM [3,4,10]. Most XRD results have shown that P3HT crystals in P3HT:PCBM films have the (1 0 0) preferred orientation, and the average crystalline size of the (1 0 0) axis increases with thermal annealing [11–14]. Preferred orientation and enlarged crystalline size of P3HT crystals were attributed to the improved performance of the solar cells upon thermal annealing. In contrast, it was recently reported that the higher crystallinity of a P3HT:PCBM film was a disadvantageous in organic photovoltaic devices because it induced more phase separation and thermally unstable morphology [15].

Despite these results, more morphological information is needed to clearly explain the device performance, mainly because most of the structural studies have been performed on P3HT:PCBM thin films without Al electrodes. The device performance improves when the blended polymer films are annealed after the deposition of an Al electrode on top of the polymer films [7]. Therefore, the structural change should be studied in the presence of an Al electrode on the blended films to determine the relationship between film structure and device performance. In addition, most of the available morphological data are limited to lateral microscopic phase separation images; information on the microstructure in the vertical direction is very limited [8–14]. The vertical connection of the separated phases is as important as the lateral phase separation, because the former is related to the collection of the charges generated at the interface between the P3HT and PCBM phases.

This paper analyzes the effects of Al electrodes on the nanostructure of P3HT:PCBM solar cell blends during thermal annealing with synchrotron X-rays, and the relationship to solar cell performance is discussed. The results clearly demonstrate that the improved solar cell performance resulting from thermal annealing in the presence of an upper Al layer is related to the crystalline properties of P3HT such as the crystal size, the volume fraction and the angular spread of crystals in the film. Among these, the improved performance is strongly affected by the angular spread of the crystals, which helps to form interpenetrated networks. In addition, the polymer film surface structure is significantly different when the Al layer is present. A thin layer between the Al electrode and the blended film is formed by Al diffusion into the organic layer during thermal annealing, assisting in the formation of interpenetrated networks.

## 2. Experimental

P3HT was obtained from RIEKE metals (Mw = 55–60 kg/mol, 93% RR), and PEDOT:PSS was obtained from Baytron P. P3HT and PCBM were blended at a ratio of 1:0.65 by weight using a chlorobenzene (18 mg of P3HT:PCBM with 1000 ml chlorobenzene) solvent. A 40 nm PEDOT:PSS film was spin-coated on a glass substrate and baked for 1 min at 140 °C on a hot plate. Blended P3HT:PCBM films were spin-coated to a thickness of 70 nm. The samples were thermally annealed on a hot plate in a glove box for 30 min at different temperatures.

Al electrode layers were thermally evaporated onto P3HT:PCBM/PEDOT:PSS/Glass samples. The Al thickness was 40 nm. After Al was deposited, we annealed the samples in a glove box for 30 min at different temperatures.

Grazing-incidence wide angle X-ray scattering (GI-WAXS) and X-ray reflectivity measurements were performed with a 5A beam line from Pohang Light Source (PLS) of Korea. This is a high flux beam line with an inserted multipole wiggler. X-rays coming from the wiggler are focused in the vertical direction using a collimating mirror and monochromated using a double crystal monochromator. The beam is equipped with a kappa type 6-circle diffractometer and a 2D image plate detector. The X-ray incident angle was defined with the 6-circle diffractometer, and a 2D image plate detector was used to obtain 2D diffraction patterns.

The X-ray penetration depth is dependent on the X-ray wavelength and the refractive index of the material. In the X-ray region, the refractive index of a material is defined by  $n = 1 - \delta - i\beta$  [16]. The constant  $\delta$  is the dielectric constant of a material, and  $\beta$  is defined by  $\lambda\mu/4\pi$ , where  $\mu$  is the linear absorption coefficient. With 1.069 Å X-rays, the critical angle of the P3HT:PCBM film was 0.113°, and  $\delta$  and  $\beta$  were  $1.95 \times 10^{-6}$  and  $2.15 \times 10^{-9}$ , respectively. The X-ray reflectivity curves of the films with Al layers were analyzed using Parratt's formula for Fresnel reflection in a multilayer system. We assumed that P3HT:PCBM was infinite compared with the Al layer, and the interface between Al and P3HT:PCBM was gradually varied.

## 3. Results and discussion

Two sets of solar cells based on P3HT:PCBM (1:0.65 by weight) blends were annealed at 150 °C before and after deposition of an Al electrode. Fig. 1 shows the current–voltage curves of the devices, and the device characteristics are summarized in Table 1. The power conversion efficiency (PCE) of the devices annealed prior to the deposition of an Al layer is about 1.6%. In contrast, the PCE of the

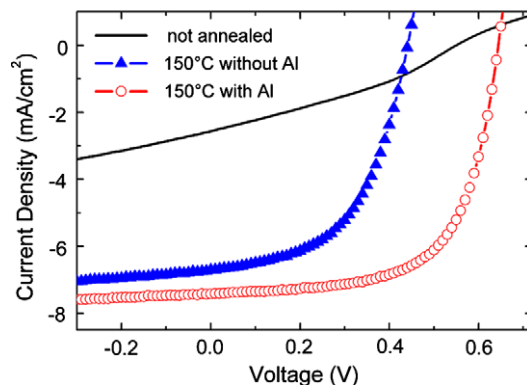


Fig. 1. Current density–voltage ( $J$ – $V$ ) characteristics of solar cells based on P3HT:PCBM blends with not annealed (solid line), annealed at 150 °C in the absence of an Al layer (blue filled triangles), and annealed at 150 °C in the presence of an Al layer (red open circles) processes. The  $J$ – $V$  characteristics were obtained under AM1.5-simulated sunlight. (For interpretation of the references to colour in this figure legend, the reader is referred to the web version of this article.)

**Table 1**

Short circuit currents ( $J_{sc}$ ), open circuit voltages ( $V_{oc}$ ), fill factors (FF), and power conversion efficiencies (PCE) of solar cells based on P3HT:PCBM blends (1:0.65 by weight) with different annealing processes.

	Not annealed	150 °C without Al	150 °C with Al
$J_{sc}$ (mA/cm <sup>2</sup> )	2.6	6.7	7.4
$V_{oc}$ (V)	0.54	0.49	0.65
FF	0.33	0.52	0.64
PCE (%)	0.5	1.6	3.0

devices annealed after Al deposition increases to 3.0% at 150 °C. This performance is similar to that in previously reported results [17,18].

Grazing-incidence X-ray scattering provided information about the film nanostructure, including the crystalline size, the number of crystals, and the crystal orientation distribution. Fig. 2a and b show the 2D X-ray diffraction images of the spin-coated (not annealed) films and the films that were thermally annealed at 150 °C in the absence of an Al layer measured at the incident angle of 0.13°, respectively. Fig. 2c and d are 2D images of not annealed and the annealed at 150 °C in the presence of an Al layer measured at the incident angle of 0.16°, respectively. These diffraction images can be analyzed based on the known crystal structure of P3HT (orthorhombic with  $a = 16.8$  Å,  $b = 3.83$  Å and  $c = 7.8$  Å with the main polymer chain parallel to the  $c$  axis and the alkyl side chain inducing a lamellar reflection along the  $a$ -axis) [19,20]. The structural information is summarized in Table 2 and Fig. 3.

The P3HT crystals grow by thermal annealing as expected and the size of the P3HT crystals is not significantly influenced by the presence of an Al layer as summarized in Table 2 and Fig. 3a. For example, annealing at 150 °C causes

the average crystal size of the edge-on crystals to increase from 15 nm to 20–25 nm in the [1 0 0] direction for both the cases. The increase in crystal size from 15 to 20 nm via thermal annealing at 150 °C is in agreement with previously reported TEM results analyzed by frequency-filtered Fourier transformation [4].

However, the presence of an Al layer during thermal annealing has a marked influence on the total amount of vertically aligned edge-on P3HT crystals. As shown in Fig. 3b, the integrated intensity of the edge-on P3HT (1 0 0) peak along the circular direction maintains almost constant or reduced a little with annealing temperature in the presence of an Al layer, whereas the integrated intensity increases to 2.5 times if the films are annealed above 120 °C in the absence of an Al layer. This fact indicates that the Al layer on the blended films disrupts improvement of the total crystallinity of P3HT.

One more significant difference is the angular spread of the P3HT crystal orientation represented by the FWHM of the edge-on P3HT (1 0 0) peak in the circular direction. The FWHM of the edge-on P3HT (1 0 0) peak increases almost linearly with annealing temperature in the presence of an Al layer, whereas it is kept constant in the absence of an Al layer. Since the intensity variation of the P3HT (1 0 0) peak in the circular direction is related to the angular spread of the P3HT crystals in a film, the presence of an Al layer during the thermal annealing reduces the preferred orientation of the P3HT crystals.

Reduction of the preferred orientation of P3HT crystals in the presence of an Al electrode is more clearly manifested in Fig. 4a, where the angular volume fractions of the P3HT crystals are plotted against the angle for a pristine film and the annealed films at 150 °C in the presence and absence of an Al electrode. The angular volume fractions were obtained from the intensity distribution in the

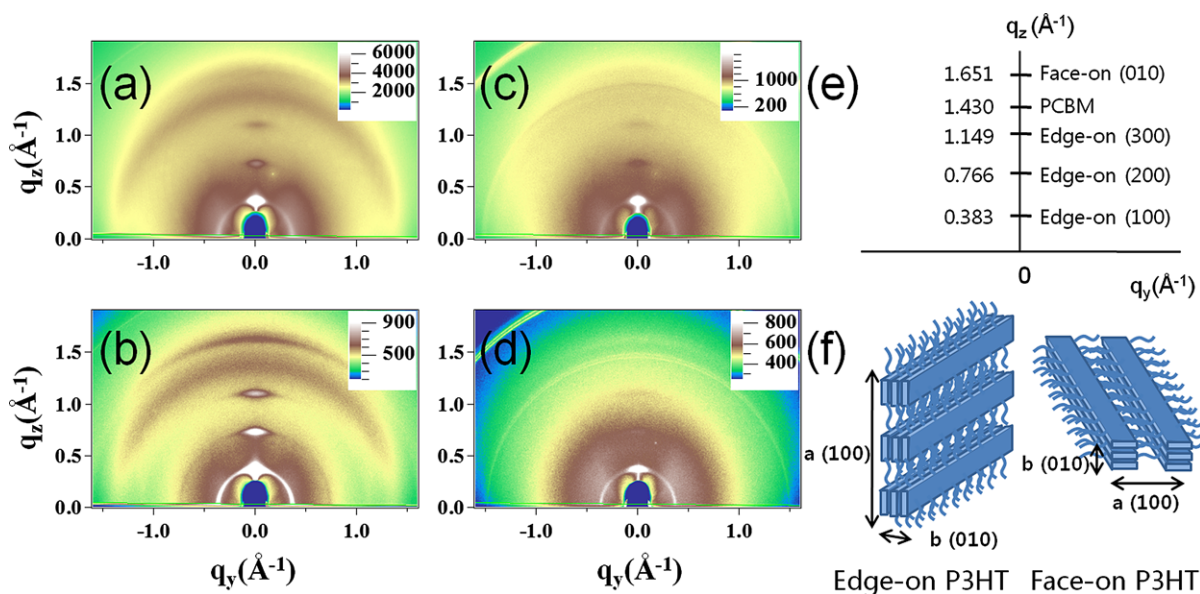


**Fig. 2.** 2D GIWAXS images of (a) not annealed and (b) annealed at 150 °C in the absence of an Al layer. (c) and (d) are images of not annealed and annealed at 150 °C in the presence of an Al layer, respectively. Indexing of the 2D images is in (e). (f) is schematic diagram of the edge-on and face-on P3HT crystals.

**Table 2**

Summary of the nanostructure of pristine (not annealed) P3HT:PCBM films and 150 °C annealed films with and without an Al layer on the surface. (ND: not detected).

	Not annealed	150°C without Al	150°C with Al
Edge-on (1 0 0) size	14 nm	20 nm	21 nm
Edge-on (0 1 0) size	2 nm	6 nm	ND
Face-on (1 0 0) size	8 nm	18 nm	23 nm
Face-on (010) size	3 nm	8 nm	ND
FWHM of (1 0 0) – preferred orientation	11.2°	10.9°	17.1°
Integrated intensity of (1 0 0)	1	2.5	0.86

P3HT (1 0 0) halo in the 2D diffraction images by counting all the crystals having the same angular orientation from the surface normal but different orientations in the in-plane direction ( $x$ - $y$  plane) under the assumption that the films are homogeneous in the in-plane direction. Angular volume fraction of the P3HT crystals is defined as the volume fraction of the P3HT crystals whose [1 0 0] direction is located between  $\theta$  and  $\theta + \delta\theta$  from surface normal of the films. Since the 2D diffraction image is the cross sectional view of the Ewald sphere of a film, the spherical integration must be performed as shown in Fig. 4b to include all

the crystals having angular orientation of  $\theta$  from the surface normal. The integration was performed numerically using the following equation. We sectioned the (1 0 0) diffraction halo of the P3HT crystals every 2° from the surface normal ( $q_z$ ,  $\theta = 0^\circ$ ) toward the in-plane direction ( $q_y$ ,  $\theta = 90^\circ$ ) for the numerical integration.

$$f_n(\theta_n) = \frac{\int_{\theta_n}^{\theta_n+\Delta\theta} q^2 I(\theta) \sin(\theta) d\theta}{\int_0^{\pi/2} q^2 I(\theta) \sin(\theta) d\theta} \approx \frac{I[(n+1)\Delta\theta] \sin[(n+1)\Delta\theta]}{\sum_{n=0}^{N-1} I(n\Delta\theta) \sin(n\Delta\theta)}$$

where  $\Delta\theta = \pi/2N$ .

Fig. 4a clearly shows the different orientational distributions of the P3HT crystals by thermal annealing in the absence and presence of an Al layer. If all crystals are randomly distributed, the angular fraction must follow the dotted line in the figure. P3HT crystals are preferentially aligned along (1 0 0) direction even in the pristine film. The preferred orientation becomes more prevalent by the thermal annealing in the absence of an Al layer, so that the main tilting angle moves to 2° with narrower angular spread than the pristine film. In contrast, the presence of an Al electrode on the film induces more random

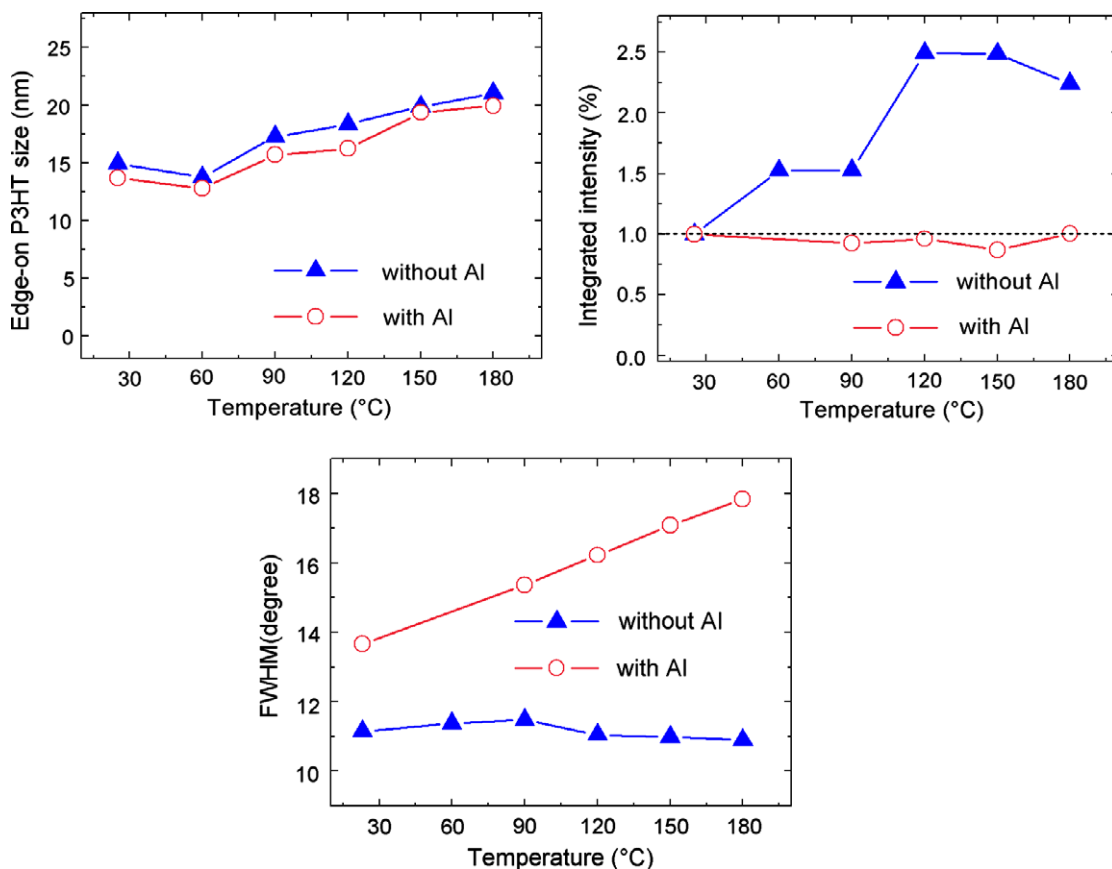


**Fig. 3.** Structural evolution of P3HT crystals in P3HT:PCBM films during annealing in the absence (filled triangle) and presence (open circle) of an Al layer; (a) the average P3HT (1 0 0) crystal size, (b) the ratio of integrated intensity of the P3HT (1 0 0) peak in the annealed film to that of the pristine film, (c) the FWHM of the P3HT (1 0 0) peak in the circular direction of the 2D diffraction images.

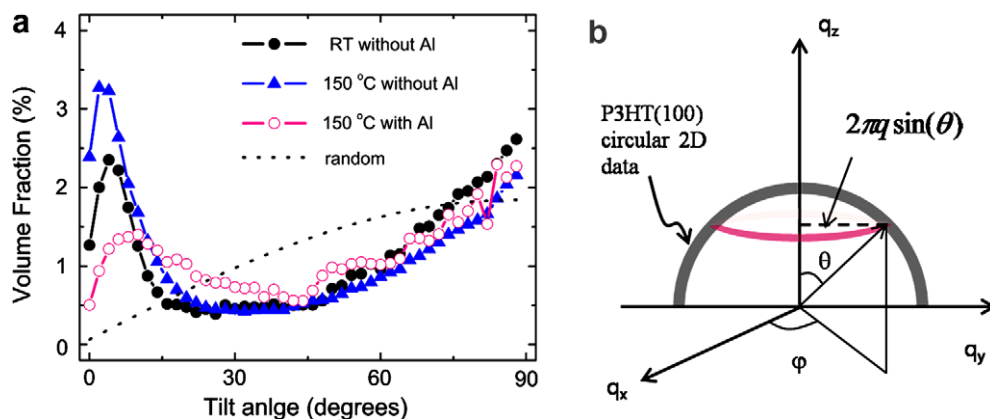


**Fig. 4.** (a) Angular volume fractions of the P3HT crystals in the pristine (black closed circle) and thermally annealed films at 150 °C in the absence (blue closed triangle) and presence (red open circle) of an Al layer. The dotted line is the curve of equally distributed crystals such as powder samples. We did not calculate the volume fraction over 86° due to surface enhancement effect. (b) Integration geometry of P3HT (1 0 0) 2D circular peak data in the spherical coordinate. (For interpretation of the references to colour in this figure legend, the reader is referred to the web version of this article.)

distribution in the crystal orientation by the thermal annealing at 150 °C, resulting in almost equal angular volume fraction against the tilting angle.

Interestingly enough, very thin amorphous like face-on P3HT layers were found in the surface region of the films in the absence of Al layer. The structural information in the surface region of the films in the absence of an Al layer were obtained by using a lower incident angle (0.1°) than the critical angle (0.113°) of the P3HT:PCBM film. The X-ray penetration depth at the incident angle of 0.1° is ~26 nm for the 1.069 Å X-rays by the calculation using Parratt's equation. The face-on crystals near the surface region (~26 nm from the surface) grow only in the lateral direction as shown in Fig. 5. The average crystal size in the [1 0 0] direction is about 23 nm after annealing at 150 °C. In contrast, the average crystal size in the [0 1 0] direction remains 0.7 nm and does not change with thermal annealing up to 180 °C. The crystals are almost plane-like, composed of a molecular bi-layer in the vertical direction.

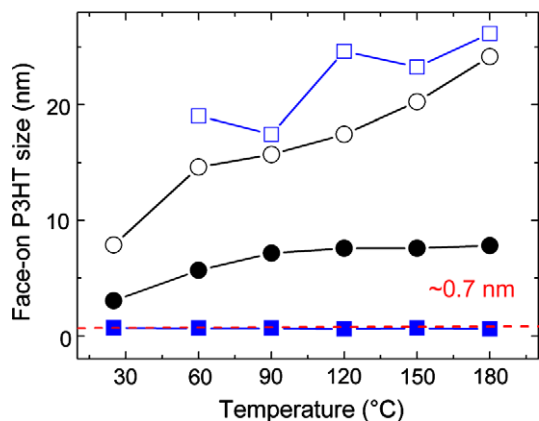


**Fig. 5.** The evolution of face-on crystals in the surface region (squares) and the bulk region (circles) in [0 1 0] direction (filled) and [1 0 0] direction (open) during thermal annealing in the absence of Al layer.

The growth of the plane-like face-on P3HT layer in the annealed film in the absence of Al layer will result in a smooth surface and it was confirmed by AFM measurements. The surface roughness of the pristine film is 0.8 nm, but it decreases to 0.5 nm after thermal annealing at 150 °C. The presence of the thin face-on P3HT layer at the surface region seem to act as a barrier for electron transport from the P3HT:PCBM matrix to the cathode if the blend films are annealed in the absence of Al.

This plane-like face-on P3HT layer was not detected if annealed in the presence of an Al electrode as evidenced by the lack of (0 1 0) peak in Fig. 2d. To check the chances of screening of the peak by the Al layer, we analyzed the X-ray penetration depth and intensity ratios. X-ray path length in the 40 nm thick Al layer is about 28 μm at 0.16° incident angle, and the X-ray penetration depth of Al layer is about 200 μm in the wavelength of 1.069 Å which was used in this experiment. This X-ray penetration depth is long enough to detect (0 1 0) peak in the presence of Al layer if the layer exist. Moreover intensity ratio of (0 1 0) peak to (2 0 0) peak in the annealed films in the absence of an Al layer (Fig. 2b) is 0.68. This value is much higher than the intensity ratio of the background to (2 0 0) peak in the annealed films in the presence of an Al layer (Fig. 2d) which is 0.31. Therefore we can safely say that the plane-like face-on P3HT layer is not formed if the film is annealed in the presence of an Al layer.

The nanostructural differences in the P3HT:PCBM films thermally annealed in the presence of an Al layer result from the interface between the Al and P3HT:PCBM layers. We performed X-ray reflectivity measurements for the as-cast and 150 °C annealed films with Al layers and could get mass density profiles by analysis [21]. The mass density profile showed that a thin interlayer is formed at the interface between the Al and P3HT:PCBM layers, even before thermal annealing. The thickness of the intermediate layer increases gradually up to ~17 nm with increasing annealing temperature due to inter-diffusion of Al atoms into the organic layer. This Al diffusion might restrict the lateral growth of the face-on P3HT crystals near the surface and

reduce the total crystallinity and the preferred orientation of the P3HT crystals in the blended film.

To understand the relationship between the structure and the device performance, we analyzed  $J$ - $V$  characteristics of pre annealed and post annealed devices at 150 °C for 30 min. The pre annealed device shows the power conversion efficiency (PCE) of 1.6%, the short circuit current ( $J_{sc}$ ) of 6.69 mA/cm<sup>2</sup>, the open circuit voltage ( $V_{oc}$ ) of 0.49 V, and the fill factor (FF) of 0.52, while the post annealed device shows PCE of 3.0%,  $J_{sc}$  of 7.4 mA/cm<sup>2</sup>, the  $V_{oc}$  of 0.65, FF of 0.64, respectively. The series resistance ( $R_s$ ) of the pre annealed device was 4.48 Ω cm<sup>2</sup>, while it was 1.76 Ω cm<sup>2</sup> in the post annealed device. The increase of the short circuit current and the fill factor in the post annealed device seems to be related to the improved interpenetrating networks and the formation of better  $p$ - $n$  junctions by the donor/acceptor molecules between the cathode and anode in the annealed film in the presence of an Al layer due to more random distribution than the annealed film in the absence of an Al layer. The decrease of the series resistance in the post annealed films must be related to the interface properties between Al electrode layer and P3HT:PCBM layer. It was published that Al-PCBM complex could be formed at the interface between the Al layer and the active layer by post annealing [2]. The diffusion of Al atoms into the active layer may be related to the formation of Al-PCBM complex, and the lateral growth of face-on P3HT near surface region seems to restrict the formation of Al-PCBM complex in the pre annealed device. As a result, the series resistance is lower in the post annealed device than the pre annealed device.

#### 4. Conclusion

In summary, our results demonstrate that the crystal size itself is not the main factor improving device performance in P3HT:PCBM bulk heterojunction solar cells. Another important factor is the orientational distribution of the P3HT crystals. The presence of an Al layer on top of the P3HT:PCBM layer reduces the preferential orientation and total crystallinity of the P3HT crystals during thermal annealing, aiding in the formation of interpenetrating networks. Al inter-diffusion may play a role in disrupting the alignment of P3HT crystals. In addition, face-on P3HT crystals in the surface region affect device performance. These very thin P3HT layer grow laterally during thermal treatment in the absence of an Al electrode and act as a barrier for electron transport from the P3HT:PCBM matrix to the cathode. The lateral growth of the face-on P3HT crystals

near the surface region might be restricted by Al inter-diffusion. An interlayer is formed at the interface between organic layer and the Al electrode through inter-diffusion Al into the organic layer if annealed in the presence of an Al electrode. As a result of all the combined effects, devices annealed in the presence of an Al layer perform better than devices annealed without an Al layer.

#### Acknowledgements

This work was supported by the NCRC Grant (R15-2008-006-00000-0) and WCU program (R31-2008-000-10075-0) through National Research Foundation of Korea funded by the Ministry of Education.

#### References

- [1] F. Padinger, R.S. Rittberger, N.S. Sariciftci, *Adv. Funct. Mater.* 13 (2003) 85.
- [2] W. Ma, C. Yang, X. Gong, K.L. Lee, A.J. Heeger, *Adv. Funct. Mater.* 15 (2005) 1617.
- [3] X. Yang, J. Loos, S.C. Veenstra, W.J.H. Verhees, M.M. Wienk, J.M. Kroon, M.A.J. Michels, R.A.J. Janssen, *Nano Lett.* 5 (2005) 579.
- [4] W. Ma, C. Yang, A.J. Heeger, *Adv. Mater.* 19 (2007) 1387.
- [5] S.E. Shaheen, C.J. Brabec, N.S. Sariciftci, F. Padinger, T. Fromherz, J.C. Hummelen, *Appl. Phys. Lett.* 78 (2001) 841.
- [6] H. Hoppe, N.S. Sariciftci, *J. Mater. Res.* 19 (2004) 1924.
- [7] M. Al-Ibrahim, O. Ambacher, S. Sensfuss, G. Gobsch, *Appl. Phys. Lett.* 86 (2005) 201120.
- [8] P.J. Brown, D.S. Thomas, A. Köhler, J. Wilson, J.-S. Kim, C. Ramsdale, H. Sirringhaus, R.H. Friend, *Phys. Rev. B* 67 (2003) 064203.
- [9] D. Chirvase, J. Parisi, J.C. Hummelen, V. Dyakonov, *Nanotechnology* 15 (2004) 1317.
- [10] M. Brinkmann, H.-C. Wittmann, *Adv. Mater.* 18 (2006) 860.
- [11] T. Erb, U. Zhokhavets, G. Gobsch, S. Raleva, B. Stühn, P. Schilinsky, C. Waldauf, C.J. Brabec, *Adv. Funct. Mater.* 15 (2005) 1193.
- [12] Y.K. Kim, S. Cook, S.M. Tuladhar, S.A. Choulis, J. Nelson, J.R. Durrant, D.C. Bradley, M. Giles, I. McCulloch, C.-S. Ha, M.H. Lee, *Nat. Mater.* 5 (2006) 197.
- [13] H. Yang, T. Shin, Z. Bao, C.Y. Ryu, *J. Polym. Sci. B* 45 (2007) 1303.
- [14] L.H. Nguyen, H. Hoppe, T. Erb, S. Günes, G. Gobsch, N.S. Sariciftci, *Adv. Funct. Mater.* 17 (2007) 1071.
- [15] C.H. Woo, B.C. Thompson, B.J. Kim, M.F. Tony, J.M.J. Fréchet, *J. Am. Chem. Soc.* 130 (2008) 16324.
- [16] L.G. Parratt, *Phys. Rev.* 95 (1954) 359.
- [17] W. Wang, H.B. Wu, C.Y. Yang, C. Luo, Y. Zhang, J.W. Chen, Y. Cao, *Appl. Phys. Lett.* 90 (2007) 183512.
- [18] Y.K. Kim, S.A. Choulis, J. Nelson, D.C. Bradley, S. Cook, J.R. Durrant, *Appl. Phys. Lett.* 86 (2005) 063502.
- [19] E.J. Samuelsen, J. Mädelén, *Handbook of organic conductive molecules and polymers*, in: H.S. Nalwa (Ed.), *Conductive Polymers: Spectroscopy and Physical Properties*, first ed., vol. 3, Wiley, Weinheim, 1997.
- [20] J.-F. Chang, J. Clark, N. Zhao, H. Sirringhaus, D.W. Breiby, J.W. Andreasen, M.M. Nielsen, M. Giles, M. Heeney, I. McCulloch, *Phys. Rev. B* 74 (2006) 115318.
- [21] H.J. Kim, H.H. Lee, J.-J. Kim, *Macromol. Rapid Commun.* 30 (2009) 1269.

the simplest and most manufacturable device configurations will require optimized semiconductor performance in “bottom-contact” TFT geometries, in which the semiconductor is deposited on the D–S contacts [6]. In either configuration, the device is turned on only when a voltage is applied between the S–G electrodes giving rise to accumulated charges in the semiconductor channel. Key TFT parameters include the field-effect mobility ( $\mu$ ) and the current on/off ratio ( $I_{\text{on}}/I_{\text{off}}$ ), which quantify the average charge carrier drift velocity per unit electric field and D–S current gain when the device is turned on, respectively. Applications require the field-effect mobility and on/off ratio to be as high as possible.

In this paper we report the optical, electrochemical, and structural characteristics of benzodithiophene-based compounds **1–5** (Fig. 1) as well as their thin-film optical, morphological, and TFT semiconductor properties. Compounds **1** and **2** are tetrathia-[7]-helicenes ([7]-TH), that are chiral molecules with an helical shape, whereas compounds **3–5** are olefins substituted at the positions 1 and 2 of the double bond with benzodithiophene units. This helical shape could provide unique charge transport properties as observed for DNA and oligophenylureas [6c]. The geometry of the double bond is *Z* in alkene **3**, whereas alkenes **4** and **5** were obtained as pure *E* isomers. During the present study, a paper appeared in the literature reporting on the semiconducting properties of compound **4**, together with some morphological characterizations [7]. Some compounds of this family have interesting optical and electronic properties and both theoretical and experimental work have shown that they are potential candidates for nonlinear optic applications [8–10]. In particular, some of us are involved in the design and establishment of appropriate synthetic methodologies to achieve various substituted tetrathia-[7]-helicenes as well as their olefinic precursors, such as alkenes **4** and **5**, from which helicenes can be easily obtained through an oxidative photochemical cyclization. Tetrathia-[7]-helicenes are thermally and configurationally very stable chiral compounds [11] and can

be easily functionalized in the positions 2 and 13 of the two terminal thiophene rings, as well as in the central arene ring of the helical system (*i.e.* positions 7 and 8). This allows the introduction of different functional groups in a regioselective manner and therefore enables the tuning of their steric and electronic properties. Contrary to helicenes **1** and **2**, alkenes **4** and **5** are not chiral due to the complete planarity of the  $\pi$ -conjugated system. The two electron-withdrawing perfluorinated chains mostly employed to induce n-channel transport have been introduced in compound **5** in order to compare its properties with those of compound **4** [12]. The syntheses of compounds **1–4** have been reported previously [13] and here we describe only synthetic optimization of new compound **5**. In addition, the full chemical and physical characterization of compounds **1–5** (Fig. 1), morphological analysis of the corresponding films and the TFT performance are described.

## 2. Experimental

### 2.1. Reagents and methods

Reagents obtained from commercial sources were used without further purification. Before being used, the THF was dried by distillation over sodium wires/benzophenone, and the butyl lithium solutions in hexane were titrated. Unless otherwise stated, all of the reactions were performed under an inert atmosphere, after the glassware had been flame-dried. In order to monitor the progress of the reactions, thin layer chromatography (TLC) was performed using Merck silica gel 60 F254 pre-coated plates. Flash chromatography was performed using Merck silica gel 60, 230–400 mesh. Melting points were determined by means of a Büchi B 540 apparatus and are uncorrected. The IR spectra were recorded on a Perkin–Elmer FT-IR 1725X and only noteworthy absorption bands are listed. Solution emission and absorption spectra were obtained with a Cary 1 Ultraviolet/Visible Spectrometer and a PTI QM2 Fluores-

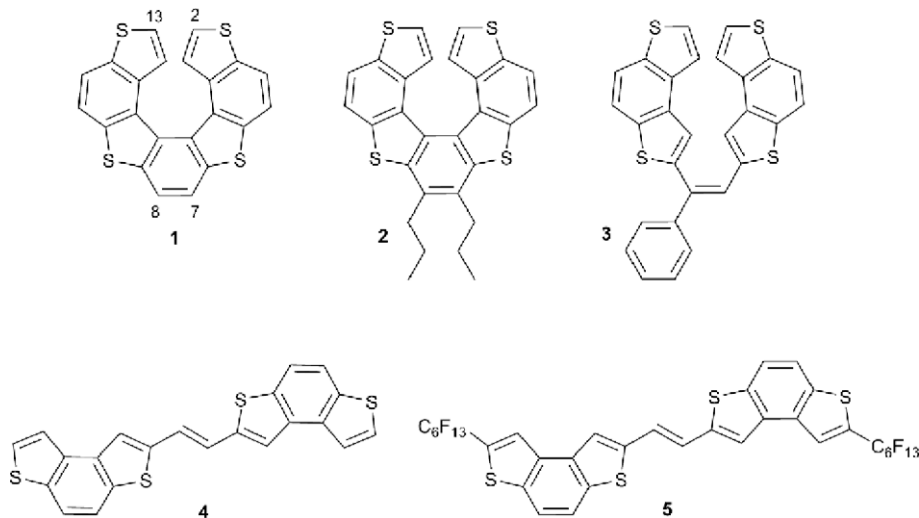


Fig. 1. Structures of the compounds **1–5** employed in this study.



cence Instrument. The mass spectra were recorded on LCO Advantage Thermo equipped with ion trap and APCI source in 50–2000  $m/z$  range. High-resolution mass spectra were recorded on a Vg Analytical 7070 EQ.  $^1\text{H}$  NMR (300 and 200 MHz) and  $^{13}\text{C}$  NMR (75 MHz) spectra were recorded on Bruker AC 300, Bruker AC 200 and Bruker AMX 300.

## 2.2. Synthesis

### 2.2.1. 2-Tridecafluorohexyl-benzo-[1,2b;4,3b']-dithiophene (compound 7) [12]

A suspension of Cu (1.473 g, 23.16 mmol, 5.23 equiv.) in dry DMSO (14.7 mL) was heated at 125 °C for 15 min under nitrogen atmosphere. Tridecafluorohexyliodide (2.41 mL, 11.07 mmol, 2.5 equiv.) was added dropwise into the suspension while keeping the temperature below 135 °C. The suspension was heated at 125 °C for 45 min and then a solution of 2-iodo-benzodithiophene **6** (1.4 g, 4.43 mmol, 1 equiv.) in 9.1 mL of DMSO was added dropwise at 115 °C. The mixture was stirred at 115 °C for 6 h. The reaction was quenched with 45 mL of cold water and extracted with ether (1 × 100 mL, 2 × 20 mL). The combined organic phases were then washed with water. The organic phase was separated and dried over  $\text{Na}_2\text{SO}_4$ , and the solvent was evaporated under reduced pressure affording 2.40 g of crude reaction mixture as a solid. The mixture was purified by means of gravimetric column chromatography, eluent light petroleum, to give the expected compound **7** in 78% yield (1.76 g) together with the disubstituted derivative **8** in 8% yield (295 mg).

**Compound 7:** HRMS calcd. for  $\text{C}_{16}\text{H}_5\text{F}_{13}\text{S}_2$ : 507.96251, found 507.9631; mp (hexane): 64–65 °C;  $^1\text{H}$  NMR (300 MHz,  $\text{CDCl}_3$ ) = 7.65 (d,  $J$  = 5.4 Hz, 1H), 7.74 (d,  $J$  = 5.4 Hz, 2H), 7.81 (d,  $J$  = 8.7 Hz, 2H), 7.94 (d,  $J$  = 8.7 Hz, 2H), 8.05 (s, 1H) ppm.  $^{13}\text{C}$  NMR (75 MHz,  $\text{CDCl}_3$ ) = 105.0, 108.1, 111.6, 115.5, 119.6 (m,  $\text{C}_q\text{F}$ ); 118.6, 121.7, 122.0, 125.8, 128.2 (CHar); 129.9 (t,  $^2J$  = 28.1 Hz,  $\text{C}_q\text{CF}$ ), 133.6, 135.6, 137.6, 138.6 (Cq) ppm;  $^{19}\text{F}$  NMR (282.23 MHz,  $\text{CDCl}_3$ ) = -81.2 (s, 3F), -102.0 (s, 2F), -121.8 (s, 4F), -123.1 (s, 2F), -126.5 (s, 2F); MS (EI):  $m/z$  (%) = 508 ( $\text{M}^+$ , 50), 489 ( $[\text{M}-\text{F}]^+$ , 15), 239 ( $[\text{M}-(\text{C}_5\text{F}_{11})]^+$ , 100).

**Compound 8:** HRMS calcd. for  $\text{C}_{22}\text{H}_4\text{F}_{26}\text{S}_2$ : 825.93393, found 825.9325; mp (hexane): 57–58 °C;  $^1\text{H}$  NMR (300 MHz,  $\text{CDCl}_3$ ) = 7.95 (s, 2H), 8.1s (s, 2H) ppm.  $^{13}\text{C}$  NMR (75 MHz,  $\text{CDCl}_3$ ) = 107.2, 111.3, 115.0, 118.5 (m,  $\text{C}_q\text{F}$ ); 120.8, 124.9 (CHar); 131.1 (t,  $^2J$  = 28.5 Hz,  $\text{C}_q\text{CF}$ ), 133.8, 138.9 (Cq) ppm;  $^{19}\text{F}$  NMR (282.23 MHz,  $\text{CDCl}_3$ ) = -81.2 (s, 3F), -102.1 (s, 2F), -121.7 (s, 4F), -123.1 (s, 2F), -126.4 (s, 2F); MS (EI):  $m/z$  (%) = 826 ( $\text{M}^+$ , 50), 807 ( $[\text{M}-\text{F}]^+$ , 20), 776 ( $[\text{M}-(\text{CF}_2)]^+$ , 15), 757 ( $[\text{M}-(\text{CF}_3)]^+$ , 5), 557 ( $[\text{M}-(\text{C}_5\text{F}_{11})]^+$ , 100), 507 ( $[\text{M}-(\text{C}_6\text{F}_{13})]^+$ , 15).

### 2.2.2. 7-Tridecafluoroethyl-benzo-[1,2b;4,3b']-dithiophene-2-carboxaldehyde (compound 9)

A *n*-BuLi solution in hexane (1.47 M, 1.56 mL, 2.29 mmol; 1.15 equiv.) was added dropwise under stirring and nitrogen atmosphere to a solution of **8** (1.01 g, 1.99 mmol) in dry THF (12 mL) at -78 °C. The solution was stirred for 30 min at -78 °C and then treated with dry DMF (0.31 mL, 3.97 mmol, 2 equiv.). The progress of the reaction was monitored by TLC (light petroleum–AcOEt

9.5:0.5;  $R_f$  **8** = 0.75;  $R_f$  **9** = 0.38). After 30 min at -78 °C, the solution was quenched with a saturated aqueous solution of  $\text{NH}_4\text{Cl}$  (10 mL). The mixture was taken up with  $\text{CH}_2\text{Cl}_2$  (40 mL) and the aqueous phase extracted twice with 5 mL of  $\text{CH}_2\text{Cl}_2$ . The organic phase was washed with water and dried over  $\text{Na}_2\text{SO}_4$ ; the solvent was removed under reduced pressure affording 1.07 g of compound **9** as pale yellow solid in quantitative yield. HRMS calcd. for  $\text{C}_{17}\text{H}_5\text{F}_{13}\text{OS}_2$ : 535.95743; found: 535.95874; mp 161–163 °C.  $^1\text{H}$  NMR (300 MHz,  $\text{CDCl}_3$ ) = 7.95 (d,  $J$  = 9.0 Hz, 1H), 7.99 (d,  $J$  = 9.0 Hz, 1H), 8.11 (s, 1H), 8.41 (s, 1H), 10.17 (s, 1H, CHO) ppm.  $^{13}\text{C}$  NMR (75 MHz,  $\text{CDCl}_3$ ) = 108.1, 111.5, 115.5, 119.5 (m,  $\text{C}_q\text{F}$ ); 122.1, 122.7, 125.4, 131.2 (CHarom), 131.8 (t,  $^2J$  = 28.6 Hz,  $\text{C}_q\text{CF}$ ), 134.7, 134.9, 139.2, 141.5, 144.6, (Cq), 184.5 (CHO) ppm;  $^{19}\text{F}$  NMR (282.23 MHz,  $\text{CDCl}_3$ ) = -81.1 (s, 3F), -102.2 (s, 2F), -121.7 (s, 4F), -123.1 (s, 2F), -126.5 (s, 2F); IR (Nujol): 1669  $\text{cm}^{-1}$  (C=O); MS (EI):  $m/z$  (%) = 536 ( $\text{M}^+$ , 65), 267 ( $[\text{M}-(\text{C}_5\text{F}_{11})]^+$ , 100), 238 ( $[\text{M}-(\text{CHO}+\text{C}_5\text{F}_{11})]^+$ , 10).

### 2.2.3. 1,2-Bis-(7-tridecafluorohexyl-benzo-[1,2b;4,3b']-dithiophen-2-yl)-ethene (compound 5)

To a stirred solution of **9** (342 mg, 0.638 mmol, 1 equiv.) in 6.8 mL of dry THF at -5 °C, pure  $\text{TiCl}_4$  (0.083 mL, 0.765 mmol, 1.2 equiv.) was added dropwise. After 30 min, at -5 °C, 104 mg of powdered Zn (1.59 mmol, 2.5 equiv.) was added and the suspension was stirred for 15 min. The mixture was refluxed for 1.5 h. After removing the solvent at reduced pressure, 10 mL of HCl 37%/water (1/1 v/v) was added at RT and the suspension stirred for 1 h, then filtered and the solid washed with cold MeOH affording pure **5** in 85% yield as a yellow solid (280 mg).

**Compound 5:** HRMS calcd. for  $\text{C}_{34}\text{H}_{10}\text{F}_{26}\text{S}_4$ : 1039.92501, found 1039.92660; mp: 223–225 °C;  $^1\text{H}$  NMR (300 MHz, THF-D8) = 7.44 (s, 2H, CH=), 7.93 (d,  $J$  = 8.7 Hz, 2H), 7.97 (d,  $J$  = 8.7 Hz, 2H), 8.00 (s, 2H), 8.34 (s, 2H);  $^{13}\text{C}$  NMR (75 MHz, THF-D8) = 108.3, 112.3, 116.3, 120.0 (m,  $\text{C}_q\text{F}$ ); 120.0, 122.3, 123.1, 125.2, 127.3 (CHar), 129.7 (t,  $^2J$  = 28.2 Hz,  $\text{C}_q\text{CF}$ ), 134.2, 137.0, 137.9, 139.6, 144.5, (Cq) ppm;  $^{19}\text{F}$  NMR (282.23 MHz, THF-D8) = -80.7 (s, 3F), -101.0 (s, 2F), -120.9 (s, 4F), -122.3 (s, 2F), -127.7 (s, 2F); MS (EI):  $m/z$  (%) = 1040 ( $\text{M}^+$ , 100), 1021 ( $[\text{M}-\text{F}]^+$ , 10), 771 ( $[\text{M}-(\text{C}_5\text{F}_{11})]^+$ , 15), 552 ( $[\text{M}-(\text{C}_9\text{F}_{20})]^+$ , 5), 520 ( $[\text{M}-(\text{C}_{10}\text{F}_{21})]^+$ , 10), 502 ( $[\text{M}-(\text{C}_{10}\text{F}_{22})]^+$ , 5), 251 ( $[(\text{M}-(\text{C}_{10}\text{F}_{22}))/2]^+$ , 50); UV/Vis ( $\text{CH}_2\text{Cl}_2$ ):  $\lambda_{\text{max}}$  = 419, 395, 374, 355 nm.

## 2.3. Electrochemistry

Cyclic voltammetry was performed in an electrolyte solution of 0.1 M tetrabutylammonium hexafluorophosphate ( $\text{Bu}_4\text{N}^+\text{PF}_6^-$ ) in THF with scan rates between 70 and 100 mV/s. A ferrocene/ferrocenium redox couple was used as an internal standard and potentials obtained in reference to a silver electrode were converted to the saturated calomel electrode (SCE) scale.

## 2.4. Device fabrication

Prime grade p-doped silicon wafers (100) having 300 nm thermally grown oxide (Montco Semiconductors)

were cleaned by sonication in ethanol (200 proof) for 3 min and by oxygen plasma treatment for 5 min. Hexamethyldisilazane (HMDS) was deposited by placing the cleaned SiO<sub>2</sub> substrates into a N<sub>2</sub>-refilled chamber saturated with HMDS vapor for 72 h. Organic compounds were vacuum-deposited ( $3 \times 10^{-6}$  Torr) at a growth rate of 0.2–0.3 Å s<sup>-1</sup> at various substrate temperatures ( $T_{DS}$ ), 25, 55, and 90 °C. Grown films were ~500 Å thick (as determined by a calibrated in situ quartz crystal monitor). For TFT device fabrication, top-contact electrodes (700 Å) were deposited by evaporating gold (pressure  $<1 \times 10^{-6}$  Torr); channel dimensions were 100 μm (L) by 5000 μm (W).

### 2.5. Thin film characterization

Thin films were analyzed by wide-angle X-ray diffraction (XRD), using standard  $\theta$ - $2\theta$  techniques, with monochromated Cu K $\alpha$  radiation. Atomic force microscopy (AFM) images are collected using a NT-MDT Solver Scanning Probe Microscope in the tapping mode using Si cantilever with the samples kept in air. UV–visible absorption and photoluminescence (PL) spectra for films of compound **5** were obtained with a Cary 1 Ultraviolet/Visible Spectrometer and a PTI QM2 Fluorescence Instrument. Except compound **5**, for all the thin films of other compounds, UV–visible absorption spectra were recorded with a JASCO V-550 spectrophotometer and PL spectra were collected in transmission by a Hamamatsu multichannel optical analyzer exciting the samples **1**, **2**, **3** with the 355 nm line of a 10 Hz, 25 pulse duration, Q-switched Quantel Nd:YAG laser and sample **4** with a Nichia laser diode module with emission at 405 nm. The Nd:YAG laser beam energy per pulse was 1.3 μJ and the laser diode beam power was 40 mW. A GG420 cut-off filter is used for truncating the 405 nm excitation without modulating the PL emission. All the PL measurements were carried out in high vacuum.

### 2.6. Single crystal X-ray diffraction of compound **3**

The intensity data of compound **3** were collected at 173 K on a ENRAF NONIUS CAD 4 single crystal diffractometer using a graphite monochromated Cu K $\alpha$  radiation. Crystallographic and experimental details of the structure are summarized in Table S1. The structure was solved by Fourier methods and refined by full-matrix least-squares procedures, first with isotropic thermal parameters and then with anisotropic thermal parameters in the last cycles of refinement for all the non-hydrogen atoms (M. Sheldrick, SHELXL-97, Program for Crystal Structure Refinement, University of Göttingen, Germany, 1997). The hydrogen atoms were introduced into the geometrically calculated positions and refined riding on the corresponding parent atoms.

### 2.7. Electrical measurements

Electrical measurements were carried out under vacuum ( $<1 \times 10^{-5}$  Torr) using a Keithly 6430 subfemtometer and a Keithly 2400 source meter, operated by a local Labview program and GPIB communication. Triaxial and/or

coaxial shielding was incorporated into Signatone probe stations to minimize the noise level.

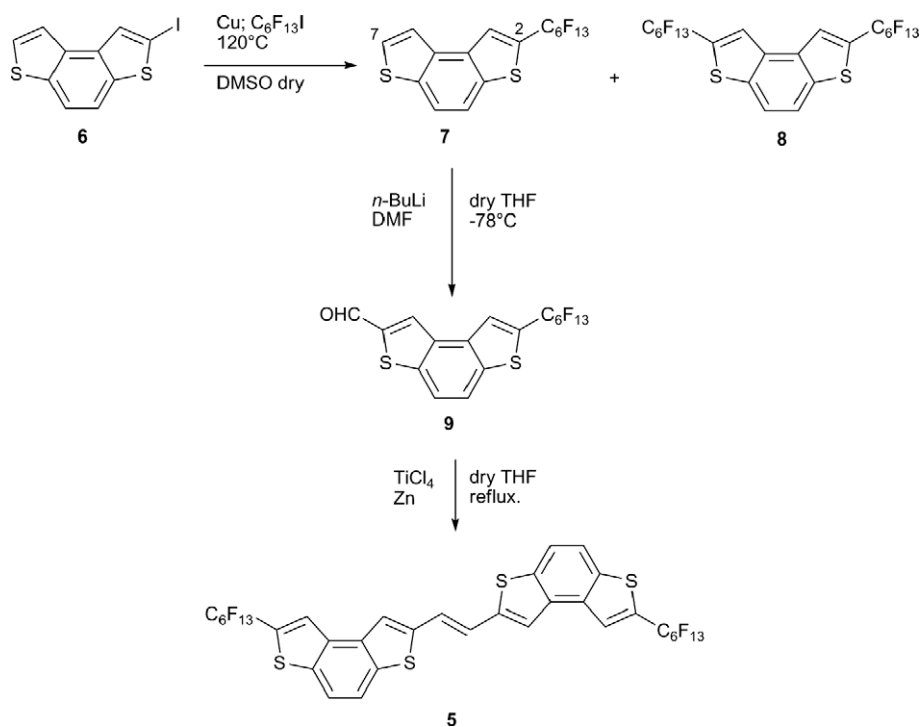
## 3. Results and discussion

### 3.1. Synthesis of compound **5**

The synthesis of polyfluorinated alkene **5** was accomplished as reported in Scheme 1. Considering that compound **5** is a symmetrically substituted alkene, an appropriate methodology is a McMurry reductive coupling of the aldehyde **9**. In fact, during our research to find suitable methodologies for the preparation of symmetrically substituted 1,2-bis(benzodithienyl)ethenes [13b,d], we verified that this method is simple, versatile, and efficient enabling the achievement of **5** from **9** in one-step. The synthesis of aldehyde **9** starts from 2-iodobenzodithiophene **6** where the perfluorohexyl chain was attached through a Cu-mediated coupling with tridecafluoro-1-iodohexane, in DMSO at 125 °C [12]. In this way, compound **7** was obtained in 78% yield as white solid, together with a small amount (8%) of the disubstituted derivative **8**. Aldehyde **9** was then obtained from **7** by deprotonating the free  $\alpha$ -position of the thiophene ring (position 7) and the resulting anion was reacted with DMF as formylating reagent. In this way, **9** was isolated in quantitative yield as a light yellow solid. The last step of the synthesis consists of the McMurry reductive coupling of aldehyde **9** using TiCl<sub>4</sub>/Zn reductive reagent. Pure *E* isomer **5** was obtained in 85% yield as yellow solid.

### 3.2. Optical properties

Optical absorption and emission maxima of compounds **1–5** were performed in solution (Fig. 2A) and as thin films on glass substrates (Fig. 2B, vide infra thin-film deposition condition). In CH<sub>2</sub>Cl<sub>2</sub>, compounds **1** and **2** exhibit very similar absorption spectra with two absorption maxima located at 368 and 387 nm for **1** and 370 and 390 nm for **2**. Note that there is a small (~3 nm) bathochromic shift going from **1** to **2** in agreement with the electron-donating nature of the propyl substituents. Thin-film absorption spectra of **1** and **2** are also very similar and exhibit two absorption maxima at 378 and 398 nm for **1** and 377 and 397 nm for **2**. A small bathochromic shift (< 10 nm) is observed going from solution to the thin film, evidence of J-aggregate formation [14]. Compound **3** in solution exhibits three major absorptions located at 364 and 380 nm, very close to those of compounds **1** and **2**, and the third peak falls at far longer wavelength (416 nm). The thin-film optical spectrum of compound **3** also exhibits three absorption maxima at 384, 406, and 436 nm, which are red-shifted by ~20 nm compared to those in solution. This result may be accounted by formation of J-aggregates or conjugated core planarization. Alkenes **4** and **5** also show similar absorption spectra in solution with absorption maxima located at 370, 391, and 415 nm for **4** and 373, 394, and 418 nm for **5**. The strong absorption maxima at ~415 nm, which is not present in compounds **1–3** spectra is a clear signature of the *E* isomers.[15] Thin films of compound **4** and



Scheme 1. Synthetic route to compound 5.

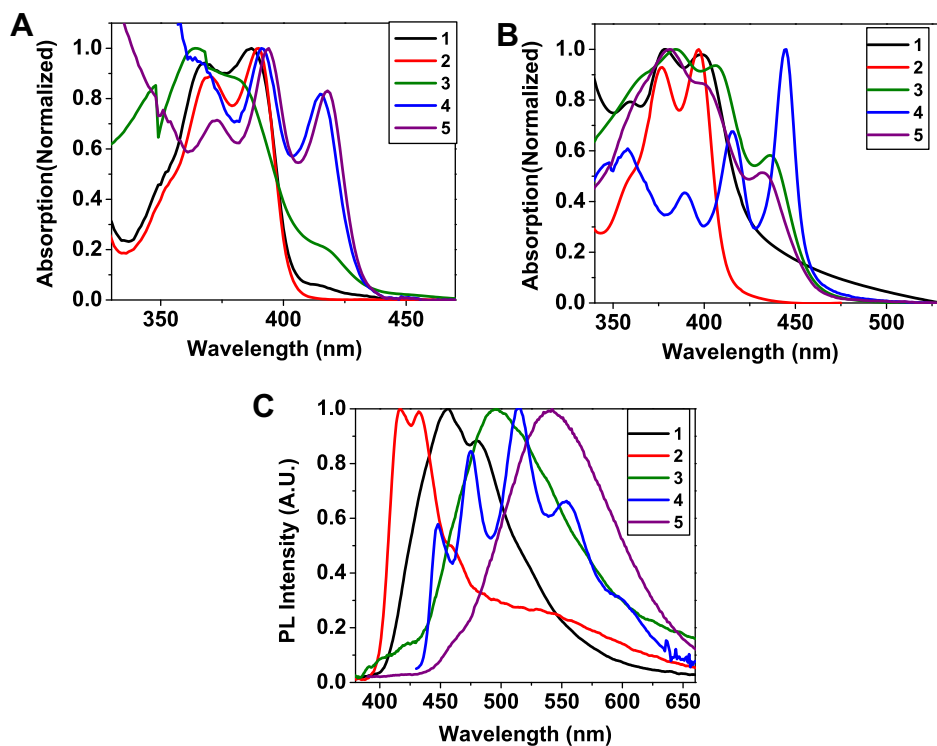


Fig. 2. UV-visible absorption spectra of compounds 1–5 in  $\text{CH}_2\text{Cl}_2$  solution (A), as thin films on glass substrates (B), and photoluminescence emission spectra as thin films on glass substrates (C).

**5** exhibit absorption maxima at 357, 386, 415, and 445 nm for **4** and 382, 399, and 432 nm for **5** with strong absorption at >410 nm.

Thin film photoluminescence emission spectra of all compounds are shown in Fig. 2C. Thin films of compounds **1** and **2** exhibit two emission peaks located at 456 and 478 nm for **1** and 417 and 432 nm for **2**. Compound **3** shows one emission maximum at 498 nm. Compounds **4** and **5** have multiple peaks at 448, 475, 515, and 555 nm for **4** and at 468 and 542 nm for **5**. Compound **4** exhibits very small Stokes shifts of ~3 nm between the absorption and emission maxima compared to those of compounds **1–3**; this suggests a greater core rigidity of thin film phase affording TFT active device (vide infra) [16]. Band gaps for the present compounds are estimated from the low-energy band edges of the thin-film optical spectra, taking 10% of the maximum as the band edge (Table 1). The optical band gaps of compounds **1–5** are estimated to be 2.9, 3.0, 2.7, 2.7, and 2.7 eV, respectively.

### 3.3. Electrochemical properties

Oxidation and reduction potentials for the present compounds were measured by cyclic voltammetry (CV). Cyclic voltammograms of the compounds **1–5** in solution are shown in Fig. 3, and electrochemical data are summarized in Table 2. Compounds **1–3** exhibit onset oxidation potentials of ~1.5, ~1.3, and ~1.0 V, respectively (vs. SCE) without obvious reduction peaks. On the other hand, compounds **4** and **5** exhibit one reduction located at -1.7 and -1.5 V, respectively, but no oxidations.

**Table 1**

Solution (in CH<sub>2</sub>Cl<sub>2</sub>) and film optical absorption maxima, film emission maxima ( $\lambda$ , nm), and energy gaps ( $E_g$ , eV) of compounds **1–5**.

Compound	$\lambda_{\text{sol}}^{\text{ab}}$ (nm)	$\lambda_{\text{film}}^{\text{ab}}$ (nm)	$\lambda_{\text{film}}^{\text{em}}$ (nm)	$E_g$ (eV) <sup>a</sup>	
				Sol	Film
<b>1</b>	368, 387	359, 378, 398	456, 478	3.1	2.9
<b>2</b>	370, 390	377, 397	417, 432	3.1	3.0
<b>3</b>	364, 380, 416	384, 406, 436	498	2.9	2.7
<b>4</b>	370, 391, 415	357, 386, 415, 445	448, 475, 515, 555	2.9	2.7
<b>5</b>	373, 394, 418	382, 399, 432	468, 542	2.9	2.7

<sup>a</sup> Optical band gap estimated from the low-energy band edge in the film optical spectrum. Concentrations are 10<sup>-4</sup>–10<sup>-6</sup> M.

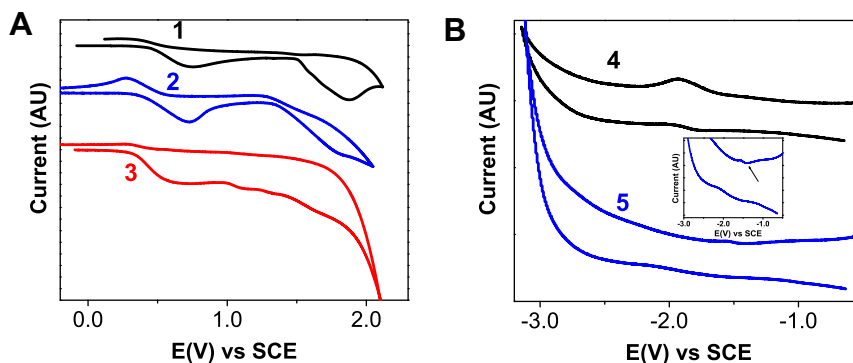


**Fig. 3.** Cyclic voltammograms of compounds **1–5** in 0.1 M Bu<sub>4</sub>N<sup>+</sup>PF<sub>6</sub><sup>-</sup> solution in THF at a scan rate of 100 mV/s. In all experiments, ferrocene is used as the internal standard (first peak in the CV scan). Inset: enlarged CV plot for compound **5** indicating reduction peak.

**Table 2**

Electrochemical (in THF) and energetic properties of compounds **1–5**.

Compound	$E_{\text{ox}}^{\text{onset}}$ (V) <sup>a</sup>	$E_{\text{red}}^{\text{onset}}$ (V) <sup>b</sup>	$E_{\text{HOMO}}$ (eV) <sup>c</sup>	$E_g$ (eV) <sup>c</sup>	$E_{\text{LUMO}}$ (eV) <sup>c</sup>
<b>1</b>	1.5	–	-5.9	2.9	-3.0
<b>2</b>	1.3	–	-5.7	3.0	-2.7
<b>3</b>	1.0	–	-5.4	2.7	-2.7
<b>4</b>	–	-1.7	-5.4	2.7	-2.7
<b>5</b>	–	-1.5	-5.6	2.7	-2.9

<sup>a</sup> Onset voltage for oxidation vs. SCE.

<sup>b</sup> Onset voltage for reduction vs. SCE.

<sup>c</sup>  $E_{\text{LUMO}} = E_{\text{HOMO}} + E_g$ .

From these oxidation and reduction potentials, HOMO and LUMO energies were estimated knowing that the SCE energy level is -4.4 eV below the vacuum level ( $E_{\text{HOMO}} = -E_{\text{ox}}^{\text{onset}} - 4.4$ ,  $E_{\text{LUMO}} = -E_{\text{red}}^{\text{onset}} - 4.4$ ) (Table 2) and the band gaps obtained by optical absorption data [17]. Using these relations, the HOMO values are estimated to lie at -5.9, -5.7, and -5.4 eV for **1**, **2**, and **3**, respectively. Similarly, the LUMO values are calculated as -2.7 and 2.9 eV for **4** and **5**.

### 3.4. Single crystal X-ray diffraction of compound **3**

An ortep view of compound **3** structure is shown in Fig. 4A with caption of the most important bond distances and torsion angles. In the crystal structure of compound **3**, the two benzodithiophene units lie on almost perpendicular planes with dihedral angle between the mean planes of

87.72(2)°. This is the consequence of the *Z*-isomer configuration. The phenyl ring is almost coplanar (dihedral angle of 3.42(1)°) and conjugated with one of benzodithiophenes in such a way as the (C15)C16=C17(C18,C23) double bond system.

The packing of the molecules along the *b*-axis is shown in Fig. 4B. The distances between adjacent mean planes of the conjugated systems, defined by the phenyl ring, the double bond system, and the benzodithiophene unit, are 3.719(1) and 3.192(1) Å, while those between adjacent mean planes of the other benzodithiophene unit are 3.338(1) and 3.348(1) Å. Thus, in principle, the interplanar distances could allow efficient intermolecular charge transfer. However, as shown in the Fig. 4B, the co-facial motif does not extend to the entire system with conjugations only between one thiophene and the phenyl ring and between two thiophene rings of co-facial conjugated systems (distances between the centroids of those rings being 4.017(2) and 3.632(2) Å, respectively), and between two thiophene rings and two phenyl rings of the benzodithiophene groups lying perpendicular to the conjugated system (distances between the centroids of those rings of 3.612(2) and 4.038(1) Å, respectively).

This weak interaction and small overlap between molecules fully explain the poor TFT activity of compounds **3** (vide infra). Note that the crystal structure of compound **3** confirms an NMR study reported elsewhere on an analogous alkene [13c], where the configuration in Fig. 5 is the most stable for *cis*-alkene precursors of tetrata-[7]-helicenes in solution and in solid state.

The crystal structures of compounds **1** and **2** have been already reported elsewhere [18,19]. It has been seen that only weak interactions of 3.77 and 4.038(2) Å, respectively are present between phenyl rings of adjacent molecules, indicating poor direct  $\pi$ -electrons overlap between adja-

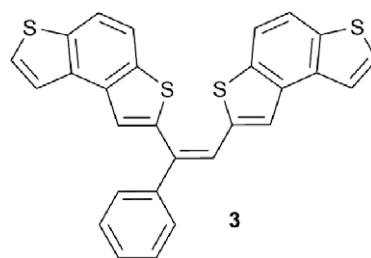


Fig. 5. Preferred conformation of compound **3** as more stable form based on single crystal XRD.

cent rings and justifying the low TFT activity of such compounds, especially of compound **2**.

### 3.5. Thin-film transistor performance

Top-contact OTFTs [100  $\mu\text{m}$  channel lengths (*L*) and 5.0 mm channel widths (*W*)] were fabricated by vapor-depositing **1–5** films on 300 nm SiO<sub>2</sub> (**Bare**) and **HMDS**-treated SiO<sub>2</sub> (**HMDS**) substrates maintained at various substrate temperatures (25, 55, and 90 °C), followed by Au deposition through a shadow mask to define the source and drain electrodes. OTFT measurements were performed under vacuum and the device performance (mobility, on/off ratio, and threshold voltage) data are summarized in Table 3. Mobilities ( $\mu$ ) were calculated in the saturation regime using the relationship:  $\mu_{\text{sat}} = (2I_{\text{sd}}L)/[WC_{\text{ox}}(V_{\text{sg}} - V_{\text{th}})^2]$ , where  $I_{\text{sd}}$  is the source-drain saturation current;  $C_{\text{ox}}$  is the areal capacitance value,  $V_{\text{sg}}$  is the gate voltage, and  $V_{\text{th}}$  is the threshold voltage. The latter can be estimated as the *x* intercept of the linear section of the plot of  $V_{\text{sg}}$  vs.  $(I_{\text{sd}})^{1/2}$ . The mobility numbers are the average of at least four chips.

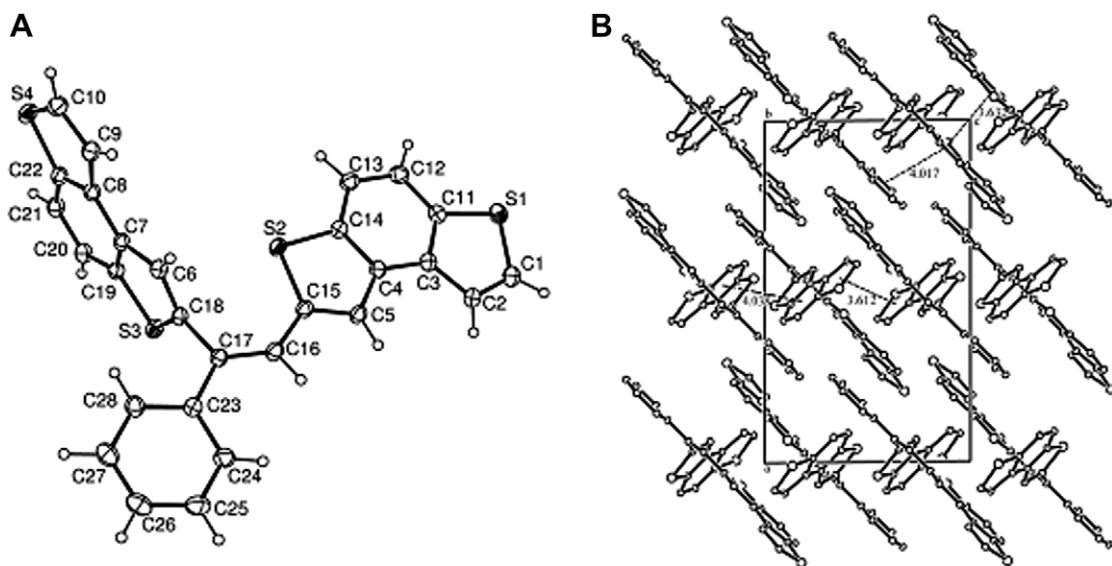


Fig. 4. (A) Ortep view of compound **3**. Ellipsoids are drawn at 30% probability level. Bond distances (Å) and torsion angles (°): C2–C3 1.430(3), C3–C4 1.422(3), C4–C5 1.425(3), C6–C7 1.433(3), C7–C8 1.416(3), C8–C9 1.434(3), C12–C13 1.379(3), C16–C17 1.352(3), C20–C21 1.374(3); S2–C15–C16–C17 14.33(1), C15–C16–C17–C18–0.90(1), C15–C16–C17–C23 178.03(1), S3–C18–C17–C23–85.08(1). (B) Molecular packing of compound **3**. View along *b*-axis.

**Table 3**

Mobilities  $\mu$ , current on/off ratios ( $I_{\text{on}}/I_{\text{off}}$ ), and threshold voltages ( $V_T$ , V) for vapor-deposited films of compounds **1–5** deposited at various substrate temperatures ( $T_D$ , °C).

Compound	$T_D$	Substrate	$\mu$	$I_{\text{on}}/I_{\text{off}}$	$V_T$
<b>1</b>	25	Bare	$1.7 \times 10^{-7}$	$10^2$	-66
<b>2</b>			–		
<b>3</b>	25	Bare		–	
	90		$4.8 \times 10^{-7}$	$10^1$	-20
	25	HMDS	$1.1 \times 10^{-5}$	$10^3$	-44
<b>4</b>	90		$1.2 \times 10^{-7}$	$10^3$	-48
	25	Bare	$9 \times 10^{-4}$	$10^6$	-49
	55		$7 \times 10^{-3}$	$10^6$	-66
	90		$3 \times 10^{-4}$	$10^6$	-46
	25	HMDS	$2 \times 10^{-2}$	$10^7$	-56
	55		$2 \times 10^{-2}$	$10^6$	-44
<b>5</b>	90		$4 \times 10^{-4}$	$10^6$	-62
			–		

With the exception of compound **4**, all the other compounds-based devices show no (**2** and **5**) or very poor (**1** and **3**) TFT activities with mobilities of  $10^{-5}$ – $10^{-7}$  cm<sup>2</sup>/Vs and on/off ratios of  $10^1$ – $10^3$ . For compound **4**, mobilities strongly depend on both dielectric surface treatment and deposition temperature ( $T_D$ ). Representative OTFT transfer and output characteristics of compound **4**-based devices are shown in Fig. 6. Overall, the devices based on compound **4** perform better on HMDS (with mobilities of  $4 \times 10^{-4}$ – $2 \times 10^{-2}$  cm<sup>2</sup>/Vs) than on Bare (with mobilities of  $3 \times 10^{-4}$ – $7 \times 10^{-3}$  cm<sup>2</sup>/Vs) substrates. All devices based on compound **4** exhibit very high current on/off ratio of  $10^6$ – $10^7$ . Considering the correlation between  $T_D$  and the device performance, 55 °C seems to be the optimum temperature affording the highest mobilities on both substrates. Deposition temperature-dependent device performance can be ascribed to the differences in film crystallinity and morphology (vide infra).

### 3.6. Film morphology and microstructure

To investigate semiconductor film microstructure, wide-angle X-ray diffraction (WAXRD) was performed on the films of compounds **1**, **3**, and **4**. The XRD spectra of **1** and **3** films exhibit no reflections in the 2–30°  $2\theta$  range,

indicating amorphous films. This result is fully in agreement with the poor device performance. Fig. 7 shows the  $\theta$ - $2\theta$  scans for **4** films deposited at  $T_D = 55$  and 85 °C on HMDS substrates, demonstrating that these vapor-deposited films are highly crystalline. The progression of Bragg reflections corresponds to a  $d$ -spacing of 18.6 Å ( $2\theta = 5.25^\circ$ ), affording an edge-on substrate molecular orientation to the substrate. Since the TFT performance of the device of **4** is quite sensitive to the substrate temperature, the XRD patterns were also examined at various  $T_D$ s. Films deposited at  $T_D = 55$  °C show much stronger intensity compared to those at  $T_D = 90$  °C, indicating higher film crystallinity in agreement with the improved device performance.

The AFM images of **1–5** films show a variety of morphological features such as tubular, grains, or smooth surface morphologies (Figs. 8 and S2). Representative AFM images of **1** and **4** films are shown in Fig. 8. Films of **1** deposited on both Bare and HMDS substrates at 25 °C exhibit tubular, nanowire-like structure. These morphological features can be understood from the analysis of the crystal packing of the racemate of compound **1**. The structure presents an alternate stacking of the two molecular enantiomers ( $P$  and  $M$ ) along the  $c$ -axis so that the two central benzene rings almost overlap in upturned positions.[18] Thus, each nanowire is likely formed by chains of alternating helicene enantiomers.

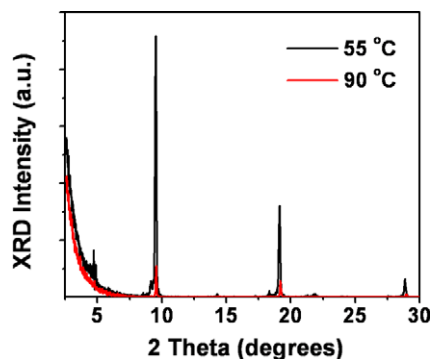


Fig. 7. Wide-angle XRD spectra of compound **4** on HMDS-treated SiO<sub>2</sub> substrate at the indicated substrate temperatures.

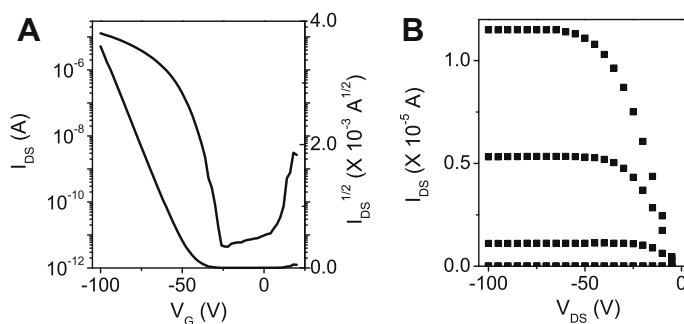
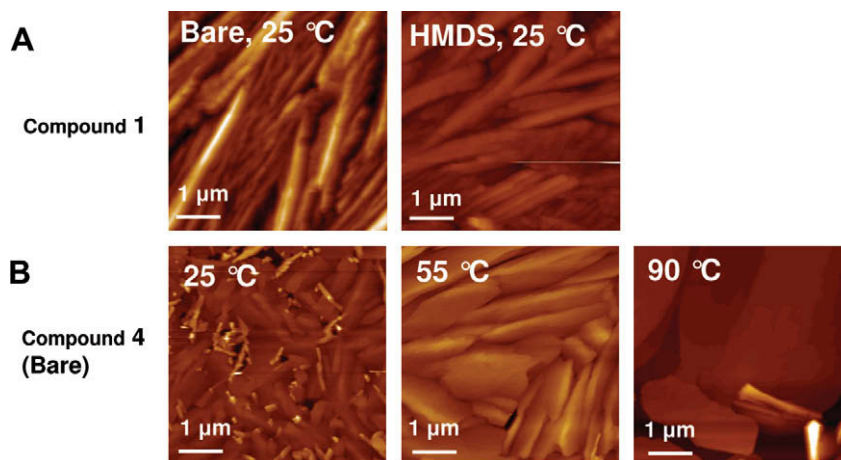


Fig. 6. OTFT performance (A: transfer B: output) characteristics of compound **4** on HMDS (films deposited at 55 °C). The gate voltage was swept at a constant  $V_{\text{DS}} = -100$  V.



**Fig. 8.** AFM images of (A) compound **1** on **Bare** (left) and on **HMDS** (right) deposited at 25 °C, (B) compound **4** on **Bare** deposited at 25 (left), 55 (middle), and 90 °C (right). The scale bar is 1  $\mu\text{m}$ .

Films of **1** grown at 90 °C afford a lot of grains possibly due to dewetting from high substrate temperature. Films of **2**, **3** and **5** exhibit smooth, amorphous morphologies indicating no or poor TFT activity.

The AFM images of films of compound **4** show somewhat different morphologies compared to those of the other compounds. From Fig. 8B, it is clear that the film growth depends significantly on the substrate temperature.

Films grown on **Bare** at low temperature (25 and 55 °C) form well-connected and faceted grains ( $>1 \mu\text{m}$ ), affording moderate field-effect mobilities. Different substrate does not affect film morphology significantly exhibiting similar morphology on **HMDS** (not shown). However at high substrate temperature, huge gaps between large grains can be seen from AFM images, possibly compromising charge transport resulting in relatively low TFT performance compared to low substrate temperature.

#### 4. Conclusions

We have synthesized and characterized two helicenes (**1**, and **2**) and three alkene (**3–5**) derivatives as semiconductors for OTFT. Compounds **1**, **2**, **3** and **5** afford poor (with the mobilities of  $10^{-5}$ – $10^{-7} \text{cm}^2/\text{Vs}$ ) or no TFT activity, probably because of the poor film crystallinity or morphology. Compound **1** exhibits nanowire-like morphology for the films grown at 25 °C, observed for the first time for vapor-deposited helicene molecule with helical shape. Compound **4** is a p-channel material with hole mobilities approaching  $0.02 \text{cm}^2/\text{Vs}$  and current on/off ratio of  $10^6$ – $10^7$ . The carrier mobilities were found to depend on the substrate deposition temperature and surface treatments, which was correlated to the corresponding film morphologies and crystallinities.

#### Acknowledgements

This work was supported by Italian Ministry MIUR under Projects FIRB-RBNE033KMA and at Bologna by EU un-

der projects FP6-Marie Curie-035859 (BIMORE) and FP6-IST-015034 (OLAS) and by CNR under CNR-DPM project PROMO, and at Northwestern by the NSF-MRSEC program through Materials Research Center (DMR-0520513). Authors thank R. Zamboni for stimulating discussions.

#### Appendix A. Supplementary data

Supplementary data associated with this article can be found, in the online version, at doi:10.1016/j.orgel.2009.08.018.

#### References

- [1] (a) V.C. Sundar, J. Zaumseil, V. Podzorov, E. Menard, R.L. Willett, T. Someya, M.E. Gershenson, J.A. Rogers, *Science* 303 (2004) 1644; (b) H. Meng, M. Bendikov, G. Mitchell, R. Helgeson, F. Wudl, Z. Bao, T. Siegrist, C. Kloc, C.-H. Chen, *Adv. Mater.* 15 (2003) 1090; (c) H. Sirringhaus, *Nature Mater.* 2 (2003) 641; (d) S.A. Ponomarenko, S. Kirchmeyer, A. Elschner, B.-H. Huisman, A. Karbach, D. Drechsler, *Adv. Funct. Mater.* 13 (2003) 591; (e) A. Afzali, C.D. Dimitrakopoulos, T. Breen, *J. Am. Chem. Soc.* 124 (2002) 8812; D.B. Mitzi, C.D. Dimitrakopoulos, L.L. Kosbar, *Chem. Mater.* 13 (2001) 3728; C.D. Dimitrakopoulos, P.R.L. Malenfant, *Adv. Mater.* 14 (2002) 99; (h) F. Wurthner, *Angew. Chem. Int. Ed.* 40 (2001) 1037; (i) J. Veres, S. Ogier, G. Lloyd, *Chem. Mater.* 16 (2004) 4543; (j) H.L. Gomes, P. Stallinga, F. Dinelli, M. Murgia, F. Biscarini, D.M. de Leeuw, M. Muccini, K. Muellen, *Polym. Adv. Technol.* 16 (2005) 227.
- [2] (a) A. Facchetti, *Mater. Today* 10 (2007) 28; C. Kim, A. Facchetti, T.J. Marks, *Science* 318 (2007) 76; (c) B.A. Jones, A. Facchetti, T.J. Marks, M.R. Wasielewski, *Chem. Mater.* 19 (2007) 2703; (d) T. Ji, M. Kathiresan, S. Nair, S. Jung, V. Natarajan, R.M.R. Vishnubhatia, V.K. Varadan, *Proc. SPIE Int. Soc. Opt. Eng.* 628 (2007) 1; (e) B. Yoo, T.O. Jung, D. Basu, A. Dodabalapur, B.A. Jones, A. Facchetti, M.R. Wasielewski, T.J. Marks, *Appl. Phys. Lett.* 88 (2006) 082104/1; (f) V. Subramanian, P.C. Chang, J.B. Lee, S.E. Molesa, S.K. Volkman, *IEEE Trans. Compon. Packag. Technol.* 28 (2005) 742; (g) P.F. Baude, D.A. Ender, M.A. Haase, T.W. Kelley, D.V. Muires, S.D. Theiss, *Appl. Phys. Lett.* 82 (2003) 3964; (h) F. Cicoira, C. Santato, F. Dinelli, M. Murgia, M.A. Loi, F. Biscarini, R. Zamboni, P. Heremans, M. Muccini, *Adv. Funct. Mater.* 15 (2005) 375; (i) D.R. Gamota, P. Brazis, X. Kalyanasundaram, J. Zhang, *Printed*

- Organic and Molecular Electronics, Kluwer Academic Publishers, NY, USA, 2004.
- [3] (a) B.S. Ong, Y. Wu, P. Liu, S. Gardner, *J. Am. Chem. Soc.* 126 (2004) 3378;  
(b) Z. Wang, J. Yuan, J. Zhang, R. Xing, D. Yan, Y. Han, *Adv. Mater.* 15 (2003) 1009;  
(c) J.H. Lee, S.H. Kim, G.H. Kim, S.C. Lim, H. Lee, J. Jang, T. Zyung, *Synth. Met.* 139 (2003) 445;  
(d) Y.-Y. Noh, J.-J. Kim, K. Yase, S. Nagamatsu, *Appl. Phys. Lett.* 83 (2003) 1243;  
(e) J. Locklin, K. Shinbo, K. Onishi, F. Kaneko, Z. Bao, R.C. Advincula, *Chem. Mater.* 15 (2003) 1404;  
(f) M. Haliq, H. Klauk, U. Zschieschang, G. Schmid, W. Radlik, W. Weber, *Adv. Mater.* 14 (2002) 1717;  
(g) C.R. Kagan, T.L. Breen, L.L. Kosbar, *Appl. Phys. Lett.* 79 (2001) 3536;  
(h) H. Sirringhaus, T. Kawase, R.H. Friend, T. Shimoda, M. Inbasekaran, W. Wu, E.P. Woo, *Science* 290 (2000) 2123;  
(i) J.A. Rogers, Z. Bao, A. Makhija, P. Braun, *Adv. Mater.* 11 (1999) 741;  
(j) Z. Bao, J.A. Rogers, H.E. Katz, *J. Mater. Chem.* 9 (1999) 1895.
- [4] (a) H. Klauk, M. Haliq, U. Zschieschang, F. Eder, G. Schmid, C. Dehm, *Appl. Phys. Lett.* 82 (2003) 4175;  
(b) H.E. Katz, X.M. Hong, A. Dodabalapur, R. Sarpeshkar, *J. Appl. Phys.* 91 (2002) 1572;  
(c) R. Singhal, W. Takashima, K. Kaneto, S.B. Samanta, S. Annapoorini, B.D. Malhotra, *Sens. Actuators, B* 86 (2002) 42;  
(d) J. Roncali, *J. Mater. Chem.* 9 (1999) 1875;  
(e) G. Velu, C. Legrand, O. Tharaud, A. Chapoton, D. Remiens, G. Horowitz, *Appl. Phys. Lett.* 79 (2001) 659.
- [5] S.M. Sze, *Semiconductor Devices: Physics and Technology*, Wiley, New York, 1985.
- [6] (a) J.A. Rogers, Z. Bao, *J. Polym. Sci. A: Polym. Chem.* 40 (2002) 3327;  
(b) H.E. Katz, Z. Bao, *J. Phys. Chem B* 104 (2000) 671;  
(c) F.D. Lewis, X. Liu, Y. Wu, X. Zuo, *J. Am. Chem. Soc.* 125 (2003) 12729.
- [7] K. Yamaguchi, K. Nagashima, S. Takamiya, M. Minami, Y. Doge, Y. Nishide, H. Osuga, K. Uno, C. Nakamoto, I. Tanaka, *Jpn. J. Appl. Phys.* 46 (2007) L727.
- [8] (a) H. Wynberg, *Acc. Chem. Res.* 4 (1971) 65;  
(b) R.H. Martin, *Angew. Chem. Int. Ed. Engl.* 13 (1974) 649;  
(c) T.J. Katz, *Angew. Chem. Int. Ed. Engl.* 39 (2000) 1921;  
(d) A. Urbano, *Angew. Chem. Int. Ed. Engl.* 42 (2003) 3986;  
(e) C. Schmuck, *Angew. Chem. Int. Ed. Engl.* 42 (2003) 2448.
- [9] (a) T. Verbiest, S. Vanelshocht, M. Kauranen, L. Hellemans, J. Snauwaert, C. Nuckolls, T.J. Katz, A. Persoons, *Science* 282 (1998) 913;  
(b) S. Sioncke, S. Van Elshocht, T. Verbiest, A. Persoons, M. Kauranen, K.E.S. Phillips, T.J. Katz, *J. Chem. Phys.* 113 (2000) 7578;  
(c) D. Beljonne, Z. Shuai, J.L. Brédas, M. Kauranen, T. Verbiest, A. Persoons, *J. Chem. Phys.* 104 (1998) 1301;  
(d) L. Minuti, A. Taticchi, A. Marrocchi, E. Gacs-Baitz, R. Galeazzi, *Eur. J. Org. Chem.* (1999) 3155;  
(e) H.S. Choi, K.S. Kim, *J. Phys. Chem.* 104 (2000) 11006.
- [10] (a) C.A. Daul, I. Ciofini, *Int. J. Quantum Chem.* 91 (2003) 297;  
(b) B. Champagne, J.-M. Andre, E. Botek, E. Licandro, S. Maiorana, A. Bossi, K. Clays, A. Persoons, *ChemPhysChem* 5 (2004) 1438;  
(c) K. Clays, K. Wostyn, A. Persoons, S. Maiorana, A. Papagni, C. Daul, V. Weber, *Chem. Phys. Lett.* 372 (2003) 438;  
(d) A. Bossi, E. Licandro, S. Maiorana, C. Rigamonti, S. Righetto, G. Richard Stephenson, M. Spassova, E. Botek, B. Champagne, *J. Phys. Chem. C* 112 (2008) 7900.
- [11] (a) A. Rajca, M. Miyasaka, *Synthesis and characterization of novel chiral conjugated materials*, in: T.J.J. Miller, U.H.F. Bunz (Eds.), *Functional Organic Materials. Syntheses, Strategies, and Applications*, Wiley-VCH, Weinheim, 2007, p. 547581;  
(b) M.B. Groen, H. Schadenberg, H. Wynberg, *J. Org. Chem.* 36 (1971) 2797 (and references therein);  
(c) K. Collins, M.P. Vachon, *Org. Biomol. Chem.* 4 (2006) 2518.
- [12] A. Facchetti, Y. Deng, A. Wang, Y. Koide, H. Sirringhaus, T.J. Marks, R.H. Friend, *Angew. Chem. Int. Ed.* 39 (2000) 4547.
- [13] (a) A. Bossi, S. Maiorana, C. Graiff, A. Tiripicchio, E. Licandro, *Eur. J. Org. Chem.* 27 (2007) 4499;  
(b) E. Licandro, C. Rigamonti, M.T. Ticozzelli, M. Monteforte, C. Baldoli, C. Giannini, S. Maiorana, *Synthesis* 21 (2006) 3670;  
(c) C. Baldoli, A. Bossi, C. Giannini, E. Licandro, S. Maiorana, D. Perdicchia, M. Schiavo, *Synlett* 7 (2005) 1137;  
(d) S. Maiorana, A. Papagni, E. Licandro, R. Annunziata, P. Paravidino, D. Perdicchia, C. Giannini, M. Bencini, K. Clays, A. Persoons, *Tetrahedron* 59 (2003) 6481.
- [14] M.-H. Yoon, A. Facchetti, C.E. Stern, T.J. Marks, *J. Am. Chem. Soc.* 128 (2006) 5792;  
(b) A. Facchetti, M. Mushrush, M.-H. Yoon, G.R. Hutchison, M.A. Ratner, T.J. Marks, *J. Am. Chem. Soc.* 126 (2004) 13859.
- [15] C.H. Choi, M. Kertesz, *J. Phys. Chem. A* 101 (1997) 3823.
- [16] N.J. Turro, *Modern Molecular Photochemistry*, University Science Books, Sausalito, CA, 1991.
- [17] Y. Zhu, R.D. Champion, S.A. Jenekhe, *Macromolecules* 39 (2006) 8712.
- [18] H. Nakagawa, A. Obata, K. Yamada, H. Kawazura, M. Konno, H. Miyame, *J. Chem. Soc., Perkin Trans. II* (1985) 1899.
- [19] A. Bossi, L. Falciola, C. Graiff, S. Maiorana, C. Rigamonti, A. Tiripicchio, E. Licandro, P.R. Mussini, *Electrochim. Acta* (2009), doi:10.1016/j.electacta.2009.02.026.



of conducting material. Remarkably, the  $\pi$ -conjugated polymer-based photorefractive composite is reported as one part excessively [11]. It is well known that  $\pi$ -conjugated polymers, due to their delocalized  $\pi$ -electron distribution, have much larger carrier mobility than those of general photorefractive polymers. Thus,  $\pi$ -conjugated polymer-based photorefractive composites are expected to exhibit faster response, owing to their high mobility. In our previous paper, we reported a novel 3,3'-dicarbazole-based non- $\pi$ -conjugated polymer (DiCz) in the main-chain, and showed adequate photorefractive properties for optical applications under moderate experimental conditions (Fig. 1) [12].

Here, we have focused our attention on preparation of a new type of NLO chromophore-doped  $\pi$ -conjugated polymer composite consisting of copoly[6,6'-bis(9-(2-ethylhexyl)carbazole-3-yl)/thieno-(2,5-*b*)thiophenyldenevinylene] (EHCzThThZ) and 2-[3-[(*E*)-2(piperidine)-1-ethenyl]-5,5-dimethyl]-2-cyclohexenyldenemalononitrile (P-IP-DC), and their optical properties [13]. It is possible that this may overcome aggregation of NLO chromophore by attaching a bulky alkyl branch group at the 9-position of the carbazole in a working device. With this mind, in this work, we extended our study to investigate the photoconductive and photorefractive properties of  $\pi$ -conjugated polymer EHCzThThZ in photorefractive composite, also in comparison to non-conjugated polymer DiCz that was investigated in Ref. [12]. It is hoped that EHCzThThZ-based photorefractive composite may endow the composite with fast photorefractive response time. We will relate the results obtained in our laboratory concerning the quantitative comparison of optical properties in EHCzThThZ composite and that obtained for a similar composite composed of DiCz composite. In order to clearly confirm the influence of different photoconducting structures, the

$\pi$ -conjugated composite was compared to a DiCz composite system with the similar weight ratio of the photorefractive ingredients, with the same NLO chromophore and photosensitizer in the photoconducting matrix. Chemical structures of these materials are provided in Fig. 1.

## 2. Experimental section

### 2.1. Materials and device fabrication

In this work, a low- $T_g$  photorefractive composite was prepared by doping the optically anisotropic chromophore, P-IP-DC, into the photoconducting polymer matrix, EHCzThThZ sensitized by  $C_{60}$ . EHCzThThZ and P-IP-DC were synthesized using previously described methods [13,7,14].  $C_{60}$  was obtained from Aldrich Chem. Co. Inc. and was used after purification by sublimation under vacuum. The composition of polymeric composite was EHCzThThZ:P-IP-DC:butyl benzyl phthalate (BBP): $C_{60}$  = 61:30:8:1 by wt.%. For sample preparation, the mixture (total 100 mg) was dissolved in 400 mg of 1,1,2,2-tetrachloroethane, and the solution was filtered through a 0.2  $\mu$ m membrane. The composite was cast on a patterned indium tin oxide (ITO) glass substrate, dried slowly for 12 h at ambient temperature, and then was vacuum dried at 30 °C for 24 h to completely remove the residual solvent. The composite was then softened on a hot plate at 100 °C and next sandwiched between ITO glasses with Teflon film spacer of 50  $\mu$ m to yield a film with a uniform thickness. The thickness of the active layer was near 50  $\mu$ m.

### 2.2. Electro-optic measurements

The electro-optic property of the polymeric composite was determined by transmission ellipsometric method

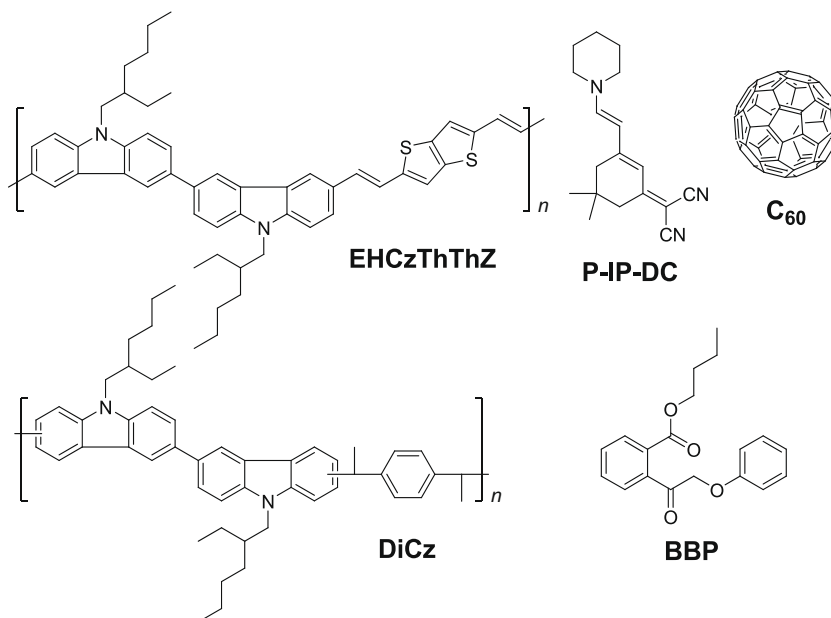


Fig. 1. There are two kinds of composites in this study.

( $I = 10 \text{ mW/cm}^2$ ). The sample tilted by  $45^\circ$  was placed between the polarizer and the analyzer with the polarization set to  $+45^\circ$  and  $-45^\circ$ , respectively. The  $\Delta n$  of composite was determined from the variation of the transmitted intensity ( $T$ ) through crossed polarizers upon the application of electric field, as described by the following equation [14]:

$$T = \sin^2 \left( \frac{2\pi}{\lambda} \cdot l \cdot \Delta n \right), \quad (1)$$

where  $\lambda$  is the wavelength and  $l$  is a distance of light path.

### 2.3. Photoconductivity measurements

The photoconductivity measurements were performed on about  $50 \mu\text{m}$  thick samples sandwiched between ITO electrodes at  $I = 13 \text{ mW/cm}^2$  using a simple DC photocurrent method [15]. The current flowing through the composite was measured using the Keithley 6485 during illumination with an operating wavelength of  $632.8 \text{ nm}$ . The dark current and photoconductivity were calculated using the following equation:

$$\sigma = I \cdot \frac{d}{VA}, \quad (2)$$

where  $I$  is current,  $d$  is the sample thickness,  $V$  is the applied voltage, and  $A$  is the laser beam area. The dark conductivity ( $\sigma_{\text{dark}}$ ), the conductivity in the presence of light ( $\sigma_{\text{light}}$ ), and the photoconductivity ( $\sigma_{\text{photo}} = \sigma_{\text{light}} - \sigma_{\text{dark}}$ ) were obtained.

### 2.4. Degenerated four-wave mixing (DFWM) measurements

Two coherent laser beams with  $\lambda = 632.8 \text{ nm}$  were irradiated on the sample in the tilted geometry at an incident angle of  $\theta = 30^\circ$  and  $60^\circ$  with respect to the sample's normal axis. The intensity of  $s$ -polarized writing beams was  $60 \text{ mW/cm}^2$ . The recorded photorefractive grating was read by a  $p$ -polarized counter-propagating beam. An attenuated reading beam with a very weak intensity of  $0.1 \text{ mW/cm}^2$  was used. The internal diffraction efficiency ( $\eta_{\text{int}}$ ) of the photorefractive material was determined using the following equation:

$$\eta_{\text{int}} = \frac{I_{\text{R,diffracted}}}{(I_{\text{R,diffracted}} + I_{\text{R,transmitted}})}, \quad (3)$$

where  $I_{\text{R,diffracted}}$  and  $I_{\text{R,transmitted}}$  are the diffracted and transmitted intensities of the reading beam, respectively. The photorefractive grating buildup time was also analyzed. The photorefractive grating buildup rate is very important for real applications such as a real-imaging and real-data processing. The buildup time of the photorefractive composites was evaluated from the buildup of the beam intensity of the DFWM measurement. The time constants,  $\tau_1$  and  $\tau_2$ , were calculated by fitting the evolution of the growth of the diffraction signal,  $\eta(t)$ . Quantitative information about the grating growth can be obtained by an empirical biexponential function of the following Eq. (4) fitted to the data of diffraction efficiency [16]:

$$\eta(t) = A_1 \left\{ 1 - \exp \left( -\frac{t}{\tau_1} \right) \right\} + A_2 \left\{ 1 - \exp \left( -\frac{t}{\tau_2} \right) \right\}, \quad (4)$$

where  $A_1$  and  $A_2$  are fitting parameters, and  $\tau_1$  and  $\tau_2$  are the fast and slow time constants, respectively.

## 3. Results and discussion

The  $T_g$  value of the current composite from the DSC data was  $T_g \sim 28^\circ\text{C}$ , which assure the facile orientation of P-IP-DC at temperatures around  $T_g$ . The mixture of the composite was sandwiched between two indium tin oxide glass plates to form a  $50 \mu\text{m}$  thick film along with a Teflon spacer. All experiments were performed near the  $T_g$  of photorefractive composite under an operating wavelength of  $632.8 \text{ nm}$ .

As given in Fig. 2, the birefringence ( $\Delta n$ ) of the photorefractive composite is increased quadratically with an external electric field. This data from the transmission ellipsometer experiments can be used to predict both the steady-state holographic contrast of the photorefractive composite and to quantify the sample. At an applied potential of  $50 \text{ V}/\mu\text{m}$ ,  $\Delta n = 2.62 \times 10^{-3}$ , which are sufficiently large values for the preparation of efficient photorefractive materials. The value of  $\Delta n$  of composite was determined from the variation of the transmitted intensity ( $T$ , Fig. 2 inset) through the crossed polarizers upon the application of the electric field, as described by the following Eq. (1). That is attributed the high birefringence due to a large dipole moment induced, as well as to the high polarizability anisotropy of the P-IP-DC chromophore [17].

The photoconductivity is governed by the photogeneration quantum efficiency and the charge mobility via an applied electric field and a light intensity. The photoconductivity increases with increasing electric field. The observed nonlinear dependence on the electric field strength is thought to be due the fact that both the quantum efficiency and the charge mobility depend strongly on the electric field strength. Photoconductivity measurements ( $\lambda = 633 \text{ nm}$ ) were carried out on the device, and showed photoconductivity of  $\sigma_{\text{photo}} = 1.19 \text{ pS/cm}$  for EHCzThThZ composite, using a light intensity of  $13 \text{ mW/cm}^2$  and an applied electric field of  $60 \text{ V}/\mu\text{m}$  (Fig. 3). Unfortunately, the EHCzThThZ composite also exhibited high dark conductivity at relatively higher electric field. The dark conductivity was calculated to be  $0.39 \text{ pS/cm}$  under an electric field of  $60 \text{ V}/\mu\text{m}$ . Comparing the photoconductivity of the EHCzThThZ composite ( $\sigma_{\text{photo}} = 0.86 \text{ pS/cm}$  under potential of  $50 \text{ V}/\mu\text{m}$ ) with that of the DiCz composite ( $\sigma_{\text{photo}} = 1.24 \text{ pS/cm}$  under a potential of  $50 \text{ V}/\mu\text{m}$ ) shows that the former is lower due to the higher dark conductivity ( $\sigma_{\text{dark}} = 0.39 \text{ pS/cm}$  under potential of  $50 \text{ V}/\mu\text{m}$ ) of EHCzThThZ composite. We observed that, when an electric field is applied to the sample,  $\sigma_{\text{dark}}$  decrease with an increase in the electric field occurs. This  $\sigma_{\text{dark}}$  in high fields may be attributed to the orientation of the NLO chromophore's under the electric field [18]. This value is found to be greater than that of the DiCz-based one, presumably due to  $\pi$ -conjugated backbone of EHCzThThZ. The EHCzThThZ polymer is probably effective for  $\pi$ -stacking of polymer rigid backbone through hydrophobic interaction between branched-chain alkyl groups. This result in higher dark conductivity than DiCz composite, suggesting that photogenerated holes should be diminished in

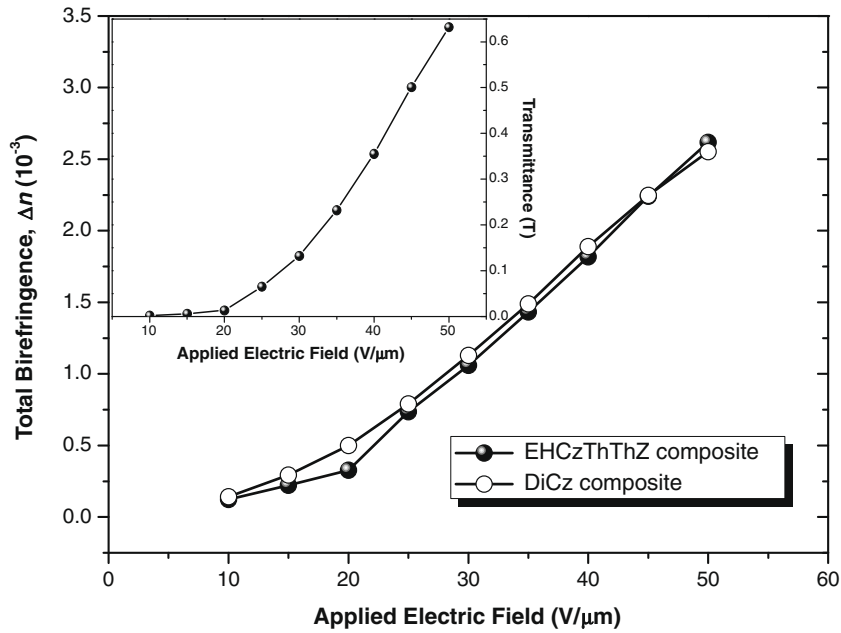


**Fig. 2.** Electric field induced birefringence of polymeric photorefractive composites versus various applied electric fields. The inset shows the transmittance for the EHCzThThZ composite on voltage applied to the device. The lines are guides for the eye.

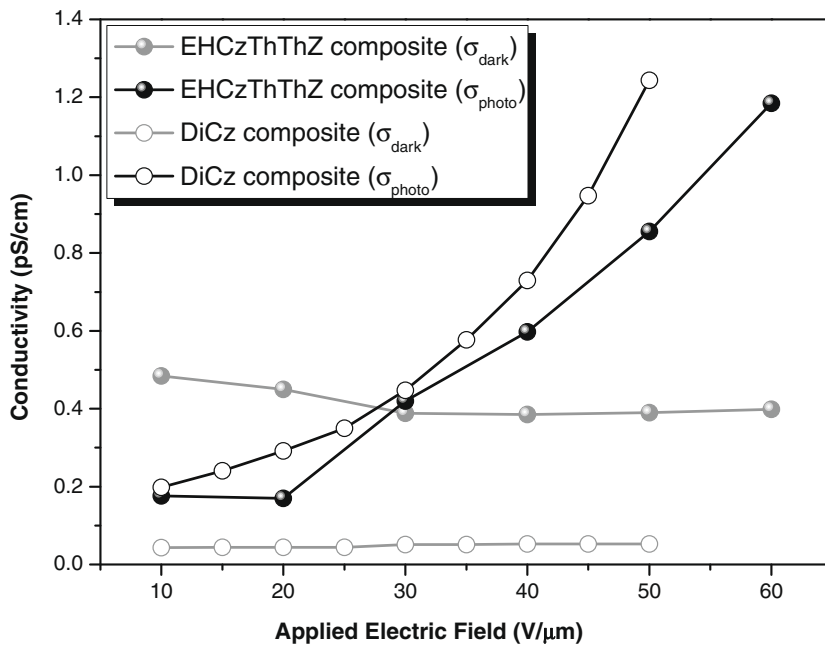


**Fig. 3.** The conductivity as a function of external electric field strength. The lines are guides for the eye.

EHCzThThZ composite, therefore, shows lower photoconductive properties. The photoconductivity was extracted as photosensitivity.

In polymeric photorefractive materials, the magnitude of space-charge field,  $|E_{SC}|$  takes the form [19]

$$|E_{SC}| = \frac{mE_q \sqrt{E_0^2 + E_d^2}}{\sqrt{E_0^2 + (E_d + E_q)^2}} \times \frac{1}{1 + \frac{\sigma_{\text{dark}}}{\sigma_{\text{photo}}}}, \quad (5)$$

where  $m = \sqrt{I_1 I_2} / (I_1 + I_2)$  is the modulation depth, where  $I_1$  and  $I_2$  is the write beams,  $E_q = eN_{\text{eff}} / (\epsilon_0 \epsilon_r K_G)$  is the trap-density-limited space-charge field, where  $N_{\text{eff}}$  is the effective trap density,  $\epsilon_r$  is the dielectric constant relative to the permittivity of free space  $\epsilon_0$ ,  $K_G$  is the grating wave vector, and  $e$  is the fundamental unit charge,  $E_d = k_B T K_G / e$  is the diffusion field, where  $k_B$  is Boltzmann's constant and  $T$  is the absolute temperature. The second part of the numerator of Eq. (5) corresponds to the conductivity con-

tribution, and this part is related to photorefractive response. As depicted in Fig. 4, this undesirable operation resulted in a maximum in the  $1/(1 + \sigma_{\text{dark}}/\sigma_{\text{photo}})$  for the EHCzThThZ composite device at  $E = 60 \text{ V}/\mu\text{m}$ , with a subsequent increase in this figure-of-merit (FOM) above these voltages. The FOM may be defined as  $Q = n^3 r_e / \epsilon_r$ , where  $n$  is the optical index of refraction,  $r_e$  is the effective electro-optic coefficient [20]. This ratio means that the photo-charge is mobile while the other is stationary, or at least one type of charge is more mobile than the other. The implications of this functioning with regard to the overall photorefractive properties will be discussed as the relevant data are presented. The photosensitivity  $S_{\text{photo}}$  (photoconductivity per unit light intensity) of EHCzThThZ composite at excitation wavelength of 632.8 nm is presented in Fig. 4 and was calculated according to the following equation:

$$S_{\text{photo}} = \frac{J_{\text{photo}}}{EI}, \quad (6)$$

where  $J_{\text{photo}}$  is the photocurrent density,  $E$  is the applied electric field,  $\sigma_{\text{photo}}$  is the photoconductivity. The photosensitivity is proportional to the carrier photogeneration rate, mobility, and life-time [21]. The photosensitivity was calculated as  $S_{\text{photo}} = 8.6 \times 10^{-11} \text{ cm}/\Omega\text{W}$  under potential of  $60 \text{ V}/\mu\text{m}$  (Fig. 4). This value is of the higher order of magnitude as the one reported in the efficient photorefractive composites for high-speed applications base on poly(*N*-vinylcarbazole) [22].

The DFWM experiment is a good choice for probing weak gratings and studying the dynamics of the photorefractive effect. The diffraction efficiency of the photorefractive material was determined using a DFWM experiment. In the DFWM experiment, the diffraction efficiency ( $\eta$ ) was determined by the ratio of the intensity of the diffracted signal to that of the incident reading beam. The

steady-state diffraction efficiency in the presence of the orientational enhancement effect is determined by the applied electric field and the space-charge field amplitude. Fig. 5 shows the electric field dependence of the diffraction efficiency. The diffraction efficiency increased with the applied electric field and the diffraction efficiency of the current composite was 37.2% at  $50 \text{ V}/\mu\text{m}$  at  $30^\circ\text{C}$ . The diffraction efficiency is rather low. This result may be explained by a previously reported study [23]. The reason for the low diffraction efficiency EHCzThThZ composite may be a low space-charge field due to a low trap density. Also, this result may be connected with highest occupied molecular orbital (HOMO) of photorefractive materials. In our photorefractive material, the HOMO level of EHCzThThZ ( $-5.24 \text{ eV}$ ) is lower than that of P-IP-DC ( $-5.32 \text{ eV}$ ), i.e., the P-IP-DC chromophore do not contribute to carrier trapping [12,24]. Therefore, the lower HOMO level of EHCzThThZ, compared with DiCz ( $-5.38 \text{ eV}$ ), may lead to slightly lower photoconductivity and space-charge field, which is consistent with our experiment results.

The response of the holographic grating formation was studied by measuring the time constants of the grating formation in the DFWM experiment. In Fig. 6, the dynamics of the diffraction grating formation process for different applied voltages is presented. Analysis of the changes in the curves' shape in function of the applied voltage allows us to affirm that there is a strong correlation between the characters of the evolution of diffracted signal and electric field. The buildup time of the photorefractive composite was evaluated from the buildup of the beam intensity of the DFWM measurement. The grating formation speed increased as the applied electric field strength increased. Fig. 7 shows the  $\tau_1$  and  $\tau_2$  of the current composite, which measured at different electric fields between 20 and  $50 \text{ V}/\mu\text{m}$ . The photorefractive speed strongly depends on

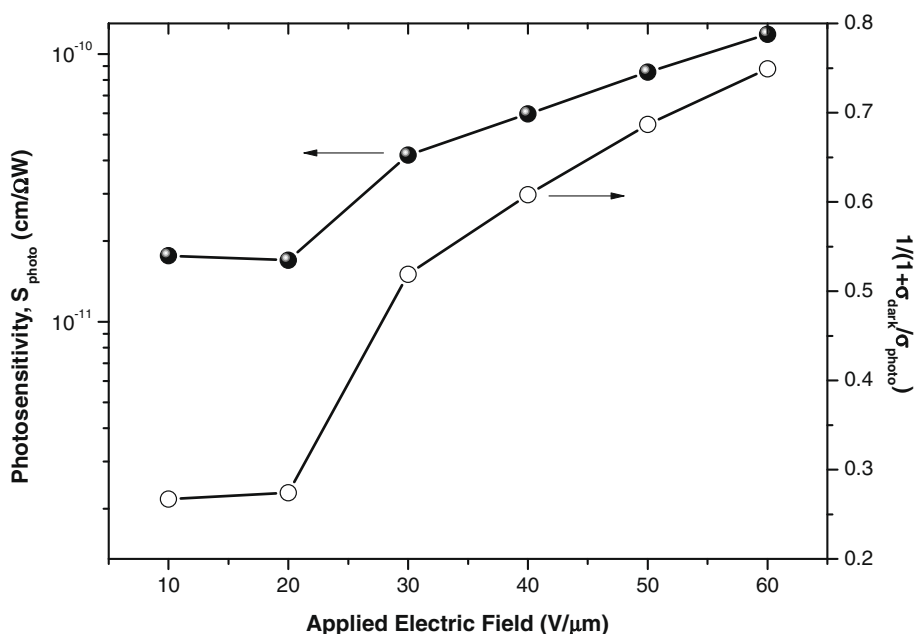


Fig. 4. Electric field dependence of photosensitivity and  $1/(1 + \sigma_{\text{photo}}/\sigma_{\text{dark}})$  for EHCzThThZ composite. The lines are guides for the eye.

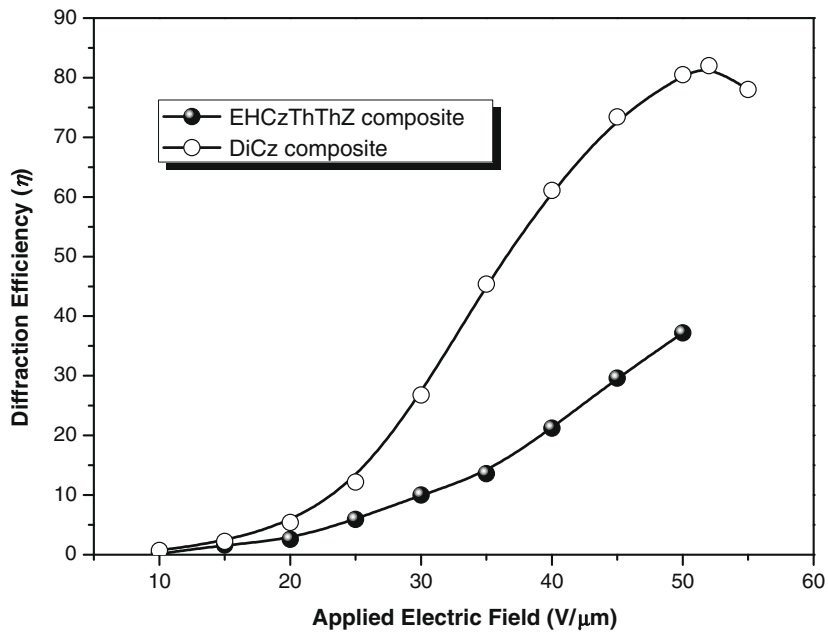


Fig. 5. Steady-state diffraction efficiency of photorefractive composites under various applied electric fields. The lines are guides for the eye.

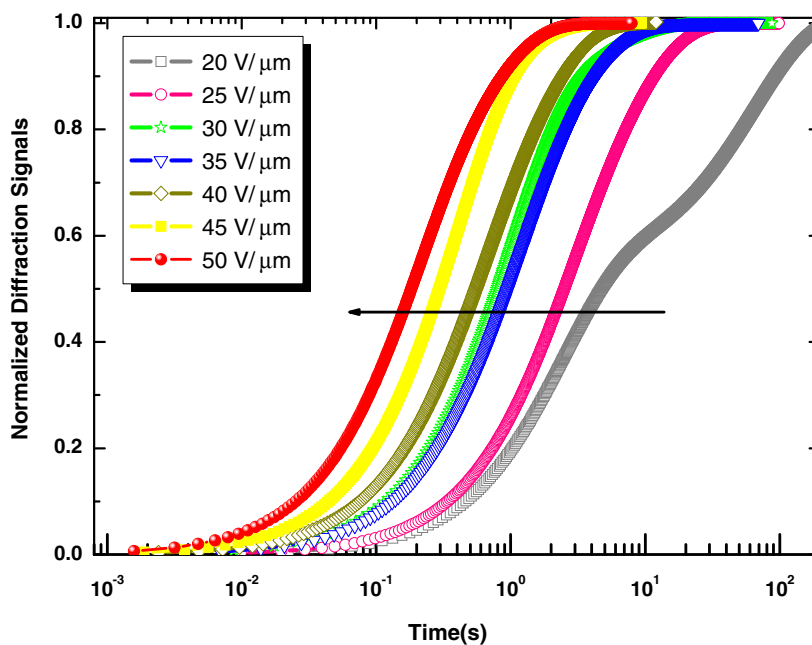


Fig. 6. The diffraction versus time of photorefractive composite for different applied voltages. The arrow indicates increasing electric field.

the photogeneration efficiency, drift mobility, NLO chromophore's mobility and other parameters.

An elevated external electric field causes faster grating formation in EHCzThThZ composite, as was expected, since the charge mobility as well as the photocharge generation efficiency increase with electric field. As displayed in Fig. 7, the moderate response time of the EHCzThThZ composite (0.16 s at 50 V/μm) having the higher  $\tau_1$  than that of DiCz composite (1.18 s at 50 V/μm) [12]. It may be considered

by the fast rate constants that the rigidity of the matrix affect the dynamics of photorefractive grating formation with the charge carrier generation and its mobility, and the hole trap density. The fast response time of EHCzThThZ composite is caused by the possibility of delocalizing charges along on polymer chain without hopping compared to the DiCz composite [25]. Since the photorefractive effect is based on the photoinduced buildup of a space-charge field in an electro-optic material, the photogenera-

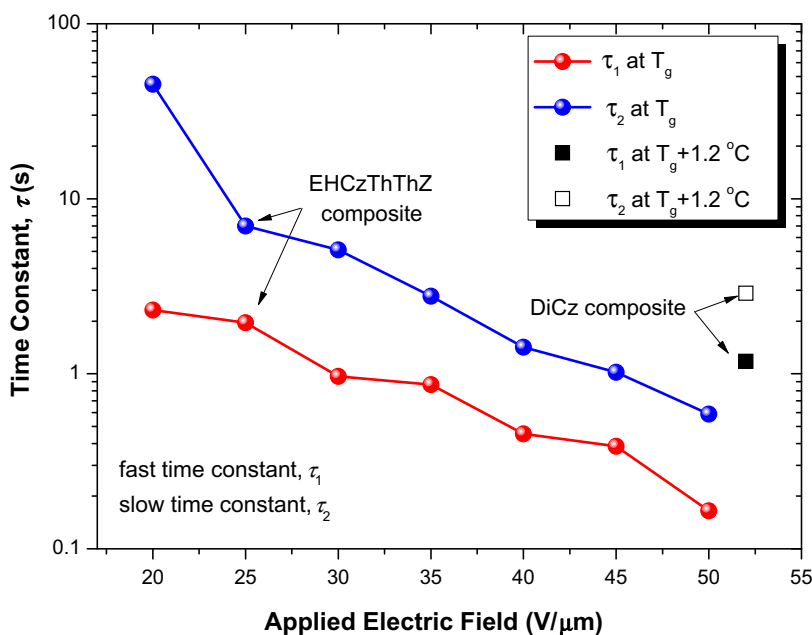


Fig. 7. Hologram buildup speed of photorefractive composite under various electric fields. The lines are guides for the eye.

Table 1

Comparative analysis of the optical properties of 50 μm thick EHCzThThZ and DiCz composites.

	$\Delta n^{a,b,c}$ ( $10^{-3}$ )	$\sigma_{\text{photo}}^{d,e,f}$ (pS/cm)	$\eta^{a,b}$ (V/μm)	$\tau_1^{a,b}$ (s)	$\tau_2^{a,b}$ (s)	
EHCzThThZ	2.62	1.19	37.2	0.16	0.58	This work
DiCz	2.62	1.24	82.5	1.18	–	[6]

<sup>a</sup> At 50 V/μm.

<sup>b</sup> At 30 °C.

<sup>c</sup> At 10 mW/cm<sup>2</sup>.

<sup>d</sup> At 13 mW/cm<sup>2</sup>.

<sup>e</sup> At 60 V/μm.

<sup>f</sup> At 27 °C.

tion of charge carriers and their subsequent migration by diffusion or drift in an electric field play a key role in determining the magnitude and speed of the photorefractive response. Table 1 provides a summary of the EHCzThThZ composite measured using optical properties.

#### 4. Conclusions

In summary, we have prepared a novel  $\pi$ -conjugated polymer-based photorefractive composite with low  $T_g$ . We emphasize the importance of taking into account the birefringence, photoconductivity, diffraction efficiency, and the speed of grating formation of  $\pi$ -conjugated polymer-based photorefractive composites in order to measure their optical properties. This composite has faster photorefractive grating formation speed due to  $\pi$ -conjugated main-chain, as compared with the non-conjugated polymer-based photorefractive composite. The EHCzThThZ composite showed a diffraction efficiency of 37.2% in moderate electric field of 50 V/μm, with a response time of the diffraction efficiency of 0.16 s in an applied field of

50 V/μm. Therefore, we believe that the photorefractive composite containing  $\pi$ -conjugated polymer shows promise as a highly efficient photorefractive material, and takes our research one step closer to the goal of finding a polymeric material that can find application in various optical devices.

#### Acknowledgements

This work was supported by the Korea Science and Engineering Foundation (KOSEF) grant funded by the Korea government (MEST) (Grant No. R11-2007-050-01003-0) and the Research fund of HYU (HYU-2008-T).

#### References

- [1] P. Günter, J.-P. Huignard, *Photorefractive Materials and Their Applications*, vols. I & II, Springer-Verlag, Berlin, 1988.
- [2] S. Tay, P.-A. Blanche, R. Voorakaranam, A.V. Tunc, W. Lin, S. Rokutanda, T. Gu, D. Flores, P. Wang, G. Li, P. St. Hilaire, J. Thomas, R.A. Norwood, M. Yamamoto, N. Peyghambarian, *Nature* 451 (2008) 594.

- [3] K. Meerholz, B.L. Volodin, B.K. Sandalphon, B. Kippelen, N. Peyghambarian, *Nature* 371 (1994) 497.
- [4] F. Würthner, S. Yao, J. Schilling, R. Wortmann, M. Redi-Abshiro, E. Mecher, F. Gallego-Gomez, *J. Am. Chem. Soc.* 123 (2001) 2810.
- [5] O. Ostroberkhova, W.E. Moerner, *Chem. Rev.* 104 (2004) 3267.
- [6] P.M. Lundquist, R. Wortmann, C. Geletneky, R.J. Twieg, M. Jurich, V.Y. Lee, C.R. Moylan, D.M. Burland, *Science* 274 (1996) 1182.
- [7] I.K. Moon, N. Kim, *Dyes Pigments* 76 (2008) 353.
- [8] C.-S. Choi, I.K. Moon, N. Kim, *Appl. Phys. Lett.* 94 (2009), 053302[1]–053302[3].
- [9] I.C. Khoo, H. Li, Y. Liang, *Opt. Lett.* 59 (1994) 142.
- [10] G.P. Wiederrecht, B.A. Yoon, M.R. Wasielewski, *Science* 270 (1995) 1794.
- [11] I.C. Khoo, J. Ding, Y. Zhang, K. Chen, A. Diaz, *Appl. Phys. Lett.* 82 (2003) 3587.
- [12] E. Mecher, C. Bräuchle, H.H. Hörhold, J.C. Hummelen, K. Meerholz, *Phys. Chem. Chem. Phys.* 1 (1999) 1749.
- [13] I.K. Moon, C.-S. Choi, N. Kim, *Polymer* 48 (2007) 3461.
- [14] I.K. Moon, C.-S. Choi, N. Kim, *J. Polym. Sci.: Part A: Polym. Chem.* 46 (2008) 1783.
- [15] H. Chun, I.K. Moon, D.-H. Shin, S. Song, N. Kim, *J. Mater. Chem.* 12 (2002) 858.
- [16] H. Hoegl, O. Sus, W. Neugebauer, German Patent 1,068,115 to Kalle A/G, 1957.
- [17] M.A. Díaz-García, D. Wright, B. Smith, E. Glazer, W.E. Moerner, *Chem. Mater.* 11 (1999) 1784.
- [18] I.K. Moon, C.-S. Choi, N. Kim, *J. Polym. Sci.: Part A: Polym. Chem.* 46 (2008) 1783.
- [19] K. Zimmerman, F. Ghebremichael, M.G. Kuzyk, *J. Appl. Phys.* 75 (1994) 1267.
- [20] J.G. Winiarz, L. Zhang, J. Park, P.N. Prasad, *J. Phys. Chem. B* 106 (2002) 967.
- [21] W.E. Moerner, S.M. Silence, *Chem. Rev.* 94 (1994) 127.
- [22] B.E. Jones, S. Ducharme, M. Liphardt, A. Goonesekera, J.M. Takacs, L. Zhang, R. Athalye, *J. Opt. Soc. Am. B* 11 (1994) 1064.
- [23] M.A. Daz-Garca, D. Wright, J.D. Casperson, B. Smith, E. Glazer, W.E. Moerner, I. Sukhomlinova, R.J. Twieg, *Chem. Mater.* 11 (1999) 1784.
- [24] H.J. Bolink, V.V. Krasnikov, P.H.J. Kouwer, G. Hadziioannou, *Chem. Mater.* 10 (1998) 3951.
- [25] L. Kulikovskiy, D. Neher, E. Mecher, K. Meerholz, H.-H. Hörhold, O. Ostroberkhova, *Phys. Rev. B* 69 (2004) 125216.

efficiencies as well as reduced roll-off [15–17]. However, there are few electron transport-type wide band-gap hosts, which resulted in limitation for introducing a mixed host structure into blue PHOLEDs. Recently, several good host materials with high electron mobility as well as triplet energy were reported, and we have taken advantage of the characteristics of these hosts to develop mixed host blue [7,18].

In this work, various mixed host structures for blue PHOLEDs were developed to study the relationship between the device performances and the combination/composition of host materials. A hole transport-type host material, 4,4',4''-tris(N-carbazolyl)triphenylamine (TcTa), was combined with an electron transport-type host material, 2-(diphenylphosphoryl)spirofluorene (SPPO1) [18] or a bipolar transport-type host material, (26DCzPPy) [7]. We found that a mixed host structure was effective to control the charge carrier injection and exciton distribution in emissive layer (EML), thus obtained highly improved and stable efficiency in blue PHOLEDs.

## 2. Experimental

A series of blue PHOLEDs in this study were fabricated using the configuration: indium tin oxide (ITO) (70 nm)/1,1-bis[(di-4-tolylamino)phenyl]cyclohexane (TAPC) (50 nm)/emissive layer (30 nm)/1,3,5-tri(m-pyrid-3-yl-phenyl)benzene (Tm3PyPB) (20 nm)/Tm3PyPB:Cs (30 nm)/LiF (1 nm)/Al (120 nm). Six different mixed host devices were prepared to investigate the effect of host material properties on device characteristics of mixed host devices. Two standard devices with single 26DCzPPy or SPPO1 host material were also fabricated as references for comparison. Bipolar transport-type 26DCzPPy (Device A) or electron transport-type SPPO1 (Device B) composition in the mixed host device were 50%, 70%, and 90%, respectively. A blue light-emitting iridium(III)bis(4,6-difluorophenyl)-pyridinato-N,C2')picolinate (Flrpic) was doped in the mixed host emissive layer and the doping concentration of Flrpic was fixed at 10%.

To achieve efficient blue PHOLEDs, effective confinements of both charge carriers and triplet excitons are necessary [7,11,13]. Therefore, TAPC and Tm3PyPB with wider triplet energy level ( $T_1 = 2.9$  and 2.78 eV, respectively, which are higher than that of Flrpic ( $T_1 = 2.62$  eV)) and low-lying the highest occupied molecular orbital (HOMO) and high-lying the lowest unoccupied molecular orbital (LUMO) energy levels, respectively, were used as a hole-transporting layer (HTL) and as an electron transporting layer (ETL), respectively. In addition, n-doped ETL (4 mol % Cesium doped TmPyPB) was introduced for effective electron injection and charge carrier balance within emissive layer because the electron mobility of Tm3PyPB ( $\sim 7.0 \times 10^{-4}$  cm<sup>2</sup>/Vs at  $2.5 \times 10^5$  V/cm) [19,20] is one to two orders of magnitude lower than the hole mobility of TAPC ( $\sim 1.0 \times 10^{-2}$  cm<sup>2</sup>/Vs at  $\sim 10^5$  V/cm) [13]. The energy level diagrams and chemical structures of materials used in this study were shown in Fig. 1.

ITO was cleaned by the standard oxygen plasma treatment. The OLED grade materials were purchased and used without further purification. All organic layers were depos-

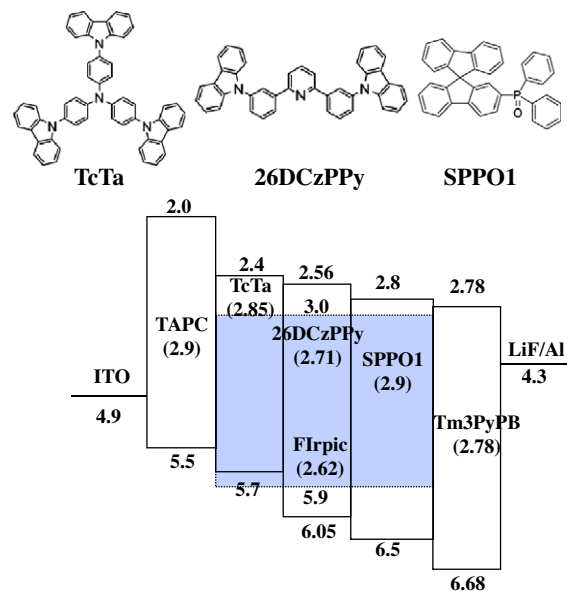


Fig. 1. Energy level diagrams and chemical structures for the materials tested in this study.

ited in a high vacuum chamber below  $5 \times 10^{-7}$  torr and thin films of LiF and Al were deposited as a cathode electrode. The OLEDs were transferred directly from vacuum into an inert environment glove-box, where they were encapsulated using a UV-curable epoxy, and a glass cap with a moisture getter. The electro-luminescence spectrum was measured using a Minolta CS-1000. The current–voltage ( $I$ – $V$ ) and luminescence–voltage ( $L$ – $V$ ) characteristics were measured with a current/voltage source/measure unit (Keithley 238) and a Minolta CS-100. Photoluminescence (PL) spectra were recorded using Spex Fluorolog-3 spectrofluorometers.

## 3. Results and discussion

The current density–voltage–luminance ( $I$ – $V$ – $L$ ) curves of the TcTa:26DCzPPy mixed host devices (Device A) are shown in Fig. 2a according to the relative content of two host materials. The current density of Device A was gradually increased with increasing TcTa content in the mixed host devices. Since Flrpic is a well-known electron transport-type triplet emitter and their relatively low-lying LUMO level compared with those of 26DCzPPy and SPPO1, the electrons injection and transport behavior in case of both Device A and B would be similar [19]. Therefore, the increased the current density with the addition of TcTa to 26DCzPPy is mainly originated from facilitated hole injection and transport from TAPC to 26DCzPPy through TcTa content. The hole injection from TAPC to 26DCzPPy was slightly restricted due to the HOMO level difference of 0.55 eV between TAPC and 26DCzPPy. However, in case of TcTa:26DCzPPy mixed host Device A, the hole injection from TAPC to EML was enhanced by TcTa addition which has higher-lying HOMO level (5.7 eV) than that of 26DCzPPy (6.05 eV). In addition, the hole mobility of TcTa is higher than that of 26DCzPPy. Therefore, increased



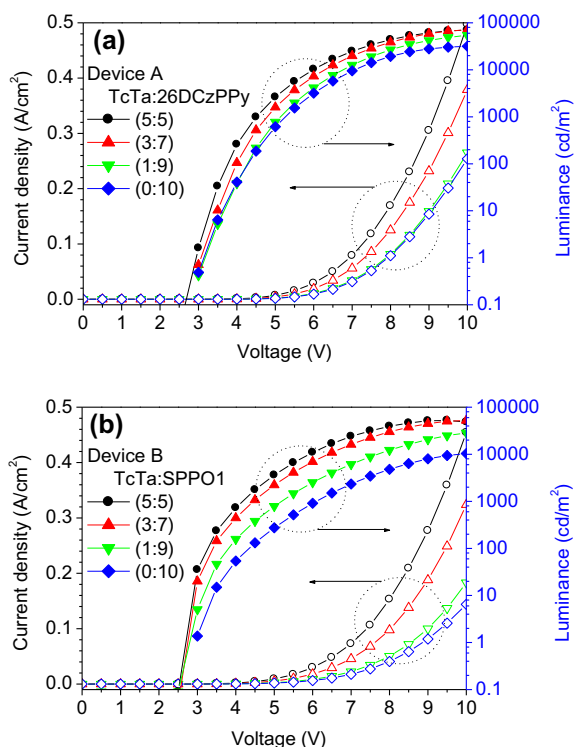


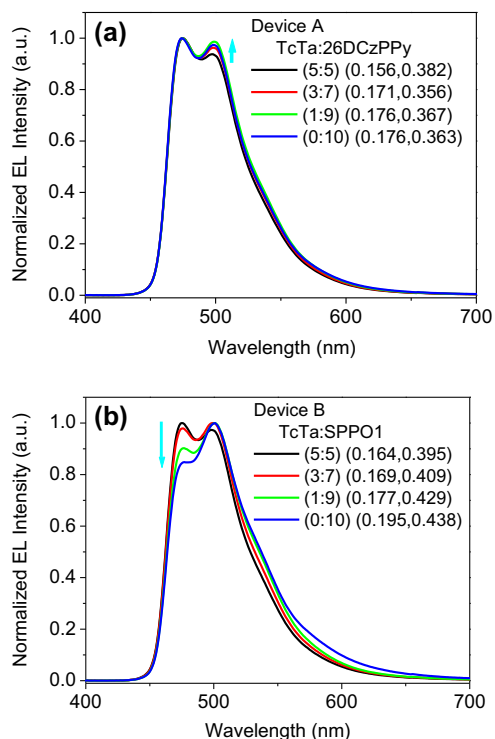
**Fig. 2.** Current density versus voltage ( $I$ - $V$ ) and voltage versus luminance ( $V$ - $L$ ) characteristics of (a) Device A (TcTa:26DCzPPy) and (b) Device B (TcTa:SPPO1).

current density in TcTa:26DCzPPy mixed host Device A could be obtained. The luminance at the same voltage was also increased as similar as the current density behavior.

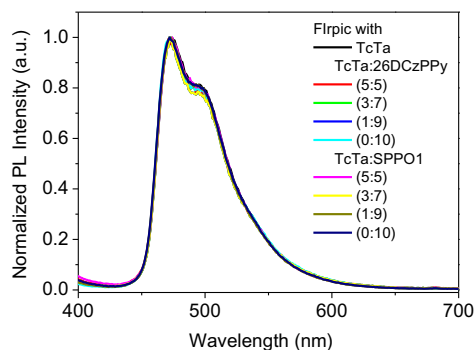
In the case of the combination of TcTa and an electron transport-type SPPO1 host (Device B), the current density as well as luminance behavior was more dramatic than those in the case of Device A as shown in Fig. 2b. This is attributed to the huge hole injection barrier (1.0 eV) from TAPC to SPPO1 and the inferior hole mobility of SPPO1 compared to 26DCzPPy [18]. Moreover, the driving voltages of Device B consequently reduced with increasing TcTa content in the mixed host devices and were 6.1, 5.2, 4.5, and 4.2 V at a luminance of 1000 cd/m<sup>2</sup>, respectively. By gathering up above results, we found that charge carrier density and injection properties in the EML were correlated with the combination/composition of the host materials, and could be controlled by device engineering.

Fig. 3 shows the electro-luminescence spectra and the Commission Internationale de L'Eclairage (CIE) coordinates of the Device A and B at a current density of 10 mA/m<sup>2</sup>. All Device A exhibited a similar maximum luminescence wavelength, near 474 nm, which is originated from the triplet emission of Flrpic emitter. However, as the TcTa content increased in the Device B, emission at 474 nm was decreased while the shoulder peak around 500 nm was increased.

These different electro-luminescence spectra could be presumed to be vibronic coupling between different host



**Fig. 3.** Normalized electro-luminescence (EL) spectra and CIE coordinates of (a) Device A (TcTa:26DCzPPy), (b) Device B (TcTa:SPPO1).



**Fig. 4.** Normalized photoluminescence (PL) spectra of the mixed host samples.

materials [21,22] and/or optical effect through the recombination zone shift [18]. Firstly, we conducted photoluminescence study to examine vibronic coupling between two host materials in the mixed host devices. Nine different mixed host samples (30 nm-thick films on quartz plate) with 10% doped Flrpic were prepared. Additionally, three reference samples with TcTa, 26DCzPPy, and SPPO1 single host were also studied for comparison. As shown in Fig. 4, we could not find any differences between the mixed host samples and reference samples. Therefore, we excluded the vibronic coupling effect as an origin of spectral change in our mixed host blue PHOLEDs. Secondly, the optical effect caused by the recombination zone change was also considered [18]. As shown in Fig. 5, we could ob-

serve the electro-luminescence changes in blue PHOLEDs with Flrpic doped single TcTa, 26DCzPPy, or SPPO1 host layers. The hole and electron recombination zone in the Device B with SPPO1 single host is positioned in the SPPO1:Flrpic EML close to the HTL side due to preferred charge (electron) carrier mobility of SPPO1 material. However, the recombination zone of the Device B with TcTa:SPPO1 mixed host structure would be shifted from the HTL/EML side to the center of the EML as increasing TcTa content in the EML. In other words, balanced exciton recombination in the EML could be achieved by using a

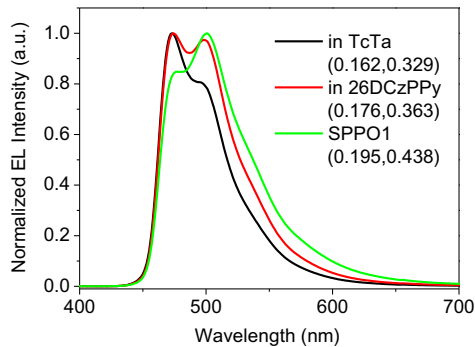


**Fig. 5.** Normalized electro-luminescence (EL) spectra of single host devices.

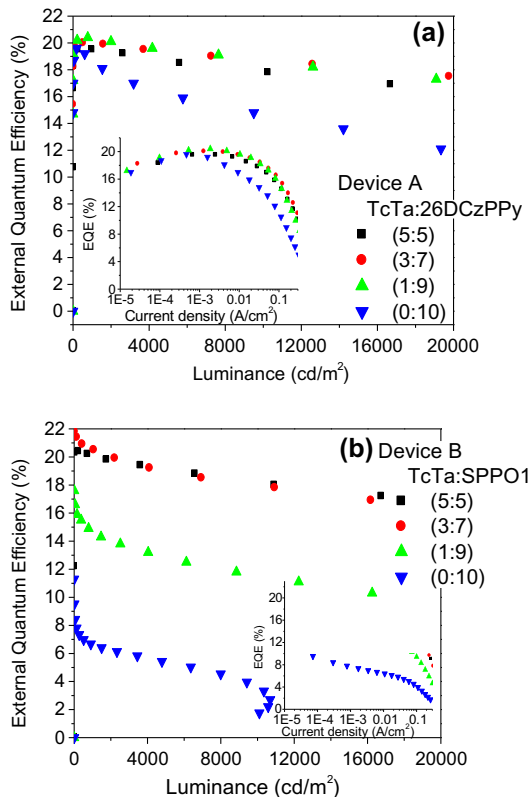


**Fig. 6.** External quantum efficiency versus luminance characteristics of (a) Device A (TcTa:26DCzPPy) and (b) Device B (TcTa:SPPO1) (Inset: EQE versus current density characteristics).

mixed host structure, in which enhancement of light-emitting efficiency was expected.

The external quantum efficiency (EQE) of the blue PHOLEDs with mixed host structure were plotted against luminance or current density in Fig. 6. Both Device A and B with mixed host structure showed highly improved performance than 26DCzPPy or SPPO1 single host devices. The maximum efficiency was obtained in the 1:9 mixed host in case of Device A (TcTa:26DCzPPy, EQE of 20.4%), while Device B (TcTa:SPPO1, EQE of 21.8%) showed the best performances in the 3:7 mixed host. Enhanced EQE in the mixed host devices is mainly due to charge carrier injection/transport balance as well as recombination region distribution within EML by the optimization of mixed host properties. [23] Moreover, these behavior were more dramatic in TcTa:SPPO1 mixed host devices because SPPO1 materials is an electron transport-type material while 26DCzPPy is a bipolar material. Additionally, the power efficiency of the mixed host devices also highly improved due to the reduced driving voltage as well as the enhanced quantum efficiency. The peak power efficiencies of Device B were improved from 28 (TcTa:SPPO1 = 0:10) to 53 lm/W (TcTa:SPPO1 = 3:7) by using mixed host structure (see Fig. 7).

It has been known that the narrow recombination zone was inferior for the efficiency roll-off due to its high exciton density which induces the triplet exciton quenching process [12,14,19]. Therefore, as shown in Fig. 6, the device performances of the single host devices at high current density region were greatly decreased. Especially, this detrimental efficiency roll-off was distinguished in the SPPO1

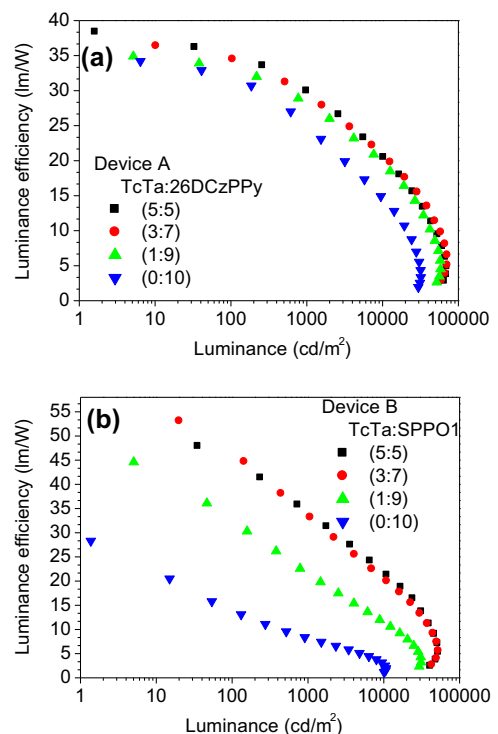


**Fig. 7.** Luminance efficiency versus luminance characteristics of (a) Device A (TcTa:26DCzPPy) and (b) Device B (TcTa:SPPO1).

single host device because SPP01 is electron transport-type material which resulted in a shallow recombination zone. However, the distributed recombination zone through balanced charge carrier injection/transport in the mixed host devices showed remarkably stable efficiency roll-off. The external quantum efficiencies of the Device A (TcTa:26DCzPPy = 1:9) and Device B (TcTa:SPP01 = 5:5) showed over 18% at a luminance of 10,000 cd/m<sup>2</sup> and decreased to half at a current density of  $J_0 = 258$  and 230 mA/cm<sup>2</sup>, respectively. Both values are better than any other efficiency roll-off values for blue electro-phosphorescent devices [19], indicating a highly reduced roll-off in efficiency.

#### 4. Conclusion

In summary, light-emitting performances of blue PHOLEDs could be enhanced by host layer engineering. Mixed host structure devices of TcTa:26DCzPPy or TcTa:SPP01 showed effective distribution of recombination zone as well as balanced charge carrier injection, which resulted in highly improved efficiency roll-off at high current density.

#### Acknowledgements

We gratefully acknowledged Prof. H.-K. Shim and Mr. M.-J. Park (Department of Chemistry of Korea Advanced Institute of Science and Technology) for PL study, and Ms. K.-I. Song and Ms. S.J. Lee (ETRI) for assistance with EL measurements. This work was supported by IT R&D program of MKE/KEIT (2009-F-016-01, Development of Eco-Emotional OLED Flat-Panel Lighting) and the future technology development program of MOCIE/KEIT (2006-10028439, OLED Lighting).

#### References

- [1] M.A. Baldo, D.F. O'Brien, Y. You, S. Shoustikov, M. Sibley, E. Thompson, S.R. Forrest, *Nature* 395 (1998) 151.
- [2] B.W. D'Andrade, S.R. Forrest, *Adv. Mater.* 16 (2004) 1595.
- [3] C. Adachi, M.A. Baldo, M.E. Thompson, S.R. Forrest, *J. Appl. Phys.* 90 (2001) 5048.
- [4] S.-O. Jeon, K.S. Yook, C.W. Joo, J.Y. Lee, K.-Y. Ko, J.-Y. Park, Y.G. Baek, *Appl. Phys. Lett.* 93 (2008) 063306.
- [5] C. Adachi, R.C. Kwong, P. Djurovich, V. Adamovich, M.A. Baldo, M.E. Thompson, S.R. Forrest, *Appl. Phys. Lett.* 79 (2001) 2082.
- [6] H. Inomata, K. Goushi, T. Masuko, T. Konno, T. Imai, H. Sasabe, J.J. Brown, C. Adachi, *Chem. Mater.* 16 (2004) 1285.
- [7] S.-J. Su, H. Sasabe, T. Takeda, J. Kido, *Chem. Mater.* 20 (2008) 1691.
- [8] R.J. Holmes, B.W. D'Andrade, S.R. Forrest, X. Ren, J. Li, M.E. Thompson, *Appl. Phys. Lett.* 83 (2003) 3818.
- [9] S. Lamansky, P. Djurovich, D. Murphy, F. Abdel-Razzaq, H. Lee, C. Adachi, P.E. Burrows, S.R. Forrest, M.E. Thompson, *J. Am. Chem. Soc.* 123 (2001) 4304.
- [10] K.S. Yook, S.O. Jeon, C.W. Joo, J.Y. Lee, *Org. Electron.* 10 (2009) 170.
- [11] J. Lee, J.-I. Lee, K.-I. Song, S.J. Lee, H.Y. Chu, *Appl. Phys. Lett.* 92 (2008) 203305.
- [12] J. Lee, J.-I. Lee, K.-I. Song, S.J. Lee, H.Y. Chu, *Appl. Phys. Lett.* 92 (2008) 133304.
- [13] S.-H. Eom, Y. Zheng, N. Chopro, J. Lee, Franky So, J. Xue, *Appl. Phys. Lett.* 93 (2008) 133309.
- [14] S. Reineke, K. Walzer, Karl Leo, *Phys. Rev. B* 75 (2007) 125328.
- [15] S.H. Kim, J. Jang, K.S. Yook, J.Y. Lee, *Appl. Phys. Lett.* 92 (2008) 023513.
- [16] S.H. Kim, J. Jang, J.Y. Lee, *Appl. Phys. Lett.* 91 (2007) 083511.
- [17] S.H. Kim, J. Jang, K.S. Yook, J.Y. Lee, M.-S. Gong, S. Ryu, G.-K. Chang, H.J. Chang, *J. Appl. Phys.* 103 (2008) 054502.
- [18] S.O. Jeon, K.S. Yook, C.W. Joo, J.Y. Lee, *Appl. Phys. Lett.* 94 (2009) 013301.
- [19] S.-J. Su, Y. Takahashi, T. Chiba, T. Takeda, J. Kido, *Adv. Funct. Mater.* 19 (2009) 1.
- [20] J. Lee, J.-I. Lee, J.Y. Lee, H.Y. Chu, *Appl. Phys. Lett.* 94 (2009) 193305.
- [21] K. Sakanoue, M. Motoda, M. Sugimoto, S. Sakaki, *J. Phys. Chem. A* 103 (1999) 5551.
- [22] A.C. Albrecht, *J. Chem. Phys.* 38 (1963) 354.
- [23] J. Lee, J.-I. Lee, H.Y. Chu, ETRI. J. (2009), doi:10.4218/etrij.09.1209.0005.

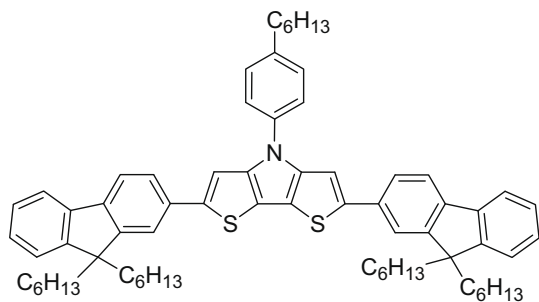


Fig. 1. Molecular structure of **DTP-FLU**.

2,6-bis[2-(9,9-dihexyl-9H-fluorene)]-*N*-(4-hexylphenyl)-dithieno[3,2-*b*:2',3'-*d*]pyrrole (**DTP-FLU**) oligomer (Fig. 1) were discussed.

## 2. Experimental section

**DTP-FLU** oligomer was synthesized by Suzuki coupling of 2,6-dibromo-*N*-(4-hexylphenyl)-dithieno[3,2-*b*:2',3'-*d*]pyrrole and 9,9-dihexyl-9H-fluorene-2-boronic acid. Scheme 1 represents the synthetic route leading to the target compound (**DTP-FLU**). The detailed synthesis, characterization, photophysical and electrochemical properties of a series of DTP derivatives are reported separately [15].

Absorption spectra were recorded using Shimadzu 1601 PC spectrophotometer and fluorescence was measured using Shimadzu RF 5301 spectrofluorophotometer. The samples for the spectroscopic studies were prepared by spin coating chloroform solution of **DTP-FLU** on a quartz substrate. The quantum yield in chloroform was measured using quinine sulfate (0.1 M H<sub>2</sub>SO<sub>4</sub>) as a reference. The solid state photoluminescence quantum yield was determined using an integrating sphere (Lab Sphere Com) with He–Cd laser (325 nm; 11 mW) as an excitation source [16].

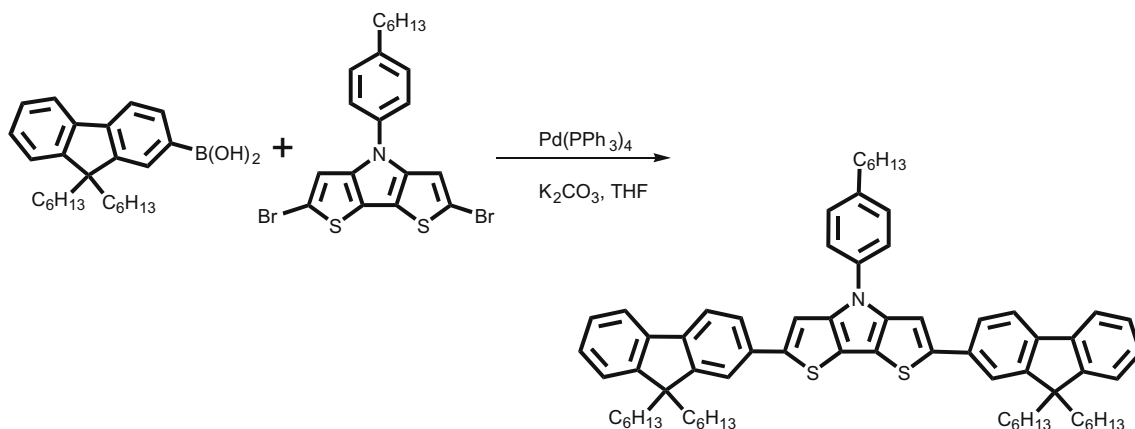
For time-of-flight photoconductivity measurement, the oligomer film samples were prepared by drop casting the chloroform solution of **DTP-FLU** (concentration: 37 mg/ml) onto an indium tin oxide (ITO) patterned glass slide in a solvent saturated environment. A 100 nm thick alumi-

num electrode was evaporated onto the **DTP-FLU** film using an Edwards thermal evaporator. The thickness of the oligomer film was measured using a surface profiler (KLA-Tencor P10 surface profiler) and it was found to be 4.4 μm. The TOF measurement system was composed of a pulsed nitrogen (N<sub>2</sub>) laser (Oriel 79074), a pulse generator (SRS-DG535), a DC voltage source (Kenwood PWR18-2), and a digital oscilloscope (Agilent-Infiniium, 1 GHz, 4 Gsa/s). The N<sub>2</sub> laser with pulse width <4 ns, and pulse repetition rate 1 Hz, was illuminated on the ITO side of the device. The photocurrent under the influence of applied electric field was monitored across a variable resistor using an oscilloscope. It was ensured that the time constant of the setup is less than the transit time ( $RC < t_{tr}$ ). The details of the TOF setup have been described elsewhere [17]. The active area of the device was 4 mm<sup>2</sup>. The sample was mounted in a temperature controlled continuous flow cryostat under vacuum of  $\sim 10^{-5}$  mbar. The charge mobilities were calculated using the relation  $\mu = d^2/Vt_T$ , where  $d$  is the thickness of the film,  $V$  is the applied voltage and  $t_T$  is the transit time. The transit time was obtained from the inflection points in a double logarithmic plot of photocurrent versus time.

## 3. Results and discussion

The solid state absorption and emission spectra of **DTP-FLU** is shown in Fig. 2. The absorption spectrum shows a broad band with a maximum around 426 nm with two shoulder peaks at 214 and 271 nm. The fluorescence spectrum in film state is characterized with emission maxima at 505 nm with full width at half maximum (FWHM) of 49 nm. The Stokes shift was found to be 79 nm. The quality of the emission spectra was assessed based on the Commission International de L'Eclairage (CIE) chromaticity coordinates (see inset of Fig. 2). The color coordinate was found to be in the green region (0.2422, 0.5019). The band gap was calculated from the onset of the absorption spectra and it was found to be 2.5 eV.

**DTP-FLU** has a strong solution state photoluminescence with a quantum efficiency of 75%. The solid state quantum yield was measured using an integrating sphere and it was



Scheme 1. Synthesis of **DTP-FLU**.

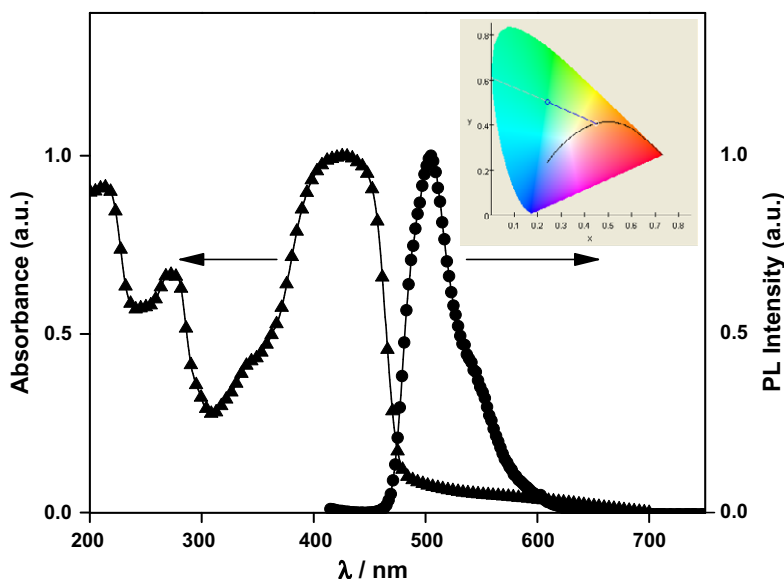


Fig. 2. Solid state absorption and emission spectra of **DTP-FLU**. Inset: CIE coordinates in film sample.

found to be 22%. The surface morphology of the **DTP-FLU** film was studied using atomic force microscopy (AFM). The experiment was performed at room temperature using a commercial AFM Nanoscope IV (Dimension 3100, Digital Instruments) in the tapping mode. The film was prepared by spin coating the **DTP-FLU** oligomer solution in chloroform on a cleaned ITO substrate. Fig. 3 shows the AFM image of the film and from the 3D view (Fig. 3D) it is noted that the film is uniform with grain size in the nanoregime.

The time-of-flight (TOF) photocurrent transients were measured to determine the carrier drift mobility by monitoring the time taken by the carriers generated at one end of the sample to reach the other end under the influence of constant electric field. The device architecture used for the TOF measurement was ITO/**DTP-FLU** (4.4 μm)/Al. Fig. 4 shows a linear plot of TOF transients for holes in **DTP-FLU** at various applied voltages at 298 K and the corresponding double logarithmic plot is shown in the inset. It

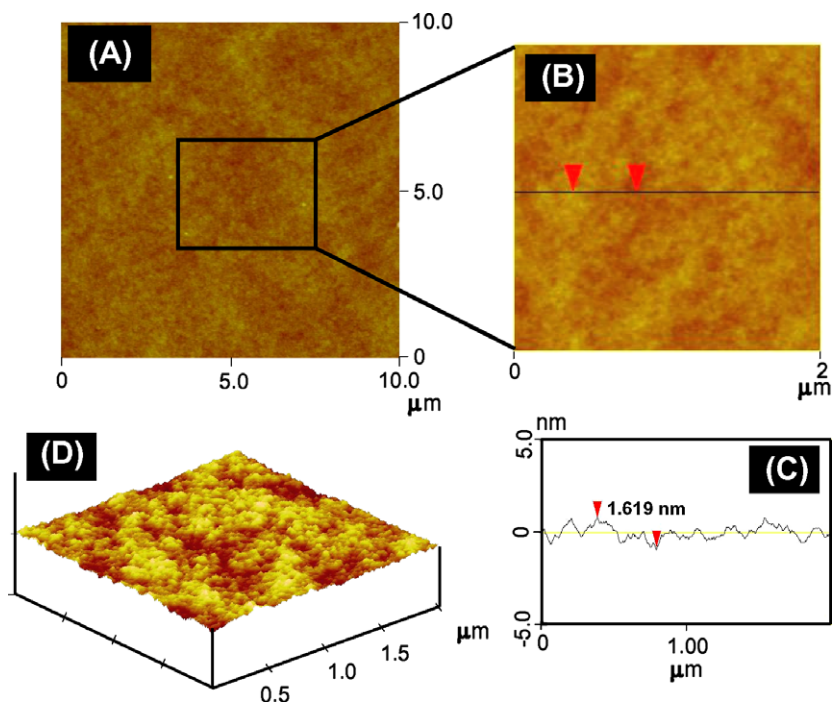


Fig. 3. (A) AFM height image of the spin coated film (10 μm × 10 μm) of **DTP-FLU** on ITO coated glass substrate. (B) magnified image of A (2 μm × 2 μm). (C) height profile of AFM image B and (D) the 3D view of the AFM image showing the surface morphology of the film.

is clear from the figure that the initial decay in the photocurrent follows a constant current plateau. This appearance of constant current plateau is due to the non-dispersive nature of the hole transport. The subsequent decay in the current is due to the holes reaching the other electrode at which they are discharged.

The transit time  $t_T$ , for the arrival of carriers were readily obtained from the inflection point in the double logarithmic plot of photocurrent versus time. The carrier mobility  $\mu$ , was extracted using the relation  $\mu = d^2/Vt_T$ . In order to get an in-depth knowledge of the transport property of **DTP-FLU**, a detailed investigation was carried out at

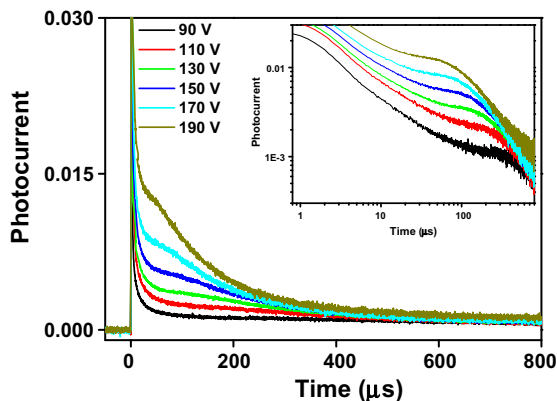


Fig. 4. Linear plot of time-of-flight hole current transients for different applied voltage in **DTP-FLU** film at 298 K. The inset shows the corresponding double-logarithmic plot.

a temperature range of 218–308 K. It is observed that at low temperature, the transport become dispersive in nature. The linear plot of TOF hole transients obtained at various temperatures are shown in Fig. 5.

At 298 K, the hole mobility was found to be  $7.7 \times 10^{-6} \text{ cm}^2/\text{Vs}$  at an applied electric field of  $2.9 \times 10^5 \text{ V/cm}$ . It is noteworthy that the field-dependences of the hole mobilities are in good agreement with the Pool-Frenkel relationship ( $\mu = \mu_{(E=0)} \exp(\gamma E^{1/2})$ ), where  $\mu_{(E=0)}$  is the zero-field mobility and  $\gamma$  is the slope of the field dependence of charge mobility, at all temperatures studied [17–20]. The Pool-Frenkel plots of hole mobility in **DTP-FLU** at various temperatures are shown in Fig. 6. The hole mobility was found to be increasing with increase in temperature. At 238 K, the hole mobility was found to be  $1.2 \times 10^{-6} \text{ cm}^2/\text{Vs}$  at an applied field of  $2.7 \times 10^5 \text{ V/cm}$ , but at 278 K the mobility was increased to  $4.1 \times 10^{-6} \text{ cm}^2/\text{Vs}$  and at 308 K, it was found to be  $8.4 \times 10^{-6} \text{ cm}^2/\text{Vs}$  with the same applied electric field. The zero-field mobility ( $\mu_{(E=0)}$ ) and  $\gamma$  were extracted from this Pool-Frenkel plot and the zero-field mobility was plotted against temperature (Fig. 7A). It is clear from the plot that the zero-field mobility increases with increase in temperature and the slope ( $\gamma$ ) decreases with increase in temperature. This illustrates the typical hopping mechanism of charge transport in **DTP-FLU**. Generally, in conjugated molecular solids, the transport of charges occurs via hopping between the localized sites on individual molecules. It is known that the disorder in energies of localized sites arises from variations in conjugation length, conformation of the molecule or intermolecular interactions. This leads to a distribution

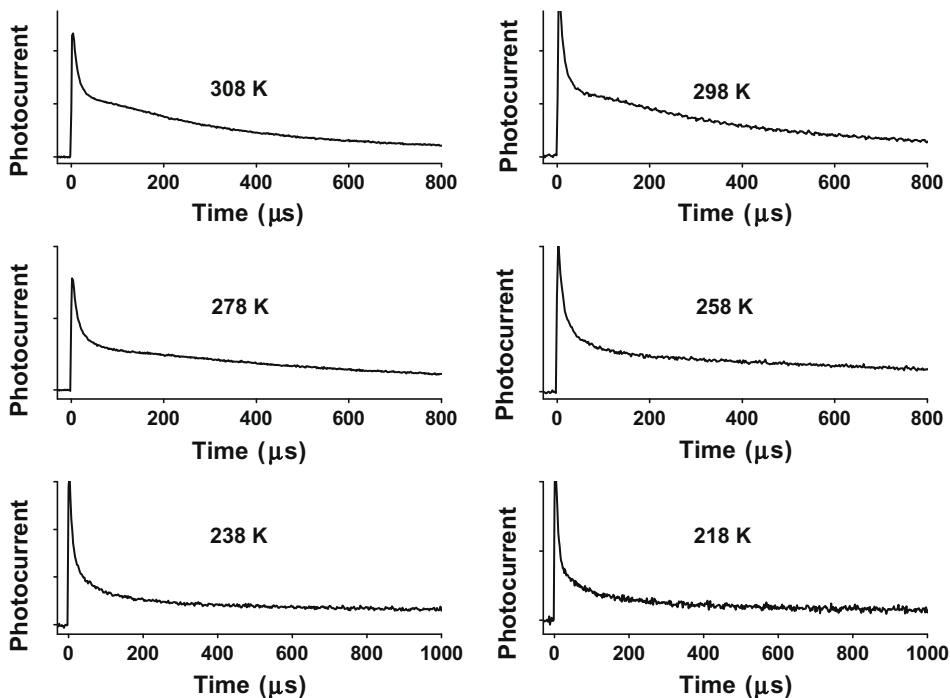


Fig. 5. Linear plot of TOF photocurrent transients at various temperatures in **DTP-FLU** (Field:  $2.7 \times 10^5 \text{ V/cm}$ ).

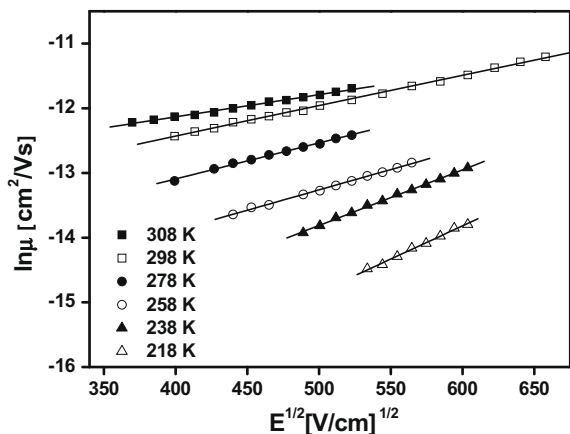


Fig. 6. Poole-Frenkel plots of hole mobility in DTP-FLU at various temperatures.

of site energies and such distributions give rise to a significant dispersion in the charge hopping times.

The mechanism of charge transport and the relation between the Gaussian energy distribution and characteristics of time-of-flight transients in disordered organic materials was interpreted by various models [21]. Gaussian disorder model (GDM), proposed by Bäessler et al. is one of the empirical expressions which has been widely used to characterize the field and temperature dependence of charge transport in amorphous organic solids [21–23]. In GDM, it is assumed that the charge transport occurs through a hopping mechanism with Gaussian distribution of energetic disorder of localized hopping sites and intermolecular positional disorder. Energetic disorder ( $\sigma$ ) and positional disorder parameter ( $\Sigma$ ) are the two crucial parameters which influence the carrier mobility [21]. The energetic disorder corresponds to the width of the Gaussian density of states and it arises from the distribution of conjugation length. The positional disorder parameter arises from the fluctuations of intermolecular distances or mutual orientation of neighboring molecules. This GDM model also accounts for the crossover from non-dispersive to dispersive transport at low temperatures [24–26]. In Gaussian model, the dependence of hole mobility on electric field and temperature can be expressed by Eq. (1) [24].

$$\mu_{\text{GDM}} = \mu_{\infty} \exp \left[ - \left( \frac{2\sigma}{3kT} \right)^2 \right] \times \exp \left[ C \left\{ \left( \frac{\sigma}{kT} \right)^2 - \Sigma^2 \right\} E^{1/2} \right] \quad (1)$$

where  $\mu_{\infty}$  is the high temperature limit of the mobility,  $\sigma$  is the energetic disorder bandwidth,  $\Sigma$  is the parameter of positional disorder and  $C$  is the empirical constant. The empirical constant indicates the hopping distances that a charge carrier has to overcome to be transferred from one site to another. The energetic disorder parameter and high temperature limit of mobility was extracted from the plot of logarithmic zero-field mobility versus  $1/T^2$  (Fig. 7A) and it was found to be  $\mu_{\infty} = 6.1 \times 10^{-4} \text{ cm}^2/\text{Vs}$  and  $\sigma = 100 \text{ meV}$ . Also the positional disorder parameter and the empirical constant  $C$  were extracted by plotting

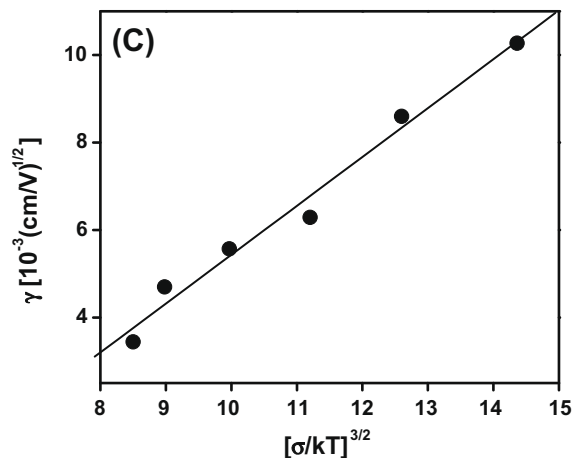
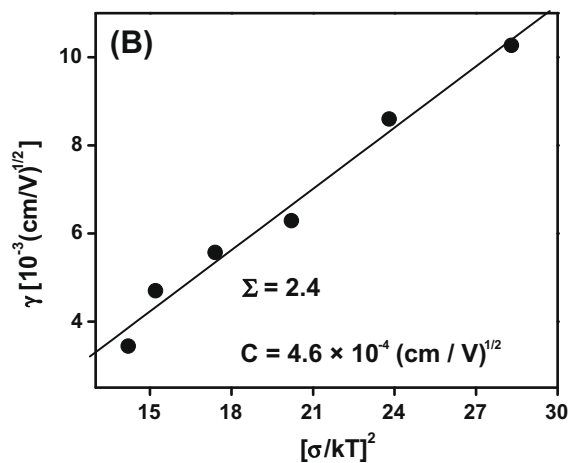
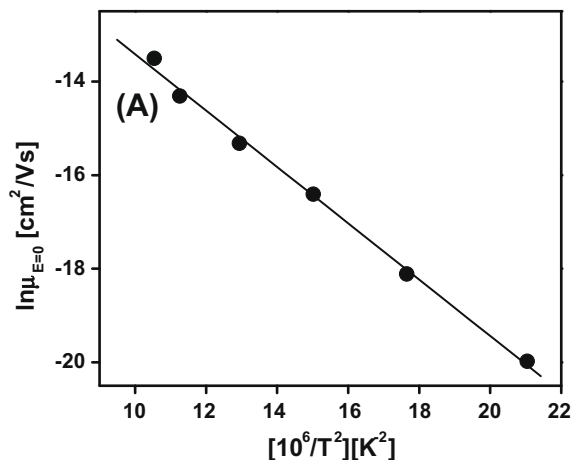


Fig. 7. (A) Temperature dependence of mobilities at zero-field in DTP-FLU. (B) The slope of the field dependence of the logarithmic mobility versus  $(\sigma/kT)^2$  the solid line is a linear fit according to Eq. (1). (C) The slope of the field dependence of the logarithmic mobility versus  $(\sigma/kT)^{3/2}$ , the solid line is a linear fit according to Eq. (2).

the slope of the field dependence ( $\gamma$ ) against  $(\sigma/kT)^2$  (see Fig. 7B) and the values of  $\Sigma$  and  $C$  were obtained from the linear fit and was found to be 2.4 and  $4.6 \times 10^{-4} \text{ (cm/V)}^{1/2}$ , respectively.

It is reported that long range correlations due to charge–dipole interaction exists in disordered organic materials [27]. But in GDM model, the correlation between the sites is not accounted. This lead to the development of another model called Correlated disorder model (CDM) which accounts for the charge–dipole interactions [28]. According to CDM, the non-dispersive mobility in correlated media can be represented by Eq. (2).

$$\mu_{\text{CDM}} = \mu_{\infty} \exp \left[ - \left( \frac{3\sigma}{5kT} \right)^2 \right] \times \exp \left[ 0.78 \left\{ \left( \frac{\sigma}{kT} \right)^{3/2} - 2 \right\} \sqrt{\frac{eaE}{\sigma}} \right] \quad (2)$$

Carrier hopping among the sites is arranged on a cubic lattice with a cell spacing  $a$ . Also the high temperature limit of mobility may have additional temperature dependence due to other less correlated sources of energy disorder or polaron effects. The major difference between GDM and CDM is the predicted temperature dependence of  $\gamma$ . Fig. 7C shows the variation of  $\gamma$  with  $(\sigma/kT)^{3/2}$  and the linear fit is according to CDM (Eq. (2)). The average cell spacing ( $a$ ) was obtained from this linear plot and it was found to be 1.4 nm. The energetic disorder parameter according to CDM model was also calculated from the plot of logarithmic zero-field mobility versus temperature (Fig. 7A) and was found to be 111 meV. The localization length for the charges was calculated by using Eq. (3) with the derived values of energetic disorder parameter,  $\mu_{\infty}$  and average cell spacing.

$$\mu_{\infty} = \frac{ea^2 v_{\text{ph}}}{\sigma} \exp \left( \frac{-2a}{L} \right) \quad (3)$$

where  $v_{\text{ph}}$  is the phonon frequency for hopping ( $\sim 10^{12} \text{ s}^{-1}$ ). The localization length was estimated to be 5 Å. The results obtained from both the models (GDM and CDM) are summarized in Table 1.

The charge transport parameters obtained from the GDM/CDM analysis are similar to the established conjugated materials such as poly (*p*-phenylenevinylene) (PPV), polyfluorene (PFO) etc [29,30]. It is interesting to note that the intersite hopping constant and energetic disorder obtained in the case of **DTP-FLU** is found to be similar to that in PFO (intersite hopping constant =  $2.4 \times 10^{-4} (\text{cm/V})^{1/2}$  and  $\sigma_{\text{GDM}} = 90 \text{ meV}$ ) [31], and in (2-methoxy-5-(2'-ethylhexyloxy)-1,4-phenylenevinylene)/C60 (MEH-PPV/C60) composite [32]. Also it is noteworthy that that the average site spacing ( $a = 1.4 \text{ nm}$ ) and the localization length ( $L = 5 \text{ Å}$ ) in **DTP-FLU** is similar to the fully conjugated materials [33]. Therefore it can be concluded that

**Table 1**

Charge transport parameters of **DTP-FLU** calculated using Gaussian disorder model (GDM) and Correlated disorder model (CDM).

Gaussian disorder model	Correlated disorder model
$\mu_{\infty, \text{GDM}}: 6.1 \times 10^{-4} \text{ cm}^2/\text{Vs}$	$\mu_{\infty, \text{CDM}}: 6.1 \times 10^{-4} \text{ cm}^2/\text{Vs}$
$C: 4.6 \times 10^{-4} (\text{cm/V})^{1/2}$	$\sigma_{\text{CDM}}: 111 \text{ meV}$
$\sigma_{\text{GDM}}: 100 \text{ meV}$	$a: 1.4 \text{ nm}$
$\Sigma: 2.4$	$L: 5 \text{ Å}$

DTP based materials have similar transport properties as that of other conjugated materials such as PFO or PPV which have potential uses in device applications. Therefore the charge transport parameters of DTP based molecules can be controlled and optimized to enable us to fine tune and fabricate the optoelectronic devices.

#### 4. Conclusion

The charge transport properties of **DTP-FLU** were studied by using time-of-flight photoconductivity method. The film morphology and photophysical properties of this oligomer was also investigated in detail. The compound is found to be hole transporting. The hole mobilities were measured over a range of temperatures from 218 to 308 K and the mobilities were in the order of  $10^{-6} \text{ cm}^2/\text{Vs}$  at all temperatures. The field and temperature dependence was analyzed by Gaussian disorder model (GDM) and Correlated disorder model (CDM) and charge transport parameters were extracted. The energetic disorder parameter and positional disorder parameter estimated using Gaussian disorder model was found to be 100 meV and 2.4, respectively. Most interestingly the transport parameters of this material are similar to the other conjugated materials such as PFO and PPV. The results indicate that dithienopyrrole-based compounds will be a promising new material for various optoelectronic applications.

#### Acknowledgment

The authors would like to thank Agency for Science, Technology and Research (A\*STAR), National University of Singapore (NUS), NUS-Nanoscience and Nanotechnology Initiative (NUSNNI) for financial support. Department of Chemistry, NUS and Institute of Materials Research and Engineering (IMRE) are acknowledged for technical support and Mr. Surani b Dolmanan for the technical assistance for solid state quantum yield measurements.

#### References

- [1] (a) S. Günes, H. Neugebauer, N.S. Sariciftci, Chem. Rev. 107 (2007) 1324; (b) Y. Shirota, H. Kageyama, Chem. Rev. 107 (2007) 953.
- [2] (a) N. Blouin, A. Michaud, M. Leclerc, Adv. Mater. 19 (2007) 2295; (b) C. Soci, I.-W. Hwang, D. Moses, Z. Zhu, D. Waller, R. Gaudiana, C.J. Brabec, A.J. Heeger, Adv. Funct. Mater. 17 (2007) 632; (c) M. Jørgensen, K. Norrman, F.C. Krebs, Sol. Energy Mater. Sol. Cells 92 (2008) 686.
- [3] J. Liu, X. Guo, L. Bu, Z. Xie, Y. Cheng, Y. Geng, L. Wang, X. Jing, F. Wang, Adv. Funct. Mater. 17 (2007) 1917.
- [4] X. Gong, M.R. Robinson, J.C. Ostrowski, D. Moses, G.C. Bazan, A.J. Heeger, Adv. Mater. 14 (2002) 581.
- [5] G. Kössmehl et al., Handbook of Oligo- and Polythiophenes, in: D. Fichou (Ed.), Wiley-VCH, Weinheim, 1999.
- [6] M. Zhang, H.N. Tsao, W. Pisula, C. Yang, A.K. Mishra, K. Müllen, J. Am. Chem. Soc. 129 (2007) 3472.
- [7] C. Vijila, N.G. Meng, C. Zhikuan, Z. Furong, C.S. Jin, J. Polym. Sci. Part B: Polym. Phys. 46 (2008) 1159.
- [8] K. Ogawa, S.C. Rasmussen, Macromolecules 39 (2006) 1771.
- [9] G. Koeckelberghs, L. De Cremer, A. Persoons, T. Verbiest, Macromolecules 40 (2007) 4173.
- [10] P. Coppo, M.L. Turner, J. Mater. Chem. 15 (2005) 1123.
- [11] G.R. Hutchison, M.A. Ratner, T.J. Marks, J. Am. Chem. Soc. 127 (2005) 2339.
- [12] W. Zhang, J. Li, L. Zou, B. Zhang, J. Qin, Z. Lu, Y.F. Poon, M.B. Chan-Park, C.M. Li, Macromolecules 41 (2008) 8953.



- [13] T.T. Steckler, X. Zhang, J. Hwang, R. Honeyager, S. Ohira, X.-H. Zhang, A. Grant, S. Ellinger, S.A. Odom, D. Sweat, D.B. Tanner, A.G. Rinzler, S. Barlow, J.-L. Brédas, B. Kippelen, S.R. Marder, J.R. Reynolds, *J. Am. Chem. Soc.* 131 (2009) 2824.
- [14] J. Liu, R. Zhang, G. Sauvé, T. Kowalewski, R.D. McCullough, *J. Am. Chem. Soc.* 130 (2008) 13167.
- [15] G. Balaji, M. Parameswaran, C. Vijila, T. Mein Jin, Z. Furong, S. Valiyaveetil, submitted for publication.
- [16] J.C. de Mello, H.F. Wittmann, R.H. Friend, *Adv. Mater.* 9 (1997) 230.
- [17] C. Vijila, B. Balakrisnan, C. Huang, Z.-K. Chen, C.-G. Zhen, M.D.J. Auch, S.J. Chua, *Chem. Phys. Lett.* 414 (2005) 393.
- [18] P.M. Borsenberger, L. Pautmeier, H. Bässler, *J. Chem. Phys.* 94 (1991) 5447.
- [19] W.D. Gill, *J. Appl. Phys.* 43 (1972) 5033.
- [20] C. Vijila, A. Pivrikas, H. Chun, C. Zhikuan, R. Österbacka, C.S. Jin, *Org. Electron.* 8 (2007) 8.
- [21] H. Bässler, *Phys. Stat. Sol. B* 15 (1993) 175.
- [22] D. Poplavskyy, J. Nelson, *J. Appl. Phys.* 93 (2003) 341.
- [23] F. Laquai, G. Wegner, C. Im, H. Bässler, S. Heun, *J. Appl. Phys.* 99 (2006) 203712.
- [24] P.M. Borsenberger, L.T. Pautmeier, H. Bässler, *Phys. Rev. B* 46 (1992) 12145.
- [25] H. Bässler, P.M. Borsenberger, *Chem. Phys.* 177 (1994) 763.
- [26] P.M. Borsenberger, L.B. Schein, *J. Phys. Chem.* 98 (1994) 233.
- [27] S.V. Novikov, D.H. Dunlap, V.M. Kenkre, P.E. Parris, V. Vannikov, *Phys. Rev. Lett.* 81 (1998) 4472.
- [28] S.J. Martin, A. Kambili, A.B. Walker, *Phys. Rev. B* 67 (2003) 165214.
- [29] H.C.F. Martens, H.B. Brom, P.W.M. Blom, H.F.M. Schoo, *Phys. Stat. Sol. b* 218 (2000) 283.
- [30] T. Kreuzis, D. Poplavskyy, S.M. Tuladhar, M. Campoy-Quiles, J. Nelson, A.J. Campbell, D.D.C. Bradley, *Phys. Rev. B* 73 (2006) 235201.
- [31] R.U.A. Khan, D. Poplavskyy, T. Kreuzis, D.D.C. Bradley, *Phys. Rev. B* 75 (2007) 035215.
- [32] Q. Shi, Y. Hou, H. Jin, Y. Li, *J. Appl. Phys.* 102 (2007) 073108.
- [33] H.C.F. Martens, P.W.M. Blom, H.F.M. Schoo, *Phys. Rev. B* 61 (2000) 7489.

metathesis reaction [24–32]. Such copolymers attracted significant attention due to the strong self-assembly induced by  $\pi$ – $\pi$  interactions and exhibited quite different ordered morphologies in comparison with the reported rod–coil block copolymers [9–21].

Polythiophene is one of the most widely explored polymers in the optoelectronic devices, especially in transistor and photovoltaic applications [33,34], because of the excellent charge-transporting mobility and highly regioregular structure. Several all-conjugated thiophene-based polymers have been reported recently [28–32]. McCullough first reported the synthesis of poly(3-hexylthiophene)(P3HT)-*block*-poly(3-dodecylthiophene) by the sequential addition of different monomers [28]. Soon after, Yokozawa and coworkers prepared an amphiphilic P3HT-*block*-poly(3-methoxyethoxyethylmethylthiophene) by the similar approach [29]. Recently, Hashimoto and his coworkers discovered that the poly[3-(2-ethylhexyl)thiophene] (P3EHT) segment in P3HT-*b*-P3EHT could promote the self-organized P3HT domains in the film state and showed a higher crystalline absorption intensity than a P3HT homopolymer [30]. The nanowire morphology of crystalline-crystalline conjugated diblock copolymer of P3HT-*block*-poly(3-octylthiophene) was developed with the aim of a photovoltaic cell application recently [32]. One of us also prepared alternative well-controlled block copolythiophenes, P3HT-*block*-poly(3-phenoxyethylthiophene) (P3HT-*b*-P3PT, Chart 1), with a nanofiber-like morphology [31]. Although the all-conjugated copolymers were successfully synthesized, the studies on the morphology and optoelectronic device characteristics are still quite limited. The nano-scaled morphologies of P3HT-*b*-P3PT could play an important role in the charge transport and optoelectronic properties.

In this study, the morphology and device characteristics of P3HT-*b*-P3PT are reported, including field-effect transistor (FET) and photovoltaic cell (PV). The polymer surface structures were explored through different solvent mixtures of chloroform (CHCl<sub>3</sub>) and dichlorobenzene (DCB). The optical absorption, FET, and PV characteristics were correlated with their surface structures. This present

study provided a new insight into the morphology and device characteristics of all conjugated block copolymers.

## 2. Experimental part

### 2.1. Materials

The monomer of 2,5-dibromo-3-phenoxyethylthiophene and the block copolythiophene of P3HT-*b*-P3PT, were prepared according to our previous report [31]. Ultra-anhydrous solvents and common organic solvents were purchased from Tedia, Merck, and J.T. Baker. Octadecyltrichlorosilane (ODTS) used as self-assembled monolayer (SAM) on the gate dielectric surface was purchased from Aldrich. P3HT (Mn: 17,730, regioregularity: 98.5%) and [6,6]-phenyl-C<sub>61</sub>-butyric acid methyl ester (PCBM) were obtained from Rieke-Metal and Nano-C, respectively. All reagents were used as received.

### 2.2. Polymer structure of P3HT-*b*-P3PT

The molecular weights of different blocks in P3HT-*b*-P3PT were well-controlled through the feed ratio of the monomers and the initiator, according to our previous report [31]. The number average molecular weight ( $M_n$ ) of the studied P3HT-*b*-P3PT estimated from GPC was around 30,100, with polydispersity index of 1.17. The degree of polymerization of P3HT and P3PT segments estimated from the <sup>1</sup>H NMR spectrum, appended in Fig. S1, were 150 and 27, respectively. The regioregularity of P3HT-*b*-P3PT was found to be 98% (P3HT block) and 69% (P3PT block), respectively, estimated from the <sup>1</sup>H NMR spectrum by comparing the signal intensities of the methylene protons next to the thiophene ring.

## 3. Characterization

UV-Vis absorption spectra of the spin-coated polymer films on quartz substrates were recorded on a Hitachi U-4100 spectrophotometer. For these thin film spectra, polymer solutions (ca. 10 mg/ml) were filtered through syringe filters with PTFE membrane (0.45  $\mu$ m pore size), then spin-coated at a speed rate of 450 rpm for 60 s onto the quartz substrate, and annealed for 10 min under nitrogen. Cyclic voltammetry (CV) was conducted with the use of a three-electrode cell in which ITO (polymer film area about 0.5  $\times$  0.7 cm<sup>2</sup>) was used as a working electrode. A platinum wire was used as an auxiliary electrode. All cell potentials were taken with the use of a homemade Ag/AgCl, KCl (sat.) reference electrode. The energy level of HOMO was determined from the onset oxidation ( $E_{\text{onset}}^{\text{ox}}$ ) based on the reference energy level of ferrocene (4.8 V below the vacuum level) according to the following relation: HOMO =  $-e(E_{\text{onset}}^{\text{ox}} - E_{\text{ferrocene}}^{1/2} + 4.8)$  (eV). The LUMO level was calculated from the HOMO and the value of optical band gap according to the relation: LUMO = HOMO +  $E_g^{\text{opt}}$  (eV) [35,36]. The thickness of the prepared polymer films was measured with an Alpha-step 500 surface profiler (TECNOR). Atomic force micrographs (AFM) of polymer films on a device surface were obtained with a Nanoscope 3D

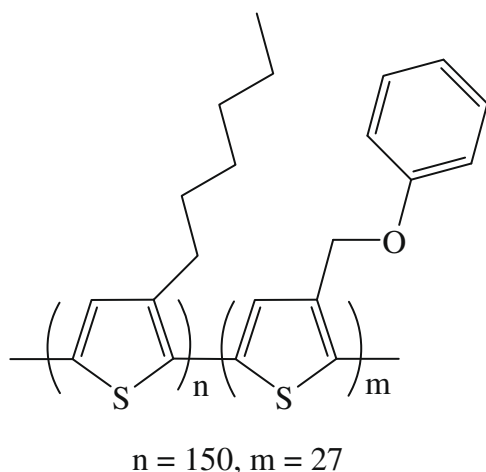


**Chart 1.** Polymer structure of the studied diblock copolythiophene, P3HT-*b*-P3PT.

Controller AFM (Digital Instruments, Santa Barbara, CA) operated in a tapping mode at room temperature. Commercial silicon cantilevers (Nanosensors, Germany) with typical force constants ( $5\text{--}37\text{ Nm}^{-1}$ ) was used and the images were taken continuously with the scan rate of 0.8 Hz.

### 3.1. Fabrication and characterization of polymer field-effect transistor

A polymer field-effect transistor was fabricated through the bottom-contact and bottom-gate geometry. A thermally grown 200 nm thickness of  $\text{SiO}_2$  was used as the gate dielectric with a capacitance of  $17\text{ nF/cm}^2$ . The source/drain regions were defined by a 130 nm thickness of Au through a shadow mask, and the channel length ( $L$ ) and width ( $W$ ) were 25 and 500  $\mu\text{m}$ , respectively. Before gilding the devices, the clean substrates were immersed in anhydrous ODTs toluene solution and left to form a self-assembled monolayer for 6 h at room temperature under nitrogen. In the following, the ODTs-treated substrate was taken out from the solution, rinsed with toluene for several times, and baked at  $100\text{ }^\circ\text{C}$  for 30 min under ambient air. The ODTs-modified substrate was kept in a dry box before use. A polymer solution (5 mg/ml) in  $\text{CHCl}_3$ , DCB, or mix-solvents was first filtered through 0.45  $\mu\text{m}$  syringe filters, spin-coated at a speed rate of 1000 rpm for 60 s onto the ODTs-modified substrate, and then annealed at  $150\text{ }^\circ\text{C}$  for 1 h under nitrogen. Output and transfer characteristics of the transistor devices were performed using a Keithley 4200 semiconductor parametric analyzer. All the electronic measurements were conducted at ambient atmosphere.

### 3.2. Fabrication and characterization of polymer photovoltaic cells

The bulk-heterojunction photovoltaic cell was fabricated through the following preparation procedures: The glass-indium tin oxide (ITO) substrate (obtained from Sanyo, Japan ( $8\ \Omega/\square$ )) was first patterned by lithograph, then cleaned with detergent, and ultrasonicated in acetone and isopropyl alcohol, and subsequently dried on a hot plate at  $120\text{ }^\circ\text{C}$  for 5 min, and finally treated with oxygen plasma for 5 min. Poly(3,4-ethylenedioxy-thiophene):poly(styrene-sulfonate) (PEDOT:PSS, Baytron P VP A14083) was passed through a 0.45  $\mu\text{m}$  filter and then spin-coated at 3000 rpm on ITO in air and dried at  $150\text{ }^\circ\text{C}$  for 30 min inside the glove box. The thickness of the prepared PEDOT:PSS film was around 30 nm. The polymer/PCBM blend was prepared by dissolving them together in  $\text{CHCl}_3$ , DCB, or mix-solvents followed by spin-coating on the top of the PEDOT:PSS layer. The device was then annealed at  $150\text{ }^\circ\text{C}$  or  $240\text{ }^\circ\text{C}$  for 10 min in glove box. Subsequently, the device was coated with a 30 nm thickness of Ca and a 100 nm thickness of Al by thermal evaporation under high vacuum ( $<10^{-6}$  torr), respectively. The active area of the device is  $4\text{ mm}^2$ .

The current–voltage ( $J$ – $V$ ) measurement of the polymer photovoltaic cell was conducted by a computer-controlled Keithley 2400 source measurement unit (SMU) with a Pecell solar simulator under the illumination of AM 1.5 G,

$100\text{ mW/cm}^2$ . The illumination intensity was calibrated by a standard Si photodiode detector with KG-5 filter.

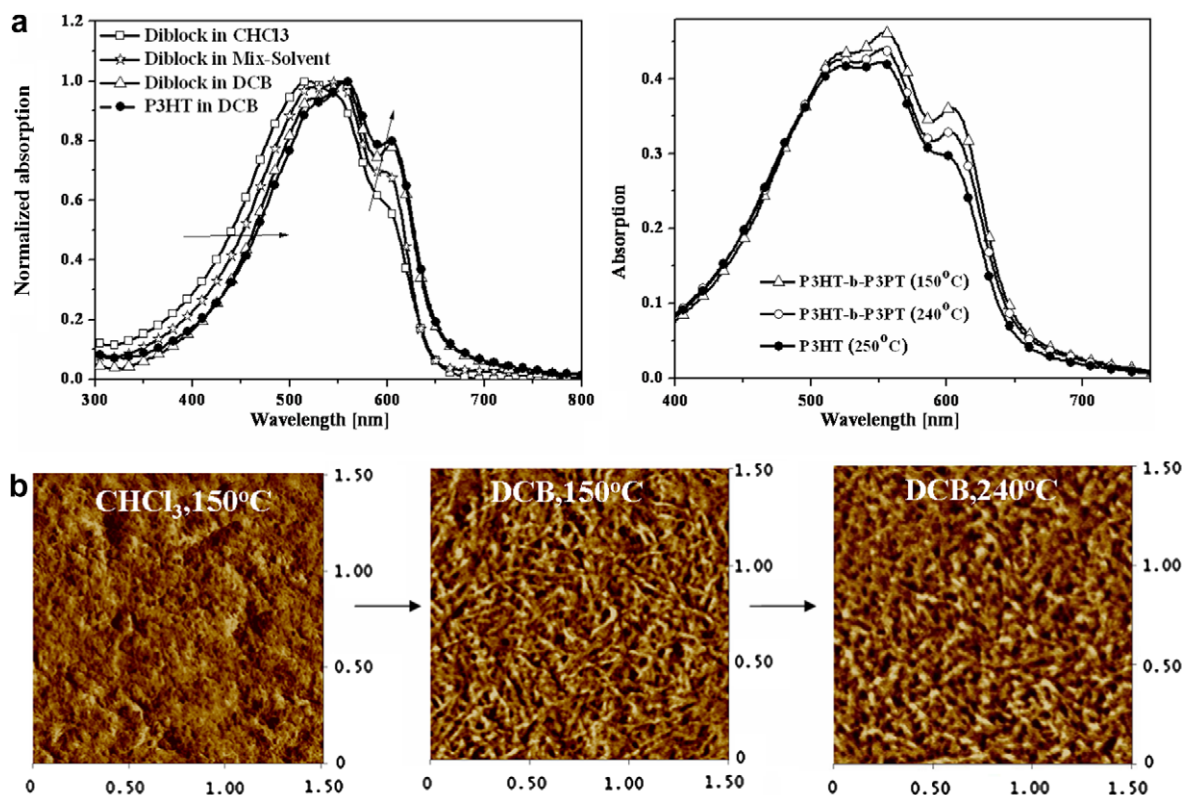
## 4. Result and discussion

### 4.1. Optical and electrochemical properties

Fig. 1(a, left) shows the UV–Vis absorption spectra of P3HT-*b*-P3PT and P3HT films cast from either  $\text{CHCl}_3$  or DCB and annealed at  $150\text{ }^\circ\text{C}$  for 10 min under nitrogen. The absorption maximum ( $\lambda_{\text{max}}$ ) of P3HT-*b*-P3PT prepared from DCB is around 554 nm with a shoulder peak around 604 nm while that from  $\text{CHCl}_3$  is around 516 nm without a clear shoulder peak. The much higher  $\lambda_{\text{max}}$  of P3HT-*b*-P3PT processed from DCB than that from  $\text{CHCl}_3$  suggests that the stronger  $\pi$ – $\pi$  interchain interaction in the former. In comparison, the  $\lambda_{\text{max}}$  of pristine P3HT prepared from DCB is around 558 nm with a shoulder peak around 605 nm. The shoulder peak around 605 nm is generally assigned to the crystalline structure, resulting from strong intermolecular interaction [30–32]. The weight fraction of P3HT to P3PT in P3HT-*b*-P3PT is around 83%. Thus, the slightly higher intensity of the shoulder peak in the pristine P3HT of Fig. 1(a, left) than that of P3HT-*b*-P3PT is as expected since P3PT is an amorphous segment from our previous study [31]. In contrast, an opposite behavior was observed after annealing at  $240\text{ }^\circ\text{C}$ , which is above the melting point of P3HT as shown in Fig. 1(a, right). P3HT-*b*-P3PT could still maintain a more intense peak around 605 nm than pristine P3HT exhibiting a significant reduction of the crystalline peak. It supports that the introduction of P3PT segments probably enhances the stability of the self-organized crystalline structure of P3HT segments.

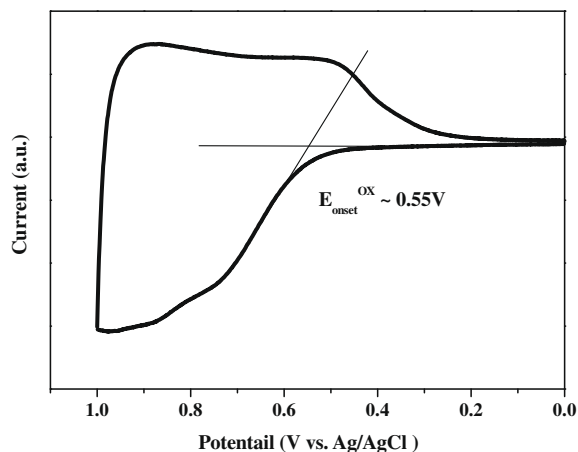
The AFM images of the prepared polymer films on quartz could further provide a detailed characterization on the polymer surface structure. The amorphous-rich polymer domain structure of the film cast from  $\text{CHCl}_3$  shown in Fig. 1b provides another evidence for the unclear shoulder peak of P3HT-*b*-P3PT in the optical absorption in Fig. 1(a, left). The volatile  $\text{CHCl}_3$  solvent is rapidly evaporated during spin-coating and thus limits the crystalline structure formation of P3HT-*b*-P3PT. However, the P3HT-*b*-P3PT film cast from DCB followed by annealing at  $150\text{ }^\circ\text{C}$  shows elongated fiber-like structure (Fig. 1b), which is almost identical to the fiber structure of pristine P3HT as shown in Figure S2. It suggests the importance of the less volatile cast solvent for the formation of crystalline domains in conjugated polymer. The polymer domain structure changes from the fiber-like to the worm-like after annealing at the elevated temperature of  $240\text{ }^\circ\text{C}$ , which is correlated with the slightly weakened intensity of the shoulder peak around 605 nm in UV–Vis absorption compared to that annealed at  $150\text{ }^\circ\text{C}$  (Fig. 1(a, right)).

Fig. 2 shows the cyclic voltammogram (CV) of the P3HT-*b*-P3PT film in acetonitrile at a potential scanning rate of  $0.1\text{ V s}^{-1}$ . The onset oxidation ( $E_{\text{onset}}^{\text{ox}}$ ) and the estimated HOMO energy level are 0.55 V and  $-4.91\text{ eV}$ , respectively. The calculated optical band gap ( $E_{\text{g}}^{\text{opt}}$ ) of P3HT-*b*-P3PT from the absorption spectrum (DCB) is about 1.91 eV. Hence, the



**Fig. 1.** (a) UV-Vis absorption spectra of P3HT on quartz processed from DCB and P3HT-*b*-P3PT (Diblock) film on quartz processed from CHCl<sub>3</sub>, CHCl<sub>3</sub>/DCB (ratio = 1:1), or DCB. The insert is the variation of UV-Vis absorption spectra of P3HT-*b*-P3PT film processed from DCB (annealed at 150 and 250 °C) and the P3HT film (annealed at 250 °C). (b) Their corresponding AFM phase images (scale: 1.5 μm × 1.5 μm) on quartz.

LUMO energy level estimated from the difference between the  $E_g^{\text{opt}}$  and HOMO energy level is  $-3.00$  eV. The  $E_g^{\text{opt}}$ , HOMO, and LUMO of P3HT-*b*-P3PT are almost identical to those of regioregular P3HT (1.9,  $-5.1$ , and  $-3.2$  eV, respectively) reported in the literature [37], but unlike some random polythiophene derivatives reported in the literatures [33].



**Fig. 2.** Cyclic voltammogram of P3HT-*b*-P3PT thin film on ITO glass at a scanning rate of  $0.1 \text{ V s}^{-1}$  in  $0.1 \text{ M TBAPF}_6$  solution.

#### 4.2. Thin film transistor characteristics

The charge-transporting mobility of P3HT-*b*-P3PT was explored by the bottom-contact and bottom-gate field-effect transistor devices. Figs. 3 and 4 show the transfer and output characteristic curves of the P3HT-*b*-P3PT films on the ODTS-modified SiO<sub>2</sub> processed from different solvents of CHCl<sub>3</sub>, CHCl<sub>3</sub>/DCB (1:1 ratio), and DCB. As shown in the figures, P3HT-*b*-P3PT exhibits typical *p*-channel output characteristics (source-drain current ( $I_d$ ) versus drain voltage ( $V_d$ ) at different gate voltages ( $V_g$ )) when operated in the accumulation mode. In the saturation region ( $V_d > V_g - V_t$ ),  $I_d$  can be described by Eq. (1) [38]:

$$I_d = \frac{WC_o\mu_h}{2L}(V_g - V_t)^2 \quad (1)$$

where  $\mu_h$  is the field-effect hole mobility,  $W$  is the channel width,  $L$  is the channel length,  $C_o$  is the capacitance per unit area of the gate dielectric layer (SiO<sub>2</sub>, 200 nm,  $C_o = 17 \text{ nF/cm}^2$ ), and  $V_t$  is the threshold voltage, respectively. The saturation region field-effect mobility of the studied copolymer was thus calculated from the transfer characteristics of the FETs involving plotting  $(I_d)^{1/2}$  versus  $V_g$ . The estimated hole mobilities of P3HT-*b*-P3PT from different solvents are listed as below:  $\sim 6.0 \times 10^{-3}$  (CHCl<sub>3</sub>),  $\sim 8.0 \times 10^{-3}$  (CHCl<sub>3</sub>/DCB = 1/1), and  $2.0 \times 10^{-2}$  (DCB). The  $I_{\text{on}}/I_{\text{off}}$  ratios of the studied TFT devices are around

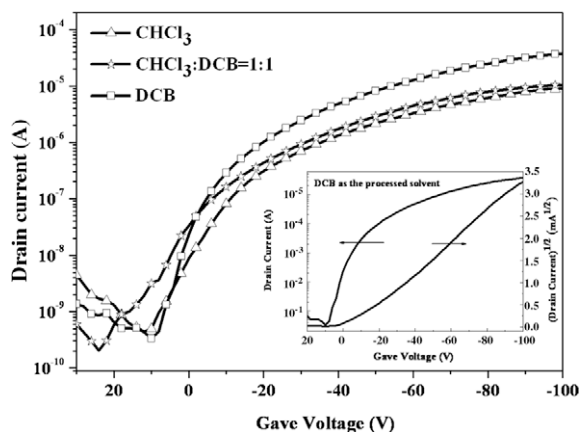


**Fig. 3.** Transfer characteristics of P3HT-*b*-P3PT device, in different processed solvents, with an ODTS-modified surface and anneal at 150 °C, where  $V_{ds} = -100$  V.

$2.1\text{--}5.5 \times 10^4$  and  $V_t$  of  $-3.0$  to  $-6.0$  V, as summarized in Table 1. It suggests that the hole mobility increases by increasing the DCB content in the processing solvent. As discussed in the optical absorption spectra, the P3HT-*b*-P3PT processed from a  $\text{CHCl}_3$  solution is largely amorphous while that from a DCB solution is mostly crystalline. It probably explains the above trend on the hole mobility with the processing solvent.

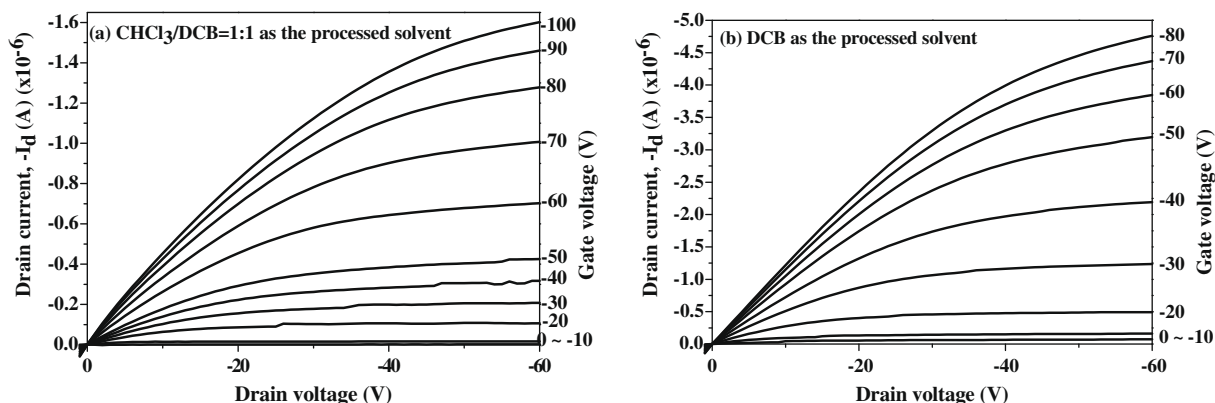
The surface structure of the P3HT-*b*-P3PT processed from different solvents may provide another insight to the above hole mobility. Fig. 5 shows the AFM images of P3HT-*b*-P3PT film on the ODTS-modified silicon surface processed from different solvents of  $\text{CHCl}_3$ ,  $\text{CHCl}_3/\text{DCB}$  (1:1 ratio), and DCB. As shown in the figure, a continuous roundish phase is observed in the polymer film processed from the  $\text{CHCl}_3$  or  $\text{CHCl}_3/\text{DCB}$  solution, but a web-like silk phase is exhibited in that processed from the DCB solution. Interestingly, the domain size of the roundish phase in polymer film decreases from 80 nm ( $\text{CHCl}_3$ ) to 40 nm ( $\text{CHCl}_3/\text{DCB}$ ). The various surface structures are probably resulted from the different volatility of  $\text{CHCl}_3$  and DCB and the miscibility between the processed solvents and

polymer blocks. Apparently, the less volatile DCB could provide enough time to rearrange the polymer chains, forming the web-like structure. Such ordered structure is similar to the pristine P3HT nanostructure with the characteristics of planar  $\pi$ -stacked chains, an elongated domain, and less grain boundary as compared to the roundish structure [39], which enhances to stabilize the *p*-channel and allow higher hole mobility. The obtained hole mobility of P3HT-*b*-P3PT is similar to that of the commercial P3HT (around  $\sim 2.0 \times 10^{-2} \text{ cm}^2 \text{ V}^{-1} \text{ S}^{-1}$  with an on/off ratio of  $\sim 2.00 \times 10^4$  and  $V_{th}$  of  $-5$  to  $5$  V under the same preparation condition and device structure) and comparable to the values reported in the literature [40–42], despite the existence of 17 wt.% of the amorphous P3PT. The above results indicate that the all conjugated block copolythiophene, P3HT-*b*-P3PT, could have a tunable hole mobility through the processing solvent.

#### 4.3. Photovoltaic cell characteristics

The BHJ solar cells based on the studied copolymer P3HT-*b*-P3PT were fabricated with a sandwich structure of ITO/PEDOT:PSS (30 nm)/polymer:PCBM/Ca (30 nm)/Al (100 nm). The  $J$ - $V$  characteristics and the related parameter of polymer solar cells prepared from the blends of polymer:PCBM (1:0.5–1:2, w/w) are shown in Fig. 6 and summarized in Table 1. The P3HT-*b*-P3PT:PCBM film in the device was also processed from three different solvent systems of  $\text{CHCl}_3$ ,  $\text{CHCl}_3/\text{DCB}$  (1:1 ratio), and DCB in order to investigate the relationship between morphology and solar cell performance [43].

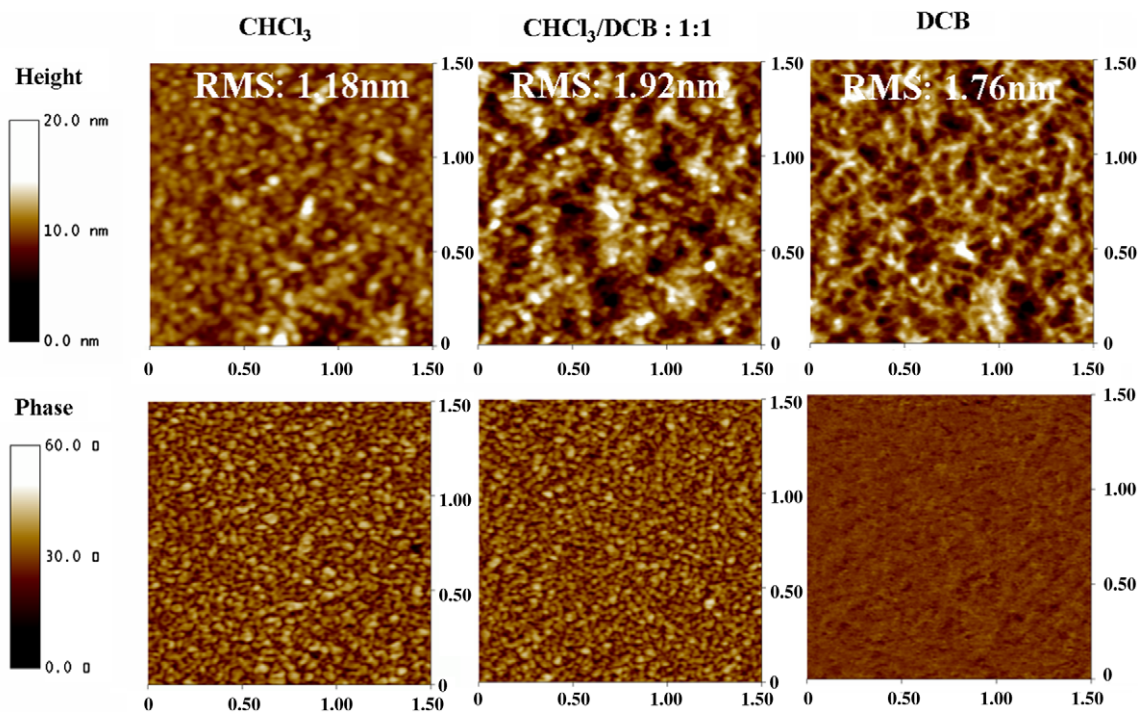
As listed in Table 1, in the case of polymer:PCBM (1:1, w/w), the photovoltaic properties of the devices fabricated from  $\text{CHCl}_3$  and  $\text{CHCl}_3/\text{DCB}$  (1:1 ratio) reveal the smaller short-circuit current ( $J_{sc}$ ) and fill factor ( $FF$ ) than the DCB fabricated devices. The power conversion efficiencies (PCE) of the photovoltaic cells are 1.88%, 2.13%, and 2.60%, for the cast solvents of  $\text{CHCl}_3$ ,  $\text{CHCl}_3/\text{DCB}$  (1:1 ratio), and DCB, respectively. The poorer performance of the former two is significantly influenced by the surface structure besides the hole mobility trend discussed above. As seen from the Fig. 7a, the domain of the polymer:PCBM (1:1) blend film onto the device processed from  $\text{CHCl}_3$  or



**Fig. 4.** Output characteristics of P3HT-*b*-P3PT device processed from (a)  $\text{CHCl}_3/\text{DCB} = 1:1$  and (b) DCB.

**Table 1**Transistor and photovoltaic characteristics of P3HT-*b*-P3PT.

Polymer	TFT – pristine polymer				Solar Cell – Polymer/PCBM				
	Processing Solvent	Mobility (cm <sup>2</sup> V <sup>-1</sup> S <sup>-1</sup> )	On/Off (-)	V <sub>th</sub> (V)	Conditions <sup>b,d</sup>	J <sub>sc</sub> (mA/cm <sup>2</sup> )	V <sub>oc</sub> (V)	FF (%)	PCE <sup>c</sup> (%)
P3HT- <i>b</i> -P3PT	CHCl <sub>3</sub>	~6.0 × 10 <sup>-3</sup>	~2.1 × 10 <sup>4</sup>	-3 to -4	CHCl <sub>3</sub> (1:1)	7.04	0.65	0.41	1.88
					CHCl <sub>3</sub> /DCB.(1:1)	7.26	0.64	0.46	2.13
	Mix-Sol. <sup>a</sup>	~8.0 × 10 <sup>-3</sup>	~3.5 × 10 <sup>4</sup>	-4 to -5	DCB (1:0.5)	7.97	0.35	0.36	1.03
					DCB (1:0.7)	8.16	0.62	0.56	2.80
	DCB	~2.0 × 10 <sup>-2</sup>	~5.5 × 10 <sup>4</sup>	-5 to -6	DCB (1:1)	7.75	0.60	0.56	2.60
					DCB (1:2)	3.10	0.59	0.52	0.95

<sup>a</sup> Mix-Sol.:CHCl<sub>3</sub>/DCB = 1:1.<sup>b</sup> All devices are annealed at 150 °C for 10 min.<sup>c</sup> The average value of power conversion efficiency is calculated from 4 pixels in the device.<sup>d</sup> The ratio in bracket is the weight ratio of polymer to PCBM.**Fig. 5.** Height (top) and phase (bottom) AFM images of the P3HT-*b*-P3PT films, in different processing solvents of (a) CHCl<sub>3</sub>, (b) CHCl<sub>3</sub>/DCB = 1:1, and (c) DCB, on ODTS-modified SiO<sub>2</sub> surface (The image sizes are 1.5 μm × 1.5 μm and the RMS is root mean square roughness.).

CHCl<sub>3</sub>/DCB solution is composed of island-like structures and shows large phase separation, which causes the drop in  $J_{sc}$  and  $FF$ . In a sharp contrast, the DCB fabricated devices retain the orderly elongated fiber-like structure induced by P3HT-*b*-P3PT, except for the case of blend ratio, polymer:PCBM (1:2), as shown in Fig. 7b. The discrepancy in surface morphology is undoubtedly resulted from the processing solvents. DCB could provide sufficient time for the polymer to form ordered structures, then filled with PCBM, and therefore form a better microphase-separation. Besides, the P3PT segment is supposed to preferably dissolve PCBM due to the better miscibility than the crystalline P3HT segment when PCBM packs the fiber-like domain. Different ratios of PCBM/P3HT-*b*-P3PT from 0.5 to 2.0 were

investigated to address the effect on the polymer structure and PCE. Fig. 7b presents the phase images of these blend films, whose RMS are all around 1 nm. All blend films, PCBM/P3HT-*b*-P3PT, with the ratio under 1.0 preserve the order structure observed in pristine P3HT-*b*-P3PT. Among them, the polymer/PCBM (1:0.7, w/w) shows the best PCE of 2.80% higher than 2.60% of polymer/PCBM (1:1, w/w). The 17% amorphous P3PT probably affects the polymer surface structure and thus the optimal blend ratio is 1:0.7, which corresponds to the weight ratio of P3HT in the block to PCBM (1:0.84). As the PCBM ratio increase to 1:2, the dark region corresponding to PCBM-rich domains become larger and more aggregated than the other blend ratios, suggesting that the order domain formed by

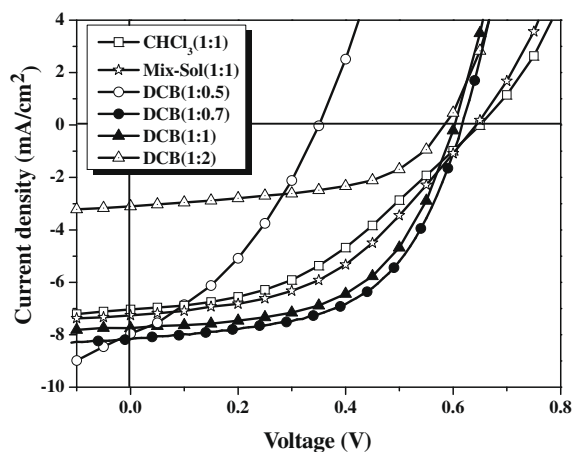


**Fig. 6.**  $J$ - $V$  characteristics of polymer solar cells with the structure of ITO/P3HT- $b$ -P3PT:PCBM/Al under the illumination of AM 1.5G, 100 mW/cm<sup>2</sup>. The ratio in bracket is the weight ratio of polymer to PCBM.

P3HT- $b$ -P3PT was destroyed at the high blend ratio of PCBM. The  $J_{sc}$  dramatically decreases to 3.10 mA/cm<sup>2</sup> at such high PCBM blend ratio. Although the polymer/PCBM (1:0.5, w/w) shows an order domain, the PV performance is inferior to those from the blend ratios of 1:0.7 and 1:1. It could be ascribed to the unbalanced carrier transport and thus efficient electron separation is not obtained. Unfortunately, the highest PCE (2.80%) based the studied P3HT- $b$ -P3PT/PCBM blend system is still lower than that (3.04%) of the commercial P3HT/PCBM (1:0.7, w/w) device under the same preparation conditions ( $J_{sc}$ : 8.60 mA/cm<sup>2</sup>,  $V_{oc}$ : 0.61 V, and FF: 0.58). It is probably due to the lower absorption coefficient of the present blend system than that of P3HT/PCBM, as shown in Fig. 8. However, the present study did address the manipulation of photo-physical properties, charge-transporting mobility and photovoltaic characteristics on such all-conjugated diblock copolymers.

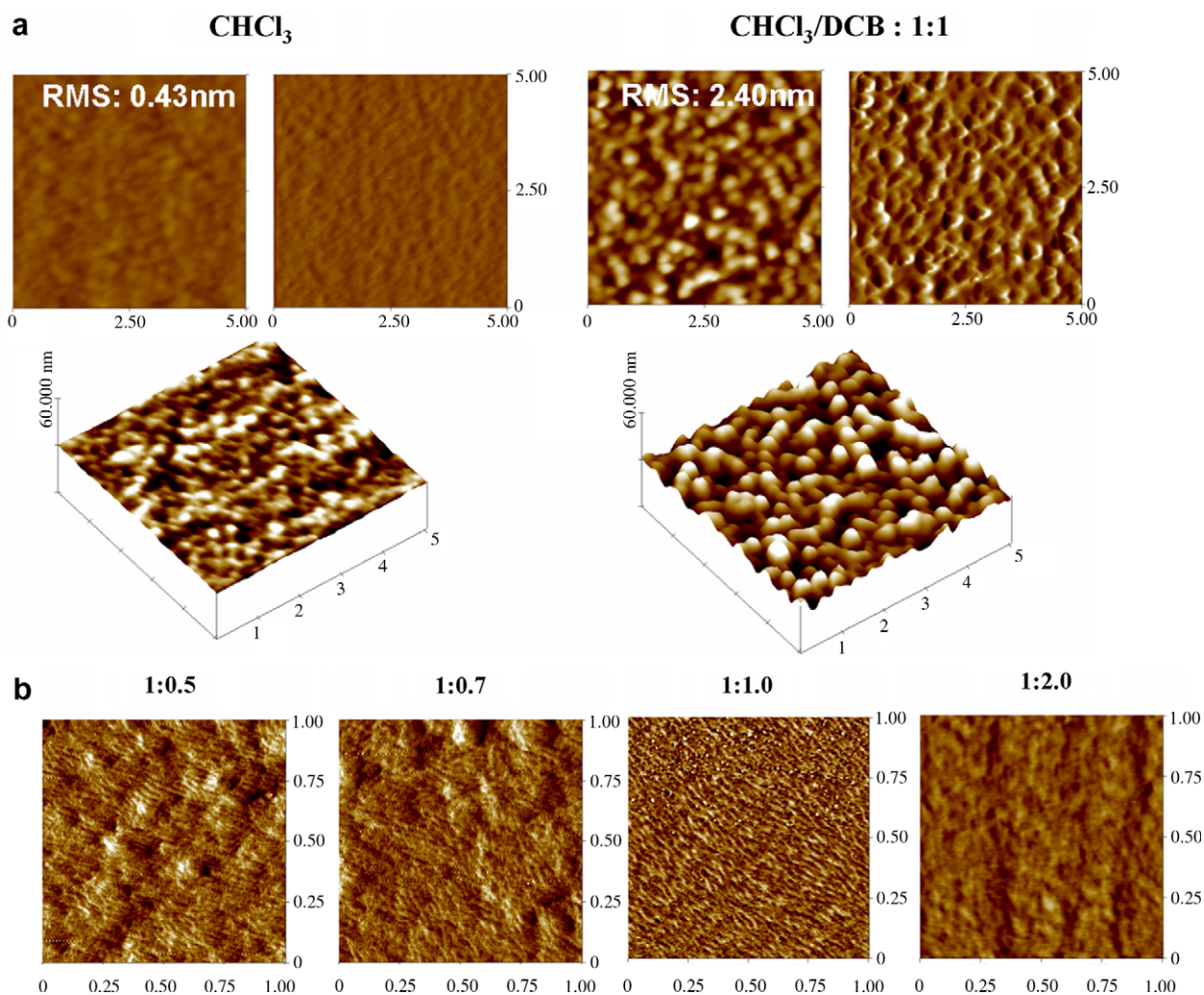


**Fig. 7.** (a) Height (left), phase (right), and its 3D images (bottom) of the P3HT- $b$ -P3PT/PCBM (1:1) blend film cast from CHCl<sub>3</sub> and CHCl<sub>3</sub>/DCB = 1:1. The image sizes are all 5  $\mu$ m  $\times$  5  $\mu$ m and the Z range is 30 nm and 60°; (b) phase images of the P3HT- $b$ -P3PT/PCBM (1:0.5–1:2.0) blend film cast from DCB. The image sizes are all 1  $\mu$ m  $\times$  1  $\mu$ m and the Z range is 10°.

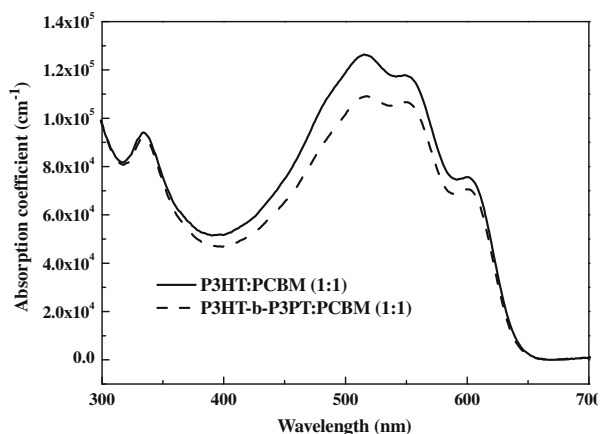


Fig. 8. UV-Vis absorption spectra of polymer:PCBM (1:1, w/w) films and their absorption coefficients calculated from Beer's law.

## 5. Conclusion

We have shown the manipulation on the surface structure and optoelectronic device applications of all-conjugated diblock copolythiophene, P3HT-*b*-P3PT, through different cast solvent mixtures. The optical absorption spectra showed the much enhanced intensity on the crystalline absorption peak from the DCB solution but not in the case of  $\text{CHCl}_3$ . The AFM images suggested that highly volatile  $\text{CHCl}_3$  led to the amorphous-rich structure, while less volatile DCB resulted in the largely orderly fiber-like structure of the P3HT-*b*-P3PT. The FET hole mobility increased from  $\sim 6.0 \times 10^{-3}$ ,  $\sim 8.0 \times 10^{-3}$  to  $2.0 \times 10^{-2} \text{ cm}^2 \text{ V}^{-1} \text{ s}^{-1}$  as the DCB content in the solvent mixture was raised. Such difference on the polymer structure and hole mobility also resulted in the variation on the power conversion efficiency (PCE) of the photovoltaic cells. The PCE of P3HT-*b*-P3PT /PCBM (1:1, w/w) based photovoltaic cells was 2.60% processed from the DCB solution was higher than 1.88% using  $\text{CHCl}_3$ . The PCE of polymer/PCBM was further improved to 2.80% at the 1:0.7 blend ratio of polymer to PCBM. The present study suggested that the photophysical properties, charge-transporting mobility and photovoltaic characteristics of all-conjugated diblock copolymers could be efficiently tuned by solvent polarity, block segment characteristic, and blend composition.

## Acknowledgements

Work at National Taiwan University (NTU) is supported by the National Science Council, Ministry of Economics Affairs of Taiwan, and Excellence research Program of NTU. T.H. at Tokyo Institute of Technology thanks Japan Society for the Promotion of Science (JSPS) for supporting this work by KAKENHI (#20850014).

## Appendix A. Supplementary data

Supplementary data associated with this article can be found, in the online version, at doi:10.1016/j.orgel.2009.08.024.

## References

- [1] M. Mofeitt, K. Khougaz, A. Eisenberg, *Acc. Chem. Res.* 29 (1996) 95.
- [2] F.S. Bates, G.H. Fredrickson, *Phys. Today* 52 (1999) 32.
- [3] P. Alexandridis, B. Lindman, *Amphiphilic Block Copolymers: Self-Assembly and Applications*, Elsevier, Amsterdam, 2000.
- [4] M.J. Fasolka, A.M. Mayes, *Annu. Rev. Mater. Res.* 31 (2001) 323.
- [5] N. Hadjichristidis, S. Pispas, G.A. Floudas, *Block Copolymers: Synthesis Strategies, Physical Properties, and Applications*, John Wiley and Sons, New Jersey, 2003.
- [6] D. Chen, M. Jiang, *Acc. Chem. Res.* 38 (2005) 494.
- [7] M. Antonietti, S. Foster, *Adv. Mater.* 15 (2003) 1323.
- [8] J.Y. Cheng, C.A. Ross, H.I. Smith, E.L. Thomas, *Adv. Mater.* 18 (2006) 2505.
- [9] M. Lee, B.K. Cho, W.C. Zin, *Chem. Rev.* 101 (2001) 3869.
- [10] F.J.M. Hoeben, P. Jonkhijm, E.W. Meijer, A.P.H.J. Schenning, *Chem. Rev.* 105 (2005) 1491.
- [11] P. Leclère, E. Hennebicq, A. Calderone, P. Brocorens, A.C. Grimsdale, K. Mullen, J.L. Brédas, R. Lazzaroni, *Prog. Polym. Sci.* 28 (2003) 55.
- [12] B.D. Olsen, R.A. Segalman, *Mater. Sci. Eng.* 62 (2008) 37.
- [13] C.A. Dai, W.C. Yen, Y.H. Lee, C.C. Ho, W.F. Su, *J. Am. Chem. Soc.* 129 (2007) 11036.
- [14] S.A. Jenekhe, X.L. Chen, *Science* 279 (1998) 1903.
- [15] B.W. Boudouris, C.D. Frisbie, M.A. Hillmyer, *Macromolecules* 41 (2008) 67.
- [16] S. Lu, T. Liu, L. Ke, D.G. Ma, S.J. Chua, W. Huang, *Macromolecules* 38 (2005) 8494.
- [17] Y.C. Tung, W.C. Wu, W.C. Chen, *Macromol. Rapid Commun.* 27 (2006) 1838.
- [18] W.C. Wu, Y. Tian, C.Y. Chen, C.S. Lee, Y.J. Sheng, W.C. Chen, A.K.Y. Jen, *Langmuir* 23 (2007) 2805.
- [19] C.H. Lin, Y.C. Tung, J. Ruokolainen, R. Mezzenga, W.C. Chen, *Macromolecules* 41 (2008) 8759.
- [20] S.T. Lin, Y.C. Tung, W.C. Chen, *J. Mater. Chem.* 18 (2008) 3985.
- [21] Y.C. Tung, W.C. Chen, *React. Funct. Polym.* 69 (2009) 507.
- [22] T. Higashihara, K. Ohshimizu, A. Hirao, M. Ueda, *Macromolecules* 41 (2008) 9505.
- [23] T. Higashihara, M. Ueda, *React. Funct. Polym.* 69 (2009) 457.
- [24] Y. Liang, H. Wang, S. Yuan, Y. Lee, L. Gan, L. Yu, *J. Mater. Chem.* 17 (2007) 2183.
- [25] U. Scherf, A. Gutacker, N. Koenen, *Acc. Chem. Res.* 41 (2008) 1086.
- [26] R.P. Barber Jr., R.D. Gomez, W.N. Herman, D.B. Romero, *Org. Electron.* 7 (2006) 508.
- [27] J.Y. Park, N. Koenen, M. Forster, R. Ponnappati, U. Scherf, R. Advincula, *Macromolecules* 41 (2008) 6169.
- [28] M.C. Iovu, E.E. Sheina, R.R. Gil, R.D. McCullough, *Macromolecules* 38 (2005) 8649.
- [29] Y. Yokozawa, I. Adachi, A. Miyakoshi, A. Yokoyama, *High Perform. Polym.* 19 (2007) 684.
- [30] Y. Zhang, K. Taiima, K. Hirota, K. Hashimoto, *J. Am. Chem. Soc.* 130 (2008) 7812.
- [31] K. Ohshimizu, M. Ueda, *Macromolecules* 41 (2008) 5289.
- [32] P.T. Wu, G. Ren, C. Li, R. Mezzenga, S.A. Jenekhe, *Macromolecules* 42 (2009) 2317.
- [33] R. Zhang, B. Li, M.C. Iovu, M. Jeffries-EL, G. Sauve, J. Cooper, S. Jia, S. Tristram-Nagle, D.M. Smilgies, D.N. Lambeth, R.D. McCullough, T. Kowalewski, *J. Am. Chem. Soc.* 128 (2006) 3480.
- [34] G. Li, V. Shrotriya, J. Huang, Y. Yao, T. Moriarty, K. Emery, Y. Yang, *Nat. Mater.* 4 (2005) 864.
- [35] Q.J. Sun, H.Q. Wang, C.H. Yang, Y.F. Li, *J. Mater. Chem.* 13 (2003) 800.
- [36] J.H. Tsai, C.C. Chueh, M.H. Lai, C.F. Wang, W.C. Chen, B.T. Ko, C. Ting, *Macromolecules* 42 (2009) 1897.
- [37] M.C. Scharber, D. Mühlbacher, M. Koppe, P. Denk, C. Waldauf, A.J. Heeger, C.J. Brabec, *Adv. Mater.* 18 (2006) 789.
- [38] G. Horowitz, *Adv. Mater.* 10 (1998) 365.
- [39] W. Geens, S.E. Shaheen, B. Wessling, C.J. Brabec, J. Poortmans, N.S. Sariciftci, *Org. Electron.* 3 (2002) 105.
- [40] Z. Bao, A. Dodabalapur, A.A. Lovinger, *Appl. Phys. Lett.* 69 (1996) 4108.
- [41] H. Yang, T.J. Shin, L. Yang, K. Cho, C.Y. Ryu, Z. Bao, *Adv. Funct. Mater.* 15 (2005) 671.
- [42] A. Zen, J. Pflaum, S. Hirschmann, W. Zhuang, F. Jaiser, U. Asawapirom, J.P. Rabe, U. Scherf, D. Neher, *Adv. Funct. Mater.* 14 (2004) 757.
- [43] F. Zhang, K.G. Jespersen, C. Björström, M. Svensson, M.R. Andersson, V. Sundström, K. Magnusson, E. Moons, A. Yartsev, O. Inganäs, *Adv. Funct. Mater.* 16 (2006) 667.



promote efficient exciton dissociation at donor/acceptor interfaces yet with bicontinuous networks to facilitate charge collection. The most efficient polymer blend solar cells utilise blends of a conjugated polymer with a methanofullerene derivate (6,6)-phenyl-C<sub>61</sub>-butyric acid (PCBM) [7,8]. The ability of P3HT to form highly ordered, nanocrystal domains in blends with PCBM is cited as one of the reasons for the high efficiency of the P3HT/fullerene system [9,10]. The structure and charge transport properties of polymer/fullerene blends have been well-studied [11–13], demonstrating efficient ambipolar charge transport [14] and the ability to form bicontinuous phases [10]. However, there are fewer reports in the literature of combined structure–transport studies of blends of two conjugated polymers [15–17]. Such investigations are of interest not only from an academic point of view, since polymer/polymer blends represent a distinct materials class to polymer/fullerene blends, but also from a technological point of view with all-polymer solar cells having the potential to contribute to development of organic photovoltaic technology. In particular, compared to polymer/fullerene blends, the use of two conjugated polymers in a polymer blend solar cell offers greater flexibility in materials design. This flexibility allows for tuning of the electronic properties of the materials (affecting the optical band gap and open circuit voltage amongst others [18]) and tailoring of the physical properties of the blend such as interfaces and phase separation [19].

Recently, we have demonstrated efficient photovoltaic operation from a blend of poly(3-hexylthiophene) (P3HT) with the polyfluorene co-polymer poly((9,9-dioctylfluorene)-2,7-diyl-alt-[4,7-bis(3-hexylthien-5-yl)-2,1,3-benzothiadiazole]-2',2''-diyl) (F8TBT) [20] (see Fig. 1 for chemical structures and energy level diagram). Power conversion efficiencies of nearly 2% were demonstrated for this blend, one of the highest for all-polymer solar cells [4]. The successful utilisation of the semicrystalline high-mobility P3HT in efficient all-polymer solar cells also represents an important development [20]. Understanding of the structure of P3HT in blends with F8TBT and its influence on hole transport is therefore important in furthering the

development of all-polymer solar cells. To this end, here we report a joint time-of-flight charge transport and X-ray diffraction study of P3HT/F8TBT blends.

## 2. Materials and methods

### 2.1. Materials, sample preparation and device fabrication

Regioregular P3HT was supplied by Merck with a molecular weight ( $M_w$ ) of 52 kg mol<sup>-1</sup>, polydispersity of 2.0 and a regioregularity of 95.6%. Regiorandom P3HT was supplied by Rieke Metals with a molecular weight of 90 kg mol<sup>-1</sup> and polydispersity of 2.4. F8TBT was supplied by Cambridge Display Technology Ltd. with molecular weight of 54 kg mol<sup>-1</sup> and polydispersity of 2.4. The glass transition temperature of F8TBT is ~360–370 K [21]. Films for both time-of-flight and X-ray diffraction studies were prepared at the same time from the same solutions, by dissolving in anhydrous chloroform at 80 mg mL<sup>-1</sup> and spin-coating in a nitrogen glovebox. Rotation speed was varied to obtain approximately the same film thickness. In particular, regioregular P3HT films were spin-coated at 1000 rpm to give a film thickness of 1.6 ± 0.2 μm, regiorandom P3HT films were spin-coated at 1000 rpm to give a film thickness of 1.8 ± 0.2 μm and F8TBT films were spin-coated at 2000 rpm to give a film thickness of 1.4 ± 0.1 μm. Blend films of regioregular P3HT and F8TBT were prepared by mixing equal volumes of 80 mg mL<sup>-1</sup> P3HT and F8TBT solutions (1:1 weight ratio) and spin-coating at 1500 rpm to give a film thickness of 1.4 ± 0.1 μm. All film thicknesses were measured with a Dektak 6 M surface profilometer. To avoid unnecessary and repetitive clarification, any reference to P3HT will henceforth refer to regioregular P3HT unless specified. Films were annealed either in the glovebox on a hotplate for 10 min at temperatures of 373, 413 or 453 K with quenching to room temperature; or *in situ* in the X-ray diffractometer (see below). Films for X-ray diffraction study were spin-coated onto cleaned silicon substrates with a 100 nm thermally grown oxide. TOF devices were fabricated with an ITO/TiO<sub>2</sub>/P3HT:F8TBT/Au architecture. TiO<sub>2</sub> (anatase) acts as a hole-blocking layer and was deposited by spray pyrolysis as follows. ITO-coated glass substrates were heated to 743 K and sprayed with the organic precursor di-iso-propoxy-titanium bis(acetylacetonate) (75 wt% in isopropanol, Aldrich) from ethanol (1:10 volume ratio). After 45 min drying on the hot plate, a thickness of 50 nm of TiO<sub>2</sub> was achieved. Au (20 nm) was deposited through vacuum evaporation in a chamber inside the glovebox at a pressure of 10<sup>-6</sup> mbar. Devices were encapsulated in the glovebox before removal and testing.

### 2.2. Time-of-flight details

Time-of-flight (TOF) measurements were performed using a Nd:YVO<sub>4</sub> Q-switched laser (AOT model YVO-25QSPX) with 500 ps pulse duration and wavelength of 532 nm near the absorption maximum of all polymers used [22]. Voltage was supplied by a battery array (9–72 V) with current recorded using a high speed current amplifier (Femto DHPA-100) and an oscilloscope (Agilent

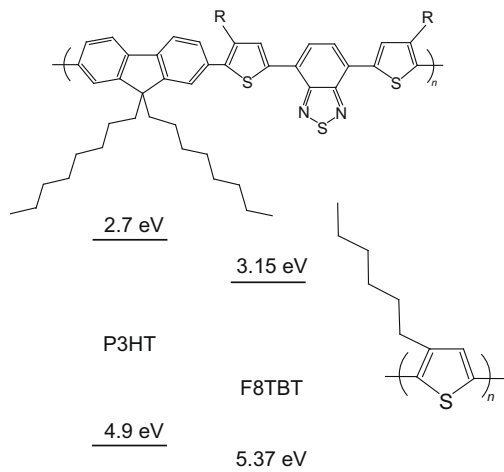


Fig. 1. Chemical structures and energy level diagram of F8TBT (R=C<sub>6</sub>H<sub>13</sub>) and P3HT.

DSO6052A). Pulse energies of less than 10 nJ/pulse were used, with the beam defocused to cover the active area of the device ( $4.5 \text{ mm}^2$ ). To avoid possible space-charge or recombination effects, the laser intensity was limited such that the collected charge was less than 10% of the capacitor charge. Transit times were estimated from the intersection of asymptotes fitted to the pre- and post-knee regions on a log–log plot of current vs. time as is standard for analysis of dispersive current transients [23]. Due to the high extinction coefficient of both polymers, the majority of light is absorbed within the first 100 nm of the film [24]. Mobility was calculated as  $\mu = d/(Et_{tr})$  where  $d$  is the thickness of the film,  $E$  is the electric field strength and  $t_{tr}$  the transit time.

### 2.3. X-ray diffraction details

X-ray diffraction (XRD) experiments have been performed on a Bruker D8 Discover diffractometer using radiation from a copper sealed tube. On the primary side polycapillary optics with a divergence of  $0.3^\circ$  and a 0.6 mm slit were used. On the secondary side conventional slit optics in combination with a graphite monochromator were mounted in front of a scintillation counter. A domed heating stage supplied by Anton Paar Ltd. [25] was used as a protective sample stage as well as for *in situ* annealing of samples *in vacuo*. Annealing in the diffractometer was performed with a ramp of 30 K/min to the anneal temperature where the temperature was held for 10 min followed by a slow cooling back to room temperature. One sample of the blend material was annealed between 373 and 453 K in subsequent steps of 20 K for 10 min at each temperature. In a final step the blend sample was annealed at 453 K for 1 hr. As a reference, one pure P3HT film was annealed at 413 K and 453 K in subsequent steps as above. All XRD measurements were performed at room temperature and in vacuum using a graphite dome to minimize degradation due to X-ray and UV radiation. Careful alignment of the sample has been performed in the primary beam to exclude misalignment errors in the experimental results.

The interplanar distances ( $d$ -values) were determined using Bragg's formula taking the  $2\theta$ -position of the experimentally observed diffraction peaks. In case of P3HT two different methods were applied (i) using the single  $2\theta$ -position of the 100 reflection and (ii) using all three diffraction peaks and correcting them towards misalignment errors. No significant difference could be observed between these two methods. Therefore, the interplanar distances of the different samples were obtained by using only the 100 diffraction peaks in order to apply the same procedure also to the blend samples where the higher order peaks were weaker. Crystal size determination was performed by using the integral peak width of the individual 100 diffraction peaks by using the Scherrer equation.

## 3. Results

### 3.1. Time-of-flight measurements

Fig. 2a presents representative time-of-flight transients of P3HT/F8TBT blends annealed at different temperatures

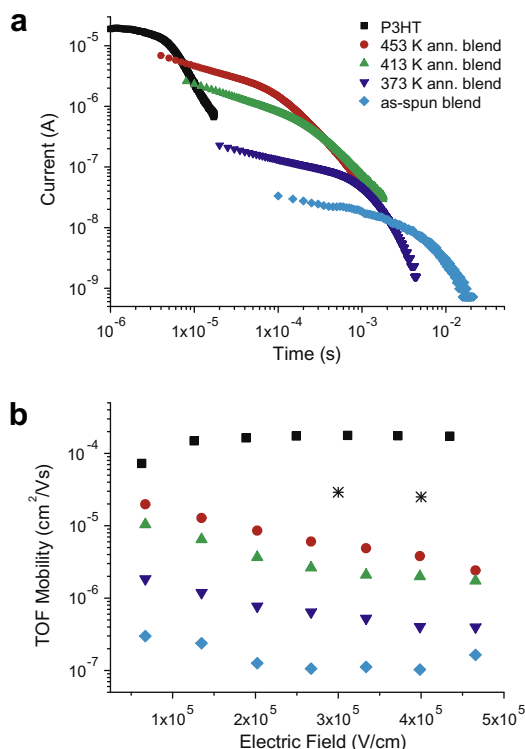


**Fig. 2.** (a) Time-of-flight (TOF) hole transients in P3HT/F8TBT blends and unblended P3HT. Squares represent the unblended P3HT hole transient, while diamonds represent the as-spun blend film, inverted triangles the 373 K annealed blend, triangles the 413 K annealed blend and circles the 453 K annealed blend. (b) Electric field dependence of the TOF mobility for as-spun and annealed P3HT/F8TBT blends and unblended P3HT using the same symbol key as for part (a) Also included are TOF mobilities measured for regiorandom P3HT (asterisks).

compared with that of an unblended P3HT film (unannealed). The transients in Fig. 2a were measured at an electric field strength of  $2.7 \times 10^5 \text{ V cm}^{-1}$  for blends and  $2.4 \times 10^5 \text{ V cm}^{-1}$  for the P3HT film. Fig. 2a shows a systematic decrease in the transit time with increasing annealing temperature for the blend films. In particular, the transit time improves from  $\sim 5 \text{ ms}$  (diamonds) to  $100 \mu\text{s}$  (circles) when the as-spun film is annealed at 453 K. The transit for the highest annealing temperature still lags that of the unblended P3HT,  $\sim 5 \mu\text{s}$  (squares). Fig. 2b plots the calculated TOF mobility of blended and unblended films as a function of electric field strength. The change in transit time of 5 ms–100  $\mu\text{s}$  corresponds to an increase in TOF mobility of nearly two orders of magnitude from  $\sim 8 \times 10^{-8}$  to  $6 \times 10^{-6} \text{ cm}^2 \text{ V}^{-1} \text{ s}^{-1}$ . The TOF mobility of the 453 K annealed blend is still over an order of magnitude less than that of the unblended P3HT film that has a TOF mobility of  $\sim 2 \times 10^{-4} \text{ cm}^2 \text{ V}^{-1} \text{ s}^{-1}$ , similar to values measured previously [23]. Examining the electric-field dependence of mobility, Fig. 2b, the blends in general exhibit a pronounced negative field dependence, compared to a relatively flat electric-field dependence of the hole mobility of unblended P3HT. The observation of a strong negative electric-field dependence in the blends compared to the unblended material may be attributed to the higher

degree of spatial disorder in the blend [26]. For comparison, we also present the TOF mobilities measured on films of regiorandom P3HT (asterisks in Fig. 2b). Despite having an amorphous film structure, the regiorandom P3HT film has a time-of-flight mobility only an order of magnitude lower than that of the regioregular film, and significantly higher than that of the 453 K annealed P3HT:F8TBT blend. This demonstrates that the lower TOF mobilities of the blend compared to the pure P3HT are related to the film microstructure and not simply the result of P3HT disorder.

We have also investigated the influence of annealing on the unblended regioregular P3HT films, Fig. 3, taken at an electric field strength of  $2.4 \times 10^{-5} \text{ cm}^2 \text{ V}^{-1} \text{ s}^{-1}$ . A systematic decrease in transit time is also seen with increasing annealing temperature, however the change in the TOF mobility is more modest, increasing from  $1.7 \times 10^{-4} \text{ cm}^2 \text{ V}^{-1} \text{ s}^{-1}$  for the unannealed film to  $\sim 3.0 \times 10^{-4} \text{ cm}^2 \text{ V}^{-1} \text{ s}^{-1}$  for the 453 K annealed film. Our observation of a large change in the P3HT hole mobility in the blend with annealing, but only a modest change in mobility in the pure P3HT film with annealing, is similar to previous observations for P3HT blended with the methanofullerene PCBM [9].

### 3.2. X-ray diffraction results

Specular X-ray diffraction experiments on the as-spun P3HT film show well pronounced 100, 200 and 300 diffraction peaks of the crystalline state without observation of an amorphous scattering contribution (Fig. 4). Annealing of the P3HT film at 413 and at 453 K induces an enhancement of the diffraction peaks in intensity together with peak narrowing. Additionally an increase in the interplanar distances is observed, consistent with previous observations [27,28]. We obtain a shift in the  $d$ -value from 1.662 nm for the as-prepared sample to 1.667 nm for the same sample after annealing at 453 K (circles in Fig. 5). We note that there is a large variation in the reported  $d$ -values of P3HT in the literature [29], but our observations are consistent with reports on similar molecular weight materials measured by Yang et al. [30] and Kline et al. [28]. The F8TBT diffraction pattern shows an amorphous

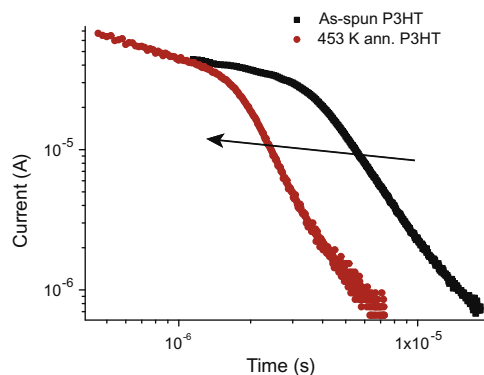


Fig. 3. Change in the dynamics of TOF hole transients of unblended P3HT with annealing.

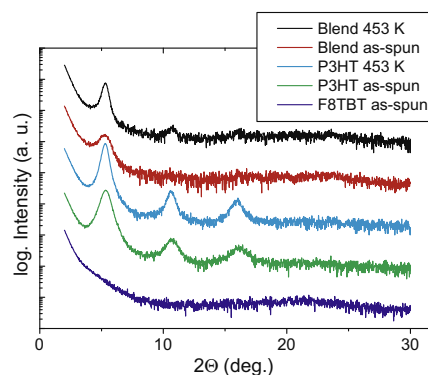


Fig. 4. Specular X-ray diffraction curves of 453 K annealed and as-spun P3HT/F8TBT films (top two curves), and P3HT films (next two curves) and of an as-spun F8TBT film (bottom curve). The curves have been shifted for clarity.

halo at around  $2\theta = 21^\circ$  which does not change after annealing. For the blend, in the as-spun state only the 100 P3HT reflection is observed together with the amorphous diffraction feature characteristic of F8TBT with a possible contribution from disordered P3HT.

Annealing of the blend leads to a more pronounced 100 diffraction peak and the emergence of second and third order peaks. In general we find a larger  $d$ -spacing for P3HT in blends compared to that measured for pure films. Furthermore, with annealing we see a general trend of decreasing  $d$ -spacing with annealing, opposite to the trend observed for pure P3HT films. Specifically, for blend samples that were annealed separately in a nitrogen atmosphere at different temperatures, the P3HT  $d$ -spacing is observed to decrease from 1.677 nm for the as-spun film to 1.668 nm for the 453 K annealed film (triangles in Fig. 5). For the case of *in situ* annealing of the same sample in the X-ray diffractometer, the  $d$ -spacing was observed to remain rather constant up to 453 K (squares in Fig. 5), but extended annealing at 453 K (for one hour) resulted in a drastic decrease of the  $d$ -value to 1.673 nm, as indicated by an arrow in Fig. 5. The differences in the trends for the two blend

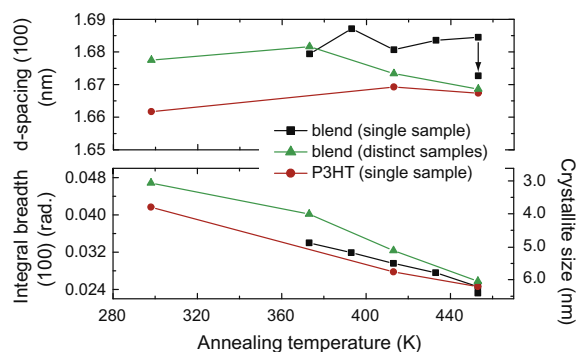


Fig. 5. The upper panel shows changes in the interplanar distances of the 100 plane with annealing for blends and unblended P3HT. The lower panel shows the effect of annealing on the integral breadth of the 100 reflection as a function of annealing temperature. The right hand axis in the lower panel displays the corresponding crystallite size calculated using the Scherrer equation.

sample sets likely arise from the different annealing procedures, with the *in situ* annealed samples gradually cooled to room temperature rather than quenched. It is interesting to note that in all cases, with annealing there appears to be a convergence of the *d*-spacing to a value of  $\sim 1.668$  nm.

For all samples, with annealing there is a significant narrowing of the 100 peak width consistent with an increase in P3HT crystallite size (lower panel in Fig. 5). As calculated using the Scherrer equation, the mean P3HT crystallite size in the unblended film increases from 3.7 nm in the as-spun state to 6.2 nm in the sample annealed at 453 K. The crystallite size in the blend increases from 3.3 nm in the as-spun film, to 3.8 nm with annealing at 373 K, to 5.0 nm with annealing at 413 K (average of two samples) and to 6.0 nm with annealing at 453 K, close to the value for 453 K annealed P3HT. The increase of the crystal size is slightly larger in case of the blends, which can be seen from the steeper negative slope of the integral breadth above 373 K (Fig. 5).

#### 4. Discussion

The experimental results reveal that the 1:1 blends of P3HT and F8TBT show a phase separation in two components with a crystalline part and an amorphous part. Within the X-ray diffraction pattern of the as-prepared sample the presence of a crystalline component is deduced from the presence of the diffraction peak at a *d*-value of 1.677 nm, while the amorphous part is clearly evident from the amorphous halo at around  $2\theta = 21^\circ$ . Since the *d*-value of the crystalline part is close to the P3HT value, it can be attributed to P3HT crystallites. However, this crystalline part cannot be formed only from pure P3HT, since the experimentally observed *d*-values as well as the relative intensities between the reflections are noticeably different. These two experimental observations reveal that the P3HT crystals in the blend are distorted. Since spin-coating is a non-equilibrium process, the packing of P3HT in the blend may be affected by solvent molecules or F8TBT molecules enclosed as impurities in the P3HT crystals. A recent report has also observed an increase in the *d*-spacing of the polythiophene poly(2,5-bis(3-tetradecylthiophen-2-yl)thieno[3,2-b]thiophene) (pBTTT) when blended with PCBM attributed to the intercalation of PCBM between the side-chains of pBTTT [31]. In contrast, blends of PCBM with P3HT show no change in the *d*-spacing of P3HT [8,32] as the side-chains in P3HT are too dense to allow intercalation of the bulky PCBM [31].

Annealing of the polymer blends leads to a gradual approach of the *d*-values of the crystalline part of the blend to that of pure P3HT. Since remaining solvent molecules within spin-coated films are evaporated at annealing temperatures well below 373 K [33], it can be inferred that the P3HT crystallites are distorted by the presence of F8TBT polymer chains. This distortion could be either a direct incorporation of F8TBT polymer chains into P3HT crystals or the intermixing of the side-chains from both types of polymers. With increasing annealing temperature the two *d*-values of blend and pure P3HT come closer which

reveals that the influence of F8TBT on P3HT packing decreases. The increasing crystallite size from 3.3 nm in the as-prepared state to 6.2 nm in the sample annealed at 453 K is a clear marker that a major re-arrangement happens during the annealing process. Such a re-arrangement would allow a reduction in the influence of F8TBT impurities on the packing of crystalline P3HT, evolving to a packing comparable to pure P3HT. We conclude that the final state of the blend consists of separated regions of amorphous F8TBT and crystalline P3HT containing only a negligible amount of F8TBT molecules as impurities.

We now turn to explain the trends in the TOF data in terms of the observed microstructure. Curiously, both unblended P3HT and P3HT/F8TBT blend films were found to have similar crystallite sizes as a function of annealing temperature. Thus the large discrepancy in general between the TOF mobilities of blended and unblended P3HT cannot be explained by differences in the size of P3HT crystallites alone. Similarly, the vast improvement in the mobility of P3HT/F8TBT films (nearly two orders of magnitude) cannot be explained in terms of variations in P3HT crystallite size in annealed blends, as only a modest change in mobility is observed in unblended P3HT for a similar change in crystallite size. As discussed in Section 3.1 where we noted the moderate TOF mobility of regiorandom P3HT films, differences in the overall degree of crystallinity of P3HT also cannot explain the orders of magnitude improvement in hole mobility in the blend with annealing. We therefore seek to explain the observed trends in terms of P3HT packing distortions and film morphology as follows.

Firstly from the X-ray diffraction measurements there is strong evidence for the presence of F8TBT chains in P3HT crystallites in as-spun and mildly annealed P3HT/F8TBT films. These F8TBT chains that are incorporated inside P3HT crystallites represent defects that may act as scattering or trapping sites for holes, impeding charge transport [34]. (We note however, that since F8TBT has a deeper HOMO, 5.37 eV, compared to P3HT, 4.9 eV, F8TBT is unlikely to act as a hole trap in itself.) Secondly, the physical structure of the blend will adversely affect hole transport particularly if P3HT crystallites are isolated due to an enclosing F8TBT phase. The observation of a strong negative electric-field dependence in the blends absent in pristine P3HT supports this assertion, with a negative electric-field dependence attributed to spatial disorder [26]. While we are unable to directly determine the crystallite content from the XRD measurements, recent photophysical studies estimate the crystallite content of unblended P3HT at 40–50% [35]. Thus in a blend with another polymer the crystallite content will be further diluted, with crystallite percolation pathways more likely in annealed films with larger crystallites than in unannealed films with smaller crystallites. Similar percolation thresholds have been observed for electron transport in blends of conjugated polymers with fullerene derivatives [14]. Given the amorphous nature of F8TBT and the propensity of P3HT to form isolated fibrils [13], it is indeed likely that the bulk morphology of the film will favour isolated P3HT domains surrounded by a continuous F8TBT phase, particularly at low anneal temperatures. Furthermore, the measured

P3HT crystallite size does not necessarily represent the P3HT aggregate size, and films annealed at higher temperatures (and/or for longer times) will therefore have the opportunity for P3HT crystallites to move and aggregate. Fig. 6 schematically presents the proposed structures of as-spun and annealed P3HT and P3HT/F8TBT films. For the case of unblended P3HT, annealing serves to increase the crystallite size, improving charge transport through a reduction in the number of inter-domain hops. However, in both unannealed and annealed P3HT films there is relatively good interconnectivity between domains with only a modest increase in mobility. For the case of unannealed P3HT/F8TBT, it is proposed that the distorted P3HT crystallites are surrounded by a continuous F8TBT phase that inhibits inter-domain hops. Hole transport relies either on inefficient inter-domain hopping possibly mediated by disordered P3HT chains that may exist as a minority component in the F8TBT phase. In contrast, in annealed P3HT/F8TBT films the crystallites have a chance to aggregate as they grow establishing interconnected percolation pathways. It is this change from isolated to interconnected domains that then accounts for the order of magnitude increase in hole mobility in the blend with annealing.

These measurements also have implications for understanding photovoltaic device performance. It is found that an annealing temperature of 413 K is required for an optimum photovoltaic performance [22]. The results here show that at this annealing temperature the film is still in an intermediate state of phase separation and purity of P3HT crystallites. Furthermore, the charge transport mobility of the P3HT phase still lags that of 453 K annealed

films that demonstrate inferior device performance [36]. Therefore it appears that it is not bulk charge transport that is primarily determining the efficiency of P3HT/F8TBT blends in solar cell devices, but rather the intermediate state of phase separation that exists in 413 K annealed films balances the two processes of charge generation (exciton diffusion and dissociation and donor/acceptor interfaces [36,37]) and charge separation (separation of bound electron–hole pairs from the donor/acceptor interface [38]). Also of interest, particularly for photovoltaic operation, is the influence of film microstructure and morphology on electron transport. However, the transport of electrons in P3HT/F8TBT blends is adversely affected by trapping effects making the observation of clean TOF transients difficult [39] and beyond the scope of this study. Curiously the intercalation of F8TBT chains in P3HT crystallites may represent a microstructural origin for electron trapping in these blends and further research is planned to investigate this.

## 5. Conclusions

We have measured the charge transport properties and microstructure of P3HT/F8TBT blends. The X-ray diffraction results reveal that P3HT/F8TBT blends show a phase separation of the two components with a crystalline part attributed to P3HT and an amorphous part attributed to F8TBT. In as-spun and mildly annealed blends, the measured  $d$ -values and relative intensities between the P3HT reflections are noticeably different to unblended P3HT indicating an incorporation of F8TBT in P3HT crystallites that distorts the crystal structure. At higher anneal temperatures the blend  $d$ -values approach that of unblended P3HT suggesting a well separated blend with almost pure P3HT crystallites. We explain the increase in hole mobility in the blend with annealing in terms of an increase in the P3HT crystallite purity and the aggregation of P3HT crystals to form percolation pathways.

## Acknowledgements

This work was supported in Cambridge by the Engineering and Physical Sciences Research Council (EP/E051804/1) and in Graz by the Austrian Research Promotion Agency (FFG) within the RPC ISOTEC. C.R.M. acknowledges Cambridge Display Technology Ltd. for the provision of F8TBT, Dr. D. Kabra for assistance with the deposition of TiO<sub>2</sub>, and I. Hwang for calculation of the optical absorption profile in the [Supplementary material](#).

## Appendix A. Supplementary material

Supplementary data associated with this article can be found, in the online version, at [doi:10.1016/j.orgel.2009.08.025](https://doi.org/10.1016/j.orgel.2009.08.025).

## References

- [1] A.C. Morteani, A.S. Dhoot, J.S. Kim, C. Silva, N.C. Greenham, C. Murphy, E. Moons, S. Ciná, J.H. Burroughes, R.H. Friend, Barrier-free

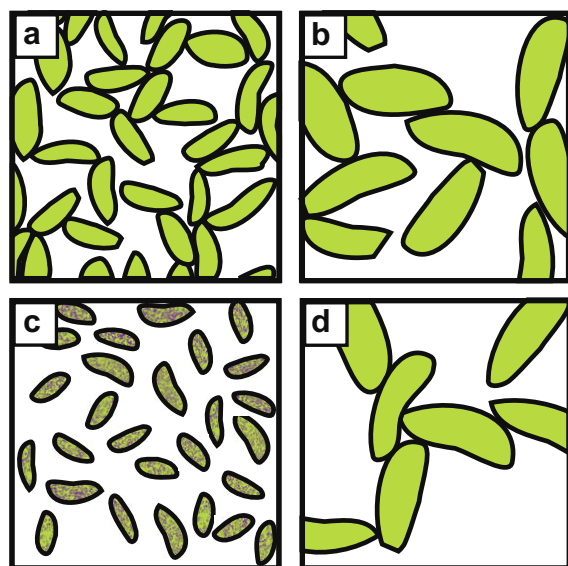


**Fig. 6.** Schematic diagram of the proposed structures of P3HT (a and b) and P3HT/F8TBT blends (c and d). (a) Presents the schematic structure of unannealed P3HT with smaller crystallite size and (b) the structure of annealed P3HT (453 K) with larger crystallite size. (c) Shows the proposed structure of unannealed P3HT/F8TBT with smaller, distorted P3HT crystals surrounded by an F8TBT matrix. (d) Shows the structure of annealed P3HT/F8TBT (453 K) with larger, pure P3HT crystallites with good interconnection.

- electron-hole capture in polymer blend heterojunction light-emitting diodes, *Adv. Mater.* 15 (2003) 1708–1712.
- [2] S. Goffri, C. Müller, N. Stingelin-Stutzmann, D.W. Breiby, C.P. Radano, R. Thompson, J.W. Andreasen, R.A.J. Janssen, H. Chanzy, M.M. Nielsen, P. Smith, H. Sirringhaus, Field-effect transistors of polymer semi-conducting/insulating blends and block-copolymers, *Nat. Mater.* 5 (2006) 950–956.
- [3] K. Asadi, D.M. De Leeuw, B. De Boer, P.W.M. Blom, Organic non-volatile memories from ferroelectric phase-separated blends, *Nat. Mater.* 7 (2008) 547–550.
- [4] S.C. Veenstra, J. Loos, J.M. Kroon, Nanoscale structure of solar cells based on pure conjugated polymer blends, *Prog. Photovolt.: Res. Appl.* 15 (2007) 727–740.
- [5] P.W.M. Blom, V.D. Mihailetschi, L.J.A. Koster, D.E. Markov, Device physics of polymer: fullerene bulk heterojunction solar cells, *Adv. Mater.* 19 (2006) 1551–1566.
- [6] D.E. Markov, E. Amsterdam, P.W.M. Blom, A.B. Sieval, J.C. Hummelen, Accurate measurement of the exciton diffusion length in a conjugated polymer using a heterostructure with a side-chain cross-linked fullerene layer, *J. Phys. Chem. A* 109 (2005) 5266–5274.
- [7] J.Y. Kim, K. Lee, N.E. Coates, D. Moses, T.Q. Nguyen, M. Dante, A.J. Heeger, Efficient tandem polymer solar cells fabricated by all-solution processing, *Science* 317 (2007) 222–225.
- [8] W. Ma, C. Yang, X. Gong, K. Lee, A.J. Heeger, Thermally stable, efficient polymer solar cells with nanoscale control of the interpenetrating network morphology, *Adv. Funct. Mater.* 15 (2005) 1617–1622.
- [9] V.D. Mihailetschi, H. Xie, B. de Boer, L.J.A. Koster, P.W.M. Blom, Charge transport and photocurrent generation in poly(3-hexylthiophene): methanofullerene bulk-heterojunction solar cells, *Adv. Funct. Mater.* 16 (2006) 699–708.
- [10] S.S. van Bavel, S. Sourty, G. de With, J. Loos, Three-dimensional nanoscale organization of bulk heterojunction polymer solar cells, *Nano Lett.* 9 (2009) 507–513.
- [11] A. Pivrikas, N.S. Sariciftci, G. Juška, R. Österbacka, A review of charge transport and recombination in polymer/fullerene organic solar cells, *Prog. Photovolt.: Res. Appl.* 15 (2007) 677–696.
- [12] M.Y. Chiu, U.S. Jeng, C.H. Su, K.S. Liang, K.H. Wei, Simultaneous use of small- and wide-angle X-ray techniques to analyze nanometerscale phase separation in polymer heterojunction solar cells, *Adv. Mater.* 20 (2008) 2573–2578.
- [13] X. Yang, J. Loos, S.C. Veenstra, W.J.H. Verhees, M.M. Wien, J.M. Kroon, M.A.J. Michels, R.A.J. Janssen, Nanoscale morphology of high-performance polymer solar cells, *Nano Lett.* 5 (2005) 579–583.
- [14] S.M. Tuladhar, D. Poplavskyy, S.A. Choulis, J.R. Durrant, D.C. Bradley, J. Nelson, Ambipolar charge transport in a methanofullerene and in poly(phenylene vinylene)/methanofullerene blend films, *Adv. Funct. Mater.* 15 (2005) 1171–1182.
- [15] M.M. Mandoc, W. Veurman, L.J.A. Koster, M.M. Koetse, J. Sweelssen, B. de Boer, P.W.M. Blom, Charge transport in MDMO-PPV: PCNEPV all-polymer solar cells, *J. Appl. Phys.* 101 (2007) 104512.
- [16] C. Yin, M. Schubert, S. Bange, B. Stiller, M. Castellani, D. Neher, M. Kumke, H.-H. Hörhold, Tuning of the excited-state properties and photovoltaic performance in PPV-based polymer blends, *J. Phys. Chem. C* 112 (2008) 14607–14617.
- [17] A. Babel, Y. Zhu, K.-F. Cheng, W.-C. Chen, S.A. Jenekhe, High electron mobility and ambipolar charge transport in binary blends of donor and acceptor conjugated polymers, *Adv. Funct. Mater.* 17 (2007) 2542–2549.
- [18] E. Bundgaard, F.C. Krebs, Low band gap polymers for organic photovoltaics, *Sol. Energy Mater. Sol. Cells* 91 (2007) 954–985.
- [19] M. Sferazza, C. Carelli, Interfaces and fluctuations in confined polymeric liquid mixtures: from immiscible to near critical systems, *J. Phys.: Condens. Matter* 19 (2007) 073102.
- [20] C.R. McNeill, A. Abrusci, J. Zaumseil, R. Wilson, M.J. McKiernan, J.J.M. Halls, N.C. Greenham, R.H. Friend, Dual electron donor/electron acceptor character of a conjugated polymer in efficient photovoltaic diodes, *Appl. Phys. Lett.* 90 (2007) 193506.
- [21] G.L. Whiting, C.R. McNeill, Unpublished results.
- [22] C.R. McNeill, J.J.M. Halls, R. Wilson, G.L. Whiting, S. Berkebile, M.G. Ramsey, R.H. Friend, N.C. Greenham, Efficient polythiophene/polyfluorene co-polymer bulk heterojunction photovoltaic devices: device physics and annealing effects, *Adv. Funct. Mater.* 18 (2008) 2309–2321.
- [23] S.A. Choulis, Y. Kim, J. Nelson, D.D.C. Bradley, M. Giles, M. Shkunov, I. McCulloch, High ambipolar and balanced carrier mobility in regioregular poly(3-hexylthiophene), *Appl. Phys. Lett.* 85 (2004) 3890–3892.
- [24] From optical simulations  $|E|^2$  drops to 1/e of its initial value 90 nm into the P3HT/F8TBT film and drops to 10% of its initial value 200 nm into the P3HT/F8TBT film. See [Supplementary material](#) for more details.
- [25] Anton Paar GmbH, DHS1100: a new high-temperature attachment for materials science in the whole orientation space, *J. Appl. Cryst.* 40 (2007) 202.
- [26] A.J. Mozer, N.S. Sariciftci, Negative electric field dependence of charge carrier drift mobility in conjugated, semiconducting polymers, *Chem. Phys. Lett.* 389 (2004) 438–442.
- [27] S. Joshi, S. Grigorian, U. Pietsch, X-ray structural and crystallinity studies of low and high molecular weight poly(3-hexylthiophene), *Phys. Status Solidi A* 205 (2008) 488–496.
- [28] R.J. Kline, M.D. McGehee, E.N. Kadnikova, J. Liu, J.M.J. Fréchet, M.F. Toney, Dependence of regioregular poly(3-hexylthiophene) film morphology and field-effect mobility on molecular weight, *Macromolecules* 38 (2005) 3312–3319.
- [29] E.J. Samuelsen, J. Mårdalen, in: H.S. Nalwa (Ed.), *Handbook of Organic Conductive Molecules and Polymers, Conductive Polymers: Spectroscopy and Physical Properties*, vol. 3, Wiley, Weinheim, 1997.
- [30] C. Yang, P. Orfino, S. Holdcroft, A phenomenological model for predicting thermochromism of regioregular and nonregioregular poly(3-alkylthiophenes), *Macromolecules* 29 (1996) 6510–6517.
- [31] A.C. Mayer, M.F. Toney, S.R. Scully, J. Rivnay, C.J. Brabec, M. Scharber, M. Koppe, M. Heeney, I. McCulloch, M.D. McGehee, Bimolecular crystals of fullerenes in conjugated polymers and the implications of molecular mixing for solar cells, *Adv. Funct. Mater.* 19 (2009) 1173–1179.
- [32] Y. Kim, S. Cook, S.M. Tuladhar, S.A. Choulis, J. Nelson, J.R. Durrant, D.D.C. Bradley, M. Giles, I. McCulloch, C.-S. Ha, M. Ree, A strong regioregularity effect in self-organising conjugated polymer films and high-efficiency polythiophene: fullerene solar cells, *Nat. Mater.* 5 (2006) 197–203.
- [33] O. Werzer, K. Matoy, P. Strohiengl, R. Resel, Temperature treatment of semiconducting polymers: an X-ray reflectivity study, *Thin Solid Films* 14 (2007) 5601–5605.
- [34] S. Verlaak, P. Heremans, Molecular microelectrostatic view on electronic states near pentacene grain boundaries, *Phys. Rev. B* 75 (2007) 115127.
- [35] J. Clark, J.F. Chang, F.C. Spano, R.H. Friend, C. Silva, Determining exciton bandwidth and film microstructure in polythiophene films using linear absorption spectroscopy, *Appl. Phys. Lett.* 94 (2009) 163306.
- [36] C.R. McNeill, A. Abrusci, I. Hwang, N.C. Greenham, Photophysics and photocurrent generation in polythiophene/polyfluorene co-polymer blends, *Adv. Funct. Mater.*, in press.
- [37] C.R. McNeill, S. Westenhoff, C. Groves, R.H. Friend, N.C. Greenham, Influence of nanoscale phase separation on the charge generation dynamics and photovoltaic performance of conjugated polymer blends – balancing charge generation and separation, *J. Phys. Chem. C* 111 (2007) 19153–19160.
- [38] V.D. Mihailetschi, L.J.A. Koster, J.C. Hummelen, P.W.M. Blom, Photocurrent generation in polymer–fullerene bulk-heterojunctions, *Phys. Rev. Lett.* 93 (2004) 216601.
- [39] C.R. McNeill, N.C. Greenham, Charge transport dynamics of polymer solar cells under operating conditions: influence of trap filling, *Appl. Phys. Lett.* 93 (2008) 203310.

grown by chemical vapor deposition (CVD) found a SWCNT/pentacene contact resistance as low as 30 k $\Omega$  cm ( $V_G = -50$  V) [18]. However, the CVD method is expensive and laborious, so solution-phase preparation of CNT films is more desirable for applications. Solution-processed CNTs have also been found to make good contact to poly(3,3'-didodecylquaterthiophene) [19], but it is not clear that this result could be expanded to pentacene, where contact resistance in bottom-contacted devices is more problematic. Here, we demonstrate transparent films of commercially-available SWCNTs produced by airbrushing from aqueous solution as electrodes for pentacene and poly-3-hexylthiophene (P3HT) thin-film transistors (TFTs). Airbrushing CNT thin films is an additive process that allows quick, large area patterning over any substrate and is compatible with ink-jet printing. CNT films deposited by spraying have been found to be rougher but exhibit similar sheet resistance for a given transparency as most other methods [14]. The channel-length-dependent output characteristics of the SWCNT-contacted TFTs on SiO<sub>2</sub>/Si substrates are used to extract the mobility  $\mu$  (0.093 cm<sup>2</sup>/Vs for pentacene, 0.014 cm<sup>2</sup>/Vs for P3HT) and contact resistivity. In the case of pentacene, we demonstrate that solution-processed SWCNT bottom-contact electrodes make moderately low-resistance (as low as 30 k $\Omega$  cm) contacts, which extends previous results for pentacene contacted by CVD-grown SWCNTs [20] to this much more easily processed material. For P3HT, we verify low contact resistance (<50 k $\Omega$  cm) bottom-contact to solution-processed SWCNTs, similar to previous results for poly(3,3'-didodecylquaterthiophene) [19]. We also demonstrate the use of solution-processed films of SWCNTs as source, drain, and gate electrodes to fabricate flexible, transparent SWCNT-contacted pentacene TFTs on plastic polyethylene terephthalate (PET) substrates.

## 2. Materials and methods

SWCNT films were prepared as follows. A dispersion of 1 mg/mL SWCNTs ("P3", carbon solutions) in 1% by wt. sodium dodecyl sulfate (SDS) and water was exfoliated by sonication for 90 min followed by differential centrifugation at 12,000 rpm for one hour to remove carbonaceous impurities [4]. The top 2/3 of the supernatant was extracted and used as the airbrush feedstock. The source/drain (S/D) electrodes of the test devices were made by using an airbrush (Aztek A470 airbrush kit) to deposit a 30–40 nm thick film onto a 500 nm-SiO<sub>2</sub>/n<sup>++</sup>-Si platform at a temperature of 165 °C. The deposited films are then soaked in water for one hour to remove surfactant, and dried with a N<sub>2</sub> gun. The SWCNT film was patterned using photolithography and O<sub>2</sub> reactive ion etching. In order to determine the organic-SWCNT contact resistance, a set of devices of varying gate length  $L$  from 3 to 1262  $\mu$ m was fabricated; the channel width  $W$  is 1.6–2.0 mm. The optical transparency of the carbon nanotube thin-film  $T$  was obtained from the ratio of the measured transparency of CNT-coated PET, prepared by airbrushing directly onto PET, to that of the PET substrate prior to nanotube coating.

Pentacene films were deposited onto the prepared electrodes in vacuum ( $<2 \times 10^{-7}$  torr) by evaporation through

a shadow mask to form the active area of the TFT. P3HT transistors were fabricated on the prepared electrodes by first vapor coating the SiO<sub>2</sub> substrate with hexamethyldisilazane and then spin casting P3HT at 1250–2000 rpm from trichlorobenzene heated to 100 °C at a concentration of 10 mg/mL followed by a vacuum bake at 100 °C for one hour [21]. The doped Si substrate acts as a back-gate electrode. All electrical characterization was done in a N<sub>2</sub> atmosphere in the dark to prevent unintentional doping during the measurements.

## 3. Results and discussion

### 3.1. Carbon nanotube thin films as transparent electrodes

Fig. 1 shows the optical transparency  $T$  of the airbrushed CNT films as a function of film sheet resistance. The airbrushed films have a sheet resistance as low as 1 k $\Omega$ /sq. for  $T = 80\%$ , and 5 k $\Omega$ /sq. for  $T = 90\%$ , compared with 0.0278 k $\Omega$ /sq. @ 80% $T$  for ITO coated glass [22]. The method of dispersing SWCNTs and subsequently spraying them to form a thin-film has been reported by several groups [12–14]. The  $T$  vs. sheet resistance behavior is in agreement with a model proposed by Hu et al. [23] which predicts.

$$\%T = \frac{100}{\left(1 + \frac{2\pi}{cR_{\square}} \frac{\sigma_{ac}}{\sigma_{dc}}\right)^2} \quad (1)$$

where  $R_{\square}$  is the sheet resistance,  $\sigma_{ac}$  is the optical conductivity,  $\sigma_{dc}$  is the dc conductivity, and  $c$  is the speed of light; a fit to Eq. (1) is shown in Fig. 1. The only free parameter used is the ratio of  $\sigma_{ac}$  to  $\sigma_{dc}$ ; we find that a ratio of 0.74  $\pm$  0.03 gives the best fit to the data. This value is slightly smaller than the value of 1 obtained by Hu et al. [23].

### 3.2. Pentacene and P3HT transistors with carbon nanotube electrodes

Scanning electron microscopy was performed on the pentacene/SWCNT TFTs after electrical measurement of

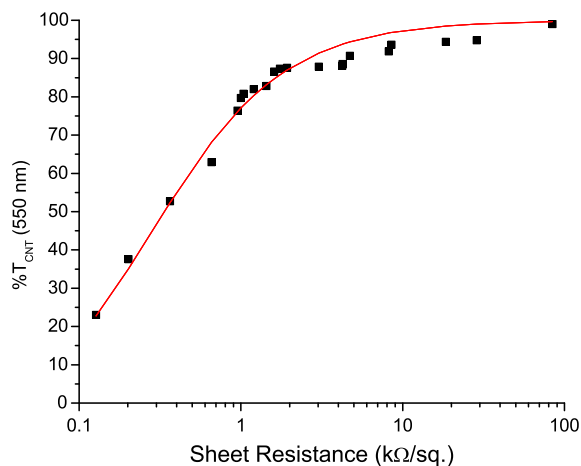


Fig. 1. The percent transparency at a wavelength of 550 nm vs. sheet resistance of airbrushed carbon nanotube films and fit using Eq. (1).

the transistors. Parts of one of the pentacene/SWCNT TFT are shown in Fig. 2a and Fig. 2b (a closeup) illustrating the morphology of the pentacene layer on both the bare SiO<sub>2</sub> as well as the CNT film. The pentacene on the bare SiO<sub>2</sub> forms ~250 nm grains separated by relatively thin grain boundaries whereas the pentacene on the CNT film forms a discontinuous film of rod-like grains. The crystal structure of these grains is unknown at this time and is the subject of further investigation.

Fig. 3a and b show output characteristics for example pentacene/SWCNT and P3HT/SWCNT TFTs, respectively. The resistance  $R$  of each device was found as a function of  $L$  and gate voltage  $V_G$  from the slope of drain current vs. drain voltage  $I(V_D)$  for  $-1 \text{ V} < V_D < 1 \text{ V}$ . A threshold voltage  $V_T$  was extracted from the conductance vs.  $V_G$  plot for each channel length; this allowed us to compare measurements performed at the same effective gate voltage  $V_G^* = V_G - V_T$ , correcting for any possible length-dependent threshold shift [24].

Fig. 4a and b show  $R$  vs.  $L$  at various values of  $V_G^*$  for the pentacene/SWCNT and P3HT/SWCNT TFTs respectively.  $R$  vs.  $L$  obeys a linear relationship  $R(L, V_G^*) = \alpha(V_G^*)L + R_c(V_G^*)$ . The intrinsic field-effect mobility may be found from  $\alpha$  [25]:

$$\mu_{FE}(V_G^*) = \frac{1}{WC_{ox}} \frac{\partial(\alpha^{-1})}{\partial V_G^*}. \quad (2)$$

The contact resistivity is defined to be  $\rho_c = R_c W$ , where  $W$  is the channel width. For pentacene/SWCNT devices,  $\rho_c$  is finite and gate voltage dependent, saturating at  $<30 \text{ k}\Omega \text{ cm}$  for  $V_G^* < -40 \text{ V}$ . Values for the contact resistance using Au bottom-contacts vary from 20 to  $110 \text{ k}\Omega \text{ cm}$  depending on the gate voltage applied, the work function and conductivity of the injecting electrode, the temperature of the substrate during deposition and the thickness of the pentacene layer [26,27]. Au top contacts exhibit contact resistances an order of magnitude smaller [27]. In our devices, the intrinsic mobility is  $0.093 \text{ cm}^2/\text{Vs}$ . On/off current ratios ( $V_D = -60 \text{ V}$ ,  $-60 \text{ V} \leq V_G \leq 60 \text{ V}$ ) were  $>10^6$ . For P3HT/SWCNT devices,  $\rho_c$  is less than  $50 \text{ k}\Omega \text{ cm}$  at all gate voltages in the ON state, higher than control devices fabricated with Au bottom-

contacts whose  $\rho_c$  is  $1\text{--}10 \text{ k}\Omega \text{ cm}$  [25,28]. Intrinsic field-effect mobility was as high as  $0.014 \text{ cm}^2/\text{Vs}$ . On/Off current ratios  $>10^5$  ( $V_D = -60 \text{ V}$ ,  $-60 \text{ V} \leq V_G \leq 50 \text{ V}$ ) were obtained for P3HT/SWCNT devices.

The bottom-contact resistance obtained with Au deposited on a relatively thin Cr or Ti wetting layer as is typically used to make bottom-contacts is higher than that for Au top contacts, and shows non-linear  $I(V_D)$  characteristics, attributed to the presence of an injection barrier [29] or disruption of the pentacene morphology at the interface of the bottom-contacts [30]. Thus our observation that bottom-contact SWCNT electrodes offer slightly lower contact resistance to pentacene might either be due to narrowing of the injection barrier due to the high electric field at the SWCNT ends [31], or by allowing better ordering of the pentacene on SiO<sub>2</sub> at the electrode interface. Given the close packing of SWCNTs in our thick (30–40 nm) SWCNT film, and the thick (500 nm) gate dielectric, we consider electric-field enhancement unlikely. We propose that SWCNT electrodes allow more favorable growth of pentacene on the neighboring SiO<sub>2</sub> substrate, or that the morphology of pentacene on the SWCNTs themselves does not give rise to a significant injection barrier. In the case of P3HT, SWCNT contacts show a contact resistance similar to that obtained with Au [25,32,33].

### 3.3. Demonstration of transparent organic thin-film transistors

Finally, we show that solution-processed SWCNT electrodes can be used to fabricate an all-carbon transparent, flexible TFT in which SWCNT films are used as the source, drain, and gate electrodes, and pentacene as the semiconductor. Cao et al. demonstrated a SWCNT-contacted pentacene thin-film transistor (TFT) on a plastic substrate using SWCNTs grown by chemical vapor deposition (CVD) and patterned by photolithography [33]. Here, SWCNT gate electrodes were airbrushed through a shadow mask onto PET (Dupont Teijin™ Melinex 454/700; thickness  $170 \sim \mu\text{m}$ ). The SWCNT gate had a sheet resistance of  $3.1 \text{ k}\Omega/\text{sq}$  and a transparency of  $>91\%$  that was interpolated from the sheet resistance vs. transparency fit using Eq. (1).

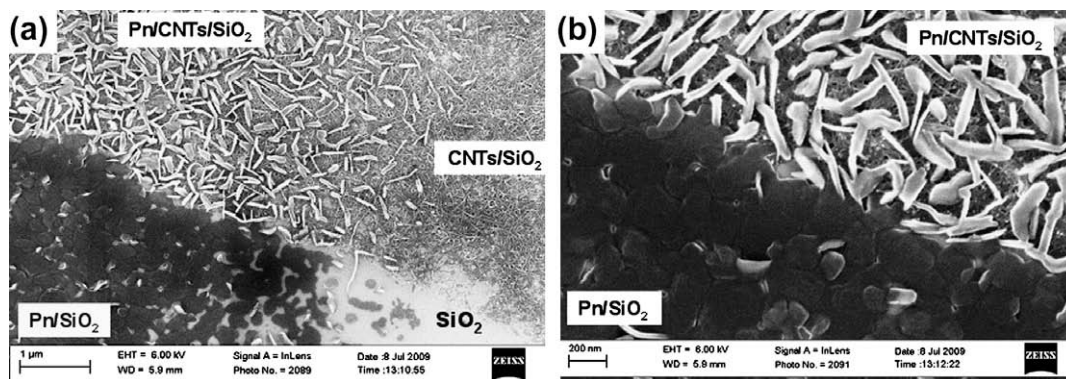
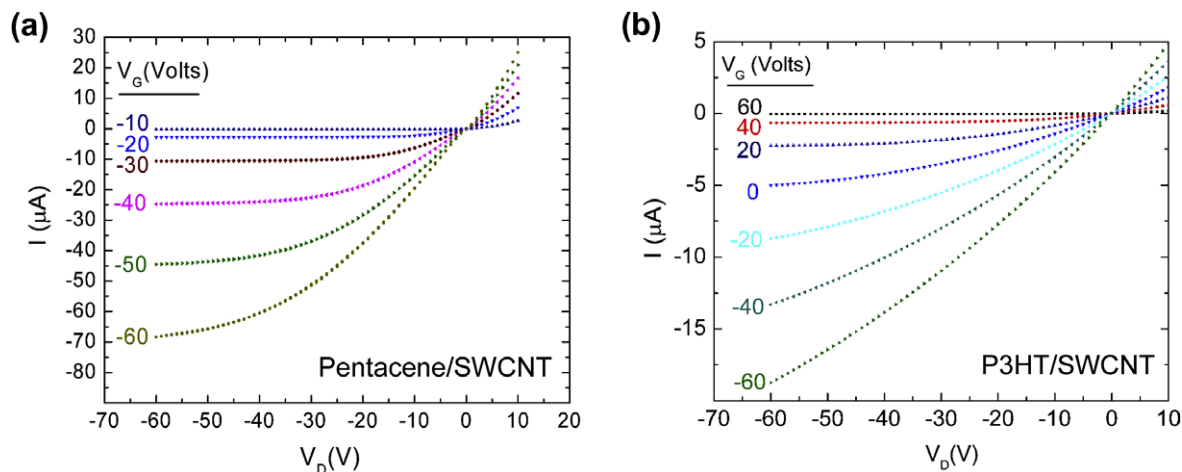
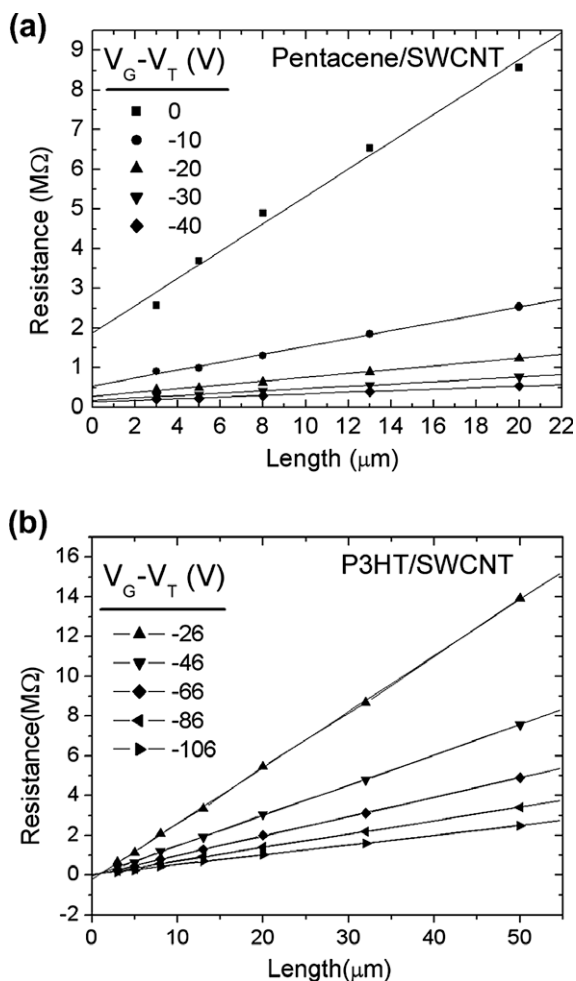


Fig. 2. Scanning electron micrographs of parts of one of the CNT/pentacene transistors showing (a) four separate areas: the bare SiO<sub>2</sub> (bottom right), the CNT film deposited on SiO<sub>2</sub> (upper right), the pentacene layer deposited on the same CNT film (upper left), the pentacene layer deposited on SiO<sub>2</sub> (bottom left) and (b) a closeup of the interface between the pentacene on SiO<sub>2</sub> and the pentacene on the CNT film.





**Fig. 3.** (a) Output characteristics of a carbon nanotube film-contacted pentacene transistor with length  $L = 20 \mu\text{m}$ , width  $W = 1600 \mu\text{m}$ . (b) Output characteristics of a poly-3-hexylthiophene thin-film transistor with carbon nanotubes electrodes with length  $L = 50 \mu\text{m}$ , width  $W = 2000 \mu\text{m}$ .



**Fig. 4.** (a) Resistance vs. channel length for effective gate voltages  $V_G - V_T = 0\text{--}60 \text{ V}$  in  $10 \text{ V}$  steps for carbon nanotube film-contacted pentacene transistors and (b) carbon nanotubes film-contacted P3HT transistors with  $V_G - V_T = -26$  to  $-106$  in  $20 \text{ V}$  steps.

To facilitate probing the CNT layer, a  $100 \text{ nm}$  Au layer was deposited onto the four sides of the CNT gate electrode. The dielectric layer was applied in two steps. In the first step, a  $1 \mu\text{m}$  thick layer of PMMA was spun cast onto a transfer substrate and printed onto the device substrate at  $500 \text{ psi}$  and  $T = 170 \text{ }^\circ\text{C}$  for three minutes [34]. In the second step, SWCNT source and drain electrodes (sheet resistance of  $1 \text{ k}\Omega/\text{sq}$  and  $T > 78\%$ ) were patterned on a  $\text{SiO}_2/\text{Si}$  transfer substrate following the scheme outlined above, coated with  $50 \text{ nm}$  of alumina (electron beam evaporation at  $2 \times 10^{-6}$  torr) followed by a  $1 \mu\text{m}$  thick spin coated layer of PMMA and then printed onto the device substrate. The alumina layer served to minimize the leakage current from the source and drain electrodes to the gate. The capacitance of the resulting gate dielectric is estimated to be  $1.33 \text{ nF}/\text{cm}^2$ . Finally,  $30 \text{ nm}$  thick pentacene was evaporated through a shadow mask as described earlier to complete the devices. Devices had a channel width of  $97\text{--}98 \mu\text{m}$  and channel length from  $37$  to  $47 \mu\text{m}$ .

Fig. 5a shows a micrograph of the completed device. The single cross-shaped CNT film acts as a common gate for all four transistors. Silver paint was applied to the ends of two of the gate contacts to facilitate repeated probing of the CNT film. Fig. 5b shows the output characteristics of the device. The field-effect mobility obtained for these devices (uncorrected for contact resistance) was as high as  $0.06 \text{ cm}^2/\text{Vs}$  with an average of  $0.04 \text{ cm}^2/\text{Vs}$ , assuming a dielectric constant for PMMA of  $3.6$ . As fabricated, the devices exhibited  $V_T > 60 \text{ V}$ , so the on/off current ratio could not be accurately determined. After aging the devices for several months in an inert environment ( $<0.1 \text{ ppm}$  moisture content) the threshold voltages shifted to between  $-10$  and  $-20 \text{ V}$  indicating diffusion of dopants out of the device over time. The on/off current ratios for the aged devices ranged from  $10^3$  to  $10^4$  ( $V_D = -60 \text{ V}$ ,  $-60 \text{ V} \leq V_G \leq 60 \text{ V}$ ), and the saturation mobility values decreased by  $10\text{--}15\%$ . The low on/off current ratios compared to devices on  $\text{SiO}_2$  are likely due to the more than four times lower gate capacitance as well as possibly charge trapping at

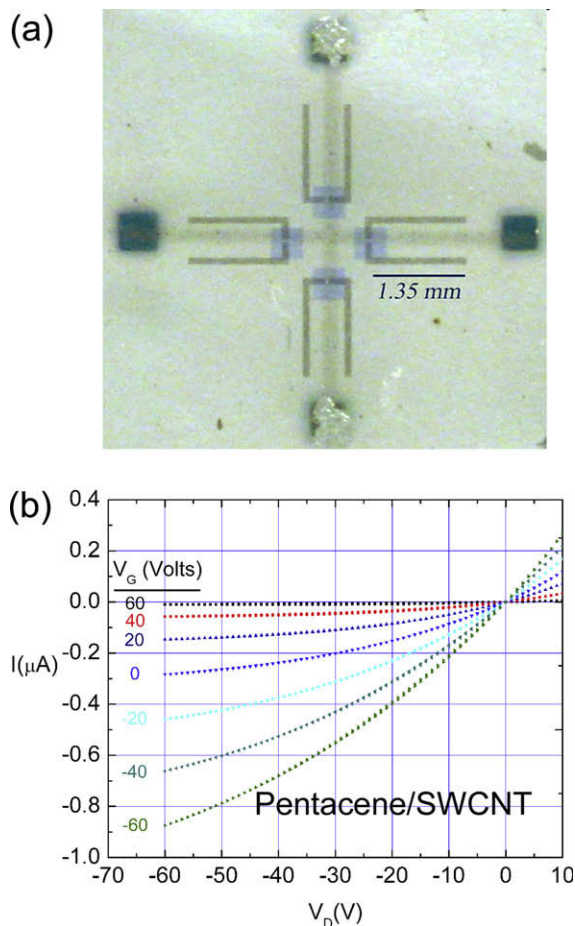


**Fig. 5.** (a) Optical micrograph of four transparent, flexible carbon nanotube film-contacted pentacene thin-film transistors (TFTs) on polyethylene terephthalate (PET) substrate. (b) Output characteristics for one of the TFTs pictured in (a).

the pentacene/ $\text{Al}_2\text{O}_3$  interface which prevent the off state from being reached.

#### 4. Conclusion

In conclusion, we have used airbrushed SWCNT films with sheet resistance below  $1 \text{ k}\Omega/\text{sq}$  at  $T = 80\%$  as electrodes to make bottom-contact pentacene transistors with contact resistance as low as  $26 \text{ k}\Omega \text{ cm}$ , lower than typically achievable with Au/Cr bottom-electrodes, and comparable to results achievable with CVD-grown CNTs. If we assume that the organic/CNT contact resistance is inversely proportional to mobility [25] even lower contact resistance should be possible with organic films optimized for higher mobility. The low contact resistance between the pentacene and CNT film is surprising given the significant differences in morphology observed for pentacene deposited on  $\text{SiO}_2$  vs. CNTs (see Fig. 2). Solution-processed SWCNT films also make bottom-contact electrodes to P3HT with contact resistance comparable to that of Au. We have also demon-

strated that solution-processed electrodes can be patterned onto a flexible plastic substrate both directly (gate electrode with transparency  $>91\%$ ) and via transfer printing (source–drain electrode), as components of a Pn TFT (with  $>78\%$  transparency) using a relatively transparent PMMA/ $\text{Al}_2\text{O}_3$  dielectric and PET substrate with a transparency of 80–90%.

#### Acknowledgements

We are grateful to Dr. D. Hines for guidance in transfer printing of carbon nanotubes and HMDS coating, Neetal Jagadeesh for assistance with calibration of the airbrush used, and Dr. V. Ballorotto for guidance on the spray coating of carbon nanotubes. This work has been supported by the Laboratory for Physical Sciences, and the UMD-MRSEC Shared Equipment Facilities, with infrastructure support from CNAM and the UMD NanoCenter.

#### References

- [1] H. Sirringhaus, *Adv. Mater.* 17 (2005) 2411.
- [2] S.R. Forrest, *Nature* 428 (2004) 911.
- [3] Y.G. Ha, E.A. You, B.J. Kim, et al., *Synth. Met.* 153 (2005) 205.
- [4] D.H. Zhang, K. Ryu, X.L. Liu, et al., *Nano Lett.* 6 (2006) 1880.
- [5] E. Cantatore, T.C.T. Geuns, G.H. Gelinck, et al., *IEEE J. Solid-State Circuits* 42 (2007) 84.
- [6] M.C. Hamilton, J. Kanicki, *IEEE J. Sel. Top. Quantum Electron.* 10 (2004) 840.
- [7] Lagemaat Jao van de, M. Barnes Teresa, Rumbles Garry, et al., *Appl. Phys. Lett.* 88 (2006) 233503.
- [8] A. Bachtold, M.S. Fuhrer, S. Plyasunov, et al., *Phys. Rev. Lett.* 84 (2000) 6082.
- [9] G. Gruner, *J. Mater. Chem.* 16 (2006) 3533.
- [10] Z.C. Wu, Z.H. Chen, X. Du, et al., *Science* 305 (2004) 1273; J.M. Bonard, T. Stora, J.P. Salvetat, et al., *Adv. Mater.* 9 (1997) 827.
- [11] M. Kaempgen, G.S. Duesberg, S. Roth, *Appl. Surf. Sci.* 252 (2005) 425; J.H. Lehman, C. Engrakul, T. Gennett, et al., *Appl. Opt.* 44 (2005) 483; H.Z. Geng, D.S. Lee, K.K. Kim, et al., *J. Korean Phys. Soc.* 53 (2008) 979.
- [12] Y.I. Song, C.M. Yang, D.Y. Kim, et al., *J. Colloid Interface Sci.* 318 (2008) 365.
- [13] H.Z. Geng, K.K. Kim, K. Lee, et al., *NANO* 2 (2007) 157; S. Paul, D.W. Kim, *Carbon* (2009).
- [14] M. Jung de Andrade, M. Dias Lima, V. Skakalova, et al., *Phys. Status Solidi (RRL) – Rapid Res. Lett.* 1 (2007).
- [15] S.F. Pei, J.H. Du, Y. Zeng, et al., *Nanotechnology* 20 (2009).
- [16] P. Fournet, D.F. O'Brien, J.N. Coleman, et al., *Synth. Met.* 121 (2001) 1683; S.P. Lee, H. Choi, K.W. Lee, et al., *J. Korean Phys. Soc.* 48 (2006) 146.
- [17] S. Chaudhary, H.W. Lu, A.M. Muller, et al., *Nano Lett.* 7 (2007) 1973; M.A. Contreras, T. Barnes, J. van de Lagemaat, et al., *J. Phys. Chem. C* 111 (2007) 14045.
- [18] Chia-Hao Chang, Chao-Hsin Chien, Jung-Yen Yang, *Appl. Phys. Lett.* 91 (2007) 083502.
- [19] Y.Y. Zhang, Y.M. Shi, F.M. Chen, et al., *Appl. Phys. Lett.* 91 (2007) 223512.
- [20] C.H. Chang, C.H. Chien, J.Y. Yang, *Appl. Phys. Lett.* 91 (2007).
- [21] J.F. Chang, B.Q. Sun, D.W. Breiby, et al., *Chem. Mater.* 16 (2004) 4772.
- [22] Y. Xu, J.S. Gao, X.M. Zheng, et al., *J. Lumin.* 122 (2007) 908.
- [23] L. Hu, D.S. Hecht, G. Gruner, *Nano Lett.* 4 (2004) 2513.
- [24] A. Benor, A. Hoppe, V. Wagner, et al., *Org. Electron.* 8 (2007) 749.
- [25] B.H. Hamadani, D. Natelson, *Appl. Phys. Lett.* 84 (2004) 443.
- [26] Vanoni Claudio, Tsujino Soichiro, A. Jung Thomas, *Appl. Phys. Lett.* 90 (2007) 193119; Kumaki Daisuke, Umeda Tokiyoshi, Tokito Shizuo, *Appl. Phys. Lett.* 92 (2008) 013301.
- [27] V. Pesavento Paul, P. Puntambekar Kanan, C. Daniel Frisbie, et al., *J. Appl. Phys.* 99 (2006) 094504.
- [28] B.H. Hamadani, D. Natelson, *J. Appl. Phys.* 95 (2004) 1227.
- [29] N. Koch, A. Kahn, J. Ghijssen, et al., *Appl. Phys. Lett.* 82 (2003) 70; P.V. Necliudov, M.S. Shur, D.J. Gundlach, et al., *J. Appl. Phys.* 88 (2000) 6594; D. Kumaki, T. Umeda, S. Tokito, *Appl. Phys. Lett.* 92 (2008).

- [30] P. Puntambekar Kanan, V. Pesavento Paul, C. Daniel Frisbie, Appl. Phys. Lett. 83 (2003) 5539.
- [31] P.F. Qi, A. Javey, M. Rolandi, et al., J. Am. Chem. Soc. 126 (2004) 11774.
- [32] L. Burgi, T.J. Richards, R.H. Friend, et al., J. Appl. Phys. 94 (2003) 6129.
- [33] Cao Qing, Zhu Zheng-Tao, G. Lemaitre Maxime, et al., Appl. Phys. Lett. 88 (2006) 113511.
- [34] D.R. Hines, V.W. Ballarotto, E.D. Williams, et al., J. Appl. Phys. 101 (2007) 024503.

mercial product that has been widely used as a hole injecting and transporting material [8–10] due to its electronic, optical and film forming properties [11–13]. Significantly, optical quality PEDOT:PSS thin films can be readily deposited on various substrates by solution processing techniques, such as spin-coating, inkjet printing, and roll-to-roll printing. [8–16].

Substantial efforts have been dedicated to develop PEDOT:PSS films with high electrical conductivity. One of the primary motivations has been that low conductivity leads to lower PLEDs performance since the average electric field across the device is decreased and Joule heating can lead to a decrease in operational lifetime [15,16]. However, high-conductivity is necessary when PEDOT:PSS films are used as the anode itself [15,17,18]. Atop ITO, PEDOT:PSS functions as a buffer layer to remedy electrical shorts and stabilize the work function. Under these conditions it is the out-of-plane resistance that contributes more significantly to the device resistance.

In this communication, we demonstrate that low conductivity PEDOT:PSS in combination with a novel high-conductivity, glycerol-modified PEDOT:PSS layer can be used to fabricate phosphorescent PLEDs with high luminous efficiency (LE), power efficiency (PE) and external quantum efficiency (EQE). This manuscript is organized as follows. The difference in PLEDs performance as function of different commercially available PEDOT:PSS formulations are provided first as a baseline measure. Subsequently, we show that the addition of glycerol as an additive during the spin-coating step leads to large increases in PEDOT:PSS conductivity. Finally, we integrate two different PEDOT:PSS layers with different electrical properties to fabricate PLEDs that displays remarkably improved LE, PE and EQE. These discoveries are anticipated to enable further improvement of the present efficiency of PLEDs and may minimize the efficiency gap relative to vacuum-deposited small molecular devices.

## 2. Experimental details

A host–guest system, consisting of poly(vinylcarbazole) (PVK) blended with 2-(4-biphenyl)-5-(4-tert-butylphenyl)-1,3,4-oxadiazole (PBD) and green emitting iridium complex, Iridium tris(2-(4-tolyl)pyridinato-*N,C*<sup>2</sup>) (Ir(mppy)<sub>3</sub>), is used as emitting layer. PVK and PBD were purchased from Aldrich and used as received. Ir(mppy)<sub>3</sub> was purchased from America Dyes Sources. The three types of PEDOT:PSS was purchased from H.C. Starck, Inc.

The fabrication of PLEDs followed well-established processes and can be referenced elsewhere [16]. For the preparation of glycerol-modified PEDOT:PSS layer, solution blending consisting of glycerol (1.0 wt%) dispersed in the commercially obtained PEDOT<sub>8000</sub> solution was dropped cast at a speed of 2000 rpm on the top of the prepared PEDOT<sub>8000</sub>. All dispersion were filtered with 0.45 μm PVDF filter before spin-coating. It is important to disperse glycerol by using a high frequency mixer. The obtained PEDOT films were then dried on a hotplate at 160 °C for 10 min. The current density–luminance–voltage (*J–L–V*) characteristic was measured using a Keithley 236 source-measurement

unit and a calibrated silicon photodiode. The luminance was calibrated by a spectrophotometer (Photo Research, Model: SpectraScan PR-705). The external quantum efficiency of device was collected by measuring the total light output in all directions in an integrating sphere (IS-080, Labsphere).

The conductivity of PEDOT:PSS film at room temperature was measured by the two-point probe or four-point probe method or *I–V* curve sweeps in dry glove box filled with N<sub>2</sub> gas using a Keithley 2410 source meter. AFM images were obtained with a Nanoscope IIIa instrument (Digital Instruments), in the tapping mode. A crystal silicon tip, with a resonant frequency of 300–350 kHz and a spring constant of 20–100 N m<sup>-1</sup> was used. The scanner was a 10 μm piezo scanner and the scan rate was 1–2 Hz. Off-line image processing and analysis (grain size, roughness) were performed using DI off-line software (Veeco Corp).

## 3. Results and discussion

Three different commercial PEDOT:PSS versions were used to fabricate phosphorescent PLEDs. The three PEDOT:PSS versions are (together with their abbreviations in this manuscript): BAYTRON P (PEDOT<sub>P</sub>), BAYTRON P Al 4083 (PEDOT<sub>4083</sub>), and BAYTRON P CH 8000 (PEDOT<sub>8000</sub>); their typical electrical conductivity are ~1 S cm<sup>-1</sup>, ~10<sup>-3</sup> S cm<sup>-1</sup> and ~10<sup>-5</sup> S cm<sup>-1</sup>, respectively [19]. The emitting layer (EML) used throughout the studies contains 70 wt% of poly(vinylcarbazole) (PVK), 29 wt% of 2-(4-biphenyl)-5-(4-tert-butylphenyl)-1,3,4-oxadiazole (PBD) and 1 wt% of Iridium tris(2-(4-tolyl)pyridinato-*N,C*<sup>2</sup>) (Ir(mppy)<sub>3</sub>). Fig. 1a presents the resulting current density–luminance–bias (*J–L–V*) characteristics. One observes that *J* is dependent on the conductivity of the PEDOT:PSS layer. The current density of the PEDOT<sub>8000</sub> device is controlled by the high resistance of the buffer layer, as a result the peak luminance of 14369 cd m<sup>-2</sup> is obtained at a current density of 52 mA cm<sup>-2</sup> (see Table 1 for a summary of relevant device characterization), much lower than that of the PEDOT<sub>P</sub> or PEDOT<sub>4083</sub> device. However, we note that this device exhibits better control over the leakage current in the small voltage region (0–3 V). For example, as shown in Fig. 1a, the leakage current before turn-on is ~10<sup>-5</sup> mA cm<sup>-2</sup>, at least 2–3 orders of magnitude lower than those of PEDOT<sub>P</sub> and PEDOT<sub>4083</sub> devices.

The luminous efficiency–current density (LE–PE–*J*) characteristics of the PLEDs described above are shown in Fig. 1b. Foremost, one can observe a peak LE of 86 cd A<sup>-1</sup> for the PEDOT<sub>8000</sub> device at 0.15 mA cm<sup>-2</sup> (6.0 V), which corresponds to an EQE of 26%. The peak PE (52 lm W<sup>-1</sup>) was obtained at 0.030 mA cm<sup>-2</sup> (5.1 V). At a high forward view luminance of 1000 cd m<sup>-2</sup>, the efficiency slightly decreased to 77 cd A<sup>-1</sup> (corresponding to an EQE of 23%) and PE still retained as high as 30 lm W<sup>-1</sup>. These performance parameters are superior relative to those observed with PEDOT<sub>P</sub> or PEDOT<sub>4083</sub> (see Table 1) and are consistent with the fact that the peak LE and EQE occur in the small current density region [20]. We also note that the efficiencies are competitive with, and even exceed, those of vacuum-deposited OLEDs reported to date [2–5]. In contrast, a peak

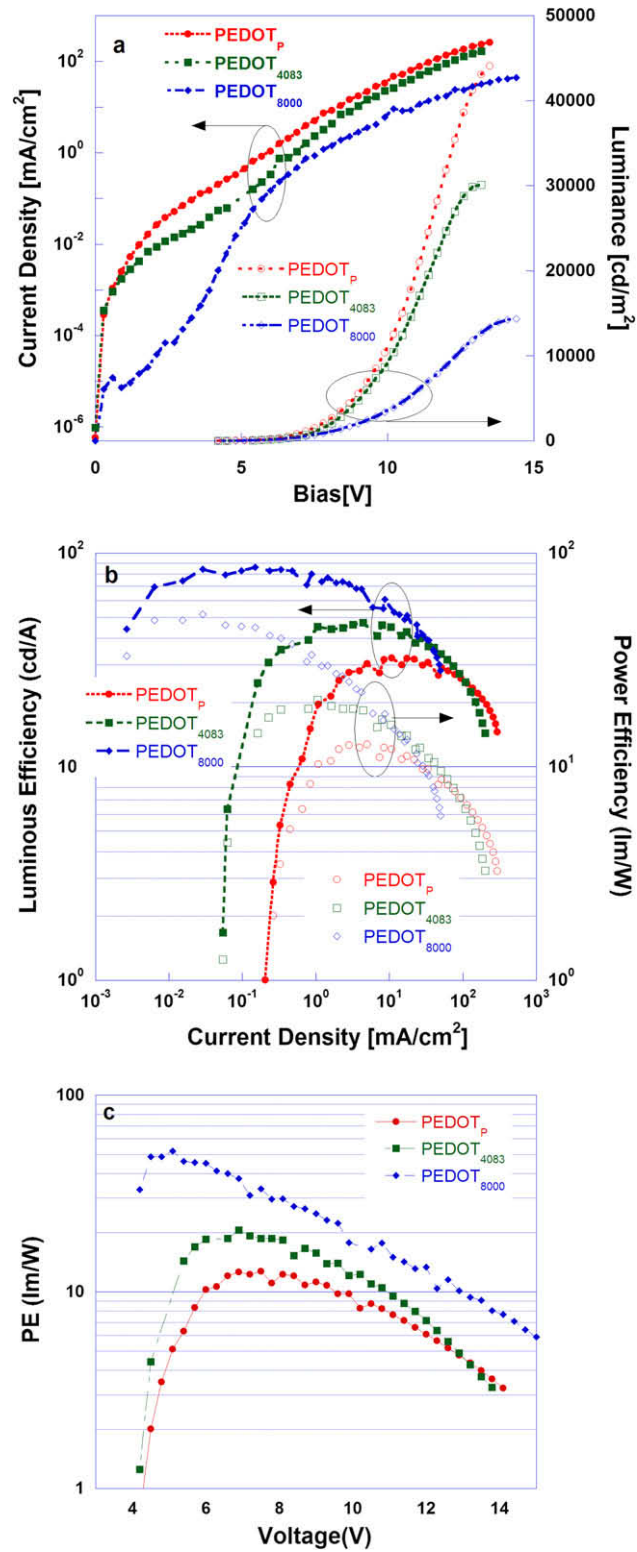


**Fig. 1.** Influence of different types of PEDOT buffer layers on the PLEDs parameters, (a) current density–voltage ( $J$ – $V$ ) characteristics (filled), luminance–voltage ( $L$ – $V$ ) characteristics (open); (b) luminous efficiency–current density ( $LE$ – $J$ ) characteristics (filled),  $PE$ – $J$  characteristics (open); (c) power efficiency–current density ( $PE$ – $J$ ) characteristics (open). Circles are for devices with PEDOT<sub>p</sub>, squares for PEDOT<sub>4083</sub>, and diamonds for PEDOT<sub>8000</sub>.

**Table 1**

Summary of PLEDs performance as a function of anode buffer layer. Device structure: ITO/PEDOT:PSS/EML/Ba/Al, EML = PVK (70 wt%):PBD (29 wt%):Ir(mppy)<sub>3</sub> (1 wt%).

Anode buffer layer	Peak LE (cd A <sup>-1</sup> )	Peak EQE (%)	Peak PE (lm W <sup>-1</sup> )	Peak lumin. (cd m <sup>-2</sup> )	Max. current density (mA cm <sup>-2</sup> )	LE@ 0.1 mA cm <sup>-2</sup> (cd A <sup>-1</sup> )	LE@ 1 mA cm <sup>-2</sup> (cd A <sup>-1</sup> )	LE@ 10 mA cm <sup>-2</sup> (cd A <sup>-1</sup> )	LE@ 100 mA cm <sup>-2</sup> (cd A <sup>-1</sup> )
PEDOT <sub>p</sub>	32	9.6	13	4.4 × 10 <sup>4</sup>	2.8 × 10 <sup>2</sup>	1.5	20	32	26
PEDOT <sub>4083</sub>	47	14	21	3.0 × 10 <sup>4</sup>	2.2 × 10 <sup>2</sup>	25	45	45	25
PEDOT <sub>8000</sub>	86	26	52	1.4 × 10 <sup>4</sup>	52	74	86	80	–
P <sub>8000</sub> + 1 wt% glycerol (1:1) (single layer)	79	24	36	1.6 × 10 <sup>4</sup>	65	51	74	58	–
P <sub>8000</sub> /P <sub>8000</sub> + 1 wt% glycerol (1:1)	76	23	47	2.6 × 10 <sup>4</sup>	1.2 × 10 <sup>2</sup>	71	74	60	26
P <sub>8000</sub> /P <sub>8000</sub> + 1 wt% glycerol (1:4)	72	21	39	3.1 × 10 <sup>4</sup>	1.9 × 10 <sup>2</sup>	63	72	60	27

LE of 47 cd A<sup>-1</sup> (EQE = 14%) at 4.4 mA cm<sup>-2</sup> (8.1 V) and a peak PE of 21 lm W<sup>-1</sup> was observed at 6.9 V for PEDOT<sub>4083</sub> device, while a peak LE of 32 cd A<sup>-1</sup> (EQE = 9.6%) at 11 mA cm<sup>-2</sup> (8.4 V) and a peak PE of 13 lm W<sup>-1</sup> at 7.5 V for the PEDOT<sub>p</sub> device. At a high forward view luminance of 1000 cd m<sup>-2</sup>, LE and PE for the PEDOT<sub>4083</sub> and PEDOT<sub>8000</sub> device are 44.7 cd A<sup>-1</sup>, 19 m W<sup>-1</sup> and 28 cd A<sup>-1</sup>, 12 lm W<sup>-1</sup>, respectively. It is very important to note, the peak LE, EQE of the PEDOT<sub>8000</sub> device are 1.8 times (=86 cd A<sup>-1</sup>/47 cd A<sup>-1</sup>) of that of route PEDOT<sub>4083</sub> device while the peak PE of the PEDOT<sub>8000</sub> device is 2.5 times (=52 lm W<sup>-1</sup>/21 lm W<sup>-1</sup>) of that of PEDOT<sub>4083</sub> device. Obviously, the above more significant enhancement in PE for PEDOT<sub>8000</sub> device is due to the combination of improved LE (Fig. 1b) and reduced power consumption (Fig. 1c).

In order to get insight of the influence of the anode buffer layer on the transport and injection of hole, and the electrical characteristics of the device, it is necessary to compare the sole current of hole. Fig. 2a presents *J*–*V* characteristics of hole-only devices with the following configuration: ITO/PEDOT:PSS/Emitting layer/Au. It is important to note that the hole carrier density of the device with PEDOT<sub>8000</sub> is 4–5 orders lower in magnitude than that of the PEDOT<sub>p</sub> device and 1–2 orders lower than that of the PEDOT<sub>4083</sub> throughout most of the applied voltage region, indicating effective attenuation of hole flux and an excellent control over electrical leakage. Given the thickness of each PEDOT layer (PEDOT<sub>p</sub>, PEDOT<sub>4083</sub>, and PEDOT<sub>8000</sub>) was 50 nm, 40 nm and 80 nm, respectively, and the nominal resistivity of these three types of PEDOT, the nominal out-of-plane resistance are 2.9 × 10<sup>-5</sup> Ω, 1.2 × 10<sup>-2</sup> Ω–1.2 × 10<sup>-1</sup> Ω, and 4.7–14 Ω, respectively (the cross section area the device is 0.17 cm<sup>2</sup> for our device). The calculation suggests that for all types of PEDOT films, their out-of-plane resistances are actually too small when compared to the intrinsic resistance of the active layer (usually in order of MΩ–GΩ as derived from *I*–*V* curve and can be treat as insulator), also smaller than the sheet resistance of ITO anode (~20 Ω), thus can be neglected. Note that the nominal out-of-plane resistances (which is too small to count) is inconsistent with Fig. 1a because the significant difference in the *J*–*V* characteristics at high voltage region. When the device is operated at high bias region, where huge amount of charge carriers are injected from the electrodes,

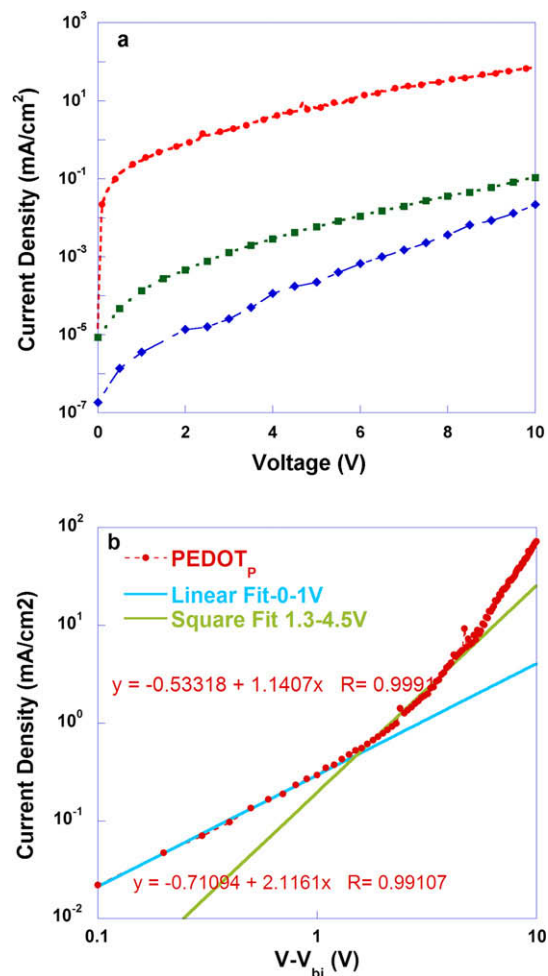


**Fig. 2.** *J*–*V* characteristics of hole-only device in ITO/different types of PEDOT/PVK (70 wt%):PBD (29 wt%):Ir(mppy)<sub>3</sub> (1 wt%)/Au configuration. (b) Double logarithmic plot of the data in (a) to show that the *J*–*V* characteristics are consistent with Ohmic law (slope = 1.1 with *R* = 0.999) at small bias region and SCLC (slope = 2.1 with *R* = 0.991) at higher bias region. Circles are for devices with PEDOT<sub>p</sub>, squares for PEDOT<sub>4083</sub>, and diamonds for PEDOT<sub>8000</sub>.

as a result of the injection, the density of free charge carriers increase accordingly, the conductivity of the active

**Table 2**

Summary of resistivity measurement of several of PEDOT films and their nominal value.

PEDOT buffer layer	PEDOT:PSS ratio	Measured normal resistivity ( $\Omega$ cm)	Measured lateral resistivity ( $\Omega$ cm)	Nominal resistivity ( $\Omega$ cm)	Normal to lateral ratio
PEDOT <sub>p</sub>	1:2.5	$(1.3 \pm 0.07) \times 10^5$	$0.66 \pm 0.22$	1.0	$2.0 \times 10^5$
PEDOT <sub>4083</sub>	1:6	$(2.9 \pm 0.09) \times 10^5$	$(1.9 \pm 0.06) \times 10^3$	500–5000	$1.6 \times 10^2$
PEDOT <sub>8000</sub>	1:20	$(4.3 \pm 0.49) \times 10^6$	$(1.9 \pm 0.33) \times 10^5$	$(1.0–3.0) \times 10^5$	22
P <sub>8000</sub> /P <sub>8000</sub> + 1 wt% glycerol (1:1)	–	$(1.6 \pm 0.54) \times 10^6$	$(4.9 \pm 0.77) \times 10^4$	–	33
P <sub>8000</sub> /P <sub>8000</sub> + 1 wt% glycerol (1:4)	–	$(1.1 \pm 0.23) \times 10^5$	$(6.2 \pm 0.85) \times 10^3$	–	$1.7 \times 10^2$

layer is significantly enhanced by several orders of magnitudes (retain as high as k $\Omega$  to hundreds of  $\Omega$ , but still much higher than that of PEDOT layer). In order to further clarify the different  $J$ – $V$  characteristics at high voltage region, direct measurement on the three types of PEDOT sandwiched between ITO and Au metal contact was performed, revealing that the actual resistance of the buffer layer are  $(3.7 \pm 0.2) \Omega$ ,  $(6.9 \pm 0.2) \Omega$ , and  $(202 \pm 23) \Omega$  for the three types of PEDOT layer in the device, and the calculated resistivity was summarized in Table 2. High resistance of the PEDOT 8000 ( $\sim(202 \pm 23) \Omega$ ), much higher than the nominal value of 4.7  $\Omega$ ) is coherent with the  $J$ – $V$  characteristics at high voltage region shown in Fig. 1a. On the other hand, our simulation shows that for PH 500 and PEDOT 4083 device, an addition resistance of 200–400  $\Omega$  (corresponding to the resistance of PEDOT 8000 layer) could shift the  $J$ – $V$  characteristics of the device towards higher voltage region, similar to that of PEDOT 8000 (not shown), but had no any influence on the small bias region due to their M $\Omega$ –G $\Omega$  of resistance, indicating that the conductivity of PEDOT layer itself only plays minor role on electrical leakage. The effective attenuation of hole flux and an excellent control over electrical leakage in the PEDOT<sub>8000</sub> devices can be attributed to a significantly reduced absolute injection efficiency [21] will occurred, which is defined as the ratio of the actual current to the ideal trap-free, space charge limited current (SCLC), is responsible for the good control over electrical leakage, hole flux attenuation and the subsequent enhanced device performance as a result of more balanced charge injection and transport [22]. This is also supported by photovoltaic measurements [6], which show identical built-in potentials ( $\pm 0.05$  V); thus the reduced absolute injection efficiency is realized via reduced injection height can be ruled out.

Furthermore, as the  $J$ – $V$  characteristics of ITO/PEDOT<sub>p</sub>/EML/Au device in Fig. 2a is replotted in double logarithmic form (Fig. 2b), one can see that the  $J$ – $V$  characteristics fit Ohm's law at small bias and the SCLC model at higher bias region, which is given by Mott–Gurney equation  $J = \frac{9}{8} \mu \epsilon \frac{V^2}{d^3}$ . [23]. Thus, direct electrical leakage bypassing the EML from irregularities of the ITO surface can be neglected: most of the hole flux is injected from the anode into the EML. One can further conclude that electrical leakage and hole flux attenuation are not realized by conductivity changes, but by the contact resistance between isolated PEDOT segments, which in turn significantly influences hole mobility and hole density since the conductivity is gi-

ven by  $\sigma = pq\mu$  [24]. These conditions result in a reduction of the absolute injection efficiency.

Despite the improved LE, EQE and PE obtained using PEDOT<sub>8000</sub>, the peak  $J$  and peak luminance are limited by the large out-of-plane resistance. In light of these challenges, we relied on recent reports that show the conductivity of PEDOT:PSS can be increased by two to three orders of magnitude if the aqueous dispersion is mixed with a small amount of additives [14–16,25–35]. Our approach consists of first spin-coating a thin layer (80 nm) of PEDOT<sub>8000</sub> atop ITO under normal experimental conditions. Subsequently, a second layer of PEDOT<sub>8000</sub> was spun coated after dilution in either 1:1 or 1:4 volume ratios with a water solution containing 1% glycerol. Partial removal of the PEDOT:PSS underlayer takes place, and the thicknesses of the resulting PEDOT:PSS films decreases from 80 nm to 50 nm (1:1), or to 23 nm (1:4). The normal resistivity of the resulting anode buffer layer film determined using  $I$ – $V$  curve sweeps is  $(1.6 \pm 0.54) \times 10^6 \Omega$  cm,  $(1.1 \pm 0.23) \times 10^5 \Omega$  cm (Table 2), in other word, the electrical conductivity of the resulting films were increased by a factor of 1.6 and 39 as compared to the film of PEDOT 8000 (Table 2).

Fig. 3a–c shows the  $J$ – $L$ – $V$ , LE–PE– $J$  and PE– $V$  characteristics of PLEDs with PEDOT<sub>8000</sub> and PEDOT<sub>8000</sub>/PEDOT<sub>8000</sub> + 1 wt% glycerol in either 1:1 or 1:4 ratios. Comparison of the data shows that peak luminance were enhanced by 79% to  $2.6 \times 10^4$  cd m<sup>–2</sup> and 113% to  $3.1 \times 10^4$  cd m<sup>–2</sup>, respectively, with the new buffer combination. More importantly, high luminous efficiency (72–76 cd A<sup>–1</sup>), high power efficiency (39–47 lm W<sup>–1</sup>) and high luminance ( $\sim 2.5 \times 10^4$ – $3.0 \times 10^4$  cd m<sup>–2</sup>) were realized. Even at ca. 10 mA cm<sup>–2</sup> one observes an efficiency of 60 cd A<sup>–1</sup>. At a high forward view luminance of 1000 cd m<sup>–2</sup>, LE and PE for the 1:1 and 1:4 devices are 71 cd A<sup>–1</sup>, 26 m W<sup>–1</sup> and 67 cd A<sup>–1</sup>, 30 lm W<sup>–1</sup>, respectively. In addition, as shown in Fig. 1b and Fig. 3b, as a result of controlling the leakage current at small biases, the LE–PE– $J$  characteristics of the PEDOT<sub>8000</sub> device and the glycerol-modified PEDOT<sub>8000</sub> device display a gradual roll-off from its peak efficiency, which is typically observed at small current region ( $\sim 0.010$ – $1.0$  mA cm<sup>–2</sup>) (Fig. 3b). In contrast, due poor control over electrical leakage current, the LE–PE– $J$  characteristics of the PEDOT<sub>p</sub> and PEDOT<sub>4083</sub> devices adopt a much sharper profile with a much steeper decline in efficiency (Fig. 1b), with the best efficiencies appearing between 1 mA cm<sup>–2</sup> and 10 mA cm<sup>–2</sup>. Also, as a result of more balanced charge carriers in the devices and reduced

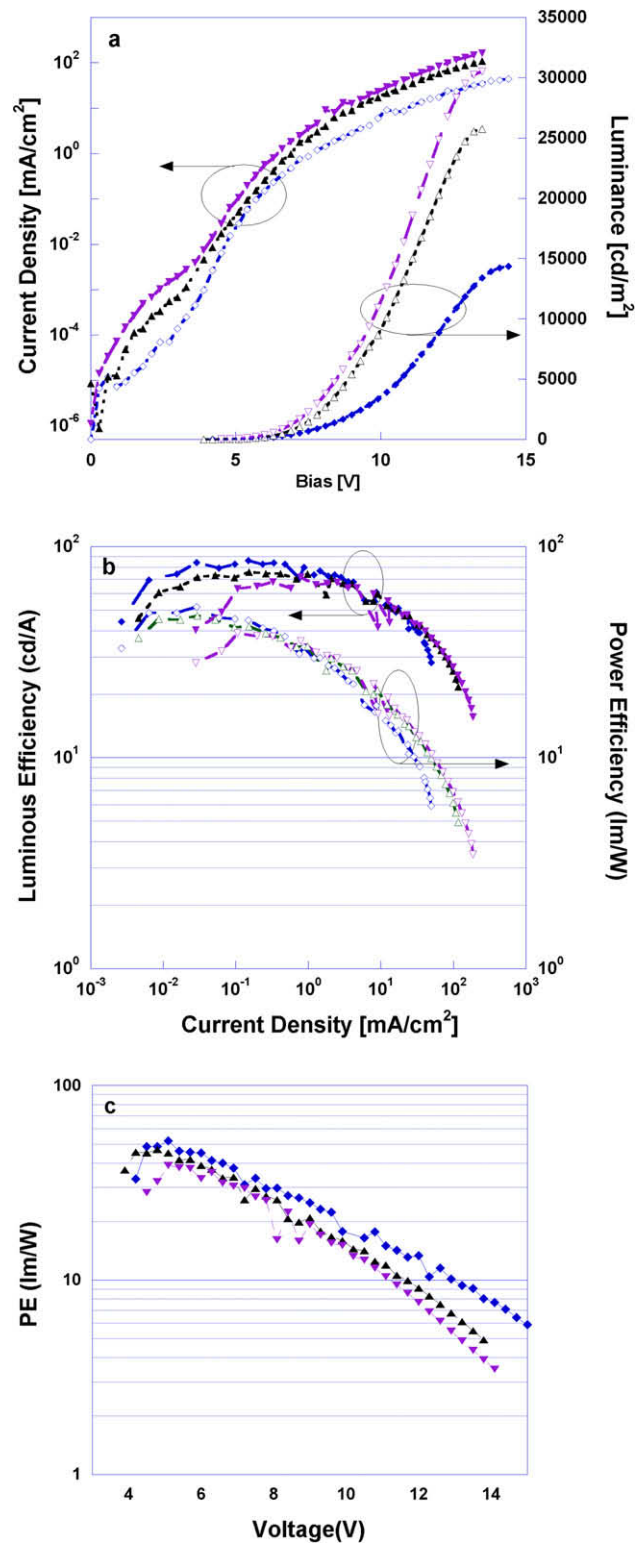


**Fig. 3.** Influence of additive on the PLEDs performance. (a) Current density–voltage ( $J$ – $V$ ) characteristics (filled) and luminance–voltage ( $L$ – $V$ ) characteristics (open); (b) luminous efficiency–current density ( $LE$ – $J$ ) characteristics (filled) and power efficiency–current density ( $PE$ – $J$ ) characteristics (open) for the devices; (c) power efficiency–current density ( $PE$ – $J$ ) characteristics. Diamonds are for PEDOT<sub>8000</sub>, upwards triangles for PEDOT<sub>8000</sub>/PEDOT<sub>8000</sub> + 1 wt% glycerol (=1:1) and downwards triangles for PEDOT<sub>8000</sub>/PEDOT<sub>8000</sub> + 1 wt% glycerol (=1:4).



power consumption, the PE-V characteristics of the PEDOT<sub>8000</sub> device and the glycerol-modified PEDOT<sub>8000</sub> device display a gradual roll-off from its peak efficiency after turn-on (4–5 V, Fig. 3c), while the peak PE for the PEDOT<sub>p</sub>

and PEDOT<sub>4083</sub> devices appeared at 7–8 V, though PE is in inverse proportion to bias.

Moreover, as summarized in Table 1, the efficiencies of the PEDOT<sub>8000</sub> device and the glycerol-modified PEDOT<sub>8000</sub>

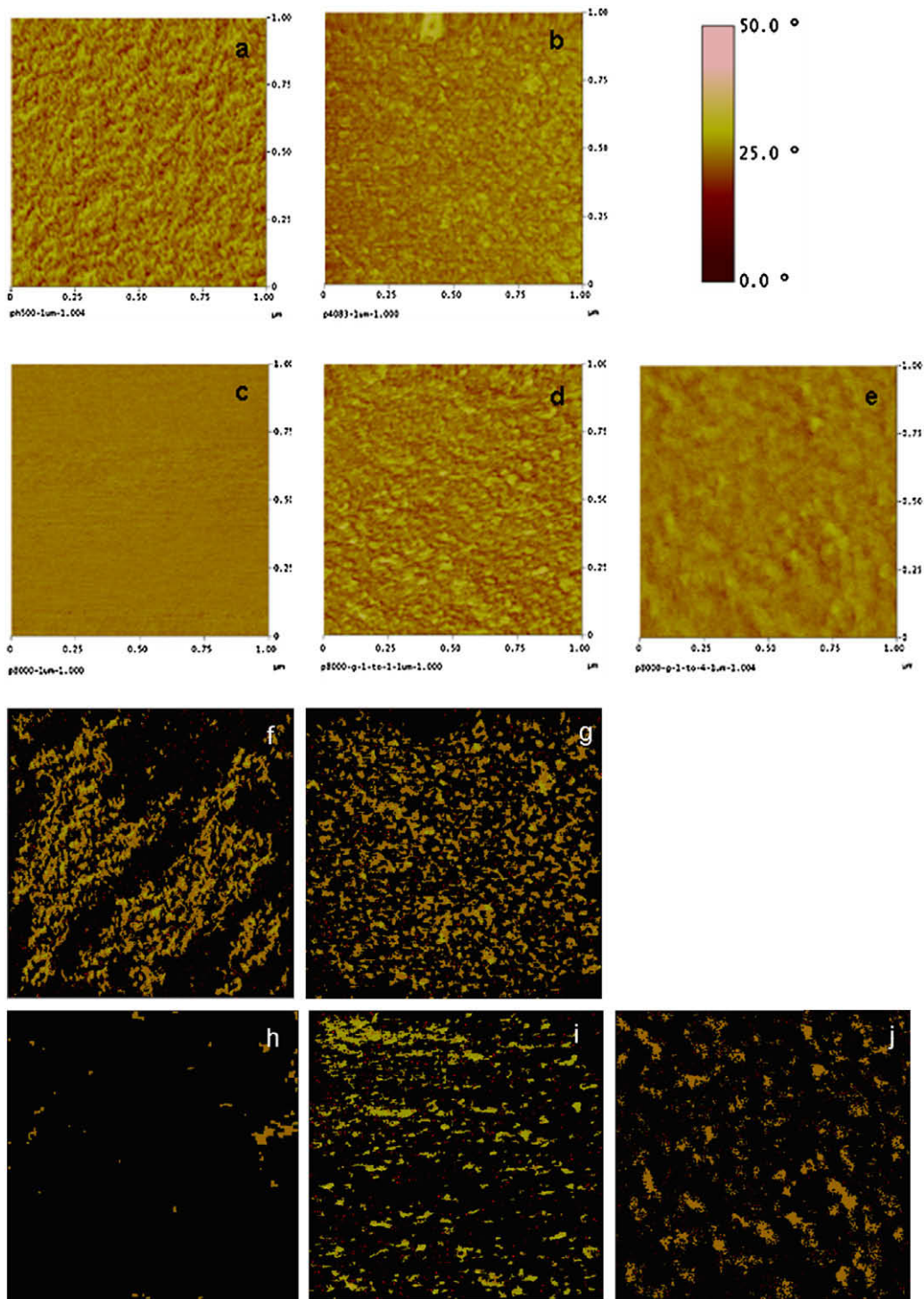


**Fig. 4.** The phase image of the PEDOT films with an area of  $1\mu\text{m} \times 1\mu\text{m}$  as obtained by tapping mode AFM. All films were obtained via spin-coating on ITO substrates and were dried at  $160^\circ\text{C}$ . Panels (a)–(e) correspond to PEDOT<sub>p</sub>, PEDOT<sub>4083</sub>, PEDOT<sub>8000</sub>, PEDOT<sub>8000</sub>/PEDOT<sub>8000</sub>:1 wt% glycerol (1:1) and PEDOT<sub>8000</sub>/PEDOT<sub>8000</sub>:1 wt% glycerol (1:4), respectively. Panels (h)–(j) correspond to the respective off-line image processing and analysis (grain size), performed by DI off-line software (Veeco Corp).

PLEDs at a series of typical current densities (ca. 0.1, 1.0, 10.0 mA cm<sup>-2</sup>) are also superior to those of PEDOT<sub>4083</sub> and PEDOT<sub>p</sub>. These data highlight the importance of controlling the leakage current, and demonstrate a novel and very simple approach to bridge the performance gap between PLEDs and OLEDs. It is also worth pointing out that if PEDOT<sub>8000</sub>:1 wt% glycerol (1:1) is directly spin-coated at top of ITO, the device performance is limited by its high resistance, similar to the neat PEDOT<sub>8000</sub> devices (Table 1).

Atomic force microscopy (AFM) was used to characterize surface morphologies of different PEDOT:PSS films. The phase images of the AFM studies obtained by tapping mode are shown in Fig. 4. Consistent with the different PEDOT:PSS ratios and mean particle/grain size in the three types of materials, for the PEDOT<sub>p</sub> film (Fig. 4a) and PEDOT<sub>4083</sub> (Fig. 4b) films, considerable surface roughness and grain-like features are visible, while a more homogenous film is observed for PEDOT<sub>8000</sub> (Fig. 4c). Phase separation of PEDOT grains and PSS matrix is observed with glycerol treatment. For example, for PEDOT<sub>8000</sub>/PEDOT<sub>8000</sub>:1 wt% glycerol (1:1) (Fig. 4d) and PEDOT<sub>8000</sub>/PEDOT<sub>8000</sub>:1 wt% glycerol (1:4) (Fig. 4e), one observes the emergence of larger grains within a three-dimensional network. These grains can be more clearly seen in Fig. 4f–j in which off-line image processing and analysis (grain size) was applied to the same scans. The observation that incorporation of glycerol leads to increase in granularity is consistent with previously reports [16,32–34]. The changes have been interpreted to be due to a decrease of the overall PSS-to-PEDOT ratio, due to an excess of PSS is washed away upon rinsing with glycerol, as revealed by X-ray and ultraviolet photoelectron spectroscopy [14,28,34,36]. In other word, as a result of excess PSS being washed away and morphology change induced by glycerol and the grains merged [14,32], a three-dimensional network of highly conducting PEDOT/PSS is formed [28,32,34], thus responsible for the enhancement of conductivity.

It is worthy pointing out that the conductivity of PEDOT:PSS film is very anisotropic [35,37–39] due to its unique morphology. Currently, the most common accepted description of film morphology of PEDOT:PSS is that PEDOT-rich grains (islands) are surrounded by lamellas formed by excess PSS [14,28,30,32,37,39]. Thus, the material has a metallic character in the plane of the film, while it behaves more like a dielectric in the direction perpendicular to the plane. Our direct measurement on these films confirm that lateral and normal conductivities may be different by 2–5 orders of magnitude (Table 2), and are consistent with previously reported measurement by a source meter in in-plane/out-of-plane configuration [37] and by conductive atomic force microscopy [39].

The concept can be applied to other emitting layers. PLEDs were fabricated containing a typical poly(*p*-phenylenevinylene) (PPV) derivative, green emitting poly [2-(4-(3',7'-dimethyloctyloxy)-phenyl)-*p*-phenylenevinylene] (P-PPV) [6], and the five types of PEDOT:PSS layers. The device performance observed vary greatly. It was found that PEDOT<sub>8000</sub> and glycerol-modified PEDOT<sub>8000</sub> devices have a peak LE of more than 25 cd A<sup>-1</sup> while 18 cd A<sup>-1</sup> for the PEDOT<sub>4083</sub> device and 3.5 cd A<sup>-1</sup> for the PEDOT<sub>p</sub> device, respectively. In contrast, with poly(9,9-di-*n*-octylfluoro-

rene-*alt*-benzothiadiazole) (F8BT) as the EML, which is a typical n-type EL polymer, [40] the reverse is observed. The PEDOT<sub>4083</sub> device is more efficient than PEDOT<sub>8000</sub> based device, fully consistent with the influence of charge carrier matchup on the efficiency via hole flux attenuation/expansion. Again, our results indicate that for most of PLEDs, in which p-type of organic semiconductor (where mobility of hole is much higher than that of electron) is used as active layer, replacement with PEDOT<sub>8000</sub> and glycerol-modified PEDOT<sub>8000</sub> can lead to significant enhancement in efficiencies, as compared to that of devices with routine PEDOT:PSS.

#### 4. Conclusions

In summary, we report a new approach for the preparation of anode buffer layer for efficient PLEDs by using glycerol to modify relative low conductivity PEDOT<sub>8000</sub>. This new type of anode buffer layer allows for a 50–60% increase in device performance in terms of luminous efficiency, and external quantum efficiency, while 90–130% in power efficiency, as compared to devices fabricated using route PEDOT:PSS with moderate conductivity, without significant loss of peak luminance. Green emitting phosphorescent PLEDs with this modified anode buffer exhibit very high efficiencies, representing a significant step forward to matching and exceeding the efficiencies reported to date with vacuum-deposited small molecular devices. We found that this enhancement stems from good control over leakage and hole flux attenuation in p-type devices, leading to more balanced charge injection and transport. Furthermore, modification with glycerol can significantly enhance the conductivity of typically low conducting types of PEDOT:PSS by a magnitude of 1–2 orders as a result of the film morphology and structure change. This modified PEDOT:PSS retains excellent properties of good control over electrical leakage, while at the same time it does not cause appreciable potential drop due to its low serial out-of-plane resistance. We anticipate that these findings can provide a simple experimental procedure for improvement of PLEDs.

#### Acknowledgements

H.B.W. and Y.C. are grateful to the Ministry of Science and Technology Project (No. 2009CB623602) and the Natural Science Foundation of China (Project No. 50433030 and U0634003) and 863 project/GD provincial project (No. 2006AA03A160, 2007A010500011) for the financial support. H.B.W. also acknowledge the China Postdoctoral Science Foundation for the financial support (20060400215).

#### References

- [1] J.H. Burroughes, D.D.C. Bradley, A.R. Brown, R.N. Marks, K. MacKay, R.H. Friend, P.L. Burn, A.B. Holmes, *Nature (London)* 347 (1990) 539.
- [2] S. Su, T. Chiba, T. Takeda, J. Kido, *Adv. Mater.* 20 (2008) 2125.
- [3] G.F. He, M. Pfeiffer, K. Leo, M. Hofmann, J. Birnstock, R. Pudzich, J. Salbeck, *Appl. Phys. Lett.* 85 (2004) 3911.

- [4] C. Adachi, M.A. Baldo, S.R. Forrest, M.E. Thompson, *Appl. Phys. Lett.* 77 (2000) 904.
- [5] Y.T. Tao, Q. Wang, C.L. Yang, Q. Wang, Z.Q. Zhang, T.T. Zou, J.G. Qin, D.G. Ma, *Angew. Chem. Int. Ed.* 47 (2008) 8104.
- [6] H. Wu, F. Huang, Y. Mo, W. Yang, D. Wang, J. Peng, Y. Cao, *Adv. Mater.* 16 (2004) 1826.
- [7] W.R. Salaneck, K. Seki, A. Kahn, J.J. Pireaux (Eds.), *Conjugated Polymer and Molecular Interfaces: Science and Technology for Photonic and Optoelectronic Applications*, Marcel Dekker, New York, 2001.
- [8] Y. Cao, G. Yu, C. Zhang, R. Menon, A.J. Heeger, *Synth. Met.* 87 (1997) 171.
- [9] L.B. Groenendaal, F. Jonas, D. Freitag, H. Pielartzik, J.R. Reynolds, *Adv. Mater.* 12 (2000) 481.
- [10] S. Kirchmeyer, K. Reuter, *J. Mater. Chem.* 15 (2005) 2077.
- [11] T.M. Brown, J.S. Kim, R.H. Friend, F. Cacialli, R. Daik, W.J. Feast, *Appl. Phys. Lett.* 75 (1999) 1680.
- [12] W. Shi, S.Q. Fan, F. Huang, W. Yang, R.S. Liu, Y. Cao, *J. Mater. Chem.* 16 (2006) 2387.
- [13] S. Ghosh, J. Rasmusson, O. Inganäs, *Adv. Mater.* 10 (1998) 1097.
- [14] S.K.M. Jonsson, J. Birgerson, X. Crispin, G. Greczynski, W. Osikowicz, A.W. Denier van der Gon, W.R. Salaneck, M. Fahlman, *Synth. Met.* 139 (2003) 1.
- [15] J. Ouyang, C.W. Chu, F.C. Chen, Q.F. Xu, Y. Yang, *Adv. Funct. Mater.* 15 (2005) 203.
- [16] J. Ouyang, Q. Xu, C.W. Chu, Y. Yang, Gang Li, J. Shinar, *Polymer* 45 (2004) 8443.
- [17] P.A. Levermore, L. Chen, X. Wang, R. Das, D.D.C. Bradley, *Adv. Mater.* 19 (2007) 2379.
- [18] K. Fehse, K. Walzer, K. Leo, W. Lövenich, A. Elschner, *Adv. Mater.* 19 (2007) 441.
- [19] <<http://www.hcstarck.com>>.
- [20] M.A. Baldo, D.F. O'Brien, Y. You, A. Shoustikov, S. Sibley, M.E. Thompson, S.R. Forrest, *Nature* 395 (1998) 151.
- [21] A.J. Campbell, D.D.C. Bradley, H. Antoniadis, *J. Appl. Phys.* 89 (2001) 3343.
- [22] S.J. Konezny, D.L. Smith, M.E. Galvin, L.J. Rothberg, *J. Appl. Phys.* 99 (2006) 064509.
- [23] M.A. Lamper, P. Mark, *Current Injection in Solids*, Academic, New York, 1970.
- [24] S.M. Sze, *Physics of Semiconductor Devices*, second ed., John Wiley & Sons, New York, 1981.
- [25] F. Zhang, M. Johansson, M.R. Andersson, J.C. Hummelen, O. Inganäs, *Adv. Mater.* 14 (2002) 662.
- [26] J.Y. Kim, J.H. Jung, D.E. Lee, J. Joo, *Synth. Met.* 126 (2002) 311.
- [27] W.H. Kim, A.J. Ma kinen, N. Nikolov, R. Shashidhar, H. Kim, Z.H. Kafafi, *Appl. Phys. Lett.* 80 (2002) 3844.
- [28] X. Crispin, S. Marciniak, W. Osikowicz, G. Zotti, A.W. Denier Van Der Gon, F. Louwet, M. Fahlman, L. Groenendaal, F.D.E. Schryver, W.R. Salaneck, *J. Polym. Sci. B: Polym. Phys.* 41 (2003) 2561.
- [29] G. Zotti, S. Zecchin, G. Schlavon, F. Louwet, L. Groenendaal, X. Crispin, W. Osikowicz, W. Salaneck, M. Fahlman, *Macromolecules* 36 (2003) 3337.
- [30] M.M. de Kok, M. Buechel, S.I.E. Vulto, P. van de Weijer, E.A. Meulenkamp, S.H.P.M. de Winter, A.J.G. Mank, H.J.M. Vorstenbosch, C.H.L. Weijtens, V. van Elsbergen, *Phys. Stat. Sol. (a)* 201 (2004) 1342.
- [31] J. Huang, P.F. Miller, J.S. Wilson, A.J. de Mello, J.C. de Mello, D.D.C. Bradley, *Adv. Funct. Mater.* 15 (2005) 290.
- [32] S. Timpanaro, M. Kemerink, F.J. Touwslager, M.M. De Kok, S. Schrader, *Chem. Phys. Lett.* 394 (2004) 339.
- [33] H.J. Snaith, H. Kenrick, M. Chiesa, R.H. Friend, *Polymer* 46 (2005) 2573.
- [34] X. Crispin, F.L.E. Jakobsson, A. Crispin, P.C.M. Grim, P. Andersson, A. Volodin, C. van Haesendonck, M. Van der Auweraer, W.R. Salaneck, M. Berggren, *Chem. Mater.* 18 (2006) 4354.
- [35] A.M. Nardes, R.A.J. Janssen, M. Kemerink, *Adv. Funct. Mater.* 18 (2008) 865.
- [36] G. Greczynski, Th. Kugler, W.R. Salaneck, *Thin Solid films* 354 (1999) 129.
- [37] A.M. Nardes, M. Kemerink, R.A.J. Janssen, J.A.M. Bastiaansen, N.M.M. Kiggen, B.M.W. Langeveld, A.J.J.M. van Breemen, M.M. de Kok, *Adv. Mater.* 19 (2007) 1196.
- [38] K.E. Aasmundtveit, E.J. Samuelsen, L.A.A. Pettersson, O. Inganäs, T. Johansson, R. Feidenhans'l, *Synth. Met.* 101 (1999) 561.
- [39] C. Ionescu-Zanetti, A. Mechler, S.A. Carter, R. Lal, *Adv. Mater.* 16 (2004) 385.
- [40] C.L. Donley, J. Zaumseil, J.W. Andreasen, M.M. Nielsen, H. Sirringhaus, R.H. Friend, J.-S. Kim, *J. Am. Chem. Soc.* 127 (2005) 12890.

Quantum–mechanical calculations based on density–functional theory (DFT) have been successful in understanding the interfacial properties of self-assembled monolayers (SAMs) chemically adsorbed on metal surfaces [15–18]; however, fewer DFT studies have been reported on weakly interacting interfacial systems, where the molecules forming the monolayer are physically adsorbed on the metal surface [19–22]. Previous DFT calculations [20,21] optimized the pentacene adsorption geometry on the Au(0 0 1) surface while assuming a flat-lying geometry of the pentacene molecules with their molecular planes parallel to the surface.

Here, we report on a DFT study of the interface made of a pentacene monolayer adsorbed on the Au(1 1 1) surface. The equilibrium structure and adsorption energy of the pentacene monolayer, the work–function change of the Au(1 1 1) surface upon pentacene adsorption, and the energy level alignment at the interface are calculated and compared with recent experimental data [3,5,7,10,12–14]. In addition, the band structures of the pentacene–Au interface are analyzed in detail to extract the electronic couplings between the HOMO level of pentacene and the gold surface and between adjacent pentacene molecules within the monolayer.

## 2. Methodology

We use a repeated–slab approach and model the Au(1 1 1) surface with a  $c(\sqrt{3} \times 6)$  surface unit cell with lateral unit cell parameters  $a = 5.11 \text{ \AA}$  and  $b = 17.71 \text{ \AA}$  along the  $\langle 112 \rangle$  and  $\langle 1\bar{1}0 \rangle$  directions. The surface unit cell parameters are derived from the optimized bulk gold lattice parameter without taking into account the Au(1 1 1) surface reconstruction [23–28], as discussed in Ref. [15]. In the direction perpendicular to the  $c$ -axis ( $\langle 111 \rangle$  direction) of the unit cell, a slab consisting of five layers of gold atoms is used to model the surface, with each layer containing 12 gold atoms (resulting in 60 gold atoms per unit cell). The gold atoms within the top two layers of the slab are fully relaxed while the bottom three layers are frozen (see the lateral view in Fig. 1a). The  $c$  lattice parameter of the unit cell is taken to be  $45.28 \text{ \AA}$ ; since the thickness of the relaxed gold slab is about  $10 \text{ \AA}$ , this leaves a vacuum gap of about  $35 \text{ \AA}$  between each repeated gold slab along the  $c$ -direction (which effectively prevents any interactions from slab to slab).

To model the monolayer coverage, each surface unit cell of the gold is made to accommodate one pentacene molecule. Interestingly, the experimental observed surface lattice parameters of the pentacene monolayer on the gold surface ( $a = 5.76 \text{ \AA}$ ,  $b = 15.3 \text{ \AA}$ ,  $\gamma = 79.1^\circ$  [10] or  $a = 5.7 \text{ \AA}$ ,  $b = 15.5 \text{ \AA}$ ,  $\gamma = 84^\circ$  [12]) are different from those of the clean gold surface unit cell. However, it would be very difficult to model two sets of non-commensurate lattice parameters in a DFT calculation under periodic boundary conditions; to take into account the lattice parameters for both the gold surface and the pentacene monolayer at the same time, a much larger super cell would need to be adopted, which would be computationally unpractical. Therefore, in the present study

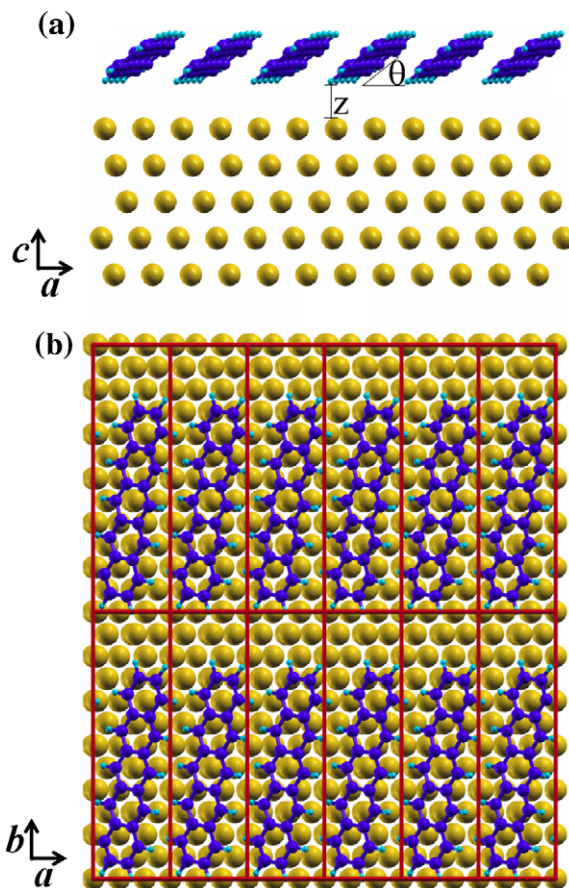


**Fig. 1.** Side view (a) and top view (b) of the relaxed structure of the pentacene–Au interface. In (a), the adsorption height  $z$  (defined as the distance between the lowest hydrogen atom of the pentacene molecule and the average height of the gold atoms in the top layer of the slab, projected along the lattice  $c$ -direction) is equal to  $3.13 \text{ \AA}$ ; the tilt angle between the pentacene molecular plane and the gold surface  $\theta$ , is equal to  $37.7^\circ$ . The surface unit cell is indicated by the red contour in (b). (For interpretation of the references in colour in this figure legend, the reader is referred to the web version of this article.)

where the  $a$  lattice parameter is taken to be  $5.11 \text{ \AA}$ , neighboring pentacene molecules are constrained to lay at a distance *ca.*  $0.6\text{--}0.65 \text{ \AA}$  shorter than the one experimentally observed; this is expected to slightly affect the optimization of the pentacene adsorption geometry due to the increased steric hindrance, as we will discuss below.

As a starting geometry, the pentacene molecules were positioned  $2.48 \text{ \AA}$  (measured as the distance between the lowest hydrogen atom of the pentacene molecule and the average height of the gold atoms in the top layer of the slab, projected along the lattice  $c$ -direction) above the clean Au(1 1 1) surface, with their molecular long axis parallel to the surface along one of the diagonals in the surface unit cell (see the top view in Fig. 1b), and the molecular plane perpendicular to the Au(1 1 1) substrate. The vacuum gap between the top atom of the pentacene molecule and the next gold slab is then larger than  $28 \text{ \AA}$ . All atoms in the pentacene molecule and in the top two layers of gold surface slab

were relaxed using a damped molecular dynamics scheme until the remaining forces were lesser than 0.03 eV/Å.

The DFT calculations were performed with plane-wave basis sets with an energy cutoff of 22 Ryd to expand the Kohn–Sham orbitals of the valence electrons; the projector augmented-wave (PAW) method [29,30] was used to describe the core electrons and valence–core interactions. The generalized gradient approximation (GGA) exchange–correlation functional of Wang and Perdew [31] was chosen since it was found earlier to perform better than other traditional functionals for weakly bonded systems [32]. All calculations were carried out using the VASP code [33]. In all slab calculations (including the Au(1 1 1) surface, the pentacene–Au interface, and the isolated pentacene monolayer where the molecules are maintained in their optimized adsorption geometry), a  $8 \times 3 \times 1$  Monkhorst–Pack  $k$ -point grid [34] was used for both geometry optimizations and total energy calculations. A Methfessel–Paxton occupation scheme [35] with a broadening of 0.2 eV was employed in all calculations.

To compute the total energy of an isolated pentacene molecule, a periodically repeated box of  $16 \times 27 \times 17 \text{ \AA}^3$  was used with the pentacene molecule sitting at the center of the box. For this large supercell, only the  $\Gamma$ -point was used in the geometry optimization and total energy calculation.

To compensate for the dipole resulting from the consideration of asymmetric slabs, a dipole sheet is introduced in the middle of the vacuum gap [36]. This procedure allows one to properly extract the electrostatic potentials on both sides away from the asymmetric slabs.

For the pentacene–Au interface, as well as for the isolated pentacene monolayer, the electronic coupling for the highest occupied molecular orbital (HOMO) or lowest un-occupied molecular orbital (LUMO) between neighboring pentacene molecules within the monolayer, was estimated from the band dispersion corresponding to each orbital. The electronic coupling between the pentacene monolayer and the Au(1 1 1) surface was extracted from the band-structure calculations by solving the following eigen-function equation based on the tight-binding model:

$$\begin{pmatrix} \varepsilon_1 & V_{12} \\ V_{12} & \varepsilon_2 \end{pmatrix} \Psi = E\Psi \quad (1)$$

where  $V_{12}$  is the electronic coupling and  $\varepsilon_1$  and  $\varepsilon_2$  denote the energies of the unperturbed states of the pentacene monolayer and Au(1 1 1) surface;  $E$  is the eigen-value of the corresponding eigen-state  $\Psi$ , which comprises the contributions of both the monolayer and the Au(1 1 1) surface. Based on the eigen-value  $E$  and eigen-state  $\Psi$  extracted from the band-structure calculations, the electronic coupling  $V_{12}$  is obtained by solving Eq. (1). Since the main goal of our band-structure calculations was to extract the electronic couplings between neighboring pentacene molecules within a monolayer and between the pentacene monolayer and the gold surface, the spin polarization and spin–orbit interactions for the gold atoms were not taken into account in these calculations.

### 3. Results and discussion

#### 3.1. Gold surface

The structure of the Au(1 1 1) surface was optimized first. After full relaxation of the top two layers of gold atoms in the slab, the work-function of the surface slab ( $\Phi_{\text{Au}}$ ) was calculated as the energy difference between the Fermi energy ( $E_{\text{F}}$ ) of the surface and the electrostatic potential energy ( $V_{\text{vac}}$ ) of an electron in the vacuum region at the distance where the potential energy has reached its asymptotic value. For the  $c(\sqrt{3} \times 6)$  surface unit cell used in our calculation, the work-function is calculated to be 5.25 eV; this value agrees very well with the reported results of 5.2–5.35 eV from both experimental [37–39] and computational studies [15,40].

#### 3.2. Pentacene adsorption geometry

Starting from the separately optimized geometries of the clean gold surface and the isolated pentacene molecule, the pentacene–Au interface system was relaxed from the starting geometry described above, in the following sequence: at first, only the pentacene monolayer was relaxed while the gold slab remained frozen; then both the pentacene monolayer and the top two layers of the gold slab were relaxed simultaneously.

After geometry optimization, the pentacene molecules are found to tilt towards the gold surface with a tilt angle  $\theta = 37.7^\circ$  due to a rotation along the molecular long axis, which remains parallel to the surface (see Fig. 1a). The molecular long axis also slightly rotates towards the  $b$ -direction of the lattice with respect to its original direction along the unit cell diagonal and forms an angle of about  $81^\circ$  with the  $a$ -direction; this value agrees very well with the  $\gamma$  angle ( $79.1^\circ$  or  $84^\circ$ ) reported from STM experiments [10,12]. The optimized tilt angle of pentacene ( $\theta = 37.7^\circ$ ) is larger than the one measured in NEXAFS experiments ( $\theta = 13^\circ$ ) [14]. This difference can be attributed to the shorter distance between neighboring pentacene molecules along the molecular short axis that we were forced to consider in our computations, as discussed in Section 2. In spite of the numerical difference in tilt angle  $\theta$ , it is clear that the pentacene molecules tend to lean towards the gold surface in the course of the geometry optimization of the interface, rather than keep the initial perpendicular orientation of the molecular plane, even though the steric hindrance can prevent reaching a more flat configuration.

The perpendicular distance between the lowest hydrogen atom of the adsorbed pentacene molecule and the gold surface (as defined in Section 2) is found to be 3.13 Å, about 0.4 Å lower than the adsorption height (3.52 Å) previously calculated for the Au(0 0 1) surface [21]. To further characterize the sensitivity of the interface to the adsorption height, the total energy of the pentacene–Au system was calculated by shifting the pentacene molecule along the  $c$ -direction around the optimized position, while keeping the optimized structures of both pentacene molecules and gold substrate. The total energy vs. the shift  $Z$  is given

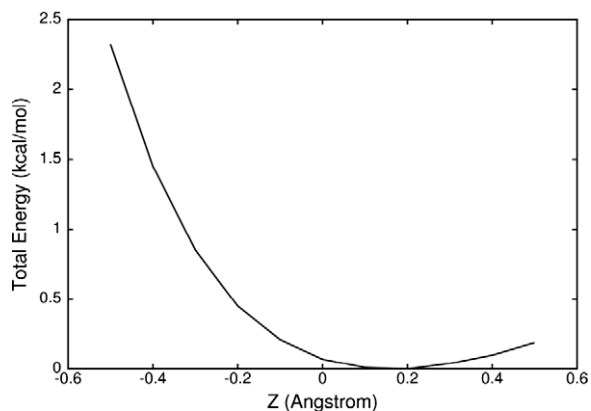


**Fig. 2.** Total energy of the pentacene–Au interface as a function of a shift of the pentacene molecules along the  $c$ -direction (the geometries of the pentacene molecules and gold slab are kept rigid);  $Z = 0$  corresponds to the fully optimized situation (we note that the extreme flatness of the potential energy surface between in the range  $Z \sim 0.0$ – $0.4$  Å does not allow for a very accurate determination of the optimal  $Z$  distance).

in Fig. 2. The main result is that the potential energy surface remains very flat for distance  $Z$  between  $-0.2$  and  $+0.5$  Å from the optimized distance. Thus, small fluctuations in pentacene–Au distance can be expected (such small fluctuations do not change the work-function of the modified Au(1 1 1) surface to any appreciable extent, see Section 3.5 below).

### 3.3. STM image

Based on the optimized structure of the pentacene–Au interface, the constant-current STM image was simulated using a tip voltage of  $-0.6$  V and compared with the experimental image reported in Ref. [12], see Fig. 3. The overall appearance of the simulated STM image is in very good agreement with experiment. In the simulated STM image, the angle formed between the molecular long axis and the  $a$ -vector (parallel to the dark zig-zag stripe) is about  $81^\circ$ , which agrees very well with the angle  $\gamma$  ( $84^\circ$ ) measured

in the STM experiment and shown in Fig. 3a [12] (note that the molecular long axis is taken as lattice vector  $b$  in Ref. [12], which corresponds to a notation different from ours).

### 3.4. Adsorption energy

The adsorption energy  $E_{\text{ads}}$  per pentacene molecule is calculated as:

$$E_{\text{ads}} = E_{\text{PEN-Au}} - E_{\text{Mol}} - E_{\text{Au}} \quad (2)$$

where  $E_{\text{PEN-Au}}$  is the energy of the pentacene–Au system,  $E_{\text{Mol}}$  is the energy of an isolated pentacene molecule and  $E_{\text{Au}}$  is the energy of the clean Au(1 1 1) slab. The adsorption energy is calculated to be  $-0.16$  eV, which is *ca.* 0.1 eV smaller than the adsorption energy ( $-0.28$  eV) calculated previously by Lee et al. [20] for a pentacene molecule adsorbed on the Au(0 0 1) surface, using the GGA functional of Perdew–Burke–Ernzerhof [41]. It was also found by these authors that the local density approximation (LDA) tends to overestimate the adsorption energy ( $-3.2$  eV for pentacene on Au(0 0 1) surface), while a GGA functional tends to underestimate it. The adsorption energy measured by temperature-programmed desorption (TPD) experiments is on the order of  $-1.1$  eV [10] for a pentacene monolayer on the Au(1 1 1) surface. The large discrepancy between the computational results and experiment is due to the lack of consideration of dispersion interactions in the exchange–correlation functional used in the present DFT approach. This is definitely an issue that warrants further improvement.

### 3.5. Work-function modification

The work-function of the gold surface modified by the pentacene monolayer was calculated in the same way as for the clean gold surface; the result is given in the upper panel of Fig. 4. Upon adsorption of the monolayer, the work-function of the modified gold surface ( $\Phi_{\text{PEN-Au}}$ ) becomes 4.29 eV; this corresponds to a work-function decrease of 0.96 eV with respect to the clean Au(1 1 1) surface ( $\Phi_{\text{Au}} = 5.25$  eV). This calculated work-function

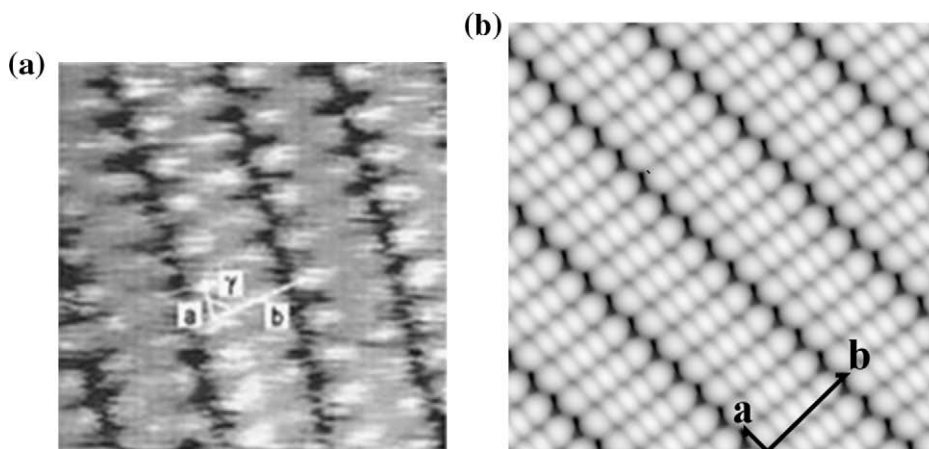


**Fig. 3.** Comparison between: (a) the experimental constant-current STM image at a bias voltage  $V_s = -0.6$  eV from Ref. [12] over an area of  $5.6$  nm  $\times$   $5.6$  nm; and (b) the calculated constant-current STM image from  $E_F$  to  $(E_F - 0.6)$  eV over an area of  $7.8$  nm  $\times$   $8.2$  nm.

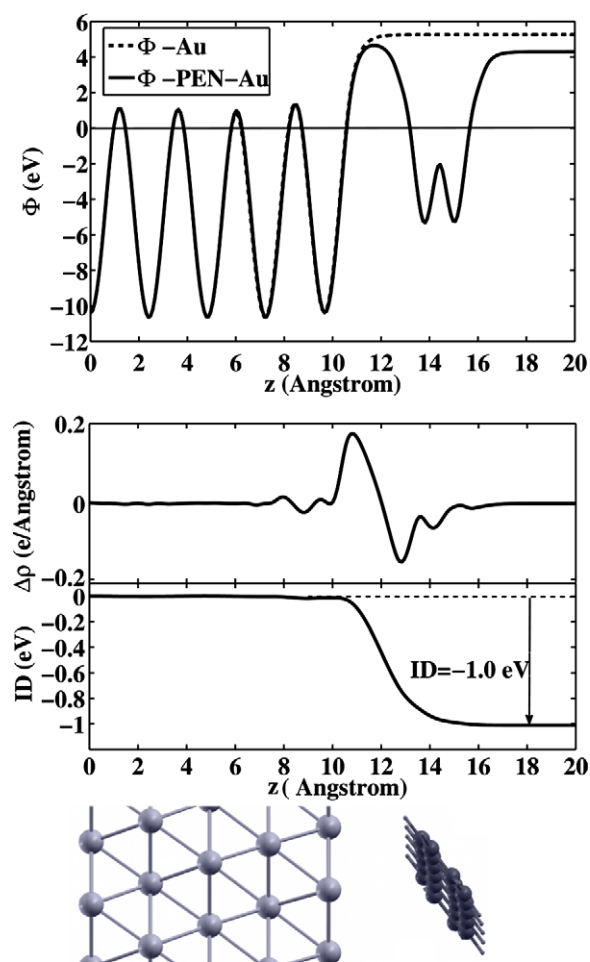


**Fig. 4.** Electrostatic potentials for the clean Au(111) surface and the pentacene–Au interface (upper panel); charge density difference upon monolayer adsorption and interface dipole (ID) obtained by solving the Poisson equation (lower panel). The Fermi level is set at zero. The locations of the gold slab and pentacene molecule are illustrated at the bottom.

modification ( $\Delta\Phi = -0.96$  eV) is in excellent agreement with the value recently reported based on angle-resolved UPS (ARUPS) experiments, there the work-function change of the clean gold surface upon adsorption of a pentacene monolayer was measured to be  $-0.95$  eV [7].

In the course of our previous theoretical work on self-assembled monolayers chemically bonded on the metal surface [15–18], the work-function change  $\Delta\Phi$  of the metal was decomposed into two largely independent contributions coming from the bond dipole around the metal–molecule bond and the electrostatic potential energy step ( $\Delta U_{\text{vac}}$ ) across the monolayer itself. Here, as expected from the non-polar character of the molecule and near-flatness of the monolayer over the surface, the contribution to the work-function change due to the potential energy step across the isolated pentacene monolayer is very small (0.04 eV). The potential energy change due to the charge redistribution within the pentacene–Au interface region (that we define here as the interface dipole, ID, since no chemical

bond is formed between the pentacene and the gold surface) can be derived by solving the Poisson equation:

$$\frac{d^2V(z)}{dz^2} = -\frac{1}{\epsilon_0} \Delta\rho(z) \quad (3a)$$

$$\Delta\rho(z) = \rho_{\text{PEN-Au}}(z) - \rho_{\text{Au}}(z) - \rho_{\text{PEN}}(z) \quad (3b)$$

where  $V(z)$  represents the electrostatic potential energy,  $\epsilon_0$  the vacuum permittivity, and  $\Delta\rho(z)$  the averaged surface-charge-density difference over the  $ab$  plane; the three terms on the r.h.s. of Eq. (3b) denote the plane-averaged surface charge densities for the pentacene–Au interface system, the clean Au(111) surface, and the isolated pentacene monolayer (evaluated with the same geometric structure as in the pentacene–Au system), respectively. The central panel of Fig. 4 shows the charge difference  $\Delta\rho$  and induced electrostatic potential energy  $V$  as a function of the distance  $z$  taken from the bottom of the slab. The charge difference  $\Delta\rho$  changes from slightly negative to positive upon crossing of the gold surface (near  $z \sim 10$  Å) and reaches a maximum at  $z \sim 11$  Å; it then becomes negative in the space between gold and pentacene ( $z \sim 12$  Å), and reaches a minimum at the lower edge of the monolayer. This evolution neatly illustrates the push-back of the gold electron density towards the surface due to pentacene adsorption, i.e., the so-called pillow effect referred to by experimentalists [7]. Correspondingly, the potential energy  $V(z)$  (see the lower panel of Fig. 4) is flat inside the gold slab, then drops abruptly by 1.0 eV in the region from  $z \sim 10$ –14 Å, and finally flattens again in the region high above the adsorbed monolayer. This potential energy change of  $-1.0$  eV is by far the dominant contribution to the total work-function change of  $-0.96$  eV, with the potential energy step ( $\Delta U_{\text{vac}}$ ) due to the pentacene monolayer providing only a very small contribution (+0.04 eV). Thus, the total work-function modification ( $\Delta\Phi$ ) can be well expressed as the sum of the vacuum potential energy step ( $\Delta U_{\text{vac}}$ ) and the interface dipole (ID):

$$\Delta\Phi = \Delta U_{\text{vac}} + \text{ID} = 0.04 - 1.00 = -0.96 \text{ eV} \quad (4)$$

This result is consistent with the conclusions obtained from our analysis of chemically bonded SAM-metal systems [15–18,42].

Since fluctuations of the pentacene–Au distance can be expected, we also calculated the total work-function modification  $\Delta\Phi$  of the pentacene–Au interface for two adsorption distances larger by 0.2 and 0.5 Å than the optimized pentacene–Au distance. The corresponding work-function modifications were calculated to be  $-0.95$  and  $-0.89$  eV, respectively, that is 0.01 and 0.07 eV smaller than for the optimized distance. Such small variations in work-function modifications are within the usual experimental resolution of UPS measurements and do not affect our main results neither qualitatively nor quantitatively.

### 3.6. Energy level alignments

The energies of the levels corresponding predominantly to pentacene molecular orbitals (MOs) in the interface system can be resolved by projecting the total density of

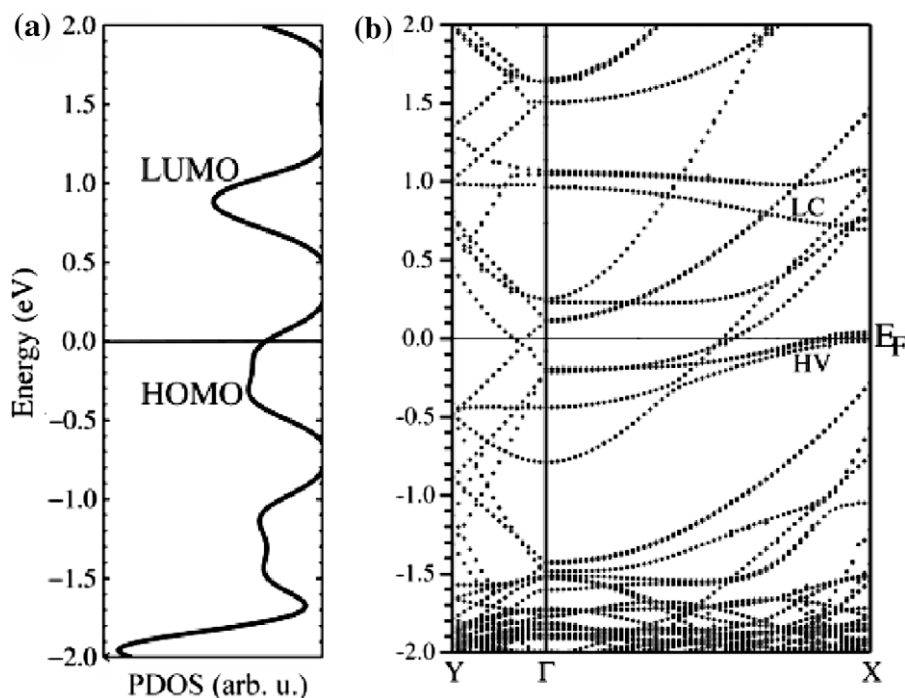


**Fig. 5.** (a) Density of states projected onto the pentacene molecule, PDOS (note that the horizontal axis runs from right to left); (b) band-structure of the pentacene–Au system along the  $\Gamma X$  ( $a$ -axis) and  $\Gamma Y$  ( $b$ -axis) directions. The Fermi energy is set at zero. For the sake of clarity, the bands comprising mainly the contributions from the  $d$ -orbitals of the gold atoms in the bulk-like states are removed from the plot.

states (DOS) into the molecular region. Fig. 5a shows the DOS projected to all carbon atoms in the pentacene monolayer for the pentacene–Au system. Below the Fermi energy ( $E_F$ ), the projected density of states (PDOS) shows a broad HOMO band spanning about 0.6 eV, with a tail extending over  $E_F$ . The LUMO band is centered at 0.9 eV above the Fermi energy, and is about 0.2 eV narrower than the HOMO band. The charge density distributions corresponding to the contributions from both the HOMO level of the pentacene molecule and the gold surface in the pentacene–Au interface system are shown in Fig. 6 and compared to the HOMO and LUMO levels of isolated pentacene in Fig. 7.

The ARUPS spectra of a pentacene monolayer on gold have recently been reported (see Fig. 1d in Ref. [7]). The calculated occupied PDOS width of 0.6 eV agrees well with the width of the pentacene HOMO band in Ref. [7]. However, there is a significant discrepancy in the energy level alignment between theory and experiment. In the ARUPS spectra, the onset of the pentacene HOMO band is found *ca.* 0.7 eV below the Fermi level of the gold surface. This discrepancy between the theoretical and experimental results is related to the lack of many-body correlation effects in the Kohn–Sham single-particle approximation used in the current DFT method; as a consequence, the excited-state energies and surface polarization response are not adequately treated and the energetic positions of molecular frontier orbitals with respect to the Fermi energy of the metal contact cannot be described accurately [43,44]. A further study based on the GW approximation [45] is currently in progress.

### 3.7. Pentacene–pentacene in-plane coupling vs. pentacene–gold coupling

To estimate the electronic coupling of the HOMO and LUMO levels between neighboring pentacene molecules within the monolayer, as well as the coupling between the monolayer and the gold surface, we calculated the band structures of the pentacene–Au system along the  $\Gamma Y$  ( $b$ -direction of the unit cell) and  $\Gamma X$  directions ( $a$ -direction of the unit cell) in reciprocal space (see Fig. 5b). Along the  $b$ -direction, since the intermolecular interactions between rows of pentacene molecules are very weak due to the large intermolecular distances (see Fig. 1), the two bands corresponding to the HOMO and LUMO levels of the pentacene monolayer (or highest valence (HV) band and lowest conduction (LC) band) are flat along  $\Gamma Y$ . Along the  $\Gamma X$  direction, the HV band shows a dispersion of *ca.* 0.43 eV (starting at *ca.* 0.4 eV below  $E_F$  from  $\Gamma$  and ending at *ca.* 0.03 eV above  $E_F$  at X). In a tight-binding context, this leads to an in-plane electronic coupling of *ca.* 0.11 eV for the HOMO level of the monolayer along the  $a$ -direction. The LC band dispersion along the same direction is about 0.27 eV, which corresponds to an in-plane electronic coupling of *ca.* 0.07 eV for the LUMO level. In addition to the smaller intramolecular electron–vibration coupling calculated for holes than electrons in the pentacene molecule [46], this result points to better transport properties for holes than for electrons along the pentacene layer.

The electronic coupling between the adsorbed monolayer and the gold surface is estimated by comparing the band structures for the gold surface in the pentacene–Au



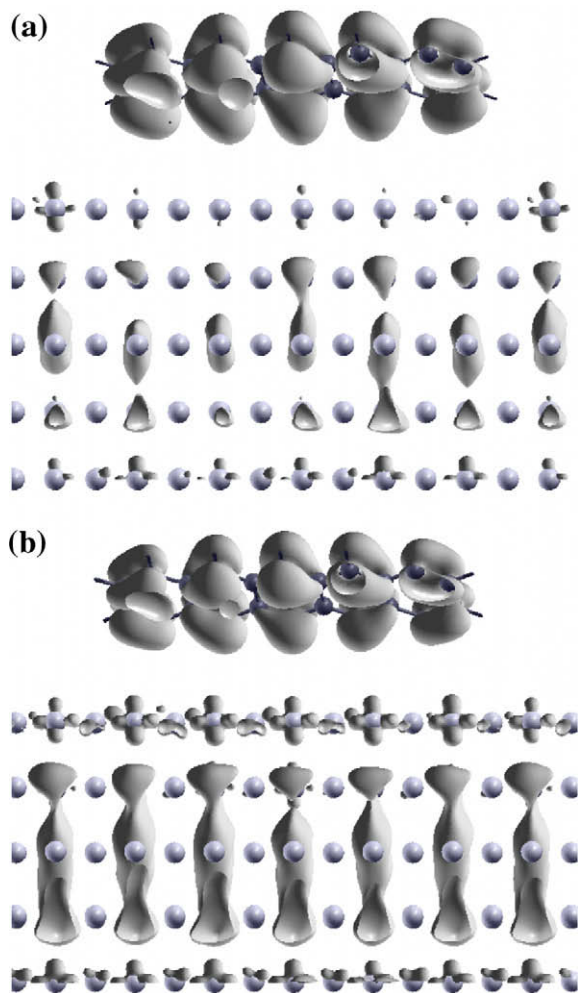


**Fig. 6.** Charge density for the pentacene–Au system corresponding to the bands near the Fermi energy at the  $X$  point in Fig. 5b: (a) illustrates the charge density for the bottom band among the three, and (b) for the top band.

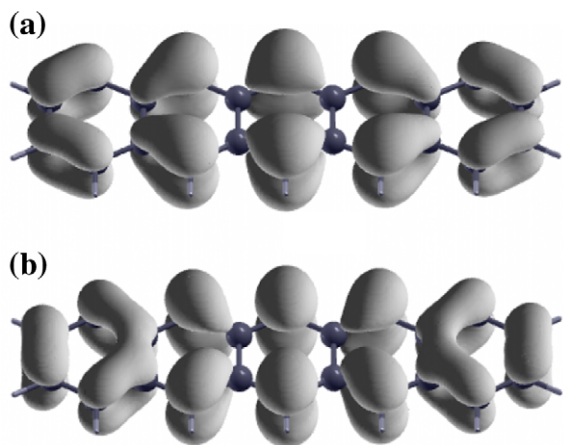


**Fig. 7.** Charge density for the isolated pentacene molecule: (a) HOMO; and (b) LUMO.

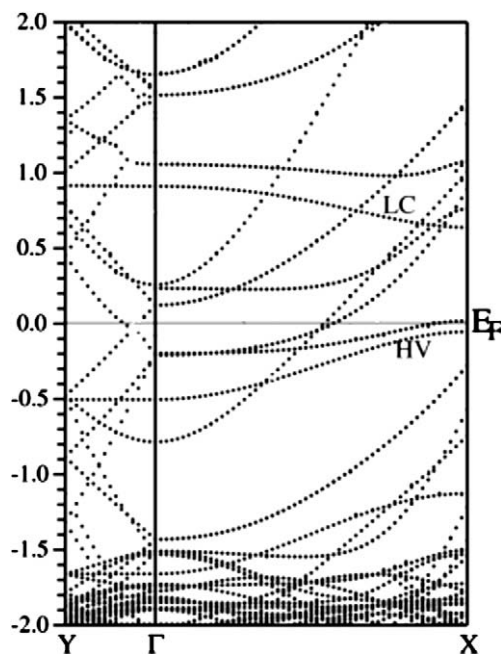


**Fig. 8.** Band-structure along the  $\Gamma X$  ( $a$ -axis) and  $\Gamma Y$  ( $b$ -axis) directions for the pentacene–gold model system where the pentacene molecule are shifted 10 Å above their optimized adsorption positions. The Fermi energy is set at zero. For the sake of clarity, the bands comprising mainly the contributions from the  $d$ -orbitals of the gold atoms in the bulk-like states are removed from the plot.

system and for a model system in which the monolayer is shifted 10 Å away from its optimized adsorption height on the gold surface (see Fig. 8). The band structures for the gold surface in both systems appear very similar, except near the Fermi energy around the  $X$  point (see Figs. 5b and 8). In the separated model system (Fig. 8), the single band above the HV band actually comprises two quasi-degenerate bands which keep their quasi-degeneracy all along the  $\Gamma X$  direction. These two bands are found to be the bonding states of  $s$ - and  $d$ -orbitals of the surface gold atoms. Interestingly, for the interacting system (Fig. 5b), we observe three bands at  $X$  near the Fermi energy. The bottom one is made of a larger contribution from the HV band of the pentacene monolayer and a smaller contribution from the  $s$ - and  $d$ -orbitals of the surface gold atoms (Fig. 6a shows the charge distribution corresponding to this band). The other two bands can be traced to the quasi-degenerate bands near the  $\Gamma$  point, which become split near the Fermi level and reach a maximum splitting (0.023 eV) at the  $X$  point; the upper of these two bands comes from a hybridization of the  $s$ - and  $d$ -orbitals of the surface gold atoms and the HV band of the pentacene monolayer (charge distribution shown in Fig. 6b), while the other one is essentially due to contributions from the surface gold atoms. This result shows that the electronic coupling between the adsorbed pentacene molecules and the gold surface is large enough to break the quasi-degeneracy of the two bands originating in the gold surface.

Applying the tight-binding approximation to the model Hamiltonian (Eq. (1)) for the top and bottom bands which comprise contributions from both the pentacene

monolayer and the gold surface, we estimate that the maximum electronic coupling between the HOMO of the pentacene molecules and the gold surface is about 0.02 eV; thus, this value is about one fifth the corresponding pentacene–pentacene electronic coupling along the *a*-direction, 0.11 eV. In our earlier work on the interface between pentacene and graphene [47], we found that: (i) the electronic coupling between pentacene and graphene is *ca.* 0.04 eV, i.e., nearly twice as large as the pentacene–gold electronic coupling; and (ii) the pentacene–pentacene in-plane coupling is  $\sim 0.01$  eV, i.e., one order of magnitude smaller than on the gold surface; on graphene, the pentacene molecular plane is parallel to the graphene sheet and the shortest distance between neighboring pentacene molecules (measured as molecular center-to-center distance along the molecular short axis) is large, about 6.3 Å. It would be interesting to evaluate how these differences in electronic coupling impact the rates of electron transfer across the interface when pentacene is deposited on gold vs. graphene/graphite.

#### 4. Conclusions

DFT calculations have been carried out to study the interface formed by a pentacene monolayer adsorbed on the gold (1 1 1) surface. The optimized geometry agrees very well with STM images. The work-function modification of the gold surface upon pentacene adsorption is calculated to be  $-0.96$  eV and is fully consistent with the results of UPS measurements. We have found that the charge distribution over the clean gold surface is altered due to pentacene adsorption and leads to a significant potential energy change at the pentacene–gold interface. Our results neatly illustrate the concept of surface-electron push-back based on UPS experiments [7].

The energy level alignment at the pentacene–gold interface has been resolved from band-structure calculations and the corresponding DOS. Although the calculations are able to reproduce the overall broadening of the pentacene HOMO level upon adsorption, the differences between our calculated values and the experimentally observed pentacene binding energy and level alignments are most likely related to the lack of many-body correlation effects in the Kohn–Sham approximation. A further study based on the GW approximation [45] is in progress to clarify this issue.

The estimated electronic interaction between the gold surface states and the pentacene HOMO level is much smaller than the one between neighboring pentacene molecules within the monolayer. We are therefore interested in the near future in determining the rates of charge transfer across the gold–pentacene interface, such as the one that can be found in pentacene-based field-effect transistors.

#### Acknowledgements

This work has been partly supported by the Science and Technology Program of the National Science Foundation

under Award DMR-0120967. We thank Drs. G. Heimel and P. Paramonov for stimulating discussions.

#### References

- [1] X.L. Chen, A.J. Lovinger, Z.N. Bao, J. Sapjeta, *Chem. Mater.* 13 (2001) 1341.
- [2] S. Lee, B. Koo, J. Shin, E. Lee, H. Park, H. Kim, *Appl. Phys. Lett.* 88 (2006) 162109.
- [3] F. Amy, C. Chan, A. Kahn, *Org. Electron.* 6 (2005) 85.
- [4] N.J. Watkins, L. Yan, Y.L. Gao, *Appl. Phys. Lett.* 80 (2002) 4384.
- [5] P.G. Schroeder, C.B. France, J.B. Park, B.A. Parkinson, *J. Appl. Phys.* 91 (2002) 3010.
- [6] N. Koch, A. Kahn, J. Ghijsen, J.J. Pireaux, J. Schwartz, R.L. Johnson, A. Elschner, *Appl. Phys. Lett.* 82 (2003) 70.
- [7] N. Koch, A. Vollmer, S. Duhm, Y. Sakamoto, T. Suzuki, *Adv. Mater.* 19 (2007) 112.
- [8] K. Ihm, B. Kim, T.H. Kang, K.J. Kim, M.H. Joo, T.H. Kim, S.S. Yoon, S. Chung, *Appl. Phys. Lett.* 89 (2006) 033504.
- [9] O. McDonald, A.A. Cafolla, D. Carty, G. Sheerin, G. Hughes, *Surf. Sci.* 600 (2006) 3217.
- [10] C.B. France, P.G. Schroeder, J.C. Forsythe, B.A. Parkinson, *Langmuir* 19 (2003) 1274.
- [11] C.B. France, P.G. Schroeder, B.A. Parkinson, *Nano Lett.* 2 (2002) 693.
- [12] J.H. Kang, X.Y. Zhu, *Appl. Phys. Lett.* 82 (2003) 3248.
- [13] J.H. Kang, X.Y. Zhu, *Chem. Mater.* 18 (2006) 1318.
- [14] D. Kafer, L. Ruppel, G. Witte, *Phys. Rev. B* 75 (2007) 085309.
- [15] G. Heimel, L. Romaner, J.L. Bredas, E. Zojer, *Surf. Sci.* 600 (2006) 4548.
- [16] G. Heimel, L. Romaner, J.L. Bredas, E. Zojer, *Phys. Rev. Lett.* 96 (2006).
- [17] G. Heimel, L. Romaner, E. Zojer, J.L. Bredas, *Nano Lett.* 7 (2007) 932.
- [18] G. Heimel, L. Romaner, E. Zojer, J.L. Bredas, *Acc. Chem. Res.* 41 (2008) 721.
- [19] M. Simeoni, S. Picozzi, B. Delley, *Surf. Sci.* 562 (2004) 43.
- [20] K. Lee, J.J. Yu, Y. Morikawa, *Phys. Rev. B* 75 (2007) 045402.
- [21] K. Lee, J.Y. Yu, *Surf. Sci.* 589 (2005) 8.
- [22] L. Romaner, G. Heimel, J.L. Bredas, A. Gerlach, F. Schreiber, R.L. Johnson, J. Zegenhagen, S. Duhm, N. Koch, E. Zojer, *Phys. Rev. Lett.* 99 (2007).
- [23] U. Harten, A.M. Lahee, J.P. Toennies, C. Woll, *Phys. Rev. Lett.* 54 (1985) 2619.
- [24] C. Woll, S. Chiang, R.J. Wilson, P.H. Lippel, *Phys. Rev. B* 39 (1989) 7988.
- [25] J.V. Barth, H. Brune, G. Ertl, R.J. Behm, *Phys. Rev. B* 42 (1990) 9307.
- [26] K.G. Huang, D. Gibbs, D.M. Zehner, A.R. Sandy, S.G.J. Mochrie, *Phys. Rev. Lett.* 65 (1990) 3313.
- [27] A.R. Sandy, S.G.J. Mochrie, D.M. Zehner, K.G. Huang, D. Gibbs, *Phys. Rev. B* 43 (1991) 4667.
- [28] N. Takeuchi, C.T. Chan, K.M. Ho, *Phys. Rev. B* 43 (1991) 13899.
- [29] P.E. Blochl, *Phys. Rev. B* 50 (1994) 17953.
- [30] G. Kresse, D. Joubert, *Phys. Rev. B* 59 (1999) 1758.
- [31] Y. Wang, J.P. Perdew, *Phys. Rev. B* 43 (1991) 8911.
- [32] S. Tsuzuki, H.P. Luthi, *J. Chem. Phys.* 114 (2001) 3949.
- [33] G. Kresse, J. Furthmuller, *Phys. Rev. B* 54 (1996) 11169.
- [34] H.J. Monkhorst, J.D. Pack, *Phys. Rev. B* 13 (1976) 5188.
- [35] M. Methfessel, A.T. Paxton, *Phys. Rev. B* 40 (1989) 3616.
- [36] J. Neugebauer, M. Scheffler, *Phys. Rev. B* 46 (1992) 16067.
- [37] D.E. Eastman, *Phys. Rev. B* 2 (1970) 1.
- [38] G.V. Hansson, S.A. Flodstrom, *Phys. Rev. B* 18 (1978) 1572.
- [39] H.B. Michaelson, *J. Appl. Phys.* 48 (1977) 4729.
- [40] V. De Renzi, R. Rousseau, D. Marchetto, R. Biagi, S. Scandolo, U. del Pennino, *Phys. Rev. Lett.* 95 (2005).
- [41] J.P. Perdew, K. Burke, M. Ernzerhof, *Phys. Rev. Lett.* 77 (1996) 3865.
- [42] L.R.G. Heimel, E. Zojer, J. Bredas, *Acc. Chem. Res.* 41 (2008).
- [43] J.B. Neaton, M.S. Hybertsen, S.G. Louie, *Phys. Rev. Lett.* 97 (2006).
- [44] M. Koentopp, K. Burke, F. Evers, *Phys. Rev. B* 73 (2006).
- [45] L. Hedin, *Phys. Rev.* 139 (1965) A796.
- [46] V. Coropceanu, M. Malagoli, D.A. da Silva, N.E. Gruhn, T.G. Bill, J.L. Bredas, *Phys. Rev. Lett.* 89 (2002).
- [47] P.B. Paramonov, V. Coropceanu, J.L. Bredas, *Phys. Rev. B* 78 (2008).

fast-switching and low-power OFETs. Since the number of tested ILs are still very limited for OFETs, further exploration is desired in quest for the best gating ILs among varieties of the existing materials.

It was reported that the components of pure ILs are not completely dissociated into ions and that considerable part of the ions form multiple-ion pairs; 30–40% of the ions form dimer and trimer which do not contribute to the ionic conduction [14–16]. As the result, it can be expected that total number of carriers accumulated at the surface of the semiconductors are reduced. To enhance the degree of dissociation of ILs, it is known that addition of highly electronegative inorganic salts is very effective; for example, in the case of lithium salts which has the strongest electrostatic interactions, only with the mole fraction of 0.15, half of multiple-ion pairs are dissociated into ions and the number of ions responsible for the ionic conduction is considerably enhanced [17–19].

To further improve the performance of the IL-gated OFETs, we introduce the binary ILs with the inclusion of lithium and potassium salts. It turned out that capacitance of the binary ILs drastically increased, especially at high-frequency. The faster ionic diffusion in response to the voltage application results mainly from the enhancement of the degree of dissociation of the ILs. Rubrene single-crystals EDL-FETs are fabricated with the binary ILs and their performance is compared with that with pure ILs. The devices show mobility as high as  $2.9 \text{ cm}^2/\text{Vs}$  with the binary ILs, indicating that good solid/liquid interfaces are possibly attained even with the inorganic salts. The results demonstrate that the binary ILs provide an effective way to achieve fast-switching, low-power, and high-mobility OFETs.

## 2. Experimental

The basal IL which we use in this experiment is 1-ethyl-3-methylimidazolium bis(fluorosulfonyl)imide ([emim][FSI]); the structures of the constituent molecules are shown in Fig. 1a. Since it has been demonstrated that the highest mobility  $9.5 \text{ cm}^2/\text{Vs}$  is achieved for the OFETs with [emim][FSI] devices [13], which is only a fraction of the values given for the air-gap transistors, the material is suited to examine the effect of the binary ILs. The binary ILs including lithium ([Li]) or potassium ([K]) salts are prepared by mixing 0.32 mol/kg of [Li][FSI] or [K][FSI] powders with [emim][FSI] to make [Li][emim][FSI] and [K][emim][FSI], respectively. The mole fraction of [Li][FSI]/[Li][emim][FSI] and [K][FSI]/[K][emim][FSI] are 0.09. It has been reported in several ILs that the degree of dissociation is enhanced with increasing the amount of lithium or potassium salts as long as mole fraction of lithium- or potassium-based ionic liquids are lower than 0.15.

We have formed a well structure of polydimethylsiloxane (PDMS) elastomer for the substrate on which a rubrene single-crystal is electrostatically attached as previously reported [12,13]. The electrodes for the gate, source, and drain are all prepared with Cr/Au films. Typical dimensions of the channel length  $L$ , channel width  $w$ , and the gap layer are  $40 \mu\text{m}$ ,  $150\text{--}200 \mu\text{m}$ , and  $25 \mu\text{m}$ , respectively. The ILs are poured underneath the rubrene single-crystal by the

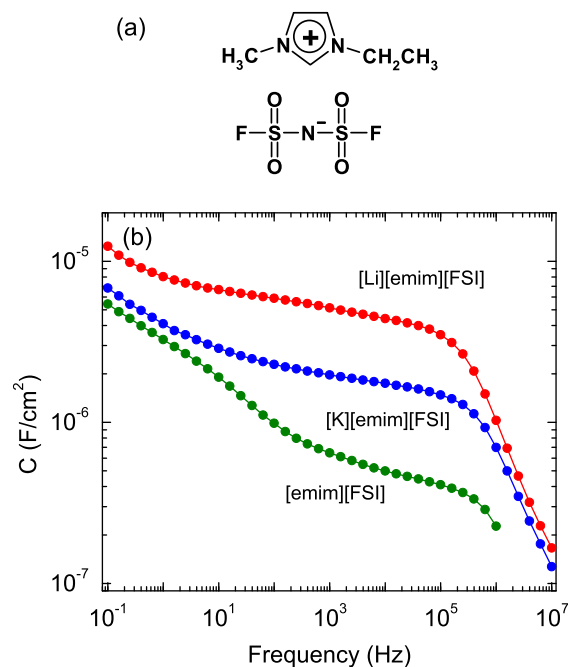


**Fig. 1.** (a) Chemical structures of [emim][FSI], (b) capacitance of the ionic liquids as a function of frequency measured by the ac impedance technique with pure [emim][FSI] (green), [K][emim][FSI] (blue) and [Li][emim][FSI] (red). (For interpretation of the references to color in this figure legend, the reader is referred to the web version of this article.)

capillary force, so that the EDLs in the ILs can induce high-density carriers at the surface of the crystal with the application of gate voltage. We use the four-terminal method to measure transfer characteristics of the device. All the measurements are done in air at room temperature with an Agilent Technology B1500A semiconductor parameter analyzer. Before we introduce the ILs, the rubrene single-crystals are characterized by measuring transistor performance with the application of gate voltage to the air-gap layer. The values of obtained mobility  $\mu$  are in the range of  $10\text{--}37 \text{ cm}^2/\text{Vs}$  with the average values around  $20 \text{ cm}^2/\text{Vs}$  [13], which is comparable to the best value ever reported for the rubrene single-crystal transistors [20,21].

EDL capacitance  $C_{EDL}$  of the ILs is measured using a test device consisting of the same PDMS substrates, where the top surface is structured with Cr/Au evaporated on the PDMS substrate. Solartron 1260 and 1296 impedance analyzers are used to obtain the frequency profiles over the range from 0.1 Hz to 10 MHz with the application of AC voltage amplitude of 5 mV. We emphasize that more than 10 devices are measured for each IL to confirm the reproducibility within the deviation of 10%.

## 3. Results and discussion

As shown in Fig. 1b, the values of the capacitance increase with decreasing frequency for all the ionic liquids. With adding lithium and potassium ions, absolute values of the capacitance in the binary ILs are enhanced particularly in the high-frequency regime and the frequency

dependence is weakened in common. It is to be emphasized that the EDL capacitance of the binary ILs does not significantly diminish with increasing frequency and remains more than  $3.5 \mu\text{F}/\text{cm}^2$  for [Li][emim][FSI] and  $1.5 \mu\text{F}/\text{cm}^2$  for [K][emim][FSI] even at 0.1 MHz: the values are only less than one order of magnitude lower than that at 0.1 Hz for the both compounds, demonstrating fast ionic diffusion in response to the voltage application. This is because that the degree of dissociation of ILs are enhanced and the number of the ions which contribute to the ion conduction is enhanced especially at high-frequency. Since the quick formation of the EDLs enables rapid accumulation of high-density carriers at the IL/semiconductor interfaces for IL-gated OFETs, the high ionic response directly relates to the fast-switching operation of OFETs in response to the gate voltage application.

The variation in the lower-frequency capacitance among the three ionic liquids is also to be addressed because the observation of the highest capacitance in [Li][emim][FSI] is reproducible for all the three measured samples, though the property gives less impact on the performance of the high-speed switching transistors. Since [Li][emim][FSI] shows larger capacitance than [K][emim][FSI], the difference possibly comes from effects of the impurities on the EDL thickness. If lithium and potassium ions by themselves are attracted to the electrodes so that they take considerable part in the EDLs with the application of the gate voltage, it can be expected that thinner EDLs are formed to enhance the capacitance in the binary ILs due to their smaller ionic radius than the main components in the ILs. As a counter effect, the stronger electrostatic interactions of the lithium and potassium ions may attract large crowds of anions, which could lead to thicker Helmholtz layers; however this effect appears to be minor in the present experiments because the observed faster ionic motion in the binary liquids is not in line with the assumption that the lithium and potassium ions moves together with anions. In addition, including influences of differences in semiconductor surfaces and inevitable inclusion of water molecules, it is to be further investigated to elucidate microscopic mechanisms of the formation of EDLs in the vicinity of the solid/binary IL interfaces.

Fig. 2 shows output characteristics of the rubrene-crystal FETs with the two binary ILs. With increasing drain voltage  $V_D$ , drain current  $I_D$  show the linear regimes and fairly good saturation behavior with the application of less than  $-0.2 \text{ V}$  for both  $V_G$  and  $V_D$ . Simultaneously measured gate leakage current  $I_G$  through the electrolytes is negligibly small as compared to the drain current  $I_D$ , that is less than  $0.1 \text{ nA}$  as long as  $|V_G|$  is less than  $0.5 \text{ V}$ . Rather large saturation current of the order of  $\mu\text{A}$  are obtained at very low gate and drain biases, demonstrating the low-voltage, high-current operation due to the high-density carrier accumulation at the IL/rubrene liquid-to-solid interfaces.

Fig. 3a and b shows typical transfer characteristics of the device with [Li][emim][FSI] and [K][emim][FSI], respectively. A sweeping rate of  $0.1 \text{ V/s}$  results in negligible hysteresis for all the ILs and is translated to the frequency of  $10 \text{ Hz}$  to change  $10 \text{ mV}$ , which is the amplitude of the capacitance measurement shown in Fig. 1. Typical turn-on voltage of the devices are  $0.40 \text{ V}$  and  $0.25 \text{ V}$  for [Li][e-

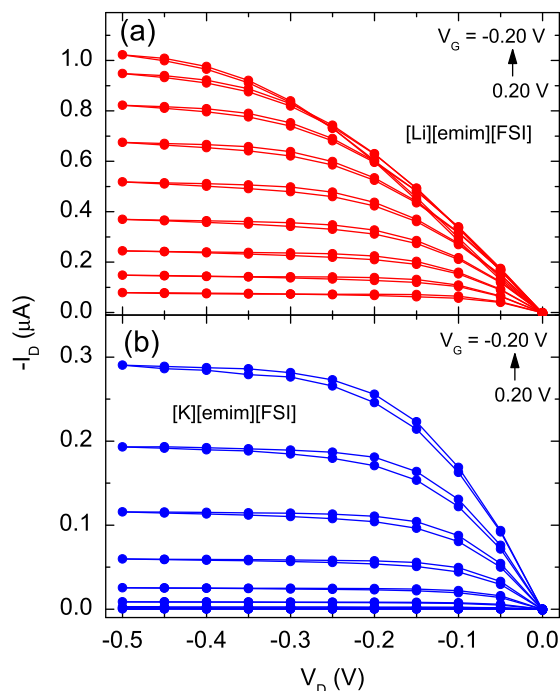


Fig. 2. Output characteristics of the devices with [Li][emim][FSI] (a) and [K][emim][FSI] (b) with different gate voltages ( $V_G = 0.20, 0.15, 0.10, 0.05, 0.00, -0.05, -0.10, -0.15, -0.20 \text{ V}$ , respectively).

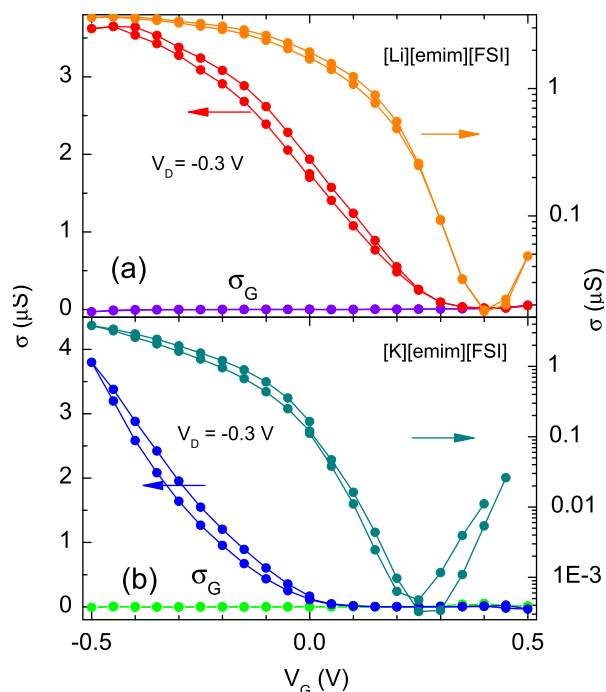


Fig. 3. Transfer characteristics of the EDL OFETs with [Li][emim][FSI] (a) and [K][emim][FSI] (b). Conductivity of gate leakage  $\sigma_G$  is also plotted.

mim][FSI] and [K][emim][FSI], respectively. We note that the turn-on voltage reproducibly shifts to positive values with the inclusion of the impurity ions among several

transistors prepared. Since lithium and a potassium salts have hydrophilic property, the shift of the turn-on voltage can be also due to inevitable inclusion of water from atmosphere or impurities in the ILs. We speculate that the impurities in the ILs and inclusion of water from atmosphere are both involved in the observation, providing additional dipoles and/or hole-trapping levels at the ILs/organic single-crystal boundaries.

The hole mobility  $\mu$  is estimated from the transfer characteristics by employing the standard formula in the Ohmic regime. Assuming the values of  $C_{EDL}$  at 10 Hz, the average mobility values are  $1.5 \text{ cm}^2/\text{Vs}$  for [Li][emim][FSI] and  $2.9 \text{ cm}^2/\text{Vs}$  for [K][emim][FSI]. These values are relatively high in the standard of ever reported EDL-gated FETs, partially due to the use of the rubrene single-crystals with high intrinsic mobility. Because of the achieved reproducibility, we can argue that the present results qualitatively follow the tendency of higher  $\mu$  with the gating ILs with smaller capacitance. Similar tendency of the decreasing  $\mu$  with increasing capacitance is reported for OFETs with *solid* dielectrics [22,23] and *ILs* [13]. At this low-frequency, the variation of  $\mu$  as function of  $C_{EDL}$  appears to be in the same trend as that for previously measured pure ILs in the [emim] families, for which the mobility systematically decreases with capacitance approximately to the power of  $-1.5$ . Since the increase in the carrier density at a certain gate voltage is compensated by more significant decrease in mobility, the overall transconductance, which is proportional to the product of mobility and capacitance, is reduced with the binary ILs. The observation still suggests that the surface of the rubrene single-crystal is not seriously damaged by using the binary ILs as was the case for the pure ILs.

In contrast to the diminished transconductance in the low-frequency region, the benefit of the binary ILs appear to be at higher frequencies than 100 Hz; capacitance is almost 10 times higher at 10 kHz for the Li-doped ILs than that for the pure ILs though  $\mu$  differs only by the factor of 6 with each other. Therefore, the devices with the binary ILs are potentially attractive for high-frequency switching, despite that the present sample dimensions are not suitable for high-frequency response because of their relatively long channel length  $L$ . If the devices with 5- $\mu\text{m}$  channel length can be developed with improved fabrication processes for example, the theoretical cut-off frequency  $f = \mu V_D / L^2$  can reach 1 MHz for the device with Li-doped ILs, as long as injection at the metal/semiconductor contacts do not cause significant delay during the on-off switching. Since the ionic motion is proportional to the inverse ionic conductance and the thickness of the ionic liquid layer in addition, development of the devices with shorter channel length and shallower well structures is under way to realize the faster-switching EDL-OFETs with the combination of high-mobility rubrene single-crystals and the Li-doped ILs.

#### 4. Conclusion

We have introduced binary ILs electrolytes for the future development of high-speed OFETs with very low oper-

ating gate voltages. As the result of comparative experiments with high-mobility rubrene single-crystal devices incorporating with and without inclusion of small amount of inorganic ions, it is shown that the EDLs are formed much more rapidly in the binary ILs and that the high-mobility rubrene surface is well preserved at the interface to the binary ILs. The above two results suggest that binary-IL gated devices can be promising candidates for fast-switching OFETs with extremely low operating gate voltage.

#### Acknowledgement

The authors would like to thank Y. Tominari for his technical assistance. We also thank I. Tsukada, and C.D. Frisbie for helpful discussion. This study was supported in part by Grants-in-Aid for Scientific Research (Nos. 17069003, 18028029, 19360009 and 20740213) from the Ministry of Education, Culture, Sports, Science, and Technology, Japan.

#### References

- [1] M.A.B.H. Susan, T. Kaneko, A. Noda, M. Watanabe, *J. Am. Chem. Soc.* 127 (2005) 4976.
- [2] S. Seki, Y. Kobayashi, H. Miyashiro, Y. Ohno, A. Usami, Y. Mita, N. Kihira, M. Watanabe, N. Terada, *J. Phys. Chem. B* 110 (2006) 10228.
- [3] S. Seki, Y. Ohno, Y. Kobayashi, H. Miyashiro, A. Usami, Y. Mita, H. Tokuda, M. Watanabe, K. Hayamizu, S. Tsuzuki, M. Hattori, N. Terada, *J. Electrochem. Soc.* 154 (2007) A173.
- [4] M.J. Panzer, C.D. Frisbie, *J. Am. Chem. Soc.* 127 (2005) 6960.
- [5] M.J. Panzer, C.D. Frisbie, *Appl. Phys. Lett.* 88 (2006) 203504.
- [6] J. Takeya, K. Yamada, K. Hara, K. Shigeto, K. Tsukagoshi, S. Ikehata, Y. Aoyagi, *Appl. Phys. Lett.* 88 (2006) 112102.
- [7] H. Shimotani, H. Asanuma, J. Takeya, Y. Iwasa, *Appl. Phys. Lett.* 89 (2006) 203501.
- [8] J. Lee, M.J. Panzer, Y. He, T.P. Lodge, C.D. Frisbie, *J. Am. Chem. Soc.* 129 (2007) 4532.
- [9] R. Misra, M. McCarthy, A.F. Hebard, *Appl. Phys. Lett.* 90 (2007) 052905.
- [10] J.H. Cho, J. Lee, Y. Xia, B. Kim, Y. He, M.J. Renn, T.P. Lodge, C.D. Frisbie, *Nat. Mater.* 7 (2008) 900.
- [11] S. Ono, S. Seki, R. Hirahara, Y. Tominari, J. Takeya, *Appl. Phys. Lett.* 92 (2008) 103313.
- [12] T. Uemura, R. Hirahara, Y. Tominari, S. Ono, S. Seki, J. Takeya, *Appl. Phys. Lett.* 93 (2008) 263305.
- [13] S. Ono, K. Miwa, S. Seki, J. Takeya, *Appl. Phys. Lett.* 94 (2009) 063301.
- [14] A. Reiche, T. Cramer, G. Fleischer, R. Sandner, F. Kremer, J. Kärger, *J. Phys. Chem. B* 102 (1998) 1861.
- [15] H.A. Every, A.G. Bishop, M. Forsyth, D.R. MacFarlane, *Electrochim. Acta* 45 (2000) 1279.
- [16] H.A. Every, A.G. Bishop, D.R. MacFarlane, G. Orädd, M. Forsyth, *Phys. Chem. Chem. Phys.* 6 (2004) 1758.
- [17] H. Tokuda, K. Ishii, M.A.B.H. Susan, S. Tsuzuki, K. Hayamizu, M. Watanabe, *J. Phys. Chem. B* 110 (2006) 2833.
- [18] K. Hayamizu, Y. Aihara, H. Nalagawa, T. Nukuda, W.S. Price, *J. Phys. Chem. B* 108 (2004) 19527.
- [19] I. Nicotera, C. Oliviero, W.A. Henderson, G.B. Appetecchi, S. Passerini, *J. Phys. Chem. B* 109 (2005) 22814.
- [20] E. Menard, V. Podzorov, S.H. Hur, A. Gaur, M.E. Gershenson, J.A. Rogers, *Adv. Mater.* 16 (2004) 2097.
- [21] J. Takeya, M. Yamagishi, Y. Tominari, R. Hirahara, Y. Nakazawa, T. Nishikawa, T. Kawase, T. Shimoda, S. Ogawa, *Appl. Phys. Lett.* 90 (2007) 102120.
- [22] A.F. Stassen, R.W.I. de Boer, N.N. Iosad, A.F. Morpurgo, *Appl. Phys. Lett.* 85 (2004) 3899.
- [23] I.N. Hulea, S. Fratini, H. Xie, C.L. Mulder, N.N. Iosad, G. Rastelli, S. Ciuchi, A.F. Morpurgo, *Nat. Mater.* 5 (2006) 982.

formulate high boiling point solvents in the active layer [15–20]. Phase separation and crystallization of the active layer were observed in OSCs with a high boiling solvent in the active layer. Peet et al. reported that the efficiency of OSCs was doubled by incorporating an alkanedithiol as the high boiling solvent [16]. The alkanedithiol dissolves the PCBM phase selectively without affecting the hole transport type polymer, resulting in phase segregation. Extensive percolating pathway formation was proposed as the main factor for the improved efficiency. Nitrobenzene [19] and 1-chloronaphthalene [20] have also been used for this purpose. Surface modification of the electrode was also successful in controlling the nanomorphology of the active layer [21–23]. Vertical segregation of the active layer was reported in the P3HT:PCBM blend depending on the surface properties of the substrate, even though the detailed device performance was not reported [21]. Other than these, Au was also successful as a modifier for the OSCs [24].

This paper reports an approach to control the nanomorphology of the P3HT:PCBM active layer. A hydrophobic fluorinated polymer, polyvinylidene fluoride (PVDF), was inserted at the interface between poly-3,4-ethylenedioxythiophene:polystyrenesulfonate (PEDOT:PSS) and P3HT:PCBM active layers. The effect of the PVDF interlayer on the morphology, crystallinity and charge transport properties of the OSCs was examined. The efficiency of the OSCs was improved by the extensive phase separation and crystallization of the active layer during thermal annealing by the hydrophobic PVDF interlayer.

## 2. Experimental

A basic OSC device configuration of indium tin oxide (ITO, 150 nm)/PEDOT:PSS(70 nm)/PVDF (4 nm)/P3HT:PCBM(1:0.7, 120 nm)/LiF(1 nm)/Al(200 nm) was used to fabricate OSCs. The PVDF was inserted at the interface between PEDOT:PSS and P3HT:PCBM. The PVDF polymer was spin-coated from a 0.05 wt.% dimethylformamide solution at a spin speed of 2000 rpm followed by baking at 160 °C for 30 min to remove the residual solvent. The P3HT:PCBM was coated from a 4 wt.% dichlorobenzene solution and the film was baked at 150 °C for 30 min. Hole-only devices of ITO/PEDOT:PSS (70 nm)/PVDF/P3HT:PCBM (120 nm)/Au (200 nm) and ITO/PEDOT:PSS (70 nm)/PVDF/PPV(80 nm)/Au (200 nm) were fabricated to monitor hole injection from the active layer to the PEDOT:PSS layer. The PPV was a super yellow<sup>®</sup> from Merck with a HOMO level of 5.2 eV. The active area of the pixel of the OSCs was 4 mm<sup>2</sup>.

The solar cell performances of the OSCs were characterized using a Keithley 2400 source measurement unit and an Abet solar cell simulator under AM1.5 condition (100 mW/cm<sup>2</sup>). The surface morphology of the PEDOT:PSS, PVDF and P3HT:PCBM blended films was analyzed by non-contact mode atomic force microscopy (AFM, XE100, PSIA Co.). The ultraviolet–visible (UV–Vis) absorption spectra were recorded using a UV–Vis spectrophotometer (Shimadzu, UV-2501PC) and the phases were examined by grazing-incidence X-ray diffraction. The cross-section of the fabricated device was analyzed by transmission electron microscopy (TEM, model JEM-2100F, Jeol Co.) after sampling using a focused ion beam method.

## 3. Results and discussion

PVDF is a well-known ferroelectric polymer with a high dielectric constant owing to the strong electron withdrawing fluorine group on the main chain [25]. It is also known as a hydrophobic polymer with a contact angle of up to 90°. The strong hydrophobic characteristics of PVDF can affect the nanomorphology of the P3HT:PCBM blend. Therefore, it was used as an interlayer between the PEDOT:PSS and P3HT:PCBM blends. PVDF can be spin-coated from a ketone or non-aromatic solvent, and can form an orthogonal film with P3HT:PCBM spin-coated from an aromatic solvent. There was no intermixing between the PVDF and P3HT:PCBM layers during spin coating of the blend. Therefore, PVDF can be applied effectively as an interlayer in the OSCs by a simple spin coating method. Although other surface modification methods, such as a self-assembled monolayer coating on the PEDOT:PSS, have been reported [21], it was difficult to modify the PEDOT:PSS surface without damaging the PEDOT:PSS layer. Compared to those methods, PVDF modification of the PEDOT:PSS is advantageous in that surface modification can be carried out by a simple spin coating of the PVDF.

PVDF was spin-coated from a 0.05 wt.% dimethylformamide solution, and its morphology after spin coating on PEDOT:PSS was examined. Fig. 1 shows AFM images of the PEDOT:PSS and PVDF coated PEDOT:PSS layers. The average surface roughness of the PVDF coated PEDOT:PSS surface was 0.89 nm, while that of the PEDOT:PSS was 0.57 nm. Although the surface roughness of the PVDF coated PEDOT:PSS was slightly higher than that of the PEDOT:PSS, the PVDF layer had a surface roughness < 1 nm. The slight increase in surface roughness of the PVDF coated PEDOT:PSS surface might be due to the minute crystallite formation in the PVDF thin film, as shown in the AFM image [25]. A small needle-like surface texture was observed in the PVDF-modified PEDOT:PSS. PVDF can form crystalline domains during film formation, which leads to an irregularity in a spin-coated film. However, crystalline domain formation is rather limited in thin films compared to that in the bulk, resulting in low surface roughness < 1 nm in PVDF coated PEDOT:PSS. PVDF thin film formation on the PEDOT:PSS also changed the surface properties from hydrophilic to hydrophobic. The contact angle of PEDOT:PSS and PVDF was 22° and 89°, respectively.

The thickness of the PVDF interlayer was measured from the transmission electron microscopy (TEM) images of the fabricated film. Fig. 2 shows a cross-section image of the PEDOT:PSS/PVDF/P3HT:PCBM. A focused ion beam method was used as a sampling method to examine the cross-section of the sample. The TEM image shows that the PEDOT:PSS and P3HT:PCBM layers were separated by a PVDF interlayer. The thickness of the PEDOT:PSS and P3HT:PCBM layers was 70 and 120 nm, respectively. The thickness of the PVDF layer, which was measured from the magnified cross-section image, was approximately 4 nm. The PVDF layer formed an almost continuous film at the interface between the PEDOT:PSS and P3HT:PCBM blend, which confirms the formation of a PVDF layer on PEDOT:PSS.

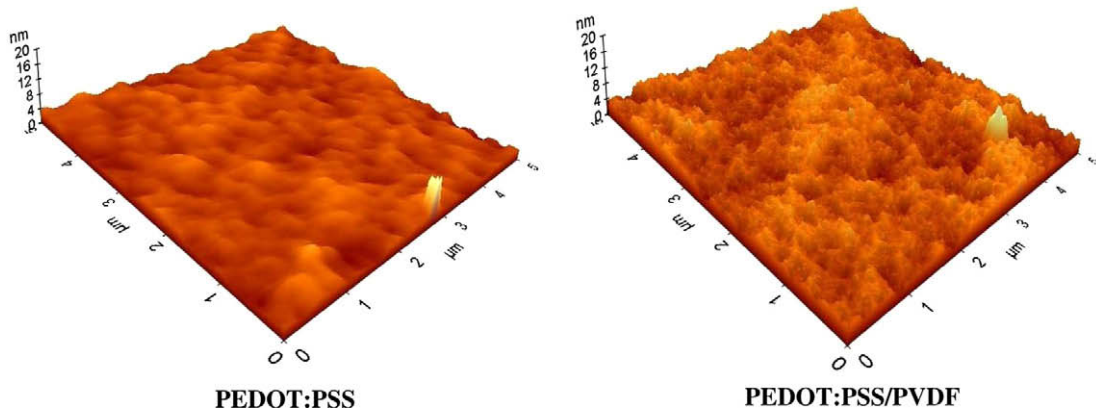


Fig. 1. Atomic force microscopic pictures of the PEDOT:PSS and PVDF coated PEDOT:PSS.

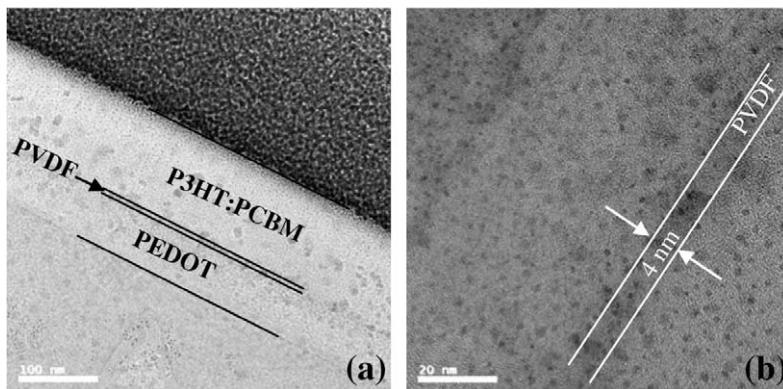


Fig. 2. Transmission electron microscopic pictures of the cross-section.

OSCs with a PVDF interlayer was fabricated to examine the effect of the PVDF layer on the device performance of P3HT:PCBM OSCs. A device architecture of ITO/PEDOT:PSS(70 nm)/PVDF/P3HT:PCBM(120 nm, 1:0.7)/LiF(1 nm)/Al(100 nm) was used, and an OSC without PVDF was also fabricated. In each device structure, two samples were fabricated with and without thermal annealing at 150 °C for 30 min. Fig. 3 presents the current density–voltage curves of the four OSCs. In the case of the OSCs without thermal annealing, the  $J_{sc}$  and fill factor of the P3HT:PCBM OSC with the PVDF interlayer were slightly lower. The reduced fill factor resulted in a low efficiency in PVDF-modified devices. This suggests that without thermal annealing, the PVDF interlayer is not effective in achieving high efficiency in the P3HT:PCBM device. The  $J_{sc}$  of the P3HT:PCBM OSCs after thermal annealing was enhanced by more than 15%, and the efficiency of the OSCs was improved by more than 10% using the PVDF interlayer. The  $J_{sc}$  and efficiency was increased from 6.5 to 7.5 mA/cm<sup>2</sup> and from 2.4% to 2.7%, respectively. In general, the  $J_{sc}$  of the OSCs depends on the energy barrier for charge transport from the P3HT:PCBM active layer to the electrodes and the morphology of the active layer including the phase morphology and crystallinity [9,10]. Therefore, the increased  $J_{sc}$  of the PVDF OSCs after thermal annealing and

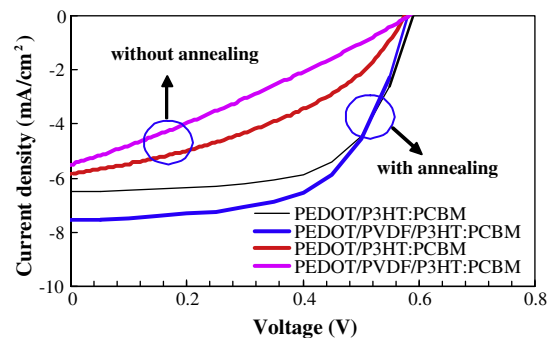


Fig. 3. Current density–voltage curves of the PEDOT/P3HT:PCBM and PEDOT/PVDF/P3HT:PCBM solar cells under illumination. Two devices were annealed at 150 °C (black and blue lines) and the other two devices were dried at room temperature (red and pink lines). (For interpretation of the references to colour in this figure legend, the reader is referred to the web version of this article.)

the reduced  $J_{sc}$  without thermal annealing might be closely related to charge transport through the interface between the PEDOT:PSS and P3HT:PCBM active layers or charge transport inside the active layer. The PVDF interlayer might alter the interfacial energy barrier between the PEDOT:PSS and P3HT:PCBM layers, affecting the  $J_{sc}$  of

the OSCs. In addition, the morphological change induced by PVDF might have a significant effect on the  $J_{sc}$  of the OSCs. The origins of the improved  $J_{sc}$  and the efficiency of the PVDF-modified OSCs after thermal annealing were examined. Compared to the  $J_{sc}$ , the open circuit voltage ( $V_{oc}$ ) of the OSC was not greatly affected by the PVDF interlayer. The  $V_{oc}$  of the OSCs was almost constant despite PVDF modification. The  $V_{oc}$  is determined typically by the HOMO level of the P3HT donor and the lowest unoccupied molecular orbital (LUMO) level of the PCBM electron acceptor in addition to the interfacial contact properties between the organic materials and electrodes. The same P3HT:PCBM active layer was used in the OSCs with and without the PVDF interlayer, which means that the  $V_{oc}$  of the OSCs may not be affected by the active layer. However, the  $V_{oc}$  from the interface between the organic layers and electrodes can be affected by the PVDF interlayer. The  $V_{oc}$  is not affected by the energy level of the electrodes assuming that ohmic contact behavior dominates charge injection from the electrodes to the organic layer [26]. In the case of the P3HT:PCBM devices used in this study, there was no difference in the interface between the electrodes and organic layers, leading to a similar  $V_{oc}$  in the two devices. The fill factor was not changed by the PVDF interlayer.

Although the  $J_{sc}$  and efficiency of the P3HT:PCBM OSCs were enhanced by the PVDF interlayer after thermal annealing, the mechanism for improving the device performances is unclear. Therefore, the origin of the improved device performances in the PVDF OSCs was examined using the device performances of the hole-only devices, light absorption and morphological analysis of the active layer. The hole-only devices of the OSCs with and without the PVDF interlayer were fabricated to confirm the origin of the high  $J_{sc}$  of the OSC with a PVDF interlayer. A device with a configuration of ITO/PEDOT:PSS/PVDF/P3HT:PCBM/Au was prepared, and the hole current density from the Au electrode to the ITO electrode was measured. The holes are transported from the P3HT:PCBM active layer to the PEDOT:PSS layer through the PVDF layer. Therefore, a comparison of the hole current density from the Au electrode to the ITO electrode can show the effect of the PVDF inter-

layer on the hole transport behavior in the OSCs. Fig. 4 shows the current density–voltage curves of the hole-only devices with and without the PVDF interlayer. The P3HT:PCBM active layer was thermally annealed at 150 °C for 30 min after spin coating. The hole current density from the Au to ITO was higher in the hole only device with the PVDF interlayer. This suggests that hole transport from the P3HT:PCBM active layer to the ITO electrode is more efficient in the OSC with the PVDF interlayer than in the OSC without the PVDF interlayer. This shows that the high  $J_{sc}$  in the PVDF OSCs is due to enhanced charge transport from the active layer to the ITO electrode. The hole current density is affected by the interface between the organic layers and the bulk charge transport properties of the active layer. However, it is unclear if the high hole current density of the OSC with the PVDF interlayer is due to an interface effect, such as band bending or a bulk effect, such as enhanced crystallinity. The hole current density reflects both the interface effect and bulk effect of the active layer because hole-only devices of the OSC were prepared under the same experimental condition as the OSC.

In order to separate the effect of the interface and bulk properties of the P3HT:PCBM active layer, hole-only devices, which were not thermally annealed at 150 °C, were fabricated because thermal treatment of the active layer induces phase separation and crystallization of the active layer. Moreover, the morphological change would be affected by the PVDF interlayer. Therefore, a comparison of the hole-only devices with the same morphology would be better for examining the interface effect by the PVDF interlayer. The P3HT:PCBM active layer, which was not thermally annealed at elevated temperatures showed an almost amorphous morphology with very little crystalline phase. In addition, the degree of phase separation of the P3HT and PCBM was similar, as shown in Fig. 7. Therefore, the bulk effect of the P3HT:PCBM active layer can be eliminated in the hole only device data of the pristine P3HT:PCBM layer without thermal annealing. A comparison of the hole current density in the P3HT:PCBM hole only device without thermal treatment shows only the interface effect of the PVDF interlayer. In addition, two hole-only devices with a polyphenylenevinylene (PPV) based amorphous active layer were also prepared to confirm the interface effect by the PVDF interlayer. The PPV polymer shows a fully amorphous morphology with a similar HOMO level as P3HT. Therefore, the interface effect of the PVDF in the OSCs can be examined indirectly. Fig. 5 shows the hole only device data of the pristine P3HT:PCBM devices without thermal treatment and the PPV devices. The hole current density of the pristine P3HT:PCBM and PPV devices decreased when a PVDF interlayer was inserted at the interface between the PEDOT:PSS and P3HT:PCBM layers or PPV. This suggests that the PVDF interlayer hinders hole transport from the organic layer to the PEDOT:PSS layer. Photoelectron spectroscopy showed that the HOMO level of the PEDOT:PSS was shifted from 5.3 to 5.4 eV by the PVDF interlayer, which has an adverse effect on hole transport from the active layer to the PEDOT:PSS. Hole transport may be facilitated in the PVDF free hole only device due to the large driving force for hole

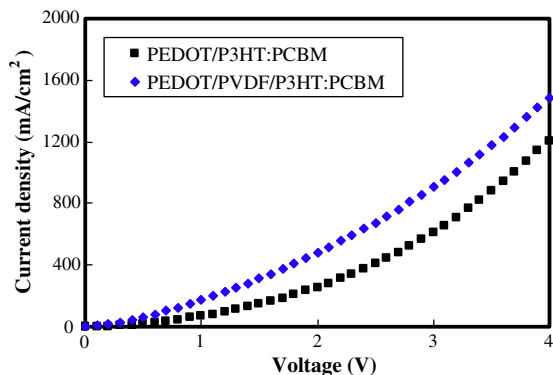


**Fig. 4.** Current density–voltage curves of the hole-only devices with a device configuration of ITO/PEDOT/P3HT:PCBM/Au and ITO/PEDOT/PVDF/P3HT:PCBM/Au. Positive bias was applied to the Au electrode and the P3HT:PCBM was annealed at 150 °C.



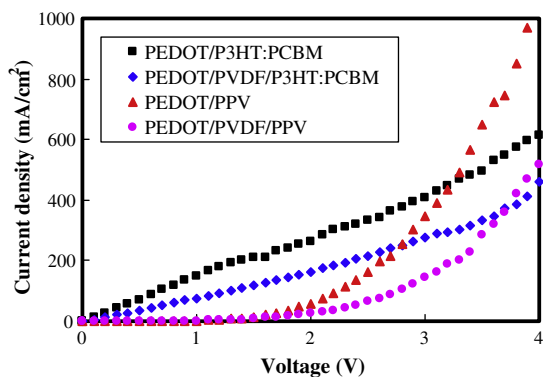


**Fig. 5.** Current density–voltage curves of the hole-only devices with a device configuration of ITO/PEDOT/P3HT:PCBM/Au and ITO/PEDOT/PVDF/P3HT:PCBM/Au. Positive bias was applied to the Au electrode and P3HT:PCBM was dried at room temperature. Hole-only devices of ITO/PEDOT/PPV/Au and ITO/PEDOT/PVDF/PPV/Au were also fabricated.

injection. There was a 0.2 eV energy barrier for hole injection from the P3HT with a HOMO level of 5.1 eV to the PEDOT:PSS with a HOMO level of 5.3 eV. However, the energy barrier for hole injection was increased from 0.2 to 0.3 eV by PVDF interlayer modification. Therefore, hole transport was reduced in the hole-only devices with the PVDF interlayer. This also explains why the bulk effect of the P3HT:PCBM, such as improved light absorption, extensive phase separation and accompanying high crystallinity by the PVDF interlayer, are responsible for the high hole current density in the PVDF-modified hole-only devices after thermal annealing. This means that the high  $J_{sc}$  of the OSCs with the PVDF interlayer is not due to the interface effect but to the bulk effect dominated by the morphology of the active layer.

UV–Vis absorption of the P3HT:PCBM film on PEDOT:PSS and PEDOT:PSS/PVDF after annealing was measured to examine the change in P3HT:PCBM bulk properties by the PVDF interlayer. Fig. 6 shows the UV–Vis absorption spectra of P3HT:PCBM. The absorption of PEDOT:PSS and PEDOT:PSS/PVDF was too weak to be observed in the UV–Vis absorption spectra and PVDF absorption was negligible. The UV–Vis absorption of the P3HT:PCBM was not changed by the PVDF interlayer after

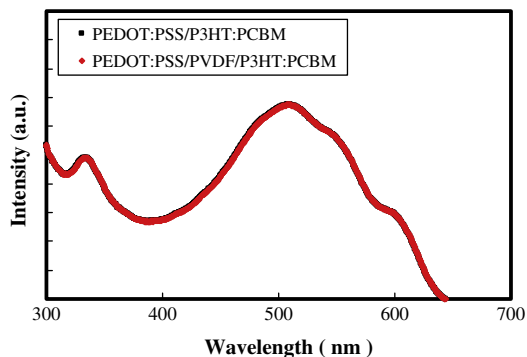


**Fig. 6.** Ultraviolet–visible absorption spectra of the PEDOT/P3HT:PCBM and PEDOT/PVDF/P3HT:PCBM films after annealing at 150 °C.

coating on the PEDOT:PSS and PEDOT:PSS/PVDF layers and thermal treatment. The PVDF did not affect the UV–Vis absorption of the P3HT:PCBM. The constant UV–Vis absorption spectra in the PEDOT:PSS/PVDF/P3HT:PCBM film after annealing suggests that the bulk absorption properties of the P3HT:PCBM active layer were not affected by the PVDF interlayer during the annealing process. This suggests that the high current density in PVDF-based OSCs is not due to increased charge generation in the active layer because strong light absorption leads to more exciton generation and charge density in the active layer.

As light absorption in the P3HT:PCBM film was not enhanced by the PVDF interlayer, the morphological change in the P3HT:PCBM layer on PVDF may be responsible for the increase in the  $J_{sc}$  of PVDF-based OSCs. Therefore, the morphology of the P3HT:PCBM film was monitored. Fig. 7 shows AFM images of the pristine and annealed P3HT:PCBM film on PEDOT:PSS and PEDOT:PSS/PVDF. The PVDF had little effect on the morphology of P3HT:PCBM, and similar AFM images were obtained in the pristine P3HT:PCBM film irrespective of the presence of a PVDF interlayer. Microscopic phase separation of the P3HT and PCBM was observed, and the domain size of each domain was small. Phase separation of the P3HT and PCBM was altered significantly by the thermal treatment, and the extent of phase separation was increased considerably after the thermal treatment. The domain size of the P3HT and PCBM was increased after the thermal treatment. In particular, the domain size of the annealed P3HT:PCBM film on PEDOT:PSS/PVDF was large due to the extensive phase separation of P3HT and PCBM. Charge transport in the blended P3HT:PCBM was enhanced by phase separation due to channel formation for the charge transport [16]. Charge hopping between the P3HT or PCBM domains was difficult due to the long distance for charge hopping, and should be minimized in order to improved charge transport in the P3HT:PCBM blend. Charge hopping between domains dominates charge transport in the P3HT:PCBM blend with a small domain size, while charge hopping between molecules dominates charge transport in the blend with a large domain size. In addition, there was excessive crystalline domain formation in the P3HT:PCBM with a large domain size. Therefore, a high current density can be obtained in the P3HT:PCBM blend with a large domain size, which explains the high  $J_{sc}$  of the PVDF OSCs. Extensive phase separation of the P3HT:PCBM after annealing on PEDOT:PSS/PVDF improved the  $J_{sc}$  of the PVDF OSCs.

The main reason for the extensive phase separation of the P3HT:PCBM on PEDOT:PSS/PVDF was the hydrophobic nature of the PVDF with a water drop contact angle of 89°. The strong hydrophobicity of PVDF induces phase separation of the P3HT and PCBM. This agrees with a report showing that the vertical phase separation of the P3HT and PCBM was induced using a self-assembled monolayer [21]. The hydrophobic self-assembled monolayer segregated the P3HT and PCBM, resulting in phase separation. Similarly, PVDF assisted in promoting the phase separation of P3HT and PCBM due to the low surface energy during the thermal annealing process. Phase separation by PVDF could not be induced in a pristine P3HT:PCBM film without thermal annealing. Therefore, phase separation during the

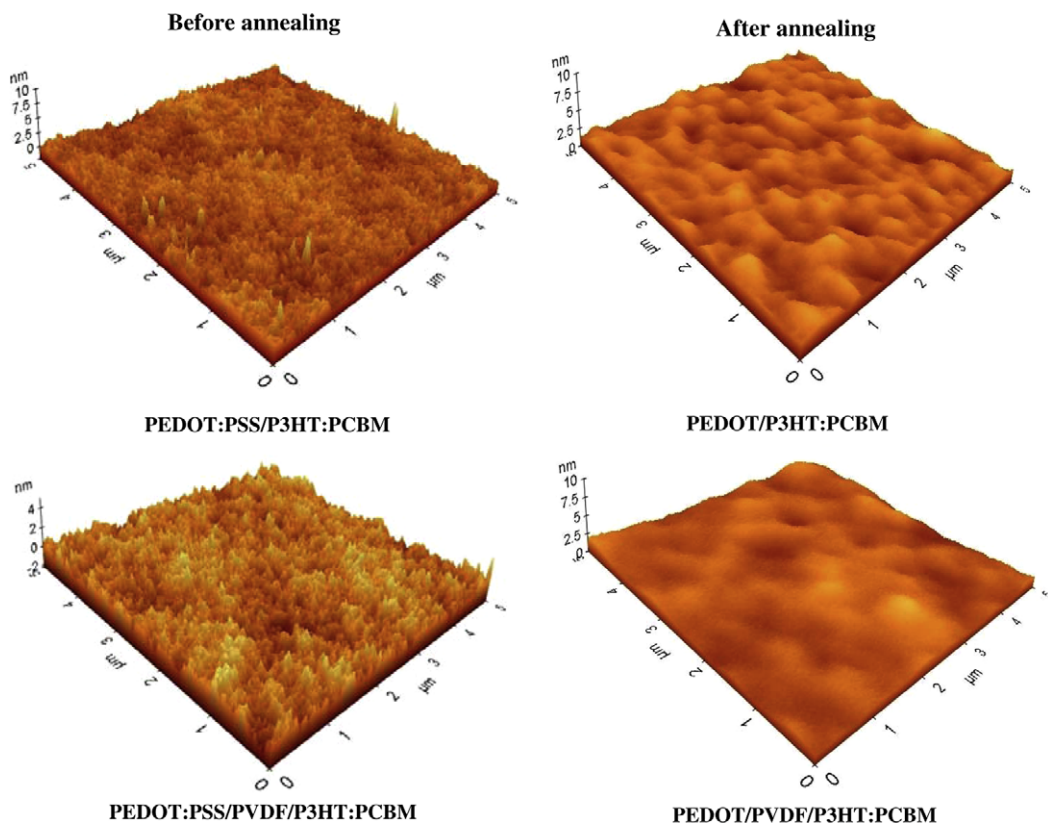


Fig. 7. Atomic force microscopic pictures of the PEDOT/P3HT:PCBM and PEDOT/PVDF/P3HT:PCBM films before and after annealing at 150 °C.

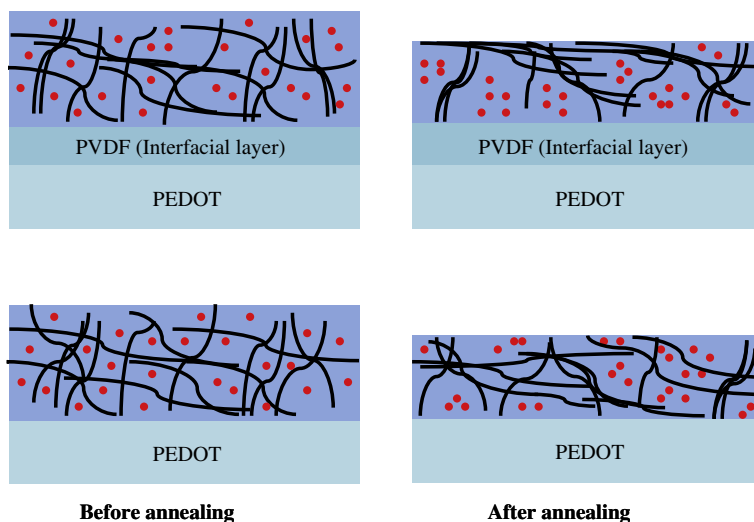


Fig. 8. Schematic diagram of the crystalline phase formation during thermal annealing process. Extensive crystallization of the P3HT and PCBM in the PVDF-modified OSCs is described after annealing.

thermal annealing process is the key factor for the increased  $J_{sc}$  in the PVDF-based OSCs. Fig. 8 shows a schematic diagram of the phase separation procedure. The P3HT:PCBM blend showed a similar morphology after spin coating on PEDOT:PSS and PVDF-modified PEDOT:PSS

without a thermal treatment. The phase separation was induced during thermal treatment of the spin-coated P3HT:PCBM film, and the degree of phase separation was high on the PVDF-modified surface due to the surface energy-induced crystallization of the P3HT:PCBM.

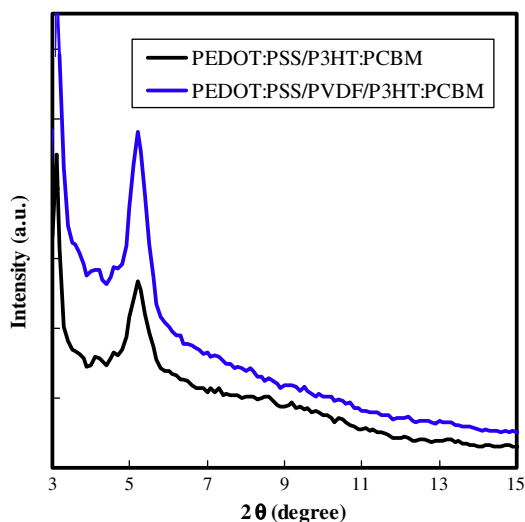


Fig. 9. X-ray diffraction pattern of the PEDOT/P3HT:PCBM and PEDOT/PVDF/P3HT:PCBM film thermally annealed at 150 °C.

Phase separation is closely related to the crystallization of the P3HT:PCBM. Therefore, the XRD patterns of the pristine and annealed P3HT:PCBM on PEDOT:PSS and PEDOT:PSS/PVDF were investigated. Fig. 9 presents the grazing-incidence XRD patterns of the P3HT:PCBM film. The intensity of the diffraction peak at  $5.2^\circ$   $2\theta$ , which was assigned to the (1 0 0) plane of P3HT, was higher in the P3HT:PCBM film annealed on PEDOT:PSS/PVDF, while it was weak in the P3HT:PCBM film annealed on PEDOT:PSS. The high intensity of the  $5.2^\circ$   $2\theta$  peak suggests that the crystallinity of the P3HT in the annealed P3HT:PCBM was increased by thermal annealing on PEDOT:PSS/PVDF. This also indicates that PVDF facilitates the phase separation of P3HT and PCBM, and film crystallization is induced during phase separation. The high crystallinity of the P3HT:PCBM film also plays a role in charge transport in the active layer, contributing to the high  $J_{sc}$  of the PVDF OSCs. Therefore, the high  $J_{sc}$  in the PVDF OSCs is due mainly to the phase separation and crystallization of P3HT:PCBM induced by the hydrophobic PVDF interlayer. The high  $J_{sc}$  improved the efficiency of the PVDF OSCs.

#### 4. Conclusions

A PVDF interlayer was introduced at the interface between the PEDOT:PSS and P3HT:PCBM layers to improve

the short circuit current and power conversion efficiency of the OSCs by inducing phase separation and crystallization of the P3HT:PCBM blend. The hydrophobicity of the PVDF thin film was responsible for the extensive phase separation and high crystallinity. The phase segregation of the P3HT:PCBM active layer was induced mainly during the thermal annealing process of the film. Therefore, the PVDF interlayer can be used as an interlayer to improve the device performance of OSCs.

#### References

- [1] C.W. Tang, S.A. VanSlyke, *Appl. Phys. Lett.* 51 (1987) 913.
- [2] J.H. Burroughes, D.D.C. Bradley, A.R. Brown, R.N. Marks, K. Mackay, R.H. Friend, P.L. Burns, A.B. Holmes, *Nature* 347 (1990) 539.
- [3] J.H. Burroughes, C.A. Jones, R.H. Friend, *Nature* 335 (1988) 137.
- [4] C.W. Tang, *Appl. Phys. Lett.* 48 (1986) 183.
- [5] W. Ma, C. Yang, A.J. Heeger, *Adv. Funct. Mater.* 15 (2005) 1617.
- [6] V.D. Mihailescu, H.X. Xie, B. de Boer, L.J.A. Koster, P.W.M. Blom, *Adv. Funct. Mater.* 16 (2006) 699.
- [7] L.H. Nguyen, H. Hoppe, T. Erb, S. Gunes, G. Gobsch, N.S. Sariciftci, *Adv. Funct. Mater.* 17 (2007) 1071.
- [8] F. Padinger, R.S. Rittberger, N.S. Sariciftci, *Adv. Funct. Mater.* 13 (2003) 85.
- [9] T. Erb, U. Zhokhavets, G. Gobsch, S. Raleva, B. Stühn, P. Schilinsky, C. Waldauf, C.J. Brabec, *Adv. Funct. Mater.* 15 (2005) 1193.
- [10] Y. Kim, S. Cook, S.M. Tuladhar, S.A. Choulis, J. Nelson, J.R. Durrant, D.D.C. Bradley, M. Giles, I. McCulloch, C.-S. Ha, M. Ree, *Nat. Mater.* 5 (2006) 197.
- [11] G. Li, Y. Yao, H. Yang, V. Shrotriya, G. Yang, Y. Yang, *Adv. Funct. Mater.* 17 (2007) 1636.
- [12] G. Li, V. Shrotriya, J. Huang, Y. Yao, T. Moriarty, K. Emery, Y. Yang, *Nat. Mater.* 4 (2005) 864.
- [13] H. Hoppe, T. Glatzel, M. Niggemann, W. Schwinger, F. Schaeffler, A. Hinsch, M.Ch. Lux-Steiner, N.S. Sariciftci, *Thin Solid Films* 511 (2006) 587.
- [14] C.-W. Chu, H. Yang, W.-J. Hou, J. Huang, G. Li, Y. Yang, *Appl. Phys. Lett.* 92 (2008) 103306.
- [15] J. Peet, C. Soci, R.C. Coffin, T.Q. Nguyen, A. Mikhailovsky, D. Moses, G.C. Bazan, *Appl. Phys. Lett.* 89 (2006) 252105.
- [16] J. Peet, J.Y. Kim, N.E. Coates, W.L. Ma, D. Moses, A.J. Heeger, G.C. Bazan, *Nat. Mater.* 6 (2007) 497.
- [17] J.K. Lee, W.L. Ma, C.J. Brabec, J. Yuen, J.S. Moon, J.Y. Kim, K. Lee, G.C. Bazan, A.J. Heeger, *J. Am. Chem. Soc.* 130 (2008) 3619.
- [18] I.-W. Hwang, S. Cho, J.Y. Kim, K. Lee, N.E. Coates, D. Moses, A.J. Heeger, *J. Appl. Phys.* 104 (2008) 033706.
- [19] A.J. Moulé, K. Meerholz, *Adv. Mater.* 20 (2008) 240.
- [20] F.-C. Chen, H.-C. Tseng, C.-J. Ko, *Appl. Phys. Lett.* 92 (2008) 103316.
- [21] M. Campoy-Quiles, T. Ferenczi, T. Agostinelli, P.G. Etchegoin, Y. Kim, T.D. Anthopoulos, P.N. Stavrinou, D.D.C. Bradley, J. Nelson, *Nat. Mater.* 7 (2008) 158.
- [22] F.-C. Chen, Y.K. Lin, C.-J. Ko, *Appl. Phys. Lett.* 92 (2008) 023307.
- [23] M.G. Harrison, J. Gruner, G.C.W. Spencer, *Phys. Rev. B* 55 (1997) 7831.
- [24] M. Park, B.D. Chin, J.W. Yu, M.S. Chun, S.H. Han, *J. Ind. Eng. Chem.* 14 (2008) 382.
- [25] Q.M. Zhang, V. Bharti, G. Kavarnos, M. Schwartz (Eds.), *Poly (Vinylidene Fluoride) (PVDF) and its Copolymers*, Encyclopedia of Smart Materials, vol. 1–2, John Wiley and Sons, 2002, pp. 807–825.
- [26] C.J. Brabec, A. Cravino, D. Meissner, N.S. Sariciftci, T. Fromherz, M.T. Rispens, L. Sanchez, J.C. Hummelen, *Adv. Funct. Mater.* 11 (2001) 374.

transport in the PVK: Au NPs hybrid memory device is dominated by the PVK matrix (i.e., by means of the hopping of holes among the carbazole groups of PVK polymer chains). The role of Au NPs is to store the electrons donated from PVK to keep the high-conductivity state stable. Hence, in the present work,  $I$ - $V$  characteristics of the Al/PVK: Au NPs/Al device are examined by fitting the  $J$ - $E$  curves to various conduction models. It is revealed that the carrier conduction is governed by the energy-band offsets at the metal–semiconductor (Al–PVK or Au–PVK) junctions. The resistive switching of the Al/PVK: Au NPs/Al device can be explained by the variation of depletion width at the Al–PVK or Au–PVK Schottky barrier junctions, owing to the change of PVK Fermi level position upon applying bias. In addition, memory retention test demonstrates that the device remains the excellent performance at 154 °C in ambient atmosphere.

## 2. Experimental procedures

The memory device had a structure shown in the inset of Fig. 1a. The polymer active layer, consisting of PVK and Au NPs, is sandwiched between Al electrodes. PVK ( $M_w = 1100000$ ,  $T_g = 220$  °C) was purchased from Sigma-Aldrich, Inc. Au NPs with a diameter of approximately 4 nm were synthesized by Brust's two-phase reaction method [14] and capped with saturated alkanethiols of 1-dodecanethiol (DT). PVK and Au NPs were mixed and dissolved in 1,2-dichlorobenzene solution with the weight ratio of Au NPs:PVK = 0.083:1. The solution was spun on the Al/glass substrate followed by a heat treatment at ~60 °C for 5 min to form the active layer. The film thickness was about 120 nm as measured with scanning electron microscope. Finally, the top aluminum electrode was deposited on the polymer active layer by electron-beam evaporation through a shadow mask. The electrode area is 0.04 mm<sup>2</sup>. The spin-coating process and electrical measurements (with Agilent 4156C semiconductor parameter analyzer) were conducted in ambient condition.

## 3. Results and discussion

Fig. 1a and b shows the  $I$ - $V$  characteristics of the PVK: Au NPs hybrid memory devices in semi-log and log-log scales, respectively. The as-fabricated device shows a high-resistance state (HRS) until the threshold voltage where the device is switched to a low-resistance state (LRS) with a current compliance of 1 mA. Once the transition is achieved, the device remains at the LRS even after the applied voltage is removed, indicative of the non-volatile switching property. The conductance of LRS is different from that of HRS by a factor of 10<sup>5</sup> at room temperature. When the current compliance is released, the device can be switched back to the HRS by the application of a positive voltage below 2 V (see Fig. 1a). For further analysis, the  $I$ - $V$  curve is replotted in a log-log scale in Fig. 1b. It can be seen that the  $I$ - $V$  characteristic in the LRS follows a linear Ohmic conduction (the slope is close to 1). The conduction behavior in the HRS is governed by Ohmic law at a low voltage region (<0.1 V) with a slope ~1. How-

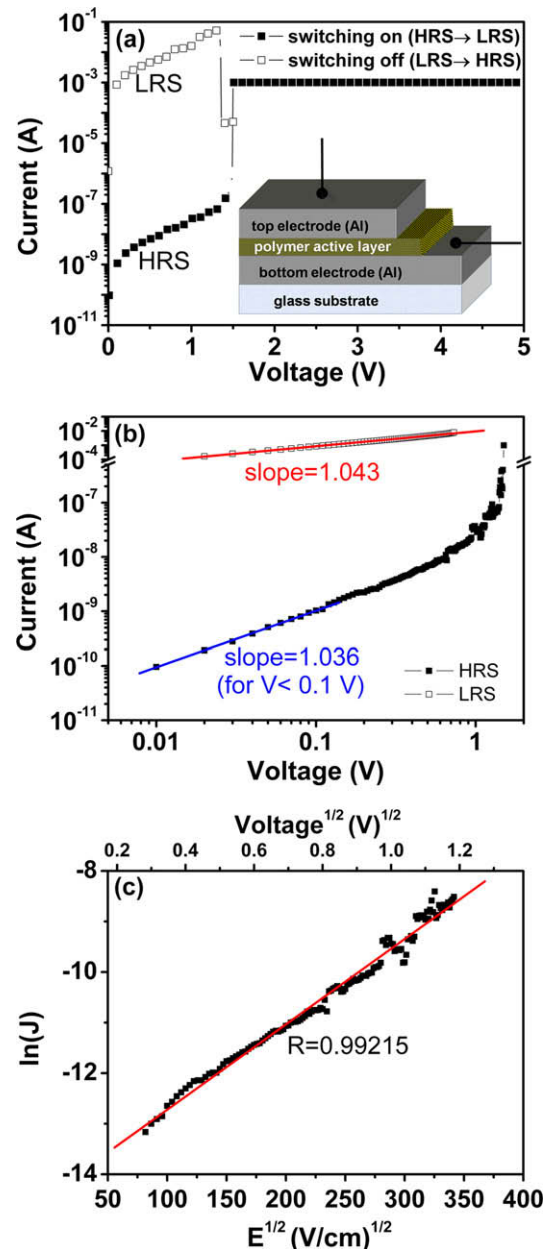


**Fig. 1.**  $I$ - $V$  characteristics of the Al/PVK: Au NPs/Al device in (a) semi-log scale and (b) log-log scale at 25 °C. The inset in (a) represents the schematic structure of the memory device. (c)  $J$ - $E$  curve (for  $V > 0.1$  V) of the Al/PVK: Au NPs/Al device at the high voltage region in the HRS fitted with the Schottky emission model.

ever, the current is not a simple straight line in the voltage region of greater than 0.1 V. This region is fitted with the Schottky emission model [15] as follows:

$$J = A^* T^2 \exp \left[ \frac{-q(\phi_B - \beta \sqrt{E})}{kT} \right], \quad (1)$$

where  $J$  is the current density,  $A^*$  is the effective Richardson constant,  $T$  is the absolute temperature,  $q$  is the elec-

tronic charge,  $\phi_B$  is the barrier height,  $\beta$  is the Schottky coefficient,  $E$  is the electric field, and  $k$  is the Boltzmann constant. A plot of  $\ln(J)$  vs.  $E^{1/2}$  indeed exhibits a linear relation, as shown in Fig. 1c, indicating that the conduction behavior in the HRS is governed by Schottky emission at the voltage greater than 0.1 V. The unipolar switching behavior and mechanism are significantly different from the space-charge-limited-conduction (SCLC) effects observed for other PVK-based memory devices so far [10,11].

To acquire further insight into the resistive switching phenomenon, the dependence of the electrical conduction property on temperature was investigated. Fig. 2a shows  $\log I$ - $\log V$  curves of the Al/PVK: Au NPs/Al memory device measured at temperatures ranging from 25 to 154 °C. The retention performance in LRS has also been examined under biased at voltage 1 V for temperatures ranging from 25 to 154 °C. The result indicates that the current remains constant as time passed for the devices tested at all individual temperatures; therefore, only the stress test in LRS for the device measured at 154 °C is presented to demonstrate the outperformed thermal stability, as shown in Fig. 2b. The memory device remains to be programmable at 154 °C, which is superior to other polymer [3,10] and even inorganic memory devices [16].

The Schottky emission mechanism is further confirmed by replotting the  $I$ - $V$  curves obtained at various tempera-

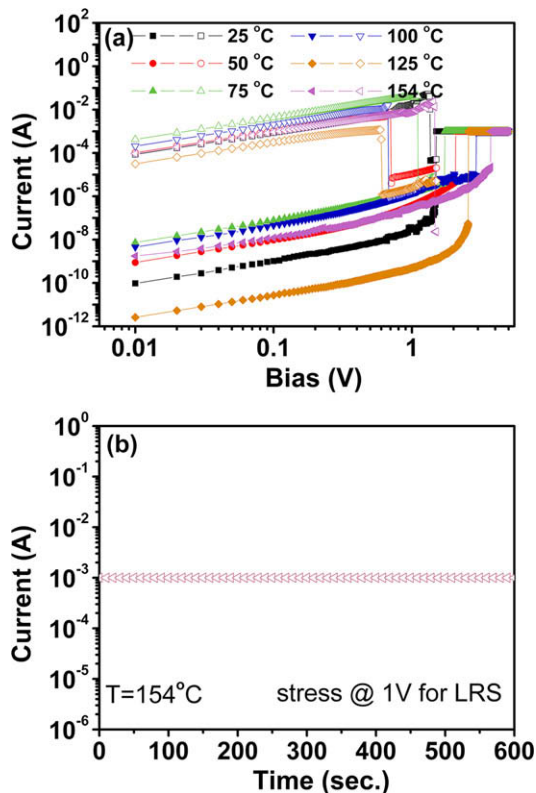


**Fig. 2.** (a)  $\log I$ - $\log V$  characteristics of the Al/PVK: Au NPs/Al device measured at temperatures ranging from 25 to 154 °C. The solid and open symbols represent the HRS and LRS, respectively. (b) Stress test (applied bias = 1.0 V) in LRS of the Al/PVK: Au NPs/Al device measured at 154 °C.

tures in form of  $\ln(J/T^2)$  vs.  $V^{1/2}$ . In the  $\ln(J/T^2)$  vs.  $V^{1/2}$  plot, the voltage range where the linear relationship holds is defined as “Schottky voltage region”. After that,  $\ln(J/T^2)$  is plotted with respect to  $1/T$  for different voltages within the Schottky voltage region, and various activation energies ( $E_{\text{act.}} = q(\phi_B - \beta d^{-1/2} V^{1/2})$ , where  $d$ : film thickness) can be extracted from the curves associated with different voltages. In the  $\ln(J/T^2)$  vs.  $1/T$  plot, one can also find that only in the temperature range 25–75 °C, the linear relationship holds well. Therefore, the Schottky emission model may not fully explain the conduction behavior of the Al/PVK: Au NPs/Al memory device when operating at high temperatures ( $T \geq 100$  °C). The reason for it is yet to be explored.

The  $E_{\text{act.}}$  is then plotted as a function of  $V^{1/2}$ , as shown in Fig. 3, to extrapolate the Schottky barrier height,  $\phi_B$ . It is found that  $\phi_B = 0.71$  and 1.89 eV for the voltage regions of  $0.1 \text{ V} \leq V \leq 0.6 \text{ V}$  and  $V \geq 1 \text{ V}$ , respectively. These two  $\phi_B$ , 0.71 and 1.89 eV, correspond nicely to the energy difference between work function of Au NPs (5.1 eV) [17] and HOMO (highest occupied molecular orbital) of PVK (5.8 eV) [18], and to the energy difference between the work function of Al electrode (3.9 eV) [19] and HOMO of PVK, respectively. The schematic energy-level diagrams for Al, Au and PVK prior to contact are shown in Fig. 4, where the Fermi levels of Al and Au, as well as the LUMO and HOMO levels of PVK are at 3.9, 5.1, 2.2 [18] and 5.8 eV, respectively. (All the energy levels are relative to the vacuum level.) After contact, Fermi level is a constant through the system at thermal equilibrium. The energy-band diagrams for the Al-PVK and Au-PVK junctions thus will depend on the position of PVK Fermi level ( $E_{F, \text{PVK}}$ ), and band bending will occur in the PVK (i.e., the semiconductor) layer. The degree of band bending in PVK shall govern the carrier transport across the Al-PVK and Au-PVK junctions, which will subsequently affect the current conduction in the resistive switching memory devices, as discussed in the following.

The position of  $E_{F, \text{PVK}}$  is dependent on the hole carrier concentration in PVK. The higher hole concentration, the closer  $E_{F, \text{PVK}}$  approaches to  $\text{HOMO}_{\text{PVK}}$ . In the pristine state, the hole concentration in PVK is relatively low. Assuming that  $E_{F, \text{PVK}} - \text{HOMO}_{\text{PVK}} = 1.0 \text{ eV}$  at the beginning of bias

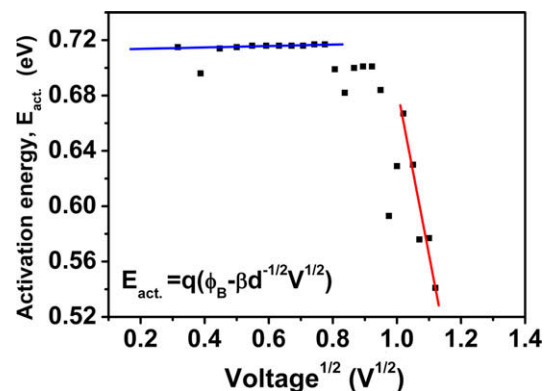


**Fig. 3.** Variation in activation energy ( $E_{\text{act.}}$ ) as a function of  $V^{1/2}$  of the Al/PVK: Au NPs/Al device.

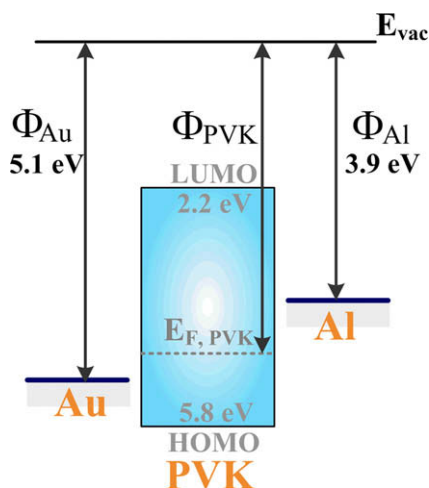


**Fig. 4.** The schematic energy-level diagram for Al, PVK, and Au prior to contact. All energy levels are in negative values with respect to the vacuum level ( $E_{vac} = 0$ ).

application. In this case,  $E_{F, Au}$  is slightly lower than  $E_{F, PVK}$ , while  $E_{F, Al}$  is higher than  $E_{F, PVK}$ . Accordingly, Au forms an Ohmic contact to PVK while Al forms a Schottky contact to PVK [20], and the schematic energy-band diagrams for Al–PVK and Au–PVK junctions is drawn in Fig. 5a. Because of the high Schottky barrier ( $\sim 1.9$  eV), it is less likely for hole

carriers to be conducted through the Al–PVK junction. However, there will be some Au NPs inevitably contacting with the Al electrodes during the device fabrication. The Au–PVK Ohmic contact provides a channel for hole conduction from the Al electrode to the HOMO of PVK, via the Au NPs, at the low voltage region. Therefore, the Ohmic conduction is observed in the HRS at the low voltage region ( $<0.1$  V).

Upon the application of external voltage, PVK carbazole groups will donate their electrons to Au NPs to increase the hole concentration and conductivity of the polymer, leading to the down-shift of  $E_{F, PVK}$  (approaching to  $HOMO_{PVK}$ ). Subsequently, the work function of PVK would be larger than that of Au, which results in the Schottky conduction at both Au–PVK junction (barrier height  $\sim 0.7$  eV) and Al–PVK junction (barrier height  $\sim 1.9$  eV), as illustrated in Fig. 5b (where  $E_{F, PVK} - HOMO_{PVK}$  is assumed to be 0.5 eV). Therefore, a Schottky barrier height of  $\sim 0.7$  eV is extracted from the  $E_{act}$  vs.  $V^{1/2}$  plot (Fig. 3) within the voltage region of 0.1–0.6 V. When the applied bias approaches 1 V, the probability for holes to surmount the energy barrier at the Al–PVK junction is enhanced. Accordingly, the Schottky barrier height extracted from the  $E_{act}$  plot (Fig. 3) corresponds adequately to the energy offset between  $E_{F, Al}$  and  $HOMO_{PVK}$  ( $\sim 1.9$  eV).

Switching of the device from the HRS to LRS can also be explained via the energy-band diagrams. As the PVK carbazole groups continuously donate electrons to Au

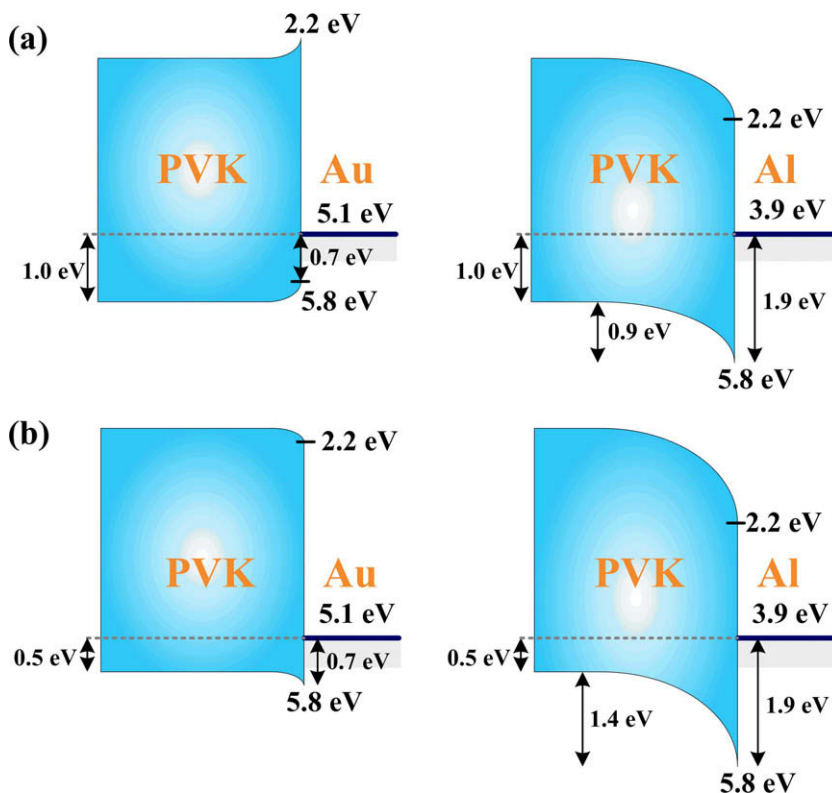


**Fig. 5.** The schematic energy-level diagrams for PVK–Au and PVK–Al junctions. Assuming that PVK possesses: (a) a rather low carrier concentration, where  $E_{F, PVK} - HOMO_{PVK} = 1.0$  eV; (b) a medium low carrier concentration, where  $E_{F, PVK} - HOMO_{PVK} = 0.5$  eV.

NPs upon applying bias, the amount of hole carriers increases. High carrier concentration will further lower  $E_{F, \text{PVK}}$  and narrow the width of depletion region at the Al–PVK Schottky barrier junction, which eventually leads to the tunneling of holes at the Al–PVK junction, as illustrated in Fig. 6a (where  $E_{F, \text{PVK}} - \text{HOMO}_{\text{PVK}} = 0.3 \text{ eV}$ ). As a result, a sharp increase of current is observed, which corresponds to the switching from HRS to LRS. The tunneling of carriers at the metal–semiconductor junction due to the thinning of depletion width of Schottky barrier may be analogous to the steep change of current of a PN diode under a large reverse bias (Zener effect). Therefore, the current increases (from HRS to LRS) abruptly.

According to the energy-level diagram, when an electron is conducted across the Au–PVK junction, it needs to overcome the energy difference (barrier) between  $E_{F, \text{Au}}$  and  $\text{LUMO}_{\text{PVK}}$ , as schematically shown in Fig. 6b. Because of the large value of  $\text{LUMO}_{\text{PVK}} - E_{F, \text{Au}}$ , the trapped electrons will be stably trapped in Au NPs. Therefore, after the memory device is switched to the LRS, a subsequent voltage scan reveals that the current instantly reaches the level of compliance current ( $I$ – $V$  curve not shown). Regarding to switching from the LRS to HRS, the current compliance needs to be released or lifted, such that the external voltage is effectively applying on the device and the hole concentration in PVK will increase with the increasing applied voltage (via the electron donation from PVK to Au NPs). Increase of hole concentration leads to thinning of the depletion region at the Au–PVK Schottky

barrier junction. Consequently, the holes will have a large probability to tunnel through the thin depletion region and neutralize the trapped electrons in Au NPs. As a result, the carrier concentration in PVK is significantly reduced and the  $E_{F, \text{PVK}}$  moves upwards, resembling the situation of Fig. 5a or b. Consequently, the device is switched back to HRS.

The work done by Song et al. [12] also utilized PVK: Au NPs hybrid as the active layer for non-volatile memory devices but the top and bottom electrodes are Al and TaN, respectively. Both Song et al.'s and our works agree that the role of Au NPs is to accept electrons donated from PVK. However, they observed bipolar switching behavior and the resistive switching is attributed to the change of the electronic states due to the formation of the electric-field-induced charge transfer complex between the PVK and Au NPs. Additionally, the conduction mechanism ( $J$ – $E$  curve fitting) was not investigated in their work. We employed Al as both top and bottom electrodes to simplify the device structure and observed unipolar switching character. The current conduction is mainly governed by Schottky emission, and the hole concentration in PVK increases via donating electrons to Au NPs upon applying electrical field. As a result, the resistive switching is correlated with the width of depletion region in Al–PVK or Au–PVK Schottky barrier junction. Because Schottky emission phenomenon is highly dependent on the electrode materials, the dissimilar observations and conclusions between Song et al.'s and our works may be attributed to the different electrode schemes of the memory devices. Definitely, the

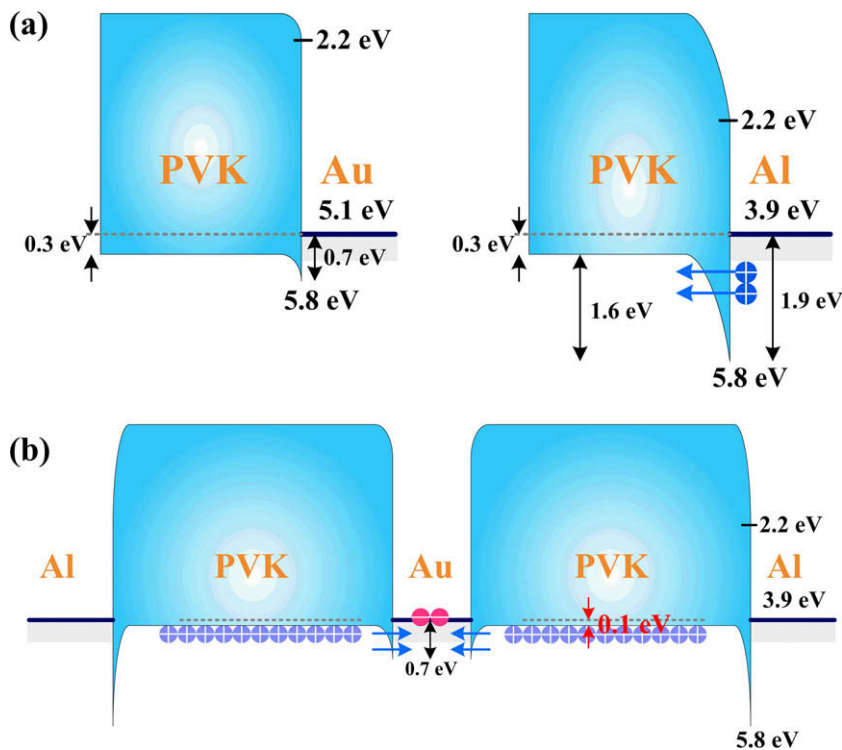


**Fig. 6.** The schematic energy-level diagrams for PVK–Au and PVK–Al junctions. Assuming that PVK possesses: (a) a high carrier concentration, where  $E_{F, \text{PVK}} - \text{HOMO}_{\text{PVK}} = 0.3 \text{ eV}$ ; (b) a very high carrier concentration, where  $E_{F, \text{PVK}} - \text{HOMO}_{\text{PVK}} = 0.1 \text{ eV}$ .

exact explanation for the dissimilarity is yet to be further explored.

#### 4. Conclusion

The Al/PVK: Au NPs/Al memory device is investigated for non-volatile memory applications with the conductance difference ratio between the HRS and LRS by a factor of  $10^5$ . Furthermore, the Au nanoparticle/PVK hybrid memory device can be programmed and exhibits excellent thermal stability at 154 °C in ambient atmosphere. It is elucidated that the carrier conduction in the HRS is mainly governed by the Schottky emission model and the barrier height is associated with the energy-band offsets at the Al–PVK or Au–PVK junction. However, the position of PVK Fermi level, characterized by the hole carrier concentration, also changes upon applying bias due to donation of electrons from PVK to Au NPs. As a result, depletion width at the Al–PVK or Au–PVK Schottky barrier junction varies with the applied bias, leading to the tunneling of carriers and subsequently inducing the resistive switching in the Au nanoparticle/PVK hybrid memory device.

#### Acknowledgements

The authors gratefully appreciate the financial support from the National Science Council of Taiwan, (Grant No. NSC-96-2628-E-006-013-MY3), NCKU Landmark Project (No. A0051) and Applied Materials Taiwan.

#### References

- [1] Y.-L. Liu, Q.-D. Ling, E.-T. Kang, K.-G. Neoh, D.-J. Liaw, K.-L. Wang, W.-T. Liou, C.-X. Zhu, D.S.-H. Chan, *J. Appl. Phys.* 105 (2009) 044501.
- [2] J. Billen, S. Steudel, R. Muller, J. Genoe, P. Heremans, *Appl. Phys. Lett.* 91 (2007) 263507.
- [3] Q.-D. Ling, E.-T. Kang, K.-G. Neoh, Y. Chen, X.-D. Zhuang, C. Zhu, D.S.H. Chan, *Appl. Phys. Lett.* 92 (2008) 143302.
- [4] H.J. Bolink, E. Coronado, J. Orozco, M. Sessolo, *Adv. Mater.* 21 (2009) 79.
- [5] K.S. Yook, S.O. Jeon, C.W. Joo, J.Y. Lee, S.H. Kim, J. Jang, *Org. Electron.* 10 (2009) 48.
- [6] P. Dimitrakakis, P. Normand, D. Tsoukalas, C. Pearson, J.H. Ahn, M.F. Mabrook, D.A. Zeze, M.C. Petty, K.T. Kamtekar, C. Wang, M.R. Bryce, M. Green, *J. Appl. Phys.* 104 (2008) 044510.
- [7] R.J. Tseng, C.O. Baker, B. Shedd, J. Huang, R.B. Kaner, J. Ouyang, Y. Yang, *Appl. Phys. Lett.* 90 (2007) 053101.
- [8] Q.-D. Ling, S.-L. Lim, Y. Song, C.-X. Zhu, D.S.-H. Chan, E.-T. Kang, K.-G. Neoh, *Langmuir* 23 (2007) 312.
- [9] B. Pradhan, S.K. Batabyal, A.J. Pal, *J. Phys. Chem. B* 110 (2006) 8274.
- [10] Y.-S. Lai, C.-H. Tu, D.-L. Kwong, J.S. Chen, *IEEE Electron Device Lett.* 27 (2006) 451.
- [11] T. Kondo, S.M. Lee, M. Malicki, B. Domercq, S.R. Marder, B. Kippelen, *Adv. Funct. Mater.* 18 (2008) 1112.
- [12] Y. Song, Q.D. Ling, S.L. Lim, E.Y.H. Teo, Y.P. Tan, L. Li, E.T. Kang, D.S.H. Chan, C. Zhu, *IEEE Electron Device Lett.* 28 (2007) 107.
- [13] P.Y. Lai, J.S. Chen, *Appl. Phys. Lett.* 93 (2008) 153305.
- [14] M. Brust, M. Walker, D. Bethell, D.J. Schiffrin, R. Whyman, *J. Chem. Soc. Chem. Commun.* (1994) 801.
- [15] S.M. Sze, *Physics of Semiconductor Devices*, second ed., Wiley, New York, 1981, p. 403.
- [16] Y.C. Shin, J. Song, K.M. Kim, B.J. Choi, S. Choi, H.J. Lee, G.H. Kim, T. Eom, C.S. Hwang, *Appl. Phys. Lett.* 92 (2008) 162904.
- [17] B. Masenelli, D. Berner, M.N. Bussac, F. Nuesch, L. Zuppiroli, *Appl. Phys. Lett.* 79 (2001) 4438.
- [18] Y. Kawamura, S. Yanagida, S.R. Forrest, *J. Appl. Phys.* 92 (2002) 87.
- [19] V.V. Afanas'ev, M. Houssa, A. Stesmans, M.M. Heyns, *J. Appl. Phys.* 91 (2002) 3079.
- [20] D.A. Neamen, *Semiconductor Physics and Devices*, third ed., McGraw-Hill, New York, 2003, pp. 326.



Pentacene-based OTFTs incorporating a PMMA gate insulator usually possess a large operating voltage ( $\sim -20$  V), related to the thickness of the PMMA layer [7,8]. It is normally difficult to produce a pinhole-free film that is  $<150$  nm in thickness because of the large free volume of the polymer. One encouraging result is that of Noh et al. who have reported devices operating at gate voltages  $<8$  V with a 30 nm thick cross-linked PMMA layer [9,10]. The particular chemical cross-linking methodology that was used, exploiting the cross-linking agent 1,6-bis(trichlorosilyl)hexane (C6-Si), is a rather demanding procedure as it requires processing in a very high purity inert atmosphere. In this work, we focus on a physical method to cross-link PMMA.

During ion-beam irradiation of polymers, both cross-linking and scission occur simultaneously, but the relative effectiveness of the two processes depends upon polymer structure and also on the linear energy transfer (LET,  $\text{eV nm}^{-1}$ ) from the radiation source [11,12]. For

example, in the case of PMMA at low LET, most radicals do not cross-link because of wide physical separation between them and chain scission predominates. Cross-linking is however possible at high LET [12] because the radical density is then higher and the separation between them is reduced. In this work, the irradiation was undertaken using a 1.515 MeV  $^4\text{He}^+$  ion beam to achieve a high LET and effective cross-linking.

## 2. Experiment

Top source and drain contact OTFTs were fabricated. Glass slides were used as substrates after cleaning sequentially in an ultrasonic bath with acetone, isopropanol and deionized water. An aluminium gate, thickness 40 nm, was defined by thermal evaporation through a shadow mask. To form the gate dielectric, a 2.44 wt% anisole (MicroChem) solution of PMMA (Mw = 93,000, Sigma-Aldrich) was spin-coated at 3000 rpm spinning speed for

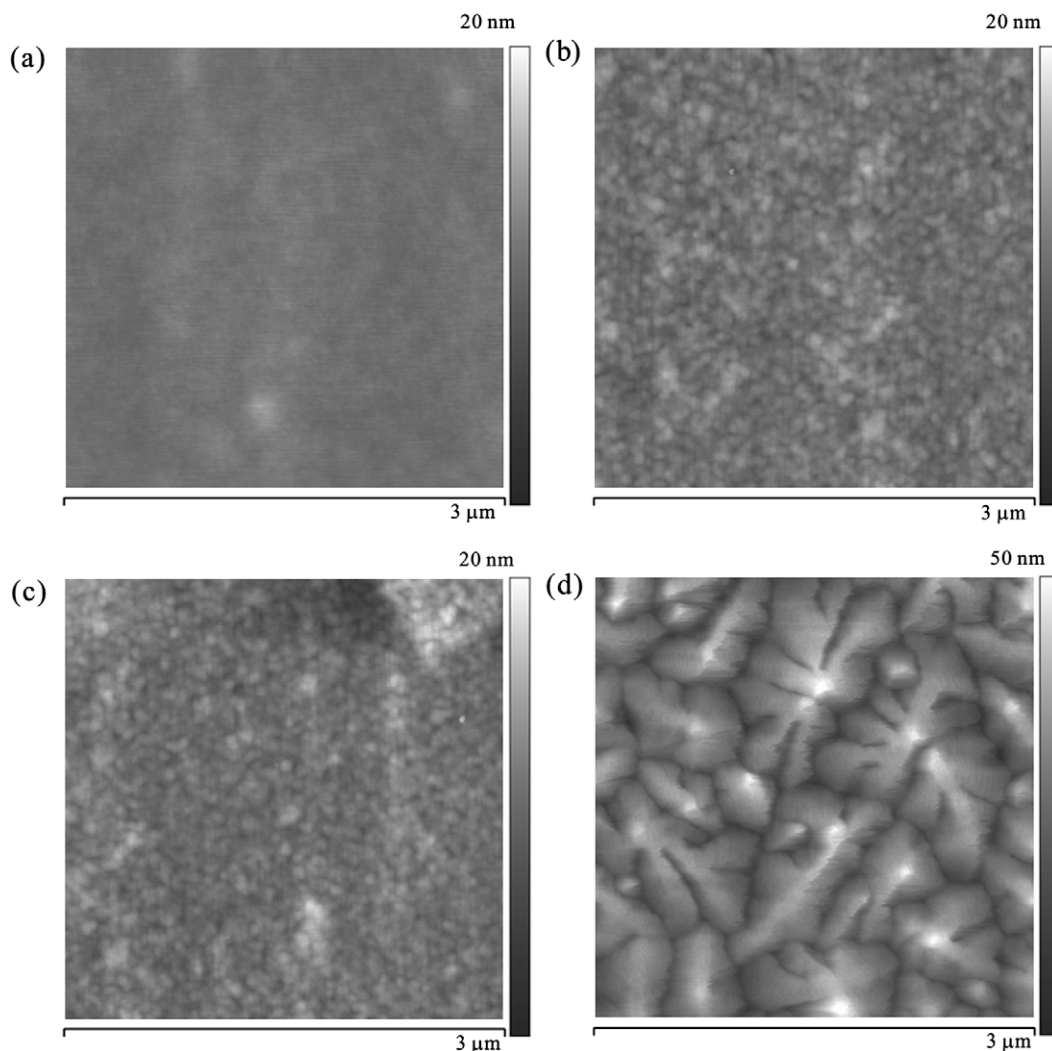


**Fig. 1.** Atomic force microscope images of (a) 57 nm thick PMMA film spin-coated onto a glass slide, (b) 33 nm thick cross-linked PMMA film by ion-beam irradiation, (c) 33 nm thick cross-linked PMMA film after development in acetone, and (d) 40 nm thick pentacene film thermally evaporated on top of the cross-linked PMMA.

50 s on Al and baked for 30 min at 120 °C; this resulted in a 57 nm thick layer with 0.65 nm rms roughness.

A 1.515 MeV  $^4\text{He}^+$  ion beam was delivered to the sample surface at 7° grazing incidence using a National Electrostatics Corporation 5SDH Pelletron accelerator. The total charge of the beam was 6  $\mu\text{C}$  per irradiated spot and the incident beam had a diameter of 2.4 mm. The irradiated area therefore was elliptical with axes of 2.4 and 19.7 mm and a total area of 37.1 mm<sup>2</sup>. The beam fluence was  $1.0 \pm 0.1 \times 10^{14}$  ions cm<sup>-2</sup>, and had an LET figure of about 220 keV  $\mu\text{m}^{-1}$  (assuming a polymer density of 1.20 g cm<sup>-3</sup>). The energy loss and range of MeV ions in solids are well-documented and may be calculated using the

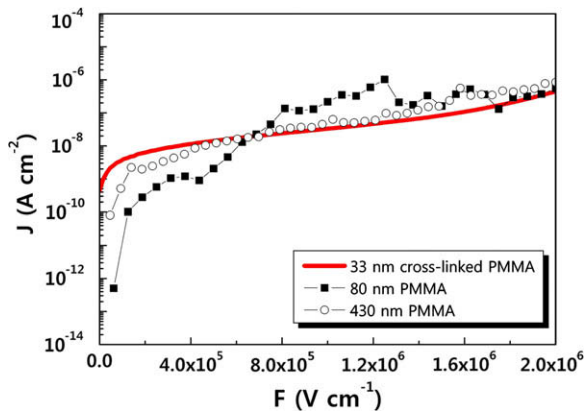


**Fig. 2.** Current density versus applied electric field for PMMA films (80 and 430 nm in thickness) and a cross-linked PMMA film (33 nm) sandwiched between aluminium and gold electrodes.

SRIM software made available by Ziegler et al. [13]. The total range of the ion beam used would be approximately 8.6  $\mu\text{m}$  in PMMA, and in our experiments the energy loss of the beam traversing 57 nm PMMA at 7° is approximately 0.1 MeV. The variation in stopping power (energy loss/distance traversed) of the ion beam over this range is <4%. Therefore, we can be confident that the level of radiation-induced cross-linking is similar throughout the film.

Pentacene (Sigma–Aldrich) was thermally deposited onto the irradiated PMMA layer at room temperature to a thickness of 40 nm using a shadow mask. The deposition rate was 0.02 nm s<sup>-1</sup> at chamber pressure of approximately  $3 \times 10^{-7}$  mbar. Finally, a further shadow mask was used to define the source and drain contacts, formed by the thermal evaporation of 40 nm of gold.

The thickness and morphologies of the various layers were studied using a Digital Instruments Nanoscope atomic force microscope. The transistor characteristics were measured under ambient conditions using an HP 4140B Picoammeter/DC Voltage source. The current versus voltage characteristics were measured using a Keithley 485 picoammeter and 2400 source meter. The capacitance versus voltage behavior was monitored with an HP4192A impedance analyser.

### 3. Results and discussion

Fig. 1 shows atomic force microscope images of the surface of a 57 nm spin-coated PMMA film (Fig. 1a), the same film (now 33 nm in thickness) following ion-beam irradiation (Fig. 1b), the irradiated PMMA film after development in acetone (Fig. 1c) and the surface of a 40 nm pentacene

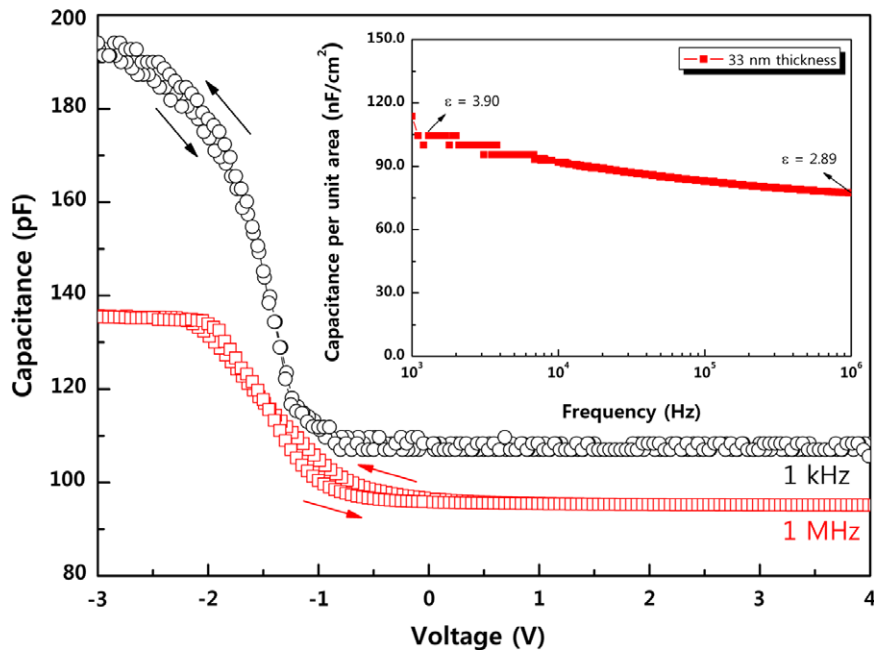


**Fig. 3.** Capacitance versus voltage characteristics, measured at 1 MHz and 1 kHz and a voltage scan rate of 0.05 V s<sup>-1</sup> for aluminium/cross-linked PMMA (33 nm)/pentacene (40 nm)/gold structure. Inset: capacitance versus frequency characteristics for 33 nm thick cross-linked PMMA layer sandwiched between the aluminium and gold electrodes.

film, which was subsequently evaporated onto the irradiated PMMA (Fig. 1d). Following irradiation, the thickness of the PMMA has been reduced by about one half and the film is no longer soluble in solvents such as acetone or iso-propyl alcohol: methyl iso-butyl ketone in a 3:1 ratio (used as a developer for PMMA). This suggests that the PMMA has become cross-linked. The ion-beam irradiation has also resulted in an increase in the rms surface roughness – from 0.65 to 1.34 nm. However, subsequent evaporation of pentacene onto cross-linked PMMA reveals a high quality film with a relatively large grain size (Fig. 1d). The cross-linked PMMA film is referred to as cPMMA in the forthcoming sections.

A parallel plate capacitor structure (Al/insulator/Au) was fabricated to investigate the dielectric properties of the cPMMA. The area of the capacitor was nominally  $1.8 \times 10^{-3} \text{ cm}^2$  (exact area values were measured and used in the calculations of current density and permittivity). Fig. 2 contrasts the current density  $J$  versus the electric field  $F$  behavior for spin-coated PMMA (80 and 430 nm

films) and for cPMMA (33 nm). The leakage current density of the cPMMA was  $<10^{-8} \text{ A cm}^{-2}$  for fields up to  $0.35 \text{ MV cm}^{-1}$  and this remained below  $10^{-6} \text{ A cm}^{-2}$  for fields up to  $2 \text{ MV cm}^{-1}$ . Similar data were measured for the uncross-linked PMMA. In a previous paper [7], we have discussed the origin of the electrical characteristics of spin-coated of PMMA films. The conclusion was that high electrical field processes, resulting from the Poole–Frenkel effect or from Schottky emission, may dominate the electrical behavior in thin films. In the case of Schottky emission, the conductivity will be limited by the electrodes, perhaps accounting for the similar conductivity values of our cross-linked and uncross-linked films. Further work is needed to clarify this point. However, for the purposes of this study, the measured leakage current densities are sufficiently small to enable a 33 nm cPMMA film to be used as the gate dielectric in an OTFT.

The capacitance,  $C$ , versus voltage,  $V$ , characteristics, measured at 1 MHz and at 1 kHz and a voltage scan rate of  $0.05 \text{ V s}^{-1}$ , for an aluminium/cPMMA/pentacene/gold

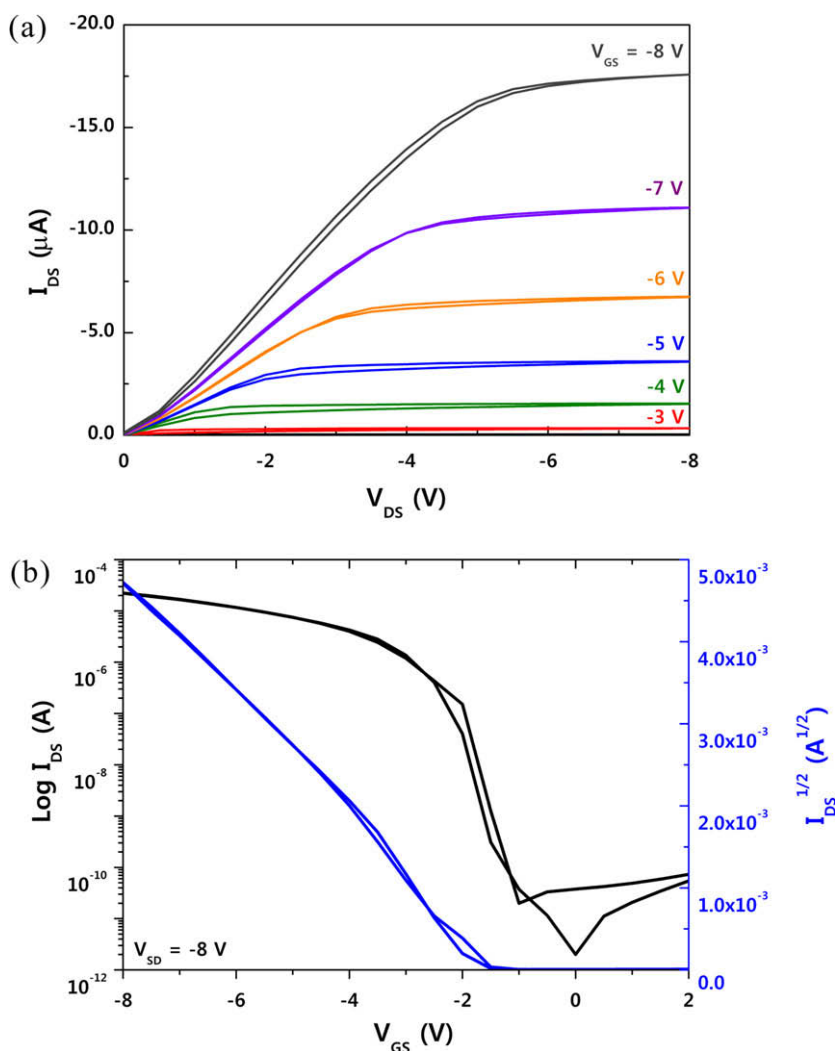


**Fig. 4.** (a) Output and (b) transfer characteristics of a pentacene-based OTFT using cross-linked PMMA as the gate dielectric. Forward and reverse voltage scans are shown for both sets of data. Device channel length =  $50 \mu\text{m}$ ; channel width =  $500 \mu\text{m}$ .

metal-insulator-semiconductor (MIS) structure are depicted in Fig. 3; the inset shows the measured capacitance per unit area as a function of frequency for a 33 nm thick cPMMA layer sandwiched between aluminium and gold electrodes. Using the latter curve, the dielectric constant of the cPMMA layer was calculated to be  $3.90 \pm 0.10$  at 1 kHz and  $2.89 \pm 0.10$  at 1 MHz. These values are almost the same as those reported for PMMA [7]. The accumulation capacitance for the MIS structure was found to scale with the cPMMA thickness and the calculated dielectric constant was the same, within experimental errors, with the value calculated from the inset of Fig. 3. The  $C$ - $V$  curves shown in Fig. 3 reveal only a very small degree of hysteresis on reversing the voltage scan direction. This is very similar to that observed with pentacene/PMMA OTFTs and is consistent with a relatively 'clean' (in an electronic sense) interface between the pentacene and the cross-linked polymer [7].

The output and transfer characteristics for an OTFT with a 33 nm cPMMA gate insulator, formed by spin-coating and ion-beam irradiation, are shown in Fig. 4 (device channel length = 50  $\mu\text{m}$ , and width = 500  $\mu\text{m}$ ). The output characteristics of the device plotted in Fig. 4a reveal the drain current,  $I_{DS}$ , as a function of source-drain voltage,  $V_{DS}$ , for different values of gate voltage,  $V_{GS}$ . The device shows excellent characteristics in the linear and saturation regions. Moreover, the thin-film transistor operates at relatively low voltages, <10 V. The transfer characteristics of the device Fig. 4b, are measured at  $V_{DS} = -8$  V. Plots are given in the form of both  $\log(I_{DS})$  versus  $V_{GS}$  and  $(I_{DS})^{1/2}$  versus  $V_{GS}$ . The on/off current ratio, threshold voltage,  $V_T$ , and sub-threshold slope for the device were  $1.1 \times 10^6$ ,  $-0.9$  V, and 219 mV decade $^{-1}$ . Such characteristics compare very favorably with other recent published data for pentacene/PMMA OTFTs, the insulator thicknesses of which are greater than reported in this work [7,8,14–16].

The field-effect mobility,  $\mu$ , was estimated in the saturation region of the transistor, using

$$I_{DS(\text{sat})} = \frac{WC_i}{2L} \mu (V_{GS} - V_T)^2 \quad (1)$$

where  $I_{DS(\text{sat})}$  is the saturated drain-source current,  $W$  and  $L$  are the channel width and length, respectively,  $C_i$  is the dielectric capacitance per unit area. The value of  $\mu$  may therefore be evaluated from a plot of  $(I_{DS(\text{sat})})^{1/2}$  versus  $V_{GS}$ . Using the data from Fig. 4b provided a mobility of  $1.1 \text{ cm}^2 \text{ V}^{-1} \text{ s}^{-1}$  (using a permittivity value of 3.9 for the cPMMA). This will be a mean value, as the field-effect mobility will vary along the channel of the OTFT. The mobility figure obtained in this work is higher than that previously obtained with thicker PMMA films [7]. Other workers on organic transistors have reported mobilities that depend on the gate voltage, even when  $V_G$  exceeds  $V_T$  [17–20]. One explanation for this phenomenon can be based on the theory described by Necliudov and coworkers [17]. According to this model, in pentacene-based OTFTs operating above threshold, most of the charge induced by the gate-source voltage is trapped and only a fraction of

the carriers participate in the current conduction. The number of accumulated carriers at the pentacene surface will depend on the gate voltage, an increase in which will result in an increase in the surface carriers. Such a process may explain the higher field-effect mobilities found with decreased thickness of gate insulator for our pentacene/PMMA OTFTs.

#### 4. Conclusions

We have been able to cross-link PMMA by ion-beam radiation and to use the resulting thin film as the gate dielectric in pentacene-based field-effect transistors. We have achieved a high-performance device, possessing a field-effect mobility of over  $1 \text{ cm}^2 \text{ V}^{-1} \text{ s}^{-1}$ , a threshold voltage of around  $-1$  V, an on/off current ratio over  $10^6$ , and a sub-threshold slope of about 220 mV decade $^{-1}$ . The cross-linking methodology using an ion beam may not seem to fit with the low-cost rationale for organic electronics noted earlier. However, the experiments reported here are feasibility studies and indicate that physical cross-linking of the PMMA gate dielectric can be used effectively to produce thin-film transistors with high carrier mobility and operating at low voltages. Other solutions, e.g. based on reactive ion etching, may prove to be more appropriate for manufacture.

#### Acknowledgements

One of us, Y. Yun, would like to thank the School of Engineering, Durham University, for the provision of a studentship.

#### References

- [1] C.D. Dimitrakopoulos, D.J. Mascaro, IBM J. Res. Dev. 45 (2001) 1.
- [2] D. Braga, G. Horowitz, Adv. Mater. 21 (2009) 1473.
- [3] O.D. Jurchescu, M. Popinciuc, B.J. Van Wees, T.T.M. Palstra, Adv. Mater. 19 (2007) 688.
- [4] H. Klauk, U. Zschieschang, J. Pflaum, M. Halik, Nature 445 (2007) 15.
- [5] M.-H. Yoon, H. Yan, A. Facchetti, T.J. Marks, J. Am. Chem. Soc. 127 (2005) 29.
- [6] Y.-S. Jang, D.-H. Kim, Y.-D. Park, J.-H. Cho, M.-K. Hwang, K.-W. Cho, Appl. Phys. Lett. 88 (2009) 072101.
- [7] Y. Yun, C. Pearson, M.C. Petty, J. Appl. Phys. 105 (2009) 034508.
- [8] T.-S. Huang, Y.-K. Su, P.-C. Wang, Appl. Phys. Lett. 91 (2007) 092116.
- [9] Y.-Y. Noh, N. Zhao, M. Caironi, H. Sirringhaus, Nat. Nanotechnol. 2 (2007) 784.
- [10] Y.-Y. Noh, H. Sirringhaus, Org. Electron. 10 (2009) 174.
- [11] A. Chapiro, Radiation Chemistry of Polymeric Systems, Interscience Publishers, New York, 1962.
- [12] E.H. Lee, G.R. Rao, L.K. Mansur, Radiat. Phys. Chem. 55 (1999) 293.
- [13] J.F. Ziegler, J.P. Biersack, U. Littmark, The Stopping Range of Ions in Solids, Pergamon Press, New York, 1985.
- [14] G.-W. Kang, K.-M. Park, J.-H. Song, C.H. Lee, D.H. Hwang, Curr. Appl. Phys. 5 (2005) 297.
- [15] K.-K. Han, S.W. Lee, H.H. Lee, Appl. Phys. Lett. 88 (2006) 233509.
- [16] J. Puigdollers, C. Voz, I. Martin, M. Vetter, A. Orpella, R. Alcubilla, Synth. Met. 146 (2004) 355.
- [17] P.V. Necliudov, M.S. Shur, D.J. Gundlach, T.N. Jackson, J. Appl. Phys. 88 (2000) 6594.
- [18] K. Seshadri, C.D. Frisbie, Appl. Phys. Lett. 78 (2001) 993.
- [19] G. Horowitz, J. Mater. Chem. 9 (1999) 2021.
- [20] J. Veres, S. Ogier, G. Lloyd, D. De Leeuw, Chem. Mater. 16 (2004) 4543.

ultrafast ( $\sim 100$  fs) hot exciton dissociation [14]. Subsequently, Virgili et al. studied the ultrafast intrachain photoexcitation in isolated polymer chains [11]. They presented the first experimental evidence of intrachain generation and recombination of free charges, and attributed the charge generation to the dissociation of some higher excited states.

Both Hendry [6] and Virgili [11] speculated that the initial excitation products are excitons and some higher excited states. However, the yields of excitons and the higher excited states have not been investigated theoretically as they are a function of the photoexciting pulse. “By-hand” exciting one electron from a low occupied molecular orbital to high empty one, An et al. considered the single-electron transition in a polymer [13]. They found that transition from the highest occupied molecular orbital (HOMO) to the lowest unoccupied molecular orbital (LUMO) results in an exciton, while transition from Below-HOMO to Above-LUMO will lead to the formation of a high-energy exciton (as called in Ref. [13] a mixed state consisting of an exciton and a polaron pair). Due to the higher energy than that of an exciton, the high-energy exciton is found to be responsible for the generation of free charges [8]. In their theoretical treatment, the excited electrons have been supposed to lie in higher energy orbitals, while the photoexciting process was neglected. So they could not give a relation between the excited states and the photoexciting pulse. In this paper, we employ an AC field to simulate a photoexcitation, through which the spontaneous electron transitions are realized. The excitation products are recognized by projecting the evolution state onto the instantaneous eigenstates of some well known excited states. The paper is organized as follows. The model and method are presented in Section 2. The results and discussions are shown in Section 3. Finally in Section 4, a summary is given.

## 2. Model and method

Here we consider the photoexcitations in a PPV molecule, which has exhibits attractive optoelectronic properties. As early as the 1990s, Choi and Rice proposed a Su-Schrieffer-Heeger (SSH)-like Hamiltonian to describe the geometry and electronic structure of PPV [15], where all the carbon atoms in the benzene rings are included. In 2007, according to the SSH-like Hamiltonian we proposed a relatively simple model for a PPV molecule [8]. That is, by a renormalization treatment for the benzene rings, a PPV molecule can be regarded as a one-dimensional chain and each PPV monomer contains six carbon atoms along the chain direction. In this work, we will continue to use the latter model, since we have found that the change between the two models has a minor effect on the photoexcited results through a comparison.

For a PPV molecule, the Hamiltonian consists of three parts

$$H = H_e + H_{latt} + H_E. \quad (1)$$

Here

$$H_e = - \sum_n t_{n,n+1} (C_{n+1}^+ C_n + C_n^+ C_{n+1}) \quad (2)$$

shows the electron hopping between the nearest-neighbor sites of the system with the spin index omitted for clarity. The transfer integral  $t_{n,n+1}$  between site  $n$  and  $n+1$  is written as

$$t_{n,n+1} = t_0 - \alpha(u_{n+1} - u_n) - t_1 \cos n\pi + t_2 \cos\left(\frac{n+1}{3}\pi\right) \cdot \delta\left(\frac{n+1}{3}, \text{int}\right), \quad (3)$$

where  $\delta\left(\frac{n+1}{3}, \text{int}\right) = 1$ , if  $\frac{n+1}{3} = \text{int}$ ; and  $\delta\left(\frac{n+1}{3}, \text{int}\right) = 0$ , if  $\frac{n+1}{3} \neq \text{int}$ . “int” means an integer.  $t_0$  represents the nearest-neighbor transfer integral for a uniform bond structure,  $\alpha$  the electron-lattice interaction constant and  $u_n$  the displacement of a unit at site  $n$ .  $t_1$  and  $t_2$  are the symmetry-breaking parameters introduced to reflect the lattice feature of a PPV monomer.  $C_n^+$  ( $C_n$ ) is the creation (annihilation) operator of an electron at site  $n$ .

$$H_{latt} = \frac{1}{2}K \sum_n (u_{n+1} - u_n)^2 + \frac{1}{2}M \sum_n \dot{u}_n^2 \quad (4)$$

describes the classical treatment of the elastic potential and kinetic energy of the sites.  $K$  denotes the elastic constant and  $M$  the mass of a site.

$$H_E = \sum_n eE(t)(na + u_n)(C_n^+ C_n - 1) \quad (5)$$

shows the photoexciting effect through a time-dependent AC field  $E(t)$ , where  $e$  is the electronic charge and  $a$  lattice constant. To numerically simulate a femtosecond electric pump pulse [6,11], we choose  $E(t)$  as a Gaussian form with width  $T$  centered at  $t_c$ ,

$$E(t) = E_0 \exp\{-[(t - t_c)/T]^2\} \cos(\omega t), \quad (6)$$

by which Streitwolf et al. have successfully investigated the formation of solitons [16].  $E_0$  and  $\omega$  separately shows the photoexciting intensity and frequency.

The evolution of an electronic state  $|\Phi_v(t)\rangle$  depends on the time-dependent Schrödinger equation

$$i\hbar \frac{\partial}{\partial t} |\Phi_v(t)\rangle = \left( H_e + \sum_n eE(t)(na + u_n)C_n^+ C_n \right) |\Phi_v(t)\rangle. \quad (7)$$

Displacement  $u_n$  is not fixed in present case due to the strong electron-lattice interactions. With the evolution of the electronic states,  $u_n$  is developed upon the Newtonian equation of motion

$$M\ddot{u}_n = -K(2u_n - u_{n+1} - u_{n-1}) + 2\alpha(\rho_{n,n+1}(t) - \rho_{n-1,n}(t)) + eE(t)(\rho_{n,n}(t) - 1) - \lambda M\dot{u}_n. \quad (8)$$

$\rho_{n,n'}(t)$  is the electronic density matrix defined as

$$\rho_{n,n'}(t) = \sum_v \Phi_{v,n}^*(t) f_v \Phi_{v,n'}(t), \quad (9)$$

where  $\Phi_{v,n}(t) = \langle n | \Phi_v(t) \rangle$ .  $f_v$  denotes the occupation of state  $|\Phi_v(t)\rangle$  and is determined by the initial electron occupation (0, 1 or 2). In Eq. (8), a damping term is introduced to describe the energy dissipation into the surrounding medium by a tuning parameter  $\lambda$  [17].

To recognize the final states after photoexcitation, we introduce instantaneous eigenstate  $|\phi_\mu(t)\rangle$ , which is obtained by the instantaneous Eigen equation

$$\left[ H_e + \sum_n eE(t)(na + u_n)C_n^+ C_n \right] |\phi_\mu(t)\rangle = \varepsilon_\mu(t) |\phi_\mu(t)\rangle, \quad (10)$$

with the Hamiltonian determined by the instantaneous site position  $u_n$ .  $\varepsilon_\mu(t)$  is the Eigen energy of instantaneous state  $|\phi_\mu(t)\rangle$ .

In present investigation, we set  $|\Phi_v(t=0)\rangle = |\phi_v(t=0)\rangle$  at beginning. When a photoexcitation is applied, the state  $|\Phi_v\rangle$  will experience an evolution determined by the coupled differential Eqs. (7) and (8), which are solved by the Runge–Kutta method of order eight with step-size control [18,19].

The actual state of the whole electronic system at any time is obtained through a Slater determinant of the occupied single-electron evolutionary wavefunction  $|\Phi_v(t)\rangle$ . It is different from the simple adiabatic approximation, where the state of the system is given by instantaneous eigenstate  $|\phi_\mu(t)\rangle$ . Therefore, the present approach is a nonadiabatic one.

### 3. Results and discussion

In the simulations, we start from a ground state, which is determined by minimizing the total energy of a PPV molecule. The parameters are set as  $\alpha = 10.29$  eV/Å,  $t_0 = 2.66$  eV,  $a = 1.22$  Å,  $K = 99$  eV/Å<sup>2</sup>, and  $M = 1349.14$  eV fs<sup>2</sup>/Å<sup>2</sup> referring to Refs. [20,21]. By adjusting the magnitudes of  $t_1$  and  $t_2$ , we get an energy gap of  $E_g = 2.8$  eV between HOMO and LUMO, in agreement with other works on pristine PPV [20,21]. If there is no any external perturbation, the molecule will keep its ground state unchanged. In this equilibrium state, we have  $|\Phi_v(t)\rangle = |\phi_v(t)\rangle = |\phi_v(t=0)\rangle$  with Eigen energy  $\varepsilon_v$ . Fig. 1 shows the schematic diagram of the molecular orbitals for a PPV molecule in a ground state, where we denote  $\varepsilon_\mu$  ( $\mu = 1, 2, \dots$ ) to be the  $\mu$ th occupied orbital counted from HOMO, and  $\varepsilon_\mu^*$  ( $\mu = 1, 2, \dots$ ) to be the  $\mu$ th unoccupied one counted from LUMO.

When the molecule is photoexcited, electrons will gain energy and  $|\Phi_v(t)\rangle$  evolves with time, which means that electrons may transit among the instantaneous eigenstates  $|\phi_\mu(t)\rangle$ . The “by-hand” simulations treat the transitions by moving electrons from the occupied orbitals to the unoccupied ones. Here let us excite the molecule with a femtosecond electric pump pulse with the form of Eq. (6), in which  $E_0$  and  $T$  is fixed to be 1.0 MV/cm and 25 fs, respectively. The final state after the photoexcitation is analyzed by calculating  $F_\mu(t) = \sum_v |f_v| \langle \phi_\mu(t) | \Phi_v(t) \rangle|^2$ , which gives the electron occupation on instantaneous eigenstate  $|\phi_\mu(t)\rangle$  at time  $t$ . The variations of  $F_\mu(t)$  reflect electron transitions among the instantaneous eigenstates. A result with photoexciting energy  $\hbar\omega = 2.7$  eV is shown in Fig. 2. At beginning, the molecule is in its ground state with electron occupation  $F_\mu(t) = f_\mu$ . A photoexcitation is applied to the molecule at  $t_c = 40$  fs. It is found that electrons on the occupied orbitals gain energy to transit to the unoccupied

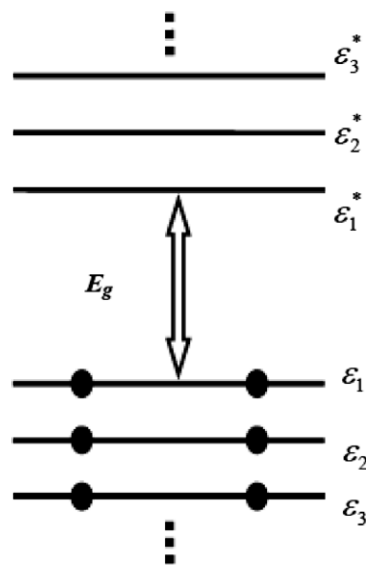


Fig. 1. Schematic diagram of the molecular orbitals for a PPV molecule in a ground state, where the filled circles indicate electrons with the spin omitted.

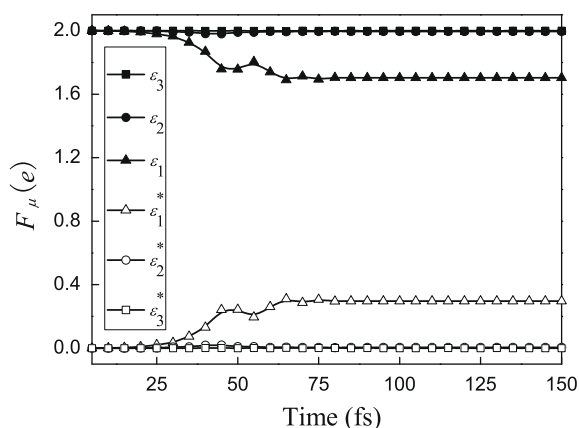
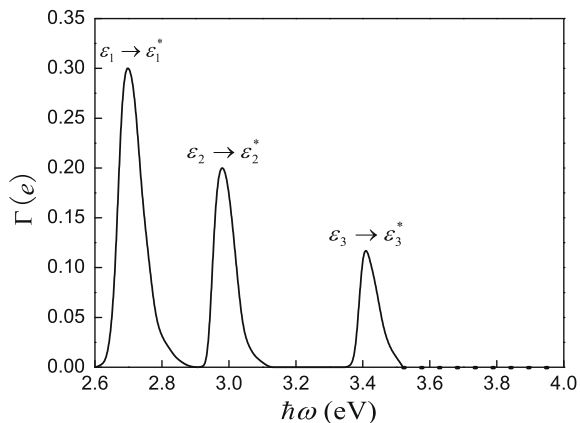


Fig. 2. Variations of occupation  $F_\mu(t)$  on the six instantaneous eigenstates near the gap during the evolution with photoexciting energy  $\hbar\omega = 2.7$  eV.

ones with different probabilities. Especially, apparent transitions take place between  $\varepsilon_1$  and  $\varepsilon_1^*$ . About 30 fs later, the transitions stop.

Transition probability of electron or distribution of  $F_\mu(t)$  is found to be dependent upon the photoexciting energy. Fig. 3 shows the dependence of the transferred electrons  $\Gamma = \sum F_\mu(\mu = \varepsilon_1^*, \varepsilon_2^*, \dots)$  on the photoexciting energy  $\hbar\omega$ . It is found that there exists a critical value of  $\hbar\omega_c = 2.6$  eV, below which electrons in the occupied orbitals can not transit to the unoccupied ones. The reason is that there is a big energy gap between HOMO and LUMO. In fact, this critical value corresponds to experimentally obtained optical energy gap [22–24]. When the photoexciting energy is larger than the critical value, electrons begin to transit. As the orbitals are discrete, the transition probab-



**Fig. 3.** Dependence of the transferred electrons  $\Gamma$  on the photoexciting energy  $\hbar\omega$ .

ity is strong only at some photoexciting energies. As shown in Fig. 3, we find that there separately appears a transition peak at  $\hbar\omega = 2.7$  eV,  $\hbar\omega = 3.0$  eV, and  $\hbar\omega = 3.4$  eV, et al. As we know, in a photoexcitation the most probable dipole-allowed transitions are those from  $\varepsilon_\mu$  to  $\varepsilon_\mu^*$  (i.e.,  $\varepsilon_\mu \rightarrow \varepsilon_\mu^*$ ). By a further check for these transition peaks, we can clearly see that the first peak corresponds to the transition  $\varepsilon_1 \rightarrow \varepsilon_1^*$  (see Fig. 2), the second one  $\varepsilon_2 \rightarrow \varepsilon_2^*$ , and the third one  $\varepsilon_3 \rightarrow \varepsilon_3^*$ , etc. For the peak value, we find that it decreases remarkably with the photoexciting energy. It shows that, in a photoexciting process, a higher-energy transition is not easy to be obtained.

It has been known that transition  $\varepsilon_1 \rightarrow \varepsilon_1^*$  with one electron will result in the formation of an exciton, while that with two electrons will produce a biexciton. But the photoexcitation can not give the ideal transitions. As shown in Fig. 3, the transferred electrons for transition  $\varepsilon_1 \rightarrow \varepsilon_1^*$  are about  $0.3e$  in present parameters. Now let us recognize the final state corresponding to the transition  $\varepsilon_1 \rightarrow \varepsilon_1^*$ , which has the highest transition probability. To do so, we calculate the projection  $i_{S_k}(t) = |\langle \phi_{S_k} | \Phi(t) \rangle|^2$  of the evolution state onto the instantaneous ground state [denoted as  $S_0(F_{\varepsilon_1^*} = 0, F_{\varepsilon_2^*} = 0)$ ], exciton [denoted as  $S_1(F_{\varepsilon_1^*} = 1, F_{\varepsilon_2^*} = 0)$ ], and biexciton [denoted as  $S_2(F_{\varepsilon_1^*} = 2, F_{\varepsilon_2^*} = 0)$ ], which gives the yield  $i_{S_k}$  of one kind state  $S_k$ . The results are shown in Fig. 4a. After the photoexcitation, it is found that the molecule may still in its ground state with a probability of 72%, or lie in an exciton with a probability of 26%, or lie in a biexciton with a probability of 2%. As we know, biexcitons have some characteristics different from those that excitons or other excited states have, such as the abnormal polarization [25]. Here the calculated yield of a biexciton is much smaller than that of an exciton, which may be related to the weak photoexciting intensity ( $E_0 = 1.0$  MV/cm in present model). For the second transition peak corresponding to  $\varepsilon_2 \rightarrow \varepsilon_2^*$ , we find that the probability in ground state is 82%. But the probability in an exciton or biexciton is nearly negligible, which means that the photoexcitation at this photoexciting energy ( $\hbar\omega = 3.0$  eV) can not get excitons or biexcitons. To recog-

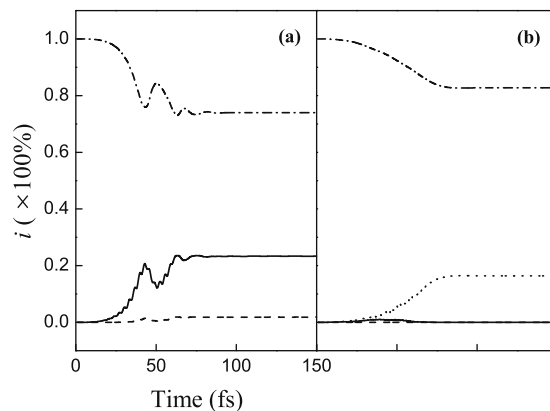


**Fig. 4.** Probabilities of the PPV molecule in a ground state (dash-dotted line), an exciton (solid line), a biexciton (dashed line), and a high-energy exciton (dotted line) during the evolution with  $\hbar\omega = 2.7$  eV (a) and  $\hbar\omega = 3.0$  eV (b), respectively.

nize the excitation product, we have to introduce another excited state. As An et al. indicated in Ref. [13], transition  $\varepsilon_2 \rightarrow \varepsilon_2^*$  will result in the formation of a high-energy exciton [denoted as  $S_3(F_{\varepsilon_1^*} = 0, F_{\varepsilon_2^*} = 1)$ ]. By projecting the evolution state onto the instantaneous state  $S_3$ , we get a yield of 18%, as shown in Fig. 4b. Hence the photoexcitation at  $\hbar\omega = 3.0$  eV produces a higher excited state or high-energy exciton. Due to the higher photoexciting energy (0.3 eV in present parameters), a high-energy exciton is found to be more easily dissociated into free charges contributing to photocurrent than an exciton [8].

For other higher energy photoexcitations, we obtain that a transition  $\varepsilon_{odd} \rightarrow \varepsilon_{odd}^*$  finally leads to the formation of excitons, while  $\varepsilon_{even} \rightarrow \varepsilon_{even}^*$  high-energy excitons. The results agree with the speculations by Hendry [6] and Virgili [11], as stated in Section 1. In addition, from Fig. 3 we can obtain a relation between the photogenerations of the two excitation products and the photoexciting energies, which is helpful for optoelectronic applications of organic semiconductors. As we know, in photovoltaic devices, such as photovoltaic cells or electrophotographic devices, one would like free charges to be efficiently produced. Since free charges result from the dissociation of high-energy excitons, we should control the photoexciting energy to improve the yield of high-energy excitons. While in light-emitting devices, one would like to suppress the formation of free charges and enhance the yield of excitons.

In actual applications, the photoexciting intensity also plays an important role for the photoexciting process. It has been experimentally observed that, at high photoexciting intensities, biexcitons will be photogenerated [26]. It means that, at a higher photoexciting intensity, biexcitons should have a higher yield. This question will be specially discussed in a future work. In addition, a superlinear dependence of the charge photogeneration (CPG) yield on the photoexciting intensity has also been reported [11]. Here we investigate the effect of the photoexciting intensity on the generation of high-energy excitons. Fig. 5 shows the dependence of the yield of high-energy excitons (corresponding to the second transition peak) on the photoexcit-

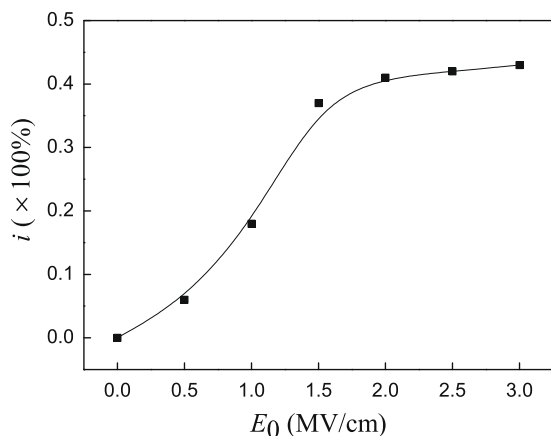


Fig. 5. Dependence of the yield of high-energy excitons on the photoexciting intensity  $E_0$ .

ing intensity  $E_0$ . An apparent superlinear increase of the yield of high-energy excitons with the photoexciting intensity is obtained when the photoexciting intensity is not strong ( $E_0 < 1.5$  MV/cm). The result is consistent with the experimental observations, if we consider that the dissociation of high-energy excitons is independent upon the photoexciting intensity. When the photoexciting intensity is strong ( $E_0 \geq 1.5$  MV/cm), the yield of high-energy excitons is found to gradually reach a constant ( $\sim 40\%$  in present parameters).

Finally, it should be stressed that, despite the model is parameterized for PPV, some molecular effects on the photoexciting process are not taken into account. An innegligible effect is the thermally-induced or solvent-induced rotations of the benzene rings out of the energetically favored planar conformation. For example, Ginder and Epstein demonstrated the importance of the ring-torsion angle in polyaniline [27]; Brédas et al. also discussed the influence of ring-torsion dimerization on the band gap of aromatic conjugated polymers [28]. Both of the two works indicate that the rotations of benzene rings can cause many interesting optoelectronic properties. In addition, an external photoexcitation or thermal perturbation must cause the quantum fluctuations of the lattices as discussed by Shuai et al. [29]. So, further investigations should be done in the future that include the molecular effects, such as the rotations of benzene rings and the quantum fluctuations of the lattices, on the excitation products and the corresponding yields in PPV.

#### 4. Summary

In summary, by numerically applying a femtosecond electric pump pulse we investigated the photoexciting process in a PPV molecule, which will be vital to understand the light-emitting efficiency and the photoconductance of organic semiconductors. We found that the initial excitation products are excitons, biexcitons, and high-energy excitons. The yields were calculated and it was found that

the photogenerations of them are determined by the photoexciting energy. A relation between their photogenerations and the photoexciting energy was obtained, which is helpful for optoelectronic applications of organic semiconductors. In addition, effect of the photoexciting intensity on the photogeneration of high-energy excitons was discussed. We found a superlinear increase of the yield of high-energy excitons with the photoexciting intensity, which is consistent with the experimental observations.

#### Acknowledgments

The authors would like to acknowledge the financial support from the National Key Basic Research Program (No. 2009CB929204), the National Natural Science Foundation (Nos. 10804062, and 10874100), the Research Fund for the Doctoral Program of Higher Education (Nos. 200804221005, and 20070422058), the China Postdoctoral Science Foundation (No. 20080431171), and the Shandong Postdoctoral Innovation Program (No. 200802028).

#### References

- [1] R.H. Friend, R.W. Gymer, A.B. Holmes, J.H. Burroughes, R.N. Marks, C. Taliani, D.D.C. Bradley, D.A. Dos Santos, J.L. Brédas, M. Lögdlund, W.R. Salaneck, *Nature (London)* 397 (1999) 121.
- [2] S.R. Forrest, *Org. Electron.* 4 (2003) 45.
- [3] C.J. Brabec, N.S. Sariciftci, J.C. Hummelen, *Adv. Funct. Mater.* 11 (2001) 15.
- [4] D. Tobjörk, N.J. Kaihovirta, T. Mäkelä, F.S. Pettersson, R. Österbacka, *Org. Electron.* 9 (2008) 931.
- [5] M. Chandross, S. Mazumdar, S. Jeglinski, X. Wei, Z.V. Vardeny, E.W. Kwock, T.M. Miller, *Phys. Rev. B* 50 (1994) 14702.
- [6] E. Hendry, J.M. Schins, L.P. Candeias, L.D.A. Siebbeles, M. Bonn, *Phys. Rev. Lett.* 92 (2004) 196601.
- [7] J.G. Müller, U. Lemmer, J. Feldmann, U. Scherf, *Phys. Rev. Lett.* 88 (2002) 147401.
- [8] K. Gao, X.J. Liu, D.S. Liu, S.J. Xie, *Phys. Rev. B* 75 (2007) 205412.
- [9] V. Gulbinas, Y. Zaushtitsyn, H. Bässler, A. Yartsev, V. Sundström, *Phys. Rev. B* 70 (2004) 035215.
- [10] D. Hertel, H. Bässler, *Chem. Phys. Chem* 9 (2008) 666.
- [11] T. Virgili, D. Marinotto, C. Manzoni, G. Cerullo, G. Lanzani, *Phys. Rev. Lett.* 94 (2005) 117402.
- [12] P.B. Miranda, D. Moses, A.J. Heeger, *Phys. Rev. B* 70 (2004) 085212.
- [13] Z. An, C.Q. Wu, X. Sun, *Phys. Rev. Lett.* 93 (2004) 216407.
- [14] D.M. Basko, E.M. Conwell, *Phys. Rev. B* 66 (2002) 155210.
- [15] H.Y. Choi, M.J. Rice, *Phys. Rev. B* 44 (1991) 10521.
- [16] H.W. Streitwolf, *Phys. Rev. B* 58 (1998) 14356.
- [17] A.A. Johansson, S. Stafström, *Phys. Rev. B* 69 (2004) 235205.
- [18] R.W. Brankin, I. Gladwell, L.F. Shampine, RKSUITE: Software for ODE IVPs, <<http://www.netlib.org>>.
- [19] Y. Li, K. Gao, Z. Sun, S. Yin, D.S. Liu, S.J. Xie, *Phys. Rev. B* 78 (2008) 014304.
- [20] H.A. Mizes, E.M. Conwell, *Phys. Rev. B* 50 (1994) 11243.
- [21] E.M. Conwell, H.A. Mizes, *Phys. Rev. B* 51 (1995) 6953.
- [22] G. Cerullo, G. Lanzani, S. De Silvestri, H.-J. Egelhaaf, L. Lüer, D. Oelkrug, *Phys. Rev. B* 62 (2000) 2429.
- [23] N.F. Colaneri, D.D.C. Bradley, R.H. Friend, P.L. Burn, A.B. Holmes, C.W. Spangler, *Phys. Rev. B* 42 (1990) 11670.
- [24] B. Kraabel, V.I. Klimov, R. Kohlman, S. Xu, H.-L. Wang, D.W. McBranch, *Phys. Rev. B* 61 (2000) 8501.
- [25] X. Sun, R.L. Fu, K. Yonemitsu, K. Nasu, *Phys. Rev. Lett.* 84 (2000) 2830.
- [26] V.I. Klimov, D.W. McBranch, N. Barashkov, J. Ferraris, *Phys. Rev. B* 58 (1998) 7654.
- [27] J.M. Ginder, A.J. Epstein, *Phys. Rev. B* 41 (1990) 10674.
- [28] J.L. Brédas, C. Quattrocchi, J. Libert, A.G. MacDiarmid, J.M. Ginder, A.J. Epstein, *Phys. Rev. B* 44 (1991) 6002.
- [29] Z. Shuai, D. Beljonne, J.L. Brédas, *Solid State Commun.* 78 (1991) 477.



trodes to the emitting materials is so similar that does not always allow sufficiently selective injection (and therefore emission) depending on the external bias. Quantum-dot-based LEDs is an alternative method to tune the outcoming light by controlling the size and shape of the quantum-dot [7]. However, the blue component is rather difficult to obtain due to the diminute dimensions of the quantum-dots required. The synergic combination of organic and inorganic semiconducting materials is a recently reported approach to obtain color tunable devices [8,9]. As we will demonstrate, the very different charge injection properties of these two dissimilar materials can also provide a fine voltage controlled color tunability. White emission in polymeric devices has also been previously reported [3,4,10], however they are either no voltage controlled, imply ternary blends or use no solution processable materials.

Therefore, we merge together two of the most promising technologies in the last decade – organic electronics and nanotechnology – to report blue to red voltage tunable emitting devices that can also be white for certain voltages. As previously mentioned, one needs the three RGB components in a white device. We obtain green and blue from the same polymer with the approach of deliberately oxidizing commercially available PFO from American Dye Source. The green band of PFO has been studied in detail by Sims et al. mainly by means of photoluminescence [9,10]. We report experimental procedures to fabricate blue and/or green emitting diodes depending on the controlled oxidation degree of PFO. In order to achieve white light, the red component arises from the addition of also commercially available CdSe/ZnS quantum dots with a diameter of 5.8 nm. The charge injection properties into PFO and QDs are that different that allows our devices to balance the Red, Green and Blue components if both, the blend composition (PFO and QD) and the PFO oxidation degree are exactly adjusted. Moreover, when this balance is broken, the same device can emit towards either blue or red depending on the externally applied voltage.

## 2. Experimental

### 2.1. Solution preparation

Fifteen milligram of PFO (American Dye Source) were dissolved in 1 mL of chlorobenzene using different procedures, in order to achieve either pure blue emission or a combination of blue and green.

- Solution preparation for non-oxidized PFO (pure blue emission): The semiconductor solution was heated at 80 °C during intervals of 10 s; enough to dissolve the polymer but preventing temperature activated oxidation. The semiconductor and the substrates were at room temperature during spin-coating process.
- Solution preparation for deliberately oxidized PFO (blue/green emission): The solution to obtain blue–green emission was stirred at 88 °C during 1 h 30'. The semiconductor was spin coated directly from the hot solution. Furthermore, after spin coating the semiconductor, the substrates were annealed at 88 °C for 5 min.

In order to prepare the PFO:QD blends, commercial dispersions of quantum dots in toluene from Evident were used (CdSe/ZnS, 5.8 nm diameter 5 mg mL<sup>-1</sup>). Different ratios of the QD dispersion were used as the percentage in volume of the initial PFO solution. Blends were stirred at 50 °C for 1 h.

### 2.2. Device fabrication and instruments

Four inch circular glass wafers completely covered with ITO from VISIONTEK were in-house structured by means of photolithography to produce 15 × 15 mm square substrates with a 7 mm wide centered ITO stripe. The ITO substrates were cleaned in acetone and isopropanol 5 min ultrasonic baths. Commercially available Baytron PEDOT:PSS Al4083 from HC Starck was spin coated on the ITO. PEDOT films were heated at 100 °C for 5 min to evaporate any residual water in the film. The either PFO or PFO:QD were spin-coated under different conditions depending on the solution used. Finally, metallic cathodes of 10 nm calcium and 200 nm silver were thermally evaporated under high vacuum (<4 × 10<sup>-6</sup> mbar) through a shadow mask, giving four diodes of 9 mm<sup>2</sup> on each substrate.

Samples were measured inside a nitrogen glove box with a Minolta CS100-A spectroradiometer applying voltages controlled by a Keithley VMU 2420.

## 3. Results and discussion

Fig. 1 shows the emission of two diodes fabricated with PFO under different conditions (see Section 2), fresh or non-oxidized, and trying to promote polymer oxidation. The emission of sample 1 (triangles) is the typical PFO blue emission habitually reported [11,12]. For sample 2 (squares) the green band grows as a function of the polymer oxidation until it becomes clearly dominant. The mechanisms to explain the green band have been previ-

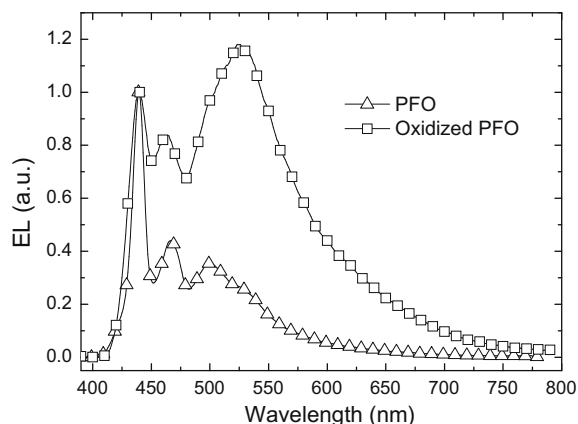


**Fig. 1.** Electroluminescence spectra measured at 8 V for different ITO/PEDOT:PSS/PFO/Ca/Ag diodes. The original PFO solution was prepared differently (see experimental details); while for triangles a minimum degree of oxidation was aimed, for squares oxidation steps were intentionally introduced.

ously reported [13,14]. It is commonly accepted that oxidation leads to a fluorenone formation (ketone (C=O)) group at the C-9 position following dealkylation. It is additionally believed that further manipulation of fluorenone-containing chains is necessary to activate the green emission. In essence, there seems to be a requirement that fluorenone groups are able to aggregate before the green emission can appear. Temperature and/or solvent assisted chain mobilization (swelling) is then envisaged to facilitate aggregation. Therefore, by modifying and controlling the solution and film preparation conditions one can achieve different color emission. Fig. 2 shows the IVL characteristics of the same two diodes. The chemical oxidation of the PFO responsible for the green emission introduces competing non-radiative processes that negatively affect the emitting properties of the device in terms of luminance. However, one can benefit from this fact to obtain outgoing color tuning by adjusting the blue and green components at wish when either the efficiency and/or efficacy of devices is not the limiting factor.

In order to also obtain the red component from the same emitting film, different amounts of a 5 mg/ml commercial dispersion of CdSe/ZnS quantum dots with diameter of 5.8 nm were added to the original PFO solution (15 mg/ml in chlorobenzene). The emission spectra of different PFO:QD combinations can be seen in Fig. 3. The triangles containing curve (70:30 in vol) denotes a nearly perfect white emission (CIE X: 0.34–0.35/Y: 0.35–0.36) while the squares containing curve (only PFO partially oxidized) and the circles containing curve (30:70) show a larger blue and red component, respectively. It has to be pointed out that devices made with PFO solutions minimally either over or under oxidized did not show white emission.

Once we have obtained the desired white emission, it is additionally possible to further tune the color by adjusting the applied voltages. Fig. 4 shows the electroluminescence spectra of a diode fabricated with a 70:30 blend at different voltages. Three different regimes can be seen in the same device depending on the applied bias. The original white emission can be modified according to the charge injection properties of each material. While small voltages exclu-

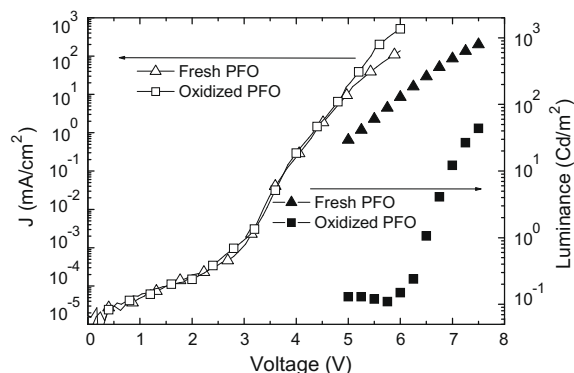


**Fig. 2.** IVL characteristics for ITO/PEDOT:PSS/PFO/Ca/Ag diodes made from different original PFO solutions as explained for Fig. 1. Triangles denote non-oxidized PFO, and squares denote deliberately oxidized PFO. Current values can be read in the left Y-axis (open symbols) and luminance values can be read in the right Y-axis (filled symbols).

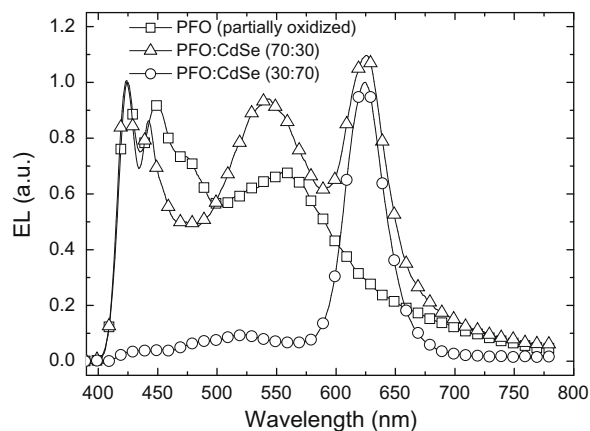


**Fig. 3.** Emission spectra at 12 V for PFO and different PFO:QD combinations. Samples were prepared as described in the Section 2. White emission (CIE X: 0.34–0.35/Y: 0.35–0.36) was achieved by precisely controlling both the oxidation degree of PFO and tuning the PFO and QD amounts in the solution.

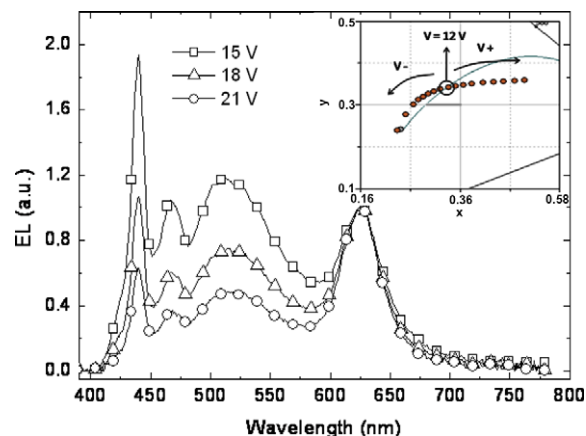


**Fig. 4.** Electroluminescence spectra for a 70:30 PFO: CdSe blend at different applied voltages. The same initially white emitting device can be tuned towards either blue or red depending on the applied bias. Increasing the voltage favors red emission from the QD while decreasing values promotes red/green emission from the partially oxidized PFO. Inset: chromatic coordinates for the emission obtained at different voltages. (For interpretation of the references to colour in this figure legend, the reader is referred to the web version of this article.)

sively allow charge injection to PFO – and therefore blue–green emission –, larger voltages induce the QD red emission.

It is noticeable – from Figs. 3 and 4 – how the green band of PFO is also affected by both the presence of QD and the applied voltage. Both effects therefore favor the formation and subsequent aggregation of fluorenone group containing polymer chains, which supporting the interpretation of Ferenczi et al. [14], triggers the green emission. Unfortunately, the chemical oxidation of PFO is not reversible, and once the green band has arisen is not removable. Fig. 5 shows the IVL characteristics of the PFO:QD diode before and after obtaining white emission. The applied

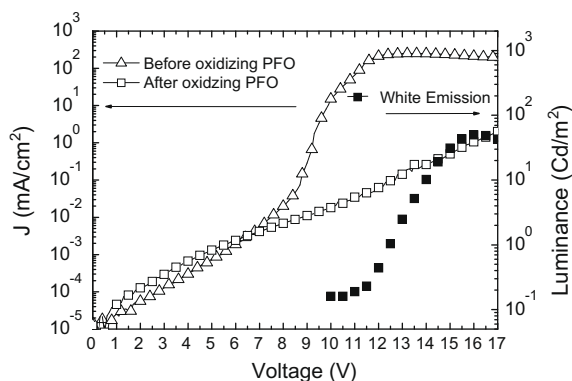


**Fig. 5.** IVL characteristics for ITO/PEDOT:PSS/PFO:QD(70:30)/Ca/Ag diodes before (triangles) and after (squares) obtaining white emission, i.e. before raising the voltage over 10 V. Current values can be read in the left Y-axis (open symbols) and luminance values can be read in the right Y-axis (filled symbols).

voltage, i.e. the current flowing through the polymer, is also believed to play a crucial role in the oxidation of the polymer. Therefore, increasing the applied voltage to obtain the red component also contributes to further oxidize the PFO. This favors the green emission also detrimenting the blue component, and makes the process non-reversible. Once we have observed white emission it is not possible to achieve blue again, but certain degree of voltage tunability between green and red is still feasible.

Voltage tunable emission has been previously reported in both polymer:QD [8] and polymer:polymer [5,6] devices. There are usually two different processes to explain color tunability from the same device. One relies on dipole–dipole interaction (Förster transfer) in which an excited state is transferred from the host to the guest if certain conditions are fulfilled. Basically, the absorption of the guest has to overlap the emission of the host. If additionally, different polymer chains are within a minimum distance (Förster radius), the whole emitted energy by the host is re-absorbed by the guest [15,16]. Therefore phase-segregation even in the nanoscale has to be avoided.

On the other hand, materials with different miscibility properties, that consequently tend to phase-segregate (like conjugated polymers and quantum dots), can also be made to simultaneously emit if they are excited at once [6]. Controlling for example the charge injection properties in both phases, it is an additional possibility to achieve voltage tunable emission. Polymers and QD tend to segregate and therefore we observe simultaneous emission from both of the components that can either be polymer (blue–green) or QD (red) biased depending on the external applied voltage.

#### 4. Conclusion

In summary, we have shown the possibility to combine organic conjugated polymers with inorganic semiconduct-

ing nanoparticles in order to fabricate white emitting diodes. Their emission can be finely tuned towards either red or blue by modifying the external applied bias. This can be achieved with a precise control of the oxidation degree of the polymer and the adequate percentage of both components – polymer and QD – in the solution. Oxidation and phase separation are controlled via specifically developed solution preparation techniques. Devices can then be processed from these solutions via a simple wet coating process. We chose spin-coating for its simplicity at lab scale, but there are no restrictions for other processes more suitable for mass production (doctor blading, inkjet printing) to result in the same desired phase segregation between polymers and quantum dots in the film. This segregation allows for the important selective charge injection to a particular material phase depending on the voltage. With this approach it is possible to cover the whole color gamut with only a single device.

#### Acknowledgements

We thank financial support from Ministerio de Educación y Ciencia under the project HOPE CSD2007-00007 (Consolider-Ingenio 2010). RP also thanks Javier Berganzo and Mikel Wolf for electronic and mechanical support, respectively.

#### References

- [1] J.H. Burroughes, D.D.C. Bradley, A.R. Brown, R.N. Marks, K. Mackay, R.H. Friend, P.L. Burns, A.B. Holmes, *Nature* 347 (1990) 539.
- [2] P.L. Burns, A.B. Holmes, A. Kraft, D.D.C. Bradley, A.R. Brown, R.H. Friend, R.W. Gymer, *Nature* 356 (1992) 47.
- [3] J. Luo, X. Li, Q. Hou, J. Peng, W. Yang, Y. Cao, *Adv. Mater.* 19 (2007) 1113.
- [4] M. Granström, O. Inganäs, *Appl. Phys. Lett.* 68 (1996) 147.
- [5] N. Ananthakrishnan, G. Padmanaban, S. Ramakrishnan, J.R. Reynolds, *Macromolecules* 38 (2005) 7660.
- [6] M. Berggren, O. Inganäs, G. Gustafsson, J. Rasmussen, M.R. Andersson, T. Hjertberg, O. Wennerström, *Nature* 372 (1994) 444.
- [7] Q.J. Sun, Y.A. Wang, L.S. Li, D. Wang, T. Zhu, J. Xu, C. Yang, Y. Li, *Nat. Photon.* 1 (2007) 717.
- [8] I.H. Campbell, B.K. Crone, *Appl. Phys. Lett.* 92 (2008) 043303.
- [9] C.-H. Chou, C.-H. Yang, C.-H. Hsu, T.-M. Chen, *J. Nanosci. Nanotechnol.* 7 (2007) 2785.
- [10] Y. Li, A. Rizzo, M. Mazzeo, L. Carbone, L. Manna, R. Cingolani, G. Gigli, *J. Appl. Phys.* 97 (2005) 113501.
- [11] M. Grell, D.D.C. Bradley, M. Inbasekaran, E.P. Woo, *Adv. Mater.* 9 (1997) 798.
- [12] A.W. Grice, D.D.C. Bradley, M.T. Bernius, M. Inbasekaran, W.W. Wu, E.P. Woo, *Appl. Phys. Lett.* 73 (1998) 629.
- [13] M. Sims, D.D.C. Bradley, M. Ariu, M. Koeberg, A. Asimakis, M. Grell, D.G. Lidzey, *Adv. Funct. Mater.* 14 (2004) 765.
- [14] T.A.M. Ferenczi, M. Sims, D.D.C. Bradley, *J. Phys.: Condens. Matter* 20 (2008) 045220.
- [15] A.R. Buckley, M.D. Rahn, J. Hill, J. Cabanillas-González, A.M. Fox, D.D.C. Bradley, *Chem. Phys. Lett.* 339 (2001) 331.
- [16] J. Cabanillas-González, T. Virgili, G. Lanzani, S. Yeates, J. Nelson, D.D.C. Bradley, *Phys. Rev. B* 71 (2005) 014211.

(LT-632) with side chains have been used in order to get uniform thin films. In addition to the molecular modification, many efforts have been made to fabricate multilayer structure by solution process, such as synthesis of cross-linked materials [3], water/methanol soluble materials [7], lamination method [8], liquid buffer layer [9], and blade coating method [10]. All-solution-processed OLEDs in multilayer device structure, hole transport layer (HTL)/emissive layer (EML)/electron transport layer (ETL), have been fabricated by blade coating without applying any cross-linked materials. In such devices the LiF/Al is used as the cathode, without any low work function metals like Ca, Ba, or Mg. The performance of the device by all-solution process is close to that by evaporation but the cost would be reduced dramatically due to the cheap solution process.

All-solution-processed multilayer blue light OLED with high device efficiency has been compared with its counterpart by vacuum deposition. Three devices with device structure of ITO/PEDOT:PSS/HTL/EML/ETL/LiF/Al were made to compare the different fabrication processes, including the device by all evaporation process (device A), the device with solution-processed HTL and evaporated EML/ETL (device B), and the device by all-solution process (device C). Four devices by all-solution process with different annealing temperatures of ETL layer, 20 °C (device C-1), 50 °C (device C-2), 70 °C (device C-3), and 90 °C (device C-4) for 10 min were made to optimize the device performance. Furthermore a device without ETL by solution process was made as comparison (device D). ITO is indium tin oxide and PED-

OT:PSS is poly-(3,4-ethylenedioxythiophene):poly-(styrenesulfonate) (CLEVIOS™ P VP CH 8000, purchased from HC Starck). PEDOT:PSS was spin coated to form a 40 nm thin film on pre-cleaned the ITO substrate and then was baked at 100 °C for 40 min. N,N'-Bis(naphthalen-1-yl)-N,N'-bis(phenyl)-9,9-dimethyl-fluorene (DMFL-NPB, from Luminescence Technology Corporation), acting as HTL, was dissolved in chlorobenzene to form a 20 nm film by blade and spin coating. LT-492 and LT-632 provided by Luminescence Technology Corporation, act as blue host and blue dopant individually. The 2 wt% LT-632 in the host LT-492 were dissolved in chlorobenzene and blade coated to form a 50 nm film on top of DMFL-NPB. Blade and spin coating is the process to use first blade coating to form the wet film and then spin coating until dried film is formed. Blade coating is the process only to use the blade coating without any spin coating. The DMFL-NPB and LT-492:LT-632 layers were baked at 120 °C for 10 min and 125 °C for 5 min in vacuum ( $10^{-3}$  torr). The 2,2',2''-(1,3,5-Benzinetriyl)-tris(1-phenyl-1-H-benzimidazole) (TPBi, from Luminescence Technology Corporation), acting as the ETL and hole blocking layer, was dissolved in methanol to form a 20 nm film by blade and spin coating. The film thickness by blade coating can be controlled by the solution concen-

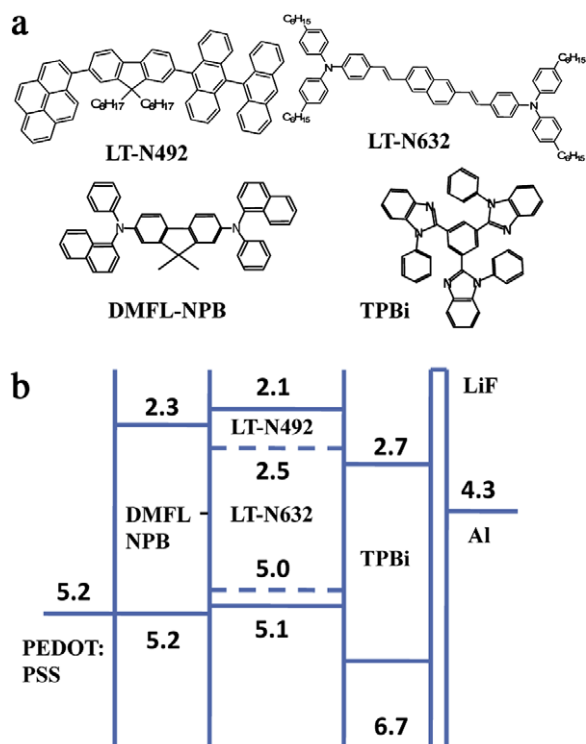


**Fig. 1.** (a) Chemical structures of the organic materials, and (b) schematic energy profile of the multilayer device structure design in this work. The numbers are in eV.

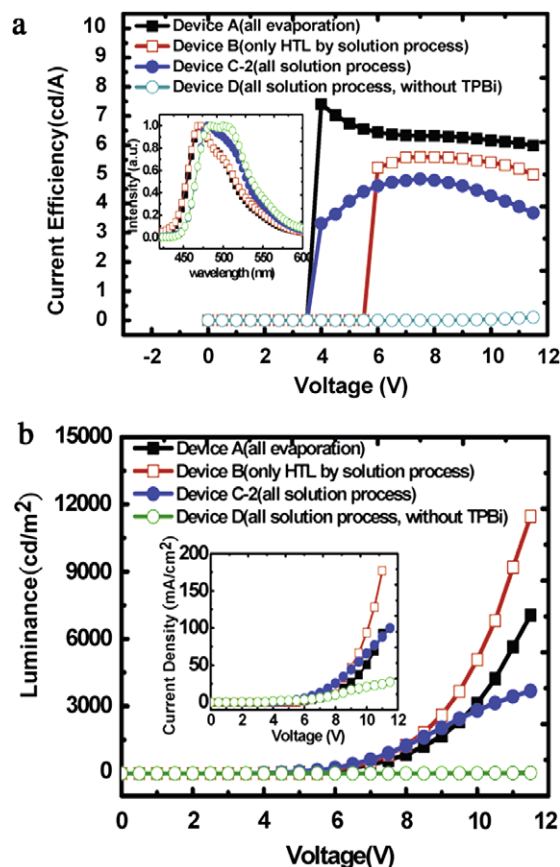


**Fig. 2.** Device performance of device A (solid square), device B (empty square), device C-2 (solid circle), and device D (empty circle). (a) The current efficiency. Inset is the electroluminescent spectra. (b) The luminance. Inset is the current density.

tration and the gap between substrate and blade coater. The film thickness by blade and spin coating can be controlled by the spin rate in addition to the solution concentration and the gap. The speed of blade coating is fixed at 10 cm/s. The film thicknesses are measured by a Kosaka ET4000 Surface Profiler. Fig. 1 shows the material chemical struc-

tures and schematic energy profile of the multilayer device structure. All the solution and annealing processes were performed in the glove box with low humidity (<5 ppm) and oxygen (<5 ppm). In device A all the organic layers were made by conventional thermal evaporation in the high vacuum chamber ( $10^{-7}$  torr) without any annealing process. All

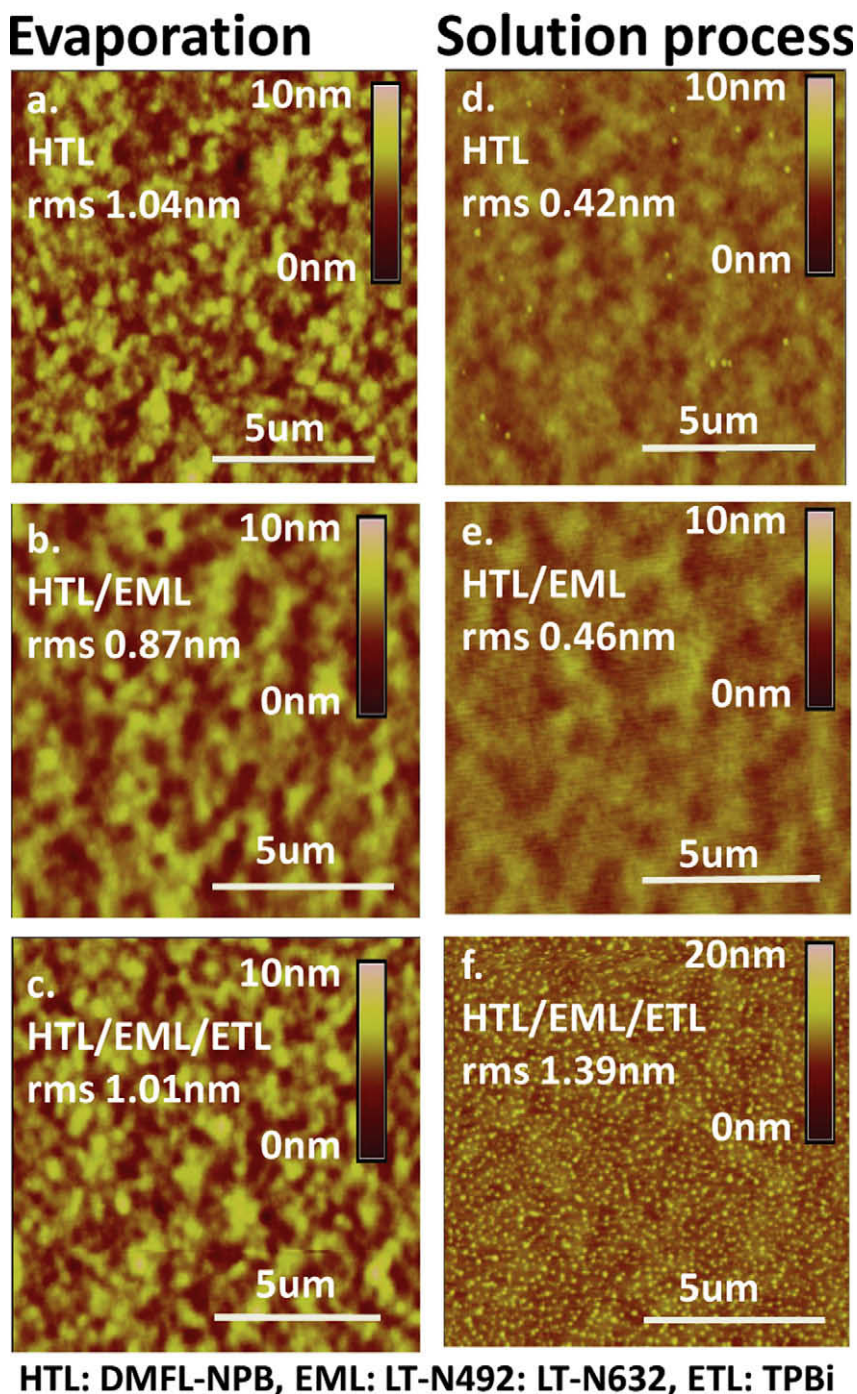


**Fig. 3.** AFM images of the (a) HTL, (b) HTL/EML, (c) HTL/EML/ETL by evaporation, and (d) HTL, (e) HTL/EML, (f) HTL/EML/ETL by solution process. The solution-processed ETL (TPBi) is annealed at 50 °C.

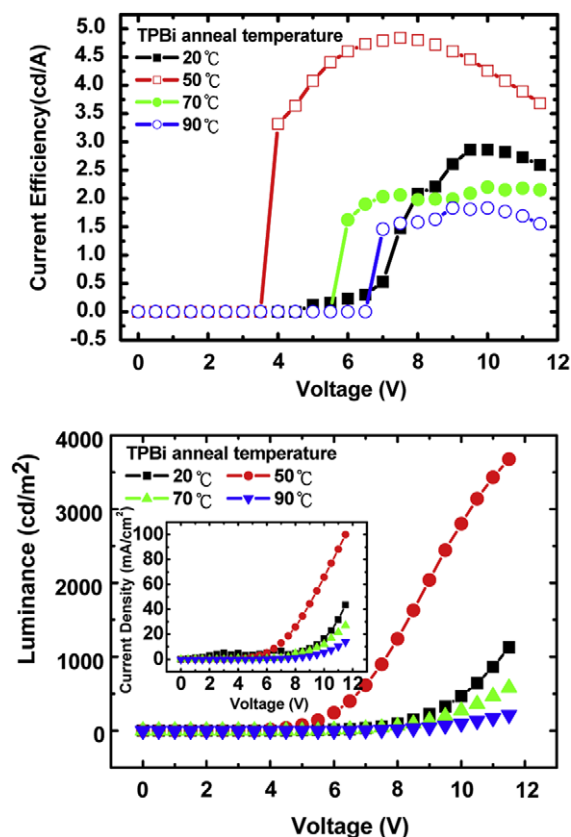


**Fig. 4.** Device performance of the all-solution-processed devices with different annealing temperature of TPBi, 20 °C (solid square), 50 °C (empty square), 70 °C (solid circle) and 90 °C (empty circle). (a) The current efficiency. Inset is the electroluminescent spectra. (b) The luminance. Inset is the current density.

the devices were coated with LiF(1 nm)/Al(100 nm) cathode and packaged in a glove box. Ionization potential is measured by cyclic voltammetry and electron affinity is calculated by ionization potential plus band gap determined by the ultraviolet absorption spectrum. The electroluminescence (EL) spectra and current–luminance–voltage ( $I$ – $L$ – $V$ ) characteristics are measured by a Photo Research PR650 spectrophotometer integrated with Keithley 2400 multimeter.

Fig. 2 shows the device performances of device A (all evaporation), device B (only HTL by solution process), de-

vice C-2 (all-solution process), and device D (all-solution process, without TPBi). While operating at 10 mA/cm<sup>2</sup>, the device efficiency is 6.3 cd/A of device A, 5.6 cd/A of device B, 4.8 cd/A of device C-2, and 0.01 cd/A of device D. The maximum luminance is 7054 cd/m<sup>2</sup> of device A, 11,460 cd/m<sup>2</sup> of device B, 3677 cd/m<sup>2</sup> of device C-2, and 26 cd/m<sup>2</sup> of device D. The maximum luminance of the devices is defined as the luminance that can be achieved of the device. The luminance will decay after this maximum luminance even the bias increases. There are some damages occurred of the devices after the maximum luminance. The device performance of device D without TPBi as ETL is obviously poor, indicating TPBi layer is required to offer efficient electron injection. As can be seen in  $I$ – $V$ – $L$  relation, the current and luminance of all-solution-processed device C-2 at low bias before 9 V are about the same as those of device B and are higher than those of all-evaporated device A. At higher bias larger than 10 V, the current and luminance of device C become saturated and lower than those of device A and device B. Moreover the electroluminescent (EL) spectra of the devices with solution-processed EML (device C-2 and device D) show red-shift compared with the devices with evaporated EML (device A and device B). This may be attributed to the slight dissolution between the HTL and EML during blade coating, which might cause exciplex formation in such mixing area. The dissolution has been verified to be less than 10 nm by measuring the total film thickness. In order to study the detail of the different processes, the microscopic morphologies of each layer of device A and device C-2 have been checked by AFM. The results are shown in Fig. 3. The roughness of the evaporated layers is 1.04 nm for DMFL-NPB, 0.87 nm for LT-492:LT-632, and 1.01 nm for TPBi. The roughness of the solution-processed layers is 0.42 nm for DMFL-NPB, 0.46 nm for LT-492:LT-632, and 1.39 nm for TPBi. The morphologies of each layer by evaporation are about the same. The uniformity of the solution-processed DMFL-NPB and LT-492:LT-632 are better than the evaporated ones but a few spots still can be seen in the solution-processed DMFL-NPB. There are even more spots shown in the solution-processed TPBi layer due to the fact that there is no side chains in the TPBi molecules. We speculate that crystallization occurs in the solution-processed DMFL-NPB and TPBi and such crystallization could be regarded as one kind of impurity, which would quench the excitons. That is the reason why the efficiency decreases in device B and even more in device C-2. On the

**Table 1**  
Performance of OLEDs in this work.

Label	HTL (DMFL-NPB)	EML (LT-492:LT-632)	ETL (TPBi)	Max. efficiency (cd/A)	Max. luminance (cd/m <sup>2</sup> )
Device A	E <sup>a</sup>	E	E	7.4(4V)	7054(11.5V)
Device B	S <sup>b</sup>	E	E	5.6(8V)	11,460(11.5V)
Device C-1	S	S	S(20 °C)	2.9(10V)	2125(13V)
Device C-2	S	S	S(50 °C)	4.8(8V)	3677(11.5V)
Device C-3	S	S	S(70 °C)	2.3(10V)	856(13V)
Device C-4	S	S	S(90 °C)	1.8(10V)	315(13V)
Device D	S	S		0.1(11.5V)	26(11.5V)

<sup>a</sup> E: evaporation.

<sup>b</sup> S: solution process.

other hand, the crystallization in DMFL-NPB may cause higher mobility in device B and device C-2, therefore the current density is higher than that of device A at lower bias range (below 9 V). While the bias increasing, the emission zone will move to the interface between EML and TPBi due to the carrier blocking effect and the excitons would be quenched by the large crystallization of TPBi. Therefore the luminance of device C-2 becomes lower at higher bias range (after 10 V). In order to optimize the all-solution-processed OLED, devices with different annealing temperatures of TPBi layer have been made, which are device C-1 (20 °C), C-2 (50 °C), device C-3 (70 °C), and device C-4 (90 °C). The results are shown in Fig. 4. The efficiencies while operating at 10 mA/cm<sup>2</sup> are 2.9 cd/A for device C-1, 4.8 cd/A for device C-2, 2.1 cd/A for device C-3, and 1.7 cd/A for device C-4. The maximum luminance are 2125 cd/m<sup>2</sup> for device C-1, 3677 cd/m<sup>2</sup> for device C-2, 856 cd/m<sup>2</sup> for device C-3, and 315 cd/m<sup>2</sup> for device C-4. The device performance of device C-1 is lower than that of device C-2, indicating that the crystallization of device C-2, as can be seen in Fig. 3f, may increase the carrier mobility and help the electron transporting. In device C-3 and device C-4 large crystallization occurs and obvious spots can be seen by naked eyes, therefore the device performances are poor due to the exciton quenching effect. the crystallization of organic film is detrimental to the device and should be avoided. The case of TPBi films annealed at 70 °C and 90 °C indeed shows the crystal formation at the scale of μm or larger in organic films which can be observed by naked eyes. The performance of the devices with TPBi at 70 °C or 90 °C shows poor efficiency. On the other hand the TPBi film at 50 °C has very small spots (much less than μm). We speculate that the films at 50 °C just start packing and cause higher carrier mobility than that annealed at 20 °C but less harmful than that with real crystals. Furthermore, according to the AFM image the morphology and roughness of HTL/EML (annealed at 125 °C, 5 min) seems to be about the same as those of HTL (annealed at 120 °C, 10 min). However the morphology and roughness changed after adding the ETL (annealed at 20 °C, 50 °C, 70 °C, or 90 °C for 10 min). Because the annealing temperature of ETL is less than that of HTL or

HTL/EML, we think the roughness and morphology change should be resulted from the crystallinity change of TPBi layer, not from other layers (HTL, EML). We suggest that vapor-quality devices from solution process can be obtained with all the small molecules including hole/electron transport and emissive materials modified with side chains to get a uniform thin film without crystallization. All the device performances are summarized in Table 1.

In conclusion we have demonstrated all-solution-processed multilayer blue OLEDs by blade coating without any cross-linked materials. This kind of device combines the advantages of small molecular organic materials and large area manufacture process with low cost. Blue organic host and guest have been used with side chains to get a uniform thin film by solution process. The performance of the solution-processed device with multilayer structure can be very close to the evaporated one, and the cost of the solution-processed can be reduced dramatically.

### Acknowledgement

This work is supported by the National Science Council of Taiwan under Grant numbers NSC96-2120-M-007-007 and NSC96-2112-M-009-036.

### References

- [1] Michael Morgenthal, *Information Display* 24 (05) (2008).
- [2] L. Hou, L. Duan, J. Qiao, W. Li, D. Zhang, Y. Qiu, *Appl. Phys. Lett.* 92 (2008) 263301.
- [3] N. Rehmman, D. Hertel, K. Meerholz, H. Becker, S. Heun, *Appl. Phys. Lett.* 91 (2007) 103507.
- [4] H. Kim, Y. Byun, R.R. Das, B.K. Choi, P.S. Ahn, *Appl. Phys. Lett.* 91 (2007) 093512.
- [5] S.C. Lo, E.B. Namdas, P.L. Burn, I.D.W. Samuel, *Macromolecules* 36 (2003) 9721.
- [6] T.D. Anthopoulos, J.P.J. Markham, E.B. Namdas, I.D.W. Samuel, S.C. Lo, P.L. Burn, *Appl. Phys. Lett.* 82 (2003) 4824.
- [7] B. Walker, A. Tamayo, J. Yang, J.Z. Brzezinski, T.Q. Nguyen, *Appl. Phys. Lett.* 93 (2008) 063302.
- [8] K.H. Kim, S.Y. Huh, S.M. Seo, H.H. Lee, *Appl. Phys. Lett.* 92 (2008) 093307.
- [9] S.R. Tseng, H.F. Meng, C.H. Yeh, H.C. Lai, S.F. Horng, H.H. Liao, C.S. Hsu, L.C. Lin, *Synth. Met.* 158 (2008) 130.
- [10] S.R. Tseng, H.F. Meng, K.C. Lee, S.F. Horng, *Appl. Phys. Lett.* 93 (2008) 153308.

gives mobility values which are anisotropic and might be far away from those in a real device because factors like disorder and experimental conditions (like nature of charge generation, electric field range and charge concentration [10]) may significantly influence mobility values.

Conventionally charge carrier mobility in organic materials has often been measured by TOF in which the transit time ( $t_{tr}$ ) of a sheet of charge carriers, flash photo-generated in a thin, initial region of the sample, is measured in a transient experiment. But  $\pi$ -conjugated polymers are slightly different in the sense that poor sample quality and low mobilities often make the TOF measurements difficult. TOF needs thick samples (in  $\mu\text{m}$  range) with optical density in excess of 10. However, the thickness of polymer solar cells is a couple of hundreds of nanometer. Therefore, the mobility values obtained from TOF experiments are not the measured values for an actual device of interest. Furthermore, the necessary conditions for the applicability of TOF techniques is that the dielectric relaxation time  $\tau_{\sigma} = \epsilon\epsilon_0/\sigma$  ( $\epsilon$  is the dielectric permittivity,  $\sigma$  is the conductivity) is larger than the charge carrier transit time,  $t_{tr} = d^2/\mu V$  (here  $d$  is the inter-electrode distance,  $\mu$  is the mobility of charge carriers,  $V$  is the magnitude of voltage), otherwise the drifting charges will relax before they reach the opposite electrode [11]. Moreover, the equilibrium charges will be sufficient to significantly redistribute the electric field inside the sample leading to anomalous electric field dependence of mobility [12]. Hence, the mobility results from TOF do not reflect the actual situation of a real solar cell device due to thick film. Hence, it can be seen that each of these mobility measurement techniques lacks the universality of application or desired accuracy.

Another method available for mobility measurements is the Charge Extraction by Linearly Increasing Voltage (CELIV) technique. The theory behind CELIV has been presented elsewhere [13]. CELIV has the advantage of being experimentally very simple and measured values are not influenced by contact barriers of sandwich sample. The CELIV method also demonstrates advantage against the popular TOF method because for CELIV it is not necessary to fulfill the TOF condition. Hence, the mobility values are for the actual OPV nanometer thick optimized films not micron thick as required in TOF. Although all methods suffer from some problems but values obtained from CELIV are inherently closer to the actual value in the device; also because CELIV is based on the charge carrier extraction current, which causes the electric field redistribution in the device.

Theoretically both electron and hole mobility measurements are possible using CELIV but it has proved to be very difficult in the past. The only restriction imposed by the experimental setup is that at least one contact of the sample should be blocking. Nonetheless, measurements have not been very straightforward as only one extraction peak is seen in CELIV. The main difficulty has been to resolve the electron and hole mobility peaks. Up until now only one of the values has reportedly been possible to extract for OPV blends [14]. The only reported data on bipolar mobility values by CELIV is by Andersson et al. [15] where they see two distinct peaks at critical acceptor loading greater than 75%.

But 75% is very high loading for the acceptor and does not represent the conditions for optimized solar cells. To identify the type of carrier they correlate their data to FET (where the polarity of charge carriers can be chosen at will), but still not all materials show obvious electron currents in FETs. Hence, a universal method is needed which can be applied to optimized films to get individual electron or hole mobility values. In this work, all measurements were performed on optimized bulk heterojunction (BHJ) active layers with a systematic variation of the donor:acceptor weight ratio over a wide range to emphasize the universality of the method and to demonstrate that this can indeed be used to study mobility in any kind of system. Appropriate blocking electrodes to block one type of carriers in the film were used in this case. This suppresses the CELIV transient corresponding to the carrier that has been blocked resulting in one broad peak converting to a sharper peak corresponding to the carrier that has not been blocked. This is, in effect, something similar to deconvolution.

However, it is an inherent problem of mobility measurement that it is very sensitive to the interface chemistry of the dielectric used [16]. Recently Quiles et al. [17] provided evidence that vertical segregation and hence transport in a polymer film depends on several processing parameters; one of them being the type of substrate used. A blocking electrode near the anode (effectively a material other than PEDOT–PSS) might change the film morphology perpendicular to the electrode. The transport characteristics and hence mobility values of the test device might then be different from those of the real devices. Hence, instead of using the blocking electrode on the anode side, it was introduced on the cathode side above the polymer layer. In this manner, the morphology of the polymer active layer was not disturbed and hence the mobility values obtained should be more reflective of the actual values.

## 2. Materials and methods

In this letter, optimized solar cells based on various poly-alkylthiophene: [6,6]-phenyl- $\text{C}_{61}$ -butyric acid methyl esters (PCBM) were fabricated. Samples of regio-regular (RR)-poly (3-butylthiophene) (RR-P3BT), RR-poly (3-octylthiophene) (RR-P3OT) and RR-poly (3-dodecylthiophene) (RR-P3DT) were investigated by the CELIV method. The materials were purchased from Reike-metals and were used without further purification. The alkylthiophenes and PCBM were separately dissolved in 1,2-dichlorobenzene, then blended together with 1: $x$  wt/wt ratio to form a 2.0 wt.% solution. The PCBM loading concentration was systematically varied with respect to the alkylthiophene polymer and hence  $x = 0.5, 1.0, 2.0$  was used. This solution was spin coated at 700 rpm for 40 s, and the wet film was dried in a covered glass Petri dish as by Li et al. [18]. The dried film was then annealed at 120 °C for 10 min in the glove box. The active film thickness was 230–250 nm measured by a Dektak 3030 profilometer. The cathode was 10 nm Ca covered by 100 nm Al. The device structure was ITO/PEDOT–PSS/BHJ/Ca/Al. The power conversion efficiency (PCE) for the different systems is shown in Table 1.



**Table 1**

Power conversion efficiency (PCE) and fill factor (FF) for BHJs of different alkylthiophene:PCBM BHJ. The leftmost column indicates ratio of alkylthiophene:PCBM. The upper values in columns 2, 3 and 4 indicate PCE while the lower values indicate FF. Device structure was ITO/PEDOT/BHJ/Ca/Al.

	P3BT	P3OT	P3DT
2:1	1.89%	2.1%	0.09%
	65.16	53.7	43.6
1:1	1.64%	0.52%	0.18%
	46.0	32.11	48.9
1:2	0.94%	0.6%	0.03%
	43.55	47.3	23.3

Successful extraction of hole mobilities is demonstrated by blocking the electrons for various poly-alkylthiophene:PCBM BHJ at varying amounts of PCBM loading percentage. This is achieved by using appropriate blocking electrode to suppress the peak for one carriers (block this carrier) thus in effect separating the electron and hole mobility peaks. The authors propose this as a generalized method which can be applied to any of the polymeric systems.

*N,N'*-bis(3-methylphenyl)-*N,N'*-diphenyl-[1,1'-biphenyl]-4,4'-diamine (TPD) (a well-known electron blocking material in small molecule solar cells as shown in Fig. 1c, with highest occupied molecular orbital (HOMO) and lowest occupied molecular orbital (LUMO) levels of 5.4 eV and 2.2 eV [19] respectively), was the material of choice to be thermally deposited between the polymer BHJ and the Ca/Al electrode. The device structure was ITO/PEDOT-PSS/BHJ/TPD/Ca/Al as shown in Fig. 1b. The TPD layer thickness was 7–8 nm and was deposited at a base pressure of  $1 \times 10^{-6}$  torr. Vacuum was broken after deposition of TPD and the film was exposed to air for less than a minute while it was loaded into another chamber for deposition of Ca/Al electrode. BHJ's as detailed in Table 1 were used in this structure. I–V curves on introduction of

additional TPD layer show a reduction in efficiency due to blocking of electrons by the TPD layer.

The experimental setup for the CELIV is shown in Fig. 1d and was the same as in Ref. [20]. A variable pulse generator Wavetek Datron 195 and a memory oscilloscope Tektronix TDS 430A were used to recode the extraction currents. In this technique charges that cause conductivity in the dark are extracted by a triangular voltage pulse [13]. The extraction field pulls charges towards the electrodes which gives rise to a current transient. The initial of the pulse current is equal to the capacitive displacement current given by:

$$j(0) = \frac{A\epsilon\epsilon_0}{d}$$

(where  $A$  is the ramp rate of voltage,  $d$  the film thickness,  $\epsilon$  is relative dielectric permittivity and  $\epsilon_0$  is the dielectric permittivity with respect to free space). By selecting the appropriate voltage rise speed ( $A = V/t$ ) the current goes over the maximum, and from the peak extraction time  $t_{\max}$  (marked by arrows in the corresponding figures) the mobility can be calculated as:

$$\mu = \frac{2d^2}{3At_{\max}^2 \left[ 1 + 0.36 \frac{\Delta j}{j(0)} \right]} \quad \text{if } \Delta j < j(0)$$

Current maxima is calculated from the zero intersect to the peak position and this excludes ohmic effects.

### 3. Results and discussion

Fig. 2a shows the CELIV transient for the structure ITO/PEDOT-PSS/P3BT:PCBM/Ca/Al. It is quite apparent that the transient peak is quite broad with poorly defined maxima for certain PCBM loading concentrations (1:1 and 2:1). It has been argued that the mobility obtained from peaks for CELIV transients corresponds to the majority carriers

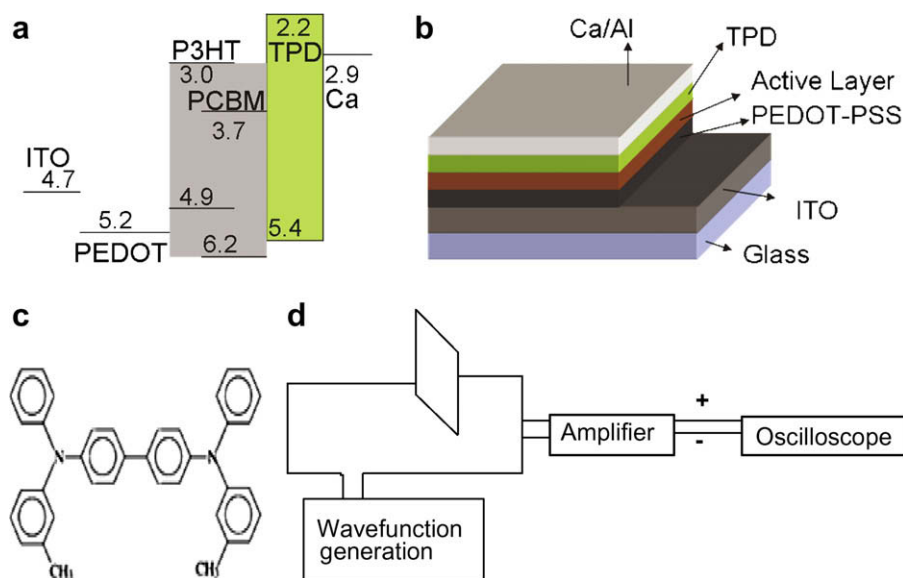


**Fig. 1.** (a) Energy diagram and (b) device structure for ITO/PEDOT/alkylthiophene:PCBM/TPD/Ca/Al, (c) chemical structure of TPD, and (d) schematic of CELIV setup used for the experiments.

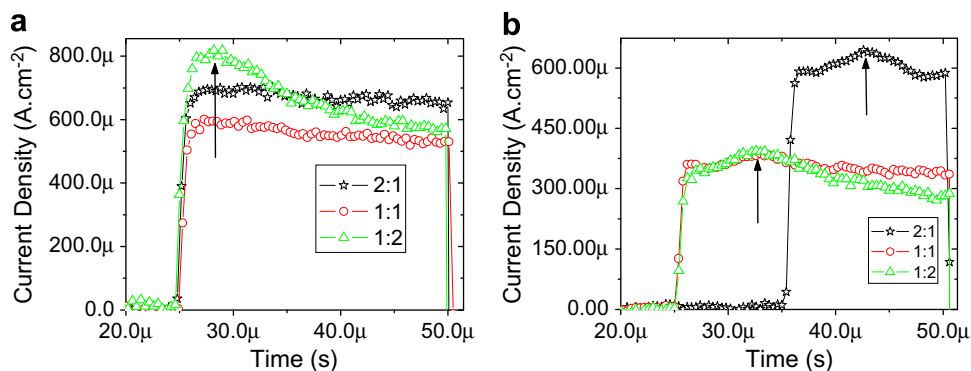


**Fig. 2.** CELIV curves for P3BT:PCBM BHJ. The device structure is (a) ITO/PEDOT:PSS/P3BT:PCBM/Ca/Al and (b) ITO/PEDOT:PSS/P3BT:PCBM/TPD/Ca/Al using a blocking electrode (TPD) at the cathode. The label in each of the subfigures indicates the ratio by weight percent (black star = 2:1, red circle = 1:1 and green triangle = 1:2) of P3BT:PCBM in the active layer. Approximate peak positions are indicated by arrows. In Fig. 2a only the mobility for ratio 1:2 ( $\Delta$ ) can be pointed by the arrow. (For interpretation of the references to colour in this figure legend, the reader is referred to the web version of this article.)

[13,21] and the integrated area under the peak gives the carrier number. However, it is difficult to extract exact mobility values from broad peaks due to uncertainty associated with  $t_{\max}$  in broad peaks (such as in Fig. 2a). These imply probably a superposition of peaks for both the carriers resulting in a particularly broad peak. Hence, if the electrons are blocked the peak corresponding to electrons should be very small (if any). Based on this underlying principle, CELIV transient for P3BT:PCBM system with the blocking TPD layer (structure ITO/PEDOT–PSS/P3BT:PCBM/TPD/Ca/Al) is shown in Fig. 2b (voltage ramp A for 2:1, 1:1 and 1:2 blends being 330, 195 and 195 kV/s). For the P3BT:PCBM ratio of 2:1 a higher ramp voltage has been applied to get a better hole peak. This will not influence the extracted mobility values. These peaks were ascribed to hole mobility as explained earlier. The calculated mobility values for the different loading concentrations of PCBM are shown in Table 2. It is to be noted that these peaks are much more prominent and sharper than those compared to those in Fig. 2a. This will be discussed in more detail later.

To test the method for more systems, similar thiophene–backbone based polymers (as P3BT) but with longer side chains (P3OT and P3DT) were used. The TPD layer was used in a similar architecture as shown in Fig. 1b to demonstrate extraction of hole mobility. The CELIV transients for these polymers with the structure ITO/PEDOT–PSS/alkylthiophene:PCBM/TPD/Ca/Al has been shown in Fig. 3 (for 2:1, 1:1 and 1:2 blends, the ramp A was 204, 270 and 230 kV/s for P3OT and 270, 195 and 230 kV/s for P3DT). A summary of the calculated values of hole mobili-

ties has been given in Table 2. It is to be noted that for 1:1 ratio of thiophene:PCBM, P3BT with the shortest four carbon alkyl side chain shows higher mobility among all three polymers under study in agreement with some previous reports [22] (measured using FET). These results agree with the correlation between mobility and the length of the alkyl side chain. Assuming the same degree of regio-regularity as well as polymerization degree for all three P3ATs, the hole mobility should increase as the length of the side chains decreases due to their contribution to the degree of intermolecular order and chain packaging density. However, this trend is not observed for 2:1 or 1:2 blends. There are also contrary reports of a non-monotonous decrease in mobility with side chain length for pure alkylthiophene polymers [23] (measured by FET). From the experimental results, it is concluded that mobility is a complex function of interlayer distance, crystallinity, crystallite size etc.; all of which will be influenced by external factors such as PCBM loading concentrations. Hence, it is all more important to study mobility values for actual solar cell devices. Therefore, results reported earlier using FET or TOF might not reflect the actual mobility values in real devices. These hole mobility values are, not surprisingly, lower than those reported by FET: approximately  $10^{-3} \text{ cm}^2 \text{ V}^{-1} \text{ s}^{-1}$  for P3OT [24] and  $2 \times 10^{-3} \text{ cm}^2 \text{ V}^{-1} \text{ s}^{-1}$  for P3DT [25]. Previous literature [26] shows that there is at least an order of magnitude difference between FET and CELIV mobility, with FET mobilities being the higher, for this class of system.

For P3BT, there seems to be an increase in hole mobility on increasing the PCBM concentration. Although on increasing the PCBM percentage, the order of mobility change is very small. This increase is less prominent in P3DT and almost absent in P3OT. Increase in hole mobility of polymers with increase in PCBM percentage has also been observed for other polymers also and has been reported earlier [27,28]. According to Pacios et al. [29], the change in film morphology upon adding PCBM molecules results in an enhanced intermolecular interaction and therefore an improved charge transfer between adjacent molecules. Though under optimized annealing conditions,

**Table 2**

Hole mobilities (unit:  $\text{cm}^2 \text{ V}^{-1} \text{ s}^{-1}$ ) extracted from CELIV peak maxima of Fig. 2 for various alkylthiophene:PCBM (given in row 1) loading conditions.

	P3BT	P3OT	P3DT
2:1	1.89 E–6	3.26 E–5	1.70 E–5
1:1	4.11 E–5	2.90 E–5	1.84 E–5
1:2	6.13 E–5	3.25 E–5	7.01 E–5

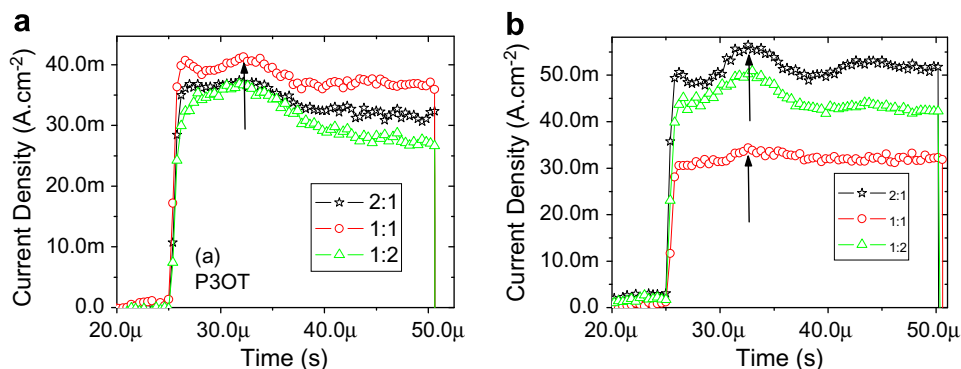


**Fig. 3.** CELIV curves for (a) P3OT:PCBM and (b) P3DT:PCBM BHJ using a blocking electrode (TPD) at the cathode. The device structure is ITO/PEDOT:PSS/P3BT:PCBM/TPD/Ca/Al. The label in each of the subfigures indicates the ratio by weight percent (black star = 2:1, red circle = 1:1 and green triangle = 1:2) of alkylthiophene:PCBM in the active layer. Approximate peak positions are indicated by arrows. (For interpretation of the references to colour in this figure legend, the reader is referred to the web version of this article.)

PCBM crystallizes out of the matrix of the BHJ [30,31], leaving the polymer chains behind which will try to reorganize and obtain an optimized morphology. Hence, for optimized devices, even on increasing PCBM loading concentration, the hole mobility should not vary by a huge factor.

For the CELIV transients shown, the peak corresponding to electrons should either be absent or highly suppressed. But on comparing the prominent hole peaks, it can be seen that some peaks are considerably sharper (distinguishable extraction time  $t_{\max}$ ), while others are still broad. It is suspected that in systems corresponding to sharp peaks (e.g. 2:1 ratio in P3BT:PCBM system), the hole and electron mobility is balanced, i.e. the peak for hole and electron mobility (even if a small one) overlap. According to Melzer et al. [32] and Li et al. [19], for high fill factors (and hence PCE) for BHJ solar cells, the charge carrier mobility should be balanced. In this case, all systems with sharp peaks indeed have considerably high fill factors (and consequently PCE) as reported in Table 1. In fact, CELIV signals for the highest fill factor for a particular donor:acceptor system have the most well defined extraction time  $t_{\max}$  for that set. Based on above arguments a mobility balance is expected for the sharp peak of 2:1 ratio for P3BT:PCBM. It has also been reported that electron mobilities increase with acceptor (PCBM) loading concentrations [33]. If this is true then the peak for electron mobility should occur at lower time scales (left shifted) on increasing PCBM loading concentration. Indeed, for this case, the curves corresponding to higher PCBM concentrations are broader than those at lower PCBM concentrations. The authors believe that the electron mobility is indeed higher at higher PCBM concentrations and hence the electron mobility peak (appearing at lower time scales) is demerged from the hole peak, broadening the overall peak.

#### 4. Conclusion

Summarizing, it has been shown in this letter that it is possible to obtain resolved hole mobility peaks through CELIV for the alkylthiophene:PCBM system by choosing the appropriate blocking electrode and the observations

agree with the existing theories. This method does not affect the organization in the polymer BHJ layer and hence it is expected that the mobility values obtained by this method will be closer to the real values. Universality of the method was demonstrated by using polymers from alkylthiophene system with varying side chain length and hole mobility for the optimized BHJ films were extracted. Since mobility is not the only factor affecting PCE, so based on these measurements no concrete conclusions for the varying performance between different alkylthiophene systems could be reached. But, it was shown, as suggested earlier, that a balance of hole and electron mobility is necessary for high fill factors. It is well known that further insight into the performance limiting properties of the solar cells can be gained by correlating the transport measurements with solar cell data. It is in this light that this method will help understand this correlation and the balance between electron and hole mobility, which is crucial to solar cells.

#### Acknowledgements

This study is sponsored by the Office of Naval Research (Grant No. N00014-04-1-0434, Program Manager Dr. Paul Armistead), Solarmer Energy Inc. and University of California Discovery Grant (Grant No. GCPO5-10208).

#### References

- [1] R. Friend, R. Gymer, A. Holmes, J. Burroughes, R. Marks, C. Taliani, D.D.C. Bradley, D.A. Dos Santos, J.L. Bredas, M. Logdlund, W.R. Salaneck, *Nature* 397 (1999) 121.
- [2] H. Katz, Z. Bao, *J. Phys. Chem. B* 104 (4) (2000) 671.
- [3] N.S. Sariciftci, H. Hoppe, *J. Mater. Res.* 19 (2004) 1924.
- [4] C.D. Dimitrakopoulos, D.J. Mascaro, *IBM J. Res. Dev.* 45 (2001) 11.
- [5] H.C.F. Martens, P.W.M. Blom, H.F.M. Schoo, *Phys. Rev. B* 61 (2000) 7489.
- [6] M. Gailberger, H. Bässler, *Phys. Rev. B* 44 (1991) 8643.
- [7] H. Bassler, *Polym. Adv. Technol.* 9 (7) (1998) 402.
- [8] G. Horowitz, *J. Mater. Res.* 19 (17) (2004) 1946.
- [9] S.A. Choulis, J. Nelson, Y. Kim, D. Poplavskyy, T. Kreouzis, J.R. Durrant, D.D.C. Bradley, *Appl. Phys. Lett.* 83 (2003) 18–3812.
- [10] C. Tanase, E.J. Meijer, P.W.M. Blom, D.M. De Leeuw, *Phys. Rev. Lett.* 91 (2003) 216601.
- [11] G. Juška, K. Genevičius, M. Viliunas, K. Arlauskas, R. Österbacka, H. Stubb, *Proc. SPIE* 4415 (2001) 145.

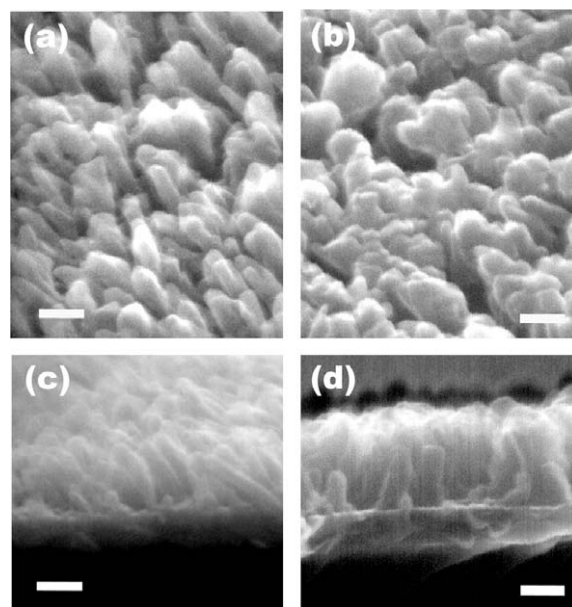
- [12] G. Juška, K. Genevičius, K. Arlauskas, R. Österbacka, *Phys. Rev. B* 65 (2002) 233208.
- [13] G. Juška, K. Arlauskas, M. Viliunas, J. Kočka, *Phys. Rev. Lett.* 84 (2000) 4946.
- [14] A.J. Mozer, N.S. Sariciftci, L. Lutsen, D. Vanderzande, R. Osterbacka, M. Westerling, G. Juska, *Appl. Phys. Lett.* 86 (2005) 112104.
- [15] L. Mattias Andersson, Fengling Zhang, Olle Inganäs, *Appl. Phys. Lett.* 89 (2006) 142111.
- [16] L.-L. Chua, J. Zaumseil, J.F. Chang, E.C.-W. Ou, P.K.-H. Ho, H. Sirringhaus, R.H. Friend, *Nature* 434 (2005) 194.
- [17] M.C. Quiles, T. Ferenczi, T. Agostinelli, P. Etchegoin, Y. Kim, T. Anthopoulos, P. Stavrinou, D. Bradley, J. Nelson, *Nat. Mater.* 7 (2008) 158.
- [18] Gang Li, Vishal Shrotriya, Jinsong Huang, Yan Yao, Tommoriarty, Keith Emery, Yang Yang, *Nat. Mater.* 4 (2005) 864.
- [19] Igor Vragović, Eva M. Calzado, María A. Díaz García, *Chem. Phys.* 332 (2007) 48.
- [20] G. Juska, K. Arlauskas, R. Osterbacka, H. Stubb, *Synth. Met.* 109 (2000) 173.
- [21] G. Juska, M. Viliunas, K. Arlauskas, N. Nekrasas, N. Wyrsh, L. Feitknecht, *J. Appl. Phys.* 89 (2001) 4971.
- [22] K. Kaneto, W.Y. Lim, W. Takashima, T. Endo, M. Rikukawa, *Jpn. J. Appl. Phys.* 39 (2000) L872.
- [23] Amit Babel, Samson A. Jenekhe, *Synth. Met.* 148 (2005) 169.
- [24] Le Huong Nguyen, Harald Hoppe, Tobias Erb, Serap Günes, Gerhard Gobsch, N. Serdar Sariciftci, *Adv. Funct. Mater.* 17 (2007) 1071.
- [25] M. Plotner, T. Wegener, S. Richter, S. Howitz, W.-J. Fischer, in: *EMRS Spring Meeting 2004, Strasbourg, 24–28 May 2004, Symposium F, F/PII.19.*
- [26] S. Scheinert, G. Paasch, M. Schrödner, H.-K. Roth, S. Sensfuss, Th. Doll, *J. Appl. Phys.* 92 (1) (2002) 330.
- [27] L. Mattias Andersson, Olle Inganäs, *Appl. Phys. Lett.* 88 (2006) 082103.
- [28] V.D. Mihailetchi, L. Kostner, P.W.M. Blom, Christian Melzer, Bert de Boer, J.K.J. Van Duren, R.A.J. Janssen, *Adv. Funct. Mater.* 15 (2005) 795.
- [29] R. Pacios, D.D.C. Bradley, J. Nelson, C.J. Brabec, *Synth. Met.* 137 (2003) 1469.
- [30] L.M. Andersson, F.L. Zhang, O. Inganäs, *Appl. Phys. Lett.* 89 (2006) 142111.
- [31] Ankit Kumar, Gang Li, Ziruo Hong, Yang Yang, *Nanotechnology* 20 (2009) 165202.
- [32] C. Melzer, E.J. Koop, V.D. Mihailetchi, P.W.M. Bloom, *Adv. Funct. Mater.* 14 (2004) 865.
- [33] T. Aernouts, P. Vanlaeke, W. Geens, J. Poortmans, P. Heremans, S. Borghs, R. Mertens, The influence of the donor/acceptor ratio on the performance of organic bulk heterojunction solar cells, in: *Presented at the E-MRS Spring Meeting, Strasbourg, France, 2003.*

layer surface, and poor contact with the top electrode [11,12]. In this letter, we report the growth of dense arrays of vertically aligned, polycrystalline copper phthalocyanine (CuPc) molecular nanorods with diameter down to 20 nm using the high vacuum oblique angle deposition (OAD) process [13–15]. By infiltrating the CuPc nanorod arrays with the acceptor of [6,6]-phenyl-C<sub>61</sub>-butyric acid methyl ester (PCBM) using spin-coating, we demonstrate interdigitated, bulk heterojunction organic PV devices with a maximum power conversion efficiency of  $\eta_p = (1.8 \pm 0.1)\%$  under 1 sun AM1.5 solar illumination, a twofold improvement over that of optimized bilayer, planar heterojunction CuPc/PCBM device.

The nanorod arrays are grown on glass substrates pre-coated with a layer of indium-tin-oxide (ITO, sheet resistance  $\sim 20 \Omega/\square$ ) in a high vacuum chamber (base pressure  $\sim 1 \times 10^{-7}$  Torr). Different from normal high vacuum deposition processes in which the ballistic molecular or atomic beam typically arrives at the substrate surface from near-normal directions, in an OAD process (also known as glancing angle deposition), [13–15] the molecular/atomic beam arrives at the surface with a large angle from the substrate normal, nearly  $90^\circ$ . Due to the self shadowing effect by the deposited molecules and the limited adatom diffusion on the substrate surface, nanorod arrays with various morphologies can be obtained by controlling the incident angle of the molecule flux as well as the surface diffusivity of the molecules [14]. In our experiments, the molecular beam incident angle from the substrate normal was  $\alpha \approx 80^\circ$  during the nanorod growth. The substrate was either stationary or rotated at a speed of  $\sim 5$  rpm.

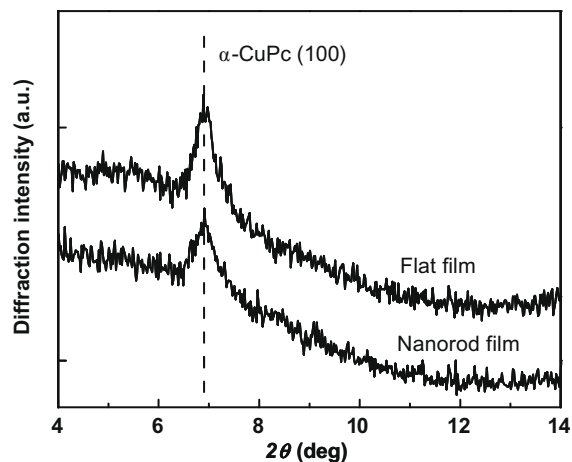
PV devices were fabricated by spin-coating PCBM solution (in chlorobenzene) onto the CuPc nanorod films at 1000 rpm for 45 s in a nitrogen glove box integrated with the vacuum system. The CuPc/PCBM composite films were then annealed at  $80^\circ\text{C}$  for 15 min to remove residual solvent and further enhance PCBM infiltration. We have not observed any significant changes in the optical, morphological or electronic properties of the CuPc films upon such quick exposure to the chlorobenzene solvent. An 8 nm thick bathocuproine (BCP) exciton-blocking layer [16] was then deposited on top of the organic active region in high vacuum, followed by a 100 nm thick aluminum cathode to complete the device and form device areas of  $4 \text{ mm}^2$ . An Agilent 4155C semiconductor parameter analyzer was used to measure the current–density–voltage ( $J$ – $V$ ) characteristics of PV devices in the dark and under simulated AM 1.5 solar illumination from an Oriel simulator equipped with a Xe-arc lamp. The light intensity was measured using a calibrated single-crystalline silicon reference cell with a KG1 filter, and the spectral mismatch factor was corrected according to the ASTM Standard E973 [17]. X-ray diffraction (XRD) patterns of the organic films were obtained using a Philips X'pert MRD diffractometer in the  $\theta$ – $2\theta$  geometry with a Cu K $\alpha$  radiation source. The film morphology was investigated using a JOEL 6335F field-emission gun scanning electron microscope (SEM).

Fig. 1a and b show the topographic SEM images of CuPc nanorod arrays grown with a stationary or rotational substrate, respectively, whereas Fig. 1c and d are the corresponding cross-sectional images. With a stationary



**Fig. 1.** Topographic ((a) and (b)) and cross-sectional ((c) and (d)) scanning electron microscope (SEM) images of CuPc nanorods grown on a stationary ((a) and (c)) or rotational ((b) and (d)) substrate. The scale bar is 100 nm in all four images.

substrate [Fig. 1a and c], slanted nanorods with 20–40 nm in diameter were grown on the ITO surface, tilting towards the direction of the incoming molecule flux during deposition [14]. On the other hand, the CuPc nanorods grown with rotational substrates have larger diameters, typically 40 to 70 nm, and are mostly in the up-right orientation. Moreover, large gaps ( $>50$  nm) between the nanorods can be occasionally observed. However, upon closer observation we have found that the larger nanorods are in fact made up of a bundle of several smaller nanorods. This is consistent with the proposed morphology evolution model of OAD growth on rotational substrate [14].



**Fig. 2.** X-ray diffraction pattern of a CuPc nanorod film with 300 nm long nanorods and a 100 nm thick flat CuPc film.

The XRD pattern of a CuPc nanorod film grown with a rotational substrate is shown in Fig. 2 along with that for a CuPc flat film deposited in the normal fashion (i.e. molecules arriving at the surface roughly from the normal direction). The XRD patterns are very similar, showing diffraction peaks at  $2\theta = 6.9^\circ$ , which suggest the existence of polycrystalline  $\alpha$ -CuPc phase in the nanorods as well as in the flat film [18,19]. The polycrystalline structure of the CuPc nanorods is important to ensure high mobility for hole transport through the donor material, leading to high collection efficiency for photogenerated holes in the PV devices.

With the obtained CuPc nanorod arrays, an interdigitated bulk heterojunction was achieved by spin-coating a chlorobenzene solution of PCBM onto the nanorod arrays. Fig. 3 shows two cross-sectional SEM images of CuPc nanorods/PCBM composite films with different PCBM loading. No obvious voids or pin-holes are observed in either film, indicating good infiltration of PCBM into the spacing between CuPc nanorods. With a high PCBM loading (30 mg/mL in chlorobenzene), the spacing between CuPc nanorods is completely filled, resulting in a relatively smooth top surface [see Fig. 3b]. However, when a much lower PCBM loading (15 mg/mL) was used, the amount of

PCBM molecules deposited was insufficient to completely fill the spacing between the CuPc nanorods, leading to a corrugated and rough surface as shown in Fig. 3a. This suggests that the CuPc nanorods still stand vertically on the substrate and the spin-coating process does not damage the contact of the nanorods with the underlying ITO electrode, which is important for hole collection in PV devices.

To fabricate PV devices, planar (i.e. flat) and/or CuPc nanorod films with 40–60 nm long nanorods were deposited. A PCBM solution with a concentration of 22 mg/mL was spin-coated on top of the CuPc films at 1000 rpm, which leads to an average PCBM layer thickness of approximately 50 nm. Fig. 4 shows the  $J$ - $V$  characteristics under 1 sun AM 1.5G illumination for PV devices based on CuPc nanorods grown with a stationary or rotational substrate (labeled as “NR-S”, and “NR-R”, respectively). The structure of the NR-R device is shown in the inset. Also shown for comparison are the characteristics of a bilayer, planar heterojunction CuPc/PCBM device (labeled as “Planar”) with a 30 nm thick flat CuPc film and a PCBM layer deposited under the same condition as the nanorod-based devices. The layer thicknesses in this bilayer device are very close to optimized [20].

As shown in Fig. 4, the short-circuit current density is  $J_{SC} = (4.4 \pm 0.2) \text{ mA/cm}^2$  for both NR-S and NR-R devices, higher than the planar heterojunction device, which is only  $(3.4 \pm 0.2) \text{ mA/cm}^2$ . The open-circuit voltage is the same for all three devices, at  $V_{OC} = 0.57 \text{ V}$ , close to the previously reported value for the same D–A material system [20]. The fill factor (FF) of the NR-S device is, however, much lower than that for the NR-R device, 0.40 vs. 0.55, which could be attributed to the differences in the nanorod array morphology. The tilted nanorods obtained with a stationary substrate may present more challenges for the complete infiltration with PCBM molecules than the mostly up-right nanorods grown with a rotational substrate. Nevertheless,

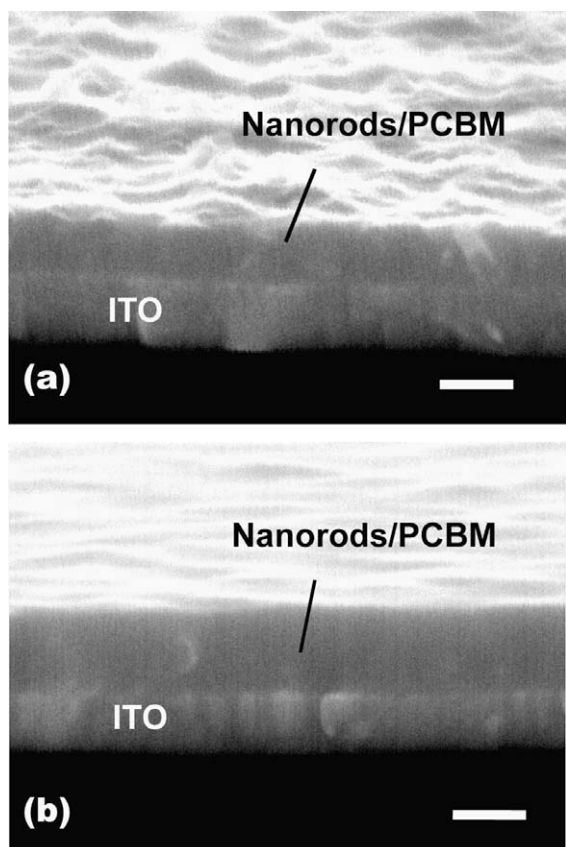


**Fig. 3.** Cross-sectional scanning electron microscope (SEM) images of CuPc nanorod/PCBM composite films with PCBM concentration of (a) 15 and (b) 30 mg/mL in the chlorobenzene solution. The scale bars are 100 nm.

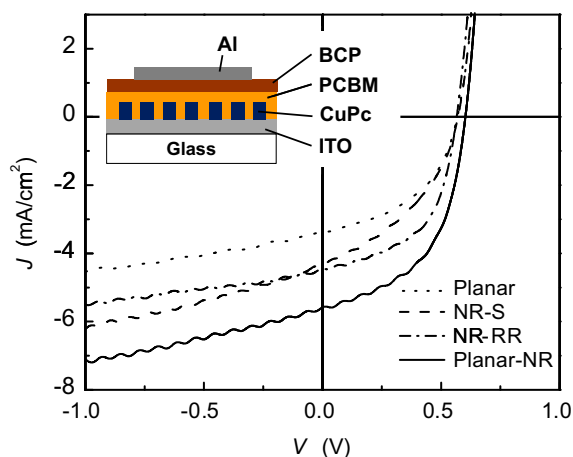


**Fig. 4.** Current-density-voltage ( $J$ - $V$ ) characteristics of four CuPc/PCBM photovoltaic cells under 1 sun AM 1.5G illumination: a bilayer cell (labeled as “Planar”) with a 30 nm thick flat CuPc film, two devices with CuPc nanorods grown on ITO with a stationary (“NR-S”) or rotational (“NR-R”) substrate, and a device with a 20 nm thick flat CuPc film followed by a nanorod film (“Planar-NR”). The inset schematically illustrates the device structure of the NR-R device.

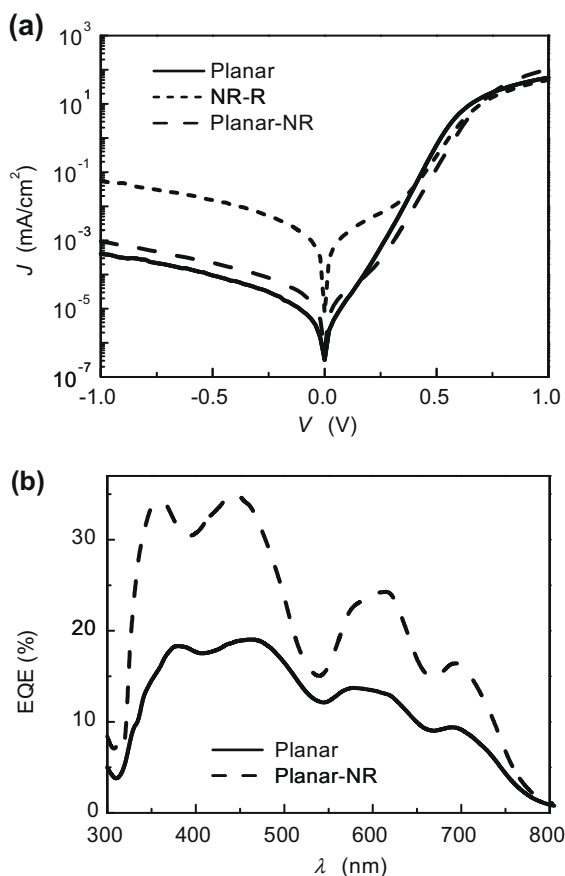


**Fig. 5.** (a) Current-density-voltage ( $J$ - $V$ ) characteristics in the dark for the Planar, NR-R, Planar-NR devices; (b) external quantum efficiency (EQE) as function of wavelength  $\lambda$  for Planar and Planar-NR devices.

the power conversion efficiency is  $\eta_p = (0.95 \pm 0.05)\%$  for the NR-S device and  $(1.4 \pm 0.1)\%$  for the NR-R device, both higher than  $\eta_p = (0.85 \pm 0.05)\%$  for the bilayer device.

To further improve the efficiency of the nanorod-based devices, a 20 nm thick planar CuPc layer was inserted between the nanorods (approximate length  $\sim 40$  nm) and the ITO. The planar layer can further improve the hole transport across the film and also provide additional absorption of the incident photons, similar to that in a planar-mixed heterojunction device [9,21]. As shown in Fig. 4,  $J_{SC}$  of this device (labeled as "Planar-NR") was improved to  $(5.6 \pm 0.3)$  mA/cm<sup>2</sup> and a high FF of 0.53 was achieved. The Planar-NR device also shows a slightly higher  $V_{OC}$  of 0.60 V, leading to a power conversion efficiency of  $\eta_p = (1.8 \pm 0.1)\%$ , approximately doubling that of the optimized bilayer CuPc/PCBM device.

Fig. 5a shows the dark  $J$ - $V$  characteristics for the Planar, NR-R, and Planar-NR devices. The NR-R device shows significantly higher leakage currents than the other two devices. The shunt resistance of the NR-R device as estimated from the dark  $J$ - $V$  characteristics around  $V = 0$  V is approximately  $5 \times 10^4 \Omega \text{ cm}^2$ , compared to approximately  $1 \times 10^7 \Omega \text{ cm}^2$  for the Planar device and  $3 \times 10^6 \Omega \text{ cm}^2$  for the Planar-NR device. The difference in

the shunt resistance can be explained by considering the direct contact of the PCBM acceptor phase with the ITO anode in the NR-R device, which provides a direct leakage path between the two electrodes. Such leakage path does not exist when a flat CuPc layer has been deposited on the ITO anode, a case for both the Planar and Planar-NR devices. These results in turn also suggest that we have achieved excellent infiltration of PCBM molecules deep into the gaps of the CuPc nanorods.

A comparison of the external quantum efficiency (EQE) for the Planar and Planar-NR devices as a function of the incident light wavelength  $\lambda$  is shown in Fig. 5b. In both the CuPc ( $550 \text{ nm} < \lambda < 800 \text{ nm}$ ) and PCBM ( $\lambda < 550 \text{ nm}$ ) absorption regions, the Planar-NR device possesses a 60–70% higher EQE than the Planar device. This efficiency increase is attributed to the increased interface area between the donor and acceptor species as enabled by the nanorod-based architecture. Note that integrating the EQE spectra shown in Fig. 5b with the standard AM1.5G solar spectrum [17] yields a 1 sun short-circuit current density of  $J_{SC} = 5.3$  mA/cm<sup>2</sup> for the Planar-NR device and 3.2 mA/cm<sup>2</sup> for the Planar device, both within the experimental errors of the actual measured  $J_{SC}$ .

In conclusion, we have demonstrated that vertically aligned polycrystalline CuPc nanorods with diameters as small as 20 nm can be grown using the oblique angle deposition method. An interdigitated bulk heterojunction structure was subsequently realized by infiltrating the CuPc nanorod array with solution processed PCBM molecules. Growth of  $\sim 40$  nm long CuPc nanorods on a thin planar CuPc film results in organic PV cells with power conversion efficiency approximately doubling that of an optimized bilayer CuPc/PCBM device. With further optimization of the nanorod growth and device fabrication processes, the structure described here could prove to be an effective architecture for very efficient organic PV cells.

## Acknowledgements

This work was supported by the National Science Foundation CAREER Program and the Solar Energy Technologies Program (SETP) of the US Department of Energy.

## References

- [1] C.W. Tang, Appl. Phys. Lett. 48 (1986) 183.
- [2] M.A. Green, K. Emery, Y. Hishikawa, W. Warta, Prog. Photovoltaics 16 (2008) 435.
- [3] P. Peumans, A. Yakimov, S.R. Forrest, J. Appl. Phys. 93 (2003) 3693.
- [4] J.J.M. Halls, C.A. Walsh, N.C. Greenham, E.A. Marsaglia, R.H. Friend, S.C. Moratti, A.B. Holmes, Nature 376 (1995) 498.
- [5] G. Yu, J. Gao, J.C. Hummelen, F. Wudl, A.J. Heeger, Science 270 (1995) 1789.
- [6] P. Peumans, S. Uchida, S.R. Forrest, Nature 425 (2003) 158.
- [7] Y. Zheng, S.K. Pregler, J.D. Myers, J.M. Ouyang, S.B. Sinnott, J.G. Xue, J. Vac. Sci. Technol. B 27 (2009) 169.
- [8] S.C. Veenstra, G.G. Malliaras, H.J. Brouwer, F.J. Esselink, V.V. Krasnikov, P.F. van Hutten, J. Wildeman, H.T. Jonkman, G.A. Sawatzky, G. Hadziioannou, Synthetic Met. 84 (1997) 971.
- [9] J. Xue, B.P. Rand, S. Uchida, S.R. Forrest, Adv. Mater. 17 (2005) 66.
- [10] F. Yang, M. Shtein, S.R. Forrest, Nat. Mater. 4 (2005) 37.
- [11] Y.S. Hsiao, W.T. Whang, S.C. Suen, J.Y. Shiu, C.P. Chen, Nanotechnology 19 (2008) 415603.
- [12] H. Xi, Z. Wei, Z. Duan, W. Xu, D. Zhu, J. Phys. Chem. C 112 (2008) 19934.
- [13] K. Robbie, J.C. Sit, M.J. Brett, J. Vac. Sci. Technol. B 16 (1998) 1115.

- [14] M.M. Hawkeye, M.J. Brett, *J. Vac. Sci. Technol. A* 25 (2007) 1317.
- [15] J.Q. Xi, M.F. Schubert, J.K. Kim, E.F. Schubert, M.F. Chen, S.Y. Lin, W. Liu, J.A. Smart, *Nat. Photonics* 1 (2007) 176.
- [16] P. Peumans, V. Bulovic, S.R. Forrest, *Appl. Phys. Lett.* 76 (2000) 3855.
- [17] Standard ASTM E973, Standard Test Method for Determination of the Spectral Mismatch Parameter between a Photovoltaic Device and a Photovoltaic Reference Cell, American Society for Testing and Materials, West Conshocken, PA, USA, 2002.
- [18] R. Prabakaran, R. Kesavamoorthy, G.L.N. Reddy, F.P. Xavier, *Phys. Status Solidi B* 229 (2002) 1175.
- [19] B.P. Rand, J. Xue, S. Uchida, S.R. Forrest, *J. Appl. Phys.* 98 (2005) 124902.
- [20] C.W. Chu, V. Shrotriya, G. Li, Y. Yang, *Appl. Phys. Lett.* 88 (2006) 153504.
- [21] J. Xue, B.P. Rand, S. Uchida, S.R. Forrest, *J. Appl. Phys.* 98 (2005) 124903.



A potential approach is to use  $\text{Cs}_2\text{CO}_3$  as the electron-injection and hole-blocking layer in  $\text{TiO}_2$  or ZnO-based devices [6,9,10]. Another approach is to improve the morphology and charge injection ability using the self-assembly monolayer (SAM) technique. SAM can adjust the work function (WF) of a substrate by producing a permanent dipole moment at interface [11,12]. As SAM links the substrate with an interfacial dipole directed towards the substrate, it would create an electric field which increases the WF of the substrate. Using this concept, numerous studies reported that the WF of the transparent substrate ITO or mirror substrate Ag is increased by linking a SAM with the high electronegativity terminal group to enhance the performance of PLEDs [11–15]. However, few reports have investigated that the WF of a cathode for I-LEDs is lowered by SAM technique.

In this study, two silane-based SAMs with different terminal groups were used to modify the  $\text{TiO}_2$  surface. The presence of an amine group at the outer surface of *N*-[3-(trimethoxysilyl)propyl]ethylenediamine (PEDA-TMS)-modified substrate induces a strong dipole due to its low electronegativity, which lowers the WF of the cathode. The performance of I-LED is enhanced by this compound. The device performance of 3-chloropropyltrimethoxysilane (CP-TMS) modified I-LED is different from that of a device modified by PEDA-TMS because the chlorine atom owns the electron-withdrawing ability. The functions of the two SAMs on the  $\text{TiO}_2$  surface are confirmed by ultraviolet photoelectron spectroscopy (UPS) measurement and electron-dominated devices. A storage test was performed on the PEDA-TMS-based device to measure the stability of both electrodes in air. The inverted device without sealing maintained a luminescence of about  $120 \text{ cd/m}^2$  after 48 h (the initial luminous was about  $124 \text{ cd/m}^2$ ).

## 2. Experimental

To fabricate the devices, ITO-coated glass substrates (received from RITEK Corp.,  $15 \Omega/\square$ ) were cleaned in an ultrasonic bath with detergent, deionized water, acetone, and isopropyl alcohol and then dried under a  $\text{N}_2$  stream. The substrates were treated using a UV/ $\text{O}_3$  photoreactor to eliminate surface contaminants. Titanium isopropoxide ( $\text{Ti}(\text{OC}_3\text{H}_7)_4$ , Aldrich, 99.999%) diluted in *n*-butyl alcohol was spin-coated onto the ITO/glass substrate at 5000 rpm for 60 s. The spin-coating process was conducted in a  $\text{N}_2$ -filled glove box. ( $\text{Ti}(\text{OC}_3\text{H}_7)_4$ ) then underwent hydrolysis and was converted to  $\text{TiO}_x$  in air for at least 1 h. The  $\text{TiO}_x$  film underwent thermal annealing at  $450^\circ\text{C}$  for 30 min to transform it into  $\text{TiO}_2$ . The glass/ITO/ $\text{TiO}_2$  substrate was immediately surface modified by immersing it in 1 wt.% PEDA-TMS (Aldrich, 97%) or CP-TMS (Aldrich, 97%) toluene solution for 2 min in an ultrasonic bath. After the reaction, the substrate was rinsed with toluene and then dried in a  $\text{N}_2$  stream. The glass/ITO/ $\text{TiO}_2$  substrates with and without SAM were then transferred into a  $\text{N}_2$ -filled glove box. High-yellow phenyl-substituted poly(*para*-phenylenevinylene) copolymer (HY-PPV)(EL emission centered at 560 nm) was spin-coated onto the substrates and used as the light-emissive layer. A  $\text{MoO}_3$  interfacial layer with a

thickness of 6 nm was thermally evaporated over the polymer, followed by the evaporation of Au(20 nm)/Ag(80 nm) at a pressure of  $10^{-6}$  torr. A conventional PLED was also fabricated for comparison. ITO/PEDOT:PSS (Baytron-P Al 4083) and Ca/Al were used as the cathode and anode part, respectively, for this PLED.

The UPS experiments were carried out in VG CLAM4, whose illumination was a non-monochromatic He(I) UV source (21.2 eV). The total energy resolution of the measurement was 0.38 eV. The entire process was performed in a multi-chamber ultrahigh vacuum (UHV) system, which included the UPS analysis chamber base ( $P_{\text{base}} \sim 8 \times 10^{-10}$  torr) and the preparation chamber ( $P_{\text{base}} \sim 9 \times 10^{-10}$  torr). The work function ( $\Phi$ ) of the films is defined as  $\Phi = h\nu - \Delta E$ , where  $h\nu$  is the photo energy (21.2 eV) and  $\Delta E$  is determined from the distance of the binding energy between the secondary electron emission cutoff edge ( $E_{\text{cut}}$ ) and the Fermi level. The current density–voltage–luminance (*J*–*V*–*L*) measurements were performed using a Keithley 2400 source measure unit and a Keithley 2000 digital multimeter with a silicon photodiode, calibrated using a Minolta LS-100 luminous meter. All measurements, except for the storage test, were performed in a  $\text{N}_2$ -filled glove box.

## 3. Results and discussion

The mechanism of silanization is shown in Fig. 1. The molecules are hydrolyzed when they come close to the  $\text{TiO}_2$  surface, which is covered with an  $\text{H}_2\text{O}$  film. Chains are then bonded to the substrate via hydrogen bonds. Water is then removed to link the silane molecule to the surface of  $\text{TiO}_2$ . The SAM substrates were analyzed using X-ray photoelectron spectroscopy (XPS) (not shown here). The feature peak of  $\text{Si}_{2p}$  is found at 103 eV [16]. The  $\text{Si}_{2p}$  peak appears on the substrates, demonstrating that the silane molecule was bound to the  $\text{TiO}_2$  surface.

UPS is a valuable tool for investigating the electronic properties of a semiconductor. Fig. 2 shows the UPS spectra of ITO/ $\text{TiO}_2$  and ITO/ $\text{TiO}_2$ /SAM substrates. The work function (WF) of a sample can be determined from UPS spectra using the difference between the photo energy and the width spectrum, the latter being given by the energetic separation of the high binding energy (secondary electron) cutoff and the Fermi level. In other words, the position of the cutoff corresponds to the position of the vacuum level relative to the Fermi level. The inset of Fig. 2 shows the emission cutoffs for these substrates. For the ITO/ $\text{TiO}_2$  substrate,  $E_{\text{cut}}$  is located at 17.08 eV. The WF of  $\text{TiO}_2$  was calculated to be 4.12 eV. Because  $\text{TiO}_2$  is N-type semiconductors, its WF is close to the molecular energy level of the conduction band. From our previous study, the band gap of  $\text{TiO}_2$  is 3.20 eV [17]. Therefore, the valance band of  $\text{TiO}_2$  was calculated to be 7.32 eV. For the PEDA-TMS-modified substrate,  $E_{\text{cut}}$  increased by about 0.32 eV to give a WF of 3.80 eV. This result is attributable to the presence of the amine group. The high electron-donating ability of the amine group polarizes electrons, which results in an interfacial dipole that is directed away from the ITO/ $\text{TiO}_2$  surface. The interfacial dipole decreases the vacuum level outside the  $\text{TiO}_2$

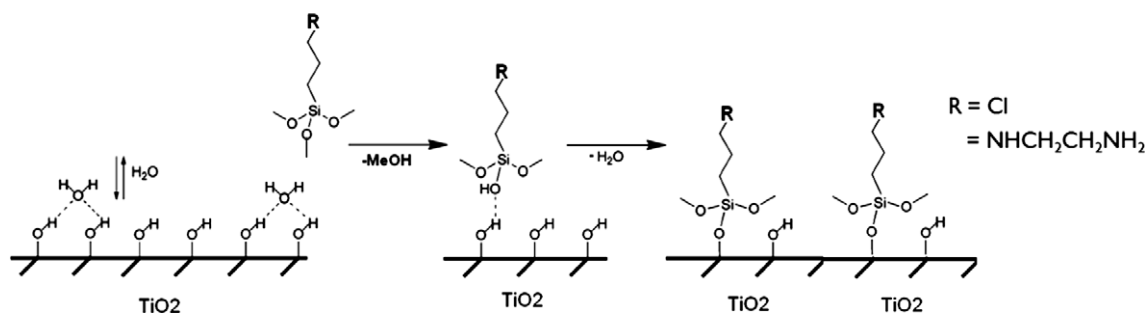


Fig. 1. Scheme for the formation of self-assembled monolayers on ITO/TiO<sub>2</sub> substrates.

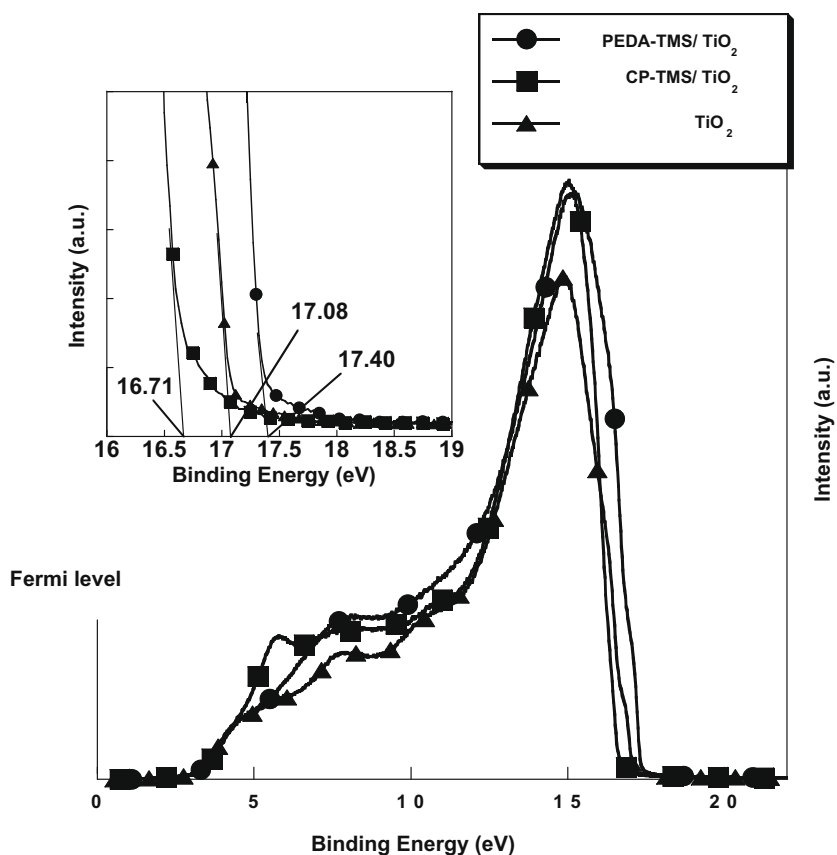


Fig. 2. UPS spectra of ITO/TiO<sub>2</sub> substrate with and without self-assembled monolayers.

layer since the Fermi level of the system is not changed. A lower vacuum level implies a lower injection barrier for electrons in the PEDA-TMS-modified device. For the CP-TMS-modified substrate,  $E_{\text{cut}}$  is 0.37 eV lower than that for the untreated TiO<sub>2</sub> surface, giving a WF of 4.49 eV. Because the chlorine atom has an electron-withdrawing ability, the polarization of electrons has the opposite effect of that for the PEDA-TMS-modified substrate. Therefore, there is a 0.69 eV gap between the PEDA-TMS and CP-TMS-modified substrates.

The effect of SAMs on electron-injection was studied using Ca/Al as a cathode. Due to the low work function of

Ca, the hole injection is inhibited and the devices should be electron-dominated. The  $J$ - $V$  curves of ITO/TiO<sub>2</sub>/HY-PPV/Ca/Al and ITO/TiO<sub>2</sub>/SAM/HY-PPV/Ca/Al are shown in Fig. 3. Because there is a high electron-injection barrier of 1.42 eV due to the energy mismatch of the LUMO of HY-PPV (2.70 eV) and the WF of ITO/TiO<sub>2</sub> cathode (4.12 eV), the current density for this device is very low even at a high driving voltage (0.38 mA/cm<sup>2</sup> at 7 V). The threshold voltage of the PEDA-TMS-modified device is greatly reduced compared to that of the base one. From UPS results, the effective dipole created by PEDA-TMS lowers the WF of the ITO/TiO<sub>2</sub> cathode by 0.32 eV, thereby eliminating the

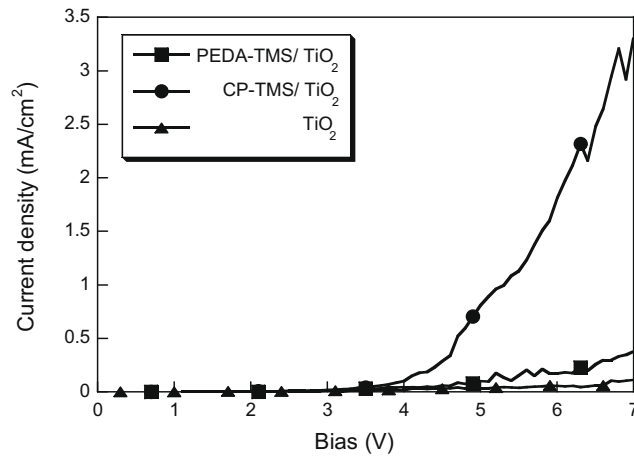


Fig. 3. Current density–voltage curves of electron-dominated devices with and without self-assembled monolayers.

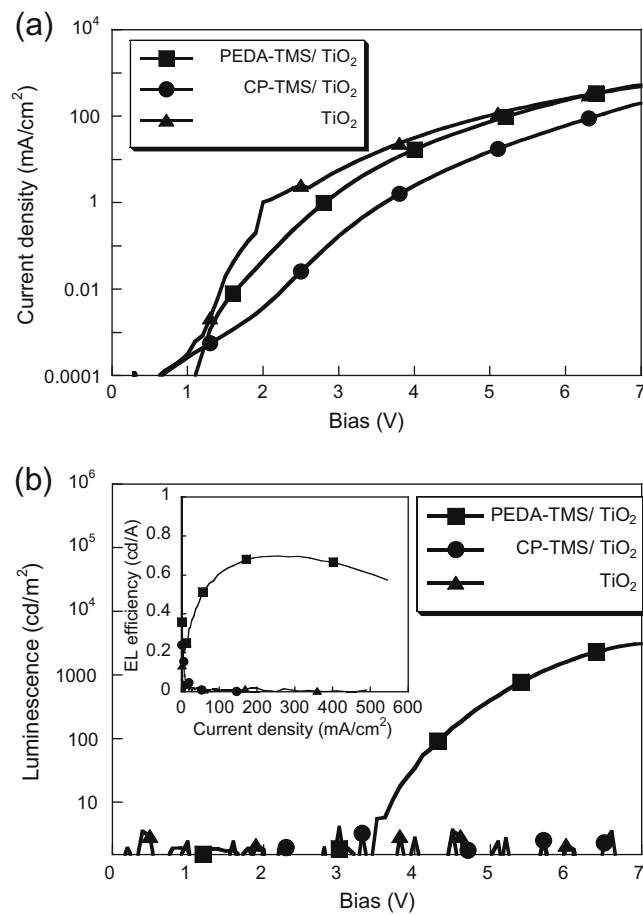


Fig. 4. (a) Current density–voltage and (b) luminescence–voltage curves of the devices with and without self-assembled monolayers. Inset: EL efficiency vs. current density.

electron-injection barrier and enhancing electron-injection into HY-PPV. In addition, the electron current is even more

suppressed by the ITO/TiO<sub>2</sub> cathode modified with CP-TMS. As demonstrated above, the effective dipole created

by this SAM increases the WF of ITO/TiO<sub>2</sub> to 4.49 eV. This modification results in an electron-injection barrier of 1.79 eV between HY-PPV and ITO/TiO<sub>2</sub>. Therefore, the electron current is almost completely suppressed.

Fig. 4a plots the  $J$ - $V$  curves of the devices with and without SAM layers. The figure shows that the driving voltage for the devices with the SAM layers is higher than that for the device without SAM layers. The majority carriers in these devices are holes because the injection barrier for holes is much lower than that for electrons. Majority carriers determine  $J$ - $V$  characteristics. Inserting SAM layers between HY-PPV and TiO<sub>2</sub> induces a higher resistance for holes, and thus produces a higher driving voltage. This indicates that SAM layers have hole-blocking capability. The  $L$ - $V$  curves and EL efficiency vs.  $J$  are shown in Fig. 4b. The light turn-on voltage for the PEDA-TMS-modified device is 3.1 V. The light intensity was 3148 cd/m<sup>2</sup> at 7 V. The EL efficiency for this device was 0.7 cd/A at 200 mA/cm<sup>2</sup>. However, no luminescence was observed for the other devices. From the results of UPS and electron-dominated devices, the enhanced EL efficiency for the PEDA-TMS-modified device is mainly attributed to the decrease in the WF of the cathode, which lowers the

injection barrier for electrons to enhance the probability of hole-electron recombination. In addition, injected electrons for the other devices are too few to emit light.

Fig. 5 shows the decays of device parameters, including light output and operating bias from the storage test without sealing. At a constant current of 0.5 mA/cm<sup>2</sup>, the inverted device has an initial brightness of about 124 cd/m<sup>2</sup> and an initial driving voltage of 5.4 V. After 48 h of exposure to air, the light output decayed by less than 1% and the driving voltage slightly increased. For the conventional device, the light decayed by more than 75% after 12 h of exposure. The improved stability for the inverted device is attributed to two factors. (1) The conventional device consists of both Ca and acidic PEDOT:PSS layer. It is well known that Ca is easily oxidized by air. The acidic PEDOT:PSS has been proven to cause corrosion of ITO in air [18]. Both of them have a negative influence on the device stability. In the inverted device, ITO/TiO<sub>2</sub>/PEDA-TMS and MoO<sub>3</sub>/Au were chosen for the cathode and anode, respectively. They are not oxidized and reacted with ITO because both electrode materials are stable in air. (2) Several groups reported that the photoluminescence (PL) in PPV-type polymers rapidly weakens when irradiated in air

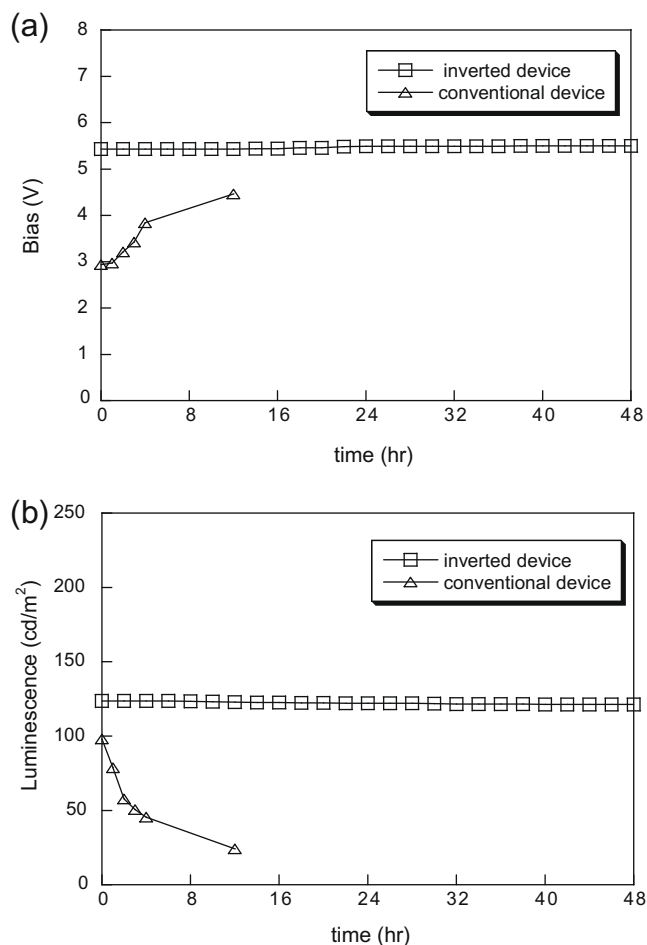


Fig. 5. Device parameters as a function of storage time for an inverted device and a conventional device: (a) bias vs. storage time and (b) luminescence vs. storage time.

[19–21]. The kinetic of the degradation depends on light, oxygen and the structure of the polymer [22,23]. TiO<sub>2</sub> has a scavenging effect due to its photocatalytic activity and intrinsic oxygen deficiency [24–26]. This can prevent the intrusion of O<sub>2</sub> or H<sub>2</sub>O into the active layer, thereby improving the lifetime of unpackaged devices exposed to air. In addition, TiO<sub>2</sub> has strong absorption in the ultraviolet region [17], so it may protect the active layer from radiation damage.

#### 4. Conclusions

A SAM technique was proposed for modifying the ITO/TiO<sub>2</sub> substrate for application in PPV-based I-PLEDs. The WF can be effectively decreased by linking the PEDA-TMS layer to the TiO<sub>2</sub> surface. The decrease is attributable to the presence of the amine group at the outer surface of TiO<sub>2</sub>, which results in an interfacial dipole that is directed away from the ITO/TiO<sub>2</sub> surface. The PEDA-TMS modified substrate can be utilized as an effective cathode to improve the electron-injection ability and EL efficiency of I-PLED. For the CP-TMS-modified substrate, a contrary result is obtained due to the presence of a chlorine atom. In addition, the emission characteristics of the PEDA-TMS modified device were almost unchanged after exposure to air for 48 h.

#### Acknowledgments

This research was supported by the National Science Council (NSC) of Taiwan (NSC-98-2221-E-006-109) and Asian office of Aerospace Research and Development (AOARD-09-4055). SN Hsieh thanks NCKU for a Post Doctor appointment as supported by the NCKU Project for promoting Academic excellence and developing world class centers (HAU 97-3-3-274). Vice President Huang and Dr. Chen from Eternal Chemical Co. Ltd., are appreciated for providing the HY-PPV polymer.

#### References

- [1] J.H. Burroughes, D.D.C. Bradley, A.R. Brown, R.N. Marks, K. Mackay, R.H. Friend, P.L. Bruns, A.B. Holmes, *Nature* 347 (1990) 539.
- [2] G. Gustafsson, Y. Cao, G.M. Treacy, F. Klavetter, N. Colaneri, A.J. Heeger, *Nature* 357 (1992) 477.
- [3] Y. Cao, I.D. Park, G. Yu, C. Zhang, A.J. Heeger, *Nature* 397 (1999) 414.
- [4] S.-Y. Chen, T.-Y. Chu, J.-F. Chen, C.-Y. Su, C.H. Chen, *Appl. Phys. Lett.* 89 (2006) 053518.
- [5] K. Morii, M. Ishida, T. Takashima, T. Shimoda, Q. Wang, M.K. Nazeeruddin, M. Graetzel, *Appl. Phys. Lett.* 89 (2006) 183510.
- [6] K. Morii, T. Takashima, S. Inoue, *Appl. Phys. Lett.* 92 (2008) 213304.
- [7] H.J. Bolink, E. Coronado, D. Repetto, M. Sessolo, E.M. Barea, J. Bisquert, G.G. Belmonte, J. Prochazka, L. Kavan, *Adv. Funct. Mater.* 18 (2008) 145.
- [8] H.J. Bolink, E. Coronado, D. Repetto, M. Sessolo, *Appl. Phys. Lett.* 91 (2007) 223501.
- [9] H.J. Bolink, E. Coronado, J. Orozco, M. Sessolo, *Adv. Mater.* 21 (2009) 79.
- [10] H.J. Bolink, E. Coronado, M. Sessolo, *Chem. Mater.* 21 (2009) 439.
- [11] S. Khodabakhsh, D. Poplavskyy, S. Heutz, J. Nelson, D.C. Bradley, H. Murata, T.S. Jones, *Adv. Funct. Mater.* 14 (2004) 1205.
- [12] B.D. Boer, A. Hadipour, M.M. Mandoc, T.V. Woudenberg, P.W.M. Blom, *Adv. Mater.* 17 (2005) 621.
- [13] M.-C. Hung, K.-Y. Wu, Y.-T. Tao, H.-W. Huang, *Appl. Phys. Lett.* 89 (2006) 203106.
- [14] K.-Y. Wu, Y.-T. Tao, H.-W. Huang, *Appl. Phys. Lett.* 90 (2007) 241104.
- [15] L.-W. Chong, Y.-L. Lee, T.-C. Wen, T.-F. Guo, *Appl. Phys. Lett.* 89 (2006) 233513.
- [16] Y. Choi, J. Noh, *Mol. Cryst. Liq. Cryst.* 492 (2008) 165.
- [17] C.Y. Li, T.C. Wen, T.H. Lee, T.F. Guo, J.C.H. Huang, Y.C. Lin, Y.J. Hsu, *J. Mater. Chem.* 19 (2009) 1643.
- [18] M.P. de Jong, L.J. van Ijzendoorn, M.J.A. de Voigt, *Appl. Phys. Lett.* 77 (2000) 2255.
- [19] M. Yan, L.J. Rothberg, F. Papadimitrakopoulos, H.E. Galvin, T.M. Miller, *Phys. Rev. Lett.* 73 (1994) 744.
- [20] R.D. Scurlock, B. Wang, P.R. Ogilby, J.R. Sheats, R.L. Clough, *J. Am. Chem. Soc.* 117 (1995) 10194.
- [21] K.Z. Xing, N. Johansson, G. Beamson, D.T. Clark, J.-L. Bredas, W.R. Salaneck, *Adv. Mater.* 9 (1997) 1027.
- [22] M. Yan, L.J. Rothberg, F. Papadimitrakopoulos, M.E. Galvin, T.M. Miller, *Phys. Rev. Lett.* 73 (1994) 744.
- [23] A.T.H. Koch, D. Beljonne, N.T. Harrison, J.L. Bredas, N. Haylett, R. Daik, W.J. Feast, R.H. Friend, *Opt. Mater.* 9 (1998) 145.
- [24] A.L. Linsebigler, G. Lu, J.T. Yates Jr., *Chem. Rev.* 95 (1995) 735.
- [25] V.E. Henrich, P.A. Cox, *The Surface Science of Metal Oxides*, Cambridge University Press, Cambridge, 1994.
- [26] C. Noguera, *Physics and Chemistry of Oxide Surfaces*, Cambridge University Press, Cambridge, 1996.

ever, while n-channel ZnO TFTs have been widely reported (for example, [1,2]), there are no reports of stable, high-mobility, p-channel devices. In contrast, p-channel organic TFTs typically have higher mobility and better stability than n-channel organic devices. While the stability and field-effect mobility of most organic TFTs are poor compared to ZnO TFTs, organic TFTs can be fabricated using very simple solution processing, which may provide a path to an inexpensive and simple to implement CMOS process.

There have been several previous reports of hybrid inorganic–organic CMOS processes. Katz et al. demonstrated CMOS inverters using amorphous silicon and  $\alpha$ -hexathienylene TFTs fabricated on separate substrates, with field-effect mobility of  $<1 \text{ cm}^2/\text{V s}$  and  $<0.03 \text{ cm}^2/\text{V s}$ , respectively [3]. Bonse et al. demonstrated ring oscillator circuits with a minimum propagation delay of  $5 \mu\text{s}$  using a-Si:H and pentacene devices fabricated on a single substrate [4]. Low-voltage ZnO–pentacene CMOS circuits were demonstrated where both the ZnO and pentacene TFT mobilities were  $\sim 1 \text{ cm}^2/\text{V s}$ , and a ZnO–pentacene inverter was shown to respond up to a 10 Hz input frequency with rise and fall times of 4 and 13 ms, respectively [5]. 5-stage hybrid CMOS ring oscillator circuits fabricated using indium gallium zinc oxide and pentacene TFTs operated with a minimum propagation delay of 1 ms/stage at 10 V [6]. All of the previous reports used vacuum-based processes to deposit the gate dielectric layer as well as both semiconducting layers. In addition, different metallization steps and patterning steps were required for the organic and inorganic semiconductor TFTs. These vacuum-based processes and additional mask steps result in a more complicated, expensive process. In addition to the complex processing, the dynamic performance of ZnO-based hybrid CMOS circuits thus far has been limited to  $>1 \text{ ms/stage}$ . In this report we demonstrate a simple 4-mask CMOS process with bifunctional Ti/Au contacts and ZnO/organic hybrid circuits operating at  $<150 \text{ ns/stage}$  at a supply voltage of 35 V.

We previously demonstrated a low-temperature (200 °C), atmospheric pressure, spatial atomic layer deposition process that allows rapid deposition (10–20 nm/min) of high-quality, uniform, and stable  $\text{Al}_2\text{O}_3$  and ZnO thin films [7]. We have also demonstrated that these films can be used to fabricate high-mobility TFTs ( $>15 \text{ cm}^2/\text{V s}$ ) and fast ring oscillators ( $<31 \text{ ns/stage}$  for  $4 \mu\text{m}$  channel length) [8]. The fast circuits, good subthreshold slopes, and device stability are consistent with low interface state densities at the  $\text{Al}_2\text{O}_3/\text{ZnO}$  interface in these TFTs [7,8]. We have also previously reported that the organic semiconductor difluoro 5,11-bis(triethylsilylethynyl) anthradithiophene (diF TES-ADT) yields a different and more ordered microstructure on and near pentafluorobenzene-thiol-treated gold electrodes than on untreated oxide surfaces, resulting in high-mobility ( $\sim 0.1\text{--}1 \text{ cm}^2/\text{V s}$ ) and a self-patterning character for diF TES-ADT TFTs and circuits [9,10]. The nature of this crystallization phenomenon and its impact on the electrical properties of the material and interfaces is related to contact treatments and molecular design and has been described in detail in several previous reports [9–12]. Using this self-patterning microstructure we demonstrated simple all-organic circuits operating at

$3.3 \mu\text{s/stage}$  with no direct patterning of the organic layer [11]. We report here an integrated approach that combines these two technologies in a simple way to form high-speed, low-temperature CMOS circuits.

## 2. Experimental

The hybrid inorganic/organic CMOS circuits were fabricated on  $2.5'' \times 2.5''$  borosilicate glass substrates, with an ion beam sputtered and photolithographically patterned chromium layer used for both the organic and inorganic TFT gates. Spatial ALD was used to deposit 150 nm of  $\text{Al}_2\text{O}_3$  and 100 nm ZnO at 200 °C and atmospheric pressure. Photolithography and wet etching were used to pattern the ZnO and  $\text{Al}_2\text{O}_3$  layers. Next, using a double-layer photoresist (Novalak/PMMA) mask, we first Ar ion beam-etched our ZnO contact surface and then deposited ion beam-sputtered Ti/Au (10/100 nm) and patterned electrodes by lift-off. The ion beam etching of the contact area improves the contact resistance to the ZnO [13]. Ti/Au was used because the Ti bottom layer makes a good contact to the n-channel ZnO and the Au top layer makes a good contact to the p-channel diF TES-ADT, minimizing the processing and mask steps required for device fabrication. The Ti/Au electrodes were then treated with the self-assembled monolayer pentafluorobenzene thiol (PFBT), and the  $\text{Al}_2\text{O}_3$  dielectric was treated with hexamethyldisilazane (HMDS). The diF TES-ADT organic semiconductor was then spin-cast from a 2.5 wt.% solution in chlorobenzene with a chlorobenzene solvent vapor ambient maintained above the sample during spin-casting to promote uniform, large grain growth on and near the near the PFBT-treated contacts [14]. The solvent spinning combined with the contact-related microstructure previously mentioned is a straightforward way to achieve a highly controlled organic crystallization. The samples received a 30 min bake at 90 °C to remove residual solvent and were then tested. All devices and circuits were measured in air. A schematic cross-section and optical micrograph of a CMOS inverter and enlarged images showing the organic thin-film differential microstructure on gold and oxide are shown in Fig. 1. The differential microstructure between the treated gold electrodes and the untreated oxide areas provides enough device isolation for simple circuit operation without direct patterning of the organic semiconductor. The entire process required no vacuum processing to deposit the semiconducting and dielectric layers and only four masks and lithography steps.

## 3. Results

Discrete n-channel ZnO and p-channel diF TES-ADT transistors were tested. The 150-nm-thick  $\text{Al}_2\text{O}_3$  layer had a dielectric constant of eight. The n-channel ZnO transistors had mobility of  $12\text{--}15 \text{ cm}^2/\text{V s}$  and threshold voltage of  $\sim 0\text{--}1 \text{ V}$ . The p-channel diF TES-ADT transistors had mobility of  $\sim 0.1\text{--}0.2 \text{ cm}^2/\text{V s}$  and threshold voltage of  $\sim 8\text{--}12 \text{ V}$ . In both transistors the off current was limited to  $\sim 1 \mu\text{A}$  due to residual leakage through the unpatterned organic layer and not through the ZnO layer which is fully

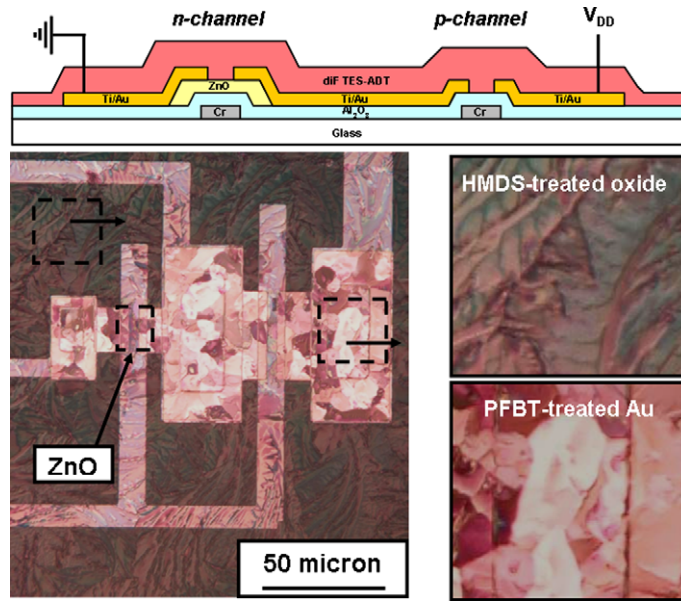


**Fig. 1.** Schematic cross-section of organic/ZnO CMOS inverter (top). Optical micrograph of CMOS inverter (bottom left) and enlarged image of diF TES-ADT microstructure on the untreated oxide area (top right) and PFBT-treated gold electrode (bottom right).

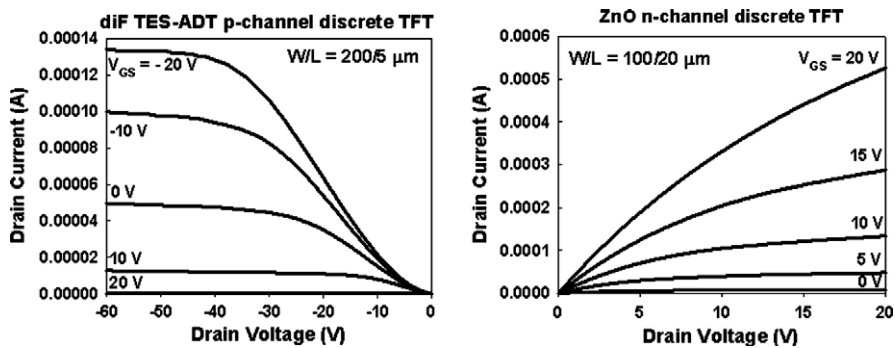


**Fig. 2.** Drain current as a function of drain voltage for several gate voltages for discrete p-channel (left) and n-channel (right) devices. The p-channel device has a field-effect mobility of  $\sim 0.1 \text{ cm}^2/\text{V s}$  and the n-channel device has a field-effect mobility of  $\sim 12 \text{ cm}^2/\text{V s}$ .

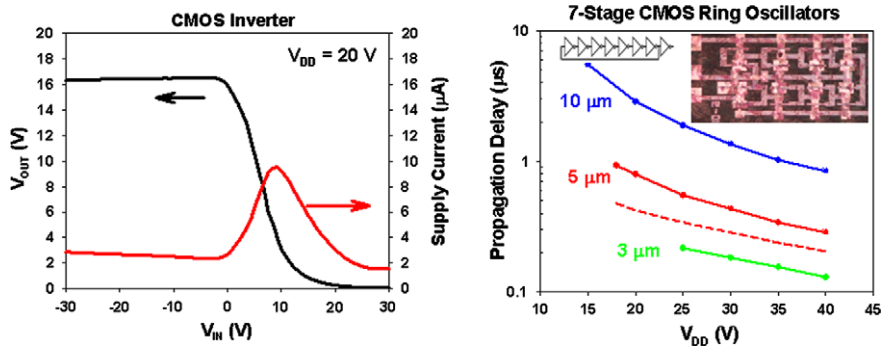


**Fig. 3.** Output voltage and supply current for a unit CMOS inverter with a beta ratio of 10 (left). Experimentally measured propagation delay as a function of channel length for 7-stage CMOS ring oscillators with AIMSpice simulated propagation delay in the dotted line (right).

depleted even at 100 nm thickness. The off current of these devices would be improved by patterning the organic layer, but the circuits operate well without patterning. In addition, because the p-channel organic material covers the ZnO layer in the n-channel device, these devices are ambipolar. However, because the mobility for the ZnO is  $\sim 100\times$  higher than the diF TES-ADT and the ZnO layer is relatively thick (100 nm), resulting in reduced gate capacitance, the p-channel channel formation in the organic layer on top of the n-channel ZnO devices has minimal impact and results mainly in a small shift in the n-channel threshold voltage ( $<3$  V). This impact would also be removed by using a patterned organic layer. Plots of the drain current as a function of drain voltage for several gate voltages are shown in Fig. 2 for both the n-channel and p-channel devices.

Fig. 3 (left) shows the characteristics of a hybrid inorganic ZnO – organic diF TES-ADT CMOS inverter. The static off current and power consumption of the circuits were limited by the unpatterned diF TES-ADT organic layer, and the supply current peak is partially due to the depletion mode organic TFT with threshold voltage of 8–12 V. In addition, the inverter was designed with a  $[W/L_{\text{p-channel}}]/[W/L_{\text{n-channel}}]$  ratio of 10, but the mobility was actually  $\sim 100\times$  larger in the n-channel device. Patterning the organic material and optimizing the circuit design would allow for substantially improved gain and power consumption. However, despite these non-idealities, the robustness of CMOS digital circuits allows acceptable operation for a range of integrated circuit applications. As an example, we fabricated simple 7-stage ring oscillators. Fig. 3 (right) shows the propagation delay as a function of supply voltage for three different TFT channel lengths. For the organic TFTs, the mobility has significant channel length dependence. This is due to the treated contact-related microstructure self-patterning which results in diF TES-ADT grains which extend completely across short channel length devices, but not longer channels, and thus in a mobility that increases with decreasing channel length. As a result the decrease in propagation delay as a function of channel length is more substantial than would be expected for a constant mobility versus channel length devices. AIMSpice [15] was used to fit  $I$ – $V$  curves for discrete  $5\ \mu\text{m}$  channel length diF-TES-ADT and ZnO TFTs and to simulate ring oscillator operation. The result is shown in Fig. 3 (right, dotted line) and shows a reasonable match to the experimental results. Because AIMSpice does not have time constants for charge states this reasonable match is evidence that slow-interface states do not dominate the electrical performance of these devices. Seven-stage ring oscillators fabricated with a beta ratio of 10,  $3\text{-}\mu\text{m}$  channel lengths, and  $1\text{-}\mu\text{m}$  gate/source and gate/drain overlaps oscillated at a frequency  $>500$  kHz, corresponding to a propagation delay of  $<150$  ns/stage at a supply voltage of 35 V.

#### 4. Conclusion

We have fabricated hybrid inorganic ZnO n-channel and organic diF TES-ADT p-channel CMOS circuits by deposit-

ing both the dielectric and semiconductor layers at atmospheric pressure and low-temperature ( $<200^\circ\text{C}$ ). The CMOS circuit fabrication process is simplified to only four masks by using bifunctional Ti/Au contacts for both the ZnO and diF TES-ADT TFTs. In addition, the functionalized organic semiconductor provided a contact-related microstructure which allowed simple circuits to operate without directly patterning the organic semiconductor layer. Thin-film transistors were formed and the n-channel ZnO had field-effect mobility of  $12\text{--}15\ \text{cm}^2/\text{Vs}$  and the p-channel diF TES-ADT had field-effect mobility of  $0.1\text{--}0.2\ \text{cm}^2/\text{Vs}$ . Using these devices seven-stage CMOS ring oscillators were fabricated and operate at  $>500$  kHz corresponding to a propagation delay  $<150$  ns/stage at a supply bias of 35 V, the fastest hybrid organic/inorganic circuits reported to date.

#### References

- [1] B. Bayraktaroglu, K. Leedy, R. Neidhard, Microwave ZnO thin-film transistors, *Electron Dev. Lett.* IEEE 29 (2008) 1024–1026.
- [2] R.L. Hoffman, ZnO-channel thin film transistors: channel mobility, *J. Appl. Phys.* 95 (2004) 5813–5820.
- [3] A. Dodabalapur, J. Baumbach, K. Baldwin, H.E. Katz, Hybrid organic/inorganic complementary circuits, *Appl. Phys. Lett.* 68 (1996) 2246–2248.
- [4] M. Bonse, D.B. Thomasson, H. Klauk, D.J. Gundlach, T.N. Jackson, Integrated a-Si:H/Pentacene inorganic/organic complementary circuits, in: Paper Presented at the Electron Devices Meeting, 1998, IEDM '98 Technical Digest, International, 1998.
- [5] M.S. Oh, D.K. Hwang, K. Lee, W.J. Choi, J.H. Kim, S. Im, S. Lee, Pentacene and ZnO hybrid channels for complementary thin-film transistor inverters operating at 2 V, *J. Appl. Phys.* 102 (2007) 076104-1–076104-3.
- [6] J.H. Na, M. Kitamura, Y. Arakawa, Organic/inorganic hybrid complementary circuits based on pentacene and amorphous indium gallium zinc oxide transistors, *Appl. Phys. Lett.* 93 (2008) 213505-1–213505-3.
- [7] D.H. Levy, D. Freeman, S.F. Nelson, P.J. Cowdery-Corvan, L.M. Irving, Stable ZnO thin film transistors by fast open air atomic layer deposition, *Appl. Phys. Lett.* 92 (2008) 192101-1–192101-3.
- [8] J. Sun, D.A. Mourey, D. Zhao, S.K. Park, S.F. Nelson, D.H. Levy, D. Freeman, P. Cowdery-Corvan, L. Tutt, T.N. Jackson, ZnO thin-film transistor ring oscillators with 31-ns propagation delay, *Electron Dev. Lett.* IEEE 29 (2008) 721–723.
- [9] D.J. Gundlach, J.E. Royer, S.K. Park, S. Subramanian, O.D. Jurchescu, B.H. Hamadani, A.J. Moad, R.J. Kline, L.C. Teague, O. Kirillov, C.A. Richter, J.G. Kushmerick, L.J. Richter, S.R. Parkin, T.N. Jackson, J.E. Anthony, Contact-induced crystallinity for high-performance soluble acene-based transistors and circuits, *Nat. Mater.* 7 (2008) 216–221.
- [10] S.K. Park, D.A. Mourey, S. Subramanian, J.E. Anthony, T.N. Jackson, High-mobility spin-cast organic thin film transistors, *Appl. Phys. Lett.* 93 (2008) 043301-1–043301-3.
- [11] S.K. Park, D.A. Mourey, S. Subramanian, J.E. Anthony, T.N. Jackson, Polymeric substrate spin-cast diF-TESADT OTFT circuits, *Electron Dev. Lett.* IEEE 29 (2008) 1004–1006.
- [12] O.D. Jurchescu, B.H. Hamadani, H.D. Xiong, S.K. Park, S. Subramanian, N.M. Zimmerman, J.E. Anthony, T.N. Jackson, D.J. Gundlach, Correlation between microstructure, electronic properties and flicker noise in organic thin film transistors, *Appl. Phys. Lett.* 92 (2008) 132103.
- [13] D.A. Mourey, S.K. Park, J. Sun, D. Zhao, S.F. Nelson, D.H. Levy, T.N. Jackson, Improved ZnO thin-film transistor contacts by contact etching, in: 2008 Electronics Materials Conference Digest, vol. 35, 2008.
- [14] D.A. Mourey, Y.Y. Li, S.K. Park, S. Subramanian, J.E. Anthony, T.N. Jackson, Enhanced solution-based organic semiconductor film growth, in: 2008 Electronics Materials Conference Digest, vol. 35, 2008.
- [15] AIM-Spice Transistor Level Circuit Simulator. [Online]. Available at <http://www.aimspice.com>.



The junction between the electrode and the organic semiconductor has a significant influence on the performance of an organic device [19]. A buffer layer is usually sandwiched at the metal–organic semiconductor interface to improve the charge-injection capability and overall device performance [20–22]. Although the output current in vertical-type transistors is dramatically enhanced when a thin buffer layer of LiF is incorporated between the emitter electrode and the organic emitter [13,23], the OFF current usually remains high – sometimes even higher than that of the device lacking a LiF layer. This behavior might be attributable to the diffusion of metal into the active layer or unfavorable chemical reactions between the organic layer and the metal electrode when operating the devices under high electric fields. Moreover, because the leakage current of a vertical transistor depends mainly on its film thickness, the presence of a thin LiF layer cannot help to reduce the leakage current. Hence, the choice of the buffer layer is a crucial factor toward improving the overall device performance.

Employing the diverse electronic properties of transition metal oxides could provide a unique opportunity to lower the energy barrier between metal and organic for the charge-injection. When a metal oxide film is sandwiched between the metal and organic semiconductor, the fundamental principle governing charge-injection at the junction is controlled by the doping concentration of the film. Therefore, a thicker film can be incorporated to prevent the diffusion of metal into the active layer and unfavorable chemical reactions between the active layer and metal electrode, while maintaining the charge-injection capability. In this Letter, we describe how the performance of organic base-modulation triodes (OBMTs) is improved after inserting a metal oxide film between the emitter electrode and the organic emitter. The OBMTs featuring molybdenic oxide (MoO<sub>3</sub>)/Al bilayer emitter electrodes exhibited increased output current; as a result, the current ON/OFF ratio reached as high as 10<sup>3</sup>, thereby allowing inverters to be prepared exhibiting higher gains.

## 2. Experimental

The structure of the OBMTs is revealed in the inset to Fig. 1. Prior to deposition, the glass substrates were cleaned using detergent, acetone, and isopropyl alcohol and then treated in a UV–ozone cleaner for 15 min. A 30-nm-thick Au layer was deposited on the glass substrate to serve as a collector electrode. A 50-nm-thick layer of copper phthalocyanine (CuPc, Luminescence Technology) was thermal deposited on the Au layer to smoothen the surface morphology and then a 270-nm-thick layer of pentacene (ca. 98% purity, Luminescence Technology), which served as the collector of the p-channel triode, was thermal evaporated. A 30-nm-thick Al strip was thermally evaporated onto the pentacene layer to function as the base electrode. A thin Al film (10 nm) was then deposited and a lithium fluoride (LiF) layer of 0.4 nm was thermally evaporated to function as a hole injection enhancement layer. A 20-nm-thick layer of *N,N'*-bis(naphthalen-1-yl)-*N,N'*-bisphenylbenzidine (NPB) was thermally evaporated to enhance the

carrier energy. Pentacene was then thermally evaporated to form the 100-nm-thick emitter layer. Finally, for comparison, three types of emitter electrodes were used: 30-nm-thick Au, 30-nm-thick Ag, and 50-nm-thick MoO<sub>3</sub>/30-nm-thick Al. The patterns of each layer were defined using different metallic shadow masks. The active area of the device, defined by the crossover between the emitter and collector electrodes, was 0.0042 cm<sup>2</sup>. The work functions of Al, Au, and Ag and the energy level of MoO<sub>3</sub> are presented schematically in Fig. 2a [20]. All organic materials were used without further purification and were deposited through thermal evaporation at a base pressure of ca. 2 × 10<sup>-6</sup> torr. The current–voltage (*I*–*V*) characteristics of the devices in a glove-box ambient (H<sub>2</sub>O and O<sub>2</sub> contents: <1 ppm) were measured using a Keithley 4200 semiconductor parameter analyzer. X-ray photoelectron spectroscopy (XPS) was performed using a PHI 5000 VersaProbe system (ULVAC-PHI Chigasaki, Japan) and a microfocused (100 μm, 25 W) Al X-ray beam with a photoelectron take-off angle of 45°.

## 3. Results and discussion

Fig. 1a displays the collector-to-emitter current (*I*<sub>CE</sub>) versus the collector-to-emitter voltage (*V*<sub>CE</sub>) characteristics of the OBMT employing MoO<sub>3</sub>/Al as the emitter electrode, with base–emitter voltages (*V*<sub>BE</sub>) ranging from 0 to –5 V at a step of 0.5 V. The value of *I*<sub>CE</sub> reached up to –16.1 μA when *V*<sub>CE</sub> and *V*<sub>BE</sub> were both –5 V. The current ON/OFF ratio, defined as *I*<sub>CE</sub> (*V*<sub>BE</sub> = –5 V)/*I*<sub>CE</sub> (*V*<sub>BE</sub> = 0 V) at *V*<sub>CE</sub> = –5 V, was ca. 3.08 × 10<sup>3</sup>. For comparison, we also tested Au and Ag as emitter electrodes. We found that the emitter electrode of the emitter–base (EB) diode had a significant influence on the electronic properties of the OBMTs. Table 1 summarizes the device parameters of the OBMTs employing Au, Ag, and MoO<sub>3</sub>/Al as emitter electrodes. The device featuring MoO<sub>3</sub>/Al as the emitter electrode had the highest ON current, while maintaining an OFF current similar to those of the other systems. Although a small energy barrier exists between Au and pentacene, metals deposited onto the pentacene surface penetrate the surface, thereby doping the upper layer of pentacene to form a metallic overlayer. Due to charge transfer across the metal/organic semiconductor interface, redistribution of electron cloud, and interfacial chemical reaction, an interface dipole forms immediately, increasing the barrier height between the metal and pentacene [24,25]. The modified MoO<sub>3</sub> layer interface provided protection against metal diffusion into the organic layer and unfavorable chemical reactions between the organic and metal electrodes; it decreased the intensity of the interface dipole and enhanced the degree of charge-injection. Besides, we also observed the output current of the device was modulated by the base current. Fig. 1b and c displays the *I*<sub>CE</sub> versus *V*<sub>CE</sub> under common-base mode and common-emitter mode. As the following two equations [16]:

$$\alpha = \frac{I_{CE} - I_{CE}(I_E = 0A)}{I_E} \quad (1)$$

$$\beta = \frac{I_{CE} - I_{CE}(I_B = 0A)}{I_B} \quad (2)$$

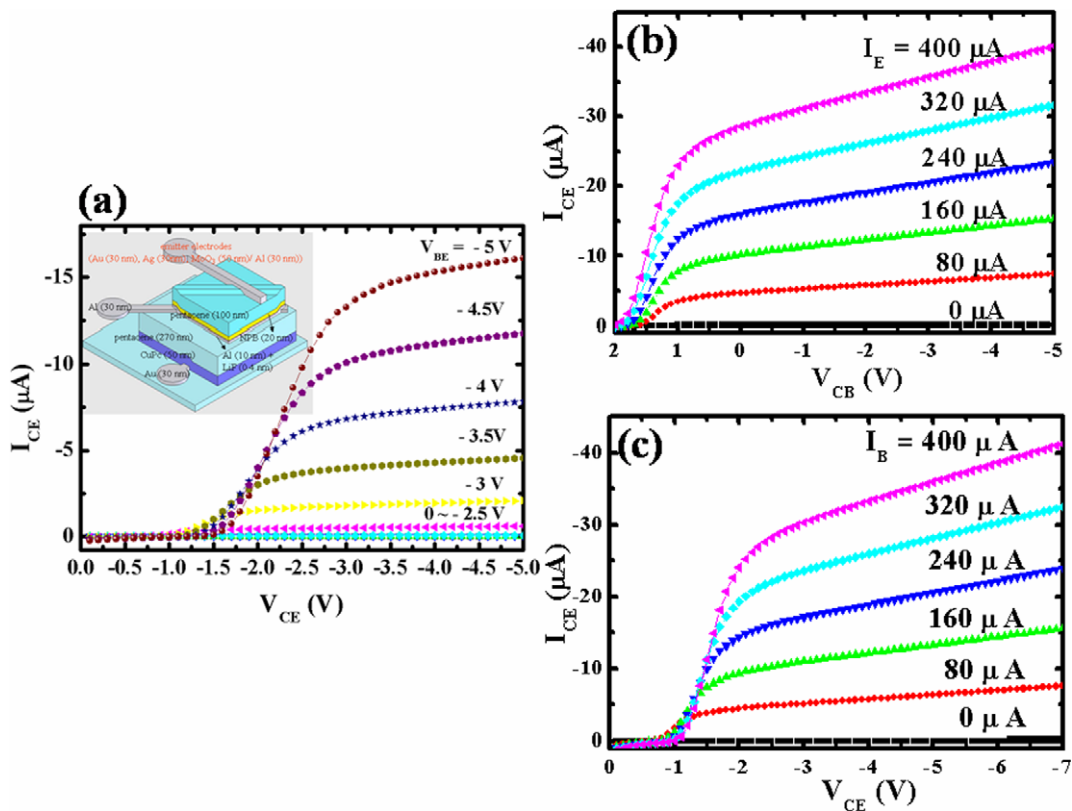


**Fig. 1.** (a) Collector-to-emitter current ( $I_{CE}$ ) plotted as a function of the collector-to-emitter voltage ( $V_{CE}$ ) for base voltages ranging from 0 to  $-5$  V at a step of  $-0.5$  V. (b)  $I_{CE}$  as a function of  $V_{CE}$  for emitter current ranging from 0 to  $400 \mu\text{A}$  under the common-base mode. (c)  $I_{CE}$  as a function of  $V_{CE}$  for base current ranging from 0 to  $400 \mu\text{A}$  under the common-emitter mode. Inset: schematic representation of the device structure with emitter electrode  $\text{MoO}_3/\text{Al}$ .

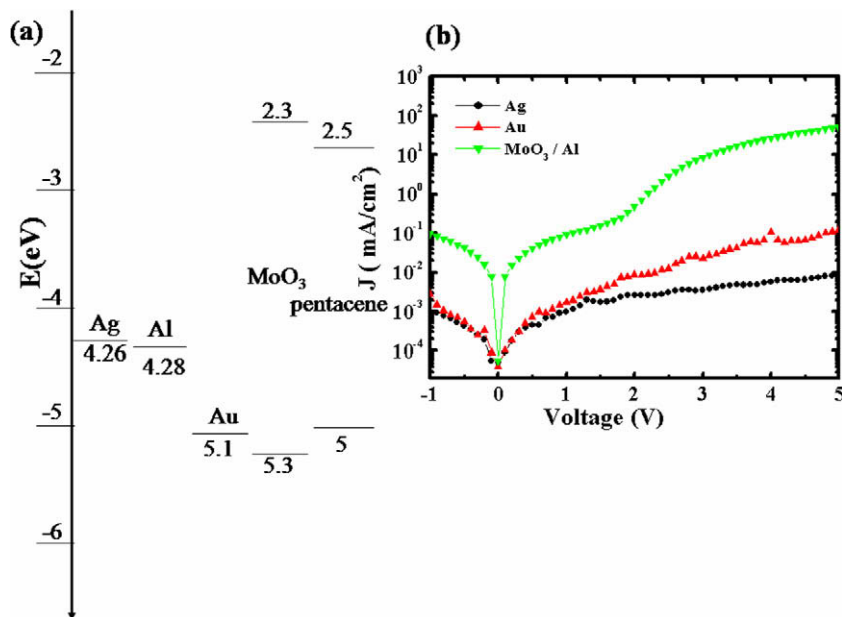


**Fig. 2.** (a) Current density ( $J$ ) versus voltage ( $V$ ) characteristics of EB diodes featuring Au, Ag, and  $\text{MoO}_3/\text{Al}$  as emitter electrodes. (b) Energy level diagrams of the organic materials and the metals.

The  $I_E$  and  $I_B$  are the input emitter current and the base current under common-base and common-emitter mode, respectively. Under Eqs. (1) and (2), the transport factor

( $\alpha$ ) of 0.1 and current gain ( $\beta$ ) of 0.1 were measured. To determine the reason why the barrier between the electrode and organic layer influenced the performance of

**Table 1**

Device performance of OBMTs featuring Au, Ag, and MoO<sub>3</sub>/Al as emitter electrodes; V<sub>CE</sub> and V<sub>B</sub> were both –5 V.

Emitter electrode	Output current (A)	OFF current (A)	Current ON/OFF ratio
Au	$3.51 \times 10^{-6}$	$4.42 \times 10^{-9}$	$7.94 \times 10^2$
Ag	$1.29 \times 10^{-8}$	$5.43 \times 10^{-9}$	2.37
MoO <sub>3</sub> /Al	$1.61 \times 10^{-5}$	$5.23 \times 10^{-9}$	$3.08 \times 10^3$

the OBMTs, we measured the current density (*J*) versus voltage (*V*) characteristics of EB diodes featuring Au, Ag, and MoO<sub>3</sub>/Al as emitter electrodes. Fig. 2b reveals that the EB diode incorporating the MoO<sub>3</sub> layer provided improved hole injection and an obvious turn-on effect at ca. 1.4 V in Fig. 1 when V<sub>BE</sub> was –5 V. For the same CB diode structure, the output current of the OBMT is determined by the currents of the forward-bias EB diode and the reverse-bias CB diode [18]. Therefore, the output current of the OBMTs was enhanced when using MoO<sub>3</sub>/Al as the emitter electrode.

Because we deposited the MoO<sub>3</sub> layer through thermal evaporation, inevitably it decomposed into various Mo species. We recorded XPS spectra to identify the chemical species present in the “MoO<sub>3</sub>” layer (Fig. 3). In Fig. 3b, we observe two measured binding energies (228.5 and 231.5 eV), suggesting that the layer included two or more Mo species. Contamination from the boat introduced into the film during thermal evaporation resulted in the shifting of the two peaks [26] from their expected values for MoO<sub>3</sub> and MoO<sub>2</sub> [27]. The intensities of the signals for MoO<sub>2</sub> and MoO<sub>3</sub> were similar, suggesting that MoO<sub>2</sub> was heavily doped into the MoO<sub>3</sub> film. Therefore, the MoO<sub>3</sub> film behaved as a degenerate semiconductor, to align the work function of the metal and the Fermi-level of the MoO<sub>3</sub> layer, with the depletion region at the MoO<sub>3</sub>–Al interface being so narrow that the carriers had a high probability of tunneling through the barrier when a suitable bias voltage was applied to the EB diode. To further demonstrate this phenomenon, we fabricated emitter electrodes featuring different thicknesses of the MoO<sub>3</sub> interfacial layer; Fig. 4 presents the *J*–*V* characteristics of the resulting EB

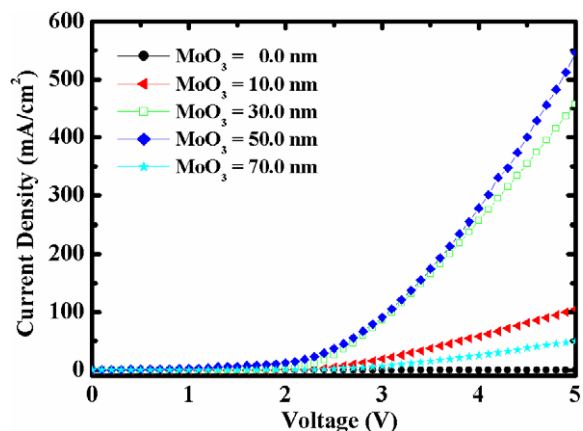


**Fig. 4.** Current density (*J*) versus voltage (*V*) characteristics of EB diodes having the structure Al (30 nm)/thin Al (10 nm)/LiF (0.4 nm)/NPB (20 nm)/pentacene (100 nm)/MoO<sub>3</sub> (0–70 nm)/Al (30 nm).

diodes. The devices employing MoO<sub>3</sub>/Al bilayers had larger current densities than that featuring the bare Al layer; the maximum value occurred at a MoO<sub>3</sub> thickness of 50 nm. Because a thicker MoO<sub>3</sub> interfacial layer would result in a longer carrier transport pathway, the probability of carrier capture would increase rapidly and the number of carriers received by the electrode would decrease. Therefore, OBMTs employing a suitable MoO<sub>3</sub> thickness would provide superior hole-injection contact and enhance the output current of the EB diode.

One of the advantages of the OBMTs requiring voltage driving is that they can be used to construct organic inverters. Fig. 5a and b displays the measured transfer characteristics of organic inverters composed of the OBMT connected with various resistances and corresponding gains, respectively. The resistance ranged from 2 to 10 MΩ at a step of 2 MΩ; a supply voltage of –5 V was applied. The inset displays the structure of a vertical OBMT with a load resistor. The corresponding gain of the inverter changed with respect to the resistance, with a maximum calculated gain of 6 arising when the OBMT was connected with a resistance of 10 MΩ. This resistor is, however, not an ideal switch; it resulted in the value of V<sub>out</sub> of the inver-

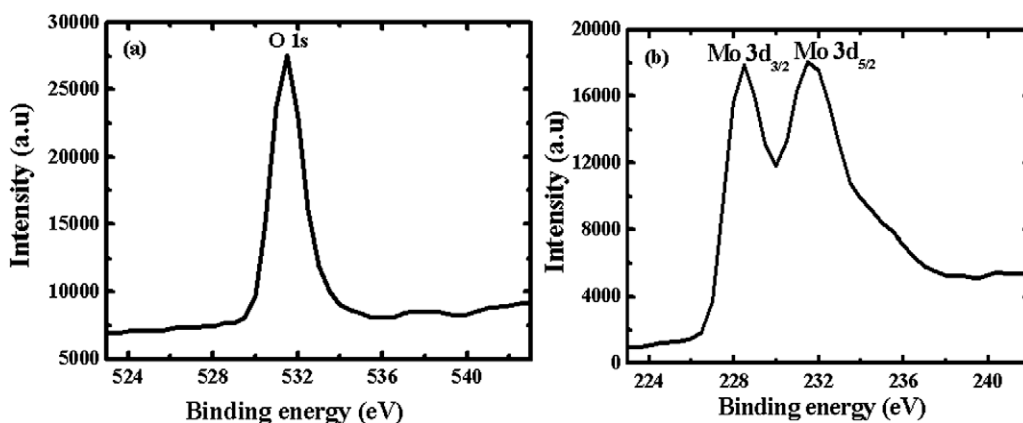


**Fig. 3.** XPS spectra of the (a) O 1s and (b) Mo 3d energy levels.

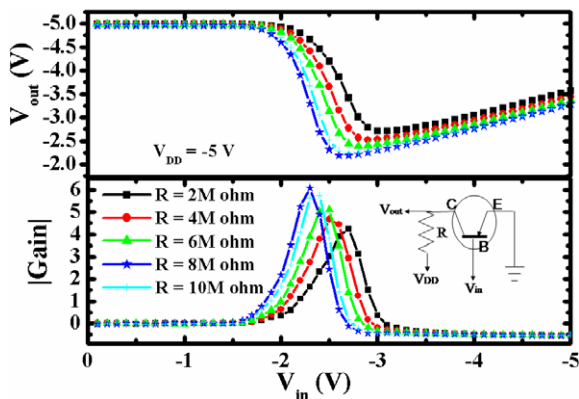


**Fig. 5.** Measured transfer characteristics and corresponding gain of inverters measured at a value of  $V_{DD}$  of  $-5$  V with resistances ranging from 2 to 10 M $\Omega$  at a step of 2 M $\Omega$ . Inset: sketch of the inverter structure and OBMT employing MoO<sub>3</sub>/Al as emitter electrode.

ter varying upon increasing  $|V_{in}|$ . To overcome this drawback, the n-type OBMT should replace the resistor to form a complementary inverter; such a study is currently under investigation.

#### 4. Conclusion

In conclusion, we have fabricated OBMTs featuring three types of emitter electrodes (Au, Ag, and MoO<sub>3</sub>/Al). The output currents of these OBMTs were strongly related to the nature of the interface between the emitter electrode and the organic semiconductor layer. XPS analysis revealed that the MoO<sub>3</sub> films formed through thermal evaporation had degenerate semiconductor characteristics, resulting in a tunnel current component at the EB diode. Therefore, the devices featuring MoO<sub>3</sub>/Al as the emitter electrode exhibited a current ON/OFF ratio of  $10^3$ . Connecting different resistances to the OBMT allowed us to prepare inverters.

#### Acknowledgment

This study was supported in part by the National Science Council, Taiwan, under grants NSC 97-2628-E-007-026-MY2 and NSC 98-2221-E-001-002.

#### References

- [1] M.G. Kane, J. Campi, M.S. Hammond, F.P. Cuomo, B. Greening, C.D. Sheraw, J.A. Nichols, D.J. Gundlach, J.R. Huang, C.C. Kuo, L. Jia, H. Klauk, T.N. Jackson, *IEEE Electron Device Lett.* 21 (2000) 34.
- [2] C.J. Drury, C.M.J. Mutsaers, C.M. Hart, M. Matters, D.M. deLeeuw, *Appl. Phys. Lett.* 73 (1998) 108.
- [3] C.D. Dimitrakopoulos, P.R.L. Malenfant, *Adv. Mater.* 14 (2002) 99.
- [4] D.J. Monsma, J.C. Lodder, T.J.A. Popma, B. Diény, *Phys. Rev. Lett.* 74 (1995) 5260.
- [5] P.F. Baude, D.A. Ender, M.A. Haase, T.W. Kelley, D.V. Muiyres, S.D. Theiss, *Appl. Phys. Lett.* 82 (2003) 3964.
- [6] C.D. Dimitrakopoulos, S. Purushothaman, J. Kymissis, A. Callegari, J.M. Shaw, *Science* 283 (1999) 822.
- [7] F.C. Chen, C.S. Chuang, Y.S. Lin, L.J. Kung, T.H. Chen, H.P. Shieh, *Org. Electron.* 7 (2006) 435.
- [8] Y.Y. Noh, N. Zhao, M. Caironi, H. Sirringhaus, *Nat. Nanotechnol.* 2 (2007) 784.
- [9] M.D. Austin, S.Y. Chou, *Appl. Phys. Lett.* 81 (2002) 4431.
- [10] K. Kudo, M. Iizuka, S. Kuniyoshi, K. Tanaka, *Thin Solid Films* 393 (2001) 362.
- [11] Y. Yang, A.J. Heeger, *Nature* 372 (1994) 344.
- [12] M.S. Meruvia, I.A. Hummelgen, M.L. Sartorelli, A.A. Pasa, W. Schwarzscher, *Appl. Phys. Lett.* 84 (2004) 3978.
- [13] K. Nakayama, S. Fujimoto, M. Yokoyama, *Appl. Phys. Lett.* 88 (2006) 153512.
- [14] S.H. Li, Z. Xu, L.P. Ma, Y. Yang, *Appl. Phys. Lett.* 91 (2007) 083507.
- [15] Y.C. Chao, M.H. Xie, M.Z. Dai, H.F. Meng, S.F. Horng, C.S. Hsu, *Appl. Phys. Lett.* 92 (2008) 093310.
- [16] C.Y. Yang, T.M. Ou, S.S. Cheng, M.C. Wu, S.Y. Lin, I.M. Chan, Y.J. Chan, *Appl. Phys. Lett.* 89 (2006) 183511.
- [17] S.S. Cheng, C.Y. Yang, Y.C. Chuang, C.W. Ou, M.C. Wu, S.Y. Lin, Y.J. Chan, *Appl. Phys. Lett.* 90 (2007) 153509.
- [18] S.S. Cheng, Y.C. Chuang, D. Kekuda, C.W. Ou, M.C. Wu, C.W. Chu, *Adv. Mater.* 21 (2009) 1860.
- [19] H. Ishii, K. Sugiyama, E. Ito, K. Seki, *Adv. Mater.* 8 (1999) 11.
- [20] C.W. Chu, S.H. Li, C.W. Chen, V. Shrotriya, Y. Yang, *Appl. Phys. Lett.* 87 (2005) 193508.
- [21] L.S. Hung, C.W. Tang, M.G. Mason, *Appl. Phys. Lett.* 70 (1997) 152.
- [22] G.L. Frey, K.J. Reynolds, R.H. Friend, *Adv. Mater.* 14 (2002) 265.
- [23] L.S. Roman, W. Mammo, L.A.A. Pettersson, M.R. Andersson, O. Inganäs, *Adv. Funct. Mater.* 10 (1998) 774.
- [24] N.J. Watkins, L. Yan, Y.L. Gao, *Appl. Phys. Lett.* 80 (2002) 4384.
- [25] H. Ishii, K. Sugiyama, E. Ito, Kazuhiko Seki, *Adv. Mater.* 11 (1999) 605.
- [26] G.D. Giuseppe, J.R. Selman, *J. Electronanal. Chem.* 559 (2003) 31.
- [27] J.F. Moulder, W.F. Stickle, P.E. Sobol, K.D. Bomben, J. Chastin, in: *Handbook of X-ray Photoelectron Spectroscopy*, Perkin-Elmer Corporation, Physical Electronics Division, Minnesota, 1992.

PEDOT:PSS showed lower resistivity, however, careful control of the doping level was required because excess doping caused phase separation and defects in PEDOT:PSS. On the other hand, Yoon and Berger [9] inserted an additional buffer layer between ITO and PEDOT:PSS to modify the contact condition. Facilitating hole collection by adjusting interface energy step resulted in an improved PCE in PSCs but an extra evaporation step in a vacuum is not a recommended method in the cost point of view.

In this study, we used external light irradiation: ultraviolet (UV) light to control not only the bulk resistance but also the contact condition of the PEDOT:PSS. This is a simple and cost-effective method compared to those attempted thus far. With a UV-irradiated PEDOT:PSS buffer layer, the PSCs showed an improved short-circuit current ( $J_{sc}$ ) and fill factor (FF) so overall performance was enhanced.

To fabricate the PSCs, an indium tin oxide glass was cleaned and then exposed to oxygen plasma for 10 min before use. A buffer layer of PEDOT:PSS (Baytron P) was then spin-coated to a thickness of  $\sim 40$  nm. After annealing the PEDOT:PSS films at  $200^\circ\text{C}$  for 5 min, they were irradiated for 20, 40, and 60 min by a UV light source (output power density of  $544\ \mu\text{W}/\text{cm}^2$ ) with its emission centered at 365 nm. An active layer composed of P3HT (Rieke Met. Inc.) and PCBM (Nano-C) (1:0.6 in weight ratio) were spin-coated from chlorobenzene with  $220\ \text{nm} \pm 5\ \text{nm}$  thin films. The prepared organic film was then thermal-annealed at  $110^\circ\text{C}$  for 10 min. Finally, LiF (0.6 nm) and Al (100 nm) electrodes were deposited under a pressure of  $5 \times 10^{-7}$  torr. The defined active area was  $9\ \text{mm}^2$  and all procedures were performed in a  $\text{N}_2$  gas-filled glove box. The current-density–voltage ( $J$ – $V$ ) curves were measured by a Keithley 2000 source-measure unit. The photocurrent was obtained under illumination from a Thermal Oriel solar simulator (AM 1.5G). The illumination intensity used was calibrated by a standard Si photodiode detector (Fraunhofer ISE, certificate no. C-ISE269).

Fig. 1 shows the current–voltage ( $J$ – $V$ ) characteristics of the devices under illumination of AM1.5G, at an overall

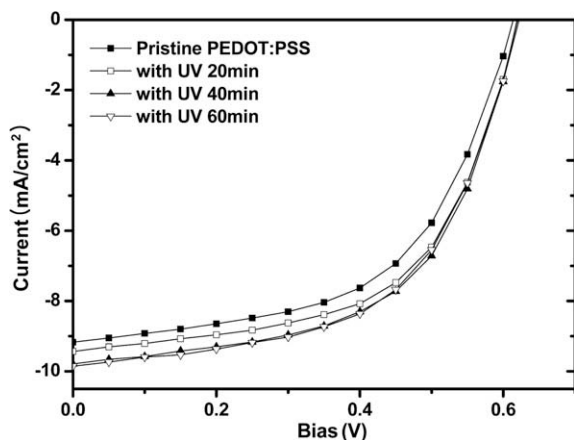


**Fig. 1.** Current–voltage characteristics of PVs with different UV irradiation times on PEDOT:PSS films: pristine PEDOT:PSS (■); with 20 min UV irradiation (□); with 40 min irradiation (▲); with 60 min UV irradiation (▽).

intensity of  $100\ \text{mW}/\text{cm}^2$  with different UV irradiation times on PEDOT:PSS films. To ensure the reproducibility, we fabricated five individual cells for each case, and photovoltaic parameters with mean deviation are summarized in Table 1. After UV irradiation, the reduced series resistance of the devices resulted in increased  $J_{sc}$  and FF values. Device without UV irradiation shows  $J_{sc}$  and FF, values of  $(9.10 \pm 0.16)\%$  and  $(54 \pm 1.2)\%$ , respectively, whereas with 40 min UV irradiation  $J_{sc}$  and FF reach to  $(9.89 \pm 0.28)\%$  and  $(57 \pm 1.5)\%$ , so calculated PCE increased from  $(3.05 \pm 0.04)\%$  to  $(3.46 \pm 0.04)\%$ . With further UV irradiation, the PCE is increased from  $(3.46 \pm 0.04)\%$  to  $(3.50 \pm 0.03)\%$ , however, the change is small respect to the irradiation time so it can be considered that the effect of UV irradiation becomes saturated after 40 min. In general, the origin of the series resistance of a photovoltaic cell can be either due to the limited charge transfer within the layers (bulk resistance) and/or charge transport between the layers (contact resistance) [10]. In the present case, all devices were fabricated in the same manner while changing only UV irradiation time, therefore it can be assumed that the reduction of series resistance comes from the bulk and/or contact resistance change of PEDOT:PSS by UV irradiation. To evaluate the effect of UV irradiation on bulk resistance of PEDOT:PSS, Raman spectroscopy and four-probe method (CMT SR2000 by A.I.T) were applied.

Fig. 2 shows the Raman spectra of PEDOT:PSS films with and without UV irradiation. The clearest difference between pristine and UV-irradiated PEDOT:PSS was the shoulder signal at  $1445\ \text{cm}^{-1}$ . The UV-irradiated PEDOT:PSS exhibited a weaker band in this region, and this indicates that the resonant structure of the PEDOT chains changes from a benzoid to a quinoid structure [11,12,16]. The benzoid structure favors coil conformation while the quinoid structure favors linear or expanded coil conformation. In the coil conformation, the  $\text{C}_\alpha$ – $\text{C}_\alpha$  bond between the two thiophene rings is similar to a  $\sigma$  bond and has a low density of conjugated  $\pi$ -electrons. Thus, the conjugated  $\pi$ -electrons are not completely delocalized so PEDOT films have a low level of charge-carrier mobility. In contrast, in the linear or coil-expanded conformation, thiophene rings in the PEDOT chains can be oriented in nearly the same plane. Therefore, the conjugated  $\pi$ -electrons are delocalized through the entire chain, giving the PEDOT films high charge-carrier mobility [11,12]. Hence, the conformational change of the PEDOT films from benzoid to quinoid results in a decrease of the bulk resistance of the PEDOT:PSS. The resistivity of the PEDOT:PSS films evaluated by the four-probe-method is summarized in Table 1.

Nextly, in order to examine the effect of the UV irradiation on PEDOT:PSS on the contact resistance of the devices, the impedance spectroscopy of the devices were measured in a dark condition [13]. Fig. 3 shows the impedance spectra of the devices at 0 V in a frequency range of  $10^{-1}\ \text{Hz}$ –10 MHz. The diameter of semi-circle on the  $Z'$  axis represents the contact resistance. The resistance of the device without UV irradiation is approximately  $0.52\ \text{M}\Omega$ , but it is decreased to 0.33, 0.27, and  $0.21\ \text{M}\Omega$  after 20, 40, and 60 min UV irradiation, respectively. This result indicates that UV irradiation reduces the interface resistance

**Table 1**

Performance of ITO/PEDOT:PSS/P3HT:PCBM/LiF/Al photovoltaic devices with different UV irradiation times under an illumination of AM1.5 (100 mW/cm<sup>2</sup>). The values of photovoltaic parameters are averaged over five individual cells.

Anode	$V_{oc}$ (V)	$J_{sc}$ (mA/cm <sup>2</sup> )	FF (%)	PCE (%)	Resistance of PEDOT:PSS film <sup>a</sup> (M $\Omega$ cm)
Pristine PEDOT:PSS	0.608 $\pm$ 0.003	9.10 $\pm$ 0.16	54 $\pm$ 1.2	3.05 $\pm$ 0.04	0.72
With UV 20 min on PEDOT:PSS	0.614 $\pm$ 0.007	9.20 $\pm$ 0.11	57 $\pm$ 1.0	3.29 $\pm$ 0.08	0.58
With UV 40 min on PEDOT:PSS	0.612 $\pm$ 0.006	9.89 $\pm$ 0.28	56 $\pm$ 1.5	3.46 $\pm$ 0.04	0.42
With UV 60 min on PEDOT:PSS	0.616 $\pm$ 0.004	9.83 $\pm$ 0.17	57 $\pm$ 1.4	3.50 $\pm$ 0.03	0.39

<sup>a</sup> Measure from the four-point probe.

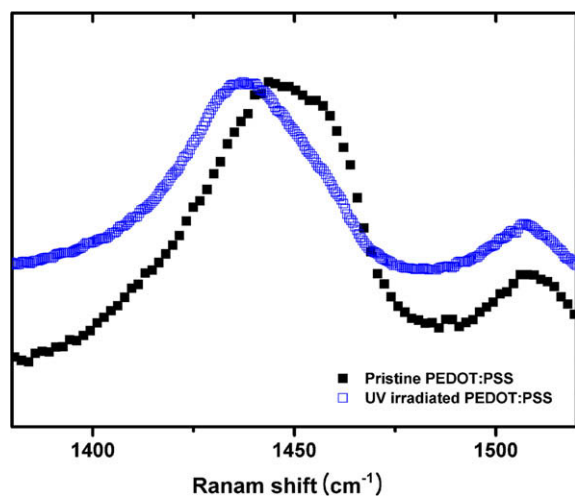


**Fig. 2.** Raman spectra of pristine PEDOT:PSS films excited using 785 nm semiconductor laser excitation.

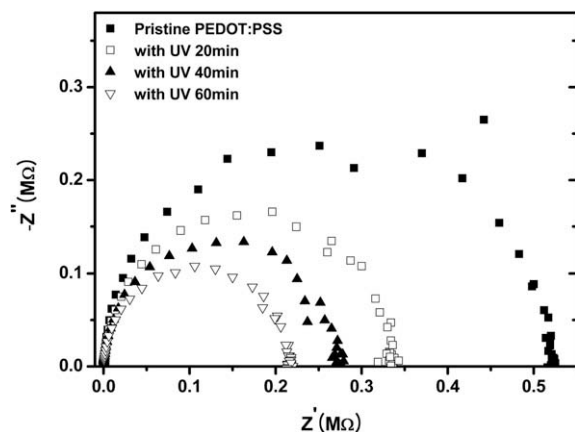


**Fig. 3.** Impedance plots of the devices: pristine PEDOT:PSS (■); with 20 min UV irradiation (□); with 40 min irradiation (▲); with 60 min UV irradiation (▽).

between the PEDOT:PSS buffer layer and the P3HT:PCBM active layer, leading to a lower device series resistance. Theoretically, hole mobility is a few orders higher than electron mobility in organic material systems such as P3HT/PCBM [14], hence, holes are accumulate in the devices and the photocurrent is governed by space-charge limited conditions [15]. However, in this case, the bulk

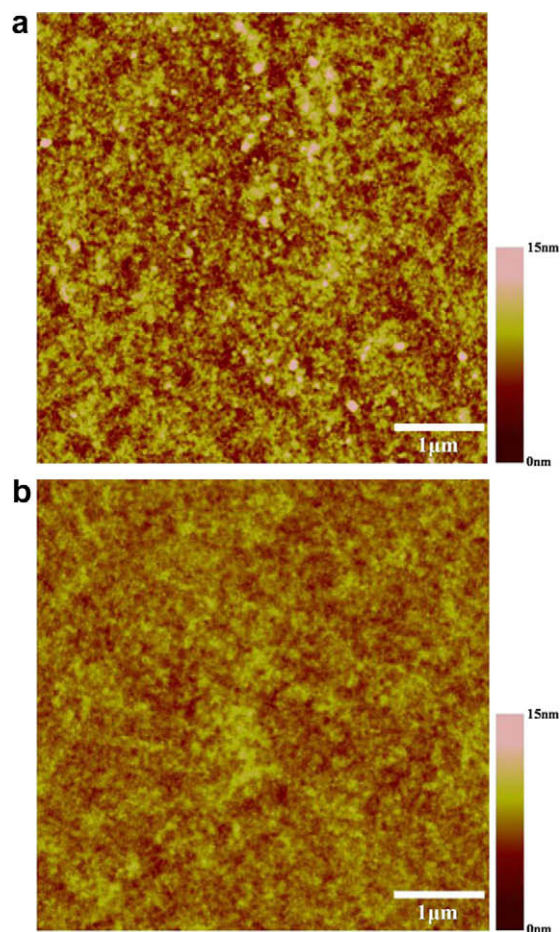


**Fig. 4.** AFM images and rms values of (a) pristine PEDOT:PSS (rms = 1.563 nm), (b) with 60 min UV irradiation (rms = 1.326 nm).

and contact resistance of PEDOT:PSS as reduced by UV irradiation promotes hole extractions so that the accumulation of holes can be decreased. This results in improved  $J_{sc}$  and FF values, as shown in Table 1 and Fig. 1. Here, the surface morphology should be noted because the roughened surface of the PEDOT:PSS also can cause an increase in the value of  $J_{sc}$  [16]. From AFM tapping mode images ( $5 \times 5 \mu\text{m}^2$ ) (Fig. 4), the root mean square (rms) roughness value of pristine PEDOT:PSS was 1.563 nm, and 1.326 nm with 60 min UV irradiation. There was no significant change in the surface morphology in the PEDOT:PSS layer after UV irradiation.

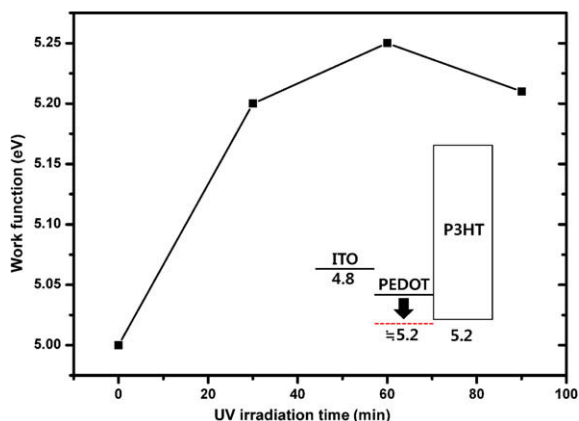


**Fig. 5.** Work function change of PEDOT:PSS layer according to the UV irradiation time. The inset is a diagram of the proposed energy level indicating work function change of the PEDOT:PSS before and after UV irradiation.

Besides these effects, UV irradiation of PEDOT:PSS film has one additional effect: an increase in work function [17]. This change in the work function can be critical to the performance of polymer PVs because it can change the hole extraction barrier between active layer and PEDOT:PSS buffer layer. Accordingly, the change in the work function by UV irradiation was examined through a Kelvin probe method. This revealed that the work function change was about 0.25 eV by 1 h UV irradiation (Fig. 5). Thus, after a UV treatment, the PEDOT:PSS films can have an extraction barrier 0.05 eV (Fig. 5, inset). There are two mechanisms for charge carrier injection/extraction at the interface, thermionic emission [18] and electron tunneling [19]. Since photovoltaic cells are operated at high temperature (around 300 K) and showed temperature-dependent current–voltage behavior [20], it can be concluded that thermionic emission dominates charge carrier extraction at the interface. For thermionic emission model,

$$J = A^* T^2 \exp(-\Phi_b/kT)$$

where  $A^*$  is Richardson constant,  $T$  is temperature (K),  $k$  is Boltzmann constant,  $\Phi_b$  is Schottky barrier height. From this equation, about 5% charge carrier can be trapped at the interface by 0.05 eV energy barrier. So if the PEDOT:PSS film with lower work function is used to eliminate the energy barrier, higher PCE can be obtained by UV irradiation.

In conclusions, this study demonstrated that the efficiency of polymer solar cells can be improved by simple

UV treatment on PEDOT:PSS buffer layer. From Raman spectroscopy, four-probe point and impedance spectroscopy measurements, it was found that UV-irradiated PEDOT:PSS films show reduction in both the bulk and contact resistance without changes of the surface morphology. This results in improved  $J_{sc}$ , FF and overall photovoltaic efficiency. From the analysis of change in work function of modified buffer layer ( $\sim 0.25$  eV), we found that higher photovoltaic performance can be obtained by adjusting buffer layer work function.

## Acknowledgement

This work was supported by ERC Grant of the Korea Science and Engineering Foundation (KOSEF) funded by the Korea Ministry of Education, Science and Technology (MEST) (No. R11-2007-045-01002-0(2009)) and KIST internal projects under contracts 2E20980. It was also partially supported by a WCU Grant from MEST (R32-2008-000-10142-0).

## References

- [1] S. Gunes, H. Neugebauer, N.S. Sariciftci, *Chem. Rev.* 107 (2007) 1324.
- [2] G. Yu, J. Hummelen, F. Wudl, A.J. Heeger, *Science* 270 (1995) 1780.
- [3] W. Ma, C. Yang, X. Gong, K. Lee, A.J. Heeger, *Adv. Funct. Mater.* 15 (2005) 1617.
- [4] G. Li, V. Shrotriya, J. Huang, Y. Yao, T. Moriarty, K. Emery, Y. Yang, *Nat. Mater.* 4 (2005) 864.
- [5] M. Reyes-Reyes, K. Kim, D.L. Carroll, *Appl. Phys. Lett.* 87 (2005) 083506.
- [6] F. Zhang, M. Johansson, M.R. Andersson, J.C. Hummelen, O. Inganäs, *Adv. Mater.* 14 (2002) 662.
- [7] C.J. Ko, Y.K. Lin, F.C. Chen, C.W. Chu, *Appl. Phys. Lett.* 90 (2007) 063509.
- [8] F.L. Zhang, A. Gadisa, O. Inganäs, M. Svensson, M.R. Andersson, *Appl. Phys. Lett.* 84 (2004) 3906.
- [9] W.-J. Yoon, P.R. Berger, *Appl. Phys. Lett.* 92 (2008) 013306.
- [10] A. Moliton, J.M. Nunzi, *Polym. Int.* 55 (2006) 583.
- [11] M. Lapkowski, A. Proń, *Synth. Met.* 110 (2000) 79.
- [12] J. Ouyang, C.W. Chu, F.C. Chen, Q. Xu, Y. Yang, *Adv. Funct. Mater.* 15 (2005) 203.
- [13] Z. Tan, C. Yang, E. Zhou, X. Wang, Y. Li, *Appl. Phys. Lett.* 91 (2007) 023509.
- [14] H. Sirringhaus, *Adv. Mater.* 17 (2005) 2411.
- [15] V.D. Mihailetchi, J. Wildeman, P.W.M. Blom, *Phys. Rev. Lett.* 94 (2005) 126602.
- [16] J.B. Emah, R.J. Curry, S.R.P. Silva, *Appl. Phys. Lett.* 93 (2008) 103301.
- [17] Y.J. Lin, F.M. Yang, C.Y. Huang, W.Y. Chou, J. Chang, Y.C. Lien, *Appl. Phys. Lett.* 91 (2007) 092127.
- [18] S.M. Sze, *Physics of Semiconductor Devices*, Wiley, New York, 1981, p. 164.
- [19] I.D. Parker, *J. Appl. Phys.* 75 (1994) 1656.
- [20] I. Riedel, J. Parisi, V. Dyakonov, L. Lutsen, D. Vanderzande, J.C. Hummelen, *Adv. Funct. Mater.* 14 (2004) 38.

# ORGANIC ELECTRONICS

materials • physics • chemistry • applications

## Editors:

Prof. Chihaya Adachi

Center for Future Chemistry, Kyushu University,  
744 Motoooka, Nishi, Fukuoka 819-0395, Japan  
Fax: +81-92-802-3294, e-mail: adachi@cstf.kyushu-u.ac.jp

Prof. Stephen R. Forrest

EECS, MS&E, and Physics, University of Michigan,  
4080 Fleming Building, 503 Thompson Street,  
Ann Arbor, MI 48109-1340, USA  
Fax: +1-734-763-0085, e-mail: stevefor@umich.edu

Prof. René Janssen

Molecular Materials and Nanosystems,  
Eindhoven University of Technology, P.O. Box 513,  
5600 MB Eindhoven, The Netherlands  
Fax: +31 40 2451036, e-mail: r.a.janssen@tue.nl

Prof. Antoine Kahn

Electrical Engineering Department,  
Princeton University, Engineering Quadrangle,  
Princeton, NJ 08544, USA

## Associate Editorial Board:

V.M. AGRANOVICH (Moscow)

N. PEYGHAMBARIAN (Tucson)

C. TALIANI (Bologna)

Y. CAO (Guangzhou)

Z. POPOVIC (Mississauga)

T. TSUTSUI (Fukuoka)

A. DODABALAPUR (Austin)

W. RIESS (Rüschlikon)

E. UMBACH (Würzburg)

M. FUJIIHARA (Yokohama)

Y. SHIROTA (Osaka)

## Founding Editors:

Prof. Donal Bradley, Prof. Stephen Forrest, Prof. Norbert Karl and Prof. Kazuhiko Seki

## Aims and scope

*Organic Electronics* is a primary journal whose interdisciplinary focus is organic materials, devices and phenomena, with application to devices such as organic light emitting diodes, thin film transistors, photovoltaic cells, etc.

Papers suitable for publication in this journal cover such topics as photoconductive and electronic properties of organic materials, thin film growth and characterization, charge and exciton transport, organic electronic and optoelectronic devices, etc.

*Organic Electronics* provides the only forum for both applied and fundamental contributions spanning the many different disciplines addressing the wide range of electronic properties and applications of organic materials. A Letters section is included for rapid publication of short articles announcing significant and highly original results.

## Advertising information

Advertising orders and enquiries can be sent to: Janine Castle, Elsevier Ltd., The Boulevard, Langford Lane, Kidlington, Oxford OX5 1GB, UK; phone: (+44) 1865 843 844; fax: (+44) 1865 853 973; e-mail: j.castle@elsevier.com. Customers in the USA and Canada can also contact: Mr Tino DeCarlo, Advertising Department, Elsevier Inc., 360 Park Avenue South, New York, NY 10010-1710, USA; phone: (+1) (212) 633 3815; fax: (+1) (212) 633 3820; e-mail: t.decarlo@elsevier.com

## Abstracted/indexed in:

Current Contents: Engineering, Technology and Applied Sciences; El Compendex Plus; Engineering Index; INSPEC; Physics Briefs; Science Citation Index, expanded; Chemistry Citation Index; Current Contents: Physics, Chemistry and Engineering Science. Also covered in the abstract and citation database SCOPUS®. Full text available on ScienceDirect®.

**USA mailing notice:** *Organic Electronics* (ISSN 1566-1199) is published monthly except for January, March, June and October by (Elsevier B.V., Radarweg 29, 1043 NX Amsterdam, The Netherlands). Periodical postage paid at Rahway, NJ and at additional mailing offices.

**USA POSTMASTER:** Send change of address to *Organic Electronics*, Elsevier Customer Service Department, 11830 Westline Industrial Drive, St. Louis, MO 63146, USA.

**AIRFREIGHT AND MAILING** in USA by Mercury International Limited, 365, Blair Road, Avenel, NJ 07001.

**Publication information:** *Organic Electronics* (ISSN 1566-1199). For 2009, Volume 10 (8 issues) is scheduled for publication. Subscription prices are available upon request from the Publisher or from the Elsevier Customer Service Department nearest you or from this journal's website: (<http://www.elsevier.com/locate/orgel>). Further information is available on this journal and other Elsevier products through Elsevier's website: (<http://www.elsevier.com>). Subscriptions are accepted on a prepaid basis only and are entered on a calendar year basis. Issues are sent by standard mail (surface within Europe, air delivery outside Europe). Priority rates are available upon request. Claims for missing issues should be made within six months of the date of dispatch.

**Orders, claims, and journal enquiries:** please contact the Elsevier Customer Service Department nearest you:

**St. Louis:** Elsevier Customer Service Department, 11830 Westline Industrial Drive, St. Louis, MO 63146, USA; phone: (877) 8397126 [toll free within the USA]; (+1) (314) 4537076 [outside the USA]; fax: (+1) (314) 5235153; e-mail: [JournalCustomerService-usa@elsevier.com](mailto:JournalCustomerService-usa@elsevier.com)

**Oxford:** Elsevier Customer Service Department, The Boulevard, Langford Lane, Kidlington OX5 1GB, UK; phone: (+44) (1865) 843434; fax: (+44) (1865) 843970; e-mail: [JournalsCustomerServiceEMEA@elsevier.com](mailto:JournalsCustomerServiceEMEA@elsevier.com)

**Tokyo:** Elsevier Customer Service Department, 4F Higashi-Azabu, 1-Chome Bldg, 1-9-15 Higashi-Azabu, Minato-ku, Tokyo 106-0044, Japan; phone: (+81) (3) 5561 5037; fax: (+81) (3) 5561 5047; e-mail: [JournalsCustomerServiceJapan@elsevier.com](mailto:JournalsCustomerServiceJapan@elsevier.com)

**Singapore:** Elsevier Customer Service Department, 3 Killiney Road, #08-01 Winsland House I, Singapore 239519; phone: (+65) 6349 0222; fax: (+65) 6733 1510; e-mail: [JournalsCustomerServiceAPAC@elsevier.com](mailto:JournalsCustomerServiceAPAC@elsevier.com)

Printed in the Netherlands

For a full and complete Guide for Authors, please go to: <http://www.elsevier.com/locate/orgel>